JANUARY/FEBRUARY 2007
Volume 18, Number 1

© *Copyright 2007 by the American Chemical Society*

Bioconjugate Chemistry

EDITORIAL: What's New

Associate Editors

Associate Editors Paul Miller, Teruo Okano, and Peter Senter have been essential to the success of the journal. Professor Okano is moving on to new responsibilities and will no longer be able to serve, but in this time of growth we have appointed three new Associate Editors to maintain and broaden our coverage of new science. The new Associate Editors are:

Ferenc Hudecz, *Department of Organic Chemistry, Eötvös Lorand University, Budapest, Hungary*

Yasuhiko Tabata, *Department of Biomaterials, Institute for Frontier Medical Sciences, Kyoto University, Japan*

Masayuki Yokoyama, *Laboratory of Polymer and Nanomedicine, Kanagawa Academy of Science and Technology, Kawasaki, Japan*

Editorial Advisory Board

Editorial Advisory Board members not only review manuscripts but also advise on journal policy. New members appointed this year are:

Darryl Bornhop, *Vanderbilt University*
Patrick Couvreur, *Université de Paris-Sud*
M. G. Finn, *The Scripps Research Institute*
Shiroh Futaki, *Kyoto University*
Wim E. Hennink, *Utrecht University*
Kazunori Kataoka, *The University of Tokyo*
Kenji Kono, *Osaka Prefecture University*
Robert Langer, *Massachusetts Institute of Technology*
Michael R. Lewis, *University of Missouri-Columbia*
Harri Lönnberg, *University of Turku*
Jong-sang Park, *Seoul National University*
Tae Gwan Park, *Korea Advanced Institute of Science and Technology*
Tariq Rana, *University of Massachusetts Medical School*
Steve Roffler, *Academia Sinica*
David A. Tirrell, *California Institute of Technology*
M. Graca H. Vicente, *Louisiana State University*
Ernst Wagner, *Ludwig Maximilian University*
Michael J. Welch, *Washington University School of Medicine*
Karen L. Wooley, *Washington University in St. Louis*

Thanks to Our Reviewers

It is a pleasure to acknowledge the contributions of the reviewers of manuscripts submitted in 2006 for publication in *Bioconjugate Chemistry*. Their unselfish service has been essential in the shaping of the 17th volume of the journal. The scientific community is fortunate that its members are willing to share their time and specialized knowledge in this way. The reviewers are listed on the following page.

Claude F. Meares

Editor-in-chief

10.1021/bc0603945 CCC: $37.00 © 2007 American Chemical Society
Published on Web 01/17/2007

List of Reviewers

Hiroshi Abe
Samuel Achilefu
Maciej Adamczyk
Achim Aigner
Kazunari Akiyoki
Roger Alberto
Nancy Allbritton
Steve Alley
Mansoor Amiji
Carolyn Anderson
David Andreu
Agnes Anne
Yasushi Arano
Alexander Augst
Don Axworthy
Manuel Baca
Marina Backer
Rumiana Bakalova
Mark Banaszak-Holl
Janina Baranowska-Korylewicz
Leonidas Bachas
Darren Baker
James Baker, Jr.
Shankar Balasubramanian
Philippe Barthelemy
Amit Basu
Serge Beaucage
Annette Beck-Sickinger
Craig Beeson
Jean-Paul Behr
David Benson
Ulrich Bickel
Dennis Benjamin
Kristian Berg
Donald Bergstrom
Gary Bignami
Otto Boerman
Alexei A. Bogdanov
Elijah Bolotin
Hans Borner
Didier Boturyn
Ned Bowden
Martin Brechbiel
Ronald Breslow
Lyudmila Bronstein
Donald Brooks
Tom Brown
Timothy Bugg
Jeff Bulte
Paolo Caliceti
D. I. Carvana
Paul Carter
Anthony Cass
David Castner
Carole Chaix
Chien-Hsing Chang
Arabinda Chaudhuri
Xiaoyuan Chen
David Corey
Patrick Couvreur
George Cox, III
Mark Davis
Clemens Decristoforo
Eric Defranq
C. de Koster
Jesus de la Fuente
Agnes Delmas
Tim Deming
Sally DeNardo
Peter Dervan
Bauke Dijkstra
Ivan Dmochowski
Abraham Domb
Svetlana Doronina
Terrence Doyle
Claudius D'Silva
Adriano Duatti
Gene Dubowchik
Yves Dufrene
William Eckelman
Michael Eisenhut
Joan Estelrich
Marian Fabian
Conan Fee
Dan Feldheim
Chan Feng
Paolo Ferruti
Gregg Fields
M. G. Finn
David Filpula
Keith Fox
John Frangioni
Shiroh Futaki
Detlaf Gabel
Hans-Joachim Gabius
Mike Gait
R. Gandhi
Elisa Garcia-Garayoa
Brian Gibney
David Goldenberg
Wayne Gombotz
David Grainger
Mark Green
Hermann Gruber
Thorfinnur Gunnlaugsson
Inga Gustafson
Rainer Haag
Michael Haka
Itaru Hamachi
Philip Hamann
Weiyue Lu
Carrie Haskell-Luevano
Ken-ichi Hatanaka
Willem Hennink
Piet Herdewijn
Greg Hermanson
Jean Herscovici
Tomasz Heyduk
Donald Hnatowich
Robert Hider
Scott Hilderbrand
Ole Hindsgaul
Robert Hoffman
Ramachandra Hosmane
Jari Hovinen
Jeffrey Hubbell
Nick Hud
Ferenc Hudecz
Stephen Husbands
Shinji Iijima
Chad Immoos
Darryl Irvine
Hitoshi Ishida
Hiro Iwata
Kenneth Jacobsen
Anna Janecka
Andreas Jaschke
Scott Jeffrey
Lee Josephson
Sylvia Jurisson
Kazunori Kataoka
Toyoji Kakuchi
Yoshiki Katayama
John Katzenellenbogen
John Keana
Kimberly Kelly
David Kerr
David Kessel
Horst Kessler
Kaisa Ketomaki
David King
Kent Kirshenbaum
Thomas Kissel
Alexander Klibanov
Toni Kline
Hisataka Kobayashi
Kazunori Kobayashi
Thomas Kodadek
Robert Kok
Kenji Kono
Jindrich Kopecek
Bert Klumperman
Heinz-Bernhard Kraatz
Felix Kratz
Kenneth Krohn
Hank Kung
Robert Langer
Luciana Lattuada
Peter Laverman
Christopher Leamon
Deborah Leckband
Robert Lee
Claus-Michael Lehr
Jason Lewis
Michael Lewis
Shuang Liu
Yu Liu
Harri Lonnberg
Angie Louie
Tao Lowe
Robert Lyon
Helmut Maecke
Hiroshi Maeda
Tetsuro Majima
Nicholas Mantis
Atsushi Maruyama
Phillip Mattingly
Julie McEarchern
Damon Meyer
Heather Maynard
Charlotte McDonagh
Igor Medintz
Oleg Melnyk
Andrew Metters
Xavier Michalet
Douglas Miller
Chad Mirkin
S. Moghimi
Sherie Morrison
François Morvan
Hong Moulton
Mark Mrksich
Klaus Muller
Regina Murphy
Yukio Nagasaki
Shinsaku Nakagawa
Michael Neeman
Dario Neri
Edward Neuwalt
Peter Nielsen
Nicole Okeley
Naoto Oku
Sean O'Malley
Tatiana Oretskaya
Chris Orvig
David Oupicky
Daniel Pack
Anja Palmans
Ravindra Pandey
Alyssa Panitch
Keykavous Parang
Jong-sang Park
Joon Park
Kinam Park
Tae Gwan Park
Blake Peterson
Catherine Picart
Gennaro Piccialli
Hans-Jurgen Pietzsch
Glenn Prestwich
Dave Puleo
Suzi Pun
David Putnam
Jeffrey Pyun
Natarajan Raju
Tariq Rana
Kenneth Raymond
Steven Regen
Theresa Reineke
Kevin Rice
Annie Roche
Steven Roffler
Buck Rogers
Keith Rose
David Rozema
Vincent Rotello
Jean-Marie Ruysschaert
Ahmad Safavy
Hideo Saji
Yogesh Sanghvi
Roger Schibli
Carsten Schmuck
Francis Schuber
John Seddon
Michael Seidman
Takeshi Serizaway
Norbert Sewald
Ajit Sharma
Lonnie Shea
John Shively
Samuel Sia
Kevin Smith
Lloyd Smith
Patrick Spicer
Caroline Springer
Jan Stegemann
Michael Sun
Julie Sutcliffe
Mary Sutherland
Francis Szoka, Jr.
Maryam Tabrizian
Shigeori Takenaka
Hitoshi Tamiaki
Timothy Tewson
David Thompson
Michael Thredgill
Werner Tjarks
Brian Toki
Don Tomalia
Pam Trail
Vladimir Trubetskoy
Ching-Hsuan Tung
Ijeoma Uchegbu
Ganesan Vaidyanathan
John Valliant
Daniel Vanerah
Johan van Lier
C. Van Nostrum
Graca Vicente
Pierre Vierling
Wynn Volkert
Ernst Wagner
Qian Wang
Marcus Weck
Ralph Weissleder
Michael Welch
Hans-Jurgen Wester
Eric Wickstrom
D. Scott Wilbur
Meir Wilchek
Chris Wilds
Jon Wolff
Martin Woodle
Anna Wu
George Wu
Kazushige Yamana
Masayuki Yokoyama
Janusz Zakrzewski
Samuel Zalipsky
Michael Zalutsky
M. Zhang
Jon Zubieta

BC0603945

In Memoriam
Robert E. Feeney
August 30, 1913 − September 21, 2006

One of the inspirations for *Bioconjugate Chemistry*, prominent specialist in the chemical modification of proteins, and unmistakable personality, Bob Feeney passed away recently. We remember him as a sprightly colleague who was never, never at a loss for words. He was likely to pop up at the most unlikely times and places, deliver a few amusing remarks, and leave us all laughing. During his years as Professor of Food Science at the University of California, Davis, Feeney had a memorable style of educating younger scientists in the treatment of biological molecules with organic reagents. What was formerly an arcane and rather mysterious set of practices has evolved into rational approaches to drug design and development. Bob Feeney was a leader of that parade and enjoyed every minute of it. We all benefited from his presence. We will miss him.

Claude F. Meares

Editor-in-Chief

BC060395X

10.1021/bc060395x CCC: $37.00 © 2007 American Chemical Society
Published on Web 12/24/2006

COMMUNICATIONS

Polyketal Microparticles: A New Delivery Vehicle for Superoxide Dismutase

Sungmun Lee,[†,§] Stephen C. Yang,[†,§] Michael J. Heffernan,[†] W. Robert Taylor,[‡] and Niren Murthy*[,†]

The Wallace H. Coulter Department of Biomedical Engineering, Georgia Institute of Technology, Atlanta, Georgia 30332, and Division of Cardiology, Department of Medicine, Emory University School of Medicine, Atlanta, Georgia 30322. Received August 21, 2006; Revised Manuscript Received November 6, 2006

There is currently great interest in developing microparticles that can enhance the delivery of proteins to macrophages. In this communication, we present a new acid-sensitive polymer for drug delivery, poly(cyclohexane-1,4-diyl acetone dimethylene ketal) (PCADK). PCADK is designed to hydrolyze, after phagocytosis by macrophages, in the acidic environment of the phagosome and enhance the intracellular delivery of phagocytosed therapeutics. Other key attributes of PCADK for drug delivery are its well-characterized degradation products and straightforward synthesis. PCADK hydrolyzes into 1,4-cyclohexanedimethanol, a compound used in food packaging, and acetone, a compound on the FDA GRAS list. PCADK was synthesized using the acetal exchange reaction between 1,4-cyclohexanedimethanol and 2,2-dimethoxypropane, and could be obtained on a multigram scale in one step. The hydrolysis kinetics of the ketal linkages in PCADK were measured by ^{1}H NMR and were determined to be pH-sensitive, having a half-life of 24.1 days at pH 4.5 and over 4 years at pH 7.4. The therapeutic enzyme superoxide dismutase (SOD), which scavenges reactive oxygen species, was encapsulated into PCADK-based microparticles using a double emulsion procedure. Cell culture experiments demonstrated that PCADK-based microparticles dramatically improved the ability of SOD to scavenge reactive oxygen species produced by macrophages. We anticipate numerous applications of PCADK in drug delivery, based on its acid sensitivity, well-characterized degradation products, and straightforward synthesis.

Reactive oxygen species (ROS) produced by macrophages play a central role in causing inflammatory diseases, such as acute liver failure, arthritis, and sepsis (*1*−*4*). Superoxide dismutase (SOD) is an enzyme that scavenges reactive oxygen species and has the potential to treat inflammatory diseases by suppressing ROS production by macrophages (*5*−*7*). Unfortunately, clinical trials with free SOD have been ineffective, due to its membrane impermeability, and SOD delivery vehicles are therefore being investigated. Liposome-based SOD delivery vehicles have shown promise for enhancing the delivery of SOD in animal models; however, their poor shelf life has prevented their progression into clinical trials (*8*, *9*). Polymeric microparticles, based on PLGA and polycaprolactone, are also being investigated for the delivery of SOD (*10*−*12*). Although polyester-based microparticles have an excellent shelf life and well-characterized degradation products, their application for the treatment of inflammatory diseases is potentially problematic because their acidic degradation products can cause inflammation (*13*).

Polymeric microparticles based on acid-degradable polymers also have the potential to enhance the delivery of SOD to macrophages. Acid-degradable polymers, such as polyorthoesters and polyacetals, hydrolyze in the acidic environment of lysosomes and phagosomes and have previously been used for intracellular drug delivery (*14*−*17*). The polyketals are a new family of acid-degradable polymers that have ketal linkages in their backbones (*18*, *19*). The polyketals have several properties that make them an attractive delivery vehicle for SOD. Polyketals degrade into neutral compounds and may avoid the inflammatory problems associated with the acidic degradation products of polyesters and polyorthoesters. Polyketals also have the potential to disrupt phagosomes, by degrading in the phagosome and osmotically destabilizing it. The ketal linkage has excellent hydrolysis kinetics for intracellular drug delivery, hydrolyzing approximately 1000 times faster at the phagosomal pH of 4.5 versus the pH 7.4 environment of the blood. Although the polyketals have potential for protein delivery to macrophages, poly(1,4-phenyleneacetone dimethylene ketal) (PPADK) is the only polyketal developed for drug delivery; however, it degrades into benzene dimethanol, an aromatic compound with potential toxicity, and new polyketals with better characterized toxicity profiles would be preferable.

In this communication, we present a new polyketal for drug delivery, poly(cyclohexane-1,4-diyl acetone dimethylene ketal) (PCADK), which degrades into acetone, a compound on the FDA GRAS list, and 1,4-cyclohexanedimethanol, a compound with an excellent toxicity profile. For example, the LD_{50} of 1,4-cyclohexanedimethanol in rats is 3200 mg/kg for an oral dosage. 1,4-cyclohexanedimethanol also does not undergo significant enzymatic transformations in vivo; for example, a 400 mg/kg peritoneal gavage of 1,4-cyclohexanedimethanol in rats led to 97.5% of it being excreted intact (*20*). In addition, 1,4-cyclohexanedimethanol is a commonly used food packaging material and has approval for human consumption as an indirect food additive (Food Contact Notification (FCN) no. 000087).

* Corresponding author. Telephone 404-385-5145, fax 404-894-4243, email: niren.murthy@bme.gatech.edu.

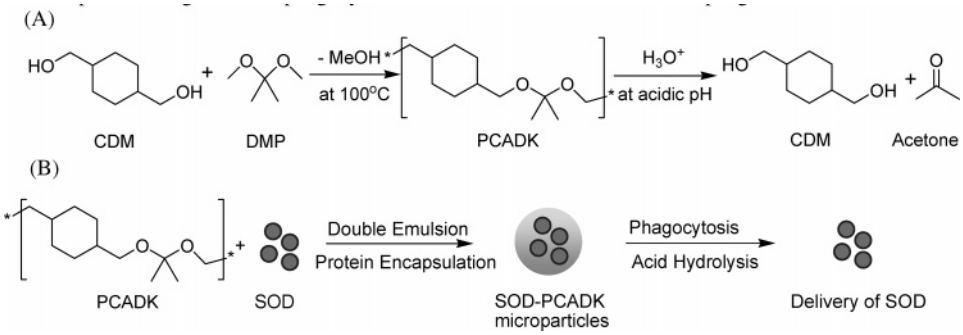
[†] Georgia Institute of Technology.

[‡] Emory University School of Medicine.

[§] Both authors contributed equally.

10.1021/bc060259s CCC: $37.00 © 2007 American Chemical Society
Published on Web 12/19/2006

Scheme 1. PCADK, a New Polymer for Drug Delivery[a]



[a] (A) Synthesis of PCADK from 1,4-cyclohexanedimethanol (CDM) and 2,2-dimethoxypropane (DMP), and acid hydrolysis of PCADK into CDM and acetone. (B) Formulation of SOD-loaded microparticles by w/o/w double emulsion. Microparticles degrade after phagocytosis, in the acidic environment of the phagosome.

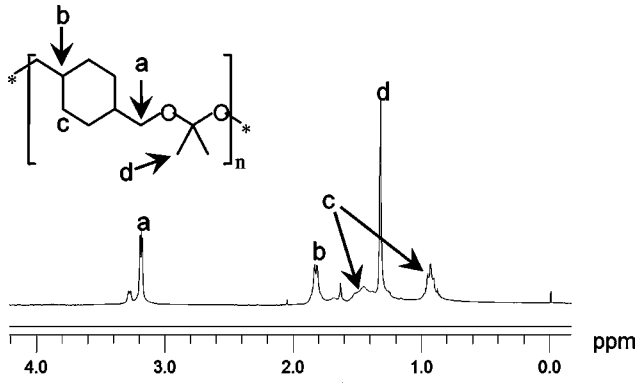


Figure 1. ^{1}H NMR of PCADK. ^{1}H NMR spectrum of PCADK in $CDCl_3$: per repeating unit, peaks at $\delta = 3.26-3.18$ (a, 4H), 1.83 (b, 2H), 1.60−0.93 (c, 8H), and 1.32 ppm (d, 6H).

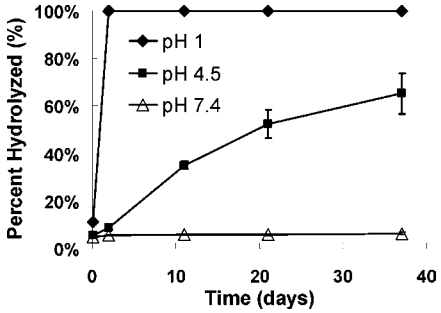


Figure 2. The hydrolysis of PCADK is pH-sensitive. Hydrolysis kinetics of PCADK (ground powder) was determined at pH 1.0, 4.5, and 7.4 at 37 °C by ^{1}H NMR. Half-lives of PCADK are 24.1 days (pH 4.5) and over 4 years (pH 7.4). PCADK was completely hydrolyzed in 2 days at pH 1.0.

In this report, SOD was encapsulated into PCADK-based microparticles via a double emulsion procedure. Cell culture experiments with macrophages demonstrated that these microparticles dramatically improved the ability of SOD to scavenge superoxide produced by macrophages. On the basis of these observations, we anticipate numerous uses for PCADK-based microparticles in drug delivery.

PCADK was synthesized, on a multigram scale, using the acetal exchange reaction between 1,4-cyclohexanedimethanol and 2,2-dimethoxypropane, as shown in Scheme 1, generating polymers with an M_w of approximately 6000 (Supporting Information Figure S1). A ^{1}H NMR spectrum of PCADK is shown in Figure 1, confirming its chemical structure. Although the acetal exchange reaction has been extensively used for the protection of alcohols, it has been rarely used for the synthesis of polyketals. In 2005, Heffernan and Murthy reported the synthesis of PPADK through the reaction of 2,2-dimethoxypropane and 1,4-benzenedimethanol (*18*). While PPADK has many of the characteristics needed for drug delivery, its degradation products have potential toxicity. PCADK, in contrast, degrades into 1,4-cyclohexanedimethanol and acetone, both of which have excellent toxicity profiles.

PCADK has ketal linkages in its backbone and should therefore degrade after phagocytosis, in the acidic environment of the phagosome. The hydrolysis kinetics of PCADK, in the form of ground powder, was measured at the pH values of 4.5 and 7.4, to estimate the behavior of PCADK-based delivery vehicles after phagocytosis. Figure 2 demonstrates that the hydrolysis of the ketal linkages in PCADK is indeed pH-sensitive, having a half-life of 24.1 days at pH 4.5 and an estimated half-life of over 4 years at pH 7.4. The hydrolysis of the ketal linkage in PCADK is considerably slower than that of a water-soluble ketal, which has a half-life of approximately 1.6 min at pH 5.0 (*21*). This observation leads us to speculate that the rate-limiting step in the hydrolysis of PCADK is the diffusion of hydronium ions into the polymer matrix, rather than the cleavage of ketal bonds. This hypothesis is further supported by the faster hydrolysis rate of the more hydrophilic polyketal, PPADK, which has a half-life of 35 h at pH 5.0.[1] This trend suggests that the hydrolysis of polyketal microparticles can be tailored by manipulating their hydrophobicity.

SOD was encapsulated into PCADK microparticles using a w/o/w double emulsion procedure. An experimental protocol was developed on the basis of procedures used to formulate SOD into PLGA-based microparticles (*10*). Briefly, a 100 μL aqueous solution of SOD (40 mg/mL) was dispersed by homogenization (21 500 rpm, 30 s) into 1.0 mL of methylene chloride, containing 125 mg of PCADK, generating a water in oil (w/o) emulsion. This w/o emulsion was then dripped into 5 mL of an 8% (w/v) aqueous polyvinyl alcohol (PVA) solution and was stirred with a homogenizer at 6000 rpm for 5 min. The resulting w/o/w emulsion was then poured into 25 mL of pH 7.4 buffer and was stirred for several hours, evaporating the methylene chloride. The resulting particles were isolated by centrifugation and freeze-dried, generating a white solid powder. The protein encapsulation efficiency of the SOD−PCADK microparticles was 36.7%, as determined by UV absorbance at 280 nm. An SEM image of the SOD−PCADK microparticles, shown in Figure 3, demonstrates that they are 3 to 15 μm in diameter, which is suitable for both intracellular and extracellular delivery. This may be beneficial in the case of SOD delivery, because superoxide causes both intracellular toxicity and extracellular tissue damage during inflammation.

[1] PCADK was determined to be more hydrophobic than PPADK on the basis of the log *P* values of their respective monomers, 0.359 for 1,4-cyclohexanedimethanol versus −0.149 for 1,4-benzenedimethanol.

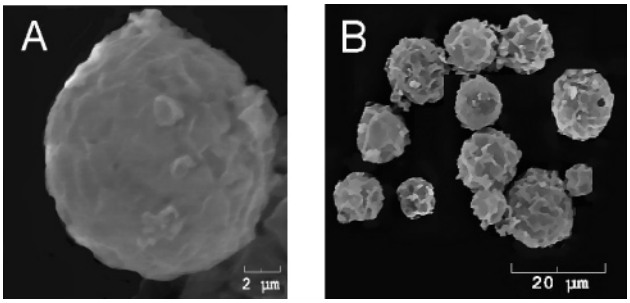


Figure 3. SEM images of SOD−PCADK microparticles: (A) 6000× magnification, (B) 1000× magnification. SEM images were taken on a Hitachi S-800.

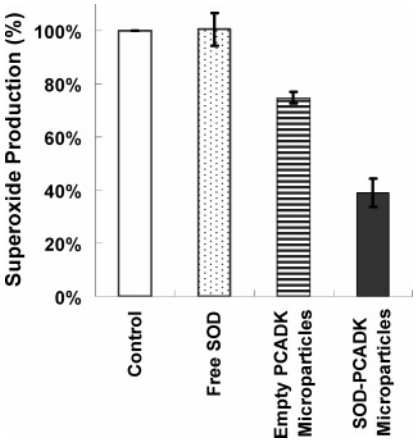


Figure 4. PCADK microparticles enhance the delivery of SOD to macrophages. Macrophages were incubated with either SOD−PCADK microparticles (black bar), empty PCADK microparticles (horizontal stripe), free SOD (dotted bar), and media only (white bar). For statistical analysis, three independent wells were measured for each sample. Significance of results was determined via the *t*-test with $p < 0.05$.

The ability of SOD−PCADK microparticles to scavenge superoxide from macrophages was investigated in cell culture. TIB-186 macrophages (1×10^5 cells/well, 96-well plate) were incubated with 0.1 mg/mL SOD−PCADK microparticles (1.14 μg SOD in 0.1 mg microparticles), free SOD (1.14 μg/mL SOD), or empty PCADK microparticles for 2 h. The cells were washed 3 times and then stimulated with 0.2 μg/mL phorbol myristate acetate (PMA) for 30 min. The superoxide production from these macrophages was then measured using a cytochrome c based assay, following the procedure of Voter et al. (*22*). Figure 4 demonstrates that free SOD by itself caused very little inhibition of superoxide production, whereas SOD−PCADK microparticles caused a 60% reduction in superoxide production. Empty microparticles also reduced superoxide production by macrophages by approximately 20%. This is most likely due to the toxicity of the particles, which caused approximately 20% toxicity under these experimental conditions (0.1 mg/mL for 2 h) as determined by an MTT assay (Supporting Information Figure S3).

In conclusion, we have developed a new acid-sensitive polyketal for drug delivery, PCADK, which is designed to hydrolyze in the acidic environment of the phagosome and enhance the intracellular delivery of phagocytosed therapeutics. Key attributes of PCADK are its well-characterized degradation products and straightforward synthesis. PCADK was synthesized on a multigram scale in one step and hydrolyzes into acetone and 1,4-cyclohexanedimethanol. The hydrolysis of PCADK is pH-sensitive, having a half-life of 24.1 days at pH 4.5 and over 4 years at pH 7.4. The therapeutic protein SOD was encapsulated into PCADK-based microparticles, 3−15 μm in size, using a double emulsion procedure. In cell culture experiments, PCADK microparticles significantly improved the ability of SOD to scavenge superoxide generated by macrophages. We anticipate widespread interest in PCADK for drug delivery, based on its acid sensitivity, well-characterized degradation products, and ease of synthesis.

ACKNOWLEDGMENT

This project was funded in part by the Georgia Tech/Emory Center for the Engineering of Living Tissues (funded by NSF-EEC-9731643), NSF-BES-0546962 CAREER AWARD, NIH UO1 HL80711-01, NIH R21 EB006418, and J&J/GT Health Care Innovation Seed Grant Proposal. Michael Heffernan is supported by an NSF Graduate Research Fellowship. Stephen Yang is supported by an NSF IGERT Fellowship.

Supporting Information Available: Additional experimental details as mentioned in the text. This material is available free of charge via the Internet at http://pubs.acs.org.

LITERATURE CITED

(1) Droge, W. (2002) Free radicals in the physiological control of cell function. *Physiol. Rev. 82*, 47−95.

(2) Hitchon, C. A., and El-Gabalawy, H. S. (2004) Oxidation in rheumatoid arthritis. *Arthritis Res. Ther. 6*, 265−78.

(3) Kamata, H., Honda, S., Maeda, S., Chang, L., Hirata, H., and Karin, M. (2005) Reactive oxygen species promote TNFalpha-induced death and sustained JNK activation by inhibiting MAP kinase phosphatases. *Cell 120*, 649−61.

(4) Victor, V. M., Rocha, M., Esplugues, J. V., and de la Fuente, M. (2005) Role of free radicals in sepsis: antioxidant therapy. *Curr. Pharm. Des. 11*, 3141−58.

(5) Cuzzocrea, S., Thiemermann, C., and Salvemini, D. (2004) Potential therapeutic effect of antioxidant therapy in shock and inflammation. *Curr. Med. Chem. 11*, 1147−62.

(6) Kinnula, V. L., and Crapo, J. D. (2003) Superoxide dismutases in the lung and human lung diseases. *Am. J. Respir. Crit. Care Med. 167*, 1600−19.

(7) Landis, G. N., and Tower, J. (2005) Superoxide dismutase evolution and life span regulation. *Mech. Ageing Dev. 126*, 365−79.

(8) Laursen, J. B., Rajagopalan, S., Galis, Z., Tarpey, M., Freeman, B. A., and Harrison, D. G. (1997) Role of superoxide in angiotensin II-induced but not catecholamine-induced hypertension. *Circulation 95*, 588−93.

(9) Luisa Corvo, M., Jorge, J. C., van't Hof, R., Cruz, M. E., Crommelin, D. J., and Storm, G. (2002) Superoxide dismutase entrapped in long-circulating liposomes: formulation design and therapeutic activity in rat adjuvant arthritis. *Biochim. Biophys. Acta 1564*, 227−36.

(10) Giovagnoli, S., Blasi, P., Ricci, M., and Rossi, C. (2004) Biodegradable microspheres as carriers for native superoxide dismutase and catalase delivery. *AAPS PharmSciTech 5*, e51.

(11) Giovagnoli, S., Luca, G., Casaburi, I., Blasi, P., Macchiarulo, G., Ricci, M., Calvitti, M., Basta, G., Calafiore, R., and Rossi, C. (2005) Long-term delivery of superoxide dismutase and catalase entrapped in poly(lactide-co-glycolide) microspheres: in vitro effects on isolated neonatal porcine pancreatic cell clusters. *J. Controlled Release 107*, 65−77.

(12) Liu, L., Ge, Y., Gao, J., and Yuan, Q. (2003) Stability of rhCu, Zn-SOD encapsulated in poly(lactide-co-glycolide) microspheres. *Zhongguo Yaoxue Zazhi (Beijing, China) 38*, 190−193.

(13) Dailey, L. A., Jekel, N., Fink, L., Gessler, T., Schmehl, T., Wittmar, M., Kissel, T., and Seeger, W. (2006) Investigation of the proinflammatory potential of biodegradable nanoparticle drug delivery systems in the lung. *Toxicol. Appl. Pharmacol. 215*, 100−8.

(14) Heller, J., and Barr, J. (2004) Poly(ortho esters)−from concept to reality. *Biomacromolecules 5*, 1625−32.

(15) Wang, C., Ge, Q., Ting, D., Nguyen, D., Shen, H. R., Chen, J., Eisen, H. N., Heller, J., Langer, R., and Putnam, D. (2004) Molecularly engineered poly(ortho ester) microspheres for enhanced delivery of DNA vaccines. *Nat. Mater. 3*, 190−6.

(16) Papisov, M. I. (2001) Acyclic polyacetals from polysaccharides: biomimetic biomedical "stealth" polymers. *ACS Symp. Ser. 786*, 301−314.

(17) Tomlinson, R., Heller, J., Brocchini, S., and Duncan, R. (2003) Polyacetal−doxorubicin conjugates designed for pH-dependent degradation. *Bioconjugate Chem. 14*, 1096−106.

(18) Heffernan, M. J., and Murthy, N. (2005) Polyketal nanoparticles: a new pH-sensitive biodegradable drug delivery vehicle. *Bioconjug Chem 16*, 1340−2.

(19) Hirai, K., Hattori, R., and Honda, J. (Konica Corporation, Japan; Konishiroku Photo Ind.) European Patent Application EP, 1999.

(20) DiVincenzo, G. D., and Ziegler, D. A. (1980) Metabolic fate of 1,4-cyclo[14C]hexanedimethanol in rats. *Toxicol. Appl. Pharmacol. 52*, 10−15.

(21) Kwon, Y. J., Standley, S. M., Goodwin, A. P., Gillies, E. R., and Frechet, J. M. (2005) Directed antigen presentation using polymeric microparticulate carriers degradable at lysosomal pH for controlled immune responses. *Mol. Pharm. 2*, 83−91.

(22) Voter, K. Z., Whitin, J. C., Torres, A., Morrow, P. E., Cox, C., Tsai, Y., Utell, M. J., and Frampton, M. W. (2001) Ozone exposure and the production of reactive oxygen species by bronchoalveolar cells in humans. *Inhal. Toxicol. 13*, 465−83.

BC060259S

N-(Iodoacetyl)-*N*′-(anthraquinon-2-oyl)-ethylenediamine (IAED): A New Heterobifunctional Reagent for the Preparation of Biochips

Satyakam Patnaik, Archana Swami, Dalip Sethi, Atul Pathak, B. S. Garg,† K. C. Gupta,* and P. Kumar*

Nucleic Acids Research Laboratory, Institute of Genomics and Integrative Biology, Mall Road, Delhi University Campus, Delhi − 110 007, India. Received August 24, 2006; Revised Manuscript Received October 23, 2006

Design and synthesis of a new heterobifunctional reagent, *N*-(iodoacetyl)-*N*′-(anthraquinon-2-oyl)-ethylenediamine (IAED), have been described for the preparation of oligonucleotide-based biochips. The performance of the featured reagent is probed by the immobilization of thiolated and thiophosphorylated oligonucleotides on modified glass microslides via two routes (routes A and B). The immobilization procedure was accelerated by performing a chemical reaction between thiolated oligomers and the iodoacetyl moiety of the reagent under microwaves (MW), where it is completed in just 10 min. The quality of the constructed oligonucleotide microarrays was tested by performing a hybridization assay with a complementary target and subsequently used for the detection of base mismatches. The immobilized probes were found to be thermally stable.

INTRODUCTION

DNA microarray (biochip) technology is one of the hottest areas of biological research today, having enormous applications in the area of monitoring of gene expression, disease diagnosis, gene mapping, detection of single nucleotide polymorphisms, and other genome analysis (*1*−*3*). For this purpose, several surface materials, viz., glass, silicon wafers, PMMA,[1] nylon, polyurethane, polypropylene, gold, and so forth, have been tried. Among them, glass has been the most preferred one owing to its features such as easy availability, handling, functionalization by well-known silane chemistry, and low intrinsic background, as well as adaptability to latest laser scanners.

Basically, two approaches, viz., in situ synthesis of oligonucleotides on the surface of choice (*4*, *5*) and post-synthesis immobilization of oligonucleotides (spotting method) (*6*−*9*), have been explored for the preparation of oligonucleotide microarrays. The first method produces high-density biochips, albeit, it lacks flexibility and involves sophisticated and expensive instruments. The second approach, employing spotting techniques that use presynthesized oligonucleotides, is widely used for most of the applications in biological research and, thus, has become the method of choice. Following the later approach, a number of reports on covalent and non-covalent attachment of oligonucleotides have appeared in the literature (*10*−*13*). Usually, this approach involves immobilization of suitably modified oligonucleotides on the surface of choice in the presence of condensing reagents. Here, the oligonucleotide is modified with a functional group that allows covalent attachment to a reactive group generated on the surface. Many of the attachment strategies are also based on heterobifunctional crosslinking reagents (*7*, *8*). A few of them, viz., NTMTA and NTPAC, have already been reported from the authors' laboratory (*10*−*12*).

* Email: kcgupta@igib.res.in; pkumar@igib.res.in.

† Department of Chemistry, University of Delhi, Delhi - 110 007, India.

[1] TET, tetrachlorofluoresceinyl; NTPAC, *N*-(3-trifluoroethanesulfonyloxypropyl)-anthraquinone-2-carboxamide; NTMTA, *N*-(2-trifuoroethanesulfonatoethyl)-*N*-(methyl)-triethoxysilylpropyl-3-amine; PMMA, polymethylmethacrylate; DMF, *N*,*N*-dimethylformamide; DMSO, dimethylsulfoxide; NHS, *N*-hydroxysucciniimde.

The use of oligonucleotide arrays is expanding beyond their high-profile role in sequencing the genome to other fundamental applications such as diseases diagnostics. To fulfill the changing requirements, alternative approaches are required for the fabrication of oligonucleotide arrays that would guarantee a high level of reproducibility and fast immobilization reaction. In search of a novel chemistry, which would respond to these specifications, we have explored the fast kinetics of reactions attained under microwaves for microarray fabrication.

Here, we describe the design, synthesis, and use of a new heterobifunctional reagent, *N*-(iodoacetyl)-*N*′-(anthraquinon-2-oyl)-ethylenediamine (IAED), for construction of oligonucleotide microarrays on a modified glass surface under microwaves, an alternative energy source (*14*−*18*) to reduce the reaction times from hours to minutes with improved selectivity and yields. The method is suitable for the preparation of oligonucleotide-based biochips without employing any additional activating/condensing reagent, making the strategy efficient and rapid. The potential of the proposed reagent has been evaluated for immobilization of oligomers via two different routes. For comparison purposes as well as to highlight the significance of the projected strategy, the immobilization of thiolated oligonucleotides was carried out under thermal conditions. The rate of reaction involving thiolated oligonucleotides and IAED was found to be much faster under MW (10 min) vs 2 h and 45 min at 45 °C for −SH and $-OPSO_2^{2-}$ oligomers, respectively. The prepared biochips (oligonucleotide microarrays) were subjected to hybridization assay using labeled complementary oligonucleotides, followed by visualization of fluorescent spots under a laser scanner. Subsequently, the biochips were also successfully used for detection of base mismatches.

EXPERIMENTAL PROCEDURES

Preparation of Modified Glass Microslides. Poly-prep glass microslides were soaked in a capping solution, acetic anhydride/triethylamine/*N*-methylimidazole/dichloroethane (1:1:0.4:6, v/v), for 1 h at 35 °C. Subsequently, the slides were rinsed thoroughly with dichloroethane (3 × 100 mL) and diethylether (2 × 100 mL), respectively, and dried under vacuum for further use.

Oligonucleotide Synthesis and Purification. Oligonucleotides were synthesized at 0.2 μmol scale on a Pharmacia Gene

10.1021/bc0602634 CCC: $37.00 © 2007 American Chemical Society
Published on Web 12/20/2006

Assembler Plus (see Supporting Information) using the standard phosphoramidite approach following the manufacturer's protocol (Pharmacia.LKB Gene Assembler Plus Manual, Uppsala, Sweden, 1988).

Buffers. (i) Reaction buffer: 0.1 M sodium phosphate, pH 8.5. (ii) Washing buffer: 0.1 M sodium phosphate, pH 7.1. (iii) Hybridization buffer: 0.1 M sodium phosphate containing 1 M sodium chloride, pH 7.1.

Preparation of *N*-(anthraquinon-2-oyl)-ethylenediamine (AED) 2. To a solution of anthraquinone-2-carboxylic acid (5.0 mmol) **1** and *N*-hydroxysuccinimide (6.0 mmol) in anhydrous *N*,*N*-dimethylformamide (DMF) (25 mL) was added DCC (6.0 mmol). The reaction was allowed to stir for 3 h at room temperature. After completion of reaction (monitored on TLC), the reaction mixture was filtered and the residue washed once with THF (5 mL). The filtrate was added dropwise to a solution of ethylenediamine (7.5 mmol) in dry tetrahydrofuran (25 mL) containing triethylamine (5 mmol). The reaction was allowed to stir for 4 h at room temperature. Then, the reaction mixture was concentrated under vacuum to a syrupy mass, which was dissolved in dichloromethane (150 mL) and washed with aqueous solutions of 5% citric acid (2 × 25 mL), 5% sodium bicarbonate (2 × 25 mL), and a saturated solution of sodium chloride (1 × 25 mL), respectively. The organic phase was collected, dried over anhydrous sodium sulfate, and, after filtration, concentrated under vacuum to obtain *N*-(anthraquinon-2-oyl)-ethylenediamine **2** as a solid material in ∼70% yield. The compound was characterized Ir, by ^{1}H NMR and mass spectroscopy. ^{1}H NMR (DMSO), δ: 2.92 (t, 2H), 3.4 (t, 2H), 7.98−8.75 (m, 7H), 9.11 (br, 1H). MS (*m*/*z*): 295.2 $(M + H)^+$. IR, ν (cm^{-1}): 1202, 1651, 2935, 3393.

Preparation of *N*-(iodoacetyl)-*N*′-(anthraquinon-2-oyl)-ethylenediamine (IAED) 3. To a solution of iodoacetic acid (2.0 mmol) and *N*-hydroxysuccinimide (2.5 mmol) in anhydrous *N*,*N*-dimethylformamide (DMF) (10 mL) was added DCC (2.5 mmol). The reaction was allowed to stir for 3 h at room temperature. After completion of reaction, dicyclohexylurea was removed by filtration, and to the filtrate, *N*-(anthraquinon-2-oyl)-ethylenediamine (1.8 mmol), dissolved in DMF (5 mL) containing triethylamine (1.8 mmol), was introduced dropwise over a period of 10 min with continuous stirring at room temperature. The reaction was allowed to stir for 4 h at room temperature. Then, it was concentrated under vacuum to a syrupy mass, which was dissolved in dichloromethane (75 mL) and washed with an aqueous solution of 5% sodium bicarbonate (2 × 25 mL) and a saturated solution of sodium chloride (1 × 25 mL), respectively. The organic phase was collected, dried over anhydrous sodium sulfate, and, after filtration, concentrated under vacuum to obtain crude *N*-(iodoacetyl)-*N*′-(anthraquinon-2-oyl)-ethylenediamine **3**. Subsequently, the crude material was purified by silica gel column chromatography to obtain the title compound in ∼80% yield. The compound was characterized Ir, by ^{1}H NMR and mass spectroscopy. ^{1}H NMR (DMSO), δ: 3.35−3.55 (m, 4H), 3.95 (s, 2H), 7.08 (br, 1H), 7.95−8.74 (m, 7H), 8.97 (br, 1H). MS (*m*/*z*): 463.3 $(M + H)^+$. IR, ν (cm^{-1}): 1286, 1670, 1709, 2931, 3317.

Determination of Threshold Concentration of Oligonucleotides on Glass Surface for Fluorescent Detection. To arrive at the threshold concentration of immobilized oligonucleotides required for visualization on a glass surface, an oligomer sequence, TET-OPO_3-d(TTC GTC ATC AAG TAG TTC CT)-OPO_3-$(CH_2)_6NHCO(CH_2)_2SH$, was serially diluted with reaction buffer, containing DMSO (10%), in five different concentrations (10, 5, 2.5, 1.0, and 0.5 μM) and applied onto an IAED-activated glass microslide (route B) in duplicate with the help of a pipettman. The spotted microslide was kept inside a microwave oven and irradiated for 10 min (30 × 20 s) (see Supporting Information). Each exposure was 20 s, followed by cooling in an ice bath for 5 s. Subsequently, the glass slide was subjected to washings with washing buffer (3 × 10 mL), dried under vacuum, and visualized under a laser scanner set at 570 nm. Similarly, thiophosphate oligomer, TET-OPO_3-d(TTC GTC ATC AAG TAG TTC CTT TTT T)-$OPSO_2^{2-}$, was immobilized on the activated glass slide and, after usual washings, visualized under a laser scanner.

Specificity of Immobilization Chemistry and Detection of Base Mismatches. Oligonucleotide sequences, viz., $HS(CH_2)_6$-OPO_3-d(CCT CTG TTC AGA TGC TCT GC), $HS(CH_2)_6OPO_3$-d(CCT CTG TTC AGA T<u>T</u>C TCT GC), $HS(CH_2)_6OPO_3$-d(CC<u>A</u> CTG TTC AGA T<u>T</u>C TC<u>T</u> GC), $HS(CH_2)_6OPO_3$-d(ACT GG<u>C</u> GTC CGT CAG <u>G</u>CA TT), were dissolved in reaction buffer containing DMSO (10%) and spotted onto an IAED-activated glass microslide (route B). The spotted slide was processed, as described above, and after drying, the slide was subjected to hybridization assay. In a glass Petri dish, the spotted glass slide was kept on a wet blotting paper, and the complementary oligomer, TET-OPO_3-d(GCA GAG CAT CTG AAC AGA GG) (25 μM dissolved in 50 μL of hybridization buffer), was spread on the spotted area. The area was covered with a coverslip, and the slide kept at 60 °C for 5 min, and later at ambient temperature for 2 h and at 10 °C for another 2 h. After removal of the coverslip, the slide was washed with washing buffer (3 × 10 mL), dried under vacuum, and subsequently, visualized under a laser scanner.

Similarly, thiophosphorylated oligomers, viz., d(CCT CTG TTC AGA TGC TCT GCT TTT T)-$OPSO_2^{2-}$, d(CCT CTG TTC AGA T<u>T</u>C TCT GCT TTT T)-$OPSO_2^{2-}$, d(CC<u>A</u> CTG TTC AGA T<u>T</u>C TCT GC)-$OPSO_2^{2-}$, d(ACT GGC GT<u>C</u> CGT CAG GCA <u>T</u>TT TTT T)-$OPSO_2^{2-}$, were immobilized and fluorescent spots visualized under a laser scanner after hybridization assay.

Under each of the above experimental conditions, the experiment was repeated 2−3 times. The immobilization and hybridization data presented are the average of these repeat experiments, and the error bars represent the percentage error (±2−4%) observed. In order to determine the immobilization and hybridization efficiencies, a calibration curve was constructed using a labeled oligomer (see Supporting Information).

RESULTS AND DISCUSSION

The present study has been undertaken with the objective to design a versatile general purpose heterobifunctional reagent to immobilize modified oligonucleotides on a variety of polymer matrices. The reactive groups in the heterobifunctional reagent were carefully selected, keeping in mind that one of the reactive groups must have reactivity toward oligonucleotides bearing a thiol or thiophosphate or phosphorothioate group, as they can easily be introduced during solid-phase synthesis of oligonucleotides using commercially available reagents and chemicals. A perusal of literature revealed that the iodoacetyl group would be an ideal choice, as it has specificity and sufficient reactivity toward these functionalities. We reckoned that the second group which would effectively functionalize a variety of polymer matrices such as polypropylene (PP), polyethylene (PE), nylon, modified glass, and so forth may be the photoactivable anthraquinone molecule which does not suffer from the intrinsic drawbacks of functionalities such as nitrenes and carbenes (*19*, *20*). Moreover, the use of anthraquinone in the synthesis of a heterobifunctional reagent has many attributes, viz., the reactions associated are fast, clean, and result in high yields. Recently, a heterobifunctional reagent, *N*-(3-trifluoroethanesulfonyloxypropyl)-anthraquinone-2-carboxamide (NTPAC), has been reported from our laboratory for the immobilization of biomolecules on various polymeric surfaces (*12*). However, its preparation requires the

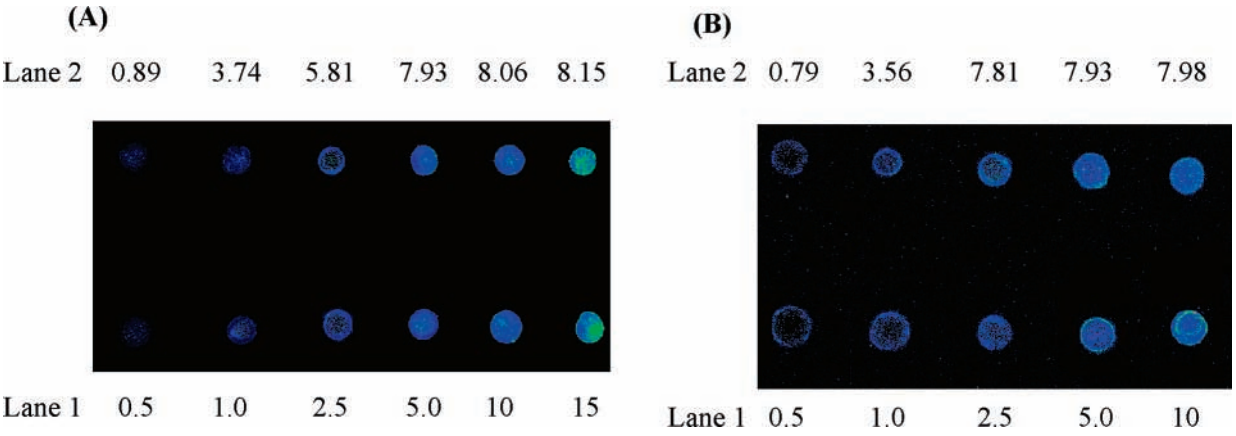


Figure 1. Fluorescence maps obtained by immobilization of (A) TET-OPO_3-d(TTC GTC ATC AAG TAG TTC CT)-OPO_3-$(CH_2)_6NHCO(CH_2)_2$-SH, (B) TET-OPO_3-d(TTC GTC ATC AAG TAG TTC CTT TTT T)-$OPSO_2^{2-}$. Lane 1 and Lane 2 depict the concentration (μM) of the immobilized probe and the immobilization efficiency (%), respectively. Slides were scanned at 85% of laser power and 80% of photomultiplier gain.

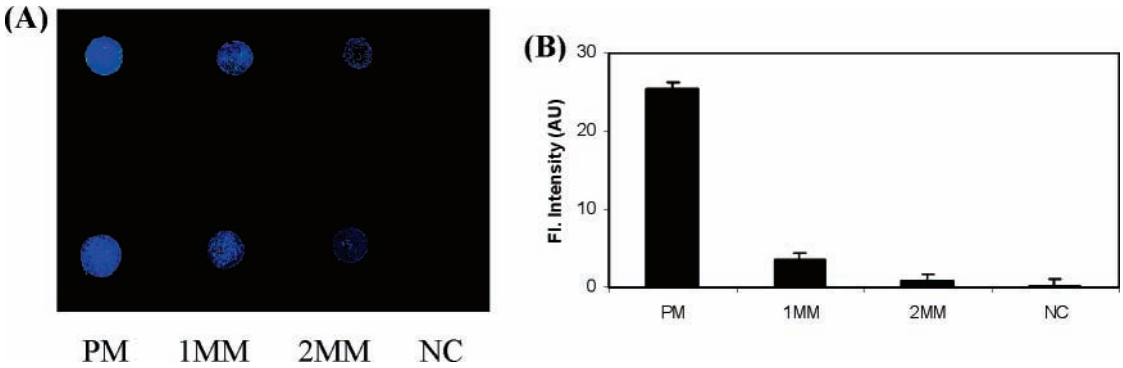
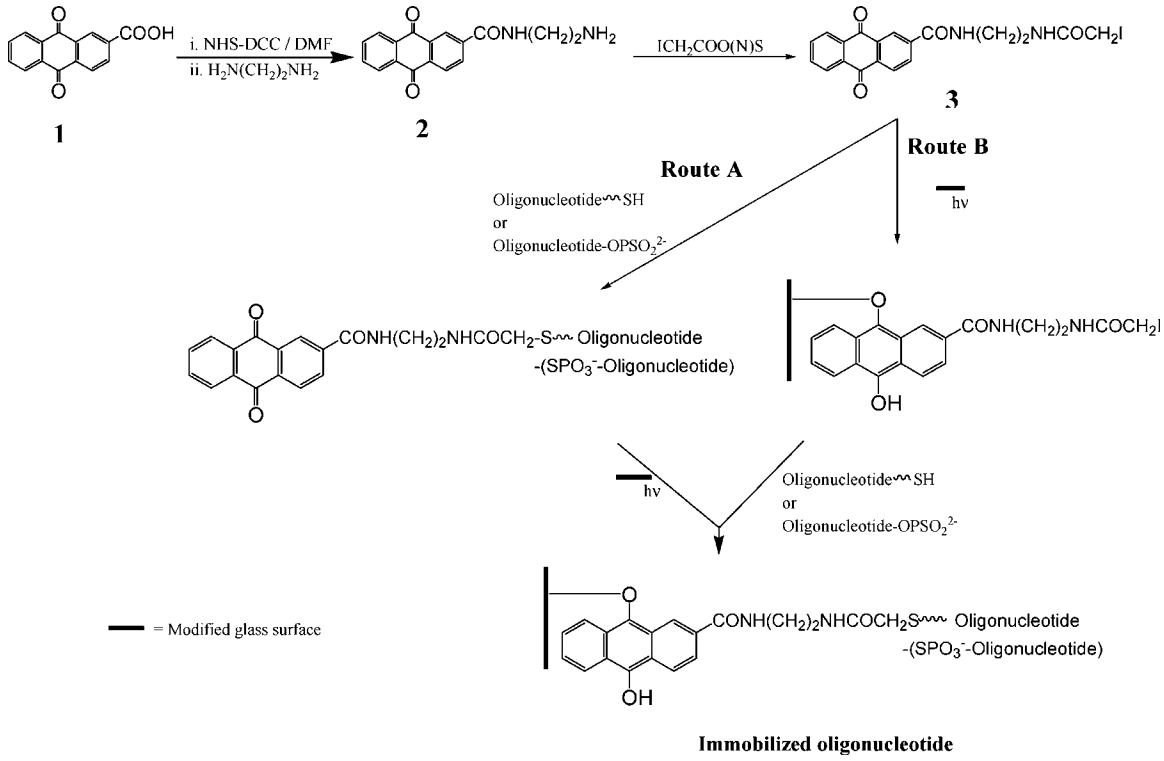


Figure 2. (A) Fluorescence map showing the detection of nucleotide mismatches and specificity of immobilization via hybridization with TET-OPO_3-d(GCA GAG CAT CTG AAC AGA GG) (25 μM). Lane 1, $HS(CH_2)_6OPO_3$-d(CCT CTG TTC AGA TGC TCT GC); Lane 2, $HS(CH_2)_6$-OPO_3-d(CCT CTG TTC AGA TTC TCT GC); Lane 3, $HS(CH_2)_6OPO_3$-d(CCA CTG TTC AGA TTC TCT GC); Lane 4, $HS(CH_2)_6OPO_3$-d(ACT GGC GTC CGT CAG GCA TT), each spotted at 5 μM. Slide was scanned at 85% of laser power and 80% of photomultiplier gain. (B) Comparison of fluorescence intensity observed with zero, single, and double mismatch in probe after hybridization with target (complementary to zero mismatch).

Scheme 1. Strategy for the Synthesis of IAED and Immobilization of Modified Oligonucleotides (−SH and -$OPSO_2^{2-}$) on Activated Glass Surface via Two Routes



use of an expensive and a highly moisture sensitive reagent, trifluoroethanesulfonyl chloride. In the present methodology, the iodoacetyl group reacts selectively with thiol functions present in modified oligonucleotides to produce a thioether/thioester linkage, and the anthraquinone moiety reacts with C−H-containing polymer surfaces under UV light, generating stable covalent bonds. Both the reactions proceed under mild conditions. However, to speed up the reaction of thiols (i.e., −SH, $-OPSO_2^{2-}$, $-OPSO_2^{-}-$) with the iodoacetyl group of IAED, reactions were performed under MW, where it completes in just 10 min with all three functionalities. The sufficient stability and high solubility of the new reagent in water-miscible solvents, such as DMF and DMSO, are among its desired features.

Synthesis of *N*-(iodoacetyl)-*N′*-(anthraquinon-2-oyl)-ethylenediamine (IAED) 3. The two-step preparation of the reagent, IAED, is illustrated in Scheme 1. In the first step, anthraquinone-2-carboxylic acid **1** was converted into its NHS ester, followed by reaction with ethylenediamine to obtain *N*-(anthraquinon-2-oyl)-ethylenediamine (AED) **2** as a solid material in ∼70% yield. The compound **2** was further reacted with iodoacetic acid-*N*-hydroxysuccinimide ester to obtain a syrupy mass, which was then purified by silica gel column chromatography to obtain the desired reagent, IAED **3**, in ∼80% yield. The reagent and its precursor were characterized by IR, ^{1}H NMR, and mass spectroscopy (vide experimental).

Threshold Concentration to Visualize Fluorescent Spots. In order to arrive at the optimal concentration required for visualization of an oligonucleotide on the modified glass microslide, an iodoacetylated glass microslide was prepared using IAED (route B). Subsequently, an oligomer, TET-OPO_3-d(TTC GTC ATC AAG TAG TTC CT)-OPO_3-$(CH_2)_6$NHCO-$(CH_2)_2$SH, was immobilized in different concentrations under MW. After usual washings with the buffer solution and drying under vacuum, the slide was subjected to scanning under a laser scanner set at 570 nm. The pictorial view of the slide is depicted in Figure 1A. The immobilization efficiency (lane 2) against each concentration (lane 1) was also determined with the help of a standard curve, which was plotted between fluorescence intensity (A.U.) of the spot vs concentration. The spots corresponding to 0.5−2.5 μM concentration were visible; however, to construct a good quality biochip, a concentration of 5 μM was selected and used for immobilization purposes. Similar data was observed in case of 3′-thiophosphorylated oligomer (Figure 1B).

Hybridization. The applicability of the projected strategy was evaluated by performing hybridization assay of slides fabricated via both the routes (A and B). (see Supporting Information).

Specificity of the Proposed Methodology. In order to demonstrate the efficacy of the proposed heterobifunctional reagent to construct biochips and to detect base mismatches, a series of oligonucleotides, viz., $HS(CH_2)_6OPO_3$-d(CCT CTG TTC AGA TGC TCT GC), $HS(CH_2)_6OPO_3$-d(CCT CTG TTC AGA T$\underline{T}$C TCT GC), $HS(CH_2)_6OPO_3$-d(CC$\underline{A}$ CTG TTC AGA T$\underline{T}$C T$\underline{C}$T GC), $HS(CH_2)_6OPO_3$-d(ACT GG$\underline{C}$ GTC CGT CAG G$\underline{C}$A TT), were covalently fixed on a modified glass slide via route B. After the usual capping and washings, the slide was subjected to hybridization with a complementary labeled oligomer, TET-OPO_3-d(GCA GAG CAT CTG AAC AGA GG). After thorough washings, the glass slide was visualized under a laser scanner. On the basis of fluorescence intensity, base mismatches were identified and the results are revealed in Figure 2A,B. The perfectly matched duplex flashed the maximum intensity (lane 1), while the spots having one (lane 2) and two (lane 3) mismatches showed fluorescence intensity values in decreasing order, and the non-complementary material (lane 4) did not glow at all. It is apparent from the results that the immobilized oligonucleotides are specific toward complementary oligonucleotides. The signal-to-noise ratio was on an average >97, as calculated from the signal obtained from hybridized (lane 1) and unhybridized oligomers (lane 4) at 5 μM concentration. Figure 3A,B depicts the results obtained with thiophosphorylated probes. The low background in this system may be attributed to the fact that the surface is not positively charged and, therefore, not prone to non-specific interactions with negatively charged oligonucleotides.

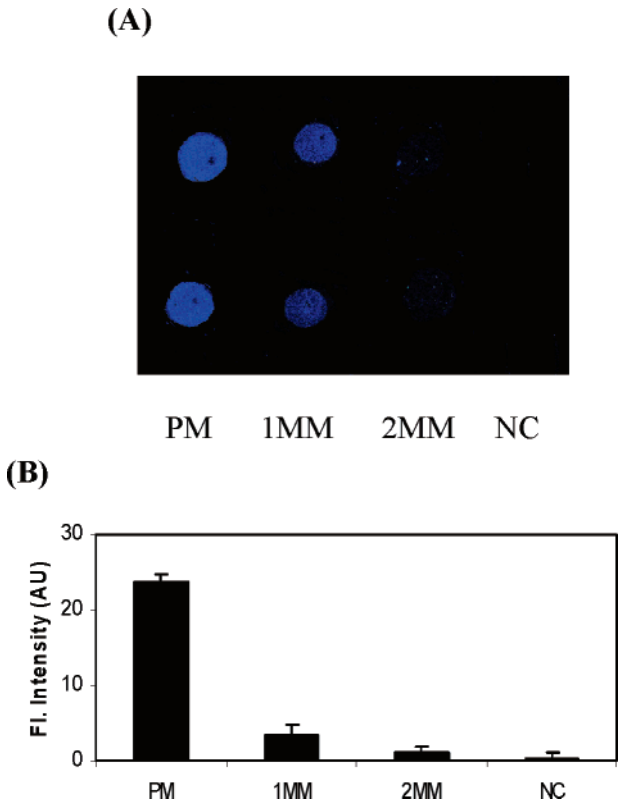


Figure 3. (A) Fluorescence map showing the detection of nucleotide mismatches and specificity of immobilization via hybridization with TET-OPO_3-d(GCA GAG CAT CTG AAC AGA GGT TTT T) (25 μM). Lane 1, d(CCT CTG TTC AGA TGC TCT GCT TTT T)-$OPSO_2^{2-}$; Lane 2, d(CCT CTG TTC AGA T$\underline{T}$C TCT GCT TTT T)-$OPSO_2^{2-}$; Lane 3, d(CC$\underline{A}$ CTG TTC AGA T$\underline{T}$C TCT GCT TTT T)-$OPSO_2^{2-}$; Lane 4, d(AC$\underline{T}$ GGC GTC CGT C$\underline{A}$G GCA TTT TTT T)-$OPSO_2^{2-}$, each spotted at 5 μM. Slide was scanned at 85% of laser power and 80% of photomultiplier gain. (B) Comparison of fluorescence intensity observed with zero, single, and double mismatch in probe after hybridization with target (complementary to zero mismatch).

Thermal Stability. The thermal stability of the constructed arrays (biochips) using the projected reagent was also evaluated by subjecting the spotted slide to PCR-like conditions. The results demonstrate that linkages employed for immobilization are stable for exploitation in biological research (see Supporting Information).

CONCLUSIONS

In summary, a new heterobifunctional reagent has been synthesized and used for fabrication of oligonucleotide microarrays on the glass surface. The preparation of the projected reagent is straightforward, and it displays sufficient stability on storage. Using the new reagent, we have demonstrated the rapid immobilization of oligonucleotides bearing mercaptoalkyl and thiophosphate functions on the uncharged glass surface. The immobilized probes are stable during PCR-like conditions. The strategy can be used for biological assays involving higher

temperatures. The data demonstrate that the featured strategy may be useful for the preparation of new devices for DNA arrays.

Supporting Information Available: Additional experimental details as indicated in the text. This material is available free of charge via the Internet at http://pubs.acs.org.

LITERATURE CITED

(1) He, Z., Wu, L., Fields, M. W., and Zhou, J. (2005) Use of microarrays with different probe sizes for monitoring gene expression. *Appl. Environ. Microbiol. 71*, 5154−5162.

(2) Napoli, C., de Nigris, F., and Sica, V. (2004) New advances in microarrays: finding the genes causally involved in disease. *Methods Mol. Med. 108*, 215−234.

(3) Martienssen, R. A., Doerge, R. W., and Colot, V. (2005) Epigenomic mapping in Arabidopsis using tiling microarrays. *Chromosome Res. 13*, 299−308.

(4) Wang, D., Gao, H., Zhang, R., Ma, X., Zhou, Y., and Cheng, J. (2005) Single nucleotide polymorphism discrimination assisted by improved base stacking hybridization using oligonucleotide microarrays. *Biotechniques 35*, 300−302.

(5) Pease, A. C., Solas, D., Sullivan, E. J., Cronin, M. T., Holmes, C. P., and Fodor, S. P. (1994) Light-generated oligonucleotide arrays for rapid DNA sequence analysis. *Proc. Natl. Acad. Sci. U.S.A. 91*, 5022−5026.

(6) Fodor, S. P.A., Read, J. L., Pirrung, M. C., Stryer, L., Lu, A. T., and Solas, D. (1991) Light directed spatially addressable parallel chemical synthesis. *Science 251*, 767−773.

(7) Pirrung, M. C. (2002) How to make DNA chip. *Angew. Chem., Int. Ed. 41*, 1276−1289.

(8) Seliger, H., Hinz, M., and Happ, E. (2003) Arrays of immobilized oligonucleotides − Contributions to nucleic acids technology. *Curr. Pharm. Biotechnol. 4*, 379−395.

(9) Kumar, P., and Gupta, K. C. (2003) A rapid method for the construction of oligonucleotide arrays. *Bioconjugate Chem. 14*, 507−512.

(10) Kumar, P., Choithani, J., and Gupta, K. C. (2004) Construction of oligonucleotide arrays on a glass surface using a heterobifunctional reagent, *N*-(2-trifluoroethanesulfonatoethyl)-*N*-(methyl)-triethoxysilylpropyl-3-amine (NTMTA). *Nucleic Acids Res. 32*, e80.

(11) Kumar, P., Agrawal, S. K., Misra, A., and Gupta, K. C. (2004) A new heterobifunctional reagent for immobilization of biomolecules on glass surface. *Biomed. Chem. Lett. 14*, 1097−1099.

(12) Kumar, P., Agarwal, S. K., and Gupta, K. C. (2004) *N*-(3-Trifluoroethanesulfonyloxypropyl)anthraquinone-2-carboxamide: A new heterobifunctional reagent for immobilization of biomolecules on a variety of polymer surfaces. *Bioconjugate Chem. 15*, 7−11.

(13) Koch, T., Jacobsen, N., Fensholdt, J., Boas, U., Fenger, M., and Jakobsen, M. H. (2000) Photochemical immobilization of anthraquinone conjugated oligonucleotides and PCR amplicons on solid surfaces. *Bioconjugate Chem. 11*, 474−483.

(14) Varma, R. S. (2002) Clay and clay-supported reagents in organic synthesis. *Tetrahedron 58*, 1235−1255.

(15) Perreux, L., and Loupy, A. (2001) A tentative rationalization of microwave effects in organic synthesis according to the reaction medium, and mechanistic considerations. *Tetrahedron 57*, 9199−9223.

(16) Kumar, P., and Gupta, K. C. (1996) Microwave-assisted synthesis of S-trityl and S-acylmercaptohexanol and their deprotection. *Chem. Lett. 8*, 635−636.

(17) Rao, N. S., Kumar, P., Chauhan, V. K., Garg, B. S., and Gupta, K. C. (2002) Microwave assisted high yielding preparation of N-protected 2′-deoxynucleosides useful for oligonucleotide synthesis. *Nucleosides, Nucleotides Nucleic Acids 21*, 393−397.

(18) Kumar, P., and Gupta, K. C. (1997) Microwave assisted rapid and clean deprotection of oligodeoxyribonucleotides. *Nucleic Acids Res. 25*, 5127−29.

(19) Yan, M., Cai, S. X., Wybourne, M. N., and Keana, J. F. W. (1993) Photochemical functionalization of polymer surfaces and the production of biomolecule-carrying micrometer-scale structures by deep UV lithography using 4-substituted perfluorophenyl azides. *J. Am. Chem. Soc. 115*, 814−816.

(20) Sigrist, H., Gao, H., and Wegmuller, B. (1992) Light dependent covalent immobilization of biomolecules on inert surfaces. *Biotechnology 10*, 1026−1028.

BC0602634

ARTICLES

Visualization of the Degradation of a Disulfide Polymer, Linear Poly(ethylenimine sulfide), for Gene Delivery

Yan Lee, Heejung Mo, Heebeom Koo, Jong-Yeun Park, Min Yi Cho, Geun-woo Jin, and Jong-Sang Park*

School of Chemistry and Molecular Engineering, Seoul National University, San 56-1, Gwanak-gu, Seoul, 151-742, Korea.
Received May 2, 2006; Revised Manuscript Received August 24, 2006

Polyethylenimine (PEI) shows high transfection efficiency and cytoxicity due to its high amine density. The new disulfide cationic polymer, linear poly(ethylenimine sulfide) (*l*-PEIS), was synthesized for efficient and safe gene delivery. As the amine density of *l*-PEIS increased, the transfection efficiency also increased. *l*-PEIS-6 and *l*-PEIS-8 show transfection efficiencies that are similar to that of PEI. However, cytotoxicity of *l*-PEIS was not observed due to the biodegradable disulfide bond. The disulfide bonds are stable in the oxidative extracellular condition and can be degraded rapidly in the reductive intracellular condition. The degradation of *l*-PEIS in HeLa cells was visualized by fluorescence microscopy using the probe−probe dequenching effect of BODIPY-FL fluorescence dye. *l*-PEIS was degraded completely within 3 h.

INTRODUCTION

Various polymers are used in the field of drug and gene delivery (*1*−*4*). Much research has concentrated on the development of a polymer with high transfection efficiency. However, high transfection efficiency often induces cytotoxicity. For example, polyethylenimine (PEI) is one of the most effective nonviral gene-delivery carriers, but its cytotoxicity is too high for in vivo gene delivery (*5*, *6*).

Polyethyleneglycol (PEG)-conjugated PEI (*7*) and low-molecular-weight PEI (*8*) have lower toxicity, but also lower transfection efficiency, than high-molecular-weight PEI (22 kDa or 25 kDa). On the basis of these results, low-molecular-weight amine derivatives have been conjugated to each other with biodegradable bonds, and the resulting polymers tested for gene delivery to determine whether a higher molecular weight would increase transfection efficiency and whether subsequent biodegradation to lower molecular weights would reduce cytotoxicity. Although the biodegradable amine derivatives reduced cytotoxicity, most of them were less efficient than PEI for transfection (*9*−*12*).

It has been reported that the exceptionally high transfection efficiency of PEI is due to the endosome buffering effect of its high amine density (*13*). Among many commercially available cationic polymers, the amine densities (Da/1N) of three representative polymers, PEI, poly(L-lysine) (PLL), and poly(amidoamine) (PAMAM) G4, are shown in Table 1. Since high amine density appears to be an important factor for high efficiency of PEI, a polymer having both a high amine density and biodegradability may be required.

Esters, acetals, orthoesters, and disulfides are the most widely used among many possible biodegradable bonds. Ester bonds in biopolymers usually are unstable in aqueous solution (*14*, *15*). Therefore, ester polymers must be manipulated carefully, and it is hard to control the release of the drugs or genes. In contrast, acetals and orthoesters can be used for controlled release because they are stable at neutral pH but degraded at acidic pH (*16*, *17*). It also has been reported that disulfide bonds are stable in the oxidative extracellular environment but are degraded rapidly in the reductive intracellular environment due to the 5 mM concentration of reduced glutathione (*18*). Thus, polymers linked with disulfide bonds can be useful for selective release in the cytosol (*19*). However, it is not known whether the polymer can be degraded in the cytosol as well as in a buffer with 5 mM glutathione. No clear proof of degradation within the cell has been presented clearly in experiments with other biodegradable polymers.

Table 1. Amine Density, M_n, and M_w of Commercially Available Cationic Polymers and *l*-PEIS Derivatives

	amine density (Da/1N)	M_n/ M_w	PD
PEI	42		
PLL	128		
PAMAM G4	113		
l-PEIS-2	89	10970/18830	1.716
l-PEIS-4	66	17150/20430	1.191
l-PEIS-6	58	7786/11340	1.457
l-PEIS-8	55	7143/11680	1.635

Therefore, we have synthesized the linear poly(ethylenimine) derivatives with disulfide bonds having various amine densities as shown in Scheme 1. In this paper, we would measure the transfection activity and cytotoxicity of these derivatives, linear poly(ethylenimine sulfide) (*l*-PEIS), and want to prove the degradation of *l*-PEIS in the cytosol as well as in the buffer with 5 mM glutathione.

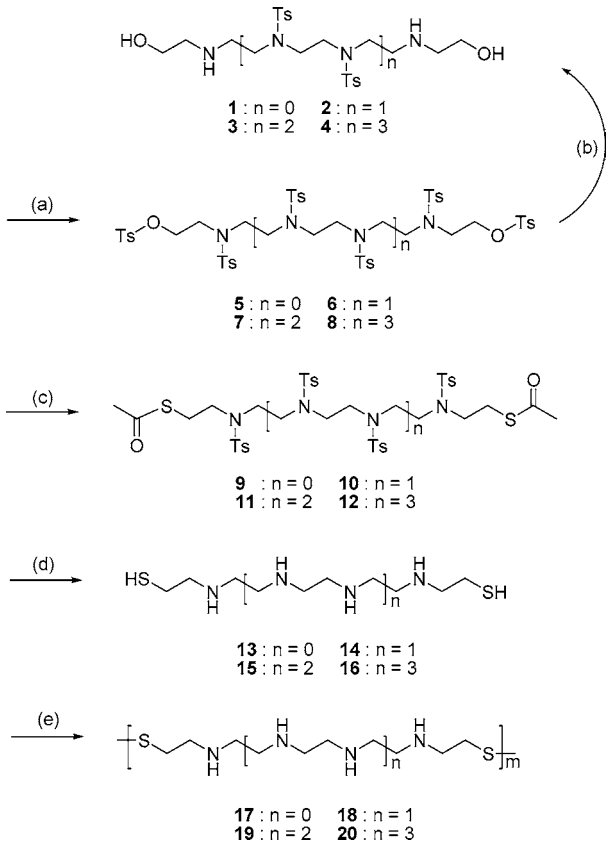
EXPERIMENTAL PROCEDURES

Materials and Reagents. *N*,*N*′-Bis(2-hydroxyethyl)ethylenediamine (**1**), *p*-toluenesulfonyl chloride (p-TsCl), 4-(dimethylamino)pyridine (DMAP), triethylamine (TEA), dichloromethane (DCM), *N*,*N*-dimethylformamide (DMF), ethanolamine, potassium thioacetate, dimethyl sulfoxide (DMSO), chloroform-*d*

* Tel: 82-2-880-6660. Fax: 82-2-877-5110. E-mail: pfjspark@plaza.snu.ac.kr.

10.1021/bc060113t CCC: $37.00 © 2007 American Chemical Society
Published on Web 12/23/2006

Scheme 1. Synthesis of *l*-PEIS-2, -4, -6, and -8[a]



[a] Conditions: (a) TsCl, DMAP, TEA/dichloromethane at 0 °C; (b) ethanolamine, dimethylformamide at 50 °C; (c) potassium thioacetate/dimethylformamide at RT; (d) phenol, 33% HBr/acetic acid at 90 °C; (e) aqueous solution under oxygen pressure at RT.

($CDCl_3$), deuterium oxide (D_2O), poly(ethylenimine) (PEI, average molecular weight 25 kDa), Hepes, and 3-[4,5-dimethylthiazol-2-yl]-2,5-diphenyltetrazolium bromide (MTT) were purchased from Sigma-Aldrich (St. Louis, MO). The Luciferase 1000 Assay System and Reporter Lysis Buffer were purchased from Promega (Madison, WI). Minimal Essential Medium (MEM), Dulbecco's Modified Eagle's Medium (DMEM), trypsin-EDTA, and antibiotic−antimycotic were purchased from GIBCO (Gaithersburg, MD). Phosphate-buffered saline (PBS) was purchased from Cambrex Bio Science (Walkersville, MD). Fetal bovine serum (FBS) was purchased from JBI (Korea). The Micro BCA Protein Assay Kit was purchased from Pierce (Rockford, IL). The BODIPY-FL STP ester was purchased from Invitrogen (Carlsbad, CA). ExGen 500 was purchased from Euromedex (France).

Synthesis of 5, 6, 7, and 8 (step a). **1**, **2**, **3**, and **4** (10 mmol) were dissolved in 40 mL dichloromethane. 4-(Dimethylamino)-pyridine (DMAP) (1 equiv, 10 mmol), triethylamine (9.2 equiv, 92 mmol), and *p*-toluenesulfonyl chloride (4.4 equiv, 44 mmol) were added. The mixture was stirred at 0 °C for 1 day. The solvent was removed by evaporation and dissolved in 100 mL chloroform. The solution was washed three times with 0.1 N HCl. The organic layer was dried with $MgSO_4$ and evaporated. The final products were obtained as white or pale yellow powder from silica column chromatography. Yield was about 60−80%. ^{1}H NMR spectra of the products were obtained using a Bruker DPX-300 NMR spectrometer (300 MHz). In the deuterium solvent, TMS (3-(trimethylsilyl)propionic acid sodium salt) was used as an internal reference (0 ppm). ^{1}H NMR (300 MHz, $CDCl_3$, δ ppm) of **5**: 2.45 (s, 12H, tosyl $-CH_3$), 3.30 (s, 4H, $-CH_2N(Ts)CH_2CH_2OTs$), 3.37 (t, 4H, $-N(Ts)CH_2CH_2OTs$), 4.14 (t, 4H, $-N(Ts)CH_2CH_2OTs$), 7.35 (d, 8H, aromatic protons of tosyl groups), 7.72 (d,d, 8H, aromatic protons of tosyl groups). ^{1}H NMR (300 MHz, $CDCl_3$, δ ppm) of **6**: 2.42 (s, 12H, *N*-tosyl $-CH_3$), 2.45 (s, 16H, *O*-tosyl $-CH_3$), 3.27 (m, 8H, $-CH_2N(Ts)CH_2CH_2OTs$), 3.43 (m, 8H, $-CH_2N(Ts)CH_2-CH_2N(Ts)CH_2CH_2OTs$), 4.16 (t, 4H, $-N(Ts)CH_2CH_2OTs$), 7.34 (m, 12H, aromatic protons of tosyl groups), 7.78 (m, 12H, aromatic protons of tosyl groups). ^{1}H NMR (300 MHz, $CDCl_3$, δ ppm) of **7**: 2.41 (s, 18H, *N*-tosyl $-CH_3$), 2.43 (s, 6H, *O*-tosyl $-CH_3$), 3.26 (m, 8H, $-CH_2N(Ts)CH_2CH_2OTs$), 3.37 (m, 16H, $-CH_2N(Ts)CH_2CH_2N(Ts)CH_2CH_2N(Ts)CH_2CH_2OTs$), 4.13 (t, 4H, $-N(Ts)CH_2CH_2OTs$), 7.31 (m, 16H, aromatic protons of tosyl groups), 7.77 (m, 16H, aromatic protons of tosyl groups). ^{1}H NMR (300 MHz, $CDCl_3$, δ ppm) of **8**: 2.43 (m, 30H, tosyl $-CH_3$), 3.28 (m, 8H, $-CH_2N(Ts)CH_2CH_2OTs$), 3.42 (m, 24H, $-CH_2N(Ts)CH_2CH_2N(Ts)CH_2CH_2N(Ts)CH_2CH_2N(Ts)CH_2CH_2-OTs$), 4.16 (t, 4H, $-N(Ts)CH_2CH_2OTs$), 7.32 (m, 20H, aromatic protons of tosyl groups), 7.83 (m, 20H, aromatic protons of tosyl groups).

Synthesis of 2, 3, and 4 (step b). **5**, **6**, and **7** (1 mmol) were dissolved in 20−30 mL DMF. After the solute was dissolved completely, ethanolamine (10 equiv, 10 mmol) was added slowly. The solution was stirred at 50 °C for 1−2 days. After evaporation, the mixture was dissolved in DMSO and evaporated again for the removal of the remaining ethanolamine.

Synthesis of 9, 10, 11, and 12 (step c). **5**, **6**, **7**, and **8** (10 mmol) were dissolved in 50 mL DMF. Potassium thioacetate (2.5 equiv) was added and stirred at RT overnight. The DMF solution was evaporated and poured into 100 mL of water. The mixture was extracted three or four times with chloroform, and the organic layer was collected, dried with $MgSO_4$, and evaporated to give the final products. Yield was about 75%. ^{1}H NMR (300 MHz, $CDCl_3$, δ ppm) of **9**: 2.34 (s, 6H, $-COCH_3$), 2.44 (s, 6H, *N*-tosyl $-CH_3$), 3.04 (t, 4H, $-N(Ts)CH_2-CH_2S-$), 3.25 (t, 4H, $-N(Ts)CH_2CH_2S-$), 3.39 (s, 4H, $-CH_2N(Ts)CH_2CH_2S-$), 7.33 (d, 4H, aromatic protons of tosyl groups), 7.75 (d, 4H, aromatic protons of tosyl groups). ^{1}H NMR (300 MHz, $CDCl_3$, δ ppm) of **10**: 2.32 (s, 6H, $-COCH_3$), 2.41 (s, 6H, inner *N*-tosyl $-CH_3$), 2.44 (s, 6H, outer *N*-tosyl $-CH_3$), 3.03 (t, 4H, $-N(Ts)CH_2CH_2S-$), 3.23 (t, $-CH_2CH_2N(Ts)CH_2-CH_2S-$), 3.37 (m, 12H, $-CH_2N(Ts)CH_2CH_2N(Ts)CH_2CH_2S-$), 7.32 (m, 8H, aromatic protons of tosyl groups), 7.77 (d, 8H, aromatic protons of tosyl groups). ^{1}H NMR (300 MHz, $CDCl_3$, δ ppm) of **11**: 2.31 (s, 6H, $-COCH_3$), 2.41 (m, 18H, *N*-tosyl $-CH_3$), 3.02 (t, 4H, $-N(Ts)CH_2CH_2S-$), 3.23 (t, 4H, $-CH_2-CH_2N(Ts)CH_2CH_2S-$), 3.36 (m, 20H, $-CH_2N(Ts)CH_2CH_2N-(Ts)CH_2CH_2N(Ts)CH_2CH_2S-$), 7.31 (m, 12H, aromatic protons of tosyl groups), 7.78 (m, 12H, aromatic protons of tosyl groups). ^{1}H NMR (300 MHz, $CDCl_3$, δ ppm) of **12**: 2.32 (s, 6H, $-COCH_3$), 2.41 (m, 24H, *N*-tosyl $-CH_3$), 3.01 (t, 4H, $-N(Ts)CH_2CH_2S-$), 3.23 (t, 4H, $-CH_2CH_2N(Ts)CH_2CH_2S-$), 3.36 (m, 28H, $-CH_2N(Ts)CH_2CH_2N(Ts)CH_2CH_2N(Ts)CH_2-CH_2N(Ts)CH_2CH_2S-$), 7.29 (m, 16H, aromatic protons of tosyl groups), 7.77 (m, 16H, aromatic protons of tosyl groups).

Tosyl and Acetyl Deprotection (step d). A solution of **9** (1 mmol) and phenol (0.41 mmol) in 33% HBr/AcOH (15.4 mL) was refluxed for 24 h. The reaction mixture was filtered, and the resulting pale brown solid was washed with ethanol. After refluxing for 1 h with ethanol, the solution was filtered and the resulting solid was washed twice with diethyl ether to obtain the pale brown powder (**13**). The syntheses of **14**, **15**, and **16** were performed in the same way. ^{1}H NMR (300 MHz, D_2O, δ ppm) of **13**: 3.03 (t, 4H, $-NHCH_2CH_2SH$), 3.41 (m, 8H, $-CH_2-NHCH_2-$). ^{1}H NMR (300 MHz, D_2O, δ ppm) of **14**: 3.07 (t, 4H, $-NHCH_2CH_2SH$), 3.23 (s, 4H, $-CH_2NH\ CH_2CH_2\ NH\ CH_2CH_2SH$), 3.32 (t, 4H, $-CH_2CH_2NHCH_2CH_2SH$), 3.45 (t, 4H, $-CH_2NHCH_2CH_2SH$), 3.55 (t, 4H, $-CH_2CH_2SH$). ^{1}H NMR (300 MHz, D_2O, δ ppm) of **15**: 3.07 (t, 4H, $-NHCH_2-$

CH_2SH), 3.22−3.32 (m, 16H, $-CH_2NHCH_2CH_2NHCH_2CH_2NHCH_2CH_2SH$), 3.39 (t, 4H, $-CH_2NHCH_2CH_2SH$), 3.52 (t, 4H, $-CH_2CH_2SH$). ^{1}H NMR (300 MHz, D_2O, δ ppm) of **16**: 3.10 (t, 4H, $-NHCH_2CH_2SH$), 3.22−3.32 (m, 24H, $-CH_2NHCH_2CH_2NHCH_2CH_2NHCH_2CH_2NHCH_2CH_2SH$), 3.39 (t, 4H, $-CH_2NHCH_2CH_2SH$), 3.52 (t, 4H, $-CH_2CH_2SH$).

Polymerization (step e). After the deprotection reactions, **13**, **14**, **15**, and **16** were dissolved in water, and the final concentrations of monomers were adjusted to 100 mM. These solutions were stirred at RT for 2 days under oxygen pressure (1 atm). The polymer solutions were evaporated, washed with diethyl ether, and dried to give the final polymer products. ^{1}H NMR (300 MHz, D_2O, δ ppm) of **17**: 3.07 (t, 4H, $-CH_2SS-$), 3.31 (t, 4H, $-CH_2CH_2SS-$), 3.54 (s, 4H, $-CH_2NHCH_2CH_2SS-$). ^{1}H NMR (300 MHz, D_2O, δ ppm) of **18**: 3.05−3.30 (m, 16H, $-CH_2NHCH_2CH_2NHCH_2CH_2SS-$), 3.45 (t, 4H, $-CH_2CH_2SS-$). ^{1}H NMR (300 MHz, D_2O, δ ppm) of **19**: 3.07−3.51 (m, 28H). ^{1}H NMR (300 MHz, D_2O, δ ppm) of **20**: 3.07−3.65 (m, 36H).

Molecular Weight Measurements of *l*-PEIS. The molecular weights of *l*-PEIS were determined by multiangle laser-light-scattering (MALLS) in combination with size-exclusion chromatography (SEC). The SEC system included a P680 HPLC pump from Dionex Corporation (Sunnyvale, CA). Polymer samples were detected by a three-angle laser-light-scattering detector (miniDAWN Tristar, 30 mW GaAs laser, 690 nm, K5 cell) and an interferometric refractometer (Optilab DSP, P10 cell) from Wyatt Technologies (Santa Barbara, CA). The MALLS system was operated by *Astra* software version 4.90. A 1% formic acid aqueous solution was used as an eluent after filtration through a 22-nm filter and degassed before use. Ultahydrogel columns (7.8 × 300 mm no. WAT011525 and no. WAT 011545) from Waters (Milford, MA) were used. The solution was delivered to a flow cell inlet at a constant flow rate of 0.4 mL/min. The d*n*/d*c* values for *l*-PEIS-2, *l*-PEIS-4, *l*-PEIS-6, and *l*-PEIS-8 are 0.1881, 0.2092, 0.1771, and 0.1649 (mL/g), which were measured by an interferometric refractometer (Optilab DSP, P10 cell) from Wyatt Technologies (Santa Barbara, CA).

Plasmid Preparation. The firefly luciferase gene was used as a reporter gene to monitor the results of gene transfection. The luciferase expression plasmid (pCN-Luci) was constructed by subcloning the cDNA of *Photinus pyralis* luciferase, with its 21-amino-acid nuclear localization signal, from the SV40 large T antigen to pCN. The pCN vector is known to result in higher expression than the vector with the CMV promoter alone. Plasmid DNA was transformed into *E. coli* TOP10 competent cells, and highly purified covalently closed circular plasmid DNA was isolated by using plasmid purification Giga kits from Qiagen (Valencia, CA) according to the manufacturer's instructions. Plasmids were precipitated with isopropyl alcohol, washed twice with a 70% ethanol solution, and resuspended in distilled water. DNA was stored at −70 °C until use.

Cell Culture. Human liver carcinoma HepG2 cells were grown in MEM, and human cervical cancer HeLa cells were maintained in DMEM. Both media contained 10% fetal bovine serum (FBS) and 1% antibiotic−antimycotic agent. The cell lines were obtained from the Korean Cell Line Bank and incubated at 37 °C in 5% CO_2.

In Vitro Transfection Assay. Cells were seeded at a density of 5 × 10^4 cells/well in 24-well plates in 600 μL of media containing 10% FBS and grown to 70−80% confluence. Prior to transfection, the medium was changed to serum-free medium. Polyplexes were formed by mixing 2 μg of plasmid DNA and polymer at different N/P ratios in 120 μL of a serum-free medium, followed by incubation for 30 min at RT. Cells were treated with the polyplex solution. After 4 h incubation at 37 °C, the medium was replaced with fresh medium containing 10% FBS. After incubation for 2 days at 37 °C, the luciferase activity of transfected cells was analyzed using a LB 9507 luminometer (Berthold, Germany), and the protein content was measured with Micro BCA assay reagents (Pierce, Rockford, IL). The transfection activities shown in Figure 1A are those at the optimum N/P ratios. The optimum N/P ratios are 8 for ExGen 500, *l*-PEIS-2, and *l*-PEIS-4, and 16 for *l*-PEIS-6 and *l*-PEIS-8.

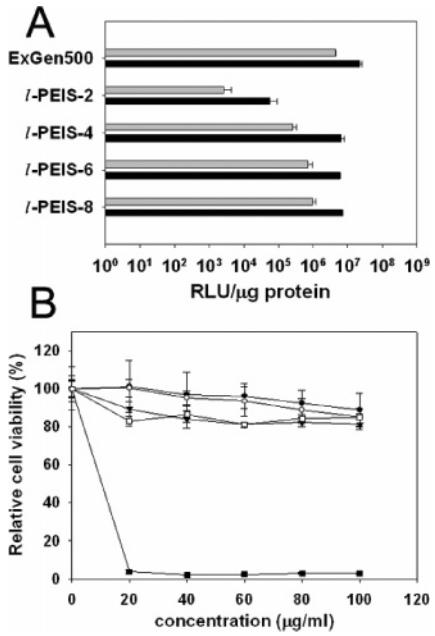


Figure 1. Transfection efficiency (A) (gray bar, HeLa; black bar, HepG2) and cytotoxicity (B) on the HeLa cell line of *l*-PEIS-2 (●), *l*-PEIS-4 (○), *l*-PEIS-6 (▼), *l*-PEIS-8 (□), and ExGen 500(■).

In Vitro Cytotoxicity Assay. MTT assay was used to measure cytotoxicity. HeLa cells were seeded in 96-well tissue culture plates at 10^4 cells/well in 90 μL DMEM medium containing 10% FBS. Cells achieving 70−80% confluence after 24 h were exposed to 10 μL of various concentrations of the polymer solutions for 4 h, after which 26 μL of stock solution of MTT (2 mg/mL in PBS) was added to each well. After 2 h of incubation at 37 °C, the media was exchanged with 150 μL of DMSO extraction buffer. The absorbance was measured at 570 nm using a microplate reader (Molecular Devices Company, Menlo Park, CA). The results were calculated as a percent absorbance to untreated control cells.

Synthesis of *l*-PEIS-BODIPY-FL. *l*-PEIS-6 (10 mg, 1.3 μmol) was dissolved in 2 mL of 5% DMSO aqueous solution. BODIPY-FL STP ester (FW = 542.19) (6 equiv, 7.7 μmols, 4.2 mg) in 200 μL of DMSO was added slowly to the solution. After stirring for 3 h at 37 °C, the solution was dialyzed against deionized water. The dialysis membrane (MWCO = 1000) was purchased from Hankook Spectrum Company. Following 24-hr dialysis, the product solution was lyophilized. The molar ratio between *l*-PEIS-6 and BODIPY was calculated from the M_n of *l*-PEIS-6 and the integration ratio in the ^{1}H NMR spectrum of *l*-PEIS-6-BOD. The molar ratio of BODIPY to *l*-PEIS-6 was 2.0 in the experiment below. The BODIPY-conjugated ExGen 500 was prepared by the same method.

The Degradation of *l*-PEIS-6 in a GSH Solution. *l*-PEIS-6 was dissolved in PBS (pH = 7.4) and combined with a glutathione solution in PBS. The final concentrations of *l*-PEIS-6 and glutathione were 1.0 mg/mL and 5 mM, respectively. The mixture was stirred at 37 °C. After some time, 500 μL was collected, and excess iodoacetic acid (10 mM) was added to prevent further degradation during the measurement of the

molecular weight. The molecular weight analysis was performed as described above for *l*-PEIS.

The Degradation of *l*-PEIS-BODIPY-FL in a GSH Solution. *l*-PEIS-BODIPY-FL was dissolved in PBS (pH = 7.4) containing 1% (v/v) DMSO. The solution was combined with a glutathione solution in PBS containing 1% DMSO. The final concentrations of *l*-PEIS-BODIPY-FL and glutathione were 10 μg/mL and 5 mM, respectively. The mixture was incubated at 37 °C. The fluorescence was measured with an FP-750 spectrofluorometer (Jasco) at RT. The excitation and emission wavelengths were 504 and 513 nm, respectively. The fluorescence of the solution was measured every 30 min.

The Degradation of *l*-PEIS-BODIPY-FL in the Cell. Cells were seeded at a density of 5×10^3 cells/well in 24-well plates in 600 μL of medium containing 10% FBS. After a 1-day incubation at 37 °C, the medium was aspirated, and 600 μL of PBS (pH = 7.4) containing 1% DMSO and *l*-PEIS-BODIPY-FL were added. The final concentration of *l*-PEIS-BODIPY-FL was 10 μg/mL. As a positive control, 5 mM glutathione was added to one well with *l*-PEIS-BODIPY-FL. As a negative control, 10 μg/mL of *l*-PEIS-6 was added to a well without *l*-PEIS-BODIPY-FL. After some time, the cells were observed with an Axiovert 25 fluorescence microscope (Carl Zeiss) with the filter set 09 (488009-0000).

RESULTS AND DISCUSSION

Synthesis of *l*-PEIS Derivatives. To obtain both high amine density and biodegradability, oligoethylenimine (*20*) or low-molecular-weight PEI (*21*) have been linked with disulfide or ester bonds in the previous reports. The resulting irregular polymers have transfection efficiencies that are somewhat satisfactory. Therefore, the linear poly(ethylenimine) derivatives with disulfide bonds having various amine densities were synthesized, as shown in Scheme 1. The number following *l*-PEIS indicates the number of internal amines in the monomer.

Secondary amine and hydroxyl groups of bis(2-hydroxyethyl) derivatives (**1**, **2**, **3**, and **4**) were tosylated by *p*-toluenesulfonyl chloride. The terminal tosyl esters were the activating groups for the next substitution reaction, and the internal tosyl amides were the protecting groups. The tosylated derivatives (**5**, **6**, **7**, and **8**) could be elongated by the substitution with two ethanolamines (**2**, **3**, and **4**) or thioacetylated (**9**, **10**, **11**, and **12**). Deprotection of tosyl amide and thioacetyl groups was performed by hydrobromic acid/acetic acid solution.

Each deprotected monomer (**17**, **18**, **19**, and **20**) was polymerized by the stirring under oxygen pressure. Molecular weights measured by gel permeation chromatography are not reliable, because polymer having high amine density can nonspecifically adsorb to the column. Therefore, the molecular weights of *l*-PEIS were measured by the multiangle laser-light-scattering method (MALLS) (*22*). The molecular weights ranged from about 10 000 to 20 000 as shown in Table 1.

Transfection Efficiency and Cytotoxicity of *l*-PEIS. *l*-PEIS-2 with two amines between the disulfide bonds has one-half the amine density (1 N per 89 Da) of PEI (1 N per 42 Da). As the number of amines between the disulfide bonds increases, the amine density of *l*-PEIS increases. *l*-PEIS-8, with a monomer of eight amines, has an amine density (1 N per 55 Da) similar to that of PEI.

Figure 1A shows the transfection efficiency of *l*-PEIS in HepG2 and HeLa cell lines as compared to that of the linear PEI derivative, ExGen 500 (22 kDa). As the amine density of *l*-PEIS increases, the transfection efficiency in both cell lines increases. *l*-PEIS-6 and *l*-PEIS-8 have amine densities and transfection efficiencies that are similar to those of ExGen 500.

The cytotoxicity of *l*-PEIS derivatives was measured in the HeLa cell line, as shown in Figure 1B. ExGen 500, with a non-biodegradable backbone, shows very high cytotoxicity at a concentration of 20 μg/mL. In contrast, all of the *l*-PEIS derivatives with degradable disulfide linkages show very low or negligible cytotoxicity at that concentration and even at concentrations of 100 μg/mL. Thus, it appears that *l*-PEIS can transfect cells with high efficiency due to its high amine density, but has low toxicity because they can be degraded into low-molecular-weight monomers with small charges.

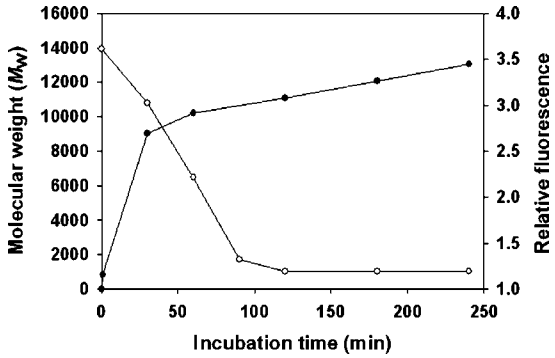


Figure 2. The decrease in molecular weight (○) and fluorescence enhancement (●) of *l*-PEIS-6.

Degradation of *l*-PEIS in a GSH Solution. Recently, we reported the degradation of poly(ethylene oxide sulfide) (PEOS), which is composed of disulfide-linked oligoethylene oxide (*23*). PEOS is degraded completely within 2 h in 5 mM glutathione buffer. By the same way, after a 37 °C incubation of *l*-PEIS-6 in 5 mM glutathione in phosphate-buffered saline, the molecular weight of a sample from the degradation buffer was measured by MALLS. As shown in Figure 2, like PEOS, *l*-PEIS-6 is degraded completely within 2 h. However, there is no clear proof of degradation within the cytosol in experiments with these and other types of biodegradable polymers.

Therefore, a fluorescence method was chosen to measure the degradation in the cytosol. BODIPY fluorescent dye is well-known for its probe−probe quenching effect. When more than two BODIPY dyes are conjugated to one molecule, the fluorescent intensity decreases sharply (*24*). However, if the molecule is degraded into small molecules and the dyes are separated, the fluorescence can be enhanced. This process is illustrated in Figure 3. BODIPY fluorescent dye has been used to measure the degradation of a BODIPY-conjugated polymer (*25*) and for the visualization of viral capsid degradation (*26*).

Two BODIPY-FL molecules were conjugated to an *l*-PEIS-6 molecule, and the recovery of fluorescence was observed during incubation under reductive conditions (Figure 2). As the molecular weight of *l*-PEIS-6-BOD decreases, its fluorescence increases more than 3-fold. Therefore, this material can be used to measure degradation within the cell.

Visualization of the Degradation of *l*-PEIS in the Cytosol. Fluorescence microscopy was used to observe the development of fluorescence in HeLa cells after addition of *l*-PEIS-6-BOD. Fluorescence in the cell interior begins to develop after 0.5 h (Figure 4A). The green fluorescence intensity of BODIPY in the cytosol increases after 2 h (Figure 4C) and is clearly shown in Figure 4E. No further increase of the fluorescence was observed after 3 h. The fluorescence outside of the cell is low in all images. However, when 5 mM of reduced glutathione is added to the cell medium as a positive control, the strong fluorescence of the *l*-PEIS-6-BOD is outside, as well as inside, the cell (Figure 4G).

Meanwhile, the fluorescence of nondegradable BODIPY-conjugated ExGen 500, a negative control, did not show any dependence upon time (Figure 4B,D,F) or the concentration of GSH (Figure 4H). Low fluorescence in the cell interior probably

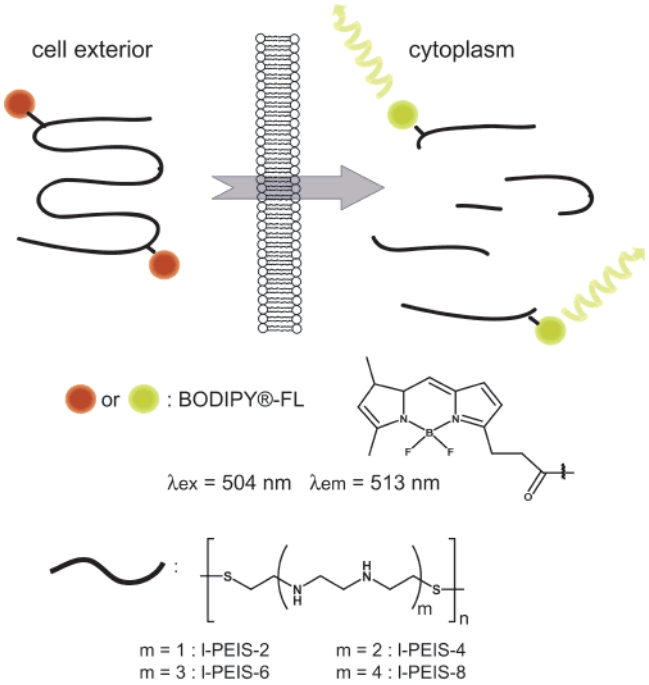


Figure 3. Structure and diagram of the intracellular degradation of *l*-PEIS.

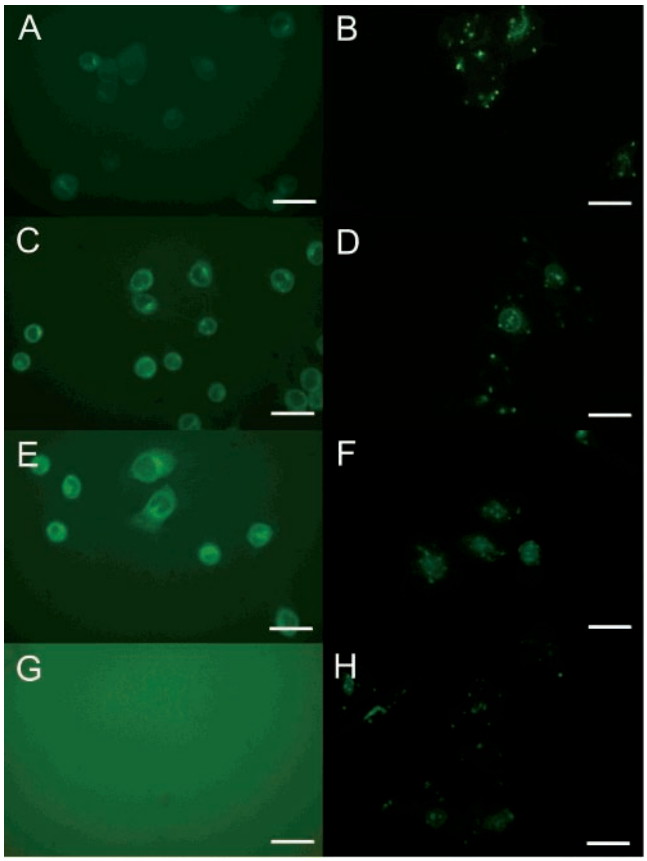


Figure 4. Fluorescence microscopic images treated with *l*-PEIS-6-BOD (A,C,E,G) and ExGen 500-BOD (B,D,F,H). After 0.5 hr (A,B), 2 hr (C,D), 3 hr (E,F), and 0.5 hr treatment with 5 mM glutathione (G,H). The white bars represent 40 μm.

originated from a portion of ExGen 500 with low density of conjugated BODIPY-FL. These results demonstrate that BODIPY-conjugated *l*-PEIS can be degraded, emitting enhanced fluorescence, in the reductive environment of the cell.

CONCLUSION

Using the characteristics of disulfide bonds—stability in the oxidative extracellular environment and degradability in the reductive intracellular environment, we have developed a disulfide derivative of poly(ethylenimine), linear poly(ethylenimine sulfide). The transfection efficiency of *l*-PEIS increases as the amine density increases. *l*-PEIS-6 and *l*-PEIS-8 have transfection efficiencies that are similar to that of PEI, without the high cytotoxicity. Above all, we have proposed methods for measuring and observing the degradation of a biodegradable polymer in the cell interior.

l-PEIS has the characteristics of an ideal nonviral gene delivery carrier: high efficiency and low toxicity. *l*-PEIS has potential applications in many gene-delivery experiments, through improvements in the efficiency, specificity, and stability in serum by cross-linking, ligand coupling, PEGylation, and so forth. In addition, the visualization and measurement of a biodegrading polymer will be of great benefit in investigations of the relationship between polymer degradation and delivery and controlled release.

ACKNOWLEDGMENT

This work was supported by the SRC-Molecular Research Center at Sungkyunkwan University (R11-2000-080-10003-0), the Korea Health 21 R&D Project of the Ministry of Health and Welfare (0405-BO02-0205-0001), and the Gene Therapy Project of the Ministry of Science and Technology (M1053403004-05N3406-00410).

Supporting Information Available: The serum dependence of the transfection efficiency of *l*-PEIS. This material is available free of charge via the Internet at http://pubs.acs.org/BC.

LITERATURE CITED

(1) Andrianov, A. K., and Payne, L. G. (1998) Polymeric carriers for oral uptake of microparticulates. *Adv. Drug Delivery Rev. 34*, 155−170.
(2) Gorman, C. (2002) Chemistry: One generation at a time. *Nature (London) 415*, 487−488.
(3) Ishii, T., Okahata, Y., and Sato, T. (2001) Mechanism of cell transfection with plasmid/chitosan complexes. *Biochim. Biophys. Acta 1514*, 51−64.
(4) Merdan, T., Kopecek, J., and Kissel, T. (2002) Prospects for cationic polymers in gene and oligonucleotide therapy against cancer. *Adv. Drug Delivery Rev. 54*, 715−758.
(5) Kircheis, R., Wightman, L., and Wagner, E. (2001) Design and gene delivery activity of modified polyethylenimines. *Adv. Drug Delivery Rev. 53*, 341−358.
(6) Uduehi, A. N., Stammberger, U., Kubisa, B., Gugger, M., Buehler, T., and Schmid, R. A. (2001) Effects of linear polyethylenimine and polyethylenimine/DNA on lung function after airway instillation to rat lungs. *Mol. Ther. 4*, 52−57.
(7) Suh, W., Han, S., Yu, L., and Kim, S. W. (2002) An angiogenic, endothelial-cell-targeted polymeric gene carrier. *Mol. Ther. 6*, 664−672.
(8) Godbey, W. T., Wu, K. K., and Mikos, A. G. (1999) Poly(ethylenimine) and its role in gene delivery. *J. Controlled Release 60*, 149−160.
(9) Lim, Y., Kim, C., Kim, K., Kim, S. W., and Park, J. (2000) Development of a safe gene delivery system using biodegradable polymer, poly[α-(4-aminobutyl)-L-glycolic acid]. *J. Am. Chem. Soc. 122*, 6524−6525.
(10) Lim, Y., Kim, S., Suh, H., and Park, J. (2002) Biodegradable, endosome disruptive, and cationic network-type polymer as a highly efficient and nontoxic gene delivery carrier. *Bioconjugate Chem. 13*, 952−957.
(11) Wang, J., Mao, H., and Leong, K. (2001) A novel biodegradable gene carrier based on polyphosphoester. *J. Am. Chem. Soc. 123*, 9480−9481.

(12) Lynn, D. M., and Langer, R. (2000) Degradable poly(*β*-amino esters): Synthesis, characterization, and self-assembly with plasmid DNA. *J. Am. Chem. Soc. 122*, 10761−10768.
(13) Boussif, O., Lezoualc'h, F., Zanta, M. A., Mergny, M. D., Scherman, D., Demeneix, B., and Behr, J. P. (1995) A versatile vector for gene and oligonucleotide transfer into cells in culture and *in vivo*: polyethylenimine, *Proc. Natl. Acad. Sci. U.S.A. 92*, 7297−7301.
(14) Lim, Y., Choi, Y. H., and Park, J. (1999) A self-destroying polycationic polymer: Biodegradable poly(4-hydroxy-L-proline ester). *J. Am. Chem. Soc. 121*, 5633−5639.
(15) Panyam, J., and Labhasetwar, V. (2003) Biodegradable nanoparticles for drug and gene delivery to cells and tissue. *Adv. Drug Delivery Rev. 55*, 329−347.
(16) Murthy, N., Thng, Y. X., Schuck, S., Xu, M. C., and Fréchet, J. M. J. (2002) A novel strategy for encapsulation and release of proteins: hydrogels and microgels with acid-labile acetal cross-linkers. *J. Am. Chem. Soc. 124*, 12398−12399.
(17) Heller, J., Barr, J., Ng, S. Y., Abdellauoi, K. S., and Gurny, R. (2002) Poly(ortho esters): Synthesis, characterization, properties and uses. *Adv. Drug Delivery Rev. 54*, 1015−1039.
(18) Kakizawa, Y., Harada, A., and Kataoka, K. (1999) Environment-sensitive stabilization of core−shell structured polyion complex micelle by reversible cross-linking of the core through disulfide bond. *J. Am. Chem. Soc. 121*, 11247−11248.
(19) Oupicky, D., Parker, A. L., and Seymour, L. W. (2002) Laterally stabilized complexes of DNA with linear reducible polycations: Strategy for triggered intracellular activation of DNA delivery vectors. *J. Am. Chem. Soc. 124*, 8−9.
(20) Trubetskoy, V. S., Budker, V. G., Hanson, L. J., Slattum, P. M., Wolff, J. A., and Hagstrom, J. E. (1998) Self-assembly of DNA−polymer complexes using template polymerization. *Nucleic Acids Res. 26*, 4178−4185.
(21) Gosselin, M. A., Guo, W., and Lee, R. J. (2001) Efficient gene transfer using reversibly cross-linked low molecular weight polyethylenimine. *Bioconjugate Chem. 12*, 989−994.
(22) Fischer, D., Harpe, A., Kunath, K., Petersen, H., Li, Y., and Kissel, T. (2002) Copolymers of ethylene imine and *N*-(2-hydroxyethyl)-ethylene imine as tools to study effects of polymer structure on physicochemical and biological properties of DNA complexes. *Bioconjugate Chem. 13*, 1124−1133.
(23) Lee, Y., Koo, H., Jin, G., Mo, H., Cho, M. Y., Park, J., Choi, J. S., and Park, J. S. (2005) Poly(ethylene oxide sulfide): new poly(ethylene glycol) derivatives degradable in reductive conditions. *Biomacromolecules 6*, 24−26.
(24) Hermanson, G. T. (1996) *Bioconjugate Techniques*, Academic Press, London, pp 341−342.
(25) Haugland, R. P., and Zhou, M. (2000) Dye labeled polymers as reagents for measuring polymer degradation. U.S. Patent 5,719,031.
(26) Poian, A. T. D., Gomes, A. M. O., and Coelho-Sampaio, T. (1998) Kinetics of intracellular viral disassembly and processing probed by Bodipy fluorescence dequenching. *J. Virol. Methods 70*, 45−58.

BC060113T

Poly(glycoamidoamine)s for Gene Delivery. Structural Effects on Cellular Internalization, Buffering Capacity, and Gene Expression

Yemin Liu and Theresa M. Reineke*

Department of Chemistry, University of Cincinnati, Cincinnati, Ohio 45221-0172. Received February 3, 2006; Revised Manuscript Received August 17, 2006

The study of polymeric nucleic acid delivery vehicles has recently grown because of their promise for many biomedical applications. In an effort to understand how the chemical traits of polymers affect the biological mechanisms of nucleic acid delivery, we have calculated the buffering capacity in the physiological pH range of a series of 10 poly(glycoamidoamine)s with systematic structural variations in the amine stoichiometry (from 1 to 4), carbohydrate moiety (D-glucarate or L-tartarate), and amine spacer (ethylene or butylene) within their repeat units. In addition, we have compared the buffering capacity of these polymeric vectors to their polyplex (polymer−DNA complex) stability, cellular internalization, and gene expression profiles to understand the parameters that are important for increasing gene delivery efficiency. The results indicate that the buffering capacity is not always the primary characteristic that determines the gene delivery efficiency for all the poly(glycoamidoamine)s. We have found that the buffering capacity may affect the gene delivery efficiency only when analogous structures containing the same number of amines but different carbohydrates are compared. We reveal that the cellular internalization is the key step in the gene delivery process with systems containing different amine stoichiometry. Also, increasing the number of methylene groups between the secondary amines increases toxicity to a large degree. This systematic and heuristic approach of studying the correlations between structural variables and gene delivery efficiency will facilitate the development of effective synthetic vectors for specific nucleic acid delivery applications.

INTRODUCTION

Synthetic polymers that exhibit positively charged functionalities at physiological pH (e.g., amine groups) readily bind to the negatively charged phosphate groups in nucleic acids and can serve as carriers to deliver genetic materials into cells. It has been shown that the complex (also named polyplex) formed between polymers and DNA can associate with the negatively charged cell surface membrane and trigger uptake via endocytosis (*1*). The study of synthetic nucleic acid carriers has become extremely important to the areas of gene therapy, genetic vaccines, siRNA, and oligonucleotide drugs (*2*−*4*). For this reason, developing polycations as practical delivery vectors has recently grown because of their simplicity of use, ease of large-scale production, and lack of eliciting an immune response in vivo (*5*). However, the chemical traits of polymers can significantly affect the mechanisms and kinetics involved with cellular uptake via endocytosis and intracellular trafficking. To date, general chemical structure−biological property relationships are poorly understood, which has hampered efforts to produce highly efficient nonviral gene delivery vectors by a systematic and rational approach.

The "proton sponge" theory has been a main hypothesis in the field of polymeric gene delivery that has been used to explain how polyplexes are released into the cytoplasm from endocytic vesicles. This theory states that after polyplexes are endocytosed, the polycations can buffer the acidification event by absorbing protons, which causes a further influx of HCl to compensate for this extra buffering capacity. This leads to an osmotic influx of water, endosome membrane disruption due to vesicle swelling, and release of polyplexes into the cytoplasm (*6*). According to the proton sponge theory, the buffering capacity of polymeric vectors is a key characteristic to interpret and estimate the transfection efficiency. Theoretically, the higher the polymer buffering capacity, the greater the osmotic effect, which increases endosomal disruption. This theory is valid for polyethylenimine (PEI) and some other polymers containing amine groups, such as poly(amidoamine) dendrimers (*7*) and histidylated polylysine (*8*). However, several recent studies have shown that the proton sponge mechanism does not always hold true for polymeric vectors. For example, Pack et al. revealed that decreasing the buffering capacity of PEI by acetylating the amines actually increased gene expression (*9*). Hennink et al. found that the enhanced buffering capacity in polydiamine methacrylate did not increase the gene delivery (*10*). Davis et al. did not observe a correlation between the buffering capacity and gene expression within a series of β-cyclodextrin-containing polymers and modified PEI (*11*). To address this contradiction, Duncan et al. have demonstrated that optimization of the counterion within a series of poly(amidoamine)s (PAAs) was significant for pH-dependent endosomal membrane permeability (*12*). It has also been suggested that the biological properties of tailored PAAs are mediated predominantly by cell membrane interaction and not by the proton sponge effect (*13*, *14*).

Our group has recently created a library of carbohydrate-containing polymers that we have termed poly(glycoamidoamine)s and studied the correlation between the polymer structure and the bioactivity toward gene delivery (e.g., cytotoxicity and gene delivery efficiency) (*15*−*18*). Although we have found that these structures all retain high biocompatibility, the delivery efficacy was significantly affected by the number of amines within the polymer repeat units. When the amine number in the repeat unit was increased from 1 to 4, a significant enhancement in gene expression was found. In those studies, we assumed that the improvement in delivery efficacy upon increasing the amine density was due to a higher buffering capacity of the polymer within the physiological pH range. In the present study, we further investigate how the structural traits

* To whom correspondence should be addressed. E-mail: Theresa.Reineke@uc.edu.

10.1021/bc060029d CCC: $37.00 © 2007 American Chemical Society
Published on Web 11/15/2006

of these polymeric vectors are related to their abilities to buffer the endosomal environment and enhance the delivery efficacy. Here, the buffering capacity of a subset of these poly(glycoamidoamine)s with systematic variations in the amine stoichiometry (from 1 to 4), carbohydrate moiety (D-glucarate or L-tartarate), and amine spacer (ethylene or butylene) has been calculated in the physiological pH range through nonlinear fitting of titration data. In this study, the D-glucarate and L-tartarate polymers were chosen because their monomer precursors (D-glucaric acid and L-tartaric acid) are both natural sugar acids. In addition to the buffering capacity, we have also characterized the polyplex stability, the cellular internalization, and luciferase gene expression with BHK-21 cells for each type of polyplex. Herein, we demonstrate that both the cellular uptake and endosomal release are essential steps in the delivery of genetic material mediated by poly(glycoamidoamine)s. For example, when analogous structures containing the same carbohydrate unit but different amine stoichiometry are compared, the gene delivery efficiency is highly dependent on the cellular uptake efficiency, but not the buffering capacity. Yet, when analogous structures containing the same amine number but a different carbohydrate unit are compared, the structures with higher buffering capacity tend to yield higher gene expression values. This examination has provided insights into the physiochemical properties of poly(glycoamidoamine)s and their relationship to the "proton sponge" hypothesis, which is essential to the future rational design of effective delivery vehicles.

EXPERIMENTAL PROCEDURES

General. All reagents used in the synthesis, if not specified, were obtained from Acros (Morris Plain, NJ). Esterified D-glucaric acid (**D**) was synthesized according to reported procedures (*19*). Melting points of polymers were measured with a Netzsch simultaneous TG-DTA/DSC apparatus (Selb/Bayern, Germany). IR spectra were taken with a Perkin-Elmer Spectrum One Fourier transform infrared spectrometer (Boston, MA) as KBr pellets. NMR spectra were collected on a Bruker AV-400 MHz spectrometer (Billerica, MA). Plasmid DNA (pDNA) gWiz-Luc and pCMVβ were purchased from Aldevron (Fargo, ND) and PlasmidFactory (Bielefeld, Germany), respectively. Heparin was purchased from Sigma (St. Louis, MO) as heparin ammonium salt from porcine intestinal mucosa. Dulbecco's Modified Eagle medium (DMEM), reduced serum medium (Opti-MEM), supplements, nuclease-free water, and phosphate-buffered saline (PBS) were purchased from Invitrogen (Carlsbad, CA). BHK-21 cells were purchased from ATCC (Rockville, MD) and cultured according to ATCC specifications in DMEM (supplemented with 10% FBS, 100 units/mg penicillin, 100 μg/mL streptomycin, and 0.25 μg/mL amphotericin) in 5% CO_2 at 37 °C. All polyplexes were prepared in nuclease-free water unless otherwise specified. N/P ratios (the ratio of the number of amines/phosphates from pDNA) were calculated by using the number of amine groups in the polymer repeat unit (and not the amide nitrogens).

Polymerization. The poly(glycoamidoamine)s **D1**−**D4** and **T1**−**T4** were synthesized as previously described (*17*, *18*). The spermine-based polymers were synthesized through condensation polymerization of esterified D-glucaric acid (**D**), or dimethyl L-tartarate (**T**) with spermine (**S**) in methanol at room temperature as detailed below (*19*, *20*). After polymerization, each product was dissolved in ultrapure water, exhaustively dialyzed to purity in a Spectra Por 1000 molecular weight cutoff membrane (Rancho Dominguez, CA), and then lyophilized to dryness with a Flexi-dry MP lyophilizer (Stone Ridge, NY).

Poly(D-glucaramido-*N*,*N*′-bispropyl-diaminobutane) (DS). Spermine (0.09 g, 0.42 mmol) was mixed with esterified D-glucaric acid (0.10 g, 0.42 mmol) in 2.8 mL of methanol and stirred at room temperature for 48 h. Yield: 0.05 g, 0.13 mmol, 31%. mp: 194.2 °C (dec). IR (KBr): 3356 cm^{-1} (O−H and N−H stretching), 2939 cm^{-1} and 2870 cm^{-1} (C−H stretching), 1651 cm^{-1} (amide C═O stretching), 1539 cm^{-1} (amide N−H bending), 1476−1398 cm^{-1} (CH_2 scissoring), 1350 cm^{-1} and 1285 cm^{-1} (CH_2 twisting and wagging), 1110 cm^{-1} and 1048 cm^{-1} (amine C−N stretching). ^{1}H NMR (D_2O): δ 4.24 (d, 1H), 4.14 (d, 1H), 4.02 (t, 1H), 3.86 (t, 1H), 3.21 (br, 4H), 2.70 (br, 8H), 1.72 (br, 4H), 1.52 (br, 4H).

Poly(L-tartaramido-*N*,*N*′-bispropyl-diaminobutane) (TS). Spermine (0.11 g, 0.56 mmol) was mixed with dimethyl L-tartarate (0.10 g, 0.56 mmol) in 1.2 mL of methanol and stirred at room temperature for 48 h. Yield: 0.03 g, 0.10 mmol, 16%. mp: 221.5 °C (dec). IR (KBr): 3366 cm^{-1} (O−H and N−H stretching), 2939 cm^{-1} and 2870 cm^{-1} (C−H stretching), 1650 cm^{-1} (amide C═O stretching), 1540 cm^{-1} (amide N−H bending), 1476 − 1400 cm^{-1} (CH_2 scissoring), 1355 cm^{-1} and 1285 cm^{-1} (CH_2 twisting and wagging), 1114 cm^{-1} and 1047 cm^{-1} (amine C−N stretching). ^{1}H NMR (D_2O): δ 4.42 (s, 2H), 3.21 (br, 4H), 2.62 (br, 8H), 1.67 (br, 4H), 1.47 (br, 4H).

Gel Permeation Chromatography (GPC). The molecular weight, polydispersity index, and Mark−Houwink−Sakurada (MHS) parameter α for each polymer were measured with a Viscotek GPCmax Instrument (Houston, TX) equipped with a ViscoGEL $GMPW_{XL}$ column coupled to a triple detection system (static light scattering, viscometry and refractive index). Mobile phase (0.5 M sodium acetate, pH 5.5) was prepared in ultrapure water containing 20% acetonitrile. Each sample (100 μL, 10−15 mg/mL) was dissolved in the mobile phase, immediately injected onto the column, and eluted at 1.0 mL/min.

Titration of the Poly(glycoamidoamine)s. Each poly(glycoamidoamine) was dissolved in 5 mL PBS (pH = 7.4). The concentration of each polymer was expressed in terms of total concentration of amine groups and was kept between 0.064 and 0.068 M for each polymer solution. This polymer concentration was calculated by assuming that each endosome is 200 nm, one polyplex is endocytosed, and each polyplex formulated at an N/P ratio of 15 consists of one pDNA molecule (gWizLuc, 6.7 kbp). The titration of each polymer solution was performed with an aqueous solution of HCl (0.1 M standard) in thermo-stat flasks. The temperature was maintained at 37 °C throughout each titration with a Fisher Scientific isotherm circulator model 3016 (Pittsburgh, PA). The pH values were recorded with an Accumet pH meter model AB15 (Pittsburgh, PA). Nonlinear regression of the experimental data was performed with the software Graphpad Prism 4.0 (San Diego, CA).

Zeta Potential Measurements. The poly(glycoamidoamine)s were dissolved in PBS buffer as described for titration experiments and adjusted to various pH conditions between 3.5−8.5 using an aqueous solution of HCl (0.1 M standard). The zeta potential values were measured at 37 °C with laser doppler velocimetry (633 nm) on a Zetasizer (Nano ZS) instrument (Malvern Instruments, Worcs, UK).

Heparin Competitive Displacement Assay. This experiment was performed as previous described for **D4** (*16*), and **T4** (*15*). In brief, each polymer (10 μL) was combined with pCMVβ (1 μg in 10 μL of H_2O) to form polyplexes at N/P = 20. The polyplexes were allowed to incubate for 30 min. A series of heparin solutions were prepared by diluting aliquots of a heparin stock solution (2700 μg/mL). The polyplex solutions were then incubated with 10 μL of each heparin solution above for 15 min. After the addition of loading buffer (1 μL), an aliquot (10 μL) of each sample was subjected to electrophoresis in a 0.6% agarose gel containing 60 μg of ethidium bromide/100 mL TAE buffer (40 mM Tris-acetate, 1 mM EDTA).

Salt-Induced Polyplex Dissociation. Polyplexes were prepared as described above in the heparin competitive displace-

ment assay and diluted with water to a concentration of 0.3 μg of DNA/100 μL solution. PicoGreen (Molecular Probes, Eugene, OR) solutions were prepared by 200-fold dilution with 10 mM HEPES (Sigma, St. Louis, MO) buffer containing various concentrations of NaCl. After the polyplex solution was arrayed into a Costar black flat-bottom 96-well plate, 100 μL of the PicoGreen solutions were added to each well to achieve the desired concentration of NaCl. The fluorescence of PicoGreen (excitation 485 nm, emission 535 nm) for each sample was measured with a TECAN US plate reader (Research Triangle Park, NC). Fractional dye exclusion was determined by the following relationship:

$$\text{Dye Exclusion} = 1 - (F_{\text{sample}} - F_{\text{blank}})/(F_{\text{DNAonly}} - F_{\text{blank}})$$

Luciferase Reporter Gene Transfection and Cell Viability Assays. Prior to transfection, BHK-21 cells were seeded at 5 $\times$ 10^4 cells/well in 24-well plates and were incubated for 24 h. Polymer solutions (150 μL) were incubated with gWiz-Luc (150 μL, 0.02 μg/μL) at N/P ratios of 5, 10, 15, 20, 25, and 30 at room temperature for 1 h to form the polyplexes. The mixtures were then diluted to 900 μL with serum-free media (Opti-MEM, pH = 7.2). Each well of cells was transfected with 300 μL of the polyplex solution containing 1 μg of gWiz-Luc pDNA complexed with each poly(glycoamidoamine) at N/P ratios between 0 (pDNA only) and 30 in triplicate. Untransfected cells and cells transfected with naked gWiz-Luc (1 μg of pDNA, N/P = 0) were used as negative controls. Four hours after the transfection, 800 μL of the supplemented DMEM was added to each well. Twenty-four hours after transfection, the media was replaced with fresh supplemented DMEM (1 mL). Forty-seven hours after initial transfection, the media was removed and the cells were washed with 500 μL of PBS and treated with cell culture lysis buffer (Promega, Madison, WI). The amount of protein in the cell lysates (as milligram of protein) was determined against a standard curve of bovine serum albumin (98%, Sigma, St. Louis, MO), using a Bio-Rad DC protein assay kit (Hercules, CA).

Cell lysates were analyzed for luciferase activity with Promega's luciferase assay reagent (Madison, WI). For each sample, luminescence was measured over 10 s in duplicate with a luminometer (GENios Pro, TECAN US, Research Triangle Park, NC), and the average was utilized. The cell viability profiles were characterized by the amount of protein in the cell lysates. The protein levels of the transfected cells were normalized to the protein amount obtained for untransfected cells.

Flow Cytometry. pCMVβ was labeled with a Cy5 nucleic acid labeling kit (Mirus, Madison, WI), and purified by QIAquick PCR purification kit (QIAGEN, Valencia, CA). BHK-21 cells were seeded on 12-well plates at 1.0 $\times$ 10^5 cells/well and allowed to incubate in supplemented DMEM at 37 °C and 5% CO_2 for 24 h. The polyplexes were prepared by combining 100 μL of Cy5 labeled pCMVβ (0.02 μg/μL) and 100 μL of **D1**−**D4** or **T1**−**T4** at the N/P values of maximum luciferase gene expression (N/P = 20 for **D1**, and N/P = 30 for **D2**−**D4** and **T1**−**T4)**. The cells were then transfected with 0.2 mL of polyplex solution (2 μg of pDNA/well) in 0.4 mL of serum-free media (Opti-MEM). The cells were incubated with each solution for 4 h to allow endocytosis and internalization of the polyplexes. After transfection, the cells were rinsed with PBS multiple times to remove the cell surface bound polyplexes. Supplemented DMEM was then added and the cells were incubated for another 30 min to allow further polyplex internalization. Four and half hours after initial transfection, the cells were trypsinized, pelleted, and resuspended in PBS containing 2% FBS for fluorescent activated cell sorting (FACS) analysis. A FACSCalibur (Becton Dickenson, San Jose, CA) equipped with a helium-neon laser to excite Cy5 (633 nm) was used. Five thousand events were collected twice for each sample. The positive fluorescence level was established by visual inspection of the histogram of untransfected cells such that less than 1% appeared in the positive region.

RESULTS AND DISCUSSION

The intracellular delivery of genetic materials involves a complex pathway requiring several biological steps: (i) cell membrane binding; (ii) cellular uptake via endocytosis; (iii) endosomal release and vector unpacking; and (iv) nuclear entry and gene expression (*21*). The biological properties of polycationic vectors, such as binding affinity to DNA, cell membrane binding and entry, and the buffering capacity of polymers in the endosome may influence the gene delivery efficiency (and gene expression) by affecting different stages in the cellular trafficking pathway. Previous studies have shown that subtle structural differences, such as the addition of one ethyl amine group in the repeat unit, can significantly affect the delivery efficacy (*15*−*18*). Here, we have further investigated the polymer structural effects on the polyplex stability, the polymer buffering capacity under physiological pH, cellular internalization of polyplexes, and the luciferase gene expression with BHK-21 cells. We show that an increase in the polymer buffering capacity within the physiological pH range does not necessarily correlate to an increase in gene expression, indicating that the buffering capacity is not always the main characteristic that determines the efficiency for all the poly(glycoamidoamine) delivery vectors. This study provides more insight into the rational design of poly(glycoamidoamine) gene delivery vectors for various applications.

Synthesis and Characterization of Poly(glycoamidoamine)s. D1−**D4** and **T1**−**T4** were synthesized as previously described (*17*, *18*) and named according to the carbohydrate moieties (**D** for D-glucarate; **T** for L-tartarate) and the number of amine groups (**1**−**4**) in the repeat units. As shown in Figure 1, the amine groups are separated by an ethylene group in **D1**−**D4** and **T1**−**T4**. In the polymers synthesized with spermine, **DS** and **TS**, the adjacent amines are separated by a butylene group, which makes the distance between the amine groups twice as long as that in **D2** and **T2**. Also, in the **DS** and **TS** structures, a propane group separates the amine groups from the amides in the repeat unit. As shown in Table 1, the polymerization conditions were optimized so all of the structures had similar degrees of polymerization between 11 and 14 (*17*, *18*). This ensured that the results obtained in this study were not affected by differences in the degrees of polymerization.

Titration of the Poly(glycoamidoamine)s and Nonlinear Regression. In an effort to understand how the polymer buffering capacity affects their DNA delivery efficiency as a function of polymer structure, titration experiments were performed to calculate the fraction of protonated amines in each structure. The poly(glycoamidoamine)s were titrated in PBS at 37 °C to simulate the intracellular environment. Because the protonation of an amine is concentration dependent (*22*), the titrations were performed within the approximate concentration range that would be encountered in an endosome. This concentration range was chosen by assuming that the average endosome diameter of BHK-21 cells is about 200 nm (*23*) and that each endosome could only entrap one polyplex during endocytosis [the polyplex sizes formed with these structures are between 100−500 nm (*16*)]. According to these assumptions, the theoretical polymer concentration in an endosome, where the polyplexes would have been formulated at an N/P = 15 (and consist of one plasmid), was approximately 0.064−0.068 M. As shown in Figure 2, the experimental data were plotted as pH vs volume of added HCl. The nonlinear regression fitting of the titration data was carried

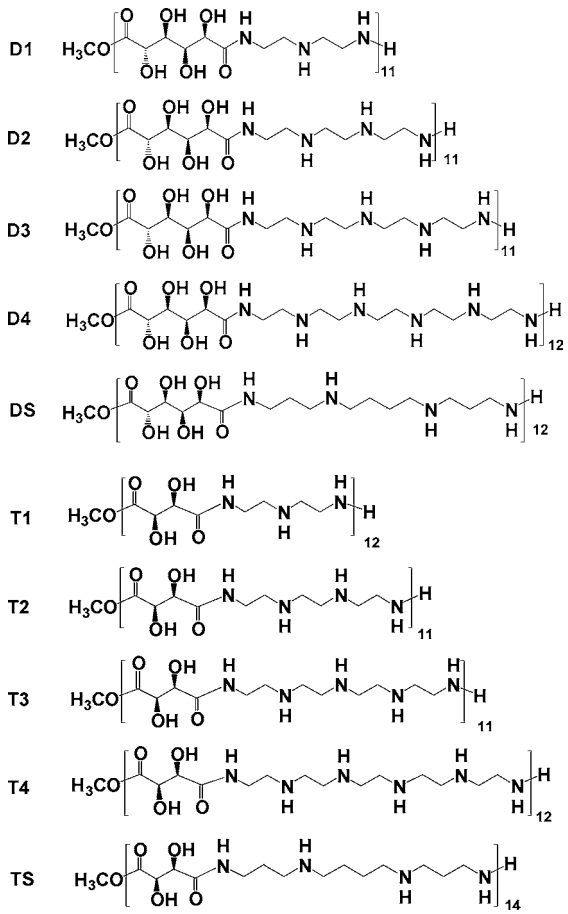


Figure 1. Structures of poly(glycoamidoamine)s.

Table 1. MHS Parameter (α), Molecular Weight (M_w), Polydispersity (M_w/M_n), and Degree of Polymerization (n) Data for the Poly(glycoamidoamine)s

polymer	a	M_w (kDa)	M_w/M_n	n
D1	0.68	3.0	2.0	11
D2	0.67	3.4	1.4	11
D3	0.64	3.9	1.4	11
D4	0.61	4.9	1.6	12
DS	0.66	4.4	1.4	12
T1	0.73	2.7	1.3	12
T2	0.76	2.9	1.3	11
T3	0.77	3.2	1.2	11
T4	0.83	4.3	1.2	12
TS	0.76	4.5	1.2	14

out according to a modified method (*22*), using equilibrium constants [K_{a1}, K_{a2}, and K_{a3} for phosphoric acid (eqs 1−3), K_w of water (eq 4), and K_a of the amine groups (eq 5)] as well as charge (eq 6) and mass balances (eqs 7−11). In these equations, N stands for an amine group in the polymers, whereas v_0 and v represent the initial volume of the polymer solutions (5 mL in PBS) and the volume of the added HCl solution (where $[HCl]_0 = 0.1$ M), respectively. In addition, we assumed that the amide groups [−HN−C(═O)] are not protonated in the pH range of titration (pH > 2), where pK_a value of a protonated amide [$-H_2N^+-C(=O)$] is much lower than 2 (e.g., p$K_a = -0.51$ for acetamide) (*24*). The components of PBS and available equilibrium constants are listed in Table 2.

Equilibrium constants:

$$K_{a1} = \frac{[H_2PO_4^-][H^+]}{[H_3PO_4]} \quad (1)$$

$$K_{a2} = \frac{[HPO_4^{2-}][H^+]}{[H_2PO_4^-]} \quad (2)$$

$$K_{a3} = \frac{[PO_4^{3-}][H^+]}{[HPO_4^{2-}]} \quad (3)$$

$$K_w = [H^+][OH^-] \quad (4)$$

$$K_a = \frac{[N][H^+]}{[NH^+]} \quad (5)$$

Charge balance:

$$[K^+] + [H^+] + [Na^+] + [NH^+] = [Cl^-] + [H_2PO_4^-] + 2[HPO_4^{2-}] + 3[PO_4^{3-}] + [OH^-] \quad (6)$$

Mass balance:

$$[NH^+] + [N] = \frac{v_0}{v_0 + v}[N]_0 \quad (7)$$

$$[Cl^-] = \frac{v}{v_0 + v}[HCl]_0 + \frac{v_0}{v_0 + v}[Cl^-]_0 \quad (8)$$

$$[H_3PO_4] + [H_2PO_4^-] + [HPO_4^{2-}] + [PO_4^{3-}] = \frac{v_0}{v_0 + v}([H_2PO_4^-]_0 + [HPO_4^{2-}]_0) \quad (9)$$

$$[K^+] = \frac{v_0}{v_0 + v}[K^+]_0 \quad (10)$$

$$[Na^+] = \frac{v_0}{v_0 + v}[Na^+]_0 \quad (11)$$

On the basis of these equations, eq 12 was derived:

$$v = v_0 \frac{[H^+] + \dfrac{[N]_0}{1 + K_a/[H^+]} + [K^+]_0 + [Na^+]_0 - [Cl^-]_0 - \dfrac{K_w}{[H^+]} - A}{[HCl]_0 + \dfrac{K_w}{[H^+]} - [H^+]} \quad (12)$$

where

$$A = [H_2PO_4^-] + 2[HPO_4^{2-}] + 3[PO_4^{3-}] = \frac{\dfrac{[H^+]}{K_{a2}} + 3\dfrac{K_{a3}}{[H^+]} + 2}{1 + \dfrac{K_{a3}}{[H^+]} + \dfrac{[H^+]}{K_{a2}}\left(1 + \dfrac{[H^+]}{K_{a1}}\right)}([H_2PO_4^-]_0 + [HPO_4^{2-}]_0)$$

Obviously, the ionization constant K_a of all individual amine groups present in the polymer structures will not be equivalent. One reason is that there are different types of amines in the polymer structures, such as primary amines (oligo-amine monomer-based termination groups of the polymer chain), and

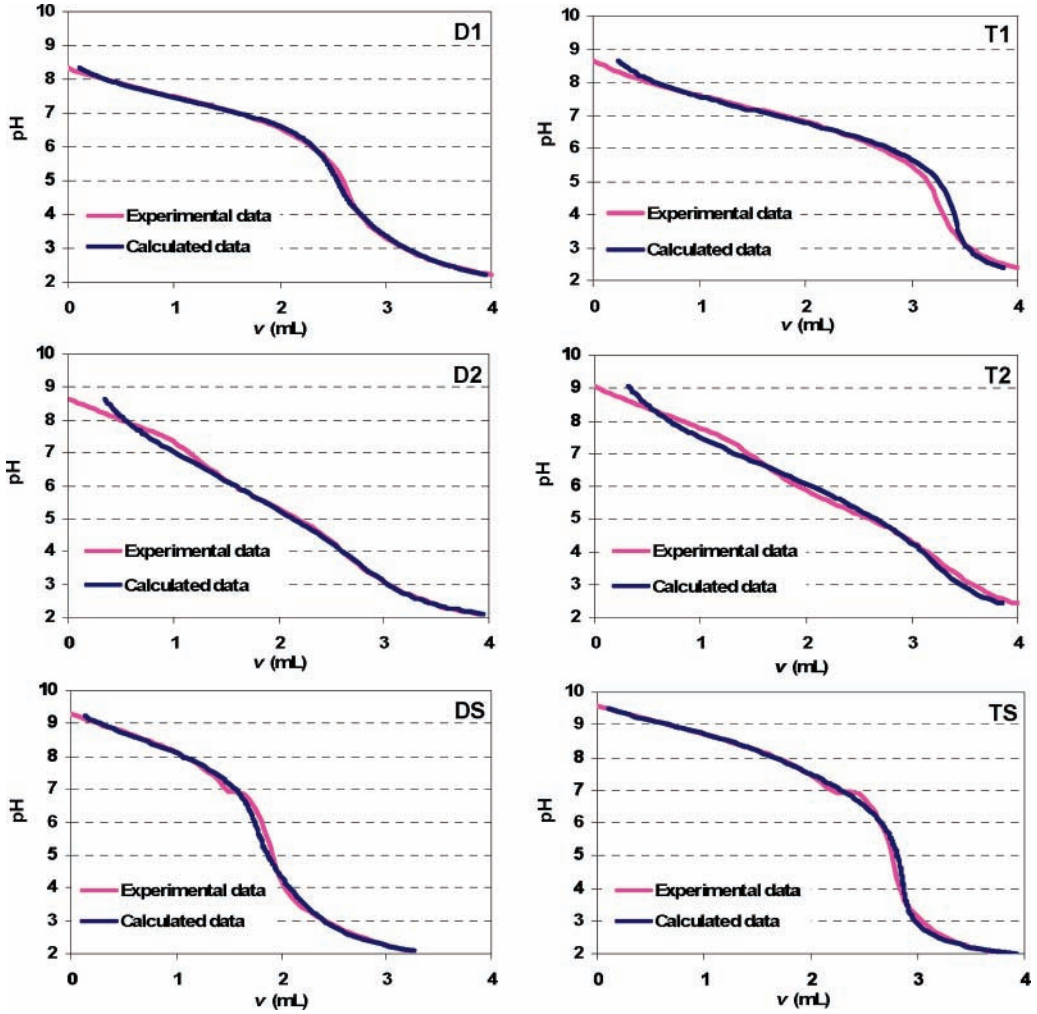


Figure 2. The titration plots (pH vs volume of added HCl) of **D1**, **D2**, **DS**, **T1**, **T2**, and **TS**. The pink lines indicate the experimental data; the blue lines indicate the calculated data after nonlinear regression using eq 14 and the hypothesized relationship between log Q and pH (eqs 16 or 17).

Table 2. Components of PBS and Equilibrium Constants

components of PBS[a] (mol/L)					equilibrium constants[b]			
$[K^+]_0$	$[Na^+]_0$	$[Cl^-]_0$	$[H_2PO_4^-]_0$	$[HPO_4^{2-}]_0$	K_{a1}	K_{a2}	K_{a3}	K_w
1.06×10^{-3}	1.60×10^{-1}	1.54×10^{-1}	1.06×10^{-3}	2.97×10^{-3}	7.58×10^{-3}	6.17×10^{-8}	4.79×10^{-13}	1.00×10^{-14}

[a] Subscript "0" indicates the initial ion concentrations. [b] Taken from ref *24*.

secondary amines (backbone of the polymer chain). The other reason is that the protonation of an amine group electrostatically suppresses the protonation of neighboring amines. In this study, to determine the total protonated fraction of all amine groups regardless of K_a values, the parameter quotient Q was introduced (eq 13) and was defined as the ratio of the fraction of unprotonated amine groups to the fraction of protonated amines (*22*). Therefore, eq 12 was modified to eq 14 to substitute K_a with quotient Q.

$$Q = \frac{[N]}{[NH^+]} = \frac{f_N}{f_{NH^+}} \tag{13}$$

$$v = v_0 \frac{[H^+] + \frac{[N]_0}{1+Q} + [K^+]_0 + [Na^+]_0 - [Cl^-]_0 - \frac{K_w}{[H^+]} - A}{[HCl]_0 + \frac{K_w}{[H^+]} - [H^+]} \tag{14}$$

From the parameter quotient Q, the total protonated fraction of the amine groups (f_{NH^+}) in the polymer structures at various pH values can be calculated (eq 15):

$$f_{NH^+} = \frac{1}{1+Q} \tag{15}$$

$$\log Q = \alpha pH + \beta \tag{16}$$

$$\log Q = \alpha pH^{\beta} + \gamma pH^{(\beta-1)} + \delta pH^{(\beta-2)} + \epsilon \tag{17}$$

On the basis of the shapes of experimental titration plots (Figure 2), we assumed a linear correlation between log Q and pH (eq 16) for polymers **D2**−**D4** and **T1**−**T4**, and a nonlinear correlation between log Q and pH (eq 17) for **D1**, **DS**, and **TS**. Equation 14 and the hypothesized correlations between log Q and pH for each polymer (eq 16 or eq 17) were combined, and the nonlinear regression of experimental titration data was calculated using software GraphPad Prism 4.0. The goodness of fit (R^2) and the estimated parameters ($\alpha - \epsilon$) from nonlinear regression are summarized in Table 3. The R^2 values for all of

Table 3. Goodness of Fit (R^2) and Calculated Parameters for the Titration of Poly(glycoamidoamine)s

polymers	R^2	α	β	γ	δ	ϵ
D1	0.999	$1.08 \pm 0.22 \times 10^{-2}$	3.58 ± 0.10	$-1.54 \pm 0.32 \times 10^{-1}$	$6.72 \pm 1.51 \times 10^{-1}$	-2.56 ± 0.22
D2	0.993	$2.92 \pm 0.05 \times 10^{-1}$	-1.66 ± 0.03			
D3	0.986	$2.30 \pm 0.05 \times 10^{-1}$	-1.16 ± 0.03			
D4	0.984	$1.99 \pm 0.05 \times 10^{-1}$	$-8.65 \pm 0.25 \times 10^{-1}$			
DS	0.998	$2.18 \pm 0.66 \times 10^{-4}$	5.13 ± 0.16	$-3.36 \pm 0.99 \times 10^{-3}$	$1.41 \pm 0.42 \times 10^{-2}$	$-4.43 \pm 0.22 \times 10^{-1}$
T1	0.995	$6.27 \pm 0.12 \times 10^{-1}$	-4.38 ± 0.09			
T2	0.988	$3.31 \pm 0.08 \times 10^{-1}$	-2.07 ± 0.05			
T3	0.982	$2.55 \pm 0.07 \times 10^{-1}$	-1.42 ± 0.04			
T4	0.989	$2.21 \pm 0.05 \times 10^{-1}$	-1.09 ± 0.03			
TS	0.998	$1.92 \pm 1.88 \times 10^{-8}$	$1.07 \pm 0.05 \times 10^{1}$	$-3.55 \pm 3.47 \times 10^{-8}$	$1.70 \pm 1.67 \times 10^{-7}$	$-6.16 \pm 0.08 \times 10^{-1}$

the fits are higher than 0.98, indicating satisfactory nonlinear regression of the experimental data. Figure 2 shows the overlay of the experimental titration plots and the calculated plots. The data for polymers **D3**−**D4** and **T3**−**T4** were not shown because the plot shapes were very similar to those obtained for **D2** and **T2**. The calculated data correlated well with the experimental data.

Effects of Carbohydrate Moiety and Amine Unit on the Protonation of Polymers. As previously mentioned, because the protonation of an amine is concentration dependent (*22*), a series of assumptions were made to approximate the initial concentration of amine groups in an endosome for each poly(glycoamidoamine). The polymer was dissolved in PBS such that the amine concentration was between 0.064−0.068 M to compare how the protonation of the amines is affected by the chemical structure. The protonated fraction of amines for each polymer within the physiological pH range between pH = 7.5 (pH of extracelluar space) and pH = 4.5 (pH of intracellular lysosomes) was calculated from eq 15, and the resulting data were plotted vs pH (Figure 3). From these data, it was obvious that the protonation of the polymers increased as the pH decreased from pH 7.5 to pH 4.5. In addition, three trends were noticed: (i) the protonated fraction of total amine groups in the molecules increased as the amine stoichiometry in the structural repeat units decreased (**D1** > **D2** > **D3** > **D4** and **T1** > **T2** > **T3** > **T4**, Figure 3a,b); (ii) the L-tartarate polymers (**T1**−**T4**, Figure 3b; **TS**, Figure 3c) revealed a higher protonated fraction than the corresponding D-glucarate polymers (**D1**−**D4**, Figure 3a; **DS**, Figure 3c); (iii) as the pH decreased, the protonation of **D2** and **T2** increased faster than their spermine-based analogues (**DS** and **TS**). As shown in Figure 3c, the protonated fraction of amines for the spermine-based polymers was compared to their analogues synthesized from triethylenetetramine. At pH = 7.5, the spermine analogues had a higher protonated fraction (**DS** > **D2**, **TS** > **T2**); however, as the pH decreased to 4.5, a different trend was observed. Polymer **D2** revealed a higher protonated fraction than **DS**, but the fraction of protonated amines for polymer **T2** was equivalent to **TS**.

As previously discussed, within a polymer repeat unit, the presence of a cationic ammonium group will electrostatically suppress the protonation of neighboring amines. An "intra-repeat unit interaction" between cationic ammonium groups and unprotonated amines may explain the first trend that is observed when the polymers within each carbohydrate family (**D1**−**D4** and **T1**−**T4**) are compared. The further protonation of amines within a repeat unit is strongly disfavored when one cationic ammonium group is present. Thus, as the number of amines within a repeat unit is increased, a decrease in the protonated fraction is observed. Similarly, an "inter-repeat unit interaction" of protonated amine groups may explain the second trend observed when L-tartarate polymers (have higher protonation) are compared to their corresponding D-glucarate polymers (have lower protonation). There is a significant overall structural difference between the **T** and **D** series of polymers. The L-tartarate polymers polymerize in a stereoregular manner (due to the symmetry of the L-tartarate monomer); however, the D-glucarate polymers polymerize in an atactic fashion. The stereoregularity of the L-tartarate moiety renders the backbones of these polymers to be more rigid than the D-glucarate polymers

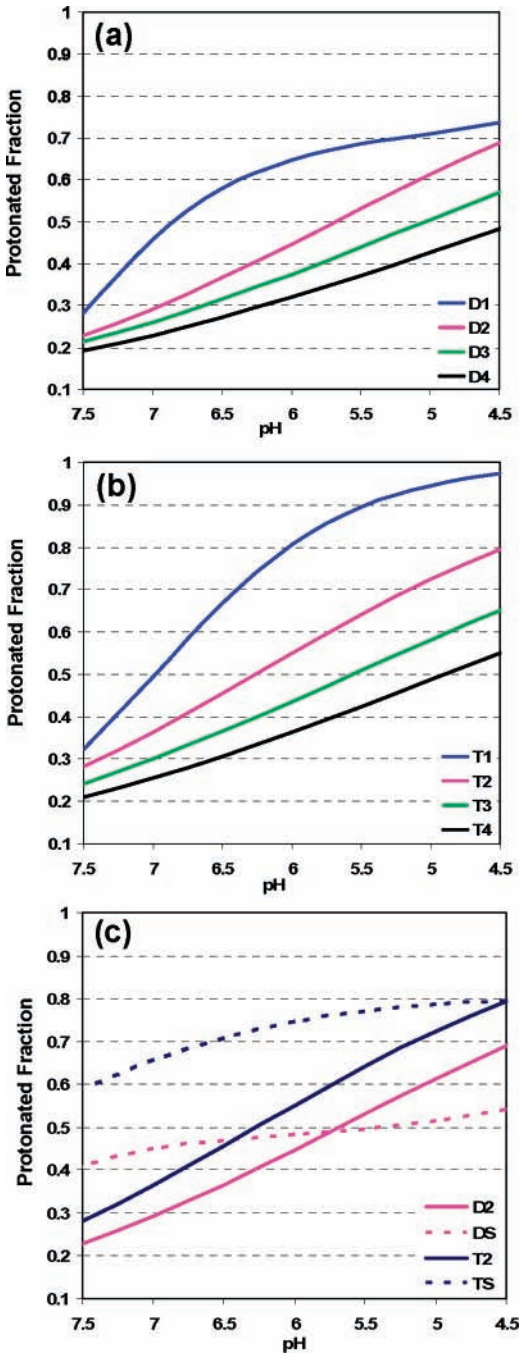


Figure 3. The protonated fraction of amines vs pH for the poly(glycoamidoamine)s calculated from eqs 14−17. (a) Plots for **D1**−**D4**; (b) plots for **T1**−**T4**; (c) comparison of calculated protonated fraction for **DS** and **TS** with **D2** and **T2**.

(*16*, *25*), which is supported by the higher MHS values (α = 0.73−0.83) observed for **T1**−**T4** and **TS** listed in Table 1 (*16*). Consequently, within the secondary structures of the L-tartarate polymers, the distance between oligoamine repeat units is likely greater than that in the D-glucarate polymers because of this stiffness. According to viscosity measurements, the D-glucarate polymers appear to form more random coil-like structures in solution (MHS values between 0.61−0.68), where the smaller distance between repeat units may electrostatically suppress amine protonation via this "inter-repeat unit interaction". With less influence from inter-repeat unit amine groups, the L-tartarate polymers should have a higher degree of protonation in the physiological pH range than the D-glucarate polymers. Lastly, the third trend observed with the spermine based polymers (**DS** and **TS**) may be attributed to a cyclic conformation that the repeat unit may adopt, which is stabilized by H-bonding. Spermine moieties can cyclize, which is induced by delocalization of the cationic charge on the ammonium group with the other unprotonated amine within the same repeat unit and is made possible by the flexible butylene spacer between the amine groups. This cyclization event has been previously observed by Karpas et al. (*26*) where spermine molecules can form a seven-membered ring stabilized by a hydrogen bond between the two central amine groups. Such cyclization within the **DS** and **TS** polymer structures may cause the protonation of the second amine group to be disfavored, thus resulting in a lower fraction of protonated amines with decreasing pH (e.g., 4.5). In addition, the increased hydrophobicity of the spermine moiety may also contribute to the reduced accessibility of the second amine group when titrated in aqueous solution (*27*).

Changes in the protonation of a polycation result in charge variations within the macromolecule that can be characterized by zeta potential measurements. We hypothesized that plotting the zeta potential values as a function of pH for polymers **D2**, **DS**, **T2**, and **TS** would reveal similar trends as the plots of the protonated fraction values (Figure 3c), thus confirming the titration results obtained for these polymers. We tested this hypothesis and found that the L-tartarate polymers had higher zeta potential values than the D-glucarate polymers within the whole endosomal pH range (Figure 4). These data were consistent with the calculated protonation values shown in Figure 3c. For **DS** and **TS**, the zeta potential values increased slower (as the pH decreased) than the zeta potential values for **D2** and **T2**. At higher pH, **DS** and **TS** showed higher zeta potential values (indicating a higher cationic charge), while at lower pH, they had similar zeta potential values to **D2** and **T2**, respectively. These results support the data obtained from the titrations of these polymers and the previously discussed theories regarding electrostatic suppression of amine protonation via "inter-repeat unit interaction" for the D-glucarate polymers and proton-induced cyclization for the spermine polymers.

Buffering Capacity. The buffering capacity of each polymer (Table 4) was calculated via eq 18 by determining the differences in the protonated amine fractions between pH 7.5 (extracellular pH) and pH 4.5 (intracellular lysosome pH). The buffering capacity is the percentage of amines that can be protonated during the acidification event in the endosomes.

$$\text{buffering capacity} = [f_{NH^+}(\text{pH } 4.5) - f_{NH^+}(\text{pH } 7.5)] \times 100\% \quad (18)$$

As shown in Table 4, the L-tartarate-based polymers (**T** series) have a higher buffering capacity than D-glucarate polymer analogues (**D** series), which, again, is likely due to their stiff chain character and the fact that the protonation of the D-glucarate polymers is suppressed by more inter-repeat unit interaction. In addition, the buffering capacity of the polymers in this pH range generally decreased as the number of amines increased in the repeat unit (e.g., **T1** (56.4%) > **T2** (51.2%) > **T3** (40.8%) > **T4** (34.0%)]. The trends for both the **D** and **T** series were similar to those found when the protonated fraction was correlated to the polymer structures (Figure 3). It should be noted that the buffering capacity is a function of the protonated fraction of a polymer. Even though polymer structural variations are reflected in their buffer capacities, the correlations between the buffering capacity and the polymer structures are not as direct as the correlation between their protonated fractions and structural variations. Thus, if the polymer already has a high protonated fraction of amines at pH 7.5, the buffering capacity will be lower because there are fewer amines available to be further protonated. For this reason, it was observed that the buffering capacities for the D-glucarate polymers had a slightly different trend compared to that of the L-tartarate polymers [**D2** (46.2%) > **D1** (45.4%) > **D3** (35.7%) > **D4** (29.2%), Table 4]. The spermine-based polymers had the lowest buffering capacity in each series (13.2% for **DS** and 20.5% for **TS**). Again, this may be explained by the proton-induced cyclization theory, where the protonation of one amine group in the spermine moiety limits the ability of the other amine to be protonated. This leads to a slower increase in the protonated fraction with a decrease in pH.

Heparin- and Salt-Induced Polyplex Dissociation. The stability of the polyplexes formed between polymer and pDNA under physiological environments is one of the properties that can affect the efficacy of intracellular pDNA delivery. The ideal polyplex should be resistant to premature pDNA release during transport yet still retain the ability to unpack the genetic materials after delivery. As previously hypothesized, if the polyplexes are not stable from the dissociation during cell surface-binding to negatively charged cell membrane glycosaminoglycans (such as heparin or heparan sulfate), they may release pDNA before cellular uptake (*16*, *28*). One way to examine polyplex stability is through the heparin displacement assays, where heparin is used to simulate the cell membrane glycosaminoglycans. After the polyplexes were formulated in water, they were exposed to heparin solutions of different concentrations and then run on agarose gels to examine the heparin concentration that promoted dissociation of pDNA from

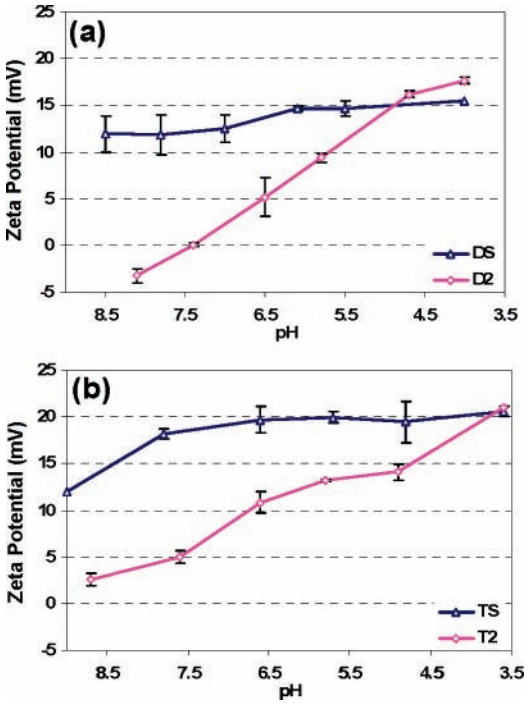


Figure 4. Plots of the zeta potential values vs pH for (a) **D2** and **DS**; (b) **T2** and **TS**.

Table 4. Percentage of Amines Protonated at pH 7.5 and 4.5 and the Buffering Capacity of the Poly(glycoamidoamine)s Calculated with eq 18

	D1	D2	D3	D4	DS	T1	T2	T3	T4	TS
$f_{NH^+} \times 100\%$ (pH 7.5)	28.2%	22.7%	21.2%	19.1%	41.0%	32.2%	28.1%	24.2%	21.0%	59.2%
$f_{NH^+} \times 100\%$ (pH 4.5)	73.6%	68.9%	56.9%	48.3%	54.2%	97.3%	79.3%	65.0%	55.0%	79.7%
buffering capacity	45.4%	46.2%	35.7%	29.2%	13.2%	65.1%	51.2%	40.8%	34.0%	20.5%

the poly(glycoamidoamine)s. In this experiment, if higher heparin concentrations are needed to dissociate the polyplexes, then the polyplexes are likely more stable and have less premature pDNA release than polyplexes that dissociate at lower heparin concentrations. It was observed that the heparin concentration needed to dissociate polyplexes formed with polymers **D1**−**D4** increased as the amine number increased in the repeat unit (Figure 5a). Such a trend was not observed with **T1**−**T4** polyplexes. Polymer **T3** revealed the highest binding affinity (heparin concentration needed to release pDNA was 700 μg/mL), while **T4** yielded the lowest affinity (heparin concentration needed to release pDNA was 560 μg/mL). The polyplexes formed with spermine-based polymers, **DS** and **TS**, required an even higher heparin concentration (700 and 960 μg/mL, respectively) to dissociate than those of **D1**−**D4** and **T1**−**T4**. This may be explained by the fact that the longer spacer between the amine groups in the repeat unit of **DS** and **TS** leads to a higher protonated amine fraction at pH = 7.5 (Table 4), which facilitates stronger electrostatic interactions with pDNA. In addition, polyplexes formed with the **T** polymers revealed a higher stability than their **D** analogues, which may be a result of the higher cationic charge exhibited by the **T** series polymer (increases electrostatic interactions) and the closer spacing of the amine groups (enhances cooperative binding).

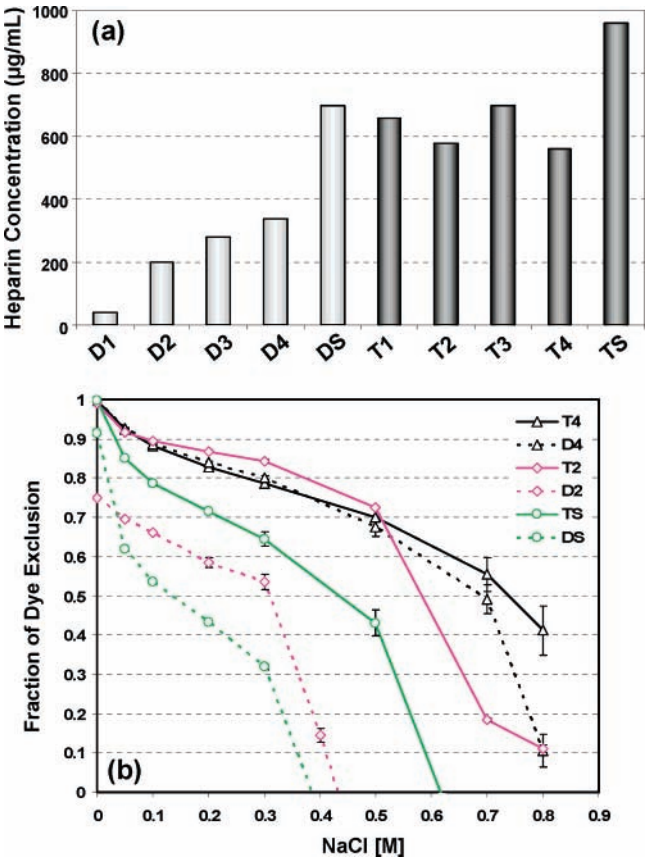


Figure 5. (a) Heparin concentration needed (μg/mL) to release pDNA from polyplexes formed with each of the poly(glycoamidoamine)s. (b) The fraction of dye exclusion [(1 − fraction of PicoGreen intercalation normalized to PicoGreen intercalation of naked pDNA)] when polyplexes formed with **T4**, **D4**, **T2**, **D2**, **TS**, and **DS** are exposed to different concentrations of NaCl.

Unpacking of the loaded genetic materials after the delivery has been hypothesized as another barrier in the transfection process (*29*, *30*), because various proteins need to access pDNA to promote gene expression. To evaluate the vector unpacking properties of poly(glycoamidoamine)s, the binding interaction between the polymer and pDNA were studied by the intercalation of PicoGreen, a dsDNA dye, as a function of NaCl concentration (*29*). Increased salt concentrations can destabilize the binding between polymer and DNA due to the decreased electrostatic interaction. This leads to decomplexation and/or pDNA release, thus increasing PicoGreen intercalation and enhancing fluorescence. As shown in Figure 5b, without NaCl addition (0 point, HEPES buffer only), the PicoGreen did not intercalate into pDNA molecules carried by vectors **T4**, **D4**, **T2**, and **TS**, resulting in almost 100% PicoGreen exclusion. However, for polyplexes formed with polymers **D2** and **DS**, we observed some PicoGreen inclusion in HEPES buffer only, signifying weaker binding. The concentrations of NaCl that allowed 50% dye inclusion (50% PicoGreen excluded) for polymers **T4**, **D4**, **T2**, **TS**, **D2**, and **DS** were roughly 0.75, 0.70, 0.60, 0.45, 0.30, and 0.15 M, respectively. Polyplexes formed with L-tartarate polymers generally had a higher fraction of PicoGreen excluded than their D-glucarate analogues under various NaCl concentrations. This indicates that the **T** polymers can facilitate more stable pDNA binding than the **D** polymers, which is consistent with the results of the heparin displacement assay. Although the greater stability of the **T** polyplexes can help to stabilize the polyplexes from the glycosaminoglycan dissociation, it also may hinder the DNA unpacking process. When the amine stoichiometry effects were compared, polyplexes formed with **D4** were observed to be more stable (higher PicoGreen exclusion) under various salt concentrations than **D2**. However, polyplexes formed with **T4** had similar exclusion as **T2** polyplexes below 0.5 M NaCl, and higher exclusion than **T2** polyplexes when the salt concentration was above 0.5 M. These observations are also consistent with the heparin displacement assay, where **D4** required a higher heparin concentration to cause polyplex dissociation than **D2**, and the heparin concentrations needed to dissociate **T4** and **T2** were very similar. When the amine spacer effects were compared, spermine based polymers **DS** and **TS** had significant lower PicoGreen exclusion (higher inclusion) than their analogues **D2** and **T2**, indicating easier vector unpacking. This was a surprise because **DS** and **TS** showed the strongest pDNA binding in the heparin displacement assay. Thus polyplexes of **DS** and **TS** may not only have higher resistance from dissociation by cell membrane glycosaminoglycans but also unpack the pDNA more easily than their analogues, **D2** and **T2**, after cell membrane entry.

Correlations Between Buffering Capacity and Gene Delivery Efficiency. The gene delivery efficiency represented by the maximum luciferase gene expression in BHK-21 cells for polymers **D1**−**D4** and **T1**−**T4** [previously published in reference (*17*, *18*)], and their buffering capacities (Table 4) are overlaid in Figure 6. First, when the amine stoichiometry was considered, it was noticed that as the number of amines in the repeat unit increased, the overall buffering capacity decreased while the gene delivery efficiency significantly increased [statistical significances of gene expression are shown with * (e.g., **T4** vs **T3**) in Figure 6]. In general, there was not a positive correlation relating a high buffering capacity to an increase in

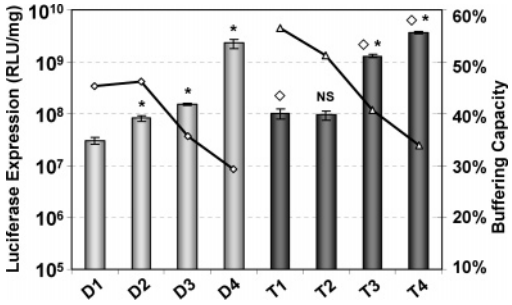


Figure 6. Maximum luciferase gene expression (bars) and buffering capacity (lines) for the polymeric vectors **D1**−**D4** and **T1**−**T4** (polyplexes formulated at N/P = 30 for all vectors except **D1**, which yielded max expression at N/P = 20). Statistical significances in luciferase expression are shown with * or ◇ as $p < 0.05$. The symbol * indicates that a significant difference in gene expression was observed between polymers with the same carbohydrate moiety but having a variation of one amine group in the repeat unit (e.g., **D4** vs **D3**). The symbol ◇ indicates that a significant difference in gene expression was observed between polymers with the same amine stoichiometry but different carbohydrate moieties (e.g., **D4** vs **T4**). The symbol NS in the chart indicates that the gene expression of **T2** is not statistically higher than **T1** or **D2**.

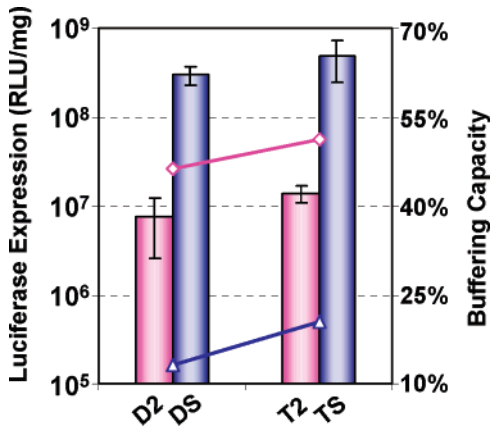


Figure 7. Luciferase gene expression (bars) and buffering capacity (lines) for the polymeric vectors **D2** and **T2** (pink), as well as **DS** and **TS** (blue) at N/P = 10.

gene delivery efficiency in this case. These results go against the relationship predicted by the proton sponge theory (*6*).

Second, when the relationship between the buffering capacity and delivery efficiency was compared between analogous structures in the **T** and **D** series, the **T** polymers had slightly higher buffering capacities and higher gene expression values than their **D** analogues [statistical significances of gene expression are shown with ◇ (e.g., **T4** vs **D4**) in Figure 6], which is consistent with the proton sponge theory in this study. An exception to this trend was found when the delivery efficiency and buffering capacity data for polymers **T2** and **D2** were compared.

Third, when the structural variation of spacer length between the amine groups was considered (e.g., **DS** vs **D2** or **TS** vs **T2**), **DS** and **TS** showed lower buffering capacities than **D2** and **T2**. However, **DS** and **TS** facilitated higher gene expression than **D2** and **T2** (Figure 7). These results go against the proton sponge theory again (*6*). This observation may be attributed to the higher stability in the presence of heparin and easier salt-induced unpacking properties of vectors **DS** and **TS** when compared to **D2** and **T2**, which may lead to an increase in the polyplex amount entering the cells and increased pDNA unpacking after cellular entry. In addition, **TS** had a higher buffering capacity and higher gene expression values than **DS**, which was consistent with the previous observed phenomena when the relationship between the buffering capacity and delivery efficiency was compared between analogous structures in the **T** and **D** series. It should be noted that these data were compared at N/P = 10 due to the high cytotoxicity (low cell survival) exhibited by the spermine-based polymers **DS** and **TS** at N/P ratios higher than 10 (see cell viability data in Figure 8).

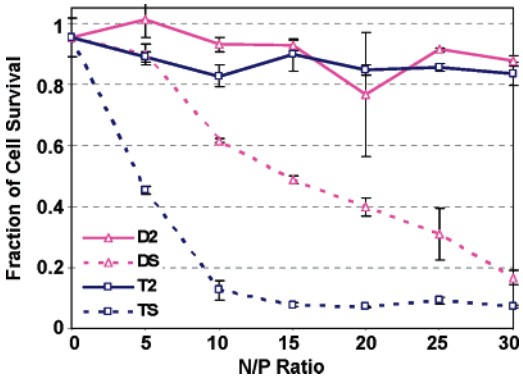


Figure 8. Fraction of cell survival of **D2**, **DS**, **T2**, and **TS** at N/P ratios between 0 (pDNA only) and 30.

Cell Viability. As previously described (*17*, *18*), a high fraction of cell survival was retained (typically greater than 80%) after cellular exposure to polyplexes formed with **D1**−**D4** and **T1**−**T4** at the N/P ratios required for maximum gene expression (N/P = 30 for **D2**−**D4** and **T1** − **T4**; N/P = 20 for **D1**). Here, the cytotoxicity profiles of **D2**, **DS**, **T2**, and **TS** were compared (Figure 8). As reported previously, the fraction of cell survival with **D2** and **T2** was greater than 80% even at high N/P ratio such as 30. However, polyplexes formed with **DS** and **TS** revealed significant toxicity, where **TS** revealed higher toxicity than **DS**. At the N/P ratios of maximum gene expression for **DS** and **TS** (N/P = 30 and 10, respectively), only 17 and 13% cell survival was retained, respectively. Spermine-based polymers have been reported to yield high cytotoxicity by inhibiting the uptake of oligoamines such as putrescine, spermidine, and spermine, which play essential regulatory roles in cell growth and differentiation (*31*). Here, the extremely high cytotoxicity observed with **DS** and **TS** may be caused by the same mechanism. Although **DS** and **TS** do not exhibit the proper biocompatibility for effective gene delivery, they may be promising to be utilized as anticancer drugs to suppress tumor cell proliferation by blocking the transmembrane transport of oligoamines (*31*).

Cellular Uptake of Polyplexes. To explain why the overall buffering capacity decreased while the gene delivery efficiency increased (when the amine stoichiometry was considered) for the poly(glycoamidoamine)s, we performed flow cytometry to quantify the cellular internalization of Cy5-labeled pDNA complexed with polymers **D1**−**D4** and **T1**−**T4** at the N/P ratios required for maximum gene expression. This experiment yields the number of cells that uptake pDNA, as well as the average intensity of fluorescence (relative amount of pDNA) in the cells. The cells were incubated with each polyplex solution for 4 h to allow endocytosis. After removing the cell surface-bound polyplexes and further incubating for 30 min, the cells were trypsinized and isolated for FACS analysis. The flow histograms of BHK-21 cells are shown in Figure 9a (**D1**−**D4**) and 9b (**T1**−**T4**). The mean fluorescence intensity and the percentage of positive cells are shown in Figure 9c. When comparing the polymers in the **D** or **T** series, both the number of transfected cells and the mean fluorescence intensity increased with the increasing of the number of amine units in the polymer repeat unit, with the exception of polymer **T1**, which is not understood at this time. This indicates that in general the cellular internalization of the polyplexes is enhanced when the number of amines is increased in the polymer repeat unit. This observation

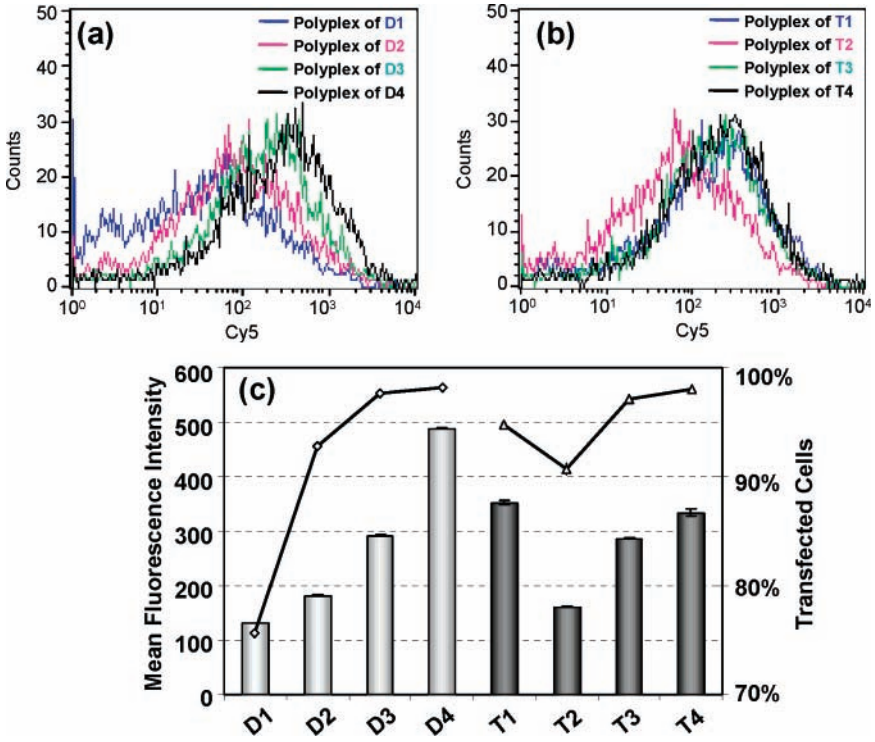


Figure 9. Cellular uptake of Cy5-labeled pDNA complexed with **D1**−**D4**, and **T1**−**T4**. (a) Flow histogram of BHK-21 cells after transfection with polyplexes of **D1**−**D4**. (b) Flow histogram of BHK-21 cells after transfection with polyplexes of **T1**−**T4**. (c) Mean fluorescence intensity (bars) and the percentage of cells positive for Cy5 (lines).

may be attributed to the spacing of the amine blocks along the polymer backbones. Negatively charged proteoglycans found on the cell surface are believed to play an integral role in mediating cellular uptake of cationic polyplexes (*28*). If more polyplexes are internalized, more pDNA enters the cells to be expressed. Different cell types have diverse distributions of proteoglycans on their surfaces. Polymers with higher amine stoichiometry may facilitate better BHK-21 cell surface binding and endosomal membrane disruption through multivalent interactions with these membrane proteins. The increased interaction of these polymers with the cell surface could result in higher polyplex uptake. After the cellular uptake, endosomal escape could then occur through polymer−proteoglycan chelation (could form leaky holes in the endosomal membrane leading to endosomal escape) and increased gene expression (shown in Figure 6). Banaszak Holl et al. have shown that PAMAM dendrimers with terminal amine groups can strongly interact via electrostatic interactions with negatively charged phospholipids, which can induce defects in the cellular membrane and cause membrane leakage (*32*). A similar interaction may also allow leakage of endosomal contents into the cytoplasm. Further experiments to study this effect are ongoing in our lab.

When the results were compared between analogous structures in the **T** and **D** series, we did not observe systematically higher cellular uptake of polyplexes formed with **T1**−**T4** when compared to the **D1**−**D4** systems (Figure 9c). For example, **T1** yielded higher cellular uptake and transfected a greater percentage of cells than **D1**. However, **D2**−**D4** yielded higher cellular uptake and transfected more BHK-21 cells than **T2**−**T4** (for **D3**, **D4**, **T3**, and **T4**, the percentages of positive cells were higher than 95%). Here, it is interesting to note that the **T** series (**T1**−**T4**) generally yield higher gene expression values than their **D1**−**D4** analogues (Figure 6). This result further indicates that the greater buffering capacity and higher protonation capacity of these materials in the endosomal pH range could allow osmotic release and/or electrostatic defect formation in the endosomal membrane, facilitating vesicle release, which does agree with the proton sponge hypothesis.

CONCLUSION

In this study, we have calculated the buffering capacity of polymers with systematic variations in the carbohydrate moiety (D-glucarate or L-tartarate), amine stoichiometry (from 1 to 4), and amine spacer (ethylene or butylene) within the physiological pH range through nonlinear fitting of titration data. By analyzing these data, along with polyplex stability, flow cytometry, and reporter gene expression studies, we sought to further understand how and why structural variables within poly(glycoamidoamine)s affect cellular internalization, buffering capacity, and gene delivery efficiency in BHK-21 cells. We have found that the tested structural variables differentially influence the biological properties of the polymers in a case-specific manner. When comparing poly(glycoamidoamine)s that have the same carbohydrate moiety but different amine stoichiometry (e.g., **D3** vs **D4**), there is no correlation between the buffering capacity and the delivery efficacy. The cellular uptake of polyplexes seems to be the key step in the gene delivery process that determines their efficacy in this case. Polyplexes formed with polymers containing a higher number of amines in the repeat unit clearly facilitate greater cellular uptake. This observation is likely due to the increased multivalent interaction of the amine groups with the cell surface. This stronger interaction of the polymers with cell surface proteoglycans may also aid endosomal release of the polyplexes. These structures may chelate the cell surface proteins and/or insert into membranes and form leaky regions in the endosomes. This, in turn, would promote higher gene expression. Similar observations between the cellular uptake and the gene delivery efficiency were also obtained by Lim et al. in a series of chitosan vectors (*33*).

When polymers that have the same amine stoichiometry but different carbohydrate moieties (e.g., **D4** vs **T4**) are compared, it appears that the buffering capacity and the higher cationic character are the key properties that determine the gene expression level. Structures with an enhanced buffering capacity can increase endosomal release according to the proton sponge hypothesis. Also, the higher amine density materials (**T** series

polymers have shorter molecular distance between the oligoamine moieties, which leads to a higher amine density than **D** series) could possibly cause release via membrane defect formation.

For the polymers containing the same carbohydrate and amine stoichiometry but a different amine spacer, no correlations are observed between the gene delivery efficacy and buffering capacity. The buffering capacity of spermine-based polymers (butylene spacer) is dramatically decreased (possibly by proton-induced cyclization), while the gene expression is increased. This may be due to the higher stability in the presence of heparin and easier vector unpacking properties of spermine based polyplexes. Although these properties are promising, the high toxicity exhibited by the spermine-based polymers (possibly by inhibiting the uptake of oligoamines that are essential to cell growth and differentiation) inhibits their use for many applications.

Our findings indicate the buffering capacity cannot effectively predict the gene delivery efficiency since the polymer structure can have a profound effect on many biological properties such as the polyplex stability, cellular uptake, and gene expression. A systematic and heuristic approach to study the correlations between the polymer structural variables and gene delivery efficiency seems to be a more direct and effective way toward determining the most effective synthetic gene delivery vectors for particular applications (*18*, *34*). Even though correlations that try to connect the physical properties of polymers to the gene delivery process (e.g., "proton sponge" theory) may not be generally valid for the large number of emerging synthetic delivery vectors, they have played a valuable role in inspiring the synthesis of many novel molecular structures.

ACKNOWLEDGMENT

We sincerely thank Professor Ann E. Hagerman for providing the thermostat flasks in the titration experiments, and Professor Ruth Duncan for helpful discussions about endosomal trafficking of nonviral delivery systems. We gratefully acknowledge funding of this work from the National Institutes of Health (1-R21-EB003938-01), National Science Foundation Career Award (CHE-0449774), the Beckman Young Investigators Program, and the UC Institute for Nanoscale Science and Technology. Yemin Liu thanks the University of Cincinnati for the Chemical Sensors and Laws-Stecker graduate fellowships.

LITERATURE CITED

(1) Wiethoff, C. M., and Middaugh, C. R. (2003) Barriers to nonviral gene delivery. *J. Pharm. Sci. 92*, 203−217.

(2) Wagner, E. (2004) Strategies to improve DNA polyplexes for in vivo gene transfer: Will "artificial viruses" be the answer? *Pharm. Res. 21*, 8−14.

(3) Davis, M. E. (2002) Non-viral gene delivery systems. *Curr. Opin. Biotechnol. 13*, 128−131.

(4) Rubanyi, G. M. (2001) The future of human gene therapy. *Mol. Aspects Med. 22*, 113−142.

(5) Anwer, K., Rhee, B. G., and Mendiratta, S. K. (2003) Recent progress in polymeric gene delivery systems. *Crit. Rev. Ther. Drug Carr. Syst. 20*, 249−293.

(6) Boussif, O., Lezoualc′h, F., Zanta, M. A., Mergny, M. D., Scherman, D., Demeneix, B., and Behr, J. (1995) A versatile vector for gene and oligonucleotide transfer into cells in culture and in vivo: Polyethylenimine. *Proc. Natl. Acad. Sci. U.S.A. 92*, 7297−7301.

(7) Haensler, J., and Szoka, F. C. (1993) Polyamidoamine cascade polymers mediate efficient transfection of cells in culture. *Bioconjugate Chem. 4*, 372−379.

(8) Midoux, P., and Monsigny, M. (1999) Efficient gene transfer by histidylated polylysine/pDNA complexes. *Bioconjugate Chem. 10*, 406−411.

(9) Forrest, M. L., Meister, G. E., Koerber, J. T., and Pack, D. W. (2004) Partial acetylation of polyethylenimine enhances in vitro gene delivery. *Pharm. Res. 21*, 365−371.

(10) Funhoff, A. M., Nostrum, C. F. v., Koning, G. A., Schuurmans-Nieuwenbroek, N. M. E., Crommelin, D. J. A., and Hennink, W. E. (2004) Endosomal escape of polymeric gene delivery complexes is not always enhanced by polymers buffering at low pH. *Biomacromolecules 5*, 32−39.

(11) Kulkarni, R. P., Mishra, S., Fraser, S. E., and Davis, M. E. (2005) Single cell kinetics of intracellular, nonviral, nucleic acid delivery vehicle acidification and trafficking. *Bioconjugate Chem. 16*, 986−994.

(12) Wan, K., Malgesini, B., Verpilio, I., Ferruti, P., Griffiths, P. C., Paul, A., Hann, A. C., and Duncan, R. (2004) Poly(amidoamine) salt form: effect on pH-dependent membrane activity and polymer conformation in solution. *Biomacromolecules 5*, 1102−1109.

(13) Griffiths, P. C., Paul, A., Khayat, Z., Wan, K., King, S. M., Grillo, I., Schweins, R., Ferruti, P., Franchini, J., and Duncan, R. (2004) Understanding the mechanism of action of poly(amidoamine)s as endosomolytic polymers: correlation of physicochemical and biological properties. *Biomacromolecules 5*, 1422−1427.

(14) Ferruti, P., Manzoni, S., Richardson, S. C. W., Duncan, R., Pattrick, N. G., Mendichi, R., and Casolaro, M. (2000) Amphoteric linear poly(amido-amine)s as endosomolytic polymers: correlation between physicochemical and biological properties. *Macromolecules 33*, 7793−7800.

(15) Liu, Y., and Reineke, T. M. (2006) Poly(glycoamidoamine)s for gene delivery. Stability of polyplexes and efficacy with cardiomyoblast cells. *Bioconjugate Chem. 17*, 101−108.

(16) Liu, Y., and Reineke, T. M. (2005) Hydroxyl stereochemistry and amine number within poly(glycoamidoamine)s affect intracellular DNA delivery. *J. Am. Chem. Soc. 127*, 3004−3015.

(17) Liu, Y., Wenning, L., Lynch, M., and Reineke, T. M. (2005) Gene delivery with novel poly(L-tartaramidoamine)s. In *Polymeric Drug Delivery Volume I - Particulate Drug Carriers* (Svenson, S., Ed.), American Chemical Society, Washington DC.

(18) Liu, Y., Wenning, L., Lynch, M., and Reineke, T. M. (2004) New poly(D-glucaramidoamine)s induce DNA nanoparticle formation and efficient gene delivery into mammalian cells. *J. Am. Chem. Soc. 126*, 7422−7423.

(19) Kiely, D. E., Chen, L., and Lin, T. (1994) Hydroxylated nylons based on unprotected esterified D-glucaric acid by simple condensation reaction. *J. Am. Chem. Soc. 116*, 571−578.

(20) Ogata, N., Sanui, K., Hosoda, Y., and Nakamura, H. (1976) Active polycondensation of diethyl 2, 3, 4, 5-tetrahydroxyadipate with diamines. *J. Polym. Sci. Polym. Chem. Ed.* 14, 783−792.

(21) Medina-Kauwe, L. K., Xie, J., and Hamm-Alvarez, S. (2005) Intracellular trafficking of nonviral vectors. *Gene Ther. 12*, 1734−1751.

(22) Suh, J., Paik, H., and Hwang, B. K. (1994) Ionization of poly(ethylenimine) and poly(allylamine) at various pH's. *Bioorg. Chem. 22*, 318−327.

(23) Marsh, M., Griffiths, G., Dean, G. E., Mellman, I., and Helenius, A. (1986) Three-dimensional structure of endosomes in BHK-21 cells. *Proc. Natl. Acad. Sci. U.S.A. 83*, 2899−2903.

(24) Jencks, W. P., and Regenstein, J. (1975) Ionization constants of acids and bases. In *Handbook of Biochemistry and Molecular Biology: Physical and Chemical Data* (Fasman, G. D., Ed.) pp 306 and 345, CRC Press: Cleveland.

(25) Inoue, T., Ryu, D., Osaki, K., and Takebe, T. (1999) Viscoelasticity and birefringence of syndiotactic polystyrene. I. Dynamic measurement in supercooled state. *J. Polym. Sci. B: Polym. Phys. 37*, 399−404.

(26) Karpas, Z., Bell, S. E., Wang, Y.-F., Walsh, M., and Eiceman, G. A. (1994) The structure of protonated diamines and polyamines. *Struct. Chem. 5*, 135−140.

(27) Gojlo, E., Smiechowski, M., and Stangret, J. (2005) The common effect of hydrophobic and electrophilic types of hydration dependent on protonation in the sec-butylamine/HCl/H_2O system studied by FTIR spectroscopy. *J. Mol. Struct. 744−747*, 809−814.

(28) Mislick, K. A., and Baldeschwieler, J. D. (1996) Evidence for the role of proteoglycans in cation-mediated gene transfer. *Proc. Natl. Acad. Sci. U.S.A. 93*, 12349−12354.

(29) Akinc, A., Thomas, M., Klibanov, A. M., and Langer, R. (2005) Exploring polyethylenimine-mediated DNA transfection and the proton sponge hypothesis. *J. Gene Med. 7*, 657−663.
(30) Schaffer, D. V., Fidelman, N. A., Dan, N., and Lauffenburger, D. A. (2000) Vector unpacking as a potential barrier for receptor-mediated polyplex gene delivery. *Biotechnol. Bioeng. 67*, 598−606.
(31) Aziz, S. M., Gosland, M. P., Crooks, P. A., Olson, J. W., and Gillespie, M. N. (1995) A novel polymeric spermine conjugate inhibits polyamine transport in pulmonary artery smooth muscle cells. *J. Pharmacol. Exp. Ther. 274*, 181−186.
(32) Hong, S., Bielinska, A. U., Mecke, A., Keszler, B., Beals, J. L., Shi, X., Balogh, L., Orr, B. G., Baker, J. R., and Holl, M. M. B. (2004) Interaction of poly(amidoamine) dendrimers with supported lipid bilayers and cells: Hole formation and the relation to transport. *Bioconjugate Chem. 15*, 774−782.
(33) Huang, M., Fong, C., Khor, E., and Lim, L. (2005) Transfection efficiency of chitosan vectors: Effect of polymer molecular weight and degree of deacetylation. *J. Control. Release 106*, 391−406.
(34) Wood, K. C., Little, S. R., Langer, R., and Hammond, P. T. (2005) A family of hierarchically self-assembling linear-dendrictic hybrid polymers for highly efficient targeted gene delivery. *Angew. Chem. Int. Ed.* 44, 6704−6708.

BC060029D

Tat-Functionalized Near-Infrared Emissive Polymersomes for Dendritic Cell Labeling

Natalie A. Christian,[†] Michael C. Milone,[‡,§] Shraddha S. Ranka,[†] Guizhi Li,[||] Paul R. Frail,[||] Kevin P. Davis,[⊥] Frank S. Bates,[⊥] Michael J. Therien,[||] P. Peter Ghoroghchian,[†,||] Carl H. June,[‡,§] and Daniel A. Hammer*[,†]

School of Engineering and Applied Science, Department of Bioengineering, Abramson Family Cancer Research Institute, Department of Pathology and Laboratory Medicine, and Department of Chemistry, University of Pennsylvania, Philadelphia, Pennsylvania 19104, and Department of Chemical Engineering and Materials Science, University of Minnesota, Minneapolis, Minnesota 55455. Received May 17, 2006; Revised Manuscript Received September 28, 2006

Dendritic cells (DCs) play a pivotal role in both immune tolerance and the initiation of immunological responses. The ability to track DCs in vivo is imperative for the development of DC-based cellular therapies and to advance our understanding of DC function and pathophysiology. Here, we conjugate a cell permeable peptide, Tat, to near-infrared (NIR) emissive polymersomes in order to enable efficient intracellular delivery for future DC tracking with these optical probes. NIR imaging allows quantitative, repetitive, in vivo detection of fluorophore-laden cells, at centimeter tissue depths without disturbing cellular function. Flow cytometry and confocal microscopy results indicate that Tat-mediated polymersome delivery to DCs is concentration and time dependent, resulting in punctate intracellular localization. Further, loading cells with Tat NIR emissive polymersomes does not interfere with cytokine-induced DC maturation and has modest effects on DC viability, but has a significant effect on mature DC-induced activation of naive T cells. We observe significant uptake of NIR emissive polymersomes when conjugated to the peptide, with a lower detection limit of 5000 labeled DCs. The extent of polymersome delivery is estimated as 70 000 ± 10 000 vesicles/cell, equivalent to 0.7 ± 0.1 fmol of NIR fluorophore. Our studies will enable future in vivo tracking of ex vivo labeled DCs by NIR fluorescence based imaging.

INTRODUCTION

Dendritic cells (DCs)[1] play a pivotal role in both initiation and regulation of immune responses (*1*−*4*). Immature DCs (iDCs) specialize in sampling the tissue microenvironment for pathogens. Upon encountering pathogens, DCs mature by upregulating adhesion and antigen presenting molecules, thereby enabling migration to local lymphoid tissue and subsequent activation of antigen specific B and T cells (*5*). This central role in the immune response has highlighted the ability of DCs to generate potent anticancer activity and has motivated the development of cell-based vaccines using ex vivo generated DCs. DC-based vaccines have shown promising results in preclinical models (*6*−*9*). However, several obstacles and questions remain before they can be viable therapies. At present, only 1−5% of intradermally administered mature DCs reach peripheral lymph nodes (*6*). Current studies are limited by a lack of intricate knowledge of both DC trafficking and how to best manipulate such cells for optimal therapeutic outcomes (*10*). In addition, clinical trials lack standard methods for evaluating DC treatment efficacy.

The development of in vivo cellular tracking techniques is imperative to ultimately advancing DC-based therapy. By utilizing imaging methods for cellular tracking, numerous aspects of DC therapy could be evaluated including DC sources, maturation states, antigen delivery methods, activation stimuli, routes of administration, and the doses and frequencies of DC vaccinations (*11*). In addition, basic dendritic cell biology could be addressed to expand our understanding of DC function and dysfunction.

Relatively few studies have attempted to track DCs mainly due to the low concentration of this specialized cell type (0.5−1.5% of peripheral blood mononuclear cells (PBMC)) (*12*). Current noninvasive, in vivo imaging modalities employed to follow DCs include magnetic resonance imaging (MRI), scintigraphic imaging (*13*), and ^{19}F-MRI (*14*). Conventional ^{1}H-MRI-based cell tracking typically utilizes iron oxide, a T_2-weighted ("negative") contrast agent, while scintigraphic imaging utilizes γ-emitting radionuclides such as ^{111}In-oxine. Both MRI and scintigraphy were used by de Vries et al. to track DCs loaded with tumor-derived peptides in stage III melanoma patients (*13*). MRI provides exquisite anatomical detail while scintigraphic imaging offers superior sensitivity but with low spatial resolution. By combining these techniques, the investigators were successful in detecting 1.5×10^5 cells (*13*). Neverthe-

* Corresponding author. E-mail: hammer@seas.upenn.edu. Phone: 215-573-6761. Fax: 215-573-2071. Mailing address: 210 S. 33rd St., 240 Skirkanich, Philadelphia, Pennsylvania 19104.

[†] School of Engineering and Applied Science, Department of Bioengineering, University of Pennsylvania.

[‡] Department of Pathology and Laboratory Medicine, University of Pennsylvania.

[§] Abramson Family Cancer Research Institute, University of Pennsylvania.

[||] Department of Chemistry, University of Pennsylvania.

[⊥] Department of Chemical Engineering and Materials Science, University of Minnesota.

[1] Abbreviations: CD, cluster designation; DC, dendritic cell; EOIS, ExPlore Optix Imaging System; FITC, fluorescein; GFP, green fluorescent protein; GM-CSF, granulocyte colony stimulating factor; GY, grays; iDC, immature dendritic cell; IL, interleukin; mDC, mature dendritic cell; MHC, major histocompatibility complex (class I or II); MLR, mixed lymphocyte reaction; MRI, magnetic resonance imaging; NIR, near-infrared; NIRF, near-infrared fluorophores; OB, poly(ethyleneoxide)-*b*-poly(butadiene) block copolymer; PBD, poly(butadiene); PBMC, peripheral blood mononuclear cells; PBS, phosphate buffered saline; PE, phycoerythrin; PEO, poly(ethyleneoxide); PFA, paraformaldehyde; PGE_2, prostaglandin; PZn, (porphinato)zinc macrocycle; SC, succinimidyl carbonate; TEM, transmission electron microscopy; TNF-α, tumor necrosis factor alpha.

10.1021/bc0601267 CCC: $37.00 © 2007 American Chemical Society
Published on Web 11/22/2006

less these techniques are inherently limited. ^{1}H-MRI imaging is not quantitative, requires millimolar concentrations of contrast agent, and is subject to artifacts due to the negative contrast. Scintigraphy requires potentially harmful radioisotopes and lacks spatial resolution. The difficulty of detecting negatively contrasted cells by MRI has motivated the use of perfluoropolyether (PFPE) particles that create positive contrast with ^{19}F-MRI (given the lack of endogenous ^{19}F). During the same imaging session, an ^{1}H-MRI image can also be acquired to assess the anatomical location of the cells. With this approach, Ahrens et al. successfully detected 2×10^5 cells/voxel (*14*).

Fluorescence-based imaging of cells labeled with near-infrared fluorophores (NIRFs) is an alternative noninvasive imaging modality capable of cell tracking. This approach is comparable to labeling cells with fluorescent tags and performing immunohistochemistry on fixed tissue slices at selected endpoints. With NIR imaging, however, the fluorophore-laden cells can be detected in vivo at centimeter tissue depths, repeatedly, without disturbing cellular function. Additional benefits of optical imaging include extremely high sensitivity (sub-nanomolar concentrations of exogenous contrast agents), fast acquisition times, low patient risk, and the potential mobility and low cost of optical imaging hardware in comparison to MRI or scintigraphy (*15*, *16*).

Recently, our lab developed near-infrared emissive polymersomes (NIR-OBs), self-assembled polymeric vesicles with porphyrin-based NIRFs loaded within their hydrophobic membranes (*17*, *18*). Both the polymer, poly(ethylene oxide(1300)-*b*-butadiene(2500)) (OB), and porphyrin-based NIRF, meso-to-meso ethyne-bridged oligomeric (porphinato)zinc(II) chromophore (**PZn$_n$** species) macrocycles, are fully biocompatible (*19*−*24*). NIR-OB vesicles are multifaceted with mechanically robust membranes, have an ability to sequester both hydrophobic and hydrophilic reagents, possess 100% PEGylated surfaces for coupling to bioactive moieties, and are tunable from 50 nm to 10 μm in diameter (*25*, *26*). Further, a single 200 nm diameter NIR-OB vesicle having less than 3 mol % loading of **PZn$_n$** NIR fluorophores possesses ≥2500 membrane-bilayer dispersed copies of these emitters, creating an unparalleled fluorescent contrast agent suitable for in vivo applications.

These NIR-OB polymersome characteristics led us to investigate the application of these optical agents for cell tracking. In order to optimize the intracellular delivery of polymersomes, we coupled the vesicles to HIV-derived Tat, a highly cationic peptide shown to enhance cellular delivery of nanoparticles (*27*−*35*). A schematic of the Tat-NIR-OB vesicle is presented in Figure 1. The goals of this study include maximizing cellular delivery of Tat-NIR-OB polymersomes to DCs, investigating the effect of polymersome loading on cellular function, and evaluating the detection sensitivity of the labeled cells using a preclinical imager.

EXPERIMENTAL PROCEDURES

Synthesis of Succinamidyl Carbonate Modified Polymer. The PEO terminal hydroxyl of the copolymer was derivatized with succinimidyl carbonate (SC) as presented in Scheme 1 and according to the procedure established by Miron and Wilchek (*36*). Briefly, disuccinimidyl carbonate was mixed with copolymer, PEO(1300)-*b*-PBD(2500) (Polymer Source Inc., Montreal, Quebec), in dioxane. The reaction was catalyzed upon the addition of 4-(dimethylamino)pyridine and stirred overnight at room temperature. The activated polymer (SC-PEO-*b*-PBD) was then precipitated using diethyl ether and purified using high performance liquid chromatography. The final product was vacuum-dried and stored under argon gas at 4 °C until use. The extent of derivatization of the polymer was determined by ^{1}H-NMR (data not shown).

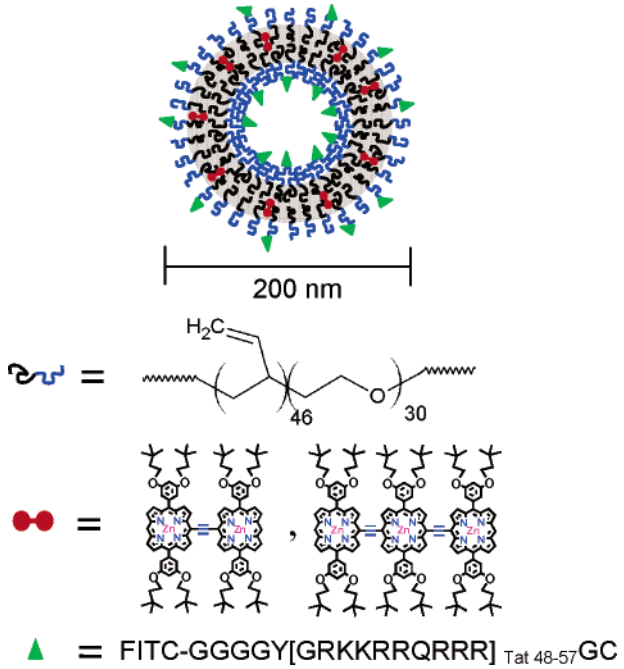
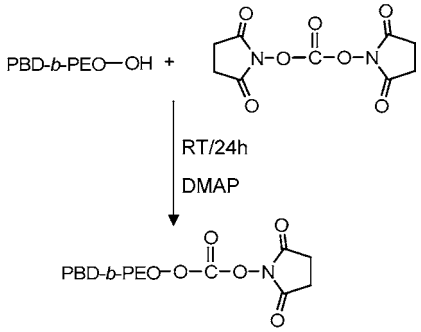


Figure 1. Tat-conjugated NIR emissive polymersomes. The FITC-Tat peptide (▲) is covalently conjugated to the terminal PEG moiety while the NIR emissive fluorophore (●—●) segregates to the hydrophobic bilayer core during self-assembly.

Scheme 1. Reaction Scheme for Terminal Hydroxyl Derivatization to Succinimidyl Carbonate



Tat Conjugation. SC-PEO-*b*-PBD polymer (MW = 3925) was dissolved in methylene chloride and added to nonderivatized PEO-PBD (MW = 3800) to achieve a 10 mol % mixture of the SC-PEO-*b*-PBD. This polymer blend was dried under vacuum and subsequently resuspended in 1 mL of anhydrous methanol. Tat (1760 Da) or FITC-Tat (2260 Da) (Alta Bioscience, Birmingham, U.K.) was then added, in a 1:1 molar ratio with the reactive polymer, and kept overnight at 4 °C. Nonconjugated Tat was removed following polymersome formation by extensive dialysis in isotonic phosphate buffered saline, pH 7.4. Finally, conjugation was verified by ^{1}H-NMR (data not shown) and confocal microscopy.

Polymersome Formulation. All NIRF-laden polymersomes were prepared as described by Ghoroghchian et al. (*17*, *18*). In brief, the selected polymer and fluorophore were dissolved in methylene chloride at a 40:1 molar ratio of polymer to NIRF. The solution was then plated onto a roughened Teflon film and dried under vacuum overnight. Polymersomes were formed upon the addition of 285 mOsm sucrose solution and either heated (60 °C for 48 h) or sonicated (1 h), in a bath sonicator. Heating yielded micron-sized polymersomes for confocal microscopic evaluation while sonication yielded nanoscale polymersomes utilized in the cellular uptake studies. A narrow size distribution of nanosized polymersomes was achieved with serial extrusion using a Liposofast Basic hand-held extruder equipped with 400,

200, and 100 nm polycarbonate membranes (Avestin Inc., Ottawa, Ontario).

In this work, the polymer component was either 10 mol % Tat-PEO-PBD with 90 mol % PEO-PBD or pure PEO-PBD. Polymersomes loaded with the porphyrin-based NIR fluorophores, **PZn_2**, were utilized for in vitro flow cytometry and confocal studies, while those that dispersed **PZn_3** ($\lambda_{excitation}$ = 785 nm, $\lambda_{emission}$ = 800 nm) were used for NIR optical imaging of cell populations. NIR emissive polymersomes were prepared using a 40:1 polymer:**PZn_n** molar ratio. The concentration of the **PZn_n** emitter in the polymersomal membrane was quantified via the established extinction coefficients of the far red absorbance of these species, λ_{PZn2} = 708 nm and λ_{PZn3} = 795 nm (*18*, *21*−*24*). Upon measurement of fluorophore absorbance in solution, the concentration of **PZn** was obtained using Beer's Law and previously established extinction coefficients ($\epsilon_{PZn2(708nm)}$ = 59 000 M^{-1} cm^{-1}, $\epsilon_{PZn3(795nm)}$ = 125 000 M^{-1} cm^{-1}) (*17*). Finally, the polymer concentration was directly related to the porphyrin concentration by the initial molar ratio deposited as a thin film (40:1 polymer:porphyrin) (*37*).

Dendritic Cell Preparation. Immature dendritic cells (iDCs) were prepared from human peripheral blood mononuclear cells (PBMC). PBMC were isolated by Ficoll−Paque density-gradient centrifugation on day 0. Plastic adherence at 37 °C for 90 min was used to separate adherent monocytes from nonadherent lymphocytes. The adherent cells were cultured for 6 days in serum free AIM-V media containing recombinant GM-CSF at 800 U/mL (Leukine, Berlex Laboratories) and recombinant IL-4 at 500 U/mL (Cytokine Inc). Cytokines were replenished on day 3 of culture. Immature DCs were recovered on day 6 by washing with cold PBS and gentle pipetting. A Multisizer3 Coulter Counter (Beckman Coulter, Fullerton, CA) and trypan blue exclusion were used to determine viable cell concentrations. Cells were resuspended in media (phenol free RPMI supplemented with 10% FCS, 1% HEPES, and 1% penicillin/streptomycin) and plated at a final cell concentration of 1 × 10^6 DC/mL.

Cell Treatments with Polymersomes. DCs were incubated in media (37 °C, 5% CO_2) with either PBS (control), NIR emissive polymersomes, or Tat NIR emissive polymersomes at controlled concentrations (50 μM to 800 μM polymer) over various time intervals (1−24 h). Following incubation, cells were collected using two cold PBS (4 °C) washes. An additional volume of PBS was added (>30× cell incubation volume) before centrifugation (5 min, 1700 rpm). The polymersome containing supernatant was then removed and the wash cycle subsequently repeated twice. Labeled cells were either used immediately as described, returned to culture in fresh media, or fixed with 2% PFA in PBS and stored at 4 °C.

Dendritic Cell Maturation Treatment. Dendritic cell maturation was induced with a cytokine mixture containing GM-CSF (800 U/mL), IL-4 (500 U/mL), TNF-α (10 ng/mL), IL-6 (0.15 μg/mL), IL-1β (10 ng/mL), and PGE_2 (1 μg/mL). In parallel, immature DCs were maintained with the addition of only GM-CSF and IL-4. Both treatments were added to culture 5 h after polymersome addition and incubated overnight.

Confocal Laser Scanning Microscopy (LSM). Fluorescence scanning confocal microscope images were obtained with a Carl Zeiss LSM-510 Meta confocal microscope (Oberkochen, Germany) equipped with a C-Apochromat 40×/1.2 W objective. Both FITC and **PZn_2** excitation were achieved with a 488 nm argon laser. Fluorescence emission was captured using either 505−530 nm band-pass (FITC) or 650 nm long-pass (**PZn_2**) filters. Cells were kept on ice and imaged by directly plating live cells (10 μL) on a glass slide and covering with coverslip. Images were modified for contrast and brightness using Photoshop software (Adobe Systems, San Jose, CA).

Cryogenic Transmission Electron Microscopy (Cryo-TEM). Nanometric Tat functionalized polymersomes were formulated as described above. Vitreous samples were prepared within a controlled environment vitrification system (CEVS) (*38*). A droplet of solution (~10 μL) was deposited on a copper TEM grid coated with a porous polymer film. A thin film (<300 nm) was obtained by blotting with filter paper. After allowing the sample sufficient time to relax from any residual stresses imparted during blotting (~30 s), the grid was plunge cooled in liquid ethane at its freezing point (−180 °C), resulting in vitrification of the aqueous film. Sample grids were examined in a JEOL 1210 transmission electron microscope operating at 120 kV, and images were recorded with a Gatan 724 multiscan digital camera.

Dynamic Light Scattering (DLS). A photon correlator spectrometer (DynaPro-LSR, ProteinSolutions, Lakewood, NJ) was used to measure the hydrodynamic radius of prepared vesicles. Quartz cuvettes were filled with 50 μL of polymersome suspensions and were thermostatically controlled at 25 °C throughout the experiment. All DLS measurements were made at a scattering angle of 90°. Data analysis was performed using DYNAMICS software provided by ProteinSolutions. The results are given as hydrodynamic radius versus percent intensity.

Flow Cytometry. A BD FACSCalibur flow cytometer (BD Biosciences, Franklin Lakes, NJ) was employed to determine both the extent of fluorescent labeling achieved by NIR emissive polymersome uptake and the DC maturation state as assessed by surface molecule phenotyping. DCs were gated using the forward versus side scatter parameters. All experiments analyzed a minimum of 10 000 DC events. The NIR fluorophores were excited using an argon ion laser (15 mW, 488 nm) and probed with fluorescence detection in the FL3 channel (650 nm long-pass filter).

For phenotypic analysis, cells were first incubated with human serum (15 min, 4 °C) to block nonspecific Fc-receptor binding. Subsequently, cells were incubated for 30 min at 4 °C with the following antibodies: FITC-CD3, CD14, CD16, CD19, PE-CD86, PE-CD83, or isotype controls. Following incubation, cells were washed and fixed with 2% PFA prior to data acquisition.

Mixed Lymphocyte Reaction (MLR). Dendritic cell function was assayed by a mixed lymphocyte reaction in a 96-well plate. Three 2-fold serial dilutions of treated DCs (stimulator cells) were plated in triplicate for each treatment. Stimulator cells were irradiated with 30 GY prior to coculture with 50 000 responder PBMC per well in serum free AIM-V media. T-cell proliferation was assessed by ^{3}H-thymidine incorporation over the last day of coculture (day 3). Anti-CD3/CD28 coated paramagnetic beads (M450 Dynal, Invitrogen) were used as a positive control for T-cell proliferation with a 3:1 bead to responder PBMC ratio (*39*).

Near-Infrared Molecular Imaging with ExPlore Optix Imaging System (EOIS). Dendritic cell populations were imaged with an ExPlore Optix Imaging System (GE Healthcare-Advanced Research Technologies Inc.; Schenectady, NY) for preclinical optical molecular imaging. Cell detection studies were performed in an opaque 96-well plate (BD Falcon, Franklin Lakes, NJ). Labeled cells were plated at dilutions of 50 000, 5000, or 500 cells per well. NIR emissive polymersomes were plated in parallel with 5-fold dilutions ranging from 10 to 0.08 pmol of fluorophore per well for calibration purposes.

Images were acquired with the following parameters: 785 nm excitation laser, 803 μW laser power, 850 ± 50 nm band-pass filter, 2 s integration time, 1.5 mm step size, and 37 °C stage temperature. Images were analyzed with Analysis WorkStation 1.1.3.0 (Advanced Research Technologies, Quebec, Canada).

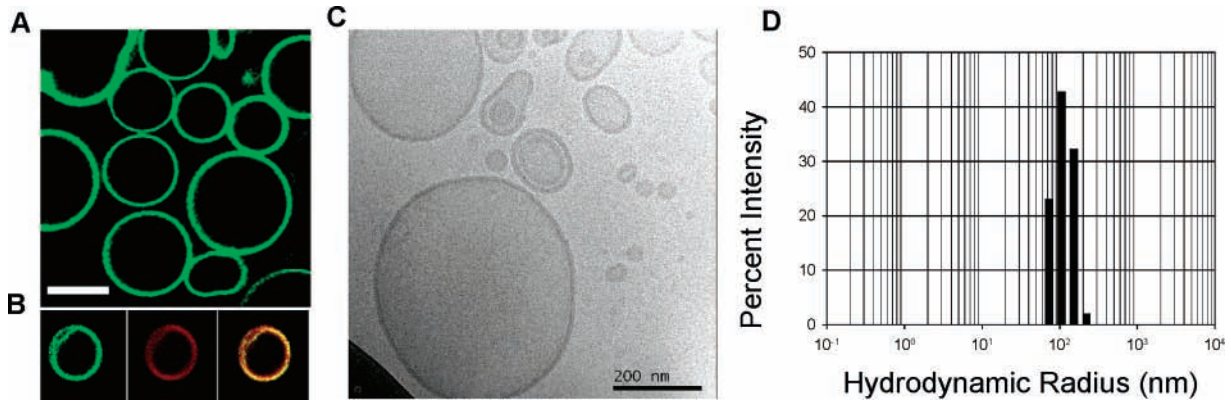


Figure 2. Tat-conjugated NIR emissive polymersome characterization. (A, B) Confocal LSM images of micron-size polymersomes. (A) FITC-Tat functionalized vesicle and (B) FITC-Tat functionalized vesicle surface with NIRF (**PZn$_2$**) loaded within the membrane. Green = FITC, red = NIRF, yellow = fluorophore colocalization; scale bar = 10 μm. (C) Cryo-TEM image of nanometer-sized Tat-conjugated polymersomes. (D) Representative DLS size distribution for serially extruded Tat-conjugated polymersomes.

The average photon count per well was correlated to fluorophore concentration using the calibration samples (n = 4). This calibration allowed estimation of the fluorophore number per cell. The number of polymersomes per cell was then computed using the molar conversion of NIRF to polymer chains (1:40) and the geometric approximation of 220 000 polymer chains per 200 nm vesicle (1 chain/nm^2).

RESULTS AND DISCUSSION

Tat NIR Polymersome Visualization. Conjugation of Tat peptide to the polymersome surface was confirmed by confocal microscopy. In Figure 2A, FITC-Tat is observed at the vesicle membrane. All visualized vesicles were fluorescently labeled, suggesting that the reacted polymer is evenly dispersed during polymersome self-assembly. The addition of the NIR fluorophore, **PZn$_2$**, to the polymer film yields similar FITC-Tat membrane functionalization (Figure 2B, green). **PZn$_2$** also localizes within the polymersome membrane (Figure 2B, red). The hydrophobic nature of this fluorophore drives its segregation into the hydrophobic core of the bilayer during polymersome formation. The presence of both FITC-Tat and NIR fluorophore within the same vesicle suggests that the fluorophore does not interfere with peptide presentation nor does the peptide interfere with fluorophore loading and fluorescence. Cellular delivery of polymersomes was studied using approximately 200 nm vesicles prepared by serial extrusion. We employed cryo-TEM to confirm vesicle morphology of these nanometric Tat−polymersomes. As observed in Figure 2C, vesicle morphology is maintained with Tat peptide conjugation.

Polymersome Size Distribution by DLS. The final distribution of vesicle sizes was measured using DLS with a representative histogram presented in Figure 2D. The mean hydrodynamic radius of the presented Tat−polymersome distribution is 115 ± 34 nm. This characterization was performed for all preparations as a quality control measure to guarantee that each batch contained equivalent size vesicles.

Cellular Localization of Tat−Polymersomes by Confocal LSM. We imaged live DCs incubated with FITC-Tat conjugated NIR polymersomes to visualize both the conjugated peptide and polymer cargo independently. In Figure 3, serial confocal z-slices of a single DC incubated for 3 h are presented to demonstrate the cellular distribution of FITC-Tat (green) and NIR emissive polymersomes (red). Predominantly, the intracellular peptide and polymersomes colocalize in a punctate distribution and appear blocked from nuclear entry. This colocalization suggests that the peptide remains in association with the polymersome once internalized. The serial slices show that the polymersomes distribute both to the cell surface and throughout the intracellular volume. These results agree with the current understanding of Tat-mediated cellular delivery.

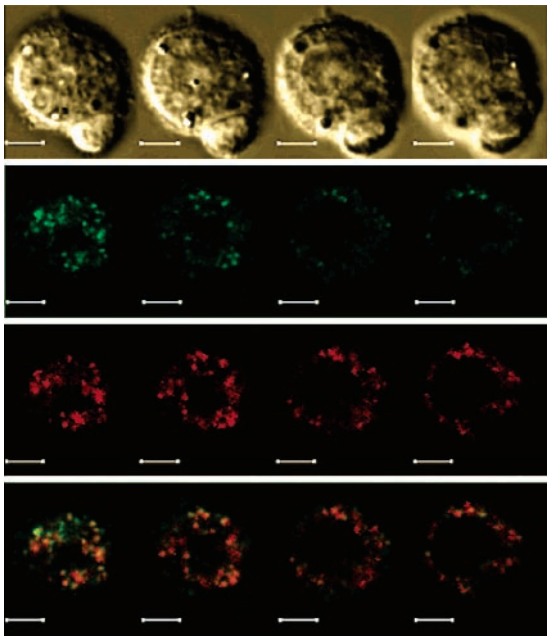


Figure 3. Confocal LSM images of an immature dendritic cell labeled with FITC-Tat NIR emissive polymersomes. (FITC = green, NIRF (**PZn$_2$**) = red.) Cells were incubated for 3 h with 100 μM polymer. Consecutive z-slices (Δ 2 μm) are presented from left to right. Scale bar is 5 μm. The DC is in contact with a lymphocyte; note that the lymphocyte does not load with polymersomes.

While initial studies suggested that Tat directed translocation of the attached cargo across the membrane into the cytoplasm, recent investigations point toward intracellular entry through typical membrane internalization pathways including endocytosis and macropinocytosis (*33*, *40*−*42*). These pathways result in punctate localization in intracellular vesicles as was observed by both Ferrari and Sandgren in CHO cells (*43*, *44*). More specifically, Ferrari utilized real time imaging to follow the distribution of Tat-GFP in CHO cells. This study found that Tat-GFP localized in intracellular vesicles accumulated in the perinuclear space as observed for polymersomes.

Concentration and Time Dependence of Tat NIR Emissive Polymersome Uptake. In order to maximize the intracellular uptake of polymersomes necessary for optimal cellular labeling, the effects of varying both the polymersome concentration and incubation time on DC uptake were examined. Flow cytometry was used to measure the intensity of cellular-associated **PZn$_2$**-

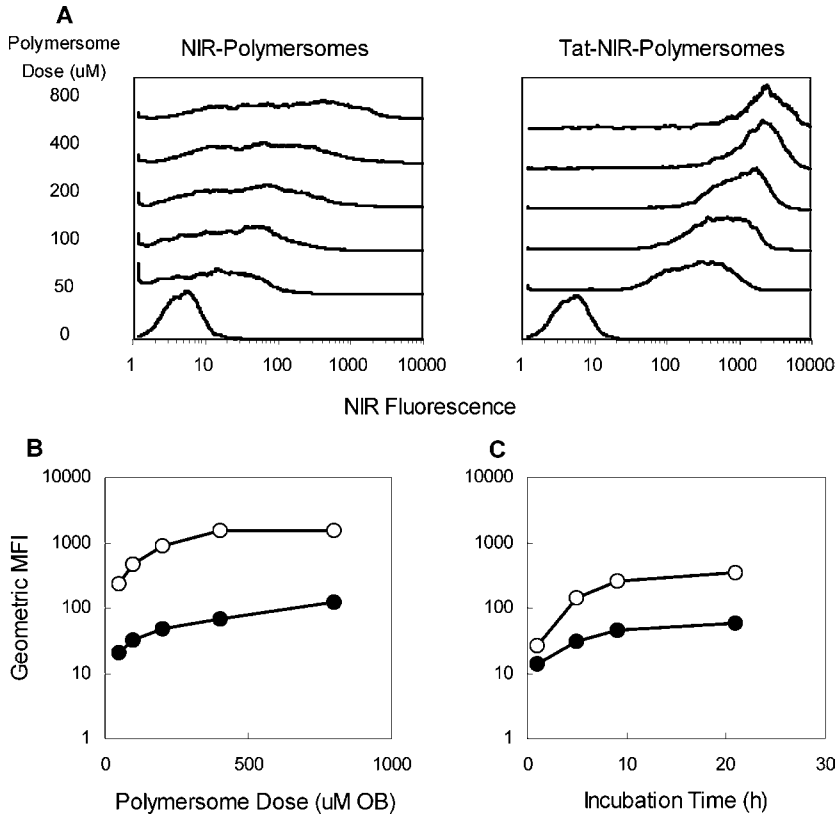


Figure 4. (A) Representative histograms for DCs treated overnight with either control or Tat-conjugated NIR emissive polymersomes at the indicated polymer dose. (B) Geometric mean fluorescent intensity of the presented histograms versus polymersome dose for immature DCs treated with control NIR emissive polymersomes (●) or Tat-conjugated NIR emissive polymersomes (○). (C) Geometric mean fluorescent intensity of 10,000 DCs as a function of incubation time. (200 μM OB)

based fluorescence following cell incubation and washing. These experiments evaluated the uptake of both Tat-conjugated polymersomes and nonfunctionalized controls (polymersomes with a 100% PEO brush) in order to distinguish the impact of Tat conjugation on intracellular delivery. The histograms presented in Figure 4A demonstrate clear Tat- and dose-dependent DC uptake.

In the absence of conjugated Tat, the extent of uptake varies greatly among the cell populations as indicated by the broad distribution of cellular fluorescence. In contrast, cells labeled with Tat NIR emissive polymersomes display a narrow distribution with a much lower coefficient of variation (CV). Tat-mediated intracellular delivery therefore generates a more uniformly labeled DC population. The concentration dependence of DC uptake is also evident for both Tat-conjugated and nonconjugated (control) polymersomes. The uptake of Tat NIR emissive polymersomes becomes saturated after an overnight incubation with a concentration of 400 μM polymer. This saturation is clearly observed in Figure 4B where the geometric mean fluorescence intensities of the presented histograms are plotted against the treatment concentration. In addition, Figure 4C shows the time dependence of polymersome uptake. The extent of dendritic cell labeling reaches half-maximal fluorescent intensity at 7 h for control NIR emissive polymersomes (MFI_{max} = 58), and at 5 h for Tat-conjugated NIR emissive polymersomes (MFI_{max} = 350).

Effect of Polymersome Labeling on Dendritic Cell Function. In order to determine the effects of polymersomes on DC function and viability, we studied the ability of immature dendritic cells to undergo cytokine-induced maturation and activate naive lymphocytes. In the presence of cytokines, immature dendritic cells (iDCs) are induced to differentiate into mature dendritic cells (mDCs), or professional antigen presenting cells (*45*). In vivo, this maturation is induced by an encounter with foreign antigen and results in DC migration to nearby lymph nodes with subsequent activation of T cells. In vitro, the addition of GM-CSF, IL-4, TNF-α, IL-6, IL-1β, and PGE_2 directs this maturation pathway, which can be evaluated by identifying a change in expression of the surface molecules: CD86 and CD83 (*46*). CD86 is a costimulatory molecule required for antigen presentation while CD83 is an accepted marker for mature dendritic cells with a function that remains to be fully elucidated (*47*). The expression levels of these molecules and the absence of other lymphoid lineage markers (CD3, T cell; CD14, monocyte; CD19, B cell; CD56, natural killer cell; and CD66b, granulocyte) were assayed via flow cytometry. Dendritic cells were selected according to their forward and side scatter properties and lack of lineage markers as shown in Figure 5A. In the left column of Figure 5B, untreated iDCs (thick line) were CD83−/CD86+ while mDCs (thin line) were CD83+/CD86++. It is clear that the maturation treatment upregulates both CD83 and CD86 as expected. Remarkably, dendritic cells treated with either control or Tat-conjugated NIR emissive polymersomes, presented in the middle and right columns, respectively, show nearly identical shifts in surface expression when compared to cells treated with media alone. In addition, the immature phenotype is maintained for cells incubated with both polymersome treatments. These results demonstrate that internalized NIR emissive polymersomes do not interfere with iDC differentiation into DCs with a mature phenotype.

The viability of treated cells is essential for cell tracking studies. Here, we assessed dendritic cell viability by trypan blue exclusion as a function of treatment, incubation time, and maturation state. Figure 6 shows that only an overnight incubation with Tat-conjugated NIR emissive polymersomes caused a measurable but not overwhelming amount of cytotoxicity, ~25%. This cytotoxicity is independent of maturation

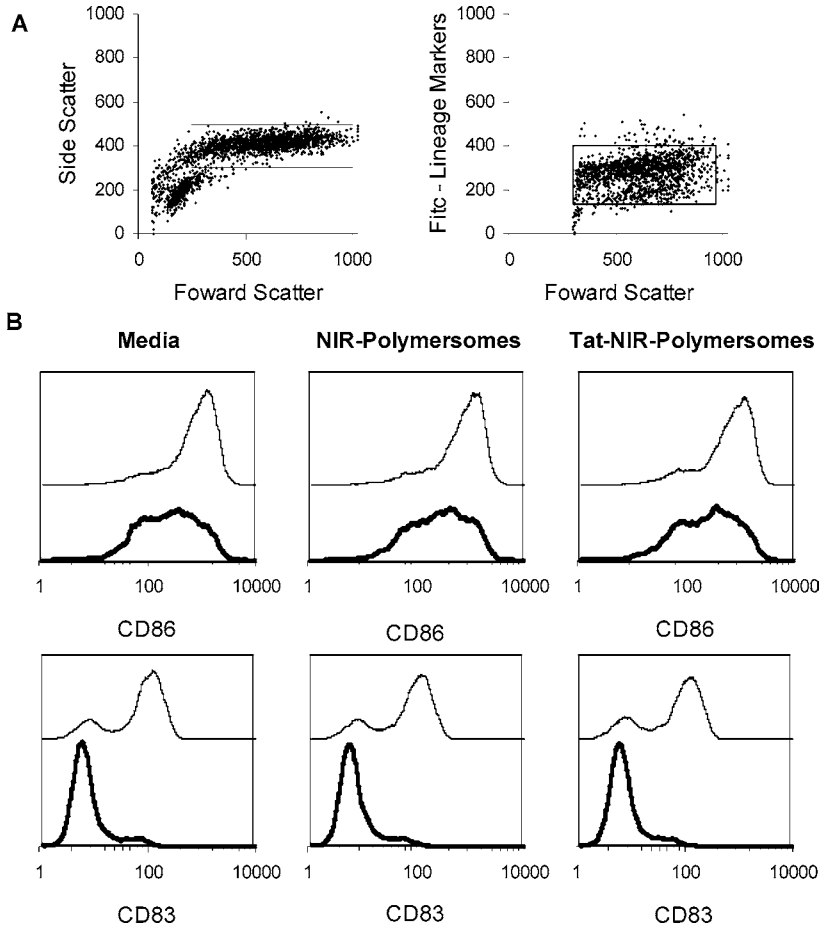


Figure 5. Dendritic cell phenotype characterization by flow cytometry. (A) DC gating approach. Cells were first selected by forward versus side scattering parameters and second for lineage negative status. (B) For each of the treatments (Media, control polymersomes, Tat-conjugated NIR-emisisve polymersomes), cells were maintained with a maturation cocktail (thin line) or in culture with only GM-CSF/IL-4 (wide line).

state. The high level of uptake that occurs with an overnight incubation of Tat-conjugated vesicles is likely responsible for this moderate cytotoxic effect. Similar levels of toxicity have been observed in other Tat-mediated particle delivery systems (*35*, *48*).

While surface marker phenotyping suggests that the iDC to mDC differentiation is unaltered by either control or Tat-conjugated NIR emissive polymersomes, we sought to confirm these results with an allogeneic mixed leukocyte reaction (MLR) (*49*, *50*). Both iDCs and mDCs labeled with polymersomes were assayed to detect any effect of internalized polymersomes on cellular activity. The MLR assay measures the ability of DCs to stimulate naive alloreactive T-cell proliferation. In our work, T-cell proliferation was measured radioactively via ^{3}H-thymidine incorporation into dividing T cells. The stimulatory activity results for iDCs and mDCs are presented in Figure 7A and 7B, respectively. For all cases, T-cell proliferation increases monotonically with DC number. This result confirms that DC activity is maintained with polymersome labeling. The ability of immature DCs to stimulate T-cell proliferation was relatively unaffected by treatment with Tat-polymersomes (Figure 7A). Mature DCs treated with Tat-conjugated NIR emissive polymersomes, however, stimulated a significantly lower level of T-cell proliferation relative to non-Tat-labeled polymersomes. Mature DCs treated with NIR polymersome lacking Tat showed a significant increase in T-cell proliferation. The factors contributing to the result with Tat−polymersomes remain unclear. For example, cell membrane associated polymersomes may sterically interfere with mature DC−T lymphocyte interactions, or a decrease in viable Tat−polymersome laden mature DCs over the course of the MLR assay could reduce the apparent stimulation capacity. Further investigation is merited to determine the cause for this weakened stimulation. Nonetheless, DCs labeled with Tat-conjugated NIR emissive polymersomes maintain the ability to stimulate T-cell proliferation. However, if the ultimate goal is to ensure T-cell proliferation, NIR-labeled polymersomes lacking Tat would be sufficient.

Cell Associated NIR Emissive Polymersome Stability. Effective cellular tracking requires that the probes remain associated with the cell of interest during longitudinal in vivo imaging. As such, we studied the stability of labeled cell fluorescence, for both iDCs and mDCs incubated with Tat-conjugated NIR emissive polymersomes, over the course of 3 days using flow cytometry. In Figure 8, the cellular geometric mean fluorescent intensity is plotted against time post removal of polymersome treatment (day 0). As expected, immature DCs take up a greater number of Tat-conjugated NIR emissive polymersomes per cell. This cellular fluorescence appears to initially decrease during the first 24-hour period following the wash but stabilizes by day 2. A similar profile is observed for mDCs labeled with Tat-conjugated NIR emissive polymersomes. In contrast, the fluorescence for DCs labeled with control NIR emissive polymersomes is stable. In examining the initial loss in DC-associated fluorescence during the first 24 h, we trypsinized a subpopulation of cells that had undergone each treatment condition in order to remove any surface associated polymersomes. These trypsinized cells displayed a fluorescent signal intensity equivalent to the stabilized levels observed for nontrypsinized cells. These results suggest that DC surface-associated polymersomes shed over time, while fully internalized polymersomes are stably incorporated over the course of 3 days. The percent of internalized polymersomes varied between

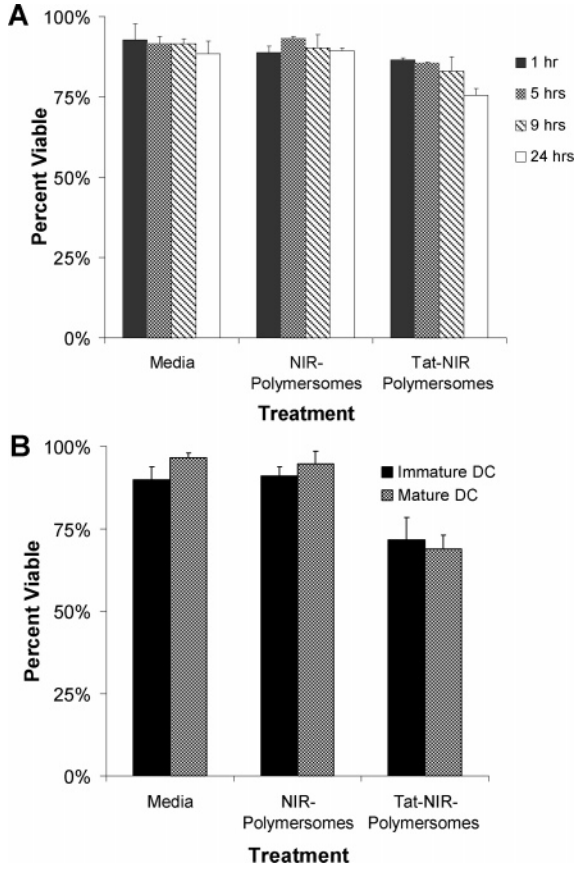


Figure 6. Cell viability as a function of treatment condition. (A) Immature DC labeled with NIR emissive polymersomes (100 μM polymer) for the indicated times. (B) DC treated for 24 h with NIR emissive polymersomes (200 μM polymer) either with or without maturation cytokines. Error bars indicate standard deviation.

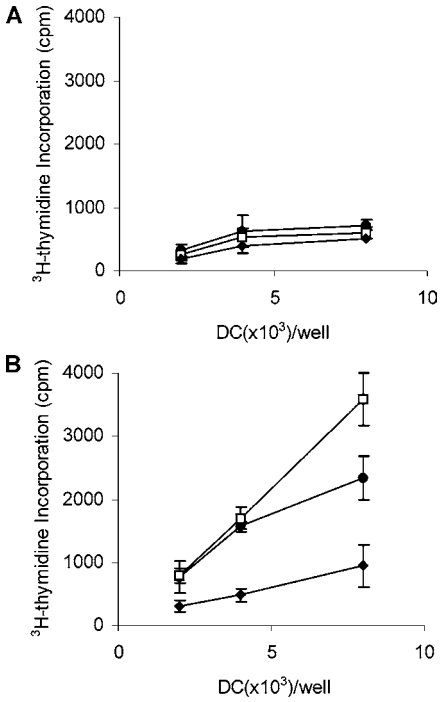


Figure 7. Representative result for mixed lymphocyte reaction (MLR). Relative T-cell proliferation (measured via ^{3}H-thymidine incorporation) is presented as a function of dendritic cell number for iDCs (A) or mDCs (B) and the following incubation treatments: (□) PBS, (●) control NIR emissive polymersomes, (◆) Tat-conjugated NIR emissive polymersomes. Error bars indicate the standard deviation of triplicate wells.

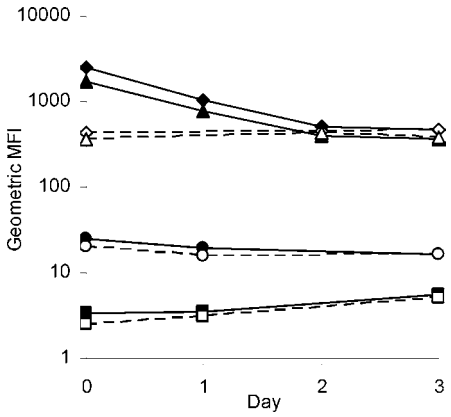


Figure 8. Geometric mean fluorescence intensity (MFI) of labeled DCs following an overnight incubation and removal of extracellular polymersomes on day 0. Cells were washed each day with subpopulations collected for analysis. Surface associated polymersomes were either undisturbed (solid line) or removed by trypsinization (dotted line). Treatment conditions include (◆) Tat-conjugated NIR emissive polymersomes, (▲) Tat-conjugated NIR emissive polymersomes + maturation cytokines, (●) control NIR emissive polymersomes, and (■) PBS control. The corresponding open circles indicate trypsinized cells from the same treatment group.

experiments with a range of 15−50% of the cell associated polymersomes. The inconsistency is likely due to Tat NIR polymersome and cell donor batch to batch variability.

In Vitro Optical Imaging of Labeled Dendritic Cells. Ultimately, in vivo fluorescence-based imaging of labeled DCs is expected to depend on the extent of NIR emissive polymersome uptake, the cellular density at a particular location, and the tissue depth of the labeled cells. In preparation for such studies, we sought to investigate, in vitro, the cell number and maturation state dependence of DCs labeled with **PZn$_3$**-based NIR emissive polymersomes. The NIR excitation and emission wavelength maxima for **PZn$_3$** make it an optimal molecular probe for in vivo optical imaging (*17*, *18*, *20*). A representative image of plated cells is presented in Figure 9A. A population of 5000 labeled DC is visible in a single well. Assuming that these cells are evenly distributed within the well, we estimate the lower limit for detection as ∼150 cells/mm^2. A calibration of the number of NIR fluorophores versus total photon counts per well (Figure 9B) enables estimation of the amount of fluorophore associated with each cell population, and ultimately a number of polymersomes per cell (see Experimental Procedures). A single immature DC can be effectively labeled with 0.7 ± 0.1 fmol of NIRF, equivalent to 70 000 ± 10 000 polymersomes/DC. The number of polymersomes per cell as a function of maturation state and treatment is presented in Figure 9C. Again, the extent of NIR emissive polymersome uptake is strongly dependent upon Tat conjugation, with iDCs taking up the greatest numbers of polymersomes.

Since both EOIS imaging and flow cytometry measure the fluorescence per cell, we compared results from each of these assays by normalizing individual values with the maximum fluorescence signal intensity observed in each method. These results are presented in Table 1 and show that the independent assays are in close agreement. In both assays, the extent of labeling is greatest for iDCs labeled with Tat-conjugated NIR emissive polymersomes followed closely by mDCs labeled with the same treatment. Cellular labeling levels in the absence of Tat are an order of magnitude lower. The corroboration of both the NIR imaging and flow cytometry-based assays shows the reliability of our imaging methods.

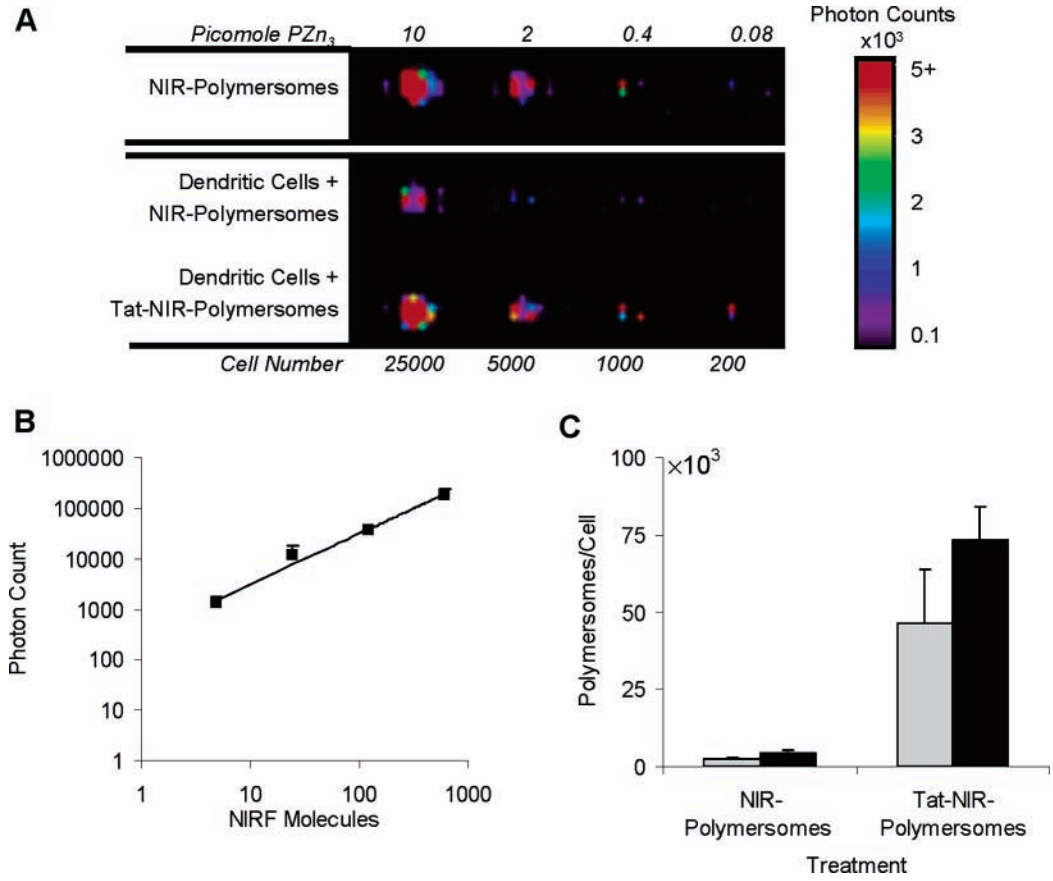


Figure 9. (A) Representative EOIS image of 96-well plate with 5-fold serial dilutions of immature DCs and control polymersomes. (B) Fluorescence calibration with total photon counts versus the number of fluorophore molecules (**PZn_3**) per well ($n = 4$). Error bars indicate standard deviation, linear fit $R^2 = 0.99$. (C) The calculated number of polymersomes per cell as a function of cellular treatment condition. Error bars represent standard deviation.

Table 1. Comparison of Fluorescence per Cell Value Generated from EOIS Image or Flow Cytometry Analysis

	normalized fluorescence/cell	
	NIR polymersomes	Tat NIR polymersomes
	EOIS[a]	
immature DC	0.06 ± 0.01	1.00 ± 0.14
mature DC	0.03 ± 0.01	0.63 ± 0.23
	Flow Cytometry[b]	
immature DC	0.06	1.00
mature DC	0.06	0.66

[a] Normalized average photon counts per cell (mean ± SD). [b] Normalized geometric mean fluorescence of 10 000 events.

CONCLUSIONS

This study demonstrates that NIR emissive polymersomes are promising reagents for cellular tracking. Intracellular delivery of these agents was significantly enhanced by conjugation to the Tat peptide. Upon incubation of the Tat-coupled NIR emissive polymersome with dendritic cells, it was found that DC uptake of the probes was predictably saturated after reasonable incubation times or high concentrations. Maximum polymersome uptake was achieved in immature DCs incubated with Tat-coupled NIR emissive polymersome at a 400 μM concentration of polymer for >10 h. In addition, we established that neither control nor Tat-conjugated NIR emissive polymersomes interfere with DC maturation and that Tat NIR polymersome uptake only modestly affects DC viability but significantly affects T-cell stimulation. Fully internalized vesicles were found to localize in endocytic compartments and remain associated with the cell for at least 3 days. Upon in vitro imaging of the labeled DCs a lower detection limit of approximately 5000 cells per well, or ~150 DC/mm^2, was established.

In addition to incorporating porphyrin-based NIRFs in their thick hydrophobic membranes, polymersomes can encapsulate a range of molecules including doxorubicin (*51*, *54*), high molecular weight dextrans (*25*), and hemoglobin (*52*) within their internal aqueous cavities. While the unmodified PEO surfaces of the polymersomes are immunologically invisible (*19*), it might be possible to build in antigenic features. For dendritic cell applications, polymersomes could potentially encapsulate antigens or cytokine cocktails thereby serving simultaneously as an antigen and contrast agent delivery vehicle. It is interesting to note that liposome-based antigen delivery is more immunogenic than antigen alone. This effect is attributed to the particulate nature of liposomes which more closely mimic the uptake of viruses or bacteria (*53*). It is possible that polymersomes would possess this adjuvant quality as well.

While PEO-PBD is a biocompatible polymer, it is unlikely that it will be implemented clinically. Fully biodegradable polymersomes, however, have also been developed using polyethyleneglycol-*block*-polycaprolactone (PEO-PCL) as the constituted vesicle forming material (*54*). These acid-labile vesicles would potentially enable endocytic escape and cytoplasmic delivery of the encapsulated reagents that would be advantageous for cross-presentation of peptide via both MHC I and MHC II antigen presenting molecules. In addition, exchanging the functional moiety on the polymersome surface for a dendritic cell targeting peptide could allow in situ delivery of antigen and NIRF. McGuire et al. isolated a targeting peptide (TPXS52.1) from a peptide library designed to target Langerhans cells (LCs), the DC variant found in skin (*55*). When presented on the surface of liposomes, this peptide was able to target LCs

in vivo. In situ DC delivery is attractive because it reduces the high cost of ex vivo cell culture for each patient.

In conclusion, the results of the current study clearly establish NIR emissive polymersomes as useful cell tracking reagents for future small animal studies. Further, the use of degradable polymersomes or DC targeting peptides may generate multifunctional polymersomes suitable for clinical applications.

ACKNOWLEDGMENT

This work was supported by NSF GRF, MRSEC DMR05-20020, NIH EB003457-01, and NIH R01CA105216. Imaging was performed at the Bioluminescence Molecular Imaging Core facility at the University of Pennsylvania (supported in part by NIH Grant CA 105008).

LITERATURE CITED

(1) Granucci, F., Foti, M., and Ricciardi-Castagnoli, P. (2005) Dendritic cell biology. *Adv Immunol. 88*, 193−233.

(2) Steinman, R. M. (1991) The dendritic cell system and its role in immunogenicity. *Annu. Rev. Immunol. 9*, 271−296.

(3) Steinman, R. M. (2001) Dendritic cells and the control of immunity: enhancing the efficiency of antigen presentation. *Mt. Sinai J. Med. 68*, 160−166.

(4) Zitvogel, L. (2002) Dendritic and natural killer cells cooperate in the control/switch of innate immunity. *J. Exp. Med. 195*, F9−14.

(5) Henri, S., Vremec, D., Kamath, A., Waithman, J., Williams, S., Benoist, C., Burnham, K., Saeland, S., Handman, E., and Shortman, K. (2001) The dendritic cell populations of mouse lymph nodes. *J. Immunol. 167*, 741−748.

(6) de Vries, I. J. M., Lesterhuis, W. J., Scharenborg, N. M., Engelen, L. P. H., Ruiter, D. J., Gerritsen, M. J. P., Croockewit, S., Britten, C. M., Torensma, R., Adema, G. J., Figdor, C. G., and Punt, C. J. A. (2003) Maturation of dendritic cells is a prerequisite for inducing immune responses in advanced melanoma patients. *Clin. Cancer Res. 9*, 5091−5100.

(7) Schuler-Thurner, B., Schultz, E. S., Berger, T. G., Weinlich, G., Ebner, S., Woerl, P., Bender, A., Feuerstein, B., Fritsch, P. O., Romani, N., and Schuler, G. (2003) Rapid induction of tumor-specific type 1 T helper cells in metastatic melanoma patients by vaccination with mature, cryopreserved, peptide-loaded monocyte-derived dendritic cells (vol 195, pg 1279, 2002). *J. Exp. Med. 197*, 395−395.

(8) Mackensen, A., Herbst, B., Chen, J. L., Kohler, G., Noppen, C., Herr, W., Spagnoli, G. C., Cerundolo, V., and Lindemann, A. (2000) Phase I study in melanoma patients of a vaccine with peptide-pulsed dendritic cells generated in vitro from CD34(+) hematopoietic progenitor cells. *Int. J. Cancer 86*, 385−392.

(9) Nestle, F. O., Alijagic, S., Gilliet, M., Sun, Y. S., Grabbe, S., Dummer, R., Burg, G., and Schadendorf, D. (1998) Vaccination of melanoma patients with peptide- or tumor lysate-pulsed dendritic cells. *Nat. Med. 4*, 328−332.

(10) Turtle, C. J., and DN, H. (2004) Dendritic cells in tumor immunology and immunotherapy. *Curr. Drug Targets 5*, 17−39.

(11) Figdor, C. G., de Vries, I. J. M., Lesterhuis, W. J., and Melief, C. J. M. (2004) Dendritic cell immunotherapy: mapping the way. *Nat. Med. 10*, 475−480.

(12) Hart, D. N. (2001) Dendritic cells and their emerging clinical applications. *Pathology 33*, 479−492.

(13) de Vries, I. J. M., Lesterhuis, W. J., Barentsz, J. O., Verdijk, P., van Krieken, J. H., Boerman, O. C., Oyen, W. J. G., Bonenkamp, J. J., Boezeman, J. B., Adema, G. J., Bulte, J. W. M., Scheenen, T. W. J., Punt, C. J. A., Heerschap, A., and Figdor, C. G. (2005) Magnetic resonance tracking of dendritic cells in melanoma patients for monitoring of cellular therapy. *Nat. Biotechnol. 23*, 1407−1413.

(14) Ahrens, E. T., Flores, R., Xu, H. Y., and Morel, P. A. (2005) In vivo imaging platform for tracking immunotherapeutic cells. *Nat. Biotechnol. 23*, 983−987.

(15) Sokolov, K., Aaron, J., Hsu, B., Nida, D., Gillenwater, A., Follen, M., MacAulay, C., Adler-Storthz, K., Korgel, B., Descour, M., Pasqualini, R., Arap, W., Lam, W., and Richards-Kortum, R. (2003) Optical systems for in vivo molecular imaging of cancer. *Technol. Cancer Res. Treat. 2*, 491−504.

(16) Weissleder, R., and Mahmood, U. (2001) Molecular imaging. *Radiology 219*, 316−333.

(17) Ghoroghchian, P. P., Frail, P. R., Susumu, K., Blessington, D., Brannan, A. K., Bates, F. S., Chance, B., Hammer, D. A., and Therien, M. J. (2005) Near-infrared-emissive polymersomes: Self-assembled soft matter for in vivo optical imaging. *Proc. Natl. Acad. Sci. U.S.A. 102*, 2922−2927.

(18) Ghoroghchian, P. P., Frail, P. R., Susumu, K., Park, T. H., Wu, S. P., Uyeda, H. T., Hammer, D. A., and Therien, M. J. (2005) Broad spectral domain fluorescence wavelength modulation of visible and near-infrared emissive polymersomes. *J. Am. Chem. Soc. 127*, 15388−15390.

(19) Photos, P. J., Bacakova, L., Discher, B., Bates, F. S., and Discher, D. E. (2003) Polymer vesicles in vivo: correlations with PEG molecular weight. *J Controlled Release 90*, 323−334.

(20) Wu, S. P., Lee, I., Ghoroghchian, P. P., Frail, P. R., Zheng, G., Glickson, J. D., and Therien, M. J. (2005) Near-infrared optical imaging of B16 melanoma cells via low-density lipoprotein-mediated uptake and delivery of high emission dipole strength tris[(porphinato)zinc(II)] fluorophores. *Bioconjugate Chem. 16*, 542−550.

(21) Rubtsov, I. V., Susumu, K., Rubtsov, G. I., and Therien, M. J. (2003) Ultrafast singlet excited-state polarization in electronically asymmetric ethyne-bridged bis[(porphinato)zinc(II)] complexes. *J. Am. Chem. Soc. 125*, 2687−2696.

(22) Susumu, K., and Therien, M. J. (2002) Decoupling optical and potentiometric band gaps in pi-conjugated materials. *J. Am. Chem. Soc. 124*, 8550−8552.

(23) Lin, V. S. Y., and Therien, M. J. (1995) The role of porphyrin-to-porphyrin linkage topology in the extensive modulation of the absorptive and emissive properties of a series of ethynyl- and butadiynyl-bridged bis- and tris(porphinato)zinc chromophores. *Chem.—Eur. J. 1*, 645−651.

(24) Lin, V. S. Y., Dimagno, S. G., and Therien, M. J. (1994) Highly Conjugated, Acetylenyl Bridged Porphyrins—New Models For Light-Harvesting Antenna Systems. *Science 264*, 1105−1111.

(25) Discher, B. M., Won, Y. Y., Ege, D. S., Lee, J. C. M., Bates, F. S., Discher, D. E., and Hammer, D. A. (1999) Polymersomes: Tough vesicles made from diblock copolymers. *Science 284*, 1143−1146.

(26) Lin, J. J., Silas, J. A., Bermudez, H., Milam, V. T., Bates, F. S., and Hammer, D. A. (2004) The effect of polymer chain length and surface density on the adhesiveness of functionalized polymersomes. *Langmuir 20*, 5493−5500.

(27) Gupta, B., Levchenko, T. S., and Torchilin, V. P. (2005) Intracellular delivery of large molecules and small particles by cell-penetrating proteins and peptides. *Adv. Drug Delivery Rev. 57*, 637−651.

(28) Kircher, M. F., Allport, J. R., Zhao, M., Josephson, L., Lichtman, A. H., and Weissleder, R. (2002) Intracellular magnetic labeling with CLIO-Tat for efficient in vivo tracking of cytotoxic T cells by MR imaging. *Radiology 225*, 453−453.

(29) Levchenko, T. S., Rammohan, R., Volodina, N., and Torchilin, V. P. (2003) In *Liposomes*, Part B, pp 339−349, Academic Press Inc., San Diego.

(30) Lewin, M., Carlesso, N., Tung, C. H., Tang, X. W., Cory, D., Scadden, D. T., and Weissleder, R. (2000) Tat peptide-derivatized magnetic nanoparticles allow in vivo tracking and recovery of progenitor cells. *Nat. Biotechnol. 18*, 410−414.

(31) Torchilin, V. P. (2002) TAT peptide-modified liposomes for intracellular delivery of drugs and DNA. *Cell. Mol. Biol. Lett 7*, 265−267.

(32) Torchilin, V. P., and Levchenko, T. S. (2003) TAT-liposomes: A novel intracellular drug carrier. *Curr. Protein Pept. Sci. 4*, 133−140.

(33) Vives, E. (2003) Cellular uptake of the Tat peptide: an endocytosis mechanism following ionic interactions. *J. Mol. Recognit. 16*, 265−271.

(34) Vives, E., Richard, J. P., Rispal, C., and Lebleu, B. (2003) TAT peptide internalization: Seeking the mechanism of entry. *Curr. Protein Pept. Sci. 4*, 125−132.

(35) de la Fuente, J., and Berry, C. (2005) Tat Peptide as an Efficient Molecule To Translocate Gold Nanoparticles into the Cell Nucleus. *Bioconjugate Chem. 16*, 1176−1180.

(36) Miron, T., and Wilchek, M. (1993) A simplified method for the preparation of succinimidyl carbonate polyethylene glycol for coupling to proteins. *Bioconjugate Chem 4*, 568−569.
(37) Ghoroghchian, P. P., Lin, J. J., Brannan, A. K., Frail, P. R.; Bates, F. S., Therien, M. J., and Hammer, D. A. (2006) Quantitative membrane loading of polymer vesicles. *Soft Matter 2*, 973−980.
(38) Bellare, J. R., Davis, H. T., Scriven, L. E., and Talmon, Y. (1988) *Electron Microsc. Tech. 10*, 87−111.
(39) Levine, B. L., Bernstein, W. B., Connors, M., Craighead, N., Lindsten, T., Thompson, C. B., and June, C. H. (1997) Effects of CD28 costimulation on long-term proliferation of CD4(+) T cells in the absence of exogenous feeder cells. *J. Immunol. 159*, 5921−5930.
(40) Green, I., Christison, R., Voyce, C. J., Bundell, K. R., and Lindsay, M. A. (2003) Protein transduction domains: are they delivering? *Trends Pharmacol. Sci. 24*, 213−215.
(41) Richard, J. P., Melikov, K., Vives, E., Ramos, C., Verbeure, B., Gait, M. J., Chernomordik, L. V., and Lebleu, B. (2003) Cell-penetrating peptides−A reevaluation of the mechanism of cellular uptake. *J. Biol. Chem. 278*, 585−590.
(42) Vives, E. (2005) Present and future of cell-penetrating peptide mediated delivery systems: "Is the Trojan horse too wild to go only to Troy?" *J. Controlled Release 109*, 77−85.
(43) Ferrari, A., Pellegrini, V., Arcangeli, C., Fittipaldi, A., Giacca, M., and Beltram, F. (2003) Caveolae-mediated internalization of extracellular HIV-1 tat fusion proteins visualized in real time. *Mol. Ther. 8*, 284−294.
(44) Sandgren, S., Cheng, F., and Belting, M. (2002) Nuclear targeting of macromolecular polyanions by an HIV-Tat derived peptide−Role for cell-surface proteoglycans. *J. Biol. Chem. 277*, 38877−38883.
(45) Syme, R., and Gluck, S. (2001) Generation of dendritic cells: role of cytokines and potential clinical applications. *Transfus. Apheresis Sci. 24*, 117−124.
(46) Jonuleit, H., Kuhn, U., Muller, G., Steinbrink, K., Paragnik, L., Schmitt, E., Knop, J., and Enk, A. H. (1997) Pro-inflammatory cytokines and prostaglandins induce maturation of potent immunostimulatory dendritic cells under fetal calf serum-free conditions. *Eur. J. Immunol. 27*, 3135−3142.
(47) Morse, M., Zhou, L. J., Tedder, T., Lyerly, H. K., and Smith, C. (1995) CD83 is a marker for mature dendritic cells (DC) generated from peripheral blood mononuclear cells (PBMC). *Blood 86*, 1279−1279.
(48) Jones, S. W., Christison, R., Bundell, K., Voyce, C. J., Brockbank, S. M. V., Newham, P., and Lindsay, M. A. (2005) Characterisation of cell-penetrating peptide-mediated peptide delivery. *Br. J. Pharmacol. 145*, 1093−1102.
(49) Kuntz, M. M., I. J. B., Weksler, M. E. (1976) Lymphocyte transformation induced by autologous cells, IV. Human T-lymphocyte proliferation induced by autologous or allogeneic non-T lymphocytes. *J. Exp. Med. 143*, 1042.
(50) Opelz, G., K. M., Takasugi, M., Terasaki, P. I. (1976) Autologous stimulation of human lymphocyte subpopulations. *J. Exp. Med. 142*, 1327.
(51) Ahmed, F., and Discher, D. E. (2004) Self-porating polymersomes of PEG-PLA and PEG-PCL: hydrolysis-triggered controlled release vesicles. *J. Controlled Release 96*, 37−53.
(52) Arifin, D. R., and Palmer, A. F. (2005) Polymersome encapsulated hemoglobin: A novel type of oxygen carrier. *Biomacromolecules 6*, 2172−2181.
(53) Brewer, J. M., Pollock, K. G. J., Tetley, L., and Russell, D. G. (2004) Vesicle size influences the trafficking, processing, and presentation of antigens in lipid vesicles. *J. Immunol. 173*, 6143−6150.
(54) Ghoroghchian, P. P., Li, G. Z., Levine, D. H., Davis, K. P., Bates, F. S., Hammer, D. A., and Therien, M. J. (2006) Bioresorbable vesicles formed through spontaneous self-assembly of amphiphilic poly(ethylene oxide)-block-polycaprolactone. *Macromolecules 39*, 1673−1675.
(55) McGuire, M. J., Sykes, K. F., Samli, K. N., Timares, L., Barry, M. A., Stemke-Hale, K., Tagliaferri, F., Logan, M., Jansa, K., Takashima, A., Brown, K. C., and Johnston, S. A. (2004) A library-selected, Langerhans cell-targeting peptide enhances an immune response. *DNA Cell Biol. 23*, 742−752.

BC0601267

Tumor Cell Targeting of Transferrin−PEG−TNF-α Conjugate via a Receptor-Mediated Delivery System: Design, Synthesis, and Biological Evaluation

Yan-Yan Jiang, Chen Liu, Ming-Huang Hong, Sai-Jie Zhu, and Yuan-Ying Pei*

Department of Pharmaceutics, School of Pharmacy, Fudan University, Shanghai, China, 200032. Received May 25, 2006; Revised Manuscript Received October 9, 2006

PEGylation is a procedure of growing interest for enhancing the therapeutic and biotechnological potential of peptides and proteins. Transferrin (Tf) has been proposed to be useful for targeting cancer cells. The aim of this study was to modify PEGylated recombinant human tumor necrosis factor alpha (PEG−TNF-α) with Tf to form Tf−PEG−TNF-α conjugates, which would maintain the advantages of PEGylation and also achieve the function of active targeting to tumor cells. In PEGylation reactions with 5-, 20-, 40-, and 60-fold molar excess of 3.4 kDa *N*-hydroxysuccinimide-PEG-maleimide (PT1, PT2, PT3, and PT4, respectively), PEG−TNF-α conjugates with different PEG chains were synthesized. A perfusion chromatography technique using a cation-exchange column was introduced to purify PEG−TNF-α conjugates. PT4 with about five PEG chains was selected as a lead candidate due to highest extent of PEGylation and maximum reaction yield. Thiolated Tf was conjugated to the maleimide group at the distal end of the PEG chains on the PEG−TNF-α conjugates, with the resulting Tf−PEG−TNF-α conjugates after purification containing approximately one Tf ligand on one TNF-α molecule. The conjugate of Tf and PT4 (TPT4) was selected to assess the specificity and affinity to transferrin receptor (TfR) on two kinds of tumor cells, K562 and KB. Both the receptor binding assays and the competition experiments were performed using radioligand binding analysis. The results demonstrated that TPT4 as well as Tf bound specifically to the TfR on the tumor cell surface and the affinity of the conjugate to TfR was similar to that of native Tf. In contrast, PEG−TNF-α demonstrated no specificity. The biodistribution and antitumor effects were investigated in S-180 tumor-bearing mice. It was found that TPT4 could markedly alter in vivo behavioral characteristics of TNF-α. Compared with TNF-α and PT4, extravasated TPT4 in tumor tissues exhibited a significantly delayed blood clearance and the highest intratumoral TNF-α levels. Furthermore, the inhibitory rate of tumor of TPT4 enhanced 5.3- and 1.8-fold over that of TNF-α and PT4, indicating that TPT4 exhibited the highest antitumor activity. These results suggested that Tf−PEG−TNF-α was a useful long circulating conjugate with the capabilities of specific receptor binding resulting in enhanced antitumor activity of TNF-α.

INTRODUCTION

Tumor necrosis factor alpha (TNF-α), an antitumor cytokine, has numerous bioactivities such as direct cytotoxicity against various tumor cells, activation of immune antitumor response, and selective impairment of tumor vascular endothelial cells (*1*). However, very high doses of TNF-α as a systemic antitumor agent were required to obtain the sufficient clinical potency, since TNF-α can be rapidly cleared from the blood and is widely distributed to various tissues. As a result, TNF-α exhibits severe toxic side effects to patients (*2*, *3*). These drawbacks are also found in the clinical applications of other bioactive proteins (*4*).

An approach that may solve these problems is the use of polyethylene glycol (PEG)-conjugated proteins (*5*). Our previous studies have shown that PEGylated TNF-α was more effective than its corresponding unmodified parent molecule while the accumulated level of PEG−TNF-α in the tumor was not significantly higher than that in normal organs including liver, spleen, lung, and kidney (*6*, *7*). This phenomenon may be due to the passive and nonspecific process of PEG−TNF-α extravasation, which is improved by the prolonged residence time of the protein in circulation and repeated passages through the tumor microvascular bed.

To improve this nonspecific targeting of PEGylation, ligand−receptor-mediated delivery systems to cell surface receptors (*8*, *9*) is a potentially desirable approach to treat diseased but spare healthy cells. Transferrin (Tf) holds promise as a targeting agent because of the larger number of transferrin receptors (TfRs) on the surface of tumor cells (*10*). Tf is potentially important as a targeting ligand to deliver a wide range of drugs, including anticancer drugs, peptides, proteins, and even genes, into malignant cells that overexpress TfRs (*11*−*16*). In the current report, a targeting TNF-α delivery system was devised. Thiolated Tf was bound to the maleimide group at the distal end of PEG−TNF-α to form a Tf−PEG−TNF-α conjugate. The binding of the Tf conjugate to TfR on K562 and KB cells was performed by using radioligand binding analysis. The specificity and affinity of the conjugate for TfR were assessed and compared with native Tf. Aiming at expanding the application of TNF-α, ^{125}I-labeled Tf−PEG−TNF-α was prepared, and tumor localization in S-180 tumor-bearing mice after intravenous injection was compared with those of ^{125}I-labeled TNF-α and PEG−TNF-α, respectively. On the basis of the findings in biodistribution studies, the antitumor effect of Tf−PEG−TNF-α was investigated and compared with free TNF-α and PEG−TNF-α on S-180 tumor-bearing mice. The results of this study will provide fundamental information enabling us to design useful Tf−PEG−TNF-α conjugate with the double effect from passive and active mechanisms.

EXPERIMENTAL PROCEDURES

Reagents and Assays. Recombinant human tumor necrosis factor-α (TNF-α, MW 17 kDa, IP = 8.0) was obtained from

* Author for correspondence. Yan-Ying Pei, 138 Yi Xue Yuan Rd, Shanghai 200032, China, Tel.: +86-21-54237186, Fax: +86-21-54237186, E-mail: yypei@shmu.edu.cn.

10.1021/bc060135f CCC: $37.00 © 2007 American Chemical Society
Published on Web 11/23/2006

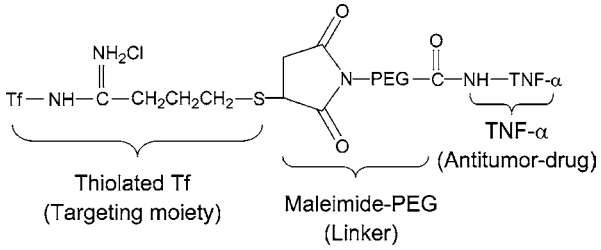


Figure 1. Design of Tf−PEG−TNF-α conjugate.

Department of Neurobiology, Second Military Medical University (Shanghai, China). *N*-hydroxysuccinimide-PEG-maleimide (NHS-PEG-MAL; MW 3.4 kDa) was from Nektar Therapeutics (San Carlos, CA). The concentration of TNF-α was estimated using bovine serum albumin as a standard using the Bradford dye assay (*17*), and the average number of PEG molecules on the conjugate was determined by spectrophotometric analysis (*18*). Human transferrin (iron-free, Tf) with MW 76−81 kDa was purchased from Sigma (St. Louis, MO) and modified with 2-iminothiolane (Traut's Reagent from Sigma). The amount of free mercapto groups was determined using the Ellman assay at 412 nm (*19*) using 5,5′-dithiobis(2-nitrobenzoic acid) (Sigma). HiTrap Desalting and HiPrep 16/60 Sephacryl S-200HR prepacked gel filtration columns for protein purification and separation were obtained from Amersham Biosciences (Stockholm, Sweden). $Na^{125}I$ was purchased from Sigma. Other reagents and solvents were of analytical grade. The specific radioactivity of the radiocompound was assessed in an autogamma instrument (Packard Instruments, CT). The radiochemical purity was determined using thin-layer chromatography.

Radiolabeling of Proteins. The Tf and purified PEG−TNF-α were labeled with ^{125}I using a protocol based on the use of Iodogen for the following experiments. Briefly, human Tf (300 μg) in 30 μL of PB (0.1 M potassium phosphate buffer, pH 7.2) was layered over a freshly prepared film of Iodogen (100 μg) and incubated for 8 min at 4 °C in presence of 0.5 mCi of $Na^{125}I$. PEG−TNF-α (100 μg based on TNF-α) in 90 μL of PB was iodinated with 3 mCi of $Na^{125}I$ accordingly. The reaction mixtures were brought up to 0.1 mL volume with PBS, and the unbound ^{125}I was removed by gel filtration chromatography on a Sephadex G-25 PD 10 column equilibrated with HB (30 mM HEPES, pH 8.5) for ^{125}I-Tf and HBS (20 mM HEPES with 150 mM NaCl, pH 7.1) for PEG−^{125}I−TNF-α (^{125}I-PT), respectively. The specific activity of ^{125}I-Tf was approximately 92 kCi/mol, and that of PEG−^{125}I−TNF-α was 87 kCi/mol. Both radiocompounds were obtained in 95% yield with a radiochemical purity higher than 99%.

Design and Synthesis of Tf−PEG−TNF-α Conjugate. The design of the conjugate is shown in Figure 1. TNF-α, the antitumor protein, was modified with 3.4 kDa PEG via an amide bond. The other end of PEG is linked to Tf, the targeting moiety.

The conjugate was synthesized in three steps. Step 1: PEGylation of TNF-α (PEG−TNF-α) using the NHS group of the NHS−PEG-maleimide. Step 2: Thiolation of Tf (Tf−SH). Step 3: Conjugation of Tf−SH to PEG−TNF-α utilizing the maleimide group of the PEG−TNF-α conjugate. The PEGylation reaction mixtures contained TNF-α (23.5 nmol, 0.40 mg/mL) and NHS−PEG−MAL reagent at a 1:5, 1:20, 1:40, and 1:60 molar ratios in 1 mL of 15 mM HEPES pH 8.0, for samples PT1, PT2, PT3, and PT4, respectively. The reactions were carried out at 4 °C for 0.25, 0.5, 1.0, 1.5, and 2.0 h, respectively. SDS-PAGE of the PEG−TNF-α mixture using 14% polyacrylamide on a Mini-PROTEIN III cell system (Bio-Rad, Hercules, CA) was carried out as described (*20*). TNF-α, as a control protein, and the PEG−TNF-α mixture equivalent to 26.7 μg of protein were run on the gels. Gel-separated proteins were stained with Coomassie brilliant blue R250. The molecular weights of the conjugated and unconjugated proteins were estimated relative to molecular weight markers.

The ImageMaster VDS-CL system (Amersham Pharmacia Biotech, Sweden) was used for acquisition of the digital image from the SDS-PAGE gels using the white light tray. Image data was imported into a PC using the Image Capture Kit and ImageMaster VDS Software. The integrated optical densities (IOD) were determined for the full width of each protein band. The amount of unconjugated protein in each gel was estimated by contrasting the IOD value with that of the control protein band. The percentage of PEGylated protein (*P*%) was calculated by the formula

$$P\% = \frac{\mathrm{IOD_c} - \mathrm{IOD_u}}{\mathrm{IOD_c}} \times 100\%$$

where IOD_c and IOD_u represent the IOD values of control protein and the remaining unconjugated protein, respectively.

Purification of PEG−TNF-α conjugates for the reaction products at 1 h was carried out by cation-exchange perfusion chromatography. The entire mixture was subjected to semi-preparative HPLC (BioCAD 700E, Applied Biosystems) using a POROS 20 HS column (20 μm, 100 × 4.6 mm i.d., 1.66 mL). The flow rate was 1.5 mL/min, with the mobile phase starting from 50% deionized water and 50% solvent A (5 mM NaH_2PO_4−Na_2HPO_4, pH 6.8) (0−2 min) to 50% solvent A and 50% solvent B (3 M NaCl in solvent A) at 33 min. The absorbance of protein and MAL−PEG−NHS was detected at 280 nm. The reaction mixture was separated into three fractions (see Figure 4). To identify the components in the three fractions, PT1 was subject to electrophoresis using SDS-PAGE. Each fraction of PT1 at 1 h was collected and loaded on 14% SDS−polyacrylamide gels. The gels were stained with Coomassie brilliant blue (for protein) and with barium iodide solution (for PEG) (*21*).

The fraction of the PEG−TNF-α peak between 0.3 and 0.8 M NaCl was collected, the solution was concentrated, and the buffer replaced simultaneously with HBS using an Amicon Ultra-4 centrifugal filter device (cutoff 5 kDa, Millipore, Bedford, MA). The purified PEG−TNF-α conjugates in HBS (PT1−PT4) were collected, where the molar ratios of TNF-α/PEG were 1:1.9, 1:2.6, 1:3.7, and 1:4.8, respectively. The yields based on TNF-α were 18.9% (PT1), 50.4% (PT2), 60.8% (PT3), and 85.7% (PT4), respectively.

To determine the amount of Tf attached to PEG−TNF-α in the third step, Tf was radioiodinated as described above. The ^{125}I-Tf solution in HB was supplemented with unlabeled Tf to a concentration of 250 μM. A calibration curve of ^{125}I-Tf was constructed by a linear regression analysis between the measured cpm values and the known concentrations of ^{125}I-Tf.

A solution of 0.25 μmol of ^{125}I-Tf in 1.0 mL of HB was mixed under argon with a solution of 1.95 μmol of 2-iminothiolane in 150 μL of 15 mM HEPES (pH 8.5). After 3 h at room temperature, purification was performed by gel filtration (Hitrap desalting column) under argon with HBS, at a flow rate of 1.5 mL/min. 4.5 mL, containing the desalted protein, was collected and concentrated using an Amicon Ultra-4 centrifugal filter device (cutoff 10 kDa, Millipore). The resulting 2.5 mL of product (^{125}I-Tf-SH) contained 0.19 μmol of ^{125}I-Tf modified with 0.59 μmol of thiolane linker (molar ratio of 1:3.1). The ^{125}I-Tf-SH solution was mixed under argon with PEG−TNF-α in 1.5 mL of HBS, at a molar ratio of 1:1.2 (maleimide linker/SH group) and kept under argon for 24 h at 4 °C. The reaction mixture and ^{125}I-Tf-SH were loaded separately onto a column of Sephacryl S-200 HR (HiPrep 16/60). The elution of product was monitored by the absorbance at 280 nm and the radioactivity of the fractions. The ^{125}I-Tf−PEG−TNF-α fraction was collected and concentrated using a centrifugal filter device (cutoff

5 kDa, Millipore). The purified ^{125}I-Tf−PEG−TNF-α conjugates for the reactions between Tf-SH and PT1−PT4 had molar ratios of Tf/PEG/TNF-α of 0.8:1.9:1 (TPT1), 0.9:2.6:1 (TPT2), 0.9:3.7:1 (TPT3), and 1.1:4.8:1 (TPT4), respectively. The radiochemical purity of each conjugate was higher than 98%. The yields of TPT1, TPT2, TPT3, and TPT4 conjugates based on TNF-α were 38.6%, 40.1%, 42.3%, and 52.7%, respectively.

Cell Culture. The cell lines, including human erythroleukemia K562 cells, human epidermoid carcinoma KB cells, and normal human hepatocyte L02 cells, were purchased from the Institute of Biochemistry and Cell Biology, Shanghai Institutes for Biological Sciences, Chinese Academy of Sciences (Shanghai, China). Cells were grown in fresh RPMI-1640 (Gibco) medium supplemented with 10% (v/v) heat-inactivated fetal calf serum (FCS), 2 mM glutamine, and 0.1 mg/mL of both penicillin and streptomycin, at 37 °C in humidified air containing 5% CO_2. All experiments were performed on cells in the logarithmic phase of growth. For subculture, monolayer cells (KB cells and L02 cells) were dispersed with 0.25% trypsin plus 1 mM EDTA at 37 °C for 30 min. The cells were collected by centrifugation and resuspended in fresh medium. Cell growth did not show any appreciable change under all the experimental conditions. Cell viability was checked at the end of the treatments using the Trypan blue exclusion method and was found to be consistently >95%.

In order to wash out the endogenous Tf, the cells were washed twice with ice-cold RPMI-1640 medium supplemented with 1% bovine serum albumin (BSA/RPMI) before the experiments.

Receptor Binding. To assess the targeting potential of TNF-α conjugates, ^{125}I-PT4 was modified by Tf−SH using the same procedure as described above. After Tf−PEG−^{125}I−TNF-α (^{125}I-TPT4) was purified, iron incorporation into ^{125}I-TPT4, as well as into ^{125}I-Tf, was carried out by addition of 1.25 μL of 10 mM iron (III) citrate buffer (containing 200 mM citrate and adjusted to pH 7.8 with sodium bicarbonate) per milligram of transferrin. To remove the excess iron (III), the ^{125}I-Tf-Fe_2 or ^{125}I-TPT4-Fe_2 was treated with HBS in the centrifugal filter device (cutoff 10 kDa, Millipore) and centrifuged twice at 7000 × *g* at 4 °C for 10 min.

For binding assays, K562 cells (1.5×10^6), KB cells (2×10^6), and L02 cells (2×10^6) in 0.5 mL fresh BSA/RPMI were incubated at 4 °C for 2 h with 0.5 mL of ^{125}I-labeled ligands (0.31−59 nM based on Tf concentration) while shaking. After incubation, 1 mL of ice-cold BSA/RPMI medium was added to terminate the binding. The cells were then centrifuged at 4 °C for 10 min at 3000 × *g*. The radioactivity incorporated was counted in cellular pellet with a γ-counter after twice being washed in the same medium. To correct for nonspecific binding, control assays were performed in parallel by addition of a 100-fold molar excess of unlabeled Tf for 5 min before the addition of the radiolabeled ligand. Specific binding was calculated by subtracting nonspecific binding from total binding. The maximum number of binding sites per cell (B_{max}) and the apparent dissociation constant (K_d) were calculated using an iterative, nonlinear, least-squares curve fitting program (*GraphPad Prism 4.0*, GraphPad Software, San Diego, CA).

To assess the specific binding of TPT4 to TfR, competitive binding assays were performed: K562 cells (1.5×10^6 /mL in BSA/RPMI) were incubated at 4 °C for 2 h while shaking, with the addition of 3.1×10^{-9} M ^{125}I-Tf-Fe_2 and different concentrations (from 10^{-11} to 10^{-6} M) of unlabeled ligands (Tf-Fe_2, TPT4-Fe_2, or PT4). After centrifuging and washing, ^{125}I radioactivity was measured to obtain the specifically bound tracer activity (*B*) at each competitor concentration and the maximum binding, carried out without unlabeled competitor (B_0). The corresponding competition curves were obtained by plotting B/B_0 versus the log concentration of each competitor. The analysis of competition assays and the calculation of ED_{50} (effective dose) was performed using the *GraphPad Prism* program.

Tumor Models. Female Kunming strain mice (18−22 g) were supplied by Shanghai Experimental Animal Center, Chinese Academy of Sciences (Shanghai, China). The animals were acclimatized at a temperature of 25 ± 2 °C and a relative humidity of 70 ± 5% under natural light/dark conditions for one week before dosing. Sarcoma 180 (S-80) cells were collected from the Kunming mice which were transplanted with S180 cells in the intraperitoneal cavity. Mice at 6 weeks of age were injected subcutaneously in the right armpit with 10^6 S180 cells suspended in PBS. Tumors were permitted to reach 8−10 mm in diameter (7 d after implant) before initiation of the studies.

Biodistribution and Antitumor Effects in Mice. For biodistribution experiments, the S-180 tumor-bearing mice received ^{125}I-TNF-α, ^{125}I-PT4, and ^{125}I-TPT4. Each animal was given intravenously the dose of 0.4 μg TNF-α with a trace of ^{125}I (~5 μCi). Mice ($n = 5$ per time point) were sacrificed after defined time periods, and then tissues were collected, wet-weighed, and counted in a γ-counter.

In vivo anticancer activity was evaluated against S-180 solid tumors in mice. Five groups of mice ($n = 10$ per group) were used, and S-180 cells were implanted subcutaneously into the armpits of the mice. After 2 d, the mice were injected intravenously with saline, TNF-α, PT4, and TPT4 once every 2 days (8 times) for 16 days, respectively. Groups 1−2 (control groups) were treated with saline, and groups 3−5 (treatment groups) with TNF-α, PT4, and TPT4 at the dose of 0.67 μg per mouse. Tumor volumes (V_t = [major axis] × [minor axis]^2 × 1/2) were measured in two perpendicular directions every 2 days. The inhibitory rate of tumor (IR) was calculated using the following equation:

$$\mathrm{IR} = \frac{[(V_t \text{ of control group}) - (V_t \text{ of treatment group})]}{(V_t \text{ of control group})} \times 100\%$$

The experimental design of this study was approved by the appropriate ethical committee on animal study in Fudan University.

RESULTS

Characterization of PEGylated TNF-α. To assess the effect of the molar ratio of PEG on the degree of PEGylation of TNF-α, and to select an appropriate reaction time, the PEG−TNF-α conjugates produced under the different reaction conditions were analyzed by SDS-PAGE. SDS-PAGE profiles (Figure 2) show that the reaction mixtures contained different PEG−TNF-α conjugates along with some unconjugated TNF-α. The molecular weight (MW) of each band was estimated relative to molecular weight markers. The MW of unconjugated TNF-α was 16.9 kDa. The PEG−TNF-α was separated into three major bands, band A (24.1 kDa), B (30.9 kDa), and C (39.9 kDa). On the basis of the apparent MW of the PEGylated TNF-α conjugates on SDS-PAGE, we estimate that they contain over two, four, and six PEG molecules, respectively. The amount of conjugated protein increased significantly with an increase in the molar ratio of PEG to protein, since the band intensity of the unconjugated protein (band TNF in lanes 3−7) reduced as the PEG concentration was increased.

The level of the unconjugated protein in the SDS-PAGE gels was quantified using the ImageMaster VDS-CL system (Figure 3). The peak labeled TNF represents unconjugated TNF-α, while peaks A, B, and C refer to the major conjugated species. The IOD value of the unconjugated TNF-α (peak labeled TNF) was

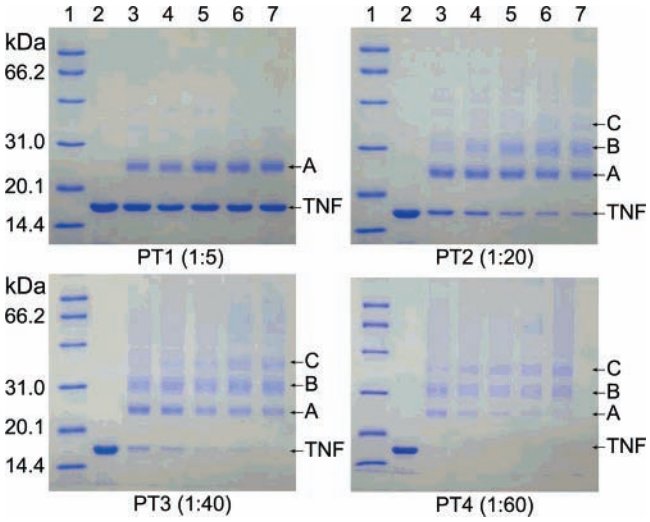


Figure 2. SDS-PAGE profiles of native (lane 2) and PEGylated TNF-α for different reaction times (0.25, 0.5, 1.0, 1.5, and 2.0 h on lanes 3−7, respectively). PEGylation of TNF-α was carried out using different molar ratios of TNF-α to PEG (PT1, 1:5; PT2, 1:20; PT3, 1:40; and PT4, 1:60 PEG/TNF-α, respectively). Molecular weight markers are shown in lane 1 on each gel. The various bands of PEGylated TNF-α are shown as A, B, and C.

determined, and the percentage of unconjugated protein (*P*%) calculated and used to indirectly represent the degree of PEGylated TNF-α. The *P*% values increased from about 20% for PT1 (1:5 TNF-α/PEG) to over 95% for PT4 (1:60 TNF-α/PEG), indicating that the degree of PEGylation increased with an increase in the molar ratio of NHS−PEG−MAL to TNF-α. Moreover, the *P*% values increased only slightly after 1.0 h of incubation, and we therefore chose this reaction time for the preparation of the PEG−TNF-α conjugates.

For purification of PEG−TNF-α, a perfusion chromatography technique was developed to separate the reaction products of TNF-α and NHS−PEG−MAL. Figure 4 shows that the crude reaction product was separated into three fractions (peaks Fr1, Fr2, and Fr3). Comparison to the chromatograms of NHS−PEG−MAL and TNF-α (Figure 4a,b) showed that the retention times of peak Fr1 and peak Fr3 were identical to those of NHS−PEG−MAL and TNF-α, respectively, while that of peak Fr2 was between those of peak Fr1 and peak Fr3. Presumably, the fractions of peaks Fr1, Fr2, and Fr3 were free NHS−PEG−MAL, PEG−TNF-α conjugates, and free TNF-α, respectively.

Identification of the components in the fractions was further confirmed by staining the gel after electrophoresis. Figure 5 shows that the staining was very selective and specific for PEG and protein. Only free or protein-bound PEG was stained by barium iodide solution. As shown in Figure 5A, the bands of the NHS−PEG−MAL standard (PEG), Fr1, and Fr2 were visible after barium iodide staining, and the mobility of Fr1 band was consistent with that of PEG band, whereas the Fr2 band had a lower mobility. The TNF-α standard (TNF) and the unconjugated protein (Fr3) were not stained with barium iodide (Figure 5A), but were with Coomassie blue (Figure 5B). Moreover, the band of Fr1 was not detected using Coomassie blue, while the components of Fr2 were stained and had a lower mobility than the TNF-α standard (Figure 5B). These results indicated that peaks Fr1, Fr2, and Fr3 correspond to the fractions of the excess free NHS−PEG−MAL, PEG−TNF-α, conjugates and free TNF-α, respectively.

Synthesis of Tf−PEG−TNF-α Conjugates. After the conjugation reactions of ^{125}I-Tf-SH to PT1−PT4, excess free ^{125}I-Tf-SH was removed by gel filtration using a Sephacryl S-200 HR column. The elution profiles of the reaction mixture of ^{125}I-Tf-SH and PT4 were monitored for absorbance at 280 nm and radioactivity. The ^{125}I-Tf−PEG−TNF-α conjugate was eluted first, followed by a separate peak corresponding to unreacted ^{125}I-Tf-SH. Additionally, no unreacted PEG−TNF-α was observed. All purified Tf−PEG−TNF-α conjugates contained approximately one Tf ligand per TNF-α molecule.

Specificity and Affinity of Tf−PEG−TNF-α for TfR. To compare the binding characteristics of Tf to the TfRs on the surface of normal and tumor cells, ligand binding assays were carried out at 4 °C. Assuming one type of binding site, the equilibrium binding of ^{125}I-Tf-Fe$_2$ to three kinds of cells resulted in a saturation isotherm, and Scatchard plots of the data gave a nonlinear regression line from which the values of K_d and B_{max} were calculated (Table 1).

The B_{max} of Tf on L02 cells was about 10-fold smaller than that on K562 cells and KB cells, while the apparent K_d values of Tf−receptor binding for L02 cells was approximately 4-fold higher than that for both tumor cell lines. These results indicate that both Tf receptor levels and Tf binding affinity on tumor cells were far higher than on the normal cells. Therefore, Tf was capable of binding to tumor cells more effectively than to normal cells, providing a useful targeting agent for antitumor drugs to tumor cell lines.

As shown in Table 1, the B_{max} values of ^{125}I-TPT4-Fe$_2$ on K562 cells and KB cells were slightly smaller than that of Tf-Fe$_2$ on the corresponding cells. The apparent K_d values of ^{125}I-TPT4-Fe$_2$ on both K562 cells and KB cells were similar to that of ^{125}I-Tf-Fe$_2$ on the corresponding cells. Additionally, it was found that the binding amount of PEG−TNF-α to both tumor cells was only 20% of that of Tf (data not shown). The above results suggest that Tf−PEG−TNF-α as well as native Tf was bound specifically, probably by TfR, while the binding of PEG−TNF-α to tumor cells may be nonspecific.

To determine the role of TfR in conjugate binding, competition experiments were conducted on K562 cells with varying amounts of unlabeled ligands (Tf-Fe$_2$, TPT4-Fe$_2$, or PT4) and a constant amount of ^{125}I-Tf-Fe$_2$. The monophasic nature of the inhibition curves (Figure 6) confirms a single population of binding sites. Competition curves showed similar decreases of ^{125}I-Tf-Fe$_2$ binding with increasing concentrations of either Tf-Fe$_2$ or TPT4-Fe$_2$. Using the *GraphPad Prism* program, ED_{50} values were calculated: 3.1 nM for Tf-Fe$_2$ and 5.4 nM for TPT4-Fe$_2$. The data showed that the inhibition of binding of ^{125}I-Tf-Fe$_2$ to the surface of K562 cells was dependent upon the concentration of Tf-Fe$_2$ and TPT4-Fe$_2$, indicating that the Tf conjugate and native Tf compete for the same receptor. This result was supported by the observation that the ligand−receptor interactions, Tf-Fe$_2$-TfR and TPT4-Fe$_2$-TfR, exhibited dissociation constants of the same order of magnitude. In contrast, when PT (10^{-11} to 10^{-6} M) was used as competitor, ^{125}I-Tf-Fe$_2$ binding did not change. As a result, the binding of TPT4-Fe$_2$ to TfRs is indeed receptor-specific, but PEGylated TNF-α (PT4) cannot specifically bind to TfR due to the absence of the corresponding Tf ligand.

In Vivo Evaluation. Since S-180 cells were one of the classical tumor models for a long time and their surface overexpress transferrin receptors (*22*), S-180 tumor-bearing mice were selected as animal models in this study. The distribution profiles of free drug and its conjugates in S-180 solid tumor-bearing mice after intravenous administration were shown in Figure 7. It was found that free TNF-α showed the lowest plasma levels as compared with TPT4 and PT4 at the same time points after dosing. Moreover, the plasma levels of free TNF-α were decreased by 36-fold from 0.25 h (539 cpm/mg) to 12 h (15 cpm/mg), indicating that free drug was quickly removed from the circulating system. In contrast, TPT4 and PT4 exhibited a significantly delayed blood clearance, and the plasma levels were decreased by 4.5-fold for TPT4 (from 1134

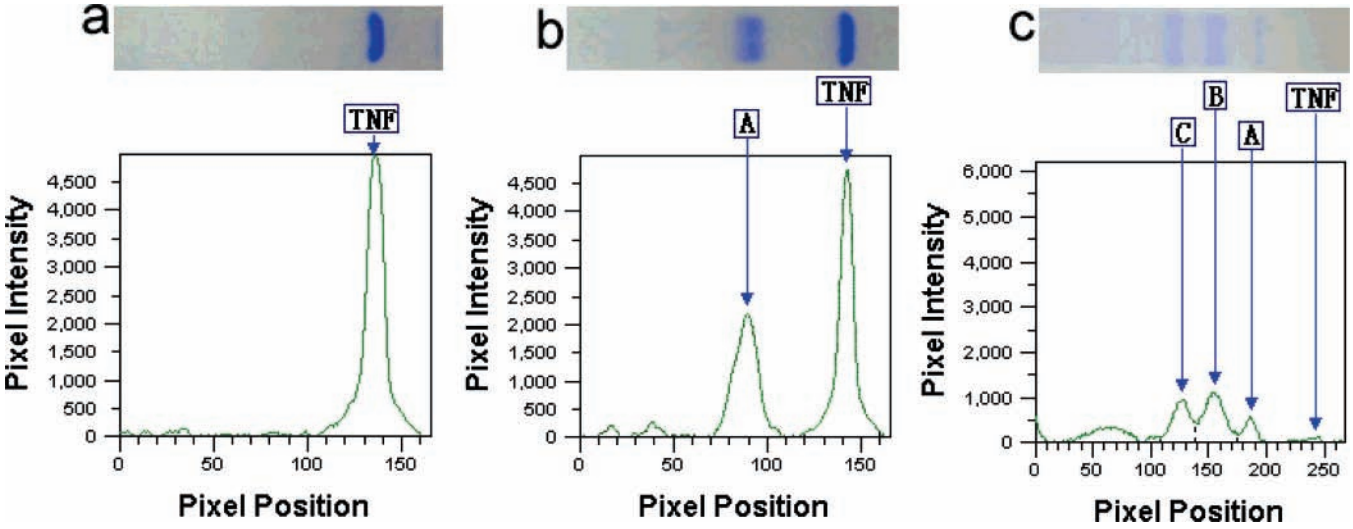


Figure 3. Profiles of band detection based on the gel image intensity using ImageMaster bioimaging system. (a) control protein (based on 26.7 μg TNF-α); (b) reaction mixture PT1 (1:5 TNF-α/PEG), and (c) PT4 (1:60 TNF-α/PEG).

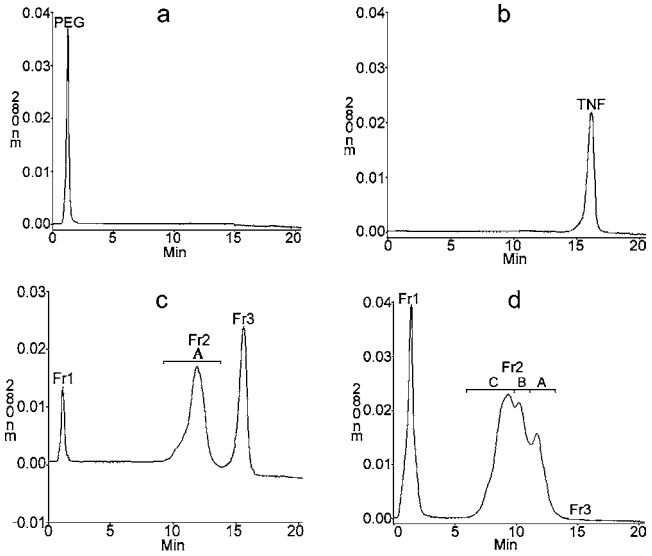


Figure 4. Purification of PEG−TNF-α conjugates by cation-exchange perfusion chromatography. NHS−PEG−MAL (a), TNF-α (b), and the crude reaction mixture of TNF-α/PEG molar ratios of 1:5 (c) and 1:60 (d) were purified on a POROS 20 HS column. The reaction mixture was separated into three fractions identified as NHS−PEG−MAL (Fr1), PEG−TNF-α (Fr2), and TNF-α (Fr3).

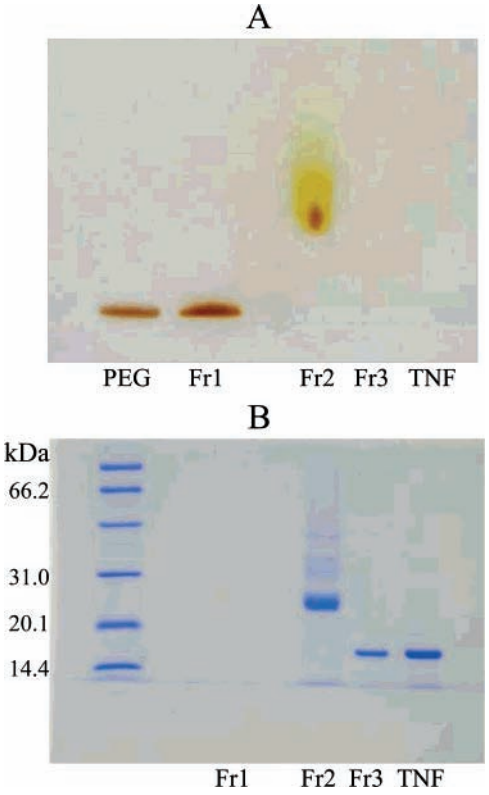


Figure 5. Identification of the three fractions of PT1 corresponding to Figure 4c by SDS-PAGE. Gel A was stained for protein with Coomassie blue, whereas gel B was stained for PEG with barium iodide solution. Two SDS-gels were loaded as follows: left lane, NHS−PEG−MAL (A) and protein markers (B); right lane (TNF), TNF-α; lanes Fr1, Fr2, and Fr3, fractions corresponding to peaks Fr1, Fr2, and Fr3.

cpm/mg to 253 cpm/mg) and 6.6-fold for PT4 (from 1043 cpm/mg to 157 cpm/mg), respectively. At 0.25 h after intravenous injection, free TNF-α was mainly distributed to normal tissues, successively: kidney > liver > lung > spleen. The tumor accumulation of TNF-α was very low, but that of TPT4 was remarkably higher than free TNF-α and PT4 ($P < 0.05$). At 2 h after administration, free TNF-α was gradually eliminated from all tissues including the S-180 tumors. There were no large differences in distribution of the TNF-α conjugates compared with free TNF-α in normal tissues. However, the TNF-α levels in tumor for TPT4 and PT4 were time-dependently increased. Tumor accumulation of TPT4 and PT4 were dramatically increased at 2 h after injection, which were about 5- and 3-fold over that of free TNF-α ($P < 0.01$), respectively. In particular, the TNF-α levels for TPT4 in tumor were much higher than those in all normal tissues examined ($P < 0.01$), while the differences between the TNF-α levels in tumor and normal tissues were found to be little for PT4. At 12 h after dosing, the tumor took up only small amounts of free TNF-α, whereas the tumor accumulation of TPT4 was still significantly higher than free TNF-α and PT4.

The inhibitory action of the TNF-α conjugates against S-180 solid tumors in mice was shown in Figure 8. A control group of 20 mice injected with saline solution induced the average tumor volume of 9.79 ± 2.38 cm^3 on day 17 after tumor cells inoculation. The TNF-α group at dose of 0.67 μg per mouse exhibited the average tumor of 8.52 ± 1.95 cm^3 on day 17, indicating that tumor volume was insignificantly suppressed as compared with the control group ($P > 0.05$). In the case of the PT4 treatment group, average tumor volume on day 17 (6.03

Table 1. Binding Parameters of ^{125}I-Tf-Fe$_2$ and ^{125}I-TPT4-Fe$_2$ on K562 Cells, KB Cells, and L02 Cells at 4 °C (n = 3)

ligand	cell lines	B_{max} ($\times 10^4$ sites/cell)	K_d (nmol/L)	goodness of fit (R^2)
Tf	K562	17.2 ± 0.7	8.9 ± 0.5	0.9717
	KB	13.5 ± 0.6	9.6 ± 1.3	0.9838
	L02	1.5 ± 0.1	35.4 ± 2.8	0.9866
TPT4	K562	14.7 ± 1.1	9.2 ± 0.4	0.9826
	KB	11.1 ± 1.0	10.5 ± 2.2	0.9855

± 0.75 cm^3) was smaller than that of the control group (P = 0.02) and the TNF-α group (P = 0.03). For the TPT4 group, the obvious antitumor response was observed from day 11 after inoculation as compared with the TNF-α group (P < 0.05). Moreover, the average tumor volume of the TPT4 group on day 17 was 3.02 ± 1.71 cm^3, which was significantly smaller than that of the control group (P = 0.0007), TNF-α group (P = 0.0008), or PT4 group (P = 0.002).

The IR was calculated on the basis of average tumor volume on day 17 after tumor cells inoculation. The IR values of the TNF-α, PT4, and TPT4 treatment groups were 12.95%, 38.42%, and 69.11%, respectively. The IR of TPT4 enhanced 5.3- and 1.8-fold over that of TNF-α and PT4 (P < 0.01), indicating that TPT4 exhibited the highest antitumor activity. No side effect was observed, such as decrease in body weight, in any mice administered TPT4.

DISCUSSION

Ligand−receptor-mediated delivery systems have received major attention in the past few years (*23*, *24*), because naturally occurring ligands are not only able to achieve site-specific targeting to ligand-specific biosites, but are also biodegradable, and potentially nontoxic and nonimmunogenic. Some of the expected advantages of transferrin−drug conjugates are a preferable tissue distribution, prolonged half-life of the drug in the plasma, and controlled drug release from the conjugates (*10*). PEG has been used widely to increase the circulation half-life of rapidly eliminated drug, to impart enhanced permeability and retention (EPR) (*25*), to increase passive targeting of anticancer drugs, and to act as a spacer in numerous delivery systems like PEG-grafted liposomes and nanoparticles (*26*).

This paper proposes a new targeted conjugate for delivering TNF-α specifically to tumor cells by coupling Tf to TNF-α via a PEG linker. The combination of active targeting, based on the use of ligands, and passive targeting, based on the PEGylation due to EPR, may provide a tumor-selective targeting strategy. To our knowledge, this is the first report of Tf-mediated TNF-α targeting to tumor cells.

The conjugate, Tf−PEG−TNF-α, was successfully synthesized using a simplified three-step procedure as shown in Scheme 1. In the first step, TNF-α was modified with the heterobifunctional (α-maleimide-ω-*N*-hydroxysuccinimide ester) 3.4 kDa PEG derivative via the formation of an amide bond

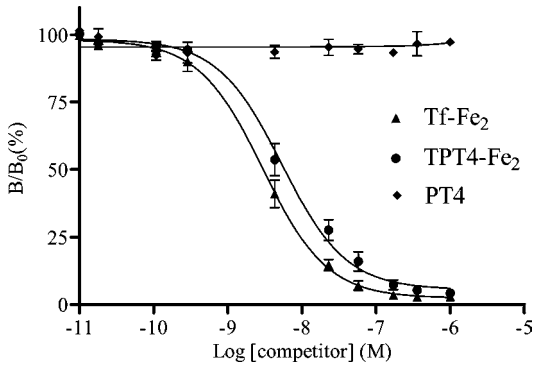


Figure 6. Competition curves among ^{125}I-Tf-Fe$_2$ and Tf-Fe$_2$, TPT4-Fe$_2$, and PT4 for the binding to K562 surface Tf receptors. The *y*-axis corresponded to B/B_0 (B = dpm corresponding to tracer bound at each competitor concentration; B_0 = dpm measured in absence of competitor), and the *x*-axis to the competitor logarithmic concentration.

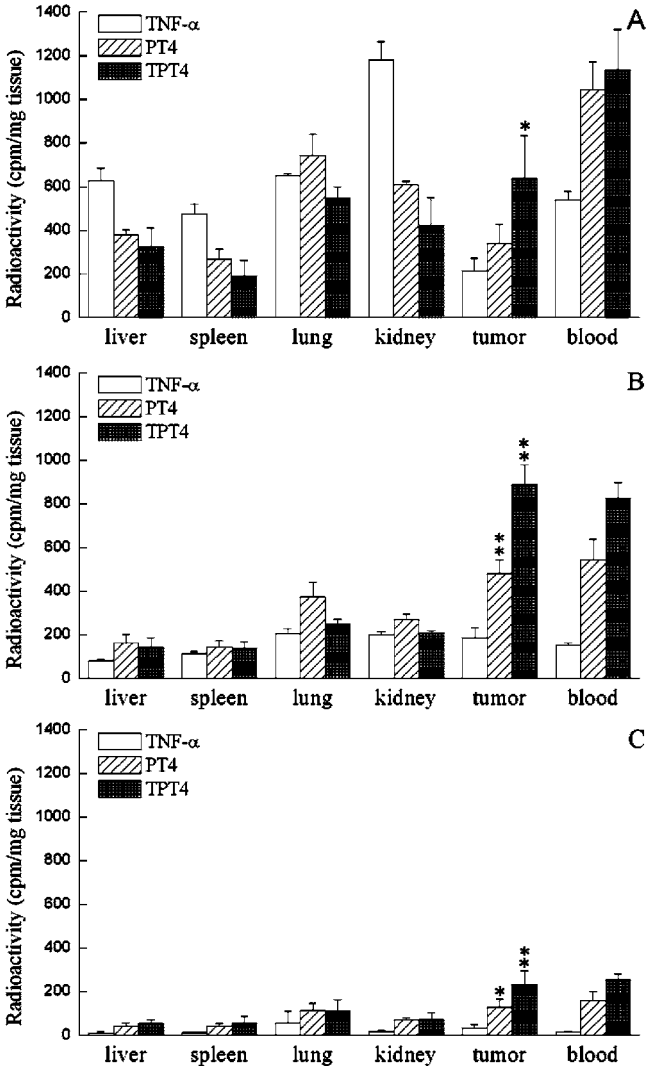


Figure 7. Tissue distribution of free TNF-α, PT4, and TPT4 in mice at 0.25 h (A), 2 h (B), and 12 h (C) after intravenous administration. Each value is the mean ± SD (n = 5). Statistical significance compared to free TNF-α: * P < 0.05, ** P < 0.01.

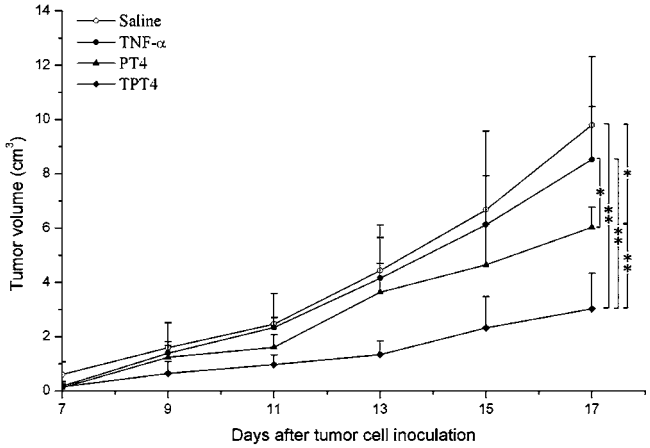
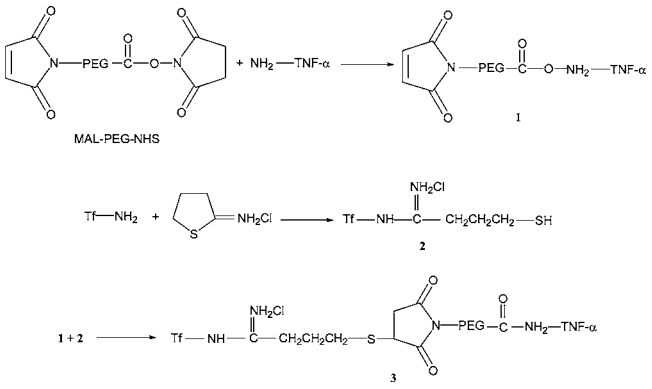


Figure 8. Antitumor effect (in terms of tumor growth) of TPT4 (◆), PT4 (▲), and free TNF-α (●) on S-180 solid tumors. Control mice were injected with 0.9% (w/v) NaCl (○). Tumor volume was monitored, mean ± SD are presented; n = 20 animals in control group, n = 10 animals per group in all treatment groups. *P < 0.05; **P < 0.01.

Scheme 1. Synthesis of PEG−TNF-α (1), Tf−SH (2), and Tf−PEG−TNF-α (3)



between amino groups of TNF-α and the terminal *N*-hydroxylsuccinimide (NHS) group of NHS−PEG−MAL. In the second step, the reaction of Tf with 2-iminothiolane was carried out to form Tf-SH. In the third step, the Tf−PEG−TNF-α conjugate was prepared by reacting the maleimide group at the distal end of the PEG chain in the TNF-α conjugate with thiolated transferrin. The HS group adds to the double bond of the maleimide group in a fast and selective reaction forming a stable thioether bond.

For the first step, it was necessary to estimate the degree of PEGylated TNF-α. In this study, an ImageMaster VDS-CL system, equipped with a multifunction bioimaging station designed for quick and accurate photodocumentation of electrophoretic results, was used to quantify proteins in SDS-PAGE gel bands. It was reported that the PEG chains attached to the protein surface would interfere with the effect of Coomassie blue staining (*27*). This phenomenon was also observed in our experiments. As seen in Figure 2, the PEG−protein band color (bands A, B, and C) with a high degree of PEGylation is rather pale (particularly in sample PT4) compared to that with a low degree of PEGylation. For this reason, the quantitative analysis of PEGylated protein based on the PEG−protein band intensity in SDS-PAGE gels was not appropriate. On the contrary, it is reliable to quantify unconjugated TNF-α compared with the control protein based on the IOD value of the free protein band. Therefore, the percentage of PEGylated TNF-α (*P*%) used to represent the degree of PEGylation can be accurately calculated. This method might be applicable to the other PEGylated protein for its simplicity.

Purification of PEGylated biomacromolecules (peptides, proteins, etc.) is a challenge due to the complexity of conjugates, heterogeneous population of molecules (*28*), and unstable structure of the resulting conjugate. Furthermore, the purification protocol must not alter or decrease the biological activity of the bioconjugates. Several purification protocols have been described including reverse-phase high-performance liquid chromatography (*29*), ion-exchange chromatography (*30*, *31*), size-exclusion chromatography (*32*, *33*), and affinity chromatography (*34*), most of which are time-consuming and result in poor yields. Perfusion chromatography is a technique based on fluid dynamics for reducing stagnant mobile-phase mass transfer in liquid chromatography and thereby reducing peak broadening. This technique involves the flow of liquid through a noncompressible porous chromatographic particle (POROS Media, PerSeptive Biosystems) with 6000−8000 Å pores which transect the particle (*35*). It therefore has high dynamic capacity, high resolution, and separation speed typically 10−100-fold faster than that obtained with conventional media. Perfusion chromatography has been shown in the past to be ideally suited for purification of large biomolecules (*36*−*38*). In this study, perfusion ion-exchange chromatography was used for rapid purification of the PEGylated TNF-α. The PEGylated protein was separated from excess free protein and PEG. The excess free PEG was eluted first before the gradient due to its electrical neutrality, while the free protein was retained on the cation-exchange column due to its positive charges until it was eluted with a salt gradient. By contrast, the PEG−TNF-α peaks A, B, and C, were eluted between free TNF-α and PEG due to the reduced charge. Since the PEG−TNF-α peak was well-resolved from free TNF-α and PEG, this method can be easily scaled up. Also, since the analysis time for the entire procedure was short (less than 20 min), larger amounts of sample can be obtained by simply repeating the procedure several times.

Many studies have demonstrated that the residence time in the bloodstream of PEG−protein conjugates increases according to the molecular size (*7*, *26*). Among those, Chapman et al. indicated that the increase is governed by the total polymer mass, regardless of the number of chains or the polymer molecular weight (*39*). In addition, size enlargement promotes the accumulation into tumor tissues by the passive EPR mechanism. With a few exceptions, the molecular weights of PEGs used for synthesis of biologically active conjugates are in the range 2−20 kDa (*40*). According to these reports and our previous studies, it is reasonable to speculate that conjugates with few low-molecular-weight 3.4 kDa PEG chains, such as PT1, may be unable to achieve a longer circulating half-life and a better tumor targeting as compared to conjugates with about five 3.4 kDa PEG chains (PT4). Therefore, PT4 with a maximum reaction yield was selected as a lead candidate, intending to produce conjugates with multiple PEGs attached to achieve the benefits similar to the ones afforded by a single larger PEG.

The thiolation of Tf and conjugation of Tf-SH to PEG−TNF-α were carried out according to the published procedures (*41*, *16*). After preparation of ^{125}I-PT4 and ^{125}I-TPT4-Fe_2, the binding parameters of the conjugates to tumor cell receptors were determined. It was found that the numbers of binding sites and the competitive ability of the TPT4-Fe_2 conjugate were slightly smaller than that of Tf-Fe_2. It may be postulated that the chemical modification of Tf with PT results in molecule size enlargement, which in turn sterically hinders Tf−receptor binding. However, the TPT4-Fe_2-TfR and Tf-Fe_2-TfR complexes exhibit the K_d, B_{max}, and ED_{50} values on the same order of magnitude, which would be unable to induce remarkable differences in specificity and affinity.

Successful treatment of cancer by TNF-α requires the selective delivery of relatively high concentration of TNF-α to tumor tissue. The Tf−PEG−TNF-α conjugate prepared in this study appears to satisfy these requirements and should be very useful for cancer therapy. It was found that in vivo behavior of TNF-α was altered by PEG and Tf modifications. Owing to rapid clearance of free TNF-α from the circulation, uptake of free TNF-α in tumor tissue exhibited the smallest levels as compared with those of TPT4 and PT4. In contrast, the tumor accumulation of TPT4 and PT4 were time-dependently increased, and the order of the accumulation amount in tumor was TPT4 > PT4 > TNF-α.

The highest tumor accumulation of Tf−PEG−TNF-α resulted in its maximal antitumor effect. As observed in Figure 8, the tumor volume of the TNF-α group was insignificantly different from that of the saline group during the experiment, indicating that a dose of 0.67 μg per mouse for the TNF-α group was not effective for tumor growth inhibition. However, this problem did not arise with PT4 or TPT4, which had significant antitumor response at a dose of 0.67 μg, especially TPT4, which showed the maximal antitumor effect. It is important to discuss why TPT4 had the greatest antitumor potency as compared with PT4 and TNF-α. It is well-known that TNF-α must bind to the extracellular domain of TNF-α receptor type I (TNF−RI, p55)

for intracellular signal transduction to occur leading to apoptosis or programmed cell death (*42*). We speculated that extravasated Tf−PEG−TNF-α in the tumor was likely to bind to two receptor types (Tf receptor and TNF-α receptor) on the tumor cell surface. Owing to specific recognition by overexpressed Tf receptors on tumor cell surface and PEGylation by the passive EPR mechanism, the accumulation amount of Tf−PEG−TNF-α at the tumor site was higher than that of TNF-α and PEG−TNF-α. Moreover, the PEG molecule as a spacer between TNF-α and Tf is a flexible long chain and could offer chances to make the TNF-α molecule move randomly. When Tf at the distal terminal of the PEG chain on Tf−PEG−TNF-α binds to the Tf receptor on the tumor cell surface, TNF-α at another terminal would also have chances to bind to the extracellular TNF receptor simultaneously. In general, the time course of cytokines binding to the membrane receptor and initiating signal transduction is transient, whereas that of internalization via ligand−receptor-mediated endocytosis is much longer. Thus, it could be reasonably speculated that antitumor activity of Tf−PEG−TNF-α mediated via TNF receptor had occurred before it was internalized into tumor cells via Tf receptor-mediated endocytosis. Therefore, it was confident that Tf−PEG−TNF-α, as a more potent systemic antitumor therapeutic agent than PEGylated TNF-α, not only improved the therapeutic index of TNF-α, but also obviated the need for repeated high doses. Of course, the identification of the mechanism of antitumor effects of the Tf−PEG−TNF-α is the subject for further studies.

In summary, a novel strategy for the formation of transferrin−PEG−TNF-α conjugate by coupling Tf to PEG−TNF-α using PEG as a spacer was established. The overall procedures were performed in neutral medium at 4 °C. These mild conditions of synthesis and purification would be suitable for the preparation of other protein conjugates. The conjugate could bind specifically to the transferrin receptor and exhibit similar affinity to tumor cells as native transferrin. As compared with TNF-α and PEG−TNF-α, Tf−PEG−TNF-α exhibited a significantly delayed blood clearance, the highest tumor accumulation, and the maximal antitumor activity. The increase of accumulation in tumors could be mainly governed by two mechanisms: active targeting using the Tf ligand and passive targeting by the EPR effect. Thus, the design of Tf−PEG−TNF-α conjugate could potentially provide a tumor-selective targeting strategy. Such targeting Tf−PEG−drug conjugates should be useful for systemic antitumor therapy.

ACKNOWLEDGMENT

This work was supported by the National Natural Science Foundation of China, No. 30271551. The authors thank Professor Jian-Hua Zhu (Department of Radiopharmacy, Fudan University, Shanghai, China) for assistance in labeling proteins and measuring radioactivity.

LITERATURE CITED

(1) Carswell, E. A., Old, L. J., Kassel, R. L., Green, S., Fiore, N., and Williamson, B. (1975) An endotoxin-induced serum factor that causes necrosis of tumors. *Proc. Natl. Acad. Sci. U.S.A. 72*, 3666−3670.

(2) Pfreundschuh, M. G., Steinmetz, H. T., Tüschen, R., Schenk, V., Diehl, V., and Schaadt, M. (1989) Phase I study of intratumoral application of recombinant human tumor necrosis factor. *Eur. J. Cancer Clin. Oncol. 25*, 379−388.

(3) Lienard, D., Ewalenko, P., Delmotte, J. J., Renard, N., Lejeune, F. J. (1992) High-dose recombinant tumor necrosis factor alpha in combination with interferon gamma and melphalan in isolation perfusion of the limbs for melanoma and sarcoma. *J. Clin. Oncol. 10*, 52−60.

(4) Yoshioka, Y., Tsutsumi, Y., Ikemizu, S., Yamamoto, Y., Shibata, H., Nishibata, T., Mukai, Y., Okamoto, T., Taniai, M., Kawamura, M., Abe, Y., Nakagawa, S., Nagata, S., Yamagata, Y., and Mayumi, T. (2004) Optimal site-specific PEGylation of mutant TNF-a improves its antitumor potency. *Biochem. Biophys. Res. Commun. 315*, 808−814.

(5) Bailon, P., and Berthold, W. (1998) Polyethylene glycol-conjugated pharmaceutical proteins. *Pharm. Sci. Technol. Today 1*, 352−356.

(6) Li, Y. P., Pei, Y. Y., Ding, J., Shen, Z. M., Zhang, X. Y., Gu, Z. H., and Zhou, J. J. (2001) PEGylated recombinant human tumor necrosis factor alpha: preparation and anti-tumor potency. *Acta Pharmacol. Sin. 22*, 549−555.

(7) Li, Y. P., Pei, Y. Y., Zhou, Z. H., Zhang, X. Y., Gu, Z. H., Ding, J., Gao, X. J., and Zhu, J. H. (2001) Pegylated recombinant human tumor necrosis factor alpha: pharmacokinetics and anti-tumor effects. *Biol. Pharm. Bull. 24*, 666−670.

(8) Han, H., and Amidon, G. (2000) Targeted prodrug design to optimize drug delivery. *AAPS PharmSci. 2*, 1−11.

(9) Allen, T. M. (2002) Ligand-targeted therapeutics in anticancer therapy. *Nat. Rev. Cancer 2*, 750−763.

(10) Li, H., Sun, H., and Qian, Z. M. (2002) The role of the transferrin−transferrin-receptor system in drug delivery and targeting. *Trends Pharmacol. Sci. 23*, 206−209.

(11) Maruyama, K., Ishida, O., Kasaoka, S., Takizawa, T., Utoguchi, N., Shinohara, A., Chiba, M., Kobayashi, H., Eriguchi, M., and Yanagie, H. (2004) Intracellular targeting of sodium mercaptoundecahydrododecaborate (BSH) to solid tumors by transferrin-PEG liposomes, for boron neutron-capture therapy (BNCT). *J. Controlled Release 98*, 195−207.

(12) Fritzer, M., Szekeres, T., Szüts, V., Jarayam, H. N., and Goldenberg, H. (1996) Cytotoxic effects of a doxorubicin-transferrin conjugate in multidrug-resistant KB cells. *Biochem. Pharmacol. 51*, 489−493.

(13) Citores, L., Ferreras, J. M., Muñoz, R., Benítez, J., Jiménez, P., and Girbés, T. (2002) Targeting cancer cells with transferrin conjugates containing the non-toxic type 2 ribosome-inactivating proteins nigrin b or ebulin l. *Cancer Lett. 184*, 29−35.

(14) Ali, S. A., Joao, H. C., Hammerschmid, F., Eder, J., and Steinkasserer, A. (1999) Transferrin trojan horses as a rational approach for the biological delivery of therapeutic peptide domains. *J. Biol. Chem. 274*, 24066−24073.

(15) Dash, P. R., Read, M. L., Fisher, K. D., Howard, K. A., Wolfert, M., Oupicky, D., Subr, V., Strohalm, J., Ulbrich, K., and Seymour, L. W. (2000) Decreased binding to proteins and cells of polymeric gene delivery vectors surface modified with a multivalent hydrophilic polymer and retargeting through attachment of transferrin. *J. Biol. Chem. 275*, 3793−3802.

(16) Kursa, M., Walker, G. F., Roessler, V., Ogris, M., Roedl, W., Kircheis, R., and Wagner, E. (2003) Novel shielded transferrin-polyethylene glycol-polyethylenimine/DNA complexes for systemic tumor-targeted gene transfer. *Bioconjugate Chem. 14*, 222−231.

(17) Bradford, M. M. (1976) A rapid and sensitive method for the quantification of protein utilizing the principles of protein-dye binding. *Anal. Biochem. 72*, 248−254.

(18) Barker, T. H., Klinger, M. M., Feldman, D. S., Fuller, G. M., and Hagood, J. S. (2001) Spectrophotometric analysis for determining the average number of poly(ethylene) glycol molecules on PEGylated proteins utilizing a protein digestion step. *Anal. Biochem. 290*, 382−385.

(19) Riddles, P. W., Blakeley, R. L., and Zerner, B. (1979) Ellman's reagent: 5,5-dithiobis(2-nitrobenzoic acid)−a reexamination. *Anal. Biochem. 94*, 75−81.

(20) Laemmli, U. K. (1970) Cleavage of structure proteins during the assembly of the head of bacteriaphage T4. *Nature (London) 227*, 680−685.

(21) Kurfürst, M. M. (1992) Detection and molecular weight determination of polyethylene glycol-modified hirudin by staining after sodium dodecyl sulfate-polyacrylamide gel electrophoresis. *Anal. Biochem. 200*, 244−248.

(22) Tanaka, T., Shiramoto, S., Miyashita, M., Fujishima, Y., and Kaneo, Y. (2000) Tumor targeting based on the effect of enhanced permeability and retention (EPR) and the mechanism of receptor-mediated endocytosis (RME). *Int. J. Pharm. 277*, 39−61.

(23) Vyas, S. P., and Sihorkar, V. (2000) Endogenous carriers and ligands in non-immunogenic site specific drug delivery. *Adv. Drug Delivery Rev. 43*, 101−164.

(24) Vyas, S. P., Singh, A., and Sihorkar, V. (2001) Ligand-receptor-mediated drug delivery: an emerging paradigm in cellular drug targeting. *Crit. Rev. Ther. Drug Carrier Syst. 18*, 1−76.
(25) Maeda, H. (2001) The enhanced permeability and retention (EPR) effect in tumor vasculature: the key role of tumor-selective macromolecular drug targeting. *Adv. Enzyme Regul. 41*, 189−207.
(26) Caliceti, P., and Veronese, F. M. (2003) Pharmacokinetic and biodistribution properties of poly(ethylene glycol)−protein conjugates. *Adv. Drug Delivery Rev. 55*, 1261−1277.
(27) McGoff, P., Baziotis, A. C., and Maskiewicz, R. (1988) Analysis of polyethylene glycol modified superoxide dismutase by chromatographic, electrophoresis, light scattering, chemical and enzymatic methods. *Chem. Pharm. Bull. 36*, 3079−3091.
(28) Wang, Y. S., Youngster, S., Grace, M., Bausch, J., Bordens, R., and Wyss, D. F. (2002) Structural and biological characterization of pegylated recombinant interferon alpha-2b and its therapeutic implications. *Adv. Drug Delivery Rev. 54*, 547−570.
(29) Chen, X. Y., Park, R., Shahinian, A. H., Bading, J. R., and Conti, P. S. (2004) Pharmacokinetics and tumor retention of ^{125}I-labeled RGD peptide are improved by PEGylation. *Nucl. Med. Biol. 31*, 11−19.
(30) Hinds, K., Koh, J. J., Joss, L., Liu, F., Baudys, M., and Kim, S. W. (2000) Synthesis and characterization of poly(ethylene glycol)−insulin conjugates. *Bioconjugate Chem. 11*, 195−201.
(31) Guiotto, A., Pozzobon, M., Sanavio, C., Schiavon, O., Orsolini, P., and Veronese, F. M. (2002) An improved procedure for the synthesis of branched polyethylene glycols (PEGs) with the reporter dipeptide Met-βAla for protein conjugation. *Bioorg. Med. Chem. Lett. 12*, 177−180.
(32) Na, D. H., and Lee, K. C. (2004) Capillary electrophoretic characterization of PEGylated human parathyroid hormone with matrix-assisted laser desorption/ionization time-of-flight mass spectrometry. *Anal. Biochem. 331*, 322−328.
(33) Yoshioka, Y., Tsutsumi, Y., Ikemizu, S., Yamamoto, Y., Shibata, H., Nishibata, T., Mukai, Y., Okamoto, T., Taniai, M., Kawamura, M., Abe, Y., Nakagawa, S., Nagata, S., Yamagata, Y., and Mayumi, T. (2004) Optimal site-specific PEGylation of mutant TNF-a improves its antitumor potency. *Biochem. Biophys. Res. Commun. 315*, 808−814.
(34) Topchieva, I. N., Sorokina, E. M., Efremova, N. V., Ksenofontov, A. L., and Kurganov, B. I. (2000) Noncovalent adducts of poly(ethylene glycols) with proteins. *Bioconjugate Chem. 11*, 22−29.
(35) Malik, P., and Strominger, J. L. (2000) Perfusion chromatography for very rapid purification of class I and II MHC proteins. *J. Immunol. Methods 234*, 83−88.
(36) McCarthy, E., Vella, G., Mhatre, R., and Lim, Y. P. (1996) Rapid purification and monitoring of immunoglobulin M from ascites by perfusion ion-exchange chromatography. *J. Chromatogr., A 743*, 163−170.
(37) García, M. C., Marina, M. L., and Torre, M. (2000) Perfusion chromatography: an emergent technique for the analysis of food proteins. *J. Chromatogr., A 880*, 169−187.
(38) Careri, M., and Mangia, A. (2003) Analysis of food proteins and peptides by chromatography and mass spectrometry. *J. Chromatogr., A 1000*, 609−635.
(39) Chapman, A. P., Antoniw, P., Spitali, M., West, S., Stephens, S., and King, D. J. (1999) Therapeutic antibody fragments with prolonged in vivo half-lives. *Nat. Biotechnol. 17*, 780−783.
(40) Esposito, P., Barbero, L., Caccia, P., Caliceti, P., D'Antonio, M., Piquet, G., and Veronese, F. M. (2003) PEGylation of growth hormone-releasing hormone (GRF) analogues. *Adv. Drug Delivery Rev. 55*, 1279−1291.
(41) Kratz, F., Beyer, U., Schumacher, P., Krüger, M., Zahn, H., Roth, T., Fiebig, H. H., and Unger, C. (1997) Synthesis of new maleimide derivatives of daunorubicin and biological activity of acid labile transferrin conjugates. *Bioorg. Med. Chem. Lett. 7*, 617−622.
(42) Mocelllin, S., Rossi, C. R., Pilati, P., and Nitti, D. (2005) Tumor necrosis factor, cancer and anticancer therapy. *Cytokine Growth Factor Rev. 16*, 35−53.

BC060135F

Stability of Cell-Penetrating Peptide−Morpholino Oligomer Conjugates in Human Serum and in Cells

Derek S. Youngblood, Susie A. Hatlevig, Jed N. Hassinger, Patrick L. Iversen, and Hong M. Moulton*

AVI BioPharma, Incorporated, 4575 SW Research Way, Corvallis, Oregon 97333. Received May 25, 2006; Revised Manuscript Received October 25, 2006

Cell penetrating peptides (CPPs) have been shown to enhance the cellular uptake of antisense oligonucleotides (AOs). However, the effectiveness of the CPPs for cytoplasmic or nuclear delivery of therapeutic AOs must take into account the possible entrapment of the CPP−AO conjugates in endosomes/lysosomes and the overall stability of the CPP−AO conjugates to enzymes. This includes the stabilities of the CPPs and AOs themselves as well as the linkage between them. In this study, we investigated the effects of several structural features of arginine-rich CPPs on the metabolic stability of CPP conjugated to phosphorodiamidate morpholino oligomers (PMOs) in human serum and in cells. Those structural features include amino acid configurations (D or L), incorporation of non-α-amino acids, peptide sequences, and types of linkages between CPPs and PMOs. Using matrix-assisted laser desorption ionization time-of-flight mass spectrometry, we found that the stability of the CPP portion was varied although the PMO portion of the conjugate was completely stable both in cells and in human serum. D-Configuration CPPs were completely stable, while L-CPPs were degraded in both serum and HeLa cells. Insertions of 6-aminohexanoic acid residues (X) into an R_8 peptide increased the corresponding CPP's serum stability with the degree of stability being dependent upon the positions of X. However, X-containing CPPs were degraded rapidly intracellularly. Insertions of β-alanines (B) into the R_8 peptide increased its serum stability and intracellular stability. An amide or a maleimide linkage was stable in both serum and cells; however, an unhindered disulfide linkage was not stable in either. By using fluorescent microscopy, flow cytometry, and an antisense splice correction assay, the cellular uptakes of an X-containing conjugate and its fragments were compared to their antisense activities. We found that a large fraction of the conjugate was trapped within vesicles and the degraded fragments cannot escape from the vesicles. This study indicates that the incorporation of non-α-amino acids into L-CPPs can increase the metabolic stability of CPP−PMOs without using costly D-CPPs. However, the position and type of non-α-amino acids affect the degree of stability extracellularly and intracellularly. In addition, this study reveals that the degradation of an X-containing CPP−PMO conjugate is a more rapid process than degradation of a B-containing conjugate. Last, the endosomal/lysosomal trapping limits the effectiveness of a CPP−PMO conjugate, and the stability of the CPP is one of the factors affecting the ability of the conjugate to escape the endosomes/lysosomes.

INTRODUCTION

Antisense oligonucleotide analogs (AOs[1]) must be present at a sufficient concentration in the cytoplasm or in the nucleus to inhibit mRNA translation or to alter pre-mRNA splicing. The therapeutic potential of these molecules has been limited by a lack of suitable in vivo delivery methods. The discovery of the cell-penetrating property of HIV Tat (*1*−*3*) and antennapedia proteins (*4*) has stimulated efforts to develop cell-penetrating peptides (CPPs) as a delivery technology (*5*−*8*). The CPP-based approach is a simple and elegant delivery method, because these are short peptides of 10−30 amino acid residues which are easily manufactured and are capable of being conjugated to an AO cargo in a quality-controlled manner.

A class of CPPs under study is the Tat-like peptides, rich in the basic amino acids lysine and arginine (*9*, *10*). The arginine-rich CPPs enhance cellular delivery of uncharged AOs such as phosphorodiamidate morpholino oligomers (PMOs) (*11*) and peptide nucleic acids (PNAs) (*12*). Conjugation of PMOs to the $(RXR)_4$ (X = 6-aminohexanoic acid) or R_9F_2 CPPs enhanced the PMOs' abilities to cause exon skipping in dog muscle cells and in human tissue carrying Duchenne muscular dystrophy (*13*, *14*), as well as to inhibit replications of various viruses (*15*−*20*). A Tat−PNA conjugate inhibited HIV-1 Tat-dependent transactivation in cells (*21*). However, high (micromolar) concentrations of CPP−PMO or CPP−PNA conjugates are required for these biological effects. Recent studies of internalization mechanisms of these conjugates revealed that they are taken up by endocytotic mechanisms and the majority of conjugates are trapped within the endosome/lysosome compartments (*21*−*23*), consistent with the observations for the free Tat and oligoarginine peptides (*24*−*26*). An effective CPP−AO conjugate should be (i) stable in blood, (ii) efficiently taken up by cells, (iii) able to effectively escape from endosomes/lysosomes, (iv) non- or minimally toxic, and (v) target-specific. Factors that likely affect these properties include the metabolic stability of a conjugate in circulation and in cells, the structural features of a CPP, the linkage between a CPP and an AO. Studies of CPP structure−activity relationships (SARs) will give insights into factors affecting these properties.

Here, we investigated several SAR features of CPPs on the metabolic stabilities of CPP−PMO conjugates in both human serum and cells. These include amino acid configurations, incorporation of non-α-amino acids, amino acid sequences, and

* Corresponding author. Hong M. Moulton, Ph.D. Email: moulton@avibio.com. Phone: (541) 753-3635. FAX: (541) 754-3545.

[1] The abbreviations used are as follows: CPP, cell penetrating peptide; HPLC, high pressure liquid chromatography; MALDI-TOF MS, matrix-assisted laser desorption ionization time-of-flight mass spectrometry; *m*/*z*, mass-to-charge ratio; PBS, phosphate buffered saline; PMO, phosphorodiamidate morpholino oligomer; PMOF, carboxyfluorescein covalently conjugated at 3′-end of PMO; PNA, peptide−nucleic acid; AO, antisense oligonucleotide analog.

10.1021/bc060138s CCC: $37.00 © 2007 American Chemical Society
Published on Web 12/10/2006

types of linkages between CPPs and PMOs. In addition, the cellular uptake and antisense activities of a conjugate and its fragments were determined in an attempt to correlate the stability and the activity.

EXPERIMENTAL PROCEDURES

Synthesis of CPP−PMO Conjugates. The sequences and nomenclature of CPPs and PMOs are listed in Table 1. Both CPPs and PMOs were synthesized at AVI BioPharma to >90% purity. PMO syntheses have been described previously (*11*, *27*), while the CPPs were synthesized using standard Fmoc chemistry (*28*). The method for the conjugation of CPPs and PMOs through a thioether (maleimide), a disulfide, or an amide linker has been described previously (*8*, *29*, *22*).

Short peptides simulating enzymolysis fragments of CPPs were conjugated to the PMO in the same manner as described previously (*22*), with the exception that the N-terminus was blocked with Fmoc during conjugation. After conjugation, the N-terminus was unblocked by adding the crude reaction mixture to a tenfold volumetric excess of concentrated ammonium hydroxide and allowing the mixture to react at 45 °C for 24 h. The truncated peptide conjugates were purified by strong cation-exchange HPLC using a 4.6 × 100 mm Source 15s tricorn column (GE Healthcare, Piscataway, NJ) and the following run conditions: buffer A (20 mM NaOAc/25% CH_3CN), buffer B (1.0 M NaCl, 20 mM NaOAc/25% CH_3CN), gradient (0−15% B in 11.25 min), and flow rate of 1.3 mL/min. The XB dipeptide conjugate was further purified by reverse-phase HPLC using a 4.6 × 150 mm PLRP-S column (Polymer Labs, Amherst, MA) and the following run conditions: buffer A (20 mM NH_4OAc), buffer B (20 mM NH_4OAc, 60% CH_3CN), gradient (10−80% B in 34.5 min), and flow rate of 1.0 mL/min. After purification, both conjugates were desalted using the reverse-phase columns as described above.

The final products were analyzed by matrix-assisted laser desorption ionization time-of-flight mass spectrometry (MALDI-TOF MS). The purity of conjugates was determined by HPLC using a Propac SCX-10 column (Dionex, Sunnyside, CA) with the following run conditions: buffer A (15 mM KH_2PO_4/25%CH_3CN), buffer B (15 mM KH_2PO_4/1.5 M KCl/ 25%CH_3CN), gradient (10−100% B in 15 min), and flow rate at 1 mL/min.

Cell Lines. HeLa (ATCC, Manassas, VA) and HeLa pLuc705 (pLuc705) cells (Gene Tools, Philomath, OR) were cultured in RPMI 1640 supplemented with 2 mM glutamine, 100 μg/mL streptomycin, 100 U/mL penicillin, and 10% fetal bovine serum (Hyclone, Logan, UT).

Extraction of CPP−PMO Conjugates from Human Serum. CPP−PMO (10 nmol) conjugates were incubated in 100 μL pooled human serum (Innovative Research, Inc., Southfield, MI) at 37 °C for 2 and 24 h. Samples were diluted to 300 μL with guanidinium−HCl solution (10 mL of 1 M guanidinium−HCl with 1 tablet of complete *mini* protease inhibitor cocktail (Roche Diagnostics, Alameda, CA)). Samples were further diluted with 600 μL ice-cold CH_3CN and centrifuged at 14 000*g* for 3 min. The supernatant was collected and lyophilized.

Extraction of Cell-Internalized CPP−PMO Conjugate. pLuc cells were seeded at 3×10^6 cells in a T-75 cm^2 flask and incubated at 37 °C for 24 h. The medium was replaced with fresh medium for control samples or with fresh medium containing a conjugate (10 μM) for test samples, and the cells were incubated at 37 °C for a designated time. The flask was washed with 1× sterile PBS twice. Cells were treated with 5 mL trypsin solution (0.25%, Hyclone) for 10 min at 37 °C, and trypsin activity was stopped by addition of the culture medium. The sample was centrifuged for 3 min at 2000*g*. The supernatant was removed, and the cells were washed with PBS and centrifuged three more times. The final cell pellet was reconstituted in 300 μL of the guanidinium−HCl solution.

Table 1. Sequences and Nomenclature of CPPs and PMOs

name	sequence	length
	peptides	
R_9F_2C	NH_2-RRRRRRRRRFFC−$CONH_2$	12
D-R_9F_2C[a]	NH_2-RRRRRRRRRFFC−$CONH_2$	12
R_9F_2XB[b]	NH_2-RRRRRRRRRFFXB−COOH	13
D-R_9F_2X	NH_2-RRRRRRRRRFFX−COOH	12
$(RXR)_4C$	NH_2-RXRRXRRXRRXRC−$CONH_2$	13
$(RXR)_4XB$	NH_2-RXRRXRRXRRXRXB−COOH	14
D-$(RXR)_4XB$[c]	NH_2-RXRRXRRXRRXRXB−COOH	14
Tat	NH_2-CYGRKKRRGRRR-$CONH_2$	12
$(RX)_8B$	NH_2-RXRXRXRXRXRXRXRXB−COOH	17
$(RB)_8B$	NH_2-RBRBRBRBRBRBRBRBB−COOH	17
	PMO[d]	
PMO	5′-CCT CTT ACC TCA GTT ACA−3′-acetyl	18
PMOF	5′-CCT CTT ACC TCA GTT ACA−3′-fluorescein	18

[a] The peptide consists of amino acids with the D configuration. [b] X = 6-aminohexanoic acid; B = β-alanine. [c] The peptide contains D-arginines. [d] This sequence targets a mutant splice site at nucleotide 705 of the human globin β-thalassemic intron 2.

Two separate controls were undertaken. A "background" control consisted of a cell pellet, without a conjugate, reconstituted in 300 μL of the guanidinium−HCl solution spiked with 30 μL H_2O. A "post-treatment degradation control" consisted of a cell pellet, without a conjugate, reconstituted in 300 μL of the guanidinium−HCl solution spiked with 30 μL of a conjugate at 10 μM. Cells were lysed by a freeze-and-thaw method: 5 min incubation in a dry ice−acetone bath and 5 min in a room-temperature water bath, repeated three times. Cellular debris was precipitated out by adding 600 μL of ice-cold CH_3CN. The samples were centrifuged at 14 000*g* for 3 min, and the supernatant was collected and lyophilized.

Characterization of Extracted Products by MALDI-TOF MS. All reagents were purchased from Sigma-Aldrich unless specified. Lyophilized samples were reconstituted in 20 μL H_2O and kept on dry ice. The well plate was precrystallized with matrix solution: approximately 1 μL of matrix solution was placed on each well of a stainless steel well plate (Applied Biosystems, Foster City, CA), some crystallization was allowed by air-drying the solvent, and then the plate was lightly wiped with a Kimwipe. Samples were kept on dry ice for up to 1 h, thawed, immediately diluted 1:10 in water, placed into matrix solution, and spotted on the precrystallized well plate. The matrices employed were 3,5-dimethoxy-4-hydroxycinnamic acid (sinapic acid, SA), 2,4,6-trihydroxyphenone monohydrate (THAP) (98%), and α-cyano-4-hydroxycinnamic acid (CHCA) (Waters, Milford, MA). SA/Amp was prepared as a supersaturated solution by placing 10 ± 1 mg into a 1.7 mL microcentrifuge tube and adding 1 mL 1:2 acetonitrile/water, then 120 μL 0.5 M ammonium phosphate (≥99%). THAP/DiAmCit was prepared by dissolving 10 ± 1 mg into a 1.7 mL microcentrifuge tube and adding 1 mL 1:1:1 acetonitrile/water/citric acid (0.2 M, diammonium salt) (98%). The CHCA/AmP solution was prepared by placing 2.0 ± 0.2 mg into a 1.7 mL microcentrifuge tube and adding 1 mL 2:3 acetonitrile/0.1% trifluoroacetic acid (99%), then 60 μL 0.5 M ammonium phosphate. All matrices were mixed, then spun down using a microcentrifuge. One microliter of sample solution was taken up into 4 μL SA/AmP, 3 μL THAP/DiAmCit, or 4 μL CHCA/AmP. If sample-in-matrix crystallization was poor, an additional microliter of matrix solution was added to the top of the sample on the well plate, and the mixture was swirled with a pipet tip. After air-drying, the wells were washed with water by placing approximately 1 μL H_2O onto each well and then pulling it up with a fresh pipet tip.

All mass spectrometric analyses were performed on a Voyager DE-PRO Biospectrometry Workstation MALDI-TOF MS (Applied Biosystems), and the instrument was calibrated before each run of samples (Applied Biosystems Sequazyme Peptide Mass Standards Kit). System calibration checks were also performed before and after each run of samples. Mass accuracy is within 0.05%. Instrument parameters were as follows: 337 nm nitrogen laser in positive ion mode with linear detection; acceleration voltage, 25 kV; grid voltage, 95%; guide wire, 0.05%; extraction delay, 400 ns; shots, 100−200.

Determination of Extraction Efficiency. Extraction efficiencies of conjugates from human serum or cells were determined by fluorescent spectroscopy. The fluorescence of each sample was determined by mixing 5 μL of serum or cell lysate and 95 μL of 0.1 M Na_2CO_3 (pH 11) and measuring with a Flx 800 microplate fluorescence/luminescence reader (Bio-tek, Winooski, Vermont) with excitation at 485 nm and emission at 524 nm. A standard curve was determined for each conjugate using the same buffer and measurement conditions as those for the serum and lysate samples.

Cellular Uptakes and Antisense Activities of $(RX)_8B$−PMOF and Its Degraded Fragments. PLuc705 cells were seeded at 0.5×10^6 cells in a six-well plate (VWR, Bisbane, CA) and incubated at 37 °C for 24 h. The medium was replaced with 1.5 mL fresh medium containing a test compound (10 μM), in triplicate. Samples were allowed to incubate in the presence of the compound at 37 °C for 24 h (nonscraped), or cells were lifted from the bottom of the well with a rubber spatula (scraped). Scraped cells were triturated several times to mix, combined with replicates, and centrifuged for 7 min at 272*g*. The supernatant was removed, and the cells were washed with PBS and reconstituted in medium, equally replated (in triplicate) in a new six-well plate and incubated at 37 °C for 24 h.

All samples were harvested by rinsing each well with 1 mL PBS, incubating in 500 μL trypsin at 37 °C for 10 min, and neutralized with 700 μL media. Each sample was aliquoted to three portions: (i) a 200 μL aliquot was taken for determining cell viability and for fluorescent microscopy, (ii) a 500 μL aliquot was taken for determining luciferase activity, and (iii) a 500 μL aliquot was taken for flow cytometry. Cell viability was determined by trypan blue exclusion assay using a cell viability analyzer (Vi-Cell, Beckman Coulter, Fullerton, CA). Cells were imaged directly in the culture medium without fixation with a Nikon Diaphot 300 inverted microscope. Images were captured with an Olympus digital camera and processed using *MagnaFire* software (Optronics, Goleta, CA). To determine luciferase activity, the 500 μL aliquot was centrifuged 5 min at 1000*g*, supernatant was removed, and the cells were reconstituted in 300 μL lysis reagent (Promega, Madison, WI) and then incubated at 4 °C for 20 min. The cell debris was removed from the lysate by centrifugation for 5 min at 2000*g*. The protein concentration and luciferase activity were determined on lysate as described elsewhere (*8*). The 500 μL aliquot for flow cytometry was centrifuged for 3 min at 2000*g*, supernatant was removed, and the cells were washed with 1 mL PBS twice, reconstituted in PBS buffer containing 1% FBS, and then analyzed by a FC 500 Beckman Coulter cytometry. Data were analyzed using *FCS Express 2* (De Novo Software, Thornhill, Ontario, Canada).

RESULTS

CPP−PMO Conjugates. The nomenclature and characterization of the CPP−PMO conjugates are listed in Table 2 (see Table 1 for peptide and PMO sequences). HPLC and MS analyses reveal that the final product contained >84% CPP conjugated to the full-length PMO with the balance composed of conjugates with incomplete sequences of PMO and a small amount of the unconjugated full-length and incomplete PMOs. MS analysis shows that the *m*/*z* values of the major peaks match the calculated molecular weights of the desired conjugates. To assess the effect of the linker on the stability of CPP−PMO conjugates, three types of linker were used for the conjugation: thioether (maleimide), amide, and disulfide (see Figure 1 for structures).

Table 2. CPP−PMO Conjugates, Linker Type, Calculated Average Molecular Weight of Protonated Molecule $(M + H)^+$, Observed Mass to Charge Ratio (*m*/*z*), and Percent Purity by HPLC

conjugate	linkage	calculated $(M + H)^+$	observed *m*/*z*	% purity
	The R_9F_2 Panel			
R_9F_2C−PMOF	thioether	8373	8374	85
D-R_9F_2C−PMO	thioether	8058	8058	88
R_9F2XB-PMOF	amide	8271	8272	91
D-R_9F2X-PMOF	amide	8200	8201	93
D-R_9F2X-PMO	amide	7885	7886	84
	The RXR Panel			
$(RXR)_4$XB−PMOF	amide	8273	8276	88
D-$(RXR)_4$XB−PMOF	amide	8273	8276	93
D-$(RXR)_4$XB−PMO	amide	7958	7959	86
$(RXR)_4$C−S−S−PMOF	disufide	8257	8256	87
	Others			
Tat-PMOF	thioether	8172	8174	87
$(RX)_8$B−PMOF	amide	8614	8616	94
$(RB)_8$B−PMOF	amide	8276	8278	88

Extraction Efficiency of CPP−PMO Conjugates. We first determined the validity of the guanidinium−HCl/CH_3CN extraction procedure in both human serum and cells. We reasoned that guanidinium moieties should inhibit binding of CPPs to proteins and other cellular components based on the observation that guanidinium−HCl (1 M) effectively eluted >95% CPP−PMO conjugates from a CM−sepharose strong cation exchange column. The extraction efficiency was only 5% if the procedure was performed without guanidinium−HCl (data not shown). PMO and CPP−PMO conjugates have excellent solubility in H_2O containing 50% CH_3CN (unpublished data), and the addition of CH_3CN precipitates most proteins and other cellular components leaving the conjugate or PMO in solution. Therefore, a high-concentration guanidinium−HCl washing step followed by a CH_3CN precipitation step was included in the procedure. Protease inhibitors were added to the guanidinium−HCl solution to preclude post-treatment protease activities.

To determine the amount of a conjugate in the extracted sample, the fluorescence of the extract was compared to the standard curve of the conjugate stock solution. The percent recovery of each conjugate was calculated from the nanomoles of recovered sample compared to the nanomoles of added sample. The carboxyfluorescein-tagged conjugates were incubated in human serum for either 2 or 24 h at 37 °C. The recoveries from serum were 50−70% for all conjugated and unconjugated (PMOF) samples except for $(RXR)_4$C−S−S−PMOF (16%) and $(RB)_8$B−PMOF (40%) (Figure 2A). The low extraction efficiency of $(RXR)_4$C−S−S−PMOF is likely due to the loss of one of the degradation products, HS−PMOF (see Table 3), since its free thiol group is very reactive toward cysteine-containing serum proteins and the reaction products (protein-PMOF conjugates) are insoluble in the extraction solution. After a similar analysis in cell lysate samples was performed, the extraction efficiencies were between 50% and 80% for all samples except for Tat−PMOF (32%), R_9F_2C−PMOF (45%), and $(RXR)_4$C−S−S−PMOF (40%) (Figure 2B).

This percent recovery is a conservative estimate, and the actual recovery should be higher because the loss in fluorescence caused by the photobleaching of the fluorescein tag and any loss in the plastic vials used for incubation and extraction were not accounted for. These losses averaged about 15% (data not

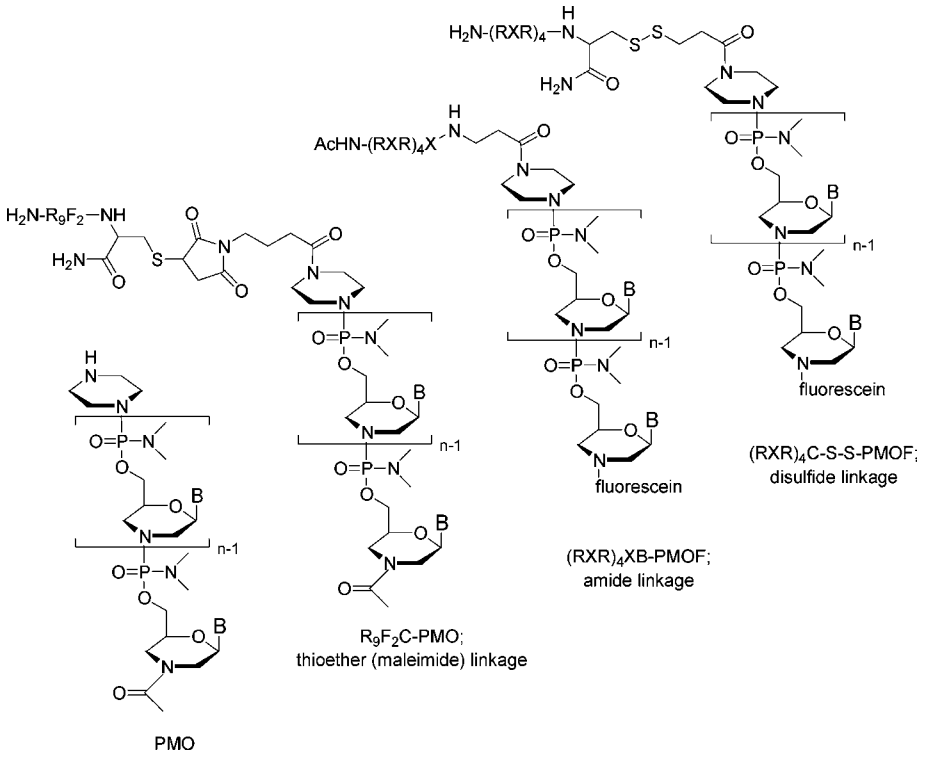


Figure 1. Structures of 3′-acetyl PMO (PMO) and CPP−PMO conjugates with maleimide (R_9F_2C−PMO), amide ($(RXR)_4$-PMOF), and disulfide ($(RXR)_4C$−S−S−PMOF) linkages.

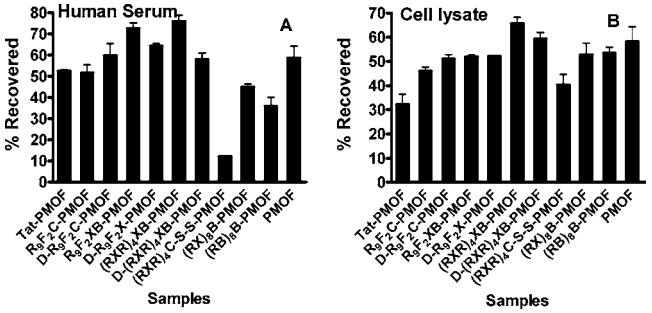


Figure 2. Extraction efficiency of the conjugates from human serum (A) and pLuc705 cells (B). (A) Human serum was spiked with 10 nmol of a CPP−PMOF conjugate and incubated at 37 °C for 24 h. (B) Cells in a T75 flask were harvested and spiked with 0.3 nmol of CPP−PMOF. The cells were lysed and the conjugate extracted. The quantity of nanomoles recovered was calculated from the fluorescence of the extract of a sample (background-subtracted) and the standard curve of the sample. The quantity of nanomoles recovered was normalized to the nanomoles added, and the data are presented as the percent recovery: mean ± SD from triplicate samples of two independent experiments ($n = 6$).

shown) and were determined by spiking the conjugates into equivalent volumes of water and then processing using the same recovery procedure as that for the treatment samples.

Effects of MALDI-TOF MS Matrices on Analysis. The MALDI-TOF MS matrix solution plays a key role in the efficiency of crystallization and ionization of particular classes of compounds (*30*). High molecular weight compounds such as PMOs and conjugates are usually analyzed using sinapic acid (SA) matrix, while lower molecular weight compounds are often analyzed in 2,4,6-trihydroxyphenone monohydrate (THAP) and α-cyano-4-hydroxycinnamic acid (CHCA) matrices, the latter especially being used for peptides and proteins. It is also known that mass discrimination effects can occur due to different rates of crystallization and/or ionization with mixtures of components (*31*). Since the possibility exists for free peptide, free PMO, and conjugate to be present in a sample, all three matrices were employed in this study to optimize identification.

Cell lysate extract was co-spiked with PMOF and either R_9F_2C−PMOF, $(RXR)_4$XB−PMOF, or $(RX)_8$B−PMOF at PMOF/CPP−PMOF molar ratios of 1:1, 1:0.75, 1:0.5, and 1:0.25. Examples of the MS spectra of a mixture of PMOF and $(RXR)_4$XB−PMOF are shown in Figure 3. The PMO peak (*m*/*z* of 6345) is clearly observed using SA and THAP matrices but is less intense using a CHCA matrix due to its poor ionization in this matrix. All conjugate peaks (*m*/*z* of 8275) were clearly observed in all three matrices with the peptide portion of the conjugate allowing good ionization in CHCA. The intensity of the conjugate peak decreases with a corresponding decrease in conjugate concentration, but at a concentration at $^1/_4$ of the PMOF concentration, the conjugate is still identifiable in all three matrices (Figure 3B).

Stability of CPP−PMO Conjugates in Human Serum. Effects of CPP sequences, amino acid configurations, and linker types on the stability of CPP−PMO conjugates in human serum were determined by MALDI-TOF MS. We studied several different CPP sequences composed of α-amino acids (L- or D-configurations), β-amino acids (β-alanine, B), and/or ϵ-amino acids (6-aminohexanoic acid, X) that were linked to the PMO by a thioether (maleimide), an amide, or a disulfide linkage (Figure 1).

The PMO portion of the conjugates was completely stable in human serum, consistent with a published report (*32*). The stability of the CPP portion of the conjugates depends on the sequences and amino acid configurations of the CPPs (Table 3). As expected, the CPPs composed of all D-amino acids, D-R_9F_2C and D-R_9F_2X, were stable even with 24 h serum treatment. This was also true of the CPPs composed of L-arginines (Arg) with the RX or RB repeats, $(RX)_8$B and $(RB)_8$B, and the one composed of D-Arg and X residues, D-$(RXR)_4$XB. However, replacement of D-Arg with L-Arg decreased the latter peptide's stability; $(RXR)_4$XB was stable to 2 h treatment but was partially degraded after 24 h treatment. The degradation products have *m*/*z* values corresponding to $(RXR)_3$-, $(RXR)_2$-, and RXR−PMOF conjugates, indicating the protease cleavage sites occur between each adjacent arginine

Table 3. Conjugate Stability in Human Serum[a]

intact conjugate		in human serum			
	calcd $(M+H)^+$	obsd *m/z*	peak identification	2 h	24 h
		The R_9F_2 panel			
D-R_9F_2C−PMO	8058	8058	D-R_9F_2C-GMBS−PMO	D	D
R_9F_2C−PMOF	8373	7239	R_2F_2C−PMOF	D	D
		7083	RF_2C−PMOF	D	D
		6927	F_2C−PMOF	D	D
D-R_9F_2X−PMOF	8200	8201	D-R_9F_2X−PMOF	D	D
R_9F_2XB−PMOF	8271	7138	R_2F_2XB−PMOF	D	D
		6982	RF_2XB−PMOF	D	D
		6826	F_2XB−PMOF	D	D
		The $(RXR)_4$ Panel			
D-$(RXR)_4$XB−PMOF	8273	8273	D-$(RXR)_4$XB−PMOF	D	D
$(RXR)_4$XB−PMOF	8273	8275	$(RXR)_4$XB−PMOF	D	D
		7807	$(RXR)_3$XB−PMOF	ND	D
		7381	$(RXR)_2$XB−PMOF	ND	D
		6956	$(RXR)_1$XB−PMOF	ND	D
$(RXR)_4$C−S−S−PMOF	8257	8256	$(RXR)_4$C−S−S−PMOF	D	ND
		6558	C−S−S−PMOF	D	D
		6436	HS−PMOF	D	D
		Others			
Tat-PMOF	8172	8174	Tat-PMOF	D	ND
		6632	C−PMOF	D	D
$(RX)_8$B−PMOF	8614	8614	$(RX)_8$B−PMOF	D	D
$(RB)_8$B−PMOF	8276	8278	$(RB)_8$B−PMOF	D	D

[a]After 2 and 24 h incubations, the samples were analyzed by MALDI-TOF MS, and the identities of the observed *m/z* peaks were determined. D = detected; ND = not detected. Two independent experiments were performed on duplicate samples for each conjugate ($n = 4$), and observed products were found in all replicates of each experiment.

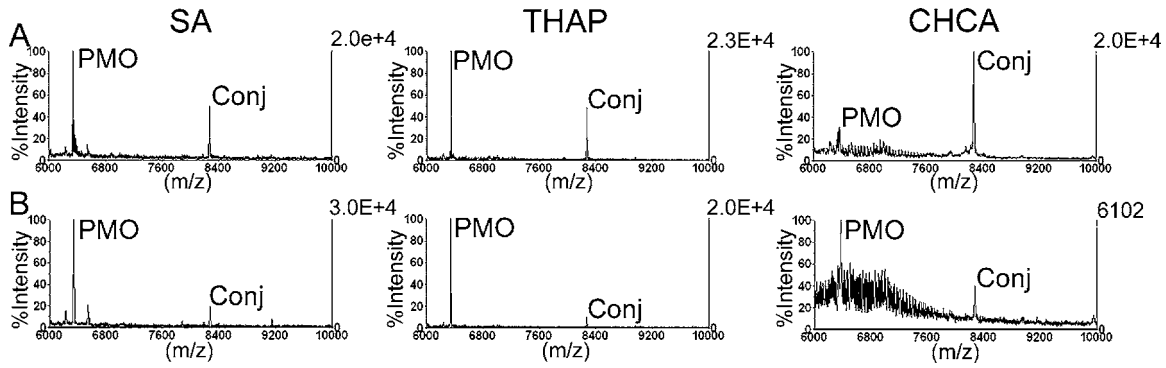


Figure 3. Matrix effect on identification of a mixture of PMO and the $(RXR)_4$XB−PMOF conjugate (Conj). pLuc705 cells were grown in the same manner outlined for the internalization study. (A) 20 μL of cell lysate extract was co-spiked with 0.3 nmol PMOF (*m/z* = 6345) and 0.25 nmol $(RXR)_4$XB−PMOF (*m/z* = 8275). (B) 20 μL of cell lysate extract was co-spiked with 0.3 nmol PMOF and 0.075 nmol $(RXR)_4$XB−PMOF. The samples were analyzed by MALDI-TOF MS in SA, THAP, and CHCA matrices. The spectra above display *m/z* corresponding to the calculated molecular weights of these compounds.

(Figure 4). The CPP−PMOF with Tat, R_9F_2C, and R_9F_2XB sequences were the least stable. Tat−PMOF was mostly degraded to C−PMOF within 2 h with no partially degraded products observed. Degradation products of R_9F_2C−PMOF were seen within the 2 h treatment and identified as R_2F_2C-, RF_2C-, and F_2C−PMOF, and the intact CPP conjugate peak had completely disappeared after the 24 h treatment. These results indicate that incorporation of non-α-amino acids into a CPP sequence can increase its serum stability. However, the degree of stability is affected by the positions of the non-α-amino acids.

Three types of linkages, thioether, disulfide, and amide, were assayed for their stability in the serum. Both thioether (used in R_9F_2C−PMOF) and amide linkages (used in R_9F_2XB−PMOF and $(RXR)_4$XB−PMOF) reveal no evidence of breakage. However, the unhindered disulfide linkage (used in $(RXR)_4$C−S−S−PMOF) was not stable as shown by appearance of the *m/z* peak corresponding to HS−PMOF, the degradation product produced by removal of the $(RXR)_4$C−SH portion from the $(RXR)_4$C−S−S−PMOF conjugate.

Intracellular Stability of CPP−PMO Conjugates. The above conjugates were studied for their intracellular stability. In order to ensure that only internalized conjugates were analyzed, a proteolysis treatment followed by a wash step prior to the cell lysis procedure was used to eliminate cell-bound material (*33*). In addition to using protease inhibitors in the lysis solution to eliminate the possibility of post-treatment degradation, a parallel "post-treatment degradation control" sample was constructed for each conjugate.

The post-treatment degradation control samples were from cells undergoing exactly the same procedure as the treatment samples, except the conjugate was not added to the treatment flask. Instead, the conjugate was spiked into the cells collected in a tube following the trypsin treatment step and prior to the lysis, extraction, and precipitation procedure. The amount of a conjugate spiked into control cells was based on the amount that was internalized in the treatment sample (about 0.3 nmol) as determined by measuring the background-subtracted fluorescence of cells treated with the CPP−PMOF. The MS spectra of the control samples for all conjugates show only peaks corresponding to intact conjugates, demonstrating that the conjugates were not degraded by the post-treatment procedure. An example set of MS spectra is shown in Figure 5A for

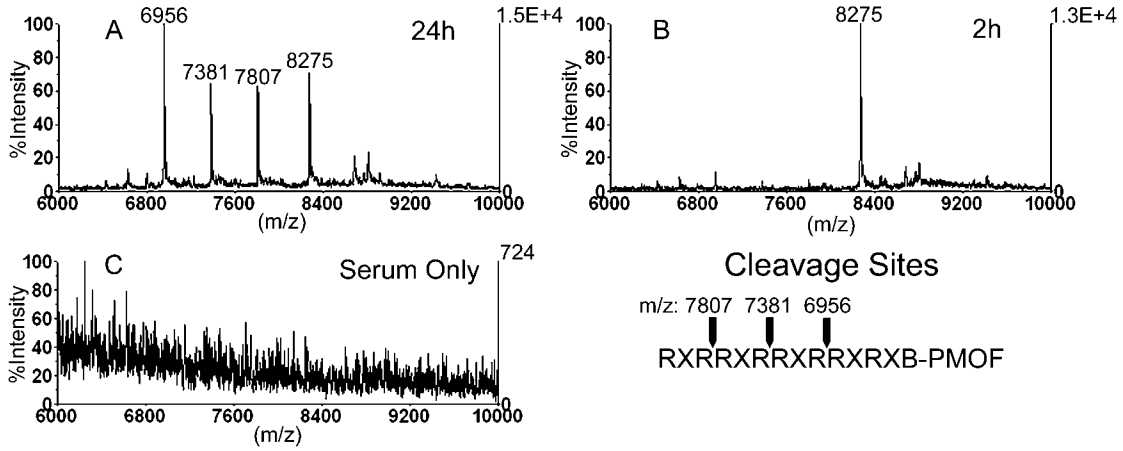


Figure 4. The stability of $(RXR)_4XB-PMOF$ in human serum. The human serum samples were treated with the conjugate for 24 h (A), 2 h (B), and without the conjugate (C) at 37 °C. The extracted materials were analyzed by MALDI-TOF MS. The spectra of the samples using the THAP matrix are shown here. The cleavage sites of the conjugate corresponding to 2 h treatment are indicated by the arrows.

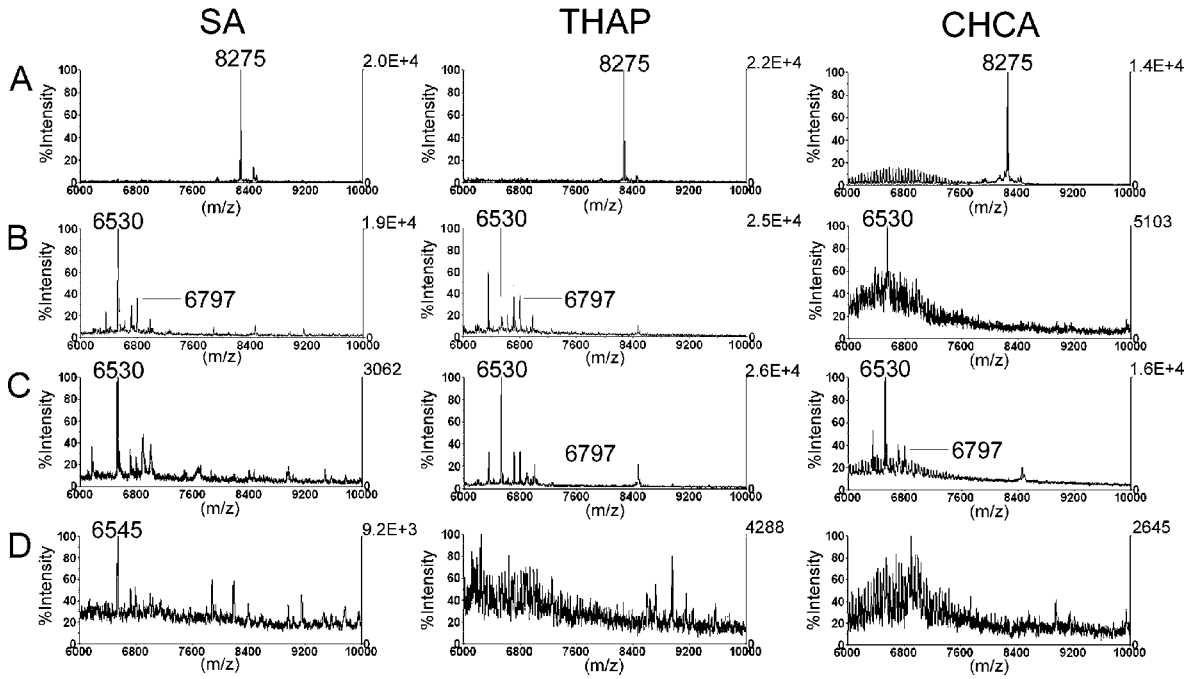


Figure 5. Mass spectra of cells treated with $(RXR)_4XB-PMOF$. (A) pLuc705 cells were harvested then spiked with 0.3 nmol of the conjugate, immediately followed by the lysis/extraction procedure (post-treatment degradation control). (B) pLuc705 cells were treated with 10 μM of the conjugate for 24 h, harvested, lysed, and extracted. (C) An extract of the wild-type HeLa cells treated with 10 μM of the conjugate for 24 h. (D) An extract of pLuc705 cells treated with vehicle control H_2O without a conjugate (background control). All extracted materials were subjected to MALDI-TOF MS analysis in SA, THAP, and CHCA matrices.

$(RXR)_4XB-PMOF$. The result indicates that the post-treatment procedure is a valid method for extraction and analysis of internalized conjugates.

All samples were analyzed using all three MS matrices. The results for internalized conjugates after 24 h of treatment are summarized in Table 4, and the corresponding MS spectra are shown in Figures 5 and 6. The mass spectra of internalized $(RXR)_4XB-PMOF$ analyzed in three matrices are shown in Figure 5B,C for pLuc705 and wild-type HeLa cells, respectively. Figure 5D shows spectra of the "background control" lysate extract. Figure 6 shows spectra of internalized R_9F_2C, $(RX)_8B$, $(RB)_8B$, D-$(RXR)_4XB$, and Tat conjugates.

The MALDI-TOF MS analysis of the PMO portion of all CPP–PMO conjugates reveals no observable peaks corresponding to the degraded PMO. To our knowledge, this is the first study that shows PMOs are totally stable intracellularly. The CPP portion of the conjugates with D-amino acids, D-R_9F_2C, D-R_9F_2X, and D-$(RXR)_4XB$ (Table 4, Figure 6D for D-$(RXR)_4$-PMO), are also stable. Cells treated with Tat, R_9F_2C, R_9F_2X, $(RXR)_4XB$, and $(RX)_8$ conjugates produced spectra containing no identifiable intact conjugate peaks in any of the three matrices (Figure 5B,C and Figure 6). Tat–PMOF, $R_9F_2C-PMOF$, and $R_9F_2XB-PMOF$ were degraded to C–PMOF, C–PMOF, and XB–PMOF, respectively (Figure 6 and Table 4). $(RX)_8B-PMOF$ was degraded to XB–PMOF (Figure 6B). The major degradation product of $(RXR)_4XB-PMOF$ was XB–PMOF with a minor product corresponding to XRXB–PMOF (Figure 5B). The $(RB)_8B-PMOF$ spectrum contains *m*/*z* peaks corresponding to BB–PMOF and intact conjugate (Figure 6C). $(RB)_8B-PMOF$ is the only conjugate not composed of D-amino acids to contain a significant amount of identifiable intact conjugate.

Because the above studies were carried out in HeLa pLuc705 cells that are stably transfected with the pLuc705 plasmid, the pre-mRNA target for the PMO (*34*), we investigated whether the degradation event is related to the RNA targeting process.

Table 4. Conjugate Intracellular Stability[a]

intact conjugate		in HeLa pLuc cells			
name	calcd $(M + H)^+$	obsd *m/z*	peak identification	24 h treatment	1 h treatment
		R_9F_2 Panel			
D-R_9F_2C−PMO	8058	8057	D-R_9F_2C−PMO	D	NA
R_9F_2C−PMOF	8374	6633	C−PMOF	D	NA
D-R_9F_2X−PMO	7885	7884	D-R_9F_2X−PMO	D	NA
R_9F_2XB−PMOF	8271	6530	XB−PMOF	D	NA
		$(RXR)_4$ Panel			
D-$(RXR)_4$XB−PMO	7958	7958	D-$(RXR)_4$XB−PMO	D	NA
$(RXR)_4$XB−PMOF	8275	6799	XRXB−PMOF	D	D
		6530	XB−PMOF	D	D
$(RXR)_4$C−S−S−PMOF	8257	6434	HS−PMOF	D	NA
		Others			
Tat-PMOF	8172	6633	C−PMOF	D	NA
$(RX)_8$B−PMOF	8614	6799	XRXB−PMOF	ND	D
		6530	XB−PMOF	D	D
$(RB)_8$B−PMOF	8276	8278	$(RB)_8$B−PMOF	D	NA
		6487	BB−PMOF	D	NA

[a]HeLa pLuc705 cells incubated in 10 μM conjugate for 24 and 1 h at 37 °C were trpsinized, washed, and lysed, and the PMO and any remaining portion of CPP were recovered. Samples were analyzed by MALDI-TOF MS, and the observed *m/z* peaks were identified. The table shows the peptide sequences and their calculated mass of the intact conjugates and the observed single-ionization *m/z* peaks of the cell-internalized recovered sample. At least two complete independent experiments were performed on duplicate samples for each conjugate ($n = 4$), and observed products were found in all replicates of each experiment. D = detected; ND = not detected; NA = not available.

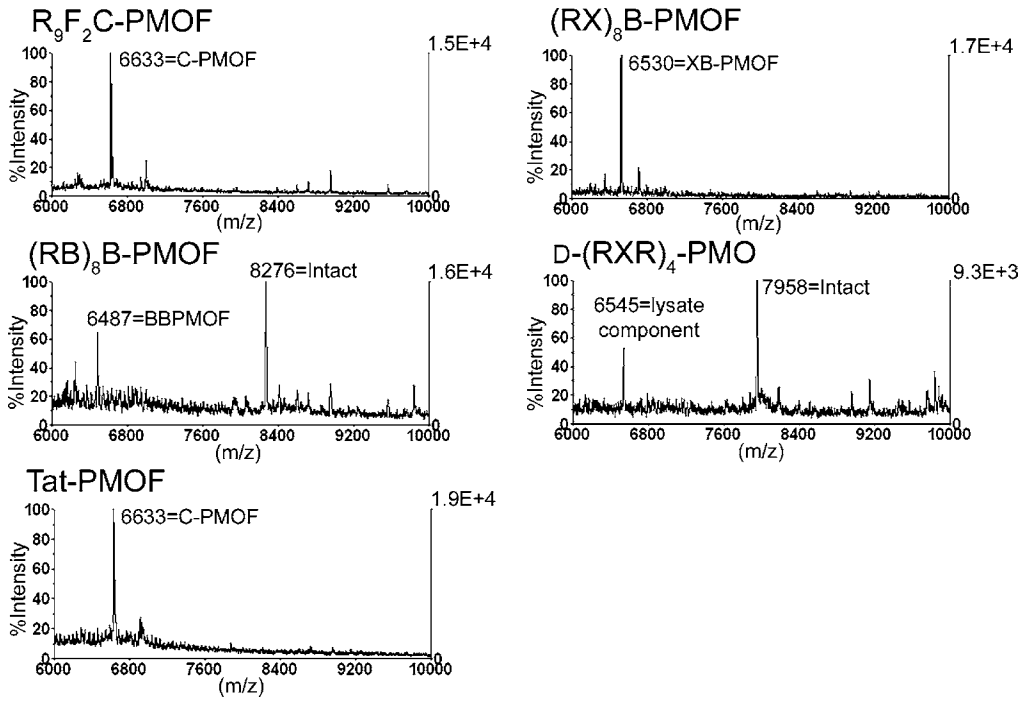


Figure 6. Intracellular stability of CPP−PMO conjugates. MALDI-TOF mass spectra of extracts of the pLuc705 cells treated with 10 μM of R_9F_2C−PMOF, $(RX)_8$B−PMOF, $(RB)_8$B−PMOF, D-$(RXR)_4$−PMO, or Tat−PMOF conjugate. The peak identifications are indicated in the graphs.

$(RXR)_4$−PMOF was incubated in wild-type HeLa cells which do not have the pLuc705 plasmid. The spectra from the wild-type HeLa cells treated with $(RXR)_4$−PMOF displayed the same *m/z* peaks as those from the HeLa pLuc705 cells (Figure 5C), indicating that conjugate degradation is not related to the RNA targeting process.

The intracellular stabilities of $(RXR)_4$XB−PMOF and $(RX)_8$B−PMOF conjugates were also studied for shorter treatment times, treating pLuc705 cells with the conjugates for 1 and 5 h. For both conjugates at both time points, the major observed *m/z* peak corresponds to degradation product XB−PMOF with a minor peak for XRXB−PMOF (Table 4). These peaks were clearly identifiable in the SA matrix for both time points, while they are less intense in the THAP matrix for the 1 h time point and not identifiable in the CHCA matrix (data not shown), although the 24 h time point gives spectra with identifiable peaks in all three matrices (Figure 5 and Figure 6). This is likely due to higher concentrations of the materials recovered, since the uptake of the conjugate is a time-dependent process (*22*). In any case, the degraded peaks are identifiable in all three time points for both conjugates, and the peaks corresponding to the intact conjugates were not observed. This indicates that degradation is a fairly quick process.

Cellular Uptakes and Antisense Activities of $(RX)_8$−PMOF and the Degraded Fragments. To understand whether the CPP degradation affects the activity of a CPP−PMO, we determined the cellular uptakes and antisense activities of the $(RX)_8$−PMOF conjugate and its fragments, XRXB−PMOF and XB−PMOF. The compounds were delivered with or without mechanically scraping cells (*35*). After the cells were treated

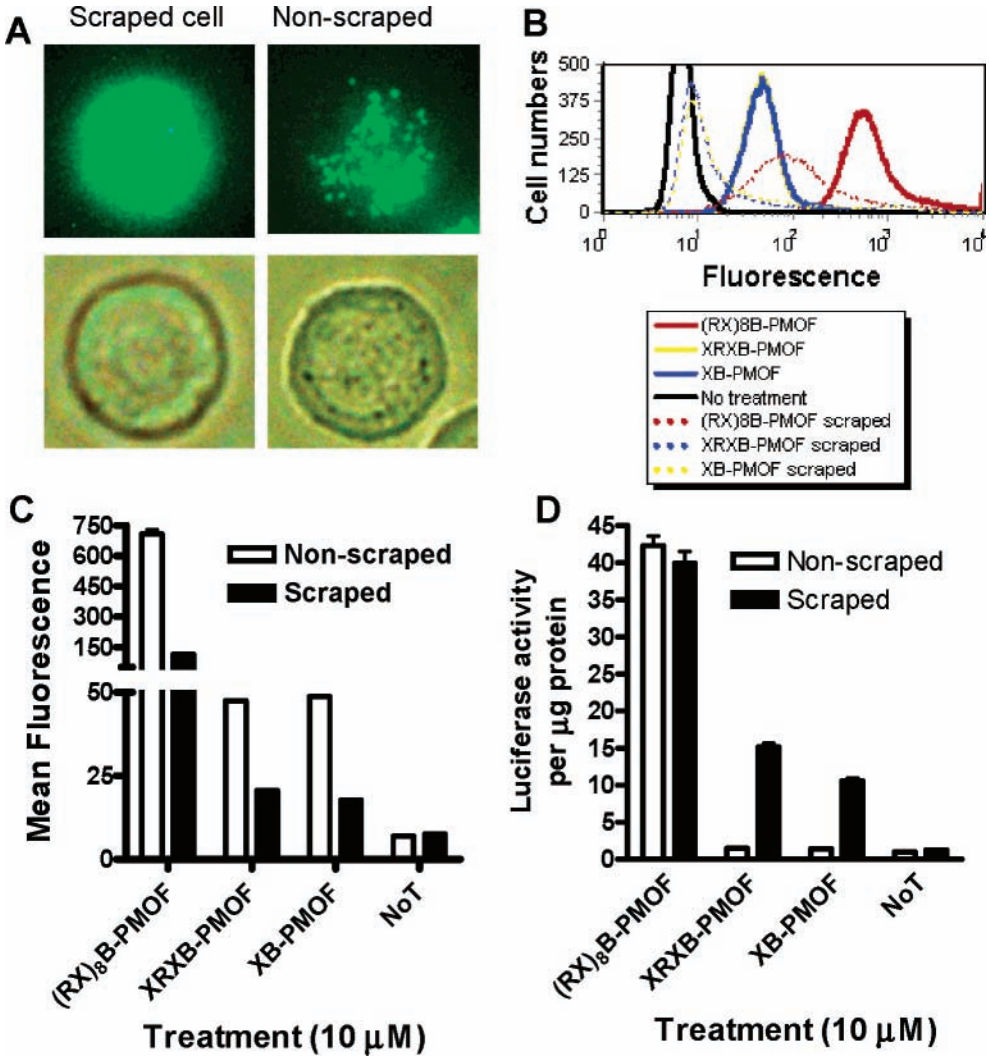


Figure 7. Cellular uptakes and antisense activities of $(RX)_8$−PMOF and the degraded fragments. Nonscraped treatment: 10 μM of the full-length conjugate or fragments in the cultural medium were added to the HeLa pLuc705 cells. Scraped treatment: 10 μM of the full-length conjugate or fragments in the cultural medium were added to cells and immediately followed by scraping, washing, and plating cells. Cells that had undergone both treatments were incubated for 24 h, washed, trypsinized, washed, and divided for the following assays. (A) Fluorescent and light images (400×) of scraped (left panel) and nonscraped (right panel) live cells treated with $(RX)_8$B−PMOF. (B) Flow cytometry histograms of scraped (dot lines) and nonscraped (solid lines) cells treated with $(RX)_8$−PMOF (red) and the fragments XRXB−PMOF (yellow) and XB−PMOF (blue). 20 000 events were collected for each histogram, and the data were presented without gating. (C) The bar graph of the mean fluorescence of scraped (black) and nonscraped (empty) cells. Each bar represents an average of fluorescence ± SEM from triplicate samples. (D) Luciferase activities of scraped (black bars) and nonscraped (empty bars) treated with the conjugate and fragments. Each bar represents an average of fluorescence ± SEM from triplicate samples.

with a compound for 24 h, the cells from each well were harvested for the determination of cell viability, cellular uptake by fluorescent microscopy, and flow cytometry as well as the antisense activity.

The harvested cells had 97−99% viable cells for all treatments as determined by a trypan blue exclusion assay. Fluorescent microscopy revealed that the scraped cells treated with $(RX)_8$−PMOF exhibited diffused fluorescence throughout the cells, while the nonscraped cells had generally brighter but punctate fluorescence as seen in the image in Figure 7A. This indicates that the majority of the compound was sequestered within vesicles and/or cellular compartments other than the cytosol and nucleus. Flow cytometry showed that nonscraped cells had higher amounts of the internalized conjugate and fragments than the scraped cells. Figure 7B and 7C show fluorescence histograms and the corresponding bar graphs of the treated cells. The nonscraped cells treated with the full-length conjugate had the highest fluorescence with mean fluorescence (MF) of 709, while the scraped cells treated with the conjugates had a much lower fluorescence (MF of 104), more than 6-fold lower. Similar trends were observed for the two fragment treatments with nonscraped cells having higher MF than scraped cells. The antisense activity was determined by the splice correction assay developed by R. Kole's group (*34*). The conjugate-treated scraped and nonscraped cells had a similar luciferase activity at approximately 40-fold over the background. The fragment-treated scraped cells produced the activity at 11−15-fold above the background, while the fragment-treated nonscraped cells had no activity (Figure 7D).

DISCUSSION

Although CPP-based delivery of therapeutic AOs is a promising technology, its effectiveness is hampered by entrapment of CPP−AO conjugates in endosomal and lysosomal compartments, as shown for the Tat− and oligoarginine−AO conjugates (*21*−*23*). Various approaches have been undertaken to induce endosomal release of CPP−AO conjugates, including the use of chloroquine (*23*), calcium ions (*36*), and a photochemical method (*37*). These approaches are not easy to use in vivo. An alternative approach is to design more effective CPPs.

We have shown that a $(RXR)_4$−PMO conjugate could escape from these compartments more effectively than the corresponding Tat− and R_9F_2−PMO conjugates (*22*). The stabilities of these conjugates in circulation and in cells are largely unknown.

SAR studies addressing enzymatic stability may assist in designing CPPs that are stable in blood, are inexpensive to manufacture, and can effectively escape from endosomes/lysosomes. As a first step in the use of SAR studies to search for more effective CPPs, we investigated several structural features of CPPs that may affect the metabolic stabilities of CPP conjugated to a therapeutically relevant AO analog (PMO): (i) amino acid configurations (L vs D), (ii) non-α-amino acids, (iii) sequences, and (iv) linker types. MALDI-TOF MS was used to analyze the samples due to its sensitivity, its tolerance to salts and impurities, and its quick analysis time.

We undertook several steps to ensure that the data from these studies are valid. First, we determined that the sample extraction/preparation procedure is adequate for MALDI-TOF MS analysis. The extraction/preparation procedure generally recovered 65−85% of PMO after taking into account the losses in vials and fluorescence photobleaching. We also controlled for any procedure-related degradation and showed that the procedure causes no detectable post-treatment degradation. We then determined the matrix effects and the relative sensitivity of MALDI-TOF MS analysis of the PMO and the conjugates in these matrices with cotitration experiments. Finally, all samples were analyzed in three matrices to take into account any mass discrimination or crystallization effects. The interpretations of MS data were based on the peak identifications from the spectra of all three matrices.

In human serum, the PMO portion of the CPP−PMO conjugates was completely stable while the CPP portions and the linkage varied. The stability of the CPP portion was ranked in the order of D-CPPs = $(RX)_8B$ = $(RB)_8B$ > $(RXR)_4$ > R_9F_2 = Tat. D-CPP conjugates were completely stable, while the L-CPP conjugates may not be, in agreement with the report of D-pVEC analogs (*38*). The utility of a D-CPP as a drug carrier may be limited by the cost of D-amino acids. CPPs consisting of non-α-amino acids interspersed with L-amino acids are an alternative for increasing blood stability with lower cost. Although insertions of *β*-alanine or 6-aminohexanoic acid into R_8 sequences increased the serum stability of R_8 (Table 3), the degree of stability was affected by the positions of these amino acids. The sequences containing no adjacent arginines, $(RX)_8B$ and $(RB)_8B$, were completely stable, while ones containing RR motifs, $(RXR)_4$, R_9F_2, and Tat were less stable, with the cleavages occurring at the amide bonds between adjacent arginines (Figure 4).

The stability of the linkage between a CPP and a PMO was ranked in the order of amide = maleimide > disulfide. No cleavage occurred at the amide or maleimide linkage, but cleavage occurred at the disulfide linkage (Tables 3 and 4). These results are consistent with other reports that an unhindered disulfide bond is not stable in blood circulation (*39*, *40*), and so it is not useful for conjugating therapeutic AOs.

In HeLa cells, the stability of the PMO portion of the CPP−PMO conjugates was excellent with no degraded products observed; the stability of the CPP portion of the conjugates was ranked in the order of D-CPPs > $(RB)_8B$ > $(RX)_8B$ = $(RXR)_4$ = R_9F_2 = Tat. No degradation products were seen for D-CPP conjugates, and no intact conjugates were observed for any L-CPP conjugates made of α-amino acids. The intact conjugate was observed for the $(RB)_8B$−PMO along with a degraded fragment after 24 h treatment, indicating that *β*-alanine increased the intracellular stability of L-CPPs. The degradation of $(RX)_8B$−PMO or $(RXR)_4$−PMO in cells was relatively rapid in contrast to degradation of these conjugates in human serum. After only 1 h treatment within cells, neither full-length conjugate was observed. Cleavage between R and X residues was observed for both CPP conjugates, and this was not seen in human serum.

We hypothesize that the rapid intracellular degradation of the conjugates may be a factor that limits the effectiveness of CPPs as AO carriers. In an attempt to address this issue, the activities of $(RX)_8B$−PMOF and its degraded fragments obtained by two delivery methods, with or without mechanically scraping cells, were compared. Mechanically scraping cells produces transient holes in the cell membranes, which permits a CPP−PMO to directly enter the cytosol/nucleus (*35*), bypassing an endosomal entry route. In nonscraped cells, the conjugate and the fragments were likely taken in by an endocytosis route, as has been shown for a similar conjugate $(RXR)_4$−PMOF (*22*).

Nonscraped cells took up $(RX)_8$−PMO much more efficiently than the scraped cells, as indicated by their >6-fold higher fluorescence (Figure 7C). However, the luciferase activities, an indicator for the antisense activity of PMO in nucleus, of the two treatments were similar (Figure 7D). In addition, the fluorescence signal of nonscraped cells was punctate compared to the diffuse signal of scraped cells (Figure 7A). These results indicate that a large fraction of internalized conjugate in the nonscraped cells was trapped within the vesicles and was not available for the pre-mRNA target in the nuclei. The cell extracts analyzed by mass spectrometry contained no full-length conjugate (Table 4), indicating that the observed fluorescent signal corresponded, at least largely, to the degraded fragments.

To address whether the observed fragments, with a major portion of the CPP degraded, can escape from endosomal/lysosomal compartments, we synthesized the fragments of $(RX)_8$−PMOF and compared their activities in nonscraped and scraped cells. The nonscraped cells treated with either of the two fragments had no luciferase activity despite their 7-fold higher fluorescence over the background. In contrast, the scraped cells treated with the fragments had luciferase activity at 11−15-fold over the background with only 2-fold over-background fluorescence. This indicates that, if the degradation occurs prior to escaping from vesicles, the internalized fragments in the nonscraped cells could not escape to reach the nucleus despite their higher cellular uptake. If they could escape the vesicles and reach the nucleus, the fragments would produce antisense activity as seen with the scraped cells.

Despite these results, a fraction of full-length or nearly full-length conjugate must be able to escape from the endosomes/lysosomes over time in order to explain the sequence-specific activities of CPP−PMO conjugates reported by our and other laboratories (*13*−*22*). Our extraction or analysis techniques may not be sensitive enough to detect a small amount of intact conjugate that has escaped. Alternatively, it is possible that escaped conjugates could be degraded in the cytosol or nucleus after they escaped from the vesicles.

At this point, the mechanisms of endosomal escaping of CPP-AO conjugates are not understood. Our results here suggest that the CPP stability is one of the several possible factors that affect its escaping ability. Other factors may include the structure, hydrophobicity/hydrophilicity, and charge density of CPP−AO conjugates. SAR studies are underway to further understand the relative importance of these aspects.

In summary, this study provides a method for determining the stability of CPP−AO conjugates in human serum and inside of cells. It shows that the stability of a CPP−cargo conjugate is affected by amino acid configurations of CPPs as well as the type of linkage to the cargo. Insertions of non-α-amino acids into L-CPP sequences increase their serum stability, which may increase the potential of CPPs as carriers for therapeutic drugs without using costly D-amino acids. In addition, we have found that degradation of the CPPs containing 6-aminohexanoic acid

was a faster process than for the CPP containing β-alanine. The degraded fragments did not escape effectively from the endosomes/lysosomes, and the majority of conjugates internalized were not available for the target. The instability of a CPP likely contributes to the endosomal trapping. Last, the study shows that PMO is completely stable both in cells and in human serum.

ACKNOWLEDGMENT

We would like to thank Dr. Jon D. Moulton for the critical reading of the manuscript. We are grateful to the chemistry team at AVI BioPharma for the synthesis, purification, and analysis of peptides and PMO.

LITERATURE CITED

(1) Fawell, S., Seery, J., Daikh, Y., Moore, C., Chen, L. L., Pepinsky, B., and Barsoum, J. (1994) Tat-mediated delivery of heterologous proteins into cells. *Proc. Natl. Acad. Sci. U.S.A. 91*, 664−668.

(2) Ruben, S., Perkins, A., Purcell, R., Joung, K., Sia, R., Burghoff, R., Haseltine, W. A., and Rosen, C. A. (1989) Structural and functional characterization of human immunodeficiency virus tat protein. *J. Virol. 63*, 1−8.

(3) Vives, E., Brodin, P., and Lebleu, B. (1997) A truncated HIV-1 Tat protein basic domain rapidly translocates through the plasma membrane and accumulates in the cell nucleus. *J. Biol. Chem. 272*, 16010−16017.

(4) Derossi, D., Joliot, A. H., Chassaing, G., and Prochiantz, A. (1994) The third helix of the Antennapedia homeodomain translocates through biological membranes. *J. Biol. Chem. 269*, 10444−10450.

(5) Futaki, S. (2005) Membrane-permeable arginine-rich peptides and the translocation mechanisms. *Adv. Drug Delivery Rev. 57*, 547−558.

(6) Gait, M. J. (2003) Peptide-mediated cellular delivery of antisense oligonucleotides and their analogues. *Cell Mol. Life Sci. 60*, 844−853.

(7) Koppelhus, U., and Nielsen, P. E. (2003) Cellular delivery of peptide nucleic acid (PNA). *Adv. Drug Delivery Rev. 55*, 267−280.

(8) Moulton, H. M., Nelson, M. H., Hatlevig, S. A., Reddy, M. T., and Iversen, P. L. (2004) Cellular uptake of antisense morpholino oligomers conjugated to arginine-rich peptides. *Bioconjugate Chem. 15*, 290−299.

(9) Futaki, S. (2006) Oligoarginine vectors for intracellular delivery: design and cellular-uptake mechanisms. *Biopolymers 84*, 241−249.

(10) Rothbard, J. B., Kreider, E., VanDeusen, C. L., Wright, L., Wylie, B. L., and Wender, P. A. (2002) Arginine-rich molecular transporters for drug delivery: role of backbone spacing in cellular uptake. *J. Med. Chem. 45*, 3612−3618.

(11) Summerton, J., and Weller, D. (1997) Morpholino antisense oligomers: design, preparation, and properties. *Antisense Nucleic Acid Drug Dev. 7*, 187−195.

(12) Nielsen, P. E., Egholm, M., Berg, R. H., and Buchardt, O. (1991) Sequence-selective recognition of DNA by strand displacement with a thymine-substituted polyamide. *Science 254*, 1497−1500.

(13) McClorey, G., Moulton, H. M., Iversen, P. L., Fletcher, S., and Wilton, S. D. (2006) Antisense oligonucleotide-induced exon skipping restores dystrophin expression in vitro in a canine model of DMD. *Gene Ther. 13* (19), 1373−1381.

(14) McClorey, G., Fall, A. M., Moulton, H. M., Iversen, P. L., Rasko, J. E., Ryan, M., Fletcher, S., and Wilton, S. D. (2006) Induced dystrophin exon skipping in human muscle explants. *Neuromuscular Disord. 16*, 583−590.

(15) Enterlein, S., Warfield, K. L., Swenson, D. L., Stein, D. A., Smith, J. L., Gamble, C. S., Kroeker, A. D., Iversen, P. L., Bavari, S., and Muhlberger, E. (2006) VP35 knockdown inhibits Ebola virus amplification and protects against lethal infection in mice. *Antimicrob. Agents Chemother. 50*, 984−993.

(16) Holden, K. L., Stein, D. A., Pierson, T. C., Ahmed, A. A., Clyde, K., Iversen, P. L., and Harris, E. (2006) Inhibition of dengue virus translation and RNA synthesis by a morpholino oligomer targeted to the top of the terminal 3′ stem-loop structure. *Virology 344*, 439−452.

(17) Alonso, M., Stein, D. A., Thomann, E., Moulton, H. M., Leong, J. C., Iversen, P. L., and Mourich, D. V. (2005) Inhibition of infectious haematopoietic necrosis virus in cell cultures with peptide-conjugated morpholino oligomers. *J. Fish Dis. 28*, 399−410.

(18) Neuman, B. W., Stein, D. A., Kroeker, A. D., Churchill, M. J., Kim, A. M., Kuhn, P., Dawson, P., Moulton, H. M., Bestwick, R. K., Iversen, P. L., and Buchmeier, M. J. (2005) Inhibition, escape, and attenuated growth of severe acute respiratory syndrome coronavirus treated with antisense morpholino oligomers. *J. Virol. 79*, 9665−9676.

(19) Kinney, R. M., Huang, C. Y., Rose, B. C., Kroeker, A. D., Dreher, T. W., Iversen, P. L., and Stein, D. A. (2005) Inhibition of dengue virus serotypes 1 to 4 in vero cell cultures with morpholino oligomers. *J. Virol. 79*, 5116−5128.

(20) Deas, T. S., Binduga-Gajewska, I., Tilgner, M., Ren, P., Stein, D. A., Moulton, H. M., Iversen, P. L., Kauffman, E. B., Kramer, L. D., and Shi, P. Y. (2005) Inhibition of flavivirus infections by antisense oligomers specifically suppressing viral translation and RNA replication. *J. Virol. 79*, 4599−4609.

(21) Turner, J. J., Ivanova, G. D., Verbeure, B., Williams, D., Arzumanov, A. A., Abes, S., Lebleu, B., and Gait, M. J. (2005) Cell-penetrating peptide conjugates of peptide nucleic acids (PNA) as inhibitors of HIV-1 Tat-dependent trans-activation in cells. *Nucleic Acids Res. 33*, 6837−6849.

(22) Abes, S., Moulton, H. M., Clair, P., Prevot, P., Youngblood, D. S., Wu, R. P., Iversen, P. L., and Lebleu, B. Vectorization of morpholino oligomers by the (R-Ahx-R)4 peptide allows efficient splicing correction in the absence of endosomolytic agents. *J. Controlled Release,* in press.

(23) Abes, S., Williams, D., Prevot, P., Thierry, A., Gait, M. J., and Lebleu, B. (2006) Endosome trapping limits the efficiency of splicing correction by PNA-oligolysine conjugates. *J. Controlled Release 110*, 595−604.

(24) Richard, J. P., Melikov, K., Brooks, H., Prevot, P., Lebleu, B., and Chernomordik, L. V. (2005) Cellular uptake of unconjugated TAT peptide involves clathrin-dependent endocytosis and heparan sulfate receptors. *J. Biol. Chem. 280*, 15300−15306.

(25) Thoren, P. E., Persson, D., Isakson, P., Goksor, M., Onfelt, A., and Norden, B. (2003) Uptake of analogs of penetratin, Tat(48−60) and oligoarginine in live cells. *Biochem. Biophys. Res. Commun. 307*, 100−107.

(26) Vives, E., Richard, J. P., Rispal, C., and Lebleu, B. (2003) TAT peptide internalization: seeking the mechanism of entry. *Curr. Protein Pept. Sci. 4*, 125−132.

(27) Summerton, J., and Weller, D. (1993) Uncharged morpholino-based polymers having phosphorus containing chiral intersubunit linkages. U.S. Patent 5,185,444.

(28) Chan, W., and White, P., Eds. (2000) *Fmoc Solid Phase Peptide Synthesis; A Practical Approach*, Oxford University Press, New York.

(29) Moulton, H. M., Hase, M. C., Smith, K. M., and Iversen, P. L. (2003) HIV Tat peptide enhances cellular delivery of antisense morpholino oligomers. *Antisense Nucleic Acid Drug Dev. 13*, 31−43.

(30) Hoffman, E., and Stroobant, V., Eds. (2002) *Mass Spectrometery, Principals and Applications*, 2nd ed., John H. Wiley & Sons, Ltd., Chichester.

(31) Cohen, S. L., and Chait, B. T. (1996) Influence of Matrix Solution Conditions on the MALDI-MS Analysis of Peptides and Proteins. *Anal. Chem. 68*, 31−37.

(32) Hudziak, R. M., Barofsky, E., Barofsky, D. F., Weller, D. L., Huang, S. B., and Weller, D. D. (1996) Resistance of morpholino phosphorodiamidate oligomers to enzymatic degradation. *Antisense Nucleic Acid Drug Dev. 6*, 267−272.

(33) Richard, J. P., Melikov, K., Vives, E., Ramos, C., Verbeure, B., Gait, M. J., Chernomordik, L. V., and Lebleu, B. (2003) Cell-penetrating peptides. A reevaluation of the mechanism of cellular uptake. *J. Biol. Chem. 278*, 585−590.

(34) Kang, S. H., Cho, M. J., and Kole, R. (1998) Up-regulation of luciferase gene expression with antisense oligonucleotides: implications and applications in functional assay development. *Biochemistry 37*, 6235−6239.

(35) Partridge, M., Vincent, A., Matthews, P., Puma, J., Stein, D., and Summerton, J. (1996) A simple method for delivering morpholino antisense oligos into the cytoplasm of cells. *Antisense Nucleic Acid Drug Dev. 6*, *169*−175.

(36) Shiraishi, T., Pankratova, S., and Nielsen, P. E. (2005) Calcium ions effectively enhance the effect of antisense peptide nucleic acids conjugated to cationic tat and oligoarginine peptides. *Chem. Biol. 12*, 923−929.

(37) Shiraishi, T., and Nielsen, P. E. (2006) Photochemically enhanced cellular delivery of cell penetrating peptide-PNA conjugates. *FEBS Lett. 580*, 1451−1456.

(38) Elmquist, A., and Langel, U. (2003) In vitro uptake and stability study of pVEC and its all-D analog. *Biol. Chem. 384*, 387−393.

(39) Ghetie, V., Till, M. A., Ghetie, M. A., Tucker, T., Porter, J., Patzer, E. J., Richardson, J. A., Uhr, J. W., and Vitetta, E. S. (1990) Preparation and characterization of conjugates of recombinant CD4 and deglycosylated ricin A chain using different cross-linkers. *Bioconjugate Chem. 1*, 24−31.

(40) Thorpe, P. E., Wallace, P. M., Knowles, P. P., Relf, M. G., Brown, A. N., Watson, G. J., Knyba, R. E., Wawrzynczak, E. J., and Blakey, D. C. (1987) New coupling agents for the synthesis of immunotoxins containing a hindered disulfide bond with improved stability in vivo. *Cancer Res. 47*, 5924−5931.

BC060138S

Site-Specific PEGylation of Protein Disulfide Bonds Using a Three-Carbon Bridge

Sibu Balan,[†] Ji-won Choi,[‡] Antony Godwin,[†] Ian Teo,[‡] Carlos M. Laborde,[†] Sibylle Heidelberger,[§] Mire Zloh,[§] Sunil Shaunak,*[,‡] and Steve Brocchini*[,†]

Department of Pharmaceutics, The School of Pharmacy, University of London, 29/39 Brunswick Square, London WC1N 1AX, Faculty of Medicine, Imperial College London, Hammersmith Hospital, Ducane Road, London W12 0NN, and Department of Pharmaceutical and Biological Chemistry, The School of Pharmacy, University of London, 29/39 Brunswick Square, London WC1N 1AX, U.K. Received May 31, 2006; Revised Manuscript Received September 8, 2006

The covalent conjugation of a functionalized poly(ethylene glycol) (PEG) to multiple nucleophilic amine residues results in a heterogeneous mixture of PEG positional isomers. Their physicochemical, biological, and pharmaceutical properties vary with the site of conjugation of PEG. Yields are low because of inefficient conjugation chemistry and production costs high because of complex purification procedures. Our solution to these fundamental problems in PEGylating proteins has been to exploit the latent conjugation selectivity of the two sulfur atoms that are derived from the ubiquitous disulfide bonds of proteins. This approach to PEGylation involves two steps: (1) disulfide reduction to release the two cysteine thiols and (2) re-forming the disulfide by bis-alkylation via a three-carbon bridge to which PEG was covalently attached. During this process, irreversible denaturation of the protein did not occur. Mechanistically, the conjugation is conducted by a sequential, interactive bis-alkylation using α,β-unsaturated β′-monosulfone functionalized PEG reagents. The combination of (a) maintaining the protein's tertiary structure after disulfide reduction, (b) the mechanism for bis-thiol selectivity of the PEG reagent, and (c) the steric shielding of PEG ensure that only one PEG molecule is conjugated at each disulfide bond. PEG was site-specifically conjugated via a three-carbon bridge to 2 equiv of the tripeptide glutathione, the cyclic peptide hormone somatostatin, the tetrameric protein L-asparaginase, and to the disulfides in interferon α-2b (IFN). SDS-PAGE, mass spectral, and NMR analyses were used to confirm conjugation, thiol selectivity, and connectivity. The biological activity of the L-asparaginase did not change after the attachment of four PEG molecules. In the case of IFN, a small reduction in biological activity was seen with the single-bridged IFN (without PEG attached). A significantly larger reduction in biological activity was seen with the three-carbon disulfide single-bridged PEG-IFNs and with the double-bridged IFN (without PEG attached). The reduction of the PEG-IFN's in vitro biological activity was a consequence of the steric shielding caused by PEG, and it was comparable to that seen with all other forms of PEG-IFNs reported. However, when a three-carbon bridge was used to attach PEG, our PEG-IFN's biological activity was found to be independent of the length of the PEG. This property has not previously been described for PEG-IFNs. Our studies therefore suggest that peptides, proteins, enzymes, and antibody fragments can be site-specifically PEGylated across a native disulfide bond using three-carbon bridges without destroying their tertiary structure or abolishing their biological activity. The stoichiometric efficiency of this approach also enables recycling of any unreacted protein. It therefore offers the potential to make PEGylated biopharmaceuticals as cost-effective medicines for global use.

INTRODUCTION

Covalent conjugates of poly(ethylene glycol) (PEG) with amino residues of native proteins are typically mixtures of positional isomers (*1*−*5*). The relative amount of each PEG−protein isomer depends upon the PEG's terminal chemical functionality, its molecular weight, its morphology, and the specific reaction conditions used for conjugation (*6*). Some amine-specific PEG reagents (e.g., active esters, carbonates, isocyanates) also have a short half-life in aqueous solution, while others are inefficient for conjugating proteins (e.g., aldehydes). Typically, a large stoichiometric excess of the PEG reagent is required. These characteristics often lead to complex purification procedures for removing the excess PEG and the unwanted protein side products.

* Joint senior and corresponding authors. E-mail address (S.B.): steve.brocchini@pharmacy.ac.uk. E-mail address (S.S.): s.shaunak@imperial.ac.uk.

[†] Department of Pharmaceutics, The School of Pharmacy, University of London.

[‡] Imperial College London.

[§] Department of Pharmaceutical and Biological Chemistry, The School of Pharmacy, University of London.

Conjugation strategies and PEG reagents have been developed to address the important issue of site specificity (*7*−*18*). Of these, thiol-specific reagents are notable because some of them can lead to efficient conjugation reactions. However, in order to utilize thiol-specific PEG reagents, it has become necessary to recombinantly engineer a new and free cysteine into the protein (*19*). This is technically demanding and expensive, and the presence of an accessible free thiol often leads to disulfide scrambling, protein misfolding, and an increased propensity for irreversible protein aggregatation during its purification.

Our approach is particularly relevant to those therapeutic proteins whose mode of action is via cell surface receptors because they often have paired disulfides but seldom have a free cysteine residue (*20*). Typically, these proteins have an even number of cysteines that pair up as disulfides (*21*−*23*). Our strategy exploits the chemical reactivity of *both* of the sulfur atoms in an accessible disulfide bond. While disulfides influence a protein's properties in subtle and complex ways (*24*), the accessible disulfides typically contribute to the stability of the protein rather than to its structure or its function (*21*). In contrast, the disulfides that are present in a protein's hydrophobic interior

10.1021/bc0601471 CCC: $37.00 © 2007 American Chemical Society
Published on Web 11/29/2006

(*21*, *25*) typically contribute to the maintenance of its tight packing and its function. Although there are examples where chemical modification of a disulfide results in a major loss of tertiary structure (*26*) and biological activity (*27*−*29*), there are also examples where chemical modification, especially of accessible disulfides, does not lead to a loss of protein structure or activity (*30*, *31*).

We have found that mild reduction of an accessible native disulfide bond to liberate the cysteine thiols can be followed by PEGylation with a bis(thiol)-specific reagent. This leads to the bridging of the two cysteine thiols with PEG attached. We have recently shown that (i) a single intrachain three-carbon bridge (with and without PEG attached) can be inserted across a native disulfide bond in interferon α-2b (IFN), and (ii) a single interchain three-carbon disulfide bridge with PEG attached can be inserted into an anti-CD4 antibody fragment using PEG monosulfone. There is no disruption of the tertiary structure or the biological activity of either protein (*32*, *33*). We now report further details of the synthesis of the disulfide bridging PEGylation reagents and their use with (i) reduced glutathione, (ii) somatostatin, (iii) the multimeric protein L-asparaginase, and (iv) interferon α-2b (IFN).

EXPERIMENTAL SECTION

Materials. Reduced (GSH) and oxidized (GSSG) glutathione, somatostatin, dithiothreitol (DTT), tris(2-carboxyethyl) phosphine (TCEP-HCl), *O*-(2-aminoalkyl)-*O*′-methyl poly(ethylene glycol) 5 kDa, *E. coli*-derived L-asparaginase (L-asparagine amidohydrolase, E.C. 3.5.1.1) and the commercial PEG−L-asparaginase were from Sigma-Aldrich. The IFN is in clinical use as Shanferon (Shantha Biotechnics, India). It is manufactured using a yeast-based protein expression system, and it shows chemical and biological equivalence to the NIBSC (U.K.) international biological standard (*34*). *O*-(2-aminoethyl)-*O*′-methyl poly(ethylene glycol) (10 and 20 kDa) were purchased from NOF Corporation, Japan. Superdex 200 prep grade, Sephadex G-25 desalting (PD-10), HiTrap SP FF cation exchange, and HiTrap Q FF anion exchange columns were from GE Healthcare. All other reagents and solvents were purchased from Sigma-Aldrich and used as received.

Preparation of 4-[2,2-bis[(*p*-tolylsulfonyl)methyl]acetyl) Benzoic Acid−NHS Ester 2. Under an argon atmosphere, a stirred mixture of 4-(2,2-bis[(*p*-tolylsulfonyl)methyl]acetyl) benzoic acid **1** (2.00 g, 4.0 mmol) prepared as described (*35*, *36*), *N*-Hydroxysuccinimide (0.483 g, 4.2 mmol, NHS) and anhydrous dichloromethane (5 mL) were cooled using an ice bath. Neat 1,3-diisopropylcarbodiimide (657 μL, 4.2 mmol, DIPC) was then added dropwise. A further 60 μL of DIPC was added after 1.5 h. After 3 h, the reaction mixture was passed through a nonabsorbent cotton wool filter. The homogeneous filtrate was diluted with dichloromethane (∼30 mL), washed with water (2 × 15 mL), and dried with magnesium sulfate. Gravity filtration followed by removal of volatiles under vacuum gave the desired active NHS ester **2** as a solid product (1.89 g, 79% yield).

^{1}H NMR: ($CDCl_3$, 400 MHz) δ 2.48 (s, 6H, CH_3), 2.94 (s, 4H, CH_2CH_2), 3.56 (A2B2X, 4H, CH_2C), 4.38 (quintet, 1H, C*H*, J = 6.3 MHz), 7.37, 7.70 (AB q, SO_2Ar, 8H, J = 8.0 and 8.3 MHz, respectively), 7.76, 8.14 (AB q, CO*Ar*, 4H, J = 8.6 MHz).

^{13}C NMR: ($CDCl_3$, 400 MHz) δ 195.29, 168.92, 160.95, 145.63, 139.11, 135.29, 130.92, 130.24, 129.59, 128.73, 128.28, 55.67, 35.89, 25.70, 21.70.

MALDI-TOF-MS: m/z = 620.3070 ± 0.43 RSD $[M + H]^+$.

Preparation of PEG Bis(sulfone) 3. To anhydrous dichloromethane (4 mL) in an argon atmosphere was added 4-(2,2-bis[(*p*-tolylsulfonyl)methyl]acetyl) benzoic acid−NHS ester **2** (300 mg, 503 μmol). This solution was cooled with an ice bath, and to this was added an anhydrous dichloromethane (5 mL) solution of *O*-(2-aminoethyl)-*O*′-methyl poly(ethylene glycol) (5000 g/mol) (0.5 g, 100 μmol). The reaction solution was stirred for 48 h. Volatiles were removed under vacuum, and the crude solid PEG bis(sulfone) **3** was redissolved in acetone (15 mL) with gentle warming. The stirred solution was then cooled in an ice bath to precipitate the desired product **3**, which was isolated using a no 3 sintered glass funnel and washed with chilled acetone (∼30 mL). Drying in vacuo gave the PEG bis-(sulfone) **3** as a white solid product (0.46 g, 84% yield).

^{1}H NMR: ($CDCl_3$, 400 MHz) δ 2.49 (s, 6H, CH_3Ar), 3.38 (s, 3H, CH_3OPEG), 3.44−3.84 (m, PEG + 4H, CH_2SO_2), 4.34 C*H*CO (qn, 1H, C*H*CO), 7.36, 7.69 (AB q, SO_2Ar, 4H, J = 8.3 MHz), 7.64, 7.81 (AB q, CO*Ar*, 4H, J = 8.3 MHz).

^{13}C NMR: ($CDCl_3$, 500 MHz) δ 195.11, 166.14, 145.51, 139.43, 136.19, 135.37, 130.19, 128.63, 128.31, 127.68, 71.94, 70.57, 69.59, 59.01, 55.56, 40.01, 35.61, 21.72.

Preparation of PEG Bis(sulfone) 3 Directly from Bis-(sulfone) Carboxylic Acid 1. To a Schlenk flask containing *O*-(2-aminoethyl)-*O*′-methyl poly(ethylene glycol) (5000 g/mol, 0.5 g, 0.33 equiv, 100 μmol) was added 4-(2,2-bis[(*p*-tolylsulfonyl)methyl]acetyl) benzoic acid **1** (150 mg, 1 equiv, 300 μmol) and *N*,*N*′-dicyclohexylcarbodiimide (62 mg, 1 equiv, 300 μmol). The flask was sealed with a rubber septum and then subjected to high vacuum for 30 min through the side arm. Argon was introduced into the flask, which was then placed in an ice bath to cool the solution. Anhydrous dichloromethane (10 mL) was injected and the contents stirred to form a homogeneous solution that was allowed to warm slowly to room temperature. The reaction mixture was then stirred for 3 h and filtered through a sintered glass filter no 3 to remove insoluble dicyclohexylurea. Dichloromethane was removed from the filtrate by rotoevaporation, and the viscous crude product residue was redissolved in acetone (20 mL) with gentle warming. The flask was then placed in a dry ice bath for 5 min to precipitate the product, which was isolated by filtration (no 3 sintered glass) and dried in vacuo to afford the desired PEG bis(sulfone) **3** as a white solid product (0.4 g, 73%).

^{1}H NMR: ($CDCl_3$, 400 MHz) δ 2.49 (s, 6H, CH_3Ar), 3.38 (s, 3H, CH_3OPEG), 3.44−3.84 (m, PEG + 4H, CH_2SO_2), 4.34 C*H*CO (qn, 1H, C*H*CO), 7.36, 7.69 (AB q, SO_2Ar, 4H, J = 8.3 MHz), 7.64, 7.81 (AB q, CO*Ar*, 4H, J = 8.3 MHz).

^{13}C NMR: ($CDCl_3$, 500 MHz) δ 195.11, 166.14, 145.51, 139.43, 136.19, 135.37, 130.19, 128.63, 128.31, 127.68, 71.94, 70.57, 69.59, 59.01, 55.56, 40.01, 35.61, 21.72.

Preparation of PEG Monosulfone 4. The PEG bis(sulfone) **3** (∼5500 g/mol, 0.20 g, 36 μmol) was dissolved in 10 mL of sodium phosphate buffer, pH 7.8 (20 mg/mL), and incubated overnight at ambient temperature. The reaction solution was added to a reverse-phase (C-18) packed sintered glass funnel that had been pre-equilibrated with deionized water. Water was removed from the filter by vacuum. The column was then washed with 25% aqueous acetonitrile to remove the buffer salts and the eliminated sulfinic acid. The reaction mixture was eluted with 75% aqueous acetonitrile and the filtrate freeze-dried to obtain the PEG monosulfone **4** (which was 80% pure by ^{1}H NMR with the remainder being the starting PEG bis(sulfone) **3**) as a white solid (0.16 g, 82% yield).

^{1}H NMR: ($CDCl_3$, 400 MHz) δ 2.35 (s, 3H, CH_3Ar), 3.31 (s, 3H, CH_3OPEG), 3.39−3.76 (m, PEG), 4.28 (s, 2H, CH_2-SO_2), 5.93, 6.22 (s, 2H, CH_2═C), 7.26, 7.64 (AB q, SO_2Ar, 4H, J = 8.3 and 8.6 MHz, respectively), 7.72, 7.81 (AB q, CO*Ar*, 4H, J = 8.1 and 8.3 MHz, respectively).

Conjugation of PEG to Reduced Glutathione (GSH). A microfuge tube was charged with PEG bis(sulfone) **3** (16 mg, 2.91 μmol, 1 equiv, 5500 g/mol) and GSH (2 mg, 2.24 equiv,

6.51 μmol) followed by 900 μL of 50 mM sodium phosphate buffer, pH 7.8, containing 10 mM EDTA. The tube was gently shaken to dissolve the solids and left for 18 h at ambient temperature. To ensure complete reaction, 100 μL of 1 N NaOH was added. The solution (1 mL) was loaded onto a PD-10 desalting column pre-equilibrated with 90:10 (v/v) H_2O/D_2O and the elution (1 mL) discarded. Additions of 1 mL each of fresh 90:10 (v/v) H_2O/D_2O to the PD-10 column were made while collecting the eluting 1 mL fractions separately. Each eluted 1 mL fraction was analyzed by UV absorbance at 215 nm. Typically, the initial two fractions which did not contain the conjugate (wash volume 2 mL) were discarded. The third fraction with the maximum amount of reaction product was analyzed by ^{1}H NMR with water suppression, 2D [^{1}H,^{1}H]-TOCSY, and 2D [^{1}H,^{1}H] NOESY.

PEGylation of Somatostatin. The PEG bis(sulfone) **3** (25 mg, 4.55 μmol, 5500 g/mol**)** was incubated in 50 mM sodium phosphate buffer (1 mL), pH 7.8, for 20 h and purified by reverse-phase (C-18) HPLC using a gradient of 30−60% acetonitrile in 30 min at a flow rate of 1 mL/min with UV detection at 215 nm. The collected fraction was subjected to freeze-drying to obtain the PEG monosulfone **4** (0.7 mg). Somatostatin (0.25 mg/mL in 50 mM sodium phosphate buffer, 0.15 μmol, pH 6.2) was disulfide-reduced with 1 equiv of TCEP-HCl (*37*) for 1 h at ambient temperature. PEG monosulfone **4** (0.7 mg, 0.13 μmol, 0.86 equiv) was added to the reduced peptide. The reaction solution was gently mixed and left overnight at 4 °C. The solution was then loaded onto a PD-10 desalting column pre-equilibrated with deionized water and the elution (1 mL) discarded. Additions of 1 mL each of fresh deionized water were made to the PD-10 column while collecting the eluting 1 mL fractions separately. Each eluted 1 mL fraction was analyzed by UV absorbance at 215 nm. Typically, the initial two elution fractions, which did not contain the conjugate (wash volume 2 mL), were discarded. The third fraction, which had the maximum amount of conjugate, was analyzed by MALDI-TOF-MS. A control reaction was conducted with somatostatin that was not previously incubated with TCEP-HCl and was followed by PD-10 desalting. MALDI-TOF-MS analysis showed only the presence of the PEG reagent, indicating that the conjugation reaction had not occurred. Unreacted somatostatin was removed during the desalting step.

Preparation of a Three-Carbon Disulfide-Bridged Somatostatin. Carboxylic acid bis(sulfone) **1** (5.7 mg) was incubated in 2:3 (v/v) acetonitrile/50 mM sodium phosphate buffer, pH 8.0 (1 mL), for 24 h. The rate of formation of the corresponding monosulfone was monitored by ^{1}H NMR (data not shown), and the pH was then adjusted to 6.2 using 1 N HCl. Somatostatin (0.25 mg/mL, 1 mL) in 2:3 (v/v) acetonitrile/50 mM sodium phosphate buffer, pH 6.2, was disulfide-reduced using 2 equiv of TCEP−HCl for 1 h at ambient temperature. The solution containing ∼1.4 equiv of the monosulfone moiety was added to the reduced peptide. The reaction solution was gently shaken and left overnight at 4 °C. It was then subjected to freeze-drying to remove volatiles. The solids were resolubilized in water and filtered (0.2 μm). The filtrate was subjected to reverse-phase (C-18) HPLC using acetonitrile/water solvent system (gradient: 20−40% acetonitrile in 10 min) containing 0.05% trifluoroacetic acid (TFA) with UV detection at 215 nm. The peptide peak (retention time 8.03 min; chromatogram not shown) was collected and mass-analyzed.

PEGylation of L-Asparaginase. To a solution of L-asparaginase (0.5 mg/mL, 1 mL) in 50 mM sodium phosphate buffer, pH 7.8, containing 10 mM EDTA was added DTT (100 mM, 15.4 mg). The solution was incubated for 30 min at ambient temperature and then loaded onto a PD-10 desalting column pre-equilibrated with 50 mM sodium phosphate buffer, pH 7.8, containing 10 mM EDTA and the elution (1 mL) discarded. Fresh 2 mL buffer (wash volume) was then added to the PD-10 and the elution discarded again. More fresh 2.5 mL buffer was added while collecting the elution for PEGylation. To the reduced protein solution (∼0.19 mg/mL, 2.5 mL; yield was 96% of the starting protein concentration) was added PEG monosulfone **4** (1.3 equiv for each disulfide) as a freshly prepared 20 mg/mL solution in 50 mM sodium phosphate buffer, and the solution was allowed to react for 16 h at 4 °C (approximately 5, 10, and 20 μL PEG monosulfone solution for 5, 10, and 20 kDa PEGylation reactions, respectively). The reaction solution (2.5 mL) was buffer-exchanged to 50 mM Tris buffer, pH 8.6, using a PD-10 desalting column (giving 0.13 mg/mL, 3.5 mL; yield 91% of the starting concentration). The solution was then loaded onto a HiTrap Q FF 1 mL column aided by a peristaltic pump. The column was washed manually using a syringe with 5 mL (2 column volumes) of fresh 50 mM Tris buffer, pH 8.6. The pure conjugate eluted on washing the column with 1 M sodium chloride in 50 mM Tris buffer (2.0 mL). The conjugates were further characterized by size exclusion chromatography (SEC) using a Superdex 200 prep grade column.

PEGylation of IFN. To a solution of IFN (0.5 mg/mL, 1 mL) in 50 mM sodium phosphate buffer, pH 7.8, containing 10 mM EDTA was added DTT (100 mM, 15.4 mg). The solution after incubation for 30 min at ambient temperature was loaded onto a PD-10 desalting column pre-equilibrated with 50 mM sodium phosphate buffer, pH 7.8, containing 10 mM EDTA and the elution (1 mL) discarded. Fresh 2 mL buffer (wash volume) was then added to the PD-10 and the elution discarded again. Further fresh buffer (2.5 mL) was added while collecting the elution for PEGylation. To the reduced protein solution (∼0.19 mg/mL, 2.5 mL; yield 96% of protein remaining) was added 1 equiv of 10 kDa PEG monosulfone **4** or 10 kDa PEG bis(sulfone) **3** (13 μL of a freshly prepared 20 mg/mL solution in 50 mM sodium phosphate buffer, pH 7.8), and the solution was allowed to react for 16 h at 4 °C. Glutathione refolding solution (50 μL of 50 mM GSH/50 mM GSSG solution to yield a reaction concentration of 1 mM GSH/1 mM GSSG) (*38*) was added to the reaction mixture and allowed to incubate for 24 h at 4 °C. The reaction solution (2.5 mL) was buffer-exchanged to 20 mM sodium acetate, pH 4.0, using a PD-10 desalting column. The resulting 3.5 mL solution had a protein concentration of 0.13 mg/mL (91% of protein remaining). The solution was then loaded onto a HiTrap SP FF 1 mL column aided by a peristaltic pump. The column was washed manually using a syringe with 5 mL (2 column volumes) of fresh 20 mM sodium acetate buffer, pH 4.0. The pure conjugate eluted on washing the column with 1 M sodium chloride in 20 mM sodium acetate buffer (0.185 mg/mL, 2 mL, yield 74%). The conjugates were further isolated by size exclusion chromatography (SEC) using a Superdex 200 prep grade column, and the yields with PEG monosulfone **4** (10 kDa, 1 equiv) were as follows: three-carbon disulfide single-bridged 10 kDa PEG−IFN, 64.3%; three-carbon disulfide double-bridged 10 kDa PEG−IFN, 17.4%; IFN, 13.4%; and aggregated IFN, 4.8%. The yields with PEG bis(sulfone) **3** (10 kDa, 1 equiv) were as follows: three-carbon disulfide single-bridged 10 kDa PEG−IFN, 56.69%; three-carbon disulfide double-bridged 10 kDa PEG−IFN, 8.69%; IFN, 32.36%; and aggregated IFN, 2.25%.

Preparation of Three-Carbon Disulfide Double-Bridged IFNs. To a solution of IFN (0.2 mg/mL, 1 mL) in 50 mM sodium phosphate buffer at pH 7.8 containing 10 mM EDTA was added dithiothreitol (DTT, 100 mM, 15.4 mg). The solution after incubation for 30 min at ambient temperature was loaded onto a PD-10 desalting column pre-equilibrated with 50 mM sodium phosphate buffer, pH 7.8, containing 10 mM EDTA and the elution (1 mL) discarded. Fresh 2 mL buffer (wash

volume) was then added to the PD-10 and the elution discarded again. More fresh 2 mL buffer was added while collecting the elution for reaction. To the solution containing the reduced IFN (~75 μg/mL, 2 mL) was then added 8 equiv of the carboxylic acid bis(sulfone) **1** as a solution in acetonitrile (50 μL of 0.625 mg/mL). The mixture was gently shaken and incubated for 2 h at 4 °C. The reaction solution was made up to 2.5 mL and then buffer-exchanged to 20 mM sodium acetate, pH 4.0, using a PD-10 desalting column to obtain the three-carbon double-bridged IFN (3.5 mL, ~40 μg/mL).

MALDI-TOF-MS. Mass spectra were acquired using an Applied Biosystems Voyager System DE PRO MALDI-TOF mass spectrometer using a nitrogen laser. The matrix was a saturated solution of α-cyano-4-hydroxycinnamic acid in a 50:50 mixture of acetonitrile and water containing 0.1% trifluoroacetic acid. Sample and matrix were mixed 1:1, and 1 μL was spotted onto a 100-well sample plate. All spectra were acquired in positive mode over the range 600−2500 Da under reflectron conditions (20 kV accelerating voltage, 350 ns extraction delay time) and 2−100 kDa under linear conditions (25 kV accelerating voltage, 750 ns extraction delay time).

Tryptic Digestion and MALDI-TOF Analysis. IFN and the bridged IFN solutions (1 mL each of 0.2 mg/mL in 10 mM sodium phosphate buffer, pH 8.0) were concentrated to 200 μL using Vivaspin 6 mL concentrators (Sartorius). Sequencing grade modified trypsin (50 μL of 0.2 mg/mL, Promega) was added to each of the samples followed by incubation at 37 °C for 14 h. To each solution was added acetonitrile (30 μL), and the incubation continued at 37 °C for another 4 h. Finally, each digest was diluted with 220 μL of acetonitrile and the resulting samples analyzed using a Voyager MALDI-TOF-MS. High-resolution reflectron mode was used to observe low molecular masses. Low-resolution linear mode was used to observe high molecular masses.

NMR Spectroscopy. NMR spectra of all reactants were obtained on a Bruker Avance 400 MHz spectrometer, while the spectra of glutathione and conjugates were acquired using a Bruker Avance 500 MHz. Both instruments were equipped with a 5 mm BBO probe including *Z*-axis pulse field gradients. Assignments for the ^{1}H spectra of peptides were achieved using standard sequential assignment procedures of protein spectra (*39*). 2D [^{1}H,^{1}H]TOCSY (*40*) were acquired employing 60 ms mixing time and 2D [^{1}H,^{1}H] NOESY (*41*) employing mixing times from 100 to 300 ms. NMR spectra were processed using Bruker *NMR Suite 3.5* and Amix *Viewer 3.1.5* (Bruker Biospin GmbH). Chemical shifts were referenced to the residual solvent signals when the sample was dissolved in an organic solvent and to sodium trimethylsilyl-(2*H*4)-propionate (TSP) when it was dissolved in D_2O/H_2O.

Enzymatic Assay for L-Asparaginase. The concentration of the PEG−L-asparaginase was determined by microBCA protein assay using an L-asparaginase standard curve. The enzymatic activities of L-asparaginase, our PEGylated L-asparaginase, and the commercially available PEGylated L-asparaginase (15 μg/mL) were determined by measuring ammonia formation (i.e., hydrolysis of L-asparagine to L-aspartic acid and ammonia) after incubation with 10 mM L-asparagine in 50 mM Tris-HCl buffer (pH 8.6) for 30 min at 37 °C (*42*, *43*). The reaction was stopped by the addition of 1.5 M trichloroacetic acid and Nessler's reagent. The ammonia that was produced was determined using ammonium sulfate as a standard.

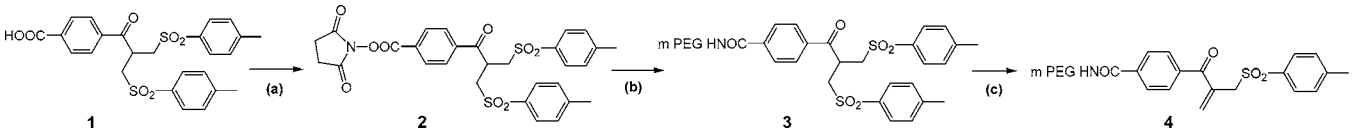
Antigenicity Assay for L-Asparaginase. The concentration of PEGylated (20 kDa) L-asparaginase was determined with a microBCA protein assay using an L-asparaginase standard curve. Enzyme immunoassay plates (96-well) were coated overnight at 4 °C with 10 μg/mL each of L-asparaginase (Sigma-Aldrich), PEG−L-asparaginase, and commercial PEG−L-asparaginase conjugate (Sigma-Aldrich) in 0.2 M carbonate coating buffer solution, pH 9.6. The plate wells were then washed four times with 0.5% v/v solution of Tween20 in PBS (PBS-T). A 0.5% BSA in PBS (200 μL) solution was added to the wells and incubated at 37 °C for 1 h. The wells were then washed with PBS-T. Rabbit anti-asparaginase polyclonal antibody (Chemicon Int., U.S.A.) (100 μL of a 1:1000 dilution) was added and incubated for 1 h at 37 °C. After washing with PBS-T, an anti-rabbit IgG−horseradish peroxidase conjugate (Sigma-Aldrich), which had been diluted 1500-fold in PBS-T, was added and incubated for 1 h at 37 °C. After washing, 100 μL of tetramethylbenzidine, 0.03% v/v hydrogen peroxide solution in 0.1 M sodium acetate buffer, pH 6.0, was added and incubated for 5 min at ambient temperature. The reaction was stopped using 100 μL of 2.5 M sulfuric acid and absorbance measured at 405 nm.

In Vitro IFN Antiviral Assay. The human lung fibroblast cell line A549 was maintained in DMEM media supplemented with 10% fetal calf serum (FCS), 50 units/mL penicillin, and 50 μg/mL streptomycin. For the antiviral assay, A549 cells were resuspended at 0.3×10^6 cells in assay media and then aliquotted at 50 μL/well into 96-well microtiter plates. Twelve hours later, 50 μL of each protein sample was prepared in assay media and added to the test wells in serial doubling dilutions. Each protein sample was tested in quadruplicate. Control wells contained either cells (negative control) or cells and virus (positive control). The plates were then incubated overnight at 37 °C. The media was then removed and the cells infected with encephalomyocarditis virus (EMCV) for 1 h after resuspending the virus in 50 μL/well of DMEM supplemented with 2% FCS, penicillin, and streptomycin. Assay media containing EMCV was then removed and 100 μL of fresh assay media added to each well. On the next day, the positive control wells were monitored until there was cell death in 80% of the wells. Each well was then washed twice with PBS and 50 μL 4% formaldehyde/0.1% methyl violet 2B solution added for 30 min. The plates were then washed twice with PBS and air-dried. The dye used was solubilized by agitation with 10% SDS (50 μL/well) and the OD measured at 570 nm.

2′,5′-Oligoadenylate Synthetase mRNA Assay. Molt-4 cells were grown in RPMI 1640 media supplemented with 10% FCS, penicillin, and streptomycin, and resuspended at 10^6 cells/mL. They were then aliquoted into a 48-well tissue culture plate at 1 mL/well. Protein samples were added in serial doubling dilutions and the plates incubated for 24 h. The cells were then washed and the mRNA (200 ng) extracted using a total mRNA extraction kit (Nucleospin RNA II, Machery-Nagel, Germany) in accordance with the manufacturer's instructions. Fifty microliters of the total RNA extract was then reverse-transcribed for 2 h to generate the cDNA. Quantitative PCR was performed on 60 ng of this cDNA for 2′,5′-oligoadenylate synthetase (2′,5′-OAS) using a RotorGene 3000 real-time PCR machine (Corbett Research, U.K.). The forward and reverse primers used were GGC TAT AAA CCT AAC CCC CAA ATC and AGC TTC CCA AGC TTC TTC TTA CAA, respectively. The PCR amplification conditions used were denaturation at 95 °C for 3 s, annealing at 59 °C for 5 s, extension of 72 °C for 8 s, and fluorescence acquisition at 83 °C for 5 s. Melting curve analysis was performed over the range 72−95 °C. mRNA quantitation was achieved by coamplifying with an in-house plasmid containing the 2′5′-OAS gene sequence.

Molecular Modeling Studies. All computational studies were carried out using integrated molecular modeling package *Maestro v6.5* (Maestro) and *Macromodel v9.1* (*44*). The OPLS-2005 force field (*45*) was used with extended cutoff values for nonbonded interactions (Van der Waals, 8 Å; electrostatic, 20

Scheme 1. Preparation of PEG Monosulfone 4[a]



[a] (a) DIPC, NHS; (b) methoxy-PEG-NH_2; (c) 50 mM sodium phosphate buffer, pH 7.8.

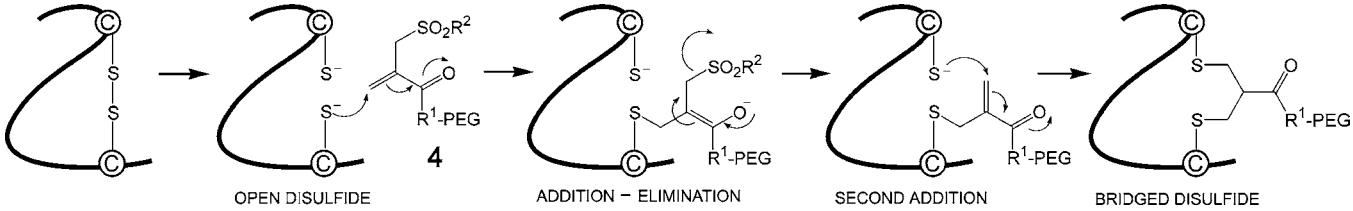


Figure 1. Site-specific PEGylation of a protein disulfide bond. The disulfide was reduced, and this was followed by reaction with a monofunctionalized PEG that was capable of sequential, interactive bis-alkylation. Mechanistically, PEGylation involves a first thiol addition to a PEG monosulfone followed by sulfinic acid elimination to generate a second double bond, which then undergoes a second thiol addition to complete the conjugation.

Å; and hydrogen bond, 4 Å). Solvent effects were considered as an aqueous generalized Born/surface area (GB/SA) solvent model (*46*). All protein and peptide models were subjected to the modified stochastic simulation protocol at 300 K used for proteins with chemically modified disulfides (*32*): 1500 steps of conjugated gradient minimization, time step of 1 ps, equilibration time of 10 ps, and 2000 ps of simulation time using the SHAKE algorithm for all bonds to hydrogen atoms. Snapshots of molecular structures were recorded at every 20 ps during simulations and energy minimized.

PEG with linker subunit was constructed as a linear chain comprising 230 monomers (10 kDa) and the simulation performed using the parameters defined above—except that molecular dynamics was used instead of stochastic dynamics. The 3D structure of the IFN was obtained as described (*33*) and imported using the *Maestro* program. Hydrogen atoms were added and the structure subjected to 1500 steps of gradient minimization using the AMBER force field and *Macromodel v8.5* (*44*). Water was defined as an aqueous generalized Born/surface area (GB/SA) solvent model to consider the solvent effect. The IFN with a three-carbon bridge across Cys1-Cys98 and across Cys29-Cys138 was built and subjected to the modified stochastic simulation protocol used for proteins with chemically modified disulfides (*32*). The initial 100 steps of conjugate gradient minimization using OPLS-2005 force field and GB/SA solvent model were used to remove clashes between added atoms and the rest of the protein. This was followed by equilibrating models at 300 K for 1 ps and stochastic simulation of 2000 ps in 1.0 fs steps at 300 K. The SHAKE algorithm was applied to bonds containing hydrogen atoms. Snapshots of the molecular structures were recorded every 2 ps during simulations and energy minimized. The modeled structure was compared to IFN α-2a by calculating the root-mean-square displacement (rmsd) values. They were determined using the McLachlan algorithm (*47*) as implemented in the program *ProFit v1.8* (*48*). The molecular model of IFN with both disulfide bonds reduced was subjected to the molecular simulation protocol, and the final snapshot structure was used to build the IFN model with a PEG attached at Cys1-Cys98 and at Cys29-Cys138. This model was subjected to the stochastic dynamics protocol after removing initial clashes between atoms.

RESULTS AND DISCUSSION

Thiol-Specific Bis-Alkylation. Our approach to protein PEGylation involves the mild reduction of a protein disulfide to free the two cysteine sulfur atoms followed by reaction with the bis-thiol-specific PEG reagent **4** (*33*). The conjugating moiety of the PEG reagent **4** (Scheme 1) is a substituted propenyl system. It contains a thiol-specific bis-alkylating group which comprises a carbonyl electron withdrawing group, an α,β-unsaturated double bond, and a β′ leaving sulfonyl group. The latter is susceptible to elimination. This juxtaposition of chemical functionality allows for a sequence of interactive and sequential addition−elimination reactions (Figure 1) that can occur at neutral or slightly acidic pH with the two free thiols that are derived from a reduced disulfide bond (*33*). Lawton et al. (*35, 36, 49, 50*) first demonstrated that this type of chemical functionality could undergo bis-thiol alkylation to cross-link proteins (e.g., ribonuclease (*49*) and antibodies (*35, 36*)). Wilbur et al. subsequently examined this functionality with antibody fragments (*51*). Other substituted propenyl systems capable of bis-alkylation with nucleophiles have also been used in organic synthesis (e.g., refs 50, 52−56 and references therein).

Our results show that appending the bis-alkylating functionality to the terminus of PEG (*33*), as shown in structure **4**, results in a water-soluble reagent that is more susceptible to an intramolecular protein thiol-specific reaction. Competitive intermolecular alkylation reactions are unlikely to occur, because the conjugation reaction occurs in aqueous conditions. This ensures that the protein's tertiary structure is maintained after the gentle reduction of a disulfide. It is also important to keep the free thiols close to each other because (a) this ensures that irreversible denaturation or aggregation of the protein does not occur during the conjugation reaction with the PEG monosulfone **4** (*33*) and (b) disulfide scrambling reactions do not occur when more than one disulfide is reduced.

The PEG monosulfone **4** is fundamentally different from the other PEGylation regents that can undergo conjugation reactions with two thiols. The dithiol reactive PEGylation reagents that have been described have two separate thiol-accepting moieties (e.g., two maleimides (*10, 57*)), which are chemically independent and which are not capable of the controlled sequential reactions of PEG monosulfone **4**. In addition, the distance between the sites for addition of the two sulfur atoms with these other reagents is much greater than the distance for our three-carbon bridge. Therefore, these reagents are unable to rebridge reduced disulfides in the way that our PEG monosulfone **4** can bridge the reduced disulfide bond.

Synthesis of PEG Conjugation Reagents. The PEG monosulfone **4** was prepared from the known carboxylic acid bis(sulfone) acid **1** (*35, 36, 50*) (Scheme 1). Coupling of methoxyamino-terminated PEG was routinely accomplished using the active ester bis(sulfone) **2** or by direct carbodiimide-mediated coupling with acid bis(sulfone) **1**. The synthesis of PEG monosulfone **4** was accomplished by incubation of the PEG bis(sulfone) **3** (25 mg/mL) in 50 mM sodium phosphate buffer

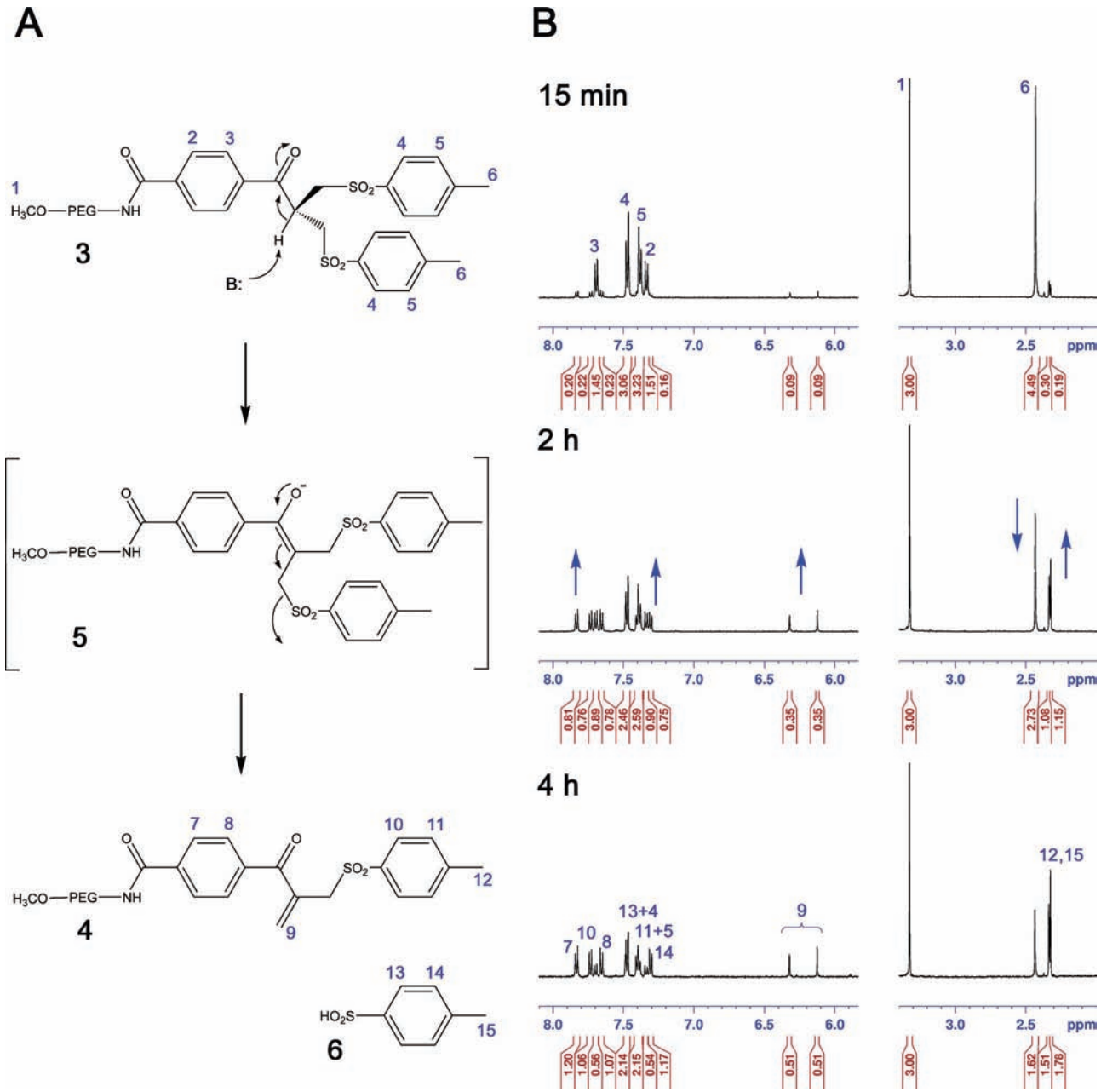


Figure 2. A. Elimination of toluene sulfinic acid **6** from PEG bis(sulfone) **3** via the enolate **5** to generate PEG monosulfone **4** is required for the first thiol addition reaction to occur. B. The elimination reaction was monitored by ^{1}H NMR in 50 mM phosphate buffer in D_2O (pH 7.2) with 51% conversion to PEG monosulfone **4** observed after 4 h as calculated by integration of the geminal vinylic protons. Typically, overnight incubation at ambient temperature was required for maximum conversion of the reagent.

(pH 7.8) and purified by RP-HPLC. PEG bis(sulfone) **3** undergoes elimination of toluene sulfinic acid **6** to give the PEG monosulfone **4** at pH values of 7.0 or higher. The elimination reaction was monitored by ^{1}H NMR (Figure 2) and reverse-phase RP-HPLC (Figure 3). The rate at which this elimination reaction occurred from the PEG bis(sulfone) **3** was dependent on pH and temperature (Figure 4). Although a decreased rate of elimination was observed at pH 6.0, this suggested that PEGylation could also be conducted at a slightly acidic pH value as was seen for somatostatin at pH 6.3 (see below).

These observations indicate that the rate to generate the double bond in the PEG monosulfone **4** can be tailored to the protein thiol's reactivity after disulfide reduction. Therefore, PEGylation was usually conducted using the PEG bis(sulfone) **3** which gave the monosulfone **4** in situ. This means that the optimized conjugation conditions can be tailored to balance the rate of the first elimination with the rate of the first thiolate addition reaction and thereby avoid the competitive conjugation of PEG to each of the thiols that are derived from a disulfide. When it is necessary to conduct PEGylation at an acidic pH value (because of issues related to protein solubility or stability, such as those described for somatostatin below), it is best to isolate and use the PEG monosulfone **4** directly in the conjugation reaction.

Bis-Thiol Selectivity of the Reagents. The tripeptide GSH was used to study the thiol reactivity and selectivity of the PEG bis(sulfone) **3** in the aqueous conditions that would typically be used for proteins. The conjugate, $PEG(SG)_2$ (Figure 5A) was derived from 2 equiv of GSH (each possessing one cysteine thiol), and it was purified by desalting column. The two glutathione molecules were conjugated to PEG via a three-carbon bridge. The conjugate structure (Figure 5A) was characterized and compared to oxidized glutathione (GSSG) by 1D and 2D ^{1}H NMR analysis. The set of 1D and 2D ^{1}H NMR spectra of GSSG was acquired and assigned using the standard procedure for proteins. The amide region of the 1D spectrum

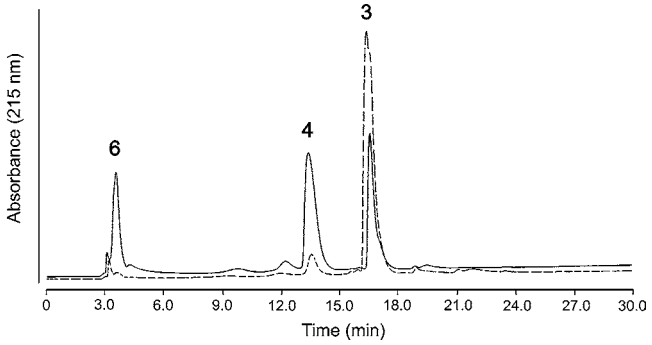


Figure 3. Reverse-phase HPLC chromatograms at $t = 15$ min (broken line) and $t = 5$ h (solid line) for the elimination of toluene sulfinic acid **6** from PEG bis(sulfone) **3** to give PEG monosulfone **4**. The elimination reaction was conducted in 50 mM phosphate buffer, pH 7.8, at ambient temperature.

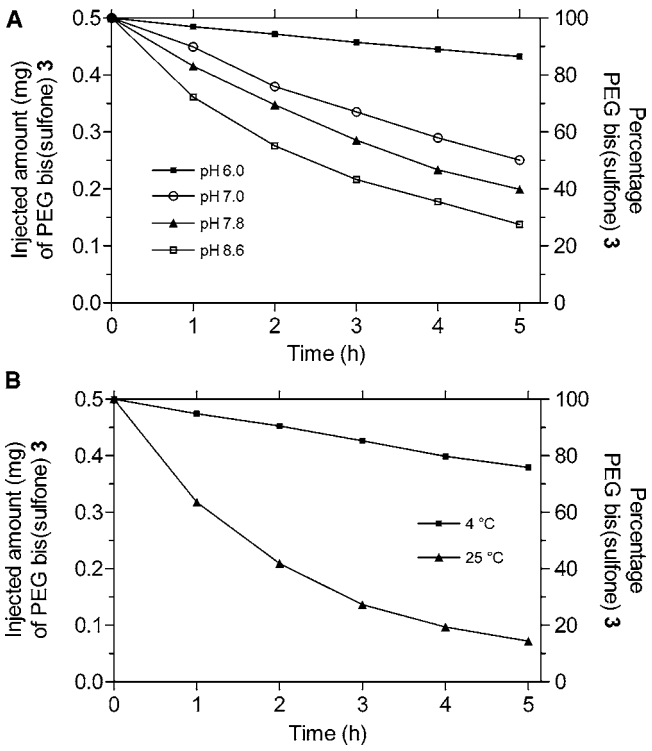


Figure 4. Effect of (**A**) pH on elimination of PEG bis-sulfone **3** (25 mg/mL) at 25 °C and (**B**) temperature on elimination of PEG bis-sulfone **3** (10 mg/mL) as monitored by reversed phase-HPLC using a C_{18} Phenomenex column (5 μm, 250 × 4.6 mm). Solvent A: acetonitrile containing 0.05% CF_3COOH (TFA), Solvent B: water containing 0.05% TFA. The gradient used was 30−60% B in 30 min with a flow rate of 1 mL/min at room temperature. UV detection was at 215 nm. The sample injection volumes for the temperature experiments were adjusted to give PEG bis(sulfone) **3** in the amount of 0.5 mg per injection.

had only two peaks: the doublet for NH of Cys and the triplet for the NH of Gly. The presence of only one set of peaks in both regions of the NMR spectra (amide and side chain) indicated that the two peptide chains of the tripeptide were connected by thiol ether bonds with a similar conformation. The two β-methylene protons of Cys are nonequivalent (2.8−3.25 ppm) in GSSG due to the restricted rotation of the disulfide bone. These methylene protons are the same in GSH where there is free rotation of the Cys side chain.

The assignment of NMR spectra for PEGylated glutathione ($PEG(SG)_2$) was achieved by observing spin system patterns in TOCSY (Figure 5B) for Cys and Gly. These corresponded to the NH doublet of Cys at 8.3 ppm and the NH triplet of Gly 8.05 ppm. The NOESY cross-peak at 8.39 and 4.45 ppm (Figure 5C) confirmed the sequential connectivity between the α-hydrogen of Cys (*) and NH of Gly. The triplet for the NH of the amide in the PEG reagent was at 8.7 ppm. This signal had a cross-peak in the TOCSY spectrum to the methylene hydrogen atoms of PEG at 3.7 ppm. This confirmed that the two GSH tripeptides and the PEG were in solution, while the 1:2 ratio for the integration of amide hydrogen atoms of the PEG reagent and the amide hydrogen atoms of the peptides was consistent with that expected for conjugation. Furthermore, the Cys β-methylene hydrogen atoms were nonequivalent, indicating the loss of free rotation seen in GSH and that the sulfur atoms were no longer in the form of free thiols. These β-hydrogen atoms from the two Cys residues are diasterotropic and without free rotation. They are therefore not magnetically equivalent, and they display slightly different chemical shifts. The possibility of conjugation on the NH_2 of the N-terminal can be ruled out, as no new peak for the hydrogen atom as a consequence of amine alkylation was observed and the keto α-proton was at ∼4.1 ppm.

The reaction of PEG bis(sulfone) **3** with reduced glutathione after overnight incubation and purification showed only the presence of the PEG−$(GS)_2$ conjugate. No unreacted PEG bis or monosulfone (**3** or **4**) was seen. If the reaction had been stopped earlier (e.g., 5 h), there was a mixture of $PEG(SG)_2$ conjugate and PEG bis(sulfone) **3**. There was no evidence of a monoglutathione adduct or of the PEG monosulfone **4**. This indicated that the second elimination−addition reaction to give a PEG alkenyl monoglutathione intermediate was thermodynamically driven and that this compound was consumed to give the final $PEG(SG)_2$ conjugate.

Mono-PEGylation of the Cyclic Peptide Somatostatin. Somatostatin is a naturally occurring cyclic peptide hormone with 14 amino acid residues (molecular mass 1637.9 Da) and a disulfide bond between Cys3 and Cys14. The disulfide reduction of somatostatin was accomplished with equimolar TCEP−HCl, pH 6.2, at ambient temperature. Reduction at higher pH values caused the peptide to precipitate out of solution. TCEP−HCl (*37*) was ideal for disulfide reduction at acidic pH values, and it could be used at stoichiometric equivalence. Once oxidized, TCEP was not nucleophilic, and it did not react with PEG monosulfone **4**; therefore, its removal (*58*) before conjugation was unnecessary.

The disulfide-bridging PEGylation of the reduced somatostatin was performed using an equimolar amount of the PEG monosulfone **4**. Further purification by simple desalting and MALDI-TOF-MS analysis indicated the presence of PEG−somatostatin (Figure 6C). To determine whether the three-carbon linker without PEG attached could be inserted, the conjugation was also performed with the carboxylic acid monosulfone, which was obtained from the carboxylic acid bis(sulfone) **1**. As removal of PEG from the reagent led to a loss of water solubility, this conjugation reaction was performed in a 2:3 (v/v) acetonitrile and 50 mM sodium phosphate buffer mixed-solvent system at pH 6.2. The three-carbon bridged somatostatin was analyzed by MALDI-TOF. The increase in mass of 190 Da confirmed the presence of 4-[2,2-bis(methylene acetyl)]-benzoic acid (Figure 6B). This suggested that the bis-alkylation reaction of the monosulfone moiety with somatostatin could occur at a slightly acidic pH. These experiments also showed that the PEG monosulfone **4** could be used for site-specific PEGylation in acidic pH conditions.

PEGylation of the Multimeric Protein L-Asparaginase. *E. coli* derived L-asparaginase is a protein (MW 133−138 kDa) that consists of four identical subunits, each of which contains 326 amino acids and a single disulfide bond between Cys77-Cys105 (*59*, *60*). L-Asparaginase must exist in its tetrameric

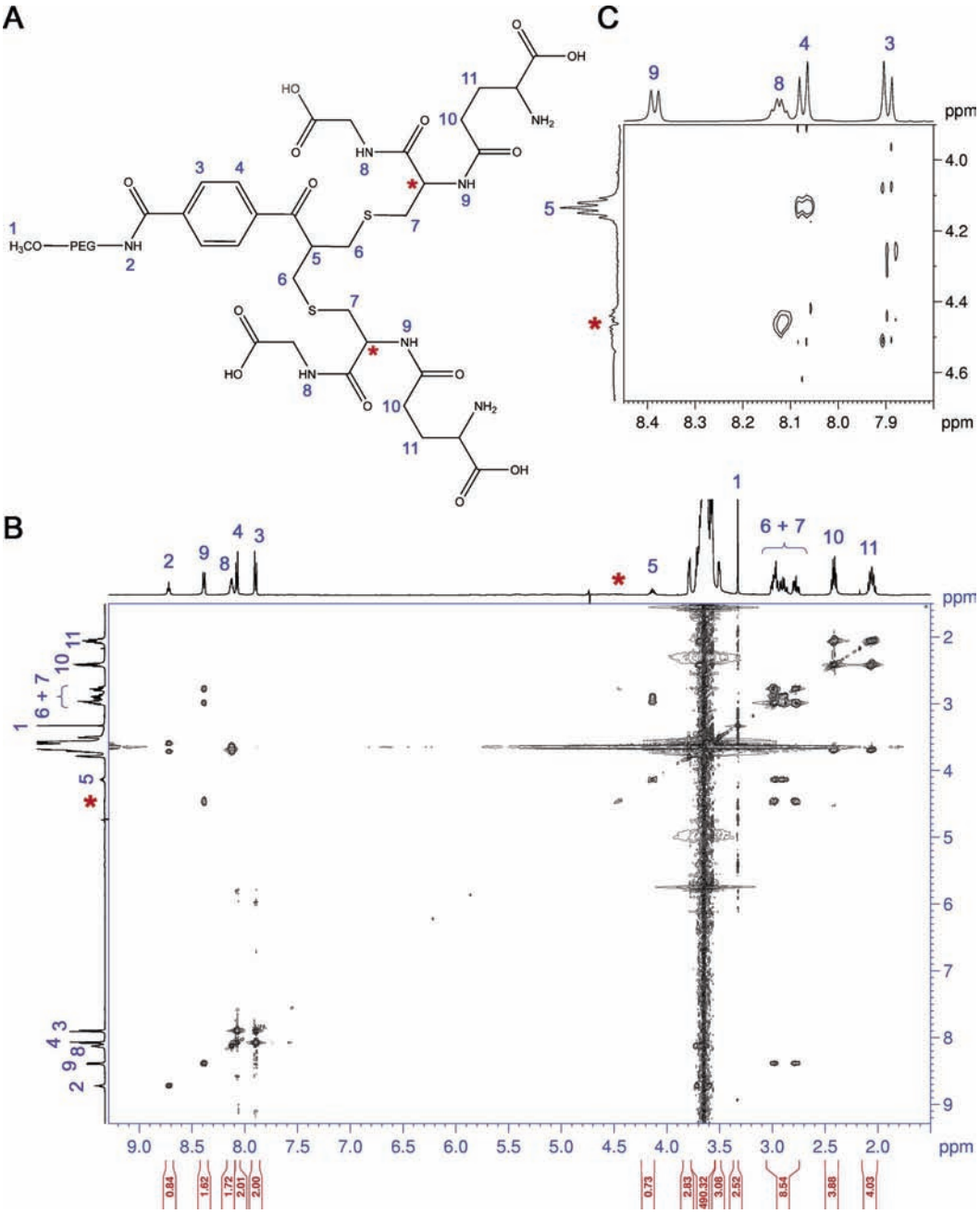


Figure 5. Thiol selectivity of PEGylation was demonstrated with reduced glutathione (GSH) to give PEG−$(SG)_2$. A. Chemical structure of PEG−$(SG)_2$; bond connectivity of the cysteine thiols was confirmed by ^{1}H-TOCSY as shown in B and ^{1}H-NOESY as shown in C.

form to display its biological activity. Structurally, the disulfide is accessible, because it lies on the outer edge of the protein and it is distant from the protein's enzymatic site (*61*). This explains why the L-asparaginase tetramer remains biologically active after reduction and carboxymethylation of its disulfides (*31*). We have PEGylated asparaginase to determine the biological effect of inserting a three-carbon bridge with PEG attached into each of the four subunits of this multimeric protein.

PEGylation of reduced L-asparaginase was examined with PEG monosulfones **4** of varying molecular weight (i.e., 5, 10, and 20 kDa as shown in Figure 7A, lanes 4, 5, and 6). The native L-asparaginase was seen at ~35 kDa on SDS-PAGE gels because of dissociation of the tetramer into the four monomers (Figure 7A, lane 2). The reduced protein displayed an apparently larger size than the unreduced protein (Figure 7A, lane 3). PEGylation only occurred if the L-asparaginase was first incubated with DTT (Figure 7A, lanes 7−9). Conjugation with 1.3 equiv of the PEG monosulfone **4** to each disulfide gave nearly quantitative conversion to the mono-PEGylated L-asparaginase monomer (Figure 7A, lanes 4−6).

Anion exchange chromatography followed by SEC−HPLC was used to purify PEG−L-asparaginase. Single peaks eluted with different retention times depending upon the size of the PEG (Figure 7B). MALDI-TOF-MS (Figure 7C,D) was used to confirm the mass of the PEG−L-asparaginase. The enzymatic activity of L-asparaginase and our PEG−L-asparaginase were similar irrespective of the size of PEG attached (Figure 8A). In an enzyme immunoassay (Figure 8B) that was based upon the use of a rabbit anti-asparaginase polyclonal antibody, the in vitro antigenicity of the PEG−L-asparaginase was similar to that of L-asparaginase. A representative, computationally calculated structure of PEG−L-asparaginase is shown in Figure 8C. These results are consistent with the site-selective conjugation of PEG to a site that is distant to the enzyme's antigenic site.

E. coli derived L-asparaginase cannot be used as a safe therapeutic drug in man, because it causes severe hypersensitiv-

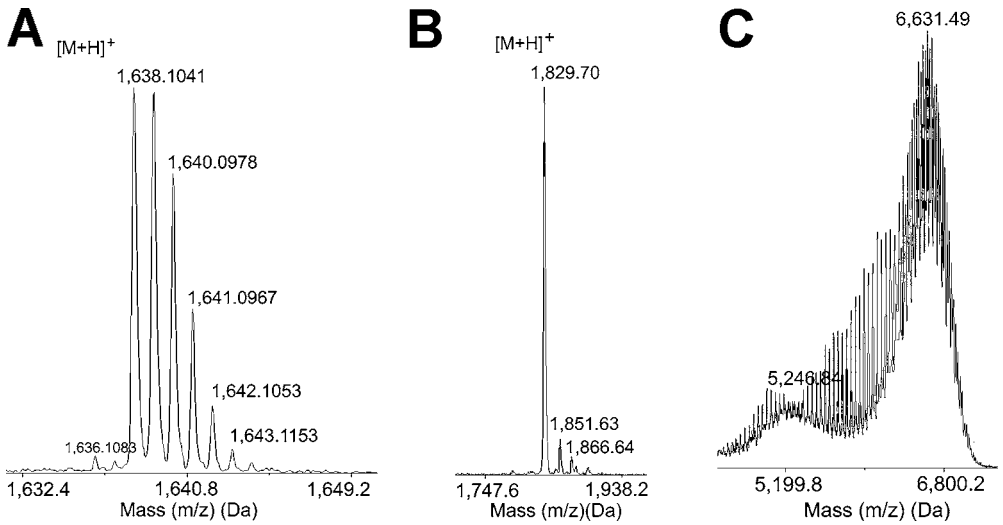


Figure 6. MALDI-TOF-MS: A. Native somatostatin showing its isotope signals. B. Three-carbon disulfide bridged somatostatin with its salt adducts. C. Reaction mixture of PEGylated somatostatin. Also seen is the unreacted PEG in the region of 5246 Da.

ity reactions. This is due to its multiple antigenic sites (*62*). PEGylation has been used to reduce this antigenicity and thereby enable its use for the treatment of acute lymphoblastic leukemia and of lymphomas (*63*, *64*). We have found that, after disulfide site-specific PEGylation, our PEGylated L-asparaginase retained its enzymatic activity and its antigenicity, irrespective of the size of PEG attached. In contrast, commercially available amine PEGylated L-asparaginase had lower enzymatic activity and was less antigenic (Figure 8B). This could be due either to the amine-based site of PEGylation of the commercially available PEG−L-asparaginase and/or to it having ∼40 molecules of 5 kDa PEGs per protein molecule. Our results show that it is possible to attach four PEG molecules to sites on a protein that are distant to its biologically active site using disulfide site-specific PEGylation without disrupting its biological activity. In this context, we have also illustrated the biological benefits of PEGylating at sites that are distant to a protein's receptor binding site by PEGylating the interchain disulfide of an antibody fragment to CD4. Both the anti-HIV-1 activity and the antigenicity of the PEGylated antibody fragment were preserved (*33*).

Three-Carbon Disulfide Single- and Double-Bridged PEGylation of IFN. We have already shown that a single native disulfide in IFN can be modified by site-specific bis-alkylation of two cysteine sulfur atoms to form a three-carbon bridged PEGylated IFN (*33*). The yield of three-carbon disulfide single-bridged PEG−IFN was high (65%). It was a mixture of the two isomers Cys1-CC[PEG]C-Cys98 and Cys29-CC[PEG]C-Cys138. The tertiary structure of IFN was retained. The stability of the three-carbon bridge was maintained under reducing conditions, at temperatures up to 90 °C, and in human serum for 24 h at 4 °C. It also had a prolonged circulation half-life in vivo of 12 h compared to 1 h for IFN.

In contrast to the multimeric L-asparaginase described above, IFN also provided an opportunity to determine the effect of introducing two PEGylated bridges into a monomeric protein. In molecular modeling studies, both disulfide bonds were replaced with three-carbon bridges linked by thioether bonds from the respective cysteines and the modified structure subjected to simulations of 2000 ps. A C-2 substituted *p*-benzoic acid acetophenone was also placed in the carbon bridge to mimic the entire linking moiety that was used for PEGylation. The conformations were recorded every 20 ps, and they resulted in a trajectory that was analyzed by calculating the rmsd values for the backbones of the starting model of IFN and for each conformation of the modified protein at the different time frames. A plot of the calculated rmsd values versus time indicated that the overall structures deviated by <4 Å from the native conformation (Figure 9A). All of the conformations were then superimposed and a ribbon plot created with the positions of the linkers at different time points shown in CPK representation (Figure 9B). These results showed that the double-bridged IFN retained its primary, secondary (i.e., helices), and tertiary structure.

The carbon bridge between Cys29-Cys138 had a lower conformational flexibility than the bridge between Cys1-Cys98 because of the restricted movements of the interhelical connecting loops. The aromatic moiety at C-2 of the carbon bridge between Cys1-Cys98 had greater freedom to move, because the N-terminal was not constrained by interactions. This resulted in greater conformational space sampling by the C-2 benzoic acid causing different interactions with the surface of the protein. These results show that the insertion of a carbon bridge that was linked by thioether bonds displayed greater conformational mobility than the native disulfide bond, and they could explain how the three-carbon bridge modified IFN was able to retain its tertiary structure.

As an example of reagent efficiency, IFN was then conjugated with 2 equiv of PEG monosulfone **4** to give the three-carbon disulfide double-bridged PEG−IFN. In order to define the structural and biological effects of the three-carbon bridges (i.e., without PEG attached) and to aid the mass-spectral analysis, a double-bridged IFN adduct was also prepared from the carboxylic acid bis(sulfone) **1**. This reaction had to be conducted in a mixed organic−aqueous solvent system to solubilize the carboxylic acid sulfone **1**. In the case of the bis(sulfone) **1**, the SDS-PAGE gel showed that the disulfide-reduced IFN had a larger apparent size, which was a consequence of the open disulfides (Figure 10A, lane 3) when compared to (a) IFN (Figure 10A, lane 2) and (b) the double-bridged IFN in which conjugation and formation of the two bridges had occurred (Figure 10A, lane 4). MALDI-TOF-MS analysis showed that the mass of the IFN had increased by 380 Da, thereby confirming the insertion of two bridges of 190 Da each (Figure 10B). Tryptic digestion of the IFN and the double-bridged IFN followed by MALDI-TOF-MS of the fragments confirmed the site-specific insertion of a carbon bridge at Cys1-Cys98 and at Cys29-Cys138 (Figure 10C,D).

Stoichiometrically efficient PEGylation reactions could be conducted with either PEG monosulfone **4** or PEG bis(sulfone) **3**. When 1 equiv of the PEG monosulfone 20 kDa **4** was used for the conjugation, a mixture of the three-carbon disulfide

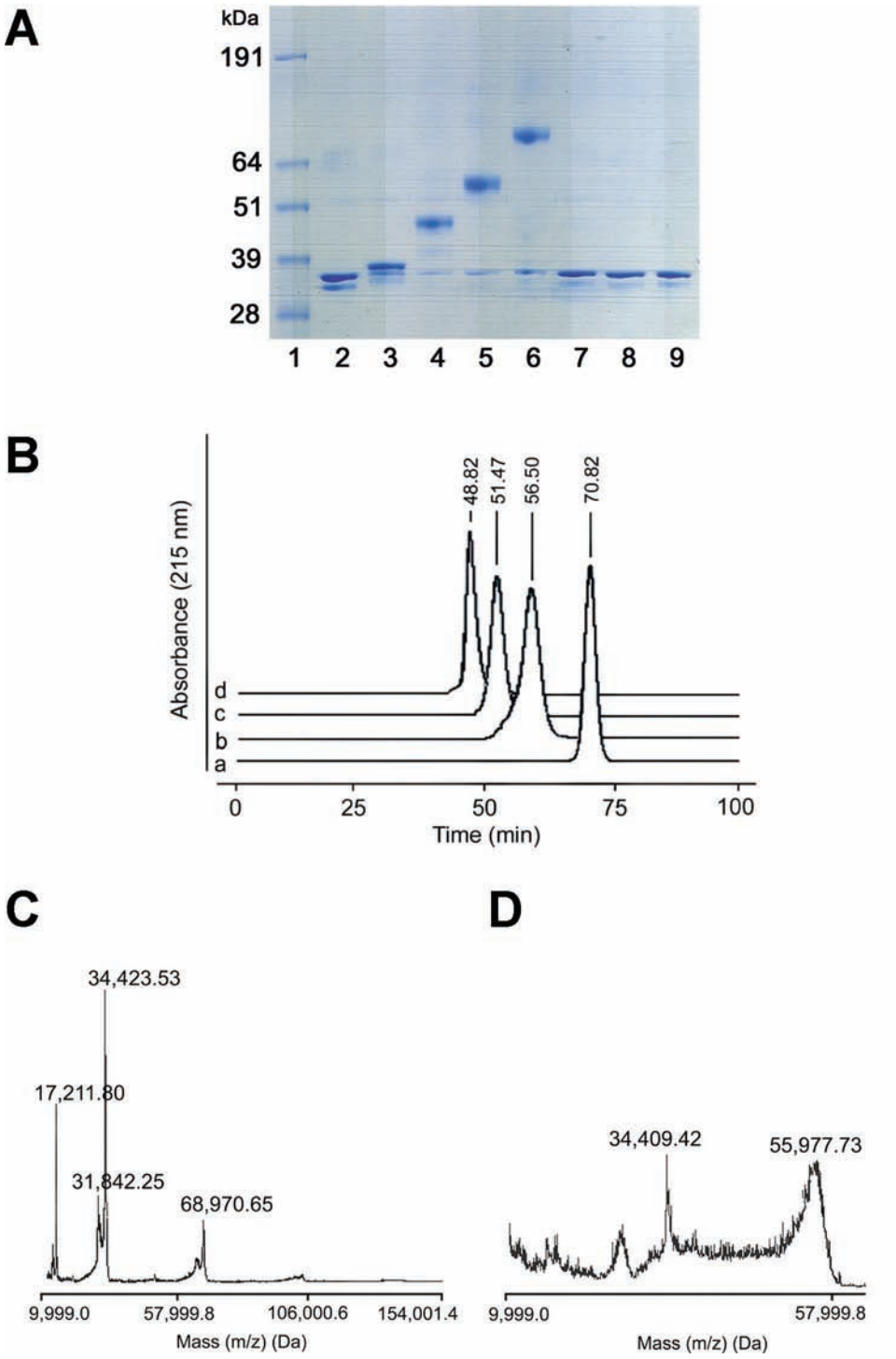


Figure 7. A. SDS-PAGE gel stained with colloidal blue to show the L-asparaginase three-carbon disulfide-bridged PEGylation reactions. Lane 1: prestained markers. Lane 2: L-asparaginase. Lane 3L disulfide-reduced L-asparaginase. Lane 4: 5 kDa PEGylation reaction. Lane 5: 10 kDa PEGylation reaction. Lane 6: 20 kDa PEGylation reaction. Lanes 7−9: control reactions with 5 kDa, 10 kDa, and 20 kDa PEG reagents **4**, respectively, in which the L-asparaginase was not reduced. Dissociation of the tetramer on SDS-PAGE resulted in monomeric L-asparaginase, and it was observed as two bands. UnPEGylated monomers of L-asparaginase (16% by densitometry) were seen in lanes 4−6. B. Size exclusion chromatography of L-asparaginase and the three-carbon disulfide-bridged PEG−L-asparaginase on a Superdex 200 prep grade column. The protein elutes in a tetrameric form: (a) L-asparaginase at 70.57 min; (b) 5 kDa PEG−L-asparaginase at 56.50 min; (c) 10 kDa PEG−L-asparaginase at 51.47 min; (d) 20 kDa PEG−L-asparaginase at 48.82 min. C. MALDI-TOF-MS of L-asparaginase ionized as a monomer with a MW range of 31 842−34 423 Da. D. MALDI-TOF-MS of the three-carbon disulfide-bridged 20 kDa PEG−L-asparaginase.

single-bridged PEG−IFN (65%), three-carbon disulfide double-bridged PEG−IFN (23.5%), IFN (4.9%), and aggregated IFN (6.6%) was obtained (*33*). When 1 equiv of the 10 kDa PEG monosulfone **4** was used for the conjugation, a mixture of the three-carbon disulfide single-bridged PEG−IFN (64.3%), three-carbon disulfide double-bridged PEG−IFN (17.4%), IFN (13.4%), and aggregated IFN (4.8%) was obtained (Figure 11B). When 1.5 equiv of PEG monosulfone **4** was used, a mixture of the three-carbon disulfide double-bridged PEG−IFN (61%) and the three-carbon disulfide single-bridged PEG−IFN (38%) was obtained (Figure 11C). There was no residual IFN, and only 1% of the IFN was aggregated.

When 1 equiv of PEG bis(sulfone) **3** was used, the conjugation reaction was similar and the three-carbon disulfide single-

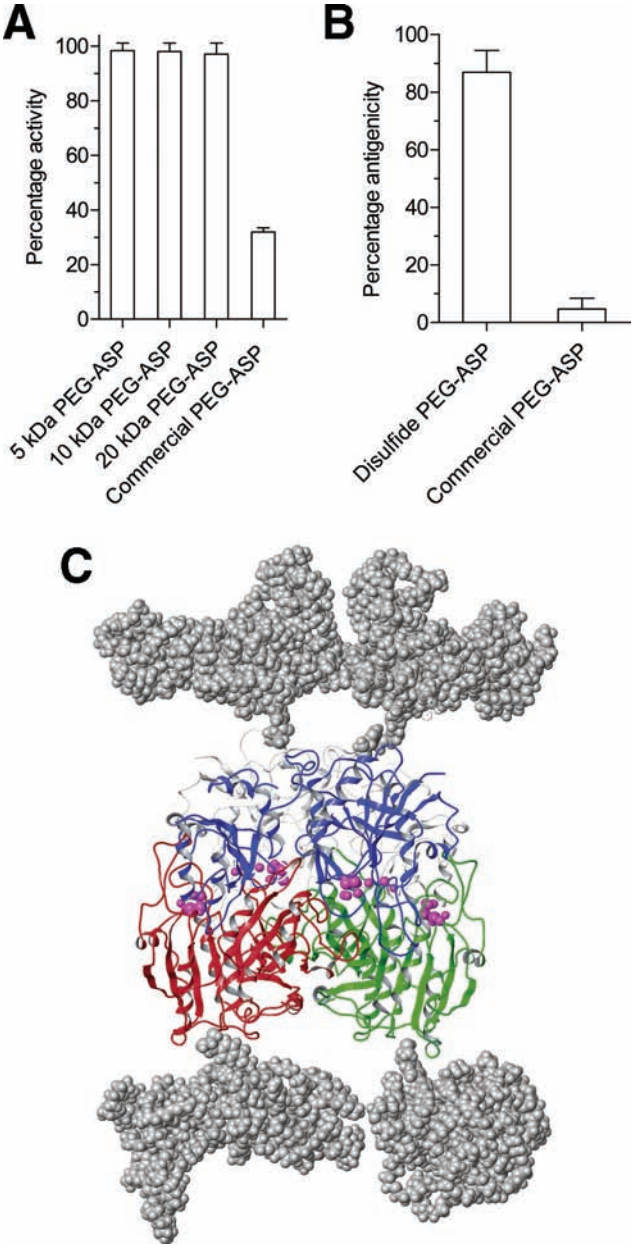


Figure 8. Evaluation of the in vitro biological properties of PEG−L-asparaginase: A. Enzymatic activity. B. Antigenicity. C. Tetrameric 10 kDa PEG−L-asparaginase (PDB 4ECA) was stochastically modeled with implicit solvent. A PEG molecule was conjugated at each of the four disulfides. The substrate aspartic acid is shown in pink.

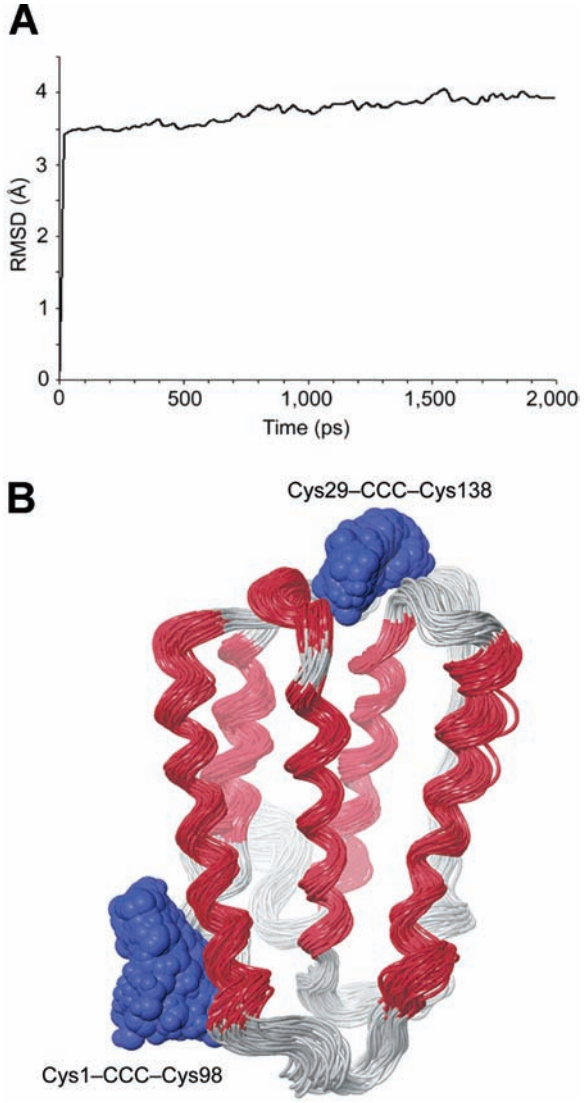


Figure 9. A. Stochastic simulation of the double-bridged IFN (2000 ps). The rmsd plot of the backbone molecules of the modified IFN was calculated using the native conformation of IFN α-2a (PDB 1ITF). B. Backbone plots of the chemically modified IFN α-2b in CPK representation. The three-carbon disulfide bridges are shown in blue.

bridged PEG-IFN was the main product (Figure 11A, lane 4). When 2 equiv of the PEG bis(sulfone) **3** was used (Figure 11A, lane 5), the three-carbon disulfide double-bridged PEG−IFN was the main product. In order to produce the three-carbon disulfide double-bridged PEG−IFN, the disulfide-reduced IFN was allowed to react with the PEG bis(sulfone) **3** immediately after the protein had been separated from the reducing agent and stored overnight at 4 °C. The PEG−IFN conjugates were purified by cation exchange chromatography followed by size exclusion chromatography and then analyzed by MALDI-TOF-MS (Figure 12A,B with the reference MALDI of IFN shown in Figure 12C). The presence of IFN in the PEG−IFN was confirmed by silver stain and by Western immunoblotting with an anti-IFN antibody (Figure 13). This study also confirmed the absence of un-PEGylated IFN in these particular fractions. As both disulfides were reduced for the mono-PEGylation of IFN, it was also necessary to reoxidize any cysteines that had not been PEGylated with glutathione. This led to increased amounts of the three-carbon disulfide single-bridged PEG−IFN and of IFN. Aggregation of the reduced IFN was not observed in 50 mM sodium phosphate buffer, pH 7.8, containing 10 mM EDTA. However, aggregation was found after buffer exchange of the non-glutathione-treated reaction mixture to 20 mM sodium acetate buffer, pH 4.0. Reannealing of the open disulfides with glutathione (1 mM GSH/1 mM GSSG) decreased the formation of aggregates while buffer exchanged to 20 mM sodium acetate buffer, pH 4.0 (Figure 14).

The biological effects of modified IFNs were studied using the A549-EMC antiviral assay and the 2′,5′-OAS mRNA induction assay (Figure 15A−D). The unreacted IFN after purification had an ED_{50} of 17 (antiviral) to 38 (2′,5′-OAS mRNA) pg/mL. The addition of a single three-carbon bridge (i.e., single-bridged IFN) reduced this slightly (given the doubling dilution format of the assays) to 41 (antiviral ED_{50}) to 97 (2′,5′-OAS mRNA ED_{50}) pg/mL. This is a remarkably small change in antiviral activity, given our expectation at the outset of our studies that manipulation of a disulfide bond would severely disrupt the biological activity of IFN. The addition of a single PEG molecule (i.e., three-carbon disulfide single-bridged PEG−IFN) reduced it significantly to 175−265 pg/mL (antiviral assay ED_{50} for the 20 and 10 kDa PEGs) and

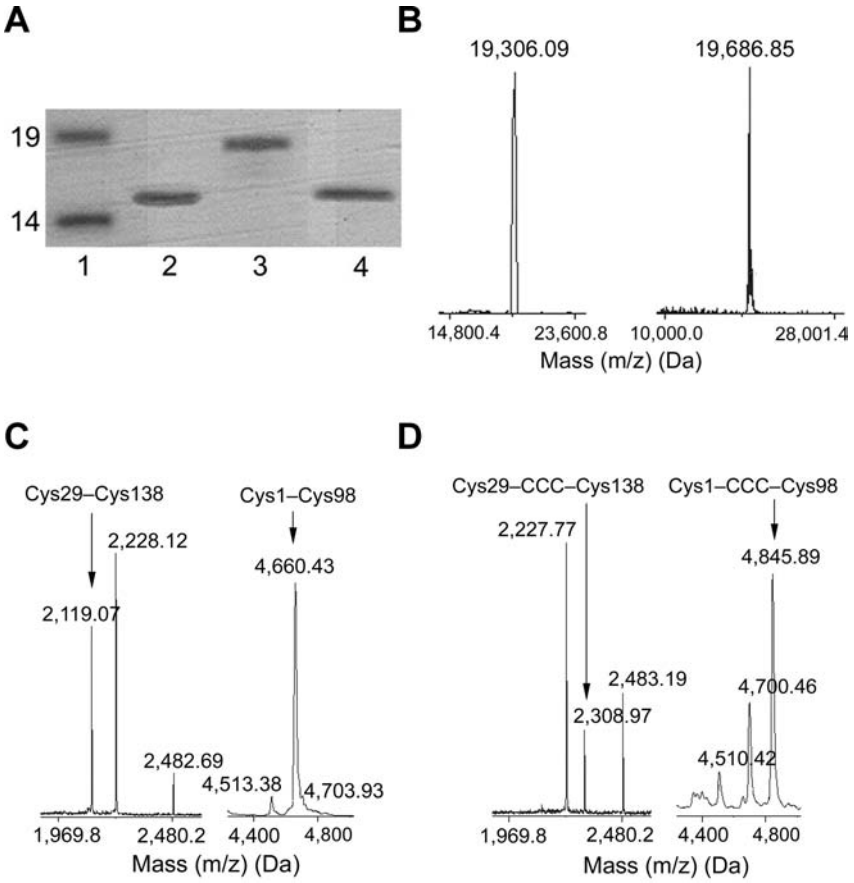


Figure 10. A. Silver stain of a 12% bis−tris SDS-PAGE gel of the double-bridged IFN reaction mixture to which PEG was not attached. Lane 1: prestained standards. Lane 2: IFN. Lane 3: disulfide reduced IFN (control for 2 h). Lane 4: double-bridged IFN after reaction with carboxylic acid bis(sulfone) **1** for 2 h. B. MALDI-TOF-MS of IFN (19 306 Da, left) and the double-bridged IFN (19 686 Da, right) showing an increase in MW of 380 Da that was due to the insertion of 2 three-carbon bridges of 190 Da each. C. MALDI-TOF-MS of trypsin-digested IFN showing the peptide fragments containing Cys29-Cys138 and Cys1-Cys98. D. MALDI-TOF-MS of the trypsin-digested double-bridged IFN showing the peptide fragments containing Cys29-CCC-Cys138 and Cys1-CCC-Cys98.

338−441 pg/mL (2′,5′-OAS mRNA ED_{50} for the 10 and 20 kDa PEGs, respectively). The length of the PEG had no effect on the biological activity of the PEG−IFN. Taken together, these results show that the insertion of a single three-carbon disulfide bridge into IFN contributed ∼11%, and the addition of PEG to that bridge contributed ∼89% to the reduction in the in vitro biological activities of the single-bridged PEG−IFNs. Therefore, the antiviral activity of our three-carbon disulfide single-bridged PEG−IFN was ∼8% of IFN and, as such, is the same as the reported activity of the mono-PEGylated IFN (∼7% of IFN) in clinical use (*65*−*69*).

The insertion of two three-carbon bridges in IFN (i.e., double-bridged IFN) caused a significant reduction in the biological activity of IFN (104 pg/mL (antiviral assay ED_{50}) and 414 pg/mL (2′,5′-OAS mRNA ED_{50}); Figure 15A−D). This was a surprising biological result, given that our molecular modeling studies had shown that the double-bridged IFN retained its primary, secondary (i.e., helices), and tertiary structure. It is possible that, as the experiment to add the two three-carbon linkers to IFN (without PEG attached) was conducted in the presence of acetonitrile (in order to solubilize the conjugation reagent shown as structure **1**), the IFNs receptor binding domains might have been significantly disrupted. This study was necessary in order to complete our mass spectral analysis (Figure 10 and (*33*)). The reduction in the biological activity of the double-bridged IFN was similar to that of adding a PEG molecule to a single-bridged IFN (175−265 pg/mL (antiviral assay ED_{50}) and 338−441 pg/mL (2′,5′-OAS mRNA ED_{50})). While the three-carbon disulfide double-bridged PEG−IFNs had only ∼2% of the activity of IFN, once again, we found that the length of the PEG had no effect on the biological activity of the PEG−IFN; the three-carbon disulfide double-bridged 10 kDa PEG−IFN had an antiviral ED_{50} of 639 pg/mL and the three-carbon disulfide single-bridged 20 kDa PEG−IFN had an antiviral ED_{50} of 697 pg/mL. Therefore, in the case of IFN, it was better to increase the MW of a single PEG molecule to optimize the molecule's pharmacokinetic profile rather than attach a second PEG molecule to the protein. This property has not previously been described for PEG−IFNs, presumably because each PEG reagent used for amine conjugation of IFN gives a different mixture of positional PEG−IFN isomers.

The reduction of the in vitro biological activity of the PEG−IFNs is a consequence of the steric shielding caused by PEG, and it is seen with all the PEG−IFNs described in the literature that have been biologically evaluated (*6*, *65*−*69*). The complex nature of the binding of IFN to its receptor (i.e., at least two receptor−ligand interactions occur) is disrupted by the presence of PEG, which is at least as large in solution as the IFN (*70*). When amine PEGylation is used, reduction of the antiviral activity of the IFN can be minimized by attaching a very short PEG to certain residues, but this is at the expense of a considerably reduced in vivo half-life. In the clinical context, the increase in the in vivo half-life of IFN to at least 12 h (*68*) is more important than the reduction in its in vitro antiviral activity, because the markedly enhanced in vivo therapeutic efficacy of IFN more than compensates for the reduced biological activity seen in vitro. This is the case for all of the IFNs that have been described in the literature (*65*−*69*). Therefore, the decrease in the in vitro activity and the decrease

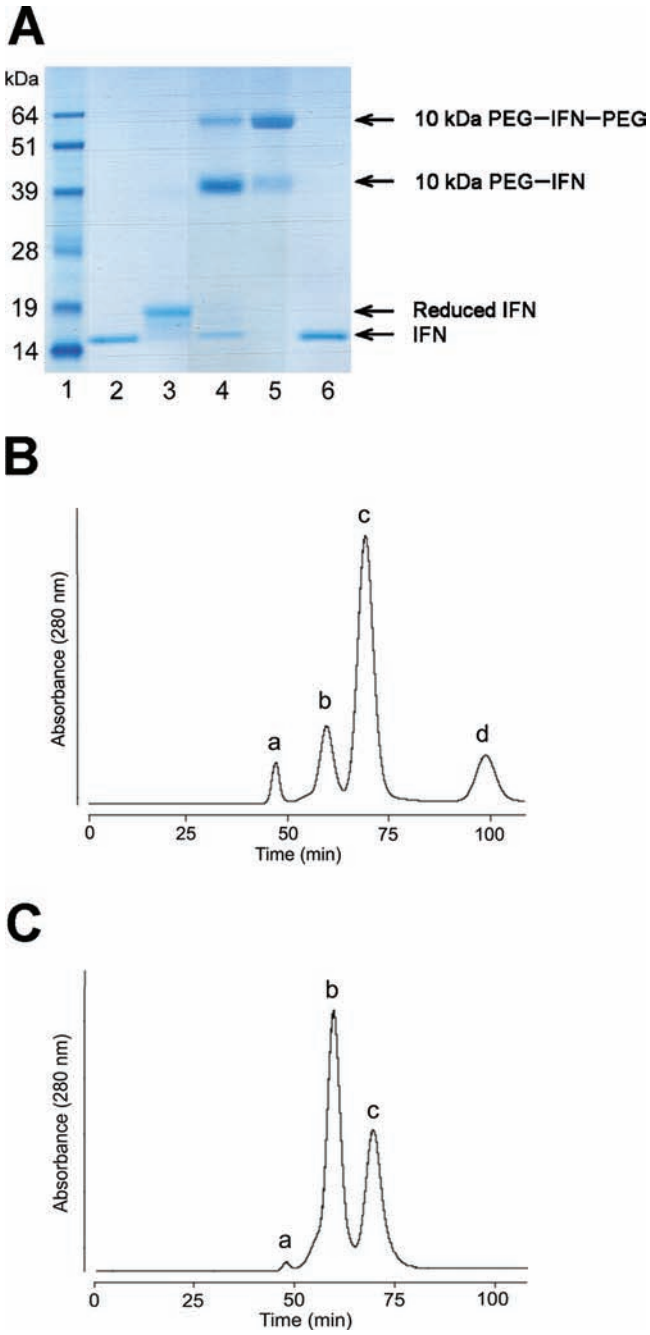


Figure 11. A. Colloidal blue stain of 12% bis−tris SDS-PAGE gel of the three-carbon disulfide double-bridged PEG−IFN. Lane 1: prestained standards. Lane 2: IFN. Lane 3: disulfide reduced IFN. Lane 4: disulfide reduced IFN with 1 equiv of PEG monosulfone **4** (10 kDa). Glutathione was used to refold the IFN. Lane 5: disulfide reduced IFN with 2 equiv of PEG monosulfone **4**. Lane 6: control reaction of IFN without prior disulfide reduction with 2 equiv of PEG monosulfone **4**. B. Size exclusion chromatography of the IFN PEGylation reaction with 1 equiv of PEG monosulfone **4**. C. Size exclusion chromatography of the IFN PEGylation reaction with 1.5 equiv of PEG monosulfone **4**. Eluting peaks are (a) aggregates, (b) three-carbon disulfide double-bridged PEG-IFN, (c) three-carbon disulfide single-bridged PEG-IFN, and (d) IFN.

in the in vivo clearance of a PEG−IFN are a direct consequence of the presence of PEG.

Using BIAcore measurements and cell binding assays, Kubetzko et al. (*71*) have recently shown that attachment of a 20 kDa PEG to an antibody fragment distal to the binding region results in a 5-fold reduction in the apparent affinity of the PEGylated antibody fragment for its receptor. This was due to a reduction in the association rate of the PEGylated molecule

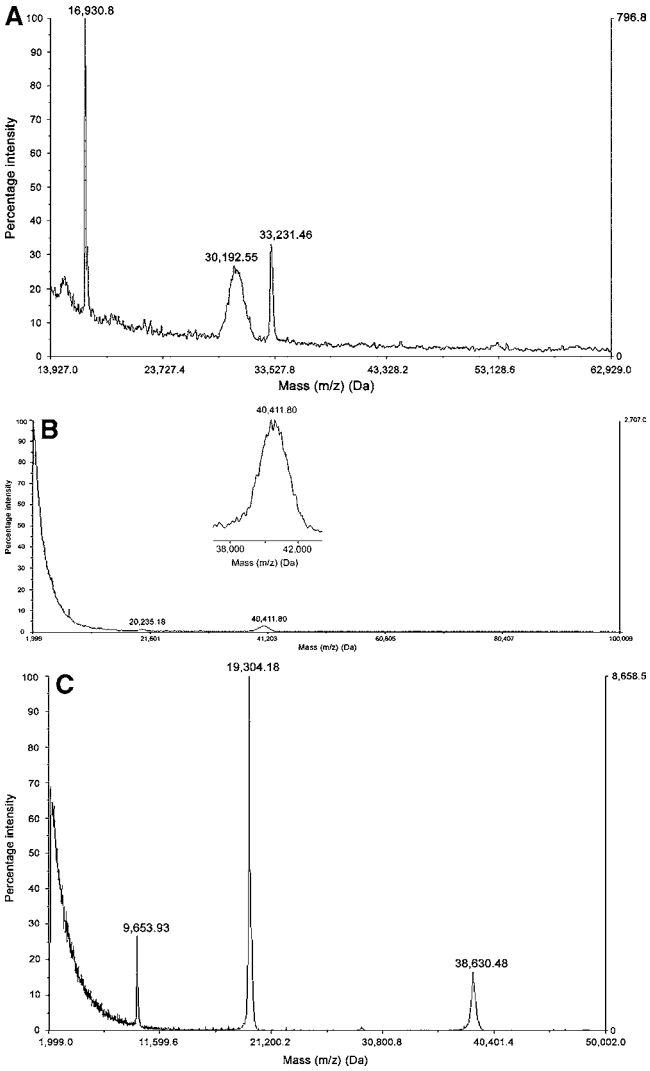


Figure 12. A. MALDI-TOF-MS of the three-carbon disulfide single-bridged 10 kDa PEG−IFN with the reference protein of doubly charged BSA seen at 33 231 Da. B. MALDI-TOF-MS of the three-carbon disulfide double-bridged 10 kDa PEG−IFN. The expanded region indicates the signal for the three-carbon disulfide double-bridged PEG−IFN. F. MALDI-TOF-MS of IFN.

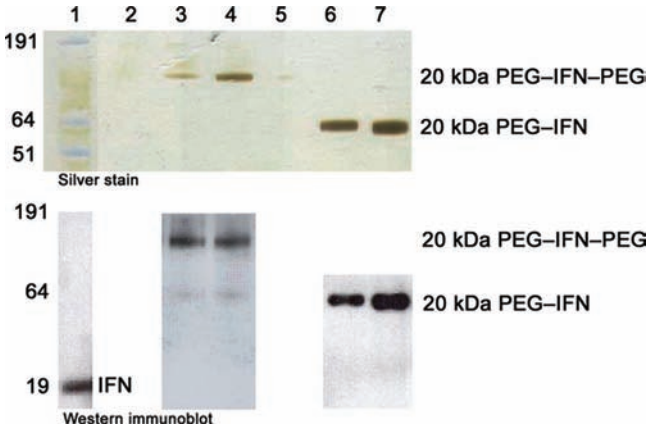


Figure 13. Silver stain and Western immunoblot with an anti-IFN antibody to confirm the presence of IFN in the PEGylated fractions, and the absence of un-PEGylated IFN (at 19 kDa) in these fractions. Lanes 1: MW markers in kDa. SEC−HPLC fractions (lane 2) 29−31 min; (lane 3) 31−33 min; (lane 4) 33−35 min; (lane 5) 35−37 min; (lane 6) 37−39 min; (lane 7) 39−41 min; (lane 8) 41−43 min.

for its receptor with no change in the dissociation rate. There was also a strong effect of the 20 kDa PEG on the hydrodynamic

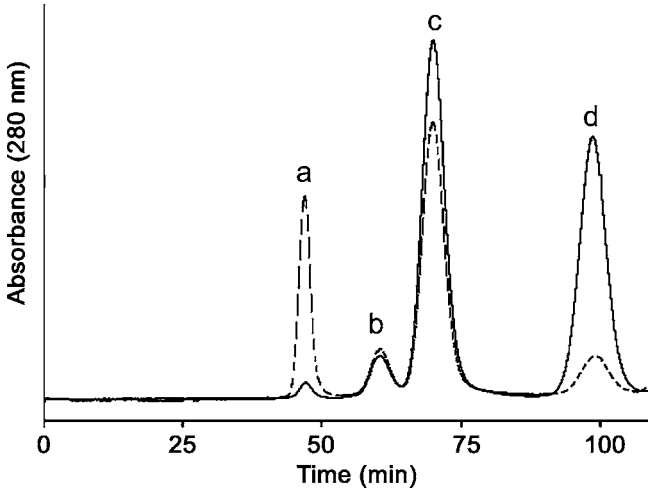


Figure 14. The addition of glutathione (solid line) to the reaction mixture after incubation of the fully reduced IFN with the PEG bis-(sulfone) **3**. Glutathione was used to reoxidize the unreacted cysteine thiols. When glutathione was not added, there was increased aggregation of the IFN (dotted line). Eluting peaks are (a) Aggregates, (b) three-carbon disulfide double-bridged PEG-IFN, (c) three-carbon disulfide single-bridged PEG-IFN and (d) IFN.

properties of the conjugated protein with its hydrodynamic radius becoming much larger than would be expected for the PEG-associated increase in molecular mass. While only a modest effect was seen with a 5 kDa PEG, conjugates modified with a 20 kDa PEG displayed a 100-fold reduction in the association rate. Their modeling studies also suggested that PEGylation results in <7% of a PEGylated molecule being available for binding to its receptor at any moment in time. The remainder has intramolecularly blocked binding interfaces and is in rapid equilibrium with the functional molecule. Although this reduces the observed association rate, all of the PEGylated molecules can eventually bind to the receptor. Similar and related observations have been made for PEG−IFN (*6*, *69*). In addition, the PEGylated molecules intermolecularly block the attachment of neighboring molecules, causing an apparent reduction in the number of binding sites, minimizing protein aggregation, and increasing protein stability (*72*). This masking of proteins by PEG also explains their lower immunogenicity, lower toxicity, and longer circulation half-life.

CONCLUSION

PEGylation reagents that undergo sequential bis-alkylation with two thiols are described and shown to undergo site-specific conjugation with the cysteine sulfur atoms that are liberated by

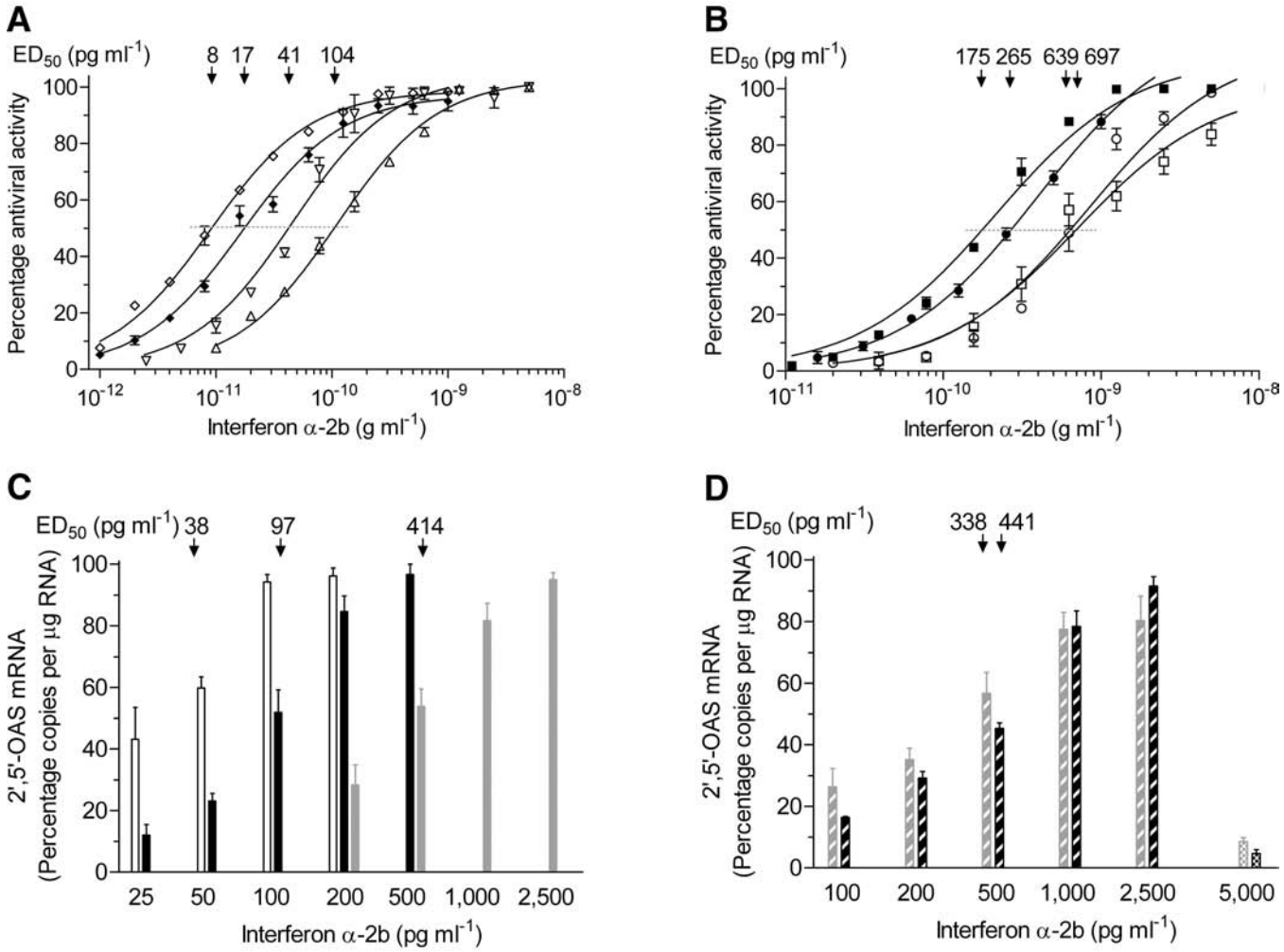


Figure 15. A,B. Antiviral activity in A549 cells infected with EMC virus with the ED_{50} shown ($n = 6$). Symbols: IFN (◇), unreacted IFN (◆), single-bridged IFN (▽), double-bridged IFN (△), three-carbon disulfide single-bridged 10 kDa PEG−IFN (●), three-carbon disulfide single-bridged 20 kDa PEG−IFN (■), three-carbon disulfide double-bridged 10 kDa PEG−IFN (○), three-carbon disulfide double-bridged 20 kDa PEG−IFN (□). C,D. 2′,5′-OAS mRNA expression in Molt-4 cells ($n = 3$), Symbols: IFN (white bars), single-bridged IFN (black bars), double-bridged IFN (gray bars), three-carbon disulfide single-bridged 10 kDa PEG−IFN (gray striped bars), three-carbon disulfide single-bridged 20 kDa PEG−IFN (black striped bars).

the mild reduction of a protein's disulfide bond. Most therapeutic proteins, antibody fragments, and enzymes have at least one disulfide bond which can be modified using disulfide site-specific PEGylation without disrupting either their tertiary structure or their biological activity (*33*). This approach does not require the incorporation of a new cysteine into the protein to exploit selective thiol conjugation chemistry. As our approach is stoichiometrically very efficient and enables the recycling of any unreacted protein, it offers the potential to make cost-effective PEGylated biopharmaceuticals as global medicines. In this context, clinical trials are now in progress with our three-carbon disulfide single-bridged PEG−IFN as a cost-effective treatment for the epidemic of hepatitis C in developing countries.

ACKNOWLEDGMENT

We are grateful to the Wellcome Trust (068309), BBSRC-UK (BB/D003636/1) and PolyTherics for funding, and to The School of Pharmacy and Avecia for contributing towards the costs of S. Balan's Ph.D. studies.

LITERATURE CITED

(1) Harris, J., and Chess, R. (2003) Effect of Pegylation on pharmaceuticals. *Nat. Rev. Drug Discovery 2* (3), 214−221.

(2) Zalipsky, S. (1995) Chemistry of poly(ethylene glycol) conjugates with biologically active molecules. *Adv. Drug Delivery Rev. 16*, 157−182.

(3) Greenwald, R., Choe, Y., McGuire, J., and Conover, C. (2003) Effective drug delivery by PEGylated drug conjugates. *Adv. Drug Delivery Rev. 55*, 217−250.

(4) Pasut, G., Guiotto, A., and Veronese F. (2004) Protein, peptide and non-peptide drug PEGylation for therapeutic application. *Expert Opin. Ther. Pat. 14* (5), 1−36.

(5) Veronese, F., and Pasut G. (2005) PEGylation, successful approach to drug delivery. *Drug Discovery Today 10* (21), 1451−1458.

(6) Grace, M., Lee, S., Bradshaw, S., Chapman, J., Spond, J., Cox, S., DeLorenzo, M., Brassard, D., Wylie, D., Cannon-Carlson, S., Cullen, C., Indelicato, S., Voloch, M., and Bordens, R. (2005) Site of pegylation and polyethylene glycol molecule size attenuate interferon-a antiviral and antiproliferative activities through the JAK/STAT signaling pathway. *J. Biol. Chem. 280* (8), 6327−6336.

(7) Woghiren, C., Sharma, B., and Stein S. (1993) Protected thio-poly(ethylene glycol): A new activated polymer for reversible protein modification. *Bioconjugate Chem. 4* (5), 314−318.

(8) Kinstler, O., Brems, D., Lauren, S., Paige, A., Hamburger, J., and Treuheit, M. (1996) Characterization and stability of N-terminally PEGylated rhG-CSF. *Pharm. Res. 13* (7), 996−1002.

(9) Kinstler, O., Molineux, G., Treuheit, M., Ladd, D., and Gegg, C. (2002) Mono-N-terminal poly(ethylene glycol)-protein conjugates. *Adv. Drug Delivery Rev. 54* (4), 477−485.

(10) Chapman, A. (2002) PEGylated antibodies and antibody fragments for improved therapy: a review. *Adv. Drug Delivery Rev. 54*, 531−545.

(11) Wylie, D., Voloch, M., Lee, S., Liu, Y., Cannon−Carlson, S., Cutler, C., and Pramanik, B. (2001) Carboxyalkylated histidine is a pH-dependent product of pegylation with SC-PEG. *Pharm. Res. 18*, 1354−1360.

(12) Manjula, B., Tsai, A., Upadhya, R., Perumalsamy, K., Smith, P., Malavalli, A., Vandegriff, I., Winslow, R., Intaglietta, I., Prabhakaran, M., Friedman, J., and Acharya, A. (2003) Site-specific PEGylation of hemoglobin at cys-93: Correlation between the colligative properties of the PEGylated protein and the length of the conjugated PEG chain. *Bioconjugate Chem. 14*, 464−472.

(13) Lee, H., Jang, H., Ryu, S., and Park, T. (2003) N-terminal site-specific mono-PEGylation of epidermal growth factor. *Pharm. Res. 20* (5), 818−825.

(14) Yamamoto, Y., Tsutsumi, Y., Yoshioka, Y., Nishibata, T., Kobayashi, K., Okamoto, T., Mukai, Y., Shimizu, T., Nakagawa, S., Nagata, S., and Mayumi, T. (2003) Site-specific PEGylation of a lysine-deficient TNF-alpha with full bioactivity. *Nat. Biotechnol. 21*, 546−552.

(15) Gentle, I., DeSouza, D., and Baca, M. (2004) Direct production of proteins with N-terminal cysteine for site-specific conjugation. *Bioconjugate Chem. 15*, 658−663.

(16) Edwards, C., Martin, S., Seely, J., Kinstler, O., Buckel, S., Bendele, A., Cosenza, M., Feige, U., and Kohno, T. (2003) Design of PEGylated soluble tumor necrosis factor receptor type I (PEG sTNF-RI) for chronic inflammatory diseases. *Adv. Drug Delivery Rev. 55* (10), 1315−1336.

(17) Sato, H., Yamamoto, K., Hayashi, E., and Takahara, Y. (2000) Transflutaminase-mediated dual and site-specific incorporation of poly(ethylene glycol) derivatives into a chimeric interleukin-2. *Bioconjugate Chem. 11*, 502−509.

(18) Sato, H. (2002) Enzymatic procedure for site-specific pegylation of proteins. *Adv. Drug Delivery Rev. 54*, 487−504.

(19) Rosendahl, M., Doherty, D., Smith, S., Carlson, S., Chlipala, E., and Cox, G. (2005) A long-acting, highly potent interferon a-2 conjugate created using site-specific PEGylation. *Bioconjugate Chem. 16*, 200−207.

(20) Pavlou, A., and Reichert, J. (2004) Recombinant protein therapeutics- success rates, market trends and values to 2010. *Nat. Biotechnol. 22*, 1513−1519.

(21) Thornton, J. (1981) Disulphide bridges in globular proteins. *J. Mol. Biol. 151*, 261−287.

(22) Petersen, M., Jonson, P., and Petersen S. (1999) Amino acid neighbours and detailed conformational analysis of cysteines in proteins. *Protein Eng. 12* (7), 535−548.

(23) Leung, H., Xu, G., Narayan, M., and Scheraga, H. (2005) Impact of an easily reducible disulfide bond on the oxidative folding rate of multi-disulfide-containing proteins. *J. Peptide Res. 65*, 47−54.

(24) Betz, S. (1993) Disulfide bonds and the stability of globular proteins. *Protein Sci. 2*, 1551−1558.

(25) Saunders, A., Young, G., and Pielak, G. (1993) Polarity of disulfide bonds. *Protein Sci. 2*, 1183−1184.

(26) Bewley, T., Brovetto-Cruz, J., and Li, C. (1969) Human pituitary growth hormone. Physicochemical investigations of the native and reduced-alkylated protein. *Biochemistry 8* (12), 4701−4708.

(27) Wedemeyer, W., Welker, E., Narayan, M., and Scheraga, H. (2000) Disulfide bonds and protein folding. *Biochemistry 39*, 4207−4216.

(28) Rajarathnam, K., Sykes, B., Dewald, B., Baggiolini, M., and Clark-Lewis, I. (1999) Disulfide bridges in interleukin-8 probed using non-natural disulfide analogues: dissociation of roles in structure from function. *Biochemistry 38*, 7653−7658.

(29) Zhu, H., Dupureur, C., Zhang, B., and Tsai, M. (1995) Phospholipase A2 engineering. The roles of disulfide bonds in structure, conformational stability, and catalytic function? *Biochemistry 34*, 15307−15314.

(30) Morehead, H., Johnston, P., and Wetzel, R. (1984) Roles of the 29-138 disulfide bond of subtype A of human a interferon in its antiviral activity and conformational stability. *Biochemistry 23*, 2500−2507.

(31) Todokoro, K., Saito, T., Obata, M., Yamazaki, S., and Tamaura, Y. (1975) Studies on conformation and antigenicity of reduced S-methylated asparaginase in comparison with asparaginase. *FEBS Lett. 60*, 259−262.

(32) Godwin, A., Choi, J., Pedone, E., Balan, S., Jumnah, R., Shaunak, S., Brocchini, S., and Zloh, M. (2006) Molecular dyamics simulations of proteins with chemically modified disulfide bonds. *Theor. Chem. Acc.* DOI: 10.1007/s00214-006-0134-0.

(33) Shaunak, S., Godwin, A., Choi, J., Balan, S., Pedone, E., Vijayarangam, D., Heidelberger, S., Teo, I., Zloh, M., and Brocchini, S. (2006) Site-specific PEGylation of native disulfide bonds in therapeutic proteins. *Nat. Chem. Biol 2*, 312−313.

(34) Meager, A., Gaines, D., Zoon, K., and Mire-Sluis, A. (2001) Establishment of new and replacement World Health Organization international biological standards for human interferon alpha and omega. *J. Immunol. Methods 257*, 17−33.

(35) Liberatore, F., Comeau, R., McKearin, J., Pearson, D., Belonga, B., Brocchini, S., Kath, J., Phillips, T., Oswell, K., and Lawton, R. (1990) Site directed modification and cross-linking of a monoclonal antibody with equilibrium transfer alkylating cross-link reagents. *Bioconjugate Chem. 1*, 36−50.

(36) de Rosario, R., Brocchini, S., Lawton, R., Wahl, R., and Smith, R. (1990) Sulfydral site-specific cross-linking of a monoclonal

antibody by a fluorescent equilibrium transfer alkylating cross-link reagent. *Bioconjugate Chem. 1*, 51−65.
(37) Burns, J., Butler, J., Moran, J., and Whitesides, G. (1991) Selective reduction of disulfides by tris(2-carboxyethy1)phosphine. *J. Org. Chem. 56*, 2648−2650.
(38) Fahey, E., Chaudhuri, J., and Binding, P. (2000) Refolding of low molecular weight urokinase plasminogen activator by dilution and size exlusion chromatography. A comparative study. *Sep. Sci. Technol. 35* (11), 1743−1760.
(39) Wüthrich, K. (1986) *NMR of the Proteins and Nucleic Acids*, Wiley, New York.
(40) Bax, A., and Davis, D. (1985) MLEV-17-based two-dimensional homonuclear magnetization transfer spectroscopy. *J. Magn. Reson. 65*, 355−360.
(41) Jeener, J., Meier, B., Ernst, B., and Ernst, R. (1979) Investigation of exchange processes by 2-dimensional NMR-spectroscopy. *J. Chem. Phys. 71*, 4546−4553.
(42) Mashburn, L., and Wriston, J. (1964) Tumor inhibitory effect of L-asparaginase from *Escherichia coli*. *Arch. Biochem. Biophys. 105*, 450−452.
(43) Soares, A., Guimaraes, G., Polakiewicz, B., Pitombo, R., and Abrahao-Neto, J. (2002) Effects of polyethylene glycol attachment on physicochemical and biological stability of *E. coli* L-asparaginase. *Int. J. Pharm. 237*, 163−170.
(44) Mohamadi, F., Richards, N., Guida, W., Liskamp, R., Lipton, M., Caufield, C., Chang, G., Hendrickson, T., and Still, W. (1990) Macromodel - an integrated software system for modeling organic and bioorganic molecules using molecular mechanics. *J. Comput. Chem. 11*, 440−467.
(45) Jorgensen, W., Maxwell D., and Tirado-Rives (1996) Development and testing of the OPLS all-atom force field on conformational energetics and properties of organic liquids. *J. Am. Chem. Soc. 118*, 11225−11236.
(46) Still, W., Tempczyk, A., Hawley, R., and Hendrickson, T. (1990) Semianalytical treatment of solvation for molecular mechanics and dynamics. *J. Am. Chem. Soc. 112* (16), 6127−6129.
(47) McLachlan, A. (1982) Rapid comparison of protein structures. *Acta Crystallogr., Sect. A 38*, 871−873.
(48) Martin A. (2005) *Profit*, version 1.8; http://www.bioinf.org.uk/software/profit/.
(49) Mitra, S., and Lawton, R. (1979) Reagents for the cross-linking of proteins by equilibrium transfer alkylation. *J. Am. Chem. Soc. 101* (11), 3097−3110.
(50) Brocchini, S., Eberle, M., and Lawton, R. (1988) Molecular yardsticks. Synthesis of extended equilibrium transfer alkylating cross-link reagents and their use in the formation of macrocycles. *J. Am. Chem. Soc. 110*, 5211.
(51) Wilbur, D., Stray, J., Hamlin, D., Curtis, D., and Vessella, R. (1994) Monoclonal antibody Fab′ fragment cross-linking using equilibrium transfer alkylation reagents. A strategy for site-specific conjugation of diagnostic and therapeutic agents with F(ab′)2 fragments. *Bioconjugate Chem. 5*, 220−235.
(52) Kim, S., and Lim, C. (2002) Tin-free radical-mediated C-C bond formations with alkyl allyl sulfones as radical precursors. *Angew. Chem., Int. Ed. 41* (17), 3265−3267.
(53) Pan, Y., Hutchinson, D., Nantz, M., and Fuchs, P. (1989) Synthesis via vinyl sulfones. 34. Sn2′ additions of cuprates to sulfone and ester-polarized cyclopentenylic systems. *Tetrahedron 45* (2), 467−478.
(54) Seebach, D., and Knochel, P. (1984) 2′-nitro-2′-propen-1-yl 2, 2-dimethylpropanoate (NPP), a multiple coupling reagent. *Helv. Chim. Acta 67* (1), 261−283.
(55) Nelson, R., and Lawton, R. (1966) On the α,α′ annelation of cyclic ketones. *J. Am. Chem. Soc. 88* (16), 3884−3885.
(56) Padwa, A., Kline, D., Murphree, S., and Yeske, P. (1992) Use of 2,3-bis(phenylsulfonyl)-l-propene as a multicoupling reagent. *J. Org. Chem. 57*, 298−306.
(57) Casey, J., Pedley, R., King, D., Boden, R., Chapman, A., Yarranton, G., and Begent, R. (2000) Improved tumour targeting of di-Fab′ fragments modified with polyethylene glycol. *Tumor Targeting 4*, 235−244.
(58) Shafer, D., Inman, J., and Lees, A. (2000) Reaction of Tris(2-carboxyethyl)phosphine (TCEP) with Maleimide and a-Haloacyl Groups: Anomalous Elution of TCEP by Gel Filtration. *Anal. Biochem. 282*, 161−164.
(59) Ho, P., Milikin, E., Bobbitt, J., Grinnan, E., Burck, P., Frank, B., Boeck, L., and Squires, R. (1970) Crystalline L-asparaginase from *Escherichia coli* B. I. Purification and chemical characterisation. *J. Biol. Chem. 245*, 3708−3715.
(60) Swain, A., Jaskolski, M., Housset, D., Rao, J., and Wlodawer, A. (1993) Crystal-structure of *Escherichia coli* L-asparaginase, an enzyme used in cancer-therapy. *Proc. Natl. Acad. Sci. U.S.A. 90*, 1474−1478.
(61) Palm, G., Lubkowski, J., Derst, C., Schleper, S., Rohm, K., and Wlodawer, A. (1996) A covalently bound catalytic intermediate in *Escherichia coli* asparaginase: crystal structure of a Thr-89-Val mutant. *FEBS Lett. 390*, 211−216.
(62) Killander, D., Dohlwitz, A., Engstedt, L., Franzen, S., Gahrton, G., Gullbring, B., Holm, G., Holmgren, A., Hoglund, S., Killander, A., Lockner, D., Mellstedt, H., Moe, P., Palmblad, J., Reizenstein, P., Skarberg, K., Swedberg, B., Uden, A., Wadman, B., Wide, L., and Ahstrom, L. (1976) Hypersensitive reactions and antibody formation during L-asparaginase treatment of children and adults with acute leukemia. *Cancer 37*, 220−228.
(63) Kamisaki, Y., Wada, H., Yagura, T., Matsushima, A., and Inada, Y. (1981) Reduction in immunogenicity and clearance rate of *Escherichia coli* L-asparaginase by modification with monomethoxy-polyethylene glycol. *J. Pharmacol. Exp. Ther. 216*, 410−414.
(64) Yoshimoto, T., Nishimura, H., Saito, Y., Sakurai, K., Kamisaki, Y., Wada, H., Sako, M., Tsujino, G., and Inada, Y. (1986) Characterization of Polyethylene Glycol-Modified L-Asparaginase from *Escherichia coli* and Its Application to Therapy of Leukemia. *Jpn. J. Cancer Res. 77*, 1264−1270.
(65) Bailon, P., Palleroni, A., Schaffer, C., Spence, C., Fung, W., Porter, J. E., Ehrlich, G., Pan, W., Xu, Z., Modi, M., Farid, A., and Berthold, W. (2001) Rational design of a potent, long-lasting form of interferon: A 40 kDa branched polyethylene glycol-conjugated interferon α-2a for the treatment of Hepatitis C. *Bioconjugate Chem. 12*, 195−202.
(66) Grace, M., Youngster, S., Gitlin, G., Sydor, W., Xie, L., Westreich, L., Jacobs, S., Brassard, D., Bausch, J., and Bordens, R. (2001) Structural and biologic characterization of pegylated recombinant IFN-a2b. *J. Interferon Cytokine Res. 21*, 1103−1115.
(67) Rajender, R., Modi, M., and Pedder, S. (2002) Use of peginterferon alfa-2a (40 KD) (Pegasys) for the treatment of Hepatitis C. *Adv. Drug Delivery Rev. 54*, 571−586.
(68) Youngster, S., Wang, Y., Grace, M., Bausch, J., Bordens, R., and Wyss, D. (2002) Structure, biology, and therapeutic implications of pegylated interferon alpha-2b. *Curr. Pharm. Des. 8*, 2139−2157.
(69) Dhalluin, C., Ross, A., Huber, W., Gerber, P., Brugger, D., Gsell, B., and Senn, H. (2005) Structural, kinetic, and thermodynamic analysis of the binding of the 40 kDa PEG-interferon-alpha 2a and its individual positional isomers to the extracellular domain of the receptor IFNAR2. *Bioconjugate Chem. 16*, 518−527.
(70) Piehler, J., Roisman, L., and Schreiber, G. (2000) New structural and functional aspects of the type I interferon-receptor interaction revealed by comprehensive mutational analysis of the binding interface. *J. Biol. Chem. 275*, 40425−40433.
(71) Kubetzko, S., Sarkar, C., and Pluckthun, A. (2005) Protein PEGylation decreases observed target association rates via a dual blocking mechanism. *Mol. Pharmacol. 68*, 1439−1454.
(72) Dhalluin, C., Ross, A., Leuthold, L., Foser, S., Gsell, B., Muller, F., and Senn, H. (2005) Structural and biophysical characterization of the 40 kDa PEG-interferon-α2a and its individual positional isomers. *Bioconjugate Chem. 16*, 504−517.

BC0601471

Incorporation of CpG Oligonucleotide Ligand into Protein-Loaded Particle Vaccines Promotes Antigen-Specific CD8 T-Cell Immunity

Stephany M. Standley,[†,§] Ines Mende,[‡,§] Sarah L. Goh,[†,||] Young Jik Kwon,[†,⊥] Tristan T. Beaudette,[†] Edgar G. Engleman,[‡] and Jean M. J. Fréchet*[,†]

Department of Chemistry, University of California, Berkeley, California 94729-1460, and Department of Pathology, Stanford University School of Medicine, Palo Alto, California. Received June 12, 2006; Revised Manuscript Received November 1, 2006

The development of multicomponent biotherapeutic carriers is an important challenge in the field of drug delivery, particularly in the area of protein-based vaccines. While the delivery of protein antigens to antigen presenting cells (APCs) is crucial for this type of vaccination, the incorporation of additional adjuvants may be just as important in order to generate more potent immune responses. This article presents the synthesis and biological evaluation of carrier particles that both deliver a protein payload to APCs and display receptor ligands for the enhancement of APC immunostimulation. Particles displaying CpG oligonucleotide ligands for Toll-like receptor 9 were synthesized. The addition of CpG DNA to the particles led to a 45-fold increase in the secretion of interleukin-12, a cytokine that aids in T-cell activation, and a significant increase in the expression of costimulatory molecules by APCs. Moreover, vaccination with particles containing both ovalbumin (OVA) and CpG DNA induced a superior OVA-specific CD8 T-cell response in vivo, as measured by increased OVA-specific CD8 T-cell proliferation, secretion of the proinflammatory cytokine IFN-γ, and the induction of OVA-specific cytotoxicity.

INTRODUCTION

The development of multicomponent drug carriers is an important objective of drug delivery research, especially in the area of protein-based vaccines. To generate protective immunity, these vaccines need to deliver protein antigens to antigen presenting cells (APCs). In previous work, we have described acid-degradable particles that accomplish this goal on the basis of a cross-linked polymer network encapsulating a model protein, ovalbumin (OVA) (*1*, *2*). The particles were designed to degrade in the mildly acidic environment of lysosomes after phagocytosis by APCs, followed by release of the protein payload into the cytoplasm for MHC class I processing, presumably due to destabilization of the lysosomal membrane caused by the swelling and breakdown of the particles into many molecules.

While it is clear that antigen delivery is a key step in developing protein-based vaccines, a number of additional steps can contribute greatly to the generation of a more potent immune response. One such step is the stimulation of APCs for increased expression of costimulatory molecules and cytokines that aid in T-cell activation. This process can be initiated by binding receptors, such as the Toll-like receptor 9 (TLR9).

One pattern that is recognized by the immune system as nonself is unmethylated CpG dinucleotides, as these motifs, in which a cytidine is linked via a phosphodiester bond to guanosine, are common in bacterial DNA but are suppressed in vertebrates. CpG sequences in vertebrate DNA are typically methylated, whereas significantly less methylation is observed in bacterial DNA (*3*). Short, single-stranded DNA containing these unmethylated dinucleotide motifs, called CpG oligonucleotides, has been shown to possess immunostimulatory properties (*4*). They bind to the TLR9, which is found in lysosomal compartments of APCs, triggering both maturation of APCs and cytokine release (*5*−*7*). Moreover, TLR signals induced by TLR agonists, such as CpG, play a crucial role in reversing tumor-induced T-cell tolerance (*8*, *9*). Previous studies have analyzed the length and sequence of CpG oligonucleotides necessary to generate an optimal immunostimulatory response (*5*, *10*).

Our aim was to investigate the potential of multicomponent delivery systems that can both release an OVA payload and display receptor ligands for protein-based vaccine applications. Therefore, a CpG oligonucleotide ligand was conjugated to the acid-degradable particles to aid in APC immunostimulation. Incorporation of this adjuvant was achieved by modifying the particle preparation protocol to include a ligand monomer in the copolymerization with acid-degradable cross-linker **1** and acrylamide (Scheme 1) (*1*, *2*). One advantage of this tailorable vaccine carrier is that it ensures that the oligonucleotide and protein will be delivered to the same APC. Once the new particles were obtained, their effects on dendritic cells (DCs), the most potent APCs capable of inducing immunity, and on the induction of an OVA-specific T-cell response were investigated. DC maturation and cytokine production experiments were performed to determine the effect of CpG incorporation.

EXPERIMENTAL PROCEDURES

General Methods. Monomers, surfactants, and reagents were purchased from Aldrich (Milwaukee, WI) or Sigma (St. Louis, MO) and used without further purification unless otherwise noted. Cascade Blue was obtained from Molecular Probes (Eugene, OR). Water for buffers was purified to a resistance of 18 MΩ using a Barnstead NANOpure DIamond purification system. MALDI-TOF data was collected on a PerSeptive

* Prof. Jean M. J. Fréchet, 718 Latimer Hall, University of California, Berkeley Department of Chemistry, Berkeley, CA 94720-1460. E-mail: frechet@berkeley.edu. Tel: (510) 643-3077. Fax: (510) 643-3079.

[†] University of California, Berkeley.

[‡] Stanford University School of Medicine.

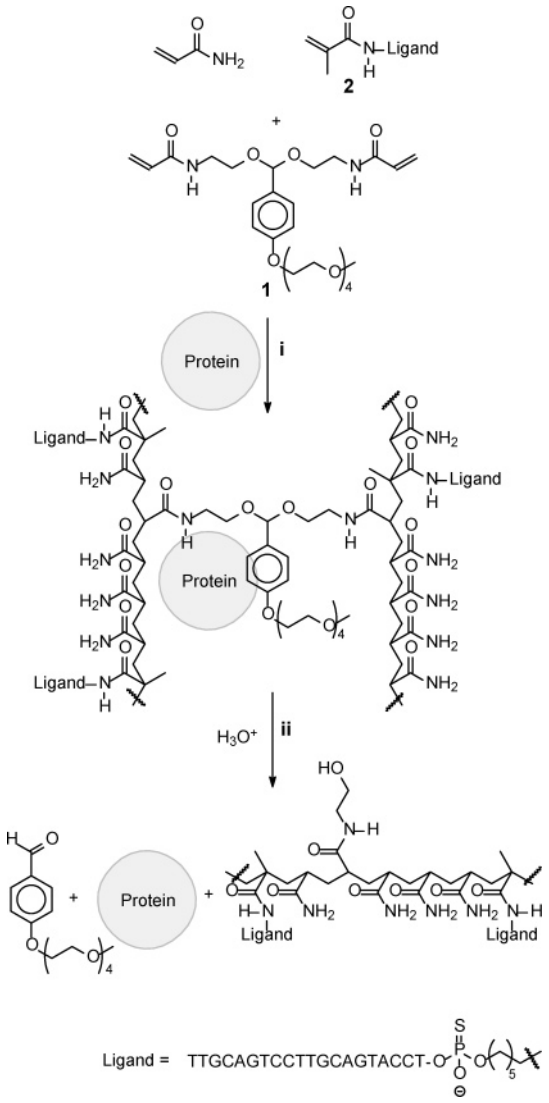
[§] These authors made equal contributions.

[||] Current address: Prof. S. L. Goh, Department of Chemistry, Williams College, Williamstown, MA.

[⊥] Current address: Prof. Y. J. Kwon, Department of Biomedical Engineering, Case Western University, Cleveland, OH.

10.1021/bc060165i CCC: $37.00 © 2007 American Chemical Society
Published on Web 12/23/2006

Scheme 1. Synthesis and Degradation of Acid-Sensitive Particles Displaying CpG Ligands[a]



[a] (i) Inverse emulsion polymerization. (ii) Acetal hydrolysis.

Biosystems Voyager-DE instrument (Applied Biosystems, Foster City, CA) in negative ion mode: accelerating voltage, 25 000 V; grid, 95%; guide wire, 0.1%; delay time, 550 ns. MALDI samples were prepared using a matrix of 0.1 M ammonium citrate and 0.35 M 3-hydroxypicolinic acid in a 1:1 mixture of acetonitrile and water (*11*). Absorbance and fluorescence readings were taken on a SPECTRAmax 190 and SPECTRAmax Gemini XS microplate readers (Molecular Devices, Sunnyvale, CA). Particles were imaged using a scanning electron microscope (WDX ISI-ds130C, Microspec Corporation, Inc.) at 15 kV after drying and sputter-coating with a 20 nm gold film.

Acid-Degradable Cross-Linker (1) was prepared as described elsewhere (*2*).

Synthesis of CpG Oligonucleotide Macromonomer (2). The phosphorothioate oligonucleotide was synthesized on solid phase on a 1 μmol scale with 500 Å controlled pore glass support using an Expedite 8909 DNA Synthesizer (Applied Biosystems, Foster City, CA) and UltraMILD phosphoramidites (Glen Research Corporation, Sterling, VA). A sulfurizing step was substituted in the oxidation cycle, using Beaucage's Reagent, 3*H*-1,2-benzodithiole-3-one-1,1-dioxide, to generate a phosphorothioate as the internucleotide linkage (*12*). To add the polymerizable moiety, the 5′ end was modified on the solid phase with an Acrydite Amidite ((6-*N*-methylacryl)-aminohexyl-(*O*-2-cyanoethyl)-(*N*,*N*-diisopropyl) phosphoramidite, Matrix Technologies, Hudson, NH) to generate a methacrylamide-derivatized oligonucleotide. The sequence was cleaved from the solid support under basic conditions of concentrated NH_4OH at room temperature (rt) for 4 h. Solvent was removed using a vacuum concentrator, and crude oligonucleotide was taken up in 500 μL of H_2O. After filtering off the support resin, the sample was purified by reverse-phase HPLC (1100 series, Agilent Technologies, Palo Alto, CA) using 0.1 M triethylammonium acetate buffer pH 7.0 containing 5% acetonitrile and a gradient of 0% to 30% acetonitrile over 10 min at 1 mL/min with a Zorbax 300 SB-C18 column (9.14 mm × 25 cm, Agilent). The desired fractions were collected and lyophilized. The sample was then taken up in 100 μL of H_2O and further purified by ethanol precipitation with 10 μL of 3 M ammonium acetate and 1 mL of ethanol. The resulting DNA pellet was recovered by centrifugation at 4 °C for 30 min and then dried in air. $[M - H]^-$ m/z = 6626.6. Found MALDI-TOF: $[M - H]^-$ m/z = 6640.5.

Protein-Loaded Particle Preparation. To synthesize the degradable particles, an inverse emulsion free radical polymerization technique was utilized (*1*, *2*). Acrylamide, cross-linker **1,** and polymerizable ligand **2** were dissolved in 0.3 M phosphate buffer (pH 8, 250 μL). Then, OVA (7 mg, ovalbumin labeled with Cascade Blue or unlabeled) and ammonium peroxodisulfate (6.5 mg) were dissolved in this aqueous solution. The organic phase consisted of a 3 wt % surfactant solution in hexanes, using a 3:1 weight ratio of Span 80 (sorbitan monooleate) and Tween 80 (poly(ethylene glycol) sorbitan monooleate). The aqueous monomer solution (250 μL) was added to 2.5 mL of the organic phase, and the two phases were emulsified by sonicating for 30 s using a Branson Sonifier 450 with an output setting of 2 and a duty cycle of 40%. Polymerization was initiated by the addition of *N*,*N*,*N*′,*N*′-tetramethylethylenediamine (25 μL), and the mixture stirred at rt for 10 min. The particles were isolated by centrifugation, rinsed with hexanes, washed four times with acetone, and then centrifuged. The solvent was decanted and the particles dried overnight in vacuo. Particles that did not contain protein were made in the same manner, omitting OVA.

Unmodified OVA-Particles. The monomer composition contained 62.3 mg of acrylamide and 62.8 mg of cross-linker **1** dissolved in the aqueous phase.

CpG−OVA-Particles. Here, the aqueous phase consisted of 62.2 mg of acrylamide, 62.8 mg of cross-linker **1**, and 4 mg of monomer **2** in 250 μL of the phosphate buffer.

Protein Encapsulation Measurements. The protein loading was determined by preparing particles with Cascade Blue labeled OVA. Particle hydrolysis and quantification of OVA were conducted as described previously (*2*).

Oligonucleotide Quantification. Oligonucleotide quantification assays were performed using OliGreen (Molecular Probes, Eugene, OR). To quantify the amount of oligonucleotide incorporated into the particles, the beads were dispersed in 300 mM sodium phosphate buffer pH 7.4 at a concentration of 1 mg/mL. The particles were then collected as a pellet by centrifuging for 10 min. The wash supernatant was removed by pipet, and an equivalent volume of acidic buffer (pH 5.0, 300 mM acetic acid) was added to maintain the concentration. The sample was then left at rt overnight, and the hydrolyzed solution analyzed for the concentration of DNA by incubating with OliGreen, and the fluorescence of the resulting solution was quantified.

Interleukin-12 Enzyme Linked Immunosorbent Assay. Bone marrow derived dendritic cells (BMDCs) were isolated as previously described (*13*, *14*). BMDCs were plated at a density of 2×10^4 cells/well and incubated overnight in 100

μL of a 1 mg/mL solution of particles in media. Control wells consisted of untreated cells and cells exposed to particles without OVA. The media was then analyzed using an ELISA assay for interleukin-12 (Pierce, Rockford, IL). Absorbance values were measured at $\lambda = 450$ nm and corrected using $\lambda = 550$ nm as a background reference. Interleukin concentrations were calculated using a standard curve. The Student's *t*-test was used to determine statistical significance.

Analysis of DC Surface Marker Expression. BMDCs were incubated in 6-well plates at the density of 2×10^6 cells/well. After overnight cultivation, cells were further incubated with 1 mL of a 1 mg/mL solution of various particles encapsulating OVA to examine immunostimulatory effects. After incubating overnight, cells were washed, trypsinized, and treated with anti-mouse CD16/CD32 (Fcγ III/II) for 1 h to prevent nonspecific adsorption. The cells were then stained with R-Phycoethrin-labeled monoclonal antibodies specific to mouse CD40, 80, 86, and H-2K^b (MHC I) and I-A^b (MHC II) (all from Pharmingen, San Diego, CA) at 4 °C for 2 h. Relative expressions of surface molecules were analyzed and compared with fluorescence intensity determined by flow cytometry.

Animals. Male C57Bl/6 mice and CD45.1 congenic C57Bl/6 mice, 6 to 8 weeks of age, were purchased from the Jackson Laboratory (Bar Harbor, ME). The 1100Mjb mice (OT-I mice) express an H-2K^b restricted T-cell receptor (TCR) specific for the octamer peptide SIINFEKL (ovalbumin 257−264) (*15*). All mice were housed in the Stanford Animal facility in accordance with the NIH guidelines.

In Vitro T-Cell Priming Studies. For in vitro T-cell proliferation, 6×10^4 DC derived from d5 bone marrow cultures were incubated with 500 μg/mL particles (corresponding to a concentration of 20 μg/mL OVA) with or without addition of the DC activator CpG (30 μg/mL). After overnight culture, DCs were washed twice and co-cultured with 3×10^5 naive SIINFEKL(ovalbumin $_{257-264}$) /H-2K^b-specific OT−I T-cells isolated from the spleens of TCR transgenic OT-I mice for 5 d. After restimulation of the T-cells using SIINFEKL-pulsed irradiated spleen cells (30 Gy) for 3 d, T-cell proliferation was measured by ^{3}H thymidine incorporation. 1 μCi of ^{3}H thymidine was added to each well of the culture. Cells were harvested 18 h later, and ^{3}H thymidine uptake was measured in a Microbeta counter (Wallac, Gaithersburg, MD). Results are presented as the mean of triplicate cultures ± standard deviation.

In Vivo T-Cell Proliferation Assay. CD45.1$^+$ C57Bl/6 mice received subcutaneous injections of 125 μg particle in 200 μL PBS into the right flank followed by adoptive transfer of 5×10^6 CD45.2$^+$ OT-I T-cells 24 h later. The OT-I T-cells were labeled with 10 μM 5-(and-6)-carboxyfluorescein diacetate, succinimidyl ester (CFSE) (Molecular Probes) prior to adoptive transfer in order to follow their proliferation by CFSE dilution. Mice vaccinated with corresponding amounts of free OVA or free OVA plus free CpG served as controls. Three days after adoptive transfer, draining inguinal lymph nodes were harvested from vaccinated mice, and single cell suspensions were stained with fluorochrome-labeled monoclonal antibodies against CD45.2, TCR, and CD8α (all Pharmingen San Diego, CA). The CFSE proliferation profile of gated CD45.2$^+$ CD8 T-cells was determined by flow cytometry.

IFN-γ ELISPOT Assay. C57Bl/6 mice were vaccinated with 1.25 mg of particle samples in 200 μL PBS or corresponding amounts of OVA and CpG. Splenocytes were isolated 10 d after vaccination. After lysis of red blood cells, splenocytes were resuspended at a final concentration of 1×10^7 cells/mL in RPMI/10% FBS, and 100 μL of this cell suspension were then cultivated at 37 °C for 24 h in ELISPOT plates coated with anti-mouse IFN-γ with or without 10 μg/mL SIINFEKL. IFN-γ secreting cells were then detected using the anti-mouse IFN-γ ELISPOT Kit (R&D Systems, Inc., Minneapolis, MN) according to manufacterer's protocol. Results are presented as the mean of triplicate cultures + standard deviation.

Cytotoxicity Assay. C57Bl/6 mice (6 mice total per group) were vaccinated with 1.25 mg of particle samples in 200 μL PBS or corresponding amounts of OVA and CpG. At day 7 after vaccination, mice were injected intravenously with 5×10^6 CFSE-labeled target cells consisting of 50% SIINFEKL-pulsed splenocytes labeled with 5 μM CFSE and 50% unpulsed splenocytes labeled with 0.5 μM CFSE. Mice were bled 18 h after adoptive transfer, and the CFSE profile of transferred cells was determined by flow cytometry for analysis of OVA-specific cytotoxicity.

RESULTS AND DISCUSSION

Synthesis of CpG Macromonomer. The preparation of immunostimulatory CpG particles began with the synthesis of the methacrylamide-modified oligonucleotide **2**. The sequence chosen for incorporation, TCCATGACGTTCCTGACGTT, was previously shown (*16*) to induce DC maturation and cytokine secretion and has also been used as a coadjuvant for protein-based therapy, demonstrating an enhanced efficiency of vaccination. This sequence was also chosen because it is well-tolerated when administered in vivo (*16*). CpG macromonomer **2** was synthesized in a solid-phase synthesizer. A sulfurizing step was substituted in the oxidation cycle to generate phosphorothioates as the internucleotide linkages, because this linkage is known to be less susceptible than native phosphate bonds to enzymatic cleavage by nucleases prevalent in serum and within the cell cytoplasm (*17*). The polymerizable end group was added by coupling Acrydite Amidite, a methacrylamide-based phosphoramidite, to the 5′ end. The polymerizable handle of **2** enabled its covalent attachment to the polymer network, which was necessary because, unlike the protein antigens, the CpG sequence is too small to be physically entrapped into the particle and would therefore diffuse out of the particle if unbound (see Supporting Information). The macromonomer was purified by reverse-phase HPLC and was further characterized by matrix-assisted laser desorption ionization time-of-flight mass spectrometry (MALDI-TOF MS). The observed molecular weight of 6640.5 agrees within 0.2% with the calculated value of 6626.6.

Preparation of CpG-Containing Particles. Multicomponent particles encapsulating OVA and including CpG ligands conjugated throughout the polymer network (CpG−OVA-particles) were successfully synthesized and characterized to investigate the possibility of enhancing APC activation using a TLR9 agonist. The synthetic flexibility of the inverse emulsion particle preparation process enabled the addition of functional monomers, such as **2**, to the polymerization mixture. Therefore, compound **2** was copolymerized with acrylamide and acid-sensitive cross-linker **1** under conditions similar to those described previously (*2*), forming protein-loaded polymer particles with the CpG ligand covalently attached throughout the polymer scaffold (Scheme 1). In this process, monomers and protein were dissolved in a slightly basic aqueous buffer to prevent cross-linker hydrolysis, and the aqueous phase was then dispersed as droplets in hexanes. Free radical polymerization was initiated within the aqueous droplets, resulting in cross-linked hydrophilic polymer particles encapsulating OVA (*1, 2*).

SEM images showed that the particles were 250−500 nm in diameter in the dry state (Figure 1), as observed previously for ligand free particles. Protein encapsulation measurements indicated a loading of 40 μg OVA/mg particles. Oligonucleotide incorporation was measured by hydrolyzing a sample of particles and analyzing the concentration of DNA using OliGreen, a

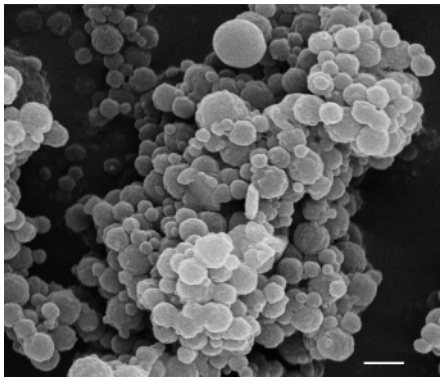


Figure 1. SEM image of CpG-particles. Scale bar = 500 nm.

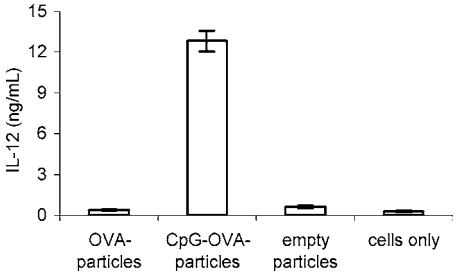


Figure 2. Interleukin-12 production by BMDCs incubated with particles.

fluorescent dye that binds to single-stranded DNA. The oligonucleotide content in the particles was 25 μg CpG DNA/mg particle. Alteration of the DNA during free radical polymerization was not expected to occur, because both oligonucleotides and plasmid DNA have previously been shown to be stable under these polymerization conditions (see Supporting Information) (*18*).

Unmodified OVA-particles free of CpG DNA were also prepared using the inverse emulsion method by omitting monomer **2**. These particles contain the same mole percent cross-linking and protein loading as the functionalized particles described above.

DC Activation by CpG−OVA-Particles. The APC receptor associated with generating potent immune responses we investigated is the TLR9, which binds CpG oligonucleotides and triggers DC activation. Soon after encountering the CpG danger signal, a DC maturation process is initiated in which the cells become less proficient at antigen uptake but increase their antigen presentation capabilities. This immunostimulation serves to enhance the effect of protein-based vaccines by inducing the production of cytokines, such as interleukin 12 (IL-12), which aid in T-cell activation (*19*−*21*). The expression of surface costimulatory molecules also rises, turning mature DCs into potent T-lymphocyte activators (*22*). Previous studies have shown that combining immunostimulatory DNA sequences with protein-based vaccines leads to a more effective therapy (*16*, *23*, *24*).

The effect of CpG−OVA-particles on the activation of DCs was investigated by analyzing cytokine secretion levels. Particle samples were incubated with murine BMDCs, and the levels of IL-12 secreted were recorded as a measure of immunostimulation (Figure 2). Unmodified OVA-particles and CpG−OVA-particles and empty particles that contained neither protein nor ligands were tested. This study revealed that the addition of immunostimulatory CpG moieties to the particles had a highly significant influence on the secretion of IL-12, with 45 times more cytokine produced than was the case for the other particle samples or for cells incubated without particles ($p < 0.001$). The other particle samples produced IL-12 cytokine levels

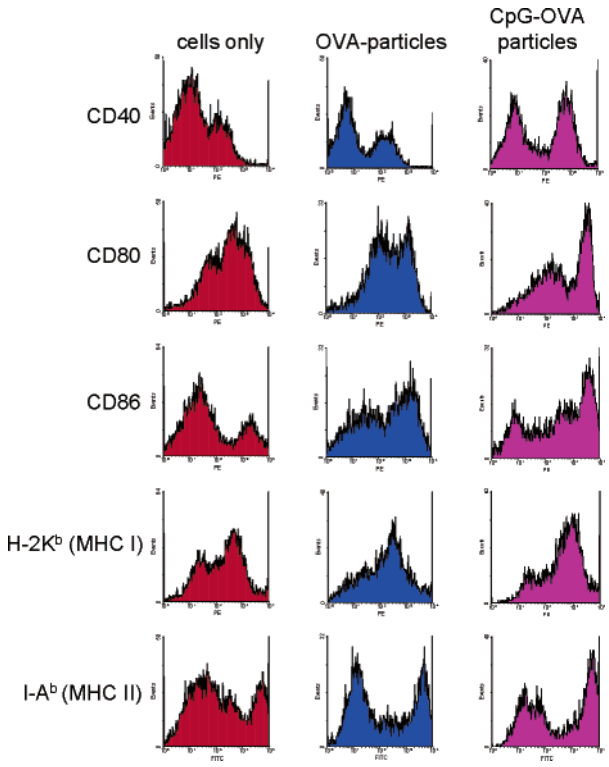


Figure 3. Surface marker expression by BMDCs incubated with particle samples. For each individual graph, the *y*-axis is number of events, *x*-axis is fluorescence.

comparable to the endogenous secretion of cells alone. Therefore, this CpG modification should enhance the vaccine efficiency of the particle system, because the secretion of this activating cytokine is expected to promote highly effective T-cell responses.

Flow cytometry was used to monitor DC maturation after exposure to the various particle formulations. Murine BMDCs were incubated with two different particle samples: OVA-particles and CpG−OVA-particles. Multiple cell surface markers associated with dendritic cell activation such as CD40, CD80, CD86, MHC I (H-2K^b), and MHC II (I-A^b) molecules, were stained with the corresponding fluorescently labeled antibodies, and the cells were analyzed by flow cytometry to determine the immunostimulatory effects of the particles. A shift to the right and increase in intensity of the peaks in Figure 3 indicate an increase in the expression of the surface molecule. Unmodified OVA-particles enhanced CD40, CD80, CD86, and MHC II expression compared to cells incubated without particles, indicating moderate DC maturation. CpG−OVA-particles significantly increased expression of surface markers CD40, CD80, and CD86 compared to the unmodified particles but had a similar response for MHC II. MHC I expression for the CpG−OVA-particle sample was also slightly upregulated. The CpG−OVA-particles generated the strongest response, demonstrating that the oligonucleotide provides an additional danger signal that initiates the transformation of immature DCs, which are efficient at antigen capture, to mature DCs, which are proficient at antigen presentation and T-cell activation. These studies indicate that the presence of CpG on the protein-loaded particles leads to strong immunostimulation, which should in turn lead to more effective therapy.

T-Cell Priming by Antigen-Loaded DC Requires CpG. As the particles were designed to specifically deliver antigen into the MHC class I presentation for induction of primary antigen-specific CD8 T-cell responses, we decided to study the capacity of BMDCs pulsed with different particle samples to induce the proliferation of naïve SIINFEKL(ovalbumin$_{257-264}$)/

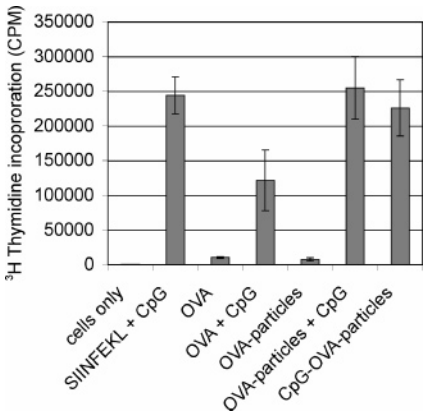


Figure 4. BMDCs loaded with OVA-particles and activated by CpG prime OVA-specific CD8 T-cells in vitro.

H-2K^b-specific CD8 T-cells isolated from TCR transgenic OT-I mice. As shown in Figure 4, only BMDCs pulsed with CpG−OVA-particles efficiently stimulated the proliferation of naïve CD8 OT-I T-cells in vitro. T-cell stimulatory capacity by BMDCs pulsed with OVA-particles could be rescued by the addition of CpG to the BMDC culture, thus demonstrating that the lack of T-cell proliferation is due to insufficient DC activation and not because of a failure of antigen delivery (Figure 4). These results indicate that codelivery of a TLR agonist, such as CpG, together with the antigen is essential to induce a primary antigen-specific T-cell response.

Induction of OVA-Specific T-Cell Immunity by CpG-Particles In Vivo. As DC activation seems to be critical for T-cell priming, and in vitro studies have limited capacity to predict the efficacy of vaccines due to the complexity of the immune system, we decided to further explore the capacity of CpG−OVA-particles to induce T-cell responses in vivo. Consistent with the in vitro results, CFSE-labeled CD45.2$^+$ naïve OT-I T-cells transferred into CD45.1$^+$ C57Bl/6 recipient mice proliferated best after vaccination with CpG−OVA-particles compared to unmodified OVA-particles or even free OVA + free CpG (Figure 5), as measured by the dilution of the CFSE with each cell division. Vaccination with empty particles induced no significant T-cell proliferation.

In order to determine if OVA-specific CD8$^+$ T-cells induced after vaccination with particles are functional, we decided to quantify IFN-γ secreting cells present in the spleen by an IFN-γ-ELISPOT assay upon stimulation with the CD8 T-cell epitope SIINFEKL. IFN-γ represents a proinflammatory cytokine that promotes antitumor immunity by inhibition of tumor cell proliferation and angiogenesis (*25*). Vaccination with CpG−OVA-particles resulted in the highest number of IFN-γ-secreting cells upon stimulation with SIINFEKL compared to plain OVA-particles or a mixture of free OVA + free CpG demonstrating that SIINFEKL/H-2k^b-specific CD8 T-cells are not only expanded after vaccination but are capable to respond with IFN-γ secretion upon TCR stimulation (Figure 6). Low numbers of IFN-γ-secreting cells were observed in the absence of SIINFEKL peptide, which proves that the immune response induced by the CpG−OVA-particles is specific for ovalbumin (Figure 6). Moreover, vaccination with CpG−OVA-particles induced at least twice as many IFN-γ-secreting cells in response to SIINFEKL stimulation compared to a mixture of OVA-particles and free CpG, consistent with reports that codelivery of antigen and TLR agonist to the same antigen-presenting cell is important for generating optimal immune responses (*23*, *26*). It is likely that the current experiments underestimate the true potential of the CpG-particles, as an arbitrary CpG concentration was used to generate these particles and the optimal CpG load has yet to be determined. We expect that future studies will show that the amount of CpG needed for optimal vaccination effect can be significantly lowered if CpG is linked to the particles compared

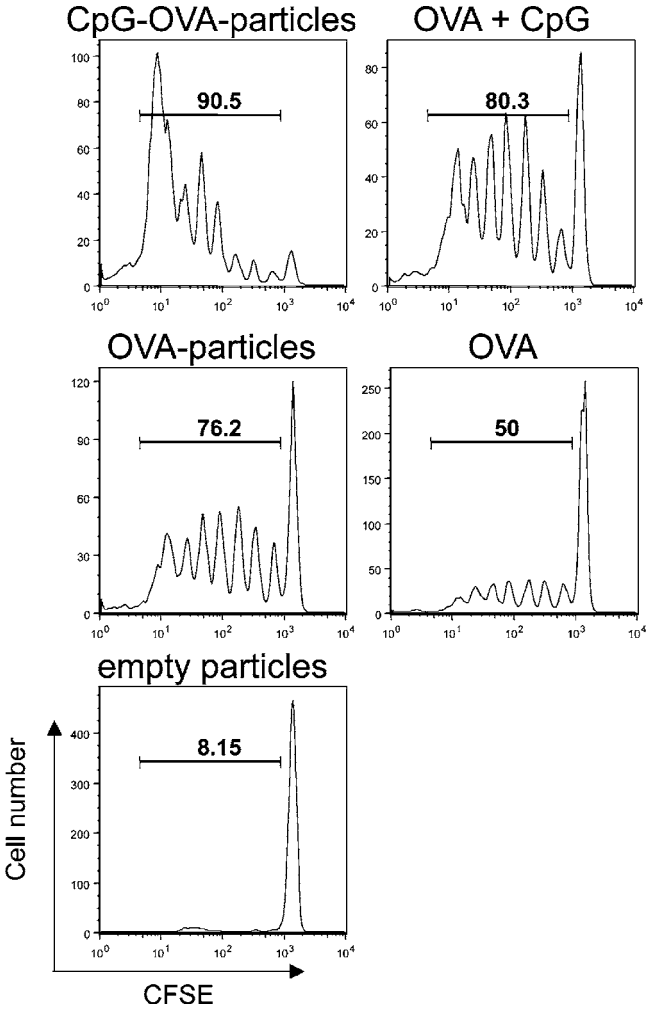


Figure 5. In vivo proliferation of SIINFEKL(ovalbumin$_{257-264}$)/H-2K^b-specific naïve CD8 T-cells induced by CpG−OVA-particles. Histograms show CFSE profiles of gated CD45.2$^+$ CD8$^+$ T-cells isolated from the lymph nodes of vaccinated mice 3 d after adoptive transfer. Numbers represent the percentages of the proliferating cells of total OT-I T-cells. Experiments were performed three times with similar results.

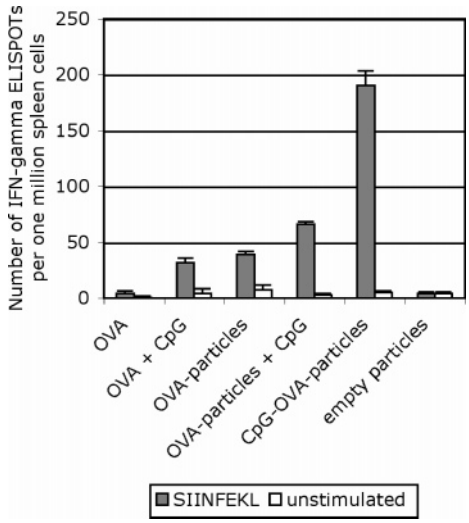


Figure 6. Vaccination with CpG−OVA-particles leads to potent IFN-γ secretion upon stimulation with the OVA-derived peptide (SIINFEKL). Data are representative of two experiments with similar results.

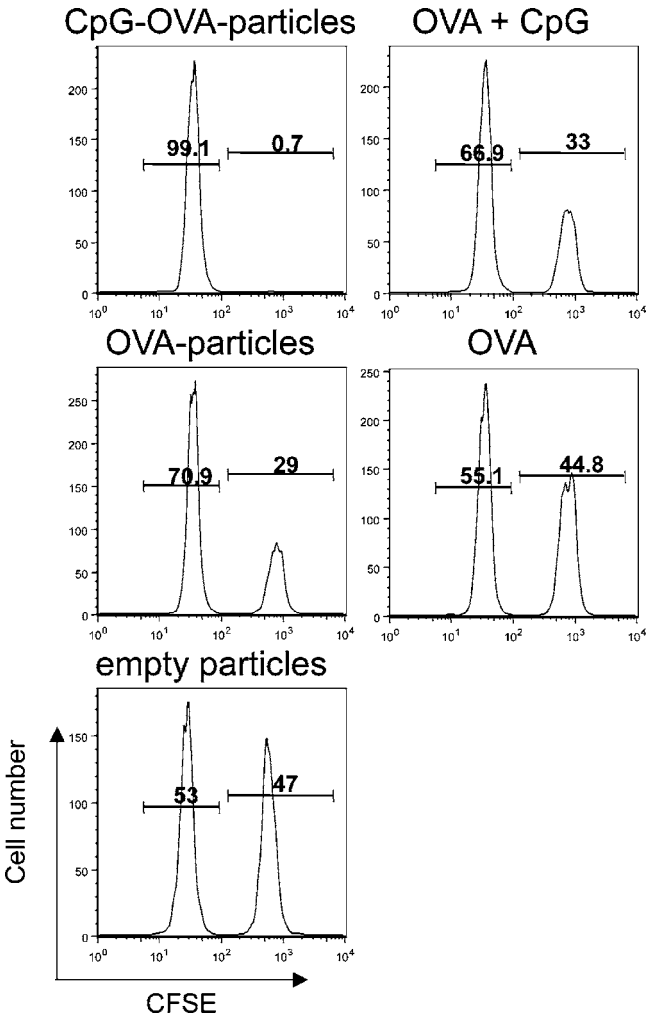


Figure 7. CpG−OVA-particles induce specific lysis of SIINFEKL-pulsed cells in vivo. Histograms show percentages of remaining SIINFEKL-pulsed spleen cells (right peak) versus unpulsed spleen cells (left peak) of total transferred cells. Data are representative of three experiments with similar results.

to the use of free CpG as an adjuvant, thus reducing the risk of toxicity caused by CpG-induced systemic inflammation (*27*).

In addition to cytokine secretion, the induction of antigen-specific cytotoxic effector cells represents probably the most important criterion for evaluating vaccine efficacy, as antigen-specific lysis of cells (e.g., tumor cells, virus-infected cells) is desirable in many vaccine applications and is especially critical for antitumor immunity. In order to measure OVA-specific cytotoxicity, C57Bl/6 mice were vaccinated by subcutaneous injection with 1.25 mg samples of particle or corresponding amounts of OVA and CpG followed by intravenous injection of an equal mixture of SIINFEKL-pulsed and unpulsed CFSE-labeled C57Bl/6 spleen cells. As SIINFEKL-pulsed cells were labeled with a higher CFSE concentration than the unpulsed spleen cells prior to injection, OVA-specific cytotoxicity can be measured by flow cytometric analysis of blood cells obtained from vaccinated mice. At 18 h after transfer, mice vaccinated with CpG−OVA-particles lacked nearly completely the CFSE high population of SIINFEKL-pulsed spleen cells in the blood, indicating that high numbers of SIINFEKL/H-2k^b-specific cytototoxic effector cells were present in these mice (Figure 7). In contrast, no OVA-specific cytotoxicity was induced after vaccination with empty particles or OVA alone (*28*), as SIINFEKL-pulsed (high CFSE concentration) and unpulsed spleen cells (low CFSE concentration) were still present at similar levels.

CONCLUSION

Protein-loaded particles incorporating CpG oligonucleotide ligands designed to trigger DC maturation and activation were successfully prepared using an inverse emulsion polymerization procedure. Incorporation of the CpG sequence into the particles significantly increased DC IL-12 secretion and costimulatory molecule expression when compared to analogous but CpG free particles. CpG-modified particles also induced a strong antigen-specific T-cell immunity in vivo, which was superior to both plain OVA-particles and a mixture of free OVA plus free CpG. This enhanced DC immunostimulation should lead to more effective vaccine therapies. In future studies, it will be critical to determine the optimal CpG ligand density in a particle formulation for maximum vaccine efficacy.

ACKNOWLEDGMENT

We thank the National Institutes of Health (grant RO1 EB005824) for funding of this research. We also thank Dr. Kelly Flook (Lawrence Berkeley National Laboratory, Berkeley, CA) for assisting with SEM images and Steve Guillaudeu for assistance with oligonucleotide purification.

Supporting Information Available: The contents include the synthesis of oligonucleotide-containing hydrogels, an analysis of oligonucleotide integrity after exposure to free radical polymerization conditions, and the comparison of encapsulation of free vs polymerizable oligonucleotides in the particles. This material is available free of charge via the Internet at http://pubs.acs.org/BC.

LITERATURE CITED

(1) Murthy, N., Xu, M., Schuck, S., Kunisawa, J., Shastri, N., and Fréchet, J. M. J. (2003) A macromolecular delivery vehicle for protein-based vaccines: acid-degradable protein-loaded microgels. *Proc. Natl. Acad. Sci. U.S.A. 100*, 4995−5000.

(2) Standley, S., Kwon, Y. J., Murthy, N., Kunisawa, J., Shastri, N., Guillaudeu, S., Lau, L., and Fréchet, J. M. J. (2004) Acid-degradable particles for protein-based vaccines: enhanced survival rate for tumor challenged mice using ovalbumin model. *Bioconjugate Chem. 15*, 1281−1288.

(3) Krieg, A. M., Yi, A., Matson, S.; Waldschmidt, T. J., Bishop, G. A., Teasdale, R., Koretzky, G. A., and Klinman, D. M. (1995) CpG motifs in bacterial DNA trigger direct B-cell activation. *Nature (London) 374*, 546−549.

(4) Sparwasser, T., Koch, E., Vabulas, R. M., Heeg, K., Lipford, G. B., Ellwart, J. W., and Wagner, H. (1998) Bacterial DNA and immunostimulatory CpG oligonucleotides trigger maturation and activation of murine dendritic cells. *Eur. J. Immunol. 28*, 2045−2054.

(5) Chuang, T., Lee, J., Kline, L., Mathison, J. C., and Ulevitch, R. J. (2002) Toll-like receptor 9 mediates CpG-DNA signaling. *J. Leukocyte Biol. 71*, 538−544.

(6) Bauer, S., and Wagner, H. (2002) Bacterial CpG-DNA licenses TLR9. *Curr. Top. Microbiol. Immunol. 270*, 145−154.

(7) Kaisho, T., and Akira, S. (2002) Toll-like receptors as adjuvant receptors. *Biochim. Biophys. Acta 1589*, 1−13.

(8) Yang, Y., Huang, C. T., Huang, X., and Pardoll, D. M. (2004) Persistent Toll-like receptor signals are required for reversal of regulatory T cell-mediated CD8 tolerance. *Nat. Immunol. 5*, 508−15.

(9) Mende, I., and Engleman, E. G. (2005) Breaking tolerance to tumors with dendritic cell-based immunotherapy. *Ann. N. Y. Acad. Sci. 1058*, 96−104.

(10) Kirsch, J. D., Yi, A., Spitz, D. R., and Krieg, A. M. (2002) Accumulation of glutathione disulfide mediates NF-κB activation during immune stimulation with CpG DNA. *Antisense Nucleic Acid Drug Dev. 12*, 327−340.

(11) Wu, K. J., Steding, A., and Becker, C. H. (1993) Matrix-assisted laser desorption time-of-flight mass spectrometry of oligonucleotides

using 3-hydroxypicolinic acid as an ultraviolet-sensitive matrix. *Rapid Commun. Mass Spectrom. 7*, 142−146.
(12) Iyer, R. P., Egan, W., Regan, J. B., and Beaucage, S. L. (1990) 3H-1,2-Benzodithiole-3-one 1,1-dioxide as an improved sulfurizing reagent in the solid-phase synthesis of oligodeoxyribonucleoside phosphorothioates. *J. Am. Chem. Soc. 112*, 1253−1254.
(13) Kwon, Y. J., Standley, S. M., Goh, S. L., and Fréchet, J. M. J. (2005) Enhanced antigen presentation and immunostimulation of dendritic cells using acid-degradable cationic nanoparticles. *J. Controlled Release 105*, 199−212.
(14) Stier, E. M., Mandal, M., and Lee, K. D. (2005) Differential cytosolic delivery and presentation of antigen by listeriolysin O-liposomes to macrophages and dendritic cells. *Mol. Pharm. 2*, 74−82.
(15) Hogquist, K. A., Jameson, S. C., Heath, W. R., Howard, J. L., Bevan, M. J., and Carbone, F. R. (1994) T cell receptor antagonist peptides induce positive selection. *Cell 76*, 17−27.
(16) Merad, M., Sugie, T., Engleman, E. G., and Fong, L. (2002) In vivo manipulation of dendritic cells to induce therapeutic immunity. *Blood 99*, 1676−1682.
(17) Eckstein, F. (1985) Nucleoside phosphorothioates. *Annu. Rev. Biochem. 54*, 367−402.
(18) Goh, S. L., Murthy, N., Xu, M., and Fréchet, J. M. J. (2004) Cross-linked microparticles as carriers for the delivery of plasmid DNA for vaccine development. *Bioconjugate Chem. 15*, 467−474.
(19) Hemmi, H., Takeuchi, O., Kawai, T., Kaisho, T., Sato, S., Sanjo, H., Matsumoto, M., Hoshino, K., Wagner, H., Takeda, K., and Akira, S. (2000) A Toll-like receptor recognizes bacterial DNA. *Nature (London) 408*, 740−745.
(20) Klinman, D. M., Yi, A., Beaucage, S. L., Conover, J., and Krieg, A. M. (1996) CpG motifs present in bacterial DNA rapidly induce lymphocytes to secrete interleukin 6, interleukin 12, and interferon γ. *Proc. Natl. Acad. Sci. U.S.A. 93*, 2879−2883.
(21) Krieg, A. M., Love-Homan, L., Yi, A., and Harty, J. T. (1998) CpG DNA induces sustained IL-12 expression in vivo and resistance to *Listeria monocytogenes* challenge. *J. Immunol. 161*, 2428−2434.
(22) Guermonprez, P., Valladeau, J., Zitvogel, L., Théry, C., and Amigorena, S. (2002) Antigen presentation and T cell stimulation by dendritic cells. *Annu. Rev. Immunol. 20*, 621−667.
(23) Heit, A., Schmitz, F., O'Keeffe, M., Staib, C., Busch, D. H., Wagner, H., and Huster, K. M. (2005) Protective CD8 T cell immunity triggered by CpG-protein conjugates competes with the efficacy of live vaccines. *J. Immunol. 174*, 4373−4380.
(24) Speiser, D. E., Liénard, D., Rufer, N., Rubio-Godoy, V., Rimoldi, D., Lejeune, F., Krieg, A. M., Cerottini, J., and Romero, P. (2005) Rapid and strong human $CD8^+$ T cell responses to vaccination with peptide, IFA, and CpG oligodeoxynucleotide 7909. *J. Clin. Invest. 115*, 739−746.
(25) Ikeda, H., Old, L. J., Schreiber, R. D. (2002) The roles of IFN gamma in protection against tumor development and cancer immunoediting. *Cytokine Growth Factor Rev. 13*, 95−109.
(26) Klinman, D. M. (2004) Immunotherapeutic uses of CpG oligodeoxynucleotides. *Nat. Rev. Immunol. 4*, 249−259.
(27) Marshak-Rothstein, A. (2006) Toll-like receptors in systemic autoimmune disease. *Nat. Rev. Immunol. 6*, 823−835.
(28) Murthy, N., Thng, Y. X., Schuck, S., Xu, M. C., Fréchet, J. M. J. (2002) A novel strategy for encapsulation and release of proteins: Hydrogels and microgels with acid-labile acetal crosslinkers. *J. Am. Chem. Soc. 124*, 12398−12399.

BC060165I

Influence of Different Spacers on the Biological Profile of a DOTA−Somatostatin Analogue

Patricia Antunes,[†] Mihaela Ginj,[†] Martin A. Walter,[†] Jianhua Chen,[†] Jean-Claude Reubi,[‡] and Helmut R. Maecke*,[†]

Division of Radiological Chemistry, Department of Radiology, University Hospital Basel, and Divison of Cell Biology and Experimental Cancer Research, Institute of Pathology, University of Berne, Switzerland. Received June 13, 2006; Revised Manuscript Received October 19, 2006

Radiolabeled somatostatin analogues have been successfully used for targeted radiotherapy and for imaging of somatostatin receptor (sst_{1-5})-positive tumors. Nevertheless, these analogues are subject to improving their tumor-to-nontarget ratio to enhance their diagnostic or therapeutic properties, preventing nephrotoxicity. In order to understand the influence of lipophilicity and charge on the pharmacokinetic profile of [1,4,7,10-tetraazacyclododecane-1,4,7,10-tetraacetic acid (DOTA)]−somatostatin-based radioligands such as [DOTA,1-Nal^3]−octreotide (DOTA−NOC), different spacers (X) based on 8-amino-3,6-dioxaoctanoic acid (PEG_2), 15-amino-4,7,10,13-tetraoxapentadecanoic acid (PEG_4), *N*-acetyl glucosamine (GlcNAc), triglycine, β-alanine, aspartic acid, and lysine were introduced between the chelator DOTA and the peptide NOC. All DOTA−X−NOC conjugates were synthesized by Fmoc solid-phase synthesis. The partition coefficient (log *D*) at pH = 7.4 indicated that higher hydrophilicity than [^{111}In-DOTA]−NOC was achieved with the introduction of the mentioned spacers, except with triglycine and β-alanine. The high affinity of [In^{III}-DOTA]−NOC for human sst_2 ($hsst_2$) was preserved with the structural modifications, while an overall drop for $hsst_3$ affinity was observed, except in the case of [In^{III}-DOTA]−β-Ala−NOC. The new conjugates preserved the good affinity for $hsst_5$, except for [In^{III}-DOTA]−Asn(GlcNAc)−NOC, which showed decreased affinity. A significant 1.2-fold improvement in the specific internalization rate in AR4-2J rat pancreatic tumor cells (sst_2 receptor expression) at 4 h was achieved with the introduction of Asp as a spacer in the parent compound. In sst_3-expressing HEK cells, the specific internalization rate at 4 h for [^{111}In-DOTA]−NOC (13.1% ± 0.3%) was maintained with [^{111}In-DOTA]−β-Ala−NOC (14.0% ± 1.8%), but the remaining derivatives showed <2% specific internalization. Biodistribution studies were performed with Lewis rats bearing the AR4-2J rat pancreatic tumor. In comparison to [^{111}In-DOTA]−NOC (2.96% ± 0.48% IA/g), the specific uptake in the tumor at 4 h p.i. was significantly improved for the ^{111}In-labeled sugar analogue (4.17% ± 0.46% IA/g), which among all the new derivatives presented the best tumor-to-kidney ratio (1.9).

INTRODUCTION

A new challenge in nuclear oncology came with the advent of radiolabeled regulatory peptides having favorable pharmacokinetics and specific targeting characteristics (*1*). The importance of these ligands is endorsed by the overexpression of their receptors in cancerous tissue (*2*). Among an array of relevant peptides, somatostatin derivatives established themselves as successful radiopharmaceuticals. The five somatostatin receptor subtypes (sst)[1] are overexpressed and widely distributed in cancerous tissues, in a homogeneous or heterogeneous manner (*3*, *4*). In addition, there is a considerable variation in sst subtype expression between different tumor types and among tumors of the same type (*3*, *4*). The most frequently overexpressed sst receptor in human tumors is sst_2 (*5*). Nevertheless, there are exceptions, namely, in inactive pituitary adenomas and in thymomas where sst_3 is predominantly expressed (*3*, *6*). Human lung tumors were shown not only to overexpress sst_5, but also sst_2 and sst_3 (*7*).

Somatostatin-based peptides labeled with radiohalogens, like fluorine-18 (^{18}F-octreotide) (*8*), or conjugated with a bifunctional chelator suitable for labeling with radiometals such as ^{111}In, $^{67/68}$Ga, ^{90}Y, or lanthanides, like ^{177}Lu, have been investigated for applications in PET and SPECT or in peptide receptor-mediated radionuclide therapy (PRRT) (*9*, *10*). For the visualization of neuroendocrine tumors, [^{123}I-Tyr^3]-octreotide ([^{123}I]-TOC) was tested clinically (*11*), giving somewhat disappointing results due to its in vivo deiodination and unfavorable pharmacokinetics. It showed extensive hepatic uptake, which led to a high background in the abdomen (*12*, *13*). Later, an extensive clinical study comparing [^{123}I]-TOC with [^{111}In-DTPA]-octreotide (OctreoScan) demonstrated that the ^{111}In-labeled

* Helmut R. Maecke, Division of Radiological Chemistry, University Hospital Basel, Petersgraben 4, CH-4031 Basel, Switzerland, E-mail: hmaecke@uhbs.ch, Tel.: +41-61-2654699, Fax: +41-61-2655559.

[†] University Hospital Basel.

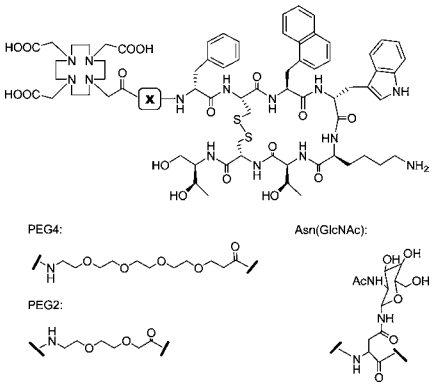
[‡] University of Berne.

[1] Abbreviations: CPM, counts per minute; DMEM, Dulbecco's Modified Eagle's Medium; DIPEA, *N*,*N*-diisopropylethylamine; DIC, *N*,*N*′-diisopropylcarbodiimide; DCM, dichloromethane; DMF, *N*,*N*-dimethylformamide; DOTA, 1,4,7,10-tetraazacyclododecane-1,4,7,10-tetraacetic acid; DTPA, diethylenetriaminepentaacetic acid; ESI-MS, electrospray ionization mass spectrometry; FBS, fetal bovine serum; FDA, Food and Drug Administration; Fmoc-Asn(Ac_3AcNH-β-Glc)-OH, *N*-α-Fmoc-*N*-β-(3,4,6-tri-O-acetyl-2-(acetylamino)-deoxy-2-β-glucopyranosyl)-L-asparagine; HATU, *O*-(7-azabenzotriazol-1-yl)-*N*,*N*,*N*′,*N*′-tetramethyluronium hexafluorophosphate; HEK, human embryonic kidney; HOBt, *N*-hydroxybenzotriazole; IA, injected activity, GlcNAc, *N*-acetyl glucosamine; NMP, *N*-methyl-2-pyrrolidone; OK, opossum kidney; p.i., postinjection; PBS, phosphate-buffered saline; PEG, polyethylene glycol; PEG_2, 8-amino-3,6-dioxaoctanoic acid; PEG_4, 15-amino-4,7,10,13-tetraoxapentadecanoic acid; PET, positron emission tomography; PRRT, peptide receptor radionuclide therapy; SPECT, single-photon emission computerized tomography; SPPS, solid-phase peptide synthesis; sst, somatostatin receptor subtype; sst_y, somatostatin receptor subtype *Y* (*Y* = 1, 2, 3, 4, or 5); TFA, trifluoroacetic acid; TFE, trifluoroethanol; TIS, triisopropylsilane.

10.1021/bc0601673 CCC: $37.00 © 2007 American Chemical Society
Published on Web 12/15/2006

Chart 1. Structural Formula of DOTA−X−NOC Conjugates and Some Spacers (X) Used in This Study

Compound	X
DOTA-NOC *(30)*, **1**	-
DOTA-PEG_4-NOC, **2**	PEG_4
DOTA-PEG_2-NOC, **3**	PEG_2
DOTA-β-Ala-NOC, **4**	β-Ala
DOTA-$(Gly)_3$-NOC, **5**	$(Gly)_3$
DOTA-Asn(GlcNAc)-NOC, **6**	Asn(GlcNAc)
DOTA-Asp-NOC, **7**	Asp
DOTA-Lys-NOC, **8**	Lys



ligand is mainly excreted via the kidneys; it has a better pharmacokinetic profile and higher sensitivity regarding the localization of neuroendocrine tumors (*14*). Nowadays, OctreoScan, an FDA approved agent, is successfully used to visualize and stage sst-positive tumors (*15*). Nevertheless, this radiotracer presents a limited binding affinity profile: from the five somatostatin receptor subtypes, [^{111}In-DTPA]-octreotide binds with low affinity to $hsst_3$ and $hsst_5$ ($IC_{50} = 182 \pm 13$ nM and 237 ± 52 nM, respectively) and with intermediate affinity to $hsst_2$ ($IC_{50} = 22 \pm 3.6$ nM) (*3*, *5*). Moreover, for therapeutic applications a β-emitter such as yttrium-90 is desirable. But, as the complex [^{90}Y-DTPA] is unstable in vivo, DTPA was replaced by DOTA, a chelator, which shows much higher kinetic inertness when complexed with yttrium (*16*−*18*). Several DOTA-octreotide derivatives with improved features compared to OctreoScan were reported (*19*, *20*). One superior example is [DOTA,Tyr^3]-octreotide (DOTA−TOC). Clinical trials with [^{111}In]-, [^{177}Lu], or [^{90}Y]-labeled DOTA−TOC have shown good tumor uptake and therapeutic effectiveness (*21*−*24*). However, the potential nephrotoxicity continues to be a drawback of these radiopharmaceuticals (*25*), and [Y^{III}-DOTA]−TOC binds with an affinity worth considering only to $hsst_2$ ($IC_{50} = 11.4 \pm 1.7$ nM) (*5*). Although PRRT with these analogues is one of the most valuable methods regarding therapy of neuroendocrine tumors, the low tumor sensitivity to radiation requires a high dose, which is limited by the high kidney uptake.

However, to cope with nephrotoxicity, amino acid infusion is currently used in the clinic (*26*). Those amino acids, usually lysine/arginine, show a blocking effect, as they most likely bind to the negative charges on the extracellular domain of the megalin/cubilin system, which might be one of the major causes for the accumulation of renal radioactivity (*27*, *28*). At the same time, it is of major importance to increase the tumor uptake. Strategies like the introduction of a spacer based on a cathepsin-B-labile peptide sequence between DOTA and [Tyr^3]-octreotate (TATE) could improve the in vitro retention time in AR4-2J tumor cells without affecting the binding affinity (*29*). The tumor uptake can also be improved by extending the sst profile of the radiotracer. A new ligand [DOTA,1-Nal^3]-octreotide (DOTA−NOC) was developed, which showed high affinity for $hsst_2$, $hsst_3$, and $hsst_5$, when complexed with In^{III}/Y^{III}; its increase of tumor uptake in relation to [^{111}In-DOTA]−TOC was verified by preclinical and clinical studies performed with [^{68}Ga]-, [^{111}In]-, and [^{177}Lu]-labeled DOTA−NOC (*30*−*34*). In spite of that, therapeutic clinical studies showed that it is still necessary to use amino acid infusions to effectively decrease the kidney uptake. Also, in some cases, [^{111}In/^{177}Lu-DOTA]−NOC exhibits higher background activity than [^{111}In-DOTA]−TOC (*30*), probably due to the higher lipophilicity of radiolabeled DOTA−NOC (*30*, *31*).

As shown in the examples specified, several somatostatin-based radioligands were developed with improved pharmacokinetics compared to [^{111}In-DTPA]-octreotide. However, the structural factors influencing the pharmacokinetic profile of these radioligands are not fully understood yet.

In this systematic study, we examine how the introduction of different spacers (X) between the chelator and the peptide in DOTA−NOC (Chart 1) modulates its properties, such as lipophilicity and charge, and how these changes influence its pharmacokinetic profile. In this evaluation, special attention was paid to the tumor-to-kidney ratio.

EXPERIMENTAL PROCEDURES

Reagents. H-Thr(tBu)-ol-(2-chloro-trityl)-resin was purchased from Advanced ChemTech (Giessen, Germany). All Fmoc-amino acids were obtained from NovaBiochem AG (Läufelfingen, Switzerland), Bachem (Bubendorf, Switzerland), and Neosystems (France), with the exception of Fmoc-PEG_4-OH that was commercially available from Quanta Biodesign (Powell, U.S.A.). DOTA(tBu)$_3$ was acquired from Macrocyclics (Richardson, Texas). [^{111}In]Cl_3 was purchased from Mallinckrodt Med. (Petten, The Netherlands). Other chemicals and solvents were obtained from commercial sources and used without further purification.

Instrumentation. Solid-phase peptide synthesis was performed on a semiautomatic peptide synthesizer commercially available from Rink Combichem (Bubendorf, Switzerland). Analytical reversed-phase high-performance liquid chromatography (RP-HPLC) was carried out on a Hewlett-Packard 1050 HPLC system (Waldbronn, Germany) coupled to a multiwavelength detector and a flow-through Berthold LB506C1 γ-detector. Preparative HPLC was performed on a Bischof HPLC system (Metrohm AG, Switzerland) with HPLC pumps 2250 and a Lambda 1010 UV detector (Metrohm AG, Switzerland). Analytical RP-HPLC and preparative HPLC were performed using CC250/4 Nucleosil 120-3C18 columns from Macherey-Nagel and a VP250/21 Nucleosil 200-5C15 column, respectively. Both columns were eluted with a gradient system of mixtures of H_2O with 0.1% trifluoroacetic acid (TFA) (solvent A) and acetonitrile (solvent B). Electrospray ionization mass spectrometry (ESI-MS) was carried out with a Finnigan SSQ 7000 spectrometer (Bremen, Germany). Lyophilization was performed on a Christ α1−2 lyophilisator (Osterode, Germany). Quantitative γ-counting was performed on a COBRA 5003 γ-system well counter from Packard Instruments (Switzerland).

Syntheses. DOTA−NOC was synthesized by standard Fmoc SPPS techniques on H-Thr(tBu)-ol-(2-chloro-trityl)-resin as reported previously (*30*). The same resin-based synthetic methods were used to develop new DOTA−X−NOC derivatives. All Fmoc-amino acid couplings were completed after 2 h, with the exception of Fmoc-PEG_2-OH, Fmoc-PEG_4-OH, and Fmoc-Asn(Ac_3AcNH-β-Glc)-OH whose reaction times were extended to 16−24 h. DOTA(tBu)$_3$ (2.5 equiv relative to the

peptide−resin) was conjugated to the *N*-terminus of the peptide using HATU activation (2.5 equiv) in NMP. The pH was adjusted to 7−8 using DIPEA. Double couplings of DOTA(tBu)$_3$ were performed for the PEG$_4$ derivative. The reaction time for the chelator conjugation usually was 5 h and increased to 18−24 h for derivatives with spacers like PEG$_2$, PEG$_4$, and the sugar moiety. The protected conjugates were cleaved from the resin with 0.5% TFA, 0.5% H_2O, and 20% TFE in DCM. Then, the Cys-Cys disulfide bond formation was achieved with excess of I_2 (10 equiv) in MeOH/H_2O = 9:1. The peptides were deprotected with 5% H_2O, 3% thioanisole, and 3% TIS in TFA for 4−5 h. In the sugar derivative, the O-acetyl groups were cleaved with a solution of N_2H_4/MeOH/H_2O (3:3:4) for 15 min. All compounds were purified by HPLC, lyophilized, and characterized by ESI-MS and RP-HPLC.

[In^{III}-DOTA]−X−NOC. DOTA−X−NOC analogues were complexed with [In^{III}]Cl$_3$, using the following procedure: Approximately 1 mg of the DOTA−X−NOC in 150 μL of 0.2 M sodium acetate buffer (pH 5) and 3 equiv of [In^{III}]Cl$_3$ were incubated at 95 °C for 25 min. After cooling, the complex was purified over a SepPak C18 cartridge (Millipore, Switzerland) preconditioned with 10 mL of MeOH and 10 mL of H_2O. The cartridge was washed with H_2O to remove the excess of [In^{III}]Cl$_3$, followed by the elution with MeOH to recover the desired [In^{III}-DOTA]−X−NOC. After evaporation of MeOH and lyophilization, the In^{III} complexes were characterized by ESI-MS and RP-HPLC with a flow of 0.75 mL/min and a linear gradient: 0−30 min, 10% B to 60% B.

Radiotracers. The radiopeptides were prepared (*9*) by dissolving 10 μg of the DOTA−X−NOC in 150 μL of 0.2 M sodium acetate buffer (pH 5); after addition of [^{111}In]Cl$_3$ (37−148 MBq), the solution was incubated at 95 °C for 25 min to afford the radioligand with a specific activity up to 28 GBq/μmol. [In^{III}]Cl$_3$ was then added and incubated at 95 °C for 25 min. In all cases, a quality control was performed by RP-HPLC with a flow of 0.75 mL/min and a linear gradient: 0−30 min, 10% B to 60% B. For all the preclinical studies, the labeling was performed as described in this section, with an exception for biodistribution studies, where the labeling was carried out accordingly without the addition of [In^{III}]Cl$_3$.

Serum Stability. To 1 mL of freshly prepared human serum, previously equilibrated in a 5% CO_2 (95% air) environment at 37 °C, 0.6 nmol of [^{111}In-DOTA]−X−NOC was added. The mixture was incubated in a 5% CO_2, 37 °C environment. At different time points, 100 μL aliquots (in triplicate) were removed and treated with 200 μL of EtOH. Samples were then cooled (4 °C) and centrifuged for 15 min at 500 *g* and 4 °C to precipitate serum proteins. The supernatants were removed, and the sediment was washed twice with 1 mL of EtOH. The activity in the ethanolic phase and in the proteic precipitate was measured in a γ-counter. Both counts were compared to give the percentage of peptides not bound to proteins or radiometal transferred to serum proteins. The supernatant was checked by HPLC using the equipment mentioned above.

Receptor Binding Assays. CHO-K1 and CCL39 cells stably expressing human sst$_{1-5}$ were grown as described previously (*5*). All culture reagents were supplied by GIBCO/BRL and Life Technologies (Grand Island, NY). Cell membrane pellets were prepared, and receptor autoradiography was performed on pellet sections (mounted on microscope slides) as described in detail previously (*5*). For each of the tested compounds, complete displacement experiments were performed with the universal somatostatin radioligand [^{125}I][Leu^8,D-Trp^{22},Tyr^{25}]somatostatin-28 using increasing concentrations of the unlabeled peptide ranging from 0.1 to 1000 nM. Somatostatin-28 was run in parallel as a control using the same increasing concentrations. IC$_{50}$ values were calculated after quantification of the data using a computer-assisted image processing system. Tissue standards (autoradiographic [^{125}I]microscales Amersham, U.K.) containing known amounts of isotopes, cross-calibrated to tissue-equivalent ligand concentrations, were used for quantification (*5*). The concentrations of the peptide solutions were measured by UV spectroscopy (ϵ_{NOC} 280 nm = 9855 dm^3 mol^{-1} cm^{-1}).

Lipophilicity. Determination of log $D_{(pH=7.4)}$ was performed by the "shake-flask" method: to a solution containing 500 μL of octanol and 500 μL of PBS (pH 7.4) (obtained from saturated octanol-PBS solution), 10 μL of 100 nM [^{111}In-DOTA]−X−NOC derivatives were added. The resulting solutions were vortexed at room temperature and centrifuged at 3000 rpm for 10 min. Aliquots of 100 μL were removed from the octanol and from the saline phase, and the activity measured in a γ-counter. The lipophilicity was calculated as the average log ratio value of the radioactivity in the organic fraction and the PBS fraction from the three samples.

Cell Culture. AR4-2J rat pancreatic tumor cells expressing sst$_2$ were cultured in high-glucose DMEM, enriched with 4 mM glutamine, 10% FBS, amino acids, vitamins, and penicillin−streptomycin from BioConcept (Allschwil, Switzerland). Human embryonic kidney 293 cells stably expressing rat sst$_3$ (HEK-sst$_3$) and sst$_5$ (HEK-sst$_5$) receptors (a gift from Dr. S. Schulz, Magdeburg, Germany) (*32*) were grown in DMEM supplemented with 10% fetal bovine serum, penicillin−streptomycin, and G418 (500 μg/mL). Cells were maintained in a humidified 5% CO_2/air atmosphere at 37 °C. The viability of the cells was assessed using trypan blue stain and counted under a microscope with a "Neubauer's counting chamber".

Internalization Studies. Cells (10^6/well) were distributed in six-well plates at 37 °C in a 5% CO_2/air atmosphere for one night in culture medium (DMEM with 10% FBS). The medium was removed; the cells were washed and incubated for 1 h, with internalization medium (DMEM with 1% FBS) under the same conditions as described above. Approximately 0.02 MBq/well of the radioligand (2.5 pmol/well) was added to the medium, and the cells were incubated at 37 °C, 5% CO_2, with and without excess of NOC (1 μM) to determine nonspecific internalization. At appropriate time periods, the internalization was stopped by removing the medium and washing the cells with ice-cold PBS. To remove the receptor-bound radioligand, an acid wash was carried out twice with a 0.1 M glycine buffer pH 2.8 for 10 min on ice. This procedure permits one to distinguish between membrane-bound (acid-releasable) and internalized radioligand (acid-resistant). Finally, cells were solubilized with 1 N NaOH and incubated for 10 min at 37 °C. The radioactivity of the culture medium, the receptor-bound, and the internalized fractions were measured in a γ-counter.

Externalization Studies. For externalization experiments, the AR4-2J cells (10^6/well) were incubated with 2.5 pmol/well of radioligand. After 2 h internalization at 37 °C and 5% CO_2, the medium was removed and the cells were washed twice with cold PBS. An acid wash was performed, as described in the previous section. Internalization medium (3 mL) was added to each well, and the cells were incubated at 37 °C. At different time points, the external medium was collected and exchanged with 37 °C fresh medium. Thereafter, the cells were treated with 1 N NaOH to extract the internalized radioligand. The radioactivity of the external medium and of the internalized radioligand fractions was quantified in a γ-counter. The recycled fraction was expressed as a percentage of the total internalized amount per 1 million cells.

Biodistribution. All animal experiments were performed in compliance with the Swiss laws on animal protection (approval no. 789). Six-week-old Lewis male rats were implanted subcutaneously with 10 to 12 million of AR4-2J rat pancreatic tumor cells freshly suspended in PBS. Fourteen days after the

Table 1. Analytical Data of DOTA−X−NOC and log $D_{(pH=7.4)}$ for Their ^{111}In Derivatives[a]

compound number	*m/z* calcd. (Da)	*m/z* meas. (Da)	T_R (min)	log *D* [b] (pH = 7.4)
1 (*30*)	1454.6	1477.7 [M + Na^+]	20.77	−2.06 ± 0.30
2	1702.9	1741.9 [M + K^+]	24.19	−2.92 ± 0.17[c]
3	1600.9	1639.1 [M + K^+]	23.99	−2.46 ± 0.04[c]
4	1526.8	1527.9 [M + H^+]	23.20	−2.13 ± 0.00
5	1626.9	1665.4 [M + K^+]	23.28	−1.97 ± 0.06
6	1772.9	1774.3 [M + H^+]	21.87	−3.39 ± 0.14[c]
7	1570.8	1609.1 [M + K^+]	20.80	−2.68 ± 0.07[c]
8	1583.8	1622.9 [M + K^+]	19.40	−2.95 ± 0.10[c]

[a] Elution system: flow 0.75 mL/min; A, 0.1% TFA in H_2O; B, MeCN; linear gradient: 0−30 min, 10% B to 60% B. T_R, elution time. [b] Log *D*, partition coefficient between 1-octanol to PBS (pH = 7.4), for the corresponding [^{111}In derivatives]. [c] Significant differences ($p < 0.05$) between ^{111}In-**1** and other ^{111}In derivatives.

inoculation, the animals were injected in the femoral vein, under anesthesia, with 2−3 MBq of 0.34 nmol [^{111}In-DOTA]−X−NOC diluted in saline solution. For the determination of nonspecific uptake in tumor or receptor-positive organs, rats were coinjected in the femoral vein with 100 μg DOTA−NOC and with the radiotracer in 100 μL saline. At 4 h and 24 h p.i., rats were sacrificed under anesthesia. Tissue samples of blood and organs of interest were collected, weighed, and their radioactivity measured by use of a γ-counter. The percentage of injected activity per gram (% IA/g) was calculated for each tissue. The total counts injected per animal were determined by extrapolation from counts of an aliquot taken from the injected solution. Urine samples were analyzed for possible metabolites by RP-HPLC.

Scintigraphy. For imaging, 0.34 nmol/100 μL of [^{111}In-DOTA]−PEG_4−NOC (3 MBq) was injected into the femoral vein of an AR4-2J tumor-bearing Lewis male rat. The same procedure was applied to another rat coinjected with the same amount of radiotracer and 100 μg/100 μL (64.7 nmol) DOTA−NOC. Four hours after injection, rats were anesthesized and images were acquired in the prone position using a γ-camera equipped with a medium-energy parallel hole collimator (Basicam, Siemens, Erlangen, Germany).

Statistical Method. The correlation between binding affinities and rates of specific internalization was tested using linear regression analysis on *Microsoft Excel*. All data are expressed as the mean ± standard deviation (mean ± SD), otherwise stated. Data comparisons are performed using the Student's t-test where differences at the 95% confidence level ($p < 0.05$) were considered statistically significant.

RESULTS

Syntheses. The synthesis of DOTA−NOC and the new compounds was achieved by Fmoc-based SPPS protocols. With the introduction of spacers, the overall yield of around 30% achieved for DOTA−NOC (*29*) decreased to 17−18% based on the first Fmoc cleavage. All compounds were characterized by ESI-MS and RP-HPLC (Table 1).

Lipophilicity. Log *D* values were determined by the "shake-flask" method using 1-octanol-to-PBS (pH 7.4). The partition coefficient of [^{111}In-DOTA]−NOC (−2.06 ± 0.2) at pH = 7.4 is similar to ^{111}In-**4** and ^{111}In-**5** (−2.13 ± 0.00 and −1.97 ± 0.06) and significantly higher than for the other radiopeptides (Table 1).

Somatostatin Receptor Affinity Profiles. In vitro binding studies were performed using cells stably expressing human sst_1−sst_5 ($hsst_{1-5}$). Affinity profiles of the [In^{III}-DOTA]−X−NOC analogues are summarized in Table 2, with native somatostatin 28 (SS28) as the control peptide, which binds with high affinity to all five hsst subtypes. All newly synthesized compounds bind specifically to $hsst_2$ with IC_{50} values ranging from 1.7 to 5.2 nM. Moderate affinity to $hsst_3$ was found for In^{III}-**4** (33.5 ± 4.9 nM), whereas the IC_{50} values of $hsst_3$ for the remaining analogues were >80 nM. IC_{50} values for $hsst_5$ were found to vary between 3.8 and 44.9 nM.

Serum Stability. Incubation of [^{111}In-DOTA]−NOC and its derivatives in fresh serum at 37 °C showed high metabolic stability with more than 98% of intact analogues after 24 h of incubation.

Internalization/Externalization Studies. The uptake of the new ^{111}In-labeled DOTA−X−NOC conjugates was evaluated using AR4-2J (exclusive sst_2-expression) and HEK-sst_3 cells. All radiolabeled compounds showed time-dependent uptake into AR4-2J cells with high specific internalization rates, as shown in Table 3. After 4 h, ^{111}In-**1** showed 23.9% ± 0.10% specific uptake, and ^{111}In-**4** and ^{111}In-**7** presented 17.50% ± 0.36% and 29.41% ± 3.30%, respectively. Equivalence in the specific internalization rate was observed between ^{111}In-**2** (14.03% ± 0.21%) and ^{111}In-**8** (13.00% ± 1.65%), or between ^{111}In-**3** (19.89% ± 0.92%), ^{111}In-**5** (20.37% ± 0.98%), and ^{111}In-**6** (20.33% ± 0.15%). No internalization in HEK-sst_5 was observed at physiological conditions, receptor subsaturation conditions.

The externalization kinetics was assessed after 2 h of internalization of the radioligand, showing time-dependent behavior (Table 4). Within 4 h, 46.50% ± 1.40% of ^{111}In-**1** were externalized, similar to ^{111}In-**6** (43.74% ± 0.67%) and ^{111}In-**7** (41.70% ± 3.60%). The other radioligands presented 57.32% to 77.52% release from the AR4-2J cells within 4 h. The assessment of the specific internalization rate of the new compounds into sst_3-expressing cells was performed using HEK-sst_3. During 4 h, [^{111}In-DOTA]−NOC and [^{111}In-DOTA]−β-Ala−NOC internalized 14.0% ± 1.8% and 13.1% ± 0.3%, respectively, while all the other radiopeptides showed <2% specific internalization (Table 3).

Biodistribution Studies. Biodistribution was performed in AR4-2J tumor-bearing rats at 4 h and 24 h p.i. to assess the specific uptake of all new radiotracers in sst-receptor-positive and -negative organs (Table 5). The main excretion organ was the kidney for all conjugates. ^{111}In-**6** showed a high uptake in the tumor and in sst-positive organs. Also, in the case of ^{111}In-**2** and ^{111}In-**5**, the adrenals, pancreas, stomach, and pituitary exhibit rather high uptake. The tumor-to-kidney ratio at 4 h p.i. (Figure 1) for ^{111}In-**1** is 2.16, followed by ^{111}In-**6** (1.90), ^{111}In-**5** (1.48), ^{111}In-**2** (1.45), ^{111}In-**7** (0.96), ^{111}In-**4** (0.94), ^{111}In-**3** (0.58), and finally ^{111}In-**8** (0.17).

The coinjection of 68.7 nmol/100 μL of DOTA−NOC with 0.34 nmol/100 μL of the radiolabeled peptide provided a significant blocking for sst-positive organs, as shown for the pancreas and the AR4-2J rat pancreatic tumor (Figure 2).

For all [^{111}In-DOTA]−X−NOC derivatives, urine sample analysis by analytical RP-HPLC at 4 h p.i. showed intact radioligands, which at 24 h p.i were completely degraded (data not shown).

Imaging of Tumor-Bearing Rats. Figure 3 shows the γ-scintigraphy of two Lewis rats bearing AR4-2J tumors 4 h after injection of ^{111}In-**2** without and with (blocked) coinjection of In^{III}-**1** as a blocking agent. This in vivo experiment showed selective binding of ^{111}In-**2** to pancreas and tumor as evidenced by the effective blocking of sst. Although the kidneys and bladder are visible, the fast clearance of this radiotracer from other sst-negative organs is remarkable.

DISCUSSION

Despite all the efforts to improve the pharmacological properties of somatostatin-based radiotracers, at present their effectiveness for targeted radionuclide therapy still is somewhat limited by the pharmacokinetics. Therefore, it is of interest to

Table 2. Affinity Profiles of ^{111}In-DOTA−X−NOC Derivatives (IC_{50})[a] for Human sst_{1-5} Receptors

compound	$hsst_1$	$hsst_2$	$hsst_3$	$hsst_4$	$hsst_5$
SS−28	3.8 ± 0.3 (10)	2.5 ± 0.3 (11)	5.7 ± 0.6 (10)	4.2 ± 0.3 (11)	3.7 ± 0.4 (11)
In^{III}-**1** (*30*)	>10 000 (3)	2.9 ± 0.1 (3)	8.0 ± 2.0 (3)	227.0 ± 18.0 (3)	11.2 ± 3.5 (3)
In^{III}-**2**	>1000 (2)	5.2 ± 0.3 (3)	343.5 ± 44.5 (2)	>1000 (2)	15.9 ± 2.1 (3)
In^{III}-**3**	>1000 (2)	3.5 ± 0.7 (2)	377.5 ± 155.5 (2)	>1000 (2)	23.7 ± 8.7 (3)
In^{III}-**4**	>1000 (2)	4.7 ± 0.4 (2)	33.5 ± 3.5 (2)	>1000 (2)	8.6 ± 3.4 (2)
In^{III}-**5**	>1000 (2)	5.0 ± 0.2 (3)	291.0 ± 53.1 (3)	>1000 (2)	15.6 ± 0.2 (3)
In^{III}-**6**	>1000 (2)	4.6 ± 0.8 (3)	>1000 (2)	>1000 (2)	44.9 ± 2.6 (3)
In^{III}-**7**	>1000 (2)	1.7 ± 0.1 (2)	66.7 ± 27.5 (2)	369.5 ± 169.5 (2)	9.3 ± 2.7 (3)
In^{III}-**8**	>1000 (2)	4.6 ± 2.0 (2)	77.0 ± 43.0 (2)	243.0 ± 46.0 (2)	3.8 ± 2.2 (2)

[a] IC_{50} values are in nM (mean ± SEM). Number of independent studies is given in parentheses. SS-28 was used as control.

Table 3. Comparison of Internalization Rate of ^{111}In-DOTA−X−NOC Derivatives (±SD) into AR4-2J and HEK-sst_3 Cells[a]

	Internalization Time (min)				
	AR4-2J cells				HEK-sst_3 cells
compound	30	60	120	240	240
^{111}In-**1** (*30*)	4.90 ± 0.20	8.40 ± 0.00	14.10 ± 0.70	23.90 ± 0.10	13.10 ± 0.30
^{111}In-**2**	2.12 ± 0.45	3.40 ± 0.97	7.38 ± 0.89	14.03 ± 0.21[b]	0.80 ± 0.20[b]
^{111}In-**3**	3.86 ± 0.43	6.66 ± 1.06	10.59 ± 1.06	19.89 ± 0.92[b]	1.90 ± 0.20[b]
^{111}In-**4**	2.80 ± 0.39	4.80 ± 0.59	11.20 ± 0.56	17.50 ± 0.36[b]	14.0 ± 1.80
^{111}In-**5**	3.07 ± 0.20	5.07 ± 0.40	10.57 ± 0.38	20.37 ± 0.98[b]	0.70 ± 0.10[b]
^{111}In-**6**	4.54 ± 0.25	7.68 ± 0.24	12.72 ± 0.43	20.33 ± 0.15[b]	
^{111}In-**7**	9.28 ± 1.23	13.46 ± 2.40	19.23 ± 2.30	29.41 ± 3.30[b]	1.80 ± 0.50[b]
^{111}In-**8**	2.00 ± 0.01	4.00 ± 0.49	8.20 ± 1.32	13.00 ± 1.65[b]	1.20 ± 0.50[b]

[a] Values and standard deviations are the result of three independent experiments with triplicates in each experiment and are expressed as specific internalization (percentage of activity added to 1 million cells at 1.67 nM concentration, 37 °C). [b] Significant differences ($p < 0.05$) between ^{111}In-**1** and other ^{111}In derivatives.

Table 4. Comparison of Externalization Rate of ^{111}In-DOTA−X−NOC Derivatives (±SD) from AR4-2J Cells after 120 min Internalization at 37 °C[a]

	externalization time (min)			
compound	30	60	120	240
^{111}In-**1** (*30*)	14.69 ± 0.40	27.02 ± 1.20	38.00 ± 1.50	46.48 ± 1.40
^{111}In-**2**	8.85 ± 1.50	16.73 ± 4.24	33.11 ± 6.23	57.32 ± 2.80[b]
^{111}In-**3**	47.08 ± 1.68	57.33 ± 1.06	68.59 ± 2.25	77.52 ± 3.00[b]
^{111}In-**4**	24.61 ± 0.97	37.92 ± 0.53	51.70 ± 0.21	64.14 ± 2.31[b]
^{111}In-**5**	29.99 ± 4.07	42.24 ± 24	51.32 ± 5.44	66.29 ± 3.82[b]
^{111}In-**6**	7.04 ± 0.17	13.96 ± 1.63	25.92 ± 1.99	43.74 ± 0.67
^{111}In-**7**	17.28 ± 1.86	25.55 ± 2.49	33.35 ± 3.32	41.67 ± 3.59
^{111}In-**8**	23.17 ± 1.06	35.92 ± 2.30	48.80 ± 4.31	62.34 ± 4.86[b]

[a] Values and standard deviations are the result of three independent experiments with triplicates in each experiment (percentage of activity added to 1 million cells at 1.67 nM concentration, 37 °C). [b] Significant differences ($p < 0.05$) between ^{111}In-**1** and other ^{111}In derivatives.

understand the pharmacologic properties as a function of different structural parameters. This knowledge may allow predictable ligand functionalization to modulate the pharmacokinetic profile of the sst radiotracers in order to obtain high tumor-to-nontumor ratios.

We performed a systematic study by introducing different spacers between DOTA and NOC to understand their influence on the pharmacokinetics. ^{111}In/^{90}Y-DOTA−NOC was shown to have a broader somatostatin receptor affinity profile than first- and second-generation somatostatin-based radioligands (*30*). In addition, DOTA−NOC labeled to different radionuclides showed superior tumor localization in patients (*30*−*32*) but also a higher general background uptake leading to a higher myelotoxicity in some early therapy attempts (*36*). The latter is possibly due to the higher lipophilicity of radiolabeled DOTA−NOC. Therefore, we decided to use this peptide and introduce different spacer molecules to study their influence on the pharmacokinetics with emphasis on tumor-to-kidney as well as tumor-to-background ratio.

To study the increase in hydrophilicity of radiolabeled DOTA−NOC while preserving its overall net charge, strategies involving its derivatization through polyethylene glycol units or carbohydration were chosen. For that purpose, we employed an asparagine side chain modified with *N*-acetyl glucosamine and two PEGs with different lengths (PEG_2 and PEG_4), ready to use in SPPS protocols. To modulate the overall charge of the radiopeptide with simultaneous increase of hydrophilicity, aspartic acid and lysine were selected. A triglycine spacer was also chosen, as the insertion of this type of cleavable linkers was already successfully employed in the modification of antibodies. The introduction of a spacer based on a triglycine unit between DOTA and $F(ab')_2$ enhanced the tumor uptake, upholding the kidney uptake with the increment of the tumor-to-kidney ratio from 0.7 ± 0.3 to 1.3 ± 0.2 (*37*).

As expected, log $D_{(pH=7.4)}$ values show significantly reduced lipophilicity of the modified ^{111}In-**1** conjugates, with exception for ^{111}In-**4** and ^{111}In-**5**.

The introduction of the spacer influenced the binding affinities to the hsst subtypes in different ways. In general, the $hsst_2$ affinities of the new [In-DOTA]−X−NOC peptides are only marginally influenced by the spacers, except for the neutral compound, ^{111}In-**7**, showing a significant improvement of the $hsst_2$ affinity by a factor of 1.7. The affinity to $hsst_5$ also is not substantially influenced by the spacers, and as for the parent radiopeptide, no affinity to $hsst_1$ and $hsst_4$ was found. Surprisingly, one outcome of the present study is the almost complete loss of $hsst_3$ affinity of the [In^{III}-DOTA]−X−NOC peptides. It is difficult to understand the influence of the spacers on the $hsst_3$ affinity. The spacers increase both the flexibility and the hydrophilicity of the peptides. Higher hydrophilicities explaining the loss of hsst affinity would parallel earlier studies from our laboratories where we showed that lowering the hydrophilicity of DOTA-peptides leads to increased affinity to the $hsst_3$ subtype (*5*, *30*). Only a few structural/conformational studies in solution or in the solid state have been performed with this group of metallopeptides, and only octreotide was studied by X-ray diffraction (*38*). We have recently performed ^{1}H and ^{13}C solution NMR studies along with modeling studies to potentially understand the difference in sst_2 affinity and tumor uptake between [^{67}Ga-DOTA^0,Tyr^3]-octreotide and [^{90}Y-DOTA^0,Tyr^3]-octreotide (*39*). This study showed that the different coordination

Table 5. Biodistribution in AR4-2J Tumor-Bearing Rats at 4 h and 24 h p.i. of [^{111}In-DOTA]−X−NOC Conjugates[a]

	^{111}In-**1**		^{111}In-**2**		^{111}In-**3**		^{111}In-**4**
site	4 h	24 h	4 h	24 h	4 h	24 h	4 h
blood	0.02 ± 0.00	0.01 ± 0.00	0.04 ± 0.01[b]	0.02 ± 0.00[b]	0.05 ± 0.00[b]	0.02 ± 0.01	0.06 ± 0.04
tumor	2.96 ± 0.48	2.65 ± 0.41	3.56 ± 1.03	2.56 ± 0.72	1.47 ± 0.46[b]	1.12 ± 0.03[b]	2.45 ± 0.37
kidneys	1.37 ± 0.21	1.27 ± 0.10	2.46 ± 0.23[b]	3.37 ± 1.03[b]	2.54 ± 0.20[b]	2.94 ± 0.16[b]	2.60 ± 0.10[b]
adrenals	8.24 ± 1.16	1.01 ± 0.17	11.96 ± 0.40[b]	12.44 ± 1.40[b]	6.93 ± 0.90	6.68 ± 0.86[b]	11.23 ± 0.47[b]
pancreas	7.94 ± 0.71	4.04 ± 0.29	7.08 ± 0.43	5.06 ± 0.81	1.97 ± 0.14[b]	1.62 ± 0.26[b]	4.65 ± 0.87[b]
liver	0.21 ± 0.04	0.15 ± 0.01	0.64 ± 0.12[b]	0.56 ± 0.20[b]	1.80 ± 0.30[b]	1.57 ± 0.29[b]	0.71 ± 0.05[b]
pituitary	6.21 ± 0.73	5.44 ± 0.79	13.98 ± 2.62[b]	10.07 ± 1.97[b]	7.24 ± 1.00	7.51 ± 0.86[b]	5.51 ± 0.34

	^{111}In-**5**		^{111}In-**6**		^{111}In-**7**		^{111}In-**8**
site	4 h	24 h	4 h	24 h	4 h	24 h	4 h
blood	0.10 ± 0.01[b]	0.03 ± 0.00[b]	0.05 ± 0.02	0.03 ± 0.00[b]	0.05 ± 0.00[b]	0.01 ± 0.01	0.11 ± 0.00[b]
tumor	2.96 ± 0.63	2.03 ± 0.43	4.17 ± 0.46[b]	3.31 ± 0.28	1.98 ± 0.09[b]	1.18 ± 0.25[b]	2.20 ± 0.47
kidneys	2.00 ± 0.24[b]	3.13 ± 0.23[b]	2.19 ± 0.27[b]	2.62 ± 0.50 [b]	2.07 ± 0.16[b]	2.31 ± 0.27[b]	12.96 ± 0.68[b]
adrenals	12.79 ± 1.23[b]	11.99 ± 1.25[b]	21.08 ± 1.24[b]	10.38 ± 2.29[b]	1.85 ± 0.24[b]	1.20 ± 0.38	3.00 ± 0.24[b]
pancreas	5.72 ± 0.75[b]	4.30 ± 0.51[b]	9.31 ± 1.41	5.36 ± 0.68[b]	6.81 ± 0.41	3.35 ± 0.91	5.87 ± 0.24[b]
liver	1.57 ± 0.22[b]	1.42 ± 0.10[b]	0.30 ± 0.07	0.27 ± 0.06[b]	0.30 ± 0.04	0.22 ± 0.03[b]	0.55 ± 0.02[b]
pituitary	17.66 ± 1.91[b]	20.11 ± 1.35[b]	9.62 ± 0.76[b]	11.55 ± 2.16[b]	6.25 ± 1.03	6.30 ± 0.31	4.56 ± 0.03[b]

[a] Values are the mean of % IA/g ± SD for groups of 3−6 animals. [b] Significant differences ($p < 0.05$) between ^{111}In-**1** and other ^{111}In derivatives.

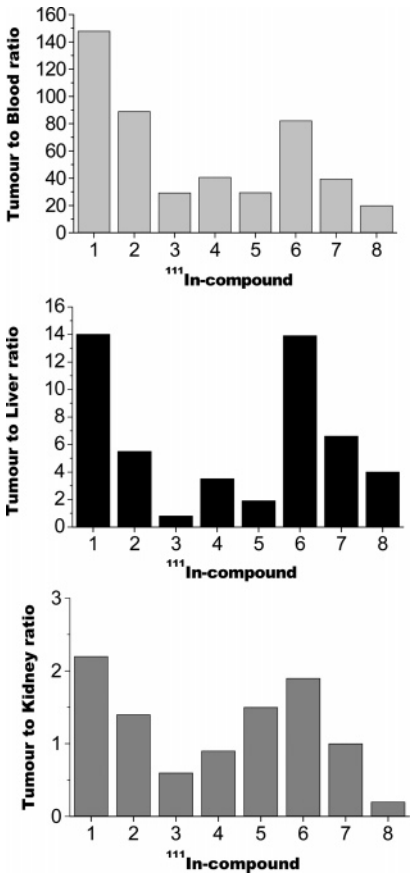


Figure 1. Tumor-to-blood, tumor-to-liver, and tumor-to-kidney ratios for [^{111}In-DOTA]−X−NOC conjugates at 4 h p.i.

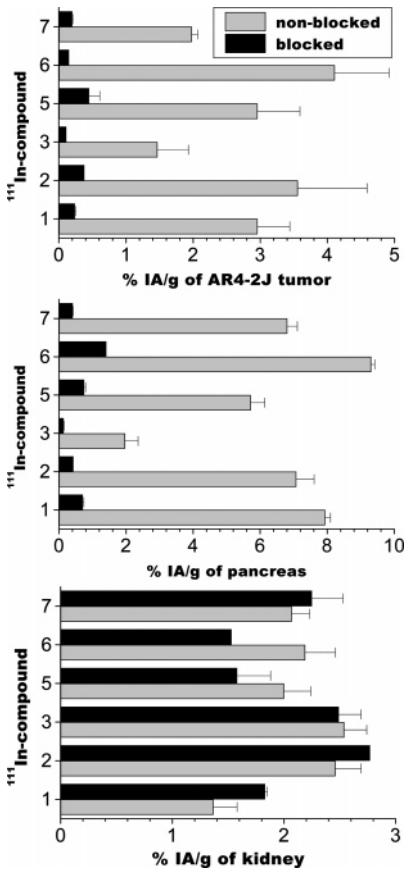


Figure 2. Comparison of biodistribution at 4 h p.i. of some ^{111}In compounds in AR4-2J rat pancreatic tumor, kidney, and pancreas without (nonblocked) and with (blocked) coinjection of excess In^{III}-**1**.

chemistry of Ga^{3+} vs Y^{3+} (6-coordinate and 8-coordinate, respectively) causes differences for the "spacing" D-Phe[1] residue leading to two conformers: they were identified as cis−trans isomers at the amide bond between DOTA and D-Phe[1]. The peptidic part could be characterized by a fast equilibrium of two predominant conformations displaying a helical and sheet-like structure not greatly influenced by the two metals incorporated. Additional conformational analysis is necessary to possibly understand the conformational contribution to subtle differences in biological potency of the metallopeptides.

The internalization of the radioligands in AR4-2J cells clearly correlates with their $hsst_2$ affinity as demonstrated in Figure 4. The best $hsst_2$ affinity of ^{111}In-**7** visibly induces an increased internalization by a factor of 1.2 at 4 h compared to ^{111}In-**1**. The radioligand array used herein presented no internalization into sst_5-transfected cells (HEK-sst_5). This confirms earlier data from our group (*40*) and from Cescato et al. (*41*) who studied sst_5 internalization with high-affinity agonists using immunocytochemical methods. In regard to $hsst_3$ affinity, ^{111}In-**4** was the only tracer that could conserve a moderate affinity for this receptor with a good internalization rate into HEK-sst_3 cells comparable to ^{111}In-**1**. ^{111}In-**5** and the most hydrophilic compounds show low affinities to $hsst_3$ corresponding with their

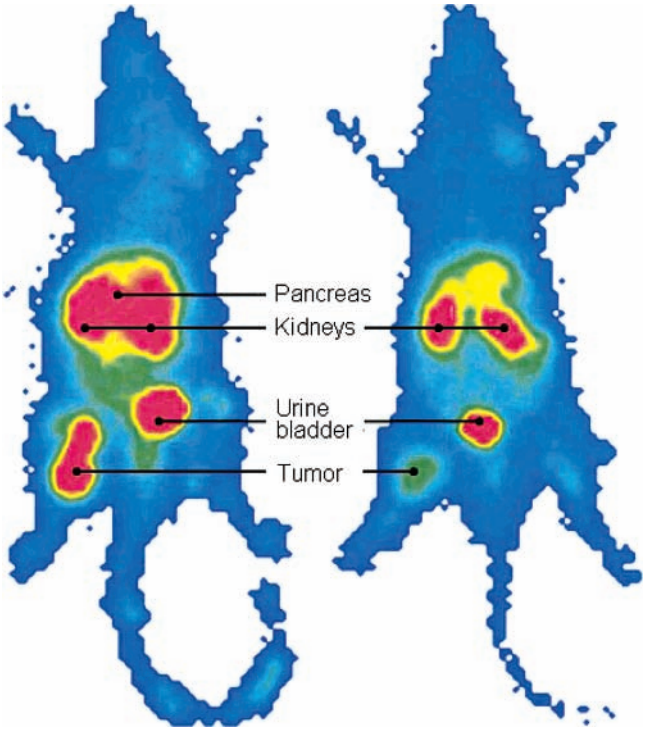


Figure 3. Scintigraphy of two male Lewis rats bearing AR4-2J rat pancreatic tumors after 4 h p.i. of ^{111}In-**2** with (right animal) and without (left animal) coinjection with excess of In^{III}-**1**.

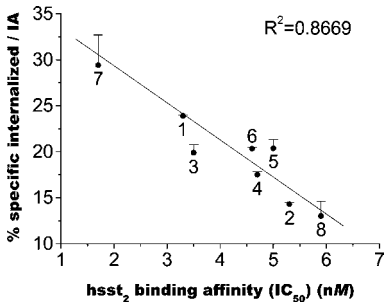


Figure 4. Correlation of rate of internalization at 4 h (% specific internalized/10^6 cells) and $hsst_2$ binding affinity for all metallopeptides involved in this study.

low internalization in HEK-sst_3 cells. In biodistribution studies, the AR4-2J tumor uptake values at 4 h p.i. of ^{111}In-**2**,**4**,**5**,**8** were equivalent to those of ^{111}In-**1**, despite their lower rates of internalization into AR4-2J cells in comparison to ^{111}In-**1**. Unpredictably, the specific uptake in sst-positive organs like the adrenals and the pancreas was in general higher for ^{111}In-**2**,**4**,**5**,**6** compared to ^{111}In-**1**. The contrary was observed for ^{111}In-**3** where the specific uptake in sst-positive organs was lower than for ^{111}In-**1**, as has already been described for [^{125}I]-(PEG_2-octreotate) (*42*). The uptake in the tumor and sst-positive organs is specific as demonstrated by blocking studies using a large excess of DOTA−NOC (Figure 2 and Figure 3). ^{111}In-**6** showed a 1.4-fold increase in the tumor uptake compared to ^{111}In-**1**. Higher tumor uptake was also achieved when glucose was introduced N-terminally into [^{125}I]-TOC via an Amidori reaction (*43*, *44*). This increase was accompanied by a significant 1.6-fold increase in kidney uptake from ^{111}In-**1** to ^{111}In-**6** and an unchanged hepatobiliary radioactivity accumulation.

The optimal features found in our in vitro affinity and internalization studies with ^{111}In-**7** were not conferred into a higher specific tumor uptake in vivo; in fact, tumor uptake decreased 1.5-fold and the kidney uptake increased also 1.5-fold compared to ^{111}In-**1**. Therefore, we could not confirm what previous studies have shown concerning the lowering of the renal accumulation by the introduction of a negative charge between DTPA and a somatostatin-based peptide (*45*, *46*). Moreover, our findings validate previous studies done in our laboratory, showing higher kidney uptake for the negatively charged conjugates (*47*). As expected, the introduction of a positive charge (Lys) into DOTA−NOC significantly increased the kidney uptake, potentially due to megalin (*48*).

Despite the enhancement of the hydrophilicity of most of the new radiopeptides, ^{111}In-**1** presents the lowest renal accumulation among all ligands. This indicates that other elimination mechanisms not controlled by hydrophilicity are active.

CONCLUSIONS

The structural tuning performed in DOTA−NOC did not result in a straightforward correlation between in vivo and in vitro studies, but it indicated a high impact of hydrophilicity and charge on its pharmacokinetic profile. An increased hydrophilicity seems to lead to a lower $hsst_3$ affinity, also resulting in a decreased internalization into sst_3-expressing cells. The excretion profile was found not to depend on the lipophilic character, while it is strongly influenced by the addition of a positive charge leading to a significantly higher renal uptake. Nevertheless, all the new compounds still bind with high affinity to $hsst_2$ and present a high specific internalization into sst_2-expressing cells. This study also indicates that carbohydration of metallopeptides, similar to iodinated radiopeptides, may lead to a higher tumor uptake as for the sugar derivative presented here. They deserve more attention if new conjugates with improved pharmacokinetics will be designed. We hypothesize that, concerning sst_2-overexpressing tumors, ^{111}In/^{90}Y/^{177}Lu-**6** may be superior to ^{111}In/^{90}Y/^{177}Lu-**1** regarding the therapeutic window, as it has a very similar tumor-to-kidney ratio (1.9 vs 2.1) but a higher tumor uptake. Its higher hydrophilicity may lower the background detected in the clinical trials with radiolabeled DOTA−NOC.

ACKNOWLEDGMENT

P. Antunes acknowledges the Ph.D. Fellowship of the Fundação para a Ciência e Tecnologia (ref SFRH/BD/3136/2000). In addition, P. Antunes, M. Ginj, M. Walter, and H. Maecke acknowledge the support from the Swiss National Science Foundation project 3100A0-100390, BBW No. C00.0091, and BBT project 4668.1 EUS. The support provided by Novartis Pharma in respect of ESI-MS analysis is gratefully acknowledged. We thank Dr. S. Schulz for the sst_3-transfected human embryonic kidney 293 cells. The authors thank K. Hinni and S. Tschumi for biological technical assistance. This work was performed within the COST B12 action. The technical personnel of nuclear medicine are acknowledged for imaging the rats.

Supporting Information Available: Additional experimental data. This material is available free of charge via the Internet at http://pubs.acs.org.

LITERATURE CITED

(1) Reubi, J. C. (2003) Peptide receptors as molecular targets for cancer diagnosis and therapy. *Endocr. Rev. 24*, 389−427.

(2) Reubi, J. C. (1995) Neuropeptide receptors in health and disease: the molecular basis for in vivo imaging. *J. Nucl. Med. 36*, 1825−1835.

(3) Reubi, J. C., Waser, B., Schaer, J. C., and Laissue, J. A. (2001) Somatostatin receptor sst1-sst5 expression in normal and neoplastic human tissues using receptor autoradiography with subtype-selective ligands. *Eur. J. Nucl. Med. Mol. Imaging 28*, 836−846.

(4) Reubi, J. C., Laissue, J., Krenning, E., and Lamberts, S. W. (1992) Somatostatin receptor sst1-sst5 expression in human cancer: inci-

dence, characteristics, functional correlates and clinical implications. *J. Steroid Biochem. Mol. Biol. 43*, 27−35.
(5) Reubi, J., Schär, J. C., Waser, B., Wenger, S., Heppeler, A., Schmitt, J. S., and Maecke, H. R. (2000) Affinity profiles for human somatostatin receptor SST1-SST5 of somatostatin radiotracers selected for scintigraphic and radiotherapeutic use. *Eur. J. Nucl. Med. Mol. Imaging 27*, 273−282.
(6) Ferone, D., Van Hagen, M. P., Kwekkeboom, D. J., Van Koetsveld, P. M., Mooy, D. M., Lichtenauer Kaligis, E., Schönbrunn, A., Colao, A., Lamberts, S. W. J., and Hofland, L. J. (2000) Somatostatin receptor subtypes in human thymoma and inhibition of cell proliferation by octreotide in vitro. *J. Clin. Endocrinol. Metab. 85*, 1719−1726.
(7) Papotti, M., Croce, S., Bello, M., Bongiovanni, M., Allia, E., Schindler, M., and Bussolati, G. (2001) Expression of somatostatin receptor types 2, 3 and 5 in biopsies and surgical specimens of human lung tumours. *Virchows Arch. 439*, 787−797.
(8) Wester, H. J., Brockmann, J., Rösch, F., Wutz, W., Herzog, H., Smith-Jones, P., Stolz, B., Bruns, C., and Stöcklin, G. (1997) PET-Pharmacokinetics of ^{18}F-octreotide: a comparison with ^{67}Ga-DFO-octreotide and ^{86}Y-DTPA-octreotide. *Nucl. Med. Biol. 24*, 275−286.
(9) Eisenwiener, K. P., Prata, M. I., Buschmann, I., Zhang, H., Santos, A. C., Wenger, S., Reubi, J. C., and Mäcke, H. R. (2002) NODAGATOC, a new chelator coupled somatostatin analogue labeled with [$^{67/68}$Ga] and [^{111}In] for SPECT, PET, and targeted therapeutic applications of somatostatin receptor (hsst2) expressing tumors. *Bioconjugate Chem. 13*, 530−541.
(10) Lamberts, W. J. S., Herder, W. W., and Hofland, L. J. (2002) Somatostatin analogs in the diagnosis and treatment of cancer. *Trends Endocrinol. Metab. 13*, 451−457.
(11) O'Connor, M. K., Kvols, L. K., Brown, M. L., Hung, J. C., Hayostek, R. J., Cho, D. S., and Vetter, R. J. (1992) Dosimetry and biodistribution of a iodine-123 labeled somatostatin analog in patients with neuroendocrine tumors. *J. Nucl. Med. 33*, 1613−1619.
(12) Bakker, W. H., Krenning, E. P., Breemann, W. A., Kooij, P. P., Reubi, J. C., Koper, J. W., de Jong, M., Lameris, J. S., Visser, T. J., and Lamberts, S. W. (1991) In vivo use of a radioiodinated somatostatin analogue: dynamics, metabolism and binding to somatostatin receptor-positive tumors in man. *J. Nucl. Med. 32*, 1184−1189.
(13) Bakker, W. H., Breemann, W. A., van der Pluijm, M. E., de Jong, M., Visser, T. J., and Krenning, E. P. (1996) Iodine-131 labeled octreotide: not an option for somatostatin receptor therapy. *Eur. J. Nucl. Med. Mol. Imaging 23*, 775−781.
(14) Krenning, E. P., Kwekkeboom, D. J., Bakker, W. H., Breeman, W. A. P., Kooij, P. P. M., Oei, H. Y., van Hagen, M., Postema, P. T. E., de Jong, M., Reubi, J. C., Visser, T. J., Reijs, E. M., Hofland, L. J., Koper, J. W., and Lamberts, S. W. J. (1993) Somatostatin receptor scintigraphy with [^{111}In-DTPA-D-Phe^{1}]- and [^{123}I-Tyr^{3}]-octreotide: the Rotterdam experience with more than 1000 patients. *Eur. J. Nucl. Med. Mol. Imaging 20*, 716−731.
(15) Gibril, F., Reynolds, J. C., Doppman, J. L., Chen, C. C., David, J. V., Weber, C. A., Stewart, C. A., and Jensen, R. T. (1996) Somatostatin receptor scintigraphy: its sensitivity compared with that of other imaging methods in detecting primary and metastatic gastrinomas: a prospective study. *Ann. Intern. Med. 125*, 24−26.
(16) Harrison, A., Walker, C. A., Parker, D., Jankowski, K. J., Cox, J. P. L., Craig, A. S., Sansom, J. M., Beeley, N. R. A., Boyce, R. A., Chaplin, L., Eaton, M. A. W., Farnsworth, A. P. H., Millar, K., Millican, A. T., Randall, A. M., Rhind, S. K., Secher, D. S., and Turner, A. (1991) The in vivo release of ^{90}Y from cyclic and acyclic ligand-antibody conjugates. *Nucl. Med. Biol.: Int. J. Radiat. Appl. Instrum. Part B 18*, 469−476.
(17) Moi, M. K., and Meares, C. F. (1988) The peptide way to macrocyclic bifunctional chelating agents: synthesis of 2-(*p*-nitrobenzyl)-1,4,7,10-tetraazacyclododecane-*N*,*N*′,*N*″,*N*‴-tetraacetic acid and study of its yttrium(III) complex. *J. Am. Chem. Soc. 110*, 6266−6267.
(18) McMurry, T. J., Pippin, C. G., Wu, C., Deal, K. A., Brechbiel, M. W., Mirzadeh, S., and Gansow, O. A. (1998) Physical parameters and biological stability of yttrium(III) diethylenetriaminepentaacetic acid derivative conjugates. *J. Med. Chem. 41*, 3546−3549.
(19) Kwekkeboom, D. J., Bakker, W. H., Kooij, P. P., Konijnenberg, M. W., Srinivasan, A., Erion, J. L., Schmidt, M. A., Bugaj, J. L., de Jong, M., and Krenning, E. P. (2001) [^{177}Lu-DOTA^{0},Tyr^{3}]octreotate: comparison with [^{111}In-DTPA^{0}]octreotide in patients. *Eur. J. Nucl. Med. 28*, 1319−1325.
(20) Ginj, M., Chen, J., Walter, M. A., Eltschinger, V., Reubi, J. C., and Maecke, H. R. (2005) Preclinical evaluation of new and highly potent analogues of octreotide for predictive imaging and targeted radiotherapy. *Clin. Cancer Res. 11*, 1136−1145.
(21) Otte, A., Jermann, E., Behe, M., Goetze, M., Bucher, H. C., Roser, H. W., Heppeler, A., Mueller-Brand, J., and Maecke, H. R. (1997) DOTATOC: a powerful new tool for receptor-mediated radionuclide therapy. *Eur. J. Nucl. Med. Mol. Imaging 24*, 792−795.
(22) Otte, A., Mueller-Brand, J., Dellas, S., Nitzsche, E. U., Herrmann, R., and Maecke, H. R. (1998) Yttrium-90-labeled somatostatin analogue for cancer treatment. *Lancet 351*, 417−418.
(23) de Jong, M., Breeman, W. A. P., Valkema, R., Bernard, B. F., and Krenning, E. P. (2004) Combination radionuclide therapy using ^{177}Lu and ^{90}Y-labeled somatostatin analogs. *J. Nucl. Med. 45* (suppl), 1S−5S.
(24) Paganelli, G., Bodei, L., Junak, D. H., Rocca, P., Papi, S., Sierra, M. L., Gatti, M., Chinol, M., Bartolomei, M., Fiorenza, M., Grana, C. (2002) ^{90}Y−DOTA−D-Phe^{1}−Tyr^{3}−Octreotide in therapy of neuroendocrine malignancies. *Pept. Sci. 66*, 393−398.
(25) Otte, A., Hermann, R., Heppeler, A., Behe, M., Jermann, E., Powell, P., Maecke, H. R., and Muller, J. (1999) Yttrium-90 DOTATOC: first clinical results. *Eur. J. Nucl. Med. 26*, 1439−1447.
(26) Bernard, B. F., Krenning, E. P., Breeman, W. A., Rolleman, E. J., Bakker, W. H., Visser, T. J., Mäcke, H., and de Jong, M. (1997) D-Lysine reduction of indium-111 octreotide and yttrium-90 octreotide renal uptake. *J. Nucl. Med. 38*, 1929−1933.
(27) Barone, R., van der Smissen, P., Devuyst, O., Beaujean, V., Pauwels, S., Courtoy, P. J., and Jamar, F. (2005) Endocytosis of the somatostatin analogue, octreotide, be the proximal tubule-derived opossum kidney (OK) cell line. *Kidney Int. 67*, 969−976.
(28) Melis, M., Bernard, B. F., Barone, R., Visser, T. J., Krenning, E. P., and de Jong, M. (2004) Localization and mechanism of retention of radiolabelled somatostatin analogues in rat kidney. *Eur. J. Nucl. Med. Mol. Imaging 31* (suppl. 2), S280.
(29) Whetstone, P. A., Akizawa, H., and Meares, C. F. (2004) Evaluation of cleavable (Tyr^{3})-octreotate derivatives for longer intracellular probe residence. *Bioconjugate Chem. 15*, 647−657.
(30) Wild, D., Schmitt, J. S., Ginj, M., Mäcke, H. R., Bernard, B. F., Krenning, E., de Jong, M., Wenger, S., and Reubi, J. C. (2003) DOTA-NOC, a high-affinity ligand of somatostatin receptor subtypes 2, 3 and 5 for labeling with various radiometals. *Eur. J. Nucl. Med. Mol. Imaging 30*, 1338−1347.
(31) Valkema, R., Froberg, A. C., Bakker, W. H., Maecke, H. R., Breeman, W. A., Kooij, P. P., de Jong, M., Jong, L. C., and Krenning, E. P. (2005) Peptide receptor radionuclide therapy (PRRT) with Lu-177-DOTANOC and peptide receptor scintigraphy (PRS) with In-111-DOTANOC and Ga-68-DOTANOC. *J. Nucl. Med. 46* (Suppl. 2), 151P.
(32) Hofmann, M., Oei, M. L., Boerner, A. R., Maecke, H., Gworski, L., Knapp, W. H., and Krause, T. (2005) Comparison of Ga-68-DOTATOC and Ga-68-DOTANOC for radiopeptide PET. *Nuklearmedizin 44*, A58.
(33) Baum, R. P., Schmuecking, M., Niesen, A., and Roesch, F. (2005) Ga-68 DOTA-1-Nal3-octreotide (DOTA-NOC) receptor PET/CT imaging for the diagnosis of neuroendocrine tumors and follow-up after peptide receptor radiotherapy: experience in 240 patients. *J. Nucl. Med. 46* (Suppl. 2), 201P.
(34) Wild, D., Mäcke, H. R., Waser, B., Reubi, J. C., Ginj, M., Rasch, H., Müller-Brand, J., and Hofmann, M. (2005) ^{68}Ga-DOTANOC: a first compound for PET imaging with high affinity for somatostatin receptor subtypes 2 and 5. *Eur. J. Nucl. Med. Mol. Imaging 32*, 724.
(35) Tulipano, G., Stumm, R., Pfeiffer, M., Kreienkamp, H. J., Hollt, V., and Schulz, S. (2004) Differential β-arrestin trafficking and endosomal sorting of somatostatin receptor subtypes. *J. Biol. Chem. 27*, 21374−21382.
(36) Baum, R. P., Junak, D. H., and Jarzab, B. (2005) Is Y^{90}/Lu^{177}-DOTA-NOC therapy safe? Preliminary results of early toxicity. *J. Nucl. Med. 46* (Suppl. 2), 448P.
(37) Zimmermann, K., Gianollini, S., Schubiger, P. A., and Novak-Hofer, I. (1999) A triglycine linker improves tumor uptake and biodistribution of 67-Cu-labeled anti-neuroblastoma Mab chCE7 F(ab′)2 Fragments. *Nucl. Med. Biol. 26*, 943−950.

(38) Pohl, E., Heine, A., Sheldrick, G. M., Dauter, Z., Schneider, T., Wilson, K. S., and Kallen, J. (1995) Comparison of different X-ray data-collection systems using the crystal structure of octreotide. *Acta Crystallogr., Sect D 51*, 60−68.

(39) Deshmukh, M. V., Voll, G., Kühlewein, A., Mäcke, H., Schmitt, J., Kessler, H., and Gemmecker, G. (2005) NMR studies reveal structural differences between the gallium and yttrium complexes of DOTA-D-Phe^{1}-Tyr^{3}-octreotide. *J. Med. Chem. 48*, 1506−1514.

(40) Ginj, M., Schmitt, J. S., Chen, J., Waser, B., Reubi, J. C., De Jong, M., Schulz, S., and Maecke, H. R. (2006) Design, synthesis, and biological evaluation of somatostatin-based radiopeptides. *Chem. Biol. 13*, 1081−1090.

(41) Cescato, R., Schulz, S., Waser, B., Eltschinger, V., Rivier, J. E., Wester, H. J., Culler, M., Ginj, M., Liu, Q., Schonbrunn, A., and Reubi, J. C. (2006) Internalization of sst2, sst3 and sst5 receptors: Effects of somatostatin agonists and antagonists. *J. Nucl. Med. 47*, 502−511.

(42) Wang, Q., Graham, K., Schauer, T., Fietz, T., Mohamed, A., Liu, X., Hoffend, J., Haberkorn, U., Eisenhut, M., and Mier, W. (2004) Pharmacological properties of hydrophilic and lipophilic derivatives of octreotate. *Nucl. Med. Biol. 31*, 21−30.

(43) Schottelius, M., Wester, H. J., Reubi, J. C., Senekowitsch-Schmidtke, R., and Schwaiger, M. (2002) Improvement of pharmacokinetics of radioiodinated Tyr^{3}-octreotide by conjugation with carbohydrates. *Bioconjugate Chem. 13*, 1021−1030.

(44) Schottelius, M., Rau, F., Reubi, J. C., Schwaiger, M., and Wester, H. J. (2005) Modulation of pharmacokinetics of radioiodinated sugar-conjugated somatostatin analogues by variation of peptide net charge and carbohydration chemistry. *Bioconjugate Chem. 16*, 429−437.

(45) Akizawa, H., Arano, Y., Mifune, M., Iwadoc, A., Saitoa, Y., Mukaid, T., Ueharab, T., Onoe, M., Fujiokae, Y., Ogawae, K., Kisof, Y., and Sajie, H. (2001) Effect of molecular charges on renal uptake of ^{111}In-DTPA-conjugated peptides. *Nucl. Med. Biol. 28*, 761−768.

(46) Akizawa, H., Takimoto, H., Saito, M., Iwado, A., Mifune, M., Saito, Y., Uehara, T., Arano, Y., Mukai, T., Hanaoka, H., and Sajid, H. (2004) Effect of carboxylation of N-terminal phenylalanine of ^{111}In-DTPA (diethylenetriaminepentaacetic acid)-octreotide on accumulation of radioactivity in kidney. *Biol. Pharm. Bull. 27*, 271−272.

(47) Froidevaux, S., Eberle, A. N., Christe, M., Sumanovski, L., Heppeler, A., Schmitt, J. S., Eisenwiener, K., Beglinger, C., and Maecke, H. R. (2002) Neuroendocrine tumor targeting study of novel gallium labeled somatostatin radiopeptides in a rat pancreatic tumor model. *Int. J. Cancer 98*, 930−937.

(48) Christensen, E. I., and Birn, H. (2002) Megalin and cubilin: multifunctional endocytic receptors. *Nat. Rev. Mol. Cell Biol. 3*, 258−268.

BC0601673

Synthesis, DNA Interaction, and Cytotoxic Activity of a Novel Proflavine−Dithiazolidinone Pharmacophore

Ladislav Janovec,[†] Danica Sabolová,[‡] Mária Kožurková,[‡] Helena Paulíková,[§] Pavol Kristian,[†] Ján Ungvarský,[†] Erika Moravčíková,[§] Mária Bajdichová,[§] Dušan Podhradský,[‡] and Ján Imrich*[,†]

Department of Organic Chemistry, Department of Biochemistry, Institute of Chemistry, Faculty of Science, P.J. Šafárik University, Moyzesova 11, SK-04167 Košice, Slovak Republic, and Department of Biochemistry and Microbiology, Faculty of Chemical and Food Technology, Slovak Technical University, Radlinského 9, SK-81237 Bratislava, Slovak Republic. Received June 16, 2006; Revised Manuscript Received September 21, 2006

Five novel proflavine−dithiazolidinone derivatives **4a**−**4e** have been designed and synthesized by the reaction of dialkyl acridin-3,6-diyl dithioureas **3a**−**3e** with methyl bromoacetate. The binding affinity of dithiazolidinone hydrochlorides **5a**−**5e** with calf thymus DNA and plasmid (pUC19) DNA was investigated by a variety of spectroscopic techniques including UV−vis, fluorescence, and CD spectroscopy. The effects of **5a**−**5e** on the thermal denaturation profiles of calf thymus DNA were also studied. From spectrophotometric and spectrofluorimetric titrations, the binding constants for the pUC19 DNA−drug complexes were determined ($K = 6.2-2.2 \times 10^4$ M^{-1}). In vitro cytotoxic activities of compounds **5a**−**5e** toward murine leukemia cell line L1210 and human uterus carcinoma HeLa cells were also examined. 2′,2″-[(Acridin-3,6-diyl)diimino]-3′,3″-dipropyl-1,3-dithiazolidin-4-one hydrochloride (**5b**) showed the highest activity against these cells with IC_{50} values of 6.3 μM and 12.9 μM over the course of 72 h.

INTRODUCTION

The interactions of small organic molecules with nucleic acids have been the focus of enhanced interest for DNA complexes over the past three decades (*1*). The understanding and recognition of the mode of action has allowed considerable progress to be made in the area of anticancer drug design, including acridinyl derivatives (*2*−*8*). One of the earliest and most well-known agents possessing a mutagenic effect toward DNA and inhibition of protein synthesis (*9*) is 3,6-diaminoacridine (proflavine, **1**). As a consequence, simple acridine compounds such as **1** have been used as antibacterial agents (*10*) and as probes to examine mutagenesis (*11*). Recently, the interaction of **1** with herring sperm DNA was investigated by cyclic voltametry and UV−vis spectroscopy to determine the binding constant (*12*). In our previous work, we observed the binding affinities and estimated the binding constants for *N*-(acridin-9-ylthiocarbamoyl)amino acids with plasmid DNA (pUC 19) (*13*). These findings inspired us to exploit the considerable intercalation capability of the highly fluorescent proflavine chromophore and prepare novel DNA-binding compounds in combination with the biologically active thiazolidinone skeleton. We wanted to ascertain the influence of structural changes on the intercalation properties, in particular, with reference to alkyl chain elongation. UV−vis spectrophotometry, fluorescence titration, circular dichroism (CD), and quantum chemical calculations (AM1) were all used to study the interaction of the compounds with DNA. The anticancer inhibitory effects were also tested against two tumor cell lines, viz., murine leukemia L1210 and human uterus carcinoma HeLa cells.

* Corresponding author. Ján Imrich, Department of Organic Chemistry, Institute of Chemistry, Faculty of Science, P. J. Šafárik University, Moyzesova 11, SK-04167 Košice, Slovak Republic. Tel. +421-55-905727892. E-mail: jimrich@kosice.upjs.sk.

[†] Department of Organic Chemistry, P.J. Šafárik University.

[‡] Department of Biochemistry, P.J. Šafárik University.

[§] Slovak Technical University.

EXPERIMENTAL PROCEDURES

Materials and Instrumental Techniques. Plasmid isolation and purification processes have been described in detail previously (*14*). Solutions of calf thymus DNA (Sigma Chemical Co.) in TE (Tris-EDTA) buffer were sonicated for 5 min and the DNA concentration determined by absorbance at 260 nm. The purity of the DNA was determined by monitoring the value of A_{260}/A_{280}. UV−vis spectra were measured on a Varian Cary 100 UV−vis spectrophotometer in 0.1 M Tris buffer. Fluorescence measurements were made using a Varian Cary Eclipse spectrofluorometer with a slit width of 10 nm for the excitation and emission beams. Fluorescence intensity is expressed in arbitrary units. Thermal denaturation studies were conducted using a Varian Cary 100 UV−vis spectrophotometer supplied with a thermostatic cell holder. The temperature was controlled by a thermostatic bath (±0.1 °C). CD spectra were recorded on a Jasco J-810 spectropolarimeter in 1 cm quartz cuvettes and are the mean result of three scans from which the buffer background had been electronically subtracted.

AM1 quantum chemical calculations were performed using the Gamess (version 6) program package (*15*).

The binding affinities were calculated using absorbance spectra according to the method of McGhee and von Hippel using data points from a Scatchard plot (*16*, *17*). The binding data were fitted using *Grafit 4* software.

^{1}H (400 MHz) and ^{13}C (100 MHz) NMR spectra were measured on a Varian Mercury Plus NMR spectrometer at room temperature in $CDCl_3$ using TMS as an internal standard (0 ppm for both nuclei). IR spectra were recorded on a Specord 75 IR spectrophotometer (Zeiss, Jena) as KBr discs (0.8 mg/300 mg KBr). Melting points were determined with a Koffler hot-stage apparatus and are uncorrected. Elemental analyses were performed on a Perkin-Elmer CHN 2400 analyzer. Reactions were monitored by thin-layer chromatography (TLC) using Silufol plates with detection at 254 nm. Preparative column chromatography was conducted using Kiesegel Merck 60 column, type

10.1021/bc060168v CCC: $37.00 © 2007 American Chemical Society
Published on Web 11/07/2006

9385 (grain size 250 nm), or aluminum oxide Merck 90 neutral (grain size 200 nm).

Murine leukemia cell line (L1210) and human uterus carcinoma cells (HeLa) were obtained from the American Type Culture Collection (Rockville, MD). The L1210 cell line was kept in a RPMI 1640 medium supplemented with 10% fetal calf serum (FCS) (Grand Island Biological Co., Grand Island, NY), penicillin (100 units/mL), and streptomycin (100 μg/mL). HeLa cells were grown as monolayers in DMEM (Dulbecco's Modified Eagle's Medium, Sigma) supplemented with 10% FCS and antibiotics penicillin (100 units/mL) and streptomycin (100 μg/mL). Trypsin (0.25%, Boehringer, Mannheim) was routinely used for subculture. The cells were incubated at 37 °C in a humidified atmosphere of 5% CO_2/95% air. Cell viability in the presence or absence of the experimental agent was determined using the MTT (3-(4,5-dimethylthiazol-2-yl)-2,5-dimethyl tetrazolium bromide; Sigma) microculture tetrazolium assay as described previously (*18, 19*). Cells harvested in the log phase of growth were counted and seeded (2.5×10^4 cells/100 μL well) in 96-well microtiter plates. After 24 h of incubation at 37 °C and 5% CO_2, cultures were treated with varying concentrations of a drug. After 45 h or 69 h exposure to the compound, MTT (50 μL, 1 mg/mL) was added to each well. After 3 h, the cell cultures were centrifuged, the supernatant discarded, and then the resulting pellets thoroughly extracted into 200 μL of DMSO. Absorption at 540 nm was recorded using the MicroPlate Reader (Labsystem Multiscan, Multisoft, Finland). The MTT assay was performed three times for each compound.

DNA fragmentation in HeLa and L1210 cells was measured after extraction of the DNA from a constant number of cells. After treatment of both cells lines for 24 h, 2×10^6 cells were collected and washed twice with cold PBS, resuspended in 200 μL TE lytic solution (10 mM Tris (pH 8.0), 1 mM EDTA, 0.5% Triton X-100) and incubated for 10 min with RNase (2.5 mg/mL) at 50 °C and then with proteinase K (2.5 mg/mL) for 30 min at 50 °C. The DNA was extracted with NaCl (1 mM), EDTA (1 mM), and 2-propanol (200 μL) for 6 h at −20 °C. After centrifugation, the DNA precipitates were washed with ethanol, resuspended in TE (Tris-EDTA) buffer and then separated by electrophoresis over a 1.5% agarose gel containing ethidium bromide (0.5 μg/mL) and the running buffer TAE (40 mM Tris-acetate, 1 mM EDTA, pH 8.0). The gel was run at 6 V/cm for 45 min after which it was photographed under UV transillumination.

Synthesis of 3,6-Diisothiocyanatoacridine (2). An aqueous solution (40 mL) of Na_2CO_3 (400 mg) was added dropwise during 1 h to a well-mixed suspension of 3,6-diaminoacridine hemisulfate hydrate (500 mg, 1.93 mmol) and thiophosgene (0.296 mL, 3.87 mmol) in chloroform (50 mL). Following this, a saturated aqueous solution of $NaHCO_3$ was slowly added until pH 8 was attained (approximately 2 h). The organic layer was then separated and the water layer extracted with chloroform (3×15 mL). The combined organic fractions were collected and dried over $CaCl_2$. After filtration, the solution was evaporated in vacuo leaving behind the dark red crude product (approximately 500 mg). The crude product was then taken up in chloroform (100 mL) and purified by flash chromatography over neutral alumina using chloroform (50 mL) as the eluent to provide 300 mg of dark yellow solid product. Yield: 60%, mp 195−197 °C. IR (KBr, cm^{-1}): 2012 (NCS), 1607 (C═C). ^{1}H NMR ($CDCl_3$, TMS/ppm): δ 8.73 (s, 1H, C*H*-9), 7.99 (m, 2H, C*H*-4,5), 7.97 (m, 2H, C*H*-1,8), 7.38 (dd, 2H, C*H*-2,7, J = 1.70 Hz, J = 8.90 Hz). ^{13}C NMR ($CDCl_3$, TMS/ppm): δ 149.12 (C-4a,10a), 138.57 (NCS), 136.41 (C-9), 133.98 (C-3,6), 130.12 (C-1,8), 124.97 (C-8a,9a), 124.74 (C-2,7), 124.16 (C-4,5). Anal. calculated for $C_{15}H_7N_3S_2$ (293.37): C, 61.41; H, 2.41; N, 14.32. Found: C, 61.37; H, 2.37; N, 14.13.

General Procedure for the Preparation of 1′,1″-(Acridin-3,6-diyl)-3′,3″-dialkyldithioureas 3a−3e. To a methanol (3 mL) suspension of 3,6-diisothiocyanatoacridine (50 mg, 0.17 mmol), a ten-molar excess of the appropriate amine was added. The reaction mixture was stirred for approximately 1 h while the progress of the reaction was monitored by TLC (toluene/acetone 3:1) until completion. The solid product was filtered off and dried in vacuo.

1′,1″-(Acridin-3,6-diyl)-3′,3″-diethyldithiourea (**3a**). Yield: 65%, mp 228−230 °C. ^{1}H NMR (DMSO, TMS/ppm): δ 9.93 (bs, 2H, 2 × N*H*), 8.86 (s, 1H, C*H*-9), 8.27 (s, 2H, C*H*-4,5), 8.21 (bs, 2H, 2 × N*H*), 8.02 (d, 2H, C*H*-1,8, J = 9.20 Hz), 7.59 (d, 2H, C*H*-2,7, J = 9.20 Hz), 3.53−3.60 (m, 4H, 2 × NC*H*$_2$), 1.18 (t, 6H, 2 × C*H*$_3$, J = 7.04 Hz). ^{13}C NMR (DMSO, TMS/ppm): δ 179.78 (CS), 149.27, 141.25, 134.95, 128.56, 122.59, 122.45, 115.91, 48.49 (NCH_2), 13.92 (CH_3). Anal. calculated for $C_{19}H_{21}N_5S_2$ (383.54): C, 59.50; H, 5.52; N, 18.26. Found: C, 59.30; H, 5.25; N, 18.20.

1′,1″-(Acridin-3,6-diyl)-3′,3″-dipropyldithiourea (**3b**). Yield: 62%, mp 222−223 °C. ^{1}H NMR (DMSO, TMS/ppm): δ 9.93 (bs, 2H, 2 × N*H*), 8.86 (s, 1H, C*H*-9), 8.32 (s, 2H, C*H*-4,5), 8.21 (bs, 2H, 2 × N*H*), 8.02 (d, 2H, C*H*-1,8, J = 8.60 Hz), 7.59 (d, 2H, C*H*-2,7, J = 8.60 Hz), 3.46−3.53 (m, 4H, 2 × NC*H*$_2$), 1.56−1.66 (m, 4H, 2 × C*H*$_2$), 0.94 (t, 6H, 2 × C*H*$_3$, J = 7.81 Hz). ^{13}C NMR (DMSO, TMS/ppm): δ 180.08 (CS), 149.21, 141.40, 135.02, 128.54, 122.57, 122.43, 115.78, 45.62 (NCH_2), 21.55 (CH_2), 11.37 (CH_3). Anal. calculated for $C_{21}H_{25}N_5S_2$ (411.59): C, 61.28; H, 6.12; N, 17.02. Found: C, 61.05; H, 5.95; N, 17.38.

1′,1″-(Acridin-3,6-diyl)-3′,3″-dibutyldithiourea (**3c**). Yield: 61%, mp 218−220 °C. ^{1}H NMR (DMSO, TMS/ppm): δ 9.92 (bs, 2H, 2 × N*H*), 8.85 (s, 1H, C*H*-9), 8.30 (s, 2H, C*H*-4,5), 8.19 (bs, 2H, 2 × N*H*), 8.01 (d, 2H, C*H*-1,8, J = 8.80 Hz), 7.58 (d, 2H, C*H*-2,7, J = 8.80 Hz), 3.50−3.57 (m, 4H, 2 × NC*H*$_2$), 1.55−1.62 (m, 4H, 2 × C*H*$_2$), 1.32−1.42 (m, 4H, 2 × C*H*$_2$), 0.93 (t, 6H, 2 × C*H*$_3$, J = 7.60 Hz). ^{13}C NMR (DMSO, TMS/ppm): δ 180.00 (CS), 149.31, 141.29, 134.88, 128.51, 122.56, 122.44, 115.84, 43.54 (NCH_2), 30.33 (CH_2), 19.57 (CH_2), 13.65 (CH_3). Anal. calculated for $C_{23}H_{29}N_5S_2$ (439.65): C, 62.84; H, 6.65; N, 15.93. Found: C, 62.52; H, 6.33; N, 16.18.

1′,1″-(Acridin-3,6-diyl)-3′,3″-dipentyldithiourea (**3d**). Yield: 60%, mp 232−233 °C. ^{1}H NMR (DMSO, TMS/ppm): δ 9.89 (bs, 2H, 2 × N*H*), 8.85 (s, 1H, C*H*-9), 8.29 (s, 2H, C*H*-4,5), 8.17 (bs, 2H, 2 × N*H*), 8.01 (d, 2H, C*H*-1,8, J = 8.80 Hz), 7.58 (d, 2H, C*H*-2,7, J = 8.80 Hz), 3.51−3.56 (m, 4H, 2 × NC*H*$_2$), 1.57−1.64 (m, 4H, 2 × C*H*$_2$), 1.32−1.37 (m, 8H, 4 × C*H*$_2$), 0.91 (t, 6H, 2 × C*H*$_3$, J = 6.0 Hz). ^{13}C NMR (DMSO, TMS/ppm): δ 180.03 (CS), 149.31, 141.31, 134.89, 128.49, 122.56, 122.39, 115.86, 43.82 (NCH_2), 28.57 (CH_2), 27.89 (CH_2), 21.80 (CH_2), 13.84 (CH_3). Anal. calculated for $C_{25}H_{33}N_5S_2$ (467.70): C, 64.20; H, 7.11; N, 14.97. Found: C, 64.51; H, 7.36; N, 14.83.

1′,1″-(Acridin-3,6-diyl)-3′,3″-dihexyldithiourea (**3e**). Yield: 60%, mp 212−214 °C. ^{1}H NMR (DMSO, TMS/ppm): δ 9.89 (bs, 2H, 2 × N*H*), 8.86 (s, 1H, C*H*-9), 8.29 (s, 2H, C*H*-4,5), 8.18 (bs, 2H, 2 × N*H*), 8.01 (d, 2H, C*H*-1,8, J = 9.00 Hz), 7.58 (d, 2H, C*H*-2,7, J = 9.00 Hz), 3.50−3.55 (m, 4H, 2 × NC*H*$_2$), 1.56−1.63 (m, 4H, 2 × C*H*$_2$), 1.30−1.37 (m, 12H, 6 × C*H*$_2$), 0.89 (t, 6H, 2 × C*H*$_3$, J = 6.80 Hz). ^{13}C NMR (DMSO, TMS/ppm): δ 180.01 (CS), 149.27, 141.17, 134.84, 128.39, 122.36, 122.43, 115.70, 43.87 (NCH_2), 30.92 (CH_2), 28.16 (CH_2), 26.06 (CH_2), 21.98 (CH_2), 13.84 (CH_3). Anal. calculated for $C_{27}H_{37}N_5S_2$ (495.76): C, 65.42; H, 7.52; N, 14.13. Found: C, 65.19; H, 7.25; N, 14.20.

General Procedure for the Preparation of 2′,2″-[(Acridin-3,6-diyl)diimino]-3′,3″-dialkyl-1,3-dithiazolidin-4-ones 4a−4e and the Corresponding Hydrochlorides 5a−5e. To a

dichloromethane (3 mL) suspension of the appropriate thiourea (0.13 mmol), triethylamine (0.04 mL, 0.286 mmol) was added. The mixture was stirred well for 10 min, followed by the addition of methyl bromoacetate (0.03 mL, 0.316 mmol), and monitored by TLC (toluene−acetone 3:1) until completion, at which time the reaction mixture was homogeneous. The solvent was evaporated in vacuo and the crude product purified over silica gel (toluene−acetone 3:1 as eluent). To produce **5**, the product **4** was dissolved in acetone (0.5 mL), and an equimolar solution of HCl in methanol (1 mL of 35% hydrochloric acid in 9 mL of methanol) was added. The mixture was stirred for 1 h followed by the addition of diethyl ether. The resulting precipitant was filtered off and dried in vacuo.

2′,2″-[(Acridin-3,6-diyl)diimino]-3′,3″-diethyl-1,3-dithiazolidin-4-one (**4a**). Yield: 71%; yellow oil. ^{1}H NMR ($CDCl_3$, TMS/ppm): δ 8.68 (s, 1H, C*H*-9), 7.98 (d, 2H, C*H*-1,8, J = 8.80 Hz), 7.70 (s, 2H, C*H*-4,5), 7.20 (d, 2H, C*H*-2,7, J = 8.80 Hz), 3.99 (q, 4H, 2 × NCH_2, J = 7.20 Hz), 3.84 (s, 4H, 2 × SCH_2), 1.36 (t, 6H, 2 × CH_3, J = 7.20 Hz). ^{13}C NMR ($CDCl_3$, TMS/ppm): δ 171.53 (CO), 155.03 (CN), 150.14, 150.05, 135.72, 129.58, 124.04, 122.88, 116.96, 38.44 (NCH_2), 32.88 (SCH_2), 12.55 (CH_3). Anal. calculated for **5a**, $C_{23}H_{21}N_5O_2S_2$·HCl, yellow solid (500.05), mp 215−216 °C: C, 55.25; H, 4.43; N, 14.01. Found: C, 55.43; H, 4.39; N, 13.89.

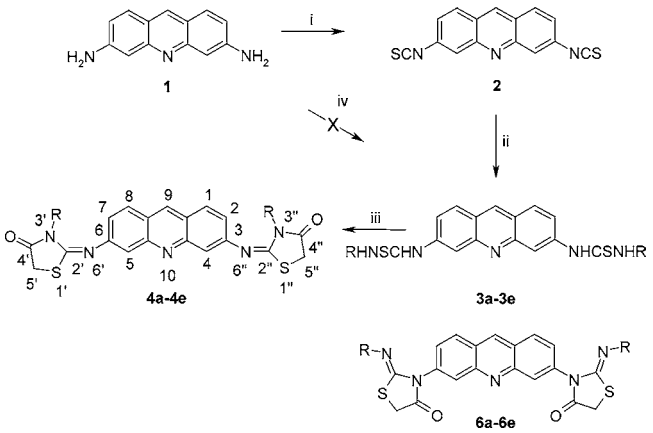
2′,2″-[(Acridin-3,6-diyl)diimino]-3′,3″-dipropyl-1,3-dithiazolidin-4-one (**4b**). Yield: 65%; yellow oil. ^{1}H NMR ($CDCl_3$, TMS/ppm): δ 8.69 (s, 1H, C*H*-9), 7.97 (d, 2H, C*H*-1,8, J = 8.80 Hz), 7.74 (s, 2H, C*H*-4,5), 7.20 (d, 2H, C*H*-2,7, J = 8.80 Hz), 3.89 (t, 4H, 2 × NCH_2, J = 7.20 Hz), 3.84 (s, 4H, 2 × SCH_2), 1.77−1.86 (m, 4H, 2 × CH_2), 1.02 (t, 6H, 2 × CH_3, J = 7.20 Hz). ^{13}C NMR ($CDCl_3$, TMS/ppm): δ 171.72 (CO), 155.12 (CN), 150.25, 149.87, 135.14, 129.84, 123.05, 122.55, 116.35, 43.66 (NCH_2), 32.38 (SCH_2), 19.79 (CH_2), 10.91 (CH_3). Anal. calculated for **5b**, $C_{25}H_{25}N_5O_2S_2$·HCl, yellow solid (528.10), mp 178−180 °C: C, 56.86; H, 4.96; N, 13.26. Found: C, 56.70; H, 4.89; N, 13.29.

2′,2″-[(Acridin-3,6-diyl)diimino]-3′,3″-dibutyl-1,3-dithiazolidin-4-one (**4c**). Yield: 63%; yellow oil. ^{1}H NMR ($CDCl_3$, TMS/ppm): δ 8.73 (s, 1H, C*H*-9), 7.99 (d, 2H, C*H*-1,8, J = 8.80 Hz), 7.78 (s, 2H, C*H*-4,5), 7.22 (d, 2H, C*H*-2,7, J = 8.80 Hz), 3.92 (t, 4H, 2 × NCH_2, J = 7.20 Hz), 3.85 (s, 4H, 2 × SCH_2), 1.72−1.80 (m, 4H, 2 × CH_2), 1.33−1.48 (m, 4H, 2 × CH_2), 0.99 (t, 6H, 2 × CH_3, J = 7.20 Hz). ^{13}C NMR ($CDCl_3$, TMS/ppm): δ 171.76 (CO), 155.31 (CN), 150.33, 149.88, 135.90, 129.60, 124.00, 122.90, 116.78, 43.19 (NCH_2), 32.85 (SCH_2), 29.36 (CH_2), 20.12 (CH_2), 13.82 (CH_3). Anal. calculated for **5c**, $C_{27}H_{29}N_5O_2S_2$·HCl, yellow solid (556.15), mp 156−158 °C: C, 58.31; H, 5.44; N, 12.59. Found: C, 58.48; H, 5.56; N, 13.22.

2′,2″-[(Acridin-3,6-diyl)diimino]-3′,3″-dipentyl-1,3-dithiazolidin-4-one (**4d**). Yield: 61%, yellow oil. ^{1}H NMR ($CDCl_3$, TMS/ppm): δ 8.67 (s, 1H, C*H*-9), 7.96 (d, 2H, C*H*-1,8, J = 8.80 Hz), 7.69 (s, 2H, C*H*-4,5), 7.18 (d, 2H, C*H*-2,7, J = 8.80 Hz), 3.90 (t, 4H, 2 × NCH_2, J = 7.20 Hz), 3.83 (s, 4H, 2 × SCH_2), 1.74−1.81 (m, 4H, 2 × CH_2), 1.36−1.43 (m, 8H, 4 × CH_2), 0.93 (t, 6H, 2 × CH_3, J = 6.40 Hz). ^{13}C NMR ($CDCl_3$, TMS/ppm): δ 171.71 (CO), 155.24 (CN), 150.25, 149.88, 135.79, 129.57, 123.99, 122.87, 116.86, 43.38 (NCH_2), 32.84 (SCH_2), 28.93 (CH_2), 26.89 (CH_2), 22.35 (CH_2), 13.98 (CH_3). Anal. calculated for **5d**, $C_{29}H_{33}N_5O_2S_2$·HCl, yellow solid (584.21), mp 175−176 °C: C, 59.62; H, 5.87; N, 11.99. Found: C, 59.33; H, 5.68; N, 12.03.

2′,2″-[(Acridin-3,6-diyl)diimino]-3,3″-dihexyl-1,3-dithiazolidin-4-one (**4e**). Yield: 58%, yellow oil. ^{1}H NMR ($CDCl_3$, TMS/ppm): δ 8.68 (s, 1H, C*H*-9), 7.97 (d, 2H, C*H*-1,8, J = 8.80 Hz), 7.70 (s, 2H, C*H*-4,5), 7.19 (d, 2H, H-2,7, J = 8.80 Hz), 3.91 (t, 4H, 2 × NCH_2, J = 7.20 Hz), 3.83 (s, 4H, 2 × SCH_2), 1.73−1.81 (m, 4H, 2 × CH_2), 1.32−1.43 (m, 12H, 6 × CH_2), 0.91 (t, 6H, 2 × CH_3, J = 6.80 Hz). ^{13}C NMR ($CDCl_3$, TMS/ppm): δ 171.71 (CO), 155.27 (CN), 150.31, 149.86, 135.88, 129.58, 123.97, 122.89, 116.86, 43.44 (NCH_2), 32.84 (SCH_2), 31.45 (CH_2), 27.19 (CH_2), 26.51 (CH_2), 22.56 (CH_2), 14.04 (CH_3). Anal. calculated for **5e**, $C_{31}H_{37}N_5O_2S_2$·HCl, yellow solid (612.26), mp 118−120 °C: C, 60.81; H, 6.26; N, 11.44. Found: C, 60.98; H, 6.25; N, 11.59.

Scheme 1. Synthesis of the Novel Proflavine Derivatives 4a−4e[a]



[a] Reagents and conditions: R = ethyl - **a**; *n*-propyl - **b**; *n*-butyl - **c**; *n*-pentyl - **d**; *n*-hexyl - **e**; (i) $CSCl_2$, $CHCl_3/H_2O$, Na_2CO_3, RT; (ii) RNH_2, CH_3OH, RT; (iii) $BrCH_2CO_2CH_3$, CH_2Cl_2, RT; (iv) RNCS, CH_2Cl_2, RT.

RESULTS

Synthesis of the Novel Proflavine Derivatives 4a−4e. The reaction course for the synthesis of 2′,2″-[(acridin-3,6-diyl)-diimino]-3′,3″-dialkyl-1,3-dithiazolidin-4-ones **4a**−**4e** is depicted in Scheme 1. Physicochemical values as well as the methods used for the structure determination are given in the Experimental Procedures section.

Spectroscopic Properties. The absorption spectra of proflavine derivatives **5a**−**5e** with pUC19 DNA all exhibited broad absorption bands in the region 250−500 nm and the spectra of the acridine derivatives significant absorption peaks in the range 350−460 nm. Figure 1 provides an example illustrating the characteristic changes in the absorption spectra during titration

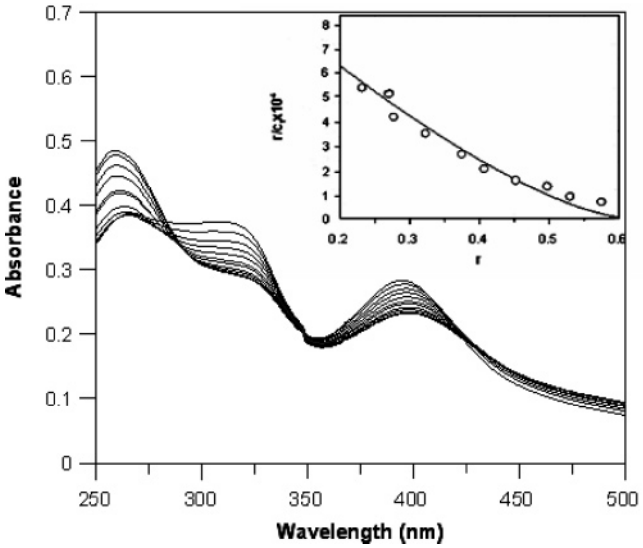


Figure 1. Absorption titration of compound **5b** (2.6 μM) in 0.1 M Tris buffer (pH 7.4) with increasing concentration of pUC19 DNA (from top to bottom: 0, 2, 4, 6, 8, 10, 12, 14, 16, 18, and 20 μM bp). Inset: Scatchard plot of **5b** complexation.

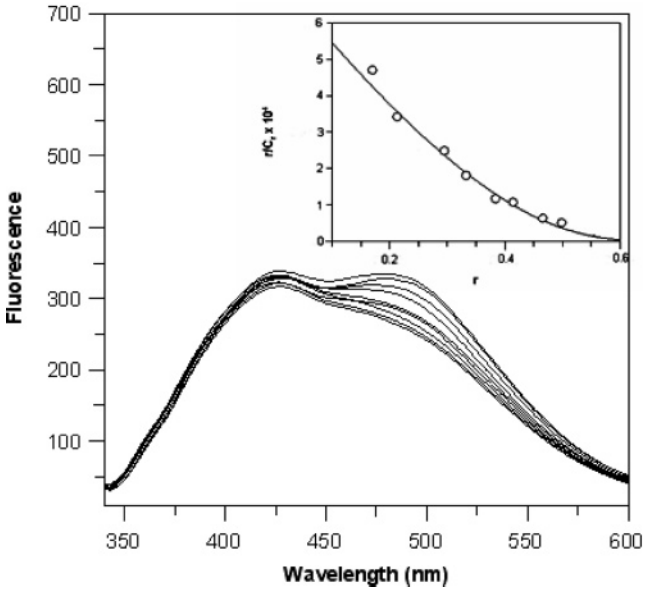


Figure 2. Changes in emission fluorescence spectra of **5b** (5.2 μM) in 0.1 M Tris buffer (pH 7.4) with increasing concentration of pUC19 DNA from top to bottom: 0, 25, 41, 62, 83, 101, 124, 145, and 163 μM bp; λ_{ex} = 320 nm. Inset: Scatchard plot of **5b** complexation.

of compound **5b** with increasing amounts of pUC19 DNA. The binding of the drugs to DNA was characterized by bathochromic shifts and marked hypochromism. The red shift of the drug absorption band was pronounced with **5c** and **5d**, whereas only mild shifts occurred for **5a**, **5b**, and **5e** (Table 1).

The representative fluorescence spectra of **5b** with pUC19 DNA were obtained by the addition of the DNA to the drug solution which resulted in a decrease of fluorescence (Figure 2). Similar fluorescence quenching was observed for all investigated derivatives.

Binding parameters for the interactions of **5a**−**5e** with DNA obtained from spectrophotometric and spectrofluorimetric analysis are summarized in Table 2. Correlation of the chain length (Å) of the alkyl substituents in **5a**−**5e** with the DNA binding constants *K* obtained from spectrophotometry ($k = -2.135$; $r = 0.965$; $S = 0.572$) and spectrofluorimetry ($k = -1.512$; $r = 0.983$; $S = 0.159$) are depicted in Figure 3.

As seen in Figure 4, the addition of **5b** to calf thymus DNA induced a slight increase of the CD signal centered at 275 nm

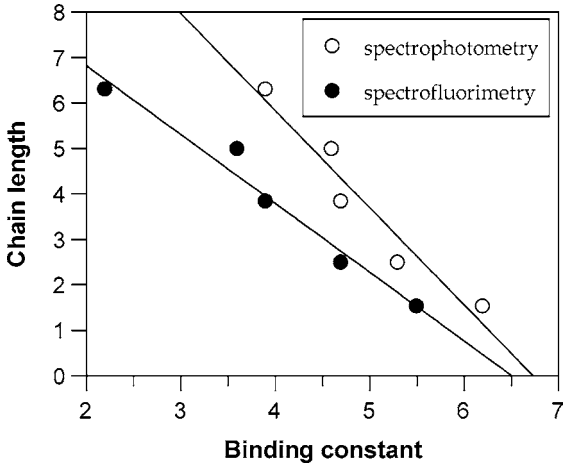


Figure 3. Correlation of the chain length (Å) of the alkyl substituents in **5a**−**5e** with the DNA binding constants *K* obtained from spectrophotometry ($k = -2.135$; $r = 0.965$; $S = 0.572$) and spectrofluorimetry ($k = -1.512$; $r = 0.983$; $S = 0.159$).

and the negative peak at 243 nm. Similar CD changes were also observed for the complexes with the other drugs.

Figure 5 provides thermal denaturation curves of DNA melting experiments for the calf thymus DNA in the presence of **5a**−**5e**, whose T_m values are presented in Table 1.

AM1 Calculations. To establish the steric structure of the intercalators under study, AM1 calculations were performed (Figure 6, Table 3).

Cytotoxic Activity in Vitro. The inhibitory effects of compounds **5a**−**5e** against two tumor cell lines (L1210, HeLa) were tested and the resulting concentration−response curve plotted. The concentrations that produced 25% (IC_{25}) or 50% (IC_{50}) inhibition of cell viability were calculated and the results collected in Table 4. Effects of **5b** on the viability of HeLa (A) and L1210 cells (B) incubated for 0−72 h without (control) or with 0−100 μM **5b** are shown in Figure 7. Changes of cells morphology have been examined using fluorescent and light microscopy (Figure 8). The induction of apoptosis by **5b** in L1210 and HeLa cells has been evaluated by electrophoresis of fragmented DNA (Figure 9).

DISCUSSION

We report an efficient strategy for the synthesis of novel proflavine−dithiazolidinone derivatives. As the starting com-

Table 1. UV−vis DNA Binding Properties

	λ_{max} (nm)			hypochromism	T_m[a]
compound	free	bound	$\Delta\lambda$	%	(°C)
5a	381	383	2	23	80
5b	393	397	4	22.7	79
5c	393	400	7	29.0	79
5d	396	406	10	18.2	78
5e	390	392	2	22.8	77

[a] T_m measurements were performed in BPE buffer pH 7.1 (6 mM Na_2HPO_4, 2 mM NaH_2PO_4, 1 mM EDTA) using 10 μM drug and 20 μM bp calf thymus DNA with a heating rate of 1 °C min^{-1}.

Table 2. Photophysical and Binding Parameters of 5a−5e from Spectrophotometric and Spectrofluorimetric Analysis

	spectrophotometry		spectrofluorimetry		λ_{em}		ΔG^b
compd	$K \times 10^4$	n	$K \times 10^4$	n	(nm)	Φ_f[a]	(kJ mol^{-1})
5a	6.2 ± 0.2	2.1 ± 0.5	5.5 ± 0.3	2.4 ± 0.4	420, 460	0.75	−27.3
5b	5.3 ± 0.4	2.3 ± 0.4	4.7 ± 0.3	2.8 ± 0.5	420, 500	0.51	−26.9
5c	4.7 ± 0.2	2.7 ± 0.3	3.9 ± 0.2	3.3 ± 0.3	430, 490	0.94	−26.6
5d	4.6 ± 0.3	2.6 ± 0.5	3.6 ± 0.4	3.0 ± 0.4	420, 490	0.89	−26.6
5e	3.9 ± 0.4	3.2 ± 0.8	2.2 ± 0.3	3.9 ± 0.6	425, 500	1	−26.2

[a] The fluorescence quantum yields were calculated using 2′,2″-[(acridin-3,6-diyl)diimino]-3′,3″-dihexyl-1,3-dithiazolidin-4-one hydrochloride (**5e**) as a standard ($\Phi_f = 1$). [b] The standard Gibb's free energy change ($\Delta G° = -RT \ln K$) for derivatives **5a**−**5e** is approximately −26.52 kJ mol^{-1} at 25 °C, thereby indicating the spontaneity of the binding with DNA.

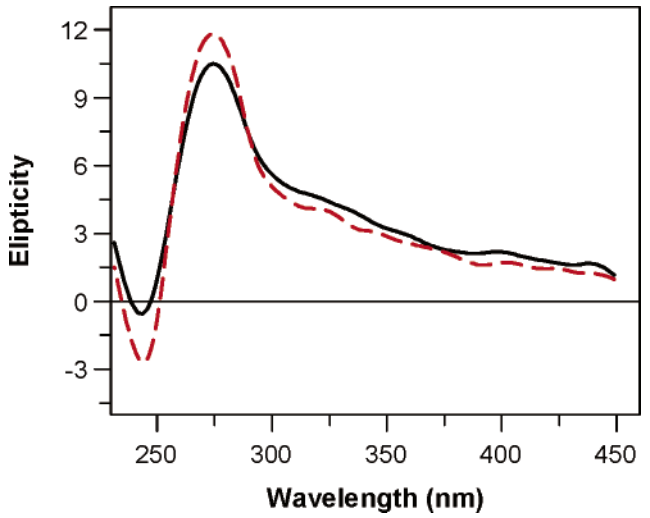


Figure 4. Circular dichroism spectra of the calf thymus DNA (20 μM) (solid line) in the absence and in the presence of **5b** (10 μM) (dashed line) in 0.1 M Tris buffer (pH 7.4).

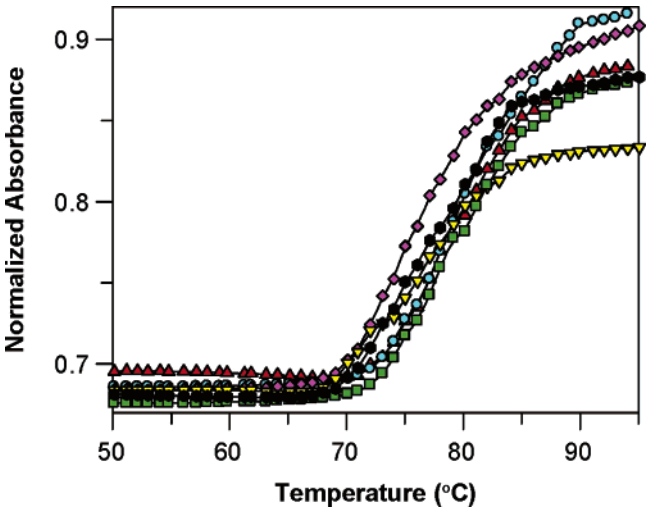


Figure 5. Melting curves of calf thymus DNA (violet ◇) with **5a** (light blue ○), **5b** (black ●), **5c** (red △), **5d** (yellow ▽), and **5e** (green □) measured at 260 nm in BPE buffer pH = 7.1.

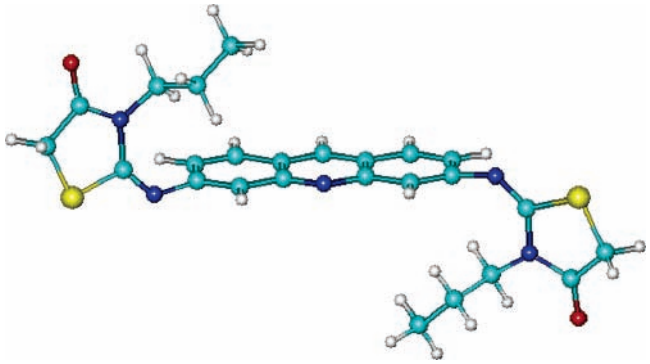


Figure 6. Minimum-energy conformation of the propyl−proflavine derivative **4b** obtained using Gamess software. Color code for the atoms: dark blue, nitrogen; light blue, carbon; red, oxygen; yellow, sulfur.

pound for the preparation of newly designed intercalators, the commercially available proflavine hemisulfate was used. We attempted to prepare the intermediate thioureas **3a**−**3e** by the treatment of the free base proflavine (**1**) with aliphatic isothiocyanates to incorporate aliphatic chains into the resulting structures. The free base was obtained by the addition of triethylamine to the solution of proflavine hemisulphate in a mixture DMSO/methanol, then poured into brine, and the resulting precipitate filtered off and dried overnight in vacuo. Unfortunately, the reaction of **1** did not proceed even with a ten-molar excess of ethylisothiocyanate and 30 h heating. In addition, proflavine (**1**) as the free base underwent decomposition during the course of the reaction, and an attempt to carry out the reaction with free base **1** released in situ also failed. The reason for these failures is probably the poor nucleophilicity of the amino group in **1** and the low electrophilicity of the NCS carbon of the alkylisothiocyanates. The problem was circumvented by preparing thioureas **3a**−**3e** using a reverse approach via reaction of the corresponding alkyl amines with the novel synthon, 3,6-diisothiocyanatoacridine (**2**) (*20*). To obtain a higher yield of **2**, the synthesis was reduced to a one-pot procedure by in situ reaction of free base **1** with thiophosgene.

Table 3. Structural and Electronic Features of Proflavine−Thiazolidinone Derivatives 4a−4e

structural/electronic parameters	compound				
	4a	**4b**	**4c**	**4d**	**4e**
φ (C4−C3−N6′−C2′)	104.57°	104.60°	105.56°	105.08°	105.28°
φ (C5−C6−N6″−C2″)	104.33°	104.63°	105.51°	104.94°	105.07°
alkyl chain length (Å)	1.52	2.48	3.83	4.98	6.29
dipole moment (D)	2.02	1.98	1.92	1.89	1.88

Diisothiocyanate **2** reacted readily with the amines in methanol, whereas in chloroform, toluene, and methylene chloride, decomposition of the products was observed. The obtained thioureas **3a**−**3e** were filtered off and dried in vacuo. Because of their low stability, they were immediately employed after drying in the subsequent reaction. Aliphatic nonbranched amines were used to study the structural dependence of the chain length vs DNA intercalation capability of the final products **5a**−**5e**. For the preparation of the corresponding thiazolidin-4-ones **5a**−**5e**, our previous experience with the regioselectivity of thiazolidin-4-one formation was exploited (*21*). The synthesis was performed by the reaction of methyl bromoacetate with thioureas **3a**−**3e** in the presence of triethylamine under anhydrous conditions; the resulting products **4a**−**4e** were obtained pure by column chromatography over silica gel. The regioselective formation of the product **4a** was proven by a gHMBC NMR experiment revealing a cross peak between the methylene signal of the ethyl group and the carbonyl carbon. In the case of compounds **4b**−**4e**, the structure was verified by the presence of a SCH_2 signal at ca. 3.8 ppm, typical for regioisomers analogous to **4** (*21*−*23*). To enhance their water solubility, the products **4a**−**4e** were converted to their corresponding hydrochlorides **5a**−**5e**. The alternative regioisomers **6a**−**6e** were not observed.

Electronic absorption spectra of the synthesized derivatives exhibited significant absorptions in the range 350−460 nm, which are typical for transitions between the π-electronic energy levels of the acridine ring.

To obtain additional information on the new proflavine derivatives **5a**−**5e**, fluorescence measurements were also performed. The fluorescence spectra of the proflavine derivatives **5a**−**5e** each exhibited a broad absorption band in the range 350−600 nm. Differences were found in the fluorescence intensities of the compounds with the highest intensity displayed by the derivative **5e**.

Binding constants (K) and neighbor exclusion parameters (n) clearly indicate a direct dependence between the structural changes and the resulting intercalation capability. Because n ranges from 2.1 to 3.9, multiple-site binding is occurring which affects interaction at the neighboring sites. Aslanoglu (*12*) determined the binding constant ($K = 2.32 \times 10^4$ M^{-1}) and the binding site size ($n = 2.07$ bp) for the interaction between proflavine and DNA. Our binding constants determined by UV−vis measurements ranged above this from 3.9 to 6.2×10^4 M^{-1}

Table 4. Effect of 5a−5e on the Viability[a] of HeLa and L1210 Cells

	L1210				HeLa			
	48 h		72 h		48 h		72 h	
IC (μM)	IC_{25}	IC_{50}	IC_{25}	IC_{50}	IC_{25}	IC_{50}	IC_{25}	IC_{50}
5a	2.6 ± 0.4	8.2 ± 0.5	3.5 ± 1.1	11.0 ± 1.7	3.0 ± 0.3	15.5 ± 1.0	3.0 ± 0.4	12.5 ± 0.9
5b	2.8 ± 0.5	6.7 ± 1.6	2.8 ± 0.3	6.3 ± 1.0	2.8 ± 0.5	20.3 ± 0.3	5.3 ± 1.1	12.9 ± 0.3
5c	2.8 ± 0.5	8.5 ± 0.7	4.0 ± 0.9	20.5 ± 0.8	11.5 ± 0.9	ND	5.0 ± 0.8	25.0 ± 1.0
5d	10.0 ± 0.8	100.0 ± 0.5	10.5 ± 1.0	100.0 ± 1.0	23.0 ± 1.0	ND	4.0 ± 0.5	57.0 ± 0.9
5e	25.0 ± 1.0	100.0 ± 0.5	45.0 ± 0.7	90.0 ± 1.2	27.0 ± 0.5	ND	3.1 ± 0.5	78.0 ± 0.8

[a] Cell viability was evaluated by MTT assay. Cells were incubated for 0−72 h without (control) or with 0−100 μM of compound. IC_{25} and IC_{50} are concentrations that produced 25% and 50%, respectively, inhibition of cell viability. ND: inhibition was not obtained (IC_{50} > 100 μM). Results are expressed as a mean ± S.D. (n = 3).

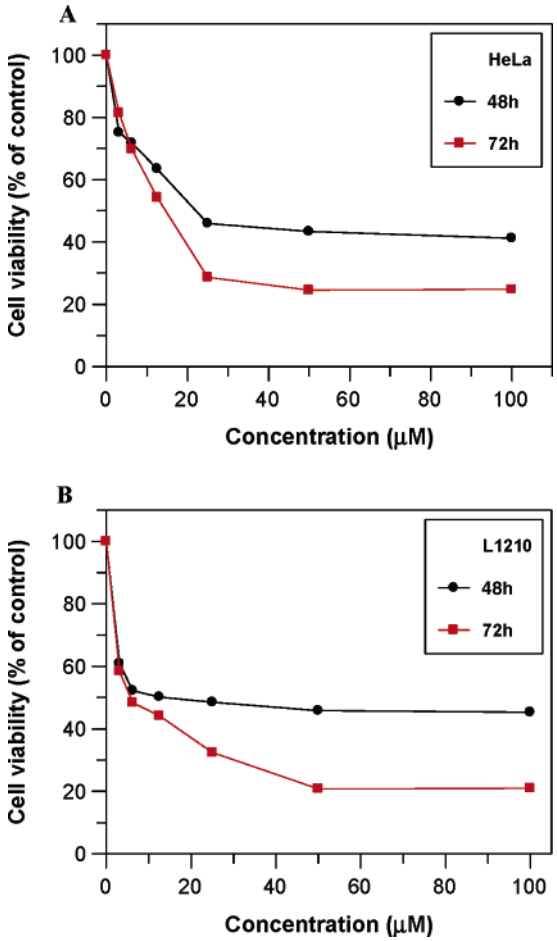


Figure 7. Effects of **5b** on the viability of HeLa (A) and L1210 cells (B). Cells were incubated for 0−72 h without (control) or with 0−100 μM **5b**. Cell viability was evaluated by MTT assay. Results are expressed as a percentage of the control.

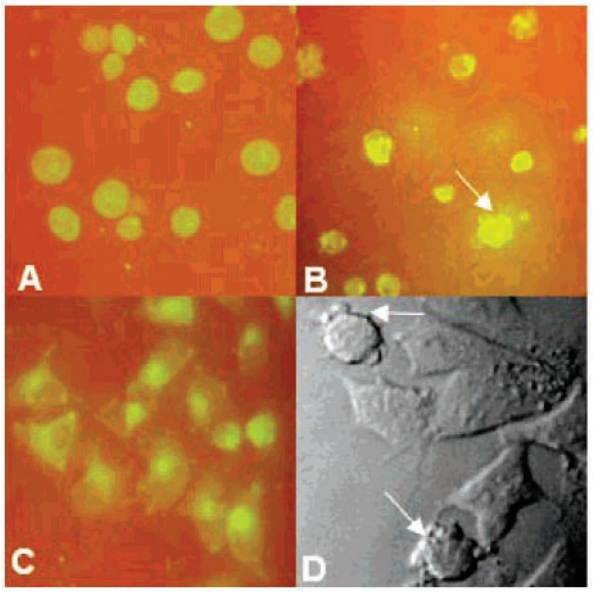


Figure 8. Morphology of leukemia cells L1210 (A,B) and cervical carcinoma HeLa cells (C,D) treated with **5b** (24 h incubation, 10 μM). Magnification 400×. Image A: control L1210 cells stained with Hoechst 44433 and propidium iodide. Images A, B, and C were obtained using a fluorescence microscope and image D using a light microscope. Arrows indicate membrane blebbing.

and by spectrofluorimetry from 2.2 to 5.5 × 10^4 M^{-1} while the binding site sizes were similar to the value determined by Aslanoglu. The slight changes are induced by the thiazolidinone moiety on the proflavine skeleton which is supposed to stabilize the double helix DNA structure. This interpretation was also supported by thermal denaturation studies.

The melting of DNA is a phenomenon observed when the double-stranded DNA molecules are heated and separate into two single strands; it occurs due to the disruption of the intermolecular forces such as $\pi-\pi$ stacking and hydrogen-bonding interactions between the DNA base pairs. DNA melting experiments revealed that the T_m of calf thymus DNA (76 °C) increases in the presence of **5a**−**5e** to within the range 77−80 °C. An increase in the helix stabilization is due to intercalation of proflavine−dithiazolidinone derivatives into DNA.

To elucidate the drug binding mechanism, CD was also used. It is one of the spectroscopic methods most amenable for determining a drug-binding mode. Changes in the CD spectrum of DNA as a result of complexation can often be ascribed to alteration of the DNA structure. Agents intercalating into the DNA generally give no induced CD or weakly negative signals in the drug absorption band (*24*). Our observations suggest that intercalation exists between **5a**−**5e** and calf thymus DNA.

To determine the steric effects of the drugs, AM1 calculations were performed. From these studies, it was deduced that the structure depicted in Figure 6 is the most suitable for DNA intercalation. The results indicate that steric influence on the size of the binding constants is negligible, as the values of the analogous dihedral angles of the thiazolidin-4-one and proflavine rings were nearly identical. However, Joseph et al. demonstrated that, by introducing a subtle steric factor, one could alter the DNA binding properties of aryl-substituted acridinium derivatives (*25*).

The values of the dipole moments, which are related to some extent to the polarity, can be considered a measure of lipophilicity of **5a**−**5e** (Table 3). Despite only small differences in the values of the binding constants, we have found that there exists a linear correlation between the chain length (Å) and binding ability.

The cells showed different responses to the tested compounds, though the L1210 cells appeared to be more sensitive than the HeLa cells. The results clearly indicate that substances **5a**−**5c** possess strong cytotoxic effects toward cancer cell lines. In the present study, **5b** is one of the most effective compounds in

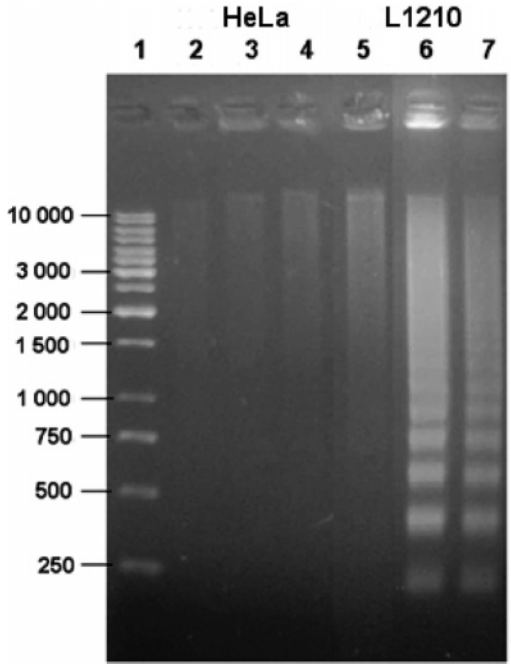


Figure 9. Agarose gel electrophoresis of DNA fragments from cells treated with **5b**. HeLa and L1210 cells were incubated with **5b** (5 or 10 μM) for 24 h. DNA fragmentation was visualized by ethidium bromide after DNA agarose gel electrophoresis. Lane 1: size marker (10000−250 bp). HeLa cells: lane 2, control; lane 3, treated with 5 μM **5b**; lane 4, treated with 10 μM **5b**. L1210: lane 5, control; lane 6, treated with 5 μM **5b**; lane 7, treated with 10 μM **5b**.

terms of its ability to inhibit proliferation in a time- and dose-dependent manner (IC_{50} 6.3 and 12.9 μM; 72 h treatment). Incubation of cells in the presence of **5b** at concentrations higher than 3 μM resulted in significant growth inhibition. The ability of **5b** to inhibit cancer cell proliferation and the aforementioned properties of drug binding into DNA suggests that this compound could cause apoptosis, also known as programmed cell death. Apoptosis is characterized by distinct morphological features such as cell shrinkage, chromatin condensation, plasma membrane blebbing, oligonucleosomal DNA fragmentation, and finally, the breakdown of the cell into smaller units.

Changes in cell morphology were examined using fluorescent microscopy to predict mode of death induced by **5b**. The fluorescence of **5b** is sufficient for intracellular localization of this drug and propidium iodide was utilized for identification of necrotic cells. The altered morphology of L1210 cells was evident after 24 h treatment with 10 μM **5b** (20% of necrotic cells), and this compound was accumulated by L1210 cells which clearly exhibited cytoplasmic blebbing (a hallmark of apoptosis) and shape irregularity (Figure 8B). When human cervical carcinoma HeLa cells were treated with 10 μM **5b**, the nuclei and the cytoplasms exhibited green fluorescence (Figure 8C), and although necrotic features were not observed, membrane blebbing was evident (Figure 8D).

In addition to characteristic changes in morphology, the induction of apoptosis by **5b** in L1210 and HeLa cells has been evaluated by electrophoresis of fragmented DNA. L1210 cells cultured with **5b** (5 μM or 10 μM) for 24 h exhibited a characteristic DNA ladder pattern of apoptosis. Negligible cleavage of DNA into nucleosomal fragments was seen with **5b**-treated HeLa cells. Since drug action usually requires internalization of the drug, a high rate of uptake of the most potent antiproliferative drug **5b** by L1210 was confirmed (about 50% of **5b** was accumulated after rapid incubation of the cells with the compound).

A linear correlation between the binding constants of **5a**−**5e** to DNA and the length of the alkyl chain has been established whereby the binding affinity decreases with increasing length of the side chain. All of the compounds displayed cytotoxic activity in vitro and inhibited the growth of cancer cells. We can therefore summarize that the newly synthesized molecules afford interesting possibilities to develop novel DNA-targeted anticancer agents.

ACKNOWLEDGMENT

This work was supported by the Slovak Grant Agency VEGA, grants no.1/1274/04, 1/1173/04, 1/ 1272/04, and 1/2471/05 and by the State NMR Programme no. 2003SP200280203. Dr. Karel D. Klika is thanked for correction of the language and assistance in manuscript preparation.

LITERATURE CITED

(1) Mountzouris, J. A., and Hurley, L. H. (1996) Small molecule-DNA interaction. In *Bioorganic Chemistry: Nucleic Acids* (Hecht, S. M., Ed.) p 288, Oxford University Press, New York.
(2) Waring, M. J. (1981) DNA modification and cancer. *Annu. Rev. Biochem. 50*, 159−192.
(3) Demeunynck, M., Charmantray, F., and Martelli, A. (2001) Interest of acridine derivatives in the anticancer chemotherapy. *Curr. Pharm. Des. 7*, 1703−1724.
(4) Denny, W. A. (2002) Acridine derivatives as chemotherapeutic agents. *Curr. Med. Chem. 9*, 1655−1665.
(5) Charmantray, F., Demeunynck, M., Carrez, D., Croisy, A., Lansiaux, A., Bailly, C., and Colson, P. (2003) 4-Hydroxymethyl-3-aminoacridine derivatives as a new family of anticancer agents. *J. Med. Chem. 13*, 967−977.
(6) Denny, W. A. (2004) Chemotherapeutic effects of acridine derivatives. *Med. Chem. 1*, 1655−1665.
(7) Dias, N., Goossens, J. F., Baldeyrou, B., Lansiaux, A., Colson, P., Di Salvo, A., Bernal, J., Turnbull, A., Mincher, D. J., and Bailly, C. (2005) Oxoazabenzo[de]anthracenes conjugated to amino acids: Synthesis and evaluation as DNA-binding antitumor agents. *Bioconjugate Chem. 16*, 949−958.
(8) Martínez, R., and Chacón-García, L. (2005) The search of DNA-intercalators as antitumoral drugs: What worked and what did not work. *Curr. Med. Chem. 12*, 11345−1359.
(9) Weinstein, B., and Finkelstein, I. H. (1967) Proflavine inhibition of protein synthesis. *J. Biol. Chem. 242*, 3757−3762.
(10) Wainwright, M. (2001) Acridine − a neglected antibacterial chromophore. *J. Antimicrob. Chemother. 47*, 1−13.
(11) Ferguson, L. R., and Denny, W. A. (1991) The genetic toxicology of acridines. *Mutat. Res. 258*, 123−160.
(12) Aslanoglu, M. (2006) Electrochemical and spectroscopic studies of the intercalation of proflavine with DNA. *Anal. Science. 22*, 439−443.
(13) Sabolová, D., Kožurková, M., Kristian, P., Danihel, I., Podhradský, D., and Imrich, J. (2006) Determination of the binding affinities of plasmid DNA using fluorescent intercalators possessing an acridine skeleton. *Inter. J. Biol. Macromol. 38*, 94−98.
(14) Víglaský, V., Valle, F., Adamčík, J., Antalík, M., Joab, I., Podhradský, D., and Dietler, G. (2003) Anthracycline-dependent heat-induced transition from positive to negative supercoiled DNA. *Electrophoresis 24*, 1703−1711.
(15) Schmidt, M. W., Baldridge, K. K., Boatz, J. A., Elbert, S. T., Gordon, M. S., Jensen, J. H., Koseki, S., Matsunaga, N., Nguyen, K. A., Su, S. J., Windus, T. L., Dupuis, M., and Montgomery, J. A. (1993) Gamess, version 22, Nov. 2004 (R1). *J. Comput. Chem. 14*, 1347−1363.
(16) McGhee, J., von Hippel, P. (1974) Theoretical aspects of DNA-protein interactions: co-operative and non-co-operative binding of large ligands to a one-dimensional homogeneous lattice. *J. Mol. Biol. 86*, 469−489.
(17) Jenkins, T. C. (1997) Optical absorbance and fluorescence techniques for measuring DNA-drug interaction. In *Methods in Molecular Biology* (Fox, K. R., Ed.) Vol. 90: Drug-DNA interaction protocol, Chapt. 14, Humana Press, Totowa, New Jersey.
(18) Alley, M. C., and Scudiero, D. A. (1988) Feasibility of drug screening with panels of human tumor cell lines. Using a microculture tetrazolium assay. *Cancer Res. 48*, 589−601.

(19) Carmichael, J., DeGraff, W. G., Gazdar, A. F., Minna, J. D., and Mitchell, J. B. (1987) Evaluation of a tetrazolium-based semiautomated colormetric assays: assessment of chemisensitivity testing. *Cancer Res. 47*, 936−942.

(20) Kristian, P., Antoš, K., Hulka, A., Nemec, P., and Drobnica, L. (1961) Isothiocyanates VIII. Study of the synthesis of diisothiocyanato- and aminoisothiocyanatoacridines. *Chem. Zvesti 15*, 731−739 (in Slovak). (1963) *Chem. Abstr. 58*, 5635.

(21) Klika, K. D., Janovec, L., Imrich, J., Suchár, G., Kristian, P., Sillanpaä, R., and Pihlaja, K. (2002) Regioselective synthesis of 2-imino-1,3-thiazolidin-4-ones by treatment of N-(anthracen-9-yl)-N′-ethylthiourea with bromoacetic acid derivatives. *Eur. J. Org. Chem.*, 1248−1255.

(22) Klika, K. D., Valtamo, P., Janovec, L., Suchár, G., Kristian, P., Imrich, J., Kivelä, H., Alföldi, J., and Pihlaja, K. (2004) Regioselective syntheses, structural characterization, and electron ionization mass spectrometric behavior of regioisomeric 2,3-disubstituted 2-imino-1,3-thiazolidin-4-ones. *Rapid Commun. Mass Spectrom. 18*, 87−95.

(23) Balentová, E., Imrich, J., Bernát, J., Suchá, L., Vilková, M., Prónayová, N., Kristian, P., Pihlaja, K., and Klika, K. D. (2006) Stereochemistry, tautomerism, and reactions of acridinyl thiosemicarbazides in the synthesis of 1,3-thiazolidines. *J. Heterocycl. Chem. 43*, 645−656.

(24) Dias, N., Jacquemard, U., Baldeyrou, B., Lansiaux, A., Goossens, J. F., Bailly, C., Routier, S., and Merour, J. Y. (2005) Synthesis of 2,6-diphenylpyrazine derivatives and their DNA binding and cytotoxic properties. *Eur. J. Med. Chem. 40*, 1206−1213.

(25) Joseph, J., Kuruvilla, E., Achuthan, A. T., Ramaiah, D., Schuster, G. B. (2004) Tuning of intercalation and electron-transfer processes between DNA and acridinium derivatives through steric effects. *Bioconjugate Chem. 15*, 1230−1235.

BC060168V

Synthesis of Cetuximab-Immunoliposomes via a Cholesterol-Based Membrane Anchor for Targeting of EGFR

Xiaogang Pan,[†,‡] Gong Wu,[§] Weiliang Yang,[§] Rolf F. Barth,[§,⊥] Werner Tjarks,[||,⊥] and Robert J. Lee*[,†,‡,⊥]

Division of Pharmaceutics, College of Pharmacy, NSF Nanoscale Science and Engineering Center (NSEC), Center for Affordable Nanoengineering of Polymeric Biomedical Devices (CANPBD), Department of Pathology, Division of Medicinal Chemistry and Pharmacognosy, College of Pharmacy, and NCI Comprehensive Cancer Center (CCC), The Ohio State University, Columbus, Ohio. Received June 18, 2006; Revised Manuscript Received October 5, 2006

The objective of the present study was to construct epidermal growth factor receptor (EGFR) targeting cetuximab-immunoliposomes (ILs) for targeted delivery of boron compounds to EGFR(+) glioma cells for neutron capture therapy. The ILs were synthesized by using a novel cholesterol-based membrane anchor, maleimido-PEG-cholesterol (Mal-PEG-Chol), to incorporate cetuximab into liposomes by either surface conjugation or a post-insertion method. For post-insertion, the transfer efficiency of MAb conjugates from micelles to liposome was examined at varying temperatures, $mPEG_{2000}$-DSPE ratios, and micelle-to-liposome lipid ratios. Following this, the cetuximab-ILs were evaluated for targeted delivery of the encapsulated boron anion, dodecahydro-*closo*-dodecaborate (2−) ($B_{12}H_{12}^{2-}$), to human EGFR gene transfected $F98_{EGFR}$ glioma cells as potential delivery agents for boron neutron capture therapy (BNCT). In addition, cellular uptake of cetuximab-ILs, encapsulating a fluorescence dye, was analyzed by confocal fluorescence microscopy and flow cytometry, and boron content was quantified by ICP−MS. Much greater (∼8-fold) cellular uptake of boron was obtained using cetuximab-ILs in EGFR(+) $F98_{EGFR}$ compared with nontargeted human IgG-ILs. On the basis of these observations, we have concluded that cholesterol can serve as an effective anchor for MAb in liposomes, and cetuximab-ILs are potentially useful delivery vehicles for BNCT of gliomas.

INTRODUCTION

Boron neutron capture therapy (BNCT) is a binary therapeutic modality based on tumor-selective delivery of boron-10 followed by external radiation with low energy (e.g., ∼0.025 keV) thermal neutrons. The resulting neutron capture and fission reactions produces high linear energy transfer (LET) α-particles and recoiling ^{7}Li nuclei ($^{10}B + {}^{1}n \rightarrow [{}^{11}*B] \rightarrow {}^{4}He\ (\alpha) + {}^{7}Li +$ 2.39 MeV), which are highly lethal to both proliferating and nonproliferating cells. Currently, BNCT primarily has been used to treat high-grade brain tumors, such as glioblastoma multiforme (GBM) and anaplastic astrocytomas (AA) (*1*−*3*). The efficacy of BNCT is highly dependent upon the selective delivery of a sufficient amount of ^{10}B (∼20 μg/g tumor) to tumor cells to sustain a lethal ^{10}B (n, α)^{7}Li capture reaction (*4*, *5*).

Liposomes, which are spherical vehicles formed by a phospholipid bilayer, are attractive drug carriers due to their biocompatibility and capacity to carry both hydrophobic and hydrophilic drugs (*6*, *7*). Encapsulation of drugs into liposomes significantly alters their pharmacokinetics and biodistribution, which may result in reduced toxicity and an expanded therapeutic window. Nontargeted liposomes rely on "passive targeting" to accumulate in solid tumors due to their porous vascular endothelium, reduced lymphatic drainage, and the resulting enhanced permeability and retention (EPR) effect (*8*, *9*). In order to increase tumor-specific delivery, liposomes can be linked to tumor targeting ligands (*10*) such as antibodies to produce immunoliposomes (ILs) (*11*, *12*), receptor ligands such as folate, transferrin, and epidermal growth factor (EGF)-liposomes (*13*, *14*), as well as peptides such as RGD-liposomes (*15*, *16*).

The EGF receptor (EGFR) frequently is overexpressed in GBM and AA but is undetectable or weakly expressed in the normal brain (*17*, *18*). Therefore, EGFR is an attractive molecular target for the specific delivery of therapeutic agents to high-grade gliomas. Delivery of ^{10}B-containing agents via liposomes conjugated to the anti-EGFR monoclonal antibody (MAb) cetuximab (C225) and L8A4, which is directed against $EGFR_{vIII}$, is an attractive approach for BNCT because of their high payload capacity (*4*, *19*). The use of EGFR-targeting boron-containing bioconjugates as delivery agents for BNCT of brain tumors has been a major focus of our laboratories (*4*, *19*−*22*). Highly boronated polyamidoamine (PAMAM) dendrimers have been linked to either EGF (*19*), cetuximab (*22*), or L8A4 (*23*) for targeted delivery of ^{10}B to gliomas. In order to bypass the blood−brain barrier, the bioconjugates have been administered by either direct intratumoral (i.t.) injection (*19*) or by convection-enhanced delivery (CED) (*21*, *23*). These studies, carried out in rats bearing either EGFR or $EGFR_{vIII}$ human gene transfected rat gliomas, designated $F98_{EGFR}$ or $F98_{EGFRvIII}$, respectively, have resulted in a doubling or tripling of the mean survival times (MST) compared to untreated control animals, thereby establishing *proof-of-principle* for the use of these agents.

To construct ILs, antibodies can be linked to the liposome surface via noncovalent or covalent coupling (*10*). Noncovalent coupling usually is accomplished by using biotinylated antibodies, which are bound to avidin-derivatized liposomes (*25*,

* Author to whom correspondence should be addressed: Robert J. Lee, Ph.D., The Ohio State University, College of Pharmacy, Division of Pharmaceutics, 500 W 12th Ave., Columbus, Ohio 43210; Tel: 614-292-4172; Fax: 614-292-7766; E-mail: lee.1339@osu.edu.

† Division of Pharmaceutics, College of Pharmacy.

‡ NSF Nanoscale Science and Engineering Center (NSEC), Center for Affordable Nanoengineering of Polymeric Biomedical Devices (CANPBD).

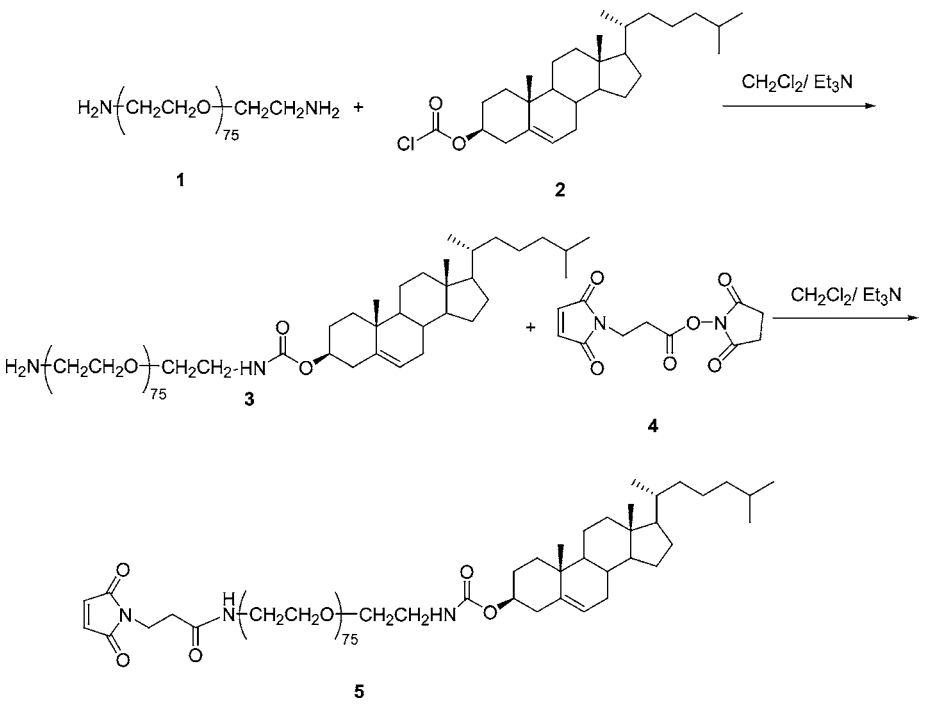
§ Department of Pathology.

|| Division of Medicinal Chemistry and Pharmacognosy, College of Pharmacy.

⊥ NCI Comprehensive Cancer Center (CCC).

10.1021/bc060174r CCC: $37.00 © 2007 American Chemical Society
Published on Web 12/21/2006

Scheme 1. Synthetic Scheme for Mal-PEG-Chol



26). Covalent coupling utilizes a variety of bioconjugation techniques, such as the forming of thioether, disulfide, or amide bonds between lipids and the antibody molecules (*27*). In general, antibodies can be directly linked to liposomes through covalent conjugation to functional groups on the liposome surface (*28*), or they can be post-inserted into preformed liposomes via micelles of an antibody−lipid conjugate (*29*, *30*).

Liposomes typically consist of phospholipids and cholesterol, both of which are potentially suitable for anchoring receptor-targeting ligands to its lipid bilayer. For example, both phospholipid- and cholesterol-anchored folate (folate-PEG-DSPE, folate-PEG-Chol) have been used in the preparation of folate receptor targeted liposomes (*31*, *32*). In this report, we have evaluated a new cholesterol derivative, maleimido-PEG-cholesterol (Mal-PEG-Chol), for the anchoring of cetuximab (C225) in ILs. Furthermore, the EGFR-targeting efficiency and subsequent internalization of the C225-ILs by the EGFR overexpressing $F98_{EGFR}$ cells have been determined both by fluorescence microscopy and by flow cytometry. Our results, described in detail in the following report, have demonstrated that ILs potentially could be useful delivery vehicles for BNCT of gliomas.

EXPERIMENTAL PROCEDURES

Materials. Hydrogenated soy phosphatidylcholine (HSPC), methoxy-poly(ethylene glycol)$_{2000}$-phosphatidylethanolamine ($mPEG_{2000}$-DSPE), were purchased from Avanti Polar Lipids (Alabaster, AL). Cholesterol (Chol), cholesteryl chloroformate, sheep IgG, 2-iminothiolane (Traut's reagent), mercaptoethylamine·HCl (MEA), ninhydrin, PEG_{3350}-bis-amine, 4-(2-hydroxyethyl)-1-piperazine ethanesulfonic acid (HEPES), 8-hydroxypyrenetrisulfonic acid trisodium salt (HPTS), Sepharose CL-4B resin, and triethylamine (TEA) were purchased from Sigma-Aldrich Co. (St. Louis, MO). Octadecylrhodamine B (R18) was purchased from Molecular Probes (Eugene, OR). Dilithium-dodecahydro-*closo*-dodecaborate ($Li_2B_{12}H_{12}$) was obtained as a gift from Callery Chemical Company (Pittsburgh, PA). DMEM, fetal bovine serum (FBS), and antibiotics were purchased from Life Technologies (Grand Island, NY). Sephadex LH20 resin and PD-10 desalting columns were purchased from GE Healthcare (Piscataway, NY). Bradford protein assay kit and *N*-[β-maleimidopropyloxy]succinimide ester (BMPS) were purchased from Peirce Chemical Co. (Rockford, IL). Polycarbonate membranes were obtained from Avestin, Inc. (Ottawa, ON, Canada). Cetuximab (C225) was generously provided by Dr. Daniel Hicklin at ImClone Systems, Inc. (New York, NY). All other chemicals were of reagent grade.

Cell Culture. Parental (wild-type) $F98_{WT}$ glioma cell line (*33*) and human EGFR gene transfected $F98_{EGFR}$ glioma cell lines, expressing 10^5 receptor sites per cell (*19*), were cultured as a mononlayer in DMEM media supplemented with 100 units/mL penicillin, 100 μM/mL streptomycin, 200 mg/mL of Geneticin, and 10% FBS in a humidified atmosphere containing 5% CO_2 at 37 °C.

Synthesis of Maleimido-PEG-Cholesterol (Mal-PEG-Chol) (5). The synthetic scheme for of Mal-PEG-Chol (**5**) is shown in Scheme 1. PEG_{3350}-bis-amine (**1**) (335 mg, 0.1 mmol) was dissolved in anhydrous CH_2Cl_2 (30 mL) and TEA (14 μL, 0.1 mmol). Then, cholesteryl chloroformate (**2**) (49 mg, 0.11 mmol, 1.1 equiv), also dissolved in anhydrous CH_2Cl_2 (2 mL), was slowly added. After 4 h reaction at room temperature, thin layer chromatography (TLC) analysis (mobile phase $CHCl_3$/MeOH/H_2O at 3:1:0.2, visualized with ninhydrin and $KMnO_4$ staining) indicated the formation of dicholesteryl (Chol-PEG-Chol) (R_f = 0.65), monocholesteryl (Chol-PEG-NH_2) (**3**) (R_f = 0.47), and unreacted PEG-bis-amine (R_f = 0.12). The reaction mixtures were separated by silica gel column chromatography using a step gradient of methanol (0−20%) in chloroform. The fractions containing monocholesteryl PEG (Chol-PEG-NH_2) (**3**) were pooled and evaporated to dryness under vacuum to yield 56% product. The MALDI mass spectrum of (**3**) showed a series of 44-Da spaced lines, corresponding to the mass of a single ethylene oxide unit, that were centered around 3819. ^{1}H NMR ($CDCl_3$, 300 MHz) δ (ppm): 5.31 (d, 1H), 4.68 (m, 1H), 3.70−3.50 (br, m, PEG protons, ∼320H), 2.46 (d, 2H), 2.04−1.05 (m, Chol protons, ∼26H), 1.00 (s, 3H), 0.91 (d, 3H), 0.86 (d, 6H), 0.683 (s, 3H).

Monocholesteryl PEG (**3**) (30 mg, 7.9 μmol) and BMPS (**4**) (3.2 mg, 11.8 μmol, 1.5 equiv) were dissolved in anhydrous CH_2Cl_2 (20 mL) under N_2 and under darkness. After 1 h,

ninhydrin assay showed the disappearance of the free primary amine group. The reaction was quenched by ethylenediamine, and the reaction mixture was concentrated on a rotary evaporator and then passed through a Sephadex LH20 column, using CH_2Cl_2/MeOH (1:1 v/v) as the mobile phase. Fractions containing product Mal-PEG-Chol (**5**) (identified by $KMnO_4$ staining) were pooled and dried by rotary evaporation. The yield was 93%. Analytical data for (**5**): MALDI showed cluster of peaks centered around 3992. ^{1}H NMR ($CDCl_3$, 300 MHz) δ (ppm): 6.70 (s, 2H), 5.31 (d, 1H), 4.68 (m, 1H), 3.80−3.50 (br, m, PEG protons, ∼312H), 2.46 (d, 2H), 2.04−1.00 (m, Chol protons, ∼26H), 0.99 (s, 3H), 0.90 (d, 3H), 0.85 (d, 6H), 0.663 (s, 3H).

Preparation of Immunoliposomes. *Liposome Preparation.* Unilamellar liposomes were prepared by the polycarbonate membrane extrusion method (*34*). A chloroform solution of lipids consisting of HSPC/Chol/$mPEG_{2000}$-DSPE (60:40:1−4 mol %), with or without Mal-PEG-Chol (0.5 mol %), was dried into a thin film in a round-bottom flask on a rotary evaporator and then further dried for 2 h under vacuum. The resulting thin lipid film was hydrated in 1 mL of a solution of fluorescent dye HPTS (25 mM, in PBS, pH 7.4). The resulting suspension was subjected to five cycles of freezing and thawing and extruded five times through a track-etched polycarbonate membrane with a pore size of 100 nm using a Lipex Extruder (Northern Lipids, Vancouver, Canada). Unentrapped HPTS was separated from liposomes by gel filtration on a 10 mL PD-10 desalting column equilibrated in PBS (pH 7.4). Liposome size was determined by dynamic light scattering on a Nicomp Particle Sizer model 370. The mean liposome diameter obtained by this method was 106.1 ± 35.6 nm by volume-weighted averaging. The phospholipid content was measured using a colorimetric assay (*35*). The liposomes were stored at 4 °C until use.

For boron uptake studies, dodecahydro-*closo*-dodecaborate (2−) ($B_{12}H_{12}^{2-}$) (50 mM) was encapsulated in liposomes by the extrusion method described above. The boronated liposomes were sterilized by passing through a 0.22 μm filter and stored at 4 °C.

Construction of C225-ILs. ILs were constructed by conjugation with either an intact MAb or an Fab′ fragment. MAb (IgG, as nontargeting control MAb, and C225, as the targeting MAb) were thiolated for 1 h at room temperature by reacting with 5-fold excess of Traut's reagent in degassed HEPES buffer (20 mM HEPES, 140 mM NaCl, 2 mM EDTA, pH 8.0). Unreacted Traut's reagent was removed by PD-10 column and eluted with degassed HEPES buffer (pH 6.5). The thiolated MAb was stored at 4 °C and used within 1 h of preparation.

For direct coupling of MAb to liposomes, thiolated MAb (or Fab′ fragment) was added to preformed liposomes (HSPC/Chol/$mPEG_{2000}$-DSPE/Mal-PEG-Chol at 60:40:2:0.5 mole ratio) at 40 μg MAb per micromole of lipids, and then gently shaken at room temperature for 4 h under N_2. Excess maleimide groups were quenched by incubation with MEA (1 mM) for 30 min at room temperature. Unbound MAb and MEA were then removed by Sepharose CL-4B gel filtration. A Bradford protein assay was performed to determine the coupling efficiency (*36*).

Fab′ fragments of C225 were produced, as described by Mamot et al. (*37*). Briefly, intact C225 was digested with pepsin (at a C225 to pepsin weight ratio of 1:20) in 0.1 M sodium citrate buffer (pH 4.5) at 37 °C for 4 h, followed by dialysis against HEPES buffer (pH 6.5). The resulting C225-F(ab)$_2$ fragment was reduced by MEA (15 mM) under N_2 for 15 min and then purified by PD-10 gel filtration.

ILs also were constructed by the post-insertion method. First, liposomes composed of HSPC/Chol (60:40, mole ratio) and varying amounts of $mPEG_{2000}$-DSPE were prepared by extrusion, as described above. To synthesize MAb−lipid micelle conjugate, Mal-PEG-Chol was dissolved in chloroform and dried into a thin film in a round-bottom flask on a rotary evaporator and then further dried overnight under vacuum. The lipid film was then rehydrated with degassed HEPES buffer (pH 6.5) at a concentration above the critical micelle concentration (cmc) of Mal-PEG-Chol with gentle vortexing, followed by incubation at 60 °C. Mal-PEG-Chol micelles were mixed with thiolated MAb (or Fab′ fragment) at 40 μg MAb (or 80 μg Fab′) per microgram of lipid and gently shaken for 4 h at room temperature. This was followed by quenching of free thiols by MEA (1 mM) and PD-10 gel filtration. The resulting MAb-PEG-Chol micelles were evaluated for efficiency of MAb transfer into preformed liposomes under varying conditions, including temperatures (37 °C and 60 °C), percentages of $mPEG_{2000}$-DSPE (1, 2, 3, and 4 mol %), and micelle-to-liposome lipid ratios (up to 1:10). Unincorporated MAb-PEG-Chol micelles were separated from ILs by Sepharose CL-4B gel filtration. Bradford protein assays were performed to determine the antibody content of ILs which enabled calculation of incorporation efficiency.

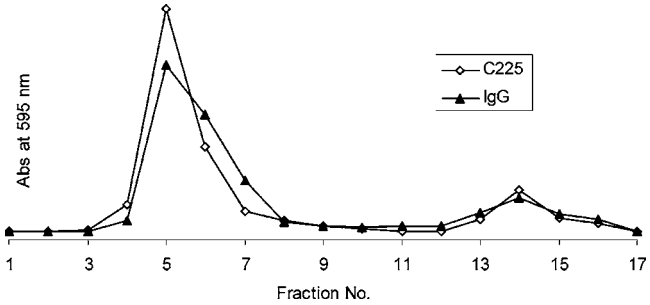


Figure 1. Elution profiles of ILs constructed with Mal-PEG-Chol and unbound MAbs. The reaction mixture was loaded onto a Sepharose CL-4B gel filtration column and eluted with PBS (pH 7.4). The peak in fractions 4−8 represents the C225 or IgG ILs. Fractions 12−17 are free, unbound C225 and IgG. Each fraction contained 0.5 mL. The protein content was measured by Bradford protein assay, which measures absorbance at 595 nm.

Binding and Internalization of Liposomes. $F98_{EGFR}$ and $F98_{WT}$ cells, cultured as monolayers in T75 flasks, were harvested by treatment with PBS containing 5 mM EDTA. The detached cells were pelleted by centrifugation at 1000 rpm for 5 min, resuspended in serum-supplemented media at a density of 2.5×10^5 cell/mL, and then aliquoted into 1.5-mL microcentrifuge tubes. Cells were incubated for 2 h at 37 °C under gentle shaking with either targeted or nontargeted ILs (at 5 μM phospholipid concentration) encapsulating HPTS. After washing three times with PBS (pH 7.4), the cells were kept on ice and subjected to flow cytometric analysis on a BD FACS Calibur analyzer and visualization by laser scanning confocal microscopy on a Zeiss 510 META microscope.

Kinetic analysis of cell surface bound and endocytosed ILs was performed as described previously (*12*, *38*). $F98_{EGFR}$ glioma cells were incubated with HPTS-loaded C225-ILs for 2 h at 37 °C, washed with ice-cold PBS, and then harvested with PBS-EDTA. Due to the pH sensitivity of HPTS and the relatively low internal pH of endosomes (pH 4−5), surface binding and internalization of ILs were quantified on the basis of measurement of the ratio between fluorescence intensity at excitation wavelengths (λ_{ex}) of 413 nm (isosbestic point) and 454 nm.

For quantitation of boron uptake, $F98_{EGFR}$ glioma cells (10^6 cells/mL) were incubated with IgG or C225 ILs, prepared by post-insertion method, encapsulating $Li_2B_{12}H_{12}$ for 2 h at 37 °C. These liposomes had 144 and 117 μg boron/mL and mean diameters of 135.6 ± 41.5 and 126.8 ± 39.5 nm, respectively. After washing with PBS (pH 7.4) three times, the cells were subjected to boron content analysis by inductively coupled

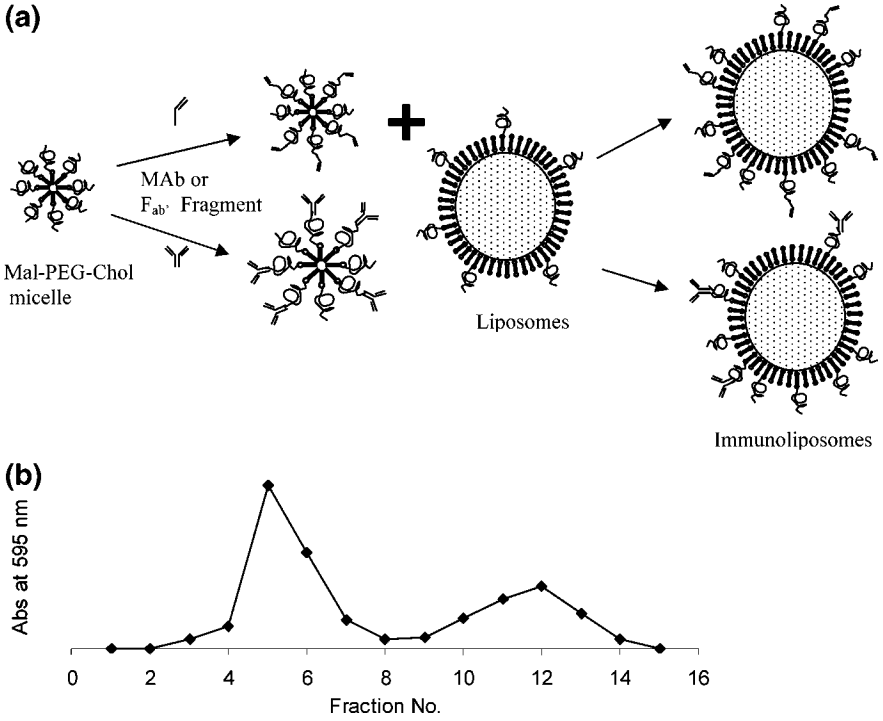


Figure 2. Post-insertion method for IL construction. (a) Schematic representation of post-insertion method for IL construction. Antibodies or antibody fragments are coupled to micelles formed by Chol-PEG-Mal and then incubated with preformed boron-loaded liposomes to form ILs. (b) A typical elution profiles of IgG-ILs constructed by post-insertion method at 60 °C for 1 h. IgG micelles were formed by coupling thiolated IgG with Mal-PEG-Chol micelles. After post-insertion, the mixture was loaded onto a Sepharose CL-4B gel filtration column and eluted with PBS (pH 7.4). The peak of fractions 4−7 represents the IgG-ILs. Fractions 9−14 are IgG−lipid micelles. Each fraction contained 0.5 mL. The protein content was measured by Bradford protein assay, which measures absorbance at 595 nm.

plasma mass spectroscopy (ICP−MS) on a Perkin-Elmer Sciex ELAN 6000.

RESULTS

Synthesis of Immunoliposomes (ILs). *Direct Coupling.* Liposomes, composed of HSPC/Chol/PEG-DSPE/Mal-PEG-Chol (60:35:5:0.5, mol %), were prepared by the lipid hydration and extrusion method and had a mean diameter of ∼100 nm. Thiolated antibodies (IgG and C225) were reacted with the maleimide group on the distal termini of PEG chains on these liposomes to form thioether linkages, yielding ∼25−35 μg MAb per micromole of lipid (Figure 1).

Post-insertion. The cmc of Mal-PEG-Chol was evaluated by monitoring changes in turbidity via OD at 254 nm, as previously described (*39*). Regression analysis indicated that micelles were formed at 2 μM (data not shown). To investigate whether micelles, formed by MAb conjugates with cholesterol anchors, could be incorporated into preformed liposomes, their transfer efficiency was examined at varying incubation temperatures, $mPEG_{2000}$-DSPE contents in the liposome, and micelle-to-liposome lipid ratios (Figure 2a). Sepharose CL-4B gel filtration chromatography was used to determine the amount of MAb incorporated into liposomes. Unincorporated micelles were eluted in a broad peak, which was well-separated from ILs that were eluted in the void volume (Figure 2b).

The incorporation of MAb into preformed liposomes was determined at 37 °C and at 60 °C. The incorporation rate at 60 °C was higher than that at 37 °C (Table 1). This was expected, since 60 °C is above the transition temperature of the bilayer, which would facilitate lipid transfer. Concomitantly, the mean diameters of the particles also were increased at 60 °C, possibly due to lipid exchange (Table 1).

The presence of $mPEG_{2000}$-DSPE, which sterically stabilized the liposomes, adversely affected the incorporation efficiency of the MAb (Table 1). The higher the $mPEG_{2000}$-DSPE content of the liposomes, the lower the efficiency of MAb insertion into the liposomes. In liposomes containing 4 mol % of $mPEG_{2000}$-DSPE, the insertion of MAb was significantly inhibited, even at 60 °C. In contrast, MAb insertion efficiency was minimal at 37 °C, when $mPEG_{2000}$-DSPE content exceeded 2 mol %.

Saturation of MAb insertion was observed at high micelle-to-liposome lipid ratios. The percent of MAb incorporation at the ratio of 1:30 was close to that at the ratio of 1:10 (Table 2), which indicated that incorporation had essentially reached a

Table 1. Increase in IL Size and IgG-PEG-Chol Incorporation Efficiency at Different $mPEG_{2000}$-DSPE Content[a]

mol % of $mPEG_{2000}$-DSPE in liposomes	particle size increase %		MAb insertion efficiency %	
	60 °C	37 °C	60 °C	37 °C
1	28	18	75	23
2	24	9	58	18
3	19	7	53	8
4	6	4	35	3

[a] Unilamellar preformed liposomes composed of HSPC/Chol (60:40, mole ratio) and various $mPEG_{2000}$-DSPE (1, 2, 3, and 4 mol %) were prepared by thin film hydration-extrusion, as described in the Experimental Procedures section. Micelles were incubated with liposome (1:30, lipid molar ratio) for 1 h at 37 °C or 60 °C.

Table 2. Effect of Micelle-to-Liposome Lipid Ratio on IgG-PEG-Chol Incorporation into Preformed Liposomes[a]

micelle-to-liposome lipid molar ratio	% Mab incorporated
1:100	72
1:30	55
1:15	36
1:10	21

[a] The liposomes, composed of HSPC/Chol/$mPEG_{2000}$-DSPE (60:40:2 mole ratio) were incubated with the micelles at 60 °C for 1 h.

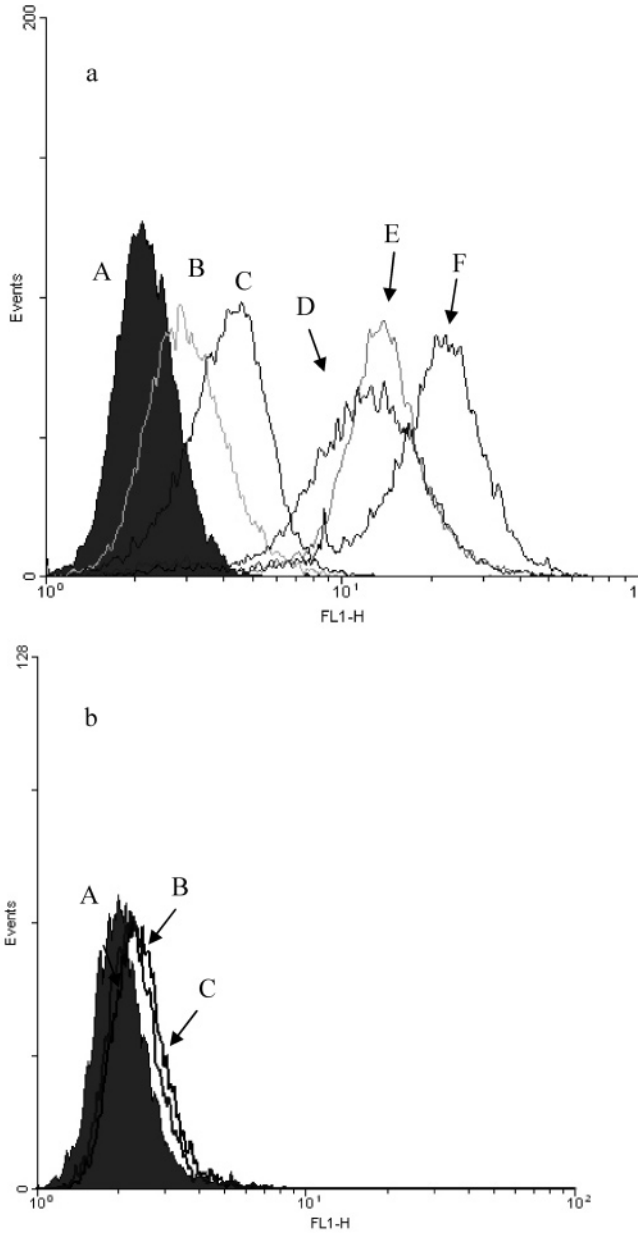


Figure 3. Binding of ILs to $F98_{EGFR}$ cells evaluated by flow cytometric assay. (a) ILs encapsulating HPTS were incubated with cells for 2 h at 37 °C, washed three times, and stored on ice until analysis: (A) untreated $F98_{EGFR}$ cells, (B) IgG-ILs, (C) C225-ILs with free C225 as a blocking agent, (D) C225-ILs prepared by post-insertion method with preformed liposomes containing 2 mol % $mPEG_{2000}$-DSPE, (E) C225-Fab′ ILs constructed by post-insertion with preformed liposomes containing 2 mol % $mPEG_{2000}$-DSPE, and (F) C225-ILs prepared by direct coupling. (b) C225-Fab′ ILs with non-EGFR-expressing $F98_{WT}$ cells: (A) untreated $F98_{WT}$ cells, (B) C225-Fab′ ILs plus free C225, and (C) C225-Fab′ ILs.

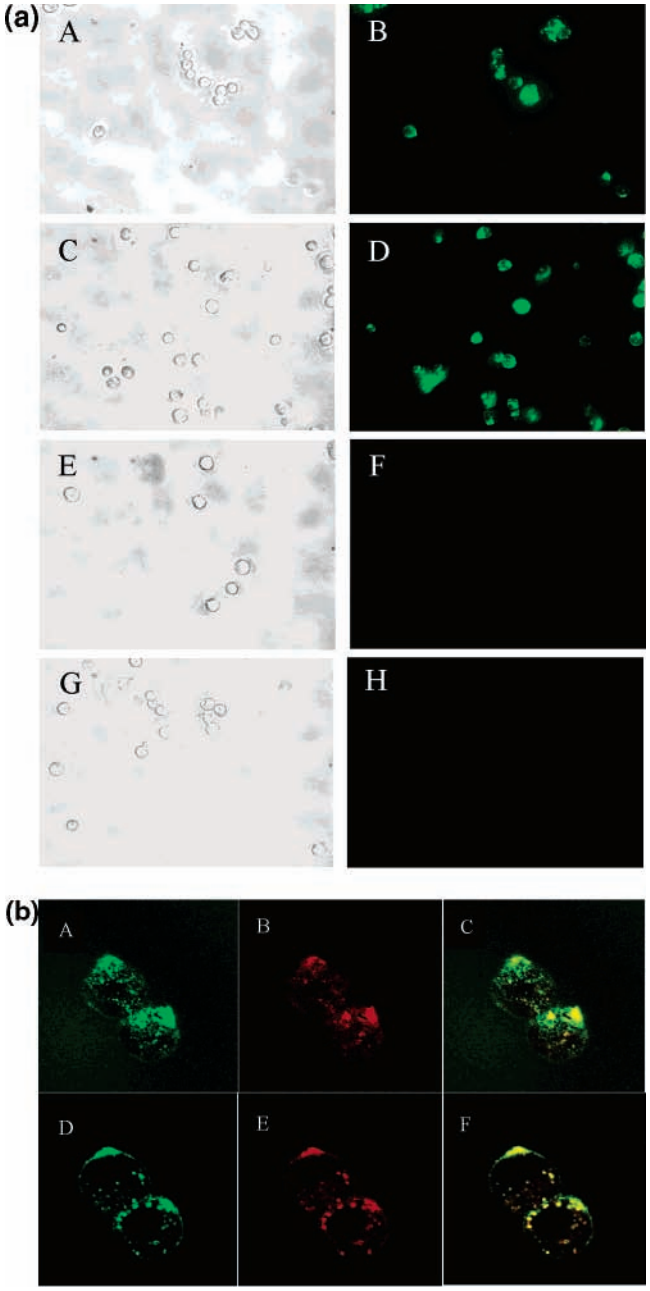


Figure 4. Fluorescence micrographs of F98 cells treated with Ils. (a) Internalization of C225-Fab′ ILs and nontargeted IgG-Fab′ ILs in EGFR-expressing $F98_{EGFR}$ cells. $F98_{EGFR}$ cells were incubated with C225-Fab′ or IgG-Fab′ ILs, containing HPTS fluorescent dye for 2 h at 37 °C. Left panels show cells visualized in the phase contract mode; right panels show cells visualized in the fluorescence mode: (A,B) $F98_{EGFR}$ cells treated with C225-Fab′ ILs constructed by directed coupling; (C,D) $F98_{EGFR}$ cells treated with C225-Fab′ ILs prepared by post-insertion method; (E,F) $F98_{EGFR}$ cells treated with nontargeted IgG-Fab′ ILs; (G,H) $F98_{WT}$ cells with C225-Fab′ ILs. (b) Confocal micrographs of $F98_{EGFR}$ cells incubated with C225-Fab′ ILs constructed by post-insertion method with preformed liposomes containing 2 mol % $mPEG_{2000}$-DSPE. The ILs were loaded with HPTS and labeled with R18. Left column, green HPTS fluoresence; central column, red rhodamine fluorescence; right column, superimposed images. (A−C) Top-view image showing cell surface-bound liposomes; (D−F) central stack image showing liposomes accumulated in the endosomal compartments.

plateau. The micelles of Fab′ also were prepared by the same method, and the incorporation rate was close to that of the whole MAb. Approximately 60% C225-Fab′ was transferred to liposomes containing 2 mol % of $mPEG_{2000}$-DSPE with micelle-to-liposome lipid ratio of 1:30, following incubation at 60 °C for 1 h.

Cellular Binding and Internalization. Cellular binding and internalization of ILs were evaluated by flow cytometry in $F98_{WT}$ and $F98_{EGFR}$ rat glioma cells. In this study, IgG-ILs and C225-ILs, constructed by direct coupling or by the post-insertion method, were loaded with fluorescent dye HPTS and incubated with the cells for 2 h at 37 °C. The uptake of C225-ILs was 10-fold higher than that of the nontargeted IgG-ILs. In a competitive binding assay, free C225 was added, which significantly reduced binding of C225-ILs by $F98_{EGFR}$ cells (Figure 3a). Both directly coupled and post-inserted C225 in the liposomes appeared to greatly increase liposome binding to EGFR-expressing $F98_{EGFR}$ cells but not to $F98_{WT}$ cells. Mean-

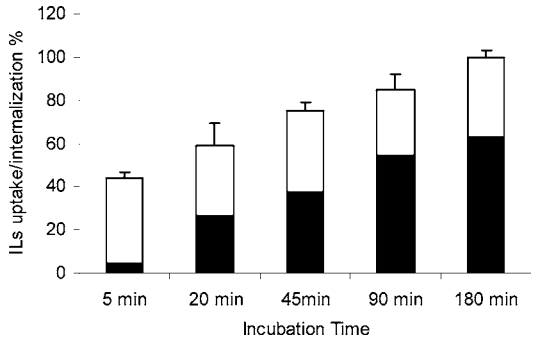


Figure 5. Kinetics of C225-Fab′ IL internalization in the EGFR overexpressing $F98_{EGFR}$ cells. C225-Fab′ ILs were constructed by post-insertion method with preformed liposomes containing 2 mol % $mPEG_{2000}$-DSPE and loaded with pH-sensitive dye HPTS and incubated with $F98_{EGFR}$ cells at 37 °C. At various time points, the sample was analyzed by measuring the fluorescence intensity at excitation wavelengths of 454 and 413 nm. Surface-bound fraction □; internalized fraction ■. The 180 min time point was set at 100%; $n = 3$.

while, C225-Fab′ liposomes, constructed by the post-insertion method, were evaluated using $F98_{WT}$ and $F98_{EGFR}$ cells. The C225-Fab′ containing liposomes showed extensive binding to $F98_{EGFR}$ cells but minimal binding to $F98_{WT}$ cells (Figure 3b). These results clearly demonstrated selective uptake of anti-EGFR ILs between two congenic cell lines based on differing EGFR expression levels.

Confocal fluorescence microscopy was used to visualize the binding and subsequent intracellular localization of C225-Fab′ ILs by F98 cells. $F98_{EGFR}$ cells, incubated with ILs prepared by either direct coupling or the post-insertion method, both showed high levels of fluorescence. In contrast, cells exposed to nontargeted IgG-Fab′ ILs showed little fluorescence (Figure 4a, A−F). Finally, the C225-Fab′ ILs did not show significant binding to non-EGFR expressing $F98_{WT}$ cells (Figure 4a, G and H). Overall, the results of the confocal fluorescence microscopy studies were consistent with those of the flow cytometric assays.

C225-Fab′ liposomes, containing 2 mol % PEG_{2000}-DSPE prepared by the post-insertion method, were loaded with pH-sensitive fluorophore HPTS in the aqueous core and labeled with octadecyl rhodamine B (R18) (0.5 mol %) in the lipid bilayer. These liposomes were incubated with $F98_{EGFR}$ cells for 2 h at 37 °C. Fluorescence was distributed throughout the cell, including cell plasma membrane, intracellular vesicles, and the cytosol (Figure 4b). Superimposition of fluorescence images based on HPTS and R18 indicated that the fluorescence was not due to HPTS leakage or R18 lipid exchange.

The pH sensitivity of the HPTS absorption spectrum allowed for the simultaneous analyses of both surface-bound (neutral pH) and endosome-localized (low pH) liposomes based on the I445/413 nm excitation ratios. C225-Fab′ liposomes bound to $F98_{EGFR}$ cells were detected within 5 min of incubation. Meanwhile, intracellular accumulation was observed within 20 min (Figure 5). The results clearly showed increasing lysosomal uptake of the liposomes over a 3-h incubation period.

For quantitative analysis of boron uptake, boron-loaded C225-ILs delivered ∼8 times more boron (509.75 ± 148.85 μg B/10^9 F98 cells) to $F98_{EGFR}$ cells than nontargeted IgG-ILs (61.00 ± 1.76 μg B/10^9 F98 Cells), greatly exceeding the required level of boron (∼20 μg/g tissue) for NCT (*1*).

DISCUSSION

A novel cholesterol-based anchor (Mal-PEG-Chol (**5**)) has been synthesized for the attachment of receptor-targeting ligands to the lipid bilayer of liposomes. Factors affecting post-insertion efficiency, in vitro targeting, internalization of IgG-ILs, anti-EGFR C225-ILs, C225-Fab′-ILs, and their drug carrying capacity were evaluated in EGFR(−) $F98_{wt}$ and EGFR overexpressing $F98_{EGFR}$ cells. Functionalization of liposomes with receptor-targeting ligands previously had been carried out by using phosphatidylethanolamine (PE) derivatives as anchors to the lipid bilayer. These have included Mal-PEG-DSPE, Hz-PEG-DSPE, and PDP-PEG-DSPE (*40*). Cholesterol, which is less expensive than PE-based lipids, is a major component of the biological membranes. PEG-Chol derivatives have been used for the preparation of sterically stabilized liposomes with long circulating time (*41*). We previously prepared a cholesterol-based folate conjugate, folate-PEG-Chol, which was successfully used for the construction of folate receptor targeted liposomes (*32*). Carrion et al. have used cholesterol derivatized with SPDP for the preparation of ILs (*42*). The present data have clearly demonstrated that cholesterol is an attractive alternative to PE as an effective lipid anchor for the construction of ILs. The strategy for the synthesis of Mal-PEG-Chol (**5**) from readily available starting materials is simple and efficient. The maleimide group in the cholesterol derivative proved to be especially useful for conjugation to Fab′ fragments, which contain a free thiol group. Moreover, MAbs-PEG-Chol in micelles was found to be efficiently incorporated into preformed liposomes during post-insertion, which is a convenient method for the construction of targeted liposomes.

The use of C225-ILs as ^{10}B delivery vehicles for BNCT of GBM is particularly attractive due to the potential synergy between the high LET radiation produced in the ^{10}B (n, α)^{7}Li neutron capture and the potential signal transduction cascade that ILs upon multivalent binding of the ILs to the cellular EGFRs. Therefore, C225-ILs also were evaluated in vitro as boron delivery vehicles with EGFR expressing $F98_{EGFR}$ glioma cells. The excellent cell-targeting capabilities of anti-EGFR ILs was demonstrated by fluorescence microscopy and flow cytometry. Nontargeted IgG-ILs showed only minimal fluorescence, while C225-ILs showed preferential binding and internalization by $F98_{EGFR}$ cells, which was indicative of EGFR-specific binding and subsequent endocytosis. Another important feature of ILs as boron delivery vehicles was their ability to selectively target only those cells overexpressing EGFR, which was demonstrated by the low binding and uptake by $F98_{WT}$ cells. In the present study, the boron-rich compound, dodecaborate anion ($B_{12}H_{12}^{2-}$) was used. This previously has been encapsulated in RGD-liposomes for the delivery of ^{10}B to human umbilical vein endothelial cells (HUVEC) (*16*). In the present study, boronated C225-ILs delivered 509.75 ± 148 μg ^{10}B per 10^9 (∼1 g) $F98_{EGFR}$ cells, which was ∼8 times greater than the amount delivered by nontargeted IgG-liposomes. This exceeded the therapeutically required amount of ^{10}B (∼20 μg/g tissue).

In conclusion, our studies have demonstrated that both MAbs and Fab′ fragments could be efficiently linked to Mal-PEG-Chol. The resulting MAb and Fab′-PEG-Chol bioconjugates could be efficiently incorporated into preformed liposome to yield ILs by the post-insertion method. C225-ILs were internalized by EGFR overexpressing $F98_{EGFR}$ cells in vitro, presumably by receptor-mediated endocytosis, resulting in the selective and efficient intracellular delivery of boron. This approach could also be applied to the delivery of other therapeutic agents to EGFR-positive tumor cells. In vivo studies are planned to further explore the tumor-targeting potential of anti-EGFR ILs for potential use for BNCT and stereotactic synchrotron radiotherapy (*43*, *44*).

ACKNOWLEDGMENT

This work was supported in part by NSF grant EEC-0425626 and NIH grants I RO1-CA098945 (to R.F. Barth) and P30CA16058.

LITERATURE CITED

(1) Barth, R. F., Coderre, J. A., Vicente, M. G., and Blue, T. E. (2005) Boron neutron capture therapy of cancer: current status and future prospects. *Clin. Cancer Res. 11*, 3987−4002.

(2) Barth, R. F. (2003) A critical assessment of boron neutron capture therapy: an overview. *J. Neurooncol. 62*, 1−210.

(3) Zamenhof, R. G., Coderre, J. A., Rivard, M. J., and Patel, H. (2004) Topics in neutron capture therapy. Proceedings of the eleventh world congress on neutron capture therapy. *Appl. Radiat. Isot. 61*, 731−1130.

(4) Wu, G., Barth, R. F., Yang, W., Lee, R. J., Tjarks, W., Backer, M. V., and Backer, J. M. (2006) Boron containing macromolecules and nanovehicles as delivery agents for neutron capture therapy. *Anticancer Agents Med. Chem. 6*, 167−84.

(5) Vicente, M. G. H. (2006) Boron in medicinal chemistry. *Anticancer Agents Med. Chem. 6*, 73−181.

(6) Pan, X. Q., Wang, H., Shukla, S., Sekido, M., Adams, D. M., Tjarks, W., Barth, R. F., and Lee, R. J. (2002) Boron-containing folate receptor-targeted liposomes as potential delivery agents for neutron capture therapy. *Bioconjugate Chem. 13*, 435−42.

(7) Sudimack, J. J., Adams, D., Rotaru, J., Shukla, S., Yan, J., Sekido, M., Barth, R. F., Tjarks, W., and Lee, R. J. (2002) Folate receptor-mediated liposomal delivery of a lipophilic boron agent to tumor cells in vitro for neutron capture therapy. *Pharm. Res. 19*, 1502−8.

(8) Jain, R. K. (2001) Delivery of molecular medicine to solid tumors: lessons from in vivo imaging of gene expression and function. *J. Controlled Release 74*, 7−25.

(9) Pan, X., and Lee, R. J. (2004) Tumour-selective drug delivery via folate receptor-targeted liposomes. *Exp. Opin. Drug Delivery 1*, 7−17.

(10) Sapra, P., and Allen, T. M. (2003) Ligand-targeted liposomal anticancer drugs. *Prog. Lipid Res. 42*, 439−62.

(11) Leserman, L. D., Machy, P., and Barbet, J. (1981) Cell-specific drug transfer from liposomes bearing monoclonal-antibodies. *Nature (London) 293*, 226−228.

(12) Kirpotin, D., Park, J. W., Hong, K., Zalipsky, S., Li, W. L., Carter, P., Benz, C. C., and Papahadjopoulos, D. (1997) Sterically stabilized anti-HER2 immunoliposomes: design and targeting to human breast cancer cells in vitro. *Biochemistry 36*, 66−75.

(13) Xu, L., Pirollo, K. F., and Chang, E. H. (1997) Transferrin-liposome-mediated p53 sensitization of squamous cell carcinoma of the head and neck to radiation in vitro. *Hum. Gene Ther. 8*, 467−75.

(14) Bohl Kullberg, E., Bergstrand, N., Carlsson, J., Edwards, K., Johnsson, M., Sjöberg, S., and Gedda, L. (2002) Development of EGF-conjugated liposomes for targeted delivery of boronated DNA-binding agents. *Bioconjugate Chem. 13*, 737−43.

(15) Janssen, A. P., Schiffelers, R. M., ten Hagen, T. L., Koning, G. A., Schraa, A. J., Kok, R. J., Storm, G., and Molema, G. (2003) Peptide-targeted PEG-liposomes in anti-angiogenic therapy. *Int. J. Pharm. 254*, 55−8.

(16) Koning, G. A., Fretz, M. M., Woroniecka, U., Storm, G., and Krijger, G. C. (2004) Targeting liposomes to tumor endothelial cells for neutron capture therapy. *Appl. Radiat. Isot. 61*, 963−7.

(17) Sauter, G., Maeda, T., Waldman, F. M., Davis, R. L., and Feuerstein, B. G. (1996) Patterns of epidermal growth factor receptor amplification in malignant gliomas. *Am. J. Pathol. 148*, 1047−53.

(18) Schwechheimer, K., Huang, S., and Cavenee, W. K. (1995) EGFR gene amplification−rearrangement in human glioblastomas. *Int. J. Cancer 62*, 145−8.

(19) Barth, R. F., Yang, W., Adams, D. M., Rotaru, J. H., Shukla, S., Sekido, M., Tjarks, W., Fenstermaker, R. A., Ciesielski, M., Nawrocky, M. M., and Coderre, J. A. (2002) Molecular targeting of the epidermal growth factor receptor for neutron capture therapy of gliomas. *Cancer Res. 62*, 3159−66.

(20) Wu, G., Barth, R. F., Yang, W., Chatterjee, M., Tjarks, W., Ciesielski, M. J., and Fenstermaker, R. A. (2004) Site-specific conjugation of boron-containing dendrimers to anti-EGF receptor monoclonal antibody cetuximab (IMC-C225) and its evaluation as a potential delivery agent for neutron capture therapy. *Bioconjugate Chem. 15*, 185−94.

(21) Yang, W., Barth, R. F., Wu, G., Ciesielski, M. J., Fenstermaker, R. A., Moffat, B. A., Ross, B. D., and Wikstrand, C. J. (2005) Development of a syngeneic rat brain tumor model expressing EGFRvIII and its use for molecular targeting studies with monoclonal antibody L8A4. *Clin. Cancer Res. 11*, 341−50.

(22) Barth, R. F., Wu, G., Yang, W., Binns, P. J., Riley, K. J., Patel, H., Coderre, J. A., Tjarks, W., Bandyopadhyaya, A. K., Thirumamagal, B. T., Ciesielski, M. J., and Fenstermaker, R. A. (2004) Neutron capture therapy of epidermal growth factor (+) gliomas using boronated cetuximab (IMC-C225) as a delivery agent. *Appl. Radiat. Isot. 61*, 899−903.

(23) Yang, W., Barth, R. F., Wu, G., Kawabata, S., Sferra, T. J., Bandyopadhyaya, A. K., Tjarks, W., Ferketich, A. K., Moeschberger, M. L., Binns, P. J., Riley, K. J., Coderre, J. A., Ciesielski, M. J., Fenstermaker, R. A., and Wikstrand, C. J. (2006) Molecular targeting and treatment of EGFRvIII-positive gliomas using boronated monoclonal antibody L8A4. *Clin. Cancer Res. 12*, 3792−802.

(24) Bobo, R. H., Laske, D. W., Akbasak, A., Morrison, P. F., Dedrick, R. L., and Oldfield, E. H. (1994) Convection-enhanced delivery of macromolecules in the brain. *Proc. Natl. Acad. Sci. U.S.A. 91*, 2076−80.

(25) Phillips, N. C., and Tsoukas, C. (1990) Immunoliposome targeting to CD4+ cells in human blood. *Cancer Detect. Prev. 14*, 383−90.

(26) Schnyder, A., Krahenbuhl, S., Torok, M., Drewe, J., and Huwyler, J. (2004) Targeting of skeletal muscle in vitro using biotinylated immunoliposomes. *Biochem. J. 377*, 61−7.

(27) Park, J. W., Hong, K., Kirpotin, D. B., Papahadjopoulos, D., and Benz, C. C. (1997) Immunoliposomes for cancer treatment. *Adv. Pharmacol. 40*, 399−435.

(28) Zalipsky, S., Hansen, C. B., Lopes de Menezes, D. E., and Allen, T. M. (1996) Long-circulating, polyethylene glycol-grafted immunoliposomes. *J. Controlled Release 39*, 153−161.

(29) Ishida, T., Iden, D. L., and Allen, T. M. (1999) A combinatorial approach to producing sterically stabilized (Stealth) immunoliposomal drugs. *FEBS Lett. 460*, 129−33.

(30) Iden, D. L., and Allen, T. M. (2001) In vitro and in vivo comparison of immunoliposomes made by conventional coupling techniques with those made by a new post-insertion approach. *Biochim. Biophys. Acta 1513*, 207−16.

(31) Lee, R. J., and Low, P. S. (1994) Delivery of liposomes into cultured KB cells via folate receptor-mediated endocytosis. *J. Biol. Chem. 269*, 3198−204.

(32) Guo, W. J., Lee, T., Sudimack, J., and Lee, R. J. (2000) Receptor-specific delivery of liposomes via folate-PEG-Chol. *J. Liposome Res. 10*, 179−195.

(33) Barth, R. F. (1998) Rat brain tumor models in experimental neuro-oncology: the 9L, C6, T9, F98, RG2 (D74), RT-2 and CNS-1 gliomas. *J. Neurooncol. 36*, 91−102.

(34) Olson, F., Hunt, C. A., Szoka, F. C., Vail, W. J., and Papahadjopulos, D. (1979) Preparation of liposomes of defined size distribution by extrusion through polycarbonate membranes. *Biochim. Biophs. Acta 557*, 9−23.

(35) Chen, P. S., Toribara, T. Y., and Warner, H. (1956) Microdetermination of phosphorus. *Anal. Chem. 28*, 1756−58.

(36) Bradford, M. M. (1974) A rapid and sensitive for the quantitation of microgram quantities of protein utilizing the principle of protein-dye binding. *Anal. Biochem. 72*, 248−254.

(37) Mamot, C., Drummond, D. C., Greiser, U., Hong, K., Kirpotin, D. B., Marks, J. D., and Park, J. W. (2003) Epidermal growth factor receptor (EGFR)-targeted immunoliposomes mediate specific and efficient drug delivery to EGFR- and EGFRvIII-overexpressing tumor cells. *Cancer Res. 63*, 3154−61.

(38) Straubinger, R. M., Papahadjopoulos, D., and Hong, K. L. (1990) Endocytosis and intracellular fate of liposomes using pyranine as a probe. *Biochemistry 29*, 4929−39.

(39) Bhadra, D., Bhadra, S., and Jain, N. K. (2005) Pegylated lysine based copolymeric dendritic micelles for solubilization and delivery of artemether. *J. Pharm. Pharm. Sci. 8*, 467−82.

(40) Nobs, L., Buchegger, F., Gurny, R., and Allemann, E. (2004) Current methods for attaching targeting ligands to liposomes and nanoparticles. *J. Pharm. Sci. 93*, 1980−92.

(41) Beugin, S., Edwards, K., Karlsson, G., Ollivon, M., and Lesieur, S. (1998) New sterically stabilized vesicles based on nonionic surfactant, cholesterol, and poly(ethylene glycol)-cholesterol conjugates. *Biophys. J. 74*, 3198−210.

(42) Carrion, C., Domingo, J. C., and de Madariaga, M. A. (2001) Preparation of long-circulating immunoliposomes using PEG-

cholesterol conjugates: effect of the spacer arm between PEG and cholesterol on liposomal characteristics. *Chem. Phys. Lipids 113*, 97−110.

(43) Biston, M. C., Joubert, A., Adam, J. F., Elleaume, H., Bohic, S., Charvet, A. M., Esteve, F., Foray, N., and Balosso, J. (2004) Cure of Fisher rats bearing radioresistant F98 glioma treated with cisplatinum and irradiated with monochromatic synchrotron X-rays. *Cancer Res. 64*, 2317−23.

(44) Adam, J. F., Joubert, A., Biston, M. C., Charvet, A. M., Peoc'h, M., Le Bas, J. F., Balosso, J., Esteve, F., and Elleaume, H. (2006) Prolonged survival of Fischer rats bearing F98 glioma after iodine-enhanced synchrotron stereotactic radiotherapy. *Int. J. Radiat. Oncol. Biol. Phys. 64*, 603−11.

BC060174R

Enzymatic and Nonenzymatic Synthesis of Glutathione Conjugates: Application to the Understanding of a Parasite's Defense System and Alternative to the Discovery of Potent Glutathione *S*-Transferase Inhibitors

Wei-Jen Lo,[†,#] Yu-Ching Chiou,[§,#] Yu-Ting Hsu,[‡] Wing See Lam,[‡] Ming-Yun Chang,[§] Shu-Chuan Jao,[⊥] and Wen-Shan Li*[,‡]

Department of Chemistry & Biochemistry, National Chung Cheng University, Chia-Yi 621, Taiwan, Department of Chemistry, National Taiwan Normal University, Taipei 116, Taiwan, Institute of Biological Chemistry, Academia Sinica, Taipei 115, Taiwan, and Institute of Chemistry, Academia Sinica, Taipei 115, Taiwan. Received June 18, 2006; Revised Manuscript Received November 27, 2006

A primary pathway for metabolism of electrophilic compounds in *Schistosoma japonicum* involves glutathione *S*-transferase (*Sj*GST)-catalyzed formation of glutathione (GSH) conjugates. As part of a program aimed at gaining a better understanding of the defense system of parasites, a series of aromatic halides (**1**−**8**), aliphatic halides (**9**, **10**), epoxides (**11**−**20**), α,*β*-unsaturated esters (**21**, **22**), and α,*β*-unsaturated amides (**23**, **24**) were prepared, and their participation in glutathione conjugate formation was evaluated. Products from enzymatic and nonenzymatic reactions of these substances with glutathione were characterized and quantified by using reverse-phase high-performance liquid chromatography (HPLC), NMR, and fast atom bombardment mass spectrometry (FAB-MS) analysis. Mechanisms for formation of specific mono(glutathionyl) or bis(glutathionyl) conjugates are proposed. Although the results of this effort indicate that *Sj*GST does not catalyze addition or substitution reactions of **1**, **3**, **4**, **7**−**9**, **11**−**13**, **15**−**17**, **19**−**21**, and **24**, they demonstrate that **2**, **5**, **6**, **14**, **18**, and **23** undergo efficient enzyme-catalyzed conjugation reactions. The k_{cat} values for *Sj*GST with **23** and **18** are about 886-fold and 14-fold, respectively, larger than that for **5**. This observation suggests that **23** is a good substrate in comparison to other electrophiles. Furthermore, the initially formed conjugation product, **23a**, is also a substrate for *Sj*GST in a process that forms the bis(glutathionyl) conjugate **23b**. Products arising by enzymatic and nonenzymatic pathways are generated under the conditions of *Sj*GST-activated GSH conjugation. Interestingly, production of nonenzymatic GSH conjugates with electrophilic substrates often overwhelms the activity of the enzyme. The nonenzymatic GSH conjugates, **9a**−**11a**, **16a**, **21a**, and **22a**, are inhibitors of *Sj*GST with respective IC_{50} values of 1.95, 75.5, 0.96, 19.0, 152, and 0.36 μM, and they display moderate inhibitory activities against human GSTA2. Direct evidence has been gained for substrate inhibition by **10** toward *Sj*GST and GSTA2 that is more potent than that of its GSH conjugate **10a**. The significance of this work is found in the development of a convenient NMR-based technique that can be used to characterize glutathione conjugates derived from small molecule libraries as part of efforts aimed at uncovering specific potent *Sj*GST and GSTA2 inhibitors. This method has potential in applications to the identification of novel inhibitors of other GST targets that are of chemotherapeutic interest.

INTRODUCTION

Because it serves as the preferred substrate for different glutathione (GSH)-related enzymes (*1*−*4*) involved in demonstrated detoxification pathways, GSH (*γ*-Glu-Cys-Gly) has garnered considerable medicinal interest. Also this substance is the precursor of a prooxidant species (thiyl radical) in the main pathway for intracellular antioxidant defense (*5*−*7*). GSH, the most abundant natural tripeptide (1−10 mM), forms covalent bonds with electrophilic molecules (endogenous and exogenous xenobiotics) through its sulfhydryl group leading to the generation of more hydrophilic GSH conjugates (*8*). The resulting GSH conjugates are generally considered to be metabolites in the defense system of the cell (*9*−*10*). Furthermore, these conjugates play a medicinal role as bioactive agents (*e.g.*, inhibitors of therapeutic enzymes (*11*−*13*), antiprotozoal agents against parasites (*14*, *15*), and enzyme-activated prodrugs (*16*−*19*)).

Glutathione *S*-transferases (GSTs), a family of GSH-dependent enzymes, participate in detoxification processes by catalyzing the conjugation of GSH to a wide variety of xenobiotics. Cytosolic GSTs in mammals were originally divided into the α, *κ*, *μ*, *ω*, *π*, *σ*, *θ*, and *ζ* classes on the basis of their biofunctional properties and sequence identities. *Schistosoma japonicum* GST (*Sj*GST), having a similar structure to members of the *μ* class of cytosolic GSTs, plays a key role in the primary defense system of parasites. This enzyme has several biochemical functions, which are common to the α, *μ*, and *π* classes (*20*, *21*). Gaining greater knowledge about *Sj*GST catalysis and the way a broad variety of substrates bind in its hydrophobic binding site (H site) are important components of understanding glutathione-dependent metabolism in the worm *S. japonicum*, a parasite that causes the tropical disease schistosomiasis, which infects 200 million people and causes 280 000 deaths in the world annually (*21*−*28*).

Herein, we report the results of an investigation aimed at determining possible metabolites and mechanistic pathways for *Sj*GST-catalyzed conjugation reactions of various electrophiles. In the effort, enzymatic and nonenzymatic conjugation reactions of glutathione with the electrophiles were explored. The results of this study show that GSH conjugates arising from nonenzy-

* To whom correspondence should be addressed. Phone: 886-2-27898662. Fax: 886-2-27831237. E-mail: wenshan@chem.sinica.edu.tw.
† National Chung Cheng University.
# These authors contributed equally to this work.
§ National Taiwan Normal University.
‡ Institute of Chemistry, Academia Sinica.
⊥ Institute of Biological Chemistry, Academia Sinica.

10.1021/bc0601727 CCC: $37.00 © 2007 American Chemical Society
Published on Web 12/21/2006

matic rather than enzymatic coupling reactions are micromolar to nanomolar inhibitors of *Sj*GST and its human counterpart hGSTA2.

EXPERIMENTAL PROCEDURES

Analytical Instrumentation and Characterization Techniques. NMR spectra were recorded on Bruker AMX400, AV400, or AV500 MHz instruments. Chemical shifts were reported in ppm and are referenced to the chemical shift of residual solvent. Mass spectra were obtained on a fast atom bombardment (FAB) JMS-700 double focusing mass spectrometer (JEOL, Tokyo, Japan), MALDI Voyager DE-PRO (Applied Biosystems, Houston, TX), and ESI Finnigan LCQ mass spectrometer (Thermo Finnigan, San Jose, CA) in negative mode. Chromatography was performed at room temperature using a high-performance liquid chromatography (HPLC) Breeze system consisting of a Waters model 1525 binary pump system with a Vydac 214SP510 C18 (10 mm × 250 mm, 5 μm) or a Waters Symmetry C18 (3.9 mm × 150 mm, 5 μm) column equilibrated in H_2O/CH_3CN as eluents, at a flow rate of 1 mL/min. GSH conjugate elution was recorded with the use of an online Waters 2487 UV dual absorbance detector that measured simultaneously the absorbance at 220 and 254 nm, unless indicated otherwise. The HPLC fraction containing the conjugate product was dried in a vacuum concentrator (Speedvac SC110, Savant Instruments, Holbrook, NY). The absorbances of all samples for *Sj*GST assays were measured at 340 nm using a SpectraMax Plus384 plate reader (Molecular Devices, Sunnyvale, CA).

Materials. Unless stated otherwise, all chemicals and reagents were purchased from Acros and used as provided. Restriction enzymes were obtained from New England Biolabs. Minipreps and gel extraction DNA purification kits were obtained from Qiagen. *Escherichia coli* strains BL21(DE3) and Rosetta(DE3) and plasmids pET-15b and pET-28a were from Novagen. Oligonucleotide synthesis and DNA sequencing reactions were conducted by using MDBio. HisTrap affinity and PD-10 columns were purchased from Amersham Biosciences. 2-Chloromethyl-4-nitrophenol, *R*-(+)-3-chlorostyrene oxide, methyl-*trans*-3-(4-methoxyphenyl)glycidate, 7-oxabicyclo[4,1,0]heptan-2-one, and sodium phosphate (NaH_2PO_4) were purchased from Sigma-Aldrich. 1,3,5-Triacryloyl-hexahydro-*s*-triazine was purchased from TCI-EP, and ethacrynic acid (EA) was purchased from MP. Crotonic anhydride and 2-bromo-4-nitroacetophenone were purchased from TCI.

Screening Assay of GSH Conjugate Formation (Table 1). *(a) With SjGST*. A typical reaction included GSH (7.7 mg, 25 μmol) in H_2O (46.5 mL), 1 M sodium phosphate (pH 7.0, 1 mL), and *Sj*GST (0.42 mg). Reactions were started by adding the corresponding electrophile (25 μmol) in methanol (2.5 mL) to a mixed solution of enzyme, GSH, and buffer (25 °C preincubated). Reactions were stopped after 10 min or 5 h by the addition of acetone (40 mL). After evaporation of the organic solvent, each solution was washed with dichloromethane (4 × 20 mL) to remove unreacted electrophiles, and the aqueous layer was concentrated *in vacuo*. The crude GSH conjugates were characterized by ^{1}H NMR spectroscopy (Figure 1) and reverse-phase HPLC analysis. In order to observe the enzymatic formation of the GSH conjugates from electrophiles **6** and **14**, the same procedure was carried out at pH 6.5 and 4 °C to reduce the rate of nonenzymatic reaction.

(*b) Without SjGST*. Nonenzymatic reactions were preformed by using the same protocol as that described in the enzymatic reaction except that *Sj*GST was not included.

Synthesis of GSH Conjugates. *(a) Enzymatic synthesis*. To 285 mL of reaction solution, containing 0.3 μM *Sj*GST, 20 mM sodium phosphate, and 0.5 mM GSH (pH 7.0), was added 15 mL of a methanol solution containing 10 mM of the corresponding electrophile. The mixture was shaken at 25 °C until the completion of the reaction (monitored by TLC) and washed with dichloromethane (4 × 50 mL) to remove the unreacted electrophile. The aqueous layer was concentrated *in vacuo*, and the residue was triturated with 20 mL of H_2O. The triturate was poured into a centrifuge tube with cold acetone (30 mL) at −15 °C, allowed to stand for 15 min, and centrifuged at 4000 rpm for 10 min. The supernatant was concentrated under reduced pressure to remove acetone. The resulting aqueous solution was dialyzed (SpectraPor, MWCO 100) against H_2O for 18 h. The dialysate was concentrated, and the residue obtained was subjected to reverse-phase HPLC. The eluant was lyophilized to afford the pure product as a white powder.

(b) Nonenzymatic synthesis. All GSH conjugates were prepared by using the same protocol as that described in the enzymatic synthesis except *Sj*GST was not included.

Table 1. Nucleophilic Substitution and Addition Reactions in the Presence or Absence of *Sj*GST[a]

		without enzyme[b]		*Sj*GST[b]		
substrate	glutathione conjugate	10 min, %	5 h, %	10 min, %	5 h, %	reaction type[c]
1	*e*	0	0	0	0	N
2	**2a**	0	*f*	99 ± 2	99 ± 2	M
3	*e*	0	0	0	0	N
4	*e*	0	0	0	0	N
5	**5a**	0	0	0	23 ± 3	E
6	**6a**	50 ± 3[d]	99 ± 1[d]	25 ± 2[d]		M
7	*e*	0	0	0	0	N
8	**8a**	0	23 ± 2	0	0	C
9	**9a**	8 ± 1	13 ± 2	0	0	C
10	**10a**	99 ± 2	99 ± 1			X
11	**11a**	0	42 ± 4	0	0	C
12	*e*	0	0	0	0	N
13	*e*	0	0	0	0	N
14	**14a**	0[d] (−)[b]	0[d] (99)[b]	0[d]	99 ± 2[d]	M[b], E[d]
15	*e*	0	0	0	0	N
16	**16a**	0	11 ± 1	0	0	C
17	*e*	0	0	0	0	N
18	**18a**	0	0	83 ± 4	83 ± 2	E
19	*e*	0	0	0	0	N
20	*e*	0	0	0	0	N
21	**21a**		20 ± 1		0	C
22	**22a**	99 ± 1	99 ± 2			X
23	**23a**	0	0		99 ± 1	E
24	*e*	0	0	0	0	N

[a] Values shown are averages of integral ratios from two independent NMR experiments. [b] Reactions were carried out in 0.5 mM GSH and 20 mM sodium phosphate buffer (pH 7.0) at 25 °C in the presence or absence of enzyme for 10 min or 5 h. [c] Reaction type: N (no reaction in both chemical and enzymatic reaction), E (enzymatic reaction only), M (mixed reactions including chemical and enzymatic reaction), C (chemical reaction only), X (chemical reaction but cannot confirm the existence of enzymatic reaction). [d] Reactions were performed in sodium phosphate buffer (pH 6.5) at 4 °C. [e] No products were detected under the same conditions. [f] Trace.

Characterization of Electrophilic Substrates and GSH Conjugates. *N-(5-Chloro-2-nitrophenyl)-N-(cyclopropylmethyl)-amine (**1**).* ^{1}H NMR (400 MHz, $CDCl_3$): δ 8.07 (d, J = 9.1 Hz, 1H), 7.27 (d, J = 2.1 Hz, 1H), 6.63 (dd, J = 2.1 Hz, J = 9.1 Hz, 1H), 2.55−2.52 (m, 1H), 1.54 (br, 1H), 0.95−0.90 (m, 2H), 0.67−0.63 (m, 2H). ^{13}C NMR (100 MHz, $CDCl_3$): δ 142.5, 127.9, 116.5, 114.7, 24.5, 7.9. HRMS-FAB: calcd for $C_9H_{10}O_2N_2Cl$ $(M + H)^+$ 213.0431; found 213.0431.

*8-Chloro-10-propylbenzo[g]pteridine-2,4(3H,10H)-dione (**8**).* ^{1}H NMR (400 MHz, D_2O): δ 8.46 (s, 1H), 8.23 (d, J = 9.3 Hz, 1H), 7.58−7.57 (m, 1H), 4.59 (t, J = 7.6 Hz, 2H), 1.95−1.85 (m, 2H), 1.13 (t, J = 7.4 Hz, 3H). ^{13}C NMR (100 MHz, DMSO-d_6): δ 159.6, 155.6, 150.5, 139.6, 138.8, 133.5, 133.4, 133.3, 126.3, 115.9, 45.7, 19.7, 10.9. HRMS-FAB: calcd for $C_{13}H_{12}O_2N_4Cl$ $(M + H)^+$ 291.0649; found 291.0653.

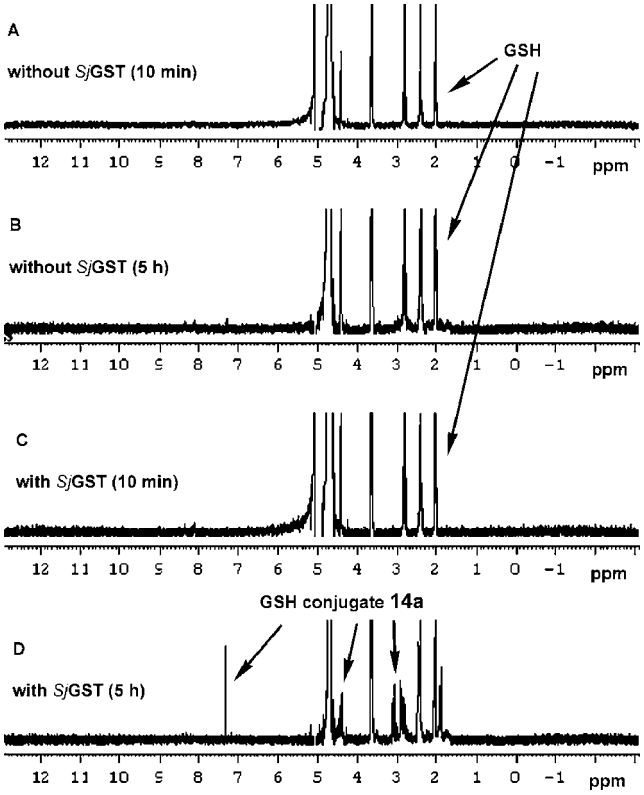


Figure 1. ^{1}H NMR spectra of the chemical conjugation product mixture from **14** and GSH for 10 min (A) and 5 h (B) and of the conjugation product mixture of **14** and GSH catalyzed by *Sj*GST for 10 min (C) and 5 h (D).

*17-Hydroxy-10,13,17-trimethyl-tetradecahydro-20-oxa-cyclopropa[4,5]cyclopenta[a]-phenanthren-3-one (**16**).* ^{1}H NMR (400 MHz, $CDCl_3$): δ 4.07 (br, 1H, OH), 2.90 (s, 1H), 2.30−0.8 (m, 28H). ^{13}C NMR (100 MHz, $CDCl_3$): δ 206.8, 81.3, 70.2, 62.8, 50.0, 46.5, 45.5, 38.7, 37.2, 35.8, 32.4, 31.1, 29.9, 29.7, 26.1, 25.7, 23.1, 21.1, 20.9, 13.8. HRMS-FAB: calcd for $C_{20}H_{31}O_3$ $(M + H)^+$ 319.2273; found 319.2265.

*N-(5-Chloro-2-nitrophenyl)-N-propylamine (**26**).* ^{1}H NMR (400 MHz, $CDCl_3$): δ 8.08 (d, J = 9.1 Hz, 1H), 6.81 (s, 1H), 6.56 (dd, J = 2.1 Hz, J = 9.1 Hz, 1H), 3.25−3.21 (m, 2H), 1.78−1.73 (m, 2H), 1.05 (t, J = 7.4 Hz, 3H). ^{13}C NMR (100 MHz, $CDCl_3$): δ 145.9, 142.7, 130.3, 128.2, 115.5, 113.1, 44.8, 22.0, 11.4. HRMS-FAB: calcd for $C_9H_{12}O_2N_2Cl$ $(M + H)^+$ 215.0587; found 215.0582.

*N-(2-Amino-5-chlorophenyl)-N-propylamine (**27**).* ^{1}H NMR (400 MHz, $CDCl_3$): δ 8.09 (d, J = 9.1 Hz, 1H), 6.81 (d, J = 2.1 Hz, 1H), 6.56 (dd, J = 2.1 Hz, J = 9.1 Hz, 1H), 3.25−3.20 (m, 2H) 1.79−1.71 (m, 2H) 1.04 (t, J = 7.4 Hz, 3H). ^{13}C NMR (100 MHz, $CDCl_3$): δ 139.1, 132.2, 125.9, 117.6, 117.3, 111.6, 45.9, 22.6, 11.7. HRMS-FAB: calcd for $C_9H_{13}N_2Cl$ $(M + H)^+$ 184.0767; found 184.0764.

*2-Glutathionyl-5-nitropyridine (**5a**).* ^{1}H NMR (400 MHz, D_2O): δ 9.26 (d, J = 2.6 Hz, 1H), 8.42 (dd, J = 2.6 Hz, J = 8.9 Hz, 1H), 7.56 (d, J = 8.9 Hz, 1H), 4.82 (br, 1H), 4.06−4.04 (m, 1H), 3.98 (s, 2H), 3.85 (dd, J = 5.2 Hz, J = 14.5 Hz, 1H), 3.58 (dd, J = 8.2 Hz, J = 14.5 Hz, 1H), 2.54−2.50 (m, 2H), 2.19−2.15 (m, 2H). ^{13}C NMR (100 MHz, DMSO-d_6): δ 171.2, 170.4, 170.0, 169.7, 165.9, 144.3, 140.8, 130.8, 121.2, 52.2, 51.1, 40.6, 31.6, 30.7, 26.0. HRMS-FAB: calcd for $C_{15}H_{20}O_8N_5S$ $(M + H)^+$ 430.1033; found 430.1028.

*2-Glutathionyl-3,5-dinitropyridine (**6a**).* ^{1}H NMR (500 MHz, D_2O): δ 9.55 (s, 1H), 9.08 (s, 1H), 8.62 (br, 2H, NH), 4.66 (br, 1H), 3.88 (br, 1H), 3.74 (s, 2H), 3.45 (s, 1H), 2.29 (br, 2H), 1.90−1.84 (m, 2H). ^{13}C NMR (125 MHz, DMSO-d_6): δ 172.3, 171.4, 170.9, 170.7, 163.2, 148.3, 141.3, 140.7, 129.9, 53.4, 51.6, 41.6, 33.5, 31.8, 27.1. HRMS-FAB: calcd for $C_{15}H_{19}O_{10}N_6S$ $(M + H)^+$ 475.0883; found 475.0879.

*8-Glutathionyl-10-propylisoalloxazine (**8a**).* ^{1}H NMR (500 MHz, DMSO-d_6): δ 11.3 (s, 1H, NH), 8.65 (br, 1H, NH), 8.55 (d, J= 8.2 Hz, 1H, NH), 7.99 (d, J = 8.6 Hz, 1H), 7.72 (s, 1H), 7.55 (d, J = 8.6 Hz, 1H), 4.63−4.57 (m, 3H), 3.81−3.73 (m, 3H), 2.35 (br, 3H), 1.97−1.96 (m, 2H), 1.77−1.72 (m, 2H), 1.02 (t, J = 7.3 Hz, 3H). ^{13}C NMR (125 MHz, DMSO-d_6): δ 171.6, 170.8, 170.7, 169.9, 159.9, 155.8, 150.6, 147.2, 136.7, 133.2, 131.9, 124.5, 111.3, 51.9, 51.7, 45.5, 40.9, 33.3, 30.8, 26.0, 19.8, 11.0. HRMS-FAB: calcd for $C_{23}H_{28}O_8N_7S$ $(M + H)^+$ 562.1720; found 562.1720.

*2-(Glutathionylmethyl)-4-nitrophenol (**9a**).* ^{1}H NMR (500 MHz, DMSO-d_6): δ 8.46 (t, J = 5.7 Hz, 1H), 8.32 (d, J = 8.4 Hz, 1H), 8.13 (s, 1H), 7.98 (dd, J = 2.9 Hz, J = 8.9 Hz, 1H, NH), 7.02 (d, J = 8.9 Hz, 1H, NH), 4.53−4.49 (m, 1H), 3.74−3.71 (m, 3H), 3.48 (t, J = 6.5 Hz, 1H), 2.86 (dd, J = 4.6 Hz, J = 13.6 Hz, 1H), 2.64 (dd, J = 8.9 Hz, J = 13.6 Hz, 1H), 2.35−2.32 (m, 2H), 1.97−1.94 (m, 2H). ^{13}C NMR (125 MHz, DMSO-d_6): δ 171.3, 170.6, 170.3, 162.6, 162.4, 138.4, 125.9, 125.5, 124.2, 115.1, 52.6, 51.9, 40.6, 30.9, 29.1, 26.3. HRMS-FAB: calcd for $C_{17}H_{23}O_9N_4S$ $(M + H)^+$ 459.1186; found 459.1191.

*2-Glutathionyl-1-(4-nitrophenyl)ethanone (**10a**).* ^{1}H NMR (400 MHz, D_2O): δ 8.38−8.35 (m, 2H), 8.20−8.18 (m, 2H), 4.60−4.56 (m, 1H), 4.19 (s, 2H), 4.08−4.06 (m, 1H), 3.97 (s, 2H), 3.13 (dd, J = 5.2 Hz, J = 14.2 Hz, 1H), 2.96 (dd, J = 8.8 Hz, J = 14.2 Hz, 1H), 2.58−2.54 (m, 2H), 2.23−2.17 (m, 2H). ^{13}C NMR (100 MHz, D_2O): δ 196.9, 174.5, 173.1, 172.6, 150.6, 139.8, 130.1, 124.2, 53.1, 52.9, 41.3, 33.3, 31.2, 25.8. HRMS-FAB: calcd for $C_{18}H_{23}O_9N_4S$ $(M + H)^+$ 471.1186; found 471.1193.

*2-(3-Chlorophenyl)-2-glutathionylethanol (**11a**).* ^{1}H NMR (400 MHz, D_2O): δ 7.47 (s, 1H), 7.37−7.31 (m, 3H), 4.28−4.25 (m, 1H), 4.08−3.99 (m, 2H), 3.97 (s, 2H), 3.89−3.86 (m, 2H), 3.08 (dd, J = 4.2 Hz, J = 11.1 Hz, 1H), 2.83 (dd, J = 6.8 Hz, J = 11.1 Hz, 1H), 2.51−2.48 (m, 2H), 2.17−2.14 (m, 2H). ^{13}C NMR (100 MHz, D_2O): δ 174.1, 173.0, 172.7, 171.9, 142.1, 134.0, 130.4, 128.0, 126.7, 64.7, 53.0, 52.6, 51.4, 41.2, 32.7, 31.0, 25.7. HRMS-FAB: calcd for $C_{18}H_{25}O_7N_3ClS$ $(M + H)^+$ 462.1102; found 462.1091.

*2-Glutathionylcyclohex-2-en-1-one (**14a**).* ^{1}H NMR (500 MHz, D_2O): δ 7.46 (t, J = 4.3 Hz, 1H), 4.55−4.54 (m, 1H), 4.08 (t, J = 6.5 Hz, 1H), 4.02 (s, 2H), 3.2 (dd, J = 5.1 Hz, J = 14.1 Hz, 1H), 3.00 (dd, J = 8.5 Hz, J = 14.1 Hz, 1H), 2.63−2.54 (m, 6H), 2.27−2.24 (m, 2H), 2.05−2.03 (m, 2H). ^{13}C NMR (100 MHz, D_2O): δ 200.7, 174.2, 172.8, 172.4, 171.8, 156.6, 131.2, 52.4, 41.0, 37.9, 32.6, 30.9, 27.2, 25.5, 21.8. HRMS-FAB: calcd for $C_{16}H_{24}O_7N_3S$ $(M + H)^+$ 402.1335; found 402.1341.

*17-Hydroxy-4-glutathionyl-10,13,17-trimethyl-1,2,6,7,8,9,10,-11,12,13,14,15,16,17-tetradecahydro-cyclopenta[a]phenanthren-3-one (**16a**).* ^{1}H NMR (400 MHz, D_2O): δ 4.19 (dd, J = 4.6 Hz, J = 9.3 Hz, 1H), 4.06 (t, J = 6.6 Hz, 1H), 3.93 (s, 2H), 3.48 (d, J = 13.7 Hz, 1H), 3.07 (dd, J = 4.6 Hz, J = 13.9 Hz, 1H), 2.76 (dd, J = 9.6, J = 13.9 Hz, 1H), 2.61−2.55 (m, 3H), 2.44−2.40 (m, 1H), 2.23−2.17 (m, 3H), 2.03−2.00 (m, 1H), 1.90−1.80 (m, 2H), 1.67−1.63 (m, 2H), 1.54−1.43 (m, 5H), 1.30−1.21 (m, 5H), 1.12−1.06 (m, 4H), 0.87−0.81 (m, 4H). ^{13}C NMR (100 MHz, D_2O): δ 199.1, 181.9, 174.0, 172.6, 172.4, 171.7, 125.6, 81.8, 54.5, 53.0, 52.3, 49.9, 45.2, 41.9, 41.0, 37.5, 35.5, 34.3, 33.9, 33.8, 31.8, 31.1, 25.5, 24.8, 22.7, 20.3, 17.2, 13.6. HRMS-FAB: calcd for $C_{30}H_{46}O_8N_3S$ $(M + H)^+$ 608.3006; found 608.3014.

*Methyl 3-Glutathionyl-2-hydroxy-3-(4-methoxyphenyl)propanoate (**18a**). Isomer 1:* ^{1}H NMR (400 MHz, D_2O): δ 7.33

(d, $J = 8.6$ Hz, 2H), 6.93 (d, $J = 8.6$ Hz, 2H), 4.70−4.69 (m, 1H), 4.34 (d, $J = 4.9$ Hz, 1H), 4.29 (dd, $J = 5.4$ Hz, $J = 8.9$ Hz, 1H), 3.95−3.92 (m, 3H), 3.80 (s, 3H), 3.65 (s, 3H), 3.06 (dd, $J = 4.9$ Hz, $J = 14.4$ Hz, 1H), 2.81 (dd, $J = 8.9$ Hz, $J = 14.4$ Hz, 1H), 2.45 (t, $J = 7.4$ Hz, 2H), 2.12−2.08 (m, 2H). ^{13}C NMR (100 MHz, D_2O) : δ 174.1, 173.5, 172.6, 172.2, 171.4, 158.7, 130.1, 129.0, 114.7, 73.1, 55.2, 52.8, 52.5, 52.1, 51.5, 40.9, 32.1, 30.8, 25.4. HRMS-FAB: calcd for $C_{21}H_{30}O_{10}N_3S$ $(M + H)^+$ 516.1652; found 516.1645.

Isomer 2: ^{1}H NMR (400 MHz, D_2O): δ 7.35 (d, $J = 8.7$ Hz, 2H), 6.96 (d, $J = 8.7$ Hz, 2H), 4.67−4.66 (m, 1H), 4.47 (dd, $J = 5.4$ Hz, $J = 9.0$ Hz, 1H), 4.31 (d, $J = 5.4$ Hz, 1H), 3.92 (s, 3H), 3.82−3.80 (m, 4H), 3.65 (s, 2H) 2.83 (dd, $J = 5.4$ Hz, $J = 14.3$ Hz, 1H), 2.77 (dd, $J = 9.0$ Hz, $J = 14.3$ Hz, 1H), 2.52−2.48 (m, 2H), 2.18−2.16 (m, 2H). ^{13}C NMR (125 MHz, D_2O): δ 173.9, 173.6, 172.8, 172.6, 171.8, 158.6, 130.1, 129.7, 113.9, 73.4, 55.4, 52.6, 52.5, 52.4, 51.8, 41.0, 32.7, 30.8, 25.5. HRMS-FAB: calcd for $C_{21}H_{30}O_{10}N_3S$ $(M + H)^+$ 516.1652; found 516.1645.

*2-Glutathionylmethyl-2-cyclohexenone (**21a**).* Compound **21a** was characterized as previously described by Creighton and coworkers (see refs *42*−*45*). ^{1}H NMR (400 MHz, D_2O): δ 7.16 (t, $J = 3.6$ Hz, 1H), 4.54 (dd, $J = 5.3$ Hz, $J = 8.6$ Hz, 1H), 4.09 (t, $J = 6.6$ Hz, 1H), 3.99 (s, 2H), 3.30 (s, 2H), 2.96 (dd, $J = 5.1$ Hz, $J = 14.0$ Hz, 1H), 2.78 (dd, $J = 8.8$ Hz, $J = 14.0$ Hz, 1H), 2.64−2.51 (m, 2H), 2.48−2.43 (m, 4H), 2.30−2.15 (m, 2H), 2.06−1.94 (m, 2H). ^{13}C NMR (100 MHz, D_2O): δ 203.3, 174.2, 172.7, 172.6, 171.3, 152.9, 134.2, 52.8, 51.9, 40.9, 37.7, 32.4, 30.8, 29.9, 25.6, 25.3, 22.1. HRMS-FAB: calcd for $C_{17}H_{26}O_7N_3S$ $(M + H)^+$ 416.1502; found 416.1501.

*{2,3-Dichloro-4-[2-(glutathionylmethyl)butanoyl]phenoxy}-acetic Acid (**22a**).* ^{1}H NMR (500 MHz, D_2O): δ 7.46 (d, $J = 8.3$ Hz, 1H), 6.94 (d, $J = 8.3$ Hz, 1H), 4.54 (dd, $J = 6.6$ Hz, $J = 10.5$ Hz, 1H), 4.09 (t, $J = 8.1$ Hz, 1H), 4.01−3.92 (m, 2H), 3.43−3.41 (m, 1H), 2.96 (dd, $J = 5.1$ Hz, $J = 13.7$ Hz 1H), 2.87−2.81 (m, 2H), 2.70−2.55 (m, 3H), 2.23−2.20 (m, 2H), 2.05 (s, 1H), 1.62−1.45 (m, 2H), 0.73 (t, $J = 5.8$ Hz, 3H). ^{13}C NMR (100 MHz, D_2O): δ 205.7, 174.0, 172.8, 172.4, 171.5, 156.3, 132.8, 131.2, 128.6, 123.2, 111.3, 65.9, 53.2, 52.4, 51.7, 41.2, 34.1, 32.5, 31.2, 25.6, 24.4, 10.5, 0.9. HRMS-FAB: calcd for $C_{23}H_{30}O_{10}N_3Cl_2S$ $(M + H)^+$ 610.1029; found 610.1022.

*1,3-Diacryloyl-5-(3-glutathionylpropanoyl)-1,3,5-triazinane (**23a**).* ^{1}H NMR (400 MHz, D_2O): δ 6.77 (m, 2H), 6.23 (m, 2H), 5.90 (m, 2H), 5.46−5.42 (m, 6H), 4.55−4.52 (m, 1H), 4.05 (t, $J = 5.9$ Hz, 4H), 3.98 (s, 2H), 3.00 (dd, $J = 5.4$ Hz, $J = 14.2$ Hz, 1H), 2.85−2.79 (m, 5H), 2.60−2.51 (m, 2H), 2.28−2.15 (m, 2H). ^{13}C NMR (100 MHz, D_2O): δ 174.1, 172.1, 172.6, 171.3, 167.6, 130.8, 126.3, 56.5, 52.9, 52.0, 40.9, 32.9, 32.5, 30.7, 26.7, 25.3. HRMS-FAB: calcd for $C_{22}H_{33}O_9N_6S$ $(M + H)^+$ 557.2024; found 557.2030.

*1-Acryloyl-3,5-bis(3-glutathionylpropanoyl)-1,3,5-triazinane (**23b**).* ^{1}H NMR (400 MHz, D_2O): δ 6.79−6.75 (dd, $J = 10.4$ Hz, $J = 16.7$ Hz, 1H), 6.25−6.21 (d, $J = 16.7$ Hz, 1H), 5.92−5.90 (d, $J = 10.4$ Hz, 1H), 5.43−5.37 (m, 6H), 4.56 (m, 2H), 4.00−3.97 (m, 6H), 3.00−2.99 (m, 2H), 2.87−2.81 (m, 10H), 2.58−2.53 (m, 4H), 2.21−2.18 (m, 4H). ^{13}C NMR (100 MHz, D_2O): δ 174.2, 172.8, 172.6, 172.4, 171.4, 167.6, 130.8, 126.4, 56.6, 56.4, 53.0, 52.1, 41.1, 33.1, 32.6, 30.9, 26.8, 25.4. HRMS-FAB: calcd for $C_{32}H_{50}O_{15}N_9S_2$ $(M + H)^+$ 864.2868; found 864.2867.

Expression and Purification of *Sj*GST. *E. coli* pET-15b−GST was cloned, expressed, and purified by using the previously described procedures (*28*) and stored in 20% glycerol at −80 °C.

Cloning, Expression, and Purification of Human GSTA2. Total RNA isolated from HeLa cells was subjected to oligo-(dT)-directed cDNA synthesis. The resulting cDNA population was used as a template, and primers *Sna*BI−*Nde*I−hGSTA2-S and hGSTA2-*Sac*I-A were used in PCR to obtain the hGSTA2 transcripts. The resulting full-length hGSTA2 cDNA was cloned into pET-28a using the *Nde*I/*Sac*I restriction sites. The plasmid containing the hGSTA2 was confirmed by sequence analysis. The overnight culture of *E. coli* Rosetta(DE3) clones carrying recombinant hGSTA2 plasmid was diluted 1:100 with fresh LB medium and grown until $A_{600} = 0.9$ was attained. The synthesis of recombinant hGSTA2 was induced by addition of 1 mM isopropyl-β-D-thiogalactopyranoside (IPTG) (Amresco) and then incubation was continued for 5 h at 30 °C. The bacteria were collected by centrifugation for 10 min at 6000 rpm. The protein was then purified using HisTrap affinity column and exchanged to 20 mM Tris-HCl (pH 7.6) by passing PD-10 column twice. The purity of hGSTA2 was confirmed by SDS−PAGE. The resulting hGSTA2 was added to 16% glycerol before storage at −80 °C.

Table 2. Catalytic Rate Constants (k_{cat}) for the Reactions of *Sj*GST with Substrates 2, 5, 14, 18, and 23

substrate	conjugate product	k_{cat} (s^{-1})	relative k_{cat}
5	**5a**	0.044 ± 0.007^a	1
18	**18a**	0.63 ± 0.14^a	14
23	**23a**	39 ± 9.9^a	886
2	**2a**	187 ± 35^b	
14	**14a**	0.037 ± 0.002^b	

[a] Conditions: 0.5 mM GSH, 20 mM sodium phosphate (pH 7.0), 25 °C. [b] Conditions: 0.5 mM GSH, 20 mM sodium phosphate (pH 6.5), 4 °C.

Determination of Catalytic Turnover Constant for Various Electrophiles (2, 5, 14, 18, and 23; Table 2). Enzymatic reaction mixtures, containing 0.5 mM GSH, various amounts of *Sj*GST (depending on the rate of reaction in different electrophile), and 95 mL of 20 mM sodium phosphate buffer (pH 7.0), were mixed with 5 mL of methanol solutions of the corresponding electrophiles (10 mM). Aliquots were removed from each mixture at five appropriate time points (*e.g.*, 2, 4, 6, 8, and 10 min for electrophile **23**) and mixed with 80 mL of acetone. After concentration, the resulting aqueous solutions were washed with dichloromethane (4 × 30 mL) to remove unreacted electrophile, and the aqueous layer was concentrated *in vacuo*. The reaction mixtures were then analyzed by using ^{1}H NMR spectroscopy to determine the distributions of GSH conjugates and GSH. The presaturation technique was used to suppress the water signal, and a total of 32 000 data points were collected per scan over a spectral width of 12 ppm. The concentration of GSH conjugate was determined from the integral ratio of GSH conjugate/GSH based on original concentration of glutathione. Initial reaction velocities were calculated over time spans that are within the linear range, and data were transferred into Excel for calculations of k_{cat}.

Determination of *Sj*GST Specific Activities and Inhibition of *Sj*GST. The specific activity of *Sj*GST with 1 mM 1-chloro-2,4-dinitrobenzene (CDNB) as a substrate was determined at pH 6.5 and 30 °C. Product formation was monitored by absorption spectroscopy (340 nm) (*28*). *Sj*GST inhibition assays were performed as previously described (*28*). Various concentrations of inhibitors, ranging from 10 nM to 500 μM, in DMSO were incubated with *Sj*GST for 3 min prior to initiation by the addition of 1 mM GSH.

hGSTA2 Activity and IC_{50} Determinations. hGSTA2 activity and IC_{50} values were determined spectrophotometrically at 340 nm and according to the procedure of Habig *et al.* (*29*). Recombinant hGSTA2 was incubated with or without inhibitor in the presence of 1 mM CDNB in ethanol (1% ethanol in assay mix) at 30 °C for 3 min in 0.1 M potassium phosphate buffer (pH 6.5). For the determination of IC_{50} values, six different

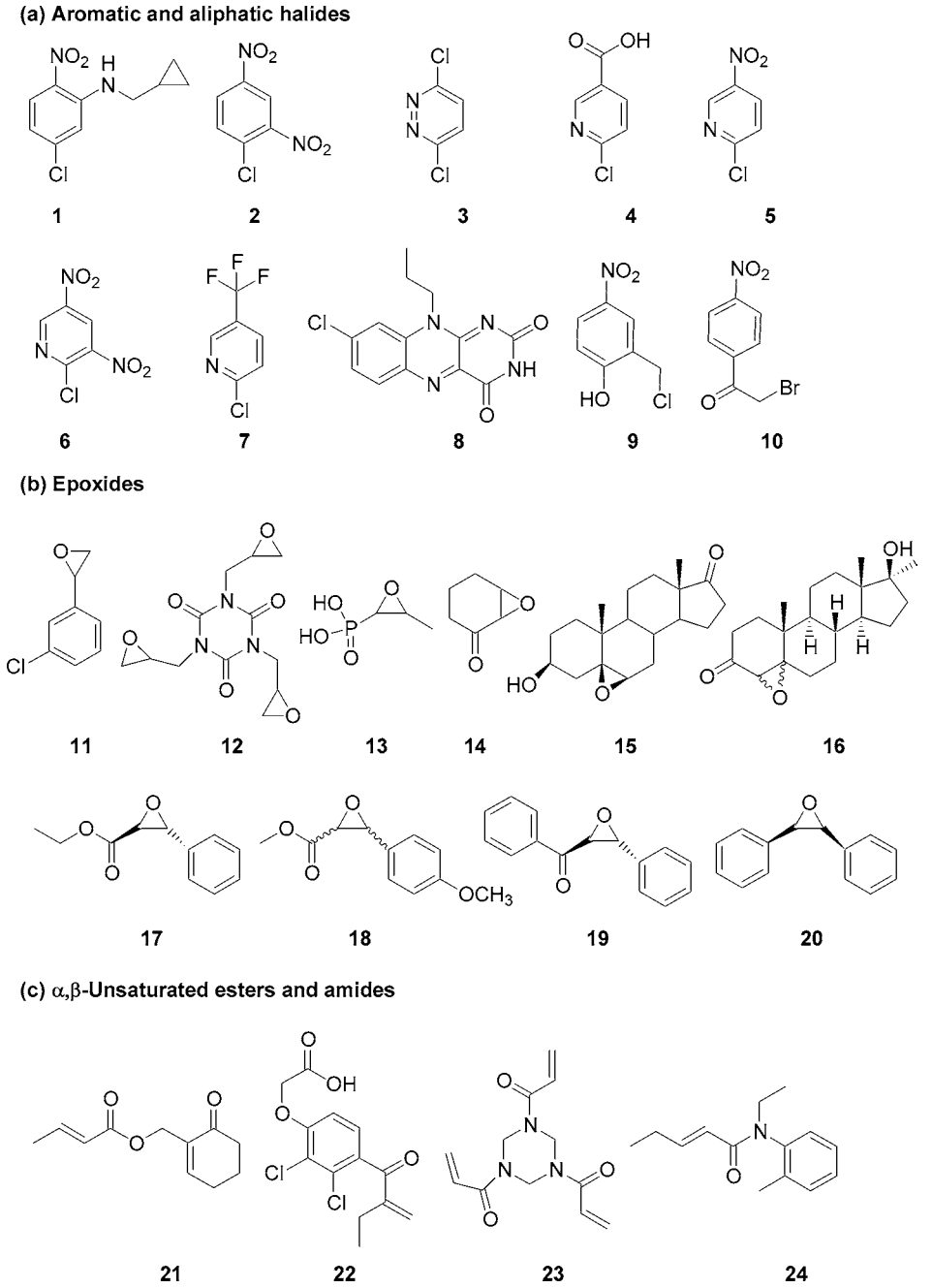


Figure 2. Chemical structures of the electrophiles.

inhibitor concentrations were tested (depending on inhibitor efficacy). The reactions were initiated by the addition of 0.25 mM GSH.

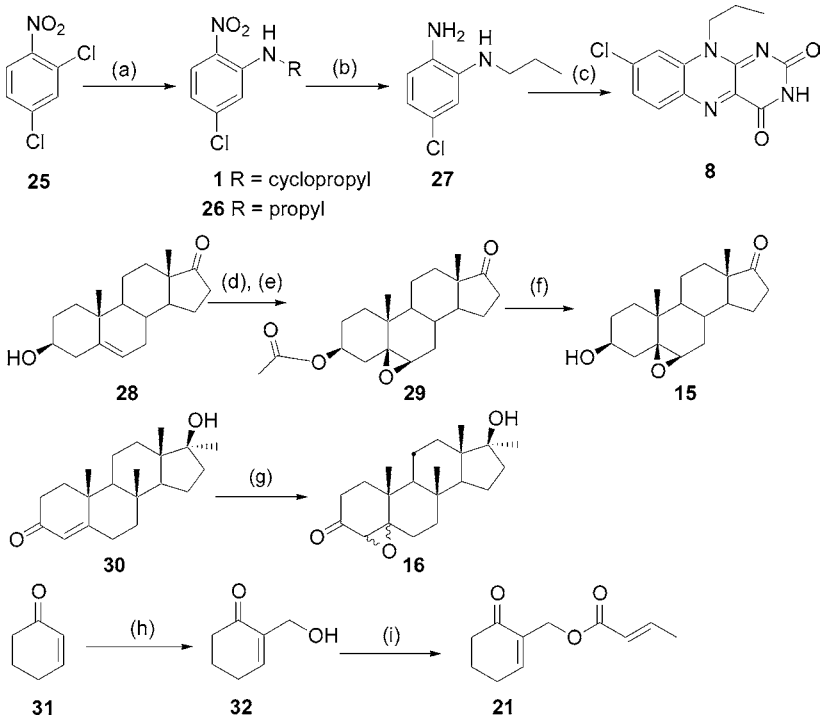
RESULTS AND DISCUSSION

Preparation and Catalytic Reaction Promoted by *Sj*GST. *Sj*GST was expressed and purified to homogeneity (SDS−PAGE) by using the protocol we previously described (*28*). The products of *Sj*GST-catalyzed reactions of the electrophilic substrates **1**−**24** with GSH were characterized by using ^{1}H NMR spectroscopy. In addition, the inhibitory properties of **9**−**11** and **22** toward *Sj*GST were determined. Finally, nonenzymatic products, **9a**−**11a**, **16a**, **21a**, and **22a**, inhibiting the activity of *Sj*GST were studied.

Selection of Substrate Library and Synthesis of Electrophilic Substrates. The common electrophilic substrates of the GSTs include epoxides, aliphatic and aromatic halides, α,*β*-unsaturated carbonyl compounds, and alkenes (*8*, *30*). The electrophilic substrates **1**−**24** (Figure 2), used in this study, include aromatic halides (**1**−**8**), aliphatic halides (**9**, **10**), epoxides (**11**−**20**), and α,*β*-unsaturated esters (**21**, **22**) and amides (**23**, **24**). The routes used for syntheses of **1**, **8**, **15**, **16**, and **21** are outlined in Scheme 1, while the other substances used are commercially available.

The cyclopropane **1** and flavin analog **8** used in this effort were synthesized starting with 2,4-dichloronitrobenzene (**25**). Regioselective aromatic substitution reactions (*31*) of **25** with cyclopropylamine or *n*-propylamine in the presence of K_2CO_3 afford **1** and **26**, respectively. Catalytic hydrogenation of **26** (methanol at 0 °C, 10% Pd/C and ammonium formate) results in dehalogenation of the arene ring. Consequently, diamine **27** was prepared by reacting **26** with Raney nickel in the presence of hydrazine at 70 °C (*32*). Condensation of **27** with alloxan monohydrate in acetic acid and boric acid under an anaerobic conditions (*33*) provides the desired flavin analogue **8**. The preparation of **15** began with acetylation of the Δ^5-unsaturated

Scheme 1. Synthetic Routes Used To Prepare the Electrophilic Substrates 1, 8, 15, 16, and 21[a]



[a] Reagents and conditions: (a) cyclopropylamine/*n*-propylamine, K_2CO_3, DMF, 90 °C, 57%; (b) RaNi, hydrazine, MeOH, 70 °C, 70%; (c) alloxan monohydrate, H_3BO_3, HOAc, 56%; (d) acetic anhydride, pyridine, 97% (e) $KMnO_4$, $CuSO_4 \cdot 5H_2O$, CH_2Cl_2, *t*-butyl alcohol, H_2O, 50%; (f) NaOMe, MeOH, 90%; (g) 30% H_2O_2, 10% NaOH, MeOH, 0 °C, 64%; (h) DMAP, CH_2O, THF, rt, 62%; (i) DMAP, crotonic anhydride, pyridine, rt, 89%.

sterol **28** followed by selective epoxidation with $KMnO_4$−$CuSO_4$ in dichloromethane containing a catalytic amount of water and *tert*-butyl alcohol. This produced the steroidal *β*-epoxide **29** (*34*). Removal of the acetyl group gave compound **15**. Alkaline hydrogen peroxide-promoted epoxidation of **30** at 0 °C afforded a mixture of the corresponding α- and *β*-epoxides **16** (*35*). Baylis−Hillman reaction (formaldehyde and 4-(dimethylamine)pyridine) of cyclohex-2-enone (**31**) was used to produce the hydroxymethyl-cyclohexenone **32**. Esterification of **32** by crotonic anhydride afforded **21** (*36*).

Identification of Glutathione Conjugates Formed in Nonenzymatic Reactions. Nonenzymatic conjugation of glutathione is one of the mechanisms associated with the development of drug resistance. Therefore, an understanding of the nonenzymatic reactivity of selected substrates with GSH could provide clues about the chemical basis for conjugation. To investigate whether nonenzymatic substrate−GSH conjugation processes, observed in aqueous solution reactions, would also be important under physiological conditions, reactions of the electrophiles in 20 mM phosphate buffer (pH 7.0) at 25 °C in the presence of 0.5 mM glutathione were explored. Formation of glutathione conjugates were monitored by using ^{1}H NMR spectroscopy. Among the substances tested, **6**, **8**−**11**, **16**, **21**, and **22** (Figure 2) were found to undergo adduct formation producing the respective conjugates **6a**, **8a**−**11a**, **16a**, **21a**, and **22a** (Table 1 and Figure 3). This suggests that these electrophilic substrates have a high potential for generating nonenzymatic metabolites under physiological conditions. Interestingly, the other compounds were found to be stable in the presence of glutathione up to 5 h under the conditions employed.

***Sj*GST-Catalyzed Formation of Glutathione Conjugates.** In view of the protective function of *Sj*GST against potentially toxic foreign chemicals, we carried out studies to elucidate the nature of the conjugation reactions that this enzyme catalyzes with selected substrates. ^{1}H NMR spectroscopic analysis was used for this purpose, and the contributions of nonenzymatic conjugation reactions were taken into account. The results, summarized in Table 1, show that electrophiles **5**, **18**, and **23** (Figure 2) participate in *Sj*GST-catalyzed reactions with glutathione to form the respective adducts **5a**, **18a**, and **23a** (Figure 3). In each of these cases, no reaction occurs in the absence of the enzyme. In addition, *Sj*GST catalyzed the reaction of glutathione with **2** to give **2a**. The nonenzymatic contribution to this process is negligible (Table 1). For substrates **6**, **10**, **14**, and **22** (Figure 2), where incubation with glutathione at room temperature leads to fast reactions, the *Sj*GST-catalyzed processes were conducted in phosphate buffer (pH 6.5) at 4 °C to retard the competition from nonenzymatic reactions. The results show that under these conditions enzyme-catalyzed GSH conjugation is the primary route followed for **14** leading to **14a** and only a minor pathway for the conversion of **6** to **6a** (Table 1). On the other hand, it is not possible to distinguish between enzymatic and nonenzymatic reactions of **10** and **22** owing to the high rates of the latter processes. The accumulated observations demonstrate that **2**, **5**, **6**, **14**, **18**, and **23** are good substrates for *Sj*GST and that **1**, **3**, **4**, **7**−**9**, **11**−**13**, **15**−**17**, **19**−**21**, and **24** are not. This is the case even though some members of the latter group of electrophiles, including **8**−**11**, **16**, **21**, and **22**, undergo nonenzymatic reactions with glutathione to form GSH conjugates (Table 1).

Structural Identification of Glutathione Conjugates and Mechanistic Studies. Studies were conducted to elucidate the chemical structures and mechanisms of formation of the GSH conjugates. Reverse-phase HPLC was used to separate products **2a**, **5a**, **6a**, **14a**, **18a**, and **23a** from mixtures generated by *Sj*GST-catalyzed reactions of the electrophilic substrates **2**, **5**, **6**, **14**, **18**, and **23** with GSH. Assignments of the structures of **2a**, **5a**, and **6a** (Figure 3) were made by using ^{1}H, ^{13}C NMR, and HRMS methods. For the more complex GSH conjugates, **14a**, **18a**, and **23a**, structural determinations were made by using a combination of MS and two-dimensional NMR spectroscopic techniques. In Figure 4 is displayed the HPLC chromatogram

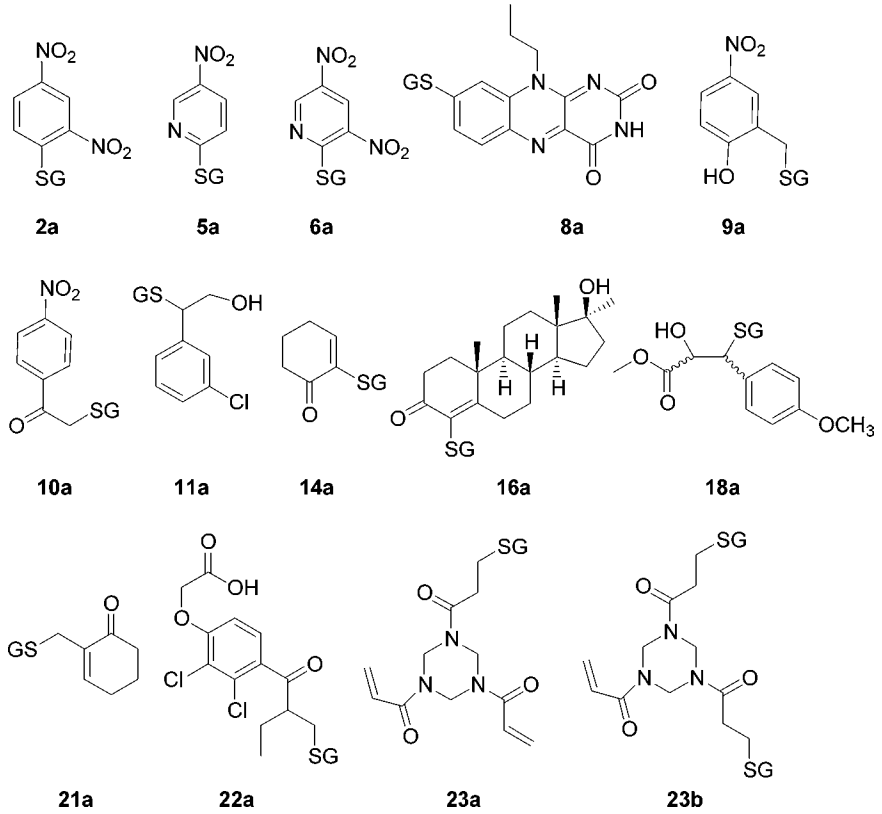


Figure 3. Structures of glutathione conjugates derived from nonenzymatic and enzymatic reactions.

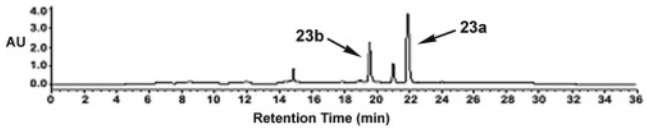


Figure 4. Reverse-phase HPLC chromatogram ($\lambda = 220$ nm) of the product mixture from *Sj*GST-catalyzed conjugation of **23**. Fractions were collected and identified with FAB-MS. The peaks containing the mono(glutathionyl) conjugate **23a** and bis(glutathionyl) conjugate **23b** are indicated with arrows.

of the mixture formed by reaction of **23** with *Sj*GST. The fractions corresponding to the peaks with retention times of 14.9, 19.2, 21.1, and 22.0 min were individually collected, lyophilized, and analyzed by fast atom bombardment (FAB) mass spectrometry and NMR spectroscopic methods (^{1}H and ^{13}C NMR, heteronuclear multiple-quantum coherence (HMQC), and heteronuclear multiple-bond correlation (HMBC)). FAB-MS analysis showed that two substances corresponding to GSH−**23** conjugates are formed in this process, a bis(glutathionyl) conjugate **23b** (retention time of 19.2 min) with $[M + H]^+$ ion at *m*/*z* 864 and a mono(glutathionyl) conjugate **23a** (retention time of 22.0 min) with $[M + H]^+$ ion at *m*/*z* 557 (Figure 5). The ratio of **23b**/**23a** is *ca.* 1:3 after 5 h as determined by integration of the well-resolved HPLC peaks. Only **23a** (without formation of **23b**) is observed to form during short reaction times, indicating that **23** most likely undergoes enzymatic activation *in vitro* to form the mono(glutathionyl) intermediate, **23a**. This substance then reacts with GSH to form the bis-(glutathionyl) conjugate, **23b**. This finding shows that the enzyme catalyzes Michael addition reactions of GSH with both **23** and **23a**. MS analysis indicates that no other types of GSH conjugates are formed in this process.

*Sj*GST was found to promote GSH conjugation reactions of the *cis* and *trans* isomers of epoxide **18**. The two products formed in these reactions were purified by reverse-phase HPLC (retention times 21.8 and 23.7 min) and found to have identical molecular ions ($[M + H]^+ = 516$). This is consistent with the assignment of *erythro* and *threo* structures of **18a** to these substances (Scheme 2). ^{1}H NMR and ^{13}C NMR spectra of these adducts are in agreement with the proposed structures, reported to form in Lewis acid-catalyzed reactions of the epoxides (*37*). *Sj*GST-catalyzed ring opening of the *cis* and *trans* isomers of epoxide **18** is expected to yield the *erythro* and *threo* isomers, respectively (Scheme 2).

Incubation of **14**, GSH, and *Sj*GST in phosphate buffer (pH 6.5) at 4 °C gives rise to **14a**, a substance that has a *m*/*z* of 402 ($[M + H]^+$). This corresponds to a substance formed by loss of one molecule of water from an initially formed GSH conjugate **33** (Scheme 3). The ^{1}H NMR spectrum of **14a** contains a chemical shift at 7.46 ppm (1 H) indicating the presence of an olefinic methine hydrogen, which is assigned to the β-proton of the α,β-unsaturated ketone moiety in **14a**. The observation of a methine proton (H-3) as a triplet (1H) with a coupling constant of 4.3 Hz, arising by coupling with C-4 methylene protons, further confirms this assignment. Additional evidence for the assignment of the structure of **14a** comes from analysis of 2D NMR (HMQC and ^{1}H−^{1}H correlation spectroscopy (COSY)) data. The HMQC spectrum of this substance shows a correlation between H-3 (7.46 ppm) and H-4a/H-4b (2.54 ppm) and carbon signals at δ 156.6 ppm (C-3) and 27.2 ppm (C-4), respectively. In the ^{1}H−^{1}H COSY spectrum (Figure 6), the H-3 methine triplet at δ 7.46 ppm shows a cross-peak at δ 2.54 ppm, attributed to the H-4a/H-4b methylene protons. These results confirm that the α,β-epoxylketone **14** undergoes *Sj*GST-catalyzed addition of glutathione to the C-α position and that the initially formed β-hydroxy sulfide **33** spontaneously loses water to produce the alkenyl sulfide **14a** (Scheme 3). It is also noteworthy that a similar mechanistic pathway is followed in the nonenzymatic reaction of **14** and in other reactions between α,β-epoxylketones and alkyl/aryl thiols (*38*).

Nonenzymatically generated GSH conjugates **8a**−**11a**, **16a**, **21a**, and **22a** were purified by reverse-phase HPLC and analyzed by using FAB-MS. The observation of *m*/*z* values of 562 ([M

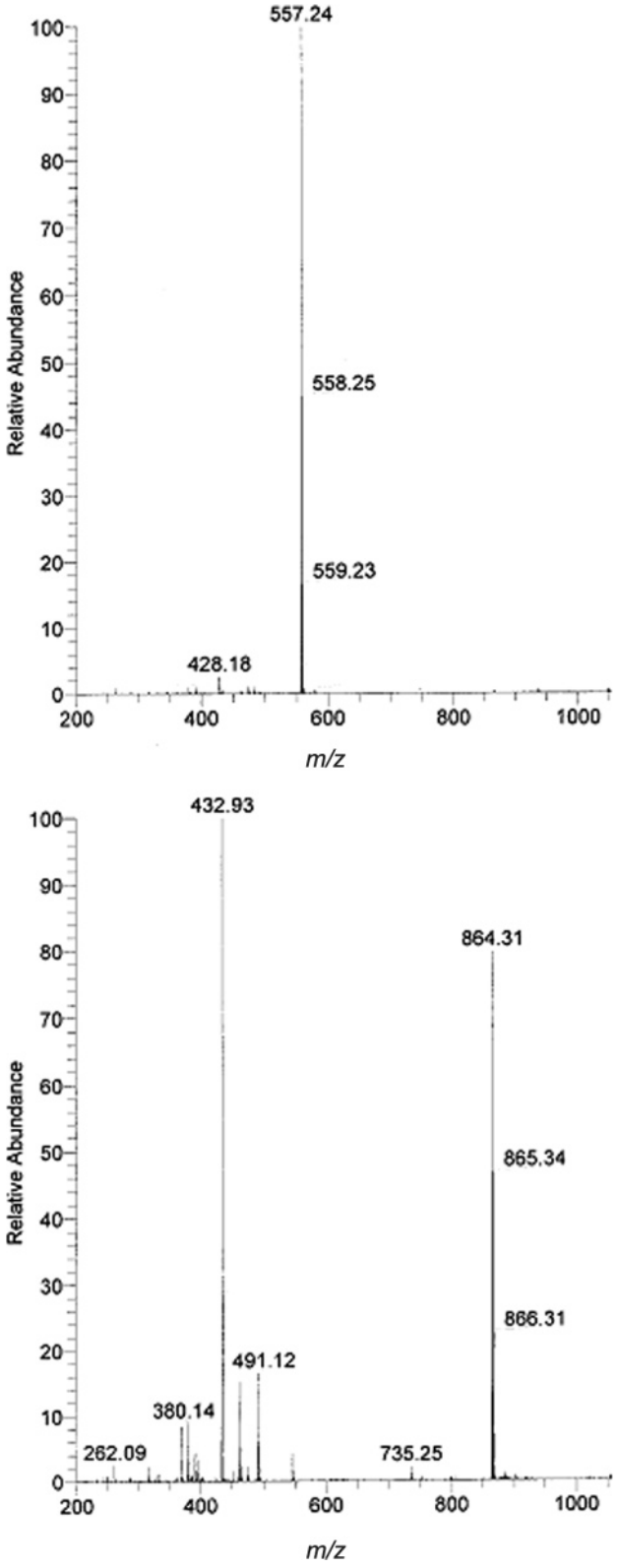


Figure 5. FAB-MS of the parent ions $[M + H]^+$ of mono(glutathionyl) conjugate **23a** and bis(glutathionyl) conjugate **23b** at *m*/*z* 557 and 864, respectively.

$+ H]^+$) for **8a**, *m*/*z* of 459 ($[M + H]^+$) for **9a**, *m*/*z* of 471 ($[M + H]^+$) for **10a**, *m*/*z* of 462 ($[M + H]^+$) for **11a**, and *m*/*z* of 610 ($[M + H]^+$) for **22a** (*39*) shows that they all are glutathione adducts. Also, **16a** and **21a**, obtained from HPLC peaks eluting at 25.82 and 6.63 min, respectively, have molecular weights of 608.3006/608.3014 and 416.1502/416.1501 (calculated molecular weight/measured molecular weight). These results indicate

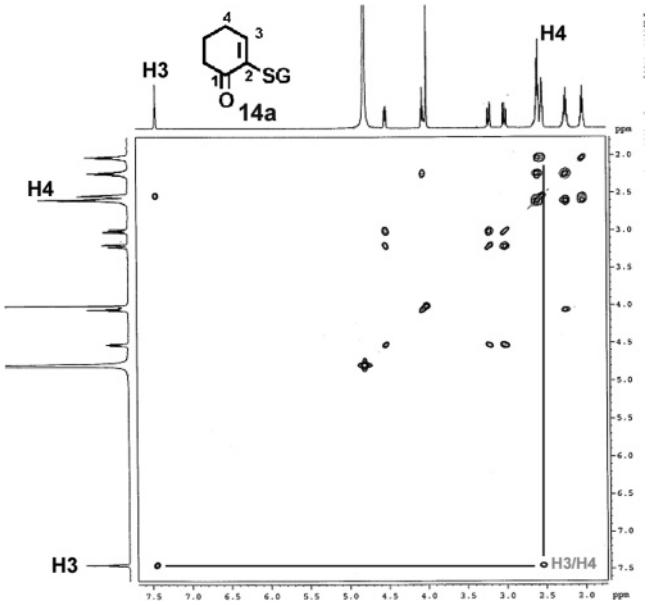


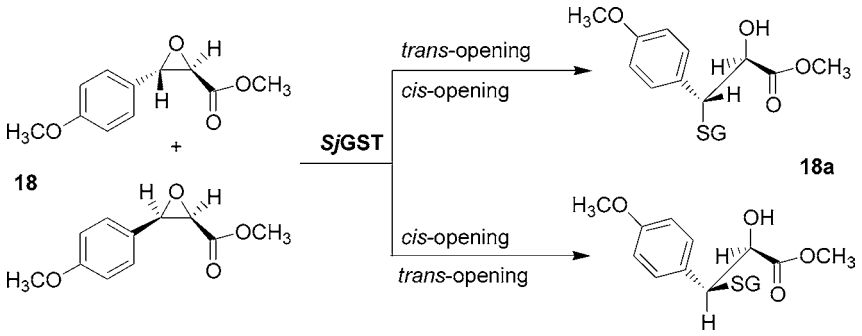
Figure 6. $[^1H,^1H]$-COSY NMR spectrum of GSH conjugate **14a** with assigned cross-peak of the H-3 methine and H-4 methylene protons (underlined).

that **16a** might be produced by loss of water from the intermediate GSH conjugate **34** (Scheme 4). The ^{13}C NMR spectrum of **16a** closely resembles that of *N*-(13-(*t*-butoxycarbonylamino)-4,7,10-trioxatridecanyl)-3-(pregn-4-ene-3,20-dione-4-yl)thiopropanamide (Chart 1) (*40*), in which the α,β-unsaturated carbon resonances at 125.6 (4-C) and 171.7 (5-C) ppm are characteristic of an alkenyl thiol. The chemical shifts associated with an alkenyl thiol moiety are observed in the ^{13}C NMR spectrum of **14a** and aromatase inhibitors (*41*). The ^1H NMR spectrum of **21a** contains a resonance at δ 7.16 ppm (triplet) indicating the presence of H3 of an β,γ-unsaturated 2-cyclohexenone. Moreover, the ^1H and ^{13}C NMR spectra of **21a** match those reported for **21a** (see the Supporting Information) from human glutathione transferase-catalyzed conversion of **21**, which arises by addition of glutathione to form the exocyclic enone intermediate, **35** (Scheme 5) (*42*−*45*).

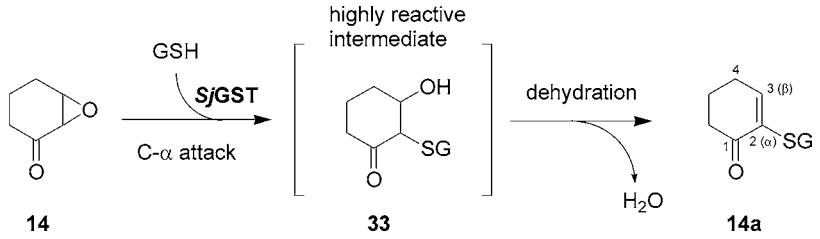
Kinetics of Glutathione Conjugate Formation. *Sj*GST was observed to accelerate the reaction of GSH with the electrophilic substrates **5**, **14**, **18**, and **23**. To determine which substrate reactions are sufficiently kinetically competent for *in vivo* metabolism, we measured k_{cat} values for *Sj*GST-catalyzed conjugation of **5**, **18**, and **23** in phosphate buffer (20 mM, pH 7.0) at 25 °C. In these processes, the amounts of products formed increased in a linear manner with increasing incubation times up to 10 or 50 min (data not shown). For these substrates, k_{cat} values were determined by measuring the initial rates of the GSH conjugation reactions as functions of substrate concentrations. The results of triplicate experiments are summarized in Table 2. The k_{cat} values for **23** and **18** are about 886-fold and about 14-fold larger than that for **5**, respectively. Due to the considerable amount of nonenzymatic reaction seen with **14**, the k_{cat} (0.037 ± 0.002 s^{-1}) was obtained in sodium phosphate buffer (20 mM, pH 6.5) at 4 °C. Similarly, the k_{cat} (187 ± 35 s^{-1}) value for **2** was measured under the same conditions due to the fast enzymatic reaction and the detectable nonenzymatic reaction. Among the electrophilic substrates tested except **2**, the reactivity order as determined by k_{cat} is **23** > **18** > **5** > **14**. Based on these results, it can be concluded that *Sj*GST might contribute to the detoxification of 1,3,5-triacryloylhexahydro-1,3,5-triazine (**23**) *in vivo*.

Inhibition of *Sj*GST by Nonenzymatically Derived GSH Conjugates 9a−11a, 16a, 21a, and 22a and Electrophilic

Scheme 2. Proposed Mechanism for *Sj*GST-Catalyzed GSH Conjugate 18a Formation



Scheme 3. Proposed Pathway for the Formation of GSH Conjugate 14a



Scheme 4. Proposed Pathway for the Conversion of 16 to 16a via Intermediate 34

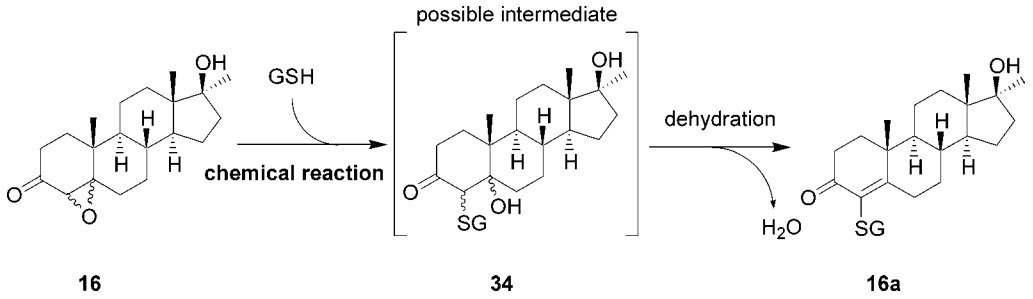
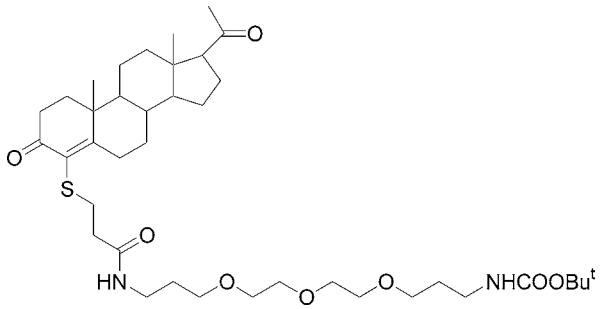


Chart 1. Chemical Structure of *N*-(13-(*t*-Butoxycarbonylamino)-4,7,10-trioxatridecanyl)-3-(pregn-4-ene-3,20-dione-4-yl)thiopropanamide



Substrates (9−11 and 22). The results of a number of earlier efforts have demonstrated that glutathione protects against the cytotoxicity of anticancer agents by causing either an increased level of GSH-mediated nucleophilic attack or an elevation in the level of cellular GST-catalyzed GSH conjugation. GSH conjugates are usually good inhibitors of GSTs *in vitro* or *in vivo*. Based on these reports, it was important to determine whether the nonenzymatically generated glutathione adducts have an effect on the *Sj*GST-catalyzed reactions. Additionally, the electrophilic substrates themselves might also play an inhibitory role in *Sj*GST-promoted reactions. To determine whether nonenzymatic products or electrophilic substrates could inhibit *Sj*GST, we incubated the enzyme with the nonenzymatic GSH conjugates **9a**−**11a**, **16a**, **21a**, and **22a** and the electrophiles **9**−**11** and **22** along with 0.25 mM GSH and 1 mM CDNB. The results, summarized in Table 3, show that nonenzymatic GSH conjugates **9a**−**11a**, **16a**, **21a**, and **22a** are inhibitors of *Sj*GST; **9a**−**11a**, **16a**, and **22a** displayed IC_{50} values of 1.95, 75.5, 0.96, 19.0, and 0.36 μM, which represent respective 78-, 2-, 158-, 8-, and 422-fold inhibitory enhancements over **21a** (IC_{50} = 152 μM). Together, the data serve to explain why conjugation reactions of some of electrophilic substrates are not catalyzed by *Sj*GST when the formation of nonenzymatic GSH conjugates occurs rapidly.

The ethacrynic acid **22** (EA) at concentrations in the 5 μM range is a significant inhibitor of *Sj*GST (*ca.* 80%). In contrast, when this substance is used in the 0.5 μM range, it is displays less efficient inhibition (*ca.* 45%). However, the adduct **22a** is a significant inhibitor of *Sj*GST (*ca.* 70%) even when it is used at the lower end of this concentration range (Figure 7). The results support the proposal that **22a**, owing to its rapid rate of formation, is able to efficiently inhibit the *Sj*GST process when low concentrations of **22** are used.

Results from studies of the inhibitory effects of substrates **9**−**11** and **22** are shown in Table 3, where the inhibitory data displayed are not corrected for contributions from the formation of glutathione conjugates. Both the substrate **10** and its GSH conjugate **10a** are micromolar inhibitors of *Sj*GST, with **10** being slightly more potent (IC_{50} = 65.0 μM) than **10a** (IC_{50} = 75.5 μM). It is interesting to note that this is the only example uncovered in this study that unambiguously provides direct evidence of substrate inhibition toward *Sj*GST. As expected, **22** has an IC_{50} value more than 2-fold lower than that of its GSH conjugate **22a** (IC_{50} = 0.36 μM) at 0.87 μM. This result is in line with the previous conclusion (see above) that the effect of **22a** on *Sj*GST occurs when low concentrations of **22** are used. Substrates **9** and **11** are weak *Sj*GST inhibitors (IC_{50} >

Scheme 5. Possible Enzymatic (*42*−*45*) and Nonenzymatic Conversion (This Study) of 21 to GSH Conjugate 21a

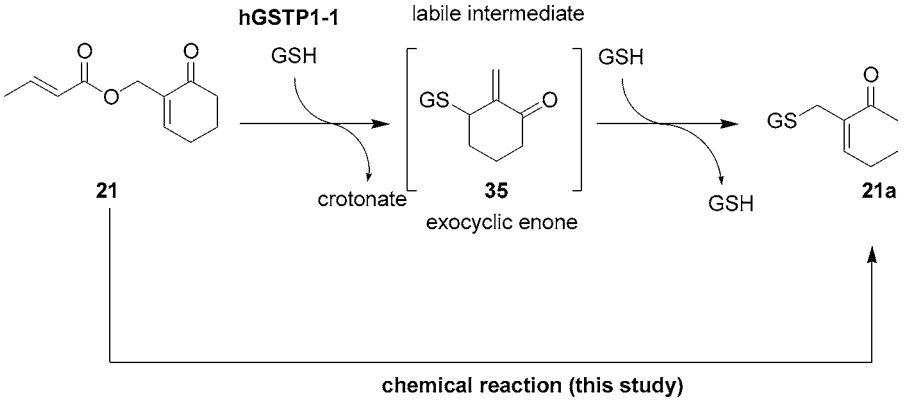


Table 3. Inhibition of *Sj*GST and hGSTA2 by Substrates and Nonezymatic Glutathione Conjugates

	IC_{50}[a] (μM)	
inhibitor	*Sj*GST	hGSTA2
9	>10 (14)[b]	>500 (5)[c]
10	65.0 ± 0.1	56 ± 13
11	>500 (27)[c]	>500 (0)[c]
22	0.87 ± 0.08	4.24 ± 0.47
9a	1.95 ± 0.07	5.65 ± 1.00
10a	75.5 ± 0.71	>250 (43)[d]
11a	0.96 ± 0.71	141 ± 37
16a	19.0 ± 7.2	10.5 ± 0.3
21a	152 ± 26	20 ± 7
22a	0.36 ± 0.01	2.08 ± 0.25

[a] Inhibitor concentration at which half-maximal enzyme activity is obtained (IC_{50}, mean ± SEM, $n = 3$). [b] The percent (%) inhibition, in parentheses, at 10 μM is expressed as the percent (%) inhibition of enzyme activity without correction for the contribution of the formation of glutathione conjugate. [c] The percent (%) inhibition, in parentheses, at 500 μM is expressed as the percent (%) inhibition of enzyme activity without correction for the contribution of the formation of glutathione conjugate. [d] The percent (%) inhibition, in parentheses, at 250 μM is expressed as the percent (%) inhibition of enzyme activity without correction for the contribution of the formation of glutathione conjugate.

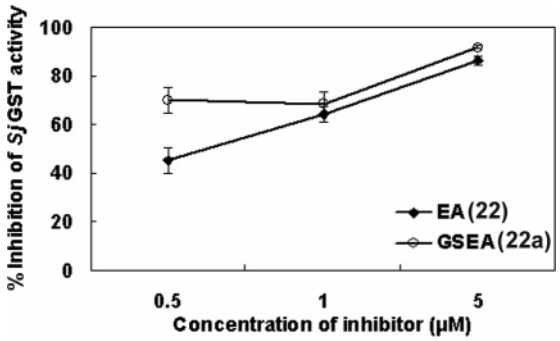


Figure 7. The inhibitory effects of EA **22** (0.5−5.0 μM) and GSEA **22a** (0.5−5.0 μM) on *Sj*GST activity. The data are expressed as % inhibition of *Sj*GST activity by **22** and **22a**.

10 μM for **9** with 14% inhibition at 10 μM, IC_{50} > 500 μM for **11** with 27% inhibition at 500 μM).

Cloning, Expression, Purification, and Characterization of Human GSTA2. Total RNA isolated from HeLa cells was subjected to oligo(dT)-directed cDNA synthesis. The resulting cDNA population was used as template in PCR to obtain the hGSTA2 transcripts (Figure 8A). The *E. coli* Rosetta(DE3) clone carrying recombinant hGSTA2 plasmid was expressed, and the hGSTA2 proteins were purified using HisTrap affinity column (Figure 8B). The specific activity of hGSTA2 (33.4 ± 0.6 μmol/(min·mg)) was measured by using the spectrophotometric assay procedure. The results show that the recombinant His-tagged protein has a higher specific activity than that reported earlier (*46*, *47*).

Inhibition of Human GSTA2 by Nonenzymatic GSH Conjugates and Selected Electrophilic Substrates. Given that nonenzymatic GSH conjugates **9a**−**11a**, **16a**, **21a**, and **22a** and electrophilic substrates **9**−**11** and **22** show inhibitory activity toward *Sj*GST, we examined the inhibition of hGSTA2 by these compounds. The results demonstrate that hGSTA2 is inhibited by these nonenzymatic GSH conjugates and electrophilic substrates in the same manner as is *Sj*GST. It is important to note that the conjugate **22a** is at least 2- to 120-fold more potent than the other conjugates (Table 3). Interestingly, the results reveal that **22a** is a potent inhibitor of human GSTA2 with an IC_{50} value of 2.08 μM, which is similar to the value (2.3 μM) obtained from the human GSTA1-1 inhibition assay (*48*). As expected, substrate **10** displays at least 4-fold greater inhibitory potency than that of the corresponding GSH conjugate **10a**. This observation indicates that the glutathionyl moiety in **10a** is not required for binding to hGSTA2. This contrasts with other substrate/GSH conjugate pairs (*e.g.*, **9**/**9a**, **11**/**11a**, and **22**/**22a**) where attachment of the glutathionyl group to substrate does enhance binding in the active site of GSTA2. As is evident from inspection of the data in Table 3, **11a** and **21a** and **22a** are potent and selective inhibitors of *Sj*GST and GSTA2, respectively.

In conclusion, the results of the study described herein demonstrate that electrophilic compounds, including aliphatic and aromatic halides (**2**, **5**, and **6**), epoxides (**14** and **18**), and an α,*β*-unsaturated carbonyl compound (**23**), undergo *Sj*GST-catalyzed *in vitro* reactions with glutathione to form the corresponding mono(glutathionyl) or bis(glutathionyl) conjugates. By using reverse-phase HPLC, NMR, and FAB-MS analysis, GSH conjugates formed in the enzymatic reactions

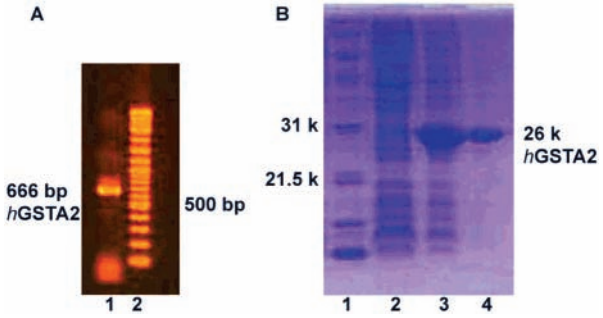


Figure 8. (A) hGSTA2 PCR products using HeLa cells total cDNA as template. Using RT-PCR, a 666-bp product corresponding to human GSTA2 was observed (lane 1). A 1-Kb DNA ladder is shown in lane 2. (B) Preparations of hGSTA2 are shown at various stages of purification on a Coomassie-stained 10% SDS−PAGE gel. Lane 1, marker; lane 2, cell extract before induction; lane 3, before purification; lane 4, hGSTA2 proteins eluted from HisTrap affinity column.

and in nonenzymatic processes were characterized and quantified. In comparison to other electrophiles except **2**, **23** was found to be a good substrate for *Sj*GST and the initially formed conjugation product **23a** also undergoes *Sj*GST-catalyzed glutathione conjugation to form **23b**. Additionally, we have demonstrated that both enzymatic and nonenzymatic products are produced under the conditions used for *Sj*GST-activated GSH conjugation. Moreover, the nonenzymatic GSH conjugates and electrophilic substrates probed in this effort have been found to inhibit catalysis by *Sj*GST. Also, these substances exhibit significant inhibitory activity against the human GST isozyme, hGSTA2. These inhibitors have considerable promise in explorations of the physiological relevance of hGST-mediated drug resistance in tumor cells.

ACKNOWLEDGMENT

We thanks Dr. Y.-J. Chen for generously providing us with total RNA of Hela cells. We thank the National Science Council (Grant NSC 94-2113-M-001-017) and Academia Sinica (Program Project AS-92-TP-A04) for financial support.

Supporting Information Available: Analytical data (^{1}H, ^{13}C NMR, and mass spectra) for **5a**−**23a**. This material is available free of charge via the Internet at http://pubs.acs.org.

LITERATURE CITED

(1) McIlwain, C. C., Townsend, D. M., and Tew, K. D. (2006) Glutathione S-transferase polymorphisms: cancer incidence and therapy. *Oncogene 25*, 1639−1648.

(2) Angelucci, F., Baiocco, P., Brunori, M., Gourlay, L., Morea, V., and Bellelli, A. (2005) Insights into the catalytic mechanism of glutathione S-transferase: The lesson from *Schistosoma haematobium*. *Structure 13*, 1241−1246.

(3) Balendiran, G. K., Dabur, R., and Fraser, D. (2004) The role of glutathione in cancer. *Cell Biochem. Funct. 22*, 343−352.

(4) Salinas, A. E., and Wong, M. G. (1999) Glutathione S-transferases-a review. *Curr. Med. Chem. 6*, 279−309.

(5) Wu, G., Fang, Y.-Z., Yang, S., Lupton, J. R., and Turner, N. D. (2004) Glutathione metabolism and its implications for health. *J. Nutr. 134*, 489−492.

(6) Paolicchi, A., Dominici, S., Pieri, L., Maellaro, E., and Pompella, A. (2002) Glutathione catabolism as a signaling mechanism. *Biochem. Pharmacol. 64*, 1027−1035.

(7) Stark, A. A., Zeiger, E., and Pagano, D. A. (1993) Glutathione metabolism by γ-glutamyltranspeptidase leads to lipid peroxidation: Characterization of the system and relevance to hepatocarcinogenesis. *Carcinogenesis 14*, 183−189.

(8) Mannervik, B., and Danielson, U. H. (1988) Glutathione transferases-structure and catalytic activity. *Crit. Rev. Biochem. 23*, 283−337.

(9) Hayes, J. D., Flanagan, J. U., and Jowsey, I. R. (2005) Glutathione transferases. *Annu. Rev. Pharmacol. 45*, 51−88.

(10) Hayes, J. D., and McLellan, L. I. (1999) Glutathione and glutathione-dependent enzymes represent a co-ordinately regulated defence against oxidative stress. *Free Radical Res. 31*, 273−300.

(11) Dirven, H. A. A. M., van Ommen, B., and van Bladeren, P. J. (1996) Glutathione conjugation of alkylating cytostatic drugs with a nitrogen mustard group and the role of glutathione S-transferases. *Chem. Res. Toxicol. 9*, 351−360.

(12) Burg, D., and Mulder, G. J. (2002) Glutathione conjugates and their synthetic derivatives as inhibitors of glutathione-dependent enzymes involved in cancer and drug resistance. *Drug Metab. Rev. 34*, 821−863.

(13) Cacciatore, I., Caccuri, A. M., Cocco, A., De Maria, F., Di Stefano, A., Luisi, G., Pinnen, F., Ricci, G., Sozio, P., and Turella, P. (2005) Potent isozyme-selective inhibition of human glutathione S-transferase A1−1. by a novel glutathione S-conjugate. *Amino Acids 29*, 255−261.

(14) Daunes, S., D'Silva, C., Kendrick, H., Yardley, V., and Croft, S. L. (2001) QSAR study on the contribution of log P and Es to the in vitro antiprotozoal activity of glutathione derivatives. *J. Med. Chem. 44*, 2976−2983.

(15) D'Silva, C., Daunes, S., Rock, P., Yardley, V., and Croft, S. L. (2000) Structure−activity study on the in vitro antiprotozoal activity of glutathione derivatives. *J. Med. Chem. 43*, 2072−2078.

(16) Satyam, A., Hocker, M. D., Kane-Maguire, K. A., Morgan, A. S., Villar, H. O., and Lyttle, M. H. (1996) Design, synthesis, and evaluation of latent alkylating agents activated by glutathione S-transferase. *J. Med. Chem. 39*, 1736−1747.

(17) Joseph, E., Ganem, B., Eiseman, J. L., Creighton, D. J. (2005) Selective inhibition of MCF-7piGST breast tumors using glutathione transferase-derived 2-methylene-cycloalkenones. *J. Med. Chem. 48*, 6549−6552.

(18) Rooseboom, M., Commandeur, J. N. M., and Vermeulen, N. P. E. (2004) Enzyme-catalyzed activation of anticancer prodrugs. *Pharmacol. Rev. 56*, 53−102.

(19) Rosen, L. S., Brown, J., Laxa, B., Boulos, L., Reiswig, L., Henner, W. D., Lum, R. T., Schow, S. R., Maack, C. A., Keck, J. G., Mascavage, J. C., Dombroski, J. A., Gomez, R. F., and Brown, G. L. (2003) Phase I study of TLK286 (glutathione S-transferase P1−1 activated glutathione analogue) in advanced refractory solid malignancies. *Clin. Cancer Res. 9*, 1628−1638.

(20) Nebert, D. W., and Vasiliou, V. (2004) Analysis of the glutathione S-transferase (GST) gene family. *Hum. Genomics 1*, 460−464.

(21) Hu, W., Yan, Q., Shen, D.-K., Liu, F., Zhu, Z.-D., Song, H.-D., Xu, X.-R., Wang, Z.-J., Rong, Y.-P., Zeng, L.-C., Wu, J., Zhang, X., Wang, J.-J., Xu, X.-N., Wang, S.-Y., Fu, G., Zhang, X.-L., Wang, Z.-Q., Brindley, P. J., McManus, D. P., Xue, C.-L., Feng, Z., Chen, Z., and Han, Z.-G. (2003) Evolutionary and biomedical implications of a *Schistosoma japonicum* complementary DNA resource. *Nat. Genet. 35*, 139−147.

(22) Mascie-Taylor, C. G. N., and Karim, E. (2003) The burden of chronic disease. *Science 302*, 1921−1923.

(23) Nwaka, S., and Ridley, R. G. (2003) Science & society: Virtual drug discovery and development for neglected diseases through public-private partnerships. *Nat. Rev. Drug Discovery 2*, 919−928.

(24) Kensler, T. W., Qian, G.-S., Chen, J.-G., and Groopman, J. D. (2003) Translational strategies for cancer prevention in liver. *Nat. Rev. Cancer 3*, 321−329.

(25) Kohn, A. B., Anderson, P. A. V., Roberts-Misterly, J. M., and Greenberg, R. M. (2001) Schistosome calcium channel β subunits. Unusual modulatory effects and potential role in the action of the antischistosomal drug praziquantel. *J. Biol. Chem. 276*, 36873−36876.

(26) Utzinger, J., Xiao, S., Keiser, J., Chen, M., Zheng, J., and Tanner, M. (2001) Current progress in the development and use of artemether for chemoprophylaxis of major human schistosome parasites. *Curr. Med. Chem. 8*, 1841−1859.

(27) Woolhouse, M. E. J., and Hagan, P. (1999) Seeking the ghost of worms past. *Nat. Med. 5*, 1225−1227.

(28) Jao, S.-C., Chen, J., Yang, K., and Li, W.-S. (2006) Design of potent inhibitors for *Schistosoma japonica* glutathione S-transferase. *Bioorg. Med. Chem. 14*, 304−318.

(29) Habig, W. H., and Jakoby, W. B. (1981) Assays for determination of glutathione S-transferase. *Methods Enzymol. 77*, 398−405.

(30) Dirven, H. A. A. M., van Ommen, B., and van Bladeren, P. J. (1996) Glutathione conjugation of alkylating cytostatic drugs with a nitrogen mustard group and the role of glutathione S-transferases. *Chem. Res. Toxicol. 9*, 351−360.

(31) Li, W.-S., Zhang, N., and Sayre, L. M. (2001) N^1,N^{10}-Ethylene-bridged high-potential flavins: synthesis, characterization, and reactivity. *Tetrahedron 57*, 4507−4522.

(32) Breslin, H. J., Kukla, M. J., Kromis, T., Cullis, H., De Knaep, F., Pauwels, R., Andries, K., De Clercq, E., Janssen, M. A. C., and Janssen, P. A. J. (1999) Synthesis and anti-HIV activity of 1,3,4,5-tetrahydro-2H-1,4-benzodiazepin-2-one (TBO) derivatives. Truncated 4,5,6,7-tetrahydro-5-methylimidazo[4,5,1-jk][1,4]benzodiazepin-2(1,H)-ones (TIBO) analogues. *Bioorg. Med. Chem. 7*, 2427−2436.

(33) Kumar, V., Woode, K. A., Bryan, R. F., and Averill, B. A. (1986) Evidence for a competing condensation reaction in the alloxan synthesis of flavins: synthesis and crystal and molecular structures of 7-chloro-8-methylalloxazine and 7,10-dimethyl-8-[(2-hydroxyethyl)thio]isoalloxazine. *J. Am. Chem. Soc. 108*, 490−496.

(34) Syamala, M. S., Das, J., Baskaran, S., and Chandrasekaran, S. (1992) A novel and highly β-selective epoxidation of Δ5-unsaturated steroids with permanganate ion. *J. Org. Chem. 57*, 1928−1930.

(35) Ringold, H. J., Batres, E., Mancera, O., and Rosenkranz, G. (1956) Steroids. LXXXII. Synthesis of 4-halo hormone analogs. *J. Org. Chem. 21*, 1432−1435.

(36) Hamilton, D. S., Zhang, X., Ding, Z., Hubatsch, I., Mannervik, B., Houk, K. N., Ganem, B., and Creighton, D. J. (2003) Mechanism of the glutathione transferase-catalyzed conversion of antitumor 2-crotonyloxymethyl-2-cycloalkenones to GSH adducts. *J. Am. Chem. Soc. 125*, 15049−15058.

(37) Hashiyama, T. (2000) Applications of Lewis acids for the efficient syntheses of diltiazem, cephems, and taxoids. *Med. Res. Rev. 20*, 485−501.

(38) Fringuelli, F., Pizzo, F., and Vaccaro, L. (2004) NaOH-catalyzed thiolysis of epoxyketones in water. A key step in the synthesis of target molecules starting from unsaturated ketones. *J. Org. Chem. 69*, 2315−2321.

(39) Dietze, E. C., Grillo, M. P., Kalhorn, T., Nieslanik, B. S., Jochheim, C. M., and Atkins, W. M. (1998) Thiol ester hydrolysis catalyzed by glutathione S-transferase A1-1. *Biochemistry 37*, 14948−14957.

(40) Mitchell, J. S., Wu, Y., Cook, C. J., and Main, L. (2005) Sensitivity enhancement of surface plasmon resonance biosensing of small molecules. *Anal. Biochem. 343*, 125−135.

(41) Lesuisse, D., Gourvest, J. F., Hartmann, C., Tric, B., Benslimane, O., Philibert, D., and Vevert, J. P. (1992) Synthesis and evaluation of a new series of mechanism-based aromatase inhibitors. *J. Med. Chem. 35*, 1588−1597.

(42) Hamilton, D. S., Zhang, X., Ding, Z., Hubatsch, I., Mannervik, B., Houk, K. N., Ganem, B., and Creighton, D. J. (2003) Mechanism of the glutathione transferase-catalyzed conversion of antitumor 2-crotonyloxymethyl-2-cycloalkenones to GSH adducts. *J. Am. Chem. Soc. 125*, 15049−15058.

(43) Joseph, E., Eiseman, J. L., Hamilton, D. S., Wang, H., Tak, H., Ding, Z., Ganem, B., and Creighton, D. J. (2003) Molecular basis of the antitumor activities of 2-crotonyloxymethyl-2-cycloalkenones. *J. Med. Chem. 46*, 194−196.

(44) Hamilton, D. S., Ding, Z., Ganem, B., and Creighton, D. J. (2002) Glutathionyl transferase catalyzed addition of glutathione to COMC: A new hypothesis for antitumor activity. *Org. Lett. 4*, 1209−1212.

(45) Zhang, Q., Ding, Z., Creighton, D. J., Ganem, B., and Fabris, D. (2002) Alkylation of nucleic acids by the antitumor agent COMC. *Org. Lett. 4*, 1459−1462.

(46) Yang, Y., Cheng, J. Z., Singhal, S. S., Saini, M., Pandya, U., Awasthi, S., and Awasthi, Y. C. (2001) Role of glutathione *S*-transferases in protection against lipid peroxidation. Overexpression of hGSTA2-2 in K562 cells protects against hydrogen peroxide-induced apoptosis and inhibits JNK and caspase 3 activation. *J. Biol. Chem. 276*, 19220−19230.

(47) Zhao, T., Singhal, S. S., Piper, J. T., Cheng, J., Pandya, U., Clark-Wronski, J., Awasthi, S., and Awasthi, Y. C. (1999) The role of human glutathione S-transferases hGSTA1-1 and hGSTA2-2 in protection against oxidative stress. *Arch. Biochem. Biophys. 367*, 216−224.

(48) Burg, D., Riepsaame, J., Pont, C., Mulder, G., and van de Water, B. (2006) Peptide-bond modified glutathione conjugate analogs modulate GST pi function in GSH-conjugation, drug sensitivity and JNK signaling. *Biochem. Pharmacol. 71*, 268−277.

BC0601727

Copper-Activated DNA Photocleavage by a Pyridine-Linked Bis-Acridine Intercalator

María-José Fernández,[†] Beth Wilson,[‡] Marta Palacios,[†] María-Melia Rodrigo,[§] Kathryn B. Grant,*[,‡] and Antonio Lorente*[,†]

Departamento de Química Orgánica and Departamento de Química-Física, Universidad de Alcalá, 28871-Alcalá de Henares, Madrid, Spain, and Department of Chemistry, Center for Biotechnology and Drug Design, Georgia State University, P.O. Box 4098, Atlanta, Georgia 30303-4098. Received June 26, 2006; Revised Manuscript Received October 16, 2006

We report the synthesis of new photonuclease **4** consisting of two acridine rings joined by a pyridine-based copper binding linker. We have shown that photocleavage of plasmid DNA is markedly enhanced when this ligand is irradiated in the presence of copper(II) (419 nm, 22 °C, pH 7.0). Viscometric data indicate that **4** binds to DNA by monofunctional intercalation, and equilibrium dialysis provides an estimated binding constant of 1.13 $\times$ 10^5 M^{-1} for its association with calf thymus DNA. In competition dialysis experiments, **4** exhibits preferential binding to GC-rich DNA sequences. When Cu(II) is added at a ligand to metal ratio of 1:1, electrospray ionization mass spectrometry demonstrates that compound **4** undergoes complex formation, while thermal melting studies show a 10 °C increase in the T_m of calf thymus DNA. Groove binding and intercalation are suggested by viscometric data. Finally, colorimetric and scavenger experiments indicate that the generation of Cu(I), H_2O_2, and superoxide contributes to the production of DNA frank strand breaks by the Cu(II) complex of **4**. Whereas the strand breaks are distributed in a relatively uniform fashion over the four DNA bases, subsequent piperidine treatment of the photolysis reactions shows that alkaline labile lesions occur predominantly at guanine.

INTRODUCTION

The design and synthesis of small molecules that bind to and cleave nucleic acids are still major challenges. These artificial nucleases have important applications as tools in molecular biology and as potential therapeutic agents for the treatment of cancer and viral diseases. DNA cleavage is often associated with redox-active or photoactivated transition metal complexes (*1*−*3*). To date, a number of metal complexes capable of inducing double-stranded DNA lesions have been developed (*4*−*7*).

Photosensitization of intercalating units can promote DNA damage by three main mechanisms: (a) electron transfer from DNA nucleobases, especially guanine, to a photochemically excited state of the intercalator, (b) photogeneration of hydroxyl radicals, an intermediate reactive species which can abstract hydrogen atoms from the DNA sugar backbone, and (c) preferential oxidation of guanines by singlet molecular oxygen generated through energy transfer from an electronically excited photosensitizer (*8*−*11*). In some cases, photoreduction of metal complexes is an important step in DNA cleavage reactions (*12*−*16*).

Photochemical DNA-cleaving molecules can be used as photonucleases, as photofootprinting agents, and as drugs in photodynamic therapy. Copper exists at micromolar levels in serum and other biological fluids (*17*) and is closely associated with nucleic acids and chromosomes (*18*−*20*), where it is thought to play a role in regulating gene expression (*21*, *22*). Taking this into account, photonucleases which bind to copper may be of greater utility at the cellular level in comparison to photonucleases containing other transition metals or to chemical nucleases which require an external reducing agent. Accordingly, a number of references on copper binding complexes with photolytic activity have appeared in the literature (*14*−*15*, *23*−*35*). While in vivo levels of free copper are tightly controlled by proteins (*36*−*38*), the kinetically labile nature of this metal allows ion exchange between small ligands and proteins to take place (*38*, *39*).

Herein, we present the synthesis, characterization, and DNA photocleaving properties of a pyridine-linked bis-acridine intercalator (**4**). We have found that **4** is a good DNA photocleaver, but that cleavage efficiency is markedly enhanced in the presence of Cu(II), converting pUC19 plasmid DNA into its nicked and linear forms upon exposure to visible light (419 nm, pH 7.0, 22 °C). Use of the colorimetric reagent bathocuproinedisulfonic acid disodium salt hydrate (BCS) indicates that the DNA photocleavage reaction involves acridine-sensitized photoreduction of Cu(II) to Cu(I).

MATERIALS AND METHODS

General Procedures. Merck silica gel 60 (230−400 ASTM mesh) was employed for flash column chromatography. TLC was performed on precoated aluminum silica gel plates (Merck or Macherey-Nagel 60F254 0.25 mm). Melting points were determined in an Electrothermal digital IA9100 apparatus. Infrared spectra were taken on an FT−IR Perkin-Elmer 1725X spectrophotometer. All ^1H and ^{13}C NMR spectra were recorded at 300 and 75 MHz, respectively, on a Varian Mercury-VX-300 spectrometer. Chemical shifts are reported in parts per million (ppm) using the residual peaks of either chloroform (δ 7.26 and 77.0 ppm) or methanol (δ 3.30 and 49.0 ppm) as an internal reference. Carbon and proton assignments were based on HSQC and HMBC experiments. CI mass spectra were generated on a Hewlett-Packard HP-5988a spectrometer at 70 eV. An Automass Multi GC/API/MS Finnigan spectrometer was used for ESI mass spectra. Elemental analyses were performed with a Heraeus CHN analyzer. A Cary Bio100 UV−visible

* Corresponding authors. E-mail: antonio.lorente@uah.es; Fax: 34 91 885 46 86 (A.L.). E-mail: kbgrant@gsu.edu; Fax: 1-404-651-1416 (K.B.G.).

[†] Departamento de Química Orgánica, Universidad de Alcalá.

[‡] Georgia State University.

[§] Departamento de Química-Física, Universidad de Alcalá.

10.1021/bc0601828 CCC: $37.00 © 2007 American Chemical Society
Published on Web 12/24/2006

spectrophotometer (Varian) was used to plot thermal melting curves, while all other UV−visible spectra were recorded with a Shimadzu UV-1601 or a Lambda 18 Perkin-Elmer spectrophotometer. DNA photolysis reactions were run in an aerobically ventilated Rayonet Photochemical Reactor fitted with eight RPR−4190 Å lamps (The Southern New England Ultraviolet Company).

Reagents were of the highest available purity and were used without further purification. L-Ascorbic acid, catalase, copper(II) chloride dihydrate, sodium phosphate monobasic and dibasic salts, and superoxide dismutase were purchased from Sigma. Glycogen and G-50 Sephadex columns were from Roche Applied Science. Sequenase Version 2.0, Sequenase Stop Solution, and [^{35}S]dATPαS were supplied by Amersham Biosciences. *Eco*RI and *Fsp*I restriction endonucleases were from New England Biolabs. All other chemicals including bathocuproinedisulfonic acid disodium salt hydrate, dimethyl sulfoxide, ethanol, ethidium bromide, D-mannitol, piperidine, and sodium azide were obtained from the Aldrich Chemical Company. Both 2,6-bis[(2-hydroxyethyl)methylaminomethyl]-pyridine (**1**) (*40*) and (6-amino-3-acridinyl)carbamic acid methyl ester (**3**) (*41*) were prepared according to reported procedures.

Transformation of *E. coli* competent cells (Stratagene, XL-1 blue) with pUC19 plasmid DNA (Sigma) and growth of bacterial cultures were performed according to established methods (*42*). Purification of the plasmid DNA was accomplished using a Qiagen Plasmid Mega Kit. All enzymes were used according to manufacturer's instructions in the buffers supplied.

2,6-Bis[(2-chloroethyl)methylaminomethyl]pyridine (2). Thionyl chloride (10 mL) was added to 348 mg (1.32 mmol) of 2,6-bis[(2-hydroxyethyl)methylaminomethyl]pyridine (**1**). The reaction mixture was stirred at room temperature for 24 h and then was concentrated at reduced pressure, affording a syrup characterized as **2**·HCl. IR (film): ν 3393, 2968, 2666, 1598, 1463, 1407, 1217, 1160, 756 cm^{-1}. ^{1}H-NMR (CD_3OD): δ 8.04 (t, J = 7.7 Hz, H4), 7.56 (d, J = 7.7 Hz, 2H, H3, H5), 4.62 and 4.80 (AB, 4H, J = 14 Hz, CH_2-pyr), 4.12 (t, J = 6.4 Hz, 4H, CH_2Cl), 3.69 (m, 4H, CH_2N), 3.01 (s, 6H, CH_3). ^{13}C-NMR (CD_3OD): δ 151.44 (C2, C6), 140.92 (C4), 125.41 (C3, C5), 60.54 (CH_2-pyr), 58.33 (CH_2N), 42.21 (CH_3), 38.04 (CH_2Cl). To a solution of 1.23 g (3.08 mmol) of **2**·HCl in methanol (20 mL), 1.14 g (10.78 mmol) of Na_2CO_3 was added. The mixture was stirred for 3 h and then concentrated to dryness. The residue was treated with dichloromethane (25 mL), and the mixture was washed three times with water (10 mL). The organic layer was dried over $MgSO_4$, filtered, and concentrated at reduced pressure to yield **2** as a brown oil (580 mg, 65%). IR (film): ν 2950, 2795, 1591, 1577, 1455, 1353, 1305, 1262, 1118, 1062, 739 cm^{-1}. ^{1}H-NMR ($CDCl_3$): δ 7.65 (t, J = 7.7 Hz, 1H, H4), 7.35 (d, J = 7.7 Hz, 2H, H3, H5), 3.73 (s, 4H, CH_2-pyr), 3.59 (t, J = 6.9 Hz, 4H, CH_2Cl), 2.81 (t, J = 6.9 Hz, 4H, CH_2N), 2.35 (s, 6H, CH_3). ^{13}C-NMR ($CDCl_3$): δ 158.23 (C2, C6), 136.93 (C4), 121.31 (C3, C5), 63.59 (CH_2-pyr), 58.69 (CH_2N), 42.59 (CH_3), 41.56 (CH_2Cl). MS (CI) m/z 290 ([M + H]$^+$, 39%), 254 (100) (calcd $C_{13}H_{21}Cl_2N_3$ 289.1). Anal. Calcd for $C_{13}H_{21}Cl_2N_3$: C, 53.80; H, 7.29; N, 14.48; Cl 24.43. Found: C, 53.94; H, 7.09; N, 14.77.

2,6-Bis{[((6-amino-acridin-3-yl)methoxycarbonylamino)-ethyl]methylaminomethyl}pyridine (**4**). To a solution of (6-amino-3-acridinyl)carbamic acid methyl ester (**3**) (184 mg, 0.69 mmol) in dry DMF (5 mL), 80% NaH (41 mg, 1.38 mmol) was added. The reaction mixture was stirred under an argon atmosphere for 20 min, and then a solution of 2,6-bis[(2-chloroethyl)methylaminomethyl]pyridine (**2**) (100 mg, 0.345 mmol) in dry DMF (6 mL) was added. The reaction mixture was heated at 50 °C for 20 h, and then concentrated at reduced pressure. The crude product thus obtained was purified by flash column chromatography on silica gel using ethyl acetate/acetone/triethylamine (5:3:1), affording unreacted carbamate **3**. Continued elution with ethyl acetate/methanol/triethylamine (10:2:1) afforded the desired product as an oil. The product was then dissolved in chloroform and precipitated with diethyl ether, affording 81 mg (31%) of an orange solid. Mp: 128−130 °C. IR (KBr): ν 3414, 1702, 1638, 1612, 1459, 1383, 1158 cm^{-1}. ^{1}H-NMR ($CDCl_3$): δ 8.49 (s, 2H, H9), 7.85 (d, J = 2.2 Hz, 2H, H4), 7.80 (d, J = 9.0 Hz, 2H, H1), 7.77 (d, J = 9.0 Hz, 2H, H8), 7.35 (t, J = 7.7 Hz, 1H, H4 pyr), 7.30 (dd, J = 9.0, 2.2 Hz, 2H, H2), 7.19 (d, J = 2.2 Hz, 2H, H5), 7.09 (d, J = 7.7 Hz, 2H, H3, H5 pyr), 7.00 (dd, J = 9.0, 2.2 Hz, 2H, H7), 3.95 (t, J = 6.9 Hz, 4H, CH_2N-acridine), 3.68 (s, 6H, OCH_3), 3.55 (s, 4H, CH_2-pyr), 2.63 (t, J = 6.9 Hz, 4H, CH_2NMe), 2.17 (s, 6H, NCH_3). ^{13}C-NMR ($CDCl_3$): δ 158.40 (C2, C6 pyr), 155.86 (CO), 151.16 (C10a), 149.51 (C4a), 148.65 (C6), 143.57 (C3), 136.57 (C4 pyr), 135.42 (C9), 129.72 (C8), 128.57 (C1), 124.63 (C2), 124.06 (C4), 123.20 (C9a), 121.94 (C8a), 120.82 (C3, C5 pyr), 120.15 (C7), 106.00 (C5), 63.77 (CH_2-pyr), 55.46 (CH_2NMe), 52.96 (OCH_3), 48.31 (CH_2N-acridine), 42.52 (NCH_3). MS (ESI) m/z 752 [M + H]$^+$ (calcd for $C_{43}H_{45}N_9O_4$ 751.36). Anal. Calcd for $C_{43}H_{45}N_9O_4$: C, 68.69; H, 6.03; N, 16.77. Found: C, 68.81; H, 6.13; N, 16.49. A stock solution of **4** was prepared in dimethyl sulfoxide (purity ≥99.9%) and was stored at −20 °C until use.

Viscometric Titrations. UltraPure Calf Thymus DNA (Invitrogen Catalog Number 15633−019, average size ≤2000 bp, 10 mg/mL in ddH_2O) was used without further purification. Viscosity experiments were conducted in a Cannon-Ubbelohde size 75 capillary viscometer immersed in a thermostated, circulating water bath maintained at 25 ± 0.2 °C. Compound **4** was titrated in buffer A: 6 mM Na_2HPO_4, 2 mM NaH_2PO_4, 1 mM Na_2EDTA, and 15 mM NaCl (pH 7.0). Alternatively, Cu(II) and Cu(II)−**4** (ligand to metal ratio of 1:1) were titrated in buffer B: 20 mM sodium phosphate (pH 7.0). In three separate titrations, a total of five 10-μL aliquots of each of the following three stock solutions were sequentially added to 1000 μL of the appropriate buffer in the viscometer containing 200 μM bp calf thymus (CT) DNA: (i) **4** (400 μM in buffer A); (ii) Cu(II)−**4** (400 μM each, in buffer B), and Cu(II) (400 μM in buffer B). After each sequential addition, the resulting solution was allowed to equilibrate for 15 min before the flow time was recorded with a stopwatch. (The final concentrations of **4**, Cu(II)−**4**, and Cu(II) ranged from 4 to 20 μM in each of the three titrations.) The flow times of the buffer and then of the DNA in the buffer were also recorded. All measurements were averaged over four trials to an accuracy of ±0.2 s. After subtracting the averaged flow time of the buffer, DNA (η_0) and dye-DNA (η) averaged flow times were plotted as $(\eta/\eta_o)^{1/3}$ versus the molar ratio r of dye to DNA bp (*43*). Slopes were generated by conducting linear least-square fits to these data (*KaleidaGraph* version 3.6.4 software).

Competition Dialysis Assay. Calf thymus (CT), *Clostridium perfringens* (CP), and *Micrococcus lysodeikticus* (ML) DNAs and the synthetic polynucleotides poly(dA)-poly(dT), [poly-(dGdC)]$_2$, and [poly(dAdT)]$_2$ were purchased from Sigma and were used without further purification. A buffer containing 6 mM Na_2HPO_4, 2 mM NaH_2PO_4, 1 mM Na_2EDTA, and 185 mM NaCl (pH 7.0) was utilized in the preparation of all nucleic acid stock solutions. The concentrations of the nucleic acid solutions were determined by UV−visible spectrophotometry using the λ_{max} values and extinction coefficients listed in Table S1 (Supporting Information). In a buffer consisting of 6 mM Na_2HPO_4, 2 mM NaH_2PO_4, 1 mM Na_2EDTA, and 15 mM NaCl (pH 7.0), competition dialysis experiments were performed as described by Chaires (*44*, *45*). For each dialysis assay, a 0.5 mL volume of DNA (75 μM bp DNA in buffer; Table S1) was

pipetted into one of six individual Spectra/Por DispoDialyzer units (S135062, Spectrum Laboratories, Inc.). The six dialysis units were then placed in a beaker containing 225 mL of a 1.5 μM solution of **4** in buffer. The beaker was covered with Parafilm and wrapped in foil, and its contents were allowed to equilibrate with continuous stirring for 24 h at room temperature (20−22 °C). At the end of the equilibration period, the DNA solutions inside the dialysis units were carefully transferred to microcentrifuge tubes, and a 10.0% (w/v) stock solution of sodium dodecyl sulfate (SDS) was added to give a final concentration of 1.0% (w/v). The DNA−SDS solutions were allowed to equilibrate for 2 h, after which the total concentration of ligand **4** (C_t) was determined by UV−visible absorbance measurements using the extinction coefficient for free ligand **4** in the presence of 1.0% SDS ($\epsilon_{451} = 22\,716\ M^{-1}\ cm^{-1}$). An appropriate correction for the slight dilution of the sample resulting from the addition of SDS stock solution was made. The concentration of free ligand **4** (C_f; $\epsilon_{451} = 12\,500\ M^{-1}\ cm^{-1}$) was also determined spectrophotometrically using an aliquot of the dialysate solution. The amount of DNA-bound **4** (C_b) was calculated by the difference ($C_b = C_t - C_f$).

Thermal Melting Studies. Individual 3 mL solutions containing 15 μM bp of calf thymus DNA (Invitrogen cat. #15633−019) in 20 mM sodium phosphate buffer pH 7.0 or in 20 mM sodium phosphate buffer pH 7.0, 10 μM **4**, and/or 10 μM $CuCl_2$ were placed in 3 mL (1 cm) quartz cuvettes (Starna). The DNA was then denatured by increasing the temperature from 25 °C to 100 °C at a rate of 0.5 °C min^{-1}, while absorbance was monitored at 260 nm. *KaleidaGraph* version 3.5 software was used to approximate the first derivative of $\Delta A_{260}/\Delta T$ vs temperature, where the T_m value for each melting transition was marked by the maximum of the first derivative plot.

Photocleavage of Supercoiled Plasmid DNA. Concentration profile reactions were conducted in a volume of 20 μL as follows. A total of 38 μM bp of pUC19 plasmid DNA in 20 mM sodium phosphate buffer pH 7.0 or in 20 mM sodium phosphate buffer pH 7.0, 50 μM, 30 μM, 20 μM, 10 μM, 5 μM, or 2 μM of $CuCl_2$ and/or 1 mol equiv (50 μM, 30 μM, 20 μM, 10 μM, 5 μM, or 2 μM) of **4** was irradiated for 50 min at 419 nm and 22 °C. A parallel control reaction consisting of 20 mM sodium phosphate buffer pH 7.0, 38 μM bp of pUC19, 50 μM of $CuCl_2$, and 50 μM of **4** was kept in the dark for 50 min.

Individual time course reactions were conducted in a volume of 20 μL. A total of 38 μM bp of pUC19 plasmid DNA in 20 mM sodium phosphate buffer pH 7.0 or in 20 mM sodium phosphate buffer pH 7.0, 50 μM $CuCl_2$, and/or 50 μM **4** was irradiated at 419 nm and 22 °C. The 20 μL reactions were removed from the Rayonet Photochemical Reactor at 10, 20, 30, 40, or 50 min time intervals. Parallel controls consisting of 20 mM sodium phosphate buffer pH 7.0, 38 μM bp of pUC19 plasmid, 50 μM of $CuCl_2$, and/or 50 μM of **4** were kept in the dark for 50 min.

After the addition of 3 μL of electrophoresis loading buffer to the photocleavage reactions (15.0% (w/v) Ficoll, 0.025% (w/v) bromophenol blue), cleavage products were separated on a 1.0% nondenaturing agarose gel stained with ethidium bromide (0.5 μg/mL). To determine the percent conversion of supercoiled plasmid DNA to nicked and linear forms, the gel was visualized on a transilluminator set at 302 nm, photographed, and then quantitated using *ImageQuant* v. 5.2 software (Amersham Biosciences).

Colorimetric Detection of Copper(I). A series of 500 μL reactions was prepared in which each contained 20 mM sodium phosphate buffer pH 7.0 and one or more of the following reagents: 50 μM of **4**, 50 μM of $CuCl_2$, and 38 μM bp of pUC19 plasmid DNA. The samples were irradiated at 419 nm in the absence and presence of 100 μM of bathocuproinedisulfonic acid disodium salt hydrate, while a parallel set of reactions was kept in the dark. After 50 min, the solutions were visually examined for color change, placed in 500 μL quartz cuvettes, and monitored between 200 and 600 nm for evidence of Cu(I)−bathocuproine complex formation. As a positive control, 500 μL samples containing 20 mM sodium phosphate buffer pH 7.0 and 100 μM bathocuproinedisulfonic acid disodium salt hydrate in the presence of 50 μM $CuCl_2$ or 50 μM $CuCl_2$ and 50 μM L-ascorbic acid were reacted at 22 °C for 1 min, after which, UV−visible spectra were recorded.

Inhibition of DNA Photocleavage. Twenty microliter reactions containing 20 mM sodium phosphate buffer pH 7.0, 38 μM bp pUC19 plasmid DNA, 50 μM of **4**, and 50 μM of $CuCl_2$ were irradiated at 419 nm for 50 min in the presence of either 100 mM sodium azide, 100 mM D-mannitol, 100 U superoxide dismutase, 100 U catalase, or 100 μM bathocuproinedisulfonic acid disodium salt hydrate. Reaction products were then resolved on a 1.0% nondenaturing agarose gel and quantitated as described above. The percent inhibition of DNA photocleavage was calculated on the basis of a comparison to parallel reactions run in the absence of scavenger or chelator.

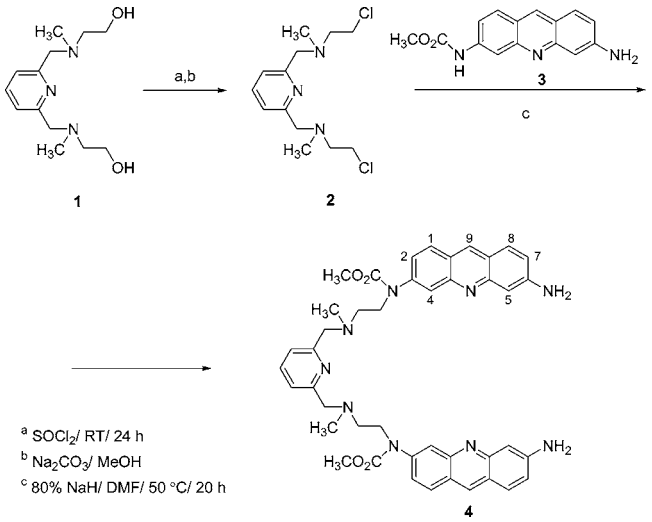
DNA Photocleavage at Nucleotide Resolution. *Eco*RI linearized pUC19 plasmid was 3′-end-labeled using *Sequenase* version 2.0 and [^{35}S]dATPαS according to an established laboratory protocol (*46*). Unincorporated nucleotides were removed with a G-50 Sephadex spun column. The DNA was then digested with *Fsp*I to produce a restriction fragment 138 bp in length and resolved on a 2.0% agarose gel. The fragment was excised, and DNA was isolated using a QIAquick Gel Extraction Kit purchased from Qiagen. The purified DNA was stored in a total volume of 400 μL of deionized, distilled water at −78 °C.

Typical photocleavage reactions contained 15 μM bp of the 138 bp DNA fragment in 20 mM sodium phosphate buffer pH 7.0 or in 20 mM sodium phosphate buffer pH 7.0, 5 μM **4** and 5 μM $CuCl_2$ (50 μL total volume). The samples were irradiated for 2 h at 419 nm, after which, DNA was precipitated with 40 μg glycogen/2.5 volumes EtOH, and washed with 70.0% EtOH. A duplicate set of reactions was precipitated, dissolved in 100 μL of 1.0% piperidine, heated at 90 °C for 30 min, and then lyophilized to dryness. Cleavage products without and with piperidine treatment were dissolved in 4 μL of Sequenase Stop Solution (95.0% (v/v) deionized formamide, 10 mM EDTA, 0.1% (w/v) xylene cyanol and 0.1% (w/v) bromophenol blue), denatured for 3 min at 95 °C, and resolved on a 10.0% denaturing polyacrylamide gel adjacent to G, G + A, and T chemical sequencing reactions. To determine yields, the gel was scanned with a *FujiFilm Image Reader* v. 2.01 Gel Imaging System. The resulting storage-phosphor autoradiogram was quantitated using *FujiFilm ImageGauge* v. 3.41 software. The DNA sequencing reactions were performed as previously described (*46*).

RESULTS AND DISCUSSION

Our approach to the design of ligand **4** combines a 2,6-bis-(aminomethyl)pyridine-based copper binding moiety and two photochemically active 3,6-acridinediamine groups as DNA recognition elements. The ligand 2,6-bis(aminomethyl)pyridine and its amino-*N*-substituted analogs form stable 1:1 complexes with Cu(II) ($\log Q_{Cu(II)} = 15.2-15.7$, equilibrium quotient $Q = [ML]/[M][L]$; refs 47 and 48). Alternatively, acridine orange, proflavin, and other 3,6-acridinediamines intercalate into DNA and, upon irradiation with visible light, efficiently effect DNA photocleavage (*16*, *49*−*51*). Therefore, the acridine rings of **4** were intended to increase DNA binding and to initiate DNA photocleavage. We also took into account that cleavage levels might be enhanced by acridine-sensitized photoreduction of pyridine-bound copper(II).

Scheme 1. Synthesis of Ligand 4



Synthesis of Ligand 4. Compound **4** was obtained from 2,6-bis[(2-hydroxyethyl)methylaminomethyl]pyridine (**1**) (*40*), which upon treatment with thionyl chloride at room temperature for 24 h, followed by basification with sodium carbonate, afforded 2,6-bis[(2-chloroethyl)methylaminomethyl]pyridine (**2**) as a brown oil in 65% yield. Compound **2** was reacted with (6-amino-3-acridinyl)carbamic acid methyl ester (**3**) (*41*) in anhydrous DMF with 80% NaH as base at 50 °C for 20 h (Scheme 1). Purification of the crude product afforded **4** in 31% yield.

Viscometric Analysis. In order to test for the intercalating ability of **4** and to further examine its behavior as a groove binder or as a mono- or bis-intercalator, DNA viscosity measurements were conducted. In the process of intercalation, helical DNA unwinds to accommodate planar aromatic ring systems that become inserted in between DNA base pairs. This process is accompanied by an effective increase in contour length that adds to the intrinsic viscosity of the DNA polymer. Because groove binding compounds do not markedly lengthen helical DNA, there is no significant change in viscosity (*52*). Consequently, viscometric titrations represent a highly reliable method for establishing the binding modes of DNA interacting ligands (*52*).

The viscometry data for compound **4** and copper(II) are presented as plots of $(\eta/\eta_o)^{1/3}$ versus r (the molar ratio of added compound to DNA base pairs) according to the theory of Cohen and Eisenberg (*43*). Figure 1 shows that compound **4** increases the relative viscosity of calf thymus DNA as a function of increasing r and that the slope (0.82) obtained from the $(\eta/\eta_o)^{1/3}$ versus r plot falls within the range expected for monofunctional intercalators (*53*). It is conceivable that the lowest-energy conformation of **4** is incompatible with the neighbor exclusion principle and therefore permits the intercalation of only one acridine ring. In contrast, the viscometric data of copper(II) with CT DNA yield slopes of −0.12 and 0.41 in the absence and presence of 1 mol equiv of **4**, respectively. The observed reduction in slope from 0.82 to 0.41 may indicate that interaction of the compound's 2,6-bis(aminomethyl)pyridine linker with copper(II) induces a conformational change that introduces a competing, non-intercalative DNA binding mode, most likely groove binding. Notwithstanding, the increase in the apparent DNA contour length by the copper(II) complex of **4** is still substantial, suggesting some degree of intercalative binding (*54*).

Electrospray Ionization Mass Spectrometry. Our next goal was to obtain direct evidence of copper(II) complex formation. Ligand **4** was reacted with $CuCl_2$ in HPLC-grade methanol at a ligand to metal ratio of 1:1 (90 min, 22 °C), after which a positive-ion electrospray (ESI) mass spectrum was recorded (Figure S1 in Supporting Information). Isotopic distributions of molecular ions corresponding to the following 1:1 metallic complexes were observed: (i) $[\mathbf{4}HCuCl]^{2+}$ between 425 and 428 *m*/*z* (calcd for $[C_{43}H_{46}N_9O_4CuCl]^{2+}$ 425.13); (ii) $[\mathbf{4}CuCl]^{1+}$ between 849 and 855 *m*/*z* (calcd for $[C_{43}H_{45}N_9O_4CuCl]^{1+}$ 849.26); and (iii) $[\mathbf{4}HCuCl_2]^{1+}$ between 885 and 892 *m*/*z* (calcd for $[C_{43}H_{46}N_9O_4CuCl_2]^{1+}$ 885.24).

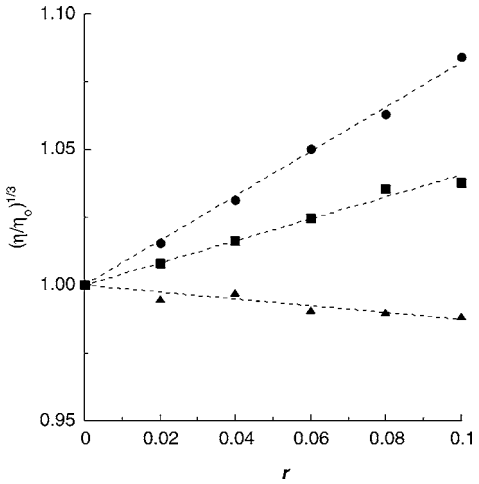


Figure 1. Change in relative viscosity $(\eta/\eta_o)^{1/3}$ of CT DNA as a function of r, the molar ratio of compound to DNA base pairs. Viscometric titrations were conducted in the presence of (i) compound **4** (•; slope = 0.82; 6 mM Na_2HPO_4, 2 mM NaH_2PO_4, 1 mM Na_2EDTA, and 15 mM NaCl buffer pH 7.0); (ii) compound **4** and copper(II) at a ligand to metal ratio of 1:1 (■; slope = 0.41; 20 mM sodium phosphate buffer pH 7.0); (iii) copper(II) (▲; slope = −0.12; 20 mM sodium phosphate buffer pH 7.0).

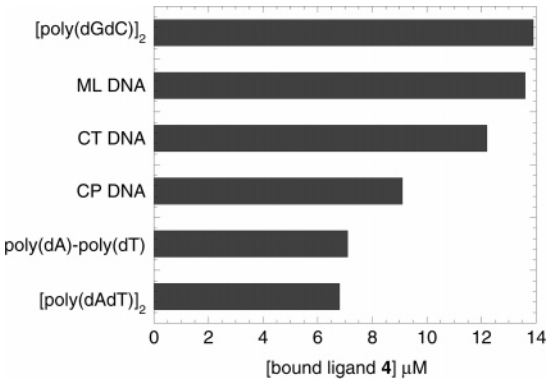


Figure 2. The bar graph indicates the concentrations of DNA-bound ligand **4** detected after a 24 h equilibration in competition binding dialysis studies of six DNA sequences.

Competition Dialysis. The results of dialysis experiments are depicted in a bar graph which shows the concentrations of ligand **4** bound to calf thymus, *Clostridium perfringens*, and *Micrococcus lysodeikticus* DNAs and to the synthetic, double-helical polynucleotides poly(dA)-poly(dT), $[poly(dGdC)]_2$, and $[poly(dAdT)]_2$ (Table S1, Figure 2). The data were obtained after equilibrating 1.5 μM of **4** (in the dialysate solution) and 75 μM bp of nucleic acid (in each sample dialysis unit) for 24 h. At the end of the equilibration period, UV−visible spectra were recorded in order to determine the concentrations of free ligand **4** and DNA-bound **4**. The amount of the DNA-bound ligand was averaged over three trials, and the estimated error was between 5% and 10% for each nucleic acid structure tested. The competition dialysis data were then used to calculate the apparent association constants of ligand **4**, given by $K_{app} = C_b/C_f$ [DNA], where C_b and C_f are the DNA-bound and free ligand

Table 1. Apparent Association Constants Obtained by Competition Dialysis[a]

deoxyribonucleic acid	$K_{app} \times 10^5\ M^{-1}$
$[poly(dGdC)]_2$ (100% GC)	1.30
ML DNA (72% GC)	1.26
CT DNA (42% GC)	1.13
CP DNA (31% GC)	0.85
poly(dA)-poly(dT) (0% GC)	0.66
$[poly(dAdT)]_2$ (0% GC)	0.63

[a] The abbreviations ML DNA, CT DNA, and CP DNA correspond to *Micrococcus lysodeikticus*, calf thymus, and *Clostridium perfringens* DNAs, respectively.

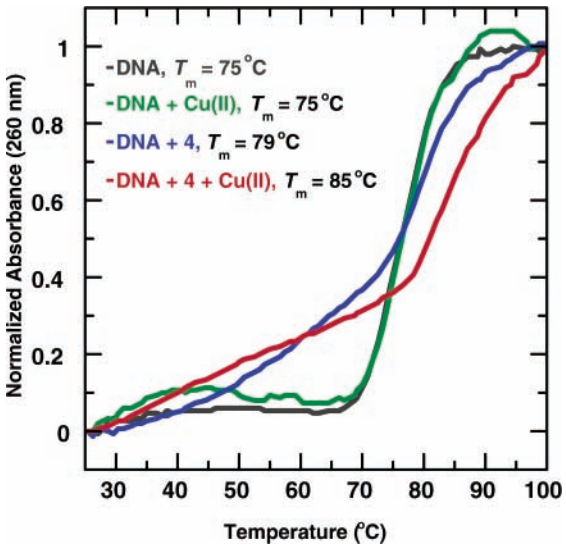


Figure 3. Thermal melting curves and T_m values of 15 μM bp calf thymus DNA in the absence and presence of 10 μM **4** and/or 10 μM $CuCl_2$ (20 mM sodium phosphate buffer pH 7.0).

concentrations, respectively, and [DNA] is the concentration of DNA in molar base pairs (Table 1).[1] Clearly, the data in Figure 2 and Table 1 indicate that ligand **4** shows a preference for GC base pairs as exemplified by an increase in levels of binding to ML DNA (71% GC, $K_{app} = 1.26 \times 10^5\ M^{-1}$) relative to CP DNA (31% GC; $K_{app} = 0.85 \times 10^5\ M^{-1}$).

Thermal Melting Studies. The majority of DNA intercalators bind to double-helical DNA through a combination of $\pi-\pi$ stacking and electrostatic interactions. As a consequence, double-helical DNA is stabilized, and the melting temperature (T_m) of the duplex is increased as a function of the increasing binding affinity of the intercalator (*55*). Melting temperature (T_m) values of 15 μM bp calf thymus DNA in 20 mM sodium phosphate buffer pH 7.0 were derived from thermal melting curves recorded at 260 nm (Figure 3). While 10 μM of Cu(II) had no effect in the absence of the ligand, 10 μM of **4** increased the T_m of calf thymus DNA by 4 °C and 10 °C in the absence and presence of 10 μM concentrations of Cu(II), respectively. Taken together, these data indicate that **4** binds to double-helical DNA, thereby increasing its stability. Duplex stability is then further enhanced by the interaction of **4** with copper(II). In light of the above viscometric data, this result would appear to suggest that groove binding and intercalation of **4** in the presence of Cu(II) might stabilize duplex DNA to a greater degree than

[1] Competition dialysis experiments were conducted at room temperature in sodium phosphate buffer pH 7.0. Under these conditions, the UV−vis spectra of the Cu(II) complex of **4** and of ligand **4** were found to be nearly superimposable. Therefore, the K_{app} of the Cu(II) complex of **4** could not be accurately determined by competition dialysis because the concentration of the Cu(II) complex of **4** versus that of **4** could not be ascertained.

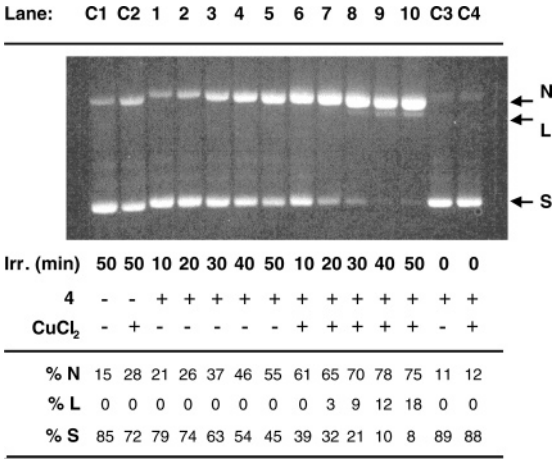


Figure 4. A photograph of a 1.0% nondenaturing agarose gel showing photocleavage of pUC19 plasmid DNA in the presence of 50 μM of **4** without and with 50 μM of $CuCl_2$ (22 °C, pH 7.0). C1 and C2 correspond to DNA irradiated at 419 nm, without and with $CuCl_2$, respectively (no **4**). C3 and C4 correspond to DNA treated for 50 min with **4,** without and with $CuCl_2$, respectively (no *hν*). Lanes 1−10 correspond to DNA irradiated at 419 nm for 10, 20, 30, 40, and 50 min in the presence of **4**, without and with $CuCl_2$. The above yields corresponding to C1, C2, Lane 5, and Lane 10 were averaged over three trials with standard deviations of ±3%, ±5%, ±3%, and ±2%, respectively. S, L, and N designate supercoiled, linear, and nicked forms of pUC19 plasmid DNA.

simple monointercalation. It is also conceivable that complex formation with positively charged copper might enhance electrostatic interactions between **4** and the negatively charged phosphate backbone of the DNA duplex. Notwithstanding, the increase in T_m observed when Cu(II) is added to **4** indicates that the apparent DNA association constant K_{app} of the Cu(II) complex of **4** is higher than the K_{app} of the free ligand **4**.[1] The small increases in low-temperature absorbance produced by compound **4** and its Cu(II) complex probably arise from thermally induced changes in the ratio of DNA-bound ligand to free ligand (Figure 3; ref 56).

Photocleavage of Supercoiled Plasmid DNA. To detect the formation of DNA frank strand breaks,[2] a preliminary concentration profile was conducted in which individual samples containing 38 μM bp of pUC19 plasmid DNA in 20 mM sodium phosphate buffer pH 7.0 were equilibrated with 50 μM to 2 μM of **4** in the absence and presence of 1 mol equiv of $CuCl_2$. The samples were irradiated for 50 min at 419 nm and 22 °C in an aerobically ventilated Rayonet Photochemical Reactor, after which, DNA photocleavage products were resolved on a 1.0% nondenaturing agarose gel. The results of the profile showed that 1 mol equiv of Cu(II) enhanced DNA photocleavage produced by 50 to 20 μM concentrations of compound **4** in a concentration-dependent fashion, with maximum levels of photocleavage occurring in the 50 μM reaction (Figure S2 in Supporting Information).

DNA photocleavage as a function of time was studied next. Reactions consisting of 20 mM sodium phosphate buffer pH 7.0 with 38 μM bp pUC19 plasmid DNA, 50 μM of compound **4**, and 50 μM of $CuCl_2$ were irradiated as described above, except that the reactions were removed at 10 to 50 min time points prior to agarose gel electrophoresis. While 50 μM of intercalator **4** clearly demonstrated time-dependent DNA photocleavage (Figure 4, lanes 1 to 5), reaction yields were markedly enhanced at all time points upon the addition of

[2] DNA frank strand breaks are defined as single- or double-stranded DNA breaks directly induced by the effects of a cleaving reagent, in the absence of subsequent treatment with alkaline or with a secondary amine such as piperidine.

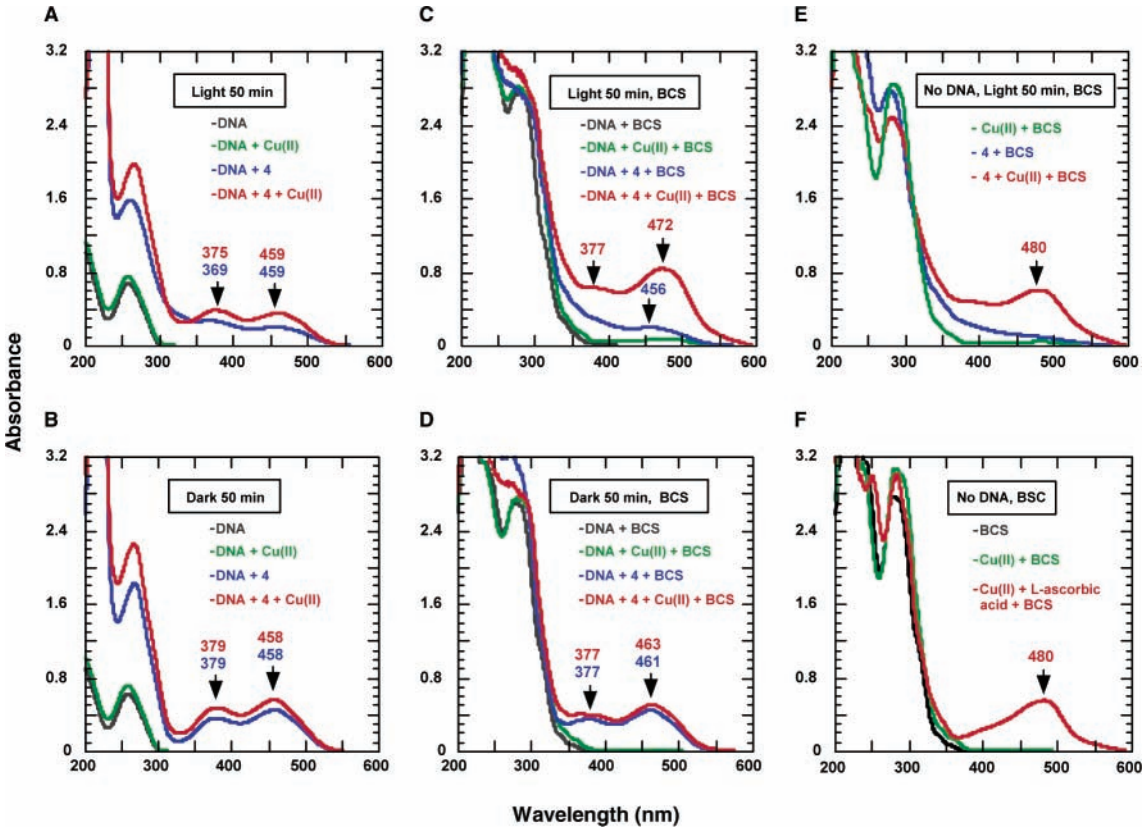


Figure 5. UV−visible spectra to assay for Cu(I)-BCS complex formation in 20 mM sodium phosphate buffer pH 7.0, 22 °C.

equivalent concentrations of $CuCl_2$ (Figure 4, lanes 6 to 10). (Virtually no cleavage was observed in parallel control reactions run in the dark; Figure 4, lanes C3 and C4.) Notably, after 50 min of irradiation, supercoiled plasmid was converted into 28% nicked DNA in the presence of Cu(II)/buffer, 55% nicked in **4**/buffer, and 75% nicked plus 18% linear when **4**/Cu(II)/buffer were present in combination (Figure 4, lanes C2, 5, and 10, respectively). Taking into consideration that 15% of photonicked DNA was produced in buffer alone, it is evident that ligand **4** and Cu(II) interact in a synergistic rather than additive fashion. Because photoreduction of Fe(III) is readily effected with visible light by means of electron transfer from the photochemically excited triplet states of acridine orange and other 3,6-diaminoacridines (*57*, *58*), we hypothesized that a potential source of synergism might involve acridine-sensitized photoreduction of pyridine-bound Cu(II). Subsequent reaction of Cu(I) with O_2 would be expected to generate DNA cleaving, reactive oxygen species (*59*−*61*).

Colorimetric Detection of Copper(I). Our next goal was to obtain experimental evidence that would substantiate photoreduction of Cu(II) by ligand **4**. We utilized a colorimetric assay based on bathocuproinedisulfonic acid disodium salt hydrate (BCS), which forms a 2:1 stable, brightly colored orange complex with Cu(I) (λ_{max} = 480 nm; ϵ = 13 500 M^{-1} cm^{-1}; ref 62). Photolysis reactions in 20 mM sodium phosphate buffer pH 7.0 were irradiated at 419 nm and 22 °C for 50 min in the presence of one or more of the following reagents: 50 μM **4**, 50 μM $CuCl_2$, 38 μM bp pUC19 plasmid DNA, and 100 μM BCS; after which UV−visible spectra were immediately recorded (Figure 5). Parallel reactions run in the dark were used as negative controls (Figure 5B,D). As a control for BCS−Cu(I) complex formation, 100 μM BCS was reacted with 50 μM $CuCl_2$ in the absence and presence of 50 μM of the reducing agent L-ascorbic acid (Figure 5F).

As expected, the addition of BCS to Cu(II) produced a bright orange color and signature 480 nm absorption in the L-ascorbic acid control reaction (Figure 5F), but not in any of the dark DNA reactions (even those containing **4** and/or Cu(II); Figure 5B,D), and not in any reactions in which BCS was omitted (Figure 5A,B). However, the DNA reaction irradiated in the presence of ligand **4**, Cu(II), and BCS produced a significant orange color change. In addition, a strong hyperchromic absorption band indicative of the formation of a BCS−Cu(I) complex was observed at 472 nm (Figure 5C: DNA + **4** + Cu(II) + BCS). (Spectral overlap with **4** and/or one of its photoproducts most likely accounts for the 8-nm blue shift relative to 480 nm: Figure 5C compared to Figure 5E,F.) Importantly, there was no evidence of BCS−Cu(I) complex formation when **4** was omitted from the photocleavage reaction (Figure 5C: DNA + Cu(II) + BCS). When DNA was left out, significant absorption and color were still produced (Figure 5E: **4** + Cu(II) + BCS). Therefore, the BCS data collectively indicate that bis-acridine ligand **4** sensitizes photoreduction of Cu(II) to Cu(I) and that DNA is not required for photoreduction.

Inhibition of DNA Photocleavage. To further investigate mechanism(s) underlying the Cu(II)-assisted formation of DNA frank strand breaks, we conducted the following inhibition experiments. Individual photocleavage reactions consisted of 38 μM bp of pUC19 plasmid DNA, 50 μM of **4**, and 50 μM of $CuCl_2$ pre-equilibrated with one of the following reagents: the singlet oxygen ($^1O_2$) scavenger sodium azide, the hydroxyl radical (•OH) scavenger D-mannitol, the hydrogen peroxide (H_2O_2) scavenger catalase, the superoxide (O_2•$^-$) scavenger superoxide dismutase (SOD), and the Cu(I)-specific chelating agent BCS. From examination of the data in Table 2, it is evident that sodium azide, catalase, and BCS blocked frank stand break formation to a significant degree, while D-mannitol was almost completely ineffective. Intermediate levels of inhibition were produced by SOD, indicating that superoxide contributes to photocleavage. (SOD produces H_2O_2, which can itself play a part in cleavage and thereby lower inhibition by this enzyme.) Although the piperidine-labile lesion 8-hydroxyguanosine is the

Table 2. Average % Inhibition of DNA Photocleavage by Scavengers and BCS[a]

scavenger/chelator	species targeted	percent inhibition
D-mannitol (100 mM)	•OH	5 ± 1
superoxide dismutase (100 U)	O_2•$^-$	29 ± 1
(BCS 100 μM)	Cu(I)	51 ± 2[b]
catalase (100 U)	H_2O_2	56 ± 2
sodium azide (100 mM)	$^1O_2$	61 ± 3

[a] Individual reactions consisting of 38 μM bp of pUC19 plasmid DNA equilibrated with 50 μM of **4** and 50 μM of $CuCl_2$, and one of the above reagents were irradiated under aerobic conditions at 419 nm for 50 min at 22 °C. Percent inhibition was averaged over three trials with error reported as standard deviation. Final reagent concentrations are in parenthesis. [b] In control experiments, we observed direct photocleavage of DNA by BCS in the absence of **4** (data not shown). Therefore, the 51% inhibition produced by BCS may be lower than the actual % inhibition value.

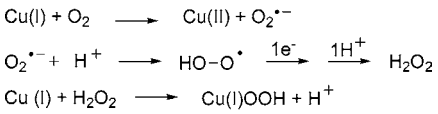


Figure 6. A proposed model in which superoxide (O_2•$^-$), hydrogen peroxide (H_2O_2), and Cu(I) contribute to the formation of a Cu(I)-peroxide complex.

primary form of DNA damage produced by singlet oxygen, the relative efficiency of sodium azide implies that singlet oxygen may play a major role: singlet oxygen is capable of cleaving DNA directly by producing frank strand breaks at guanine bases (*63*). However, because frank strand breaks account for no more than 5% of total DNA damage produced by $^1O_2$ (*64*), it is conceivable that cleavage inhibition by sodium azide involves a copper−peroxide-type complex (*60*) of ligand **4**. The relatively strongly inhibitory effects of catalase and of the Cu(I)-specific chelating agent BCS clearly indicate that hydrogen peroxide and Cu(I) participate in DNA photocleavage. Alternatively, the ineffectiveness of the hydroxyl radical scavenger D-mannitol suggests that freely diffusible hydroxyl radicals do not make a significant contribution. This latter result is consistent with the majority of literature reports in which copper−peroxide-type complexes rather than hydroxyl radicals were found to be the principal reactive species involved in DNA cleavage by Cu(II)/Cu(I) redox cycling systems (*59*−*61*, *65*). A mechanism consistent with the above photocleavage inhibition data is shown in Figure 6 (*61*). It is conceivable that Cu(II) bound to the pyridine linker of ligand **4** is photoreduced to Cu(I), which in turn reacts with hydrogen peroxide to produce a DNA-damaging Cu(I)-peroxide complex. Because the colorimetric BCS assay detected Cu(I) only when **4** was present, it can also be inferred that DNA photocleavage involves acridine-sensitized photoreduction of Cu(II) to Cu(I).

DNA Photocleavage at Nucleotide Resolution. In order to map the sequence specificity of Cu(II)-assisted DNA photocleavage, pUC19 plasmid was linearized with *Eco*RI, 3′-end-labeled with [^{35}S]dATPαS, and then cut with *Fsp*I to produce a 138 bp restriction fragment (*58*). Reactions containing 15 μM bp of the radiolabeled DNA fragment in the absence and presence of 5 μM **4** and 5 μM $CuCl_2$ were irradiated at 419 nm for 2 h (20 mM sodium phosphate buffer pH 7.0). Half of the reactions were subsequently treated with 1.0% piperidine (90 °C, 30 min) in order to produce strand breaks at alkaline-labile lesions in the DNA. Products were electrophoresed adjacent to G, G + A, and T chemical sequencing reactions on a 10.0% denaturing polyacrylamide gel, after which, cleavage patterns were analyzed. Shown in Figure 7 are cleavage plots of a representative 40 bp sequence within the radiolabeled restriction fragment. The top 20 bases producing the highest levels of

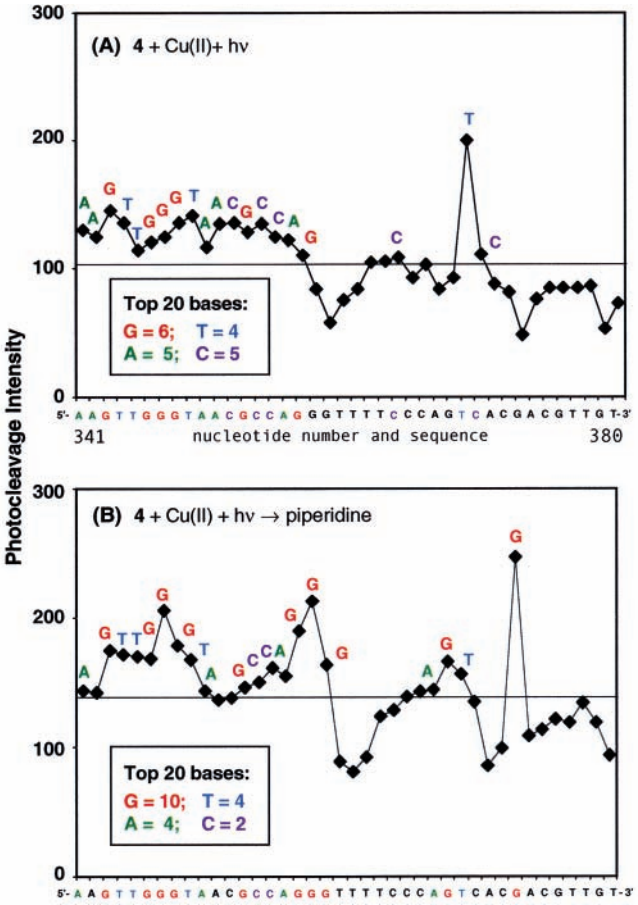


Figure 7. Cleavage plots of a representative 40 bp DNA sequence. Photocleavage intensities as a function of DNA base were calculated by quantitating a storage-phosphor autoradiogram of DNA photocleavage products resolved on a 10.0% denaturing polyacrylamide gel (Figure S3 in Supporting Information). A total of 15 μM bp of ^{35}S 3′-end labeled 138 bp restriction fragment was irradiated at 419 nm in the presence of 5 μM **4** and 5 μM $CuCl_2$ without (A) and with (B) subsequent piperidine treatment. The ordinate is in units of $f_a - f_c$, where f_a is the fractional cleavage intensity produced in the photocleavage reaction and f_c is fractional cleavage intensity in a parallel control reaction in which DNA was irradiated in the absence of the Cu(II) complex of compound **4,** without (A) and with (B) the piperidine treatment. A horizontal line has been drawn through each plot in order to identify the top 20 DNA bases (inset) producing the highest levels of cleavage.

photocleavage appear in the inset of each plot. In the absence of piperidine, it is evident that the Cu(II) complex of **4** almost always produces frank strand breaks without a marked base preference (Figure 7A). This result suggests that photocleavage may involve hydrogen atom abstraction from deoxyribose. Because sugar residues are present in every nucleotide, reagents which function by hydrogen atom abstraction are expected to cleave at all nearby DNA sequences irrespective of base composition (*11*). Singlet oxygen and direct electron transfer from DNA nucleobases produce DNA damage predominately at guanine bases (*11*, *63*) and are therefore unlikely to have made overriding contributions to the formation of frank strand breaks. Alternatively, the cleavage pattern was changed after the DNA photolysis reactions were treated with piperidine, showing preferential damage at guanine. This result indicates that alkaline-labile lesions were formed at guanine bases, either through the production of singlet oxygen and/or by direct electron transfer from DNA (Figure 7B).

CONCLUSION

In summary, our data indicate that Cu(II) markedly enhances DNA photocleavage by ligand **4** under near-physiological

conditions of temperature and pH. Although the precise cleavage mechanism is unknown, at this time we believe that the formation of frank strand breaks may involve acridine-sensitized photoreduction of Cu(II) to Cu(I) followed by reaction of **4**/Cu(I) with hydrogen peroxide to form a copper−peroxide complex. Considering the bioavailability of copper at the cellular level, copper-based photonucleases are advantageous in comparison to complexes based on other metals or to chemical nucleases which require an external reducing agent for their activity. To the best of our knowledge, bis-acridine **4** is only the third example of a photonuclease that has been shown to cleave DNA by a process that involves direct photochemical reduction of copper (*14*, *15*). Our future work will focus on mechanistic studies and on synthetic endeavors to develop new copper-based photonucleases for use in chemical and medical applications.

ACKNOWLEDGMENT

We thank Timothy C. Laeger, Prof. Marcus W. Germann, and Prof. W. David Wilson for their assistance (Georgia State University). Support of this research by the CAM-UAH (2005-012; A.L.), the CAM (GR-MAT 2004-0810; M.-M.R.), the National Science Foundation (CHE-9984772; K.B.G.), and the American Chemical Society Petroleum Research Fund (32897-G3; K.B.G.) is gratefully acknowledged.

Supporting Information Available: Table S1, the λ_{max} values and extinction coefficients of nucleic acid samples used in competition dialysis experiments; Figure S1, ESI mass spectra of compound **4** and of 1:1 metallic complexes formed between compound **4** and Cu(II); Figure S2, concentration profile: percent photocleavage of pUC19 plasmid DNA in the absence and presence of 50 μM to 2 μM concentrations of $CuCl_2$ and/or compound **4**; Figure S3, storage-phosphor autoradiogram of a 10.0% denaturing polyacrylamide gel showing DNA photocleavage products at nucleotide resolution. This material is available free of charge via the Internet at http://pubs.acs.org/BC.

LITERATURE CITED

(1) Barton, J. K. (1986) Metals and DNA: molecular left-handed complements. *Science 233*, 727−734.
(2) Pyle, A. M., and Barton, J. K. (1990) Probing nucleic acids with transition metal complexes. *Prog. Inorg. Chem. 38*, 413−475.
(3) Erkkila, K. E., Odom, D. T., and Barton, J. K. (1999) Recognition and reaction of metallointercalators with DNA. *Chem. Rev. 99*, 2777−2795.
(4) Huber, P. W. (1993) Chemical nucleases: their use in studying RNA structure and RNA-protein interactions. *FASEB J. 7*, 1367−1375.
(5) Pratviel, G., Bernadou, J., and Meunier, B. (1995) Carbon-hydrogen bond of DNA sugar units as targets for chemical nucleases and drugs. *Angew. Chem., Int. Ed. Engl. 34*, 746−769.
(6) Burrows, C. J., and Muller, J. G. (1998) Oxidative nucleobase modifications leading to strand scission. *Chem. Rev. 98*, 1109−1151.
(7) Pratviel, G., Bernadou, J., and Meunier, B. (1998) DNA and RNA cleavage by metal complexes. *Adv. Inorg. Chem. 45*, 251−312.
(8) Cadet, J., and Vigny, P. (1990) The Photochemistry of Nucleic Acids. *Bioorganic Photochemistry* (Morrison, H., Ed.) Vol. 1, pp 1−272, Wiley, New York.
(9) Kochevar, I. E., and Dunn, D. A. (1990) Photosensitized Reactions of DNA: Cleavage and Addition. *Bioorganic Photochemistry* (Morrison, H., Ed.) Vol. 1, pp 273−315, Wiley, New York.
(10) Saito, I., and Nakatani, K. (1996) Design of DNA-cleaving agents. *Bull. Chem. Soc. Jpn. 69*, 3007−3019.
(11) Armitage, B. (1998) Photocleavage of nucleic acids. *Chem. Rev. 98*, 1171−1200.
(12) Barton, J. K., and Raphael, A. L. (1984) Photoactivated stereospecific cleavage of double-helical DNA by cobalt(III) complexes. *J. Am. Chem. Soc. 106*, 2466−2468.
(13) Subramanian, R., and Meares, C. F. (1986) Photosensitization of cobalt bleomycin. *J. Am. Chem. Soc. 108*, 6427−6429.
(14) Kuwahara, J., Suzuki, T., Funakoshi, K., and Sugiura, Y. (1986) Photosensitive DNA cleavage and phage inactivation by copper(II)-camptothecin. *Biochemistry 25*, 1216−1221.
(15) Gude, L., Fernández, M. J., Grant, K. B., and Lorente, A. (2005) Syntheses and copper(II)-dependent DNA photocleavage by acridine and anthracene 1,10-phenanthroline conjugate systems. *Org. Biomol. Chem. 3*, 1856−1862.
(16) Wilson, B., Gude, L., Fernández, M.-J., Lorente, A., and Grant, K. B. (2005) Tunable DNA photocleavage by an imidazole-acridine conjugate. *Inorg. Chem. 44*, *6159*−6173.
(17) Spector, W. S. (1956) *Handbook of Biological Data*, p 52, W. B. Saunders Company, Philadelphia.
(18) Wacker, W. E. C., and Vallee, B. L. (1959) Nucleic acids and metals. I. Chromium, manganese, nickel, iron, and other metals in ribonucleic acid from diverse biological sources. *J. Biol. Chem. 234*, 3257−3262.
(19) Cantor, K. P., and Hearst, J. E. (1966) Isolation and partial characterization of metaphase chromosomes of a mouse ascites tumor. *Proc. Natl. Acad. Sci. U.S.A. 55*, 642−649.
(20) Bryan, S. E., Vizard, D. L., Beary, D. A., LaBiche, R. A., and Hardy, K. J. (1981) Partitioning of zinc and copper within subnuclear nucleoprotein particles. *Nucleic Acids Res. 9*, 5811−5823.
(21) Fürst P., and Hamer, D. (1989) Cooperative activation of a eukaryotic transcription factor: interaction between Cu(I) and yeast ACE1 protein. *Proc. Natl. Acad. Sci. U.S.A.* 86, 5267−5271.
(22) Thiele, D. J. (1992) Metal-regulated transcription in eukaryotes. *Nucleic Acids Res. 20*, 1183−1191.
(23) Mc Millin, D. R., and McNett, K. M. (1998) Photoprocesses of copper complexes that bind to DNA. *Chem. Rev. 98*, 1201−1219.
(24) Eppley, H. J., Lato, S. M., Ellington, A. D., and Zaleski, J. M. (1999) Transition metal kinamycin model as a DNA photocleaver for hypoxic environments: bis(9-diazo-4,5-diazafluorene)copper(II) nitrate. *Chem. Commun.* 2405−2406.
(25) Benites, P. J., Holmberg, R. C., Rawat, D. S., Kraft, B. J., Klein, L. J. Peters, D. G., Thorp, H. H., and Zaleski, J. M. (2003) Metal-ligand charge-transfer-promoted photoelectronic Bergman cyclization of copper metalloenediynes: photochemical DNA cleavage via C-4′ H-atom abstraction. *J. Am. Chem. Soc. 125*, 6434−6446.
(26) Dhar, S., and Chakravarty, A. R. (2003) Efficient visible light induced nuclease activity of a ternary mono-1,10-phenanthroline copper(II) complex containing 2-(methylthio)ethylsalicylaldimine. *Inorg. Chem. 42*, 2483−2485.
(27) Dhar, S., Senapati, D., Das, P. K., Chattopadhyay, P., Nethaji, M., and Chakravarty, A. R. (2003) Ternary copper complexes for photocleavage of DNA by red light: direct evidence for sulfur-to-copper charge transfer and d-d band involvement. *J. Am. Chem. Soc. 125*, 12118−12124.
(28) Dhar, S., Senapati, D., Reddy, P. A., Das, P. K., and Chakravarty, A. R. (2003) Metal-assisted red light-induced efficient DNA cleavage by dipyridoquinoxaline-copper(II) complex. *Chem. Commun.* 2452−2453.
(29) Vaidyanathan, V. G., and Nair, B. N. (2003) Oxidative cleavage of DNA by tridentate copper (II) complex. *J. Inorg. Biochem. 93*, 271−276.
(30) Gupta, T., Dhar, S., Nethaji, M., and Chakravarty, A. R. (2004) Bis(dipyridophenazine)copper(II) complex as major groove directing synthetic hydrolase. *Dalton Trans.* 1896−1900.
(31) Reddy, P. A., Santra, B. K., Nethaji, M., and Chakravarty, A. R. (2004) Metal-assisted light-induced DNA cleavage activity of 2-(methylthio)phenylsalicylaldimine Schiff base copper(II) complexes having planar heterocyclic bases. *J. Inorg. Biochem. 98*, 377−386.
(32) Dhar, S, and Chakravarty, A. R. (2005) Photosensitizer in a molecular bowl: steric protection enhancing the photonuclease activity of copper(II) scorpionates. *Inorg. Chem. 44*, 2582−2584.
(33) Dhar, S., Nethaji, M., and Chakravarty, A. R. (2005) Effect of charge transfer bands on the photo-induced DNA cleavage activity of [1-(2-thiazolylazo)-2-naphtholato]copper(II) complexes. *J. Inorg. Biochem. 99*, 805−812.
(34) Patra, A. K., Dhar, S., Nethaji, M., and Chakravarty, A. R. (2005) Metal-assisted red light-induced DNA cleavage by ternary L-methionine copper(II) complexes of planar heterocyclic bases. *Dalton Trans.* 896−902.

(35) Patra, A. K., Nethaji, M., and Chakravarty, A. R. (2005) Red-light photosensitized cleavage of DNA by (L-lysine)(phenanthroline base)copper(II) complexes. *Dalton Trans.* 2798−2804.
(36) Halliwell, B., and Gutteridge, J. M. C. (1984) Oxygen toxicity, oxygen radicals, transition metals and disease. *Biochem. J. 219*, 1−14.
(37) Linder, M. C. (1991) *Biochemistry of Copper*, Plenum Press, New York.
(38) Peña, M. M., Lee, J., and Thiele, D. J. (1999) A delicate balance: homeostatic control of copper uptake and distribution. *J. Nutr. 129*, 1251−1260.
(39) Chevion, M. (1988) A site-specific mechanism for free radical induced biological damage: the essential role of redox-active transition metals. *Free Radical Biol. Med. 5*, 27−37.
(40) Kady, I. O., and Tan, B. (1995) Metal-catalyzed intramolecular hydrolysis of phosphate esters. *Tetrahedron Lett. 36*, 4031−4034.
(41) Lorente, A., Fernández-Saiz, M., Espinosa, J.-F., Jaime, C., Lehn, J.-M., and Vigneron, J.-P. (1995) Cyclo-bis-intercalands with acridine subunits linked by rigid spacers. *Tetrahedron Lett. 36*, 5261−5264.
(42) Sambrook, J., Fritsch, E. F., and Maniatis, T. (1989) *Molecular Cloning: A Laboratory Manual*, 2nd ed., Cold Spring Harbor Laboratory, Cold Spring Harbor, NY.
(43) Cohen, G., and Eisenberg, H. (1969) Viscosity and sedimentation study of sonicated DNA-proflavine complexes. *Biopolymers 8*, 45−55.
(44) Ren, J., and Chaires, J. B. (2001) Rapid screening of structurally selective ligand binding to nucleic acids. *Methods Enzymol. 340*, 99−108.
(45) Chaires, J. B. (2002) A competition dialysis assay for the study of structure-selective ligand binding to nucleic acids. *Current Protocols in Nucleic Acid Chemistry*, pp 8.8.1−8.3.8, John Wiley & Sons, New York.
(46) Yang, X., and Grant, K. B. (2002) Chemical sequencing of restriction fragments 3′-end-labeled with [^{35}S]dATPαS. *J. Biochem. Biophys. Methods 50*, 123−128.
(47) Couturier, Y., and Petitfaux, C. (1978) Composition and stability of copper complexes and pyridine amine-copper complexes. XI. Comparison of monopyridine mono- and diamines. *Bull. Soc. Chim. Fr. 11−12*, Pt. 1, 435−441.
(48) Garcia Basallote, M., and Martell, A. E. (1988) New multidentate ligands. 29. Stabilities of metal complexes of the binucleating macrocyclic ligand BISBAMP and dioxygen affinity of its dinuclear cobalt(II) complex. *Inorg. Chem. 27, 4219*−4224.
(49) Freifelder, D., Davison, P. F., and Geiduschek, E. P. (1961) Damage by visible light to the acridine orange−DNA complex. *Biophys. J. 1*, 389−400.
(50) Piette, J., López, M., Calberg-Bacq, C. M., and Van, de Vorst, A. (1981) Mechanism for strand-break induction in DNA-proflavine complexes exposed to visible light. *Int. J. Radiat. Biol. 40*, 427−433.
(51) Espinosa, J.-F., Fernández, M.-J., Grant, K. B., Gude, L., Rodrigo, M.-M., and Lorente, A. (2004) Synthesis, DNA intercalation and europium(III)-triggered DNA photocleavage by a bis-proflavine succinamide conjugate. *Tetrahedron Lett. 45*, 4017−4020.
(52) Suh, D., and Chaires, J. B. (1995) Criteria for the mode of binding of DNA binding agents. *Bioorg. Med. Chem. 3*, 723−728.
(53) Chaires, J. B., Leng, F., Przewloka, T., Fokt, I., Ling, Y-H., Pérez-Soler, R., and Priebe, W. (1997) Structure-based design of a new bisintercalating anthracycline antibiotic. *J. Med. Chem. 40*, 261−266.
(54) Pilch, D. S., Kirolos, M. A., Liu, X., Plum, G. E., and Breslauer, K. J. (1995) Berenil [1,3-bis(4′-amidinophenyl)triazene] binding to DNA duplexes and to a RNA duplex: evidence for both intercalative and minor groove binding properties. *Biochemistry 34*, 9962−9976.
(55) Wilson, W. D., Tanious, F. A., and Fernández-Saiz, M. (1997) Evaluation of Drug-Nucleic Acid Interactions by Thermal Melting Curves. In *Drug-DNA Interaction Protocols* (K. R. Fox, Ed.) Humana Press, New Jersey.
(56) Satyanarayana, S., Dabrowiak, J. C., and Chaires, J. B. (1993) Tris(phenanthroline)ruthenium(II) enantiomer interactions with DNA: mode and specificity of binding. *Biochemistry 32*, 2573−2584.
(57) Oster, G. K., and Oster, G. (1959) Photoreduction of metal ions by visible light. *J. Am. Chem. Soc. 81*, 5543−5545.
(58) Kellmann, A. (1974) Primary photochemical processes of cationic acridine orange in aqueous solution studied by flash photolysis. *Photochem. Photobiol. 20*, 103−108.
(59) Yamamoto, K., and Kawanishi. S. (1989) Hydroxyl free radical is not the main active species in site-specific DNA damage induce by copper(II) ion and hydrogen peroxide. *J. Biol. Chem. 264*, 15435−15440.
(60) Li, Y., and Trush, M. A. (1993) DNA damage resulting from the oxidation of hydroquinone by copper: role for a Cu(II)/Cu(I) redox cycle and reactive oxygen generation. *Carcinogenesis* 1303−1311.
(61) Oikawa, S., and Kawanishi, S. (1998) Distinct mechanisms of site-specific DNA damage induced by endogenous reductants in the presence of iron(III) and copper(II). *Biochim. Biophys. Acta 1399*, 19−30.
(62) Wong, A., Huang, H.-C., and Crooke, S. T. (1984) Mechanism of deoxyribonucleic acid breakage induced by 4′-(9-acridinylamino)-methanesulfon-m-anisidide and copper: role for cuprous ion and oxygen free radicals. *Biochemistry 23*, 2946−2952.
(63) Devasagayam, T. P., Steenken, S., Obendorf, M. S., Schulz, W. A., and Sies, H. (1991) Formation of 8-hydroxy(deoxy)guanosine and generation of strand breaks at guanine residues in DNA by singlet oxygen. *Biochemistry 30*, 6283−6289.
(64) Di Mascio, P., Wefers, H., Do-Thi, H. P., Lafleur, M. V., and Sies, H. (1989) Singlet molecular oxygen causes loss of biological activity in plasmid and bacteriophage DNA and induces single-strand breaks. *Biochim. Biophys. Acta. 1007*, 151−157.
(65) Masarwa, M., Cohen, H., Meyerstein, D., Hickman, D. L., Bakac, A., and Espenson, J. H. (1988) Reactions of low-valent transition-metal complexes with hydrogen peroxide. Are they "Fenton-like" or not? 1. The case of Cu^{+} aq and Cr^{2+} aq. *J. Am. Chem. Soc. 110*, 4293−4297.

BC0601828

Synthesis of Cell-Penetrating Conjugates of Calpain Activator Peptides

Zoltán Bánóczi,[†] Ágnes Tantos,[‡] Attila Farkas,[‡] Péter Tompa,[‡] Péter Friedrich,[‡] and Ferenc Hudecz*[,†,§]

Research Group of Peptide Chemistry, Eötvös L. University, Hungarian Academy of Sciences, P.O. Box 32, 1518 Budapest 112 Hungary, Institute of Enzymology, Biological Research Center, Hungarian Academic of Sciences, 1518, Budapest, P.O. Box 7, Hungary, and Department of Organic Chemistry, Eötvös L. University, Budapest, Hungary.
Received July 5, 2006; Revised Manuscript Received October 31, 2006

Calpains, the intracellular proteolytic enzymes, play important roles in various processes in cells. The lack of calpain or its overexpression is thought to be an underlying factor in some diseases. In this study, we report the synthesis of a new group of cell-penetrating calpastatin−peptide conjugates with the activating capacity of m-calpain intracellularly. In these constructs, peptides related to the calpastatin A or C subunit with the capabiliy of activation of isolated m-calpain was covalently conjugated to the C-terminal of penetratin via amide, thioether, or disulfide bond. These conjugates were prepared by solid-phase synthesis and/or by chemical ligation and properly characterized (MS, HPLC). Our results using isolated m-calpain suggest that conjugation does not interfere with the enzyme-activating effect of the calpastatin peptides; in fact, the efficiency of the conjugates was markedly higher. The conjugates with different bonds showed essentially the same level of activation. Internalization experiments with fluorophore (4-[7-hydroxycoumaryl] acetic acid (Hca) at the N-terminal of penetratin and/or 5(6)-carboxyfluorescein (cf)) labeled conjugates show that these constructs are taken up by COS-7 cells. Using cell lysates produced after incubation with the 1:1 (mol/mol) mixture of calpastatin A and C peptide conjugates, we found a significant calpain activating effect. We also noticed that the conjugate even with a disulfide bond between the components seems to be stable and activate m-calpain after intracellular translocation under the conditions studied. To the best of our knowledge, this is the first report to describe conjugates with an m-calpain activating effect on isolated enzymes and more importantly within living cells after transmembrane delivery. Thus, these conjugates seem to be appropriate as molecular tools to activate intracellular m-calpain and to study calpain functions in living cells.

INTRODUCTION

Calpains are intracellular cysteine proteases whose catalytic site is analogous to those of papain-like proteases (*1*, *2*). In mammals, the family has 14 members showing various patterns of expression. The ubiquitous forms are the μ- and m-calpains (calpains 1 and 2, respectively). Calpains play crucial roles in cell adhesion and motility, exocytosis, signal transduction, cell cycle progression, and regulation of gene expression (*3*−*7*). Their activation leads to the limited proteolytic modification of a variety of substrate proteins. However, the overactivation of calpains is associated with the pathogenesis of a wide range of disorders (*8*).

The activation of calpain by Ca^{2+} binding is mechanistically clear, but the key aspects of activation in vivo are still enigmatic. Namely, calpains require nonphysiologically high Ca^{2+} concentrations in vitro (*9*). Various mechanisms have been proposed for calpain sensitization to Ca^{2+} in the cell. One may be the fragmentation of calpastatin, the endogenous inhibitor of calpains. Calpastatin contains four inhibitory domains (*10*). Each domain contains three short, conserved sequences of about 20 amino acids, termed subdomains A, B, and C. Functional studies showed that only subdomain B is responsible for inhibition of calpains (*11*, *12*). Subdomains A and C exert no inhibitory effect on calpain (*12*−*14*). However, peptides corresponding to subdomain A (S^{12}GKSGMDAALDDLIDTLGG^{31}) or subdomain C (S^{86}KPIGPDDAIDALSSDFTS^{105}) significantly activate both human erythrocyte μ-calpain and rat m-calpain and increased the Ca^{2+} sensitivity in vitro (*15*). Peptides, when applied separately, activate the enzyme, but their 1:1 (mol/mol) mixture exhibited the maximal effect. On the basis of these findings, it was postulated that calpastatin might be fragmented, and the fragments could play a role in calpain activation in vivo.

In the extensive studies on calpains physiological function, almost invariably calpain inhibitors were used. These, however, lack strict specificity. They may react with the proteosome, lysosomal proteinases, or even with nonproteolytic enzymes (*16*, *17*). In general, the results obtained with calpain inhibitors cannot always be unequivocally attributed to the action of calpain. In contrast, peptides derived from calpastatins A and C are likely to be specific to calpain.

In recent years, several oligopeptides of natural and/or synthetic origin have been described with cell membrane penetrating capability. The first peptide sequences came from the HIV-1 Tat (*18*, *19*) and the antennapedia protein of *Drosophila* (*20*). These peptides can cross the cell membrane with different cargos (peptides, peptide−nucleic acid, oligonucleotide) (*21*).

There have been efforts to prepare specific calpain inhibitors based on calpastatin and cell-penetrating peptides capable of transmembrane trafficking of covalently attached cargo (*22*−*24*). The alternative strategy was to produce, by genetic manipulation, fusion constructs containing the cell-penetrating motif and the sequence derived from calpastatin (*25*). In these studies, calpastatin or its inhibitory region was joined with cell-penetrating peptides. Croce et al. developed an inhibitor of calpain by conjugating with amide bond the minimal inhibitory

* Ferenc Hudecz, Ph.D., D.Sc., Research Group of Peptide Chemistry, Hungarian Academy of Sciences, Eötvös L. University, Budapest 112, POB 32, H-1518 Hungary. Fax: 36-1-372-2620. Tel: 36-1-372 2828. Email: fhudecz@ludens.elte.hu.

[†] Research Group of Peptide Chemistry, Eötvös L. University.

[‡] Biological Research Center, Hungarian Academic of Sciences.

[§] Department of Organic Chemistry, Eötvös L. University.

10.1021/bc0601976 CCC: $37.00 © 2007 American Chemical Society
Published on Web 12/23/2006

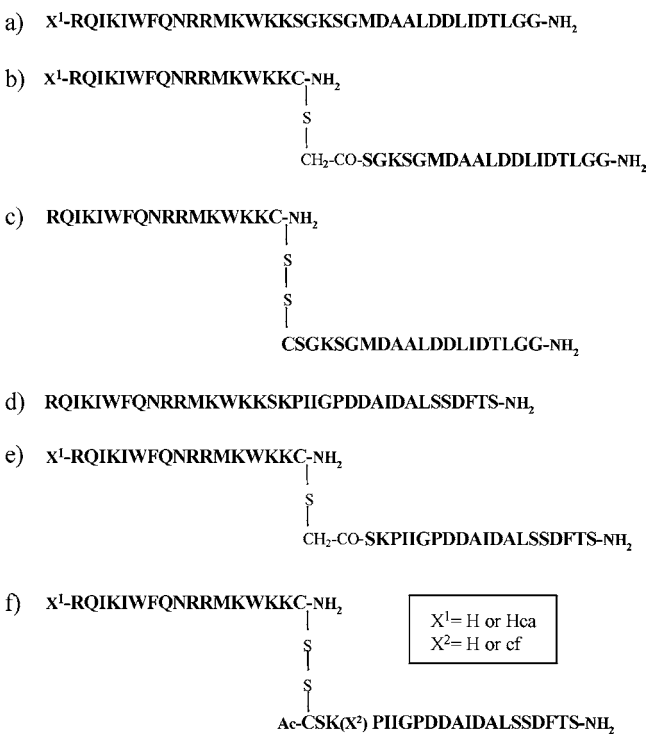


Figure 1. Outline of the structure of the penetratin−calpastatin A (a−c) and penetratin−calpastatin C (d−f) conjugates with amide (a,d), thioether (b,e), or disulfide (c,f) linkage.

sequence (EKLGERDDTIPPEYRELLEKKTGV) of calpastatin to the C-terminal of the signal-sequence-based penetrating peptide, AAVALLPAVLLALLAP. Using this chimera and a set of peptidyl calpain inhibitors, with appropriate specificity controls, it was demonstrated that calpain regulates platelet degranulation, aggregation, and spreading (*22*).

The peptide related to subdomain B of calpastatin (DPMSSTYIEELGKREVTIPPKYRELLA) was prepared with N-terminal 11-mer arginine also via amide bond by solid-phase peptide synthesis (*23*). The conjugated calpastatin peptide was able to inhibit calpain activity in a primary culture of rat cortical neurons. In the other study, the same calpastatin peptide with Cys at the N-terminal was coupled to penetratin containing Cys at the N-terminal position by disulfide bond (*24*). This conjugate was also able to penetrate LCLC 103H cells and inhibit calpain activation in vivo. Sengoku et al. fused the full-length calpastatin or calpastatin subdomain I (115−248 residues) with the Tat peptide (Tat_{47-57}, YGRKKRRQRRR) and observed that the fusion proteins were able to enter primary rat cortical neurons and also exhibited a potent m-calpain inhibitory effect in a cell-free activity assay but did not influence the activity of intracellular calpain (*25*). The authors found that the fusion protein with Tat peptide was taken up by the endosomal route, which might be in relation to the loss of inhibitory property of the cargo.

In the present work, our aim was to prepare a new class of calpastatin peptide conjugates in which the related peptide (calpastatin A or calpastatin C) with calpain-activating properties is conjugated with the well-known cell-penetrating peptide, penetratin. In contrast to the impermeable calpastatin A and C peptides, we expected that these contructs will possess membrane translocating properties and provide activation of calpain intracellularly. The conjugation of calpastatin A and C peptides was carried out via amide, thioether, and disulfide bond formation to study the effect of linkage between the components on both calpain activation and cellular uptake. In these constructs, penetratin (RQIKIWFQNRRMKWKK) was at the N-terminus as outlined in Figure 1. Conjugates with amide bond were built up by solid-phase peptide synthesis. For conjugates with thioether or disulfide bonds, nonprotected peptide fragments with added N- or C-terminal Cys residues were prepared, and appropriate ligation techniques were utilized in solution. Here, we report on our findings that the calpain-activating properties of calpastatin peptides were not only preserved after conjugation with penetratin but significantly increased in both cell-free (isolated enzyme) and cellular assays. Internalization experiments with fluorophore (4-[7-hydroxycoumaryl] acetic acid (Hca) at the N-terminal of penetratin and/or 5(6)-carboxyfluorescein (cf)) labeled conjugates show that these constructs are taken up by COS-7 cells We found that a conjugate even with disulfide bonds between the components seems to be stable and can activate calpain after intracellular translocation.

EXPERIMENTAL PROCEDURES

All amino acid derivatives were purchased from Novobiochem (Laufelfingen, Switzerland) and Reanal (Budapest, Hungary), while *p*-cresol, thioanisole, 1,8-diazabicyclo[5.4.0]undec-7-ene (DBU), piperidine, *N*,*N*′-diisopropylethylamine (DIEA), tris(hydroxymethyl)aminomethane (Tris), trifluoroacetic acid (TFA), triisopropylsilane (TIS), 1-hidroxybenztriazole (HOBt), *N*,*N*′-diisopropylcarbodiimide (DIC), *N*,*N*′-dicyclohexylcarbodiimide (DCC), 5(6)-carboxyfluorescein (cf), 4-[7-hydroxycoumaryl] acetic acid (Hca), and hydrogen fluoride (HF) were Fluka (Buchs, Switzerland) products. The 4-methylbenzhydrylamine (MBHA, 1.4 mmol/g) and Rink amide resin (0.64 mmol/g) were purchased from Novobiochem (Laufelfingen, Switzerland). Solvents (DMF, DCM, diethyl ether, acetonitrile) for syntheses and purification were obtained from Reanal (Budapest, Hungary). The chloroacetic acid pentachlorophenyl ester and the 5(6)-carboxyfluorescein pentachlorophenyl ester were prepared in our laboratory.

Synthesis of Calpastatin Peptides. Calpastatin A peptide with N-terminal Cys residue ($C(Npys)S^{12}$GKSGMDAALDDLIDTLGG^{31}) was synthesized manually by solid-phase methodology on MBHA resin (0.5 g, 1.4 mmol/g). The amino acid side-chain protecting groups were benzyl ether for Ser and Thr and cyclohexyl ester for Asp. The side chain of Lys was protected with *tert*-butyloxycarbonyl group, and of Cys was protected by 3-nitro-2-pyridinesulfenyl (Npys) group.

The synthesis was carried out by the Boc/Bzl strategy up to the incorporation of Asp at position 18. Then, the Fmoc/^{t}Bu strategy was applied. The N^{α}-Boc group was removed with 33% TFA in DCM (2 + 20 min) followed by washing with DCM (5 × 0.5 min), neutralization with 10% DIEA in DCM (3 × 1 min), and DCM washing again (4 × 0.5 min). For coupling, amino acid derivatives and DCC and HOBt dissolved in a minimal amount of DCM−DMF 4:1 (v/v) mixture were used in 3 molar excess for the resin capacity. The reaction proceeded at room temperature (RT) for 60 min. Then, the resin was washed (DMF 2 × 0.5 min, DCM 3 × 0.5 min). The efficiency of coupling was checked by ninhydrin (*26*) or isatin (*27*) tests. The N^{α}-Fmoc group was removed with 2% piperidine plus 2% DBU in DMF (2 + 2 + 5 + 10 min) followed by washing with DMF (8 × 0.5 min). For coupling, amino acid derivatives and DIC and HOBt dissolved in DMF were used in 3-fold molar excess for the resin capacity. The reaction proceeded at RT for 60 min. Then, the resin was washed (DMF 2 × 0.5 min, DCM 3 × 0.5 min). Finally Boc-Cys(Npys) was added as the N-terminal residue. The Boc group was removed by 33% TFA in DCM in the presence of 0.5 g Met as a scavenger. The peptide was cleaved from the resin by 10 mL HF using 0.5 g *p*-cresol scavenger at 0 °C for 1.5 h. Crude products were precipitated with dry diethyl ether, filtered, washed, dissolved in 10% acetic acid, and freeze-dried.

The N^{α}-choloroacetylated calpastatin A peptide (ClAc−S^{12}-GKSGMDAALDDLIDTLGG^{31}) was synthesized manually by

solid-phase methodology on Rink amide resin (0.1 g, 0.64 mmol/g) using the Fmoc/^{t}Bu strategy. The amino acid side-chain protecting groups were *tert*-butyl ether for Thr and Ser and *tert*-butyl ester for Asp. The side chain of Lys was protected with the *tert*-butyloxycarbonyl group. After the removal of the last N^α-Fmoc group, a chloroacetic group was introduced to the N-terminal of the peptidyl resin using 5 molar excess chloroacetic acid pentachlorophenyl ester dissolved in DMF at RT for 10 h (*28*). Chloroacetylated peptide was removed from the resin by cleavage with 10 mL TFA containing 0.5 g phenol, 0.5 mL distilled water, 0.5 mL thioanisole, and 0.6 mL TIS as scavengers. The crude product was precipitated by dry diethyl ether, dissolved in 10% acetic acid, and freeze-dried.

The calpastatin C peptide (Ac−C(Npys)S^{86}KPIGPDDAIDALSSDPFTS^{105}) was synthesized manually by solid-phase methodology on MBHA resin (0.2 g, 1.4 mmol/g) using Boc/Bzl strategy. The amino acid side-chain protecting groups were benzyl ether for Ser and Thr and cyclohexyl ester for Asp. The side chain of Lys was protected with a 2-chlorobenzyloxycarbonyl group. After the cleavage of the last Boc group, the N-terminus was acetylated by acetic anhydride in DMF in the presence of DIEA (1:1 = mol/mol). The acetylated peptide was cleaved from the resin by 10 mL HF using 0.5 g *p*-cresol scavenger at 0 °C for 1.5 h. The crude product was precipitated with dry diethyl ether, filtered, washed, dissolved in 10% acetic acid, and freeze-dried.

Choloroacetylated calpastatin C peptide (ClAc−S^{86}KPIGPDDAIDALSSDPFTS^{105}) was prepared manually by solid-phase methodology on MBHA resin (0.15 g, 1.4 mmol/g) as described above. After the removal of the last N^α-Boc group, the peptidyl resin was chloroacetylated by 5 molar excess of chloroacetic acid pentachlorophenyl ester dissolved in DMF for 10 h. The peptide was cleaved from the resin by 10 mL HF using 0.5 g *p*-cresol scavenger at 0 °C for 1.5 h. The crude product was precipitated with dry diethyl ether, filtered, washed, dissolved in 10% acetic acid, and freeze-dried.

The fluorophore-labeled calpastatin C peptide (Ac−C(Npys)-S^{86}K(cf)PIGPDDAIDALSSDPFTS^{105}) was prepared in solution using 5(6)-carboxyfluorescein pentachlorophenyl ester. 5 mg (2.2 μmol) calpastatin C peptide was dissolved in 0.5 mL DMF. 2.8 mg (4.4 μmol) 5(6)-carboxyfluorescein pentachlorophenyl ester and 0.7 μL (4 μmol) DIEA were added to the solution. The reaction was carried out at RT overnight.

The crude peptides were purified by RP-HPLC (see below).

Synthesis of Penetratin Peptides with C-Terminal Cys. Penetratin with C-terminal Cys (RQIKIWFQNRRMKWKKC) was synthesized manually by solid-phase methodology on Rink amide resin (0.5 g, 0.64 mmol/g) using the Fmoc/^{t}Bu strategy as described above. The amino acid side-chain protecting groups were trityl for Asn, Gln, and Cys and the 2,2,4,6,7-pentamethyldihydrobenzofuran-5-sulfonyl group for Arg. The side chain of Lys was protected with the *tert*-butyloxycarbonyl group. After assembly, the peptide was cleaved from the resin with 10 mL TFA using 0.75 g phenol, 0.5 mL distilled water, 0.5 mL thioanisole, and 0.25 mL ethandithiol as scavengers. The crude product was precipitated by dry diethyl ether, dissolved in 10% acetic acid, and freeze-dried.

4-[7-Hydroxycoumaryl]acetic acid (Hca)-labeled penetratin C peptide (Hca−penetratinC) was synthesized the same way, but after the cleavage of the last N^α-Fmoc group, Hca was introduced into the sequence using the same coupling reagents and conditions as amino acid derivatives. Labeled penetratin C peptide was cleaved from the resin as the penetratin. The peptides were purified by RP-HPLC.

Synthesis of Calpastatin Conjugates. Conjugates with an amide bond were prepared manually by solid-phase methodology using the Fmoc/^{t}Bu strategy on Rink amide resin (0.05 and 0.1 g, 0.64 mmol/g). The amino acid side-chain protecting groups were trityl for Asn, Gln, and Cys and the 2,2,4,6,7-pentamethyldihydrobenzofuran-5-sulfonyl group for Arg. The side chain of Lys was protected with the *tert*-butyloxycarbonyl group. The amino acid side chains of Thr and Ser were protected by *tert*-butyl ether and that of Asp by *tert*-butyl ester. The peptides were cleaved from the resin by 10 mL TFA using 0.75 g phenol, 0.5 mL distilled water, 0.5 mL thioanisole, and 0.25 ethandithiol as scavengers. The crude products were precipitated by dry diethyl ether, dissolved in 10% acetic acid, and freeze-dried. Hca-labeled penetratin−calpastatin A conjugate with an amide bond was prepared the same way, but after the cleavage of the last N^α-Fmoc group, Hca was introduced into the sequence using the same coupling reagents and conditions as amino acid derivatives. The labeled conjugate was cleaved from the resin as the unlabeled one.

Conjugates with a thioether bond were prepared in solution. 15 mg penetratin C (6.4 μmol) or Hca−penetratinC (5.9 μmol) peptides were added in small portions into the buffered (0.1 M TRIS, pH 8.1) solution of 10 mg (5 μmol) chloroacetylated calpastatin A or C peptide (c = 1 mg/mL) every 15 min. The reaction mixture was stirred at RT and followed by RP-HPLC. After 5 h, the solution was freeze-dried.

The synthesis of conjugates with a disulfide bond was carried out in 0.16 M phosphate buffer (pH = 6). 15 mg (6.4 μmol) penetratin C was added in small portions into the buffered solution of 10 mg (4.8 and 4.5 mmol) calpastatin A or C peptides (c = 2 mg/mL) every 15 min. The reaction mixture was stirred at RT and followed by RP-HPLC. Dual-labeled Hca−penetratinCys−Cyscalpastatin(cf)C conjugate with a disulfide bond was prepared in the same way.

All crude conjugates were purified by RP-HPLC as described below.

Reverse-Phase High-Performance Liquid Chromatography (RP-HPLC). Analytical HPLC was performed on a Knauer (Herbert Knauer GmbH, Berlin, Germany) system using a Phenomenex SYNERGI MAX-RP column (250 × 4.6 mm i.d., 4 μm silica, 80 Å pore size) (Torrance, CA) as a stationary phase. Linear-gradient elution (0 min 0% B; 5 min 0% B; 50 min 90% B) was generated using 0.1% TFA in water as eluent A and 0.1% TFA in acetonitrile−water (80:20, V/V) as eluent B. A flow rate of 1 mL/min was applied at ambient temperature. Peaks were detected at λ = 220 nm. The samples were dissolved in eluent B. The crude products were purified on a semipreparative Phenomenex Jupiter C18 column (250 × 10 mm i.d., 10 μm silica, 300 Å pore size) (Torrance, CA). The flow rate was 4 mL/min. The following gradients were applied: 0 min 30% B, 5 min 30% B, and 50 min 75% B for calpastatin A and its conjugates; 0 min 20% B, 5 min 20% B, and 50 min 60% B for calpastatin C, its conjugates, and penetratin.

Amino Acid Analysis. The amino acid composition of peptides was determined by amino acid analysis using a Beckman (Fullerton, CA) model 6300 amino acid analyzer. Prior to analysis, the samples were hydrolyzed in 6 M HCl in sealed and evacuated tubes at 110 °C for 24 h.

Mass Spectrometry. Positive-ion electrospray ionization mass spectrometric analysis was performed on a Bruker Esquire 3000 plus (Germany). The samples were dissolved in acetonitrile−water (50:50, v/v) containing 0.1% acetic acid.

Activation of Calpain in Vitro. Activity of purified recombinant m-calpain was measured in a Jasco FP-6300 spectrofluorometer (Essex, U.K.) in a 3 × 3 mm quartz cuvette, continuously recording the increase of fluorescence corresponding to the cleavage of the substrate FRET (DABCYL-TPLK-SPPPSPR-EDANS) (*29*). The excitation wavelength was 320 nm, and emission was monitored at 480 nm. Reactions were

set up in a final volume of 50 μL at room temperature. Data were recorded for 60 s.

Comparison of the Calpain-Activating Capacity of Conjugates. Maximum activity was measured at 5 mM free Ca^{2+} concentration. Reaction mixtures contained 50 mM Tris-HCl (pH 7.5), 150 mM NaCl, 1 mM EDTA, 2 mM benzamidine, 0.2 mM phenylmethylsulphonyl fluoride and 15 mM β-mercaptoethanol, 200 μM substrate, and 0.2 μM m-calpain. The reaction was started by the rapid mixing of $CaCl_2$ into the sample immediately before starting the measurement. Activation by the conjugates was measured under the same conditions, with the sole difference in the free Ca^{2+} concentration, which was 0.1 mM in these cases. Conjugates were used at 75 μM concentration.

Calpain Activation with the Conjugates with Amide Bond. m-Calpain activity was measured as described above. Different concentrations (0, 5 10, 20, 30, 50, and 100 μM) of the conjugates were used at a constant (0.1 mM) free Ca^{+} level.

Uptake of Fluorescent-Labeled Penetratin−Calpastatin Conjugates. COS-7 cells were grown in Dulbecco's modified Eagle's medium (Sigma) at 37 °C and 5% CO_2 content. Peptides or peptide conjugates were dissolved in a minimal amount of 10% (v/v) acetic acid and diluted with 0.01 M PBS (pH = 7.4) and used at a final concentration of 330 μM. Cells were incubated for 4 h with peptides, then washed with PBS. The fluorescence of cells after fixation (3% paraformaldehyde for 10 min) or without fixation were mounted with MOWIOL 4−88 (Calbiochem) and analyzed by a Leica DMLS fluorescent microscope equipped with a Spot RT color digital camera (Diagnostic Instruments, Livingston, U.K.). According to the type of fluorophores, the Chroma UV and narrow-band GFP filters (Chroma Technology Corp, Rockingham, VT) were used.

Flow Cytometry Analysis of Cellular Uptake. The stock solution of conjugate labeled with 5(6)-carboxyfluorescein dissolved in HPMI (c = 0.4 mM) was used for the treatment of COS-7 cells. Cells were seeded in 24-well plate, and before treatment, the cells were washed with PBS, and they were incubated with the 5(6)-carboxyfluorescein-labeled compound (c = 10 μM) for 1, 1.5, and 3 h at 37 °C. After incubation, cells were washed three times with PBS, trypsinized for 10 min, and resuspended in HPMI. The increase in COS-7 cell fluorescence following incubation was monitored by flow cytometry (BD LSR II, BD Bioscience, San Jose, CA). Data were analyzed with *FACSDiva* software.

Measurement of Endogenous Calpain Activity in COS-7 Cell Lysate. The COS-7 cells were treated with 330 μM conjugates at 37 °C for 4 h. Confluent cells were than washed three times with 0.01 M PBS (pH = 7.4) and were scraped in 1 mL of ice-cold 0.01 mM PBS (pH = 7.4). Cells were collected by centrifugation at 1500 × g at 4 °C for 2 min, resuspended in a 0.1 M Tris-HCl buffer containing 5 mM EDTA, 1 mM dithioerythritol, 5 mM benzamidine, 0.5 mM phenylmethylsulfonyl fluoride, and 10 mM β-mercaptoethanol and sonicated (16 μm, MSE sonicator, West Sussex, U.K.) four times for 10 s with 1 min breaks. The cell lysate was than centrifuged at 15 000 × g at 4 °C for 20 min to remove the cell debris, and the supernatant was used for fluorometric calpain activity measurements as described above. In these experiments, either 1 mM EDTA containing 1 mM $CaCl_2$ or 10 mM $CaCl_2$ was added to 30 μL of lysates. The change in fluorescence intensity was monitored with the FRET peptide substrate (*29*).

RESULTS AND DISCUSSION

Calpains are important proteases involved in several intracellular processes. In studying their function, mainly inhibitors have been used so far. These, however, are not specific for calpains; therefore, the results obtained cannot always be unequivocally associated with the action of calpain (*16*, *17*). We have demonstrated earlier that peptides corresponding to two regions of calpastatin, the protein inhibitor of calpains, exert activation on isolated calpains (*15*). This effect may also be utilized to study calpain function in living cells. To achieve this, we have produced conjugates containing calpastatin peptides derived from subdomains A and C (*12*) as well as cell-penetrating peptide, penetratin (*20*), in the N-terminal part for transmembrane delivery. Here, we report on the synthesis of a new set of penetratin conjugates with an amide, thioether, or disulfide bond between the components (Figure 1). The amide and thioether linkages are considered stable in the cell, while the disulfide bond could be cleaved in the reducing environment of the cytoplasm (*30*). These conjugates were assayed for their calpain activation properties using isolated m-calpain and also COS-7 cell lysate after incubation with the test compounds. We have demonstrated that fluorescent-labeled penetratin conjugates enter cells, and the nature of the covalent linkage between the components has no marked effect on the calpain activation and membrane translocation of the conjugates.

Synthesis of Calpastatin Conjugates. Conjugates, including the 4-[7-hydroxycoumaryl]acetic acid (Hca) labeled variant of penetratin−calpastatin A, with an amide bond were prepared by solid-phase synthesis on Rink amide resin to produce peptide−amides by the Fmoc/^{t}Bu strategy. The completed conjugates were cleaved from the resin by the TFA cleavage mixture. The compounds were obtained without any difficulties, and their characteristics are summarized in Table 1.

Conjugates with a disulfide or thioether bond were prepared in solution. Considering that none of the partner molecules contain the Cys residue, the original sequences were modified by the incorporation of Cys at an adequate position. First, penetratin and Hca−penetratin elongated at the C-terminal by a Cys residue was synthesized on Rink amide resin by the Fmoc/^{t}Bu strategy and used for conjugates with either disulfide or thioether linkages. The peptides were removed from the resin by the TFA/phenol/thioanizol/EDT/water cleavage mixture. Simultaneously, calpastatin A and C peptide amides extended with a Cys at their N-terminal were also produced on the solid phase.

To build up the heterodimer via disulfide bond, the 3-nitro-2-pyridinesulfenyl (Npys) group was used in the calpastatin peptides as a thiol-blocking group. The Npys group was originally proposed for the protection of amino and/or hydroxyl functions during solid-phase peptide synthesis (*31*, *32*). The greatest potential of Npys, however, has gradually been realized to lie in the side-chain protection of Cys (*31*). Indeed, the most attractive feature of Npys is its dual character as an S-protecting and S-activating group. The calpastatin C derivative with Npys-protected and N-acetylated Cys was synthesized on MBHA resin by the Boc/Bzl strategy. However, in the case of the calpastatin A peptide, from position Asp^{18}, the Fmoc/^{t}Bu strategy was used. This combination of Boc/Bzl and Fmoc/^{t}Bu strategies is to avoid oxidation-related side reactions of Met. After completion of the assembly of the sequences, the HF/*p*-cresol cleavage mixture was used for detachment of the peptides from the resin. The calpastatin C peptide labeled with 5(6)-carboxyfluorescein (cf) at the ϵ-amino group of the Lys residue at position 87 was produced after the detachment of the peptide from the resin in DMF solution by using the active ester derivative of cf. The peptides were characterized and used in the conjugation reaction (Table 1.).

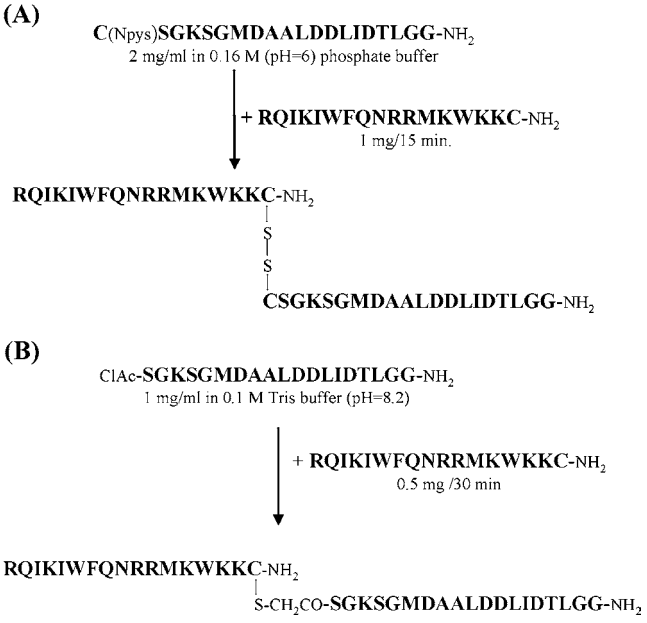
For conjugate preparation, the coupling procedure between the Cys(Npys) peptide and the free SH groups of the protein or polypeptide are usually carried out in solution under acidic conditions (pH 4.5−7.0) to prevent the oxidation of the thiol−peptide (*33*). In our case, the Cys(Npys) containing calpastatin

Table 1. Characteristics of Calpastatin Conjugates and Their Precursors

compounds	code	bond	$[M + H]^+$ [a] calculated [measured]	R_t [b] [min]
H−C(Npys)S^{12}GKSGMDAALDDLIDTLGG^{31}-NH_2	CysCalpA		2092.4 [2092.2]	34.9
ClAc-SGKSGMDAALDDLIDTLGG-NH_2	ClAcCalpA		1912.5 [1913.0]	36.9
Ac−C(Npys)SKPIGPDDAIDALSSDFTS-NH_2	CysCalpC		2235.0 [2235.0]	31.5
Ac−C(Npys)S^{86}K(cf)PIGPDDAIDALSSDFTS^{105}-NH_2 [c]	CysCalp(cf)C		2593.5 [2593.3]	34.4
ClAc-SKPIGPDDAIDALSSDFTS-NH_2	ClAcCalpC		2013.0 [2013.0]	31.9
H-RQIKIWFQNRRMKWKKC-NH_2	PenetratinCys		2349.0 [2349.0]	25.5
Hca-RQIKIWFQNRRMKWKKC-NH_2	Hca-PenetratinCys		2551.9 [2551.5]	28.7
PenetratinCys-CysCalpC		disulfide	4427.3 [4427.0]	28.6
PenetratinCys-CysCalpA		disulfide	4285.1 [4285.0]	31.5
Penetratin-CalpC		amide	4165.0 [4165.0]	28.1
Penetratin-CalpA		amide	4066.5 [4067.0]	32.2
PenetratinCys(CalpC)		thioether	4325.0 [4325.0]	28.4
PenetratinCys(CalpA)		thioether	4226.0 [4226.2]	31.8
Hca-Penetratin-CalpA		amide	4266.8 [4267.0]	33.2
Hca-PenetratinCys(CalpA)		thioether	4427.0 [4427.0]	35.0
Hca-PenetratinCys(CalpC)		thioether	4526.0 [4526.8]	29.4
Hca-PenetratinCys-CysCalp(cf)C		disulfide	4987.7 [4988.2]	30.4

[a] ESI-MS analysis was carried out on a Bruker Esquire 3000 plus (Germany). The samples were dissolved in acetonitrile−water (50:50, v/v), 0.1% acetic acid. [b] HPLC retention time, column: Phenomenex SYNERGI MAX-RP (250 × 4.6 mm, 4 μm, 80 Å). Linear gradient elution: 0 min 0% B; 5 min 0% B; 50 min 90% B with eluent A (0.1% TFA in water) and eluent B (0.1% TFA in acetonitrile−water (80:20, v/v)) was used at a flow rate of 1 mL/min at ambient temperature. Peaks were detected at λ = 220 nm. [c] cf, 5(6)-carboxyfluorescein.

Scheme 1. Outline of the Synthesis of Conjugates with Disulfide (a) or Thioether (b) Bond



A or C peptide was dissolved in 0.16 M phosphate buffer (pH = 6.0) at 2 mg/mL concentration, and penetratin with unprotected C-terminal Cys was added in small portions into this solution as outlined in Scheme 1. The advancement of the reaction was monitored by RP-HPLC, and after completion, the conjugates were purified and characterized (Table 1). Under the conditions used, we found a negligible amount of penetratin dimer.

Conjugation resulting in a thioether bond is a simple method, which can be carried out even with unprotected fragments. For this reaction, penetratin with C-terminal Cys and calpastatin peptides chloroacetylated at their N-terminal were produced. The chloroacetylated calpastatin A was synthesized on Rink amide resin by the Fmoc/^{t}Bu strategy and cleaved from the resin by TFA in the presence of scavengers. It should be noted that EDT was replaced by TIS as a scavenger. Considering the differences in the sequence, the chloroacetylated calpastatin C was synthesized on MBHA resin by the Boc/Bzl strategy and cleaved from the resin by HF. It is important to notice that the chloroacetyl group is stable under the normal HF deprotection conditions, even in the presence of appropriate thiols as scavengers (*34*). The peptides were properly characterized and used in the conjugation reaction (Table 1). Since the reaction of the thiol and Cl−Ac group is fast and selective enough, the protection of the side-chain functional groups in the peptide is not necessary. The thioether bond forms rapidly under mild alkaline conditions (*35*); therefore, the reaction was carried out in 0.1 M Tris buffer (pH 8.1) as outlined in Scheme 1. In most cases, this reaction is faster than the competing oxidation, which could lead to disulfide bridge formation. To avoid this side reaction, the choloroacetylated peptides were dissolved in the buffer, and the Cys-containing penetratin with or without the N-Hca-label was added in small portions into the mixture. We essentially did not observe formation of the oxidized product. It should be noted that this side reaction could be dependent on the position of Cys in the peptide chain (*36*).

In Vitro Activation of Calpain. We have demonstrated earlier that the calpastatin A and C peptides can activate the isolated m-calpain in vitro (*15*). This activating effect was the most pronounced when a 1:1 (mol/mol) mixture of both peptides was used for incubation with calpain. Therefore, using the same assay (*15*), we have performed a comparative study to investigate the effect of conjugation on the enzyme activation effect of calpastatin A plus C peptides. Conjugates with different bonds were also compared for activation of isolated rat m-calpain. The activity of isolated enzyme measured at 5 mM Ca^{2+} concentration was taken as the positive control (100%) (Figure 2, column A), while activation observed in the presence of 0.1 mM Ca^{2+} concentration was considered the "negative" one (2.4%) (Figure 2, column B). At this low Ca^{2+} concentration, the calpain activity was tested in the presence of peptide or conjugate mixtures at equimolar concentration. The mixture of free calpastatin A and C peptides moderately increased the enzyme activity to 9.4% (Figure 2C). A more pronounced effect was observed in the case of the conjugate mixtures (Figure 2D−F). All three samples induced a much higher level of activation of isolated m-calpain (41.7−54.1%). The results show that the conjugation of the calpastatin A and C peptides with penetratin at the N-terminal increased, rather then decreased, the activating potential of the peptides. Penetratin alone had no influence on the calpain activity (data are not shown). Seemingly, the type of linkage between the calpastatin A or C peptides and penetratin had no significant influence on the calpain-activating effect. Perhaps conjugates with an amide bond possessed a slightly higher effect (54.1%). The concentration dependence of calpain

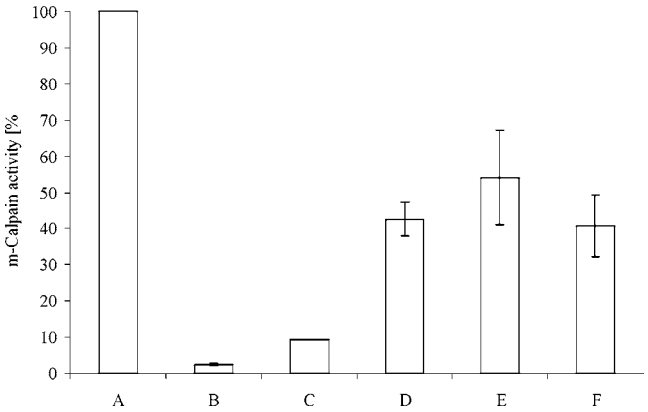


Figure 2. Activation of purified m-calpain with the mixture of calpastatin A and C peptides and with penetratin−calpastatin A and C conjugates. The m-calpain activity was measured at 5 mM $CaCl_2$ (A), at 0.1 mM $CaCl_2$ (B) concentration in the presence of the mixture of 75 μM calpastatin A + 75 μM calpastatin C peptides (C), at 75 μM penetartin−calpastatin A + 75 μM penetratin−calpastatin C conjugates with disulfide bond (D), at 75 μM penetratin−calpastatin A + 75 μM penetratin−calpastatin C conjugates with amide bond (E), and at 75 μM penetratin−calpastatin A + 75 μM penetratin−calpastatin C conjugates with thioether bond (F).

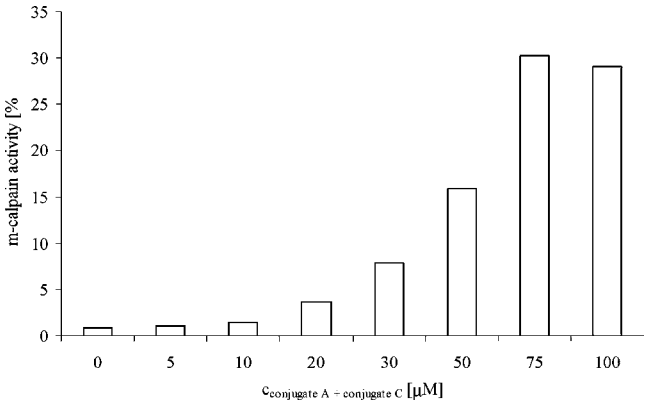


Figure 3. Activity of m-calpain at 0.1 mM $CaCl_2$ using different concentrations of the mixture of penetratin−calpastatin A and C conjugates with amide bond. For details, see Experimental Procedures.

activation was further studied by the mixture of penetratin−calpastatin A and C conjugates with amide bonds (Figure 3.). The m-calpain was measured in the presence of 0.1 mM Ca^{2+} concentration after the addition of 5−100 μM conjugate mixture. The concentration versus activity curve obtained has a sigmoidal pattern, like in the case of the mixture of free calpastatin A and C peptides (*15*). The effect reaches its maximum value at ∼75 μM. These data indicate that the presence of the penetratin sequence is beneficial for the activation of m-calpain perhaps by promoting the binding of calpastatin peptides to calpain. However, further studies are needed to understand the mechanism of action.

Uptake of Penetratin Conjugates. We studied the membrane translocation of conjugates by COS-7 cell by fluorescent microscopy and also by FACS analysis as a function of time. In these experiments, the internalization ability of the conjugates with different bonds was tested. COS-7 cells were incubated with 330 μM Hca−penetratin−CalpA or Hca−penetratinCys-(CalpC) conjugates containing the amide or thioether linkage, respectively. After 4 h at RT, the cells were examined with and without fixation by fluorescent microscopy. The Hca-related fluorescence detected showed that both kinds of conjugates could penetrate into the COS-7 cells and distribute nearly homogeneously in the cells (Figure 4). It should be noted that no effect of fixation on the translocation of Hca−penetratinCys-

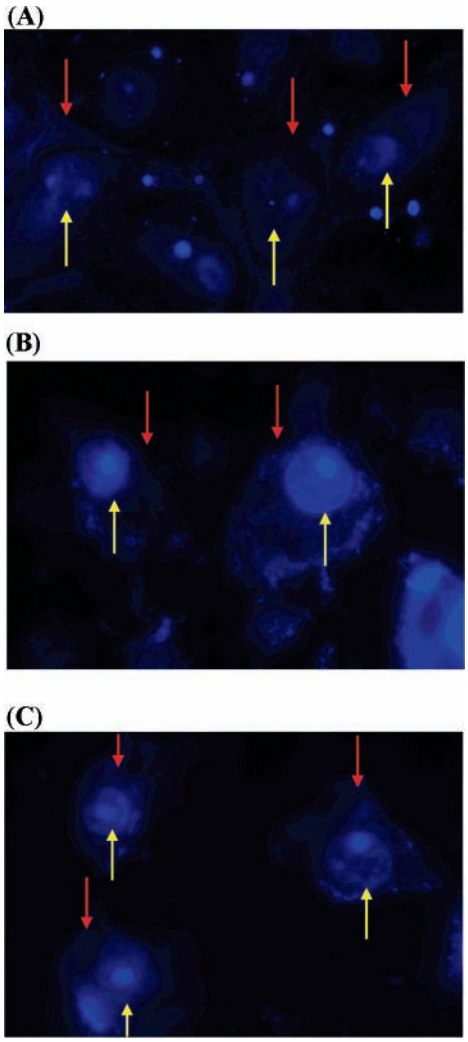


Figure 4. Uptake of Hca−penetratin−calpastatin peptide conjugates by COS-7 cells with (A,B) or without (C) fixation. Hca−penetratin−CalpA conjugate with amide bond (A); Hca−penetratinC−CalpC conjugate with thioether bond (B); and Hca−penetratinC−CalpC conjugate with thioether bond (C). COS-7 cells were treated with 330 μM solution of the conjugate at 37 °C for 4 h. Cells were fixed, and fluorescence was visualized on a Leica DMLS fluorescent microscope. Cell bodies and the nucleus can be distinguished, the conjugates distribute nearly homogeneously in the cells, and the nucleolus is most dense. Red arrows indicate cells, while yellow ones indicate the nucleus. The strong blue patches are aggregates of the conjugates outside the cells. Fixed and living cells provided essentially the same microscopic result, as can be seen in parts B and C.

(CalpC) conjugate was observed under the conditions studied. Similar findings could be detected with other conjugates (data not shown). To study the stability of the disulfide bond, COS-7 cells were also treated with the dual-labeled Hca−penetratin-Cys−CysCalp(cf)C conjugate as described above. The conjugate showed essentially the same cellular uptake and intracellular distribution as compared to conjugates with amide or thioether linkages (Figure 5). The signals derived from both fluorophores inside the cells provided practically the same pattern, suggesting similar intracellular distribution. Apparently, the disulfide bond was stable under the experimental conditions. Furthermore, these data suggest that by this construct calpastatin peptide can be efficiently transported into COS-7 cells. In order to study the viability of cells under conditions used for uptake studies, MTT-based cytotoxicity experiments were carried out. We found that, after the treatment with the conjugate for 3 h, almost 80% of the COS-7 cells were alive, indicating that the 330 μM concentration of the conjugate is not harmful.

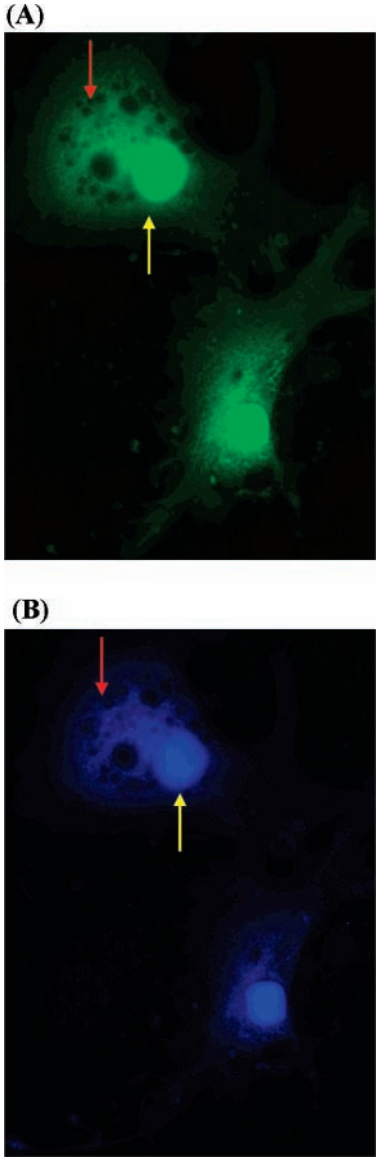


Figure 5. Uptake of double-labeled Hca−penetratinCys−CysCalp-(cf)C conjugate with disulfide bond by COS-7 cells. Signal of the 5(6)-carboxyfluorescein (A). Signal of the Hca (B). COS-7 cells were treated with 330 μM solution of the conjugate at 37 °C for 4 h. Then, fixed cells were visualized on a Leica DMLS fluorescent microscope. Red arrows indicate cells, while yellow ones indicate the nucleus. The conjugate distributes nearly homogeneously in the cell body; the nucleus is denser. Fixed and living cells gave essentially the same microscopic images.

Time dependence of the dual-labeled conjugate was examined by flow cytometry after 1, 1.5, and 3 h treatment of COS-7 cells with the compound under the conditions described above. Data obtained are shown in Figure 6, for a typical experiment. The internalization of the conjugate by cells was in direct proportion to the duration of the incubation time. Even after 1 h, uptake could be demonstrated (*F*(mean): 6), which increases after 1.5 h (*F*(mean): 90) and seems to be saturable since only modest elevation of fluorescence intensity was detected after 3 h (*F*(mean): 200) treatment. For detailed analysis and characterization of the mechanism of internalization, further studies (e.g., temperature dependence, inhibition) are in progress.

Calpain Activity in COS-7 Cell Lysate. In order to study the intracellular calpain-activating potency of conjugate, COS-7 cells were treated with the 1:1 (mol/mol) mixture of penetratin−calpastatin A and C conjugates containing an amide bond at 37 °C for 4 h. Cells without treatment were used as controls. After

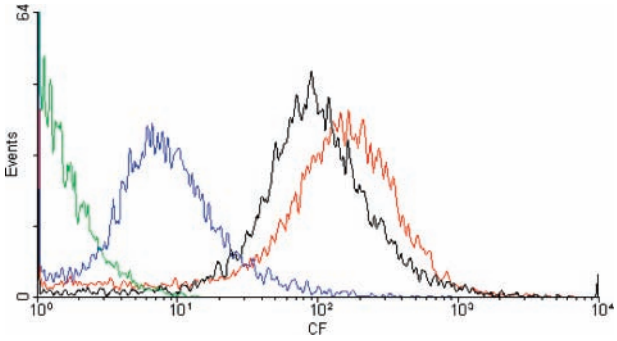


Figure 6. Uptake of the 5(6)-carboxyfluorescein (cf) labeled penetratin−calpastatin C conjugate by COS-7 cells. Cells were treated with a solution of the Hca−penetratinCys−CysCalp(cf)C conjugate with disulfide bond at $c = 10$ μM for 60 min (blue), 90 min (black), and 180 min (red). The fluorescence intensity was measured by FACS analysis. The green line represents the untreated control. For details, see Experimental Procedures.

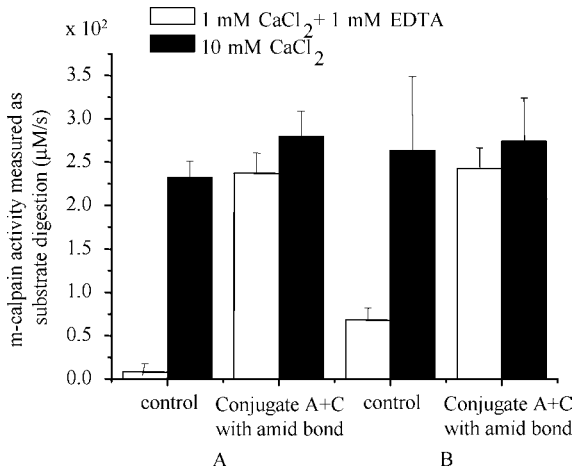


Figure 7. Calpain activity in COS-7 cell lysate in the presence or absence (control) of the mixture of penetratin−calpastatin A plus C conjugates with amide bond. COS-7 cells were treated with the mixture of penetratin−calpastatin A and C conjugates with amide bond using $c = 330$ μM (final), at 37 °C for 4 h. Cells were lysed, and calpain activity was measured in the presence of 1 mM EDTA and 1 mM $CaCl_2$, or of 10 mM $CaCl_2$. The activity of lysates were measured immediately (A) or after 30 min at RT (B). Each column represents the mean value of three independent measurements.

this period of time, the cells were washed and lysated, and the supernatant was used for fluorometric calpain activity measurements in the presence of 1 mM EDTA and 1 mM $CaCl_2$, or of 10 mM $CaCl_2$. Results are shown in Figure 7. Each column represents the mean value of three independent measurements. The activity of lysates was measured immediately (Figure 7A) or after 30 min at RT (Figure 7B). In the case of measurements immediately after cytolysis, calpain activity was only noticeable at 10 mM $CaCl_2$ concentration. However, the calpain activity in the cell lysate treated with the conjugate mixture was clearly higher at both low and high $CaCl_2$ concentrations as compared to the untreated control. We recorded essentially the same tendency in the case of experiments performed after 30 min. These results suggest that the calpastatin conjugates not only before cellular uptake but also after internalization possess a calpain-activating effect.

CONCLUSIONS

In this study, we report the synthesis of a novel group of cell-penetrating calpastatin−peptide conjugates. In these constructs, peptides related to the calpastatin A or C subunit with in vitro calpain-activating capacity were covalently conjugated

to N-terminal penetratin via amide, thioether, or disulfide bond. Our results show that conjugation does not interfere with the m-calpain-activating effect of the calpastatin peptides; in fact, the efficiency of the conjugates was markedly higher. The conjugates with different bonds showed essentially the same level of activation of isolated m-calpain. We have demonstrated that the penetratin conjugates are internalized by COS-7 cells, and the 1:1 (mol/mol) mixture of calpastatin A and C peptides retained their calpain-activating effect even inside the cells. By the help of the dual-labeled penetratin−calpastatin C conjugate, we proved that the disulfide bond is stable enough to transport the attached cargo into the cells under the conditions studied. To the best of our knowledge, this is the first report to describe conjugates with m-calpain-activating effect on isolated enzyme and more importantly within living cells after transmembrane delivery. Thus, these conjugates seem to be appropriate as molecular tools to activate intracellular calpain and to study calpain functions in living cells.

ACKNOWLEDGMENT

These studies were supported by grants from the Hungarian Research Fund (OTKA no. T-043576), from the Hungarian Ministry of Education (Medichem2, NFKP 1/A/005/2004), and from GVOP-2.2.1.-2004-04-0005/2.0.

LITERATURE CITED

(1) Sorimachi, H., Ishiura, S., and Suzuki, K. (1997) Structure and physiological function of calpains. *Biochem. J. 328*, 721−732.

(2) Sorimachi, H., and Suzuki, K. (2001) The structure of calpain. *J. Biochem. (Tokyo) 129*, 653−664.

(3) Goll, D. E., Thompson, V., Li, F. H., Wei, W., and Cong, J. (2003) The calpain system. *Physiol. Rev. 83*, 731−801.

(4) Glading, A., Lauffenburger, D. A., and Wells, A. (2002) Cutting to the chase: calpain proteases in cell motility. *Trends Cell Biol. 12*, 46−54.

(5) Sato, K., and Kawashima, S. (2001) Calpain function in the modulation of signal transduction molecules. *Biol. Chem. 382*, 743−751.

(6) Rutledge, T. W., and Whiteheart, S. W. (2002) SNAP-23 is a target for calpain cleavage in activated platelets. *J. Biol. Chem. 277*, 37009−37015.

(7) Franco, S. J., and Huttenlocher, A. (2005) Regulating cell migration: calpains make the cut. *J. Cell Sci. 118*, 3829−3838.

(8) Huang, Y., and Wang, K. K. (2001) The calpain family and human disease. *Trends Mol. Med. 7*, 355−362.

(9) Baki, A., Tompa, P., Alexa, A., Molnar, O., and Friedrich, P. (1996) Autolysis parallels activation of μ-calpain, *Biochem. J. 318*, 897−901.

(10) Maki, M., Takano, E., Mori, H., Sato, A., Murachi, T., and Hatanaka, M. (1987) All 4 internally repetitive domains of pig calpastatin posses inhibitory activities against calpain-I and calpain-II. *FEBS Lett. 223*, 174−180.

(11) Maki, M., Bagaci, H., Hamaguchi, K., Ueda, M., Murachi, T., and Hatanaka, M. (1989) Inhibition of calpain by a synthetic oligopeptide corresponding to an exon of the human calpastatin gene. *J. Biol. Chem. 264*, 18866−18869.

(12) Takano, E., Ma, H., Yang, H. Q., Maki, M., and Hatanaka, M. (1995) Preference of calcium-dependent interactions between calmodulin-like domains of calpain and calpastatin subdomains. *FEBS Lett. 362*, 93−97.

(13) Ma, H., Yang, H. Q., Takano, E., Hatanaka, M., and Maki, M. (1994) Amino-terminal conserved region in proteinase inhibitor domain of calpastatin potentiates its calpain inhibitory activity by interacting with calmodulin-like domain of the proteinase. *J. Biol. Chem. 269*, 24430−24436.

(14) Maki, M., Takano, E., Osawa, T., Ooi, T., Murachi, T., and Hatanaka, M. (1988) Analysis of structure-function relationship of pig calpastatin by expression of mutated cDNAs in *Escherichia coli*. *J. Biol. Chem. 263*, 10254−10261.

(15) Tompa, P., Mucsi, Z., Orosz, Gy., and Friedrich, P. (2002) Calpastatin subdomains A and C are activators of calpain. *J. Biol. Chem. 277*, 9022−9026.

(16) Wang, K. K., and Yuen, P. W. (1994) Calpain inhibition: an overview of its therapeutic potential. *Trends Pharmacol. Sci. 15*, 412−419.

(17) Donkor, I. O. (2000) A survey of calpain inhibitors. *Curr. Med. Chem. 7*, 1171−1188.

(18) Frankel, A. D., and Pabo, C. O. (1988) Cellular uptake of the Tat protein from human immunodeficiency virus. *Cell 55*, 1189−1193.

(19) Green, M., and Loewenstein, P. M. (1988) Autonomous functional domains of chemically synthesized human munodeficiency virus Tat trans-activator protein. *Cell 55*, 1179−1186.

(20) Joliot, A., Pernelle, C., Deagostini-Bazin, H., and Prochiantz, A. (1991) Antennapedia homeobox peptide regulates neural morphogenesis. *Proc. Natl. Acad. Sci. U.S.A. 88*, 1864−1868.

(21) Hudecz, F., Bánóczi, Z., and Csík, G. (2005) Medium-sized peptides as built in carriers for biologically active compounds. *Med. Res. Rev. 25*, 679−736.

(22) Croce, K., Flaumenhaft, R., Riversi, M., Furie, B., Furie, B. C., Herman, I. M., and Potter, D. (1999) A. Inhibition of calpain blocks platelet secretion, aggregation, and spreading. *J. Biol. Chem. 274*, 36321−36327.

(23) Wu, H. Y., Tomizawa, K., Matsushita, M., Lu, Y. F., Li, S. T., and Matsui, H. (2003) Poly-arginine-fused calpastatin peptide, a living cell membrane-permeable and specific inhibitor for calpain. *Neurosci. Res. 47*, 131−135.

(24) Gil-Parrado, S., Assfalg-Machleidt, I., Fiorino, F., Deluca, D., Pfeiler, D., Schaschke, N., Moroder, L., and Machleidt, W. (2003) Calpastatin exon 1B-derived peptide, a selective inhibitor of calpain: enhancing cell permeability by conjugation with penetratin. *Biol. Chem. 384*, 395−402.

(25) Sengoku, T., Bondada, V., Hassane, D., Dubal, S., and Geddes, J. W. (2004) Tat-calpastatin fusion proteins transduce primary rat cortical neurons but do not inhibit cellular calpain activity. *Exp. Neurol. 188*, 161−170.

(26) Kaiser, E., Colescott, R. L., Bossinger, C. D., and Cook, P. I. (1970) Color test of detection of free amino groups in the solid phase synthesis of peptides. *Anal. Biochem. 34*, 595−598.

(27) Kaiser, E., Bossinger, C. D., Colescott, R. L., and Olsen, D. B. (1980) Color test for terminal prolyl residues in the solid phase synthesis of peptides. *Anal. Chim. Acta 118*, 149−151.

(28) Mezö, G., de Oliveira, E., Krikorian, D., Feijlbrief, M., Jakab, A., Tsikaris, V., Sakarellos, C., Welling−Wester, S., Andreu, D., and Hudecz, F. (2003) Synthesis and comparision of antibody recognition of conjugates containing herpes simplex virus type 1 glycoprotein D epitope VII. *Bioconjugate Chem. 14*, 1260−1269.

(29) Tompa, P., Buzder-Lantos, P., Tantos, A., Farkas, A., Szilagyi, A., Banoczi, Z., Hudecz, F., and Friedrich, P. (2004) On the sequential determinants of calpain cleavage. *J. Biol. Chem. 279*, 20775−20785.

(30) Saito, G., Swanson, J. A., and Lee, K. D. (2003) Drug delivery strategy utilizing conjugation via reversible disulfide linkages: role and site of cellular reducing activities. *Adv. Drug Delivery Rev. 55*, 199−215.

(31) Matsueda, R., and Walter, R. (1980) 3-Nitro-2-piridinesulfenyl (Npys) group. *Int. J. Pept. Protein Res. 16*, 392−401.

(32) Matsueda, R., Kimura, T., Kaiser, E. T., and Matsueda, G. R. (1981) 3-Nitro-2-pyridinesulfenyl group for protection and activation of the thiol function of cystein. *Chem. Lett*. 737−740.

(33) Mezö, G., Mihala, N., Andreu, D., and Hudecz, F. (2000) Conjugation of epitope peptides to branched chain polypeptides via Cys(Npys). *Bioconjugate Chem. 11*, 484−491.

(34) Ivanov, B. B., and Robey, A. F. (1996) Effective use of free thiols as scavengers for HF cocktails to deprotect bromo- and chloroacetyl synthetic peptides. *Pept. Res. 9*, 305−307.

(35) Robey, A. F., and Fields, L. R. (1989) Automated synthesis of *N*-bromoacethyl-modified peptides for preparation of synthetic peptide polymers, peptide-protein conjugates and cyclic peptides. *Anal. Biochem. 177*, 373−377.

(36) Mezö, G., Manea, M., Jakab, A., Kapuvári, B., Bösze, Sz., Schlosser, G., Przybylski, M., and Hudecz, F. (2004) Synthesis and structural characterization of bioactive peptide conjugates using thioether linkage approaches. *J. Pept. Sci. 10*, 701−713.

BC0601976

Novel Bioreducible Poly(amido amine)s for Highly Efficient Gene Delivery

Chao Lin,[†] Zhiyuan Zhong,*[,†] Martin C. Lok,[‡] Xulin Jiang,[‡] Wim E. Hennink,[‡] Jan Feijen,[†] and Johan F. J. Engbersen*[,†]

Department of Biomedical Chemistry and Department of Polymer Chemistry and Biomaterials, Institute for Biomedical Technology (BMTI), Faculty of Science and Technology, University of Twente, P.O. Box 217, 7500 AE Enschede, The Netherlands, and Department of Pharmaceutics, Utrecht Institute for Pharmaceutical Science (UIPS), Utrecht University, P.O. Box 80082, 3508 TB, Utrecht, The Netherlands. Received July 6, 2006; Revised Manuscript Received November 8, 2006

A series of novel bioreducible poly(amido amine)s containing multiple disulfide linkages (SS-PAAs) were synthesized and evaluated as nonviral gene vectors. These linear SS-PAAs could be easily obtained by Michael-type polyaddition of various primary amines to the disulfide-containing cystamine bisacrylamide. The SS-PAA polymers are relatively stable in medium mimicking physiological conditions (pH 7.4, 150 mM PBS, 37 °C), but are rapidly degraded in the presence of 2.5 mM DTT, mimicking the intracellular reductive environment (pH 7.4, [R−SH] = 5 mM, 37 °C). The polymers efficiently condense DNA into nanoscaled (<200 nm) and positively charged (>+20 mV) polyplexes that are stable under neutral conditions but are rapidly destabilized in a reductive environment, as was revealed by both dynamic light scatting measurement and agarose gel assays. Moreover, most of the poly(amido amine)s possess buffer capacities in the pH range pH 7.4−5.1 that are even higher than polyethylenimine (pEI), a property that may favorably contribute to the endosomal escape of the polyplexes. Polyplexes of four of the seven SS-PAAs studied were able to transfect COS-7 cells in vitro with transfection efficiencies significantly higher than those of branched pEI, being one of the most effective polymeric gene carriers reported to date. Importantly, also in the presence of serum, a high level of gene expression could be observed when the incubation time was elongated from 1 h to 4 h. XTT assays showed that SS-PAAs and their polyplexes possess essentially no or only very low cytotoxicity at concentrations where the highest transfection activity is observed. The results indicate that bioreducible poly(amido amine)s have excellent properties for the development of highly potent and nontoxic polymeric gene carriers.

1. INTRODUCTION

A prerequisite for the success of human gene therapy is the availability of safe and efficient gene delivery systems (*1*−*3*). Although viral vectors can efficiently deliver therapeutic nucleotides into cells, clinical application of these vectors is associated with considerable safety and immunogenicity risks. In the past decade, cationic polymers have emerged as important synthetic alternatives, as they have many potential advantages such as absence of specific immune response, large DNA loading capacity, and the ease of large-scale production (*4*−*6*). The currently investigated polymeric gene delivery systems, however, have not yet advanced to clinical evaluation, mainly because of their inferior transfection ability and high degrees of toxicity (*7*−*9*). Improvements have been aimed at developing polymeric vectors that are hydrolytically degradable (*10*−*15*), and a particular example of that approach is the large library of linear poly(β-amino ester)s synthesized and screened by Langer and co-workers (*16*−*18*). Indeed, these hydrolyzable carrier systems generally display decreased cytotoxicity by avoiding the accumulation of positively charged high molecular weight polymers in cells. Degradation of the polymeric vector was also proposed to increase the transfection efficiency by facilitating the unpacking of the polymer/DNA complexes (polyplexes) after endocytosis. The latter process has been identified as one of the major barriers for efficient transfection for many nonviral gene delivery systems (*6*, *19*). However, in the design of hydrolytically degradable carriers, a compromise has to be found between hydrolytic stability in the extracellular environment and fast degradation inside the cell, and this conflicting requirement might explain that in practice the transfection performance of many degradable systems has not improved as compared to their nondegradable counterparts. Furthermore, polymers which are very sensitive for hydrolysis may give difficulties in vector handling and further modification (*20*).

Poly(amido amine)s (PAAs) are hydrolytically much more stable than poly(amino ester)s, and important improvement of the extracellular stability is obtained with these polymers. Generally, linear PAAs have good water solubility and biodegradability, which makes these polymers interesting for biomedical applications, including drug and gene delivery, as was recently pointed out by Ferruti and Duncan et al. (*21*, *22*). These authors reported that an amphiprotic PAA with carboxylic acid side groups give a transfection efficiency comparable to that of 25 kDa branched polyethylenimine (pEI) (*23*), and a conformational change of this polymer upon protonation in the endosomes was proposed to contribute to the endosomal escape of the polyplexes (*24*). The degradation of PAAs under physiological conditions is, however, very slow, and it can be expected that amide hydrolysis does not contribute to the intracellular release of DNA from polyplexes of this polymer.

In this paper, we report a novel family of linear poly(amido amine)s containing repetitive disulfide linkages in their main chain (SS-PAAs) as highly efficient intracellularly degradable gene delivery vectors. These SS-PAAs are relatively stable in the extracellular setting but are prone to fast degradation in a reductive environment analogous to that in the cytoplasm (Scheme 1). Remarkably, the polyplexes based on these SS-PAAs were essentially nontoxic, and a number of them showed

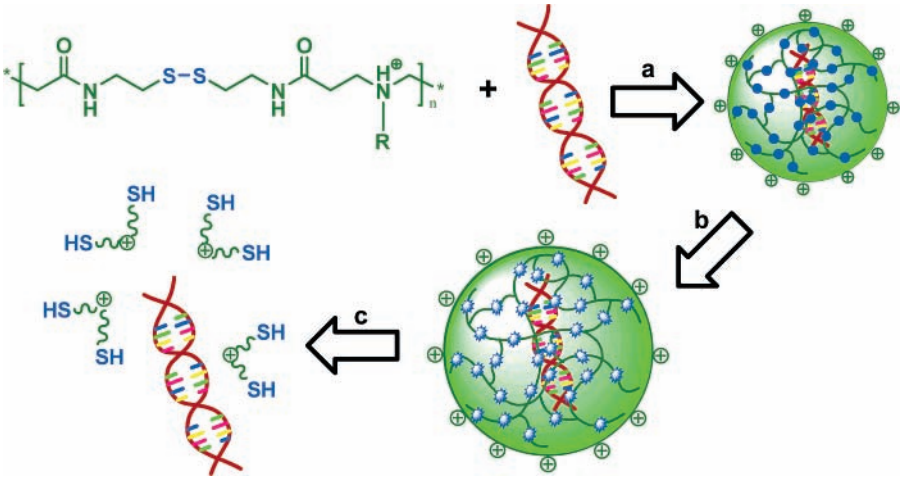
* To whom correspondence should be addressed. Phone: (+31) 53−489-2926. Fax: (+31) 53−489-2479. E-mail: j.f.j.engbersen@utwente.nl (J.F.J. Engbersen), z.zhong@utwente.nl (Z.Y. Zhong).

[†] University of Twente.

[‡] Utrecht University.

10.1021/bc060200l CCC: $37.00 © 2007 American Chemical Society
Published on Web 12/22/2006

Scheme 1. The Concept of DNA Condensation and Subsequent Intracellular Release[a]



[a] (a) Formation of SS-PAAs/DNA polyplexes that are stable in the extracellular environment. (b) Intracellular reduction of the disulfide linkages in the polymer of the polyplex. (c) Dissociation of DNA from the degraded polymer.

transfection efficiencies in COS-7 cells much higher than those of 25 kDa branched pEI, one of the most effective gene delivery polymers reported to date.

It has been well-established that disulfide linkages can be rapidly cleaved in the intracellular compartment due to the presence of relatively high concentrations of glutathione and thioredoxin reductases. This phenomenon has been successfully exploited for the intracellular release of carrier-conjugated therapeutics (*25*−*28*), and cross-linking of various polymer (*29*−*31*), lipid (*32*, *33*), and peptide (*34*, *35*) based carrier systems. However, only a few reports have appeared on disulfide-containing polymers applied for reduction-triggered gene delivery. Read and Seymour et al. (*36*, *37*) showed that reducible cationic polypeptides $(Cys\text{-}Lys_{10}\text{-}Cys)_n$ give a 187-fold higher level of gene expression than nonreducible polylysine. Significant improvement of the transfection efficiency could also be obtained by Middoux et al. (*38*) by substitution of the amino groups of polylysine with 3-(2-aminoethyldithio)propionyl residues. Lee et al. (*39*, *40*) reported that disulfide cross-linking of low molecular weight pEI results in largely improved transfection properties, attaining levels comparable to 25 kDa branched pEI, while maintaining low degrees of cytotoxicity. During the study described in this paper, Ferruti et al. reported the synthesis and chemical characterization of two disulfide-containing poly(amido amine)s derived from 2-methyl piperazine with *N*,*N*-bisacryloyl cystamine and *N*,*N*-bisacryloyl (L)-cystine, respectively (*22*).

Here, we describe the synthesis of a novel series of functionalized poly(amido amine)s with disulfide linkages in their main chain and the evaluation of their chemical and biophysical properties in relation to their capacity as gene delivery vectors. The influence of variation in the side groups of the polymers and the favorable effect of the presence of the disulfide linkages on the transfection efficiency and cytotoxicity is illustrated.

2. EXPERIMENTAL PROCEDURES

2.1. Materials. All monomers, 4-amino-1-butanol (ABOL, Aldrich), 5-amino-1-pentanol (APOL, Aldrich), *N*,*N*-dimethyl-1,3-ethylenediamine (DMEA, Aldrich), 2-(2-aminoethoxy) ethanol (AEEOL, Aldrich), 3-methoxypropylamine (MOPA, Aldrich), 3-morpholinopropylamine (MPA, Aldrich), histamine (Fluka), dithiothreitol (DTT, Sigma), *N*,*N*′-methylenebisacrylamide (MBA, Aldrich), 1,4-bis(acryloyl)piperazine (BAP, Aldrich), *N*,*N*′-hexamethylenebisacrylamide (HMBA, Polysciences, U.S.A), *N*,*N*′-cystaminebisacrylamide (CBA, Polysciences, U.S.A.), branched polyethylenimine (B-pEI, M_w 25 kDa, Aldrich) were purchased in the highest purity and used without further purification. The plasmid pCMVLacZ, containing a bacterial LacZ gene preceded by a nuclear localization signal under control of a CMV promoter, was purchased from Plasmid Factory (Bielefeld, Germany). pDMAEMA (M_w 1.94×10^5 Da) was synthesized as described previously (*41*).

2.2. Synthesis of Bioreducible Poly(amido amine)s (SS-PAAs). SS-PAAs were synthesized by polyaddition of a primary amine to *N*,*N*′-cystaminebisacrylamide (CBA). In a typical experiment, CBA (0.250 g, 1.1 mM) and histamine (HIS) (0.145 g, 1.1 mM) were added into a brown reaction flask and dissolved in methanol/water mixture (1.1 mL, 4/1 v/v). Polymerization was carried out in the dark at 45 °C under nitrogen atmosphere. The reaction mixture became homogeneous in less than 2 h. The reaction was allowed to proceed for 10 days yielding a viscous solution. Subsequently, 10 mol % excess HIS (0.0145 g, 0.11 mM) was added to consume any unreacted acrylamide groups, and stirring was continued for 2 days at 45 °C. The resulting solution was diluted with 30 mL water, acidified with 6 M HCl aqueous solution to pH ∼3, and then purified by ultrafiltration operation (1000 g/mol cutoff) with acidic deionized water (pH ∼4). The polymers in their HCl−salt form were collected as solid powder after freeze-drying (0.14 g, 35%). The same experiment procedure was applied to the synthesis of p(MBA-HIS), p(BAP-HIS), and p(HMBA-HIS) polymers, but water instead of methanol/water as a solvent was used for p(MBA-HIS) and p(BAP-HIS) polymers. The yields of these polymers ranged from 25% to 35% after ultrafiltration.

2.3. Polymer Characterizations. The ^1H spectra of the synthesized SS-PAAs (in D_2O), recorded on a Varian Inova spectrometer operating at 300 MHz, are given in the Supporting Information.

The molecular weight and polydispersity of the SS-PAAs were determined by GPC relative to PEO standards (Polymer Labs) as described by Jiang et al. (*42*). In short, GPC measurements were performed using a Waters 2695 LC system (Milford, MA) and two thermostated (30 °C) PL aquagel-OH 30 columns (8 μm, 300 × 7.5 mm, Polymer Labs, with a low-molar-mass separation range (200−40 000)). Data were collected using a differential refractometer (model 2414). 0.3 M NaAc aqueous solution (pH 4.4) plus methanol (70/30 v/v) was used as eluent at a flow rate of 0.5 mL/min. (The GPC data of the polymers are given in the Supporting Information.)

The buffering capacity of the SS-PAAs was determined by acid−base titration. Therefore, a known amount of poly(amido amine), which was isolated as its HCl salt with 0.25 mmol of

protonable amine groups, was dissolved in 5 mL of 150 mM NaCl aqueous solution. The pH of the polymer solution was set at 2.0, and the solution was titrated with 0.1 M NaOH solution using an automatic titrator (Metrohm 702 SM Titrino). For comparison, branched PEI ($M_w = 25$ kDa) dissolved in 150 mM aqueous solution adjusted to pH 2.0, was also titrated using the same method. The buffering capacity is defined as the percentage of (protonable) amine groups becoming protonated from pH 7.4 to 5.1 and can be calculated from the following equation (*43*):

$$\text{Buffer capacity (\%)} = \frac{\Delta V_{\text{NaOH}} \times 0.1\ \text{M}}{N\ \text{mol}} \times 100\%$$

wherein ΔV_{NaOH} is the volume of NaOH solution (0.1 M) required to bring the pH value of the polymer solution from 5.1 to 7.4, and N mol (0.25 mmol), is the total moles of protonable amine groups in the known amount of poly(amido amine) polymer.

2.4. Polymer Degradation Studies. In the polymer degradation studies, pABOL was selected as a representative polymer. For the estimation of the rate of hydrolytic degradation, 20 mg of pABOL (0.05 mmol in monomeric units) was dissolved in 2 mL of PBS buffer pH 7.4, and the obtained homogeneous solution was incubated at 37 °C. Aliquots of the solution (100 μL) were taken at regular time intervals (24 h) and analyzed by GPC measurements. For the reductive degradation study, 2 mg of pABOL (0.005 mmol in monomeric units) was dissolved in 0.5 mL PBS buffer pH 7.4, and then DTT (0.0025 mmol) in 0.5 mL of PBS buffer (final [R−SH] = 5 mM) was added. The obtained homogeneous solution (1 mL) was incubated at 37 °C, and aliquots of the solution (50 μL) were taken at regular time intervals (5 min) and analyzed by GPC measurements (see Supporting Information).

2.5. Particle Size and ζ-Potential Measurements. SS-PAA/plasmid DNA polyplexes at a polymer/DNA mass ratio of 48/1 were prepared by adding a HEPES buffer solution (20 mM, pH 7.4, 5 wt % glucose) of poly(amido amine)s (800 μL, 900 μg/mL) to a HEPES buffer solution (20 mM, pH 7.4, 5 wt % glucose) of plasmid DNA (200 μL, 75 μg/mL), followed by vortexing for 5 s and incubating at room temperature for 30 min. The surface charge and the size of polyplexes were measured at 25 °C with a Zetasizer 2000 instrument and a Zetasizer 4000, respectively (Malvern Instruments Ltd., Malvern, U.K.).

2.6. Agarose Gel Retardation. Polyplexes were made by adding 10 μL of polymer solution (various concentrations in 20 mM HEPES buffered saline (HBS)) to 10 μL plasmid solution (80 μg/mL in HBS buffer, pH 7.4), followed by vortexing for 5 s, and the dispersions were incubated for 30 min at room temperature. Next, 10 μL of HBS buffer solution (as control) or HBS buffer containing DTT was added to give final 2.5 mM DDT in the resultant solution, and the dispersions were incubated for 30 min. After addition of 5 μL of 6× loading buffer containing bromophenol (Ferments), 10 μL of this mixture was applied onto a 0.7% agarose gel containing 0.5 μg/mL ethidium bromide. After development of the gel, DNA was visualized with a UV lamp using a GelDoc system (Imago).

2.7. In Vitro Transfection and Cell Viability Assays. Transfection experiments were performed with COS-7 cells (SV-40 transformed African green monkey kidney cells) by using the plasmid pCMV-LacZ as reporter gene as reported previously (*41, 44*). Two parallel transfection series, one for the determination of reporter gene expression (β-galactosidase) and the other for the evaluation of cell viability by XTT assay, were carried out in separate 96-well plates (ca.1.0×10^4 cells per well). Different polymer/plasmid DNA weight ratios ranging from 0.75 /1 to 96 /1 (w/w) were used to prepare polyplexes. In brief, the polyplexes were prepared by adding a HEPES buffer solution (20 mM, 130 mM NaCl, pH 7.4, 200 μL) of poly(amido amine)s with varying concentrations (from 9.4 to 1200 μg/mL) to a HEPES buffer solution (20 mM, 130 mM NaCl, pH 7.4, 50 μL) of plasmid DNA (50 μg/mL), followed by gentle shaking and incubating at room temperature for 30 min. The incubations of the polyplexes with the cells were performed in either the presence or absence of 5.0% serum. All transfection and toxicity assays were carried out in triplicate. In a standard transfection experiment, the cells were incubated with desired amounts of polyplexes (100 μL dispersion with 1 μg plasmid DNA per well) for 1 h at 37 °C in a humidified 5% CO_2-containing atmosphere. Next, the polyplexes were removed. 100-μL fresh culture medium was added, and the cells were cultured for 2 days. The transfection efficiency was determined by measuring the enzyme activity of β-galactosidase using the ONPG assay (*41*). A pDMAEMA/DNA formulation prepared at a polymer/DNA ratio of 3/1 (w/w) was used as a reference. The number of viable cells was measured using an XTT assay (*45*). The XTT value for untreated cells (i.e., cells not exposed to transfection systems) was taken as 100% cell viability.

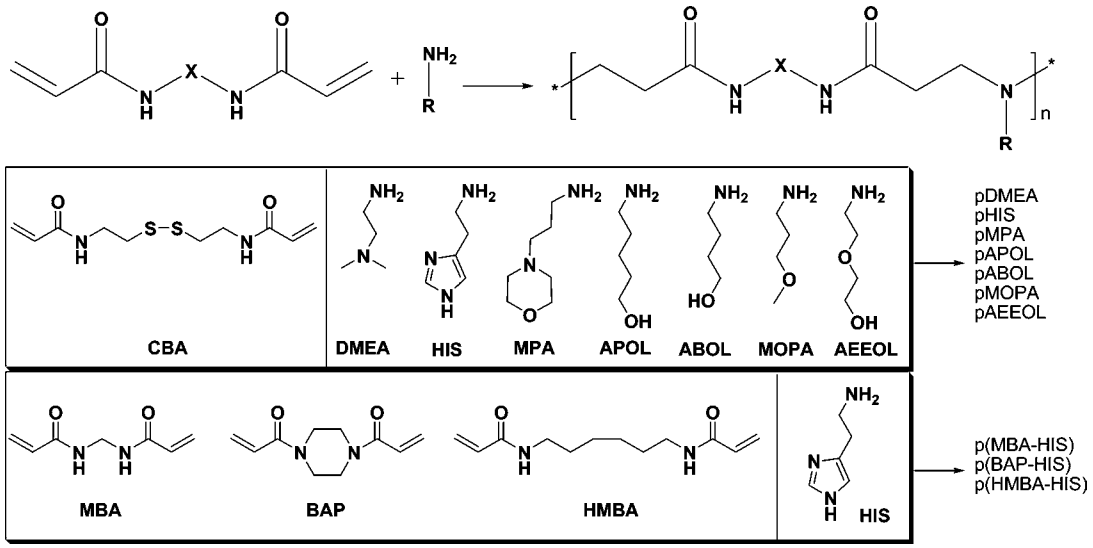
The influence of transfection time on the transfection efficiency of pABOL/pDNA polyplexes at a mass ratio of 54/1 was examined by using the same transfection experiment operation mentioned above; in this case, the polyplexes were incubated with COS-7 cells in varying transfection times (1, 2, or 4 h).

The XTT assay on the cytotoxicity of poly(amido amine) polymers (i.e., pABOL and pAPOL) was carried out with same operation steps mentioned above; in this case, only plain polymer in varying concentration from 9.4 to 600 μg/mL was incubated with COS-7 cells.

3. RESULTS AND DISCUSSION

3.1 Synthesis and Characterization of SS-PAAs. Seven different bioreducible poly(amido amine) polymers with repetitive disulfide linkages in their main chain (SS-PAAs) were synthesized via Michael addition of the corresponding primary amine monomers to *N*,*N*′-cystamine bisacrylamide (Scheme 2). Furthermore, for use as control polymers, three poly(amido amine)s lacking the disulfide linkages were prepared from polyaddition of histamine (HIS) to *N*,*N*′-methylenebisacrylamide (MBA), 1,4-bis(acryloyl)piperazine (BAP), and *N*,*N*′-hexamethylenebisacrylamide (HMBA), respectively (Scheme 2). The Michael-type addition of the difunctional amine to the conjugated acrylamide bond is compatible with a diversity of functional groups, and therefore this reaction allows the introduction of a large variety of side groups in the polymer. In our study, we have selected a number of side groups that appeared to be favorable in a gene delivery screening of a large library of poly(amino ester)s by Langer et al. (*17*). Since the addition polymerization is a stepwise process, equal monomer ratios were used in the synthesis in order to obtain PAAs of highest theoretical molecular weight. In the final stage of the reaction, an excess of the amine monomer was added in order to ensure that all potentially toxic acrylamide end groups are consumed and the polymers have only amino end groups. All 10 PAAs were finally isolated in their HCl−salt form and are readily soluble in water, alcohols, and dimethyl sulfoxide, but not in chloroform or ether. The ^{1}H NMR spectra of the polymers were in full accordance with the expected structures. Moreover, the absence of any proton signals between 5 and 7 ppm shows that the polymer did not contain any residual acrylamide end groups. Gel permeation chromatography (GPC) measurements showed that the weight-average molecular weights (M_w) of these

Scheme 2. Synthesis of Bioreducible Poly(amido amine)s (SS-PAAs) and Nonreducible Control Polymers (p(MBA-HIS), p(BAP-HIS), and p(HMBA-HIS))[a]



[a] SS-PAAs were coded in terms of the used primary amine monomer.

Table 1. Characteristics of Poly(amido amine)s: Weight-Average Molecular Weight (M_w), Polydispersity Index (PDI), and Buffer Capacity[a] in the Range pH 5.1−7.4

polymers	M_w (kDa)	PDI	buffer capacity in the range pH 5.1−7.4 (%)
pDMEA	8.70	1.41	13
pHIS	7.84	1.89	58
pMPA	7.60	1.53	59
pAPOL	3.57	1.26	74
pABOL	5.24	1.29	72
pMOPA	3.15	1.35	74
pAEEOL	3.54	1.63	75
p(MBA-HIS)	26.2	2.51	62
p(BAP-HIS)	17.4	2.31	72
p(HMBA-HIS)	7.7	1.57	66
branched pEI[b]	9.54	1.47	24

[a] Conditions: 5 mL of a solution of the polymer (50 mM in amino nitrogen atoms) was titrated with 0.1 M NaOH solution. [b] The absolute weight-average molecular weight of branched pEI is 25KDa.

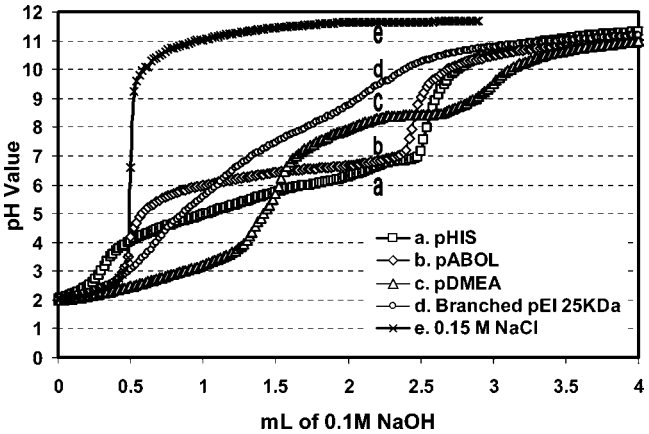


Figure 1. Titration curves obtained by titrating aqueous solutions (pH 2, adjusted with 1 M HCl) of poly(amido amine)•HCl salt (50 mM amino nitrogen atoms) in 150 mM aqueous NaCl with 0.1 M NaOH. For comparison, the titration curve of branched pEI 25 kDa is also presented.

SS-PAAs were in the range from 3000 to 8000 g/mol, with polydispersity indexes (PDI) ranging from 1.26 to 2.51 (Table 1).

It is assumed that the buffering effect of cationic polymers like pEI facilitates the endosomal escape of polyplexes (proton sponge hypothesis) (*46*, *47*). The buffer capacity of the SS-PAA polymers, defined as the percentage of amine groups that becomes protonated on decrease of the pH from 7.4 to 5.1 (i.e., the pH change from the extracellular environment to the lower pH of the endosomes), was measured by acid−base titration (Table 1 and Figure 1). All SS-PAAs, except pDMEA, showed excellent buffer capacity ranging from 42% to 75% protonation, which is significantly higher than that of pEI (24%). Interestingly, pDMEA possessing the dimethylamino group in the side chain has only poor buffer capacity (13%), whereas polymers like pABOL, lacking a proton-acceptor side group show good buffer capacities. The presence of the protonated dimethylamino group in pDMEA (pK_a ~8.5) may largely suppress the protonation of the tertiary nitrogen in the polymer backbone, resulting in a low buffer capacity. The high buffer capacities of the SS-PAAs, as well as their large change in the degree of protonation, may play an important role in the endosomal escape of SS-PAAs/DNA polyplexes and consequently may favorably contribute to the high transfection efficiency of these polymers (vide infra).

The hydrolytic and reductive degradation profiles of the SS-PAAs, using pABOL as a representative example, were investigated in buffer solution (pH 7.4, 150 mM) at 37 °C in the absence and presence of the reduction agent dithiothreitol (DTT, 2.5 mM), mimicking the physiological and intracellular environment, respectively. Monitoring of the decrease in M_w of the polymer by GPC measurements revealed that the pABOL polymer only slowly degrades under physiological conditions, with 5% decrease of M_w after 3 days and 60% decrease after 20 days, which is, as expected, much slower than that of branched and linear poly(amino ester)s (*16*, *20*). However, in the presence of 2.5 mM DTT, a very rapid degradation of the pABOL polymer was observed, and degradation was completed within 5 min. These results suggest that SS-PAA-based polyplexes will not be prone to hydrolytic destabilization under physiological conditions, but can rapidly disintegrate by reductive cleavage of the disulfide linkages in an intracellular reductive environment.

3.2. DNA Condensation and Release. A requirement for cationic polymers to function as gene delivery vectors is that they are able to condense DNA into nanosized polyplexes. Dynamic light scattering (DLS) and ζ-potential measurements show that five SS-PAAs condense DNA at a polymer/DNA mass ratio of 48/1 into polyplexes with small particle size (<200 nm)

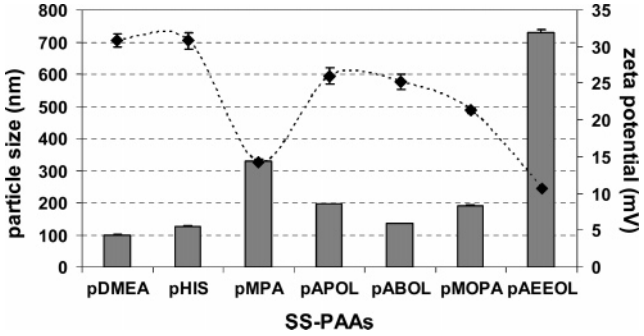


Figure 2. Average particle size (solid bars) and ζ potential (◆) of polyplexes formed with various SS-PAAs and DNA at a polymer/DNA mass ratio of 48/1.

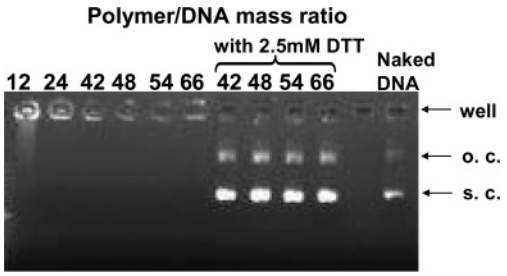


Figure 3. Agarose gel electrophoresis of pAPOL/pDNA polyplexes prepared at different polymer/DNA mass ratios before and after addition of DTT (final concentration of 2.5 mM). o.c. = open circular, s.c. = supercoiled form of plasmid DNA.

and positive surface charge (>+20 mV) (Figure 2). The smallest size and a relatively high surface charge was observed for the polyplexes of pDMEA containing protonated dimethylamino moieties, whereas polyplexes of pMPA and pAEEOL, containing an ether moiety, display a relatively large particle size and a low surface charge. The condensation ability of the SS-PAAs gives the following tendency: pDMEA, pHIS > pAPOL, pABOL, pMOPA > pMPA, pAEEOL. Obviously, the charge density of the polymers plays an important role in their complexation capacity. Polymers pDMEA and pHIS with (partially) protonated side groups, possessing the highest charge density, give polyplexes of small particle size and high surface charge. However, comparison of pABOL and pAPOL with pAEEOL also shows that subtle changes in side chain structure, like the introduction of an ether oxygen in the side chain, have large effects on the condensation ability and surface charge.

For efficient gene transfer, DNA should eventually be released from the polymeric vector. It has been reported that insufficient unpacking of polyplexes can form a major barrier in the transfection process (*6*, *19*). Consequently, the rapid cleavage of the disulfide linkages in the intracellular reductive environment (containing 0.1−10 mM glutathione) is biologically relevant to induce fast dissociation of SS-PAA-based polyplexes and efficient DNA release, leading to increased levels of gene expression. In order to prove the concept of efficient release of DNA from the polyplexes upon disulfide reduction, the complexation−decomplexation behavior of polyplexes based on the 7 PAAs was investigated by agarose gel retardation. A typical example is given in Figure 3, which shows that the migration of negatively charged DNA is retarded by positively charged pAPOL polymer at polymer/DNA mass ratios at and above 24/1. As expected, incubation of the polyplexes for 30 min to dithiothreitol (DTT, 2.5 mM), mimicking the reducing intracellular environment, resulted in total DNA release even at higher ratios of 42/1 and 66/1. The same behavior was observed for the other SS-PAA-based polyplexes, except pAEEOL. However, DNA release did not occur with polyplexes based on the nonreducible control polymers and branched pEI under otherwise identical conditions (data not shown). The concept of fast polyplex destabilization in a reductive environment is further supported by DLS measurements that show that the size of pAPOL-based polyplexes rapidly increases from 200 nm to more than 1 μm within 10 min after the addition of DTT, whereas the size of polyplexes based on the reference polymers remain stable in the presence of DTT.

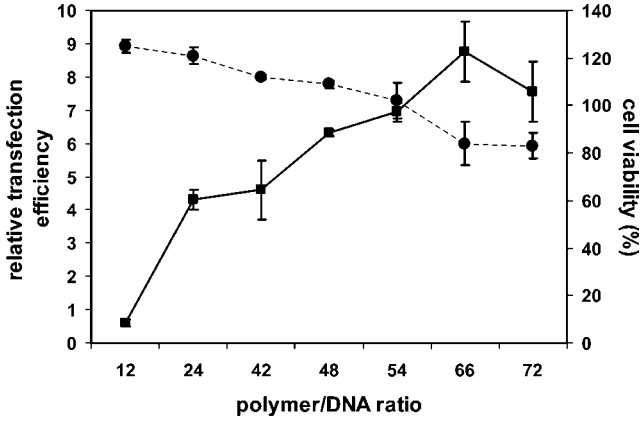


Figure 4. Relative transfection efficiencies (■) and corresponding cell viabilities (●) for pAPOL-based polyplexes formed at various polymer/DNA mass ratios. Transfection efficiencies were normalized to that of pDMAEMA/DNA complexes at a ratio of 3/1 (w/w) (i.e., the transfection efficiency of pDMAEMA polyplexes at their optimal polymer/DNA ratio of 3/1 (w/w) was taken as 1.0). Cell viability was determined by the XTT assay. The data were expressed as mean values (standard deviations) of three experiments.

3.3. In Vitro Transfection Efficiency and Cytotoxicity. The transfection of polyplexes based on the seven SS-PAAs was studied in vitro by using COS-7 cells and the plasmid pCMV-LacZ as reporter gene. Transfection efficiencies were optimized as a function of polymer/DNA mass ratios, ranging from 0.75/1 to 96/1 (Figure 4). As a typical example, a bell-shaped transfection curve was observed for pAPOL-based polyplexes with increasing mass ratios. The optimal transfection of the polyplexes was revealed at a mass ratio of 66/1 (N/P ≈ 50) with an efficiency of about ninefold higher than that of the polyplexes of poly(2-(dimethylamino)ethyl methacrylate) (pDMAEMA) at their optimal (3/1) ratio (*41*). Moreover, remarkably high gene expressions are accompanied with essentially absent or only very low cytotoxicities (≥85% cell viability) (Figure 4).

Figure 5A shows that four of the seven SS-PAAs polyplexes transfect COS-7 cells, with transfection efficiencies higher than that of 25 kDa branched pEI, being the "golden standard". All of these four polymers exhibit considerable buffer capacity (Table 1). In the series of polymers, it appears that the polymers with more hydrophobic side groups give higher transfection, as the transfection efficiency increases in the sequence: pAPOL, pABOL > pMOPA ≫ pAEEOL. Notably, the low transfection efficiency of the polyplexes based on pDMEA, pMPA, and pAEEOL coincides with their less favorable biophysical characteristics, i.e., low buffer capacity, low surface charge, and large particle size, respectively. In the series of the histamine-based polymers, it is clear that polyplexes of the disulfide-containing pHIS show a much higher transfection efficiency and a lower cytotoxicity than those of the control PAAs, indicating that reductive disulfide cleavage indeed plays an important role in the gene delivery process.

It is well-known that the presence of serum often causes aggregation of polyplexes, resulting in decreased transfection efficiencies (*48*). As is shown in Figure 5A, the presence of 5% serum decreases the transfection efficiency of polyplexes of 25 kDa branched pEI ca. 2 times, and even larger effects are observed for polymers like pAPOL. However, it should be noted

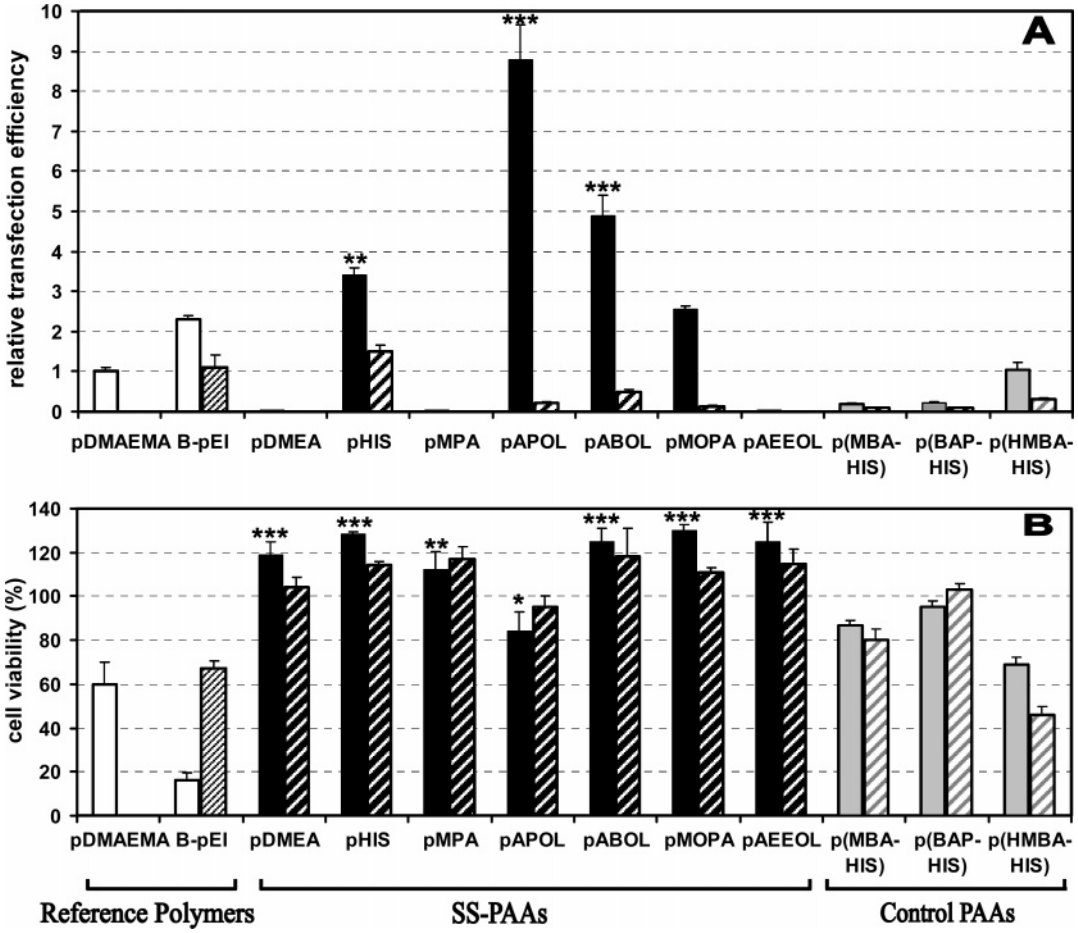


Figure 5. Relative transfection efficiencies (A) and corresponding cell viabilities (B) of polyplexes formed with various poly(amido amine)s and DNA in COS-7 cells at optimized polymer/DNA mass ratios in the absence (solid bars) and presence (slashed bars) of 5% serum. Polymer/DNA ratios for the disulfide containing SS-PAAs p(HIS), p(APOL), p(ABOL), and p(MOPA) were 12/1, 66/1, 54/1, and 48/1 respectively. The transfection efficiency of pDMAEMA polyplexes in the absence of serum at the optimal polymer/DNA ratio of 3/1 (w/w) was taken as reference (set at 1.0). Polyplexes of 25 kDa branched pEI (B-pEI) at an optimized mass ratios of 6/1 was also measured for comparison. Polyplexes of the PAAs without disulfide linkages, p(MBA-HIS), p(BAP-HIS), and p(HMBA-HIS) at optimized mass ratios of 6/1, 96/1, and 48/1, respectively, were used as a control. Cell viability was determined by the XTT assay. The data were expressed as mean values (standard deviations) of three experiments. (Student's *t*-test, $*p < 0.05$, $**p < 0.01$, $***p < 0.001$, poly(amido amine) vs B-pEI).

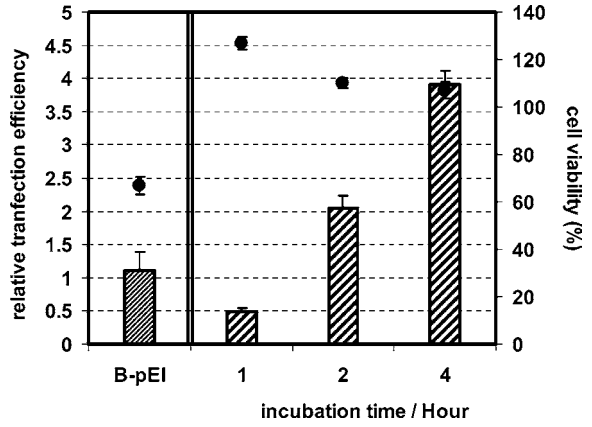


Figure 6. Effect of cell incubation time on transfection efficiency (slashed bars) and corresponding cell viability (●) of pABOL-based polyplexes in COS-7 at an optimized polymer/DNA mass ratio of 54/1 in the presence of 5 wt % serum. The transfection efficiency of pDMAEMA polyplexes in the absence of serum at their optimal polymer/DNA mass ratio of 3/1 was taken as 1.0. Polyplexes of 25 kDa branched pEI (B-pEI) at an optimized mass ratios of 6/1 in the presence of 5 wt % serum were used as a control. Cell viability was determined by the XTT assay. The data were expressed as mean values (standard deviations) of three experiments.

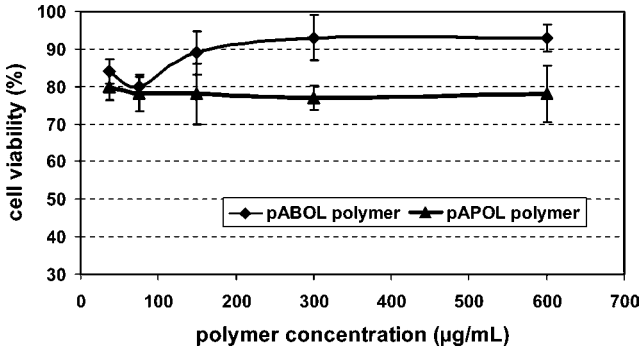


Figure 7. Cell viability of pABOL (◆) and pAPOL (▲) in COS-7 cells at varying polymer concentrations. Cell viability was determined by the XTT assay. The data were expressed as mean values (standard deviations) of three experiments.

that the transfection efficiencies given in this figure were not optimized for serum conditions and that the low toxicity profiles of the PAAs allow considerable optimization by increasing the incubation time of the cells with the polyplexes. For example, a remarkable increase of about 8 times in transfection efficiency of pABOL-based polyplexes is observed in the presence of 5% serum when the incubation time is increased from 1 h to 4 h (Figure 6).

The cell viability experiments, as evaluated by XTT assay, showed that the SS-PAA-based polyplexes are essentially nontoxic (~100% cell viability), illustrating superior properties compared to 25 kDa branched pEI (20% cell viability) and the

control polymers (70−95% cell viability) at polymer/DNA mass ratios of highest transfection efficiency (Figure 5B). As was tested for pABOL and pAPOL also, the plain polymers have a much lower cytotoxicity than 25 kDa branched pEI (IC_{50} of ~30 μg/mL); even at the high concentration of 600 μg/mL, about 80% of the cells retain their metabolic activity (Figure 7).

4. CONCLUSIONS

We have demonstrated that the novel family of functionalized poly(amido amine)s containing repetitive disulfide linkages in their main chain (SS-PAAs) have very promising characteristics for the development of highly potent and nontoxic gene carriers. Their easy and versatile synthesis is compatible with the use of a large variety of functionalized amine monomers, allowing large variation in the structure of the polymers. This enables the tuning of various chemical and biophysical properties important for efficient gene delivery as well as the attachment of stealth polymers and homing devices for gene delivery in vivo. These latter modifications are the subject of current studies.

Supporting Information Available: ^{1}H NMR and GPC data of the poly(amido amine)s. This material is available free of charge via the Internet at http://pubs.acs.org.

LITERATURE CITED

(1) Anderson, W. F. (1998) Human gene therapy. *Nature (London) 392*, 25−30.

(2) Thomas, C. E., Ehrhardt, A., and Kay, M. A. (2003) Progress and problems with the use of viral vectors for gene therapy. *Nat. Rev. Genet. 4*, 346−358.

(3) Verma, M., and Somia, N. (1997) Gene therapy - promises, problems and prospects. *Nature (London) 389*, 239−242.

(4) Li, S., and Huang, L. (2000) Non-viral gene therapy: promises and challenges. *Gene Ther. 7*, 31−34.

(5) Luo, D., and Saltzman, W. M. (2000) Synthetic DNA delivery systems. *Nat. Biotechnol. 18*, 33−37.

(6) Pack, D. W., Hoffman, A. S., Pun, S., and Stayton, P. S. (2005) Design and development of polymers for gene delivery. *Nat. Rev. Drug Discovery 4*, 581−593.

(7) Han, S., Mahato, R. I., Sung, Y. K., and Kim, S. W. (2000) Development of biomaterials for gene therapy. *Mol. Ther. 2*, 302−317.

(8) Merdan, T., Kopecek, J., and Kissel, T. (2002) Prospects for cationic polymers in gene and oligonucleotide therapy against cancer. *Adv. Drug Delivery Rev. 54*, 715−758.

(9) Anwer, K., Rhee, B. G., and Mendiratta, S. K. (2003) Recent progress in polymeric gene delivery systems. *Crit. Rev. Ther. Drug Carrier Syst. 20*, 249−293.

(10) Lim, Y. B., Choi, Y. H., and Park, J. S. (1999) A self-destroying polycationic polymer: biodegradable poly(4-hydroxy-l-proline ester). *J. Am. Chem. Soc. 121*, 5633−5639.

(11) Putnam, D., and Langer, R. (1999) Poly(4-hydroxy-l-proline ester): low temperature polycondensation and plasmid DNA complexation. *Macromolecules 32*, 3658−3662.

(12) Lim, Y. B., Kim, C. H., Kim, K., Kim, S. W., and Park, J. S. (2000) Development of a safe gene delivery system using biodegradable polymer, poly[α-(4-aminobutyl)-L-glycolic acid]. *J. Am. Chem. Soc. 122*, 6524−6525.

(13) Lim, Y. B., Kim, S. M., Lee, Y., Lee, W. K., Yang, T. G., Lee, M. J., Suh, H., and Park, J. S. (2001) Cationic hyperbranched poly(amino ester): A novel class of DNA condensing molecule with cationic surface, biodegradable three-dimensional structure, and tertiary amine groups in the interior. *J. Am. Chem. Soc. 123*, 2460−2461.

(14) Liu, Y., Wu, D. C., Ma, Y. X., Tang, G. P., Wang, S., He, C. B., Chung, T. S., and Goh, S. (2003) Novel poly(amino ester)s obtained from Michael addition polymerizations of trifunctional amine monomers with diacrylates: safe and efficient DNA carriers. *Chem. Commun. 20*, 2630−2631.

(15) Luten, J., van Steenis, J. H., van Someren, R., Kemmink, J., Schuurmans-Nieuwenbroek, N. M. E., Koning, G. A., Crommelin, D. J. A., van Nostrum, C. F., and Hennink, W. E. (2003) Water-soluble biodegradable cationic polyphosphazenes for gene delivery. *J. Controlled Release 89*, 483−497.

(16) Lynn, D. M., and Langer, R. (2000) Degradable poly(β-amino esters): synthesis, characterization, and self-assembly with plasmid DNA. *J. Am. Chem. Soc. 122*, 10761−10768.

(17) Anderson, D. G., Lynn, D. M., and Langer, R. (2003) Semi-automated synthesis and screening of a large library of degradable cationic polymers for gene delivery. *Angew. Chem., Int. Ed. 42*, 3153-3158.

(18) Anderson, D. G., Akinc, A., Hossain, N., and Langer, R. (2005) Structure/property studies of polymeric gene delivery using a library of poly(beta-amino esters). *Mol. Ther. 11*, 426−434.

(19) Schaffer, D. V., Fidelman, N. A., Dan, N., and Lauffenburger, D. A. (2000) Vector unpacking as a potential barrier for receptor mediated polyplex gene delivery. *Biotechnol. Bioeng. 67*, 598−606.

(20) Zhong, Z. Y., Song, Y., Engbersen, J. F. J., Lok, M. C. Hennink, W. E., and Feijen, J. (2005) A versatile family of degradable non-viral gene carriers based on hyperbranched poly(ester amine)s. *J. Controlled Release 109*, 317−329.

(21) Ferruti, P., Marchisio, M., and Duncan, A., R. (2002) Poly(amido-amine)s: Biomedical applications. *Macromol. Rapid Commun. 23*, 332−355.

(22) Emilitri, E., Ranucci, E., and Ferruti, P. (2005) New poly-(amidoamine)s containing disulfide linkages in their main chain. *J. Polym. Sci., Part A: Polym. Chem. 43*, 1404−1416.

(23) Richardson, S. C. W., Pattrick, N. G., Man, Y. K. S., Ferruti, P., and Duncan, R. (2001) Poly(amido amine)s as potential nonviral vectors: Ability to form interpolyelectrolyte complexes and to mediate transfection in vitro. *Biomacromolecules 2*, 1023−1028.

(24) Ferruti, P., Manzoni, S., Richardson, S. C. W., Duncan, R., Pattrick, N. G., Mendichi, R., and Casolaro, M. (2000) Amphoteric linear poly(amido-amine)s as endosomolytic polymers: correlation between physicochemical and biological properties. *Macromolecules 33*, 7793−7800.

(25) Saito, G., Swanson, J. A., and Lee, K-D. (2003) Drug delivery strategy utilizing conjugation via reversible disulfide linkages: role and site of cellular reducing activities. *Adv. Drug. Delivery Rev. 55*, 199−215.

(26) Filipovska, A., Eccles, M. R., Smith, R. A. J., and Murphy, M. P. (2004) Delivery of antisense peptide nucleic acids (PNAs) to the cytosol by disulphide conjugation to a lipophilic cation. *FEBS Lett. 556*, 180−186.

(27) Muratovska, A., and Eccles, M. R. (2004) Conjugate for efficient delivery of short interfering RNA (siRNA) into mammalian cells. *FEBS Lett. 558*, 63−68.

(28) Oishi, M., Hayama, T., Akiyama, Y., Takae, S., Harada, A., Yarnasaki, Y., Nagatsugi, F., Sasaki, S., Nagasaki, Y., and Kataoka, K. (2005) Supramolecular assemblies for the cytoplasmic delivery of antisense oligodeoxynucleotide: Polylon complex (PIC) micelles based on poly(ethylene glycol)-SS-oligodeoxynucleotide conjugate. *Biomacromolecules 6*, 2449−2454.

(29) Kakizawa, Y., Harada, A. and Kataoka, K. (1999) Environment-sensitive stabilization of core-shell structured polyion complex micelle by reversible cross-linking of the core through disulfide bond, block catiomer polyplexes with regulated densities of charge and disulfide cross-linking directed to enhance gene expression. *J. Am. Chem. Soc. 121*, 11247−11248.

(30) Miyata, K., Kakizawa, Y., Nishiyama, N., Harada, A., Yamasaki, Y., Koyama, H., and Kataoka, K. (2004) Block catiomer polyplexes with regulated densities of charge and disulfide cross-linking directed to enhance gene expression. *J. Am. Chem. Soc. 126*, 2355−2361.

(31) Li, Y. T., Lokitz, B. S., Armes, S. P., and McCormick, C. L. (2006) Synthesis of reversible shell cross-linked micelles for controlled release of bioactive agents. *Macromolecules 39*, 2726−2728.

(32) Chittimalla, C., Zammut-Italiano, L., Zuber, G., and Behr, J. P. (2005) Monomolecular DNA nanoparticles for intravenous delivery of genes. *J. Am. Chem. Soc. 127*, 11436−11441.

(33) Hirko, A., Tang, F. X, and Hughes, J. A. (2003) Cationic lipid vectors for plasmid DNA delivery. *Curr. Med. Chem. 10*, 1185−1193.

(34) Trentin, D., Hubell, J., and Hall, H. (2005) Non-viral gene delivery for local and controlled DNA release. *J. Controlled Release 102*, 263−275.
(35) Kwok, K. Y., Park, Y., Yang, Y. S., Mckenzie, D. L., Liu, Y. H., and Rice, K. C. (2003) In vivo gene transfer using sulfhydryl cross-linked PEG-peptide/glycopeptides DNA condensates. *J. Pharm. Sci. 92*, 1174−1185.
(36) Oupicky, D., Parker, A. L., and Seymour, L. W. (2002) Laterally stabilized complexes of DNA with linear reducible polycations: strategy for triggered intracellular activation of DNA delivery vectors. *J. Am. Chem. Soc. 124*, 8−9.
(37) Read, M. L., Singh, S., Ahmed, Z., Stevenson, M., Briggs, S. S., Oupicky, D., Barrett, L. B., Spice, R., Kendall, M., Berry, M., Preece, J. A., Logan, A., and Seymour, L. W. (2005) A versatile reducible polycation-based system for efficient delivery of a broad range of nucleic acids. *Nucleic Acid Res. 33*, e86.
(38) Pichon, C., LeCam, E., Guerin, B., Coulaud, D., Delain, E., and Midoux, P. (2002) Poly[Lys-(AEDTP)]: A cationic polymer that allows dissociation of pDNA/cationic polymer complexes in a reductive medium and enhances polyfection. *Bioconjugate Chem. 13*, 76−82.
(39) Gosselin, M. A., Guo, W. and Lee, R. J. (2002) Incorporation of reversibly cross-linked polyplexes into LPDII vectors for gene delivery. *Bioconjugate Chem. 13*, 1044−1053.
(40) Gosselin, M. A., Guo, W., and Lee, R. J. (2001) Efficient gene transfer using reversibly cross-linked low molecular weight polyethylenimine. *Bioconjugate Chem. 12*, 989−994.
(41) Cherng, J., van de Wetering, P., Talsma, P., H., Crommelin, D. J. A., and Hennink, W. E. (1996) Effect of size and serum proteins on transfection efficiency of poly((2-dimethylamino)ethyl methacrylate)-plasmid nanoparticles. *Pharm. Res. 13*, 1038−1042.
(42) Jiang, X. L., van der Horst, A., van Steenbergen, M. J., Akeroyd, N., van Nostrum, C. F., Schoenmakers, P. J., and Hennink, W. E. (2006) Molar-mass characterization of cationic polymers for gene delivery by aqueous size-exclusion chromatography. *Pharm. Res. 23*, 595−603.
(43) Zhong, Z. Y., Feijen, J., Lok, M. C., Hennink, W. E., Christensen, L. V., Yockman, J. W., Kim, Y.-H., and Kim, S. W. (2005) Low molecular weight linear polyethylenimine-b-poly(ethylene glycol)-b-polyethylenimine triblock copolymers: synthesis, characterization, and in vitro gene transfer properties. *Biomacromolecules 6*, 3440−3448.
(44) Arigita, C., Zuidam, N. J., Crommelin, D. J. A., and Hennink, W. E. (1999) Association and dissociation characteristics of polymer/DNA complexes used for gene delivery. *Pharm. Res. 16*, 1534−1541.
(45) Scudiero, D. A., Shoemaker, R. H., Paull, K. D., Monks, A., Tierney, S., Nofziger, T. H., Currens, M. J., Seniff, D., and Boyd, M. R. (1988) Evaluation of a soluble tetrazolium formazan assay for cell-growth and drug sensitivity in culture using human and other tumor-cell lines. *Cancer Res. 48*, 4827−4833.
(46) Sonawane, N. D., Szoka, F. C., and Verkman, A. S. (2003) Chloride accumulation and swelling in endosomes enhances DNA transfer by polyamine-DNA polyplexes. *J. Biol. Chem. 278*, 44826−44831.
(47) Boussif, O., Lezoualch, F., Zanta, M. A., Mergny, M. D., Scherman, D., Demeneix, B., and Behr, J. P. (1995) A versatile vector for gene and oligonucleotide transfer into cells in culture and in vivo: polyethylenimine. *Proc. Natl. Acad. Sci. U.S.A. 92*, 7297−7301.
(48) Audouy, S., Molema, G., de Leij, L., and Hoekstra, D. (2000) Serum as modulator of lipoplex-mediated gene transfection: dependence of amphiphile, cell type and complex stability. *J. Gene Med. 2*, 465−476.

BC060200L

Sugar−Quantum Dot Conjugates for a Selective and Sensitive Detection of Lectins

Ponnusamy Babu, Sharmistha Sinha, and Avadhesha Surolia*

National Institute of Immunology, Aruna Asaf Ali Marg, New Delhi 110067, India. Received July 9, 2006; Revised Manuscript Received November 13, 2006

One-pot synthesized neoglycoconjugates with a reactive thiol group are introduced here for functionalization with carbohydrates for solubilization and stabilization of CdSe−ZnS quantum dots in aqueous solution. Three different sizes of quantum dots (QDs) with lactose, melibiose, and maltotriose on their surface have been utilized, for the first time, for lectin detection through agglutination assay. The sugar−QDs thus synthesized were characterized by transmission election microscopy (TEM), fluorescence, and absorption spectroscopy. Agglutination of sugar−QDs by three different lectins occurred through specific multivalent carbohydrate−lectin interactions and was studied extensively by monitoring the scattered light at 600 nm. This assay was very selective, which has been demonstrated by a more selective binding of soybean agglutinin (SBA) with melibiose−QD, as compared to lactose−QD, and specific deagglutination caused by α-D-galactose, while α-D-mannose did not show any effect. The detection sensitivity of the maltotriose−QD was tested with Concanavalin A (ConA), and as little as 100 nM of the lectin was detected using light scattering. The detection sensitivity of this protocol has been enhanced considerably by the fluorescence properties of QDs. This agglutination process seems to occur through formation of smaller soluble aggregates, which further associate to form larger aggregates.

INTRODUCTION

Lectins are proteins or glycoproteins of nonimmune origin that bind to mono/oligosaccharides with a high degree of stereospecificity. Since this carbohydrate recognition is very selective and often multivalent, lectins have been implicated in many important functions like cell−cell interactions, homing of leukocytes, host pathogen interactions, biosynthesis and quality control of glycoproteins, immune response, malignancy, and metastasis (*1*, *2*). Lectins also find applications in bioanalytical chemistry and molecular biology (*3*).

Agglutination refers to the process of clumping of cells, such as bacteria or red blood cells, in the presence of an antibody or a lectin (*4*). As this clumping reaction occurs rapidly, agglutination has become an important tool in microbiology and bioanalytical chemistry to identify blood groups, antigens, antibodies, prion proteins (*5*), bacteria such as *S. aureus* (*6*), and metal ions (*7*). Agglutination of erythrocytes has been the preliminary and rapid detection method for lectins since its discovery in the 19th century (*8*−*9*). Hemagglutination assay is qualitative, subjective, requires animal bleeding, and is not very sensitive. Various strategies have been adopted to develop an alternative method for agglutination assay. Although suitably derivatized carbohydrate lysozymes were able to detect nanograms of lectins, this strategy is not a direct method and could not be applied for the determination of the affinities of oligosaccharides (*10*). Carbohydrate-functionalized poly(*p*-phenylene ethynylene) (*11*−*13*) and commercially available Latex particles (*14*) have also been used for agglutination. A few reports of mono- or oligosaccharide functionalized gold (*15*−*16*) and semiconductor (*17*−*18*) nanomaterials have been explored for the study of carbohydrate-binding proteins. Penadés et al., very recently, have reported an excellent account of synthesis and application of various glyconanoparticles published so far in the literature (*19*).

Quantum dots (QDs) are semiconductor nanocrystals, which display very interesting optical properties such as single-wavelength excitation, size-dependent narrow emission, high luminescence, and low photobleaching. These properties make quantum dots very attractive candidates for biolabeling. However, insolubility in water has limited the utility of QDs in bioimaging, thus necessitating work on functionalization and solubilization to exploit QDs in imaging applications. Micellar (*20*), polymer encapsulation (*21*) and covalent coupling to thiol containing hydrophilic functional derivatives (*22*) are the two extreme strategies used frequently for the solubilization and functionalization of CdSe−ZnS QDs. Bioconjugated QDs have been utilized in various fields of in vivo bioimaging including early cancer detection (*23*), multiplexed optical coding (*24*), signal transduction (*25*), sensing (*26*), imaging (*27*), and in Western blot analysis (*28*). Some of the advantages of these nanomaterials in biodetection and biodiagnostics are (i) small size (1−100 nm) and large surface-to-volume-ratio, (ii) physical properties tailored readily according to the end application, (iii) unusual target binding properties, and (iv) structural robustness (*29*).

Here, we report a simple and easy-to-perform detection assay for lectins using a two-step-synthesized, water-soluble, carbohydrate conjugated core−shell CdSe−ZnS quantum dots. This non-erythrocyte agglutination strategy is versatile, reversible, selective, and highly sensitive to lectin detection.

EXPERIMENTAL PROCEDURES

^{1}H NMR spectra were recorded on a Bruker AMX-400 MHz spectrometer, and the mass spectra were recorded on Bruker Daltonics ESI mass spectrometer. The lectins, SBA and Jacalin, were isolated to homogeneity from soybean and jack beans, respectively. Concanavalin A and other chemicals were obtained from Sigma-Aldrich. All the agglutination assays involving

* National Institute of Immunology, Aruna Asaf Ali Marg, New Delhi 110067, India. Tel: +91-11-26717102/03; Fax: +91-11-26162125. E-mail: surolia@nii.res.in.

10.1021/bc060204q CCC: $37.00 © 2007 American Chemical Society
Published on Web 12/22/2006

ConA was prepared in pH 7.2 HEPES (0.1 M) buffer containing NaCl (0.15 M), Ca^{2+}, and Mg^{2+} (10 mM each); SBA and jacalin were prepared in pH 7.4 phosphate salined buffer (20 mM).

Synthesis of Core−Shell CdSe−ZnS Quantum Dots and Surface Modification with Pyridine. Core−shell CdSe−ZnS nanocrystals emitting green (QD-555), orange (QD-589), and red (QD-613) light were synthesized in one pot following a literature procedure (*30*) with slight modification (see Supporting Information).

The surface exchange of TOPO-capped QDs with pyridine was performed by heating a solution of CdSe−ZnS in chloroform with pyridine (three times the volume of chloroform) at 60 °C in an open vial for 3 h. The pyridine solution was precipitated with hexane and centrifuged. The obtained precipitate was redissolved in pyridine, and this stock solution was used for further reactions.

Preparation of Neoglycoconjugates of 2-Aminoethanethiol. For the synthesis of thiol-appended sugar molecules, reducing sugars were reductively aminated with 2-aminoethanethiol. Briefly, 2-aminoethanethiol hydrochloride (125 mg) was dissolved in water (100 μL) in a screw-capped vial (airtight), and pH was adjusted to ∼7.5 (by adding aqueous NaOH solution). To this, $NaCNBH_3$ (40 mg, 0.64 mmol) and a solution of sugar (0.04 mmol) in water (100 μL) were added, and the reaction mixture was heated at 90 °C with stirring. After 1 h, the reaction mixture was cooled to room temperature. The solution was concentrated in speedvac, and the obtained solid was extracted with absolute ethanol (three times) to remove excess starting material. The product was further purified in a Sephadex G-10 column (2 × 17.5 cm) by eluting with water. The products contained ∼5% of compound with a disulfide bond between the product and 2-aminoethane thiol. However, the presence of the disulfide compound is not expected to affect the conjugation with QDs, and hence, no further treatment of these compounds prior to the coupling with QDs was carried out. The compounds were characterized by ^{1}H NMR and ESI-MS.

***β*-D-Galactopyranosyl-(1→4)-(1-deoxy-D-glucityl)-(1→N)-cysteamine 1.** Yield 85%. ^{1}H NMR (400 MHz, D_2O): δ 4.39 (d, J = 7.8 Hz, 1H), 3.9 (m, 1H), 3.85−3.8 (m, 2H), 3.79−3.74 (m, 3H), 3.72−3.65 (m, 3H), 3.64−3.54 (m, 3H), 3.52 (m, 1H), 3.2−2.8 (br. m, 5H). The mass (*m/z*) values calculated for $C_{14}H_{29}NO_{10}S$: 404.16 $(M + 1)^+$, observed 404.1.

α-D-Galactopyranosyl-(1→4)-(1-deoxy-D-glucityl)-(1→N)-cysteamine 2. Yield 88%. ^{1}H NMR (400 MHz, D_2O): δ 4.8 (d, J = 2.76 Hz, 1H), 3.92−3.82 (m, 3H), 3.80−3.73 (m, 3H), 3.73−3.64 (m, 3H), 3.64−3.55 (m, 3H), 3.53 (br. d, J = 8.2, 1H), 3.2−2.8 (br. m, 5H). The mass (*m/z*) values calculated for $C_{14}H_{29}NO_{10}S$: 404.16 $(M + 1)^+$, observed 404.1.

α-D-Glucopyranosyl-(1→4)-α-D-Glucopyranosyl-(1→4)(1-deoxy-D-glucityl)-(1→N)-cysteamine 2. Yield 91%. ^{1}H NMR (400 MHz, D_2O): δ 5.27 (d, J = 3.4 Hz, 1H), 4.99 (d, J = 3.3 Hz, 1H), 4.13 (m, 1H), 3.87−3.84 (m, 3H), 3.75 (m. 2H), 3.72−3.66 (m, 4H), 3.64 (br. d, J = 4.1, 2H), 3.60 (br. s, 1H), 3.59−3.41 (m, 5H), 3.37−3.32 (m, 1H), 3.28 (br. t, J = 9.24 Hz, 1H), 3.15 (br. s, 2H), 2.94 (t, J = 6.34 Hz, 1H). The mass (*m/z*) values calculated for $C_{20}H_{39}NO_{15}S$: 566.21 $(M + 1)^+$, observed 566.2.

Surface Capping of CdSe−ZnS QDs with Neoglycoconjugates. Water solubilization and surface functionalization of CdSe−ZnS was achieved in a single step by covalently coupling QDs with thiol-derivatized sugar molecules. The excess of thiol-appended sugar derivative (**2**, 8 mg) was dissolved in doubled distilled water (50 μL) and DMSO (200 μL) in a microcentrifuge tube. To this solution was added a known concentration of pyridine-capped CdSe−ZnS (QD-589, 2.5 mg) in pyridine (200 μL). The thiol coupling with the ZnS shell of CdSe−ZnS was initiated by adding tetramethylammonium hydroxide (∼5 μL, pH ≈ 10.5) in methanol. The whole mixture was quickly vortexed and centrifuged. The obtained precipitate was resuspended in 50 μL of distilled water and centrifuged (15 000 rpm for 5 min) again. Resuspension and centrifugation were repeated three times to remove excess sugar derivatives. Finally, the precipitate was dissolved in water at pH ≈ 7 (by adding ∼3 μL of 10% AcOH/water) to get a clear solution. The concentration of carbohydrate-capped QD particles was estimated using the extinction coefficients of 0.736×10^5, 3.159×10^5, and 1.531×10^6 M^{-1} cm^{-1} at 350 nm for QD-555, QD-589, and QD-613, respectively (*31*).

For the preparation of a variable number of melibiose per QD particle, a solution of melibiose thiol derivative (20 mg) in 100 μL of water was prepared. From that stock solution, 2, 8, 30, and 40 μL were transferred to four different microcentrifuge tubes and dried. These samples were used for conjugation with QD-589 as described earlier.

Estimation of Concentration of Carbohydrates per Sugar−QD. The concentration of carbohydrate molecules coated on CdSe−ZnS was determined by the phenol-sulfuric acid method using a microtiter plate (*32*). The concentration of sugar molecules in each well was determined by the following procedure. Sugar−QD solution (50 μL) was added to the microtiter plate, followed by quick addition of concentrated sulfuric acid (150 μL) and freshly prepared aqueous phenol solution (5% w/v, 30 μL). The microtiter plate was carefully heated in a water bath at 90 °C. After 5 min, the plate was cooled at room temperature for another 5 min before measuring the absorbance at 490 nm. S−QD solution and sulfuric acid were used as a control. The concentration of sugar (nmol/well) was estimated by comparing the sample absorption with a standard curve. The number of sugar molecules per QD particle was calculated from the ratio of the concentration of sugar and the concentration of CdSe−ZnS QD particles.

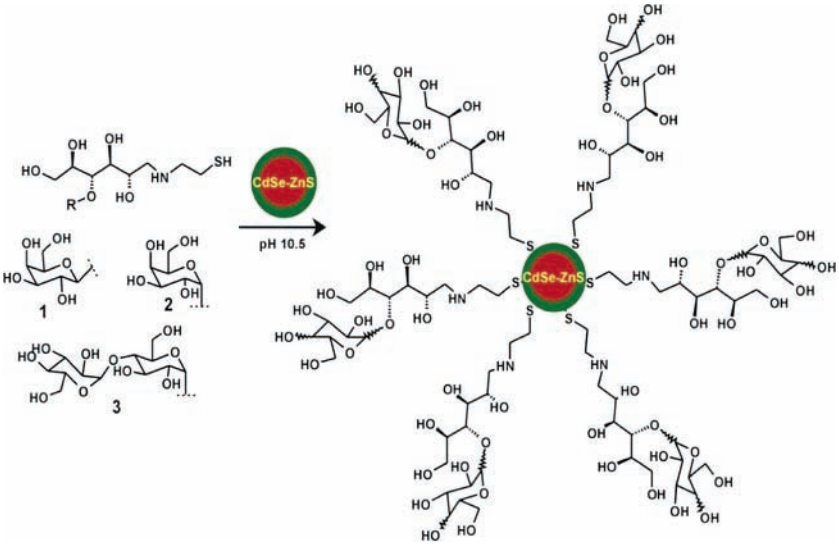
Kinetic Study of Agglutination of S−QDs by Lectins. When the sugar/sweet−QDs (S−QDs) were mixed with lectins, the clear solution slowly turned turbid, and after ∼2 h, the colloidal mass settled down at the bottom of the cuvette or microcentrifuge tube. Since this agglutination reaction occurred through the formation of aggregates of lectins binding to multivalent sugar-dots, we monitored the kinetics of agglutination by measuring the scattered light at 600 nm (in 1 cm cell). For example, a known concentration of lectin in the appropriate buffer was mixed with a solution of S−QD in the same buffer (total volume 120 μL), and the change in absorbance was monitored. An exponential growth curve was obtained as a function of time. The kinetic data were best fitted with $f = y_0 + a(1 - e^{-bx})$ equation, and the apparent rate constants were obtained. At high concentrations of QD and/or lectin, the apparent absorbance increases to a maximum and starts to decrease, which is due to the precipitation of agglutinated product.

Electron Microscope. TEM images were recorded in a TECHNAI F30 instrument with an acceleration voltage of 200 KV. The aqueous sample solutions were loaded in 200-mesh carbon-coated copper grids and stained with 2% uranyl acetate solution. The grids were dried completely before imaging.

RESULTS AND DISCUSSION

Synthesis of Neoglycoconjugates and Functionalization of QDs. The strategy adopted here for the preparation of carbohydrate-functionalized QDs was to first prepare sugar derivatives with reactive sulfhydryl groups and then couple them to CdSe−ZnS quantum dots. Hence, reducing sugars D-melibiose (Gal-1-α-4-Glc), D-lactose (Gal-1-β-4-Glc), and D-maltotriose (Glc-1-α-4-Glc-1-α-4-Glc) were reacted with an excess of 2-amino-

Scheme 1. Schematic Representation of Synthesis of Neoglycoconjugate CdSe−ZnS QD Constructs



ethanethiol hydrochloride salt at 90 °C, and subsequent in situ imine reduction by sodium cyanoborohydride furnished the corresponding carbohydrates with a thiol arm. This synthetic protocol consisted of two steps and therefore has an advantage over some of the other reported methods, where multiple-step, protection, and deprotection strategies were employed (*33*−*36*). Moreover, this neoglycoconjugation method can be applied to higher oligosaccharides as well. In these neoglycoconjugates, the reducing end of the sugar unit became acyclic and the nonreducible part remained cyclic (with retention of stereochemistry). We anticipated that these carbohydrate−thiol derivatives are appropriate molecules not only for the solubilization of quantum dots but also for the functionalization of the periphery in a single step. Furthermore, attachments of two or more sugar−thiol molecules to QDs resulted in the formation of a dendritic architecture with multiple functional carbohydrates on the surface (Scheme 1). The acyclic hydroxylated spacer chain would also reduce the diffusion of oxygen molecules, thereby protecting the CdSe−ZnS dots from surface oxidation. Thus, these multi-carbohydrate nanoparticles have tremendous potential in a number of applications in analytical chemistry.

The covalent coupling reaction of carbohydrate−thiol molecules with three different sizes (555-QD (OD = 3.5 nm), 589-QD (3.8 nm), and 613-QD (4.3 nm)) of CdSe−ZnS QDs was achieved at higher pH (see Experimental Procedures). The sugar−quantum dots were soluble in water at around neutral pH but not above pH 8. The water-soluble sugar−QDs were characterized by TEM, fluorescence microscopy, and absorption spectroscopy. Furthermore, these S−QDs emitted bright green (555-QD), orange (589-QD), and red (613-QD) colors upon excitation (at 400 nm). The number of sugar molecules present on the QD surface was estimated by the simple and very sensitive phenol-sulfuric acid method (see Experimental Procedures). To our expectation, these S−QDs were agglutinated by lectins rapidly and very selectively. The agglutinated product was reversibly deagglutinated/disaggregated by addition of selective carbohydrate molecules. This reversal of agglutination demonstrated that the interaction between the S−QDs and lectin is specific and reversible. The agglutinated products were characterized by TEM (Figure 1).

Effect of the Number of Sugar Molecules per Particle and Size of QDs on Agglutination. Our initial aim was to estimate the stability and agglutinability of various carbohydrate-capped CdSe−ZnS quantum dots. Hence, a series of S−QDs with varying number of melibiose−neoglycoconjugate (MB, **2**), approximately 2, 4, 6, 12, and 18 molecules per QD-589 particle, were prepared by appropriately changing the concentration of **2** (see Experimental Procedures). The ability of 589-MB-QDs to remain stable in solution (without aggregation) was monitored at room temperature and found to be <20, 47, 52, 72, and 180 h for QDs with 2, 4, 6, 12, and 18 molecules of **2** per particle, respectively. Thus, the stability of S−QDs increased upon increasing the number of sugar units. However, all the S−QD solutions were stable for months when kept in the dark at 4 °C. The agglutination efficiency of a variable number of melibiose-coated 589-QD was studied with an excess of Jacalin (533 μM)—an α-galactose specific lectin. A plot of variable numbers of melibiose-containing 589-MB−QDs as a function of the agglutination rate constant showed a linear behavior (Figure 2). Reversal of agglutination occurred when α-D-galactose (14 mM) was added to the agglutinated product of 589-MB−QDs and Jacalin (data not shown). These results suggested that, as the number of melibiose−neoglycoconjugate per QD increased, because of the multivalent nature, a greater number of lectins bound to S−QDs through specific carbohydrate-mediated interaction.

In order to study the effect of agglutination on the size of CdSe−ZnS QDs, 589-QD and 613-QD were surface-modified with **2**. The concentrations of melibiose conjugate and QD were adjusted to get an approximately equal number of average melibiose per unit area of particles of two different sizes of QDs. The mean numbers of melibiose moieties per unit area (percentage) of QD are 34.7 and 35 for 589-MB−QD and 613-MB−QD, respectively. The agglutination assay was performed, keeping concentrations of QD (6.4 μM) and Jacalin (107 μM) constant. The obtained data were fitted, and apparent rate constant values for orange and red emitting MB−QDs are 4.585

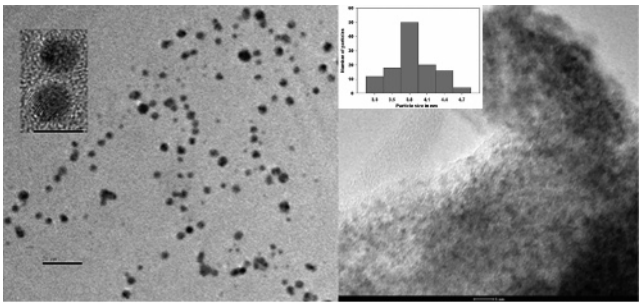


Figure 1. TEM images of melibiose−QD-589 conjugate (left, scale bar 20 nm), inset scale bar 5 nm, and its agglutinated product with jacalin (right, scale bar 5 nm; negatively strained with uranyl acetate). Inset graph shows the histogram of the TEM.

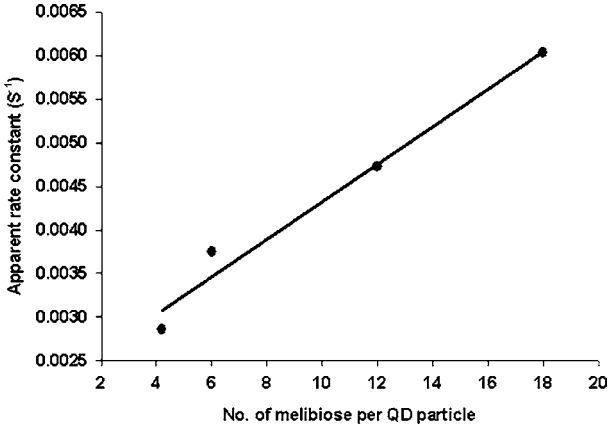


Figure 2. A plot of apparent rate constant of agglutination of 589-MB−QD by Jacalin (533 μM) as a function of number of melibiose molecules per QD particle.

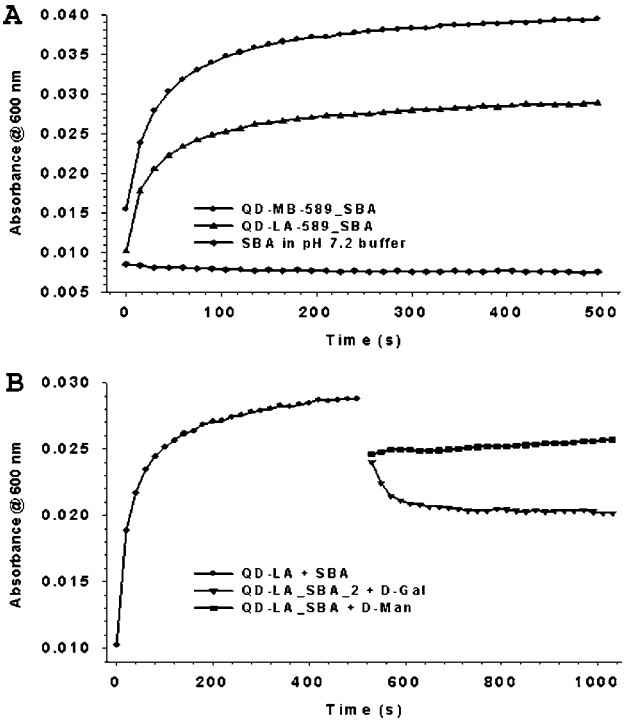


Figure 3. (A) Kinetics of agglutination of 589-MB−QD (5.9 μM particles) and 589-LA−QD (7.1 μM particles) by SBA (5.0 μM). (B) Deagglutination of the 589-LA−QD−SBA agglutinated product by α-D-Gal (100 mM) and α-D-Man (100 mM).

$\times 10^{-3}$ and 12.6×10^{-3} s^{-1}, respectively. Hence, an increase in the QD size appears to increase the apparent rate of agglutination, presumably because of the increase in the surface area and subsequently more accessible carbohydrate units.

Stereospecific Binding of S−QDs with Lectins. In order to assess the stereospecificity of the S−QD based agglutination assay, we studied the agglutinability of 589-MB−QD and 589-LA−QD (α-D-lactose−thiol−QD) with soybean agglutinin (25 μM). The binding constant of SBA with Me-α-Gal is slightly higher (1.2 times) compared to Me-β-Gal (*37*). The agglutination kinetics data of 589-LA−QD (6.8 μM, 6 LA/QD) and 589-MB−QD (6.8 μM, 6 MB/QD) with SBA indeed showed that MB−QD was able to agglutinate slightly more effectively than LA−QD (Figure 3A). The better agglutination observed for 589-LA−QD with SBA was ascertained when only α-D-galactose (7.7 mM) was able to deagglutinate, while α-D-mannose (7.7 mM) did not show any effect (Figure 3B). In order to further

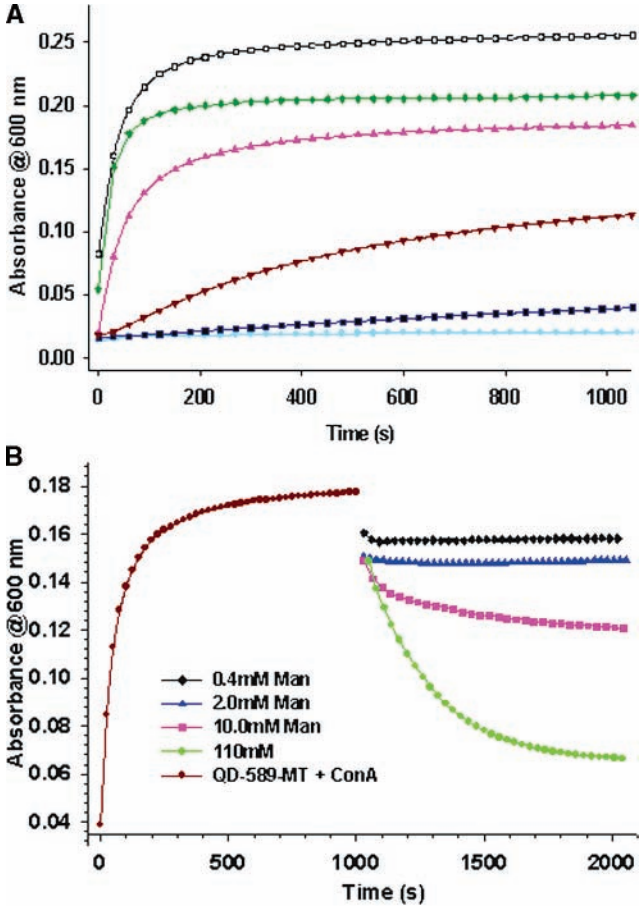


Figure 4. (A) Kinetic study of agglutination of 589-MT−QD (13.0 μM particles) by varying concentrations of ConA (top to bottom: 7.3, 3.6, 1.0, 0.5, 0.2, 0.1 μM). (B) Disaggregation study of agglutinated product of 589-MT−QD (13.0 μM particles) and ConA with variable concentrations of α-D-mannose.

confirm the specificity of the sugar−QDs, an agglutination experiment was performed between lacto−QD/melibio−DQ and ConA, and maltotrio−QD with Jacalin/SBA. In both cross combinations, we did not observe any agglutination. These studies suggest that even after conjugation to QDs the stereospecific binding and selectivity of the neoglycoconjugates toward lectins are retained.

Sensitivity of S−QD Based Agglutination Assay. In order to establish the detection sensitivity of the S−QD assay for agglutination, 589-MT−QD (D-maltotriose−thiol−QD) and a glucose-binding lectin Concanavalin A were studied. Here, the concentration of 589-MT−QD (13 μM, ~10.8 MT per particle) was kept constant, and the ConA concentration was varied from 7.3 μM to 100 nM. As the concentration of ConA decreased, the extent of agglutination also reduced, which is reflected in the intensity of the scattered light. Notably, we were able to follow the agglutination reaction between a very low concentration (100 nM) of ConA and 589-MT−QD by monitoring the change in absorbance at 600 nm (Figure 4A). We have also studied the inhibition or deagglutination by adding a variable concentration of α-D-mannose from 0.4 mM to 110 mM to the preformed agglutinated product of ConA 1.0 μM and MT-QD (13 μM). As the concentration of D-mannose was increased, the degree of deagglutination also increased (Figure 4B). These results again proved that agglutination is due to a very specific interaction between the lectin and the carbohydrates on the surface of QDs.

Sensitive Fluorescence Detection for Agglutination. Although studies discussed so far were primarily based on light

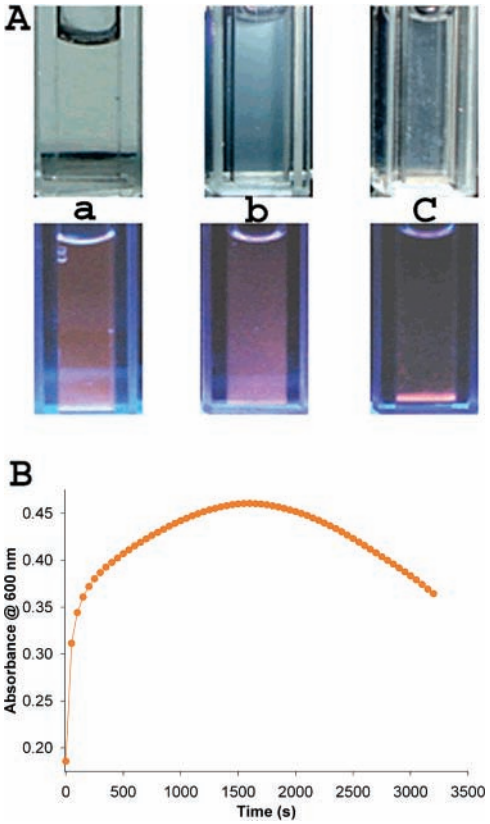


Figure 5. (A) Photographs of (a) 589-MT−QD alone, (b) 5 min after ConA addition (10 μM, pH 7.2 HEPES buffer), (c) 2 h after ConA addition, taken under white (top) and UV light (bottom). (B) Change in the absorbance of 589-MT−QD (0.103 μM particles) immediately after mixing with ConA (5 μM) as a function of time.

scattering data, the use of CdSe−ZnS quantum dots for sugar conjugation and agglutination assay can be rationalized as follows. First of all, the S−QDs are smaller in size. The larger surface-to-volume ratio allows the attachment of a greater number of functional groups. Second, the CdSe−ZnS QDs can easily be functionalized through a variety of chemical and noncovalent methods. In addition, the fluorescence property of QDs allow for a more sensitive detection of the agglutination. Thus, we tried to use fluorescence spectroscopy to study agglutination kinetics and to improve the detection limit of lectins. However, the data obtained from the fluorescence experiments could not be interpreted satisfactorily because of the simultaneous occurrence of various processes, like scattering and precipitation, and so forth, during the course of the experiment. Nevertheless, we went ahead and used a UV transilluminator for visual detection of lectins upon agglutination. In fact, agglutination of MT−QD by <100 nM of ConA was detected under UV irradiation, which was barely seen under normal light. This study thus confirms that sugar−QDs can be used for the detection of very small amounts of carbohydrate-binding proteins with high sensitivity. Furthermore, snapshots of the agglutination at various intervals may reveal insights into the process of agglutination which can be correlated with kinetic studies. The top row of Figure 5A shows the pictures of (a) QD-589−MT solution, (b) QD-589−MT and ConA (10 μM) 5 min after mixing, (c) and 2 h after mixing in a 200 μL fluorescence cuvette under white light, while the pictures at the bottom row are those of respective samples under UV illumination (see Supporting Information for emission spectra). It is quite evident from the above results that the detection of agglutinated products by quantum dot fluorescence has more advantages in terms of detection sensitivity and the ease with which the experiments are conducted.

On the basis of the kinetic studies (Figure 5B), the agglutination process of sugar−QDs by lectins can be hypothesized to occur in a stepwise manner as shown graphically (Figure 6). At first, soluble smaller S−QD−lectin aggregates are formed through specific interaction of carbohydrates and multivalent lectins, which lead to an increase in turbidity and consequently an increase in the scattering. Further association of the smaller aggregates into much larger aggregates induces the precipitation and subsequent decrease in the absorbance at longer time scales as observed experimentally.

CONCLUSIONS

The results reported here demonstrate that di- and oligosaccharides can be covalently attached via thiol functionality to CdSe−ZnS quantum dots without using protection and deprotection in two steps. The water-soluble, sugar-functionalized QDs were selectively agglutinated by lectins, which indicates that the synthesized neoglycoconjugates retain their lectin specificity. The selective deagglutination by specific sugars showed that this process is reversible and selective. The sensitivity of this nanomaterial-based assay was extended to nanomolar concentrations of the analyte—a lectin. Moreso, the value of this method has been enhanced further by using fluorescence properties of QDs. The present work not only has implications in the area of nanomaterials in analytical context but has a broad potential to study various carbohydrate−protein interactions, which are of considerable interest in both medicine and biology.

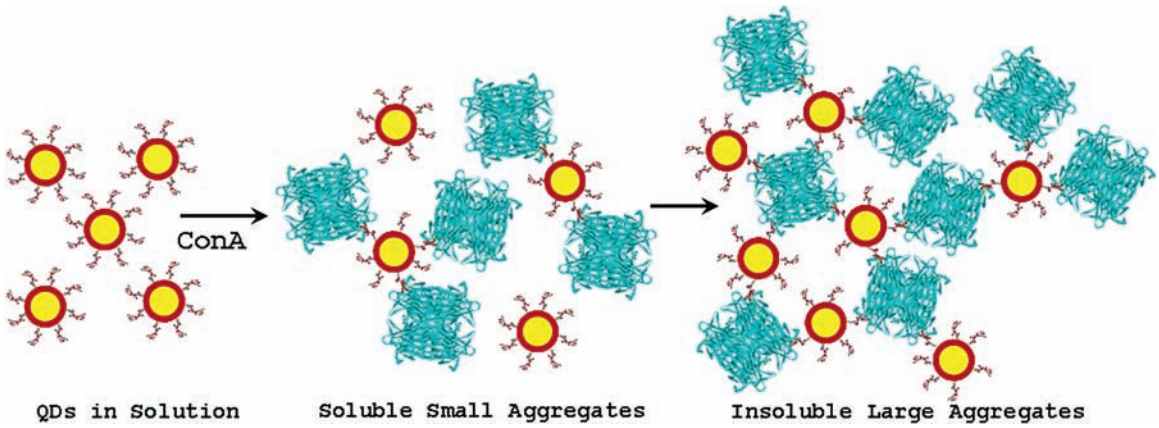


Figure 6. Graphical representation of agglutination of MT−QD-589 by ConA tetramer.

ACKNOWLEDGMENT

This work is supported by a grant from the Department of Biotechnology, Government of India, to A.S. The authors thank Nano Centre, IISc, Bangalore, for recording TEM images. A.S. holds J C Bose Fellowship of the Department of Science and Technology, Government of India. S.S. thanks Council for Scientific and Industrial Research, India, for a fellowship.

Supporting Information Available: The contents included are (1) procedure for the synthesis of TOPO stabilized QDs, (2) emission spectra of three different sugar−QDs in water, (3) mass spectra of compounds **1**−**3**, (4) comparison of fluorescence spectra of 589-MT−QD in water and after mixing with ConA. This material is available free of charge via the Internet at http://pubs.acs.org/BC.

LITERATURE CITED

(1) Lis, H., and Sharon, N. (1998) Lectins: carbohydrate-specific proteins that mediate cellular recognition. *Chem. Rev. 98*, 637−674.
(2) Haltiwanger, R. S., and Lowe, J. B. (2004) Role of glycosilation in development. *Annu. Rev. Biochem. 73*, 491−537.
(3) Lowe, J. B., and Marth, J. D. (2003) The biochemistry of plant lectins (phytohemagglutinins). *Annu. Rev. Biochem. 72*, 643−691.
(4) Lundquist, J. L., and Toone, E. J. (2002) The cluster glycoside effect. *Chem. Rev. 102*, 555−578.
(5) Lee, I. S., Long, J. R., Prusiner, S. B., and Safar, J. G. (2005) Selective precipitation of prions by polyoxometalate complexes. *J. Am. Chem. Soc. 127*, 13802−13803.
(6) Kanai, M., Mortell, K. H., and Kiessling, L. L. (1997) Varying the size of multivalent ligands: the dependence of concanavalin a binding on neoglycopolymer length. *J. Am. Chem. Soc. 119*, 9931−9932.
(7) Kim, I.-B., and Bunz, U. H. F. (2006) Modulating the sensory response of a conjugated polymer by proteins: an agglutination assay for mercury ions in water. *J. Am. Chem. Soc. 128*, 2818−2819.
(8) Gupta, R. K., Sharma, S. B., Ahuja, S., and Saxena, S. N. (1991) Indirect (passive) haemagglutination test for assay of antigen and antibody. *Acta Microbiol. Hung. 38*, 81−90.
(9) Burger, M. M. (1974) Assays for agglutination with lectins. *Methods Enzymol. 32*, 615−621.
(10) Ghosh, M., Bachhawat, K., and Surolia, A. (1979) A rapid and sensitive assay for detection of nanogram qantities of casto-bean (*Ricinus communis*) lectins. *Biochem. J. 183*, 185−188.
(11) Disney, M. D., Zheng, J., Swager, T. M., and Seeberger, P. H. (2004) Detection of bacteria with carbohydrate-functionalized fluorescent polymers. *J. Am. Chem. Soc. 126*, 13343−13346.
(12) Kim, I. B., Wilson, J. N., and Bunz, U. H. F. (2005) Mannose-substituted PPEs detect lectins: a model for ricin sensing. *Chem. Commun.* 1273−1275.
(13) Kelly, T. L., Lam, M. C. W., and Wolf, M. O. (2006) Carbohydrate-labeled fluorescent microparticles and their binding to lectins. *Bioconjugate Chem. 17*, 575−578.
(14) Koo, H. C., Park, Y. H., Ahn, J., Waters, W. R., Hamilton, M. J., Barrington, G., Mosaad, A. A., Palmer, M. V., Shin, S., and Davis, W. C. (2004) New latex bead agglutination assay for differential diagnosis of cattle infected with mycobacterium bovis and mycobacterium avium subspecies paratuberculosis. *Clin. Diagn. Lab. Immunol. 11*, 1070−1074.
(15) Otsuka, H., Akiyama, Y., Nagasaki, Y., and Kataoka, K. (2001) Quantitative and reversible lectin-induced association of gold nanoparticles modified with α-lactosyl-ω-mercapto-poly(ethylene glycol). *J. Am. Chem. Soc. 123*, 8226−8230.
(16) de la Fuente, J. M., Eaton, P., Barrientos, A. G., Menéndez, M., and Penadés, S. (2005) Thermodynamic evidence for Ca^{2+}-mediated self-aggregation of lewis X gold glyconanoparticles. A model for cell adhesion via carbohydrate-carbohydrate interaction. *J. Am. Chem. Soc. 127*, 6192−6197.
(17) Chen, Y., Ji, T., and Rosenzweig, Z. (2003) Synthesis of glyconanospheres containing luminescent CdSe-ZnS quantum dots. *Nano Lett. 3*, 581−583.
(18) de la Fuente, J. M., and Penadés, S. (2005) Glyco-quantum dots: A new luminescent system with multivalent carbohydrate display. *Tetrahedron: Asymmetry 16*, 387−391.
(19) de la Fuente, J. M., and Penadés, S. (2006) Glyconanoparticles: Types, synthesis and applications in glycoscience, biomedicine and material science. *Biochim. Biophys. Acta 1760*, 636−651.
(20) Dubertret, B., Skourides, S., Norris, D. J., Noireaux, V., Brivanlou, A. H., and Libchaber, A. (2002) In vivo imaging of quantum dots encapsulated in phospholipids micelles. *Science 298*, 1759−1762.
(21) Gao, X., Cui, Y., Levenson, R. M., Chung, L. W. K., and Nie, S. (2004) In vivo cancer targeting and imaging with semiconductor quantum dots. *Nat. Biotechnol. 22*, 969−976.
(22) Chan, W. C. W., and Nie, S. (1998) Quantum dot bioconjugates for ultrasensitive nonisotopic detection. *Science 281*, 2016−2018.
(23) Wu, X., Liu, H., Liu, J., Haley, K. N., Treadway, J. A., Larson, J. P., Ge, N., Peale, F., and Bruchez, M. P. (2003) Immunofluorescent labeling of cancer marker Her2 and other cellular targets with semiconductor quantum dots. *Nat. Biotechnol. 21*, 41−46.
(24) Han, M., Gao, X., Su, J. Z. and Nie, S. (2001) Quantum dot-tagged microbeads for multiplexed optical coding of biomolecules. *Nat. Biotechnol. 19*, 631−635.
(25) Lidke, D. S., Nagy, P., Heintzmann, R., Arndt-Jovin, D. J., Post, J. N., Grecco, H. E., Jares-Erijman, E. A., and Jovin, T. M. (2004) Quantum dot ligands provide new insights into erbB/HER receptor-mediated signal transduction. *Nat. Biotechnol. 22*, 198−203.
(26) Medints, I. L., Clapp, A. R., Mattoussi, H., Goldman, E. R., Fisher, B., and Mauro, J. M. (2003) Self-assembled nanoscale biosensors based on quantum dot FRET donors. *Nat. Mater. 2*, 630−638.
(27) Michalet, X., Pinaud, F. F., Bentolila, L. A., Tsay, J. M., Doose, S., Li, J. J., Sundaresan, G., Wu, A. M., Gambhir, S. S., and Weiss, S. (2005) Quantum dots for live cells, in vivo imaging, and diagnostics. *Science 307*, 538−544.
(28) Zhelev, Z., Bakalova, R., Ohba, H., Jose, R., Imai, Y., and Baba, Y. (2006) Uncoated, broad fluorescent, and size-homogeneous CdSe quantum dots for bioanalyses. *Anal. Chem. 78*, 321−330.
(29) Rosi, N. L., and Mirkin, C. A. (2005) Nanostructures in biodiagnostics. *Chem. Rev. 105*, 1547−1562.
(30) Peng, Z. A., and Peng, X. (2001) Formation of high-quality CdTe, CdSe, and CdS nanocrystals using CdO as precursor. *J. Am. Chem. Soc. 123*, 183−184.
(31) Leatherdale, C. A., Woo, W.-K., Mikulec, F. V., and Bawendi, M. G. (2002) On the absorption cross section of CdSe nanocrystal quantum dots. *J. Phys. Chem. 106*, 7619−7622.
(32) Masuko, T., and Minami, A. (2005) Carbohydrate analysis by a phenol-sulfuric acid method in microplate format. *Anal. Biochem. 339*, 69−72.
(33) Osaki, F., Kanamori, T., Sando, S., Sera, T., and Aoyama, Y. (2004) A quantum dot conjugated sugar ball and its cellular uptake. On the size effects of endocytosis in the subviral region. *J. Am. Chem. Soc. 126*, 6520−6521.
(34) Halkes, K. M., de Souza, A. C., Maljaars, E. P., Gerwig, G. J., and Kamerling, J. P. (2005) A facile method for the preparation of gold glyconanoparticles from free oligosaccharides and their applicability in carbohydrate-protein interaction studies. *Eur. J. Org. Chem.* 3650−3659.
(35) Sun, X.-L., Cui, W., Haller, C., and Chaikof, E. L. (2004) Site-specific multivalent carbohydrate labeling of quantum dots and magnetic beads. *ChemBioChem 5*, 1593−1596.
(36) Robinson, A., Fang, J.-M., Chou, P.-T., Liao, K.-W., Chu, R.-M., and Lee, S.-J. (2005) Probing lectin and sperm with carbohydrate-modified quantum dots. *ChemBioChem 6*, 1899−1905.
(37) Swamy, M. J., Sastry, M. V. K., Khan, M. I., and Surolia, A. (1986) Thermodynamic and kinetic studies on saccharide binding to soya-bean agglutinin. *Biochem. J. 234*, 515−522.

BC060204Q

Ricin Antitoxins Based on Lyotropic Mesophases Containing Galactose Amphiphiles

P. G. Hartley,*,† M. R. Alderton,‡ R. M. Dawson,‡ and D. Wells†

CSIRO Molecular & Health Technologies, Private Bag 10, Clayton South, Victoria 3169, Australia, and Defence Science and Technology Organisation, PO Box 4331, Melbourne, Victoria 3001, Australia. Received July 14, 2006; Revised Manuscript Received November 14, 2006

Lyotropic mesophases of the inverse hexagonal or cubic type are nanostructured materials that result from the self-assembly of amphiphilic surfactant molecules in water. The extremely large area of the surfactant−water interface inherent within these structures makes them attractive media for sorbent or encapsulant systems. Here, we report on the development of a new class of polyvalent materials that are based on the incorporation of bioactive ligands within lyotropic mesophases. In particular, we have studied the potential for these materials to behave as polyvalent antitoxins by incorporating synthetic galactose amphiphiles, which mimic the natural cell surface ligand for the protein toxin ricin. The study demonstrates that cubic morphology lyotropic mesophases containing galactose amphiphiles exhibit high specificity ricin uptake, with favorably high dissociation constants and high capacities. We suggest that lyotropic mesophase polyvalent ligands are thus promising materials for the incorporation of a broad range of cell surface recognition moieties and hence may have wide applicability as materials capable of partaking in biological recognition processes.

INTRODUCTION

Polyvalent ligand−receptor interactions are employed in many biological recognition processes (*1*). There has been recent interest in designing synthetic polyvalent inhibitors for the therapeutic inactivation of biological entities, including viruses, bacteria, and toxins. In such systems, molecular architectures are employed to act as scaffolds for the presentation of high densities of bioactive ligands. These polyvalent ligands act to saturate receptor sites on the target, thereby blocking its ability to bind to cellular recognition sites, reducing uptake and cytotoxicity. Of particular interest have been polyvalent ligand systems based on synthetic branched polymer architectures such as dendrimers. Such systems are currently under commercial development for antiviral and microbiocidal applications (*2*).

Pathogenic protein toxins are produced by a number of microbial species such as *Clostridium botulinim*, *Vibrio cholera*, and *Shigella* species (*3*). Numerous plant protein toxins with pathogenic activity have also been identified (*4*). Within the latter family, the toxin ricin, derived from the castor bean plant *Ricinus communis*, has unprecedented toxicity and has been utilized as the active agent within immunotoxins (*5*) and as a potent poison or biowarfare agent (*6*, *7*).

Both plant and bacterial toxins act by binding with high specificity to cell surface moieties. This recognition process then triggers cellular uptake *via* several possible routes, resulting in the transport of the cytotoxic component of the toxin to its site of action.

In the case of ricin, the cell binding component (ricin B chain) specifically attaches to multiple cell surface galactose moieties and facilitates internalization of the cytotoxic A chain within the cell, which acts to disrupt ribosomal function (*5*).

The spontaneous self-assembly of certain lipid and synthetic surfactant molecular architectures results in the formation of extended three-dimensional hydrated structures in solution (*8*−*12*). Under certain circumstances, these structures exist in equilibrium with an excess of solution and are thus stable against dilution. In particular, the structures of the lyotropic mesophases of glyceryl monooleate (monoolein) and 3,7,11,15,-tetramethyl-1,2,3-hexadecanetriol (phytantriol) have been extensively studied, and proposed for use in drug delivery formulations (*13*−*17*).

These materials also possess attractive properties with respect to the development of polyvalent ligand systems. Most notably, they exhibit an extraordinarily large surfactant−water interface, which is potentially available for incorporation of biological or chemical functionality. Additionally, the formulation of lyotropic mesophase colloidal dispersions has been demonstrated in several systems (*10*, *11*, *15*, *18*, *19*). These low viscosity dispersions are readily amenable to *in vivo* administration.

In an earlier paper, we studied the ricin binding activity of a number of dendrimer systems derivatized with pendent galactose functional groups (*20*). We also introduced a new class of polyvalent ligand, in the form of the biofunctionalized lyotropic mesophase, which compared favorably with the dendrimer systems with regard to ricin binding.

In the current study, we have developed a variety of novel synthetic surfactant systems, which form dilutable lyotropic mesophases and which incorporate high concentrations of biologically active ligands for ricin based on galactose surfactants. We discuss the role of surfactant chemical and anomeric structure in determining the efficacy of these materials for ricin binding and uptake. The broad aim of this work is to demonstrate unequivocally the potential for employing lyotropic mesophase systems as a new class of polyvalent ligands.

EXPERIMENTAL PROCEDURES

Surfactant Synthesis and Formulation. Synthesis and chemical characterization information for the novel galactose surfactants discussed in this paper are available in the Supporting Information. In particular, synthesis was directed toward surfactants that possessed alkylation of galactose at the C1 position.

* To whom correspondence should be addressed. Tel: +61 3 9545 2595. Fax: +61 3 9545 8106. E-mail: patrick.hartley@csiro.au.

† CSIRO Molecular & Health Technologies.

‡ Defence Science and Technology Organisation.

10.1021/bc060216b CCC: $37.00 © 2007 American Chemical Society
Published on Web 12/23/2006

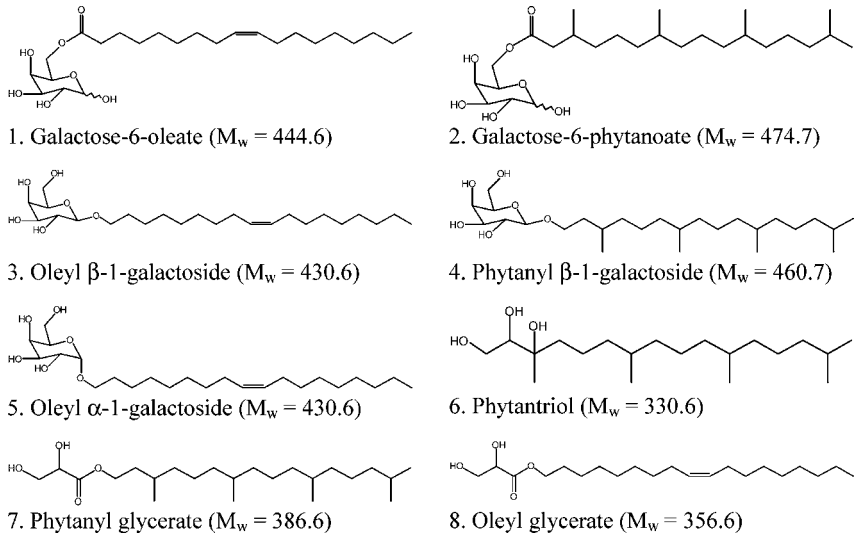


Figure 1. Structures of surfactant amphiphiles used in this study. Galactose-6-oleate existed as a solid (melting point 90−98 °C). Galactose-6-phytanoate and all galactosides (oleyl α and *β* and phytanyl *β*) existed as viscous mesomeric liquids at room temperature.

In this way, free galactose functionality in the C3−C6 positions is retained, and it is these positions that are known to be important in galactose binding to ricin (*21*). C6 alkylations were also performed for comparative purposes. The various surfactants employed in this study are shown in Figure 1. Mixed surfactant formulations were prepared by dissolving the appropriate proportions of each compound in dichloromethane to a total surfactant concentration of ∼40−100 mg/mL. Phytantriol was obtained from Sigma-Aldrich Pty. Ltd. Castle Hill, NSW. All water used in these experiments was Milli-Q grade.

Surfactant Lyotropic Phase Behavior. *Water Penetration Behavior.* Small samples of each surfactant were sandwiched beneath a coverslip on a microscope slide and stabilized at room temperature prior to addition of water at the edge of the coverslip. Capillary action drew the water between the two glass surfaces to surround the surfactant island. The optical behavior of the surfactant−water interface was observed during water penetration using an Olympus IMT-2 microscope equipped with crossed polarizing lenses. The sample was then heated at 2 °C/min or less in a Mettler FP82HT hot stage controlled by a FP90 central processor and changes in the optical textures at the surfactant−water interface were monitored and correlated with phase structures according to established correlations (*22*). Water penetration scans were usually performed in the temperature range 22−99 °C. Images were captured *via* a video camera, and observations were noted concerning viscosity of any observed mesophase forms.

Further detailed confirmation of the structure of selected surfactant mesophases was obtained using small-angle X-ray scattering (SAXS). Samples of surfactant in excess water solution were loaded into a small sample cell consisting of two very thin mica windows separated by a 1 mm stainless steel spacer ring. A Bruker "nanostar" SAXS camera equipped with a position sensitive 2-D "Hi-Star" detector using point collimated copper Kα radiation was employed. Experiments were performed under vacuum or under a helium atmosphere to minimize background scattering. Sample transmissions were estimated using a glassy carbon standard, which avoided the need to remove the instrument beam stop and thus protect the detector.

Data acquisition was performed at a sample-to-detector distance of 23 cm, which allowed analysis of intensity behavior over the wavevector range $0.0498\ \text{Å}^{-1} \le q \le 0.950\ \text{Å}^{-1}$. The scattering profiles of the empty sample geometries were subtracted from the final scattering profile of the sample (per-pixel subtraction) after first correcting for the intensity of the X-ray beam.

Ricin Binding Efficiency. Ricin binding to lyotropic mesophases was facilitated by the addition of 10 *μ*L aliquots of ∼49 mg/mL surfactant solutions in dichloromethane or dichloromethane−methanol to glass test tubes and allowing the solvent to evaporate. The final mass of surfactant deposited in the tubes was in the range 0.43−1.28 mg. Ricin solutions, of known concentrations between 6.25 and 200 ng/mL in blocking buffer (130 *μ*L, 0.25% bovine serum albumin in 0.05%Tween/PBS, pH 7.4), were added to the tubes, and they were placed on a rocker platform and gently oscillated for 24 h at room temperature. Aliquots (100 *μ*L) of the supernatants from these tubes were then assayed for ricin, as described below. Aliquots (100 *μ*L) of ricin control solutions (known ricin concentrations) were also analyzed in each experiment.

Ricin concentrations in control and test solutions were quantified using an enzyme-linked immunosorbent based microtiter plate binding assay described elsewhere (*23*).

Briefly, Nunc microtiter test plates were prepared by treating overnight with 0.1 mL per well of 2 *μ*g/mL of the ricin binding protein asialofetuin in 0.1 M carbonate/bicarbonate buffer, pH 9.6. After washing with PBS−Tween and incubating 1 h with blocking buffer, the plates were incubated sequentially for 1 h each with ricin-containing control and test solutions, followed by rabbit anti-ricin antibody (1:15 000 dilution), and goat anti-rabbit IgG alkaline phosphatase conjugate (1:4000 dilution), each in blocking buffer, with washing of the plate with PBS−Tween 3 times after each incubation. An additional wash with distilled water followed the incubation with antibody−enzyme conjugate. The substrate for alkaline phosphatase (*p*-nitrophenyl phosphate in Tris buffer) was then added, and the rate of increase of absorbance at 405 nm was recorded for either 17.5 min (at 2.5 min intervals) or 55 min (at 5 min intervals) with a Titertek-Plus MS212 plate reader. All incubations were at room temperature (approximately 20 °C).

The known ricin concentration control solutions were used to construct a calibration curve for solution ricin concentration versus absorbance change per minute (Abs/min) for each ELISA assay. Calibration curves were recorded to accompany each ricin binding experiment, in order to reduce errors resulting from solution preparation and handling. The calibration curve data was conveniently fit in the ricin concentration limit 0−100 ng/mL using a logarithmic relationship, $\text{Abs/min} = A + B\ \ln[\text{ricin}]$. The *A* and *B* factors in this relationship were obtained from the linear plot of Abs/min vs ln[ricin] for control solutions. These factors were then used to derive a residual ricin concentration (final [ricin]) in test solutions (i.e., ricin solutions that were

exposed to lyotropic mesophase samples). In this way, the relationship between initial [ricin] and final [ricin] following exposure to lyotropic mesophase samples was quantified.

The ricin affinity constants (K_a) and dissociation constants ($K_d = 1/K_a$) for the different mesophase formulations were ascertained from the ELISA assay data by assuming 1:1 binding and using the initial and final equilibrium solution ricin concentrations ($[ricin]_{in}$ and $[ricin]_{eq}$) with the initial concentration of galactose surfactant monomers within the mesophase ($[active]_{in}$), in the relationship: $K_a = [\text{bound ricin}]_{eq}/([\text{unbound active}]_{eq}[ricin]_{eq})$, where $[\text{bound ricin}]_{eq} = [ricin]_{in} - [ricin]_{eq}$ and $[\text{unbound active}]_{eq} = [active]_{in} - [\text{bound ricin}]$.

RESULTS

A number of surfactant amphiphiles possessing a galactose headgroup that might be capable of self-assembling into lyotropic mesophases of the cubic or inverse hexagonal type were synthesized (Figure 1). The approach was based on employing hydrophobic moieties (phytanyl and oleyl groups) found in surfactants that exhibit these mesophase behaviors (*9*, *14*). Once produced, we found that addition of water to these materials at room temperature resulted in the formation of myelinic lamellar phases, as determined by polarizing light microscopy.

Since we were seeking to produce materials that existed in the dilutable cubic or inverse hexagonal mesophase phase forms, a second approach was adopted that relied on incorporation of the galactose surfactants within binary surfactant mixtures. Secondary "matrix surfactants" were selected for these mixtures on the basis of their known propensity to support mesophase formation.

The phase behavior properties of these matrix surfactants are described in detail elsewhere (*10*, *14*). To summarize, oleyl glycerate (OG) shows a viscous anisotropic phase (inverse hexagonal, H_{II}) in equilibrium with water above 22 °C, which melts into a mobile isotropic phase at 66−73 °C (inverse micellar, L_{II}). Phytanyl glycerate (PG) also forms an H_{II} phase spontaneously in equilibrium with water, which melts at a slightly lower temperature, 39.5 °C.

Phytantriol exhibits a cubic phase in equilibrium with water over a broad temperature range with an inverse hexagonal phase appearing at higher temperatures (*14*). In our measurements, the cubic−inverse hexagonal phase transition occurred at 54.5 °C, which contrasts with a literature value of 44 °C (*14*). From discussions with other researchers, we understand that these elevated phase transition temperatures for different phytantriol samples are not an uncommon observation.

Addition of water at room temperature to mixtures of monoalkyl galactose surfactants with matrix surfactants yielded a number of systems, which exhibited lyotropic mesophase behavior of the desired type (cubic and inverse hexagonal, see Figure 2 and Table 1).

We found that the mesophase behavior of these mixtures could be manipulated by adjusting the ratios of the component surfactants. The aim of this approach was to obtain mixtures in which a high concentration of galactose surfactant could be incorporated within a dilutable mesophase material while retaining the mesophase structure. As such, the compositions (Figure 2 and Table 1) represent the upper limit of galactose surfactant concentrations that could be added while retaining the desired mesophase structure, as determined by the polarizing microscopy−water penetration technique.

We found that high concentrations of the galactose surfactants (20−50%) could be incorporated within these mixtures. This is an important observation, since it suggests that a high surfactant−water interfacial concentration of ligand (galactose) should be available for binding to the protein toxin ricin within the mesophase structure, which was the aim of this work.

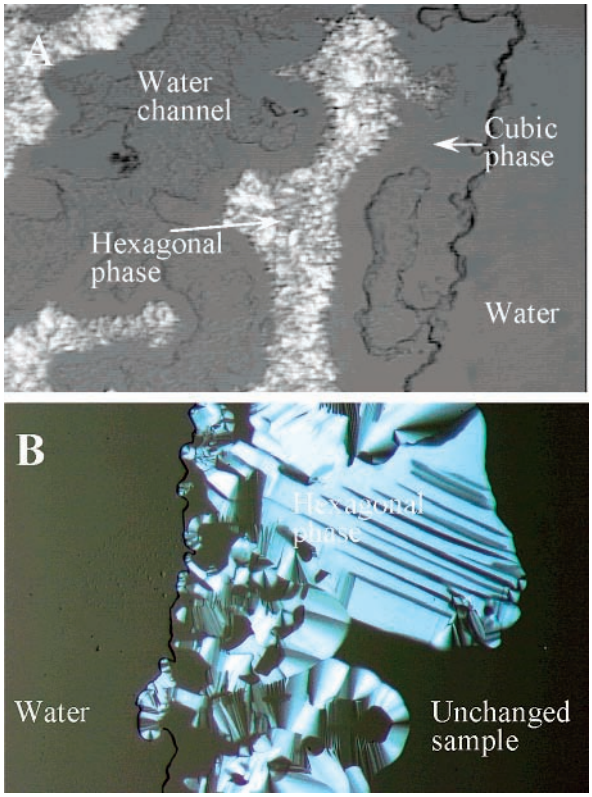


Figure 2. Lyotropic phase behavior as viewed through cross polarizers. The optical textures are used to assign mesophase forms. The viscosity of both the isotropic and anisotropic phases is clear from the "rough" nature of the interface of the phases with water and is a hallmark of dilutable mesophases of the inverse type. Panel A shows water penetration behavior of 40% oleyl α-1-galactoside/60% oleyl glycerate initial penetration at room temperature (25 °C). Panel B shows the water penetration behavior of 20% oleyl α-1-galactoside/80% oleyl glycerate at room temperature for 30 min (23 °C).

Broadly speaking, the phase behavior of the mixed surfactant systems appears to lie between the behavior of the two isolated components. This can be rationalized by considering the curvature of the surfactant−water interface, according to the model suggested by Israelachvili (*24*). Isolated galactosyl surfactants preferentially form lamellar phases (of minimal curvature), while the matrix surfactants discussed above preferentially form structures of greater (inverse) curvature, the cubic and inverse hexagonal phases.

For mixtures comprising >20% galactose surfactants in oleyl glycerate, addition of the lamellar-preferring galactoside reduces the preference for the negatively curved inverse hexagonal phase, yielding a cubic phase in equilibrium with water. We postulate that the low concentration of galactoside in the 20% oleyl α-1-galactoside/oleyl glycerate mixture is insufficient to significantly alter the phase behavior from the pure oleyl glycerate system; hence the inverse hexagonal phase is retained. We note the absence of phase behavior data for one of the surfactant mixtures prepared, namely, 40% oleyl β-1-galactoside/60% oleyl glycerate. This surfactant was prepared in quantities sufficient only for ricin binding analysis (see later). The phase behavior for this mixture is expected to be qualitatively similar to 40% oleyl β-1-galactoside/60% oleyl glycerate, which showed a cubic phase in equilibrium with water at all temperatures studied.

When phytanyl glycerate was employed as the matrix surfactant, the effect of adding the galactoside surfactants was less marked, and the inverse hexagonal phase was retained in

Table 1. Summary of Compositions and Lyotropic Phase Behavior Observed through Cross Polarizers Using Water Penetration Analysis

sample	optical textures observed	temperature range	likely phases present
40% galactose-6-oleate/60% oleyl glycerate	100% water		
	viscous isotropic	RT to 65 °C	cubic (C_{II})
	viscous isotropic	RT to >100 °C	cubic (C_{II})
	isotropic	24−92 °C	cubic (C_{II})
	anisotropic	RT to 92 °C	lamellar (L_α)
	isotropic	24−100 °C	inverse micellar (L_{II})
	100% surfactant		
40% galactose-6-phytanoate/60% phytanyl glycerate	100% water		
	anisotropic	RT to 99 °C	inverse hexagonal (H_{II})
	100% surfactant		
20% oleyl α-1-galactoside/80% oleyl glycerate	100% water		
	anisotropic	RT to 88 °C	inverse hexagonal
	mobile isotropic	>81 °C	inverse micellar (L_{II})
	100% surfactant		
40% oleyl α-1-galactoside/60% oleyl glycerate	100% water		
	viscous isotropic	>RT	cubic (C_{II})
	anisotropic	RT to 42°	lamellar (L_α)
	100% surfactant		
50% phytanyl *β*-1-galactoside/50% phytanyl glycerate	100% water		
	anisotropic	RT to 100 °C	inverse hexagonal (H_{II})
	100% surfactant		
30% oleyl α-1-galactoside/70% phytantriol	100% water		
	viscous isotropic	40−78 °C	cubic (C_{II})
	second viscous isotropic	RT to 78 °C	cubic (C_{II})
	anisotropic	RT to 68 °C	lamellar (L_α)
	mobile isotropic	>68 °C	inverse micellar (L_{II})
	100% surfactant		
40% phytanyl *β*-1-galactoside/60% phytantriol	100% water		
	viscous isotropic	RT to 100 °C	cubic (C_{II})
	second viscous isotropic	RT to 100 °C	cubic (C_{II})
	anisotropic	RT to 78 °C	lamellar (L_α)
	100% surfactant		

most cases. This suggests that the phytanyl-chained surfactants exhibit more robust inverse phases, probably due to the large volume occupied by the hydrophobe, and the disorder that it confers within self-assembly structures.

The addition of galactosides to the less negatively curved matrix surfactant phytantriol (cubic phase), results in a slight reduction in the curvature relative to the pure phytantriol system. This manifests itself in the elimination of the high temperature inverse hexagonal phase of phytantriol, as was observed in phytantriol mixtures comprising 30% oleyl α-1-galactoside or 40% phytanyl-*β*-1-galactoside. These mixtures also showed the presence of a lamellar phase at lower water contents, which is also a feature of the pure phytantriol−water phase diagram.

In order to study the structural properties of the mesophase systems in more detail, small-angle X-ray scattering (SAXS) was employed on a selection of the samples, which were prepared in equilibrium with excess water, and analyzed at room temperature (Figure 3). As expected from the polarizing microscopy optical texture observations, the 50% phytanyl glycerate/50% phytanyl *β*-1-galactoside in equilibrium with excess water at room temperature (∼22 °C), exhibited Bragg reflections with scattering vector (q) spacings consistent with the (inverse) hexagonal phase ($1{:}\sqrt{3}{:}\sqrt{4}$). SAXS analysis of the 40% phytanyl *β*-1-galactoside/60% phytantriol, 30% oleyl α-1-galactoside/70% phytantriol and 40% oleyl α-1-galactoside/60% oleyl glycerate mixtures in equilibrium with excess water revealed *Pn*3*m* cubic symmetry (Bragg peak spacings $\sqrt{2}{:}\sqrt{3}{:}\sqrt{4}{:}\sqrt{6}{:}\sqrt{8}{:}\sqrt{9}$), (*25*) again consistent with the polarizing microscopic observation of viscous isotropic phases in these systems.

SAXS analysis also allows the quantification of structural parameters associated with lyotropic mesophases (*25*). The lattice parameter, a, is readily derived from the q spacings of the Bragg reflections (Figure 3). The straight line relationship again reinforces the assignment of the *Pn*3*m* space group for the cubic phases (Figure 3B−D). The lattice parameter for the inverse hexagonal phase (Figure 3A) was obtained from the scattering vector position of the initial [10] reflection *via* the relationship $a = q(\sqrt{3}/4\pi)$.

Lattice parameters supply information regarding the center-to-center distances of repeating structural units within the mesophases. Larger lattice parameters indicate larger center to center distances, implying a more expanded mesophase structure (*26*). For the inverse hexagonal phase, this can readily be envisaged as the distance between the centers of adjacent aqueous channels. For inverse cubic phases, it corresponds to the cubic unit cell dimension. Considering the similarity between the various surfactant molecular dimensions involved in this study, changes in the lattice parameter within the cubic phases can reasonably be assumed to correlate with the diameter of aqueous channels within the structure. The addition of galactoside surfactants dramatically increases the lattice parameter from the previously described value of 64−66 Å for pure phytantriol (*14*) to values for the mixtures of 90.9−93.5 Å (Figure 3). Expansion of the mesophase structure is to be expected for the addition of the relatively bulky sugar headgroups possessed by the galactoside surfactants, causing reduced negative interfacial curvature, as discussed earlier. The phytantriol-derived mesophases do possess somewhat narrower aqueous channel diameters than the corresponding oleyl glycerate mixture, with the largest lattice spacing encountered for 40% oleyl α-1-galactoside/60% oleyl glycerate (a = 121.2 Å).

The inverse hexagonal phase structure based on phytanyl glycerate possesses the most compressed (narrowest) unit cell (a = 60 Å). These are important observations with regard to understanding the optimal mesophase structures for protein uptake within mesophase polyvalent ligands, as will be discussed later.

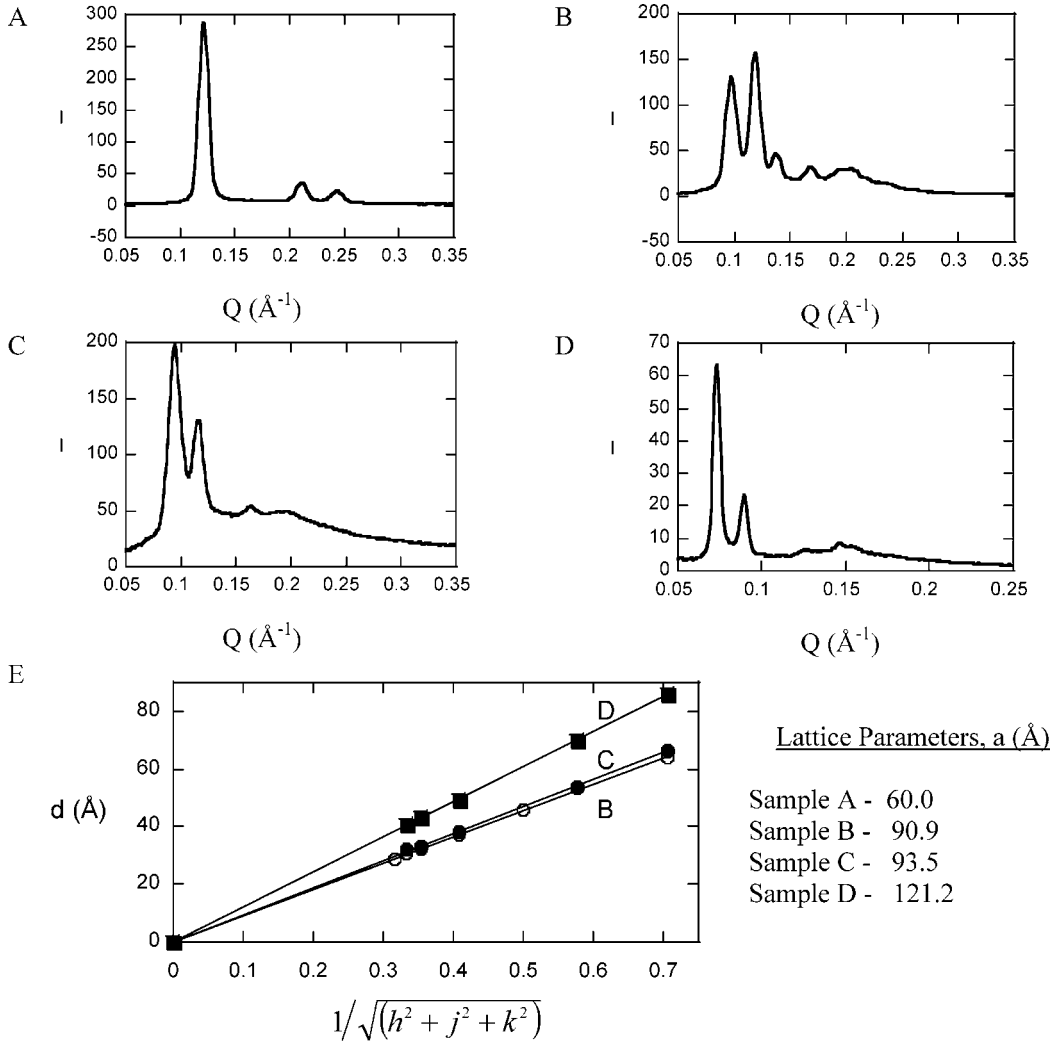


Figure 3. SAXS data for different surfactant formulations recorded at room temperature (22 °C): (A) 50% phytanyl β-1-galactoside/50% phytanyl glycerate; (B) 40% phytanyl β-1-galactoside/60% phytantriol; (C) 30% oleyl α-1-galactoside/70% phytantriol; (D) 40% oleyl α-1-galactoside/60% oleyl glycerate; (E) plots used to derive lattice parameters from SAXS data for cubic phase mixtures; *h*, *j*, and *k* refer to the Miller indices for *Pn*3*m* symmetry assigned to each peak in the scattering data.

The ricin binding exhibited by surfactant mixtures possessing inverse hexagonal mesophase morphology was examined using the enzyme-linked immunosorbent binding assay (ELISA) described in the methods (Figure 4). This assay measures the residual ricin in solution following exposure of known ricin concentration solutions to small samples of mesophase formulations.

A control measurement for a pure phytantriol mesophase sample shows that the galactoside-free mesophase has little or no affinity for the ricin in solution, since final [ricin] approximates initial [ricin] over the initial ricin concentration range studied. A similar poor affinity for ricin is demonstrated for mesophase samples containing galactose-6-phytanoate. Measurable reduction in [ricin] is however observed for mesophases containing galactosides possessing alkyl groups attached at the C1 carbon of the sugar (phytanyl β-1-galactoside and oleyl α-1-galactoside). Referring to Table 2, we find that the maximum proportion of ricin removed from solution for these inverse hexagonal materials is 39.6%, (for the 20% oleyl α-1-galactoside/oleyl glycerate formulation). The linear nature of the initial versus final ricin concentration relationship indicates that an equilibrium between bound and unbound ricin exists in these systems. The lack of an observable plateau in the binding relationship also suggests that these systems are not saturated at the ricin concentrations that we have investigated. The equilibrium nature of the ricin binding to the mesophase systems permits calculation of the affinity constant for ricin binding, as described in the methods section (Table 2).

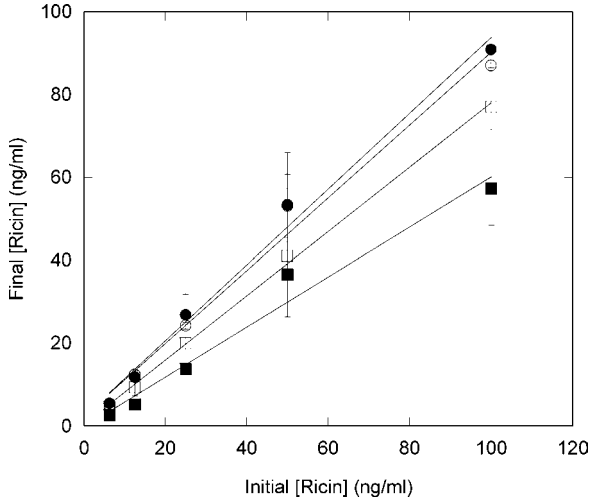


Figure 4. Ricin binding assay data for inverse hexagonal phase structures (with phytantriol control): (●) phytantriol (control); (○) 40% galactose-6-phytanoate/phytanyl glycerate; (□) 50% phytanyl β-1-galactoside/phytanyl glycerate; (■) 20% oleyl α-1-galactoside/oleyl glycerate.

Table 2. Efficiency of Removal of Ricin from Solution by Mesophase Formulations with Calculated Affinity and Dissociation Constants

composition	% ricin removed	K_a (M^{-1})	K_d (mM)
phytantriol (control)	8.6	8.3	120
Inverse Hexagonal Mesophase Mixtures			
40% galactose-6-phytanoate/ phytanyl glycerate	12.2	43.7	23
50% phytanyl β-1-galactoside/ phytanyl glycerate	22.4	70.6	14
20% oleyl α-1-galactoside/ oleyl glycerate	39.6	374.5	2.7
Inverse Cubic Mesophase Mixtures			
40% galactose-6-oleate/ oleyl glycerate	40.5	200.7	5.0
40% oleyl α-1-galactoside/ 60% oleyl glycerate	80.3	1164.2	0.86
40% oleyl β-1-galactoside/ oleyl glycerate	85.1	1631.2	0.610
40% phytanyl β-1-galactoside/ 60% phytantriol	90.3	2844.6	0.35
30% oleyl α-1-galactoside/ phytantriol	91.3	3996.2	0.25

The inverse cubic mesophase formulations showed considerably different ricin binding behavior (Figure 5). When incorporated within a cubic mesophase, galactose-6-oleate is able to bind a significant quantity of ricin from solution (40.5%), which is in contrast to the analogous galactose-6-phytanoate, when contained within an inverse hexagonal mesophase (12.2%, Figure 4).

However, it is again the C1-substituted galactose surfactants that show the most dramatically increased potency for binding ricin when contained within inverse cubic mesophase structures (Figure 5 and Table 2). These materials are capable of binding 80−91.3% of ricin in solution over the concentration range studied. The optimal ricin binding activity (91.3%) was observed for a 30% oleyl α-1-galactoside/phytantriol mixture.

The most unequivocal observation from this data is the superior ability of cubic phase materials to absorb ricin. A direct comparison between different mesophase forms possessing identical ligands may be made by comparing the 40−50% phytanyl β-1-galactoside containing inverse hexagonal and inverse cubic mesophases. Here, despite decreasing the galactoside concentration by 10% in moving from inverse hexagonal to inverse cubic morphologies, a 40-fold decrease in ricin dissociation constant (K_d) is observed (14 mM for 50:50 phytanyl β-1-galactoside/phytanyl glycerate versus 0.35 mM for 40:60 phytanyl β-1-galactoside/phytantriol). A similar comparison can be made between oleyl α-1-galactoside/phytantriol formulations. Twenty percent oleyl α-1-galactoside (inverse hexagonal phase) yields $K_d = 2.7$ mM, while 30% oleyl α-1-galactoside (cubic phase) gives $K_d = 0.25$ mM.

DISCUSSION

The high affinity for ricin of the cubic morphology galactoside mixtures may be explained through analysis of the SAXS data. The typical lattice parameters for the cubic mesophases are on the order of 9.1−12.1 nm (Figure 3) versus 6 nm for the inverse hexagonal mesophase of 50% phytanyl glycerate/50% phytanyl β-1-galactoside. A significantly increased pore diameter within the cubic phase for the phytantriol-based systems is therefore observed. We propose that this allows greater diffusion of the ricin protein (whose longest dimension is on the order of 12 nm according to crystallographic data (*21*)) within the mesophase aqueous channels and hence greater opportunity to bind to the ligands immobilized therein. This further suggests that the mesophases incorporate a molecular size exclusion capability, which may have implications for other delivery and uptake applications (*17*). Further work is currently underway in our laboratory to probe this phenomenon.

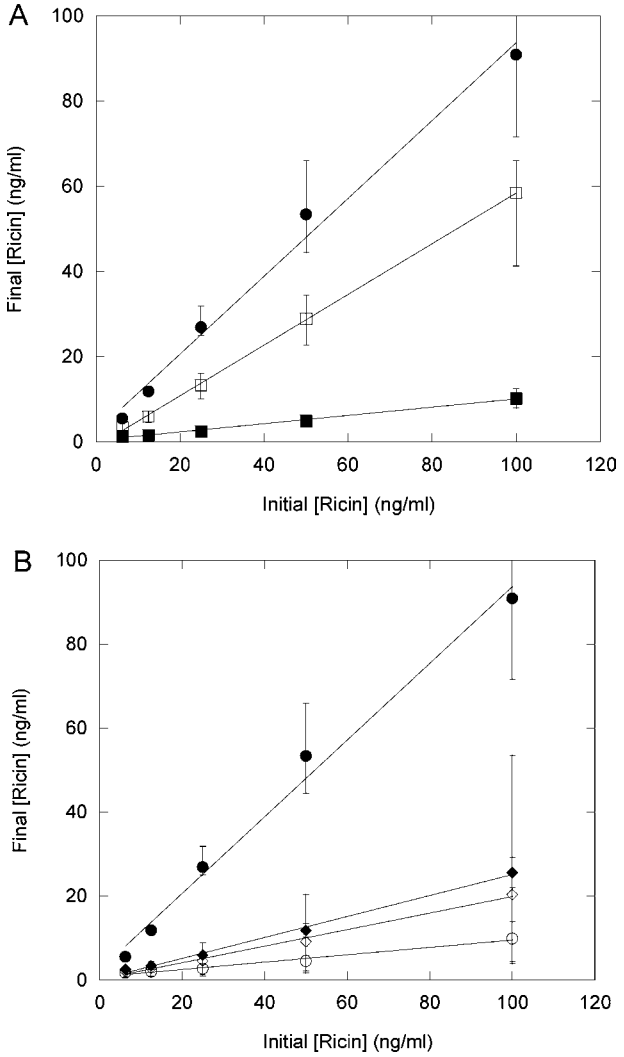


Figure 5. Ricin binding asay data: inverse cubic structures (with phytantriol control): (A) ●, phytantriol (control); □, 40% galactose-6-oleate/oleyl glycerate (cubic phase 24−100 °C); ■, 40% phytanyl β-1-galactoside/60% phytantriol (cubic phase 24−100 °C); (B) ●, phytantriol (control); ◇, 40% oleyl α-1-galactoside/60% oleyl glycerate; ◆, 40% oleyl β-1-galactoside/oleyl glycerate; ○, 30% oleyl α-1-galactoside/phytantriol.

In the current work, the role of the anomeric form of the galactose ligand on ricin binding was also probed. The data indicates that the anomeric conformation of the galactoside has little influence on mesophase ricin binding, since little difference in ricin binding was observed between oleyl α-1 and oleyl β-1 surfactant containing mesophases. This observation contrasts with earlier evaluation of methyl-substituted galactose inhibitors of ricin, which indicated that the β anomer of the methyl-substituted sugar exhibited significantly greater binding to ricin (*27*).

Comparing binding data between the C6 and C1 alkylated galactose surfactants reveals that alkylation at the C1 position is optimal for ricin binding. This is not surprising, given that the major protein−sugar interactions for ricin appear to occur through the C3, C4, and C6 OH groups (*21*).

An indicative lower limit to the ricin binding capacity of the mesophases investigated here is obtained by assuming 100% binding of a 130 μL aliquot of 100 ng/mL ricin by approximately 1 mg of mesophase. This yields a capacity of ∼13 μg of ricin per gram of mesophase. It is important to reiterate

that this represents a lowest limit to binding capacity. Work is currently underway to define the upper limits of mesophase binding capacity for ricin; however, it is interesting to note that the lethal dose (LD_{50}) of ricin for humans is on the order of 0.1−1 μg/kg (*28*).

We note that the kinetics of ricin binding have not been explored in the current study, since the measurements were performed after a 24 h incubation period. This is clearly a key consideration for the development of either an effective antitoxin or sequestration material. Preliminary measurements suggest that equilibrium ricin binding is attained within 5−10 h of incubation with ricin solutions. The kinetics of binding will be critically dependent on the diffusion of ricin within the mesophase, which in turn will depend on the surface area of the mesophase in contact with ricin binding solution. Given that these materials can be readily prepared in microparticulate dispersion form (*10*), we would anticipate that dramatic improvements in binding kinetics should be achievable. Further work is underway to prepare these materials in dispersion form and elucidate the ricin binding kinetics in such systems.

In summary, we have prepared a number of dilutable (i.e., insoluble) mesophase materials, incorporating the biological ligand galactose, which is known to specifically bind the B-chain of the protein toxin ricin. The aim of this work was to demonstrate that lyotropic mesophases can be effective in the selective separation of biological solutes, by virtue of their internally mobile structure and high interfacial area with respect to water. The self-assembly behavior exhibited by these systems has been characterized by polarizing microscopy and small-angle X-ray scattering. Specific ricin uptake characteristics have been measured by means of a modified ELISA assay. Mesophase materials composed of C1 alkylated galactose surfactants that formed cubic phase structures were found to be highly effective at the specific extraction of ricin from solution. This efficacy was not found for inverse hexagonal mesophase structures. This is explained on the basis of the structural parameters of the different mesophase forms. We postulate that the more open cubic mesophase structure permits in-diffusion and uptake of the toxin more readily. Ricin assay data shows that in all cases, binding occurs *via* an equilibrium that can be manipulated through changes in mesophase structural form or ligand chemistry. In these studies, 0.49 mg samples of mesophase materials were capable of removing in excess of 90% of ricin from a 100 ng/mL ricin solution, with a corresponding dissociation constant of 0.25 mM, which compares favorably with literature values for dissociation constants measured for the active component of the natural cell surface receptor, galactose (0.15−0.6 mM) (*23*).

While this binding efficiency is at the lower level of that required to compete with cell surface receptors for ricin binding *in vivo*, these data show that synthetic mesophase materials represent promising systems for ricin sequestration. Optimization of these systems by, for example, improving accessibility for ricin binding by incorporating spacer groups between surfactant alkyl chains and galactose moieties can readily be envisaged.

In forthcoming publications, we demonstrate the incorporation of biological lipid ligands into mesophase materials and their increased effectiveness in the extraction of ricin from solution. Work is now underway to determine the efficacy of these materials in cytotoxicity inhibition assays and to form dispersions from them. The ease with which mesophase materials can be prepared further offers an economic route to their development. The fact that self-assembled mesophase forms mimic to some extent the surface properties of the plasma membrane of the cell offers the possibility of exploring many cell surface recognition processes using this approach.

ACKNOWLEDGMENT

We thank Dr. Jamie Booth and Prof. Suresh Bhargava of RMIT, Melbourne, for assistance with SAXS measurements. We also thank Dr. Peter Gray of DSTO for valuable discussions.

Supporting Information Available: Details of galactose surfactant synthesis and characterization. This material is available free of charge *via* the Internet at http://pubs.acs.org/BC.

LITERATURE CITED

(1) Mammen, M., Choi, S.-K., and Whitesides, G. M. (1998) Polyvalent interactions in biological systems: Implications for design and use of multivalent ligands and inhibitors. *Angew. Chem., Int. Ed. 37*, 2754−2794.

(2) Bourne, N., Stanberry, L. R., Kern, E. R., Holan, G., Matthews, B., and Bernstein, D. I. (2000) Dendrimers, a new class of candidate topical microbicides with activity against herpes simplex virus infection. *Antimicrob. Agents Chemother. 44*, 2471−2474.

(3) Todar, K. (2006) *Todar's Online Textbook of Bacteriology*, www.textbookofbacteriology.net.

(4) Harborne, J. B., Baxter, H., and Moss, G. P. Eds., (1996) *Dictionary of Plant Toxins*, Wiley, Chichester, U.K.

(5) Lord, J. M., Roberts, L. M., and Robertus, J. D. (1994) Ricin: structure, mode of action, and some current applications. *FASEB J. 8*, 201−208.

(6) Crompton, R., and Gall, D. (1980) Georgi Markov: Death in a pellet. *Med.-Leg. J. 48*, 51−62.

(7) Knight, B. (1979) Ricin-a potent homicidal poison. *Br. Med. J. 278*, 350−351.

(8) Larsson, K. (1967) Structure of mesomorphic phases and micelles in aqueous glyceride systems. *Z. Phys. Chem. 56*, 173−198.

(9) Qiu, H., and Caffrey, M. (1998) Lyotropic and thermotropic phase behavior of hydrated monoacylglycerols: Structure characterization of monovaccenin. *J. Phys. Chem. B 102*, 4819−4829.

(10) Fong, C., Krodkiewska, I., Wells, D., Boyd, B. J., Booth, J., Bhargava, S., McDowall, A., and Hartley, P. G. (2005) Submicron dispersions of hexosomes based on novel glycerate surfactants. *Aust. J. Chem 58*, 683−687.

(11) Fong, C., Wells, D., Krodkiewska, I., Hartley, P. G., and Drummond, C. J. (2006) New role for urea as a surfactant headgroup promoting self-assembly in water. *Chem. Mater. 18*, 594−597.

(12) Baba, T., Minamikawa, H., and Hato, M. (2001) Hydration and molecular motions in synthetic phytanyl-chained glycolipid vesicle membranes. *Biophys. J. 81*, 3377−3386.

(13) Briggs, J., Chung, H., and Caffrey, M. (1996) The temperature-composition phase diagram and mesophase structure characterization of the monoolein/water system. *J. Phys. II Fr. 6*, 723−751.

(14) Barauskas, J., and Landh, T. (2003) Phase behavior of the phytantriol/water system. *Langmuir 19*, 9562−9565.

(15) Larsson, K. (1997) Cubosomes and hexosomes for drug delivery. *Proc. Int. Symp. Controlled Release Bioact. Mater.* 198−199.

(16) Barauskas, J., Johnsson, M., and Tiberg, F. (2005) Self-assembled lipid superstructures: Beyond vesicles and liposomes. *Nano Lett. 5*, 1615−1619.

(17) Clogston, J., and Caffrey, M. (2005) Controlling release from the lipidic cubic phase. Amino acids, peptides, proteins and nucleic acids. *J. Controlled Release 107*, 97−111.

(18) Spicer, P. T., Hayden, K. L., Lynch, M. L., Ofori-Boateng, A., and Burns, J. L. (2001) Novel process for producing cubic liquid crystalline nanoparticles (cubosomes). *Langmuir 17*, 5748−5756.

(19) Zhao, X. Y., Zhang, J., Zheng, L. Q., and Li, D. H. (2004) Studies of cubosomes as a sustained drug delivery system. *J. Dispersion Sci. Technol. 25*, 795−799.

(20) Dawson, R. M., Alderton, M. R., Wells, D., and Hartley, P. G. (2006) Monovalent and polyvalent carbohydrate inhibitors of ricin binding to a model of the cell-surface receptor. *J. Appl. Toxicol. 26*, 247−252.

(21) Montfort, W., Villafrancas, J. E., Monzingo, A. F., Ernst, S. R., Katzin, B., Rutenber, E., Xuong, N. H., Hamlin, R., and Robertus, J. D. (1987) The three-dimensional structure of ricin at 2.8 Å. *J. Biol. Chem. 262*, 5398−5403.

(22) Rosevear, F. B. (1954) The microscopy of the liquid crystalline neat and middle phases of soaps and synthetic detergents. *J. Am. Oil Chem. Soc. 31*, 628−639.

(23) Dawson, R. M., Paddle, B. M., and Alderton, M. R. (1999) Characterization of the asialofetuin microtitre plate-binding assay for evaluating inhibitors of ricin lectin activity. *J. Appl. Toxicol. 19*, 307−312.

(24) Israelachvili, J. (1994) The science and applications of emulsions − an overview. *Colloids Surf., A 91*, 1−8.

(25) Sun, R. G., and Zhang, J. (2004) The cubic phase of phosphatidylethanolamine by small angle x-ray scattering. *J. Appl. Phys. D 37*, 463−467.

(26) Hyde, S., Andersson, S., Larsson, K., Blum, Z., Landh, T., Lidin, S., and Ninham, B. W. (1997) *The Language of Shape*, Elsevier Science B.V., Amsterdam.

(27) Sharma, S., Bharadwaj, S., Surolia, A., and Podder, S. K. (1998) Evaluation of the stoichiometry and energetics of carbohydrate binding to Ricinus communis agglutinin: a calorimetric study. *Biochem. J. 333*, 539−542.

(28) Hicks, R. P., Hartell, M. G., Nichols, D. A., Bhattacharjee, A. K., van Hamont, J. E., and Skillman, D. R. (2005) The medicinal chemistry of botulinum, ricin and anthrax toxins. *Curr. Med. Chem. 12*, 667−690.

BC060216B

Sequence-Specific Targeting of RNA with an Oligonucleotide−Neomycin Conjugate

Irudayasamy Charles,† Hongjuan Xi, and Dev P. Arya*

Laboratories of Medicinal Chemistry, Clemson University, Clemson, South Carolina 29634. Received August 9, 2006; Revised Manuscript Received September 22, 2006

The synthesis of neomycin covalently attached at the C5-position of 2′-deoxyuridine is reported. The synthesis outlined allows for incorporation of an aminoglycoside (neomycin) at any given site in an oligonucleotide (ODN) where a thymidine (or uridine) is present. Incorporation of this modified base into an oligonucleotide, which is complementary to a seven-bases-long α-sarcin loop RNA sequence, leads to enhanced duplex hybridization. The increase in T_m for this duplex ($\Delta T_m = 6$ °C) suggests a favorable interaction of neomycin within the duplex groove. CD spectroscopy shows that the modified duplex adopts an A-type confirmation. ITC measurements indicate the additive effects of ODN and neomycin binding to the RNA target ($K_a = 4.5 \times 10^7$ M^{-1}). The enhanced stability of the hybrid duplex from this neomycin−ODN conjugate originates primarily from the enthalpic contribution of neomycin {$\Delta\Delta H_{obs} = -7.21$ kcal/mol ($\Delta H_{neomycin\ conjugated} - \Delta H_{nonconjugated}$)} binding to the hybrid duplex. The short linker length allows for selective stabilization of the hybrid duplex over the hybrid triplex. The results described here open up new avenues in the design and synthesis of nucleo−aminoglycoside−conjugates (N−Ag−C) where the inclusion of any number of aminoglycoside (neomycin) molecules per oligonucleotide can be accomplished.

INTRODUCTION

Aminoglycoside antibiotics interact with a variety of RNA molecules and exhibit bactericidal activity by inducing the misreading of codons (*1*, *2*) as well as inhibition of translocation (*3*). A number of RNA molecules have been known to interact with aminoglycosides; group I introns (*4*, *5*), ribonuclease P RNA (*6*), hairpin ribozyme (*7*, *8*), hammerhead ribozyme (*9*−*11*), hepatitis delta virus ribozyme (*12*, *13*), untranslated region of thymidylate synthase mRNA (*14*), hTR RNA component (*15*), human mRNAs and both reverse response element and transactivating response element RNA motifs of HIV-1 (*16*−*19*). We have identified neomycin (Figure 1) as the most potent DNA/RNA/hybrid triplex stabilizing groove binder (*20*, *21*). Neomycin, an aminoglycoside, had largely been known to bind different RNA structures (*10*, *14*, *22*−*24*). Recent studies from our laboratory have, however, revealed that aminoglycosides (in particular, neomycin) can bind to other A-form structures (*25*). The stabilization of the poly(dA)•2poly(dT) (*20*), small triplexes (*26*), DNA•RNA hybrid duplexes, RNA triplex, and hybrid triple helices (*27*) by neomycin has recently been reported by us. Aminoglycosides most likely bind in the major groove of these structures (much like RNA, as the A-form nucleic acids have a narrower major groove) (*25*, *28*).

Carbohydate (Neomycin)−DNA Conjugates. In contrast to abundant glycosylated protein and lipids in nature, few examples of glycosylayted nucleic acids have been reported. A few reports discuss glycosylated nucleosides (*29*−*31*) and their role in gene expression (*32*, *33*). The presence of these glycosylated nucleosides modulates the functions of *Escherichia coli* bacteriophages of the T-even series (*34*), genome of *Trypanosoma brucei (*a protozoan found in phages and known to cause African sleeping sickness) (*35*), and *Diplonema* (a small phagotrophic marine flagellate) (*36*). These reports in carbohydrate−nucleic acid interactions have also ignited interest in the development of such conjugates. The importance of aminoglycosides in the recognition of nucleic acids prompted us to design, synthesize, and evaluate aminoglycoside−oligonucleotide conjugates. If carbohydrates (aminoglycosides) can be conjugated to DNA without affecting the structure and stability of DNA, and bind to their nucleic acid target (RNA) with specificity, then these conjugates will be of interest as a new class of artificial glycoconjugate materials applicable to cell-targeted gene therapy techniques. A few examples are also known in which carbohydrate ligands have been used to increase the uptake of antisense oligonucleotides (*38*). These examples include the use of mannosylated polylysine (*39*) and galactosylated polylysine (*40*) in receptor-mediated endocytosis of antisense oligonucleotides. We have recently shown that neomycin assists in the lipid-mediated delivery of plasmid DNA and oligonucleotides (*41*). Delivery of oligonucleotides has been a major impediment in the

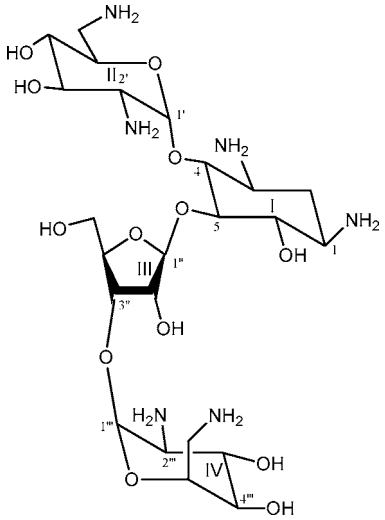


Figure 1. Structure of neomycin.

* Corresponding author. dparya@clemson.edu; 864-656-1106; Fax 864-656-6613.

† Current address: Ambion, Inc., Austin, Texas.

10.1021/bc060249r CCC: $37.00 © 2007 American Chemical Society
Published on Web 11/09/2006

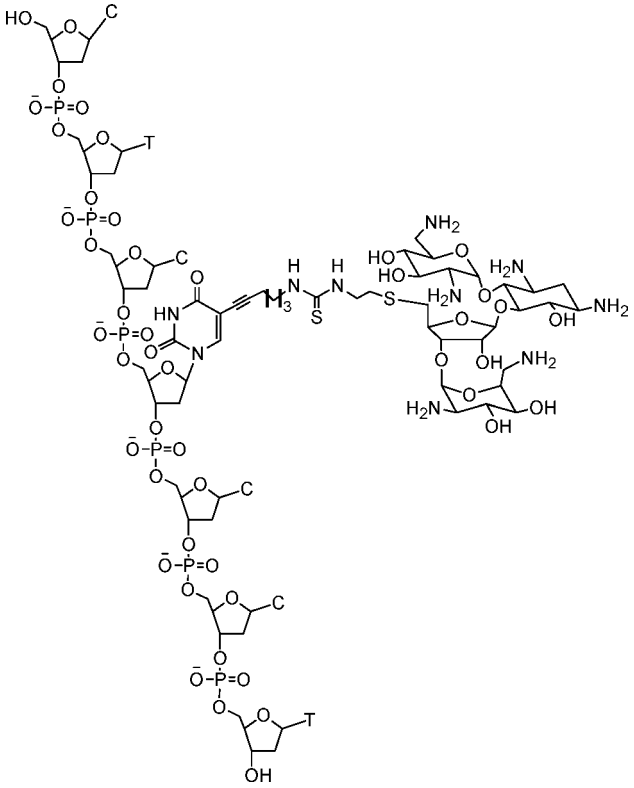


Figure 2. Structure of the 7mer−neo conjugate.

development of all nucleic acid based drugs. We recently showed that neomycin, an aminoglycoside antibiotic, when combined with a cationic lipid preparation, like DOTAP, enhances transfection efficiency of both reporter plasmids and oligonucleotides and results in a significant increase in transgene expression (*41*).

To take advantage of these unique findings of aminoglycoside−nucleic acid interaction, we have initiated the development of aminoglycoside−nucleic acid conjugates. Recently, we reported synthesis of neomycin conjugates in which neomycin was conjugated at the 5′-end of the nucleic acid analogs (DNA/PNA) via thiourea linkage (*42*, *43*). The application of such conjugates, however, is limited, as the drug can be added only at the 5′-end of the oligomer. The applicability of conjugating a drug molecule to any given site in an oligonucleotide can be accomplished if the drug is attached to the base or sugar using an appropriate linker, leaving 5′- and 3′-ends free for suitable oligomer elongation. With this methodology, the addition of drug−phosphoramidite conjugates to the growing strand during oligonucleotide synthesis can be monitored using trityl monitor. Herein, we describe an efficient phosphoramidite-based method for the synthesis of neomycin attached to the C5-position of 2′-deoxyuridine through a hexynyl linker, its extension to oligonucleotide−neomycin synthesis (Figure 2), and its hybridization with a complementary RNA structure. These conjugates will be referred to as nucleo−aminoglycoside conjugates (N−Ag−C), of which the first example, nucleo−neomycin conjugate (N-Neo-C), is reported here.

Selection of Target RNA. Among functionally active 16S rRNA target sites, A-site (*1*, *44*−*47*) and α-sarcin loop (*47*−*50*) are important, as they have a profound effect on protein synthesis. The α-sarcin loop is the region where α-sarcin catalyzes the hydrolysis of the phosphodiester bond that links its eighth and ninth residues (*50*). This causes improper binding of ribosomes to elongation factors, which eventually terminates protein synthesis (*47*). The importance of this single phosphodiester linkage emphasizes the significance of the α-sarcin loop as an attractive target for antisense oligonucleotides. We therefore chose this target for our initial studies.

EXPERIMENTAL PROCEDURES

Materials. All commercial reagents were used without further purification. Pyridine, methylene chloride, and *N*,*N*-dimethylformamide (DMF) were refluxed over calcium hydride and distilled. All reactions were carried out in oven-dried glassware under N_2/argon atmosphere. All reactions were monitored by thin-layer chromatography (TLC) with precoated silica gel on glass plate. Visualization of the TLC plate was achieved with either UV light or spraying ethanolic ninhydrin solution followed by heating the plate with a heat gun. ICN silica gel 32−63 (60 Å) was used for column chromatography. ^{1}H NMR spectra were recorded by using either 300 MHz or 500 MHz NMR. IR was recorded on a Nicolet Magna-IR Spectrometer 550 as a solution of either 1,2-dichloroethane or CCl_4, and the peaks corresponding to the solvent was subtracted manually. MALDI-TOF mass was recorded on a Bruker Daltonics OmniFLEX Bench-Top MALDI-TOF mass spectrometer. Preparative anion exchange HPLC was carried out on a Phenomenex SAX 80 Å column (10 × 250 mm, 5μ), and for analytical anion exchange HPLC, a Waters Gen-Pak FAX (4.6 × 100 mm) column was used. Preparative and analytical RP-HPLC were carried out with Alltima C8 100 Å (250 × 4.6 mm, 10μ) column.

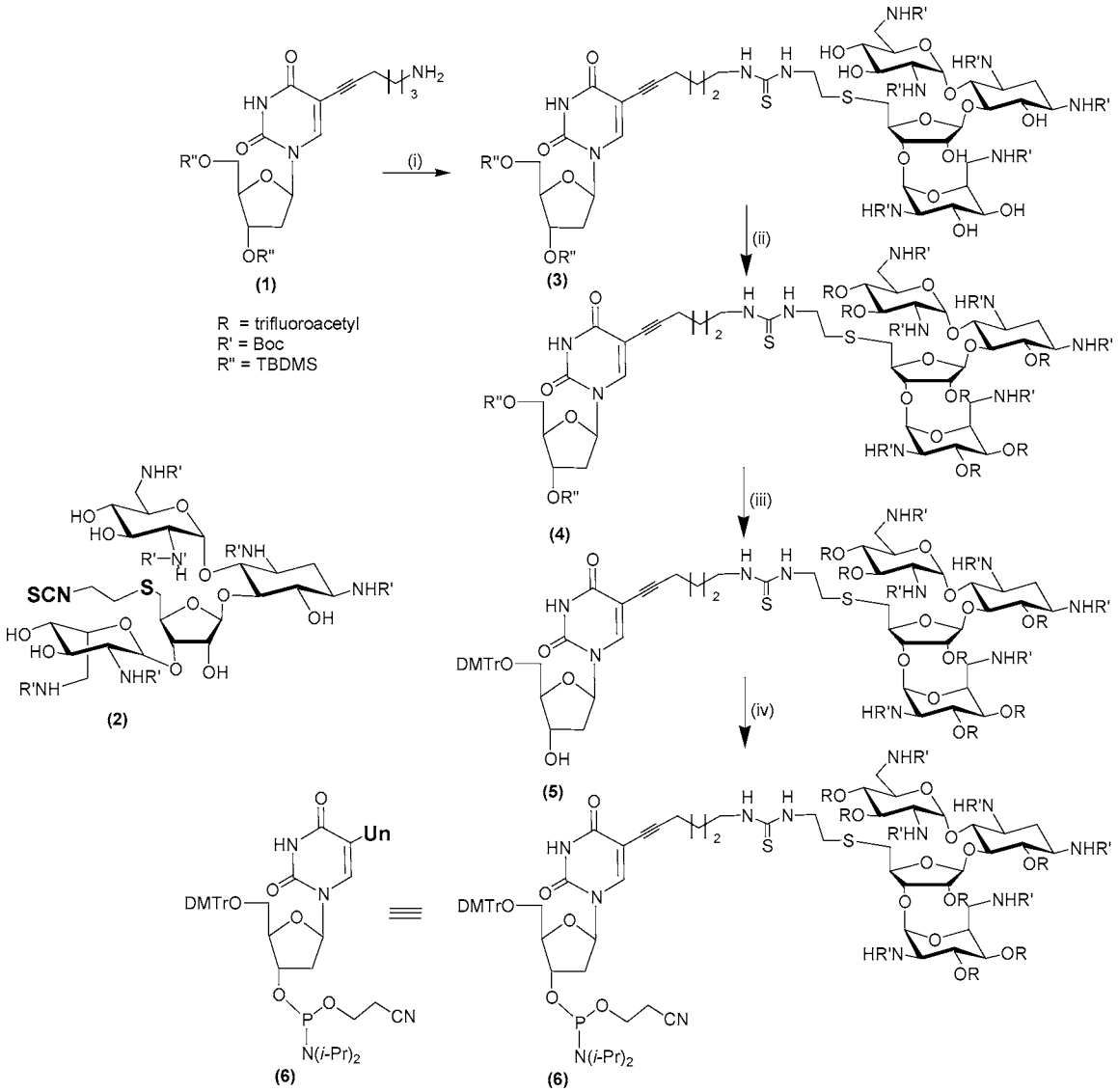
Please see Supporting Information for experimental procedures for synthesis of monomers. 7mer DNAs (dY, N-dY, and dY′) were synthesized on Expedite Nucleic Acid System (8909) and purified by HPLC. RNA (rR) was purchased from Dharmacon, Inc., (Lafayette, CO) and was used without further purification (lot numbers COFRA-0001 and CHAIB-0001). The concentrations of all the nucleic acid solutions were determined spectrophotometrically using the following extinction coefficients (on a per strand basis, M^{-1} cm^{-1}): e_{260} = 81 900 for rR, and e_{260} = 54 000 for dY. Neomycin (lot 129H0918) was purchased from Sigma (St. Louis, MO) and was used without further purification.

UV Spectroscopy. UV spectra were recorded at λ = 200−300 nm on a Cary 1E UV/vis spectrophotometer equipped with temperature programming. Spectrophotometer stability and λ alignment were checked prior to initiation of each melting point experiment. For accurate T_m determinations, first-derivative functions were used. Data were recorded every 1.0 °C. In all UV experiments, the samples were heated from 20 to 95 °C at a rate of 5 °C/min, annealed (95 to 5 °C, at a rate of 0.2 °C/min), and again melted (5 to 90 °C, at a rate of 0.2 °C/min), and the samples were brought back to 25 °C at a rate of 5 °C/min. During melting and annealing, the absorbance of each solution was monitored at the following wavelengths: 260, 280, and 284 nm. The second melting stage was used for calculating melting temperature.

CD Spectroscopy. All CD experiments were conducted at 15 °C on a JASCO J-810 spectropolarimeter equipped with a thermoelectrically controlled cell holder. A quartz cell with a 1 cm path length was used in the CD studies. CD spectra were recorded as an average of 3 scans from 220 to 320 nm with data recorded in 1 nm increments with an averaging time of 2 s. The hybrid duplex solution was incubated at 4 °C for 16 h before CD titration. After each addition of 5 μL of neomycin (1 mM) to a 2 mL solution of hybrid duplex (10 μM per duplex), the solution was inverted 3 times to ensure thorough mixing and incubated for 3 min prior to scanning. Buffer conditions for CD titration are as follows: 10 mM sodium cacodylate, 0.5 mM EDTA, 60 mM total Na^+, and pH 6.0.

ITC Measurements. Isothermal titration calorimetric measurements were performed at 10 °C on a MicroCal VP-ITC (MicroCal, Inc.; Northampton, MA). In a typical experiment, 5

Scheme 1[a]



[a] Reagents and conditions: (i) (a) Neo−S-CH_2CH_2SCN, DMAP, pyridine (76%); (ii) $(CF_3CO_2)O$, *i*-Pr_2EtN, CH_2Cl_2 (75%); (iii) TBAF, DMF; and then DMTrCl, pyridine, DMAP (78%); (iv) $NCCH_2CH_2OP[N(i\text{-}Pr)_2]_2$, bis(diisopropylammonium) tetrazolide and CH_2Cl_2 (89%).

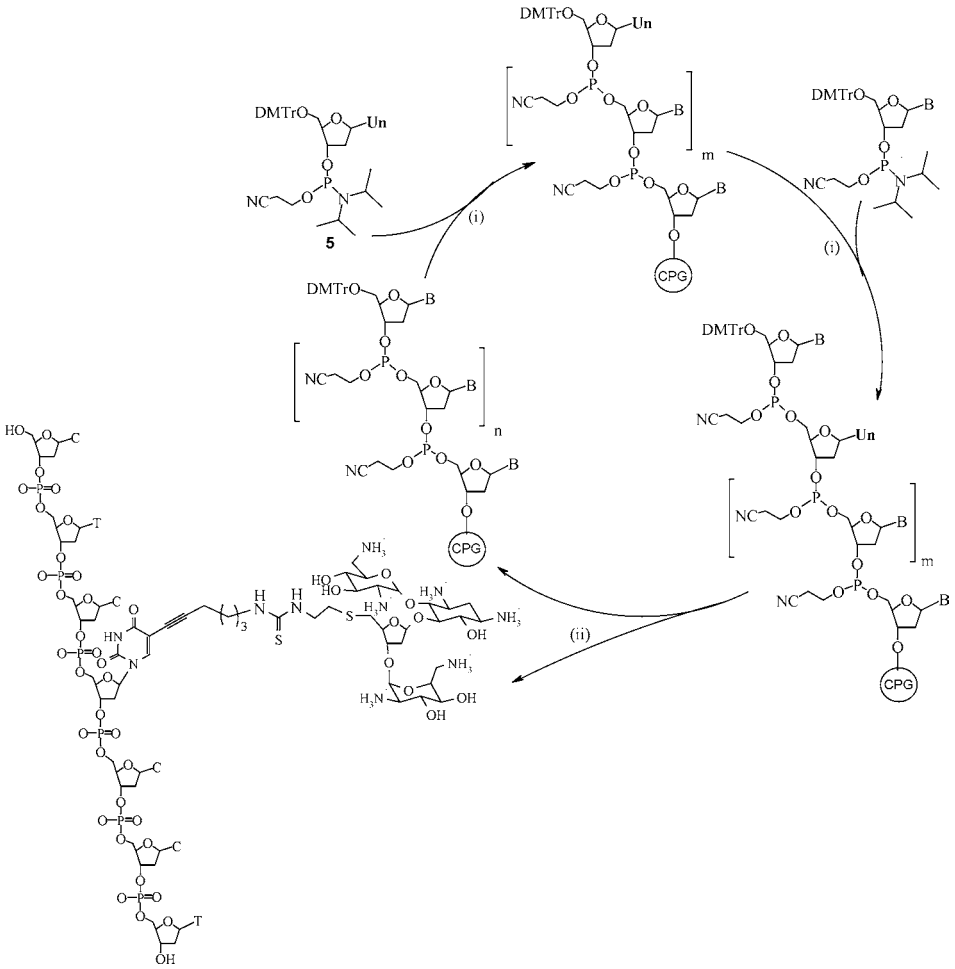
μL aliquots of 200 μM single strand were injected from a rotating syringe (300 rpm) into an isothermal sample chamber containing 1.42 mL of a RNA solution that was 20 μM per strand. Each experiment was accompanied by control experiments in which 5 μL aliquots of the single strands were titrated into buffer. The duration of each injection was 5.0 s, and the delay between each injection was 300 s. The initial delay prior to the first injection of 2 μL was 60 s. Each injection generated a heat burst curve (microcalories per second vs seconds). The area under each curve was determined by integration using the *Origin 5.0* software (MicroCal, Inc.; Northampton, MA) to obtain a measure of the heat associated with that injection. The buffer used in the experiment was 10 mM sodium cacodylate, 0.5 mM EDTA, 60 mM total Na^+, and pH 7.0.

Covalent Attachment of Neomycin to an Oligonucleotide. The oligonucleotide synthesis (1 μM) was carried out on Expedite Nucleic Acid Synthesis System (8909) using standard phosphoramidite chemistry (*51*). The coupling of deoxyuridine−neomycin conjugate 6 (0.2 M) to the oligomer was carried out for 30 min. After the oligomer synthesis, the CPG column was dried using argon gas. Then, the conjugate was detached from the solid support using NH_4OH, and the resulting solution was evaporated. The lyophilized sample was treated with 1 mL of 1,4-dioxane solution containing 3% CF_3CO_2H and 1% *m*-cresol (v/v/v %). After 30 min, the conjugate (Scheme 2) was precipitated with 10 mL of diethyl ether and the precipitate was washed with 3 × 10 mL of diethyl ether. The solution was evaporated, and the residue was resuspended in triethylammonium acetate buffer 10 mM and extracted twice with ether. Ether was removed, and the aqueous layer was dried under vacuum for 1 h. The solid was redissolved in 1 mL of water, purified by anion-exchange chromatography, and lyophilized.

RESULTS AND DISCUSSION

Design. Our design is based on a computer model of neomycin bound to the hybrid duplex major groove, shown in Figure 3. There are two ways of approaching the major groove: either through a 5′-OH conjugation or through conjugation with a base. Only one neomycin can be conjugated through 5′-OH conjugation, which left the 5-uridine position as the desirable site for conjugation of multiple neomycins. The linker length (12 atoms between 5-uridine and neomycin 5′-CH_2-) chosen by us allows enough flexibility for neomycin to fit into the major groove and maintain the favorable contacts. Our previous results show that the amino groups on rings I, II, and

Scheme 2. Synthesis of 7mer−Neo Conjugate N−Neo−C[a]



[a] (i) Deprotection with 4% trichloroacetic acid in CH_2Cl_2, and coupling with **3** in the presence of 1*H*-tetrazole followed by capping with acetic anhydride isn pyridine/THF solution, and oxidation with I_2 in THF/H_2O/pyridine solution; (ii) β-elimination followed by deprotection from the solid support using conc. NH_4OH; (c) 1,4-dioxane solution containing 3% CF_3CO_2H and 1% *m*-cresol (v/v/v %).

IV (Figure 1) of neomycin are necessary in stabilizing and recognizing various nucleic acid forms (aminoglycosides without any of these amines do not stabilize A-form structures as efficiently) (*20*).

Synthesis. On the basis of prior results mentioned above, the 5″-OH on ring III of neomycin was modified to neomycin isothiocyanate **2** as described in our earlier report (*42*). The precursor **1** was prepared from 2′-deoxyuridine by following a literature procedure (*52*). Then, neomycin isothiocyanate **2** was coupled with hexynylamino group of the modified 2′-deoxyuridine **1** to give conjugate **3** with an isothiourea linkage (Scheme 1). The hydroxyl groups on the neomycin molecule need to be protected in order to use phosphoramidite chemistry. The literature survey shows that the hydroxyl groups on aminoglycosides can be protected with an acetyl group (*53*). Deacylation can be carried out at the end of the oligonucleotide-conjugate synthesis with aqueous ammonia treatment, which can also perform the following in a single step: cleavage of the oligonucleotide from the solid support and β-elimination. Thus, the hydroxyl groups on neomycin were protected with a trifluoroacetyl group to get acetylated neomycin **4** in 75% yields. Deprotection of *t*-butyl dimethylsilyl (TBDMS) groups on the sugar with tetrabutylammonium fluoride (TBAF) followed by protection of 5′-hydroxyl group with DMTr-Cl in the presence of DMAP in pyridine gave the required TBDMS-free compound **5** in 78% yield. Further reaction of compound **5** with 2-cyanoethyl-*N*,*N*,*N*′,*N*′-tetraisopropyl phosphoramidite in the presence of bis-(diisopropylammonium) tetrazolide gave phosphoramidite **6** in good yields (*54*). For synthesis and characterization of compounds **1**−**6**, please see Supporting Information.

After synthesizing phosphoramidite **6**, the 7mer oligonucleotide (Figure 1) was prepared on a CPG column using standard phosphoramidite synthesis protocols (Scheme 2) (*51*). After introducing three bases, the modified base was coupled with the oligonucleotide on the solid support for 30 min, which was followed by the addition of the remaining three bases. Then, the conjugate was detached from the solid support using NH_4OH and purified by preparative reverse phase HPLC using a triethylammonium acetate buffer. The dried sample was treated with 1,4-dioxane solution containing 3% CF_3CO_2H and 1% *m*-cresol (v/v/v %). After 30 min, the deprotected conjugate was precipitated and washed with excess diethyl ether. The deprotected conjugate was finally purified by preparative anion exchange HPLC using a Tris-HCl buffer. As shown in Figure 4, neomycin-conjugated DNA elutes faster than the unmodified DNA. The identity of the conjugate (N-dY) was confirmed by MALDI−TOF mass spectrometry (MS (MALDI−TOF) *m*/*z* calcd $[M + H]^+$ 2795, found −2796.21, Figure 5).

Evidence of Incorporation of a Modified Base. The base composition of the conjugate was determined by complete enzymatic hydrolysis using snake-venom phosphodiesterase followed by alkaline phosphatase and subsequent reverse phase HPLC chromatography. The modified and unmodified oligonucleotides (0.2 A_{260} unit) were subjected to digestion with snake venom phosphodiesterase (10 units/mL) and alkaline phosphatase (100 units/mL) in 50 μL of 50 mM Tris-HCl buffer

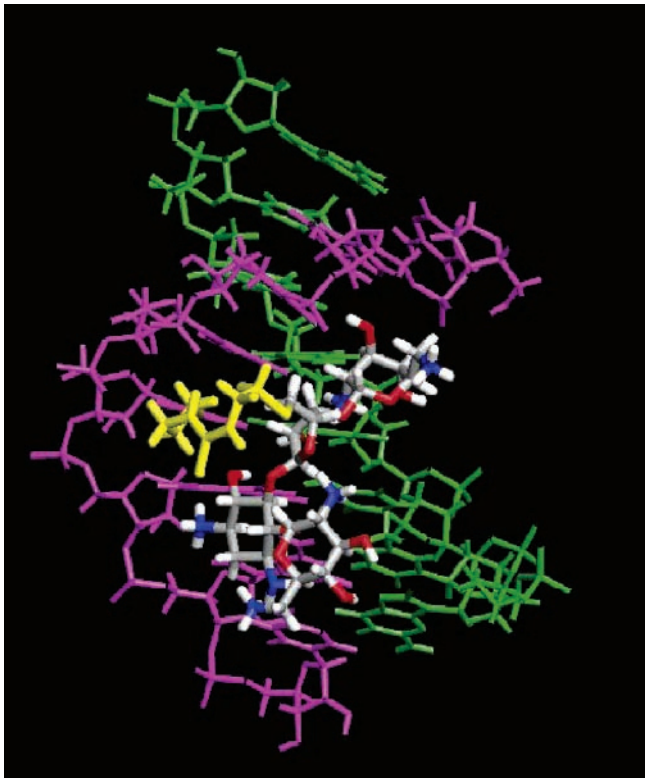


Figure 3. A model of neomycin−7mer DNA conjugate. The linker is shown in yellow and neomycin is shown in atom colors. The molecule was generated from a NMR solution structure file (PDB: 124D). The structure was optimized with *Maestro* program using the AMBER* force field to a gradient of 0.05 kJ/mol Å. The continuum GB/SA model of water, as implemented in *MacroModel*, has been used in all calculations. The force field atomic charges were used for the hybrid duplex. Neomycin was built and optimized in *MacroModel* as described previously (*21*).

(pH 7.2) containing 10 mM $MgCl_2$ at 37 °C for 24 h. The reaction mixtures were analyzed by reverse phase HPLC. As shown in Figure 6, an extra peak appears at approximately 10 min, which integrates to a base ratio of 1 (X = dU−neomycin conjugate) compared to base ratio of 4 (dC) to 2 (dT). In the unmodified DNA, only two peaks elute, with ratios of 4(dC)/3(dT).

Spectroscopic Studies of Interaction of Single Strand RNA with N−Neo Conjugate. We then investigated using UV thermal denaturation studies to determine if the stabilization shown by neomycin can also be observed with the neomycin−DNA conjugate. Covalent conjugation of a large molecule like neomycin can easily lead to unfavorable base/backbone contacts, if the molecule is not placed in the major groove with needed flexibility. The thermal denaturation of the rR•dY1 duplex (Scheme 3) in the absence and presence of 4 μM of neomycin was carried out in the presence of various concentrations of sodium ions (Table 1). In the absence of NaCl, the hybrid duplex (rR•dY1) melts at 26.3 °C. As the NaCl concentration was increased (0−100 mM), the T_m of the hybrid duplex increased from 26.3 °C to 30.0 °C. With 60 mM NaCl, the hybrid duplex showed a T_m of 28.1 °C. The presence of 4 μM of neomycin at 60 mM NaCl increases the T_m of the hybrid duplex (rR•dY) by 3.2 °C (Figure 7). When the DNA strand (dY1) was replaced with the modified oligonucleotide−neomycin conjugate (N-dY), the ΔT_m of the hybrid duplex (rR•N-dY) was 6.9 °C (with 60 mM NaCl) compared to the hybrid duplex (rR•dY1) without neomycin. Control experiments with just the amino linker led to a 1.8 °C change in T_m (see Supporting Information).

Sequence Specificity of the Conjugate. The effect of neomycin on the presence of a mismatch in this duplex (mismatch present on strand-rR^1) was also carried out. The mismatch was chosen on the RNA base which is complementary to the modified base. The presence of a single mismatch on the RNA strand decreases the melting temperature of the hybrid duplex (rR^1•dY1) from 35.3 °C to 8 °C when there is 4 μM of neomycin and 60 mM NaCl present in the solution. The mismatch penalty was similarly observed with the hybrid duplex (rR^1•N-dY) (with neomycin−oligonucleotide conjugate (N-dY) as one of the DNA strands) showing a T_m of 8 °C. This clearly suggests that neomycin's presence does not disrupt the Watson−Crick hybridization and the stabilization seen by neomycin is dependent on the retention of this fidelity leading to the A-form hybrid duplex.

Conformation of the Resulting Hybrid Duplex: Circular Dichroism (CD) Studies. The interaction of the aminoglycoside with hybrid nucleic acids can be monitored by CD spectroscopy. Depending upon the nature of the spectrum obtained from the CD scan, one can predict whether the complex exists in A-, B-, or canonical forms. The literature shows the preference of aminoglycosides for nucleic acids with A-like conformation (*55*−*58*). In some cases, transition of B- to A-conformation has also been observed with aminoglycosides, a phenomenon observed with cationic ligands such as spermine and $Co(NH_3)_6^{3+}$ (*59*, *60*). In a recent report, a complex formed between an 8-base-pair hybrid duplex and paramomycin was shown to exist in an A-like canonical conformation (*61*). Our earlier competition dialysis results have shown the preference of neomycin conjugates for A-form nucleic acids. The CD spectra of both the hybrid duplexes ((rR•dY1 and (rR•N-dY) were therefore analyzed. The spectra show that the conjugate shifts the maximum in the CD spectrum from 275 nm to 271 nm when compared to nonconjugated hybrid duplex (Figure 8). This observation suggests that the conjugate hybrid duplex prefers to be in canonical A-form (*61*−*64*) and retains the form exhibited by the unmodified RNA•DNA hybrid duplex.

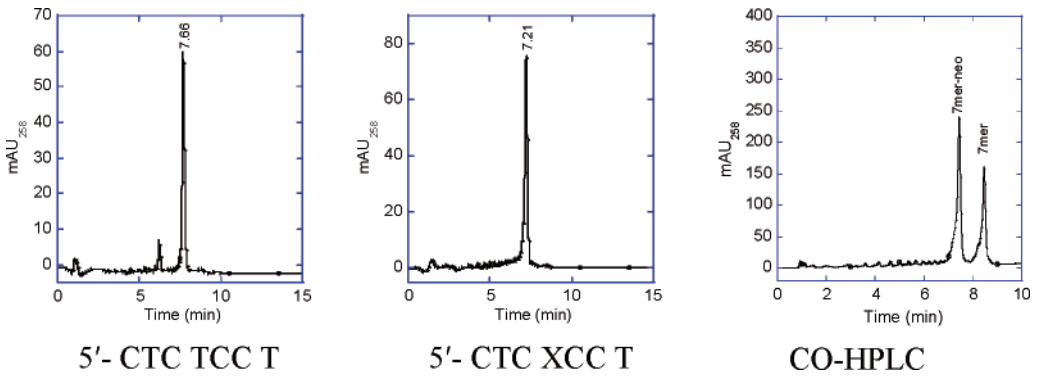


Figure 4. Conditions. Buffer A: 25 mM tris-HCl and 1 mM EDTA, pH = 8.0. Buffer B: buffer A + 1 M $NaClO_4$, pH = 8.0. 2% buffer B in buffer A for 2 min; 2−40% during 15 min; flow rate was 0.75 mL/min. X corresponds to deoxyuridine−neomycin conjugate base.

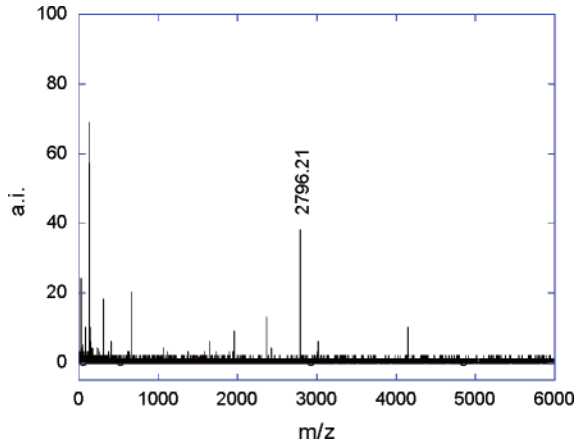


Figure 5. MALDI-TOF profile of 7mer−neomycin conjugate recorded with picolinic acid as the matrix and ammonium tartarate as the co-matrix.

Thermodynamic Basis of Interaction of Neomycin with the Target: Isothermal Titration Calorimetry. The effect of neomycin binding to the host rR•dY duplex was also studied using ITC experiments. The experiment was conducted at 15 °C in sodium cacodylate buffer at pH 6.0. Each injection gave the corresponding heat burst curve, and integration of the areas under these curves corresponds to the associated injection heats. These injection heats were subtracted from the dilution heats, which were obtained by two separate blank titrations of the corresponding drug vs buffer and the duplex vs buffer.

The thermodynamic properties for the binding of the conjugate N-dY with RNA (rR) were determined with the help of isothermal calorimetry. Monophasic transition was observed when N-dY conjugate was titrated against rR, and the injection heat data was fit with a model for a single binding site (Figure 9). For comparison, a titration of rR against nonconjugated DNA (dY1) was also carried also out, and the results are presented in Table 2.

The results show that rR single strand prefers to form the duplex approximately two times more with the N-dY conjugate than the nonconjugated dY single strand. A 2-fold change

Scheme 3. Base Sequences Used in the Present Study[a]

rY : 5'-r(C U C U C C U)
rR : 3'-r(G A G A G G A)
rR[1] : 3'-r(G A G U G G A)
dR : 3'-d(G A G A G G A)
dY1 : 5'-d(C T C T C C T)
dY2 : 5'-d(T C C T C T C)
N-dY : 5'-d(C T C X C C T)

[a] X indicates the presence of neomycin conjugated to 2′-deoxyuridine at the 5-position.

Table 1. UV Melting Profiles of the 7-mer Hybrid Duplex in the Presence of Various Concentrations of NaCl[a]

		T_m (°C)		
	concn of NaCl (mM)	without neomycin	with 4 μM neomycin	with N−Neo−C
1	0	26.3	30.0	32.1
2	10	27.1	31.1	32.1
3	25	27.1	31.1	32.3
4	60	28.1	31.3	35.0
5	100	30.0	31.0	36.1

[a] Solution conditions: [DNA] = 4 μM per strand; 10 mM sodium cacodylate buffer, 0.5 mM EDTA, pH 7.0. Samples were heated from 5 to 90 °C at 0.2 °C/min, and were brought back to 20 °C at a rate of 5 °C/min.

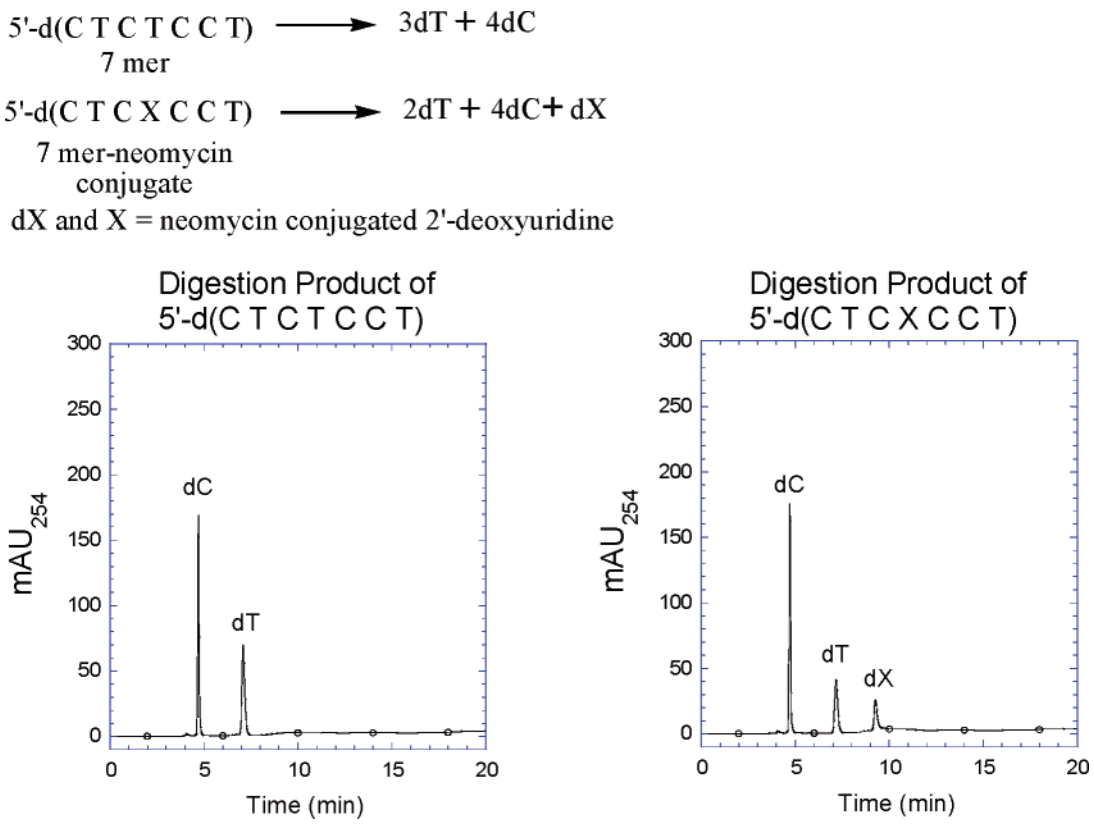


Figure 6. Conditions. Buffer A: 100 mM triethylammonium acetate and 5% of acetonitrile. Buffer B: 95% of acetonitrile and 5% of 100 mM triethylammonium acetate, pH = 7.0; 1−10% of buffer B over buffer A during 15 min, flow rate was 0.5 mL/min; 10−23% during 8 min, flow rate was 1.0 mL/min.

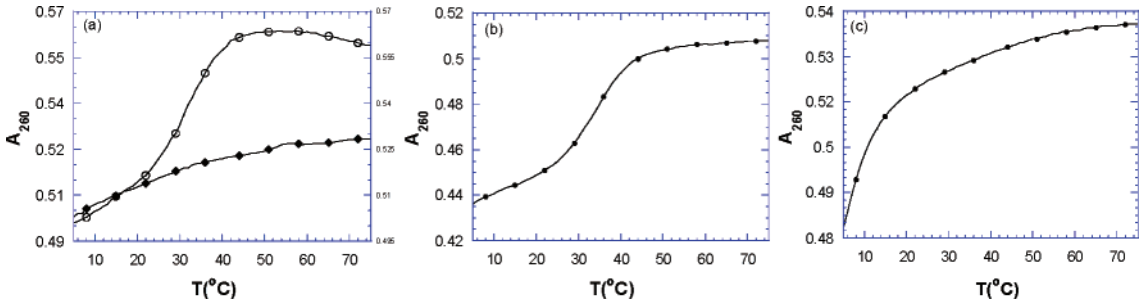


Figure 7. UV melting profiles of (a) rR•dY1 hybrid duplex in the absence (filled squares) and presence of 4 μM of neomycin (open circles); (b) rR•N-dY hybrid duplex; (c) rR^1•N-dY hybrid duplex. The spectra were recorded at 260 nm in the presence of 60 mM Na^+ ion concentration. [DNA] = 4 μM/strand. Buffer conditions: 10 mM sodium cacodylate, 0.1 mM EDTA, pH 7.0. The melting rate was 0.2 °C/min.

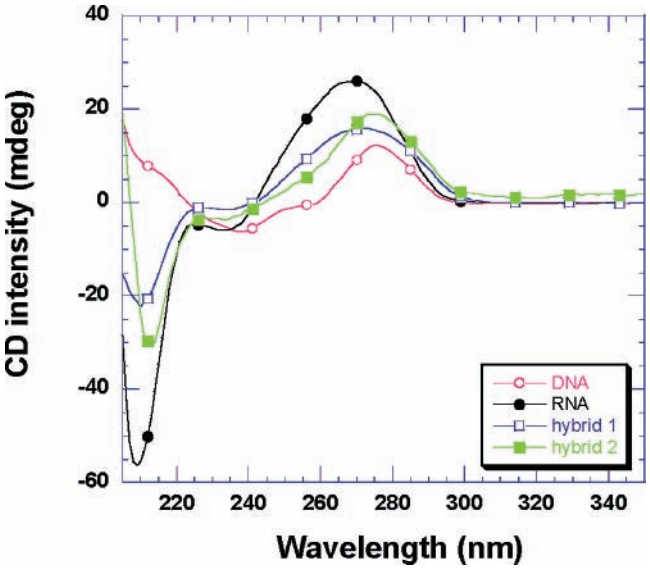


Figure 8. CD scans of 10 μM DNA duplex (dR·dY1, open circle), RNA duplex (rR·rY, filled circle), hybrid 1 (rR·N-dY, open square), and hybrid 2 (rR·dY1, filled square) at 10 °C. Buffer conditions: 10 mM sodium cacodylate, 0.5 mM EDTA, 60 mM total Na^+, and pH 7.0.

reflects the synergistic effect of DNA and covalently bound neomycin on the duplex structure. The increased stability of the duplex is driven mainly by a larger and more negative enthalpy {$\Delta\Delta H_{obs} = -7.21$ kcal/mol ($\Delta H_{neomycin\ conjugated} - \Delta H_{nonconjugated}$)}. This increase in enthalpy matches the enthalpy of interaction of aminoglycoside binding to the hybrid duplex (*61*). Interestingly, lowering the pH (to pH 6.0) leads to a decrease in K_a, such that the effect of neomycin conjugation is almost negligent (please see Supporting Information). Normally, when neomycin binds to a nucleic acid target, loss of pH leads to a lowering of binding-induced protonation (less favorable enthalpy of binding), but that is compensated by a favorable entropy such that the overall affinity of the drug to nucleic acid decreases slightly as the pH is lowered (please see Supporting Information) (*65*). Conjugation of neomycin to DNA in N−Neo−Cs leads to a similar decrease in $\Delta\Delta H$ (−7.2 kcal/mol at pH 7.0 to −5.5 kcal/mol at pH 6.0), but covalent attachment of neomycin does not allow for a favorable change in entropy as the pH is lowered. The unfavorable entropy changes in binding are dominated by the binding of larger DNA oligomer to its RNA target and are affected almost equally for dY1 and N-dY binding when the pH is lowered. The binding results of N-dY to RNA is also of interest in light of the general problem of the attribution and additivity of the binding free energies of ligand substituents. In general, if a ligand molecule A and ligand molecule B bind to a receptor, ligand A−B is then expected to bind so that the binding constant of A−B equals the product of two individual binding constants. DNA (dY) binds to RNA with 100 nM affinity, whereas neomycin shows very little binding to small single strand RNA. Therefore, the conjugation of the two, as observed here, is not expected to result in a major change in DNA to RNA binding constant at room temperature. The increase in T_m of the duplex, as seen with the effect of neomycin on the hybrid duplex, is retained with this conjugation. Neomycin binding to the target is therefore dependent on the ability of the single strand DNA to bind single strand RNA and form the hybrid duplex. A corollary to the discussion is also that neomycin conjugation to DNA is not likely to result in a lack of sequence specificity in RNA binding. We have previously shown the ability of neomycin to stabilize DNA and RNA triplexes as well (*27*). We therefore investigated if conjugation of neomycin to DNA using this linker will allow for triplex stabilization (dY1•rR•dY2). Addition of a third strand DNA or RNA, in the absence of neomycin, does not result in the formation of the triplex, since such triplexes only form with much longer sequences in high salt conditions. We have previously shown the ability of neomycin to induce intermolecular DNA triplexes with at least 16 base pairs (*26*). Addition of high concentrations of neomycin did not induce the formation of the 7-base-pair triplex (dY1•rR•dY2 or dY1•dY•dY2). When the studies were conducted with neomycin-linked DNA, no change in the T_m (UV or CD melting; please see Supporting Information) was observed. These results substantiate our model where a shorter linker, such as used here, allows a better fit of neomycin to the hybrid duplex, whereas longer linkers are better suited for reaching into the triplex Watson−Hoogsteen groove (*26*). The short size of the triplex also contributes to its instability, and more direct comparisons of duplex vs triplex stabilization can only be carried out with longer sequences. Nevertheless, using the appropriate linker and sequence design, one can, in principle, make the N−Neo−Cs specific for targeting a single strand RNA or a duplex DNA/RNA target. Additionally, variation of linker lengths in future studies are also likely to lead to much larger affinity increases per neomycin conjugation.

CONCLUSION

To investigate the advantage of nucleic acid based specificity coupled with aminoglycoside charge/shape complementarity, we have initiated the development of aminoglycoside−nucleic acid conjugates (N−Ag−Cs) (*42*, *43*, *66*, *67*). This report focuses on the development of such conjugates and their binding to a biologically relevant target—ribosomal RNA.

In conclusion, we have synthesized a modified oligonucleotide, where an aminoglycoside is covalently linked to one of the bases of a 7-base-long oligonucleotide. When we began this work, there was considerable doubt that a large molecule such as neomycin can be placed in the major groove of an RNA duplex using a covalent linkage. This report is the first of its kind that shows the ability of such a large covalently linked

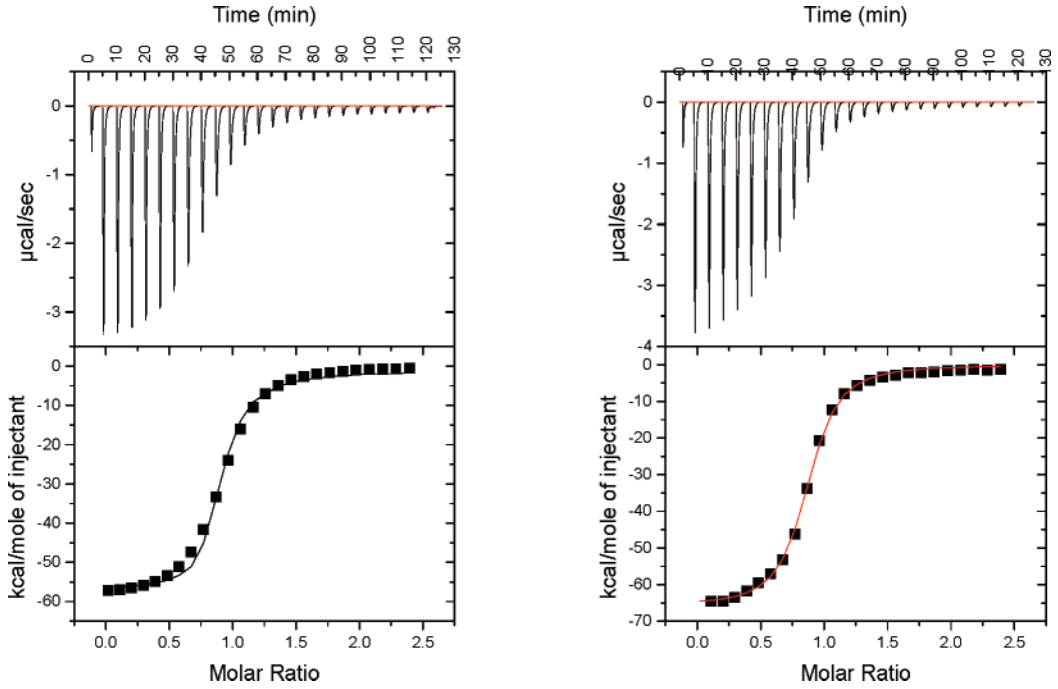


Figure 9. ITC profile of rR single strand titrated against (a) dY single strand (b) neomycin conjugate (N-dY) at 10 °C and pH 7.0 in sodium cacodylate buffer. Buffer conditions: 10 mM sodium cacodylate, 0.1 mM EDTA, pH 7.0 and 60 mM total Na^+ ions. Each heat burst curve is a result of a 10 μL injection of 200 μM of rR into 15 μM of N-dY solution. A plot of corrected ITC injection heats as a function of the [rR]/[N-dY] ratio (r_{dup}). The heats were derived by subtraction of the heats obtained by the titration of rR SS against the N-dY SS with the heats obtained by blank titration of the corresponding buffer vs buffer. The data points reflect the experimental injection heats, while the line denotes calculated fit using a model for one set of binding.

Table 2. Binding Parameters for the Complexation of the rR SS (single strand) with N−dY SS in Cacodylate Buffer at pH 7.0 and a Temperature of 10 °C Obtained from ITC

duplex	N	K_a (M^{-1})	ΔH_{obs} (kcal/mol)	$T\Delta S$ (kcal/mol)
rR•dY	0.97 ± 0.01	$2.8 \times 10^6 \pm 3.8 \times 10^5$	-58.7 ± 0.9	−50.4
rR•N-dY	0.93 ± 0.01	$5.0 \times 10^6 \pm 2.3 \times 10^5$	-65.9 ± 0.5	−54.5

carbohydrate (neomycin) to aid in RNA•DNA hybrid complexation. In addition, we have demonstrated that the N−Neo− conjugate and a 7-base-long RNA sequence present in the α-sarcin loop can form a stable hybrid duplex. The stability of the rR•dY1 hybrid duplex with 1 equiv of neomycin is comparable to the stability of the rR•N-dY hybrid duplex. The presence of a single mismatch decreases the melting temperature of both neomycin conjugated and nonconjugated hybrid duplexes. This is an important finding, as it supports the fact that association of the conjugate is driven by DNA−RNA base-pair association and not through non-sequence-specific electrostatic interactions between neomycin and the phosphodiester linkages. The linker length used here does not induce the formation of the short triplexes and will thus be specific for RNA targeting as opposed to duplex DNA targeting. Since the formation of such hybrid duplexes can be used to control gene expression by inhibition of the steps of translation, slicing, or by activation of RNase H leading to degradation of the mRNA, these conjugates have potential applications that include drug and oligonucleotide delivery to a specific RNA site.

The design, construction, and preliminary analysis of a new class of carbohydrate−DNA conjugates, which we term nucleoaminoglycoconjugates (N−Ag−C), has been described. The example shown here—a nucleoneomycinconjugate (N−Neo−C)—illustrates that these aminoglycoside−DNA hybrids are efficiently synthesized, chemically stable, and behave similarly to an unmodified DNA strand in solution. The synthetic methodology described here allows for inclusion of any number of aminoglycoside (neomycin) molecules per oligonucleotide. These conjugates can provide a platform for the development of a new form of hybrid biomaterials. They combine the unique specificity of nucleic acids and the recognition/binding ability of the aminoglycosides. N−Neo−Cs could have enormous potential in oligonucleotide therapeutic strategies (duplex as well as triplex approaches) and in the engineering of novel DNA-based materials. These applications will be further investigated and reported in due course.

ACKNOWLEDGMENT

Financial support for this work was provided by NSF-CAREER (CHE/MCB-0134972) awarded to D.P.A.

Supporting Information Available: UV and CD scans/melts, synthesis and characterization of intermediates (23 pages). This material is available free of charge via the Internet at http://pubs.acs.org.

LITERATURE CITED

(1) Recht, M. I., Fourmy, D., Blanchard, S. C., Dahlquist, K. D., and Puglisi, J. D. (1996) RNA sequence determinants for aminoglycoside binding to an A-site rRNA model oligonucleotide. *J. Mol. Biol. 262,* 421−36.

(2) Purohit, P., and Stern, S. (1994) Interactions of a small RNA with antibiotic and RNA ligands of the 30S subunit. *Nature (London) 370,* 659−62.

(3) Davies, J., and Davis, B. D. (1968) Misreading of ribonucleic acid code words induced by aminoglycoside antibiotics. The effect of drug concentration. *J. Biol. Chem. 243,* 3312−6.

(4) von Ahsen, U., and Noller, H. F. (1993) Footprinting the sites of interaction of antibiotics with catalytic group I intron RNA. *Science 260,* 1500−3.

(5) Hoch, I., Berens, C., Westhof, E., and Schroeder, R. (1998) Antibiotic inhibition of RNA catalysis: Neomycin B binds to the catalytic core of the td group I intron displacing essential metal ions. *J. Mol. Biol. 282*, 557−569.

(6) Mikkelsen, N. E., Brannvall, M., Virtanen, A., and Kirsebom, L. A. (1999) Inhibition of RNase P RNA cleavage by aminoglycosides. *Proc. Natl. Acad. Sci. U.S.A. 96*, 6155−60.

(7) Walter, F., Murchie, A. I., Thomson, J. B., and Lilley, D. M. (1998) Structure and activity of the hairpin ribozyme in its natural junction conformation: Effect of metal ions. *Biochemistry 37*, 14195−203.

(8) Earnshaw, D. J., and Gait, M. J. (1998) Hairpin ribozyme cleavage catalyzed by aminoglycoside antibiotics and the polyamine spermine in the absence of metal ions. *Nucleic Acids Res. 26*, 5551−61.

(9) Tor, Y., Hermann, T., and Westhof, E. (1998) Deciphering RNA recognition: aminoglycoside binding to the hammerhead ribozyme. *Chem. Biol. 5*, R277−83.

(10) Stage, T. K., Hertel, K. J., and Uhlenbeck, O. C. (1995) Inhibition of the hammerhead ribozyme by neomycin. *RNA 1*, 95−101.

(11) Clouet-d'Orval, B., Stage, T. K., and Uhlenbeck, O. C. (1995) Neomycin inhibition of the hammerhead ribozyme involves ionic interactions. *Biochemistry 34*, 11186−90.

(12) Rogers, J., Chang, A. H., von Ahsen, U., Schroeder, R., and Davies, J. (1996) Inhibition of the self-cleavage reaction of the human hepatitis delta virus ribozyme by antibiotics. *J. Mol. Biol. 259*, 916−25.

(13) Chia, J. S., Wu, H. L., Wang, H. W., Chen, D. S., and Chen, P. J. (1997) Inhibition of hepatitis delta virus genomic ribozyme self-cleavage by aminoglycosides. *J. Biomed. Sci. 4*, 208−216.

(14) Tok, J. B. H., Cho, J., and Rando, R. R. (1999) Aminoglycoside antibiotics are able to specifically bind the 5′-untranslated region of thymidylate synthase messenger RNA. *Biochemistry 38*, 199−206.

(15) Gan, H. H., Pasquali, S., and Schlick, T. (2003) Exploring the repertoire of RNA secondary motifs using graph theory; implications for RNA design. *Nucleic Acids Res 31*, 2926−43.

(16) Faber, C., Sticht, H. Schweimer, K., and Rosch, P. (2000) Structural Rearrangements of HIV-1 Tat-Responsive RNA upon Binding of Neomycin B. *J. Biol. Chem. 275*, 20660−6.

(17) Zapp, M. L., Stern, S., and Green, M. R. (1993) Small molecules that selectively block RNA binding of HIV-1 Rev protein inhibit Rev function and viral production. *Cell 74*, 969−78.

(18) Mei, H.-Y., Galan, A. A., Halim, N. S., Mack, D. P., Moreland, D. W., Sanders, K. B., Truong, H. N., and Czarnik, A. W. (1995) Inhibition of an HIV-1 Tat-derived peptide binding to TAR RNA by aminoglycoside antibiotics. *Bioorg. Med. Chem. Lett. 5*, 2755−60.

(19) Hermann, T., and Westhof, E. (1998) Saccharide-RNA recognition. *Biopolymers 48*, 155−65.

(20) Arya, D. P., and Coffee, R. L., Jr. (2000) DNA triple helix stabilization by aminoglycoside antibiotics. *Bioorg. Med. Chem. Lett. 10*, 1897−9.

(21) Arya, D. P., Xue, L., and Tennant, P. (2003) Combining the Best in Triplex Recognition: Synthesis and Nucleic Acid Binding of a BQQ-Neomycin Conjugate. *J. Am. Chem. Soc. 125*, 8070−8071.

(22) Hermann, T., and Westhof, E. (1998) Saccharide-RNA recognition. *Biopolymers 48*, 155−165.

(23) Chow, C. S., and Bogdan, F. M. (1997) A structural basis for RNA-ligand interactions. *Chem. Rev. 97*, 1489−1514.

(24) Tor, Y., Hermann, T., and Westhof, E. (1998) Deciphering RNA recognition: aminoglycoside binding to the hammerhead ribozyme. *Chem. Biol. 5*, R277−R283.

(25) Arya, D. P., Xue, L., and Willis, B. (2003) Aminoglycoside preference is for A-form nucleic acids, not just RNA: Results from a competition dialysis study. *J. Am. Chem. Soc. 125*, 10148−10149.

(26) Arya, D. P., Micovic, L., Charles, I., Coffee, R. L., Jr., Willis, B., and Xue, L. (2003) Neomycin binding to DNA triplex Watson-Hoogsteen (W-H) groove: A model. *J. Am. Chem. Soc. 125*, 3733−3744.

(27) Arya, D. P., Coffee, R. L., Jr. and Charles, I. (2001) Neomycin-induced hybrid triplex formation. *J. Am. Chem. Soc. 123*, 11093−11094.

(28) Arya, D. P. (2005) In *Topics Curr. Chem: DNA Binders* (Chaires, J. B. and Waring, M. J., Eds.) pp 149−178, Springer-Verlag, Heidelburg.

(29) Lichtenstein, J., and Cohen, S. S. (1960) Nucleotides derived from enzymic digests of nucleic acids of T2, T4 and T6 bacteriophages. *J. Biol. Chem. 235*, 1134−41.

(30) Lehman, I. R., and Pratt, E. A. (1960) Structure of the glucosylated hydroxymethylcytosine nucleotides of coliphages T2, T4 and T6. *J. Biol. Chem. 235*, 3254−9.

(31) Ehrlich, M., and Ehrlich, K. C. (1981) A novel, highly modified, bacteriophage DNA in which thymine is partly replaced by a phosphoglucuronate moiety covalently bound to 5-(4′, 5′-dihydroxypentyl)uracil. *J. Biol. Chem. 256*, 9966−72.

(32) Borst, P., and van Leeuwen, F. (1997) b-D-glucosyl-hydroxymethyluracil, a novel base in African trypanosomes and other Kinetoplastida. *Mol. Biochem. Parasitol. 90*, 1−8.

(33) van Leeuwen, F., Kieft, R., Cross, M., and Borst, P. (2000) Tandemly repeated DNA is a target for the partial replacement of thymine by b-d-glucosyl-hydroxymethyluracil in *Trypanosoma brucei*. *Mol. Biochem. Parasitol. 109*, 133−145.

(34) Kornberg, A., and Baker, T. A. (1992) *DNA Replication*, W. H. Freeman Co., New York.

(35) Gommers-Ampt, J. H., Van Leeuwen, F., de Beer, A. L. J., Vliegenthart, J., Dizdaroglu, M., Kowalak, J. A., Crain, P. F., and Borst, P. (1993) b-D-Glucosyl-hydroxymethyluracil: A novel modified base present in the DNA of the parasitic protozoan *T. brucei*. *Cell 75*, 1129−36.

(36) Van Leeuwen, F., Taylor, M. C., Mondragon, A., Moreau, H., Gibson, W., Kieft, R., and Borst, P. (1998) b-D-Glucosyl-hydroxymethyluracil is a conserved DNA modification in kinetoplastid protozoans and is abundant in their telomeres. *Proc. Natl. Acad. Sci. U.S.A. 95*, 2366−2371.

(37) Dubber, M., and Frechet, J. M. J. (2003) Solid-phase synthesis of multivalent glycoconjugates on a DNA synthesizer. *Bioconjugate Chem. 14*, 239−246.

(38) Akhtar, S., Hughes, M. D., Khan, A., Bibby, M., Hussain, M., Nawaz, Q., Double, J., and Sayyed, P. (2000) The delivery of antisense therapeutics. *Adv. Drug Delivery Rev. 44*, 3−21.

(39) Liang, W., Shi, X., Deshpande, D., Malanga, C. J., and Rojanasakul, Y. (1996) Oligonucelotide targeting to alveolar macrophages by mannose receptor mediated endocytosis. *Biochim. Biophys. Acta 1279*, 227−234.

(40) Biessen, E. A. L., Vietsch, H., Rump, E. T., Fluiter, K., Kuiper, J., Bijsterbosch, M. K., and Berkel, T. J. C. V. (1999) Targeted delivery of oligodeoxynucleotides to parenchymal liver cells in vivo. *Biochem. J. 340*, 783−792.

(41) Napoli, S., Carbone, G. M., Catapano, C., Shaw, N., and Arya, D. P. (2005) Neomycin improves cationic lipid-mediated transfection of DNA in human cells. *Bioorg. Med. Chem. Lett. 15*, 3467−3469.

(42) Charles, I., Xue, L., and Arya, D. P. (2002) Synthesis of aminoglycoside-DNA conjugates. *Bioorg. Med. Chem. Lett. 12*, 1259−62.

(43) Charles, I., and Arya, D. P. (2005) Synthesis of neomycin-DNA/peptide nucleic acid conjugates. *J. Carbohydr. Chem. 24*, 143−157.

(44) Carter, A. P., Clemons, W. M., Brodersen, D. E., Morgan-Warren, R. J., Wimberly, B. T., and Ramakrishnan, V. (2000) Functional insights from the structure of the 30S ribosomal subunit and its interactions with antibiotics. *Nature (London) 407*, 340−8.

(45) Fourmy, D., Recht, M. I., Blanchard, S. C., and Puglisi, J. D. (1996) Structure of the A site of *Escherichia coli* 16S ribosomal RNA complexed with an aminoglycoside antibiotic. *Science 274*, 1367−71.

(46) Fourmy, D., Recht, M. I., and Puglisi, J. D. (1998) Binding of neomycin-class aminoglycoside antibiotics to the A-site of 16 S rRNA. *J. Mol. Biol. 277*, 347−62.

(47) Hausner, T. P., Atmadja, J., and Nierhaus, K. H. (1987) Evidence that the G2661 region of 23S rRNA is located at the ribosomal binding sites of both elongation factors. *Biochimie 69*, 911−23.

(48) Hill, W. E., Camp, D. G., Tapprich, W. E., and Tassanakajohn, A. (1988) Probing ribosome structure and function using short oligodeoxyribonucleotides. *Methods Enzymol. 164*, 401−19.

(49) Steitz, J. A., and Jakes, K. (1975) How ribosomes select initiator regions in mRNA: base pair formation between the 3′ terminus of 16S rRNA and the mRNA during initiation of protein synthesis in *Escherichia coli*. *Proc. Natl. Acad. Sci. U.S.A. 72*, 4734−8.

(50) Endo, Y., and Wool, I. G. (1982) The site of action of alpha-sarcin on eukaryotic ribosomes. The sequence at the alpha-sarcin cleavage site in 28 S ribosomal ribonucleic acid. *J. Biol. Chem. 257*, 9054−60.
(51) Beaucage, S. L., and Iyer, R. P. (1992) Advances in the synthesis of oligonucleotides by the phosphoramidite approach. *Tetrahedron 48*, 2223−311.
(52) Kahl, J. D., and Greenberg, M. M. (1999) Introducing structural diversity in oligonucleotides via photolabile, convertible C5-substituted nucleotides. *J. Am. Chem. Soc. 121*, 597−604.
(53) Tona, R., Bertolini, R., and Hunziker, J. (2000) Synthesis of aminoglycoside-modified oligonucleotides. *Org. Lett. 2*, 1693−6.
(54) Bannwarth, W. (1988) Solid phase synthesis of oligonucleotides containing phosphoramidate internucleotide linkages and their specific chemical cleavage. *Helv. Chim. Acta 71*, 1517.
(55) Xi, H., and Arya, D. P. (2005) Recognition of triple helical nucleic acids by aminoglycosides. *Curr. Med. Chem. Anticancer Agents 5*, 327−38.
(56) Arya, D. P., Coffee, R. L., Jr., Willis, B., and Abramovitch, A. I. (2001) Aminoglycoside-nucleic acid interactions: Remarkable stabilization of DNA and RNA triple helices by neomycin. *J. Am. Chem. Soc. 123*, 5385−5395.
(57) Willis, B., and Arya, D. P. (2006) Recognition of B-DNA by Neomycin-Hoechst 33258 Conjugates. *Biochemistry 45*, 10217−10232.
(58) Arnott, S., Bond, P. J., Selsing, E., and Smith, P. J. C. (1976) Models of triple-stranded polynucleotides with optimized stereochemistry. *Nucleic Acids Res. 3*, 2459−70.
(59) Robinson, H., and Wang, A. H. J. (1996) Neomycin, spermine and hexaamminecobalt(III) share common structural motifs in converting B- to A-DNA. *Nucleic Acids Res. 24*, 676−82.
(60) Xu, Q., Shoemaker, R. K., and Braunlin, W. H. (1993) Induction of B-A transitions of deoxyoligonucleotides by multivalent cations in dilute aqueous solution. *Biophys. J. 65*, 1039−49.
(61) Barbieri, C. M., Li, T.-K., Guo, S., Wang, G., Shallop, A. J., Pan, W., Yang, G., Gaffney, B. L., Jones, R. A., and Pilch, D. S. (2003) Aminoglycoside Complexation with a DNA.RNA Hybrid Duplex: The Thermodynamics of Recognition and Inhibition of RNA Processing Enzymes. *J. Am. Chem. Soc. 125*, 6469−6477.
(62) Ivanov, V. I., Minchenkova, L. E., Shchelkina, A. K., and Poletaev, A. I. (1973) Different conformations of double-stranded nucleic acid in solution as revealed by circular dichroism. *Biopolymers 12*, 89−110.
(63) Gray, D. M., Ratliff, R. L., and Vaughan, M. R. (1992) Circular dichroism spectroscopy of DNA. *Methods Enzymol. 211*, 389−406.
(64) Gray, D. M., and Ratliff, R. L. (1975) Circular dichroism spectra of poly[d(AC):d(GT)], poly[r(AC):r(GU)] and hybrids poly[d(AC):r(GU)] and poly[r(AC):d(GT)] in the presence of ethanol. *Biopolymers 14*, 487−98.
(65) Kaul, M., and Pilch, D. S. (2002) Thermodynamics of Aminoglycoside-rRNA Recognition: The Binding of Neomycin-Class Aminoglycosides to the A Site of 16S rRNA. *Biochemistry 41*, 7695−7706.
(66) Willis, B., and Arya, D. P. (2006) Major groove recognition of DNA by carbohydrates. *Curr. Org. Chem., Carbohydr. Drug Design 10*, 663−673.
(67) Willis, B., and Arya, D. P. (2006) An expanding view of aminoglycoside-nucleic acid interactions. *Adv. Carb. Chem. Biochem*, pp 263−314, Chapt. 6, Vol. 60.

BC060249R

Protein Delivery by the Cell-Penetrating Peptide YTA2

Helena Myrberg,*,† Maria Lindgren,‡ and Ülo Langel†

Department of Neurochemistry, Stockholm University, Svante Arrhenius v. 21A, SE-106 91 Stockholm, Sweden, and Cepep II AB, Box 45029, SE-104 30 Stockholm, Sweden. Received August 30, 2006; Revised Manuscript Received November 13, 2006

In most cases, the transport of cell-penetrating peptide (CPP) with a cargo molecule over the plasma membrane requires a cross-linking of the cargo molecule to the peptide. Lately, a method of cargo delivery, coincubation with CPP, has been applied. We have studied uptake and toxicity of the CPP, YTA2, in the Bowes human melanoma cell line and human MDA-MB-231 breast cancer cell line and compared the results with known cell-penetrating peptides. The results show that fluoresceinyl YTA2 is taken up by the Bowes cells with 3.23 nmol/mg protein and shows low membrane toxicity to the cells with an EC50 of 60 μM. Furthermore, we show that YTA2 is capable of delivering cargo proteins, such as β-galactosidase and tetramethyl rhodamine iso-thiocyanate (TRITC) labeled streptavidin into cells by coincubation. The delivery of TRITC-labeled streptavidin was quantified to 42.4 pmol streptavidin/mg protein. The delivery of proteins into the cells by mere coincubation is an advantage, since the chemical coupling between the CPP and the cargo molecule, which adds time-consuming synthesis and purification steps, can be omitted. In addition, the flexibility in CPP cargo delivery is increased.

INTRODUCTION

In the past decade, cell-penetrating peptides (CPPs[1]), also called protein transduction domains (PTDs), have drawn major attention for their capability to translocate the cellular membranes (for review, see ref 1). CPPs also have the aptitude of transporting conjugated cargoes over different cellular membranes both in vivo and in vitro (*2*, *3*). So far, most CPPs require a cross-linking to their cargo to be able to transport it inside the cell (*4*, *5*). In the case of a chemical coupling, it demands additional attention when synthesizing and purifying the peptide−cargo complexes and is therefore time-consuming. The presence of a conjugated peptide might also affect the cargo inside the cell. Morris et al. developed a new technique for protein delivery based on a peptide, Pep-1 (*6*). Pep-1 has the capability to deliver different peptides, proteins, and antibodies inside different cells, in vivo and in vitro, without any chemical coupling between the cargo and Pep-1 (*7*). The same group, Morris et al., has also developed other peptides, MPG and Pep-2, that have been shown to deliver nucleic acids, oligonucleotides and HypNA-*p*PNAs, respectively, by mere coincubation (*8*−*10*).

We have studied the uptake and toxicity of the CPP YTA2 (*11*) and compared the results with known CPPs. Interestingly, YTA2, like Pep-1, also has the capability to deliver proteins into cells by simply coincubation of the peptide−protein with the cells. The proteins that are used in this study are a 119 kDa subunit of β-galactosidase and TRITC-labeled streptavidin with a molecular weight of 66 kDa. β-Galactosidase is a protein consisting of four subunits. In this work, one 119 kDa subunit has been used. β-Galactosidase is the gene product of lacZ and catalyzes the hydrolysis of X-gal while blue color is produced (*12*). The cells that have been successfully transfected with β-galactosidase will, due to appearance of a blue color, be easily visualized by light microscope. The other protein used, streptavidin, is a tetramer that is a mainly neutral and a nonglycosylated protein. In this study, we have used TRITC-labeled streptavidin to quantify the uptake of YTA2 coincubated with the TRITC-labeled streptavidin.

The disclosure that YTA2 can deliver, e.g., proteins, inside cells by mere coincubation is an advantage, since the need of a chemical coupling between the CPP and the cargo molecule might no longer be necessary for transport over the cell membrane in vitro.

MATERIALS AND METHODS

Cell Culture. The human breast cancer cell line MDA-MB-231 was cultured in RPMI-1640 and Bowes human melanoma cells (ATCC CRL-9607) in MEM media with Glutamax I (InVitrogen, Sweden) supplemented with 10% fetal bovine serum, sodium pyruvate (1 mM), penicillin (100 U/mL), streptomycin (100 μg/mL), and 1% nonessential amino acids. All cells were incubated at 37 °C in 5% CO_2.

Quantitative Uptake of Peptide. Bowes and MDA-MB-231 cells (100 000 cells/well) was seeded on a 12-well plate 2 days before the experiment. On the day of the experiment, the cells were washed with HEPES-buffered Krebs Ringer solution (HKR) (2 × 1 mL) and exposed to drug solution (500 μL, 5μM) for 30 min at 37 °C. Cells were washed (2 × HKR) whereafter trypsin (200 μL) was added and incubated for 5 min at 37 °C. HKR was added (1000 μL), and cells were transferred to Eppendorf tubes and centrifuged (10 min, 1000 *g*). Cells were lysed in sodium hydroxide solution (0.1 M, 300 μL) for 45 min and centrifuged (10 min, 10 000 *g*). The fluorescence (492/518 nm) was measured with SPEKTRAmax GEMINI XS spectrofluorometric plate reader (Molecular Devices). The amount of internalized peptide was normalized against the amount of protein (Lowry BioRad, U.S.A.).

Membrane Integrity. The assay was performed using the CytoTox-ONE Homogeneous Membrane Integrity Assay (Prome-

* To whom correspondence should be addressed. Neurochemistry, Stockholm University, Svante Arrhenius v. 21 A, 106 91 Stockholm, Sweden, Tel: (+46-8-164196), Fax: (+46-8-161371), E-mail: helenam@neurochem.su.se.

† Stockholm University.

‡ Cepep II AB.

[1] Abbreviations: CPP, cell-penetrating peptide; Fl, fluoresceinyl; HKR, Hepes-buffered Krebs Ringer solution; PBS, phosphate buffered saline; RT, room temperature; TRITC, tetramethyl rhodamine isothiocyanate.

10.1021/bc060266g CCC: $37.00 © 2007 American Chemical Society
Published on Web 12/22/2006

ga, Madison, WI), which is based on the measurement of lactate dehydrogenase leaking from cells with damaged membrane. The cells were seeded on 12-well plates 2 days before the experiment, with 100 000 cells/well in 1 mL of the respective medium. On the day of the experiment, the cells were washed twice with 0.5 mL HKR and exposed to drug solution (500 μL, 5 μM), or 0.1% Triton X-100 in HKR (500 μL) for 30 min at 37 °C. Then, 100 μL of the exposure solution was transferred to a black polypropylene FluoroNunc plate, and CytoTox-ONE reagent (100 μL) was added. The mixture was incubated for 10 min at room temperature (RT), and fluorescence was measured (560/590 nm) in the spectrofluorometric plate reader.

Cell Viability. Bowes cells (20 000 cells/well) were seeded on a 48-well plate 2 days before the experiment. The cells were exposed to peptides in different concentrations in full media containing 1% FBS for 48 h at 37 °C. The plate was cooled to RT, and CellTiter-Glo Reagent (Promega) was added. The plate was incubated for 10 min at RT whereafter the luminescence was measured with SPEKTRAmax GEMINI XS spectrofluorometric plate reader (Molecular Devices).

Protein Transfection with β-Galactosidase. Cells (100 000 cells/well) were seeded the day before the experiment on a 24-well plate. β-Galactosidase (1 μL, 0.25 μg/μl) was mixed with phosphate buffered saline (PBS) (50 μL). Peptides (3.5 μL or 6 μL, 1 mM) were mixed with H_2O (50 μL). The β-galactosidase solution was mixed with the peptide solution and incubated for 30 min at RT. The cells were washed with PBS. The peptide−protein solution was added to the cells whereafter serum-free media (100 μL) was added and cells were incubated for 60 min at 37 °C. At this time, complete media (150 μL) was added to the cells, and incubation was continued for 90 min at 37 °C.

β-Galactosidase Staining. Cells were fixed and stained according to the β-galactosidase staining kit (Active Motif). Cells were fixed in PBS containing 0.7% formaldehyde and 0.05% glutaraldehyde for 10 min at RT. Cells were washed three times with PBS and stained with a solution of PBS containing potassium ferricyanide (40 mM), potassium ferrocyanide (40 mM), magnesium chloride (20 mM), and 2 mg/mL of X-gal for 90 min at 37 °C. Cells were studied under a phase-contrast microscope (Olympus) at 300× magnification and imaged using a CCD camera (Olympus DP50).

Quantitative Protein Transfection with TRITC-Labeled Streptavidin. Cells (100 000 cells/well) were seeded 2 days before experiment on a 12-well plate. TRITC-labeled streptavidin (purchased from Zymed Laboratories) (1 μL, 1 μg/μl) was mixed with PBS (100 μL). Peptides (3.5 μL, 1 mM) were mixed with H_2O (100 μL). The TRITC-labeled streptavidin solution was mixed with the peptide solution and incubated for 30 min at RT. The cells were washed with PBS (1 × 0.5 mL). The peptide−protein solution was added to the cells whereafter serum-free media (150 μL) was added, and the cells were incubated for 60 min at 37 °C. Complete media (200 μL) was added to cells, and incubation was continued for 90 min at 37 °C. Cells were washed (2 × PBS) whereafter trypsin (200 μL) was added and incubated for 5 min at 37 °C. PBS was added (1000 μL), and cells were transferred to Eppendorf tubes and centrifuged (10 min, 1000 *g*). Cells were lysed in sodium hydroxide solution (0.1 M, 300 μL) for 45 min and centrifuged (10 min, 10 000 *g*). The fluorescence (550/570 nm) was measured with SPEKTRAmax GEMINI XS spectrofluorometric plate reader (Molecular Devices). The amount of internalized peptide was normalized against the amount of protein (Lowry BioRad, U.S.A.).

RESULTS

Quantitative Uptake of Fluoresceinyl Peptides. The uptake of fluoresceinyl YTA2 was studied and compared with penetratin, *p*VEC, TP10, and Tat, well-characterized fluoresceinyl CPPs. Fluoresceinyl peptides at a concentration of 5 μM were added to cells and incubated at 37 °C for 30 min whereafter the amount of internalized peptide was normalized against the amount of total protein content (Figure 1). The uptake was studied in two different cell lines, Bowes human melanoma cell line and human MDA-MB-231 breast cancer cell line. For all studied peptides, the amount of internalized peptide is slightly higher in the MDA-MB-231 cells than in the Bowes cells, but the peptides show a similar pattern in both cell lines. For clarity, only the internalization into the Bowes cells will be discussed. The amount of internalized peptide is lowest, 0.064 nmol peptide/mg protein, for the Tat peptide, slightly higher for TP10 and penetratin with 1.57 and 2.32 nmol peptide/mg protein, respectively. The peptides internalizing with the highest amounts appear to be *p*VEC and YTA2 with 7.79 and 3.23 nmol peptide/mg protein, respectively. Since the amount of a peptide inside the cell may be connected to the toxicity of the peptide, we continued with two different membrane toxicity studies.

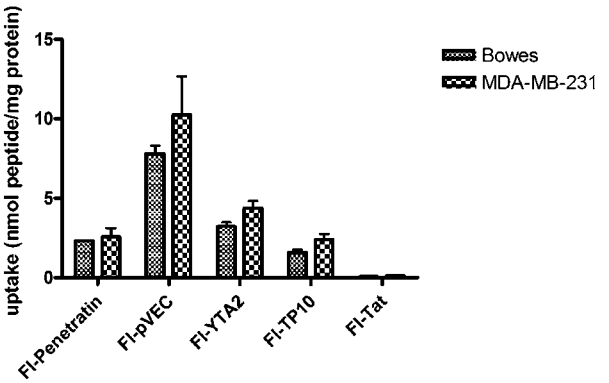


Figure 1. Uptake in nanomoles of fluoresceinyl (Fl) peptides in Bowes cells and MDA-MB-231 cells. Cells were exposed to a 5 μM peptide solution for 30 min whereafter the peptide attached to the cell membrane was removed by trypsination. Cells were lysed in sodium hydroxide solution, the fluorescence (492/518 nm) was measured, and the amount of internalized peptide was normalized against the amount of protein.

Lactate Dehydrogenase Leakage. To investigate if the cell-penetrating capacity was not due to toxicity of the peptides, two different toxicity assays were used. First, we studied the amount of disrupted membranes by means of the amount of leaked lactate dehydrogenase (LDH) in the HKR−peptide solution that was added to the cells. LDH is an enzyme that exists in the cytosole in eukaryotic cells. If LDH can be detected outside the cells, it is a mark of damaged cell membranes. The peptides were studied at 5 μM, and the LDH leakage of lysed cells was set to 100%. Figure 2 shows the Triton X-100-induced LDH leakage. The LDH leakage is studied in Bowes cells and MDA-MB-231 cells, and all studied peptides show the same pattern in both cell lines, but with a slightly higher effect in the MDA-MB-231 cells. Here, only the LDH leakage from the Bowes cells will be discussed. The peptides YTA2 and *p*VEC that had the highest amount of internalized peptides also show the highest LDH leakage with 5.56% and 1.66%, respectively. TP10, Penetratin, and Tat show less membrane toxicity with 1.63%, 0.59%, and 0.37%, respectively. This indicates that to some extent the membrane toxicity and the amount of internalized peptide are related to each other. The LDH leakage of Pep-1 was also studied and measured to only 0.47%. From a general point of view, an LDH leakage below 10% is no major membrane leakage (*13*).

Measurement of ATP Content. To investigate concentration-dependent toxicity, CellTiter-Glo has been used to study the amount of viable cells. This assay uses luciferase to measure the ATP content of the cells after incubation with the peptide in different concentrations (Figure 3). The ATP content is

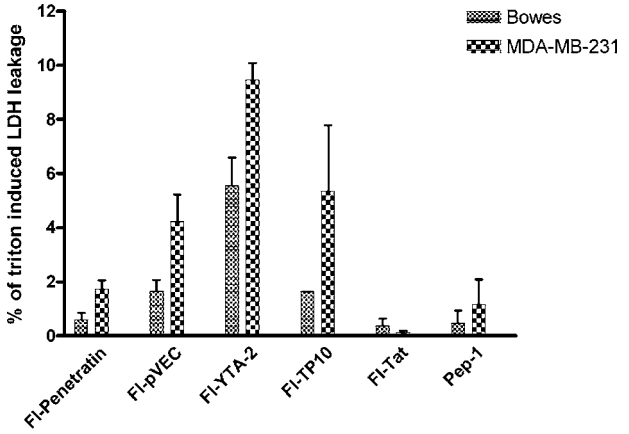


Figure 2. LDH leakage from Bowes cells and MDA-MB-231 cells. Cells were exposed to a 5 μM peptide solution for 30 min whereafter the amount of lactate dehydrogenase in the supernatant was measured (560/590 nm).

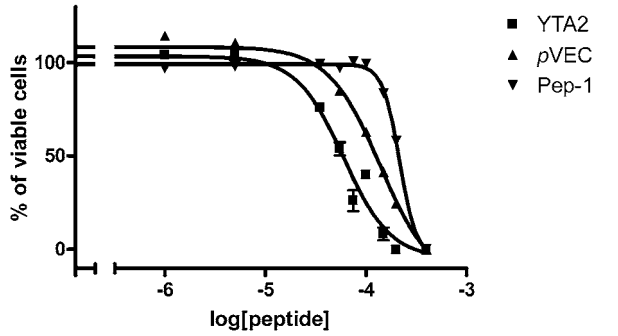


Figure 3. Cytotoxicity based on the ATP level in the Bowes cells. Cells were exposed to different concentration of drug in media containing 1% fetal bovine serum, for 48 h.

relative to the amount of viable, metabolically active cells. We studied the toxicity of the peptides after incubation for 48 h. Figure 3 gives the EC50 values of *p*VEC, Pep-1, and YTA2, that is 138 μM, 216 μM, and 60 μM, respectively. This suggests that the peptides are not toxic at the concentrations where we study uptake of fluoresceinyl peptides and peptide−protein complexes. To sum up, the uptake of peptide and peptide−protein complexes can not only be due to damaged cell membranes and thereby damaged cells.

Protein Transfection with *β*-Galactosidase. We studied whether YTA2 is capable of delivering proteins inside cells without chemical coupling between the peptide and the cargo protein. The peptides were first coincubated with the 119 kDa subunit of β-galactosidase and then added to the cells. Cells were fixed and stained according to the β-galactosidase staining kit (Active Motif). Figure 4 shows the delivery of β-galactosidase inside Bowes cells. The delivery of β-galactosidase with YTA2 (Figure 4C,D) was compared to the delivery of β-galactosidase with *p*VEC (Figure 4E,F) and Pep-1 (Figure 4A,B). *p*VEC (*14*) is another well-characterized CPP, and Pep-1 is also a CPP with the additional well-known capability to deliver proteins inside cells by coincubation. YTA2 is at the least as effective as Pep-1 to deliver β-galactosidase inside Bowes cells, while *p*VEC appears not to be as efficient. Merely β-galactosidase was used as a negative control (Figure 4G,H), and as expected, no uptake of β-galactosidase was detected.

Quantitative Protein Transfection with TRITC-Labeled Streptavidin. The amount of delivered protein by coincubation between the peptides YTA2 and Pep-1 with the protein TRITC-labeled streptavidin was investigated. The peptides were coincubated with 66 kDa streptavidin and then added to the cells. The result is presented in Figure 5 where internalized streptavidin is normalized against the amount of total protein in the cell culture well. The pattern of the result is similar in both Bowes cells and MDA-MB-231 cells, and for clarity, only the results in the Bowes cells will be discussed. YTA2 and Pep-1 have the ability to deliver TRITC-labeled streptavidin with 42.4 and 70.9 pmol of internalized streptavidin/mg protein, respectively. However, in contrast to the uptake with β-galactosidase

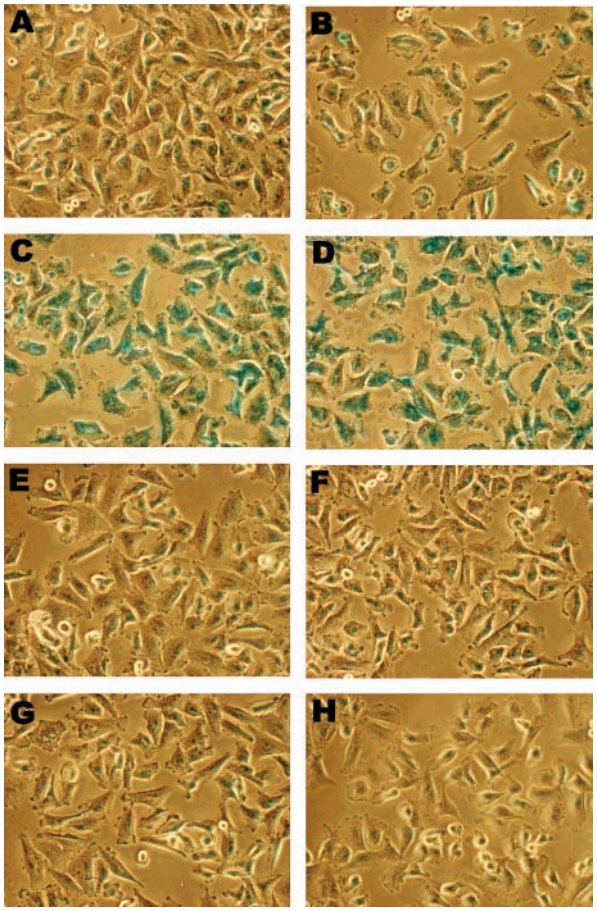


Figure 4. Uptake of β-galactosidase in Bowes cells. Cells were exposed to a peptide protein complex solution for 3 h whereafter cells were fixed and stained according to the β-galactosidase staining kit (Active Motif). In parts A−H, the amount of β-galactosidase is 8.4 pmol. In the left column, the peptide amount is 3.5 nmol, and in the right column, the peptide amount is 6 nmol. Parts A and B show coincubated β-galactosidase and Pep-1. Parts C and D show coincubated β-galactosidase and YTA2. Parts E and F show coincubated β-galactosidase and *p*VEC. Parts G and H show merely β-galactosidase.

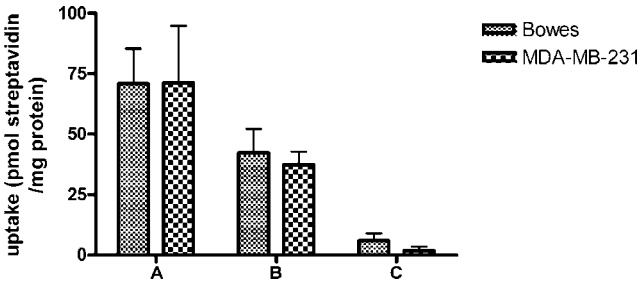


Figure 5. Uptake in picomoles of TRITC-labeled streptavidin in Bowes cells and MDA-MB-231 cells. Bar A shows coincubated TRITC-labeled streptavidin and Pep-1. Bar B shows TRITC-labeled streptavidin and YTA2. Bar C shows merely TRITC-labeled streptavidin. Cells were exposed to a peptide (3.5 nmol) and protein (15 pmol) solution for 3 h whereafter the protein attached to the cell membrane was removed by trypsination. Cells were lysed in sodium hydroxide, the fluorescence (550/570 nm) was measured, and the amount of internalized TRITC-labeled streptavidin was normalized against the amount of protein in the well.

Table 1. Sequences and Experimental Data of Selected Cell-Penetrating Peptides

peptide	sequence	peptide uptake, nmol peptide/ mg protein[a]		LDH leakage,[b] %		EC50 of peptide[c] μM	protein uptake[d]	protein uptake, pmol streptavidin/ mg protein[e]	
YTA2	YTAIAWVKAFIRKLRK-amide	3.23	4.38	5.56	9.46	60	+++	42.4	37.4
Pep−1	KETWWETWWTEWSQPKKKRKV-cysteamide	n.s.	n.s.	0.47	1.18	215	++	70.9	71.9
*p*VEC	LLIILRRRIRKQAHAHSK-amide	7.79	8.12	1.66	4.22	138	+	n.s.	n.s.
Penetratin	RQIKIWFQNRRMKWKK-amide	2.32	2.56	0.59	1.74	n.s.[f]	n.s.	n.s.	n.s.
TP10	AGYLLGKINLKALAALAKKIL-amide	1.57	2.40	1.63	5.36	n.s.	n.s.	n.s.	n.s.
Tat	GRKKRRQRRRPPQ-amide	0.06	0.12	0.37	0.13	n.s.	n.s.	n.s.	n.s.

[a] Amount of intracellular fluoresceinyl peptide normalized against the protein content in the well. Left column shows the uptake in Bowes cells, and right column shows uptake in MDA-MB-231 cells. [b] LDH leakage from cells treated with 5 μM fluoresceinyl peptide (Pep-1 without fluoresceinyl moiety). 100% is set to LDH leakage from cells treated with 0.1% Triton X-100. Left column shows the LDH leakage from Bowes cells, and right column shows LDH leakage from MDA-MB-231 cells. [c] EC50 on Bowes cells treated with increasing concentration of peptides. [d] Determination by microscopy of uptake of β-galactosidase coincubated with peptide. The + indicates minimal uptake and then increasing amount of uptake from + to +++. [e] Amount of intracellular TRITC-labeled streptavidin coincubated with peptide. The amount of TRITC-labeled streptavidin is normalized against the protein content in the well. Left column shows the uptake in Bowes cells, and right column shows uptake in MDA-MB-231 cells. [f] n.s. stands for not studied.

where YTA2 seemed to be superior to Pep-1 to deliver proteins inside cells, here Pep-1 is better than YTA2 to deliver streptavidin over the cell membrane. This difference is probably due to the difference between the two proteins β-galactosidase and TRITC-labeled streptavidin. Merely TRITC-labeled streptavidin was used as a negative control, and as expected, no uptake of TRITC-labeled streptavidin was detected.

DISCUSSION

The discovery and development of CPPs has tremendously facilitated the transport and delivery of conjugated cargoes over the cell membrane (for review, see ref 1). CPPs can be divided into different classes depending on their origin. There are CPPs derived from naturally occurring peptides/proteins (TAT, antennapedia, and *p*VEC) (*14*−*17*), chimeric peptides (transportan) (*18*), and synthetic peptides (Pep-1, YTA2) (*6*, *11*). Common for all classes is that the CPPs are short peptide sequences, less than 30 amino acids, and that the peptides are often highly rich in basic amino acid residues (*1*). The translocation mechanism of CPPs has been debated for a long time and was at the start believed to be receptor- and endocytosis-independent (*19*). Nowadays, different types of endocytosis seem to be important for the uptake of CPPs (*20*−*22*).

Morris et al. developed a new technique based on coincubation of the CPP Pep-1, with the cargo that should be transported over the cell membrane (*6*). In this way, the CPP and the cargo form a complex which can be transported over the cell membrane, and once inside the cell, the cargo will be released from the CPP (*6*, *7*). This finding is of great importance, since the chemical coupling between the peptide and the cargo is no longer needed. This chemical coupling requires additional attention when synthesizing the peptide−cargo complex, and the CPP might also affect the cargo inside the cell.

Pep-1 is an amphipathic peptide consisting of 21 amino acids from 3 different domains. One domain is hydrophobic with 5 tryptophan residues, which seem to be important for forming hydrophobic interactions with proteins. The other domain is hydrophilic with 5 lysine residues that improve the cellular delivery of the peptide. This hydrophilic domain originates from the nuclear localization sequence of simian virus 40 (SV-40) large T-antigens. The hydrophobic and hydrophilic domains are separated by a short sequence of 3 amino acids (serine, glutamine, and proline) (*6*).

YTA2 (*11*) is a CPP with similar uptake abilities to those of penetratin (*17*, *19*), *p*VEC (*14*), TP10 (*23*), and Tat (*15*), other well-characterized fluoresceinyl CPPs (Table 1). The CPP YTA2 was designed according to a method outlined in Hällbrink et al. (*24*). In short, new transport peptides were designed by extending an amino acid sequence corresponding to a matrix metalloprotease-2 substrate (*25*). The seeding peptide sequence was selected from an already published phage library screening, with the aim to find a higher selectivity for matrix metalloprotease-2 over several other matrix metalloproteases. The original sequence was SGESLAY-YTA (*25*), with the hyphen representing the protease cleavage site. The newly designed CPP was named YTA2 after the substrate sequence. The CPP YTA2 was designed for a new approach to overcome the setback of drug resistance by conjugating of a cell-penetrating peptide and the cytostatic agent methotrexate.

The uptake of fluoresceinyl peptide was studied in two different cell lines, Bowes human melanoma cell line and human MDA-MB-231 breast cancer cell line. The uptake shows a similar pattern in both cell lines. After incubating the peptides with the cells, peptides bound to the outside of the cell membrane were removed by trypsination. Before measuring the fluorescence of internalized peptide, the lysed cells were centrifuged to eliminate the possibility of peptide in the cell membrane. To confirm that the cell-penetrating ability was not due to toxicity of YTA2, two different toxicity studies were performed. First, we studied membrane leakage, or acute toxicity, of lactate dehydrogenase from the cytosole. Since almost no LDH could be detected outside the cells, it could be concluded that the cell membranes were not damaged, i.e., leaky. A longer exposure- and concentration-dependent toxicity study was made to describe the amount of living, metabolically active cells dependent on the amount of ATP produced. Moreover, this study shows that YTA2 is not toxic at the concentrations used in the peptide and protein uptake studies. Hence, the fluoresceinyl−YTA2 uptake and the protein−YTA2 uptake are likely due to cell-penetrating abilities of the YTA2.

To investigate whether YTA2, just as Pep-1, has the ability to deliver proteins over the cell membrane, YTA2 was coincubated with two different proteins, β-galactosidase and TRITC-labeled streptavidin, whereafter the complexes were added to the cells. The uptake of β-galactosidase was studied under a phase-contrast microscope, and it showed that YTA2 is at least as effective as Pep-1 at delivering β-galactosidase inside the Bowes cells. TRITC-labeled streptavidin was used to quantify the uptake of the coincubated peptide−protein complex. Here, YTA2 appears to be approximately half as effective as Pep-1 at delivering TRITC-labeled streptavidin inside cells. This indicates that the uptake of protein seems to be dependent on which protein is delivered.

In summary, we have characterized the cell-penetrating ability of YTA2 and confirmed that the cell-penetrating ability is not just due to the toxicity. It was also established that a chemical coupling between YTA2 and the cargo is not needed for transport of the cargo, in this case, β-galactosidase and TRITC-

labeled streptavidin, over the cellular membrane in vitro. This finding facilitates, in respect to both time and synthesis, the transport of proteins over the cellular membrane.

ACKNOWLEDGMENT

This work was funded by European Community (LSHB-CT-2005-018961), VR-NT, and VR-Med (Swedish Research Council) and CePep II AB.

LITERATURE CITED

(1) Järver, P., and Langel, Ü. (2006) Cell-penetrating peptides−a brief introduction. *Biochim. Biophys. Acta 1758*, 260−263.
(2) Lindgren, M., Hällbrink, M., Prochiantz, A., and Langel, Ü. (2000) Cell-penetrating peptides. *Trends Pharmacol. Sci. 21*, 99−103.
(3) Schwarze, S. R., Ho, A., Vocero-Akbani, A., and Dowdy, S. F. (1999) In vivo protein transduction: delivery of a biologically active protein into the mouse. *Science 285*, 1569−1572.
(4) Hällbrink, M., Florén, A., Elmquist, A., Pooga, M., Bartfai, T., and Langel, Ü. (2001) Cargo delivery kinetics of cell-penetrating peptides. *Biochim. Biophys. Acta 1515*, 101−109.
(5) Nagahara, H., Vocero-Akbani, A. M., Snyder, E. L., Ho, A., Latham, D. G., Lissy, N. A., Becker-Hapak, M., Ezhevsky, S. A., and Dowdy, S. F. (1998) Transduction of full-length TAT fusion proteins into mammalian cells: TAT-p27Kip1 induces cell migration. *Nat. Med. 4*, 1449−1452.
(6) Morris, M. C., Depollier, J., Mery, J., Heitz, F., and Divita, G. (2001) A peptide carrier for the delivery of biologically active proteins into mammalian cells. *Nat. Biotechnol. 19*, 1173−1176.
(7) Gros, E., Deshayes, S., Morris, M. C., Aldrian-Herrada, G., Depollier, J., Heitz, F., and Divita, G. (2006) A non-covalent peptide-based strategy for protein and peptide nucleic acid transduction. *Biochim. Biophys. Acta 1758*, 384−393.
(8) Morris, M. C., Vidal, P., Chaloin, L., Heitz, F., and Divita, G. (1997) A new peptide vector for efficient delivery of oligonucleotides into mammalian cells. *Nucleic Acids Res. 25*, 2730−2736.
(9) Morris, M. C., Chaloin, L., Mery, J., Heitz, F., and Divita, G. (1999) A novel potent strategy for gene delivery using a single peptide vector as a carrier. *Nucleic Acids Res. 27*, 3510−3517.
(10) Morris, M. C., Chaloin, L., Choob, M., Archdeacon, J., Heitz, F., and Divita, G. (2004) Combination of a new generation of PNAs with a peptide-based carrier enables efficient targeting of cell cycle progression. *Gene Ther. 11*, 757−764.
(11) Lindgren, M., Rosenthal-Aizman, K., Saar, K., Eiríksdóttir, E., Jiang, Y., Sassian, M., Östlund, P., Hällbrink, M., and Langel, Ü. (2006) Overcoming methotrexate resistance in breast cancer tumour cells by the use of a new cell-penetrating peptide. *Biochem. Pharmacol. 71*, 416−425.
(12) Matthews, B. W. (2005) The structure of *E. coli* β-galactosidase. *C. R. Biol. 328*, 549−556.
(13) Saar, K., Lindgren, M., Hansen, M., Eiríksdóttir, E., Jiang, Y., Rosenthal-Aizman, K., Sassian, M., and Langel, Ü. (2005) Cell-penetrating peptides: a comparative membrane toxicity study. *Anal. Biochem. 345*, 55−65.
(14) Elmquist, A., Lindgren, M., Bartfai, T., and Langel, Ü. (2001) VE-cadherin-derived cell-penetrating peptide, pVEC, with carrier functions. *Exp. Cell Res. 269*, 237−244.
(15) Vives, E., Brodin, P., and Lebleu, B. (1997) A truncated HIV-1 Tat protein basic domain rapidly translocates through the plasma membrane and accumulates in the cell nucleus. *J. Biol. Chem. 272*, 16010−16017.
(16) Derossi, D., Calvet, S., Trembleau, A., Brunissen, A., Chassaing, G., and Prochiantz, A. (1996) Cell internalization of the third helix of the Antennapedia homeodomain is receptor-independent. *J. Biol. Chem. 271*, 18188−18193.
(17) Fischer, P. M., Zhelev, N. Z., Wang, S., Melville, J. E., Fahraeus, R., and Lane, D. P. (2000) Structure-activity relationship of truncated and substituted analogues of the intracellular delivery vector Penetratin. *J. Pept. Res. 55*, 163−172.
(18) Pooga, M., Kut, C., Kihlmark, M., Hällbrink, M., Fernaeus, S., Raid, R., LAnd, T., Hallberg, E., Bartfai, T., and Langel, Ü. (2001) Cellular translocation of proteins by transportan. *FASEB J. 15*, 1451−1453.
(19) Derossi, D., Joliot, A. H., Chassaing, G., and Prochiantz, A. (1994) The third helix of the Antennapedia homeodomain translocates through biological membranes. *J. Biol. Chem. 269*, 10444−10450.
(20) Wadia, J. S., Stan, R. V., and Dowdy, S. F. (2004) Transducible TAT-HA fusogenic peptide enhances escape of TAT-fusion proteins after lipid raft macropinocytosis. *Nat. Med. 10*, 310−315.
(21) Säälik, P., Elmquist, A., Hansen, M., Padari, K., Saar, K., Viht, K., Langel, Ü., and Pooga, M. (2004) Protein cargo delivery properties of cell-penetrating peptides. A comparative study. *Bioconjugate Chem. 15*, 1246−1253.
(22) Thorén, P. E., Persson, D., Isakson, P., Goksor, M., Önfelt, A., and Nordén, B. (2003) Uptake of analogs of penetratin, Tat(48−60.) and oligoarginine in live cells. *Biochem. Biophys. Res. Commun. 307*, 100−107.
(23) Soomets, U., Lindgren, M., Gallet, X., Hällbrink, M., Elmquist, A., Balaspiri, L., Zorko, M., Pooga, M., Brasseur, R., and Langel, Ü. (2000) Deletion analogues of transportan. *Biochim. Biophys. Acta 1467*, 165−176.
(24) Hällbrink, M., Kilk, K., Elmquist, A., Lundberg, P., Lindgren, M., Jiang, Y., Pooga, M., Soomets, U., and Langel, Ü. (2005) Prediction of cell-penetrating peptides. *Int. J. Pept. Res. Ther. 11*, 249−259.
(25) Chen, E. I., Kridel, S. J., Howard, E. W., Li, W., Godzik, A., and Smith, J. W. (2002) A unique substrate recognition profile for matrix metalloproteinase-2. *J. Biol. Chem. 277*, 4485−4491.

BC060266G

Development of Tissue Plasminogen Activator Specific "On Demand Cleavable" (ODC) Linkers for Radioimmunotherapy by Screening One-Bead-One-Compound Combinatorial Peptide Libraries

Pappanaicken R. Kumaresan,[†] Arutselvan Natarajan,[‡] Aimin Song,[†] Xiaobing Wang,[†] Ruiwu Liu,[†] Gerald DeNardo,[‡] Sally DeNardo,[‡] and Kit S. Lam*,[†]

Division of Hematology and Oncology, and Radiodiagnosis and Therapy, Department of Internal Medicine, UC Davis Cancer Center, University of California Davis, School of Medicine, Sacramento, California 95817. Received August 31, 2006; Revised Manuscript Received November 7, 2006

New strategies are needed to protect normal organs from radiation in cancer radioimmunotherapy (RIT). This can be achieved by rapid clearance of radiometal in the circulation after accumulation of radioimmunoconjugates (RIC) in the tumor. Our strategy is to place highly efficient and specific cleavable linkers between radiometal chelates and the tumor targeting agents. Such linkers must be resistant to cleavage by enzymes present in the plasma and the tumor. After radiotargeting agents have accumulated in the tumor, a cleaving agent can be administered "on demand" to cleave a specific linker, resulting in the release of radiometal from the circulating RIC in a form that will have rapid renal clearance. We have selected TNKase, a thrombolytic agent approved for patient use, as our model on-demand cleaving agent. To identify TNKase-specific linkers, we screened fluorescent-quenched random "one-bead-one-compound" (OBOC) combinatorial peptide libraries. D-Amino acid containing peptides that were specific for TNKase but were resistant to cleavage by plasma and tumor-associated proteases were identified. One of these peptide substrates (rqYKYkf) was used to link the DOTA chelate to ChL6, a monoclonal antibody known to target breast cancer. This antibody conjugate was stable in plasma for 7 days while preserving the immunoreactivity to intact tumor cells. The addition of TNKase at clinical achievable plasma level (10 μg/mL) resulted in the release of 28% of the radiometal from the radioimmunoconjugate within 72 h. This lead linker, after further optimization to increase its response to TNKase, may be useful in the development of more effective radioimmunotherapeutic and radioimaging agents.

INTRODUCTION

Radioimmunotherapy (RIT)[1], in which a targeting agent is conjugated to a radiometal, is a promising approach to treat cancer (*1*−*3*). However, its potential is limited by radiation exposure to normal organs, particularly bone marrow (*4*−*6*). One approach to clear nontargeted radioactivity is to increase renal excretion of circulating radiometal from the body after tumor targeting (*7*−*9*). Immunoadsorption has been utilized to remove circulating radioimmunoconjugates (RIC) and reduce radiation dose to normal tissues (*10*). Removal of free circulating RIC after adequate tumor uptake has been tried preclinically and clinically with modest success (*11*, *12*). DeNardo *et al.* used a similar approach by treating B-cell lymphoma patients using ^{131}I Lym-1, an anti-lymphoma monoclonal antibody, with and without immunoadsorption (*13*, *14*). Results for two patients receiving RIT with immunoadsorption on four occasions demonstrated that RIC was reduced by 75% in blood and by 50% in the bone marrow when their plasma was pumped through an anti-gammaglobulin column for removing the circulating ^{131}I Lym-1 antibodies. It is clear that a large portion of the RIC can be removed with this approach. However, the procedure is cumbersome and expensive, and there is need for a simpler strategy.

Various forms of pretargeting RIT delivery have been developed to overcome this problem and used in clinical trials, for example, by administering tumor targeting molecules that bind subsequently injected radiochelates. The small radiochelates that do not bind to the tumor are cleared quickly from body. This results in a high therapeutic index (tumor dose vs normal tissue dose) (*15*−*18*). However, continued circulating pretargeting molecules have presented interference in tumor targeting of the radiochelates; clearing agents, such as biotin-*N*-acetyl-galactosamine for the antibody−strepavidin conjugates, have resulted in effective radiochelate tumor targeting (*15*−*17*). Although pretargeting approaches have great promise, these systems require multiple injections and administration of reagents at specific time points. Some of the reagents used in such systems, e.g., streptavidin, can be immunogenic. Another approach is to introduce a cleavable linker between the targeting agent and the radiochelate. For example, RIC with linkers cleavable by endogenous proteases such as liver-specific cathepsin-D or by an exogenous hydrolytic enzyme β-lactamase have been reported (*19*−*21*).

Repeated usage of exogenous enzymes of nonhuman source, such as β-lactamase, however, may elicit an immune response. An ideal on-demand cleavable (ODC) enzyme should be of human origin and be primarily restricted to the intravascular space so that only the circulating radioconjugates will be cleaved. Recombinant tissue plasminogen activator (t-PA),

* Corresponding author. Kit S. Lam, M.D., Ph.D., Professor of Medicine, Chief, Division of Hematology & Oncology, UC Davis Cancer Center, 4501 X Street, Sacramento, CA 95817. Tel: (916)-734-8012. Fax: (916)734-7946. E-mail: kit.lam@ucdmc.ucdavis.edu.

[†] Division of Hematology and Oncology.

[‡] Radiodiagnosis and Therapy, Division of Hematology and Oncology.

[1] Abbreviations: RIT, radioimmunotherapy; RIC, radioimmunoconjugates; ODC, on-demand cleavable; OBOC, one-bead-one-compound; t-PA, tissue plasminogen activator; ChL6, chimeric mAb; DOTA, 1,4,7,10-tetraazacyclododecane-1,4,7,10-tetraacetic acid; CAE, cellulose acetate electrophoresis. Standard single-letter abbreviation for amino acids is used. Upper case letters represent L-amino acids; lower case letters represent D-amino acids.

10.1021/bc0602681 CCC: $37.00 © 2007 American Chemical Society
Published on Web 12/23/2006

currently used as a thrombolytic agent in patients (TNKase) provides these characteristics (*22*). Thus, the aim of this study is to develop TNKase substrates with high specificity and efficiency that can be used as an ODC linker between radiometal chelate and tumor targeting agents such as mAbs.

In this study, we have shown that currently known TNKase peptide substrates are not stable in plasma and cancer cell supernatants. We have utilized the one-bead-one-compound (OBOC) combinatorial library method (*23*, *24*) to develop an ODC linker that is highly susceptible to TNKase but highly resistant to other proteases in plasma or in a tumor. In this study, we have selected one such TNKase peptide substrate as a lead ODC linker and have evaluated its potential to reduce radiation to normal tissues.

EXPERIMENTAL PROCEDURES

Materials and Instruments. PEGA resin (0.40 mmol/g) was purchased from Polymer Laboratories (Amherst, MA). Boc-2-Abz-OH and Boc-Tyr(3-NO2)-OH were purchased from ChemImpex (Wood Dale, IL). All other amino acid derivatives and HOBt (1-hydroxybenzotriazole) were purchased from SynPep (Dublin, CA). DOTA-NHS-ester (1,4,7,10-tetraazacyclododecane-1,4,7,10-tetraacetic acid mono(*N*-hydroxysuccinimide ester) and DOTA-mono-NHS-tris(*t*-Bu)-ester-(1,4,7,10-tetraazacyclododecane-1,4,7-tris(*t*-butyl acetate)-10-acetic acid mono(*N*-hydroxysuccinimide ester)) were purchased from Macrocyclics (Dallas, TX). DIC (*N*,*N*′ diisopropylcarbodiimide) was purchased from Advanced ChemTech (Louisville, KY). DMF (*N*,*N*′-dimethylformamide), DCM (dichloromethane), MeOH (methanol), diethyl ether, and acetonitrile were purchased from Fisher (Houston, TX). All other chemical reagents were purchased from Aldrich (Milwaukee, WI). Analytical HPLC analyses (Vydac column, 4.6 mm × 250 mm, 5 μm, 300 Å, C_{18}, 1.0 mL/min) and preparative HPLC purification (Vydac column, 20 mm × 250 mm, 5 μm, 300 Å, C_{18}, 7.0 mL/min, 45 min gradient) were performed on a Beckman System Gold HPLC system (Fullerton, CA). MALDI-TOF MS analysis was performed on a Bruker BIFLEX III mass spectrometer (Billerica, MA). All of the experiments are carried out at room temperature unless otherwise noted. ChL6 (Bristol-Myers Squibb Pharmaceutical Research Institute, Seattle, WA) was a chimera consisting of human IgG1-constant regions and the murine L6 MAb antigen-variable region. Carrier-free ^{111}In(MDS Nordion, Vancouver, Canada) was purchased as chloride in 0.05 M HCl solution. Sephadex G50-80 (Pharmacia, Uppsala, Sweden), molecular sieving high-performance liquid chromatography (HPLC) (Beckman Coulter System Gold 127; Beckman, San Ramon, CA; SEC-3000 molecular sieving column), cellulose acetate electrophoresis (CAE) (Gelman Sciences, Inc., Ann Arbor, MI) were used for purification and characterization of RIC. TNKase was purchased from Genentech (San Francisco, CA) and reconstituted with distilled water to get 10 mg/mL concentration. The reconstituted samples were stored in −80 °C in aliquots.

Synthesis of "Fluorescent-Quenched" Peptide Library. An OBOC combinatorial library, containing random Y(NO_2)-peptide-K(Abz), was synthesized on PEGA resin with a standard "split-mix" approach (*25*). The following fluorescent-quenched libraries were prepared on PEGA beads: Y(NO_2)-xxxxxxx-K(Abz), Y(NO_2)-xxXxx-K(Abz), Y(NO_2)-xxxXXxxx-K(Abz), and Y(NO_2)-xxXXXxx-K(Abz). For these random peptides, Y(NO_2) represents 3-nitrotyrosine, K(Abz) represents lysine bearing a 2-aminobenzoyl group on its ϵ-amino group, X represents one of 19 natural L-amino acids excluding cysteine, and x represents one of the D-isomers of 18 natural L-amino acids plus glycine. Theoretically, there are $19^7 = 8.9 \times 10^8$ possible permutations of peptide sequences in this library.

Screening and Sequencing. Four different combinatorial libraries were screened against TNKase enzyme. Approximately 1 mL of the beads (about 325 000 beads) was used in each screening experiment, and a total of 1 million beads from each library were screened. Fluorescent-quenched combinatorial libraries were first incubated with pooled plasma, isolated from citrate-treated human blood obtained from normal volunteers. The beads were incubated with 50% plasma containing PBS overnight at 37 °C with occasional shaking. Beads with peptides that were labile in plasma and therefore fluoresced and those beads that autofluoresced were removed by a fluorescence bead sorter (COPAS, Union Biometrica). The remaining nonfluorescent beads were washed several times with PBS to remove plasma proteins. 10 μg/mL TNKase in PBS was added and incubated for 1 h at 37 °C with occasional shaking. After 1 h, beads were incubated with 8 M guanidine HCl to terminate the enzyme activity and washed with water several times to remove all the proteins attached on the beads. Positive fluorescent beads were picked under a fluorescent microscope at 360/410 excitation/emission spectrum and sequenced with Edman chemistry using an automatic microsequencer (ABI, Procise 494). On the basis of the plasma stability and TNKase susceptibility, 12 peptides were selected as candidate substrates for TNKase. For in vitro stability assay, the selected candidates were synthesized as soluble fluorescent-quenched substrates without tethering to beads as described below.

Synthesis of Individual "Fluorescent-Quenched" ODC Linkers. Rink amide MBHA resin (70 mg, 0.09 mmol) was swollen in DMF overnight. The supernatant was removed, and 20% piperidine solution in DMF (2 mL) was added to the resin. The mixture was agitated for 15 min, and the supernatant was drained. This process was repeated. The resin was thoroughly washed with DMF, MeOH, and DMF. Fmoc-Lys(Alloc)-OH (122.2 mg, 0.27 mmol), HOBt (36.5 mg, 0.27 mmol), and DIC (42.3 μL, 0.27 mmol) in DMF (2 mL) were added to the resin. The resulting mixture was agitated until the ninhydrin test was negative. The resin was washed with DMF, MeOH, and DCM. In the presence of argon, a solution of $PhSiH_3$ (266.5 μL, 2.16 mmol) in DCM (1 mL) was added to the resin, followed by a solution of $Pd(PPh_3)_4$ (26.0 mg, 0.0225 mmol) in DCM (2.2 mL). The mixture was shaken in an argon atmosphere for 30 min. This process was repeated. The supernatant was removed, and the resin was washed thoroughly with DCM, DMF, MeOH, and DMF. To the resin was added a solution of Boc-2-Abz-OH (64.1 mg, 0.27 mmol), HOBt (36.5 mg, 0.27 mmol), and DIC (42.3 μL, 0.27 mmol) in DMF (2 mL). The resulting mixture was agitated until the ninhydrin test was negative. The supernatant was removed. The resin was washed with DMF, and the α-Fmoc protecting group of the lysine was removed by piperidine treatment as described above. The peptide was then synthesized on the α-amino group of the lysine using standard Fmoc chemistry. Boc-Tyr(3-NO2)-OH was used as the last amino acid. After the peptide sequence was finished, the resin was washed with DMF, MeOH, and DCM, and then dried under vacuum. 4 mL of cleavage mixture (TFA (trifluoroacetic acid)/phenol/thioanisole/water/TIS (triisopropylsilane), 82.5:7.5:5:5:2.5, v/w/v/v/v) was added to the dried resin at 0 °C. The mixture was slowly warmed to room temperature and allowed to mix for 6 h. The supernatant was then collected, and the resin was washed with TFA (3 × 1 mL). The combined supernatants were concentrated to 1 mL under a stream of nitrogen. The peptide was precipitated by dilution with ethyl ether (10 mL), separated by centrifugation, washed with ethyl ether, and dried under vacuum. The crude peptide was analyzed and purified by HPLC and characterized by MALDI-TOF MS.

Synthesis of DOTA-ODC Linker with an Aminooxyacetyl (Aoa) Group. The DOTA-ODC linker (DOTA-spacer-rqYKYkf-

spacer-K(Aoa)-NH_2) was synthesized using a procedure similar to the synthesis of fluorescent-quenched peptides. After the Alloc deprotection, instead of Boc-2-Abz-OH, Boc-Aoa-OH was coupled to the ϵ-amino group of the lysine. The α-Fmoc protecting group was then removed by piperidine treatment as described above. To increase ODC accessibility for TNKase digestion, a short hydrophilic spacer was introduced on both sides of the ODC linker. This linear hydrophilic spacer has a diamine component at the N-terminal end derived from 2,2′(ethylenedioxy)-bis(ethylamine) and an anhydride component at the C-terminal end derived from succinic anhydride, respectively (*26*). A Fmoc-protected spacer was coupled to the α-amino group of the lysine using our previously published procedure (*26*). After the coupling of the last amino acid, the N-terminus Fmoc protection group was removed by piperidine treatment. An additional spacer was introduced between the DOTA and the peptide. After Fmoc deprotection, the resin was incubated with a solution of DOTA-NHS-ester (112.0 mg, 0.135 mmol) and DIEA (156.8 μL, 0.9 mmol) until the ninhydrin test was negative. The peptide was released from the resin and purified using the procedure described above. A total of 26 mg of DOTA-spacer-rqYKYkf-spacer-K(Aoa)-NH_2 was obtained from 200 mg of resin (yield 14%), and mass (2088.1) was calculated by MALDI-TOF MS $(M + H)^+$. All the substrates were purified by preparative HPLC, and purity was verified by both analytical and MALDI-TOF mass spectrometry. The products that showed $\geq$95% purity were taken for the TNKase susceptibility and stability assay.

Linker Stability Analysis. 100 nmol/mL of fluorescent-quenched ODC linkers were incubated in PBS containing 10% human plasma at 37 °C. The susceptibility was monitored every hour in a fluorescence plate reader (Tecan) at 360/410 nm excitation/emission spectrum. The ODC linker that was stable in plasma overnight was taken for further stability analysis. For this, the cell culture supernatant was isolated from several cancer cell lines (approximately 1−5 million cells/mL) that were split 1 day before the collection. 100 nmol/mL of the ODC linkers was incubated with the cancer cell culture supernatant, and its susceptibility was monitored in a fluorescence plate reader at 360/410 nm excitation/emission spectrum. ODC linkers that were stable in both plasma and various cancer cell culture supernatants were taken for the TNKase susceptibility assay.

TNKase Susceptibility Assay. Potential ODC linkers (100 nmol/mL) were incubated with TNKase (10 μg/mL) in PBS at 37 °C with occasional shaking. To simulate the in vivo condition, plasma was added (10%) in the assay medium. The susceptibility was monitored at various time intervals at 360/410 nm excitation/emission spectrum using a Tecan fluorescence plate reader. The entire assay was done in triplicate, and two independent experiments were performed.

Antibody-Linker Conjugation and MALDI-MS Analysis. For on-demand cleavable studies, ChL6, an antibody targeted against tumor antigen expressed in colon, lung, and breast cancer cells, was used (*27*, *28*). DOTA-ODC-aminoxyamine was conjugated with ChL6 by the ketone−oxime method developed in our lab (*29*). In brief, primary amines (mainly lysine) present ChL6 mAb was coupled with levulinic succinimidyl esters by incubating a 1:30 molar ratio in 40 mM TEA, pH 8.0, for 5 h in a cold room. The uncoupled levulinic succinimidyl esters were removed by dialysis with 40 mM TEA, pH 5.5 buffer. ChL6 was equilibrated with 40 mM TEA, pH 5.5, and incubated with 20 molar excess of DOTA-ODC-ONH_2 linkers for 5−12 h. To verify that ChL6 Ab was conjugated, a small aliquot was removed at various time intervals, and the degree of conjugation was determined by the expected mass shift in MALDI-TOF MS.

Estimation of Metal-Chelatable DOTA (c) per MAb (a) in RIC. The DOTA−ODC−ChL6 conjugate was purified by Sephadex G50 column chromatography (*30*) and was tested for its pyrogen-free status by standard procedures. DOTA−ODC−ChL6 was assayed in triplicate by cobalt metal binding assay to determine the ratio of the metal chelatable DOTA-ODC (chelate) per ChL6 (c/a) (*30*−*32*). Generally, an aliquot of DOTA−ODC−ChL6 (480 μg, 3 nmol) dissolved in 0.1 M tetramethylammonium phosphate buffer at pH 7.0 was treated with excess standardized aqueous solution of $^{57}CoCl_2$ (ICN Radiochemicals, Irvine, CA) and incubated for 30 min at room temperature. To this reaction mixture, aqueous EDTA solution (Fisher Scientific, Fair Lawn, NJ) was added to a final concentration of 10 mM and incubated for 15 min to complex with excess unbound cobalt ions. This EDTA chased mixture was purified by a Penefsky column. The concentration of the $^{57}Co/CoCl_2$-chelated DOTA−ODC−ChL6 was determined by radiation counting using a γ counter against a known quantity of the standardized $^{57}CoCl_2$ solution. The metal-chelatable DOTA was calculated as the ratio of the molar concentration of the ^{57}Co-DOTA−ODC−ChL6 (chelate) and ChL6 (MAb).

Radiolabeling of DOTA−ODC−ChL6 and Quality Control (QA). To prepare RIC, DOTA−ODC−ChL6 and ^{111}In were combined in 0.1 M ammonium acetate (pH 5.3) and incubated for 30 min at 37 °C. To scavenge unbound ^{111}In, EDTA was added to a final concentration of 10 mM for 30 min at room temperature. The final RIC was purified by molecular sieving chromatography. QA of the RIC was established by SEC-3000 HPLC, cellulose acetate electrophoresis (CAE), and immunoreactivity (*32*, *33*).

Immunoreactivity, Plasma Stability, and TNKase Cleavage Assay. ^{111}In-DOTA−ODC−ChL6 was incubated with ChL6 antibody-binding breast cancer cells (HBT 3477) and ChL6 nonbinding lymphoma cancer cells (Raji). Immune reactivity was assayed by performing a competitive assay against lightly iodinated ^{125}I-ChL6. Approximately 1 million cells were incubated for 1 h and washed with PBS to remove any unbound antibody. This experiment was carried out in triplicate and repeated twice. The cells were counted using a β counter. The in vitro plasma stability of RIC was evaluated by mixing 10 μg of ^{111}In-DOTA−ODC−ChL6 incubated in freshly prepared human plasma (1:1 v/v dilution; total volume, 1 mL) at 37 °C in a humidified incubator maintained at 5% CO_2 and 95% air. At various intervals (1, 3, 5, 7, 9, 13, and 14 days), aliquots were taken and analyzed by CAE and high-performance liquid chromatography (*32*, *33*). For TNKase susceptibility assay, RIC (0.39 μCi/μg)) was incubated in human plasma with and without TNKase at the clinical dosage level (10 μg/mL). Plasma samples were fractioned by HPLC. Radioactivity and UV absorption (280 nm) from each fraction were monitored. The degree of susceptibility was calculated by either decreased radioactivity to the peak corresponding to the ChL6 mAb or increased radioactivity to the fractions corresponding to the peptide peak.

RESULTS

Identification of TNKase (t-PA) Specific Substrates. To be effective, ODC linkers need to be (i) stable to proteases present in the plasma, (ii) stable to proteases present in normal tissues and tumor, and (iii) highly susceptible to TNKase. Prior to screening with TNKase, the four OBOC fluorescent-quenched combinatorial libraries were prescreened with human plasma so that those beads with peptides susceptible to plasma could be identified and removed. A library with more L-amino acids in their structure yielded more positive beads. In fact, about 10−15% of the bead library (xxXXXxx) became fluorescent after mixing with plasma for 1 h at room temperature. Fluorescent beads from the plasma-treated peptide libraries were physically removed either manually or by passing through a fluorescence bead sorter (COPAS); the residual beads were

Table 1. TNKase Substrates Identified from OBOC Libraries

P_4	P_3	P_2	P_1	↓	P_1'	P_2'	P_3'	P_4' [a]
C	P	G	R		V	V	G	G[b]
	P	F	R		G	S	A[c]	
x	x	X	X		X	x	x[d]	
y	v	R	K		Q	w	k	
p	d	A	R		K	f	n	
p	k	G	K		K	G	e	
l	r	N	K		K	G	G	
f	l	H	K		S	r	i	
f	r	Q	K		W	G	k	
G	r	F	K		M	a	t	
	p	G	R		R	H	k	p
k	q	Y	K		Y	k	l[e]	
r	q	Y	K		Y	k	f[e]	
G	r	Y	K		G	k	s[e]	

↓; [a] depicts the TNKase cleaving site on peptides and P and P′ amino acids positions are numbered accordingly. [b] Peptide substrate derived from t-PA cleaving site of its native substrate plasminogen. [c] Peptide substrate derived from phage display library. [d] Structure of OBOC combinatorial library. [e] Motifs identified by aligning 3 peptide substrate homologues based on the cleavage site.

screened with TNKase. Similar to the plasma experiment, the xxXXXxx peptide library yielded more positive beads than the xxxXXxxx library. xxXxx and xxxxxxx libraries, on the other hand, were totally resistant to digestion by TNKase. Since only a portion of the peptides on each positive bead were cleaved by the enzyme, there were enough intact peptides left on each bead for sequence determination. On the basis of the microsequencing result (Edman degradation), we determined the precise TNKase cleavage site. The amino acid sequences of the 12 TNKase-susceptible peptides isolated from the xxXXXxx bead library are shown in Table 1.

All twelve peptides except one were found to be cleaved at the peptide bond between the fourth and fifth residues. One peptide (pGRRHkp) was cleaved between the third and fourth residues. In both cases, the peptides were all cleaved between two L-amino acids. This is not unexpected, as peptide bonds between two D-amino acids or one D- and one L-amino acid are generally resistant to proteolysis. Table 1 also includes the peptide sequence (PGRVVGG) of the cleavage site of plasminogen, the native substrate for TNKase, and a peptide substrate, PFRGSA, identified by the phage-display peptide library method. The P_1 position of all fourteen peptides was found to contain either an Arg or a Lys. Tyr and Phe are the preferred amino acids in the P_2 position. Eight of the twelve substrates have one basic residue (D-Arg or D-Lys) at either the P_3 or P_4 position. Similarly, there is at least one basic residue in position P_1', P_2', or P_3'. Peptides rqYKYkf and kqYKYkl share the same structural homology.

Stability in Biological Fluids. For in vitro stability and susceptibility studies, the identified candidates were synthesized in a free form that is not tethered to beads to rule out steric effects of beads on TNKase digestion. As shown in Figure 1, all the peptides listed in Table 1 were stable in plasma over a 12 h period except for PFRGSA (phage display peptide) and GrFKMat. Peptides yvRKQwk, kqYKYkl, flHKSri, frQKWGk, and rqYKYkf were susceptible to TNKase digestion. Of these, rqYKYkf, frQKWGk, and yvRKQwk were the most susceptible and were completely cleaved within 1 h of TNKase addition (10 μg/mL). Since an effective ODC linker needs to be stable to proteolytic enzymes at the tumor site, we evaluated the susceptibility of these peptide substrates against tissue culture supernatants from various cancer cell lines: pancreatic cancer (Panc1), prostate cancer (PC3), B-cell lymphomas (Raji, Ramos), T-cell lymphomas (Jurkat), and normal immortalized hepatocytes (PHH) (Figure 2). Even though most of the peptides showed stability up to 5 h in the supernatant, peptides flHKSri and rqYKYkf were stable in cancer cell supernatants and plasma for at least 10 h. Out of these two peptides, rqYKYkf was more susceptible to TNKase (Figure 1), and this peptide (Table 1) was also identified twice from library screening. Therefore, we elect rqYKYkf as the first prototype ODC linker for further characterization.

Conjugation and Radiolabeling. Peptide rqYKYkf was derivatized with DOTA and conjugated to a chimeric ChL6 antibody for radiolabeling and in vitro susceptibility studies with TNKase. Prior to conjugation, ChL6 was analyzed by HPLC, CAE, and PAGE, and its purity was found to be over 95% (data not shown). After conjugation, as revealed by MALDI-TOF mass spectrometry, the number of DOTA peptides conjugated to ChL6 was determined to be 1−3 (Figure 3). $^{57}Co/CoCl_2$ was utilized, which demonstrated that 0.5 c/a was available to chelate radiometal. The ^{111}In-DOTA−ODC−ChL6 was purified by Sephadex-G50 column chromatography, and the purity was confirmed by the HPLC and CAE radioactive profiles.

Linker Stability and Immunoreactivity Studies. The plasma stability and TNKase susceptibility of ^{111}In-DOTA−ODC−ChL6 was assayed in vitro prior to in vivo study. ^{111}In-

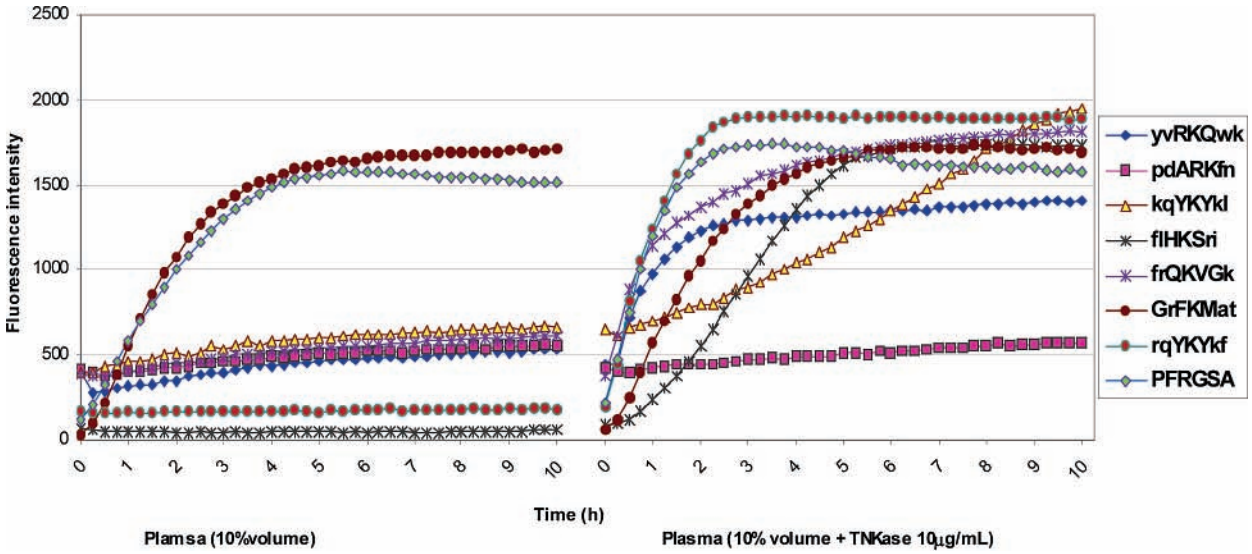


Figure 1. The fluorescence intensity of the ODC-peptides (100 nmol/mL) with plasma (10%) alone is shown on the left. On the right, the fluorescence intensity of the peptides (100 nmol/mL) with 10% of plasma containing 10 μg/mL of TNKase. Peptide "rqYKYkf" is stable in plasma and highly susceptible to TNKase digestion.

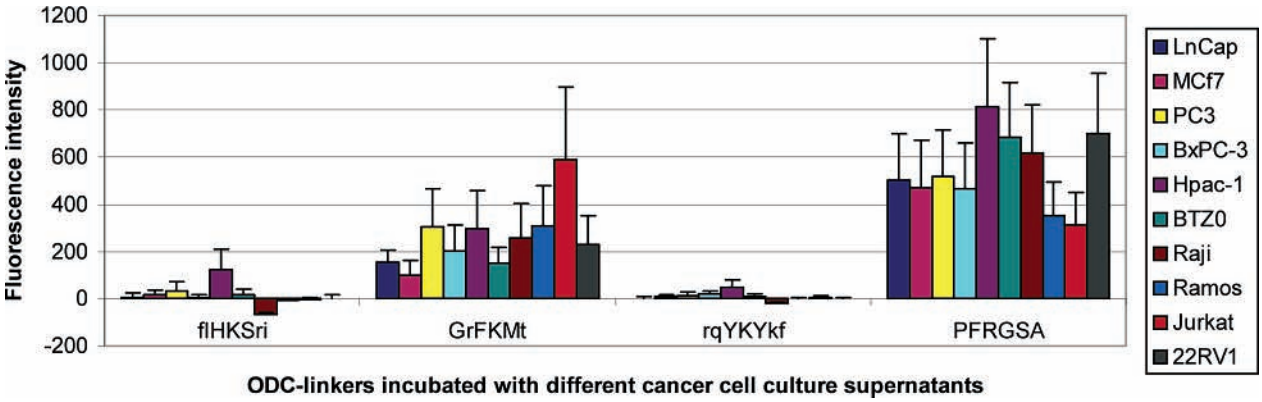


Figure 2. The ODC-linker (rqYKYkf) demonstrated notable stability, while others demonstrated varying degrees of susceptibility to enzymes present in these cell supernatants.

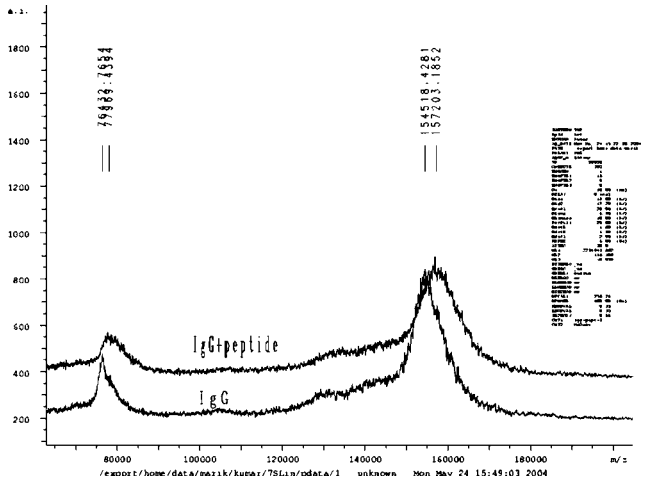


Figure 3. ChL6 antibody mass spectrum is designated as IgG and ChL6−ODC−DOTA mass spectrum designated as IgG + peptide. On the basis of the mass spectrum, we estimate that ~1 to 3 peptides were conjugated per antibody (calculated by shift in mass).

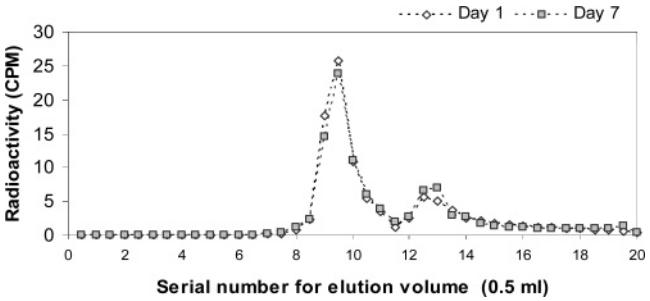


Figure 4. HPLC analysis was performed at UV 280 nm, and each 0.5 mL fraction was collected and radioactivity was counted. The radioactive profiles of ^{111}In-DOTA−ODC−ChL6 with human plasma at days 1 and 7 are identical. Thus, the RIC was essentially stable for a minimum of 6 days.

DOTA−ODC−ChL6 was monitored for 14 days in plasma. Stability of the conjugated ODC-linker in RIC was assessed by HPLC for radioactive and protein peak. Figure 4 showed that the RIC was intact for 7 days (Figure 4). The appearance of small MW species at days 1 and 7 was due to a small amount (≤5%) of ^{111}In-EDTA present in the original preparation. CAE and HPLC analysis indicated that ≥95% of the radiometal was associated with RIC, and ≥98% of RIC was in monomeric form (Figure 5). The appearance of a small percentage of radioactivity on small molecular peaks was noticed after 7 days of incubation with plasma. ^{111}In-DOTA−ODC−ChL6 selectively bound to specific breast cancer cells (HBT) and did not bind to negative control cells (Raji). Immunoreactivity of the ^{111}In-DOTA−

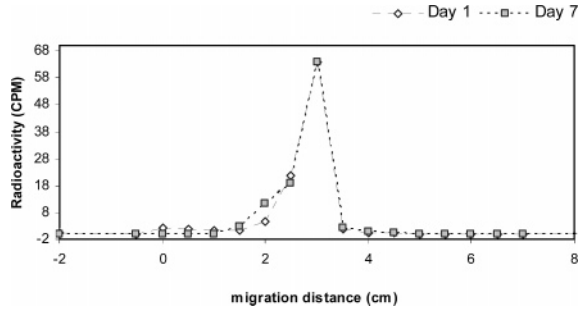


Figure 5. Cellulose acetate electophoresis (CAE): 45 min analysis was carried out at pH 8.6, with CAE strip. After 45 min, the strips were cut at 0.5 cm of each and counted on a γ counter. The radioactivity traces represented are migration patterns of ^{111}In-DOTA−ODC−ChL6 on CAE strips of days 1 and 7 with human plasma. The traces are identical. No radioactivity was observed in the lower molecular weight region for any breakdown product.

ODC−ChL6 on HBT cells was greater than 50%, whereas it was only 6% to Raji cells. In the competitive assay, the RIC competed with ^{125}I-labeled ChL6. This further suggests that conjugating the ODC linker to the antibody did not alter its antigen binding site (data not shown). ^{111}In-DOTA−ODC−ChL6 was incubated in plasma with and without TNKase at 37 °C, and we found that 10−15% and 28% of the radiometal were released from ChL6−ODC−DOTA conjugates at the clinical dosage level in 2 and 72 h, respectively (Figure 6).

DISCUSSION

To protect vital organs in myeloablative RIT, an equal amount of unlabeled mAb is preinfused before the radiolabeled mAb infusion. The unlabeled mAb will saturate nonspecific antibody-binding sites and Fc receptors in the host body, that will aid labeled mAb in targeting the tumor and reduce nonspecific binding during targeting. In spite of that, radioactive uptake in normal organs is still very high, resulting in bone marrow abalation (*34*, *35*), and nonhematological toxicity such as lung, gastrointestinal, liver, and kidney toxicity (*36*−*39*). It has been proven that complete removal of radioimmunoconjugates from circulation after tumor targeting is the best way to protect the vital organs. Various methods have been developed, but none has reached the clinic because of practical difficulties and cost associated with the techniques. Thus, to date, no optimal strategy has been developed to limit the radiation toxicity to normal organs. Introduction of cathepsin-D degradable linkers between Ab and radiometal-DOTA-chelate has shown partial protection for the liver that is dose-limiting for myeloablative RIT using radiometals (*20*). Pretargeting approaches are promising but have limitations. The administration of exogenous protease from a nonhuman source, such as β-lactamase, has been shown to

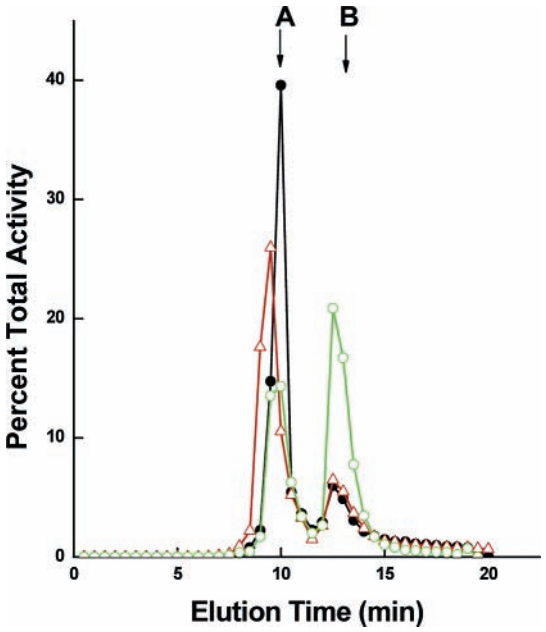
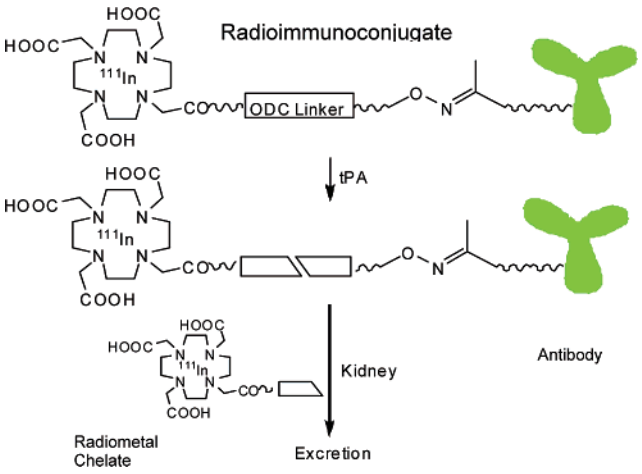


Figure 6. ^{111}In-DOTA−ODC−ChL6 was incubated with human plasma containing 10 μg/mL of TNKase. HPLC radiochromatograms are shown from samples, before (●) and after [2 h (red △) and 72 h (green ○)] the addition of TNKase. Peak A: ^{111}In-DOTA−ODC−ChL6, 150 kD. Peak B: ^{111}In-DOTA−ODC, 5 kD. At 10 μg/mL, TNKase digested 28% of RIC by 72 h.

Scheme 1. Schematic Representation of ODC Linker Hypothesis



cleave the radioconjugates in circulation; however, radioconjugates at tumor sites are also cleaved, suggesting that such agents should be active only in circulation in order to be effective (*21*).

In this study, we provide an alternative novel approach to lower radiation exposure to all normal organs by producing radioimmunoconjugates with TNKase-susceptible "on-demand cleavable" (ODC) linkers. After adequate uptake of radiometal in the tumor, TNKase can be administered intravenously to cleave the ODC linker, resulting in the release of radiometal-DOTA-chelate from the circulating RIC for renal excretion (Scheme 1). Consequently, the unbound radiometal-DOTA-chelate can be rapidly eliminated from the circulation, resulting in diminished toxicity to normal organs. TNKase was chosen over other proteases as an on-demand cleavage agent because (i) it has already been used safely for several years as a thrombolytic agent (*22*, *40*), (ii) it has one known physiological substrate, plasminogen (*41*), (iii) it is already commercially available in both the short-acting (Ativase) and longer-acting forms (TNKase) (*42*), and (iv) its volume of distribution is very similar to the blood volume, indicating that the enzyme resides predominantly within the intravascular space. Bleeding is the main side effect of the t-PA therapy at clinical dosage (10 μg/mL), so we intend to use only one-tenth of the clinical dosage (1 μg/mL) or less, by developing highly susceptible ODC linkers.

A linear peptide substrate derived from the primary sequence of plasminogen (t-PA's physiological substrate) is not cleaved efficiently as intact plasminogen, suggesting that it is not a good candidate for an ODC linker (*43*, *44*). Ding *et al.* described the use of phage-display combinatorial peptide libraries to identify PFGRSA peptide as an efficient substrate for t-PA (*44*). However, this peptide is also highly susceptible to cleavage by proteases present in plasma (Figure 1) and cancer cell supernatants (Figure 2). Thus, it is unsuitable for use as an ODC linker. One main reason that PFGRSA is rapidly degraded in human plasma and cancer cell supernatant is that it is an all L-amino acid peptide. Every peptide bond within this hexapeptide is a potential cleavage site for the numerous proteases present in plasma or tissue proteases. In order to eliminate many of the unwanted cleavage sites by other proteases but still retain appropriate amino acid side chains at the P_2, P_3, P_4, P_2', P_3', and P_4' sites for specific interaction with TNKase, we needed to develop peptide libraries with a combination of D-amino acids and L-amino acids. This is impossible with phage-display libraries but can be easily accomplished with synthetic peptide libraries such as the OBOC combinatorial peptide library method.

Screening an OBOC library is one of the best strategies to identify potential enzyme substrates and novel cancer-specific targeting ligands. We have recently reported the use of the focused OBOC library strategy to develop a lymphoma-targeting ligand with binding affinity of approximately 2 pM (*45*, *46*). By screening the OBOC libraries with a fluorescence-quench assay, we identified unique peptide linkers that were susceptible to TNKase cleavage but stable in human plasma and cancer cell supernatants. One of these peptides rqYKYkf, containing both D- and L-amino acids, is particularly promising, as it can be completely degraded by TNKase within 2 h, resulting in an enzyme level that is clinically achievable (10 μg/mL), and yet it is stable in plasma and cancer cell supernatants. When rqYKYkf was used as an ODC linker to ligate DOTA to ChL6 antibody and DOTA was labeled with ^{111}In, only 28% of the radiometal was released from the RIC after incubation with TNKase (10 μg/mL) for 72 h. The less-efficient cleavage of rqYKYkf when linked to an antibody when compared to a solution peptide may in part be explained by steric hindrance caused by the antibody molecule or by the DOTA.

CONCLUSION AND FUTURE PLAN

We have demonstrated that highly specific and efficient ODC-peptide linkers can be discovered through screening OBOC combinatorial peptide libraries containing both D- and L-amino acids. To improve the efficiency of on-demand cleavage by eliminating possible steric hindrance caused by DOTA and/or the antibody molecule, we plan to insert short PEG linkers between DOTA and rqYKYkf and between rqYKYkf and the antibody. We also plan to link two rqYKYkf peptides serially so that cleavage of any of the two peptides will lead to radiometal-DOTA-chelate release. Furthermore, we plan to design focused OBOC libraries based on the rqYKYkf sequence and use a more stringent screening method, e.g., a much lower dose of TNKase (1μg/mL), to further optimize a highly specific and efficient substrate for TNKase.

ACKNOWLEDGMENT

This work was supported by PO1 grant (CA47829) from NIH. The authors thank Jan Marik for help in mass spectrometry analysis, Gary Mirick for performing immunoreactivity assay, and Amanda Enstrom for help in manuscript preparation.

LITERATURE CITED

(1) Denardo, S. J., Richman, C. M., Goldstein, D. S., Shen, S., Salako, Q., Kukis, D. L., Meares, C. F., Yuan, A., Welborn, J. L., and Denardo, G. L. (1997) Yttrium-90/indium-111-DOTA-peptide-chimeric L6: pharmacokinetics, dosimetry and initial results in patients with incurable breast cancer. *Anticancer Res. 17*, 1735−1744.

(2) DeNardo, G. L., Kukis, D. L., Shen, S., DeNardo, D. A., Meares, C. F., and DeNardo, S. J. (1999) ^{67}Cu-versus ^{131}I-labeled Lym-1 antibody: comparative pharmacokinetics and dosimetry in patients with non-Hodgkin's lymphoma. *Clin. Cancer Res. 5*, 533−541.

(3) Press, O. W., Shan, D., Howell-Clark, J., Eary, J., Appelbaum, F., Matthew, D., Hinman, L., Shochat, D., and Bernstein, I. D. (1996) Comparative metabolism and retension of iodine-125, yttrium-90, and indium-111 radioimmunoconjugates by cancer cells. *Cancer Res. 56*, 2123−2129.

(4) Breitz, H. (2002) Dosimetry in a myeloablative setting. *Cancer Biother. Radiopharm. 17*, 119−128.

(5) Bouchet, L. G., Bolch, W. E., Blanco, H. P., Wessels, B. W., Siegel, J. A., Rajon, D. A., Clairand, I., and Sgouros, G. (2003) MIRD pamphlet no. 19: Absorbed fractions and radionuclide values for six age-dependent multiregion models of the kidney. *J. Nucl. Med. 44*, 1113−1147.

(6) Wessels, B. W., Bolch, W. E., Bouchet, L. G., Breitz, H. B., DeNardo, G. L., Meredith, R. F., Stabin, M. G., and Sgouros, G. (2004) Bone marrow dosimetry using blood-based models for radiolabeled antibody therapy: A multiinstitutional comparison. *J. Nucl. Med. 45*, 1725−1733.

(7) Goodwin, D. A., and Meares, C. F. (2001) Advances in pretargeting biotechnology. *Biotechnol. Adv. 19*, 435−450.

(8) Paganelli, G. (2005) Pretargeted radioimmunotherapy. *Ernst Schering Res. Found. Workshop 49*, 73−84.

(9) Breitz, H. B., Fisher, D. R., Goris, M. L., Knox, S., Ratliff, B., Murtha, A. D., and Weiden, P. L. (1999) Radiation absorbed dose estimation for 90Y-DOTA-biotin with pretargeted NR-LU-10/streptavidin. *Cancer Biother. Radiopharm. 14*, 381−395.

(10) Norrgren, K., Strand, S. E., Nilsson, R., Lindgren, L., and Sjogren, H. O. (1993) A general, extracorporeal immunoadsorption method to increase the tumor-to-normal tissue ratio in radioimmunoimaging and radioimmunotherapy. *J. Nucl. Med. 34*, 448−454.

(11) Dienhart, D. G., Kasliwal, R., Lear, J. L., Johnson, T. K., Bloedow, D. C., Hartmann, C., Seligman, P. A., Miller, G. J., Glenn, S. D., Mcateer, M. J., Thickman, D., Feyerabend, A., Maddock, E. N., Maddock, S. W., and Bunn, P. A. (1994) Extracorporeal immunoadsorption of radiolabeled monoclonal-antibody - a method for reduction of background radioactivity and its potential role during the radioimmunotherapy of cancer. *Antibody Immunoconjugates and Radiopharmaceuticals 7*, 225−252.

(12) Tennvall, J., Garkavij, M., Chen, J., Sjogren, H. O., and Strand, S. E. (1997) Improving tumor-to-normal-tissue ratios of antibodies by extracorporeal immunoadsorption based on the avidin-biotin concept: development of a new treatment strategy applied to monoclonal antibodies murine L6 and chimeric BR96. *Cancer 80*, 2411−2418.

(13) Denardo, G. L., Denardo, S. J., Meares, C. F., Kukis, D., Diril, H., Mccall, M. J., Adams, G. P., Mausner, L. F., Moody, D. C., and Deshpande, S. V. (1991) Pharmacokinetics of copper-67 conjugated Lym-1, a potential therapeutic radioimmunoconjugate, in mice and in patients with lymphoma. *Antibody Immunoconjugates and Radiopharmaceuticals 4*, 777−785.

(14) Denardo, G. L., Maddock, S. W., Sgouros, G., Scheibe, P. O., and Denardo, S. J. (1993) Immunoadsorption - an enhancement strategy for radioimmunotherapy. *J. Nucl. Med. 34*, 1020−1027.

(15) Chang, C. H., Sharkey, R. M., Rossi, E. A., Karacay, H., McBride, W., Hansen, H. J., Chatal, J. F., Barbet, J., and Goldenberg, D. M. (2002) Molecular advances in pretargeting radioimunotherapy with bispecific antibodies. *Mol. Cancer Ther. 1*, 553−563.

(16) Boerman, O. C., van Schaijk, F. G., Oyen, W. J., and Corstens, F. H. (2003) Pretargeted radioimmunotherapy of cancer: progress step by step. *J. Nucl. Med. 44*, 400−411.

(17) Gruaz-Guyon, A., Raguin, O., and Barbet, J. (2005) Recent advances in pretargeted radioimmunotherapy. *Curr. Med. Chem. 12*, 319−338.

(18) Weiden, P. L., Breitz, H. B., Press: O., Appelbaum, J. W., Bryan, J. K., Gaffigan, S., Stone, D., Axworthy, D., Fisher, D., and Reno, J. (2000) Pretargeted radioimmunotherapy (PRIT (TM)) for treatment of non-Hodgkin's lymphoma (NHL): Initial phase I/II study results. *Cancer Biother. Radiopharm. 15*, 15−29.

(19) Meares, C. F., McCall, M. J., Deshpande, S. V., DeNardo, S. J., and Goodwin, D. A. (1988) Chelate radiochemistry: cleavable linkers lead to altered levels of radioactivity in the liver. *Int. J. Cancer Suppl. 2*, 99−102.

(20) DeNardo, G. L., DeNardo, S. J., Peterson, J. J., Miers, L. A., Lam, K. S., Hartmann-Siantar, C., and Lamborn, K. R. (2003) Preclinical evaluation of cathepsin-degradable peptide linkers for radioimmunoconjugates. *Clin. Cancer Res. 9*, 3865S−72S.

(21) Beeson, C., Butrynski, J. E., Hart, M. J., Nourigat, C., Matthews, D. C., Press, O. W., Senter, P. D., and Bernstein, I. D. (2003) Conditionally cleavable radioimmunoconjugates: a novel approach for the release of radioisotopes from radioimmunoconjugates. *Bioconjugate Chem. 14*, 927−933.

(22) Davydov, L., and Cheng, J. W. (2001) Tenecteplase: a review. *Clin. Ther. 23*, 982−97; discussion 981.

(23) Lam, K. S., Salmon, S. E., Hersh, E. M., Hruby, V. J., Kazmierski, W. M., and Knapp, R. J. (1991) A new type of synthetic peptide library for identifying ligand-binding activity. *Nature (London) 354*, 82−84.

(24) Lam, K. S., Lebl, M., and Krchnak, V. (1997) The "one-bead-one-compound'' combinatorial library method. *Chem. Rev. 97*, 411−448.

(25) Meldal, M., Svendsen, I., Breddam, K., and Auzanneau, F. I. (1994) Portion-mixing peptide libraries of quenched fluorogenic substrates for complete subsite mapping of endoprotease specificity. *Proc. Natl. Acad. Sci. U.S.A. 91*, 3314−3318.

(26) Song, A. M., Wang, X. B., Zhang, J. H., Marik, J., Lebrilla, C. B., and Lam, K. S. (2004) Synthesis of hydrophilic and flexible linkers for peptide derivatization in solid phase. *Bioorg. Med. Chem. Lett. 14*, 161−165.

(27) Goodman, G. E., Hellstrom, I., Yelton, D. E., Murray, J. L., Ohara, S., Meaker, E., Zeigler, L., Palazollo, P., Nicaise, C., Usakewicz, J., and Hellstrom, K. E. (1993) Phase-I trial of chimeric (human-mouse) monoclonal-antibody L6 in patients with non-small-cell lung, colon, and breast-cancer. *Cancer Immunol. Immunother. 36*, 267−273.

(28) Denardo, S. J., Mirick, G. R., Kroger, L. A., Ogrady, L. F., Erickson, K. L., Yuan, A., Lamborn, K. R., Hellstrom, I., Hellstrom, K. E., and Denardo, G. L. (1994) The biologic window for chimeric L6 radioimmunotherapy. *Cancer 73*, 1023−1032.

(29) Xu, Q., Miyamoto, S., and Lam, K. S. (2004) A novel approach to chemical microarray using ketone-modified macromolecular scaffolds: application in micro cell-adhesion assay. *Mol. Diversity 8*, 301−310.

(30) Meares, C. F., McCall, M. J., Reardan, D. T., Goodwin, D. A., Diamanti, C. I., and McTigue, M. (1984) Conjugation of antibodies with bifunctional chelating agents: isothiocyanate and bromoacetamide reagents, methods of analysis, and subsequent addition of metal ions. *Anal. Biochem. 142*, 68−78.

(31) Goodwin, D. A., Meares, C. F., Watanabe, N., Mctigue, M., Chaovapong, W., Ransone, C. M., Renn, O., Greiner, D. P., Kukis, D. L., and Kronenberger, S. I. (1994) Pharmacokinetics of pretargeted monoclonal-antibody 2d12.5 and Y-88 Janus-2-(*p*-nitrobenzyl)-1,4,7,10-tetraazacyclododecanetetraacetic acid (DOTA) in Balb/C mice with Khjj mouse adenocarcinoma - a model for Y-90 *Cancer Res. 54*, 5937−5946.

(32) Kukis, D. L., DeNardo, G. L., DeNardo, S. J., Mirick, G. R., Miers, L. A., Greiner, D. P., and Meares, C. F. (1995) Effect of the extent of chelate substitution on the immunoreactivity and biodistribution of 2IT-BAT-Lym-1 immunoconjugates. *Cancer Res. 55*, 878−884.

(33) Moi, M. K., Meares, C. F., DeNardo, S. J. (1988) The peptide way to macrocyclic bifunctional chelating agents: synthesis of 2-(*p*-nitrobenzyl)-1,4,7,10-tetraazacyclododecane-*N*,*N*′,*N*′′,*N*′′′-tetraacetic acid and study of its yttrium (III) complex. *J. Am. Chem. Soc. 110*, 6266−6267.

(34) Lim, S. M., DeNardo, G. L., DeNardo, D. A., Shen, S., Yuan, A., O'Donnell, R. T., and DeNardo, S. J. (1997) Prediction of myelotoxicity using radiation doses to marrow from body, blood and marrow sources. *J. Nucl. Med. 38*, 1374−1378.

(35) Breitz, H. B., Fisher, D. R., and Wessels, B. W. (1998) Marrow toxicity and radiation absorbed dose estimates from rhenium-186-labeled monoclonal antibody. *J. Nucl. Med. 39*, 1746−1751.

(36) Divgi, C. R., Bander, N. H., Scott, A. M., O'Donoghue, J. A., Sgouros, G., Welt, S., Finn, R. D., Morrissey, F., Capitelli, P., Williams, J. M., Deland, D., Nakhre, A., Oosterwijk, E., Gulec, S., Graham, M. C., Larson, S. M., and Old, L. J. (1998) Phase I/II radioimmunotherapy trial with iodine-131-labeled monoclonal antibody G250 in metastatic renal cell carcinoma. *Clin. Cancer Res. 4*, 2729−2739.

(37) Behr, T. M., Sharkey, R. M., Sgouros, G., Blumenthal, R. D., Dunn, R. M., Kolbert, K., Griffiths, G. L., Siegel, J. A., Becker, W. S., and Goldenberg, D. M. (1997) Overcoming the nephrotoxicity of radiometal-labeled immunoconjugates - Improved cancer therapy administered to a nude mouse model in relation to the internal radiation dosimetry. *Cancer 80*, 2591−2610.

(38) Press, O. W., Appelbaum, F. R., Eary, J. F., and Bernstein, I. D. (1995) Radiolabeled antibody therapy of lymphomas. *Important Adv. Oncol.* 157−171.

(39) Press, O. W., Eary, J. F., Appelbaum, F. R., Martin, P. J., Nelp, W. B., Glenn, S., Fisher, D. R., Porter, B., Matthews, D. C., Gooley, T., and Bernstein, I. D. (1995) Phase II trial of 131I-B1 (anti-CD20) antibody therapy with autologous stem cell transplantation for relapsed B cell lymphomas. *Lancet 346*, 336−340.

(40) Guerra, D. R., Karha, J., and Gibson, C. M. (2003) Safety and efficacy of tenecteplase in acute myocardial infarction. *Expert Opin. Pharmacother. 4*, 791−798.

(41) Madison, E. L., Coombs, G. S., and Corey, D. R. (1995) Substrate-specificity of tissue-type plasminogen-activator - characterization of the fibrin independent specificity of T-Pa for plasminogen. *J. Biol. Chem. 270*, 7558−7562.

(42) Modi, N. B., Fox, N. L., Clow, F. W., Tanswell, P., Cannon, C. P., Van, de Werf, F., and Braunwald, E. (2000) Pharmacokinetics and pharmacodynamics of tenecteplase: results from a phase II study in patients with acute myocardial infarction. *J. Clin. Pharmacol. 40*, 508−515.

(43) Madison, E. L. (1994) Probing structure-function-relationships of tissue-type plasminogen-activator by site-specific mutagenesis. *Fibrinolysis 8*, 221−236.

(44) Ding, L., Coombs, G. S., Strandberg, L., Navre, M., Corey, D. R., and Madison, E. L. (1995) Origins of the specificity of tissue-type plasminogen activator. *Proc. Natl. Acad. Sci. U.S.A. 92*, 7627−7631.

(45) Peng, L., Liu, R. W., Marik, J., Wang, X. B., Takada, Y., and Lam, K. S. (2006) Combinatorial chemistry identifies high-affinity peptidomimetics against α(4)β(1) integrin for in vivo tumor imaging. *Nat. Chem. Biol. 2*, 381−389.

(46) Peng, L., Liu, R., Wang, X., Marik, J., Takada, Y., and Lam, K. S. (2005) High affinity high specificity α4 β1 integrin targeting peptides for lymphoid cancers. *Biopolymers 80*, 559−559.

BC0602681

Encapsulated Magnetic Nanoparticles as Supports for Proteins and Recyclable Biocatalysts

Aimee R. Herdt, Byeong-Su Kim, and T. Andrew Taton*

University of Minnesota, Department of Chemistry, 207 Pleasant Street SE, Minneapolis, Minnesota 55455.
Received July 14, 2006; Revised Manuscript Received November 13, 2006

This paper describes the bioconjugation of histidine-tagged enzymes and other proteins to the surface of composite "magnetomicelles" consisting of magnetic γ-Fe_2O_3 nanoparticles encapsulated within cross-linked polystyrene-*block*-polyacrylate copolymer micelle shells. Free carboxylic acid groups on the magnetomicelle surface were converted to Cu^{2+}-iminodiacetic acid (IDA) for protein capture. The conjugation of T4 DNA ligase and enhanced green fluorescent protein to magnetomicelles revealed that proteins were captured with a high surface density and could be magnetically separated from reaction mixtures and subsequently released from the nanoparticle surface. Additionally, bioconjugation of T7 RNA polymerase yielded a functional enzyme that maintained its biological activity and could be recycled for up to three subsequent transcription reactions. We propose that protein−magnetomicelle bioconjugates are effective for protein bioseparation and enzymatic recycling and further strengthen the idea that nanoparticle surfaces have utility in protein immobilization.

INTRODUCTION

Protein-modified particles (*1*), both microparticles and nanoparticles, have many biotechnological uses, including protein separation and purification, protein detection and analysis, in vivo imaging, bioelectrodes and biosensors, and biocatalytic transformations (*2*−*7*). Particle-bound enzymes are of special interest as recyclable catalysts. In principle, magnetic nanoparticles should be excellent solid supports for enzymes (*8*); nanoparticle supports inherently maximize the surface area available for enzyme attachment, and magnetic nanoparticles with sufficient magnetization are easily recovered from aqueous suspension by applying a static magnetic field. One significant challenge to practical use of magnetic nanoparticles as enzyme supports is the availability of general bioconjugate chemistries for connecting proteins to particles. Current methods for attaching proteins to particles include physical adsorption/deposition (*9*, *10*), entrapment (*11*, *12*), cross-linking (*5*), and covalent attachment (*13*). One attractive strategy for specifically conjugating proteins to particles uses fusion tags to attach a specific locus, usually the N- or C-terminus, to reactive or coordinating groups on the particle surface (*14*−*17*). For example, Xu and co-workers recently demonstrated that hexahistidine (His_6)-tagged GFP could be selectively captured onto nitriloacetic acid (NTA)-modified FePt (*18*) or M/Fe_2O_3 (M = Co or $SmCo_{5.2}$) (*19*) nanoparticles when appropriate ligands were covalently installed on the particle surfaces.

In order to control the stability and surface functionality of magnetic nanoparticles, our group has developed a method for the encapsulation of hydrophobic γ-Fe_2O_3 particles (d = 10.9 nm) in amphiphilic polystyrene$_{250}$-*block*-poly(acrylic acid$_{13}$) (PS_{250}-*b*-PAA_{13}) block copolymer (*20*). The outer PAA block of the micelles renders these nanostructures water-soluble and displays carboxylic acid groups used to (*1*) permanently fix the micelle shell with EDC-activated 2,2′-(ethylenedioxy)bis(ethylamine) cross-linker and (*2*) facilitate the attachment of biomolecules. Herein, we demonstrate the covalent immobilization of proteins onto these hybrid nanoscale materials, termed "magnetomicelles", by attaching iminodiacetic acid (IDA) to the micelle surface, and use the functionalized Cu^{2+}-IDA magnetomicelles to selectively capture His_6-tagged proteins (Scheme 1) (*18*, *21*). We establish that the encapsulated magnetic nanoparticles are suitable for biological environments and permit the external manipulation of conjugated biomolecules. Specifically, we report the bioseparation of His_6-tagged T4 DNA ligase (T4 DNAL) and enhanced green fluorescent protein (EGFP). In addition, we show that T7 RNA polymerase (T7 RNAP) maintains enzyme activity while conjugated to magnetomicelles and that the enzyme bioconjugate is recoverable for recycled enzyme use.

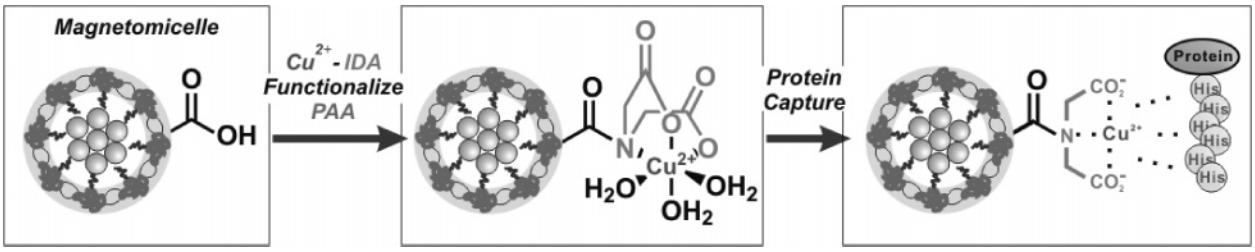
EXPERIMENTAL PROCEDURES

Magnetomicelle Preparation and Functionalization. Magnetomicelles were prepared as previously reported (*20*). Briefly, magnetomicelles were prepared from 10.9 nm γ-Fe_2O_3 magnetic nanoparticles ($[\gamma\text{-}Fe_2O_3]_{initial}$ = 0.30 mg/mL in 50:50 DMF/THF) and PS_{250}-*b*-PAA_{13} ($[PS_{250}\text{-}b\text{-}PAA_{13}]_{final} = 2.0 \times 10^{-2}$ mg/mL). Assembled, copolymer-coated particles were exposed to 1-ethyl-3-(3-dimethylaminopropyl)-carbodiimide (EDC) to activate 50% of the PAA block carboxylates, followed by 2,2′-(ethylenedioxy)bis(ethylamine) to cross-link these carboxylates. For IDA functionalization, 5.0 mL of magnetomicelle solution (effective carboxylic acid groups in PAA block = 2.41×10^{-8} mol) was mixed with 21.5 μL of freshly prepared EDC solution (1.0 mg/mL in H_2O, 3.0 equiv to carboxylic acid groups in the PAA block) with vigorous stirring. After 30 min of activation, 31.4 μL of *N*-hydroxysulfosuccinimide sodium salt (sulfo-NHS) (1.0 mg/mL in H_2O, 6.0 equiv to carboxylic acid groups in the PAA block) was added to the suspension. Solutions were stirred for 1.5 h, and the suspension was added dropwise to 32 μL of iminodiacetic acid (IDA) (1.0 mg/mL in H_2O, 10 equiv to carboxylic acid groups in the PAA block) in 1.0 mL of 10 mM $Na_2CO_3/NaHCO_3$ buffer (pH 9.5) (*22*). The solution was vigorously mixed for 24 h at room temperature and dialyzed against diH_2O (Spectra/Por 4 Regenerated Cellulose Membrane, MWCO = 12−14K) over 48 h. To this solution was added 7.2 μL of aqueous $CuSO_4 \cdot 5H_2O$ (10 mg/mL in H_2O, 10 equiv of carboxylic acid groups in the PAA block), and the mixture was

* Author to whom correspondence should be addressed. E-mail: taton@chem.umn.edu.

10.1021/bc060215j CCC: $37.00 © 2007 American Chemical Society
Published on Web 12/13/2006

Scheme 1. Protein−Magnetomicelle Bioconjugaton



allowed to stand for 3 h to load IDA groups with Cu^{2+}; excess reagents were removed with extensive dialysis.

Characterization of Functionalized Magnetomicelles. Transmission electron microscopy (TEM) images were obtained on a JEOL 1210 electron microscope equipped with a Gatan video camera and a Gatan Multiscan CCD camera (1024 × 1024 pixels). Magnetomicelle solutions were dropped onto 300-mesh Formvar-graphite-coated copper TEM grids (Electron Microscopy Science, Hartfield, PA) and air-dried for TEM imaging. All images were obtained at an operating voltage of 120 kV.

Protein Preparation, Purification. Recombinant T4 DNA ligase (BL21(DE3)p-lysS, p3H11) (*23*), EGFP (pBAD-18-Cm) (*24*), and T7 RNA polymerase (M15:pDMI.1, p6HRNAP) (*25*), all containing His_6 fusion tags, were overexpressed in *E. coli* according to previously published protocols. Proteins were purified by affinity chromatography using Ni^{2+}-NTA-agarose resin (Qiagen) and eluted with imidazole-containing buffer. Product protein solutions were buffer-exchanged and concentrated by centrifugal dialysis using Centriprep YM-10 tubes (Amicon, Bedford, MA) and stored at −20 °C. Proteins were analyzed by 8% SDS-PAGE and their concentrations estimated by standard BCA protein assay.

Bioconjugate Preparation and Magnetic Separation. Suspensions of Cu^{2+}-IDA magnetomicelles were mixed with His_6-tagged proteins in Eppendorf tubes for 2 h at 4 °C. Magnets (NdFeB magnet, 0.14 T) were applied to the bottom and one side edge of the tubes for 1 h, and the supernatant (top 70% of solution) was pipetted away, in order to isolate the magnetomicelle−protein conjugates from unconjugated, free protein. The magnetomicelle−protein bioconjugates were then washed two to four times with diH_2O prior to protein analysis, elution, or enzymatic reaction. To wash, the magnet was removed from the bottom of the Eppendorf tube, residue was resuspended in an equal volume diH_2O, the magnets were reapplied for 1 h, and the supernatant (top 50%) was pipetted away.

T4 DNA Ligase−Magnetomicelle Assay. 450 μL of Cu^{2+}-IDA magnetomicelle solution was mixed with T4 DNAL and 10% SDS for a total reaction volume of 500 μL. Reactions were treated as described above in Bioconjugate Preparation and Magnetic Separation. T4 DNAL could be eluted from the magnetomicelles by resuspending magnetically separated residue in 75 μL 1 M imidazole, followed by a round of magnetic separation. The flow-through, washes, and final elution fraction were dialyzed overnight against diH_2O using Slide-A-Lyzer Mini Dialysis units (Pierce, Rockford, IL) at 4 °C. Dialyzed samples were lyophilized to dryness and resuspended in 10 μL for gel analysis by 8% SDS-PAGE. In control experiments, magnetomicelles were treated as described above, except that IDA and Cu^{2+} were omitted.

GFP−Magnetomicelle Assay. 200 μL of Cu^{2+}-IDA magnetomicelle solution was mixed with EGFP. Reactions were treated as described in Bioconjugate Preparation and Magnetic Separation. All washes and the final 60 μL fraction of EGFP−magnetomicelle bioconjugates were resuspended to 140 μL for fluorescence analysis. EGFP−magnetomicelle data reported is the average of six individual experiments. The steady-state fluorescence measurements were obtained with a Quantamaster Fluorimeter (PTI London, Ontario) at room temperature, using an excitation wavelength of 395 nm and emission and excitation slit widths of 2 nm. In all experiments, the raw average of two emission scans was reported. An EGFP fluorescence calibration curve was generated by magnetically separating 200 μL of nonfunctionalized magnetomicelle suspension, then removing 60 μL of the supernantant. The resulting 140 μL of micelle solution was mixed with known amounts of EGFP and the fluorescence intensity measured.

T7 RNA Polymerase Activity. 200 μL of Cu^{2+}-IDA magnetomicelle solution was mixed with T7 RNAP. Reactions were treated as described in Bioconjugate Preparation and Magnetic Separation. The final 60 μL fraction of T7 RNAP−magnetomicelle bioconjugates were added to transcription reactions, performed at 37 °C for 4 h, in the presence of 10× transcription buffer (0.4 M Tris·Cl, pH 8.0, 60 mM $MgCl_2$, 0.01 M spermidine, 0.1% 1090 Triton, BSA and DTT), 4 mM each NTPs, 1 μM template DNA, 20 mM $MgCl_2$, and 10 mM DTT for a final reaction volume of 100 μL. Template DNA was (i) a 155-mer, PCR-generated synthetic template containing the DNA sequence for the T7 RNAP promoter or (ii) plasmid DNA (3.4 kb), which contains the T7 RNA promoter and the DNA template for *E. coli* $tRNA^{Pro}$ RNA (76-mer) (*26*). Plasmid DNA was digested with *Bst*N1 and gel-purified prior to transcription. For T7 RNAP−magnetomicelle recycling experiments, after the first transcription reaction, the reaction solution was magnetically separated and 70% of the free reaction solution was removed (70 μL) for gel analysis. The remaining 30 μL of T7 RNAP−magnetomicelle bioconjugates were resuspended to 120 μL with diH_2O and treated according to Bioconjugation Preparation and Magnetic Separation, described above. The final 60 μL was reused in a second transcription reaction. Transcription products (RNA) were analyzed by denaturing 12% PAGE. Control experiments were preformed as described above, except that all the fractions were collected without the application of the magnets. In addition, reactions were run with unconjugated T7 RNAP and T7 RNAP mixed with magnetomicelles that were not washed from T7 RNAP free in solution.

RESULTS

On the basis of our previous studies on the synthesis and functionalization of copolymer micelle-encapsulated nanoparticles (*20, 27, 28*), we anticipated that γ-Fe_2O_3 magnetomicelles would be excellent supports for proteins. Encapsulation of γ-Fe_2O_3 magnetic nanoparticles within cross-linked surfactant shells makes it possible to take advantage of the nanoparticles' intrinsic properties without the need to develop specific chemistries for directly attaching proteins to the nanoparticle surface. The surfactant shell also stabilizes the particles to physical and chemical manipulation in biological buffers and protects proteins from direct contact with the core nanoparticle surfaces. In this study, we used magnetomicelles in which 50% of the PAA carboxylates were cross-linked, leaving the other 50% available for bioconjugation.

The bioconjugate chemistry used in this study is based on immobilized metal affinity chromatography (IMAC), a common

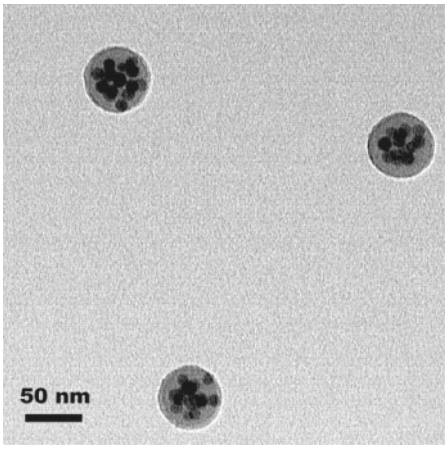


Figure 1. Representative TEM micrograph of Cu^{2+}-IDA functionalized magnetomicelles. Multiple γ-Fe_2O_3 nanoparticles are confined within each polymer micelle core, and the average Cu^{2+}-IDA magnetomicelle diameter is 50 nm.

technique for the purification of recombinant proteins (*29*, *30*). In IMAC, His_6−protein fusions are initially bound to Ni^{2+}- or Co^{2+}-loaded nitriloacetic acid (NTA) groups on functionalized resin and can be subsequently eluted from the support by exposure to imidazole solution. Interactions between His_6 tags and metal-NTA groups have recently been used to capture proteins on the surfaces of various types of nanostructures, including gold (*21*) and magnetic nanoparticles (*18*, *19*) and magnetic nanorods (*31*). We chose to functionalize magnetomicelles with Cu^{2+}-IDA rather than Ni^{2+}- or Co^{2+}-NTA due to its higher binding affinity for the polyhistidine fusion tag (*32*, *33*). Magnetomicelle carboxylates were converted to IDA groups via EDC coupling. Particles were then exposed to Cu^{2+} and washed to prepare them for protein loading. TEM micrographs of Cu^{2+}-IDA functionalized magnetomicelles appeared identical to those taken prior to functionalization (Figure 1). Further characterization by X-ray photoelectron spectroscopy (XPS) confirmed the presence of copper in dialyzed Cu^{2+}-IDA magnetomicelle preparations. By contrast, control samples in which EDC was omitted from the magnetomicelle functionalization exhibited no XPS peak corresponding to copper (data not shown). This experiment indicates that IDA functionalization was required to bind Cu^{2+}. Suspensions of Cu^{2+}-IDA magnetomicelles were stable for at least several months but were typically bound to proteins soon after synthesis. Assuming that functionalization with IDA was similar to that of primary amines studied previously in our group, we estimate that several hundred Cu^{2+}-IDA molecules can be attached to the surface of a single, 50-nm magnetomicelle (*20*).

We initially evaluated Cu^{2+}-IDA magnetomicelles as protein supports by using them to capture His_6-tagged T4 DNA ligase (T4 DNAL). These experiments were designed to mimic standard, column-based IMAC protein purification protocols. Proteins were first captured by suspended nanoparticles, which were washed to remove unbound protein. Then, an IMAC-competing ligand, imidazole, was added to elute the protein from its nanoparticle supports (*34*). In all experiments, excess T4 DNAL was added to the functionalized magnetomicelles to saturate the particles with protein. Numerous cycles of magnetic separation and washing were used to remove unbound protein. The supernatant recovered from each step of protein bioconjugation and purification was analyzed by gel electrophoresis (Figure 2a). Excess unbound protein was recovered only in initial washing steps; subsequent magnetic separations and redispersion showed no loss of bound T4 DNAL to the supernatant. Elution with imidazole, however, yielded a single band on the SDS-PAGE gel corresponding to pure T4 DNAL.

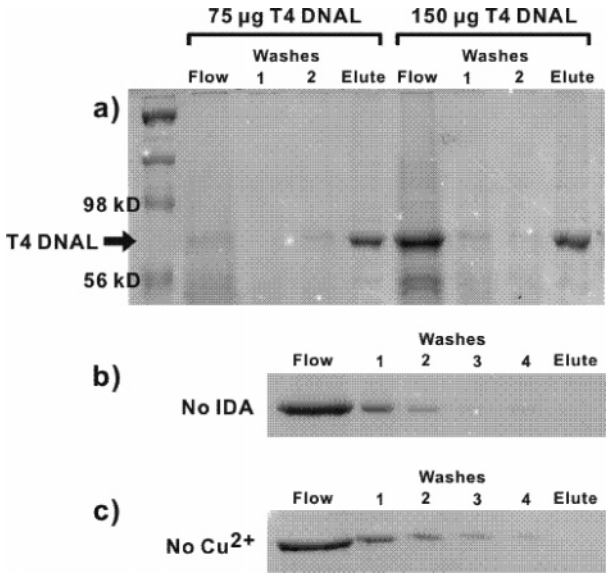


Figure 2. SDS-PAGE gel of T4 DNA ligase (68 kD) captured and isolated from ~2 × 1011 magnetomicelles (400 μL magnetomicelle solution), where (a) micelles were conjugated with varying amounts of T4 DNA ligase, or where (b) IDA or (c) Cu^{2+} was omitted from the preparation. Flow: Unbound material collected from supernatant after initial conjugation. Washes: Material collected from diH_2O wash steps. Elute: Material collected after exposure to 500 μM imidazole.

The binding capacity for T4 DNAL was dependent on the magnetomicelle concentration, such that the amount of T4 DNAL captured by equal suspensions of magnetomicelles was qualitatively reproducible, regardless of the amount of protein initially mixed with the nanoparticles. For example, magnetomicelle preparations mixed with 75 or 150 μg of T4 DNAL eluted similar quantities of protein after T4 DNAL−magnetomicelle purification (Figure 2a, elute lanes; additional data not shown).

Control experiments verified the specificity of the interaction between the Cu^{2+}-loaded IDA groups and the His_6 tags. In general, proteins lacking His_6 fusion tags did not bind to the surfaces of magnetomicelles. As a result, when particles were mixed with impure preparations of T4 DNAL, the imidazole-eluted protein was always observed to be more pure than the starting material by SDS-PAGE analysis (Figure 2a; additional data not shown). In addition, control experiments in which magnetomicelles were either not functionalized with IDA or not loaded with Cu^{2+}, exposed to T4 DNAL, and then subjected to elution conditions showed negligible protein capture. Instead, the T4 DNAL mixed with these preparations was recovered from the reaction solution during magnetic separation and washing (Figure 2b,c). This data confirms that the interaction between the particle-bound Cu^{2+}-IDA groups and the His_6 tag is highly specific. Similar work on monolithic, PAA-coated surfaces that had been modified with metal-NTA groups has shown low nonspecific binding in the absence of metal or ligand (*35*).

In order to quantify the protein bound to magnetomicelles, we analyzed particles conjugated to His_6-tagged enhanced green fluorescent protein (EGFP). The intrinsic fluorescence of GFP has been previously used in protein attachment to surfaces (*36*, *37*), supported membranes (*38*), and particles (*18*, *39*). Here, to further quantify the effectiveness of magnetomicelle protein loading, as well as to verify protein integrity after conjugation, His_6-tagged EGFP was captured by the magnetomicelles. As with His_6-T4 DNAL, gel electrophoresis experiments demonstrated that His_6-EGFP could be bound to the magnetomicelle surface and eluted with imidazole (*34*).

The conjugation and surface density of His_6-EGFP was also monitored by fluorescence spectroscopy. Overall, the fluores-

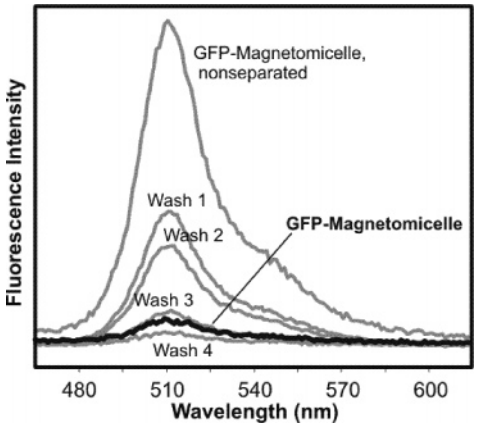


Figure 3. Fluorescence spectra of GFP−magnetomicelles, prior to magnetic separation, after all subsequent washes and after recovery of the bioconjugate solution. Bioconjugates were washed until the fluorescence intensity was negligible (wash 4), followed by GFP−magnetomicelle analysis.

cence spectrum of EGFP was not affected by conjugation to the particles. After mixing His_6-EGFP with the magnetomicelle suspension, the mixture was magnetically separated and washed until the supernatant exhibited no significant fluorescence (Figure 3). Then, the fluorescence signal from the EGFP−magnetomicelle bioconjugates was measured. When limiting amounts of His_6-EGFP were added to the preparation, the fluorescence intensity of these suspensions increased with increasing EGFP concentration. At the saturating concentration of His_6-EGFP, we estimate that 300 molecules of EGFP are attached to each 50-nm-diameter magnetomicelle in solution, based on the final fluorescence intensity of the suspension, or one molecule of EGFP per 26 nm^2 of particle surface. Given that GFP has a footprint of 12 nm^2 (*40*), this corresponds to a fairly high surface density of attached protein. The high density of conjugated EGFP molecules is consistent with our previous study, which indicated that around 600 molecules of NH_2-(ethylene glycol)$_5$-fluorescein functionalized the surface of a single magnetomicelle (*20*). The fluorescence intensity of the conjugates also suggests that EGFP remains intact while conjugated to the surface of the magnetomicelles, due to the retention of the protein's intrinsic fluorescence. Attaching GFP to magnetomicelles gives us a quantitative way to measure the magnetomicelle−protein loading capacity.

In order for magnetic nanoparticles to be useful as supports for enzymes, the bound enzyme must maintain its native activity even after repeated physical manipulation. A variety of enzymes have been used as models for evaluating the activity of particle-bound enzymes, including *Candida rugosa* lipase (*41*), horseradish peroxidase (*21*, *42*), proteases (*43*, *44*), and glucose oxidase (*3*). To test the use of magnetomicelles as recyclable supports for enzymes used in molecular biology, we used magnetomicelles in conjunction with an enzyme routinely used for the in vitro transcription of RNA, T7 RNA polymerase (T7 RNAP). Like most enzymes in molecular biology protocols, T7 RNAP is by far the most expensive reagent used in a transcription reaction, and we expected that attaching the enzyme to magnetomicelles would allow it to be recycled after use. However, T7 RNAP is susceptible to inhibition by a variety or reaction contaminants (*45*), and so we first tested whether transcription was inhibited by the magnetomicelle supports. Cu^{2+}-IDA magnetomicelles (with no protein attached) were added to otherwise ordinary transcription reactions of two separate dsDNA templates: a 155-nt, linear template that generates a 135-mer mRNA, and 3.4 kb plasmid that yields the 76-mer $tRNA^{Pro}$ (*26*). Gel electropherograms of the RNA

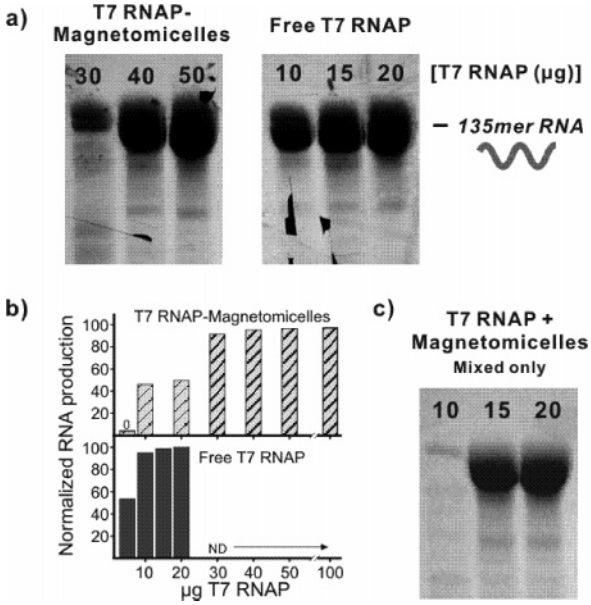


Figure 4. (a) Representative urea-PAGE gel images of RNA produced by T7 RNAP−magnetomicelles or free T7 RNAP, at concentrations where the enzyme was the limiting reagent. (b) Graphical analysis of densitometry studies of numerous gel images. Transcription data for free T7 RNAP at concentrations above 20 μg were not determined (ND), because the maximum level of RNA production was reached by 20 μg of enzyme. The data was normalized, such that the RNA generated with 20 μg of free T7 RNAP was set to 100%. No RNA was detected with 5 μg of T7 RNAP bound to the magnetomicelles. (c) Urea-PAGE gel of RNA produced when magnetomicelle suspension was added to a transcription reaction already in progress.

products produced in the absence or presence of Cu^{2+}-IDA magnetomicelles were indistinguishable (data not shown).

Additional experiments with magnetomicelle-bound RNA polymerase demonstrate that these materials are active, recoverable catalysts for transcription. Magnetomicelles were loaded with His_6-T7 RNAP, washed exhaustively, and used in place of free T7 RNAP to transcribe the two DNA templates described above. Conjugated T7 RNAP successfully transcribed both linear and plasmid DNA to RNA under standard reaction conditions (*34*). Cu^{2+}-IDA magnetomicelles that had been incubated with T7 RNAP that lacked a His_6 tag, by contrast, failed to catalyze DNA transcription (*34*). We conclude that, as was true for His_6-T4 DNAL and His_6-GFP, the hexahistidine tag is required to conjugate T7 RNAP to Cu^{2+}-IDA magnetomicelles and nonspecific adsorption of active catalyst was not significant.

In order to relate the activity of T7 RNAP−magnetomicelles to that of free T7 RNAP, we compared the amount of RNA product generated in side-by-side reactions using both catalysts. Experiments were conducted in which the enzyme was a limiting reagent for RNA production, and in all cases, the amount of DNA template was held constant at 1 μM. As is true for T7 RNAP alone, increasing concentrations of RNAP-loaded magnetomicelles increased transcription efficiency (Figure 4a). Collectively, using densitometry to quantify the amount of RNA produced, these transcription assays reveal that efficient transcription requires 3−4 times the amount of T7 RNAP to be conjugated to the magnetomicelle surfaces versus free enzyme in solution (Figure 4b). However, we found that any manipulation of the standard transcription reaction, including adding magnetomicelles to a transcription reaction already in progress, causes a slight decrease in RNA production (Figure 4c). As a result, it is possible that the magnetomicelle solution is slightly inhibitory to T7 RNAP, regardless of its bound or unbound state, or causes RNA degradation, perhaps due to the presence of RNases.

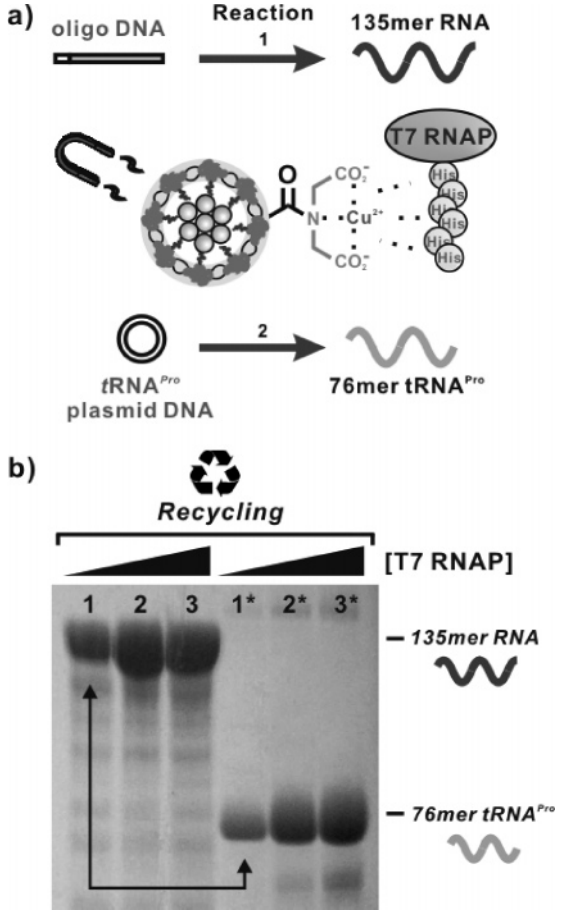


Figure 5. (a) T7 RNAP−magnetomicelle recycling scheme. (b) Urea-PAGE gel of RNA produced by T7 RNAP−magnetomicelles. Starred lanes represent the second reaction performed with the recycled T7 RNAP−magnetomicelle bioconjugates from the similarly numbered but unstarred lanes. The concentration of T7 RNAP conjugated to the magnetomicelles increased from lanes 1−3.

Consequently, to further justify the utility of our protein−magnetomicelle bioconjugates, we tested the recyclability of the conjugates. Recycling biologically relevant enzymes, for as little as one or two subsequent assays, could greatly reduce experimental times and costs. To test whether magnetomicelle-bound enzymes could be recycled and reused without contamination from prior reactions, we designed a transcription assay using T7 RNAP−magnetomicelles and the two different DNA templates (for 135-nt mRNA and 76-nt $tRNA^{Pro}$) described above. The first reaction was performed in the presence of one DNA template, followed by magnetic separation of the T7 RNAP−magnetomicelles, removal of the RNA product generated, washing, and a second transcription with the separated bioconjugates and the opposite DNA template (Figure 5a). Incomplete washing of the recycled T7 RNAP−magnetomiclles would be assayed by the production of the first RNA product in the second reaction. As a result, up to four T7 RNAP−magnetomicelle washes were required to remove DNA contamination in a second reaction (*34*). To our surprise, T7 RNAP−magnetomicelles successfully transcribed RNA up to three times, although only the first two reactions produced levels of RNA with no qualitative loss in T7 RNAP activity (Figure 5b). Additionally, the amount of RNA produced from recycled T7 RNAP was dependent on the concentration of T7 RNAP conjugated to the magnetomicelle surface. The recovery and reuse of T7 RNAP is significant, considering the complexity of the transcription reaction and the fragility of T7 RNAP.

DISCUSSION

Nanoparticle-supported proteins have considerable potential in a variety of biotechnological areas, mostly limited by the bioconjugation chemistries available for joining proteins and particles and the biocompatibility of the protein for the solid support. In the present study, we have proposed a new composite nanostructure suitable for protein bioseparation and enzymatic recycling. Our method takes advantage of IMAC chemistry and requires His-tagged recombinant proteins for attachment to encapsulated, magnetic γ-Fe_2O_3 particles. Specifically, using His_6-tagged T4 DNAL, we demonstrated reproducible binding capacity on the surface of the magnetomicelles and specific protein capture through the His_6-Cu^{2+}-IDA interaction. This highly specific protein attachment is likely a factor for the retention of enzyme function in subsequent experiments. We argue that these nanoparticle supports should be versatile, as the carboxylic acid groups available on the surface of the magnetomicelles could be further functionalized to recognize other distinctive protein features for bioconjugation and could in turn provide additional scenarios for specific protein capture.

Additionally, by quantifying the amount of His_6-EGFP conjugated to a magnetomicelle surface, we revealed large loading capacities of bound, intact protein. The high surface-to-volume ratio afforded by conjugating proteins to nanoparticle supports is a clear advantage over other solid-supported enzyme techniques. Furthermore, the Cu^{+2}-IDA magnetomicelles utilized in these examples were prepared by cross-linking 50% of available carboxylic acid groups prior to Cu^{+2}-IDA functionalization and subsequent protein attachment. We envision that this system could be modified to accommodate more or fewer IDA groups to tailor the number of conjugated proteins.

Most importantly, Cu^{+2}-IDA magnetomicelles were biocompatible in transcription reactions performed with bound T7 RNAP, with only subtle losses in enzyme activity. This lower activity could be due to enzyme denaturation or a structural change at the particle surface, as has been previously demonstrated for adsorbed protein−nanoparticle conjugates (*10*), or a portion of the bound protein may be less accessible for catalysis than in free solution. Although the loss in RNA production after T7 RNAP bioconjugation to magnetomicelles was not favorable, we are optimistic that magnetomicelle supports could be applicable for the conjugation of other proteins. Reports of catalyst activity on magnetic supports is diverse for particle-bound enzymes, ranging from a significant or complete loss in activity to an increase in catalytic function (*41*, *46*−*48*). Therefore, despite the variability in surface-bound enzyme activity, there remains great interest in the potential for magnetic enzyme carriers that permit easy enzyme separation and reuse.

Recyclable biocatalysts are becoming more widely used for organic transformations in industrially relevant reactions (*6*). Our work, by contrast, is one of the first examples of magnetic recycling of an enzyme used in a molecular biology transformation under strict biological conditions. In principle, our enzyme−magnetomicelle system could be broadly applied for the separation and reuse of a variety of enzymes under diverse reaction conditions. In addition to the advantages that protein−magnetomicelles offer to protein separation, analysis, and enzyme reuse, we envision that proteins attached to the surface of magnetomicelles could also facilitate targeted, magnetic drug delivery (*49*) or be used in in vivo imaging systems (*50*, *51*).

ACKNOWLEDGMENT

We would like to acknowledge the NIH (EB003809) for support of this research; A.R.H. also acknowledges Abbey E. Rosen and the Karin Musier-Forsyth group for their generous gift of the $tRNA^{pro}$ plasmid DNA, as well as clones for T4

DNAL and T7 RNAP. Additionally, A.R.H. would also like to thank Jennifer Maynard for the EGFP clone. K.B.S. thanks Dr. Taewoon Cha for XPS analysis.

Supporting Information Available: Additional figures. This material is available free of charge via the Internet at http://pubs.acs.org.

LITERATURE CITED

(1) Niemeyer, C. M. (2001) Nanoparticle, proteins, and nucleic acids: biotechnology meets materials science. *Angew. Chem., Int. Ed. 40*, 4128−4158.

(2) Gao, X., Cui, Y., Levenson, R. M., Chung, L. W., and Nie, S. (2004) In vivo cancer targeting and imaging with semiconductor quantum dots. *Nat. Biotechnol. 22*, 969−76.

(3) Xiao, Y., Patolsky, F., Katz, E. Hainfeld, J. F., and Willner, I. (2003) "Plugging into enzymes": nanowiring of redox enzymes by a gold nanoparticle. *Science 299*, 1877−1881.

(4) Tannous, B. A., Grimm, J., Perry, K. F., Chen, J. W., Weissleder, R., and Breakefield, X. O. (2006) Metabolic biotinylation of cell surface receptors for in vivo imaging. *Nat. Methods 3*, 391−396.

(5) Cao, L., van Langen, L., and Sheldon, R. A. (2003) Immobilized enzymes: carrier-bound or carrier-free? *Curr. Opin. Biotechnol. 14*, 387−394.

(6) Bornscheuer, U. T. (2003) Immobilizing enzymes: How to create more suitable biocatalysts. *Angew. Chem., Int. Ed. 42*, 3336−3337.

(7) You, C.-C., Verma, A., and Rotello, V. M. (2006) Engineering the nanoparticle-biomacromolecule interface. *Soft Matter 2*, 190−204.

(8) Carpenter, E. E. (2001) Iron nanoparticles as potential magnetic carriers. *J. Magn. Magn. Mater. 225*, 17−20.

(9) Li, J., Wang, J., Gavalas, V. G., Atwood, D. A., and Bachas, L. G. (2003) Alumina-pepsin hybrid nanoparticles with orientation-specific enzyme coupling. *Nano Lett. 3*, 55−58.

(10) Vertegel, A. A., Siegel, R. W., and Dordick, J. S. (2004) Silica nanoparticle size influences the structure and enzymatic activity of adsorbed lysozyme. *Langmuir 20*, 6800−6807.

(11) Lei, C., Shin, Y., Liu, J., and Ackerman, E. J. (2002) Entrapping enzyme in a functionalized nanoporous support. *J. Am. Chem. Soc. 124*, 11242−11243.

(12) Kulkarni, S., Schilli, C., Mueller, A. H. E., Hoffman, A. S., and Stayton, P. S. (2004) Reversible meso-scale smart polymer−protein particles of controlled sizes. *Bioconjugate Chem. 15*, 747−753.

(13) Huang, S.-H., Liao, M.-H., and Chen, D.-H. (2003) Direct binding and characterization of lipase onto magnetic nanoparticles. *Biotechnol. Prog. 19*, 1095−1100.

(14) Johnson, D. L., and Martin, L. L. (2005) Controlling protein orientation at interfaces using histidine tags: an alternative to Ni/NTA. *J. Am. Chem. Soc. 127*, 2018−2019.

(15) Lata, S., and Piehler, J. (2005) Stable and functional immobilization of histidine-tagged proteins via multivalent chelator headgroups on a molecular poly(ethylene glycol) brush. *Anal. Chem. 77*, 1096−1105.

(16) Wang, Y., and Caruso, F. (2005) Mesoporous silica spheres as supports for enzyme immobilization and encapsulation. *Chem. Mater. 17*, 953−961.

(17) Meziani, M. J., Pathak, P., Harruff, B. A., Hurezeanu, R., and Sun, Y.-P. (2005) Direct conjugation of semiconductor nanoparticles with proteins. *Langmuir 21*, 2008−2011.

(18) Xu, C., Xu, K., Gu, H., Zhong, X., Guo, Z., Zheng, R., Zhang, X., and Xu, B. (2004) Nitrilotriacetic acid-modified magnetic nanoparticles as a general agent to bind histidine-tagged proteins. *J. Am. Chem. Soc. 126*, 3392−3393.

(19) Xu, C., Xu, K., Gu, H., Zheng, R., Liu, H., Zhang, X., Guo, Z., and Xu, B. (2004) Dopamine as a robust anchor to immobilize functional molecules on the iron oxide shell of magnetic nanoparticles. *J. Am. Chem. Soc. 126*, 9938−9939.

(20) Kim, B.-S., Qiu, J.-M., Wang, J.-P., and Taton, T. A. (2005) Magnetomicelles: composite nanostructures from magnetic nanoparticles and cross-linked amphiphilic block copolymers. *Nano Lett. 5*, 1987−1991.

(21) Abad, J. M., Mertens, S. F. L., Pita, M., Fernandez, V. M., and Schiffrin, D. J. (2005) Functionalization of thioctic acid-capped gold nanoparticles for specific immobilization of histidine-tagged proteins. *J. Am. Chem. Soc. 127*, 5689−5694.

(22) Ausubel, F. M. B. R., Kingston, R. E., Moore, D. D., Seidman, J. G., Smith, J. A., Struhl, K. (1999) *Short Protocols in Molecular Biology*, 4th ed., John Wiley & Sons: New York.

(23) Strobel, S. A., and Cech, T. R. (1995) Minor groove recognition of the conserved G.U pair at the *Tetrahymena* ribozyme reaction site. *Science 267*, 675−9.

(24) Cormack, B. P., Valdivia, R. H., and Falkow, S. (1996) FACS-optimized mutants of the green fluorescent protein (GFP). *Gene 173*, 33−38.

(25) Ellinger, T., and Ehricht, R. (1998) Single-step purification of T7 RNA polymerase with a 6-histidine tag. [Erratum to document cited in CA129:64701]. *BioTechniques 25*, 640.

(26) Stehlin, C., Burke, B., Yang, F., Liu, H., Shiba, K., and Musier-Forsyth, K. (1998) Species-specific differences in the operational RNA code for aminoacylation of tRNAPro. *Biochemistry 37*, 8605−8613.

(27) Kang, Y., and Taton, T. A. (2005) Controlling shell thickness in core-shell gold nanoparticles via surface-templated adsorption of block copolymer surfactants. *Macromolecules 38*, 6115−6121.

(28) Kang, Y., and Taton, T. A. (2005) Core/shell gold nanoparticles by self-assembly and crosslinking of micellar, block-copolymer shells. *Angew. Chem., Int. Ed. 44*, 409−412.

(29) Porath, J., Carlsson, J., Olsson, I., and Belfrage, G. (1975) Metal chelate affinity chromatography, a new approach to protein fractionation. *Nature (London) 258*, 598−9.

(30) Chaga, G. S. (2001) Twenty-five years of immobilized metal ion affinity chromatography: past, present and future. *J. Biochem. Biophys. Methods 49*, 313−334.

(31) Lee, K. B., Park, S., and Mirkin, C. A. (2004) Multicomponent magnetic nanorods for biomolecular separations. *Angew. Chem., Int. Ed. 43*, 3048−3050.

(32) Pack, D. W., Chen, G. H., Maloney, K. M., Chen, C. T., and Arnold, F. H. (1997) A metal-chelating lipid for 2D protein crystallization via coordination of surface histidines. *J. Am. Chem. Soc. 119*, 2479−2487.

(33) Shnek, D. R., Pack, D. W., Sasaki, D. Y., and Arnold, F. H. (1994) Specific protein attachment to artificial membranes via coordination to lipid-bound copper(II). *Langmuir 10*, 2382−2388.

(34) See Supporting Information for details.

(35) Dai, J., Bao, Z., Sun, L., Hong, S. U., Baker, G. L., and Bruening, M. L. (2006) High-capacity binding of proteins by poly(acrylic acid) brushes and their derivatives. *Langmuir 22*, 4274−4281.

(36) Schmid, E. L., Keller, T. A., Dienes, Z., and Vogel, H. (1997) Reversible oriented surface immobilization of functional proteins on oxide surfaces. *Anal. Chem. 69*, 1979−1985.

(37) Cha, T., Guo, A., Jun, Y., Pei, D., and Zhu, X.-Y. (2004) Immobilization of oriented protein molecules on poly(ethylene glycol)-coated Si(111). *Proteomics 4*, 1965−1976.

(38) Tanaka, M., and Sackmann, E. (2005) Polymer-supported membranes as models of the cell surface. *Nature (London) 437*, 656−663.

(39) Anikin, K., Roecker, C., Wittemann, A., Wiedenmann, J., Ballauff, M., and Nienhaus, G. U. (2005) Polyelectrolyte-mediated protein adsorption: fluorescent protein binding to individual polyelectrolyte nanospheres. *J. Phys. Chem. B 109*, 5418−5420.

(40) Yang, F., Moss, L. G., and Phillips, G. N. (1996) The molecular structure of green fluorescent protein. *Nat. Biotechnol. 14*, 1246−1251.

(41) Dyal, A., Loos, K., Noto, M., Chang, S. W., Spagnoli, C., Shafi, K. V. P. M., Ulman, A., Cowman, M., and Gross, R. A. (2003) Activity of *Candida rugosa* lipase immobilized on γ-Fe_2O_3 magnetic nanoparticles. *J. Am. Chem. Soc. 125*, 1684−1685.

(42) Long, M. S., and Keating, C. D. (2006) Nanoparticle conjugation increases protein partitioning in aqueous two-phase systems. *Anal. Chem. 78*, 379−386.

(43) Jia, H., Zhu, G., and Wang, P. (2003) Catalytic behaviors of enzymes attached to nanoparticles: the effect of particle mobility. *Biotechnol. Bioeng. 84*, 406−414.

(44) Phadtare, S., Vinod, V. P., Mukhopadhyay, K., Kumar, A., Rao, M., Chaudhari, R. V., and Sastry, M. (2004) Immobilization and

biocatalytic activity of fungal protease on gold nanoparticle-loaded zeolite microspheres. *Biotechnol. Bioeng. 85*, 629−637.
(45) Chamberlin, M., and Ring, J. (1973) Characterization of T7-specific ribonucleic acid polymerase. II. Inhibitors of the enzyme and their application to the study of the enzymatic reaction. *J. Biol. Chem. 248*, 2245−50.
(46) Rossi, L. M., Quach, A. D., and Rosenzweig, Z. (2004) Glucose oxidase-magnetite nanoparticle bioconjugate for glucose sensing. *Anal. Bioanal. Chem. 380*, 606−613.
(47) Krogh, T. N., Berg, T., and Hojrup, P. (1999) Protein analysis using enzymes immobilized to paramagnetic beads. *Anal. Biochem. 274*, 153−162.
(48) Kouassi, G. K., Irudayaraj, J., and McCarty, G. (2005) Examination of cholesterol oxidase attachment to magnetic nanoparticles. *J. Nanobiotechnol.,* 3:1.
(49) Son, S. J., Reichel, J., He, B., Schuchman, M., and Lee, S. B. (2005) Magnetic nanotubes for magnetic-field-assisted bioseparation, biointeraction, and drug delivery. *J. Am. Chem. Soc. 127*, 7316−7317.
(50) Lewin, M., Carlesso, N., Tung, C.-H., Tang, X.-W., Cory, D., Scadden, D. T., and Weissleder, R. (2000) Tat peptide-derivatized magnetic nanoparticles allow in vivo tracking and recovery of progenitor cells. *Nat. Biotechnol. 18*, 410−414.
(51) Xie, H.-Y., Zuo, C., Liu, Y., Zhang, Z.-L., Pang, D.-W., Li, X.-L., Gong, J.-P., Dickinson, C., and Zhou, W. (2005) Cell-targeting multifunctional nanospheres with both fluorescence and magnetism. *Small 1*, 506−509.

BC060215J

Design, Synthesis, and Evaluation of [^{188}Re]Organorhenium-Labeled Antibody Fragments with Renal Enzyme-Cleavable Linkage for Low Renal Radioactivity Levels

Tomoya Uehara,[†] Miho Koike,[†] Hideo Nakata,[†] Hiroshi Hanaoka,[‡] Yasuhiko Iida,[‡] Kazuyuki Hashimoto,[#] Hiromichi Akizawa,[†] Keigo Endo,[‡] and Yasushi Arano*[,†]

Graduate School of Pharmaceutical Sciences, Chiba University, 1-8-1 Inohana, Chuo-ku, Chiba 260-8675, Japan, Gunma University, School of Medicine, 3-39-22 Showa-cho, Maebashi, 371-8511, Japan, and Japan Atomic Energy Agency, Tokai-mura, Ibaraki 319-1195, Japan. Received July 27, 2006; Revised Manuscript Received November 17, 2006

Renal localization of radiolabeled antibody fragments constitutes a problem in targeted imaging and radiotherapy. We have reported that Fab fragments labeled with 3′-[^{131}I]iodohippuryl N^{ϵ}-maleoyl-lysine (HML) showed markedly low renal radioactivity levels even shortly after injection, due to a rapid and selective release of *m*-[^{131}I]iodohippuric acid by the action of brush border enzymes. To estimate the applicability of the molecular design to metallic radionuclides, [^{188}Re]tricarbonyl(cyclopentadienylcarbonate)rhenium ([^{188}Re]CpTR-COOH) was conjugated with N^{ϵ}-tert-butoxycarbonyl-glycyl-lysine or N^{ϵ}-maleoyl-glycyl-lysine to prepare [^{188}Re]CpTR-GK-Boc or [^{188}Re]CpTR-GK. The cleavage of the glycyl-lysine linkage of the two compounds generates a glycine conjugate of [^{188}Re]-CpTR-COOH ([^{188}Re]CpTR-Gly), which possesses in vivo behaviors similar to those of *m*-iodohippuric acid. The hydrolysis rate of the peptide bond in [^{188}Re]CpTR-GK-Boc was compared with that in 3′-[^{125}I]iodohippuryl N^{ϵ}-Boc-lysine ([^{125}I]HL-Boc) using brush border membrane vesicles (BBMVs) prepared from rat kidneys. [^{188}Re]-CpTR-GK was conjugated to thiolated Fab fragments to prepare [^{188}Re]CpTR-GK-Fab. The biodistribution of radioactivity after injection of [^{188}Re]CpTR-GK-Fab was compared with that of [^{125}I]HML-Fab and [^{188}Re]CpTR-Fab prepared by conjugating *N*-hydroxysuccinimidyl ester of [^{188}Re]CpTR-COOH with antibody fragments. While [^{188}Re]CpTR-GK-Boc liberated [^{188}Re]CpTR-Gly in BBMVs, [^{125}I]HL-Boc liberated *m*-[^{125}I]iodohippuric acid at a much faster rate. In addition, although [^{125}I]HL-Boc was hydrolyzed by both metalloenzymes and nonmetalloenzymes, metalloenzymes were responsible for the cleavage of the peptide linkage in [^{188}Re]CpTR-GK-Boc. In biodistribution studies, [^{188}Re]CpTR-GK-Fab exhibited significantly lower renal radioactivity levels than did [^{188}Re]CpTR-Fab. However, the renal radioactivity levels of [^{188}Re]CpTR-GK-Fab were slightly higher than those of [^{125}I]HML-Fab. The analysis of urine samples collected for 6 h postinjection of [^{188}Re]CpTR-GK-Fab showed that [^{188}Re]CpTR-Gly was the major radiometabolite. In tumor-bearing mice, [^{188}Re]CpTR-GK-Fab significantly reduced renal radioactivity levels without impairing the radioactivity levels in tumor. These findings indicate that the molecular design of HML can be applied to metallic radionuclides by using a radiometal chelate of high inertness and by designing a radiometabolite of high urinary excretion when released from antibody fragments following cleavage of a glycyl-lysine linkage. This study also indicates that a change in chemical structure of a radiolabel attached to a glycyl-lysine linkage significantly affected enzymes involved in the hydrolysis reaction. Since there are many kinds of enzymes that cleave a variety of peptide linkages on the renal brush border membrane, selection of a peptide linkage optimal to a radiometal chelate of interest may provide radiolabeled antibody fragments that exhibit renal radioactivity levels similar to those of [^{131}I]HML-labeled ones. The in vitro system using BBMVs might be useful for selecting an appropriate peptide linkage.

INTRODUCTION

When injected into body, radiolabeled antibody fragments and peptides show high and persistent localization of radioactivity in the kidneys from early postinjection times, which impairs diagnostic accuracy and limits therapeutic potential (*1*−*5*). To circumvent the problem, we have developed a radioiodination reagent for antibody fragments, 3′-iodohippuryl N^{ϵ}-maleoyl-L-lysine (HML, Figure 1A), based on the hypothesis that the glycyl-lysine linkage in HML would be cleaved by the action of enzymes present on the lumen of renal tubules while the antibody fragments are taken up by renal cells (*6*). Indeed, [^{131}I]-HML-conjugated Fab fragments (Figure 1) significantly reduced renal radioactivity levels shortly after injection without impairing radioactivity levels in the tumor (*6, 7*). Subsequent in vivo and in vitro studies supported that the cleavage of the glycyl-lysine linkage occurred at the membrane fraction of renal cells (*8*) and that enzymes on the renal brush border membrane were responsible for cleaving the glycyl-lysine linkage in HML (*9*).

Since high and persistent radioactivity levels in the kidney are observed with antibody fragments and peptides particularly labeled with metallic radionuclides (*4, 10*−*13*), application of the molecular design of HML to metallic radionuclides constitutes an attractive approach to reduce renal radioactivity levels. Recently, Li et al. developed bifunctional chelating agents with glycyl-lysine linkages to reduce renal radioactivity levels of ^{111}In-labeled diabodies (*14*). Although one of the ^{111}In-labeled diabodies significantly reduced renal radioactivity levels, further reduction in the renal radioactivity levels was required for clinical application.

* To whom correspondence should be addressed. Tel: +81-43-226-2896. Fax: +81-43-226-2897. E-mail: arano@p.chiba-u.ac.jp.
[†] Chiba University.
[‡] Gunma University.
[#] Japan Atomic Energy Agency.

10.1021/bc0602329 CCC: $37.00 © 2007 American Chemical Society
Published on Web 12/22/2006

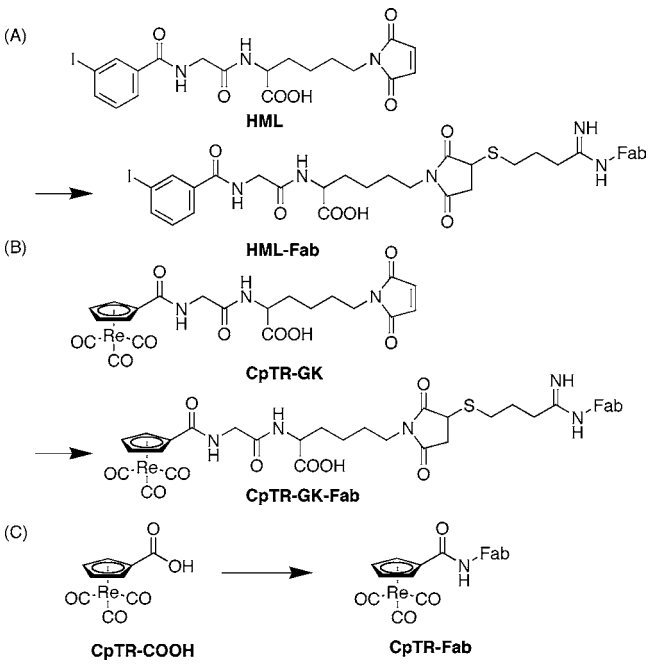


Figure 1. Chemical structures of (A) HML, (B) CpTR-GK, and (C) CpTR-COOH and their Fab conjugates. Both HML and CpTR-GK were conjugated to thiol groups of 2-iminothiolane-modifided Fab fragments, while CpTR-COOH was coupled directly to amine residues of Fab fragments.

Since HML was designed to liberate a radiometabolite of urinary excretion from covalently conjugated antibody fragments by the action of renal brush border enzymes, a radiometal chelate released from antibody molecules following cleavage of a glycyl-lysine linkage should possess biological behaviors similar to those of *m*-iodohippuric acid. In addition, our prior study indicates the involvement of some metalloenzymes in cleaving the glycyl-lysine linkage in HML (*9*). Since the majority of chelating agents in radiolabeled antibody fragments are free of radiometal ions, care should be taken so as not to inactivate metalloenzymes on the renal brush border membrane. On these bases, we estimated applicability of the molecular design of HML to metallic radionuclides using organorhenium compounds, due to their extremely high chemical inertness (*15*). Our previous study also indicated that [188Re]tricarbonyl-(cyclopentadienylcarbonate)rhenium ([188Re]CpTR-COOH) was metabolized to glycine conjugate ([188Re]CpTR-Gly) in vivo and that [188Re]CpTR-Gly possessed in vivo behaviors similar to those of *m*-iodohippuric acid (*16*). In addition, chemical structures of CpTR-Gly and its derivatives are well-characterized using non-radioactivity rhenium compounds.

In this study, [188Re]CpTR-COOH was coupled with N^{ϵ}-maleoyl-glycyl-lysine or N^{ϵ}-*tert*-butoxycarbonyl-glycyl-lysine to prepare [188Re]CpTR-GK or [188Re]CpTR-GK-Boc (Figure 1B). In vitro hydrolysis rates of the glycyl-lysine linkages in [188Re]CpTR-GK-Boc and 3′-[125I]iodohippuryl N^{ϵ}-Boc-lysine ([125I]HL-Boc) were compared using renal brush border membrane vesicles (BBMVs) (*9*). The biodistribution of radioactivity was compared after injection of Fab fragments conjugated with [188Re]CpTR-GK, [125I]HML, or [188Re]CpTR-COOH (Figure 1) to estimate in vivo cleavage of the glycyl-lysine linkage in [188Re]CpTR-GK. The applicability of the molecular design of HML to metallic radionuclides was assessed, and future application of the strategy will be discussed.

EXPERIMENTAL PROCEDURES

Materials. 188W was supplied as [188W]Na_2WO_4 in sodium hydroxide solution (17−29 MBq/mL) by the Japan Atomic Energy Agency (Tokai-Mura, Japan). 188Re was eluted from a 188W/188Re generator system prepared by the method of Callahan et al. (*17, 18*). Reversed-phase HPLC (RP-HPLC) was performed with a Cosmosil 5C_{18}-AR-300 column (4.6 × 150 mm, Nacalai Tesque, Kyoto, Japan) at a flow rate of 1 mL/min with a gradient mobile phase starting from 80% A (0.1% aqueous trifluoroacetic acid (TFA)) and 20% B (acetonitrile with 0.1% TFA) to 20% A and 80% B at 30 min (solvent system 1) or from 100% A (water) and 0% B (acetonitrile) to 0% A and 100% B at 30 min (solvent system 2). Size-exclusion HPLC (SE-HPLC) was performed using a Cosmosil Diol-300 column (7.5 × 600 mm, Nacalai Tesque) eluted with 0.1 M phosphate buffer (pH 6.8) at a flow rate of 1 mL/min. Each eluent was collected with a fraction collector (RadiFlac, GE healthcare bioscience, Tokyo, Japan) at 30-s intervals, and the radioactivity levels in each fraction (500 μL) were determined with an auto well gamma counter (ARC-380M, Aloka, Tokyo). TLC analyses were performed with silica plates (Silica gel 60 F_{254}, Merck, Tokyo) developed with chloroform (solvent system 3) or 80% methanol (solvent system 4). 188Re complexes were purified by SepPak plus cartridge (C_{18} short body, 360 mg/cartridge, Waters, Tokyo) activated with 6 mL each of ethanol and water prior to use. Proton nuclear magnetic resonance (^{1}H-NMR) spectra were recorded on a JEOL JNM-ALPHA 400 spectrometer (JEOL Ltd., Tokyo) with tetramethylsilane as an internal standard. FAB-MS was taken on a JEOL JMS-HX-110A mass spectrometer (JEOL Ltd., Tokyo). Elemental analyses were performed by PE-2400 (Perkin-Elmer Japan, Tokyo). Two masses were reported for rhenium-containing fragments to indicate the significant isotopic abundances of both 185Re and 187Re. Each peak was observed to have the proper relative abundances. The following compounds were prepared as described previously: [188Re]tricarbonyl(cyclopentadienylcarbonate)rhenium ([188Re]-CpTR-COOH), non-radioactive CpTR-COOH and [188Re]tricarbonyl[(cyclopentadienylcarbonyl amino)-acetic acid]rhenium ([188Re]CpTR-Gly) (*16*), *N*-methoxycarbonylmaleimide (**5**) (*19*), 3-(tri-*n*-butylstannyl)hippuric acid, 3-iodohippuric acid, and [125I]HML-Fab (*20*) and 3′-[125I]iodohippuryl N^{ϵ}-*tert*-butoxycarbonyl-L-lysine ([125I]HL-Boc) (*9*). Human carcinoembryonic antigen (CEA)-positive human gastric cancer strain (MKN-45) and a monoclonal antibody against CEA (1B2) were supplied by Immuno-Biological Laboratories Co. Ltd. (Takasaki, Japan). Other reagents were of reagent grade and used as received.

Tumor and Monoclonal Antibody. CEA-positive human gastric cancer strain MKN-45 was transplanted into subcutaneously and pieces of tumor tissue (∼0.5 g) were used for the in vivo study. The Fab fragment of monoclonal antibody against CEA (1B2) was prepared using a Fab preparation kit (ImmunoPure IgG_1 Fab and $F(ab')_2$ Preparation kit, Pierce, Rockford, USA).

Synthesis of N^{α}-(*tert*-Butoxycarbonyl)-glycyl-N^{ϵ}-carbobenzoxy-L-lysine-*tert*-butyl Ester (3). *N*-(*tert*-Butoxycarbonyl)-glycine (**1**) (2.8 g, 16.1 mmol), N^{ϵ}-carbobenzoxy-L- lysine-*tert*-butyl ester hydrochloride (**2**) (5.0 g, 13.4 mmol), and 1-hydroxybenzotriazole (HOBt, 2.4 g, 16.1 mmol) were dissolved in dimethylformamide (DMF, 80 mL). After the sample was cooled to 0 °C, 1-(3-dimethylaminopropyl)-3-ethylcarbodiimide hydrochloride (EDC, 4.26 g, 22.5 mmol) and diisopropylethylamine (DIEA, 6.1 mL, 35.9 mmol) in DMF (20 mL) was added dropwise to the solution, and the reaction mixture was stirred for 4 h at 0 °C. After the sample was stirred overnight at room temperature, the solvent was removed in vacuo, and the residue was dissolved in ethyl acetate (20 mL). The organic phase was washed with 1% H_2SO_4 (20 mL × 3), saturated NaCl solution (20 mL × 3) and saturated $NaHCO_3$ solution (20 mL× 3), successively, and dried over anhydrous $CaSO_4$. After the solvent was removed, the residue was purified with silica gel chroma-

tography using a mixture of chloroform and methanol (9:1) as an eluent to produce compound **3** (4.7 g, 71.2%) as a colorless oil. ^{1}H-NMR ($CDCl_3$): δ 1.25−1.81 (6H, m, $(CH_2)_3$), 1.40−1.43 (9H, s, Boc), 1.40−1.43 (9H, s, *tert*-butyl), 3.14 (2H, t, CH_2), 3.75 (2H, d, CH_2), 4.37 (1H, q, CH), 4.93 (1H, s, NH), 5.07 (2H, s, CH_2), 5.14 (1H, s, NH), 6.58 (1H, s, NH), 7.22−7.33 (5H, m, phenyl); FAB-MS $(M + H)^+$: *m/z* 494, Found: 494.

Synthesis of N^{α}-(*tert*-Butoxycarbonyl)-glycyl-L-lysine-*tert*-butyl Ester (4). Compound **3** (4.7 g, 9.6 mmol) and 10% Pd on activated carbon (0.9 g) in 13% aqueous methanol was stirred under a hydrogen atmosphere for 2 h. The catalyst was removed by filtration, and the filtrate was evaporated in vacuo to provide compound **4** (3.1 g, 90%) as a colorless oil. ^{1}H-NMR (CD_3OD): δ 1.33−1.95 (6H, m, $(CH_2)_3$), 1.48−1.49 (9H, s, Boc), 1.48−1.49 (9H, s, *tert*-butyl), 2.94 (2H, t, CH_2), 3.77 (2H, d, CH_2), 4.35 (1H, s, CH); FAB-MS $(M + H)^+$: *m/z* 360, Found: 360.

Synthesis of N^{α}-(*tert*-Butoxycarbonyl)-glycyl-N^{ϵ}-maleoyl-L-lysine-*tert*-butyl Ester (6). Compound **6** was synthesized according to the procedure described previously with slight modifications (*19*). To a solution of compound **4** (1.37 g, 3.8 mmol) in saturated $NaHCO_3$ (18.8 mL) was added a solution of compound **5** (0.71 g, 4.6 mmol) dissolved in tetrahydrofuran (37.6 mL) at 0 °C, and the reaction mixture was stirred for 2 h while the pH was maintained at 8.7 by the addition of 2 N NaOH. After the solution was acidified to pH 3−4 with conc. H_2SO_4, crude compound **6** was extracted with ethyl acetate (20 mL × 3) and dried over anhydrous $CaSO_4$. After the solvent was removed in vacuo, the residue was purified with silica gel chromatography using a mixture of chloroform and methanol (99:1) as an eluent to produce compound **6** (1.05 g, 61.7%) as a colorless oil. ^{1}H-NMR ($CDCl_3$): δ 1.18−1.76 (6H, m, $(CH_2)_3$), 1.36−1.40 (9H, s, Boc), 1.36−1.40 (9H, s, *tert*-butyl), 3.40 (2H, t, CH_2), 3.73 (2H, d, CH_2), 4.37 (1H, q, CH), 5.34 (1H, s, NH), 6.62 (2H, s, maleimide), 6.69 (1H, s, NH); FAB-MS $(M + H)^+$: *m/z* 440, Found: 440.

Synthesis of Glycyl-N^{ϵ}-maleoyl-L-lysine-*tert*-butyl Ester Hydrochloride (7). Compound **7** was synthesized according to the procedure of Kinoshita et al. (*21*) with slight modifications. Compound **6** (180 mg, 0.68 mmol) and anisole (0.5 mL) was dissolved in HCOOH (8.5 mL) and ether (1.0 mL) at 0 °C. After the sample was stirred at 15−17 °C for 3 h, the solvent was evaporated in vacuo. The residue was purified with reversed phase chromatography using a mixture of acetonitrile containing 0.01% HCl and water containing 0.01% HCl (20:80) as an eluent. The combined fractions were lyophilized to produce compound **7** (30 mg, 16.7%) as a white solid. ^{1}H-NMR (CD_3OD): δ 1.37−1.76 (6H, m, $(CH_2)_3$), 1.36−1.50 (9H, s, *tert*-butyl), 3.54 (2H, t, CH_2), 3.77 (2H, d, CH_2), 4.34 (1H, q, CH), 6.85 (2H, s, maleimide); FAB-MS $(M + H)^+$: *m/z* 340, Found: 340.

Synthesis of Tricarbonyl(cyclopentadienylcarbonyl glycyl-N^{ϵ}-maleoyl-L-lysine-*tert*-butyl ester)rhenium (8). CpTR-COOH (189.4 mg, 0.5 mmol), compound **7** (250 mg, 0.65 mmol) and HOBt (101.1 mg, 0.75 mmol) were dissolved in DMF (5 mL) at 0 °C, and a solution of EDC (118.8 mg, 0.62 mmol) in DMF (1 mL) and DIEA (217 μL, 1.27 mmol) were successively added to the solution. The reaction mixture was stirred for 4 h at 0 °C and overnight at room temperature. After the solvent was removed in vacuo, the residue was dissolved in ethyl acetate (20 mL), and the organic layer was successively washed with 1% H_2SO_4 (20 mL × 3), saturated NaCl (20 mL × 3), and saturated $NaHCO_3$ (20 mL × 3). After the sample was dried over anhydrous $CaSO_4$, the solvent was evaporated in vacuo, and the residue was purified by silica gel chromatography using a mixture of ethyl acetate:hexane (3:1) as an eluent to produce compound **8** (40 mg, 11.4%) as a colorless oil. ^{1}H-NMR ($CDCl_3$): δ 1.21−1.82 (6H, m, $(CH_2)_3$), 1.43 (9H, s, *tert*-butyl), 3.46−3.50 (2H, t, CH_2), 4.00 (2H, d, CH_2), 4.37−4.40 (1H, q, CH), 5.33−6.00 (4H, t, Cp), 6.67 (2H, s, maleimide), 6.77 (1H, d, NH), 7.30 (1H, t, NH); FAB-MS $(M + H)^+$: *m/z* 700/702, Found: 700/702.

Synthesis of Tricarbonyl(cyclopentadienylcarbonyl glycyl-N^{ϵ}-maleoyl-L-lysine)rhenium (CpTR-GK). Compound **8** (10 mg, 14.3 μmol) and anisole (25 μL) were dissolved in TFA (475 μL), and the mixture was stirred for 1 h. After the solvent was removed with a stream of N_2 gas, the residue was purified by RP-HPLC using solvent system 2 to produce CpTR-GK (4.6 mg, 50%). ^{1}H-NMR (CD_3OD): δ 1.21−1.82 (6H, m, $(CH_2)_3$), 3.46−3.50 (2H, t, CH_2), 4.15 (2H, d, CH_2), 4.46 (1H, q, CH), 5.37−6.08 (4H, t, Cp), 6.67 (2H, s, maleimide), 7.56 (1H, t, NH); FAB-MS $(M + H)^+$: *m/z* 644/646, Found: 644/646. Anal. ($C_{21}H_{21}N_3O_9Re$): C, H, N.

Synthesis of Carbobenzoxy-glycyl-N^{ϵ}-*tert*-butoxycarbonyl-L-lysine Methyl Ester (11). Carbobenzoxy-glycine (**9**) (84 mg, 0.40 mmol), N^{ϵ}-*tert*-butoxycarbonyl-L-lysine methyl ester hydrochloride (**10**) (100 mg, 0.34 mmol) and HOBt (54 mg, 0.40 mmol) were dissolved in DMF (5 mL) and cooled to −5 °C. A solution of EDC (77 mg, 0.40 mmol) in DMF (0.5 mL) and triethylamine (TEA; 56 μL, 0.40 mmol) were added to the solution, and the mixture was stirred for 3 h on ice. After the sample was stirred for an additional 6 h at room temperature, the solvent was removed in vacuo. The residue was resolved in chloroform (5 mL), and the organic phase was successively washed with 1% citric acid (5 mL × 3) and saturated $NaHCO_3$ (5 mL × 3) and was dried over anhydrous $CaSO_4$. After the solvent was removed in vacuo, compound **11** was obtained as a white solid (141 mg, 89.1%). ^{1}H-NMR ($CDCl_3$): δ 1.12−1.83 (15H, overlapped, Boc, $(CH_2)_3$), 3.06 (2H, d, CH_2), 3.71 (3H, s, OCH_3), 3.91 (2H, d, CH_2), 4.59 (1H, d, CH), 4.77 (1H, s, NH), 5.12 (2H, s, CH_2), 5.76 (1H, s, NH), 6.88 (1H, s, NH), 7.31 (5H, multi, aromatic); FAB-MS $(M + H)^+$: *m/z* 452, Found: 452.

Synthesis of Tricarbonyl(cyclopentadienylcarbonyl glycyl-N^{ϵ}-*tert*-butoxycarbonyl-L-lysine-methyl ester)rhenium (13). Compound **11** (67.7 g, 150 mmol) and 10% Pd on activated carbon (0.9 g) was dissolved in 5% aqueous methanol (2 mL), and the mixture was stirred under a hydrogen atmosphere for 12 h. The catalyst was removed by filtration, and the filtrate was evaporated in vacuo to produce crude compound **12**.

A mixture of crude compound **12** (47.6 mg, 150 mmol), CpTR-COOH (68.3 mg, 180 mmol), and HOBt (24.3 mg, 180 mmol) was dissolved in DMF (5 mL), and the mixture was cooled to −5 °C. A solution of EDC (48.3 mg, 0.25 mmol) in DMF (0.5 mL) and TEA (35 μL, 0.1.68 mmol) were added to the solution before reaction mixture was stirred for 3 h on ice. After the sample was stirred for an additional 6 h at room temperature, the solvent was removed in vacuo. The residue dissolved in chloroform (5 mL) was successively washed with 1% H_2SO_4 (5 mL × 3) and saturated $NaHCO_3$ (5 mL × 3) and dried over anhydrous $CaSO_4$. After the solvent was removed in vacuo, compound **13** was obtained as a white solid (53 mg, 53.5%). ^{1}H-NMR ($CDCl_3$) δ: 1.29−1.82 (15H, Boc, $(CH_2)_3$), 3.01 (2H, d, CH_2), 3.66 (3H, s, OCH_3), 3.96 (2H, d, CH_2), 4.46 (1H, d, CH), 4.77 (1H, s, NH), 5.32−5.99 (4H, t, Cp), 7.10 (1H, s, NH), 7.61 (1H, s, NH); FAB-MS $(M + H)^+$: *m/z* 678/680, Found 678/680.

Synthesis of Tricarbonyl(cyclopentadienylcarbonyl glycyl-N^{ϵ}-*tert*-butoxycarbonyl-L-lysine)rhenium (CpTR-GK-Boc). A solution of 2 N NaOH (600 μL) was added dropwise to a solution of compound **13** (53 mg, 14.7 μmol) in dioxane (300 μL). After the sample stood for 30 min at room temperature, the pH of the solution was adjusted to 3 by 5.6 N H_2SO_4 (about 240 μL). The reaction mixture was loaded onto SepPak plus

cartridge, and the cartridge was washed with water (5 mL) and eluted with acetonitrile (3 mL). The first elution acetonitrile fraction (100 μL) was discarded, and the combined eluents were evaporated in vacuo to provide CpTR-GK-Boc as a white solid (51.5 mg, 57.1%). ^{1}H-NMR (CD_3OD) δ: 1.44−1.90 (15H, Boc, $(CH_2)_3$), 3.04 (2H, t, CH_2), 3.85 (2H, d, CH_2), 4.42 (1H, d, CH), 5.60−6.12 (4H, t, Cp); FAB-MS $(M + Na)^+$: *m*/*z* 686/688, Found 686/688, Anal: ($C_{22}H_{28}N_3O_9Re$): C, H, N.

Radiosynthesis of [188Re]tricarbonyl(cyclopentadienylcarbonyl glycyl-N^ϵ-maleoyl-L-lysine-*tert*-butyl ester)rhenium ([188Re]Compound 8). A mixture of [188Re]CpTR-COOH, HOBt (2.0 mg, 14.8 μmol), and EDC (2.0 mg, 10.2 μmol) in dichloromethane (200 μL) was stirred for 5 min. The solvent was then removed in vacuo, and the residue dissolved in DMF (150 μL) was added to a mixture of compound **7** (1.5 mg, 4.0 μmol) and DIEA (0.17 μL, 1.0 μmol) in DMF (50 μL). After the sample stood for 20 min, acetic acid (100 μL) was added dropwise to the solution, and the pH was adjusted to 6.5−7.5 with saturated $NaHCO_3$. After the sample stood for 10 min, the reaction mixture was loaded onto a SepPak plus cartridge. The cartridge was successively washed with 0.01 M phosphate buffer (pH 8.0, 5 mL), 0.01 M phosphate buffer (pH 6.0, 5 mL), and water (5 mL) before the product was eluted with acetonitrile (3 mL). The first elution acetonitrile fraction (100 μL) was discarded, and the combined eluents were evaporated in vacuo to produce [188Re]compound **8** in radiochemical yield and purity of 54% and over 95%.

Radiosynthesis of [188Re]Tricarbonyl(cyclopentadienylcarbonyl glycyl-N^ϵ-maleoyl-L-lysine)rhenium ([188Re]CpTR-GK). [188Re]compound **8** and anisole (10 μL) were dissolved in TFA (190 μL). After the sample stood for 10 min, the solvent was removed by a stream of N_2 gas. The residue was dissolved in 0.1 M phosphate buffer (pH 6.5, 100 μL) and subjected to RP-HPLC purification (solvent system 2) to produce [188Re]-CpTR-GK in radiochemical yield and purity of 73% and over 95%.

Radiosynthesis of [188Re]tricarbonyl(cyclopentadienylcarbonyl glycyl-N^ϵ-*tert*-butoxycarbonyl-L-lysine)rhenium ([188Re]CpTR-GK-Boc). To a solution of [188Re]CpTR-COOH in dichloromethane (200 μL) was added HOBt (1.0 mg, 14.8 μmol) and DCC (1.0 mg, 4.8 μmol). After the sample stood for 5 min, the solvent was removed in vacuo, and the residue was added to a solution of compound **12** (1 mg, 3.2 μmol) in DMF (200 μL). After the sample stood for 20 min, a solution of 2 N NaOH (600 μL) was added dropwise to the solution, and the reaction mixture was kept for 10 min. A solution of 5.6 N H_2SO_4 (240 μL) was added to the solution before the solution was loaded onto a SepPak plus cartridge. The cartridge was washed with water (5 mL) and eluted with acetonitrile (3 mL). The first elution acetonitrile fraction (100 μL) was discarded, and the combined eluents were evaporated in vacuo to produce [188Re]CpTR-GK-Boc in radiochemical yield and purity of 92% and over 95%.

Preparation of 188Re-Labeled Fab Fragments. A solution of Fab (200 μL, 2 mg/mL) in well-degassed 0.16 M borate buffer (pH 8.0) containing 2 mM EDTA was allowed to react with 7.2 μL of 2-iminothiolane (2-IT) solution (1 mg/mL) prepared in the same buffer. After gentle agitation of the reaction mixture for 30 min at room temperature, excess 2-IT was removed by a centrifuged column procedure using Sephadex G-50 equilibrated and eluted with 0.1 M phosphate buffer (pH 6.5) containing 2 mM EDTA. Aliquots of this mixture were sampled to estimate the number of thiol groups with 2,2′-dipyridiyl disulfide (*22*). The filtrate (100 μL) was then added to a reaction vial containing freshly prepared [188Re]CpTR-GK. After gentle agitation of the reaction mixture for 1.5 h at room temperature, 14.8 μL of iodoacetamide (10 mg/mL) in 0.1 M phosphate buffer (pH 6.5) were added. The reaction mixture was further incubated for 30 min to alkylate the unreacted thiol groups. [188Re]CpTR-GK-Fab was subsequently purified by the centrifuged column procedure, equilibrated, and eluted with 0.5 M acetate buffer (pH 6.0). [188Re]CpTR-GK-Fab was diluted with saline prior to the animal study.

[188Re]CpTR-COOH was also conjugated to Fab fragment according to the procedure of Spraudau et al. (*23*) with slight modification as follows. *N*-Hydroxysuccinimide (1.0 mg) and DCC (1.0 mg) were added successively to a solution of [188Re]-CpTR-COOH in dichloromethane (200 μL), and the reaction mixture was stirred for 5 min. After purification by RP-HPLC (solvent system 2), the solvent was removed in vacuo, and the residues were dissolved in DMF (10 μL). This solution was then added to a solution of Fab fragment (2 mg/mL, 100 μL) in 0.16 M borate buffer pH 8.0. After gentle agitation of the reaction mixture for 2 h at 4 °C, [188Re]CpTR-Fab was obtained by the centrifuged column procedure, as described above. Radiochemical purities of radiolabeled Fab fragments were also determined by SE-HPLC.

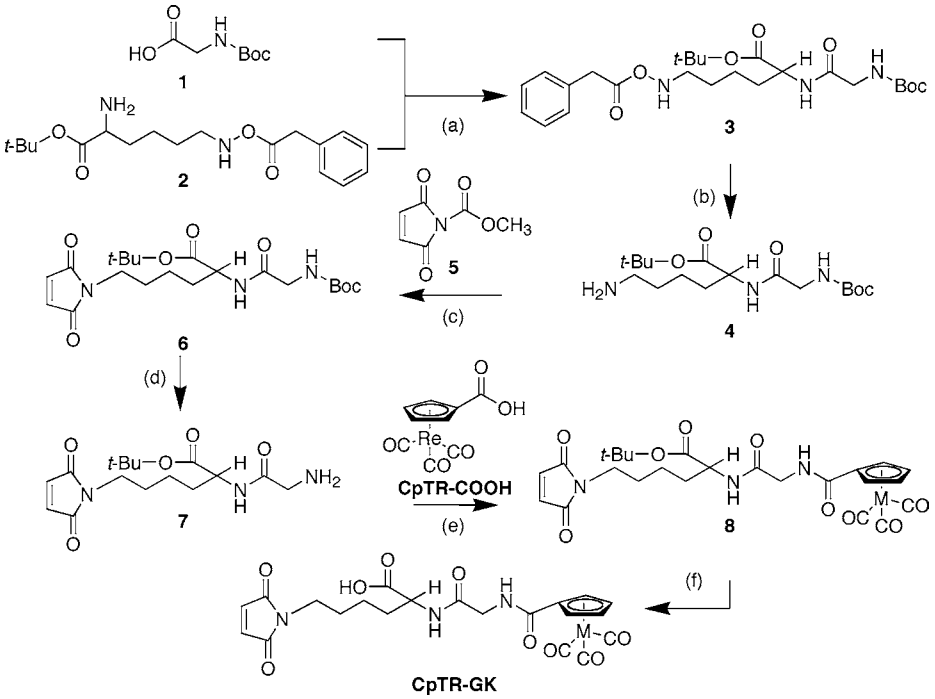
Preparation of Brush Border Membrane Vesicles (BBMVs). BBMVs were isolated from the renal cortex of male Wistar rats according to the Mg/EGTA precipitation method reported previously (*9*). For incubation studies, the vesicles were diluted with 0.1 M phosphate buffer (pH 7.0) to give the final protein concentration of 10 mg/mL. The γ-glutamyltransferase and aminopeptidase activities on BBMVs were 5.69 μmol (mg of protein)$^{-1}$ min^{-1} and 639 nmol (mg of protein)$^{-1}$ min^{-1}, respectively, when determined using L-γ-glutamyl-*p*-nitroanilide (*22*) and L-leucine-*p*-nitroanilide as substrates (*24*). The β-galactosidase activity on BBMVs was not detected when determined using *p*-nitrophenyl-β-D-galactopyranoside as a substrate (*25*), indicating that BBMVs were free from cross-contamination by lysosomal enzymes.

In Vitro Studies. A solution of BBMVs (20 μL) was preincubated for 2 h at 4 °C, followed by the addition of [125I]HL-Boc or [188Re]CpTR-GK-Boc (20 μL) in 0.1 M phosphate buffer (pH 7.0). After incubation for 3 h at 37 °C, samples were taken from the solution and analyzed by RP-HPLC (solvent system 1 or 2) after ultrafiltration through a 10 kDa cutoff membrane (Microcon-10, Millipore, Tokyo). Similar studies were performed in the presence of an activator (Co^{2+}) or an inhibitor (DL-2-mercaptomethyl-3-guanidinoethylthiopropanoic acid: MGTA) for brush border enzymes (*26*, *27*) at a final concentration of 1 mM, as reported previously (*9*).

Biodistribution of Radiolabeled Fab Fragments. The biodistribution of radioactivity after intravenous administration of [188Re]CpTR-GK-Fab, [188Re]CpTR-Fab, or [125I]HML-Fab (0.3 μCi, 100 μL) to 6-week-old mice was determined at 10 and 30 min, 1, 3, and 6 h postinjection. Groups of 3−4 mice, each receiving 20 μg of Fab fragments, were used for the experiments. Organs of interest were removed and weighed, and the radioactivity counts were determined with an auto well gamma counter. Urine and feces were colleted for 6 h postinjection, and the radioactivity counts were also determined. The radiolabeled species excreted in the urine for 6 h postinjection of [188Re]CpTR-GK-Fab were analyzed by SE-HPLC after filtration through a polycarbonate membrane with a pore diameter of 0.45 μm (Cosmonice Filter, Nacalai Tesque) and RP-HPLC (solvent system 1) after filtration through a 10 kDa cutoff ultrafiltration membrane (Microcon-10, Millipore).

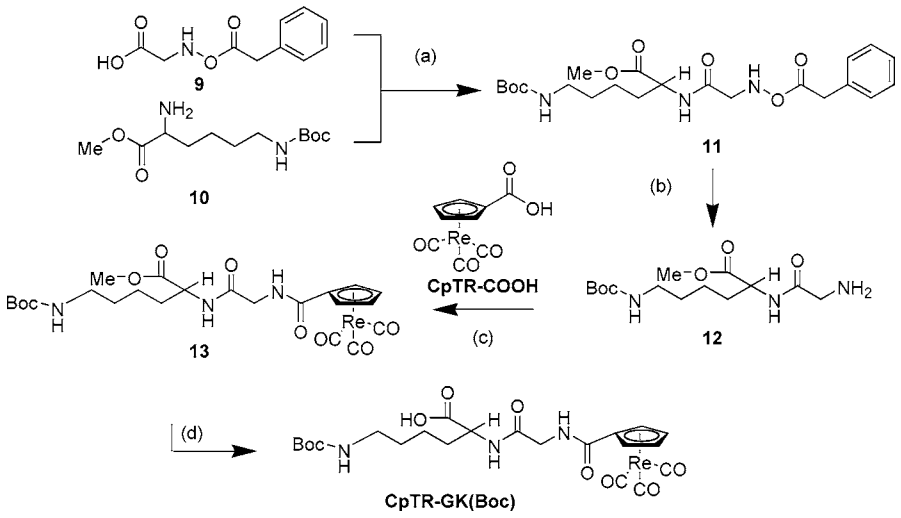
Athymic mice bearing an MKN-45 tumor were also treated intravenously with 100 μL of [188Re]CpTR-GK-Fab, [188Re]-CpTR-Fab, or [125I]HML-Fab, prepared as described above. The animals were sacrificed at 3 h postinjection (6−7 mice). Organs of interest were removed and weighed, and the radioactivity counts in each tissue were determined.

Scheme 1. Synthetic Procedure for CpTR-GK[a]



[a] Reagents: (a) HOBt, EDC, DIEA; (b) 10% Pd/C; (c) saturated $NaHCO_3$ solution, pH 8.7; (d) HCOOH, anisole; (e) HOBt, EDC, DIEA; (f) TFA, anisole.

Scheme 2. Synthetic Procedure for CpTR-GK-Boc[a]



[a] Reagents: (a) HOBt, EDC, TEA; (b) 10%Pd/C; (c) HOBt, EDC, TEA; (d) 2 N NaOH.

Statistical Analysis. Data are expressed as the means ± SD where appropriate. Results were statistically analyzed using the unpaired Student's *t*-test. Differences were considered statistically significant when p was <0.05.

RESULTS

Preparation of [^{188}Re]CpTR Derivatives and Its Fab Conjugates. [^{188}Re]CpTR-GK was synthesized according to the procedure outlined in Scheme 1. A key intermediate compound (compound **7**) was prepared by selective deprotection of N^{α}-Boc group in compound **6** by HCOOH (*21*). [^{188}Re]CpTR-GK was obtained by the reaction of [^{188}Re]CpTR-COOH with compound **7**. The low molecular weight model substrate, [^{188}Re]-CpTR-GK-Boc, was synthesized by the reaction of compound **12** with [^{188}Re]CpTR-COOH, followed by the hydrolysis of methyl ester, as outlined in Scheme 2. Similar synthetic procedures were employed for the preparation of non-radioactive rhenium compounds.

The treatment of Fab fragments with 2-IT introduced two thiol groups per molecule of Fab, as determined by 2,2′-dipyridyl disulfide. The conjugation of [^{188}Re]CpTR-GK with Fab fragments was performed by reacting the thiolated Fab fragments with maleimide groups of [^{188}Re]CpTR-GK. After purification by centrifuged column procedure, [^{188}Re]CpTR-GK-Fab was obtained with a radiochemical yield and purity of 21% and over 95%, as determined by TLC (solvent system 4). [^{188}Re]CpTR-Fab was prepared by the active ester method with a radiochemical yield and purity of 31% and over 95%, as determined by TLC (solvent system 4). Both [^{188}Re]CpTR-GK-Fab and [^{188}Re]CpTR-Fab showed SE-HPLC retention times similar to that of unmodified Fab fragment (19.5 min), as shown in Figure 2.

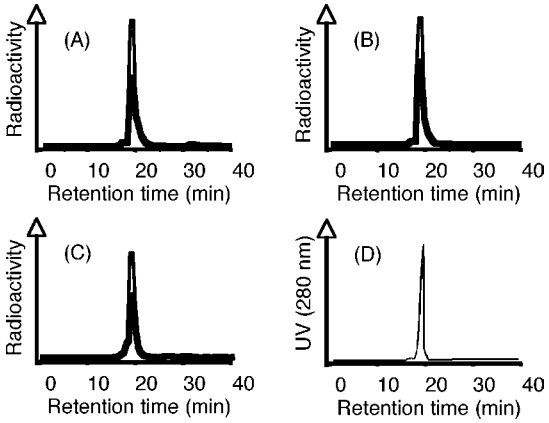


Figure 2. Radiochromatograms of (A) [188Re]CpTR-GK-Fab, (B) [188Re]CpTR-Fab, and (C) [125I]HML-Fab by SE-HPLC. The three radiolabeled Fab fragments showed SE-HPLC retention times similar to that of unmodified Fab fragment (19.5 min) as determined by the UV (280 nm) trace (D).

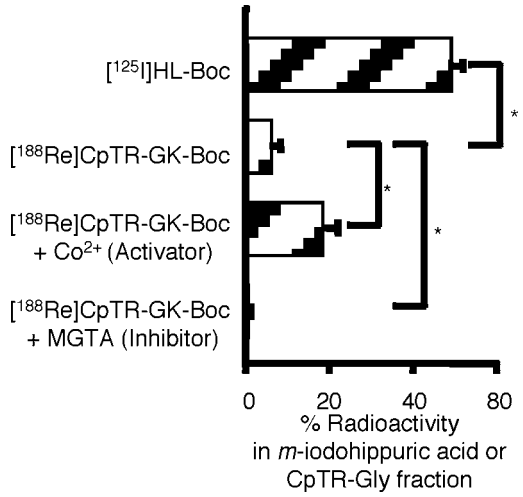


Figure 3. The amount of [188Re]CpTR-Gly or *m*-[125I]iodohippuric acid liberated from [188Re]CpTR-GK-Boc or [125I]HL-Boc after incubation with BBMVs for 3 h at 37 °C. [188Re]CpTR-GK-Boc was also incubated with BBMVs for 3 h at 37 °C in the presence of Co^{2+} or MGTA. Significance was determined by unpaired Student's *t*-test (*: $p < 0.05$ compared to [188Re]CpTR-GK-Boc).

Reactivities of [188Re]CpTR-GK-Boc with Enzymes on BBMVs. Figure 3 shows the percentage of radioactivity in the fraction of CpTR-Gly or *m*-iodohippuric acid after incubation of [188Re]CpTR-GK-Boc or [125I]HL-Boc with BBMVs at 37 °C for 3 h, respectively. The rate of [188Re]CpTR-Gly release from [188Re]CpTR-GK-Boc was significantly ($p < 0.05$) slower than that of *m*-[125I]iodohippuric acid from [125I]HL-Boc. The rate of [188Re]CpTR-Gly release significantly ($p < 0.05$) increased when [188Re]CpTR-GK-Boc was incubated with BBMVs in the presence of Co^{2+}, whereas the [188Re]CpTR-Gly release was almost completely inhibited in the presence of MGTA.

Biodistribution Studies. The biodistribution of radioactivity after simultaneous injection of [188Re]CpTR-GK-Fab and [125I]HML-Fab, or [188Re]CpTR-Fab and [125I]HML-Fab to normal mice is summarized in Table 1. The biodistribution of [125I]-HML-Fab was expressed as a mean of the two studies. No significant differences were observed in the radioactivity levels in the blood between the three radiolabeled Fab fragments up to 3 h postinjection. However, significant differences were observed in renal radioactivity levels between the two 188Re-labeled Fab fragments. Although [188Re]CpTR-Fab showed high radioactivity levels in the kidney and reached its peak at 30 min (41.69% ID/g), [188Re]CpTR-GK-Fab showed significantly lower renal radioactivity levels at all postinjection time points examined. However, [188Re]CpTR-GK-Fab showed higher renal radioactivity levels when compared with [125I]HML-Fab at all postinjection intervals. The kidney-to-blood ratios of radioactivity of the three radiolabeled Fab fragments are summarized in Figure 4. [188Re]CpTR-Fab showed the highest kidney-to-blood ratios of radioactivity, reaching a peaked ratio of 7.1 at 3 h postinjection. In contrast, [188Re]CpTR-GK-Fab and [125I]HML-Fab exhibited almost constant radioactivity ratios of about 1.6 and 1 from 10 min to 6 h postinjection.

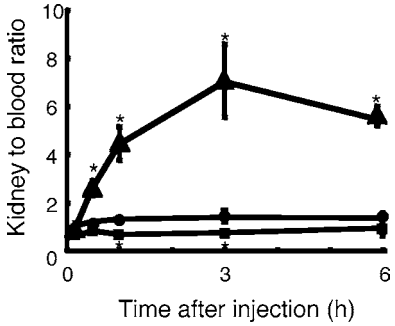


Figure 4. Comparison of the kidney-to-blood ratios of radioactivity after injection of [188Re]CpTR-GK-Fab (circle), [188Re]CpTR-Fab (triangle), and [125I]HML-Fab (square) to normal mice. Significances were determined by unpaired Student's *t*-test (*: $p < 0.05$ compared to [188Re]CpTR-GK-Fab).

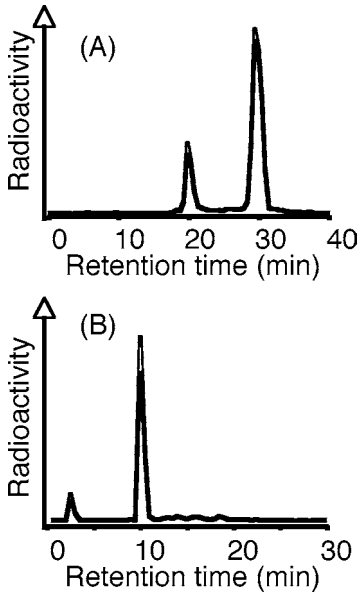


Figure 5. Radiochromatograms of urine sample collected for 6 h postinjection of [188Re]CpTR-GK-Fab (A) by SE-HPLC after filtration through a 0.45 μm polycarbonate membrane and (B) by RP-HPLC after filtration though a 10 kDa cutoff membrane.

Figure 5 shows the radiochromatograms of urine samples collected for 6 h postinjection of [188Re]CpTR-GK-Fab when analyzed by SE-HPLC (Figure 5A) and RP-HPLC (Figure 5B). On SE-HPLC, 73% of the radioactivity was observed in the low molecular weight fractions with over 20% being eluted in fractions similar to those of intact [188Re]CpTR-GK-Fab. On RP-HPLC, 72% of radioactivity in the low molecular weight fractions of the urine samples was observed with a retention time of 10.5 min, identical to that of CpTR-Gly.

The biodistribution of radioactivity after the administration of [188Re]CpTR-GK-Fab, [188Re]CpTR-Fab, or [125I]HML-Fab in nude mice bearing an MKN-45 tumor is summarized in Figure 6. No significant differences were observed in the radioactivity levels in the tumor and blood among the three radiolabeled antibodies. However, [188Re]CpTR-GK-Fab reg-

Table 1. Biodistribution of Radioactivity in Mice after Injections of [^{188}Re]CpTR-GK-Fab, [^{188}Re]CpTR-Fab, and [^{125}I]HML-Fab[a]

	time after injection				
	10 min	30 min	1 h	3 h	6 h
			[^{188}Re]CpTR-GK-Fab		
blood	23.93 (3.32)	11.31 (0.42)	6.43 (0.61)	3.26 (0.38)	1.66 (0.14)
liver	5.79 (0.06)	4.05 (0.52)	3.46 (0.22)	2.05 (0.59)	1.29 (0.14)
kidney	16.30 (1.01)	12.16 (1.06)	8.62 (0.32)	5.05 (0.47)	2.47 (0.38)
intestine	0.77 (0.07)	0.97 (0.08)	1.09 (0.14)	1.16 (0.19)	0.76 (0.10)
stomach[b]	0.44 (0.08)	0.51 (0.09)	0.57 (0.09)	0.63 (0.36)	0.35 (0.07)
urine[b]					45.33 (2.29)
feces[b]					2.01 (0.52)
			[^{188}Re]CpTR-Fab		
blood	23.80 (2.33)	13.44 (1.97)	6.22 (1.53)	2.65 (0.29)	1.03 (0.17)[c]
liver	6.23 (1.13)	4.08 (0.54)	2.92 (1.53)	2.31 (0.23)	1.27 (0.22)
kidney	27.59 (6.45)[c]	41.69 (7.16)[c]	33.86 (0.81)[c]	18.54 (1.66)[c]	5.89 (0.89)[c]
intestine	1.13 (0.19)	1.35 (0.21)[c]	1.40 (0.18)	1.99 (0.26)[c]	0.92 (0.18)
stomach[b]	0.30 (0.07)	0.46 (0.10)	0.62 (0.07)	0.54 (0.12)	0.29 (0.09)
urine[b]					44.05 (5.60)
feces[b]					4.49 (1.40)
			[^{125}I]HML-Fab		
blood	22.76 (2.63)	11.34 (0.85)	7.47 (0.71)	3.35 (0.73)	1.69 (0.17)
liver	5.42 (0.36)	2.47 (0.22)[c]	1.66 (0.21)[c]	0.64 (0.08)[c]	0.47 (0.11)[c]
kidney	14.87 (1.69)[c]	9.86 (1.02)[c]	6.46 (1.24)[c]	2.68 (0.93)[c]	1.72 (0.07)[c]
intestine	0.88 (0.23)	1.04 (0.11)	1.10 (0.12)	0.65 (0.13)[c]	0.23 (0.03)[c]
stomach[b]	0.43 (0.04)	0.49 (0.05)	0.43 (0.07)	0.41 (0.06)	0.27 (0.08)
urine[b]					55.45 (8.27)
feces[b]					2.57 (1.44)

[a] Tissue radioactivity is expressed as % ID/g [for each group, $n = 3-4$; results are expressed as the mean (SD). [b] Expressed as %ID. [c] Significance determined by unpaired Student's *t*-test; $p < 0.05$ compared to [^{188}Re]CpTR-GK-Fab.

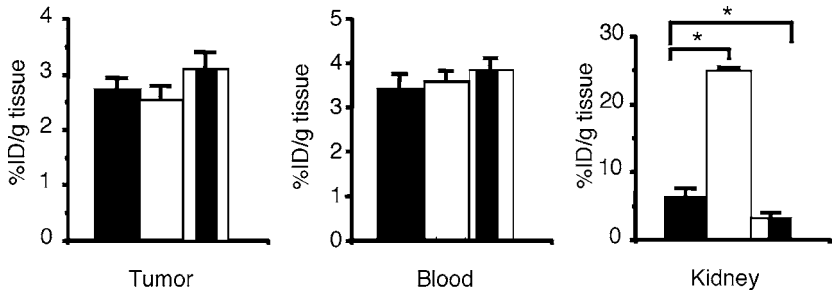


Figure 6. Radioactivity levels in the tumor, blood and kidney at 3 h postinjection of [^{188}Re]CpTR-GK-Fab (solid bar), [^{188}Re]CpTR-Fab (open bar), and [^{125}I]HML-Fab (stripe bar) into nude mice bearing MKN-45 tumor. Significances were determined by unpaired Student's *t*-test (*: $p < 0.05$ compared to [^{188}Re]CpTR-GK-Fab).

istered significantly lower radioactivity level in the kidney than did [^{188}Re]CpTR-Fab. [^{188}Re]CpTR-GK-Fab also showed renal radioactivity slightly higher than did [^{125}I]HML-Fab.

DISCUSSION

Our prior studies of the stability of metabolizable ester bonds in radiolabeled antibodies showed the involvement of many parameters that affect esterase-mediated hydrolysis of the chemical bonds. These include chemical structures of linkages and radiolabels attached to ester bonds, distance between an ester bond and an antibody molecule, and molecular size of antibody molecules (*28*, *29*). These parameters may also be involved in cleaving a glycyl-lysine linkage by enzymes on renal brush border membrane. Indeed, Li et al. documented an importance of the nature of chemical linkage from the antibody fragment to the lysine group in cleaving the glycyl-lysine linkage (*14*). Since the application of the molecular design of HML to metallic radionuclides should accompany a significant change in chemical structure of radiolabels, *m*-iodobenzene in HML or HL-Boc was replaced with CpTR to prepare CpTR-GK or CpTR-GK-Boc, respectively (Figure 1). The effect of a change in a radiolabel on brush border enzyme-mediated hydrolysis rate and renal radioactivity levels was estimated.

The significantly slower rate of [^{188}Re]CpTR-Gly release from [^{188}Re]CpTR-GK-Boc than that of *m*-[^{125}I]iodohippuric acid from [^{125}I]HL-Boc indicated that the change in a radiolabel from *m*-iodobenzene to CpTR significantly impaired recognition and cleavage of the glycyl-lysine linkage by enzymes on BBMVs (Figure 3). In addition, while the glycyl-lysine linkage in HL-Boc was cleaved by both metalloenzymes and nonmetalloenzymes (*9*), the peptide linkage in CpTR-GK-Boc was predominantly cleaved by metalloenzymes, as indicated by the facilitated [^{188}Re]CpTR-Gly release by the addition of an activator for metalloenzymes (Co^{2+}) and almost complete inhibition of [^{188}Re]CpTR-Gly release by the addition of an inhibitor for metalloenzymes, MGTA (Figure 3). These results indicate that a change in the size and the shape of a radiolabel attached to a glycyl-lysine linkage significantly affected enzymes involved in the hydrolysis reaction.

In biodistribution studies, the three radiolabeled Fab fragments exhibited similar radioactivity levels in the blood from 10 min to 3 h, indicating that similar radioactive portions of the three radiolabeled Fab fragments would be filtered through the glomerulus and transported to the proximal tubules of the kidney during these intervals (Table 1). However, significant differences were observed in renal radioactivity levels between [^{188}Re]-CpTR-GK-Fab and [^{188}Re]CpTR-Fab. This was more clearly demonstrated when the kidney-to-blood ratios of radioactivity were compared (Figure 4). In addition, [^{188}Re]CpTR-Gly was excreted as the major radiometabolite in the urine following

injection of [188Re]CpTR-GK-Fab (Figure 5). These studies along with the in vitro studies indicate that the low renal radioactivity levels by [188Re]CpTR-GK-Fab would be attributable to a release of [188Re]CpTR-Gly by the action of enzymes on renal brush border membrane.

Since in vivo behaviors of [188Re]CpTR-Gly are similar to those of *m*-[125I]iodohippuric acid (*16*), the different renal radioactivity levels between the simultaneously administered [188Re]CpTR-GK-Fab and [125I]HML-Fab would reflect in vivo cleavage of the glycyl-lysine linkage of the two radiolabeled Fab fragments by enzymes on renal brush border membrane. As expected from the in vitro studies using BBMVs, [188Re]-CpTR-GK-Fab showed higher renal radioactivity levels than did [125I]HML-Fab. However, the differences in the renal radioactivity levels of the two radiolabeled Fab fragments were smaller than those expected from the in vitro studies. The differences in densities of the enzymes between the two experiments might account for the discrepancy. In addition, the glycyl-lysine linkage in [188Re]CpTR-GK-Fab might gain access to enzymes on brush border enzymes during the internalization process of the antibodies into renal cells, which may have facilitated the cleavage of the linkage in vivo.

The ability of [188Re]CpTR-GK to reduce the renal radioactivity levels without impairing the radioactivity levels in the tumor was demonstrated in biodistribution study in nude mice model (Figure 6). [188Re]CpTR-GK-Fab exhibited radioactivity levels in the blood and tumor similar to those of [188Re]CpTR-Fab and [125I]HML-Fab, indicating that the three radiolabeled Fab fragments possessed similar binding affinities to tumor cells in vivo. However, the renal radioactivity levels of [188Re]CpTR-GK-Fab was significantly lower than those of [188Re]CpTR-Fab. These findings suggest that [188Re]CpTR-GK may constitute a useful radiolabeling agent for antibody fragments if a new chemistry to prepare [188Re]CpTR-GK in high yields with easier procedure can be developed.

In conclusion, the findings in this study indicate that the molecular design of HML can be applicable to metallic radionuclides by using a radiometal chelate of high inertness and by designing a radiometabolite of high urinary excretion following cleavage of a glycyl-lysine linkage. This study also indicates that a change in chemical structure of a radiolabel attached to a glycyl-lysine linkage significantly affected enzymes responsible for the hydrolysis reaction. There are many kinds of enzymes on renal brush border membranes, and they recognize and cleave a variety of peptide linkages. The key concept of HML is to liberate a designed radiometabolite of urinary excretion from covalently conjugated antibody fragments or peptides by the action of enzymes present on lumen of renal tubules. Thus, the peptide linkage should be optimized to a radiometal chelate of interest so that a designed radiometabolite of urinary excretion can rapidly and selectively be released from antibody molecules by the action of enzymes on the renal brush border membrane. The in vitro system using renal brush border membrane vesicles might be useful to select an appropriate peptide linkage from a variety of candidates.

ACKNOWLEDGMENT

The authors appreciate Immuno-Biological Laboratories Co. Ltd. for providing a monoclonal antibody, 1B2, and CEA-positive tumor cells, MKN-45. This study was supported in part by a grant-in-aid for scientific research (B), scientific research on priority area, and exploratory research from the Ministry of Education, Culture, Sports, Science and Technology, Japan, and a grant-in-aid from the Fugaku Trust for Medicinal Research. The authors are also grateful to Mr. Takio Kobayashi for financial support.

Supporting Information Available: Elemental analyses data. This material is available free of charge via the Internet at http://pubs.acs.org/BC.

LITERATURE CITED

(1) Li, S. L., Liang, S. J., Guo, N., Wu, A. M., and Fujita-Yamaguchi, Y. (2000) Single-chain antibodies against human insulin-like growth factor I receptor: expression, purification, and effect on tumor growth. *Cancer Immunol. Immunother. 49*, 243−252.

(2) Ray, K., Embleton, M. J., Jailkhani, B. L., Bhan, M. K., and Kumar, R. (2001) Selection of single chain variable fragments (scFv) against the glycoprotein antigen of the rabies virus from a human synthetic scFv phage display library and their fusion with the Fc region of human IgG_1. *Clin. Exp. Immunol. 125*, 94−101.

(3) Choi, C. W., Lang, L., Lee, J. T., Webber, K. O., Yoo, T. M., Chang, H. K., Le, N., Jagoda, E., Paik, C. H., Pastan, I., Eckelman, W. C., and Carrasquillo, J. A. (1995) Biodistribution of F-18- and I-125-labeled anti-Tac disulfide-stabilized Fv fragments in nude mice with interleukin 2 alpha receptor-positive tumor xenografts. *Cancer Res. 55*, 5323−5329.

(4) Wu, C., Jagoda, E., Brechbiel, M., Webber, K. O., Pastan, I., Gansow, O., and Eckelman, W. C. (1997) Biodistribution and Catabolism of Ga-67-Labeled Anti-Tac dsFv Fragment. *Bioconjugate Chem. 8*, 365−369.

(5) Ultee, M. E., Bridger, G. J., Abrams, M. J., Longley, C. B., Burton, C. A., Larsen, S. K., Henson, G. W., Padmanabhan, S., Gaul, F. E., and Schwartz, D. A. (1997) Tumor imaging with Technetium-99m-labeled hydrazinonicotinamide-Fab′ conjugates. *J. Nucl. Med. 38*, 133−138.

(6) Arano, Y., Fujioka, Y., Akizawa, H., Ono, M., Uehara, T., Wakisaka, K., Nakayama, M., Sakahara, H., Konishi, J., and Saji, H. (1999) Chemical design of radiolabeled antibody fragments for low renal radioactivity levels. *Cancer Res. 59*, 128−134.

(7) Nakamoto, Y., Sakahara, H., Saga, T., Sato, N., Zhao, S., Arano, Y., Fujioka, Y., Saji, H., and Konishi, J. (1999) A novel immunoscintigraphy technique using metabolizable linker with angiotensin II treatment. *Br. J. Cancer 79*, 1794−1799.

(8) Fujioka, Y., Arano, Y., Ono, M., Uehara, T., Ogawa, K., Namba, S., Saga, T., Nakamoto, Y., Mukai, T., Konishi, J., and Saji, H. (2001) Renal metabolism of 3′-iodohippuryl N^{ϵ}-maleoyl-L-lysine (HML)-conjugated Fab fragments. *Bioconjugate Chem. 12*, 178−185.

(9) Fujioka, Y., Satake, S., Uehara, T., Mukai, T., Akizawa, H., Ogawa, K., Saji, H., Endo, K., and Arano, Y. (2005) In vitro system to estimate renal brush border enzyme-mediated cleavage of peptide linkages for designing radiolabeled antibody fragments of low renal radioactivity levels. *Bioconjugate Chem. 16*, 1610−1616.

(10) Akizawa, H., Arano, Y., Mifune, M., Iwado, A., Saito, Y., Uehara, T., Ono, M., Fujioka, Y., Ogawa, K., Kiso, Y., and Saji, H. (2001) Significance of 111In-DTPA chelate in renal radioactivity levels of 111In-DTPA-conjugated peptides. *Nucl. Med. Biol. 28*, 459−468.

(11) Akizawa, H., Arano, Y., Uezono, T., Ono, M., Fujioka, Y., Uehara, T., Yokoyama, A., Akaji, K., Kiso, Y., Koizumi, M., and Saji, H. (1998) Renal metabolism of 111In-DTPA-D-Phe1-octreotide in vivo. *Bioconjugate Chem. 9*, 662−670.

(12) Duncan, J. R., Stephenson, M. T., Wu, H. P., and Anderson, C. J. (1997) Indium-111-diethylenetriaminepentaacetic acid-octreotide is delivered in vivo to pancreatic, tumor cell, renal, and hepatocyte lysosomes. *Cancer Res. 57*, 659−671.

(13) Rogers, B. E., Franano, F. N., Duncan, J. R., Edwards, W. B., Anderson, C. J., Connett, J. M., and Welch, M. J. (1995) Identification of metabolites of In-111-diethylenetriaminepentaacetic acid monoclonal antibodies and antibody fragments in vivo. *Cancer Res. 55*, S5714−S5720.

(14) Li, L., Olafsen, T., Anderson, A. L., Wu, A., Raubitschek, A. A., and Shively, J. E. (2002) Reduction of kidney uptake in radiometal labeled peptide linkers conjugated to recombinant antibody fragments. Site-specific conjugation of DOTA-peptides to a Cys-diabody. *Bioconjugate Chem. 13*, 985−995.

(15) Schibli, R., and Schubiger, P. A. (2002) Current use and future potential of organometallic radiopharmaceuticals. *Eur. J. Nucl. Med. Mol. Imaging 29*, 1529−1542.
(16) Uehara, T., Koike, M., Nakata, H., Miyamoto, S., Motoishi, S., Hashimoto, K., Oku, N., Nakayama, M., and Arano, Y. (2003) In vivo recognition of cyclopentadienyltricarbonylrhenium (CpTR) derivatives. *Nucl. Med. Biol. 30*, 327−334.
(17) Callahan, A. P., Rice, D. E., and Knapp, F. F. J. (1989) A radionuclide generator system based on the adsorption of sodium or potassium [^{188}W]tungstate on alumina gives good yields of rhenium-188 for radiolabeling of therapeutic agents. *NUC-COM-PACT 20, 3-4*, 6.
(18) Kobayashi, K., Motoishi, S., Terunuma, K., Rauf, A. A., and Hashimoto, K. (2000) Production of ^{186,188}Re and recovery of tungsten from spent ^{188}W/^{188}Re generator. *Radiochemistry 42*, 551−554.
(19) Arano, Y., Matsushima, H., Tagawa, M., Koizumi, M., Endo, K., Konishi, J., and Yokoyama, A. (1991) A novel bifunctional metabolizable linker for the conjugation of antibodies with radionuclides. *Bioconjugate Chem. 2*, 71−76.
(20) Wakisaka, K., Arano, Y., Uezono, T., Akizawa, H., Ono, M., Kawai, K., Ohmomo, Y., Nakayama, M., and Saji, H. (1997) A novel radioiodination reagent for protein radiopharmaceuticals with L-lysine as a plasma-stable metabolizable linkage to liberate *m*-iodohippuric acid after lysosomal proteolysis. *J. Med. Chem. 40*, 2643−2652.
(21) Kinoshita, H. (1974) Selective cleavage of N-t-Butoxycarbonyl protecting group. *Chem. Lett.* 631−634.
(22) Grassetti, D. R., and Murray, J. F., Jr. (1967) Determination of sulfhydryl groups with 2,2′- or 4,4′-dithiodipyridine. *Arch. Biochem. Biophys. 119*, 41−49.
(23) Spradau, T. W., and Katzenellenbogen, J. A. (1998) Protein and peptide labeling with (cyclopentadienyl)tricarbonyl rhenium and technetium. *Bioconjugate Chem. 9*, 765−772.
(24) Kramers, M. T., and Robinson, G. B. (1979) Studies on the structure of the rabbit kidney brush border. *Eur. J. Biochem. 99*, 345−351.
(25) Wallner, S. J., and Walker, J. E. (1975) Glycosidases in cell wall-degrading extracts of ripening tomato fruits. *Plant Physiol. 55*, 94−98.
(26) Deddish, P. A., Skidgel, R. A., and Erdos, E. G. (1989) Enhanced Co^{2+} activation and inhibitor binding of carboxypeptidase M at low pH. Similarity to carboxypeptidase H (enkephalin convertase). *Biochem. J. 261*, 289−291.
(27) Skidgel, R. A., Davis, R. M., and Tan, F. (1989) Human carboxypeptidase M. Purification and characterization of a membrane-bound carboxypeptidase that cleaves peptide hormones. *J. Biol. Chem. 264*, 2236−2241.
(28) Arano, Y., Inoue, T., Mukai, T., Wakisaka, K., Sakahara, H., Konishi, J., and Yokoyama, A. (1994) Discriminated release of a hippurate-like radiometal chelate in nontarget tissues for target-selective radioactivity localization using pH-dependent dissociation of reduced antibody. *J. Nucl. Med. 35*, 326−333.
(29) Arano, Y., Wakisaka, K., Mukai, T., Uezono, T., Motonari, H., Akizawa, H., Kairiyama, C., Ohmomo, Y., Tanaka, C., Ishiyama, M., Sakahara, H., Konishi, J., and Yokoyama, A. (1996) Stability of a metabolizable ester bond in radioimmunoconjugates. *Nucl. Med. Biol. 23*, 129−136.

BC0602329

Applications of Tailored Ferrocenyl Molecules as Electrochemical Probes of Biochemical Interactions

Isabelle Tranchant,[⊥,‡] Anne-Cécile Hervé,[†,§] Stephen Carlisle,[†] Phillip Lowe,[†,#] Christopher J. Slevin,[†,#] Camilla Forssten,[†] John Dilleen,[†,#] Alethea B. Tabor,[⊥] David E. Williams,*[,†,||] and Helen C. Hailes*[,⊥]

Department of Chemistry, University College London, 20 Gordon Street, London WC1H 0AJ, U.K., and Unipath Ltd, Priory Business Park, Bedford, MK44 3UP, U.K. Received February 17, 2006; Revised Manuscript Received August 31, 2006

The development of electrochemical probes useful for investigating the occupancy by other molecules of sites on complex proteins such as human serum albumin (HSA) is described. Ferrocenyl-(oxoethylene)-fatty acid compounds of different fatty acid chain length probed different binding sites on HSA. The interaction could be changed from one primarily with a drug binding site, when the probe was ferrocene methanol, to one predominantly with medium-chain fatty acid binding sites, by adding an (oxoethylene)-fatty acid substituents. Finally, the interaction could be changed to one interacting primarily with high-affinity long-chain fatty acid binding sites, as the fatty acid chain length in ferrocene-(oxoethylene)-fatty acid molecules increased. These results strongly implied that the binding could be further tailored by relatively simple modifications to the probe, for example, by changing the balance of hydrophobicity and hydrophilicity. The possibility of a procedure using mass-produced electrochemical cells to determine the fractional occupancy of different sites on HSA is demonstrated.

INTRODUCTION

Serum albumin is of significance as a carrier for small molecules in blood (*1*, *2*). Arguably, the fractional occupancy of different binding sites on albumin could be an important medical diagnostic indicator (*1*, *3*). In particular, the binding of fatty acid to serum albumin is an important interaction in mammalian metabolism. It has previously been demonstrated that the binding of fatty acids to human serum albumin (HSA) influences the binding of a number of other drug and biomolecules in the body (*4*). The ability of serum albumin to bind a number of medium- and long-chain fatty acids simultaneously enables it to be an effective carrier for these molecules, which play a key role in cell functioning. The buffer capacity of albumin for fatty acid concentration in the blood has been proposed as a significant diagnostic indicator, for cardiac ischemia (*5*). Fatty acids are also known to bind to a number of other proteins, particularly the class of fatty acid binding proteins (FABP) (*6*). The work reported here has aimed to provide probes for fatty acid interactions with proteins, which are complementary to other methods such as the electronic spin resonance (ESR) spectroscopy method using binding of the spin-probe 16-doxyl stearate, described in ref *3*. Our focus has been to develop electrochemical methods, in view of their instrumental convenience. Here we demonstrate the principle of electrochemical probes of site occupancy and that implementation in mass-produced electrochemical cells is feasible, while highlighting some of the challenges raised by such procedures.

* Author to whom correspondence should be addressed: E-mail: david.williams@auckland.ac.nz (D.E.W.); h.c.hailes@ucl.ac.uk (H.C.H.); fax: +44 (0)20 7679 7463.

[⊥] University College London.

[†] Unipath Ltd.

[§] Current address: Diatos NV, Brusselsestraat 69, B-3000 Leuven, Belgium.

[‡] Current address: Diatos SA, Therapeutic Chemistry Department, 3-5 Impasse Reille, 75014 Paris, France.

[#] Current address: Sterling Medical Innovations, Unit 10, Scion House, Stirling University Innovation Park, Stirling, FK9 4NF.

[||] Current address: Department of Chemistry, University of Auckland, Private Bag, Auckland, New Zealand.

Fatty acid−protein interactions and, in particular, fatty acid−HSA interactions have been studied by various methods including X-ray crystallography (*7*), in which distinct binding sites for a range of fatty acids were identified. HSA has been specifically labeled with a fluorescent molecule and used to study oleate binding (*8*). The binding of a fluorescently labeled fatty acid such as 11-(dansylamino)undecanoic acid (DAUDA) to HSA (*9*) and to FABP (*10*) was studied by measuring the fluorescent signal response to the changing microenvironment around the fluorescent moiety on binding. DAUDA was also used to investigate the binding of other fatty acids as well as other molecules such as bilirubin in competitive studies with HSA (*9*). Equilibrium dialysis has been used with radiolabeled fatty acids to study the binding of a range of fatty acids to albumin (*11*); analysis was done in terms of a multiple non-interacting binding sites. Binding of a range of fatty acids to an acrylodan modified FABP (ADIFAB) has been characterized by fluorescence, and subsequently the binding characteristics of these fatty acids to HSA was determined by using the modified FABP to determine the free fatty acid concentration in the presence of HSA (*12*).

We have previously demonstrated the design and synthesis of a range of molecules consisting of a functional group that confers some specific biochemical activity, linked to an electrochemical label, to enable the reporting of activity (*13*). The two groups were linked by a spacer group, which was chosen to influence the solubility and enhance the electrochemical properties of the molecule, and may also improve the biochemical functionality through structural or specific chemical interactions. We report here the use of a range of molecules based on the earlier design, consisting of a fatty acid group, linked to a solubilizing spacer group, which in turn is linked to a ferrocene based electrochemically active signaling moiety, of the general structure **1** shown in Figure 1. The ideal structural characteristics were identified in compound **2**, as an amide at linker **A**, carbamate at linker **B**, and a short poly(ethylene glycol) (PEG) unit, for investigating fatty acid binding to a number of fatty acid binding molecules.

In this paper, we illustrate how *m*, the length of the fatty acid, may be varied (compounds synthesized for $m = 2, 5, 7,$

10.1021/bc060039e CCC: $37.00 © 2007 American Chemical Society
Published on Web 11/11/2006

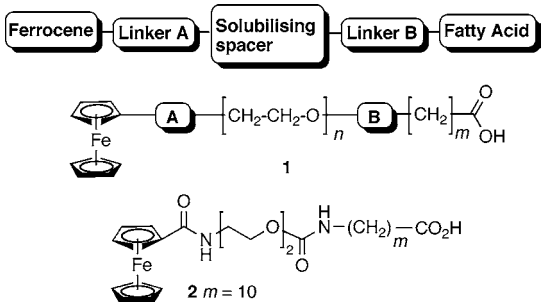
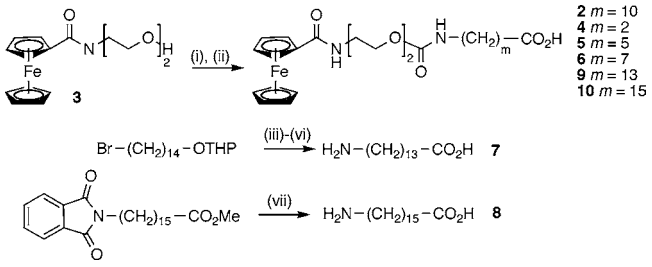


Figure 1. Ferrocene multifunctional conjugates.

Scheme 1. Synthesis of Ferrocene Conjugates with Chain Lengths ($m + 1$)[a]



[a] (i) DSC, CH_3CN, 87%; (ii) amino acid, THF/H_2O, 30−80%; (iii) potassium phthalimide, DMF, 58%; (iv) HCl, MeOH, 67%; (v) CrO_3, H_2SO_4, 50%; (vi) N_2H_4, EtOH, reflux, 4 h, 80%; (vii) N_2H_4, EtOH, reflux, 3 h, then NaOH, 84%.

10, 13, and 15) to allow us to study specifically the interactions of different fatty acids with proteins, particularly albumin. The approach is a general one, so that other small molecules might be electrochemically labeled using similar methods. One of the key aspects is the use of carefully chosen signaling, linker, and spacer groups to deliver a compound that has fast electrochemistry at a potential accessible in biologically relevant media such as blood and plasma and which has the desired solubility, stability, and probe characteristics. This work is related in concept to the studies using fluorescently labeled fatty acids (*9*). However, the earlier studies on DAUDA (*9*) showed it interacting with the bilirubin site rather than the fatty acid binding sites of albumin. Hence, we have varied the length of the labeled fatty acid and to some extent altered the balance of aromatic, aliphatic, hydrophobic, and hydrophilic elements to provide a range of probes that might access different sites on HSA.

Comparison with theory for noninteracting multiple binding sites (*11*, *12*, *14*, *15*), using binding constants already determined for fatty acids to HSA, allowed investigation of the competitive binding of labeled fatty acids with natural fatty acids and demonstrated the feasibility of using instrumentally simple methods and mass-produced electrochemical cells to probe fractional occupancy of different sites on HSA.

EXPERIMENTAL PROCEDURES

Syntheses of Compounds Based on the General Structure, 2, but with Different Numbers of Carbons in the Fatty Chain. The ferrocene PEG-amide **3** was activated (*13*) as the *N*-hydroxysuccinimidyl (NHS) ester, which was isolated, and then coupled with the commercially available amino acids β-alanine, 6-aminohexanoic acid, 8-aminooctanoic acid, to give **4**, **5**, and **6** in 40−80% yield (Scheme 1). Two longer chain analogues were prepared using 14-aminotetradecanoic acid and 16-aminohexadecanoic acid, which were synthesized via the phthalimides using established synthetic manipulations (*16*, *17*). 14-Aminotetradecanoic acid (**7**) was prepared from 1-bromo-14-(tetrahydropyran-2-yloxy)tetradecane via the addition of phthalimide, OTHP deprotection, oxidation using Jones' reagent to the acid, and finally removal of the phthalimide group using hydrazine. 16-Aminohexadecanoic acid (**8**) was prepared in 84% overall yield from methyl 16-phthalimide hexadecanoate through removal of the phthalimide group and hydrolysis of the ester. 14-Tetradecanoic acid (**7**) and 16-aminohexadecanoic acid (**8**) were coupled with the NHS ester of **3** as before to give the PEG conjugates **9** and **10**, respectively (Scheme 1).

Materials. Unless otherwise noted, solvents and reagents were reagent grade from commercial suppliers and used without further purification. Tetrahydrofuran (THF) was dried by distillation from a sodium/benzophenone suspension under a dry N_2 atmosphere. CH_2Cl_2 was dried by distillation from CaH_2 under a dry N_2 atmosphere. All moisture-sensitive reactions were performed under a nitrogen atmosphere using oven-dried glassware. Reactions were monitored by TLC on Kieselgel 60 F_{254} plates with detection by UV, or permanganate, ninhydrin, and phosphomolybdic acid stains. Flash column chromatography was carried out using silica gel (particle size 40−63 μm). Melting points are uncorrected. ^{1}H NMR and ^{13}C NMR spectra were recorded in $CDCl_3$ at the field indicated unless otherwise indicated. 1-Bromo-14-(tetrahydropyran-2-yloxy)tetradecane was prepared as previously described (*18*). Methyl 16-phthalimide hexadecanoate was prepared as previously reported (*19*).

3-(Ferrocenoylamide-3-oxapentanyloxycarbonylamino)-propanoic Acid (4). The reaction was carried out under anhydrous conditions. Compound **3** was activated as the *N*-hydroxysuccinimide ester (NHS) as previously described (*13*). The NHS intermediate (150 mg, 0.33 mmol) was dissolved in DMF (2 mL), and triethylamine (54 μL, 0.39 mmol) was added. To this solution was added β-alanine (30 mg, 0.33 mmol), dissolved in a mixture of water/DMF (3.3 mL/1.3 mL). The reaction was stirred at room temperature (rt) for 18 h, and the solvents were then evaporated in vacuo. The resulting oil was purified by flash silica chromatography (5% methanol in CH_2Cl_2) to afford **4** (102 mg, 73%) as an orange oil. ^{1}H NMR (300 MHz; methanol-d_4) 2.25 (t, 2H, J 6.1 Hz, CH_2CO_2H), 3.18 (m, 2H, CH_2NH), 3.32 (dt, J 10.3 and 5.2 Hz, 2H, CH_2NH), 3.44 (t, J 5.2 Hz, 2H, CH_2O), 3.49 (t, J 5.2 Hz, 2H, m, CH_2O), 3.99 (m, 2H, C_5H_2), 4.03 (m, 2H, CH_2OCO), 4.17 (s, 5H, C_5H_5), 4.57 (m, 2H, C_5H_2); ^{13}C NMR (75 MHz; methanol-d_4) 34.2, 36.4, 39.3, 63.6, 68.0, 69.3, 69.6, 69.7, 70.5, 75.0, 156.7 (C═O carbamate), 171.7 (C═O amide), 174.6 (C═O acid); m/z HRMS calculated for $C_{19}H_{24}N_2O_6FeNa$ $(MNa)^+$ 455.08760, found (ES+) 455.08592.

6-(Ferrocenoylamide-3-oxapentanyloxycarbonylamino)-hexanoic Acid (5). The reaction was carried out under anhydrous conditions. Compound **3** was activated as the *N*-hydroxysuccinimide ester as previously described (*13*). The NHS intermediate (50 mg, 0.11 mmol) was dissolved in DMF (0.7 mL) and triethylamine (18 μL, 0.13 mmol) was added. To this solution was added 6-aminohexanoic acid (15 mg, 0.11 mmol), dissolved in a mixture of water/DMF (1.1 mL/0.4 mL). The reaction was stirred at rt for 18 h, and the solvents were then evaporated in vacuo. The resulting oil was purified by flash silica chromatography (5% methanol in CH_2Cl_2) to afford **5** (42 mg, 80%) as an orange oil. ^{1}H NMR (300 MHz; $CDCl_3$) 1.33 (quin, J 7.2 Hz, 2H), 1.47 (quin, J 7.2 Hz, 2H), 1.61 (quin, J 7.2 Hz, 2H), 2.33 (t, 2H, J 7.2 Hz, CH_2CO_2H), 3.12 (m, 2H, CH_2NH), 3.54 (m, 2H, CH_2NH), 3.65 (m, 4H, CH_2O), 4.19 (s, 5H, C_5H_5), 4.22 (m, 2H, CH_2OCO), 4.33 (m, 2H, C_5H_2), 4.73 (m, 2H, C_5H_2), 5.04 (m, 1H, NH), 6.59 (m, 1H, NH); ^{13}C NMR (75 MHz; $CDCl_3$) 25.8, 29.4, 29.7, 34.1, 39.3, 39.6, 63.9, 68.4, 69.7, 69.8, 70.5, 72.3, 75.7, 156.5 (C═O carbamate), 171.0 (C═O amide), 177.9 (C═O acid); m/z HRMS calculated for $C_{22}H_{31}N_2O_6Fe$ M^+ 474.14532, found (ES+) 474.14527.

8-(Ferrocenoylamide-3-oxapentanyloxycarbonylamino)-octanoic Acid (6). The reaction was carried out under anhydrous conditions. Compound **3** was activated as the *N*-hydroxysuc-

cinimide ester as previously described (*13*). The NHS intermediate (150 mg, 0.33 mmol) was dissolved in DMF (2 mL) and triethylamine (55 μL, 0.39 mmol) was added. To this solution was added 6-aminooctanoic acid (15 mg, 0.11 mmol), dissolved in a mixture of water/DMF (3.3 mL/1.3 mL). The reaction was stirred at rt for 18 h and the solvents were then evaporated in vacuo. The resulting oil was purified by flash silica chromatography (5% methanol in CH_2Cl_2) to afford **6** (63 mg, 40%) as an orange oil. ^{1}H NMR (300 MHz; $CDCl_3$) 1.28 (m, 6H), 1.39 (quin, *J* 6.6 Hz, 2H), 1.60 (quin, *J* 5.8 Hz, 2H), 2.31 (t, 2H, *J* 6.6 Hz, CH_2CO_2H), 3.09 (dt, *J* 6.8 and 5.8 Hz, 2H, CH_2-NH), 3.55 (dt, *J* 5.3 and 4.9 Hz, 2H, CH_2NH), 3.65 (m, 4H, CH_2O), 4.19 (s, 5H, C_5H_5), 4.20 (t, *J* 4.5 Hz, 2H, CH_2OCO), 4.31 (m, 2H, C_5H_2), 4.71 (m, 2H, C_5H_2), 4.90 (br m, NH), 6.59 (br m, 1H, NH); ^{13}C NMR (75 MHz; $CDCl_3$) 24.7, 26.5, 28.78, 28.79, 29.7, 34.0, 39.4, 41.0, 63.7, 68.3, 69.7, 69.8, 70.1, 70.5, 75.8, 156.5 (C═O carbamate), 171.0 (C═O amide), 177.9 (C═O acid); *m/z* HRMS calculated for $C_{24}H_{34}N_2O_6Fe$ M^+ 502.17661, found (FAB$^+$) 502.17918.

14-Aminotetradecanoic Acid (7). The reaction was carried out under anhydrous conditions. 1-Bromo-14-(tetrahydropyran-2-yloxy)tetradecane (63 mg, 0.17 mmol) and potassium phthalimide (48 mg, 0.26 mmol) in DMF (1 mL) were heated at 40 °C for 4 h. Water (10 mL) was added, and the product was extracted into CH_2Cl_2 (3 × 10 mL). The organic phase was dried ($MgSO_4$) and evaporated to give 2-(14-tetrahydropyran-2-yloxy-tetradecyl)-isoindole-1,3-dione (64 mg, 58%) which was used without further purification. ^{1}H NMR (300 MHz; $CDCl_3$) 1.25 (m, 20H), 1.51 (m, 6H), 1.62 (m, 4H), 3.33 (m, 2H), 3.45 (m, 2H), 3.68 (m, 2H, CH_2O), 4.52 (m, 1H, CHO), 7.68 (m, 2H, ArH), 7.78 (m, 2H, ArH); ^{13}C NMR (75 MHz; $CDCl_3$) 19.8, 25.5−31.7 (signals superimposed), 38.0, 62.3, 67.7, 99.4, 123.0, 132.1, 134.3, 168.4 (C═O); *m/z* (ES+) 466 (MNa^+, 25%), 377 (100).

To 2-(14-tetrahydropyran-2-yloxy-tetradecyl)-isoindole-1,3-dione (64 mg, 0.15 mmol) in methanol (2 mL) was added dilute hydrochloric acid (6 N; 0.5 mL). The reaction was heated at reflux for 2 h, ether was added (20 mL) and the solution washed with sodium carbonate solution (2 × 20 mL), saturated sodium chloride solution (1 × 20 mL) and dried ($MgSO_4$). After evaporation in vacuo, the product was purified by flash silica chromatography (hexane/EtOAc, 1:1) to give 2-(14-hydroxy-tetradecyl)-isoindole-1,3-dione (37 mg, 67%) (*17*). ^{1}H NMR (300 MHz; $CDCl_3$) 1.29 (m, 18H), 1.60 (m, 6H), 3.60 (m, 4H), 7.68 (m, 2H, ArH), 7.78 (m, 2H, ArH); ^{13}C NMR (75 MHz; $CDCl_3$) 25.7−29.6 (signals superimposed), 32.8, 38.1, 63.1, 123.2, 132.2, 133.8, 168.5 (C═O); *m/z* (ES+) 360 (MH^+, 10%).

To 2-(14-hydroxytetradecyl)-isoindole-1,3-dione (37 mg, 0.10 mmol) in acetone (1 mL) was added Jones reagent (0.085 mL; for 1 mL of Jones reagent- 0.23 mL H_2SO_4, 270 mg CrO_3, 0.77 mL H_2O). The reaction was stirred at rt for 1 h, 2-propanol (5 mL) was added and the mixture diluted with water (5 mL), then the acetone removed in vacuo. The solution was extracted with CH_2Cl_2 (2 × 20 mL), dried ($MgSO_4$) and evaporated, then purified by flash silica chromatography (hexane/EtOAc, 3:2) to give 14-(1,3-dioxo-1,3-dihydroisoindol-2-yl)tetradecanoic acid (20 mg, 50%). ^{1}H NMR (300 MHz; $CDCl_3$) 1.22 (m, 18H), 1.57 (m, 4H), 2.26 (m, 2H), 3.63 (m, 2H, CH_2N), 7.68 (m, 2H, ArH), 7.78 (m, 2H, ArH); ^{13}C NMR (75 MHz; $CDCl_3$) 25.7−29.6 (signals superimposed), 32.4, 34.1, 38.1, 123.2, 132.2, 133.8, 168.5 (C═O), 171.3 (C═O acid).

Hydrazine hydrate (0.25 mL, 0.50 mmol) was added to 14-(1,3-dioxo-1,3-dihydroisoindol-2-yl)-tetradecanoic acid (20 mg, 0.05 mmol) in ethanol (1 mL). The reaction was heated at reflux for 4 h, and the solvents were evaporated in vacuo. The residue was dissolved in CH_2Cl_2, and the precipitated phthalimide was removed by filtration. The CH_2Cl_2 was removed in vacuo to give 14-aminotetradecanoic acid (**7**) (10 mg, 80%) (*16*) as a colorless solid. mp 176−178 °C (CH_2Cl_2); ^{1}H NMR (300 MHz; $CDCl_3$) 1.10 (m, 18H), 1.36 (m, 4H), 2.05 (t, *J* 7.5 Hz, 2H, CH_2CO_2H), 2.57 (m, 2H, CH_2N); ^{13}C NMR (75 MHz; $CDCl_3$) 25.7−29.6 (signals superimposed), 32.9, 34.1, 40.1, 171.2 (C═O acid); *m/z* (ES+) 261 ($M^+ + H_2O$, 100%), 258 ($M^+ + NH_3$, 21), 244 (MH^+, 5).

16-Aminohexadecanoic Acid Hydrochloride (8). A solution of methyl 16-phthalimide hexadecanoate (*19*) (200 mg, 0.48 mmol) and hydrazine hydrate (97 mg, 1.94 mmol) in ethanol (5 mL) was heated at reflux for 3 h. The solvents were evaporated in vacuo, the residue was dissolved in ethanol (5 mL) and dilute hydrochloric acid (2 N; 0.5 mL), and the mixture was heated at reflux for a further 3 h. Ethanol (2 mL) was removed in vacuo and the precipitated phthalimide removed by filtration. Dilute sodium hydroxide solution (6 N; 0.5 mL) was added to the filtrate and the mixture was stirred for 4 h, then neutralized with 2 N hydrochloric acid solution. The remaining ethanol was removed in vacuo, and the suspension was filtered, then washed with water (20 mL) and CH_2Cl_2 (3 × 10 mL) to give **8** (*16*) as a colorless powder (125 mg, 84%), which was used directly in the next step (see synthesis of **10** below).

14-(Ferrocenoylamide-3-oxapentanyloxycarbonylamino)-tetradecanoic Acid (9). The reaction was carried out under anhydrous conditions. Compound **3** was activated as the *N*-hydroxysuccinimide ester as previously described (*13*). The NHS intermediate (38 mg, 0.08 mmol) was dissolved in THF (1 mL) and triethylamine (14 μL, 0.09 mmol) was added. To this solution was added **7** (10 mg, 0.04 mmol), in a mixture of water/DMF (1 mL/1.3 mL). The reaction was stirred at rt for 18 h, and the solvents were evaporated in vacuo. The resulting oil was purified by flash silica chromatography (5% methanol in CH_2Cl_2) to afford **9** (2 mg, 62%) as an orange oil. ^{1}H NMR (300 MHz; $CDCl_3$) 1.13 (m, 18H), 1.46 (m, 4H), 2.15 (t, 2H, *J* 7.5 Hz, CH_2CO_2H), 3.08 (m, 2H, CH_2NH), 3.54 (m, 2H, CH_2-NH), 3.65 (m, 4H, CH_2O), 4.21 (s, 5H, C_5H_5), 4.23 (m, 2H, CH_2OCO), 4.32 (m, 2H, C_5H_2), 4.72 (m, 2H, C_5H_2), 4.90 (br m, 1H, NH), 6.59 (br m, 1H, NH); *m/z* (ES+) 609 (MNa^+, 10%), 340 (100).

16-(Ferrocenoylamide-3-oxapentanyloxycarbonylamino)-hexadecanoic Acid (10). The reaction was carried out under anhydrous conditions. Compound **3** was activated as the *N*-hydroxysuccinimide ester as previously described (*13*). The NHS intermediate (50 mg, 0.11 mmol) was dissolved in THF (5 mL), and triethylamine (34 μL, 0.24 mmol) and **8** (37 mg, 0.12 mmol) in a mixture of water/THF (3 mL/2 mL) were added. The reaction was stirred at rt for 18 h, and the solvents were evaporated in vacuo. The resulting oil was solubilized in EtOAc (20 mL), washed with water (2 × 20 mL), dried (Na_2SO_4), evaporated, and purified by flash silica chromatography (100% EtOAc, then EtOAc/methanol 90:10) to afford **10** (20 mg, 30%) as an orange oil. ^{1}H NMR (300 MHz; $CDCl_3$) 1.26 (m, 20H), 1.45 (m, 2H), 1.65 (m, 2H), 2.38 (t, 2H, *J* 7.5 Hz, CH_2CO_2H), 3.15 (m, 2H, CH_2NH), 3.59 (m, 2H, CH_2NH), 3.64 (m, 2H, CH_2O), 3.70 (m, CH_2O), 4.21 (s, 5H, C_5H_5), 4.26 (m, 2H, CH_2-OCO), 4.34 (m, 2H, C_5H_2), 4.72 (m, 3H, C_5H_2 + NH), 6.25 (br m, 1H, NH); *m/z* HRMS calculated for $C_{32}H_{50}N_2O_6FeNa$ $(MNa)^+$ 637.29105, found (ES+) 637.28895.

Electrochemistry. *Materials and Cells.* The basic reagents were phosphate buffered saline (PBS: 0.01 M phosphate buffer, 0.137 M NaCl, 0.0027 M KCl, pH 7.4), sodium oleate, human serum albumin (all Sigma) and Nafion perfluorinated ion-exchange resin 10 wt % dispersion in water (Aldrich). All solutions were filtered using a 0.2 μm cutoff filter. All measurements were performed with electrodes screen-printed onto alumina tiles using polymer-bonded, heat-cured inks (Gwent Electronic Materials Ltd), with the cell area defined by

over-printing an insulator with a circular hole to expose the electrodes: carbon working (area = 3.0×10^{-2} cm^2) and counter electrodes and a silver/silver chloride reference electrode. In repeat measurements of cyclic voltammetry of the ferrocene probe molecules in PBS, cells mass-produced in this way reproduced peak currents to better than ± 15% and $E_{1/2}$ to better than ± 5 mV (2 standard deviations). Nafion coating of the electrodes was achieved by pipetting 3 μL of a 1% v/v dilution in water of the as-supplied Nafion solution onto the cell so as to cover the entire exposed disc with the working, counter and reference electrodes. The resulting assembly was left to dry at room temperature in the dark. The volume and dilution required were determined empirically. Given the cell area (0.12 cm^2) this implied a fully dense membrane thickness of approximately 0.1 μm. When the sample was fully swollen in water, the thickness would be significantly greater. The electrode coating method was not optimized and introduced a degree of variability into the results (variation in peak current ± 20%). All electrochemical measurements were performed with a general purpose electrochemical system (Autolab: Eco Chemie B.V Netherlands).

For measurement, 20 μL of sample was applied to the sample/working area of the electrode ensuring complete coverage of the working, counter, and reference electrodes. All samples were premixed before being applied to the electrode, and a new electrode tile was used for each measurement. All ferrocene-labeled fatty acid probe molecule stock solutions were dissolved in methanol due to poor solubility at high concentrations in PBS. Subsequent dilutions were made with PBS, and the final concentration of methanol was no more than 5% v/v. Methanol binds weakly to albumin through the methylene group (*20*) and will probably compete on the drug binding sites. This competition will introduce an error into the determination of binding constants, which is assessed in the Discussion. Cyclic voltammetry measurements were made immediately on uncoated electrodes and after a 2 min period on Nafion-coated electrodes. All potentials are quoted with respect to the Ag/AgCl reference electrode in the measurement solution. The potential ramp was a digitally generated staircase. Cyclic voltammetry scan parameters were as follows, hold at 0 V for 5 s, start potential 0 V, vertex potential 0.7 V, staircase step potential 0.002 V, and scan rate 0.05 V s^{-1}.

Electrochemical System Design. The binding of the probe to a protein, the competition with other molecules in the solution, and measurement through electrochemistry is overall a complicated system. The electrochemical process has a second-order reaction preceding the electrochemical step and probably another following. Also, as we showed in our previous paper (*13*), the ferricenium product can decompose to electrochemically inactive species.

$$\mathrm{E} + \mathrm{A} \underset{k_a}{\overset{k_d}{\rightleftharpoons}} \mathrm{EA}$$

$$\mathrm{E} \leftrightharpoons \mathrm{E}^+ + \mathrm{e}^-$$

$$\mathrm{E}^+ + \mathrm{A} \underset{k_{a,1}}{\overset{k_{d,1}}{\rightleftharpoons}} \mathrm{E}^+\mathrm{A}$$

$$\mathrm{E}^+ \xrightarrow[k_2]{} \text{products} \qquad (1)$$

The behavior is determined by the value of the characteristic time constants for the chemical processes relative to the characteristic time constant for the electrochemical experiment, which for cyclic voltammetry is $\upsilon F/RT$ where υ denotes the potential scan rate, F is Faraday's constant, R is the gas constant and T is the Kelvin temperature. If the electrochemistry is fast, so that E and E$^+$ (eq 1) can be considered at equilibrium at the electrode surface, with concentrations determined by the Nernst equation, then the ratio of electrochemical to chemical rate constants is $V = \upsilon F/(RT\{(k_{a,1} + k_{a,2})c_{E,T} + k_{d,1} + k_{d,2} + k_2\})$ where $c_{E,T} = c_E + c_{E^+} + c_{EA} + c_{E^+A}$ is the total concentration of the species E. With decrease of V below unity, reactions in the boundary layer on the time scale of the scan have a profound effect on the wave shape and peak height in cyclic voltammetry. Literature data for fatty acid binding (*21*) show one should expect $k_{a,1}c_{E,T} + k_{d,1} \sim 1$ s^{-1}, and hence for potential scan rates around 50 mV s^{-1}, indeed $V \sim 1$.

Although the full system is complex, the behavior can be calculated easily using finite difference solution of the diffusion−reaction equations. We used a spreadsheet to do this. Figure 2 illustrates the wave shift that could be caused, calculated using representative parameters deduced in Results and from the literature. Figure 2 also shows that, in these circumstances, the concentration of "unbound" probe in the presence of protein cannot be obtained by using a simple calibration in the absence of the protein. Therefore, for quantitation of the equilibrium solution concentrations of the probe, E, the complicating effects of the preceding and following chemical reactions need to be avoided. While in principle a sufficiently high scan rate would suffice, quantitation is most conveniently achieved by use of a membrane that defines the boundary layer and excludes the protein from it. Figure 2 also illustrates the theoretical effect of a membrane on the voltammetry of a second-order CEC process. If the membrane is sufficiently thick, then the concentration changes of E and E$^+$ near the surface, that determine the electrochemical response, are confined within the membrane and are largely uninfluenced by the protein. The peak current, though obviously dependent on the membrane thickness, the diffusion coefficient of E and E$^+$ within the membrane and the decomposition rate of E$^+$ within the membrane, becomes the same for the same bulk solution concentration of free label whether or not protein is present. The theory shows that even a very thin membrane could allow deduction of the bulk solution concentration of free label from a calibration made in the absence of protein, without too much error. A compromise is clearly achievable wherein the voltammetry can be simplified and a reasonable calibration obtained without too much diminution of the peak current.

A suitably chosen membrane also has the advantage of mitigating the effects of protein and probe adsorption on the electrode surface. Proteins adsorb strongly on carbon and can unfold across the hydrophobic surface. There is also the possibility that the long-chain fatty acid analogues used as electrochemical probes could adsorb on a hydrophobic carbon surface. These considerations all indicate the use of a hydrophilic, protein-excluding membrane over the electrode. The major interferences in electrochemistry in blood are due to the anionic species ascorbate and uric acid. A cationic membrane should exclude these species. We indeed found that a Nafion membrane essentially eliminated the interference, and in view of the other considerations outlined above, used such coated electrodes for the measurements reported here.

RESULTS

Electrochemical Characterization. In the previous paper (*13*) the optimal linkers **A** and **B** and the ferrocene solubilizing group were identified in order to obtain molecules with the desired electrochemistry, solubility and stability. The selected structure **2** consisted of a monosubstituted ferrocene with an amide bond linking the cyclopentadienyl ring to a short (two unit) PEG spacer group, linked to the fatty acid through a carbamate bond (Figure 1).

Compounds **4**−**6** (m = 2, 5, 7) showed half-wave potentials at approximately 350 mV Ag/AgCl (Table 1). A further increase

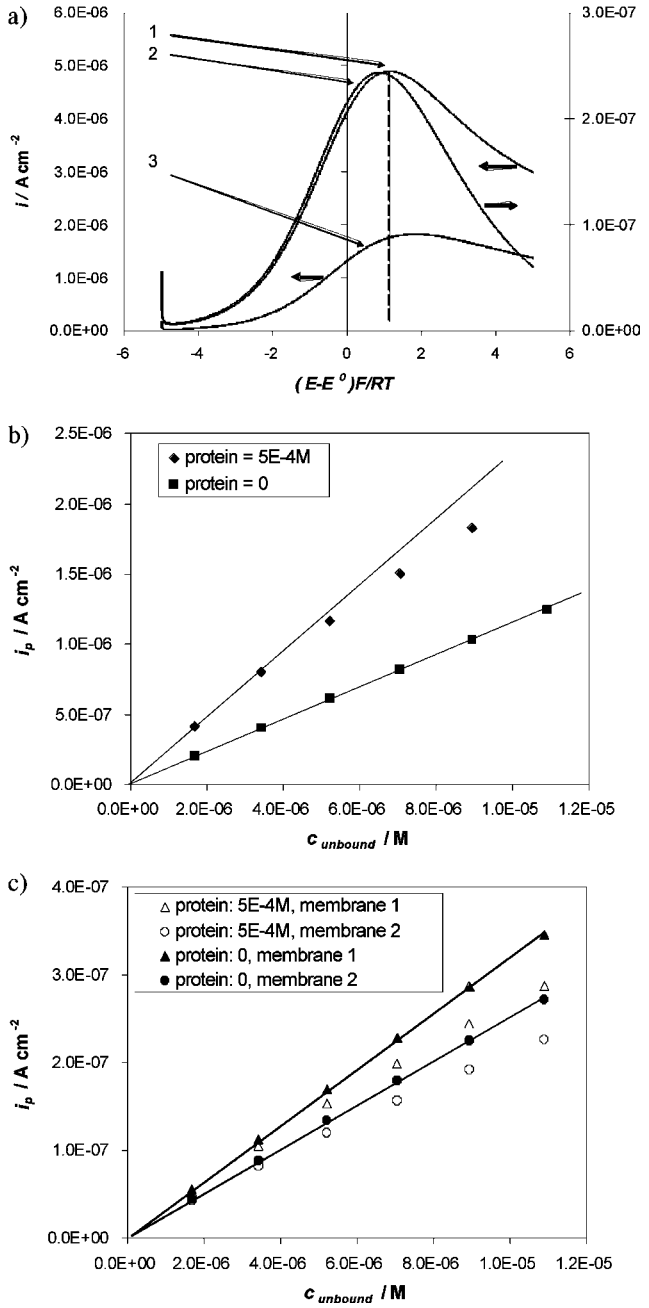


Figure 2. Effects of the CEC process described by eqs 1 on linear sweep voltammetry, illustrating the effect of a membrane. (a) Simulation of linear sweep voltammetry. 1: E only, no membrane; 2: E, protein, and membrane 1 (current density on right-hand axis); 3: E and protein, no membrane. (b) Simulated voltammetric peak current density, i_p, dependence on the concentration of electrochemically active species, E, that is not bound to protein, $c_{unbound}$, in the absence of a membrane, showing that a calibration deduced in the absence of protein would result in a significant error in $c_{unbound}$; (c) as for (b), but with a membrane covering the electrode, illustrating that, with a sufficiently thick membrane a calibration deduced in the absence of protein would give a reasonably reliable measure of $c_{unbound}$. Parameters assumed: $c_{E,T} = 5 \times 10^{-5}$ mol dm^{-3}, $c_{A,T} = c_A + c_{EA} + c_{E^+A} = 5 \times 10^{-4}$ mol dm^{-3}, $k_d = k_{d,1} = 1$ s^{-1}, binding constant, $K = k_d/k_a = k_{d,1}/k_{a,1} = 1 \times 10^{-4}$ mol dm^{-3}, solution diffusion coefficients of E and E^+ 1×10^{-6} cm^2 s^{-1}, scan rate 50 mV s^{-1}, start potential $F(E - E^0)/RT = -5$. Assumed membrane characteristics are that protein, A, is totally excluded and membrane 1, thickness 5×10^{-4} cm, diffusion coefficient of E and E^+ 1×10^{-7} cm^2 s^{-1}; membrane 2: thickness 1×10^{-3}cm, diffusion coefficient of E and E^+ 5×10^{-8} cm^2 s^{-1}. The diffusion coefficients of the protein species A, EA, and E^+A are assumed much less than those of the electrochemically active species E and E^+. The decomposition of E^+ is neglected.

Table 1. Electrochemical Data for the Probe Molecules[a]

compd	*m*	$E_{1/2}$/V Ag,AgCl	$E_{a,p} - E_{a,p/2}$/V	$E_{a,p} - E_{c,}/V_p$	$I_{c,p}/I_{a,p}$
4	2	0.349	0.063	0.074	0.88
5	5	0.356	0.065	0.072	0.91
6	7	0.351	0.061	0.071	0.91
2	10	0.363	0.059	0.072	0.65
9	13	0.379	0.071	0.095	0.43
10	15	0.507	0.105	0.125	0.06

[a] 50 mM in PBS with MeOH content for **10** = 5%, others approximately 1−2%, on uncoated screen-printed carbon electrodes, recorded at 50 mV s^{-1} scan rate. $E_{1/2}$ was taken as the mean of the peak potentials for anodic and cathodic peaks. The peak current ratio was determined by the extrapolation method illustrated in ref *22*.

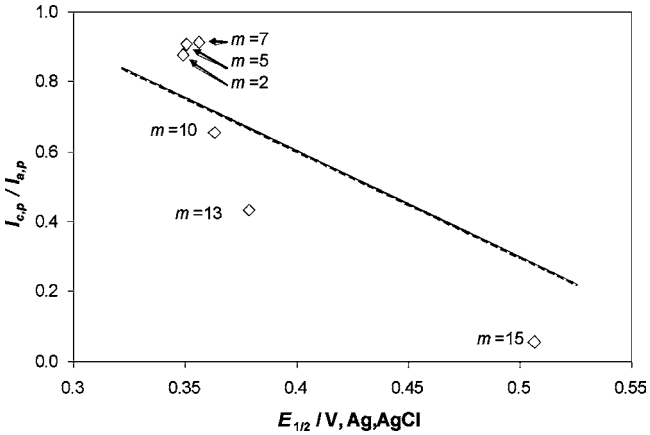


Figure 3. Correlation of peak current ratio $I_{c,p}/I_{a,p}$ with half-wave potential $E_{1/2}$ for the ferrocene probe molecules. The dotted line illustrates the correlation for the series of different compounds given in ref *13*.

in *m* caused $E_{1/2}$ to move anodic. For a given concentration, the peak current generally increased with increasing *m*. When the length of the carbon chain in the fatty acid was longer than C11 (e.g., compound **10**) the oxidation potential shifted significantly anodic and the ferricenium reduction wave virtually disappeared. As noted in a previous paper (*13*), there was a systematic trend of half-wave potential, $E_{1/2}$ and anodic/cathodic peak current ratio with the length of the substituent chain (Figure 3). These effects are consistent with the trend in electrochemical behavior that was identified in previous work (*13*). The difference between the potential at the anodic peak and that at half the peak current, $E_{a,p} - E_{a,p/2}$, was ~60 mV for $m = 10$ or less, and somewhat higher for greater *m*, (Table 1).

Figure 4 shows the effect of the Nafion membrane on the voltammetry of the ferrocene compounds. The half-wave potential was shifted significantly cathodic, to around 0.28 V Ag/AgCl and the variation in $E_{1/2}$ with substituent chain length was eliminated. The cathodic peak height, for reduction of ferricenium, was significantly increased.

Binding to Human Serum Albumin. The ferrocene labeled fatty acid probe molecules investigated were ferrocene methanol ($FcCH_2OH$), **4** ($m = 2$), **5** ($m = 5$), **6** ($m = 7$), **2** ($m = 10$), and **10** ($m = 15$). Experiments with no membrane coating the electrodes showed the expected effects of the CEC process on the wave shape in cyclic voltammetry, different for different chain lengths, *m* (Figure 5). The effects on the peak position and wave shape were eliminated by the use of the Nafion membrane (Figure 5). Therefore, in view of the theory given in the System Design section, the membrane coating used was assumed sufficiently thick to allow reasonably reliable determination of the concentration of the probe free in solution, based on a calibration made in the absence of protein.

The binding of the ferrocene labeled poly(oxoethylene)-fatty acid probe molecules as a function of the number of carbons in

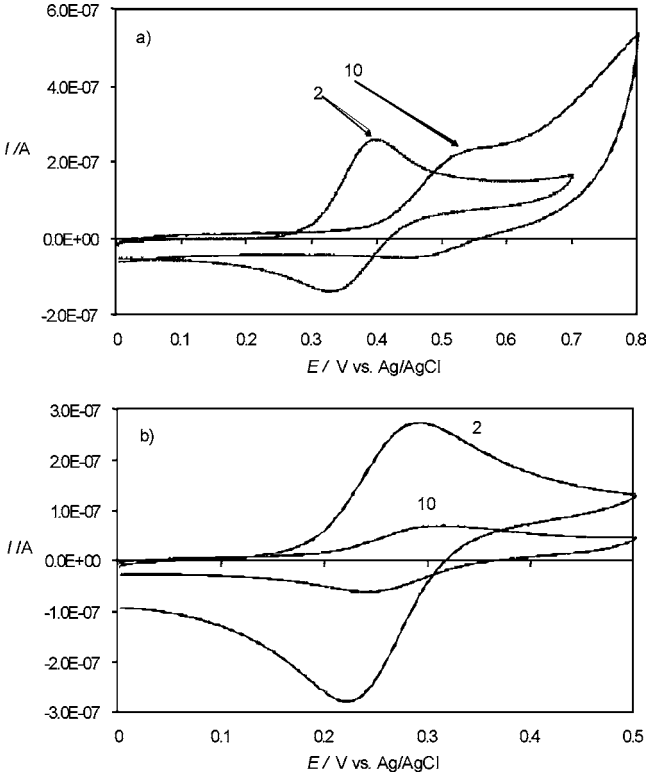


Figure 4. Cyclic voltammetry of ferrocenyl compounds illustrating the effect of a Nafion membrane. The curves are labeled with the compound number. (a) On uncoated electrodes; (b) on Nafion-coated electrodes. Compounds 2 and 10 at 50 μM in PBS with MeOH content 10 = 5%, 2 = 2%, recorded at 50 mV s^{-1} scan rate.

the fatty acid chain is further illustrated in Figure 6. The degree of binding of the probes to HSA can be changed by varying the fatty acid carbon chain length, as expected. The data show a gradual decrease in the degree of binding from 15 to 5 carbons. There was little detectable binding for two and five carbons. However, $FcCH_2OH$ (no poly(oxoethylene) chain) did bind to HSA.

Electrochemical Probe of Site Occupancy on HSA. We explored the possibility of an electrochemical measurement of site occupancy on albumin, using **2** ($m = 10$) and **10** ($m = 15$), as examples of a medium chain length and a long-chain length probe, respectively, competing with decanoate and oleate. Figures 7 and 8 show the amount of free **2** and **10**, respectively, taken from I_p in cyclic voltammetry on membrane-coated electrodes, in a solution containing different concentrations of HSA. Comparison has been made with the calculated amounts that would be bound, based on the binding constants of other fatty acids given by Spector et al. (*11*) (multiple binding sites and different binding constants to each site). Compound **2** did not bind as strongly to HSA as a fatty acid of similar chain length such as decanoate, but more like one with eight methylene groups. The binding of **2** was also well-represented by a three-site model, each site having dissociation constant, $K_d = 1 \times 10^{-4}$ mol dm^{-3}. However, the measurements at higher albumin concentration showed unbound probe concentration, determined electrochemically in the manner described, higher than expected. Figure 7 also illustrates that the fluorescent probe 11-(dansyl-amino)undecanoic acid (DAUDA) bound much more strongly to HSA than either the electrochemical probe, or fatty acids of similar chain length. Compound **10**, with 15 methylene groups in the hydrocarbon chain, bound with similar strength to a fatty acid with 12−14 methylene groups. Curry et al. (*7*) described seven binding sites for fatty acids on albumin. A simple model in which **10** binds equally to seven sites gave reasonable

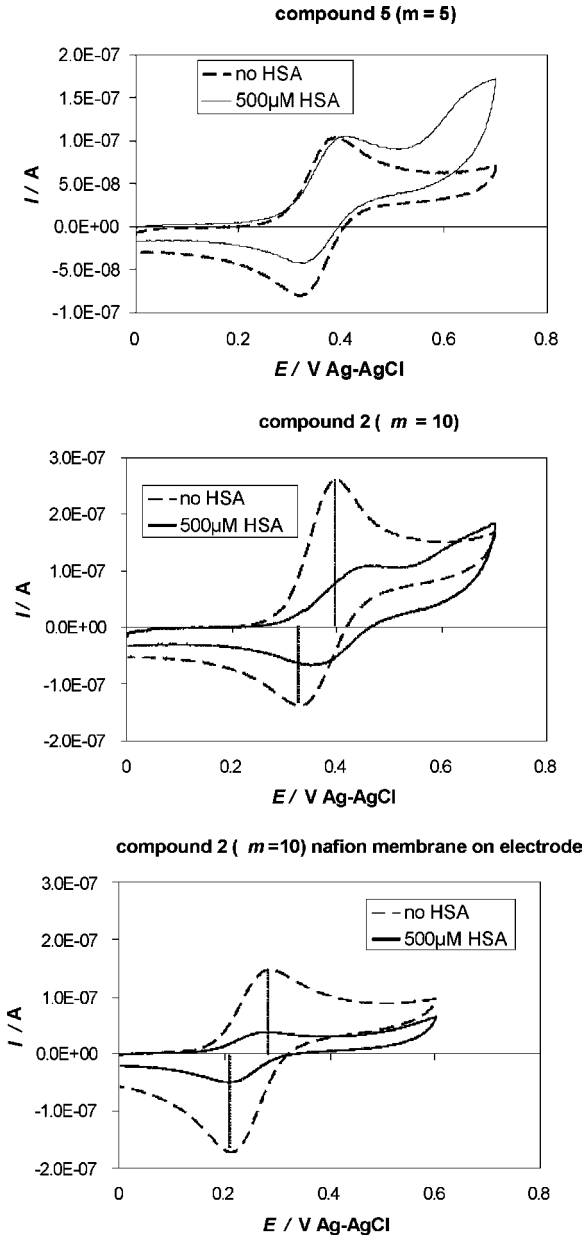


Figure 5. Effect of HSA on cyclic voltammetry of **2** and **5** at uncoated carbon electrodes and of **2** at a Nafion-coated electrode. The dotted lines are added to show the change in peak positions. PBS; compound concentration 50 μM, 50 mV s^{-1}.

agreement to the data with $K_d = 5 \times 10^{-6}$ mol dm^{-3}. Again, the measurement at highest albumin concentration showed a higher than expected unbound probe concentration, determined electrochemically in the manner described.

The competition of compounds **2** and **10** with fatty acids for binding sites on HSA is shown in Figures 9−11. Comparison is made with theoretical predictions assuming binding to different classes of site on HSA. The binding constants determined using the stepwise equilibrium model for oleate (*12*) and decanoate (*11*) have been used.

In competition with decanoate, there was a steady increase in the concentration of **2** in the solution with an increasing molar ratio of decanoate to albumin. However, even when decanoate was at 10 times excess of HSA, there was still significant **2** bound to HSA. Competition of **2** with oleate showed a different pattern of behavior. For molar ratios oleate/HSA up to approximately 5, **2** was not significantly displaced by oleate. At higher ratios, **2** was completely displaced by oleate. The behavior of compound **10** was different, as expected. At low molar ratio

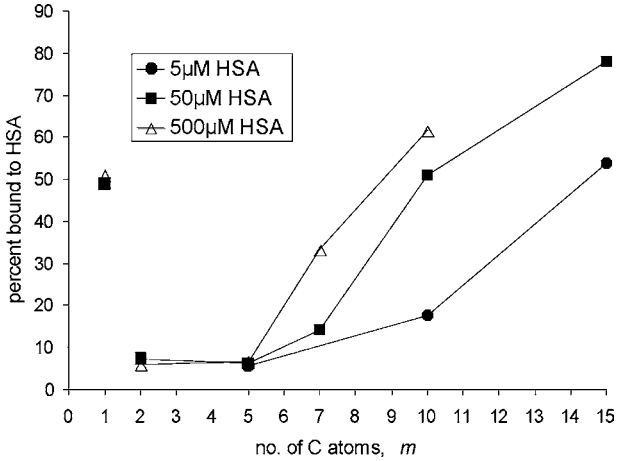


Figure 6. Binding of ferrocene labeled fatty acid probes (50 μM) to HSA, determined by the % decrease in anodic peak height in cyclic voltammetry on membrane-covered electrodes, as a function of the number of carbon atoms in the fatty acid chain. The points for $m = 1$ are for $FcCH_2OH$ (ferrocene methanol).

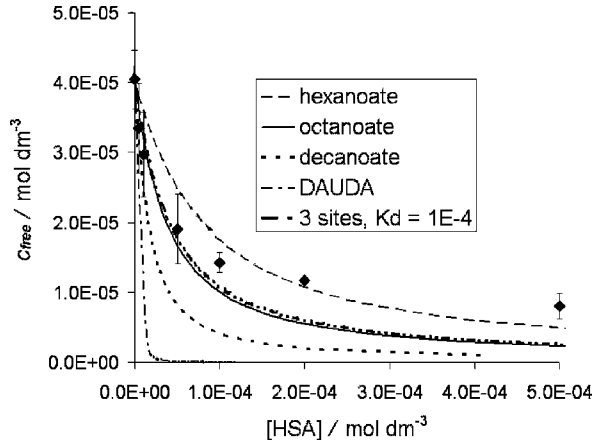


Figure 7. Measurement of bulk solution unbound concentration of compound **2**, c_{free}, (symbols) by cyclic voltammetry at a Nafion-coated carbon electrode, as a function of concentration of HSA, [HSA]. Total concentration of **2** in the solution 40 μM. Solid lines show c_{free} calculated at the same total concentration for different fatty acids, for 11-(dansylamino)undecanoic acid (DAUDA), using literature values for the binding constants (*9*, *11*), and for a simple three-site binding model with each site having $K_d = 1 \times 10^{-4}$ mol dm^{-3}.

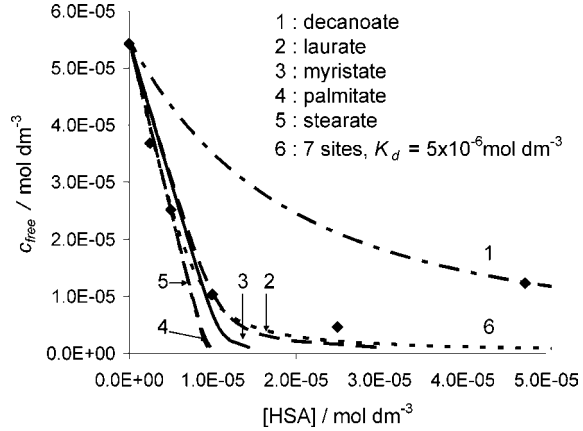


Figure 8. Measurement of bulk solution unbound concentration of compound **10**, c_{free}, (symbols) by cyclic voltammetry at a Nafion-coated carbon electrode, as a function of concentration of HSA, [HSA]. Total concentration of **10** in the solution 55 μM. Solid lines show c_{free} calculated at the same total concentration for different fatty acids, using literature values for the binding constants (*11*, *12*).

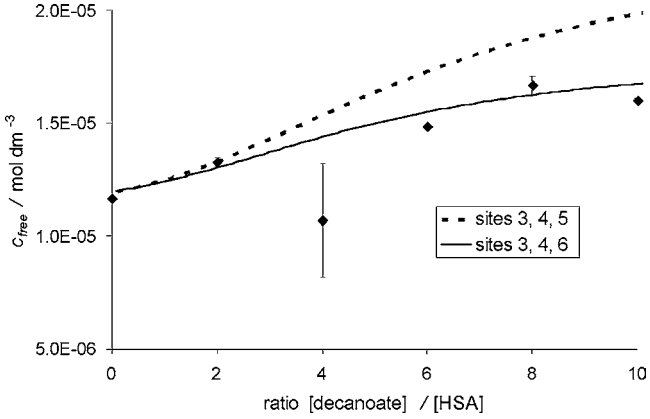


Figure 9. Competition of **2** with decanoate for sites on HSA. $[\mathbf{2}]_{total} = 25$ μM, and $[HSA]_{total} = 50$ μM. Solid lines correspond to calculated values of the concentration of **2** free in the solution, c_{free}, assuming that decanoate binds to HSA at five sites according to Spector et al. (*11*), numbered in order of decreasing affinity, and that **2** binds to three of them, specified in the legend, with $K_d = 1 \times 10^{-4}$ mol dm^{-3}. Site 6 in the calculation is an additional site for which it is assumed that **2** binds but decanoate does not; c_{free} determined from I_p in cyclic voltammetry at Nafion-coated carbon electrodes.

oleate/HSA, the solution concentration of **10** increased, indicating its displacement from the higher affinity sites. Compound **10** was essentially completely displaced into solution at molar ratio oleate/HSA > 8.

DISCUSSION

Electrochemistry of the Ferrocenes. In our previous paper (*13*), we deduced that the electrochemical behavior of variously substituted ferrocenes was strongly determined by the effect of the substituent on the stability of the ferricenium cation. The ability of the substituent to disperse the positive charge on ferricenium, and steric effects that caused the two cyclopentadiene rings to move out of coplanarity were also identified as important. The peak shape, as measured by the difference between peak and half-peak potential, indicated that the electrochemical reaction was fast on the time scale of the scan in cyclic voltammetry. The ratio of cathodic to anodic peak current implied decomposition of the ferricenium product in the boundary layer near the electrode. The behavior reported here (Figure 3, Table 1) is consistent with this interpretation. The peak potential difference implied that the electrochemical process was fast in comparison with the time scale of the scan, perhaps decreasing in rate with increasing chain length, *m*. The variation of half-wave potential and peak current ratio indicated decreasing stability of the ferricenium cation with increasing substituent chain length. The observed increase of anodic peak current with increasing substituent chain length is similarly consistent with the interpretation: increasing the size of the molecule should decrease the diffusion coefficient and so decrease the peak current; however, if the electrochemistry is fast and the product decomposes then the peak current would be increased.

Effect of the Nafion Membrane on the Electrochemistry of the Ferrocenes. The increase of the cathodic peak current, the cathodic shift of the wave, and the removal of the effect of the chain length on the half-wave potential and peak current ratio (Figure 4) can be interpreted simply as a consequence of stabilization of the ferricenium cation in the membrane. The cathodic peak current is significantly increased. We showed, by holding the potential at the anodic limit of the scan for a time, that ferricenium could be accumulated in the cation exchange membrane. The decrease in current with increasing *m* is attributable to interaction of the hydrocarbon chain with

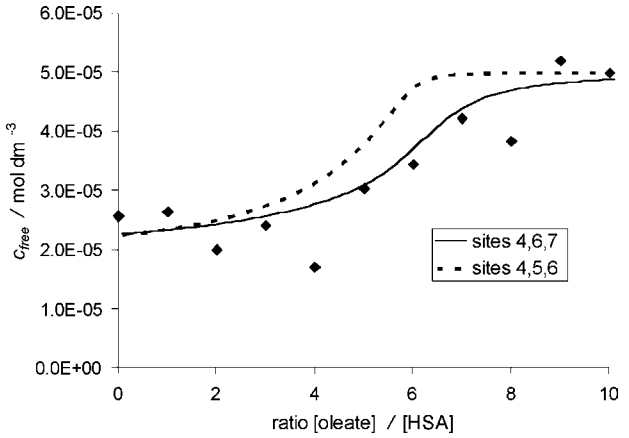


Figure 10. Competition of **2** with oleate for sites on HSA. $[\mathbf{2}]_{total} = 50\ \mu M$, and $[HSA]_{total} = 50\ \mu M$. Solid lines correspond to calculated values of concentration of **2** free in the solution, c_{free}, assuming that oleate binds to HSA at seven sites numbered in order of decreasing affinity, and that **2** binds to three of them, specified in the legend, with $K_d = 1 \times 10^{-4}$ mol dm^{-3}. Sites 1−6 in the calculation are those identified by Richieri et al. (*12*). Site 7 is an assumed additional weak binding site with $K_d = 1 \times 10^{-5}$ mol dm^{-3}; c_{free} determined from I_p in cyclic voltammetry at Nafion-coated carbon electrodes.

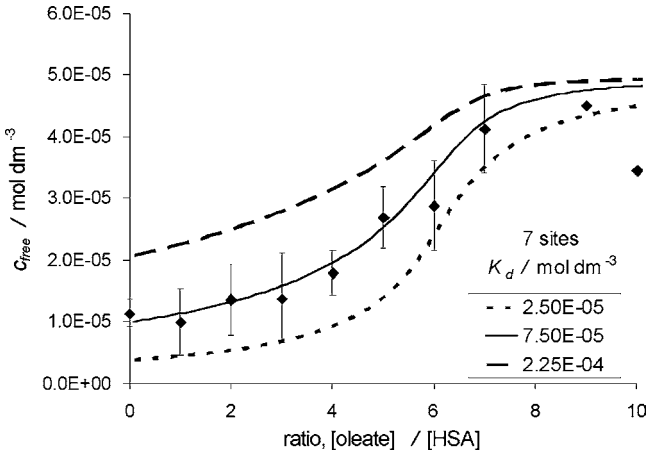


Figure 11. Competition of **10** with oleate for sites on HSA $[\mathbf{10}]_{total} = 50\ \mu M$, and $[HSA]_{total} = 50\ \mu M$. Symbols give the concentration of **10** free in the solution, c_{free}, determined from I_p in cyclic voltammetry at Nafion-coated carbon electrodes. Solid lines correspond to calculated values c_{free} assuming that oleate binds to HSA at seven sites numbered in order of decreasing affinity. Sites 1−6 in the calculation are those identified by Richieri et al. (*11*). Site 7 is an additional weak binding site with assumed $K_d = 1 \times 10^{-5}$ mol dm^{-3}. Compound **10** is assumed to bind to all seven sites with equal binding constant, K_d, specified in the legend.

the polymer membrane decreasing the diffusion coefficient through the membrane.

Electrochemistry in the Presence of Albumin. The effects on cyclic voltammetry at an uncoated electrode (Figure 5) were consistent with a dissociation rate of any complex increasing significantly, and a binding affinity decreasing significantly with decreasing chain length. The decrease in the presence of albumin of cathodic peak current relative to anodic peak current indicated that the ferricenium cation was also complexed by albumin. For compound **2**, taken with the estimates of binding constant deduced below, the effect on the voltammetry was consistent with a dissociation rate constant $\sim 1\ s^{-1}$, which is consistent with values reported in the literature (*21*). With a Nafion membrane, the protein had no effect on either the peak position or the relative peak height. On the basis of the theory given under Electrochemical System Design, it was therefore reasonable to assume that calibration in the absence of protein would give a reliable measure of the unbound concentration of the probe. However, the theory (Figure 2) also showed that this assumption could fail as the unbound concentration increased. The assumption could also fail at higher protein concentration. The effect would be to indicate a free probe concentration higher than that actually present, because the effect of the complexation with protein would be to increase the concentration gradients in the boundary layer immediately outside the membrane and hence increase the observed current.

Binding of the Ferrocene Probes to Albumin. There appeared to be three effects operative (Figure 6): binding of the ferrocene group, binding of the hydrocarbon chain, and the effect of the poly(oxoethylene) part of the chain in decreasing the binding to albumin. With $m = 7$, 10, 15 (compounds **6**, **2**, and **10**), the carboxylic acid chain was long enough to interact with the fatty acid binding sites of HSA, and the observed good binding of these molecules to HSA is likely to be due to the fatty acid part. The result with ferrocene methanol showed that ferrocene itself could bind reasonably strongly to HSA. Albumin has sites that bind drug molecules (*2*), for example, paracetamol and aspirin, which have a conjugated ring as does ferrocene, and one of these sites may be involved in the ferrocene binding. The results show that the addition to ferrocene of a PEG chain, if this was terminated by a sufficiently short carboxylic acid chain ($m = 2$, 5: compounds **4** and **5**), prevented the ferrocene from binding to HSA. A likely explanation is improved solvation by water conferred by the PEG. However, effects caused by the chain and the carbamate linking group such as steric hindrance of binding, or restriction in the orientation of the ferrocene with respect to the protein, cannot be discounted.

Figures 7 and 8 show that the system can reasonably measure the binding of the probes to albumin, although with a deviation from the expected behavior at high protein concentration. The deviation is expected in view of the theory above, and the solution to the problem would be to increase the membrane thickness. The binding of the ferrocene probes was similar to that of fatty acids with a slightly shorter chain length. We can attribute the reduction in binding affinity to the steric effects of the carbamate linker and the affinity for water conferred by the short PEG chain. The result indicates the possibility of fine-tuning the probe by altering the balance of hydrophilicity and hydrophobicity in the molecule. The behavior contrasts to that of DAUDA. Wilton (*9*) has interpreted data on binding to HSA of DAUDA, a fluorescently labeled fatty acid with 10 CH_2 units in the carbon chain, to deduce three binding sites with $K_d < 10^{-7}$ M at the high-affinity site, and $K_d = 8 \times 10^{-7}$ M at the other two sites (*8*). The calculated binding of DAUDA to HSA, using the K_d given by Wilton, plotted in Figure 7, demonstrates the much stronger binding of that compound than either fatty acids or the ferrocene probe of similar chain length. As noted below, the bilirubin binding site was deduced as one major binding site for DAUDA implying that, for this compound, binding was dominated by the effect of the large aromatic fluorescent label.

The competition studies (Figures 9−11) showed that the ferrocene probes did indeed bind to the fatty acid binding sites of albumin, with behavior modified by the presence of PEG and carbamate linker. Thus, Figure 9 shows that **2** bound to the sites accessed by decanoate, since it could be displaced from albumin by decanoate. However, compound **2** was not completely displaced, implying the presence of another site. The ferrocene probe appeared to bind weakly to a site not accessed by fatty acids. Given the binding observed for ferrocene methanol, it is reasonable to presume that this was a site that bound the cyclopentadienyl ring, perhaps one of the drug binding sites. Figure 9 shows that it is possible to make quantitative comparison with a site binding model and deduce the binding constants. Reliable deduction of the binding constants would

require further development of the electrochemical method and better design of the membrane coating of the electrode.

Figure 10 shows that the high-affinity sites accessed by oleate were not accessed by **2**. Compound **2** could only access sites with low affinity for oleate, from which it was displaced at a sufficiently high oleate/HSA ratio. The results are consistent with previous measurements carried out with DAUDA (10 CH_2 fatty acid chain). Wilton (*9*) deduced that DAUDA does not bind to the high-affinity sites for long-chain fatty acids, since it was displaced only at higher fatty acid/HSA ratios. Similarly, DAUDA was not completely displaced by medium-chain fatty acids. However, bilirubin displaced DAUDA significantly indicating that DAUDA shared with this molecule its major binding site, termed drug site I (*2*). As noted above, it is probable that compound **2** also bound weakly at this site, perhaps through the ferrocene group.

Extending the fatty acid chain of the ferrocene allowed these probes to access the high-affinity binding sites for long-chain fatty acids. Figure 11 shows that compound **10** was displaced from HSA at low molar ratios of oleate to HSA. Hence, this compound accessed the highest affinity sites for oleate. As indicated in Figure 11, the data could be interpreted with a simple competitive binding model assuming seven binding sites accessible to both species—the six sites identified by Richieri et al. (*12*) together with an additional weak binding site to account for the data when oleate/HSA > 6.

Interaction with Methanol. The possible interaction with methanol used to introduce the probes and consequently present at concentrations up to 5% v/v is a complication that does not, however, affect the major conclusions of the work. Alcohols have a large effect on albumin in acid solution, promoting α-helix formation. However, the effects at neutral pH are small (*23*). Lubas et al. (*20*) showed a weak interaction of methanol with albumin, through the methylene group. By using the ethanol binding constant reported by Avdulov et al. (*24*) and comparing the results for methanol and ethanol in ref *20*, an approximate binding constant for methanol can be deduced: 0.17 mol dm^{-3}. Ha et al. (*25*) showed that ethanol could displace drugs such as warfarin from HSA. However, Rosenberg et al. (*23*) showed no effect of ethanol on the binding of methyl orange to HSA. The effect of methanol will be less than that of ethanol (*20*). If the added methanol competed equally with the probes for all the binding sites, with a binding constant of 0.17 mol dm^{-3}, then the binding constants for the probes, deduced above, could be a factor of 10 times too high. If, however, the methanol competed only for the drug binding site where we have deduced that the ferrocene group also bound, then only the estimate of binding constant for this site would be in error, although it could be substantially so.

CONCLUSION

We have shown how to design both an instrumentally simple electrochemical system and a set of probe molecules that can be used to determine the occupancy of different classes of fatty acid binding sites on human serum albumin. We have shown how variation in the fatty acid chain length on the probe results in interaction with different classes of sites on HSA and deduced that the interaction can be changed from primarily with a drug binding site, when the probe is ferrocene methanol, to one interacting primarily with medium-chain fatty acid binding sites, by adding a poly(oxoethylene)-fatty acid substituent, to one interacting primarily with high-affinity long-chain fatty acid binding sites as the fatty acid chain length in ferrocene-poly-(oxoethylene)-fatty acid molecules is increased. The results strongly imply that the binding could be further tailored by relatively simple modifications to the probe, for example, to change the balance of hydrophobicity and hydrophilicity. The approach is a general one, in that other small molecules might be electrochemically labeled using similar methods and these probe molecules used to access different classes of binding sites.

ACKNOWLEDGMENT

We thank Unipath for funding (IT) and for permission to publish this article.

LITERATURE CITED

(1) Peters, T. (1996) *All About Albumin: Biochemistry, Genetics and Medical Applications*, Academic Press: San Diego.

(2) (a) Ghuman, J., Zunszain, P. A., Petitpas, I., Bhattacharya, A. A., Otagiri, M., and Curry, S. (2005) Structural basis of the drug-binding specificity of human serum albumin. *J. Mol. Biol.* 353, 38−52. (b) Curry, S. (2002) Beyond expansion: structural studies of the transport roles of human serum albumin. *Vox Sang. 83*, 315−319. (c) Emerson, T. E. (1989) Unique features of albumin − a brief review. *Crit. Care Med. 17*, 690−694. (d) Kragh-Hansen, U., Chuang, V. T. G., and Otagiri, M. (2002) Practical aspects of the ligand-binding and enzymatic properties of human serum albumin. *Biol. Pharm. Bull. 25*, 695−704. (e) Fasano, M., Curry, C., Terreno, E., Galliano, M., Fanali, G., Narciso, P., Notari, S., and Ascenzi, P. (2005) The extraordinary ligand binding properties of human serum albumin. *Life 57*, 787−796.

(3) (a) Seidel, P., Gurachevsky, A., Muravsky, V., Schnurr, K., Seibt, G., and Matthes, G. (2005) Recognition of malignant processes with neural nets from ESR spectra of serum albumin. *Z. Med. Phys. 15*, 265−272. (b) Muravskaya, E. V., Lapko, A. G., and Muravskii, V. A. (2003) Modification of transport function of plasma albumin during atherosclerosis and diabetes mellitus. *Bull. Exp. Biol. Med. 135*, 433−435.

(4) Zatón, A. M. L., Ferrer, J. M., Ruizde G.orda, J. C., and Marquín, M. A. (1995) Binding of coumarins to site I of human serum albumin. Effects of fatty acids. *Chem.−Biol. Interact. 97*, 169−174.

(5) (a) Apple, F. S., Kleinfeld, A. M., and Adams, J. (2004) Unbound free fatty acid concentrations are increased in cardiac ischemia. *Clin. Proteomics 1*, 41−44. (b) Kleinfeld, A. (2003) Diagnostic markers for ischemia. *PCT Int. Appl.*, WO 2003025571.

(6) Hamilton, J. A. (2002) How fatty acids bind to proteins: the inside story from protein structures. *Prostaglandins, Leukotrienes Essent. Fatty Acids 67*, 65−72.

(7) (a) Curry, S., Brick, P., and Franks, N. P. (1999) Fatty acid binding to human serum albumin: new insights from crystallographic studies. *Biochim. Biophys. Acta 1441*, 131−140. (b) Petitpas, I., Grüne, T., Bhattacharya, and A. A., Curry, S. (2001) Crystal Structures of Human Serum Albumin Complexed with Monounsaturated and Polyunsaturated Fatty Acids. *J. Mol. Biol. 314*, 955−960. (c) Bhattacharya, A. A., Grüne, T., and Curry, S. (2000) Crystallographic analysis reveals common modes of binding of medium and long-chain fatty acids to human serum albumin. *J. Mol. Biol. 303*, 721−732. (d) Sacchettini, J. C., Gordon, J. I., and Banaszak, L. J. (1989) Crystal structure of rat intestinal fatty acid binding protein. Refinement and analysis of the Escherichia coli-derived protein with bound palmitate. *J. Mol. Biol. 208*, 327−339. (e) Simard, J. R., Zunszain, P. A., Ha, C. E., Yang, J. S., Bhagavan, N. V., Petitpas, I., Curry, S., and Hamilton, J. A. (2005) Locating high-affinity fatty acid-binding sites on albumin by X-ray crystallography and NMR spectroscopy. *Proc. Natl. Acad. Sci. U.S.A. 102*, 17958−17963.

(8) Narazaki, R., Maruyama, T., and Otagiri, M. (1997) Probing the cysteine 34 residue in human serum albumin using fluorescence techniques. *Biochem. Biophys. Acta 1338*, 275−281.

(9) Wilton, D. C. (1990) The fatty acid analogue 11-(dansylamino)-undecanoic acid is a fluorescent probe for the bilirubin-binding sites of albumin and not for the high-affinity fatty acid-binding sites. *Biochem. J. 270*, 163−166.

(10) (a) Kennedy, M. W., Scott, J. C., Lo, S., Beauchamp, J., and McManus, D. P. (2000) Sj-FABPc fatty-acid-binding protein of the human blood fluke *Schistosoma japonicum*: structural and functional characterisation and unusual solvent exposure of a portal-proximal tryptophan residue. *Biochem. J. 349*, 377−384. (b) Veerkamp, J. H., van Moerkerk, H. T. B., Prisen, C. F. M., and van Kuppevelt,

T. H. (1999) Structural and functional studies on different human FABP types. *Mol. Cell. Biochem. 192*, 137−142.

(11) (a) Spector, A. A. (1975) Fatty acid binding to plasma albumin. *J. Lipid Res.* 16, 165−179. (b) Ashbrook, J. D., Spector, A. A., and Fletcher, J. E. (1972) Medium chain fatty acid binding to human plasma albumin. *J. Biol. Chem. 247*, 7038−7042. (c) Ashbrook, J. D., Spector, A. A., Santos, E. C., and Fletcher, J. E. (1975) Long chain fatty acid binding to human plasma albumin. *J. Biol. Chem. 250*, 2333−2338.

(12) Richieri, G. V., Anel, A., and Kleinfeld, A. M. (1993) Interactions of long-chain fatty acids and albumin: determination of free fatty acid levels using the fluorescent probe ADIFAB. *Biochemistry 32*, 7574−7580.

(13) Tranchant, I., Hervé, A. -C., Carlisle, S., Lowe, P., Slevin, C. J., Forssten, C., Dilleen, J., Williams, D. E., Tabor, A. B., and Hailes, H. C. (2006) Design and synthesis of ferrocene probe molecules for detection by electrochemical methods. *Bioconjugate Chem.* 17, 1256−1264.

(14) Klotz, I. M., Walker, F. M., and Pivan, R. B. (1946) The binding of organic ions by proteins. *J. Am. Chem. Soc. 68*, 1486−1490.

(15) Abumrad, N. A., Perkins, R. C., Park, J. H., and Park, C. H. (1981) Mechanism of long chain fatty acid permeation in the isolated adipocyte. *J. Biol. Chem. 256*, 9183−9191.

(16) Huenig, S., Graessmann, W., Luecke, E., and Brenninger, W. (1967) Syntheses with enamines. XIV. Synthesis of long-chain α-amino acids. *Chem. Ber. 100*, 3039−3044.

(17) Oshida, N., Mimaki, Y., Satoh, H., Yokoyama, S., Muraki, Y., Nishimura, K., Hamada, T., Sakurai, E., Sakai, H., Sugai, T., Tonoike, T., and Itoh, K. Preparation of pyridinecarboxamide derivatives as brain protectants. PCT Int. Appl. 1998, WO 9822439.

(18) Dobner, B., and Nuhn, P. (1991) Synthesis of deuterium-labeled methyl branched fatty-acids. *Chem. Phys. Lipids 60*, 21−28.

(19) Takahashi, T., Mizuno, T., Ido, T., Iwata, R., and Watanabe, K.-I. (2003) Improved synthesis of pure [18F]fluoro-compounds for PET studies from bromo-compounds. *Appl. Radiat. Isotopes 58*, 557−566.

(20) Lubas, B., Soltysik-Rasek, M., and Lesniewska, I. (1979) Proton NMR study of association of monovalent and divalent alcohols with bovine serum albumin. *Biochemistry 18*, 4943−4951.

(21) Demant, E. J. F., Richieri, G. V., and Kleinfeld, A. M. (2002) Stopped-flow kinetic analysis of long-chain fatty acid dissociation from bovine serum albumin. *Biochem. J. 363*, 809−815.

(22) Southampton Electrochemistry Group (1990) *Instrumental Methods in Electrochemistry*, p 182, Ellis Horwood, Chichester, U.K.

(23) Rosenberg, R. M., Rogers, D. W., Haebig, J. E., and Steck, T. L. (1962) The interaction of serum albumin with ethanol. *Arch. Biochem. Biophys. 97*, 433−441.

(24) Avdulov, N. A., Chochina, S. V., Daragan, V. A., Schroeder, F., Mayo, K. H., and Wood, W. G. (1996) Direct binding of ethanol to bovine serum albumin: A fluorescent and C-13 NMR multiplet relaxation study. *Biochemistry 35*, 340−347.

(25) Ha, C. E., Petersen, C. E., Park, D. S., Harohalli, K., and Bhagavan, N. V. (2000) Investigations of the effects of ethanol on warfarin binding to human serum albumin. *J. Biomed. Sci. 7*, 114−121.

BC060039E

Neighboring Group-Controlled Hydrolysis: Towards "Designer" Drug Release Biomaterials

Colin P. McCoy,* Ryan J. Morrow, Christopher R. Edwards, David S. Jones, and Sean P. Gorman

School of Pharmacy, Queen's University Belfast, Belfast BT9 7BL, U.K. Received August 1, 2006; Revised Manuscript Received October 17, 2006

To give the first demonstration of neighboring group-controlled drug delivery rates, a series of novel, polymerizable ester drug conjugates was synthesized and fully characterized. The monomers are suitable for copolymerization in biomaterials where control of drug release rate is critical to prophylaxis or obviation of infection. The incorporation of neighboring group moieties differing in nucleophilicity, geometry, and steric bulk in the conjugates allowed the rate of ester hydrolysis, and hence drug liberation, to be rationally and widely controlled. Solutions (2.5×10^{-5} mol dm^{-3}) of ester conjugates of nalidixic acid incorporating pyridyl, amino, and phenyl neighboring groups hydrolyzed according to first-order kinetics, with rate constants between $3.00 \pm 0.12 \times 10^{-5}$ s^{-1} (fastest) and $4.50 \pm 0.31 \times 10^{-6}$ s^{-1} (slowest). The hydrolysis was characterized using UV−visible spectroscopy. When copolymerized with poly(methyl methacrylate), free drug was shown to elute from the resulting materials, with the rate of release being controlled by the nature of the conjugate, as in solution. The controlled molecular architecture demonstrated by this system offers an attractive class of drug conjugate for the delivery of drugs from polymeric biomaterials such as bone cements in terms of both sustained, prolonged drug release and minimization of mechanical compromise as a result of release. We consider these results to be the rationale for the development of "designer" drug release biomaterials, where the rate of required release can be controlled by predetermined molecular architecture.

INTRODUCTION

The design of enhanced performance, particularly drug eluting, bone cement biomaterials is an area of active current interest. Clinically used poly(methyl methacrylate) (PMMA)-based acrylic bone cements use a strategy of direct incorporation of a particulate anti-infective agent (typically gentamicin) as prophylaxis against postoperative infection. Particulate drug incorporation represents a suboptimal strategy for two main reasons. First, release is initially a burst from near-surface (*1*) and is not prolonged (*2*, *3*). Second, the voids left by this initial release act as stress foci for the bulk PMMA material, which act as nucleation sites for cracks (*4*−*6*). These cracks can subsequently propagate and compromise the mechanical function of the cement (*7*). Additionally, the development of these cracks exposes small amounts of additional particulate drug for release, which then elute at subtherapeutic levels, potentially leading to the emergence of resistant infective organisms.

A rational strategy to improve this situation is therefore to develop labile drug−polymer conjugates, whereby the copolymerization of the appropriate conjugate allows drug to be liberated from a pendant side chain of the main polymer chain. Such release would move toward elimination of the development of stress foci for crack formation, as a particulate drug is no longer dissolved from the release matrix. Additionally, if the rate of liberation of drug from the drug−polymer conjugate can be controlled, materials can be developed which offer sustained release over longer periods than that offered by current technology. Suitable, labile functional groups which undergo hydrolysis at a variety of rates under differing conditions are esters or amides. However, such bonds are frequently very stable, resulting in an extremely slow bond cleavage and subsequent slow release of drug. Attempts to overcome this problem have included the use of enzymatically sensitive spacers between the drug and polymer which are designed to break in vivo and thus improve the release profile (*8*). However, such enzyme-dependent systems require specific, predictable biological conditions, which are frequently not found in biological systems. This can lead to unpredictable drug liberation profiles. Consequently, conjugates which do not rely upon biological enzymes to control the drug release rate make attractive target systems. In particular, hydrolysis of an appropriate drug from a polymer backbone to which it is covalently attached via an ester group is appropriate for adaptation to the fields of bone cement and non-blood contact biomaterials, where esterases are absent, to give both improved release profiles and mechanical properties to drug-eluting drug particle-incorporated strategies in current clinical use. By controlling the rate of drug liberation, the development of "designer" biomaterials, where drug release rate can be controlled precisely and as required clinically, will be possible.

A technology which can be adapted to provide control of the hydrolysis rate for drug−polymer conjugates is that of neighboring group-assisted hydrolysis. In this established technology, an intramolecular nucleophile can accelerate the rate of hydrolysis of a hydrolytically labile functional group, such as an ester (*9*) or amide (*10*). The process involves incorporating a neighboring group (NG) moiety in an appropriate geometry so as to facilitate intramolecular reaction at the carbonyl carbon of the labile group. This process is termed neighboring group participation (NGP). To accelerate NGP-assisted hydrolysis, the NG must contain a nucleophile, such as that found on the lone pair of a nitrogen atom in an amine (*11*), a sulfur atom in a thiol or thioacetal (*12*), or a nitrogen-containing heterocycle such as imidazolyl or pyridyl (*13*, *14*). Phenolate NGs can similarly provide an intramolecular nucleophile through the oxygen bearing a negative charge (*15*). The molecule must also be able to adopt a conformation whereby minimum strain is required to facilitate the attack of the NG at the carbonyl carbon. NGs

* To whom correspondence should be addressed. E-mail: c.mccoy@qub.ac.uk.

10.1021/bc060238y CCC: $37.00 © 2007 American Chemical Society
Published on Web 12/09/2006

which form pseudo five- or six-membered rings during the first mechanistic stage of the hydrolysis reaction have been reported to be particularly successful at accelerating overall hydrolysis rates. As an example, Bruice et al. found that the hydrolysis of 4-(2′-acetoxyphenyl)-imidazole was approximately 10^3 times faster with the intramolecular assistance of an imidazolyl group in a pseudo six-membered ring position than without assistance (*16*).

To apply this technology to enhanced release profile bone cements and related medical device biomaterials, it is first necessary to fully elucidate the effect of different neighboring groups and the conformations adopted during NGP on hydrolysis rates for discrete molecular species (i.e., in solution). Once these effects are fully understood, they inform their performance as pendant drug−polymer conjugates, where additional factors such as porosity and surface density must be considered together with the NGP effect. The current study therefore presents the first account of neighboring group-assisted drug release and examines the effect in solution of various NG-containing drug conjugates of nalidixic acid, an appropriate model quinoline antibiotic. We also demonstrate the drug elution behavior of conjugate-incorporated PMMA biomaterials.

METHODS AND MATERIALS

Materials. Pyridine-2-carboxaldehyde, pyridine-3-carboxaldehyde, benzaldehyde, allylmagnesium bromide, *N*-phenylethanolamine, triethylamine, allyl bromide, ethyl chloroformate, methyl methacrylate, and benzoyl peroxide were obtained from Aldrich Chemical Co., Poole, Dorset, U.K. Anhydrous magnesium sulfate, nalidixic acid, hydrochloric acid, and sodium hydroxide were obtained from BDH Chemicals Ltd., Poole, Dorset, U.K. Ethyl acetate, hexane, benzene, acetone, anhydrous dichloromethane, and anhydrous tetrahydrofuran (THF) were of analytical grade and were obtained from Lab-Scan Limited, Dublin, Ireland. Nuclear magnetic resonance spectra were recorded on a General Electric GN-Ω500 instrument operating at 500 MHz. Chemical shifts are given in parts per million (ppm, δ), downfield of tetramethylsilane (TMS), used as an internal standard. A Nicolet Protégé 460 Fourier Transform infrared (FTIR) spectrometer interfaced with *Omnic E.S.P.* software was used to record infrared spectra as potassium bromide discs (Sigma, Poole, Dorset, U.K.) from 4000 cm^{-1} to 400 cm^{-1}. Mass spectra were recorded on a Finnegan MAT 900 XLT high-resolution double focusing mass spectrometer operating at 70 eV. Melting points were recorded on an Electrothermal 9100 melting point apparatus and are uncorrected. Elemental analysis was carried out using a Perkin-Elmer PE-240 automatic CHN analyzer.

Synthesis of 1-Pyridin-2-yl-but-3-en-1-ol, 1. Pyridine-2-carboxaldehyde (2.00 g, 1.78 mL, 18.7 mmol) was dissolved in dry ether (180 mL) in a three-necked round-bottomed flask. Allylmagnesium bromide (24 mmol, 24.0 mL) was injected through a septum, and the reaction mixture was stirred under a stream of dry nitrogen for 2 h. After this time, the reaction was quenched with water (10 mL). A further 100 mL of water was added to the mixture and the product extracted with ethyl acetate (3 × 50 mL). The combined organic phases were dried over anhydrous magnesium sulfate, filtered, and evaporated to dryness under reduced pressure. The crude product was purified by flash chromatography over silica gel using ethyl acetate/hexane (2:3 v/v) as the mobile phase to afford 2.17 g (78%) of a yellow oil. IR (KBr, cm^{-1}): 3369 (OH), 3075 (=C−H), 2907 (C−H), 1641 (C=C), 1595, 1571 (Ar C=C), 1064 (CO), 1001, 916. NMR δ ^{1}H ($CDCl_3$): 2.51 (1H, m, C*H*^{1}CH^{2}CH=CH_2); 2.62 (1H, m, CH^{1}C*H*^{2}CH=CH_2); 4.47 (1H, s, OH); 4.82 (1H, t, J = 4.8 Hz, CH_2−C*H*−OH); 5.08 (2H, m, CH=*CH_2*); 5.82 (1H, m, C*H*=CH_2); 7.18 (1H, m, Ar−H); 7.31 (1H, d, J = 7.5 Hz, Ar−H); 7.67 (1H, d,d, J_1 = 7.7 Hz, J_2 = 7.8 Hz, Ar−H); 8.52 (1H, d, J = 4.9 Hz, Ar−H).

Synthesis of 1-Pyridin-3-yl-but-3-ene-1-ol, 2. This was prepared by a method analogous to that used for **1**, using pyridine-3-carboxaldehyde (2.00 g, 1.78 mL, 18.7 mmol) in place of pyridine-2-carboxaldehyde. The product was purified by flash chromatography over silica gel using ethyl acetate as the mobile phase to afford 2.11 g (76%) of a pale orange oil. IR (KBr, cm^{-1}): 3213 (OH), 3077 (=C−H), 1580 (Ar C=C), 1427, 1061 (CO), 1028 (CN), 918. NMR δ ^{1}H ($CDCl_3$): 2.52 (2H, m, C*H*$_2$CH=CH_2); 4.03 (1H, s, OH); 4.75 (1H, t, J = 6.5 Hz, CH_2−C*H*−OH); 5.12 (2H, m, CH=C*H*$_2$); 5.75 (1H, m, C*H*=CH_2); 7.25 (1H, m, Ar−H); 7.70 (1H, d, J = 7.9 Hz, Ar−H); 8.37 (1H, d, J = 4.8 Hz, Ar−H); 8.44 (1H, s, Ar−H).

Synthesis of *N*-Allyl, *N*-Phenyl-2-aminoethanol, 3. *N*-Phenylethanolamine (1.00 g, 0.92 mL, 7.3 mmol) was dissolved in benzene (20 mL). To this solution, triethylamine (7.3 mmol, 1.01 mL) and allyl bromide (7.3 mmol, 0.62 mL) were added. This solution was stirred for 24 h. Benzene was evaporated under reduced pressure, and the reaction mixture dissolved in acetone (20 mL) and cooled in ice for 1 h. This caused precipitation of triethylammonium bromide which was removed by filtration and the filtrate evaporated to dryness under reduced pressure. The product was purified by flash chromatography over silica gel with a mobile phase of ethyl acetate/hexane (2:3 v/v) to afford 0.57 g (44%) of yellow oil. IR (KBr, cm^{-1}): 3384 (OH), 2879 (C−H), 1598 (Ar C=C), 1505, 1037 (CO), 748 (Ar−H). NMR δ ^{1}H ($CDCl_3$): 2.01 (1H, s, OH); 3.49 (2H, t, J = 5.8 Hz, NCH_2CH_2OH); 3.77 (2H, t, J = 5.8 Hz, N*C*H$_2$CH$_2$-OH); 3.09 (2H, d, J = 5 Hz, NC*H*$_2$CH=CH_2); 5.16 (2H, m, CH=C*H*$_2$); 5.75 (1H, m, C*H*=CH_2); 6.70 (1H, m, Ar−H); 6.75 (2H, d, J = 8 Hz, Ar−H); 7.20 (2H, m, Ar−H).

Synthesis of 1-Phenyl But-3-en-1-ol, 4. This was prepared by a method analogous to that used for **1**, using benzaldehyde (1.98 g, 1.89 mL, 18.7 mmol) in place of pyridine-2-carboxaldehyde. The product was purified by flash chromatography over silica gel using ethyl acetate/hexane (4:1 v/v) as the mobile phase to afford 2.44 g (88%) of pale yellow oil. IR (KBr, cm^{-1}): 3381 (OH), 3075 (=C−H), 3029 (Ar−H), 2906 (C−H), 1640 (C=C), 1047 (CO), 1000 (CN), 757 (Ar−H). NMR δ ^{1}H ($CDCl_3$): 2.00 (1H, s, OH); 2.46 (2H, m, C*H*$_2$CH=CH_2); 4.68 (1H, t, J = 7.1 Hz, CH_2−C*H*−OH); 5.15 (2H, m, CH=C*H*$_2$); 5.79 (1H, m, C*H*=CH_2); 7.36 (5H, m, Ar−H).

Synthesis of [(1-Ethyl-7-methyl-4-oxo-1,4-dihydro-[1,8]-naphthyridine-3-carbonyl)-amino]-acetic Acid Ethyl Ester, 6. 1-Ethyl-7-methyl-4-oxo-1,4-dihydro-1,8-naphthyridine-3-carboxylic acid (nalidixic acid, 3.65 g, 15.7mmol) was dissolved in anhydrous dichloromethane (100 mL). Triethylamine (3.11 mL, 2.26 g, 22.3 mmol) and ethyl chloroformate (2.03 mL, 2.30 g, 21.2 mmol) were added, and the solution was allowed to stir at ambient temperature for 30 min. The reaction mixture was washed with 0.20 M HCl (2 × 20 mL) and water (1 × 40 mL). The organic phase was dried over anhydrous magnesium sulfate, filtered, and evaporated to dryness under reduced pressure. Recrystallization from acetonitrile gave a white solid (3.36 g, 70.4%). Melting point 122−124 °C. IR (KBr, cm^{-1}): 1014 (C−O stretch), 1174 (O=C−O−C stretch), 1243 (C=O stretch), 1609 (phenyl). NMR δ ^{1}H ($CDCl_3$): 1.31 (3H, t, C$^{15}H_3$); 1.41 (3H, t, C$^{11}H_3$); 2.61 (3H, s, C$^9H_3$); 4.37 (2H, q, C$^{14}H_2$); 4.48 (2H, q, C$^{10}H_2$); 7.3 (1H, d, C^6*H*); 8.67 (1H, d, C^5*H*); 8.69 (1H, s, C^2*H*).

Synthesis of Drug Conjugates. The appropriate alcohol from **1**−**4** (8.0 mmol) was dissolved in dry THF (100 mL), and sodium hydride (8.8 mmol, 0.211 g) was added. The solution was refluxed for 1 h and cooled to ambient temperature. **6** (8.0 mmol, 2.43 g) was added over 15 min, and the reaction mixture stirred for a further 10 min. Ethanol (5 mL) was added to the

solution to deactivate any residual sodium hydride. The reaction mixture was evaporated to dryness under reduced pressure, ethyl acetate (70 mL) was added to the oily residue, and any solid material was removed by filtration to precipitate and remove any nalidixic acid that was present in the reaction mixture. The product was purified by flash chromatography over silica gel using ethyl acetate as the mobile phase in each case to give conjugates **7**−**10** from alcohols **1**−**4**, respectively.

*Conjugate **7**: 1-Ethyl-7-methyl-4-oxo-1,4-dihydro-1,8-naphthyridine-3-carboxylic Acid 1-Pyridin-2-yl-but-3-enyl Ester.* Yield 34.6%. mp 118−120 °C. IR (KBr, cm^{-1}): 1727 (OC═O), 1619 (C═O), 1439, 1590 Ar C═C), 1082 (C−O), 806 (Ar−H). NMR δ ^{1}H ($CDCl_3$): 1.50 (3H, t, J = 7.33 NCH_2CH_3); 2.66 (3H, s, Ar−C*H*$_3$); 2.89 (2H, m, C*H*$_2$CH═CH$_2$); 4.47 (2H, m, N−C*H*$_2$CH$_3$); 5.09 (2H, d,d, J_1 = 10.2 Hz, J_2 = 15.2 Hz, CH═C*H*$_2$); 5.89 (1H, m, C*H*═CH$_2$); 6.17 (1H, t, J = 7.2 Hz, CO_2−C*H*−pyridyl); 7.18 (1H, m, Ar−H); 7.24 (1H, d, J = 8.1 Hz, Ar−H); 7.7 (2H, m, Ar−H); 8.57 (1H, d, J = 4.5 Hz, Ar−H); 8.65 (2H, m, Ar−H and C═C*H*). Anal. Calcd for $C_{21}H_{21}N_3O_3$ (%): C, 69.41; H, 5.82; N, 11.56. Found: C, 69.81; H, 5.80; N, 11.37.

*Conjugate **8**: 1-Ethyl-7-methyl-4-oxo-1,4-dihydro-1,8-naphthyridine-3-carboxylic Acid 1-Pyridin-3-yl-but-3-enyl Ester.* Yield 38.2%. mp 132−134 °C. IR (KBr, cm^{-1}): 1713 (OC═O), 1624 (C═O), 1442, 1084 (C−O), 805 (Ar−H). NMR δ ^{1}H ($CDCl_3$): 1.47 (3H, t, J = 7.2 Hz, NCH_2CH_3); 2.66 (3H, s,-Ar−C*H*$_3$); 2.74 (1H, m, C*H*^{1}CH^{2}CH═CH$_2$); 2.86 (1H, m, CH^{1}C*H*^{2}CH═CH$_2$); 4.47 (2H, m, N−C*H*$_2$CH$_3$); 5.09 (2H, m, CH═C*H*$_2$); 5.82 (1H, m, C*H*═CH$_2$); 6.10 (1H, t, J = 6.7 Hz, CO_2−C*H*−pyridyl); 7.24 (1H, d, J = 7.5 Hz, Ar−H); 7.30 (1H, m, Ar−H); 7.93 (1H, d, J = 7.9 Hz, Ar−H); 8.52 (1H, d, J = 4.8 Hz, Ar−H); 8.58 (1H, s, Ar−H); 8.66 (1H, d, J = 8.1 Hz, Ar−H); 8.69 (1H, s, *C═CH*). Anal. Calcd for $C_{21}H_{21}N_3O_3$ (%): C, 69.41; H, 5.82; N, 11.56. Found: C, 69.76; H, 5.94; N, 11.46.

*Conjugate **9**: 1-Ethyl-7-methyl-4-oxo-1,4-dihydro-1,8-naphthyridine-3-carboxylic Acid 2-(Allylphenylamino)-ethyl Ester.* Yield 29.6%. mp 93−94 °C. IR (KBr, cm^{-1}): 1719 (OC═O), 1631 (C═O), 1611 (C═C), 1593 and 1505 (Ar C═C), 1442, 1086, 805. NMR δ ^{1}H ($CDCl_3$): 1.44 (3H, t, J = 7.2 Hz, NCH_2CH_3); 2.66 (3H, s, Ar−C*H*$_3$); 3.75 (2H, t, J = 6.6 Hz, $CO_2CH_2CH_2$); 4.04 (2H, d, J = 4.8 Hz, C*H*$_2$CH═CH$_2$); 4.38 (2H, q, J = 7.2 Hz, N−C*H*$_2$CH$_3$); 4.49 (2H, t, J = 6.6 Hz, $CO_2CH_2CH_2$N); 5.16 (2H, m, CH═C*H*$_2$); 5.85 (1H, m, C*H*═CH$_2$); 6.67 (1H, t, J = 6.4 Hz, Ar−H); 6.82 (2H, d, J = 8.8 Hz, Ar−H); 7.23 (3H, m, Ar−H); 8.49 (1H, s, *C═CH*); 8.67 (1H, d, J = 8.1 Hz, Ar−H). Anal. Calcd for $C_{23}H_{25}N_3O_3$ (%): C, 70.57; H, 6.44; N, 10.73. Found: C, 70.75; H, 6.45; N, 10.64.

*Conjugate **10**: 1-Ethyl-7-methyl-4-oxo-1,4-dihydro-1,8-naphthyridine-3-carboxylic Acid 1-Phenyl -but-3-enyl Ester.* Yield 32.0%. mp 124−126 °C. IR (KBr, cm^{-1}): 1724 (OC═O), 1617 (C═O), 1442, 1082 (C−O), 806 (Ar−H). NMR δ ^{1}H ($CDCl_3$): 1.45 (3H, t, J = 7.2 Hz, NCH_2CH_3); 2.64 (3H, s, Ar−C*H*$_3$); 2.65−2.84 (2H, m, *CH*$_2$CH═CH$_2$); 4.45 (2H, m, N−C*H*$_2$CH$_3$); 5.09 (2H, m, CH═C*H*$_2$); 5.85 (1H, m, C*H*═CH$_2$); 6.07 (1H, t, J = 7.2 Hz, CO_2−C*H*−Ph); 7.23−7.28 (2H, m, Ar−H); 7.35 (2H, t, J = 7.8 Hz, Ar−H); 7.5 (2H, d, J = 7.6 Hz, Ar−H); 8.57 (1H, s, C═C*H*); 8.66 (1H, d, J = 8.1 Hz, Ar−H). Anal. Calcd for $C_{23}H_{25}N_3O_3$ (%): C, 70.57; H, 6.43; N, 10.73. Found: C, 70.84; H, 6.65; N, 10.79.

Synthesis of PMMA−Drug Conjugate Copolymers. Methyl methacrylate (MMA) (20 mL) was washed with 0.10 M sodium hydroxide (3 × 20 mL) followed by deionized water (3 × 20 mL) to remove monomethyl ether hydroquinone inhibitor. The MMA layer was isolated, dried over anhydrous magnesium sulfate, and filtered. To a stirred solution of this MMA (12.0 g), the appropriate conjugate from **7**−**10** (4% w/w), a loading equivalent to that used in commercial bone cement biomaterials, and benzoyl peroxide (1% w/w) were added. The mixture was injected into a mold comprising two glass plates separated with 1 mm medical grade silicone tubing lined with release liner. The molds were incubated at 60 °C for 2 h. The resulting polymer sheets were washed with deionized water for 12 h to remove residual MMA.

Characterization of Hydrolysis of Conjugates 7−**10.** A solution of each of the conjugates **7**−**10** (10 mL, 2.5 × 10^{-5} mol dm^{-3}) was prepared in acetonitrile, and aqueous sodium hydroxide solution (0.10 mol dm^{-3}, 1.0 mL) was added. Hydrolysis was characterized by recording UV−visible absorption spectra between 200−400 nm using a Perkin-Elmer LAMBDA 650 UV−visible spectrophotometer at various time intervals for each solution in a 1 cm path length quartz cuvette.

Subsequently, to characterize the products of hydrolysis, the solvent was removed under reduced pressure, yielding a colorless oil. Separation of the products by preparative-scale thin layer chromatography using ethyl acetate as the eluant allowed the identification of the products by means of ^{1}H NMR, infrared spectroscopy, and mass spectrometry.

In Vitro Characterization of Drug Release from Copolymers. Copolymers were cut into 1 cm × 1 cm square samples and suspended using a needle in phosphate buffered saline (pH 7.4, 10.0 mL, 0.254 M ionic strength). Samples were incubated in an orbital incubator at 37.4 ± 0.1 °C for defined periods and the release of nalidixic acid quantified using UV−visible spectroscopy. At each sampling, the copolymers were transferred to fresh, prewarmed buffer to maintain sink conditions. For each copolymer, only nalidixic acid could be detected in the release medium. The identity of nalidixic acid was confirmed by ^{1}H NMR and mass spectrometry following preparative-scale thin layer chromatography following release.

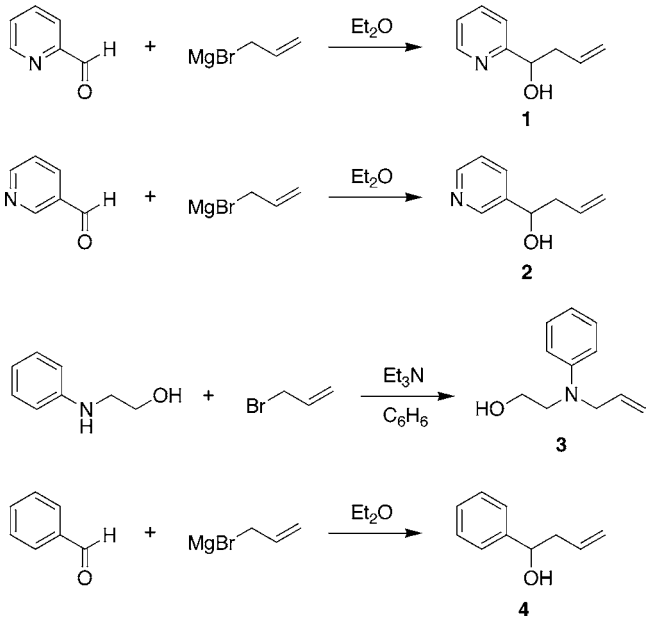
Statistical Analysis. Differences in the hydrolysis rates, amount released from copolymers, and percentage hydrolysis at 60 min were statistically evaluated using the Kruskal-Wallis test. Individual differences between conjugates were identified using Dunn's test. In all cases, at least three replicates were analyzed and $p \leq 0.05$ denoted significance.

RESULTS AND DISCUSSION

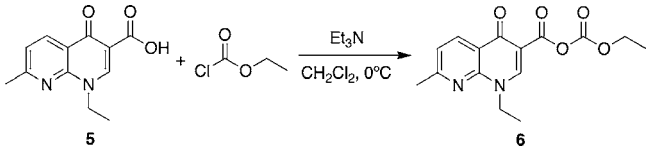
Synthesis and Characterization of Drug Conjugates. A series of novel, polymerizable conjugates of nalidixic acid (1-ethyl-7-methyl-4-oxo-1,4-dihydro-1,8-naphthyridine-3-carboxylic acid), **5**, was synthesized by a three-step process. First, a series of four alcohols, **1**−**4**, were prepared from commercial materials via Grignard reaction with allylmagnesium bromide as summarized in Scheme 1. Alcohols **1**, **2**, and **4** were prepared from pyridine-2-carboxaldehyde, pyridine-3-carboxaldehyde, and benzaldehyde, respectively, in high yield (76−88%). Alcohol **3** was prepared from *N*-phenyl ethanolamine and allyl bromide using triethylamine as a base in dry benzene. Following workup and purification by column chromatography, all alcohols were characterized by FTIR and ^{1}H NMR spectroscopies and were determined to be analytically pure and suitable for use in subsequent syntheses.

The second synthetic step involved synthesis of a suitably reactive derivative of nalidixic acid, **5**, for coupling with alcohols **1**−**4**. Direct esterification, even under catalytic conditions, of nalidixic acid is unsuccessful due to the relatively strong intramolecular hydrogen bond between the hydrogen of the carboxylic acid group with the carbonyl oxygen of the carbonyl group of the naphthyridine ring. The stability of this intramolecular hydrogen bond can be ascribed to the cyclic pseudo six-membered ring geometry which the hydrogen-bonded system adopts (*17*). Additionally, synthesis of a reactive acyl chloride derivative has been hampered by the reactivity of the methyl

Scheme 1. Synthesis of Alcohol Intermediates 1−4



Scheme 2. Synthesis of 6, a Mixed Anhydride of Nalidixic Acid, 5



group directly attached to the naphthyridine ring toward thionyl chloride and phosphorus oxychloride, resulting in chlorination of the methyl group preferentially to production of acyl chloride (*17*). Attempts at esterification using coupling reagents dicyclohexylcarbodiimide (DCC) and 1-(3-dimethylaminopropyl)-3-ethylcarbodiimide (EDCI) also failed, which we ascribe to the inhibition of formation of the required imide intermediate by the intramolecular hydrogen bond. A successful strategy for the synthesis of amides of nalidixic acid has employed a mixed anhydride as a reactive intermediate (*18*, *19*). We have adapted this strategy to the synthesis of esters of nalidixic acid by isolating the mixed anhydride formed by the reaction of nalidixic acid with ethyl chloroformate, as shown in Scheme 2, and subsequently reacting this anhydride with an appropriate deprotonated alcohol. Reaction of nalidixic acid with ethyl chloroformate in dichloromethane at 0 °C in the presence of triethylamine gave mixed anhydride, **6**, after workup in 70% yield.

The third, convergent step of the synthesis involved coupling of the mixed anhydride of nalidixic acid, **6**, with each of the alcohols **1**−**4** separately, to give conjugates **7**−**10** as summarized in Scheme 3. To achieve efficient reaction, each alcohol was deprotonated with sodium hydride, and nucleophilic attack of the resulting alkoxide with the reactive carbonyl carbon of **6** yielded the corresponding drug conjugate in good yield following workup and purification by column chromatography. Each conjugate was fully characterized using FTIR and ^{1}H NMR spectroscopies, mass spectrometry, and elemental analysis, and each was determined to be analytically pure. All alcohols and conjugates were synthesized as racemates.

Nalidixic acid, a broad-spectrum quinoline antibiotic, was chosen as the model antibiotic to demonstrate the system, as it is active against typical pathogens found in infected, cemented hip arthroplasties (*20*). The design of synthesized conjugates **7**−**10** is such that each conjugate incorporates nalidixic acid covalently linked via an ester functionality to a moiety (a vinyl group) capable of taking part in free radical polymerization with, for example, acrylates, methacrylates (as used in bone cements), and related free-radical polymerization biomaterials (*21*). Additionally, a further moiety is included in each conjugate which is designed to either accelerate or retard the rate of liberation of nalidixic acid by hydrolysis. This moiety, separated from the ester via an inert spacer and termed the neighboring group (NG), is varied in the conjugates studied to explore how variations in two key factors—intramolecular nucleophilicity (for facilitated hydrolysis) and steric bulk (for hindered hydrolysis)—affect the rate of drug release. A schematic representation of the molecular design is shown in Figure 1.

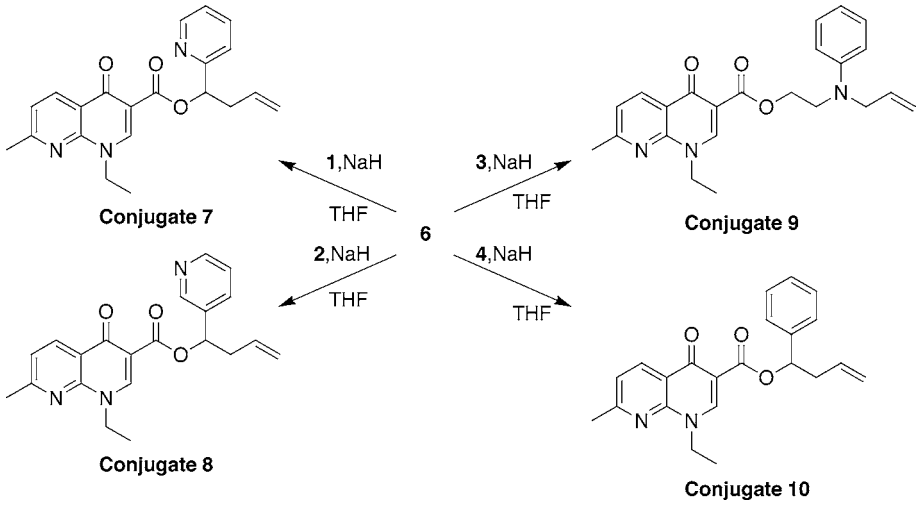
Conjugates **7** and **8** incorporate a pyridyl moiety which is either 2- or 3-substituted with respect to the potential nitrogen nucleophile. Conjugate **10** shares the steric geometry of these conjugates but lacks the intramolecular nucleophile. Conjugate **9** offers a different (amino) intramolecular nucleophile and was thus expected to offer a further, different rate of hydrolysis. The conjugates were thus designed to exemplify how the ability to act as an intramolecular nucleophile and steric bulk can be simultaneously controlled to give a wide control of hydrolysis, and hence drug release, rates. The choice of and geometry of intramolecular nucleophile were informed by related neighboring group participation ester hydrolysis systems incorporating amines, pyridyl (*14*), and other nucleophilic moieties such as imidazole (*16*) and related moieties (*13*).

Characterization of Drug Liberation in Solution. To characterize the drug liberation behavior of the conjugates, hydrolysis studies were carried out in acetonitrile solution containing 1% (v/v) water. Overlaid UV−visible spectra for each of the conjugates **7**−**10** at various times during the course of hydrolysis show very similar behavior for each conjugate. As a representative example, overlaid spectra for conjugate **8** are shown in Figure 2.

Prior to hydrolysis, all conjugates show maxima at 231, 257, and 335 nm (334 nm for conjugate **7** and 336 nm for conjugate **10**) with a shoulder at 326 nm (325 nm for conjugate **7**). As hydrolysis progresses, these bands show a hypsochromic shift, and the longest-wavelength band with a shoulder resolves, with a hypsochromic shift of 3 nm, to a single band. During the hydrolysis, the spectra for each conjugate show an isosbestic point at 344, 345, 345, and 342 nm for conjugates **7**−**10**, respectively. The closely similar spectral trends for conjugates **7**−**10** indicate that similar processes occur for each conjugate. Such spectral changes, with a clear isosbestic point, indicate that a single reaction is taking place with no side reactions. The longest-wavelength absorption is, for all conjugates, due to the nalidixate chromophore, which has an extended π-system. Large wavelength changes upon hydrolysis are not expected, as nalidixic acid, with the same π-system, is liberated. The observed 3-nm hypsochromic shift, together with a broadening of the band, indicates the loss of a small, stabilizing interaction arising from the relevant NG. This stabilization may arise from the nonbonded nitrogen lone pair in conjugates **7**−**9** or, more likely, a small degree of overlap with the aromatic π-system for all conjugates, which is lost upon hydrolysis. Monitoring of absorbance changes with time at an appropriate wavelength therefore provides a sensitive probe to the progress of the hydrolysis reaction. Quantification of the first-order rate constant using spectral data at either 257 nm or 334 nm ($r^2 > 0.99$ in all cases) and the percentage hydrolysis completed after 1 h is shown in Table 1. The only significant difference between the conjugates is the time required for the hydrolysis reaction to proceed to completion, which is ascribed to the nature of the neighboring group.

At the conclusion of the hydrolysis experiments, chromatographic separation and identification of the reaction products

Scheme 3. Synthesis of Drug Conjugate Monomers 7−10



showed that free nalidixic acid was liberated in all cases. This is in agreement with related NGP hydrolyses reported in the literature and indicates that drug is liberated in the manner expected.

Data from Table 1 demonstrate that the nature of the neighboring group has a very significant effect on the drug liberation characteristics of each conjugate. The order of hydrolysis rate from fastest to slowest is conjugate **9** > **8** > **7** > **10**, which is reflected in the percentage of hydrolysis shown in each system after 1 h. After this time, 48.8% of conjugate **9** is hydrolyzed in comparison to 11.1% for conjugate **10**. The strong influence of the neighboring group on the hydrolysis rate can be rationalized in terms of the nucleophile strength and relative stability of the required intramolecular intermediate. Conjugate **9**, which hydrolyzes most rapidly, has the strongest potential nucleophile of the series. As an aliphatic amine, its NG is significantly more basic than the pyridyl NGs of conjugates **7** and **8**. Additionally, the nature of the intermediate can be predicted from the examination of precision space-filling Corey−Pauling−Koltun (CPK) molecular models (Harvard Apparatus, Massachusetts) (*22*). These models use accurate bond angles according to both the nature and the hybridization of both atoms participating in that bond and also accurately reflect typical van der Waals atomic radii. As such, space-filling CPK models are considered accurate to within 0.3 Å (*23*). Models show that intramolecular attack of the amine for conjugate **9** is conformationally accessible through an unstrained five-membered intermediate. This conformation is therefore expected to be readily thermally accessible in solution; hence, hydrolysis can proceed relatively rapidly.

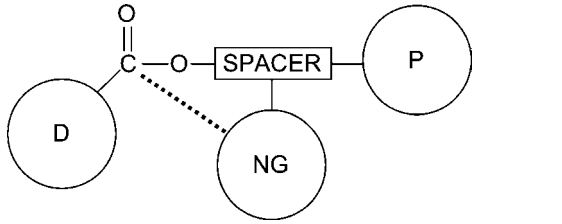


Figure 1. Schematic representation of design of neighboring group-controlled drug ester conjugates where D = drug, NG = neighboring group, and P = polymerizable group. Interaction of NG with the ester group is indicated by a dashed line.

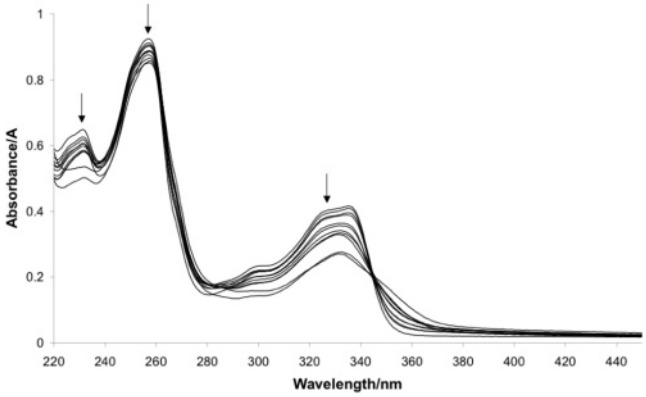


Figure 2. Overlaid UV−visible spectra of conjugate **8** after various times during hydrolysis in acetonitrile containing 1% (v/v) 0.10 M aqueous sodium hydroxide. The spectral changes are representative of conjugates **7**−**10**. Arrows indicate trends in spectral change with time. Spectra shown were recorded at times of 0, 0.25, 0.5, 1, 2, 3, 4, 5, 6, 9, and 25 h.

Table 1. Hydrolysis Rate Constants and Percentage Hydrolysis after 60 Min for Conjugates 7−10

conjugate	hydrolysis rate constant k (s^{-1})	hydrolysis after 60 min (%)
7	$7.51 \pm 0.52 \times 10^{-6}$	12.5%
8	$1.79 \pm 0.39 \times 10^{-5}$	30.1%
9	$3.00 \pm 0.12 \times 10^{-5}$	48.8%
10	$4.50 \pm 0.31 \times 10^{-6}$	11.1%

The trend in hydrolysis rate also implies that the 3-pyridyl NG conjugate, **8**, participates more readily as an intramolecular nucleophile than the 2-pyridyl NG conjugate, **7**. This is not necessarily expected from a simple examination of the structures; however, a more detailed examination using space-filling molecular models allows a rationale for this behavior to be achieved. For intramolecular nucleophilic reaction of the pyridyl nitrogen with the ester carbonyl carbon, a pseudo five-membered ring must form as an intermediate for conjugate **7**, while a pseudo six-membered ring must form for conjugate **8**. Six-membered species are usually considered marginally more stable than five-membered species. Additionally, in the case of conjugate **7**, the geometry of the nitrogen lone pair is such that it cannot be in line with the rear side of the carbonyl carbon−oxygen σ bond, which is optimal for nucleophilic attack. Conversely, conjugate **8** can achieve this geometry, and the more rapid observed drug release can thus be accounted for in terms of this improved geometry for reaction compared to conjugate **7**, given that the nature of the nucleophiles for conjugates **7** and **8** are the same. Conjugate **10**, which lacks an intramolecular nucleophile, but has almost identical steric considerations as conjugates **7** and **8**, is observed to have the slowest hydrolysis rate. This conjugate demonstrates that each of the conjugates

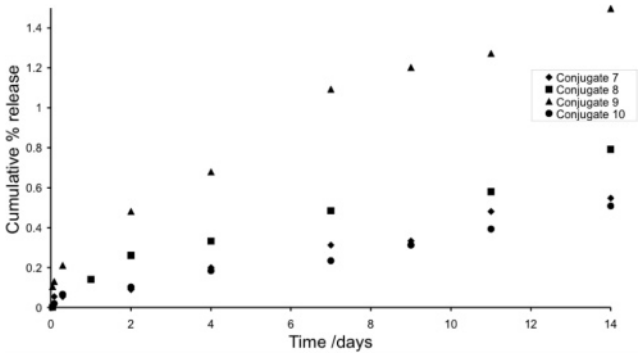


Figure 3. Plot of cumulative release with time for copolymers of MMA with conjugates **7**−**10**. Error bars (±1 standard deviation), in all cases, were less than the indicated point size and have been omitted for clarity.

with an intramolecular nucleophile shows an accelerated hydrolysis rate.

Characterization of Drug Liberation from Copolymers. To characterize the in vitro drug liberation behavior of the conjugates in model bone cement biomaterials, conjugates **7**−**10** were each copolymerized separately with methyl methacrylate with a conjugate loading of 4% (w/w), which is a similar drug loading to commercial drug-eluting PMMA bone cements (*1*−*4*). Release into phosphate buffered saline over 14 days demonstrated that only nalidixic acid was released. The conjugate design is such that the neighboring group remains covalently attached to the copolymer backbone following hydrolysis and is not observed in the release medium, which is important, as only the active drug is released and thus bioavailable. Quantitation of the cumulative relative amount of nalidixic acid released from each copolymer at various times is shown in Figure 3.

Importantly, Figure 3 demonstrates that the polymeric matrices give the same order of kinetic release as seen in solution, with the relative release rate decreasing in the order conjugate **9** > **8** > **7** > **10**. This reinforces the mechanism of drug liberation and demonstrates that NGP-controlled hydrolysis can applied to polymeric biomaterials. The observed release is primarily from the copolymer surface, as PMMA-based materials are hydrophobic and show only a small degree of subsurface ingress of water. The resulting reduced steric availability of water, and use of physiological pH, leads to a slower release rate than that in solution while retaining the neighboring group-controlled trend in release rate.

As release is from the material surface only, 0.5−1.5% of the total incorporated drug is released over 14 days. This is in line with the surface release of drug from drug-incorporated PMMA biomaterials (*1*). Prolonged release from these copolymers introduces several additional considerations, such as the formation of cracks and voids, common in drug-eluting PMMA-based biomaterials (*4*−*6*), which provides additional, fresh polymer surface for hydrolytic release, and the consideration of relatively slow drug diffusion from nonsurface, hydrated subsurface areas of the copolymers, which adds an additional phase of release to the hydrolysis-induced surface release demonstrated here (*1*). Such considerations, particularly of crack and void formation, relate to the important biomaterial considerations of tensile properties (*7*). The mechanical, porosity, and diffusion aspects are beyond the scope of this paper and will be published elsewhere with data on prolonged release.

The system demonstrated here is well-suited to relatively nonporous biomaterials such as PMMA-based bone cement, where surface burst release currently observed would be minimized by the judicious combination of conjugates in a composite biomaterial giving different release rates of the same drug, depending on the nature of the neighboring group, to give a sustained release profile. In conventional, drug-incorporated systems, the rapid (<1 day) burst of release from the surface, followed by elution of low, subinhibitory amounts of drug, makes their clinical performance nonideal. Also, as particulate drug is not dissolved during release in the present system, fewer stress foci and nucleation sites for crack formation and propagation will be formed using this technology, thereby improving mechanical performance.

In conclusion, this study demonstrates the rational synthesis and characterizes the solution hydrolysis of a range of drug conjugates suitable for subsequent copolymerization in biomaterials for acrylate-based bone cements or other medical device biomaterials, where release from current materials is not optimal. The kinetic control of drug liberation rate translates to PMMA-based conjugate copolymers. The ability to control the rate of drug release by neighboring group participation-assisted hydrolysis through the judicious choice of intramolecular nucleophile is shown to give a greater than an order of magnitude control of the release rate. This paradigm is also of general applicability to the design of sustained release formulations.

ACKNOWLEDGMENT

This study was funded by the Engineering and Physical Sciences Research Council (U.K.) under grant GR/N63604/01 and the European Social Fund. The receipt of a Royal Society University Research Fellowship (to McCoy) and use of the EPSRC National Mass Spectrometry Service Centre, Swansea, are acknowledged.

Supporting Information Available: Discussion of ^{1}H NMR data for **1**−**4** and **7**−**10**. Mass spectrometry data for **1**−**4** and **7**−**10** and for nalidixic acid isolated from hydrolysis of conjugates **7**−**10** and released from copolymers containing conjugates. This material is available free of charge via the Internet at http://pubs.acs.org.

LITERATURE CITED

(1) Torrado, S., Paloma, F., and Frutos, G. (2001) Gentamicin bone cements: characterisation and release (in vitro and in vivo assays). *Int. J. Pharm. 217*, 57−69.

(2) Cabanillas, P. F., Pena, E. D., Barrales-Rienda, J. M., and Frutos, G. (2000) Validation and in vitro characterization of antibiotic-loaded bone cement release. *Int. J. Pharm. 209*, 15−26.

(3) Baker, A. S., and Greenham, L. W. (1988) Release of gentamicin from acrylic bone-cement - elution and diffusion studies. *J. Bone Joint Surg. 70A*, 1551−1557.

(4) Schurman, D. J., Trindade, C., Hirshman, H. P., Moser, K., Kajiyama, G., and Stevens, P. (1978) Antibiotic-acrylic bone cement composites - studies of gentamicin and palacos. *J. Bone Joint Surg. 60A*, 978−984.

(5) Lautenschlager, E. P., Marshall, G. W., Marks, K. E., Schwartz, J., and Nelson, C. L. (1976) Mechanical strength of acrylic bone cements impregnated with antibiotics. *J. Biomed. Mater. Res. 10*, 837−845.

(6) Lautenschlager, E. P., Jacobs, J. J., Marshall, G. W., and Meyer, P. R. (1976) Mechanical properties of bone cements containing large doses of antibiotic powders. *J. Biomed. Mater. Res. 10*, 929−938.

(7) Dunne, N. J., Orr, J. F., Mushipe, M. T., and Eveleigh, R. J. (2003) The relationship between porosity and fatigue characteristics of bone cements. *Biomaterials 24*, 239−245.

(8) Harada, M., Sakakibara, H., Yano, T., Suzuki, T., and Okuno, S. (2000) Determinants for the drug release from T-0128, camptothecin analogue-carboxymethyl dextran conjugate. *J. Controlled Release 69*, 399−412.

(9) Frerot, E., Herbal, K., and Herrmann, A. (2003) Controlled stepwise release of fragrance alcohols from dendrimer-based 2-carbamoylbenzoates by neighbouring group participation. *Eur. J. Org. Chem. 6*, 967−971.

(10) Chandrasekhar, S., and Gopalan, S. S. (2000) Neighbouring group participation by amide N-H and its possible biological significance. *J. Chem. Res. S 11*, 504−505.
(11) Leung, M. K. (1993) Amine-catalyzed intramolecular imidization of alkyl and aryl phthalamates - kinetics and mechanism in deuteriated chloroform. *J. Chem. Soc., Perkin Trans. 2*, 2329−2335.
(12) Gibson, M., Goodman, J. M., Farrugia, L. J., and Hartley, R. C. (2003) Controlling neighbouring group participation from thioacetals. *Tetrahedron Lett. 44*, 2841−2844.
(13) Fife, T. H., Bambery, R. J., and DeMark, B. R. (1978) Intramolecular nucleophilic attack by imidazole on aliphatic and phenolic esters of *o*-(2-imidazoyl)benzoic acid. Relationship of anion and neutral species attack. *J. Am. Chem. Soc. 100*, 5500−5507.
(14) Fife, T. H., and Hutchins, J. E. C. (1981) Effect of nucleophile basicity on intramolecular nucleophilic aminolysis reactions of carbonate diesters. *J. Am. Chem. Soc. 103*, 4194−4199.
(15) Capon, B., McDowell, S. T., and Rafferty, W. V. (1971) Comparison of neighbouring group participation by phenolic and alcoholic hydroxy-groups in ester hydrolysis. *J. Chem. Soc. D 8*, 389−391.
(16) Bruice, T. C., and Sturtevant, J. M. (1959) Imidazole catalysis. V. The intramolecular participation of the imidazolyl group in the hydrolysis of some esters and the amide of γ-(4-imidazolyl)-butyric acid and 4-(2′-acetoxyethyl)-imidazole. *J. Am. Chem. Soc. 81*, 2860−2870.
(17) Ghosh, M. (1990) Monomers and polymers of nalidixic acid. *Progress in Biomedical Polymers* (Gebelin, C. G., and Dunn, R. L., Eds.) pp 335−345, Plenum, New York.
(18) Aboul-Fadl, T., and Fouad, E. A. (1996) Synthesis and in vitro investigations of nalidixic acid amides of amino acid esters as prodrugs. *Pharmazie 51*, 30−33.
(19) Singh, R., and Geetanjali, S. (2005) Synthesis of selected novel covalently linked flavoquinolones. *Synthesis 14*, 2315−2320.
(20) Von Rosenstiel, N., and Adam, D. (1994) Quinolone antibacterials - an update of their pharmacology and therapeutic use. *Drugs 47*, 872−901.
(21) Matsumura, S., Ii, S., Shigeno, H., Tanaka, T., Okuda, F., Shimura, Y., and Toshima, K. (1993) Molecular design of biodegradable functional polymers. 3. biodegradability and functionality of poly-[(sodium acrylate)-co-(vinyl alcohol)]. *Makromol. Chem. Macromol. Chem. Phys. 194*, 3237−3246.
(22) Francoeur, E. (1997) The forgotten tool: the design and use of molecular models. *Soc. Studies Sci. 27*, 7−40.
(23) Koltun, W. (1965) Precision space-filling atomic models. *Biopolymers 3*, 665−679.

BC060238Y

Synthesis and Biological Evaluation of a New Type of ^{99m}Technetium-Labeled Fatty Acid for Myocardial Metabolism Imaging

Martin Walther,*,† Christian M. Jung,† Ralf Bergmann,† Jens Pietzsch,† Katrin Rode,† Karim Fahmy,‡ Peter Mirtschink,§ Sebastian Stehr,⊥ Anke Heintz,⊥ Gerd Wunderlich,∥ Werner Kraus,# Hans-Juergen Pietzsch,† Joachim Kropp,▽ Andreas Deussen,§ and Hartmut Spies†

Institute of Radiopharmacy, Research Center Dresden-Rossendorf, PF 510119, D-01314 Dresden, Germany, Institute of Radiation Physics, Research Center Dresden-Rossendorf, PF 510119, D-01314 Dresden, Germany, Institute of Physiology, Technical University Dresden, Carl Gustav Carus University Hospital, D-01307 Dresden, Germany, Department of Anesthesiology, TU Dresden, University Hospital, D-01307 Dresden, Germany, Department of Nuclear Medicine, TU Dresden, University Hospital, D-01307 Dresden, Germany, Federal Institute for Materials Research and Testing (BAM), D-12205 Berlin, Germany, Department of Nuclear Medicine, Carl-Thiem Hospital, D-03048 Cottbus, Germany. Received May 10, 2006; Revised Manuscript Received September 25, 2006

Technetium-labeled fatty acids intended for myocardial metabolism imaging and the respective rhenium model complexes were synthesized according to the "4 + 1" mixed-ligand approach and investigated *in vitro* and *in vivo*. The non-radioactive rhenium model complexes were characterized by NMR, IR, and EA, and the geometrical impact of the chelate unit on the integrity of the fatty acid head structure was determined by single-crystal X-ray analyses. To estimate the diagnostic value of the ^{99m}Tc-labeled fatty acids, the compounds were investigated in experiments *in vitro* and in biodistribution studies using male Wistar rats. The new fatty acid tracers contain the metal core in the oxidation states +3, well-wrapped in a trigonal-bipyramidal coordination moiety, which is attached at the ω-position of a fatty acid chain. This structural feature is considered to be a good imitation of the well-established iodinated phenyl fatty acids. High heart extraction in perfused heart studies (up to 26% injected dose (ID)) and noticeable heart uptake of the ^{99m}Tc tracers *in vivo* being in the order of 2% ID/g at 5 min (postinjection, pi.), accompanied by a good heart to blood ratio of 8, confirms that the new Tc compounds are suitable as fatty acid tracers.

INTRODUCTION

The present work aims at the development of new technetium-based radiopharmaceuticals that are suited for the noninvasive diagnosis of myocardial diseases. In particular, efforts have been directed toward the design, synthesis, and biological evaluation of ^{99m}Tc-labeled fatty acids (Tc−FAs) searching for representatives that show biodistribution patterns similar to the well-known iodophenyl FA (*1*, *2*). Such technetium compounds are of potential use as tracers for myocardial FA metabolism single-photon emission tomography (SPET) imaging. Despite many attempts, an appropriate technetium FA is still not available (*3*).

The crucial point in developing Tc-"labeled" FAs is the impact of the metal technetium on the structure and biological properties of the FA. Therefore, the successful design of Tc−FAs requires a chelating moiety that enables strong binding of the FA to the metal center but at the same time preserves the physiological integrity of the FA.

The recent progress in coordination chemistry of technetium provided a variety of new neutral and small-sized mixed-ligand Tc chelate types that can be used for this purpose. They form almost exclusively square-pyramidal Tc(V)-oxo complexes of tetradentate ligands (*4*) and in some rare cases strong lipophilic Tc(I)-carbonyl species (*5*, *6*). Our preliminary approach to label FAs with technetium was based on oxotechnetium(V) complexes as well (*7*, *8*). All these systems suffer from the fact that molecular properties and the *in vivo* patterns of biomolecule−chelate conjugates are strongly influenced by the presence of the polar metal-oxo unit, making them unsuitable for mimicking FAs.

Previously, we have developed mixed-ligand Tc(III) and Re(III) complexes with a "4 + 1" donor atom arrangement, where the metal is coordinated by both a tripodal tetradentate ligand and a monodentate ligand (*9*) (Figure 1).

The "4 + 1" approach was applied for Tc−FAs as shown exemplarily for the dodecanoic acid technetium derivative with $n = 4$, [12-[isocyano-κC]dodecanoic acid][2,2′,2″-(nitrilo-κN)-triethanethiolato(3−)-κS]technetium(III) (IUPAC name). Such Tc complexes seem to be a promising alternative to the oxotechnetium-derived chelates, since they are rather lipophilic and highly stable, particularly toward challenging SH agents (*10*). Therefore, we have focused on this system to design Tc−FA compounds. The coordination chemistry of technetium with the FA-coupled ligands as well as *in vitro* and *in vivo* evaluations of their applicability as radiotracers is described.

EXPERIMENTAL PROCEDURES

Chemicals. Commercially available substances and all solvents were of reagent grade and used without further purification. Bis(triphenylphosphine)palladium(II) chloride, ω-amino undecanoic acid and ω-amino dodecanoic acid were purchased from Aldrich (Taufkirchen, Germany). Syntheses of the tetradentate tripodal ligand tris(2-mercaptoethyl)amine (NS_3) and the rhenium precursor complex designated **RePMe$_2$Ph** have been reported elsewhere (*11*). (Since all the complexes differ

* To whom correspondence should be addressed. Fax: +49 351 260 3232. E-mail: m.walther@fzd.de.

† Institute of Radiopharmacy, Research Center Dresden-Rossendorf.

‡ Institute of Radiation Physics, Research Center Dresden-Rossendorf.

§ Institute of Physiology, Technical University Dresden.

⊥ Department of Anesthesiology, Technical University Dresden.

∥ Department of Nuclear Medicine, Technical University Dresden.

Federal Institute for Materials Research and Testing (BAM).

▽ Carl-Thiem Hospital Cottbus.

10.1021/bc0601222 CCC: $37.00 © 2007 American Chemical Society
Published on Web 12/22/2006

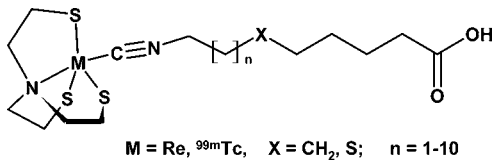


Figure 1. General formula for "4 + 1"-Tc/Re−FA.

only in the nature of the monodentate ligand, the abbreviation "**ReMonodentate**" is used throughout the text.) Tris(2-mercaptoethyl)amine was isolated and applied as the oxalate. Sodium pertechnetate ($Na^{99m}TcO_4$) was eluted from a $^{99}Mo/^{99m}Tc$ generator (Mallingkrodt, Le Petten, The Netherlands).

Instrumentation. Nuclear magnetic resonance spectra were recorded on a 400 MHz Varian Inova 400 spectrometer. The ^1H and ^{13}C chemical shifts are reported relative to residual solvent signals or TMS as reference. Mass-spectrometric measurements were performed with a Micromass tandem quadropole mass spectrometer (Quadro LC) operating in the MS mode. Mass-spectral data were recorded in the positive ESI mode. About 10^{-4} mol of the sample dissolved in 1.0 mL of methanol or acetonitrile were injected at a flow rate of 5 mL/min. Element analyses were performed on a LECO Element Analyzer CHNS-932. UV/vis spectra were recorded on a SPECORD S10 spectrometer (Carl Zeiss Jena). HPLC analysis and purification of ^{99m}technetium complexes were performed using a Perkin-Elmer instrument consisting of a Turbo LC system with a quaternary pump (series 200 LC pump) and a programmable absorbance detector model 785A. Nonradioactive rhenium complexes were monitored by their UV absorption at 254 nm, and ^{99m}technetium complexes by γ-ray detection (Bohrloch, NaI(Tl) crystal).

General Procedure for Alkyl ω-(Formylamino)alkanoates (3a−d, 11a−e, and 16). ω-Methoxy ω-oxoalkan-1-aminium chloride (5 mmol) was dissolved in 20 mL of methanol, 20 mL of ethyl formate, and 750 μL (5.4 mmol) of triethylamine and heated under reflux for 36 h. After removal of the solvent, the remaining white residue was dissolved with chloroform, and this solution was washed with water before separation.

Ethyl 8-(Formylamino)octanoate (3a). Yield: 50% colorless oil. Anal. ($C_{11}H_{21}NO_3$ (215.29)): calcd C 61.37%, H 9.83%, N, 6.51%; found C 61.31%, H 10.04%, N 6.48%. ^1H NMR (400 MHz, $CDCl_3$): 8.14 (s, 1H), 5.6 (s, H), 4.09 (q, 2H, OC*H*$_2$-CH$_3$, J = 7.2 Hz), 3.26 (t, 2H, C*H*$_2$CN, J = 6.8 Hz) 2.26 (t, 2H, C*H*$_2$, J = 7.5 Hz), 1.48−1.60 (m, 8H, 4xC*H*$_2$), 1.22 (t, 3H, OCH$_2$C*H*$_3$, J = 7.1 Hz). ^{13}C NMR (100.6 MHz, $CDCl_3$): 174.1 (*C*OO), 161.4 (*O* = *C*), 60.4 (O*C*H$_2$CH$_3$), 38.3 (*C*H$_2$N), 34.5, 29.6, 29.1, 29.0, 26.8, 25.0, 14.5 (OCH$_2$*C*H$_3$). IR (KBr, cm^{-1}): 2019 ν(N≡C), 1732 ν(C═O). MS (ESI/MeOH): m/z (%) = 216 (100) $[C_{11}H_{22}NO_3]^+$.

Methyl 11-(Formylamino)undecanoate (3b). Yield: 90% colorless solid. Mp: 41 °C. Anal. ($C_{13}H_{25}NO_3$ (243.35)): calcd C 64.16%, H 10.35%, N, 5.76%; found C 64.32%, H 10.24%, N 5.68%. ^1H NMR (MeOH-d_4): 8.01 (s, 1H, NCHO), 3.65 (s, 3H, OCH$_3$), 3.20 (t, ^3J = 7.0 Hz, 2H, CH$_2$N), 2.31 (t, ^3J = 7.4 Hz, 2H, CH$_2$COO), 1.65−1.55 (m, 2H, CH$_2$), 1.55−1.46 (m, 2H, CH$_2$), 1.39−1.26 (m, 12H, 6×CH$_2$). ^{13}C NMR (MeOH-d_4): δ 176.0 (COO), 163.7 (NCHO), 52.0 (OCH$_3$), 39.0 (CH$_2$N), 34.8 (CH$_2$COO), 30.6, 30.5, 30.3 (3C), 30.2, 27.9, 26.0. IR (KBr, cm^{-1}): 3277, 3063 ν(NH), 1737 ν(C═O, ester), 1647 ν(C═O, amide), 1174 ν(C−O).

Methyl 12-(Formylamino)dodecanoate (3c). Yield: 92% colorless solid. Mp: 52 °C. Anal. ($C_{14}H_{27}NO_3$ (257.37)): calcd C 65.33%, H 10.57%, N 5.44%; found C 65.19%, H 10.20%; N 5.36%. ^1H NMR (MeOH-d_4): 8.01 (s, 1H, NCHO), 3.65 (s, 3H, OCH$_3$), 3.20 (t, ^3J = 7.0 Hz, 2H, CH$_2$N), 2.31 (t, ^3J = 7.4 Hz, 2H, CH$_2$COO), 1.66−1.55 (m, 2H, CH$_2$), 1.55−1.46 (m, 2H, CH$_2$), 1.40−1.26 (m, 14H, 7×CH$_2$). ^{13}C NMR (MeOH-d_4): δ 176.0 (COO), 163.7 (NCHO), 52.0 (OCH$_3$), 39.0 (CH$_2$N), 34.8 (CH$_2$COO), 30.6 (2C), 30.5, 30.4, 30.3 (2C), 30.2, 27.9, 26.0. IR (KBr, cm^{-1}): 3280, 3081 ν(NH), 1740 ν(C═O, ester), 1650 ν(C═O, amide), 1175 ν(C−O).

Methyl 15-(Formylamino)pentadecanoate (3d). Yield 88% colorless solid. Mp: 60 °C. Anal. ($C_{17}H_{33}NO_3$ (299.45)): calcd C 68.19%, H 11.11%, N 4.68%; found C 68.29%, H 10.82%; N 4.66%. ^1H NMR (MeOH-d_4): 8.01 (s, 1H, NC*H*O), 3.65 (s, 3H, OC*H*$_3$), 3.20 (t, ^3J = 6.9 Hz, 2H, C*H*$_2$N), 2.31 (t, ^3J = 7.4 Hz, 2H, C*H*$_2$COO), 1.65−1.55 (m, 2H, C*H*$_2$), 1.55−1.46 (m, 2H, C*H*$_2$), 1.39−1.26 (m, 20H, 10×C*H*$_2$). ^{13}C NMR (MeOH-d_4): 176.0 (*C*OO), 163.7 (N*C*HO), 52.0 (O*C*H$_3$), 39.0 (*C*H$_2$N), 34.8 (*C*H$_2$COO), 30.7 (5C), 30.6, 30.4 (3C), 30.2, 27.9, 26.0. IR (KBr, cm^{-1}): 3296, 3069 ν(NH), 1739 ν(C═O, ester), 1646 ν(C═O, amide), 1176 ν(C−O).

Methyl 5-{[5-(Formylamino)pentyl]thio}pentanoate (11a). Yield: 73% colorless solid. Mp: 25 °C. Eluent: $CHCl_3$/EtOAc = 2/1. Anal. ($C_{12}H_{23}NO_3S$ (261.39)): calcd C 55.14%, H 8.87%, N, 5.36%, S 12.27%; found C 54.33%, H 8.84%, N 5.77%, S 12.22%. ^1H NMR (400 MHz, MeOH-d_4): 8.02 (s, 1H, NC*H*O), 3.66 (s, 3H, OC*H*$_3$), 3.22 (t, ^3J = 6.8 Hz, 2H, C*H*$_2$N), 2.52 (2×t, $^3J_1$ = 7.1 Hz, $^3J_2$ = 7.3 Hz, 4H, C*H*$_2$SC*H*$_2$), 2.35 (t, ^3J = 7.3 Hz, 2H, C*H*$_2$COO), 1.75−1.66 (m, 2H, C*H*$_2$), 1.65−1.49 (m, 6H, 3×C*H*$_2$), 1.48−1.39 (m, 2H, C*H*$_2$). ^{13}C NMR (MeOH-d_4): 175.7 (*C*OO), 163.7 (N*C*HO), 52.0 (O*C*H$_3$), 38.8 (*C*H$_2$N), 34.3 (*C*H$_2$COO), 32.6, 32.4, 30.3, 30.0, 29.9, 27.0, 25.1.

Methyl 5-{[6-(Formylamino)hexyl]thio}pentanoate (11b). Yield: 72% colorless solid. Mp: 31 °C. Eluent: $CHCl_3$/EtOAc = 10/3. Anal. ($C_{13}H_{25}NO_3S$ (275.41)): calcd C 56.69%, H 9.15%, N, 5.09%, S 11.64%; found C 56.15%, H 9.27%, N 5.28%, S 11.56%. ^1H NMR (MeOH-d_4): 8.02 (s, 1H, NC*H*O), 3.66 (s, 3H, OC*H*$_3$), 3.21 (t, ^3J = 6.9 Hz, 2H, C*H*$_2$N), 2.52 (t, ^3J = 7.0 Hz, 2H, C*H*$_2$SCH$_2$), 2.51 (t, ^3J = 7.2 Hz, 2H, CH$_2$-SC*H*$_2$), 2.35 (t, ^3J = 7.3 Hz, 2H, C*H*$_2$COO), 1.75−1.65 (m, 2H, C*H*$_2$), 1.65−1.48 (m, 6H, 3×C*H*$_2$), 1.48−1.31 (m, 4H, 2×C*H*$_2$). ^{13}C NMR (MeOH-d_4): 175.7 (*C*OO), 163.7 (N*C*HO), 52.0 (O*C*H$_3$), 38.9 (*C*H$_2$N), 34.3 (*C*H$_2$COO), 32.7, 32.4, 30.6, 30.3, 30.1, 29.5, 27.5, 25.1.

Methyl 5-{[7-(Formylamino)heptyl]thio}pentanoate (11c). Yield: 67% colorless solid. Mp: 36−37 °C. Eluent: $CHCl_3$/EtOAc = 5/1. Anal. ($C_{14}H_{27}NO_3S$ (289.44)): calcd C 58.10%, H 9.40%, N, 4.84%, S 11.08%; found C 58.03%, H 9.51%, N 4.84%, S 10.92%. ^1H NMR (MeOH-d_4): 8.02 (s, 1H, NC*H*O), 3.66 (s, 3H, OC*H*$_3$), 3.21 (t, ^3J = 6.9 Hz, 2H, C*H*$_2$N), 2.52 (t, ^3J = 7.1 Hz, 2H, C*H*$_2$SCH$_2$), 2.51 (t, ^3J = 7.2 Hz, 2H, CH$_2$-SC*H*$_2$), 2.35 (t, ^3J = 7.2 Hz, 2H, C*H*$_2$COO), 1.75−1.66 (m, 2H, C*H*$_2$), 1.64−1.48 (m, 6H, 3×C*H*$_2$), 1.47−1.32 (m, 6H, 3×C*H*$_2$). ^{13}C NMR (MeOH-d_4): 175.7 (*C*OO), 163.7 (N*C*HO), 52.0 (O*C*H$_3$), 38.9 (*C*H$_2$N), 34.3 (*C*H$_2$COO), 32.7, 32.4, 30.6, 30.3, 30.1, 29.9, 29.8, 27.8, 25.1. IR (KBr, cm^{-1}): 3290, 3032 ν(NH), 1731 ν(C═O, ester), 1646 ν(C═O, amide), 1175 ν(C−O).

Methyl 5-{[9-(Formylamino)nonyl]thio}pentanoate (11d). Yield: 69% colorless solid. Mp: 48 °C. Eluent 1: $CHCl_3$/EtOAc = 4/1. Eluent 2: *n*-hexane/acetone = 5/2. Anal. ($C_{16}H_{31}NO_3S$ (317.49)): calcd C 60.53%, H 9.84%, N, 4.41%, S 10.10%; found C 60.80%, H 9.74%, N 4.38%, S 10.22%. ^1H NMR (MeOH-d_4): 8.01 (s, 1H, NC*H*O), 3.66 (s, 3H, OC*H*$_3$), 3.21 (t, ^3J = 6.9 Hz, 2H, C*H*$_2$N), 2.51 (t, ^3J = 7.1 Hz, 2H, C*H*$_2$SCH$_2$), 2.50 (t, ^3J = 7.3 Hz, 2H, CH$_2$SC*H*$_2$), 2.35 (t, ^3J = 7.3 Hz, 2H, C*H*$_2$COO), 1.75−1.66 (m, 2H, C*H*$_2$), 1.64−1.47 (m, 6H, 3×C*H*$_2$), 1.44−1.29 (m, 10H, 5×C*H*$_2$). ^{13}C NMR (MeOH-d_4): 175.7 (*C*OO), 163.7 (N*C*HO), 52.0 (O*C*H$_3$), 39.0 (*C*H$_2$N), 34.3 (*C*H$_2$COO), 32.8, 32.4, 30.7, 30.6, 30.3 (2C), 30.2, 30.1, 29.8, 27.9, 25.1. IR (KBr, cm^{-1}): 3293, 3030 ν(NH), 1731 ν(C═O, ester), 1646 ν(C═O, amide), 1175 ν(C−O).

Methyl 5-{[11-(Formylamino)undecyl]thio}pentanoate (11e). Yield: 69% colorless solid. Mp: 58 °C. Eluent: *n*-hexane /acetone = 5/2. Anal. ($C_{18}H_{35}NO_3S$ (345.55)): calcd C 62.57%, H 10.21%, N, 4.05%, S 9.28%; found C 62.42%, H 10.10%, N 4.02%, S 9.40%. ^{1}H NMR (MeOH-d_4): 8.01 (s, 1H, NC*H*O), 3.66 (s, 3H, OCH_3), 3.20 (t, ^3J = 7.0 Hz, 2H, CH_2N), 2.51 (t, ^3J = 7.0 Hz, 2H, CH_2SCH$_2$), 2.50 (t, ^3J = 7.3 Hz, 2H, CH$_2$-SCH_2), 2.35 (t, ^3J = 7.2 Hz, 2H, CH_2COO), 1.76−1.66 (m, 2H, CH_2), 1.64−1.47 (m, 6H, 3×CH_2), 1.44−1.28 (m, 14H, 7×CH_2). ^{13}C NMR (MeOH-d_4): 175.7 (*C*OO), 163.7 (N*C*HO), 52.0 (O*C*H$_3$), 39.0 (*C*H$_2$N), 34.3 (*C*H$_2$COO), 32.8, 32.4, 30.7, 30.6 (3C), 30.4 (2C), 30.3, 30.1, 29.9, 27.9, 25.1. IR (KBr, cm^{-1}): 3295, 3028 ν(NH), 1729 ν(C═O, ester), 1646 ν(C═O, amide), 1175 ν(C−O).

Phenylene-Inserted FA Body by Sonogashira Coupling. To the ice-cooled (0 °C) solution of 6-phthalimido-1-hexine **13** (2.5 mmol) and p-iodophenylethylacetate **14** (1.8 mmol) in acetonitrile (10 mL) was added triethylamine (5 mmol) followed by the addition of bis(triphenyl-phosphine)palladium(II) chloride (0.15 mmol) and CuI (0.025 g) under an argon atmosphere. The reaction mixture was stirred for 30 min at 0 °C and then at room temperature for 2 h. The orange-colored solution was concentrated under reduced pressure, and the residue was partitioned between 5% citric acid (50 mL) and ethyl acetate (50 mL). The organic layer was washed with 5% citric acid (3 × 15 mL) and water, dried with Na_2SO_4, and concentrated. The crude product was purified by column chromatography on silica gel (hexane/ethylacetate, 3:2).

Ethyl {4-[6-(1,3-Dioxo-1,3-dihydro-2*H*-isoindol-2-yl)hexynyl]-phenyl}acetate (15). Yield: 68% of orange waxy solid. Anal. ($C_{24}H_{23}NO_4$ (389.44)): calcd C, 74.02; H, 5.95; N, 3.60; found C, 73.98; H, 5.86; N, 3.37. IR (KBr): 1770.1, 1717 C═O, 1615.3, 1397.4. ^{1}H NMR (400 MHz, $CDCl_3$): 1.21 (t, 3H, CH_3, J = 7.14 Hz), 1.62 (m, 2H, CH_2), 1.80−1.84 (m, 2H, CH_2), 2.44 (t, 2H, CH_2, J = 7.05 Hz), 3.55 (s, 2H, CH_2COOEt), 3.72 (t, 2H, CH_2N, J = 7.05 Hz), 4.09−4.14 (q, 2H, CH_2), 7.15 (d, 2H, phenyl, J = 8.06 Hz), 7.30 (d, 2H, phenyl, J = 8.24 Hz), 7.66−7.69 (m, 2H, phthalimide), 7.79−7.83 (m, 2H, phthalimide). ^{13}C NMR (100.6 MHz, $CDCl_3$): 14.4, 19.2, 26.1, 28.0, 37.7, 41.5, 61.1, 81.0. 89.7, 122.8, 123.4, 129.3, 131.9, 132.3, 133.7, 134.1, 168.6, 171.5. ESI MS (MeOH): *m*/*z* (%) = 412 (100) $[C_{24}H_{23}NNaO_4]^+$.

Ethyl {4-[6-(Formylamino)hexyl]phenyl}acetate (16). The catalytic reduction of **15** (711 mg = 1.828 mmol) was accomplished in 10 mL of methanol under addition of 150 mg of 10% palladium on charcoal under pressure of 1.5 bar H_2 in a 150 mL autoclave and stirring at room temperature for 12 h. After filtration of the mixture, the solvent was removed *in vacuo*, and the waxy residue was redissolved in 15 mL of ethanol. The addition of 1.1 equiv of hydrazine hydrate and 2 h refluxation leads to the desired substituted ω-amino fatty acid ester. This crude product was used for the general formylation procedure. Yield: 78% colorless oil. Anal. ($C_{17}H_{25}NO_3$ (291.39)): calcd C 70.07%, H 8.65%, N, 4.81%; found C 70.22%, H 8.34%, N 4.77%. ^{1}H NMR ($CDCl_3$): 8.14 (s, 1H, NC*H*O), 7.32 (d, 2H, phenyl, J = 7.82 Hz), 7.18 (d, 2H, phenyl, J = 8.10 Hz), 5.63 (s, 1H, N*H*), 4.16−4.08 (q, 2H, OCH_2CH$_3$), 3.56 (s, 2H, CH_2-Ph), 3.21 (t, 2H, CH_2N, J = 6.98 Hz), 2.58 (t, 2H, CH_2, J = 7.78 Hz), 1.71−1.59 (m, 8H, 4xCH_2), 1.22 (t, 3H, OCH$_2$CH_3, J = 7.08 Hz). ^{13}C NMR ($CDCl_3$): 171.5 (*C*OOEt), 161.4 (N*C*HO), 133.9, 131.9, 129.1, 128.9, 61.1 (O*C*H$_2$CH$_3$), 39.8 (*C*H$_2$N), 35.5, 31.1, 29.2, 28.3, 27.6, 26.2, 14.2 (OCH$_2$*C*H$_3$). ESI-MS (MeOH): *m*/*z* (%) = 292 (100) $[C_{17}H_{26}NO_3]^+$.

General Procedure for Alkyl ω-Alkyl-isocyanoalkanoates (4a−d, 12a−e, and 17) Methyl ω-(formylamino)alkanoate (1.5 mmol) was dissolved in 15 mL of anhydrous pyridine, and 330 mg (1.73 mmol) of *p*-toluenesulfonyl chloride was added under ice cooling. After having been stirred for 1.5 h at 0 °C, the mixture was transferred in a flask filled with 75 g of ice. After the temperature was slowly raised above the freezing point, the oily product was extracted three times with diethyl ether, and the organic layer was washed with a saturated solution of sodium chloride. The product was purified by column chromatography on silica gel 60 using a mixture of diethyl ether and *n*-hexane (2:5) as eluent.

Ethyl 8-Isocyanooctanoate (4a). Yield: 81% colorless oil. Anal. ($C_{11}H_{19}NO_2$ (197.28)): calcd C 66.97%, H 9.71%, N 7.10%; found C 66.64%, H 9.92%, N 6.98%. ^{1}H NMR (400 MHz, $CDCl_3$): 4.07 (q, 2H, OCH_2CH$_3$, J = 7.1 Hz), 3.35 (tt, 2H, CH_2CN, J = 6.6, 1.9 Hz,) 2.26 (t, 2H, CH_2, J = 7.4 Hz), 1.56−1.68 (m, 8H, 4xCH_2), 1.23 (t, 3H, OCH$_2$CH_3, J = 7.1 Hz). ^{13}C NMR (100.6 MHz, $CDCl_3$): 173.9 (*C*OO), 155.9 (N≡*C*), 60.4 (O*C*H$_2$CH$_3$), 41.7 (*C*H$_2$N), 34.4, 29.2, 28.6, 26.4, 24.9, 14.5 (OCH$_2$*C*H$_3$). MS (ESI/MeOH): *m*/*z* (%) = 220 (100) $[C_{11}H_{19}NO_2Na]^+$.

Methyl 11-Isocyanoundecanoate (4b). Yield: 76% colorless oil. Anal. ($C_{13}H_{23}NO_2$ (225.33)): calcd C 69.29%, H 10.29%, N 6.22%; found C 69.23%, H 9.94%, N 6.25%. ^{1}H NMR (400 MHz, $CDCl_3$): 3.66 (s, 3H, OCH_3), 3.37 (tt, $^2J_{NH}$ = 1.9 Hz, $^3J_{HH}$ = 6.8 Hz, 2H, CH_2N), 2.29 (t, ^3J = 7.5 Hz, 2H, CH_2-COO), 1.72−1.55 (m, 4H, 2×CH_2), 1.47−1.36 (m, 2H, CH_2), 1.35−1.23 (m, 10H, 5×CH_2). ^{13}C NMR (100 MHz, $CDCl_3$): 174.3 (*C*OO), 155.5 (t, $^1J_{NC}$ = 6.1 Hz, N≡*C*), 51.4 (O*C*H$_3$), 41.5 (t, $^1J_{NC}$ = 6.5 Hz, *C*H$_2$N), 34.0 (*C*H$_2$COO), 29.2 (2C), 29.1, 29.0 (2C), 28.6, 26.2, 24.9.

Methyl 12-Isocyanododecanoate (4c). Yield: 80% colorless oil. Anal. ($C_{14}H_{25}NO_2$ (239.36)): calcd C 70.25%, H 10.53%, N 5.85%; found C 70.01%, H 10.17%, N 5.92%. ^{1}H NMR (400 MHz, $CDCl_3$): 3.65 (s, 3H, OCH_3), 3.36 (tt, $^2J_{NH}$ = 1.9 Hz, $^3J_{HH}$ = 6.8 Hz, 2H, CH_2N), 2.29 (t, ^3J = 7.5 Hz, 2H, CH_2-COO), 1.72−1.55 (m, 4H, 2×CH_2), 1.47−1.36 (m, 2H, CH_2), 1.35−1.22 (m, 12H, 6×CH_2). ^{13}C NMR (100 MHz, $CDCl_3$): 174.3 (*C*OO), 155.5 (t, $^1J_{NC}$ = 6.1 Hz, N≡*C*), 51.4 (O*C*H$_3$), 41.5 (t, $^1J_{NC}$ = 6.5 Hz, *C*H$_2$N), 34.0 (*C*H$_2$COO), 29.3 (3C), 29.1, 29.0 (2C), 28.6, 26.2, 24.9.

Methyl 15-Isocyanopentadecanoate (4d). Yield: 81% colorless oil. Anal. ($C_{17}H_{31}NO_2$ (281.44)): calcd C 72.55%, H 11.11%, N 4.98%; found C 72.61%, H 11.13%, N 4.88%. ^{1}H NMR ($CDCl_3$) 3.66 (s, 3H, OCH_3), 3.36 (tt, $^2J_{NH}$ = 1.9 Hz, $^3J_{HH}$ = 6.8 Hz, 2H, CH_2N), 2.30 (t, ^3J = 7.6 Hz, 2H, CH_2-COO), 1.72−1.54 (m, 4H, 2×CH_2), 1.47−1.37 (m, 2H, CH_2), 1.37−1.21 (m, 18H, 9×CH_2). ^{13}C NMR ($CDCl_3$) 174.5 (*C*OO), 155.7 (t, $^1J_{NC}$ = 6.0 Hz, N≡*C*), 51.4 (O*C*H$_3$), 41.6 (t, $^1J_{NC}$ = 6.1 Hz, *C*H$_2$N), 34.1 (*C*H$_2$COO), 29.6, 29.5 (3C), 29.4, 29.3, 29.2, 29.1 (2C), 28.7, 26.3, 24.9. IR (KBr, cm^{-1}): 2148 ν(N≡C), 1728 ν(C═O), 1163 ν(C−O).

Methyl 5-[(5-Isocyanopentyl)thio]pentanoate (12a). Yield: 73% colorless oil. Anal. ($C_{12}H_{21}NO_2S$ (243.37)): calcd C 59.22%, H 8.70%, N 5.76%, S 13.80%; found C 59.17%, H 8.49%, N 6.05%, S 13.30%. ^{1}H NMR ($CDCl_3$) 3.64 (s, 3H, OCH_3), 3.37 (tt, $^2J_{NH}$ = 2.0 Hz, $^3J_{HH}$ = 6.6 Hz, 2H, CH_2N), 2.49 (2×t, $^3J_1$ = 7.1 Hz, $^3J_2$ = 7.2 Hz, 4H, CH_2SCH_2), 2.31 (t, ^3J = 7.3 Hz, 2H, CH_2COO), 1.75−1.64 (m, 4H, 2×CH_2), 1.63−1.47 (m, 6H, 3×CH_2). ^{13}C NMR ($CDCl_3$) 173.7 (*C*OO), 155.8 (t, $^1J_{NC}$ = 5.7 Hz, N≡*C*), 51.4 (O*C*H$_3$), 41.3 (t, $^1J_{NC}$ = 6.5 Hz, *C*H$_2$N), 33.4 (*C*H$_2$COO), 31.6 (2C), 28.9, 28.6 (2C), 25.4, 24.0.

Methyl 5-[(6-Isocyanohexyl)thio]pentanoate (12b). Yield: 77% colorless oil. Anal. ($C_{13}H_{23}N\ O_2S$ (257.40)): calcd C 60.66%, H 9.01%, N 5.44%, S 12.46%; found C 60.64%, H 9.01%, N 5.78%, S 12.42%. ^{1}H NMR ($CDCl_3$): 3.64 (s, 3H, OCH_3), 3.37 (tt, $^2J_{NH}$ = 2.0 Hz, $^3J_{HH}$ = 6.7 Hz, 2H, CH_2N), 2.49 (2×t, $^3J_1$ = 7.2 Hz, $^3J_2$ = 7.3 Hz, 4H, CH_2SCH_2), 2.31 (t, ^3J = 7.3 Hz, 2H, CH_2COO), 1.75−1.53 (m, 8H, 4×CH_2), 1.49−1.34 (m, 4H, 2×CH_2). ^{13}C NMR ($CDCl_3$): 173.7 (*C*OO), 155.6

(t, $^1J_{NC}$ = 5.7 Hz, N≡*C*), 51.4 (O*C*H$_3$), 41.4 (t, $^1J_{NC}$ = 6.5 Hz, *C*H$_2$N), 33.5 (*C*H$_2$COO), 31.8, 31.6, 29.2, 28.9 (2C), 27.8, 25.9, 24.0.

Methyl 5-[(7-Isocyanoheptyl)thio]pentanoate (12c). Yield: 80% colorless oil. Anal. ($C_{14}H_{25}NO_2S$ (271.42)): calcd C 61.59%, H 9.28%, N 5.16%, S 11.81%; found C 62.11%, H 9.05%, N 5.38%, S 11.88%. ^{1}H NMR ($CDCl_3$): 3.65 (s, 3H, OC*H*$_3$), 3.36 (tt, $^2J_{NH}$ = 2.0 Hz, $^3J_{HH}$ = 6.7 Hz, 2H, C*H*$_2$N), 2.49 (t, ^3J = 7.2 Hz, 2H, C*H*$_2$SCH$_2$), 2.48 (t, ^3J = 7.3 Hz, 2H, CH$_2$SC*H*$_2$), 2.32 (t, ^3J = 7.4 Hz, 2H, C*H*$_2$COO), 1.76−1.52 (m, 8H, 4×C*H*$_2$), 1.48−1.27 (m, 6H, 3×C*H*$_2$). ^{13}C NMR ($CDCl_3$) 173.8 (*C*OO), 155.6 (t, $^1J_{NC}$ = 6.1 Hz, N≡*C*), 51.5 (O*C*H$_3$), 41.4 (t, $^1J_{NC}$ = 6.5 Hz, *C*H$_2$N), 33.5 (*C*H$_2$COO), 31.9, 31.6, 29.3, 29.0, 28.9, 28.5, 28.2, 26.1, 24.0.

Methyl 5-[(9-Isocyanononyl)thio]pentanoate (12d). Yield: 75% colorless oil. Anal. ($C_{16}H_{29}NO_2S$ (299.48)): calcd C 64.17%, H 9.76%, N 4.68%, S 10.71%; found C 63.82%, H 9.96%, N 4.94%, S 10.78%. ^{1}H NMR ($CDCl_3$): 3.65 (s, 3H, OC*H*$_3$), 3.36 (tt, $^2J_{NH}$ = 2.0 Hz, $^3J_{HH}$ = 6.7 Hz, 2H, C*H*$_2$N), 2.50 (t, ^3J = 7.2 Hz, 2H, C*H*$_2$SCH$_2$), 2.48 (t, ^3J = 7.4 Hz, 2H, CH$_2$SC*H*$_2$), 2.32 (t, ^3J = 7.4 Hz, 2H, C*H*$_2$COO), 1.76−1.51 (m, 8H, 4×C*H*$_2$), 1.46−1.25 (m, 10H, 5×C*H*$_2$). ^{13}C NMR ($CDCl_3$): 173.8 (*C*OO), 155.5 (t, $^1J_{NC}$ = 5.7 Hz, N≡*C*), 51.5 (O*C*H$_3$), 41.5 (t, $^1J_{NC}$ = 6.5 Hz, *C*H$_2$N), 33.5 (*C*H$_2$COO), 32.0, 31.6, 29.5, 29.2, 29.0 (3C), 28.7, 28.6, 26.2, 24.1.

Methyl 5-[(11-Isocyanoundecyl)thio]pentanoate (12e). Yield: 78% colorless wax. Anal. ($C_{18}H_{33}NO_2S$ (327.53)): calcd C 66.01%, H 10.16%, N 4.28%, S 9.79%; found C 65.88%, H 10.11%, N 4.25%, S 9.85%. ^{1}H NMR ($CDCl_3$): 3.66 (s, 3H, OC*H*$_3$), 3.37 (tt, $^2J_{NH}$ = 2.0 Hz, $^3J_{HH}$ = 6.7 Hz, 2H, C*H*$_2$N), 2.50 (t, ^3J = 7.3 Hz, 2H, C*H*$_2$SCH$_2$), 2.48 (t, ^3J = 7.6 Hz, 2H, CH$_2$SC*H*$_2$), 2.32 (t, ^3J = 7.3 Hz, 2H, C*H*$_2$COO), 1.77−1.50 (m, 8H, 4×C*H*$_2$), 1.47−1.22 (m, 14H, 7×C*H*$_2$). ^{13}C NMR ($CDCl_3$): 173.8 (*C*OO), 155.5 (t, $^1J_{NC}$ = 5.7 Hz, N≡*C*), 51.5 (O*C*H$_3$), 41.5 (t, $^1J_{NC}$ = 6.1 Hz, *C*H$_2$N), 33.6 (*C*H$_2$COO), 32.1, 31.6, 29.6, 29.4 (2C), 29.3, 29.2, 29.0 (2C), 28.8, 28.6, 26.3, 24.1. IR (KBr, cm^{-1}): 2153 ν(N≡C), 1729 ν(C═O), 1173 ν-(C−O).

Ethyl [4-(6-Isocyanohexyl)phenyl]acetate (17). Yield: 73% colorless oil. Anal. ($C_{17}H_{23}NO_2$ (273.38)): calcd C 74.69%, H 8.48%, N, 5.12%; found C 74.34%, H 8.41%, N 4.98%. ^{1}H NMR ($CDCl_3$): 7.18 (d, 2H, phenyl, J = 7.87 Hz), 7.13 (d, 2H, phenyl, J = 8.92 Hz), 4.15 (q, 2H, OC*H*$_2$CH$_3$), 3.57 (s, 2H, C*H*$_2$Ph), 3.36 (t, 2H, C*H*$_2$CN, J = 6.92 Hz) 2.59 (t, 2H, C*H*$_2$, J = 7.86 Hz), 1.49−1.80 (m, 8H, 4xC*H*$_2$), 1.25 (t, 3H, OCH$_2$C*H*$_3$, J = 7.06 Hz). ^{13}C NMR ($CDCl_3$): 172.0 (*C*OO), 155.8 (N≡*C*), 132.7, 131.8, 129.4, 128.8, 61.0 (O*C*H$_2$CH$_3$), 41.2 (*C*H$_2$N), 35.6, 31.3, 29.2, 28.5, 27.7, 26.4, 14.4 (OCH$_2$*C*H$_3$). ESI-MS (MeOH): m/z (%) = 296 (100) $[C_{17}H_{23}NO_2Na]^+$.

General Procedure for the Synthesis of "4 + 1"-Re−FA Complexes. A 65 mg (125 μmol) sample of **RePMe$_2$Ph** was dissolved in 6 mL of CH_2Cl_2 and 155 mmol (1.24 equiv) of alkyl isocyanoalkanoate **4**, **12**, or **17** dissolved in further 4 mL of CH_2Cl_2 was added. The mixture was stirred 12 h at room temperature. The solvent was stripped *in vacuo*, and the complex was purified by column chromatography ($CHCl_3$/acetone = 20/1). Dissolved in 10 mL of dioxane and stirred with 2 mL 0.5 N sodium hydroxide 48 h at rt, the ester functions were saponified. After neutralization with 1 N citric acid, the solvent was removed *in vacuo*. Further purification was carried out by column chromatography ($CHCl_3$/acetone/AcOH = 90/10/0.1)

[8-[Isocyano-κC]octanoic acid][2,2′,2″-(nitrilo-κN)triethanethiolato(3-)-κS]rhenium(III) (ReC8−FA). Yield: 61% dark green solid. Mp: 52 °C. Anal. ($C_{15}H_{27}N_2O_2ReS_3$ (549.79)): calcd C 32.77%, H 4.95%, N 5.10%, S 17.50%; found C 32.52%, H 5.04%, N 5.05%, S 17.32%. ^{1}H NMR (400 MHz, $CDCl_3$): 4.74 (t, ^3J = 6.5 Hz, 2H, C*H*$_2$NC), 3.34−2.50 (bs, 12H, N(C*H*$_2$C*H*$_2$S)$_3$), 2.27 (t, ^3J = 7.6 Hz, 2H, C*H*$_2$COO), 1.76−1.58 (m, 8H, 4xC*H*$_2$). ^{13}C NMR (100.6 MHz, $CDCl_3$): 177.1 (*C*OO), 163.5 (N≡*C*), 59.6 (3C, N(*C*H$_2$)$_3$), 45.2 (*C*H$_2$NC), 44.9 (3C, Re(S*C*H$_2$)$_3$), 34.5 (*C*H$_2$COO), 29.4, 28.6, 26.7, 24.5. IR (KBr, cm^{-1}): 2035 ν(N≡C), 1710 ν(C═O). ESI-MS (MeOH): m/z (%) = 572 (100) $[C_{15}H_{26}N_2NaO_2ReS_3]^+$.

[11-[Isocyano-κC]undecanoic acid][2,2′,2″-(nitrilo-κN)triethanethiolato(3-)-κS]rhenium(III) (ReC11−FA). Yield: 72% dark green solid. Mp: 158 °C. Anal. ($C_{18}H_{33}N_2O_2ReS_3$ (591.88)): calcd C 36.53%, H 5.62%, N 4.73%, S 16.25%; found C 36.50%, H 5.76%, N 4.73%, S 16.21%. ^{1}H NMR ($CDCl_3$, 25 °C, TMS): 4.78 (t, ^3J = 6.5 Hz, 2H, C*H*$_2$NC), 3.3−2.6 (bs, 12H, N(C*H*$_2$C*H*$_2$S)$_3$), 2.34 (t, ^3J = 7.6 Hz, 2H, C*H*$_2$-COO), 1.84−1.73 (m, 2H, C*H*$_2$), 1.69−1.50 (m, 4H, 2×C*H*$_2$), 1.41−1.20 (m, 10H, 5×C*H*$_2$). ^{13}C NMR (100 MHz, $CDCl_3$, 25 °C, TMS): δ 178.3 (*C*OO), 162.4 (N≡*C*), 59.4 (3C, N(*C*H$_2$)$_3$), 45.0 (*C*H$_2$NC), 44.7 (3C, Re(S*C*H$_2$)$_3$), 33.8 (*C*H$_2$-COO), 33.0, 29.4, 29.3, 29.2, 29.0 (2C), 26.7, 24.7. IR (KBr, cm^{-1}): 2039 ν(N≡C), 1713 ν(C═O).

[12-[Isocyano-κC]dodecanoic acid][2,2′,2″-(nitrilo-κN)triethanethiolato-κS]rhenium(III) (ReC12−FA). Yield: 77% dark green solid. Mp: 115 °C. Anal. ($C_{19}H_{35}N_2O_2ReS_3$ (605.90)): calcd C 37.66%, H 5.82%, N 4.62%, S 15.88%; found C 37.62%, H 5.61%, N 4.20%, S 15.98%. ^{1}H NMR ($CDCl_3$): δ 4.78 (t, ^3J = 6.6 Hz, 2H, C*H*$_2$NC), 3.3−2.6 (bs, 12H, N(C*H*$_2$C*H*$_2$S)$_3$), 2.34 (t, ^3J = 7.5 Hz, 2H, C*H*$_2$COO), 1.84−1.72 (m, 2H, C*H*$_2$), 1.68−1.50 (m, 4H, 2×C*H*$_2$), 1.41−1.20 (m, 12H, 6×C*H*$_2$). ^{13}C NMR (100 MHz, $CDCl_3$): 179.1 (*C*OO), 162.5 (N≡*C*), 59.4 (3C, N(*C*H$_2$)$_3$), 45.0 (*C*H$_2$NC), 44.7 (3C, Re(S*C*H$_2$)$_3$), 33.9 (*C*H$_2$COO), 33.0, 29.5, 29.4 (2C), 29.2, 29.0 (2C), 26.7, 24.7. IR (KBr, cm^{-1}): 2038 ν(N≡C), 1710 ν(C═O).

[15-[Isocyano-κC]pentadecanoic acid][2,2′,2″-(nitrilo-κN)-triethanethiolato-κS]rhenium(III) (ReC15−FA). Yield: 78% dark-green crystals. Mp: 146 °C. Anal. ($C_{22}H_{41}N_2O_2ReS_3$ (647.98)): calcd C 40.78%, H 6.38%, N 4.32%, S 14.85%; found C 40.70%, H 6.25%, N 4.32%, S 14.79%. ^{1}H NMR ($CDCl_3$): 4.78 (t, ^3J = 6.6 Hz, 2H, C*H*$_2$NC), 3.3−2.6 (bs, 12H, N(C*H*$_2$C*H*$_2$S)$_3$), 2.35 (t, ^3J = 7.6 Hz, 2H, C*H*$_2$COO), 1.83−1.74 (m, 2H, C*H*$_2$), 1.68−1.50 (m, 4H, 2×C*H*$_2$), 1.40−1.20 (m, 18H, 9×C*H*$_2$). ^{13}C NMR ($CDCl_3$): 178.0 (*C*OO), 162.3 (N≡*C*), 59.4 (3C, N(*C*H$_2$)$_3$), 45.0 (*C*H$_2$NC), 44.7 (3C, Re(S*C*H$_2$)$_3$), 33.7 (*C*H$_2$COO), 33.0, 29.6 (4C), 29.5, 29.4, 29.2, 29.1 (2C), 26.7, 24.7. IR (KBr, cm^{-1}): 2038 ν(N≡C), 1707 ν(C═O).

(5-{[5-(Isocyano-κC)pentyl]thio}pentanoic acid)[2,2′,2″-(nitrilo-κN)triethanethiolato(3-)-κS] rhenium(III) (ReC10S−FA). Yield: 68% dark green solid. Mp: 116 °C. Anal. ($C_{17}H_{31}N_2O_2ReS_4$ (609.92)): calcd C 33.48%, H 5.12%, N 4.59%, S 21.03%; found C 33.32%, H 5.08%, N 4.46%, S 20.81%. ^{1}H NMR ($CDCl_3$): δ 4.79 (t, ^3J = 6.3 Hz, 2H, C*H*$_2$-NC), 3.3−2.6 (bs, 12H, N(C*H*$_2$C*H*$_2$S)$_3$), 2.55 (t, ^3J = 7.8 Hz, 2H, C*H*$_2$SCH$_2$), 2.53 (t, ^3J = 7.2 Hz, 2H, CH$_2$SC*H*$_2$), 2.38 (t, ^3J = 7.2 Hz, 2H, C*H*$_2$COO), 1.88−1.78 (m, 2H, C*H*$_2$), 1.78−1.58 (m, 8H, 4×C*H*$_2$). ^{13}C NMR ($CDCl_3$): δ 177.6 (*C*OO), 164.1 (N≡*C*), 59.3 (3C, N(*C*H$_2$)$_3$), 44.9 (*C*H$_2$NC), 44.6 (3C, Re(S*C*H$_2$)$_3$), 33.2 (*C*H$_2$COO), 32.6, 31.9, 31.5, 29.2, 28.9, 26.1, 23.8. IR (KBr, cm^{-1}): 2039 ν(N≡C), 1712 ν(C═O).

(5-{[6-(Isocyano-κC)hexyl]thio}pentanoic acid)[2,2′,2″-(nitrilo-κN)triethanethiolato(3-)-κS] rhenium(III) (ReC11S−FA). Yield: 71% dark green solid. Mp: 115 °C. Anal. ($C_{18}H_{33}N_2O_2ReS_4$ (623.94)): calcd C 34.65%, H 5.33%, N 4.49%, S 20.56%; found C 34.78%, H 5.33%, N 4.38%, S 20.67%. ^{1}H NMR ($CDCl_3$): 4.79 (t, ^3J = 6.4 Hz, 2H, C*H*$_2$-NC), 3.3−2.6 (bs, 12H, N(C*H*$_2$C*H*$_2$S)$_3$), 2.52 (t, ^3J = 7.3 Hz, 4H, C*H*$_2$SC*H*$_2$), 2.38 (t, ^3J = 7.3 Hz, 2H, C*H*$_2$COO), 1.86−1.69 (m, 4H, 2×C*H*$_2$), 1.69−1.56 (m, 6H, 3×C*H*$_2$), 1.52−1.41 (m, 2H, C*H*$_2$). ^{13}C NMR ($CDCl_3$): 177.1 (*C*OO), 163.4 (N≡*C*), 59.4 (3C, N(*C*H$_2$)$_3$), 45.0 (*C*H$_2$NC), 44.7 (3C, Re(S*C*H$_2$)$_3$),

33.1 (*C*H_2COO), 32.9, 32.0, 31.5, 29.6, 28.9, 28.3, 26.3, 23.9. IR (KBr, cm^{-1}): 1989 ν(N≡C), 1706 ν(C═O).

(5-{[7-(Isocyano-κ*C*)heptyl]thio}pentanoic acid)[2,2′,2″-(nitrilo-κ*N*)triethanethiolato(3−)-κ*S*] rhenium(III) (ReC12S−FA). Yield: 75% dark green solid. Mp: 111 °C. Anal. ($C_{19}H_{35}N_2O_2ReS_4$ (637.97)): calcd C 35.77%, H 5.53%, N 4.39%, S 20.11%; found C 35.94%, H 5.90%, N 4.38%, S 20.06%. ^{1}H NMR ($CDCl_3$): 4.78 (t, ^3J = 6.4 Hz, 2H, CH_2-NC), 3.3−2.6 (bs, 12H, N(CH_2CH_2S)$_3$), 2.52 (t, ^3J = 7.2 Hz, 2H, CH_2SCH_2), 2.49 (t, ^3J = 7.5 Hz, 2H, CH_2SCH_2), 2.38 (t, ^3J = 7.3 Hz, 2H, CH_2COO), 1.85−1.69 (m, 4H, 2×CH_2), 1.69−1.52 (m, 6H, 3×CH_2), 1.48−1.32 (m, 4H, 2×CH_2). ^{13}C NMR ($CDCl_3$): 178.0 (*C*OO), 163.1 (N≡*C*), 59.4 (3C, N(*C*H_2)$_3$), 45.0 (*C*H_2NC), 44.7 (3C, Re(S*C*H_2)$_3$), 33.3 (*C*H_2COO), 32.9, 32.1, 31.6, 29.6, 28.9, 28.8, 28.6, 26.6, 23.8. IR (KBr, cm^{-1}): 2038 ν(N≡C), 1704 ν(C═O).

(5-{[9-(Isocyano-κ*C*)nonyl]thio}pentanoic acid)[2,2′,2″-(nitrilo-κ*N*)triethanethiolato(3−)-κ*S*] rhenium(III) (ReC14S−FA). Yield: 78% dark green solid. Mp: 94 °C. Anal. ($C_{21}H_{39}N_2O_2ReS_4$ (666.02)): calcd C 37.78%, H 5.90%, N 4.21%, S 19.26%; found C 37.95%, H 5.74%, N 4.22%, S 19.23%. ^{1}H NMR ($CDCl_3$): 4.78 (t, ^3J = 6.5 Hz, 2H, CH_2-NC), 3.3−2.6 (bs, 12H, N(CH_2CH_2S)$_3$), 2.52 (t, ^3J = 7.1 Hz, 2H, CH_2SCH_2), 2.48 (t, ^3J = 7.5 Hz, 2H, CH_2SCH_2), 2.38 (t, ^3J = 7.3 Hz, 2H, CH_2COO), 1.83−1.69 (m, 4H, 2×CH_2), 1.69−1.50 (m, 6H, 3×CH_2), 1.42−1.24 (m, 8H, 4×CH_2). ^{13}C NMR ($CDCl_3$): 178.7 (*C*OO), 162.7 (N≡*C*), 59.4 (3C, N(*C*H_2)$_3$), 45.0 (*C*H_2NC), 44.7 (3C, Re(S*C*H_2)$_3$), 33.4 (*C*H_2COO), 33.0, 32.1, 31.6, 29.7, 29.3, 29.1, 28.9 (3C), 26.6, 23.8. IR (KBr, cm^{-1}): 2040 ν(N≡C), 1702 ν(C═O).

(5-{[11-(Isocyano-κ*C*)undecyl]thio}pentanoic acid)[2,2′,2″-(nitrilo-κ*N*)triethanethiolato(3-)-κ*S*] rhenium(III) (ReC16S−FA). Yield: 75% dark green solid. Mp: 100 °C. Anal. ($C_{23}H_{43}N_2O_2ReS_4$ (694.08)): calcd C 39.80%, H 6.24%, N 4.04%, S 18.48%; found C 39.89%, H 6.26%, N 3.86%, S 18.54%. ^{1}H NMR ($CDCl_3$): 4.78 (t, ^3J = 6.6 Hz, 2H, CH_2-NC), 3.3−2.6 (bs, 12H, N(CH_2CH_2S)$_3$), 2.52 (t, ^3J = 7.2 Hz, 2H, CH_2SCH_2), 2.49 (t, ^3J = 7.5 Hz, 2H, CH_2SCH_2), 2.38 (t, ^3J = 7.3 Hz, 2H, CH_2COO), 1.83−1.69 (m, 4H, 2×CH_2), 1.69−1.50 (m, 6H, 3×CH_2), 1.41−1.22 (m, 12H, 6×CH_2). ^{13}C NMR ($CDCl_3$): 177.6 (*C*OO), 162.4 (N≡*C*), 59.4 (3C, N(*C*H_2)$_3$), 45.0 (*C*H_2NC), 44.7 (3C, Re(S*C*H_2)$_3$), 33.2 (*C*H_2COO), 33.0, 32.1, 31.6, 29.7, 29.5 (2C), 29.4, 29.2, 29.0 (3C), 26.7, 23.8. IR (KBr, cm^{-1}): 2040 ν(N≡C), 1710 ν(C═O).

({4-[6-(Isocyano-κ*C*)hexyl]phenyl}acetic acid)[2,2′,2″-(nitrilo-κ*N*)triethanethiolato(3-)-κ*S*]rhenium(III) (ReCPh1−FA). Yield: 63% dark green solid. Mp: 114 °C. Anal. ($C_{21}H_{31}N_2O_2ReS_3$ (625.88)): calcd C 40.33%, H 4.99%, N 4.48%, S 15.37%; found C 40.41%, H 5.07%, N 4.39%, S 15.24%. ^{1}H NMR ($CDCl_3$): 7.22 (d, 2H, phenyl, J = 8.24 Hz), 7.12 (d, 2H, phenyl, J = 8.06 Hz), 4.76 (t, 2H, CH_2CN, J = 6.41 Hz), 3.55 (s, 2H, CH_2Ph), 3.3−2.6 (bs, 12H, N(CH_2CH_2S)$_3$), 2.58 (t, 2H, CH_2, J = 7.87 Hz), 1.79−1.83 (m, 4H, 2xCH_2), 1.61 (m, 4H, 2xCH_2). ^{13}C NMR ($CDCl_3$): 172.1(*C*OO), 163.4 (N≡*C*), 133.0, 129.3, 128.8, 126.4, 59.6, 45.2 (*C*H_2N), 44.9, 41.3, 33.2, 35.7, 31.5, 28.9, 26.7. IR (KBr, cm^{-1}): 2010 ν(N≡C), 1711 ν(C═O). ESI-MS (MeOH): *m*/*z* (%) = 648 (100) $[C_{21}H_{31}N_2NaO_2ReS_3]^+$.

General Procedure for Cu(I) Complex Preparation. A well-stirred mixture of the corresponding isocyanide (4 mmol) and copper(I) chloride (1 mmol) in 10 mL of MeOH was refluxed for 10 min. After stirring over a period of 1 h at ambient temperature, the resulting solution was concentrated *in vacuo*. The residue was extracted with $CHCl_3$, filtered off, and dried *in vacuo* (purification of this crude product can be done by recrystallization from Et_2O, EtOAc/hexane).

[Cu(methyl 11-isocyanoundecanoate)$_4$]Cl (4bCu). Crystallized from diethyl ether. Yield: 85%. Mp: 46 °C. ^{1}H NMR (400 MHz, $CDCl_3$): 1.24 (m, 10H, CH_2), 1.36 (m, 2H, CH_2), 1.58 (m, 2H, CH_2), 1.69 (m, 2H, CH_2), 2.26 (t, 2H, CH_2COOMe, J = 7.6 Hz), 3.46 (broad, 2H, CH_2NC), 3.63 (s, 3H, CH_3). ^{13}C NMR (100.6 MHz, $CDCl_3$): 25.1, 26.6, 28.8, 28.9, 29.3, 29.4, 29.5, 29.5, 34.3, 43.1, 51.7, 142.0, 174.5. IR (KBr): 2178.6 N≡C, 1737.0 C═O. ESI-MS (MeOH): *m*/*z* (%) = 964 (10) $[C_{52}H_{92}CuN_4O_8]^+$, 739 (100) $[C_{39}H_{69}CuN_3O_6]^+$, 514 (40) $[C_{26}H_{46}CuN_2O_4]^+$.

[Cu(methyl 12-isocyanododecanoate)$_4$]Cl (4cCu). Recrystallized from ethyl acetate overlaid with hexane. Yield: 80%. Mp: 57 °C. ^{1}H NMR ($CDCl_3$): 1.24 (m, 12H, CH_2), 1.37 (m, 2H, CH_2), 1.58 (m, 2H, CH_2), 1.70 (m, 2H, CH_2), 2.27 (t, 2H, CH_2COOMe, J = 7.5 Hz), 3.48 (broad, 2H, CH_2NC), 3.63 (s, 3H, CH_3). ^{13}C NMR ($CDCl_3$): 25.1, 26.6, 28.8, 28.9, 29.3, 29.4, 29.5, 29.6, 29.7, 34.3, 43.1, 51.7, 142.4 (broad, after 40 960 scans visible), 174.5. IR (KBr): 2199.6 ν(N≡C), 1740.1 ν(C═O). ESI-MS (MeOH): *m*/*z* (%) = 1076 (6) $[C_{60}H_{108}CuN_4O_8]^+$, 823 (100) $[C_{45}H_{81}CuN_3O_6]^+$, 570 (50) $[C_{30}H_{54}CuN_2O_4]^+$.

[Cu(methyl 15-isocyanopentadecanoate)$_4$]Cl (4dCu). Recrystallized from diethyl ether. Yield: 92%. Mp: 78 °C. Anal. ($C_{68}H_{124}ClCuN_4O_8$ (1224.73)): calcd C 66.69%, H 10.21%, N 4.57%, Cl 2.89%; found C 66.52%, H 10.09%, N 4.39%. ^{1}H NMR (400 MHz, $CDCl_3$): 1.21−1.24 (m, 18H, CH_2), 1.37 (m, 2H, CH_2), 1.58 (m, 2H, CH_2), 1.70 (m, 2H, CH_2), 2.26 (t, 2H, CH_2COOMe, J = 7.5 Hz), 3.47 (broad, 2H, CH_2NC,), 3.63 (s, 3H, CH_3). ^{13}C NMR (100.6 MHz, $CDCl_3$): 25.1, 26.6, 28.8, 28.9, 29.3, 29.4, 29.5, 29.6, 29.7, 29.8, 29.8, 29.8, 34.3, 43.1, 51.6, 141.9 (broad), 174.5. IR (KBr): 2179.1 ν(N≡C), 1737.2 ν(C═O). ESI-MS (MeOH): *m*/*z* (%) = 1188 (2) $[C_{68}H_{124}CuN_4O_8]^+$, 907 (20) $[C_{51}H_{93}CuN_3O_6]^+$, 626 (100) $[C_{34}H_{62}CuN_2O_4]^+$.

(Cu{methyl 5-[(7-isocyanheptyl)thio]pentanoate}$_4$)Cl (12c-CuCl). Yield: 90% oily product. ^{1}H NMR (400 MHz, $CDCl_3$): 1.21−1.40 (m, 6H, CH_2), 1.52−1.59 (m, 4H, CH_2), 1.67−1.72 (m, 4H, CH_2), 2.29 (t, 2H, CH_2 CH_2COOMe, J = 7.5 Hz), 2.46 (m, 4H, CH_2SCH_2), 3.50 (broad, 2H, CH_2NC), 3.62 (s, 3H, CH_3). ^{13}C NMR (100.6 MHz, $CDCl_3$): 24.3, 26.5, 28.5, 28.7, 28.8, 29.3, 29.6, 32.0, 32.3, 33.8, 43.1, 51.6, 143.6 (broad), 173.9. IR (KBr): 2196.6 ν(N≡C), 1739.2 ν(C═O). ESI-MS (MeOH): *m*/*z* (%) = 1148 (10) $[C_{56}H_{100}CuN_4O_8S_4]^+$.

General Radiolabeling Procedure. The procedure is exemplified for the ^{99m}TcC11−FA (C11): 0.5 mL of pertechnetate solution (100−500 MBq generator eluate) was added to a before prepared EDTA kit, which contains 1 mg of EDTA, 0.04 mg of stannous(II) chloride and 5 mg of mannitol. After 20 min tempering by 37 °C, a purity control by TLC (silica gel/acetone) followed. In most cases, the ^{99m}Tc(III)−EDTA complex was recovered with over 99% radiochemical purity. The EDTA complex solution was added to a mixture of 0.3 mg of 2,2,2-nitrilotris(ethanethiol) (oxalate), dissolved in 0.1 mL of water and 0.05 mg of tetra(methyl 11-isocyanoundecanoate)copper-(I) chloride in 0.2 mL of *n*-propanol, and kept for 30 min at 90 °C. Subsequently the ester function was saponified by addition of 0.1 mL of 1 N sodium hydroxide to the reaction mixture kept at 75 °C for 10 min. After neutralization with 1 N hydrochloric acid, the ^{99m}Tc−FA complex was purified by semipreparative HPLC (Hypersil RP-18, eluent methanol/0.01 M phosphate buffer, pH 7.4; gradient in 10 min from 60 → 100% methanol; flow rates 2 mL/min (semipreparative), 1 mL/min (analytical); retention time between 7 and 8 min). After the removal of methanol by vacuum evaporation 200 μL of propylene glycol was added. The radiochemical yield was 85%.

X-ray Data Collection and Processing. The X-ray data were collected at room temperature (293 K or 273 K) on a SMART-CCD diffractometer (SIEMENS), using graphite monochroma-

Table 1. Crystallographic Data for X-ray Diffraction Studies of Rhenium FA and the Copper Complexes, ReC15−FA, Re12b, and 4cCu

	ReC15−FA	Re12b	4cCu
formula	$C_{22}H_{41}N_2O_2ReS_3$	$C_{19}H_{35}N_2O_2ReS_4$	$C_{56}H_{100}ClCuN_4O_{10}$
formula weight	647.95	637.93	1088.44
crystal system	triclinic	triclinic	monoclinic
space group	$P\bar{1}$	$P\bar{1}$	$C2$
a [Å]	7.428(7)	8.395(3)	59.700(3)
b [Å]	7.450(7)	10.638(5)	5.380(6)
c [Å]	26.86(3)	14.340(6)	11.060(17)
α [deg]	84.922(18)	90.887(7)	90
β [deg]	86.814(18)	98.677(8)	90.900(10)
γ [deg]	63.600(18)	99.176(7)	90
volume [Å^3]	1326(2)	1248.8(9)	3552(7)
Z	2	2	2
T [K]	293(2)	293(2)	293(2)
ρ [g/cm^3]	1.623	1.697	1.018
absorption coeff. [mm^{-1}]	4.838	5.217	0.391
F(000)	652	636	1184
λ (Mo Kα) [Å]	0.710 73	0.710 73	0.710 73
crystal size [mm^3]	0.8 × 0.4 × 0.02	0.5 × 0.25 × 0.12	0.45 × 0.02 × 0.015
θ-range from data collection	2.28−22.00	1.44−25.00	1.84−25.00
index ranges	$-6 \le h \le 7$	$-9 \le h \le 9$	$-70 \le h \le 69$
	$-7 \le k \le 7$	$-10 \le k \le 12$	$-6 \le k \le 6$
	$-27 \le l \le 28$	$-14 \le l \le 17$	$-13 \le l \le 9$
reflections collected	5056	6347	8761
independent reflections	3221	4337	5798
goodness-of-fit on F^2	0.859	1.039	0.729
R [$I > 2\sigma(I)$]	R1 = 0.0397	R1 = 0.0559	R1 = 0.0977
	wR2 = 0.1069	wR2 = 0.1498	wR2 = 0.2319
R (all data)	R1 = 0.0449	R1 = 0.0641	R1 = 0.1692
	wR2 = 0.1104	wR2 = 0.1559	wR2 = 0.2594

tized Mo Kα radiation (λ = 0.710 73 Å). A summary of the crystallographic data of **ReC15−FA**, **Re12b**, and **4cCu** is given in Table 1. The structures were solved by direct methods. After anisotropic refinement of the non-hydrogen atoms, the hydrogen positions were calculated according to ideal geometries. Empirical absorption corrections were made. Most of the calculations were carried out in the SHELXTL system with some local modifications. Selected bond lengths and angles are reported in figure legends of the crystal structures. CCDC 287047 (**ReC15−FA**), CCDC 287049 (**Re12b**), and CCDC 287048 (**4cCu**) contain the supplementary crystallographic data for this paper. These files can be obtained free of charge via http://www.ccdc.cam.ac.uk/data_request/cif, by emailing data_request@ccdc.cam.ac.uk, or by contacting The Cambridge Crystallographic Data Centre, 12 Union Road, Cambridge CB2 1EZ, U.K.; fax: +44 1223 336033.

Determination of the Surface Activity in Aqueous Solution. *Sample Preparation.* For surface tension, **ReC12−FA** was vacuum-dried from 1 mM $CHCl_3$ solution overnight and redissolved in ethanol at 5 mM. A portion (20 μL) was added to 580 μL of distilled water, and surface tension was determined using a KIBRON μ-trough. Subsequent dilutions by a factor of 2 were made and measured in the same way. The effect of residual ethanol was found to be less than 4 mN/m.

For FTIR, phosphatidylcholine and **ReC12−FA** compound were dissolved in chloroform in a ratio of 50:1 lipid/rhenium−FA and vacuum-dried overnight. Distilled water (1 mL) was added; the mixture was homogenized and sonicated in a bath sonicater (5 min). The resulting suspension was extruded through a polycarbonate filter (0.2 μm) using an Avestin extruder. Large unilamellar vesicles obtained in this way were dried on a diamond attenuated total reflectance (ATR) cell (Resultec). Infrared spectra were obtained from this liposome film at room temperature with a VECTOR 22 FTIR spectrophotometer (BRUKER, Karlsruhe) using 2 cm^{-1} resolution (256 scans). Samples were exposed to an atmosphere of either saturated H_2O or D_2O to observe isotope-sensitive absorptions. The effect of pH was studied by adding defined amounts of unbuffered solutions of NaOH or HCl at pH 9 and pH 2, respectively, and evaporating the water.

Activation of Tc−FA Tracers by Acyl-CoA Synthetase. The activation of ^{99m}Tc-labeled fatty acids by acyl-CoA synthetase was determined in cell extracts obtained from cultured human hepatoma cell line HepG2 and in isolated rat mitochondria. The cultivation of HepG2 cells and isolation of mitochondria from rat liver homogenates were performed according to established standard protocols. ^{99m}Tc-labeled FAs, for example, $^{99m}TcNS_3$C12−FA, were added to 1 mL of reaction mixtures containing 200 mM Tris-HCL, pH 7.5, 8 mM $MgCl_2$, 2 mM EDTA, 20 mM sodium fluoride, 0.1% Triton X-100, and 0.2 mM dithiothreitol with and without 0.5 mM ATP and 0.5 mM CoA (*12*, *13*). The reactions were initiated by adding either the cell extracts or the isolated mitochondria and terminated by a mixture of 2-propanol, *n*-heptane, and 1 M H_2SO_4 (40:10:1). Separation of hydrophilic and lipophilic reaction products was performed by triplicate extraction with 2.0 mL of *n*-heptane. The radioactivity of the separated phases was measured using an activimeter for ^{99m}Tc. Furthermore, all phases were analyzed by HPLC, TLC, and ESI-MS analyses.

Isolated Heart Preparation. An isolated retrogradely perfused Langendorff rat heart preparation (*14*) was used in our study. The investigation conformed to the guidelines of the German Regulations for Animal Welfare. The protocol was approved by the local Ethical Committee for Animal Experiments. Male and female Wistar rats (n = 22, 200−250 g) purchased from Charles River (Sulzfeld, Germany) were used. Anesthesia was performed in two steps: After resting in a diethyl chamber for a short time, deep anesthesia was achieved by an intraperitoneal (ip) injection of 2−3 mL of urethane (15%). In addition, 1000 U/kg ip heparin was injected. Hearts were rapidly removed during continuous cooling (Krebs−Henseleit buffer (KHB), 4 °C) and mounted within 1 min via the aorta vertically on a perfusion cannula. Perfusion was immediately started according to the Langendorff technique (*14*) with a modified KHB containing the following (mmol/L): NaCl 116, KCl 4.6, $MgSO_4$ 1.2, KH_2PO_4 1.2, $NaHCO_3$ 25, $CaCl_2$ 2.5, glucose 11, and pyruvate 2. The buffer was equilibrated with a 95% O_2/5% CO_2 gas mixture (resulting pH 7.38) and FA-free bovine albumin (0.1%, 14.9 μmol/L) and maintained at 37 °C. The pulmonary artery was catheterized to permit

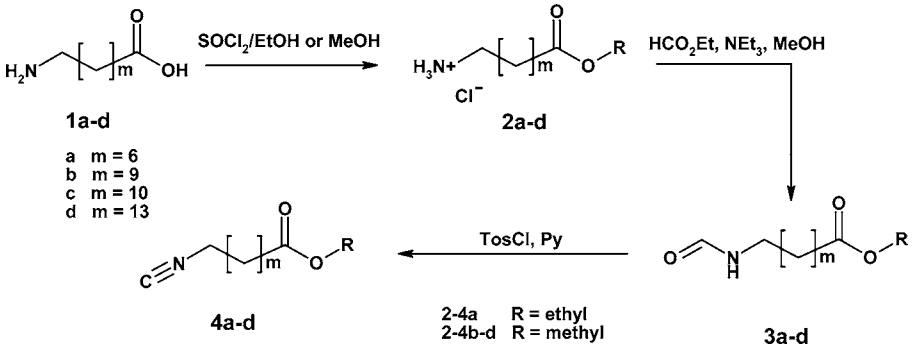


Figure 2. Synthesis of alkyl isocyano alkanoates **4a**−**d**.

anaerobic collection of the coronary venous effluent perfusate. Total coronary flow was measured using an ultrasonic transit-time flowmeter (T206, Transonic Systems Inc., Ithaca, NY) inserted in the arterial perfusion line and kept constant at 10 mL/min. Coronary perfusion pressure (CPP) was measured through a pressure transducer (Gould Statham, USA) connected to the perfusion cannula. Heart rate was calculated manually from a CPP print-out. "Arterial" and "venous" perfusate samples collected anaerobically were analyzed for pO_2, pCO_2, pH, and HCO_3^- (AVL 990S, AVL Scientific Corporation, Roswell, GA) before each intervention. At the start of interventions, the perfusion pressure and heart rate were stable at 91 ± 4 mmHg and 270 ± 6 beats/min, respectively. The influent O_2 tension was 510 mmHg. After 30 min of steady-state perfusion with 10 mL/min of normotherm KHB enriched with 0.1% albumin, isolated hearts were perfused with FA tracers for 180 s in a 1:1000 ratio. The venous effluent perfusate was collected in intervals of 15 s for 225 s following the start of tracer infusion. Perfusion was stopped, the heart was dissected into atria and ventricle compartments, and γ-activity was measured. A total of seven compounds were tested in this way.

***In Vivo* Stability of FA Tracers.** *In vivo* experiments in rats were performed to investigate the stability of FA tracers. Briefly, ^{99m}Tc-labeled FA (50 MBq) were administered intravenously into male Wistar rats (Kyoto−Wistar strain; aged 5−6 weeks; 150 ± 15 g). At 60 min postinjection (pi.), the animals were sacrificed and plasma samples and organ homogenates (liver, intestine) were obtained. Analysis was performed by radio-HPLC (Hewlett-Packard series 1050, LiChroCART RP18 reversed phase, 7 μm particle size, 250 mm × 4 mm).

Biodistribution Studies in Rats. All animal experiments were carried out with male Wistar rats (Kyoto−Wistar strain; aged 5−6 weeks; 150 ± 15 g) according to the guidelines of the German Regulations for Animal Welfare. The protocol was approved by the local Ethical Committee for Animal Experiments. Animals were kept under a 12 h light−dark cycle and fed with commercial animal diet and water *ad libitum*.

For biodistribution studies, the complexes were injected into the tail vein of the animals under light ether anesthesia. The injection volume of ^{99m}Tc−FA solution (0.5 MBq; radiochemical purity >96%) was 0.5 mL. Biodistribution was determined in groups of eight rats sacrificed 5 and 60 min pi. by heart puncture under ether anesthesia. Organs and tissues of interest were rapidly excised and weighed, and the radioactivity was determined (Cobra II gamma counter, Canberra-Packard, Meriden, CT). The accumulated radioactivity in organs and tissues was calculated as the percentage of the injected dose per organ (%ID/organ) or per gram of tissue (%ID/g tissue). Data are given as mean ± standard deviation (SD) of four animals.

Statistical Analysis. All data are presented as means ± standard deviations (SD). Statistical analyses were carried out using SPSS software for MS Windows (Release 11.0, SPSS Inc., Chicago, IL) using ANOVA and LSD *post hoc* adjustment. The error probability $p < 0.05$ was taken to indicate a statistical significance.

RESULTS AND DISCUSSION

1. Synthesis of Isocyano-Functionalized Fatty Acids and Derived "4 + 1" ^{99m}Tc/Re Complexes. The development of Tc/Re(III)-labeled FA analogues making use of the "4 + 1" mixed-ligand concept can be accomplished by the metal coordination with the tetradentate (tripodal) tris(2-mercaptoethyl)amine and one exchangeable monodentate neutral ligand; the latter should combine σ-donor and π-acceptor properties. Both the isocyanide and phosphane functionality fulfill this requirement (*9*, *15*, *16*). In this study, we have preferred sterically less demanding long-chain alkanoate substituted isocyanides to mimic FA. The instability of the free isocyano-substituted acids requires the conversion of the appropriate carboxyl group into the alkyl ester during the ligand synthesis and the complex preparation. The alkyl isocyano alkanoates **4a**−**d** were synthesized according to Figure 2.

In the first step, the ω-amino-FAs **1** were transformed into their alkyl ester hydrochloride form **2** by reaction with thionylchloride in ethanol or methanol. The appropriate ω-methoxy-ω-oxoalkane-1-aminium chlorides **2** were converted into the corresponding formamides **3** via the reaction with ethylformate in presence of triethylamine. The formation of the isocyano function follows the method described by Corey *et al.* (*17*). using tosylchloride and pyridine as dehydrating agents. The long-range couplings of the CH_2 protons to the ^{14}N (tt, $^2J_{NH}$ = 1.9 Hz, $^3J_{HH}$ = 6.8 Hz, 2H, CH_2N) in the neighborhood of the isocyano group (*18*) are characteristic ^{1}H NMR signals for alkyl isocyano compounds (for examples of ^{1}H and ^{13}C NMR spectra, see Supporting Information) and can be used as an analytical probe.

The thia-inserted FA derivatives (Figure 3) were generated in a six step procedure starting from the commercially available 5-bromovaleric acid **5** related to the preparation of the mercapto-substituted FA ligands (*7*). After nucleophilic substitution of the terminal halogenide by a mercapto unit **6**, the FA body **8** was built up by coupling to a ω-bromo-1-alkanol **7** under basic conditions. Conversion of the hydroxyl group into the bromide **9** was accomplished via an adapted version of the Appel reaction (*19*). With a further nucleophilic substitution of the bromide atom in **9** by azide, subsequent reduction to an amino function, and the analogous conversion of the amino group (formylation to **11a**−**e**, dehydration), the isocyano fatty acid ligands **12a**−**e** were accessible in good yields.

Spectroscopic data (IR, ^{1}H NMR, ^{13}C NMR), as well as element analyses, confirm the expected structures.

Isocyano-Substituted FA Containing a Phenylene Blocking Group. The insertion of a phenylene group into the FA chain appears as an experimentally easily accessible and alternative route for the induction of metabolic interferences in analogy to the already described iodine-labeled derivative ^{123}I-PHIPA (*20*).

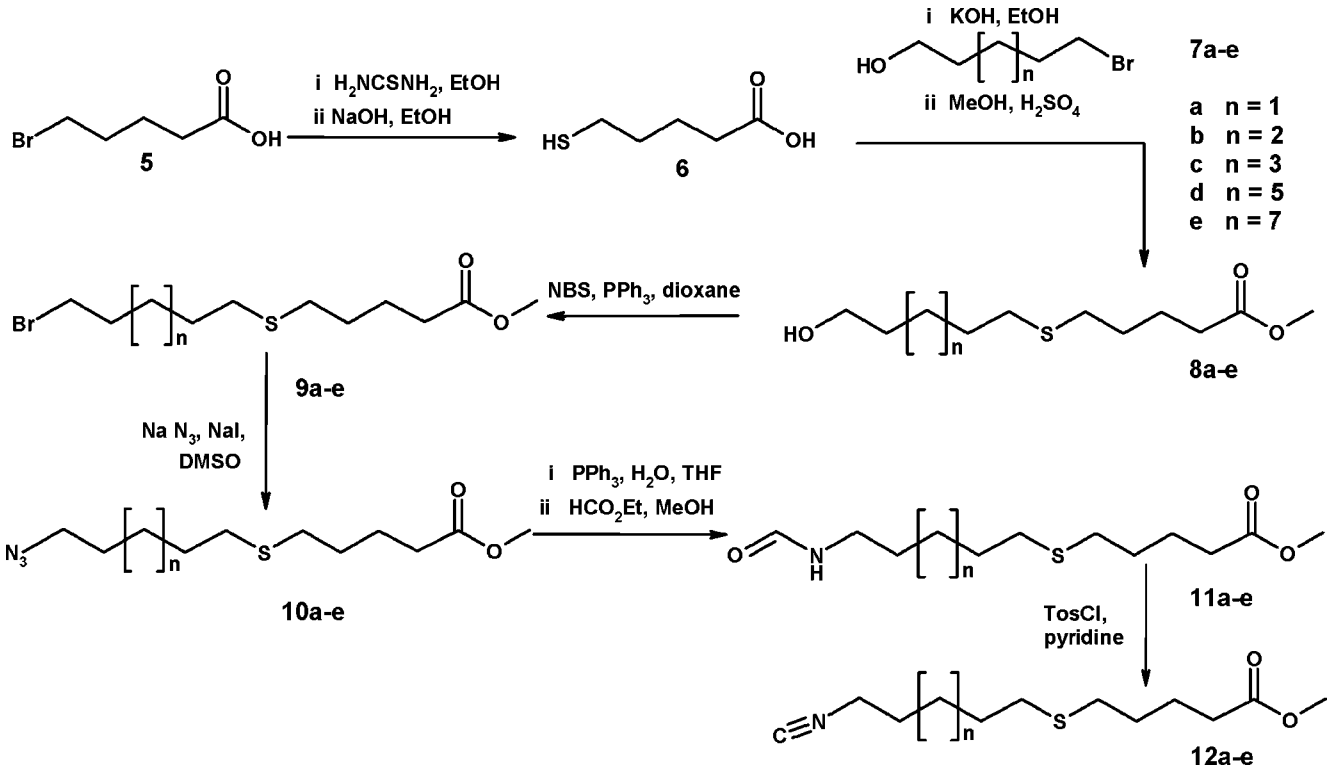


Figure 3. Synthesis of the sulfur-containing isocyano FA ligands **12a**−**e**.

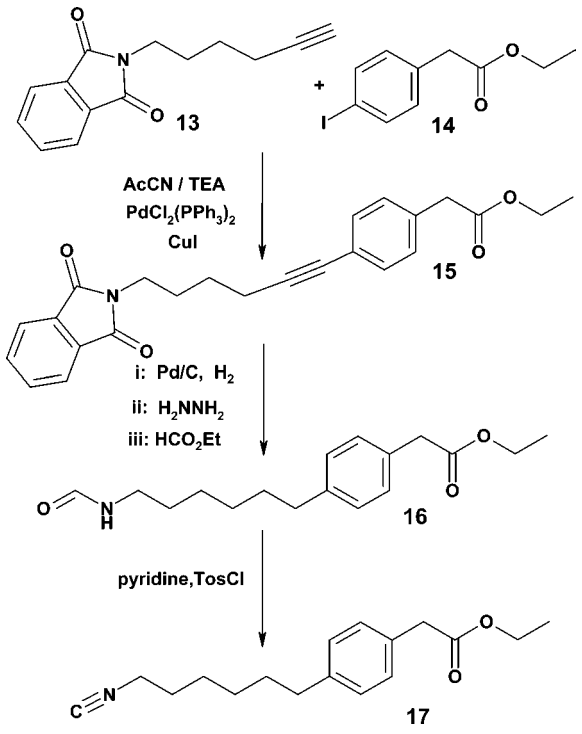


Figure 4. Example of a phenylene-bridged ω-isocyano FA **17**.

Thus, we developed a synthesis of ω-isocyano phenylene-inserted FA. The new phenylene-inserted FA **17** (Figure 4) was prepared starting from the commercially available end-standing alkine 6-phthalimido-1-hexine **13** and *p*-iodophenylethylacetate **14** by Sonogashira coupling (*21*) to the phenyl-substituted alkyne **15**. The catalytic reduction of the triple bond and the liberation of the amine unit with hydrazine hydrate resulted in the saturated amino FA ester. According to the analogous conversion of the amino group (formylation to **16**, dehydration as in former experiments), the isocyanide **17** was accessible in suitable yield. Spectroscopic data (^{1}H NMR, ^{13}C NMR, MS) were collected and confirm the expected structure.

Isocyano FA Ester Copper(I) Complexes. Additional advantages for handling and storage of isocyano FA ligands have been achieved by their conversion into the corresponding copper(I) complexes (*22*). Isocyanido copper(I) complexes are described as alternative sources of isocyanides, especially as precursors for the commonly used ^{99m}Tc routine radiopharmaceuticals ^{99m}Tc(I) SESTAMIBI (*23*).

The desired complexes are easily accessible by mixing the isocyanide solution with a copper(I) chloride solution in methanol in the appropriate 4:1 ratio (Figure 5).

The crystal structure in Figure 6 reveals the expected tetrahedral geometry of the copper(I) complex despite the long chain FA ester substituents on the isocyano ligands. The C−N distances of around 116 pm in the coordinating isocyano groups (exemplary N(2)−C(15) 115.9(5) pm) are characteristic for the bond order of three and appear unchanged compared with free isocyanides (*22*).

The ^{13}C NMR signals of the four chemically equivalent isocyano carbon atoms of the copper(I) complexes are positioned around 142 ppm but are difficult to locate because of their broad line width, $h_{1/2}$, of up to 50 Hz (see Supporting Information Figure 2). The reason for this strong broadening of the resonance signals should be the presence of the $^{63/65}$Cu-quadrupole nuclei as has been described for Cu(I)-phosphane complexes (*24*).

"4 + 1" Re and ^{99m}Tc Complexes. The "4 + 1" rhenium(III) phosphane complex **RePMe$_2$Ph** serving as precursor in the manner described (*11*) reacts in dichloromethane with the appropriate alkyl isocyanoalkanoate **4**, **12**, or **17** to the ester compound, which leads to the desired model complex of the free FA after saponification (Figure 7, additional analytical data of isolated ester compounds **Re4b**−**d** and **Re12a**−**e** were given in Supporting Information). These nonradioactive rhenium

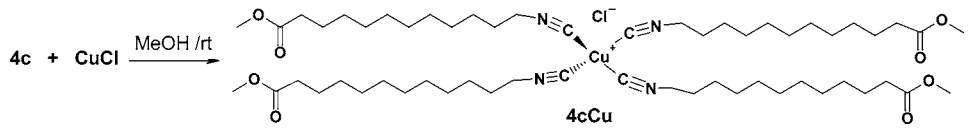


Figure 5. Preparation of the isocyano FA ester copper(I) complex **4cCu**.

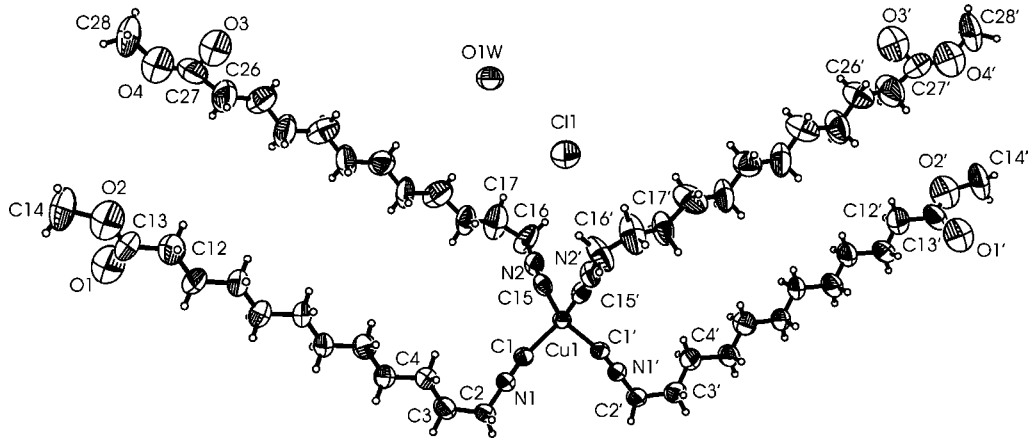


Figure 6. Molecular structure of the FA copper(I) complex **4cCu.** Selected bond lengths [pm] and angels [deg]: Cu−C(15) 198.0(5), N(2)−C(15) 115.9(5), C(15)−N(2)−C(16) 175.1(5).

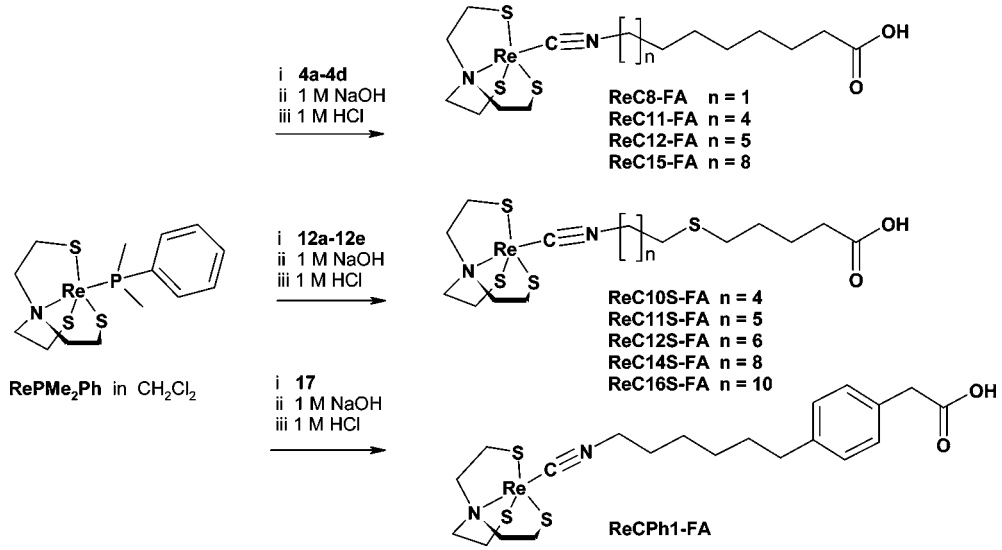


Figure 7. Synthesis of the rhenium FA model complexes.

complexes were used as reference compounds for the chemical characterization and identification of the corresponding ^{99m}Tc complexes especially by comparison of the retention times on HPLC.

The different chemical properties of the (acid-) labile free isocyanides, of the rhenium complexes with high stability in a large pH range, and of the quite stable copper(I) complexes correlate with different spectroscopic behaviors. Both types of isocyano complexes show opposite changes of the chemical shifts of the isocyano carbon atom, depending on the metal type. In comparison to the free isocyanide **4d** (155.7 ppm), the rhenium complex **ReC15−FA** shows a noticeable low field shift to 162.5 ppm compared with the high field shift to 142.2 ppm in the copper(I) complex **4dCu** (for selected extracts of ^{13}C NMR spectra see Supporting Information). The same general tendency is seen in the absorption bands of the different isocyano groups in the appropriate IR spectra of **4d** (2148 cm^{-1}), **ReC15−FA** (2038 cm^{-1}), and **4dCu** (2179 cm^{-1}). These results indicate a slightly reduced CN bond order in the Re complexes: the isocyano carbon tends to sp^2-character caused by back-donation. This contrasts the sp character of the carbon atom in the CN triple bond of the isocyano copper(I) complexes, where back-donation in Cu(I)- or Ag(I)-isocyano complexes plays a minor role (*25*). This explanation was supplemented and confirmed further by the crystal structure data of **4cCu** and **ReC15−FA**.

Structural Characterization of the Re Model Complexes. Figures 8 and 9 show examples for the ester complex **Re12b**, as well as the FA complex **ReC15−FA**. A summary of the crystallographic data is given in Table 1, and selected bond lengths and angles are reported in the figure legends. Both complexes crystallize in the triclinic space group $P\bar{1}$, and crystals contain no solvents or other interactions. The two complexes adopt a trigonal-bipyramidal geometry where the three NS_3 thiolate sulfurs form the trigonal plane and the amine nitrogen of the tetradentate ligand and the isocyano carbon occupy the apical positions. The N2−C7 bond lengths of 119.3(16) pm and 118.9(13) for the isocyano ligands in **Re12b** and **ReC15−FA**, respectively, show the expected prolongation compared with the isocyano FA copper(I) complex.

The molecular structure of **ReC15−FA** obtained by X-ray structure analysis is presented in Figure 9. The carbon chain of

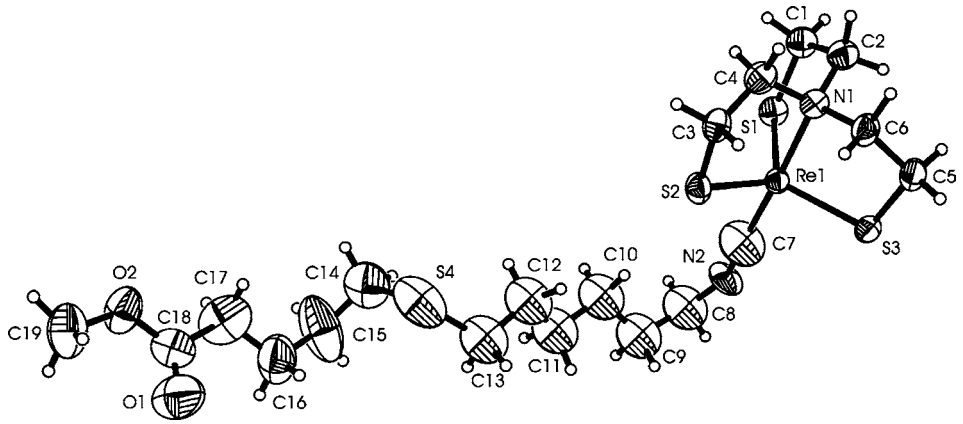


Figure 8. ReC11S−FA-methyl ester (**Re12b**). Selected bond lengths [pm] and angels [deg]: Re−C(7) 195.1(12), N(2)−C(7) 119.3(16), Re−N(1) 220.1(8), C(7)−Re−N(1) 178.5(4), N(2)−C(7)−Re 177.9(12).

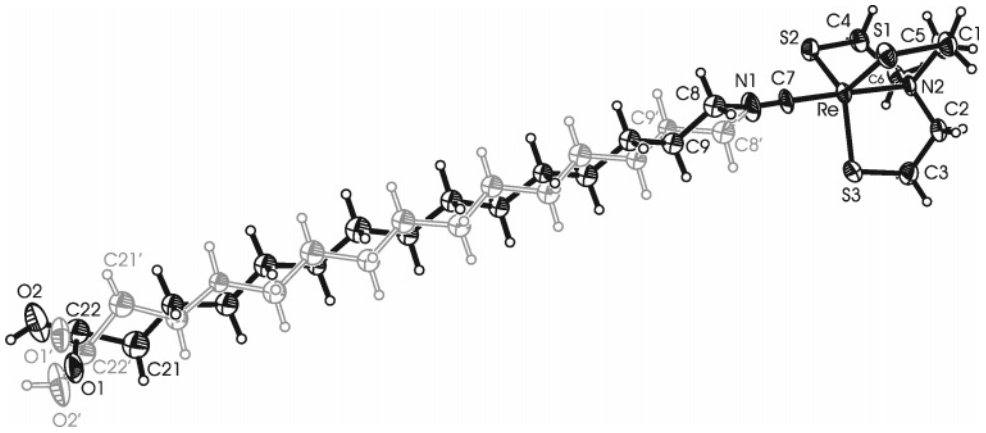


Figure 9. The molecular structure of the **ReC15−FA** model complex. Selected bond lengths [pm] and angels [deg]: Re−N(2) 217.8(8), Re−C(7) 190.7(10), N(1)−C(7) 118.9(13), C(7)−Re−N(2) 177.3(4), N(1)−C(7)−Re 176.8(10).

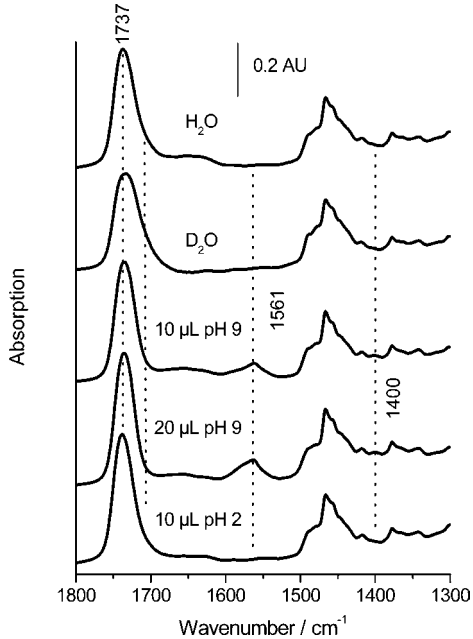


Figure 10. FTIR spectra of **ReC12−FA**-reconstituted liposomes: (a) dried from H_2O; (b) dried from D_2O; (c) dried after addition of 10 μL of NaOH (10 μM); (d) dried after addition of 20 μL of NaOH (10 μM); (e) same sample as in panel d after addition of 10 μL of HCl (10 mM).

the complex **ReC15−FA** is positionally disordered over two positions. Dimers are formed in the crystal structure and are stabilized by H-bonds (O2−O1 = 265.8 pm; O2′−O1′ = 261.5 pm).

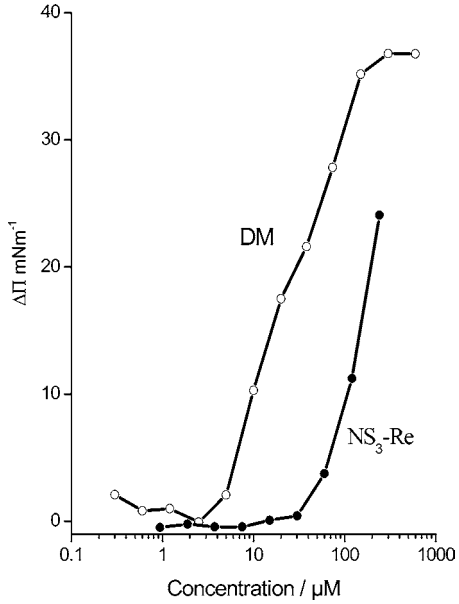


Figure 11. Concentration dependence of surface tension at the air−water interface. DM = dodecyl-β-D-maltoside; NS_3−Re = **ReC12−FA**.

Physicochemical Characterization: Determination of the Surface Activity in Aqueous Solution. Transport and membrane passage of lipophilic Tc/Re−FAs are influenced to a high extent by hydrophobicity/hydrophilicity relations at the lipid−water interface. Therefore, their amphipathic nature was assessed by surface tension measurements, which revealed the surface activity of this kind of compound as exemplified for the rhenium

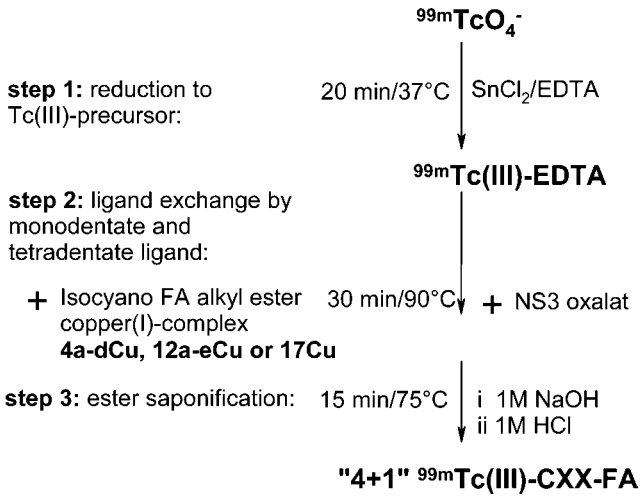


Figure 12. "4 + 1" ^{99m}Tc−FA preparations on nca level.

model complex **ReC12−FA.** The surface tension of water is decreased by 20−25 mN/m at 200 μM concentration of **ReC12−FA**. For comparison, a comparable change of the surface tension is observed with the detergent *n*-dodecyl β-D-maltoside at 20 μM. The amphipathic nature of **ReC12−FA** suggests that, when incorporated into liposomes, the transmembrane positioning will match hydrophobicity/hydrophilicity at the lipid−water interface. Accordingly, the free carboxylic acid is likely to be exposed to the aqueous phase near the lipid head groups, whereas the rhenium chelate is more likely to be buried within the lipid acyl chains. To address this question, the aqueous accessibility and titratability of the carboxyl group was determined by FTIR spectroscopy (Figures 10 and 11). FTIR spectra of **ReC12−FA**-reconstituted liposomes exhibit a strong ester carbonyl vibration at 1737 cm^{-1}. Upon H/D exchange, the center of the peak shifts to 1733 cm^{-1} and the low-frequency part of the band broadens. These spectral alterations indicate the additional presence of non-ester carbonyls from protonated/deuterated carboxylic acids in which the C═O stretching mode is coupled to OH bending. The coupling is abolished in D_2O, leading to the down shift of the C═O stretching frequency in the liposomes when dried from a D_2O atmosphere. To further prove the presence of a carboxylic acid group and to determine its solvent accessibility, we have recorded IR spectra at different pH. Addition of small amounts of 10 μM NaOH (pH 9) followed by evaporation of water to ambient humidity induces spectral changes consistent with deprotonation of a carboxylic acid group. The strong 1737 cm^{-1} band becomes narrower at the low-frequency side with increasing addition of base. Simultaneously, a band at 1560 cm^{-1}, not present in the original liposome spectra, appears and increases with addition of base. These spectral changes evidence the deprotonation of a carboxylic acid, causing the disappearance of its C═O stretching mode around 1730 cm^{-1} (i.e., at a position also deduced from H/D exchange) and a concomitant appearance of the antisymmetric COO^- mode at 1561 cm^{-1} during the transition from a COOH to a COO^- group. Consistent with this interpretation, also the weaker absorption increase of the symmetric COO^- mode upon addition of base can be identified at 1400 cm^{-1}, although on a broad background. As expected for a titration-dependent signal, the spectral changes are completely reversed by acidification (addition of small amounts of 10 mM HCl, pH 2), which also re-establishes the band broadening in the 1700−1730 cm^{-1} range, where the C═O stretch of protonated carboxyl groups overlaps with the ester carbonyl absorption. The only carboxylic group present in the sample is that of **ReC12−FA**. Since the FTIR data evidence its titration, it must be exposed to the liposome surface. This indicates that the rhenium-carrying moiety is buried in the hydrophobic core of the lipid bilayer, whereas the polar carboxylic acid group is positioned close to the polar lipid head groups, where it can exchange protons (deuterons) with the environment.

Preparation of No-Carrier-Added (nca) ^{99m}Tc−FA. The nca preparation of the "4 + 1" ^{99m}Tc−FA was carried out in a three-step procedure and based on the use of ^{99m}Tc(III)−EDTA complexes as precursors, which react with the NS3-ligand (as oxalate) and the copper(I) complex of the isocyano fatty acid ester at 90 °C (Figure 12). After saponification of the ester function the radiochemical yields range from 50% to 80% depending on the FA chain length. Purification is carried out by HPLC and can be controlled by radio-TLC. Under the above-mentioned conditions, the radiochemical yields in case of the **C11** derivative were about 80%. Figure 13 illustrates the TLC characterization of selected ^{99m}Tc−FA.

2. In vitro studies. *Metabolism of Tc−FA: Activation by Acyl-CoA Synthetase.* The activation of Tc−FA by acyl-CoA synthetase was investigated for selected Tc−FA to ascertain their potential acceptability as metabolism tracers. Figure 14 shows radio-HPLC chromatograms of **C12** tracer in enzyme reaction mixture containing ATP and CoA in both the aqueous phase (B) and the heptane phase (C).

The data indicate that the Tc−FA (chromatogram A) was activated by acyl-CoA synthetase in cell extracts. The aqueous phase (chromatogram B) contained one major hydrophilic metabolite, suspected to be the corresponding FA−acyl-CoA.

These data show the formation of a FA−acyl-CoA conjugate and confirm in part our results from experiments using the

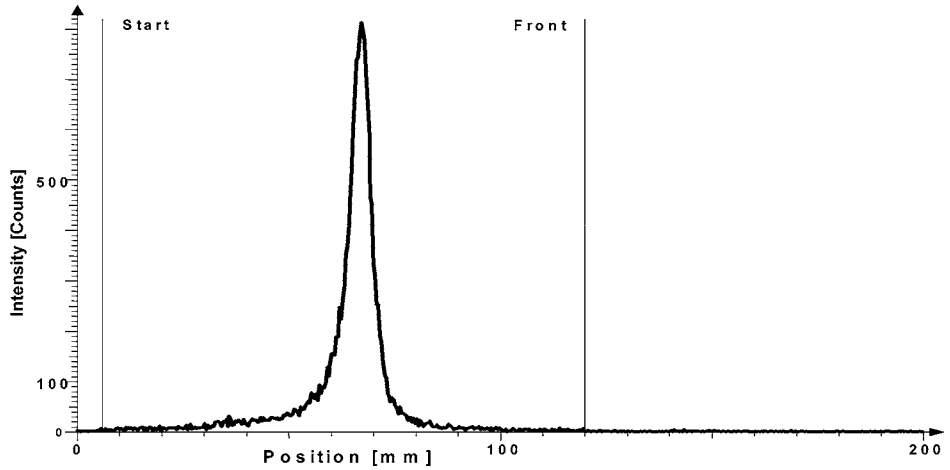
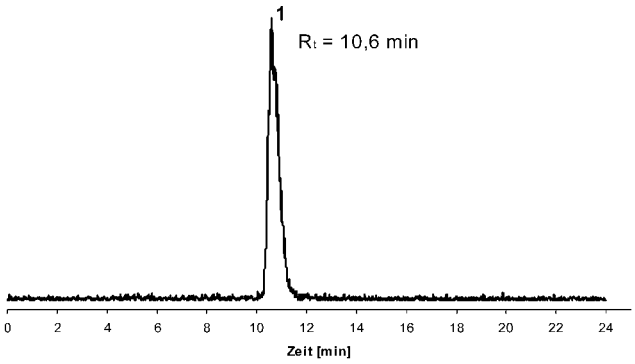
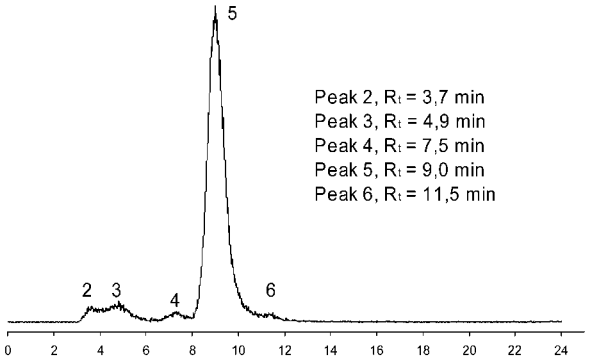


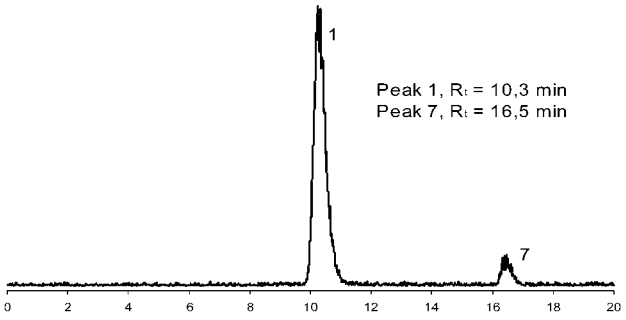
Figure 13. Radio-TLC characterization of ^{99m}TcC11−FA (**C11**), CH_3CN/H_2O + 0.1% TFA, 8/2, RP 18 R_f value = 0.65.



A) Radioactivity chromatogram (RC) of original ^{99m}TcNS$_3$C12-FA



B) RC of the aqueous phase of enzyme reaction mixture containing both ATP and CoA



C) RC of the heptane phase of enzyme reaction mixture containing both ATP and CoA

Figure 14. Representative radio-HPLC analysis of the activation of TcNS$_3$C12−FA (**C12**) by acyl CoA-synthetase in HepG2 cell extracts.

^{99m}TcNS$_3$C12−FA (**C12**). Similar results have been obtained with rat liver mitochondria.

To confirm the identity of the suspected product, ESI-MS analyses were carried out with the corresponding nonradioactive **ReC12−FA**. For ESI-MS analysis, the **ReC12−FA** was applied to the enzyme reaction mixture (see Supporting Information Figure 3). Figure 3a of Supporting Information shows the spectrum of the original **ReC12−FA** before and Figure 3b that after application to HepG2 cell extracts. This spectrum reveals unequivocally the presence of the **ReC12−FA**−acyl-CoA conjugate.

Metabolism of Tc−FA: Degradation of Fatty Acid Moiety from C12 to C2. The ^{99m}TcC12−FA (**C12**) was injected into Wistar rats, and samples were taken from plasma and intestine (homogenated) 60 min pi. Figure 15 shows the radio-HPLC chromatograms of the respective samples. As seen in Figure 15, the Tc−FA was completely metabolized *in vivo* to form one major metabolite. We hypothesize that this metabolite is the **C2−FA** (^{99m}TcNS$_3$−tripod−CN−CH$_2$−COOH), which has been designated **Tc4** in previous studies on its synthesis, stability, and biodistribution studies (*10*). The reported stability of the isocyano ester complex **Tc4** in rat plasma and the biodistribution study are obviously equivalent to investigations of the free **C2** fatty acid generated by the well-known very fast ester cleavage in rat plasma (*27*). This assumption is supported by HPLC analysis showing coelution of the corresponding rhenium **ReC2−FA** (*9*) at the same retention time as the radioactive metabolite.

The metabolic *in vivo* studies reveal the complete β-oxidation within 1 h. This is consistent with observations made with Tc-tripod-derived tracers, showing that the chelate remains unattacked in metabolic studies. However, liver activity is mainly responsible for metabolism, and the contribution of the heart has to be proven.

Extraction Studies on Perfused Rat Heart. Experiments on isolated perfused rat hearts provide a simple and well reproducible approach to detect promising ^{99m}Tc compounds in biodistribution experiments. Although many compounds have been

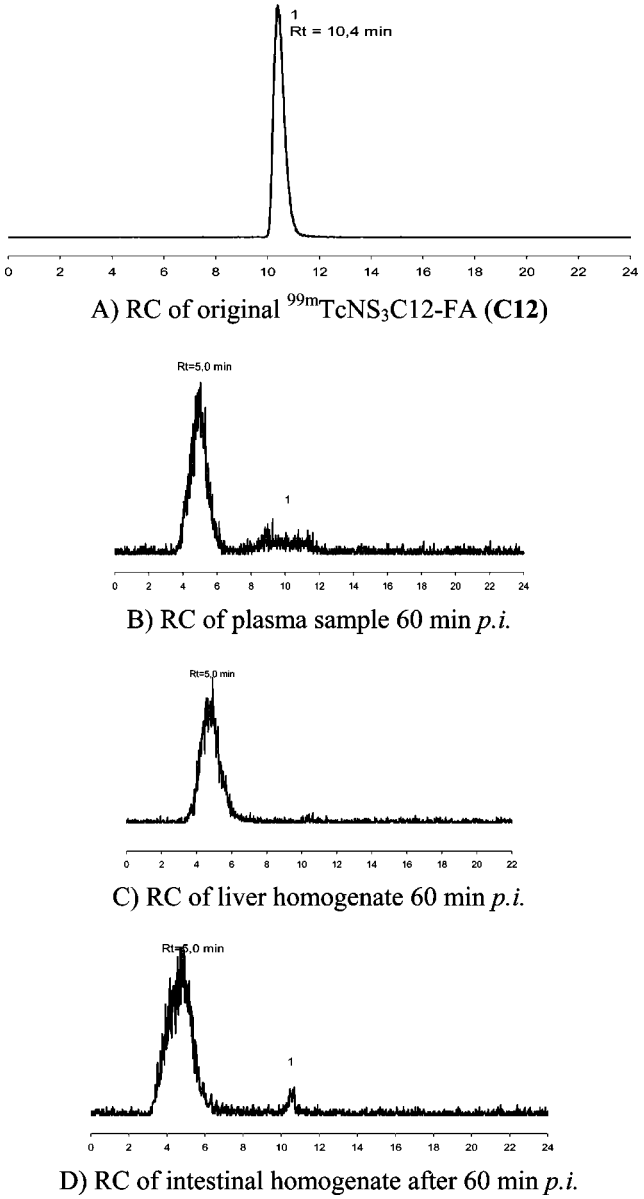


Figure 15. Representative radio-HPLC analysis of plasma samples and organ homogenates 60 min after *iv* administration of ^{99m}TcC12−FA (**C12**) in male Wistar rats.

synthesized, the ideal structure of a Tc−FA compound with high ventricular extraction (and a designated lower liver uptake) is not entirely clear. It is known, however, that the ventricular extraction primarily depends on the type of FA, the chain length, and the lipophilicity.

In the isolated beating heart model, the investigated compounds showed slightly different results compared with the biodistribution studies. Here, the highest ventricular extraction was obtained with the **C11** compound (26.65% ± 3.71%, n = 12), followed by the **C12** (24.42% ± 4.92%, n = 5) and **C11S** (23.38% ± 4.86%, n = 5) FA complexes. These extraction rates were much higher than those achieved with the established iodinated FA **^{123}IPPA** (15.51% ± 1.10%, n = 5). Shortening of the fatty acid chain length down to **C8** or lengthening it up to **C15** resulted in significantly lower extraction rates (5.96% ± 0.72% and 3.21% ± 1.10%, respectively, n = 4 for each compound; Figure 16). The synthesized phenylene inserted **CPh1** FA showed a poor myocardial extraction of only 3.83% ± 0.33% (n = 2).

Biodistribution Studies. Figure 17a,b summarizes the distribution of ^{99m}Tc radioactivity (decay-corrected) in male Wistar rats

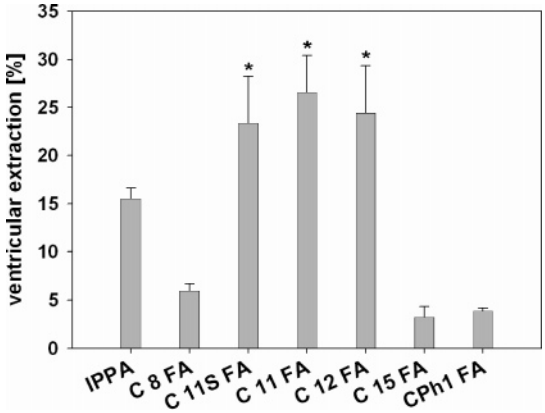


Figure 16. Ventricular extraction (in % of infused activity) of selected ^{99m}Tc-labeled FA compared with **^{123}IPPA** (mean ± SD, ∗ denotes p < 0.05 ANOVA *post hoc* LSD vs all other substances).

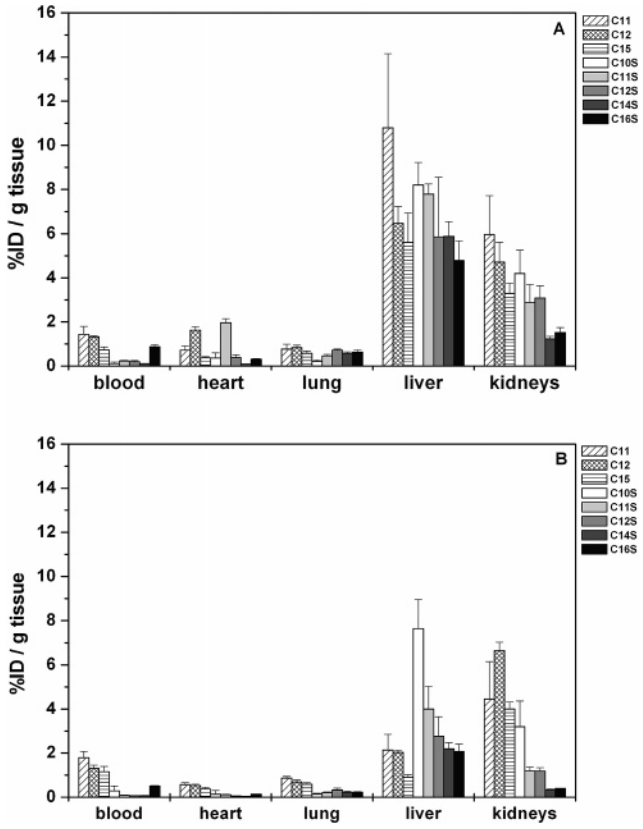


Figure 17. Biodistribution of ^{99m}Tc radioactivity concentration (%ID/g tissue) in male Wistar rats (n = 4) at 5 min (A) and 60 min (B) after intravenous injection of ^{99m}Tc-labeled FA.

after a single intravenous injection of various ^{99m}Tc-labeled FA. Data were obtained at 5 and 60 min pi.

A very rapid disappearance of ^{99m}Tc radioactivity concentration from the blood circulation was observed for all compounds. **C11S** showed the highest uptake with 2% ID/g tissue in the rat heart followed by **C12** and **C11** with 1.6% and 0.7% ID/g tissue.

Only **C11S** and **C12** showed a heart/blood ratio greater than one up to 5 min pi. (Figure 18). Remarkably, the heart/blood ratio of **C11S** was 8.6 ± 0.1 at 5 min and still 1.3 ± 0.1 at 60 min.

In principle, these *in vivo* findings show some parallels to the data obtained by *in vitro* investigation using the perfused rat heart model. "4 + 1"-Tc−FA with chain lengths close to C12 exhibits the highest heart uptake. However, in contrast to the 2-fold ventricular *in vitro* uptake, the heart extraction rate at 5 min pi. reached maximally 30−40% of the described *in*

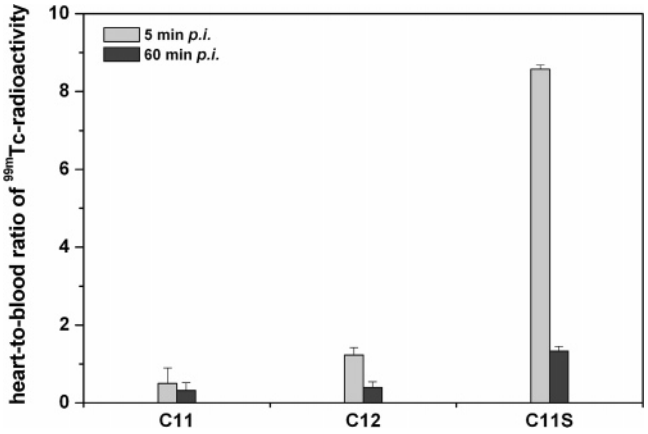


Figure 18. Heart : blood ratio of ^{99m}Tc-radioactivity in male Wistar rats ($n = 4$) at 5 and 60 min after intravenous injection of ^{99m}Tc-labeled FA **C11**, **C12**, and **C11S**.

vivo values from different iodophenyl−FA (*26*). This effect is caused by the concurrent high liver affinity accompanied by slow liver clearance. The direct comparison with recent results of other Tc−FA investigations (*4*, *5*) is not possible because of the use of different species (mice versus rats) in the biodistribution studies.

Liver and kidneys are mainly responsible for fast removal of ^{99m}Tc radioactivity from the circulation. At 5 min after injection, approximately 50% of the injected dose is liver-associated. A substantial fraction is cleared by the kidneys and approximately 6% of the injected dose is kidney-associated at 5 min pi. Overall, fast systemic clearance of ^{99m}Tc radioactivity after injection of ^{99m}Tc-labeled FA in the rat is explained by the rapid hepatobiliary and renal elimination of ^{99m}Tc radioactivity.

On the other hand, the low mean accumulation of ^{99m}Tc radioactivity in the thyroid gland (<0.07% ID at 5 min; <0.07% ID at 60 min) and the stomach (<1.7% ID at 5 min; <3.9% ID at 60 min), which both express the sodium iodide transporter is indicative of a very low abundance of pertechnetate *in vivo*.

CONCLUSION

Ten ^{99m}Tc-labeled FAs and their corresponding nonradioactive rhenium model complexes have been prepared according to the "4 + 1" mixed-ligand approach, where the metal is coordinated by both a tetradentate NS_3 chelator and a monodentate isocyano FA coligand. The FA bodies varied in their chain length and by sulfur or phenylene insertion in order to introduce two different sites of potential metabolic interference. The Re complexes have been fully characterized by spectroscopic methods, and in the case of both the Re−C11S−FA methyl ester (**Re12b**) and the **ReC15−FA**, the structure was confirmed additionally by X-ray crystallography. Furthermore, the surface activity in aqueous solution was determined for the **ReC12−FA** exemplarily and compared with the known detergent *n*-dodecyl β-D-maltoside. An important fact in the labeling procedure with technetium-99m is the conversion of the isocyano ligands **4**, **12**, and **17** into their copper(I) complexes **4Cu**, **12Cu**, and **17Cu.** This allows improvements of both handling of the ligands and, as a consequence, of the nca ^{99m}Tc−FA preparation. Experiments on isolated perfused rat hearts showed very high ventricular extraction rates of the FA complexes, in the order **C11** compound (26.65% ± 3.71%, $n = 12$), **C12** (24.42% ± 4.92%, $n = 5$), and **C11S** (23.38% ± 4.86%, $n = 5$). These extraction rates exceed considerably those achieved with the established iodinated FA **^{123}IPPA** (15.51% ± 1.10%). Biodistribution studies in Wistar rats reveal a heart uptake of 2% ID/g 5 min pi. and heart/blood ratio of 8.6 ± 0.1 at 5 min pi. for **C11S**. In this respect, the tracer **C11S** is superior to other described Tc−FA mimics in biodistribution studies. The heart/liver ratio of 0.25 ± 0.1 at 5 min pi. has to be improved, which may be achieved by alterations of the FA binding mode to the "4 + 1" chelate unit and variations of the chelate position in the FA chain. Corresponding studies and investigations aiming at the activation of other FA tracers, as well as the identification of metabolites *in vitro* and *in vivo*, are currently underway.

ACKNOWLEDGMENT

This study was supported by an intramural grant (MedDrive program 2003) funded by the Medical Faculty Carl Gustav Carus, by the DFG (Deutsche Forschungsgemeinschaft) Grant SP 401, and by Nihon Medi-Physics Co., Inc. 9-8 Rokutanjicho, Nishinomiya-shi, Hyogo, 662-0918, Japan. The authors are grateful to Regina Herrlich, Mareike Barth, and Sandra Tuchscheerer-Hoffmeister for their expert technical assistance.

Supporting Information Available: ^{1}H NMR spectra of **4b**, ^{13}C NMR of **4d**, **Re4d**, and **4dCu**, analytical data for **Re4b−Re4d** and **Re12a−Re12e**, and ESI-MS spectrum showing the **ReC12−FA**−acyl-CoA conjugate. This material is available free of charge via the Internet at http://pubs.acs.org.

LITERATURE CITED

(1) Evans, J. R., Gunton, R. W., Baker, R. G., Beanlands, D. S., and Spears, J. C. (1965) Use of radioiodinated fatty acids for photoscans of the heart. *Circ. Res. 16*, 1−10.

(2) Knapp, F. F., Jr., and Kropp, J. (1995) Iodine-123-labelled fatty acids for myocardial single-photon emission tomography: current status and future perspectives. *Eur. J. Nucl. Med. 22* (4), 361−381.

(3) Mach, R. H., Kung, H. F., Jungwiwattanaporn, P., and Guo, Y.-Z. (1991) Synthesis and biodistribution of a new class of Tc-99m-labeled fatty acid analogues for myocardial imaging. *Nucl. Med. Biol. 18*, 215−226.

(4) Magata, Y., Kawaguchi, T., Ukon, M., Yamamura, N., Uehara, T., Ogawa, K., Arano, Y., Temma, T., Mukai, T., Tadamura, E., and Saji, H. (2004) A Tc-99m-labeled long chain fatty acid derivative for myocardial imaging. *Bioconjugate Chem. 15* (2), 389−393.

(5) Chu, T., Zhang, Y., Liu, X., Wang, Y., Hu, S., and Wang, X. (2004) Synthesis and biodistribution of ^{99m}Tc-carbonyltechnetiumlabeled fatty acids. *Appl. Radiat. Isot. 60* (6), 845−850.

(6) Lee, B. C., Choe, Y. S., Chi, D. Y., Paik, J.-I., Lee, K.-H., Choi, Y., and Kim, B.-T. (2004) 8-Cyclopentadienyltricarbonyl ^{99m}Tc 8-Oxooctanoic Acid: A Novel Radiotracer for Evaluation of Medium Chain Fatty Acid Metabolism in the Liver. *Bioconjugate Chem. 15*, 121−127.

(7) Jung, C. M., Kraus, W., Leibnitz, P., Pietzsch, H.-J., Kropp, J., and Spies, H. (2002) Syntheses and First Crystal Structures of Rhenium Complexes Derived from ω - Functionalized Fatty Acids as Model Compounds of Technetium Tracers for Myocardial Metabolism Imaging. *Eur. J. Inorg. Chem*., 1219−1225.

(8) Heintz, A., Jung, C. M., Stehr, S., Mirtschink, P., Walther, M., Pietzsch, J., Bergmann, R., Pietzsch, H.-J., Spies, H., Wunderlich, G., Kropp, J., and Deussen, A. (2006) Myocardial uptake and biodistribution of technetium labeled fatty acid analogues. *Nucl. Med. Comm.*, accepted.

(9) Spies, H., Glaser, M., Pietzsch, H.-J., Hahn, F. E., Kintzel, O., and Lügger, T. (1994) Trigonal-Bipyramidal Technetium and Rhenium Complexes with Tetradentate NS_3 Tripod. *Angew. Chem. 106*, 1416−1419; *Angew. Chem., Int. Ed. Engl. 33*, 1354−1356.

(10) Pietzsch, H.-J., Gupta, A., Syhre, R., Leibnitz, P., and Spies, H. (2001) Mixed-ligand technetium(III) complexes with tetradentate/monodentate NS3/isocyanide coordination: A new nonpolar technetium chelate system for the design of neutral and lipophilic complexes stable in vivo. *Bioconjugate Chem. 12*, 583−544.

(11) Spies, H., Glaser, M., Pietzsch, H.-J., Hahn, F. E., and Lügger, T. (1995) Synthesis and reactions of trigonal-bipyramidal rhenium and technetium complexes with a tripodal, tetradentate NS3 ligand. *Inorg. Chim. Acta 240*, 465−478.

(12) Black, P. N., Concetta, C., DiRusso, C. C., Sherin, D., MacColl, R., Knudsen, J., and Weimar, J. D. (2000) Affinity Labeling Fatty Acyl-CoA Synthetase with 9-p-Azidophenoxy Nonanoic Acid and the Identification of the Fatty Acid-binding Site. *J. Biol. Chem. 275*, 38547−38553.

(13) Watkins, P. A., Lu, J. F., Steinberg, S. J., Gould, S. J., Smith, K. D., and Braiterman, L. T. (1998) Disruption of the *Saccharomyces cerevisiae FAT1* Gene Decreases Very Long-chain Fatty Acyl-CoA Synthetase Activity and Elevates Intracellular Very Long-chain Fatty Acid Concentrations. *J. Biol. Chem. 273*, 18210−18219.

(14) Langendorff, O. (1895) Investigations on alive mammalian heart. *Pflügers Arch. 61*, 291−332.

(15) Seifert, S., Künstler, J.-U., Schiller, E., Pietzsch, H.-J., Pawelke, B., Bergmann, R., and Spies, H. (2004) Novel Procedures for Preparing ^{99m}Tc(III) Complexes with Tetradentate/Monodentate Coordination of Varying Lipophilicity and Adaptation to ^{188}Re Analogues. *Bioconjugate Chem. 15*, 856−863.

(16) Schiller, E., Seifert, S., Tisato, F., Refosco, F., Kraus, W., Spies, H., and Pietzsch, H.-J. (2005) Mixed-Ligand Rhenium-188 Complexes with Tetradentate/ Monodentate NS3/P ('4 + 1') Coordination: Relation of Structure with Antioxidation Stability. *Bioconjugate Chem. 16*, 634−643.

(17) Hertler, W. R., and Corey, E. J. (1958) A Novel Preparation of Isonitriles. *J. Org. Chem. 23*, 1221−1222.

(18) Kuntz, I. D., Jr., Schleyer, P.v.R., and Allerhand, A. (1961) Long-Range N14−H1. Nuclear-Resonance Coupling in Isonitriles. *J. Chem. Phys. 35*, 1533−1534.

(19) Appel, R. (1975) Tertiary Phosphane/Tetrachloromethane, a Versatile Reagent for Chlorination, Dehydration, and P−N Linkage. *Angew. Chem. 87*, 863−874; *Angew. Chem., Int. Ed. Engl. 14*, 801−811.

(20) (a) Eisenhut, M., and Liefhold, J. (1988) Radioiodinated p-Phenylene Bridged Fatty Acids as New Myocardial Imaging Agents: Syntheses and Biodistribution in Rats, *Appl. Radiat. Isot. 39*, 639−649. (b) Eisenhut, M., Lehmann, W. D., Hull, W. E., Just, W. W., Hoffend, J., Zehelein, J., and Zimmermann, R. (1997) Trapping and Metabolism of Radioiodinated PHIPA 3−10. in the Rat Myocardium, *J. Nucl. Med. 38*, 1864−1869. (c) Zehelein, J., Zimmermann, R., Bubeck, B., Eisenhut, M., Kübler, W., and Georgi, P. (1994) SPECT I-123 PHIPA Imaging in Patients with Chronic Artery Disease: A Comparative Study with Thallium-201. *Eur. J. Nucl. Med. 21* (347), 811.

(21) Nagarajan, S. R., Devadas, B., Zupec, M. E., Freeman, S. K., Brown, D. L., Lu, H.-F., Mehta, P. P., Kishore, N. S., McWherter, C. A., Getman, D. P., Gordon, J. I., and Sikorski, J. A. (1997) Conformationally Constrained [p-(ω-Aminoalkyl)phenacetyl]-L-SERYL-L-lysyl Dipeptide Amides as Potent Peptidomimetic Inhibitors of Candida albicans and Human Myristoyl-CoA: Protein N-Myristoyl Transferase. *J. Med. Chem. 40*, 1422−1438.

(22) Deicas, B., Gambino, D., Kremer, C., Kremer, E., Mombrú, A., Suescun, L., Mariezcurrena, R., González, O., Rey, A., Mallo, L., and León A (1997) Synthesis, characterization and spectroscopic properties of $[Cu^{I}(alkylisocyanide)_4]BF_4$ complexes. X-ray crystal structures of $[Cu(MIBI)_4]BF_4$ and $[Cu(CPI)_4]BF_4$. *Polyhedron 16* (14), 2397−2403.

(23) Lee, T.-W., Su, C.-S., and Ting, G. (1996) Synthesis, reactivity and ^{99m}Tc labelling of 2-alkoxyisobutylisonitrile. *Appl. Radiat. Isot. 47* (2), 207−210.

(24) Gonschorowsky, M., Merz, K., and Driess, M. (2006) Cyclohexylbis(hydroxymethyl)phosphane: A Hydrophilic Phosphane Capable of Forming Novel Hydrogen-Bonding Networks. *Eur. J. Inorg. Chem.* 455−463.

(25) Cotton, A., and Zingales, F. J. (1961) The Donor-Acceptor Properties of Isonitriles as Estimated by Infrared Study. *J. Am. Chem. Soc. 83*, 351−355.

(26) (a) Ambrose, K. R., Owen, B. A., Goodmann, M. M., and Knapp, F. F., Jr. (1987) Evaluation of the metabolism in rat hearts of two new radioiodinated 3-methyl-branched fatty acid myocardial imaging agents. *Eur. J. Nucl. Med. 12*, 486−491. (b) Knapp, F. F., Jr., Goodman, M. M., Callahan, A. P., and Kirsch, G. (1986) Radioiodinated 15-(p-Iodophenyl) 3,3-Dimethylpentadecanoic Acid: A Useful New Agent to Evaluate Myocardial Fatty Acid Uptake. *J. Nucl. Med. 27*, 521−531. (c) Mokler, F. T., Lin, Q., Luo, H., McPherson, D. W., Beets, A. L., Bockisch, A., Kropp, J., and Knapp, F. F., Jr. (1999) Dual-Label Studies with [125I]-3(R)/[131I]-3(S)-BMIPP Show Similar Metabolism in Rat Tissues. *J. Nucl. Med. 40* (11), 1918−1927.

(27) (a) Kronauge, F., Noska, M. A., Davison, A., Holman, B. L., and Jones, A. G. (1992) Interspecies variation in biodistribution of technetium (2-carbomethoxy-2-isocyanopropane)6+. *J. Nucl. Med. 33*, 1357−1365. (b) Seifert, S., Syhre, R., Spies, H., and Johannsen, B. (1997) Enzymatic Hydrolysis of Ester Groups of Mixed-Ligand Oxorhenium (V) and Oxotechnetium (V) Complexes. *Appl. Radiat. Isot. 48* (8), 1052−1057.

BC0601222

Fluorescent Ligands for the Hemagglutinin of Influenza A: Synthesis and Ligand Binding Assays

V. Ranjit N. Munasinghe,[†] John E. T. Corrie,*[,†] Geoff Kelly,[‡] and Stephen R. Martin[†]

MRC National Institute for Medical Research, The Ridgeway, Mill Hill, London NW7 1AA, U.K., and MRC Biomedical NMR Centre, The Ridgeway, Mill Hill, London NW7 1AA, U.K. Received June 22, 2006; Revised Manuscript Received September 21, 2006

Two fluorescent conjugates of sialic acid have been prepared, with a convenient synthetic route that involves preparation of an unsaturated benzyl ester by cross-metathesis, followed by combined hydrogenation/ hydrogenolysis to provide a sialoside bearing a δ-carboxybutyl group, suitable for coupling with the chosen fluorophores. The fluorescent conjugates bound to bromelain-cleaved hemagglutinin (BHA) with affinities in the low μM range. Binding was accompanied by ~4.5-fold fluorescence enhancement for the dansyl conjugate **1** and ~3-fold fluorescence quenching for the pyrene conjugate **3**.

INTRODUCTION

The influenza A virus is a cause of significant human disease and can on occasion result in devastating pandemics, as in the 1918 outbreak that caused at least 20 million deaths worldwide (*1*). The infection process is initiated by hemagglutinin on the viral surface binding to terminal α-sialosides of glycoproteins and glycolipids on the surface of the target cell (see ref *2* for a recent review). It is believed that the aquatic bird population is a reservoir for the virus (*3*). Avian viruses bind preferentially to sialosides with an α2,3-linkage (*4*), whereas those subtypes of the virus that have caused human pandemics recognize α2,6-linked sialosides (*5*), and changes in binding specificity as a result of mutations are likely required for human infection.

As part of studies of viral infectivity, we wished to develop a fluorescence-based assay system that might have potential to evaluate affinities of hemagglutinins from different viral strains for relevant sialosides. Three types of fluorescent sialoside ligands have been previously described, one with a dansyl group attached via a linker to position 4 of the sialoside and an additional naphthyl group linked to the anomeric position to enhance the affinity for hemagglutinin (*6*), a second with a range of aromatic species (not all fluorescent) attached in the α-orientation to the glycosidic position via linkers of different lengths (*7*), and a third with a dansyl group linked via a spacer at the 9-position (*8*). Among these derivatives, only that with the 4-O-linked dansyl group has a report of its fluorescence properties (*6*) upon binding to hemagglutinin. It showed only a small (<20%) change in fluorescence intensity upon binding, although larger fluorescence anisotropy changes enabled competitive titrations to be performed with several related compounds. For our purpose, the compounds linked at the glycosidic position seemed the most likely to have differential competitive binding with sialosides of different regiochemistry, and we therefore aimed to prepare compounds **1**−**3** shown in Figure 1. These target compounds were chosen for the following reasons: the dansyl derivative **1** had been prepared in previous work (*7*) so could be considered as a reference material, although the previous study gave little experimental detail. The coumarin derivative **2** was selected because of our use of this fluorophore as an environmentally sensitive probe in other applications (e.g., *9*, *10*), and the pyrene compound **3** was chosen because previous work (*7*) suggested that an increased number of aromatic rings in the attached fluorophore resulted in increased affinity for hemagglutinin. For reasons discussed below, we were only able to prepare compounds **1** and **3**, and the binding properties of these two compounds were tested with BHA, the trimeric, soluble portion of hemagglutinin released from the virus by bromelain digestion (*11*).

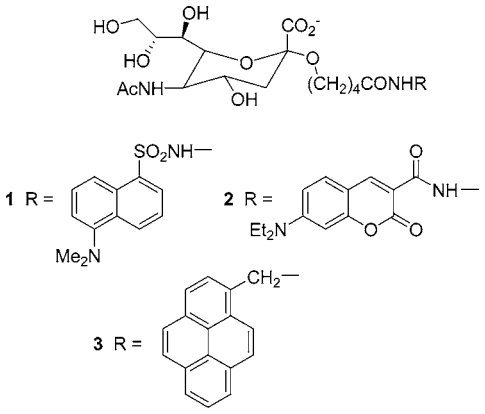


Figure 1. Target structures of fluorescent sialoside conjugates.

EXPERIMENTAL PROCEDURES

General Details. Reagents were purchased from Sigma-Aldrich, except for benzyl acrylate from Lancaster Synthesis and *N*-acetylneuraminic acid from Quisuo Biotech Co. Ltd, Shenzhen, China (http://www.sialicacid.com). Silver salicylate (*12*) and the chlorosugar **11** (*13*) were prepared by previously described methods. Flash chromatography was on Merck type 9385 silica gel. Preparative reverse-phase HPLC was carried out on a 2 × 30 cm column (Waters C_{18} packing, Cat. No. 20594) using mobile phases described below, at flow rates of 2 mL min^{-1}. Analytical reverse-phase HPLC was on a Merck Lichrospher 250 × 4 mm RP8 column at flow rates of 1.5 mL min^{-1}. Detection for both preparative and analytical work was at 254 nm. 1D ^{1}H NMR spectra were determined on JEOL FX90Q or Varian Unityplus 500 spectrometers for solutions in

* Corresponding author. Phone (+44) 208 906 2276. Fax: (+44) 208 906 4477. E-mail: jcorrie@nimr.mrc.ac.uk.
[†] MRC National Institute for Medical Research.
[‡] MRC Biomedical NMR Centre.

10.1021/bc060178w CCC: $37.00 © 2007 American Chemical Society
Published on Web 11/29/2006

$CDCl_3$ with TMS as internal reference, unless otherwise specified. 2D spectra used to assign resonances in compounds **1** and **3** were run on Varian Inova and UnityPlus spectrometers operating at 500−800 MHz. Methods used were $^1H-^1H$ COSY, $^1H\{^{13}C\}$-HSQC, HMBC, HSQC−TOCSY, plus 1D ^{13}C and 1D $^1H\{^1H\}$ steady-state NOE spectra.

Fluorescence measurements were made using a Spex Fluoromax fluorimeter and titrations were performed with BHA derived from X-31 (H3N2) influenza A virus. The BHA concentration was determined from absorption at 280 nm using an extinction coefficient of 1.5 cm^{-1} $(mg/mL)^{-1}$ and a monomer molecular weight of 69.5 kDa.

(4-Carboxy-1-butyl) 2,3,4,6-Tetra-*O*-acetyl-*β*-D-glucopyranoside (8). A mixture of benzyl acrylate (0.89 mL, 5.82 mmol), but-3-enyl 2,3,4,6-tetra-*O*-acetyl-*β*-D-glucopyranoside **6** (*14*) (1.22 g, 3.03 mmol), and Grubbs second generation catalyst (110 mg, 0.13 mmol) in CH_2Cl_2 (14.6 mL) was refluxed for 8 h. The solution was evaporated and flash chromatography (Et_2O−hexanes 4:1) gave 5-benzyloxy-5-oxopent-3-en-1-yl 2,3,4,6-tetra-*O*-acetyl-*β*-D-glucopyranoside **7** as an oil (1.34 g, 82%); ^1H NMR δ 7.32−7.37 (m, 5H, ArH), 6.95 (dt, J = 15.7, 6.8 Hz, 1H, C*H*═CHCO), 5.92 (dt, J = 15.7, 1.7 Hz, 1H, CH═C*H*CO), 5.19 (t, J = 9.5 Hz, 1H, H-3), 5.16 (s, 2H, PhCH_2), 5.08 (t, J = 9.7 Hz, 1H, H-4), 4.98 (dd, J = 9.6, 7.9 Hz, 1H, H-2), 4.51 (d, J = 7.9 Hz, 1H, H-1), 4.25 (dd, J = 12.3, 4.7 Hz, 1H, H-6), 4.14 (dd, J = 12.3, 2.4 Hz, 1H, H-6′), 4.00 (dt, J = 9.7, 5.7 Hz, 1H, pentenoyl-H5), 3.69 (ddd, J = 9.7, 4.7, 2.4 Hz, 1H, H-5), 3.59 (ddd, J = 9.7, 7.7, 5.6 Hz, 1H, pentenoyl-H5′), 2.42−2.55 (m, 2H, OCH_2CH_2), 2.08 (s, 3H, Ac), 2.02 (s, 3H, Ac), 2.00 (s, 3H, Ac), 1.96 (s, 3H, Ac). The spectrum reported above is that of the *E*-isomer. A small proportion (7%) of the *Z*-isomer was present, as shown by integration of the signal at 6.29 p.p.m (J = 11.5, 7.3 Hz) from the *β*-position of the unsaturated ester. The proton on the α-position was at 5.91 ppm (J = 11.5, 1.5 Hz) and was partly overlapped by the much larger signal for the same proton of the *E*-isomer.

Without further characterization, a solution of this material (1.0 g, 1.87 mmol) in EtOH (80 mL) was hydrogenated over 10% Pd−C at room temperature for 1 h, then filtered and evaporated to give **8** as a foam (0.81 g, 97%); ^1H NMR δ 5.21 (t, J = 9.6 Hz, 1H, H-3), 5.08 (t, J = 9.8 Hz, 1H, H-4), 4.98 (dd, J = 9.6, 7.8 Hz, 1H, H-2), 4.50 (d, J = 7.8 Hz, 1H, H-1), 4.27 (dd, J = 12.2, 4.4 Hz, 1H, H-6), 4.15 (dd, J = 12.2, 2.4 Hz, 1H, H-6′), 3.87−3.89 (m, 1H, pentanoyl-H5), 3.69−3.72 (m, 1H, H-5), 3.48−3.51 (m, 1H, pentanoyl-H5′), 2.26−2.31 (m, 2H, CH_2CO), 2.09 (s, 3H, Ac), 2.05 (s, 3H, Ac), 2.03 (s, 3H, Ac), 2.01 (s, 3H, Ac), 1.59−1.68 (br m, 4H, CH_2CH_2); HRMS: *m*/*z* calcd for $(C_{19}H_{28}O_{12} + H)^+$, 449.1653; found, 449.1665. This compound has been reported in a patent application (*15*) but without details of its NMR spectrum.

7-Diethylamino-2-oxo-2*H*-chromene-3-carbohydrazide (9). An ice-cold solution of 7-diethylamino-2-oxo-2*H*-chromene-3-carboxylic acid (*16*) (0.26 g, 1.0 mmol) and Bu_3N (360 μL, 1.51 mmol) in dry DMF (10 mL) was treated with isobutyl chloroformate (135 μL, 1.04 mmol), and the solution was stirred for 0.5 h at 0 °C. *tert*-Butyl carbazate (0.145 g, 1.1 mmol) was added, and the reaction was brought to room temperature and stirred overnight. The solution was diluted with Et_2O washed with water, 1 M HCl, saturated $NaHCO_3$, and brine, dried, and evaporated. Flash chromatography (EtOAc−hexanes 1:1) and crystallization (EtOH) gave *tert*-butyl 2-(7-diethylamino-2-oxo-2*H*-chromene-3-carbonyl)hydrazinecarboxylate as yellow crystals (0.28 g, 75%), mp 195.5−197 °C; ^1H NMR δ (90 MHz, $CDCl_3$) 8.68 (s, 1H, H-4), 7.42 (d, J = 8.8 Hz, 1H, H-5), 6.65 (dd, J = 8.8, 2.6 Hz, 1H, H-6), 6.65 (br s, 1H, NH), 3.46 (q, J = 7.0 Hz, 4H, CH_2), 1.51 (s, 9H, CH_3), 1.25 (t, J = 7.0 Hz, CH_3). Anal. Found: C, 60.52; H, 6.97; N, 10.96. $C_{19}H_{25}N_3O_5$ requires C, 60.79; H, 6.71; N, 11.19%.

The above compound (1.84 g, 4.91 mmol) was dissolved in TFA (25 mL) and kept for 1 h at room temperature. The TFA was evaporated, and the residue was partitioned between $CHCl_3$ and saturated $NaHCO_3$. The organic layer was dried and evaporated to give **9** as yellow crystals (1.25 g, 4.54 mmol, 92%), mp 162−165 °C ($CHCl_3$−hexanes), (lit. mp (*17*) 160−165 °C).

5-[2-(7-Diethylamino-2-oxo-2*H*-chromene-3-carbonyl)hydrazino]-5-oxo-1-pentyl 2,3,4,6-Tetra-*O*-acetyl-*β*-D-glucopyranoside (10) and Its Hydrolysis. A solution of **8** (0.28 g, 0.62 mmol), 1-hydroxybenzotriazole (92 mg, 0.68 mmol), and 1-(3-dimethylaminopropyl)-3-ethylcarbodiimide hydrochloride (130 mg, 0.68 mmol) in CH_2Cl_2 (5 mL) was stirred for 3 h at room temperature. A solution of **9** (196 mg, 0.71 mmol) in CH_2Cl_2 (2.5 mL) was added, and the mixture was stirred overnight at room temperature. The solution was diluted with CH_2Cl_2, washed with water and brine, dried, evaporated, and flash chromatographed (MeOH−$CHCl_3$ 4:96) to give **10** (0.36 g, 0.51 mmol, 83%); ^1H NMR δ 10.93 (d, J = 5.5 Hz, 1H, NH), 8.65 (s, 1H, H-4′), 8.38 (d, J = 5.5 Hz, 1H, NH), 7.43 (d, J = 9.2 Hz, 1H, H-5′), 6.65 (dd, J = 9.2, 2.4 Hz, 1H, H-6′), 6.51 (d, J = 2.4 Hz, 1H, H-8′), 5.22 (t, J = 9.6 Hz, 1H, H-3), 5.09 (t, J = 9.6 Hz, 1H, H-4), 5.01 (dd, J = 9.7, 8.2 Hz, 1H, H-2), 4.51 (d, J = 8.2 Hz, 1H, H-1), 4.26 (dd, J = 12.3, 4.4 Hz, 1H, H-6), 4.18 (dd, J = 12.3, 2.4 Hz, 1H, H-6′), 3.92 (dt, J = 9.5, 6.0 Hz, 1H, pentanoyl-H5), 3.70 (ddd, J = 9.9, 4.4, 2.4 Hz, 1H, H-5), 3.54 (dt, J = 9.5, 6.1 Hz, 1H, pentanoyl-H5′), 3.46 (q, J = 7.2 Hz, 4H, CH_2Me), 2.28−2.40 (m, 2H, CH_2CO), 2.10 (s, 3H, Ac), 2.07 (s, 3H, Ac), 2.02 (s, 3H, Ac), 2.00 (s, 3H, Ac), 1.79 (m, 2H, CH_2CH_2CO), 1.69 (m, 2H, C$H_2CH_2CH_2CO$), 1.25 (t, J = 7.2 Hz, 6H, Me); assignments were confirmed by a COSY spectrum. HRMS: *m*/*z* calcd for $(C_{33}H_{43}N_3O_{14} + H)^+$, 706.2818; found, 706.2786.

NaOH (0.69 mL) (2 M aq) was added to a solution of **10** (0.21 g, 0.3 mmol) in MeOH (1.9 mL) at room temperature. TLC analysis (MeOH−$CHCl_3$ 1:9) after 5 min showed a strong yellow spot that had the same R_f as 7-diethylamino-2-oxo-2*H*-chromene-3-carboxylic acid, and a more polar but much less intense yellow spot. After 30 min, the latter spot was absent from the reaction mixture, and only the spot corresponding to the above acid was observed under visible or UV illumination.

Methyl [But-3-enyl 4,7,8,9-Tetra-*O*-acetyl-5-(acetylamino)-3,5-dideoxy-D-glycero-α-D-galacto-2-nonulopyranosid]-onate (5b). Silver salicylate (0.69 g, 2.81 mmol) was added to a stirred solution of the chloro sugar **11** (2.16 mmol) in a mixture of dry benzene and 3-buten-1-ol (1:1, 14.4 mL). The flask was flushed with nitrogen, sealed, and stirred in the dark at room temperature for 4.5 days. The solution was diluted with $CHCl_3$ (30 mL) and filtered through a small pad of Celite, and the filter cake was washed with MeOH−$CHCl_3$ (1:9; 10 mL). The total filtrate was evaporated and the residue was dissolved in ether and washed with 5% aq sodium thiosulfate, water, 0.1 M NaOH (×2), and water, dried, evaporated, and flash chromatographed (MeOH−$CHCl_3$ 3:97) to give **5b** (0.47 g, 0.86 mmol, 40%); ^1H NMR δ 5.80 (ddt, J = 17.1, 10.4, 6.6 Hz, 1H, C*H*═CH_2), 5.40 (ddd, J = 8.5, 5.9, 3.0 Hz, 1H, H-8), 5.33 (dd, J = 8.3, 2.0 Hz, 1H, H-7), 5.14 (d, J = 9.6 Hz, 1H, NH), 5.09 (dq, J = 17.1, 1.5 Hz, 1H, ═CH), 5.04, (dq, J = 10.4, 1.5 Hz, 1H, ═CH), 4.85 (ddd, J = 12.3, 9.6, 4.4 Hz, 1H, H-4), 4.31 (dd, J = 12.3, 2.8 Hz, 1H, H-9), 4.04−4.13 (m, 3H, H-5, H-6, H-9′), 3.83 (dt, J = 9.3, 6.5 Hz, 1H, butenyl-H5), 3.80 (s, 3H, OMe), 3.29 (dt, J = 9.3, 6.6 Hz, 1H, butenyl-H4′), 2.59 (dd, J = 12.7, 4.6 Hz, 1H, H-3_{eq}), 2.29−2.33 (m, 2H, OCH_2CH_2), 2.03 (s, 3H, Ac), 2.04 (s, 3H, Ac), 2.14 (s, 3H, Ac), 2.15 (s, 3H, Ac), 1.96 (t, J = 12.7 Hz, 1H, H-3_{ax}), 1.88 (s, 3H, NAc).

This compound has been reported previously (*18*) but without NMR details.

Methyl [4-Carboxy-1-butyl 4,7,8,9-Tetra-*O*-acetyl-5-(acetylamino)-3,5-dideoxy-D-glycero-α-D-galacto-2-nonulopyranosid]onate (4). Benzyl acrylate (0.27 mL, 1.76 mmol) was added to a mixture of **5b** (0.5 g, 0.92 mmol) and Grubbs second generation catalyst (53 mg, 0.062 mmol) in CH_2Cl_2 (4.4 mL), and the solution was refluxed for 8 h, evaporated to ~1 mL, and flash chromatographed (MeOH−$CHCl_3$ 2.5:97.5) to give methyl [5-benzyloxy-5-oxopent-3-en-1-yl 4,7,8,9-tetra-*O*-acetyl-5-(acetylamino)-3,5-dideoxy-D-glycero-α-D-galacto-2-nonulopyranosid]onate (0.46 g, 0.68 mmol, 74%); ^{1}H NMR δ 7.31−7.39 (m, 5H, Ar-H), 6.98 (dt, J = 15.7, 6.5 Hz, 1H, C*H*═CHCO), 5.95 (d, 1H, J = 15.7 Hz, CH═C*H*CO), 5.39 (ddd, J = 8.5, 5.9, 3.0 Hz, 1H, H-8), 5.31 (dd, J = 8.3, 2.0 Hz, 1H, H-7), 5.18 (s, 2H, CH_2Ph), 5.11 (d, J = 10.1 Hz, 1H, NH), 4.85 (ddd, J = 12.3, 9.6, 4.4 Hz, 1H, H-4), 4.29 (dd, J = 12.4, 2.6 Hz, 1H, H-9), 4.02−4.13 (m, 3H, H-5, H-6, H-9′), 3.91 (dt, J = 9.7, 5.7 Hz, 1H, pentenoyl-H5), 3.76 (s, 3H, OMe), 3.34 (dt, J = 9.7, 5.6 Hz, 1H, pentenoyl-H5′), 2.57 (dd, J = 12.8, 4.6 Hz, 1H, H-3$_{eq}$), 2.42−2.50 (m, 2H, CH_2CH_2O), 2.14 (s, 3H, Ac), 2.13 (s, 3H, Ac), 2.03 (s, 3H, Ac), 2.02 (s, 3H, Ac), 1.92−1.96 (m, 1H, H-3$_{ax}$), 1.88 (s, 3H, NAc). A solution of this material (0.43 g, 0.635 mmol) in EtOH (27 mL) was hydrogenated at room temperature over 10% Pd−C (~45 min), then filtered through Celite and evaporated to give **4** as a white foam (0.37 g, 0.63 mmol, 100%); ^{1}H NMR δ 5.41 (ddd, J = 8.5, 5.9, 3.0 Hz, 1H, H-8), 5.30 (dd, J = 8.7, 1.8 Hz, 1H, H-7), 5.16 (d, J = 9.5 Hz, 1H, NH), 4.85 (ddd, J = 12.3, 9.6, 4.4 Hz, 1H, H-4), 4.32 (dd, J = 12.5, 2.4 Hz, 1H, H-9), 4.05−4.12 (m, 3H, H-5, H-6, H-9′), 3.80 (s, 3H, OMe), 3.78 (dt, J = 9.3, 6.5 Hz, 1H, pentanoyl-H5), 3.26 (dt, J = 9.5, 6.1 Hz, 1H, pentanoyl-H5′), 2.57 (dd, J = 12.9, 4.6 Hz, 1H, H-3$_{eq}$), 2.36−2.43 (m, 2H, CH_2CO), 2.15 (s, 3H, Ac), 2.15 (s, 3H, Ac), 2.04 (s, 3H, Ac), 2.03 (s, 3H, Ac), 1.95 (t, J = 12.7 Hz, 1H, H-3$_{ax}$), 1.89 (s, 3H, NAc), 1.59−1.76 (m, 4H, CH_2CH_2). This material has been reported previously (*7*) but without NMR details.

[5-{2-[(5-Dimethylamino-1-naphthalenyl)sulfonyl]hydrazino}-5-oxo-1-pentyl 5-(Acetylamino)-3,5-dideoxy-D-glycero-α-D-galacto-2-nonulopyranosid]onic Acid (1). A mixture of **4** (0.68 g, 1.15 mmol), 1-hydroxybenzotriazole (173 mg, 1.28 mmol), and EDC (245 mg, 1.28 mmol) was stirred in dry CH_2Cl_2 (28 mL) for 3 h at room temperature. Dansyl hydrazine (340 mg, 1.28 mmol) and DMAP (156 mg, 1.28 mmol) were added, and the solution was stirred at room temperature for 4 days. The solution was diluted with CH_2Cl_2 (150 mL) and washed successively with saturated aq $NaHCO_3$, H_2O, and brine, dried, and evaporated to give a yellow-green foam that contained two fluorescent spots on TLC (MeOH−$CHCl_3$ 2.5:97.5), of which the less polar corresponded to dansyl hydrazine. Flash chromatography (MeOH−$CHCl_3$ as above) gave the more polar component (0.42 g), which was dissolved in methanol (45 mL), mixed with 1 M aq NaOH (5 mL), and kept at room temperature for 3 h. Glacial acetic acid (1 mL) was added, and the solution was concentrated to ~10 mL and then diluted to 50 mL with 25 mM Na phosphate, pH 6, and adjusted to pH 6. Analytical reverse-phase HPLC (mobile phase: 25 mM Na phosphate, pH 6−MeCN 3:1 v/v) showed a major peak, t_R 3.0 min, assigned as the required compound **1** and a very small peak (t_R 11.9 min), assigned as the methyl ester of **1** since it had been present in gradually diminishing amount during the alkaline hydrolysis.

The solution was pumped onto the preparative reverse-phase HPLC column (previously equilibrated in 25 mM Na phosphate, pH 6), and the column was eluted with 25 mM Na phosphate, pH 6, for 2 h and then with 25 mM Na phosphate, pH 6−MeCN (5:1 v/v) for 2 h to elute **1**. Analysis by reverse-phase HPLC as above showed essentially a single peak with no later eluting material. Combined fractions containing the required conjugate were quantified by UV−visible spectroscopy [based on ϵ_{330} 4600 M^{-1} cm^{-1} for the dansyl chromophore in aqueous solvent (*16*)], and the solution was evaporated to remove acetonitrile. The residue was dissolved in water, adjusted to pH 6, and reapplied to the preparative HPLC column, again equilibrated in 25 mM Na phosphate, pH 6. The column was eluted with this buffer for 3 h and then with water. After some very minor contaminants that eluted with water up to 2.5 h, the dansyl conjugate began to elute after ~3.5 h, and the mobile phase was changed to water−MeCN (4:1 v/v) to elute the majority of the material. The combined fractions were concentrated under vacuum to remove acetonitrile and finally lyophilized. The residue was dissolved in water (19.5 mL), and the solution (19.8 mM, i.e., 386 μmol, 34%) was stored at −20 °C. ^{1}H NMR δ (D_2O, acetone reference) 8.54 (d, J = 8.5 Hz, 1H, Ar-H4), 8.45 (d, J = 8.9 Hz, 1H, Ar-H8), 8.31 (d, J = 7.3 Hz, 1H, Ar-H2), 7.72 (t, J = 8.2 Hz, 1H, Ar-H7), 7.71 (t, J = 7.9 Hz, 1H, Ar-H3), 7.44 (d, J = 7.6 Hz, 1H, Ar-H6), 3.85−3.89 (m, 2H; centers of signals within this envelope were assigned as follows: 3.87, H-9; 3.86, H-8), 3.79 (t, J = 10.1 Hz, 1H, H-5), 3.63−3.70 (m, 3H; centers of signals within this envelope were assigned as follows: 3.66, H-4,6; 3.65, H-9′), 3.55−3.61 (m, 2H; centers of signals within this envelope were assigned as follows: 3.59, H-8; 3.57, pentanoyl-H5), 3.28 (dt, J = 9.5, 6.4 Hz, 1H, pentanoyl-H5′), 2.89 (s, 6H, NMe_2), 2.71 (dd, J = 12.2, 4.6 Hz, 1H, H-3$_{eq}$), 2.04 (s, 3H, NHAc), 1.99 (t, J = 7.2 Hz, 2H, pentanoyl-H2), 1.60 (t, J = 12.2 Hz, 1H, H-3$_{ax}$), 1.23 (quintet, J = 7.5 Hz, 2H, pentanoyl-H3), 1.14−1.19 (m, 2H, pentanoyl-H4); ^{13}C NMR δ (D_2O, acetone ref) 178.1 (CH_3*C*O), 177.5 (pentanoyl-C1), 176.3 (C-1), 153.3 (Ar-C5), 134.5 (Ar-Cq), 134.3 (Ar-C2), 133.8 (Ar-C4), 132.8 (Ar-Cq), 131.4 (Ar-C7), 131.3 (Ar-Cq), 126.7 (Ar-C3), 122.4 (Ar-C9), 118.7 (Ar-C6), 103.4 (C-2), 75.4 (C-6), 74.6 (C-7), 71.1 (C-4), 71.0 (C-8), 66.6 (pentanoyl-C5), 65.4 (C-9), 54.6 (C-5), 47.7 (NMe_2), 43.2 (C-3), 35.1 (pentanoyl-C2), 30.7 (pentanoyl-C4), 24.7 (Me), 24.0 (pentanoyl-C3); LRMS *m*/*z*: calcd for $(C_{27}H_{39}N_4O_{12}S)^-$, 655.2; found *m*/*z* 655.4.

[5-(Pyren-1-ylmethylamino)-5-oxo-1-pentyl 5-(Acetylamino)-3,5-dideoxy-D-glycero-α-D-galacto-2-nonulopyranosid]onic Acid (3). 1-Pyrenemethylamine (165 mg, 0.71 mmol) was coupled with **4** (367 mg, 0.62 mmol) as described above for the dansyl conjugate **1**. After incubation overnight at room temperature, the reaction mixture was diluted with CH_2Cl_2, washed with 1 M HCl, saturated $NaHCO_3$, H_2O, and brine, dried, and evaporated. Flash chromatography (MeOH−$CHCl_3$ 3:97) gave a pale brown oil (0.44 g), that on TLC [MeOH−$CHCl_3$ (1:9)] had one principal product, R_f 0.4. Without further purification, this material was dissolved in MeOH (45 mL) and mixed with 1 M aq NaOH (5 mL). After 3 h at room temperature, the solution was treated with glacial AcOH (5 mL), concentrated to ~10 mL, and then diluted to 50 mL with 25 mM sodium phosphate, pH 6, and adjusted to pH 6. Analytical reverse-phase HPLC (mobile phase: 25 mM Na phosphate, pH 6−MeCN 2:1 v/v) showed a major peak, t_R 3.6 min, assigned as the required compound **3** and a very small peak at t_R 13.6 min, assigned as the methyl ester of **3** (see similar comment for **1** above). The solution was pumped onto the preparative reverse-phase HPLC column (previously equilibrated in 25 mM sodium phosphate, pH 6), and the column was eluted with the same buffer for 1.5 h. The mobile phase was changed to 25 mM sodium phosphate, pH 6−MeCN (4:1) for 2.5 h and then to 25 mM sodium phosphate, pH 6−MeCN (3.5:1). The product eluted in the latter solvent. Fractions were analyzed by reverse-phase HPLC as above, and those containing only **3** were combined and quantified by UV spectroscopy (based on the reported (*19*) absorbance coefficient of ϵ_{342} 35700 M^{-1} cm^{-1} for a water-

soluble 1-alkylpyrene compound). The solution containing **3** (201 μmol) was evaporated, dissolved in water (20 mL), adjusted to pH 6, and reapplied to the preparative HPLC column (equilibrated with 25 mM sodium phosphate, pH 6). The column was eluted with the same buffer for 1 h, and the mobile phase was changed to water for 1.5 h and then to $H_2O-MeCN$ (4:1) for 2.5 h. Fractions containing **3** were analyzed and quantified as above (186 μmol), the solution was evaporated and then re-evaporated from water (2×10 mL) to remove all acetonitrile, and the residue was dissolved in water (19 mL, 9.8 mM) and stored at -20 °C. ^{1}H NMR δ (D_2O, acetone reference) 8.13 (d, $J = 7.6$ Hz, 1H, Ar-H6 or 8), 8.11 (d, $J = 7.6$ Hz, 1H, Ar-H8 or 6), 7.98 (t, $J = 7.6$ Hz, 1H, Ar-H7), 7.96 (d, $J = 7.8$ Hz, 1H, Ar-H), 7.94 (d, $J = 9.5$ Hz, 1H, Ar-H), 7.92 (d, $J = 9.5$ Hz, 1H, Ar-H), 7.88 (d, 1H, $J = 9.5$ Hz, 1H, Ar-H), 7.85 (d, 1H, $J = 9.5$ Hz, 1H, Ar-H), 7.74 (d, 1H, $J = 7.8$ Hz, 1H, Ar-H), 4.69 (s, 2H, ArCH_2), 3.54−3.81 (m, 8H; centers of signals within this envelope were assigned as follows from 2D experiments: 3.79, H-7; 3.76, H-9; 3.69, H-5; 3.65, pentanoyl-H5; 3.63, H-4; 3.62, H-6; 3.57, H-9′; 3.55, H-8), 3.37 (dt, $J =$ 9.5, 6.5 Hz, pentanoyl-H5′), 2.65 (dd, $J = 12.3$, 4.5 Hz, 1H, H-3_{eq}), 2.20 (t, $J = 7.6$ Hz, 2H, pentanoyl-H2), 2.02 (s, 3H, Me), 1.60 (quintet, $J = 7.5$ Hz, 2H, pentanoyl-H3), 1.51 (t, $J = 12.1$ Hz, 1H, H-3_{ax}), 1.46 (quintet, $J = 7.5$ Hz, 2H, pentanoyl-H4); ^{13}C NMR δ (D_2O, acetone reference) 178.6 (pentanoyl-C1), 177.6 (CH_3CO), 176.4 (C-1), 133.5 (Ar-C), 133.1 ($2 \times$ Ar-C), 132.9 (Ar-C), 130.5 (Ar-C), 130.2 (Ar-CH), 130.0 (Ar-CH), 129.8 (Ar-CH), 129.2 (Ar-CH), 129.0 (Ar-C7), 128.0 (Ar-C6 & C8), 127.4 (Ar-CH), 126.5 (Ar-C), 126.4 (Ar-C), 125.0 (Ar-CH), 103.3 (C-2), 75.4 (C-6), 74.5 (C-7), 71.0 (C-4,8), 66.7 (pentanoyl-C5), 65.2 (C-9), 54.5 (C-5), 43.8 (CH_2NH), 42.9 (C-3), 37.7 (pentanoyl-C2), 30.7 (pentanoyl-C4), 24.7 (pentanoyl-C3), 24.5 (Me); LRMS *m/z*: calcd for $(C_{33}H_{37}N_2O_{10})^-$, 621.2; found, *m/z* 621.3.

Hemagglutinin Binding Assays. Dissociation constants for binding of the sialic acid conjugates **1** and **3** to X31-BHA were determined at 20 °C in phosphate-buffered saline, pH 7.4 (140 mM NaCl, 10 mM KCl, 20 mM phosphate), using direct fluorometric titrations. Measurements were made at constant probe concentration (1.9 μM for **1** and 1.25 μM for **3**). Excitation/emission wavelengths were 321/521 nm for **1** and 340/394 nm for **3**. The titrations were fit to the equation:

$$\text{fluorescence} = F_{(SA)}[SA] + F_{(BHA\cdot SA)}[BHA\cdot SA]$$

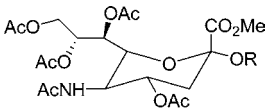
where the F values are the appropriate molar fluorescence intensities and SA is the relevant sialic acid derivative. A value for the dissociation constant (K_d) was obtained from a nonlinear least-squares fit to this equation with concentrations calculated by solving:

$$[BHA\cdot SA]^2 - (K_d + [BHA_T] + [SA_T])[BHA\cdot SA] + [BHA_T][SA_T] = 0$$

where BHA_T and SA_T are the total concentrations of BHA and sialic acid conjugate, respectively.

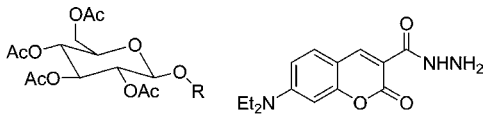
RESULTS AND DISCUSSION

Synthesis of the proposed compounds required the functionalized α-sialoside **4** as the key intermediate. Many related sialosides have been described, with functional groups such as amino, hydroxyl, formyl, thioalkyl, and carboxyl, as well as olefins, at the end of an oligomethylene chain (see ref *20* for typical examples). In the previous synthesis of **1**, the acid **4** was obtained by synthesis of olefin **5a**, which was then oxidized to **4** with potassium permanganate (*7*). Although this approach has been used elsewhere in synthesis of sialosides, we aimed



4 R = $(CH_2)_4CO_2H$
5a R = $(CH_2)_3CH{=}CH_2$
5b R = $(CH_2)_2CH{=}CH_2$

Figure 2. Structures of compounds **4** and **5a**,**b**.



6 R = $(CH_2)_2CH{=}CH_2$
7 R = $(CH_2)_2CH{=}CHCO_2Bn$
8 R = $(CH_2)_4CO_2H$

9

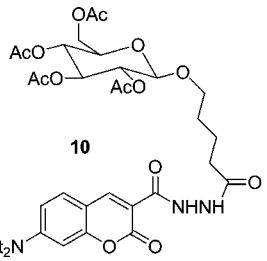


Figure 3. Structures of compounds relevant to synthesis of a model for compound **2**.

to apply current methods in our work to simplify access to the required compounds and therefore began our studies with a convenient model glucoside.

Following precedents described above, we planned to install the linker chain onto the sugar by a Koenigs−Knorr procedure, using an unsaturated alcohol to provide a site for further functionalization. Subsequently, it seemed likely that olefin cross-metathesis (*21*) using benzyl acrylate, followed by hydrogenation to reduce the double bond and concurrently cleave the benzyl ester, would allow ready access to the required carboxylic acid side chain. There are numerous previous examples of this combined hydrogenation/hydrogenolysis procedure (e.g., *22*) although the substituted benzyl acrylates used have generally been assembled by routes other than cross-metathesis. As a convenient model, we used the readily accessible 3-butenyl glucoside **6** (*14*) that underwent clean cross-metathesis with benzyl acrylate in the presence of Grubbs second generation catalyst (*23*) to give the unsaturated ester **7** as a mix (93:7) of *E* and *Z* isomers. Hydrogenation then gave the saturated acid **8** in near-quantitative yield. To check the remainder of the intended synthesis of **1**−**3**, this crude acid was coupled with the hydrazide **9** and the product **10** was subjected to mild base treatment in the expectation of hydrolyzing the acetyl groups from the sugar. In practice, we found that the C−N bond between the coumarin and the hydrazine moiety was rapidly cleaved, releasing the coumarin-3-carboxylic acid. We had previously encountered unexpected lability of this C−N bond in an amide of a related coumarin-3-carboxylic acid (*24*), but the present results imply that any coumarin-3-carboxamide system is vulnerable to hydrolysis under relatively mild alkaline conditions. Results from other reactions of 3-acylated coumarins support this view (*25*). It thus seemed certain that construction of the related sialoside conjugate **2** would encounter the same problem, and we therefore restricted subsequent work to compounds **1** and **3**.

With the basic methodology established, we turned to the sialosides themselves. Although there is a large literature on O-sialylation [reviewed in ref *26*], it required several trials to

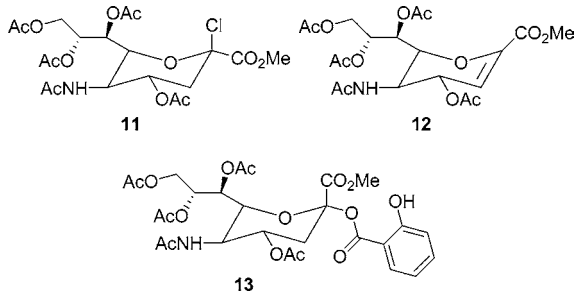


Figure 4. Structures of compounds **11**−**13** used as starting material or formed as byproducts during synthesis of compounds **1** and **3**.

establish convenient and reliable methods for our purpose. We summarize these conclusions here as an aid to other workers. *N*-Acetylneuraminic acid was peracetylated and converted to its methyl ester as described (*27*) in 73% overall yield. Subsequent transformation to the β-chloro sugar **11** was readily and best achieved with anhydrous HCl in cold dichloromethane, as previously described (*13*). This convenient method routinely gave material of excellent quality for use in glycosylation reactions and in our hands was more satisfactory than alternative procedures using acetyl chloride (e.g., *27*).

To optimize the glycosylation of but-3-en-1-ol with **11**, we surveyed three promoter reagents, namely mercury(II) cyanide as previously used by Toogood et al. (*7*) in their preparation of fluorescent sialic acid conjugates, silver carbonate, and silver salicylate [both reviewed in ref *26*]. As expected, mercury(II) cyanide gave a mixture of α- and β-glycosides (~1:1 ratio) and was not investigated further. Silver carbonate in CH_2Cl_2 gave a product mix of the dehydro sugar **12** and the α- and β-glycosides, in which **12** constituted ~13% of the mixture while the α:β ratio was ~85:15. While this was reasonably satisfactory, we found that the extent of reaction was very dependent on the batch of commercial silver carbonate, and significant quantities of unreacted **11** were frequently present, despite prolonged reaction times or increased amounts of promoter. In contrast, silver salicylate routinely resulted in complete reaction of **11**, giving a product mix that contained only ~3% of the dehydro sugar **12** and an anomeric ratio of the glycosides that was >99:1 in favor of the required α-product **5b**. Under our conditions, 20−30% of the total product was the salicylate ester **13**, but this compound was easily removed during workup by washing the organic extract with dilute sodium hydroxide. The byproduct was identified as the ester **13** rather than the isomeric aryl glycoside principally because of a sharp singlet at δ 10.1 that exchanged with D_2O and was consistent with a phenolic hydroxyl rather than a carboxylic acid. Both types of byproduct (i.e., ester or aryl glycoside) have been observed in other glycosylations mediated by silver salicylate (*28*).

The olefin **5b** was smoothly transformed to the acid **4** by the sequence of olefin cross-metathesis and hydrogenation/hydrogenolysis described above, and the crude acid was coupled with either dansyl hydrazine or 1-pyrenemethylamine in carbodiimide-mediated reactions. Subsequent alkaline hydrolysis gave the required conjugates **1** and **3** that were each purified by reverse-phase HPLC, and each compound was used in fluorescence titrations with BHA.

The emission spectrum of the dansyl conjugate **1** (Figure 5A) has a single broad band with an emission maximum at approximately 524 nm. Its binding to BHA results in ~4.5-fold intensification of the fluorescence at saturation (see below) and a small blue shift to ~521 nm. The emission spectrum of **3** (Figure 6A) shows two sharp bands at 376 and 395 nm, with a broad long wavelength shoulder at ~416 nm. Its binding to BHA quenches the fluorescence ~3-fold at saturation (see below),

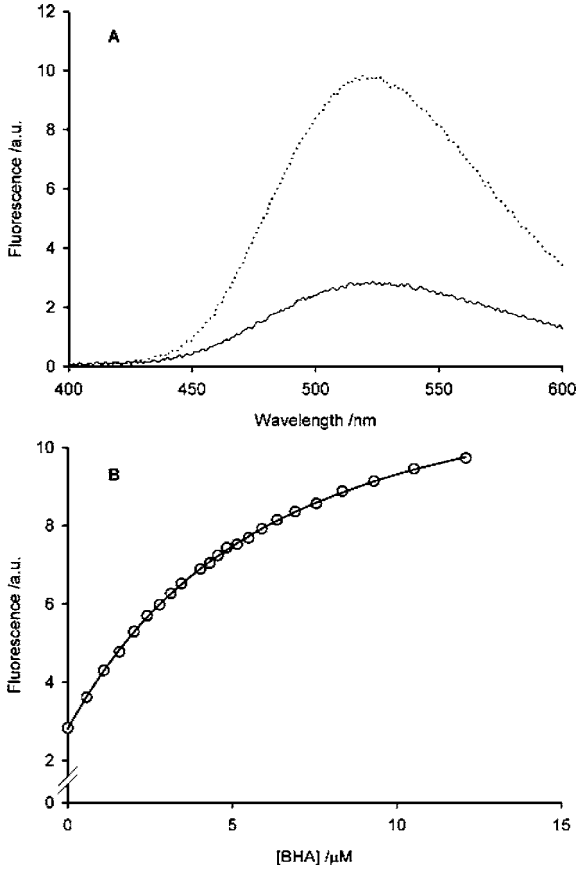


Figure 5. (A) The emission spectrum of the dansyl conjugate **1** (1.9 μM) in the absence (solid line) and presence (dotted line) of 12.5 μM BHA trimer. (B) Fluorescence intensity at 521 nm as a function of the concentration of BHA trimer. Excitation was at 321 nm.

with no significant change in band shape. These changes in fluorescence were used to estimate affinities and stoichiometries for the binding of the compounds to BHA. However, to be able to determine binding stoichiometry it would be necessary to perform titrations at concentrations that are typically at least 3-fold higher than K_d for the ligand, in order that essentially all the BHA added in the early part of the titration is saturated with ligand. This was impractical in the present experiments, where for reasons of availability we were unable to use high enough concentrations of BHA to make unambiguous determinations of stoichiometry. We therefore analyzed the titration data for two plausible models: a one-site model in which there is a single binding site for sialic acid in the BHA trimer and a three-site model in which each monomer within the trimer contains a site for binding. In the latter case we assumed that these sites were identical and noninteracting.

For **1**, the fit using the one-site model (Figure 5B) gave $K_d = 4.7 \pm 0.7$ μM and $F_{(BHA\cdot\mathbf{1})}/F_{(\mathbf{1})} = 4.58 \pm 0.45$; the corresponding values for the three-site model were $K_d = 17.9 \pm 2.4$ μM and $F_{(BHA\cdot\mathbf{1})}/F_{\mathbf{1})} = 4.83 \pm 0.59$. The computed best fit for the one-site model (shown as the solid line in Figure 5B) is marginally better than that for the three-site model (not shown) as judged by χ^2 values of 1.09 and 1.43, respectively. For **3**, analysis using the one-site model gave $K_d = 2.3 \pm 0.4$ μM and a fluorescence intensity ratio $F_{(BHA\cdot\mathbf{3})}/F_{(\mathbf{3})}$ of 0.31 ± 0.02. The corresponding values for the analysis using the three-site model were $K_d = 8.7 \pm 1.7$ μM and $F_{(BHA\cdot\mathbf{3})}/F_{(\mathbf{3})} = 0.28 \pm 0.03$. As above, the best fit for the one-site model (shown as the solid line in Figure 6B) is marginally better than that for the three-site model (not shown) as judged by χ^2 values of 1.23 and 1.69, respectively, but the differences are too small to distinguish between the models.

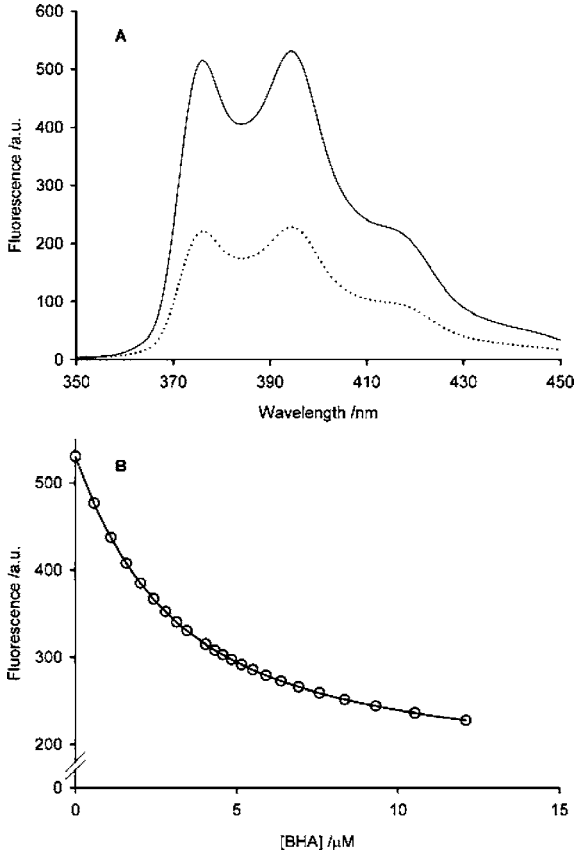


Figure 6. (A) The emission spectrum of the pyrenyl conjugate **3** (1.25 μM) in the absence (solid line) and presence (dotted line) of 12.5 μM BHA trimer. (B) Fluorescence intensity at 394 nm as a function of the concentration of BHA trimer. Excitation was at 340 nm.

The binding of BHA to the pyrene conjugate is only 2-fold tighter than for the dansyl one, which is somewhat different from expectations based on previous data (*7*), in which a trend to higher affinity was associated with an increased number of aromatic rings in the fluorophore (or related pendent group). However, two factors may explain this divergence from the earlier results. First, those data were derived from hemagglutination inhibition experiments, and it has been noted that such assays may not give identical results to fluorescence assays (*20d*). Second, although the dansyl conjugate **1** described here was identical to that in the earlier study, the series of aromatic hydrocarbon conjugates described previously had six-carbon linkers to the sialic acid rather than the four-carbon one in the present pyrene conjugate **3**. The previous data suggest that the linker length can influence the binding constant for these compounds, but there are insufficient data to draw definitive conclusions.

Both compounds show much tighter binding (low μM range) than simple α-methyl sialoside [K_d 2.8 mM (*7*)], implying that the fluorophores and/or linker have interactions with hemagglutinin. Although it seems most probable that the sialic acid moiety does bind to the specific binding site of hemagglutinin, positive demonstration of this will be required and studies to obtain structural evidence for specific binding are planned. These and further application of the binding assays will be described elsewhere.

ACKNOWLEDGMENT

We thank the Division of Virology (NIMR) for provision of BHA. We are grateful to the EPSRC Mass Spectrometry Centre, Swansea, for low-resolution negative ion spectra, and to the MRC Biomedical NMR Centre for access to facilities.

LITERATURE CITED

(1) Reid, A. H., Taubenberger, J. K., and Fanning, T. G. (2001) The 1918 Spanish influenza: integrating history and biology. *Microbes Infect. 3*, 81−87.

(2) Skehel, J. J., and Wiley, D. C. (2000) Receptor binding and membrane fusion in virus entry: the influenza hemagglutinin. *Annu. Rev. Biochem. 69*, 531−569.

(3) Webster, R. G. (1999) 1918 Spanish influenza: the secrets remain elusive. *Proc. Natl. Acad. Sci. U.S.A. 96*, 1164−1166.

(4) Ha, Y., Stevens, D. J., Skehel, J. J., and Wiley, D. C. (2001) X-ray structures of H5 avian and H9 swine influenza virus hemagglutinins bound to avian and human receptor analogs. *Proc. Natl. Acad. Sci. U.S.A. 98*, 11181−11186.

(5) Matrosovich, M., Tuzikov, A., Bovin, N., Gambaryan, A., Klimov, A., Castrucci, M. R., Donatelli, I., and Kawaoka, Y. (2000) Early alterations of the receptor binding properties of H1, H2 and H3 avian influenza virus hemagglutinins after their introduction into mammals. *J. Virol. 74*, 8502−8512.

(6) Weinhold, E. G., and Knowles, J. R. (1992) Design and evaluation of a tightly binding fluorescent ligand for influenza A hemagglutinin. *J. Am. Chem. Soc. 114*, 9270−9275.

(7) Toogood, P. L., Galliker, P. K., Glick, G. D., and Knowles, J. R. (1991) Monovalent sialosides that bind tightly to influenza A virus. *J. Med. Chem. 34*, 3138−3140.

(8) Fitz, W., and Wong, C. H. (1994) Combined use of subtilisin and *N*-acetylneuraminic acid aldolase for the synthesis of a fluorescent sialic acid. *J. Org. Chem. 59*, 8279−8280.

(9) Brune, M., Hunter, J. L., Howell, S. A., Martin, S. R., Hazlett, T. L., Corrie, J. E. T., and Webb, M. R. (1998) The mechanism of the coumarin-labeled phosphate binding protein, as a probe of inorganic phosphate in the submicromolar range. *Biochemistry 37*, 10370−10380.

(10) Webb, M. R., Reid, G. P., Munasinghe, V. R. N., and Corrie, J. E. T. (2004) A series of related nucleotide analogues that aids optimization of fluorescence signals to probe the mechanism of P-loop ATPases, such as actomyosin. *Biochemistry 43*, 14463−14471.

(11) Brand, C. M., and Skehel, J. J. (1972) Crystalline antigen from influenza-virus envelope. *Nature, New Biol. 238*, 145−147.

(12) van der Vleugel, D. J. M., van Heeswijk, W. A. R., and Vliegent-Hart, J. F. G. (1982) A facile preparation of alkyl α-glycosides of the methyl ester of *N*-acetyl-D-neuraminic acid. *Carbohydr. Res. 102*, 121−130.

(13) Kononov, L. O., and Magnusson, G. (1998) Synthesis of methyl and allyl α-glycosides of *N*-acetylneuraminic acid in the absence of added promoter. *Acta Chem. Scand. 52*, 141−144.

(14) Rodebaugh, R., and Fraser-Reid, B. (1996) Evidence for cyclic bromonium ion transfer in electrophilic bromination of alkenes: Reaction of ω-alkenyl glycosides with aqueous *N*-bromosuccinimide. *Tetrahedron 52*, 7663−7678.

(15) Platzek, J., Graske, K. D., and Niedballa, U. (2003) Method for producing peracylated 1-*O*-glycosides. PCT Appl. WO 03006474.

(16) Corrie, J. E. T. (1994) Thiol-reactive probes for protein labelling. *J. Chem. Soc., Perkin Trans. 1* 2975−2982.

(17) Takechi, H., Oda, Y., Nishizono, N., Oda, K., and Machida, M. (2000) Screening search for organic fluorophores: syntheses and fluorescence properties of 3-azolyl-7-diethylaminocoumarin derivatives. *Chem. Pharm. Bull. 48*, 1702−1710.

(18) Allanson, N. M., Davidson, A. H., Floyd, C. D., and Martin, F. M. (1994) The synthesis of novel mimics of the sialyl-Lewis-X determinant. *Tetrahedron Asymmetry 5*, 2061−2076.

(19) Cardona, C. M., Wilkes, T., Ong, W., Kaifer, A. E., McCarley, T. D., Pandey, S., Baker, G. A., Kane, M. N., Baker, S. N., and Bright, F. V. (2002) Dendrimers functionalized with a single pyrene label: synthesis, photophysics, and fluorescence quenching. *J. Phys. Chem. A 106*, 8649−8656.

(20) (a) Roy, R., and LaFerrière, C. (1990) Synthesis of protein conjugates and analogues of *N*-acetylneuraminic acid. *Can. J. Chem. 68*, 2045−2054. (b) McAuliffe, J. C., Rabuka, D., and Hindsgaul, O. (2002) Synthesis of *O*-glycolyl-linked neuraminic acids through a spirocyclic intermediate. *Org. Lett. 4*, 3067−3069. (c) Matsuoka, K., Kurosawa, H., Esumi, Y., Terunuma, D., and Kuzuhara, H. (2000) Introduction of monosaccharides having functional groups onto a carbosilane dendrimer: A broadly applicable one-pot reaction

in liquid ammonia involving Birch reduction and subsequent S_N2 reaction. *Carbohydr. Res. 329*, 765−772. (d) Lees, W. J., Spaltenstein, A., Kingery-Wood, J. E., and Whitesides, G. M. (1994) Polyacrylamides bearing pendant α-silaoside groups strongly inhibit agglutination of erythrocytes by influenza A virus: multivalency and steric stabilization of particulate biological systems. *J. Med. Chem. 37*, 3419−3433.

(21) Trnka, T. M., and Grubbs, R. H. (2001) The development of $L_2X_2Ru{=}CHR$ olefin metathesis catalysts: an organometallic success story. *Acc. Chem. Res. 34*, 18−29.

(22) Nicolaou, K. C., Hwang, C. K., Marron, B. E., DeFrees, S. A., Couladouros, E. A., Abe, Y., Carroll, P. J., and Snyder, J. P. (1990) Bridging of macrodithionolactones to bicyclic systems. Synthesis and modeling of oxapolycyclic frameworks. *J. Am. Chem. Soc. 112*, 3040−4054.

(23) Chattergee, A. K., Morgan, J. P., Scholl, M., and Grubbs, R. H. (2000) Synthesis of functionalized olefins by cross and ring-closing metatheses. *J. Am. Chem. Soc. 122*, 3783−3784.

(24) Corrie, J. E. T., Munasinghe, V. R. N., and Rettig, W. (2000) Synthesis and fluorescence properties of substituted 7-amino-coumarin-3-carboxylate derivatives. *J. Heterocycl. Chem. 37*, 1447−1455.

(25) (a) Nemeryuk, M. P., Dimitrova, V. D., Sedov, A. L., and Traven, V. F. (1997) Unusual "replacement" of carbonyl containing functions of position 3 of coumarin by a cyano group. *Chem. Heterocycl. Compd. 33*, 1234−1235. (b) Nemeryuk, M. P., Dimitrova, V. D., Anisimova, O. S., Sedov, A. L., Soloveva, N. P., and Traven, V. F. (2005) Conversions of coumarins accompanied by intermediate opening and recyclization of the lactone ring. Study of the interaction of malonic acid hydrazide and amide derivatives with 3-acyl (3-cyano, 3-ethoxycarbonyl)coumarins. *Chem. Heterocycl. Compd. 41*, 1255−1266.

(26) (a) Boons, G.-J., and Demchenko, A. V. (2000) Recent advances in *O*-sialylation. *Chem. Rev. 100*, 4539−4565. (b) Ross, D. K., and Linhardt, R. J. (2004) Sialic acid donors: chemical synthesis and glycosylation. *Curr. Org. Chem. 1*, 31−46.

(27) Marra, A., and Sinay, P. (1989) Acetylation of *N*-acetylneuraminic acid and its methyl ester. *Carbohydr. Res. 190*, 317−322.

(28) Wulff, G., Krüger, W., and Röhle, G. (1971) Die Umsetzung von α-acetobromglucose mit den Silbersalzen von Hydroxycarbonsäuren. *Chem. Ber. 104*, 1387−1399.

BC060178W

Fluoro-pegylated (FPEG) Imaging Agents Targeting Aβ Aggregates

Karin A. Stephenson, Rajesh Chandra, Zhi-Ping Zhuang, Catherine Hou, Shunichi Oya, Mei-Ping Kung, and Hank F. Kung*

Departments of Radiology, University of Pennsylvania, 3700 Market Street, Room 305, Philadelphia, Pennsylvania 19104. Received August 1, 2006; Revised Manuscript Received November 2, 2006

A novel approach of producing positron emission tomography (PET) imaging agents through the formation of bioconjugates based on a pegylation−fluorination strategy resulting in fluoro-pegylated (FPEG) molecules is reported. This approach offers a simple and easy method by which to incorporate ^{18}F in the target molecule without an appreciable increase in the lipophilicity. After ^{18}F labeling, this convenient approach leads to PET imaging probes binding to Aβ aggregates in the brain (an important factor associated with Alzheimer's disease) using the known core structures, such as [2-(4-dimethylaminophenyl)-vinyl]-benzoxazol **(3′)** or 2-phenylbenzothiazole (**4**). This approach appears to be effective in some core structures, but it cannot be uniformly applied to all structures.

INTRODUCTION

Alzheimer's disease (AD) is an important neurodegenerative disorder of the brain affecting millions of older Americans, and yet the diagnosis of this disease based on neurological observations is often difficult and unreliable. The only definitive diagnosis of the disease is by pathological examination of postmortem staining of affected brain tissues. The presence of β-amyloid (Aβ) aggregates in the brain is generally accepted as the hallmark of AD (*1*−*4*). Recent success in developing radionuclide-labeled agents targeting the Aβ aggregates provides a window of opportunity to improve the diagnosis of AD (*5*−*8*). Preliminary reports of positron emission tomography (PET) imaging suggested that 4-*N*-methylamino-4′-hydroxystilbene ([^{11}C]**1**, SB-13) (*9*) and [^{11}C] 2-(4′-(methylaminophenyl)-6-hydroxybenzothiazole ([^{11}C]**4**, also known as PIB) (*10*) (Figure 1) showed differential uptake and retention in the brain of AD patients as compared to controls. Since ^{11}C is a positron emitting isotope with $T_{1/2}$ = 20 min, which limits its usefulness for widespread clinical application, efforts are being made to develop comparable agents labeled with a longer half-life isotope—^{18}F ($T_{1/2}$ = 110 min). Preliminary studies with [^{18}F]-2-(1-(2-(*N*-(2-fluoroethyl)-*N*-methylamino)naphthalen-6-yl)ethylidene)malononitrile ([^{18}F]FDDNP) (*7*) showed differential uptake and retention in the brain of AD patients, but this a highly lipophilic tracer, binding to both tangles and plaques, making it difficult to measure the specific signal contribution from plaques. In 2002, Mathis et al. reported a series of [^{18}F]-fluoroalkoxy-BTA-1 derivatives, which showed excellent binding affinities and brain penetration (*11*). Two other potential series of Aβ-specific imaging agents, 6-iodo-2-(4′-dimethylamino)phenylimidazo[1,2-*a*]pyridine (**2**, IMPY) (*12*−*14*) and 2-(4-methylaminostyryl)-6-(2-fluoroethoxy)benzoxazole (**3**, BF-168) (*15*, *16*), have also shown high specific binding affinities to Aβ aggregates of AD brain homogenates (K_i < 10 nM; see Table 1).

We are interested in replacing the labeling isotope with ^{18}F, but the challenge is to maintain the Aβ aggregate-binding affinity and maintain suitable in vivo kinetics of the agents with sufficient selective uptake in the brain (*6*, *17*). Incorporating a radioactive fluoride atom (^{18}F) is typically accomplished using either electrophilic or nucleophilic conditions (*18*−*20*). Fluoride nucleophilic displacement reactions are advantageous, as they often result in higher yields and higher specific activities and the fluoride can be produced more readily (*19*, *20*). [^{18}F] fluoride can be added via an SN2-type reaction with good leaving groups such as either the mesylate or tosylate precursor. One of the commonly used methods to append a fluorine atom involves adding a fluoroethyl or fluoropropyl group to the target compound. However, when these short fluoro alkyl chains were added to the core structures, the results were sometimes not promising. This is often due to an increase in lipophilicity; the resulting ^{18}F-labeled agents tend to have a higher nonspecific binding to the Aβ aggregates. To circumvent these undesirable effects, we have exploited a novel approach by using fluoro-

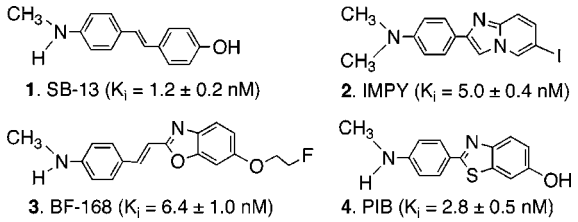


Figure 1. Structures of four imaging agents (**1**−**4**) targeting Aβ aggregates in the brain. The K_i values indicate the in vitro binding affinity to Aβ aggregates (*15*, *27*, *31*).

Table 1. Inhibition Constants (K_i, nM) of Compounds on [^{125}I]IMPY Binding to AD Brain Homogenates[a]

compounds	K_i (nM)	log P[b]	compounds	K_i (nM)	log P[b]
(1) SB−13	1.2 ± 0.2[c]	2.36	(2) IMPY	5.0 ± 0.4[d]	2.19
1a (SB n = 2)[c]	2.9 ± 0.2	2.53	**12a** (IMPY n = 1)	16 ± 2.0	
1b (SB n = 3)[c]	6.7 ± 0.3	2.41	**12b** (IMPY n = 2)	31 ± 9.0	
1c (SB n = 4)[c]	4.4 ± 0.8	2.05	**12c** (IMPY n = 3)	30 ± 2.5	2.69
1d (SB n = 5)[c]	6.8 ± 0.8	2.27	**12d** (IMPY n = 6)	96 ± 14	
			12e (IMPY n = 8)	387 ± 12	
(4) PIB	2.8 ± 0.5[e]	1.3	(3) BF−168	6.4 ± 1.0[f]	
5a (PIB n = 2)	2.2 ± 0.5	3.04	**8a** (BF n = 1)	12 ± 0.5	
5b (PIB n = 3)	3.8 ± 0.5	3.04	**8b** (BF n = 3)	14.5 ± 5.0	2.93
5c (PIB n = 6)	4.7 ± 0.9	2.99	**8c** (BF n = 6)	10.0 ± 0.2	
5d (PIB n = 8)	9.0 ± 1.8		**8d** (BF n = 8)	6.0 ± 0.6	

[a] Values K_i (nM) are the mean ± SEM of three independent experiments, each in duplicate. [b] log P = log of partition coefficient between 1-octanol and buffer. [c] ref 21. [d] ref 33. [e] ref 6. [f] ref 15.

* Corresponding author. Tel: (215) 662-3096; FAX: (215) 349-5035; E-mail: kunghf@sunmac.spect.upenn.edu.

10.1021/bc060239q CCC: $37.00 © 2007 American Chemical Society
Published on Web 12/23/2006

pegylation (FPEG) of the core structures for ^{18}F labeling of stilbene derivatives (*21*). It is generally assumed that the *p-N*-methylaminophenyl or the *p-N,N*-dimethylaminophenyl group is critical for binding affinity; modification on the opposite end of these core structures may not alter the binding affinity (*17*).

Pegylation (PEG) is a common approach for changing in vivo pharmacokinetics of various biologically interesting proteins or peptides, through which the in vivo stability and pharmacokinetics can be improved, leading to better therapeutics (*22*, *23*). Recently, the "pegylation" technique has been applied to modify the pharmacokinetic properties of radiopharmaceuticals (*24*, *25*). Conjugating PEG macromolecules (high molecular weight PEGs, $M_w = 10\,000-20\,000$) to labeled peptides may be efficacious in changing biodistribution in vivo and leading to improvements in specific localization of agents targeting peripheral tissues. However, it will be ineffective to use macromolecular PEG-conjugated radiopharmaceuticals as imaging agents for the brain due to the limitation of such macromolecules to cross the blood−brain barrier. In an attempt to modulate the lipophilicity of ^{18}F-labeled stilbene derivatives (*21*, *26*), we have adopted a novel approach by adding a short length of FPEG ($n = 2-5$) and capping the end of the ethylene glycol chain with a fluorine atom (*21*). The resulting FPEG derivatives of SB-13 displayed excellent Aβ aggregate-binding affinities and high brain penetrations. The success of this FPEG approach has prompted us to expand this simple strategy to different Aβ-targeting small core structures (**1**−**4**).

In this report, we explored fluoro-pegylated compounds with IMPY (**2**), BF168 (**3**), and PIB (**4**) core structures with various chain lengths ($n = 1-8$) for biological evaluations. F-18 radiolabelings were attempted on several compounds with each core ([^{18}F]**5a**−**c** for PIB, [^{18}F]**12c** for IMPY, and [^{18}F]**8b** for BF168), and the initial biodistributions and autoradiograms of [^{18}F]**5a**−**c** were obtained. Reported herein is a structure−binding activity study of attaching a short chain length FPEG ($n \leq 8$) to these molecules for labeling with ^{18}F and concomitantly maintaining in vitro binding affinities and in vivo biological properties.

EXPERIMENTAL PROCEDURES

General. All reagents in the syntheses were commercial products used without further purification unless otherwise indicated. ^{1}H NMR spectra were obtained on a Bruker DPX spectrometer (200 MHz) in $CDCl_3$ unless otherwise indicated. Chemical shifts are reported as δ values (parts per million) relative to internal TMS. Coupling constants are reported in hertz. The multiplicity is defined by s (singlet), d (doublet), t (triplet), br (broad), and m (multiplet). High-resolution electron ionization (HREI) mass spectra were performed at the McMaster Regional Centre for Mass Spectrometry using a Micromass/Waters GCT instrument (GC-EI/CI time-of-flight mass spectrometer). Semipreparative HPLC was performed using a Phenomenex Gemini C18 column [(5.0 × 250 mm, 5 μm); acetonitrile/water 70/30; flow rate 3 mL/min] and analytical HPLC conditions using a Phenomenex Gemini C18 analytical column [(5.0 × 250 mm, 5 μm); acetonitrile/water 80/20; flow rate 1 mL/min)].

Synthesis of 2-(4′-(methylaminophenyl)-6-hydroxybenzothiazole (PIB, 4) Derivatives. Compound **4** (2-(4′-(methylaminophenyl)-6-hydroxybenzothiazole (PIB) was prepared using the approach of Mathis and co-workers (*27*). Monomethylation was accomplished via standard reported procedures (*28*) to yield **4** that was used in the subsequent steps.

*General Procedure for the Pegylation of **4**.* To a solution of **4** (1 equiv) in anhydrous *N,N*-dimethylformamide (2 mL/0.1 mmol of **4**) in a microwavable vial (from Biotage) was added anhydrous cesium carbonate (2.5 equiv) and the mixture stirred at room temperature under argon for 30 min. Pegylation agent (1.2 equiv) followed by sodium iodide (1.5 equiv) were then added to the vial. The vial was then sealed and subjected to microwave irradiation (Biotage Initiator system). The microwave conditions were 200 °C for 10 min with 10 s pre-stirring. After cooling the reaction mixture to room temperature, the vial was opened, the contents were transferred to a round-bottom flask, and the volatiles were removed under reduced pressure. The residue was extracted with ethyl acetate (3 × 10 mL), and the ethyl acetate layer was washed with water (1 × 10 mL) and brine (1 × 10 mL). The organic layer, after drying over anhydrous magnesium sulfate, was evaporated, and the residue was purified on silica PTLC (PTLC) to afford the corresponding PEGylated derivatives.

*Preparation of Compounds **5a**−**d**.* Treatment of *4* with the fluoromesylates according to the general procedure afforded compounds **5a**−**d**.

2-[4′-(Methylamino)phenyl]-6-[2-(2-fluoroethoxy)ethoxy]benzothiazole (**5a**). Yield: 84%. (PTLC, 50% ethyl acetate in hexane). ^{1}H NMR (200 MHz, $CDCl_3$): δ 7.83−7.89 (3H, m), 7.33 (1H, d, $J = 2.5$ Hz), 7.06 (1H, dd, $J = 8.9$, 2.5 Hz), 6.63 (2H, d, $J = 8.9$ Hz), 4.60 (2H, dt, $J = 47.6$, 4.2 Hz), 4.21 (2H, t, $J = 4.5$ Hz), 3.89−3.94 (3H, m), 3.76 (1H, d, $J = 4.2$ Hz), 2.90 (3H, s). HRMS (EI) *m/z* calcd. for $[C_{18}H_{19}FN_2O_2S]^+$ 346.1151, found 346.1141.

2-[4′-(Methylamino)phenyl]-6-(2-(2-(2-fluoroethoxy)ethoxy)-ethoxy)benzothiazole (**5b**). Yield: 78%. (PTLC, 60% ethyl acetate in hexane). ^{1}H NMR (200 MHz, $CDCl_3$): δ 7.82−7.88 (3H, m), 7.32 (1H, d, $J = 2.5$ Hz), 7.05 (1H, dd, $J = 8.8$, 2.5 Hz), 6.63 (2H, d, $J = 8.8$ Hz), 4.56 (2H, dt, $J = 47.6$, 4.2 Hz), 4.19 (2H, t, $J = 4.5$ Hz), 3.65−3.88 (8H, m), 2.89 (3H, s). HRMS (EI) *m/z* calcd. for $[C_{20}H_{23}FN_2O_3S]^+$ 390.1413, found 390.1386.

2-[4′-(Methylamino)phenyl]-6-(2-(2-(2-(2-(2-(2-fluoroethoxy)ethoxy)ethoxy)ethoxy)ethoxy)ethoxy)benzothiazole (**5c**). Yield: 72%. (PTLC, 80% ethyl acetate in hexane). ^{1}H NMR (200 MHz, $CDCl_3$): δ 7.82−7.87 (3H, m), 7.33 (1H, d, $J =$ 2.4 Hz), 7.05 (1H, dd, $J = 8.8$, 2.4 Hz), 6.63 (2H, d, $J = 8.8$ Hz), 4.54 (2H, dt, $J = 47.6$, 4.1 Hz), 4.18 (2H, t, $J = 4.5$ Hz), 3.65−3.90 (20H, m), 2.89 (3H, s). HRMS (EI) *m/z* calcd. for $[C_{26}H_{35}FN_2O_6S]^+$ 522.2200, found 522.2175.

2-[4′-(Methylamino)phenyl]-6-(2-(2-(2-(2-(2-(2-(2-fluoro-ethoxy)ethoxy)ethoxy)ethoxy)ethoxy)ethoxy)ethoxy)-benzothiazole (**5d**). Yield: 71%. (PTLC, ethyl acetate). ^{1}H NMR (200 MHz, $CDCl_3$): δ 7.81−7.87 (3H, m), 7.33 (1H, d, $J =$ 2.4 Hz), 7.05 (1H, dd, $J = 8.8$, 2.4 Hz), 6.63 (2H, d, $J = 8.8$ Hz), 4.55 (2H, dt, $J = 47.7$, 4.2 Hz), 4.19 (2H, t, $J = 4.4$ Hz), 3.63−3.90 (28H, m), 2.89 (3H, s). HRMS (EI) *m/z* calcd. for $[C_{30}H_{43}FN_2O_8S]^+$ 610.2724, found 610.2705.

*Preparation of Compounds **6a**−**c**.* Treatment of **4** with hydroxymesylates according to the general procedure afforded compounds **6a**−**c**.

2-(2-(2-(4-Methylaminophenyl)benzothiazol-6-yloxy)ethoxy)-ethanol (**6a**). Yield: 82%. (PTLC, 1% methanol in dichloromethane). ^{1}H NMR (200 MHz, $CDCl_3$): δ 7.85−7.89 (3H, m), 7.33 (1H, d, $J = 2.4$ Hz), 7.06 (1H, dd, $J = 8.8$, 2.4 Hz), 6.64 (2H, d, $J = 8.8$ Hz), 4.20 (2H, d, $J = 4.3$ Hz), 3.90 (2H, d, $J = 4.6$ Hz), 3.69−3.78 (m, 4H), 2.90 (s, 3H). HRMS (EI) *m/z* calcd. for $[C_{18}H_{20}N_2O_3S]^+$ 344.1195, found 344.1188.

2-(2-(2-(2-(4-Methylaminophenyl)benzothiazol-6-yloxy]ethoxy)-ethoxy)ethanol (**6b**). Yield: 74%. (PTLC, 1% methanol in dichloromethane). ^{1}H NMR (200 MHz, $CDCl_3$): δ 7.83−7.88 (3H, m), 7.31 (1H, d, $J = 2.5$ Hz), 7.05 (1H, dd, $J = 8.8$, 2.5 Hz), 6.63 (2H, d, $J = 8.8$ Hz), 4.19 (2H, t, $J = 4.5$ Hz), 3.88 (2H, t, $J = 4.6$ Hz) 3.58−3.78 (8H, m), 2.90 (3H, s). HRMS (EI) *m/z* calcd. for $[C_{20}H_{24}N_2O_4S]^+$ 388.1457, found 388.1444.

2-(2-(2-(2-(2-(2-(4-Methylaminophenyl)benzothiazol-6-yloxy)ethoxy)ethoxy)ethoxy)ethoxy)ethoxy)ethanol (**6c**). Yield: 66%. (PTLC, 2% methanol in dichloromethane). ^{1}H NMR (200 MHz, $CDCl_3$): δ 7.83−7.88 (s, 3H), 7.33 (1H, d, J = 2.41 Hz), 7.06 (1H, dd, J = 8.8, 2.5 Hz), 6.63 (2H, d, J = 8.8 Hz), 4.19 (2H, t, J = 4.5 Hz), 3.88 (2H, t, J = 4.8 Hz), 3.56−3.53 (20H, m), 2.90 (3H, s). HRMS (EI) *m*/*z* calcd. for $[C_{26}H_{36}N_2O_7S]^+$ 520.2243, found 520.2282.

*Preparation of Compounds **7a**−**c**.* Alkylation of **4** with *tert*-butyldimethylsilyl protected mesylates as per the general procedure afforded compounds **7a**−**c**.

2-[4′-(Methylamino)phenyl]-6-(2-(2-*tert*-butyldimethylsilyloxyethoxy)ethoxy)benzothiazole (**7a**). Yield: 70%. (PTLC, 50% ethyl acetate in hexane). ^{1}H NMR (200 MHz, $CDCl_3$): δ 7.84−7.88 (3H, m), 7.32 (1H, d, J = 2.4 Hz), 7.06 (1H, dd, J = 8.8, 2.4 Hz), 6.64 (2H, d, J = 8.8 Hz), 4.20 (2H, d, J = 4.3 Hz), 3.90 (2H, d, J = 4.6 Hz), 3.64−3.78 (m, 4H), 2.90 (s, 3H), 0.88 (9H, s), 0.05 (6H, s).

2-[4′-(Methylamino)phenyl]-6-(2-(2-(2-*tert*-butyldimethylsilyloxyethoxy)ethoxy)ethoxy)benzothiazole (**7b**). Yield: 62%. (PTLC, 60% ethyl acetate in hexane). ^{1}H NMR (200 MHz, $CDCl_3$): δ 7.82−7.87 (3H, m), 7.30 (1H, d, J = 2.5 Hz), 7.05 (1H, dd, J = 8.8, 2.5 Hz), 6.62 (2H, d, J = 8.8 Hz), 4.21 (2H, t, J = 4.5 Hz), 3.88 (2H, t, J = 4.6 Hz), 3.58−3.74 (8H, m), 2.90 (3H, s), 0.88 (9H, s), 0.05 (6H, s).

2-[4′-(Methylamino)phenyl]-6-(2-(2-(2-(2-(2-(2-*tert*-butyldimethylsilyloxyethoxy)ethoxy)ethoxy)ethoxy)ethoxy)ethoxy)benzothiazole (**7c**). Yield: 55%. (PTLC, 80% ethyl acetate in hexane). ^{1}H NMR (200 MHz, $CDCl_3$): δ 7.85−7.89 (3H, m), 7.32 (1H, d, J = 2.4 Hz), 7.05 (1H, dd, J = 8.4, 2.4 Hz), 6.64 (2H, d, J = 8.4 Hz), 4.19 (2H, t, J = 4.7 Hz), 3.88 (2H, t, J = 4.9 Hz), 3.44−3.77 (20H, m), 2.90 (3H, s), 0.88 (9H, s), 0.05 (6H, s).

General Procedure for the Preparation of Compounds 10a−c. *General Procedure for Boc Protection to Form 7′(a−c).* Compounds **7a**−**c** (1 equiv) were dissolved in anhydrous tetrahydrofuran (10 mL/mmol of **7**), and to the resulting solution, di-*tert*-butyldicarbonate (2 equiv) and 4-dimethylaminopyridine (catalytic) were added and the mixture heated to reflux. After 16 h, another batch of di-*tert*-butyldicarbonate (1 equiv) was added and the mixture was further refluxed for another 20 h. The reaction mixture was then cooled to room temperature, and the solvent was removed under reduced pressure. The residue was taken in ethyl acetate (25 mL/mmol of **6**), washed successively with water (1 × 10 mL) and brine (1 × 10 mL), and dried over anhydrous magnesium sulfate. The residue after removing the solvent was purified by silica PTLC.

2-[4′-(*N*-*tert*-Butyloxycarbonyl-*N*-methylamino)phenyl]-6-(2-(2-*tert*-butyldimethylsilyloxyethoxy)ethoxy)benzothiazole (**7′a**). Yield: 55%. (PTLC, 20% ethyl acetate in hexane). ^{1}H NMR (200 MHz, $CDCl_3$): δ 7.91−8.01 (3H, m), 7.34−7.38 (3H, m), 7.08 (1H, dd, J = 8.8, 2.4 Hz), 4.22 (2H, d, J = 4.3 Hz), 3.89 (2H, d, J = 4.6 Hz), 3.60−3.76 (m, 4H), 3.02 (s, 3H), 1.47 (9H, s), 0.88 (9H, s), 0.05 (6H, s).

2-[4′-(*N*-*tert*-Butyloxycarbonyl-*N*-methylamino)-phenyl]-6-(2-(2-(2-*tert*-butyldimethylsilyloxyethoxy)ethoxy)-ethoxy)benzothiazole (**7′b**). Yield: 48%. (PTLC, 30% ethyl acetate in hexane). ^{1}H NMR (200 MHz, $CDCl_3$): δ 7.90−7.99 (3H, m), 7.34−7.37 (3H, m), 7.06 (1H, dd, J = 8.6, 2.5 Hz), 4.20 (2H, t, J = 4.5 Hz), 3.88 (2H, t, J = 4.6 Hz), 3.54−3.69 (8H, m), 3.01 (3H, s), 1.46 (9H, s), 0.88 (9H, s), 0.05 (6H, s).

2-[4′-(*N*-*tert*-Butyloxycarbonyl-*N*-methylamino)phenyl]-6-(2-(2-(2-(2-(2-*tert*-butyldimethylsilyloxyethoxy)ethoxy)ethoxy)-ethoxy)ethoxy)ethoxy)benzothiazole (**7′c**). Yield: 40%. (PTLC, 50% ethyl acetate in hexane). ^{1}H NMR (200 MHz, $CDCl_3$): δ 7.92−8.01 (3H, m), 7.36−7.40 (3H, m), 7.05 (1H, dd, J = 8.4, 2.4 Hz), 4.20 (2H, t, J = 4.7 Hz), 3.88 (2H, t, J = 4.9 Hz), 3.44−3.77 (20H, m), 3.02 (3H, s), 1.47 (9H, s), 0.88 (9H, s), 0.05 (6H, s).

*General Procedure for Deprotection Followed by Preparation of the Mesylate Derivatives **10a**−**c**.* *tert*-Butyl carbonate (BOC) protected compounds **7′a**−**c** were dissolved in anhydrous tetrahydrofuran (3 mL/0.1 mmol of **7′**), and the resulting solution was cooled to 0 °C. Tetrabutylammonium fluoride (2 equiv, 1 M in tetrahydrofuran) was added to the ice cold solution and stirred at the same temperature for 15 min followed by room temperature for 2 h. The solvent was then removed, and the residue dissolved in ethyl acetate (30 mL) and washed with water (1 × 10 mL), brine (1 × 10 mL), and dried over anhydrous magnesium sulfate. The resultant solution was then concentrated and redissolved in anhydrous dichloromethane (1 mL/0.1 mmol of **7′**). Anhydrous triethylamine (4 equiv) was then added and the mixture cooled in an ice−acetone bath (∼ −5 °C). Methanesulfonyl choride (3 equiv) was added and the mixture stirred at the same temperature for 15 min. The reaction mixture was brought to room temperature gradually and stirred for an additional 2 h. It was then quenched with ice and extracted with dichloromethane (3 × 5 mL). The organic layer after drying over anhydrous magnesium sulfate was purified by silica PTLC.

2-(4′-(*N*-*tert*-Butyloxycabonyl-*N*-methylamino)phenyl)-6-(2-(2-methylsulfonyloxyethoxy)ethoxy)benzothiazole (**10a**). Yield: 92%. (PTLC, 1% methanol in dichlormethane, 92%). ^{1}H NMR (200 MHz, $CDCl_3$): δ 7.91−8.01 (3H, m), 7.34−7.38 (3H, m), 7.08 (1H, dd, J = 8.8, 2.4 Hz), 4.39−4.44 (2H, m), 4.19−4.23 (2H, m), 3.84−3.89 (4H, m), 3.30 (3H, s), 3.05 (3H, s), 1.47 (9H, s).

2-(4′-(*N*-tert-Butyloxycarbonyl-*N*-methylamino)phenyl]-6-(2-(2-(2- methylsulfonyloxyethoxy)ethoxy)ethoxy)benzothiazole (**10b**). Yield: 95%. (PTLC, 1% methanol in dichloromethane, 95%). ^{1}H NMR (200 MHz, $CDCl_3$): δ 7.90−8.01 (3H, m), 7.33−7.38 (3H, m), 7.09 (1H, dd, J = 8.8, 2.5 Hz), 4.35−4.39 (2H, m), 4.17−4.22 (2H, m), 3.86−3.91 (2H, m), 3.69−3.80 (6H, m), 3.31 (3H, s), 3.05 (3H, s), 1.47 (9H, s).

2-[4′-(*N*-tert-Butyloxycarbonyl-*N*-methylamino)phenyl]-6-(2-(2-(2-(2-(2- methylsulfonyloxyethoxy)ethoxy)ethoxy)ethoxy)-ethoxy)ethoxy)benzothiazole (**10c**). Yield: 90%. (PTLC, 2% methanol in dichloromethane). ^{1}H NMR (200 MHz, $CDCl_3$): δ 7.91−8.01 (3H, m), 7.34−7.38 (3H, m), 7.11 (1H, dd, J = 8.8, 2.4 Hz), 4.33−4.38 (2H, m), 4.18−4.23 (2H, m), 3.87−3.92 (2H, m), 3.62−3.78 (18 H, m), 3.31 (3H, s), 3.06 (3H, s), 1.47 (9H, s).

Preparation of [2-(4-dimethylaminophenyl)vinyl]benzoxazol Derivatives. *2-(2-(4-dimethylaminophenyl)vinyl)benzoxazol-6-ol (3′).* 2-Methylbenzoxazol-6-ol (prepared following Schreiner and co-workers method (*29*)) (1.7 mmol) was dissolved in anhydrous tetrahydrofuran (8 mL) and cooled to 0 °C. Trimethylsilyl chloride (1.8 mmol) and diisopropylethylamine (1.84 mmol) were then added and the resultant solution stirred for 2 h at room temperature. After cooling to −78 °C, sodium hexamethyldisilazane (11.7 mmol, 1.0 M solution in tetrahydrofuran) was added slowly over 1.5 h and then stirred at −78 °C for an additional hour. 4-(Dimethylamino)benzaldehyde was then added and the reaction allowed to warm to room temperature overnight. The reaction was then poured into a 1 M solution of sodium hydrogen sulfate and extracted with ethyl acetate. The organic layer was then washed with brine, dried over magnesium sulfate, and concentrated to yield a yellow solid that was purified using column chromatography (3% methanol in dichloromethane). Yield: 45%. ^{1}H NMR (200 MHz, $CDCl_3$): δ 7.57 (2H, d, J = 8.9 Hz), 7.55 (1H, d, J = 16.0 Hz), 7.43 (1H, d, J = 8.5 Hz), 6.99 (1H, d, J = 2.1 Hz), 6.89 (1H, d, J = 16.0 Hz), 6.78 (1H, dd, J = 8.5, 2.1 Hz), 6.73 (2H, d, J = 8.9 Hz), 2.98 (6H, s). HRMS (EI) *m*/*z* calcd. for $[C_{17}H_{16}N_2O_2]^+$ 280.1212, found 280.1205.

*General Procedure for Pegylation of **3′***. To a solution of **3′** (1 equiv) in anhydrous *N*,*N*-dimethylformamide (2 mL) in a microwavable vial (from Biotage) was added potassium carbonate (3.0 equiv) and pegylating agent (1.2−1.5 equiv). The vial was sealed and subjected to microwave irradiation (Biotage Initiator system) at 200 °C for 10 min with 10 s pre-stirring and with fixed hold time "on". After cooling the reaction mixture to room temperature, the vial was opened and the contents poured into water and extracted with ethyl acetate (3 × 10 mL). The ethyl acetate layer was washed with water (2 × 10 mL) and brine (2 × 10 mL). The organic phase was then dried over anhydrous sodium sulfate and evaporated. The residue was purified by silica PTLC to afford the corresponding PEGylated derivatives (**8a**−**d**).

6-(2-Fluoroethoxy)-[2-(4-dimethylaminophenyl)vinyl]benzoxazol (**8a**). Yield: 68%. ^{1}H NMR (200 MHz, $CDCl_3$): δ 7.64 (1H, d, J = 16.2 Hz), 7.54 (1H, d, J = 8.7 Hz), 7.47 (2H, d, J = 8.8 Hz), 7.06 (1H, d, J = 2.3 Hz), 6.93 (1H, dd, J = 8.7, 2.3 Hz), 6.80 (1H, d, J = 16.2 Hz), 6.72 (2H, d, J = 8.8 Hz), 4.78 (2H, dt, J = 47.4, 4.0 Hz), 4.26 (2H, dt, J = 27.7, 4.0 Hz), 3.02 (6H, s). HRMS (EI) *m*/*z* calcd. for $[C_{19}H_{19}FN_2O_2]^+$ 326.1434, found 326.1431.

6-(2-(2-(2-Fluoroethoxy)ethoxy)ethoxy)-[2-(4-dimethylaminophenyl)vinyl]benzoxazol (**8b**). Yield: 71%. ^{1}H NMR (200 MHz, $CDCl_3$): δ 7.63 (1H, d, J = 16.2 Hz), 7.52 (1H, d, J = 8.8 Hz), 7.47 (2H, d, J = 9.0 Hz), 7.06 (1H, d, J = 2.1 Hz), 6.92 (1H, dd, J = 8.8, 2.1 Hz), 6.80 (1H, d, J = 16.2 Hz), 6.72 (2H, d, J = 9.0 Hz), 4.57 (2H, dt, J = 47.6, 4.1 Hz), 4.19 (2H, t, J = 4.5 Hz), 3.92−3.67 (10H, m), 3.02 (6H, s). HRMS (EI) *m*/*z* calcd. for $[C_{23}H_{27}FN_2O_4]^+$ 414.1955, found 414.1946.

6-(2-(2-(2-(2-(2-Fluoroethoxy)ethoxy)ethoxy)ethoxy)ethoxy)-[2-(4-dimethylaminophenyl)vinyl]benzoxazol (**8c**). Yield: 66%. ^{1}H NMR (200 MHz, $CDCl_3$): δ 7.63 (1H, d, J = 16.2 Hz), 7.51 (1H, d, J = 8.1 Hz), 7.46 (2H, d, J = 8.7 Hz), 7.05 (1H, d, J = 2.1 Hz), 6.91 (1H, dd, J = 8.1, 2.1 Hz), 6.80 (1H, d, J = 16.2 Hz), 6.71 (2H, d, J = 8.7 Hz), 4.54 (2H, dt, J = 47.5, 3.8 Hz), 4.17 (2H, t, J = 5.1 Hz), 3.90−3.65 (20H, m), 3.02 (6H, s). HRMS (EI) *m*/*z* calcd. for $[C_{29}H_{39}FN_2O_7]^+$ 546.2741, found 546.2740.

6-(2-(2-(2-(2-(2-(2-(2-Fluoroethoxy)ethoxy)ethoxy)ethoxy)ethoxy)ethoxy)ethoxy)[2(4-dimethylaminophenyl)vinyl]-benzoxazol (**8d**). Yield: 95%. ^{1}H NMR (200 MHz, $CDCl_3$): δ 7.62 (1H, d, J = 16.2 Hz), 7.50 (1H, d, J = 8.6 Hz), 7.48 (2H, d, J = 8.9 Hz), 7.08 (1H, d, J = 2.2 Hz), 6.92 (1H, dd, J = 8.6, 2.2 Hz), 6.80 (1H, d, J = 16.2 Hz), 6.73 (2H, d, J = 8.9 Hz), 4.53 (2H, dt, J = 47.7, 4.0 Hz), 4.17 (2H, t, J = 4.39 Hz), 3.87−3.59 (30H, m), 3.02 (6H, s). HRMS (EI) *m*/*z* calcd. for $[C_{33}H_{47}FN_2O_9]^+$ 634.3266, found 634.3242.

*Preparation of 2-(2-(2-(2-(4-(dimethylamino)styryl)benzoxazol-6-yloxy)ethoxy)ethoxy)ethanol (**9**).* To a solution of **3′** (1 equiv) in anhydrous *N*,*N*-dimethylformamide (2 mL) in a microwavable vial (from Biotage) was added potassium carbonate (3.0 equiv) and 2-(2-(2-chloroethoxy)ethoxy)ethanol (1.5 equiv). The vial was sealed and subjected to microwave irradiation (Biotage Initiator system) at 200 °C for 10 min with 10 s pre-stirring and with fixed hold time "on". After cooling the reaction mixture to room temperature, the vial was opened and the contents poured into water and extracted with ethyl acetate (3 × 10 mL). The ethyl acetate layer was washed with water (2 × 10 mL) and brine (2 × 10 mL). The organic phase was then dried over anhydrous sodium sulfate and evaporated. The residue was purified by silica PTLC (25% hexanes in ethyl acetate) to afford the corresponding hydroxy PEGylated derivative (**9**) in 80% yield. ^{1}H NMR (200 MHz, $CDCl_3$): δ 7.61 (1H, d, J = 16.2 Hz), 7.52 (1H, d, J = 8.8 Hz), 7.48 (2H, d, J = 9.0 Hz), 7.05 (1H, d, J = 2.2 Hz), 6.92 (1H, dd, J = 8.8, 2.2 Hz), 6.80 (1H, d, J = 16.2 Hz), 6.72 (2H, d, J = 9.0 Hz), 4.17 (2H, t, J = 4.4 Hz), 3.88 (2H, t, J = 4.4 Hz), 3.76−3.59 (8H, m), 3.00 (6H, s).

*Preparation of 2-(2-(2-(2-(4-(dimethylamino)styryl)benzoxazol-6-yloxy)ethoxy)ethoxy)ethyl methanesulfonate (**11**).* Compound **9** was dissolved in dichloromethane, followed by the addition of triethylamine (4.0 equiv). Methanesulfonyl chloride was then added via a syringe and the resultant solution stirred for 3 h at room temperature. The solution was then poured into water and extracted with dichloromethane, washed with brine, and dried over sodium sulfate. The residue was purified via silica PTLC (25% hexanes in ethyl acetate) to afford the mesylated precursor (**11**) in 75% yield. ^{1}H NMR (200 MHz, $CDCl_3$): δ 7.63 (1H, d, J = 16.2 Hz), 7.52 (1H, d, J = 8.8 Hz), 7.48 (2H, d, J = 9.0 Hz), 7.05 (1H, d, J = 2.1 Hz), 6.92 (1H, dd, J = 8.8, 2.1 Hz), 6.80 (1H, d, J = 16.2 Hz), 6.72 (2H, d, J = 9.0 Hz), 4.37 (2H, t, J = 4.4 Hz), 4.19 (2H, t, J = 4.4 Hz), 3.87 (2H, t, J = 4.3 Hz), 3.79−3.61 (6H, m), 3.05 (3H, s), 3.02 (6H, s).

Synthesis of 6-Iodo-2-(4′-dimethylamino)phenylimidazo-[1,2-*a*]pyridine (IMPY) (2) Derivatives. Preparation of **2** (IMPY core) has been described elsewhere (*30*). The general procedure for the synthesis of 6-FPEG substituted-IMPY conjugates was accomplished using the following procedures.

Method A. Conventional synthesis: The mixture of **2** (prepared as reported previously (*30*)), fluoro-polyglycols (2−5 equiv), CuI (10% mol), Cs_2CO_3 (2 equiv), 1,10-phenanthroline (20% mol) in toluene (1 mL/0.1 mmol **2**) was stirred in a sealed tube for 48 h. The solvent was then removed and the residue purified by silica PTLC (ethyl acetate or 95% dichloromethane/5% methanol as the developing solvent) to give the desired product.

Method B. Microwave synthesis: The mixture of reactants and reagents described above in a sealed tube was put in the microwave oven at the following conditions: 170 °C, 60 min, normal absorption level (yields were similar to those used for the conventional synthesis).

6-(2-Fluoroethoxy)-2-(4-dimethylamino)phenylimidazo[1,2-a]pyridine (**12a**). Yield: 17%. (Method A) ^{1}H NMR (200 MHz, $CDCl_3$): δ 7.78 (2H, d, J = 8.8 Hz), 7.68 (1H, d, J = 2.2 Hz), 7.67 (1H, s), 7.50 (1H, d, J = 9.7 Hz), 6.96 (1H, dd, J = 9.7, 2.2 Hz), 6.74 (2H, d, J = 8.8 Hz), 4.75 (2H, dt, J = 47.7, 4.1 Hz), 4.16 (2H, dt, J = 25.9, 4.1 Hz), d 2.99 (6H, s). HRMS (EI) *m*/*z* calcd. for $[C_{17}H_{19}FN_3O]^+$ $(M + H)^+$ 300.1512, found 300.1500.

6-(2-(2-Fluoroethoxy)ethoxy)-2-(4-dimethylamino)phenylimidazo[1,2-*a*]pyridine (**12b**). Yield: 59%. (Method A) ^{1}H NMR (200 MHz, $CDCl_3$): δ 7.78 (2H, d, J = 8.8 Hz). 7.66 (1H, d, J = 2.2 Hz), 7.64 (1H, s), 7.46 (1H, d, J = 9.7 Hz), 6.94 (1H, dd, J = 9.7, 2.2 Hz), 6.76 (2H, d, J = 8.8 Hz), 4.59 (2H, dt, J = 47.6, 4.1 Hz), 4.08 (2H, t, J = 4.2 Hz), 3.88 (2H, t, J = 4.2 Hz), 3.80 (2H, dt, J = 25.9, 4.1 Hz), 2.98 (6H, s). HRMS (EI) *m*/*z* calcd. for $[C_{19}H_{23}FN_3O_2]^+$ $(M + H)^+$ 344.1774, found 344.1768.

6-(2-(2-(2-Fluoroethoxy)ethoxy)ethoxy)-2-(4-dimethylamino)-phenylimidazo[1,2-*a*] pyridine (**12c**). Yield: 60%. (Method A) ^{1}H NMR (200 MHz, $CDCl_3$): δ 7.77 (2H, d, J = 8.8 Hz), 7.65 (1H, d, J = 2.2 Hz), 7.63 (1H, s), 7.45 (1H, d, J = 9.7 Hz), 6.93 (1H, dd, J = 9.7, 2.2 Hz), 6.75 (2H, d, J = 8.8 Hz), 4.54 (2H, dt, J = 47.7, 4.1 Hz), 4.06 (2H, t, J = 4.6 Hz), 3.82 (2H, t, J = 4.6 Hz), 3.70−3.59 (6H, m), 2.97 (6H, s). HRMS (EI) *m*/*z* calcd. for $[C_{21}H_{27}FN_3O_3]^+$ $(M + H)^+$ 388.2036, found 388.2032.

6-(2-(2-(2-(2-(2-Fluoroethoxy)ethoxy)ethoxy)ethoxy)ethoxy)-2-(4-dimethylamino)phenylimidazo[1,2-*a*]pyridine (**12d**). Yield: 18%. (Method A) ^{1}H NMR (200 MHz, $CDCl_3$): δ 7.78 (2H, d, J = 8.8 Hz), 7.71 (1H, d, J = 1.9 Hz), 7.67 (1H, s), 7.48 (1H, d, J = 9.7 Hz), 6.93 (1H, dd, J = 9.7, 2.2 Hz), 6.76

(2H, d, $J = 8.8$ Hz), 4.53 (2H, dt, $J = 47.7$, 4.1 Hz), 4.09 (2H, t, $J = 4.6$ Hz), 3.85 (2H, t, $J = 4.6$ Hz), 3.89−3.64 (18H, m), 2.98 (6H, s). HRMS (EI) *m/z* calcd. for $[C_{27}H_{39}FN_3O_6]$ $(M + H)^+$ 520.2823, found 520.2808.

6-(2-(2-(2-(2-(2-(2-(2-(2-Fluoroethoxy)ethoxy)ethoxy)ethoxy)-ethoxy)ethoxy)ethoxy)ethoxy)-2-(4-dimethylamino)phenylimidazo[1,2-*a*]pyridine (**12e**). Yield: 58%. (Method A) ^{1}H NMR (200 MHz, $CDCl_3$): δ 7.75 (2H, d, $J = 8.8$ Hz), 7.68 (1H, d, $J = 1.9$ Hz), 7.62 (1H, s), 7.52 (1H, d, $J = 9.7$ Hz), 6.95 (1H, dd, $J = 9.7$, 2.2 Hz), 6.71 (2H, d, $J = 8.8$ Hz), 4.50 (2H, dt, $J = 47.7$, 4.0 Hz), 4.07 (2H, t, $J = 4.6$ Hz), 3.64−3.85 (28H, m), 2.95 (6H, s). HRMS (EI) *m/z* calcd. for $[C_{31}H_{47}FN_3O_8]^+$ $(M + H)^+$ 608.3347, found 608.3329.

*Synthesis of 2-(2-(2-(2-(4-(Dimethylamino)phenyl)imidazo-[1,2-a]pyridin-6-yloxy)ethoxy)ethoxy)ethanol (**13**).* Method 1. The mixture of **2** (prepared as reported previously (*30*)) (36 mg, 0.1 mmol), triethylene glycol (135 mg, 1mmol), CuI (19 mg, 0.1 mmol), Cs_2CO_3 (65 mg, 0.2 mmol), and 1,10-phenanthroline (927 mg, 0.15 mmol) in toluene (1 mL) was reacted in MW (170 °C, absorption: normal) for 1 h. The solvent was removed, and the residue was purified by silica PTLC (CH_2Cl_2/MeOH = 95:5) to give 28 mg of product (73.6%).

Method 2. The above mixture was stirred at 120 °C in a sealed tube for 48 h. The same workup as described in Method 1 gave the desired product in 36% yield.

^{1}H NMR (200 MHz, $CDCl_3$): d 7.75 (2H, d, $J = 7.8$ Hz), 7.67 (2H, s), 7.58 (2H, d, $J = 9.2$ Hz), 6.96 (2H, d, $J = 8.9$ Hz), 6.69 (2H, d, $J = 7.8$ Hz), 4.07 (2H, t, $J = 4.5$ Hz), 3.84 (2H, t, $J = 4.5$ Hz), 3.71−3.76 (6H, m), 3.61 (2H, t, $J = 4.5$ Hz), 2.95 (6H, s).

*Synthesis of 2-(2-(2-(2-(4-(Dimethylamino)phenyl)imidazo-[1,2-a]pyridin-6-yloxy)ethoxy)ethoxy)ethyl 4-Methylbenzene-sulfonate (**14**).* To a solution of **13** (45 mg, 0.12 mmol) dissolved in pyridine (1 mL) was added tosyl chloride (45 mg, 0.24 mmol) in solid form at 0 °C followed by DMAP (10 mg), and the resultant solution stirred at room temperature for 3 h. The reaction mixture was then poured into ice water and the mixture extracted with a mixed solvent (CH_2Cl_2/MeOH = 95:5). The combined organic solvent was dried over Na_2SO_4, filtered, and the filtrate concentrated to yield the crude product which was purified by silica PTLC (CH_2Cl_2/MeOH = 95:5) to give 29 mg of product (46%). ^{1}H NMR (200 MHz, $CDCl_3$): d 7.77 (2H, d, $J = 8.7$ Hz), 7.70 (1H, d, $J = 2.2$ Hz), 7.67 (1H, s), 7.48 (2H, d, $J = 9.6$ Hz), 7.29 (2H, d, $J = 8.2$ Hz), 6.94 (2H, dd, $J = 9.7$, 2.1 Hz), 6.76 (2H, d, $J = 8.8$ Hz), 4.16 (2H, t, $J = 4.7$ Hz), 4.07 (2H, t, $J = 4.6$ Hz), 3.83 (2H, t, $J = 4.6$ Hz), 3.53−3.69 (6H, m), 2.98 (6H, s), 2.40 (3H, s).

Radiochemistry. *General Procedure for ^{18}F Labeling of **10a**.* [^{18}F]Fluoride was produced by the JSW-type BC3015 cyclotron at the Cyclotron Facility, University of Pennsylvania, using ^{18}O-(p,n)^{18}F reaction. An [^{18}O]-enriched aqueous solution of [^{18}F]-fluoride was passed through a Sep-Pak Light quaternary methyl ammonium (QMA) cartridge (Waters) and the cartridge dried by airflow. The ^{18}F activity was then eluted using 1.2 mL of a Kryptofix 222/potassium carbonate solution, which is made up of 22 mg of Kryptofix 222 and 4.6 mg of potassium carbonate in acetonitrile/water (1.77/0.23). The solvent was removed under a stream of nitrogen at 120 °C and the residue azeotropically dried twice with 1 mL of anhydrous acetonitrile, also at 120 °C. The mesylate precursor (**10a**) (0.5, 1, 3, and 6 mg) was then dissolved in 0.2 mL of dimethyl sulfoxide and added to the reaction vessel containing the dry ^{18}F. The reaction was subsequently carried out under different temperatures for different time periods as shown in Table 2. 10% aqueous HCl (0.5 mL) was then added and the resultant mixture heated for an additional 10 min. Following completion of the reaction, water (2 mL) was added and the resultant solution loaded onto a Waters Oasis HLB cartridge (3 cm^3) previously washed with 2 × 3 mL ethanol and 2 × 3 mL of water. The cartridge was washed with 4 mL of water and the crude product eluted with 2 mL of acetonitrile. The Waters C18 Sep Pak could be used alternatively. However, the recovery yield of radioactivity by acetonitrile was lower.

Table 2. Optimization Studies for Compound [^{18}F]5a, Examining the Effect of Precursor Mass, Temperature, and Time for Traditional Heating vs Microwave Heating Strategies

entry	heating method	precursor mass (mg)	time (min)	temperature (°C)	radiochemical yield (%)
1	oil	0.5	4	120	32
2	oil	1	4	120	50
3	oil	3	4	120	50
4	oil	6	4	120	30
5	oil	1	8	120	59
6	oil	1	12	120	64
7	oil	1	16	120	62
8	oil	1	4	75	17
9	oil	1	4	90	26
10	oil	1	4	105	45
11	MW (80W)	0.25	1	100	24
12	MW (80W)	0.5	1	100	30
13	MW (80W)	1	1	100	41
14	MW (80W)	3	1	100	24
15	MW (80W)	1	2	100	42
16	MW (80W)	1	3	100	40
17	MW (80W)	1	4	100	60
18	MW (80W)	1	1	90	54
19	MW (80W)	1	1	110	52
20	MW (80W)	1	1	130	48
21	MW (80W)	1	1	150	43

Acetonitrile solution was then injected onto a semipreparative HPLC for purification. The retention time of the major hydrolysis byproduct ($R_t = 3.6$ min) was well-resolved from the desired ^{18}F-labeled product ($R_t = 5.2$ min), which was isolated in >99% radiochemical purity, and the specific activity was estimated to be 500−1000 Ci/mmol after purification (specific activity was estimated by comparing UV peak intensity of purified [^{18}F]**5a** with reference to a nonradioactive compound of known concentration). Radiochemical yields are summarized in Table 2.

*General Procedure for ^{18}F Labeling of **10b**, **10c**, **11**, and **14**.* Compounds **10b**, **10c**, **11**, and **14** were labeled with ^{18}F using the similarly described procedure for **10a**. Subsequent Boc deprotection was carried out for **10b** and **10c**. For all these compounds, the reaction was carried out at 120 °C for 4 min, which is the optimum condition with regard to time and temperature.

The crude reaction was purified via HPLC using the same conditions (except **11**, which used the same columns with solvent composition acetonitrile/water 60/40 at the same flow rate). Radiochemical yields ranged between 11% and 35%, and all were isolated in good radiochemical purity (>90%) with the exception of [^{18}F]**8b** wherein a second peak was evident within minutes of isolation. Specific activities for [^{18}F]**5b**, **c**, and [^{18}F]**12c** ranged between 800 and 1500 Ci/mmol.

Preparation of Brain Tissue Homogenates. Postmortem brain tissues were obtained from AD patients at autopsy, and neuropathological diagnosis was confirmed by current criteria (NIA-Reagan Institute Consensus Group, 1997). Homogenates were then prepared from dissected gray matter from AD patients in phosphate buffered saline (PBS, pH 7.4) at the concentration of approximately 100 mg wet tissue/mL (motor-driven glass homogenizer with setting of 6 for 30 s). The homogenates were aliquoted into 1-mL portions and stored at −70 °C for 6−12 months without loss of binding signal.

Binding Studies. As reported previously, [^{125}I]IMPY (*12*), with 2200 Ci/mmol specific activity and greater than 95%

radiochemical purity, was prepared using the standard iodo-destannylation reaction and purified by a simplified C-4 minicolumn (*12*). Binding assays were carried out in 12 × 75 mm borosilicate glass tubes. The reaction mixture contained 50 μL of brain homogenates (20−50 μg), 50 μL of [^{125}I]IMPY (0.04−0.06 nM diluted in PBS), and 50 μL of inhibitors (10^{-5}−10^{-10} M diluted serially in PBS containing 0.1% bovine serum albumin, BSA) in a final volume of 1 mL. Nonspecific binding was defined in the presence of IMPY (600 nM) in the same assay tubes. The mixture was incubated at 37 °C for 2 h, and the bound and free radioactivity were separated by vacuum filtration through Whatman GF/B filters using a Brandel M-24R cell harvester followed by 2 × 3 mL washes of PBS at room temperature. Filters containing the bound ^{125}I ligand were assayed for radioactivity content in a γ counter (Packard 5000) with 70% counting efficiency. Under the assay conditions, the specifically bound fraction was less than 15% of the total radioactivity. The results of inhibition experiments were subjected to nonlinear regression analysis using EBDA by which K_i values were calculated.

Film Autoradiography. Brain sections from AD subjects were mounted onto glass slides and incubated with F-18 tracers (300 000−600 000 cpm /200 μL) for 1 h at room temperature. The sections were then washed in saturated Li_2CO_3 in 40% EtOH (two 2-min washes) and in 40% EtOH (2 min) followed by rinsing with water for 30 s. After drying, the F-18 labeled sections were exposed to Kodak MR film overnight.

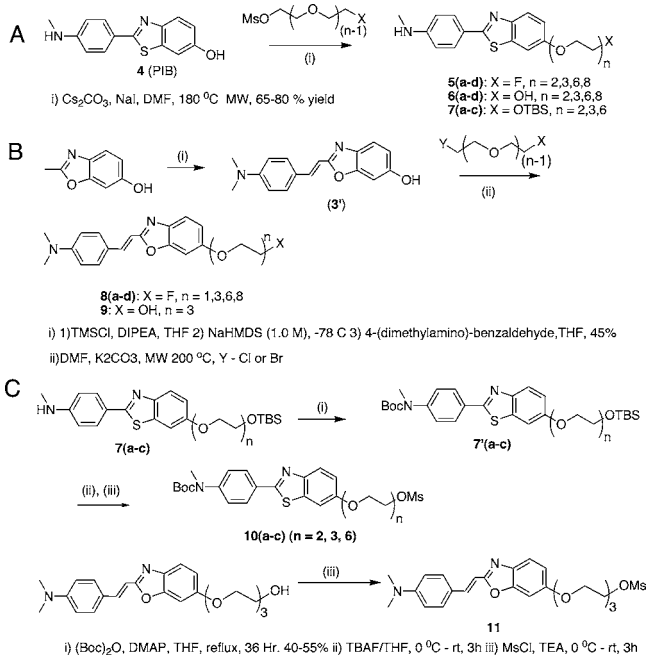
Partition Coefficient. Partition coefficients were measured by mixing the [^{18}F]-labeled sample with 3 g each of 1-octanol and buffer (0.1 M phosphate, pH 7.4) in a test tube. The two layers in the test tube were vortexed for 3 min followed by centrifugation for 5 min at room temperature. The radioactivity content values of two weighed samples (0.5 g each) from the 1-octanol and buffer layers were counted in a well counter. The partition coefficient was determined by calculating the ratio of cpm/g of 1-octanol to that of buffer. A sample from the 1-octanol layer was repartitioned with buffer solution, and each layer was counted again. This procedure was repeated until a consistent value of partition coefficient values was obtained (usually the third or fourth partition). The measurements were repeated three times.

Biodistribution Studies in Normal Mice. While under isoflurane anesthesia, 0.15 mL of a saline solution containing the [^{18}F] tracers (10−20 uCi) was injected directly into the lateral tail vein of male ICR mice. The mice (n = 3 for each time point) were sacrificed by cervical dislocation. At 2, 30, 60, and 120 min postinjection, organs of interest were removed, weighed, and assayed for radioactivity content with an automatic γ counter. The percentage dose per organ was calculated by a comparison of the tissue counts to counts of 1% of initial dose (100 times diluted aliquots of the injected material). Total activities of blood and bone were calculated under the assumption that they were 7% and 14% of the body weight, respectively. The % dose/g of samples was calculated by comparing the sample counts with the count of the diluted initial dose.

RESULTS AND DISCUSSION

One of the major advantages of our FPEG approach is incorporation of the fluoro tag at the end of a polyethylene glycol chain. The preparation of these compounds is readily achieved in a relatively simple and straightforward manner. In this report, we describe the FPEG derivatives of three cores: PIB (**4**), [2-(4-dimethylaminophenyl)vinyl]benzoxazol (**3′**), and IMPY (**2**), previously reported as imaging agents for Aβ aggregates (*10*, *12*−*16*). Syntheses of core compounds **2** and **4** and polyethylene glycol precursors were accomplished following literature procedures with minor modifications (*21*, *26*). Compound **3′** was

Scheme 1. Syntheses of FPEG Conjugates and Radiolabeling Precursors

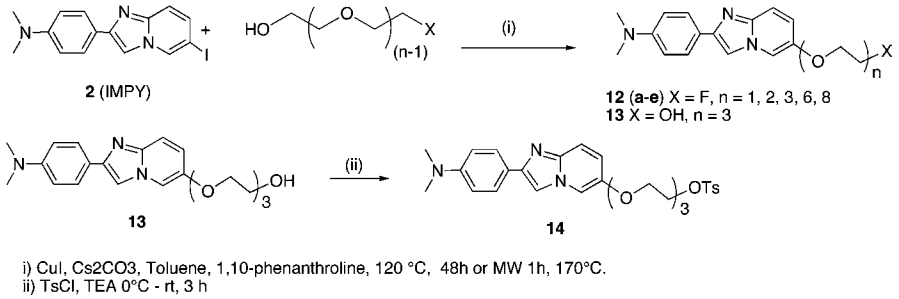


prepared from 6-hydroxy-2-methylbenzoxazole followed by in situ trimethylsilyl protection of the phenolic OH, deprotonation, and condensation with *N*,*N*′-dimethylaminobenzaldehyde as described during the synthesis of similar compounds by Schreiner and co-workers (Scheme 1) (*29*). Conjugation of the free phenolic hydroxy groups to compounds **3′** and **4** with various oligoethylene glycol precursors was accomplished under microwave irradiation in good yields (68−95%) (Scheme 1A and B). By utilizing the same methodology, the radiofluorination precursors can be generated quickly and efficiently, conveniently allowing the radioactive fluoride to be added in the last step of the synthesis. Preparation of the mesylate precursor was generated following synthesis of the hydroxy derivative using a similar microwave procedure (Scheme 2C). It was important to also prepare and identify the hydroxy derivatives of FPEG, as they compete for binding to β-amyloid plaques and they are the major byproducts during radiolabeling.

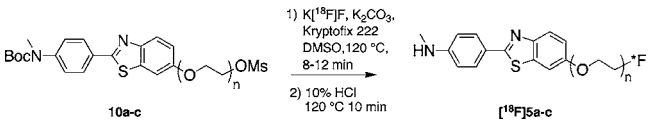
The synthetic versatility of this strategy was further demonstrated with conjugates of compound **2** wherein FPEG was conjugated to **2** via a copper-catalyzed coupling reaction with the aryl iodide and corresponding fluoro/hydroxy PEG derivative (Scheme 3). The desired FPEG derivatives were prepared in moderate to good yields (17−60%).

In vitro binding studies to evaluate the binding affinities of the FPEG conjugates (**5a**−**d**, **8a**−**d**, and **12a**−**e**) to Aβ aggregates were carried out in AD brain homogenate with [^{125}I]-IMPY (**2**) as the ligand (*31*) (Table 1). Previous experience in preparing FPEG−stilbene (**1**) derivatives suggested that FPEG n = 3 was an ideal compromise between the addition of PEG groups to reduce lipophilicity and the need for a small neutral molecule to maintain good brain penetration (*21*). However, when similar n = 3 derivatives (**5b**, **8b**, and **12c**) were prepared and evaluated in vitro, it was evident this was not always the case. Only **5b** and **8b** retained high binding affinities for the n = 3 FPEG conjugates with K_i values of 3.8 and 14.5 nM, respectively. Compound **12c** was not nearly as potent, with a K_i value of 30 nM. In fact, further derivatization of **12** only increased the K_i (96 and 387 nM for **12d** and **12e**, respectively) (i.e., reducing the binding affinity), while the other core compounds remained highly potent in their binding affinities. On the basis of these initial in vitro results, FPEG conjugation

Scheme 2. Synthesis of FPEG-IMPY Conjugates 12a−e, 13, and the Corresponding Precursor 14 for Radiolabeling



Scheme 3. ^{18}F Radiolabeling of 10a−c



clearly failed for conjugates **12a**−**e** (IMPY (**2**) derivatives) but was quite successful with the other two core compounds (PIB conjugates **5a**−**d** and BF conjugates **8a**−**d**).

^{18}F labeling was performed on either the mesyl or tosyl precursors undergoing a nucleophilic displacement reaction with the fluoride anion. Radiolabeling with ^{18}F was successfully performed on all core structures from precursors **10a**−**c** (Scheme 3), **11**, and **14** to generate [^{18}F]**5a**−**c**, [^{18}F]**8b**, and [^{18}F]**12c**, respectively. We labeled FPEG conjugates $n = 3$ initially on the basis of our past experience and success using this approach (*21*, *26*). Both core conjugates [^{18}F]**12c** (IMPY, **2**) and [^{18}F]**5b** (PIB, **4**) were labeled in moderate yields (30−35%) and with good radiochemical purities (>90%) from the tosyl and mesyl precursors, respectively. Retention times of the ^{18}F-labeled products (R_t([^{18}F]**12c**) = 6.5 min and R_t([^{18}F]**5b**) = 8.0 min) were well-separated from the major hydrolysis products (R_t = 4.0 and 4.5 min). An example of HPLC profile is shown in Figure 3. The preparation was about 80−90 min, and the specific activity for all prepared ^{18}F compounds was estimated to be 500−1500 Ci/mmol at the end of synthesis. Radiolabeled [^{18}F]-**8b**, which was prepared from the mesylate precursor in moderate radiochemical yield (23%), unfortunately could not be prepared in good radiochemical purity due to the instability of this compound. The formation of a second peak was evident within minutes of labeling upon standing at room temperature in ethanol or the acetonitrile/water HPLC solvent mixture. These results are consistent with those found by Shimadzu et al. during their labeling of a similar substrate (*32*). They attributed the formation of a second peak to the facile formation of *E* and *Z* isomers (*32*). On the basis of the promising in vitro binding affinities of **5a**−**d** and initial labeling results of [^{18}F]**5b**, we then prepared both [^{18}F]**5a** and [^{18}F]**5c** using the standard approach in good yields (35% and 11%, respectively) and purity (>98%).

For many years, use of mesylate precursors for radiofluorination chemistry has been demonstrated (*19*); however, the utility of these precursors for radiolabeling FPEG conjugates is relatively new. In order to study the radiofluorination reaction with FPEG, we prepared a large batch of precursor **10a** and evaluated the effects of precursor mass, temperature, reaction time, and sep-pak purification strategies.

Initially, using 1 mg of precursor **10a** dissolved in 250 μL of DMSO, the reaction temperature was varied from 75 °C to 120 °C using standard oil-bath heating for 4 min. Deprotection of the Boc protecting group was then achieved by adding 10% HCl and heating for 10 min. Water was then added (2 mL) and the solution loaded onto an Oasis HLB sep-pak cartridge. Following washing with water, the crude labeled product was eluted with 2 mL of acetonitrile and injected onto the HPLC. Labeling yields were highest at 120 °C (Table 2). Next, the amount of precursor (**10a**) was varied from 0.5 mg to 6 mg with oil-bath heating at 120 °C for 4 min. Boc deprotection was then accomplished as described above, leading to radiochemical yields ranging from 30% to 50%, with the highest between 1 and 3 mg. The final study performed with traditional oil-bath heating evaluated the effect of increasing the reaction times from 4 min to 16 min using 1 mg of precursor and heating at 120 °C. We found that reaction times from 8 min to 16 min all led to high radiochemical yields of greater than 59%. The radiochemical purity for all reactions was greater than 98%.

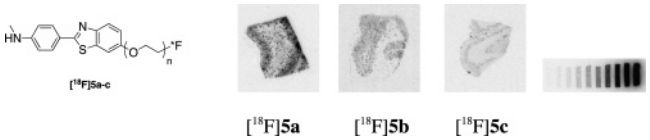
Microwave heating methods were also studied in the same manner, evaluating the effect of precursor mass, increased temperatures, and reaction times. In general, the precursor mass did not have an affect when ranging between 0.25 and 3 mg. Increasing the reaction times from 1 to 4 min showed significant improvement in the radiochemical yield (up to 60% with 4 min at 80 W, 100 °C using 1 mg of precursor dissolved in 250 μL of DMSO), while increasing the temperature at a constant power level seemed to decrease the yields (Table 2).

From these studies, it is evident that both traditional oil-bath and microwave heating strategies can prepare radiolabeled [^{18}F]-**5a** (FPEG PIB, $n = 2$) conjugates in good radiochemical yields (60−64%). The optimized oil bath conditions are 1−3 mg of precursor heated at 120 °C for 12 min, followed by the standard deprotection. Traditional oil-bath heating is still preferred in our hands, as it has led to more reproducible results.

The lipophilicity (log *P*) of the labeled tracers ([^{18}F]**5a**−**c**, **8b**, and **12c**) was evaluated, as log *P* values between 0 and 3 can often indicate good blood−brain barrier penetration. The log *P* value of [^{18}F]**12c** was 2.69, and that of the parent compound, IMPY (**2**), was 2.19 (*33*), suggesting that addition of the FPEG unit does not significantly change the lipophilicity of the compound. Furthermore, all ^{18}F-labeled tracers were within an appropriate range (log *P* values between 2.69 and 3.04, Table 1) and similar to those of the stilbene−FPEG conjugates (log $P = 2.05-2.53$) (*21*).

The binding of these radiofluorinated probes to Aβ plaques in AD brain sections was evaluated by in vitro autoradiography and labeling of Aβ plaques in confirmed AD brain sections was observed for [^{18}F]**5a**−**c**. [^{18}F]**5a** especially displayed a superior Aβ plaque labeling showing a strong signal and a low background (Figure 2). The results strongly confirm the binding of these ^{18}F tracers to the Aβ aggregates in the brain of AD patients. Similarly, [^{18}F]**8b** was able to label the plaques using the mixture of isomers (data not shown). However, unlike the other conjugates, [^{18}F]**12c** did not display a significant labeling under similar labeling conditions (data not shown).

Biodistribution studies in normal mice with [^{18}F]**5a**−**c** (displayed in Table 3) and [^{18}F]**12c** were performed. [^{18}F]**8b** was not evaluated for the distribution study on the basis of the higher molecular weight, lower brain penetration of the parent core (**3**, BF-168) (*15*, *16*), and the facile racemization seen during labeling. We use normal mice as a convenient animal model to evaluate the brain penetration of these ^{18}F tracers.



[^{18}F]**5a** [^{18}F]**5b** [^{18}F]**5c**

Figure 2. In vitro autoradiography of brain cortical sections from confirmed AD patients labeled with [^{18}F]**5a**−**c.** The Aβ plaques, known to be a hallmark of AD, were distinctively labeled with all ^{18}F tracers.

Table 3. Biodistribution in Normal Mice of [^{18}F] Tracers[a]

[^{18}F]**5a**

organ	2 min	30 min	1 h	2 h
blood	3.37 ± 0.46	3.60 ± 0.13	4.55 ± 0.40	4.38 ± 0.14
heart	8.32 ± 0.37	3.49 ± 0.27	3.81 ± 0.25	3.59 ± 0.03
muscle	0.82 ± 0.12	2.83 ± 0.22	2.76 ± 0.17	2.36 ± 0.11
lung	7.79 ± 0.34	3.91 ± 0.28	3.84 ± 0.55	3.63 ± 0.15
kidney	13.02 ± 1.04	4.54 ± 0.62	3.98 ± 0.24	3.18 ± 0.16
spleen	6.92 ± 0.79	3.93 ± 0.29	3.87 ± 0.61	3.32 ± 0.16
liver	19.02 ± 1.06	7.98 ± 0.60	6.35 ± 0.46	5.05 ± 0.43
skin	1.08 ± 0.22	3.14 ± 0.22	3.15 ± 0.28	2.62 ± 0.16
brain	10.27 ± 1.30	4.59 ± 0.47	3.94 ± 0.04	3.86 ± 0.35
bone	1.69 ± 0.21	2.28 ± 0.20	3.17 ± 0.39	6.35 ± 1.32

[^{18}F]**5b**

organ	2 min	30 min	1 h	2 h
blood	6.29 ± 1.19	3.41 ± 0.07	3.91 ± 0.23	4.04 ± 0.45
heart	6.26 ± 1.12	3.22± 0.33	3.06 ± 0.15	2.50 ± 0.09
muscle	1.40 ± 0.11	1.92± 0.34	1.58 ± 0.13	1.38 ± 0.11
lung	7.35 ± 1.50	3.94± 0.29	3.63 ± 0.25	3.24 ± 0.10
kidney	9.02 ± 0.77	5.27± 0.77	3.97 ± 0.25	2.97 ± 0.07
spleen	5.24 ± 0.67	2.66± 0.14	2.84 ± 0.13	2.46 ± 0.05
liver	21.84 ± 1.56	13.75± 1.88	11.22 ± 0.82	9.13 ± 1.11
skin	2.09 ± 0.22	2.27± 0.17	1.92 ± 0.13	1.57 ± 0.06
brain	5.53 ± 0.56	2.33± 0.15	2.18 ± 0.09	1.96 ± 0.13
bone	2.13 ± 0.16	1.48± 0.03	1.82 ± 0.04	2.41 ± 0.28

[^{18}F]**5c**

organ	2 min	30 min	1 h	2 h
blood	3.54 ± 0.12	2.52 ± 0.29	2.46 ± 0.29	1.54 ± 0.19
heart	9.37 ± 0.18	2.11 ± 0.27	1.82 ± 0.28	1.19 ± 0.15
muscle	1.60 ± 0.98	1.87 ± 0.38	1.52 ± 0.24	0.93 ± 0.07
lung	4.68 ± 0.27	2.41 ± 0.37	2.08 ± 0.32	1.24 ± 0.16
kidney	23.00 ± 0.89	5.01 ± 0.84	3.50 ± 0.86	1.27 ± 0.08
spleen	4.74 ± 0.23	2.05 ± 0.18	1.87 ± 0.26	1.13 ± 0.16
liver	12.43 ± 1.11	3.94 ± 0.29	2.86 ± 0.38	1.67 ± 0.32
skin	0.95 ± 0.12	2.14 ± 1.03	1.42 ± 0.14	0.91 ± 0.10
brain	2.57 ± 0.12	1.69 ± 0.23	1.80 ± 0.25	1.29 ± 0.17
bone	1.68 ± 0.60	1.20 ± 0.29	1.68 ± 0.17	2.31 ± 0.37

[a] % dose/g, avg of 3 mice ± SD.

Normal mice are not expected to have Aβ plaques in the brain, and therefore an ideal compound will have a high initial brain uptake that washes out quickly, because there are no plaques to cause retention of Aβ aggregate specific probes. [^{18}F]**5a**−**c** were all able to penetrate the blood−brain barrier with [^{18}F]**5a** showing the highest initial brain uptake (10.27% dose/g at 2 min post iv injection) and a fast washout (3.94% dose/g at 60 min post iv injection). [^{18}F]**5b** also displayed a good initial brain uptake and washout (5.53% and 2.18% dose/g at 2 and 60 min post iv injection, respectively). The brain uptakes of these compounds ([^{18}F]**5a**,**b)** are similar to those of the stilbene series (6.6−8.1% dose/g at 2 min post iv injection and 1.2−2.62% dose/g at 60 min post iv injection, (*21*)). However, the washout rate of this series of compounds is slower compared to that of the stilbene derivatives. Rapid initial brain uptake in normal mouse brain coupled with a fast washout are highly desirable properties for Aβ plaque-targeting imaging agent, as these would lead to high signal to background ratios. Unlike [^{18}F]**5a** and **b**, [^{18}F]**5c** showed a much lower initial brain uptake (1.68% dose/g), indicating low penetration of the compound through the intact blood−brain barrier. The poor penetration of [^{18}F]**5c** (FPEG $n = 6$) led us to not pursue the studies using the further extended chain length of $n = 8$ (**5d**). It was also observed that in vivo defluorination was likely occurring with [^{18}F]**5a**, because the bone uptake increased with time (6.35% dose/g at 2 h) but was minimal with [^{18}F]**5b** and [^{18}F]**5c**. In addition, the biodistribution of [^{18}F]**12e** was performed and showed low brain uptake and slow washout (results not shown), further confirming that FPEG conjugation with the IMPY core is not successful.

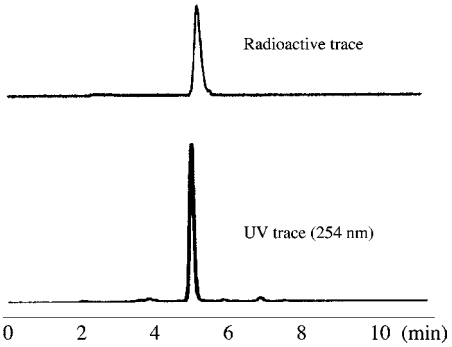


Figure 3. HPLC profiles of [^{18}F]**5a** (top) and **5a** (bottom). HPLC condition: Agilent 1100 series; Phenomenex Gemini C-18 analytical column CH_3CN/water 8/2 1 mL/min. $t_R = 4.80$ min (UV), 5.03 min (γ). The slight difference in retention time between UV and γ is due to the sequential configuration of the detector system.

Our approach toward preparing ^{18}F-labeled FPEG tracers is based on four critically important attributes: 1. The end-capped fluoropegylation with a short PEG chain ($n = 2-5$) connecting to the core structure will lead to a small and neutral molecule that can penetrate the intact blood−brain barrier. 2. The FPEG derivatives retain high binding affinities with K_i values comparable to those of the parent compounds in most cases but are not universally applicable. 3. The fluorine atom at one end of the pegylation chain can be readily labeled through the use of a simple nucleophilic substitution reaction of either the *O*-mesylate or *O*-tosylate group by ^{18}F fluoride in moderate to good radiochemical yields. It is also revealed that precise optimization of reaction conditions (amount of precursor, reaction time, and temperature) are needed to maximize the radiochemical yield. The resulting ^{18}F-labeled FPEG compounds are relatively stable in vivo after an iv injection. These unique features may provide a suitable approach for the preparation of other novel ^{18}F-labeled tracers.

In summary, we present here examples of a novel approach toward preparing PET imaging agents via a fluorinated pegylation approach. These examples illustrate a simple, efficient, and highly flexible methodology. This approach has proven effective for two core structures, but unfortunately, it was not universally applicable. However, the full power of this approach toward the development of other novel ^{18}F-labeled imaging agents is yet to be explored, and it will be interesting and exciting to see its application to other new imaging agents.

ACKNOWLEDGMENT

This work was supported by the grants from the National Institute of Health (AG021868 to M.P.K. and AG-22559 to H.F.K.).

LITERATURE CITED

(1) Selkoe, D. J. (2000) Imaging Alzheimer's amyloid. *Nat. Biotechnol. 18*, 823−824.
(2) Hardy, J., and Selkoe, D. J. (2002) The amyloid hypothesis of Alzheimer's disease: progress and problems on the road to therapeutics. *Science 297*, 353−356.
(3) Golde, T. E. (2005) The Abeta hypothesis: leading us to rationally-designed therapeutic strategies for the treatment or prevention of Alzheimer disease. *Brain Pathol. 15*, 84−7.

(4) Petkova, A. T., Leapman, R. D., Guo, Z., Yau, W.-M., Mattson, M. P., and Tycko, R. (2005) Self-propagating, molecular-level polymorphism in alzheimer's {beta}-amyloid fibrils. *Science 307*, 262−265.
(5) Mathis, C. A., Klunk, W. E., Price, J. C., and DeKosky, S. T. (2005) Imaging technology for neurodegenerative diseases: progress toward detection of specific pathologies. *Arch. Neurol. 62*, 196−200.
(6) Mathis, C. A., Wang, Y., and Klunk, W. E. (2004) Imaging b-amyloid plaques and neurofibrillary tangles in the aging human brain. *Curr. Pharm. Des. 10*, 1469−1492.
(7) Shoghi-Jadid, K., Barrio, J. R., Kepe, V., Wu, H. M., Small, G. W., Phelps, M. E., and Huang, S. C. (2005) Imaging beta-amyloid fibrils in Alzheimer's disease: a critical analysis through simulation of amyloid fibril polymerization. *Nucl. Med. Biol. 32*, 337−51.
(8) Shoghi-Jadid, K., Small, G. W., Agdeppa, E. D., Kepe, V., Ercoli, L. M., Siddarth, P., Read, S., Satyamurthy, N., Petric, A., Huang, S. C., Barrio, J. R., Liu, J., Flores-Torres, S., and Cole, G. M. (2002) Localization of neurofibrillary tangles and beta-amyloid plaques in the brains of living patients with Alzheimer disease: Binding characteristics of radiofluorinated 6-dialkylamino-2-naphthylethylidene derivatives as positron emission tomography imaging probes for beta-amyloid plaques in Alzheimer disease. *Am. J. Geriatr. Psychiatry 10*, 24−35.
(9) Verhoeff, N. P., Wilson, A. A., Takeshita, S., Trop, L., Hussey, D., Singh, K., Kung, H. F., Kung, M.-P., and Houle, S. (2004) In vivo imaging of Alzheimer disease beta-amyloid with [11C]SB-13 PET. *Am. J. Geriatr. Psychiatry 12*, 584−595.
(10) Klunk, W. E., Engler, H., Nordberg, A., Wang, Y., Blomqvist, G., Holt, D. P., Bergstrom, M., Savitcheva, I., Huang, G.-f., Estrada, S., Ausen, B., Debnath, M. L., Barletta, J., Price, J. C., Sandell, J., Lopresti, B. J., Wall, A., Koivisto, P., Antoni, G., Mathis, C. A., and Langstrom, B. (2004) Imaging brain amyloid in Alzheimer's disease with Pittsburgh Compound-B. *Ann. Neurol. 55*, 306−319.
(11) Mathis, C. A., Holt, D. P., Wang, Y., Huang, G. F., Debnath, M. L., and Klunk, W. E. (2002) 18F-labeled thioflavin-T analogs for amyloid assessment. *J. Nucl. Med. 43*, 166P.
(12) Kung, M.-P., Hou, C., Zhuang, Z.-P., Cross, A. J., Maier, D. L., and Kung, H. F. (2004) Characterization of IMPY as a potential imaging agent for b-amyloid plaques in double transgenic PSAPP mice. *Eur. J. Nucl. Med. Mol. Imaging 31*, 1136−1145.
(13) Zhuang, Z.-P., Kung, M.-P., Hou, C., Skovronsky, D., Gur, T. L., Trojanowski, J. Q., Lee, V. M.-Y., and Kung, H. F. (2001) Radioiodinated styrylbenzenes and thioflavins as probes for amyloid aggregates. *J. Med. Chem. 44*, 1905−1914.
(14) Cai, L., Chin, F. T., Pike, V. W., Toyama, H., Liow, J.-S., Zoghbi, S. S., Modell, K., Briard, E., Shetty, U. H., Sinclair, K., Donohue, S., Tipre, D., Kung, M.-P., Dagostin, C., Widdowson, D. A., Green, M., Gao, W., Herman, M. M., Ichise, M., and Innis, R. B. (2004) Synthesis and evaluation of two ^{18}F-labeled 6-iodo-2-(4′-N,N-dimethylamino)phenylimidazo[1,2-a]pyridine derivatives as prospective radioligands for b-amyloid in alzheimer's disease. *J. Med. Chem. 47*, 2208−2218.
(15) Okamura, N., Suemoto, T., Shimadzu, H., Suzuki, M., Shiomitsu, T., Akatsu, H., Yamamoto, T., Staufenbiel, M., Yanai, K., Arai, H., Sasaki, H., Kudo, Y., and Sawada, T. (2004) Styrylbenzoxazole derivatives for in vivo imaging of amyloid plaques in the brain. *J. Neurosci. 24*, 2535−2541.
(16) Zhuang, Z.-P., Kung, M.-P., Hou, C., Plossel, K., Skovronsky, D., Gur, T. L., Trojanowski, J. Q., Lee, V. M.-Y., and Kung, H. F. (2001) IBOX(2-(4′-dimethylaminophenyl)-6-iodobenzoxazole): a ligand for imaging amyloid plaques in the brain. *Nucl. Med. Biol. 28*, 887−894.
(17) Kung, H. F., Lee, C.-W., Zhuang, Z. P., Kung, M. P., Hou, C., and Plossl, K. (2001) Novel stilbenes as probes for amyloid plaques. *J. Am. Chem. Soc. 123*, 12740−12741.
(18) Kilbourn, M. R. (1990) *Fluorine-18 Labeling of Radiopharmaceuticals*, National Academy Press, Washington, DC.
(19) Elsinga, P. H. (2002) Radiopharmaceutical chemistry for positron emission tomography. *Methods 27*, 208−17.
(20) Lasne, M.-C., Perrio, C. C., Rouden, J., Barre, L., Roeda, D., Dolle, F. D. R., and Crouzel, C. (2002) Chemistry of β+-emitting compounds based on fluorine-18. *Top. Curr. Chem. 222*, 201−258.
(21) Zhang, W., Oya, S., Kung, M. P., Hou, C., Maier, D. L., and Kung, H. F. (2005) F-18 PEG Stilbenes as PET Imaging agents targeting Aβ aggregates in the brain. *Nucl. Med. Biol. 32*, 799−809.
(22) Roberts, M. J., Bentley, M. D., and Harris, J. M. (2002) Chemistry for peptide and protein PEGylation. *Adv. Drug Delivery Rev. 54*, 459−76.
(23) Harris, J. M., and Chess, R. B. (2003) Effect of pegylation on pharmaceuticals. *Nat. Rev. Drug Discov. 2*, 214−21.
(24) Chen, X., Hou, Y., Tohme, M., Park, R., Khankaldyyan, V., Gonzales-Gomez, I., Bading, J. R., Laug, W. E., Conti, P. S., Haubner, R., Wester, H. J., Burkhart, F., Senekowitsch-Schmidtke, R., Weber, W., Goodman, S. L., Kessler, H., and Schwaiger, M. (2004) Pegylated Arg-Gly-Asp peptide: 64Cu labeling and PET imaging of brain tumor alphavbeta3-integrin expression. *J. Nucl. Med. 45*, 1776−83.
(25) Chen, X., Park, R., Hou, Y., Khankaldyyan, V., Gonzales-Gomez, I., Tohme, M., Bading, J. R., Laug, W. E., Conti, P. S., Haubner, R., Wester, H. J., Burkhart, F., Senekowitsch-Schmidtke, R., Weber, W., Goodman, S. L., Kessler, H., and Schwaiger, M. (2004) MicroPET imaging of brain tumor angiogenesis with 18F-labeled PEGylated RGD peptide. *Eur. J. Nucl. Med. Mol. Imaging 31*, 1081−9.
(26) Zhang, W., Oya, S., Kung, M. P., Hou, C., Maier, D. L., and Kung, H. F. (2005) F-18 stilbenes as PET imaging agents for detecting beta-amyloid plaques in the brain. *J. Med. Chem. 48*, 5980−8.
(27) Mathis, C. A., Wang, Y., Holt, D. P., Huang, G.-f., Debnath, M. L., and Klunk, W. E. (2003) Synthesis and evaluation of ^{11}C-labeled 6-substituted 2-arylbenzothiazoles as amyloid imaging agents. *J. Med. Chem. 46*, 2740−2754.
(28) Barluenga, J., Bayon, A. M., and Asensio, G. (1984) A new specific method for the monomethylation of primary amines. *J. Chem. Soc., Chem. Commun.* 1334−1335.
(29) Schreiner, E. P., Wolff, B., Winiski, A. P., and Billich, A. (2003) 6-(2-adamantan-2-ylidene-hydroxybenzoxazole)-O-sulfamate: a potent non-steroidal irreversible inhibitor of human steroid sulfatase. *Bioorg. Med. Chem. Lett. 13*, 4313−6.
(30) Zhuang, Z. P., Kung, M. P., Wilson, A., Lee, C. W., Plossl, K., Hou, C., Holtzman, D. M., and Kung, H. F. (2003) Structure-activity relationship of imidazo[1,2-a]pyridines as ligands for detecting beta-amyloid plaques in the brain. *J. Med. Chem. 46*, 237−243.
(31) Kung, M.-P., Hou, C., Zhuang, Z.-P., Skovronsky, D., and Kung, H. F. (2004) Binding of two potential imaging agents targeting amyloid plaques in postmortem brain tissues of patients with Alzheimer's disease. *Brain Res. 1025*, 89−105.
(32) Shimadzu, H., Suemoto, T., Suzuki, M., Shiomitsu, T., Okamura, N., Kudo, Y., and Sawada, T. (2004) Novel probes for imaging amyloid-b: F-18 and C-11 labeling of 2-(4-aminostyryl)benzoxazole derivatives. *J. Labelled Compd. Radiopharm. 47*, 181−190.
(33) Kung, M. P., Hou, C., Zhuang, Z.-P., Zhang, B., Skovronsky, D. M., Gur, T., Lee, V. M.-Y., Trojanowski, J. Q., and Kung, H. F. (2002) IMPY: An improved thioflavin-T derivative for in vivo labeling of b-amyloid plaques. *Brain Res. 956*, 202−210.

BC060239Q

Self-Assembled Monolayers with Latent Aldehydes for Protein Immobilization

Christoph D. Hahn,[†] Christa Leitner,[†] Theo Weinbrenner,[†] Robert Schlapak,[§] Ali Tinazli,[‡] Robert Tampé,[‡] Bernd Lackner,[#] Christian Steindl,[#] Peter Hinterdorfer,[†] Hermann J. Gruber,[†] and Martin Hölzl*[,†]

Institute of Biophysics and Institute of Organic Chemistry, University of Linz, Altenberger Strasse 69, A-4040 Linz, Austria, Center for Biomedical Nanotechnology, Upper Austrian Research GmbH, A-4020 Linz, Austria, and Institute of Biochemistry, Biocenter, Johann Wolfgang Goethe-University, Max-von-Laue-Strasse 9, D-60438 Frankfurt, Germany. Received September 18, 2006; Revised Manuscript Received November 28, 2006

Aldehyde functions are widely used for immobilization of biomolecules on glass surfaces but have found little attention for biofunctionalization of self-assembled monolayers (SAMs) on gold, due to interference between thiol and aldehyde functions. This problem was recently solved by synthesis of an alkanethiol that carried a vicinal diol group [Jang et al. (2003) *Nano Lett. 3*, 691−694]. The latter served as a latent aldehyde function that was unmasked by short exposure of the vicinal diol-terminated SAM to aqueous periodate. However, the synthesis of the new vicinal diol-terminated alkane thiol was time-consuming and had an overall yield of ∼3.5%. In the present study, a general modular strategy was introduced by which SAM components with vicinal diol functions were rapidly synthesized with high yield: this was accomplished by amide bond formation between a SAM-forming carboxylic acid (exemplified by lipoic acid and 16-mercaptohexadecanoic acid) with 3-aminopropane-1,2-diol, using suitable protecting groups. The disulfide or free thiol group afforded SAM formation on gold and, after periodate oxidation of the vicinal diol functions, proteins were covalently bound via their lysine residues. At 1 mg/mL protein concentration, complete surface coverage was reached within minutes. No further protein was bound by nonspecific adsorption, but cognate proteins were specifically bound with high capacity. Pyrogallol-*O*-hexadecanoic acid and 10-undecenoic acid were also coupled with 3-aminopropane-1,2-diol by amide bond formation, thereby producing latent aldehyde-containing SAM components for metal oxides and hydrogen-terminated silicon, respectively, to show the general usefulness of the new synthetic design.

INTRODUCTION

Functionalized self-assembled monolayers (SAMs)[1] on gold surfaces are key elements in many affinity biosensors and biocatalytic sensors (*1*−*5*). Moreover, functionalized gold surfaces are increasingly used for cell arrays (*6*−*8*) and for chip assays, whether readout is label-dependent (*9*−*12*) or via label-free detection (*4*, *13*−*14*) or MALDI-MS (*15*−*16*). Functionalization of gold is facilitated by selective binding of thiol or disulfide groups toward gold; thus, densely packed SAMs can be formed with a wide range of physical properties and chemical functionalities, or a mixture of functional groups, at the exposed surface (*4*).

SAMs with selective coupling functions, such as biotin (*17*−*21*), maleimide (*9*, *12*), NTA (*22*−*24*), hydroquinone (*10*, *25*), acetylene (*26*), and suicide inhibitors, (*27*) have been developed for selective, oriented, and/or triggered binding of probe molecules that then serve as capture probes in sensors and chip assays. Complementary coupling functions, such as biotin, free thiols, His_6 tags, cyclopentadiene, azide, or enzyme domains, respectively, are required on the probe molecules, which may be present in particular cases but not in general.

In contrast to these selective coupling functions, amino-reactive coupling functions are almost generally applicable, for the following reasons: (i) Most proteins can be immobilized via one/few of their many lysine residues without impeding protein function. (ii) DNA probes with reactive aliphatic NH_2 groups are easily obtained by standard methods and commercially supplied in this form. (iii) Many other natural or synthetic ligands are also available with primary amino groups for coupling to amino-reactive SAMs (*28*−*29*). (iv) Amino-reactive groups on a SAM can easily be adapted with other coupling functions such as reactive disulfides (*30*) or hydrazide (*31*).

SAMs with reactive carboxyls are the most widely used kind of amino-reactive SAMs. In some cases, the SAMs have been

* To whom correspondence may be addressed at the Institute of Biophysics in Linz. Phone: +43 (732) 2468-9271. Fax: +43 (732) 2468-9270. E-mail: martinhoelzl@yahoo.de.

[†] Institute of Biophysics, University of Linz.

[#] Institute of Organic Chemistry, University of Linz.

[§] Upper Austrian Research GmbH.

[‡] Johann Wolfgang Goethe-University.

[1] Abbreviations: Ac-Pygal, 2,2-dimethyl-1,3-benzodioxole-4-ol; AcS-HDA, 16-(acetylthio)-hexadecanoic acid; APD, 3-aminopropane-1,2-diol; APD-ac, 2,2-dimethyl-1,3-dioxolan-4-methanamine (**2** in Figures 1 and 3); biotin-cap-NHS, *N*-succinimidyl 6-(biotinamido)-caproate; BSA, bovine serum albumine; DOPA, 3,4-dihydroxy-L-phenylalanine; EDC, *N*-ethyl-*N*′-(3-dimethylaminopropyl)-carbodiimide; FC1 and FC2, flow cell 1 and 2 of the BIAcore X setup; IgG, immunoglobulin G; ITO, indium-tin oxide; Lip-APD, *N*-(2,3-dihydroxypropyl)-5-(1,2-dithiolane-3-yl)-pentanamide; Lip-APD-ac, *N*-(2,2-dimethyl-1,3-dioxolan-4-yl-methyl)-5-(1,2-dithiolan-3-yl)-pentanamide; Lip-NH_2, lipoamide = thioctic acid amide; MALDI-MS, matrix-assisted laser desorption ionization mass spectrometry; MHD-APD, *N*-(2,3-dihydroxypropyl)-16-mercapto-hexadecanamide; NHS, *N*-hydroxysuccinimide; OEG, oligo(ethylene glycol); NTA, *N*,*N*,*N*-nitrilotriacetic acid; PBS, phosphate-buffered saline; PEG, poly(ethylene glycol); Pygal-HD, 3-hexadecanyloxy-catechol; Pygal-HDA-APD, *rac*-3-(16-oxo-17-aza-19,20-dihydroxyeicosanyloxy)-catechol; RU, resonance unit (1 RU = 0.0001° surface plasmon resonance angle shift in the BIAcore); SAM, self-assembled monolayer; SC1, standard cleaning solution no. 1 (5/1/1 mixture of water/25% ammonia/30% H_2O_2); SDS, sodium dodecyl sulfate; SPR, surface plasmon resonance; TEA, *N*,*N*,*N*-triethylamine; THF, tetrahydrofuran; TSTU, *N*,*N*,*N*′,*N*′-tetramethyl-*O*-(*N*-succinimidyl)-uronium tetrafluoroborate.

10.1021/bc060292e CCC: $37.00 © 2007 American Chemical Society
Published on Web 12/22/2006

formed with the carboxyl groups present in their activated form, for example, as NHS ester (*32*−*33*). More often, SAMs have been activated shortly before ligand coupling, for example, with EDC and NHS (*21*, *22*, *28*, *29*). This activation step is simple and efficient, and the same applies to subsequent amide bond formation with a primary amine. Nevertheless, this method has problematic aspects: First, the activation reagent (EDC) and the transiently formed NHS ester are very sensitive to hydrolysis (*34*); thus, the timing of EDC dissolution, carboxyl activation, and amine coupling is critical (*35*), which complicates application of this method in automated systems, especially in microspotting. Second, nonactivated carboxyls or hydrolyzed NHS esters are present as negatively charged carboxylate functions which are strongly adsorptive toward proteins in simple SAMs (*36*−*37*), weakly adsorptive in OEG-terminated SAMs (*28*), or strongly repulsive in case of dextran-coated SAMs (*35*). Third, the kinetics of NHS ester hydrolysis, the coupling of amines to NHS esters, and the above named adsorption/repulsion effects are dependent on pH, and in addition the coupling protocols have to be optimized for individual proteins (*35*).

These complications are eliminated if aldehyde functions are used in place of activated carboxyls because aldehydes have no electric charge, they are spontaneously reactive toward amino groups over a wide pH range, and their reactivity is retained for a long time under ambient conditions (*9*, *36*−*40*). However, a new problem was encountered when forming aldehyde-terminated SAMs on gold: the free thiol needed for chemisorption toward gold is known to reversibly form a hemithioacetal with a free aldehyde function (*38*). Fortunately, this effect has been shown not to impede SAM formation, at least with 5-mercaptopentanal, which actually gave an aldehyde-terminated SAM on gold although a large fraction of the SAM component was present as the cyclic 2-hydroxypentamethylene sulfide (*38*).

The problem of hemithioacetal formation from thiol and aldehyde was altogether avoided in two other approaches: In the first method, the thiol was oxidized into a disulfide before the aldehyde function was generated in the synthesis of the SAM component (*9*). Disulfides are known to form the same kind of SAMs on gold as do free thiols, only the kinetics of chemisorption is somewhat reduced (*41*). Another group of authors has obviously used the same strategy (*36*, *37*, *39*) even though these authors stated to have worked with 3-mercapto-1-propanal and 11-mercapto-1-undecanal. More likely, the actual compounds were 3,3′-dithio-*bis*-propanal and 11,11′-dithio-*bis*-undecanal because the aldehyde function had been prepared by oxidation of 3-mercapto-1-propanol and 11-mercapto-1-undecanol with pyridinium dichromate (*36*) and because the closely similar reagents pyridinium or picolinium chlorochromate will first oxidize all free thiols into disulfides before they will even start to oxidize alcohol groups into aldehydes (*42*, *43*). For the particular application, the disulfide form was the better choice anyway, and only for the critical interpretation of the data (*36*, *37*, *39*) are these considerations important.

In the second method, the SAM has been formed with a latent, rather than an actual, aldehyde function, thereby avoiding mutual interference between free thiol and aldehyde (*40*). A vicinal diol group was used as a latent aldehyde, permitting the aldehyde function to easily be generated after SAM formation by use of sodium metaperiodate (*40*). While the latter strategy offers an elegant route to aldehyde-terminated SAMs, the major drawback of the above study (*40*) was the long synthetic scheme and the low overall yield (∼3.5%) of the SAM component. We therefore looked for an easier synthesis of alkanethiol derivatives with a vicinal diol on the second end of the molecule. As shown below, this was accomplished by introducing the vicinal diol in the form of 3-aminopropane-1,2-diol (APD), preferably with the vicinal diol group protected as acetonide (APD-ac, **2**, see Figures 1 and 3).

EXPERIMENTAL PROCEDURES

Compounds **3**, **4**, **7**, **8**, **11**, **12**, **13**, **14**, **15**, and **17** were synthesized by standard procedures (see Figures 1, 3, 5, and 6), as described in detail in Supporting Information. Preparation of biotin-IgG by reaction of goat IgG (Sigma I-5256) with biotin-cap-NHS is also described in Supporting Information. Affinity-purified streptavidin (Fluka 85878), fatty acid-free BSA (Roche 775 827) and 99% pure D-biotin (Sigma B-4501) were used. D-Biotin (10 mM) was dissolved in 50 mM Na_2HPO_4, (final pH ∼7.2) and aliquots for single use were stored at −20 °C.

SAMs were formed on commercial gold slides (BIAcore SIA kit) that had been pretreated either by sonication in ethanol (see legend to Figure 4) or by two cycles of boiling in SC1 (water/25% ammonia/30% H_2O_2 = 5/1/1) at 70−80 °C for 20 min and rinsing (5×) in ultrapure water (Milli-Q50) after each SC1 treatment (as in Figure 2 and in Supporting Information) (*24*, *44*). The chips were dried with a stream of nitrogen and incubated in a thiol solution (0.1−1 mM) either overnight or for 36 h, as specified in the figure legends. Unless stated otherwise, the chips were rinsed in ethanol (3×) and water (3×), with 3 min of sonication each in the third rinsing cycle. The chips were stored in water at 4 °C for up to 3 days. Before use, chips with intact Lip-APD-ac (**3**) were deprotected by incubation in a 1:1 mixture of THF and 1 M HCl (90 min), followed by rinsing in THF (3×), ethanol (3×), and water (3×) and applying 3 min of sonication in the third rinsing cycle with ethanol and water each.

SAMs with vicinal diol termini were incubated for 30 min in the dark in a freshly prepared solution of 50 mM $NaIO_4$ in buffer 5.5 (100 mM sodium acetate, pH 5.5 adjusted with HCl). After being rinsed in water (5×), the chip was blown dry with nitrogen gas and mounted in the BIAcore X setup. Degassed PBS (140 mM NaCl, 2.7 mM KCl, 10 mM Na_2HPO_4, 1.8 mM KH_2PO_4, pH 7.3) was run over the chip at 5 μL/min until the SPR readout from the two flow cells (solid and dotted trace for FC1 and FC2, respectively, in Figures 2 and 4) remained constant. This took <30 min for SAMs of oxidized MHD-APD (**9**) and <2 h for SAMs of oxidized Lip-APD (**5**). Meanwhile, a 1 M solution of $NaCNBH_3$ was prepared by dissolving 32 mg of $NaCNBH_3$ in 0.5 mL of 10 mM NaOH.

For covalent coupling of proteins to the aldehyde chip, 150 μL of protein (1 mg/mL in PBS) was mixed with 3 μL of 1 M $NaCNBH_3$, 140 μL thereof were pulled into the yellow tip of a digital pipet, another 10 μL of air was pulled into the lower end of the yellow tip, and all was loaded into the sample loop, the air bubble serving to replace all old liquid from the sample loop, as recommended by BIAcore. The content of the 100 μL sample loop was then injected onto the chip by the system at a flow rate of 5 μL/min. Unlabeled IgG was applied to flow cell 2 only (FC2, dotted trace in the figures), with no flow in FC1. Vice versa, biotin-IgG was applied to FC1 only. Then, BSA was applied to both flow cells, the flow serially passing through FC1 and FC2 with a time delay of a few seconds.

Noncovalent binding of proteins (streptavidin and biotin-IgG, always at 2 μM protein concentration) to immobilized biotin-IgG (in FC1, solid traces in Figures 2 and 4) and unlabeled IgG (in FC2, dotted traces in Figures 2 and 4) was measured in PBS at a flow of 10 μL/min, the flow passing the two measuring cells with a time delay of a few seconds. "Blocked streptavidin" was used as a negative control for streptavidin; it was prepared by mixing 150 μL of 2 μM streptavidin with 3 μL of 10 mM

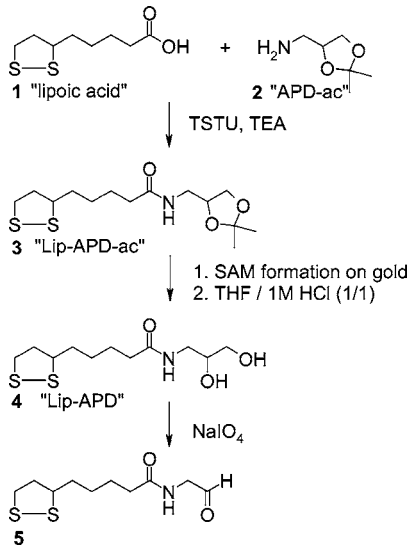


Figure 1. Conjugation of lipoic acid (**1**) with APD-ac (**2**), followed by SAM formation on gold, acetonide cleavage, and periodate treatment to generate an aldehyde SAM.

D-biotin, resulting in a final biotin concentration of 0.2 mM. Unlabeled goat IgG was used as a negative control for biotin-IgG.

RESULTS AND DISCUSSION

Lipoic Acid Derivative with Latent Aldehyde Function. The goal of this study was to devise an easy method to equip SAM forming molecules with a vicinal diol group that can be converted into an aldehyde by periodate treatment after SAM formation. In the literature, we found examples in which APD had been coupled to nitrophenyl esters (*45*, *46*), yielding a stable urethane with a vicinal diol group (comparable to the amide **4** in Figure 1). This provoked the idea to couple APD with a carboxyl-terminated SAM component and thereby to obtain a new SAM component with a terminal vicinal diol (Gruber et al., Austrian patent application 1469/2006). Fortunately, many fatty acids with terminal thiols or disulfides, as well as lipoic acid (see **1** in Figure 1), are known to form stable SAMs on gold. We therefore attempted direct coupling of APD to the NHS ester of lipoic acid (**1**), but this reaction gave a mixture of products, none of which had the desired structure (according to the NMR spectrum, data not shown). In contrast, the protected form of APD (APD-ac, **2**) was easily coupled to NHS-activated lipoic acid (**1**), resulting in pure amide conjugate (Lip-APD-ac, **3**) after extraction (see Figure 1 and Supporting Information). In our first batch, this product could also be deprotected to give pure Lip-APD (**4** in Figure 1), which was mixed with 19 parts (w/w) of lipoamide (Lip-NH_2) and successfully used to form a mixed SAM with periodate-reactive vicinal diol groups on its surface (see Figure 8S in Supporting Information). In several subsequent batches, however, a considerable fraction of the deprotected product (**4**) contained polymeric fractions, as judged from the smaller elution volume in comparison to product (**4**) when the mixture was gel filtered in methanol on Sephadex LH-20 (1.5 × 95 cm column, 0.4 mL/min). The inclination of lipoic acid and its derivatives toward polymerization has been described before (*47*, *48*). Removal of the polymerized components was possible by gel filtration in methanol on Sephadex LH-20 (data not shown), but the yield of pure **4** was low, and after storage at −20 °C the polymerized components (R_f < $R_{f,\text{product}} = 0.58$ in chloroform/methanol/25% ammonia, 70/30/4, v/v/v) were seen again.

In contrast to Lip-APD (**4**), the protected form Lip-APD-ac (**3**) showed no sign of polymerization during synthesis and storage; therefore, it was decided to form the SAM with protected Lip-APD-ac (as in Figure 2). The acetonide function of (**3**) was cleaved on the chip by incubation of the SAM in the usual deprotection reagent for 90 min (see Figure 1). After being washed with ethanol and water, the chip was also incubated in metaperiodate for 30 min, washed with water, dried, and mounted in the BIAcore X setup. This system has two flow cells (FC1 and FC2, see solid and dotted traces in Figures 2 and 4) that can be operated in series, in which case the buffer (or sample) passes FC1 and FC2 with a few seconds delay in between. Alternatively, FC1 or FC2 can individually be addressed, in which case the entrance to the other flow cell is always blocked.

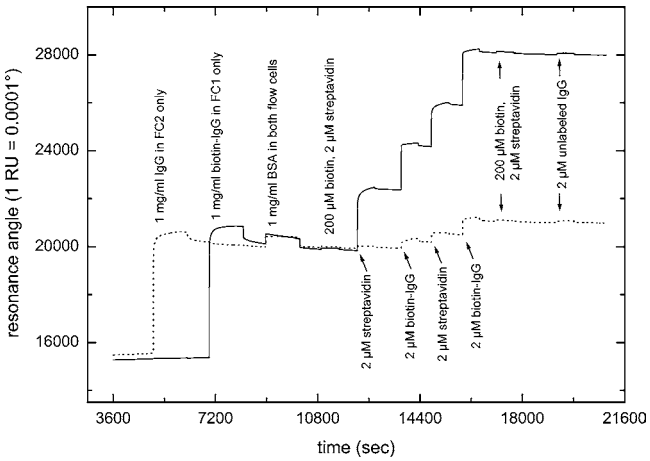


Figure 2. Functionalization and characterization of a sensor chip with a SAM of Lip-APD-ac (**3**) on gold. The SAM was formed by overnight incubation in ethanol containing 1 mM Lip-APD-ac (**4**), rinsed, and sequentially treated with THF/1 M HCl (1/1) and 50 mM periodate (see Experimental Section). For covalent coupling, 100 µL of protein solution (always at 1 mg/mL, with 20 mM $NaCNBH_3$) was applied at a flow of 5 µL/min. For noncovalent binding (after $t = 10800$ s), 100 µL of protein solution (2 µM of streptavidin or biotin-IgG or unlabeled IgG) was applied at a flow of 10 µL/min. Blocked streptavidin contained 200 µM of D-biotin besides 2 µM of streptavidin.

Figure 2 depicts the sensorgrams (SPR angles of FC1 and FC2 versus time) for a chip with a SAM of compound **5** (see Figure 1) prepared as described in the previous paragraph. In the first step, unlabeled goat IgG (1 mg/mL, with 20 mM $NaCNBH_3$) was injected into the control cell only (FC2, dotted trace in Figure 2). After 20 min, the injection (100 µL) was over, and uncoupled IgG was removed by PBS flow. The sensorgram shows that over 4000 RU of unlabeled IgG were immobilized in FC2, which is more than the 2500 RU observed for a monolayer of IgG molecules immobilized in the side-on orientation (*28*). The same efficiency of immobilization was also observed when biotin-IgG was injected into FC1 only (solid trace). From then on, both flow cells were operated in series, i.e., exposed to the same buffer or sample almost simultaneously. Injection of BSA (1 mg/mL, with 20 mM $NaCNBH_3$) gave no additional immobilization of protein in any flow cell; thus, the initial exposure to IgG or biotin-IgG had sufficed to completely cover the chip surface with protein.

The functionalized chip was then tested for specific capture and/or nonspecific adsorption of different proteins. First, "blocked streptavidin" (200 µM D-biotin and 2 µM streptavidin) was injected. This caused no SPR angle shift in any of the two flow cells, proving complete absence of nonspecific binding. Unblocked streptavidin, however, was vigorously bound in FC1 (solid trace in Figure 2, +2500 RU step increase after washout), while very little streptavidin was bound to unlabeled IgG in the control cell (dotted line, +18 RU). The streptavidin-covered surface, in turn, showed high affinity for biotin-IgG (solid line), and binding was similarly strong in another cycle of streptavidin

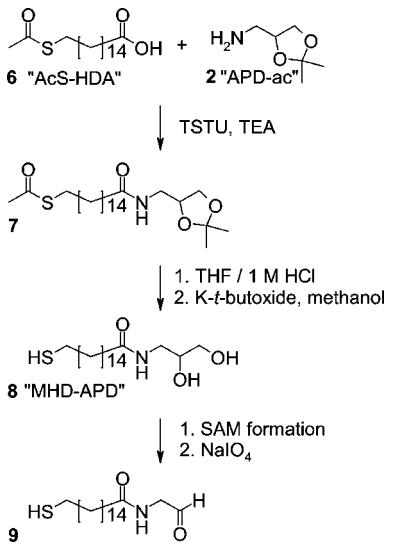


Figure 3. Conjugation of AcS-HDA (**6**) with APD-ac (**2**), followed by acetonid cleavage, SAM formation on gold, and periodate treatment to generate an aldehyde SAM.

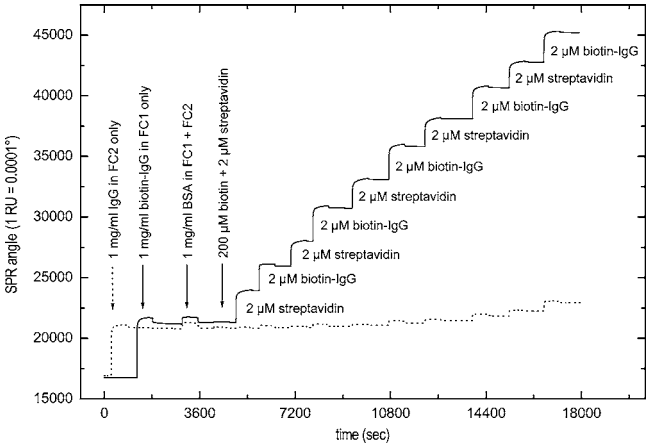


Figure 4. Functionalization and characterization of a sensor chip with a SAM of MHD-APD (**8**) on gold. The commercial gold slide had been sonicated in ethanol, washed with chloroform/methanol (3/1), incubated overnight in a chloroform/methanol (3/1) solution of 1 mM MHD-APD (**8**), and washed with chloroform/methanol (3/1, 2/2, 1/3, 0/4) and methanol/water (3/1, 2/2, 1/3, 0/4), followed by periodate treatment outside the BIAcore setup, as usual (see Experimental Section). After the chip was mounted in the BIAcore X setup, PBS was run over the chip at 5 μL/min. The protocol for covalent binding of IgG (in FC2, dotted line) or biotin-IgG (in FC1, solid line) and of BSA (in both flow cells) was the same as in Figure 2. The protocol for alternating binding of streptavidin and biotin-IgG was equal to the protocol in Figure 2, except that five double layers were prepared instead of two. Absence of nonspecific binding was tested with blocked streptavidin (containing 200 μM D-biotin) before protein multilayer formation.

and subsequent biotin-IgG injection. For easy visualization of the protein multilayer formed in FC1, a sketch is offered in Supporting Information (Figure 7S).

At first sight, there appears to be significant nonspecific binding of protein in the control cell. A closer look, however, reveals that this was exclusively caused by specific binding to the biotin binding sites of streptavidin. This is concluded from the fact that neither blocked streptavidin (i.e., with 200 μM D-biotin) nor unlabeled IgG showed any significant binding in FC1 and FC2, whether measured immediately after the BSA injection or at the end of the total injection sequence (see Figure 2). A possible explanation for the paradoxical behavior of "specific binding in the control cell" is the hypothesis that the unlabeled goat IgG in FC2 (dotted line) contained traces of biotinylated protein which caused a progressive buildup of undesired *specific* binding in the control cell in the alternating injections of streptavidin and biotin-IgG. This interaction, however, was fully dependent on the availability of empty biotin-binding sites in streptavidin, as demonstrated by the complete blocking of streptavidin binding by 200 μM D-biotin, as well as by the complete absence of unlabeled IgG binding at the end of the injection sequence.

Mercaptohexadecanoic Acid Derivative with Latent Aldehyde Function. Admittedly, the use of Lip-APD-ac (**3**) for preparation of SAMs with latent aldehydes has two practical disadvantages: (i) Each chip must be incubated for 90 min in the THF/HCl mixture, and the organic solvent must be removed by careful rinsing and sonication. (ii) After periodate treatment and insertion in the SPR setup, another 90 min of rinsing with PBS is required to obtain a stable baseline. Since these problems were caused by the imminent polymerization tendency of the lipoyl residue in **3** upon acid treatment (see above), we synthesized an analogous molecule (**7**, Figure 3) in which lipoic acid was replaced by AcS-HDA (**6**, Figure 3), a well-known precursor for gold-selective SAM components (*44*, *49*). The conjugate (**7**) was sequentially treated with acid to deprotect the vicinal diol and with base to hydrolyze the thioester protecting group, resulting in an alkanethiol derivative (**8**) which was stable during storage.

Compound **8** was used to form SAMs with latent aldehyde functions, and the vicinal diol group was oxidized with metaperiodate to generate reactive aldehyde groups (**9**), either before insertion of the chip into the SPR setup (Figure 4) or inside the SPR setup (Figure 9S in Supporting Information).

The protocol and the data in Figure 4 were closely similar to those in Figure 2; that is, unlabeled IgG was first immobilized in the control cell (FC2, dotted trace), followed by coupling of biotin-IgG in FC1 (solid trace in Figure 4), and the step increases (+4000 RU for IgG and +3900 RU for biotin-IgG) were quite similar as in Figure 2. The chip surfaces in FC1 and FC2 were completely covered with biotin-IgG and IgG, respectively, as is concluded from the fact that neither BSA nor blocked streptavidin were measurably bound in the next two injections. Moreover, the IgG-covered surface in FC2 (dotted trace) proved to be inert in several alternating injections of streptavidin and biotin-IgG, except that after several such cycles some initially adsorbed traces of streptavidin and/or biotin-IgG caused a gradual buildup of clusters with alternating layers of streptavidin and biotin-IgG in the control cell also (dotted trace). Unblocked streptavidin, however, is avidly bound to the biotin-IgG surface in FC1 (solid line), followed by strong binding of biotin-IgG in the next injection. In the five cycles of alternating streptavidin and biotin-IgG injection, the step increases per protein layer were rather constant, indicating the formation of a dense protein monolayer in each injection.

Finally the stability of the protein multilayer was tested by 100 μL injections of D-biotin (200 μM, in PBS), of acetic acid (100 mM, in water), and of SDS (0.5%, in water), none of which could remove a significant amount of bound protein (data not shown). Similarly, SDS (0.5%) could not remove IgG that had been bound and fixed (with 20 mM $NaCNBH_3$) to a chip surface with periodate-treated MHD-APD, whereas before periodate treatment, the same chip had shown weak adsorption of IgG all of which had been removed by 0.5% SDS (see Figure 10S in Supporting Information).

Monolayer Components with Latent Aldehydes for Metal Oxides and Hydrogen-Terminated Silicon. Alkane derivatives with terminal phosphate or phosphonate groups are known to form stable SAMs on metal oxides, such as titanium oxide, tantalum oxide, or ITO, which are increasingly used in bio-

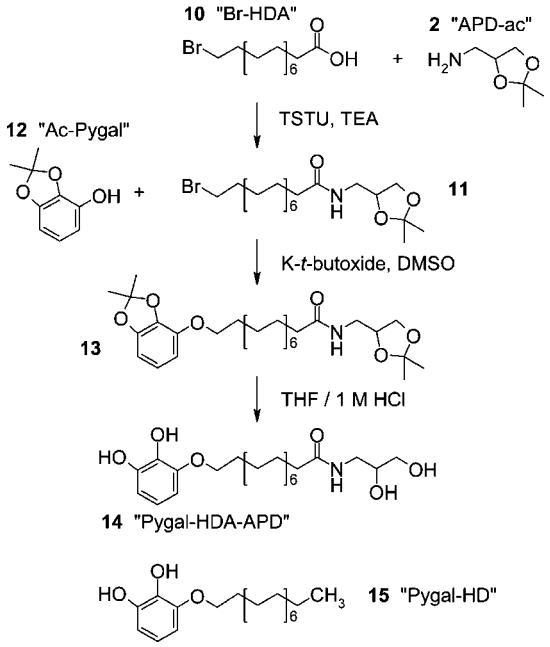


Figure 5. Synthesis of a heterobifunctional SAM component with a catechol function on one end and a latent aldehyde on the other end. The amide conjugate (**11**) of Br-HDA (**10**) and APD-ac (**2**) was used to alkylate Ac-Pygal (**12**). Removal of the acetonide functions from **13** gave the final product Pygal-HDA-APD (**14**). By analogy, the hydrophobic SAM component Pygal-HD (**15**) was synthesized by alkylation of Ac-Pygal (**12**) with 1-bromohexadecane and cleavage of the acetonide function.

sensors and biochips (*4*). Recently, catechol functions were also shown to confer tight binding to metal oxides, at least of PEG chains with 1−3 terminal DOPA residues (*50*). As shown in Figure 5, we have introduced the catechol function on the hydrophobic end of hexadecanoic acid by forming an ether bond between acetonide-protected pyrogallol (**12**) and the amide conjugate (**11**) of 16-bromohexadecanoic acid (**10**) and APD-ac (**2**). Removal of the acetonide functions on both ends of **13** gave the final product (**14**), which contains a catechol function for binding to metal oxides and an aliphatic vicinal diol that serves as a latent aldehyde. For preliminary studies, the monofunctional pyrogallol-*O*-hexadecyl ether (**15**) was also synthesized and chemisorbed from a 3 mM solution in ethanol (36 h at room temperature) to ITO-covered glass slides that had been cautiously precleaned in SC1 (2 × 10 min at 40 °C). These slides indeed showed contact angles of 84 ± 5°, in contrast to the 47 ± 2° measured on control slides that had been incubated in pure ethanol. This result has encouraged further studies with the bifunctional SAM component **14** which are underway.

In recent years, monolayers of 1-alkenes and their derivatives on hydrogen-terminated silicon have become increasingly popular (*4*). When the monolayer was formed at high temperature, only aprotic molecules such as 1-alkenes or esters of 10-undecenoic acid were uniformly bound to Si−H with their terminal vinyl group (*51*). In contrast, monolayers with unprotected carboxyl- or hydroxyl-terminated 1-alkenes could directly be prepared when using UV light (*52*) or a nitroxide catalyst (*53*) for grafting at room temperature; nevertheless, esters are preferred over free carboxylates and Boc-protected amines over free amino groups (*54*). On the basis of these findings, we devised a 10-undecenoic acid derivative with a latent aldehyde function by coupling 10-undecenoic acid (**11**) with APD-ac (**2**). Functional studies have not yet been conducted because hydrogen-terminated silicon is presently outside of our topical interest, yet compound **17** and analogous monolayer components (e.g., with −NH−PEG−CO− between the undecenoyl residue

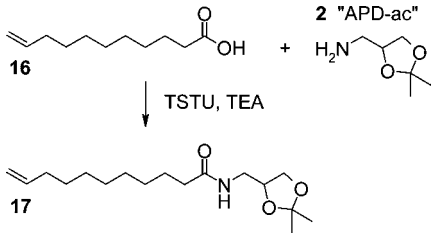


Figure 6. Synthesis of a heterobifunctional SAM component (**17**) with a double bond on one end and a latent aldehyde on the other end.

and APD, see below) should be of high interest to others working in this field. As in case of Lip-APD-ac (**3**, see Figures 1 and 2), SAM formation with the acetonide form and subsequent deprotection with mild acid appear most appropriate to arrive at a SAM with vicinal diol groups, i.e., with latent aldehyde functions.

CONCLUSIONS

This study offers a versatile design for SAM components with latent aldehyde functions: amide bond formation between a SAM-forming carboxylic acid with 3-amino-1,2-propanediol (APD). Usually it will be preferable to couple APD with the vicinal diol in its protected form (APD-ac, **2**). Some SAM-forming carboxylic acids, however, can be used in their final form, as exemplified by lipoic acid (see Figure 1) and 10-undecenoic acid (see Figure 6), and the disulfidic forms of ω-mercapto-fatty acids would be further candidates for this simple route. Alternatively, the SAM-forming function needs to be protected while forming the amide bond with APD-ac, as can be seen in Figure 3 where the thiol function was protected as thioester that was easily unmasked in the last step. A third variant of the same basic strategy is shown in Figure 5. In this case, a precursor of the SAM-forming carboxylic acid (Br-HDA, **10**) was first coupled to APD-ac (**2**), and only then the SAM-forming function (the catechol) was attached by O-alkylation, taking advantage of the high stability of the amide bond and the acetonide protecting group in **11** under basic conditions. Given the wide variety of SAM-forming carboxylic acids and their precursors, the attachment of APD or APD-ac appears to be a fairly general method to prepare SAM components with latent aldehyde functions for most types of inorganic surfaces. Moreover, we have shown that insertion of NH_2-PEG-COOH between the SAM-forming carboxylic acid and APD produces protein-resistant SAMs with latent aldehyde functions (Hölzl et al., submitted manuscript, Austrian patent application 1469/2006), indicating further extensions of the simple modular design principle.

ACKNOWLEDGMENT

Consulting in NMR spectroscopy by Norbert Müller is gratefully acknowledged. This work was supported by the Austrian Science Foundation (projects P15295, N00104) and (A.T.) by the Deutsche Forschungsgemeinschaft (DFG, FOR495) and the Bundesministerium für Bildung und Forschung (BMBF, Programm Nanobiotechnologie).

Supporting Information Available: Syntheses of compounds **3**, **4**, **7**, **8**, **11**, **12**, **13**, **14**, **15**, and **17**. Preparation of biotin-IgG. Preparation and characterization of a mixed SAM (95/5, w/w) of Lip-NH_2 and Lip-APD (**4**). Oxidation of a SAM of MHD-APD (**8**) inside the BIAcore X setup. Proof of covalent coupling of protein to oxidized MHD-APD (**9**) as opposed to mere adsorption to nonoxidized MHD-APD (**8**). This material is available free of charge via the Internet at http://pubs.acs.org.

LITERATURE CITED

(1) Chaki, N. K., and Vijayamohanan, K. (2002) Self-assembled monolayers as a tunable platform for biosensor applications. *Biosens. Bioelectron. 17*, 1−12.

(2) Gooding, J. J., Mearns, F., Yang, W. R., and Liu, J. Q. (2003) Self-assembled monolayers into the 21st century: Recent advances and applications. *Electroanalysis 15*, 81−96.

(3) Karlsson, R. (2004) SPR for molecular interaction analysis: a review of emerging application areas. *J. Mol. Recognit. 17*, 151−161.

(4) Love, J. C., Estroff, L. A., Kriebel, J. K., Nuzzo, R. G., and Whitesides, G. M. (2005) Self-assembled monolayers of thiolates on metals as a form of nanotechnology. *Chem. Rev. 105*, 1103−1170.

(5) Riu, J., Maroto, A., and Rius, F. X. (2006) Nanosensors in environmental analysis. *Talanta 69*, 288−301.

(6) Chen, C. S., Ostuni, E., Whitesides, G. M., and Ingber, D. E. (2000) Using self-assembled monolayers to pattern ECM proteins and cells on substrates. *Methods Mol. Biol. 139*, 209−219.

(7) Falconnet, D., Csucs, G., Michelle Grandin, H., and Textor, M. (2006) Surface engineering approaches to micropattern surfaces for cell-based assays. *Biomaterials 27*, 3044−3063.

(8) Mrksich, M. (1998) Tailored substrates for studies of attached cell culture. *Cell. Mol. Life Sci. 54*, 653−662.

(9) Peelen, D., and Smith, L. M. (2005) Immobilization of amine-modified oligonucleotides on aldehyde-terminated alkanethiol monolayers on gold. *Langmuir 21*, 266−271.

(10) Houseman, B., Huh, J., Kron, S., and Mrksich, M. (2002) Peptide chips for the quantitative evaluation of protein kinase activity. *Nat. Biotechnol. 20*, 270−274.

(11) Houseman, B. T., and Mrksich, M. (2002) Carbohydrate arrays for the evaluation of protein binding and enzymatic modification. *Chem. Biol. 9*, 443−454.

(12) Houseman, B. T., Gawalt, E. S., and Mrksich, M. (2003) Maleimide-functionalized self-assembled monolayers for the preparation of peptide and carbohydrate biochips. *Langmuir 19*, 1522−1531.

(13) Haake, H., Schutz, A., and Gauglitz, G. (2000) Label-free detection of biomolecular interaction by optical sensors. *Fresenius J. Anal. Chem. 366*, 576−585.

(14) Brockman, J. M., Nelson, B. P., and Corn, R. M. (2000) Surface plasmon resonance imaging measurements of ultrathin organic films. *Annu. Rev. Phys. Chem. 51*, 41−63.

(15) Su, J., and Mrksich, M. (2002) Using mass spectrometry to characterize self-assembled monolayers presenting peptides, proteins, and carbohydrates. *Angew. Chem. Int. Ed. Engl. 41*, 4715−4718.

(16) Mouradian, S., Nelson, C. M., and Smith, L. M. (1996) A Self-assembled matrix monolayer for UV-MALDI mass spectrometry. *J. Am. Chem. Soc. 118*, 8639−8645.

(17) Ryan, D., Parviz, B. A., Linder, V., Semetey, V., Sia, S. K., Su, J., Mrksich, M., and Whitesides, G. M. (2004) Patterning multiple aligned self-assembled monolayers using light. *Langmuir 20*, 9080−9088.

(18) Boozer, C., Yu, Q., Chen, S., Lee, C.-Y., Homola, J., Yee, S. S., and Jiang, S. (2003) Surface functionalization for self-referencing surface plasmon resonance (SPR) biosensors by multi-step self-assembly. *Sens. Actuators B: Chem. 90*, 22−30.

(19) Jung, L. S., Nelson, K. E., Stayton, P. S., and Campbell, C. T. (2000) Binding and dissociation kinetics of wild-type and mutant streptavidins on mixed biotin-containing alkylthiolate monolayers. *Langmuir 16*, 9421−9432.

(20) Nelson, K. E., Gamble, L., Jung, L. S., Boeckl, M. S., Naeemi, E., Golledge, S. L., Sasaki, T., Castner, D. G., Campbell, C. T., and Stayton, P. S. (2001) Surface characterization of mixed self-assembled monolayers designed for streptavidin immobilization. *Langmuir 17*, 2807−2816.

(21) Su, X. D., Wu, Y. J., Robelek, R., and Knoll, W. (2005) Surface plasmon resonance spectroscopy and quartz crystal microbalance study of streptavidin film structure effects on biotinylated DNA assembly and target DNA hybridization. *Langmuir 21*, 348−353.

(22) Madoz-Gurpide, J., Abad, J. M., Fernandez-Recio, J., Velez, M., Vazquez, L., Gomez-Moreno, C., and Fernandez, V. M. (2000) Modulation of electroenzymatic NADPH oxidation through oriented immobilization of ferredoxin:NADP(+) reductase onto modified gold electrodes. *J. Am. Chem. Soc. 122*, 9808−9817.

(23) Sigal, G. B., Bamdad, C., Barberis, A., Strominger, J., and Whitesides, G. M. (1996) A self-assembled monolayer for the binding and study of histidine-tagged proteins by surface plasmon resonance. *Anal. Chem. 68*, 490−497.

(24) Tinazli, A., Tang, J., Valiokas, R., Picuric, S., Lata, S., Piehler, J., Liedberg, B., and Tampé, R. (2005) High-affinity chelator thiols for switchable and oriented immobilization of histidine-tagged proteins: a generic platform for protein chip technologies. *Chem. Eur. J. 11*, 5249−5259.

(25) Yousaf, M. N., and Mrksich, M. (1999) Diels-Alder reaction for the selective immobilization of protein to electroactive self-assembled monolayers. *J. Am. Chem. Soc. 121*, 4286−4287.

(26) Lee, J. K., Chi, Y. S., and Choi, I. S. (2004) Reactivity of acetylenyl-terminated self-assembled monolayers on gold: Triazole formation. *Langmuir 20*, 3844−3847.

(27) Hodneland, C. D., Lee, Y. S., Min, D. H., and Mrksich, M. (2002) Selective immobilization of proteins to self-assembled monolayers presenting active site-directed capture ligands. *Proc. Natl. Acad. Sci. U.S.A. 99*, 5048−5052.

(28) Lahiri, J., Isaacs, L., Tien, J., and Whitesides, G. M. (1999) A strategy for the generation of surfaces presenting ligands for studies of binding based on an active ester as a common reactive intermediate: A surface plasmon resonance study. *Anal. Chem. 71*, 777−790.

(29) Lahiri, J., Ostuni, E., and Whitesides, G. M. (1999) Patterning ligands on reactive SAMs by microcontact printing. *Langmuir 15*, 2055−2060.

(30) Löfas, S., Johnsson, B., Edstrom, A., Hansson, A., Lindquist, G., Hillgren, R.-M. M., and Stigh, L. (1995) Methods for site controlled coupling to carboxymethyldextran surfaces in surface plasmon resonance sensors. *Biosens. Bioelectron. 10*, 813−822.

(31) Johnsson, B., Löfas, S., Lindquist, G., Edstrom, A., Müller-Hillgren, R. M., and Hansson, A. (1995) Comparison of methods for immobilization to carboxymethyl dextran sensor surfaces by analysis of the specific activity of monoclonal antibodies. *J. Mol. Recognit. 8*, 125−131.

(32) Wagner, P., Hegner, M., Kernen, P., Zaugg, F., and Semenza, G. (1996) Covalent immobilization of native biomolecules onto Au(111) via N-hydroxysuccinimide ester functionalized self-assembled monolayers for scanning probe microscopy. *Biophys. J. 70*, 2052−2066.

(33) Wilkop, T., Wang, Z. Z., and Cheng, Q. (2004) Analysis of μ-contact printed protein patterns by SPR imaging with a LED light source. *Langmuir 20*, 11141−11148.

(34) Tournier, E. J. M., Wallach, J., and Blond, P. (1998) Sulfo-succinimidyl 4-(*N*-maleimidomethyl)-1-cyclohexane carboxylate as a bifunctional immobilization agent. Optimization of the coupling conditions. *Anal. Chim. Acta 361*, 33−44.

(35) Johnsson, B., Löfas, S., and Lindquist, G. (1991) Immobilization of proteins to a carboxymethyldextran-modified gold surface for biospecific interaction analysis in surface plasmon resonance sensors. *Anal. Biochem. 198*, 268−277.

(36) Wadu-Mesthrige, K., Xu, S., Amro, N. A., Liu, G.-Y. (1999) Fabrication and imaging of nanometer-sized protein patterns. *Langmuir 15*, 8580−8583.

(37) Wadu-Mesthrige, K., Amro, N. A., Garno, J. C., Xu, S., and Liu, G. Y. (2001) Fabrication of nanometer-sized protein patterns using atomic force microscopy and selective immobilization. *Biophys. J. 80*, 1891−1899.

(38) Horton, R. C., Herne, T. M., and Myles, D. C. (1997) Aldehyde-terminated self-assembled monolayers on gold: Immobilization of amines onto gold surfaces. *J. Am. Chem. Soc. 119*, 12980−12981.

(39) Liu, G. Y., and Amro, N. A. (2002) Positioning protein molecules on surfaces: a nanoengineering approach to supramolecular chemistry. *Proc. Natl. Acad. Sci. U.S.A. 99*, 5165−5170.

(40) Jang, C.-H., Stevens, B. D., Phillips, R., Calter, M. A., and Ducker, W. A. (2003) A strategy for the sequential patterning of proteins: Catalytically active multiprotein nanofabrication. *Nano Lett. 3*, 691−694.

(41) Bain, C. D., Biebuyck, H. A., and Whitesides, G. M. (1989) Comparison of self-assembled monolayers on gold: Coadsorption of thiols and disulfides. *Langmuir 5*, 723−727.

(42) Khodaei, M. M., Salehi, P., Goodarzi, M., and Yazdanipour, A. (2004) γ-PCC and γ-PCC-SiO_2 as efficient reagents for oxidation of thiols to disulfides. *Synth. Commun. 34*, 3661−3666.
(43) Salehi, P., Farrokhi, A., and Gholizadeh, M. (2001) Oxidative coupling of thiols by pyridinium chlorochromate in solution and solvent free conditions. *Synth. Commun. 31*, 2777−2781.
(44) Valiokas, R., Svedhem, S., Svensson, S. C. T., and Liedberg, B. (1999) Self-assembled monolayers of oligo(ethylene glycol)-terminated and amide group containing alkanethiolates on gold. *Langmuir 18*, 3390−3394.
(45) Caillant, D., Vandoorne, F., and Schacht, E. (1998) A new approach to dextran derivatives with pendant aldehyde groups. *React. Polym. 8*, 126−136.
(46) Vandoorne, F., Loccufier, J., and Schacht, E. (1989) Functionalization of α-halogen-ω-methoxypoly(oxyethylene). 1. A new method for the conversion of hydroxyl end groups into aldehyde groups. *Makromol. Chem., Rapid Commun. 10*, 271−275.
(47) Barltrop, J. A., Hayes, P. M., and Calvin, M. (1954) The chemistry of 1,2-dithiolane (trimethylene disulfide) as a model for the primary quantum conversion act in photosynthesis. *J. Am. Chem. Soc. 76*, 4348−4367.
(48) Wagner, A. F., Walton, E., Boxer, G. E., Pruss, M. P., Holly, F. W., and Folkers, K. (1956) Properties and derivatives of α-lipoic acid. *J. Am. Chem. Soc. 79*, 5079−5081.
(49) Svedhem, S., Hollander, C. A., Shi, J., Konradsson, P., Liedberg, B., and Svensson, S. C. T. (2001) Synthesis of a series of oligo(ethylene glycol)-terminated alkanethiol amides designed to address structure and stability of biosensing interfaces. *J. Org. Chem. 66*, 4494−4503.
(50) Dalsin, J. L., Lin, L., Tosatti, S., Vörös, J., Textor, M., and Messersmith, P. B. (2005) Protein resistance of titanium oxide surface modified by biologically inspired mPEG-DOPA. *Langmuir 21*, 640−646.
(51) Sieval, A. B., Demirel, A. L., Nissink, J. W. M., Linford, M. R., van der Maas, J. H., de Jeu, W. H., Zuilhof, H., and Sudhölter, E. J. R (1998) Highly stable Si-C linked functionalized monolayers on the silicon (100) surface. *Langmuir 14*, 1759−1768.
(52) Voicu, R., Boukherroub, R., Bartzoka, V., Ward, T., Wojtyk, J. T. C., and Wayner, D. D. M. (2004) Formation, characterization, and chemistry of undecanoic acid-terminated silicon surfaces: Patterning and immobilization of DNA. *Langmuir 20*, 11713−11720.
(53) Perring, M., Dutta, S., Arafat, S., Mitchell, M., Kenis, P. J. A., and Bowden, N. B. (2005) Simple methods for the direct assembly, functionalization, and patterming of acid-terminated monolayers on Si(111). *Langmuir 21*, 10537−10544.
(54) Mengistu, T. Z., Goel, V., Horton, J. H., and Morin, S. (2006) Chemical force titrations of functionalized Si(111) surfaces. *Langmuir 22*, 5301−5307.

BC060292E

3,4,6-Tri-*O*-acetyl-2-deoxy-2-[^{18}F]fluoroglucopyranosyl Phenylthiosulfonate: A Thiol-Reactive Agent for the Chemoselective ^{18}F-Glycosylation of Peptides

Olaf Prante,*[‡] Jürgen Einsiedel,[†] Roland Haubner,[§] Peter Gmeiner,[†] Hans-Jürgen Wester,[#] Torsten Kuwert,[‡] and Simone Maschauer[‡]

Laboratory of Molecular Imaging, Clinic of Nuclear Medicine, Friedrich-Alexander University, 91054 Erlangen, Germany, Department of Medicinal Chemistry, Emil Fischer Center, Friedrich-Alexander University, 91052 Erlangen, Germany, Universitätsklinik für Nuklearmedizin, Medizinische Universität Innsbruck, 6020 Innsbruck, Austria, and Department of Nuclear Medicine, Klinikum rechts der Isar, Technische Universität München, 81675 Munich, Germany. Received October 29, 2006

3,4,5-Tri-*O*-acetyl-2-[^{18}F]fluoro-2-deoxy-D-glucopyranosyl 1-phenylthiosulfonate (Ac_3-[^{18}F]FGlc-PTS) was developed as a thiol-reactive labeling reagent for the site-specific ^{18}F-glycosylation of peptides. Taking advantage of highly accessible 1,3,4,6-tetra-*O*-acetyl-2-deoxy-2-[^{18}F]fluoroglucopyranose, a three-step radiochemical pathway was investigated and optimized, providing Ac_3-[^{18}F]FGlc-PTS in a radiochemical yield of about 33% in 90 min (decay-corrected and based on starting [^{18}F]fluoride). Ac_3-[^{18}F]FGlc-PTS was reacted with the model pentapeptide CAKAY, confirming chemoselectivity and excellent conjugation yields of >90% under mild reaction conditions. The optimized method was adopted to the ^{18}F-glycosylation of the $\alpha_v\beta_3$-affine peptide c(RGDfC), achieving high conjugation yields (95%, decay-corrected). The $\alpha_v\beta_3$ binding affinity of the glycosylated c(RGDfC) remained uninfluenced as determined by competition binding studies versus ^{125}I-echistatin using both isolated $\alpha_v\beta_3$ and human umbilical vein endothelial cells ($K_i = 68 \pm 10$ nM ($\alpha_v\beta_3$) versus $K_i = 77 \pm 4$ nM (HUVEC)). The whole radiosynthetic procedure, including the preparation of the ^{18}F-glycosylating reagent Ac_3-[^{18}F]FGlc-PTS, peptide ligation, and final HPLC purification, provided a decay-uncorrected radiochemical yield of 13% after a total synthesis time of 130 min. Ac_3-[^{18}F]FGlc-PTS represents a novel ^{18}F-labeling reagent for the mild chemoselective ^{18}F-glycosylation of peptides indicating its potential for the design and development of ^{18}F-labeled bioactive S-glycopeptides suitable to study their pharmacokinetics in vivo by positron emission tomography (PET).

INTRODUCTION

Positron emission tomography (PET) using peptide-based radiopharmaceuticals has gained considerable importance in the field of nuclear medicine and radiopharmaceutical sciences (*1*, *2*). In particular, the increasing knowledge about improved automated solid-phase peptide synthesis and advanced methods for structure−activity relationship studies of receptor-specific peptides accelerated the development of suitable candidates as agents for diagnostic and also therapeutic applications. Furthermore, the positron emitter fluorine-18 has been characterized as a suitable nuclide for radiochemical approaches toward peptide labeling. The short-lived positron emitter fluorine-18 has excellent physical characteristics, such as a relatively low positron energy of 635 keV, limiting the patient's absorbed dose, and a prolonged half-life of 109.7 min allowing extended and multistep radiochemical syntheses and prolonged PET imaging protocols. These features support an exceptional position of ^{18}F as a beneficial PET radionuclide in comparison with alternative positron emitters such as ^{11}C or ^{13}N.

Moreover, the development of new ^{18}F-labeled prosthetic groups for the radiofluorination of peptides strongly increased the availability of peptide-based radiopharmaceuticals for PET over the past years. A commonly used strategy to label peptides relies on the use of *N*-succinimidyl-4-[^{18}F]fluorobenzoate ([^{18}F]SFB) targeting the N-terminus or lysine side chains of the target peptide. According to Wester et al., [^{18}F]SFB can be efficiently prepared by a simplified method affording an overall radiochemical yield ranging between 50% and 60% based on [^{18}F]fluoride within a preparation time of 35 min (*3*). Besides [^{18}F]SFB, 4-nitrophenyl 2-[^{18}F]fluoropropionate proved to be an effective and suitable ^{18}F-acylation agent. The prevalent application of these two ^{18}F-labeled prosthetic groups has resulted in a large number of ^{18}F-labeled peptide-based imaging agents, such as [^{18}F](D-Phe^1)octreotide (*4*), [^{18}F]galacto-RGD (*5*), [^{18}F]FB−PEG−RGD (*6*), [^{18}F]NT(8−13) (*7*), [^{18}F](Nle^4, D-Phe^7)-α-MSH) (*8*), and ^{18}FB−AHx−insulin (*9*). Among these, [^{18}F]galacto-RGD already provided promising results for the noninvasive assessment of $\alpha_v\beta_3$ expression on tumor and endothelial cells in patients with malignant tumors by PET (*10*).

The development of chemoselective ^{18}F-labeling strategies that are favorable for routine large scale syntheses of short-lived ^{18}F-labeled radiopharmaceuticals have been intensively studied in recent years. For instance, [^{18}F]fluorothiols have been prepared for the chemoselective labeling of N-terminal chloroacetylated peptides (*11*). Recently, Poethko et al. developed a convenient ^{18}F-labeling method for peptides by oxime conjugation of [^{18}F]fluorobenzaldehyde with unprotected aminooxy peptides yielding chemoselectively labeled RGD peptides and somatostatin analogs (*12*). Moreover, chemoselective ^{18}F-labeling strategies being based on the radiosynthesis of ^{18}F-labeled maleimide derivatives as thiol-reactive reagents were investigated (*13*, *14*). Toyokuni et al. reported the ^{18}F-radiosynthesis of a new heterobifunctional maleimide derivative, namely, *N*-[4-(aminooxy)butyl]maleimide ([^{18}F]FBABM, Figure

* Corresponding author. Mailing address: Laboratory of Molecular Imaging, Clinic of Nuclear Medicine, Friedrich-Alexander University, Schwabachanlage 6, D-91054 Erlangen, Germany. Tel: +49-09131-8534440. Fax: +49-09131-8534325. E-mail: olaf.prante@nuklear.imed.uni-erlangen.de.

‡ Clinic of Nuclear Medicine, Friedrich-Alexander University.

† Emil Fischer Center, Friedrich-Alexander University.

§ Medizinische Universität Innsbruck.

Technische Universität München.

10.1021/bc060340v CCC: $37.00 © 2007 American Chemical Society
Published on Web 12/23/2006

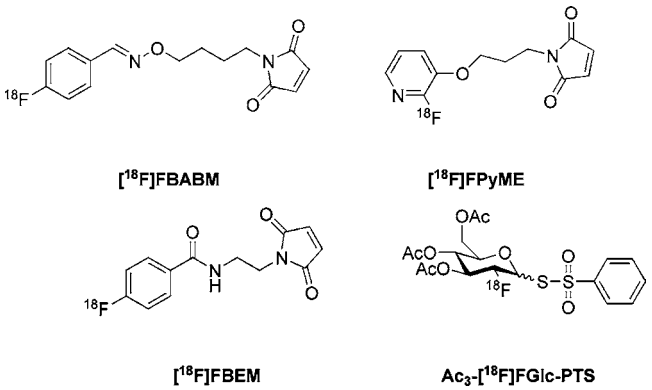


Figure 1. Chemical structures of ^{18}F-labeled thiol-reactive prosthetic groups for site-selective ^{18}F-labeling of peptides: *N*-[4-(aminooxy)-butyl]maleimide ([^{18}F]FBABM (*13*)), 1-[3-(2-fluoropyridin-3-yloxy)-propyl]pyrrole-2,5-dione ([^{18}F]FPyME (*14*)), *N*-[2-(4-[^{18}F]fluorobenz-amido)ethyl]maleimide ([^{18}F]FBEM (*15*)), and 3,4,6-tetra-*O*-acetyl-2-deoxy-2-[^{18}F]fluoro-glucopyranosyl phenylthiosulfonate (Ac_3-[^{18}F]FGlc-PTS (**[^{18}F]2**), this work).

1), within a two-step synthesis that was followed by a conjugation step with the cysteine-containing peptide in phosphate-buffered saline (*13*). Using this strategy, radiochemical yields (RCYs) of 70% for the model compound glutathione were possible, whereas for a 5′-thiol-functionalized oligodeoxynucleotide only 5% (decay-corrected) RCY was achieved.

Meanwhile, de Bruin et al. developed the alternative pyridinyl-substituted maleimide reagent [^{18}F]FPyME (Figure 1) for the prosthetic ^{18}F-labeling of peptides via conjugation with a thiol function (*14*). A three-step process is needed for the preparation of [^{18}F]FPyME, advantegeously making use of a nucleophilic heteroaromatic substitution in ortho position of the pyridinyl moiety, followed by cleavage of an *N*-BOC protective group and ultimately maleimide formation. This strategy provides a RCY of about 30% for the preparation of [^{18}F]FPyME and a non-decay-corrected yield of 65% for the final conjugation of target peptides (*14*). More recently, a similar approach for the radiosynthesis of a thiol-reactive ^{18}F-labeled maleimide starting from [^{18}F]SFB has been described (*15*). [^{18}F]SFB was isolated and subsequently converted to the benzamide derivative [^{18}F]FBEM (Figure 1, non-decay-corrected RCY of about 5% within 150 min), which was suitable for ^{18}F-labeling of thiolated RGD peptides. Following this 200 min procedure, the overall decay-corrected RCY was 20% including two HPLC purification steps.

2-Deoxy-2-[^{18}F]fluoroglucose ([^{18}F]FDG) represents by far the most frequently used radiopharmaceutical for PET imaging in nuclear medicine, not least because of its highly efficient radiosynthesis (*16*). Despite its very high availability, only few approaches toward a chemoselective glycoconjugation of an ^{18}F-labeled glycosyl donor with peptides have been described in previous short communications (*17*, *18*). Such a strategy could be beneficial for the development of ^{18}F-labeled glycopeptides as PET tracers with improved biokinetics, since glycosylation of peptides has often been shown to enhance bioavailability and improve blood−brain barrier (BBB) permeability and in vivo clearance properties (*19*−*21*). As an extension to the available ^{18}F-labeling agents, we recently investigated the applicability of tetra-O-acetylated 2-[^{18}F]fluoro-2-deoxy-glucopyranose as a ^{18}F-glycosylation reagent (*22*, *23*). However, this approach did not include a chemoselective ligation of the glycosyl residue and suffered from the necessity of Lewis acids as promotors.

The aim of this study was to develop a thiol-reactive ^{18}F-labeled glycosyl donor for a chemoselective ^{18}F-glycosylation approach. Besides maleimide-activated carbohydrates (*24*), glycosyl 1-phenylthiosulfonates (*25*) have recently been reported to be well-suited for site-specific glycosylation of cysteine-containing peptides and proteins. In this study, we present the radiosynthesis of 3,4,6-tri-*O*-acetyl-2-deoxy-2-[^{18}F]fluoroglucopyranosyl phenylthiosulfonate (Ac_3-[^{18}F]FGlc-PTS, Figure 1) as a new ^{18}F-labeled thiol-reactive glycosyl donor for ^{18}F-glycosylation of peptides and its application for bioconjugation using the cyclic peptide c(RGDfC). Furthermore, we studied the in-vitro binding affinities of the glycosylated RGD peptide using immobilized $\alpha_v\beta_3$ integrin and human endothelial cells.

EXPERIMENTAL PROCEDURES

General. All chemicals and reagents were of analytical grade and obtained from commercial sources if not stated otherwise. *N*,*N*′-Dimethylformamide (DMF), dichloromethane (CH_2Cl_2), acetonitrile, and dimethyl sulfoxide (DMSO) were obtained from Fluka as SureSeal bottles. Benzotriazol-1-yl-oxy-tris-pyrrolidino-phosphonium hexafluorophosphate (PyBOP) and *N*-hydroxy-benzotriazole (HOBt) were purchased from Bachem. [^{18}F]-Fluoride was obtained from PET Net GmbH (Erlangen, Germany). ^{125}I-Echistatin was purchased from Amersham Biosciences (GE Healthcare, Germany). Purified $\alpha_v\beta_3$ integrin was obtained as a Triton X-100 formulation from Chemicon Europe (Southampton, U.K.). Radio-thin layer chromatography (radio-TLC) was carried out on plastic sheets using ethyl actetate/*n*-hexane (1:1, v/v) as eluent (Polygram, Sil G/UV_{254}, Macherey Nagel). Analytical HPLC was performed on an Agilent 1100 system with a quarternary pump and variable wavelength detector and radio-HPLC detector D505TR (Canberra Packard). Computer analysis of the HPLC data was performed using FLO-One software (Canberra Packard). Electronic autoradiography (Instant Imager, Canberra Packard) was used to analyze radio-TLC data. Electron-spray-ionization (ESI) mass spectrometry analysis was performed using a Bruker esquire 2000 instrument. LC-MS analyses were performed on an Agilent 1100 series analytic HPLC system coupled to a Bruker esquire 2000 mass spectrometer. Matrix-assisted laser desorption/ionization time-of-flight (MALDI) mass spectrometry was performed using a MALDI-3 apparatus (Kratos Instruments) at the Department of Nuclear Medicine of the University of Heidelberg. NMR spectra were recorded on a Varian Gemini-300 system for ^{19}F NMR (Deutero GmbH, Germany) and on a Bruker Avance 600 system for ^{1}H NMR. The syntheses of the ^{18}F-labeling precursor 1,3,4,6-tetra-*O*-acetyl-2-*O*-trifluoromethanesulfonyl-β-D-mannopyranose (*26*) and of 3,4,6-tri-*O*-acetyl-2-deoxy-2-fluoro-α-D-glucopyranose 1-bromide (**1**) were described elsewhere (*22*).

Peptide syntheses. *CAKAY*. The peptide synthesis was achieved by manual solid-phase techniques, when microwave irradiation (Discover reactor, CEM corporation) supported short reaction times and enhanced coupling effectivities. Fmoc-Tyr(*t*-Bu)-Wang resin (Fluka) with a loading of 0.8 mmol/g was used as the solid support incorporating amino acids as their N^{α}-(9-fluorenylmethyloxycarbonyl) (Fmoc)-protected derivatives. For the protection of the amino acid side chains, *tert*-butoxycarbonyl (Boc) and trityl (Trt) were used for lysine and cysteine, respectively. Elongation of the peptide chain was done by repetitive cycles of Fmoc deprotection applying 20% piperidine in DMF (microwave irradiation 5 × 5 s, 100 W), followed by five washings with DMF and subsequent peptide coupling employing 5 equiv of the corresponding Fmoc-amino acid/PyBOP/diisopropylamine and 7.5 equiv of HOBt, dissolved in a minimum amount of DMF (irradiation 15 × 10 s, 50 W). Between every irradiation step, cooling of the reaction mixture to a temperature of −10 °C was achieved by sufficient agitation in an ethanol−ice bath. Cysteine was introduced as the pentafluorophenyl ester (Fmoc-Cys(Trt)-OPfp, Fluka) and solely used as a solution in DMF without any additive. After each acylation step, the solid support was washed five times with

DMF. Subsequently, the N-terminal Fmoc residue was deprotected as described above, the resin was rinsed 10 times with CH_2Cl_2 and dried under vacuum. Cleavage from the resin was performed by using a mixture of trifluoroacetic acid (TFA)/phenol/water/thioanisole/ethanedithiole/triisopropylsilane 81.5:5:5:5:2.5:2 for 2 h. After evaporation of the solvent, the peptide was precipitated and washed four times in *t*-butyl methyl ether, while N_2 was bubbled through the suspension before each washing. Purification of the crude material was done using preparative RP-HPLC (Agilent 1100 preparative series, column Zorbax 300 SB-C18, 21.2 mm × 250 mm, 7 μm particles). The eluting system was 0.1% TFA in acetonitrile (A) and 0.1% TFA in water (B) applying a linear gradient from 5.0% to 6.3% A over 15 min at a flow rate of 21.2 mL/min. Chemical purity of CAKAY was 96% as determined by HPLC (Lichrosorb RP-18, 250 mm × 4.6 mm, 1.5 mL/min, 10−100% acetonitrile in water (0.1% TFA) over 40 min; t_R = 4.23 min). ESI-MS: *m/z* 555.3 $[M + H]^+$.

Cyclic RGD Peptides. c(RGDfC) and c(RGDfS) were synthesized by Fmoc-assisted peptide solid-phase synthesis using a trityl chloride polystyrene (TCP) resin (PepChem, Tübingen, Germany). Loading of the TCP resin, synthesis of the peptide, subsequent cyclization, and deprotection were carried out following the protocol described elsewhere (*5*, *19*, *27*). Side-chain protection was 2,2,4,6,7-pentamethyldihydrobenzofuran-5-sulfonyl (Pbf) for arginine, *tert*-butyl (tBu) for aspartic acid and serine, and trityl (Trt) for cysteine. Chemical purities of cyclic RGD peptides were ≥96% as determined by HPLC and LC-MS. c(RGDfS): HPLC Lichrosorb RP-18, 250 mm × 4.6 mm, 1 mL/min, 0−50% acetonitrile in water (0.1% TFA) over 30 min, t_R(c(RGDfS)) = 15.5 min; ESI-MS *m/z* 563.2 $[M + H]^+$. c(RGDfC): HPLC Lichrosorb RP-18, 250 mm × 4.6 mm, 1.5 mL/min, 10−100% acetonitrile in water (0.1% TFA) over 40 min, t_R = 8.8 min; ESI-MS *m/z* 579.3 $[M + H]^+$, 601.2 $[M + Na]^+$; LC-MS 579.0 $[M + H]^+$.

Sodium Phenylthiosulfonate (NaPTS). The synthesis of NaPTS was performed as described by Gamblin et al. (*25*). Sodium benzenesulfinate (2 g, 12 mmol) and 390 mg (12 mmol) of sulfur were dissolved in 12 mL of anhydrous pyridine to give a yellow suspension. The reaction was stirred in a nitrogen atmosphere at room temperature for 1 h until a white suspension occurred. The mixture was filtered and washed with anhydrous diethyl ether. The crude product was crystallized from ethanol to yield 2.1 g (11 mmol, 92%) of NaPTS as a white solid. ^{1}H NMR (360 MHz, DMSO-d_6): δ 7.76−7.71 (m, 2H), 7.38−7.31 (m, 3H). ESI-MS: *m/z* 173.2 $[M- Na]^-$, 219.1 $[M + Na]^+$.

*3,4,6-Tri-O-acetyl-2-deoxy-2-fluoro-β-*D*-glucopyranosyl Phenylthiosulfonate, **2** (Ac$_3$-FGlc-PTS).* 3,4,6-Tri-*O*-acetyl-2-deoxy-2-fluoro-α-D-glucopyranosyl bromide (207 mg, 558 μmol, **1**) was dissolved in 5 mL of acetonitrile and 216 mg (1.1 mmol) of NaPTS and 18 mg (558 μmol) of tetrabutylammonium bromide (TBABr) were added. The mixture was stirred at 70 °C under a nitrogen atmosphere for 1.5 h. Afterward the solvent was removed in vacuo, the residue was partitioned between CH_2Cl_2 and water, and the aqueous phase was re-extracted with CH_2Cl_2. The combined organic phases were dried over Na_2SO_4, and the solvent was removed in vacuo. The resulting residue was purified by flash column chromatography (ethyl acetate/hexane 1:1) to afford 189 mg (407 μmol, 72%) of Ac$_3$-FGlc-PTS (**2**) as a yellow oil. TLC: ethyl acetate/hexane 1:1, R_f = 0.6. HPLC (Lichrosorb RP-18, 250 mm × 4.6 mm, 1.5 mL/min, 10−100% acetonitrile in water (0.1% TFA) over 40 min): t_R = 21.52 min. ^{1}H NMR (360 MHz, DMSO-d_6): δ 8.04−7.94 (m, 2H, Ar−H), 7.81−7.64 (m, 3H, Ar−H), 6.33 (d, 0.2H (α), H-1, $J_{1,2}$ = 5.8 Hz), 5.73 (dd, 1H (β), H-1, $J_{1,2}$ = 9.4 Hz, $J_{1,F}$ = 2.0 Hz), 5.62 (dt, 1H, H-3, $J_{3,F}$ = 14.8 Hz, $J_{2,3} = J_{3,4}$ = 9.7 Hz), 4.85 (t(dd), 1H, H-4, $J_{4,5} = J_{4,3}$ = 9.7 Hz), 4.79 (ddd, 1H, H-2, $J_{2,F}$ = 50.0 Hz, $J_{2,3}$ = 9.7 Hz, $J_{2,1}$ = 9.4 Hz), 4.14 (ddd, 1H, H-5, $J_{5,4}$ = 9.7 Hz, $J_{5,6a}$ = 4.6 Hz, $J_{5,6b}$ = 2.3 Hz), 4.02 (dd, 1H, H-6a, $J_{6a,6b}$ = 12.6 Hz, $J_{6a,5}$ = 4.6 Hz), 3.68 (dd, 1H, H-6b, $J_{6a,6b}$ = 12.6 Hz, $J_{6b,5}$ = 2.3 Hz), 2.03 (s, 3H, OAc), 1.98 (s, 3H, OAc), 1.95 (s, 3H, OAc). ^{19}F NMR (DMSO-d_6): δ −192.51 (dd, $J_{F,2}$ = 49.8 Hz, $J_{F,3}$ = 14.9 Hz, α-anomer), −191.93 (ddd, $J_{F,2}$ = 50.0 Hz, $J_{F,3}$ = 14.8 Hz, $J_{F,1}$ = 2.0 Hz, β-anomer); α/β = 20:80. ESI-MS: *m/z* 465.0 $[M + H]^+$, 487.0 $[M + Na]^+$.

L-*(S-3,4,6-Tri-O-acetyl-2-deoxy-2-fluoro-β-*D*-glucopyranosyl disulfide)-cysteinyl-*L*-alanyl-*L*-lysyl-*L*-alanyl-*L*-tyrosine, **3** (C(S,S′-Ac$_3$-FGlc)AKAY).* To a solution of 1.3 mg (2.3 μmol) of CAKAY in 1 mL of buffer (50 mM Tris, pH 7.7) was added 19 mg (40 μmol) of Ac$_3$-FGlc-PTS (**2**) in 100 μL of acetonitrile/water, 8:2. After the reaction time of 30 min, the absence of free thiol was shown by Ellman's analysis, and the product was isolated by semipreparative HPLC (Lichrosorb RP-18, 125 mm × 8 mm, 4 mL/min, 10−100% acetonitrile in water (0.1% TFA) over 40 min) and subsequently lyophilized to afford C(S,S′-Ac$_3$-FGlc)AKAY (**3**) (1.8 mg, 2 μmol, 90%) as a white powder. HPLC (Lichrosorb RP-18, 250 mm × 4.6 mm, 1.5 mL/min, 10−100% acetonitrile in water (0.1% TFA) over 40 min, 220 nm): t_R = 9.7 min. ^{1}H NMR (600 MHz, DMSO-d_6): δ 9.23 (b, 1H, COOH), 8.69 (d, 1H, $J_{HN/H\alpha}$ = 7.5 Hz, NH), 8.12 (d, 1H, $J_{HN/H\alpha}$ = 8.0 Hz, NH), 8.10 (d, 1H, $J_{HN/H\alpha}$ = 7.8 Hz, NH), 7.83 (d, 1H, $J_{HN/H\alpha}$ = 7.4 Hz, NH), 7.67 (b, 1H, NH_2), 7.01 (m, 2H, Ar-Tyr), 6.65 (m, 2H, Ar-Tyr), 5.53 (dt, 1H, $J_{3,F}$ = 14.1 Hz, $J_{3,2} = J_{3,4}$ = 9.5 Hz, H-3), 5.17 (dd, 1H, $J_{1,2}$ = 9.5 Hz, $J_{1,F}$ = 1.8 Hz, H-1, β-anomer), 4.94 (t(dd), 1H, $J_{4,3} = J_{4,5}$ = 9.5 Hz, H-4), 4.73 (dt(ddd), 1H, $J_{2,F}$ = 49.7 Hz, $J_{2,1} = J_{2,3}$ = 9.5 Hz, H-2, β-anomer), 4.54 (q, 1H, $J_{H\alpha/H\beta}$ = 6.1 Hz, α-CH), 4.39 (p, 1H, *J* = 7.5 Hz, α-CH), 4.32−4.07 (m, 5H, 3 × α-CH, H-5, H-6a, H-6b), 3.23 (dd, 1H, $J_{H\beta/H\beta}$ = 14.0 Hz, $J_{H\beta/H\alpha}$ = 6.1 Hz, β-CH), 3.09 (dd, 1H, $J_{H\beta/H\beta}$ = 14.0 Hz, $J_{H\beta/H\alpha}$ = 7.5 Hz, β-CH), 2.90 (dd, 1H, $J_{H\beta/H\beta}$ = 14.0 Hz, $J_{H\beta/H\alpha}$ = 5.4 Hz, β-CH), 2.79 (dd, 1H, $J_{H\beta/H\beta}$ = 14.0 Hz, $J_{H\beta/H\alpha}$ = 8.3 Hz, β-CH), 2.73 (b, 2H, H^{ϵ}-Lys), 2.05 (s, 3H, OAc), 2.00 (s, 3H, OAc), 1.99 (s, 3H, OAc), 1.51 (d, 4H, β-CH-Lys, γ-CH-Lys), 1.29 (m, 2H, H^{δ}-Lys), 1.25 (d, 3H, β-CH_3-Ala, $J_{H\beta/H\alpha}$ = 7.0 Hz), 1.19 (d, 3H, β-CH_3-Ala, $J_{H\beta/H\alpha}$ = 7.0 Hz). ESI-MS: *m/z* 877.4 $[M + H]^+$, 439.3 $[M + 2H]^{2+}$.

*Cyclo[*L*-arginyl-*L*-glycyl-*L*-asparagyl-*D*-phenylalanyl-*L*-(S-3,4,6-tri-O-acetyl-2-deoxy-2-fluoro-β-*D*-glucopyranosyl disulfide) cysteine], **4** (c(RGDfC(S,S′-Ac$_3$-FGlc))).* To a solution of 1.3 mg (2.2 μmol) of c(RGDfC) in 1 mL of buffer (50 mM Tris, pH 7.7) was added 18.5 mg (40 μmol) of Ac$_3$-FGlc-PTS (**2**) in 100 μL of acetonitrile/water, 8:2. After a reaction time of 30 min, the absence of free thiol was shown by Ellman's analysis, and the product was isolated as described for C(S,S′-Ac$_3$-FGlc)AKAY (**3**) to afford 1.8 mg (2 μmol, 90%) of c(RGDfC(S,S′-Ac$_3$-FGlc)) (**4**) as a white powder. HPLC (Lichrosorb RP-18, 250 mm × 4.6 mm, 1.5 mL/min, 10−100% acetonitrile in water (0.1% TFA) over 40 min, 220 nm): t_R = 14.9 min. ^{1}H NMR (600 MHz, DMSO-d_6: δ 8.71 (1H, b, COOH-Asp), 8.42 (dd, 1H, $J_{HN/H\alpha}$ = 7.5 Hz, $J_{HN/H\alpha}$ = 4.2 Hz, NH-Gly), 8.23 (d, 1H, $J_{HN/H\alpha}$ = 7.7 Hz, NH-D-Phe), 8.09 (d, 1H, $J_{HN/H\alpha}$ = 7.2 Hz, NH-Cys), 8.06 (d, 1H, $J_{HN/H\alpha}$ = 7.2 Hz, NH-Asp), 7.73 (d, 1H, $J_{HN/H\alpha}$ = 8.2 Hz, NH-Arg), 7.44 (t(dd), 1H, *J* = 5.6 Hz, HN^{ϵ}-Arg), 7.26−7.14 (m, 7H, 5 × H-Ar (D-Phe), 2 × NH/NH_2-Arg), 5.50 (dt, 1H, $J_{3,F}$ = 14.3 Hz, $J_{3,2} = J_{3,4}$ = 9.3 Hz, H-3), 5.02 (dd, 1H, $J_{1,2}$ = 9.3 Hz, $J_{1,F}$ = 1.4 Hz, H-1, β-anomer), 4.92 (t(dd), 1H, $J_{4,3} = J_{4,5}$ = 9.3 Hz, H-4), 4.70 (dt(ddd), 1H, $J_{2,F}$ = 49.5 Hz, $J_{2,1} = J_{2,3}$ = 9.3 Hz, H-2, β-anomer), 4.63 (ddd, 1H, $J_{H\alpha/H\beta}$ = 6.0 Hz, $J_{H\alpha/H\beta}$ = 8.5 Hz, $J_{H\alpha/HN}$ = 7.2 Hz, α-CH-Asp), 4.47−4.40 (m, 2H, α-CH-D-Phe, α-CH-Cys), 4.21−4.01 (m, 5H, H-5, H-6a, H-6b, α-CH-Gly, α-CH-Arg), 3.25 (dd, 1H, $J_{H\alpha/H\alpha}$ = 14.9 Hz, $J_{H\alpha/HN}$ = 4.2 Hz,

α-CH-Gly), 3.08 (m, 3H, β-CH-Cys, δ-CH_2-Arg), 3.00 (dd, 1H, $J_{H\beta/H\beta}$ = 13.6 Hz, $J_{H\beta/H\alpha}$ = 8.1 Hz, β-CH-D-Phe), 2.86 (dd, 1H, $J_{H\beta/H\beta}$ = 13.6 Hz, $J_{H\beta/H\alpha}$ = 10.0 Hz, β-CH-Cys), 2.79 (dd, 1H, $J_{H\beta/H\beta}$ = 13.6 Hz, $J_{H\beta/H\alpha}$ = 5.7 Hz, β-CH-D-Phe), 2.70 (dd, 1H, $J_{H\beta/H\beta}$ = 16.2 Hz, $J_{H\beta/H\alpha}$ = 8.5 Hz, β-CH-Asp), 2.38 (dd, 1H, $J_{H\beta/H\beta}$ = 16.2 Hz, $J_{H\beta/H\alpha}$ = 6.0 Hz, β-CH-Asp), 2.05 (s, 3H, OAc), 2.00 (s, 3H, OAc), 1.99 (s, 3H, OAc), 1.72 (m, 1H, β-CH-Arg), 1.49−1.35 (m, 3H, γ-CH_2-Arg, β-CH-Arg). ^{19}F NMR (282 MHz, DMSO-d_6): δ −192.13 (ddd, $J_{F,2}$ = 49.5 Hz, $J_{F,3}$ = 14.3 Hz, $J_{F,1}$ = 1.4 Hz, β-anomer). MALDI: *m/z* 900.6. ESI-MS: *m/z* 901.3 $[M + H]^+$, 922.7 $[M + Na]^+$.

Ellman's Analysis. The absence of the free thiol was shown using Ellman's test (*28*). An aliquot (10 μL) of the reaction mixture was diluted in 990 μL of phosphate buffer (0.1 M NaH_2PO_4, pH 8). Subsequently, 90 μL of this solution was added to 60 μL of Ellman's reagent (10 mM 5,5′-dithio-bis(2-nitrobenzoic acid) in phosphate buffer) in a 96-well plate. After incubation for 30 min at room temperature, the optical density was measured at 450 nm using an ELISA reader. A calibration curve was measured using cysteine as the reference in concentrations of 0, 5, 10, 20, 30, 40, 50, and 60 μM in phosphate buffer.

Solid-Phase Receptor Binding Assay. The receptor binding assay was performed following the procedure described by Orlando and Cheresh (*29*) with slight modifications. Commercially available purified $\alpha_v\beta_3$ (Chemicon International) was diluted at 250 ng/mL in coating buffer (25 mM Tris-HCl, 150 mM NaCl, 1 mM $CaCl_2$, 0.5 mM $MgCl_2$, 1 mM $MnCl_2$, pH 7.4), and an aliquot of 100 μL/well was added to a 96-well microtiter plate (Maxisorb, Nunc, Wiesbaden, Germany) and incubated overnight at 4 °C. The wells were washed once with 200 μL of blocking buffer (coating buffer + 1% (w/v) bovine serum albumin) and incubated an additional 2 h with 200 μL of blocking buffer at room temperature. The plate was rinsed twice with binding buffer (coating buffer with 0.1% (w/v) bovine serum albumin) and incubated in the presence of varied amounts of competing ligand (0.5 pM to 500 nM echistatin; 0.05 nM to 50 μM RGD peptide) for 3 h with 370 Bq/well (0.05 nM) ^{125}I-echistatin (Amersham, Germany) in a total volume of 100 μL of binding buffer. After the incubation time, the wells were washed three times with binding buffer, and bound ^{125}I-echistatin was solubilized with hot 2 N NaOH. Radioactivity in the resulting suspension was measured by a γ-counter (Wallac Wizard). Nonspecific binding was measured in the presence of 200-fold molar excess of echistatin and was substracted from total binding to yield specific binding. When ^{125}I-echistatin incubations were performed without receptor, negligible nonspecific adsorption (0.04%) to the microtiter well was detected. Each data point is an average of values from triplicate wells. All measurements were repeated at least three times. K_i values were calculated by use of the software program GraphPad Prism in consideration of the equation for "heterologous competitive binding with ligand depletion".

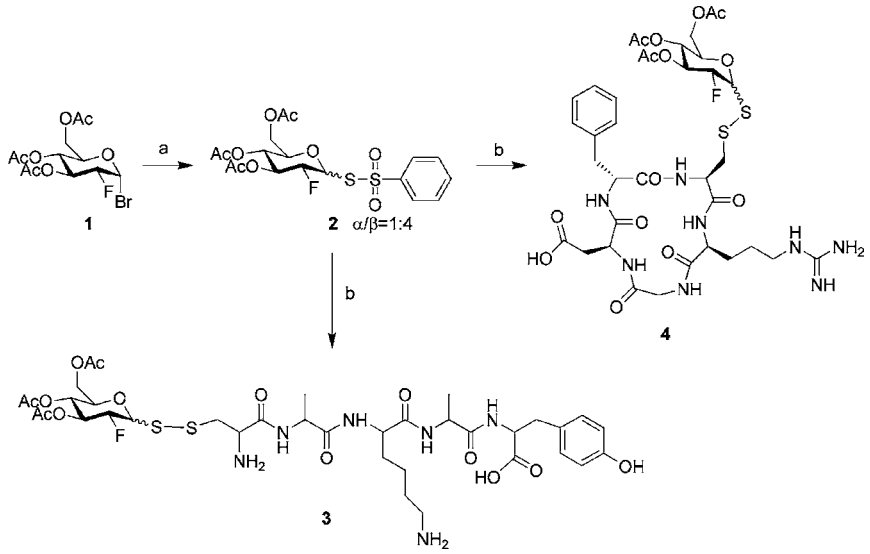
Cell Binding Assay. Human umbilical vein endothelial cells (HUVEC) (Cambrex, Walkersville, MD) were cultured in endothelial growth medium (EGM) (endothelial basal medium (EBM) supplemented with SingleQuotKits (1 mL/L hEGF, 0.4 mL/L hydrocortisone, 1 mL/L VEGF, 4 mL/L hFGF-B (with heparin), 1 mL/L R^3-IGF-1, 1 mL/L ascorbic acid, 1 mL/L GA-1000, 50 mL/L fetal calf serum, Cambrex) as described previously (*30*) and used in passage 5−8. For cell binding assay, HUVEC were harvested and suspended in EGM at a concentration of 500 000 cells per Eppendorf tube. Each Eppendorf tube was centrifuged at 210*g* for 4 min. After the cells were blocked with blocking buffer for 15 min at room temperature, they were washed twice with binding buffer. Subsequently, the HUVEC were incubated on a shaker in the presence of varied amounts of competing ligand (0.5 pM to 500 nM echistatin; 0.05 nM to 50 μM RGD peptide) with 370 Bq/Eppendorf tube (0.025 nM) ^{125}I-echistatin (Amersham, Germany) in a total volume of 200 μL of binding buffer. After the incubation time of 1 h, cells were rinsed three times with binding buffer, the supernatant was sucked off, and the cell pellets with bound ^{125}I-echistatin were transferred to counting tubes for measuring the radioactivity with a γ-counter (Wallac Wizard). Nonspecific binding was measured in the presence of 200-fold molar excess of echistatin and was substracted from total binding to yield specific binding. Each data point is an average of values from triplicate or quadruplicate wells. All measurements were repeated at least three times. K_i values were calculated by use of the software program GraphPad Prism in consideration of the equation for "heterologous competitive binding with ligand depletion".

Radiosynthesis of 3,4,6-Tetra-*O*-acetyl-2-deoxy-2-[^{18}F]-fluoro-glucopyranosyl Phenylthiosulfonate, [^{18}F]2 (Ac_3-[^{18}F]-FGlc-PTS). Starting from [^{18}F]fluoride (500 MBq), 3,4,6-tri-*O*-acetyl-2-deoxy-2-[^{18}F]fluoro-glucopyranosyl bromide (**[^{18}F]1**) was synthesized in 45 min as described elsewhere (*22*, *23*). The bromide **[^{18}F]1** (275 MBq) was fixed on a RP-18 cartridge (Merck Lichrolut, 100 mg), eluted with 1.0 mL of acetonitrile in a new reaction vessel, and dried in a stream of nitrogen. Subsequently, 10 mg (50 μmol) of NaPTS and 5 mg (15 μmol) of dry TBABr in 200 μL of anhydrous acetonitrile and 50 μL of DMF was added. The reaction mixture was stirred at 70 °C for 20 min, diluted with 250 μL of water, and transferred to a semipreparative HPLC system (Kromasil C8, 125 mm × 8 mm, 4 mL/min, 40−100% acetonitrile in water (0.1% TFA) over 40 min). Subsequent solid-phase extraction (SPE, Merck Lichrolut, 100 mg) yielded 95 MBq of Ac_3-[^{18}F]FGlc-PTS (**[^{18}F]2**) after 45 min (related to [^{18}F]fluoride). The chemical identity was confirmed by analytical gradient HPLC by reference to Ac_3-FGlc-PTS (**2**) (Lichrosorb RP-18, 250 mm × 4.6 mm, 1.5 mL/min, 10−100% acetonitrile in water (0.1% TFA) over 40 min, t_R = 21.7 min).

Radiosynthesis of L-(*S*-3,4,6-tri-*O*-acetyl-2-deoxy-2-[^{18}F]-fluoro-glucopyranosyl disulfide)-cysteinyl-L-alanyl-L-lysyl-L-alanyl-L-tyrosine, [^{18}F]3 (C(S,S′-Ac_3-[^{18}F]FGlc)AKAY). To a solution of 95 MBq of Ac_3-[^{18}F]FGlc-PTS (**[^{18}F]2**) in 100 μL of acetonitrile/buffer (1:1, 50 mM Tris, pH 7.7) was added 200 nmol of CAKAY dissolved in 100 μL of 50 mM Tris buffer (pH 7.7) at room temperature. The reaction was complete within 15 min (RCY 90−95%) as determined by analytical HPLC (Lichrosorb RP-18, 250 mm × 4.6 mm, 1.5 mL/min, 10−100% acetonitrile in water (0.1% TFA) over 40 min; t_R(C(S,S′-Ac_3-[^{18}F]FGlc)AKAY, **[^{18}F]3**) = 9.7 min. The chemical identity of C(S,S′-Ac_3-[^{18}F]FGlc)AKAY (**[^{18}F]3**) was confirmed by analytical gradient HPLC by co-injection with the reference compound C(S,S′-Ac_3-FGlc)AKAY (**3**).

Radiosynthesis of Cyclo[L-arginyl-L-glycyl-L-asparagyl-D-phenylalanyl-L-(*S*-3,4,6-tri-*O*-acetyl-2-deoxy-2-[^{18}F]fluoro-glucopyranosyl disulfide) cysteine], [^{18}F]4 (c(RGDfC(S,S′-Ac_3-[^{18}F]FGlc))). To a solution of 95 MBq of Ac_3-[^{18}F]FGlc-PTS (**[^{18}F]2**) in 100 μL of acetonitrile/buffer (1:1, 50 mM Tris, pH 7.7) was added 200 nmol of c(RGDfC) dissolved in 100 μL of 50 mM Tris buffer (pH 7.7) at room temperature. The reaction was complete within 15 min (RCY 90−95%) as determined by analytical HPLC (Lichrosorb RP-18, 250 mm × 4.6 mm, 1.5 mL/min, 10−100% acetonitrile in water (0.1% TFA) over 40 min; t_R(c(RGDfC(S,S′-Ac_3-[^{18}F]FGlc)), **[^{18}F]4**) = 14.9 min). The reaction mixture was diluted with 300 μL of acetonitrile/water (1:9) and subjected to semipreparative HPLC (Lichrosorb RP-18, 125 mm × 8 mm, 4 mL/min, 10−100% acetonitrile in water (0.1% TFA) over 40 min). The product fraction was diluted with water (1:10), and the product was isolated by solid-phase extraction (C18-cartridge, Merck, 100

Scheme 1. Synthesis of the Glycosyl Donor Ac_3-FGlc-PTS (2) and Subsequent Glycosylation Reaction Using Cysteine-Containing Peptides[a]



[a] Reaction conditions: (a) NaPTS, acetonitrile, 70 °C; (b) 50 mM Tris buffer (pH 7.7, containing 7% CH_3CN), 1 mM CAKAY or 1 mM c(RGDfC).

mg). After elution of the product with acetonitrile, the solvent was evaporated in vacuo, and PBS was added to obtain a solution for further experimental use. Starting from 500 MBq of [^{18}F]fluoride, this procedure yielded about 65 MBq of c(RGDfC(S,S′-Ac_3-[^{18}F]FGlc)) (**[^{18}F]4**) after a total synthesis time of 130 min. The chemical identity of c(RGDfC(S,S′-Ac_3-[^{18}F]FGlc)) (**[^{18}F]4**) was confirmed by analytical gradient HPLC by co-injection with the reference compound c(RGDfC(S,S′-Ac_3-FGlc)) (**4**).

Metabolic Stability. c(RGDfC(S,S′-Ac_3-[^{18}F]FGlc)) (**[^{18}F]4**) dissolved in 200 μL of PBS was added to 2 mL of human serum and incubated at 37 °C. Aliquots (100 μL) were taken at various time intervals (5−90 min) and quenched in 500 μL of methanol/CH_2Cl_2 (1:1). The samples were centrifuged, and the supernatants were analyzed by radio-TLC (ethyl acetate/hexane 1:1).

RESULTS AND DISCUSSION

Chemistry. Glycosyl phenylthiosulfonates have been introduced as suitable glycosyl donors for the glycoconjugation of thiols, peptides, and proteins (*25*). These reagents provided enhanced stability under basic conditions compared with the earlier described methanethiosulfonates (*31*). In this paper, we adopted the synthesis of glycosyl phenylthiosulfonates to provide the 2-deoxy-2-fluoro-glycosyl derivative **2** that served as a reference compound for the corresponding ^{18}F-labeled analog (Ac_3-[^{18}F]FGlc-PTS (**[^{18}F]2**), Figure 1). The synthesis of the glycosylating reagent 3,4,6-tri-*O*-acetyl-2-fluoro-2-deoxy-β-D-glucopyranosyl 1-phenylthiosulfonate (**2**) is outlined in Scheme 1. Starting from tetraacetylated 2-deoxy-2-fluoro-β-D-glucopyranose, which was available by acetylation of an anomeric mixture of mannose and subsequent fluorination with diethylamino sulfur trifluoride (DAST), the initial α-bromide (**1**) was easily obtained in 90% yield by reaction with HBr at room temperature as previously described (*23*). Following the procedure of Gamblin et al. (*25*), displacement of the halide from **1** using NaPTS in acetonitrile at 70 °C readily afforded Ac_3-FGlc-PTS (**2**) in 70% yield. Ac_3-FGlc-PTS (**2**) consisted of a β/α anomeric ratio of >80:20 as analyzed by ^{19}F NMR spectroscopy.

Glycosylation properties of the resulting 2-deoxy-2-fluoro-glycosyl donor (**2**) were evaluated using the model peptide CAKAY and the $\alpha_v\beta_3$ targeting c(RGDfC). The glycosylation of cysteine-containing peptides using glycosyl phenylthiosulfonates proceeds via a highly specific and quantitative coupling reaction of the thiol function, that is, cysteine β-SH, and the thiosulfonate moiety resulting in the formation of a disulfide bond (*32*). On the one hand, the peptide CAKAY was chosen to demonstrate the chemoselectivity of Ac_3-FGlc-PTS (**2**) and also to optimize ^{18}F-labeling conditions (see paragraph below). On the other hand, the cyclic RGD peptide was selected because of its biological relevance (*33*) allowing study of the influence of S-glycosylation on $\alpha_v\beta_3$ binding affinity in vitro. Glycosylation of CAKAY and c(RGDfC) with Ac_3-FGlc-PTS (**2**) were carried out under similar reaction conditions using an aqueous buffer system (pH 7.7; for details, see Scheme 1). Ligations proceeded rapidly within 30 min and quantitatively, as confirmed by monitoring the reaction progress by titration of residual free thiol groups with Ellman's reagent (*28*). Both S-glycosylated peptides, C(S,S′-Ac_3-FGlc)AKAY (**3**) and c(RGDfC(S,S′-Ac_3-FGlc)) (**4**), were isolated by RP-HPLC, and their structures were confirmed by NMR spectroscopy, ESI-MS, and, in the case of c(RGDfC(S,S′-Ac_3-FGlc)) (**4**), MALDI mass spectroscopy. Importantly, the prevailing β-anomeric configuration as given by Ac_3-FGlc-PTS (**2**) was retained in the S-glycosidic linked products C(S,S′-Ac_3-FGlc)AKAY (**3**) and c(RGDfC(S,S′-Ac_3-FGlc)) (**4**). Hence, the anomeric stereochemistry was maintained during the glycosylation process, which is consistent with the observation that α- and β-glycosyl thiols also do not mutarotate even under basic reaction conditions (*34*). Noteworthy, the determination of the anomeric configuration of such 2-deoxy-2-fluoro-glycoconjugates was simplified because of the fluorine substituent at C-2, since the $^3J_{F,1}$ coupling constant provides an excellent tool to distinguish between α ($^3J_{F,1}$ < 0.5 Hz) and β ($^3J_{F,1} \approx$ 2.5 Hz) configuration by ^{19}F NMR spectroscopy.

In Vitro Binding Assays. In order to compare the affinities of c(RGDfS), c(RGDfC), and the S-glycosylated derivative c(RGDfC(S,S′-Ac_3-FGlc)) (**4**) to $\alpha_v\beta_3$ integrin, competitive displacement assays were performed (Figure 2). It is well-known that the disintegrin echistatin displays high affinity for $\alpha_v\beta_3$ and also for other integrins, such as $\alpha_8\beta_1$ and $\alpha_{3/5/v}\beta_1$ with K_i values ranging between 1 and 4 nM (*35*, *36*). Besides echistatin, we introduced c(RGDfS) as a competitor of ^{125}I-echistatin binding in our experiments, since this cyclic RGD peptide has already been characterized as an inhibitor of vitronectin binding to

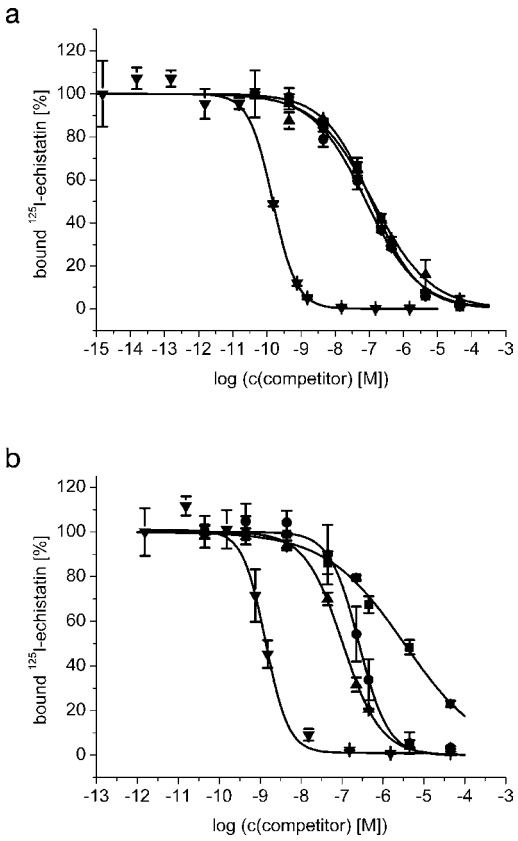


Figure 2. Effect of the concentration of unlabeled echistatin (▼), c(RGDfS) (■), c(RGDfC) (●), and c(RGDfC(S,S′-Ac$_3$-FGlc)) (**4,** ▲) on ^{125}I-echistatin binding in a competition binding experiment using (a) immobilized $\alpha_v\beta_3$ integrin or (b) human endothelial cells (HUVEC). Data are from four independent experiments each performed in triplicate or quadruplicate ($n = 12-16$).

Table 1. Binding Affinities of RGD Peptides to Immobilized $\alpha_v\beta_3$ and to HUVEC[a]

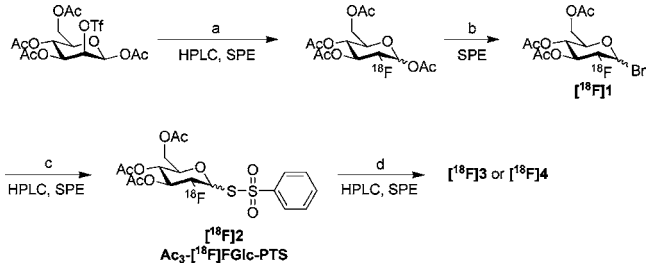
compound	K_i (nM) $\alpha_v\beta_3$	K_i (nM) HUVEC
echistatin	0.052 ± 0.001	0.43 ± 0.11
c(RGDfS)	53 ± 12	541 ± 99
c(RGDfC)	41 ± 0.5	241 ± 40
c(RGDfC(S,S′-Ac$_3$-FGlc)) (**4**)	68 ± 10	77 ± 4

[a] Values are given as mean ± standard deviation from four independent experiments performed in triplicate or quadruplicate.

isolated $\alpha_v\beta_3$ ($IC_{50} = 12$ nM (*27*)). Therefore, c(RGDfS) represents a structurally related RGD peptide that was used as a reasonable reference compound to assess the influence of glycosylation on $\alpha_v\beta_3$ binding affinity by comparing c(RGDfC-(S,S′-Ac$_3$-FGlc)) (**4**) with its non-glycosylated analog c(RGDfC).

In the presence of echistatin, c(RGDfS), c(RGDfC), and c(RGDfC(S,S′-Ac$_3$-FGlc)) (**4**) binding of ^{125}I-echistatin to immobilized $\alpha_v\beta_3$ integrin was inhibited in a concentration-dependent manner. All of the peptides demonstrated the capability to completely inhibit ^{125}I-echistatin binding to isolated $\alpha_v\beta_3$ integrin (Figure 2a). Due to a significant change of the free radioligand concentration during the incubation period, we used an equation for curve analysis that considered this finding. The obtained K_i values are presented in Table 1. Chen et al. also tested RGD peptides using the same in-vitro assay and found K_i values of 30−70 nM (*37*). Using the $\alpha_v\beta_3$ solid-phase binding assay, we obtained K_i values within the same range for all tested cyclic peptides (column 2, Table 1), which are also comparable with Chen's data. Moreover, these data confirm that $\alpha_v\beta_3$ binding affinity is not substantially impaired by S-glycosylation of the cysteine moiety in c(RGDfC).

Scheme 2. Radiosynthetic Pathway for the Chemoselective ^{18}F-Glycosylation of CAKAY or c(RGDfC) Using the Thiol-Reactive Reagent Ac$_3$-[^{18}F]FGlc-PTS ([^{18}F]2)[a]



[a] Reaction conditions: (a) [K⊂222]$^+$[^{18}F]F$^-$, 9 mg (20 μmol) of 1,3,4,6-tetra-*O*-acetyl-2-*O*-trifluoromethanesulfonyl-β-D-mannopyranose, 500 μL of acetonitrile, $T = 85$ °C, $t = 5$ min (*16*); (b) 33% HBr/AcOH, rt; (c) 200 mM NaPTS, 60 mM TBABr, acetonitrile/DMF, 4:1 (v/v), $T = 70$ °C, $t = 20$ min; (d) 50 mM Tris buffer (pH 7.7)/acetonitrile, 3:1 (v/v), 1 mM CAKAY or 1 mM c(RGDfC).

In addition, we performed a competition study using human endothelial cells, in order to qualitatively assess the binding affinity of the peptides under investigation to interfering receptors in a comparative experiment (Figure 2b). We chose human umbilical vein endothelial cells (HUVEC), since the expression of various integrins, such as $\alpha_2\beta_1$, $\alpha_3\beta_1$, $\alpha_v\beta_1$, and $\alpha_v\beta_3$ is well-known for this cell type (*38*). As shown in Figure 2b and Table 1, the peptides c(RGDfS) and c(RGDfC) revealed significant differences in K_i values when comparing $\alpha_v\beta_3$ binding results to the values obtained from HUVEC binding experiments. In particular, the curve for inhibition of ^{125}I-echistatin binding to HUVEC by c(RGDfS) showed a decreased steepness with a Hill slope factor lower than 1. This finding clearly indicated the presence of additional low-affinity binding sites for c(RGDfS) and c(RGDfC) on HUVEC. In contrast, the K_i value of the glycosylated derivative c(RGDfC(S,S′-Ac$_3$-FGlc)) (**4**) was determined to be almost unchanged, when comparing the K_i value obtained from competition studies using pure $\alpha_v\beta_3$ with that of HUVEC binding experiments (Table 1). However, the assay using HUVEC cells cannot discriminate between different integrins present on the cell surface, but it provided additional information, that the affinity of the S-glycosylated peptide c(RGDfC(S,S′-Ac$_3$-FGlc)) (**4**) toward ^{125}I-echistatin binding sites was not significantly affected.

Radiosynthesis of the ^{18}F-Labeled Glycosyl Donor Ac$_3$-[^{18}F]FGlc-PTS ([^{18}F]2). Our radiochemical synthesis of Ac$_3$-[^{18}F]FGlc-PTS (**[^{18}F]2**) was based on the first step of the [^{18}F]FDG synthesis (*16*), as shown in Scheme 2. Starting from 1,3,4,6-tetra-*O*-acetyl-2-*O*-trifluoromethanesulfonyl-β-D-mannopyranose (*26*), cryptate-assisted nucleophilic substitution was performed at 85 °C for 5 min following the procedure of Hamacher et al. (*16*). After solid phase (SiO_2) purification and semipreparative RP-HPLC (*22*), no-carrier-added tetraacetylated 2-deoxy-2-[^{18}F]fluoroglucose was converted into the α-bromide **[^{18}F]1** using HBr in acetic acid as previously reported (*23*). **[^{18}F]1** was generally obtained in a 55% non-decay-corrected yield within 45 min starting from [^{18}F]fluoride, providing adequate quantities for the following reaction steps. The reaction conditions for the conversion of **[^{18}F]1** to the phenylthiosulfonate Ac$_3$-[^{18}F]FGlc-PTS (**[^{18}F]3**) were studied in detail by varying the reaction solvent, the reaction time, the concentration of the promoter TBABr, and the amount of NaPTS used. As shown in Figure 3, the use of acetonitrile/DMF (4:1) resulted in highest radiochemical yields for the synthesis of Ac$_3$-[^{18}F]FGlc-PTS (**[^{18}F]2**) (approximately 47% related to **[^{18}F]1**) within a reaction time of 20 min, whereas acetonitrile alone, acetonitrile/DMSO (4:1), and DMF turned out to be less suitable. Presumably, this is due to an improved solubility of NaPTS in acetonitrile/DMF. Moreover, it turned out that important factors for an optimized

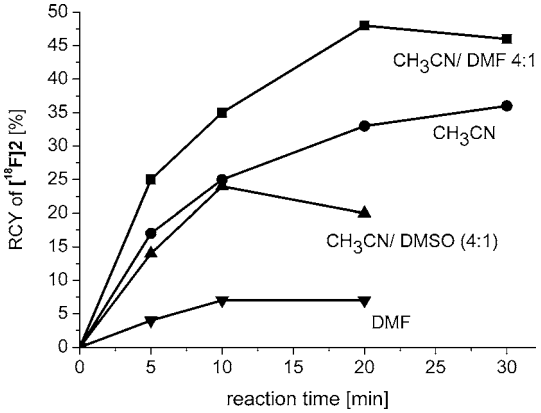


Figure 3. Dependence of the radiochemical yield (RCY, decay-corrected and related to **[^{18}F]1**) of the ^{18}F-labeled glycosyl donor Ac_3-[^{18}F]FGlc-PTS (**[^{18}F]2**) on the reaction solvent.

RCY are (a) the use of recrystallized and intensively dried NaPTS for the reaction with **[^{18}F]1** (in general, moisture has to be excluded, since limited RCY (<10%) of Ac_3-[^{18}F]FGlc-PTS (**[^{18}F]2**) were obtained when insufficiently dried NaPTS was used), (b) that reaction temperatures >100 °C should be avoided, due to an accelerated degradation of Ac_3-[^{18}F]FGlc-PTS (**[^{18}F]-2**) with higher temperatures, and (c) the presence of TBABr as promoter (data not shown). Under optimized reaction conditions (200 mM NaPTS, 60 mM TBABr, acetonitrile/DMF (4:1), 70 °C, 20 min), the ^{18}F-labeled glycosylating reagent Ac_3-[^{18}F]-FGlc-PTS (**[^{18}F]2**) was isolated in 33% decay-corrected RCY (related to [^{18}F]fluoride) after semipreparative HPLC.

^{18}F-Glycosylation of CAKAY and c(RGDfC). In a set of preceding experiments in order to assess the ^{18}F-labeling ability of Ac_3-[^{18}F]FGlc-PTS (**[^{18}F]2**), varied concentrations of CAKAY were used in the conjugation step (Scheme 2, step d). As shown in Figure 4, a peptide precursor concentration of 1 mM in aqueous buffer (pH 7.7) was adequate to achieve a RCY of C(S,S′-Ac_3-[^{18}F]FGlc)AKAY) (**[^{18}F]3**) of about 95% (related to Ac_3-[^{18}F]FGlc-PTS (**[^{18}F]2**)) as determined by radio-HPLC within a reaction time of 15 min. With adoption of these optimized coupling conditions for the chemoselective S-glycosylation of c(RGDfC) using Ac_3-[^{18}F]FGlc-PTS (**[^{18}F]2**), quantitative ligation yielding c(RGDfC(S,S′-Ac_3-[^{18}F]FGlc)) (**[^{18}F]4**) was successfully demonstrated. It should be mentioned that a possible complication in the synthesis of mixed disulfides, such as c(RGDfC(S,S′-Ac_3-[^{18}F]FGlc)) (**[^{18}F]4**), is the formation of a peptide−peptide disulfide (*32*). This could occur via a disulfide exchange reaction between c(RGDfC(S,S′-Ac_3-[^{18}F]FGlc)) (**[^{18}F]4**) and the peptide thiol, which is present in excess under no-carrier-added reaction conditions. However, such a reaction pathway would result in the degradation of the ^{18}F-glycosylated product, which we did not observe by radio-HPLC analysis in our experiments, even after a prolonged reaction time of 30 min (Figure 4a). Thus, the conjugation proceeded efficiently in 95% coupling yield (decay corrected), illustrating the excellent ability of Ac_3-[^{18}F]FGlc-PTS (**[^{18}F]2**) as a thiol-reactive ^{18}F-labeling agent for cysteine-containing peptides under mild reaction conditions. Both ^{18}F-labeled peptides, C(S,S′-Ac_3-[^{18}F]FGlc)-AKAY (**[^{18}F]3**) and c(RGDfC(S,S′-Ac_3-[^{18}F]FGlc)) (**[^{18}F]4**), were characterized by reference to the respective ^{19}F-substituted standards C(S,S′-Ac_3-FGlc)AKAY (**3**) and c(RGDfC(S,S′-Ac_3-FGlc)) (**4**) and co-injection using HPLC (Figure 5). The overall-radiochemical yield of C(S,S′-Ac_3-[^{18}F]FGlc)AKAY (**[^{18}F]3**) and c(RGDfC(S,S′-Ac_3-[^{18}F]FGlc)) (**[^{18}F]4**) was about 13% (decay-uncorrected and related to [^{18}F]fluoride) after a total synthesis time of 130 min, following a three-step procedure (Scheme 2). Finally, to verify the stability of the formed glycosidic bond toward degradation, we performed incubation

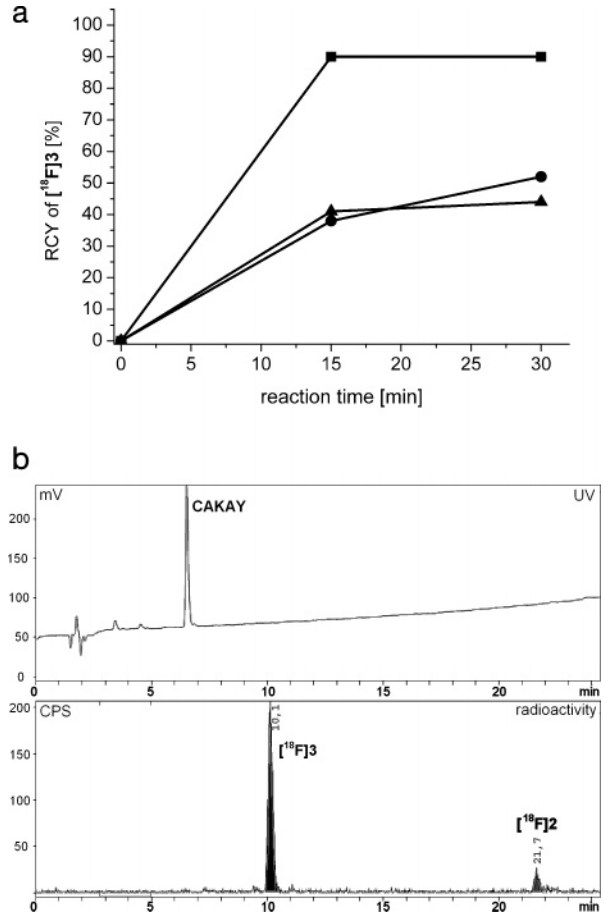


Figure 4. (a) Dependence of the radiochemical yield (RCY) of C(S,S′-Ac_3-[^{18}F]FGlc)AKAY (**[^{18}F]3**) for ^{18}F-glycosylation of CAKAY using Ac_3-[^{18}F]FGlc-PTS (**[^{18}F]2**) on the concentration of CAKAY (10 μM (▲), 0.1 mM (●), and 1 mM (■)) and (b) representative HPLC analysis of a sample withdrawn from the reaction mixture containing 1 mM CAKAY after 15 min.

experiments with c(RGDfC(S,S′-Ac_3-[^{18}F]FGlc)) (**[^{18}F]4**) using human serum at 37 °C. Radio-TLC of the incubation mixture revealed no cleavage of the carbohydrate moiety of the glycopeptide c(RGDfC(S,S′-Ac_3-[^{18}F]FGlc)) (**[^{18}F]4**), thereby indicating high in-vitro metabolic stability of c(RGDfC(S,S′-Ac_3-[^{18}F]FGlc)) (**[^{18}F]4**) for at least 90 min (>98%). This finding is consistent with the known resistance of thioglycosides to chemical and enzymatic hydrolysis (*39*).

In comparison with chemoselective ^{18}F-radiolabeling methods using maleimide derivatives (*13*−*15*), our approach provided radiochemical yields within the same range, additionally gaining the opportunity to perform glycosylation and ^{18}F-labeling of peptide target compounds simultaneously within the same reaction step. In our study, we successfully developed a suitable radiosynthesis for the novel ^{18}F-labeled glycosyl donor Ac_3-[^{18}F]FGlc-PTS (**[^{18}F]2**) and focused on the optimization of the ligation of **[^{18}F]2** with cysteine-containing peptides. In view of the rapid and chemoselective conjugation under mild reaction conditions, together with the improved stability of S-linked glycopeptides toward acid/base or enzyme-mediated hydrolysis compared with their O-linked counterparts (*39*), the ^{18}F-glycosylation reaction described herein could find valuable use in the radiosynthesis of ^{18}F-labeled S-glycopeptides to study their pharmacokinetics by PET. The development of a facilitated radiochemical procedure for an efficient automated synthesis of fully unprotected ^{18}F-labeled glycopeptides taking advantage of this mild ligation procedure is a topic of further studies.

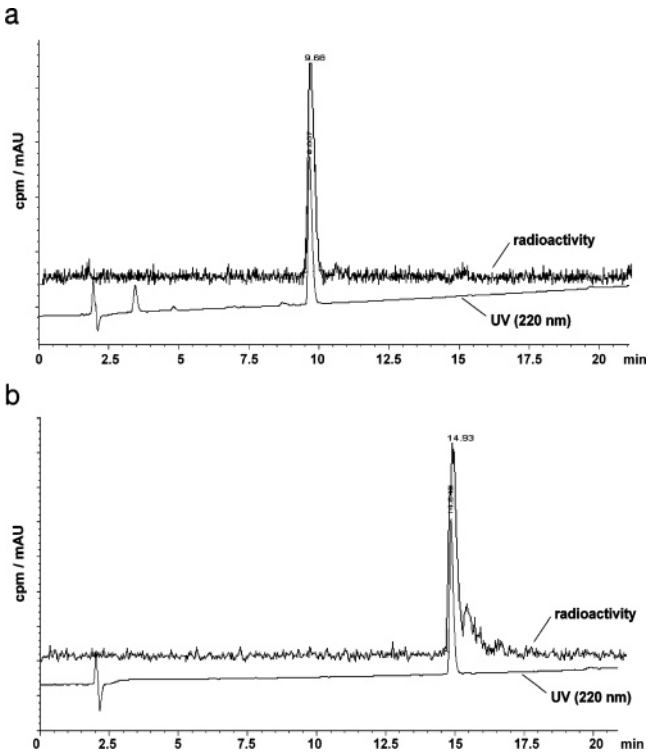


Figure 5. Analytical HPLC profiles of (a) the ^{18}F-labeled CAKAY **[^{18}F]3** coinjected with the standard C(S,S′-Ac_3-FGlc)AKAY (**3**) and (b) the ^{18}F-labeled peptide c(RGDfC(S,S′-Ac_3-[^{18}F]FGlc)) (**[^{18}F]4**) coinjected with the standard c(RGDfC(S,S′-Ac_3-FGlc)) (**4**). HPLC column and elution protocol: Lichrosorb RP-18, 250 mm × 4.6 mm, 1.5 mL/min, 10−100% CH_3CN in water (0.1% TFA) over 40 min.

CONCLUSION

Ac_3-[^{18}F]FGlc-PTS, a novel phenylthiosulfonate derivative of [^{18}F]FDG, has been introduced as a new thiol-reactive ^{18}F-glycosylation reagent for labeling of peptides. This strategy combines both site-specific ^{18}F-labeling and glycosylation of a cysteine-containing target peptide. As illustrated by glycosylation of c(RGDfC), the in-vitro $\alpha_v\beta_3$ binding affinity of this representative peptide remained unaffected, providing evidence for the suitability of this ^{18}F-glycosylation method. Due to the excellent yield for the conjugation step between cysteine-containing peptides and the ^{18}F-labeled glycosyl phenylthiosulfonate, this method is promising for the design and development of ^{18}F-labeled bioactive glycopeptides.

ACKNOWLEDGMENT

The authors thank Dr. Walter Mier (Department of Nuclear Medicine, University of Heidelberg) for performing MALDI mass spectrometry and Stephan Schwarz (Medizinische Universität Innsbruck) for excellent technical assistance. This work was supported by the ELAN-Fonds of the Friedrich-Alexander-Universität Erlangen-Nürnberg (Grant 06.01.04.1).

LITERATURE CITED

(1) Massoud, T. F., and Gambhir, S. S. (2003) Molecular imaging in living subjects: seeing fundamental biological processes in a new light. *Genes Dev. 17*, 545−580.

(2) Okarvi, S. M. (2004) Peptide-based radiopharmaceuticals: future tools for diagnostic imaging of cancers and other diseases. *Med. Res. Rev. 24*, 357−397.

(3) Wester, H. J., Hamacher, K., and Stöcklin, G. (1996) A comparative study of N.C.A. fluorine-18 labeling of proteins via acylation and photochemical conjugation. *Nucl. Med. Biol. 23*, 365−372.

(4) Wester, H. J., Brockmann, J., Rösch, F., Wutz, W., Herzog, H., Smith-Jones, P., Stolz, B., Bruns, C., and Stöcklin, G. (1997) PET-pharmacokinetics of ^{18}F-octreotide: A comparison with ^{67}Ga-DFO- and ^{86}Y-DTPA-octreotide. *Nucl. Med. Biol. 24*, 275−286.

(5) Haubner, R., Kuhnast, B., Mang, C., Weber, W. A., Kessler, H., Wester, H. J., and Schwaiger, M. (2004) [^{18}F]Galacto-RGD: synthesis, radiolabeling, metabolic stability, and radiation dose estimates. *Bioconjugate Chem. 15*, 61−69.

(6) Chen, X., PArk, R., Hou, Y., Khankaldyyan, V., Gonzales-Gomez, I., Tohme, M., Bading, J. R., Laug, W. E., and Conti, P. S. (2004) MicroPET imaging of brain tumor angiogenesis with ^{18}F-labeled PEGylated RGD peptide. *Eur. J. Nucl. Med. Mol. Imaging 31*, 1081−1089.

(7) Bergmann, R., Scheunemann, M., Heichert, C., Mading, P., Wittrisch, H., Kretzschmar, M., Rodig, H., Tourwé, D., Iterbeke, K., Chavatte, K., Zips, D., Reubi, J. C., and Johannsen, B. (2002) Biodistribution and catabolism of ^{18}F-labeled neurotensin(8−13.) analogs. *Nucl. Med. Biol. 29*, 61−72.

(8) Vaidyanathan, G., and Zalutsky, M. R. (1994) Improved synthesis of N-succinimidyl 4-[^{18}F]fluorobenzoate and its application to the labeling of a monoclonal antibody fragment. *Bioconjugate Chem. 5*, 352−356.

(9) Guenther, K. J., Yoganathan, S., Garofalo, R., Kawabata, T., Strack, T., Labiris, R., Dolovich, M., Chirakal, R., and Valliant, J. F. (2006) Synthesis and in vitro evaluation of ^{18}F- and ^{19}F-labeled insulin: A new radiotracer for PET-based molecular imaging studies. *J. Med. Chem. 49*, 1466−1474.

(10) Haubner, R., Weber, W. A., Beer, A. J., Vabuliene, E., Reim, D., Sarbia, M., Becker, K. F., Goebel, M., Hein, R., Wester, H. J., Kessler, H., and Schwaiger, M. (2005) Noninvasive visualization of the activated $\alpha_v\beta_3$ integrin in cancer patients by positron emission tomography and [^{18}F]Galacto-RGD. *PLoS Med. 2*, e70.

(11) Glaser, M., Karlsen, H., Solbakken, M., Arukwe, J., Brady, F., Luthra, S. K., and Cuthbertson, A. (2004) ^{18}F-fluorothiols: A new approach to label peptides chemoselectively as potential tracers for positron emission tomography. *Bioconjugate Chem. 15*, 1447−1453.

(12) Poethko, T., Schottelius, M., Thumshirn, G., Hersel, U., Herz, M., Henriksen, G., Kessler, H., Schwaiger, M., and Wester, H. J. (2004) Two-step methodology for high-yield routine radiohalogenation of peptides: ^{18}F-labeled RGD and octreotide analogs. *J. Nucl. Med. 45*, 892−902.

(13) Toyokuni, T., Walsh, J. C., Dominguez, A., Phelps, M. E., Barrio, J. R., Gambhir, S. S., and Satyamurthy, N. (2003) Synthesis of a new heterobifunctional linker, *N*-[4-(aminooxy)butyl]maleimide, for facile access to a thiol-reactive ^{18}F-labeling agent. *Bioconjugate Chem. 14*, 1253−1259.

(14) de Bruin, B., Kuhnast, B., Hinnen, F., Yaouancq, L., Amessou, M., Johannes, L., Samson, A., Boisgard, R., Tavitian, B., and Dollé, F. (2005) 1-[3-(2-[^{18}F]Fluoropyridin-3-yloxy)propyl]pyrrole-2,5-dione: design, synthesis, and radiosynthesis of a new [^{18}F]fluoropyridine-based maleimide reagent for the labeling of peptides and proteins. *Bioconjugate Chem. 16*, 406−420.

(15) Cai, W., Zhang, X., Wu, Y., and Chen, X. (2006) A thiol-reactive ^{18}F-labeling agent, *N*-[2-(4-^{18}F-fluorobenzamido)ethyl]maleimide, and synthesis of RGD peptide-based tracer for PET imaging of $\alpha_v\beta_3$ integrin expression. *J. Nucl. Med. 47*, 1172−1180.

(16) Hamacher, K., Coenen, H. H., and Stöcklin, G. (1986) Efficient stereospecific synthesis of no-carrier-added 2-[^{18}F]-fluoro-2-deoxy-D-glucose using aminopolyether supported nucleophilic substitution. *J. Nucl. Med. 27*, 235−238.

(17) Prante, O., Hamacher, K., and Coenen, H. H. (1999) Chemoenzymatic n.c.a. synthesis of the coenzyme uridine diphospho-2-deoxy-2-[^{18}F]fluoro-α-D-glucose. *J. Labelled Compd. Radiopharm. 42*, S111.

(18) Berndt, M., Pietzsch, J., Bergmann, R., and Wuest, F. (2006) A novel role for [^{18}F]FDG: Synthesis and application of a [^{18}F]FDG-based prosthetic group for peptide and protein labeling. *J. Nucl. Med. 47*, 29P.

(19) Haubner, R., Wester, H. J., Burkhart, F., Senekowitsch-Schmidtke, R., Weber, W., Goodman, S. L., Kessler, H., and Schwaiger, M.

(2001) Glycosylated RGD-containing peptides: Tracer for tumor targeting and angiogenesis imaging with improved biokinetics. *J. Nucl. Med. 42*, 326−336.
(20) Schottelius, M., Rau, F., Reubi, J. C., Schwaiger, M., and Wester, H.-J. (2005) Modulation of pharmacokinetics of radioiodinated sugar-conjugated somatostatin analogues by variation of peptide net charge and carbohydration chemistry. *Bioconjugate Chem. 16*, 429−437.
(21) Egleton, R. D., Davis, T. P. (2005) Development of neuropeptide drugs that cross the blood-brain barrier. *NeuroRx 2*, 44−53.
(22) Maschauer, S., Pischetsrieder, M., Kuwert, T., and Prante, O. (2005) Utility of 1,3,4,6-tetra-*O*-acetyl-2-deoxy-2-[^{18}F]fluoroglucopyranoside for no-carrier-added ^{18}F-glycosylation of amino acids. *J. Labelled Compd. Radiopharm. 48*, 701−719.
(23) Maschauer, S., Kuwert, T., and Prante, O. (2006) ^{18}F-glycosylation using Koenigs-Knorr conditions: A comparative study. *J. Labelled Compd. Radiopharm. 49*, 101−108.
(24) Ni, J., Singh, S., and Wang, L. X. (2003) Synthesis of maleimide-activated carbohydrates as chemoselective tags for site-specific glycosylation of peptides and proteins. *Bioconjugate Chem. 14*, 232−238.
(25) Gamblin, D. P., Garnier, P., Ward, S. J., Oldham, N. J., Fairbanks, A. J., and Davis, B. G. (2003) Glycosyl phenylthiosulfonates (Glyco-PTS): Novel reagents for glycoprotein synthesis. *Org. Biomol. Chem. 1*, 3642−3644.
(26) Hamacher, K. (1984) Phase-transfer catalysed synthesis of 4-S-β-D-glucopyranosyl-4-thio-D-glucopyranose (thiocellobiose) and 2-S-β-D-glucopyranosyl-2-thio-D-glucopyranose (thiosophorose). *Carbohydr. Res. 128*, 291−295.
(27) Haubner, R., Gratias, R., Diefenbach, B., Goodman, S. L., Jonczyk, A., and Kessler, H. (1996) Structural and functional aspects of RGD-containing cyclic pentapeptides as highly potent and selective integrin $\alpha_v\beta_3$ antagonists. *J. Am. Chem. Soc. 118*, 7461−7472.
(28) Ellman, G. L., Courtney, K. D., Andres, V., Jr., and Feather-Stone, R. M. (1961) A new and rapid colorimetric determination of acetylcholinesterase activity. *Biochem. Pharmacol. 7*, 88−95.
(29) Orlando, R. A., and Cheresh, D. A. (1991) Arginine-glycine-aspartic acid binding leading to molecular stabilization between integrin $\alpha_v\beta_3$ and its ligand. *J. Biol. Chem. 266*, 19543−19550.
(30) Maschauer, S., Prante, O., Hoffmann, M., Deichen, J. T., and Kuwert, T. (2004) Characterization of ^{18}F-FDG uptake in human endothelial cells in vitro. *J. Nucl. Med. 45*, 455−460.
(31) Davis, B. G., Maughan, M. A. T., Green, M. P., Ullman, A., and Jones, J. B. (2000) Glycomethanethiosulfonates: Powerful reagents for protein glycosylation. *Tetrahedron: Asymmetry 11*, 245−262.
(32) Wynn, R., and Richards, F. M. (1995) Chemical modification of protein thiols: Formation of mixed disulfides. *Methods Enzymol. 251*, 351−356.
(33) Ruoslahti, E., and Pierschbacher, M. D. (1987) New perspectives in cell adhesion: RGD and integrins. *Science 238*, 491−497.
(34) MacDougall, J. M., Zhang, X. D., Polgar, W. E., Khroyan, T. V., Toll, L., and Cashman, J. R. (2004) Design, chemical synthesis, and biological evaluation of thiosaccharide analogues of morphine- and codeine-6-glucuronide. *J. Med. Chem. 47*, 5809−5815.
(35) Thibault, G. (2000) Sodium dodecyl sulfate-stable complexes of echistatin and RGD-dependent integrins: A novel approach to study integrins. *Mol. Pharmacol. 58*, 1137−1145.
(36) Kumar, C. C., Nie, H., Rogers, C. P., Malkowski, M., Maxwell, E., Catino, J. J., and Armstrong, L. (1997) Biochemical characterization of the binding of echistatin to integrin a_vb_3 receptor. *J. Pharmacol. Exp. Ther. 283*, 843−853.
(37) Chen, X., Hou, Y., Tohme, M., Park, R., Khankaldyyan, V., Gonzales-Gomez, I., Bading, J. R., Laug, W. E., and Conti, P. S. (2004) Pegylated Arg-Gly-Asp peptide: ^{64}Cu labeling and PET imaging of brain tumor $\alpha_v\beta_3$-integrin expression. *J. Nucl. Med. 45*, 1776−1783.
(38) Luscinskas, F. W., and Lawler, J. (1994) Integrins as dynamic regulators of vascular function. *FASEB J. 8*, 929−938.
(39) Pachamuthu, K., and Schmidt, R. R. (2006) Synthetic routes to thiooligosaccharides and thioglycopeptides. *Chem. Rev. 106*, 160−187.

BC060340V

TECHNICAL NOTES

Soluble Camptothecin Derivatives Prepared by Click Cycloaddition Chemistry on Functional Aliphatic Polyesters

Bryan Parrish and Todd Emrick*

Polymer Science & Engineering Department, University of Massachusetts, Conte Center for Polymer Research, Amherst, Massachusetts 01003. Received July 6, 2006; Revised Manuscript Received October 19, 2006

Aliphatic polyesters are of interest as biomaterials and drug-delivery vehicles, as their ability to degrade under physiological conditions provides a mechanism for both drug release and clearance of the polymer from the body. Presented here is the synthesis of a polyester−drug graft copolymer conjugate, enabled by click cycloaddition of azide-functionalized camptothecin derivatives with alkyne-functionalized aliphatic polyesters. Further grafting of residual alkyne groups with azide-terminated poly(ethylene oxide) gave a water-soluble polyester−camptothecin conjugate. Control over PEGylation and drug loading, inherent to the graft copolymer design, opens versatile routes to new materials with potential utility in polymer therapeutics.

INTRODUCTION

Central issues associated with chemotherapy include the methods and mechanisms by which drugs are introduced to the body and delivered to cancer tissue (*1*−*3*). As potent anticancer drugs such as doxorubicin, camptothecin, and paclitaxel have poor aqueous solubility, and in some cases short-term aqueous stability, introduction of these drugs into the bloodstream is enhanced by modification of their chemical structures or by their encapsulation in liposomal or polymeric formulations (*4*). In order to improve delivery efficiency and avoid high levels of dosing to achieve therapeutic drug levels, new conjugation methods to attach drugs to polymer materials are needed (*5*−*6*).

A number of polymer−drug conjugates have been reported to enhance drug solubility and stability in aqueous media, in turn providing longer circulation time of the drug in the bloodstream relative to the nonconjugated drugs (*7*−*10*). In addition, the high molecular weight of the polymer−drug conjugates enables tumor targeting by the enhanced permeability and retention effect (*11*). Polymer−drug conjugates that utilize poly(ethylene glycol) (PEG), *N*-(2-hydroxypropyl)methacrylamide (HPMA), and poly(glutamic acid) (PGA) as the polymeric component have been investigated, as have a variety of polymer architectures including linear, graft, and dendritic systems (*12*−*17*). The conjugates are too large to permeate the vasculature of healthy tissue, and thus preferably enter the leaky vasculature of cancerous tissue, where they accumulate due to poor lymphatic drainage in this environment. Following localization in cancer tissue, the polymer−drug conjugates can be taken up by cancer cells through endocytosis, then may be delivered to the lysosomal compartment. The relatively acidic environment of the lysosome makes attractive the use of acid-cleavable linking groups between the polymer and the drug (*18*).

Here, we present the synthesis of a water-soluble form of camptothecin by its conjugation to a PEGylated aliphatic polyester graft copolymer. Aliphatic polyesters are particularly attractive as biomaterials and drug delivery vehicles, as their in vivo degradation products are relatively benign (*19*). However, conventional aliphatic polyesters are insoluble in water, and thus not inherently well-suited for aqueous-based injectable formulations. Moreover, water-soluble PEG−aliphatic polyester diblock copolymers have drug carrying capabilities limited to physical encapsulation and/or substitution at the PEG chain end(s) with one (or two) drug molecules.

EXPERIMENTAL PROCEDURES

Materials. 6-Bromohexanoic acid (98%), bromotris(triphenylphosphine) copper(I) (98%), 20(*S*)-camptothecin (95%), copper(II) sulfate pentahydrate (>98.0%), *N*,*N*′-dicyclohexylcarbodiimide (DCC) (99%), *N*,*N*-diisopropylethylamine (≥99%), (4-(dimethylamino)pyridine (DMAP) (99%), and sodium azide (99.5%) were obtained from Aldrich. Sodium ascorbate (crystalline) was purchased from Source Naturals. Dialysis tubing (Spectra/Por Membrane MWCO 6−8000) was obtained from VWR. CH_2Cl_2 was washed according to standard procedures and distilled over CaH_2. All other materials were used without further purification.

Instrumentation. NMR spectra were recorded on $CDCl_3$ solutions using a Bruker DPX300 or Bruker Avance400 spectrometer ($\omega^{13}_C = 0.25^*\omega^1_H$) with residual solvent signal as calibration. Molecular weights and polydispersity indices were measured by gel permeation chromatography in THF relative to polystyrene standards (Scientific Polymer Products M_n = 503, 700, 1306, 2300, 4760, 12 400, 196 700, and 556 000 g/mol) on a system equipped with a three-column set (Polymer Laboratories 300 × 7.5 mm; 5 μm; 10^{-5}, 10^{-4}, and 10^{-3} Å pore sizes) and a refractive-index detector (HP 1047A) at room temperature with a flow rate of 1 mL/min. High-resolution mass spectral (HRMS) data were obtained on a JEOL JMS700 MStation. IR absorbance data was obtained on a Perkin-Elmer Spectrum One FT−IR spectrometer equipped with a universal ATR sampling accessory.

Synthesis of 6-Azidohexanoic Acid (2). 6-Bromohexanoic acid (5.0 g, 25.6 mmol) and sodium azide (8.37 g, 128 mmol)

* Corresponding author. E-mail: tsemrick@mail.pse.umass.edu.

10.1021/bc060201d CCC: $37.00 © 2007 American Chemical Society
Published on Web 12/13/2006

were dissolved in DMSO and stirred at room temperature for 8 h. The reaction mixture was then dissolved in CH_2Cl_2, washed with water, brine, and $NaHCO_{4(aq)}$, dried over $MgSO_4$, and concentrated by rotary evaporation. Residual DMSO was removed by Kugelrohr distillation at 120 °C. Distillation at 160 °C gave 6-azidohexanoic acid **2** as a colorless liquid (2.98 g, 74%). MS-ESI (*m*/*z*): $[M + Na]^+$ calculated for $C_6H_{11}N_3O_2$ 180.1, found 180.1. ^{1}H NMR ($CDCl_3$, 300 MHz): δ ($CHCl_3$ = 7.26 ppm) 11.43 (br, 1H, COO*H*), 3.28 (t, 2H, CH_2N$_3$), 2.38 (t, 2H, CH_2COOH), 1.65 (m, 4H, CH$_2$CH_2CH$_2$CH_2CH$_2$), 1.43 (m, 2H, CH$_2$CH$_2$CH_2CH$_2$CH$_2$) ppm. ^{13}C NMR ($CDCl_3$, 75 MHz): δ ($CHCl_3$ = 77.0 ppm) 180.1 (*C*═O), 51.2 (*C*H$_2$N$_3$), 33.9 (*C*H$_2$COOH), 28.5 (*C*H$_2$CH$_2$N$_3$), 26.2 (*C*H$_2$CH$_2$CH$_2$N$_3$), 24.2 (*C*H$_2$CH$_2$COOH) ppm. IR(ATR): N═N═N 2090 cm^{-1}.

Synthesis of Camptothecin Azide (3) Camptothecin (100 mg, 0.27 mmol), 6-azidohexanoic acid **2** (85 mg, 0.54 mmol), and DMAP (4 mg) were dissolved in CH_2Cl_2 (5 mL). DCC (110 mg, 5.4×10^{-1} mmol) was added, and the solution was stirred at room temperature for 8 h. The reaction mixture was then precipitated into diethyl ether (50 mL) and isolated by filtration. Recrystallization from MeOH/CH_2Cl_2 (95:5) gave camptothecin azide **3** as a slightly yellow, crystalline solid (114 mg, 87%). HRMS-EI (*m*/*z*): $[M]^+$ calculated for $C_{26}H_{25}N_5O_5$ 487.186, found 487.186. ^{1}H NMR ($CDCl_3$, 300 MHz): δ ($CHCl_3$ = 7.26 ppm) 8.40 (s, 1H, C-16*H*), 8.23 (d, J = 8.4 Hz, 1H, C-18*H*), 7.95 (d, J = 8.4 Hz, 1H, C-21*H*), 7.84 (t, J = 6.8 Hz, 1H, C-19*H*), 7.67 (t, J = 7.6 Hz, 1H, C-20*H*), 7.21 (s, 1H, C-25*H*), 5.70 (d, J = 17.2 Hz, 1H, C-11H_2), 5.43 (d, J = 17.2 Hz, 1H, C-11H_2), 5.29 (s, 2H, C-14*H*), 3.22 (t, J = 6.8 Hz, 2H, C-1H_2), 2.51 (m, 2H, C-5H_2), 2.28 (m, 1H, C-8H_2) 2.16 (m, 1H, C-8H_2), 1.67 (m, 2H, C-2H_2), 1.62 (m, 2H, C-4H_2), 1.43 (m, 2H, C-3H_2), 0.98 (t, J = 7.2 Hz, 2H, C-9H_3) ppm. ^{13}C NMR ($CDCl_3$, 75 MHz): δ ($CHCl_3$ = 77.0 ppm) 172.5 (*C*═O$_{\text{lactone C−10}}$), 167.7 (*C*═O$_{\text{ester C−6}}$), 157.5, 152.5, 149.0, 146.4, 146.0, 131.4, 130.9, 129.7, 128.6, 128.4, 128.3, 128.2, 120.4, 96.0, 75.9, 67.2, 51.3 (*C*H$_2$N$_{3\ C-1}$), 50.1, 33.7, 32.0, 28.6, 26.2, 24.3, 7.7 (*C*H$_{3\ C-9}$) ppm. IR (ATR): N═N═N 2096 cm^{-1}.

Synthesis of Polyester−Camptothecin Conjugate (4). Aliphatic polyester **1** (52 mol % acetylene, $M_n = 9.2 \times 10^3$ g/mol, PDI = 1.17, 500 mg, 2.1 mmol acetylene) was dissolved in CH_2Cl_2 (2 mL) in a small reaction vessel. Camptothecin azide **3** (205 mg, 0.42 mmol, *N*,*N*-diisopropylethylamine (31 μL, 0.16 mmol), and bromotris(triphenylphosphine) copper(I) (77 mg, 8.4×10^{-2} mmol), to target 20 mol % camptothecin grafting, were then added sequentially, and the reaction mixture was stirred at room temperature for 48 h. The crude reaction mixture was precipitated into ether (50 mL) and isolated by filtration. The resulting solid was then dissolved in CH_2Cl_2 (2 mL) and dialyzed against pure CH_2Cl_2 (400 mL) for 48 h. Removal of the solvent and washing with cold hexanes (5 mL) afforded polyester−camptothecin conjugate **4** as a slightly yellow, viscous liquid (580 mg, 82%). GPC (THF): $M_n = 14.3 \times 10^3$ g/mol, PDI = 1.19, 18 mol % camptothecin grafting. ^{1}H NMR ($CDCl_3$, 300 MHz): δ ($CHCl_3$ = 7.26 ppm) 8.41 (s, 1H, camptothecin **3** C-16*H*), 8.20 (d, J = 8.3 Hz, 1H, camptothecin **3** C-18*H*), 7.94 (d, J = 8.3 Hz, 1H, camptothecin **3** C-21*H*), 7.86 (t, J = 6.9 Hz, 1H, camptothecin **3** C-19*H*), 7.67 (m, 1H, camptothecin **3** C-20*H*), 7.37 (m, 1H, R$_2$C═C*H*), 7.19 (s, 1H, camptothecin **3** C-25*H*), 5.68 (d, J = 15.2 Hz, 1H, camptothecin **3** C-11H_2), 5.40 (d, J = 15.3 Hz, 1H, camptothecin **3** C-11H_2), 5.29 (s, 2H, camptothecin **3** C-14*H*), 4.25 (br, 2H, CH_2NR$_2$ camptothecin **3**), 4.04 (br, 4H, CH_2OC═O polyester), 3.22 (t, J = 6.6 Hz, 2H, camptothecin **3** C-1H_2), 3.01 (br, 2H, R$_2$CHCH_2 polyester), 2.51 (m, 2H, camptothecin **3** C-5H_2), 2.35 (br, 4H, C═OC*H* polyester + C═OCH_2 polyester + camptothecin **3** C-8H_2), 2.15 (m, 1H, camptothecin **3** C-8H_2), 2.03 (m, 1H, C≡C*H* polyester), 1.65 (br m, 12H, CH_2CH_2CH$_2$O polyester + CH_2CH$_2$CH_2CH$_2$O polyester + camptothecin **3** C-2H_2 + camptothecin **3** C-4H_2), 1.36 (br m, 4H, CH_2CH$_2$CH$_2$O polyester + camptothecin **3** C-3H_2), 0.95 (t, J = 7.1 Hz, 2H, camptothecin **3** C-9H_3) ppm. ^{13}C NMR ($CDCl_3$, 75 MHz): δ ($CHCl_3$ = 77.0 ppm) 174.2 (*C*═O polyester), 173.4 (*C*═O polyester), 172.5 (*C*═O camptothecin **3** C-10), 167.6 (*C*═O camptothecin **3** C-6), 157.5, 152.5, 149.0, 146.4, 146.0, 144.5, 131.4, 130.9, 129.7, 128.6, 128.3, 128.3, 128.2, 122.5, 120.4, 96.0, 75.9, 67.2, 64.6, 64.1, 53.3, 50.1, 49.9, 44.7, 34.1, 33.7, 32.1, 28.6, 28.4, 27.6, 26.2, 25.9, 25.4, 24.5, 24.3, 7.7 (*C*H$_3$ camptothecin **3** C-9) ppm.

Synthesis of PEG-Grafted Polyester−Camptothecin Conjugate (5). Polyester−camptothecin conjugate **4** (580 mg, 1.4 mmol acetylene) was dissolved in a minimal amount of acetone and added by syringe to a rapidly stirred solution of azide-functionalized PEG-1100 (1.8 g, 1.5 mmol) in water (2 mL). Sodium ascorbate (120 mg, 6.0×10^{-1} mmol) and copper(II) sulfate (150 mg, 6.0×10^{-1} mmol) were added, and the resulting dispersion was heated to 80 °C overnight. The crude reaction mixture was then diluted with water (50 mL) and extracted five times with CH_2Cl_2 (50 mL). The combined organics were dried over $MgSO_4$ and concentrated by rotary evaporation. The resulting solid was then dissolved in PBS (2 mL) and dialyzed against pure PBS for 48 h to remove residual PEG-azide. After removal of the solvent, the product was dissolved in acetone (2 mL) and precipitated into cold hexanes (50 mL). The product was isolated by filtration and dried in a vacuum oven overnight to give PEG-grafted polyester−camptothecin conjugate **5** as an off-white powder (1.80 g, 76%). GPC (THF): $M_n = 23.5 \times 10^3$ g/mol, PDI = 1.20. ^{1}H NMR ($CDCl_3$, 300 MHz): δ ($CHCl_3$ = 7.26 ppm) 8.42 (s, 1H, camptothecin **3** C-16*H*), 8.17 (d, J = 8.3 Hz, 1H, camptothecin **3** C-18*H*), 7.94 (d, J = 8.3 Hz, 1H, camptothecin **3** C-21*H*), 7.84 (t, J = 6.7 Hz, 1H, camptothecin **3** C-19*H*), 7.66 (m, 1H, camptothecin **3** C-20*H*), 7.51 (br, 1H, R$_2$C═C*H* PEG), 7.46 (br, 1H, R$_2$C═C*H* camptothecin), 7.18 (s, 1H, camptothecin **3** C-25*H*), 5.66 (d, J = 14.9 Hz, 1H, camptothecin **3** C-11H_2), 5.40 (d, J = 14.9 Hz, 1H, camptothecin **3** C-11H_2), 5.28 (s, 2H, camptothecin **3** C-14*H*), 4.48 (m, 2H, R$_2$NCH_2), 4.26 (br, 2H, CH_2NR$_2$ camptothecin **3**), 4.02 (br, 2H, CH_2OC═O polyester), 3.84 (t, J = 5.15 Hz, 2H, R$_2$NCH$_2$CH_2), 3.61 (br m, 96H, CH_2CH_2O PEG), 3.43 (t. J = 5.44 Hz, 2H, CH_2OCH$_3$ PEG), 3.37 (s, 3H, CH_3 PEG), 3.20 (t, J = 6.6 Hz, 2H, camptothecin **3** C-1H_2), 3.00 (br, 2H, R$_2$CHCH_2 polyester), 2.48 (m, 2H, camptothecin **3** C-5H_2), 2.27 (br, 4H, C═OC*H* polyester + C═OCH_2 polyester + camptothecin **3** C-8H_2), 2.15 (m, 1H, camptothecin **3** C-8H_2), 1.66 (br m, 12H, CH_2CH_2CH$_2$O polyester + CH_2CH$_2$CH_2CH$_2$O polyester + camptothecin **3** C-2H_2 + camptothecin **3** C-4H_2), 1.35 (br m, 4H, CH_2CH$_2$-CH$_2$O polyester + camptothecin **3** C-3H_2), 0.91 (t, J = 7.1 Hz, 2H, camptothecin **3** C-9H_3) ppm. ^{13}C NMR ($CDCl_3$, 75 MHz): δ ($CHCl_3$ = 77.0 ppm) 174.1 (*C*═O polyester), 173.3 (*C*═O polyester), 172.5 (*C*═O camptothecin **3** C-10), 167.7 (*C*═O camptothecin **3** C-6), 157.5, 152.3, 149.1, 146.4, 146.0, 144.5, 131.3, 130.9, 129.7, 128.6, 128.2, 128.3, 128.2, 122.5, 120.4, 96.0, 75.9, 71.7 (*C*H$_2$OCH$_3$ PEG), 70.4 (*C*H$_2$CH$_2$O PEG), 69.2, 67.2, 64.7, 64.1, 58.6 (*C*H$_3$ PEG), 53.3, 50.1, 49.8, 44.7, 34.0, 33.7, 32.0, 28.6, 28.4, 27.5, 26.2, 25.9, 25.4, 24.5, 24.3, 7.8 (*C*H$_3$ camptothecin **3** C-9) ppm.

RESULTS AND DISCUSSION

We recently reported the preparation of novel, water-soluble PEGylated aliphatic polyester graft copolymers by the controlled ring-opening polymerization of alkyne-functionalized lactones, followed by PEGylation of the polyester by click chemistry with azide-terminated PEG (*20*). Tailored graft densities of PEG were achieved by copolymerization of unfunctionalized lactones (i.e., ϵ-caprolactone) with the acetylene-functionalized derivatives. These aliphatic polyesters proved soluble in water when ~25

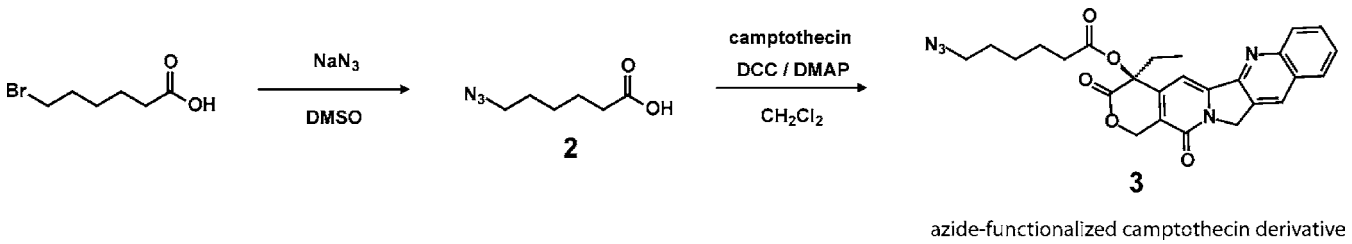


Figure 1. Synthesis of azide-functionalized camptothecin derivative **3** by carbodiimide coupling of camptothecin with 6-azidohexanoic acid **2**.

mol % of the monomer units in the backbone were grafted with PEG 1100 g/mol (~70 wt % PEG), using click chemistry. This provides the opportunity to intentionally leave unreacted acetylene in the backbone for additional click cycloaddition reactions. Click chemistry is useful for functionalization of aliphatic polyesters, as unlike the wide variety of acid- or base-induced chemistries, the mild nature of click chemistry allows it to occur in the absence of polyester degradation. The particular click chemistry employed here is the Cu(I)-catalyzed cycloaddition of azides and alkynes to give triazoles, which has been demonstrated, for example, by Sharpless and Fokin (*21*) to be efficient, selective, and tolerant of many functional groups, and thus advantageous not only for maintaining the integrity of the polyester backbone following conjugation but also potentially for conjugation of a variety of therapeutic drugs to the polymer backbone, as such drugs often contain numerous types of functionality that could interfere with conventional organic coupling reactions. In this study, we demonstrate the synthesis of water-soluble PEG- and camptothecin-functionalized aliphatic polyesters, where both PEGylation and camptothecin grafting is accomplished using click chemistry. For the camptothecin coupling, it was necessary to prepare the requisite azide derivative of the drug.

Sn(II)-mediated ring-opening copolymerization of α-propargyl-δ-valerolactone and ϵ-caprolactone was conducted to give aliphatic polyester **1** with a nearly 1:1 ratio of the two monomers, as confirmed by integration of the ^{1}H NMR spectrum of the polymer. Gel permeation chromatography of polyester **1**, performed in THF against polystyrene molecular weight standards, gave an estimated number-average molecular weight (M_n) of 9200 g/mol and a polydispersity index (PDI, M_w/M_n) of 1.17. Click cycloaddition of camptothecin to the alkyne-functionalized polyester required the synthesis of an azide-functionalized camptothecin derivative. For this, esterification of camptothecin at the 20-OH position was carried out, as upon cleavage of the ester bond in aqueous-based delivery applications, the drug would be released in its active, unmodified form. Moreover, Greenwald and co-workers recently reported that PEG-esterification of camptothecin at the 20-OH position led to stabilization of the drug in its lactone form under physiological conditions, as characterized by NMR and UV−vis spectroscopy (*22*). Buffer hydrolysis experiments at different pH values further demonstrated that camptothecin remained in its lactone form until exocylic ester cleavage, at which point the active drug was released. Thus, on the basis of Greenwald's important study, we chose to integrate azides onto camptothecin using an ester linkage at the 20-OH position, for both enhanced aqueous stability of the conjugate and the ultimate release of free, unmodified camptothecin, leaving behind the degradable aliphatic polyester.

Azide-functionalized camptothecin **3** was prepared as shown in Figure 1. 6-Azidohexanoic acid **2** was obtained by nucleophilic substitution of 6-bromohexanoic acid with sodium azide in 74% yield after purification by Kugelrohr distillation. Compound **2** was characterized by ^{1}H NMR spectroscopy (methylene triplet $-CH_2N_3$ at 3.28 ppm, shifted slightly relative to the $-CH_2Br$ methylene group of the starting material at 3.42 ppm), ^{13}C NMR spectroscopy ($-CH_2N_3$ at 51.2 ppm), infrared spectrometry (azide signal at 2108 cm^{-1}), and mass spectrometry (MS ESI (*m*/*z*) $[M + Na]^+$ calcd 180.1, found 180.1). While azide **2** was reported previously as a synthetic intermediate (*23*), its detailed synthesis and characterization were not. α,ω-Azide-carboxylic acid **2** was then used to esterify camptothecin at the 20-OH position, using dicyclohexylcarbodiimide coupling conditions. This esterification occurred readily at room temperature in dichloromethane to give azide-functionalized camptothecin **3** in 87% yield after purification by crystallization from 95:5 MeOH/CH_2Cl_2. The structure of **3** was confirmed by ^{1}H and ^{13}C NMR spectroscopy, FTIR spectrometry (azide signal at 2096 cm^{-1}), and high-resolution mass spectrometry (HRMS-EI (*m*/*z*): $[M]^+$ calculated for $C_{26}H_{25}N_5O_5$ 487.186, found 487.186.

Coupling of acetylene-functionalized polyester **1** with camptothecin azide **3** was then performed by targeting 20 mol % camptothecin incorporation (or one camptothecin per five monomer repeat units). Initial attempts to use aqueous click chemistry for this coupling were unsuccessful, due to the poor aqueous solubility of both components. Thus, organic soluble copper(I) catalysts for click chemistry were used as alternatives (*24*−*25*); bromotris(triphenylphosphine) copper(I) with *N*,*N*-diisopropylethylamine in dichloromethane solution was found to be effective for the cycloaddition of camptothecin azide **3** and acetylene-functionalized polyester **1**, as shown in Figure 2a. The reaction was complete in 48 h, at which point the crude polymer−drug conjugate was precipitated into ether. The resulting solid was dissolved in CH_2Cl_2 and dialyzed against pure CH_2Cl_2 using a Spectra/Por Membrane MWCO 6−8000. Removal of the solvent and washing with cold hexanes gave polyester−camptothecin conjugate **4** as a slightly yellow, viscous liquid in 82% yield. ^{1}H NMR spectroscopy of **4** revealed signals characteristic of both camptothecin and the aliphatic polyester backbone, with new signals at 7.37 and 4.25 ppm, corresponding to the triazole proton $R_2C{=}CHR$ and the methylene group adjacent to the triazole CH_2NR, respectively. The relative integrations of the signals at 4.04 ppm (CH_2O polyester backbone) and 4.25 ppm (CH_2-triazole) indicated a nearly quantitative incorporation of camptothecin azide **3** into the polyester backbone. GPC analysis in THF indicated a substantial increase in molecular weight, from $M_n \approx 9200$ g/mol before conjugation to ~14 300 after conjugation of the drug. The narrow polydispersity (PDI = 1.19) of the polyester−camptothecin product demonstrated that these click cycloaddition conjugation conditions caused no substantial degradation of the polyester, a key feature of click chemistry that makes it especially attractive for polyester modification.

While these hydrophobic polymer−drug conjugates can in principle be used to prepare hydrophobic aliphatic polyester microparticles with covalently bound camptothecin, further grafting, for example, with PEG, is necessary to impart water solubility to the conjugate. In the ^{1}H NMR spectrum of **4**, the signal at 2.03 ppm ($-C{\equiv}C-H$) indicated the presence of substantial residual alkyne (~30−35 mol %) available for further coupling, as expected from the use of camptothecin azide **3** as the limiting reagent. Click cycloaddition of these residual acetylene groups with azide-terminated PEG (*19*) (i.e., CH_3O-

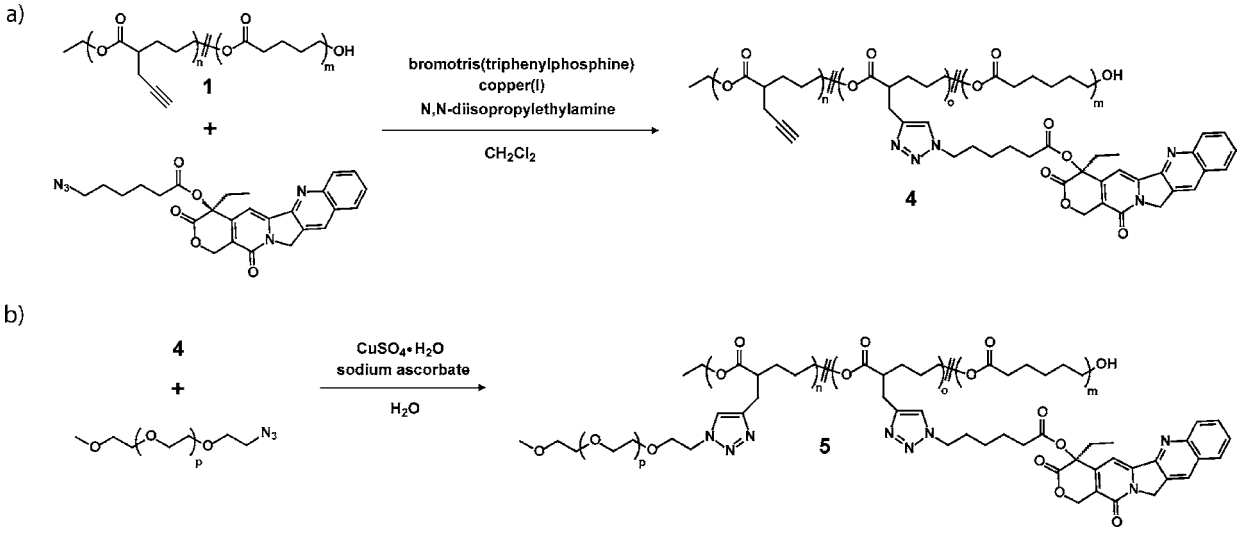


Figure 2. (a) Preparation of hydrophobic polyester−camptothecin conjugate **4** by click cycloaddition of azide-functionalized **3** to acetylene-functionalized copolymer **1** and (b) preparation of hydrophilic PEG-grafted polyester−camptothecin conjugate **5** by further grafting of conjugate **3** with PEG−azide.

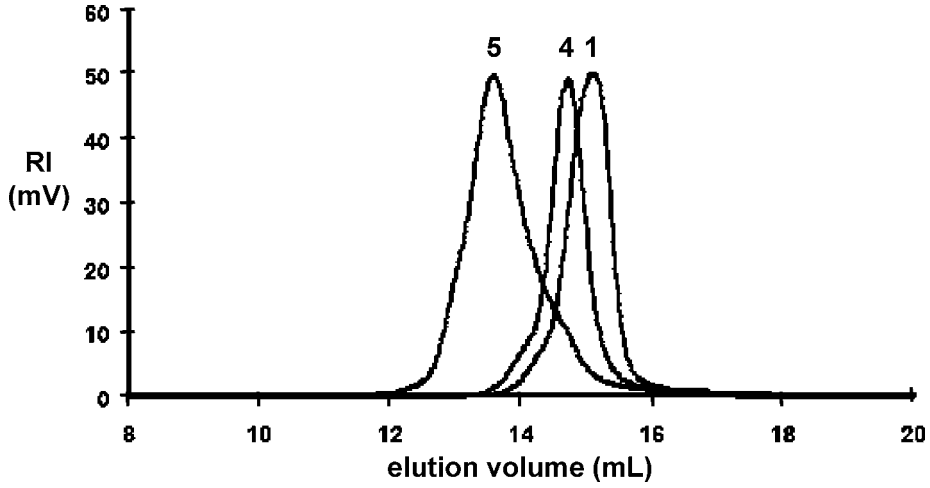


Figure 3. Gel permeation chromatography traces (THF relative to polystyrene standards) of acetylene-functionalized polyester **1**, polyester−camptothecin conjugate **4**, and PEG-grafted polyester−camptothecin conjugate **5**.

PEG−N_3; M_n = 1100), as shown in Figure 2b, was performed successfully in water. The acetylene-containing polyester was dissolved in a minimal amount of acetone, then added to a rapidly stirred, aqueous solution of azide-terminated PEG to ensure good dispersion. Copper sulfate and sodium ascorbate were then added, and the resulting reaction mixture heated to 80 °C and stirred overnight. Purification of the PEGylated camptothecin−polyester conjugate **5** was performed by extraction into CH_2Cl_2, dialysis in phosphate buffered saline, and finally precipitation into cold hexanes to give a slightly yellow, semicrystalline solid in 74% yield. Successful grafting of both the PEG and camptothecin components onto the aliphatic polyester backbone was confirmed by ^{1}H NMR spectroscopy of **5**, by the triazole proton resonance from the camptothecin (7.36 ppm, $R_2C{=}CHR$) and PEG (7.51 ppm, $R_2C{=}CHR$) grafts, as well as methylene signals at 4.26 and 4.48 ppm, corresponding to the R_2NCH_2 groups from the camptothecin and PEG grafts, respectively. The relative integrations of the NMR signals at 4.46 (2H−PEG), 4.23 (2H−camptothecin), and 4.04 (2H−polyester backbone) ppm indicated a grafting density, in terms of percent monomers containing the grafts, of ∼18% camptothecin and ∼33% PEG. GPC analysis of **5**, shown in Figure 3, gave an estimated M_n of ∼23 500 g/mol, a significant increase over the polyester−camptothecin conjugate **4**. Moreover, the narrow polydispersity of **4** was maintained in **5** (PDI ≈ 1.20), again confirming the absence of degradation reactions during the coupling procedure.

Importantly, PEG grafting had a tremendous influence on the solubility properties of the polyester−camptothecin conjugate **5**, which proved highly soluble in water, as well as many organic solvents (e.g., acetone, DMSO, and CH_2Cl_2), due to the amphiphilicity of PEG. The water solubility of this conjugate, coupled with the biodegradable features of the polyester backbone, holds potential for enhancing the ability of camptothecin to be used in polymer therapeutics. Future studies will center on active targeting of the conjugate by the incorporation of oligopeptide sequences (*26*), as well as pH-dependent release of camptothecin from the backbone and in vitro cytotoxicity toward cancer cell lines. In addition, the convenient synthesis of camptothecin azide **3** reported here may prove useful for click cycloaddition to other polymer scaffolds, oligopeptide sequences, and/or modified proteins.

ACKNOWLEDGMENT

The authors gratefully acknowledge financial support from the Army Research Laboratory through a MURI award, the National Science Foundation (Collaborative Research in Chemistry award, CHE-0404575), and a gift from PMUSA.

Supporting Information Available: NMR spectra of 6-azidohexanoic acid **2**, azide-functionalized camptothecin derivative **3**, hydrophobic polyester−camptothecin conjugate **4**, and PEG-grafted polyester−camptothecin conjugate **5**. This material is available free of charge via the Internet at http://pubs.acs.org.

LITERATURE CITED

(1) Pantazis, P. (1995) The water-insoluble camptothecin analogues: Promising drugs for the effective treatment of haematological malignancies. *Leukemia Res. 19*, 775−778.

(2) Raghavan, D., Koczwara, B., and Javle, M. (1997) Evolving strategies of cytotoxic chemotherapy for advanced prostate cancer. *Eur. J. Cancer 33*, 566−574.

(3) Langer, R. (1990) New methods of drug delivery. *Science 249*, 1527−1533.

(4) Hatefi, A., Knight, D., and Amsden, B. (2004) A biodegradable injectable thermoplastic for localized camptothecin delivery. *J. Pharm. Sci. 93*, 1195−1204.

(5) Huang, P. S., and Oliff, A. (2001) Drug-targeting strategies in cancer therapy. *Curr. Opin. Genet. Dev. 11*, 104−110.

(6) Duncan, R. (2003) The dawning era of polymer therapeutics. *Nat. Rev. Drug Discovery 5*, 347−360.

(7) Maeda, H., Seymor, L. W., and Miyamoto, Y. (1992) Conjugates of anticancer agents and polymers: advantages of macromolecular therapeutics in vivo. *Bioconjugate Chem. 3*, 351−362.

(8) Duncan, R., Dimitrijevic, S., and Evagorou, E. G. (1996) The role of polymer conjugates in the diagnosis and treatment of cancer. *STP Pharma Sci. 6*, 237−263.

(9) Padilla De Jesús, O. L., Ihre, H. R., Gagne, L., Fréchet, J. M. J., and Szoka, Jr., F. C. (2002) Polyester dendritic systems for drug delivery applications: in vitro and in vivo evaluation. *Bioconjugate Chem. 13*, 453−461.

(10) Duncan, R., Ringsdorf, H., Satchi-Fainaro, R. (2006) Polymer therapeutics: Polymers as drugs, drug and protein conjugates and gene delivery systems: Past, present and future opportunities. *Adv. Polym. Sci. 192*, 1−8.

(11) Maeda, H., Wu, J., Sawa, T., Matsumura, Y., and Hori, K. (2000) Tumor vascular permeability and the EPR effect in macromolecular therapeutics: a review. *J. Controlled Release 65*, 271−284.

(12) Greenwald, R. B., Conover, C. D., and Choe, Y. H. (2000) Poly(ethylene glycol) conjugated drugs and prodrugs: a comprehensive review. *Crit. Rev. Ther. Drug Carrier Syst. 17*, 101−161.

(13) Vasey, P. A., Kaye, S. B., Morrison, R., Twelves, C., Wilson, P., Duncan, R., Thomson, A. H., Murray, L. S., Hilditch, T. E., Murray, T., Burtles, S., Fraier, D., Frigerio, E., and Cassidy, J. (1999) Phase I clinical and pharmacokinetic study of PK1 [N-(2-hydroxypropyl)-methacrylamide copolymer doxorubicin]: first member of a new class of chemotherapeutic agents − drug polymer conjugates. *Clin. Cancer Res. 5*, 83−94.

(14) Li, C., Yu, D. F., Newman, R. A., Cabral, F., Stephens, L. C., Hunter, N., Milas, L., and Wallace, S. (1998) Complete regression of well-established tumors using a novel water-soluble poly(L-glutamic acid) paclitaxel conjugate. *Cancer Res. 58*, 2404−2409.

(15) Greenwald, R. B., Choe, Y. H., McGuire, J., and Conover, C. D. (2003) Effective drug delivery by PEGylated drug conjugates. *Adv. Drug Delivery Rev. 55*, 217−250.

(16) Andersson, L., Davies, J., Duncan, R., Ferruti, P., Ford, J., Kneller, S., Mendichi, R., Pasut, G., Schiavon, O., Summerford, C., Tirk, A., Veronese, F. M., Vincenzi, V., and Wu, G. (2005) Poly(ethylene glycol)−poly(ester-carbonate) block copolymers carrying PEG-peptidyl-doxorubicin pendant side chains: synthesis and evaluation as anticancer conjugates. *Biomacromolecules 6*, 914−926.

(17) Ihre, H. R., Padilla De Jesús, O. L., Szoka, Jr., F. C., and Fréchet, J. M. J. (2002) Polyester dendritic systems for drug delivery applications: design, synthesis, and characterization. *Bioconjugate Chem. 13*, 443−452.

(18) Gillies, E. R., Goodwin, A. P., Fréchet, J. M. J. (2004) Acetals as pH-sensitive linkages for drug delivery. *Bioconjugate Chem. 15*, 1254−1263.

(19) Gilding, D. K., Reed, A. M. (1979) Biodegradable polymers for use in surgery−polyglycolic/poly(lactic acid) homo- and copolymers: 1. *Polymer 20*, 1459−1464.

(20) Parrish, B., Breitenkamp, R. B., and Emrick, T. (2005) PEG- and peptide-grafted aliphatic polyesters by click chemistry. *J. Am. Chem. Soc. 127*, 7404−7410.

(21) Rostovtsev, V. V., Green, L. G., Fokin, V. V., and Sharpless, K. B. (2002) A stepwise Huisgen cycloaddition precess: Copper(I)-catalyzed regioselective "ligation" of azides and terminal alkynes. *Angew. Chem., Int. Ed. 41*, 2596−2599.

(22) Zhao, H., Lee, C., Sai, P., Choe, Y. H., Boro, M., Pendri, A., Guan, S., and Greenwald, R. B. (2000) 20-O-acylcamptothecin derivatives: evidence for lactone stabilization. *J. Org. Chem. 65*, 4601−4606.

(23) Charon, D., Mondange, M., Pons, J.-F., Blay, K. L., and Chaby, R. (1998) Synthesis and in vitro activities of a spacer-containing glycophospholipid ligand of a lipopolysaccharide receptor involved in endotoxin tolerance. *Bioorg. Med. Chem. 6*, 755−765.

(24) Wu, P., Feldman, A. K., Nugent, A. K., Hawker, C. J., Scheel, A., Voit, B., Pyun, J., Fréchet, J. M. J., Sharpless, K. B., and Fokin, V. V. (2004) Efficiency and fidelity in a click-chemistry route to triazole dendrimers by the copper(I)-catalyzed ligation of azides and alkynes. *Angew. Chem., Int. Ed. 43*, 3928−3932.

(25) Malkoch, M., Schleicher, K., Drockenmuller, E., Hawker, C. J., Russell, T. P., Wu, P., and Fokin, V. V. (2005) Structurally diverse dendritic libraries: a highly efficient functionalization approach using click-chemistry. *Macromolecules 38*, 3663−3678.

(26) Goun, E. A., Shinde, R., Dehnert, K. W., Adams-Bond, A., Wender, P. A., Contag, C. H., and Franc, B. L. (2006) Intracellular cargo delivery by an octaarginine transporter adapted to target prostate cancer cells through cell surface protease activation. *Bioconjugate Chem. 17*, 787−796.

BC060201D

Direct Ring Conjugation of Catecholamines and Their Immunological Interactions

John S. Mitchell,[†,‡] Yinqiu Wu,*[,†] Christian J. Cook,[†] and Lyndsay Main[‡]

Bioengineering Sector, HortResearch, East Street, Private Bag 3123, Hamilton, New Zealand, and Department of Chemistry, University of Waikato, Private Bag 3105, Hamilton, New Zealand. Received July 17, 2006; Revised Manuscript Received October 26, 2006

Catecholamine derivatives were synthesized with potential applications as coating antigens in biosensors or in the raising of specific antibodies. Thioether-bridged derivatives of the catecholamines dopamine, norepinephrine, and epinephrine that attach carboxylic acid functionalities directly to the aromatic ring via an easily incremented linker chain were synthesized by an electrochemical method. These derivatives were purified by convenient ion-exchange chromatography, exact positions of conjugation determined by NMR, and a dopamine derivative immobilized in situ in a BIAcore surface plasmon resonance (SPR) biosensor and its antibody binding studied in comparison with immobilization via the catecholamine primary amine. Binding of an antibody raised to an amine-conjugated protein conjugate showed clear distinction between conjugations at different positions on the catecholamine, illustrating the importance of rational conjugate design in immunosensing of the catecholamines.

INTRODUCTION

For small molecules with few functional groups and relatively simple shape, such as the catecholamine neurotransmitters, the formation of conjugates to the molecule for recognition by specific antibodies or for the generation of specific antibodies requires a conjugation that does not disrupt existing functional groups and has the minimum effect on the overall shape of the hapten. To date, conjugations of the catecholamines have relied upon attachment via the primary amine of the neurotransmitter, principally through the formation of a glutaraldehyde-mediated linkage (*1*−*4*) or through Mannich conjugations *ortho* to the hydroxyl moieties (*5*). Glutaraldehyde and carbodiimide conjugations compromise the primary amine and have been shown to alter the charge state in the hapten and sterically alter the hapten structure (*6*). Furthermore, antibodies raised to such conjugates have been demonstrated to bind much more strongly to the original conjugate than to the free catecholamine (*3*). Similar binding has also been observed with Mannich conjugation (*5*, *7*), and Mannich reactions require protection of the primary amine before conjugation and result in a mixture of isomeric conjugation products (*8*, *9*).

There is a clear need to develop a new conjugation technique for attachment to catecholamines that is not via existing functional groups and for which purified products with a known conjugation position can be produced. Such conjugations when used to link the antigen to a carrier protein could in the future be used to raise specific antibodies able to recognize all the functional groups of the antigen that would have extensive applications in neurological and immunological research and immunoassay development.

This conjugation technique could also be used in the formation of biosensor surfaces for detection of important catecholamines in biological fluid. Catecholamine immunoassay in body fluids is important for evaluation of the activity of the sympathetic nervous system (*10*) and for supporting diagnosis of many diseases including the biochemical detection of catecholamine-secreting tumors such as pheochromocytoma (*11*). Catecholamine biosensors to date have usually relied upon immobilization of antibodies or enzymes on sensor surfaces mainly for electrochemical detection (*12*, *13*), but the ability to conjugate the antigen to a sensor surface and still retain specific antibody binding would allow a range of optical biosensor formats to be used. Flow-through surface plasmon resonance (SPR)[11] immunoassay and antibody and receptor binding studies require a high mass agent to bind to the surface to generate the signal (*14*, *15*), which means that the small-molecule antigen must be immobilized to the sensory surface or a high mass label (*16*, *17*). Until now, there has been no means of doing this for the catecholamines without substantially compromising the existing functional groups on the molecule that are essential to specific antibody or receptor recognition. The attachment of colorimetric, fluorescent, and enzymatic labels to the catecholamines to produce conjugates capable of strong and specific recognition by receptors in biological samples would also benefit from this type of conjugation.

Thioether conjugation direct to the aromatic rings of the catecholamines offers a potential route for production of conjugates that retain the original antigen functional groups intact. Such conjugations using cysteine and glutathione are known in nature for the metabolism of catecholamines (*18*−*20*) and estrogens (*21*) but have not been used as a synthetic method for conjugations used in antibody binding. We report the synthesis of a range of thioether conjugates direct to the aromatic ring of the catecholamines dopamine, norepinephrine, and epinephrine and the ion-exchange purification of these and clear identification of the conjugation position by NMR. We also report the antibody binding interactions of dopamine-conjugated surface plasmon resonance (SPR) biosensor surfaces and examine the effect of different ring conjugation positions and linker lengths on antibody binding.

EXPERIMENTAL PROCEDURES

General. All chemicals were purchased from Sigma Aldrich (Milwaukee, WI). The dopamine was used as the racemate, and

* Corresponding author. Tel.: +64-7-858-4751. Fax: +64-7-858-4705. E-mail address: ywu@hortresearch.co.nz.

† HortResearch.

‡ University of Waikato.

[1]Abbreviations: SPR, surface plasmon resonance; TFA, trifluoroacetic acid; COSY, homonuclear correlated spectroscopy; NOESY, nuclear overhauser enhancement spectroscopy; MPA, 3-mercaptopropionic acid; MUA, 11-mercaptoundecanoic acid; NHS, *N*-hydroxysuccinimide.

10.1021/bc0602174 CCC: $37.00 © 2007 American Chemical Society
Published on Web 12/22/2006

the norepinephrine bitartrate and epinephrine were used as the R-isomer. All solvents were analytical grade except for HPLC solvents (HPLC grade). The silica gel for column chromatography was Merck 60 Å, grade 9385, 230−400 mesh. Melting point determinations were done using a Reichert Thermopan instrument and were uncorrected. ^{1}H, ^{13}C, and DEPT 135 NMR spectra were obtained on Bruker AC300 300 MHz and Bruker Avance 400 MHz spectrometers. Chemical shifts (ppm) were referenced to tetramethylsilane. Low-resolution mass spectra were obtained on a VG Platform II electrospray mass spectrometer (ESI-MS). High-resolution mass spectra were obtained on a VG-70SE mass spectrometer with *MASPEC 2* data analysis software. BIAcore SPR analysis was done on a BIAcore 3000 instrument (BIAcore, Inc., Piscataway, NJ) using CM5 research-grade chips and 10 mM (*N*-[2-hydroxyethyl]piperazine-*N*′-[2-ethanesulfonic acid]), 150 mM NaCl with 0.11% w/v ethylenediaminetetraacetic acid, and 0.05% v/v P-20 surfactant, pH 7.4, as running buffer. All BIAcore experiments were performed at 25 °C. The monoclonal antibody used was mouse anti-human dopamine (US Biological, Swampscott, U.S.A., D-9000) raised to dopamine−bovine serum albumin conjugate, conjugated through the primary amine by the glutaraldehyde method, and with an affinity of $\sim 1 \times 10^7$ L/M.

HPLC was performed on a Shimadzu instrument and data analyzed using *Class-VP* software (5.032 1999). The reversed-phase HPLC column used was a Prodigy 3 μm ODS 100 × 4.6 mm, 00D-4243-E0, 111274−4 from Phenomenex (Milford, New Zealand). All mobile phases were filtered (Nylon 0.45 μm filter) and degassed before use. The mobile phases were as follows: A = 50%v/v MeCN pH 2.15 (adjusted with TFA), B = 5% MeCN pH 2.15. All experiments were done at 40 °C oven temperature and flow rate of 1 mL/min. All tubing was stainless steel. The ion-exchange column was a Dowex-50W strongly acidic cation-exchange resin column (10 g dry resin, slurry packed in deionized water with final bed dimensions of 150 mm × 15 mm). The resin was cleaned thoroughly before use with cycles of deionized water, acetone, methanol, deionized water, 2 M HCl, and deionized water and then vacuum-dried after diethyl ether wash.

Positions of attachment for the catecholamines were determined by analysis of cross-peaks in homonuclear correlated spectroscopy (COSY) and nuclear Overhauser enhancement spectroscopy (NOESY) 2D-NMR spectra. A positive cross-peak in the NOESY and no cross-peak in the COSY suggest attachment at the 5-position, no NOESY cross-peak and a cross-peak in the COSY suggest attachment at the 2-position, and no cross-peaks suggests attachment at the 6-position (numbering as indicated in Scheme 1). Analytical RP-HPLC was performed to determine compound purity using the same HPLC apparatus as above. Retention times (t_R) are provided with the compound experimentals. All reported binding response differences in SPR were analyzed by the Student's *t*-test and found to be significant ($P < 0.05$). Errors quoted are standard errors.

3-(5-(2-Aminoethyl)-2,3-dihydroxyphenylthio)propanoic Acid (1). Dopamine (30 mg, 0.158 mmol) was dissolved in 0.1 M HCl (80 mL). A 2 V potential difference was applied for 3 h between graphite bar electrodes and *o*-quinone formation monitored by HPLC. 10% v/v 3-mercaptopropionic acid (MPA) solution (413 μL, 0.473 mmol in 0.1 M HCl) was then added rapidly with vigorous stirring. After 18 h, the reaction mixture pH was adjusted to 5 with NaOH and the solution poured into the ion-exchange column. The column was flushed with deionized water until no more MPA could be seen by HPLC, and the column was then flushed with HCl (1 M) and ethanol (10% v/v). Yield: 34% (14 mg, 0.0545 mmol). mp: decomposes. IR (KBr disc): 1241, 1400, 1638, 3434. ^{1}H NMR (D_2O) δ: 2.49 (2H, t, J = 7.9 Hz, CH_2-COO^-), 2.72 (2H, t, J = 9.2 Hz, CH_2-Ar), 2.95 (2H, t, J = 7.0 Hz, CH_2-S), 3.07 (2H, t, J = 9.2 Hz, CH_2-N), 6.68 (1H, s, 2-H), 6.77 (1H, s, 6-H). ^{13}C NMR (D_2O) δ: 28.6, 32.0, 34.1, 40.6, 116.5, 120.5, 125.3, 129.3, 144, 144.5. ESI-MS *m*/*z* (MeCN/H_2O 1:1 5 V) 258.9 $[M + H]^+$. HPLC: purity 95%, t_R = 7.2 min (100% B, 0−6.5 min; 100−50% B, 6.5−11 min).

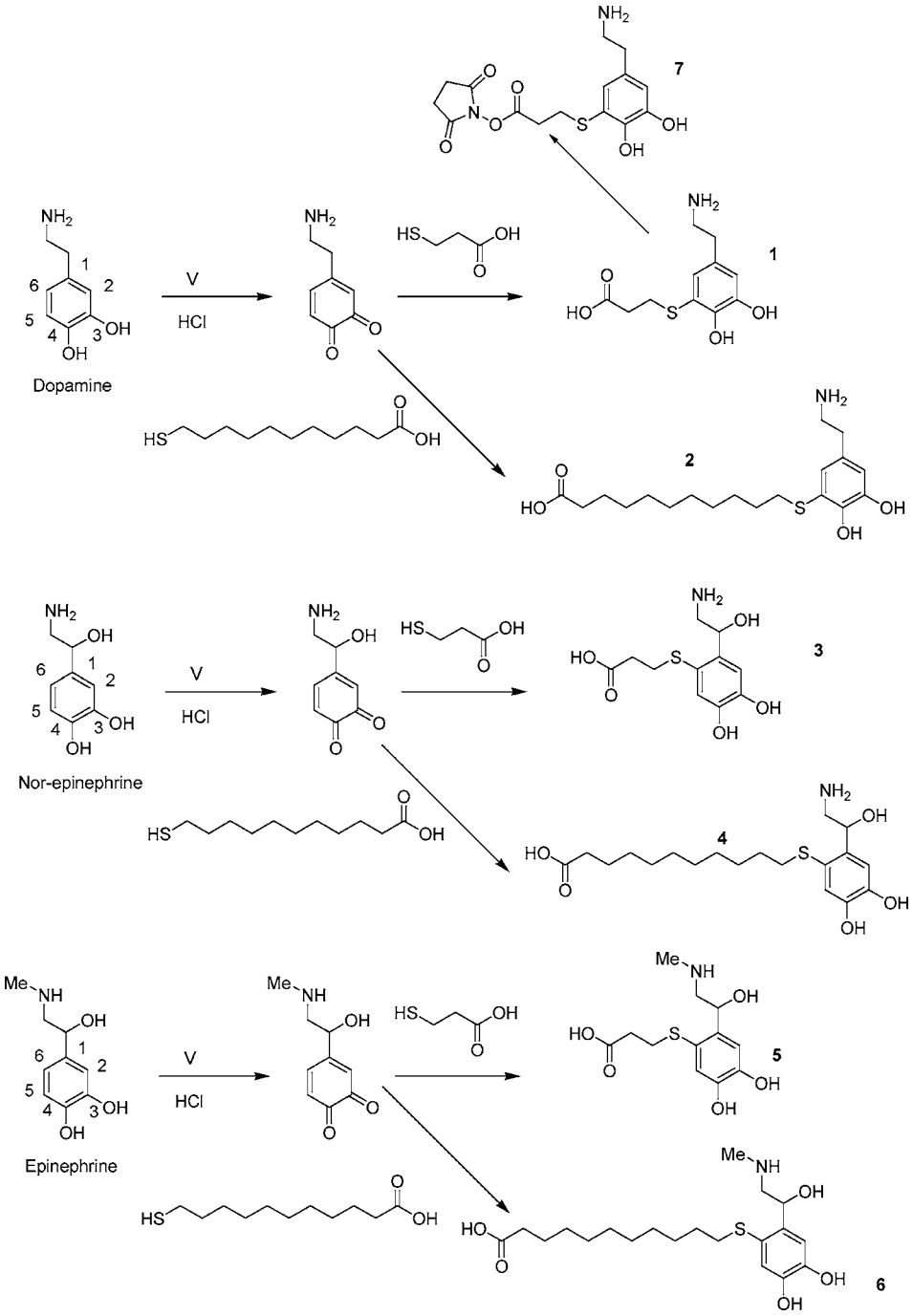
11-(5-(2-Aminoethyl)-2,3-dihydroxyphenylthio)undecanoic Acid (2). Dopamine (30 mg, 0.158 mmol) was dissolved in HCl solution (80 mL, 0.2 M in 1:1 MeCN/H_2O) and electrolyzed at 2 V with vigorous stirring for 2.5 h. 11-Mercaptoundecanoic acid (MUA) (104 mg, 0.475 mmol, in 6 mL of 50% v/v MeCN, 0.2 M HCl total) was added rapidly to the vigorously stirring solution. After 1 h, the pH was adjusted to 5 with NaOH. The solution was run into the ion-exchange column, and the column was then washed extensively with 50% v/v MeCN to remove all MUA. HPLC analysis revealed that MUA alone eluted through the column and all other compounds were retained.

The column was then eluted with the following elution scheme to separate the products and reactant chromatographically: 10% v/v EtOH 1 M HCl total, 20% v/v EtOH 1 M HCl total, 30% v/v EtOH 1 M HCl total, 40% v/v EtOH 1 M HCl total, 50% v/v EtOH 1 M HCl total, 20% v/v EtOH 2 M HCl total. Fractions were combined and solvent removed in vacuo. Yield: 16% (9.2 mg, 0.025 mmol). IR (film): 1413, 1638, 2855, 2929, 3437 cm^{-1}. ^{1}H NMR (D_2O) δ: 1.21 (10H, main chain CH_2 of MUA), 1.36 (2H, MUA), 1.56 (4H, MUA), 2.36 (2H, CH_2-COO^-), 2.87 (2H, CH_2-S), 2.88 (2H, CH_2-Ar), 3.22 (2H, CH_2-N), 6.78 (1H, m, 2-H), 6.88 (1H, m, 6-H). ^{13}C NMR (D_2O) δ: 24.3, 28.3, 32.1, 33.3, 33.9, 40.6, 115.5, 122.6, 123.8, 129.3, 143.0, 144.4, 179.1. ESI-MS *m*/*z* (CH_3CN/H_2O 1:1) 370.6 $[M + H]^+$. HRMS: Calcd. 370.2052, found 370.2047 MH^+. HPLC: purity 94%, t_R = 7.7 min (100−50% B, 0−4 min; 50−0% B, 4−8 min; 0% B 8−13.5 min).

3-(2-(2-Amino-1-hydroxyethyl)-4,5-dihydroxyphenylthio)-propanoic Acid (3). Norepinephrine bitartrate (40 mg, 0.125 mmol) was dissolved in HCl solution (80 mL; 0.1 M) and electrolyzed at 2 V until maximum conversion to *o*-quinone was observed (2 h). MPA (328 μL of 1/10 solution in 0.1 M HCl, 0.375 mmol) was added with rapid stirring. The reaction was stirred vigorously for 18 h. The reaction mixture was adjusted to pH 5 with NaOH before eluting into the ion-exchange column, the column then being flushed with deionized water until no more MPA was visible eluting from the column. The column was then eluted using the following eluant scheme: 100 mL 0.01 M HCl, 100 mL 0.1 M HCl, 100 mL 0.1 M HCl 10% v/v EtOH, 100 mL 0.2 M HCl, 460 mL 0.4 M HCl, 100 mL 0.3 M HCl 10% v/v EtOH, 100 mL 0.3 M HCl, 700 mL 0.4 M HCl. Yield 41% (14 mg, 0.0512 mmol). IR (film): 1193, 1470, 1633, 3450 cm^{-1}. ^{1}H NMR (D_2O) δ: 2.67 (2H, t, J = 7.2 Hz, CH_2-COO^-), 3.15 (2H, m, CH_2-S), 3.27 (2H, m, CH_2-N), 4.55 (1H, s, CH−OH), 6.91 (1H, s, 2-H), 7.07 (1H, s, 5-H). ^{13}C NMR (D_2O) δ: 40.5, 41.0, 123, 129, 139. ESI-MS *m*/*z* (MeCN/H_2O 1:1, 20 V) 274.3 $[M + H]^+$. HPLC: purity 94%, 3.31 min (100% B, 0−6.5 min; 100−50% B, 6.5−11 min).

11-(2-(2-Amino-1-hydroxyethyl)-4,5-dihydroxyphenylthio)undecanoic Acid (4). Norepinephrine bitartate (40 mg, 0.125 mmol) was dissolved in HCl solution (80 mL; 0.2 M in 1:1 MeCN/H_2O) and electrolyzed at 2 V until maximum conversion to *o*-quinone was observed (2 h). MUA (82 mg, 0.375 mmol in 5 mL of 0.2 M HCl in 1:1 MeCN/H_2O) was added quickly to the rapidly stirring solution. The solution was stirred for 18 h. The reaction mixture was pH-adjusted to 5 with 2 M NaOH and 0.1 M NaOH and then eluted into the column and the column flushed with 50% v/v acetonitrile in deionized water until all the MUA had eluted according to the HPLC analysis. The column was then eluted using the following elution

Scheme 1. Reaction Scheme for the Synthesis of Thioether Derivatives of the Catecholamines Dopamine, Norepinephrine, and Epinephrine Presenting Carboxylic Acid Functionalities for Linker Attachment and Conjugation



scheme: 0.4 M HCl, 0.6 M HCl, 0.6 M HCl total 10% v/v EtOH, 0.6 M HCl total 20% v/v EtOH, 0.8 M HCl total 10% v/v EtOH, 1 M HCl total 10% v/v EtOH, 1 M HCl total 20% v/v EtOH, 1 M HCl total 30% v/v EtOH, 1 M HCl total 20% v/v EtOH, 1 M HCl total 30% v/v EtOH. Yield 28% (14 mg, 0.0353 mmol). IR (film): 1456, 1616, 3394, 3429 cm^{-1}. ^1H NMR (D_2O) δ: 1.15 (12H, m, MUA chain CH_2), 1.44 (4H, m, MUA CH_2), 2.26 (2H, m, CH_2-COO^-), 2.62 (2H, m, CH_2-S), 3.10 (2H, m, $CH_2-NH_3^+$), 6.92 (1H, m, 2-H), 7.07 (1H, m, 5-H). ^{13}C NMR (D_2O) δ: 24.3, 28.7, 115.8. ESI-MS *m/z* (MeCN/H_2O, 20 V): 386.5 $[M + H]^+$. HRMS: Calcd. 386.2001, found 386.2010 (MH^+). HPLC: purity 95%, t_R = 5.77 min (100−50% B, 0−4 min; 50% B−0% B, 4−8 min; 0% B, 8−13.5 min).

3-(4,5-dihydroxy-2-(1-hydroxy-2-(methylamino)ethyl)phenylthio)propanoic Acid (5). Epinephrine (30 mg, 0.164 mmol) was dissolved in aqueous HCl (0.1 M; 80 mL) and electrolyzed at 2 V until maximum *o*-quinone formation was observed by HPLC. MPA (428 μL, 0.491 mmol diluted 1/10 in 0.1 M HCl) was then added quickly to the rapidly stirring solution and stirred for 30 min. The product was purified by silica gel column chromatography using successively MeCN, 5% v/v H_2O in MeCN, 10% v/v H_2O in MeCN, 20% v/v H_2O in MeCN, 10% 0.01 M HCl in MeCN, 10% 0.1 M HCl in MeCN, 20% 0.1 M HCl in MeCN, 10% 1 M HCl in MeCN, 20% 2 M HCl in MeCN, and 2 M HCl. Yield: 21% (10 mg, 0.035 mmol) mp: decomposes. IR (KBr disc): 1123, 1638, 3447 cm^{-1}. ^1H NMR (D_2O) δ: 2.75 (3H, s, $NH-CH_3$), 2.86 (2H, t, J = 6.7 Hz, CH_2-COO^-), 3.01 (2H, t, J = 7.1 Hz, CH_2-S), 6.91−7.09 (2H, m, aromatics). ^{13}C NMR (D_2O) δ: 16.7, 28.7, 42, 57.4, 115, 117, 126, 130, 138, 140, 167. ESI-MS *m/z* (CH_3CN/H_2O 1:1, 30 V) 288.5 $[M + H]^+$. (H_2O, 5 V): 214.5 [M-amine side chain +

H]$^+$, 306.3 [M + H_2O + H]$^+$. HPLC: purity 96%, t_R = 7.0 min (100% B, 0−6.5 min; 100−50% B, 6.5−11 min).

11-(4,5-dihydroxy-2-(1-hydroxy-2-(methylamino)ethyl)-phenylthio)undecanoic Acid (6). Epinephrine (30 mg, 0.164 mmol) was dissolved in HCl solution (80 mL; 0.2 M in 1:1 MeCN/H_2O) and electrolyzed at 2 V until maximum *o*-quinone formation was observed by HPLC. MUA (107 mg, 0.491 mmol, in 9 mL 0.2 M HCl in 1:1 MeCN/H_2O) was added to the rapidly stirring solution and stirring continued for 18 h. The reaction was separated by silica gel column chromatography using successively MeCN, 5% H_2O in MeCN, 10% H_2O in MeCN, 20% H_2O in MeCN, and 10% 0.1 M HCl in MeCN. Yield: 36% (24 mg 0.0596 mmol). mp: decomposes. IR (KBr disc): 1120, 1638, 3437 cm^{-1}. ^{1}H NMR (D_2O) δ: 1.24 (10H, s, MUA chain CH_2), 1.33 (2H, m, MUA chain CH_2), 1.51 (2H, m, MUA chain CH_2 β to COOH), 1.66 (2H, m, MUA chain CH_2 β to S), 2.23 (2H, t, J = 9.8 Hz, CH_2−COOH), 2.71 (3H, m, N−CH_3), 2.84 (2H, m, CH_2−S), 3.13 (1H, m, CH−NH), 3.21 (1H, m, CH−NH), 6.87 (2H, m, aromatic). ^{13}C NMR (D_2O + CD_3OD) δ: 24.0, 27.8, 28.3, 28.5, 28.5, 33.1, 54.6, 68.4, 113.9, 114.5, 116.4, 118.7, 132.2. ESI-MS *m/z* (MeCN/H_2O 1:1, 40 V): 454.6 [M + MeOH + Na]$^+$. HPLC: purity 96%, t_R = 7.7 min (100% B−50% B, 0−4 min; 50−0% B, 4−8 min; 0% B, 8−13.5 min).

HPLC Mobile Phase Sequences. *Compounds **1**, **3**, **5.*** Mobile phases: A, 50% v/v MeCN pH adjusted to 2.15 with trifluoroacetic acid (TFA); B, 5% v/v MeCN pH adjusted to 2.15 with TFA. Gradient: 100% B for 6.5 min, then linear gradient to 50% B until 11 min.

*Compounds **2**, **4**, **6.*** Mobile phases: A, 50% MeCN, pH 2.15 with TFA; B, 5% MeCN pH 2.15 with TFA. 1: 0−6.5 min 100% B, 6.5−14.5 min 100% B−0% B, 14.5−20 min 0% B. 2: 0−4 min 100% B−50% B, 4−8 min 50% B−0%, 13.5 min 0% B.

2,5-Dioxo-1-pyrrolidinyl-3-(5-(2-amino-1-hydroxyethyl)-2,3-dihydroxyphenylthio)propionate (7). 1 (5 mg, 0.019 mmol) was dissolved in dimethylformamide (1 mL, dimethylformamide pH adjusted to 4.2 with HCl), and dicyclohexylcarbodiimide (96 mg, 0.465 mmol in 125 μL of dimethylformamide pH 4.2) and *N*-hydroxysuccinimide (NHS) (54 mg, 0.465 mmol in 125 μL of dimethylformamide pH 4.2) were then added dropwise to the stirring solution of catecholamine. The reaction was stirred at room temperature in the dark for 3 h. The production of the ester was confirmed by ESI-MS and the raw reaction mixture used as is immediately to minimize risk of internal cyclization. ESI-MS: (MeOH, 40 V) 354.4 [M + H]$^+$.

Immobilization of SPR Flow Cells. A CM5 carboxymethylated dextran chip (BIAcore) was activated with *N*-ethyl-*N*-(3-dimethylaminopropyl)carbodiimide (EDC) and *N*-hydroxysuccinimide (NHS) (1:1, 100 μL, 5 μL/min) for each flow cell in turn. To one flow cell, 4,7,10-trioxa-1,13-tridecanediamine was injected (2 × 200 μL of 1% w/v pH 9.7 aqueous, and then 2 × 200 μL 1% w/v pH 11.3, 5 μL/min). The flow cell was then deactivated with ethanolamine (50 μL, 5 μL/min). Another flow cell was treated in the same fashion but with 1,6-hexanediamine. The flow cells were treated with NaOH and $NaHCO_3$ washes, and then into each of the two flow cells, a solution of **7** was injected (1/4 dilution in deionized water, centrifuged at 14 000 *g*, then 1 × 200 μL and 4 × 50 μL injected at 5 μL/min). Another flow cell was activated as above with ϵ-aminocaproic acid (1% w/v, pH 9.7 aqueous, 2 × 200 μL injections at 5 μL/min and then again at pH 11.3). The surface was deactivated with ethanolamine as above, equilibrated with deionized water, and then the exposed carboxylic acid groups were activated with EDC/NHS as above (200 μL). Dopamine (1% w/v, pH 5.5 aqueous, 1 × 200 μL, 4 × 50 μL, 5 μL/min, and 8 × 50 μL at pH 7.0) was then injected over the flow cell before final deactivation with ethanolamine as above.

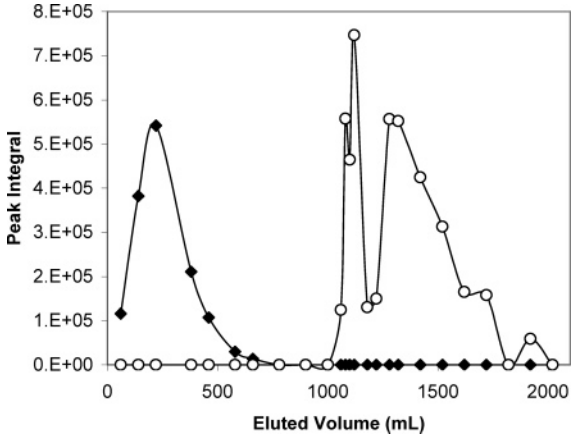


Figure 1. Ion-exchange chromatographic separation plot (peak integral vs elution volume) of dopamine (◆) and compound **2** (○).

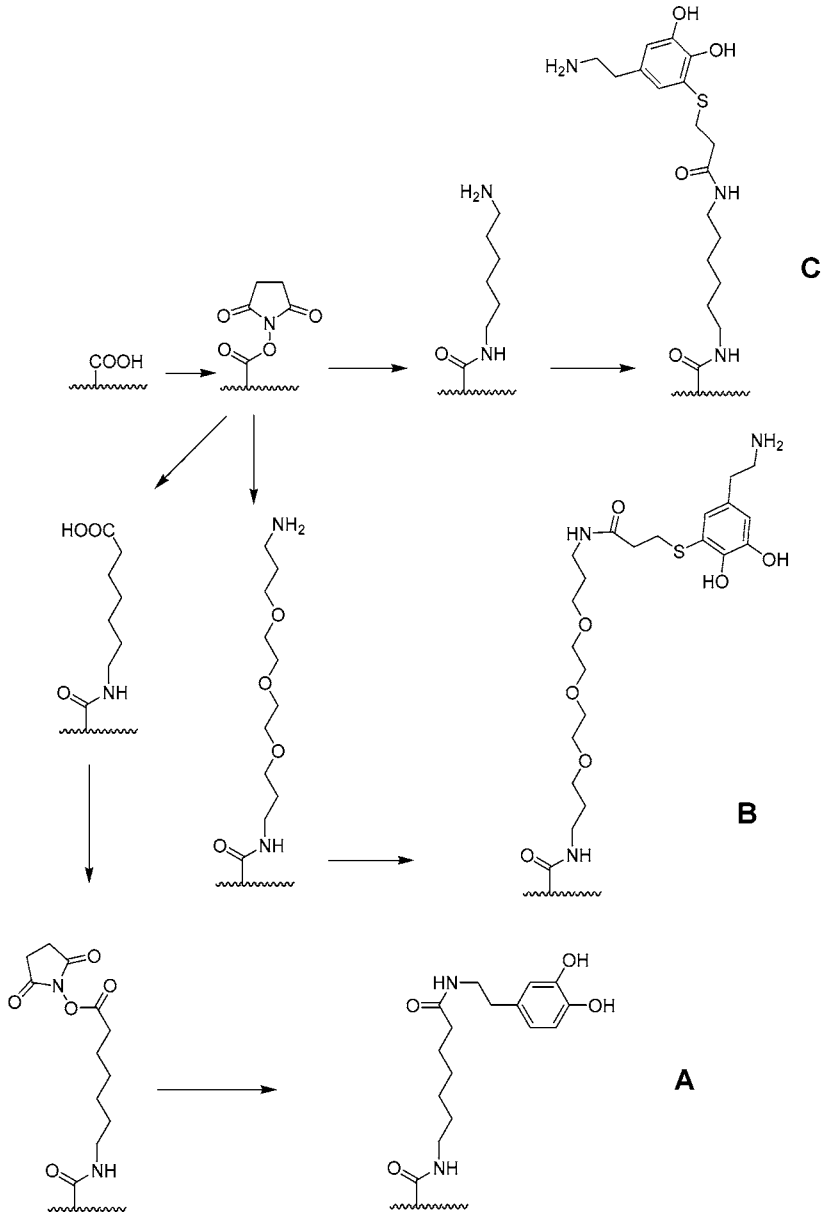
Antibody Binding Tests. 0.15 M NaCl, 0.01 M phosphate buffer pH 5.2 was used as the running buffer. Monoclonal anti-dopamine was injected (100 μg/mL and 50 μg/mL, 60 μL, 20 μL/min, three replicates each). Surfaces were regenerated with HCl solution (pH 3.5 in 20% v/v MeCN).

RESULTS AND DISCUSSION

Derivatization of Catecholamines by Thioether Linkage. Until now, there has been no reliable method for conjugating the catecholamine neurotransmitters for potential use in immunology and biosensor design such that conjugation does not compromise existing functional groups or result in an impure mixture or require protection of existing functional groups. In this study, we employed electrolysis to produce the *o*-quinones of the catecholamines dopamine, norepinephrine, and epinephrine, making use of their *o*-hydroxyl moieties and generating the intensely orange colored *o*-quinone solutions by simple application of electrical potential difference (Scheme 1). These *o*-quinones are susceptible to conjugation by thiols as has been demonstrated in biological systems with conjugation to cysteine and glutathione residues, and that has been successfully synthetically replicated for these amino acids (*22*). In this study, two different carboxylic acid bearing thiols of different chain lengths (3- and 11-carbons) were added to the catecholamines to generate a mixture of thiol-conjugated products with attachment directly to the aromatic ring of the catecholamines (Scheme 1). This reaction is envisaged to proceed by an addition mechanism with proton migration. The reaction results in a range of different products corresponding to the three substitution positions possible around the aromatic ring. This reaction method has the advantage that it is rapid: most of the reaction occurs within minutes, is one step only, and requires no complex apparatus. Conversion to the *o*-quinone can be monitored by HPLC and thiol added at the point of maximum conversion. Linker chain length can be easily adjusted as required for different applications.

The reaction mixtures next needed to be purified, and this posed significant challenges, as the product mixtures are quite complex. Ion-exchange chromatography offers an inexpensive and effective means of purifying such compounds by making use of the differing functional groups of the products and starting materials to separate them. Previously, such techniques have been applied only for very low concentrations of biological catecholamine mixtures (*23*, *24*). By use of a strongly acidic cation-exchange column, it was possible to adsorb the amine-bearing catecholamines on the column while eluting out the remaining unreacted thiol from the reaction mixture. Once all unreacted thiol had eluted as determined by HPLC, then application of mineral acid at carefully controlled concentrations

Scheme 2. Immobilization of Dopamine by Primary Amine Linkage to ϵ-Aminocaproic Acid (A), 4,7,10-Trioxa-1,13-tridecanediamine (B), and by Thioether Linkage to 1,6-Hexanediamine (C)



along with organic solvent (ethanol) to compress the elution volumes enabled chromatographic elution of the catecholamines and purification to a single product with attachment at one position only on the aromatic ring of the catecholamine.

The chromatographic purification can be traced by HPLC (Figure 1) and the product isolated to one peak by fraction collection. The resolution of the ion-exchange column was adequate to resolve one of the major products from the starting neurotransmitter and the other products with minimal overlap for dopamine and norepinephrine, but in the case of epinephrine, the polarities of products and starting materials were too close to enable complete resolution. The epinephrine products were sufficiently nonpolar to allow separation on normal-phase silica gel by flash chromatography, whereas the dopamine and norepinephrine products were too polar. The carboxylic acid bearing products could not be separated from the original catecholamine by use of an anion-exchange resin column after the cation-exchange resin, as binding to the anion-exchange column released OH^- ions, which cause oxidation of the catecholamines in situ. This separation approach allows rapid, convenient, and inexpensive purification of the catecholamine derivatives to one position of conjugation.

Position of attachment can be determined by the use of 2-dimensional NMR techniques. Homonuclear correlated spectroscopy (COSY) enabled assessment of the presence of coupling between close neighboring protons, and nuclear overhauser enhancement spectroscopy (NOESY) enabled the determination of proton pairs that were within ∼5 Å of each other. This data combined with chemical-shift increments enabled all products to be identified relative to their position of attachment around the aromatic ring. The isolated products had substitution at the position *meta* to the amine side chain (4-position in Scheme 1) for both dopamine derivatives, whereas for the norepinephrine and epinephrine derivatives, attachment was *ortho* to the amine side chain (6-position in Scheme 1). Conjugation to the position *ortho* to the amine side chain and hydroxyl moiety (position 2 in Scheme 1) is sterically disfavored by the bulk of the two neighboring groups.

Surface Plasmon Resonance Studies and Antibody Interactions. It is of interest to consider the effects of different conjugation positions and techniques on the ability of antibodies to bind to immobilized antigens. Because of the small size of the catecholamine molecules, it is envisaged that conjugation through an existing functional group will have a profound effect

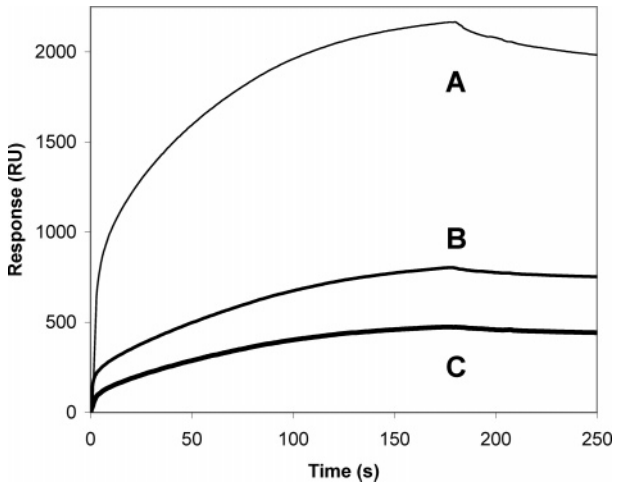


Figure 2. Antibody binding sensorgrams for surfaces immobilized by primary amine linkage to ϵ-aminocaproic acid (A), by thioether linkage to 4,7,10-trioxa-1,13-tridecanediamine (B), and by thioether linkage to 1,6-hexanediamine (C) at 100 μg/mL antibody concentration.

on the ability of the antigen to mimic the free catecholamine effectively. Commercially available antibodies have so far relied upon use of conjugates through existing functional groups to generate the antibody. In the design of possible immunobiosensors for catecholamines, it is of interest to consider how important biosensor surface conjugation techniques may be in determining antibody binding levels, signal strength, and thus assay performance. Surface plasmon resonance provides an excellent tool for assessing antibody binding properties (*14*, *25*).

In this study, dopamine was immobilized to a surface plasmon resonance biosensor surface using immobilization technology that employs in situ addition of linkers and then attachment of dopamine (Scheme 2). To attach the synthesized dopamine derivative, it is necessary to first pass a homobifunctional linker over the sensor surface to generate an amine terminus and provide further spacing from the biosensor surface. Two different linker types were selected in this instance: one was the nonpolar linker chain 1,6-hexanediamine, and the other was the more water-soluble oligoethylene glycol chain 4,7,10-trioxa-1,13-tridecanediamine. The dopamine−propanoic acid derivative (compound **1**) was attached by formation of the NHS active ester (compound **7**) and flowing the compound over the biosensor surface in large excess to ensure maximum immobilization. Conjugation via the primary amine of the dopamine was possible by first modifying the surface with attachment of the heterobifunctional linker ϵ-aminocaproic acid and then flowing dopamine over the surface (Scheme 2). This system offers a convenient in situ means of constructing a biosensor surface with the antigen spaced from the sensor surface, to ensure maximum projection in the fluid stream and thus minimizing steric hindrance to antibody binding.

The catecholamines are sensitive to base-catalyzed oxidation, and as such, the running buffer was kept acidic to help to preserve the biosensor surface. Monoclonal anti-dopamine was applied to the surfaces to assess its binding. The antibody was raised to a glutaraldehyde-linked protein conjugate through the primary amine. The sensorgrams obtained for the binding indicated clearly that the strongest binding was obtained for the surface with dopamine conjugated through the primary amine, as expected given that the antibody was raised to a conjugate through the primary amine, whereas antibody binding to the sensor surfaces with dopamine immobilization via its aromatic ring directly was only about 35% of that of the binding to the primary amine immobilized surface at 100 μg/mL antibody (Figure 2 and Table 1). Such great differences in binding response have demonstrated clearly that a catecholamine

Table 1. Surface Plasmon Resonance Binding Responses (RU) for Different mAb Concentrations for Each of the Sensor Surfaces

mAb concentration (μg/mL)	surface A (RU)	surface B (RU)	surface C (RU)
50	313 + 39	153 + 21	175 + 19
100	1670 + 210	580 + 100	650 + 140

monoclonal antibody's binding strength is strongly dependent upon the site of conjugation around the aromatic ring of the immobilized analyte relative to the site used to raise the antibody and that careful selection of immobilization conjugation position is required to maximize antibody binding signal in flow-through biosensors.

In general, immunizing haptens should be designed as a close mimic of the target molecule, retaining all functional groups, preserving as much as possible the original steric and electronic characteristics of the analyte (*26*). From our results (Figure 2 and Table 1), it is suggested that the commercial antibody, raised to a catecholamine conjugate through the existing primary amine (not a close mimic of the free catecholamine), is most likely to have much stronger recognition of coated antigens (catecholamine conjugates) through the same amine conjugation, compared with recognition of the free catecholamines having the similar chemical structure to our aromatic-linked catecholamine derivatives (B and C) where all original functional groups including primary amine were retained and which gave lower antibody-binding responses (Figure 2 and Table 1). These results support previous reports (*3*) that suggest anti-dopamine antisera raised with glutaraldehyde conjugation preferentially recognize the catechol moiety and any modification of the aromatic ring significantly disrupts binding of the antibody. Such poorer antibody binding will probably lead to poor inhibition by the free catecholamine, and thus, higher catecholamine concentrations would be required to inhibit antibody binding to any surface-bound catecholamine conjugates, which results in lower assay sensitivity. Speculatively, for development of a highly sensitive competitive assay, better antibody recognition of the full catecholamine structure or higher affinity to free catecholamine, and thus better inhibition by the catecholamine and sensitivity of detection, could potentially in the future be achieved by using the thioether attachment to the aromatic ring in protein conjugations to raise antibodies. Antibodies raised in this manner should clearly distinguish between neurotransmitters with differences in their amine side chain. Raising of such antibodies is an area of possible future research.

It is generally accepted that the type and length of the hapten spacer arm are important factors in preparation of surface coated hapten conjugates. A long spacer arm is thought to offer the ability to space the antibody binding site out from the solid surface. However, a spacer arm which is too long may cause entwining around the hapten molecules and blocking of antibody binding on the coated surface. Therefore, an optimal type and length of spacer arm should be applied. In the present study, biosensor surface bound catecholamine molecule (B) through a relatively long oligoethylene glycol (OEG) spacer arm provided a hydrophilic molecular layer as a favorable binding medium and more space for antibody binding than the surface-coated catecholamine (C) with a short hexanediamine linker. In this study, changing the type and length of the linker did not result in a statistically definitive change in binding response (Table 1), indicating that these parameters are less significant than changing conjugation position. The binding of antibody further confirms the viability of an OEG spacer arm for covalent immobilization of small molecules on a biosensor surface (*16*).

The catecholamine sensory surface is somewhat unstable, being prone to gradual oxidation, and this is shown in gradually declining binding responses on the surfaces. This instability has made the construction of an assay or full antibody saturation

curves based on these surfaces difficult, due to high variation, without the introduction of additional measures to minimize surface degradation such as the use of powerful antioxidants. Furthermore, the monoclonal antibody used has a comparatively low affinity, even to the homologous antigen (10^7 L/M), further hindering generation of saturation curves.

These studies have shown how conjugation directly to the aromatic ring of the catecholamine can be achieved with purification to a single product and without the need to protect existing functional groups, thus offering a very convenient conjugation method for biosensor design and potentially for future use in antibody generation, one that much more closely mimics the free catecholamines. These derivatives have great application for biosensor construction, and this study has shown that monoclonal antibodies raised to conjugates through the catechol primary amine can discriminate between different conjugation positions for dopamine in a flow-through type biosensor.

ACKNOWLEDGMENT

The authors thank the New Zealand Foundation for Research Science and Technology for funding this work and providing a Top Achiever Doctoral Scholarship to J. Mitchell.

LITERATURE CITED

(1) Geffard, M., Seguela, P., and Heinrich-Rock, A. M. (1984) Antisera against catecholamines: specificity studies and physicochemical data for anti-dopamine and anti-p-tyramine antibodies. *Mol. Immunol. 21*, 515−522.

(2) Chagnaud, J. L., Mons, N., Tuffet, S., Grandier-Vazeilles, X., and Geffard, M. (1987) Monoclonal antibodies against glutaraldehyde-conjugated dopamine. *J. Neurochem. 49*, 487−494.

(3) Mons, N., and Geffard, M. (1987) Specific antisera against the catecholamines: L-3,4-dihydroxyphenylalanine, dopamine, noradrenaline, and octopamine tested by an enzyme-linked immunosorbent assay. *J. Neurochem. 48*, 1826−1833.

(4) Mons, N., Danel, N., and Geffard, M. (1988) Visualization of L-dihydroxyphenylalanine in rat brain by using specific antibodies. *Brain Res. 451*, 403−407.

(5) Flurkey, K., Bolger, M. B., and Linthicum, D. S. (1985) Preparation and characterization of antisera and monoclonal antibodies to serotonergic and dopaminergic ligands. *J. Neuroimmunol. 8*, 115−127.

(6) Kazak, L. E., Etkin, A. F., Bol'shakova, T. D., Ermolin, G. A., and Babayan, S. S. (1983) Difficulties in obtaining antisera for immunological assay of catecholamines and normetanephrine. *Lab. Delo 5*, 20−22.

(7) Miwa, A., Yoshioka, M., Shirahata, A., and Tamura, Z. (1977) Preparation of specific antibodies to catecholamines and L-3,4-dihydroxyphenylalanine. I. Preparation of the conjugates. *Chem. Pharm. Bull. 25*, 1904−1910.

(8) Miwa, A., Yoshioka, M., and Tamura, Z. (1978) Preparation of specific antibodies to catecholamines and L-3,4-dihydroxyphenylalanine. II. The site of attachment on catechol moiety in the conjugates. *Chem. Pharm. Bull. 26*, 2903−2905.

(9) Miwa, A., Yoshioka, M., and Tamara, Z. (1978) Preparation of specific antibodies to catecholamines and L-3,4-dihydroxyphenylalanine. III. Preparation of antibody to epinephrine for radioimmunoassay. *Chem. Pharm. Bull. 26*, 3347−3352.

(10) Bergquist, J., Sciubisz, A., Kaczor, A., and Sillberring, J. (2002) Catecholamines and methods for their identification and quantitation in biological tissues and fluids. *J. Neurosci. Methods 113*, 1−13.

(11) Peaston, R. T., and Weinkove, C. (2004) Measurement of catecholamines and their metabolites. *Ann. Clin. Biochem. 41*, 17−38.

(12) Cook, C. J., and Devine, C. E. (1998) Antibody-based electrodes for hormonal and neurotransmitter measurements in vivo. *Electroanalysis 10*, 1108−1111.

(13) Stoica, L., Lindgren-Sjolander, A., Ruzgas, T., and Gorton, L. (2004) Biosensor based on cellobiose dehyrogenase for detection of catecholamines. *Anal. Chem. 76*, 4690−4696.

(14) Wu, Y., Mitchell, J. S., Cook, C. J. and Main, L. (2002) Evaluation of progesterone-ovalbumin conjugates with different length linkers in enzyme-linked immunosorbent assay and surface plasmon resonance-based immunoassay. *Steroids 67*, 565−572.

(15) Usami, M., Mitsunaga K., and Ohno, Y. (2002) Estrogen receptor binding assay of chemicals with a surface plasmon resonante biosensor. *J. Steroid Biochem. 81*, 47−55.

(16) Mitchell, J. S., Wu, Y., Cook, C. J., and Main, L. (2005) Sensitivity enhancement of surface plasmon resonance biosensing of small molecules. *Anal. Biochem. 343*, 125−135.

(17) Dillon, P. P., Daly, S. J., Manning, B. M., and O'Kenedy, R. (2003) Immunoassay for the determination of morphine-3-glucuronide using a surface plasmon resonance-based biosensor. *Biosens. Bioelectron. 18*, 217−227.

(18) Miller, R. T., Lau, S. S., and Monks, T. J. (1995) Metabolism of 5-(glutathione-S-yl)-alpha-methyldopamine following intracerebroventricular administration to male Sprague-Dawley rats. *Chem. Res. Toxicol. 8*, 634−641.

(19) Spencer, J. P., Jenner, P., Daniel, S. E., Lees, A. J., Marsden, D. C., and Halliwell, B. (1998) Conjugates of catecholamines with cysteine and GSH in Parkinson's disease: possible mechanisms of formation involving reactive oxygen species. *J. Neurochem. 71*, 2112−2122.

(20) Nakagomi, M., and Suzuki, E. (2000) Quantitation of catechol estrogens and their N-acetylcysteine conjugates in urine of rats and hamsters. *Chem. Res. Toxicol. 13*, 1208−1213.

(21) Cao, K., Stack, D. E., Ramanathan, R., Gross, M. L., Rogan, E. G., and Cavalieri, E. L. (1998) Synthesis and structure elucidation of estrogen quinones conjugated with cysteine, N-acetylcysteine, and glutathione. *Chem. Res. Toxicol. 11*, 909−916.

(22) Shen, X. M., Xia, B., Wrona, M. Z., and Dryhurst, G. (1996) Synthesis, redox properties, in vivo formation, and neurobehavioural effects of N-acetylcysteinyl conjugates of dopamine: possible metabolites of relevance to Parkinson's disease. *Chem. Res. Toxicol. 9*, 1117−1126.

(23) Dalmaz, Y., and Peyrin, L. (1976) Specific ion-exchange chromatography and fluorimetric assay of urinary 3-*o*-methyldopamine. *J. Chromatogr. 116*, 379−394.

(24) Atack, C. V., and Magnusson, T. (1970) Individual elution of noradrenaline (together with adrenaline), dopamine, 5-hydroxytryptamine and histamine from a single, strong cation exchange column, by means of mineral acid-organic solvent mixtures. *J. Pharm. Pharmacol. 22*, 625−627.

(25) Adamcyzk, M., Chen, Y. Y., Gebler, J. C., Johnson, D. D., Mattingly, P. G., Moore, J. A., Reddy, R. E., Wu, J., and Yu, Z. (2000) Evaluation of chemiluminescent estradiol conjugates by using a surface plasmon resonance detector. *Steroids 65*, 295−303.

(26) Marco, M., Gee, S., and Hammock, B. D. (1995) Immunochemical techniques for environmental analysis II. Antibody production and immunoassay development. *Trends Anal. Chem. 14*, 415−425.

BC0602174

A Versatile Photocleavable Bifunctional Linker for Facile Synthesis of Substrate−DNA Conjugates for the Selection of Nucleic Acid Catalysts

Dayal Saran[†] and Donald H. Burke*[,‡]

Department of Chemistry, Indiana University, Bloomington, Indiana, and Department of Molecular Microbiology and Immunology and Department of Biochemistry, University of Missouri, Columbia, Missouri 65211-7310.
Received July 20, 2006; Revised Manuscript Received October 14, 2006

Covalent photocleavable attachment of small molecules or peptides to oligonucleotides is an integral strategic element in the selection of novel nucleic acid enzymes. Here, we report the synthesis of a multipurpose, photocleavable bifunctional linker (PCBL) suitable for nucleic acid selections and other biotechnology applications. PCBL contains a photocleavable *O*-nitrobenzyl group flanked on one side by an *N*-hydroxysuccinimidyl ester (reactive toward primary amines) and on the other side by a sulfhydryl. To demonstrate the utility of PCBL, the linker was used to couple an analog of the antibiotic chloramphenicol (Cam) to the 5′ end of an amino-modified 8-mer DNA oligo. Coupling was confirmed by MALDI-TOF spectrophotometry. Decoupling was performed by irradiating the coupled species with near-UV light (approximately 360 nm), regenerating the original amino-modified oligo. Ligation of the Cam−PCBL−DNA conjugate to random-sequence RNA generated a diversity library appropriate for the selection of new ribozymes that catalyze reactions involving the tethered substrate. Coupling and decoupling of the Cam analog from the library was monitored on a trilayered organomercurial polyacrylamide gel. The coupling/decoupling strategy described here is readily generalized to many combinations of macromolecules and small molecules. For example, analogs of this small molecule−DNA conjugate can be generated as synthons for ligation to nucleic acid diversity libraries during each round of novel ribozyme selections, or they can be immobilized onto chips for addresssably reversible microarray analysis.

INTRODUCTION

Covalent modifications of nucleic acids have found broad application in chemistry and biology. In particular, there has been growing interest in the coupling of functional groups to nucleic acids. For example, conjugation of peptides to oligos has been used to improve biological stability, cellular uptake efficiency, and cell-specific targeting of antisense RNAs, aptamers, and siRNA (*1*−*4*). Nucleic acids have also been conjugated to chromophores for target detection or tertiary structural analysis, or to immobilizing agents for the production of high-density DNA arrays (*5*−*7*). Similar conjugation is also very useful in the *in vitro* selections of catalytic nucleic acids such as ribozymes that catalyze Michael addition, Diels−Alder cycloaddition, or oxidoreduction reactions (*8*, *9*).

The *in vitro* selection of ribozymes involves multiple cycles of partitioning and amplification of reactive nucleic acids from among a vast number of starting molecules (10^{14} or more). The partition often takes advantage of the conversion of a nucleic-acid-tethered substrate into a nucleic-acid-tethered product, followed by preferential purification and amplification of nucleic acids that are tethered to product. Each selection cycle increases the number of copies of catalytically active nucleic acid strands relative to nonspecifically recovered molecules, until the population is dominated by nucleic acids with autocatalytic activity. This strategy is highly effective at recovering reactive RNA species but can be limited by poor control of regiospecificity and cumbersome synthesis of substrate-linked nucleic acid libraries. Several selections that were originally intended to target nucleic-acid-tethered substrates have instead yielded ribozyme libraries dominated by species that modify themselves at internal sites on the RNA, such as 2′ hydroxyls, rather than modifying the intended substrate (*10*−*13*). This is especially problematic for catalysis of condensation reactions that label active nucleic acids with an affinity tag, such as biotin or a free sulfhydryl. Depending on the method used for recovering product-linked ribozymes, this unwanted background can be difficult to separate from the desired ribozymes.

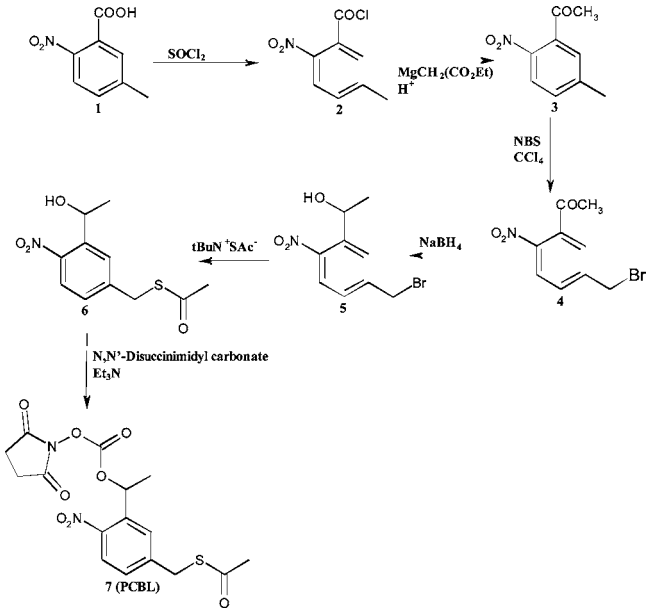
A productive strategy for overcoming this limitation has been to introduce a cleavable moiety between the RNA and the tethered substrate, such that the desired product−RNA conjugates can be easily decoupled from unreacted substrate−RNA conjugates (*14*, *15*). In this strategy, the partition step of the selection includes three stages: recovery of all nucleic acid species that have become modified during the course of the reaction (including product−RNA conjugates and internally reacted species), cleavage of the tether joining the substrate/product to the ribozyme, and elimination of all RNA species that still retain internal covalent modifications. A second limitation is that the attachment of small-molecule substrates to the nucleic acids can be challenging in the absence of considerable synthetic expertise. Although there is a limited repertoire of commercially available mono- and oligonucleotides with covalently attached pendants, such as nucleoside analogs and fluorescent dyes, the use of such reagents is not readily generalizable to the attachment of new pendants. Importantly, most attachment strategies do not allow facile reversal of the coupling using benign conditions.

The present work addresses both of these concerns by introducing a photocleavable *O*-nitrobenzyl group (ONB) into the linker. ONB derivatives are especially convenient photocleavable moieties and have been used for a variety of applications, because they are synthetically tractable and photocleave upon irradiation in the near-UV at 330−370 nm. Examples include the covalent attachment of immobilizing agent to the

* Corresponding author. burkedh@health.missouri.edu.
[†] Present address: J. Craig Venter Institute, 9704 Medical Center Drive, Rockville, Maryland 20850.
[‡] University of Missouri.

10.1021/bc060221f CCC: $37.00 © 2007 American Chemical Society
Published on Web 12/20/2006

Scheme 1. Synthesis Scheme of Photocleavable Bifunctional Linker



termini of nucleic acids and proteins for substrate surface modifications and purification and analyses (*16*−*18*), conjugation of protein toxin to an antibody for cellular delivery (*19*), protection of amines and carboxylic acid groups during chemical synthesis of amino acids and nucleotides (*20*−*22*), synthesis of many caged fluorophores, proteins, and other caged compounds (*23*), and synthesis of multifunctional mono- and dinucleotide analogs (*15*). Photoreversible fluorescent chain terminators and fluorescent oligonucleotides have been generated for DNA sequencing by synthesis (*5*, *24*, *25*), and aptamers to hepatitis C virus RNA polymerase have been immobilized to affinity chromatography columns via ONB linkers to allow photoelution of the bound polymerase (*26*).

This paper reports a time-effective, inexpensive, easy-to-use general scheme for the synthesis and evaluation of a multipurpose, photocleavable, bifunctional linker (PCBL). The PCBL can be used to couple any pair of amine-containing and thiol-reactive species, and the linkage is labile to near-UV irradiation at 360 nm under conditions that are benign for nucleic acids. The utility of the PCBL is demonstrated experimentally by coupling an analog of the antibiotic chloramphenicol (Cam) to the 5′ end of a DNA oligonucleotide and to a random-sequence RNA library and subsequently decoupling it in both contexts by near-UV irradiation.

EXPERIMENTAL PROCEDURES

Synthesis of Photocleavable Bifunctional Linker (PCBL) (Scheme 1). Photocleavable bifunctional linker was synthesized as shown in Scheme 1.

Compound 2. 5-Methyl-2-nitrobenzoic acid (**1**; 1.81 g, 0.01 mmol) and 2 drops of DMF were added to 25 mL of $SOCl_2$ and refluxed at 80 °C for 3 h under inert atmosphere. The mixture was evaporated to a yellow oil, washed after dissolving in ether, and further evaporated to dryness.

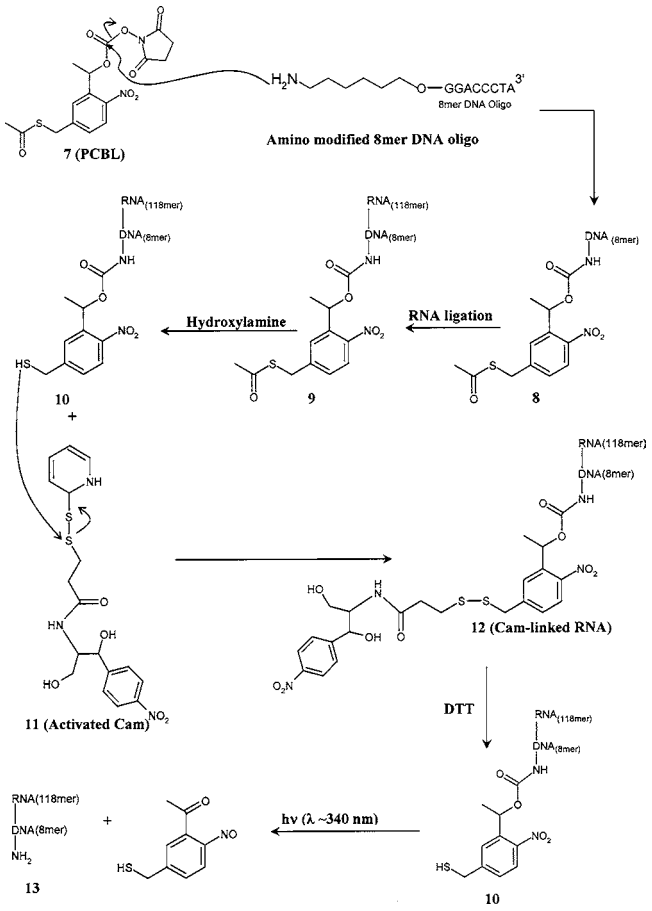
Compound 3. Compound **3** was prepared according to the procedure discussed by Reynolds et al. (*27*). Magnesium turnings (270 mg) were mixed with 0.25 mL of absolute ethanol and 0.025 mL of carbon tetrachloride in a three-neck, round-bottom flask and stirred at room temperature under inert (N_2) atmosphere. If the reaction did not start immediately (no effervescence), the flask was heated for a few minutes on a steam bath. The reaction was allowed to continue for 5 min, then 10 mL of ether was added slowly with constant stirring. A solution of 1.66 mL of diethyl malonate, 1 mL of absolute ethanol, and 1.25 mL of absolute ether was added at a rate that maintained constant boiling, and the mixture was refluxed over a steam bath until most of the magnesium was dissolved. Compound **2**, 5-methyl-2-nitrobenzoyl chloride, (0.01 mmol) was dissolved in 2.5 mL of ether and was very slowly added to the gray solution. Reflux was continued throughout the addition until the resulting green solution became too viscous to stir. The reaction mixture was cooled and dissolved in dilute sulfuric acid (0.69 mL of H_2SO_4 in 10 mL of H_2O). The ether layer was separated, and the aqueous layer was extracted with 2.06 mL of ether. Ether extracts were combined, and solvent was removed to yield crude diethyl-5-methyl-2-nitrobenzoylmalonate. A solution of 2 mL of glacial acetic acid and 0.38 mL of concentrated sulfuric acid was added, and the mixture was refluxed until no more carbon dioxide was evolved. The reaction mixture was cooled on an ice bath and made alkaline with NaOH solution, and the product 5-methyl-2-nitroacetophenone **3** was extracted with ether and purified by flash column chromatography on a column of silica (3 × 20 cm, grade 230−400 mesh, purchased from Scientific Adsorbance), using 20% ether in hexane as eluent. This product is characterized by ^{1}H NMR ($CDCl_3$) δ: 2.582 (s, 3H, CH_3), 2.637 (s, 3H, Ar−CH_3), 7.324 (s, H, ArH), 7.485 (d, H, ArH), 8.078 (d, H, ArH).

Compound 4. Synthetic protocols for compounds **4** through **6** were adapted from Senter et al. (*19*). 2 g (11 mmol) of compound **3**, 2.18 g (12.3 mmol) of *N*-bromosuccinimide, 27 mg (0.11 mmol) of benzoyl peroxide, and 20 mL of CCl_4 were mixed and refluxed for 6 h under Ar or until the succinimide produced in the reaction floated on the top of the solution. The reaction mixture was cooled and filtered, and the filtrate was evaporated to dryness. The product was further dissolved in CH_2Cl_2, washed with water, and dried. Formation of 5-Bromomethyl-2-nitroacetophenone (**4**) was confirmed by monitoring the new ^{1}H NMR (s, 2H, CH_2Br) peak at δ 4.573. Additional peaks in the NMR spectra indicated a small amount of unreacted starting material and dibrominated product, but further purification at this step was deemed unnecessary.

Compound 5. Compound **4** (2.0 g, 7.7 mmol) was dissolved in a mixture of 10 mL dioxane and 14 mL methanol and kept on ice. $NaBH_4$ (150 mg, 3.94 mmol) was added in the ice-cold solution of the reaction mixture and allowed to stir for 2 h at 0 °C. The reaction was quenched with acetone, and solvent was evaporated to dryness. The crude product was dissolved in 25 mL of $CHCl_3$, washed with brine water, and evaporated to a yellow oil. The formation of 1-(5-bromomethyl-2-nitrophenyl) ethanol (**5**) was confirmed by NMR without further purification. ^{1}H NMR ($CDCl_3$) δ: 1.582 (d, 3H, CH_3), 4.571 (s, 2H, Ar−CH_2Br), 5.458 (q, H, CHOH), 7.28 (s, H, ArH), 7.36 (d, H, ArH), 7.88 (d, H, ArH).

Compound 6. 3.28 mL (5.0 mmol) of 40% aq tetrabutylammonium hydroxide was slowly added to a solution of 0.35 mL (5.0 mmol) of thioacetic acid in 5 mL DMF at room temperature. A solution of compound **5** (1.0 g, 3.85 mmol) in 6.37 mL DMF was slowly added, and the mixture was stirred for 3 h. The solvent was evaporated, and the residue was redissolved in 25 mL ether and washed with saturated aqueous NaCl, then with saturated $NaHCO_3$, and dried under vacuum. 1-[5-(Methyl-3-*S*-acetylthioic acid ester)-2-Nitrophenyl] ethanol [**6**] was purified by silica flash column chromatography (grade 230−400 mesh, purchased from Scientific Adsorbance), using 35% ether in hexane as eluent. ^{1}H NMR ($CDCl_3$) δ: 1.582 (d, 3H, CH_3), 2.395 (s, 3H, $COCH_3$), 4.178 (s, 2H, Ar−CH_2Br), 5.458 (q, H, CHOH), 7.28 (s, H, ArH), 7.36 (d, H, ArH), 7.88 (d, H, ArH).

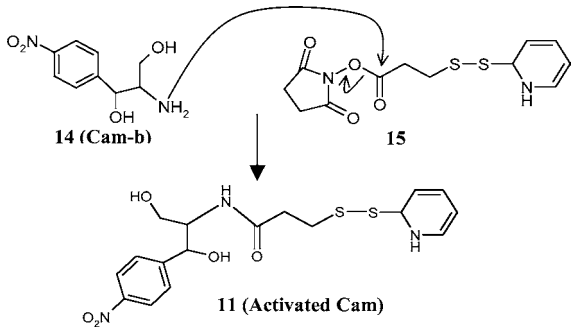
Scheme 2. Synthesis of Cam-Linked RNA Pool and Decoupling Reaction of Cam from RNA



PCBL, Final Compound (7). Compound **6** (50 mg, 0.20 mmol) was dissolved in 0.8 mL of DMF. 80 mg (0.33 mmol) of *N*,*N*′-disuccinimidyl carbonate was added, followed by 84.5 mL (0.6 mmol) of triethylamine, and the mixture was stirred for 6 h at room temperature. Solvent was evaporated to dryness, and the residue was washed thoroughly with 0.1 M $NaHCO_3$ and water. Finally, the crude product 1-[5-(methyl-3-*S*-acetyl-thioic acid ester)-2-nitrophenyl] ethyl-*N*-hydroxysuccinimidyl carbonate [**7**] was dissolved in minimum CH_2Cl_2 and purified over preparative TLC (250 μ glass-backed silica gel plate) using a solvent system of 70:30 ratio $CHCl_3/CH_3OH$. ^1H NMR ($CDCl_3$) δ: 1.79 (d, 3H, CH_3), 2.395 (s, 3H, $COCH_3$), 4.19 (s, 2H, Ar−CH_2Br), 6.41 (q, H, CHOH), 7.28 (s, H, ArH), 7.45 (d, H, ArH), 7.98 (d, H, ArH).

Synthesis of Conjugated RNA Pool (Scheme 2). 1 mM 5′ amino-modified DNA oligo was incubated with 5 mM PCBL in 80% DMSO for 12 h at room temperature. The product was purified on a 1 mL size-exclusion column (G25 Sephadex, purchased from Sigma), dried under vacuum, and resuspended in water. Ligation was performed by incubating 118 nt RNA (1 μM) carrying 70 random nucleotides (*13*) with purified PCBL-linked 8-mer DNA oligo (1.5 μM) and 24-mer DNA bridge (3 μM) in a buffer that contained 1 mM ATP and T4 DNA ligase at 37 °C for 5 h. RNA was internally radiolabeled by transcription in the presence of [α-^{32}P] UTP. The sequence of the DNA bridge (5′-GATTCGCTTTTCCCTAGGGTCC-3′) is complementary to both the 8-mer DNA oligo and to the 5′ terminal 14 nucleotides of the RNA. Deacylation was accomplished by incubating 10 μM hybrid RNA (**9**) with 25 mM hydroxylamine at pH 7.5 and purifying it on a trilayer APM gel. 10 μM of deacylated product (**10**) was incubated with 10 μM DTT (1 equiv) for 5 min. Activated Cam in 60% DMSO was added to a final concentration of 50 μM (5 equiv). The mixture was incubated for 4 h at room temperature, and the product Cam-linked RNA pool (**12**) was purified on an 8% denaturing (8 M urea) polyacrylamide gel. Activated Cam was synthesized by incubating 1 mM chloramphenicol base (Cam-b) (**14**) with 1 mM *N*-succinimidyl 3-(2-pyridyldithio)-propionate (SPDP) (**15**) in DMSO for 2 h at room temperature (Scheme 3).

Scheme 3. Activation of Cam Analog with Commercially Obtained Crosslinker



Photolysis of Conjugate from the RNA Pool. A 1 μM solution of DTT-treated, Cam-linked RNA pool in 25 mM phosphate buffer at pH 7.4 was irradiated with a hand-held, long-wavelength UV lamp (UVP, Inc., model no UVGL-25) at approximately 360 nm from a distance of 10 cm for 5 or 10 min, as indicated in the text.

RESULTS

PCBL Design and Synthesis. The photocleavable bifunctional linker (PCBL) carries two reactive groups separated by a photocleavable *O*-nitrobenzyl moiety. It was designed to permit reversible coupling of any amine-containing and sulfur-reactive species (Figure 1). The *N*-hydroxysuccinimide group is highly reactive toward primary amines, which react to form a stable carbamate. The sulfur at the other end of the PCBL is initially protected by an acetyl group to avoid premature reactivity or disulfide bond formation. Deacetylation of the thioester with hydroxylamine exposes the sulfhydryl, which is highly reactive toward numerous reagents. This PCBL reagent was synthesized as described in methods and summarized in Scheme 1.

Coupling to, and Photorelease from, a DNA Oligo. PBCL was dissolved in DMSO and allowed to react with 5′ amino-modified DNA oligo (Scheme 2). The PBCL−DNA conjugate (**8**) was purified from the reaction mixture containing DMSO and other contaminants by gel filtration on a size-exclusion column (pre-equilibrated with water), eluting with multiple 1 mL fractions of water. A second column was loaded in parallel with 5′ radiolabeled 8-mer DNA oligo to identify the elution fraction likely to contain the purified DNA. The fraction containing the DNA was concentrated, and product formation was confirmed by MALDI-TOF (Figure 2). A peak of molecular

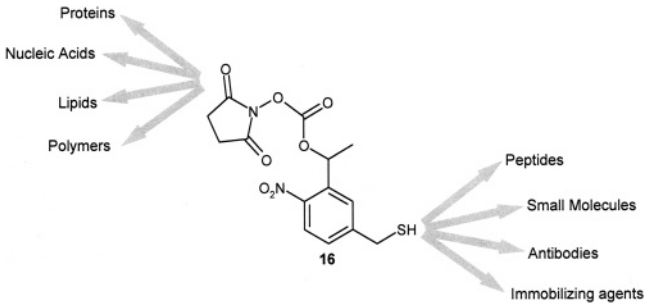


Figure 1. Some of the potential combinations of attachment of macromolecules with small molecules using PCBL [**7**].

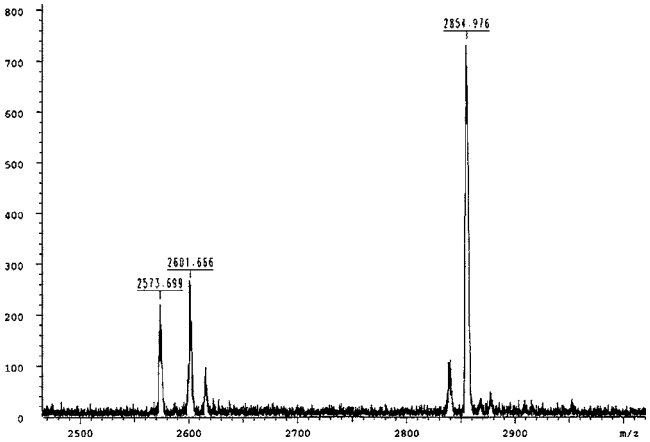


Figure 2. MALDI-TOF spectra of PBCL-linked 8-mer DNA oligo. The calculated molecular weight of the starting material (amino-linked 8-mer DNA oligo) is 2573. Reaction with PCBL is expected to increase the molecular weight by 282 (396 for PCBL minus 114 for released NHS), yielding a product with expected molecular weight of 2854. Peak at 2854.9 confirms the product formation.

weight 2573, which is the molecular weight of both the starting material and the photolytic product, was always present in the spectrum, generated by photolysis of the product by the 337 nm laser of the MALDI-TOF instrument. Essentially identical spectra were obtained irrespective of the amount of excess PCBL relative to DNA in the coupling reaction, suggesting that the peak at MW 2573 is due to photocleaved product and not to leftover starting material.

A Model Substrate-Linked RNA Library. For the PCBL to be useful in ribozyme and DNAzyme selections, it must be suitable for tethering potential substrates to a nucleic acid library, followed by releasing the substrate or product after the intended reaction. To this end, the PCBL−DNA conjugate (**8**) was enzymatically ligated to a random-sequence, radiolabeled RNA library (Scheme 2). The 118 nt input RNA and the 126 nt ligated product (**9**) were separately loaded onto a trilayer organomercurial polyacrylamide gel (*13*, *28*) in which the middle layer was doped with *N*-acryloylaminophenylmercuric chloride (APM) (*29*). The strong Hg−S interaction impedes the migration of nucleic acids carrying a free thiol. Because neither of these two input RNAs carries a free thiol, there was no appreciable material retained in the APM layer (lanes 1 and 2 of Figure 3a; columns 1 and 2 of Figure 3b). In contrast, exposing the sulfhydryl by deprotecting compound **9** with hydroxylamine to yield compound **10** resulted in retention of >60% of the input RNA in the APM layer (lane 3 of Figure 3a; column 3 of Figure 3b). PCBL attachment to the 5′ end of the DNA oligo did not affect ligation efficiency of T4 DNA ligase (data not shown). Compound **10** was purified from the APM layer and incubated with thiopropyl-activated Cam **11** (Scheme 3). To minimize the formation of disulfide via spontaneous oxidation, 1 equiv of dithiothreitol (DTT) was added to the RNA pool prior to incubating it with activated Cam. 5 equiv of activated Cam analog was used in the coupling reaction to minimize disulfide reduction of the product by unused DTT. Coupling of Cam to the library was confirmed by loading the product onto a trilayer APM gel. The Cam-coupled library (**12**) no longer carries a free thiol, and it again passed through the APM (lane 4 of Figure 3a; column 4 of Figure 3b). However, when this material was incubated with DTT to reduce the disulfide bond between the linker and the Cam, the free sulfhydryl is regenerated (**10**), and the reduced product was again retained at the APM layer (lane 5 of Figure 3a; column 5 of Figure 3b). Thus, Cam can be attached to an RNA library via ligation of a PCBL-modified oligo and released by reduction with DTT.

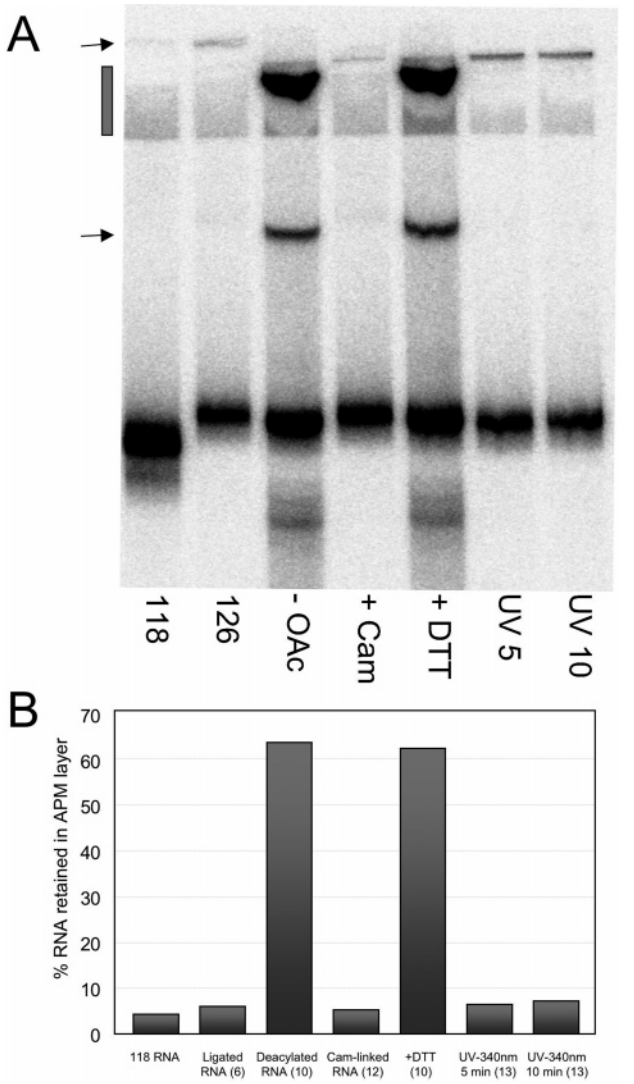


Figure 3. Attachment to, and decoupling from, random-sequence RNA library. (A) Trilayer APM gel of internally radiolabeled RNA treated as described in the text. Top arrow, wells; box, APM layer; bottom arrow, disulfide-oxidized side product. The sulfhydride can be retained in reduced form without interfering with APM electrophoresis by including tris-carboxyethyl phosphine (not shown) (*13*, *28*). (B) Percentage of internally radiolabeled RNA retained in the APM layer is plotted for individual constructs given under each column.

Photocleavage of Pendant from Library. While chemical reduction with DTT is convenient in some circumstances, it is not feasible in cases where the intended selection is based upon acquisition of a new sulfhydryl in the product or where the initial coupling is performed using thioether linkages (reaction with maleimides or iodoacetyl groups) or via interactions with inorganic compounds or surfaces (such as nanoparticles or chip arrays) rather than via a disulfide. Photocleavage is much more convenient in these cases.

To test the photodecoupling efficiency of the linker, compound **10** was purified from the APM layer and irradiated with near-UV light at 360 nm for 5 or 10 min. Decoupling of the *O*-nitrobenzyl moiety from the RNA removes the free sulfhydryl, allowing the RNA (**13**) to migrate through the APM layer. The reaction is complete within 5 min, with no additional product observed after 10 min of irradiation (lanes 6 and 7 of Figure 3a; columns 6 and 7 of Figure 3b). The results are in agreement with previous studies on the time requirements for *O*-nitrobenzyl derivative photocleavage (*16*, *17*).

DISCUSSION

We have successfully synthesized an *O*-nitrobenzyl-containing, photocleavable bifunctional linker (PCBL). This linker enabled coupling an analog of Cam to the 5′ end of an RNA library and its photorelease by near-UV irradiation. Analogs of this small molecule−DNA conjugate can be generated as synthons that are ligated to a nucleic acid diversity library during each round of a ribozyme selection. Alternatively, they could be annealed to immobilized oligonucleotides for chip array analysis. Diverse substrates can be readily coupled to nucleic acid libraries for use in novel nucleic acid enzyme selection using the PCBL. In this context, photochemical release of the tethered product (vs internal products) can be exploited to ensure regiospecific control of the reactions catalyzed by those selected ribozymes. Photocleavable, heterobifunctional crosslinkers such as PCBL and analogous compounds reported previously (*18*) are also highly versatile for applications in proteomics and nanotechnology, as they enable reversible coupling of a wide variety of other combinations of amine-containing species (oligonucleotides, peptides, proteins, fluorophores, and immobilizing agents) with thiol-reactive species (maleimides, iodoacetyl groups, activated disulfides, semiconductor surfaces, and organomercurial compounds and several metallic or semiconductor surfaces) (Figure 1).

ACKNOWLEDGMENT

The authors thank Dr. Rajesh Viswanathan and Dr. Jeffrey N. Johnston for providing the lab space and critical comments on the synthetic scheme of the synthon, and members of the Burke lab for insightful comments on the manuscript. This work was supported by Exobiology Award NAG5-12360 from NASA and by an Interdisciplinary Science Award from the David and Lucille Packard Foundation.

LITERATURE CITED

(1) Astriab-Fisher, A., Sergueev, D. S., Fisher, M., Shaw, B. R., and Juliano, R. L. (2000) Antisense inhibition of P-glycoprotein expression using peptide-oligonucleotide conjugates. *Biochem. Pharmacol. 60*, 83−90.

(2) Kwok, K. Y., Park, Y., Yang, Y., McKenzie, D. L., Liu, Y., and Rice, K. G. (2003) In vivo gene transfer using sulfhydryl cross-linked PEG-peptide/glycopeptide DNA co-condensates. *J. Pharm. Sci. 92*, 1174−85.

(3) McInnes, J. L., and Symons, R. H. (1989) *NucleicAcid Probes*, pp 33−80, CRC, Boca Raton.

(4) Rogers, F. A., Manoharan, M., Rabinovitch, P., Ward, D. C., and Glazer, P. M. (2004) Peptide conjugates for chromosomal gene targeting by triplex-forming oligonucleotides. *Nucleic Acids Res 32*, 6595−604.

(5) Bai, X., Li, Z., Jockusch, S., Turro, N. J., and Ju, J. (2003) Photocleavage of a 2-nitrobenzyl linker bridging a fluorophore to the 5′ end of DNA. *Proc. Natl. Acad. Sci. U.S.A. 100*, 409−13.

(6) Niemeyer, C. M., and Blohm, D. (1999) DNA microarrays. *Angew. Chem. Inter Ed. 38*, 2865−2869.

(7) Wojczewski, C., Stolze, K., and Engels, J. W. (1999) Fluorescent oligonucleotides - Versatile tools as probes and primers for DNA and RNA analysis. *Synlett* 1667−1678.

(8) Seelig, B., and Jaschke, A. (1999) A small catalytic RNA motif with Diels-Alderase activity. *Chem. Biol. 6*, 167−176.

(9) Tarasow, T. M., Tarasow, S. L., and Eaton, B. E. (1997) RNA-catalysed carbon-carbon bond formation. *Nature (London) 389*, 54−57.

(10) Curtis, E. A., and Bartel, D. P. (2005) New catalytic structures from an existing ribozyme. *Nat. Struct. Mol. Biol. 12*, 994−1000.

(11) Jenne, A., and Famulok, M. (1998) A novel ribozyme with ester transferase activity. *Chem. Biol. 5*, 23−34.

(12) Lorsch, J. R., and Szostak, J. W. (1994) In vitro evolution of new ribozymes with polynucleotide kinase activity. *Nature (London) 371*, 31−6.

(13) Saran, D., Nickens, D. G., and Burke, D. H. (2005) A trans acting ribozyme that phosphorylates exogenous RNA. *Biochemistry 44*, 15007−16.

(14) Eisenfuhr, A., Arora, P. S., Sengle, G., Takaoka, L. R., Nowick, J. S., and Famulok, M. (2003) A ribozyme with michaelase activity: synthesis of the substrate precursors. *Bioorg. Med. Chem. 11*, 235−49.

(15) Hausch, F., and Jäschke, A. (2001) Multifunctional dinucleotide analogs for the generation of complex RNA conjugates. *Tetrahedron 57*, 1261−1268.

(16) Bai, X., Kim, S., Li, Z., Turro, N. J., and Ju, J. (2004) Design and synthesis of a photocleavable biotinylated nucleotide for DNA analysis by mass spectrometry. *Nucleic Acids Res. 32*, 535−41.

(17) Olejnik, J., Sonar, S., Krzymanska-Olejnik, E., and Rothschild, K. J. (1995) Photocleavable biotin derivatives: a versatile approach for the isolation of biomolecules. *Proc. Natl. Acad. Sci. U.S.A. 92*, 7590−4.

(18) Yan, F., Chen, L., Tang, Q., and Wang, R. (2004) Synthesis and characterization of a photocleavable cross-linker and its application on tunable surface modification and protein photodelivery. *Bioconjugate Chem. 15*, 1030−6.

(19) Senter, P., Tansey, M., Lambert, J., and WA, B. (1985) Novel photocleavable protein crosslinking reagents and their use in the preparation of antibody-toxin conjugates. *Photochem. Photobiol. 42*, 231−237.

(20) Kaplan, J. H., Forbush, B., 3rd, and Hoffman, J. F. (1978) Rapid photolytic release of adenosine 5′-triphosphate from a protected analogue: utilization by the Na:K pump of human red blood cell ghosts. *Biochemistry 17*, 1929−35.

(21) McCray, J. A., Herbette, L., Kihara, T., and Trentham, D. R. (1980) A new approach to time-resolved studies of ATP-requiring biological systems; laser flash photolysis of caged ATP. *Proc. Natl. Acad. Sci. U.S.A. 77*, 7237−41.

(22) Patchornik, A., Amit, B., and Woodward, R. B. (1970) Photosensitive protecting groups. *J. Am. Chem. Soc. 92*, 6333−6335.

(23) Ottl, J., Gabriel, D., and Marriott, G. (1998) Preparation and photoactivation of caged fluorophores and caged proteins using a new class of heterobifunctional, photocleavable cross-linking reagents. *Bioconjugate Chem. 9*, 143−51.

(24) Ruparel, H., Bi, L., Li, Z., Bai, X., Kim, D. H., Turro, N. J., and Ju, J. (2005) Design and synthesis of a 3′-O-allyl photocleavable fluorescent nucleotide as a reversible terminator for DNA sequencing by synthesis. *Proc. Natl. Acad. Sci. U.S.A. 102*, 5932−7.

(25) Seo, T. S., Bai, X., Ruparel, H., Li, Z., Turro, N. J., and Ju, J. (2004) Photocleavable fluorescent nucleotides for DNA sequencing on a chip constructed by site-specific coupling chemistry. *Proc. Natl. Acad. Sci. U.S.A. 101*, 5488−93.

(26) Cho, S., Lee, S. H., Chung, W. J., Kim, Y. K., Lee, Y. S., and Kim, B. G. (2004) Microbead-based affinity chromatography chip using RNA aptamer modified with photocleavable linker. *Electrophoresis 25*, 3730−9.

(27) Reynolds, G. A., and Hauser, C. R. (1950) O-nitroacetophenone. *Org. Synth. 30*, 70.

(28) Rhee, S. S., and Burke, D. H. (2004) Tris(2-carboxyethyl)-phosphine stabilization of RNA: comparison with dithiothreitol for use with nucleic acid and thiophosphoryl chemistry. *Anal. Biochem. 325*, 137−143.

(29) Igloi, G. L. (1988) Interaction of transfer-RNAs and of phosphorothioate-substituted nucleic-acids with an organomercurial - probing the chemical environment of thiolated residues by affinity electrophoresis. *Biochemistry 27*, 3842−3849.

BC060221F

MARCH/APRIL 2007
Volume 18, Number 2

© *Copyright 2007 by the American Chemical Society*

Bioconjugate Chemistry

COMMUNICATIONS

Poly(vinyl alcohol) Functionalized Poly(dimethylsiloxane) Solid Surface for Immunoassay

Ling Yu,[†] Chang Ming Li,*[,†] Qin Zhou,[†] and John H. T. Luong[‡]

School of Chemical and Biomedical Engineering, Nanyang Technological University, 639798, Singapore, and Nanobiotechnology and Biosensor Group, Biotechnology Research Institute, Canada National Research Council, 6100 Royalmount Avenue, Montreal, Quebec, Canada H4P 2R2. Received April 24, 2006; Revised Manuscript Received January 29, 2007

In this communication, we describe a simple and robust method for the covalent bonding of poly(vinyl alcohol) (PVA) on a silanized poly(dimethylsiloxane) (PDMS) surface. Nonspecific adsorption of proteins via hydrophobic−hydrophobic interactions of the PVA-coated surface is greatly reduced, and biomolecules can be rapidly anchored on the PVA-coated surface with high loading and uniformity. On the basis of a sandwich immunoassay with the anti-rabbit IgG and IgG pair as a model, the detection limit for IgG is down to 1 pg/mL with linearity up to 11 μg/mL, the levels often encountered in biological, forensic, and environmental samples.

Immunoassays performed in polystyrene-based microtiter plates are superior to other heterogeneous solid-phase immunoassays with respect to sensitivity and specificity (*1*). The current trend in analytical sciences is to miniaturize the assay format to reduce the diffusion paths and the cost associated with the reagent consumption. The revolution in microfabrication has been long rooted in the polymer sciences, since the use of polymers has proven to reduce the time, complexity, and cost of prototyping and manufacturing (*2*). Poly(dimethylsiloxane), PDMS, is of particular interest in the fabrication of microfluidics (*3*) since it can be cast in a suitable mold with high fidelity. However, nonspecific interaction between contaminants and hydrophobic PDMS greatly debilitates its potential applications (*4*), i.e., a low signal-to-noise ratio in analytical procedures. Since various factors affect protein adsorption, the surface chemistry of the substrate has been studied most intensively to alleviate nonspecific protein adsorption via a plethora of surface modification procedures. In general, proteins adsorb in higher amounts at hydrophobic than at hydrophilic surfaces owing to hydrophobic interactions between the solid surface and hydrophobic domains in the protein (*5*). In particular, proteins usually give higher adsorption at methylated than at the nonmethylated counterparts. For instance, when glass surfaces are progressively hydrophobized, the adsorbed amount of fibrinogen increases from 2 to ~5 mg/m^2 (*5*). Although proteins often rely on hydrophobic interactions and electrostatic attractions in the nonspecific binding, at most surfaces, the hydrophobic interaction is the governing factor (*5*).

Polymer coatings designed to reduce protein adsorption have been used to modify a variety of polymeric substrates. The hydrophobic part of the polymers is first adsorbed onto the substrate, with the hydrophilic end serving as the barrier for protein adsorption from aqueous solutions. Poly(vinyl alcohol), or PVA, is one of the most hydrophilic polymers with stable

* Corresponding author. ecmli@ntu.edu.sg; Tel: 6567904485.
[†] Nanyang Technological University.
[‡] Canada National Research Council.

10.1021/bc060108p CCC: $37.00 © 2007 American Chemical Society
Published on Web 02/14/2007

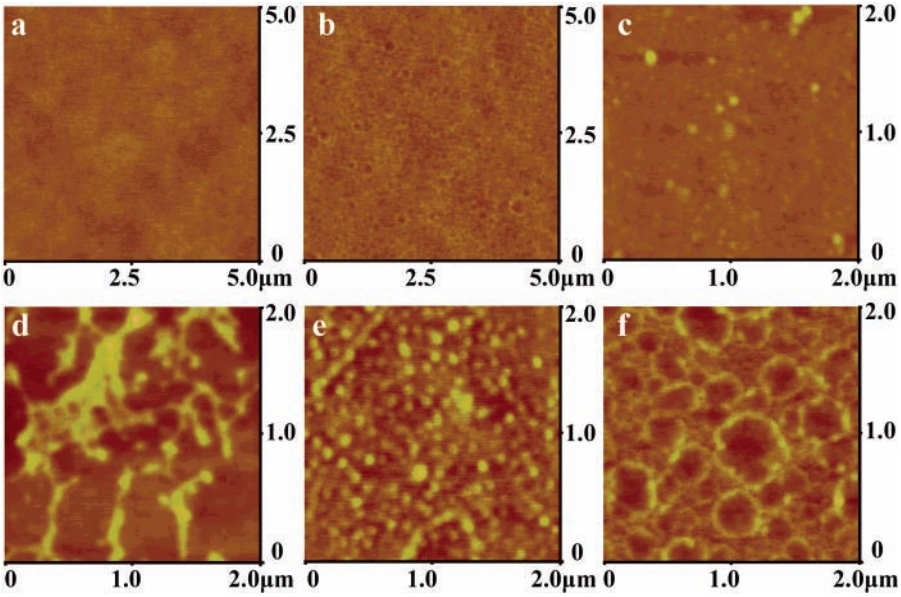


Figure 1. (a) Pristine PDMS. (b) PDMS after modification with PVA. (c) 1% BSA passive adsorption on PVA-modified surface. (d) 1% BSA passive adsorption on pristine PDMS. (e) Covalent immobilization of BSA (1%) on PVA-modified surface. (f) Covalent immobilization of bovine IgM (10 μg/mL) on PVA-modified surface.

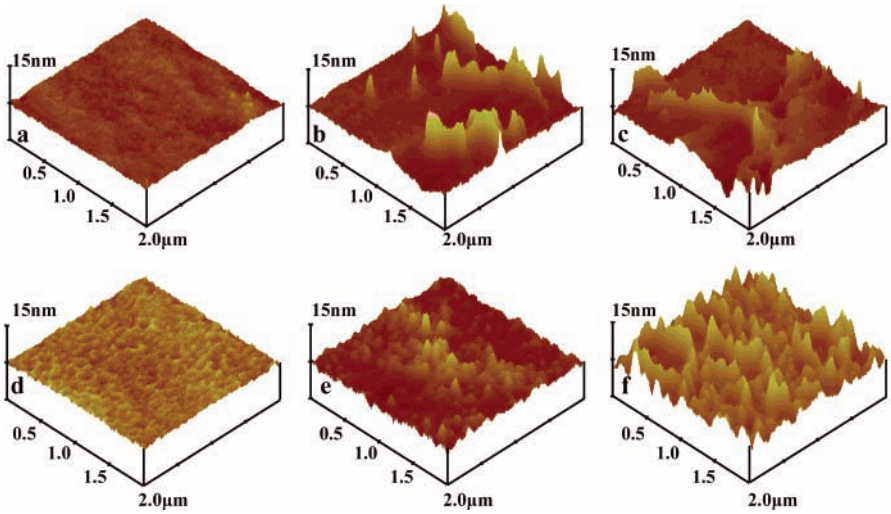


Figure 2. (a) Unmodified PDMS. (b) PDMS after 10 min of incubation with rabbit IgG. (c) After 30 min of incubation with rabbit IgG. (d) PVA-modified PDMS. (e) 10 min after covalent bonding with rabbit IgG. (f) 30 min after covalent bonding with rabbit IgG. In all experiments, the amount of IgG was 112 μg/mL.

chemical properties, good dissolution, and strong adhesion power. PVA can be irreversibly adsorbed on some hydrophobic surfaces, but less significant on PDMS (*6*). In addition, it is very difficult to produce homogeneous PVA films on a hydrophobic surface by adsorption. Nevertheless, PVA can be adsorbed on oxygen plasma treated PDMS, since the resulting surface possesses a highly hydrophilic layer with hydroxyls, silanols, and carboxylic acids. Hydrogen bonding, instead of hydrophobic interaction, is probably the dominant driving force for the PVA adsorption on such a treated PDMS surface (*7*). Notice that the functional groups generated by the oxygen plasma treatment are not stable, particularly in air. Coatings of the nonionic PVA has also proven effective in reducing adsorption of certain proteins (β-lactoglobulin and bovine serum albumin) onto polysulfone surfaces (*8*).

Here, we have prepared and silanized poly(dimethylsiloxane (PDMS) with 3-aminopropyltriethoxysilane (APTES), followed by glutaraldehyde activation to convert the amino groups on the PDMA surface to the aldehyde groups (*9*). PVA was then coupled to the aldehyde groups at pH 1 (Supporting Information). Indeed, this reaction was used by Belder et al. (*6a*) in an attempt to cross-link this polymer during the coating process and thus immobilize it into fused silica capillary in order to modify the electroosmosis flow.

In our preparation, PVA cross-linking did not occur, since only one aldehyde group was available from the bifunctional aldehyde. Therefore, we reasoned that PVA formed a firm hydrophilic layer on the glutaraldehyde-activated PDMS surface. The procedure was rapid with high coupling efficiency as discussed later by probing the morphological changes by AFM. Pristine PDMS probed by AFM exhibited a smooth, featureless, and continuous surface with a corresponding contact angle of 101.8°. After the treatment with PVA, the contact angle decreased to 71.5° and the morphology of PDMS changed from a flat feature to a surface dominated by circles (Figure 1a,b). The decrease of the contact angle was due to the hydroxyl groups of PVA immobilized on PDMS after the cross-linking process. As the crystalline PVA is characterized by doubly hydrogen bonded alcohols, the lower contact angle suggests that PVA is highly disordered and less capable of ordering or crystallizing. PVA is an atactic material but exhibits crystallinity, as the hydroxyl groups are small enough to fit into the lattice

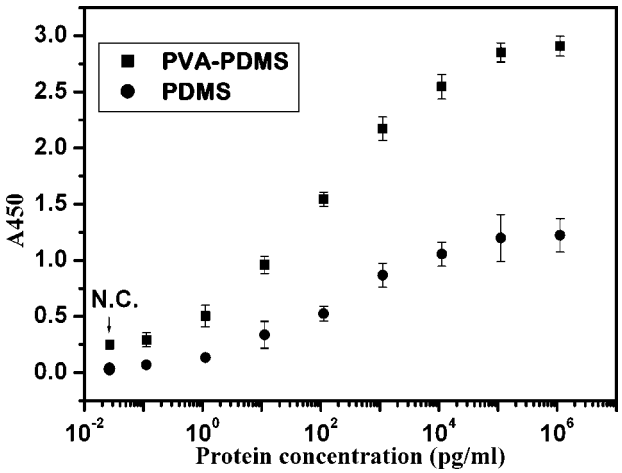


Figure 3. Sandwich ELISA results on PVA-modified PDMS and pristine PDMS.

without disrupting it. Regarding the protein nonspecific adsorption, only an insignificant amount of bovine serum albumin (BSA) or immunoglobulin was adsorbed by the PVA-modified PDMS surface (Figure 1c). In contrast, unmodified PDMS exhibited a drastic change in morphology after its exposure to such proteins, indicative of nonspecific adsorption via hydrophobic−hydrophobic interaction (Figure 1d). Such data confirmed that the modification of PDMS with PVA suppressed protein adsorption and reduced nonspecific bonding, although the immobilized surface was not totally hydrophilic, as confirmed by the value of the measured contact angle. This might be attributed to the blocking reagent application after the probe immobilization on the PVA−PDMS surface, which could not be applicable on a PDMS surface that solely relies on hydrophobic nonspecific bindings for probe immobilization. Rafati et al. (*10*) studied the interactions of a homologous series of cationic surfactants with BSA and reported that the hydrophobic interactions play an important role in the BSA-surfactant binding, whereas electrostatic interactions play only a minor one.

The PVA-modified PDMS surface was then reacted with one aldehyde group of glutaraldehyde, whereas the second aldehyde became available for coupling with bovine IgM or BSA (Supporting Information). It should be noted that glutaraldehyde might cross-link two adjacent PVA chains or even react with two hydroxyls of the same PVA molecule. Therefore, the reaction was performed with excess glutaraldehyde to ensure the availability of abundant aldehydes for the subsequent bimolecular attachment. As shown in Figure 1e, BSA (67 kDa), as represented by small dots with an average diameter of 100 nm, was distributed rather evenly on the surface. The obtained data were in agreement with the FESEM micrograph performed at low accelerating voltage (5 kV), which provided comparable resolution to conventional SEM performed at 15−25 kV (Figure S1, Supporting Information). Notice also that, with prolonged FESEM testing, PDMS is undergoing a noticeable distortion under the vacuum condition, and the twisted PDMS covers up the entire surface of the adsorbed protein. Bovine IgM (900 kDa) consists of five subunits of a Y-shaped immunoglobulin structure (900 kDa). The covalent bonding of this circular protein resulted in much larger circles; presumably, the protein was linked to the PVA backbone (Figure 1f).

AFM morphological changes were then used to monitor the kinetics of protein immobilization. The protein immobilization by covalent binding at the PVA-modified surface was completed within 30 min with an even distribution across the modified surface. In contrast, the amount of protein adsorbed nonspecifically by unmodified PDMS was much lower, and the protein distribution was nonuniform (Figure 2). A sandwich immunoassay was then conducted using the PVA-modified PDMS to anchor anti-rabbit IgG via the glutaraldehyde-activated surface for the detection of rabbit IgG. HRP-conjugated anti-rabbit IgG formed a tertiary complex with the anti IgG−IgG pair and was detected spectrophotometrically (Supporting Information). The detection range of the PVA-modified PDMS substrate was 1.12 pg/mL to 11.2 μg/mL (Figure 3), significantly wider than the unmodified PDMS surface (112 pg/mL to 11.2 μg/mL). The detection limit is also much lower than the reported value of 15 ng/mL immunoglobulins on non-PVA-treated PDMS (*11*). Together with AFM imaging, our results revealed that the PVA-modified substrate provided uniformly distributed aldehyde groups at the backbone of PVA. High densities of such functional groups coupled with the hydrophilic property of PVA led to the capture of a high amount of antibody, i.e., improved detection sensitivity as well as reduced false positive response. The tendency to capture the protein nonspecifically by unmodified PDMS resulted in a higher detection limit. Such results were not completely unexpected, since the binding sites of protein/antibody are mostly located in the hydrophobic domain and are no longer available for a target binding because of their preoccupied association with PDMS.

In brief, this communication describes a simple but effective technique to suppress nonspecific adsorption toward the development of a solid-phase material for immunoassay. Hydrophobicity of PDMS can be silanized with APTES followed by PVA coating and glutaraldehyde activation. Biomolecules can be covalently attached to the modified surface with even distribution. The application of the PVA-functionalized surface in sandwich ELISA results in excellent detection sensitivity (1 pg/mL) and linearity up to 11.2 μg/mL with negligible nonspecific protein adsorption.

Besides hydrophobic−hydrophobic interaction, nonspecific protein adsorption is affected by several factors such as protein properties (size, charge, shape, composition, and pH), surface properties (charge, chemistry, and topology), coadsorption of low-molecular-weight ions, intermolecular forces between adsorbed molecules, and strength of functional group bonds (*12*). Therefore, work is in progress to extend the applicability of the PVA-modified PDMS materials for immunoassays for pathogens with significant impact on clinical, environmental, and food monitoring. The prevention of nonspecific protein adsorption can also be exploited in many areas to enhance the performance and function of the materials including bioreactors, affinity chromatography, materials for cell colonization, and biosensors.

ACKNOWLEDGMENT

The author thanks Dr. Yu Shu Chong for conducting the FESEM experiment. The work is financially funded by Center for Advanced Bionanosystems, Nanyang Technological University.

Supporting Information Available: Experimental procedures, preparation of PDMS−PVA solid substrates, characterization of nonspecific adsorption (passive adsorption), sandwich ELISA assay, and AFM and field emission scanning electron microscopy (FESEM) micrographs. This material is available free of charge via the Internet at http://pubs.acs.org.

LITERATURE CITED

(1) (a) Hagiwara, K., Kitajima, K., Yamanaka, H., Kirisawa, R., and Iwai, H. (2004) Development of a sandwich ELISA assay for measuring bovine soluble type II IL-1 receptor (IL1R2) concentration in serum and milk. *Cytokine 32* (3−4), 132−136. (b) Li, C. M.,

Chen, W., and Yang, X. (2005) Impedance labeless detection-based polypyrrole protein biosensor. *Front. Biosci. 10*, 2518−2526.

(2) (a) Xia, Y., McClelland, J. J., Gupta, R., Qin, D., Zhao, X. M., Sohn, L. L., Celotta, R. J., and Whitesides, G. M. (1997) Replica molding using polymeric materials: a practical step toward nanomanufacturing. *Adv. Mater. 9*, 147−149. (b) Fogarty, B. A., Heppert, K. E., Cory, T. J., Hulbutta, K. R., Martin, R. S., and Lunte, S. M. (2005) Electrophoresis devices using CO_2 laser ablation. *Analyst 130* (6), 924−930.

(3) (a) McDonald, J. C., and Whitesides, G. M. (2002) Covalent micropatterning of poly(dimethylsiloxane) by photografting through a mask. *Acc. Chem. Res. 35* (7), 491−499. (b) Bao, N., Zhang, Q., Xu, J. J., and Chen, H. Y. (2005) Fabrication of poly(dimethylsiloxane) microfluidic system based on masters directly printed with an office laser printer. *J. Chromatogr., A 1089* (1−2), 270−275. (c) Wu, H., Odom, T. W., Chiu, D. T., and Whitesides, G. M. (2003) Fabrication of complex three-dimensional microchannel systems in PDMS. *J. Am. Chem. Soc. 125* (2), 554−559.

(4) (a) Hu, S., Ren, X., Bachman, M., Sims, C. E., Li, G. P., and Allbritton, N. L. (2004) Surface-directed, graft polymerization within microfluidic channels. *Anal. Chem. 76* (7), 1865−1870. (b) Lahann, J., Balcells, M., Lu, H., Rodon, T., Jensen, K. F., and Langer, R. (2003) Reactive polymer coatings: a first step toward surface engineering of microfluidic devices. *Anal. Chem. 75* (9), 2117−2122. (c) Yu, L., Li, C. M., and Zhou, Q. (2005) Efficient probe immobilization on poly (dimethylsiloxane) for sensitive detection of proteins. *Front. Biosci. 10*, 2848−2855.

(5) Holmberg, K. (2002) Control of protein adsorption at surfaces. In *Encyclopedia of Surface and Colloid Science* (Hubbard, Ed.) pp 1242, New Dekker Encyclopedia, Taylor−Francis, New York.

(6) (a) Belder, D., Deege, A., Husmann, H., Kohler, F., and Ludwig, M. (2001) Cross-linked poly(vinyl alcohol) as permanent hydrophilic column coating for capillary electrophoresis. *Electrophoresis 22*, 3813−3818. (b) Kozlov, M., Quarmyne, M., Chen, W., and McCarthy, T. J. (2003) Adsorption of poly(vinyl alcohol) onto hydrophobic substrates. A general approach for hydrophilizing and chemically activating surfaces. *Macromolecules 36*, 6054−6059.

(7) Wu, D., Luo, Y., Zhou, X., Dai, Z., and Lin, B. (2005) Multilayer poly(vinyl alcohol)-adsorbed coating on poly(dimethylsiloxane) microfluidic chips for biopolymer. *Electrophoresis 26* (1), 211−218.

(8) Bearinger, J. P., Castner, D. G., Golledge, S. L., Rezania, A., Hubchak, S., and Healy, K. E. (1997) P(AAm-co-EG) interpenetrating polymer networks grafted to oxide surfaces: surface characterization, protein adsorption, and cell detachment studies. *Langmuir 13*, 5175−5183.

(9) Weetall, H. (1976) Covalent coupling methods for inorganic support materials. *Methods Enzymol. 44*, 134−148.

(10) Rafati, A. A., Bordbar, A.-K., Gharibi, H., Amini, M.-K., and Safarpour, M.-A. (2004) The interaction of a homologous series of cationic surfactants with bovine serum albumin (BSA) studied using surfactant membrane selective electrodes. *Bull. Chem. Soc. Jpn. 77*, 1111−1116.

(11) Eteshola, E., and Balberg, M. (2004) Microfluidic ELISA: on-chip fluorescence imaging. *Biomed. Microdevices 6* (1), 7−9.

(12) (a) Andrade, J. D., and Hlady, V. (1986) Protein adsorption and materials biocompatibility - a tutorial review and suggested hypotheses. *Adv. Polym. Sci. 79*, 1−63. (b) Sadana, A. (1992) Protein adsorption and inactivation on surfaces. Influence of heterogeneities. *Chem. Rev. 92*, 1799−1818.

BC060108P

One-Pot Synthesis, Purification, and Formulation of Bionanoparticle−CpG Oligodeoxynucleotide Hepatitis B Surface Antigen Conjugate Vaccine via Tangential Flow Filtration

Krishnaswami Raja,*,† Ross McDonald,‡ Stephen Tuck,*,‡ Roberto Rodriguez,‡ Bob Milley,*,‡ and Paula Traquina‡

Department of Chemistry, The Institute for Macromolecular Assemblies, Center for Engineered Polymeric Materials, City University of New York at the College of Staten Island, 2800 Victory Boulevard, Staten Island, New York 10314, and DYNAVAX Technologies, 2929 Seventh Street, Suite 100, Berkeley, California 94710. Received May 5, 2006; Revised Manuscript Received December 1, 2006

The synthesis and characterization of a Hepatitis B virus vaccine (HBsIC−ISS) candidate composed of Hepatitis B surface antigen (HBsAg) bionanoparticles conjugated to multiple copies of immunostimulatory sequence oligodeoxynucleotides is presented. An efficient tangential flow filtration (TFF) method has been developed to purify the conjugated bionanoparticles from the excess conjugation reagents. The TFF technique presented can serve as a rapid and convenient alternative to current methods like ultracentrifugation for the separation of excess small molecule/polymeric conjugation reagents from chemically modified viruses and other viruslike particles.

The branch of bionanotechnology in which naturally occurring biomacromolecular assemblies are modified and manipulated for biomedical and material science applications is a newly emerging field of research (*1*−*4*). A few biomacromolecular assemblies like viruses and protein cages such as ferritin have been recently used as reactors for biomineralization (*3*−*5*) and as nanoscaffolds for the polyvalent display of small molecules (*6*, *7*) and synthetic polymers (*8*−*10*) Future applications and breakthroughs in the field will depend on the conjugation of novel functional polymers and ligands to biomacromolecular assemblies and the development of efficient purification methods for producing these conjugates. In this paper, we have used recombinant Hepatitis B surface antigen (HBsAg) as a nanoscaffold for polyvalent display (clinical-grade HBsAg is composed of a mixture of bionanoparticles and small aggregates of particles formed by the spontaneous self-assembly of 100−150 copies of 25.4 KD recombinant protein subunits) (*11*). HBsAg is a therapeutically relevant protein and has one covalently accessible lysine residue that can be modified with lysine-specific reagents; each protein subunit has fourteen cysteines and one lysine. The current commercial hepatitis B virus (HBV) vaccine consists of HBsAg adsorbed to alum which acts as an adjuvant. The current vaccine is preventive and requires three immunizations over 6 months. Immunostimulatory sequence oligodeoxynucleotides (ISS) are synthetic CpG DNA sequences that mimic the immunostimulatory effects of bacterial DNA (*12*). We have shown that ISS (5-TGACTGTGAACGTTCGAGATGA-3) noncovalently mixed with HBsAg serves as a potent adjuvant, and the resulting improved preventive HBV vaccine provides protective HBsAg-specific antibody titers in humans after two immunizations over a 2 month period (*13*). The covalent linkage of multiple copies of ISS to HBsAg could produce a more potent HBV vaccine. In this communication, we present the conjugation, purification (using tangential flow filtration), and characterization of a potentially therapeutic polyvalent HBsIC−ISS vaccine. Tangential flow filtration (TFF) is a pressure-driven separation technique that utilizes size-selective ultrafiltration (UF) membranes or hollow fibers to separate molecules in solution on the basis of differences in size (23). Molecular species larger than the pore size of the membrane are retained by the membrane and recirculate in the retentate loop of the TFF system (retentate fraction); molecules smaller than the pores sieve through under applied pressure and are removed from the sample and the system via the filtrate (permeate fraction) (*14*−*16*). Tangential flow filtration has been previously used to purify excess poly(vinyl alcohol) from nanoparticle dispersions generated from poly(lactide-*co*-glycolide) and poly(vinyl alcohol) (*14*). TFF has also been used to purify viruses such as influenza virus and adenovirus from host cell proteins and DNA, to concentrate viruses, and to purify virus particles from large host cell fragments (*15*,*16*). To the best of our knowledge, this is the first time TFF has been used to purify chemically modified bionanoparticles from excess bioconjugation reagents.

The synthesis of HBsIC−ISS was a challenging problem, since clinical-grade HBsAg (Green Cross Vaccine Corporation) was supplied at a low concentration for bioconjugation (1 mg/mL). The conjugation process we first adopted was to block any free cysteine residues present on HBsAg with an excess of *N*-ethyl maleimide (NEM) (see Scheme 1, **1b**). This was followed by activation of lysine residues using sulfosuccinimidyl-4-(*N*-maleimidomethyl)cyclohexane-1-carboxylate (sulfo-SMCC). This reaction modified the amino acid side chains of L-lysine residues and produced a particle polyvalently displaying maleimide groups (Scheme 1, **1c**). The excess reagents were removed by chromatography on a G-25 desalting column (GE Biosciences, Piscatway, NJ). 5′-Disulfide-linked phosphorothioate ISS (TGACTGTGAACGTTCGAGATGA-3′) was reduced with 200 mM Tris-(2-carboxyethyl)phosphine (TCEP) at room temperature for 1 h, and the residual reagents were removed by chromatography on a G-25 desalting column to produce 5′-thio-ISS. Since the concentration of **1c** was too low for effective conjugation to 5′-thio-ISS, the sample was concentrated by

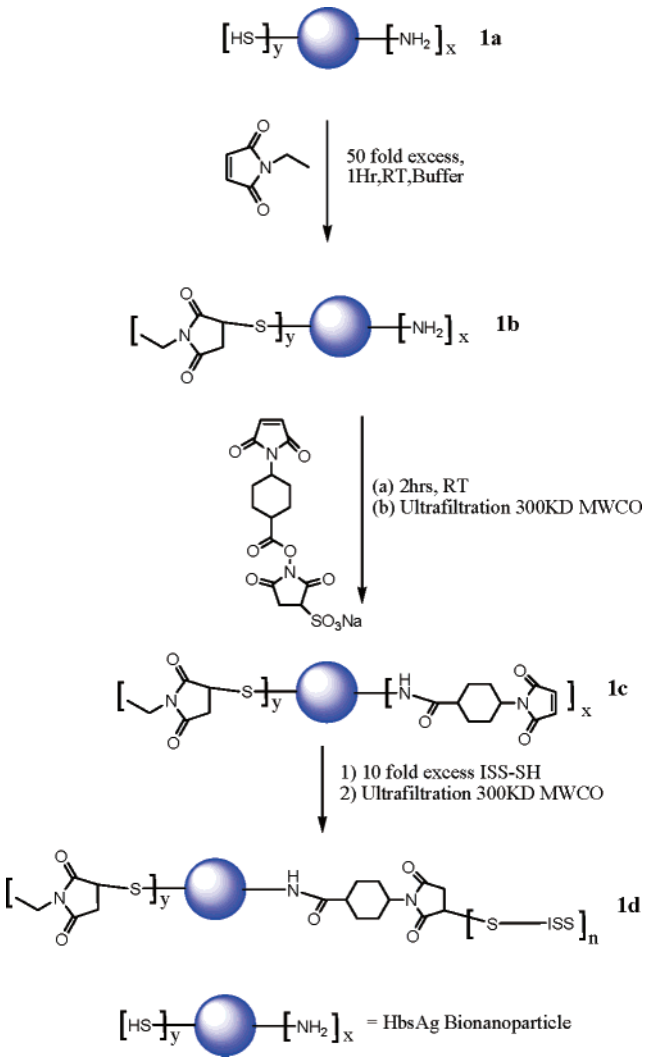
* Corresponding authors. K.R.: E-mail: raja@mail.csi.cuny.edu, Tel: 718-982−4091, Fax: 718-982−3091. S.T.; B.M.: E-mail: stuck@dvax.com, bmilley@dvax.com; Tel: 510-848−5100, Fax: 510-848−1327.

† City University of New York at the College of Staten Island.

‡ DYNAVAX Technologies.

10.1021/bc060118q CCC: $37.00 © 2007 American Chemical Society
Published on Web 02/16/2007

Scheme 1. Synthesis of HBsAg Conjugate withISS (HBsIC-ISS)



centrifugation using a centricon filter; this caused precipitation and loss of sample. The remaining concentrated sample of **1c** was conjugated to 5′-thio-ISS. After conjugation, the excess 5′-thio-ISS was removed using a Superdex HR 200 30/10 column (GE Biosciences, Piscatway, NJ) to produce the final product HBsIC−ISS (Scheme 1, **1d**). The process described above is inefficient; the overall yield for the process was very low (∼20%), and the final concentration of the product was less than 0.2 mg/mL.

To overcome these limitations, we developed a tangential flow filtration (TFF)-based process. HBsIC−ISS conjugate was synthesized and then purified via the TFF process in accordance with the steps described below and summarized in Scheme 1. The cysteine residues of HBsAg (**1a**) were capped with an excess of *N*-ethyl maleimide (NEM) to produce (**1b**). The lysine residues of **1b** were activated with excess sulfosuccinimidyl-4-(*N*-maleimidomethyl)cyclohexane-1-carboxylate (sulfo-SMCC) to produce the maleimide-labeled bionanoparticles (**1c**). Sample **1c** was conjugated with 5′-thio-ISS to produce the final conjugated product HBsIC−ISS (**1d**) (see Supporting Information). We employed a 300 kDa molecular weight cutoff cellulose membrane to retain the large nanoparticles (**1c** and **1d**) in the sample vessel (retentate fraction) (Figure 1A). Excess reagents DMSO, NEM, and sulfo-SMCC were separated from the maleimide-labeled HBsAg particle via the filtrate (permeate fractions) during constant volume diafiltration (Figure 1).

The same diafiltration process was performed after conjugation of the maleimide-labeled HBsAg with polymeric ISS (7500

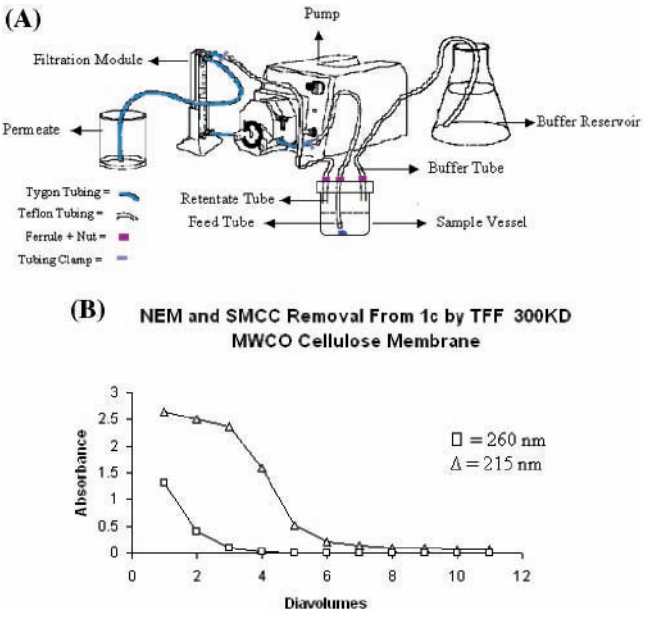


Figure 1. (A) Tangential flow filtration (TFF) setup for one-pot synthesis, purification, and formulation of conjugated HBsAg and ISS (HBsIC−ISS). (B) NEM and sulfo-SMCC removal from HBsAg−sulfoSMCC conjugate by TFF using a PXC300C50 300 kDa MWCO cellulose membrane monitored at △ = 215 nm and □ = 60 nm. The Pellicon XL picture is courtesy of Millipore Corporation.

MW) in order to remove excess 5′-thio-ISS. The extent of removal of small molecules was monitored by measuring the UV spectra of the permeate fractions at 215 nm and 260 nm after each diavolume (1 diavolume = volume of reaction mixture) (Figure 1B). The removal of unconjugated ISS was also similarly monitored (see Supporting Information). Over ∼99% removal of excess conjugation reagents was achieved in less than 1 h. The buffer used in the ISS removal step was in-house formulation buffer (PBS, pH 7.4). The final formulated vaccine was tested for endotoxin content and used for preclinical experiments. Vaccines are formulated in a buffer which is physiologically compatible; in this TFF step, both ISS purification and formulation were achieved simultaneously. The fact that 20 nm particles were retained by the 300 kDa MWCO TFF membrane was previously confirmed by performing a system qualification experiment using 20 nm green nanobeads (absorbance maximum 466 nm) as a model for HBsAg in the sample reservoir.

The overall yield of HBsIC−ISS (**1d**) was determined by a Lowry-based assay using a Biorad, Inc., DC assay kit for proteins to be 77% (see Supporting Information). The fact that the presence of DNA does not affect the DC assay was previously confirmed using a noncovalent mix of **1a** and ISS (Dynavax Technologies, unpublished results). Overall yields of HBsIC−ISS were ∼80%; in contrast, yields by conventional G25 desalting chromatography were considerably lower at ∼20% (Rodriguez, R., unpublished results). In our TFF experiment, the concentration of the final conjugated product (**1d**) was 0.9 mg/mL. This is quite remarkable because the starting concentration of the surface antigen (**1a**) was 1 mg/mL. In contrast, the conventional chromatographic approach produced HBsIC−ISS at less than 0.2 mg/mL concentration; the additional concentration step in the chromatographic approach was time-consuming and resulted in a reduced yield.

The conjugate HBsIC−ISS (**1d**) was characterized by capillary zone electrophoresis (CZE). CZE separates sample components on the basis of differences in mass/charge ratio (see Supporting Information). The highly charged conjugated product HBsIC−ISS (**1d**) eluted very early as a narrow peak at 3.7 min,

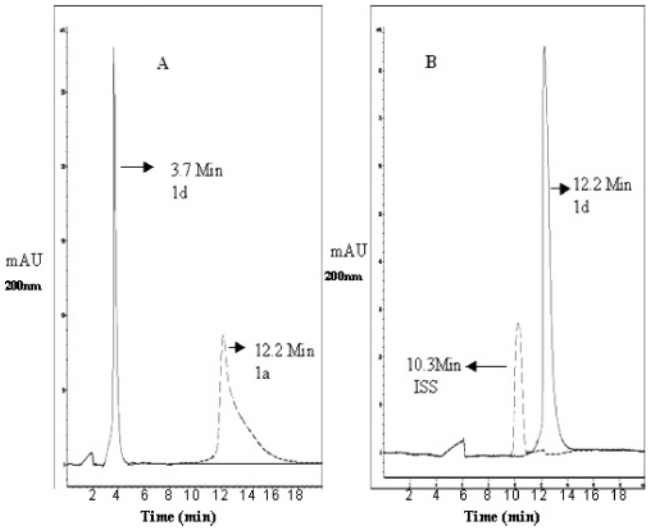


Figure 2. Capillary zone electrophoresis. (A) Separate injections of HBsIC−ISS conjugate and starting surface antigen HBsAg. (B) Separate injections of HBsIC−ISS conjugate 1d and starting 5-thio-ISS−oligodeoxy nucleotide.

and the relatively uncharged HBsAg (**1a**) eluted as a broad peak at 12.2 min (Figure 2A). A second CZE method was employed to clearly distinguish between the starting ISS and the conjugate HBsIC−ISS (**1d**) (Figure 2B).

The oligodeoxynucleotide concentration in HBsIC−ISS was determined by measuring the UV spectrum of the DNA component of the conjugate after subtracting the absorbance contribution from the protein; the validity of this approach was established by performing suitable control experiments (see Supporting Information). The oligodeoxynucleotide/protein subunit ratio in the conjugate HBsIC−ISS (**1d**) was determined to be 1/1. The modification of HBsAg by oligodeoxynucleotide (in the case of **1d**) was also confirmed by HPLC. In our HPLC experiments, we observed that the ratio of the absorbance at 215 nm to the absorbance 260 nm (A_{215}/A_{260} ratio) (using a Phenomenex BioSEp-SEC-3000 column) was more sensitive to the presence of ISS conjugated to the protein than if we used an A_{280}/A_{260} ratio. The HBsAg control sample (**1a**) and the HBsIC−ISS conjugated product (**1d**) eluted at the void volume due to their large size; the peak areas at 215 nm and 260 nm were integrated (see Supporting Information). The A_{215}/A_{260} ratios were 13.1 for the HBsAg control sample (**1a**) and 5.9 for the HBsIC−ISS sample (**1d**), indicating the presence of oligodeoxynucleotide in the conjugate. This reduced A_{215}/A_{260} ratio for the HBsIC−ISS conjugate suggests that several copies of oligodeoxynucleotide are attached to HBsAg particles; this ratio was very consistent among different batches of conjugate synthesized.

Preliminary light scattering characterization for HBsAg (**1a**) and HBsIC−ISS (**1d**) using a PSS NICOMP ZLS particle sizing system provided mean diameters of 30 nm for HBsAg (**1a**) and 40 nm for the conjugate HBsIC−ISS (**1d**), respectively (see Supporting Information). The size of recombinant HBsAg has previously been determined in the literature to be 27.5 nm using high-resolution transmission electron microscopy (*17*).

Transimssion electron microscroscopy of the HBsIC−ISS conjugate (**1d**) confirms the intact nature of the conjugated particles (see Supporting Information for TEM of **1d**).

The SEC chromatogram of HBsAg (**1a**) (Figure 3) indicates a bimodal distribution. The conjugate (**1d**) chromatogram was shifted to a slightly lower retention time (higher MW); although bimodal, the molecular weight distribution was narrower than that of unmodified HBsAg (Figure 3A). The bimodal nature of the SEC chromatogram of the clinical-grade HBsAg control sample and the HBsIC−ISS conjugate is ascribed to the presence of individual particles and small aggregates of particles. The intact nature of the particles after conjugation can be inferred from the following facts: (a) The retention times in the SEC chromatogram for both the surface antigen (commercially obtained intact particles) and the conjugate **1d** are similar, indicating that both of them are of approximately the same size. (b) The conjugate (**1d**) is retained by a 300 kDa molecular weight cutoff TFF membrane (if the particle had disassembled

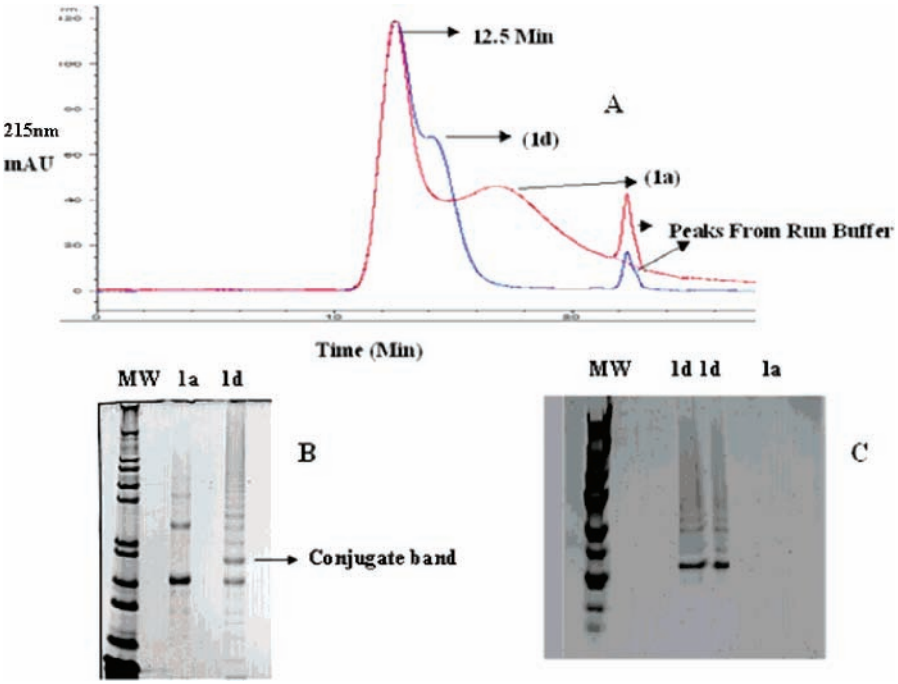


Figure 3. Characterization of HBsAg (1a) and HBsIC−ISS conjugate (1d). (A) Size-exclusion HPLC. (B) SDS PAGE analysis using Mark 12 as the molecular weight standards (MW), visualized with gel code blue protein stain; the arrow denotes the shifted band of the ISS-modified monomeric protein subunit (1d). (C) SDS PAGE analysis using Bio-Rad Blue molecular weight standards (MW), visualized with a DNA-specific silver stain kit; HBsAg (1a) which has no DNA is not visible. The DNA modified protein bands in the conjugate is visible (1d).

during conjugation, the 25.4 kDa subunits produced would be too small to be retained by the 300 kDa MWCO membrane), and (c) the preliminary light scattering data suggest sizes of ~30 nm for unmodified HBsAg (**1a**) and ~40 nm for the HBsIC−ISS conjugate (**1d**) (see Supporting Information). (d) TEM images of the HBsIC−ISS conjugate **1d** clearly indicate intact particles (see Supporting Information).

The samples were analyzed by denaturing gel electrophoresis. HBsIC−ISS conjugate (**1d**) displayed an additional band at 32 KD (Figure 3B) that corresponds to monomeric protein subunit modified by one ISS, and there are additional faint bands corresponding to ISS-modified protein multimers (a protein-specific stain was used to stain the gel shown in Figure 3b). The modification of HBsAg with ISS (DNA) in the conjugate product was further confirmed by using a DNA-specific silver stain (Figure 3C). The starting HBsAg (**1a**) was not visible, because it lacks DNA. In contrast, the ISS modified protein bands in the conjugate HBsIC−ISS (**1d**) were clearly visible (Figure 3C). The presence of faint high molecular weight protein bands observed in the SDS PAGE gels of clinical-grade HBsAg control and HBsIC−ISS conjugate is possibly due to disulfide cross-links between cysteine residues from protein subunits (each subunit has 14 cysteine residues).

The rapid TFF-based approach we present here is bound to be generally applicable in the separation of a wide range of conjugated nanoparticles from small molecules/polymer reagents and will be useful in the areas of nanomedicine and material science. The advantages of TFF over other methods of separation are that TFF is a very rapid process; a synthesis, purification, and formulation can be performed within a few hours in a single reaction vessel. The standard method of purification of bionanoparticles from excess conjugation reagents is ultracentrifugation over sucrose gradients, pelleting, and resuspension of the conjugate. This is a multistep 2 day process and requires expensive equipment (*4*−*7*) In the specific application of separating nanoparticles from small molecules/polymers, the vast difference in size between the entities makes TFF an efficient and high-yield technique. TFF is a scaleable method allowing aseptic processing; sample volumes of milliliters up to hundreds of liters could be easily processed with inexpensive equipment. Furthermore, unlike using dialysis or chromatography, TFF allows concentration of samples when run in the concentration mode. This method would be the equivalent of "flash chromatography" in contrast to "regular column chromatography" for the virus/protein cage-based chemistry community.

The biological activity of the HBsIC−ISS vaccine in mice indicates that it generates robust immune responses (antibody, Interferon-γ, and Cytotoxic T Lymphocyte); a detailed study of the biological activity is currently underway and will be reported in the future. A similar polyvalent display of ISS on other bionanoparticles like the human papilloma virus (HPV) antigen could lead to an improved vaccine against HPV infection.

ACKNOWLEDGMENT

We thank Dr. Gary Ott for many valuable discussions regarding the project.

Supporting Information Available: Synthesis, tangential flow filtration, DC protein concentration determination for HBsIC−ISS, ISS content determination for HBsIC−ISS, HPLC determination of the A_{215}/A_{260} ratio, capillary zone electrophoresis, size exclusion HPLC, SDS-PAGE, preliminary light scattering data, and transmission electron microscopy. This material is available free of charge via the Internet at http://pubs.acs.org.

LITERATURE CITED

(1) Raja, K. S., and Wang, Q. (2004) Bionanoparticles. In *Encyclopedia of Nanoscience and Nanotechnology* (James A. S., Contescu, C., and Putyera, K., Eds.) pp 331−330, Marcel Dekker, New York.
(2) Vriezema, D. M., Aragones, M. C., Elemans, J. A. A. W., Cornelissen, J. J. L. M., Rowan, A. E., and Nolte, R. J. M. (2005) Self-assembled nanoreactors. *Chem. Rev. 105* (4), 1445−1489.
(3) Douglas, T., and Young, M. (1998) Host-guest encapsulation of materials by assembled virus protein cages. *Nature (London) 393* (6681), 152−155.
(4) Douglas, T., and Young, M. (2006) Viruses: making friends with old foes. *Science 312* (5775), 873−875.
(5) Douglas, T., Strable, E., Willits, D., Aitouchen, A., Libera, M., and Young, M. (2002) Protein engineering of a viral cage for constrained nanomaterials synthesis. *Adv. Mater. 14* (6), 415−418.
(6) Wang, Q., Lin, T., Tang, L., Johnson, J. E., and Finn, M. G. (2002) Icosahedral virus particles as addressable nanoscale building blocks. *Angew. Chem., Int. Ed. 41* (3), 459−462.
(7) Raja, K. S., Wang, Q., and Finn, M. G. (2003) Icosahedral virus particles as polyvalent carbohydrate display platforms. *ChemBioChem 4* (12), 1348−1351.
(8) Raja, K. S., Wang, Q., Gonzalez, M. J., Manchester, M., Johnson, J. E., and Finn, M. G. (2003) Hybrid virus−polymer materials. 1. Synthesis and properties of PEG-decorated cowpea mosaic virus. *Biomacromolecules 4* (3), 472−476.
(9) Gupta, S. S., Raja, K. S., Kaltgrad, E., Strable, E., and Finn, M. G. (2005) Virus-glycopolymer conjugates by copper(I) catalysis of atom transfer radical polymerization and azide-alkyne cycloaddition. *Chem. Commun.* (34), 4315−4317.
(10) Schlick, T. L., Ding, Z., Kovacs, E. W., and Francis, M. B. (2005) Dual-surface modification of the tobacco mosaic virus. *J. Am. Chem. Soc. 127* (11), 3718−3723.
(11) Schirmbeck, R., and Reimann, J. (2001) Revealing the potential of DNA-based vaccination: lessons learned from the hepatitis B virus surface antigen. *Biol. Chem. 382*, 543−552.
(12) Klinman, D. M. (2004) Immunotherapeutic uses of CpG oligodeoxynucleotides. *Nat. Rev. Immunol. 4*, 249−259.
(13) Halperin, A. S., Nest, G. V., Smith, B., Abtahi, S., Whiley, H., and Eiden, J. J. (2003) A phase I study of the safety and immunogenicity of recombinant hepatitis B surface antigen co-administered with an immunostimulatory phosphorothioate oligonucleotide adjuvant, *Vaccine 21*, 2461−2467.
(14) Dalwadi, G., Benson, H. A. E., and Chen, Y. Comparison of diafiltration and tangential flow filtration for purification of nanoparticle suspensions (2005) *Pharm. Res. 22* (12), 2152−2162.
(15) Wickramasinghe, S. R., Kalbfuss, B., Zimmermann, A., Thom, V., and Reichl, U. (2005) Tangential flow microfiltration and ultrafiltration for human influenza A virus concentration and purification, *Biotechnol. Bioeng. 92* (2), 199−208.
(16) Morenweiser, R. (2005) Downstream processing of viral vectors and vaccines, *Gene Ther. 12*, S62−S72.
(17) Yamaguchi, M., Sugahara, K., Shiosaki, K., Mizokami, H., and Takeo, K. (1998) Fine structure of hepatitis B virus surface antigen produced by recombinant yeast: comparison with HBsAg of human origin. *FEMS Microbiol. Lett. 165* (2), 363.

BC060118Q

Triple-Helix Mediated Excimer and Exciplex Formation

Ivan Trkulja and Robert Häner*

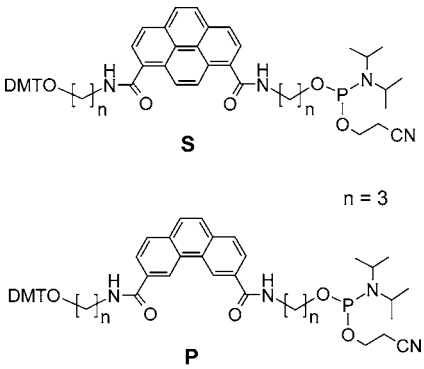
Department of Chemistry and Biochemistry, University of Bern, Freiestrasse 3, CH-3012 Bern, Switzerland. Received October 20, 2006

The synthesis and properties of triple-helical hybrids containing non-nucleosidic polyaromatic building blocks are described. Clamp-type oligonucleotides containing a non-nucleosidic pyrene linker form stable triple helices with a polypurine target strand containing a terminal pyrene or phenanthrene moiety. Stacking interactions between the unnatural building blocks enhance triplex stability and lead to strong excimer or exciplex formation, which is monitored by fluorescence spectroscopy.

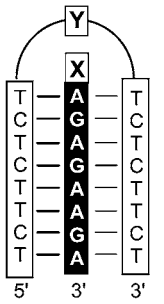
The formation of triple-helical structures is a well-documented feature of nucleic acids (*1*−*6*). Although generally limited to homopurine/homopyrimidine regions, triplex formation is of interest as a method of targeting DNA with high selectivity (*7*−*11*). In particular, synthetic oligonucleotides have been shown to adopt clamp-type motifs (*12*−*21*) in which a single-stranded homopurine strand is recognized by an oligonucleotide through simultaneous formation of Watson−Crick and Hoogsteen bonds. Aromatic linkers have also been used as loop replacements in clamps to tether the Watson−Crick and the Hoogsteen bond-forming strands of a DNA triplex (*22*, *23*). Recently, we reported the synthesis and properties of non-nucleosidic, polyaromatic building blocks and their incorporation into DNA (*24*, *25*). Interstrand stacking of such polyaromatic building blocks was subsequently shown by excimer formation (*26*) of pyrenes placed in opposite positions (*27*, *28*). The fluorescence properties of pyrene building blocks render them valuable for structural studies of the resulting oligomers and the hybrids they form (*29*−*34*). The strength of excimer formation as well as the ratio between excimer and monomer is determined by overall structure and, most importantly, the distance between the pyrene molecules. As part of our research, we designed chemically and structurally stable mimics of a triple helical structure that would bring the pyrenes and/or other aromatic moieties into a favorable position for excimer or exciplex formation. The approach makes use of a clamp-type oligomer that, upon binding to a homopurine strand, brings the two aromatic structures in close proximity. Here, we report the formation and spectroscopic properties of clamp-based triple helices with oligonucleotides containing pyrene- and phenanthrene-derived building blocks.

The synthesis of the pyrene and phenanthrene phosphoramidites **S** and **P** (Scheme 1) was performed as described (*24*, *27*). The building blocks were further used for the preparation of the oligomers **1**, **2**, and **3** by automated oligonucleotide synthesis. Incorporation of the pyrene and phenanthrene monomers proceeded with coupling yields comparable to those of the unmodified nucleotide phosphoramidites. The obtained oligomers were purified by reverse-phase HPLC and characterized by mass spectrometry (see Supporting Information). Oligonucleotides **4** and **5** were used for control purposes. Hybridization of the clamp oligonucleotides (**1** or **5**) with either of the homopurine strands (**2** to **4**) results in formation of a triple helix as illustrated in Scheme 1.

Scheme 1. Phosphoramidite Building Blocks and Pyrene- or Phenanthrene-Modified Oligonucleotides Used in This Study[a]



1 5′ TCT TCTCT **S** TCTCT TCT
2 3′ AGAAGAGA **S**
3 3′ AGAAGAGA **P**
4 3′ AGAAGAGA
5 5′ TCT TCTCT$(T)_6$TCTCT TCT



X = **S** or **P**, or (-)

Y = **S** or $(T)_6$

[a] Schematic representation of triplex formation between clamps **1** or **5** and targets **2**−**4** (for simplicity, **S** and **P** are used for both phosphoramidites as well as incorporated building blocks; DMT = 4,4′-dimethoxytrityl).

Thermal denaturation experiments revealed a strong influence of the modifications on the stability of the triple helical complex at pH 5.0 and 7.0 (Table 1). In comparison to the control triplex (**4*****5**), a slight increase in stability (ΔT_m approximately 4 °C) is observed upon introduction of a pyrene moiety (**S**) in the loop of clamp **1** observed in its complex with **4**. This increase is comparable with the one observed for phenanthrene-containing hairpin structures containing this type of building block as loop replacement (*35*). A considerably larger increase (ΔT_m = 8.6 and 10.2 °C at pH 5.0 and 7.0, respectively) in stability is found, however, when a pyrene residue is present (triplex **1*****2**). A further substantial rise in structural stability (ΔT_m = 12.8 and 17.3 °C) results from introduction of a phenanthrene modification at the 5′-end of the homopurine target strand (triplex **1*****3**). For all hybrids, a single transition was observed in the melting diagrams. Also, as expected, lower pH favors the stability of all triple helices.

The large increase in the T_m observed for all pyrene- or phenanthrene-modified hybrids is most likely the result of

* Author to whom correspondence should be addressed. Fax +41 31 631 8057; E-mail robert.haener@ioc.unibe.ch.

10.1021/bc0603283 CCC: $37.00 © 2007 American Chemical Society
Published on Web 02/20/2007

Table 1. T_m Values of Pyrene and Phenanthrene-Modified Triple Helices[a]

	pH 5.0[b]		pH 7.0[c]	
	T_m[d] [°C]	ΔT_m[e] [°C]	T_m[d] [°C]	ΔT_m[e] [°C]
1*2	55.3	8.6	33.2	10.2
1*3	59.5	12.8	40.3	17.3
1*4	50.5	3.8	27.8	4.8
4*5	46.7		23.0	

[a] Conditions: oligomer concentration 1.0 μM, 100 mM NaCl, 20 mM $MgCl_2$, temperature gradient: 0.5 °C/min. [b] 10 mM sodium acetate buffer. [c] 10 mM sodium cacodylate buffer. [d] Melting temperatures were determined from the maximum of the first derivative of the melting curve (A_{260} against temperature); exptl error: ±0.5 °C. [e] Difference in T_m relative to that of control triplex **4*5**.

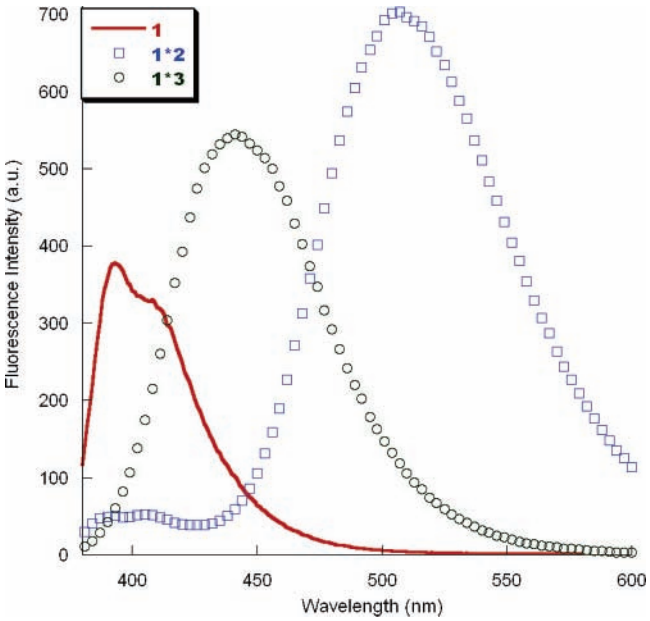


Figure 1. Fluorescence spectra of pyrene- and phenanthrene-containing triplexes **1*2** and **1*3**, as well as of the oligonucleotide **1**. Conditions: oligomer concentration 1.0 μM, 10 mM acetate buffer, 100 mM NaCl, 20 mM $MgCl_2$, pH 5.0, 25 °C. Excitation wavelength, 356 nm; excitation slit, 10 nm; emission slit, 5 nm.

favorable stacking interactions between two pyrenes (**S**/**S**) or pyrene and phenanthrene (**S**/**P**), respectively. This implies that the aromatic systems are in a favorable position for excimer and exciplex formation upon excitation, and the interactions of the aromatic residues should, thus, be observable by fluorescence spectroscopy (Figure 1). Upon excitation at 356 nm, oligonucleotide **1** shows pyrene monomer fluorescence (approximately 380−420 nm). For hybrid **1*2**, strong pyrene excimer fluorescence is observed at 500 nm. Only traces of emission at 394 nm are observed in this hybrid, indicating very efficient excimer formation. The change from monomer to excimer fluorescence is in close analogy to the findings obtained with duplex formation by pyrene-containing oligonucleotides (*27*). Surprisingly, a very strong signal with maximum intensity at 437 nm was observed for hybrid **1*3**, which can be attributed to formation of an exciplex between pyrene and phenanthrene. The high intensity of the pyrene/phenanthrene exciplex fluorescence is remarkable. Phenanthrene is known to form exciplexes with amino-substituted aromatic hydrocarbons (*36*, *37*), but to our knowledge, exciplex formation between phenanthrene and pyrene has not been described (*38*). The formation of the exciplex in hybrid **1*3** is also noteworthy in light of the interest in exciplex formation as a tool for genetic diagnostics (*39*).

Temperature-dependent fluorescence spectroscopy was carried out to monitor the change of emission at 394 nm and 500 nm

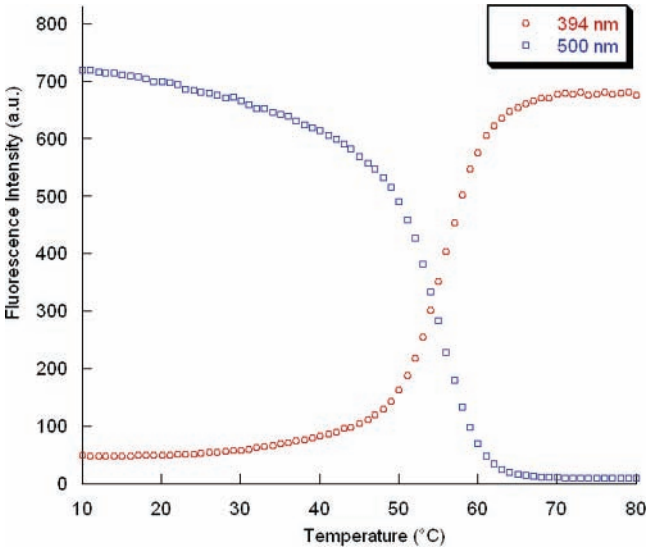


Figure 2. Temperature-dependent fluorescence measurements for triplex **1*2**; 80 °C to 10 °C at 0.5 °C /min; conditions: see Figure 1. T_m values: 55.9 °C (394 nm); 55.5 °C (500 nm).

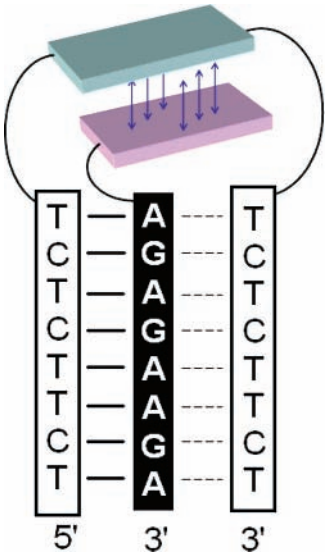


Figure 3. Illustration of triplex formation between a homopyrimidine oligonucleotide and a homopurine target strand, both modified with polyaromatic building blocks.

for hybrid **1*2** at pH 5.0 (Figure 2). Upon formation of the triple helix (80 °C to 10 °C), monomer emission decreases and excimer fluorescence increases simultaneously. The shape of the curves is coherent with the UV−Vis thermal denaturation curves, and the T_m values are in close agreement to the ones calculated from the thermal denaturation experiments monitored by UV absorbance (difference in the values is <1 °C).

Similar data were also obtained for the **1*3** hybrid by monitoring the exciplex fluorescence at 437 nm and at different pH values (see Supporting Information). This provides additional evidence that excimer or exciplex formation proceeds in close connection to the formation of the triplex helix between the oligonucleotide clamp **1** and homopurine sequences **2** and **3**, respectively. Upon association of the strands, the pyrene modification in the loop is brought in close contact to the pyrene or phenanthrene modification at the 5′-end of the homopurine strand (illustrated in Figure 3). This positioning enables the formation of an excited dimer or complex. At higher temperatures, as the strands dissociate, the excimer or exciplex fluorescence disappears and the monomer fluorescence increases.

The data show that stable triple-helix formation is possible with clamp-type oligonucleotides containing a non-nucleosidic pyrene linker. The pyrene strongly interacts with aromatic residues (pyrene or phenanthrene) attached to the target strand, resulting in a considerable increase in the T_m values (up to 17 °C at pH 7.0 against an 8-mer target strand). Pyrene−phenanthrene interactions have a more pronounced stabilizing effect than pyrene−pyrene interaction in the present system. The interactions can be monitored by fluorescence spectroscopy. Strong pyrene excimer or pyrene−phenanthrene exciplex emission is observed below the melting temperature of the hybrids. At room temperature, monomer fluorescence is completely absent, which underlines the close and tight association of the aromatic building blocks. In light of the biological relevance of the triple helix (*40*), mimics of the kind described here may serve as chemically and structurally stable analogues of naturally occurring structures. Introduction of unnatural building blocks not only increases chemical and structural stability but at the same time also leads to the generation of a fluorescent signal.

ACKNOWLEDGMENT

Financial support by the Swiss National Science Foundation (grant 200020-109482) is gratefully acknowledged.

Supporting Information Available: Experimental procedures, analytical data for modified oligomers, fluorescence spectra, and thermal denaturation curves are included. This material is available free of charge via the Internet at http://pubs.acs.org/BC.

LITERATURE CITED

(1) Felsenfeld, G., Davies, D. R., and Rich, A. (1957) Formation of a 3-stranded polynucleotide molecule. *J. Am. Chem. Soc. 79*, 2023−2024.

(2) Le Doan, T., Perrouault, L., Praseuth, D., Habhoub, N., Decout, J. L., Thuong, N. T., L'homme, J., and Hélène, C. (1987) Sequence-specific recognition, photo-cross-linking and cleavage of the DNA double helix by an oligo-[alpha]-thymidylate covalently linked to an azidoproflavine derivative. *Nucl. Acids Res. 15*, 7749−7760.

(3) Moser, H. E., and Dervan, P. B. (1987) Sequence-specific cleavage of double helical DNA by triple helix formation. *Science 238*, 645−650.

(4) Frank-Kamenetskii, M. D., and Mirkin, C. M. (1995) Triplex DNA structures. *Annu. Rev. Biochem. 64*, 65−95.

(5) Roberts, R. W., and Crothers, D. M. (1992) Stability and properties of double and triple helices - dramatic effects of RNA or DNA backbone composition. *Science 258*, 1463−1466.

(6) Häner, R., and Dervan, P. B. (1990) Single-strand DNA triple-helix formation. *Biochemistry 29*, 9761−9765.

(7) Hélène, C., and Toulmé, J. J. (1990) Specific regulation of gene expression by antisense, sense and antigene nucleic acids. *Biochim. Biophys. Acta 1049*, 99−125.

(8) Maher, L. J., III (1992) DNA Triple-helix formation - an approach to artificial gene repressors. *Bioessays 14*, 807−815.

(9) Maher, L. J., III (1996) Prospects for the therapeutic use of antigene oligonucleotides. *Cancer Invest. 14*, 66−82.

(10) Fox, K. R. (2000) Targeting DNA with triplexes. *Curr. Med. Chem. 7*, 17−37.

(11) Buchini, S., and Leumann, C. J. (2003) Recent improvements in antigene technology. *Curr. Opin. Chem. Biol. 7*, 717−726.

(12) Xodo, L. E., Manzini, G., and Quadrifoglio, F. (1990) Spectroscopic and calorimetric investigation on the DNA triplex formed by d(CTCTTCTTTCTTTTCTTTCTTCTC) and d(GAGAAGAAAGA) at acidic pH. *Nucl. Acids Res. 18*, 3557−3564.

(13) Giovannangeli, C., Thuong, N. T., and Hélène, C. (1993) Oligonucleotide clamps arrest DNA-synthesis on a single-stranded-DNA target. *Proc. Natl. Acad. Sci. U.S.A. 90*, 10013−10017.

(14) Kandimalla, E. R., and Agrawal, S. (1994) Single-strand-targeted triplex formation: stability, specificity and RNase H activation properties. *Gene 149*, 115−121.

(15) Ryan, K., and Kool, E. T. (1998) Triplex-directed self-assembly of an artificial sliding clamp on duplex DNA. *Chem. Biol. 5*, 59−67.

(16) Maksimenko, A. V., Volkov, E. M., Bertrand, J. R., Porumb, H., Malvy, C., Shabarova, Z. A., and Gottikh, M. B. (2000) Targeting of single-stranded DNA and RNA containing adjacent pyrimidine and purine tracts by triple helix formation with circular and clamp oligonucleotides. *Eur. J. Biochem. 267*, 3592−3603.

(17) Phipps, A. K., Tarkoy, M., Schultze, P., and Feigon, J. (1998) Solution structure of an intramolecular DNA triplex containing 5-(1-propynyl)-2′-deoxyuridine residues in the third strand. *Biochemistry 37*, 5820−5830.

(18) Durand, M., Peloille, S., Thuong, N. T., and Maurizot, J. C. (1992) Triple-helix formation by an oligonucleotide containing one (dA)-12 and 2 (dT)12 sequences bridged by 2 hexaethylene glycol chains. *Biochemistry 31*, 9197−9204.

(19) Bartley, J. P., Brown, T., and Lane, A. N. (1997) Solution conformation of an intramolecular DNA triplex containing a non-nucleotide linker: comparison with the DNA duplex. *Biochemistry 36*, 14502−14511.

(20) Avino, A., Frieden, M., Morales, J. C., de la Torre, B. G., Garcia, R. G., Azorin, F., Gelpi, J. L., Orozco, M., Gonzalez, C., and Eritja, R. (2002) Properties of triple helices formed by parallel-stranded hairpins containing 8-aminopurines. *Nucl. Acids Res. 30*, 2609−2619.

(21) Nadal, A., Eritja, R., Esteve, T., and Pla, M. (2005) "Parallel" and "antiparallel tail-clamps" increase the efficiency of triplex formation with structured DNA and RNA targets. *Chembiochem 6*, 1034−1042.

(22) Bevers, S., Schutte, S., and McLaughlin, L. W. (2000) Naphthalene- and perylene-based linkers for the stabilization of hairpin triplexes. *J. Am. Chem. Soc. 122*, 5905−5915.

(23) Salunkhe, M., Wu, T. F., and Letsinger, R. L. (1992) Control of folding and binding of oligonucleotides by use of a nonnucleotide linker. *J. Am. Chem. Soc. 114*, 8768−8772.

(24) Langenegger, S. M., and Häner, R. (2002) The effect of a non-nucleosidic phenanthrene building block on DNA duplex stability. *Helv. Chim. Acta 85*, 3414−3421.

(25) Langenegger, S. M., and Häner, R. (2005) A DNA mimic made of non-nucleosidic phenanthrene building blocks. *ChemBioChem 6*, 2149−2152.

(26) Winnik, F. M. (1993) Photophysics of preassociated pyrenes in aqueous polymer-solutions and in other organized media. *Chem. Rev. 93*, 587−614.

(27) Langenegger, S. M., and Häner, R. (2004) Excimer formation by interstrand stacked pyrenes. *Chem. Commun.* 2792−2793.

(28) Langenegger, S. M., and Häner, R. (2006) Selectivity in DNA interstrand-stacking. *Bioorg. Med. Chem. Lett. 16*, 5062−5065.

(29) Mayer-Enthart, E., and Wagenknecht, H. A. (2006) Structure-sensitive and self-assembled helical pyrene array based on DNA architecture. *Angew. Chem., Int. Ed. 45*, 3372−3375.

(30) Nakamura, M., Ohtoshi, Y., and Yamana, K. (2005) Helical pyrene-array along the outside of duplex RNA. *Chem. Commun.* 5163−5165.

(31) Michel, J., Bathany, K., Schmitter, J. M., Monti, J. P., and Moreau, S. (2002) New ligand combinations for the efficient stabilization of short nucleic acid hairpins. *Tetrahedron 58*, 7975−7982.

(32) Dioubankova, M. N., Malakhov, A. D., Stetsenko, D. A., Gait, M. J., Volynsky, P. E., Efremov, R. G., and Korshun, V. A. (2003) Pyrenemethyl ara-uridine-2′-carbamate: A strong interstrand excimer in the major groove of a DNA duplex. *Chembiochem 4*, 841−847.

(33) Fujimoto, K., Shimizu, H., and Inouye, M. (2004) Unambiguous detection of target DNAs by excimer-monomer switching molecular beacons. *J. Org. Chem. 69*, 3271−3275.

(34) Kashida, H., Asanuma, H., and Komiyama, M. (2006) Insertion of two pyrene moieties into oligodeoxyribonucleotides for the efficient detection of deletion polymorphisms. *Chem. Commun.* 2768−2770.

(35) Stutz, A., Langenegger, S. M., and Häner, R. (2003) Phenanthrene-derived DNA hairpin mimics. *Helv. Chim. Acta 86*, 3156−3163.

(36) Cao, H., Miyata, K., Tamura, T., Fujiwara, Y., Katsuki, A., Tung, C. H., and Tanimoto, Y. (1997) Effects of high magnetic field on the intramolecular exciplex fluorescence of chain-linked phenanthrene and dimethylaniline. *J. Phys. Chem. A 101*, 407−411.

(37) Tanimoto, Y., Hasegawa, K., Okada, N., Itoh, M., Iwai, K., Sugioka, K., Takemura, F., Nakagaki, R., and Nagakura, S. (1989) Magnetic-field effects on the intramolecular and intermolecular exciplex fluorescence of phenanthrene and dimethylaniline. *J. Phys. Chem. 93*, 3586−3594.

(38) Phenanthrene is a notable exception among the aromatic hydrocarbons because it forms excimers only under very special circumstances, see, e.g.: Nakamura, Y., Yamazaki, T., and Nishimura, J. (2005) synthesis and fluorescence spectra of oxa[3.*n*]-phenanthrenophanes. *Org. Lett. 7*, 3259−3262. Chandross, E. A., and Thomas, H. T. (1972) Excited dimer luminescence of pairs of phenanthrene molecules. *J. Am. Chem. Soc. 94*, 2421−2424. Lewis, F. D., and Burch, E. L. (1996) Excimer fluorescence from phenanthrene-9-carboxylate derivatives. *J. Photochem. Photobiol. A: Chem. 96*, 19−23.

(39) Bichenkova, E. V., Savage, H. E., Sardarian, A. R., and Douglas, K. T. (2005) Target-assembled tandem oligonucleotide systems based on exciplexes for detecting DNA mismatches and single nucleotide polymorphisms. *Biochem. Biophys. Res. Commun. 332*, 956−964.

(40) Zain, R., and Sun, J. S. (2003) Do natural DNA triple-helical structures occur and function in vivo? *Cell. Mol. Life Sci. 60*, 862−870.

BC0603283

Supplementary Information to:

Triple Helix Mediated Excimer and Exciplex Formation

Ivan Trkulja and Robert Häner*

Department of Chemistry and Biochemistry, University of Bern

Freiestrasse 3, CH-3012 Bern, Switzerland

(phone: +41 31 631 4382; e-mail: robert.haener@ioc.unibe.ch)

Experimental Section

Oligonucleotide Synthesis. Pyrene-derived phosphoramidite building block **S** and Phenanthrene-derived building block **P** were incorporated into oligonucleotides *via* standard automated oligonucleotide synthesis (ABI 394 DNA/RNA Synthesizer) using I_2/pyridine/water in the oxidation step. Coupling yields with **S** and **P** were comparable to the ones obtained with standard phosphoramidite building blocks. Average per-step-yield was between 95 and 97% for modified oligonucleotides. Oligonucleotides were purified by reverse phase HPLC and characterized by MS (Table 1). Unmodified oligonucleotides **4** and **5** were obtained from *Microsynth AG* (Balgach, Switzerland).

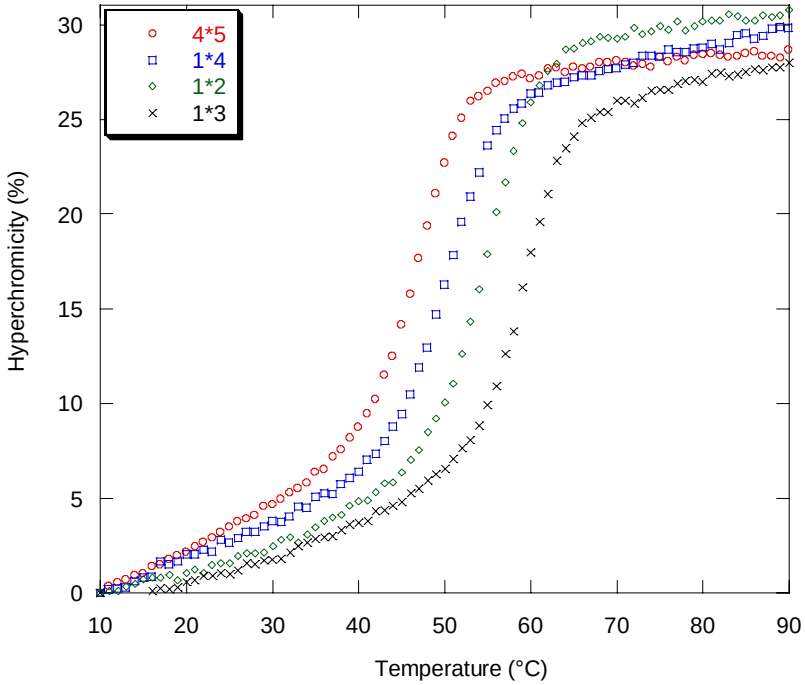
Thermal Denaturation Experiments. A *Varian Cary 3e* UV/Vis spectrophotometer equipped with a *Peltier* block temperature-controller and Varian *WinUV* software were used to determine the melting curves at 260nm, a heating-cooling-heating cycle in the temperature range 10-90ºC was applied with a temperature gradient of 0.5ºC min^{-1}. The data were collected and analyzed with *KaleidaGraph* software from Synergy Software. T_m values were determined as the maximum of the first derivative of the melting curve. Each T_m shown is the average the second (cooling) and third (heating) curve of three independent experiments; experimental error ± 0.5 ºC.

Table 1 suppl.: Molecular weight of oligonucleotides used in this study (electrospray ionisation time-of-flight, ESI-TOF, *VG Platform single quadrupole ESI-MS*).

oligonucleotide	calculated for $(M-H)^-$	found
1	5180.6	5180.6
2	2957.1	2957.2
3	2933.7	2934.1

Figure 1 suppl.: Melting curves of different triplex hybrids. Conditions: Oligomer concentration 1.0µM, 100mM NaCl, 20mM $MgCl_2$, pH 5.0 sodium acetate buffer (10mM), pH 7.0 sodium cacodylate buffer (10mM); temp. gradient: 0.5°C/min. Exptl. error: ± 0.5°C. Absorbance was measured at 260nm. **A**) triplexes **1*2, 1*3, 1*4** and **4*5** at pH 5.0, **B**) triplexes **1*2, 1*3, 1*4** and **4*5** at pH 7.0; cooling curves (90°C to 10°C) are shown.

A)



B)

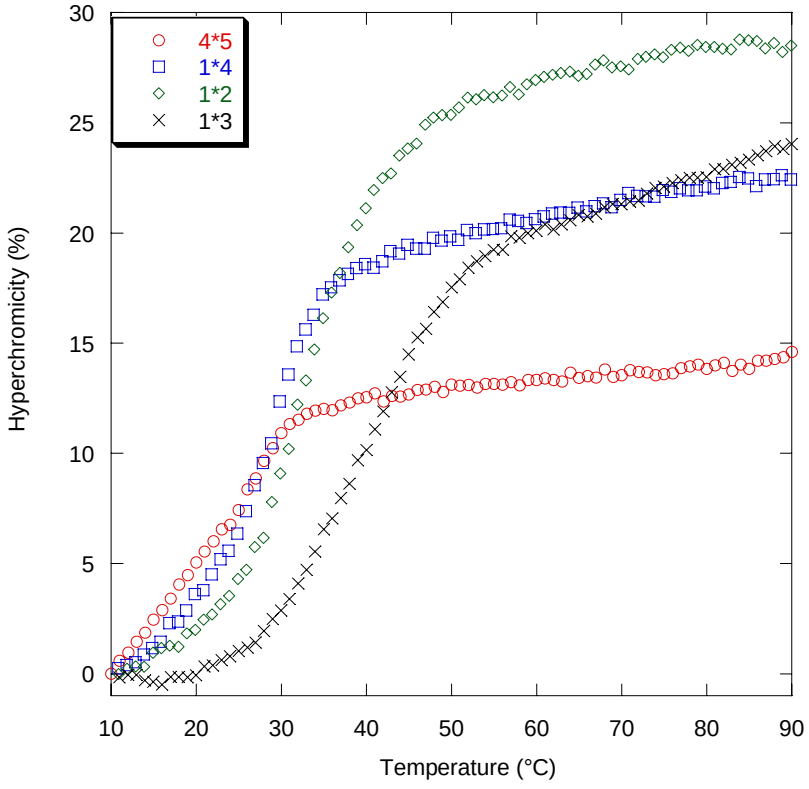
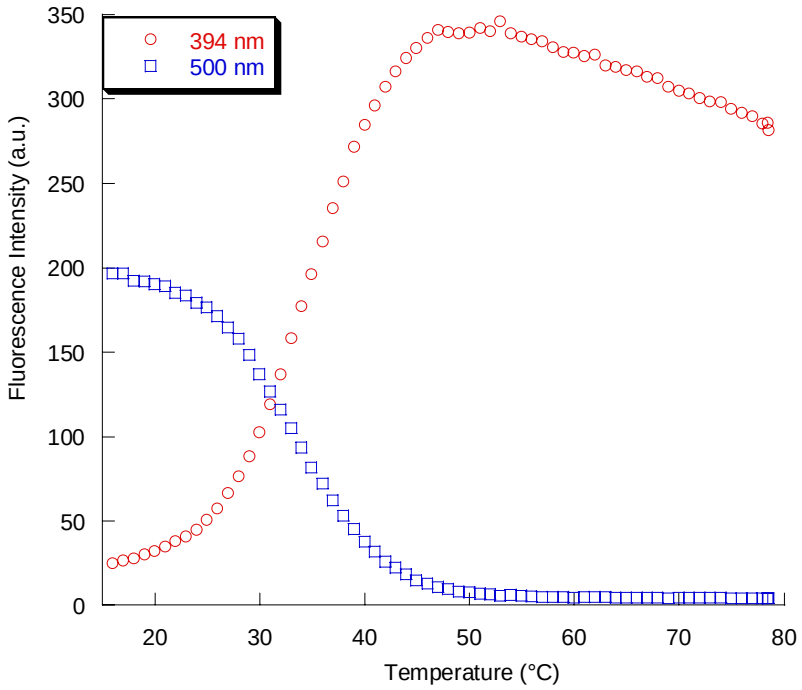
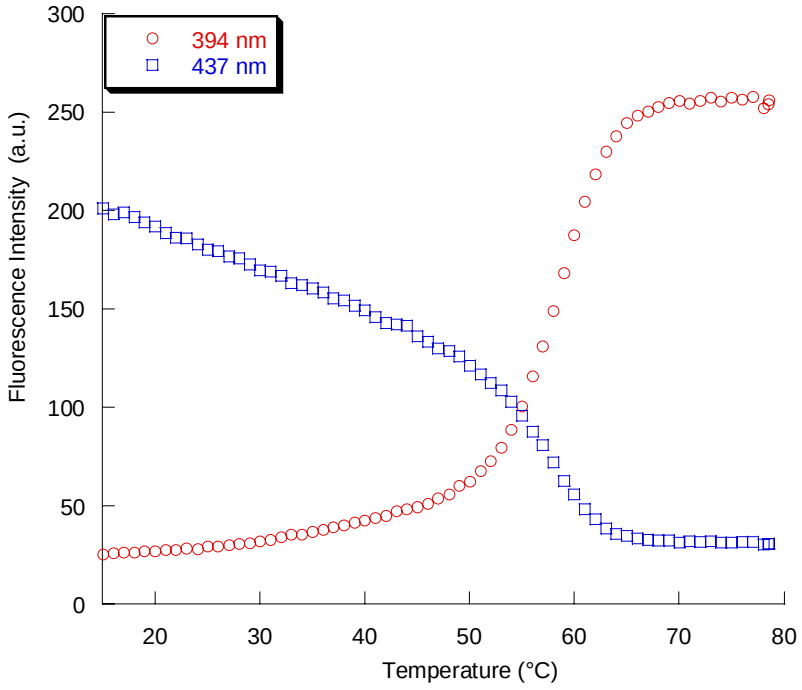


Figure 2 suppl: Temperature dependent fluorescence measurements of different triplex hybrids. Conditions: Oligomer concentration 1.0µM, l, 100mM NaCl, 20mM $MgCl_2$, pH 5.0 acetate buffer (10mM), pH 7.0 sodium cacodylate buffer (10mM). A) Triplex **1*****2**, pH = 7.0; Tm values: 34.2°C (394nm); 33.3°C (500nm). B) Triplex **1*****3**, pH 5.0, Tm values: 59.6°C (394nm); 58.8°C (437nm). C) Triplex **1*****3** pH 7.0, Tm values: 41.5°C (394nm); 36.0°C (437nm).

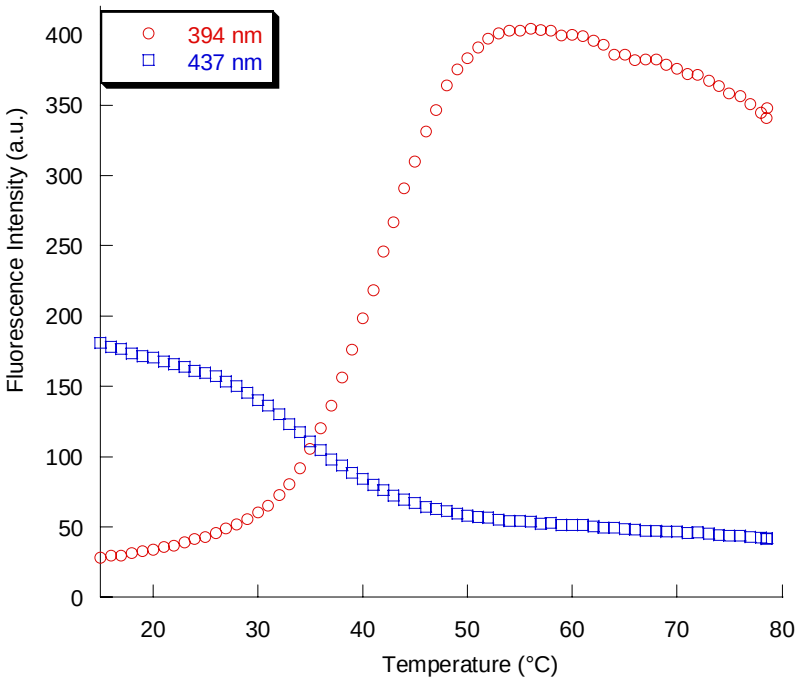
A)



B)



C)


394 nm
437 nm
Fluorescence Intensity (a.u.)
0
50
100
150
200
250
300
350
400
20
30
40
50
60
70
80
Temperature (°C)

Acidic Hydrolysis of *N*-Ethoxybenzylimidazoles (NEBIs): Potential Applications as pH-Sensitive Linkers for Drug Delivery

Seong Deok Kong,[†] Alice Luong,[†] Gerald Manorek,[‡] Stephen B. Howell,[‡] and Jerry Yang*,[†]

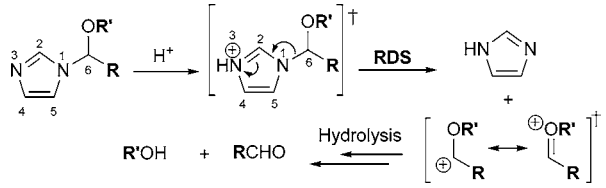
Department of Chemistry and Biochemistry, University of California, San Diego, 9500 Gilman Drive, La Jolla, California 92093-0358, and Department of Medicine and the Rebecca and John Moores Cancer Center, University of California, San Diego, 3855 Health Sciences Drive, MC 0819, La Jolla, California 92093.
Received July 20, 2006; Revised Manuscript Received November 24, 2006

This paper describes the development of a new class of N-linked imidazoles as potential pH-sensitive, cleavable linkers for use in cancer drug delivery systems. Kinetic analysis of eight derivatives of *N*-ethoxybenzylimidazoles (NEBIs) showed that their rates of hydrolysis are accelerated in mild aqueous acidic solutions compared to in solutions at normal, physiological pH. Incorporation of electron donating or electron withdrawing substituents on the phenyl ring of the NEBI resulted in the ability to tune the rates of hydrolysis under mild acidic conditions with half-lives ranging from minutes to months. A derivative of NEBI carrying doxorubicin, a widely used anticancer agent, also showed an increased rate of hydrolysis under mild acid compared to that at normal physiological pH. The doxorubicin analogue resulting from hydrolysis from the NEBI exhibited good cytotoxic activity when exposed to human ovarian cancer cells. These results demonstrate a potentially useful, general strategy for conjugating a wide range of drugs to imidazole-containing delivery vessels via NEBI functionalities for controlled release of therapeutics for drug delivery applications.

Herein, we describe the development of a class of pH-sensitive molecules that hydrolyze with tunable rates under physiological conditions. Organic functional groups that decompose slowly in an aqueous environment have attracted wide interest as potential linkers for the covalent conjugation of drugs to polymers for a range of drug delivery applications (*1*). Functional groups that decompose in mildly acidic environments, for instance, may be useful for the development of cancer drug delivery systems where an acid-sensitive group could exploit the lower extracellular pH (pH $\approx$ 6.4−6.9) of some tumor cells compared to that of blood or normal tissues (*2*) to trigger the release of therapeutic agents from suitable delivery vessels (*3*). Functional groups that cleave under mild acid may also exploit the low pH of endosomes (pH $\approx$ 5.5−6) and lysosomes (pH $\approx$ 4.5−5) to trigger the release of covalently linked therapeutics from drug delivery carriers after endocytosis by targeted cells (*4*).

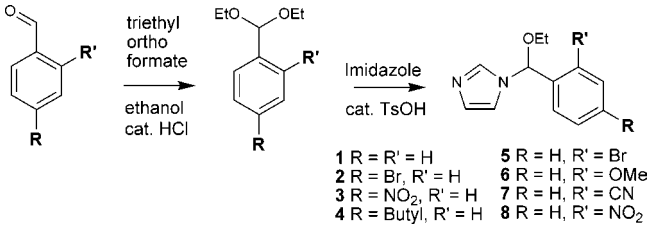
In the course of developing new drug delivery systems, we have explored the possibility of using N-linked imidazoles as functionalities that could undergo hydrolysis in aqueous acidic solutions at physiological temperature. We hypothesized that the expected difference in the protonated state of certain N-linked imidazoles in mild acid (e.g., pH = 5.5) compared to normal, physiological pH (pH = 7.4) (*5*) might be useful for initiating the rapid release of molecules (e.g., drugs) linked to imidazole-containing delivery vessels when exposed to tumor-like environments. Here, we present a study of the hydrolysis of a new class of N-linked imidazoles that cleave under physiologically relevant conditions upon protonation of the imidazole group. We designed these molecules on the basis of a previously reported (*6*) ethoxyethyl protecting group for imidazoles that was shown to be hydrolytically unstable in aqueous acidic conditions at elevated temperatures. Mechanistically, the cleavage of ethoxyethyl groups on imidazoles had been proposed to involve the protonation of the imidazole nitrogen (N3 in Scheme 1) followed by breaking of the C6−N1 bond as the rate-determining step (RDS, Scheme 1). To attain a related N-linked imidazole that could undergo acid hydrolysis at physiological temperatures, we explored whether substitution of the ethyl group (i.e., bearing the C6 carbon in Scheme 1) with benzyl groups could lower the activation energy required for this hydrolysis reaction and facilitate the cleavage of the C6−N1 bond under physiological conditions.

Scheme 1. Proposed Mechanism for the Hydrolysis of *N*-Alkoxyalkylimidazoles in aqueous acidic solutions[a]



[a] RDS = Rate-determining step.

Scheme 2. General Procedure for the Synthesis of *N*-Ethoxybenzylimidazoles (NEBIs) 1−8 from the Corresponding Benzaldehydes



We synthesized *N*-ethoxybenzylimidazole (NEBI) **1** from benzaldehyde using a simple and mild two-step procedure

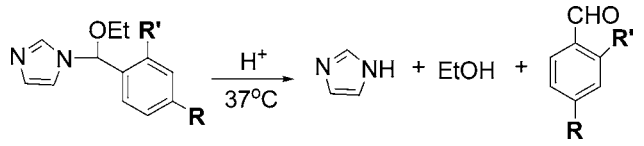
* E-mail: jerryyang@ucsd.edu. Tel: 858-534-6006; Fax: 858-534-4554.

[†] Department of Chemistry and Biochemistry.

[‡] Department of Medicine and the Rebecca and John Moores Cancer Center.

10.1021/bc060224s CCC: $37.00 © 2007 American Chemical Society
Published on Web 01/30/2007

Table 1. Half-Lives ($t_{1/2}$) and Rate Constants (k) for the Hydrolysis of NEBIs in D_2O at pD = 5.5 and pD = 7.4[a]



			pH = 5.5[b]		pH = 7.4[c]	
	R	R′	$t_{1/2}$ [h]	k [h^{-1}]	$t_{1/2}$ [h]	k [h^{-1}]
1	H	H	1.7	0.41	25	0.028
2	Br	H	16.2	0.04	270	0.003
3	NO_2	H	6900	<0.001	N/A[d]	
4	Bu	H	1.0	0.69	8.8	0.079
5	H	Br	280	0.003	2300	<0.001
6	H	OMe	0.6	1.13	5.1	0.136
7	H	CN	3500	<0.001	N/A[d]	
8	H	NO_2	6900	<0.001	N/A[d]	

[a] Rates of hydrolysis were measured by ^1H NMR. See Supporting Information for details. [b] 0.5 M MES buffer solution. [c] 0.5 M HEPES buffer. [d] No hydrolysis detected after >8 weeks.

(Scheme 2). The Supporting Information summarizes the details of the synthesis. At 37 °C in 0.5 M HEPES buffer in D_2O (pD = 7.4), we measured by ^1H NMR that **1** hydrolyzes with a half-life of 25 h to give imidazole, ethanol, and benzaldehyde as the only products detected (Scheme 1) (*7*). At 37 °C in 0.5 M MES buffer in D_2O (pD = 5.5), **1** hydrolyzed to give the same products as at higher pD (Figure 1) but with a much shorter half-life of 1.7 h for hydrolysis. Kinetic analysis indicated that the hydrolysis of **1** is first-order dependent on the concentration of **1** and zero-order dependent on the concentration of buffering agent (see Figure S1 in the Supporting Information) (*8*). As expected from the proposed mechanism shown in Scheme 1, the benzyl group (R = phenyl) appears to stabilize the transition state of the rate-determining step better than the previously reported (*6*) ethyl group (R = methyl) and, thus, facilitates hydrolysis of **1** at physiological temperatures. Having measured the pK_a of the protonated form of **5** (as a representative NEBI) to be 5.4 (*9*), the observed acceleration of the rate of hydrolysis of **1** in mild acidic solution compared to physiological pH is also consistent with the proposed mechanism (Scheme 1).

To investigate whether electronic effects might influence the rate of hydrolysis of NEBIs, we incorporated electron donating and electron withdrawing groups at the ortho or para positions of the phenyl ring and compared the rates of hydrolysis for **1**−**8**. Incorporation of an electron donating methoxy group at the ortho position in **6**, for instance, resulted in a half-life of 0.6 h for the hydrolysis of **6** at 37 °C in 0.5 M MES buffered D_2O (pD = 5.5); we observed a slower rate of hydrolysis for **6** ($t_{1/2} \approx 5$ h) at 37 °C in 0.5 M HEPES buffered D_2O (pD = 7.4) compared to the rates of hydrolysis at pD = 5.5 (Table 1). Incorporation of electron withdrawing substituents at the ortho or para positions of the phenyl ring of **1**, on the other hand, resulted in slower rates of hydrolysis in acidic and neutral solutions. Incorporation of a relatively weak electron withdrawing bromo substituent at the ortho position in **5**, for example, resulted in a significant decrease in the rate of cleavage of the NEBI moiety, with measured half-lives of 280 and 2300 h for the hydrolysis of **5** at 37 °C in buffered D_2O at pD = 5.5 and pD = 7.4, respectively. Furthermore, incorporation of strong electron withdrawing nitro substituents at the ortho or para position of the phenyl ring resulted in remarkably slow rates of hydrolysis of the NEBI moiety at 37 °C, with measured half-lives of 6900 h for both **3** and **8** in buffered D_2O at pD = 5.5 and no hydrolysis detected after >8 weeks at pD = 7.4.

To further probe the mechanism of cleavage of NEBIs in acidic solutions, we plotted the linear free energy relationship

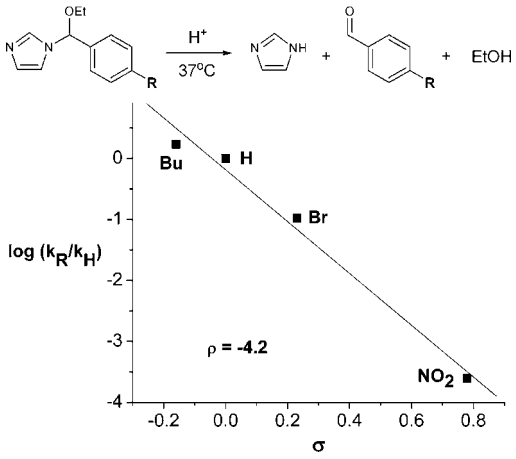


Figure 1. Linear Hammett correlation for the hydrolysis of **1**−**4** in 0.5 M MES buffered D_2O (pD = 5.5) at 37 °C, where R = *n*-butyl (Bu), H, Br, and NO_2.

(*10*) for the hydrolysis of **1**−**4** in D_2O at pD = 5.5 (Figure 1). We calculated a ρ-value of −4.2 for the hydrolysis of the NEBIs, which is consistent with an increase in positive charge (e.g., on the benzylic carbon of **1**−**8**) in the rate-determining step of the reaction. This observed linear Hammett correlation, combined with the finding that the rate of hydrolysis of **1** is independent of the concentration of buffering agent (see Figure S1 in the Supporting Information), supports a specific acid-catalyzed mechanism (*10*) for the hydrolysis of **1**−**8** as shown in Scheme 1.

With these results from kinetic and mechanistic studies in hand, we were interested in determining whether a NEBI carrying an antitumor agent—here, doxorubicin (*11*)—would also hydrolyze with accelerated rates under mild acidic solutions compared to at normal, physiological pH. We synthesized **9** by formation of an amide bond between a reactive amine group on doxorubicin and a carboxylate group on the para position of the phenyl ring of the NEBI (Figure 2). The Supporting Information describes the details of the synthesis and characterization of **9**. We measured a half-life by RP-HPLC of 55 h for the hydrolysis of **9** at 37 °C in MES buffered H_2O (pH = 5.5) (*12*). As expected, we observed a slower rate of hydrolysis of **9** ($t_{1/2}$ = 1150 h) at 37 °C in HEPES buffered H_2O (pH = 7.4) compared to the rates of hydrolysis at pH = 5.5 (Figure 2). Cytotoxicity studies indicated that **10** (i.e., the analogue of doxorubicin resulting from hydrolysis of **9** in mild acidic solutions) retains anticancer activity against human ovarian carcinoma 2008 cells with an IC_{50} of ∼12 μM (Figure 3). For comparison, compound **9** had a 2-fold higher IC_{50}, and doxorubicin had a >10-fold lower IC_{50} than **10** against this cell line. Although less potent than doxorubicin, compound **10** also has similar cytotoxic activity compared to other clinically used anticancer agents being developed for controlled release from drug delivery systems via pH-sensitive linkers (*4c*).

We have thus demonstrated that NEBIs hydrolyze in aqueous solutions at physiological temperatures with hydrolysis occurring approximately 10 times faster in mildly acidic solutions compared to solutions at normal, physiological pH. By incorporating electron donating or electron withdrawing substituents, we demonstrated the ability to tune the rates of hydrolysis of these N-linked imidazoles in mild acidic solutions with half-lives ranging from ∼30 min to >9 months. A NEBI carrying doxorubicin also exhibited accelerated rates of hydrolysis in acidic solution compared to at neutral pH, with the product of hydrolysis showing potentially useful cytotoxic activity against human cancer cells. Previous studies have shown that drugs conjugated to delivery vessels via pH-sensitive linkers with hydrolytic properties similar to those of **9** can exhibit useful

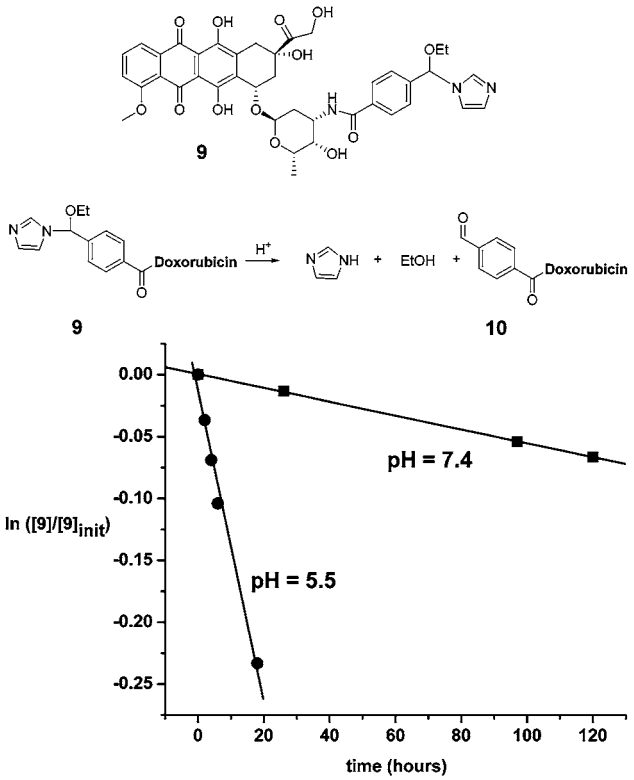


Figure 2. Hydrolysis of a NEBI conjugated with doxorubicin (**9**) in MES buffer (pH = 5.5) and HEPES buffer (pH = 7.4). The pH-dependent rate of hydrolysis of **9** to aldehyde **10** was determined by RP-HPLC. See Supporting Information for details.

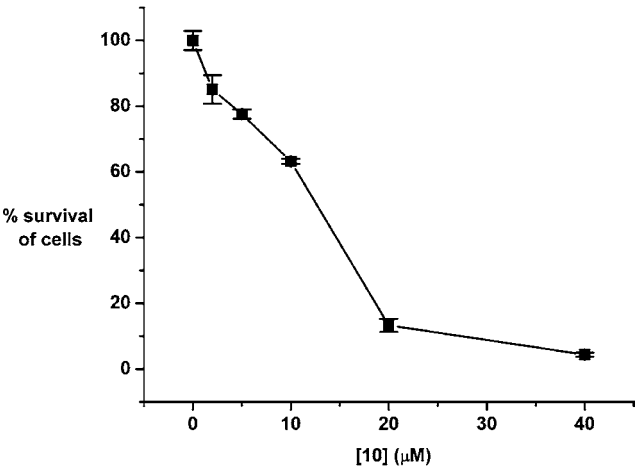


Figure 3. Concentration-dependent cytotoxicity of *N*-(4-formylbenzoyl)doxorubicin **10** on human ovarian carcinoma 2008 cells. Cells were exposed to various concentrations of **10** for 1 h, and survival was determined after a further 7 day period of growth in drug-free medium. See Supporting Information for details of the cell survival assay.

antitumor activity in vivo (*1d*). These drugs conjugated to delivery vessels using pH-sensitive linkers also showed reduced toxicity to normal, healthy tissues compared to administration of equivalent concentrations of free drug. The ability to tune the rates of hydrolysis of the NEBIs may make it possible to optimize the rate of release of drugs attached to delivery vessels via these acid-sensitive functionalities for maximal efficacy for cancer therapy.

The described N-linked imidazoles possess many desired features (*1*, *4*) for use as acid-sensitive linkers in cancer drug delivery. In addition to (1) their tunable rates of hydrolysis, (2) their nontoxic byproducts from hydrolysis (i.e., ethanol), and (3) their versatility for the range of alcohol- and amine-containing therapeutics that can be linked to drug carriers, the known ability to tune the pK_a's of protonated imidazoles (*5*) may make it possible to optimize the operational pH range of NEBIs for specific drug delivery applications. The mild conditions required to synthesize NEBIs carrying anticancer agents also provides a simple route to incorporate this functionality into tumor-targeting vessels. It may be possible, for instance, to use NEBI linkers to covalently attach therapeutics to imidazole-containing derivatives of known delivery systems (*1*, *4*) that can target tumors and exploit the endocytotic pathway for internalization in cells. The synthesis and detailed study of a range of potential therapeutic agents conjugated to drug delivery carriers via NEBI linkers is currently under way.

ACKNOWLEDGMENT

This work was partially supported by the Academic Senate, a Faculty Career Development Award, a Hellman Fellowship Award, and the Department of Chemistry and Biochemistry at UCSD and by grant #RSG-07-024-01-CDD from the American Cancer Society. S.B.H and G.M. acknowledge support from the National Institutes of Health (CA 95298). The National Science Foundation (CHE-0116662) is gratefully acknowledged for support of the mass spectrometry facilities at UCSD. The authors also thank Professor Charles Perrin for helpful discussions during the preparation of this manuscript.

Supporting Information Available: Additional experimental details and characterization of molecules. This material is available free of charge via the Internet at http://pubs.acs.org/BC.

LITERATURE CITED

(1) (a) Gillies, E. R., Goodwin, A. P., and Frechet, J. M. J. (2004) Acetals as pH-Sensitive Linkages for Drug Delivery. *Bioconjugate Chem. 15*, 1254−1283. (b) Heller, J., Barr, J., Ng, S. Y., Abdellauoi, K. S., and Gurny, R. (2002) Poly(ortho esters): synthesis, characterization, properties and uses. *Adv. Drug Delivery Rev. 54*, 1015−1039. (c) Kruger, M., Beyer, U., Schumacher, P., Unger, C., Zahn, H., and Kratz, F. (1997) Synthesis and stability of four maleimide derivatives of the anticancer drug doxorubicin for the preparation of chemoimmunoconjugates. *Chem. Pharm. Bull. 45*, 399−401. (d) Patel, V. F., Hardin, J. N., Mastro, J. M., Law, K. L., Zimmermann, J. L., Ehlhardt, W. J., Woodland, J. M., and Starling, J. J. (1996) Novel acid labile COL1 trityl-linked difluoronucleoside immunoconjugates: Synthesis, characterization, and biological activity. *Bioconjugate Chem. 7*, 497−510. (e) Greenfield, R. S., Kaneko, T., Daues, A., Edson, M. A., Fitzgerald, K. A., Olech, L. J., Grattan, J. A., Spitalny, G. L., and Braslawsky, G. R. (1990) Evaluation in vitro of adriamycin immunoconjugates synthesized using an acid-sensitive hydrazone linker. *Cancer Res. 50*, 6600−6607. (f) Shen, W. C., and Ryser, H. J. P. (1981) Cis-aconityl spacer between daunomycin and macromolecular carriers: A model of pH-sensitive linkage releasing drug from a lysosomotropic conjugate. *Biochem. Biophys. Res. Commun. 102*, 1048−1054. (g) Etrych, T., Jelinkova, M., Rihova, B., and Ulbrich, K. (2001) New HPMA copolymers containing doxorubicin bound via pH-sensitive linkage: Synthesis and preliminary in vitro and in vivo biological properties. *J. Controlled Release 73*, 89−102. (h) Walker, G. F., Fella, C., Pelisek, J., Fahrmeir, J., Boeckle, S., Ogris, M., and Wagner, E. (2005) Toward synthetic viruses: Endosomal pH-triggered deshielding of targeted polyplexes greatly enhances gene transfer *in vitro* and *in vivo*. *Mol. Ther. 11*, 418−425. (i) Tomlinson, R., Heller, J., Brocchini, S., and Duncan, R. (2003) Polyacetal-doxorubicin conjugates designed for pH-dependent degradation. *Bioconjugate Chem. 14*, 1096−1106. (j) Choi, j. S., MacKay, J. A., and Szoka, F. C., Jr. (2003) Low-pH-sensitive PEG-stabilized plasmid-lipid nanoparticles: Preparation and characterization. *Bioconjugate Chem. 14*, 420−429.

(2) (a) Ojugo, A. S. E., McSheehy, P. M. J., Stubbs, M., Alder, G., Bashford, C. L., Maxwell, R. J., Leach, M. O., Judson, I. R., and

Griffiths, J. R. (1998) Influence of pH on the uptake of 5-fluorouracil into isolated tumour cells. *Br. J. Cancer 77*, 873−879. (b) Ojugo, A. S. E., McSheehy, P. M. J., McIntyre, D. J. O., McCoy, C., Stubbs, M., Leach, M. O., Judson, I. R., and Griffiths, J. R. (1999) Measurement of the extracellular pH of solid tumours in mice by magnetic resonance spectroscopy: A comparison of exogenous ^{19}F and ^{31}P probes. *NMR Biomed. 12*, 495−504. (c) van Sluis, R., Bhujwalla, Z. M., Raghunand, N., Ballesteros, P., Alvarez, J., Cerdan, S., Galons, J.-P., and Gilles, R. J. (1999) In vivo imaging of extracellular pH using ^{1}H MRSI. *Magn. Reson. Med. 41*, 743−750.

(3) Brown, D. M. (2004) *Drug Delivery Systems in Cancer Therapy*, Humana Press, Totowa, NJ.

(4) (a) Gillies, E. R., and Frechet, J. M. J. (2005) pH-responsive copolymer assemblies for controlled release of doxorubicin. *Bioconjugate Chem. 16*, 361−368. (b) Rice, J. R., and Howell, S. B. (2004) Polymer-delivered platinum complex. *Drugs Future 29*, 561−565. (c) Lin, X., Zhang, Q., Rice, J. R., Stewart, D. R., Nowotnik, D. P., and Howell, S. B. (2004) Improved targeting of platinum chemotherapeutics: The antitumour activity of HPMA copolymer platinum agent AP5280 in murine tumour models. *Eur. J. Cancer 40*, 291−297.

(5) The pK_a values of imidazolium ions have been reported to be between 5 and 7. Bruice, T. C., and Schmir, G. L. (1958) Imidazole catalysis. 11. the reaction of substituted imidazoles with phenyl acetates in aqueous solution. *J. Am. Chem. Soc. 80*, 148−156.

(6) Manoharan, T. S., and Brown, R. S. (1988) I-(1-Ethoxyethyl): An effective protecting group for imidazole nitrogen. *J. Org. Chem. 53*, 1107−1110.

(7) For all hydrolysis studies in D_2O, we added 20−40% d_6-DMSO (v/v) to improve the solubility of the molecules. The addition of 20−40% DMSO did not affect the pH of the solutions or the rate of hydrolysis of **1**.

(8) Connors, K. A. (1990) *Chemical Kinetics: The Study of Reaction Rates in Solution*, Wiley-VCH, New York.

(9) We measured the pK_a of **5** in 50:50 H_2O/DMSO by titration of **5** with a concentrated solution of HCl. We estimated the pK_a of **5** by measuring the pH of the solution when 0.5 equiv of HCl was added.

(10) Carroll, F. A. (1998) *Perspectives on Structure and Mechanism in Organic Chemistry*, Brooks/Cole Publishing Company, Pacific Grove.

(11) Perry, M. C. (2001) *The Chemotherapy Source Book*, 3rd ed., Lipincott, Williams & Wilkins, Philadelphia. Arcamone, F. (1981) *Doxorubicin Anticancer Antibiotics*, Academic Press, New York.

(12) The observed rate of hydrolysis of **9** at pH = 5.5 is consistent with the expected value for a NEBI group containing an amide functionality attached to the para position of the phenyl ring in **1** as predicted from the linear free energy relationship shown in Figure 2 (R = CONHR′, $\sigma = 0.36$, $\log(k_R/k_H) = -1.32$).

BC060224S

Fluorescent Nanoparticles for Multiplexed Bacteria Monitoring

Lin Wang, Wenjun Zhao, Meghan B. O'Donoghue, and Weihong Tan*

Center for Research at the Bio/Nano Interface, Department of Chemistry, Shands Cancer Center and UF Genetics Institute, University of Florida, Gainesville, Florida 32611-7200. Received August 16, 2006;
Revised Manuscript Received December 14, 2006

Rapid, sensitive, and selective detection of pathogenic bacteria is extremely important for proper containment, diagnosis, and treatment of diseases like foodborne illness, sepsis, and bioterrorism. Most current bacterial detection methods are time-consuming and laborious and can detect only one bacterial pathogen at a time. We have developed a method for sensitive, multiplexed monitoring of bacterial pathogens within 30 min using multicolored FRET (fluorescence resonance energy transfer) silica NPs (nanoparticles). By varying the ratio of three tandem dyes coencapsulated into the NPs, we have synthesized NPs that emit unique colors upon excitation with a single wavelength. When these NPs were conjugated to monoclonal antibodies specific for the pathogenic bacteria species *Escherichia coli*, *Salmonella typhimurium*, and *Staphylococcus aureus*, and then incubated with small concentrations of the bacteria, simultaneous and sensitive detection of the multiple bacterial targets was achieved.

INTRODUCTION

Under the appropriate conditions, bacterial pathogens can survive and spread easily in the environment. As a result, trace concentrations (~10−100 cells) of bacterial pathogens in food, donated blood, or the environment can pose a serious threat to human health. An estimated 76 million illnesses, over 300000 hospitalizations, and over 5000 deaths are attributable to foodborne illness in the United States every year (*1*). In all of these pathogenic situations, there are several likely bacterial suspects of infection. For example, *E. coli* O157:H7, *Salmonella* spp., and *Staphyllococcus* spp. are the most common causes of foodborne illness and are responsible for 20% of deaths related to sepsis from blood transfusions (*2, 3*). Consequently, there has been a critical demand for techniques that can recognize numerous bacterial pathogens simultaneously in a single assay (multiplexing), thereby giving an early warning of bacteria contamination. However, the currently accepted bacteria detection methods require PCR amplification and/or cell culturing (*4*−*6*) which are slow, time-consuming, laborious, and have a limited ability to multiplex (*7*−*13*). Many attempts have been made to improve the sensitivity of bacterial detection of numerous strains simultaneously without the need for bacterial culturing or PCR (*14*−*18*) but have met with limited success.

To address this issue, we have developed triple-dye-doped FRET silica nanoparticles (NPs) (*19, 20*) to serve as promising substrates for multiplexed bacteria monitoring. Previously, our group has used single-dye-doped NPs for in situ pathogen quantification down to a single bacterium (*21*). These dye-doped NPs, each encapsulating ~10 000 dye molecules in a ~60 nm silica sphere, provide an extremely strong fluorescent signal for bioanalysis and are easily conjugated to biorecognition molecules, such as antibodies, for fluorescence-based immunoassays. Now, by varying the ratio of three fluorescence energy transfer tandem dyes coencapsulated into the silica NPs, excitation with a single wavelength leads to emission of numerous different colors (*20*), thereby permitting simultaneous and sensitive detection of multiple targets. The work described here assesses the use of FRET NPs for multiplexed bacterial detection. *Escherichia coli* (*E. coli*), *Salmonella typhimurium* (*ST*), and *Staphylococcus aureus* (*SA*) were used as model pathogens in our system because they are major human pathogens responsible for foodborne illness and sepsis (*22*). Thus, if routine testing of food and blood products could rapidly detect these three pathogens, both the safety and the shelf life of these products could be increased (*2, 3, 23*). Our results show that FRET NPs can be used as highly sensitive and selective platforms for sensing multiple microorganisms simultaneously.

EXPERIMENTAL PROCEDURES

Reagents and Apparatus. Biotinylated rabbit anti-*E. coli* IgG, biotinylated rabbit anti-*ST* IgG, and goat anti-rabbit IgG were ordered from Biodesign International (Saco, ME). Biotinylated rabbit anti-*SA* IgG was bought from Cortex Biochem (San Leandro, CA). NanoOrange, DAPI (4′-6-diamidino-2-phenylindole), and amine reactive dyes FAM-SE (5-carboxyfluorescein succinimidyl ester), R6G-SE (5-carboxyrhodamine 6G, succinimidyl ester), ROX-SE (6-carboxy-X-rhodamine, succinimidyl ester), and TMR-SE (carboxytetramethylrhodamine, succinimidyl ester) were ordered from Invitrogen Corporation (Carlsbad, CA). NHS−PEG_{5000}−biotin was purchased from Nektar Therapeutics (San Carlos, CA). TEOS (tetraethyl orthosilicate) and APTS [(3-aminopropyl)triethoxysilane)] were purchased from Aldrich Chemical Co., Inc. (Milwaukee, WI). Sulfo-NHS (*N*-hydroxysulfosuccinimide sodium salt) and EDC (1-ethyl-3-(3-dimethylaminopropyl)carbodiimide hydrochloride) were ordered from Pierce Chemicals (Rockford, IL). Tween-20 and MES (2-(*N*-morpholino)ethanesulfonic acid) were obtained from Sigma Chemical Co. (St. Louis, MO). Carboxylated silica microspheres (5.06 μm in diameter) were ordered from Bangs Laboratories (St. Louis, MO). All other chemicals were of analytical reagent grade. Distilled deionized water (Easy Pure LF) was used for the preparation of all aqueous solutions.

A Hitachi S-4000 scanning electron microscope was used for imaging bacteria−NP conjugates. Optical and fluorescence images were obtained on a fluorescence microscope (Zeiss, U.S.A.) and a laser scanning confocal microscope (Olympus, Japan).

NP Preparation. TMR-doped and triple-dye-doped silica NPs (diameter $\Phi = 70$ nm) were prepared through a modified Stöber

* Fax and Tel 352-846-2410; E-mail tan@chem.ufl.edu.

10.1021/bc060255n CCC: $37.00 © 2007 American Chemical Society
Published on Web 03/07/2007

synthesis method (*20*, *24*, *25*). First, amine-reactive dye molecules (TMR-SE, FAM-SE, R6G-SE, ROX-SE) were individually dissolved in 1.5 mL of anhydrous DMF (dimethylformamide), combined with an excess of APTS (molar ratio of dye to APTS = 1:2), and stirred under a dry nitrogen atmosphere for 24 h in the dark. Second, the TMR−APTS conjugate or the three tandem dye−APTS conjugates (FAM−APTS, R6G−APTS, ROX−APTS) mixed at desired ratios (1:0.5:1, 0.5:1:4, 0.5:0.5:3) were added to a clean glass reaction vessel containing 16.75 mL of ethanol and 1.275 mL of ammonium hydroxide, respectively. The mixture was stirred for 24 h. 0.71 mL of TEOS (0.00375 mol) was added afterward and stirred for another 24 h. After the reaction, the samples were centrifuged at 14 000 rpm for 30 min to collect the silica NPs. The NPs were further washed with ethanol and deionized water by centrifugation and decanted several times to remove unreacted chemicals.

NP Surface Modification. *Amine Group Modification.* After washing the NPs, approximately 10 mg of NPs were dispersed in 1 mL of deionized water with sonication and mixed with 20 μL of glacial acetic acid. 20 μL of (3-trimethoxysilylpropyl)-diethylenetriamine was added with sonication, and the suspension was stirred for 3−4 h. The particles were washed and dispersed in 10 mM MES buffer (pH = 5.5).

Carboxyl Group Modification. Carboxyl group modification was accomplished by mixing 10 mg of NPs in 1 mL of phosphate buffer (10 mM, pH 7.4) and 20 μL of carboxyethylsilanetriol sodium salt, 25% in water (Gelest, Inc., Kent, ME). The mixture was stirred for 3−4 h, washed with phosphate buffer, and dispersed in the same buffer.

NP−Antibody Bioconjugation. *Strategy A*: Carbodiimide chemistry was used to cross-link free carboxylic acid groups on NPs with amine-containing antibodies. Briefly, 100 μL of a 0.22% (w/v) suspension of COOH-modified NPs was washed by centrifuging once with deionized water. The pellet was then resuspended in 1 mL of 0.1 M MES (pH 5.5). Aqueous solutions of 10 mM sulfo-NHS and 4 mM EDC dissolved in MES buffer were freshly prepared, and 0.5 mL of each solution was immediately added to the NP solution. The NPs were incubated at room temperature with gentle agitation. After 15 min, the NPs were centrifuged and washed with 10 mM phosphate buffer (pH 7.4), then resuspended in 1.5 mL phosphate buffer, followed by addition of 50 μL of antibodies (rabbit anti-*ST*-IgG) at a concentration of 1 mg/mL. The mixture was incubated at room temperature for 2 h with gentle end-to-end shaking. NPs were washed in 10 mM phosphate buffer and then resuspended in the quenching solution (40 mM Tris−HCl with 0.05% (w/v) BSA) for 60 min to block free carboxylates. Protein-coated NPs were purified by alternately centrifuging and resuspending in phosphate buffer (10 mM, pH 7.4) with 1% BSA and stored at 4 °C until use. Covalent coupling of secondary antibodies (goat anti-rabbit-IgG) to carboxylated silica microspheres followed the same procedures.

Strategy B. Streptavidin conjugation to NPs used the above procedure except that the antibody was changed to streptavidin. After the centrifugation and washing steps, biotin-labeled antibody was added to the solution with a final concentration ratio of biotin-Ab:NP = 1000:1. The solution was allowed to gently mix for 1 h, washed, and centrifuged to remove free biotin−antibody.

Strategy C. Amine-modified NPs were reacted with the activated ester of biotin (NHS−PEG_{5000}−biotin) in the phosphate buffer for 2 h to couple biotin molecules to the NPs. The complexes were centrifuged and washed several times with phosphate buffer to remove the unbound biotin. Streptavidin and NP−biotin were then mixed at a 1000:1 ratio to ensure sufficient saturation of streptavidin on the NP surface, and the mixture was slowly shaken for 2 h. The complexes were centrifuged and washed several times with phosphate buffer to remove unbound streptavidin. Biotin-labeled antibody was further mixed into the above solution with a final concentration ratio of biotin−Ab to NP of 1000:1. The solution was allowed to gently mix for 1 h, washed, and centrifuged to remove free biotin−antibody.

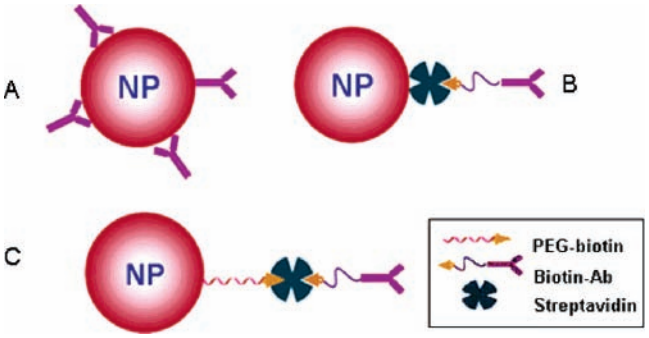


Figure 1. Schematic representation of three antibody-labeling strategies on NPs.

NP−Antibody Conjugation with Bacteria. Antibody-labeled NPs and bacteria were mixed at an experimentally optimized ratio (10 000:1), diluted in the incubation buffer (10 mM phosphate buffer, pH 7.4, 0.05% Tween-20), and gently shaken at room temperature for 30 min. The resultant product was washed three times by centrifugation (3000 rpm, 5 min) to remove all unbound antibody-conjugated NPs.

RESULTS AND DISCUSSION

Antibody Labeling Strategy Optimization. Before applying FRET NPs for multiplexed detection of pathogenic bacteria, single dye (TMR)-doped NPs were used in the initial assay to test bacteria binding efficiency and specificity. TMR-doped NPs were prepared using the Stöber method (*24*, *25*). The amine-reactive dye TMR-SE was first chemically bound to an amine-containing silane agent APTS, and then APTS and TEOS were allowed to hydrolyze and co-condense in a mixture of water, ammonia, and ethanol, resulting in TMR-doped silica NPs. The NPs were then modified with surface functional groups and covalently conjugated to antibodies specific to three bacteria individually.

Considering the effects of strong steric hindrance between the rigid NP and the bacterial surface, different antibody labeling strategies were designed (Figure 1). In strategy A, we directly immobilized monoclonal antibody onto COOH−NP surface using carbodiimide chemistry (*19*, *26*, *27*) to cross-link free carboxylic acid groups on NPs with amine-containing antibodies; in strategy B, we first linked COOH−NP surface with streptavidin as a bridge molecule (*28*), then immobilized biotin−antibody onto streptavidin; in strategy C, we immobilized NHS−PEG−biotin molecules onto NH_2-modified NPs (*20*); after incubation with streptavidin, biotin-labeled antibody was anchored onto NP surface. For strategy A, we assumed that, due to the random attachment of antibody onto the NPs, some of the antigen binding sites of the antibody may be blocked. In strategy B, the bridge molecule streptavidin was bound to the biotin attached to the antibody ensuring that the antibody recognition sites were oriented away from the NP surface, so that they do not lose their ability to bind to a target bacterium. The third strategy added hydrophilic PEG linkers between NP and antibody to further improve the NP solubility and dispersivity, and allow the conjugated biotin−antibody to extend out from the NP surface, reducing the binding steric hindrance and benefiting the binding efficiency. To verify the functionality of conjugating antibody onto NPs and mimic the bacteria−NP interaction, goat-anti-rabbit IgG-coated microspheres and rabbit

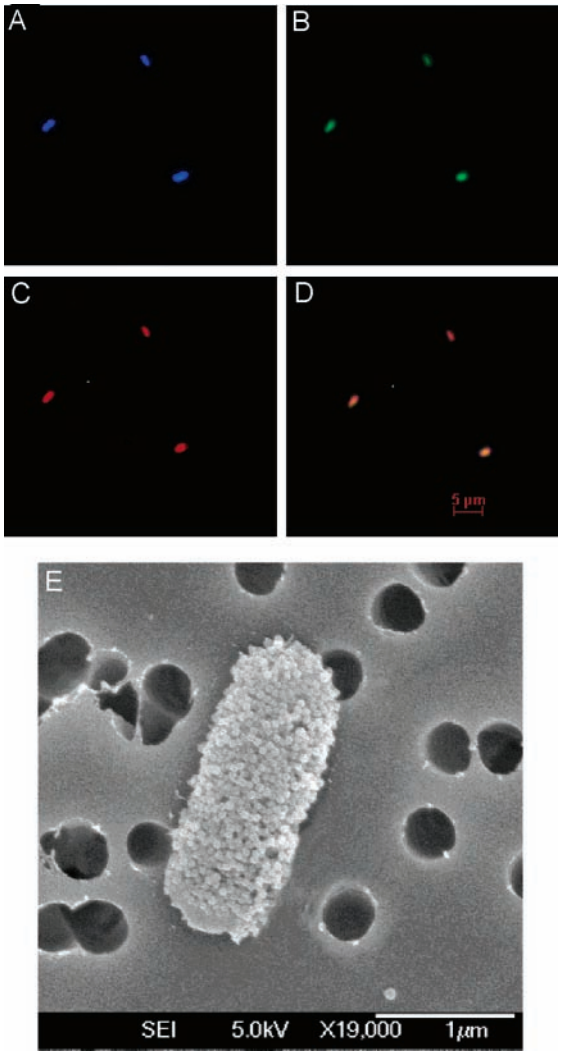


Figure 2. (A−D) *ST* bacteria conjugated with antibody-labeled TMR NPs and stained with DAPI and NanoOrange. (A) Blue channel, DAPI; (B) green channel, NanoOrange; (C) red channel, TMR; (D) combinatorial color of the three detection channels. (E) SEM image of an *ST* bacterium coated with PEG-*ST*-biotin-antibody labeled NPs.

anti-*ST*-IgG conjugated NPs prepared with the three strategies were mixed and allowed to react for 30 min. As expected, we found that NPs prepared with the third strategy exhibited the best colloidal stability and binding performance.

NP−Antibody Binding with Bacteria. *ST* was used for the initial bacteria monitoring. Anti-*ST*-IgG conjugated TMR−NPs were allowed to bind to *ST* bacteria. The resultant product was washed three times by centrifugation to remove all unbound antibody-conjugated NPs. To clarify the bacterial configuration and differentiate bacteria from NP aggregates, the *ST* bacteria were stained with DAPI (4′-6-diamidino-2-phenylindole, which stains double-stranded DNA) and NanoOrange (protein stain). Fluorescence images of the NP-coated *ST* were taken by exciting them with a 100 W mercury lamp, while three orthogonal detection channels monitored fluorescence for DAPI, NanoOrange, and TMR, respectively. Both the fluorescence and SEM images (Figure 2) display the successful binding between NPs and *ST* bacteria.

NP−Bacteria Binding Specificity. One critical issue when detecting large numbers of targets simultaneously is specificity of binding. Cross-reactivity in highly multiplexed assays will lead to potentially disastrous false positives. The next experiment was designed to specifically detect the target bacteria *ST* in the presence of other pathogenic bacteria. Before incubation with NP−antibody conjugates, only target bacteria *ST* were stained with NanoOrange. Free NanoOrange unbound to *ST* was removed by centrifugation, mixed with the other two bacteria species (*E. coli* and *SA*), and incubated with rabbit anti-*ST*-IgG-NPs. After 30 min, the sample was washed three times by centrifugation to remove free antibody-conjugated NPs that did not bind to the bacteria, and the sample was stained together with DAPI before imaging. The fluorescence image demonstrates that only those bacteria stained with NanoOrange fluoresced red due to the bound NPs, verifying that the antibody-conjugated NPs specifically associated with *ST* cell surfaces (Figure 3).

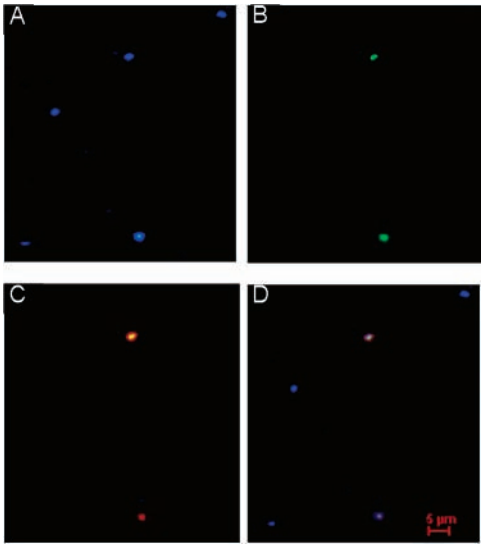


Figure 3. Fluorescence images of all three bacteria species incubated with NPs labeled with antibody to *ST*. (A) All three bacteria species were stained with DAPI. (B) Target bacteria *ST* were prestained with NanoOrange. (C) Only target bacteria *ST* fluoresced—the color of the NPs. (D) Combination of the three channels.

Simultaneous Monitoring of Multiple Bacteria. Simultaneous multiple bacteria monitoring was achieved using color-encoded FRET NPs. To prepare the FRET NPs, the three amine-reactive energy-transfer tandem dyes (FAM-SE, R6G-SE, ROX-SE) were first covalently linked to the silane coupling agent APTS. The three APTS−dye conjugates were then mixed at desired ratios (1:0.5:1, 0.5:1:4, 0.5:0.5:3), and each mixture was added to a clean glass reaction vessel containing pure ethanol and ammonium hydroxide. After stirring for 24 h, TEOS was added, and the mixture was stirred for 24 h. When the reaction was complete, the solution was centrifuged to collect the silica NPs. The NPs were further washed with ethanol and deionized water to remove the unreacted chemicals.

During the NP preparation process, the three APTS−dye conjugates were first allowed to prehydrolyze for 24 h before adding TEOS to start the colloid formation. During the prehydrolysis step, the three tandem dyes were covalently attached to one another and shortened the distance between them to the benefit of the FRET efficiency (*20*). In the FRET NPs, FAM was used as a common donor for R6G and ROX, while R6G acted as both an acceptor for FAM and a donor for ROX. By exciting at the maximum excitation wavelength for FAM (488 nm), efficient energy transfer between the three dyes in the same NP occurred, and NPs exhibited three emission peaks corresponding to the three encapsulated dyes, while the combinatorial color varies due to the different dye doping ratio. Figure 4A−C displays the fluorescence images of the three types of NPs taken under a confocal microscope. Circles a, b, and c display the fluorescence images of NPs close to the three emission peaks, while circle d exhibits the resultant combina-

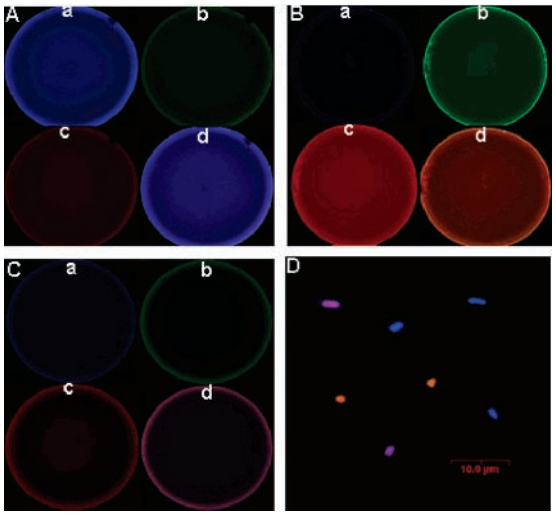


Figure 4. (A−C) Fluorescence images of three types of FRET NPs taken under a confocal microscope. (a) FAM emission channel; (b) R6G emission channel; (c) ROX emission channel; (d) combinatorial color of the three channels. The three types of NPs exhibit blue, orange, and purple colors. (D) Confocal image of three bacteria species specifically covered with the corresponding antibody labeled NPs.

torial color of the three detection channels. When excited at 488 nm, the three types of NPs fluoresce blue, orange, and purple.

These three types of FRET NPs were further conjugated with the PEG−streptavidin−biotin−IgG complex. Blue NPs were conjugated with antibody to *E. coli*; orange NPs were coated with antibody to *SA*; while the purple NPs were linked with antibody to *ST*. These three antibody-labeled NPs and three bacteria species were mixed together in the buffer (10 mM phosphate buffer, pH 7.4, 0.05% Tween-20) and incubated for 30 min. After the centrifugation and washing steps, the confocal image of the resultant bacteria−NP complexes shows that three bacteria species were specifically covered with their corresponding antibody-labeled NPs and exhibit the coding colors of the attached NPs (Figure 4D). Furthermore, using the recently established two NP assay (*29*), it is feasible to use both antibody-conjugated magnetic NPs and fluorescent NPs to achieve multiple bacteria extraction and detection.

In summary, we have been the first to apply multicolor FRET NPs for multiplexed monitoring of bacteria species. This method is fast and accurate with high sensitivity and specificity. By changing the dye doping ratios of the energy-transfer dye series, a large FRET NP bar-coding library can be built permitting multiplexed detection of numerous bacterial pathogens. By eliminating the sample enrichment and amplification steps required with current cell culture and PCR-based methods, our method can achieve the diagnosis of disease at the earliest stage of its development. Routine bacteria testing of food or blood using this method could allow for increased safety and shelf life (especially important for blood platelets whose current shelf life is 3−5 days). FRET silica NPs hold great promise to develop multiplexed bacterial detection kits.

ACKNOWLEDGMENT

This work was supported by NSF NIRT and NIH grants. The bacteria were kindly provided by Dr. Samuel Farrah of the Microbiology and Cell Science Department at University of Florida. L.W. receives support as an ACS Division of Analytical Chemistry Graduate Student Fellow sponsored by GlaxoSmith-Kline.

LITERATURE CITED

(1) Inglesby, T. V., O'Toole, T., Henderson, D. A., Bartlett, J. G., Ascher, M. S., Eitzen, E., Friedlander, A. M., Gerberding, J., Hauer, J., Hughes, J., McDade, J., Osterholm, M. T., Parker, G., Perl, T. M., Russell, P. K., and Tonat, K. (2002) Anthrax as a biological weapon, 2002: updated recommendations for management. *J. Am. Med. Assoc. 287*, 2236−2252.

(2) Brecher, M. E., and Hay, S. N. (2005) Bacterial contamination of blood components. *Clin. Microbiol. Rev. 18*, 195−204.

(3) Shorten, P. R., Pleasants, A. B., and Soboleva, T. K. (2006) Estimation of microbial growth using population measurements subject to a detection limit. *Int. J. Food Microbiol. 108*, 369−375.

(4) Stokstad, E. (2006) New disease endangers Florida's already-suffering citrus trees. *Science 312*, 523−524.

(5) Deisingh, A. K., and Thompson, M. (2004) Strategies for the detection of *Escherichia coli* O157:H7 in foods. *J. Appl. Microbiol. 96*, 419−429.

(6) Lukinmaa, S., Nakari, U. M., Ekland, M., and Siitonen, A. (2004) Application of molecular genetic methods in diagnostics and epidemiology of food-borne bacterial pathogens. *APMIS 112*, 908−929.

(7) Benjamin, R. J., and Mintz, P. D. (2005) Bacterial detection and extended platelet storage: The next step forward *Transfusion 45*, 1832−1835.

(8) Kox, L. F., Rhienthong, D., Miranda, A. M., Udomsantisuk, N., Ellis, K., van Leeuwen, J., van Heusden, S., Kuijper, S., and Kolk, A. H. (1994) A more reliable PCR for detection of *Mycobacterium tuberculosis* in clinical samples. *J. Clin. Microbiol. 32*, 672−678.

(9) Alexandre, M., and Prado, V. (2003) Detection of Shiga toxin-producing *Escherichia coli* in food. *Expert Rev. Mol. Diagn. 3*, 105−115.

(10) Bettelheim, K. A., and Beutin, L. (2003) Rapid laboratory identification and characterization of verocytotoxigenic (Shiga toxin producing) *Escherichia coli* (VTEC/STEC). *J. Appl. Microbiol. 95*, 205−217.

(11) Ibekwe, A. M., and Grieve, C. M. (2003) Detection and quantification of *Escherichia coli* O157:H7 in environmental samples by real-time PCR. *J. Appl. Microbiol. 94*, 421−431.

(12) Blajchman, M. A., Beckers, E. A., Dickmeiss, E., Lin, L., Moore, G. and Muylle, L. (2005) Bacterial detection of platelets: current problems and possible resolutions. *Transfus. Med. Rev. 19*, 259−272.

(13) Slezak, T., Kuczmarski, T., Ott, L., Torres, C., Medeiros, D., Smith, J., Truitt, B., Mulakken, N., Lam, M., Vitalis, E., Zemla, A., Zhou, C. E., and Gardner, S. (2003) Comparative genomics tools applied to bioterrorism defence. *Brief Bioinform. 4*, 133−149.

(14) Goldschmidt, M. C. (2006) The use of biosensor and microarray techniques in the rapid detection and identification of salmonellae. *J. AOAC Int. 89*, 530−537.

(15) Song, J. M., and Vo-Dinh, T. (2004) Miniaturized biochip system for detection of *E. coli* O157:H7 based on antibody-immobilized capillary reactors and enzyme-linked immunoassay. *Anal. Chim. Acta 507*, 115−121.

(16) Muhammad-Tahir, Z., and Alocilja, E. C. (2003) Fabrication of a disposable biosensor for *Escherichia coli* O157: H7 detection. *IEEE Sens. J. 3*, 345−351.

(17) Kim, J. Y., Kim, S. H., Kwon, N. H., Bae, W. K., Lim, J. Y., Koo, H. C., Kim, J. M., Noh, K. M., Jung, W. K., Park, K. T., and Park, Y. H. (2005) Isolation and identification of *Escherichia coli* O157:H7 using different detection methods and molecular determination by multiplex PCR and RAPD. *J. Vet. Sci. 6*, 7−19.

(18) Ikeda, M., Yamaguchi, N., Tani, K., and Nasu, M. (2006) Rapid and simple detection of food poisoning bacteria by bead assay with a microfluidic chip-based system. *J. Microbiol. Methods 6*, 241−247.

(19) Wang, L., Yang, C. Y., and Tan, W. H. (2005) Dual-luminophore-doped silica nanoparticles for multiplexed signaling. *Nano Lett. 5*, 37−43.

(20) Wang, L., and Tan, W. H. (2006) Multicolor FRET silica nanoparticles by single wavelength excitation. *Nano Lett. 6*, 84−88.

(21) Zhao, X. J., Hilliard, L. R., Mechery, S. J., Wang, Y., Jin, S., and Tan, W. H. (2004) A rapid bioassay for single bacterial cell quantitation using bioconjugated nanoparticles. *Proc. Natl. Acad. Sci. U.S.A. 101*, 15027−15032.

(22) Bacterial Contamination in Blood Products, American Red Cross, July 2003, http://redcrosslife.org/northatlantic/presentation072003.-ppt#23 (accessed 6/20/06).

(23) Park, Y. S., Lee, S. R., and Kim, Y. G. (2006) Detection of *Escherichia coli* O157:H7, *Salmonella spp.*, *Staphylococcus aureus* and *Listeria monocytogenes* in kimchi by multiplex polymerase chain reaction (mPCR). *J. Microbiol. 44*, 92−97.

(24) Stöber, W., Fink, A., and Bohn, E. (1968) Controlled growth of monodisperse silica spheres in the micron size range. *J. Colloid Interface Sci. 26*, 62−69.

(25) van Blaaderen, A., and Vrij, A. (1992) Synthesis and characterization of colloidal dispersions of fluorescent, monodisperse silica spheres. *Langmuir 8*, 2921−2931.

(26) Santra, S., Zhang, P., Wang, K. M., Tapec, R., and Tan, W. H. (2001) Conjugation of biomolecules with luminophore-doped silica nanoparticles for photostable biomarkers. *Anal. Chem. 73*, 4988−4993.

(27) Zhao, X. J., Tapec-Dytioco, R., and Tan, W. H. (2003) Ultrasensitive DNA detection using bioconjugated nanoparticles, *J. Am. Chem. Soc. 125*, 11474−11475.

(28) Ye, Z., Tan, M., Wang, G., and Yuan, J. (2004) Preparation, characterization, and time-resolved fluorometric application of silica-coated terbium(III) fluorescent nanoparticles. *Anal. Chem. 76*, 513−518.

(29) Herr, J. K., Smith, J. E., Medley, C. D., Shangguan, D. H., and Tan, W. H. (2006) Aptamer-conjugated nanoparticles for selective collection and detection of cancer cells. *Anal. Chem. 78*, 2918−2924.

BC060255N

ARTICLES

Employment of Cationic Solid-Lipid Nanoparticles as RNA Carriers

Giovanna Montana,[†,⊥] Maria L. Bondì,[‡,⊥] Rita Carrotta,[§,△] Pasquale Picone,[†] Emanuela F. Craparo,[∥] Pier L. San Biagio,[§] Gaetano Giammona,[∥] and Marta Di Carlo*[,†]

Istituto di Biomedicina e Immunologia Molecolare, Istituto per lo Studio dei Materiali Nanostrutturati, sezione di Palermo, and Istituto di Biofisica, Consiglio Nazionale delle Ricerche, Via Ugo La Malfa, 153, 90146 Palermo, and Dipartimento di Chimica e Tecnologie Farmaceutiche, Università di Palermo, via Archirafi, 32, 90123 Palermo, Italy. Received May 5, 2006; Revised Manuscript Received July 27, 2006

Gene transfer represents an important advance in the treatment of both genetic and acquired diseases. In this article, the suitability of cationically modified solid-lipid nanoparticles (SLN) as a nonviral vector for gene delivery was investigated, in order to obtain stable materials able to condense RNA. Cationic SLN were produced by microemulsion using Compritol ATO 888 as matrix lipid, Pluronic F68 as tenside, and dimethyldioctadecylammonium bromide (DDAB) as cationic lipid. The resulting particles were approximately 100 nm in size and showed a highly positive surface charge (+41 mV) in water. Size and shape were further characterized by scanning electron microscopy (SEM) measurements. Moreover, we utilized the sea urchin as a model system to test their applicability on a living organism. To evaluate cationic SLN ability to complex the in vitro transcribed *Paracentrotus lividus bep3* RNA, we utilized both light scattering and gel mobility experiments, and protection by nuclease degradation was also investigated. By microinjection experiment, we demonstrated that the nanoparticles do not inference with the viability of the *P. lividus* embryo and the complex nanoparticles-*bep3* permits movement of the RNA during its localization in the egg, suggesting that it could be a suitable system for gene delivery. Taken together, all these results indicate that the cationic SNL are a good RNA carrier for gene transfer system and the sea urchin a simple and versatile candidate to test biological properties of nanotechnology devices.

INTRODUCTION

Gene delivery is an area of considerable current interest for molecular medicine. DNA and proteins have been extensively investigated for their application in nanotechnology as a possible approach to gene therapy (*1*, *2*). Minor attention has been given to other important biological molecules such as RNA until now. In nature, RNA exhibits a single-stranded conformation, but it is versatile enough to form, through specific complementary sequences, stems, loops, and hairpins, providing elements of adaptability to nanotechnology that is based on a double-helical structure. The use of antisense or sense RNA is a specific and powerful tool for selectively modulating the expression of a gene target to identify loss-of-function or gain-of-function phenotypes (*3*−*8*). The use of RNA interference (RNAi), based on gene-silencing of key molecules involved in many diseases, has been an improvement in this technology (*9*). All these kinds of synthetic RNAs are generally introduced into the cells by electroporation and/or microinjection, but their poor stability is often the cause of failure. Another technology to introduce RNA molecules employs viral vectors, but undesirable effects can occur (*10*, *11*). In the past decade, many studies have shown that nonviral vectors, as cationic liposomes and polycations, are valid tools for delivering nucleic acids to specific cell types both to inhibit some undesirable gene expression or to express therapeutic proteins (*12*, *13*). The use of nonviral vectors permits one to avoid some risk factors such as pathogenesis, immunogenicity, and so forth(*14*−*16*). Among them, cationic solid-lipid nanoparticles (SLN) as a carrier system for the delivery of genetic materials may offer several technological advantages (*17*). These include excellent storage stability, relatively easy production without the use of any organic solvent, the possibility of steam sterilization and lyophilization, and large-scale production utilizing substances that are approved for use in pharmaceutical human applications (*18*−*22*). These particles consist of a lipid core bearing cationic lipids on its surface.

The aim of this study was to prepare and utilize cationically modified SLN as specific RNA carriers and to evaluate their potential as a nonviral vector for gene delivery. Moreover, we have utilized, as a living organism, the sea urchin *Paracentrotus lividus* and its *bep3* maternal messenger RNA (*23*, *24*). Among the classical model systems, the sea urchin provides a powerful model for a great variety of studies in molecular and cell biology and biochemistry. Moreover, the sea urchin occupies a key phylogenetic position as the only nonchordate detereustomes, and the results obtained on this embryo can be extrapolated and compared to those of higher eukaryotes. Eggs and embryos are transparent, allowing direct observation of cell division and movement, and specific techniques permit us to visualize the presence of exogenous nucleic acids inside the cells. Further-

* To whom correspondence may be addressed. E-mail: dicarlo@ibim.cnr.it. Tel. ++39 0916809538; fax ++39 0916809548.

[†] Istituto di Biomedicina e Immunologia Molecolare, Consiglio Nazionale delle Ricerche.

[‡] Istituto per lo Studio dei Materiali Nanostrutturati, sezione di Palermo, Consiglio Nazionale delle Ricerche.

[§] Istituto di Biofisica, Consiglio Nazionale delle Ricerche.

[△] Present address: Dipartimento di Scienze Fisiche ed Astronomiche, Università di Palermo, via Archirafi 36, 90138 Palermo.

[∥] Università di Palermo.

[⊥] These authors contributed equally to this work.

10.1021/bc0601166 CCC: $37.00 © 2007 American Chemical Society
Published on Web 01/25/2007

more, *bep3* RNA codifies for a cell surface protein, localized after fertilization at the animal pole of the *Paracentrotus lividus* egg by moving along cytoskeleton elements (*24, 25*). Thus, this RNA represents a good model to study the delivery of nucleic acids. Interestingly, it has been demonstrated that *bep3* 3′UTR, necessary for its localization, could fold in secondary structures; that is a required element for nanotechnology (*26*). The ability to form complexes between SLN and *bep3* and the effect on its mobility have been tested.

EXPERIMENTAL PROCEDURES

Materials. Compritol ATO 888 is a mixture of approximately 15% mono-, 50% di-, and 35% triglycerides of behenic acid (C_{22}). The melting point lies between 69 and 74 °C. It was a gift from Gattefossé (D-Weil am Rhein, Germany). Pluronic F68 and the cationic surfactant dimethyldioctadecylammonium bromide (DDAB) were purchased from Sigma-Aldrich.

Preparation of Solid-Lipid Nanoparticles. The SLN were prepared from a warm oil-in-water (o/w) microemulsion by using Compritol ATO 888 and DDAB as the lipid matrix. Briefly, 0.273 mmol of Compritol were heated to 10 °C above its melting point and mixed with 2.5 mL of a hot aqueous solution of Pluronic F68 (0.158 mmol) and DDAB (1.45 mmol) to form a clear microemulsion, under mechanical stirring. Then, cationic nanoparticles were obtained by dispersing under mechanical stirring at 1000 rpm the warm o/w microemulsion in cold water (2−3 °C) (organic/aqueous volume ratio equal to 1:10). The obtained cationic nanoparticles were purified by dialysis using a Visking Tubing Dialysis 18/32″ (with a molecular weight cutoff of 12 000−14 000 Da). Then, cationic nanoparticles were freeze-dried using a Modulo freeze-dryer (Labconco Corporation, Missouri). To label SLN, fluorescein free acid was added to the lipid phase during preparation of the microemulsion.

In Vitro Synthesis of the Transcript. To synthesize *bep3* RNA, the plasmid containing this clone was linearized by digestion at the Xho I site (*24*). Transcription by T7 polymerase was carried out utilizing the DIG-RNA labeling kit and DIG-UTP as the substrate according to the manufacturer's instructions in the kit (Roche). The DIG-labeled RNA probe was detected by immunoassay using an anti-digoxigenin alkaline phosphatase conjugate (anti DIG-AP) according to the manufacturer's instructions (Roche).

Preparation of Cationic SLN−RNA Complexes and RNA Retardation Assay. To four equal aliquots of a *bep3* DIG-RNA (50 ngr) solution in 5 mM Hepes, increasing amounts of nanoparticle suspensions were added to obtain the final w/w ratios of 50:1, 100:1, 200:1, and 400:1. In order to evaluate the effect of the preparation method on the nature of the obtained complexes, these were prepared also by adding the RNA solutions to the cationic SLN suspensions. All the cationic SLN−RNA complexes prepared by using both methods were characterized in terms of mean size, ζ potential, and electrophoretic mobility, and the same results were achieved.

After 30 min incubation at room temperature, RNA binding was studied by assaying for agarose gel retardation. Samples were electrophoresed through a 1% agarose gel at 80 V for 1 h. RNA was visualized by a UV transluminator using ethidium bromide staining.

Size and ζ Potential Measurements. Particle or complex size was analyzed by photon correlation spectroscopy (PCS) using a Zetasizer Nano ZS (Malvern Instrument, Herrenberg, Germany) which utilizes the noninvasive back-scattering (NIBS) technique. PCS gives information about the mean diameter of the bulk population (so-called *z*-average) and the width of distribution via the polydispersity index (PI). Samples were appropriately diluted with filtered (0.2 μm) twice-distilled water, and the readings were carried at a 173° angle with respect to the incident beam. The reported values were the averages of three measurements.

The surface charge was determined using the same equipment. The ζ potential value was measured using principles of the laser Doppler velocimetry and phase analysis light scattering (M3-PALS technique). Samples were dispersed in filtered (0.2 μm) twice-distilled water and analyzed in triplicate.

Light Scattering Measurements. A water dispersion of SLN at a final concentration of c1.2 mg/mL was filtered via a 0.45 μm filter directly into a cylindrical quartz cuvette. To study the interaction between SLN and *bep3* RNA, a small aliquot of RNA solution (about 25 ng) was added in situ into the cuvette containing the filtered SLN suspension. A Brookhaven Instrument BI200-SM goniometer, equipped with a 100 mW Ar laser tuned at $\lambda_0 = 488$ nm, was used in a temperature-controlled setup, as reported elsewhere (*27*). Simultaneous measurement of the intensity autocorrelation function and static light scattered at 90° proved the stability of the SLN suspension for 60 min. Immediately after mixing the RNA into the suspension of nanoparticles, the interaction between SLN and *bep3* RNA was monitored by time-resolved light scattering experiments. Both the intensity autocorrelation function measured at 90° and static light scattered at 90°, averaged for 3 min, were measured independently to follow the process at $T = 25$ °C. From the measured intensity autocorrelation functions, $g_2(t)$, we calculated the electric field autocorrelation functions, $g_1(t)$, considering the Siegert relation: $g_1(t) = \sqrt{g_2(t) - 1}$ (*28*). The autocorrelation functions $g_1(t)$ were analyzed using a smoothing constrained regularization method, in order to obtain the distribution $P(D)$ of the apparent diffusion coefficients D, according to the fact that $g_1(t) = \int P(D)e^{-Dq^2t}\,dD$, where q is the scattering vector defined as $q = 4\pi n/\lambda_0 \sin\theta/2$, with n the medium refractive index and θ the scattering angle (*29*). By using the Stokes Einstein relationship, $D = KT/3\pi\eta D_h$ (k is the Boltzmann's constant, T the absolute temperature, η the solvent viscosity, and D_h the *z*-averaged hydrodynamic diameter), we obtain the distribution $P(D_h)$ of the *z*-averaged hydrodynamic diameters of the species in suspension. The mean hydrodynamic diameter relative to a restricted interval of the distribution was estimated by calculating the harmonic average of the hydrodynamic diameter in the region of interest. Absolute scale for the scattered intensity was obtained by normalizing data to the toluene Rayleigh ratio at 488 nm, taken 39.6×10^{-6} cm^{-1}.

Scanning Electron Microscopy (SEM). A scanning electron microscope (SEM) (XL-30 Philips, The Netherlands) was used to evaluate both size and morphology of cationic SLN and SLN−RNA complexes obtained by using a w/w ratio of 200:1. Before the SEM analysis, the samples were coated under an argon atmosphere with a 10-nm gold thickness. The samples were stuck onto aluminum stubs, which were then fixed into a sample holder and placed in the vacuum chamber of the microscope and observed under low vacuum (10^{-3} Torr).

RNAse Degradation Assay. To evaluate the nuclease activity, the complex between cationic SLN−RNA obtained at a 200:1 w/w ratio was chosen, and the incubation was continued in the presence of 0.1, 1, and 10 u of RNAse T1 (Roche) or 0.1, 1, and 10 u of RNAse A (Roche) for an additional 30 min at room temperature. Electrophoresis of the RNA nanoparticle complex was carried out in 1% agarose gel at 80 V for 1 h. The gel was visualized by a UV transilluminator.

Microinjection in Sea Urchin Eggs. Dejellied *P. lividus* unfertilized eggs were microinjected as described by McMahon (*30*). When we microinjected the nanoparticles alone, 200 of the eggs were fertilized and left to develop for 48 h (pluteus stage). When we microinjected the complex SNL−*bep3* in the 200:1 w/w ratio, before and after fertilization the eggs were

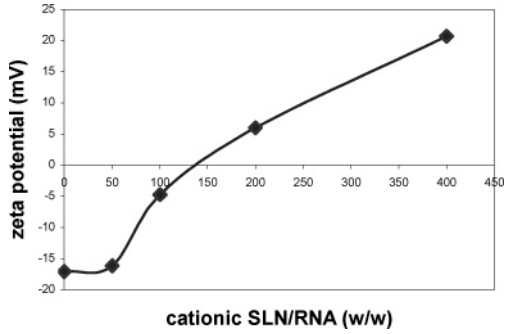


Figure 1. ζ potential values of cationic SLN−RNA complexes at different weight ratios, measured in twice-distilled water after 30 min of incubation.

fixed in 4% paraformaldeide. The presence and movement of exogenous RNA were detected by immunoassay using an anti-digoxigenin alkaline phosphatase conjugate (anti-Dig-AP) according to the manufacturer's instructions of the DIG Nucleic Acid Detection kit (Roche).

Viability Assay. Cell viability was determined using MTS assay according to manufacturer's instructions (PROMEGA). This assay uses the tetrazolium compound (3-(4,5-dimethylthiazol-2-yl)-5-(3-carboxymethoxyphenyl)-2-(4-sulfophenyl)-2*H*-tetrazolium, inner salt (MTS), and the electron coupling reagent, phenazine methosulfate (PMS). MTS is chemically reduced by cells into formazan, which is soluble in culture medium. Briefly, MTS was added to embryos at 48 h of development (pluteus stage), to a final concentration of 0.8 mg/mL, and incubated for 5 h. The measurement of the absorbance of the formazan was carried out using a spectrophotometer at 495 nm.

RESULTS

Production of Cationic SLN. The aim of this study was to prepare cationic nanoparticles consisting of Compritol, dimethyldioactadecylammonium bromide (DDAB), and Pluronic F68, to characterize them in water suspension (particle size and surface charge), and to study their interaction process with RNA. The SLN formulation was produced, as previously described, from a warm oil-in-water (o/w) microemulsion. In order to obtain a positive surface charge, a cationic lipid/surfactant DDAB was employed. The characterization of particle size by photon correlation spectroscopy (PCS) revealed that the average particle size of these particles was 100 nm (PI = 0.215). The surface charge value was highly positive (+41 mV), demonstrating the successful incorporation of DDAB onto the nanoparticle surface. The formulation was stored in the dark and at room temperature. It showed excellent storage stability, with the average particle diameter changing only by a few nanometers during 180 days (data not shown). The binding of RNA with cationic SLN was evaluated by measurements of the ζ potentials of complexes at different cationic SLN−RNA weight ratios. The trend of the ζ-potential measurements of these complexes in water as a function of SLN−RNA weight ratios is illustrated in Figure 1. It is shown that, by increasing the used weight amount of nanoparticles in the complex formation, ζ potential values increased, starting from a value of −17 mV for naked RNA, up to 20 mV, passing through a neutral condition at a SLN−RNA weight ratio of 200:1. These results confirm the good capacity of these cationic nanoparticles to complex RNA and neutralize its anionic charge.

SLNs are Able to Complex RNA. To investigate if cationic SLN can be applied in RNA nanotechnology, we followed the aggregation kinetics of the two components by light scattering. For this aim, we utilized *Paracentrotus lividus bep3* RNA whose characteristics have been described before (*24*−*26*). The static light scattered and the intensity autocorrelation functions both

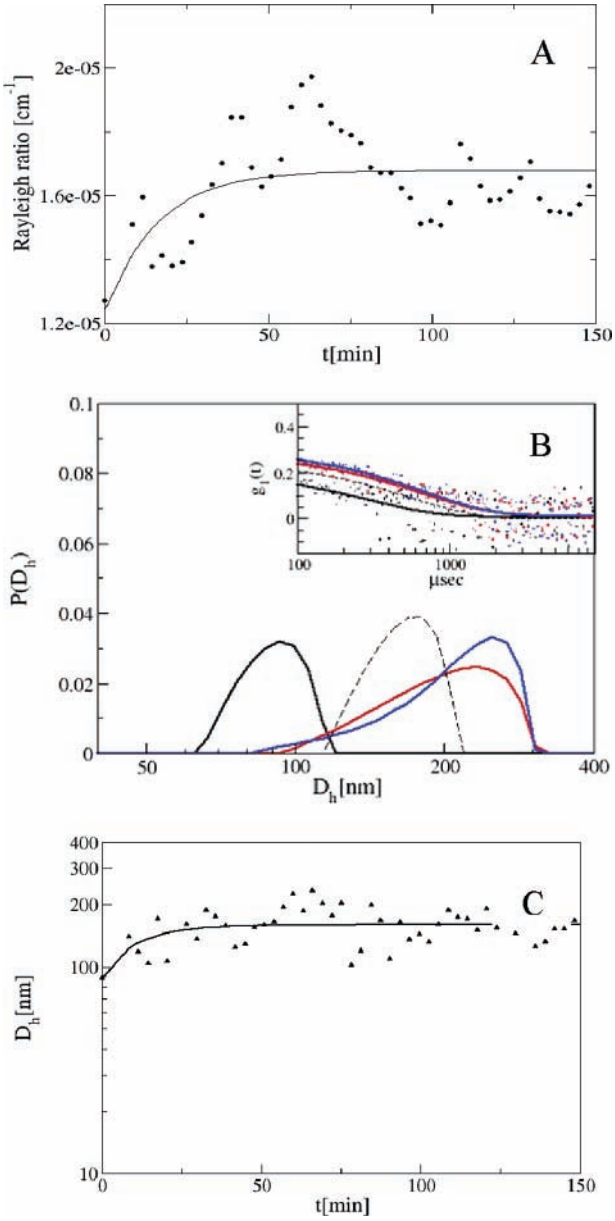


Figure 2. (A) Static light scattered at 90° after mixing of SNL and *bep3* RNA particles. The continuous line represents the best fit by using an exponential function. (B) Distribution functions of the hydrodynamic diameter, $P(D_h)$, at four different times during the kinetic process, at $t = 0$ without RNA (continuous black line), at $t = 25$ min after mixing (dashed black line), at $t = 35$ min after mixing (red line), and at $t = 155$ min after mixing (blue line). The distribution functions were obtained by using a smoothing constrained regularization method to analyze the field autocorrelation functions ($g_1(t)$ data and resulting fits are shown in the inset). (C) Time dependence of the *z*-average hydrodynamic diameter corresponding to the region 40 nm < D_h < 400 nm.

at 90° have been measured simultaneously and independently in order to follow the interaction process between SLN and *bep3* RNA. Figure 2A shows an appreciable, though noisy, Rayleigh ratio increase. The data fit, by using an exponential growth function, gives an estimate of the characteristic interaction time, τ, of 16 min and of the process saturation time on the order of 100 min.

Figure 2B reports on the distribution function of hydrodynamic diameters in the range 40−400 nm at different times during the interaction process obtained by the analysis of the field autocorrelation function data. From the field autocorrelation functions (data shown in the inset), one can notice a decay in

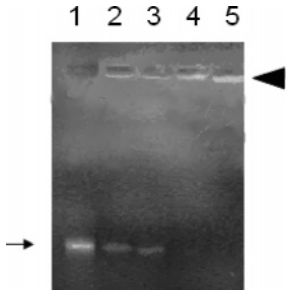


Figure 3. Binding of sense RNA to cationic nanoparticles. 50 ng of RNA was incubated with increasing amounts of cationic nanoparticles. Uncomplexed *bep3* RNA (1), cationic SLN−*bep3* complexes in a w/w ratio of 50:1 (2), 100:1 (3), 200:1 (4), and 400:1 (5). The arrow indicates the uncomplexed RNA; the arrowhead indicates the RNA trapped in the well.

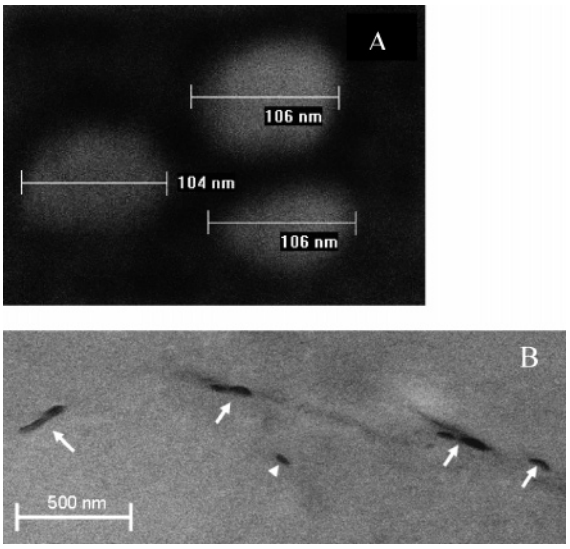


Figure 4. SEM images of (A) cationic SLN and (B) group of representative cationic SLN−RNA complexes obtained at a w/w ratio of 200:1. The arrows indicate the complexes; the arrowhead indicates the free nanoparticles.

the time interval 0.1−1 ms, corresponding to particles with hydrodynamic diameters between 40 and 400 nm, that is to SLN at the beginning ($t = 0$) and to SLN−RNA complexes later on during their formation. A faster decay due to smaller particles with hydrodynamic dimensions of about 5 nm was noticed in the autocorrelation functions (data not shown). Such a contribution, constant during the entire process, suggested the probable presence in solution of small lipid aggregates not interacting with RNA. Figure 2C shows the values of the mean hydrodynamic diameter calculated for the band of particles with hydrodynamic dimensions between 40 and 400 nm. The increase of the hydrodynamic diameter for the SLN−RNA particles has been fitted by using a function expressing an exponential growth giving a characteristic time, τ, of 13 min, a saturation time process of about 100 min, and an average diameter increase, ΔD_h, of about 80 nm.

***Bep3* RNA Mobility is Retarded by SNL.** In order to evaluate the ability of cationic SLN to bind *bep3* RNA, the RNA electrophoretic mobility shift within an agarose gel was investigated. Efficient complexation of *bep3* by cationic SNL led to immobilization and prevention of ethidium bromide intercalation with RNA. In vitro transcribed *bep3* RNA was incubated with increasing amounts of cationic SLN for 30 min. 50 to 100 weight equivalent were sufficient to bind most of RNA, while 200 to 400 completely immobilized RNA. As shown in Figure 3, *bep3* is able to form complexes with

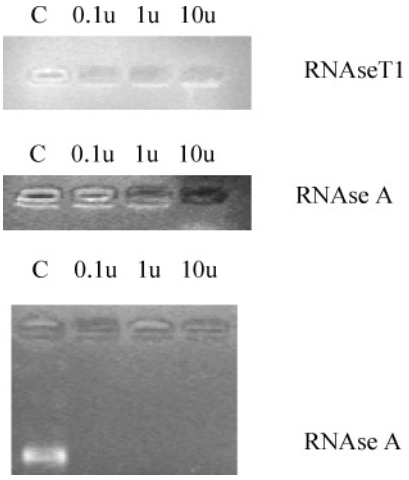


Figure 5. *bep3* RNA−SNL complex is protected by RNAse enzymatic degradation. The RNA−cationic nanoparticle complexes were incubated without (C) or with RNA T1 A or with RNAse A at different amounts (0.1; 1; 10 units). Uncomplexed RNA incubates or not (C) with RNAse A.

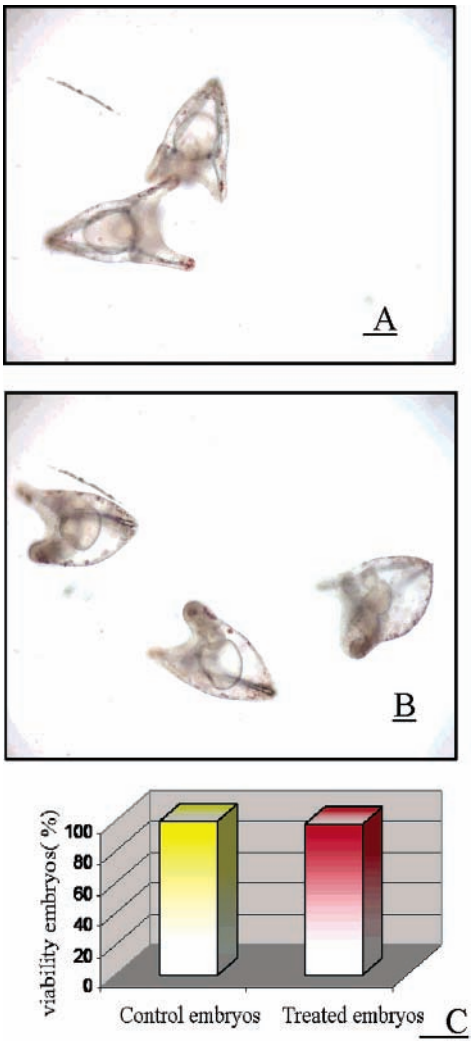


Figure 6. SNL microinjection into *Paracentrotus lividus* unfertilized eggs. Cationic nanoparticles were microinjected into unfertilized eggs and left to develop for 48 h until pluteus stage (B) as control embryos (A). (C) Vitality of microinjected embryos compared with control embryos. On the right, the percentage of survived embryos is indicated. Standard deviation is 3.

nanoparticles in a dose-dependent manner. As nanoparticle concentration increased, the RNA exhibited decreased migration

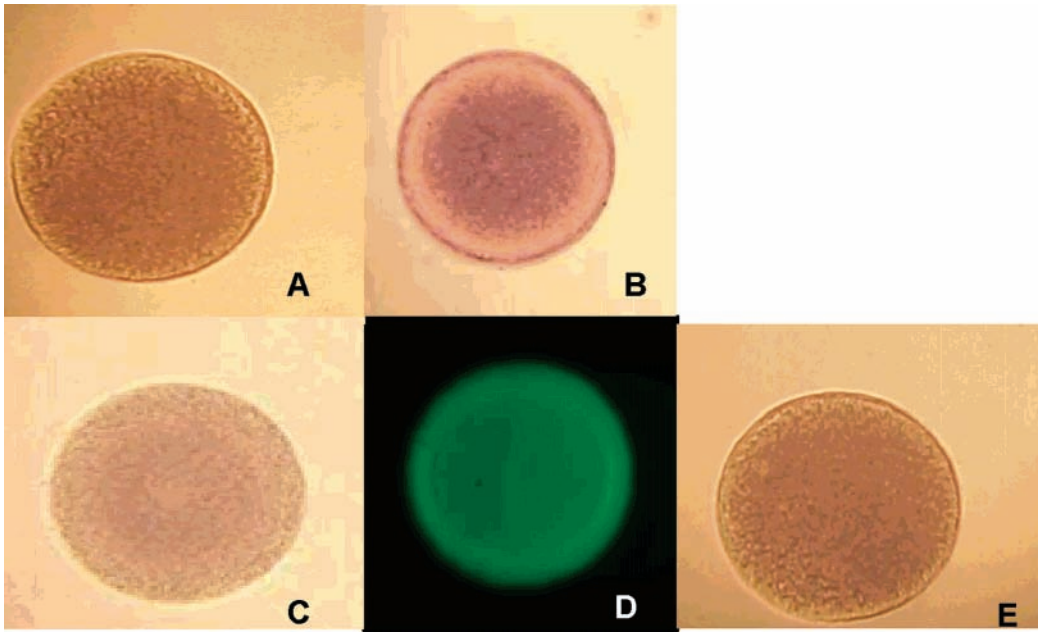


Figure 7. Localization of *bep3* RNA in *Paracentrotus lividus* unfertilized (A) or fertilized (B) eggs after microinjection with cationic nanoparticles. (C) Untreated *P. lividus* egg as control. (D) *P. lividus* egg after incubation with fluorescent SNL. (E) *P. lividus* egg after incubation with fluorescent SNL complexed to RNA and stained with anti-DIG.

strength, and when the complex was too large, it did not enter into the gel, staying trapped in the well. This behavior was probably due both to the increased mass and to the modification of the RNA's electric charges.

Cationic SLN, indeed, spontaneously reacted with the negatively charged RNA molecules by the formation of ion pairs between the hydrophobic cations and the negatively charged phosphate groups of the nucleic acid chain, forming complexes with 100% RNA molecules involved in the reaction, in a self-assembling manner. When all the RNA negative charges are neutralized by the positive charges of the SLN surface, the RNA is no longer able to migrate.

Analysis of Cationic SLN and SLN−RNA Complexes by SEM. To examine the size and the shape of the produced cationic SLN and SLN−RNA complexes obtained at a w/w ratio equal to 200:1, SEM analysis was performed on the sample. Figure 4A,B shows cationic SLNs and SLN−RNA complexes, respectively. By SEM images, we detected that the nanoparticles alone are spherical and have a diameter of approximately 100 nm (Figure 4A). Figure 4B shows an overview of SLN−RNA complexes; many coupled nanoparticles, with diameters between 200 and 300 nm, are present in the sample, indicating that the complex with RNA probably involves two or three nanoparticles. Moreover, free cationic SLN were found into the same sample (Figure 4B).

SLN Protect RNA by Enzymatic Degradation. A peculiar problem, when RNA molecules are in vitro or in vivo transferred in any type of cells, is their susceptibility toward nuclease activity. Thus, nuclease could destroy an RNA molecule before it is able to arrive to the target site. Exogenous RNA is, indeed, unstable in biological fluid or intracellular environments. To test the protection ability of the nanoparticles toward RNA by nuclease attack, we have incubated the *bep3*−SNL complex with increasing amounts until excessive concentrations of two types of ribonucleases RNAse A and RNAse T1 are reached. The difference between these two endonucleases consists of the ability of T1 to digest only unprotected RNA with respect to the ability of A to digest any RNA. After separate digestion with RNAse A and T1, the complexes underwent to electrophoresis. Results, shown in Figure 5, suggest that nanoparticles protect *bep3* RNA by RNAse T1 enzymatic degradation, while it remains exposed to digestion by RNAse A only when a huge excess, in any case not present in the cellular environment, was utilized.

Microinjection of SLN in Sea Urchin Eggs. To investigate the eventual SLN toxicity on a living organism and if they are harmful for RNA delivery, we utilized a classical model system such as the sea urchin *Paracentrotus lividus.* Different amounts of SLN were injected into *P. lividus* eggs. After fertilization, the embryos were left to develop for 48 h until the control arrived at the so-called pluteus stage (a primordial larva). Both microinjected embryos and the control showed the correct morphological aspect of this sea urchin embryonal stage, demonstrating that SLN are not toxic for this living organism (Figure 6A,B). Moreover, the viability of microinjected *P. lividus* embryos was monitored by MTS assay (Figure 6C). Successively, to investigate the RNA delivery ability of SLN, the complex SLN-*bep3* RNA in unfertilized *P. lividus* eggs was microinjected and its localization was observed before and after fertilization. The RNA movement was detected after incubation with anti-DiG, an antibody able to recognize the UTP−DIG conjugate of the in vitro transcribed *bep3*. As shown in Figure 7A, before fertilization, *bep3* RNA is distributed throughout the cytoplasm. After fertilization (see Figure 7B), instead, staining both under the cellular membrane and particularly in the subcortical region around the nucleus was detected, indicating that the SLN have not interfered with the normal movement of this RNA (*24*). Moreover, the possibility of SLN passing through the biological cellular membrane was tested. Fluorescein-loaded SLN, alone or complexed with RNA, were incubated with sea urchin eggs and after 16 h were observed with a fluorescence microscope. As shown in Figure 7D, the eggs are completely fluorescent, in particular forming a layer around the egg and indicating the perfect ability of SLN to diffuse through the cellular membrane. Finally, fluorescein-loaded SNL complexed to *bep3* were incubated with *P. lividus* eggs and the ability of the RNA to enter the SNL by diffusion was detected after incubation with anti-DIG (Figure 7E).

DISCUSSION

The emergent field of nanotechnology generally involves the characterization, modification, and assembly of organized

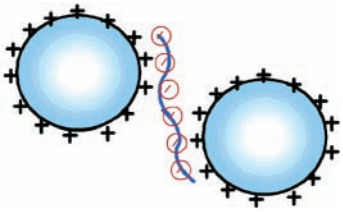


Figure 8. Schematic representation of the interaction between RNA and cationic nanoparticles in the complex.

materials on the nanoscale level. The application of nanotechnology in life sciences is already having an impact on diagnostics and gene therapy in the fight against cancer and genetic disorders. Since biological macromolecules have intrinsic features at the nanometer scale, they have the potential characteristics for formation of nanostructures or nanodevices. RNA is a particular candidate for such application and can exhibit the right versatility to form complexes with nonviral vectors such as cationic nanoparticles. The use of this kind of vector can help genetic material cross the plasmatic membrane and enter the cytoplasm of a living cell and could avoid immunogenic and cytotoxic problems. In this paper, we describe the production of a new type of cationic nanoparticle, and we test both their ability to form a complex and protect RNA and their toxicity and biocompatible properties on a living organism such as the sea urchin.

Cationic SLN have been used to incorporate RNA, and the self-assembled RNA nanostructures are formed with dimensions that fit well within the range of nanotechnology.

As measured by dynamic light scattering, the average hydrodynamic diameter of cationic SLN with RNA in a water solution can be estimated at about 100 nm. After 100 min of mixing, the increase of the average hydrodynamic diameter to about 180 nm confirms the formation of SLN−RNA complexes. From these data, which can only give averaged information, it is hard to assume any kind of model for the complex. However, an indication that very few SLN (two or three) are involved in the complex can be ruled out (Figure 8). SEM microscopy support this result, suggesting that mainly two or three SLN are involved in the complex formation with RNA (Figure 4B).

As shown in gel shift experiments, depending on the cationic SLN−RNA w/w ratio, complexes were produced in a self-assembling manner. Thus, at an SLN−RNA w/w ratio of 200:1 the negative charges on RNA, as also confirmed by ζ-potential measurements, are neutralized and the charge complex is positive. This is relevant for the bioelectrochemistry and the biodistribution of RNA−nanoparticles complexes, increasing their adsorption efficiency in the negatively charged cellular membranes. Moreover, nanoparticles are able to protect *bep3* by RNAase T1 enzymatic degradation even at high concentration and by RNAse A in concentration consistent with a cellular environment, strengthening the idea of a high affinity for RNA molecules. This might permit major RNA stability inside the cellular environments that results in a required condition for nanobiotechnology applications.

To utilize SLN for eventual medical applications, we need to understand if they have a potential toxic effect. To address this question, we decided to utilize the sea urchin as a model system. This organism is very sensitive to different chemical or environmental agents (*31*, *32*). Microinjection of cationic nanoparticles into the *Paracentrotus lividus* eggs permits normal embryonic development as observed by their high viability, regular cell cycle, and correct morphogenesis, indicating their high biocompatibility within the cellular environment. Thus, cationic SLN are composed by physiologically well tolerated ingredients, indicating that they may be suitable for pharmacological applications. Moreover, we took advantage of the characteristic movement of *bep3* RNA along the cytoskeleton to test the potential delivering ability of SLN. The observed correct biodistribution of the RNA suggests that the +/− charge ratio and the ζ potential of the complexes allows an efficient transfer of *bep3* into the cell that maintains its functionality. All these data, together with the ability of SLN to diffuse through the cellular membrane and its potential controlled release of a bioactive molecule, such as *bep3* RNA, suggest that they may have specific characteristics for being a good tool for gene delivery in human therapy.

ACKNOWLEDGMENT

We thank Mr. Alessandro Pensato for technical assistance.

LITERATURE CITED

(1) Mao, C., Sun, W., Shen, Z, and Seeman, N. C. (1999) A nanomechanical device based on the B-Z transition of DNA. *Nature (London) 397*, 144−6.

(2) Mao, C., Solis, D. J., Reiss, B. D., Kottmann, S. T., Sweeney, R. Y., Hayhurst, A., Georgiou, G., Iverson, B., and Belcher, A. M. (2004) Virus-based toolkit for the directed synthesis of magnetic and semiconducting nanowires**.** *Science 303*, 213−7.

(3) Wagner, R. W., and Fanagan, W. M. (1997) Antisense technology and prospects for therapy of viral infections and cancer. *Mol. Med. Today 3*, 31−38.

(4) Helene, C., and Toulmè, J. J. (1990) Specific regulation of gene expression by antisense, sense and antigene nucleic acids. *Biochem. Biophys. Acta 1049*, 99−125.

(5) Zon, G. (1988) Oligonucleotide analogues as potential chemotherapeutic agents. *Pharm. Res. 5*, 539−549.

(6) Walter, N. G., and Burke, J. M. (1998) The hairpin ribozyme: structure, assembly and catalysis. *Curr. Opin. Chem. Biol. 2*, 24−30.

(7) McKay, R. A., Miraglia, L. Y., Cummins, L. L., Owens, S. R., Sasmor, H., and Dean, N. M. (1999) Characterization of a potent and specific class of antisense oligonucleotide inhibitor of human protein kinase C-alpha expression. *J. Biol. Chem. 274*, 1715−1722.

(8) Monia, B. P., Sasmor, H., Jonston, J. F., Freier, S. M., Lesnik, E. A., and Muller, M. (1996) Sequence-specific antitumor activity of a phosphorothioate oligodeoxyribonucleotide targeted to human C-raf kinase supports an antisense mechanism of action in vivo. *Proc. Natl. Acad. Sci. U.S.A. 93*, 15481−15484.

(9) Jackson, A. L., Bartz, S. R., Schelter, J., Kobayashi, S. V., Burchard, J., Mao, M., Li, B., Cavet, G., and Linsley, P. S. (2003) Expression profiling reveals off-target gene regulation by RNAi. *Nat. Biotechnol. 21*, 635−7.

(10) Mir, L. M., Banon, H., and Paoletti, (1988) Introduction of definite amounts of nonpermeant molecules into living cells after electropermeabilization: direct access to the cytosol. C. *Exp. Cell Res. 175*, 15−25.

(11) Dash, P., Lotan, L., Knapp, M., Kandel, E. R., and Goelet, P. (1987) Selective elimination of mRNAs in vivo: complementary oligodeoxynucleotides promote RNA degradation by an RNase H-like activity. *Proc. Natl. Acad. Sci. U.S.A. 84*, 7896−7900.

(12) Haensler, J., and Szoka, F. C. (1993) Polyamidoamine cascade polymers mediate efficient transfection of cells in culture. *Bioconjugate Chem. 4*, 372−379.

(13) Gottschalk, S., Sparrow, J. T., Hauer, J., Mims, M. P., Leland, F. E., Woo, S. L.C., and Smith, L. C. (1996) A novel DNA-peptide complex for efficient gene transfer and expression in mammalian cells. *Gene Ther. 3*, 448−457.

(14) Kneuer, C., Sameti, M., Bakowsky, U., Schiestel, T., Schirra, H., Schmidt, H., and Lehr, C. M. (2000) A non-viral DNA delivery system based on surface modified silica-nanoparticles can efficiently transfect cells *in vitro*. *Bioconjugate Chem. 11*, 926−932.

(15) Zhou, X., and Huang, L. (1994) Liposome-mediated cytoplasmic delivery of proteins: an effective means of accessing the MHC class I-restricted antigen presentation pathway. *Biochim. Biophys. Acta 1189*, 195−203.

(16) Woodle, M.C., and Scaria, P. (2001) Sterically stabilized polyplex: ligand-mediated activity. *Curr. Opin. Colloid Interface Sci. 6*, 78−84.

(17) Tabatt, K., Sameti, M., Olbrich, C., Muller, R. H., and Lehr, C. M. (2004) Effect of cationic lipid and matrix lipid composition on solid lipid nanoparticle-mediated gene transfer. *Eur. J. Pharm. Biopharm. 57*, 155−162.
(18) Mehnert, W., and Mader, K. (2001) Solid lipid nanoparticles: production, characterization and applications. *Adv. Drug Delivery Rev. 47*, 165−196.
(19) Schwarz, C., and Mehnert, W. (1995) *Proceeding of the First World Meeting APGI/APV*, Budapest, pp 485−486.
(20) Schwarz, C., and Mehnert, W. (1997) Freeze-drying of drug-free and drug-loaded solid lipid nanoparticles (SLN). *Int. J. Pharm. 157*, 171−179.
(21) Muller, R. H., Dingler, T., Schneppe, Y., and Gohla, S. (2000) *Handbook of Pharmaceutical Controlled Release Technology* (Wise, D., ed.) pp 359−376, Marcel Dekker, New York.
(22) Muller, R. H., Mader, K., and Gohla, S. (2000) Solid lipid nanoparticles (SLN) for controlled drug delivery - a review of the state of the art. *Eur. J. Pharm. Biopharm. 50*, 61−177.
(23) Giudice, G. (1973) *Developmental biology of the sea urchin embryo*, Academic Press, New York.
(24) Montana, G., Romancino, D. P., and Di Carlo, M. (1996) Cloning, expression, and localization of a new member of a *Paracentrotus lividus* cell surface multigene family. *Mol. Reprod. Dev. 44*, 36−43.
(25) Montana, G., Bonura, A., Romancino, D. P., Sbisà, E., and Di Carlo, M. (1997) A 54-kDa protein specifically associates the 3′ untranslated region of three maternal mRNAs with the cytoskeleton of the animal part of the *Paracertrotus lividus* egg. *Eur. J. Biochem. 247*, 183−9.
(26) Montana, G., Sbisà, E., Romancino, D. P., Bonura, A., and Di Carlo, M. (1998) Folding and binding activity of the 3′UTRs of *Paracentrotus lividus* bep messengers. *FEBS Lett. 425*, 157−60.
(27) Carrotta, R., Manno, M., Bulone, D., Martorana, V., and San Biagio, P. L. (2005) Protofibril formation of amyloid beta-protein at low pH via a non-cooperative elongation mechanism. *J. Biol. Chem. 280*, 30000−30008.
(28) Berne, B. J., and Pecora, R. (1976) *Dynamic Light Scattering*, Interscience, New York.
(29) Spenanek, P. (1993) In *Dynamic light scattering: The method and some applications* (Brown, W., ed.) Clarendon Press, Oxford.
(30) McMahon, A. P., Flytzanis, C. N., Hough-Evans, B. R., Katula, K. S., Britten, R. J., and Davidson, E. H. (1985) Introduction of cloned DNA into sea urchin egg cytoplasm: replication and persistence during embryogenesis. *Dev. Biol. 108*, 420−30.
(31) Livingston, B. T., and Wilt, F. H. (1992) Phorbol esters alter cell fate during development of sea urchin embryos. *J. Cell. Biol. 119*, 1641−8.
(32) Livingston, B. T., and Wilt, F. H. (1989) Lithium evokes expression of vegetal-specific molecules in the animal blastomeres of sea urchin embryos. *Proc. Natl. Acad. Sci. U.S.A. 86*, 3669−73.

BC0601166

Synthesis and Characterization of a Novel Arginine-Grafted Dendritic Block Copolymer for Gene Delivery and Study of Its Cellular Uptake Pathway Leading to Transfection

Tae-il Kim,[†] Jung-un Baek,[†] Jae Keun Yoon,[†] Joon Sig Choi,[‡] Kwan Kim,[†] and Jong-sang Park*[,†]

School of Chemistry and Molecular Engineering, Seoul National University, San 56-1, Shillim-dong, Gwanak-gu, Seoul 151-742, and Department of Biochemistry, Chungnam National University, 220 Gung-dong, Yuseong-gu, Daejeon 305-764, Korea. Received June 2, 2006; Revised Manuscript Received November 29, 2006

We synthesized a novel arginine-grafted dendritic block copolymer, R-PAMAM-PEG-PAMAM-R G5 (PPP5-R) for gene delivery systems. Its Mw was measured as 2.74×10^4 Da by MALDI-TOF, and approximately 36 arginine residues are found to be grafted to the polymer by ^{1}H NMR. PPP5-R was able to form polyplexes with plasmid DNA, the average size of which was about 200 nm. Positive ζ-potential values (+22 to +28 mV) of PPP5-R polyplex indicate the formation of positively charged stable polyplex particles and suggest that large dendritic blocks with high positive charge may not be fully shielded by PEG chains even after PEG-coated complex formation. PPP5-R polyplex shows enhanced water solubility due to the polymer's PEG core and also shows low cytotoxicity, representing the potential for in vivo application. We identified the greatly enhanced transfection efficiency of PPP5-R in comparison with that of native PPP5 on various cell lines. Moreover, in view of the result of various cellular uptake inhibitor treatments during a transfection step, the cellular uptake of PPP5-R polyplex leading to effective transfection is thought to be not dependent on one exclusive pathway and to have the possibility of multiple pathways (caveolae-, clathrin-, and macropinocytosis-mediated pathways), contrary to the caveolae-dependent uptake of the PPP5 polyplex lacking arginine residues.

INTRODUCTION

The necessity of developing efficient gene delivery carriers is increasing gradually both in basic sciences and in clinical research fields. Viral vectors (adenoviruses, adeno-associate viruses, retroviruses, etc.) have been successfully applied to various clinical tests for gene therapy because of their high gene delivery efficiency, but their side effects such as severe pathogenicity occasionally limited further application (*1*). On the other hand, nonviral vectors have been studied as alternatives to viral vectors because of their lower cytotoxicity, nonimmunogenicity, more convenient handling, and larger capacity of gene to deliver (*2*−*4*).

However, nonviral vectors including cationic polymers and lipids show much lower transfection efficiency than viral vectors. They also need to overcome the barriers of considerable polyplex aggregation due to the decreased water solubility induced by charge neutralization through the electrostatic interaction between polycationic vectors and polyanionic DNA (*5*).

Our recent report suggested PAMAM-PEG-PAMAM (PPP[1]) as a novel triblock dendritic polymeric vector (*6*). PPP could form polyplexes with plasmid DNA showing much enhanced water solubility. However, the polymer did not show satisfactory transfection efficiency in vitro experiments, urging us to improve the efficiency of the polymer. Recently, Tat-mediated molecular delivery into cells was highlighted and is the subject of intensive research (*7*−*9*). Arginine residues of Tat peptide are thought to perform an important role for the intracellular translocation of molecular delivery (*10*). Also, the synthetic lipidic vectors with a guanidinium headgroup of arginine showed great potential for a gene delivery system (*11*). Moreover, we recently reported that the arginine conjugation of PAMAM dendrimer surfaces led to highly enhanced transfection efficiency of the polyplex (*12*). So, we designed a novel dendritic polymeric vector by conjugating arginine residues to the periphery of PPP in order to increase the transfection efficiency of the polymer, keeping the good water solubility.

Here, we report the synthesis of R-PAMAM-PEG-PAMAM-R (PPP-R), characterization of its self-assembly with plasmid DNA, and its transfection results in vitro.

Meanwhile, the cellular uptake mechanism of cell-penetrating peptides containing arginine residues was reported by many groups (*13*−*15*). However, the cellular uptake mechanism of arginine-grafted dendritic polymer/DNA complex leading to effective transfection has not been reported yet. So, we also report the cellular uptake pathway of PPP-R polyplex by comparing with that of PPP polyplex lacking arginine residues for the first time.

EXPERIMENTAL SECTION

Materials. Poly(ethylenimine) (25 kDa), methyl acrylate, ethylenediamine, *N*,*N*-diisopropylethylamine (DIPEA), piperidine, 3-[4,5-dimethylthiazol-2-yl]-2,5-diphenyltetrazolium bromide (MTT), 2,5-dihydroxybenzoic acid (DHB), and fucose were purchased from Sigma-Aldrich (St. Louis, MO). Poly(ethylene glycol)-*bis*-amine (MW 3400) was purchased from Shearwater Polymers (Huntsville, AL). *N*-Hydroxybenzotriazole (HOBt) and 2-(1*H*-benzotriazole-1-yl)-1,1,3,3-tetramethyluro-

* Corresponding author. Jong-sang Park, Ph.D. Phone: 82-2-880-6660. Fax: 82-2-877-5110. E-mail: pfjspark@plaza.snu.ac.kr.

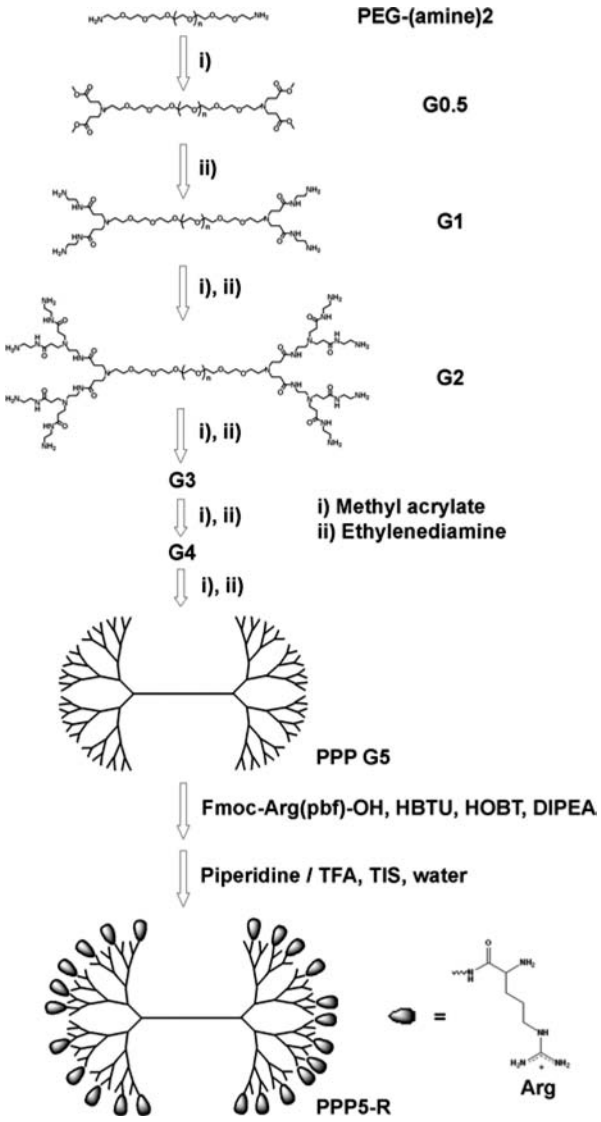
† Seoul National University.

‡ Chungnam National University.

[1] Abbreviations: PAMAM, poly(amido amine); PEG, poly(ethylene glycol); PPP, PAMAM-PEG-PAMAM; PPP-R, Arg-PAMAM-PEG-PAMAM-Arg; PEI, polyethylenimine; DHB, 2,5-dihydroxybenzoic acid; HOBt, *N*-hydroxybenzotriazole; HBTU, 2-(1*H*-benzotriazole-1-yl)-1,1,3,3-tetramethyluronium hexafluorophosphate; pbf, 2,2,4,6,7-pentamethyldihydrobenzofuran-5-sulfony; MALDI-TOF, matrix assisted laser desorption ionization-time of flight; AFM, atomic force microscopy; PBS, phosphate buffered saline; PLLD, poly(L-lysine) dendrimer.

10.1021/bc0601525 CCC: $37.00 © 2007 American Chemical Society
Published on Web 02/23/2007

Scheme 1. Synthetic Scheme of PPP5-R



nium hexafluorophosphate (HBTU) were purchased from Anaspec, Inc. (San Jose, CA). Fmoc-L-Arg(pbf)-OH was purchased from Novabiochem (San Diego, CA). Luciferase 1000 Assay System and Reporter Lysis Buffer were purchased from Promega (Madison, WI). The luciferase expression plasmid, pCN-Luci, was constructed by subcloning cDNA of *Photinus pyralis* luciferase with the 21-aminoacid nuclear localization signal from SV40 large T antigen to pCN (*16*). The GFP expression plasmid, pEGFP-N3 (4.7 kb), was purchased from BD Biosciences Clontech (Mountain View, CA). PicoGreen reagent was purchased from Molecular Probes (Eugene, OR). Fetal bovine serum (FBS), minimal essential medium (MEM), and Dulbecco's modified Eagle's medium (DMEM) were purchased from GIBCO (Gaithersburg, MD). The Micro BCA protein assay kit was purchased from Pierce (Rockford, IL). All other chemicals were purchased and used without any further purification.

Synthesis of PPP5-R. The backbone polymer, PAMAM-PEG-PAMAM G5 (PPP5) was synthesized according to the methods of our previous work (*6*). Briefly, PPP5 was synthesized using poly(ethylene glycol)-*bis*-amine(PEG) (MW 3400) as a polymeric supporter through iterative multistep reactions of Michael addition of methyl acrylate (step 1) followed by amidation of ethylenediamine (step 2) as shown in Scheme 1.

Synthesis of PPP0.5 (step 1). First, PEG was dissolved in methanol and added dropwise to 100 equiv of methyl acrylate kept at 37 °C. After 48 h, methanol and unreacted methyl acrylate were removed under vacuum. The residue was precipitated with an excess of cold ethyl ether and dried under vacuum to remove ethyl ether, leaving a white solid, PAMAM-PEG-PAMAM G 0.5 (PPP0.5). ^{1}H NMR (MeOD): δ PEG(CH_2CH_2O) = 3.63; δ PAMAM($-COOCH_3$) = 3.66; δ PAMAM($-CH_2COOCH_3$) = 2.51; δ PAMAM(protons next to tertiary amines) = 2.85.

Synthesis of PPP1 (step 2). PPP0.5 was dissolved in methanol and added dropwise to 100 equiv of ethylenediamine kept at 37 °C. After 48 h, methanol and ethylenediamine were removed under vaccum. The residue was precipitated with an excess of ethyl ether to remove residual ethylenediamine and dried under vacuum to remove ethyl ether, leaving a pale yellow solid, PAMAM-PEG-PAMAM G 1.0 (PPP1). ^{1}H NMR (D_2O): δ PEG(CH_2CH_2O) = 3.72; δ PAMAM($-CH_2CONH-$) = 2.46; δ PAMAM($-CONHCH_2-$) = 3.32; δ PAMAM(protons next to amines) = 2.6−3.0.

Synthesis of PPP1.5−PPP5. Steps 1 and 2 were consecutively repeated to obtain the higher-generation copolymers. Synthesis of higher-generation copolymer is identical to the above methods, and so we omit them and show the ^{1}H NMR result of each generation copolymer.

Synthesis of PPP1.5. ^{1}H NMR (MeOD): δ PEG(CH_2CH_2O) = 3.63; δ PAMAM($-COOCH_3$) = 3.67; δ PAMAM($-CONHCH_2-$) = 3.27; δ PAMAM($-CH_2COOCH_3$) = 2.46; δ PAMAM($-CH_2CONH-$) = 2.39; δ PAMAM(protons next to tertiary amines) = 2.6−3.0.

Synthesis of PPP2. ^{1}H NMR (D_2O): δ PEG(CH_2CH_2O) = 3.72; δ PAMAM($-CH_2CONH-$) = 2.45; δ PAMAM($-CONHCH_2-$) = 3.31; δ PAMAM(protons next to amines) = 2.6−3.0.

Synthesis of PPP2.5. ^{1}H NMR (MeOD): δ PEG(CH_2CH_2O) = 3.63; δ PAMAM($-COOCH_3$) = 3.67; δ PAMAM($-CONHCH_2-$) = 3.26; δ PAMAM($-CH_2COOCH_3$) = 2.46; δ PAMAM($-CH_2CONH-$) = 2.39; δ PAMAM(protons next to tertiary amines) = 2.6−3.0.

Synthesis of PPP3. ^{1}H NMR (D_2O): δ PEG(CH_2CH_2O) = 3.72; δ PAMAM($-CH_2CONH-$) = 2.46; δ PAMAM($-CONHCH_2-$) = 3.36; δ PAMAM(protons next to amines) = 2.6−3.0.

Synthesis of PPP3.5. ^{1}H NMR (MeOD): δ PEG(CH_2CH_2O) = 3.68; δ PAMAM($-COOCH_3$) = 3.71; δ PAMAM($-CONHCH_2-$) = 3.30; δ PAMAM($-CH_2COOCH_3$) = 2.51; δ PAMAM($-CH_2CONH-$) = 2.43; δ PAMAM(protons next to tertiary amines) = 2.6−3.0.

Synthesis of PPP4. ^{1}H NMR (D_2O): δ PEG(CH_2CH_2O) = 3.72; δ PAMAM($-CH_2CONH-$) = 2.46; δ PAMAM($-CONHCH_2-$) = 3.31; δ PAMAM(protons next to amines) = 2.6−3.0.

Synthesis of PPP4.5. ^{1}H NMR (MeOD): δ PEG(CH_2CH_2O) = 3.66; δ PAMAM($-COOCH_3$) = 3.69; δ PAMAM($-CONHCH_2-$) = 3.28; δ PAMAM($-CH_2COOCH_3$) = 2.48; δ PAMAM($-CH_2CONH-$) = 2.41; δ PAMAM(protons next to tertiary amines) = 2.5−3.0.

Synthesis of PPP5. ^{1}H NMR (D_2O): δ PEG(CH_2CH_2O) = 3.72; δ PAMAM($-CH_2CONH-$) = 2.45; δ PAMAM($-CONHCH_2-$) = 3.31; δ PAMAM(protons next to amines) = 2.6−3.0.

Synthesis of PPP5-R. Arginine coupling to the PPP5 was performed in anhydrous DMF for 1 day at room temperature with 4 equiv of HOBT, HBTU, and Fmoc-Arg(pbf)-OH and 8 equiv of DIPEA. The product was precipitated with an excess of diethyl ether three times and mixed with an equal volume of piperidine (30% in DMF) at room temperature for 20 min to remove the Fmoc groups of coupled Fmoc-Arg(pbf)-OH. The reaction mixture was precipitated again with diethyl ether and

the reagent (95:2.5:2.5, trifluoroacetic acid/triisopropylsilane/water, v/v) was used to deprotect the pbf groups of coupled arginine residues at room temperature for 6 h. After the reaction, the final product, PPP5-R, was dialyzed against ultrapure water overnight and lyophilized before use for analysis and assay.

^{1}H NMR (D_2O): δ arginine($-HCCH_2C\mathbf{H_2}CH_2NH-$) = 1.66; δ arginine($-HCC\mathbf{H_2}CH_2CH_2NH-$) = 1.86; δ PAMAM($-C\mathbf{H_2}$-$CONH-$) = 2.50; δ PAMAM(protons next to amines) = 2.7−2.9; δ arginine($-HCCH_2CH_2C\mathbf{H_2}NH-$) = 3.24; δ PAMAM($-CONHC\mathbf{H_2}-$ and $-CONHCH_2C\mathbf{H_2}NHCO-$) = 3.37; δ PEG($-C\mathbf{H_2}C\mathbf{H_2}O-$) = 3.71; δ arginine($-\mathbf{H}CCH_2CH_2CH_2NH-$) = 3.86.

^{1}H NMR Spectroscopy. ^{1}H NMR spectra of the polymers were obtained using a Bruker DPX-300 NMR spectrometer (300 MHz). For analysis, the polymer samples were dissolved in MeOD or D_2O containing 3-(trimethylsilyl)propionic-2,2,3,3-d_4 acid sodium salt as an internal reference (0 ppm).

MALDI-TOF Mass Spectroscopy. MALDI-TOF mass spectra were obtained using a Voyager-DE STR Biospectrometry Workstation (Applied Biosystems, Inc.) in the linear delayed-extraction mode. A polymer solution was prepared by dissolving 1 mg of the polymer in 1 mL of water. The matrix solution was prepared by dissolving 10 mg of matrix (DHB/fucose = 1:1) in 1 mL of the 1:1 mixture of the water and acetonitrile. The samples were prepared by mixing them to a final volume of 2 μL at various ratios.

Gel Retardation Assays. PPP5-R/plasmid complexes at various weight ratios ranging from 0.5 to 8.0 were prepared in Hepes buffered saline (10 mM Hepes, 1 mM NaCl; pH 7.4). After 30 min incubation at room temperature for the complex formation, the samples were electrophoresed on a 0.7% (w/v) agarose gel and stained in an ethidium bromide solution (0.5 μg/mL), and analyzed on a UV illuminator to show the location of the DNA.

Polymer/DNA Self-Assembly Analysis by PicoGreen Assay. PicoGreen assay was carried out to analyze the self-assembly of PPP5-R/plasmid DNA quantitatively as reported recently (*12*, *16*). Briefly, PicoGreen reagent (200×) was diluted to 200-fold in TE buffer before the experiment. 200 μL of the diluted PicoGreen stock solution was mixed with the same volume of blank solution or polyplex solution (1 μg DNA, 1× HBS) prepared at various weight ratios ranging from 0 to 10. After 2 min incubation, each solution was added to 1.6 mL of TE buffer in a test tube. Fluorescence was measured with a FP-750 spectrofluorometer (Jasco) at room temperature. Excitation and emission wavelengths were set at 480 and 520 nm, respectively. Values were represented as relative fluorescence (%) to the value of plasmid DNA.

Polyplex Size Measurements. The hydrodynamic diameters of the PPP5-R/plasmid DNA complexes were determined by light scattering. 2 mL of polyplex solutions containing 5 μg of DNA were prepared at various weight ratios ranging from 1 to 20. After 30 min incubation, polyplex sizes were measured using a Zetasizer 3000HS (Malvern Instruments, U.K.). The laser used is a nominal 5 mW HeNe laser having a 633 nm wavelength. Scattered light was detected at a 90° angle. The refractive index (1.33) and the viscosity (0.89) of ultrapure water were used at 25 °C for measurements. *Zetasizer 3000 (Advanced) Size Mode* v1.61 software was used for data acquisition. Data analysis was performed in automatic mode. Measured sizes were presented as the average values of five runs.

ζ-Potential Measurements. 2 mL of polyplex solutions containing 5 μg of DNA were prepared in Hepes buffered saline (10 mM Hepes, 1 mM NaCl; pH 7.4) at various weight ratios ranging from 0.5 to 20. After 30 min incubation, each polyplex solution was diluted to a 10 mL final volume prior to measurements. ζ-Potential measurements were carried out using a Zetasizer 3000HS (Malvern Instruments, U.K.) at 25 °C. *Zetasizer 3000 (Advanced) Zeta Mode* v1.61 software was used for data acquisition. The sampling time was set to automatic. Potential values were presented as the average values of five runs.

Atomic Force Microscopy (AFM). The particle shapes and sizes of the polymer/plasmid DNA complexes were analyzed using atomic force microscopy (Nanoscope IIIa system, Digital Instruments, Inc., Santa Barbara, CA). The samples were prepared by mixing 0.1 μg of plasmid DNA with aqueous polymer solution at various weight ratios to obtain a final DNA concentration of 10 ng/μL. After 30 min incubation, 1 μL aliquots of the complex solutions were placed on a freshly cleaved mica surface and allowed to stick for 1−2 min. Excess solution was removed by careful absorption onto filter paper, and the mica surface was further dried at room temperature for 24 h. The image mode was set to tapping mode, and the scanning speed was 1−5 Hz.

Polyplex Solubility Measurements in Water. The solubility of polyplex was evaluated by the method developed by Wadhwa et al. with a slight modification (*17*). The PAMAM-R G 4 dendrimer was used as a control reagent (*12*). Polymers were mixed with 20 μg of plasmid DNA at various weight ratios in 0.5 mL of 25 mM Hepes buffer. After incubation for 30 min at room temperature, each mixture was centrifuged for 5 min at 13000 rpm and 10 °C. Then, the absorbance of each supernatant was measured at 260 nm. The solubility was calculated as a percentage ratio of the absorbance of pure DNA solution and each supernatant.

Cytotoxicity Assay. The cytotoxicity of the polymers was measured by MTT assay. HepG2 human hepatocellular carcinoma cells were seeded in a 96-well tissue culture plate at 10^4 cells per well in 90 μL MEM medium containing 10% FBS. Cells achieving 70−80% confluence after 24 h were exposed to 10 μL of the polymer solutions having various concentrations for 24 h. Then, 26 μL of stock solution of MTT (2 mg/mL in PBS) were added to each well. After 4 h of incubation at 37 °C, each medium was removed, and 150 μL of DMSO was added to each well to dissolve the formazan crystal formed by proliferating cells. Absorbance was measured at 570 nm using a microplate reader (Molecular Devices Co., Menlo Park, CA) and recorded as a percentage relative to the value of untreated control cells.

In Vitro Transfection. HepG2, HeLa human adenocarcinoma cells were seeded at a density of 5×10^4 cells/well in a 24-well plate in a medium containing 10% FBS and grown to reach 70−80% confluence prior to transfection. C2C12 mouse myoblast cells were seeded at a density of 3×10^4 cells/well. Before transfection, the cells were rinsed with PBS, and serum-free or serum-containing medium was added to each well. The cells were treated with polyplex solution containing 2 μg of plasmid DNA at different weight ratios for 4 h at 37 °C. In the presence of serum, the cells were incubated for 24 h after transfection. After exchange of medium, cells were further incubated for 2 days after transfection. Then, the growth medium was removed, and the cells were rinsed with PBS and shaken for 30 min at room temperature in 120 μL of Reporter Lysis Buffer. Luciferase activity was measured by a luminescence assay, and a protein assay was performed using a Micro BCA Protein Assay Reagent Kit. 10 μL of the lysate was dispensed into a luminometer tube, and luciferase activity was integrated over 10 s with a 2 s measurement delay in a Lumat LB 9507 luminometer (Berthold, Germany) with an automatic injection of 50 μL of luciferase assay reagent. The final results were reported in terms of RLU/mg cellular protein.

Fluorescence Miscroscopy. HeLa cells were seeded at a density of 2×10^4 cells/well in a 24-well plate in a medium containing 10% FBS. The cells were treated with polyplex solution containing 2 μg of plasmid DNA (pEGFP-N3) at different weight ratios for 4 h at 37 °C. After exchange of medium, cells were further incubated for 24 h, and the fluorescence of expressed GFP was viewed using Axiovert 25 microscopy (Carl Zeiss, Germany). The images were obtained using *AxioVision 3.1* software.

Treatment with Inhibitors. HeLa cells were seeded at a density of 1×10^5 cells/well in a 24-well plate. After 1 day of incubation in normal conditions, cells were pretreated with genistein (200 μM) (*18*), wortmannin (100 nM) (*19*), or chlorpromazine (10 μg/mL) (*20*) for 1 h, or chloroquine (100 μM) for 30 min, before addition of polyplexes. Genistein is reported to inhibit caveolae-mediated uptake processes, and chlorpromazine is known to block clathrin-mediated endocytosis. Wortmannin is an inhibitor of phosphatidyl inositol-3-phosphate (PI3) kinase completing macropinocytosis, and chloroquine is well-known to inhibit endosome acidification. Polyplexes of PPP5 and PPP5-R, containing 2 μg of plasmid DNA, were prepared at weight ratios of 15 and 10, respectively. After 2 h of polyplex incubation, all media were washed with PBS and replaced with fresh media containing 10% serum, then cells were further incubated for 2 days before assay.

Potassium Depletion. HeLa cells were seeded at a density of 1×10^5 cells/well in a 24-well plate and treated with a procedure described by Larkin et al., which results in rapid depletion of cellular potassium (*21*). Potassium depletion of the cells is known to perturb clathrin-mediated endocytosis. After 1 day of incubation in normal conditions, cells were rinsed with K^+-free buffer (140 mM NaCl, 20 mM Hepes, 1 mM $CaCl_2$, 1 mM $MgCl_2$, 1 mg/mL D-glucose; pH 7.4) and subsequently rinsed for 5 min with hypotonic buffer (K^+-free buffer diluted 1:1 with distilled water), followed by washing three times with K^+-free buffer. Control cells were treated with buffer (K^+-free buffer + 10 mM KCl). Polyplexes were incubated with the cells for 2 h and washed with PBS. Then, all media were replaced with fresh media containing 10% serum, and cells were further incubated for 2 days before assay.

RESULTS AND DISCUSSION

Synthesis and Characterization of PPP5-R. Backbone polymer, PAMAM-PEG-PAMAM G5 (PPP5), was synthesized according to the previous report (*6*). The synthesis of PPP5 was monitored by ^{1}H NMR spectroscopy. Arginine conjugation of PPP5 was performed with the HOBt/HBTU coupling method in DMF. Fmoc groups of conjugated arginines were removed by piperidine solution, and the reagent (95:2.5:2.5, trifluoroacetic acid/triisopropylsilane/water, v/v) was used to deprotect the pbf groups of coupled arginines. Scheme 1 shows the entire synthetic procedure of PPP5-R. The synthesis of PPP5-R was confirmed by ^{1}H NMR spectroscopy and MALDI-TOF. The ^{1}H NMR spectra is shown in Figure 1.

The number of grafted arginines was calculated by comparing the NMR peak intensities between the protons of PEG and arginine. Approximately 36 molecules of arginine were found to be conjugated to 1 molecule of PPP5. From this result, the molecular weight of PPP5-R was calculated to be 2.37×10^4 Da. Meanwhile, the Mn and Mw of PPP5-R were experimentally measured using MALDI-TOF. Figure 2 shows the MALDI-TOF MS of PPP5-R. 1:1 DHB/fucose mixture, a well-known "cold" matrix was used as a matrix (*22*). The Mn was estimated to be 2.34×10^4 Da and the Mw to be 2.37×10^4 Da. The polydispersity index of the polymer was determined to be 1.01. The MALDI-TOF result was found to correspond well with the ^{1}H NMR result.

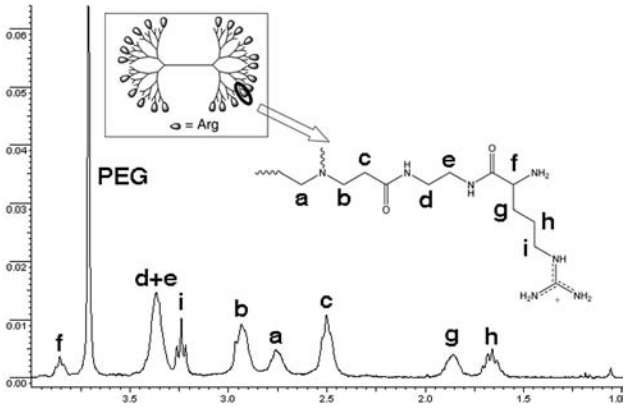


Figure 1. ^{1}H NMR spectra of PPP5-R in D_2O. Molecule in box represents PPP5-R.

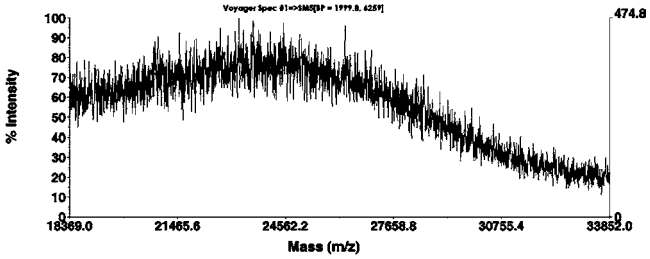


Figure 2. MALDI-TOF MS of PPP5-R.

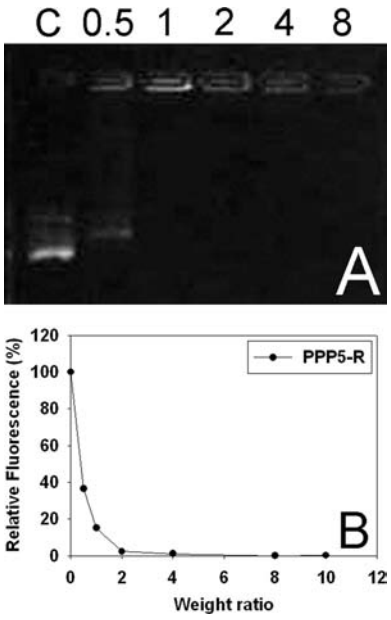


Figure 3. (a) Agarose gel retardation of PPP5-R polyplexes. The numbers represent the weight ratios of the polyplexes. C: plasmid DNA only. (b) PicoGreen reagent assay of PPP5-R polyplexes. Values were represented as relative fluorescence (%) to the value of plasmid DNA.

Self-Assembly of PPP5-R and Plasmid DNA. The self-assembly of PPP5-R and plasmid DNA was examined by agarose gel retardation assay and PicoGreen reagent assay, respectively. PicoGreen reagent is a highly sensitive probe for monitoring polymer/DNA self-assembly (*23*). Figure 3a shows the gel retardation assay result of PPP5-R. PPP5-R could retard the migration of plasmid DNA by forming polyplexes at a weight ratio of 1. Nonmigration of DNA in the gel indicates condensation of DNA by PPP5-R. In a PicoGreen reagent assay experiment (Figure 3b), the polymer is thought to possess a strong DNA condensing ability, as the relative fluorescence intensity of polyplex is abruptly decreased to 15% at a weight ratio of 1 and even to 2% at a ratio of 2.

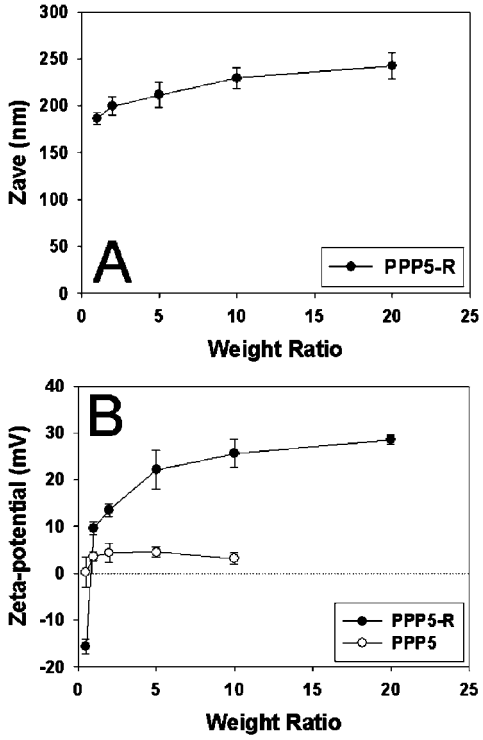


Figure 4. (a) Average size measurements of PPP5-R polyplexes. (b) ζ-Potentials of PPP5-R and PPP5 polyplexes.

Size and ζ-Potential Measurements of the PPP5-R Polyplexes. The proper size of polyplexes is thought to be essential for efficient gene delivery. We performed the average size measurements of PPP5-R polyplexes using a Zeta-sizer. Polyplexes were prepared at various weight ratios ranging from 1 to 20. As shown in Figure 4a, the average size of the polyplexes was 186 nm at a weight ratio of 1 and gradually increased to 242 nm at 20. A plateau of size values from a weight ratio of 5 indicated the formation of stable polyplexes with a size appropriate for gene delivery.

The ζ-potential values of the polyplexes were also estimated at various weight ratios ranging from 0.5 to 20 using a Zeta-sizer (Figure 4b). We also performed ζ-potential measurements for native PPP5 polyplexes to analyze the effect of the arginine modification of PPP5. The positive potential value of the polyplex is thought to be important to adhere to the negatively charged cellular membrane, leading to the intracellular uptake of the polyplex. The ζ-potential value of PPP5-R polyplex was negative (−15.6 mV) at a weight ratio of 0.5 and abruptly increased to 9.7 mV at a ratio of 1. In addition, the values were around 22−28 mV at the ranges over weight ratio 5, displaying stable complex formation with plasmid DNA. On the other hand, the ζ-potential values of PPP5 polyplex were around 3−5 mV even at a weight ratio of 10. In addition, we have reported an interesting result about the ζ-potential experiments of dendritic

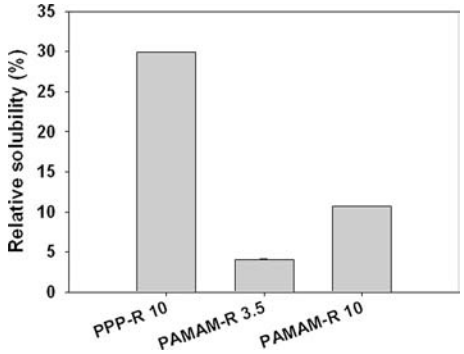


Figure 6. Water solubility of PPP5-R polyplex. The numbers represent the weight ratios of the polyplexes.

triblock copolymer, poly(L-lysine) dendrimer-PEG-poly(L-lysine) dendrimer (PLLD-PEG-PLLD) (*24*). The potential value of PLLD-PEG-PLLD polyplex did not rise to a positive value even at a charge ratio of 8, suggesting that two PLL dendrimer blocks located at each end of the copolymer self-assemble with DNA, and accordingly, the surface of the polyplex is coated with hydrophilic PEG chains. There are big differences in the pK_a value of surface functionalities and molecular size of the dendritic blocks of each block copolymer. The pK_a value of guanidine group of arginine residue is over 12, although that of the primary amine of PLLD and PAMAM is about 10. So, the dendritic blocks of PPP5-R would possess stronger positive charges than others at the same pH condition. Moreover, the molecular weights of the dendritic block of $PLLD_4$-PEG-$PLLD_4$, PPP5, and PPP5-R are about 1920, 6760, and 10 590, respectively. Therefore, it is thought that large dendritic blocks with high positive charges may not be fully shielded by PEG chains even after PEG-coated complexation.

Atomic Force Microscopy (AFM). The morphologies of PPP5-R polyplexes were observed by AFM. Polyplexes were prepared at various weight ratios ranging from 0.5 to 10. As shown in Figure 5a, PPP5-R could not condense plasmid DNA compactly, and so DNA stretched out from hundreds of nanometer-scale semicondensed polyplex cores like a corona at a weight ratio of 0.5. At a ratio of 1, the polymer could condense plasmid DNA to a complex, but we could still observe the small projections around the core, which were inferred to be a portion of noncondensed plasmid DNA (Figure 5b). At a ratio of 10, it was observed that PPP5-R could form compact spherical polyplexes with plasmid DNA with homogeneity and about a 200-nm size (Figure 5c). These results agreed well with the size measurement results obtained by Zeta-sizer.

Water Solubility. After complexation, some polyplexes show a tendency to aggregate in water because of increased hydrophobicity caused by charge neutralization, limiting their in vivo application (*5*). So, we examined the water solubility of the PPP5-R polyplex. PAMAM-R G4 was used as a control reagent because its molecular structure was identical to that of PPP5-R

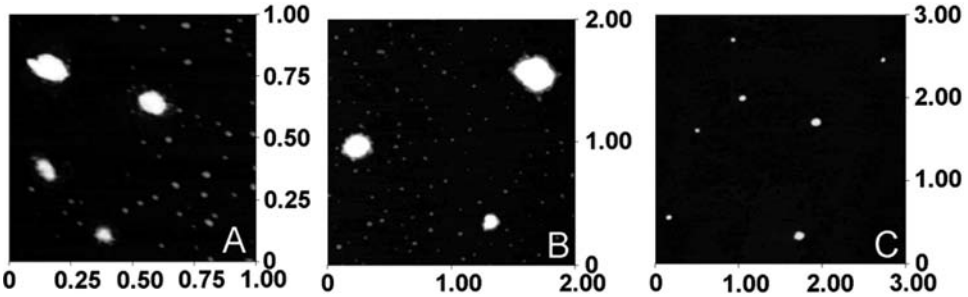


Figure 5. AFM images of PPP5-R polyplexes: at weight ratios of (a) 0.5, (b) 1, and (c) 10. The numbers around the figures represent μm-scaled sizes.

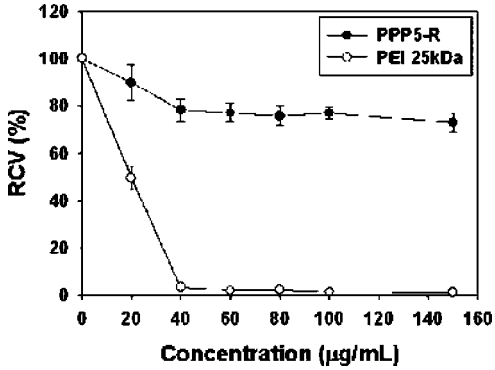


Figure 7. Cytotoxicity of PPP5-R in HepG2 cells by MTT assay. RCV: relative cell viability. Data were expressed as mean ± standard deviation ($n = 5$).

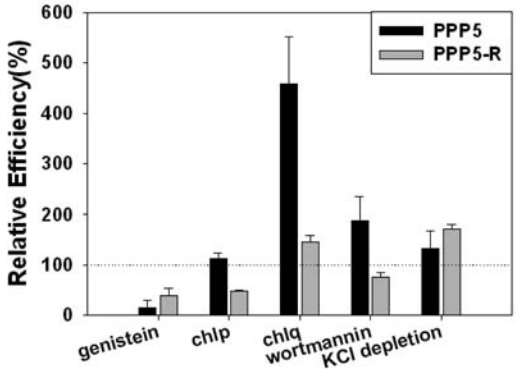


Figure 9. Relative transfection efficiency (RTE) of each polyplex in treating various cellular uptake inhibitors and in potassium depletion condition. chlp , chlorpromazine; chlq, chloroquine; RTE = experimental value/control value × 100 (%). Data were expressed as mean ± standard deviation ($n = 3$).

except the core part. As shown in Figure 6, we can find that PPP5-R polyplex has a sixfold enhanced water solubility compared to PAMAM-R G4 polyplex in an optimal ratio for transfection. From this result, it is obvious that the PEG core of PPP5-R plays an important role for increasing the water solubility of the polyplex.

Cytotoxicity. The cytotoxicity of PPP5-R was examined on HepG2 cell lines by MTT assay. PEI was used as a control. The cytotoxicity of PEI is well-known. As shown in Figure 7, cell viability of PEI was 50% at 20 μg/mL and decreased to 4% at 40 μg/mL of concentration, while PPP5-R displayed 77−90% cell viability in the same concentration range, suggesting that the cytotoxicity of PPP5-R is minimal.

Transfection Experiments. Transfection efficiency of PPP5-R was examined on HeLa, C2C12, and HepG2 cells. PEI was used as a control reagent in optimal condition. PPP5-R showed very high transfection efficiency comparable to that of PEI in the presence or absence of serum in HeLa and C2C12 cells in Figure 8a,b. The transfection efficiencies of both PEI and PPP5-R were observed to be reduced in the presence of serum. Interestingly, transfection efficiency ratios (+FBS/−FBS) of PEI were 0.03 and 0.07 in C2C12 and HeLa cells, respectively, while the ratios of PPP5-R were in a range between 0.10 and 0.23. Considering our previous data for native PPP5 (transfection efficiency ratio = 0.85−1.3) (*6*), the PEG core of the copolymers is thought to coat the surface of the polyplex and inhibit the nonspecific interaction of polyplexes with serum compartments, suppressing the reduction of the transfection efficiency. However, in the case of PPP5-R, PEG could not coat the polyplex completely, reducing its efficiency ratio, as described in the ζ-potential experiment. The transfection efficiency of PPP5-R was also compared with that of native PPP5 on HepG2 cells (Figure 8c). PPP5-R showed a transfection efficiency value 20−36 times higher than that of native PPP5.

Furthermore, we can also identify a much increased transfection activity of PPP5-R in fluorescence microscopy. A considerable number of cells expressed green fluorescence protein in treatment with PPP5-R/pEGFP polyplex (Figure 8e), unlike with PPP5/pEGFP polyplex (Figure 8d). This greatly increased transfection efficiency of PPP5-R must be due to the arginine residues grafted onto the periphery. From these results, we hypothesize that arginine residues of PPP5-R would function

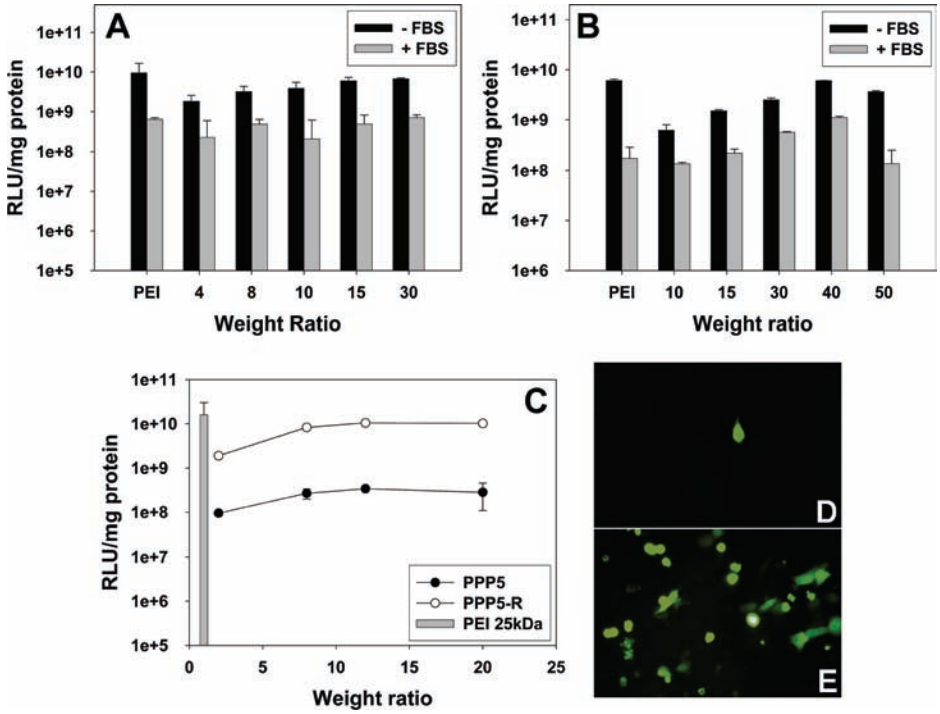
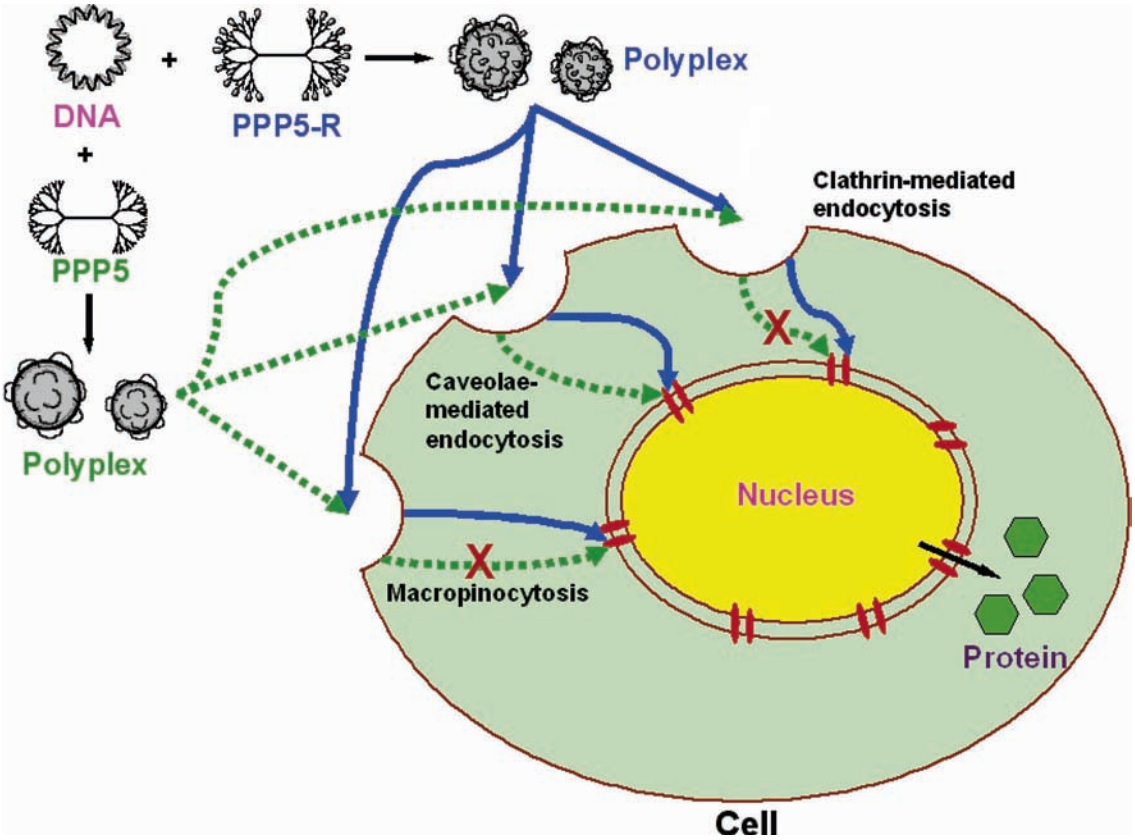


Figure 8. Transfection experiments in (a) HeLa cells, (b) C2C12 cells, and (c) HepG2 cells. PEI and PPP5 are used as control reagents. (d,e) represent GFP expression in HeLa cells by PPP5 and PPP5-R, respectively. Data were expressed as mean ± standard deviation ($n = 3$).

Scheme 2. Schematic Diagram of the Proposed Cellular Uptake Mechanism of PPP5 Polyplex and PPP5-R Polyplex



as a key to a cellular membrane gate, which guides the PPP5-R polyplex to the cellular uptake pathway for efficient transfection.

Cellular Uptake Pathway Leading to Enhanced Transfection. These transfection results raise a question about the differences of the cellular uptake pathway leading to enhanced transfection between native PPP5 and arginine-grafted PPP5-R. The cellular uptake pathway of cell-penetrating peptides containing Tat sequences and oligo-arginine peptides has been reported by many groups (*13*−*15*), but that of arginine-grafted dendritic polymer polyplex is not well-understood. We performed the transfection experiments on HeLa cells by treatment with various cellular uptake inhibitors and compared the effect in order to examine the cellular uptake pathway leading to effective transfection of PPP5 and PPP5-R polyplexes, for the first time. Genistein is reported to inhibit caveolae-mediated uptake processes (*18*), and chlorpromazine is known to block clathrin-mediated endocytosis (*20*). Wortmannin is an inhibitor of phosphatidyl inositol-3-phosphate (PI3) kinase completing macropinocytosis (*19*), and chloroquine is a well-known endosome acidification inhibitor.

Figure 9 represents the relative transfection efficiencies of PPP5 and PPP5-R polyplexes in the presence of each inhibitor. In the case of PPP5, only genistein reduced the efficiency considerably, and chlorpromazine did not affect the efficiency. The result suggests that PPP5 polyplexes entering through caveolae-mediated uptake lead the effective transfection and agrees well with the other report (*25*). In the presence of chloroquine, its enhanced efficiency leads us to believe that the cellular uptake of PPP5 polyplex also happens through clathrin-mediated endocytosis but the polyplex may not escape from the endosome efficiently, not leading to effective transfection. It is thought that chloroquine helps the PPP5 polyplex escape from the endosome by inhibiting acidification of the endosome and leading to mechanical swelling of the polymer. This view is well-supported by the previous result that the transfection efficiency of PPP5 is relatively lower in HepG2 cells lacking caveolin-1 than in 293 cells (*6*). Macropinocytosis inhibition by treatment with wortmannin led to a somewhat increased transfection efficiency of PPP5 polyplex. It is thought that this may be associated with the fact that the cellular uptake of polyplex through macropinocytosis is reported to impair the transfection efficiency (*19*).

Interestingly, unlike with PPP5, the transfection of the PPP5-R polyplex is reduced in the presence of both genistein and chlorpromazine by 39% and 47%, respectively, and is not particularly affected in the presence of chloroquine. This result represents evidence that the effective transfection of arginine-grafted dendritic polymer is carried out through the cellular uptake of both caveolae- and clathrin-mediated pathways to some degree. A relatively small effect of chloroquine on PPP5-R in comparison with PPP5 and the inhibition of transfection by chlorpromazine suggest that PPP5-R polyplex may have its own specific competency to escape from the compartments of a clathrin-dependent pathway, unlike PPP5 polyplex. Macropinocytosis inhibition by wortmannin reduced the transfection efficiency by 76%, unlike in the recent report by Nakase et al. that the cellular uptake of arginine-rich peptides was significantly suppressed by a macropinocytosis inhibitor (*26*). Our results show that arginine-rich peptide and arginine-grafted dendritic copolymer polyplex have distinct internalization mechanisms. Scheme 2 shows the proposed cellular uptake mechanisms leading to transfection of both PPP5 polyplex and PPP5-R polyplex.

Moreover, we performed the transfection experiments of both polyplexes in the depletion of potassium ion in order to confirm the chlorpromazine experimental result (Figure 9). Potassium depletion of the cells is also known to perturb clathrin-mediated endocytosis (*21*). In line with our expectations, the transfection of PPP5 polyplexes was not affected by potassium depletion, which corresponded with the chlorpromazine result. However, on the contrary, the transfection efficiency was increased about twofold in the case of PPP5-R. Discordance with the previous

chlorpromazine result leads us to preconclude that another factor could be affecting the cellular uptake of arginine-grafted dendritic polymer. Recently, Rothbard et al. reported that the membrane potential of cells strongly induces the translocation of guanidinium-rich peptides, and the membrane potential is related to the negative log value of the concentration ratio of extracellular (K_o) and intracellular (K_i) potassium ions (*27*). In KCl-containing buffer, generally K_o and K_i are known to be about 10 mM and 140 mM, respectively. In potassium depletion condition, K_o may become a micromolar concentration at most and K_i drops to 40% (about 50 mM) when polyplex solution is added after about 15 min of cell rinsing (*21*). According to Rothbard et al.'s formula, the membrane potential would become more negative in the potassium depletion condition, and it may induce more cellular uptake of polyplexes and the following enhanced transfection efficiency.

In summary, these results strongly suggest that the cellular uptake leading to the effective transfection of arginine-grafted dendritic polymer polyplex is not dependent on one exclusive pathway and has the possibility of combination of multiple pathways, unlike with the caveolae-dependent uptake of PPP5 polyplex lacking arginine residues. Therefore, this unique uptake mechanism of the PPP5-R polyplex is thought to be one of the important reasons for the enhanced transfection efficiency of the polyplex. Moreover, we are studying the nuclear localization ability of the arginine residues, which may provide another key explanation for the result. This finding would help us to understand arginine-based polymeric gene carriers and to develop more efficient gene delivery carriers in the future.

Finally, PPP5-R would be a less toxic and high transfection efficient gene delivery carrier unrelated to cell type because of its multiple uptake mechanisms. Also, it would show the potential for drug delivery systems by conjugation of drugs to the polymer due to its great cell-penetrating ability.

CONCLUSION

We synthesized a novel arginine-grafted dendritic block copolymer, R-PAMAM-PEG-PAMAM-R G5 (PPP5-R), for gene delivery systems. PPP5-R could form nanosized polyplexes with plasmid DNA, which was examined by agarose gel electrophoresis, PicoGreen reagent assay, Zeta-sizer, and AFM. The positive ζ-potential values of the PPP5-R polyplex show the formation of positively charged stable polyplex particles and suggest that large dendritic blocks with high positive charge may not be fully shielded by PEG chains even after PEG-coated complexation. The PPP5-R polyplex showed enhanced water solubility due to the PEG core and low cytotoxicity. The PPP5-R polyplex represented the greatly enhanced transfection efficiency in comparison with native PPP5 on various cell lines. By treating various cellular uptake inhibitors, we concluded that the cellular uptake leading to the effective transfection of arginine-grafted dendritic polymer PPP5-R polyplex is not dependent on one exclusive pathway and has the possibility of multiple pathways, unlike with the caveolae-dependent uptake of PPP5 polyplex lacking arginine residues. Moreover, this particular cellular uptake pathway of PPP5-R is proposed to be one of the important reasons for the enhanced transfection efficiency.

ACKNOWLEDGMENT

This work was supported by the Korea Health 21 R&D Project of The Ministry of Health & Welfare, Republic of Korea (A04-0004), the Gene Therapy Project of the Ministry of Science and Technology (M1053403004-05N3403-00410), and the KBRDG Initiative Research Program (F104AD010011-06A0401-01110).

LITERATURE CITED

(1) Kay, M. A., Liu, D., and Hoogerbrugge, P. M. (1997) Gene therapy. *Proc. Natl. Acad. Sci. U.S.A. 94*, 12744−12746.

(2) Luo, D., and Saltzman, W. M. (2000) Synthetic DNA delivery systems. *Nat. Biotechnol. 18*, 33−37.

(3) Zauner, W., Ogris, M., and Wagner, E. (1998) Polylysine-based transfection systems utilizing receptor-mediated delivery. *Adv. Drug Delivery Rev. 30*, 97−113.

(4) Veena, V., Thomas, T., and Thomas, T. J. (2002) DNA nanoparticles and development of DNA delivery vehicles for gene therapy. *Biochemistry 41*, 14085−14094.

(5) Tang, M. X., and Szoka, F. C., Jr. (1997) The influence of polymer structure on the interactions of cationic polymers with DNA and morphology of the resulting complexes. *Gene Ther. 4*, 823−832.

(6) Kim, T.-i., Seo, H. J., Choi, J. S., Jang, H. S., Baek, J. U., Kim, K., and Park, J. S. (2004) PAMAM-PEG-PAMAM: Novel triblock copolymer as a biocompatible and efficient gene delivery carrier. *Biomacromolecules 5*, 2487−2492.

(7) Brooks, H., Lebleu, B., and Vivès, E. (2005) Tat peptide-mediated cellular delivery: back to basics. *Adv. Drug Delivery Rev. 57*, 559−577.

(8) Zhao, M., and Weissleder, R. (2004) Intracellular cargo delivery using Tat peptide and derivatives. *Med. Res. Rev. 24*, 1−12.

(9) Wadia, J. S., and Dowdy, S. F. (2005) Transmembrane delivery of protein and peptide drugs by TAT-mediated transduction in the treatment of cancer. *Adv. Drug Delivery Rev. 57*, 579−596.

(10) Tung, C.-H., and Weissleder, R. (2003) Arginine containing peptides as delivery vectors. *Adv. Drug Delivery Rev. 55*, 281−294.

(11) Sen, J., and Chaudhuri, A. (2005) Design, syntheses, and transfection biology of novel non-cholesterol-based guanidinylated cationic lipids. *J. Med. Chem. 48*, 812−820.

(12) Choi, J. S., Nam, K., Park, J.-y., Kim, J.-B., Lee, J.-K., and Park, J.-s. (2004) Enhanced transfection efficiency of PAMAM dendrimer by surface modification with L-arginine. *J. Controlled Release 99*, 445−456.

(13) Richard, J. P., Melikov, K., Vivès, E., Ramos, C., Verbeure, B., Gait, M. J., Chernomordik, L. V., and Lebleu, B. (2003) Cell-penetrating peptides. A reevaluation of the mechanism of cellular uptake. *J. Biol. Chem. 278*, 585−590.

(14) Fischer, R., Kohler, K., Fotin-Mleczek, M., and Brock, R. (2004) A stepwise dissection of the intracellular fate of cationic cell-penetrating peptides. *J. Biol. Chem. 279*, 12625−12635.

(15) Fittipaldi, A., Ferrari, A., Zoppe, M., Arcangeli, C., Pellegrini, V., Beltram, F., and Giacca, M. (2003) Cell membrane lipid rafts mediate caveolar endocytosis of HIV-1 Tat fusion proteins. *J. Biol. Chem. 278*, 34141−34149.

(16) Kim, T.-i., Seo, H. J., Choi, J. S., Yoon, J. K., Baek, J.-u., Kim, K., and Park, J.-S. (2005) Synthesis of biodegradable cross-linked poly(β-amino ester) for gene delivery and its modification, inducing enhanced transfection efficiency and stepwise degradation. *Bioconjugate Chem. 16*, 1140−1148.

(17) Wadhwa, M. S., Knoell, D. L., Young, A. P., and Rice, K. G. (1995) Targeted gene delivery with a low molecular weight glycopeptide carrier. *Bioconjugate Chem. 6*, 283−291.

(18) Liu, P., and Anderson, R. G. (1999) Spatial organization of EGF receptor transmodulation by PDGF. *Biochem. Biophys. Res. Commun. 261*, 695−700.

(19) Goncalves, C., Mennesson, E., Fuchs, R., Gorvel, J.-P., Midoux, P., and Pichon, C. (2004) Macropinocytosis of polyplexes and recycling of plasmid via the clathrin-dependent pathway impair the transfection efficiency of human hepatocarcinoma cells. *Mol. Ther. 10*, 373−385.

(20) Wang, L. H., Rothberg, K. G., and Andrson, R. G. (1993) Mis-assembly of clathrin lattices on endosomes reveals a regulatory switch for coated pit formation. *J. Cell Biol. 123*, 1107−1117.

(21) Larkin, J. M., Brown, M. S., Goldstein, J. L., and Anderson, R. G. (1983) Depletion of intracellular potassium arrests coated pit

formation and receptor-mediated endocytosis in fibroblasts. *Cell 33*, 273−285.

(22) Gusev, A. I., Wilkinson, W. R., Proctor, A., and Hercules, D. M. (1995) Improvement of signal reproducibility and matrix/comatrix effects in MALDI analysis. *Anal. Chem. 67*, 1034−1041.

(23) Singer, V. L., Jones, L. J., Yue, S. T., and Haugland, R. P. (1997) Characterization of PicoGreen reagent and development of a fluorescence-based solution assay for double-stranded DNA quantitation. *Anal. Biochem. 249*, 228−238.

(24) Choi, J. S., Joo, D. K., Kim, C. H., Kim, K., and Park, J. S. (2000) Synthesis of a barbell-like triblock copolymer, poly(L-lysine) dendrimer-*block*-poly(ethylene glycol)-*block*-poly(L-lysine) dendrimer, and its self-assembly with plasmid DNA. *J. Am. Chem. Soc. 122*, 474−480.

(25) Rejman, J., Bragonzi, A., and Conese, M. (2005) Role of clathrin- and caveolae-mediated endocytosis in gene transfer mediated by lipo- and polyplexes. *Mol. Ther. 12*, 468−474.

(26) Nakase, I., Niwa, M., Takeuchi, T., Sonomura, K., Kawabata, N., Koike, Y., Takehashi, M., Tanaka, S., Ueda, K., Simpson, J. S., Jones, A. T., Sugiura, Y., and Futaki, S. (2004) Cellular uptake of arginine-rich peptides: roles for macropinocytosis and actin rearrangement. *Mol. Ther. 10*, 1011−1022.

(27) Rothbard, J. B., Jessop, T. C., Lewis, R. S., Murray, B. A., and Wender, P. A. (2004) Role of membrane potential and hydrogen bonding in the mechanism of translocation of guanidinium-rich peptides into cells. *J. Am. Chem. Soc. 126*, 9506−9507.

BC0601525

Oligothiophene Molecular Beacons

Antonella Cazzato,† Massimo L. Capobianco,* Massimo Zambianchi, Laura Favaretto, Cristian Bettini, and Giovanna Barbarella

Istituto per la Sintesi Organica e la Fotoreattività del Consiglio Nazionale delle Ricerche (ISOF-CNR), Via. P. Gobetti 101, 40129 Bologna, Italy. Received June 16, 2006; Revised Manuscript Received November 21, 2006

Oligomers of thiophene are widely studied compounds for their electronic and optoelectronic properties. Despite their strong fluorescence, their use as markers for biomolecules, especially for oligonucleotides (ONs), is still largely unexplored. Here, we describe the synthesis of a series of ON molecular beacons employing different oligothiophenes as fluorescent probes and discuss their fluorescence emissions in comparative experiments with and without dabcyl as a quencher, in their hairpin and linear conformations, and as duplexes after hybridization with a complementary target.

INTRODUCTION

Oligomers of thiophene are well-studied compounds for their (opto)electronic properties. For instance, they have been used for the preparation of thin-film-based organic devices (LED, FET, etc.) (*1*, *2*). An important characteristic of this class of compounds is that their absorption and emission wavelength can be rationally predicted and easily obtained by a careful design of their molecular structure and positioning of substituents (*3*). We have recently started a program aimed at exploring the biological potential of this class of compounds as fluorescent markers for biomolecules such as proteins (*4*) and, more recently, oligonucleotides (*5*, *6*). The use of fluorescence as a tag for oligonucleotides is a useful alternative to radioactive labeling in quantitative experiments (*7*); it also allows an easy localization of oligonucleotides in cells (*8*). The emission of a fluorescent molecule is extremely sensitive to its environment, since small conformational changes of the fluorophore due to solvent effects or to interactions with other molecules through complex formation or energy transfer (FRET) may lead to dramatic changes in emitted light (*9*). In 1996, Tyagi showed a stunning application of FRET in the field of molecular recognition using double-labeled oligonucleotides called "molecular beacons" (*10*). Probes based on this principle are oligonucleotides (ONs) that spontaneously form a hairpin structure (see Figure 1) that puts their 5′ and 3′ ends in close proximity. In such a conformation, the fluorescence of a fluorophore tagged to one of the extremities can be quenched by a suitable moiety linked to the other end through Forster's energy transfer mechanism (*11*) and other mechanisms (*9*). When the ON probe in its quenched form is hybridized with a complementary strand, its conformation changes from hairpin to a distended double helix in which the fluorophore is moved away from the quencher and the fluorescence is (at least in part) restored. In ideal conditions, the ON probe behaves like a molecular beacon (MB): a strong fluorescence emission indicates the formation of the distended duplex (hence the presence of the target), while a weak response to the exciting light reveals the hairpin structure (indicating the absence of the target).

* To whom correspondence should be addressed. E-mail: capobianco@isof.cnr.it.

† Present address: Mediteknology srl, c/o ISOF Area della Ricerca CNR, Via P. Gobetti 101, 40129 Bologna, Italy.

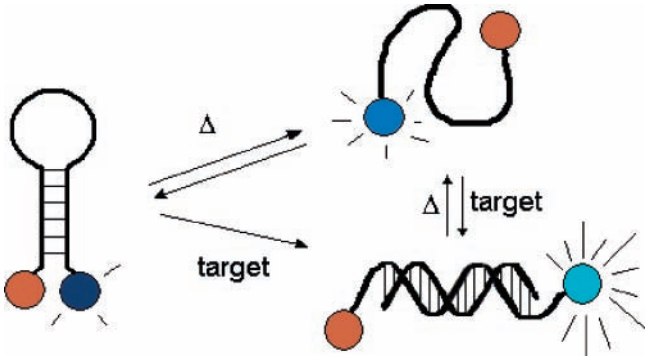


Figure 1. In the hairpin form, the fluorescence of the molecular beacon is quenched by the proximal quencher (orange circle). After denaturation by heat or after a hybridization event, the hairpin structure is broken and the quencher is moved away, restoring the fluorescence signal.

EXPERIMENTAL PROCEDURES

Synthesis and Purification of Oligonucleotides and Conjugates. The **MB** sequence was synthesized in our laboratory starting with commercial DMTr-C6-phtalimido-CPG. The compound was purified by ionic exchange chromatography on Sephacell using a gradient of triethylammonium hydrogen carbonate. Pure fractions were pooled, lyophilized several times, quantified, and split in vials of about 20 OD. The vials were eventually lyophilized and stored at −20 °C until use.

Similarly, the **dabcyl-MB** sequence was synthesized on a 10 μM scale on the same CPG, using DMTr-dabcyl-C6-amidite as the last monomer. This compound was purified on a C-18 reversed-phase column using a gradient of acetonitrile in 0.1 M of aq triethylammonium acetate. Pure fractions were collected, lyophylised several times, and split in amount of 20 OD in separate vials, stored at −20 °C.

The target sequence was purified by *n*-BuOH precipitation and found to be more than 80% pure at 260 nm by HPLC analysis on both reversed-phase and ionic exchange columns. It was kept solid at −20 °C until the moment of use.

Succinimidyl Esters. The succinimidyl esters of fluorophores **A**, **B**, and **D** (Figure 2) were synthesized according to the modalities described in ref 5. Succinimidyl esters of derivatives **C** and **E** are gifts from Mediteknology srl.

10.1021/bc060169n CCC: $37.00 © 2007 American Chemical Society
Published on Web 02/15/2007

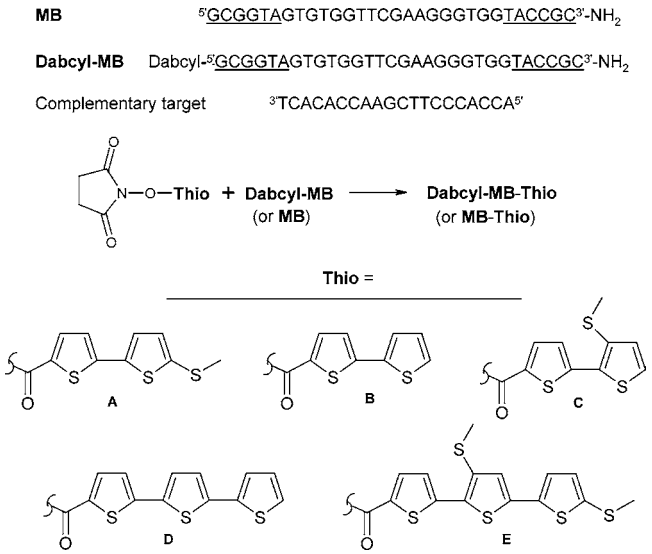


Figure 2. List of used compounds. The underlined bases form the hairpin stem.

Fluorescent ON Molecular Beacons. Fluorescent molecular beacons (with or without dabcyl) were obtained by mixing 20 OD of the corresponding 3′-amino-oligonucleotide with 1 mg of the succinimidyl ester of the oligothiophene in a buffer containing 160 μL of DMF and 18 μL of HEPES 0.2 M, pH 8.0, in water. The mixture was kept at 40 °C overnight. The reaction mixture was then diluted with 1 mL of water, and the excess of thiophene succinimidyl ester was extracted by repeated washing with dichloromethane. The aqueous phase was concentrated and purified by HPLC reversed-phase chromatography using a gradient of acetonitrile in 0.1 M aq TEAA. The collected fractions were judged more than 90% pure by absorbance at 260 nm and more than 95% pure by fluorescence detection using the appropriate λ_{ex} and λ_{em} for each compound. Usually, 5−7 OD of pure conjugate were obtained. The UV/vis profile of each conjugate was carefully checked to verify the correct incorporation of the oligothiophene and dabcyl. Finally, the identity of the ON MBs was confirmed by mass spectrometry (Bruker Esquire 3000 plus) in ESI mode with the following results: **MB-A** calcd *m*/*z* 9792.7, found 9791.4; **dabcyl-MB-A** calcd *m*/*z* 10255.1, found 10256.6; **MB-B** calcd *m*/*z* 9746.6, found 9746.3; **dabcyl-MB-B** calcd *m*/*z* 10209.0, found 10209.6; **MB-C** calcd *m*/*z* 9792.7, found 9792.7; **dabcyl-MB-C** calcd *m*/*z* 10255.1, found 10255.5; **MB-D** calcd *m*/*z* 9828.7, found 9831.2; **dabcyl-MB-D** calcd *m*/*z* 10291.1, found 10290.8; **MB-E** calcd *m*/*z* 9920.9, found 9920.0; **dabcyl-MB-E** calcd *m*/*z* 10383.3, found 10383.5.

Sample Preparation. To prevent manipulation errors, especially in the fluorescence readings, all experiments were done starting from a 1 μM concentration of the sample in a 3.0 mL fluorescence cuvette. The sample was then used for UV scan and fluorescence measurements, and then 5 μL of complementary target ON was added to the very sample to perform the hybridization experiments.

RESULTS AND DISCUSSION

In this work, we used fluorophores made of two and three thiophene rings (see Figure 2) tagged to the 3′-end of the ON strand, while the other end was kept free or conjugated to a dabcyl moiety.

The stem part of the sequence **MB** was chosen for the strong T_m found to be about 38 and 50 °C for **MB** and **dabcyl-MB** (data not shown), respectively, while its loop region was chosen to be complementary to an oligo already used by our group (*6*). The 3′-amino group was obtained by use of commercial DMTr-C6-phthalimido-CPG (Glen research). The use of dabcyl as a quencher was dictated by its large absorption region and by the commercial availability of its DMTr-dabcyl-C6-amidite (Chem Genes).

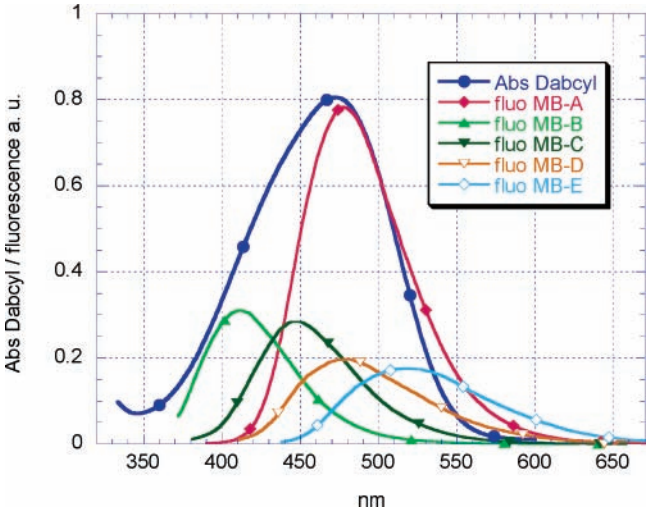


Figure 3. Superimposition of UV absorption spectrum of the dabcyl moiety of **dabcyl-MB** with fluorescence emissions of **MB-A**−**MB-E** conjugates. Each thiophene derivative was excited at its maximum excitation frequency. The intensities of the emission spectra, on an arbitrary scale, are proportional among all members. The absorption of the dabcyl derivative is also on an arbitrary scale. All fluorescence spectra were recorded at 1 μM concentration in 100 mM NaCl, 10 mM sodium cacodylate buffer pH 7.0.

Table 1. List of Maximum Frequency of Excitation and Emission of Succinimide and Oligonucleodide Derivatives

	succinimidyl ester		oligo conjugate	
entry	λ_{ex}	λ_{em}	λ_{ex}	λ_{em}
A	370	479	360	479
B	352	418	335	410
C	361	479	350	445
D	390	460	410	480
E	418	549	425	520

Oligothiophene fluorophores **A**−**D** were chosen for their intense fluorescence in water and for the overlap of their emission within the absorption range of the dabcyl as illustrated in Figure 3.

After conjugation, we noticed, in aqueous solution, some small variations at both wavelengths of absorption and emission of thiophene derivatives with respect to those of their succinimidyl ester parents in dichloromethane. A list of absorption and emission wavelength is reported in Table 1.

All the compounds were analyzed by the same methodology described below for **MB-A** and **dabcyl-MB-A**.

MB-A and **dabcyl-MB-A** were analyzed by UV at 10, 20, 30, 40, 50, 60, and 70 °C. The spectra had the expected UV/vis intensity ratio and did not shown any significant variation in the shape of the signal in the visible region, a strong indication that neither the tagged chromophore nor the quencher was involved in formation of complexes directly affected by temperature change (as would be expected in the case of intercalation of the dabcyl or thiophene moieties between base pairs of the stem of the hairpin of the molecular beacons) (see Figure 4). (A similar behavior was shown by all the other members, derivatives **B**−**E**, not shown.)

Compoud **MB-A** showed no clear melting point (from hairpin to random coil) in melting experiments, while the **dabcyl-MB-A**

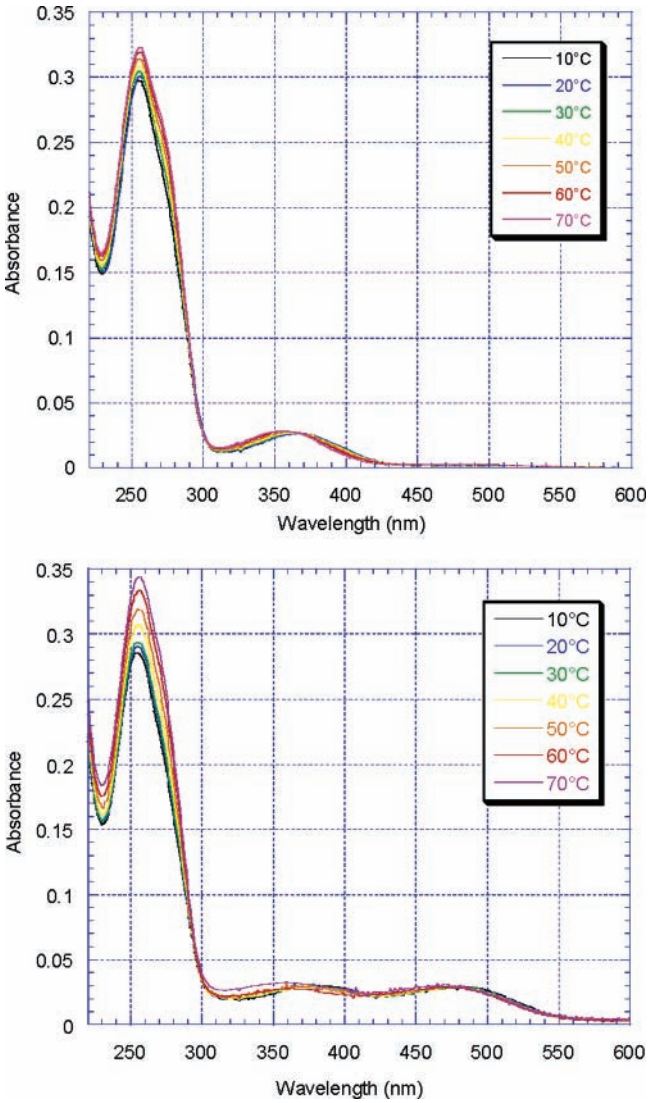


Figure 4. UV/vis scan at various *T* of **MB-A** (top panel) and **dabcyl-MB-A** (bottom panel) at 1 μM concentration in 100 mM NaCl and 10 mM sodium cacodilate pH 7.0.

showed a clear transition centered at 58 °C. (In all tested compounds, the melting point was not clearly detectable in the **MB** series, while in the **dabcyl** series, it was in the range 56−58 °C.)

Next, we analyzed the emitted fluorescence of **MB-A** and **dabcyl-MB-A** at different temperatures (Figure 5).

As expected, in the absence of dabcyl, the emission was slightly affected by heating; the intensity decreased by less than 10% from 10 to 70 °C (as in the corresponding succinimidyl parent compound; data not shown). This decrease can be attributed to a partial loss of coplanarity between the thiophene rings with heating. The **dabcyl-MB-A** showed a marked increase in fluorescence emission on going from 40 to 70 °C due to the thermal opening of the hairpin structure (molecular beacon effect). It is remarkable that even at high temperature the fluorescence emission of **dabcyl-MB-A** is lower than that of the corresponding compound without the quencher. This indicates that even in the random coil conformation the dabcyl moiety is able to quench part of the emission of the thiophene derivative **A** (dabcyl effect). This quenching was found to be independent of the concentration.

Next, we determined, by UV, the melting point of both **thiophene A** conjugates with their complementary strand (Figure 6).

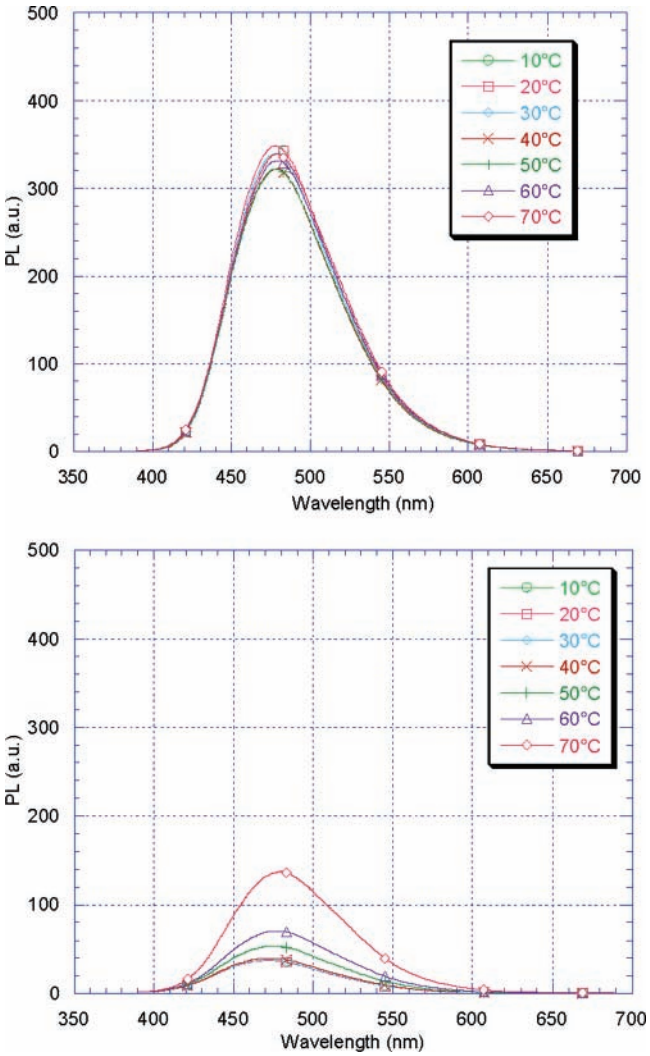


Figure 5. Variation of fluorescence with the temperature. Top panel **MB-A**; bottom panel **dabcyl-MB-A**.

Both molecular beacons showed a clear melting point (48 and 64 °C, respectively) higher than that of the hairpin, thus demonstrating that in the presence of the target the favored form is the duplex with the complementary strand.

Eventually, we studied the variation of fluorescence of the formed duplex with temperature (Figure 7).

By comparing all the above experiments, several conclusions can be drawn:

- The double labeling favors the stability of the hybrid with the target.
- The fluorescence of **MB-A** is enhanced (about 1.4 times) by hybridization (duplex effect).
- After hybridization with the target, the fluorescence of **dabcyl-MB-A** is more than 7 times higher than that of its hairpin form ("diagnostic effect": combination of molecular beacon and duplex effects).
- After hybridization, the fluorescence of **dabcyl-MB-A** is higher than that of the same compound in random coil form.

The experiments illustrated for **thiophene-A** derivatives were performed with all the compounds in Figure 2. A summary of the findings are shown in Figure 8.

Data in Figure 8 show that dabcyl is a quencher for all derivatives; however, while for derivatives **D** and **E** after hybridization with the complementary strand the fluorescence of the dabcyl derivative is equal to that of the relative compound without dabcyl, in cases **A** to **C**, the signal remains lower. This can indicate that for these derivatives the distance between the

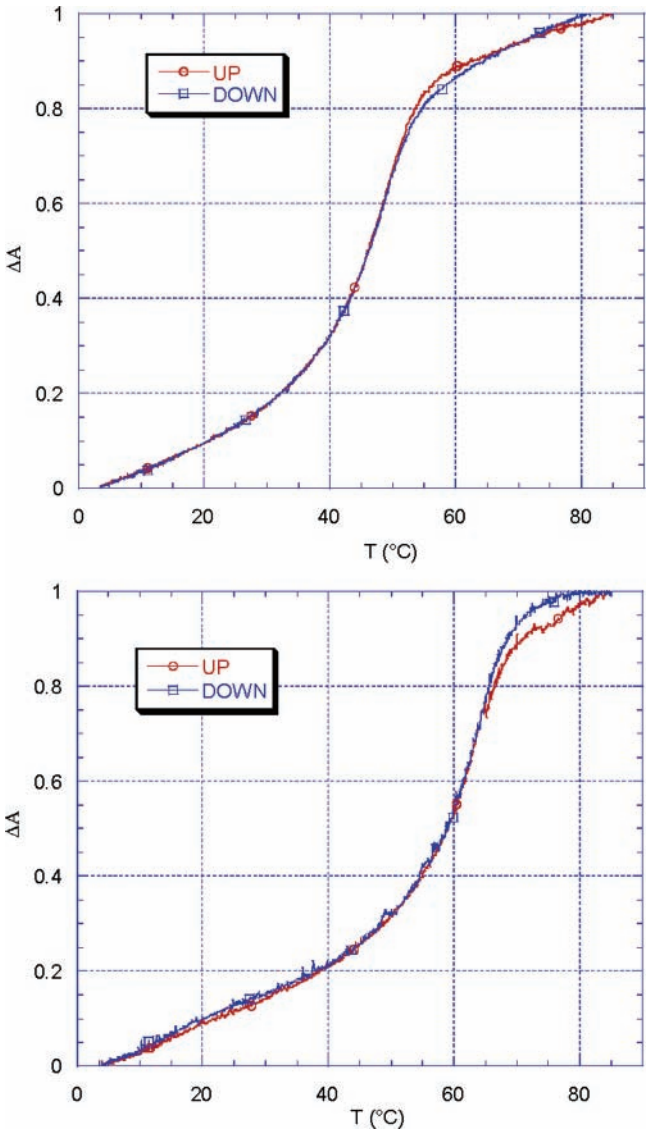


Figure 6. Melting of duplex **MB-A** (top panel) and **dabcyl-MB-A** (bottom panel) with their target (1.2 equiv). For each melting, heating and cooling curves are shown. The melting was performed on a buffer containing 100 mM NaCl and 10 mM sodium cacodilate at pH 7.0. Heating up and cooling down rates were of 0.2 °C/min. Normalized variations of absorbance were plotted.

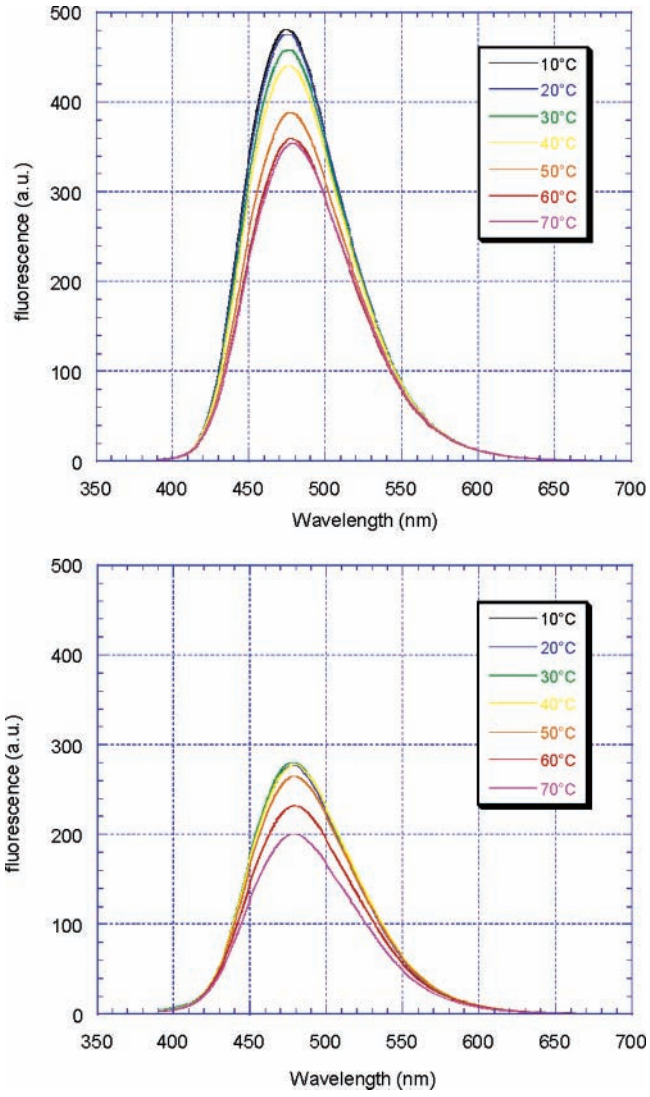


Figure 7. Variation of fluorescence emission with temperature for **MB-A** (top panel) and **dabcyl-MB-A** (bottom panel) after hybridization.

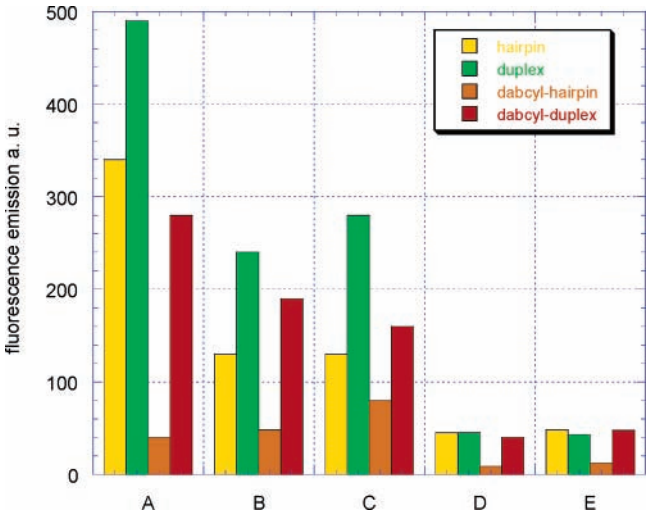


Figure 8. For each compound, the intensity of the emitted fluorescence at room temperature (on the same scale for all compounds) is reported. For each group, left to right: yellow bars, **MB hairpins**; green bars, **duplex MBs/target**; orange bars, **dabcyl-MB hairpins**; red bars, **duplex dabcyl-MBs/target**.

fluorophore and the quencher, even in the distended duplex, does not reach the Forster's radius. Oligonucleotide conjugates of **A**, **B**, and **C** are, at least within this system, quite sensitive to the hairpin−duplex transition even in absence of dabcyl as a quencher. We still do not know if this change of emission intensity depends on a possible quenching from bases on the 5′ region that came in proximity to the fluorophore in the hairpin structure (*12*, *13*) or if the formation of the duplex puts the fluorophore in a more favorable condition to increase the fluorescence quantum yield. Luckily for our systems, the molecular beacon effect and the duplex effect combine favorably to enhance the "diagnostic value" of probes **dabcyl-MB-A** and **dabcyl-MB-B**.

Derivatives **A**, **B**, and **C** (two thiophene rings) show a higher fluorescence than derivatives **D** and **E** (three thiophene rings), as well as their precursors; among the first three, derivative **A** has the strongest quantum yield.

In conclusion, we have described the fluorescence properties of a series of oligothiophene conjugated oligonucleotides. All compounds show a high fluorescence emission (they are easily detectable at 10−100 nM concentration). All derivatives are suitable for preparation of molecular beacons with dabcyl as a

quencher. Derivatives **A**−**C** are sensitive enough, at least in this system, to reveal a hybridization event even in absence of dabcyl.

ACKNOWLEDGMENT

This work was partially funded by project FIRB RBNE 03S7XZ_005 SYNERGY. We thank SPINNER (Services for the Promotion of INNovation and Research) Consortium, for support to A.C.

LITERATURE CITED

(1) Perepichka, I. F., Perepichka, D. F., Meng, H., and Wudl, F. (2005) Light-emitting polythiophenes. *Adv. Mater. 17*, 2281−2305.

(2) Yoon, M. H., Facchetti, A., Stern, C. E., and Marks, T. J. (2006) Fluorocarbon-modified organic semiconductors: Molecular architecture, electronic, and crystal structure tuning of arene-versus fluoroarene-thiophene oligomer thin-film properties. *J. Am. Chem. Soc. 128*, 5792−5801.

(3) Barbarella, G., Melucci, M., and Sotgiu, G. (2005) The versatile thiophene: An overview of recent research on thiophene-based materials. *Adv. Mater 17*, 1581−1593.

(4) Barbarella, G., Zambianchi, M., Pudova, O., Paladini, V., Ventola, A., Cipriani, F., Gigli, G., Cingolani, R., and Citro, G. (2001) Oligothiophene lsothiocyanates as a new class of fluorescent markers for biopolymers. *J. Am. Chem. Soc 123*, 11600−11607.

(5) Barbarella, G., Zambianchi, M., Ventola, A., Fabiano, E., DellaSala, F., Gigli, G., Anni, M., Bolognesi, A., Polito, L., Naldi, M., and Capobianco, M. (2006) Bright oligothiophene N-succinimidyl esters for efficient fluorescent labeling of proteins and oligonucleotides. *Bioconjugate Chem. 17*, 58−67.

(6) Capobianco, M. L., Naldi, M., Zambianchi, M., and Barbarella, G. (2005) Oligothiophene phosphoramidites for oligonucleotide labelling. *Tetrahedron Lett. 46*, 8181−8184.

(7) Powe, A. M., Fletcher, K. A., St. Luce, N. N., Lowry, M., Neal, S., McCarroll, M. E., Oldham, P. B., McGown, L. B., and Warner, I. M. (2004) Molecular fluorescence, phosphorescence, and chemiluminescence spectrometry. *Anal. Chem. 76*, 4614−34.

(8) Kocisova, E., Praus, P., Rosenberg, I., Seksek, O., Sureau, F., Stepanek, J., and Turpin, P. Y. (2004) Intracellular uptake of modified oligonucleotide studied by two fluorescence techniques. *Biopolymers 74*, 110−4.

(9) Lakowicz, J. R. (1983) *Priciples of fluorescence spectroscopy*, Plenum Press, New York.

(10) Tyagi, S., and Kramer, F. R. (1996) Molecular beacons: probes that fluoresce upon hybridization. *Nat. Biotechnol. 14*, 303−8.

(11) Stryer, L., and Haugland, R. P. (1967) Energy transfer: a spectroscopic ruler. *Proc. Natl. Acad. Sci. U.S.A. 58*, 719−26.

(12) Crockett, A. O., and Wittwer, C. T. (2001) Fluorescein-labeled oligonucleotides for real-time PCR: Using the inherent quenching of deoxyguanosine nucleotides. *Anal. Biochem. 290*, 89−97.

(13) Nazarenko, I., Pires, R., Lowe, B., Obaidy, M., and Rashtchian, A. (2002) Effect of primary and secondary structure of oligodeoxyribonucleotides on the fluorescent properties of conjugated dyes. *Nucleic Acids Res. 30*, 2089−2095.

BC060169N

Peptide-Labeled Quantum Dots for Imaging GPCRs in Whole Cells and as Single Molecules

Min Zhou,[†] Eri Nakatani,[†] Luisa S. Gronenberg,[†] Takahira Tokimoto,[†] Mary J. Wirth,[†] Victor J. Hruby,[†] Amber Roberts,[‡] Ronald M. Lynch,[‡] and Indraneel Ghosh*[,†]

Department of Chemistry and Department of Physiology, University of Arizona, Tucson, Arizona 85721. Received July 2, 2006; Revised Manuscript Received October 25, 2006

We report a robust and practical method for the preparation of water-soluble luminescent quantum dots (QDs) selectively coupled through an amine or thiol linkage to peptide ligands targeted to G-protein coupling receptors (GPCRs) and demonstrate their utility in whole-cell and single-molecule imaging. We utilized a low molecular weight (~1200 Da) diblock copolymer with acrylic acids as hydrophilic segments and amido-octyl side chains as hydrophobic segments for facile encapsulation of QDs (QD 595 and QD 514) in aqueous solutions. As proof of principle, these QDs were targeted to the human melanocortin receptor (hMCR) by chemoselectively coupling the polymer-coated QDs to either a hexapeptide analog of α-melanocyte stimulating hormone or to the highly potent MT-II ligand containing a unique amine. To label QDs with ligands lacking orthogonal amines, the diblock copolymers were readily modified with water-soluble trioxa-tridecanediamine to incorporate freely available amine functionalities. The amine-functionalized QDs underwent facile reaction with the bifunctional linker NHS−maleimide, allowing for covalent coupling to GPCR-targeted ligands modified with unique cysteines. We demonstrate the utility of these maleimide-functionalized QDs by covalent conjugation to a highly potent Deltorphin-II analog that allowed for selective cell-surface and single-molecule imaging of the human δ-opioid receptor (hDOR).

INTRODUCTION

Semiconductor nanocrystals, also called quantum dots (QDs), have received considerable attention due to their novel electronic and optical properties that are desirable for applications in biological imaging (*1*−*3*). Their broad absorption spectra, as well as their narrow and size-tunable emissions, by altering particle size, make it possible to excite all colors of QDs simultaneously with a single light source for multiplexing without substantial spectral overlap. The long photo luminescent lifetime of QDs (30−100 ns) also allow for imaging of living cells with minimal interference from background autofluorescence, while their resistance to photobleaching makes them useful for continuous monitoring of biological processes (*4*). These emerging probes can potentially aid in refining existing methods for drug targeting and in facilitating studies in basic biology (*5*, *6*).

Organometallic chemistry has provided synthetic pathways to robust, monodisperse, highly emissive nanomaterials, such as CdSe nanocrystals capped with ZnS shells. However, for biological imaging it remains challenging to choose appropriate organic coating agents to generate water-soluble QDs that maintain high luminescent quantum yields and stability. Ligand exchange is the most common method for generating water-soluble QDs; for example, simple thiol-containing molecules, such as mercaptoacetic acid, have been used to replace hydrophobic TOPO (trioctylphosphine oxide) coatings on the surface of CdSe/ZnS nanoparticles (*7*−*10*). In this case, the mercapto group thiolates the nanocrystal surface, while the carboxylic acid provides solubility. This method is simple, but the stability of the QDs in water is decreased (*11*) and the thiolation leads to eventual dissolution of the nanocrystals, resulting in the release of heavy atoms into solution (*12*). Phospholipid (*13*), polypeptide (*14*), bovine serum albumin (*15*), and silica (*12*) have also been used as capping agents but potentially lack simple and reliable methods for further bioconjugation to the targeting ligand for cell-surface imaging applications. Alternatively, amphiphilic di- and triblock copolymers for encapsulating QDs via a spontaneous self-assembly process (*16*, *17*) allow one to circumvent these potential drawbacks while maintaining the photoluminescent properties of the QD label. Besides generating water-soluble QDs, the conjugation of ligands to QDs is also critically important. Most reported methods for QD−ligand conjugation are achieved by precoupling the QDs with antibodies or streptavidin, followed by addition of hapten- or biotin-modified ligands. However, nonspecific interactions between the antibody or streptavidin with cell-surface targets are possible. Furthermore, both antibodies and streptavidin significantly increase the size of the QD complex (~50 nm), which could potentially affect accessibility to crowded cell-surface locations (*18*, *19*) and also interfere with receptor dynamics.

Though QDs are now commercially available, few robust literature methods have been reported for covalently conjugating peptide and peptidomimetic ligands to QDs. In a recent study, Schmidt and co-workers synthesized a small peptide ligand (RGD) with an added cysteine, which was directly used to coat bare quantum dot surfaces together with mercaptoacetic acid (*20*). However, the thiol coating may possibly lead to QD dissolution, as previously discussed. In more recent work, Rosenthal and co-workers coupled angiotensin II to carboxylic acid modified QDs by EDC (*21*). This method, though very useful, cannot be easily utilized when a ligand of interest contains two or more free amines and especially in instances

* Corresponding author. Indraneel Ghosh. E-mail: ghosh@email.arizona.edu. Department of Chemistry, The University of Arizona, P.O. Box 210041, 1306 E. University Blvd, Tucson, Arizona 85721-0041. Phone (520) 621-6331. Fax (520) 621-8407.

[†] Department of Chemistry.

[‡] Department of Physiology.

10.1021/bc0601929 CCC: $37.00 © 2007 American Chemical Society
Published on Web 01/17/2007

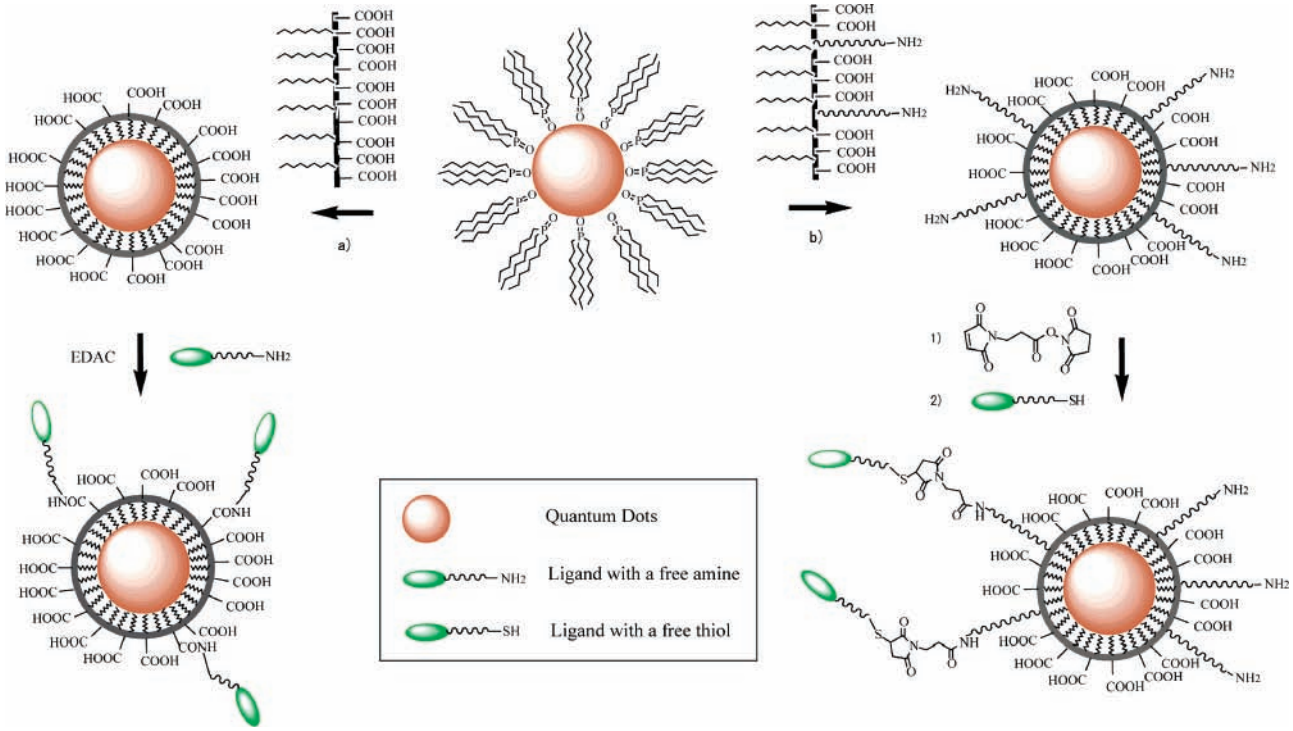


Figure 1. Synthesis of water-soluble QDs with associated ligand conjugation chemistry. (a) Carboxylic acid functionalized QDs for conjugation to ligands through EDAC coupling. (b) Amine-functionalized QDs for conjugation to thiol-containing ligands through bifunctional cross-linkers.

where the amines are important for bioactivity. Thus, it still remains challenging to optimize the chemistry as well as the process for generating water-soluble polymer-coated QDs that allow for facile covalent coupling to peptidic ligands that maintain their bioactivity.

Herein, we present a practical method for generating water-soluble QDs and the necessary chemistry for covalently coupling the QDs with G-protein couple receptor (GPCR) targeted ligands (Figure 1). GPCRs constitute a large and diverse family of proteins whose primary function is to transduce extracellular stimuli into intracellular signals. Since 50% of pharmaceuticals target GPCRs, new methods for imaging GPCRs at cell surfaces are of much interest. As proof of principle, we chose to target the QDs to the human melanocortin and δ-opioid receptors. We demonstrate the feasibility of QD514 conjugated to α-MSH analogs that effectively image melanocortin receptors overexpressed on HEK293 cells. We also demonstrate that QDs conjugated to Deltrophin-II analogs can be utilized for selectively imaging δ-opioid receptors on cell surfaces and for single-molecule imaging.

EXPERIMENTAL PROCEDURES

Instruments. QD absorbance was recorded by a Beckman DU520 instrument. Fluorescence spectra were recorded on a PTI fluorimeter (814 photomultiplier detection system and LPS-220B power supply). ^{1}H NMR spectra were recorded on a Bruker DRX-500 instrument.

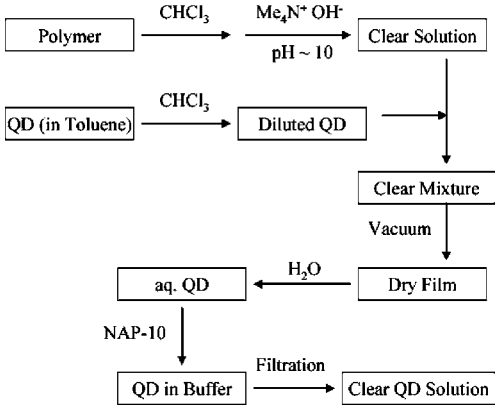
General. All Fmoc-protected amino acids, BOP, HOBt, and Rink-amide resin used for peptide synthesis were purchased from Novabiochem. Boc-AEEEA (Boc-11-amino-3,6,9-trioxaundecanoic acid) was purchased from Peptides International. Bare QDs were synthesized using published methods (*22*) or purchased from Evident Technology. All other chemicals were purchased from Aldrich. Peptides were purified by reverse-phase HPLC (Varian) using a C18 column (Vydac.)

Synthesis of Octylamine-Modified Poyacrylic Acid (OPA). *A.* 10 mL of a poly(acrylic acid) sodium salt solution (MW ~1200, 45 wt % in water) was acidified by 5 mL of 12 N HCl, followed by addition of 200 mL of acetone under stirring to precipitate NaCl. After filtration, the acetone was removed from the filtrate by vacuum. The crude product was redissolved with 20 mL of water, frozen, and lyophilized. 4.5 g of white poly(acrylic acid) solid was collected.

B. 2.16 g of poly(acrylic acid) solid (0.03 mol of carboxylic acid) and 2.85 g of 1-ethyl-3-(3-dimethylaminopropyl)carbodiimide hydrochloride (EDAC, 0.015 mol) were transferred into a 100 mL round-bottom flask. 20 mL of DMF was added to dissolve the mixture. About 1.6 mL of octylamine (0.0096 mol) was added dropwise into the reaction flask. The clear solution was stirred overnight under argon. TLC ($CH_2Cl_2/CH_3OH = 7:1$, $R_{f(\text{octylamine})} = 0.55$, $R_{f(\text{product})} = 0.24$) was used to monitor the reaction. When the reaction was complete, DMF was removed by vacuum, and the residue was mixed with 10 mL of acetone and transferred into a centrifuge tube. 25 mL of water was added, and the gummy precipitated product was separated by centrifugation (3000 rpm for 5 min) and washed with water (25 mL $\times$ 3). The solid product was dissolved in 40 mL of ethyl acetate (gentle heating 40−50 °C was applied), and a tetramethylammonium hydroxide (6.4 g in 25 mL water) solution was added to the polymer solution and stirred for 10 min, before being transferred into a separation funnel. The yellowish aqueous layer was isolated in a centrifugation tube and acidified by 1 N HCl to pH 2. The precipitate was separated by centrifugation and washed with H_2O (15 mL $\times$ 2). The sticky solid was redissolved in ethanol, at which point the ethanol was removed under vacuum and 1.63 g of the yellow solid OPA was collected (45 $\pm$ 5% of the carboxylic acids were converted to octyl amide). ^{1}H NMR (*d*-CH_3OH): δ 0.85−0.92 (m, 3H), 1.20−1.35 (m, 10H), 1.40−1.55 (m, 2H), 1.55−1.95 (m, 3.2H), 2.05−2.50 (m, 2.4H), 2.95−3.28 (m, 2H).

Synthesis of Amine-PEG-Modified Polymer (APOPA). *A. Synthesis of Mono-Boc-Protected 4,7,10-trioxatridecanediamine.* 80 g of 4,7,10-trioxatridicanediamine (0.364 mol) was dissolved in 250 mL dichloromethane in a 500 mL round-bottom flask. 3.2 g of *t*-Boc anhydride (0.0147 mol) was dissolved in 20 mL of dichloromethane and added dropwise to the diamine solution

Scheme 1. Processing QDs with Water-Soluble Amphiphilic Shells



over 4 h with stirring. After the addition, the solution was stirred overnight. The solution was reduced to 150 mL under vacuum and extracted with water (300 mL × 6) to remove excess diamine. The organic layer was dried over Na_2SO_4, and the dichloromethane was removed under vacuum. About 2.54 g of mono-Boc-protected 4,7,10-trioxatridicanediamine (oily precipitate) was collected (yield 54%). ^{1}H NMR ($CDCl_3$): δ 1.45 (s, 9H), 1.74 (m, 4H), 2.80 (t, 2H), 3.22 (m, 2H), 3.52−3.67 (m, 12H).

B. Synthesis of Amine-PEG-Modified Triblock Copolymer. 383 mg of the octylamine-modified poly(acrylic acid) (OPA, ~0.2 mmol) and 190 mg of EDAC (1 mmol) were dissolved in 6 mL DMF in a 25 mL round-bottom flask, and the solution was stirred for 10 min. 128 mg of mono-Boc-protected 4,7,-10-trioxatridecanediamine (0.4 mmol) dissolved in 1 mL DMF was added into the reaction flask. The solution was stirred overnight, and the Kaiser test (*23*) was used to monitor the reaction. When the Kaiser test indicated no free amine in solution, DMF was removed by vacuum and the residue was transferred into a centrifuge tube, which contained 20 mL of H_2O. The precipitated product was isolated by centrifugation (3500 rpm for 8 min) and washed with 5 mL of H_2O. The product was redissolved in 3 mL of ethanol, which was subsequently removed by vacuum. 8 mL of 50% TFA in dichloromethane was added to the container to dissolve the residue and remove the Boc group. After a short reaction time, the solvent was removed by vacuum. The crude oily product was redissolved with 2 mL of ethyl acetate, and the solution was added dropwise into a centrifuge tube, which contained 30 mL of cold ether. The solid product was separated by centrifugation (3500 rpm for 5 min) and washed with 20 mL of ether. After drying, 120 mg of yellowish solid APOPA was obtained (12−14% of carboxylic acids were converted to amide-PEG-amine). ^{1}H NMR ($CDCl_3$): δ 0.80−0.95 (m, 3H), 1.02−1.39 (m, 10H), 1.39−1.60 (m, 2H), 1.60−2.15 (m, 3.1H), 2.15−2.55 (m, 1.4H), 2.78−3.00 (m, 1.1H), 3.0−3.4 (m, 2.9H), 3.5−3.88 (m, 3.3H).

Process for Coating QD with Amphiphilic Polymer Shell (Scheme 1). 50 mg of the OPA was dissolved in 4 mL of dichloromethane. Tetramethylammonium hydroxide (25 wt % in methanol) was used to adjust pH to 10. 500 μL of 0.12 mM bare QD514 in toluene (λ_{em} = 514 nm, Evident) were added to the solution and stirred for several minutes, at which time the solvent was removed under vacuum. The solid was redissolved in 500 μL of water and loaded onto a NAP-10 column (Amersham Biosciences). Phosphate buffer A (10 mM, pH 7.35) was used to elute the QDs. Fluorescent fractions were combined (~2 mL) and further filtered through a 0.45 μm Acrodisc syringe filter. The filtrate was dialyzed overnight in a Slide-A-Lyzer dialysis cassette (MWCO 7000, Pierce) against 400 mL of buffer A. The final aqueous QD stock solution was stored at 4 °C. QD concentration was determined by the absorption at 496 nm (ϵ = 50 000 M^{-1} cm^{-1}) based on the first excitation state of QD514.

The same process was repeated for coating QD595 (λ_{em} = 595 nm) with OPA. Twice the amount of OPA (100 mg) was used because of the larger size of QD595 (5 nm) compared to QD514 (3.2 nm). After dialysis, 2 mL of OPA-coated QD595 was collected. (Concentrations were determined by absorbance at 586 nm, based on the first excitation state of QD595 (ϵ = 400 000 M^{-1} cm^{-1}). Primary amine modified QD514 and QD595 were prepared using a similar protocol (Scheme 1), but starting with the amine-PEG-modified polymer, APOPA.

Peptide Synthesis and Purification. All ligands (NDP, MT-II, Deltorphin-II (Ile−Ile), and CCK; see Figure 2) were synthesized by solid-phase peptide synthesis using a standard fluorenylmethoxycarbonyl (Fmoc) strategy starting with Rink amide resin (*24*). The cyclization reaction of MT-II was performed according to the method reported by Hruby et al. (*25*) in 2002. Boc-AEEEA (PEG linker) was coupled at the N-terminal of norleucine before deprotection of glutamic acid and lysine, followed by cyclization.

The final peptides were cleaved from the resin and all protecting groups were removed by cleavage cocktail (100 mg of peptide resin was treated with 1 mL of cocktail) composed of TFA and scavengers (81.5% TFA, 5% H_2O, 5% thioanisole, 5% phenol, 2.5% ethanedithiol, and 1% triisopropylsilane) for 4 h at room temperature. The solution was filtered and precipitated by transferring into a centrifuge tube containing precooled ether. After centrifugation and 3× washes with fresh ether, the white solid was collected and lyophilized to yield crude product. The crude peptides were purified by reverse-phase HPLC (Varian) using a C18 column (Vydac). Peptides were purified with a linear gradient of 20% to 80% acetonitrile containing 0.1% TFA at a flow rate of 8 mL/min, for 50 min. The purified peptides were reinjected on reverse-phase HPLC and found to be >95% pure. The k' value of each product was determined by a C18 column with a linear gradient of 20% to 80% actonitrile containing 0.1% TFA at a flow rate of 1 mL/min for 20 min.

AEEEA-Nle-Glu-His-(D)Phe-Arg-Trp-NH$_2$ (NDP α-MSH Analogue). Mass spectroscopy (ESI): observed 886.5 (calculated 886.5). k' = 0.64.

MT-II (α-MSH Analogue). Mass spectroscopy (ESI): observed 1171.5 (calculated 1171.6). k' = 0.84.

Tyr-(D)Ala-Phe-Glu-Ile-Ile-Gly−Gly-(PEG)$_2$-Cys-Gly-NH$_2$ (Deltorphin II Analogue). Mass spectroscopy (ESI): observed 1345.5 (calculated 1346.8). k' = 0.95.

AEEEA-Asp-Tyr-N-MeNle-Gly-Trp-N-MeNle-Asp-Phe-NH$_2$ (CCK−B Ligand). Mass spectroscopy (ESI): observed 1244.3 (calculated 1244.8). k' = 1.50.

Preparation of NDP−QD514. 1.1 mL of 5 μM OPA-coated QD514 (5.5 nmol) was mixed with 10 μL of EDAC solution (0.05 mg/μl) and stirred for 10 min. 170 μL of 6.4 mM NDP-α-MSH stock solution (concentration was determined by absorption at 280 nm in 8 M guanidine) was added to the coated QD514 solution with stirring. The pH was adjusted to 7−8 with 25% tetramethylammonium hydroxide in methanol, and the Kaiser test was used to monitor reaction progress. After 6 h, the Kaiser test showed no free amine in solution, and the solution was loaded on a NAP-10 column and eluted with buffer A. The fluorescent fractions (~1.5 mL) were collected and dialyzed in a MWCO 3500 dialysis cassette against 500 mL of buffer A. After 10 h, fresh buffer was used for another 10 h dialysis. The final NDP−QD514 conjugate solution was 3 μM as determined by the absorption at 496 nm, described above.

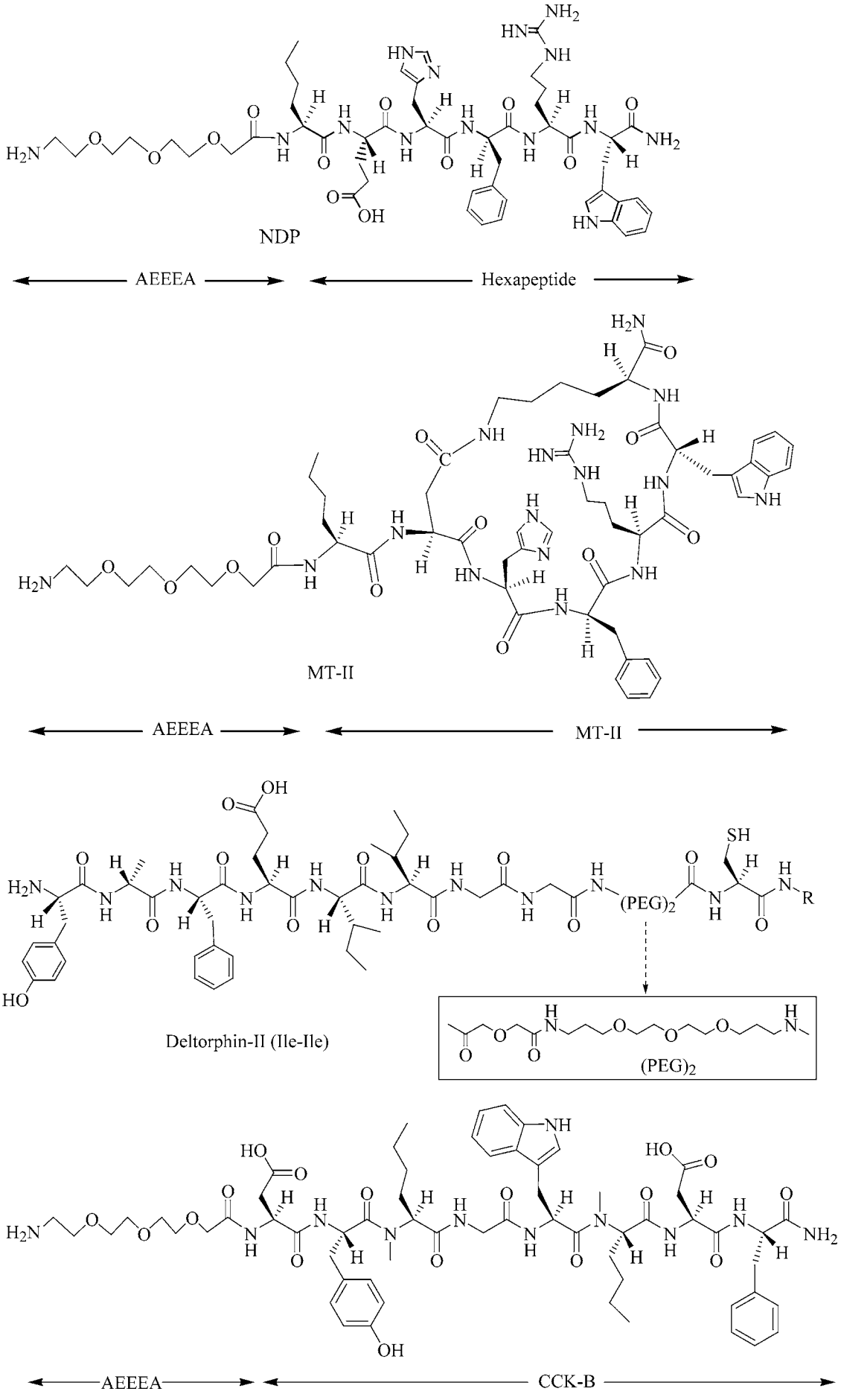


Figure 2. Structures of the GPCR-targeting ligands investigated.

Preparation of MT-II−QD595 and MT-II−QD514. 500 μL of 1.1 μM OPA-coated QD595 (0.55 nmol) was mixed with 20 μL of 2.8 mM MT-II (56 nmol) solution (concentration was determined by absorption at 280 nm in 8 M guanidine) in 80 μL of 0.1 M pH 9.2 sodium bicarbonate buffer. Under stirring, 20 μL of EDAC solution (40 mM) was added, and another 20 μL was added after 2 h. The Kaiser test was used to monitor the reaction. When the reaction was over (4−6 h), the solution was filtered with a 0.45 μm Acrodisc followed by dialysis in a MWCO 10 000 dialysis cassette against 400 mL × 2 of buffer A. Finally, ∼1.7 mL of 0.2 μM of the MT-II−QD595 conjugate solution was collected in which the ratio of MT-II to QD595 is about 100:1. The same procedure was used to conjugate MT-II to OPA-coated QD514.

Preparation of Deltorphin-II−QD595 and Deltorphin-II−QD514. 2.5 mg of *N*-(β-maleimidopropyloxyl)succinimide ester was dissolved in 1 mL DMSO to obtain a 10 mM cross-linker stock solution. 0.6 mg Deltorphin-II (Ile−Ile) was dissolved in 200 μL H_2O to obtain a 2 mM δ-opioid ligand stock solution (concentration was determined by the DTNB test based on the free thiol concentration (*26*)). 120 μL of APOPA-coated QD595 (2.8 μM, 0.33 nmol) was mixed with 10 μL of the cross-linker stock solution and incubated at room temperature for 1 h. The resultant clear solution was loaded on a NAP-10 column and eluted with buffer A. Fluorescent fractions (∼250 μL) were collected and mixed with 8 μL of the Deltorphin-II (Ile−Ile) stock solution (16 nmol) and 42 μL of buffer A. The mixture was equilibrated at room temperature for 1 h, at which time 3 μL of 100 mM β-mercaptoethanol was added to quench the unreacted maleimide. After 30 min, the reaction solution was filtered through a 0.45 μM Acrodisc and dialyzed in a MWCO 10 000 dialysis cassette against 400 mL × 2 of buffer A. The final 0.75 μM Deltorphin-II−QD595 solution was collected in which the maximal ratio of ligand/QD is about 50:1. A similar procedure was used to conjugate Deltorphin-II to APOPA-coated QD514. All QD or QD−ligand conjugate concentrations were determined as described above.

Immunocytochemistry. Cells grown on 25 mm round #1 coverslips were fixed with 3% paraformaldehyde, rinsed with 25 mM glycine, and permeabilized with 0.1% Triton X-100. The cells were incubated with the primary antibodies (rabbit polyclonal) against the δ-opioid receptor (Neuromics, Northfield, MN) or MC4R (RDI, Flanders, NJ) for 1 h at 25 °C. Cells were washed three times (5 min each) in phosphate buffered saline to remove unbound primary antibody. Since the MC4R antibody recognized an epitope on the cell exterior, live cells also were incubated with this antibody (10 μg/mL) for 5 min, washed in antibody-free buffer (2×, 5 min each), then fixed for subsequent processing. At this point, all fixed and permeabilized cells were incubated with secondary anti-rabbit IgG labeled with either Cy5 (Jackson ImmunoResearch) or FITC (Sigma) for 45 min at 25 °C. After washing, coverslips were mounted onto glass slides using a 50% glycerol/saline solution containing the antibleach agent paraphenylendiamine (0.1%). NDP−QD514 and Deltorphin-II(Ile−Ile)−QD595 were used for imaging MC4R or δ-opioid receptors as described in the results and discussion section.

For standard wide-field imaging, slides were mounted on the stage of an Olympus IX-70 microscope equipped with a 60 × 1.4 NA objective. Illumination was provided by a 100 W Hg lamp, and images were acquired using a liquid-cooled CCD camera (Roper Scientific) equipped with a Kodak CCD array (KAF1401E).

Single-Molecule Imaging: Incorporation of hDOR in Lipid Bilayer. The lipid bilayer was formed on a fused silica coverslip surface covered by a thin polyacrylamide film. It is possible to make a polymer brush of controlled thickness by the surface-initiated atom transfer radical polymerization (ATRP) (*27*, *28*). A 5-nm-thick polyacrylamide brush was prepared on the coverslip according to the same procedure previously reported (*29*). The lipid bilayer of 1-palmitoyl-2-oleoyl-*sn*-glycero-3-phosphocholine (POPC) with cholesterol (0−10%) was formed on the polyacrylamide-modified coverslip surface using a standard vesicle fusion procedure (*29*, *30*). The isolation and purification procedure of hDOR was as described previously (*29*, *31*). The receptor has a His tag and myc epitope on its C terminus, and is solubilized in buffered 1% dodecyl-β-D-maltoside solution. The hDOR solution was added into the buffer on the lipid membrane described above. This dilution of hDOR suspension allowed hDOR to be incorporated into the lipid bilayer. The lipid membrane was rinsed multiple times, then 50 mM phosphate buffer (0.5 M NaCl, pH 7.5) was added.

Single-Molecule Fluorescence Imaging. Single-molecule fluorescence imaging of the ligand binding was achieved by using a highly sensitive CCD camera coupled to an argon ion laser as an excitation source. The microscope (TE2000-U, Nikon) was designed for total internal reflection fluorescence imaging. For the excitation of the QDs, the blue line of the argon ion laser (488 nm, 0.05 mW) was used. The green line (514.5 nm, 0.26 mW) was used for Cy3 excitation. The laser beam was used to irradiate the sample in a total internal reflection mode via an oil-immersion 100× TIRF objective (NA 1.4, Nikon). A high-sensitivity CCD camera, PhotonMAX (512 × 512 pixels, Princeton Instruments), was used to detect emitted fluorescence from the QDs or Cy3 dye after reduction of stray light by the emission filter (595AF60, Omega Optical). The fluorescence image was captured as a 500 frame movie, in which the exposure (integration) time was 3 s for each frame.

RESULTS AND DISCUSSION

Design and Syntheses of Polymer-Coated QDs. For facile encapsulation of QDs, we chose to synthesize amphiphilic diblock (OPA) and triblock (APOPA) copolymers that would potentially impart solubility to the QDs in aqueous systems for biological imaging. In order to synthesize the block copolymers, we chose three different commercially available poly(acrylic acid) polymers with average molecular weights of 1200, 8000, and 100 000. For each polymer, 40% of the free acids were transformed to the hydrophobic octylamide groups such that the octyl chains would encapsulate and stabilize the QD while the unmodified carboxylic acids would provide solubility in an aqueous environment. The red QD 595 and green QD 514 were both coated with the amphiphilic diblock polymers in dichloromethane and were subsequently purified by size exclusion chromatography (NAP-10 column) followed by dialysis (Scheme 1). Nie and co-workers have recently utilized a similar strategy utilizing octylamine-modified triblock copolymer (MW 100 000, 25% of the free carboxylic acid was derivatized) as the QD coating polymer. All three copolymers afforded soluble QDs. Notably, the low molecular weight diblock polymer (MW 1200) provided the most reproducible coating for both the green and red QDs, where the copolymer contains ∼16 acid units of which 40% are modified with octylamine as evidenced by NMR. Both green and red QDs coated with this low molecular weight polymer were water-soluble and maintained high luminescence in aqueous solution. The absorption and emission spectra are very similar compared with those of TOPO-coated commercial QDs in toluene (Figure 3). We investigated whether these coatings provide extended stability and observed no changes in solubility or fluorescence over a 6 month period (stored at 4 °C). We also tested whether these coatings are stable to various pHs that may be found in different cellular environments and are also required in bioconjugation chemistries. We found that the QDs are stable between pH 3.5 and pH 10.5. Thus, our

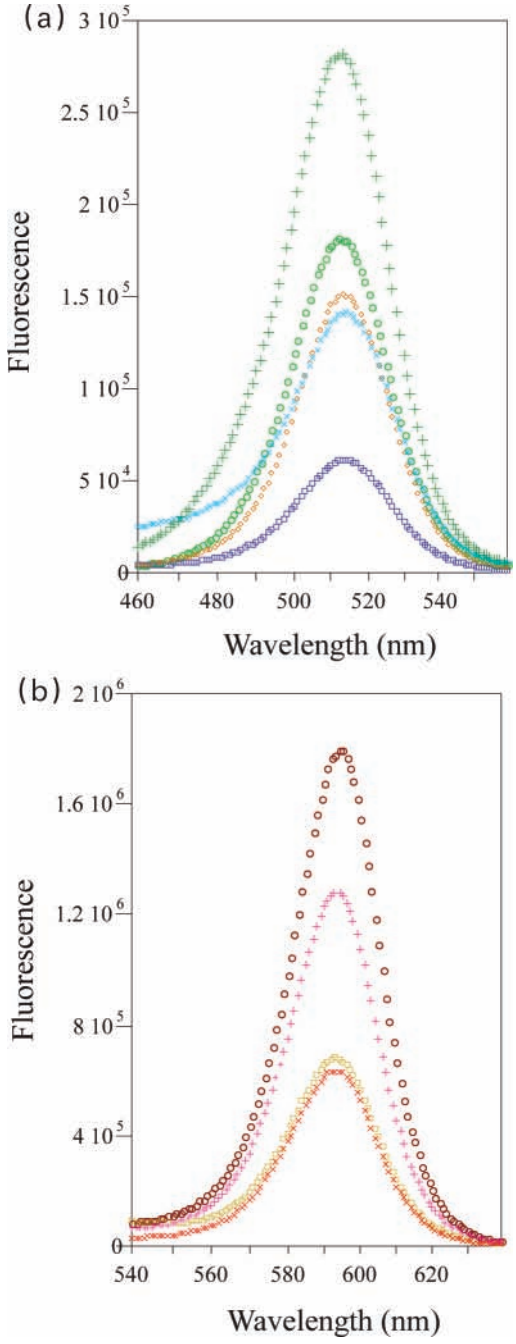


Figure 3. Photoluminescence of uncoated QDs and their GPCR−ligand conjugates. (All samples are normalized to 1 μM of QD) (a) QD514 labeled ligands (green ○, Evidot QD514; red ◇, NDP−QD514; blue □, MT-II−QD514; cyan ×, Deltorphin-II(Ile−Ile); green +, CCK-B−QD514). (b) QD595 labeled ligands. (dark red ○, Evidot QD595; yellow □, MT-II−QD595; red ×, Deltorphin-II(Ile−Ile); magenta +, CCK-B−QD595).

results provide a robust method for synthesizing stable water-soluble QDs suitable for covalent labeling with any macromolecule containing free amines via EDAC-mediated amide bond formation.

In many peptide ligands, the amino terminal and/or free amines play an important role in ligand/receptor interactions. For such ligands, the EDAC-mediated coupling to carboxylic acid functionalized QDs is not feasible. Thus, we also synthesized amino functionality containing amphiphilic copolymers as an alternate QD coating that can be further modified with standard NHS containing bifunctional cross-linkers. We chose to functionalize the 40% octylamine modified poly(acrylic acid) (OPA) with 4,7,10-trioxatridecanediamine. We protected one of the amines with *t*-Boc, while the free amine was coupled to the polymer using EDAC followed by deprotection of *t*-BOC with TFA to give the amino-modified OPA. ^{1}H NMR showed that each polymer chain contained an average of six octyl chains and two free amines. The new amino-amphiphilic polymer (APOPA) was utilized to successfully encapsulate the QDs utilizing the same protocol described for the diblock copolymer (OPA) (Scheme 1). The properties of these amine-functionalized APOPA-coated QDs were found to be very similar to the OPA-coated QDs, with excellent water solubility, stability, and luminescent properties. With both types of water-soluble QDs in hand, we turned to applying them for ligand conjugation for biological imaging.

Bioconjugation of Ligands to QDs for GPCR Imaging. In order to showcase our bioconjugation chemistries and provide useful biological reagents, we chose to target two different G-protein-coupled receptors (GPCRs), the human melanocortin receptor (hMCR) and the human δ-opioid receptor (hDOR). Cell-surface receptors, particularly GPCRs, play a central role in cellular signaling and are important targets for modern pharmaceuticals (*32*). Hence, there is a continuing demand for reliable methods to directly probe cellular localization, receptor density, and trafficking. As such, we chose ligands with high affinity for the chosen GPCRs to allow for imaging with the QD label. For hMCR targeting, we utilized two analogues of α-melanocyte-simulating hormone (α-MSH), NDP and MT-II, developed by Hruby and co-workers (*33*, *34*). NDP and MT-II (Figure 2) ligands were synthesized by standard solid-phase peptide synthesis and purified. The purified peptides were directly conjugated to the OPA copolymer coated QD514 and QD595 by utilizing the water-soluble EDAC-coupling reagent. The carboxylic acids on the QD surface were activated with EDAC followed by addition of the amine-containing ligands to generate the QD−α-MSH conjugate (Figure 1, route a). We also synthesized another potent ligand, Asp-Tyr-*N*-MeNle-Gly-Trp-*N*-MeNle-Asp-Phe-NH_2 (CCK−B), which has been shown to be a selective CCK−B-type analogue with an IC_{50} of 0.13 nM (*35*) and conjugated this ligand to our soluble QDs using the above-described methodology to yield CCK−B−QD514 and CCK−B−QD595.

In an effort to provide a general strategy for QD conjugation, we also considered the possibility that many peptide ligands could contain two or more free amines and thus not allow for selective conjugation to QDs. Alternatively, the N-terminal amine in the ligand could be important for biological activity, which would preclude the EDAC-mediated coupling reaction described above. Considering this situation, we prepared QDs coated with amine functionalities (APOPA) that could be modified by a suitable bifunctional linker, where one end provides an activated ester that can react with a free amine on the QD surface while the other end provides a maleimide that can specifically react with a unique thiol that is engineered into a ligand. To demonstrate the feasibility of this approach, we synthesized a highly potent Deltorphin-II analog, Tyr-(D)Ala-Phe-Glu-Ile-Ile-Gly (Deltorphin-II(Ile−Ile)), developed by Sasaki (*36*) to selectively target the δ-opioid receptor (K_d = 67 pM). We incorporated a short linker and a cysteine at the C-terminus of this ligand for facile conjugation at pH 6−8 to the maleimide-functionalized amine-bearing QDs (Figure 1, route b). The peptide was conjugated to the QDs to yield Deltorphin-II(Ile−Ile)−QD514 and Deltorphin-II−QD595.

Having all of the four different sets of GPCR ligand−QD conjugates in hand, we compared them to the commercial QDs in toluene. All the water-soluble ligand-modified QDs were shown to maintain high photoluminescence in aqueous conditions (Figure 3). NDP−QD514 and Deltorphin-II(Ile−Ile)−QD514 almost have the same fluorescence intensity as the bare

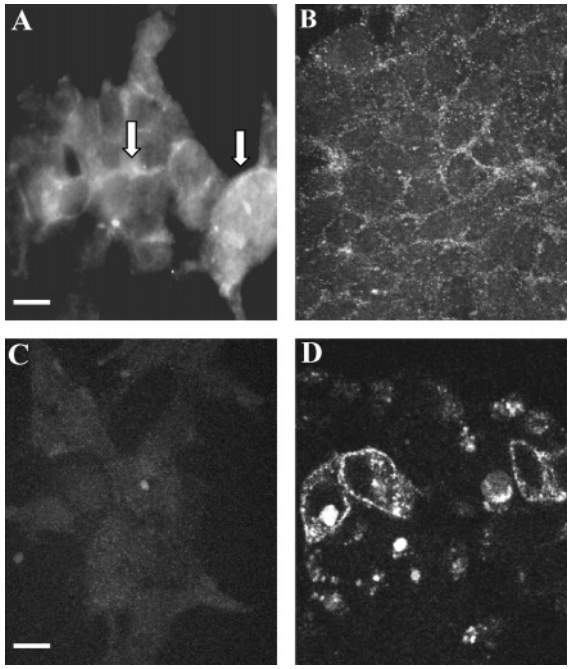


Figure 4. NDP−QD514 targeted hMC4R. (a) HEK293 cells incubated with an MC4R specific antibody after cell fixation and permeabilization showing the distribution of all expressed receptors. Arrows indicate labeling at cell membranes. (b) HEK293 cells incubated with MC4R-specific antibody prior to cell fixation showing the distribution of cell-surface expressed receptors. (c) Live HEK293 cells lacking hMC4R expression, incubated with 10^{-7} M NDP−QD514 15 min prior to imaging. (d) Live cells overexpressing the hMC4R, incubated with 10^{-7} M NDP−QD514. Scale bars = 20 μM.

QD514. The fluorescence values of MT-II−QD514, MT-II−QD595, and Deltorphin-II(Ile−Ile)−QD595 decreased to about one-third those of the bare QDs, but still high enough for bioimaging because of the strong QD photoluminescence.

GPCR Imaging Utilizing QDs. *Targeting hMC4R.* The utility of the EDAC coupling chemistry in generating ligand-modified water-soluble QDs was evaluated. NDP-QD514 was used to target overexpressed melanocortin 4 receptor (MC4R) in HEK293 cells (Figure 4). An MC4R-specific antibody was used to validate receptor expression and determine the cellular distribution of MC4R for comparison with NDP−QD514 mediated imaging. The distribution of total MC4R expression is shown in Figure 4A where cells were permeabilzied then probed with the receptor-specific antibody. This image shows the distribution of all expressed receptor. However, this antibody recognizes an extracellular epitope of the MC4R; therefore, MC4R-transfected HEK293 cells were also incubated with the receptor-specific antibody prior to fixation. Figure 4B shows the distribution of surface-expressed receptor. Control cells without receptor do not show significant fluorescence under either condition (data not shown). Having established that hMC4R was stably expressed, we turned to testing the selectivity of NDP−QD514. HEK293 cells that either did not express (Figure 4c) or expressed hMC4R (Figure 4d) were incubated with NDP−QD514 (10^{-7} M). We clearly observe cell-surface labeling by the NDP−QD514 of the HEK293 cells expressing hMC4R (Figure 4d) with almost no background labeling. These results clearly show that our small ligand labeled water-soluble QDs are easily comparable to commercial fluorescently labeled antibody-based detection methods. Importantly, most receptor antibodies are not raised against extracellular epitopes and therefore do not label only the surface receptors, but rather show the distribution of all receptors (functional or nonfunctional) including those in subcellular compartments such as seen in Figure 4A. Therefore, ligand-conjugated QDs provide an important tool for specifically evaluating the functional receptor complement on the cell surface.

Targeting hDOR. To determine the utility of the APOPA−QDs functionalized with maleimides for conjugation with thiol-bearing ligands, we tested the Deltorphin-II(Ile−Ile)−QD595 targeting to human δ-opioid receptors (hDOR) expressed in CHO cells (Figures 5 and 6). CHO cells with stably expressed receptors were incubated with 0.75 nM Deltorphin-II(Ile−Ile)−QD595 for 1 min, washed, and subsequently imaged (Figure 5). The surface distribution of hDOR can be clearly observed. Since Deltorphin-II(Ile−Ile) is a known agonist, it can activate hDOR and therefore should be internalized. Cells expressing hDOR were incubated for 1 min or 20 min with the Deltorphin-II(Ile−Ile)−QD595. Interestingly, after 1 min we only observed cell-surface labeling, while at 20 min, we can directly observe receptor internalization. As shown in Figure 5, this agonist-mediated activity is retained when the ligand is conjugated on the QD. Control experiments show no cellular labeling or receptor internalization. Thus, these results not only show that the amine-modified QDs are suitable for ligand conjugation and cellular labeling of GPCRs but that they can also be internalized in a receptor-dependent fashion.

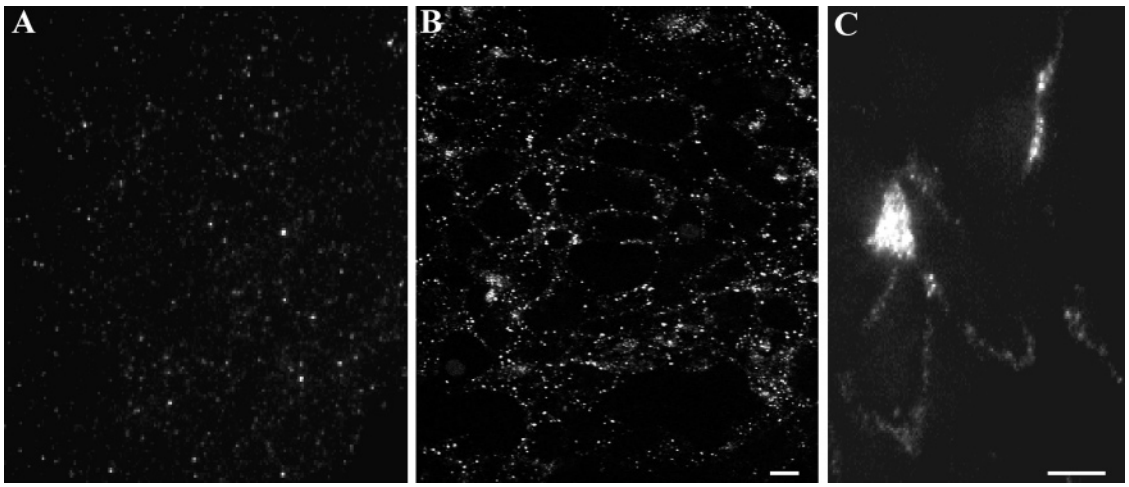


Figure 5. Images of Deltorphin-II(Ile−Ile)−QD595 mediated targeting of human δ-opioid (hDOR) expressed CHO cells. Live cells were incubated for 1 min with 0.75 nM QD−ligand. (a) Cells imaged after 1 min postincubation showing only surface labeling. (b) Cells imaged after incubating for 20 min showing significant organization of Deltorphin-II(Ile−Ile)−QD595 distribution at or near cell surfaces. Scale bars are 10 μm. (c) Image is a magnification showing distribution in four cells, 15 min following the 1 min labeling period.

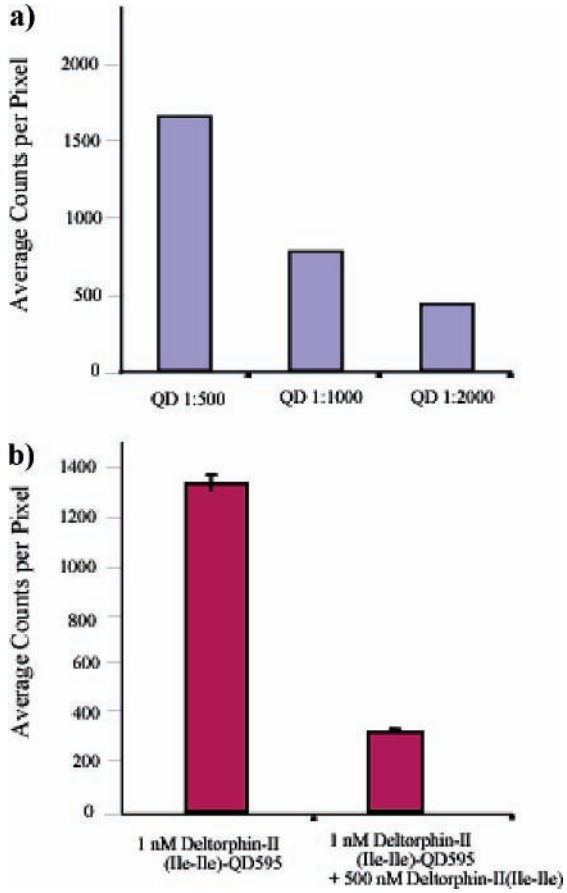


Figure 6. Specificity of Deltorphin-II(Ile−Ile)−QD595 for hDOR on CHO cells. (a) In all experiments, 500 nM of free Deltorphin-II(Ile−Ile) was mixed with varying amounts of Deltorphin-II(Ile−Ile)−QD595 and added to hDOR-expressing CHO cells. (b) Deltorphin-II(Ile−Ile)−QD595 conjugate (1.5 nM) targeting hDOR on CHO cells in the absence and presence of 500 nM of free ligand with prior incubation for 5 min. Measurements are averaged on ten cells per image and five independent images.

In the above experiments, the average number of Deltorphin-II(Ile−Ile)/QD is ∼200; thus, we expected that multivalent interaction (avidity effects) could possibly result in tighter apparent binding constants for Deltorphin-II(Ile−Ile)−QD595 when compared to free Deltorphin-II(Ile−Ile). In a first set of experiments, CHO cells overexpressing hDOR were incubated with 500 nM free Deltorphin-II(Ile−Ile) in the presence of varying concentrations of the Deltorphin-II(Ile−Ile)−QD595. Interestingly, QD−conjugate concentrations in the range 0.375−1.5 nM showed clear cellular labeling, even in the presence of 500 nM of free Deltorphin-II(Ile−Ile) ligands (Figure 6a). These data suggest that the multivalent or avidity effects increase the binding of the labeled QDs which cannot be competed off by the free ligand. In a second experiment, we envisioned that adding free ligand prior to adding QD-conjugated ligand would possibly prevent QD binding. To test this, we added 500 nM of free Deltorphin-II(Ile−Ile) ligand to the cells and incubated for 5 min prior to adding the QD−Deltorphin-(Ile−Ile). The QD−Deltorphin-II(Ile−Ile) was added for 1 min followed by washing the cells and imaging. As expected, incubation of cells with 500 nM of free Deltorphin-II(Ile−Ile) prior to adding the QD−Deltorphin-II(Ile−Ile) prevented significant QD binding as seen by the decrease in the average signal per pixel, from ∼1350 to ∼300 (Figure 6b). The competition experiments taken together establish that the QD conjugates target the hDOR specifically but with a much higher binding constant possibly due to a strong multivalent effect, which may aid in visualizing low copy number receptors. Future experiments will aim to develop approaches for controlling and measuring ligand density on QD surfaces as well as to systematically explore the utility of avidity effects.

Single-Molecule Detection of GPCRs. Single-molecule imaging has emerged as a particularly useful method for investigating receptor localization and trafficking in live cells and in model bilayers (*37*). QDs provide certain advantages over traditional fluorophores due to their broad absorption spectra, tunable emission, and resistance to photobleaching. In order to test the suitability of our ligand-conjugated QDs for single-molecule imaging studies, we chose the human δ-opioid receptor (hDOR) as a target. In these experiments, we directly compare the Deltorphin-II(Ile−Ile)−QD595 conjugate to a Deltorphin-II(Ile−Ile) ligand labeled with Cy3, a widely used fluorophore.

Purified hDOR was incorporated into an artificial lipid bilayer formed on a fused silica coverslip modified by a thin 5-nm-thick polyacrylamide brush. Single-molecule fluorescence was recorded with a total internal reflection fluorescence system, by excitation with an argon ion laser at 488 nm for QDs and 514.5 nm for Cy3. Fluorescence images for hDOR binding for both Deltorphin-II(Ile−Ile)−QD595 and Deltorphin-II(Ile−Ile)−Cy3 were captured as a 500 frame movie, in which the exposure (integration) time was 3 s for each frame. We observed that both Deltorphin-II(Ile−Ile)−QD595 and Deltorphin-II(Ile−Ile)−Cy3 had similar average residence times (bimodal: ∼30 s and hundreds of seconds) on single hDORs (Figure 7). This would at first appear to be in contradiction to the avidity effect observed at cell surfaces; however, in the single-molecule model

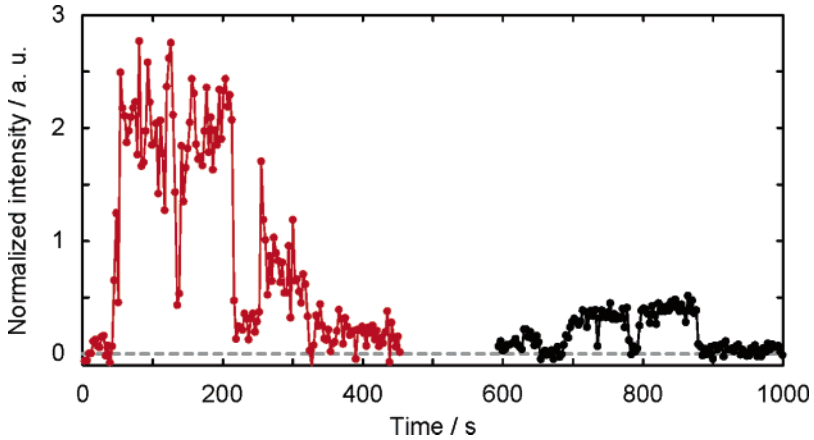


Figure 7. Comparison of fluorescence intensity of Deltorphin-II(Ile−Ile)−QD595 (red) and Deltorphin-II(Ile−Ile)−Cy3 (black) in the presence of hDOR in a lipid bilayer. (Fluorescence intensities after background subtraction.) Fluorescence is normalized at a laser power of 0.05 mW. The one-step increase and decrease indicate one single-molecule event.

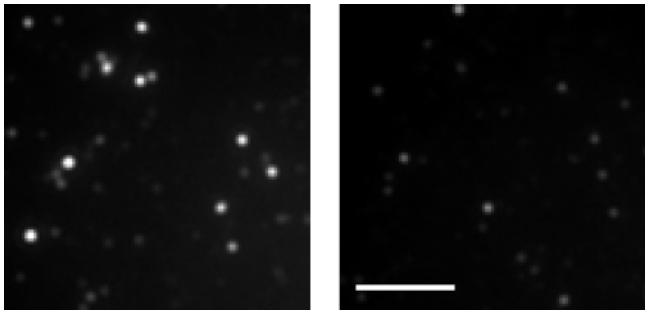


Figure 8. Specific targeting in single-molecule experiments. Cumulative fluorescence images of Deltorphin-II(Ile−Ile)−QD595 (2 nM) bound to hDOR in a lipid bilayer: (a) with and (b) without free Deltorphin-II(D-Ala2) (19 μM). (Same contrast. Image size 16 μm × 16 μm. Scale and illumination are identical in both images, and scale bar is 5 μm.) The 300-frame movies for both (a) and (b) are available online in the Supporting Information.

system, the receptors are at a very low concentration and thus several microns apart, which likely precludes multivalent binding. Most importantly, the fluorescence from QD conjugates was measured to be about sixfold stronger than that from Cy3. This increased fluorescence, combined with other advantages of the QDs such as resistance to photobleaching and multiplexing, provides a potential alternative imaging agent in single-molecule experiments for both model systems and in live cells.

We also considered the possibility that the QD conjugates could possibly bind nonspecifically to the model bilayer. Thus, in order to test the binding specificity, 2 nM of the Deltorphin-II(Ile−Ile)−QD595 conjugate was incubated with hDOR in the absence and presence of excess (19 μM) free Deltorphin-II(D-Ala2) ligand. The cumulative fluorescence images showed that free ligand significantly reduces Deltorphin-II(Ile−Ile)−QD595 from binding the hDOR (Figure 8). Thus, these experiments clearly demonstrate that observed binding is due to specific interaction of Deltorphin-II(Ile−Ile)−QD595 with the immobilized hDOR. Together with the whole-cell experiments, the single-molecule experiments also suggest that careful control experiments, with and without the targeted receptor, must be routinely performed to distinguish between specific versus nonspecific binding for ligand-targeted QDs.

In conclusion, we have developed a convenient method for synthesizing two types of water-soluble QDs with carboxylic acid and amine functionalities. We tested our approach with two different sizes of bare CdSe/ZnS QDs (QD595 and QD514). Both types of polymer-coated QDs displayed excellent solubility, stability, and fluorescence properties in a wide pH regime. We envisioned that the carboxylic acid functionalized QDs can be utilized for directly coupling amine-containing ligands, while the amine-functionalized QDs can be used for conjugating cysteine-containing ligands. Three small peptide ligands were successfully conjugated to our water-soluble QDs in order to target G-protein-coupled receptors (hMCR and hDOR). The ligand-conjugated QDs were shown to be specific for the targeted receptor and could be utilized for fluorescence imaging of receptors in cells as well as in single-molecule experiments in model bilayers. Thus, our methodology provides an expeditious route for constructing new fluorescent bioconjugates that are amenable for multiplexing and may have utility in studying the localization and trafficking of GPCRs in live cells and in single-molecule experiments.

ACKNOWLEDGMENT

We thank the Bio5, University of Arizona, and the NSF (CHE-0548264 and CHE-0433779) for supporting aspects of this research. We thank members of the Ghosh lab for helpful comments. All ligand labeled and unlabeled water-soluble QDs are freely available from the Ghosh lab for research purposes.

Supporting Information Available: Two movies showing single-molecule GPCR binding events in the presence and absence of inhibitors. This material is available free of charge via the Internet at http://pubs.acs.org.

LITERATURE CITED

(1) Michalet, X., Pinaud, F. F., Bentolila, L. A., Tsay, J. M., Doose, S., Li, J. J., Sundaresan, G., Wu, A. M., Gambhir, S. S., and Weiss, S. (2005) Quantum dots for live cells, in vivo imaging, and diagnostics. *Science 307*, 538−544.

(2) Medintz, I. L., Uyeda, H. T., Goldman, E. R., and Mattoussi, H. (2005) Quantum dot bioconjugates for imaging, labelling and sensing. *Nat. Mater. 4*, 435−446.

(3) Green, M. (2004) Semiconductor quantum dots as biological imaging agents. *Angew. Chem., Int. Ed. 43*, 4129−4131.

(4) Smith, A. M., and Nie, S. M. (2004) Chemical analysis and cellular imaging with quantum dots. *Analyst 129*, 672−677.

(5) Wu, A. M., and Senter, P. D. (2005) Arming antibodies: prospects and challenges for immunoconjugates. *Nat. Biotechnol. 23*, 1137−1146.

(6) Goodwin, D. A., and Meares, C. F. (2001) Advances in pretargeting biotechnology. *Biotechnol. Adv. 19*, 435−450.

(7) Chan, W. C. W., and Nie, S. M. (1998) Quantum dot bioconjugates for ultrasensitive nonisotopic detection. *Science 281*, 2016−2018.

(8) Mattoussi, H., Mauro, J. M., Goldman, E. R., Anderson, G. P., Sundar, V. C., Mikulec, F. V., and Bawendi, M. G. (2000) Self-assembly of CdSe-ZnS quantum dot bioconjugates using an engineered recombinant protein. *J. Am. Chem. Soc. 122*, 12142−12150.

(9) Pathak, S., Choi, S. K., Arnheim, N., and Thompson, M. E. (2001) Hydroxylated quantum dots as luminescent probes for in situ hybridization. *J. Am. Chem. Soc. 123*, 4103−4104.

(10) Ding, S. Y., Jones, M., Tucker, M. P., Nedeljkovic, J. M., Wall, J., Simon, M. N., Rumbles, G., and Himmel, M. E. (2003) Quantum dot molecules assembled with genetically engineered proteins. *Nano Lett. 3*, 1581−1585.

(11) Parak, W. J., Gerion, D., Pellegrino, T., Zanchet, D., Micheel, C., Williams, S. C., Boudreau, R., Le Gros, M. A., Larabell, C. A., and Alivisatos, A. P. (2003) Biological applications of colloidal nanocrystals. *Nanotechnology 14*, R15−R27.

(12) Gerion, D., Pinaud, F., Williams, S. C., Parak, W. J., Zanchet, D., Weiss, S., and Alivisatos, A. P. (2001) Synthesis and properties of biocompatible water-soluble silica-coated CdSe/ZnS semiconductor quantum dots. *J. Phys. Chem. B 105*, 8861−8871.

(13) Dubertret, B., Skourides, P., Norris, D. J., Noireaux, V., Brivanlou, A. H., and Libchaber, A. (2002) In vivo imaging of quantum dots encapsulated in phospholipid micelles. *Science 298*, 1759−1762.

(14) Pinaud, F., King, D., Moore, H. P., and Weiss, S. (2004) Bioactivation and cell targeting of semiconductor CdSe/ZnS nanocrystals with phytochelatin-related peptides. *J. Am. Chem. Soc. 126*, 6115−6123.

(15) Gao, X. H., Chan, W. C. W., and Nie, S. M. (2002) Quantum-dot nanocrystals for ultrasensitive biological labeling and multicolor optical encoding. *J. Biomed. Opt. 7*, 532−537.

(16) Wu, X. Y., Liu, H. J., Liu, J. Q., Haley, K. N., Treadway, J. A., Larson, J. P., Ge, N. F., Peale, F., and Bruchez, M. P. (2003) Immunofluorescent labeling of cancer marker Her2 and other cellular targets with semiconductor quantum dots. *Nat. Biotechnol. 21*, 41−46.

(17) Gao, X. H., Cui, Y. Y., Levenson, R. M., Chung, L. W. K., and Nie, S. M. (2004) In vivo cancer targeting and imaging with semiconductor quantum dots. *Nat. Biotechnol. 22*, 969−976.

(18) Howarth, M., Takao, K., Hayashi, Y., and Ting, A. Y. (2005) Targeting quantum dots to surface proteins in living cells with biotin ligase. *Proc. Natl. Acad. Sci. U.S.A. 102*, 7583−7588.

(19) Groc, L., Heine, M., Cognet, L., Brickley, K., Stephenson, F. A., Lounis, B., and Choquet, D. (2004) Differential activity-dependent regulation of the lateral mobilities of AMPA and NMDA receptors. *Nat. Neurosci. 7*, 695−696.

(20) Gomez, N., Winter, J. O., Shieh, F., Saunders, A. E., Korgel, B. A., and Schmidt, C. E. (2005) Challenges in quantum dot-neuron active interfacing. *Talanta 67*, 462−471.
(21) Tomlinson, I. D., Mason, J. N., Blakely, R. D., and Rosenthal, S. J. (2005) Peptide-conjugated quantum dots: imaging the angiotensin type 1 receptor in living cells. *Methods Mol. Biol. 303*, 51−60.
(22) Hines, M. A., and Guyot-Sionnest, P. (1996) Synthesis and characterization of strongly luminescing ZnS-capped CdSe nanocrystals. *J. Phys. Chem. 100*, 468−471.
(23) Kaiser, E., Colescot, R., Bossinge, C., and Cook, P. I. (1970) Color test for detection of free terminal amino groups in solid-phase synthesis of peptides. *Anal. Biochem. 34*, 595.
(24) Rink, H. (1987) Solid-phase synthesis of protected peptide-fragments using a trialkoxy-diphenyl-methylester resin. *Tetrahedron Lett. 28*, 3787−3790.
(25) Grieco, P., Han, G. X., Weinberg, D., MacNeil, T., Van der Ploeg, L. H. T., and Hruby, V. J. (2002) Design and synthesis of highly potent and selective melanotropin analogues of SHU9119 modified at position 6. *Biochem. Biophys. Res. Commun. 292*, 1075−1080.
(26) Hu, M. L. (1994) Measurement of protein thiol-groups and glutathione in plasma. *Methods Enzymol. 233*, 380−385.
(27) Xiao, D. Q., and Wirth, M. J. (2002) Kinetics of surface-initiated atom transfer radical polymerization of acrylamide on silica. *Macromolecules 35*, 2919−2925.
(28) Osborne, V. L., Jones, D. M., and Huck, W. T. S. (2002). Controlled growth of triblock polyelectrolyte brushes. *Chem. Commun.* 1838−1839.
(29) Smith, E. A., Coym, J. W., Cowell, S. M., Tokimoto, T., Hruby, V. J., Yamamura, H. I., and Wirth, M. J. (2005) Lipid bilayers on polyacrylamide brushes for inclusion of membrane proteins. *Langmuir 21*, 9644−9650.
(30) Cremer, P. S., and Boxer, S. G. (1999) Formation and spreading of lipid bilayers on planar glass supports. *J. Phys. Chem. B 103*, 2554−2559.
(31) Alves, I. D., Salamon, Z., Varga, E., Yamamura, H. I., Tollin, G., and Hruby, V. J. (2003) Direct observation of G-protein binding to the human delta-opioid receptor using plasmon-waveguide resonance spectroscopy. *J. Biol. Chem. 278*, 48890−48897.
(32) Marinissen, M. J., and Gutkind, J. S. (2001) G-protein-coupled receptors and signaling networks: emerging paradigms. *Trends Pharmacol. Sci. 22*, 368−376.
(33) Sawyer, T. K., Sanfilippo, P. J., Hruby, V. J., Engel, M. H., Heward, C. B., Burnett, J. B., and Hadley, M. E. (1980) 4-Norleucine, 7-D-phenylalanine-α-melanocyte-stimulating hormone - a highly potent α-melanotropin with ultralong biological-activity. *Proc. Natl. Acad. Sci. U.S.A. 77*, 5754−5758.
(34) Haskellluevano, C., Miwa, H., Dickinson, C., Hruby, V. J., Yamada, T., and Gantz, I. (1994) Binding and camp studies of melanotropin peptides with the cloned human peripheral melanocortin receptor, Hmc1r. *Biochem. Biophys. Res. Commun. 204*, 1137−1142.
(35) Hruby, V. J., Fang, S., Knapp, R., Kazmierski, W., Lui, G. K., and Yamamura, H. I. (1990) Cholecystokinin analogs with high-affinity and selectivity for brain membrane-receptors. *Int. J. Pept. Protein Res. 35*, 566−573.
(36) Sasaki, Y., Ambo, A., and Suzuki, K. (1991) [D-Ala2]Deltorphin-II analogs with high-affinity and selectivity for δ-opioid receptor. *Biochem. Biophys. Res. Commun. 180*, 822−827.
(37) Weiss, S. (1999) Fluorescence spectroscopy of single biomolecules. *Science 283*, 1676−1683.

BC0601929

Highly-Efficient Purification of Native Polyhistidine-Tagged Proteins by Multivalent NTA-Modified Magnetic Nanoparticles

Jason S. Kim,[†] C. Alexander Valencia,[‡] Rihe Liu,*[,‡] and Wenbin Lin*[,†]

Department of Chemistry and School of Pharmacy and Carolina Center for Genome Sciences, University of North Carolina, Chapel Hill, North Carolina 27599. Received July 3, 2006; Revised Manuscript Received January 2, 2007

A new bis-nitrilotriacetic acid (NTA) chelate with catechol anchor was synthesized and immobilized on superparamagnetic iron oxide nanoparticles. When loaded with Ni(II), these bis-NTA-immobilized nanoparticles were shown to bind polyhistidine (His × 6-tagged) fusion proteins in their native, folded conformations that commercial microbeads failed to bind under identical conditions. Control experiments with a mono-NTA chelate immobilized on iron oxide nanoparticles indicate a similarly high affinity for His × 6-tagged native proteins, suggesting that the high density of the mono-NTA chelate presented by the nanoparticles allows the binding of the His × 6-tag to more than one Ni-NTA moiety on the surface. This study shows that the multivalency strategy can be utilized to enhance the binding of His × 6-tagged proteins in their native, folded conformations. We further demonstrated the selective purification of His × 6-tagged proteins from crude cell lysates by using the Ni(II)-loaded iron oxide nanoparticles. The present platform is capable of efficient purification of His × 6-tagged proteins that are expressed at low levels in mammalian cells. This work thus presents a novel nanoparticle-based high-capacity protein purification system with shorter incubation times, proportionally large washes, and significantly smaller elution volumes compared to commercially available microbeads.

INTRODUCTION

As we enter the proteomic era, there is an ever-increasing need for efficient protein purification techniques that allow for direct isolation of proteins from cell lysates (*1*). Among many currently used protein purification strategies (*2*), immobilized metal affinity chromatography (IMAC) has emerged as one of the most powerful techniques for the purification of recombinant proteins (*3*). In the most common IMAC implementation, a His × 6 tag that comprises six consecutively placed histidine residues is incorporated into the C- or N-terminus of a recombinant protein. The His × 6 tag binds strongly to a divalent metal chelate such as the Ni(II) nitrilotriacetate complex (Ni-NTA) which is in turn immobilized on a resin. It is believed that four of the six coordination sites on the octahedral Ni(II) center are occupied by the NTA ligand and the remaining coordination sites are occupied by two of the six imidazole moieties in the His × 6 tag (*4*).

The IMAC strategy allows the purification of His × 6-tagged proteins in one or two steps to achieve a moderate degree of purity. Moreover, the His × 6 tag is relatively small and generally does not interfere with the native structure and function of the tagged protein. Since its discovery in the late 1980s, Ni-NTA-based IMAC has been widely used for purifying recombinant proteins, and many His × 6-tagged proteins are now commercially available. While this strategy has proven to be largely successful, a significant percentage of recombinant proteins remain difficult to purify by IMAC (*5*). Low protein expression is a key contributor to such difficulties, as the target protein concentration may be less than 0.1% of the cleared crude lysate when overexpressed in *E. coli*, and much lower when overexpressed in mammalian cells. Numerous functionally active proteins can only be expressed in mammalian cells, which poses new challenges to protein purification techniques. The target protein structure may also add to purification difficulties by blocking the His × 6-tag from the Ni-NTA moiety on the surface of microbeads. Consequently, commercial Ni-NTA resins cannot capture a large number of His × 6-tagged proteins under native conditions. To overcome this problem, purification under denaturing conditions has been used to gain full access to the His × 6-tag, but overall protein purification efficacy significantly decreases because of the unreliability and inefficiency of in vitro protein refolding to their native functional conformations.

Significant efforts have been devoted to gaining a better understanding of the Ni-NTA/His × 6-tag interactions and thus improving the IMAC protein purification efficiency over the past few years. The strength of the Ni-NTA/His × 6-tag interaction was, for example, recently assessed using scanning force microscopic techniques (*6*). Ebright et al. elegantly demonstrated enhanced binding of the His × 6-tag to a bivalent Ni-NTA system over a monovalent Ni-NTA control using fluorescence anisotropy and fluorescence resonance energy transfer measurements (*7*). Piehler et al. has further studied the enhanced affinity of multivalent Ni-NTA-derived molecules toward the histidine tag in great detail (*8*−*10*). In the present work, we wish to design a superparamagnetic iron oxide immobilized bivalent Ni-NTA chelate system with the aim of improving IMAC purification of His × 6-tagged proteins by strengthening the interactions between the His × 6-tag and the bivalent Ni-NTA chelate. The bis-Ni-NTA-immobilized nanoparticles were shown to be capable of binding His × 6-tagged proteins in their native, folded conformations that failed to bind commercial microbeads under identical conditions. We have demonstrated that the present system is superior to commercial magnetic beads in binding to His × 6-tagged proteins and is useful for isolating target proteins that are overexpressed at low levels in the mammalian cells. Control experiments with a mono-NTA chelate immobilized on iron oxide nanoparticles

* Corresponding authors. (W.L.) Phone: (919)-962-6320. Fax: (919)-962-2388. E-mail: wlin@unc.edu. (R.L.) Phone: (919)-843-3635. Fax: (919)-966-0204. E-mail: rliu@email.unc.edu.

[†] Department of Chemistry.

[‡] School of Pharmacy and Carolina Center for Genome Sciences.

10.1021/bc060195l CCC: $37.00 © 2007 American Chemical Society
Published on Web 02/21/2007

indicated a similarly high affinity for His × 6-tagged proteins, suggesting that the very high density of the mono-NTA chelate presented by the nanoparticles allows the binding of the His × 6-tag to more than one NTA moiety on the surface. Thus, this work demonstrates that the multivalency strategy can be utilized to enhance the binding of His × 6-tagged proteins in their native, folded conformations.

MATERIALS AND METHODS

General. N_α,N_α-bis(carboxymethyl)-L-lysine was purchased from Fluka. 2-(3,4-Bis-benzyloxyphenyl)ethylamine trifluoroacetate salt (Bn-DA-TFA) and N_α,N_α-bis(carboxymethyl)-L-lysine tribenzyl ester trifluoroacetate salt (Bn-NTA-lys-TFA) were prepared from literature procedures (*1*, *11*). All other chemicals were purchased from Sigma-Aldrich and used as received unless otherwise noted. Carboxy-terminated magnetic microparticles were purchased from Bangs Laboratories, Inc. Purified recombinant His × 6-endostatin (His × 6-rmES) was purchased from Calbiochem. Recombinat human His × 6-ubiquitin (His × 6-Ub) and mouse His × 6-ubiquitin C-terminal hydrolase L-1 (His × 6-UCH-L1) were from Boston Biochem. ^{1}H and ^{13}C{^{1}H} NMR spectra were obtained on a Bruker 400 MHz AVANCE or Bruker 400 MHz DRX. Mass spectra were obtained from Voyager DE-Pro MALDI-MS or HP/Agilent LC/Ion-trap MS in the Department of Chemistry at Duke University. Liquid scintillation counting experiments are performed on a Tri-Carb 2900TR liquid scintillation analyzer. SDS-PAGE gels were quantified using the AlphaEaseFC program. The molecular markers used for the SDS gels have molecular weights of 175, 83, 62, 47, 32, 25, and 16 kDa, respectively. Transmission electron microscopy (TEM) images were taken with a JEM-100CXII transmission electron microscope at 100 KV.

Synthesis of Dimethyl 5-(3,4-Bis(benzyloxy)phenethylcarbamoyl)benzene-1,3-dioate (1). To a stirring solution of benzene-1,3,5-tricarbonyltrichloride (1.7 g, 6.40 mmol) in dry CH_2Cl_2 (170 mL) at 0 °C was added Bn-DA-TFA (0.536 g, 1.20 mmol) in dry CH_2Cl_2 (100 mL) dropwise over 5 h. The solution was allowed to warm to room temperature. The solvent was removed under reduced pressure to produce a white residue. Methanol was added and stirred for a few hours. The excess methanol was removed under reduced pressure to produce a white solid. The product was isolated using flash column chromatography (ethyl acetate/hexanes, 2:3 v/v; $R_f = 0.4$). The solvents were removed under reduced pressure to yield a white solid of **1** (0.225 g, 0.408 mmol, 34.0% yield). ^{1}H NMR (400 MHz, $CDCl_3$) δ 8.75 (s, 1H), 8.52 (s, 2H), 7.40 (d, 4H), 7.29 (m, 6H), 6.90 (d, 1H), 6.81 (s, 1H), 6.72 (d, 1H), 5.11 (s, 2H), 5.01 (s, 2H), 3.92 (s, 6H), 3.64 (q, 2H), 2.83 (t, 2H). ^{13}C NMR ($CDCl_3$, 100 MHz) δ 165.4, 165.3, 149.0, 147.6, 137.2, 137.0, 135.4, 132.9, 132.0, 131.9, 130.9, 128.3, 127.7, 127.2, 121.5, 115.5, 115.3, 71.3, 71.2, 52.4, 41.4, 34.9, 31.5. MALDI-MS: $[M + H]^+$ *m*/*z* 554.0 (calcd 554.6); $[M + Na]^+$, *m*/*z* 577.2 (calcd 576.6); $[M + K]^+$ *m*/*z* 592.8 (calcd 592.7).

Synthesis of 5-(3,4-Bis(benzyloxy)phenethylcarbamoyl)-benzene-1,3-dioic acid (2). To a stirring solution of **1** (0.160, 0.289 mmol) in acetone (6 mL) was added 1 N NaOH (4 mL). After 3 h, complete deprotection was confirmed by TLC. The solution was acidified to pH 3 using 1 N HCl. The solvent was removed, and the product was stirred in H_2O. The precipitate of **2** was collected by suction filtration and recrystallized in acetone (0.145 g, 0.276 mmol, 95.5% yield). ^{1}H NMR (400 MHz, MeOD) δ 8.42 (s, 1H), 8.21 (s, 2H), 7.15−6.90 (m, 10H), 6.67 (s, 1H), 6.62 (d, 1H), 6.49 (d, 1H), 4.73 (s, 4H), 3.28 (t, 2H), 2.54 (t, 2H). ^{13}C NMR (DMSO, 100 MHz) δ 166.4, 164.6, 148.3, 146.8, 137.5, 137.4, 135.5, 132.7, 132.2, 132.0, 131.8, 128.4, 127.8, 127.7, 127.6, 127.5, 121.2, 115.2, 114.8, 70.3, 70.2, 41.1, 34.4. MALDI-MS: $[M + H]^+$ *m*/*z* 525.9 (calcd 526.6).

Synthesis of 5-(3,4-Bis(benzyloxy)phenethylcarbamoyl)-benzene-1,3-benzyl-NTA-lysine (3). The diacid **2** (0.140 g, 0.266 mmol) was stirred in dry CH_2Cl_2 (13 mL) to form a cloudy suspension. 0.40 mL of $SOCl_2$ was slowly added and stirring continued at 50 °C for 6 h to form a clear solution. The solvent was removed under reduced pressure to give the 5-(3,4-bis(benzyloxy)phenethylcarbamoyl)benzene-1,3-dioyl dichloride intermediate which was used without further purification.

To a stirring mixture of Bn-NTA-lys-TFA (0.408 g, 0.632 mmol), TEA (0.5 mL), and $CHCl_3$ (5 mL) was added a solution of 5-(3,4-bis(benzyloxy)phenethylcarbamoyl)benzene-1,3-dioyl dichloride in $CHCl_3$ (10 mL) dropwise at 0 °C. The reaction was allowed to warm to room temperature and stir overnight. After removal of solvents under reduced pressure, column chromatography (ethyl acetate/hexanes, 3:2 v/v; $R_f = 0.5$) was used to isolate a pure white solid of **3** (0.281 g, 0.181 mmol, 67.9% yield). ^{1}H NMR ($CDCl_3$, 400 MHz) δ 8.33 (s, 3H), 7.41−7.25 (m, 35H), 6.95 (t), 6.86 (d, 2H), 6.80 (s, 2H), 6.69 (d, 2H), 5.10 (s, 8H), 5.06 (s, 2H), 4.98 (s, 4H), 3.68 (s, 4H), 3.59 (t, 4H), 3.46 (t, 1H), 3.32 (t, 2H) 2.75 (t, 4H), 1,69−1.24 (m, 6H). ^{13}C NMR ($CDCl_3$, 100 MHz) δ 172.8, 171.7, 166.3, 149.3, 148.0, 137.6, 137.5, 135.9, 135.8, 135.6, 135.4, 132.4, 128.8, 128.7, 128.6, 128.5, 128.0, 127.7, 121.7, 116.2, 115.9, 71.6, 66.8, 66.7, 64.5, 53.1, 40.2, 35.4, 29.9, 28.5, 23.1. MALDI-MS: $[M + H]^+$ *m*/*z* 1556.3 (calcd 1555.8); $[M + Na]^+$, *m*/*z* 1577.5 (calcd 1577.8); $[M + K]^+$, *m*/*z* 1593.1 (calcd 1593.9).

Synthesis of 5-(3,4-Bis(hydroxy)phenethylcarbamoyl)-benzene-1,3-NTA-lysine (4). 3 (0.043 g, 0.052 mmol) was dissolved in 1.5 mL of $CHCl_3$ and 6 mL of MeOH and placed in a Parr flask with 15 mg Pd/C (10%). The mixture was shaken in a Parr reactor for 24 h under H_2 (60 psi). Upon complete deprotection, the palladium catalyst was filtered off using Celite and solvent removed under reduced pressure. The product was purified by recrystallization in MeOH/CH_2Cl_2 to give **4** in a quantitative yield. ^{1}H NMR (MeOD, 400 MHz) δ 8.29 (s, 3H), 6.60 (s, 1H), 6.59 (s, 1H), 6.47 (d, 2H), 3.71−3.21 (m, 16H), 2.68 (t, 2H), 1.63−1.45 (m, 8H), 1.18 (m, 4H). ^{13}C NMR ($CDCl_3$, 100 MHz) δ 174.1, 173.0, 168.6, 146.7, 144.7, 136.6, 132.0, 130.0, 121.1, 117.0, 116.4, 66.9, 54.3, 43.1, 40.7, 35.9, 29.8, 29.8, 24.4. MALDI-MS: $[M]^+$, *m*/*z* 833 (calcd 833.8); $[M + Na]^+$, *m*/*z* 856 (calcd 856.8).

Synthesis of Methyl 3,5-Bis(3,4-bis(benzyloxy)phenethylcarbamoyl)benzoate (5). To a stirring solution of benzene-1,3,5-tricarbonyltrichloride (0.320 g, 1.20 mmol) in dry CH_2Cl_2 (170 mL) at 0 °C was added Bn-DA-TFA (0.536 g, 1.20 mmol) in dry CH_2Cl_2 (100 mL) dropwise over 5 h. The solution was allowed to warm to room temperature. The solvent was removed under reduced pressure to produce a white residue. Methanol was added and allowed to stir for a few hours. The excess methanol was removed under reduced pressure to produce a white solid. The product was isolated using silica flash column chromatography (ethyl acetate/hexanes, 1:1 v/v; $R_f = 0.4$). The solvents were removed under reduced pressure to yield a white solid of **5** (0.298 g, 0.349 mmol, 29.0% yield). ^{1}H NMR ($CDCl_3$, 400 MHz) δ 8.44 (s, 2H), 8.28 (s, 1H), 7.45−7.25 (m, 20H), 6.88 (d, 2H), 6.81 (s, 2H), 6.71 (d, 2H), 6.56 (t, 2H), 5.10, (s, 8H), 3.88 (s, 3H), 3.60 (q, 4H), 2.80 (t, 4H). ^{13}C NMR ($CDCl_3$, 100 MHz) δ 165.6, 165.3, 148.7, 147.4, 136.9, 136.8, 135.1, 131.9, 130.5, 130.3, 129.6, 128.2, 127.6, 127.2, 127.1, 121.4, 115.4, 115.0, 71.1, 52.2, 41.3, 34.7. MALDI-MS: $[M + Na]^+$, *m*/*z* 877.0 (calcd 878.0); $[M + K]^+$, *m*/*z* 893.0 (calcd 894.1).

Synthesis of 3,5-Bis(3,4-bis(benzyloxy)phenethylcarbamoyl)benzoic acid (6). 5 (0.250 g, 0.292 mmol) was stirred in a solution of 3 mL of acetone and 1 mL of 1 M NaOH overnight. The solution was acidified to pH 3 using 1 N HCl, added dropwise. The solvent was removed, and the product was stirred in H_2O. The precipitate was collected by vacuum filtration to

give **6** in quantitative yield. ^{1}H NMR (MeOD, 400 MHz) δ 8.53 (s, 2H), 8.37 (s, 1H), 7.40−7.20 (m, 20H), 6.93 (s, 2H), 6.91 (s, 2H), 6.76 (d, 2H), 5.03 (s, 8H), 3.54 (t, 4H), 2.81 (t, 4H). ^{13}C NMR ($CDCl_3$, 100 MHz) δ 169.2, 164.9, 150.4, 148.9, 138.9, 138.8, 136.3, 134.3, 131.9, 129.8, 129.5, 128.9 128.8, 123.1, 117.2, 116.9, 72.7, 72.5, 42.8, 37.0. MALDI-MS: $[M + Na]^+$, *m/z* 863.4 (calcd 864.0).

Synthesis of Benzyl 6-(N_3, N_5-Bis(3,4-bis(benzyloxy)phenethyl)benzene-1,3,5-tricarboxamido)-2-(bis(((benzyloxy)carbonyl)methyl)amino)hexanoate (7). A mixture of Bn-NTA-lys-TFA (0.060 g, 0.071 mmol), **6** (0.075 g, 0.142 mmol), and HOBt (0.010 g, 0.074 mmol) was stirred in 3 mL anhydrous DMF for 5 min. Dicyclohexylcarbodiimide (0.015 g, 0.073 mmol) was added, and the mixture was allowed to stir overnight. The solvents were removed under reduced pressure. The product **7** was isolated with silica gel flash column chromatography (ethyl acetate/hexanes, 3/2 v/v; R_f = 0.4). Yield: 0.094 g (97.7%). ^{1}H NMR ($CDCl_3$, 400 MHz) δ 8.43 (s, 1H), 8.41 (s, 2H), 7.50−7.26 (m, 40H), 7.04 (s, 3H), 6.87 (s, 1H), 6.85 (d, 1H), 6.72 (d, 1H), 5.12 (s, 8H), 5.07 (s, 8H), 3.74 (s, 8H), 3.59 (t, 2H), 3.51 (t, 2H), 3.35 (t, 4H), 2.79 (t, 2H), 1.75−1.28 (m, 12H). ^{13}C NMR ($CDCl_3$, 100 MHz) δ 172.5, 171.5, 165.9, 148.9, 147.6, 137.2, 137.1, 135.3, 132.0, 128.5, 128.4, 128.3, 128.2, 128.1, 127.7, 127.4, 127.3, 121.5, 115.7, 115.2, 71.3, 66.5, 66.4, 64.0, 52.8, 41.5, 39.9, 35.0, 27.9, 25.5, 24.8. MALDI-MS: $[M + H]^+$, *m/z* 1356.4 (calcd 1355.6); $[M + Na]^+$, *m/z* 1378.0 (calcd 1378.6); $[M + K]^+$, *m/z* 1393.9 (calcd 1394.7).

Synthesis of 6-(N_3, N_5-Bis(3,4-dihydroxyphenethyl)benzene-1,3,5-tricarboxamido)-2-(bis(carboxymethyl)amino)hexanoic acid (8). To a solution of **7** (0.094 g, 0.069 mmol) in of 5 mL of MeOH and 10 mL of $CHCl_3$ was added 20 mg Pd/C (10%). The mixture was placed in a Parr reactor bottle and rocked for 24 h at 60 psi H_2. Upon complete deprotection, the catalyst was filtered off using Celite, and the solvents were removed under reduced pressure. **8** was purified by recrystallization in MeOH/CH_2Cl_2 in a quantitative yield. ^{1}H NMR (MeOD, 400 MHz) δ 8.34 (s, 3H), 6.69 (s, 2H), 6.67 (s, 2H), 6.56 (d, 2H), 3.64 (t, 4H), 3.60 (t, 1H), 3.33 (s, 4H), 3.29 (t, 2H), 2.77 (t, 4H), 1.90−1.50 (m, 4H), 1.27 (p, 2H). ^{13}C NMR ($CDCl_3$, 100 MHz) δ 175.3, 174.1, 168.5, 146.1, 144.7, 136.6, 132.0, 129.4, 121.1, 117.0, 116.4, 68.2, 55.1, 43.1, 40.3, 35.9, 26.4, 25.9, 23.6. MALDI-MS: $[M + H]^+$, *m/z* 724.8 (calcd 725.7); $[M + Na]^+$, *m/z* 746.8 (calcd 747.7).

Surface Modification of Iron Oxide Nanoparticles with Bis-NTA-derived Ni(II) Chelate and Mono-NTA-derived Ni-(II) Chelate. The ligand **4** (0.5 mL of a 10 mg/mL MeOH solution) was placed in 1.25 mL distilled water. To this aqueous solution was added 1 mL of iron oxide nanoparticles in *n*-hexanes (16.3 mg/mL). The two layers were sonicated for 1 h and repeatedly washed with *n*-hexanes, then methanol, until the nanoparticles were readily dispersed in distilled water. Using a magnet, the nanoparticles were collected and placed in 2 mL of distilled water. The bis-NTA-pendant ligand-immobilized nanoparticles (0.5 mL) were placed in 2 M $NiCl_2$ solution and sonicated for 1 h. The Ni(II)-loaded nanoparticles were stored in the $NiCl_2$ solution before use. Iron oxide nanoparticle modified with mono-NTA Ni(II)-loaded nanoparticles were similarly prepared.

Preparation of Ni(II)-Loaded Magnetic Microparticles. An aliquot of 0.5 mL (2.4 μmol carboxyl) BioMag Carboxyl magnetic iron oxide microparticles (~1.5 μm mean diameter, ~20 mg/mL particle concentration, ~4.8 μmol/mL carboxy-surface titration) was washed with distilled water (3 × 500 μL), then with acetone (3 × 500 μL). Aliquots of *N*-hydroxysuccinimide (NHS) (25 μL, 30 mg/mL acetone) and dicyclohexylcarbodiimide (50 μL, 50 mg/mL acetone) were added and incubated overnight. The NHS-activated particles were washed with acetone and used without further purification.

A 240 μM solution of N_α,N_α-bis(carboxymethyl)-L-lysine was prepared by dissolving 0.629 mg N_α,N_α-bis(carboxymethyl)-L-lysine in 35 μL of triethylamine, 500 μL of acetone, and 500 μL of distilled water. The NHS-activated microparticles were washed with distilled water, then placed in 100 μL of the N_α,N_α-bis(carboxymethyl)-L-lysine solution. After overnight incubation, the particles were washed with distilled water. The particles were placed in a 1 M $NiCl_2$ solution for 1 h before use.

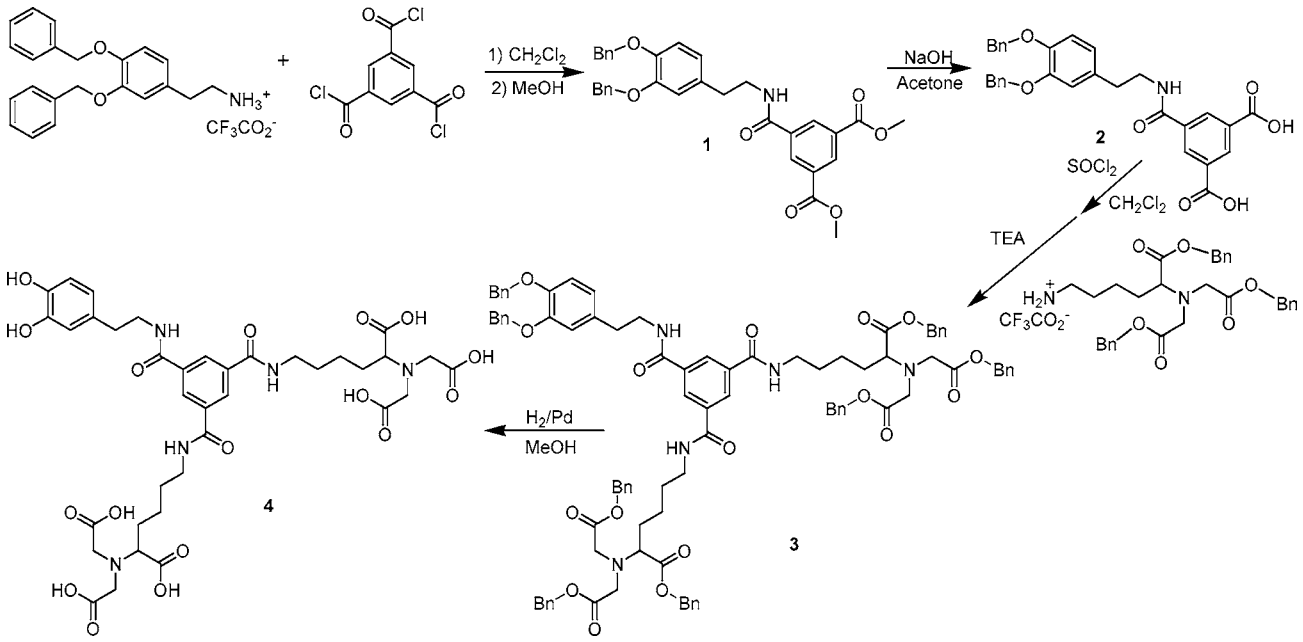
Isolation of Recombinant Mouse His × 6-Endostatin (His × 6-rmES) with Ni(II)-Loaded Nanoparticles. The Ni(II)-loaded nanoparticles (7−10 μL; 16.3 mg/mL) were washed in distilled water (3 × 50 μL) and a binding buffer (3 × 50 μL; 50 mM phosphate buffer system, 300 mM NaCl, 10 mM imidazole, pH 8.0). The washed nanoparticles were incubated with 10 μg of His × 6-rmES in 40 μL of binding buffer for 5−60 min at 4 °C. Using a centrifuge and magnet, the supernatant was collected and nanoparticles washed in 50 μL aliquots of binding buffer (FT, flow through; W1, wash 1; W2, wash 2; W3, wash 3). After the third wash, 50 μL of the elution buffer (50 mM phosphate buffer system, 300 mM NaCl, 250 mM imidazole, pH 8.0) was added and the mixture tumbled for 10 min at 4 °C. The eluents were similarly collected by centrifugation and magnetic immobilization (E1, elution 1; E2, elution 2). Nonspecifically bound protein was released from the nanoparticles by boiling at 95 °C for 4 min in a Laemmli SDS-PAGE gel loading buffer. The volumes of the aliquots were reduced in a Speedvac before loading to an SDS-PAGE (12.5%, 180 V, 50 min). After separation, the SDS-PAGE gel was stained in a Coomassie blue solution (0.1% Coomassie blue, 10% acetic acid, 40% methanol) overnight. Recombinant human His × 6-ubiquitin (His × 6-Ub) and recombinant mouse His × 6-ubiquitin C-terminal hydrolase L-1 (His × 6-UCH-L1) were isolated with Ni(II)-loaded nanoparticles in the same fashion. Protein isolation by commercial magnetic agarose beads was performed according to the manufacturer's instructions (Qiagen).

Isolation of His × 6-rmES by Ni(II)-Loaded Microparticles. The Ni(II)-loaded microparticles (10 μL, 20 mg/mL) were washed in distilled water (3 × 50 μL) and binding buffer (3 × 50 μL). The washed microparticles were incubated with 10 μg of His × 6-rmES in 40 μL of binding buffer for 60 min at 4 °C. The beads were washed and the bound protein eluted similarly. All the fractions were loaded to an SDS-PAGE for analysis as previously described.

Expression of [^{35}S]-Methionine-Labeled His × 6-GMAP-210. The gene coding a 70 kDa fragment of GMAP-210 (Golgi-associated microtubule-binding protein) was PCR-amplified from a human total RNA library (Stratagene). After introducing the T7 promoter and TMV 5′-UTR by second PCR, the cDNA was used as the template for a coupled in vitro transcription/translation (TNT) reaction in the presence of 10 μCi [^{35}S]-methionine (Perkin-Elmer) in a total volume of 25 μL for 90 min at 30 °C. Protein synthesis was confirmed by SDS-PAGE and autoradiography. The protein was stored at −80 °C until used.

Isolation of [^{35}S]-Methionine-Labeled His × 6-GMAP-210 with Ni(II)-Loaded Nanoparticles. The Ni(II)-loaded nanoparticles (10 μL; 16.3 mg/mL) were washed in distilled water (3 × 50 μL) and binding buffer (3 × 50 μL). The washed nanoparticles were incubated with 5 μL of TNT reaction mixture in 100 μL of binding buffer for 60 min at 4 °C. The nanoparticles were washed and the bound protein eluted according to the procedures detailed above. All the fractions including the remaining nanoparticles were transferred to scintillation vials for radioactivity measurements using a liquid scintillation counter. Protein isolation using commercial mag-

Scheme 1



netic agarose beads (Qiagen) was performed according to the manufacturer's instructions, and scintillation counts were measured as mentioned above.

Expression and Purification of His × 6-UGT from 293T Cells Using Nanoparticles. The cDNA corresponding to the open reading frame of *C. elegans* UGT was amplified from a *C. elegans* cDNA library (Invitrogen) using high-fidelity platinum *Pfx* DNA polymerase (Invitrogen) and sequence-specific primers with CACC at the 5′-end of the forward primer. The full-length cDNA was gel-purified and subcloned into the pcDNA3.1D/V5-His TOPO vector (Invitrogen) according to the manufacturer's instructions. The resulting gene-containing plasmid was confirmed by PCR and sequence analysis.

293T cells were cultured in Dulbecco's Minimal Essential Media (DMEM, Gibco) supplemented with 10% fetal bovine serum (FBS, Sigma), 1% L-glutamate (Gibco), and 1% penicillin/streptomycin. Cell culture was maintained at 37 °C with 5% CO_2. On the day of transfection, the preformed UGT plasmid DNA−lipofectamine complex (500 μL) in DMEM serum-free media was added directly to each well. Cells were incubated at 37 °C in 5% CO_2 for 4 h. Afterward, the media was changed and 2 mL of fresh DMEM (with 10% FBS and 1% L-glutamate) was added. After incubation at 37 °C in a 5% CO_2 incubator for a total of 24 h to allow protein expression, cells were harvested and lysed using a commercial extraction buffer (Biovision). Intact cells were removed by centrifugation, and the supernatants were cleared at 21 000 *g* for 15 min at 4 °C. Levels of protein expression were assessed by separation on SDS-PAGE gels, followed by Western blotting onto nitrocellulose membranes (Amersham Pharmacia), and probing with anti-V5 antibody (Invitrogen). The lysates that were prepared were used for binding studies.

To purify the His × 6-UGT expressed in 293T cells, the prewashed, Ni(II)-loaded nanoparticles (10 μL; 16.3 mg/mL) were incubated with 50 μL of cleared crude cell lysate (∼4 μg/μL total protein) in 50 μL of binding buffer for 15 min at 4 °C. After washing nanoparticles three times using 50 μL of binding buffer, the bound proteins were eluted using 15 μL of elution buffer. Aliquots of each fraction were loaded to an SDS-PAGE for separation. The protein was detected by Coomassie blue staining.

RESULTS AND DISCUSSION

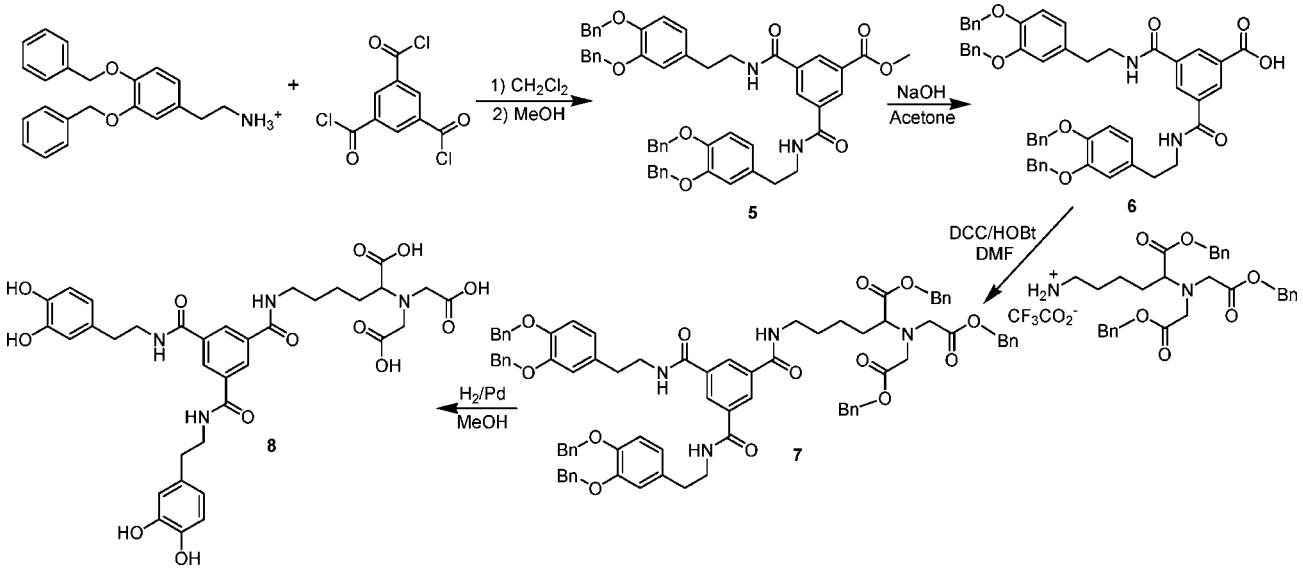
Surface Modification of Iron Oxide Nanoparticles with Bis-NTA and Mono-NTA Ni(II) Chelates. The iron oxide magnetic nanoparticles were synthesized using protocols previously described (*12*−*14*). The nanoparticles were washed in ethanol and transferred into *n*-hexanes and used without further purification. The concentration of the nanoparticles was estimated on the basis of the dry mass after the removal of the solvents. Iron oxide nanoparticles prepared by different routes gave similar results for protein binding and purification experiments.

Although a number of functional groups have been immobilized on iron oxide nanoparticles, their binding strength and their ease of surface immobilization vary significantly. Since Xu and co-workers recently demonstrated the efficient immobilization of dopamine derivatives on iron oxide nanoparticles (*15*), we have decided to use this strategy to immobilize bis-NTA Ni(II) chelate for protein purifications. The new bis-NTA ligand with a catechol group (**4**) was synthesized according to Scheme 1. Compound **4** was synthesized in 22% overall yield in four steps starting from known benzyl-protected dopamine trifluoroacetate salt and benzene-1,3,5-tricarbonyltrichloride. New compounds **1**−**4** were characterized by ^{1}H and ^{13}C{^{1}H} NMR spectroscopy and mass spectrometry.

In order to determine the effects of multivalency on protein binding, we have also prepared a new mono-NTA ligand with two catechol groups (**8**) by using a 1:1 ratio of dopamine hydrochloride and benzene-1,3,5-tricarbonyltrichloride as shown in Scheme 2. Compound **8** was synthesized in an overall yield of 28% in four steps. New compounds **5**−**8** were characterized by ^{1}H and ^{13}C{^{1}H} NMR spectroscopy and mass spectrometry.

Surface modification of iron oxide nanoparticles with new NTA-derived ligands was accomplished by simply stirring a biphasic mixture of the ligand in water and iron oxide nanoparticles in hexanes. The NTA−ligand-immobilized nanoparticles were charged with Ni(II) ions by ultrasonic mixing in 2 M $NiCl_2$. The iron oxide nanoparticles with different coatings were characterized by transmission electron microscopy (TEM). TEM images of ∼10 nm monodisperse iron oxide nanoparticles (prepared by thermal decomposition) before and after surface modifications illustrate the retention of nanoparticle size and shape and monodispersity throughout monovalent and bivalent

Scheme 2



NTA−ligand surface modification and Ni(II)-loading. Slight aggregation of Ni(II)-loaded nanoparticles was, however, observed in the TEM images (Figure 1).

Binding of His × 6-Tagged Proteins Labeled with [^{35}S]-Methionine. Immobilization of proteins onto the nanoparticles and subsequent elution were initially demonstrated with His × 6-tagged, [^{35}S]-methionine-labeled GMAP-210 protein synthesized via coupled in vitro transcription and translation (Scheme 3). In a typical binding-elution experiment, the direct lysate (DL) signal is equal to the sum of the flow through (FT), washes (W1, W2, W3), elutions (E1, E2), and residual resin signals. The signal from each fraction was measured using liquid scintillation counting.

Since only a small percentage of [^{35}S]-methionine was incorporated into the recombinant protein in the TNT reaction, a majority of the radioactivity in both the commercial beads and nanoparticle systems came from unbound free [^{35}S]-methionine in the FT (Figure 2 and Supporting Information Table S1). Following the removal of FT, the resin was washed three times until the background was low, before elution by imidazole. This scintillation counting assay demonstrates that the NTA-modified nanoparticles can specifically capture His × 6-tagged proteins followed by efficient elution with imidazole. We also examined the relative protein binding capacity of nanoparticles as compared to the commercial beads. It was found that the 10 μL (0.32% v/v suspension, assuming Fe_3O_4 density of 5.15 g/cm^3) of nanoparticles (16.3 mg/mL) had a similar binding capacity to 10 μL (5% v/v suspension) of commercial magnetic agarose beads. It appears that the unoptimized nanoparticles used in this work have higher residual radioactivity after elutions when compared to the commercial beads, presumably due to relatively strong nonspecific binding. This result was within expectation, since the commercial beads were coated with agarose, which has low nonspecific binding to proteins. We think that the nonspecific binding of the nanoparticles could be minimized if the surface is modified with hydrophilic molecules such as PEG that are known to resist nonspecific protein binding (*16*).

Binding of Overexpressed His × 6-Tagged Proteins. We next carried out protein binding studies of several commercially available recombinant His × 6-tagged proteins. One of the major problems in using Ni-NTA in protein purification is that numerous His × 6-tagged proteins can only be purified under denaturing conditions. Consequently, a complicated refolding process is needed that often results in low yield of the active protein. In this work, we focus on examining whether the NTA-modified nanoparticles can be used under native conditions to purify His × 6-tagged proteins that require denaturing conditions when commercial NTA beads are used. We used recombinant murine His × 6-endostatin as an example. Endostatin is a potent angiogenesis inhibitor that has shown therapeutic suppression of tumor-induced angiogenesis in mice implanted with tumors (*17*). O'Reilly et al. reported that recombinant murine endostatin with His × 6 tag could be expressed in *E. coli* as insoluble inclusion bodies and purified using Ni-NTA resin under denaturing conditions. Endostatin thus purified underwent an inefficient refolding process before it could be used in xenograft mouse studies. We found that the already folded endostatin could not be captured when commercial Ni(II)-NTA beads were used. As shown in Figure 3, approximately 90% of His × 6-rmES was present in the FT, and almost no protein was detected in the elutions, indicating that commercial beads failed to capture His × 6-rmES under native conditions. Significantly, Ni(II)-loaded nanoparticles readily bound His × 6-rmES without the use of denaturing conditions. A 10 μL volume of Ni(II)-loaded nanoparticles (163 μg) is found to have a binding capacity of 5.6 μg under unoptimized conditions. The His × 6-rmES was readily eluted by imidazole and was shown to be biologically active in inducing apoptosis in cow pulmonary artery endothelial cells (Supporting Information Figure S1) (*18*). Confocal microscopic images showed characteristic apoptotic rings for the cow pulmonary artery endothelial cells after annexin-V PE staining. This result indicates that milligrams of a biologically active native protein can be purified using approximately 30 mg of Ni(II)-loaded nanoparticles. We have also successfully recycled and reused the modified nanoparticles in His × 6-rmES binding without Ni(II) reloading. The recycled nanoparticle appears to have a similar binding capacity to the pristine sample on the basis of SDS-PAGE analysis (Supporting Information Figure S2).

We also compared the binding of other His × 6-tagged proteins that do not require denaturing conditions for Ni-NTA-based purifications. Ubiquitin is a protein found throughout all eukaryotic cells and plays key roles in highly specific protein degradation. The small His × 6-tagged ubiquitin (9.3 kDa) is expected to have an affinity for both the commercial beads as well as the surface-modified nanoparticles. SDS-PAGE analysis confirms the affinity of the commercial beads and the Ni(II)-loaded nanoparticles (Table 1 and Supporting Information Figure S3). Densitometry analysis shows the binding capacity of 20

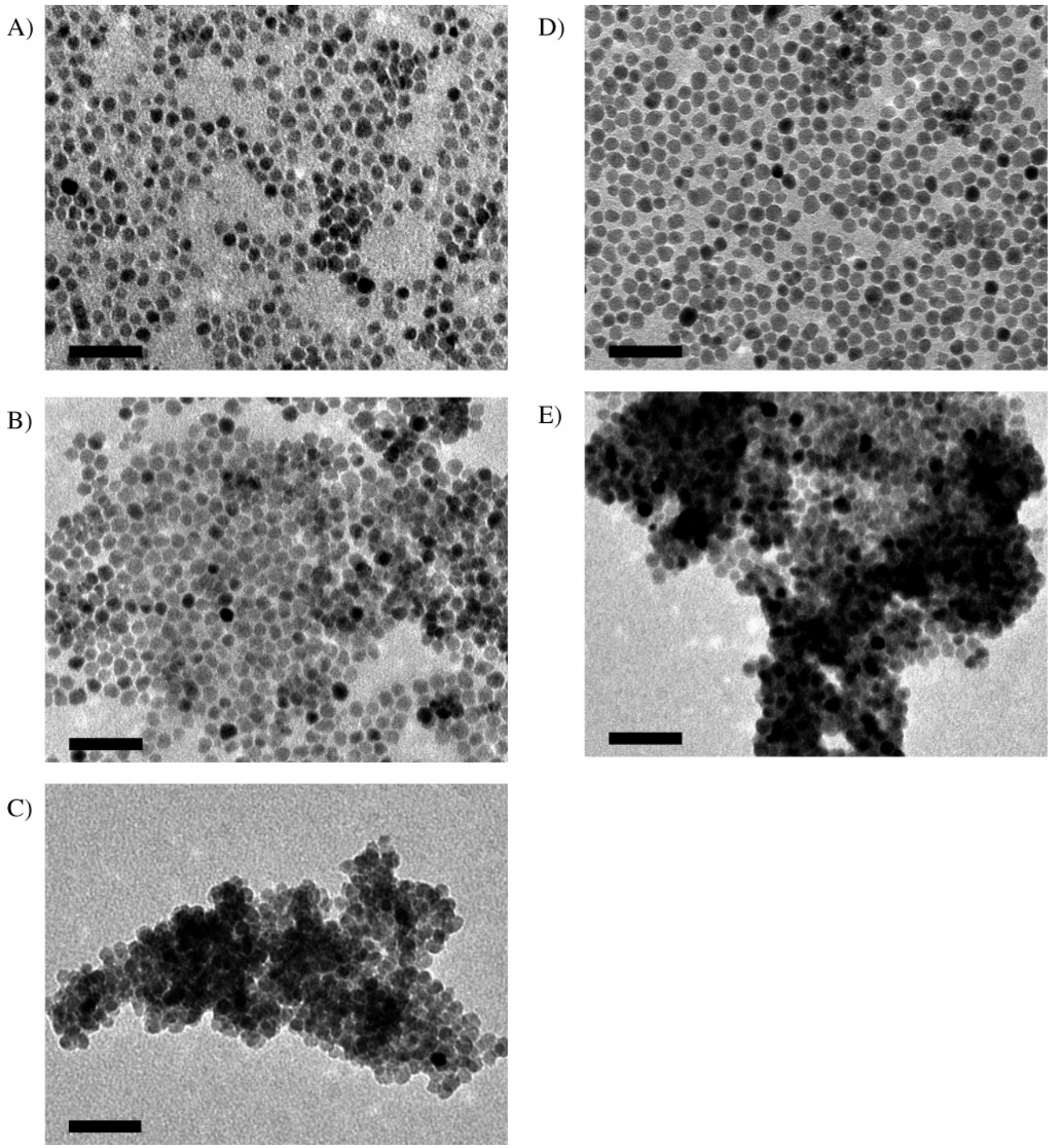
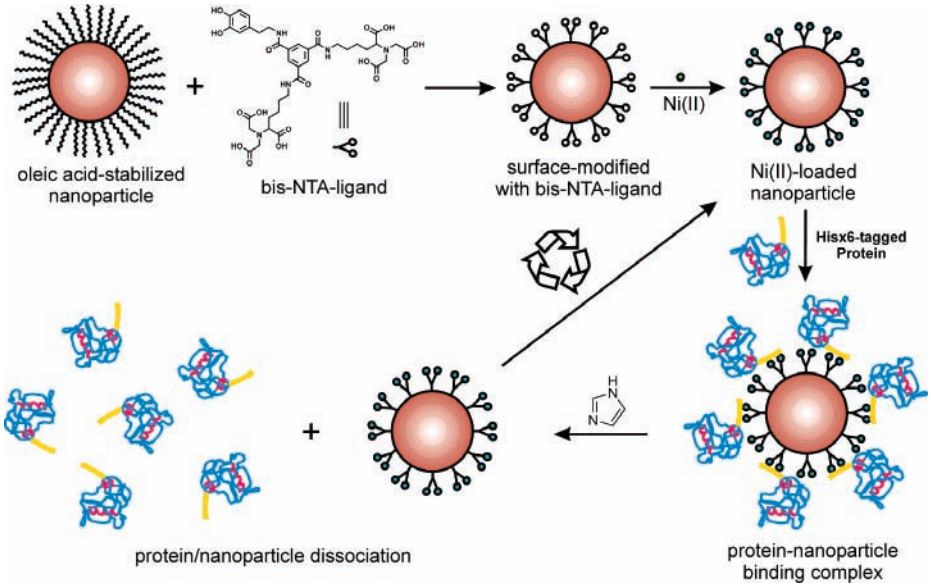


Figure 1. TEM images of monodisperse iron oxide nanoparticles (~10 nm in diameter): (A) Prepared by thermal decomposition and stabilized with oleic acid. (B) Modified with bis-NTA ligand. (C) Ni(II)-loaded bis-NTA nanoparticle. (D) Modified with mono-NTA ligand. (E) Ni(II)-loaded mono-NTA nanoparticle. The scale bar is 50 nm.

μL (5% v/v suspension) of commercial beads is 1.1 μg His × 6-Ub, while that of 10 μL (0.32% v/v suspension) of bis-NTA-Ni(II)-loaded nanoparticle is 2.3 μg. In comparing the binding of 10 μL (0.32% v/v suspension) of nanoparticle for His × 6-rmES (21.3 kDa, 5.6 μg) and 6 × His-Ub (9.3 kDa, 2.3 μg), it is estimated that the binding capacity of the Ni(II)-loaded nanoparticles is approximate 25 pmol of proteins/μL.

Binding studies on His × 6-UCH-L1 (~25 kDa) were also used to demonstrate the nanoparticle's ability to capture His × 6-enzymes (Table 1 and Supporting Information Figure S4). Binding capacities of 40 μL (5% v/v suspension) of commercial beads and 10 μL (0.32% v/v suspension) of nanoparticles are 0.06 μg and 3.48 μg His × 6-UCH-L1, respectively. One major concern in NTA microbeads based protein purification is the large elution volume that requires additional concentration steps before being used in the subsequent experiments. While lyophilization can be used to concentrate most proteins, the process reduces the biological activity of many other proteins. Ultrafiltration is another widely used method in volume reduction. However, the loss of purified proteins could be significant, presumably due to nonspecific interactions with the membrane. Our Ni(II)-loaded nanoparticles disperse well in aqueous solution, and therefore significantly smaller elution volume can be used. This advantage eliminates the need of volume reduction and makes it possible to directly use the proteins after purification. Our studies clearly demonstrated that the present magnetic,

Scheme 3



recyclable nanoparticles are able to bind important His × 6-proteins in native, active conformations with a high capacity and thus show significant advantages over the commercial microbeads. Since the chosen His × 6-proteins have a wide range of molecular weights (9387.6−74406.8 Da) and isoelectric points (5.43−9.33), we do not believe that their binding to the present Ni(II)-loaded nanoparticles are due to simple electrostatic interactions.

Purification of Recombinant His × 6-Tagged Proteins from Crude Mammalian Cell Lysate. Proteins expressed in mammalian cells are usually soluble and active, and therefore extremely useful in studying their physiological significances. The biggest drawback is that their expression levels are very low, making the purification challenging. The nanoparticle platform was previously used for protein purification from *E. coli* cell lysate (*15*), in which proteins are much more easily overexpressed. We investigated whether our NTA-loaded nanoparticles could be used to purify recombinant proteins expressed in mammalian cells. 293T cells were used to express a recombinant His × 6-UGT protein. The lysate was prepared for purification of 6 × His-UGT protein by the bis-Ni(II)-NTA modified nanoparticles. Figure 4 shows the staining of DL, FT, W3, E1, E2, and nanoparticle fractions and clearly indicates the purification of desired His × 6-tagged protein from the mammalian crude lysate. The elution E1 is significantly cleaner than the direct lysate, with few impurities. These nonspecifically bound impurities are probably due to proteins with many amino acid residues that can coordinate to the immobilized metal ion. Nonetheless, the present nanoparticle system has shown great promise in the purification of His × 6-tagged proteins from crude mammalian cell lysates.

Nonspecific Interactions. Nonspecific interactions between the protein and nanoparticles do not appear to be significant when the NTA nanoparticles are chelated with Ni(II). Table 1 shows that approximately 8.7% of His × 6-rmES remained on the Ni(II) loaded bis-NTA-modified nanoparticles after elution, slightly higher than that on commercial microbeads. Without the chelation of Ni(II), His × 6-rmES was found to have a high affinity for the bis-NTA-modified nanoparticle (Supporting Information Figure S5). Densitometry measurements show that more than 45% of the 6 × His-rmES was present in the sum of the washes and elutions, while 39% of the protein remained on the bis-NTA-modified nanoparticles.

On the other hand, freshly prepared iron oxide nanoparticles (without surface modifications) had little interaction with His × 6-rmES. Over 70% of the 10 μg of loaded protein was detected in the FT, and over 90% was detected in the sum of the FT and washes. The nanoparticles retained approximately 7% of the His × 6-rmES after elution, a significant reduction from the 39% retention of Ni(II)-free bis-NTA-modified nanoparticles. The nonspecific interaction of the rmES to the nanoparticle is thus a result of the surface modifications. To rule out the potential role of residual oleic acid on the nanoparticle surface, we carried out a binding experiment using

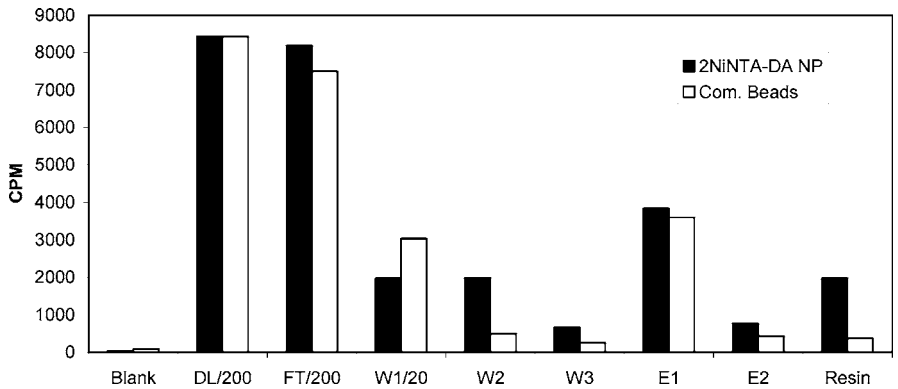


Figure 2. Graphical representation of [^{35}S]-labeled His × 6-GMAP-210 binding scintillation counting assay for bis-Ni-NTA nanoparticles (solid bars) and commercial Ni-NTA agarose beads (open bars). Fractions collected and radioactivity quantified in counts per minute (CPM). DL = direct lysate, FT = flow through, W1 = wash 1, W2 = wash 2, W3 = wash 3, E1 = elution 1, E2 = elution 2.

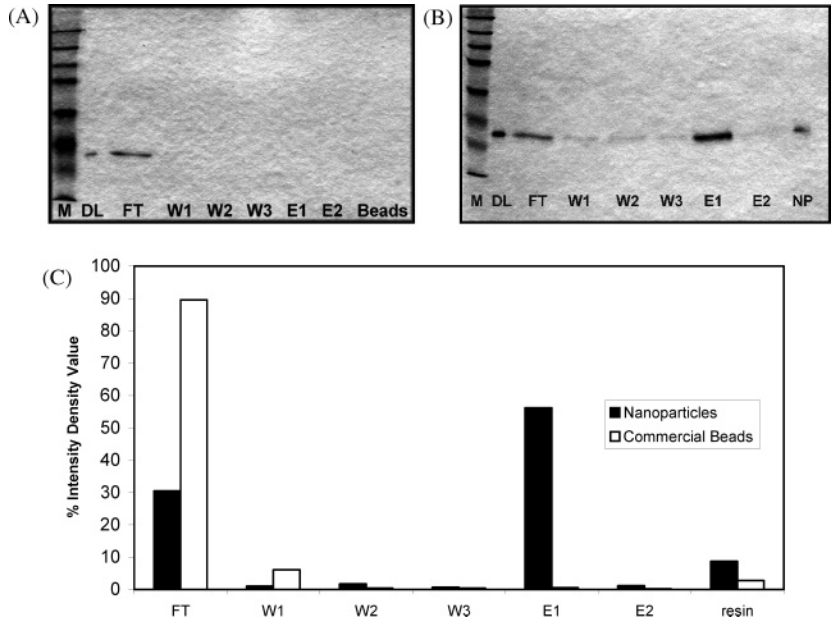


Figure 3. Binding assay of His × 6-rmES. (A) Commercial magnetic agarose beads (Qiagen): no protein was bound to the bead or eluted by imidazole. Most of the protein was washed away unbound in the FT. (B) Bis-Ni-NTA NPs: His × 6-tag protein was bound and a majority was eluted from the nanoparticles by imidazole. (C) Graphical representation of densitometry quantification of SDS-PAGE gels.

Table 1. Intensity Density Values (% IDV) Compiled from Densitometry Quantification of SDS-PAGE Results for Collected Fractions Comparing Bis-Ni-NTA-Modified Nanoparticles and Commercial Ni-NTA Agarose Beads in His × 6-Tagged Protein Binding Experiment (10 μg total protein)

	FT	W1	W2	W3	E1	E2	NP/resin
6×*His-rmES* + 2NiNTA-NP	30.48	1.05	1.70	0.67	56.20	1.21	8.70
6×*His-rmES* + Com. Beads	89.58	6.06	0.44	0.44	0.54	0.18	2.74
6×*His-Ub* + 2NiNTA-NP	26.30	18.22	9.80	3.07	23.21	7.85	11.54
6×*His-Ub* + Com. Beads	39.35	23.76	8.31	5.10	10.70	6.24	6.54
6×*His-UCH-L1* + 2NiNTA NP	31.80	12.38	1.25	1.16	34.78	3.30	15.33
6×*His-UCH-L1* + Com. Beads	83.16	6.19	0.89	0.89	0.58	0.03	8.27

particles without oleic acid stabilization. Nonspecific interaction was observed for the oleic acid-free nanoparticles as well.

As the ratio of His × 6-rmES (μg) to bis-Ni(II)-loaded NTA nanoparticle (mg) is increased from 10.2 to 61.3, the amount of nonspecifically bound protein appears to remain constant (Figure 5). The specific his-tag binding to Ni(II)-NTA occurs after the full capacity of the nonspecific interaction is reached at a 6 × His-rmES (μg) to bis-Ni(II)-loaded NTA nanoparticle (mg) ratio between 10.2 and 15.3. Maximum binding capacity of the nanoparticle via the His × 6-tag appears to have been reached with a His × 6-rmES (μg) to bis-Ni(II)-loaded NTA nanoparticle (mg) ratio of 61.3, since some 6 × His-rmES is detectable in the FT.

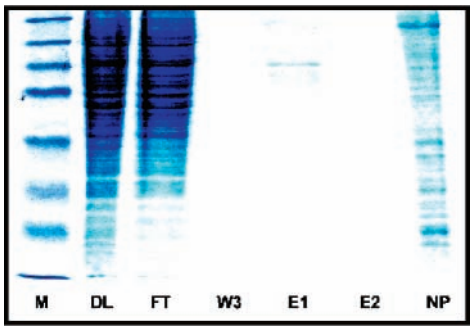


Figure 4. Mammalian cell lysate fractionation. SDS-PAGE (12.5% separation gel) results of flag-His × 6-UGT expressed in 293T cells showing marker (M), direct lysate (DL, 10% dilution), flow through (FT, 10%), wash 3 (W3), elution 1 (E1), elution 2 (E2), and protein residue on nanoparticle (NP).

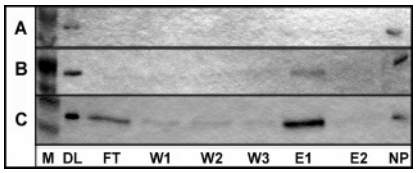


Figure 5. Preference toward nonspecific interaction before his-tag−Ni-NTA interaction demonstrated through increasing ratios of 6 × His-rmES protein (μg) to bis-Ni-NTA nanoparticle (mg) A, 10.2; B, 15.3; C, 61.3. (M = marker, FT = flow through, W1 = wash 1, W2 = wash 2, W3 = wash 3, E1 = elution 1, E2 = elution 2, NP = protein bound nonspecifically to nanoparticle.) The molecular markers have molecular weights of 25 and 16 kDa.

Various attempts were made to block the nonspecific interaction of the target protein (Supporting Information Figure S6). We first attempted to block the nonspecific binding with BSA. The surface-modified nanoparticles were preincubated with BSA before the His × 6-rmES binding experiment was performed. Unfortunately, BSA did not effectively block the His × 6-rmES nonspecific binding. An attempt to block the His × 6-rmES nonspecific interaction of the nanoparticle with a smaller protein (His × 6-Ub) did not seem to result in any noticeable improvement by SDS-PAGE analysis.

Surface Density of the Ni-NTA Chelates. The mono-NTA ligand with two dopamine anchors was synthesized to present monovalency of the Ni(II)-NTA moiety onto the nanoparticle surface. Interestingly, an SDS-PAGE binding assay of the mono-Ni(II)-NTA-modified nanoparticle showed a similarly effective binding with His × 6-rmES (Supporting Information Figure S7). Furthermore, we compared the mono- and bis-Ni(II)-NTA ligand-modified nanoparticles by elution with variable imidazole concentrations, and no significant difference was observed. Unlike commercial Ni-NTA beads, the His × 6-rmES could not be eluted from the mono- and bis-Ni(II)-NTA-modified nanoparticles at a pH as low as 4.0 (without the use of imidazole, Supporting Information Figure S8). These results are suggestive of similar binding affinity of mono- and bis-Ni(II)-NTA-modified nanoparticles, probably a result of high surface coverage of mono-Ni(II)-NTA moieties.

To demonstrate the importance of high surface coverage, we conjugated Ni(II)-NTA to micrometer-sized, carboxy-terminated commercial beads (~1.5 μm diameter). NTA-lysine was con-

jugated to the beads via the amide bond using the DCC/NHS coupling protocol. Upon loading with Ni(II), these beads were found to bind His × 6-rmES as effectively as mono- and bis-Ni(II)-NTA modified nanoparticles (Supporting Information Figure S9). This experiment unambiguously supports the notion that enhanced binding of His × 6-tagged protein can be achieved by taking advantage of the multivalency effect.

CONCLUSIONS

New bis-nitrilotriacetic acid (NTA) chelates with catechol anchors were synthesized and immobilized on superparamagnetic iron oxide nanoparticles. When loaded with Ni(II), these NTA-immobilized nanoparticles were shown to bind His × 6-tagged proteins in their native, folded conformations with retained activity that commercial microbeads fail to bind under identical conditions. A series of control experiments suggest that the multivalency strategy can be utilized to enhance the binding of His × 6-tagged proteins in their native, folded conformations. We further demonstrated the selective purification of His × 6-tagged proteins from direct cell lysates by using the Ni(II)-loaded magnetic nanoparticles. The present platform is capable of efficient purification of His × 6-tagged proteins that are expressed at low level in mammalian cells. This work thus presents a novel nanoparticle-based high-capacity protein purification system with shorter incubation times, proportionally large washes, and significantly smaller elution volumes compared to currently available microbeads.

ACKNOWLEDGMENT

We acknowledge NIH (U54-CA119343) for funding this research. We thank Mr. William J. Reiter for taking the TEM images.

Supporting Information Available: Detailed experimental procedures, data table, and figures. This material is available free of charge via the Internet at http://pubs.acs.org.

LITERATURE CITED

(1) Porath, J., and Olin, B. (1983) Immobilized metal ion affinity adsorption and immobilized metal ion affinity chromatography of biomaterials. serum protein affinities for gel-immobilized iron and nickel ions. *Biochemistry 22*, 1621−1630.

(2) Garrett, R. H., and Grisham, C. M. (1999) *Biochemistry*, 2nd ed., Saunders College Publishing, Fort Worth.

(3) Porath, J., and Kristiansen, T. (1975) Biospecific affinity chromatography and related methods. *The Proteins*, 3rd ed. (Neurath, H., and Hill, R. L., Eds.) pp 95−178, Vol. 1, Academic Press, New York.

(4) Hochuli, E., Dobeli, H., and Schacher, A. (1987) New metal chelate absorbent selective for proteins and peptides containing neighboring histidine residues. *J. Chromatogr. 411*, 177−184.

(5) Braun, P., Hu, Y., Shen, B., Halleck, A., Koundinya, M., Harlow, E., and LaBaer, J. (2002) Proteome-scale purification of human proteins from bacteria. *Proc. Natl. Acad. Sci. U.S.A. 99*, 2654−2659.

(6) Conti, M., Falini, G., and Samorì, B. (2000) How strong is the coordination bond between a histidine tag and Ni-nitrilotriacetate? An experiment of mechanochemistry on single molecules. *Angew. Chem. Int. Ed. 39*, 215−218.

(7) Kapanidis, A. N., Ebright, Y. W., and Ebright, R. H. (2001) Site-specific incorporation of fluorescent probes into protein: hexahistidine-tag-mediated fluorescent labeling using (Ni^{2+}:nitrilotriacetic acid)$_n$−fluorochrome conjugates. *J. Am. Chem. Soc. 123*, 12123−12125.

(8) Lata, S., Gavutis, M., Tampé, R., and Piehler, J. (2006) Specific and stable fluorescence labeling of histidine-tagged proteins for dissecting multi-protein complex formation. *J. Am. Chem. Soc. 128*, 2365−2372.

(9) Lata, S., Reichel, A., Brock, R., Tampé, R., and Piehler, J. (2005) High-affinity adaptors for switchable recognition of histidine-tagged proteins. *J. Am. Chem. Soc. 127*, 10205−10215.

(10) Hutshenreiter, S., Neumann, L., Rädler, U., Schmitt, L., and Tampé, R. (2003) Metal-chelating amino acids as building blocks for synthetic receptors sensing metal ions and histidine-tagged proteins. *ChemBioChem 4*, 1340−1344.

(11) Brook, M.A., and Stan, R. S. (2004) Canadian Patent Application CA 02309486.

(12) Sahoo, Y., Pizem, H., Fried, T., Golodnitsky, D., Burstein, L., Sukenik, C. N., and Markovich, G. (2001) Alkyl phosphonate/phosphate coating on magnetite nanoparticles: A comparison with fatty acids. *Langmuir 17*, 7907−7911.

(13) Sun, S. H., Murray, C. B., Weller, D., Folks, L., and Moser, A. (2000) Monodisperse FePt nanoparticles and ferromagnetic FePt nanocrystal superlattices. *Science 287*, 1989−1992.

(14) Park, J., An, K., Hwang, Y., Park, J. G., Noh, H. J., Kim, J. Y., Park, J. H., Hwang, N. M., and Hyeon, T. (2004) Ultra-large-scale syntheses of monodisperse nanocrystals. *Nat. Mater. 3*, 891−895.

(15) Xu, C., Xu, K., Gu, H., Zheng, R., Liu, H., Zhang, X., Guo, Z., and Xu, B. (2004) Dopamine as a robust anchor to immobilize functional molecules on the iron oxide shell of magnetic nanoparticles. *J. Am. Chem. Soc. 126*, 9938−9939.

(16) Bentzen, E. L., Tomlinson, I. D., Mason, J., Gresch, P., Warnement, M. R., Wright, D., Sanders-Bush, E., Blakely, R., and Rosenthal, S. J. (2005) Surface modification to reduce nonspecific binding of quantum dots in live cell assays. *Bioconjugate Chem. 16*, 1488−1494.

(17) O'Reilly, M. S., Boehm, T., Shing, Y., Fukai, N., Vasios, G., Lane, W. S., Flynn, E., Birkhead, J. R., Olsen, B. R., and Folkman, J. (1997) Endostatin: an endogenous inhibitor of angiogenesis and tumor growth. *Cell 88*, 277−285.

(18) Dhanabal, M., Ramchandran, R., Waterman, M. J., Lu, H., Knebelmann, B., Segal, M., and Sukhatme, V. P. (1999) Endostatin induces endothelial cell apoptosis. *J. Biol. Chem. 274*, 11721−11726.

BC060195L

Solid-Phase Synthesis, Bioconjugation, and Toxicology of Novel Cationic Oligopeptoids for Cellular Drug Delivery

Tina Schröder,[†,△] Katja Schmitz,[‡,△] Nicole Niemeier,[§] Teodor S. Balaban,[§] Harald F. Krug,[§] Ute Schepers,*[,‡] and Stefan Bräse*[,†]

Institut für Organische Chemie and Center for Functional Nanostructures (CFN), Universität Karlsruhe (TH), Fritz-Haber-Weg 6, D-76131 Karlsruhe, Germany, Kekulé-Institut für Organische Chemie und Biochemie, Universität Bonn, Gerhard-Domagk-Str. 1, D-53121 Bonn, Germany, and Karlsruhe Institute of Technology, Forschungszentrum Karlsruhe, Hermann-von-Helmholtz-Platz 1, D-76344 Eggenstein-Leopoldshafen, Germany. Received July 10, 2006; Revised Manuscript Received November 19, 2006

For many therapeutic applications, it has become more and more important to find synthetic compounds that have the ability to transport a variety of drugs and cargo molecules into cells and tissues. Like arginine-rich cell-penetrating peptides (CPPs), it is already known that peptide mimetics such as β-peptides and peptoids can also express a transport function. In this study, ten fluorophore-labeled chiral and achiral peptoids with different backbone lengths and side chains as well as three peptoids coupled to a therapeutically active porphyrin moiety were prepared using a highly modular solid-phase synthesis (SPP) approach. To compare the structural determinants with the cellular uptake efficiency, all peptoids were analyzed by live cell imaging. All cells show an even vesicular distribution of the internalized peptoids, also revealing that a vesicular escape into the cytosol was stronger for peptoids with longer backbones. Moreover, the uptake efficiency correlated with both the incubation time and the given concentration. Toxicology tests and uptake experiments with porphyrin-coupled peptoids indicate their suitability for application as robust and readily available drug delivery systems or intracellular probes.

INTRODUCTION

During studies on viruses in the late 1980s, it was found that HIV-1 trans-activator of transcription (Tat), a protein of 101 amino acids essential for HIV-1 replication, is rapidly taken up from the culture medium by cultured cells (*1*, *2*). It turned out that only a small proportion of the protein was responsible for the internalization of the whole protein. The relevant peptide comprises residues 49−57, which mainly are basic amino acids (*3*−*7*).

Similar properties were found for short basic domains in the *Drosophila* Antennapedia homeobox protein (*8*) and in the *Herpes simplex* protein VP22 (*9*). Thus, a rapid development was triggered, in which more peptides with the capability to enter cells were discovered, and a broad variety of cargo molecules was delivered into cultured cells.

Initial assays suggested that these peptides could directly penetrate the plasma membrane by a novel mechanism that became known as protein transduction. Therefore, the new class of peptides was referred to as protein transduction domains (PTDs). After the development of synthetic delivery peptides, the term cell-penetrating peptides (CPP) was coined to refer to naturally occurring PTDs and their functional homologs from organic synthesis (*10*−*12*).

It has been shown that cell-penetrating peptides (CPPs) have a high potential to deliver drugs and reporter molecules into cultured cells, and even into cells in fully grown organisms (*13*, *14*). However, many CPPs derived from natural polypeptide sequences do not fulfill any known function *in vivo*. Presumably, they have not been optimized by evolutionary processes. This creates the possibility to improve the cell-penetrating function of these molecules by varying their amino acid sequence. Synthetic peptides with enhanced delivery properties have already been synthesized (*6*, *15*−*19*), and the synthesis of many peptide analogs that mimic CPP function are already described (*3*, *20*−*24*). Most of these contain a majority of basic amino acids.

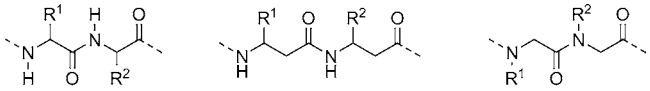
However, arginine-rich peptides are sensitive to oxidation and degradation by proteases, which requires great care to be taken when working with CPP-coupled substances. This sensitivity also reduces their lifespan, bioavailability, and blood circulation time *in vivo* making them unsuitable for oral application and preventing them to reach the target tissue. Moreover, peptides may be recognized as epitopes and trigger immunogenic responses. Peptide mimetics that circumvent these disadvantages provide a wider range of possible application in living organisms. Once the synthesis of effective structures is established, the process can further be improved to achieve structures exhibiting low toxicity and optimized pharmacokinetic properties.

As shown for natural and synthetic CPP analogs, an α-helical and amphipathic structure can be advantageous for cellular uptake (*25*). Apparently, a high density of positively charged side chains appears to be the most important feature for enhanced cellular uptake efficiency. Therefore, backbone mimetics need to be equipped with basic functional groups such as amine or guanidinium groups in order to exhibit cell-penetrating behavior.

In particular, β-peptides (*2*) have been studied intensively in recent years (Figure 1) (*24*). With one methylene unit inserted between the carboxyl group and the former α-carbon, these backbone analogs constitute higher homologs of the α-peptides (*1*). They form stable helices that are structurally more confined

* Correspondence to S.B. (braese@ioc.uka.de) or U.S. (schepers@uni-bonn.de).
† Institut für Organische Chemie, Universität Karlsruhe.
‡ Universität Bonn.
△ Contributed equally to this paper.
§ Karlsruhe Institute of Technology and Center for Functional Nanostructures (CFN), Universität Karlsruhe.

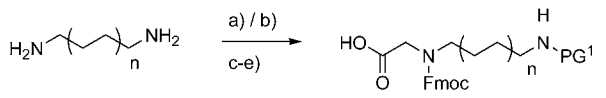
10.1021/bc0602073 CCC: $37.00 © 2007 American Chemical Society
Published on Web 02/28/2007



1 **2** **3**

Figure 1. Representative structures of peptides (**1**), β-peptides (**2**), and peptoids (**3**).

Scheme 1. Synthesis of Monomeric Building Blocks 5{*x*} (*x* = 4, 6, 8) for Peptoid Synthesis[a]



4{4}: n = 1
4{6}: n = 2
4{8}: n = 3

5a{x}: PG^1 = Boc
5b{x}: PG^1 = Ns
x = 4,6,8

[a] Reaction conditions: (a) 0.13 equiv Boc_2O, dioxane, RT, (under argon) 22.5 h; (b) 0.13 equiv *o*-nosyl chloride, dioxane, RT, (under argon) 22.5 h; (c) 3.00 equiv of NEt_3, 1.00 equiv ethyl bromoacetate, THF, RT, 16 h; (d) 4 N NaOH, MeOH, dioxane, RT, 30 min; (e) 1.00 equiv 9*H*-fluorene-9-ylmethoxycarbonyl-*N*-hydroxysuccinimide, H_2O/MeCN (1:2 (v/v)), RT, 30 min.

than those formed by α-peptides or α-peptide analogs. Furthermore, they are stable against protease degradation. It has also been shown that β-peptides equipped with amino and guanidino groups can be internalized by cultured mammalian cells (*3*). However, they are more or less resistant to clearance through the kidneys.

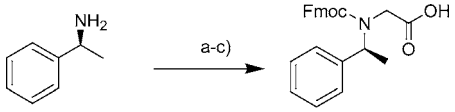
Likewise, oligo-N-alkylglycines (*3*), more commonly known as peptoids, have been subject to intensive studies to investigate cell behavior and synthetic pathways (*3*, *26*, *27*). As opposed to α-peptides, the side chains are attached to the nitrogen so that the monomers can be readily synthesized from a reaction of functionalized diamines with 2-bromoacetic acid (Figure 1). Peptoids with guanidinium headgroups attached to alkyl chains of varying lengths are taken up by mammalian cells (*3*). These peptoids have been successfully used to mimic peptide hormones, antibiotics, and receptor ligands (*28*).

Besides the studies that already exist on peptoids as molecular transporters, the aim of this study was to compare the cellular uptake efficiency and the toxicology of cargo-coupled peptoids with different chiral and achiral side chains and backbone length to design effective molecular transporters for use in drug delivery or as molecular probes for bioconjugation.

EXPERIMENTAL PROCEDURES

Synthesis of the Building Blocks. Monomeric building blocks were built up from diamines **4**{*x*} (*x* = 4, 6, 8) (90.0 mmol, 1.00 equiv) with varying lengths (C4, C6, and C8, respectively) (Scheme 1). After protecting the amino group with either *tert*-butyloxycarbonyl (Boc) (11.7 mmol, 0.13 equiv) or 2-nitrophenylsulfonyl (*o*-nosyl) (11.7 mmol, 0.13 equiv), in order to permit orthogonal deprotection of the side chains the monoprotected diamines were subsequently reacted with ethyl bromoacetate (1.00 equiv). Then, the resulting amino acetic acid esters were hydrolyzed with sodium hydroxide. The secondary amines were finally protected with 9-fluorenylmethoxycarbonyl (Fmoc) (1.00 equiv) to yield ready-to-use **5**{*x*} (*x* = 4, 6, 8) as building blocks for solid-phase synthesis (Scheme 1). An additional chiral building block **5**{**1***} was also synthesized (Scheme 2). Instead of a protected amino side chain, it contains an aromatic ring derived from (*S*)-1-phenylethylamine (**4**{**1***}) (*29*, *30*) that had been reacted with ethyl bromoacetate, hydrolyzed, and protected with Fmoc to yield a chiral monomer **5**{**1***}, which enforced steric restrictions upon the conformation of the assembled peptoid (Scheme 2).

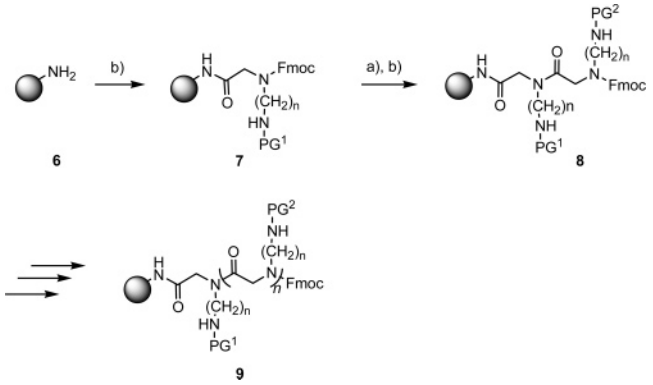
Scheme 2. Chiral Building Block 5{1*} Derived from (*S*)-1-Phenylethylamine 4{1*} in a Three-Step Synthesis[a]



4{1*} **5{1*}**

[a] Reaction conditions: (a) *tert*-butyl bromoacetate, KI, K_2CO_3, DMF; (b) 9*H*-fluorene-9-ylmethoxycarbonyl-*N*-hydroxy succinimide, THF, 0 °C − RT, 12 h; (c) HCl/H_2O, reflux, 2 h.

Scheme 3. Solid-Phase Synthesis of Peptoids[a]



6 **7** **8** **9**

[a] (a) 20% Piperidine in DMF, 3 × 2 min; (b) 2.00 equiv monomer, 2.00 equiv PyBrOP, 4.00 equiv DIPEA, CH_2Cl_2, RT, 24 h.

Solid-Phase Synthesis. *General Procedure A (Construction of the Peptoids).* For activation, the amino-functionalized Rink amide resin **6** (0.510 mmol, 1.00 equiv) was suspended in dichloromethane (5 v/v) and allowed to swell at room temperature for 30 min. After removal of the solvent, the Fmoc protection group of the linker amine was removed by incubation of the resin with 6 mL piperidine solution (20% in DMF) for 2 min. This procedure was repeated twice. For the coupling step, the crystalline Fmoc-protected building block **5a**{*x*} (**5b**{*x*}) (1.530 mmol, 3.00 equiv) was added to the resin followed by PyBrOP (1.02 mmol, 2.00 equiv) and DIPEA (2.04 mmol, 4.00 equiv), and the mixture was suspended in dichloromethane (6 mL) and shaken at room temperature for 24 h. Then, the resin was filtered and sequentially washed with MeOH/DMF/MeOH (2 cycles each), THF/MeOH/THF/MeOH/THF/pentane/dichloromethane (3 cycles each) and pentane (4 cycles). Finally, the resin was dried *in vacuo* (10^{-2} mbar) for 48 h. Coupling of the respective monomers to the growing peptoid chain proceeded under the same conditions as the attachment of the first building block to the solid support. All reaction procedures were succeeded by repetitive cycles of coupling and deprotection until a peptoid of the desired length was obtained. The procedure is outlined in Scheme 3.

General Procedure B (Labeling and Bioconjugation). Prior to attaching a fluorophore or other cargos to the peptoids, *N*-Fmoc-aminohexanoic acid was coupled as a spacer to prevent steric hindrance between fluorophore/conjugate and transporter. The immobilized peptoid was first deprotected as described in general procedure A. This step was repeated twice. For the coupling step of the spacer, *N*-Fmoc-aminohexanoic acid (0.250 mmol, 3.00 equiv) was added to the resin. PyBrOP (0.160 mmol, 2.00 equiv) and DIPEA (0.330 mmol, 4.00 equiv) were added as activating reagents and the suspension was agitated at room temperature for 24 h in 6 mL of dichloromethane. Then, the resin was filtered and washed as described in General Procedure A. Finally, the resin was dried *in vacuo* for 48 h. After reswelling of the resin and deprotection with piperidine solution (as described in General Procedure A), the fluorophore **11a**

(**11b**) or carboxyporphyrin **12** (0.250 mmol, 3.00 equiv) was attached as described in General Procedure B1.

General Procedure B1. For activation of the fluorophore, 5(6)-carboxyfluorescein (**11a**) or carboxyporphyrin **12** (0.250 mmol, 3.00 equiv) and HOBt (0.250 mmol, 3.00 equiv) were transferred into a 50 mL flask and dissolved in 2 mL of dichloromethane/DMF (1:1 (v/v)). After addition of DIC (0.250 mmol, 3.00 equiv), the mixture was shaken at room temperature for 20 min and eventually added to the prepared resin derived from General Procedure B. The suspension was agitated at room temperature for 5 h (5(6)-carboxyfluorescein (**11a**)) and 24 h (carboxyporphyrin **12**), respectively.

For rhodamine labeling, rhodamine-B-isothiocyanate (**11b**) (3.00 equiv in dichloromethane) was added to the prepared resin derived from General Procedure B, without activation. The mixture was agitated in dichloromethane/DMF (5 vol according to the initial resin volume) for 4 days.

General Procedure C (Nosyl Deprotection). For the deprotection of the nosyl-functionalized amino groups, the resin (0.090 mmol, 1.00 equiv) was suspended in dichloromethane (3 v/v) and allow to swell at room temperature for 30 min. After filtration, the resin was deprotected by treatment with 3 mL of 2-mercaptoethanol/DBU (diaza-[5.4.0]-bicycloundecene) (0.3 M) in DMF. The suspension was shaken for 45 min. The solution was removed, and the deprotection step was repeated twice. The resin was filtered, washed, and dried as described in General Procedure A.

General Procedure D (Cleavage and Isolation). For the cleavage of the peptoid from solid support, the resin was transferred into a 25 mL flask and suspended in 1 mL of TFA/TIS (95:5 (v/v)). The suspension was gently agitated at room temperature for 3 h under argon atmosphere. Then, the resin was filtered and rinsed with TFA (2 × 3 mL): The filtrates were collected and combined. The peptoid was precipitated from the filtrate by gently pivoting with 50 mL of cold diethyl ether (−78 °C). It was filtered and finally dried in vacuo.

Fluorophore-Coupled Peptoids. *Fluo-{4,4,4,4}-NH₂.* Following General Procedures A, B, and D, the tetramer was obtained as yellow solid in a yield of 0.173 g (quant). TLC (silica gel: RP-18 F_{254s}): CH_3CN/H_2O (1:1 (v/v) (+1 drop TFA)); $R_f = 0.55$. MS (FAB, matrix: glycerol), *m/z* (%) [norm: 472]: 1001 (50) $[M + H]^+$, 873 (32) $[M -$ monomer$]^+$, 745 (18) $[M - 2\times$ monomers $+ H]^+$, 600 (97) [Fluo + spacer + monomer + H]$^+$, 472 (100) [Fluo + spacer]$^+$. HRMS (FAB): exact mass ($C_{51}H_{72}N_{10}O_{11}$), calcd 1000.5382 g/mol, found 1000.5380 g/mol. IR (drift): $\nu = 3046$ (s), 2949 (s), 2088 (vs), 1679 (s), 1204 (s), 1182 (s), 1137 (s), 837 (s), 800 (s). UV/vis (CH_3OH): λ_{max} (log ϵ) = 202 (4.8), 459 (2.8).

Fluo-{6,6,6,6}-NH₂. Following General Procedures A−D, the peptoid was obtained as a brown, viscous solid in a yield of 0.051 g (46%). TLC: chloroform/methanol (5:1 (v/v)); R_f = 0.2; strong, green fluorescence in UV light. MS (FAB, matrix: mNBA), *m/z* (%): 1113 (4) $[M + H]^+$, 755 (4) [M − Fluo + H]$^+$, 486 (16) [trimer + H]$^+$, 307 (100) $[2M_a + H]^+$. HRMS (FAB): exact mass ($C_{59}H_{89}N_{10}O_{11}$), calcd 1113.671 g/mol, found 1113.667 g/mol. IR (drift): $\nu = 2942$ (w, br), 1679 (w), 1547 (w), 1468 (w), 1317 (w), 1203 (w), 1137 (w).

Rhod-{8,8,8,8}-NH₂. The dry resin was reacted as in General Procedures A, B, and D. The tetramer was obtained as a purple solid in a yield of 0.165 g (74%). TLC (silica gel: RP-18 F_{254s}): CH_3CN/H_2O (1:1 (v/v) (+1 drop TFA)); $R_f = 0.49$. MS (FAB (LR), matrix: glycerol), *m/z* (%) [norm: 867]: 1367 (6) $[H]^+$, 1183 (5) $[M -$ monomer$]^+$, 867 (100) $[M -$ Rhod$]^+$, 683 (31) [M − Rhod − monomer]$^+$, 500 (66) [Rhod]$^+$. HRMS (FAB): exact mass ($C_{46}H_{95}N_{10}O_5$), calcd 867.7487 g/mol, found 867.7484 g/mol. IR (drift): $\nu = 2940$ (s), 2864 (s), 2088 (vs), 1682 (s), 1204 (s), 1181 (s), 1137 (s). UV/vis (CH_3OH): λ_{max} (log ϵ) = 196 (4.5), 256 (3.6), 283 (3.5), 351 (2.9), 399 (2.6), 553 (4.0).

Fluo-{6,1,6,1*,6}-NH₂.* As in General Procedures A−D, the pentamer was obtained as a brown solid in a yield of 0.200 g. Strong, green fluorescence in UV light (366 nm).

Rhod-{4,4,4,4,4,4}-NH₂. The resin were treated as in General Procedures A, B, and D. The product was obtained as a red-brown solid. Yield: 0.088 g (39%). TLC (silica gel: RP-18 F_{254s}): CH_3CN/H_2O (1:1 (v/v) (+1 drop TFA)); $R_f = 0.42$. MS (FAB (LR), matrix: glycerol), *m/z* (%) [norm: 899]: 1399 (76) $[M]^+$, 1271 (22) $[M -$ monomer$]^+$, 1144 (18) [M − 2 monomers + H]$^+$, 916 (32) [M − 3× monomers + H]$^+$, 899 (100) [M− Rhod]$^+$, 888 (56) [M − 4× monomers + H]$^+$, 760 (52) [M − 5× monomers + H]$^+$. HRMS (FAB): exact mass ($C_{42}H_{87}N_{14}O_7$), calcd 899.6882 g/mol, found 899.6879 g/mol. UV/vis (CH_3OH): λ_{max} (log ϵ) = 200 (4.7), 257 (3.8), 354 (3.0), 547 (4.0).

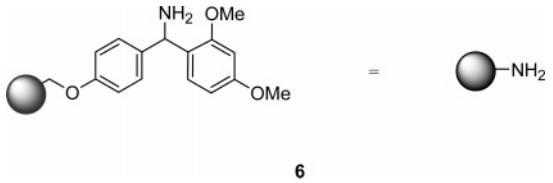
Fluo-{6,6,6,6,6,6}-NH₂. As described in General Procedures A−D, the product was obtained as a brown solid. Yield: 0.066 g (60%). TLC: chloroform/methanol (5/1); $R_f = 0.03$; strong, green fluorescence in UV light (366 nm). MS (MALDI, matrix: DHB), *m/z* (%): 1463.891 (52) [M + K]$^+$, 1447.914 (100) [M + Na]$^+$, 1425.923 (62) [M + H]$^+$, 799 (45) [pentamer + H]$^+$, 486 (6) [trimer + H]$^+$. IR (drift): $\nu = 2940$ (m, br), 2100 (vw), 1677 (m), 1466 (w), 1203 (w), 1135 (w).

Fluo-{8,4,8,4,8,4}-NH₂. The resin was reacted as in General Procedures A, B, and D. The peptoid was obtained as a red-brown solid in a yield of 0.042 g. TLC: chloroform/methanol (2/1); $R_f = 0.05$; strong, green fluorescence in UV light (366 nm). MS (MALDI, matrix: DHB), *m/z* (%): 1463.814 (31) [M + K]$^+$, 1447.914 (41) [M + Na]$^+$, 1425.863 (28) [M + H]$^+$, 771(94) [pentamer + H]$^+$, 458 (88) [trimer + H]$^+$. IR (drift): $\nu = 2937$ (w, br), 2082 (vw), 1758 (m), 1682 (w), 1457 (w), 1203 (w), 1136 (w).

Rhod-{6,6,6,6,6,6,6,6}-NH₂. Followed General Procedures A, B, and D, the product was received as a purple solid. Yield: 0.268 g (89%). TLC (silica gel: RP-18 F_{254s}): CH_3CN/H_2O (1:1 (v/v) (+1 drop TFA)); $R_f = 0.32$. MS (FAB (LR), matrix: glycerol), *m/z* (%) [norm: 1223]: 1880 (20) [M+ H]$^+$, 1722 (26) [M − monomer]$^+$, 1567 (36) [M − 2× monomers + H]$^+$, 1380 (66) [M − Rhod]$^+$, 500 (>100) [Rhod]$^+$. HR−MS (FAB (HR), matrix: glycerol), *m/z* (%): exact mass ($C_{40}H_{84}N_{11}O_5$), calcd 798.6657; found 798.6655. IR (drift): $\nu = 2945$ (s), 2868 (s), 2088 (vs), 1680 (s), 1204 (s), 1182 (s), 1136 (s). UV/vis (CH_3OH): λ_{max} (log ϵ) = 196 (4.8), 257 (3.8), 282 (3.6), 353 (3.2), 550 (4.1).

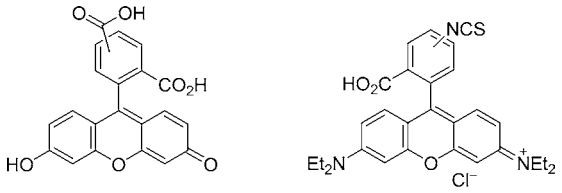
Fluo-{8,8,8,8,8,8,8,8}-NH₂. The resin was processed following General Procedures A, B, and D. Yield: 0.245 g (79%). The peptoid was a yellow-orange solid. TLC (silica gel: RP-18 F_{254s}): CH_3CN/H_2O (1:1 (v/v) (+1 drop TFA)); $R_f = 0.41$. MS (FAB (LR), matrix: glycerol), *m/z* (%) [norm: 1123]: 1960 (3) [M − H]$^+$, 1778 (20) [M − monomer + H/M* + H]$^+$, 1603 (10) [M − Fluo + H]$^+$, 1419 (98) [M − monomer − Fluo + H/M* − Fluo + H]$^+$, 938 (150) [5er + H]$^+$. HR−MS (FAB (HR), matrix: glycerol), *m/z* (%): exact mass ($C_{50}H_{104}N_{11}O_5$), calcd 938.8222; found 938.8220. IR (drift): ν = 2940 (m), 2864 (s), 2102 (vs), 1680 (m), 1204 (m), 1137 (s).

Fluo-{8,4,8,4,8,4,8,4}-NH₂. As in General Procedures A, B, and D, the product was obtained. Yield: 0.021 g. The peptoid was a brown, viscous solid. Strong, green fluorescence in UV light (366 nm). MS (MALDI, matrix: DHB), *m/z* (%): 1760.149 (33) [M + Na]$^+$, 1738.170 (15) [M + H]$^+$, 793 (100) [pentamer + Na]$^+$, 648 (89) [tetramer − NH_2 + Na]$^+$. IR (drift): ν = 2939 (m, br), 2101 (vw), 1758 (w), 1682 (m), 1472 (w), 1203 (m), 1134 (w).



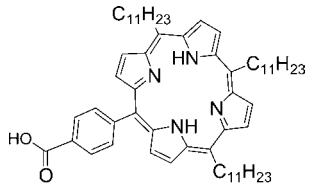
6

Figure 2. Rink amide resin **6** and its abbreviated representation.



11a **11b**

Figure 3. Structures of the fluorophores 5(6)-carboxyfluorescein **11a** (= **Fluo-OH**) and rhodamine B-isothiocyanate hydrochloride **11b** (= **Rhod** + **HCl**).



12

Figure 4. Structure of the 5-(4-carboxyphenyl)-10,15,20-triundecyl-21*H*-23*H*-porphyrin (**12**) (**Porph-OH**, carboxyporphyrin) (*37* and see Supporting Information).

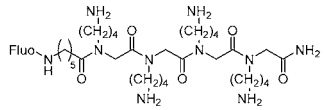
Porphyrin-Coupled Peptoids. *Porph-{4,4,4,4,4,4}-NH2.* Following General Procedures A, B, and D, the product was obtained as a dark green-blue solid. Yield: 0.109 g (63%). MS (FAB (LR), matrix: glycerol), *m*/*z* (%): 1775 (6) $[M + H^+]^+$, 1116 (1) [monomer + spacer + porphyrin]$^+$, 849 (9) [porphyrin − CO + H]$^+$. UV/vis (CH_3OH): λ_{max} (log ϵ) = 194 (4.6), 304 (3.8), 325 (3.8), 414 (5.0) 517 (3.5), 551 (3.5) 595 (3.4), 653 (3.3). IR (film on KBr): ν = 3437 (w), 3082 (w), 2927 (w), 2856 (w), 2557 (vw), 1780 (w), 1672 (w), 1495 (w), 1467 (w), 1439 (w), 1179 (w).

Porph-{6,6,6,6,6,6}-NH2. The resin was reacted as in General Procedures A, B, and D. The product was obtained as dark green-blue solid. Yield: 0.122 g (quant). MS (FAB (LR), matrix: glycerol), *m*/*z* (%): 1942 (8) $[M + H]^+$, 1786 (7) [M − $C_{11}H_{23}$]$^+$, 847 (8) [porphyrin − CO]$^+$. UV/vis (CH_3OH): λ_{max} (log ϵ) = 193 (4.7), 305 (3.9), 414 (5.1), 517 (3.7), 552 (3.5) 597 (3.4), 652 (3.4). IR (film on KBr): ν = 2929 (m), 2859 (m), 1779 (m), 1665 (m), 1495 (w), 1468 (w), 1171 (s).

Porph-{8,8,8,8,8,8}-NH2. The resin was reacted as in General Procedures A, B, and D. The product was obtained as dark green-blue solid. Yield: 0.105 g (quant). MS (FAB (LR), matrix: glycerol), *m*/*z* (%): 2111 (8) $[M + H]^+$, 847 (8) [porphyrin − CO]$^+$, 554 (4) [3× monomers + H]$^+$, 386 (6) [NH_2 + 2× monomers + H]$^+$. UV/vis (CH_3OH): λ_{max} (log ϵ) = 194 (4.7), 305 (3.9), 414 (5.1) 517 (3.7), 552 (3.6) 596 (3.5), 654 (3.4). IR (film on KBr): ν = 2931 (s), 2860 (m), 2552 (w), 1780 (s), 1665 (s), 1496 (m), 1468 (m), 1172 (vs).

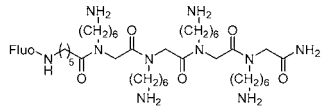
For further information and detailed experimental procedures for the synthesis of the building blocks and the solid-phase synthesis, see Supporting Information.

Purification of Peptoids. Lyophilized samples of peptoids were dissolved in methanol to yield a 10 mM stock solution. To analyze the peptoid composition, 1 μL of the stock solution was diluted in 1 mL of methanol and was analyzed by MALDI-TOF mass spectrometry. A 2 μL aliquot of the stock solution was diluted in 120 μL of low-salt buffer (5% acetonitrile, 100 mM TEAB), and 100 μL of this solution was purified chromatographically on a Nucleosil-120 RP-18 column (Knauer)

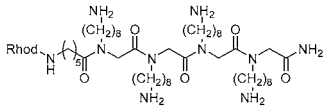


Tetramer

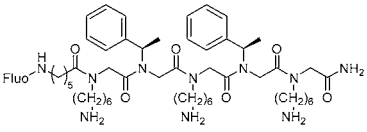
Fluo-{4,4,4,4}-NH2



Fluo-{6,6,6,6}-NH2

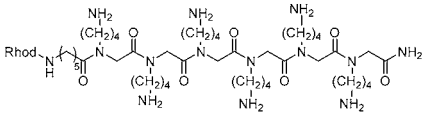


Rhod-{8,8,8,8}-NH2



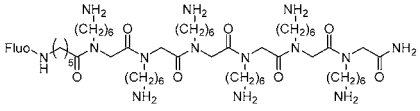
Alternating Pentamer

Fluo-{6,1*,6,1*,6}-NH2

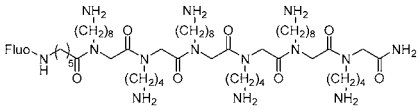


Hexamer

Rhod-{4,4,4,4,4,4}-NH2

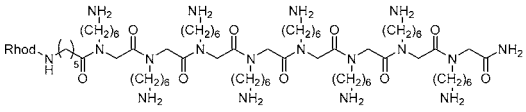


Fluo-{6,6,6,6,6,6}-NH2



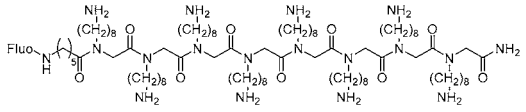
Alternating Hexamer

Fluo-{8,4,8,4,8,4}-NH2

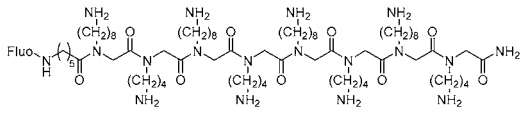


Octamer

Rhod-{6,6,6,6,6,6,6,6}-NH2



Fluo-{8,8,8,8,8,8,8,8}-NH2

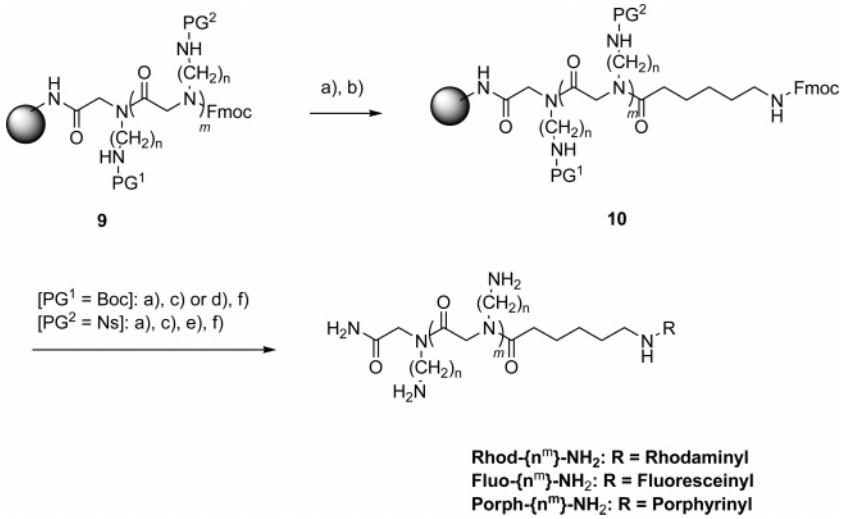


Alternating Octamer

Fluo-{8,4,8,4,8,4,8,4}-NH2

Figure 5. Fluorescein- and rhodamine-labeled peptoids **Fluo-{*n*^{m}}-NH2** and **Rhod-{*n*^{m}}-NH2** after deprotection and cleavage from the solid phase.

Scheme 4. Attachment of Fluorescein 11a and Rhodamine B Isothiocyanate 11b as Fluorophores[a]



[a] Reaction conditions: (a) 20% piperidine in DMF, 3 × 2 min; (b) 3.00 equiv Fmoc−aminohexanoic acid, 2.00 equiv PyBrOP, 4.00 equiv DIPEA in CH_2Cl_2, RT, 24 h; (c) 3.00 equiv 5(6)-carboxyfluorescein **11a**, 3.00 equiv HOBt, 3.00 equiv DIC in DMF/CH_2Cl_2 (1:1), RT, 5 h; (d) 3.00 equiv rhodamine B isothiocyanate hydrochloride **11b**, CH_2CL_2, RT, 4 d; (e) 2-mercaptoethanol/DBU (0.3 M in DMF), 45 min; (f) TFA/TIS (95:5), 3 h.

in a 60 min gradient from 5% to 80% acetonitrile (100 mM NEt_3) at a flow rate of 150 μL/min. Alternatively, the chromatography buffers were supplemented with 0.1% TFA instead of 100 mM TEAB.

Cellular Uptake of the Peptoids. For general cell culture procedures, preparation of mammalian cells and cell fixation procedures, see Supporting Information.

RESULTS

To mimic CPP function and to enhance cellular uptake, the peptide structure was altered to that of a peptoid. In spite of previous work, showing peptoid suitability as molecular transporters carrying a variety of cargo into cells, there are still many unanswered questions. For example, the correlation between backbone and side chain length is yet uncertain, and the composition, the uptake efficiency, and the mechanisms of cellular uptake are not yet elucidated. In our approach, ten different peptoids (Figure 5) with varying lengths, side chain lengths, and compositions were synthesized, as depicted in Schemes 1−4 and Figures 5 and 6. After initial experiments, the various peptoids were tested in cell culture in order to assess the effect of structural deviation patterns on uptake efficiency and cellular distribution.

The outlined syntheses are somewhat modified from those described by Bradley et al. (*31*, *32*), which are all performed on solid support. Solid-phase reactions greatly facilitate the synthesis, as the growing oligomer attached to a solid support can easily be purified from excess reactants by washing the resin with the appropriate solvents and subsequently filtering. Scheme 3 represents the outline of the peptoid synthesis on solid support using different monomeric building blocks and fluorophores or cargo. For this study, a Rink amide resin **6** (Figure 2) was chosen due to its stability at ambient conditions, the ease of the first coupling step, and the mild cleavage conditions. Moreover, the reaction conditions for almost all coupling steps are the same as for the attachment of the first building block to the resin. The outlined synthesis allowed the protection of the free amino groups of the side chains with either o-nosyl (Ns) or Boc, while the N-terminal amino group was protected with Fmoc. Fmoc has been well-established in peptide chemistry, as it can be quantitatively removed under mild conditions in a short reaction time. The peptoid-backbone synthesis was finished by either the coupling of a fluorophore or a cargo (Scheme 4, Figures 3 and 4). The fluorophore was required to monitor the cellular uptake of the different peptoids by live cell imaging. 5(6)-Carboxyfluorescein **11a** (λ_{abs} = 492 nm, λ_{em} = 517 nm) as well as rhodamine-B-isothiocyanate **11b** (λ_{abs} = 550 nm, λ_{em} = 580 nm) (Figure 3) were coupled to the peptoids (designated as **Fluo** and **Rhod**) (Figure 3) prior to cleavage from the solid phase to permit simultaneous tests of different labeled peptoids on the same cultured cells for future investigations. 6-Aminohexanoic acid was used as a linker to prevent interactions of the fluorophore or cargo with the peptoid moiety. As outlined in Scheme 4, the Fmoc-protected linker molecule was attached to the amino terminus of the peptoids under standard coupling conditions. 5(6)-Carboxyfluorescein **11a** formed a peptide bond via its carboxyl group under mild coupling conditions without detectable side reactions. In this reaction step, 1-hydroxybenzotriazole (HOBt) and diisopropylcarbodiimide (DIC) were used to activate the carboxyl function, while no activating substances were required to form the thiourea bond between rhodamine-B-isothiocyanate and the amine.

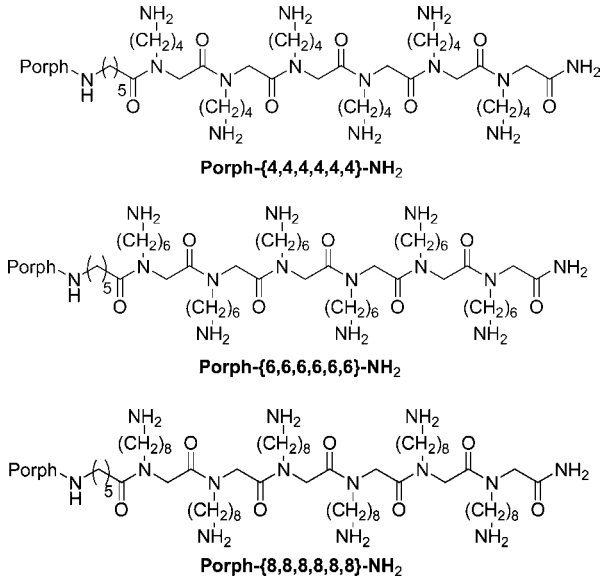


Figure 6. Peptoids conjugated with carboxyporphyrin **12** after deprotection and cleavage from the solid phase.

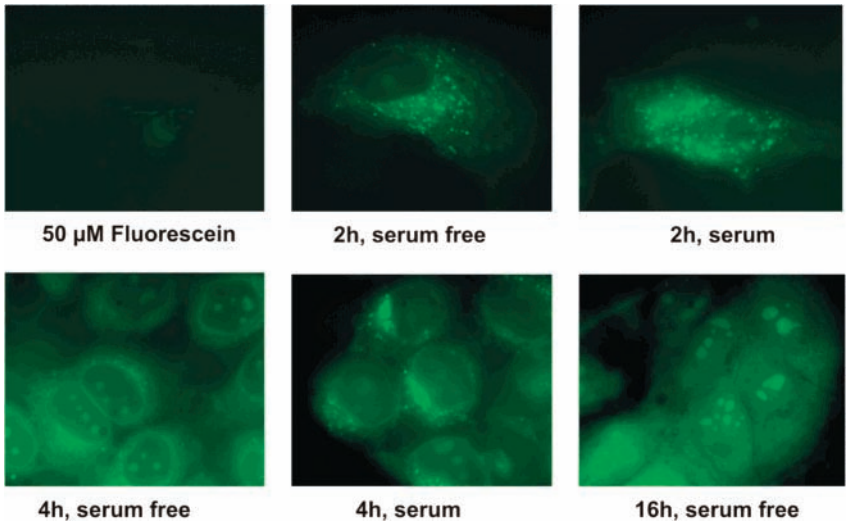


Figure 7. Decreases in serum levels led to changes in cell morphology already after 2 h of incubation. COS7 cells incubated for 2, 4, and 6 h in −FCS and +FCS culture media treated with 50 μM of hexapeptoid **Fluo**-{**6,6,6,6,6,6**}-$\mathbf{NH_2}$ are shown.

In the final step, the labeled peptoids **Rhod**-{$\boldsymbol{n^m}$}-$\mathbf{NH_2}$/**Fluo**-{$\boldsymbol{n^m}$}-$\mathbf{NH_2}$ were simultaneously deprotected and cleaved from the solid phase by treatment with trifluoroacetic acid (TFA)/triisopropyl silane (TIS). Peptoids containing the o-nosyl protection group had to be deprotected by treatment with 2-mercaptoethanol and diaza-[5.4.0]-bicycloundecene (DBU) prior to cleavage from the solid support. The free peptoids were precipitated with cold diethyl ether and dried *in vacuo*. The peptoids were characterized by nuclear magnetic resonance spectroscopy and mass spectrometry and were subjected to reversed-phase chromatography on RP-18 to reveal a purity of >95%.

Figure 5 represents the ten peptoids that were used for the study. The peptoids comprise different building blocks, which are indicated by the nomenclature used in Figure 5. Each number in the brackets indicates one monomeric building block that was synthesized from a diamine **4**{$\boldsymbol{x}$} ($x = 4, 6, 8$) of a certain chain length x (x = 4, 6, and 8 from C4, C6, and C8, respectively). As shown in Figure 5, the peptoid backbone comprises 4, 5, 6, and 8 of such building blocks. Peptoid **Fluo**-{**6,6,6,6**}-$\mathbf{NH_2}$ was composed of four monomers with C6 side chains (**5**{**6**}), in which the side chain amino groups were protected during SPPS with o-nosyl or Boc protecting groups. Likewise, peptoid **Fluo**-{**6,6,6,6,6,6**}-$\mathbf{NH_2}$ was assembled with two additional Boc-protected C6-building blocks. Peptoids **Fluo**-{**8,4,8,4,8,4**}-$\mathbf{NH_2}$ and **Fluo**-{**8,4,8,4,8,4,8,4**}-$\mathbf{NH_2}$ were synthesized with six and eight building blocks, respectively, with alternating C4 (**5b**{**4**}) and C8 (**5b**{**8**} (n = 3)) side chains (Scheme 1).

Peptoid **Fluo**-{**6,1*,6,1*,6**}-$\mathbf{NH_2}$ was synthesized as a pentamer starting with an o-nosyl protected C6-monomer **5b**{**6**} followed by an alternating sequence of two chiral building blocks **5**{**1***} and two Boc-protected C6 monomers **5**{**6**} (see Scheme 2 and 3).

The peptoids **Fluo**-{**4,4,4,4**}-$\mathbf{NH_2}$, **Rhod**-{**4,4,4,4,4,4**}-$\mathbf{NH_2}$, **Rhod**- {**6,6,6,6,6,6,6,6**}-$\mathbf{NH_2}$, **Rhod**-{**8,8,8,8**}-$\mathbf{NH_2}$, and **Fluo**-{**8,8,8,8,8,8,8,8**}-$\mathbf{NH_2}$ were synthesized with Boc-protected building blocks **5a**{**4**}, **5a**{**6**}, and **5a**{**8**} (Scheme 1).

All further experiments with the fluorescein (Fluo), rhodamine (Rhod), and porphyrin-labeled compounds were performed in the dark to avoid photobleaching of the light-sensitive chromophores. Further synthesis details can be found in the Supporting Information.

Cellular Uptake of Fluorescein-Labeled Peptoids. The fluorescein and rhodamine-labeled peptoids obtained by solid-phase synthesis were tested in cultured mammalian cells for their potential to act as molecular transporters. The minimal concentrations required for visible uptake and the maximum nontoxic concentrations were estimated. Live cell imaging by fluorescence and confocal microscopy enabled visualization of the uptake mode and intracellular localization of the internalized compounds.

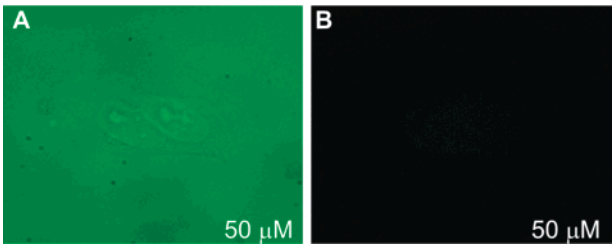


Figure 8. Uncoupled 5(6)-carboxyfluorescein **11a** was not taken up by mammalian cells. HeLa cells were incubated with 50 μM 5(6)-carboxyfluorescein **11a** for 16 h at 37 °C. The same picture was taken in transmission (A) and fluorescence mode (B).

The peptoids were tested on both human and simian cancer cell lines (HeLa and COS7, respectively), as well as on human primary fibroblasts. At the beginning of the cell culture experiments, the appropriate treatment conditions had to be determined. Serum-free media versus serum-containing media was tested, since many drug delivery and transfection reagents have been shown to be sensitive to serum due to interaction with serum proteins and other serum ingredients. On the other hand, the cells might suffer from lack of serum for prolonged times.

With reference to recent findings, which demonstrated that fixation procedures led to artifactual uptake and nuclear localization of cationic amphiphiles and other cationic molecules (*23*, *33*, *34*), cellular uptake of the amphiphilic peptoids was visualized by live cell imaging. Cells fixed with paraformaldehyde (PFA) did indeed show different intracellular distribution of the peptoids from living cells. They exhibited cytosolic staining with remarkably fewer vesicular structures and an accumulation of fluorescence in the nucleus.

To avoid fixation artifacts, all images were taken from living cells. Tetrapeptoid **Fluo**-{**6,6,6,6**}-$\mathbf{NH_2}$ was dissolved in serum-containing (+FCS) or serum-free (−FCS) culture media to yield final concentrations of 5, 10, 50, 100, and 500 nM and 1 μM, respectively. Uncoupled 5(6)-carboxyfluorescein was used as a control (Figure 8)

The cells were grown to 10−20% confluency in an eight-well LabTek chamber slide coated with fetal calf serum (FCS).

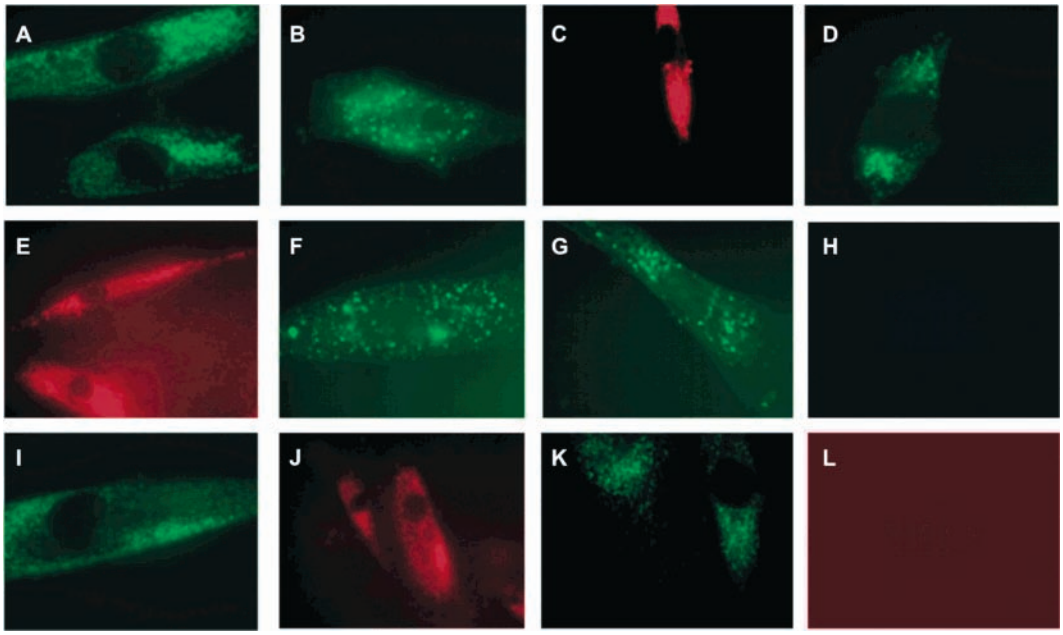


Figure 9. Comparison of the ten peptoids A, **Fluo**-{**4,4,4,4**}-NH_2; B, **Fluo**-{**6,6,6,6**}-NH_2; C, **Rhod**-{**8,8,8,8**}-NH_2; D, **Fluo**-{**6,1*,6,1*,6**}-NH_2; E, **Rhod**-{**4,4,4,4,4,4**}-NH_2; F, **Fluo**-{**6,6,6,6,6,6**}-NH_2; G, **Fluo**-{**8,4,8,4,8,4**}-NH_2; I, **Fluo**-{**8,4,8,4,8,4,8,4**}-NH_2; J, **Rhod**-{**6,6,6,6,6,6,6,6**}-NH_2; K, **Fluo**-{**8,8,8,8,8,8,8,8**}-NH_2; and as controls H, 5(6)-carboxyfluorescein, **11a**; (50 μM) and L, rhodamine-B-isothiocyanate, **11b** (50 μM). All peptoids were tested on human primary fibroblasts in a concentration of 10 μM. To visualize uptake, the cells were incubated with the peptoids solution for 24 h and analyzed by confocal microscopy.

The medium was replaced by half of the final volume of medium +FCS or −FCS, and a doubly concentrated peptoid solution in Dulbecco's Modified Eagle Medium (DMEM) was added dropwise, while constantly rocking the culture dish to ensure a homogeneous distribution of the compound. After an incubation of 5, 20, 60, or 120 min at 37 °C, the peptoid-containing medium was removed and the cells were washed with fresh medium without phenol red to facilitate the imaging.

No signal could be detected at concentrations below 1 μM, which could be attributed to the weak intensity of fluorescein fluorescence or to the small amounts taken up by the cells. Therefore, subsequent experiments were carried out at 10, 20, 50, and 100 μM as described for the related peptoid in a similar study (Figure 7) (*31*). Although these dosages were high, and despite the fact that cationic amphiphiles are mainly stored in the endosomal compartment and will eventually lead to the disruption of the latter (*35*), the experiments were still performed to determine the fate of the peptoids.

In all experiments, the fluorescent peptoids were detected in vesicular structures, in which the fluorescence accumulated. However, after short incubation, the nucleus remained devoid of fluorescence.

Similar to other cationic amphiphiles, it was assumed that the peptoids were protonated, when they reach the acidic compartments. Thus, they interacted with any kind of negatively charged lipids or aggregate, while slowly being released into the cytosol by endosomal escape, a mechanism, which is currently under investigation but not fully understood (*36*). Alternatively, the amide bond linking the fluorophore to the transporter could have been cleaved so that the nonpolar cargo molecule could diffuse into the cytosol. Apart from the staining of those vesicular structures, a perinuclear accumulation of these fluorescent structures was visible in almost all experiments.

In control experiments with hexameric **Fluo**-{**6,6,6,6,6,6**}-NH_2, prolonged incubation in FCS-depleted (−FCS) media led to significant changes in cell morphology and cell death, as depicted in Figure 7. Therefore, subsequent tests were carried out in serum-containing media.

The observed vesicular structures indicated an endocytosis-like mechanism for the uptake of the peptoids. Thus, the

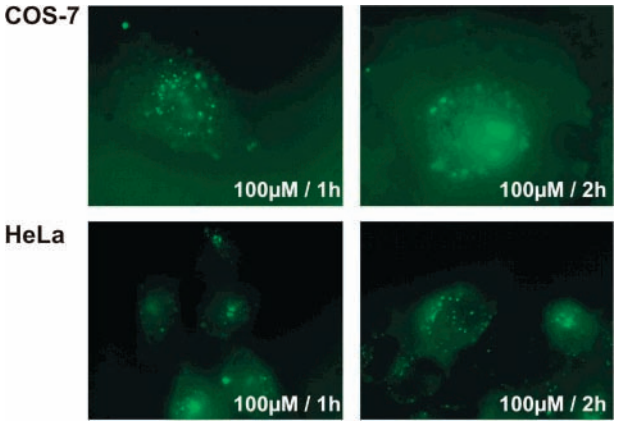


Figure 10. Treatment of COS7 (top row) and HeLa cells (bottom row) with 100 μM of the tetrameric peptoid **Fluo**-{**6,6,6,6**}-NH_2 coupled to fluorescein. Left panel: Vesicular structures accumulated in the perinuclear region can be seen after 1 h. Right panel: 2 h after treatment, the compound has entered the nucleoli of both cell types.

experiment was repeated with incubation times of 4 and 16 h, to monitor the fate of the vesicular structures and to investigate whether the fluorescent peptoids were able to escape into the cytosol. Cell treatment was facilitated by direct application of the peptoid-containing medium without rocking of the culture plate. To avoid strong background fluorescence normally observed at high peptoid concentrations, additional washing steps with 0.2% BSA solution in PBS and a short trypsin treatment were carried out.

Under the given conditions, uncoupled 5(6)-carboxyfluorescein (**11a**) was not taken up by mammalian cells, even when incubated overnight at high concentrations (16 h, Figure 8).

In further experiments, it was shown that the other fluorescein-labeled peptoids **Fluo**-{**8,4,8,4,8,4**}-NH_2, **Fluo**-{**8,4,8,4,8,4,8,4**}-NH_2, and **Fluo**-{**6,1*,6,1*,6**}-NH_2 were taken up by all cell types. Fluorescence and confocal microscopy also revealed that all peptoids had entered the interior of all cells.

At the applied concentrations of 10 μM to 100 μM, intracellular fluorescence was clearly visible (Figures 9−14).

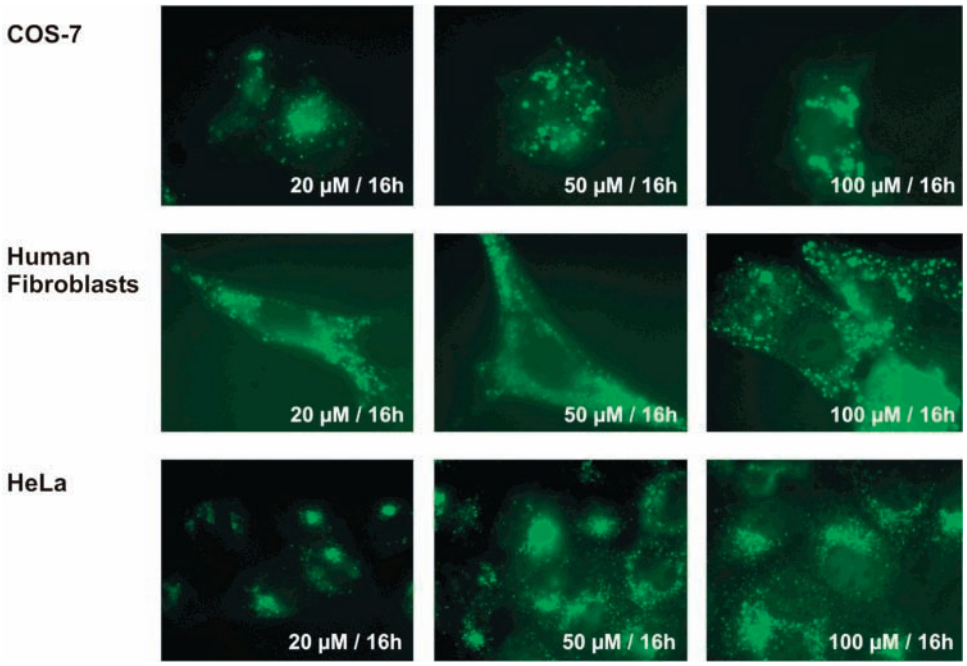


Figure 11. Overnight incubation of COS7 (top row), human fibroblasts (middle row), and HeLa-cells (bottom row) with the chiral pentameric peptoid **Fluo**-{**6,1*,6,1*,6**}-$\mathbf{NH_2}$. At concentrations of 20, 50, and 100 μM, the fluorescence was localized in vesicular structures after incubation overnight. Diffuse fluorescence was observed within the interior of all cells.

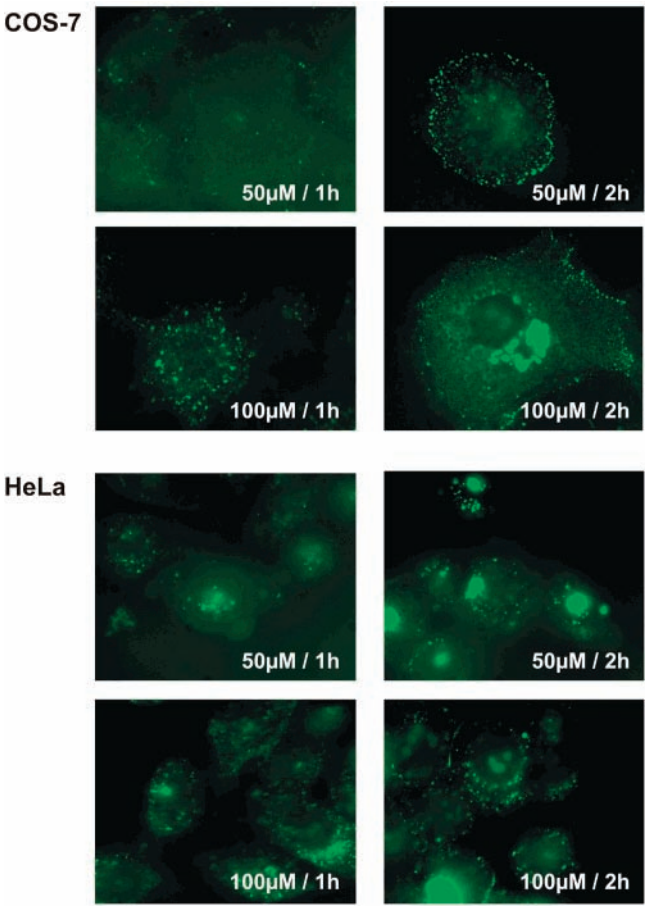


Figure 12. Overnight incubation of COS7 and HeLa cells with 100 μM of the hexameric fluorescein-labeled peptoid **Fluo**-{**6,6,6,6,6,6**}-$\mathbf{NH_2}$. Fluorescence was found concentrated in vesicular structures and more diffuse within the interior of the cells. Note the assembly of vesicular structures along the plasma membrane of the COS7 cells.

However, it is worth mentioning that the uptake rate of all tested peptoids was dependent on the applied concentration in correlation to the duration of the incubation. At lower concentrations, as low as 1−10 μM, all peptoids could only be detected after longer exposure times (24 h and longer) (Figure 9). All peptoids showed similar uptake efficiency and no significant differences in cellular distribution at 10 μM, suggesting no need for the synthesis of longer peptoids than tetramers (Figure 9). At 50−100 μM concentrations, internalization of the peptoids was already detected after 1−2 h. At these times, punctated fluorescence could be seen on the plasma membrane. Fluorescence accumulated in vesicular structures was observed throughout the cells and with higher density in the perinuclear region. After overnight incubation, cytosol staining increased. Thus, it was assumed that a minor part of the labeled molecules had escaped from the vesicles into the cytosol. Whether this was due to active transport or to rupture of the endosomal compartment requires a more detailed analysis.

The tetramer **Fluo**-{**6,6,6,6**}-$\mathbf{NH_2}$ showed a perinuclear localization of the vesicular structures and a distinct homogeneous fluorescence throughout the cells even after 1 and 2 h at 100 μM. Weak staining of the nuclei was also observed (Figure 10). The chiral pentameric peptoid **Fluo**-{**6,1*,6,1*,6**}-$\mathbf{NH_2}$ was trapped in vesicular structures. A tendency to accumulate in the perinuclear region was only observed in HeLa cells and was much less pronounced in COS7 cells. Staining of the nuclei was only visible after overnight incubation with 100 μM (Figure 11). The hexameric peptoid **Fluo**-{**6,6,6,6,6,6**}-$\mathbf{NH_2}$ was visible in vesicular structures even after 1 h of incubation at 50 and 100 μM. Remarkably, after 2 h, a clear distinction could be made among peptoids associated with the plasma membrane, peptoids accumulated in vesicular structures, and those localized in the perinuclear region (Figure 12). After treatment with the hexameric peptoid with alternating C4 and C8 side chains **Fluo**-{**8,4,8,4,8,4**}-$\mathbf{NH_2}$, an increased amount of diffuse fluorescence was observed throughout the interior of the cells, in addition to the vesicular structures of bright fluorescence. In COS7 cells and HeLa cells, these structures accumulated in the perinuclear region, which was less obvious for the fibroblasts even after overnight incubation. The nuclei of all cells were stained, with bright fluorescence in the nuclei of COS7 cells and the weakest staining in the nuclei of the fibroblasts (Figure 13). Finally, the

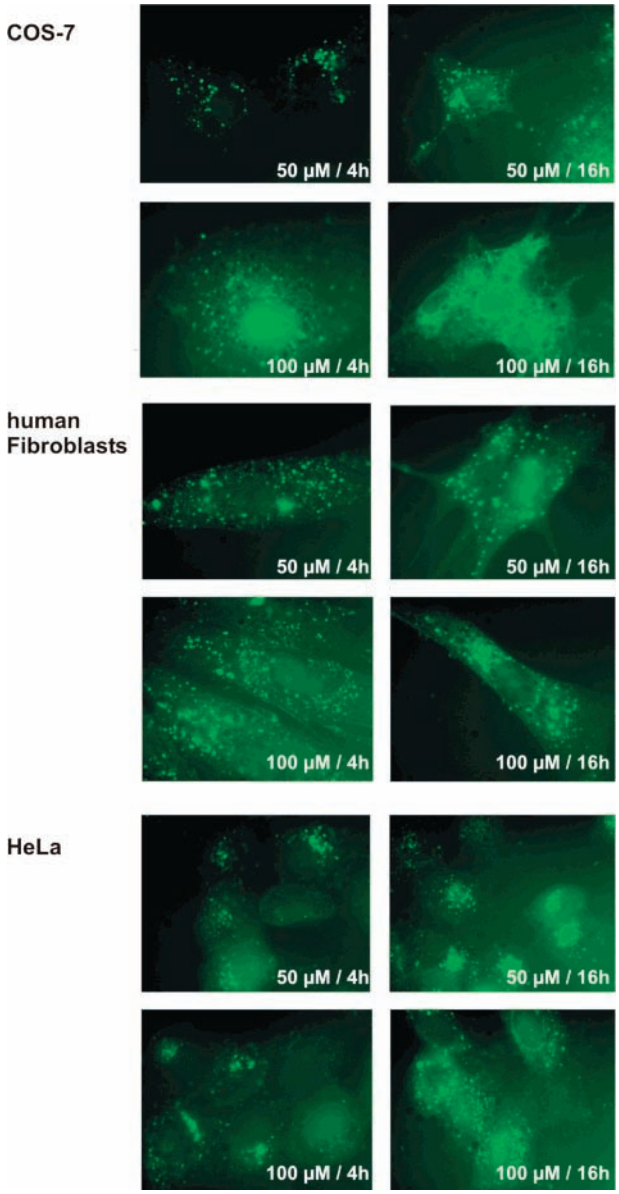


Figure 13. Treatment of COS7, human fibroblasts, and HeLa cells with the fluorescein-labeled hexameric peptoid with alternating C4 and C8 side chains **Fluo**-{**8,4,8,4,8,4**}-NH_2. In all cells, fluorescence was concentrated in vesicular structures, but a diffuse cytosol staining in the cells was also observed.

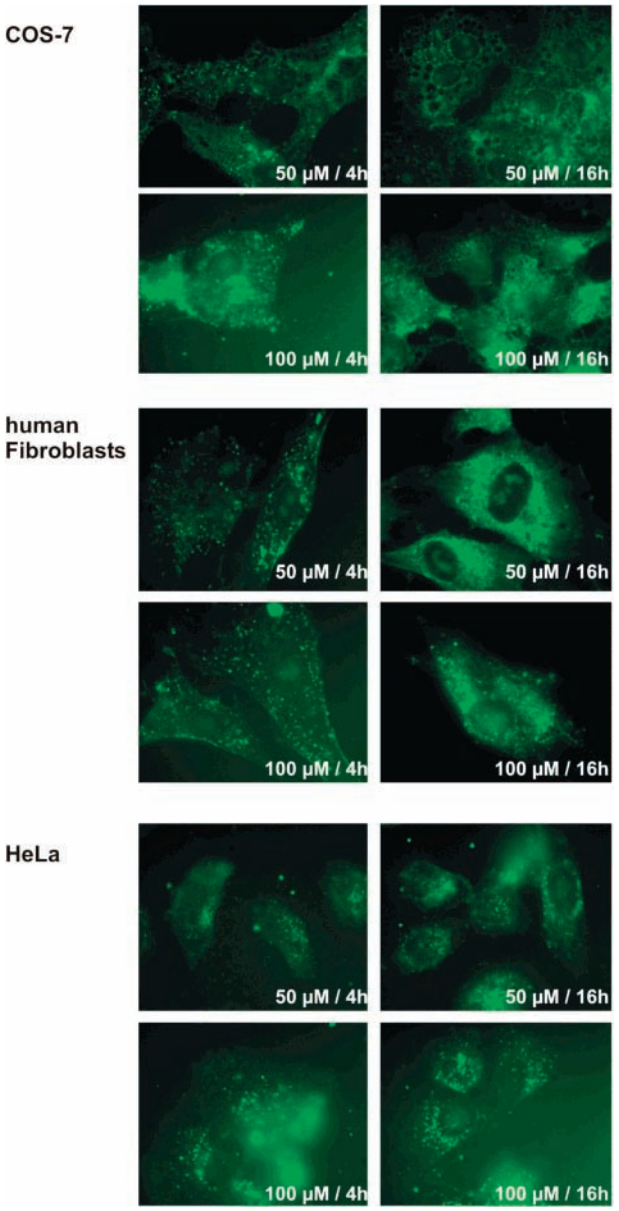


Figure 14. Treatment of COS7, human fibroblasts, and HeLa cells with the fluorescein-labeled octameric peptoid **Fluo**-{**8,4,8,4,8,4,8,4**}-NH_2. In all cell types, fluorescence was localized to vesicular structures and nuclear staining was observed. The main region of the nucleus was precluded from staining.

octameric compound **Fluo**-{**8,4,8,4,8,4,8,4**}-NH_2 exhibited the highest amount of putative cytosolic staining, while vesicular fluorescence decreased in cells with a high degree of diffuse staining. Fluorescence was weak in the nuclei. After overnight incubation, vesicular structures were found to aggregate in the perinuclear region (Figure 14).

In summary, the cytosolic stain was stronger for peptoids with longer backbones. The chimeric compound appeared to be trapped in vesicular structures with markedly less diffused fluorescence within the cytosol. With an increase in incubation time, vesicular structures redistributed their proximity from the plasma membrane to the nucleus. This tendency was markedly less pronounced for the hexamer with alternating side chain lengths than for the homohexamer. The results are summarized in Table 1.

To further examine the influence of side chain length and backbone length, three fluorescein-labeled peptoids and three rhodamine-labeled peptoids of varying side chain and backbone lengths were tested: **Fluo**-{**4,4,4,4**}-NH_2, **Rhod**-{**8,8,8,8**}-NH_2, **Rhod**-{**4,4,4,4,4,4**}-NH_2, **Fluo**-{**6,6,6,6,6,6**}-NH_2, **Rhod**-{**6,6,6,6,6,6,6,6**}-NH_2, and **Fluo**{**8,8,8,8,8,8,8,8**}-NH_2, respectively. Tests were performed in primary human fibroblasts with incubation times of 8, 24, and 48 h, respectively.

As in prior experiments, the transporter molecules were found to accumulate in vesicular structures. In general, transporters with shorter backbones exhibited a weaker uptake than those with a long backbone. The weakest uptake was observed for the tetramer **Fluo**-{**4,4,4,4**}-NH_2, while the octamers **Rhod**-{**6,6,6,6,6,6,6,6**}-NH_2 and **Fluo**{**8,8,8,8,8,8,8,8**}-NH_2 exhibited the highest uptake efficiency but are not as efficient for cytosolic and nuclear staining. Comparison with their relatives containing alternating side chains revealed a higher uptake rate of the nonalternating peptoids in the tested cell cultures.

To prove that this kind of peptoids can be used as shuttles for other cargos than fluorophores, the different peptoid building blocks were covalently coupled to 5-(4-carboxyphenyl)-10,15,-20-triundecyl-21*H*,23*H*-porphyrin (**12**) (carboxyporphyrin) (*37*)

Table 1. Comparison of Cellular Uptake of Different Peptoids

			intracellular localization			
	compound	uptake rate % of cells	vesicular	perinuclear	cytosolic	nuclear
tetramer	**Fluo**-{**4,4,4,4**}-NH_2	100	++	++	+	-
	Fluo-{**6,6,6,6**}-NH_2	100	++	++	+	++ (high conc.)
	Rhod-{**8,8,8,8**}-NH_2	100	++	++	+	-
pentamer	**Fluo**-{**6,1*,6,1*,6**}-NH_2	100	+++	+++	+	+
hexamer	**Rhod**-{**4,4,4,4,4,4**}-NH_2	100	+++	+++	++	+
	Fluo-{**6,6,6,6,6,6**}-NH_2	100	+++	+++	++	+
	Fluo-{**8,4,8,4,8,4**}-NH_2	100	+++	++	++	++ (high conc.)
	Porph-{**4,4,4,4,4,4**}-NH_2	100	+++	+++	+	-
	Porph-{**6,6,6,6,6,6**}-NH_2	100	+++	+++	+	-
	Porph-{**8,8,8,8,8,8**}-NH_2	100	+++	+++	+	-
octamer	**Rhod**-{**6,6,6,6,6,6,6,6**}-NH_2	100	+++	+++	+	-
	Fluo-{**8,4,8,4,8,4,8,4**}-NH_2	100	+++	+++	++	+++ (high conc.)
	Fluo-{**8,8,8,8,8,8,8,8**}-NH_2	100	+++	+++	+	-

(Figure 4) via a peptide bond. It is well-known that porphyrin derivatives are photosensitizers that are administered in photopdynamic therapy (PDT) to initiate a light-activated destruction of a variety of cell types, especially in tumors. Porphyrins have the ability to generate reactive oxygen species (ROS) after illumination with visible light, which leads to the destruction of all kinds of double bonds in biomacromolecules such as unsaturated lipids, DNA, RNA, and many more. However, most of the porphyrin derivatives are insoluble in polar solvents such as water, DMSO, or methanol making them unsuitable for *in vivo* applications. If the porphyrins can be carried into tumor cells, those can be destroyed by illumination. Therefore, the following peptoids **Porph**-{**4,4,4,4,4,4**}-NH_2, **Porph**-{**6,6,6,6,6,6,**}-NH_2, and **Porph**-{**8,8,8,8,8,8**}-NH_2 were synthesized by using building blocks **5a**{**4**}, **5a**{**6**}, and **5a**{**8**} (Scheme 1) and carboxyporphyrin **12** (*37*, see Supporting Information) to investigate whether the peptoid moiety is able to enhance the water solubility and the cellular uptake of the porphyrin. The cellular uptake of **Porph**-{**4,4,4,4,4,4**}-NH_2, **Porph**-{**6,6,6,6,6,6,**}-NH_2, and **Porph**-{**8,8,8,8,8,8**}-NH_2 was tested in primary fibroblasts and several tumor cell lines such as HeLa, COS-7, and neuroblastoma cells at a concentration of

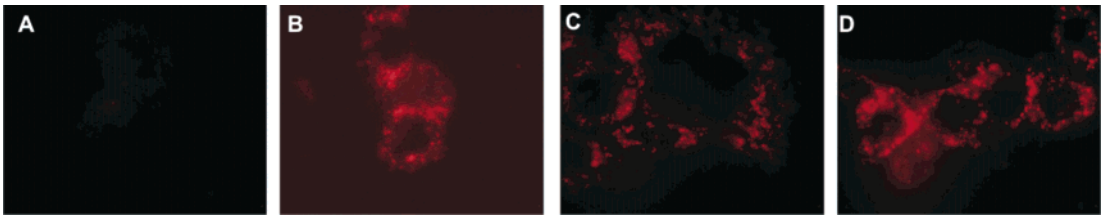


Figure 15. Confocal images of living primary fibroblasts treated as follows: A, carboxyporphyrin **12** 5 μM, 24 h; B, **Porph**-{**4,4,4,4,4,4**}-NH_2, 1 μM, 24 h; C, **Porph**-{**6,6,6,6,6,6**}-NH_2, 1 μM, 24 h; D, **Porph**-{**8,8,8,8,8,8**}-NH_2, 1 μM, 24 h.

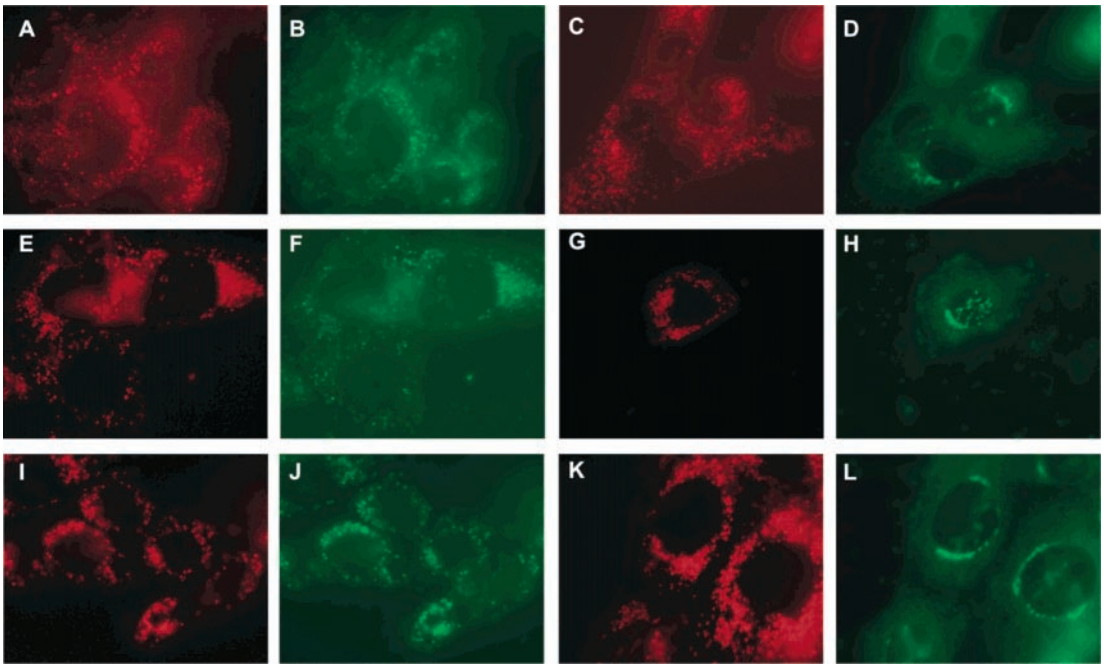


Figure 16. Confocal images of living primary fibroblasts treated as follows: A, **Porph**-{**4,4,4,4,4,4**}-NH_2, 1 μM, 24 h; B, labeling of A with Lysotracker for endosome and lysosome staining; C, **Porph**-{**4,4,4,4,4,4**}-NH_2, 1 μM, 24 h; D, labeling of C with NBD-C6-Ceramide for Golgi staining; E, **Porph**-{**6,6,6,6,6,6**}-NH_2, 1 μM, 24 h; F, labeling of E with Lysotracker; G, **Porph**-{**6,6,6,6,6,6**}-NH_2, 1 μM, 24 h; H, labeling of G with NBD-C6-Ceramide; I, **Porph**{**8,8,8,8,8,8**}-NH_2, 1 μM, 24 h; J, labeling of I with Lysotracker; K, **Porph**-{**8,8,8,8,8,8**}-NH_2, 1 μM, 24 h; L, labeling of K with NBD-C6-Ceramide.

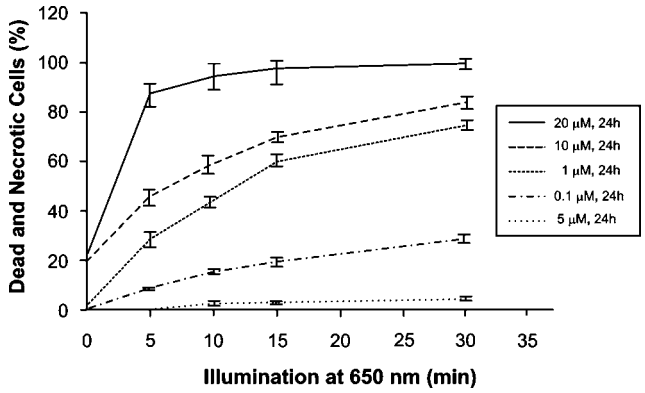


Figure 17. Quantification of the phototoxic effect of **Porph-{8,8,8,8,8,8}-NH$_2$** on primary fibroblasts. Cells were incubated with 0.1, 1, 10, and 20 μM **Porph-{8,8,8,8,8,8}-NH$_2$** and 5 μM carboxyporphyrin **12** for 24 h. Eventually, the cells were illuminated with 650 nm light for various times. Quantification of dead and necrotic cells from five independent experiments was performed after staining with propidium iodide and trypan blue. The illumination of cells in the absence of photosensitizers revealed no significant necrosis. The cells were counted in 3 × 4 random fields framed with the *Axiovision* software, and the readout was evaluated by the Student's *t* test. SD was calculated from the $n = 5$ experiments.

1−10 μM. Figure 15 shows the intracellular localization and the successful cellular uptake of all porphyrin-coupled peptoids while the unmodified carboxyporphyrin **12** was not taken up by the cells. As shown in Figure 16, **Porph-{4,4,4,4,4,4}-NH$_2$**, **Porph-{6,6,6,6,6,6,}-NH$_2$**, and **Porph-{8,8,8,8,8,8}-NH$_2$** colocalize with the endosomal compartment but with neither the Golgi apparatus nor the nucleus. After longer incubation with the *Lysotracker Green* and a chase of the lysosomal marker into the lysosomes, colocalization is not longer detectable (data not shown), revealing an endosomal accumulation.

Besides the measurement of the cellular uptake, the phototoxic effect was determined after illumination of the cells with light of 650 nm. The cells were incubated with different concentrations of **Porph-{8,8,8,8,8,8}-NH$_2$** for 24 h. A phototoxicity was already seen after 5 min of illumination, and necrosis of the cells was clearly dependent on the concentration of **Porph-{8,8,8,8,8,8}-NH$_2$** during the treatment (Figure 17). When cells are treated with 20 μM of **Porph-{8,8,8,8,8,8}-NH$_2$**, about 85% of the cells already showed severe necrosis after 5 min, while almost no cells survived the treatment for 15−30 min. Likewise, incubation with 10 μM of **Porph-{8,8,8,8,8,8}-NH$_2$** yielded 80% dead cells after 30 min.

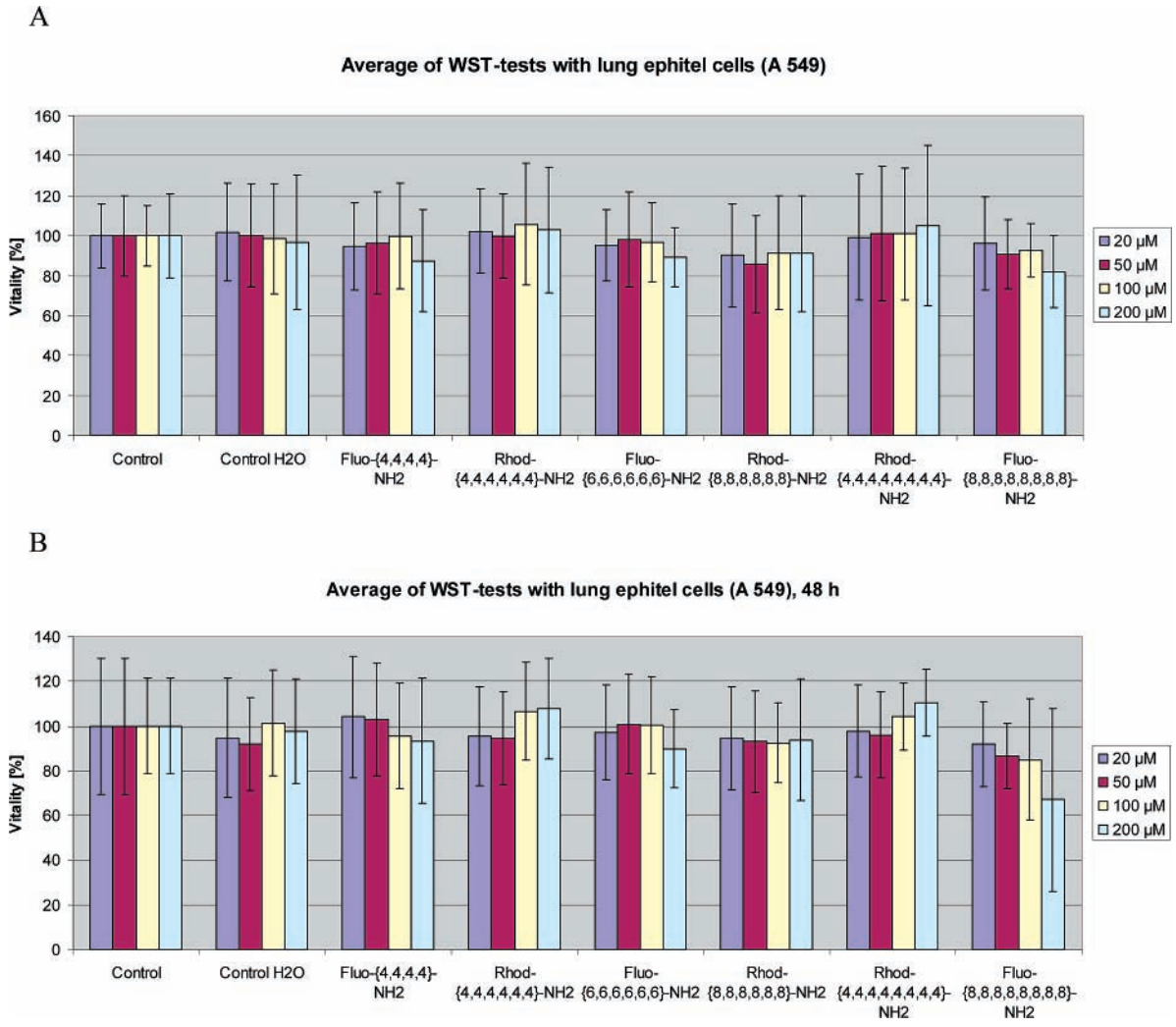


Figure 18. WST test. A. For each viability test, human epithelial lung cancer cells (A549) were grown to confluence in 96 MicroWell plates from Nunc and treated with 20, 50, 100, and 200 μM of the peptoids for 24 h at 37 °C. All experiments were carried out two to three times in quadruplicate. After incubation, the formed dyes were quantified at 450 nm by using a scanning multiwell spectrophotometer (ELISA reader). For every time point, the test was carried out twice. Untreated cells are used as positive control (100% viable), and all values from the experiment are correlated with this set of data. B. Average from WST test after incubation with the above-described peptoid concentration for 48 h.

Toxicological Tests. To verify that the synthesized peptoids could be used for in vivo applications, it is important to gain information about their toxicity toward mammalian cells. Therefore, six of the ten peptoids were tested in different cytotoxicity assays. The effects of the peptoids were investigated with the adherent human epithelial lung cancer cell line A549.

To confirm the results, three tests with different outcome or procedures were carried out. Two of the tests, MTT and WST-1, detect the viable cells by examination of the intracellular reduction potential, while the third, the LDH test, detects dead cells.

The MTT assay, which is usually used to measure cell proliferation of cancer cells, is based on the reduction of the yellow tetrazolium salt MTT (3-(4,5-dimethylthiazol-2-yl)-2,5-diphenyltetrazolium bromide) by actively growing cells to produce a blue formazan product.

The positive charge of MTT is responsible for its cellular uptake. Within the cell, the reduced pyridine nucleotide cofactor, NADH, is responsible for most MTT reduction to the blue formazan. This reduction is associated not only with mitochondria, but also with the cytoplasm and with the endosomal/lysosomal compartment and the plasma membrane (*38*). This bioreduction occurs intracellularly in viable cells only. Eventually, it can be extracted and photometrically quantified at 550 nm. The amount of formazan dye formed directly correlates to the number of metabolically active cells in the culture.

The WST-1 assay uses second-generation tetrazolium dyes that form water-soluble formazans and require an intermediate electron acceptor for reduction. The WST-1 assay is more sensitive than the MTT assay, and the results are depicted in Figure 18. WST-1, a sodium salt of 4-[3-(4-iodophenyl)-2-(4-nitrophenyl)-2*H*-5-tetrazolio]-1,3-benzene disulfonate, is oppositely charged from MTT and cannot be taken up by the cells. It was suggested that its reduction occurs at the extracellular side of the plasma membrane via trans-plasma membrane electron transport (*38*, *39*). In contrast to MTT−formazan from the MTT assay, the resulting WST-1-formazan is water-soluble and can be photometrically quantified at 450 nm. This bioreduction is largely dependent on the glycolytic production of NAD(P)H in viable cells and is thus directly correlated to the number of metabolically active cells.

In contrast the lactate dehydrogenase (LDH) assay is a marker for membrane integrity. The test is based on the measurement of cytoplasmic enzyme activity found in the supernatant of damaged cells. Lactate dehydrogenase (LDH) is a stable cytoplasmic enzyme that is present in all cells. It is rapidly released into the cell culture supernatant when the plasma membrane is damaged. It is freely floating in the cytosol, and upon membrane damage, it is released into the extracellular space, where it can reduce the tetrazolium salt INT (2-(4-iodophenyl)-3-(4-nitrophenyl)-5-phenyl-2*H*-tetrazolium chloride) to another formazan dye (*40*). LDH enzyme activity in the culture supernatant increases with the number of dead cells. The increase in supernatant LDH activity directly correlates to the amount of formed formazan.

The cells were tested in cell proliferation and viability assays according to the protocols described previously (*40*). The data shown in Figure 18 representing the results from the WST-1 test could be reproduced by the two other tests (data not shown). As shown by all viability tests, the viability of A549 cells treated with up to 200 μM of any one of the six peptoids did not differ significantly and did not increase or decrease in comparison to wild-type cells over the time period observed. This makes the peptoids suitable for the first in vivo assays.

DISCUSSION

Ten peptoids labeled with a fluorescent dye and three carriers, bioconjugated with porphyrins, were efficiently prepared using solid-phase syntheses and tested for cellular uptake in three different mammalian cell types (COS7, HeLa, human fibroblasts). Peptoids with short backbones were shown to exhibit a weaker uptake than those with long backbone lengths, with the highest ratio between uptake efficiency and cytosolic/nuclear localization being found for hexameric peptoids. In addition, a relatively short peptoid with chiral side chains also exhibited good cellular properties. Nevertheless, all carrier peptoids had cell-penetrating abilities, making these efficient structures promising transporter candidates for drug delivery.

As it is shown, no acute toxicity of the peptoids could be detected in the WST-1 assay. The results of the MTT and LDH assays (data not shown) supported this conclusion. For these tests, lung cells were taken to observe whether the transporters could be used as aerosols as well. The uptake rate was 100%.

ACKNOWLEDGMENT

This work has been performed as part of the project E1.1 of the DFG Research Center for Functional Nanostructures (CFN). Further support provided by a grant from the Ministry of Science, Research, and the Arts of Baden-Württemberg (Az: 7713.14−300). K. Schmitz was supported by the Fond der Chemischen Industrie. A special thank-you goes to Dr. Johannes Köbberling, Bayer Health Care AG, Germany, for donation of modified resins. We thank Dr. Frank Lauterwasser for supply of the monomer **5**{**1***} and Sylvia Vanderheiden for the dedicated experimental help.

Supporting Information Available: Spectroscopic and analytical data for all products not described in the text (e.g., building blocks). This material is available free of charge via the Internet at http://pubs.acs.org.

LITERATURE CITED

(1) Frankel, A. D., and Pabo, C. O. (1988) Cellular uptake of the tat protein from human immunodeficiency virus. *Cell 55*, 1189−93.

(2) Green, M., and Loewenstein, P. M. (1988) Autonomous functional domains of chemically synthesized human immunodeficiency virus tat trans-activator protein. *Cell 55*, 1179−88.

(3) Wender, P. A., Mitchell, D. J., Pattabiraman, K., Pelkey, E. T., Steinman, L., and Rothbard, J. B. (2000) The design, synthesis, and evaluation of molecules that enable or enhance cellular uptake: peptoid molecular transporters. *Proc. Natl. Acad. Sci. U.S.A. 97*, 13003−8.

(4) Fawell, S., Seery, J., Daikh, Y., Moore, C., Chen, L. L., Pepinsky, B., and Barsoum, J. (1994) Tat-mediated delivery of heterologous proteins into cells. *Proc. Natl. Acad. Sci. U.S.A. 91*, 664−8.

(5) Pepinsky, R. B., Androphy, E. J., Corina, K., Brown, R., and Barsoum, J. (1994) Specific inhibition of a human papillomavirus E2 trans-activator by intracellular delivery of its repressor. *DNA Cell Biol. 13*, 1011−9.

(6) Vives, E., Charneau, P., van Rietschoten, J., Rochat, H., and Bahraoui, E. (1994) Effects of the Tat basic domain on human immunodeficiency virus type 1 transactivation, using chemically synthesized Tat protein and Tat peptides. *J. Virol. 68*, 3343−53.

(7) Vives, E., Brodin, P., and Lebleu, B. (1997) A truncated HIV-1 Tat protein basic domain rapidly translocates through the plasma membrane and accumulates in the cell nucleus. *J. Biol. Chem. 272*, 16010−7.

(8) Derossi, D., Joliot, A. H., Chassaing, G., and Prochiantz, A. (1994) The third helix of the Antennapedia homeodomain translocates through biological membranes. *J. Biol. Chem. 269*, 10444−50.

(9) Elliott, G., and Ohare, P. (1997) Intercellular trafficking and protein delivery by a herpesvirus structural protein. *Cell 88*, 223−233.

(10) Lindgren, M., Hallbrink, M., Prochiantz, A., and Langel, U. (2000) Cell-penetrating peptides. *Trends Pharmacol. Sci. 21*, 99−103.

(11) Jeang, K. T., Xiao, H., and Rich, E. A. (1999) Multifaceted activities of the HIV-1 transactivator of transcription, Tat. *J. Biol. Chem. 274*, 28837−40.

(12) Nagahara, H., Vocero-Akbani, A. M., Snyder, E. L., Ho, A., Latham, D. G., Lissy, N. A., Becker-Hapak, M., Ezhevsky, S. A., and Dowdy, S. F. (1998) Transduction of full-length TAT fusion proteins into mammalian cells: TAT-p27Kip1 induces cell migration. *Nat. Med. 4*, 1449−52.

(13) Schwarze, S. R., and Dowdy, S. F. (2000) In vivo protein transduction: intracellular delivery of biologically active proteins, compounds and DNA. *Trends Pharmacol. Sci. 21*, 45−48.

(14) Schwarze, S. R., Hruska, K. A., and Dowdy, S. F. (2000) Protein transduction: unrestricted delivery into all cells? *Trends Cell Biol. 10*, 290−295 (review).

(15) Emi, N., Kidoaki, S., Yoshikawa, K., and Saito, H. (1997) Gene transfer mediated by polyarginine requires a formation of big carrier-complex of DNA aggregate. *Biochem. Biophys. Res. Commun. 231*, 421−4.

(16) Hallbrink, M., Floren, A., Elmquist, A., Pooga, M., Bartfai, T., and Langel, U. (2001) Cargo delivery kinetics of cell-penetrating peptides. *Biochim. Biophys. Acta 1515*, 101−9.

(17) Mi, Z., Mai, J., Lu, X., and Robbins, P. D. (2000) Characterization of a class of cationic peptides able to facilitate efficient protein transduction in vitro and in vivo. *Mol. Ther. 2*, 339−47.

(18) Ho, A., Schwarze, S. R., Mermelstein, S. J., Waksman, G., and Dowdy, S. F. (2001) Synthetic protein transduction domains: enhanced transduction potential in vitro and in vivo. *Cancer Res. 61*, 474−7.

(19) Rothbard, J. B., Garlington, S., Lin, Q., Kirschberg, T., Kreider, E., McGrane, P. L., Wender, P. A., and Khavari, P. A. (2000) Conjugation of arginine oligomers to cyclosporin A facilitates topical delivery and inhibition of inflammation. *Nat. Med. 6*, 1253−7.

(20) Wender, P. A., Rothbard, J. B., Jessop, T. C., Kreider, E. L., and Wylie, B. L. (2002) Oligocarbamate molecular transporters: design, synthesis, and biological evaluation of a new class of transporters for drug delivery. *J. Am. Chem. Soc. 124*, 13382−3.

(21) Raguse, T. L., Porter, E. A., Weisblum, B., and Gellman, S. H. (2002) Structure-activity studies of 14-helical antimicrobial beta-peptides: probing the relationship between conformational stability and antimicrobial potency. *J. Am. Chem. Soc. 124*, 12774−85.

(22) Rueping, M., Mahajan, Y., Sauer, M., and Seebach, D. (2002) Cellular uptake studies with beta-peptides. *Chem. Biochem. 3*, 257−9.

(23) Potocky, T. B., Menon, A. K., and Gellman, S. H. (2003) Cytoplasmic and nuclear delivery of a TAT-derived peptide and a beta-peptide after endocytic uptake into HeLa cells. *J. Biol. Chem. 278*, 50188−94.

(24) Rueping, M., Mahajan, Y. R., Jaun, B., and Seebach, D. (2004) Design, synthesis and structural investigations of a beta-peptide forming a 314-helix stabilized by electrostatic interactions. *Chemistry 10*, 1607−15.

(25) Wadia, J. S., and Dowdy, S. F. (2003) Modulation of cellular function by TAT mediated transduction of full length proteins. *Curr. Protein Pept. Sci. 4*, 97−104.

(26) Goff, D. A., and Zuckermann, R. N. (1992) Solid phase synthesis of highly substituted peptoid 1(2H) isoquinolinones. *Proc. Natl. Acad. Sci. U.S.A. 60*, 5748−9.

(27) Figliozzi, G. M., Goldsmith, R., Ng, S. C., Banville, S. C., and Zuckermann, R. N. (1996) Synthesis of N-substituted glycine peptoid libraries. *Methods Enzymol. 267*, 437−47.

(28) Uno, T., Beausoleil, E., Goldsmith, R. A., Levine, B. H., and Zuckermann, R. N. (1999) New submonomers for poly N-substituted glycines (peptoids). *Tetrahedron Lett. 40*, 1475−1478.

(29) Wu, C. W., Sanborn, T. J., Zuckermann, R. N., and Barron, A. E. (2001) Peptoid oligomers with alpha-chiral, aromatic side chains: effects of chain length on secondary structure. *J. Am. Chem. Soc. 123*, 2958−63.

(30) Wu, C. W., Kirshenbaum, K., Sanborn, T. J., Patch, J. A., Huang, K., Dill, K. A., Zuckermann, R. N., and Barron, A. E. (2003) Structural and spectroscopic studies of peptoid oligomers with alpha-chiral aliphatic side chains. *J. Am. Chem. Soc. 125*, 13525−30.

(31) Peretto, I., Sanchez-Martin, R. M., Wang, X. H., Ellard, J., Mittoo, S., and Bradley, M. (2003) Cell penetrable peptoid carrier vehicles: synthesis and evaluation. *Chem. Commun.* 2312−3.

(32) Kirshenbaum, K., Barron, A. E., Goldsmith, R. A., Armand, P., Bradley, E. K., Truong, K. T., Dill, K. A., Cohen, F. E., and Zuckermann, R. N. (1998) Sequence-specific polypeptoids: a diverse family of heteropolymers with stable secondary structure. *Proc. Natl. Acad. Sci. U.S.A. 95*, 4303−8.

(33) Lundberg, P., Magzoub, M., Lindberg, M., Hallbrink, M., Jarvet, J., Eriksson, L. E., Langel, U., and Graslund, A. (2002) Cell membrane translocation of the N-terminal (1−28) part of the prion protein. *Biochem. Biophys. Res. Commun. 299*, 85−90.

(34) Richard, J. P., Melikov, K., Vives, E., Ramos, C., Verbeure, B., Gait, M. J., Chernomordik, L. V., and Lebleu, B. (2003) Cell-penetrating peptides. A reevaluation of the mechanism of cellular uptake. *J. Biol. Chem. 278*, 585−90.

(35) Kichler, A., Leborgne, C., Danos, O., and Bechinger, B. (2007) Characterization of the gene transfer process mediated by histidine-rich peptides. *J. Mol. Med 85*, 191−201.

(36) Mason, A. J., Gasnier, C., Kichler, A., Prevost, G., Aunis, D., Metz-Boutigue, M. H., and Bechinger, B. (2006) Enhanced membrane disruption and antibiotic action against pathogenic bacteria by designed histidine-rich peptides at acidic pH. *Antimicrob. Agents Chemother. 50*, 3305−11.

(37) Balaban, T. S., Eichhöfer, A., and Lehn, J. M. (2000) Self-assembly by hydrogen bonding and pi-pi interactions in the crystal of a porphyrin - Attempts to mimic bacteriochlorophyll c. *Eur. J. Org. Chem.* 4047−4057.

(38) Berridge, M. V., Herst, P. M., and Tan, A. S. (2005) Tetrazolium dyes as tools in cell biology: new insights into their cellular reduction. *Biotechnol. Annu. Rev. 11*, 127−52.

(39) Berridge, M. V., and Tan, A. S. (1993) Characterization of the cellular reduction of 3-(4,5-dimethylthiazol-2-yl)-2,5-diphenyltetrazolium bromide (MTT): subcellular localization, substrate dependence, and involvement of mitochondrial electron transport in MTT reduction. *Arch. Biochem. Biophys. 303*, 474−82.

(40) Wörle-Knirsch, J. M., Pulskamp, K., and Krug, H. F. (2006) Oops they did it again! Carbon nanotubes hoax scientists in viability assays. *Nano Lett. 6*, 1261−8.

BC0602073

A Stereocomplex Platform Efficiently Detecting Antigen−Antibody Interactions

Takeshi Serizawa,*[,†,‡] Yuya Nagasaka,[†,§] Hisao Matsuno,[||] Masakazu Shimoyama,[†,⊥] and Kimio Kurita[§]

Research Center for Advanced Science and Technology (RCAST), The University of Tokyo, 4-6-1 Komaba, Meguro-ku, Tokyo 153-8904, Japan, Precursory Research for Embryonic Science and Technology (PRESTO), Japan Science and Technology Agency (JST), 4-1-8 Honcho, Kawaguchi, Saitama 332-0012, Japan, Graduate School of Science and Technology, Nihon University, 1-8-14 Surugadai, Kanda, Chiyoda-ku, Tokyo 101-8308, Japan, Komaba Open Laboratory, The University of Tokyo, 4-6-1 Komaba, Meguro-ku, Tokyo 153-8904, Japan, and Department of Applied Chemistry, Faculty of Science and Engineering, Chuo University, 1-13-27 Kasuga, Bunkyo-ku, Tokyo 112-8551, Japan. Received July 22, 2006; Revised Manuscript Received November 15, 2006

Ultrathin poly(methyl methacrylate) (PMMA) stereocomplex films with macromolecularly double-stranded regular nanostructures were prepared by layer-by-layer assembly of isotactic and syndiotactic PMMAs on solid surfaces. Antibodies were immobilized through the Fc region-capturing protein A, which had been physically adsorbed on the complex film, and the binding of antigens to immobilized antibodies was quantitatively investigated by the quartz crystal microbalance technique. Greater amounts of protein A with native forms were adsorbed on the complex film than those on conventional single-component PMMA films. Antibodies with high target-binding activities were also immobilized on the complex film. A greater amount of antigens could be detected on the complex film. The activity of protein A was maintained on the complex for a long time even within a dried state. The mechanism for the preservation of protein native forms on the complex surface was speculated by analyzing the physical adsorption of proteins with various secondary structures. Stereocomplex films can be utilized as novel coating nanomaterials for efficiently detecting protein−protein interactions.

INTRODUCTION

Efficient and reproducible observations of the interaction between proteins and biomolecules including target proteins, peptides, DNAs, and sugars on solid material surfaces are essential to develop reliable immunoassay (*1*−*3*) and high-throughput microarray/chip (*4*, *5*) systems. The first step for the observation is the immobilization of proteins on material surfaces. Covalent or noncovalent linkages based on site-specific or nonspecific interactions between proteins and surfaces have been used to stably immobilize proteins on material surfaces (*6*). The suitable immobilization method is selected on the basis of protein species and surface chemical compositions. The key technology among these methods is the maintenance of protein active forms after the immobilization on solid surfaces.

The detection of antigen−antibody interactions on material surfaces is one of the important requirements for immunoassay and microarray/chip. For these applications, antibodies have to be immobilized on surfaces, as those can bind efficiently to antigens. In this case, antigen-binding sites of antibodies should be oriented ideally to outside of the surface. For the simple noncovalent immobilization, physical adsorption of antigens or antibodies on nitrocellulose membrane (*7*), polystyrene surfaces, polylysine- or nitrocellurose-modified glass slides (*8*), and ω-functionalized self-assembled monolayers (*9*) have been employed. However, these methods lack defined orientations of proteins. In order to overcome this problem, site-specific protein A (PA) (or protein G)-Fc interactions (*10*−*15*), avidin−biotin interactions (biotinylated antibody) (*10*, *16*), duplex formation of DNAs (*17*), metal coordination (*18*), and other interactions (*19*, *20*) have been utilized for protein immobilization.

We originally developed ultrathin polymer films composed of double-stranded helical stereocomplexes (SCs) (*21*−*26*), in which isotactic (it) poly(methyl methacrylate) (PMMA) is surrounded by twice the length of syndiotactic (st) PMMA (*27*, *28*). Layer-by-layer (LbL) assembly (*29*, *30*) of stereoregular polymers of methacrylates on material surfaces resulted in the stepwise formation of SCs on surfaces, thus fabricating ultrathin complex films with regular nanostructures at macromolecular level. Since LbL assembly is simply and readily demonstrated in wet processes, ultrathin SC films with controllable thicknesses can be fabricated on various material surfaces, when substrates never dissolve into acetonitrile, a typical assembly solvent for the complex.

Our previous papers quantitatively analyzed physical adsorption of proteins such as bovine serum albumin (*31*), human serum albumin (HSA), fibrinogen, and lysozyme (*32*) on PMMA films and revealed that (1) greater amounts of proteins adsorbed on the SC film surface than those on conventionally prepared spin-coated films composed of a single PMMA component, (2) apparent adsorption constants of proteins on the complex surface were smaller than those on the conventional film, and (3) denaturation of physically adsorbed proteins might be suppressed on the complex surface, although the mechanism for the interaction between the complex surface and proteins has not been discussed. Furthermore, interactions of human whole blood with the complex surface supported un-denaturing of serum proteins adsorbed (*33*). These observations indicated that the protein adsorption property on polymer films is strongly dependent on surface-assembly structures of polymers. Note that the static contact angle of the complex surface is located between it- and st-PMMA films, thereby indicating that the film's

* To whom correspondence should be addressed, at Research Center for Advanced Science and Technology (RCAST), The University of Tokyo, Japan. Phone & Fax: +81-3-5452-5224; E-mail: t-serizawa@bionano.rcast.u-tokyo.ac.jp.

† RCAST, The University of Tokyo.

‡ JST.

§ Nihon University.

|| Komaba Open Laboratory, The University of Tokyo.

⊥ Chuo University.

10.1021/bc060225k CCC: $37.00 © 2007 American Chemical Society
Published on Web 02/14/2007

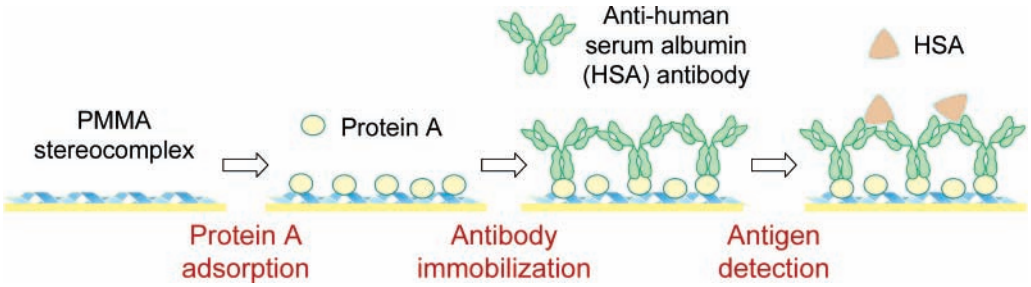


Figure 1. A schematic representation of the detection of antigen−antibody interactions on the double-stranded SC film.

Table 1. Analytical Data of Antigen−Antibody Interactions on Various Surfaces

surface	PA adsorbed/ ng cm^{-2}	Ab immobilized/ ng cm^{-2}	PA used[a]/ %	Ab + HSA[b]/ ng cm^{-2}	HSA[c] detected/ ng cm^{-2}	Ab used[d]/ %
SC	202 ± 11	457 ± 34	60	583 ± 14	126	62
it-PMMA	109 ± 25	318 ± 27	77	384 ± 30	66	50
st-PMMA	123 ± 19	320 ± 23	69	383 ± 25	63	45
at-PMMA	120 ± 11	311 ± 21	66	352 ± 16	41	32
gold	211 ± 19	367 ± 27	46	438 ± 27	71	43

[a] Percent PA used for the Ab immobilization estimated by the equation that the average molar number of Ab immobilized was divided by that of PA adsorbed, assuming 1:1 binding. [b] The sum of Ab immobilized and HSA detected. [c] Estimated by the difference of the Ab + HSA average and the immobilized Ab average. [d] Percent Ab used for the HSA detection estimated by the equation that the molar number of HSA detected was divided by the average molar number of Ab immobilized, assuming 1:1 binding.

hydrophobicity cannot interpret these observations (*21*). Since the complex film can be fabricated not only on inorganic surfaces such as glass and gold but also on organic surfaces such as polystyrene and poly(ethylene terephthalate), the complex film surface has the potential for novel platforms that efficiently detect antigen−antibody interactions, when suitable target-capturing proteins are utilized for the direct immobilization on the complex surface.

In this study, we analyzed the detection of antigens using antibodies immobilized on PA, which had been physically adsorbed on ultrathin SC films composed of stereoregular PMMA. A combination of HSA and anti-HSA rabbit polyclonal antibody (Ab) was selected as a typical model. The results were compared to conventionally prepared spin-coated films composed of a single stereoregular PMMA and a gold surface. On the basis of amounts of HSA detected on Ab-immobilized PA surfaces with other spectral and surface topological data, PA denaturing and Ab orientation were discussed. It was suggested that the physical adsorption of PA with native forms on the complex film surface is the key step for favorable oriented immobilization of antibodies through PA and subsequent antigen detection. Other antigen−antibody combinations supported the advantage of the complex surface. In order to reveal the mechanism, other proteins were adsorbed on PMMA films, and effects of the secondary structure were analyzed. Our system is schematically shown in Figure 1.

MATERIALS AND METHODS

Film Fabrication. PA adsorption, antibodies immobilization, and antigen detection were quantitatively analyzed by a 9 MHz quartz crystal microbalance (QCM) substrate with gold electrodes (4.5 mm diameter), which estimates the mass of proteins (Δm) from frequency decreases ($-\Delta F$) as follows: $-\Delta m$ [ng] $= 0.87 \times \Delta F$ [Hz] (*34*). The potential of the QCM method for the detection of antigen−antibody interactions has already been demonstrated (*15*). PMMA SC films were prepared by the alternate immersion of substrates into acetonitrile solutions of it-PMMA (M_n 19 000, M_w/M_n 1.10, >98% isotacticity) (Polymer Source) and st-PMMA (M_n 18 600, M_w/M_n 1.23, >85% syndiotacticity) (Polymer Source) at 1.7 mg mL^{-1} for 5 min each at ambient temperature, following methods previously reported (*21*). After the 14 step assembly (7 steps for each PMMA), the mean film thickness was estimated to be 4.8 nm. Atactic (at) PMMA (M_n 22 500, M_w/M_n 1.03) was purchased from Polysciences. Single-component films with 7 nm thickness were prepared by a conventional spin-casting method using a chloroform solvent (1.7 mg mL^{-1}, 2000 rpm).

Antigen−Antibody Interaction. On the film surface, PA (42 kDa, *Staphylococcus aureus*, ICN Pharmaceutical) was physically adsorbed at 1 μM in PBS (pH 7.4) for 1 h at 37 °C, and Ab (160 kDa, Sigma-Aldrich) was immobilized at 1 μM in PBS for 1 h at 37 °C. Subsequently, specific HSA (69 kDa, human serum, fatty acid and globulin free, Sigma-Aldrich) or nonspecific bovine serum albumin (66 kDa, bovine serum, fatty acid and globulin free, Sigma-Aldrich; BSA) was bound from PBS solutions for 1 h at 37 °C to immobilized antibodies and analyzed for suitable concentrations. After immersion of substrates into protein solutions, substrates were rinsed with PBS and ultrapure water and dried with nitrogen gas. Then, frequencies were measured in air, so as not to weigh solvents. PA amounts were measured in air in all experiments, since Ab were successfully immobilized in the following steps. However, antigen amounts were measured without drying (and measuring ΔF) at Ab steps, so as not to lose Ab activities (in fact, Ab in dried state did not detect antigens). Therefore, antigen amounts were estimated by the difference of total Ab immobilized plus antigen detected amounts, and Ab immobilized amounts (see Table 1). For other antigen−antibody combinations, fibrinogen (Fib) (EMD Bioscience)/anti-Fib goat antibody (Rockland Immunochemicals), avidin (Av) (Zymed Laboratories)/anti-Av rabbit antibody (Polysciences), and human chorionic gonadotropin (hCG) (Cell Sciences)/anti-hCG rabbit polyclonal antibody (Rohto Pharmaceutical) were used. The antibodies were similarly immobilized on PA-coated films at 1 μM at 37 °C, and then the antigens were detected.

Characterization Methods. The surface topology at each step was analyzed by a tapping-mode atomic force microscope (AFM) (SPM-9500J3, Shimadzu) in air at ambient temperature. The mean roughness (R_a) of each surface was estimated. The apparent binding constant between antibodies and antigens on surfaces was estimated using the following equation:

$$A = \frac{K_{app} A_{max}}{1 + K_{app}[\mathrm{HSA}]}[\mathrm{HSA}]$$

where A is the amount of HSA bound, A_{max} is the maximum A, K_{app} is the apparent binding constant. Apparent adsorption constants of PA on polymer surfaces were similarly estimated by using the aforementioned equation, as shown in previous studies. (*31, 32*) Attenuated total reflection (ATR) spectra of PA adsorbed were obtained using the refractive surface of 100 nm thick gold-coated poly(ethylene terephthalate) substrates (Tanaka Precious Metals, Japan) with a Perkin-Elmer Spectrum One (U.S.A.) in air at ambient temperature. Interferograms were co-added 50 times and Fourier transformed at a resolution of 4 cm^{-1}. Experiments were repeated three times. Note that *S*/*N* ratios of spectra obtained from the substrate were smaller than those directly obtained from the QCM gold surface.

Physical Adsorption of Proteins. Physical adsorption of HSA, citrate synthase (52 kDa, porcine heart, Sigma-Aldrich; cit. synth), horseradish peroxidase (44 kDa, horseradish, Sigma-Aldrich; HRP), cytochrome c (12 kDa, horse heart, Sigma-Aldrich; cyto. c), alkaline phosphatase (94 kDa, *E. coli*, Wako; ALP), carbonic unhydrase (30 kDa, bovine erythrocytes, Sigma-Aldrich; CA), α-chymotrypsin (25 kDa, bovine pancreas, Wako; α-CTP), green fluorescent protein (27 kDa, aeqorea victoria, prepared by our group; GFP), avidin (67 kDa, egg white, nacalai tesque), and superoxide dismutase (62 kDa, bovine erythrocytes, Sigma-Aldrich; sup. dismut) at 1 μM in PBS (except for ALP and β-Gal) at 37 °C was similarly analyzed by using the QCM method. ALP was dissolved in 50 mM Tris-HCl (pH 9.0), and β-Gal was dissolved in 50 mM phosphate buffer (pH 7.4) containing 1 mM $MgCl_2$, because the enzymatic activity will be analyzed using these solutions in the near future. Although we have already analyzed the physical adsorption of HSA on the SC film (*32*), it was analyzed again because of the difference in polymer sources. The secondary structures of these proteins were obtained from the web site of Protein Data Bank (PDB, http://www.rcsb.org/pdb/home/home.do). Experiments were repeated at least three times.

RESULTS AND DISCUSSION

Protein A Adsorption on Surfaces. Direct immobilization of antibodies on polymer films is the simplest way for detecting antigens on surfaces. Since the SC film has the potential to suppress the antibody denaturing by physical adsorption, we expected efficient detection of antigens using the antibody-immobilized complex film. Therefore, the antibody immobilization on PMMA films based on physical adsorption and antigen detected was investigated as the first system. However, antigens did not bind to the antibodies (a level of nonspecific adsorption), indicating that directed orientation of antibodies could not be realized by the simple adsorption on solid PMMA films (data not shown). Accordingly, we selected PA, which specifically binds to the Fc region of IgG, as an antibody-capturing protein, and PA was physically adsorbed on PMMA films, following previous studies (*10*−*15*). In this case, the amount and activity of immobilized PA is crucial for antibody immobilization and subsequent antigen detection.

The amounts of PA physically adsorbed on SC film surfaces, each component film, at-PMMA, and the bare gold of the QCM substrate are summarized in Table 1. These amounts were almost saturated at 1 μM and are reasonable when we consider monolayer adsorption of proteins (*35, 36*). Greater amounts of PA adsorbed on the complex film at the same PA concentration when compared to other PMMA films. The aforementioned observation is consistent with our previous results, in which greater amounts of serum proteins tend to adsorb on complex surfaces (*31, 32*). The amounts of PA on the gold surface were the same as those of the complex, within experimental error. Accordingly, the amount of PA adsorbed was strongly dependent on the film surface component.

Antibody Immobilization on Protein A-Coated Surfaces. The amounts of Ab immobilized on PA-coated surfaces and the percent of PA used for the Ab immobilization are shown in Table 1 (the percentage was estimated by assuming 1:1 binding between PA and Ab). The component obviously affected the amount of immobilized antibodies. The greatest amount of Ab was immobilized on the complex film coated with PA. The amount of Ab immobilized on the complex was 1.5 times greater than the amount observed on other PMMA films. In addition, the Ab amount on gold was clearly smaller than the amount on the complex, suggesting that certain amounts of PA adsorbed on gold were functionally denatured (this is also supported by spectral data; see below). Surface coverages of IgG were estimated to be 550 ng cm^{-2} and 200 ng cm^{-2} for all "end-on" (Fc closer to the surface) and "side-on" orientations, respectively (*37*). Therefore, it is suggested that the present surfaces are covered by Ab monolayer with different orientations. These observations indicate that the PMMA surface composed of the double-stranded SC is suitable to immobilize greater amounts of Ab through the physically adsorbed PA underlayer at the same protein concentrations.

It is noted that all PA adsorbed on polymer film surfaces are not necessary to interact with Ab, because the molecular size of PA (M_w 42 kDa) is much smaller than that of Ab (M_w 160 kDa), as schematically drawn in Figure 1. When we compare the percent of PA used for the Ab immobilization between the complex and gold surfaces, the former was estimated to be 60% and the latter was 46%, indicating that greater percents of PA adsorbed on the complex were used for the Ab immobilization. Since Ab immobilized on the complex more efficiently detects HSA than those on gold (see the percent Ab used for HSA detection in Table 1, as discussed below), favorable immobilization of Ab was not realized on gold. This means that the specific interaction between PA and the Fc region might not occur due to PA denaturing, followed by the fact that antigen HSA cannot access the binding site of Ab immobilized on PA-coated gold surfaces. On other homogeneous PMMA surfaces, greater percents of PA captured Ab in comparison to that on the complex. This observation is possibly due to the reduced steric hindrance during Ab immobilization, because the amount of PA adsorbed was smaller than that on the complex. However, the percents of Ab used for capturing HSA on homogeneous films were similarly smaller than that on the complex, thus suggesting unfavorable Ab orientation.

Antigen Detection Using Antibody-Immobilized Surfaces. Detecting amounts of antigen HSA at the same concentration (1 μM) and the percent Ab used for the HSA detection, which was estimated by assuming that a single Ab can capture a single HSA due to steric hindrance (although Ab has two sites for antigens), is also summarized in Table 1. Significantly, 2 to 3 times greater total amounts of HSA could be detected on the complex, which is significant when compared to other PMMA films and gold. Detected amounts were clearly greater than those of nonspecifically adsorbed BSA (approximately 23 ng cm^{-2}), thereby indicating that HSA interacted specifically with surface-immobilized Ab. The PA underlayer was used to immobilize Ab, and then it possibly blocked nonspecific protein adsorption. On the complex, the percent of Ab used for HSA detection was greatest in all surfaces. These observations indicate that greater amounts of Ab were immobilized on the complex, and that complex-immobilized Ab worked efficiently. Accordingly, the amount of HSA detected on the complex was maximal, even though the polymers had the same chemical structure.

In order to obtain surface topographic data of the present stepwise process, the surfaces were observed by AFM, as shown in Figure 2. AFM images revealed that the mean roughness of surfaces of the QCM, SC-coated, PA-adsorbed, Ab-immobilized,

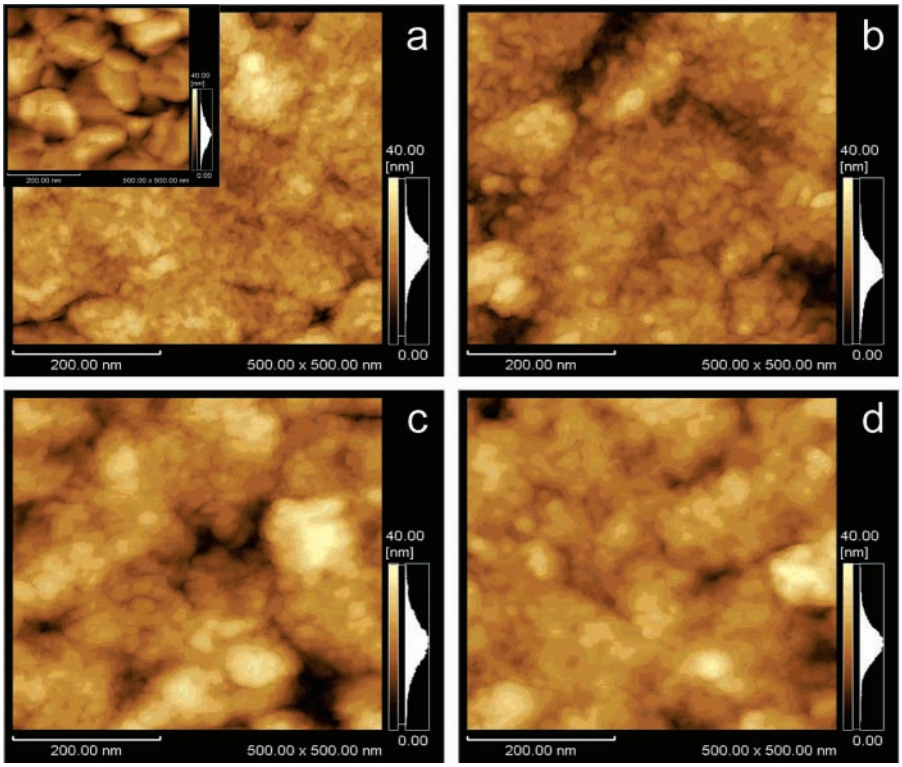


Figure 2. AFM images of (a) the SC surface, (b) the PA-adsorbed surface, (c) the Ab-immobilized surface, and (d) the surface after HSA detection. The inset in (a) shows the bare QCM surface.

and HSA (1 μM)-detected substrates were 5.6, 3.6, 3.7, 4.7, and 3.5 nm, respectively. The roughness of the gold QCM surface was diminished by the SC coating. The adsorption of PA increased the roughness of 0.1 nm. Then, the immobilization of Ab resulted in the roughness increase of 1.0 nm. Since Ab has a nonspherical extremely distorted shape, this roughness increase suggested the Ab coverage. The HSA binding regenerated the smooth surface, which is reasonable when we consider that smaller HSA covered the Ab-immobilized surface based on antigen−antibody interactions. These observations strongly suggest layer-by-layer monolayer immobilization and detection of proteins.

The dependence of HSA detected against the HSA concentration was analyzed to understand the potential for antigen detection on the SC surface, as shown in Figure 3. The dependences for all surfaces were saturated against the HSA concentration. It is obvious that detected values on the complex are greater than those detected on other conventional surfaces. Assuming a Langmuirian-type adsorption, data were fitted to obtain the apparent binding constant (K_{app}) and the maximum detecting amount (A_{max}), which can be converted to the maximum percent Ab used for HSA detection. The coefficient of variation of the fitting for the complex was 0.93. K_{app} was estimated to be 2.02×10^7 M^{-1}, which would be reasonable for the present antigen−antibody combinations. A_{max} was also estimated to be 128 ng cm^{-2}, which corresponds to the maximum percent to be 64%. On the contrary, the coefficients of variation for it-PMMA and gold were 0.66 and 0.54, respectively, Since these fittings for it-PMMA and gold seemed to be unreliable, parameters were not discussed.

The SC surface has the unique potential for maintaining protein functions. The activity of PA was surprisingly maintained even though complex films coated with PA were stored for 10 days under a dried state, as shown in Figure 4. Even after 10 days in a silica gel box at ambient temperature, Ab was similarly immobilized and detected HSA as freshly prepared. However, as expected, the detected amounts on it-

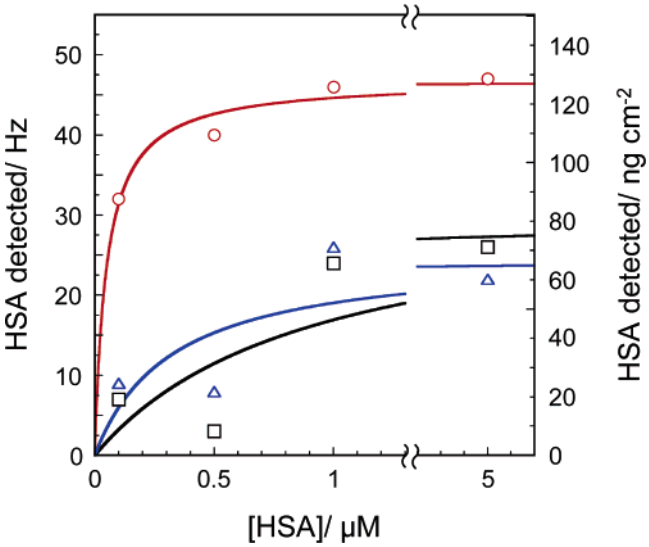


Figure 3. Dependences of the HSA concentration against HSA detected on the SC (red), it-PMMA (black), and the QCM gold (blue) surfaces. Lines show the fitting to a Langmuir isotherm.

PMMA and gold decreased to 25% and 54%, respectively. These observations mean that PA denaturation after drying was suppressed on the complex. Accordingly, the SC surface has the potential for maintaining the activity of physically adsorbed proteins. It is important to maintain the activity of proteins adsorbed on substrates for the long-term preservation of diagnostic materials and other biorelated materials. These stabilizing activities of the complex surface will be caused by the fact that PA with native forms adsorbed on the complex, as shown below. The denaturing of proteins that initially adsorbed with denatured forms on other surfaces might be accelerated in air atmosphere. ATR spectra at the amide I region of PA adsorbed on the complex hardly changed after 10 days storage (see below), supporting the maintenance of PA functions. More

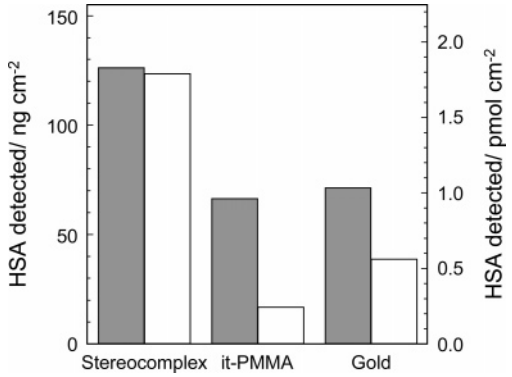


Figure 4. Amounts of detected HSA on each surfaces after adsorbed PA was maintained for 10 days in air. Gray and open bars show the detections as prepared and after 10 days, respectively.

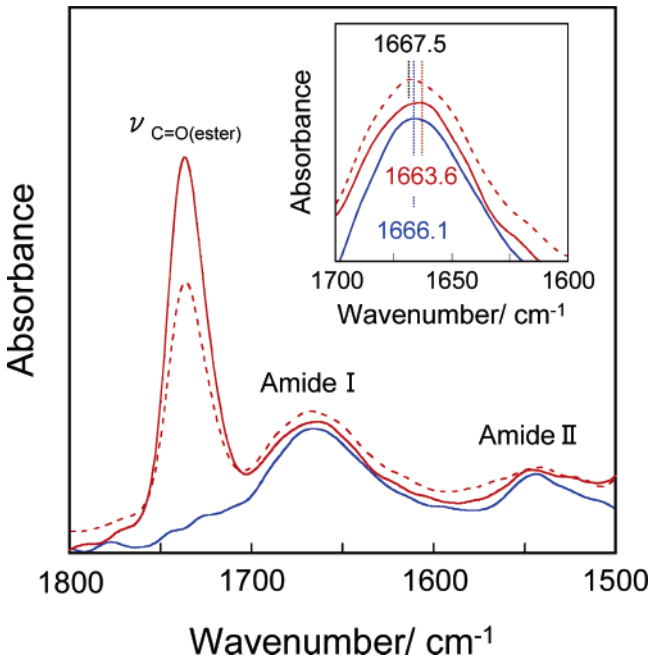


Figure 5. ATR spectra of PA adsorbed on the SC (red) and the gold QCM surface (blue), and denatured PA adsorbed on the SC (dotted).

details regarding the aforementioned dry storage of adsorbed proteins will be investigated in the near future.

Other antigens such as Fib, Av, and hCG (0.5 μM) were similarly detected using corresponding antibodies immobilized on PA-coated SC and it-PMMA surfaces. Detecting amounts on the former surface were analyzed to be 328, 129, and 148 ng cm^{-2}, while those on the latter surface were analyzed to be 252, 85, and 47 ng cm^{-2}, respectively. In all combinations, detecting amounts on the complex were clearly greater than those on it-PMMA. Accordingly, we found that the SC surface is generally valuable to detect antigen−antibody interactions.

Structural Analysis of Protein A Adsorbed on Solid Surfaces. The biological activity of the SC should be derived from the non-denaturing of PA adsorbed on complex surfaces. The long-term maintenance of PA activity is also thought to be derived from the initial non-denaturing adsorption. Therefore, the denaturing of adsorbed PA was analyzed by using ATR spectra, following previous studies (*38*−*40*). ATR spectra at the amide I region (1600−1700 cm^{-1}) of PA also supported the non-denaturation of PA on the complex, as shown in Figure 5. The peak position on the complex was observed at 1663.6 ± 0.9 cm^{-1}. On the other hand, that on gold was observed at 1667.1 ± 1.2 cm^{-1} and was the same as that for denatured PA adsorbed on the complex (1667.8 ± 0.4 cm^{-1}) and gold (1667.4 ± 1.8 cm^{-1}), respectively, within experimental error (PA was denatured in an acidic solution of pH 1 for 5 min). Previous studies suggest that peak positions for an ordered α-helix could be observed at a relatively smaller wavenumber than those for unordered α-helices and random coils (*41*−*43*). Accordingly, the aforementioned observations strongly suggest that PA on gold was relatively denatured compared to that on the complex. A greater amount of ordered α-helices in PA might be maintained on the complex.

The amide I peak position of PA on the complex after 10 days storage (1662.9 ± 1.1 cm^{-1}) was the same as that as prepared within experimental error, suggesting that changes in the ordered structure were not detected. This observation is consistent with the aforementioned maintenance of PA activities. It is noted that the decrease in PA activities on gold after storage was not supported by amide I peak shifts, possibly because of the detection limitation of protein structural changes with ATR spectra. As a consequence, ATR spectra suggested that PA native forms were maintained after the immobilization on the complex surface.

Amide I peak positions from adsorbed PA spectra obtained by an ATR method were relatively shifted to higher wavenumbers, compared to those from native PA powder (1652.6 ± 0.2 cm^{-1}). This observation is possibly due to changes in hydration states of PA on surfaces, as similarly shown in a previous study (*44*). In fact, the amide I peak position of denatured PA powder was adequately observed at 1655.4 ± 0.6 cm^{-1} and was slightly greater than that from native PA. Therefore, the aforementioned discussion about relative peak shifts for denatured PA on surfaces would be reliable.

Mechanistic Speculation of Unique Protein Adsorption on the Stereocomplex Surface. It is necessary to speculate the reason that proteins are comfortable on the complex surface. Since the hydrophobicity of the complex surface ranges between it- and st-PMMAs (*22*, *45*), the hydrophobicity must be negligible. Furthermore, since amounts of physically adsorbed proteins such as BSA (*31*), HSA, fibrinogen, lysozyme (*32*), and the present PA, which are composed of different amino acid sequences, have been ordinarily greater on the SC surface than homogeneous films; therefore, specific functional groups on protein surfaces (as well as on film surfaces) that are related to protein physical adsorption can also be negligible. On the other hand, it has been observed that apparent adsorption constants of serum proteins for the complex were ordinarily smaller than those for homogeneous films (*31*, *32*). The adsorption isotherms of PA for the complex and it-PMMA are shown in Figure 6 and were fitted to the Langmuirian adsorption to obtain adsorption constants, following our previous studies (*31*, *32*). In fact, the adsorption constant of PA for the complex was estimated to be 4.8 × 10^7 M^{-1} (coefficient of variation, 0.84) and was also smaller than 7.5 × 10^7 M^{-1} for it-PMMA (coefficient of variation, 0.94). Since adsorption constants are composed of the sum of individual interactions such as hydrogen bonding, hydrophobic, and van der Waals interactions of proteins against PMMAs, the greater numbers of contacting points are necessary for greater adsorption constants.

To interpret these interfacial phenomena, we focus on the difference in regular conformations of the film surface and proteins. The quantitative QCM analysis as well as other analytical data supported that almost all it-PMMAs on the film surface formed the SC with st-PMMAs, thus forming a 9/1 double-stranded helical assembly (*21*, *28*). On the contrary, homogeneous films simply prepared by spin-casting without thermal treatment possibly have disordered surface structures, although it- and st-PMMAs partially have 10/1 or 5/1-helical and planer zigzag or glide-plane structures, respectively (*46*). To adsorb proteins with greater adsorption constants on the

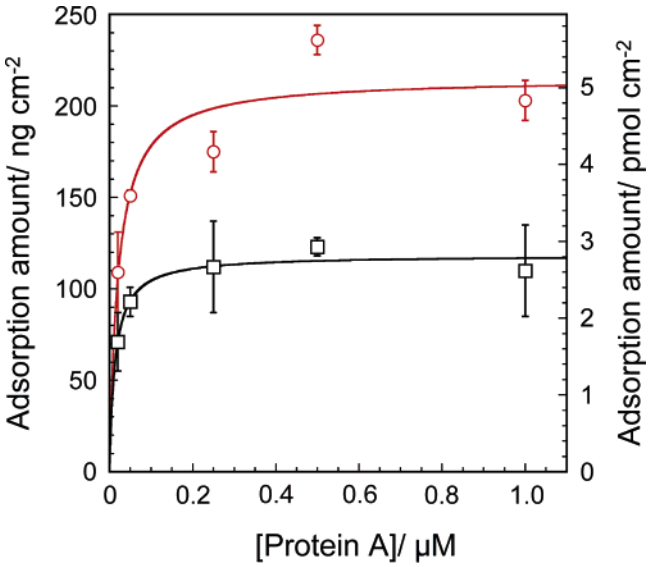


Figure 6. Adsorption isotherms for PA on the SC (red) and it-PMMA (black) surfaces.

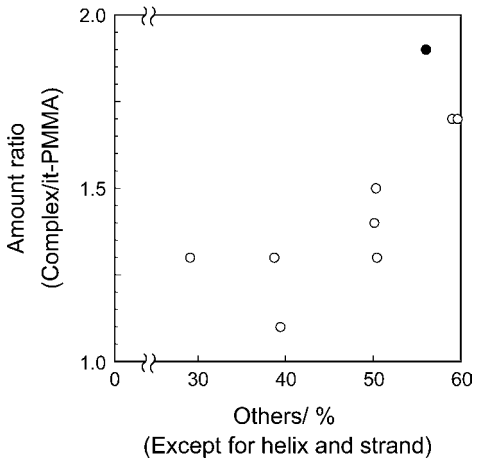


Figure 7. Dependence of the ratio of protein amounts adsorbed on the SC and it-PMMA surfaces. To estimate the ratio, the adsorption amount on the complex was divided by that on it-PMMA. Closed symbol shows the ratio of PA.

disordered surface, multiple interactions are necessary. Therefore, entropic disadvantages of the surface polymer for protein adsorption have to be compensated by enthalpy gain through the multiple interactions. The greater numbers of the interaction between the surface and PA should result in denaturing of PA native forms, followed by unfavorable Ab orientation and smaller percent of Ab used for HSA detection. In fact, the amount of PA adsorbed on gold, which has an ordered surface structure, was almost the same as that on the complex. This observation also supports the regular conformation effect of the surface on protein physical adsorption. It is, however, noted that PA adsorbed on gold was denatured by strong electrostatic interactions with free electrons on gold surfaces.

The secondary structure of proteins is the other parameter for discussing protein physical adsorption. In order to understand effects of the secondary structure on the difference in adsorption amounts on the complex and it-PMMA surfaces, we selected ten proteins (HSA (*47*), cit. synth (*48*), HRP (*49*), cyto. c (*50*), ALP (*51*), CA (*52*), α-CTP (*53*), GFP (*54*), avidin (*55*), and sup. dismut (*56*)) with different secondary structures for adsorption experiments. Amounts of proteins adsorbed at 1 μM with secondary structures, molecular weights, shapes assuming a rectangular parallelepiped, and expected adsorption amounts assuming monolayer coverage were summarized in Table 2. Except for cyto. c and α-CTP, which were ignored because they adsorbed with multilayers (the adsorption amounts on it-PMMA and the complex exceeded expected monolayer full coverage, respectively), adsorption amounts of proteins were greater on the complex than it-PMMA. These results revealed that the ratio of the amounts of adsorbed proteins on the complex and it-PMMA was independent of the secondary structure of the helix and sheet, molecular weights, and shapes. On the contrary, the ratio tended to increase with an increase in other structures such as random coil and turn, as shown in Figure 7. It is obvious that random coil is a disordered structure in proteins. Although it is difficult to conclude that the use of bulk secondary structures is reasonable to discuss protein physical adsorption, Figure 7 clearly demonstrated the relationship between the ratio and the other structure. It is noted that PA contains 56% other structures (*57*). In fact, the ratio was estimated to be 1.9, confirming the relationship. Accordingly, disordered conformation effects of protein structures as well as polymer surfaces were observed. The aforementioned advantage of the complex surface, which has regular conformations compared to conventional polymer film surfaces, was also supported.

CONCLUSIONS

Stepwise processes comprising the fabrication of functional ultrathin films, PA adsorption, Ab immobilization, and antigen detection were quantitatively monitored by the QCM method. We newly developed the SC platform for efficiently detecting antigen−antibody interactions. Amounts of adsorbed PA, immobilized antibodies, and detected antigens were greatest on the complex film surface. Percent PA and antibodies used for antibody immobilization and antigen detection, respectively, were discussed quantitatively. It was found that the greatest percents of antibodies were used for antigen detection on the complex surface. The activity of PA adsorbed on the complex surface was maintained for a long time even in air atmosphere. Unique activities were derived from the nondenaturing adsorp-

Table 2. Analytical Data of Protein Adsorption on SC and it-PMMA Surfaces

protein	adsorption amount/ng (pmol) cm^{-2} on complex	adsorption amount/ng (pmol) cm^{-2} on it-PMMA	amount ratio[a]	dimension[b]/ nm	amount expected[c]/ pmol cm^{-2}	Secondary structure[d]/% helix	strand	others
HSA	210 ± 16 (3.1)	164 ± 3 (2.5)	1.3	8.0 × 8.0 × 3.0	2.6−6.9	70.9	0.0	29.1
cit. synth	219 ± 16 (4.2)	205 ± 16 (3.9)	1.1	9.0 × 7.5 × 6.0	2.5−3.7	59.2	1.4	39.4
HRP	322 ± 74 (7.3)	213 ± 27 (4.8)	1.5	6.2 × 4.3 × 1.2	6.3−32	47.7	2.0	50.3
cyto. *c*	118 ± 25 (9.5)	200 ± 57 (16.1)	0.6	4.0 × 4.0 × 4.0	10	37.5	0.0	62.5
ALP	216 ± 19 (2.3)	153 ± 11 (1.6)	1.4	10 × 5.0 × 5.0	3.3−6.7	31.7	18.3	50.1
CA	222 ± 8 (7.4)	129 ± 27 (4.3)	1.7	4.7 × 4.1 × 4.1	8.6−9.9	14.1	26.8	59.0
α-CTP	137 ± 36 (5.5)	60 ± 16 (2.4)	2.3	9.8 × 7.0 × 7.0	2.4−3.4	11.4	32.1	56.5
GFP	230 ± 66 (8.5)	181 ± 16 (6.7)	1.3	4.2 × 2.4 × 2.4	17−29	10.7	50.7	38.7
av	128 ± 3 (1.9)	98 ± 8 (1.6)	1.3	5.6 × 5.0 × 4.0	6.0−8.3	4.9	44.7	50.4
sup. dismut	129 ± 25 (2.1)	74 ± 55 (1.2)	1.7	6.7 × 3.6 × 3.3	6.9−14	2.0	38.4	59.6

[a] Adsorption amounts on the SC surface were divided by those on the it-PMMA surface. [b] From previous papers (see text). [c] Expected adsorption amounts when assumed the monolayer full coverage. For estimation, the substrate area was divided by the cross section of proteins. [d] From PDB.

tion of PA. The mechanism for the protein adsorption on the complex surface was speculated on the basis of previous observations (*31*, *32*) and physical adsorption data of various proteins. Since the SC film can be easily prepared on solid material surfaces, the present observation will help to fabricate novel immunoassay materials and high-throughput microarray/chips and will lead to other protein-conjugated materials such as enzyme immobilization (*58*). Even though certain polymer materials have the same chemical structure, the assembly nanostructure that provides regular conformations might be one of the essential factors to regulate interactions with proteins with variable secondary structures. SC surfaces might be helpful leads to develop a new category of bioconjugated nanomaterials.

ACKNOWLEDGMENT

The authors thank Prof. M. Chikira (Chuo University) for helpful discussion on all experiments and Mr. M. Matsuda and Mr. A. Kogure (Shimadzu) for AFM measurement. This work is financially supported in part by Grant-in-Aid for Scientific Research (no. 16710089) from the Ministry of Education, Culture, Sports, Science and Technology, Japan, and by PRESTO from JST.

LITERATURE CITED

(1) Hage, D. S. (1999) Immunoassays. *Anal. Chem. 71*, 294R.
(2) Wiseman, S. B., and Singer, T. D. (2002) Applications of DNA and protein microarrays in comparative physiology. *Biotechnol. Adv. 20*, 379.
(3) Zhu, H., and Snyder, M. (2003) Protein chip technology. *Curr. Opin. Chem. Biol. 7*, 55.
(4) Kambhampati, D., Ed. (2003) *Protein Microarray Technology*, Wiley-VCH, Weinheim.
(5) Fung, E. T., Ed. (2004) *Methods in Molecular Biology, Vol. 264, Protein Arrays: Methods and Protocols*, Humana Press, Totowa.
(6) Tomizaki, K., Usui, K., and Mihara, H. (2005) Protein-detecting microarrays: current accomplishments and requirements. *ChemBioChem 6*, 782.
(7) Joos. T. O., Schrenk, M., Höpfl, P., Kröger, K., Chowdhury, U., Stoll, D., Schörner, D., Dürr, M., Herick, K., Rupp, S., Sohn, K., and Hämmerle, H. (2000) A microarray enzyme-linked immunosorbent assay for autoimmune diagnostics. *Electrophoresis 21*, 2641.
(8) Angenendt, P., Glökler, J., Sobek, J., Lehrach, H., and Cahill, D. J. (2003) Next generation of protein microarray support materials: evaluation for protein and antibody microarray applications. *J. Chromatogr., A 1009*, 97.
(9) Sethuraman, A., Han, M., Kane, R. S., and Belfort, G. (2004) Effect of surface wettability on the adhesion of proteins. *Langmuir 20*, 7779.
(10) Quinn, J., Patel, P., Fitzpatrick, B., Manning, B., Dillon, P., Daly, S., O'Kennedy, R., Alcocer, M., Lee, H., Morgan, M., and Lang, K. (1999) The use of regenerable, affinity ligand-based surfaces for immunosensor applications. *Biosens. Bioelectron. 14*, 587.
(11) Vijayendran, R. A., and Leckband, D. E. (2001) A quantitative assessment of heterogeneity for surface-immobilized proteins. *Anal. Chem. 73*, 471.
(12) Zuo, B., Li, S., Guo, Z., Zhang, J., and Chen, C. (2004) Piezoelectric immunosensor for SARS-associated coronavirus in sputum. *Anal. Chem. 76*, 3536.
(13) Oh, B.-K., Kim, Y.-K., Lee, W., Bae, Y. M., Lee, W. H., and Choi, J.-W. (2003) Immunosensor for detection of *Legionella pneumophila* using surface plasmon resonance. *Biosens. Bioelectron. 18*, 605.
(14) Starodub, N. F., Pirogova, L. V., Demchenko, A., and Nabok, A. V. (2005) Antibody immobilisation on the metal and silicon surfaces. The use of self-assembled layers and specific receptors. *Bioelectrochemistry 66*, 111.
(15) Carrigan, S. D., Scott, G., and Tabrizian, M. (2005) Real-time QCM-D immunoassay through oriented antibody immobilization using cross-linked hydrogel biointerfaces. *Langmuir 21*, 5966.
(16) Koepsel, R. R., and Russell, A. J. (2003) Directed capture of enzymes and bacteria on bioplastic films. *Biomacromolecules 4*, 850.
(17) Boozer, C., Ladd, J., Chen, S., Yu, Q., Homola, J., and Jiang, S. (2004) DNA directed protein immobilization on mixed ssDNA/oligo-(ethylene glycol) self-assembled monolayers for sensitive biosensors. *Anal. Chem. 76*, 6967.
(18) Zhu, H., Bilgin, M., Bangham, R., Hall, D., Casamayor, A., Bertone, P., Lan, N., Jansen, R., Bidlingmaier, S., Houfek, T., Mitchell, T., Miller, P., Dean, R. A., Gerstein, M., and Snyder, M. (2001) Global analysis of protein activities using proteome chips. *Science 293*, 2101.
(19) Lee, Y., Lee, E. K., Cho, Y. W., Matsui, T., Kang, I.-C., Kim, T.-S., and Han, M. H. (2003) ProteoChip: A highly sensitive protein microarray prepared by a novel method of protein immobilization for application of protein-protein interaction studies. *Proteomics 3*, 2289.
(20) Sasakura, Y., Kanda, K., Yoshimura-Suzuki, T., Matsui, T., Fukuzono, S., Han, M. H., and Shimizu, T. (2004) Protein microarray system for detecting protein-protein interactions using an anti-His-tag antibody and fluorescence scanning: Effects of the heme redox state on protein-protein interactions of heme-regulated phosphodiesterase from *Escherichia coli*. *Anal. Chem. 76*, 6521.
(21) Serizawa, T., Hamada, K.-I., Kitayama, T., Fujimoto, N., Hatada, K., and Akashi, M. (2000) Stepwise stereocomplex assembly of stereoregular poly(methyl methacrylate)s on a substrate. *J. Am Chem. Soc. 122*, 1891.
(22) Serizawa, T., Hamada, K.-I., Kitayama, T., Katsukawa, K.-I., Hatada, K., and Akashi, M. (2000) Stepwise assembly of isotactic poly(methyl methacrylate) and syndiotactic poly(methacrylic acid) on a substrate. *Langmuir 16*, 7112.
(23) Hamada, K.-I., Serizawa, T., Kitayama, T., Fujimoto, N., Hatada, K., and Akashi, M. (2001) Stepwise stereocomplex assembly of isotactic poly(methyl methacrylate) and syndiotactic poly(alkyl methacrylate)s on surfaces. *Langmuir 17*, 5513.
(24) Serizawa, T., Hamada, K.-I., Kitayama, T., and Akashi, M. (2003) Recognition of stereoregular polymers using structurally-regulated ultrathin polymer films. *Angew. Chem., Int. Ed. 42*, 1118.
(25) Serizawa, T., Hamada, K.-I., and Akashi, M. (2004) Polymerization within a molecular-scale stereoregular template. *Nature (London) 429*, 52.
(26) Hamada, K.-I., Serizawa, T., and Akashi, M. (2005) Template polymerization using artificial double-strands. *Macromolecules 38*, 6759.
(27) Spěváček, J., and Schneider, R. (1987) Aggregation of stereoregular poly(methyl methacrylates). *Adv. Colloid Interface Sci. 27*, 81.
(28) Schomaker, E., and Challa, G. (1989) Complexation of stereoregular poly(methyl methacrylates). 14. The basic structure of the stereocomplex of isotactic and syndiotactic poly(methyl methacrylate). *Macromolecules 22*, 3337.
(29) Decher, G. (1997) Fuzzy nanoassemblies: Toward layered polymeric multicomposites. *Science 277*, 1232.
(30) Decher, G., and Schlenoff, J. B., Eds. (2003) *Multilayer Thin Films*, Wiley-VCH, Weinheim.
(31) Hamada, K.-I., Yamashita, K., Serizawa, T., Kitayama, T., and Akashi, M. (2003) Adsorption of bovine serum albumin onto poly(methyl methacrylate) stereocomplex films with a molecularly regulated nano-structure. *J. Polym. Sci., Part A: Polym. Chem. 41*, 1807.
(32) Serizawa, T., Yamashita, K., and Akashi, M. (2006) Unique physical adsorption of proteins onto double stranded stereocomplex films composed of stereoregular poly(methyl methacrylate)s. *Polym. J. 38*, 503.
(33) Serizawa, T., Yamashita, K., and Akashi, M. (2004) Cell-adhesive and blood-coagulant properties of ultrathin poly(methyl methacrylate) stereocomplex films. *J. Biomater. Sci.: Polym. Ed. 15*, 511.
(34) Sauerbrey, G. (1959) The use of quartz oscillators for weighing thin layers and for microweighing. *Z. Phyzik 155*, 206.
(35) Saha, K., Bender, F., Rasmusson, A., and Gizeli, E. (2003) Probing the viscoelasticity and mass of a surface-bound protein layer with an acoustic waveguide device. *Langmuir 19*, 1304.
(36) Reimhult, E., Larsson, C., Kasemo, B., and Höök, F. (2004) Simultaneous surface plasmon resonance and quartz crystal microbalance with dissipation monitoring measurements of biomolecular adsorption events involving structural transformations and variations in coupled water. *Anal. Chem. 76*, 7211.

(37) Buijs, J., Lichtenbelt, J. W. T., Norde, W., and Lyklema, J. (1995) Adsorption of monoclonal IgGs and their $F(ab')_2$ fragments onto polymeric surfaces. *Colloids Surf., B 5*, 11.
(38) Dousseau, F., and Pézolet, M. (1990) Determination of the secondary structure content of proteins in aqueous solutions from their amide I and amide II infrared bands. Comparison between classical and partial least-squares methods. *Biochemistry 29*, 8771.
(39) Lenk, T. J., Horbett, T. A., Ratner, B. D., and Chittur, K. K. (1991) Infrared spectroscopic studies of time-dependent changes in fibrinogen adsorbed to polyurethanes. *Langmuir 7*, 1755.
(40) Buijs, J., Norde, W., and Lichtenbelt, J. W. Th. (1996) Changes in the secondary structure of adsorbed IgG and $F(ab')_2$ studied by FTIR spectroscopy. *Langmuir 12*, 1605.
(41) Iconomidou, V. A., Chryssikos, D. G., Gionis, V., Pavlidis, M. A., Paipetis, A., and Hamodrakas, S. J. (2000) Secondary structure of chorion proteins of the teleostean fish *Dentex dentex* by ATR FT-IR and FT-Raman spectroscopy. *J. Struct. Biol. 132*, 112.
(42) Ringeisen, B. R., Callahan, J., Wu, P. K.; Piqué, A., Spargo, B., McGill, R. A., Bucaro, M., Bubb, D. M., and Chrisey, D. B. (2001) Novel laser-based deposition of active protein thin films. *Langmuir 17*, 3472.
(43) Hernandez-Perez, M. A., Garapon, C., Champeaux, C., Shahgaldian, P., Coleman, A., and Mugnier, J. (2003) Pulsed laser deposition of bovine serum albumin protein thin films. *Appl. Surf. Sci. 208*−*209*, 658.
(44) Grdadolnik, J., and Maréchal, Y. (2001) Bovine serum albumin observed by infrared spectrometry. I. Methodology, structural investigation, and water uptake. *Biopolymers 62*, 40.
(45) Tretinnikov, O. N. (1997) Selective accumulation of functional groups at the film surfaces of stereoregular poly(methyl methacrylate)s. *Langmuir 13*, 2988.
(46) Tretinnikov, O. N. (1999) Wettability and microstructure of polymer surfaces. Stereochemical and conformational aspects. *J. Adhes. Sci. Technol. 13*, 1085.
(47) Sugio, S., Kashima, A., Mochizuki, S., Noda, M., and Kobayashi, K. (1999) Crystal structure of human serum albumin at 2.5 Å resolution. *Protein Eng. 12*, 439.
(48) Wiegand, G., Kukla, D., Scholze, H., Jones, T. A., and Huber, R. (1979) Crystal structure analysis of the tetragonal crystal form and preliminary molecular model of pig-heart citrate synthase. *Eur. J. Biochem. 93*, 41.
(49) Zhang, J., Chi, Q., Dong, S., and Wang, E. (1996) In situ electrochemical scanning tunnelling microscopy investigation of structure for horseradish peroxidase and its electrocatalytic property. *Bioelectrochem. Bioenerg. 39*, 267.
(50) Deere, J., Magner, E., Wall, J. G., and Hodnett, B. K. (2001) Adsorption and activity of cytochrome c on mesoporous silicates. *Chem. Commun.* 465.
(51) Kim, E. E., and Wyckoff, H. W. (1991) Reaction mechanism of alkaline phosphatase based on crystal structures two-metal ion catalysis. *J. Mol. Biol. 218*, 449.
(52) Kannan, K. K., Notstrand, B., Fridborg, K., Lovgren, S., Ohlsson, A., and Petef, M. (1975) Crystal structure of human erythrocyte carbonic anhydrase B. Three-dimensional structure at a nominal 2.2-Å resolution. *Proc. Natl. Acad. Sci. U.S.A. 72*, 51.
(53) Corey, R. B., Battfay, O., Brueckner, D. A., and Mark, F. G. (1965) Preliminary X-ray diffraction studies of crystal forms of free and inhibited chymotrypsin. *Biochim. Biophys. Acta 94*, 535.
(54) Brejc, K., Sixma, T. K., Kitts, P. A., Kain, S. R., Tsien, R. Y., Ormö, M., and Remington, S. J. (1997) Structural basis for dual excitation and photoisomerization of the aequorea victoria green fluorescent protein. *Proc. Natl. Acad. Sci. U.S.A. 94*, 2306.
(55) Pugliese, L., Coda, A., Malcovati, M., and Bolognesi, M. (1993) Three-dimensional structure of the tetragonal crystal form of egg-white avidin in its functional complex with biotin at 2.7 Å resolution. *J. Mol. Biol. 231*, 698.
(56) Tainer, J. A., Getzoff, E. D., Beem, K. M., Richardson, J. S., and Richardson, D. C. (1982) Determination and analysis of the 2 Å structure of copper, zinc superoxide dismutase. *J. Mol. Biol. 160*, 181.
(57) Lindmark, R. (1982) Estimation of the secondary structure of protein A from *S. aureus* by CD-spectroscopy. *Mol. Immunol. 19*, 957.
(58) Matsuno, H., Nagasaka, Y., Kurita, K., and Serizawa, T. Manuscript in preparation.

BC060225K

Design, Synthesis, and Characterization of pH-Sensitive PEG−PE Conjugates for Stimuli-Sensitive Pharmaceutical Nanocarriers: The Effect of Substitutes at the Hydrazone Linkage on the pH Stability of PEG−PE Conjugates

Amit A. Kale and Vladimir P. Torchilin*

Department of Pharmaceutical Sciences and Center for Pharmaceutical Biotechnology and Nanomedicine, Northeastern University, Boston, Massachusetts 02115. Received July 24, 2006; Revised Manuscript Received November 8, 2006

A set of aliphatic and aromatic aldehyde-derived hydrazone (HZ)-based acid-sensitive polyethylene glycol−phosphatidylethanolamine (PEG−PE) conjugates was synthesized and evaluated for their hydrolytic stability at neutral and slightly acidic pH values. The micelles formed by aliphatic aldehyde-based PEG−HZ−PE conjugates were found to be highly sensitive to mildly acidic pH and reasonably stable at physiologic pH, while those derived from aromatic aldehydes were highly stable at both pH values. The pH-sensitive PEG−PE conjugates with controlled pH sensitivity may find applications in biological stimuli-mediated drug targeting for building pharmaceutical nanocarriers capable of specific release of their cargo at certain pathological sites in the body (tumors, infarcts) or intracellular compartments (endosomes, cytoplasm) demonstrating decreased pH.

INTRODUCTION

The development of an optimal drug delivery systems has the utmost importance in contemporary medicine (*1*). The ultimate goal in drug delivery is to achieve therapeutic concentrations of the drug at the target site while drug concentrations at other tissues are kept in safe levels. This has particular importance in the case of cancer treatment, where the challenge is to selectively destroy the tumor without damaging normal tissues. Disease (tumor) site-specific targeting of drugs and drug carriers may, at least partially, solve the problem. The issue, however, remains how to achieve fast and effective drug release from the pharmaceutical carrier when it has already reached its target, such as a tumor (*2*−*4*). This issue is equally important when long-circulating PEGylated drug delivery systems are used (*5*−*7*), since PEG prevents normal interaction of the carrier with cells and other destabilizing factors, or when the drug carrier is intended for intracellular penetration (*8*, *9*) and a properly scheduled cytoplasmic release of the active drug is expected to prevent its degradation in lysosomes (*10*).

There are several approaches to this problem including the use of stimuli-sensitive pharmaceutical nanocarriers, which is based on the fact that many pathological sites including tumors demonstrate hyperthermia or acidification (*11*−*13*). In general, environmentally sensitive carriers exhibit dramatic changes in their swelling behavior, network structure, permeability, or stability in response to changes in the pH or ionic strength of the surrounding fluid or temperature (*14*). Such systems, for example, may include certain pH-sensitive linkages allowing for drug release, protective "coat" removal, or new functional appearance because of their fast degradation in acidified pathological sites (*15*−*17*). Different approaches have been employed to develop pH-responsive carriers, with one being the incorporation of acid-sensitive linkages between drug and ligand or into the molecules of the carrier-forming components. These include cis-aconityls (*18*, *19*), electron-rich trityls (*20*), polyketals (*21*), acetals (*22*, *23*), vinyl ethers (*24*, *25*), hydrazones (*26*−*28*), poly(ortho esters) (*29*), and thiopropionates (*30*). Such constructs may turn out to be useful for the site-specific delivery of drugs at the tumor sites (*12*), infarcts (*31*), inflammation zones (*32*), or cell cytoplasm or endosomes (*33*), since at these "acidic" sites, pH drops from the normal physiologic value of pH 7.4 to pH 6.0 and below.

We have recently demonstrated the utility of highly pH-sensitive hydrazone bond-based PEG−PE conjugates in preparing double-targeted stimuli-sensitive pharmaceutical nanocarriers (*34*). This proof-of-principle study did not, however, address an important issue of the proper coordination between two important temporal characteristics of such carriers, which are expected to demonstrate a sufficiently long lifetime under normal physiological conditions allowing for their efficient accumulation in the target, and sufficiently fast destabilization within the acidic target providing better drug penetration into the target cells. Since real practical tasks may require different times for such carriers to stay in the blood and to release their contents (or "develop" an additional function) inside the target, the need is evident to have a set of pH-sensitive conjugates capable of serving as components of stimuli-sensitive pharmaceutical nanocarriers and demonstrating variable stabilities at normal and acidic pH values.

With this in mind, we have synthesized a series of PEG−HZ−PE conjugates with different substituents at the hydrazone bond and evaluated their hydrolytic stability at normal and slightly acidic pH values. These conjugates differ from each other with respect to the exact structure of groups forming the hydrazone linkage between phospholipid and PEG. The characterization of the in vitro behavior of these conjugates has provided important information useful for future design and development of pH-sensitive nanocarriers with desired properties.

MATERIALS

1,2-Dioleoyl-*sn*-glycero-3-phosphoethanolamine, DOPE[1]; 1,2-dipalmitoyl-*sn*-glycero-3-phosphothioethanolamine (sodium salt), DPPE-SH; and 1,2-dimyristoyl-*sn*-glycero-3-phosphoethanolamine-*N*-(lissamine rhodamine B sulfonyl) ammonium salt, Rh-PE, were purchased from Avanti Polar Lipids, Alabaster (AL); (*N*-ϵ-maleimidocaproic acid) hydrazide, EMCH; 4-(4-*N*-male-

* Corresponding author. Northeastern University, Mugar Building 312, 360 Huntington Ave, Boston, MA 02115. Tel: 617 373 3206. Fax: 617 373 8886. E-mail: v.torchilin@neu.edu.

10.1021/bc060228x CCC: $37.00 © 2007 American Chemical Society
Published on Web 02/20/2007

imidophenyl)butyric acid hydrazide hydrochloride, MPBH; *N*-(κ-maleimidoundecanoic acid) hydrazide, KMUH; succinimidyl 4-(*N*-maleimidomethyl) cyclohexane-1-carboxylate, SMCC, were purchased from Pierce Biotechnology, Inc., Rockford, IL. 2-Acetamido-4-mercaptobutanoic acid hydrazide, AMBH, was purchased from Molecular Probes (Invitrogen, Carlsbad, CA); methoxy poly(ethylene) glycol butyraldehyde (MW 2000) and mPEG-SH (MW 2000) were purchased from Nektar Therapeutics (Huntsville, AL). Triethylamine was purchased from Aldrich Chemicals. 4-Succinimidyl formylbenzoate (SFB) was purchased from Molbio (Boulder, Colorado). All solvents were purchased from Fisher Scientific (HPLC grade) and used without further purification.

SYNTHESES

All reactions were monitored by TLC using 0.25 mm × 7.5 cm silica plates with UV indicator (Merck 60F-254) and mobile phase of chloroform/methanol (80:20% v/v). Phospholipid and PEG alone or their conjugates were visualized by iodine, phosphomolybdic acid, and Dragendorff spray reagents (Figure 1). Silica gel (240−360 μm) and size exclusion media, Sepharose CL4B (40−165 μm) and Sephadex G25 m (Sigma-Aldrich), were used for silica column chromatography and size exclusion chromatography, respectively.

^{1}H NMR spectra were obtained on Varian Unity AS500 instrument (500 MHz). Chemical shifts (δ) were given in ppm relative to TMS.

Hydrazide-Activated Phospholipids (3a, 3b, 3c). 22 μmol of phosphatidylthioethanolamine, **2**, were mixed with 1.5 molar excess of each acyl hydrazide linker (Table 1) in 3 mL anhydrous methanol containing 5 molar excess of triethylamine over lipid (Scheme 1). The reaction was performed at 25 °C under argon for 8 h. Solvent was removed under reduced pressure, and the residue was dissolved in chloroform and applied to a 5 mL silica gel column which had been activated (150 °C overnight) and prewashed with 20 mL of chloroform. The column was equilibrated with an additional 15 mL of chloroform followed by 5 mL of each of the chloroform/methanol mixtures, 4:0.25, 4:0.5, 4:0.75, 4:1, and 4:2, and, finally, with 6 mL of 4:3 v/v. The phosphate-containing fractions eluting in 4:l, 4:2, and 4:3 chloroform/methanol (v/v) were pooled and concentrated under reduced pressure. The yields of **3a**, **3b**, and **3c** were 65.7%, 71.9%, and 68%, respectively. The products were stored in glass ampoules as chloroform solutions under argon at −80 °C.

For the activation of phospholipid with AMBH, a maleimide derivative of phosphatidylethanolamine (PE), **7**, was prepared using SMCC (Scheme 3). In brief, PE, **6**, in chloroform was reacted with 1.5 molar excess of SMCC, **5**, over lipid in the presence of 5 molar excess of TEA under argon for 5 h. The maleimide derivative was separated from excess SMCC on silica gel column using chloroform/methanol (4:0.2 v/v) mobile phase. The elution fractions containing ninhydrin-negative and phosphorus-positive fractions were pooled and concentrated under reduced pressure. The yield of the product was 65.7%.

DOPE−maleimide was further used to synthesize the AMBH-activated derivative of phospholipid, **8**, by reacting with 1.5 molar excess of AMBH using TEA as catalyst (Scheme 4).

^{1}H NMR Spectroscopy. EMCH-Activated Phospholipid Derivative (**3a**). ^{1}H NMR (500 MHz, $CDCl_3$): δ 0.85−0.87 (t, 6H, 20), 1.25−1.32 (m, 46H), 1.39 (d, 2H, 35), 1.56−1.64 (m, 8H), 2.25 (m, 12H), 3.06−3.08 (m, 5H), 3.48 (m, 3H), 7.12−7.19 (d, 2H, 35), 7.32 (s, 3H).

MPBH-Activated Phopsholipid Derivative (**3b**). ^{1}H NMR (500 MHz, $CDCl_3$): δ 0.85−0.89 (t, 6H, 20), 1.11 (s, 5H), 1.18 (s, 12H), 1.25−1.30 (m, 44H), 1.56−1.60 (m, 8H), 2.26 (m, 4H), 3.49 (s, 1H), 7.12 (s, 1H), 7.19 (s, 2H), 7.32 (s, 4H).

KMUH-Activated Phospholipid Derivative (**3c**). ^{1}H NMR (500 MHz, $CDCl_3$): δ 0.85−0.89 (t, 6H, 20), 1.11 (s, 3H), 1.25−1.30 (m, 52H), 1.30−1.35 (m, 4H), 1.57−1.60 (m, 4H),

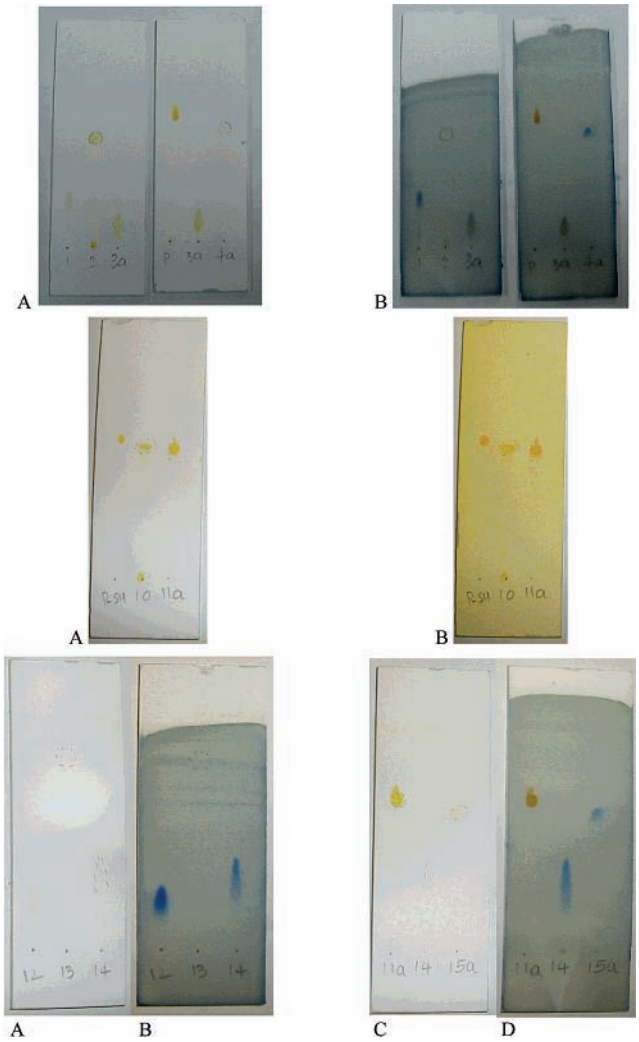


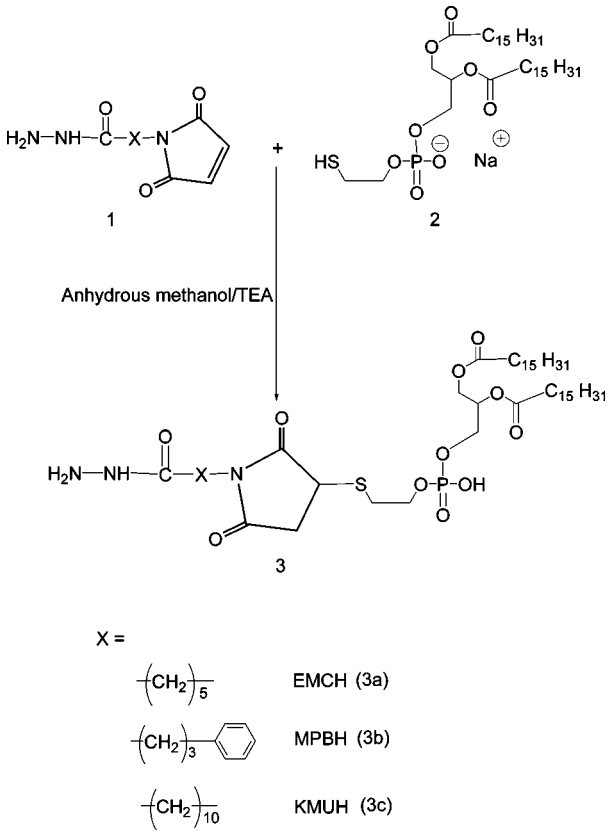
Figure 1. Representative TLC patterns of different reactants and purified products. Upper row: For Schemes 1 and 2 with iodine (A) or phosphomolybdenum spray (B) visualization. (**1**, DPPE−SH; **2**, EMCH linker; **3a**, EMCH-activated phospholipid; P, PEG-butyraldehyde; **4a**, PEG−HZ−PE conjugate). Middle row: For Scheme 6 with iodine (A) or Dragendorff spray (B) visualization. (P−SH, PEG−SH; **10**, EMCH linker; **11a**, EMCH-activated PEG). Bottom row: For Schemes 7 and 8 with iodine (A,C) or phosphomolybdenum spray (B,D) visualization. (**11a**, EMCH-activated PEG; **12**, DOPE; **13**, SFB; **14**, SFB-activated DOPE; **15a**, PEG−HZ−PE).

Table 1. Acyl Hydrazide Linkers Used in This Study

linker (X)	mol. wt.	length of spacer arm
AMBH 2-acetamido−4-mercaptobutanoic acid hydrazide	191.25	−
EMCH (*N*-ϵ-maleimidocaproic acid) hydrazide	225.24	11.8 Å
MPBH 4-(4-*N*-maleimidophenyl)butyric acid hydrazide	309.5	17.9 Å
KMUH *N*-(κ-maleimido undecanoic acid) hydrazide	295.8	19.0 Å

[1] Abbreviations: Phosphotidylethanolamine, PE; 1,2-dioleoyl-*sn*-glycero-3-phosphoethanolamine, DOPE; 1,2-dipalmitoyl-*sn*-glycero-3-phosphothioethanolamine (sodium salt), DPPE-SH; methoxy(polyethylene)glycol, PEG; hydrazone, HZ.

Scheme 1. Synthesis of Acyl Hydrazide-Activated Phospholipids



2.13−2.29 (m, 6H), 3.08−3.11 (m, 8H), 3.48 (m, 3H), 3.90−3.96 (m, 5H), 7.19 (s, 1H), 7.32 (s, 2H).

AMBH-Activated Phospholipid Derivative (**8**). ^{1}H NMR (500 MHz, $CDCl_3$): δ 0.85−0.90 (t, 6H, 25), 1.26−1.29 (m, 41H), 1.57 (s, 8H), 1.80−1.84 (m, 5H), 2.01 (m, 19H), 2.17 (d, 6H, 2.5), 2.27−2.29 (d, 5H, 10), 2.69 (s, 2H), 3.37−3.40 (m, 3H), 3.86−3.88 (m, 4H), 4.09−4.11 (m, 1H), 5.3 (m, 3H)

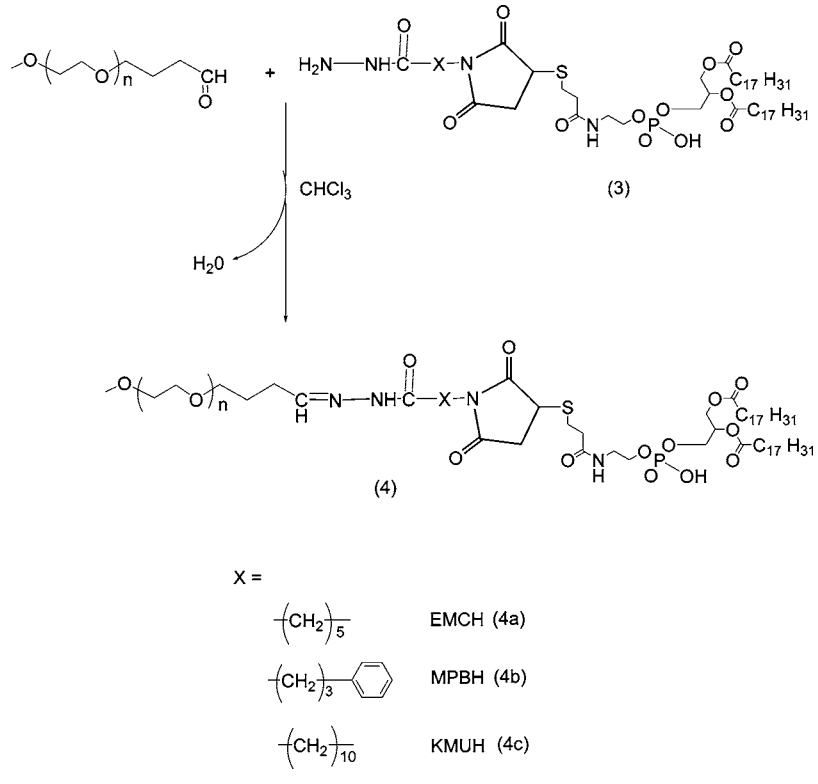
PEG−HZ−PE Conjugates (4a, 4b, 4c, 9). 21 μmol of $mPEG_{2000}$−butyraldehyde were reacted with 14 μmol of linker-activated phospholipid in 2 mL chloroform at 25 °C in a tightly closed reaction vessel (Schemes 2 and 5). After overnight stirring, chloroform was evaporated under vacuum in a rotary evaporator. The excess $mPEG_{2000}$−butyraldehyde was separated from PEG−HZ−PE conjugates using gel filtration chromatography. The gel filtration chromatography was performed using Sepharose-CL4B equilibrated overnight in pH 9−10 degassed ultrapure water (elution medium) in a 1.5 × 30 cm glass column. The thin film formed in the round-bottom flask after evaporating chloroform was hydrated with the elution medium and applied to the column. The micelles formed by PEG−HZ−PE conjugate were the first to elute from the column. Micelle-containing fractions were identified by Dragendorff spray reagent, pooled together, and kept in the freezer at −80 °C overnight before subjecting to freeze-drying. The freeze-dried PEG−HZ−PE conjugates were weighed and stored at −80 °C as chloroform solutions. The yields of **4a**, **4b**, **4c**, and **9** were 55.1%, 57.4%, 53.5%, and 61.0%, respectively.

^{1}H NMR Spectroscopy. PEG−HZ−PE Conjugate with EMCH Cross-Linker (**4a**). ^{1}H NMR (500 MHz, $CDCl_3$): δ 0.85−0.88 (t, 6H, 15), 1.25−1.27 (m, 44H), 1.55−1.60 (m, 9H), 2.12−2.20 (m, 106H), 2.68 (s, 22H), 3.37 (s, 3H), 3.49−3.59 (m, 240H), 3.90−3.92 (m, 9H), 4.2 (s, 6H), 4.67−4.7 (m, 1H), 5.31−5.33 (m, 2H).

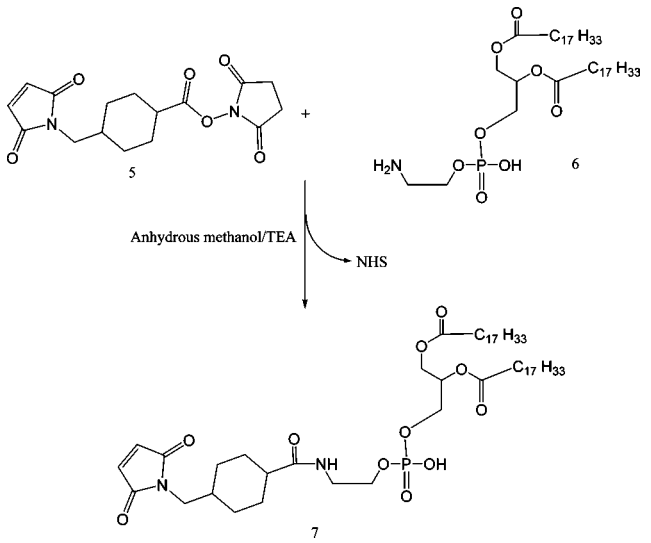
PEG−HZ−PE Conjugate with MPBH Cross-Linker (**4b**). ^{1}H NMR (500 MHz, $CDCl_3$): δ 0.87−0.94 (t, 6H, 10), 1.25 (m, 54H), 3.37 (s, 3H), 3.5−3.69 (m, 243H), 7.19 (m, 3H), 7.32 (s, 5H).

PEG−HZ−PE Conjugate with KMUH Cross-Linker (**4c**). ^{1}H NMR (500 MHz, $CDCl_3$): δ 0.85−0.88 (t, 6H, 15), 1.24−1.3 (m, 54H), 1.56−1.57 (m, 8H), 1.9−2.0 (m, 49H), 2.26−2.28 (m, 5H), 3.37 (s, 3H), 3.47−3.49 (m, 7H), 3.50−3.53 (m, 9H),

Scheme 2. Synthesis of PEG−HZ−PE Conjugates



Scheme 3. Maleimide Activation of Phosphatidylethanolamine



3.55−3.65 (m, 240H), 3.67 (s, 5H), 3.7−3.76 (m, 2H), 5.31−5.33 (m, 1H).

PEG−HZ−PE Conjugate with AMBH Cross-Linker (**9**). ^{1}H NMR (500 MHz, $CDCl_3$): δ 0.86−0.89 (t, 6H, 15), 1.29−1.32 (m, 54H), 1.68 (m, 104H), 1.99 (m, 13H), 2.15 (m, 58H), 2.33−2.34 (m, 4H), 2.46 (m, 1H), 3.0 (m, 1H), 3.37 (s, 3H), 3.54−3.57 (m, 243H), 3.77−3.78 (t, 1H, 5), 5.33−5.34 (m, 2H).

Hydrazide-Activated PEG Derivatives (11a, 11b, 11c). 40 μmol of mPEG−SH in chloroform were mixed with 2 molar excess of acyl hydrazide cross-linkers: EMCH (**10a**), MPBH (**10b**), and KMUH (**10c**) presence of 5 molar excess of triethylamine over lipid. The excess EMCH was separated from the product by size exclusion chromatography using Sephadex G25m media. The acyl hydrazide derivatives of PEG (**11a**, **11b**, **11c**) were freeze-dried, weighed (yields 80.3%, 80.5%, 84%, respectively) and stored as chloroform solutions at −80 °C.

^{1}H NMR Spectroscopy. EMCH-Activated PEG Derivative (**11a**). ^{1}H NMR (500 MHz, $CDCl_3$): δ 1.21 (s, 1H), 1.3 (s, 1H), 1.6 (m, 2H), 1.78 (s, 1H), 1.86 (s, 1H) 1.96 (s, 1H), 2.09−2.11 (m, 29H), 2.42−2.46 (m, 3H), 2.57−2.64 (m, 2H), 3.07−3.14 (m, 1H), 3.34 (s, 3H), 3.45−3.51 (m, 8H), 3.54−3.62 (m, 236H), 3.68−3.71 (t, 2H, 15), 3.73−3.75 (t, 1H, 10), 7.01−7.11 (m, 1H).

MPBH-Activated PEG Derivative (**11b**). ^{1}H NMR (500 MHz, $CDCl_3$): δ 1.25 (s, 1H), 1.71−1.8 (d, 19H, 45), 1.98 (s, 2H), 2.16−2.17 (d, 18H, 5), 2.48 (m, 1H), 2.64−2.73 (m, 2H), 3.37 (s, 3H), 3.53−3.69 (m, 183H), 7.18−7.20 (d, 1H, 10), 7.31−7.32 (d, 1H, 5).

KMUH-Activated PEG Derivative (**11c**). ^{1}H NMR (500 MHz, $CDCl_3$): δ 1.27−1.33 (m, 18H), 1.53−1.56 (m, 3H), 1.18 (s, 3H), 1.96−2.03 (m, 25H), 2.16 (m, 43H), 2.45−2.49 (m, 5H), 2.60−2.63 (t, 2H, 5), 3.11−3.17 (m, 2H), 3.37 (s, 3H), 3.48−3.68 (m, 236H).

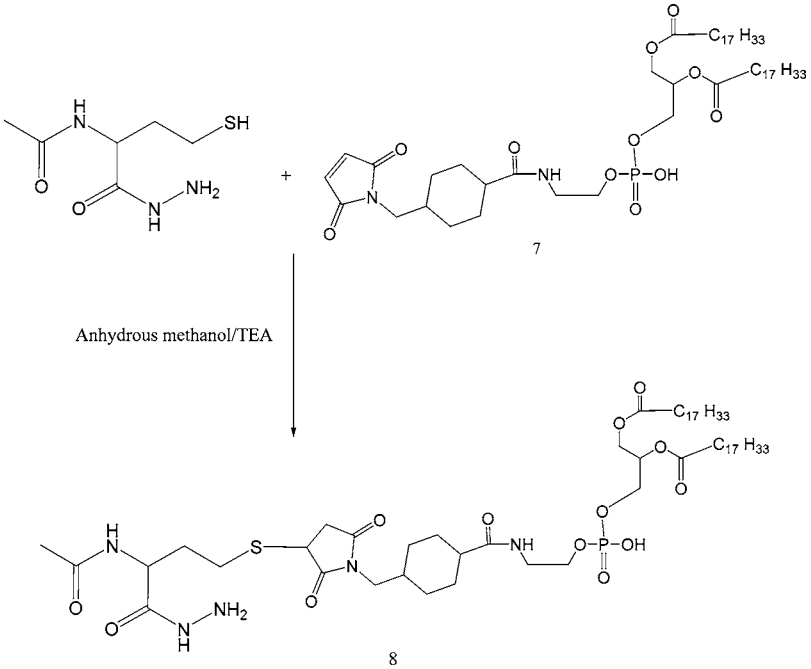
4-Succinimidylformyl Benzoate (SFB) Activated Phospholipid (14). 35 μmol of phosphatidylethanolamine, DOPE-NH_2, **12**, in chloroform were mixed with 2 molar excess of 4-succinimidylformyl benzoate, **13**, in the presence of 3 molar excess triethylamine over lipid. After stirring for 3 h, solvent was evaporated, residue was redissolved in chloroform, and product was separated on a silica gel column using acetonitrile/methanol mobile phases 4:0, 4:0.25, 4:0.5, 4:0.75, and 4:1 v/v. The fractions containing the product were identified by TLC analysis, pooled, and concentrated. The yield was 73%. The product was stored as chloroform solution at −80 °C.

^{1}H NMR Spectroscopy. SFB-Activated Phospholipid (**14**). ^{1}H NMR (500 MHz, $CDCl_3$): δ 0.85 (t, 6H, 15), 1.21−1.29 (m, 45H), 1.5 (s, 4H), 1.96 (d, 8H, 10), 2.19 (d, 4H, 25), 2.6 (s, 2H), 3.0 (m, 1H), 3.64 (m, 2H), 3.9−4.04 (m, 4H), 5.30−5.34 (m, 4H), 7.84−7.87 (t, 3H, 15), 8.05−8.13 (m, 3H), 9.98−10.05 (d, 1H, 35).

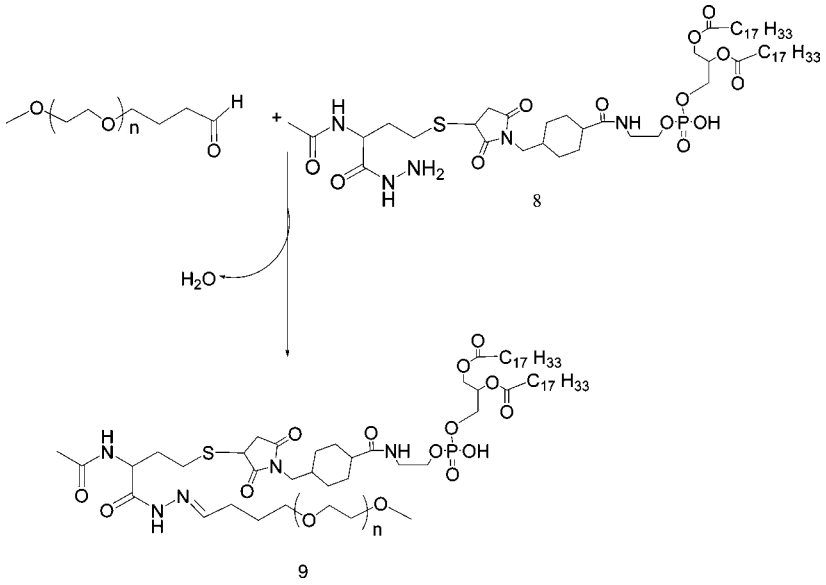
PEG−HZ−PE Conjugates (**15a**, **15b**, **15c**). 1.5 molar excess of SFB-activated phospholipid, **14**, was reacted with acyl hydrazide-derivatized PEGs, **11a**, **11b**, and **11c**, respectively, in chloroform at room temperature. After overnight stirring, chloroform was evaporated under reduced pressure. The PEG−HZ−PE conjugate was purified using size exclusion chromatography using Sepharose CL4B as described before. The yields of the conjugates **15a**, **15b**, and **15c** were 57.8%, 65.4%, and 62%, respectively.

^{1}H NMR Spectroscopy. PEG−HZ−PE Conjugate with EMCH-Activated PEG (**15a**). ^{1}H NMR (500 MHz, $CDCl_3$): δ 0.84−

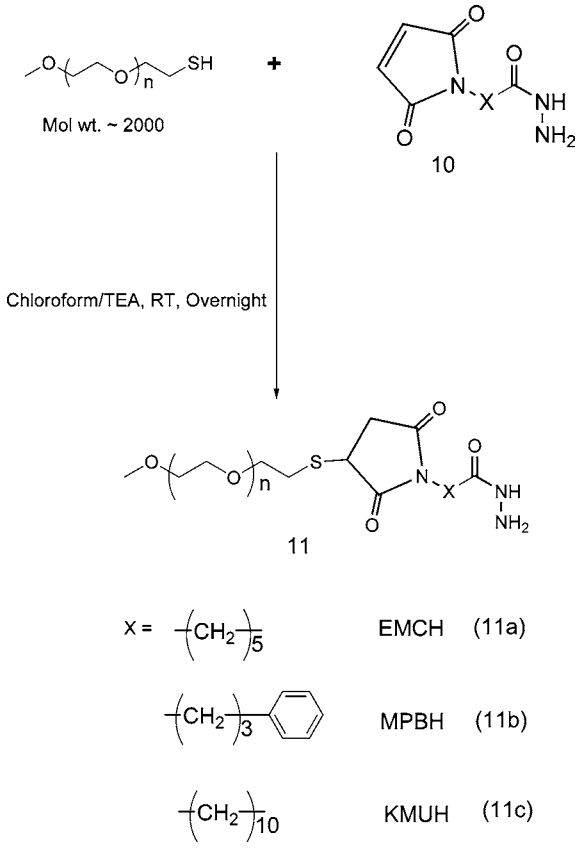
Scheme 4. AMBH-Derivatized Phospholipid via Sulfhydryl−Maleimide Addition Reaction



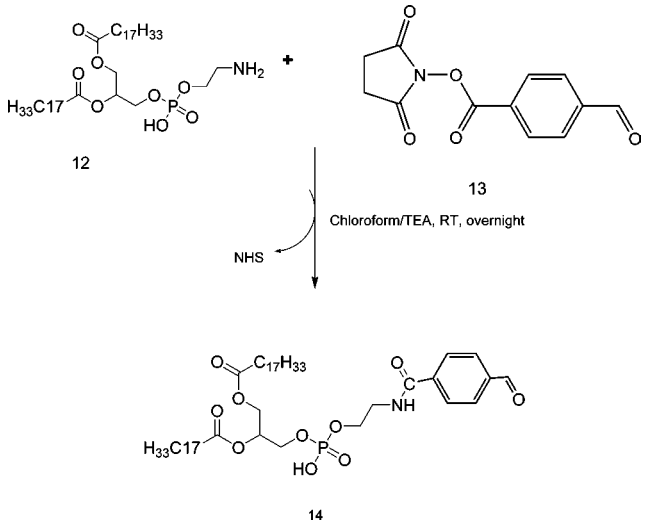
Scheme 5. Synthesis of PEG−HZ−PE Conjugate Using AMBH-Activated Phospholipid



Scheme 6. Synthesis of Acyl Hydrazide-Activated PEG



Scheme 7. SFB Activation of Phosphatidylethanolamine



0.86 (t, 6H, 10), 1.23−1.30 (m, 45H), 1.63 (s, 40H), 1.96−2.00 (m, 9H), 2.15 (s, 4H), 2.24−2.28 (q, 5H, 15), 2.53−2.55 (t, 2H), 3.35 (s, 3H), 3.55−3.66 (m, 232H), 3.75−3.76 (m, 1H), 3.98−4.04 (q, 3H, 7.5), 4.16−4.20 (m, 1H), 4.39−4.41 (m, 1H), 5.30−5.33 (m, 4H), 7.64−7.66 (d, 2H, 10), 7.75 (s, 1H), 8.0 (d, 2H, 10).

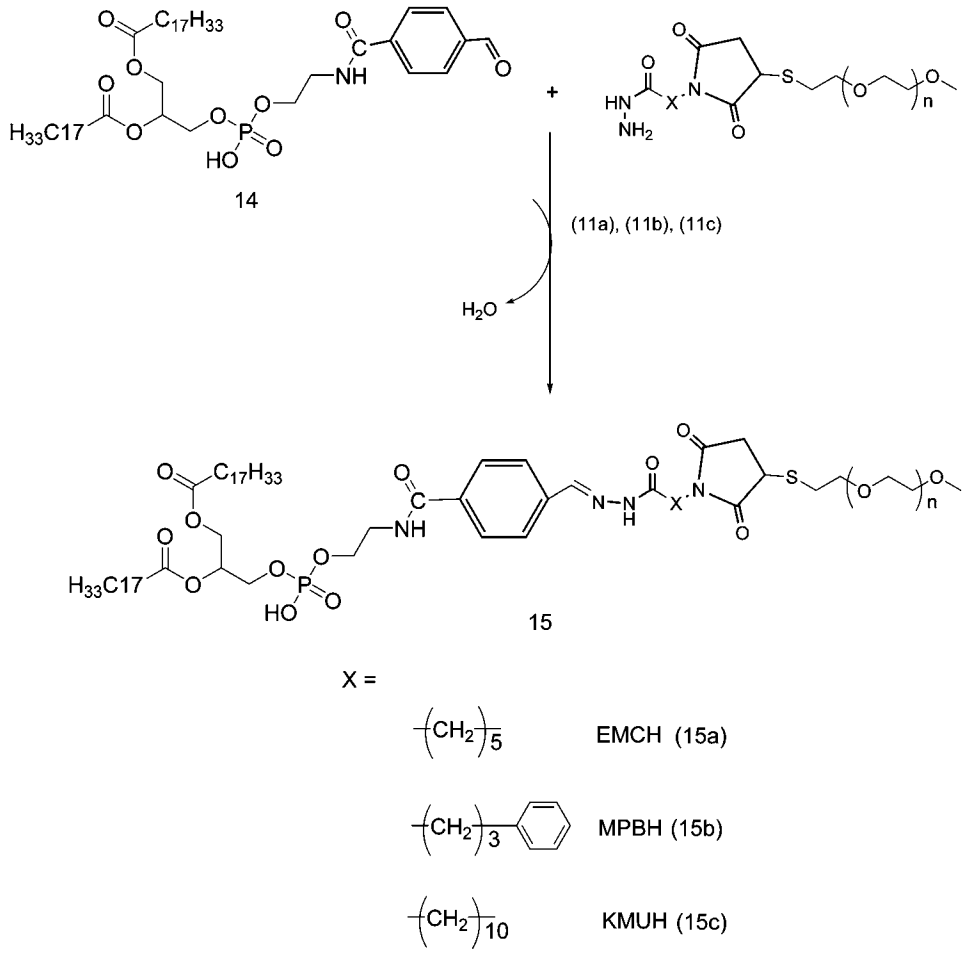
PEG−HZ−PE Conjugate with MPBH-Activated PEG (**15b**). ^{1}H NMR (500 MHz, $CDCl_3$): δ 0.86−0.88 (t, 6H, 10), 1.26 (m, 54H), 1.56−1.57 (m, 4H), 1.71 (s, 18H), 1.99−2.00 (d, 6H, 5), 2.17 (s, 1H), 2.25−2.26 (m, 3H), 3.37(s, 3H), 3.54−3.77 (m, 181H), 5.22−5.34 (m, 2H), 7.29−7.31 (d, 1H, 15), 7.58 (s, 1H), 8.01 (m, 1H).

PEG−HZ−PE Conjugate with KMUH-Activated PEG (**15c**). ^{1}H NMR (500 MHz, $CDCl_3$): δ 0.86−0.88 (t, 6H, 10), 1.26−1.28 (m, 62H), 1.55−1.65 (m, 56H), 1.99−2.00 (d, 20H, 5), 2.04 (s, 6H), 2.12 (s, 16H), 2.16 (m, 40H), 2.20 (m, 11H), 2.27−2.29 (m, 12H), 3.37 (s, 3H), 3.54−3.67 (m, 248H), 5.33 (m, 7H).

Micelle Size Measurement. The micelle size (hydrodynamic diameter) was measured by the dynamic light scattering (DLS) using a N4 Plus Submicron Particle System (Coulter Corporation, Miami, FL) at PEG−PE concentration of 10 mM.

In Vitro pH-Dependent Degradation Of PEG−HZ−PE Conjugates. The time-dependent degradation of PEG−HZ−PE micelles incubated in buffer solutions (phosphate buffered saline, pH 7.4 and pH 5.5) maintained at 37 °C was followed by HPLC using Shodex KW-804 size exclusion column as described in ref 34. In brief, the elution buffer used was pH 7.0, phosphate buffer (100 mM phosphate, 150 mM sodium sulfate), run at 1.0 mL/min. For fluorescent detection (Ex 550 nm/Em 590 nm) of micelle peak, Rh−PE (1 mol % of PEG−PE) was added to the PEG−PE conjugate in chloroform. A film was prepared by evaporating the chloroform under an argon stream and hydrated with the phosphate buffered saline, pH 7.4 or 5.5 (adjusted by precalculated quantity of 1 N HCl). A peak that represents micelle the population appeared at the retention

Scheme 8. Synthesis of PEG−HZ−PE Conjugate



time between 9 and 10 min. The degradation kinetics of micelles was assessed by following the area under the micelle curve.

DISCUSSION

Synthesis of Hydrazone-Based PEG−PE Conjugates. The success of hydrazones as pH-sensitive linkages derives from the fact that their hydrolytic stability is governed by the nature of hydrazone bond formed. Hydrazones are much more stable than imines as a result of the delocalization of the π-electrons in the former. In fact, parent hydrazones are too stable for the application in drug delivery systems, and an electron withdrawing group has to be introduced to moderate the stability by somewhat disfavoring electron delocalization throughout the molecule as compared to the parent hydrazone. Hydrazones can be prepared from aldehydes or ketones and hydrazides under very mild conditions including aqueous solutions. Hydrazone bond formation can take place even in vivo from separate fragments which self-assemble under physiological conditions (*35*).

In this work, we have applied different synthetic methods based on the use of various aldehydes that can produce the hydrazone linkage between PEG and PE. We have also conducted studies to check hydrolytic stability of hydrazones derived from aliphatic and aromatic aldehydes and different acyl hydrazides. Synthesis of aliphatic aldehyde-derived hydrazone containing PEG−PE conjugate was pursued in two steps. First, phospholipid was activated with four different acyl hydrazides. The sulfhydryl reactive group of phosphatidylthioethanolamine was reacted with maleimide end of maleimido acyl hydrazides (refer to Table 1) through Michael addition, thus providing acyl hydrazide-activated PE. mPEG−butyraldehyde, an aliphatic aldehyde, was then reacted with acyl hydrazide-activated PE to get a hydrazone-based PEG−PE conjugate. ^{1}H NMR analysis was performed on synthesized conjugates using comparisons with both starting materials.

To synthesize aromatic aldehyde-derived hydrazone, an aromatic aldehyde moiety was introduced into the phospholipid by reacting succinimidyl 4-formylbenzoate (SFB) with PE under mild alkaline conditions. The acyl hydrazide−PEG derivatives were synthesized using mPEG−SH and maleimido acyl hydrazides (EMCH, MPBH, and KMUH). The SFB-activated phospholipid was then reacted with acyl hydrazide-derivatized PEG. The identity of aromatic aldehyde derived PEG−HZ−PE conjugates was confirmed by ^{1}H NMR.

Particle Size Measurement. All synthesized conjugates spontaneously self-assemble into micelles in aqueous solutions. The typical size distribution pattern of the micelles assembles from the representative PEG−HZ−PE conjugate, **15a**, is presented in Figure 2. As the measurements indicate, **15a** exhibited the size of 8−24 nm that is characteristic for typical PEG−PE micelles (*36*, *37*). All synthesized PEG−HZ−PE conjugates followed similar micelle size and distribution pattern.

In Vitro pH-Dependent Degradation of PEG−HZ−PE Conjugates. The stability of hydrazone-based PEG−PE conjugates incubated at physiological pH 7.4 and acidic pH 5.5 in buffer solutions maintained at 37 °C was investigated by HPLC. For this purpose, the area under the micelle peak of PEG−HZ−PE (R_t = 9−10 min) was observed over a period of time. PEG−HZ−PE conjugates were derived from an aliphatic aldehyde, and different acyl hydrazides were found to be highly unstable under acidic conditions, with the micelle peak completely disappearing within 2 min incubation at pH 5.5. At the

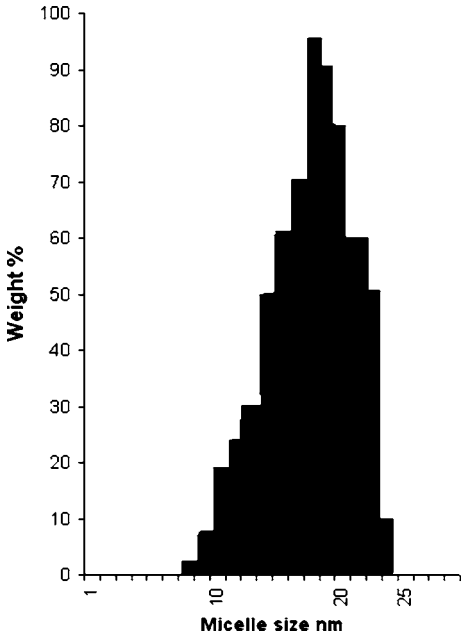


Figure 2. Typical particle size distribution pattern for PEG−HZ−PE conjugate miceles (compound **15a**).

Table 2. Half-Lives of Aliphatic Aldehyde-Based Hydrazone-Derived mPEG−HZ−PE Conjugates[a]

	half-life (min)	
mPEG−HZ−PE conjugate	pH 7.4	pH 5.5
4a	120	<2
4b	90	<2
4c	20	<2
9	150	<2

[a] In phosphate buffered saline, pH 7.4 or 5.5, at 37 °C.

Table 3. Half-Lives of Aromatic Aldehyde-Based Hydrazone-Derived mPEG−HZ−PE Conjugates[a]

	half-life (h)	
mPEG−HZ−PE conjugate	pH 7.4	pH 5.5
15a	>72 h	>48 h
15b	>72 h	>48 h
15c	>72 h	>48 h

[a] In phosphate buffered saline, pH 7.4 or 5.5, at 37 °C.

same time, these conjugates were relatively stable at physiological pH: the PEG−HZ−PE conjugate, **9**, with AMBH as cross-linker showed a half-life of 150 min, followed by EMCH, **4a**, (120 min), MPBH, **4b**, (90 min), and KMUH, **4c**, (20 min) (Table 2). The hydrolysis rate of the aliphatic aldehyde-derived hydrazone-based PEG−PE conjugates (**4a**, **4b**, **4c**, and **9**) at pH 7.4 seems to be dependent on the carbon chain length of acyl hydrazide. The increase in the number of carbon atoms in acyl hydrazide led to an increase in the rate of hydrolysis (PEG−PE conjugate **4c**, acyl hydrazide with 10 C atoms > **4a**, acyl hydrazide with 5 C atoms > **9**, acyl hydrazide with 3 C atoms). Introducing aromatic character within the carbon chain of acyl hydrazide led to an increase in the hydrolysis rate as observed in cases of **4b** and **4a** (the rate of hydrolysis of **4b** > **4a**). One has to note the precipitate (lipid) formation as hydrolysis of the hydrazone bond proceeds.

Alternatively, the PEG−HZ−PE conjugates derived from an aromatic aldehyde and acyl hydrazides were found to be highly stable at pH 7.4 and 5.5 (Table 3). The half-life values were not attained at either of those pH values even at the end of the incubation periods of 72 h at pH 7.4 and 48 h at pH 5.5 in buffer solutions maintained at 37 °C. The resistance to hydrolysis exhibited by hydrazones derived from aromatic aldehydes can be attributed to the conjugation of the π bonds of the −C═N− bond of the hydrazone with the π-bonding benzene ring. This observation supports the finding that hydrazones formed from aromatic aldehydes are more stable to acidic hydrolysis than those formed from aliphatic ones (*38*, *39*). The hydrazone hydrolysis involves the protonation of the −C═N nitrogen followed by the nucleophilic attack of water and cleavage of C−N bond of the tetrahedran intermediate (*40*). Any of these steps are determining and dependent on the pH. The substituents on the carbonyl reaction partner influence the rate of hydrolysis by altering the pK_a of the hydrazone with electron donating substituents facilitating protonation of the −C═N nitrogen (*41*). It is important to note here that "direct" PEG−PE conjugates with no HZ linkage between PEG and PE moieties used by us as controls in this study and others (*34*, *36*, *37*) do not demonstrate any hydrolysis at tested pH values over extended periods of time.

This would support the fact that PEG−HZ−PE conjugates containing a hydrazone bond derived from the aliphatic aldehyde are more prone to hydrolytic degradation. The aromatic aldehyde-derived hydrazone bond is too stable for the purpose of pH-triggered drug release. Careful selection of an aldehyde and an acyl hydrazide would be necessary for the application of the hydrazone-based chemistry for the development of pH-sensitive pharmaceutical nanocarriers with required stabilities/instabilities at normal and acidic pH values. Additional studies on the synthesis of aromatic and aliphatic ketone-derived hydrazone-based PEG−PE conjugates are currently underway in our laboratory.

ACKNOWLEDGMENT

This work was supported by NIH grant R01 EB001961 to Vladimir P. Torchilin. Authors thank Vijay S. Boddapathi and Dr. Ganesh Thakur for the technical assistance with ^{1}H NMR studies.

LITERATURE CITED

(1) Mainardes, R. M., and Silva, L. P. (2004) Drug delivery systems: past, present, and future. *Curr. Drug Targets 5*, 449−455.
(2) Nishiyama, N., Okazaki, S., Cabral, H., Miyamoto, M., Kato, Y., Sugiyama, Y., Nishio, K., Matsumura, Y., and Kataoka, K. (2003) Novel cisplatin-incorporated polymeric micelles can eradicate solid tumors in mice. *Cancer Res. 63*, 8977−8983.
(3) Kreuter, J. (1994) Drug targeting with nanoparticles. *Eur. J. Drug Metab. Pharmacokinet. 19*, 253−256.
(4) Storm, G., and Crommelin, D. J. (1997) Colloidal systems for tumor targeting. *Hybridoma 16*, 119−125.
(5) Simard, P., Hoarau, D., Khalid, M. N., Roux, E., and Leroux, J. C. (2005) Preparation and in vivo evaluation of PEGylated spherulite formulations. *Biochim. Biophys. Acta 1715*, 37−48.
(6) Francis, G. E., Delgado, C., Fisher, D., Malik, F., and Agrawal, A. K. (1996) Polyethylene glycol modification: relevance of improved methodology to tumour targeting. *J. Drug Target. 3*, 321−340.
(7) Maruyama, K. (2000) In vivo targeting by liposomes. *Biol. Pharm. Bull. 23*, 791−799.
(8) Xiong, X. B., Huang, Y., Lu, W. L., Zhang, X., Zhang, H., Nagai, T., and Zhang, Q. (2005) Intracellular delivery of doxorubicin with RGD-modified sterically stabilized liposomes for an improved antitumor efficacy: in vitro and in vivo. *J. Pharm. Sci. 94*, 1782−1793.
(9) Torchilin, V. P., Rammohan, R., Weissig, V., and Levchenko, T. S. (2001) TAT peptide on the surface of liposomes affords their efficient intracellular delivery even at low temperature and in the presence of metabolic inhibitors. *Proc. Natl. Acad. Sci. U.S.A. 98*, 8786−8791.
(10) Nori, A., and Kopecek, J. (2005) Intracellular targeting of polymer-bound drugs for cancer chemotherapy. *Adv. Drug Delivery Rev. 57*, 609−636.

(11) Jayasundar, R., and Singh, V. P. (2002) In vivo temperature measurements in brain tumors using proton MR spectroscopy. *Neurol. India 50*, 436−439.
(12) Engin, K., Leeper, D. B., Cater, J. R., Thistlethwaite, A. J., Tupchong, L., and McFarlane, J. D. (1995) Extracellular pH distribution in human tumours. *Int. J. Hyperthermia 11*, 211−216.
(13) Ojugo, A. S., McSheehy, P. M., McIntyre, D. J., McCoy, C., Stubbs, M., Leach, M. O., Judson, I. R., and Griffiths, J. R. (1999) Measurement of the extracellular pH of solid tumours in mice by magnetic resonance spectroscopy: a comparison of exogenous (19)F and (31)P probes. *NMR Biomed. 12*, 495−504.
(14) Khare, A. R., and Peppas, N. A. (1993) Release behavior of bioactive agents from pH-sensitive hydrogels. *J. Biomater. Sci. Polym. Ed. 4*, 275−289.
(15) Braslawsky, G. R., Kadow, K., Knipe, J., McGoff, K., Edson, M., Kaneko, T., and Greenfield, R. S. (1991) Adriamycin(hydrazone)-antibody conjugates require internalization and intracellular acid hydrolysis for antitumor activity. *Cancer Immunol. Immunother. 33*, 367−374.
(16) Yoo, H. S., Lee, E. A., and Park, T. G. (2002) Doxorubicin-conjugated biodegradable polymeric micelles having acid-cleavable linkages. *J. Controlled Release 82*, 17−27.
(17) Lee, E. S., Na, K., and Bae, Y. H. (2005) Super pH-sensitive multifunctional polymeric micelle. *Nano Lett. 5*, 325−329.
(18) Shen, W. C., and Ryser, H. J. (1981) cis-Aconityl spacer between daunomycin and macromolecular carriers: a model of pH-sensitive linkage releasing drug from a lysosomotropic conjugate. *Biochem. Biophys. Res. Commun. 102*, 1048−1054.
(19) Ogden, J. R., Leung, K., Kunda, S. A., Telander, M. W., Avner, B. P., Liao, S. K., Thurman, G. B., and Oldham, R. K. (1989) Immunoconjugates of doxorubicin and murine antihuman breast carcinoma monoclonal antibodies prepared via an N-hydroxysuccinimide active ester intermediate of cis-aconityl-doxorubicin: preparation and in vitro cytotoxicity. *Mol. Biother. 1*, 170−174.
(20) Patel, V. F., Hardin, J. N., Mastro, J. M., Law, K. L., Zimmermann, J. L., Ehlhardt, W. J., Woodland, J. M., and Starling, J. J. (1996) Novel acid labile COL1 trityl-linked difluoronucleoside immunoconjugates: synthesis, characterization, and biological activity. *Bioconjugate Chem. 7*, 497−510.
(21) Heffernan, M. J., and Murthy, N. (2005) Polyketal nanoparticles: a new pH-sensitive biodegradable drug delivery vehicle. *Bioconjugate Chem. 16*, 1340−1342.
(22) Gillies, E. R., and Frechet, J. M. (2005) pH-Responsive copolymer assemblies for controlled release of doxorubicin. *Bioconjugate Chem. 16*, 361−368.
(23) Gillies, E. R., Jonsson, T. B., and Frechet, J. M. (2004) Stimuli-responsive supramolecular assemblies of linear-dendritic copolymers. *J. Am. Chem. Soc. 126*, 11936−11943.
(24) Gumusderelioglu, M., and Kesgin, D. (2005) Release kinetics of bovine serum albumin from pH-sensitive poly(vinyl ether) based hydrogels. *Int. J. Pharm. 288*, 273−279.
(25) Shin, J., Shum, P., and Thompson, D. H. (2003) Acid-triggered release via dePEGylation of DOPE liposomes containing acid-labile vinyl ether PEG-lipids. *J. Controlled Release 91*, 187−200.
(26) Kratz, F., Beyer, U., Roth, T., Schutte, M. T., Unold, A., Fiebig, H. H., and Unger, C. (1998) Albumin conjugates of the anticancer drug chlorambucil: synthesis, characterization, and in vitro efficacy. *Arch. Pharm. (Weinheim) 331*, 47−53.
(27) Beyer, U., Roth, T., Schumacher, P., Maier, G., Unold, A., Frahm, A. W., Fiebig, H. H., Unger, C., and Kratz, F. (1998) Synthesis and in vitro efficacy of transferrin conjugates of the anticancer drug chlorambucil. *J. Med. Chem. 41*, 2701−2708.
(28) Di Stefano, G., Lanza, M., Kratz, F., Merina, L., and Fiume, L. (2004) A novel method for coupling doxorubicin to lactosaminated human albumin by an acid sensitive hydrazone bond: synthesis, characterization and preliminary biological properties of the conjugate. *Eur. J. Pharm. Sci. 23*, 393−397.
(29) Toncheva, V., Schacht, E., Ng, S. Y., Barr, J., and Heller, J. (2003) Use of block copolymers of poly(ortho esters) and poly (ethylene glycol) micellar carriers as potential tumour targeting systems. *J. Drug Target. 11*, 345−353.
(30) Oishi, M., Nagasaki, Y., Itaka, K., Nishiyama, N., and Kataoka, K. (2005) Lactosylated poly(ethylene glycol)-siRNA conjugate through acid-labile β-thiopropionate linkage to construct pH-sensitive polyion complex micelles achieving enhanced gene silencing in hepatoma cells. *J. Am. Chem. Soc. 127*, 1624−1625.
(31) Steenbergen, C., Deleeuw, G., Rich, T., and Williamson, J. R. (1977) Effects of acidosis and ischemia on contractility and intracellular pH of rat heart. *Circul. Res. 41*, 849−858.
(32) Frunder, H. (1949) The pH changes of living tissue during activity and inflammation. *Pharmazie 4*, 345−355.
(33) Mellman, I., Fuchs, R., and Helenius, A. (1986) Acidification of the endocytic and exocytic pathways. *Annu. Rev. Biochem. 55*, 663−700.
(34) Sawant, R. M., Hurley, J. P., Salmaso, S., Kale, A. A., Tolcheva, E., Levchenko, T., and Torchilin, V. P. (2006) "Smart" drug delivery systems: Double-targeted pH-responsive pharmaceutical nanocarriers. *Bioconjugate Chem. 17*, 943−949.
(35) Rideout, D. (1994) Self-assembling drugs: a new approach to biochemical modulation in cancer chemotherapy. *Cancer Invest. 12*, 189−202.
(36) Lukyanov, A. N., Gao, Z., Mazzola, L., and Torchilin, V. P. (2002) Polyethylene glycol-diacyllipid micelles demonstrate increased acculumation in subcutaneous tumors in mice. *Pharm. Res. 19*, 1424−1429.
(37) Lukyanov, A. N., Gao, Z., and Torchilin, V. P. (2003) Micelles from polyethylene glycol/phosphatidylethanolamine conjugates for tumor drug delivery. *J. Controlled Release 91*, 97−102.
(38) Apelgren, L. D., Bailey, D. L., Briggs, S. L., Barton, R. L., Guttman-Carlisle, D., Koppel, G. A., Nichols, C. L., Scott, W. L., Lindstrom, T. D., Baker, A. L., and Bumol, T. F. (1993) Chemoimmunoconjugate development for ovarian carcinoma therapy: preclinical studies with vinca alkaloid-monoclonal antibody constructs. *Bioconjugate Chem. 4*, 121−126.
(39) Baker, M. A., Gray, B. D., Ohlsson-Wilhelm, B. M., Carpenter, D. C., and Muirhead, K. A. (1996) Zyn-Linked colchicines: Controlled-release lipophilic prodrugs with enhanced antitumor efficacy. *J. Controlled Release 40*, 89−100.
(40) Cordes, E. H., and Jencks, W. P. (1963) The mechanism of hydrolysis of Schiff's bases derived from aliphatic amines. *J. Am. Chem. Soc. 85*, 2843−2848.
(41) Harnsberger, H. F., Cochran, E. L., and Szmant, H. H. (1955) The basicity of hydrazones. *J. Am. Chem. Soc. 77*, 5048−5050.

BC060228X

Synthetic PEGylated Glycoproteins and Their Utility in Gene Delivery

Chang-po Chen, Ji-seon Kim, Dijie Liu, Garrett R. Rettig, Marie A. McAnuff, Molly E. Martin, and Kevin G. Rice*

Division of Medicinal and Natural Products Chemistry, College of Pharmacy, University of Iowa, Iowa City, Iowa 52242.
Received July 24, 2006; Revised Manuscript Received November 13, 2006

PEGylated glycoproteins (PGPs) were synthesized by copolymerizing a Cys-terminated PEG−peptide, glycopeptide, and melittin peptide. Compositionally unique PGPs were prepared by varying the ratio of PEG−peptide (20−90%) and melittin (0−70%) with a constant amount of glycopeptide (10%). The PGPs were purified by RP-HPLC, and characterized for molecular weight and polydispersity by GPC-HPLC and SDS-PAGE and for composition by RP-HPLC following reduction to form monomeric peptides. PGPs formed DNA condensates of 200−300 nm in diameter that were administered to mice via the tail vein. Biodistribution studies confirmed their primary targeting to liver hepatocytes with a DNA metabolic half-life of 1 h. Upon stimulation by hydrodynamic dosing with saline, PGP DNA (5 μg) mediated luciferase expression in the liver detected by bioluminescence imaging (BLI) after 24 h. The level of gene expression mediated by PGP DNA was 5000-fold less than direct hydrodynamic dosing of an equivalent amount of DNA and was independent of the mol percent of melittin incorporated into the polymer, but dependent on the presence of galactose on PGP. The results establish the ability to prepare three-component gene delivery polymers that function in vivo. Further design improvements in fusogenic peptides for gene delivery and for the simultaneous use of a nuclear targeting strategy will be necessary to approach levels of expression mediated by the direct hydrodynamic dosing of DNA.

INTRODUCTION

Glycoproteins are a class of biological molecules composed of a protein backbone modified with N or O-glycans (*1*). Their functions are quite varied and often involve the interaction of the terminal sugars on the glycan with endogenous lectins on mammalian cell surfaces (*2*).

One of the earliest nonviral gene delivery systems was able to target DNA to internalize into hepatocytes via the asialoglycoprotein receptor (*3*, *4*). This delivery system was composed of an asialoglycoprotein covalently linked to polylysine. Refinement of this delivery system has been ongoing by many groups since this first demonstration. The ligand has been simplified by utilization of a cluster of the monosaccharide galactose (*5*−*7*), neoglycopeptides (*8*), or purified N-glycans (*9*−*11*). Polylysine has been substituted by PEI (*12*), chitosan (*13*), dendrimers (*14*), and synthetic peptides (*10*, *15*−*18*) containing clusters of Lys or Arg residues. In many cases, the polymers have been modified by poly(ethylene glycol) (PEG) (*10*, *19*−*22*) to render them more biocompatible for use as in vivo gene delivery agents. In all, these refinements have led to more sophisticated nonviral gene delivery systems that are smaller, more homogeneous, more modular, and better equipped to achieve subcellular targeting than their predecessors.

Two key steps to enhancing the expression of a receptor-mediated nonviral gene delivery system in vivo are (1) DNA escape from the endosome (*23*−*26*) and (2) nuclear targeting (*27*). Several studies have reported the utility of fusogenic peptides to enhance endosomal escape and gene expression in vitro (*21*, *25*, *28*), but fewer studies have reported their use in vivo (*29*, *30*), and none have reported the use of melittin in vivo. In part, the difficulty in demonstrating the utility of fusogenic peptides in vivo relates to the synthetic challenge in incorporating these into the gene delivery system so that they can be properly released within the endosomal compartment of the target cell. A further complication with testing the efficacy of fusogenic peptides in vivo is the need to simultaneously achieve efficient targeted delivery of DNA to cells and nuclear targeting of DNA, to observe appreciable gene expression in animals.

Ongoing studies from our lab have reported the development of peptides possessing terminal Cys residues that bind DNA and polymerize through disulfide bond formation (*31*, *32*). The resulting polypeptide DNA condensates mediate enhanced in vitro gene transfer, presumably by triggered release of the DNA following intracellular reduction of disulfide bonds (*33*). To test the utility of this approach in vivo, we have reported the use of a Cys-terminated glycopeptide and PEG−peptide that copolymerize on DNA, direct its biodistribution through receptor-mediated targeting to hepatocytes in mice, and produce measurable but low-level gene expression in vivo (*11*, *22*).

In the present study, we have advanced this delivery system to generate ternary peptide copolymers composed of PEG−peptide, glycopeptide, and a fusogenic melittin peptide. A detailed account of the polymerizable melittin peptide used in this study was recently reported (*34*). The resulting PEGylated glycoproteins (PGPs) are prepared with a precise stoichiometry of peptide components and have the ability to bind to DNA and mediate targeted gene delivery in vivo. Entry into hepatocytes requires careful control over the particle size of DNA condensates (*35*). Once inside the cell, the reduction of disulfide bonds should lead to the rapid dissociation of the carrier from the DNA and release of melittin in the endosome where it can function to facilitate DNA escape to the cytosol.

However, without the ability to target DNA to the nucleus, endocytosed DNA remains largely in the cytosol where it is incapable of mediating significant gene expression in quiescent hepatocytes. To stimulate gene expression, we report the utility of hydrodynamic dosing (*36*) of saline 5 min after a conventional dose of formulated DNA. This approach has allowed us to utilize bioluminescence imaging (BLI) to compare the efficiency of

* Corresponding author. E-mail: kevin-rice@uiowa.edu. Tel: 319-335-9903. Fax: 319-335-8766.

10.1021/bc060229p CCC: $37.00 © 2007 American Chemical Society
Published on Web 01/17/2007

PGP DNA relative to the direct hydrodynamic dosing of an equivalent amount of DNA.

MATERIALS AND METHODS

General Methods. Substituted Wang resin for peptide synthesis, N-terminal Fmoc-protected amino acids, 9-hydroxybenzotriazole, and diisopropylethylamine were obtained from Advanced ChemTech (Lexington, KY). *N*,*N*-Dimethylformamide, trifluoroacetic acid (TFA), acetic acid anhydride, acetonitrile, and piperidine were purchased from Fisher Scientific (Pittsburgh, PA). Tris(2-carboxyethyl)phosphine hydrochloride (TCEP), thiazole orange, poly(lysine) of varying molecular weight, and bovine testes β-galactosidase (EC 3.2.1.23) were obtained from Sigma Aldrich Co. (St Louis, MO). PEG standards were purchased from Tosoh Corp. (Tokyo, Japan). D-Luciferin and luciferase from *Photinus pyralis* were purchased from Roche Applied Science (Indianapolis, IN). Inactivated "qualified" fetal bovine serum (FBS) and Seeblue prestained peptide standard were from Invitrogen Co. (Carlsbad, CA). BCA assay kit, Blocker BSA in TBS (10×), and 1-Step NBT/BCIP were from Pierce (Rockford, IL). Precast 4−15% gradient SDS-PAGE gels (Ready Gel) were purchased from BioRad (Hercules, CA). GS-1 lectin was from EY Laboratories, Inc. (San Mateo, CA). Protran (pure nitrocellulose transfer and immobilization membrane, 0.2 μm) was from Schleicher and Schuell BioScience (Basel, Germany). pGL3 control vector, a 5.3 kb luciferase plasmid containing a SV40 promoter and enhancer, was obtained from Promega (Madison, WI). pDNA was amplified in a DH5α strain of *Escherichia coli* and purified on an endotoxin-free Qiagen megaprep column (Valencia, CA) according to the manufacturer's instructions.

Peptide Synthesis. Peptide synthesis was carried out on an Apex 396 from Advanced Chem Tech (Louisville, KY). Peptide purification was performed using a semipreparative (10 μm) C_{18} RP-HPLC column from Vydac (Hesperia, CA). Preparative HPLC was performed using a computer-interfaced HPLC and fraction collector from ISCO (Lincoln, NE). Electrospray mass spectrometry (ES-MS) was performed using an Agilent 1100 LC-MS system.

Cys-terminated melittin peptide, (**M1**) CKKKIGAVLKVLTTG LPALISWIKRKRQQKKKC, was synthesized using standard Fmoc procedures as described previously (*34*).

DNA binding peptide (**P1**) (Acm)CKKKKKKKKCKKKKKKKKKWC(Acm) (acetamidomethyl) was synthesized using standard Fmoc procedures starting from Fmoc-Cys(Acm)-Wang resin, except that N-capping with diisopropylethylamine and acetic anhydride was included after each coupling cycle to avoid truncated sequences. The peptide was cleaved from the resin and deprotected (except for the Acm protecting groups on cysteines) in 95% TFA. The peptide was then purified to homogeneity by injecting 1 μmol onto a semipreparative RP-HPLC column (2 × 25 cm) eluted at 10 mL/min with 0.1% (v/v) TFA and a gradient of acetonitrile (5−25% over 30 min) while monitoring tryptophan absorbance at 280 nm. The major peak eluting at 22 min was collected and pooled from multiple injections, concentrated by rotary evaporation, lyophilized, and stored dry at −20 °C. The purified peptides were reconstituted in 0.1% TFA, quantified by tryptophan absorbance ($\epsilon_{280\ nm}$ = 5600 M^{-1} cm^{-1}) and characterized on an Agilent 1100 LC-MS resulting in *m*/*z*: 2706.6/2706.1 (found/calculated).

An Acm-protected PEG−peptide was synthesized by reacting **P1** with PEG−maleimide (molar ratio 1:1.5) in 0.1 M sodium phosphate buffer (pH 7.0) at RT for 3 h. The PEG−peptide was purified by injection of 2 μmol onto semipreparative RP-HPLC (2 × 25 cm) eluted at 10 mL/min with 0.1% TFA and a gradient of acetonitrile (5−65% over 30 min) while detecting $Abs_{280\ nm}$. Final deprotection was accomplished by dissolving 5 μmol in 1 mL of cold TFA followed by the addition of silver tetrafluoroborate (20 mol equiv per Acm group) and anisol (10 equiv per Acm group) followed by reaction at 4 °C for 1 h with stirring. The deprotected PEG−peptide was precipitated as the silver salt in 60% (v/v) diethyl ether. The precipitate was centrifuged, then redissolved in 0.1 M acetic acid containing DTT (40 equiv per Acm group) and reacted at RT for 3 h. Following centrifugation to remove insolubles, the deprotected PEG−peptide was purified on a semipreparative RP-HPLC eluted as described above. The isolated PEG−peptide was freeze-dried and reconstituted in 0.1% TFA and reanalyzed by analytical HPLC to determine purity. The PEG−peptide was characterized by MALDI-TOF by spotting 1 μL (1 nmol) in α-cyano-4-hydroxycinnamic acid (30 mg/mL) on the target. A broad peak with an average mass of 8077 *m*/*z* was observed, consistent with the anticipated mass of the conjugate.

Acm-protected glycopeptide was synthesized by conjugating iodoacetamide triantennary *N*-glycan (*37*) and **P1** at a molar ratio of 1:1.25 in 0.2 M Tris buffer (pH 8.0) for 12 h at RT. The resulting glycopeptide was purified by a semipreparative RP-HPLC column (2 × 25 cm) eluted at 10 mL/min with 0.1% TFA and a gradient of 5−20% acetonitrile over 30 min. The peak corresponding to the glycopeptides was pooled and lyophilized. Final deprotection of the Acm groups was performed as described above. After purification on semipreparative RP-HPLC, the glycopeptide was concentrated, lyophilized, and reconstituted in 0.1% TFA, then quantified by $Abs_{280\ nm}$ ($\epsilon_{280\ nm}$ = 6930 M^{-1} cm^{-1}) and characterized by LC-MS resulting in *m*/*z*: 4773.5/4775.0 (found/calculated).

Synthesis of PGPs. Cys-terminated melittin peptide, glycopeptide, and PEG−peptide were combined in a predetermined ratio resulting in 200 nmol of total peptide in 200 μL of 0.1% TFA. The peptides were vortexed and freeze-dried, then dissolved in 16 μL of 0.1 M sodium phosphate pH 8 containing 4 μL of DMSO and reacted at RT for 48 h.

The progress of the polymerization was monitored using Ellman's method (*38*) to monitor free thiols. An aliquot (2 μL) was combined with 1 mL of DTNB solution (10 mM DTNB in 100 mM sodium phosphate pH 7.3 containing 0.5 mM EDTA) at times ranging from 1 min to 48 h. The absorbance was determined at 412 nm relative to a blank of DTNB solution.

PGPs were purified on a semipreparative RP-HPLC column (2 × 25 cm) eluted at 10 mL/min with 0.1% TFA and a gradient of 20−55% acetonitrile over 30 min. The primary peak was collected, concentrated by freeze drying, dissolved in water, and quantified by $Abs_{280\ nm}$ (ϵ = 6900 M^{-1} cm^{-1}). Agalatosyl PGP was prepared by treating the PGP 3 with β-galactosidase as reported previously (*22*). The agalactosyl PGP 3* was characterized by compositional analysis as describe below, during which LC-MS verified the complete removal of galactose from the glycopeptide.

RP-HPLC-purified PGPs (10 nmol) were prepared in 100 μL of 50 mM Tris pH 7.5 to which 50 nmol equiv of TCP was added in 10 μL of water and reacted for 3 h at RT. The product was chromatographed on analytical RP-HPLC eluted 1 mL/min with 0.1% TFA and 5−65% gradient of acetonitrile over 30 min. The glycopeptide, PEG−peptide, and melittin peptide were quantified against primary standards of each peptide to allow calculation of the peptide composition of each PGP.

The molecular weight of each PGP was determined GPC−HPLC on an Agilent 1100 HPLC system equipped with a refractive index detector and a Shodex OH Pak SB-800 HQ column (7.8 × 300 mm). Freeze-dried PGPs were dissolved in the mobile phase (10 v/v % methanol in water prepared in 0.5 M sodium chloride and 50 mM sodium phosphate pH 7), and 100 μL (10 nmol) was applied to the column. The average molecular weight (MW) was calculated relative to the elution

time of polylysine standards of 3.5, 20.4, 27.4, 66.7, and 84.0 kDa and PEG standards of 24, 50, 107, and 140 kDa.

PGPs (8 nmol) were dissolved in nondenaturing sample loading buffer containing 8 M urea, then loaded onto a 4−15% gradient SDS-PAGE without a stacking gel and run for 1.5 h at 90 V. PGPs bands were visualized by staining with coumassie followed by destaining. PGPs were also stained for PEG using Dragendorff's method (*39*). PGPs were likewise stained for galactose following transfer onto a nitrocellulose membrane in transfer buffer (10 mM $NaHCO_3$, 9.9 mM Na_2CO_3, 0.1% SDS; pH 9.9). The membrane was blocked overnight in 2.5% BSA in TBS (50 mM Tris-HCl, pH 7.4, 150 mM sodium chloride), washed three times with TBST (0.1% Tween 20 in TBS), and washed once with lectin buffer I (1 mM $CaCl_2$ and 1 mM $MgSO_4$ in TBS). The membrane was then incubated with 1 mL of alkaline phosphatase-conjugated GS-1 lectin (1 μg/mL) for 1.5 h. The unbound lectin was removed by washing with TBST three times, and the membrane was treated with 5 mL of lectin buffer II containing 100 μg/mL of nitro blue tetrazolium and 200 μg/mL of 5-bromo-4-chloro-3-indolyl phosphate.

DNA Formulation, Biodistribution, and Gene Expression. PGP binding to DNA was monitored by a fluorophore exclusion assay (*17*). PGP DNA condensates (2.5 μg in 50 μL) were prepared at 0, 0.1, 0.15, 0.3, 0.6, and 1.2 nmol of peptide monomer per μg of DNA then added to 950 μL of HBM (0.27 M mannitol, 5 mM Hepes; pH 7.5) containing 0.1 μM thiazole orange. The fluorescence of the intercalator dye was measured using an LS50B fluorometer (Perkin-Elmer, U.K.) by exciting at 500 nm while monitoring emission at 530 nm with the slit width set at 15 and 20 nm, respectively. Fluorescence blanks were subtracted from all values before data analysis.

The particle sizes of peptide DNA condensates were determined by quasi-elastic light scattering at a scatter angle of 90° on a Brookhaven ZetaPlus particle sizer. Condensates were prepared at a DNA concentration of 50 μg/mL in 400 μL of HBM at a stoichiometry of 0.3 nmol of peptide per μg of DNA corresponding to a charge ratio of approximately 2:1 for each. The mean diameter and population distribution were computed from the diffusion coefficient using a unimodal cumulate analysis supplied by the manufacturer. The zeta potential was determined as the mean of ten measurements in 5 mM Hepes pH 7.4.

Plasmid DNA was radiolabeled with ^{125}I as described previously (*40*), resulting in ^{125}I-DNA with a specific activity of 250 nCi/μg. PGP DNA biodistribution studies were conducted in ICR mice. Mice were anesthetized, and ^{125}I-DNA (2.5 μg, 0.75 μCi) condensed with 0.8 nmol PGP in 50 μL of HBM were dosed i.v. via the tail vein. After 5, 15, 30, 60, 120, 240, 360, and 480 min, mice were sacrificed by cervical dislocation; and the major organs (liver, lung, spleen, stomach, kidney, heart, large intestine, and small intestine) were harvested, rinsed with saline, and weighed. The radioactivity in each organ was determined by direct γ-counting and expressed as the percent of the dose in the target organ (*10*). The distribution of liver-targeted DNA between hepatocytes and Kupffer cells was determined following collagenase perfusion as described previously (*10*).

PGP DNA condensates were prepared for in vivo gene expression by combining 15 μg of pGL3 in 150 μL of HBM (0.27 M mannitol, 5 mM Hepes; pH 7.5) with 4.5 nmol of PGP in 150 μL of HBM while vortexing, resulting in DNA condensates possessing a calculated charge ratio (NH_4^+/PO_4^-) of 2. Triplicate mice (20 g) were administered a 100 μL tail vein dose (5 μg of DNA, 1.5 nmol of PGP), and after 5 min, a 1.8 mL dose of PBS was hydrodynamically delivered (*36*) via the tail vein to stimulate gene expression. After 24 h, the mice were dosed i.p. with 80 μL (2.4 mg) of D-luciferin, then anesthetized with isoflorane gas and imaged after 4 min on an IVIS Imaging System (Xenogen, Alameda, CA). The luminescence in the liver was quantified (photons/s/cm^2/seradian) by *Living Image* software and is presented with a pseudo-color overlay of luminescence intensity on grayscale images. The photon intensity in the liver was converted into pg of luciferase via a standard curve that was reported previously (*41*).

RESULTS

The present study prepared three Cys-terminated peptides used as monomers to polymerize into PEGylated glycoproteins (PGPs) with utility for gene transfer. This strategy would allow polymeric peptides to undergo reduction into their monomeric components after cellular internalization (*42*). We have previously utilized DNA as a template to polymerize either one or two Cys-terminated peptides into polymers (*22*, *31*). However, template polymerization becomes inherently more difficult as the number of peptide components increase. This is especially true if each peptide component possesses a different binding affinity for DNA. Thus, when preparing polymers that possess a PEG−peptide, glycopeptide, and a melittin peptide, it became desirable to polymerize, purify, and characterize the resulting PGPs prior to the formation of DNA condensates. The component PEG−peptide, glycopeptide, and melittin peptide utilized in this study and the resulting PGPs are illustrated in Figure 1.

To establish optimal polymerization conditions for multicomponent PGPs, a model peptide ($CWK_{17}C$) was used (*31*). The results obtained were similar to those reported by Seymour and colleagues using a single peptide (*43*). The polymerization reaction was monitored by RP-HPLC with the full-length polymer eluting later relative to monomeric and intermediate-length peptides. The polymerization progressed further toward completion when the peptide was concentrated to 10 mM in 100 mM sodium phosphate buffer pH 8. More dilute peptide solutions polymerized more slowly and to a lesser degree of completion. Lowering the pH to 7 or 6 caused the reaction to slow, whereas raising the pH to 9 or 10 did not increase the rate. Likewise, phosphate buffer concentrations higher than 0.1 M did not influence the rate of reaction. When applying the polymerization conditions described above to a two- or three-component polymerization to form PGPs, the same trends were observed except that the limiting solubility of the melittin peptide (**M1**) necessitated the addition of 20 v/v % DMSO, which also facilitated oxidation to form cystines.

The time course of the optimized reaction to form PGPs was monitored by Ellman's reaction to detect residual thiols (Figure 2). The results indicate that the reaction was >95% complete after 48 h at RT. Analysis of the reaction by RP-HPLC established that the glycopeptide, PEG−peptide, and melittin peptide were consumed during the 48 h of reaction with the formation of a major peak (Figure 3). PGPs were preparatively purified to remove minor earlier- or later-eluting shoulder peaks.

A calibrated GPC-HPLC was used as the primary means to measure the approximate size of each PGP. Each purified PGP appeared as single peak on a Shodex column eluted with 10% methanol and 0.5 M sodium chloride (Figure 4A−E). When using commercially available poly(lysine)s as calibrants, the average molecular weights of PGPs 1−4 were determined to be 83−106 kDa (Table 1). The average molecular weight of PGP 5 was significantly lower (35 kDa) than those of the other PGPs, most likely due to the larger ratio of **M1** in the polymer (Table 1). The average molecular weights of PGPs 1−4 were estimated to be approximately 50 kDa when using PEG standard to calibrate the GPC-HPLC (Table 1). On the basis of the monomer composition and molecular weight of each monomer, the average degree of polymerization (dp) for PGPs 1−4 was found to be 10−13 monomer peptides based on poly(lysine) standards or dp 5−6 based on PEG standards.

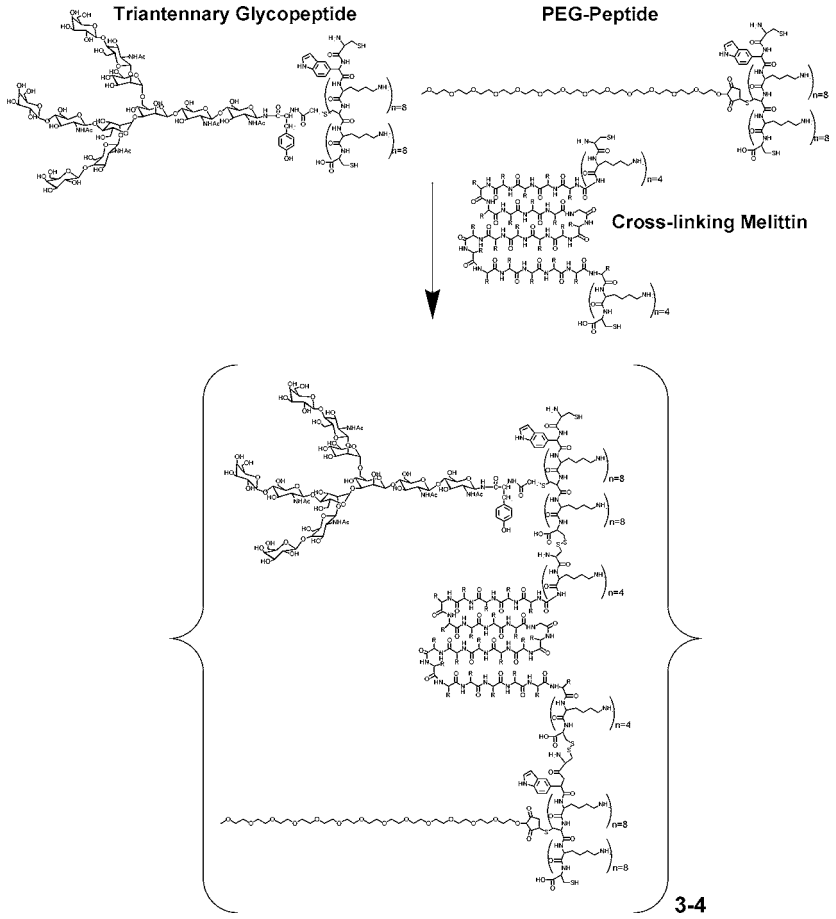


Figure 1. Structure of Cys-terminated peptides and PEGs. The structures of Cys-terminated glycopeptide, PEG−peptide, and melittin peptide are shown. Following polymerization for 48 h, the resulting PGPs, illustrated as a representative structure, were isolated by RP-HPLC and characterized for composition and molecular weight. R represents the side chains of melittin amino acids (*34*).

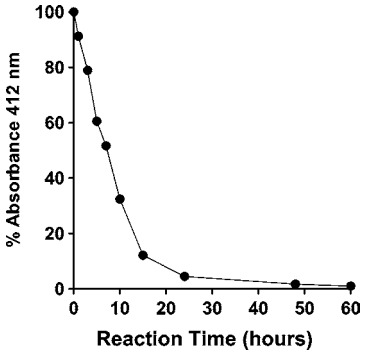


Figure 2. Kinetic analysis of polymerization reaction. The time course of the PGP polymerization reaction was measured by monitoring the number of residual thiols by Ellman's reaction. The results indicated that the reaction was >95% complete after 48 h.

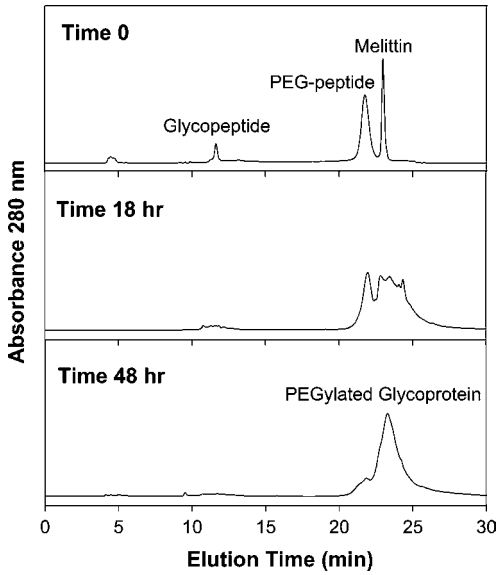


Figure 3. RP-HPLC analysis of PGP formation. The time courses of polymerization of Cys-terminated glycopeptide, PEG−peptide, and melittin peptide were monitored by RP-HPLC. The results indicate that PGPs elute slightly later than the monomeric components on RP-HPLC eluted with a gradient.

Gradient SDS-PAGE was used as a secondary measure of molecular size. As illustrated in Figure 4, PGPs 1−4 each showed a high molecular weight band of greater than 250 kDa based on protein standards stained with coumassie (Figure 4, lanes A−E), as well as Dragendorff's stain (lanes F−J) for PEG and by lectin overlay (lanes K−O) to detect for galactose-terminated N-glycans. Although the PAGE analysis established that each PGP is polymeric and contains both PEG and N-glycan, the molecular weight by PAGE appears to be overestimated. As with GPC-HPLC, the PAGE analysis of PGP 5 established that it is substantially less polymeric than the other PGPs (Figure 4, lanes E,J,O).

Each purified PGP was also characterized for the precise composition of Cys-terminated peptide in the polymer. Reduction of each PGP followed by RP-HPLC analysis led to the quantitative analysis of each peptide component (Figure 5A−E′). The results summarized in Table 1 indicate that melittin peptide was slightly overincorporated and the glycopeptide slightly underincorporated relative to the input ratio. However,

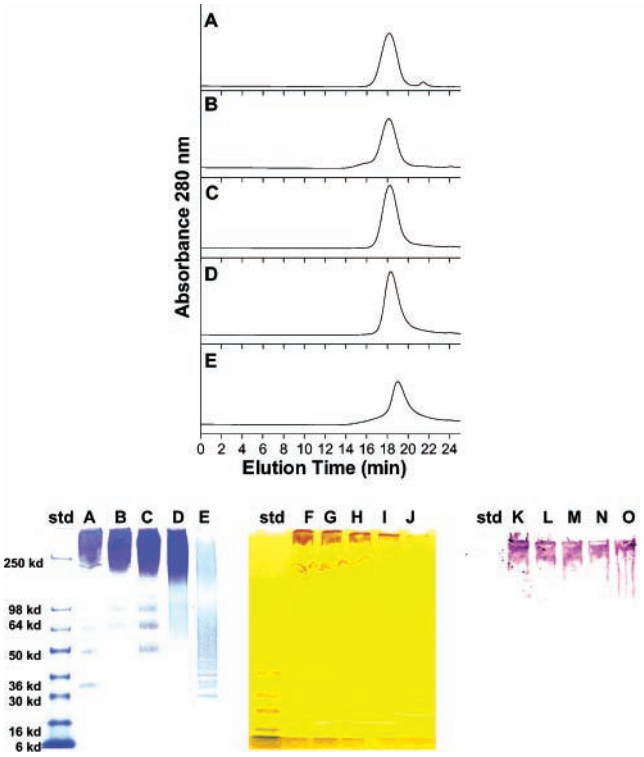


Figure 4. Molecular weight characterization of PGPs. The average molecular weight of each PGP was determined by GPC−HPLC and estimated by gradient SDS-PAGE. Panels A−E (upper) and lanes A−O (lower) represent (A,F,K) PGP 1, 90% PEG−peptide/10% glycopeptide; (B,G,L) PGP 2, 80% PEG−peptide/10% glycopeptide/10% melittin; (C,H,M) PGP 3, 70% PEG−peptide/10% glycopeptide/20% melittin; (D,I,N) PGP 4, 40% PEG−peptide/10% glycopeptide/50% melittin; (E,J,O) PGP 5, 20% PEG−peptide/10% glycopeptide/70% melittin. The gradient SDS-PAGE gel was stained with coumassie to detect protein (lanes A−E), with iodobismuthate to detect PEG (lanes F−J), and with lectin overlay to detect N-glycan (lanes K−O).

these results clearly indicate the potential to manipulate the PGP composition.

PGPs were individually combined with plasmid DNA, and the binding stoichiometry was measured by fluorophore displacement assay (not shown). On the basis of this experiment, the PGP to DNA stoichiometry was set at 0.3 nmol (based on peptide monomer) per μg of DNA, corresponding to approximately a 2:1 N/P ratio. The particle size of each PGP DNA condensate ranged from 200 to 300 nm, whereas the zeta potential was +0.5−6 mV (Table 1).

The biodistribution of tail vein dosed PGP−^{125}I-DNA revealed that each targeted the liver as the primary target site (Figure 6). Nearly 50% of the dose accumulated in the liver within 5 min following i.v. dosing. Control experiments reported previously (*10*) established that naked ^{125}I-DNA also accumulates with 50% of the dose recovered in the liver after 5 min but is rapidly metabolized and eliminated from the liver with a half-life of 30 min. Likewise, previously published biodistribution studies also established that 65% of the liver-targeted dose of naked ^{125}I-DNA was recovered from Kupffer cells and only 35% recovered from hepatocytes (*10*). In contrast, each PGP−^{125}I-DNA resulted in a slightly longer liver metabolic half-life of 1 h (Table 1). Detailed analysis of the liver targeting established that PGP DNA condensates mediated specific targeting with 60% of the dose recovered with hepatocytes and only 40% with Kupffer cells (Table 1). A control PGP that lacked galactose (PGP 3*) was deficient in specific targeting, resulting in the recovery of 62% of the dose from Kupffer cells and 38% from hepatocytes (Table 1).

To determine the influence of melittin concentration on gene transfer efficiency, each PGP DNA sample was dosed i.v. via the tail vein in mice. A conventional dose of 5 μg of DNA administered in 100 μL failed to produce luciferase gene expression after 24 h as measured by a Xenogen CCD camera (not shown). In contrast, a hydrodynamic dose of 5 μg of naked plasmid DNA in 1.8 mL of normal saline delivered via the tail vein in 5 s to 20 g mice produced 1×10^{10} light units in triplicate mice at 24 h post-DNA administration (Figure 7).

To evaluate if hydrodynamic dosing could stimulate the gene expression from DNA delivered by a conventional dose, a hydrodynamic dose of 1.8 mL of normal saline was administered in 5 s via the tail vein at 5 min post-conventional dose administration. Luciferase expression was then measured by a Xenogen CCD camera at 24 h post-administration of DNA. The results indicate that PGP DNA gained access to the liver cells and that upon stimulation by hydrodynamic dose the DNA gained access to the nucleus. A control experiment of conventionally dosed naked DNA followed by a hydrodynamic dose of saline established the complete absence of gene expression (Figure 7, Con1). This result suggests that a conventional dose of PGP DNA results in hepatocyte internalization and perhaps endosomal release, with the nuclear localization of DNA stimulated by a hydrodynamic dose of saline. Likewise, a control experiment that utilized PGP 3*, which was devoid of galactose, failed to mediate specific targeting of plasmid DNA to hepatocytes (Table 1) and greatly diminished the influence of the hydrodynamic dose of saline to stimulate gene expression (Figure 7, PGP 3*).

The magnitude of expression mediated by PGPs 1−5 DNA was approximately 5000-fold less than direct hydrodynamic dosing of an equivalent amount of DNA (5 μg). Surprisingly, the level of expression mediated by PGP DNA was independent of the amount of melittin incorporated into the PGP. The expression mediated by PGP 1, which was a copolymer of PEG−peptide and glycopeptide, was indistinguishable from that mediated by PGPs 2−5.

DISCUSSION

Receptor-mediated gene delivery holds promise as being a safe and efficient means of targeting DNA into specific cells following i.v. dosing. For nonviral gene delivery to reach its full potential, many biological barriers must be overcome from the point of dosing to crossing the nuclear membrane of the target cell. We have systematically studied receptor-mediated gene delivery aimed at targeting the liver and, in particular, hepatocytes as a model system to discover solutions to the barriers that exist for all receptor-mediated gene delivery systems. To this end, the asialoglycoprotein receptor on hepatocytes has been useful, since its cell trafficking and ligand specificity are well-understood (*44*, *45*).

We have previously demonstrated specific targeting to hepatocytes in mice via the asialoglycoprotein receptor mediated by a triantennary glycopeptide (*10*). We have also demonstrated the necessity for PEG to block protein binding and the recognition of DNA condensates by the reticuloendothelial system (*10*, *22*, *46*). Binary peptide copolymers were prepared from glycopeptides and PEG−peptides using plasmid DNA to conduct a template polymerization (*22*). One of the primary advantages of this approach is the triggered release of DNA upon reduction of the disulfide bonds within the cell. In order to cause endosomal escape, we have recently reported the design of synthetic Cys-terminated melittin peptides that bind and polymerize on DNA and mediate gene transfer in vitro (*34*). In the present study, we have selected a melittin analogue that mediated potent gene expression in vitro to incorporate into a copolymeric gene delivery system in an attempt to enhance gene expression in vivo.

Table 1. Structure, Biological, and Formulation Properties of PGP DNA

structure	monomer composition[a] (mol %)	measured composition[b] (mol %)	molecular weight (PLL),[c] (PEO)[d]	particle size[e]	zeta potential[f]	$t_{1/2}$ [g] hr	PC/NPC[h]
PGP 1	0:90:10	0:91.7:8.3	106 kDa, 50 kDa	221 ± 8	+0.5	1.1	60:40
PGP 2	10:80:10	12.8:82.5:4.7	109 kDa, 51 kDa	210 ± 13	+5	1.2	59:41
PGP 3	20:70:10	24.4:70.3:5.3	99 kDa, 47 kDa	227 ± 11	+6	1.2	65:35
PGP 4	40:50:10	44.8:46.4:8.8	83 kDa, 46 kDa	232 ± 1	+6	1.3	60:40
PGP 5	70:20:10	73.2:19.8:7.0	35 kDa, 21 kDa	295 ± 7	+5	1.1	63:37
PGP 3*[i]	20:70:10	12.6:80.9:6.5	99 kDa, 47 kDa	227 ± 11	+6	1.0	38:62

[a] Represents the input mol ratio of Cys-terminated melittin, PEG−peptide, and glycopeptide. [b] Represents the measured mol ratio of Cys-terminated melittin, PEG−peptide, and glycopeptide for each purified PGP. [c] Values are the calculated MW based on polylysine standards. [d] Values are the calculated MW based on PEG standards. [e] The mean particle size determined at a stoichiometry of 0.3 nmol of PGP per μg of DNA. The value represents the mean diameter (nm) based on unimodal analysis. [f] The zeta potential of PGP DNA condensates at a stoichiometry of 0.3 nmol of PGP per μg of DNA. [g] The metabolic half-life of PGP ^{125}I-DNA in triplicate mice. The results are derived from Figure 6. [h] The PC/NPC ratio of DNA-targeted liver. [i] Represents a control PGP 3 in which galactose has been removed.

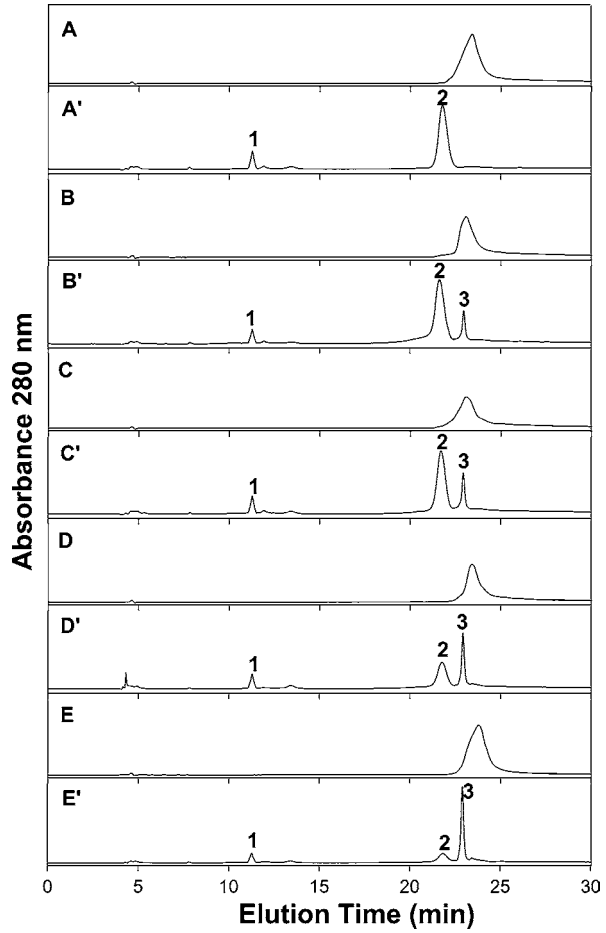


Figure 5. Compositional analysis of PGPs. The composition of each PGP was determined by RP-HPLC following reduction of the polymer with TCEP. Panels A−E illustrate the purified PEGylated glycoprotein prepared with mol composition of (A) PGP 1, 90% PEG−peptide/10% glycopeptide; (B) PGP 2, 80% PEG−peptide/10% glycopeptide/10% melittin; (C) PGP 3, 70% PEG−peptide/10% glycopeptide/20% melittin; (D) PGP 4, 40% PEG−peptide/10% glycopeptide/50% melittin; (E) PGP 5, 20% PEG−peptide/10% glycopeptide/70% melittin. Panels A′−E′ illustrate the recovery of the three peptide components from reduction with TCP. The precise compositions determined relative to standard curves are indicated in Table 1.

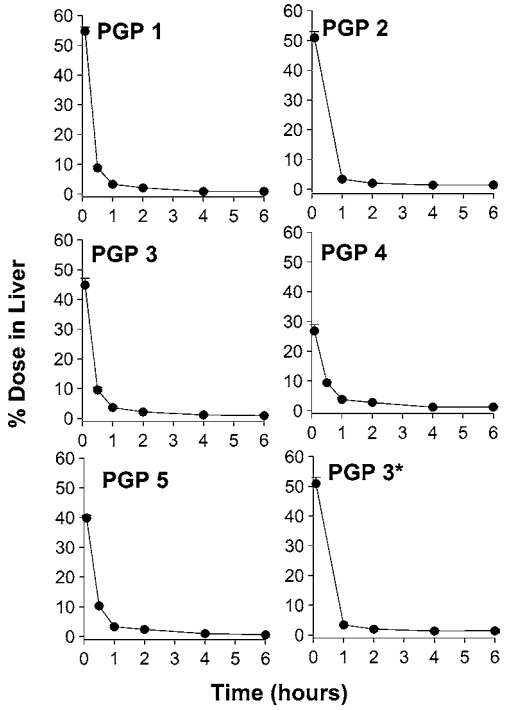


Figure 6. Biodistribution analysis of PGP DNA. The biodistribution analysis of each PGP−^{125}I-DNA condensate is compared following tail vein dosing in triplicate mice. The results establish the liver as the major target site. The liver metabolic half-life of PGP DNA is approximately 1 h, whereas naked ^{125}I-DNA dosed via the tail vein produced a similar targeting efficiency to liver but only a 0.5 h half-life. Each formulation demonstrated specific targeting to hepatocytes as indicated in Table 1, whereas a control formulation where galactose had been removed produced much lower targeting to hepatocytes.

To incorporate all three peptide components into a polymer and control their mol ratio, we found it most efficient to copolymerize concentrated mixtures of monomeric peptides followed by RP-HPLC purification of the resulting PGPs. The advantages of this approach over template polymerization are that it is not necessary that each monomer possesses DNA binding affinity, the resulting polymer can be characterized for size and composition, and more than three peptide components can be copolymerized to further increase the efficiency of gene delivery.

The de novo synthesis of PGPs 1−5 is a significant advancement toward more sophisticated gene delivery carriers that not only achieve primary targeting in vivo, but may potentially achieve secondary targeting by lysing endosomes and releasing DNA intracellularly. The molecular weight and compositional analysis of each PGP demonstrates that the polymerization results in the incorporation of 6−13 monomer peptides and the input ratio of monomer peptides closely reflects the ratio of peptides incorporated into the PGPs. At low melittin ratios, PGPs are higher molecular weight and somewhat more homogeneous, whereas at high melittin ratios, the opposite is observed. Still, each PGP was able to bind to plasmid DNA and form condensates that were of sufficiently small size to mediate specific targeting to the liver.

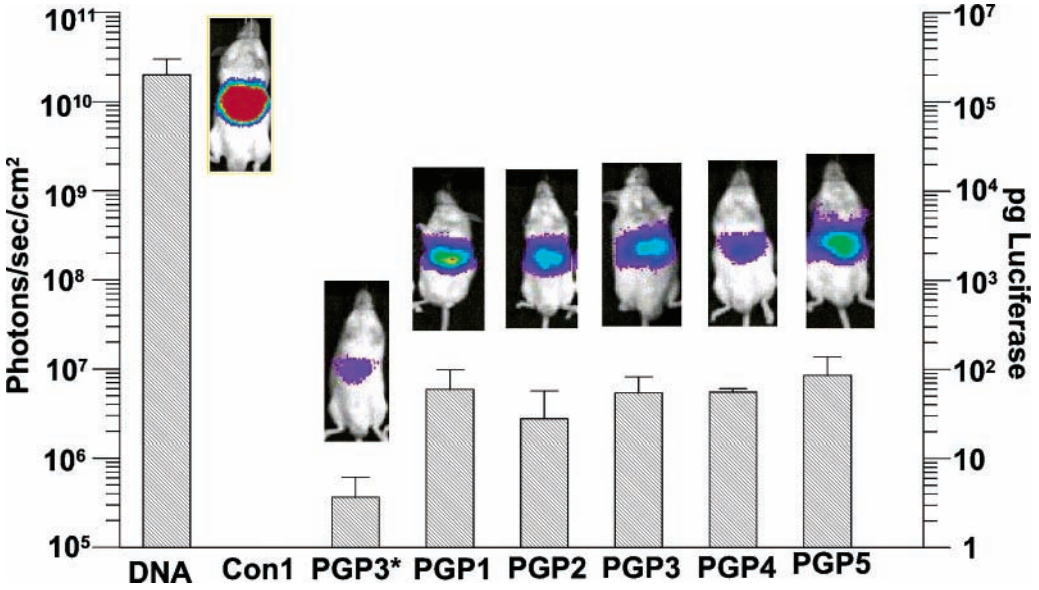


Figure 7. In vivo gene expression of PGP DNA condensates. Luciferase expression was measured by BLI 24 h following an i.v. tail vein dose of PGP DNA (5 μg) in 100 μL in triplicate mice and a subsequent hydrodynamic dose of 1.8 mL of saline administered 5 min later to stimulate nuclear uptake and gene expression. The insets illustrate representative BLI images for each treatment group. Control 1 illustrates the result of tail vein dose dosing of 5 μg of DNA in 100 μL of saline followed 5 min later by a hydrodynamic stimulation dose, resulting in no detectable luciferase expression. Likewise, PGP 3* has been modified to remove galactose, greatly reducing the specific targeting and the liver mediated gene expression. Alternatively, PGPs 1−5 demonstrate that the gene expression is independent of the amount of melittin incorporated into the PGP.

One of the difficulties in developing and testing targeted gene delivery systems in vivo is that, even if cell-type specific targeting is achieved, appreciable gene expression will not be observed unless the DNA gains access to the nucleus. This is indeed the case for PGP DNA, which fails to mediate measurable gene expression relative to direct hydrodynamic dosing of identical amounts of DNA (Figure 7).

Since hydrodynamic dosing is able to deliver a small fraction of a 5 μg DNA dose to the nucleus of mouse hepatocytes, resulting in a high level of gene expression (*36*), we rationalized that it may also stimulate the movement of cytosolic DNA to the nucleus. We tested this by measuring the luciferase gene expression after administering the PGP DNA by conventional small-volume dosing (100 μL), followed after 5 min by a hydrodynamic dose of saline that occurred after the DNA condensate had time to bind and perhaps internalize into hepatocytes via receptor-mediated endocytosis. We found that a delay 15 or 30 min prior to hydrodynamic stimulation resulted in unreliable stimulation of gene expression. The resulting expression profiles clearly establish that some of the hepatocyte-targeted DNA could be stimulated to enter the nucleus, resulting in its expression. The mechanism by which this occurs is unknown and could be similar to that by which hydrodynamic dosing delivers DNA to the nucleus (*47*), although the overall magnitude of gene expression still does not compare with direct hydrodynamic dosing.

Despite finding that hydrodynamic dosing could stimulate gene expression, we found that there was no correlation between the amount of melittin in PGPs and the magnitude of gene expression. This could result from the inability of melittin to release from the polymers during reduction or that this particular melittin analogue is not fully active in endosomal lysis in hepatocytes when entering via receptor-mediated endocytosis. In fact, the melittin analogue used in this study was found to maintain nearly full hemolytic potency at pH 7 relative to natural melittin but lost most of this activity at pH 4 (*34*). It is also possible that the lack of correlation may result from the use of hydrodynamic stimulation, which could mask the influence of melittin in vivo.

In conclusion, we have developed a modular gene delivery system by generating PGPs that function to deliver 5 μg of DNA in vivo leading to measurable gene expression in liver following hydrodynamic stimulation. However, given that hydrodynamic stimulation was essential to observe gene expression in vivo, the results point toward the need to develop more sophisticated delivery systems that are able to deliver the cytosolic DNA to the nucleus in vivo without the need for artificial intervention.

ACKNOWLEDGMENT

The authors gratefully acknowledge support for this work from NIH DK063196.

LITERATURE CITED

(1) Varki, A. (1993) Biological roles of oligosaccharides: all of the theories are correct. *Glycobiology 3*, 97−130.

(2) Lee, Y. C. (1992) Biochemistry of carbohydrate-protein interaction. *FASEB J. 6*, 3193−3200.

(3) Wu, G. Y., and Wu, C. H. (1988) Evidence for targeted gene delivery to Hep G2 hepatoma cells in vitro. *Biochemistry 27*, 887−892.

(4) Wu, G. Y., and Wu, C. H. (1988) Receptor-mediated gene delivery and expression in vivo. *J. Biol. Chem. 263*, 14621−14624.

(5) Midoux, P., Mendes, C., Legrand, A., Raimond, J., Mayer, R., Monsigny, M., and Roche, A. C. (1993) Specific gene transfer mediated by lactosylated poly-L-lysine into hepatoma cells. *Nucleic Acids Res. 21*, 871−878.

(6) Erbacher, P., Roche, A. C., Monsigny, M., and Midoux, P. (1995) Glycosylated polylysine/DNA complexes: gene transfer efficiency in relation with the size and the sugar substitution level of glycosylated polylysines and with the plasmid size. *Bioconjugate Chem. 6*, 401−410.

(7) Erbacher, P., Bousser, M. T., Raimond, J., Monsigny, M., Midoux, P., and Roche, A. C. (1996) Gene transfer by DNA/glycosylated polylysine complexes into human blood monocyte-derived macrophages. *Hum. Gene Ther. 7*, 721−729.

(8) Anwer, K., Logan, M., Tagliaferri, F., Wadhwa, M., Monera, O., Tung, C. H., Chen, W., Leonard, P., French, M., Proctor, B., Wilson, E., Singhal, A., and Rolland, A. (2000) Synthetic glycopeptide-based

delivery systems for systemic gene targeting to hepatocytes. *Pharm. Res. 17*, 451−9.
(9) Wadhwa, M. S., Knoell, D. L., Young, A. P., and Rice, K. G. (1995) Targeted gene delivery with a low molecular weight glycopeptide carrier. *Bioconjugate Chem. 6*, 283−291.
(10) Collard, W. T., Yang, Y., Kwok, K. Y., Park, Y., and Rice, K. G. (2000) Biodistribution, metabolism, and *in vivo* gene expression of low molecular weight glycopeptide polyethylene glycol peptide DNA co-condensates. *J. Pharm. Sci. 89*, 499−512.
(11) Park, Y., Kwok, K. Y., Boukarim, C., and Rice, K. G. (2002) Synthesis of sulfhydryl crosslinking poly(ethylene glycol) peptides and glycopeptides as carriers for gene delivery. *Bioconjugate Chem. 13*, 232−239.
(12) Bettinger, T., Remy, J. S., and Erbacher, P. (1999) Size reduction of galactosylated PEI/DNA complexes improves lectin-mediated gene transfer into hepatocytes. *Bioconjugate Chem. 10*, 558−61.
(13) Gao, S., Chen, J., Xu, X., Ding, Z., Yang, Y., Hua, Z., and Zhang, J. (2003) Galactosylated low molecular weight chitosan as DNA carrier for hepatocyte-targeting. *Int. J. Pharm. 255*, 57−68.
(14) Zanini, D., and Roy, R. (1998) Practical synthesis of starburst PAMAM - thiosialodendrimers for probing multivalent carbohydrate-lectin binding properties. *J. Org. Chem. 63*, 3486−3491.
(15) Niidome, T., Takaji, K., Urakawa, M., Ohmori, N., Wada, A., Hirayama, T., and Aoyagi, H. (1999) Chain length of cationic α-helical peptide sufficient for gene delivery into cells. *Bioconjugate Chem. 10*, 773−80.
(16) Plank, C., Tang, M. X., Wolfe, A. R., and Szoka, F. C., Jr. (1999) Branched cationic peptides for gene delivery: role of type and number of cationic residues in formation and in vitro activity of DNA polyplexes. *Hum. Gene Ther. 10*, 319−32.
(17) Wadhwa, M. S., Collard, W. T., Adami, R. C., McKenzie, D. L., and Rice, K. G. (1997) Peptide-mediated gene delivery: influence of peptide structure on gene expression. *Bioconjugate Chem. 8*, 81−8.
(18) Lee, H., Jeong, J. H., and Park, T. G. (2002) PEG grafted polylysine with fusogenic peptide for gene delivery: high transfection efficiency with low cytotoxicity. *J. Controlled Release 79*, 283−91.
(19) Choi, Y. H., Liu, F., Park, J. S., and Kim, S. W. (1998) Lactose-poly(ethylene glycol)-grafted poly-L-lysine as hepatoma cell-targeted gene carrier. *Bioconjugate Chem. 9*, 708−18.
(20) Ogris, M., Brunner, S., Schuller, S., Kircheis, R., and Wagner, E. (1999) PEGylated DNA/transferrin-PEI complexes: reduced interaction with blood components, extended circulation in blood and potential for systemic gene delivery. *Gene Ther. 6*, 595−605.
(21) Lee, H., Jeong, J. H., and Park, T. G. (2001) A new gene delivery formulation of polyethylenimine/DNA complexes coated with PEG conjugated fusogenic peptide. *J. Controlled Release 76*, 183−192.
(22) Kwok, K. Y., Park, Y., Yongsheng, Y., McKenzie, D. L., and Rice, K. G. (2003) In vivo gene transfer using sulfhydryl crosslinked PEG-peptide/glycopeptide DNA co-condensates. *J. Pharm. Sci. 92*, 1174−1185.
(23) Plank, C., Oberhauser, B., Mechtler, K., Koch, C., and Wagner, E. (1994) The influence of endosome-disruptive peptides on gene transfer using synthetic. *J. Biol. Chem. 269*, 12918−12924.
(24) Grosse, S., Tremeau-Bravard, A., Aron, Y., Briand, P., and Fajac, I. (2002) Intracellular rate-limiting steps of gene transfer using glycosylated polylysines in cystic fibrosis airway epithelial cells. *Gene Ther. 9*, 1000−7.
(25) Ogris, M., Carlisle, R. C., Bettinger, T., and Seymour, L. W. (2001) Melittin enables efficient vesicular escape and enhanced nuclear access of nonviral gene delivery vectors. *J. Biol. Chem. 276*, 47550−47555.
(26) Boeckel, S., Wagner, E., and Ogris, M. (2005) C-versus N-terminally linked melittin-polyethylenimine conjugates: the site of linkage strongly influences activity of DNA polyplexes. *J. Gene Med. 7*, 1335−1347.
(27) Chan, C. K., and Jans, D. A. (2002) Using nuclear targeting signals to enhance non-viral gene transfer. *Immunol. Cell Biol. 80*, 119−30.
(28) Wagner, E., Plank, C., Zatloukal, K., Cotten, M., and Birnstiel, M. L. (1992) Influenza virus hemagglutinin HA-2 N-terminal fusogenic peptides augment gene transfer by transferrin-polylysine-DNA complexes: toward a synthetic virus-like gene-transfer vehicle. *Proc. Natl. Acad. Sci. U.S.A. 89*, 7934−7938.
(29) Nishikawa, M., Yamauchi, M., Morimoto, K., Ishida, E., Takakura, Y., and Hashida, M. (2000) Heptocyte-targeted *in vivo* gene expression by intraveneous injection of plasmid DNA complexed with synthetic multi-functional gene delivery system. *Gene Ther. 7*, 548−555.
(30) Schuster, M. J., Wu, G. Y., Walton, C. M., and Wu, C. H. (1999) Multicomponent DNA carrier with a vesicular stomatitis virus G-peptide greatly enhaances liver-targeted gene expression in mice. *Bioconjugate Chem. 10*, 1075−1083.
(31) McKenzie, D. L., Kwok, K. Y., and Rice, K. G. (2000) A potent new class of reductively activated peptide gene delivery agents. *J. Biol. Chem. 275*, 9970−9977.
(32) McKenzie, D., Smiley, B., Kwok, K. Y., and Rice, K. G. (2000) Low molecular weight disulfide cross-linking peptides as nonviral gene delivery carriers. *Bioconjugate Chem 11*, 901−911.
(33) Carlisle, R. C., Etrych, T., Briggs, S. S., Preece, J. A., Ulbrich, K., and Seymour, L. W. (2004) Polymer-coated polyethylenimine/DNA Complexes designed for triggered activation by intracellular reduction. *J. Gene Med. 6*, 337−344.
(34) Chen, C.-P., Kim, J.-s., Steenblock, E., Liu, D., and Rice, K. G. (2006) Gene transfer with poly-melittin peptides. *Bioconjugate Chem. 17*, 1057−62.
(35) Rensen, P. C. N., Sliedregt, L. A. J. M., Ferns, M., Kieviet, E., Rossenberg, S. M. W. v., Leeuwen, S. H. v., Berkel, T. J. C. v., and Biessen, E. A. L. (2001) Determination of the upper size limit for uptake and processing of ligands by the asialoglycoprotein receptor on hepatocytes in vitro and in vivo. *J. Biol. Chem. 276*, 37577−37584.
(36) Liu, F., Song, Y., and Liu, D. (1999) Hydrodynamics-based transfection in animals by systemic administration of plasmid DNA. *Gene Ther. 6*, 1258−66.
(37) Collard, W. T., Evers, D. L., and McKenzie, D. L. (2000) Synthesis of homogenous glycopeptides and their utility as DNA condensing agents. *Carbohydr. Res. 323*, 176−184.
(38) Ellman, G. L. (1959) Tissue sulfhydryl groups. *Arch. Biochem. Biophys. 82*, 70−77.
(39) Dhara, D., and Chatterji, P. R. (1999) Electrophoretic transport of poly(ethylene glycol) chains through poly(acrylamide) gel. *J. Phys. Chem.* B *103*, 8458−8561.
(40) Terebesi, J., Kwok, K. Y., and Rice, K. G. (1998) Iodinated plasmid DNA as a tool for studying gene delivery. *Anal. Biochem. 263*, 120−123.
(41) Rettig, G., McAnuff, M., Kim, J., Liu, D., and Rice, K. G. (2006) Qantitative bioluminscence imaging of transgene expression in vivo. *Anal. Biochem. 335*, 90−94.
(42) Oupicky, D., Carlisle, R. C., and Seymour, L. W. (2001) Triggered intracellular activation of disulfide crosslinked polyelectrolyte gene delivery complexes with extended systemic circulation in vivo. *Gene Ther. 8*, 713−24.
(43) Oupicky, D., Parker, A. L., and Seymour, L. W. (2002) Laterally stabilized complexes of DNA with linear reducible polycations: strategy for triggered intracellular activation of DNA delivery vectors. *J. Am. Chem. Soc. 124*, 8−9.
(44) Schwartz, A. L., Bolognesi, A., and Fridovich, S. E. (1984) Recycling of the asialoglycoprotein receptor and the effect of lysosomotropic amines in hepatoma cells. *J. Cell Biol. 98*, 732−738.
(45) Schwartz, A. L., Fridovich, S. E., and Lodish, H. F. (1982) Kinetics of internalization and recycling of the asialoglycoprotein receptor in a hepatoma cell line. *J. Biol. Chem. 257*, 4230−4237.
(46) Yang, Y., Park, Y., Man, S., Liu, Y., and Rice, K. G. (2001) Cross-linked low molecular weight glycopeptide mediated gene delivery: relationship between DNA metabolic stability and the level of transient gene expression in vivo. *J. Pharm. Sci. 90*, 2010−2022.
(47) Zhang, G., Gao, X., Song, Y. K., Vollmer, R., Stolz, D. B., Gaskowski, J. Z., Dean, D. A., and Liu, D. (2004) Hydroporation as the mechanism of hydrodynamic delivery. *Gene Ther. 11*, 675−682.

BC060229P

Peptide-Based Pharmacomodulation of a Cancer-Targeted Optical Imaging and Photodynamic Therapy Agent

Klara Stefflova,[†] Hui Li,[‡] Juan Chen,[‡,§] and Gang Zheng*[,‡,§,||]

Departments of Chemistry and Radiology, University of Pennsylvania, Philadelphia, Pennsylvania 19104, and Ontario Cancer Institute, University of Toronto, MaRS Center, TMDT 5-363, 101 College Street, Toronto, Ontario M5G 1L7, Canada. Received August 18, 2006; Revised Manuscript Received November 20, 2006

We designed and synthesized a folate receptor-targeted, water-soluble, and pharmacomodulated photodynamic therapy (PDT) agent that selectively detects and destroys the targeted cancer cells while sparing normal tissue. This was achieved by minimizing the normal organ uptake (e.g., liver and spleen) and by discriminating between tumors with different levels of folate receptor (FR) expression. This construct (Pyro−peptide−Folate, PPF) is composed of three components: (1) pyropheophorbide a (Pyro) as an imaging and therapeutic agent, (2) peptide sequence as a stable linker and modulator improving the delivery efficiency, and (3) Folate as a homing molecule targeting FR-expressing cancer cells. We observed an enhanced accumulation of PPF in KB cancer cells (FR+) compared to HT 1080 cancer cells (FR−), resulting in a more effective post-PDT killing of KB cells over HT 1080 or normal CHO cells. The accumulation of PPF in KB cells can be up to 70% inhibited by an excess of free folic acid. The effect of Folate on preferential accumulation of PPF in KB tumors (KB vs HT 1080 tumors 2.5:1) was also confirmed in vivo. In contrast to that, no significant difference between the KB and HT 1080 tumor was observed in case of the untargeted probe (Pyro−peptide, PP), eliminating the potential influence of Pyro's own nonspecific affinity to cancer cells. More importantly, we found that incorporating a short peptide sequence considerably improved the delivery efficiency of the probe—a process we attributed to a possible peptide-based pharmacomodulation—as was demonstrated by a 50-fold reduction in PPF accumulation in liver and spleen when compared to a peptide-lacking probe (Pyro−K−Folate, PKF). This approach could potentially be generalized to improve the delivery efficiency of other targeted molecular imaging and photodynamic therapy agents.

INTRODUCTION

When a porphyrin-like molecule is activated by light, it relaxes to its ground state in three ways: through nonradiative decay, by emitting a photon, or transferring the energy, producing reactive oxygen species, mainly singlet oxygen (*1*). The detectable outcomes are fluorescence (*2*) and phototoxicity (*3*), making the porphyrin-based photosensitizer (PS[1]) a perfect candidate for image-guided therapy.

Curing cancer is a complicated goal, and the success of treatment is often short-term owing to the difficulty in clearing out all the cancer cells. Being able to clearly identify the cancer cells shortly before or during the treatment would most likely increase the success of the therapy, making imaging and therapy a beneficial union (*4*−*7*). We have utilized the natural connection of near-infrared (NIR) fluorescence imaging, a sensitive and accessible means of in vivo cancer detection (*2*, *8*, *9*), with photodynamic therapy (PDT), a promising cancer therapy using a laser to excite a tumor-associated photosensitizer that produces short-lived cytotoxic singlet oxygen (*10*, *11*). Although many target-specific NIR imaging and PDT agents are being developed, the common limit remains: these agents are mostly lost in organs involved in drug clearance, generating an unwanted toxicity and elevated background (*12*). Here, we propose a novel construct designed for improving the delivery efficiency of NIR imaging and PDT agents to the desired cancer cell targets with reduced normal tissue retention. It is composed of three functional modules (Scheme 1). The first is a fluorescent photosensitizer pyropheophorbide a (Pyro) for NIR imaging (with a long-wavelength absorption at 665 nm and emission at 675 and 720 nm) and PDT (over 50% singlet oxygen yield) (*13*, *14*). This semisynthetic photosensitizer, obtained by three steps from *Spirulina* algae, has minimal dark toxicity, and its derivative Photochlor is in phase I/II clinical trial (*15*).

The second component is a folate moiety, serving as a tumor-homing molecule that guides the photosensitizer into folate receptor (FR)-overexpressing cancer cells (*16*, *17*) via receptor-mediated endocytosis (*18*). FRs are mainly overexpressed on ovary, breast, colon, lung, nose, prostate, and brain cancer cells and activated macrophages (*19*) but have limited expression on normal cells (e.g., kidney, intestine, lung) with restricted accessibility for blood-circulating drugs (*20*).

The third component is a short peptide sequence GDEVDGSGK inserted between the photosensitizer and folate. It serves multiple purposes: (A) it is a stable and hydrophilic linker that prevents the separation of folate and Pyro and enhances water solubility, (B) it separates the Pyro from the Folate to avoid the hindrance of FR-targeting (*20*), (C) it serves as a pharmacomodulator for better delivery efficiency and decreased normal

* To whom correspondence should be addressed. E-mail: gang.zheng@uhnres.utoronto.ca. Phone: 1-416-581-7666. Fax: 1-416-581-7667.

[†] Department of Chemistry and, University of Pennsylvania.

[‡] Department of Radiology, University of Pennsylvania.

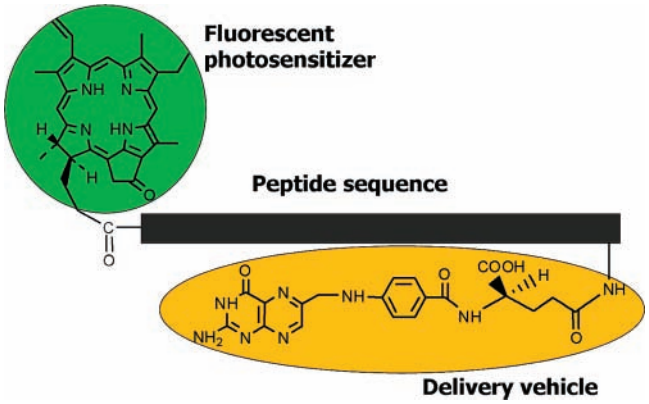
[§] Ontario Cancer Institute.

[||] Joey and Toby Tanenbaum/Brazilian Ball Chair in Prostate Cancer Research.

[1] Abbreviations: BSA, bovine serum albumin; DCM, dichloromethane; DIPEA, diisopropylethylamine; DMSO, dimethylsulfoxide; EDTA, ethylendiaminetetraacetic acid; MALDI-ToF, matrix assisted laser desorption/ionization - time of flight mass spectrometry; MTT, 3-[4,5-dimethylthiazol-2-yl]-2,5-diphenyl tetrazolium bromide; NHS, *N*-hydroxysuccinimide; NIR, near-infrared; NMP, 1-methyl-2-pyrrolidinone; PBS, phosphate-buffered saline; PDT, photodynamic therapy; PS, photosensitizer; TEAA, triethyl amine and acetic acid; TFA, trifluoroacetic acid; TIS, triisopropylsilane.

10.1021/bc0602578 CCC: $37.00 © 2007 American Chemical Society
Published on Web 02/14/2007

Scheme 1. Pyro−GDEVDGSGK−Folate Comprises Three Principal Components: (1) Fluorescent Photosensitizer Pyropheophorbide a, an Imaging and Therapeutic Agent; (2) Peptide Sequence Is a Stable and Pharmacomodulating Linker That Can Be Exchanged with Any Organelle-Targeting Sequence; and (3) Folate, Serving as a Cancer-Specific Delivery Vehicle



tissue toxicity, and (D) it is possible to exchange it with other peptide sequences for targeting subcellular organelles (*21*−*23*).

There have been many attempts to enhance the photosensitizer's efficacy by targeting "cancer fingerprints" (*24*) through association with various vehicles (*25*, *26*) like proteins (e.g., BSA targeting scavenger receptors on macrophages (*27*), transferrin (*28*), or LDL (*29*)), tumor-selective monoclonal antibodies (*30*), saccharides (*31*), aptamers (*32*), or other small molecule ligands (e.g., short peptides or peptidomimetics) (*22*, *33*−*35*). By attaching Pyro to Folate, an easy-to-conjugate, small, soluble, and nonimmunogenic tumor homing molecule (*20*) targeting cancer cells overexpressing FR (*9*, *36*, *37*), we expected to enhance the cancer specificity of Pyro. To potentiate this specificity, we have inserted a short peptide sequence to serve as a spacer, a solubilizer, and a pharmacomodulator (*38*). As a spacer, it makes the Folate more accessible to FR and, being small and hydrophilic, it decreases its retention in the excretion organs, making it more suitable for in vivo applications.

In this paper, we describe the synthesis and characterization of such agent, Pyro−GDEVDGSGK−Folate (PPF, Figure 1). We have demonstrated, both in vitro and in vivo, that all three functional modules act in synergy and thus significantly improve the delivery efficiency, reducing the potential toxicity of the probe.

MATERIALS AND METHODS

The coupling reagents HOBt (1-hydroxybenzotriazole) and HBTU (*O*-(benzotriazol-1-yl)-*N*,*N*,*N*′,*N*′-tetramethyluronium hexafluorophosphate) were purchased from ACROS and Fluka, respectively. KB cells (human epidermal cancer cells; folate receptor positive), HT 1080 cells (human fibrosarcoma cells; folate receptor negative), and CHO (chinese hamster ovary cells; folate receptor negative) were purchased from ATCC. "Complete MEM" (for HT 1080 and KB cells) consists of 85% Minimum Essential Medium (MEM), 10% fetal bovine serum, 2% of 1.5 g/L sodium bicarbonate, 1% of 200 mM L-glutamine, 1% of 0.1 mM nonessential amino acids, and 1% of 1 mM sodium pyruvate; and "MEM containing 0.8% BSA" consists of MEM supplemented with 8 g/L of bovine serum albumin. "Complete F12K" (for CHO cells) consists of 85% Ham's F12K medium (F12K), 10% fetal bovine serum, 2% of 1.5 g/L sodium bicarbonate, and 1% of 200 mM L-glutamine; and "F12K containing 0.8% BSA" consists of F12K supplemented with 8 g/L of bovine serum albumin. Compounds **3** (PP), **4** (PPF), and Pyro−K−Folate (PKF) prepared for in vivo experiments were dissolved in 1 μL DMSO and 20 μL PBS, filtered through a 0.22 μm filter and further diluted with saline to the 120−150 μL volume. For the in vitro experiments, compound **4** (PPF) and Pyro−K−Folate (PKF) were first dissolved in DMSO (no more than 0.5% of total volume), then diluted with 0.1% Tween-80 in DNA−water, filtered through a 0.22 μm filter, and further diluted with MEM containing 0.8% BSA (HT 1080 and KB cells) or F12K containing 0.8% BSA (CHO cells).

All compounds were purified by HPLC (Waters 600 controller with a 2996 photodiode array detector). The eluents were A = 0.1 M TEAA (pH 7) and B = acetonitrile, and the method used for all injections was 90% of A and 10% of B to 100% of B in 45 min with flow 1.5 mL/min on a Zorbax 300SB-C3 column. MALDI-ToF was measured on an Applied Biosystems Voyager DE mass spectrometer, and fluorescence was measured on a Perkin-Elmer LS50B luminescence spectrometer. We acquired confocal images using a Leica TCS SP2 confocal microscope and Xenogen images at the Bioluminescence Molecular Imaging Core facility at UPenn on an IVIS Xenogen Imager. The laser for PDT treatment was tuned to 670 nm with a fluence rate of 20 mW/cm^2. Mice were euthanized according to guidelines established by the Institutional Animal Care and Use Committee of the University of Pennsylvania.

Synthesis of PPF. The peptide Fmoc-GD(O-2-PhiPr)E(O-2-PhiPr)VD(O-2-PhiPr)GS(Trt)GK(Mtt) (**1**) was synthesized by manual SPPS using commercially available Fmoc amine-protected amino acids as building blocks and Sieber resin (cleavable by 2% TFA) as a solid phase, all purchased from Novabiochem. After the last Fmoc group cleavage, the resin was washed with NMP, and Pyro acid was coupled to the N-terminal glycine to give Pyro-GD(O-2-PhiPr)E(O-2-PhiPr)-VD(O-2-PhiPr)GS(Trt)GK(Mtt)-Sieber resin (**2**). The molar ratio of Pyro/HOBt/HBTU to the peptide (**1**) was 3/3/3:1, and the reaction was done in a shaker flask with a 12 h coupling time using dry NMP as a solvent. The resin was then washed with NMP, capped by 0.3 M acetylimidazol in NMP for 15 min, and washed again by an excess of NMP, DCM, and dry methanol, transferred from the shaker flask, and dried. Compound **2** (37.7 mg, 11.5 μmol) was cleaved from the resin and deprotected in one step by 2% TFA/5% TIS/DCM for 1 h to yield Pyro-GDEVDGSGK(NH_2) (**3**) with the ε-NH_2 group of the C-terminal lysine exposed. The compound was precipitated from the cleavage solution by dry ether and prepurified by a few cycles of ether precipitation−DMSO dissolving. Compound **3** (10.9 mg, 6.8 μmol) was dried under high vacuum and, without further purification, used in the next reaction. For in vivo experiments, compound **3** (PP) was purified by HPLC. The structure was confirmed by MALDI-ToF (Supporting information Figure 1A; mass calculated 1377.64, found 1377.95). Crude PP (9.3 mg, 5.8 μmol) was dissolved in 100 μL of dry 1% DIPEA/DMSO and reacted for 2 h with Folate−NHS (4.7 mg, 6 μmol) dissolved in 100 μL of dry DMSO to give Pyro−GDEVDGSGK−Folate (**4**, PPF). The reaction was concentrated by precipitation with ether and directly separated by HPLC. Purified compound **4** (11.7 mg, 5.5 μmol) was dried under high vacuum and stored at −20 °C. The purity was checked by HPLC and MALDI-ToF (mass calculated 1800.76, found 1799.79).

Synthesis of PKF. The Fmoc−Lys was coupled to the Sieber resin after activation with HOBt/HBTU in the ratio 1/1/1:3 (Fmoc−Lys/HOBt/HBTU:Sieber resin) in NMP. After the Fmoc group cleavage, the resin was washed with NMP, and Pyro−acid was coupled to the N-terminus to give Pyro−K(Mtt)−Sieber resin. The molar ratio of Pyro/HOBt/HBTU to the NH_2−K(Mtt)−Sieber resin was 3/3/3:1, and the reaction was done in a shaker flask with a 12 h coupling time using dry NMP as a solvent. The resin was then washed with NMP, capped by 0.3 M acetylimidazol in NMP for 15 min, and washed again

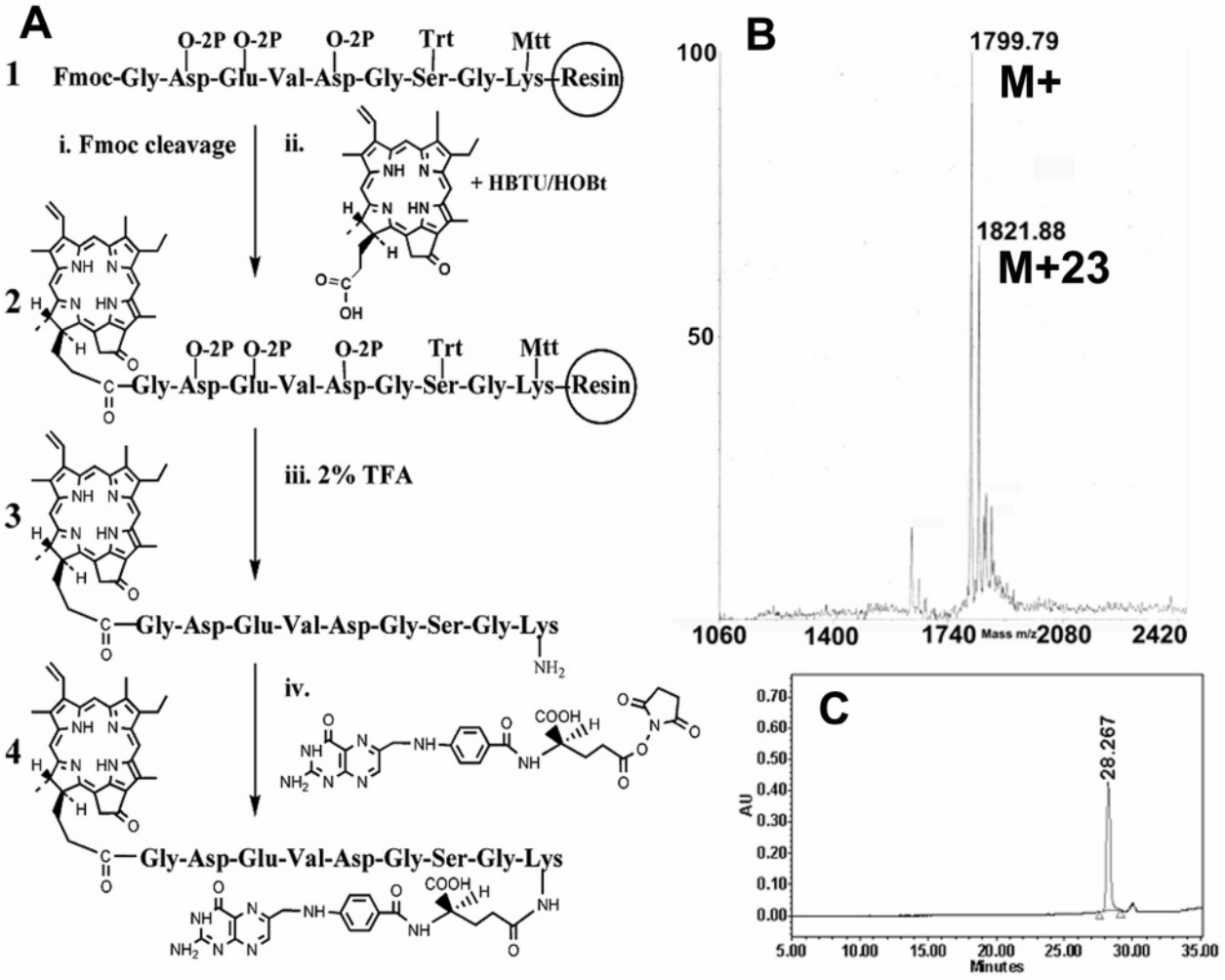


Figure 1. Synthesis (A), MALDI-ToF (B, mass calculated 1800.76, found 1799.79) and HPLC (C, absorbance at 410 nm) of Pyro−GDEVDGSGK−Folate.

by an excess of NMP, DCM, and dry methanol, transferred from the shaker flask, and dried. Pyro−K(Mtt)−Sieber resin was cleaved from the resin and the Mtt group deprotected in one step by 2% TFA/5% TIS/DCM for 1 h to yield Pyro−K−ϵNH$_2$. The compound was precipitated from the cleavage solution by dry ether and dried under high vacuum. This crude compound (21 mg, 31.7 μmol) was dissolved in 300 μL of dry 1% DIPEA/DMSO and reacted for 2 h with Folate−NHS (31.3 mg, 40 μmol) dissolved in 200 μL of dry DMSO to give Pyro−K−Folate (PKF). The reaction was concentrated and directly separated by HPLC. Purified PKF (29.8 mg, 27.5 μmol) was dried, and the purity was checked by HPLC and MALDI-ToF (Supporting information Figure 1B; mass calculated 1084.50, found 1084.18).

Confocal Microscopy. KB and HT 1080 cells were grown in 4-well Lab-Tek chamber slides (Naperville, Illinois) at a density of 50 000 cells/well and grown for 24 h in complete MEM, then rinsed with HBSS (Hank's balanced salt solution) and incubated with 50 μM PPF in 300 μL of MEM containing 0.8% BSA at 37 °C for 5 h. Cells were repeatedly rinsed with HBSS after the incubation and fixed by 1% formaldehyde in PBS for 20 min prior to scanning with confocal microscopy. The settings for confocal microscopy were as follows: 640−800 nm detector slit for detection of Pyro fluorescence, with zoom = 2, expander = 3, resolution 512 × 512, 633 nm excitation wavelength, 40× objective, 100% power, 851.1 gain, and −28.5 offset.

Flow Cytometry Experiments. KB, HT 1080, and CHO cells were seeded in T25 flasks (each flask 10^6 cells) and grown for 1 day in complete MEM (KB cells and HT 1080 cells) or complete F12K (CHO cells) medium. The cells were incubated for 12 h with 5 μM PPF or PKF in MEM containing 0.8% BSA (KB and HT 1080 cells) or F12K containing 0.8% BSA (CHO cells) 1.3 mL/flask alone or with 5 mM folic acid added, and at the end of incubation, the medium was aspirated and cells washed 3 times with 2 mL of PBS. The cells were detached by 0.25% trypsin−EDTA, fixed by 1% formaldehyde (methanol-free) in PBS, resuspended in 1 mL of PBS, and immediately analyzed on a BD LSRII machine at the Flow Cytometry Laboratory, Abramson Cancer Center, at the University of Pennsylvania focusing on Pyro fluorescence (exc. 633 nm, em. 695 nm). The gain was constant for all three samples and set so that the control cells had a fluorescent intensity between 1 and 100 AU.

Cell Viability (MTT) Assay. KB, HT 1080, and CHO cells were seeded in clear 96-well plates at a density of 50 000 cells/well in 250 μL of complete MEM (KB and HT 1080 cells) or complete F12K (CHO cells) and grown for 24 h at 37 °C. Cells were subsequently rinsed with HBSS and incubated with no or 0.5, 5, or 15 μM PPF in MEM containing 0.8% BSA (KB and HT 1080 cells) or F12K containing 0.8% BSA (CHO cells) for 24 h. Cells were then rinsed with HBSS, 100 μL/well of complete MEM was added, and the cells were either kept in the dark or treated with different light doses (5 or 10 J/cm^2) by a 670 nm laser with a 20 mW/cm^2 fluence rate. After incubation for 24 h at 37 °C, the cells were incubated for 2 h with a 0.5 mg/mL solution of MTT in complete MEM/complete F12K, that was disposed afterward and replaced with 100 μL of equal

parts of DMSO and 70% isopropanol in 0.1 M HCl. Absorbance at 570 nm was measured. Data shown are based on three different experiments, and the results were expressed as mean ± standard error.

In Vivo Imaging. Nude mice were inoculated subcutaneously with 10^7 KB cells above the right leg and 10^7 HT 1080 cells above the left leg, and the tumors were grown for about 7 days. First, three mice were initially scanned with a Xenogen IVIS imager with a Cy 5.5 filter (λ_{exc} = 615−665 nm, λ_{em} = 695−770 nm) and then intravenously injected with 50 nmol (left), 100 nmol (middle), and 150 nmol (right mouse) of PPF 60−180 μL/mouse into the tail vein. The mice were imaged 5 min, 6 h, and 24 h after injection. In order to compare the biodistribution of PP and PPF, two double tumor mice were intravenously injected with 30 nmol of PPF or 30 nmol of PP and imaged. These mice were sacrificed 26−30 h after the injection, and the organs (KB tumor, HT 1080 tumor, muscle, heart, adrenal, kidney, spleen, and liver) were imaged directly after dissection and used for biodistribution. In order to compare the biodistribution of PP, PPF, and PKF, the first mouse was injected with 30 nmol of PPF, the second with 30 nmol of PP, and the third with 15 nmol of PKF in two different experiments. The Xenogen images were obtained with the same settings (small binning, 2 s exposure time) and were compared using max = 20 000, min = 3000 for PPF and PP and max = 10 000, min = 1500 for PKF. The mice were sacrificed 26−30 h after iv, the organs were scanned by Xenogen and used for biodistribution.

Semiquantitative ex Vivo Organ Biodistribution. The mice were euthanized 26−30 h after drug injection, and the dissected organs were washed in PBS and scanned by Xenogen in a clear 24-well plate. The organs were weighed and disintegrated in DMSO/MeOH (2/3). After settling, the fluorescence was measured (excitation 650 nm, emission 670 nm) and divided by weight for each organ. This ratio of fluorescence vs weight was normalized with respect to muscle, and these semiquantitative values plotted in graphs comparing either PP and PPF (these data are based on three different experiments and the results expressed as mean ± standard error) or PP, PPF, and PKF. Statistically significant differences between KB tumor and other organs of PPF mouse are indicated with an asterisk ($P < 0.05$).

RESULTS AND DISCUSSION

Synthesis and Characterization of Pyro−GDEVDGSGK−Folate (PPF). First, Fmoc−GDEVDGSGK was synthesized according the standard solid-phase peptide synthesis (SPPS) protocol using a Sieber resin as a solid phase (**1**). The photosensitizer Pyro acid was then coupled to the N-terminus of the immobilized peptide (Figure 1A) to give Pyro−GDEVDGSGK−Sieber resin (**2**), which was cleaved from the solid phase and deprotected with 2% TFA. The folate−NHS was then coupled in a solution reaction to the ϵ-NH_2 group of C-terminal lysine of Pyro−GDEVDGSGK (PP, **3**), and the product Pyro−GDEVDGSGK−(Folate) (PPF, **4**) was characterized by MALDI-ToF (mass calculated 1800.76, found 1799.79; Figure 1B) after purification by HPLC (Figure 1C, absorbance at 410 nm).

Accumulation of Pyro−GDEVDGSGK−Folate (PPF) inside FR-Positive and -Negative Cells Monitored by Confocal Microscopy and Flow Cytometry. To confirm the preferential uptake of PPF by folate receptor-overexpressing tumor cells, KB cells (human epidermal cancer cells; folate receptor positive, FR+) and HT 1080 cells (human fibrosarcoma cells; folate receptor negative, FR−) were incubated with 50 μM PPF for 5 h, and the fluorescence of fixed cells was then monitored by confocal microscopy (Figure 2). By comparing

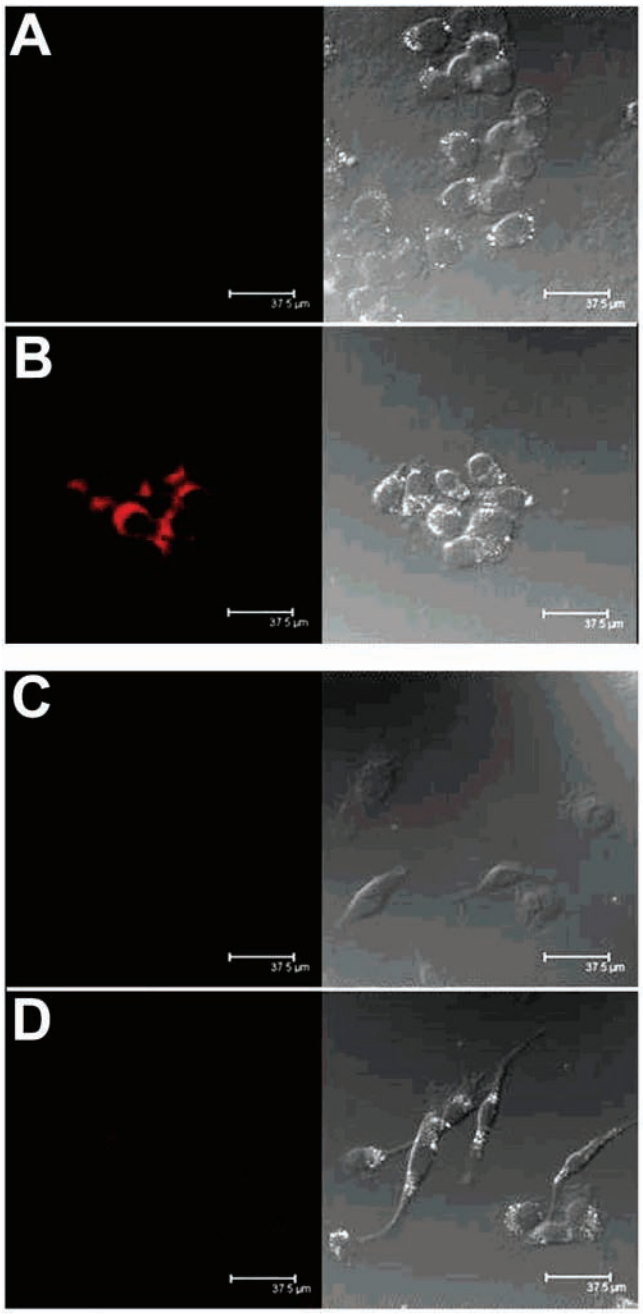


Figure 2. Accumulation of Pyro−GDEVDGSGK−Folate (PPF) in KB (FR+) vs HT 1080 (FR−) cells. (A) KB cells alone, (B) KB cells incubated with 50 μM PPF for 5 h, (C) HT 1080 cells alone, (D) HT 1080 cells incubated with 50 μM PPF for 5 h. PPF accumulates preferentially in KB cells. The scale bar represents 37.5 μm.

Figure 2B andD, it is clear that PPF accumulates more in KB cells (FR+) (Figure 2B) than in HT 1080 cells (FR−) (Figure 2D).

In order to establish the FR delivery pathway as the main uptake mechanism for PPF, the inhibition of PPF uptake was monitored by flow cytometry using an excess of free folic acid in KB, HT 1080, and CHO (chinese hamster ovary) cells. As expected, there is a minimal influence of folic acid on the uptake of PPF into HT 1080 and CHO cells (both FR−) in contrast to KB cells, where the uptake was inhibited up to 70% (Figure 3). These results suggest that (A) the main delivery pathway for PPF into the FR+ cells is via folate receptor-mediated endocytosis, (B) PPF's uptake can be inhibited up to 70% by folic acid in the case of KB cells (FR+), and (C) the remaining

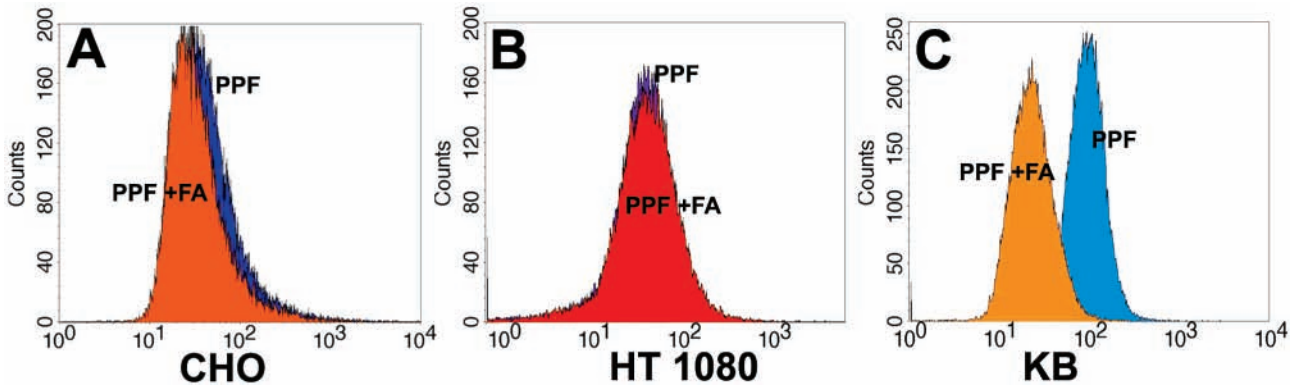


Figure 3. Monitoring the accumulation of PPF (Pyro−GDEVDGSGK−Folate) in CHO (FR−), HT 1080 (FR−), and KB (FR+) cells using flow cytometry and inhibition of this uptake with free folic acid. CHO cells (A) and HT 1080 cells (B) incubated with 5 μM PPF (blue) or 5 μM PPF and 5 mM folic acid (orange/red) show very similar uptake of PPF (695 nm fluorescence) with or without inhibition (PPF + FA vs PPF). Only KB cells (C) show significant (70%) reduction in PPF uptake when incubated with 5 μM PPF and 5 mM Folic acid (PPF, blue; vs PPF + FA, orange), suggesting that folate receptor-mediated endocytosis is the main delivery pathway for KB, but not for CHO and HT 1080 cells.

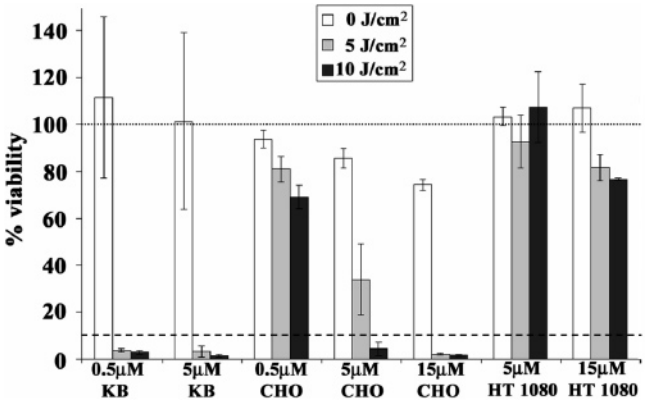


Figure 4. Viability of KB cells (FR+, cancer cells), HT 1080 cells (FR−, cancer cells), and CHO cells (FR−, normal cells) incubated with 0.5, 5, and 15 μM PPF and treated with light (5 or 10 J/cm^2) or kept in the dark (0 J/cm^2). KB cells have viability reduced below 10% when incubated with the lowest drug dose (0.5 μM) and treated with 5 J/cm^2. CHO cells reach this level of cell death for the same concentration (5 μM) only when treated with the highest light dose (10 J/cm^2), and in case of HT 1080, even the highest drug dose (15 μM) and light dose (10 J/cm^2) did not reduce their viability below 10%.

uptake of PPF to KB cells and the lower uptake of PPF to the HT 1080 and CHO cells can be attributed to the nonspecific tumor affinity of the Pyro moiety.

Selective PDT-Induced Cell Killing as a Result of FR Targeting. To compare the post-PDT viability reduction for cell lines with different levels of FR expression, KB tumor cells (FR+), HT 1080 tumor cells (FR−), and normal CHO cells (FR−) were incubated with 0.5, 5, and 15 μM **PPF** for 24 h and were then either kept in the dark or treated by PDT with 5 or 10 J/cm^2 light doses using a 670 nm tunable laser with a fluence rate of 20 mW/cm^2. The MTT study (Figure 4) shows that the viability of KB cells drops below 10% when incubated with 0.5 μM **PPF** and treated with a 5 J/cm^2 light dose. Achieving the same cell viability reduction in CHO cells requires both a 10-fold concentration (5 μM) in combination with a 2-fold light dose (10 J/cm^2). Interestingly, using the combination of the highest drug dose (15 μM) and light dose (10 J/cm^2) does not effectively kill the HT 1080 cells, suggesting an even lower accumulation of PPF or a possible PDT resistance of the HT1080 cells. This study further supports the FR-mediated PDT activity of PPF toward FR+ cancer cells.

In Vivo Discrimination between KB (FR+) and HT 1080 (FR−) Tumors. To validate the FR-targeting specificity of PPF in vivo, nude mice bearing an HT 1080 tumor (FR−) on the left flank and a KB tumor (FR+) on the right flank were used for in vivo imaging studies. Three double tumor mice were intravenously injected with 50, 100, and 150 nmol of PPF and scanned by Xenogen imager (Figure 5, using a Cy 5.5 filter) before the drug injection (prescan, Figure 5A) and after the drug injection at three different time points (5 min, 6 h, and 24 h). Five minutes after injection (Figure 5B), PPF is distributed rapidly throughout the body, carried by the blood stream. At 6 h postinjection (Figure 5C), KB tumor accumulates significantly more PPF than HT 1080, and accumulation in normal organs is considerably reduced. At 24 h postinjection (Figure 5D), the uptake of PPF in normal organs as well as the HT1080 (FR−) tumor for "50 nmol" and "100 nmol" mouse drops almost to the prescan level in contrast to a high fluorescent signal that remains in the KB tumor. These in vivo imaging studies clearly show that (A) PPF accumulates preferentially in KB tumor with respect to HT1080 tumor and other normal organs, (B) it is clear from the saturated image of the "150 nmol" mouse (Figure 5D) that PPF also accumulates in HT 1080 tumor, and (C) PPF is not toxic at the 150 nmol drug dose and is cleared quickly out of normal tissues.

The Role of Folate and Peptide Modules in Targeted Delivery of PPF. In order to examine the impact of each module on delivery efficiency and target specificity, two analogues of PPF were synthesized. One is Pyro−GDEVDGSGK (PP) that lacks the folate moiety; the other is Pyro−K−Folate (PKF) with one lysine residue replacing the short peptide sequence (Figure 6).

A. The Role of Folate Attachment for Target-Specific Delivery of PPF in Vivo. Since Pyro itself can serve as a delivery molecule (albeit with poor specificity), the in vivo imaging and biodistribution of the nontargeting Pyro−GDEVDGSGK (PP) can help to assess the true influence of folate as a tumor homing molecule. Thus, two double tumor-bearing mice in each experiment were injected with 30 nmol of PPF or with 30 nmol of PP (n = 3). The image in Figure 7 (upper left) shows that, around 6.5 h after injection of PPF (left) and PP (right), PPF accumulates significantly more in KB tumors than in HT1080 tumors, whereas PP accumulates comparably in both KB and HT 1080 tumors (see also Figure 8). The animals were sacrificed 26−30 h after injection, and the dissected organs were first imaged (Figure 7, lower left) and then homogenized. The images of the organs showed stronger fluorescence in the KB tumor from the PPF mouse, a weaker signal coming mainly from kidneys and livers of both the PPF and the PP mouse, and almost no signal from other organs.

The uptake of PPF and PP was determined by extracting the homogenized organs with DMSO/MeOH, measuring the fluorescence at 670 nm, and correcting the signal for weight (Figure

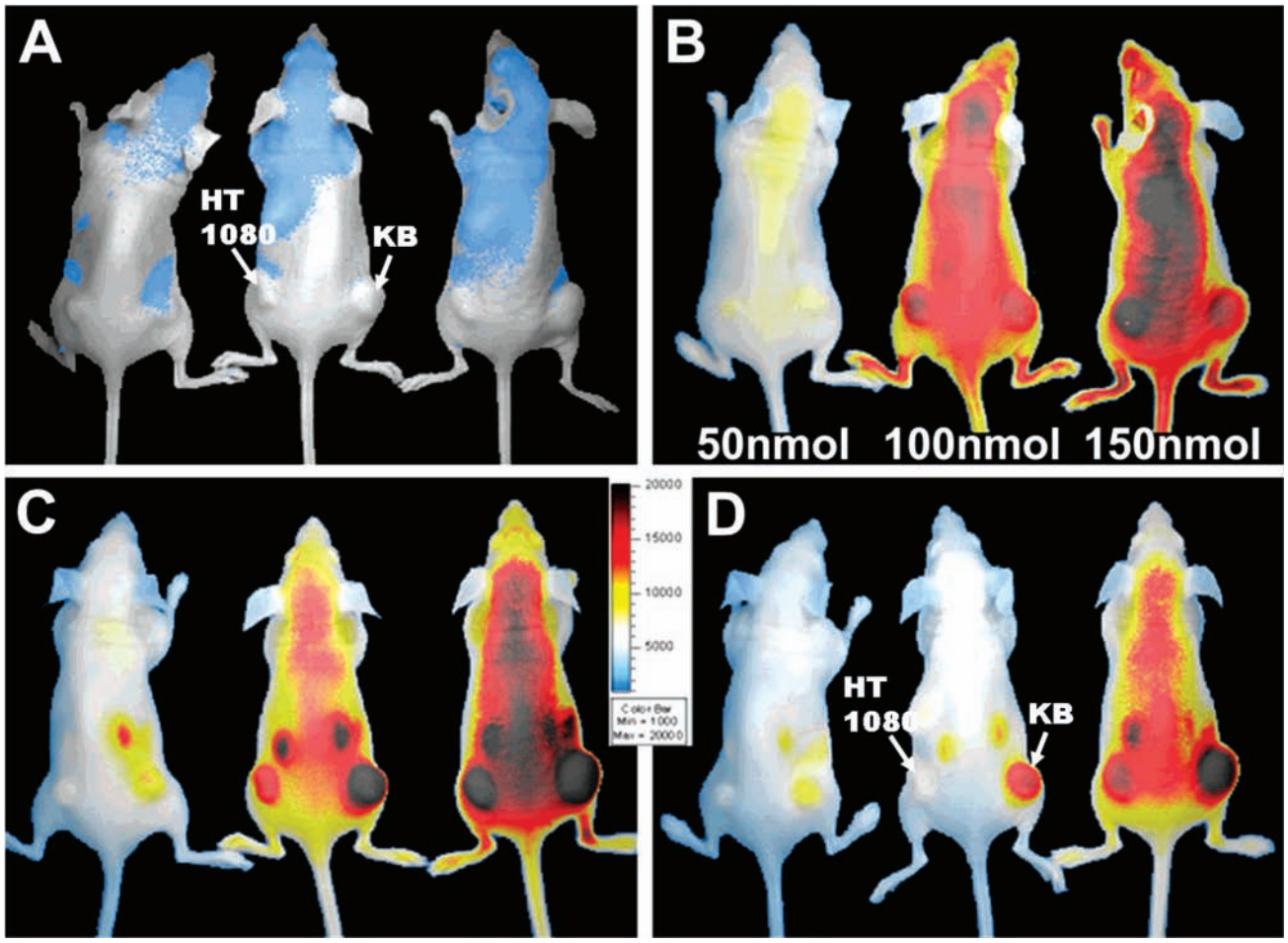


Figure 5. Monitoring fluorescence signal distribution after intravenous injection of three different doses of PPF to double tumor-bearing mice that have a KB tumor (FR+) on the right side and an HT 1080 tumor (FR−) on the left side, using a Xenogen imager. (A) Prescan, (B) 5 min after injection of 50 nmol (left mouse), 100 nmol (middle mouse) and 150 nmol (right mouse) of PPF, (C) 6 h after injection, and (D) 24 h after injection. At this point, it is clear that PPF preferentially accumulates in the KB tumor.

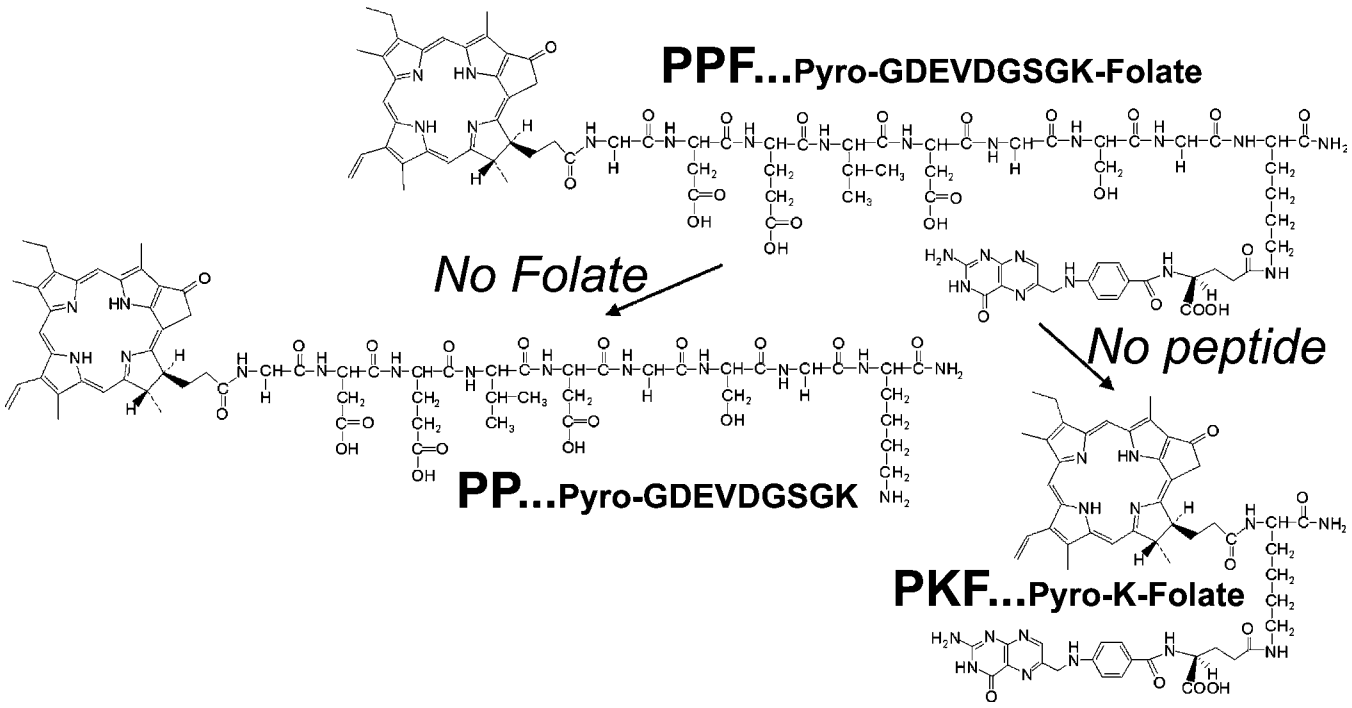


Figure 6. Structure of PPF (both peptide and folate modulation), PP (lacking the folate), and PKF (lacking the peptide module).

7, right). By examining the biodistribution of PPF after normalizing with respect to muscle, the highest fluorescence signal was found in the KB tumor. This signal is only comparable to the signal from kidney, which is known as the

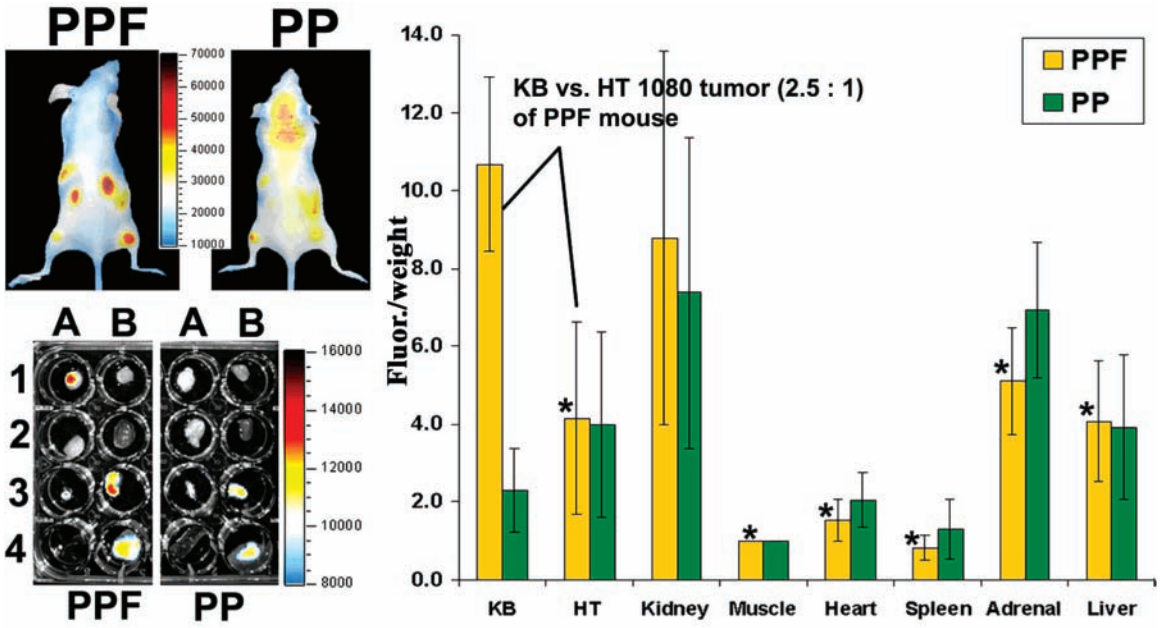


Figure 7. In vivo and ex vivo distribution of iv injected Pyro−GDEVDGSGK−Folate (PPF, targeting FR+ KB tumor) and Pyro−GDEVDGSGK (PP, no targeting). Xenogen images of double tumor mice (HT 1080 tumor left, KB tumor right) injected with PPF (left) or PP (right) at 6.5 h after injection (upper left corner) shows higher accumulation of PPF in the KB tumor. This was confirmed by images of the dissected organs (lower left corner): 1A, KB tumor; 1B, HT 1080 tumor; 2A, muscle; 2B, heart; 3A, adrenal; 3B, kidney; 4A, spleen; 4B, liver (left, PPF; and right, PP). Fluorescence from homogenized organs (right: PPF, orange; PP, green), corrected for weight and expressed as a ratio of the signal of muscle (=1), shows a significantly higher accumulation of PPF in the KB tumor than in the HT 1080 tumor but a similar distribution of nontargeting PP in both tumors. The asterisk identifies those organs of the PPF mouse whose relative fluorescence is significantly ($P < 0.05$, $n = 3$) different from that of the KB tumor, showing that the KB tumor has the highest accumulation of PPF, comparable only with kidney, while the HT 1080 tumor has an average signal that is 2.5 times lower.

major clearance pathway for folate bioconjugates. Moreover, the fluorescence signals in HT 1080 and other normal organs (adrenal, liver, heart, and spleen) were significantly lower (*$P < 0.05$) with the ratio of KB to HT 1080 on average 2.5:1. In contrast, the biodistribution of PP shows no significant difference between the HT 1080 tumors and KB tumors (or the rest of the organs), confirming the minimal role of Pyro on the PPF tumor selectivity and thus validating the importance of folate as a tumor homing molecule.

B. The Role of Peptide Modulation in Targeted Delivery of PPF. In order to clarify the role of peptide in the targeted delivery of PPF, Pyro−K−Folate (PKF) was synthesized by replacing the nine amino acid peptide sequence in PPF with a single lysine residue. The following investigations revealed the consequences of removing the peptide module. First, PKF showed the increased hydrophobicity and decreased water solubility when compared to PPF (HPLC, Supporting information Figure 2). Next, the accessibility of the folate moiety to FR in PKF vs PPF was also investigated in vitro using flow cytometry. KB, HT 1080, and CHO cells were incubated with the same concentration (5 μM) of PKF or PPF. It was observed that both PPF and PKF accumulate in HT 1080 and CHO cells (both FR−) with similar efficiency, whereas in KB cells (FR+), the efficiency of PKF uptake drops almost to 50% compared to that of PPF (Supporting information Figure 3). This indicates that the nine amino acid linker in PPF increases the efficiency of the FR-mediated uptake probably by making the folate more accessible (Supporting information Figure 4).

Perhaps the most profound effect of peptide modulation on the targeted delivery of PPF was its role in the biodistribution pattern of PPF as depicted in Figure 8 and Supporting information Figure 5. As expected, when we compare the in vivo biodistribution of PPF with that of PP, the difference in KB and HT 1080 tumor accumulation of PPF is visible at 1.5 h (Figure 8, column C) and is much more distinguishable at 6.5 h (Figure 8, column D) postinjection. This is clearly due to the effect of FR targeting by the folate moiety, which facilitates the preferential accumulation of PPF in the KB tumor (FR+), since folate-lacking PP does not distinguish between the FR+ and FR− tumors. However, what is notable is the common biodistribution pattern showing a low retention in the organs responsible for drug clearance for both PPF and PP. We attribute this finding to the peptide-based pharmacomodulation, meaning that the presence of a short peptide sequence significantly alters the pharmacokinetics and pharmacodynamics of the parent molecule. Such modulation becomes more obvious when we compare the biodistribution pattern of PPF with that of PKF (Figure 8, row 3, and Supporting information Figure 5). Even though PKF immediately after the injection (Figure 8, 3B) displays a distribution pattern very similar to that of PPF and PP (Figure 8, 1B and 2B), this pattern is drastically changed only 1.5 h postinjection (Figure 8, column C). At 6.5 h, it is clear that most PKF is retained by the excretion organs and exhibits extremely low tumor accumulation (Figure 8, 3D). In contrast, both PPF and PP are delivered to the tumors with much higher efficiency even though there is a difference in FR-targeting specificity.

The ex vivo organ biodistribution corrected for weight and normalized for muscle (Supporting information Figure 5) further confirmed this accumulation pattern. It identifies liver and spleen (followed by adrenal and kidney) as the organs accumulating most of the PKF, and when comparing the relative fluorescence intensity with both that of PPF and PP, this accumulation is approximately 50-fold higher for PKF. This pharmacomodulation highlights the positive impact of the peptide sequence on the targeted delivery of PPF by minimizing the nonspecific uptake by liver, spleen, and other organs.

Future Perspective. In principle, the target-specific, peptide-based pharmacomodulation approach described here could be applicable for improving the delivery efficiency of other cancer diagnostics and therapeutics. The versatility of this approach lies in its modular design in which any module could be easily

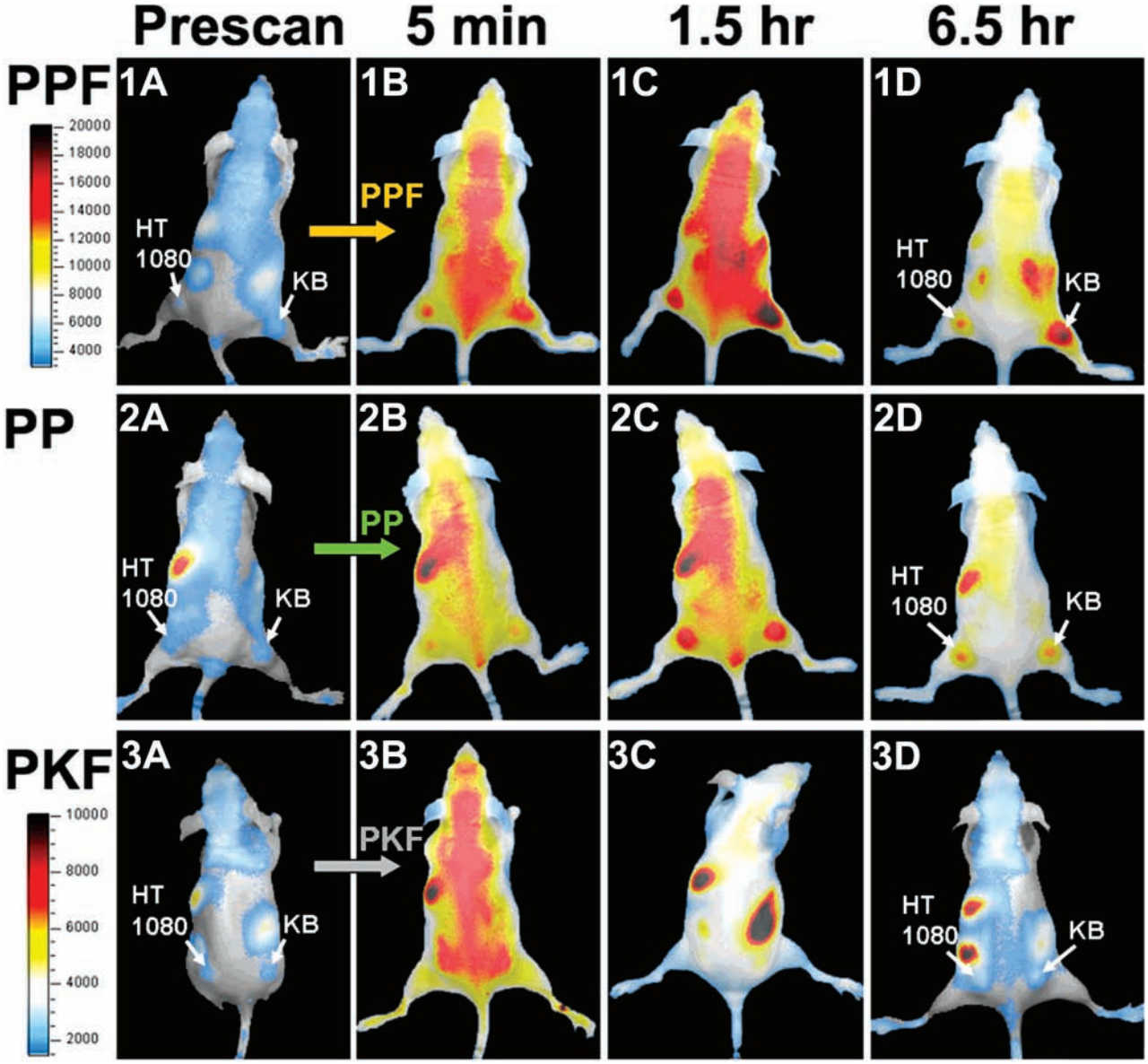


Figure 8. Double tumor mice (HT 1080 tumor, left; KB tumor, right) injected with Pyro−GDEVDGSGK−Folate (PPF, row 1), Pyro−GDEVDGSGK (PP, row 2), or Pyro−K−Folate (PKF, row 3) and imaged before the injection (Prescan, A) and 5 min (B), 1.5 h (C), and 6.5 h (D) after the drug injection. It is clear that 6.5 h after the injection PPF accumulates mostly in the KB tumor (1D) and PP equally in both tumors (2D), demonstrating the folate-introduced cancer specificity. This is in contrast to PKF (3D) that has minimal tumor accumulation and is retained in organs responsible for drug clearance, clearly identifying the peptide as the pharmacomodulating component.

replaced for a different purpose. For example, the Pyro moiety could be replaced with another photosensitizer that is active at a longer-wavelength absorption (e.g., bacteriochlorophylls (*39*) or naphthalocyanines (*40*)) or even a chemotherapeutic agent (e.g., docetaxel, etc.). The target specificity can also be modulated by exchanging the folate moiety for any small molecule ligand targeting other cancer signatures. Finally, the length and the sequence of the peptide linker could be fine-tuned to optimize the pharmacomodulation, improving not only the solubility and the target accessibility, but most importantly, also the delivery efficiency. In the future, the peptide linker could also serve as an subcellular organelle specific delivery vehicle when exchanged for different sequences.

SUMMARY

We synthesized, characterized, and evaluated a target-specific NIR imaging and PDT agent with improved target specificity and delivery efficiency. This agent is composed of three modules: a fluorescent photosensitizer Pyro for NIR imaging and PDT, folate for selective delivery, and a short peptide linker for pharmacomodulation. Although there were several previous attempts to link a dye (*9*) or a photosensitizer (*9*, *37*) to a folate moiety in order to specifically deliver the agent to cancer cells overexpressing FR, they were limited either to use in vitro or only to the imaging purposes. Here, we report a novel, modular approach using the combination of a folate-mediated targeting and a peptide-based pharmacomodulation to improve the efficiency of targeted delivery of NIR imaging and PDT agents. This study created a fluorescent photosensitizer with an excellent biodistribution pattern (folate receptor-specific tumor uptake and low accumulation in normal tissues), a crucial step toward lowering the toxicity and background signal, thus making it potentially applicable for detecting and treating cancers in patients.

ACKNOWLEDGMENT

We thank André E. X. Brown for critical comments and suggestions on the manuscript. This work was supported by the

DOD Breast Cancer Research Program DAMD17-03-1-0373 and the NIH grant U54 CA105008 (Penn NTROI).

Supporting Information Available: MALDI-ToF of PP and PKF; HPLC and UV−vis of PPF (**4**), PP (**3**), and PKF; flow cytometry of CHO, HT 1080, and KB cells incubated with 5 μM PKF or PPF; the 3D structure of PPF; ex vivo biodistribution of PPF, PP, and PKF. This material is available free of charge via the Internet at http://pubs.acs.org.

LITERATURE CITED

(1) Berg, K., Selbo, P. K., Weyergang, A., Dietze, A., Prasmickaite, L., Bonsted, A., Engesaeter, B. O., Angell-Petersen, E., Warloe, T., Frandsen, N., and Hogset, A. (2005) Porphyrin-related photosensitizers for cancer imaging and therapeutic applications. *J. Microsc. 218*, 133−147.

(2) Licha, K. (2002) Contrast agents for optical imaging. *Top. Curr. Chem. 222*, 1−29.

(3) Oleinick, N. L., and Evans, H. H. (1998) The photobiology of photodynamic therapy: cellular targets and mechanisms. *Radiat. Res. 150*, S146−156.

(4) Bogaards, A., Varma, A., Collens, S. P., Lin, A., Giles, A., Yang, V. X., Bilbao, J. M., Lilge, L. D., Muller, P. J., and Wilson, B. C. (2004) Increased brain tumor resection using fluorescence image guidance in a preclinical model. *Lasers Surg. Med. 35*, 181−190.

(5) Coleman, C. N. (2003) Linking radiation oncology and imaging through molecular biology (or now that therapy and diagnosis have separated, it's time to get together again!) *Radiology 228*, 29−35.

(6) Huang, X., El-Sayed, I. H., Qian, W., and El-Sayed, M. A. (2006) Cancer cell imaging and photothermal therapy in the near-infrared region by using gold nanorods. *J. Am. Chem. Soc. 128*, 2115−2120.

(7) Dougherty, T. J. (1987) Photosensitizers: therapy and detection of malignant tumors. *Photochem. Photobiol. 45*, 879−889.

(8) Gurfinkel, M., Thompson, A. B., Ralston, W., Troy, T. L., Moore, A. L., Moore, T. A., Gust, J. D., Tatman, D., Reynolds, J. S., Muggenburg, B., Nikula, K., Pandey, R., Mayer, R. H., Hawrysz, D. J., and Sevick-Muraca, E. M. (2000) Pharmacokinetics of ICG and HPPH-car for the detection of normal and tumor tissue using fluorescence, near-infrared reflectance imaging: a case study. *Photochem. Photobiol. 72*, 94−102.

(9) Moon, W. K., Lin, Y., O'Loughlin, T., Tang, Y., Kim, D. E., Weissleder, R., and Tung, C. H. (2003) Enhanced tumor detection using a folate receptor-targeted near-infrared fluorochrome conjugate. *Bioconjugate Chem. 14*, 539−545.

(10) Dougherty, T. J., Gomer, C. J., Henderson, B. W., Jori, G., Kessel, D., Korbelik, M., Moan, J., and Peng, Q. (1998) Photodynamic therapy. *J. Natl. Cancer Inst. 90*, 889−905.

(11) Niedre, M. J., Secord, A. J., Patterson, M. S., and Wilson, B. C. (2003) In vitro tests of the validity of singlet oxygen luminescence measurements as a dose metric in photodynamic therapy. *Cancer Res. 63*, 7986−7994.

(12) Jori, G. (1996) Tumour photosensitizers: approaches to enhance the selectivity and efficiency of photodynamic therapy. *J. Photochem. Photobiol., B 36*, 87−93.

(13) Chen, J., Stefflova, K., Neidre, M., Wilson, B., Chance, B., Glickson, J. D., and Zheng, G. (2004) Protease-triggered photosensitizing beacon based on singlet oxygen quenching and activation. *J. Am. Chem. Soc. 126*, 11450−11451.

(14) Sun, X., and Leung, W. N. (2002) Photodynamic therapy with pyropheophorbide-a methyl ester in human lung carcinoma cancer cell: efficacy, localization and apoptosis. *Photochem. Photobiol. 75*, 644−651.

(15) Bellnier, D. A., Greco, W. R., Loewen, G. M., Nava, H., Oseroff, A. R., Pandey, R. K., Tsuchida, T., and Dougherty, T. J. (2003) Population pharmacokinetics of the photodynamic therapy agent 2-[1-hexyloxyethyl]-2-devinyl pyropheophorbide-a in cancer patients. *Cancer Res. 63*, 1806−1813.

(16) Reddy, J. A., Allagadda, V. M., and Leamon, C. P. (2005) Targeting therapeutic and imaging agents to folate receptor positive tumors. *Curr. Pharm. Biotechnol. 6*, 131−150.

(17) Lu, Y., and Low, P. S. (2002) Folate-mediated delivery of macromolecular anticancer therapeutic agents. *Adv. Drug Delivery Rev. 54*, 675−693.

(18) Sabharanjak, S., and Mayor, S. (2004) Folate receptor endocytosis and trafficking. *Adv. Drug Delivery Rev. 56*, 1099−1109.

(19) Paulos, C. M., Turk, M. J., Breur, G. J., and Low, P. S. (2004) Folate receptor-mediated targeting of therapeutic and imaging agents to activated macrophages in rheumatoid arthritis. *Adv. Drug Delivery Rev. 56*, 1205−1217.

(20) Hilgenbrink, A. R., and Low, P. S. (2005) Folate receptor-mediated drug targeting: from therapeutics to diagnostics. *J. Pharm. Sci. 94*, 2135−2146.

(21) Sibrian-Vazquez, M., Jensen, T. J., Hammer, R. P., and Vicente, M. G. (2006) Peptide-mediated cell transport of water soluble porphyrin conjugates. *J. Med. Chem. 49*, 1364−1372.

(22) Rosenkranz, A. A., Jans, D. A., and Sobolev, A. S. (2000) Targeted intracellular delivery of photosensitizers to enhance photodynamic efficiency. *Immunol. Cell Biol. 78*, 452−464.

(23) Dozzo, P., Koo, M. S., Berger, S., Forte, T. M., and Kahl, S. B. (2005) Synthesis, characterization, and plasma lipoprotein association of a nucleus-targeted boronated porphyrin. *J. Med. Chem. 48*, 357−359.

(24) Hanahan, D., and Weinberg, R. A. (2000) The hallmarks of cancer. *Cell 100*, 57−70.

(25) Sharman, W. M., van Lier, J. E., and Allen, C. M. (2004) Targeted photodynamic therapy via receptor mediated delivery systems. *Adv. Drug Delivery Rev. 56*, 53−76.

(26) Konan, Y. N., Gurny, R., and Allemann, E. (2002) State of the art in the delivery of photosensitizers for photodynamic therapy. *J. Photochem. Photobiol., B 66*, 89−106.

(27) Hamblin, M. R., Miller, J. L., and Ortel, B. (2000) Scavenger-receptor targeted photodynamic therapy. *Photochem. Photobiol. 72*, 533−540.

(28) Derycke, A. S., Kamuhabwa, A., Gijsens, A., Roskams, T., De Vos, D., Kasran, A., Huwyler, J., Missiaen, L., and de Witte, P. A. (2004) Transferrin-conjugated liposome targeting of photosensitizer AlPcS4 to rat bladder carcinoma cells. *J. Natl. Cancer Inst. 96*, 1620−1630.

(29) Zheng, G., Chen, J., Li, H., and Glickson, J. D. (2005) Rerouting lipoprotein nanoparticles to selected alternate receptors for the targeted delivery of cancer diagnostic and therapeutic agents. *Proc. Natl. Acad. Sci. U.S.A. 102*, 17757−17762.

(30) Morgan, J., Gray, A. G., and Huehns, E. R. (1989) Specific targeting and toxicity of sulphonated aluminium phthalocyanine photosensitised liposomes directed to cells by monoclonal antibody in vitro. *Br. J. Cancer 59*, 366−370.

(31) Chen, X., Hui, L., Foster, D. A., and Drain, C. M. (2004) Efficient synthesis and photodynamic activity of porphyrin-saccharide conjugates: targeting and incapacitating cancer cells. *Biochemistry 43*, 10918−10929.

(32) Farokhzad, O. C., Karp, J. M., and Langer, R. (2006) Nanoparticle-aptamer bioconjugates for cancer targeting. *Expert Opin. Drug Delivery 3*, 311−324.

(33) Ichikawa, K., Hikita, T., Maeda, N., Yonezawa, S., Takeuchi, Y., Asai, T., Namba, Y., and Oku, N. (2005) Antiangiogenic photodynamic therapy (PDT) by using long-circulating liposomes modified with peptide specific to angiogenic vessels. *Biochim. Biophys. Acta 1669*, 69−74.

(34) Renno, R. Z., Terada, Y., Haddadin, M. J., Michaud, N. A., Gragoudas, E. S., and Miller, J. W. (2004) Selective photodynamic therapy by targeted verteporfin delivery to experimental choroidal neovascularization mediated by a homing peptide to vascular endothelial growth factor receptor-2. *Arch. Opthalmol. 122*, 1002−1011.

(35) Bisland, S. K., Singh, D., and Gariepy, J. (1999) Potentiation of chlorin e6 photodynamic activity in vitro with peptide-based intracellular vehicles. *Bioconjugate Chem. 10*, 982−992.

(36) Kukowska-Latallo, J. F., Candido, K. A., Cao, Z., Nigavekar, S. S., Majoros, I. J., Thomas, T. P., Balogh, L. P., Khan, M. K., and Baker, J. R., Jr. (2005) Nanoparticle targeting of anticancer drug improves therapeutic response in animal model of human epithelial cancer. *Cancer Res. 65*, 5317−5324.

(37) Schneider, R., Schmitt, F., Frochot, C., Fort, Y., Lourette, N., Guillemin, F., Muller, J. F., and Barberi-Heyob, M. (2005) Design, synthesis, and biological evaluation of folic acid targeted tetraphenylporphyrin as novel photosensitizers for selective photodynamic therapy. *Bioorg. Med. Chem. 13*, 2799−2808.

(38) Schottelius, M., Rau, F., Reubi, J. C., Schwaiger, M., and Wester, H. J. (2005) Modulation of pharmacokinetics of radioiodinated sugar-conjugated somatostatin analogues by variation of peptide net charge and carbohydration chemistry. *Bioconjugate Chem. 16*, 429−437.
(39) Zheng, G., Chen, Y., Intes, X., Chance, B., and Glickson, J. D. (2004) Contrast-enhanced near-infrared (NIR) optical imaging for subsurface cancer detection. *J. Porphyrins Phthalocyanines 8,* 1106−1117.
(40) Li, H., Marotta, D. E., Kim, S., Busch, T. M., Wileyto, E. P., and Zheng, G. (2005) High payload delivery of optical imaging and photodynamic therapy agents to tumors using phthalocyanine-reconstituted low-density lipoprotein nanoparticles. *J. Biomed. Opt. 10*, 41203.

BC0602578

Sentinel Lymph Node Imaging Using Quantum Dots in Mouse Tumor Models

Byron Ballou,*[,†,‡] Lauren A. Ernst,[†] Susan Andreko,[†] Theresa Harper,[||] James A. J. Fitzpatrick,[†,§] Alan S. Waggoner,[†,‡] and Marcel P. Bruchez[†,§,⊥]

Molecular Biosensor and Imaging Center, Department of Biological Sciences, and Department of Chemistry, Carnegie Mellon University, 4400 Fifth Avenue, Pittsburgh, Pennsylvania 15213, and Aviir, 2463 Faber Place, Palo Alto, California 94303.
Received August 22, 2006; Revised Manuscript Received November 21, 2006

We demonstrate that quantum dots injected into two model tumors rapidly migrate to sentinel lymph nodes. PEG-coated quantum dots having terminal carboxyl, amino, or methoxyl groups all migrated from the tumor to surrounding lymph nodes similarly. Passage from the tumor through lymphatics to adjacent nodes could be visualized dynamically through the skin; at least two nodes could usually be defined. Imaging during necropsy confirmed confinement of the quantum dots to the lymphatic system and demonstrated easy tagging of sentinel lymph nodes for pathology. Examination of the sentinel nodes identified by quantum dot localization showed that at least some contained metastatic tumor foci.

INTRODUCTION

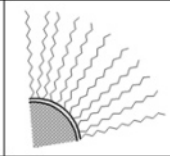
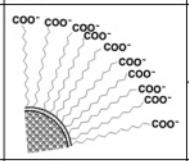
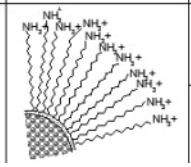
Mapping the reticuloendothelial system (RES) and locating draining lymph nodes were among the first uses of quantum dots *in vivo* (*1*−*3*). Fluorescence imaging should allow a simple optical readout, as well as higher resolution and a wider dynamic range than dye absorption or scintigraphy. For exposed tissues, the localization capability and sensitivity are potentially better than given by either visible dyes or radioactives, especially when using near-infrared emission, because of good tissue penetration and lowered background in the infrared (*3*−*5*).

Frangioni and colleagues (*3*, *6*−*9*) as well as others (*10*−*16*) have published studies showing mapping of draining lymph nodes by injection of fluorophores or fluorescently labeled macromolecules and particulates into various normal tissues. However, to our knowledge this is the first study that uses quantum dots injected into tumors to map sentinel nodes. In this paper, we also investigate whether changing the surface of PEG-conjugated quantum dots influences migration to sentinel nodes. We would expect binding and retention in lymph nodes to be influenced by surface charge, but simple drainage from the tumor volume would not.

MATERIALS AND METHODS

Quantum Dots were provided by Quantum Dot Corporation (now a division of Invitrogen). For the experiments reported here, we used 655 nm emitting ZnS−CdSe and 800 nm emitting ZnS−CdSe−CdTe core−shell quantum dots having a primary amphiphilic polymer coating (amp (*17*)), which yields highly fluorescent quantum dots with a high density of carboxyl groups on the surface. These amp-coated QDs were further substituted using poly(ethylene glycol) polymers having terminal methoxy, carboxy, or amino termini (*2*) (see Table 1). Thus, PEG-conjugated quantum dots having terminal neutral, positively charged, or negatively charged PEG surfaces could be compared as to their ability to access sentinel nodes after injection into a tumor.

Table 1. Quantum Dot Surfaces Used in this Report

Surface	Diagram	Emission wavelength, nm	Quantum yield	Hydrodynamic diameter, nm*
Methoxy-PEG		655	71%	22.6
		800	19%	*
Carboxy-PEG		655	44%	30.4
		800	17%	*
Amino-PEG		655	70%	41.2
		800	19%	*

*Measured in 0.01 M sodium borate buffer, pH 8.5. It was not possible to perform fluorescence correlation spectroscopy on the 800 nm quantum dots using our apparatus, which uses an 800 nm emitting laser for two-photon excitation. We expect the hydrodynamic diameters to be roughly similar to those of the 655 nm quantum dots.

Properties of the quantum dots are summarized in Table 1. Quantum yields were determined as described (*2*), using Rhodamine 101 as a standard, and with excitation at 530 nm. Hydrodynamic diameters were determined in 0.01 M sodium borate buffer, pH 8.5, using two-photon fluorescence correlation spectroscopy (*18*, *19*).

To minimize aggregation, all quantum dots were kept in 0.01 M sodiuim borate, pH 8.5. Just before use, the quantum dots were filtered through a 0.2 μm filter and made up to normal tonicity by addition of $^1/_9$ volume of 1.5 M NaCl, then adjusted to the desired volume by adding Dulbecco's phosphate-buffered saline (PBS).

* Corresponding author. Byron Ballou, MBIC, CMU, 4400 Fifth Avenue, Pittsburgh, PA 15213, e-mail bbal@andrew.cmu.edu. Tel: 412-268-4779. Fax: 412-268-6571.

[†] Molecular Biosensor and Imaging Center, Carnegie Mellon University.

[‡] Department of Biological Sciences, Carnegie Mellon University.

[§] Department of Chemistry, Carnegie Mellon University.

[||] Aviir.

[⊥] T.H. and M.P.B. were at Quantum Dot Corporation (now a part of Invitrogen, 29851 Willow Creek Road, Eugene OR 97402) at the time this research was done.

10.1021/bc060261j CCC: $37.00 © 2007 American Chemical Society
Published on Web 01/31/2007

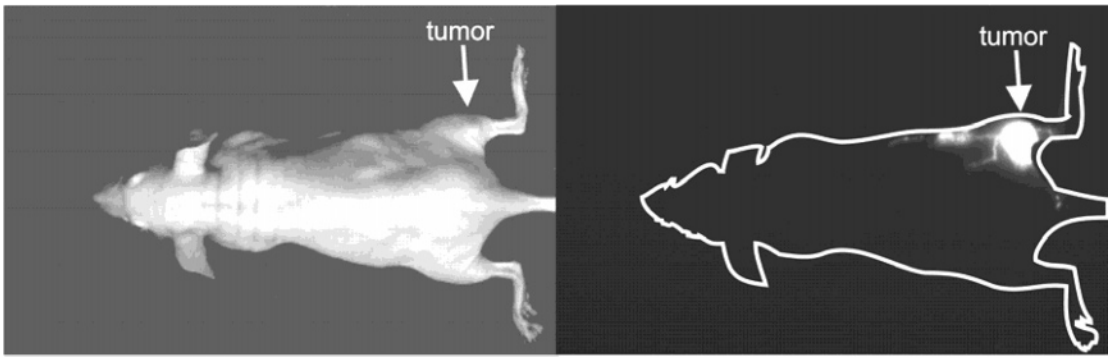


Figure 1. Nude mouse bearing M21 melanoma, dorsal view 3 min after injection into the tumor using 655 nm PEG 5k−COOH quantum dots. Left, visible light; right, fluorescence at 655 nm. Migration toward the inguinal node is already apparent.

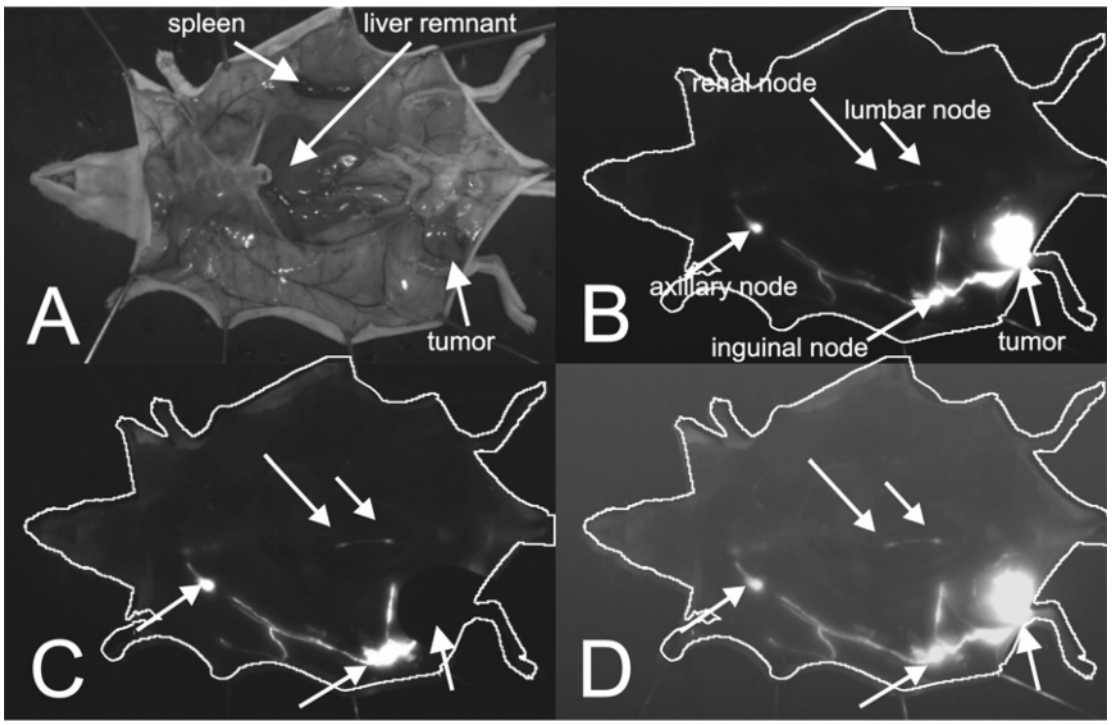


Figure 2. Same mouse as Figure 1, dissected at 40 min postinjection; ventral view. (A) Visible light. (B) Fluorescence at 655 nm. (C) Same as B, but with tumor masked. (D) Same as B, log-transformed image. Both C and D allow better display of the less bright lymphatics and smaller lymph nodes. Note drainage from tumor into lymphatics, accumulation in right inguinal, axillary, lumbar, and renal lymph nodes, but no fluorescence in the general circulation or in lymph nodes on the left side of the body. Arrows in C and D as in B; captions are omitted for clarity. We use the term "axillary" to describe lymph nodes often termed brachial (or "proper axillary") nodes as well as axillary (or "accessory axillary") nodes; in our preparations, these nodes are often not well separated (compare ref 48).

Table 2. Quantum Dot Combinations Used in This Report[a]

study	Qdot 1 surface	Qdot 1 emission	Qdot 2 surface	Qdot 2 emission
1	PEG 5k-OMe	800 nm	PEG 6k-NH2	655 nm
2	PEG 6k-NH2	655 nm	PEG 5k-OMe	800 nm
3	PEG 5k-OMe	800 nm	PEG 5k-COOH	655 nm
4	PEG 5k-COOH	655 nm	PEG 5k-OMe	800 nm

[a] Three mice were injected using each mixture.

Animals. Athymic nude mice were obtained from Harlan Sprague Dawley and were used at ages from 6 weeks to 3 months. All operations involving animals were performed in accord with institutional animal use and care regulations.

Tumors. Two tumor models were used, the M21 human melanoma (*20*, *21*) and the MH-15 mouse teratocarcinoma (*22*). For each tumor model, the tumor was grown subcutaneously in the right thigh; this location drains to the inguinal lymph node. Because the inguinal node is large and superficial, a rapid, reproducible assessment of quantum dot migration by noninvasive imaging was possible. After tumor growth to a suitable size (usually 2−4 mm diameter, 1−2 mm thick), mice were anesthetized using pentobarbital ip to effect (typically 62.5 mg/kg). Quantum dots were injected into tumors using a volume of 5−25 μL of a quantum dot preparation containing 25−100 pmol of quantum dots. The volume was adjusted to avoid noticeably inflating the tumors. In all cases, we attempted to inject directly into tumors and not into surrounding tissue. In two cases, we removed the skin over the tumor, then injected the visible tumor; no significant leakage was observed. Migration of fluorescence to the lymph nodes was identical to that reported in this paper (data not shown). We cannot exclude the possibility that a small amount of material may have leaked into subcutaneous space in some instances, but any significant

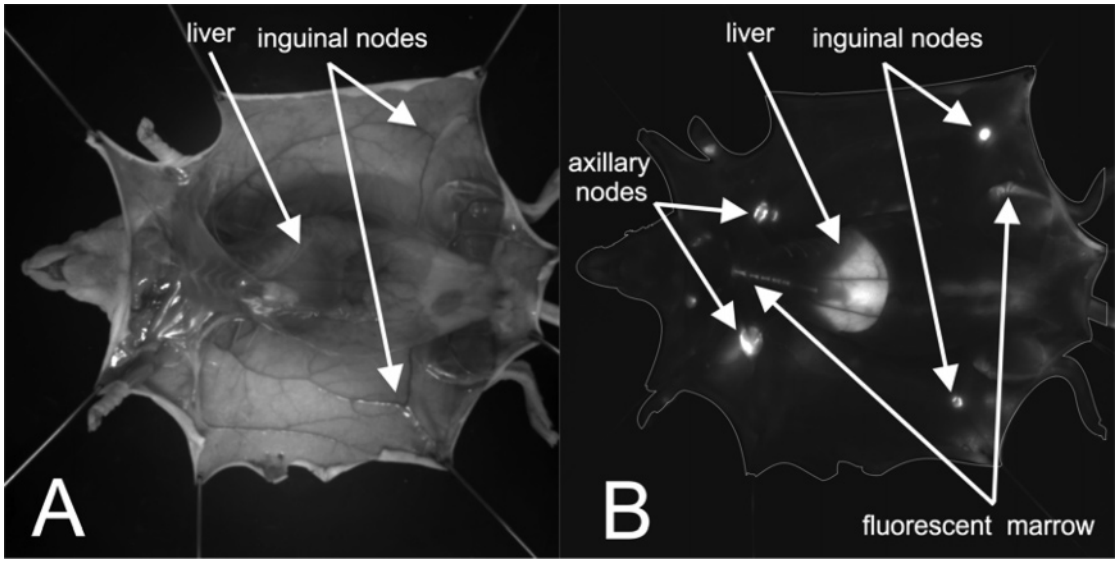


Figure 3. Mouse bearing M21 melanoma, injected sequentially in the tail vein first using 655 nm PEG 5k−COOH quantum dots, followed 20 min later by injection into the tumor using 800 nm PEG 5k−OMe quantum dots. Necropsy 90 min after tail vein injection. (A) Visible light image. (B) General labeling by IV-injected quantum dots, 655 nm window. Bone marrow, lymph nodes, and liver are prominent in the 655 window.

amount would have been detected by imaging immediately after injection. Tail vein injection was as described (*2*). Quantum dot doses given by tail vein were typically 300 pmol in 200 μL of normal saline.

Imaging. Tumors were imaged using an Andor DU 434-BR−DD cooled CCD camera (Andor Technology, South Windsor, CT 06074) equipped with a 50 mm AF Nikkor lens and any of several interference filters fitted between the lens and the CCD (filters were supplied by Chroma Technologies, Brattleboro, VT 05301). Mice were illuminated using four 450 nm emitting 5 W LEDs (Luxeon Royal Blue LXHL-MRRC, Lumileds Lighting, San Jose, CA 95131); 655 nm emitting quantum dots were imaged using a 654 nm × 24 nm interference filter. 800 nm emitting quantum dots were normally imaged using an 820 nm × 40 nm interference filter. Where the two different emitters were used together, to eliminate any residual spillover from 655 nm emitting quantum dots, 800 nm emitters were illuminated using a 250 W fiberoptic equipped halogen illuminator (Cuda Products, Jacksonville, FL 32217) filtered through a 750 nm × 30 nm interference filter, and emission was observed using an 840 nm × 20 nm filter. This resulted in much less observed emission from the 800 nm quantum dots and a higher background, but eliminated completely a small spillover (∼2%) from the 655 nm emitting quantum dots seen using the 450 nm LED illuminators and the 820 nm × 40 nm interference filter. There was no spillover from 800 nm quantum dots into the 655 nm channel.

A difficulty in displaying lymph nodes in the same image as the tumor is caused by the much greater brightness of the tumor. Either a logarithmic transform of the image or masking the tumor permits the display of small lymph nodes or faint lymphatics in the same image as the tumor. Where a log-transformed image is used, we display the original and transformed images together.

To demonstrate that transfer of quantum dots from tumors occurred through the lymphatics, lymph nodes were labeled generally by injecting animals in the tail vein, followed by injection in the tumor using a different wavelength quantum dot. This allowed us to assess whether any trapping of quantum dots had occurred by leakage from the tumor into the vascular compartment, followed by uptake into lymph nodes. In only 2 cases of a total of 27 mice examined, including the 12 mice reported in this paper, was there any indication of such leakage. Both cases involved large tumors having significant necrotic areas.

To compare the effects of surface charge on migration to sentinel nodes, a mixture of quantum dots having a methoxy−PEG surface and either a carboxy−PEG or amino−PEG surface was injected, and images were made in two different spectral windows corresponding to the neutral or charged quantum dots; the reciprocal combination was also injected. The tested combinations of emission wavelengths and surfaces are summarized in Table 2. For the results given in this paper, three mice were labeled using each combination.

Microscopy. Lymph nodes were removed at necropsy and subjected to normal paraffin embedding and staining procedures. Examination by a veterinary pathologist confirmed the presence or absence of tumor in lymph nodes. Where necessary, paraffin sections were stained using tumor-binding monoclonal antibodies: anti-SSEA-1 for the MH-15 teratocarcinoma (*22*) or 9.2.27 for the M21 melanoma (*20*).

RESULTS

In most cases, injection of quantum dots into the tumor yielded rapid transfer of fluorescence into adjacent lymph nodes, visible through the skin. Figure 1 shows that movement out of the tumor to adjacent lymphatics is rapid. Drainage toward the inguinal node can be seen through the skin almost immediately after injection. Figure 2 shows the same animal as in Figure 1, necropsied 40 min after injection. Drainage through the lymphatics to the right inguinal and axillary lymph nodes is clearly apparent. Migration of quantum dots to the right lumbar and renal nodes is also detectable. There is no labeling of the lymph nodes on the left side of the mouse. Note that Figure 1 shows a dorsal view, while all the other figures show ventral views. The tumors were always on the dorsal side of the thigh, so the tumor in the ventral images is partly obscured by the mouse thigh.

Figures 3 and 4 show that drainage to adjacent lymph nodes is not caused by any difference in ability to trap quantum dots between nodes adjacent to the tumor and more distant lymph nodes. All lymph nodes were labeled by the 655 nm PEG 5k−COOH quantum dots that were tail-vein injected; only nodes close to the tumor were labeled by the 800 nm PEG 5k−OMe quantum dots injected into the tumor. (Carboxy-terminal quantum dots were used for general labeling to ensure rapid uptake by lymph nodes (*1*, *2*).)

To determine the effect of terminal charged groups on migration from tumors to lymph nodes, neutral PEG 5k−OMe

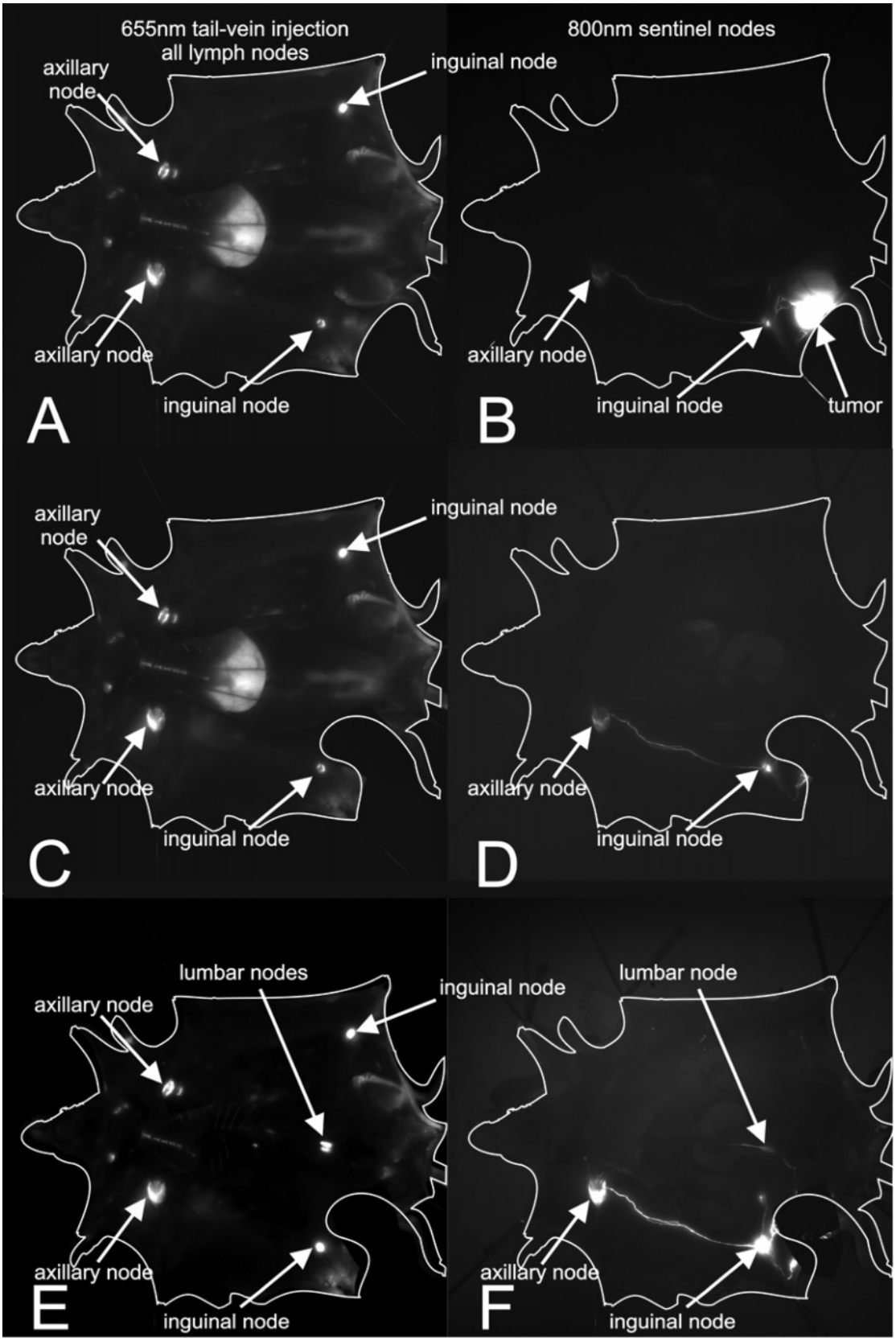


Figure 4. Same mouse as Figure 3, visualized in 655 nm window (left; A,C,E; tail-vein injection, 655 nm PEG 5k−COOH) and 800 nm window (right; B,D,F; intratumoral injection, 800 nm PEG 5k−OMe). Internal organs are removed to display all lymph nodes. (A,B) Superficial skin removed, but peritoneum intact. (A) Fluorescence of peripheral lymph nodes and liver. (B) Unilateral fluorescence of lymph nodes adjacent to tumor, no staining of liver. (C,D) Same as A,B, but with tumor masked. The lymphatic drainage from the tumor is more easily seen in D. (E,F) Most internal organs removed. Bilateral staining of lumbar and renal nodes visible in E, but only unilateral staining is visible in F.

quantum dots were injected together with either PEG 5k−COOH or PEG 6k−NH_2 quantum dots (Table 2; coprecipitation rules out injecting amino− and carboxy−PEG mixtures). Figures 5 and 6 (reciprocal combination) show that migration to sentinel nodes was similar when mixed methoxy- and carboxy-terminated PEG substituents were used. Results were also similar

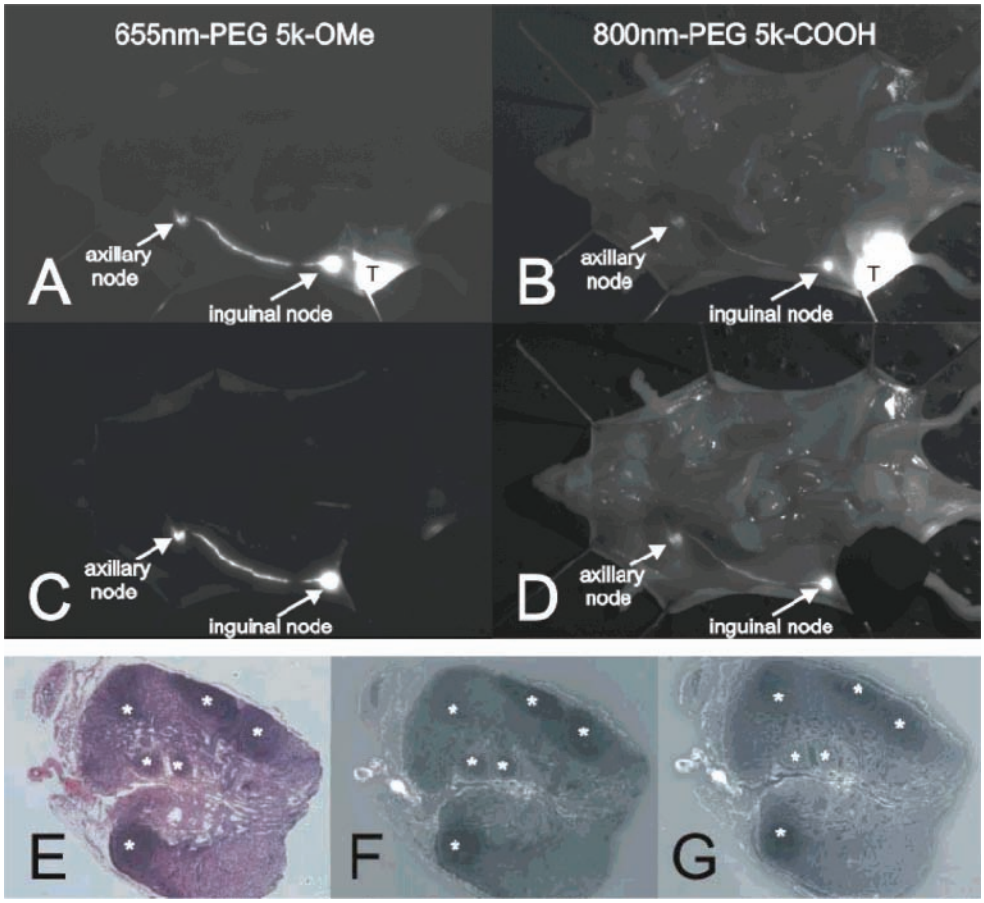


Figure 5. Quantum dots having either carboxy or methoxy surfaces migrate similarly. A mixture of 655 nm PEG 5k−OMe and 800 nm PEG 5k−COOH was injected into the tumor. Necropsy at 40 min after injection. (A) 655 nm window, tumor visible. (B) 800 nm window, tumor visible. (C) 655 nm window, tumor masked. (D) 800 nm window, tumor masked. Visibility of tumor through the leg is better using 800 nm quantum dots, but signal is lower and background is higher in B,D due to long-wavelength illumination (750 nm); however, no spillover from 655 nm quantum dots is possible. (E−G) Lymph node from mouse in Figure 5. The node was removed, fixed in buffered formalin, paraffin-embedded, and then stained using conventional hematoxylin and eosin. (E) Bright-field color image; note germinal centers (asterisks). (F) 655 nm fluorescence image (PEG 5k−OMe quantum dots). (G) 800 nm fluorescence image (PEG 5k−COOH quantum dots.) Fluorescence is confined to lymphatic vessels and sinuses.

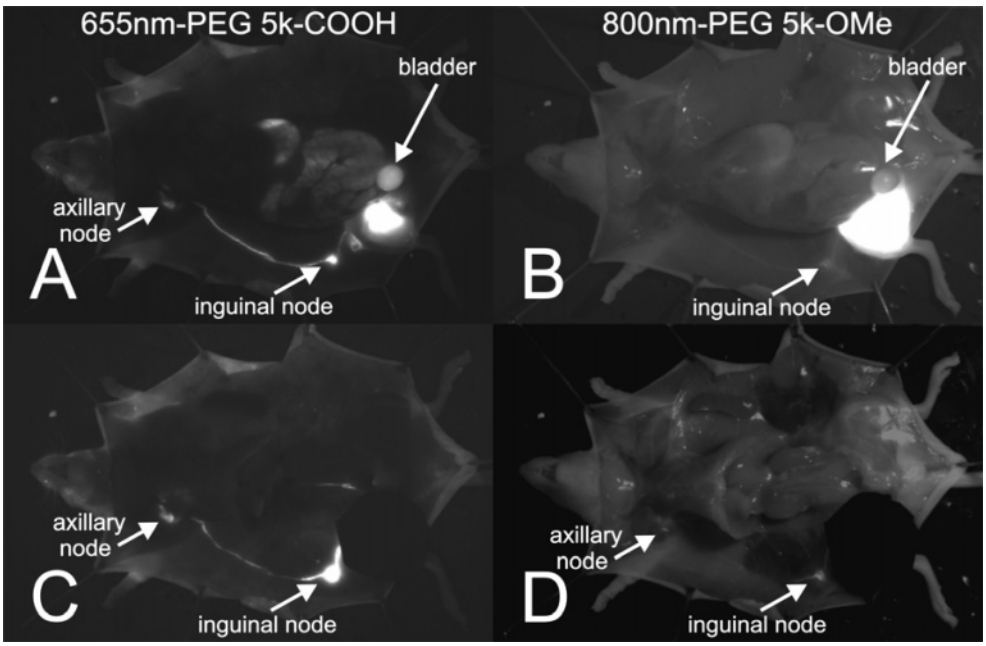


Figure 6. A mixture of 655 nm PEG 5k−COOH and 800 nm PEG 5k−OMe quantum dots was used, reciprocal to that of Figure 5. Necropsy and imaging were similar to those of Figure 5. (A) 655 nm window, tumor visible. (B) 800 nm window, tumor visible. (C) 655 nm window, tumor masked. (D) 800 nm window, tumor masked.

when injections of mixed amino- and methoxy-PEG-terminated quantum dots were used (Figure 7). Reciprocal combinations of emission wavelength and surface (Table 2) all gave similar results, so the nature of the core−shell material was unimportant.

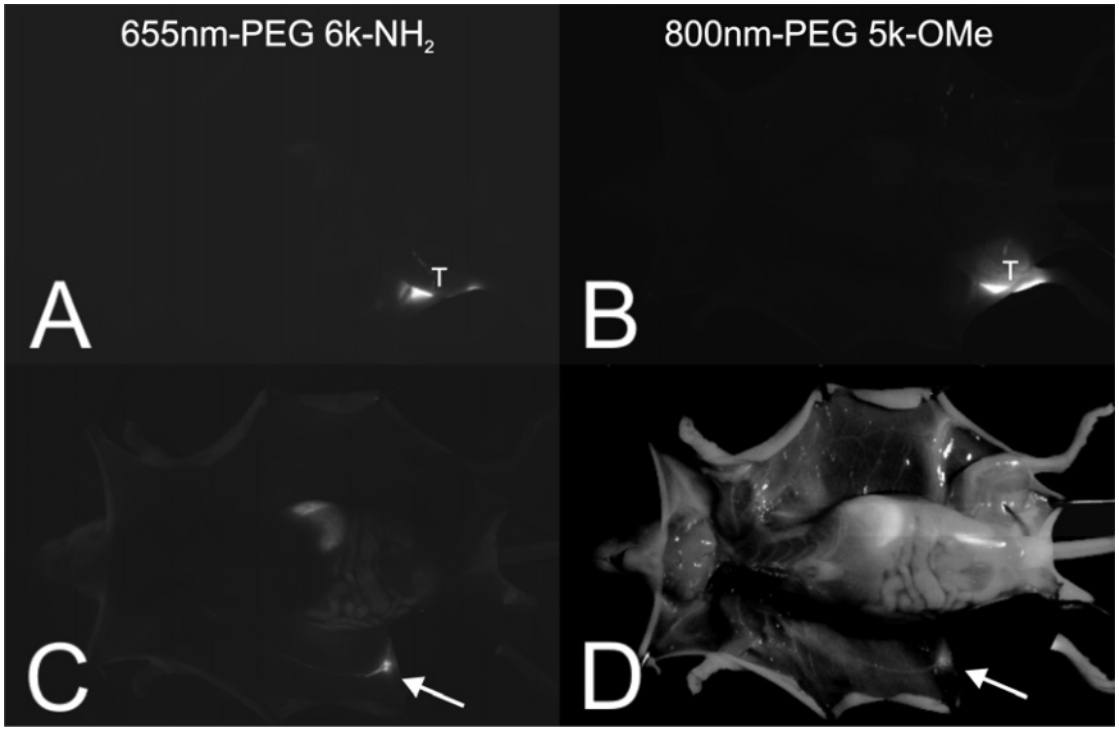


Figure 7. A mixture of 655 nm PEG 6k−NH_2 and 800 nm PEG 5k−OMe quantum dots was used. Necropsy 40 min after intratumoral injection into M21 melanoma. (A) 655 nm window, tumor visible. (B) 800 nm window, tumor visible. (C) 655 nm window, tumor masked. (D) 800 nm window, tumor masked. Quantum dots having either surface migrate similarly to adjacent inguinal node (arrows). T, tumor.

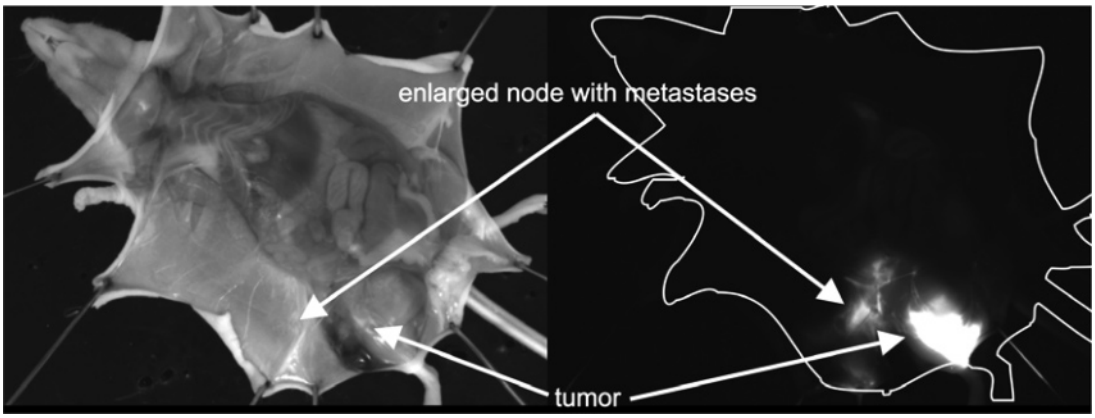


Figure 8. Nude mouse having large (~0.5 g) MH-15 teratocarcinoma, main growth dorsal to the right thigh, injected using 655 nm PEG 5k−OMe quantum dots. Ventral view. Left, visible light; right, 655 nm fluorescence. The thigh muscle has been infiltrated by the tumor, and there are local metastases to the adjacent tissue, including the right inguinal lymph node. Image taken 24 h postinjection.

Figure 8 shows the result of injecting a large MH-15 teratocarcinoma with neutral PEG-surfaced quantum dots. In this case, only the adjacent inguinal lymph node showed uptake of the quantum dots.

DISCUSSION

We have demonstrated that quantum dots define sentinel lymph nodes in mice after injection into tumors. Our results indicate that, for tumors in mice, terminal charged groups on PEG-conjugated quantum dots have little or no effect on drainage to surrounding lymph nodes. These results were surprising, since we expected that, as with whole-body imaging after intravenous injection, charged surfaces on quantum dots would increase lymph node uptake (*1*, *2*).

Our results also show that quantum dots having significantly different hydrodynamic diameters migrate similarly to lymph nodes. We would expect significant binding of intersitital tissue fluid components to the quantum dots, including enhanced binding to charged surfaces as compared to neutral PEG; this makes the results we observed even more remarkable and reinforces our belief that we are following mostly fluid flow from the tumors. On the time scale of these experiments, it is unlikely that any significant selective uptake by the lymph node occurs. Figure 5 shows that quantum dots in sentinel lymph nodes are found only on vessel boundaries and not in monocytes surrounding the germinal centers.

For visualization of superficial lymph nodes and lymphatics, or for parts of the lymphatic system exposed during necropsy, there was little difference in visibility between 655 nm emitting and 800 nm emitting quantum dots. For imaging deeper nodes or visualizing tumors through the thigh, we found 800 nm emitting quantum dots to be superior, as expected (*1*, *23*).

Frangioni and colleagues proposed the use of NIR-emitting quantum dots for sentinel lymph node mapping and demonstrated migration of quantum dots to lymph nodes when injected into normal tissues in mice. They also demonstrated that quantum dots can be used for lymph node mapping in a large animal model (pig) at centimeter depths (*3*). In subsequent

papers, this group has shown quantum dot fluorescence imaging of lymph nodes draining the lungs (*6*, *9*) and esophagus (*8*). Recently, Zimmer et al. (*24*) demonstrated that sufficiently small InAs−ZnSe quantum dots, coated using PEG−DHLA, localized in sentinel lymph nodes when injected into normal tissues. A sequence of draining lymph nodes could be labeled using these quantum dots; the authors attributed passage through the first draining lymph node to the small size of their quantum dots (>10 nm hydrodynamic diameter). In our hands, a sequence of lymph nodes was labeled using much larger, polymer-coated quantum dots; however, the bypass route through mouse lymph nodes (*25*) likely accounts for our results.

Other fluorophores used for sentinel lymph node imaging include free indocyanine green (*11*, *26*), indocyanine green adsorbed to albumin (*26*), free IRDye800CW (*26*), albumin conjugated to IRDye78 (*7*) or IRDye800CW (*8*, *26*), albumin colloid conjugated to IRDye800CW (*26*), fluorescent polystyrene microspheres (*14*, *15*), and two targeted conjugates, Cy5−vitamin B12 ("Cobalofluor") (*13*) and MECA-78, a cyanine-conjugated IgM antibody (*11*). Finally, enzyme-specific dequenching of a Cy5.5 conjugated polymer has been used to define lymph nodes (*16*, *27*). Frangioni and colleagues directly compared quantum dots to human serum albumin conjugates (*8*, *26*) and to isosulfan blue (*9*). Both quantum dots and organic fluorochromes imaged sentinel lymph nodes successfully; the quantum dots, probably because of their relatively large sizes (10−30 nm), normally targeted only the first draining lymph node, while organic dyes and smaller conjugates continued further to more distant lymph nodes (*26*) (but see ref 3.)

As compared to other methods of sentinel node location, fluorescence imaging offers improved sensitivity and greater speed, at least for lymph nodes that are close enough to the surface to be imaged or are revealed during surgery. Combining quantum dot fluorescence imaging with other noninvasive techniques (e.g., scintigraphy, MRI, or PET) would allow mapping of deep nodes; after exposure during surgery, fluorescence would then give more precise, detailed localization, potentially including microscopic levels (*3*, *28*). Alternatively, fluorescence endoscopic examination could be used during minimally invasive surgery (*8*, *13*). The equipment required for near-infrared imaging is relatively cheap and readily available, and a color video−NIR combined system has been described (*9*, *29*). Easy visualization of transport through lymphatics and accumulation in lymph nodes should be helpful for understanding the pattern of flow in the vicinity of tumors.

The ability to use multiple fluorescent emission colors may be useful in tumor diagnosis; ideally, sentinel nodes might be labeled using nonspecific quantum dots, while quantum dots conjugated to appropriate ligands and fluorescing at a different wavelength might be used to localize metastases in lymph nodes.

The advantages of quantum dots remain: very high brightness, wide range of fluorescence emission wavelengths, excitation at any wavelength below the emission wavelength, and extraordinary photostability. No organic fluorophore matches this set of advantages. Moreover, the long fluorescence lifetimes of quantum dots potentially allow nearly zero background imaging by time-gating (*30*). The difficulties remain also: relatively large size caused by the coats required for stability in aqueous solution; and potential toxicity, due either to heavy metal toxicity from dissolution of the quantum dots or to the size and surface characteristics of the nanoparticles. Several recent articles have discussed both actual and potential toxicity of quantum dots (*31*−*39*). Both major concerns are being addressed; new quantum dot compositions and coats should yield nanoparticles that are both smaller and less toxic (*24*, *40*−*47*). Molecules or particulates multiply substituted with organic dyes are good alternatives that have been demonstrated to function well for sentinel node location (*7*, *8*, *26*); however, the NIR organic fluorophores themselves may also be toxic. In our hands, the toxicity of amp-coated CdSe−ZnS quantum dots is minimal or nonexistant, as assessed by pathological examination of animals injected with quantum dots and kept for long periods (now over 2 years.) Even after this time, at least some of the quantum dots retain their fluorescence, suggesting that they remain intact ((*1*) and in preparation). We therefore believe that the clinical use of existing quantum dots, suitably purified and at low doses relevant to sentinel lymph node detection, would result in minimal toxicity, though less toxic compositions and surfaces will be welcome.

ACKNOWLEDGMENT

The authors are grateful for assistance with quantum dot manufacture by Joseph Treadway (present address Invitrogen, 29851 Willow Creek Road, Eugene OR 97402) and to B. Christoffer Lagerholm (present address Memphys, Physics Department, University of Southern Denmark, Campusvej 55, 5230 Odense M, Denmark) for assistance in infrared imaging. We are grateful to Newell R. Washburn (Department of Chemistry, Carnegie Mellon University) for use of the FCS apparatus. We also thank Lisa McGaw (Department of Biological Sciences, Carnegie Mellon University) for assistance with animal handling. This work was supported by NIH grant no. R01 EB 000364. The work at Quantum Dot Corporation was partly funded by NIST-ATP 70NANB0H3000.

LITERATURE CITED

(1) Ballou, B. (2005) Quantum dot surfaces for use in vivo and in vitro. *Curr. Top. Dev. Biol. 70*, 103−20.

(2) Ballou, B., Lagerholm, B. C., Ernst, L. A., Bruchez, M. P., and Waggoner, A. S. (2004) Noninvasive imaging of quantum dots in mice. *Bioconjugate Chem. 15*, 79−86.

(3) Kim, S., Lim, Y. T., Soltesz, E. G., De Grand, A. M., Lee, J., Nakayama, A., Parker, J. A., Mihaljevic, T., Laurence, R. G., Dor, D. M., Cohn, L. H., Bawendi, M. G., and Frangioni, J. V. (2004) Near-infrared fluorescent type II quantum dots for sentinel lymph node mapping. *Nat. Biotechnol. 22*, 93−7.

(4) Ballou, B., Ernst, L. A., and Waggoner, A. S. (2005) Fluorescence imaging of tumors in vivo. *Curr. Med. Chem. 12*, 795−805.

(5) Frangioni, J. V. (2003) In vivo near-infrared fluorescence imaging. *Curr. Opin. Chem. Biol. 7*, 626−634.

(6) Parungo, C. P., Colson, Y. L., Kim, S. W., Kim, S., Cohn, L. H., Bawendi, M. G., and Frangioni, J. V. (2005) Sentinel lymph node mapping of the pleural space. *Chest 127*, 1799−1804.

(7) Parungo, C. P., Ohnishi, S., De Grand, A. M., Laurence, R. G., Soltesz, E. G., Colson, Y. L., Kang, P. M., Mihaljevic, T., Cohn, L. H., and Frangioni, J. V. (2004) In vivo optical imaging of pleural space drainage to lymph nodes of prognostic significance. *Ann. Surg. Oncol. 11*, 1085−1092.

(8) Parungo, C. P., Ohnishi, S., Kim, S. W., Kim, S., Laurence, R. G., Soltesz, E. G., Chen, F. Y., Colson, Y. L., Cohn, L. H., Bawendi, M. G., and Frangioni, J. V. (2005) Intraoperative identification of esophageal sentinel lymph nodes with near-infrared fluorescence imaging. *J. Thorac. Cardiovasc. Surg. 129*, 844−850.

(9) Soltesz, E. G., Kim, S., Laurence, R. G., DeGrand, A. M., Parungo, C. P., Dor, D. M., Cohn, L. H., Bawendi, M. G., Frangioni, J. V., and Mihaljevic, T. (2005) Intraoperative sentinel lymph node mapping of the lung using near-infrared fluorescent quantum dots. *Ann. Thorac. Surg. 79*, 269−277; discussion 269−277.

(10) Eyles, J. E., Bramwell, V. W., Williamson, E. D., and Alpar, H. O. (2001) Microsphere translocation and immunopotentiation in systemic tissues following intranasal administration. *Vaccine 19*, 4732−4742.

(11) Kitai, T., Inomoto, T., Miwa, M., and Shikayama, T. (2005) Fluorescence navigation with indocyanine green for detecting sentinel lymph nodes in breast cancer. *Breast Cancer 12*, 211−215.

(12) Licha, K., Debus, N., Emig-Vollmer, S., Hofmann, B., Hasbach, M., Stibenz, D., Sydow, S., Schirner, M., Ebert, B., Petzelt, D., Buhrer, C., Semmler, W., and Tauber, R. (2005) Optical molecular imaging of lymph nodes using a targeted vascular contrast agent. *J. Biomed. Opt. 10*, 41205−1−41205−6.

(13) McGreevy, J. M., Cannon, M. J., and Grissom, C. B. (2003) Minimally invasive lymphatic mapping using fluorescently labeled vitamin B12. *J. Surg. Res. 111*, 38−44.

(14) Nakajima, M., Takeda, M., Kobayashi, M., Suzuki, S., and Ohuchi, N. (2005) Nano-sized fluorescent particles as new tracers for sentinel node detection: experimental model for decision of appropriate size and wavelength. *Cancer Sci. 96*, 353−356.

(15) Ueno, H., Hihara, J., Shimizu, K., Osaki, A., Yamashita, Y., Yoshida, K., and Toge, T. (2005) Experimental study on fluorescent microspheres as a tracer for sentinel node detection. *Anticancer Res. 25*, 821−825.

(16) Wunderbaldinger, P., Turetschek, K., and Bremer, C. (2003) Near-infrared fluorescence imaging of lymph nodes using a new enzyme sensing activatable macromolecular optical probe. *Eur. Radiol. 13*, 2206−2211.

(17) Wu, X., Liu, H., Liu, J., Haley, K. N., Treadway, J. A., Larson, J. P., Ge, N., Peale, F., and Bruchez, M. P. (2003) Immunofluorescent labeling of cancer marker Her2 and other cellular targets with semiconductor quantum dots. *Nat. Biotechnol. 21*, 41−46.

(18) Larson, D. R., Zipfel, W. R., Williams, R. M., Clark, S. W., Bruchez, M. P., Wise, F. W., and Webb, W. W. (2003) Water-soluble quantum dots for multiphoton fluorescence imaging in vivo. *Science 300*, 1434−1436.

(19) Yao, J., Larson, D. R., Vishwasrao, H. D., Zipfel, W. R., and Webb, W. W. (2005) Blinking and nonradiant dark fraction of water-soluble quantum dots in aqueous solution. *Proc. Natl. Acad. Sci. U.S.A. 102*, 14284−14289.

(20) Bumol, T. F., and Reisfeld, R. A. (1982) Unique glycoprotein-proteoglycan complex defined by monoclonal antibody on human melanoma cells. *Proc. Natl. Acad. Sci. U.S.A. 79*, 1245−1249.

(21) Giuliano, A. E., Irie, R. F., Morton, D. L., and Ramming, K. P. (1978) Quantitative variations in expression of oncofetal antigens on human melanomas in culture. *Proceedings of the American Association for Cancer Research 19*, 133.

(22) Ballou, B., Levine, G., Hakala, T. R., and Solter, D. (1979) Tumor location detected with radioactively labeled monoclonal antibody and external scintigraphy. *Science 206*, 844−847.

(23) Lim, Y. T., Kim, S., Nakayama, A., Stott, N. E., Bawendi, M. G., and Frangioni, J. V. (2003) Selection of quantum dot wavelengths for biomedical assays and imaging. *Mol. Imaging 2*, 50−64.

(24) Zimmer, J. P., Kim, S. W., Ohnishi, S., Tanaka, E., Frangioni, J. V., and Bawendi, M. G. (2006) Size series of small indium arsenide-zinc selenide core-shell nanocrystals and their application to in vivo imaging. *J. Am. Chem. Soc. 128*, 2526−2527.

(25) Kowala, M. C., and Schoefl, G. I. (1986) The popliteal lymph node of the mouse: internal architecture, vascular distribution and lymphatic supply. *J. Anat. 148*, 25−46.

(26) Ohnishi, S., Lomnes, S. J., Laurence, R. G., Gogbashian, A., Mariani, G., and Frangioni, J. V. (2005) Organic alternatives to quantum dots for intraoperative near-infrared fluorescent sentinel lymph node mapping. *Mol. Imaging 4*, 172−81.

(27) Josephson, L., Mahmood, U., Wunderbaldinger, P., Tang, Y., and Weissleder, R. (2003) Pan and sentinel lymph node visualization using a near-infrared fluorescent probe. *Mol. Imaging 2*, 18−23.

(28) Mulder, W. J., Koole, R., Brandwijk, R. J., Storm, G., Chin, P. T., Strijkers, G. J., de Mello, Donega, C., Nicolay, K., and Griffioen, A. W. (2006) Quantum dots with a paramagnetic coating as a bimodal molecular imaging probe. *Nano. Lett. 6*, 1−6.

(29) De Grand, A. M., and Frangioni, J. V. (2003) An operational near-infrared fluorescence imaging system prototype for large animal surgery. *Technol. Cancer Res. Treat. 2*, 553−562.

(30) Dahan, M., Laurence, T., Pinaud, F., Chemla, D. S., Alivisatos, A. P., Sauer, M., and Weiss, S. (2001) Time-gated biological imaging by use of colloidal quantum dots. *Opt. Lett. 26*, 825−827.

(31) Derfus, A. M., Chan, W. C. W., and Bhatia, S. N. (2004) Probing the cytotoxicity of semiconductor quantum dots. *Nano Lett. 4*, 11−18.

(32) Hardman, R. (2006) A toxicologic review of quantum dots: toxicity depends on physicochemical and environmental factors. *Environ. Health Perspect. 114*, 165−172.

(33) Hoshino, A., Fujioka, K., Oku, T., Suga, M., Sasaki, Y. F., Ohta, T., Yasuhara, M., Suzuki, K., and Yamamoto, K. (2004) Physicochemical properties and cellular toxicity of nanocrystal quantum dots depend on their surface modification. *Nano Lett. 4*, 2163−2169.

(34) Kirchner, C., Liedl, T., Kudera, S., Pellegrino, T., Munoz, Javier, A., Gaub, H. E., Stolzle, S., Fertig, N., and Parak, W. J. (2005) Cytotoxicity of colloidal CdSe and CdSe/ZnS nanoparticles. *Nano Lett. 5*, 331−338.

(35) Lovric, J., Cho, S. J., Winnik, F. M., and Maysinger, D. (2005) Unmodified cadmium telluride quantum dots induce reactive oxygen species formation leading to multiple organelle damage and cell death. *Chem. Biol. 12*, 1227−1234.

(36) Shiohara, A., Hoshino, A., Hanaki, K.-i., Suzuki, K., and Yamamoto, K. (2004) On the cyto-toxicity caused by quantum dots. *Microbiol. Immunol. 48*, 669−675.

(37) Tsuji, J. S., Maynard, A. D., Howard, P. C., James, J. T., Lam, C. W., Warheit, D. B., and Santamaria, A. B. (2006) Research strategies for safety evaluation of nanomaterials, part IV: risk assessment of nanoparticles. *Toxicol. Sci. 89*, 42−50.

(38) Voura, E. B., Jaiswal, J. K., Mattoussi, H., and Simon, S. M. (2004) Tracking metastatic tumor cell extravasation with quantum dot nanocrystals and fluorescence emission-scanning microscopy. *Nat. Med. 10*, 993−998.

(39) Zhang, T. T., Stilwell, J. L., Gerion, D., Ding, L. H., Elboudwarej, O., Cooke, P. A., Gray, J. W., Alivisatos, A. P., and Chen, F. F. (2006) Cellular effect of high doses of silica-coated quantum dot profiled with high throughput gene expression analysis and high content cellomics measurements. *Nano Lett. 6*, 800−808.

(40) Jurbergs, D., Rogojina, E., Mangolini, L., and Kortshagen, U. (2006) Silicon nanocrystals with ensemble quantum yields exceeding 60%. *Appl. Phys. Lett.* 88, 233116−1−233116−3.

(41) Mangolini, L., Thimsen, E., and Kortshagen, U. (2005) High-yield synthesis of luminescent silicon quantum dots in a continuous flow non-thermal plasma reactor. *Mater. Res. Soc. Symp. Proc. 862*, 307−312.

(42) Michalet, X., Pinaud, F. F., Bentolila, L. A., Tsay, J. M., Doose, S., Li, J. J., Sundaresan, G., Wu, A. M., Gambhir, S. S., and Weiss, S. (2005) Quantum dots for live cells, in vivo imaging, and diagnostics. *Science 307*, 538−544.

(43) Pinaud, F., Michalet, X., Bentolila, L. A., Tsay, J. M., Doose, S., Li, J. J., Iyer, G., and Weiss, S. (2006) Advances in fluorescence imaging with quantum dot bio-probes. *Biomaterials 27*, 1679−1687.

(44) Warner, J. H., Hoshino, A., Shiohara, A., Yamamoto, K., and Tilley, R. D. (2006) The synthesis of silicon and germanium quantum dots for biomedical applications. *Proc. SPIE—Int. Soc. Opt. Eng. 6096*, 13−20.

(45) Warner, J. H., Hoshino, A., Yamamoto, K., and Tilley, R. D. (2005) Water-soluble photoluminescent silicon quantum dots. *Angew. Chem., Int. Ed. 44*, 4550−4554.

(46) Warner, J. H., Hoshino, A., Yamamoto, K., and Tilley, R. D. (2005) The synthesis of silicon nanoparticles for biomedical applications. *Proc. SPIE—Int. Soc. Opt. Eng. 5705*, 52−59.

(47) Wolcott, A., Gerion, D., Visconte, M., Sun, J., Schwartzberg, A., Chen, S. W., and Zhang, J. Z. (2006) Silica-coated CdTe quantum dots functionalized with thiols for bioconjugation to IgG proteins. *J. Phys. Chem. B 110*, 5779−5789.

(48) Van den Broeck, W., Derore, A., and Simoens, P. (2006) Anatomy and nomenclature of murine lymph nodes: Descriptive study and nomenclatory standardization in BALB/cAnNCrl mice. *J. Immunol. Methods 312*, 12−19.

BC060261J

A New Optical and Nuclear Dual-Labeled Imaging Agent Targeting Interleukin 11 Receptor Alpha-Chain

Wei Wang,* Shi Ke, Sunkuk Kwon, Sasidhar Yallampalli, Arlin G. Cameron, Kristen E. Adams, Michel E. Mawad, and Eva M. Sevick-Muraca

Department of Radiology, Division of Molecular Imaging, Baylor College of Medicine, Houston, Texas 77030 .
Received August 30, 2006; Revised Manuscript Received January 5, 2007

Optical imaging has great potential for studying molecular recognitions both *in vivo* and *in vitro*, yet nuclear imaging is the most effective clinical molecular imaging modality. The combination of optical and nuclear imaging modalities may provide complementary information for improving diagnosis and management of diseases. In this study we developed an optical and nuclear dual-labeled imaging agent, ^{111}In-DTPA-Bz-NH-SA-K(IR-783-S-Ph-CO)-c(CGRRAGGSC)NH_2, called DLIA-IL11Rα. ^{111}In-DTPA-Bz-NH-SA is the radiotracer moiety; a near-infrared dye IR-783-S-Ph-COOH serves as the fluorescent emitter; and the cyclic peptide c(CGRRAGGSC), which is known to target interleukin 11 receptor alpha-chain (IL-11Rα), delivers the desired imaging agent to its target. Experiments revealed that the cyclic peptide c(CGRRAGGSC) continued to possess the targeting capability to IL-11Rα after the conjugation of the optical and nuclear tracers. Furthermore, the presence of the metal isotope chelator did not cause quenching of fluorescence emission. The cross validation and direct comparison of optical and nuclear imaging of a tumor was achieved using a single injection, and the preliminary results show the conjugate has tumor targeting capabilities *in vivo*.

INTRODUCTION

Near-infrared (NIR) fluorescence imaging is an active and promising area for noninvasive, *in vivo* molecular imaging (*1*−*4*). It is used to probe the expression of disease-associated biomarkers in small animals and provide real-time information about molecular events. In the wavelength range of 700−900 nm, NIR light causes minimal autofluorescence and is minimally absorbed by hemoglobin (the principal absorber of visible light) as well as by water and lipids (the principal absorbers of infrared light). Furthermore, since stable fluorophores can be reactivated by propagating excitation light, as many as 10^9 photons per second per molecule can be generated from a fluorophore with a fluorescent lifetime of one nanosecond. The sensitivity of fluorescence in microscopy is well established, and the correlation between medical imaging and pathology may be offered by optical imaging (*5*, *6*).

On the other hand, nuclear imaging techniques such as positron emission tomography (PET) and single photon emission tomography (SPECT) are currently the most effective clinical molecular imaging modalities due to their intrinsically high sensitivity at deep tissue sites and capability of quantitation. However, radionuclide imaging may suffer from low photon counts requiring long scan times as well as from a finite half-life and radiation dosage preventing longitudinal imaging in patients (*7*).

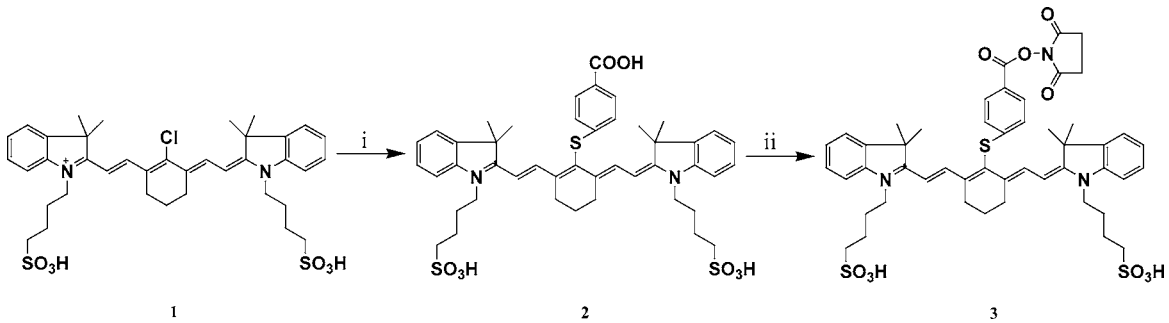
Considering the importance and advantages of both nuclear and fluorescence imaging, a combination of these two techniques provides an attractive approach for enhancing the imaging accuracy and providing complementary information for improving diagnosis and management of diseases. The strategy to achieve this goal is to develop an optical and nuclear dual-labeled imaging agent. Although NIR fluorophores and radiotracers possess excellent photophysical properties, none are tumor specific. To address this problem, a targeting moiety must be introduced to specifically deliver a dual-labeled imaging agent to diseased sites. Dual-labeled targeting imaging agents, such as the one described herein, allow cross validation and direct comparison between nuclear and fluorescence optical imaging (*8*−*10*). By combining optical imaging for enhanced photon signal count without agent half-life concerns and gamma imaging for high sensitivity at deep tissue detection, dual-labeled imaging agents could allow a comprehensive picture of the imaging agent distribution and provide a rapid and efficient imaging method for basic research and clinical diagnosis.

Small peptides represent a class of potential targeting unit candidates (*11*), since they are structurally well defined, easily synthesized, and possess faster circulatory clearance when employed in imaging agents compared to larger antibodies or proteins. Interleukin-11 (IL-11) is a multifunctional cytokine involved in various pathways in blood cells, their precursors, and many other cell types both *in vitro* and *in vivo*. The effects of IL-11 are largely mediated by the IL-11 receptor alpha-chain (IL-11Rα), which is a member of the gp130-dependent receptor group that has been associated with various unique biological actions. Experimental evidence has shown that interleukin (IL-11) and its receptor (IL-11Rα) are related to breast cancer development and progression and may play a significant role in the bone metastasis of human breast cancer (*12*−*14*). IL-11 may also be a predictor of poor prognosis in human breast cancer (*15*). Consequently, targeting of IL-11Rα positive tumors could be a useful strategy for noninvasive imaging. Using phage display technique, Arap et al. (*16*, *17*) identified the cyclic nonapeptide c(CGRRAGGSC), as a mimic motif of IL-11 and showed that it bound specifically to IL-11Rα. Herein, we report the development of a new dual-labeled imaging agent, called DLIA-IL11Rα [^{111}In-DTPA-Bz-NH-SA-K(IR-783-S−Ph−CO)-c(CGRRAGGSC)NH_2] targeting IL-11Rα based upon this cyclic nonapeptide. The radioisotope ^{111}In complexes with DTPA-Bz-NH-SA to form a radiotracer and the NIR dye (IR-783-S-Ph-CO) functions as an optical signal generator. Both are conjugated via amino functional groups of lysine to the

* To whom correspondence should be addressed. E-mail: ww1@bcm.edu. Phone +1 713 798 6017. Fax +1 713-798-2749.

10.1021/bc0602679 CCC: $37.00 © 2007 American Chemical Society
Published on Web 02/22/2007

Scheme 1. Synthesis of IR783-S−Ph−CONHS[a]



[a] Reagents and conditions: (i) 4-mercaptobenzoic acid in DMF; (ii) HOSu/DIC/DMAP (1.5/1.5/0.5) in DMF.

cyclic peptide K-c(CGRRAGGSC)NH_2. The use of this probe enables us to image the interaction between a targeting ligand and an IL-11Rα positive tumor in mice by both conventional nuclear imaging and fluorescence-enhanced optical imaging techniques. Herein, we present the chemistry, *in vitro* cell binding, and *in vivo* imaging of DLIA-IL11Rα.

EXPERIMENTAL PROCEDURES

Materials. All Fmoc-amino acids, benzotriazol-1-yl-oxy-tris-pyrrolidino-phosphonium hexafluorophosphate (PyBOP), *O*-benzotriazole-*N*,*N*,*N*′,*N*′-tetramethyl-uronium-hexafluoro-phosphate (HBTU), dimethylaminopyridine (DMAP), 1-hydroxybenzotriazole (HOBt), *N*-hydroxysuccinimide (HOSu), and Fmoc rink linker were purchased from Novabiochem (San Diego, CA); PL-DMA resin was purchased from Polymer Laboratories (Amherst, MA); piperidine, *N*,*N*-diisopropylethylamine (DIPEA), ethylenediamine, triethylsilane (TES), 1,3-diisopropylcarbodiimide (DIC), IR-783 and succinic anhydride were purchased from Sigma-Aldrich Chemical (St. Louis, MO); *p*-aminobenzyl-diethylenetriamine-penta-(acetic acid-*t*-butyl ester) was purchased from Macrocyclics (Dallas, TX); trifluoroacetic acid (TFA), *N*-methylmorpholine (NMM), indium chloride, and all other solvents were purchased from VWR (San Dimas, CA); indium^{111} chloride ($^{111}InCl_3$) was purchased from Perkin-Elmer (Billerica, MA). 10% serum was purchased from Invitrogen Corporate (Carlsbad, CA). Mouse whole blood was purchased from Pel-Freez Biological (Fayetteville, AR).

Analyses. Analytical high-performance liquid chromatography (HPLC) was performed on an Agilent 1100 HPLC system equipped with a Varian reverse phase C-18 analytical column (R0086200CG) at a flow rate of 1 mL/min. Samples were eluted with H_2O/acetonitrile containing 0.1% TFA varying from three linear gradients (A: 0−40% in 30 min; B: 10−80% in 30 min; C: 30−100% in 30 min). Preparative HPLC was performed on a Varian Prostar 210 HPLC equipped with a 25 × 2.5-cm Varian reverse phase C-18 preparative column (R0080220CB). Matrix-assisted laser desorption ionization mass spectrometry (MALDI) and electrospray ionization mass spectrometry (ESI) were performed by the Protein Chemistry Core Laboratory at Baylor College of Medicine. Fluorescence properties were measured on a Spex Fluorolog III spectrophotometer from HORIBA Jobin Yvon, Inc. (Edison, NJ).

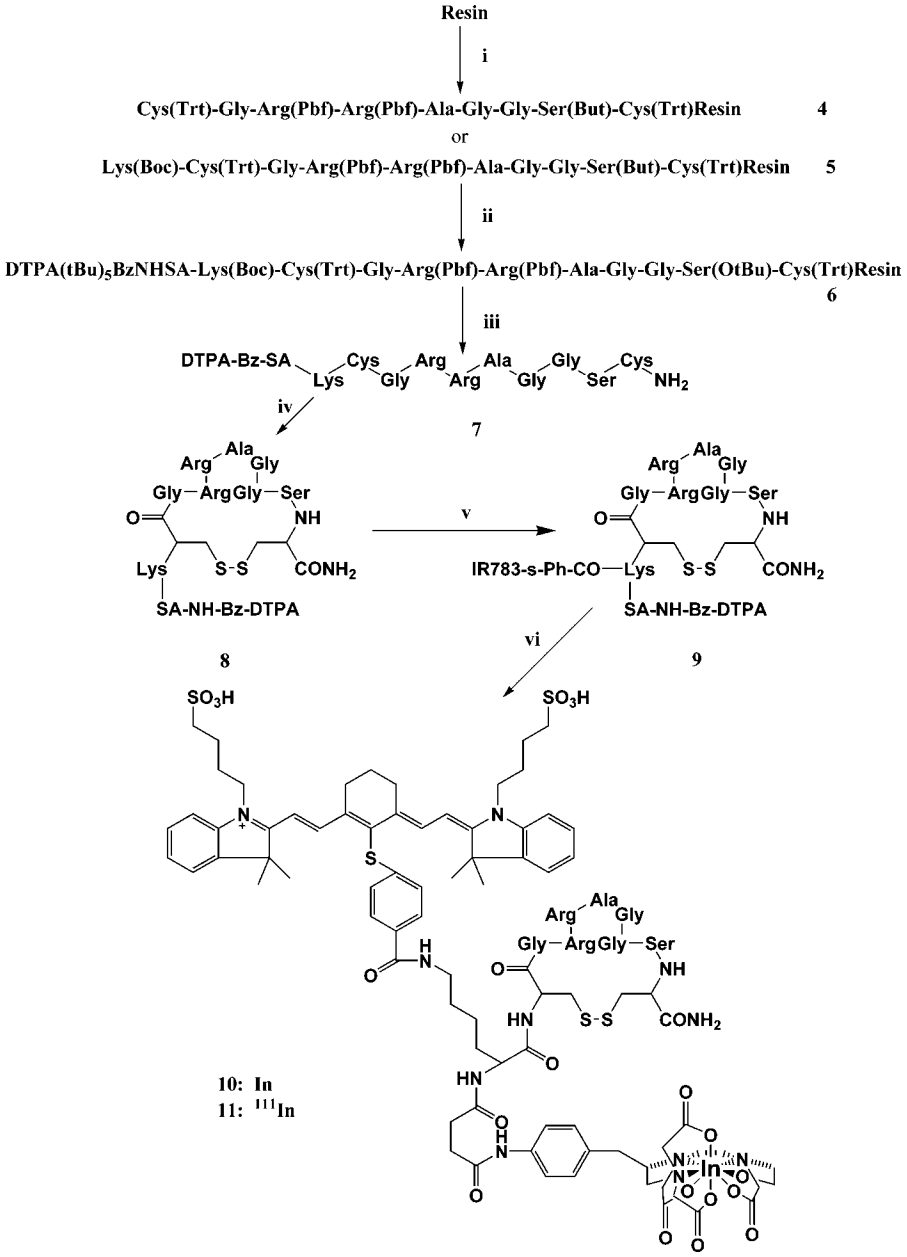
Synthesis of *p*-Succinamidobenzyl-diethylenetriamine-penta-(acetic acid-*t*-butyl ester) [DTPA(OtBu)5-Bz-NH-SA]. Synthesis of DTPA(OtBu)5-Bz-NH-SA was conducted according to previously published procedures (*18*). DTPA(OtBu)5-Bz-NH_2(1.0 mmol) was dissolved in 10 mL of DMF/DCM (1/5). Succinic anhydride (1.0 mmol) and DIPEA (0.2 mL) were added to the solution. The mixture was stirred at room temperature for 4 h. After evaporation of the solvents under vacuum, the residue was dissolved in ethyl acetate, washed with 2% $KHSO_4$ and brine, and then dried over $MgSO_4$. After filtration, ethyl acetate was removed to yield a white powder. ESI for $C_{45}H_{74}N_4O_{13}$ calcd. $[M + H]^+$ 879. 53; found 879. 4; HPLC (gradient C) retention time 23.98 min.

Synthesis of 2-(2-(2-(4-Carboxyphenylthio)-3-(2-(3,3-dimethyl-1-(4-sulfobutyl)indolin-2-ylidene)ethylidene)cyclohex-1-enyl)vinyl)-3,3-dimethyl-1-(4-sulfobutyl)-3H-indolium [IR-783-S-Ph-COOH] (*2*) (Scheme 1). IR-783 (**1**) (250 mg, 0.33 mmol) and 4-mercaptobenzoic acid (156 mg, 1 mmol) were dissolved in 5 mL of DMF and stirred overnight at room temperature. After the solvent was removed, the residue was dissolved in MeOH and then precipitated in ether. The solid was filtered out and further purified with flash chromatography with ethyl acetate and methanol. MALDI for $C_{45}H_{53}N_2O_8S_3^+$ calcd. $[M]^+$ 845. 30; found 845. 30; HPLC (gradient B) retention time 18.56 min; Ex/Em 794/810 in MeOH.

Synthesis of 2-(2-(3-(2-(3,3-dimethyl-1-(4-sulfobutyl)indolin-2-ylidene)ethylidene)-2-(4-((2,5-dioxopyrrolidin-1-yloxy)-carbonyl)-phenylthio)cyclohex-1-enyl)vinyl)-3,3-dimethyl-1-(4-sulfobutyl)-3H-indolium [IR-783-S-Ph-CO-NHS] (*3*) (Scheme 1). IR-783-S-Ph-COOH (**2**) (200 mg, 0.24 mmol), DIC (56 μL, 0.36 mmol), HOSu (42 mg, 0.36 mmol), and DMAP (15 mg, 0.12 mmol) were dissolved in 5 mL of DMF and stirred overnight at room temperature. After the solvent was removed, the residue was dissolved in MeOH and then precipitated in ether. The solid was filtered out and purified with reverse phase HPLC. MALDI for $C_{49}H_{56}N_3O_{10}S_3^+$ calcd. $[M]^+$ 942. 31; found 942. 30; HPLC (gradient B) retention time 20.27 min.

Synthesis of cyclic peptide c(Cys-Gly-Arg-Arg-Ala-Gly-Gly-Ser-Cys)NH_2 (*4*) and its DTPA chelating conjugate DTPA-Bz-NH-SA-Lys-c(Cys-Gly-Arg-Arg-Ala-Gly-Gly-Ser-Cys)NH_2 (*8*) (Scheme 2). First, Fmoc-rink linker was attached to PL-DMA resin, which had been treated with ethylenediamine overnight. The linear peptide Cys-Gly-Arg-Arg-Ala-Gly-Gly-Ser-Cys-NH_2 and its conjugate DTPA-Bz-SA-Lys-Cys-Gly-Arg-Arg-Ala-Gly-Gly-Ser-Cys-NH_2 were synthesized using Symphony synthesizer from Protein Technologies, Inc. (Tucson, AZ) following Fmoc standard procedure. The protecting groups of amino acid side chains were t-butyloxycarbonyl (Boc) for Lys, trityl (Trt) for Cys, 2,2,4,6,7-pentamethyl-dihydrobenzofurane-5-sulfonyl (Pbf) for Arg, t-butyl (tBu) for Ser and t-butoxy (tBuO) for DTPA. Each amino acid was sequentially coupled on solid support using HBTU, HOBt, and NMM as coupling reagents. The conjugation of DTPA$(OtBu)_5$-Bz-NH-SA to the linear peptide Lys(Boc)-Cys(Trt)-Gly-Arg(Pbf)-Arg(Pbf)-Ala-Gly-Gly-Ser(But)-Cys(Trt)-resin was achieved in the presence of PyBOP, HOBt, and DIPEA. Cyclization between Cys−Cys for peptide **4** and **8** was achieved in NH_4OH solution (pH 9. 5) after linear peptides were cleaved from the support using TFA/H_2O/TES (94/2/4). The products were purified by reverse phase HPLC. MALDI for c(CGRRAGGSC)NH_2 (*4*) ($C_{30}H_{54}N_{16}O_{10}S_2$) calcd. $[M + H]^+$ 863. 37; found 863. 37; HPLC (gradient A) retention time 8.71 min. MALDI for DTPA-Bz-NH-SA-K-

Scheme 2. Synthesis of ^{111}In-DTPA-Bz−NH-SA-Lys(IR783-S−Ph−CO)-c(CGRRAGGSC)NH$_2$[a]



[a] Reagents and conditions: (i) Fmoc solid-phase peptide synthesis; (ii) DTPA(But)$_5$-Bz−NH-SA/PyBOP/HOBt/DIPEA (3:3:3:6 Eq) in DMF; (iii) TFA/H_2O/TES (95:1:4); (iv) H_4NOH basic solution (pH 9. 5); (v) IR-783-S-Ph_CONHS in DMF with 10% DIPEA; (vi) $^{111}InCl_3$ or $InCl_3$ in NaOAc (0. 1 N).

c(CGRRAGGSC)NH$_2$ (*8*) ($C_{61}H_{98}N_{22}O_{23}S_2$) calcd [M + H]$^+$ 1571. 66; found 1571. 70; HPLC (gradient A) retention time 13.24 min.

Synthesis of DTPA-Bz-NH-SA-K(IR783-S-Ph-CO)-c(CGRRAGGSC)NH$_2$ (*9*) (Scheme 2). Conjugation of IR783-S-Ph-CONHS (**3**) to ω-NH$_2$ of Lys in DTPA-Bz-NH-SA-K-c(CGRRAGGSC)NH$_2$ was carried out in DIPEA/DMF(1/9) solution overnight. After the solvent was removed, the residue was washed with ether several times. The product was purified by reversed phase HPLC. MALDI for $C_{106}H_{149}N_{24}O_{30}S_5$ calcd. [M]$^+$ 2397. 95; found 2397. 94; HPLC (gradient B) retention time 18.19 min; Ex/Em 794/810 in MeOH.

Cold and Radioactive Indium Labeling of DTPA-Bz-NH-SA-Lys(IR783-S-Ph-CO)-c(CGRRAGGSC)NH$_2$ to Yield DLIA-IL11Rα (*10, 11*) (Scheme 2). DTPA-Bz-NH-SA-K(IR-783-S-Ph-CO)-c(CGRRAGGSC)NH$_2$ (9) in 0.1 N sodium acetate solution was mixed with an aqueous solution of cold $InCl_3$ or radioactive $^{111}InCl_3$ for 30 min. The purity of the labeled compound was analyzed using an HPLC system equipped with a radiometric detector from Bioscan (Washington, DC). MALDI for $C_{106}H_{146}InN_{24}O_{30}S_5$ calcd. [M]$^+$ 2509. 83; found 2509.9; HPLC (gradient B) retention time 17.39 min; Ex/Em 794/810 in MeOH.

Peptide Stability Test in Serum. DTPA-Bz-NH-SA-K-c(CGRRAGGSC)NH$_2$ (**8**) (1 mg) was incubated in 1 mL of culture medium containing 10% of fetal serum albumin at 37 °C. At various time intervals, 50 μL aliquot was injected into an HPLC system. The samples were eluted with water and acetonitrile containing 0.1% TFA varying from 0 to 40% over 30 min and detected with a diode array UV/vis detector at 230 and 275 nm.

Peptide Stability Test in Mouse Whole Blood. DTPA-Bz-NH-SA-K-c(CGRRAGGSC)-NH$_2$ (**8**) (1 mg) was incubated in 200 μL of mouse whole blood at 37 °C. At various time intervals, 20 μL of the mixture was added into 100 μL of PBS and then centrifuged. 50 μL of the supernatant was injected

into an HPLC system. The samples were eluted with water and acetonitrile containing 0.1% TFA varying from 0 to 40% over 30 min and detected with a diode array UV/vis detector at 230 and 275 nm.

Cell Binding Study of Imaging Agent. Human breast cancer that expresses IL-11Rα (MDA-MB-231) was purchased from American Type Culture Collection (Manassas, VA). A highly metastatic subline MDA-MB-231 (1833) was a kindly donated by Dr. Massaque at the Memorial Sloan-Kettering Cancer Center. The cells were cultured in MDEM DMEM/F12 (Invitrogen, Carlsbad, CA) with 10% FBS (Hyclone, Logan, UT) in a humidified incubator maintained at 37 °C with 5% CO_2. In vitro cell binding was performed on both cell lines. A solution (1 μM) of dual-labeled imaging agent was incubated with cells for 10 min at 37 °C. The cells were fixed and stained with 1 μM of Sytox Green in 95% ethanol for 15 min at 4 °C. Images were recorded by a Leica fluorescent microscope (Model: DM6000 B, Leica Microsystems GmbH, Ernst-Leitz-Strasse, Germany) equipped with 100 W xenon lamp and fluorescent filters.

Autocrine Stimulation. MDA-MB-231 cells that express IL-11 Rα were first co-incubated and stimulated by 0.5 mg/mL of IL-11 (Neumega, Oprelvekin, Wyeth Pharmaceuticals Inc. Philadelphia, PA) for 18 h. DLIA-IL11Rα was then added to achieve a final concentration of 1 μM for 10 min at 37 C. Cells were washed 3 times with PBS. The autocrine stimulatory effect of IL-11 was determined by measuring the intensity of bound DLIA-IL11Rα normalized by cell number for both stimulated and untreated cells. Statistical analysis was performed using SAS software version 9.0 (SAS Institute Inc., Cary, NC) for Microsoft Windows. The difference between normalized intensities of stimulated and unstimulated cells was compared using the one-way ANOVA. The significant value (p) was set at 0.5.

***In Vivo* NIR Optical and Nuclear Imaging Studies of Imaging Agent.** Human breast cancer xenografts were injected s.c. with 1×10^6 MDA-MB-231 cells on the hindlimb. Tumor growth occurred over 3−4 weeks reaching 7−8 mm in diameter. At this size, 2 nmol of DLIA-IL11Rα was injected intravenously into the tail vein of the mice. Mice were imaged on a Siemens Preclinical microCAT II for SPECT/CT. The integration time for SPECT was 20 min and CT required 8 min. *In vivo* fluorescence-based optical imaging was accomplished by illuminating the animal with light from a laser diode (80 mW at 785 nm light) expanded to an approximately 8-cm-diameter circular area. The re-emitted fluorescent light was collected by an electron-multiplying charge-coupled device (EMCCD) camera (model PhotoMAX:512B, Princeton Instruments, Trenton, NJ). The resolution of the EMCCD camera was 16×16 μm in a 512×512 pixels square frame-transfer format. Filter sets used in this study included a bandpass filter (830 nm center wavelength) to transmit fluorescent emission and holographic filter (785 nm center wavelength) to reject reflected excitation light. Image acquisition was accomplished using V++ software from Digital Optics (Auckland, New Zealand). Data processing and analysis were accomplished using Matlab software from The MathWorks, Inc. (Natick, MA). The integration time for each image was 800 ms. The whole body images were taken at 24 h after the injection and 48 h after the injection, mice were sacrificed and images of the excised organs were taken. Three-dimension SPECT/CT and images/movies were reconstructed by Amira (version 3.1, Konrad-Zuse-Zentrum fur Informationstechnik Berlin, Germany).

RESULTS AND DISCUSSION

Chemistry. In this study, the cyclic nonapeptide c(CGRRAGGSC)NH_2 was selected as targeting molecule. To develop an optical and nuclear dual-labeled targeting imaging agent based upon this targeting molecule, it is necessary to introduce a fluorophore, which serves as an optical imaging component, and to select a suitable bifunctional chelator, which is able to be coupled to a targeting compound and capable of forming a stable complex with a radiometal ion.

Cyanine dyes are most commonly used as NIR fluorophores. IR-783-S-Ph-CONHS (**3**) was selected as NIR fluorescence reaction agent for this study, due to its increased chemical stability over IR-783-S-(CH2)2-CONHS (*19*). Compound **3** was prepared from a commercially available cyanine dye IR-783 (**1**). First, the chlorine on IR-783 was replaced with S-Ph-COOH (Scheme 1) using a similar method as Strekowski et al. described (*20*) to form compound **2**. Next, the reaction of compound **2** with HOSu yielded the desired compound **3**, which can be directly applied for conjugation with an amino functional group.

Diethylenetriaminepenta-acetic acid (DTPA) is one of the well-known radiometal chelating agents for such radionuclides as ^{111}In and ^{90}Y. The DTPA derivative DTPA$(OtBu)_5$-Bz-NH-SA (*18*) was selected as a chelating compound. The advantage of this reagent is that it can be easily conjugated to peptides on a solid support and still possesses five carboxylates for radiometal chelation.

The reaction scheme and the structure of dual-labeled targeting imaging agent [In-DTPA-Bz-NH-SA-K(IR-783-S-Ph-CO)-c(CGRRAGGSC)NH_2] are summarized in Scheme 2. The synthesis procedure can be divided into six major parts. The first three parts were carried out on solid support. The latter three parts were performed in solution phase. The linear protective peptides on resin, Cys(Trt)-Gly-Arg(Pbf)-Arg(Pbf)-Ala-Gly-Gly-Ser(But)-Cys(Trt)-resin (**4**) and Lys(Boc)-Cys(Trt)-Gly-Arg(Pbf)-Arg(Pbf)-Ala-Gly-Gly-Ser(But)-Cys(Trt)-resin (**5**), were synthesized using Fmoc solid-phase chemistry (part 1). DTPA$(OtBu)_5$-Bz-NH-SA was coupled to the linear peptide Lys(Boc)-Cys(Trt)-Gly-Arg(Pbf)-Arg(Pbf)-Ala-Gly-Gly-Ser-(But)-Cys(Trt)-resin (**6**) through α-amino functional group of lysine (part 2). After deprotection and cleavage of the compounds from the solid support (part 3), the side chain−side chain cyclization between cysteine and cysteine of peptide CGRRAGGSCNH_2 or its conjugate DTPA-Bz-NH-SA-K-CGRRAGGSCNH_2 (**8**) was achieved through disulfide bridge formation (part 4).

An important consideration in selecting cyclic peptide c(CGRRAGGSC)NH_2 as the targeting agent to IL-11Rα was the peptide stability, since it may be degraded by enzymes in vivo. Consequently, the stability test of DTPA-Bz-SA-K-c(CGRRAGGSC)NH_2 (**8**) was carried out in two different media: 10% fetal serum albumin serum and mouse whole blood. The peak areas from HPLC analysis of the conjugate (**8**) were quantified, and the stability was expressed as a percentage of individual peak area at different incubation times divided by the peak area at the initial incubation time. The results indicated that compound **8** was 20% degraded when incubated in a serum-containing culture medium at 37 °C over 24 h, while 50% degradation was observed when incubated in mouse whole blood. Although modification of the peptide can be carried out later to improve the stability, the data demonstrated that the stability of the peptide chelator complex is sufficient for this study, since imaging was to be accomplished within 24 h.

After validating the stability of DTPA-Bz-SA-K-c(CGRRAGGSC)NH_2, conjugation of dye (IR-783-S-Ph-CO-NHS) to compound **8** through ε-amino functional group of lysine was performed in a basic solution (part 5). In the last step (part 6), DTPA-Bz-SA-K(IRdye783-S-Ph-CO)-c(CGRRAGGSC)NH_2 (**9**) was separately labeled with cold indium or with radioactive isotope. The non-radioactive compound **10** was selected for

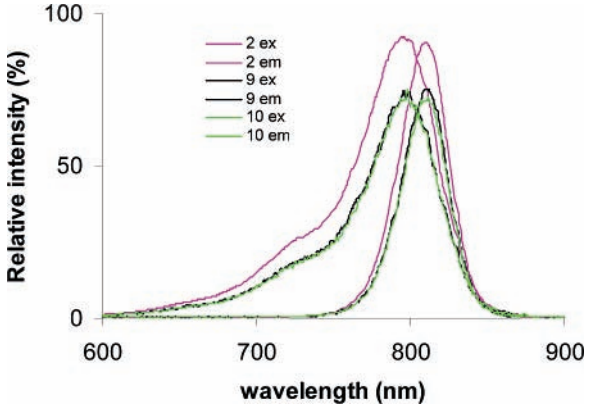


Figure 1. Excitation and emission fluorescence spectra of compound **2** (IR-783-S−Ph-COOH), compound **9** [DTPA-Bz-SA-K(IR-783-S-Ph-CO)-c(CGRRAGGGSC)NH_2] and compound **10** [In-DTPA-Bz-SA-K(IR-783-S-Ph-CO)-c(CGRRAGGSC)NH_2] at 1 μM in MeOH at wavelength Ex/Em 795/810 nm.

examination of fluorescence properties and cell studies, while the radiolabeled conjugate **11** was used for the *in vivo* imaging study.

The fluorescence properties of compounds IR783-S-Ph-COOH (**2**), DTPA-Bz-NH-SA-Lys(IR783-S-Ph-CO)-c(CGRRAGGSC)NH_2 (**9**) and In-DTPA-Bz-NH-SA-Lys(IR783-S-Ph-CO)-c(CGRRAGGSC)NH_2 (**10**) were evaluated. Upon comparing compounds **2** and **9**, we found that the excitation and emission spectra of conjugate **9** remained unchanged (Figure 1). However, after the conjugation of dye to DTPA-cyclopeptide the signal intensity was reduced to 84%. Nevertheless, the spectra in Figure 1 demonstrate that the metal chelation of compound **9** to form compound **10** did not impact fluorescence spectra.

Cell Binding Study of Imaging Agent. To evaluate DLIA-IL11Rα as a potential targeting molecule for *in vivo* imaging, the binding ability to IL-11 receptor was examined *in vitro*. Figure 2 illustrates cell binding of the imaging agent **10** to IL-11Rα positive MDA MB-231 and its subline 1833. The cell nuclei were stained with Sytox green, while the red halo arose from the imaging agent associated with the membrane expression of IL-11Rα. Furthermore, cell stimulation study was carried out using the MDA-MB-231 cell line (*21*). The results show that conjugate **10** binding to stimulated cells was statistically significant higher than binding to nonstimulated cells. These preliminary data reveal that the targeting ability of cyclic peptide c(CGRRAGGSC)NH_2 to IL-11Rα was retained after introducing the nuclear and optical tracers.

***In Vivo* NIR Optical and Nuclear Imaging.** Further demonstration of the targeting feasibility of DLIA-IL11Rα as an imaging agent was performed *in vivo*. Figure 3 demonstrates white light, SPECT/CT, and NIR optical images of the same mouse bearing subcutaneous MDA-MB-231 tumor 24 h after administration of the imaging agent. The white light shows the location of the tumor in the hind leg of the animal. The SPECT/CT and NIR optical imaging illustrate the uptake of the imaging agent in the region of the tumor. In addition, each of the images display uptake of the agent in the abdominal area, presumably within the kidneys as indicated from the NIR planar imaging. It is important to note that the NIR imaging is not tomographic and therefore is directly comparable to the gamma scintigraphy. SPECT/CT on the other hand provides the three-dimensional image of the location of the imaging agent based upon the indium signature. The tomographic SPECT/CT has resolution on the order of 2 mm and consequently may not provide the same information as the NIR images. Furthermore, since light is attenuated in blood born tissues such as the liver, the NIR

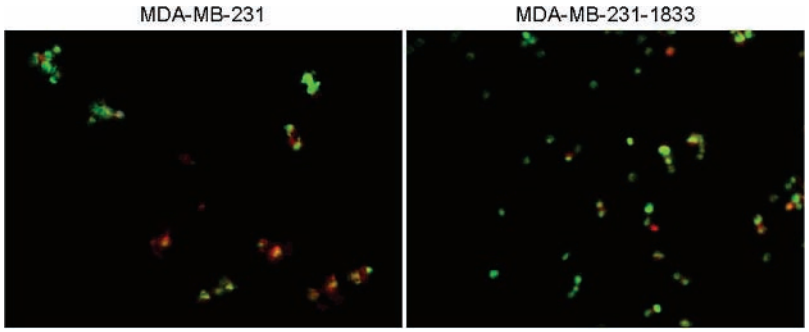


Figure 2. Cell binding study: Two human breast cancer cell lines (MDA-MB-231 and MDA-MB-231-1833) that express IL-11Rα receptor were incubated with 1 μM of DLIA-IL11Rα. Green (Sytox green) represents cell nuclei, and red (NIR imaging agent) represents conjugate bound to the cells.

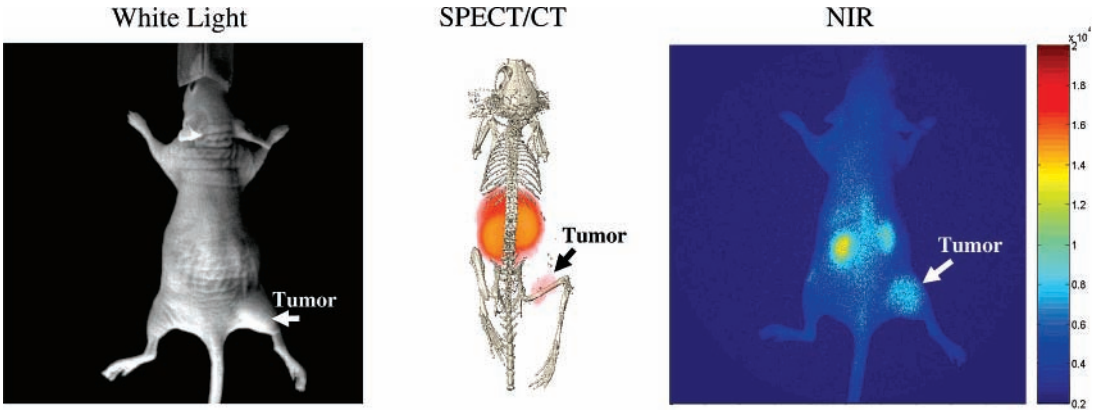


Figure 3. SPECT/CT and NIR imaging. Mice bearing human breast cancer xenograft (MDA-MB-231) were injected with 2 nmol of the conjugate DLIA-IL-11Rα i.v. Representative images show results 24 h after injection. Tumors (arrows) show more conjugate uptake than muscle in both SPECT/CT and NIR images. High signal intensity in kidneys showed the excretion route of this agent even at very low injection dose.

imaging may not provide the same depth specificity of the indium label. When tissues are excised and counted for gamma emission, we found that the tumor to muscle, liver to muscle, and kidney to muscle ratios were 2.12, 2.62, 10.42. To date, we have not conducted biodistribution or pharmacological studies to determine the optimal dose or timing for imaging. The high kidney signal counts may reflect excretion routes and therefore suggest that a lower dose/longer post administration imaging time is warranted. While these *in vitro* scintigraphy counts provide an absolute measure of the deposition of the imaging agent within the body, there is no validated method for quantifying the uptake on the basis of NIR fluorescence. Development of quantitative methods for NIR imaging and tomography depend upon the development of dual-labeled imaging agents to further improve optical imaging techniques.

CONCLUSION

We successfully developed and deployed a new optical and nuclear dual-labeled targeting imaging agent DLIA-IL11Rα [In-DTPA-Bz-NH-SA-K(IR-783-S-Ph-CO)c(CGRRAGGSC)-NH_2] against IL-11Rα expressed in cancer as well as in other processes associated with disease. Our data indicate that the cyclic peptide c(CGRRAGGSC)NH_2 is a feasible targeting agent of IL-11Rα for diagnostic cancer imaging. As shown in our in vitro cell study, introduction of two imaging tracers to cyclic peptide c(CGRRAGGSC)NH_2 did not alter the targeting capability of the peptide to IL-11Rα. Furthermore, indium isotope chelation did not cause any quenching on fluorescence emission of imaging agent **10** relative to the nonchelated compound **9**. Even through peptides usually have lower binding affinity than antibodies, we found that injection of 2 nmol of DLIA-IL11Rα was sufficient to observe specific binding in tumor region. Furthermore, we found that the preliminary *in vivo* imaging by optical and radionuclear methods were consistent. Before DLIA-IL11Rα can be validated as a potential imaging agent, the optimal dose and biodistribution remain to be determined.

ACKNOWLEDGMENT

This research was supported, in part, by the Department of Radiology at Baylor College of Medicine and National Institutes of Health Grant R01 EB003132.

LITERATURE CITED

(1) Ntziachristos, V., Bremer, C., and Weissleder, R. (2003) Fluorescence imaging with near-infrared light: new technological advances that enable *in vivo* molecular imaging. *Eur. Radiol. 13*, 195−208.
(2) Sevick-Muraca, E. M., Houston, J. P., and Gurfinkel, M. (2002) Fluorescence-enhanced, near infrared diagnostic imaging with contrast agents. *Curr. Opin. Chem. Biol. 6*, 642−650.
(3) Shah, K., and Weissleder, R. (2005) Molecular optical imaging: applications leading to the development of present day therapeutics. *NeuroRx 2*, 215−25.
(4) Wu, Y., Cai, W., and Chen, X. (2006) Near-infrared fluorescence imaging of tumor integrin alpha (v)beta (3) expression with Cy7-labeled RGD multimers. *Mol. Imaging Biol. 8*, 226−236.
(5) Godavarty, A., Eppstein, M. J., Zhang, C., and Sevick-Muraca, E. M. (2005) Detection of single and multiple targets in tissue phantoms with fluorescence-enhanced optical imaging: feasibility study. *Radiology 235*, 148−154.
(6) Joshi, A., Bangerth, W., and SevickMuraca, E. M. (2004) Adaptive finite element based tomography for fluorescence optical imaging in tissue. *Opt. Express 12*, 5402−5417.
(7) Weissleder, R., and Mahmood, U. (2001) Molecular imaging. *Radiology 219*, 316−333.
(8) Houston, J. P., Ke, S.; Wang, W., Li, C., and Sevick-Muraca, E. M. (2005) Quality analysis of *in vivo* near-infrared fluorescence and conventional gamma images acquired using a dual-labeled tumor-targeting probe. *J. Biomed. Opt. 10*, 054010.
(9) Li, C., Wang, W., Wu, Q., Ke, S., Houston, J., Sevick-Muraca, E., Dong, L., Chow, D., Charnsangavej, C., and Gelovani, J. G. (2006) Dual optical and nuclear imaging in human melanoma xenografts using a single targeted imaging probe. *Nucl. Med. Biol. 33*, 349−358.
(10) Zhang, Z., Liang, K., Bloch, S., Berezin, M., and Achilefu, S. (2005) Monomolecular multimodal fluorescence-radioisotope imaging agents. *Bioconjugate Chem 16*, 1232−1239.
(11) Stefanidakis, M., and Koivunen, E. (2004) Peptide-mediated delivery of therapeutic and imaging agents into mammalian cells. *Curr. Pharm. Des. 10*, 3033−3044.
(12) Kang, Y., He, W., Tulley, S., Gupta, G. P., Serganova, I., Chen, C. R., Manova-Todorova, K., Blasberg, R., Gerald, W. L., and Massague, J. (2005) Breast cancer bone metastasis mediated by the Smad tumor suppressor pathway. *Proc. Natl. Acad. Sci. U.S.A. 102*, 13909−13914.
(13) Lacroix, M., Siwek, B., Marie, P. J., and Body, J. J. (1998) Production and regulation of interleukin-11 by breast cancer cells. *Cancer Lett. 127*, 29−35.
(14) Morinaga, Y., Fujita, N., Ohishi, K., Zhang, Y., and Tsuruo, T. (1998) Suppression of interleukin-11-mediated bone resorption by cyclooxygenases inhibitors. *J. Cell. Physiol. 175*, 247−254.
(15) Hanavadi, S., Martin, T. A., Watkins, G., Mansel, R. E., and Jiang, W. G. (2006) Expression of interleukin 11 and its receptor and their prognostic value in human breast cancer. *Ann. Surg. Oncol. 13*, 802−808.
(16) Zurita, A. J., Troncoso, P., Cardo-Vila, M., Logothetis, C. J., Pasqualini, R., and Arap, W. (2004) Combinatorial screenings in patients: the interleukin-11 receptor alpha as a candidate target in the progression of human prostate cancer. *Cancer Res. 64*, 435−439.
(17) Arap, W., Kolonin, M. G., Trepel, M., Lahdenranta, J., Cardo-Vila, M., Giordano, R. J., Mintz, P. J., Ardelt, P. U., Yao, V. J., Vidal, C. I., Chen, L., Flamm, A., Valtanen, H., Weavind, L. M., Hicks, M. E., Pollock, R. E., Botz, G. H., Bucana, C. D., Koivunen, E., Cahill, D., Troncoso, P., Baggerly, K. A., Pentz, R. D., Do, K. A., Logothetis, C. J., and Pasqualini, R. (2002) Steps toward mapping the human vasculature by phage display. *Nat. Med. 8*, 121−127.
(18) Wang, W.;, McMurray, J. S., Wu, Q., Campbell, M. L., and Li, C. (2005) Convenient solid-phase synthesis of diethylenetriamine-penta-acetic acid (DTPA)- conjugated cyclic RGD peptide analogues. *Cancer Biother. Radiopharm. 20*, 547−556.
(19) Hilderbrand, S. A., Kelly, K. A., Weissleder, R., and Tung, C. H. (2005) Monofunctional near-infrared fluorochromes for imaging applications. *Bioconjugate Chem. 16*, 1275−1281.
(20) Strekowski, L., Gorecki, T., Mason, J. C., Lee, H., and Patonay, G. (2001) New heptamethine cyanine reagents for labeling of biomolecules with a near-infrared chromophore. *Heterocycl. Commun. 7*, 117−122.
(21) Ke, S. (2007) IL-11 receptor, in preparation.

BC0602679

Dendritic Molecular Transporters Provide Control of Delivery to Intracellular Compartments

Kui Huang,[†,§] Bryan Voss,[‡,§] Disha Kumar,[†] Heidi E. Hamm,*[,‡] and Eva Harth*[,†,‡]

Department of Chemistry, Vanderbilt University, 7619 Stevenson Center, Nashville, Tennessee 37235, and Department of Pharmacology, Vanderbilt University Medical Center, 442 Robinson Research Building, Nashville, Tennessee 37232-6600 .
Received September 13, 2006; Revised Manuscript Received November 16, 2006

Novel biocompatible macromolecular vectors were developed that not only enable transport of bioactive cargo across the cell membrane but also control the delivery into defined intracellular compartments. This work describes the synthesis and design of two non-peptidic fluorescently labeled Newkome-type dendrimers, differentiated over a varied alkyl spacer with guanidine end moieties. The internalization of the fluorescein-labeled molecular transporter into mammalian cells showed strong subcellular localizations, evident with both live cells and fixed cells costained with DAPI, a nuclear stain. We observed that the subcellular distribution of these vectors varied significantly, as one of the vectors concentrates in the nucleus (**FD-1**) while the other (**FD-2**) concentrates in the cytosol. All experiments performed with NIH-3T3 fibroblasts and human microvascular endothelial cells (HMEC) showed similar results. The differential localization patterns of the two molecular transporters can be controlled through the variation of alkyl spacer length at the terminal generation of the dendrimer. Intracellular delivery of bioactive entities into specific subcellular locations, utilizing this practical approach, might overcome limitations in drug delivery and pioneer future technologies in drug transport.

INTRODUCTION

The development of novel approaches that facilitate cellular uptake of a variety of physiologically and therapeutically active agents relies on the elucidation of new molecular transporter/translocator molecules and methodologies. In the past several years, strategies to overcome the limiting uptake of the plasma membrane have included cell-permeable peptide vectors (*1*−*4*), such as Tat peptide and other various arginine-rich oligopeptides (*5*−*9*). HIV−Tat peptide (R_{49}KKRRQRRR$_{57}$) and its arginine-rich derivatives have been given much attention, primarily due to their high efficiency, short sequence, and capabilities of transporting various types of molecular structures, such as small molecular weight compounds, oligonucleotides, magnetic beads, plasmid DNA, and even a full 129 kDa protein, across the membranes of most cell types (*10*−*16*). In particular, uptake assays of oligoarginines identified nona-arginines as being superior over traditional Tat peptides. The subcellular localization profile of synthetic oligoarginine peptides appeared to be in both the cytoplasm and nucleus, which is similar to that of HIV−Tat (49−57) (*7*, *13*, *17*−*19*). However, our goal is to develop novel therapeutic strategies to deliver drugs directly to intracellular sites such as the nucleus or the cytosol, in order to limit unwanted intracellular probe metabolism and transport and reduce nonspecific effects, toxicity and dosage levels. Alternative delivery tools for drug delivery, gene therapy, and vaccine delivery are in high demand to overcome current limitations.

One attempt to develop transport vectors has been the investigation of selected lysine−arginine-rich human-derived peptide vectors (*20*). It was found that these peptides, once inside the cell, enable accumulation of therapeutic molecules in the cytoplasm or nucleus, depending on the specific vector used. However, these peptide or peptoid-based molecular transporters are limited again by high cost, scalability, solubility, and stability.

We sought to exploit non-peptidic branched architectures based on the reported observation that branched-chain arginine peptides resulted in different patterns of cellular localization (*21*). Dendritic structures have been recognized to be ideal building blocks for biomedical applications because of their monodispersity, high loading capacity, large-scale production, and bioconjugation capability (*22*−*24*). Despite numerous reports about the importance of guanidinium groups in the peptidic backbone of oligoarginines, relatively few attempts have been made using guanidine groups in branched dendritic scaffolds (*25*, *26*). For example, a recent paper by Wender et al. (*26*) employs the use of triamine-based diamino acids to form a series of octa-arginine dendrimers that show differences in uptake efficiency related to the structural flexibility of the dendritic architecture. In contrast to this study, we directed our efforts to develop dendritic structures which mimic features of branched polyarginines but provide means to target and control intracellular delivery. We investigated intracellular distributions and the time course of uptake in vivo with two different mammalian cell lines using confocal microscopy.

We proposed that for a molecular transporter to possess the aforementioned features the constitution of the dendritic backbone had to be one of the most compact, highly branched, and biocompatible structures possible. Through mimicking a regular peptidic backbone, by the implementation of highly symmetric macromolecular peripheries, the critical presentation of the guanidino groups to the biological systems are controlled by the length of the alkyl spacer. We focused on these parameters for two main reasons. One, the length and flexibility of the spacer in dendritic transporter have thus far been connected with enhanced and rapid cellular uptake, and two, factors for

* To whom correspondance should be addressed: (E.H.) E-mail: eva.harth@vanderbilt.edu. Phone: 615-343-3405. Fax: 615-343-1234. (H.E.H.) E-mail: heidi.hamm@vanderbilt.edu. Phone: 615-343-3533. Fax: 615-343-1084.

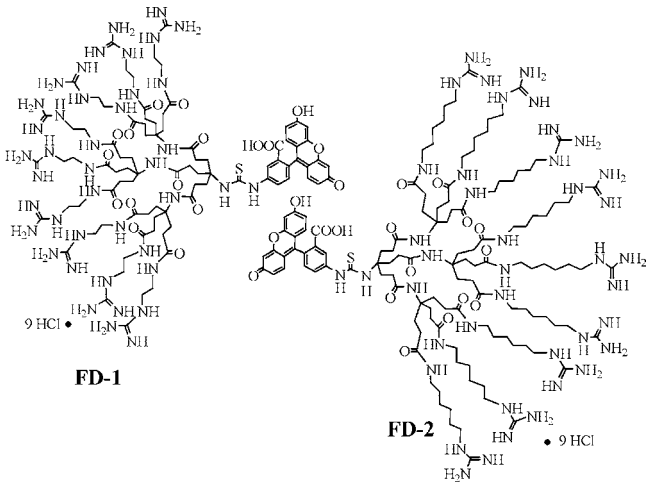
† Vanderbilt University.

‡ Vanderbilt University Medical Center.

§ Both authors contributed equally to this work.

10.1021/bc060287a CCC: $37.00 © 2007 American Chemical Society
Published on Web 02/07/2007

Scheme 1. Structures of FD-1 and FD-2



regulating intracellular specification have been unclear. Therefore, we sought to design and synthesize macromolecules with a differentiated flexible spacer to the guanidine functionality, but with a high-density arrangement on a symmetric and compact dendritic macromolecule.

In this study, we utilized the classic Newkome-type dendrimer as the structural building block, a compact yet highly branched structure in which the necessary nine end functionalities can be achieved in just one generation of dendritic growth (*11*, *27*). We report the design and synthesis of Newkome-type probe transporters, functionalized with guanidine end moieties and differentiated over a varied alkyl spacer to the scaffold, with a fluorophore conjugated to the focal point as the sample cargo molecule. We demonstrate the cell-penetrating capabilities of two new fluorescent macromolecular conjugates, FITC−dendrimer 1 (**FD-1**) and FITC−dendrimer 2 (**FD-2**), shown in Scheme 1. Interestingly, while these molecules feature similar, high levels of cellular uptake, they differ considerably in their subcellular localization (cytoplasm vs nucleus). There is a high potential for these molecular transporter molecules in both basic biomedical research and the clinical setting, as they could be used for the highly targeted delivery of a variety of bioactive molecules, thereby avoiding some of the common caveats of other drug delivery approaches, such as toxicity and limited cargo delivery (*16*).

EXPERIMENTAL PROCEDURES

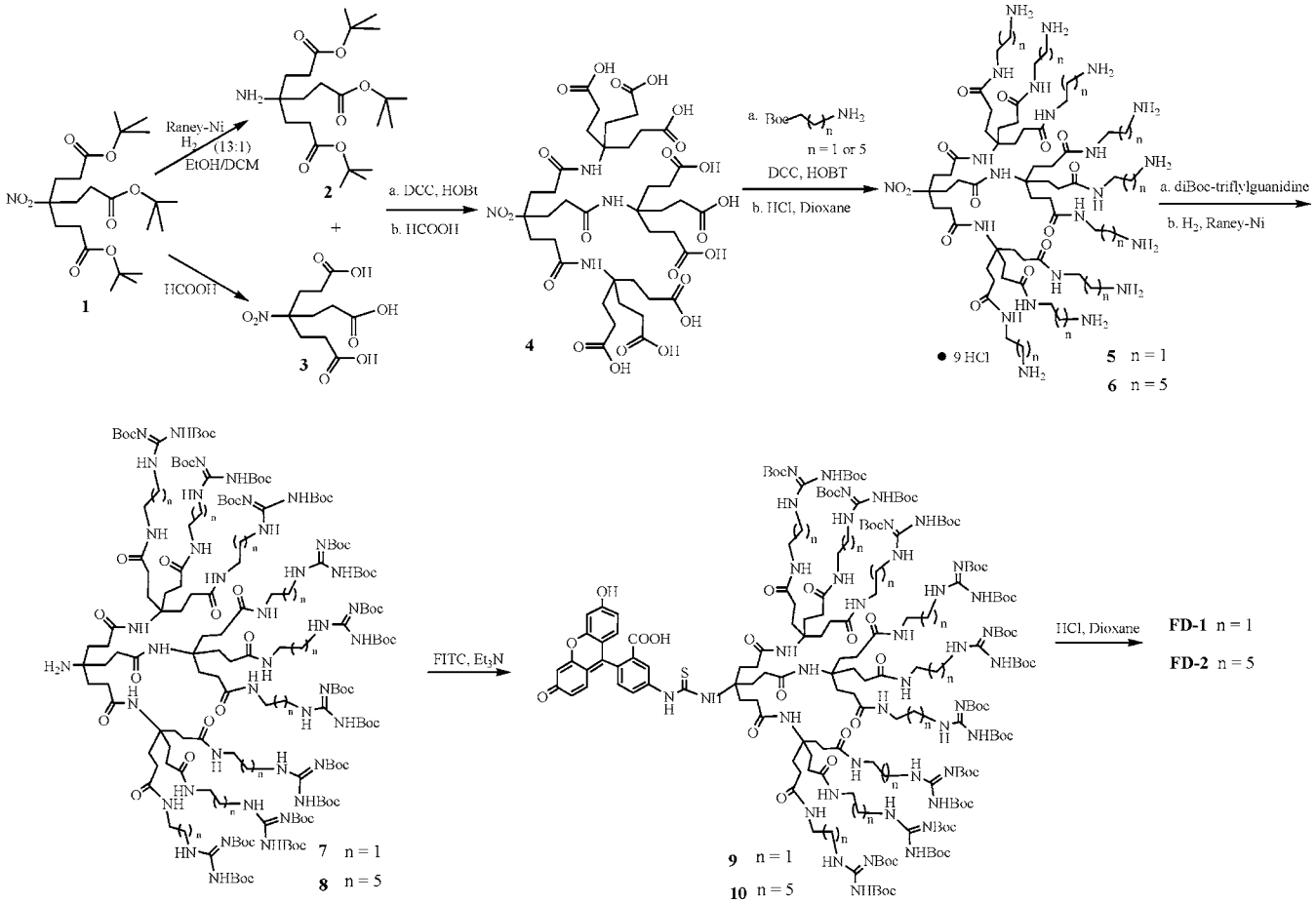
Materials and Methods. All reagents and solvents were purchased from commercial sources and were used as received, unless otherwise stated. Spectra/Por Biotech cellulose ester and regenerated cellulose dialysis membranes were purchased from Spectrum Laboratories, Inc. Di-*tert*-butyl-4-[2-(*tert*-butoxycarbonyl)ethyl]-4-nitroheptanedicarboxylate **1** and 4-nitro-4-[2-(carboxyethyl)]heptanediacid **3** (Scheme 2) were prepared using a previously described method (*27*). Analytical TLC was carried out on Merck 250 μM silica gel 60 F_{254} plates, and spots were located by UV light or treatment with iodine. Column chromatography was conducted by silica gel (60−200 mesh) from Fisher Scientific. All NMR spectra were measured on a 400 MHz Bruker FT−NMR spectrometer. MALDI-MS were carried out on a Perspective Biosystems Voyager-DE STR (Framingham, MA) equipped with delayed extraction technology operating in linear mode (MALDI-MS data of known compounds not shown). 2′,4′,6′-Trihydroxyacetophenone (THAP) or 2,5-dihydroxybenzoic acid (DHBA) was used as the matrix with a matrix/analyte ratio of 1000:1. Reverse-phase high-performance liquid chromatography (RP-HPLC) was carried out with a Varian Prostar 210/215 HPLC using either an analytical column (Vydak, C18, 150 × 4.6 mm) or a preparative column (Alltec Alltima, C18, 250 × 22 mm). The products were eluted using a solvent gradient (solvent A = 0.05% TFA/H_2O; solvent B = 0.05% TFA/CH_3CN).

Synthesis of Di-*tert*-butyl-4-[2-(*tert*-butoxycarbonyl)ethyl]-4-aminoheptanedicarboxylate, "Behera's Amine" 2 (*27*). A solution of nitrotriester **1** (6.00 g, 0.0135 mol) in ethanol/dichloromethane (13:1, 140 mL) in a Parr hydrogenation bottle with 4 g of Raney-Nickel was stirred at 60 psi for 24 h at room temperature. The suspension was carefully filtered through Celite, and the removal of the solvent under reduced pressure gave the crude product. The residue was dissolved in dichloromethane (120 mL), and the resulting organic solution was washed sequentially with saturated $NaHCO_3$ (120 mL) and water (120 mL) and dried over anhydrous Na_2SO_4. The solvent was evaporated under reduced pressure to yield aminotriester **2** (5.2 g, 93%). ^{1}H NMR (400 MHz, $CDCl_3$): δ = 1.44 (s, CH_3, 27H), 1.95 (t, CH_2, 6H), 2.43 (t, CH_2, 6H). ^{13}C NMR (400 MHz, $CDCl_3$): δ = 27.98 (*C*H_3), 29.46 (*C*H_2CO), 31.47 (C*C*H_2), 56.99 (*C*NH_2), 80.96 (*C*CH_3), 172.30 (*C*O_2).

Synthesis of 9 Cascade:nitromethane [3]:(2-aza-3-oxopenylidyne):propionic acid 4 (*27*). To a solution of nitrotriacid **3** (0.65 g, 2.35 mmol) in dry THF (50 mL), 1-hydrobenzotriazole (HOBt) (0.96 g, 7.10 mmol), DCC (1.46 g, 7.10 mmol), and aminotriester **2** (3.54 g, 8.5 mmol) were added sequentially. The solution was stirred at room temperature for 40 h, then filtered and concentrated under reduced pressure. The crude product was purified by flash column chromatography, eluting with hexane/ethyl acetate (3:2) to yield the desired denron (3.00 g, 86%). ^{1}H NMR (400 MHz, $CDCl_3$): δ = 1.44 (m, CH_3, 81H), 1.95 (m, CH_2, 18H), 2.21 (m, CH_2, 30H), 6.20 (s, N*H*, 3H). ^{13}C NMR (400 MHz, $CDCl_3$): δ = 28.04, 29.74, 29.85, 31.28, 57.56, 80.69, 92.47, 170.46, 172.76. The dendron (1.47 g, 1 mmol) was stirred in 15 mL of formic acid overnight at room temperature. After the solvent was evaporated under reduced pressure, toluene was added and concentrated in vacuo to remove any residue of formic acid to give a white nona-acid **4** (0.95 g, 100%). ^{1}H NMR (400 MHz, DMSO): δ = 1.81 (m, CH_2, 18H), 2.11 (m, CH_2, 30H), 7.29 (s, N*H*, 3H), 12.10 (br, COO*H*). ^{13}C NMR (400 MHz, DMSO): δ = 28.03, 29.03, 30.08, 56.41, 93.31, 170.43, 174.42.

Synthesis of 9 Cascade:nitromethane [3]:(2-aza-3-oxopenylidyne):[propionic acid-(2-aminoethyl)amide] HCl Salt 5. To a solution of nona-acid **4** (2.12 g, 0.0022 mol) in DMF (30 mL), HOBt (2.68 g, 0.0198 mol) and DCC (4.09 g, 0.0198 mol) were added, and the solution was cooled to 0 °C. *N*-Boc-ethylenediamine (3.49 g, 0.0218 mol) in DMF (5 mL) was added dropwise, and the mixture was stirred for 48 h at room temperature, filtered, and concentrated under reduced pressure. The residue was dissolved in dichloromethane (100 mL), and the resulting organic solution was washed sequentially with 1 N HCl (100 mL), saturated $NaHCO_3$ (100 mL), and water (100 mL) and dried over anhydrous Na_2SO_4. The solvent was evaporated under reduced pressure, and the crude residue was purified by flash column chromatography eluting with 2% methanol in dichloromethane and gradually increasing to 10% methanol in dichloromethane to yield a white solid (2.5 g, 51%). ^{1}H NMR (400 MHz, CD_3OD): δ = 1.44 (m, CH_3, 81H), 1.80−2.10 (m, CH_2, 48H), 3.0−3.2 (m, CH_2, 36H), 6.20 (m, N*H*, 3H), 6.46 (m, N*H*, 8H), 7.71 (m, N*H*, 8H). ^{13}C NMR (400 MHz, CD_3OD): δ = 28.40, 31.24, 31.44, 31.80, 32.09, 40.66, 40.97, 59.14, 80.13, 94.42, 158.48, 173.48, 175.91. MALDI MS: calculated for $C_{103}H_{187}N_{22}O_{32}$ (M + Na^+), 2268.9; found, 2270.5. The resulting solid was dissolved in 1,4-dioxane (40 mL), the solution was cooled to 0 °C, and 4 M HCl in dioxane (40 mL) was added and stirred for 1 h at room temperature. Removal of the solvent under reduced pressure gave **5** as a white

Scheme 2. Synthetic Scheme for FITC−Dendrimer Conjugates



solid (1.86 g, 100%). ^{1}H NMR (400 MHz, D_2O/CD_3OD): δ = 1.70−2.15 (m, CH_2, 48H), 3.30 (m, CH_2, 18H), 3.36 (m, CH_2, 18H). ^{13}C NMR (400 MHz, D_2O/CD_3OD): δ = 27.61, 27.98, 28.86, 35.11, 37.41, 56.29, 92.01, 171.84, 174.98. MALDI MS: calculated for $C_{58}H_{124}Cl_9N_{22}O_{14}$ ($M + H^+$), 1673.9; found, 1674.8.

Synthesis of 9 Cascade:nitromethane [3]:(2-aza-3-oxopenylidyne):[propionic acid-(6-aminohexyl)amide] HCl Salt 6. To a solution of nona-acid **4** (1.2 g, 0.0012 mol) in DMF (20 mL), HOBt (1.514 g, 0.0112 mol) and DCC (2.311 g, 0.0112 mol) were added and the solution cooled to 0 °C. *N*-Boc-1,6-diaminohexane (2.66 g, 0.0123 mol) in DMF (5 mL) was added dropwise, and the mixture was stirred for 48 h at room temperature, filtered, and concentrated under reduced pressure to give the crude product. The residue was dissolved in dichloromethane (80 mL), and the solution was washed with 1 N HCl (80 mL), saturated $NaHCO_3$ (80 mL), and water (80 mL) and dried over anhydrous Na_2SO_4. The solution was concentrated under reduced pressure, and the crude product was purified by flash column chromatography eluting with 2% methanol in dichloromethane and gradually increasing to 10% methanol in dichloromethane to yield a white solid (1.68 g, 49%). ^{1}H NMR (400 MHz, CD_3OD): δ = 1.2−1.6 (m, CH_3, CH_2, 153H), 1.80−2.10 (m, CH_2, 48H), 3.0−3.2 (m, CH_2, 36H). ^{13}C NMR (400 MHz, CD_3OD): δ = 27.54, 28.85, 30.37, 30.90, 31.28, 31.60, 32.14, 40.58, 41.24, 59.13, 79.30, 94.30, 158.49, 173.50, 175.56. MALDI MS: calculated for $C_{139}H_{259}N_{22}O_{32}$ ($M + H^+$) 2750.7; found, 2784.03. The product was then dissolved in 1,4-dioxane (40 mL) and the solution cooled to 0 °C; 4 M HCl in dioxane (40 mL) was added and stirred for 1 h at room temperature. Removal of the solvent under reduced pressure gave **6** as a white solid (1.32 g, 100%). ^{1}H NMR (400 MHz, D_2O/CD_3OD): δ = 1.10−1.60 (m, CH_2, 72H), 1.7−2.2 (m, CH_2, 48H), 3.30 (m, CH_2, 18H), 3.36 (m, CH_2, 18H). ^{13}C NMR (400 MHz, D_2O/CD_3OD): δ = 26.89, 27.42, 28.21, 28.90, 35.03, 37.68, 56.28, 91.89, 172.3, 175.50. MALDI MS: calculated for $C_{94}H_{196}Cl_9N_{22}O_{14}$ ($M + H^+$), 2177.8; found, 2177.6.

Synthesis of 9 Cascade:nitromethane [3]:(2-aza-3-oxopenylidyne):propionic acid-(2-(1,3-bis-(*tert*-butoxycarboyl)guanidino)ethyl)amide 7. The resulting HCl salt of **5** (1.53 g, 0.92 mmol) was dissolved in methanol (80 mL), and the solution was cooled to 0 °C. Et_3N (3.5 mL) was added, followed by *N*,*N*′-diBoc-*N*′′-triflylguanidine (4.2 g, 10.73 mmol), and the mixture was stirred for 24 h at room temperature. After the solvent was evaporated under reduced pressure, the residue was dissolved in dichloromethane (100 mL), and the solution was washed with 1 N HCl (100 mL), water (100 mL), and dried over anhydrous Na_2SO_4. After removal of the solvent under reduced pressure, the crude product was purified by flash column chromatography starting with 2% methanol in dichloromethane and gradually increasing to 10% methanol in dichloromethane to yield a white solid (2.88 g, 90%). ^{1}H NMR (400 MHz, CD_3OD): δ = 1.45 (m, CH_3, 81H), 1.51 (m, CH_3, 81H), 1.90−2.25 (m, CH_2, 48H), 3.30−3.52 (m, CH_2, 36H). ^{13}C NMR (400 MHz, CD_3OD): δ = 28.37, 28.67, 31.32, 31.67, 32.06, 39.74, 41.24, 59.02, 80.23, 84.35, 94.31, 153.91, 157.737, 164.38, 173.33, 175.87. MALDI MS: calculated for $C_{157}H_{278}N_{40}O_{48}$ (M^+), 3524.1; found, 3573.4. The resulting white solid (0.352 g, 0.10 mmol) was dissolved in ethanol (40 mL) and transferred into a hydrogenation vessel containing Raney-Nickel catalyst (5 g), and the suspension was stirred at 65 psi for 48 h at room temperature. After filtration through Celite, the solvent was removed under reduced presssure to give a **7** as a white solid (0.28 g, 80%). ^{1}H NMR of **7** (400 MHz, CD_3OD): δ = 1.46 (m, CH_3, 81H), 1.51 (m, CH_3, 81H), 1.90−2.25 (m, CH_2, 48H), 3.30−3.55 (m, CH_2, 36H). ^{13}C NMR (400 MHz, CD_3OD): δ

= 28.37, 28.67, 31.40, 31.76, 39.76, 41.27, 54.0, 58.86, 80.32, 84.37, 153.97, 157.81, 164.4, 175.61, 176.02. MALDI MS: calculated for $C_{157}H_{278}N_{40}O_{48}$ ($M + H^+$), 3495.1; found, 3496.3.

Synthesis of 9 Cascade:nitromethane [3]:(2-aza-3-oxopenylidyne):propionic acid-(6-(1,3-bis-(*tert*-butoxycarboyl)guanidino)hexyl)amide 8. The resulting HCl salt **6** (0.838 g, 0.385 mmol) was dissolved in methanol (50 mL), and the solution was cooled to 0 °C. Et_3N (1.45 mL) was added, followed by *N*,*N*′-diBoc-*N*′′-triflylguanidine (1.765 g, 4.51 mmol), and the solution was stirred at room temperature for 24 h and the solvent evaporated under reduced pressure. The crude product was purified by flash column chromatography eluting with 2% methanol in dichloromethane and gradually increasing to 10% methanol in dichloromethane to give a white solid (1.40 g, 91%). ^{1}H NMR (400 MHz, CD_3OD): δ = 1.15−1.55 (m, 234H), 1.70−2.15 (m, C*H*$_2$, 48H), 3.29−3.30 (m, C*H*$_2$, 36H). ^{13}C NMR (400 MHz, CD_3OD): δ = 27.70, 27.62, 28.33, 28.67, 30.08, 30.33, 31.30, 31.60, 40.48, 40.62, 41.27, 54.5, 59.14, 80.25, 84.40, 154.22, 157.49, 164.53, 173.50, 175.53. MALDI MS: calculated for $C_{193}H_{349}N_{40}O_{50}$ ($M + H^+$), 4030.1; found, 4031.8. The white solid (0.40 g, 0.10 mmol) was dissolved in ethanol (40 mL) and transferred into a hydrogenation bottle containing Raney-Nickel catalyst (5 g), and the suspension was stirred at 65 psi for 72 h at room temperature. After filtration through Celite, the solution was evaporated to under reduced pressure to give a white solid **8** (0.32 g, 80%). ^{1}H NMR of **8** (400 MHz, CD_3OD): δ = 1.46 (m, C*H*$_3$, 81H), 1.51 (m, C*H*$_3$, 81H), 1.90−2.25 (m, C*H*$_2$, 48H), 3.30−3.55 (m, C*H*$_2$, 36H). ^{13}C NMR (400 MHz, CD_3OD): δ = 28.37, 28.67, 31.40, 31.76, 39.76, 41.27, 54.0, 58.86, 80.32, 84.37, 153.97, 157.81, 164.4, 175.61, 176.02. MALDI MS: calculated for $C_{193}H_{350}N_{40}O_{48}$ ($M + H^+$), 4000.1; found, 4007.8.

Synthesis of 9 Cascade:fluoresceinylmethane [3]:(2-aza-3-oxopenylidyne):propionic acid-(2-guanidino)ethyl)amide HCl Salt FD-1. Fluorescein isothiocyanate (FITC, 0.14 g, 0.36 mmol) in DMF (1 mL) was added to a 1:1 mixture of DMF/dichloromethane (10 mL) containing dendron **7** (0.23 g, 0.066 mmol). The mixture was cooled to 0 °C, Et_3N (0.092 mL, 0.66 mmol) was added, and the solution was stirred overnight at room temperature. After removal of the solvent under reduced pressure, the residue was dissolved in dichloromethane (15 mL), and the resulting solution was washed with 1 N HCl (15 mL) and water (15 mL) and dried over anhydrous Na_2SO_4. The solution was concentrated under reduced pressure to afford the yellow solid of 9 cascade:fluoresceinylmethane[3]:(2-aza-3-oxopenylidyne):propionic acid−(2-(1,3-bis-(*tert*-butoxycarboyl)-guanidino)ethyl)amide **9** (0.23 g, 91%). ^{1}H NMR (400 MHz, CD_3OD): δ = 1.46 (m, C*H*$_3$, 81H), 1.51 (m, C*H*$_3$, 81H), 1.90−2.25 (m, C*H*$_2$, 48H), 3.30−3.55 (m, C*H*$_2$, 36H), 6.52−6.72 (br, 4H), 7.15 (br, 1H), 7.5 (br, 2H), 7.72 (br, 1H), 8.4 (br, 1H). MALDI MS: calculated for $C_{179}H_{294}N_{41}O_{53}S$, ($M + H^+$), 3899.5; found, 3901.9. The resulting yellow solid (200 mg, 0.052 mmol) was dissolved in 1,4-dioxane (10 mL), and the solution was cooled to 0 °C. 4 M HCl in dioxane (10 mL) was added, and the mixture was stirred overnight at room temperature. After removal of the solvent under reduced pressure, the residue was dissolved in water, the insoluble precipitate was filtered off, and the filtrate was concentrated under reduced pressure. The crude product was purified by RP-HPLC using a solvent gradient (solvent A = 0.05% TFA/H_2O; solvent B = 0.05% TFA/CH_3CN) to give water-soluble **FD-1** (50 mg, 44%). Alternatively, the crude product could be purified by dialysis, as described for FD-2, to give a pure compound. ^{1}H NMR (400 MHz, D_2O): δ = 1.85−2.30 (m, C*H*$_2$, 48H), 3.10−3.30 (m, C*H*$_2$, 36H), 6.9 (br, 2H), 7.10−7.2 (m, 3H), 7.4 (s, 2H), 7.5 (br, 1H), 8.1 (s, 1H). MALDI MS: calculated for $C_{89}H_{157}Cl_9N_{41}O_{17}S$, ($M + H^+$), 2425.6; found, 2427.20.

Synthesis of 9 Cascade:fluoresceinylmethane [3]:(2-aza-3-oxopenylidyne):propionic acid-(6-guanidino)hexyl)amide HCl Salt FD-2. FITC (0.096 g, 0.2256 mmol) in DMF (1 mL) was added to 1:1 mixture of DMF/dichloromethane (10 mL) containing nona-(Boc-guanidinohexyl) dendron amine **8** (0.300 g, 0.075 mmol). The mixture was cooled to 0 °C, Et_3N (72 μL) was added, and the solution was stirred overnight at room temperature. After removal of the solvent under reduced pressure, the residue was dissolved in dichloromethane (15 mL), and the resulting solution was washed with 1 N HCl (15 mL) and water (15 mL) and dried over anhydrous Na_2SO_4. The solvent was evaporated at reduced pressure, and the crude product was dissolved in methanol and purified by dialysis against methanol with SpectraPor Biotech regenerated cellulose membranes (MWCO = 3500) for 24 h. Removal of the methanol in vacuo gave a yellow solid of 9 cascade:fluoresceinylmethane[3]:(2-aza-3-oxopenylidyne):propionic acid−(6-(1,3-bis-(*tert*-butoxycarboyl)guanidino)hexyl)amide **10** (290 mg, 88%). ^{1}H NMR (400 MHz, CD_3OD): δ = 1.20−1.7 (m, C*H*$_3$, C*H*$_2$, 234H), 1.89−2.30 (m, C*H*$_2$, 48H), 3.10−3.40 (m, C*H*$_2$, 36H), 6.52−6.72 (br, 4H), 7.15 (br, 1H), 7.5−7.72 (br, 3H), 8.1 (br, 1H). MALDI MS: calculated for $C_{215}H_{366}N_{41}O_{53}S$, ($M + H^+$), 4405.5; found, 4406.7. The resulting yellow solid (200 mg, 0.052 mmol) was dissolved in 1,4-dioxane (10 mL) and the solution cooled to 0 °C; 4 M HCl in dioxane (10 mL) was added and the solution stirred overnight at room temperature. The precipitate was filtered off and dried to give the crude product. The solid was redissolved in water, insoluble precipitate was filtered off, and the filtrate was dialyzed against water with SpectraPor Biotech cellulose ester membranes (MWCO = 1000) for 48 h and lyophilized to yield water-soluble **FD-2** (127 mg, 96%). ^{1}H NMR (400 MHz, D_2O): δ = 1.1−1.50 (m, C*H*$_2$, 72H), 1.50−2.20 (m, C*H*$_2$, 48H), 3.10−3.30 (m, C*H*$_2$, 36H), 6.5−6.7 (br, 6H), 7.10 (m, 1H), 7.5 (br, 3H). MALDI MS: calculated for $C_{124}H_{226}Cl_9N_{41}O_{17}S$ (M^+), 2914.5; found, 2914.6.

Uptake Experiment Protocol. Fluorescent dendrimer uptake by mammalian cells was assessed using NIH-3T3 cells (American Type Culture Collection) and HMEC (human microvascular endothelial cells—Centers for Disease Control) grown on gelatin-coated coverslips and a Zeiss LSM 510 confocal microscope. NIH-3T3 cells were grown in DMEM (Invitrogen) supplemented with 10% FBS (Invitrogen), and HMEC were grown in MCDB-131 media (Mediatech) supplemented with 5% FBS (Invitrogen) and 2 mM L-glutamine (Invitrogen). A time course of fluorescent dendrimer entry into NIH-3T3 cells and HMEC was completed in triplicate as previously described for Tat peptides (*21*). Briefly, the cells were treated with the dendrimer molecules for the series of incubation times, washed three times with PBS, fixed with 3% paraformaldehyde at room temperature for 10 min, and analyzed using confocal microscopy. In order to confirm the data, these experiments were also completed without fixing the cells. These experiments were completed through the use of the VUMC Cell Imaging Resource (supported by CA68485 and DK20593).

DAPI Staining. NIH-3T3 cells grown on gelatin-coated coverslips were treated with **FD-1** (10 μM), **FD-2** (10 μM), or vehicle (water) for 60 min at 37 °C, washed, and fixed as previously described above (*21*). After the cells were permeabilized with 0.1% Triton X-100 and washed twice with PBS, they were incubated with 0.5 μg/mL of 4′,6-diamidino-2-phenylindole (DAPI—Invitrogen) for 30 min at room temperature in the dark. The coverslips were then washed twice with PBS and mounted. A Nikon fluorescent microscope with a UV filter was then used to image the samples.

TUNEL Assay. NIH-3T3 cells grown on gelatin-coated coverslips were treated with **FD-1** or **FD-2** (10 μM), vehicle (water), or 50% methanol (positive control for apoptosis) for

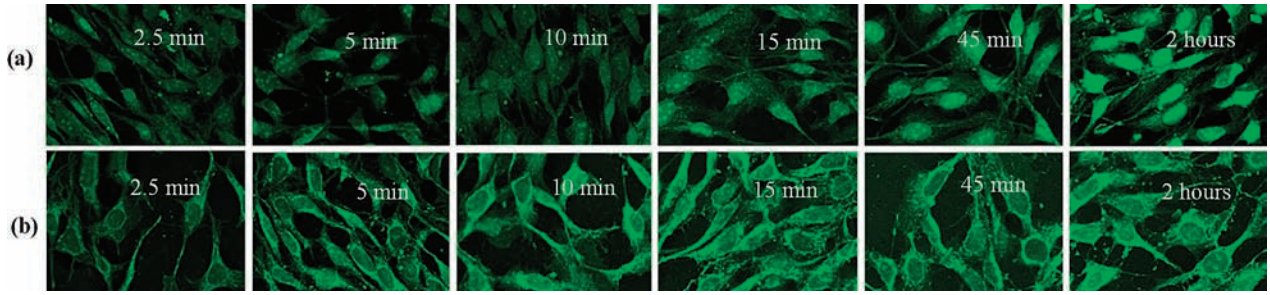


Figure 1. Time course of internalization of (a) **FD-1** and (b) **FD-2** into NIH-3T3 cells (fixed) at 37 °C. The conjugate concentration was 10 μM.

1 h at 37 °C and washed and fixed as previously described (*28*). An additional positive control involved the addition of DNAseI (New England BioLabs) to vehicle-treated cells that had been permeabilized with 0.1% Triton X-100 (Sigma). In order to label apoptotic nuclei, an in situ cell death detection kit with tetramethyl rhodamine (TMR-red) labeled dUTP (Roche Diagnostics) was used. The number of apoptotic nuclei in the **FD-1** and **FD-2** treated samples as compared to the positive and negative controls were measured with a Zeiss LSM-510 Confocal Microscope.

RESULTS AND DISCUSSION

In developing a new molecular transporter for targeted subcellular delivery of cargo molecules, we were drawn to the Newkome-type dendrimers, which are typically 1→3 C-branched polyamide macromolecules. These molecules are built from a "Behera's amine" monomer or its derivatives, that can be easily attached to a great variety of starting cores, surfaces, and polymers. Although the Newkome-type dendrimer is well-known, one of the drawbacks for a broader application is the elaborate synthesis of the monomer **2**. We efficiently synthesized the amine monomer **2** through improved hydrogenation of nitroester **1** and workup procedures of known literature methods (*27*). The synthesis of the dendron scaffold began with nitro-triacid monomer **3** reacting with "Behara's amine" monomer **2**, achieving the necessary nine end functionalities in only one generation of dendritic growth (Scheme 2). After the *t*-butyl groups were removed, the [G-1] nona-acid scaffold **4** was obtained in high yields. In order to introduce the guanidinium groups to the periphery of the dendrimer and provide diversity in the presentation of the guanidine groups to biological membranes, the carboxylic acid groups were first converted into Boc-protected amine groups. This was completed by reaction with a short alkyl linker (*N*-Boc-ethylendiamine) or a longer alkyl linker (*N*-Boc-1,6-diaminehexane), through established amide coupling reactions. After removal of the Boc groups, the nine free amines **5** or **6** were reacted with the guandinylating reagent (*29*) to give the guanidinylated dendritic scaffold in high yield (Scheme 2).

For preliminary uptake studies, a fluorescent probe was conjugated to the focal point of the molecular transporter, which served also as the test cargo molecule. The attachment of the fluorescein isothiocyanate (FITC) moiety to the guanidinylated scaffold started with a successful reduction of the nitro group at the focal point to an amino group via hydrogenation at room temperature in quantitative yields to form **7** or **8**. The free amino group was then directly reacted with FITC to form the Boc-protected FITC-labeled guanidino dendrimers **9** or **10**. After deprotection of the Boc-protected guanidine groups, FITC-labeled dendritic molecules were obtained and further purified by dialysis or HPLC, yielding pure **FD-1** and **FD-2**.

The two FITC−dendrimer conjugates were found to be highly water-soluble and were investigated for their capability to translocate through cell membranes. Internalization of **FD-1** and **FD-2** in mammalian cells was assessed using two different

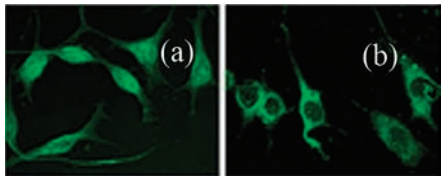


Figure 2. Confocal microscopy of (a) **FD-1** and (b) **FD-2** into unfixed NIH-3T3 cells at 37 °C. The conjugate concentration was 10 μM.

mammalian cell lines, NIH-3T3 fibroblasts and human microvascular endothelial cells (HMEC). Figure 1 shows the time course of uptake of **FD-1** and **FD-2** into NIH-3T3 fibroblasts at 37 °C. In this time course, the cells were treated with **FD-1** or **FD-2** for the series of time points shown, then washed, fixed with paraformaldehyde, and analyzed using confocal microscopy. The fluorescence was clearly observed within the cells 2.5 min after the addition of conjugates to the medium, which is comparable to the uptake rate of Tat−peptide (*13*, *21*). Furthermore, the extent of internalization increased in an incubation time-dependent manner, and the fluorescence intensity of cells treated with **FD-2** was near saturation after 10 min. However, the fluorescence intensity of cells treated with **FD-1** did not approach saturation until longer time points (45 min to 2 h). Interestingly, **FD-1** and **FD-2** exhibited differential patterns of subcellular localization, as **FD-1** appeared to concentrate in the nucleus with punctuated patterns similar to that of HIV Tat peptide, whereas **FD-2** appeared to concentrate in the cytosol. These data suggest that guanidine-rich **FD-1** and **FD-2,** bearing dendritic backbones, are internalized into cells in a similar manner to Tat peptides, but the length of the spacer at the terminal generation of the dendrimer not only controls the uptake rate (*30*), it also regulates the subcellular localization of the molecule and its putative cargo. For instance, the uptake levels of **FD-2** appeared to be generally higher than those of **FD-1** after the same incubation time at the same concentration. Therefore, the dendrimer with a hexyl spacer seems to cross the cell membrane faster than the molecule with an ethyl chain. As pointed out before, **FD-1** with the short spacer appeared to be localized mainly in the nucleus, whereas **FD-2**, with its longer spacer, was observed to reside mainly in the cytosol.

Fixed cells are usually used for confocal microscopy to obtain clear images, but recent studies indicate that cell fixation might lead to the artifactual redistribution of highly charged peptides (*31*, *32*). For this reason, the intracellular localization of **FD-1** and **FD-2** were also assessed using unfixed NIH-3T3 fibroblasts. In these experiments, the cells were treated with **FD-1** or **FD-2**, washed, and analyzed using confocal microscopy. The confocal images (Figure 2) showed that the distribution pattern of the fluorescent conjugates was consistent with that seen in fixed cells: **FD-1** with the short spacer appeared to be highly concentrated in the nucleus; while **FD-2**, with its longer spacer, was observed mainly in the cytosol. These experimental results strengthen the hypothesis that the cellular localization of **FD-1** and **FD-2** by fibroblasts is dominated to a high extent by the

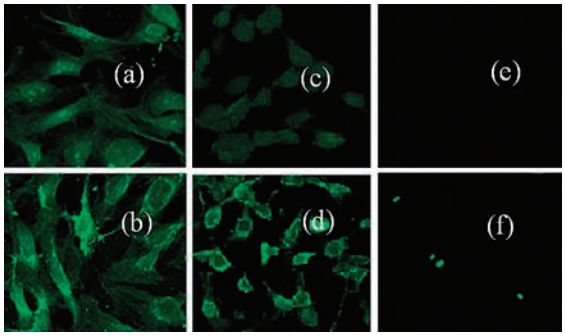


Figure 3. Confocal microscopy of human microvascular endothelial cells (HMEC) treated with (a) 10 μM of **FD-1** for 10 min at 37 °C; (b) 10 μM of **FD-2** for 10 min at 37 °C; (c) 10 μM of **FD-1** for 10 min at 4 °C; (d) 10 μM of **FD-2** for 10 min at 4 °C; (e) fluorescein isothiocyanate (FITC) for 1 h at 37 °C; (f) 10 μM of Boc-protected guanidinylated **FD-2** for 1 h.

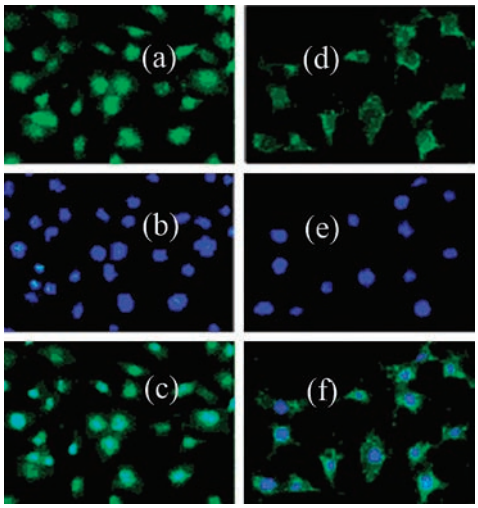


Figure 4. (a−f) NIH-3T3 cells were treated with **FD-1** (10 μM), **FD-2** (10 μM), or vehicle (water) for 60 min at 37 °C. Then, the cells were incubated with 0.5 μg/mL of 4′,6-diamidino-2-phenylindole (DAPI) for 30 min at room temperature in the dark.

length of the linker between the guanidine headgroups and the dendritic backbone. These results were confirmed with HMEC cells (Figure 3a,b).

The subcellular localization of **FD-1** and **FD-2** was further assessed by determining colocalization with the DAPI DNA stain. The 3T3 cells were treated with **FD-1** or **FD-2** and the nuclei were stained with DAPI, followed by the imaging of the cells with a fluorescent microscope equipped with a UV filter. **FD-1** colocalizes with DAPI (Figure 4a−c) to a much greater extent than **FD-2** (Figure 4d−f). These data provide solid evidence of the disparate subcelluar localization of the synthesized carriers, with **FD-1** concentrated mainly in the nucleus and **FD-2** concentrated in the cytosol.

In order to evaluate the effect of the guanidinium groups and the macromolecular dendritic structure on cellular uptake, control experiments were performed. HMEC were treated with free FITC and Boc-protected guanidinylated **FD-2**-dendrimer **10**. In the same time course of cellular uptake corresponding to the experiments of **FD-1** and **FD-2,** we observed extremely weak or no fluorescence for both compounds, as shown in Figure 3e,f. These observations suggest that the nanoscale hole formation mechanism (*33*), as previously proposed for the PAMAM dendrimer uptake mechanism, could be excluded and that the guanidino groups play a critical role in the cell permeability.

Additionally, we assessed the effect of temperature on the internalization of **FD-1** and **FD-2.** Figure 3c,d shows that the

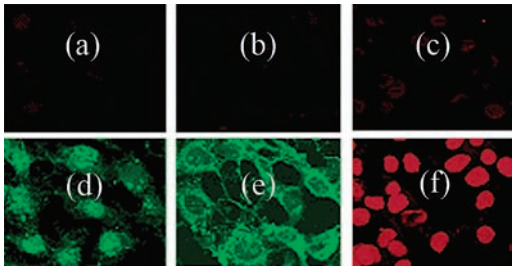


Figure 5. (a) **FD-1** + TMR − dUTP (red filter). (b) **FD-2** + TMR− dUTP (red filter). (c) Vehicle (water) + TMR − dUTP = negative control (red filter). (d) **FD-1** + TMR − dUTP (green filter). (e) **FD-2** + TMR − dUTP (green filter). (f) 50% Methanol + TMR− dUTP = positive control (red filter).

two conjugates are able to internalize into cells not only at 37 °C, but also at 4 °C, and no significant decrease in fluorescence intensity was observed. Although the exact translocation mechanism of guanidinylated peptides such as Tat and its derivatives remains controversial, these experiments suggest that active transport across the membrane is not needed and demonstrate that the internalization mechanism of the dendrimer carriers is similar to that of Tat and its derivatives.

The cytotoxicity of **FD-1** and **FD-2** was assessed using a well-characterized TUNEL assay and confocal microscopy to ensure the biocompatibility for further utilization. Neither **FD-1** nor **FD-2** caused 3T3 cell apoptosis in the dose range tested, with the highest dose being 10 μM for 60 min (Figure 5d,e), as only background staining of the nuclei (Figure 5a **FD-1**, red channel; Figure 5b, **FD-2**, red channel) similar to that of the negative control samples (Figure 5c) occurred. DNAse I (data not shown) and 50% methanol (Figure 5e) were used as the positive control treatments, as both cause nicks in the genomic DNA, and the nuclei of these cells were highly apoptotic as denoted by their strong staining pattern. Additionally, HMEC treated with 10 μM **FD-1** or **FD-2** for 60 min had no defect in intracellular calcium mobilization, as measured by the flex station, upon thrombin receptor stimulation when compared to HMEC treated with water (data not shown). These data suggest that **FD-1** and **FD-2**, at the experimental conditions tested, are not cytotoxic and are therefore ideal molecular carriers for the transport of putative bioactive cargo molecules.

CONCLUSION

In this report, we have described the synthesis of two novel dendritic molecular transporters, **FD-1** and **FD-2**, and investigated their uptake rate and intracellular distribution in mammalian cell lines using confocal microscopy. The design features of this macromolecule display a compact, biocompatible Newkome dendrimer scaffold with guanidine groups differentiated over an alkyl spacer. The combination of flexible spacer units conjugated to a highly symmetric dendritic backbone affords an increased density presentation of critical guanidine groups on the scaffold, without neglecting the necessity of structural flexibility for cellular uptake. We observed that the shorter alkyl spacer of **FD-1** directed the uptake of the transporter mainly into the nucleus, while **FD-2**, with the longer alkyl spacer, concentrated its fluorescent cargo in the cytosol. The critical role of the length of the hydrophobic alkyspacer, in this particular macromolecular design, has never been shown and allows for the directed subcellular delivery of bioactive cargo molecules utilizing scalable, biocompatible macromolecular carriers. Our results suggest that the synthetic approach of these molecular transporters and their unique targeting abilities will advance the development of novel vaccine vectors and drug delivery systems to overcome the limitations of current technologies.

ACKNOWLEDGMENT

We acknowledge gratefully Vanderbilt University for a junior faculty startup fund (E.H.) and the National Institutes of Health supporting this work (NIH EY06062, EY10291, HL84388) (H.H.). B.V. was supported by an American Heart Association pre-doctoral fellowship.

LITERATURE CITED

(1) Langel, Ü. (2002) *Cell-penetrating peptides: Processes and applications*. CRC Press, London.
(2) Lindsay, M. A. (2002) Peptide-mediated cell delivery: application in protein target validation. *Curr. Opin. Pharmacol. 2*, 587−594.
(3) Bennett, R. P., and Dalby, B. (2002) Protein delivery using VP22. *Nat. Biotechnol. 20*, 20−20.
(4) Derossi, D., Joliot, A. H., Chassaing, G., and Prochiantz, A. (1994) The 3rd helix of the antennapedia homeodomain translocates through biological-membranes. *J. Biol. Chem. 269*, 10444−10450.
(5) Joliot, A., and Prochiantz, A. (2004) Transduction peptides: from technology to physiology. *Nat. Cell Biol. 6*, 189−196.
(6) Fukati, S. (2006) Oligoargine vectors for intracellular delivery: design and cellular-uptake mechanisms. *Biopolymers 84*, 241−249.
(7) Rothbard, J. B., Jessop, T. C., and Wender, P. A. (2005) Adaptive translocation: the role of hydrogen bonding and membrane potential in the uptake of guanidinium-rich transporters into cells. *Adv. Drug Delivery Rev. 57*, 495−504.
(8) Brooks, H., Lebleu, B., and Vives, E. (2005) Tat peptide-mediated cellular delivery: back to basics. *Adv. Drug Delivery Rev. 57*, 559−577.
(9) Snyder, E. L., and Dowdy, S. F. (2004) Cell penetrating peptides in drug delivery. *Pharm. Res. 21*, 389−393.
(10) Wadia, J. S., Stan, R. V., and Dowdy, S. F. (2004) Transducible TAT-HA fusogenic peptide enhances escape of TAT-fusion proteins after lipid raft macropinocytosis. *Nat. Med. 10*, 310−315.
(11) Wender, P. A., Mitchell, D. J., Pattabiraman, K., Pelkey, E. T., Steinman, L., and Rothbard, J. B. (2000) The design, synthesis, and evaluation of molecules that enable or enhance cellular uptake: peptoid molecular transporters. *Proc. Natl. Acad. Sci. U.S.A. 97*, 13003−13008.
(12) Zhao, M., and Weissleder, R. (2004) Intracellular cargo delivery using tat peptide and derivatives. *Med. Res. Rev. 24*, 1−12.
(13) Vives, E., Brodin, P., and Lebleu, B. (1997) A truncated HIV-1 Tat protein basic domain rapidly translocates through the plasma membrane and accumulates in the cell nucleus. *J. Biol. Chem. 272*, 16010−16017.
(14) Fischer, P. M., Krausz, E., and Lane, D. P. (2001) Cellular delivery of impermeable effector molecules in the form of conjugates with peptides capable of mediating membrane translocation. *Bioconjugate Chem. 12*, 825−841.
(15) de la Fuente, J. M., and Berry, C. C. (2005) Tat peptide as an efficient molecule to translocate gold nanoparticles into the cell nucleus. *Bioconjugate Chem. 16*, 1176−1180.
(16) Torchilin, V. P., Levchenko, T. S., Rammohan, R., Volodina, N., Papahadjopoulos-Sternberg, B., and D'Souza, G. G. M. (2003) Cell transfection in vitro and in vivo with nontoxic TAT peptide-liposome-DNA complexes. *Proc. Natl. Acad. Sci. U.S.A. 100*, 1972−1977.
(17) Futaki, S., Suzuki, T., Ohashi, W., Yagami, T., Tanaka, S., Ueda, K., and Sugiura, Y. (2001) Arginine-rich peptides - An abundant source of membrane-permeable peptides having potential as carriers for intracellular protein delivery. *J. Biol. Chem. 276*, 5836−5840.
(18) Nori, A., Jensen, K. D., Tijerina, M., Kopeckova, P., and Kopecek, J. (2003) Tat-conjugated synthetic macromolecules facilitate cytoplasmic drug delivery to human ovarian carcinoma cells. *Bioconjugate Chem. 14*, 44−50.
(19) Torchilin, V. P. (2006) Recent approaches to intracellular delivery of drugs and DNA organelle targeting. *Annu. Rev. Biomed. Eng. 8*, 343−375.
(20) De Coupade, C., Fittipaldi, A., Chagnas, V., Michel, M., Carlier, S., Tasciott, E., Darmon, A., Ravel, D., Kearsey, J., Giacca, M., and Cailler, F. (2005) Novel human-derived cell-penetrating peptides for specific subcellular delivery of therapeutic biomolecules. *Biochem. J. 390*, 407−418.
(21) Futaki, S., Nakase, I., Suzuki, T., Youjun, Y., and Sugiura, Y. (2002) Translocation of branched-chain arginine peptides through cell membranes: flexibility in the spatial disposition of positive charges in membrane-permeable peptides. *Biochemistry 41*, 7925−7930.
(22) Gillies, E. R., and Frechet, J. M. J. (2005) Dendrimers and dendritic polymers in drug delivery. *Drug Discovery Today 10*, 35−43.
(23) Lee, C. C., MacKay, J. A., Frechet, J. M. J., and Szoka, F. C. (2005) Designing dendrimers for biological applications. *Nat. Biotechnol. 23*, 1517−1526.
(24) Tomalia, D. A., Naylor, A. M., and Goddard, W. A. (1990) Starburst dendrimers - molecular-level control of size, shape, surface-chemistry, topology, and flexibility from atoms to macroscopic matter. *Angew. Chem., Int. Ed. Engl. 29*, 138−175.
(25) Chung, H., Harms, G., Seong, C. M., Choi, B. H., Min, C., Taulane, J. P., and Goodman, M. (2004) Dendritic oligoguanidines as intracellular translocators. *Biopolymers 76*, 83−96.
(26) Wender, P. A., Kreider, E., Pelkey, E. T., Rothbard, J., and VanDeusen, C. L. (2005) Dendrimeric molecular transporters: synthesis and evaluation of tunable polyguanidino dendrimers that facilitate cellular uptake. *Org. Lett. 7*, 4815−4818.
(27) Newkome, G. R., Behera, R. K., Moorefield, C. N., and Baker, G. R. (1991) Cascade polymers: synthesis and characterization of one-directional arborols based on adamantane. *J. Org. Chem. 56*, 7162−7167.
(28) Nori, A., Jensen, K. D., Tijerina, M., Kopečcková, P., and Kopeček, J. (2003) Tat-conjugated synthetic macromolecules facilitate cytoplasmic drug delivery to human ovarian carcinoma cells. *Bioconjugate Chem. 14*, 44−50.
(29) Feichtinger, K., Sings, H. L., Baker, T. J., Matthews, K., and Goodman, M. (1998) Triurethane-protected guanidines and triflyldiurethane-protected guanidines: new reagents for guanidinylation reactions. *J. Org. Chem. 63*, 8432−8439.
(30) Wender, P. A., Kreider, E., Pelkey, E. T., Steinman, L., Rothbard, J. B., and VanDeusen, C. L. (2005) Dendritic molecular transporters: synthesis and evaluation of tunable polyguanidino dendrimers that facilitate cellular uptake. *Org. Lett. 7*, 4815−4818.
(31) Richard, J. P., Melikov, K., Vives, E., Ramos, C., Verbeure, B., Gait, M. J., Chernomordik, L. V., and Lebleu, B. (2003) Cell-penetrating peptides - a reevaluation of the mechanism of cellular uptake. *J. Biol. Chem. 278*, 585−590.
(32) Lundberg, M., and Johansson, M. (2002) Positively charged DNA-binding proteins cause apparent cell membrane translocation. *Biochem. Biophys. Res. Commun. 291*, 367−371.
(33) Hong, S. P., Bielinska, A. U., Mecke, A., Keszler, B., Beals, J. L., Shi, X. Y., Balogh, L., Orr, B. G., Baker, J. R., and Holl, M. M. B. (2004) Interaction of poly(amidoamine) dendrimers with supported lipid bilayers and cells: hole formation and the relation to transport. *Bioconjugate Chem. 15*, 774−782.

BC060287A

Synthesis and Properties of Cell-Targeted Zn(II)−Phthalocyanine−Peptide Conjugates

Martha Sibrian-Vazquez,[†] Javier Ortiz,[‡] Irina V. Nesterova,[†] Fernando Fernández-Lázaro,[‡] Angela Sastre-Santos,*[,‡] Steven A. Soper,*[,†] and M. Graça H. Vicente*[,†]

Department of Chemistry, Louisiana State University, Baton Rouge, Louisiana 70803, and División de Química Orgánica, Instituto de Bioingeniería, Universidad Miguel Hernández, 03202 Elche, Spain. Received September 22, 2006; Revised Manuscript Received November 29, 2006

Two Zn−Pc−peptide conjugates bearing either a short linker or a long PEG−linker between the macrocycle and a bifunctional peptide containing the nucleoplasmin and HIV-1 Tat 48−60 sequences have been synthesized in order to increase the Pc cell-targeting ability and to evaluate the effect of the linker. The presence of the peptide chain increased the water solubility of the Pc macrocycle and, consequently, its fluorescence in aqueous solutions. The highest fluorescence quantum yields were observed at low pH (5.0) for both conjugates and were always higher for the conjugate bearing the short linker. Both conjugates were found to have low dark cytotoxicity toward human HEp2 cells ($IC_{50} > 77\ \mu M$) but were highly phototoxic ($IC_{50} < 2\ \mu M$ at 1 J cm^{-2}). The conjugate bearing the long PEG−linker accumulated the most within cells (26 times more than the unconjugated Zn−Pc), followed by the short linker conjugate (17 times more than the unconjugated Zn−Pc). Both conjugates were found to localized preferentially within the cell lysosomes.

INTRODUCTION

Photodynamic therapy (PDT) is a binary modality for cancer treatment that involves the activation of photosensitizer-containing tissue with light (*1*). Since neither the photosensitizer nor the light has a toxic effect when used alone, PDT has the potential for being highly selective for tumor tissue. Phthalocyanines (Pcs[1]) are promising photosensitizers for use in PDT because they typically exhibit strong light absorptions in the near-infrared (650−750 nm) and often have high quantum yields of singlet oxygen formation (*2*, *3*). These characteristics are important, because red light penetrates significantly deeper into tissues than visible light and singlet oxygen is considered a key species in PDT-induced cell death. Nevertheless, the biological efficacy of a photosensitizer is often determined by its subcellular distribution within cancer cells, which in turn depends on the structural characteristics and physicochemical properties of the photosensitizer (*4*). Therefore, depending on the nature of the peripheric substituents, the centrally chelated metal ion, the overall molecular charge, and the formulation vehicle, Pc-based sensitizers can be localized within certain compartments of cells, such as in the lysosomes, mitochondria, ER, or the Golgi complex (*5*). A significant disadvantage of Pc-based photosensitizers is their strong tendency for aggregation in solution, especially in water and other polar solvents, due to the hydrophobic nature of the Pc macrocycle. Phthalocyanine aggregation not only reduces their solubility in aqueous solutions, but also decreases their fluorescence and singlet oxygen quantum yields and consequently their photosensitizing activity (*6*).

In order to reduce Pc aggregation and to increase their solubility and biological efficacy, hydrophilic groups have been introduced at the Pc macrocycle periphery, for example, multiple carboxylic acids (*7*), sulfonic acids (*8*), or polyoxyethylene groups (*9*). Another strategy involves the conjugation of Pc macrocycles to biomolecules, such as oligonucleotides (*10*, *11*), antibodies (*12*−*15*), proteins (*16*−*19*), cyclodextrins (*20*), and epidermal growth factors (EGF) (*21*). Although improved biological efficiency has been achieved with some of the above Pc conjugates, the use of peptide signaling sequences, with the exception of EGF peptides, to direct the delivery of Pc-based photosensitizers within cancer cells and into sensitive organelles has not been fully explored. This strategy is based on the natural ability of certain proteins and peptide sequences for crossing cellular membranes and specifically targets sensitive organelles, such as the mitochondria, ER, and cell nuclei. Examples of desirable peptide signaling sequences to be conjugated to Pc macrocycles include fusogenic or cell-penetrating peptides, nuclear localization sequences (NLS), and bifunctional signaling sequences (*22*−*26*). Among these, the bifunctional peptides contain a minimum sequence for translocation across cellular membranes and a signaling sequence to direct the movement of the molecule from the cytoplasm to a target organelle, for example, containing both a fusogenic and an NLS peptide sequences. We have recently shown that porphyrin−peptide conjugates bearing either NLS, fusogenic, or bifunctional peptides exhibit increased cellular uptake and improved biological efficacy in cells in culture (*27*). We now report the synthesis and photophysical and biological evaluation of two cationic Pcs and two new Pc conjugates to a bifunctional peptide containing the bipartite NLS nucleoplasmin (*28*) and the fusogenic peptide sequence corresponding to the human

* E-mail: vicente@lsu.edu.
[†] Louisiana State University.
[‡] Universidad Miguel Hernández.

[1] Abbreviations: Pc, phthalocyanine; DBN, 1,5-diazabicyclo[4.3.0]-non-5-ene; DMAE, dimethylaminoethanol; 3-NOBA, 3-nitrobenzylalcohol; HOBt, 1-hydroxybenzotriazole; DMF, *N*,*N*-dimethylformamide; Et_3N, triethylamine; CCA, α-cyano-4-hydroxycinnamic acid; TFA, trifluoroacetic acid; DIEA, *N*,*N*-diisopropylethylamine; TBTU, 2-(1*H*-benzotriazole-1-yl)-1,1,3,3-tetramethyluronium tetrafluoroborate; TIS, triisopropyl silane; DMSO, dimethyl sulfoxide; NHS, *N*-hydroxy succinimide, Boc, *t*-butoxy carbonyl; Fmoc, fluorenylmethoxy carbonyl; HEPES, 4-(2-hydroxyethyl)-1-piperazine ethanesulfonic acid; PBS, phosphate buffered saline; FBS, fetal bovine serum; MEM, modified Eagle's medium; TFE, trifluoroethanol.

10.1021/bc060297b CCC: $37.00 © 2007 American Chemical Society
Published on Web 02/06/2007

immunodeficiency virus I transcriptional activator (HIV-1 Tat, 48−60) (*24*).

EXPERIMENTAL PROCEDURES

Syntheses. Unless otherwise indicated, all commercially available starting materials were used directly without further purification. All reactions were monitored by TLC using Sorbent Technologies 0.25 mm silica gel plates with or without UV indicator (60F-254). Silica gel Sorbent Technologies 32−63 μm was used for flash column chromatography. ^{1}H NMR spectra were obtained on either an ARX-300 Bruker spectrometer or a Bruker AVANCE DRX-500. Chemical shifts (δ) are given in ppm. Electronic absorption spectra were measured on either a Perkin-Elmer Lambda 35 UV−vis spectrophotometer or a Helios Gamma spectrophotometer. IR spectra were recorded with a Nicolet Impact 400D spectrophotometer. Mass spectra were obtained on either a MAT 900 (Finnigan-MAT Gmbh, Bremen Instrument, FAB-MS) spectrometer or a Bruker ProFlex III MALDI-TOF mass spectrometer using CCA or dithranol as the matrix. Elemental analyses were performed on a Thermo Finnigan Flash 1112 CHN elemental analyzer. HPLC analyses were carried out on a Dionex system containing a P680 pump and a UVD340U detector. Semipreparative HPLC was carried out using a Luna C_{18} 100 Å, 5 μm, 10 × 250 mm (Phenomenex, U.S.A.) column and a stepwise gradient; analytical HPLC was carried out using a Delta Pak C_{18} 300 Å, 5 μm, 3.9 × 150 mm (Waters, U.S.A.) column and a stepwise gradient.

Peptide Synthesis. The peptide sequence KRPAATKK-AGQAKKKLEDPRKKRRQRRRPPQG was prepared on an automated peptide synthesizer (Applied Biosystems Pioneer, Peptide Synthesis System, U.S.A.) on a 0.2 mmol scale using the Fmoc strategy of solid-phase peptide synthesis. A 4-fold excess of the Fmoc-protected amino acids were coupled to the PAL−PEG−PS resin using PyBOP/TBTU as the activating agents. After the final coupling and the successive removal of the Fmoc group, the resin was washed with DMF and isopropanol and then dried under vacuum. The dried resin containing the protected peptide sequence was used in the coupling reaction to the Pc derivatives.

Zn−Pc 1. A mixture of 4-(2-*tert*-butoxycarbonylaminoethoxy)phthalonitrile (50 mg, 0.174 mmol), $Zn(CH_3CO_2)_2{\cdot}2H_2O$ (19.3 mg, 0.087 mmol), DMAE (0.2 mL), and a drop of DBN was refluxed for 5 h under argon. The green solution obtained was cooled, then methanol (4 mL) was added and the solvents were evaporated. The crude product was purified by column chromatography (methanol/CH_2Cl_2 3/97) affording 30 mg of pure **1**. Yield: 57%. UV−vis (DMF), λ_{max} (log ϵ): 354 (4.76), 612 (4.42), 679 (5.10). IR (KBr): 3361, 2976, 2931, 1705, 1609, 1491, 1392, 1241, 1171, 1095, 747 cm^{-1}. ^{1}H NMR (DMF-d_7): δ = 1.48−1.50 (m, 36H, $(CH_3)_3C$), 3.80 (m, 8H, CH_2N), 4.64−4.72 (m, 8H, CH_2O), 7.32 (broad s, 4H, NH), 7.80−7.87 (m, 4H, ArH), 8.95−9.01 (m, 4H, ArH), 9.30−9.37 (m, 4H, ArH). FAB-MS (3-NOBA) *m*/*z* 1212 (M^+). Calcd for $C_{60}H_{68}N_{12}O_{12}Zn{\cdot}2H_2O$: C, 57.62%; H, 5.80%; N, 13.44%. Found: C, 57.70%; H, 6.02%; N, 13.11%.

Zn−Pc 2. Phthalocyanine **1** (25 mg, 0.022 mmol) was dissolved in a mixture of CH_2Cl_2 (0.3 mL) and TFA (0.3 mL) at 0 °C and then room temperature for 2 h. The solvent was removed at reduced pressure, and the residue was treated with 2 M NaOH, extracted with ethyl acetate (3 × 5 mL), and dried over magnesium sulfate. After evaporating the solvent, the tetramino-subtituted Pc was obtained as a blue powder. This compound was dissolved in 2 M HCl (2 mL), the solvent was removed by azeotropic distillation with toluene, and the residue was dried under vacuum to obtain Pc **2** as a green powder. Yield: 11 mg, 52%. UV−vis (DMF), λ_{max} (log ϵ): 354 (4.79), 631 (4.54), 683 (4.91). IR (KBr): 3600−2000, 1606, 1482, 1335, 1242, 1120, 1009 cm^{-1}. ^{1}H NMR (TFA-d_1): δ = 4.04 (m, 8H, CH_2O), 4.95 (m, 8H, CH_2N), 7.97 (m, 4H, ArH), 9.09 (m, 4H, ArH), 9.46 (m, 4H, ArH). MALDI-TOF MS (dithranol) *m*/*z* 813 $(M + H)^+$. HR MALDI-TOF *m*/*z* 812.22693 (M^+), calcd for $C_{40}H_{36}N_{12}O_4Zn$ 812.22685.

Zn−Pc 3. Phthalocyanine **3** was prepared by statistical condensation of 4-*tert*-butylphthalonitrile (385 mg, 2.09 mmol) and 4-(2-*tert*-butoxycarbonylaminoethoxy)phthalonitrile (200 mg, 0.696 mmol) in the presence of $Zn(CH_3CO_2)_2{\cdot}2H_2O$ (306 mg, 1.39 mmol), DMAE (3.2 mL), and two drops of DBN. The crude phthalocyanine was purified by column chromatography using hexane/ethyl acetate 4:1 for elution affording 58 mg (9%) of protected Zn−Pc. This compound (30 mg, 0.033 mmol) was stirred at 0 °C for 2 h in a mixture of CH_2Cl_2 (0.3 mL) and TFA (0.3 mL). The solvent was removed, and the resulting residue was treated with 2 M NaOH, extracted with ethyl acetate, and washed with water, affording 22 mg of Zn−Pc **3a**. To this compound, an equivalent of HCl and diethyl ether (2 mL) were added. The mixture was sonicated and the solvents removed, yielding 18 mg of Zn−Pc **3b** (67%). UV−vis (DMF), λ_{max} (log ϵ): 677 (5.34), 610 (4.58), 350 (4.88). IR (KBr): 3399, 2957, 2904, 2866, 1611, 1489, 1328, 1229, 1090, 1047, 748 cm^{-1}. ^{1}H NMR (TFA-d_1): δ = 1.80 (s, 27H, $(CH_3)_3C$), 4.04 (m, 2H, CH_2O), 4.96 (m, 2H, CH_2N), 8.00 (m, 1H, ArH), 8.59−8.64 (m, 3H, ArH), 9.15−9.18 (m, 1H, ArH), 9.42−9.50 (m, 4H, ArH), 9.58−9.67 (m, 3H, ArH). MALDI-TOF (dithranol) *m*/*z* 804 $(M + H)^+$.

Zn−Pc 4. Diglycolic anhydride (2 mg, 0.0186 mmol) was added to a solution of Pc **3a** (10 mg, 0.0124 mmol) in DMF (100 μL), and the solution stirred overnight at room temperature. The reaction mixture was diluted with CH_2Cl_2 (1 mL) and hexanes (2 mL) until precipitation occurred. The dark green solid was washed with hexanes (3 × 2 mL) and warm water until neutral pH. The solid residue was dissolved in $CHCl_3$, dried over Na_2SO_4, the solvent evaporated, and the solid residue dried under vacuum to yield 11 mg (97%) of Pc **4**. ^{1}H NMR (DMF-d_7, 250 MHz): δ =1.77 (s, 27H, $(CH_3)_3C$), 3.95 (s, 2H, CH_2), 4.32 (s, 2H, CH_2O), 4.54 (s, 2H, CH_2N), 4.69 (s, 2H, CH_2O), 7.78−7.95 (m, 2H, ArH), 8.35−8.44 (m, 4H, ArH), 9.05 (d, 1H, J = 8.30 Hz, ArH), 9.33−9.43 (m, 4H, ArH), 9.53−9.57 (m, 3H, ArH). MALDI-TOF MS *m*/*z* 920.409 ($M + H^+$), calcd for $C_{50}H_{50}N_9O_5Zn$ 920.315.

Zn−Pc Conjugate 5. Peptidyl resin (0.0032 mmol) was introduced into a glass synthesizer, swelled in DMF for 1 h, and then washed with DMF (2 × 5 mL). To the peptidyl resin was added 300 μL of a solution containing 0.0064 mmol of Pc **4**, 0.193 mmol of DIEA, 0.0064 mmol of HOBt, and 0.0064 mmol of TBTU. The reaction mixture was shaken overnight at room temperature and then filtered to give a blue resin. The resin was washed to remove unreacted Pc, first with DMF until the filtrate was colorless, then with CH_2Cl_2 and methanol, before being dried under vacuum. Cleavage and deprotection was carried out by treatment of the dried resin with 2 mL of a mixture of TFA/phenol/TIS/H_2O, 88/5/2/5, at room temperature for 4 h. The resin was filtered, washed with TFA (3 × 2 mL), and the filtrates combined and evaporated under vacuum to give a blue residue. Addition of cold Et_2O yielded a blue−green precipitate, which was washed repeatedly with Et_2O and dried under vacuum. The purification of the Pc−peptide conjugate was achieved by reverse-phase HPLC on a Luna C_{18} semi-preparative column (10 × 250 mm, 5 μm) (Phenomenex, U.S.A.) using a solvent system of water and acetonitrile both containing 0.1% TFA, with a stepwise gradient from 50% to 95%. The fraction containing the conjugate was collected and lyophilized to yield pure conjugate. The purity of the Pc−peptide conjugate was >95% as obtained by HPLC on an analytical Delta Pak C_{18} (3.9 × 150 mm, 5 μm) column. Yield: 12.3 mg,

57%. HPLC, $t_r = 16.04$ min. MALDI-TOF MS *m/z* 4670.643 ($M + H^+$), calcd for $C_{210}H_{339}N_{74}O_{44}Zn$ 4669.592.

Zn−Pc Conjugate 6. To a solution of Pc **4** (15 mg, 0.0167 mmol) in 200 μL of DMF was added DIEA (13 mg, 0.1 mmol), followed by the addition of HOBt (2.5 mg, 0.0167 mmol) and TBTU (5 mg, 0.0167 mmol). The reaction mixture was stirred for 2 min, and then $NH_2CH_2CH_2(OCH_2CH_2)_5OCH_2CO_2{}^tBu$ (6.6 mg, 0.0167 mmol) was added in one portion. Stirring was continued for 24 h at room temperature and then the reaction mixture diluted with ethyl acetate (25 mL). The organic phase was washed with water (100 mL), saturated aqueous $NaHCO_3$ (100 mL), water (100 mL), then dried over Na_2SO_4, filtered, and the solvent evaporated under vacuum to leave a blue residue. The Pc conjugate was isolated by flash chromatography on silica gel using ethyl acetate followed by $CHCl_3$/MeOH 9/1. Yield 8.6 mg, 40%. MALDI-TOF MS *m/z* 1242.518 ($M - C_4H_9$), calcd for $C_{64}H_{76}N_{10}O_{12}Zn$ 1242.738. The protected Pc conjugate was dissolved in 1 mL of $CHCl_3$/TFA 1/1 and stirred at room temperature for 4 h. The solvent was evaporated, and the dark blue residue was triturated with cold Et_2O. The dark blue residue was dried under vacuum to give 8.2 mg, quantitative yield of the title conjugate. MALDI-TOF MS *m/z* 1242.618 (M^+), calcd for $C_{64}H_{76}N_{10}O_{12}Zn$ 1242.738. Conjugation to the peptide sequence was performed on the solid phase as described above. Because this conjugate was sensitive to acid conditions, after separation by reverse-phase HPLC, the fraction corresponding to the Pc conjugate was neutralized with triethylamine. After lyophilization, the blue residue was redissolved in water, and any excess of Et_3N or $Et_3NH^+CF_3COO^-$ salt was removed by gel filtration on Sephadex G-25 (PD-10 desalting column, GE) using water as the eluent. The fraction containing the Pc conjugate was lyophilized to yield the pure conjugate as a blue solid (6.6 mg, 42%). HPLC, $t_r = 12.50$ min. MALDI-TOF MS *m/z* 4995.527 ($M + Na^+$), calcd for $C_{224}H_{365}N_{75}O_{50}ZnNa$ 4996.7577.

CD Studies. The CD measurements were carried out on a AVIV 620S Circular Dichroism Spectrometer, at a scan speed of 10 nm/min using quartz cells with 1 mm path length. 20 μM Pc−peptide conjugate solutions were prepared in water/TFE 9/1, and the pH adjusted to 7.0 using 0.1 M NaOH. All spectra correspond to an average of three separate experiments. All spectra were corrected by the baseline obtained for Pc−peptide conjugate free solutions.

Photophysical studies. All absorption spectra were acquired using a Perkin-Elmer Lambda 25 UV−vis spectrophotometer with 10 mm path length quartz cuvettes. Corresponding diluents were utilized as reference solutions. Emission spectra were obtained using a Fluorolog 3 spectrofluorometer. The optical density of solutions used for emission studies was below 0.05 at the excitation wavelength to eliminate inner filter effects. All the measurements were performed within 3 h of solution preparation. Anhydrous DMSO (Biotech grade) was purchased from Sigma-Aldrich and sodium phosphate from EMD. Milli-Q water (resistance 18 MΩ) was prepared in-house. Stock solutions (10 mM) of Pcs **2** and **3b** and conjugates **5** and **6** were prepared in DMSO The aqueous solutions were prepared by spiking 1.5−2 μL of the corresponding stock solutions into 1 mL of phosphate buffer. Phosphate buffers (100 mM) were prepared by dissolving appropriate amounts of the dibasic sodium phosphate in H_2O and adjusting pH using HCl and/or NaOH.

Calculations. The quantum yields were calculated using a secondary standard approach (*29*, *30*) with methylene blue, a dye with excitation/emission wavelengths similar to Pcs, and an established quantum yield. According to this approach, the integrated fluorescence intensity of the analyte (I) and standard (I_R), the optical density of the analyte (OD) and the standard (OD_R), and the refractive index of analyte solvent (n) and standard solvent (n_R) are related to the quantum yield of the analyte (Q) as

$$Q = Q_R \frac{I}{I_R} \frac{OD_R}{OD} \frac{n^2}{{n_R}^2}$$

where Q_R is a quantum yield of the reference standard (0.03 for methylene blue). To account for incomplete spectra, the bands were extrapolated using appropriate fitting models whenever necessary.

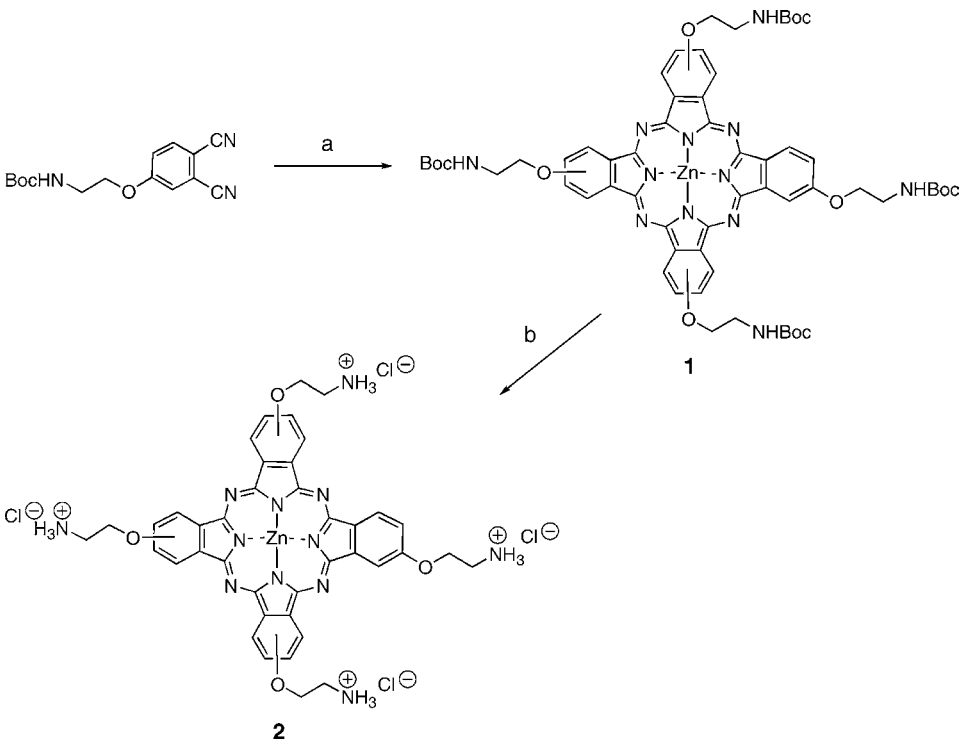
Cell Culture. All tissue culture media and reagents were obtained from Invitrogen. Human HEp2 cells were obtained from ATCC and maintained in a 50:50 mixture of DMEM/advanced MEM containing 5% FBS. The cells were subcultured biweekly to maintain subconfluent stocks.

Time-Dependent Cellular Uptake. HEp2 cells were plated at 10 000 per well in a Costar 96 well plate and allowed to grow 36 h. Conjugate stocks of Pcs **2** and **3b** were prepared in DMSO, and Pc conjugates **5** and **6** were prepared in water at a concentration of 10 mM and then diluted into medium to final working concentrations. The cells were exposed to 10 μM of each conjugate for 0, 1, 2, 4, 8, and 24 h. At the end of the incubation period, the loading medium was removed and the cells were washed with 200 μL of PBS. Cells were solubilized upon addition of 100 μL of 0.25% Triton X-100 (Calbiochem) in PBS. To determine the Pc concentrations, fluorescence emission was read at 690/710 nm (excitation/emission) using a BMG FLUOstar plate reader. The cell numbers were quantified using the CyQuant reagent (Molecular Probes).

Cytotoxicity. The HEp2 cells were plated as described above and allowed 36−48 h to attach. For the dark cytotoxicity experiments, the cells were exposed to increasing concentrations of Pc conjugate up to 100 μM and incubated for 24 h. The loading medium was then removed, and medium containing Cell Titer Blue (Promega) was added to the cells as per manufacturer's instructions. The dark cell toxicity was then measured by reading the fluorescence at 520/584 nm using a BMG FLUOstar plate reader. The signal was normalized to 100% viable (untreated) cells and 0% viable (treated with 0.2% saponin from Sigma) cells. For the phototoxicity experiments, the HEp2 cells were prepared as described above, treated with Pc conjugate concentrations of 0, 0.625, 1.25, 2.5, 5, and 10 μM and incubated for 24 h. After compound loading, the medium was removed and replaced with medium containing 50 mM HEPES (pH 7.4). The cells were then placed on ice and exposed to light from a 100 W halogen lamp filtered through a 610 nm long pass filter (Chroma) for 20 min. An inverted plate lid filled with water to a depth of 5 mm acted as an IR filter. The total light dose was approximately 1 J cm^{-2}. The cells were returned to the incubator overnight and assayed for toxicity as described above.

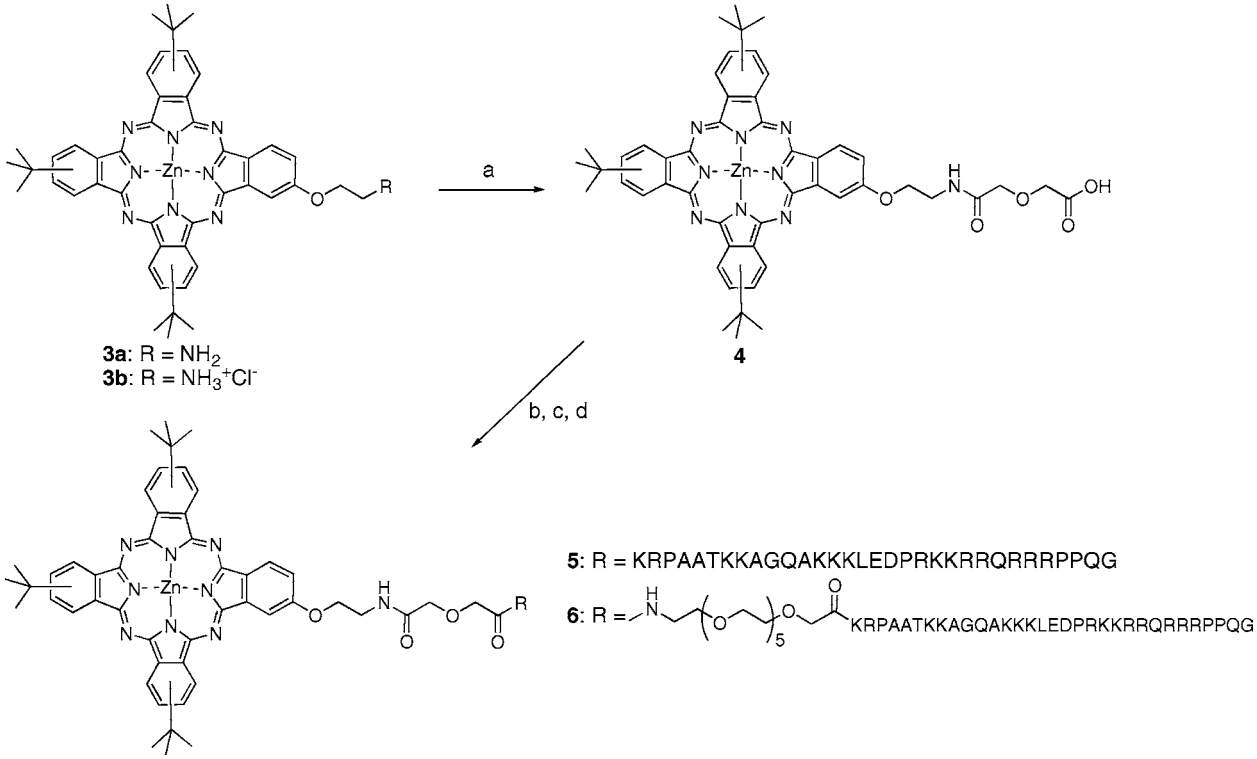
Microscopy. The HEp2 cells were plated on LabTek 2 chamber coverslips and incubated for 36 h before being exposed to 10 μM of Pc and incubated for 24 h. For the colocalization experiments, the cells were incubated for 24 h concurrently with Pc and one of the following organelle tracers for 30 min: MitoTracker Green at 250 nM (mitochondria), LysoSensor Green at 50 nM (lysosomes), $DiOC_6$ at 5 μg/mL (ER), and BODIPY FL C_5-ceramide at 50 nM (Golgi network). The slides were washed three times with growth medium, and new medium containing 50 mM HEPES (pH 7.4) was added. Fluorescent microscopy was performed using a Zeiss Axiovert 200M inverted fluorescence microscope fitted with standard FITC and Texas Red filter sets (Chroma). The images were aquired with a Zeiss Axiocam MRM CCD camera fitted to the microscope.

Scheme 1 [a]



[a] Conditions: (a) $Zn(OAc)_2 \cdot 2H_2O$, DBN, DMAE (57%); (b) TFA/CH_2Cl_2 rt/2h, then NaOH followed by HCl (52%).

Scheme 2 [a]



[a] Conditions: (a) diglycolic anhydride/DMF rt/24 h (97%); (b) HOBt/TBTU/DIEA/peptidyl-PEG-PAL resin/DMF 24 h, then TFA/H_2O/phenol/TIS 88/5/5/2 (42−57%); (c) HOBt/TBTU/DIEA/$NH_2CH_2CH_2(OCH_2CH_2)_5OCH_2CO_2{}^tBu$/DMF, rt/24 h (40%); (d) $TFA/CHCl_3$ 1/1, 4 h/rt, quantitative yield.

RESULTS

Synthesis. The synthetic route to water-soluble Zn−Pc **2** is shown in Scheme 1. Zn−Pc **2** was prepared in good yield from Zn−Pc **1** by deprotection of the Boc groups using TFA, followed by neutralization with NaOH to afford the tetra-amino-substituted Pc and final treatment with HCl. The tetraBoc-protected Zn−Pc **1** was synthesized in 57% yield by tetramerization of 4-(2-*tert*-butoxycarbonylaminoethoxy)phthalonitrile using zinc acetate as the template, DMAE as the solvent, and DBN as the catalyst, following a standard procedure for the synthesis of Pcs (*31*). Zn−Pc **3**, containing either a single amino group (**3a**) or quaternary ammonium salt (**3b**) (upon acidifica-

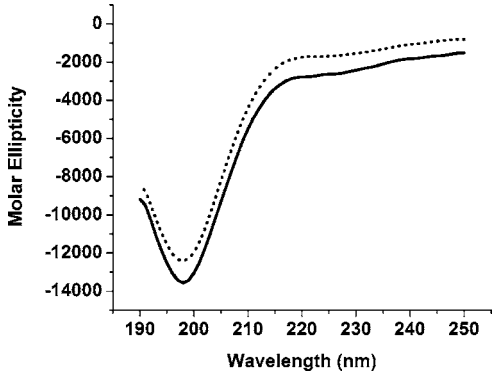


Figure 1. Pc conjugates **5** (full line) and **6** (dotted line) in TFE/H_2O 1/9 at pH 7.0 and 20 μM concentration. The molar ellipticity is given in deg cm^2 dmol^{-1}, cell path was 0.1 cm, and the temperature 25 °C.

tion), was also prepared following a known methodology (*31*). Two Pc−peptide conjugates were prepared from amino-Pc **3a** as shown in Scheme 2 in order to improve its water solubility and to reduce Pc aggregation in aqueous media. Conjugates **5** and **6** were designed to contain a bifunctional peptide bearing both an NLS and cell-penetrating peptide sequences attached to the Pc via either a short (9 atom) or long (30 atom) linker. The NLS corresponding to nucleoplasmin (*32*) and the HIV-1 Tat 48−60 cell-penetrating sequence (*24*) were chosen in order to obtain amphiphilic Pc conjugates **5** and **6** with higher cell-penetrating ability and improved biological activity. This bifunctional nucleoplasmin−HIV-1 Tat peptide sequence, KRPAATKKAGQAKKKLEDPRKKRRQRRRPPQG, was synthesized using Fmoc solid-phase synthesis methodology (*33*), and the heterofunctional PEG linker $^tBuO_2CCH_2O(CH_2CH_2O)_5CH_2CH_2NH_2$ was prepared as previously described in the literature (*34*). The reaction of Pc **3a** with diglycolic anhydride in DMF gave Pc **4** in 97% yield (Scheme 2), thus providing a free carboxylic acid group for conjugation to either the peptide or the Boc-protected PEG linker. The coupling of the hydroxybenzotriazole ester of Pc **4** with $^tBuO_2CCH_2O(CH_2CH_2O)_5CH_2CH_2NH_2$ in solution using TBTU as the coupling agent gave the corresponding Boc-protected PEG−Pc in 40% yield after purification by flash chromatography on silica gel. The deprotection of the Boc group in $CHCl_3$/TFA 1:1 was achieved in quantitative yield. The solid-phase conjugation of the carboxylate-functionalized Pcs to the bifunctional peptide produced conjugates **5** and **6**, respectively, bearing either a short or a PEG-containing long linker between the peptide and the Pc moieties. The carboxylates were initially converted to the corresponding reactive hydroxybenzotriazole esters and then coupled to the peptidyl−PAL−PEG−PS resin using TBTU as the coupling agent; after cleavage and deprotection from the solid support using TFA/phenol/TIS/H_2O, 88/5/2/5, the water-soluble Pc conjugates **5** and **6** were isolated by reverse-phase HPLC in 57% and 42% yield, respectively.

The structures of the Pc conjugates **5** and **6** were confirmed by MS, NMR, CD, and UV−vis and fluorescence spectrophotometry (vide infra). CD was used to determine the secondary structure of the peptide sequences on the Pc conjugates in solution. The CD spectra of conjugates **5** and **6** in water/TFE 9/1 at pH 7.00 were measured in the amide region (190−250 nm). As shown in Figure 1, both conjugates show negative Cotton effects; for Pc **5**, $[\Phi]_{MRW} = -13\,560$ deg cm^2 dmol^{-1} at 198 nm, and for Pc **6**, $[\Phi]_{MRW} = -12\,416$ deg cm^2 dmol^{-1} at 198 nm. These CD spectra indicate that the peptide sequences conjugated to the Pc macrocycle by either the short or long linkage adopt random coil conformations under the conditions studied; peptides adopting a random coil structure usually exhibit a single negative Cotton effect at 198 nm (for example, for polylysine at pH 7, $[\Phi]_{MRW} = -41\,900$ deg cm^2 dmol^{-1} at 197 nm (*35*)).

Photophysical Studies. The spectral characteristics observed for Zn−Pcs **2** and **3b** and conjugates **5** and **6** in DMSO and water at different pH values are summarized in Table 1. The absorption and emission properties for the Pcs and conjugates studied were found to be strongly dependent on their structure and aggregation state. With the exception of Pc **2**, where partial aggregation was observed in DMSO as noted from the relatively strong absorption band appearing at 628 nm (Supporting Information Figure S3), no evidence of aggregation was observed in DMSO for Pc **3b** or the Pc conjugates **5** and **6** (Supporting Informatio Figures S4−S6). However, in buffered aqueous solutions, both Pcs **2** and **3b** were strongly aggregated as evidenced in the broadening of the Q-band absorption and bathochromic and hypsochromic shifts (Supporting Information Figures S3 and S4). Pc **3b** did not exhibit fluorescence at any of the pH values investigated (5.0, 6.0, 7.0, 7.4, and 8.0), while Pc **2** fluoresced only at pH 5.0 but with a very small quantum yield (0.00011; see Table 1). In DMSO, the fluorescence quantum yield determined for Pc **3b** was 10 times higher than that of Pc **2**, although the observed Stokes shift was smaller for **3b** (see Table 1). The absorption spectra for Pc conjugates

Table 1. Spectral Properties of Pcs 2, 3b, 5, and 6 at Different pH and in DMSO[a]

	absorption				fluorescence											
	absorption maxima				emission maximum				Stokes shift, nm				quantum yield ($\times 10^{-2}$)			
medium (pH)	**2**	**3b**	**5**	**6**	**2**	**3b**	**5**	**6**	**2**	**3b**	**5**	**6**	**2**	**3b**	**5**	**6**
aqueous (5.0)	336	336	335	335	686	NF	693	692	12	NF	15	7	0.011	NF	0.030	0.019
	634	632	633	636												
	674	678	678	685												
aqueous (6.0)	337	336	335	335	NF	NF	694	692	NF	NF	16	7	NF	NF	0.016	0.011
	625	632	633	632												
		679	678	685												
aqueous (7.0)	336	336	335	335	NF	NF	693	692	NF	NF	15	7	NF	NF	0.0099	0.008
	624	632	633	630												
		682	678	685												
aqueous (7.4)	337	337	335	335	NF	NF	694	691	NF	NF	16	6	NF	NF	0.0091	0.007
	622	632	633	630												
		681	678	685												
aqueous (8.0)	337	336	335	335	NF	NF	693	690	NF	NF	14	5	NF	NF	0.0096	0.008
	624	612	634	632												
		681	679	685												
DMSO	353	354	353	355	689	684	684	684	9	4	4	4	2	20	14	17
	628	613	613	612												
	680	680	680	680												

[a] NF = Nonfluorescent.

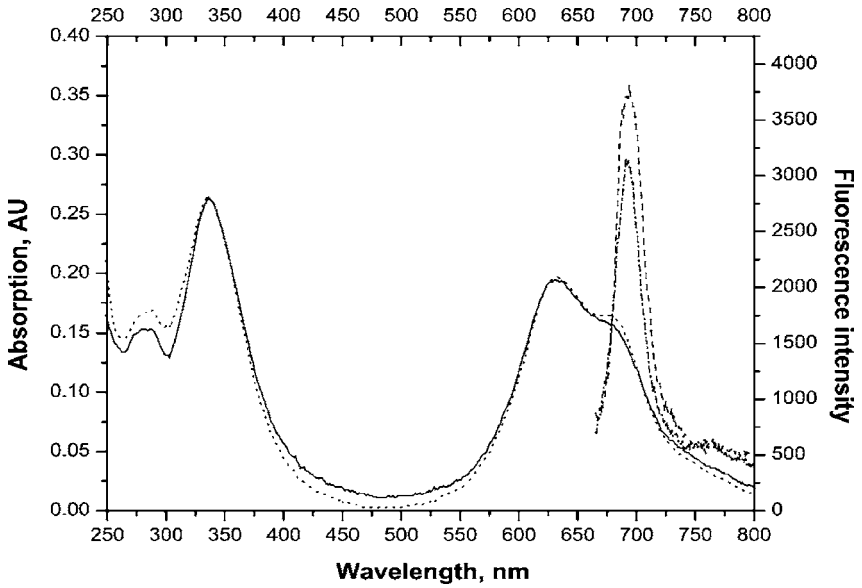


Figure 2. Absorption and emission spectra of Pcs **5** and **6** in 100 mM phosphate buffer, pH 7.4: absorption of **5** (dot line), absorption of **6** (solid line), emission of **5** (dash line), emission of **6** (dash−dot line).

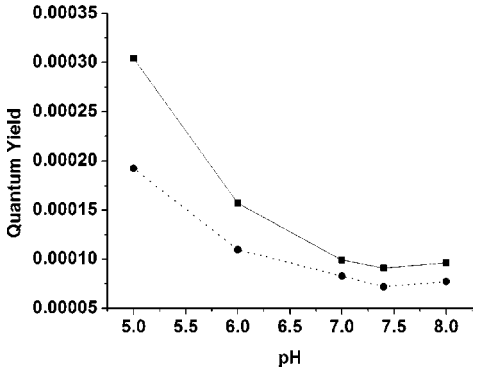


Figure 3. Fluorescence quantum yields in 100 mM phosphate buffer at different pH values of Pc conjugate **5** (full line) and Pc conjugate **6** (dot line).

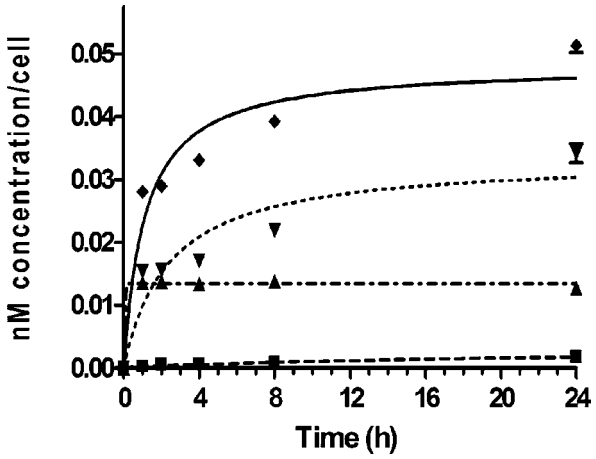


Figure 4. Time-dependent uptake of Pcs **2** (dash−dot−dash), **3b** (dash), conjugate **5** (dot), and conjugate **6** (full line) at 10 μM by HEp2 cells.

5 and **6** in aqueous solutions (Figure 2 and Supporting Information Figures S5 and S6) also showed evidence of ground-state aggregation as indicated by the blue-shifted and broad Q bands. No significant effect of the pH on the position and shape of the absorption bands was observed within the range studied for Pc conjugates **5** and **6** (Supporting Information Figures S3 and S4). Nevertheless, both Pc conjugates **5** and **6** fluoresced in aqueous solutions at all pH values studied (Figure 2 and Supporting Information Figures S5 and S6). The fluorescence quantum yields for Pc conjugates **5** and **6** were found to be 0.14 and 0.17 in DMSO, respectively, and these compounds also displayed measured fluorescence in all the pH values investigated but were generally found to increase as the pH value was decreased (see Figure 3). Pc conjugate **5** exhibited a higher quantum yield at all pH values studied compared to Pc conjugate **6**.

Cellular Studies. The results obtained for the time-dependent uptake of Zn−Pcs **2** and **3b** and conjugates **5** and **6** at a concentration of 10 μM in human HEp2 cells are shown in Figure 4. As expected, Pc conjugates **5** and **6** bearing the bifunctional peptide nucleoplasmin-HIV-1 Tat 48−60 accumulated to a significantly higher extent within cells than Pcs **2** and **3b**. The extent of conjugate uptake was dependent on the nature of the linker between the Pc and the peptide moieties; conjugate **6** containing a long PEG−linker was taken up by cells to a higher extent than conjugate **5**, which possesses a short linker. On the other hand, the cellular uptake of the unconjugated Zn−Pcs **2** and **3b** depended significantly on the number of quaternary ammonium groups at the Pc periphery, i.e., Zn−Pc **2** exhibited higher uptake than Zn−Pc **3b**, bearing only one quaternary ammonium group. Similar uptake kinetics were observed for Pc conjugates **5** and **6**; both conjugates accumulated rapidly in the first 2 h, and from 2 to 24 h, their uptake was considerably slower. Zn−Pc **2** also accumulated within cells very rapidly in the first 30 min, and after this time, a plateau was reached. On the other hand, Zn−Pc **3b** accumulated steadily over time during the 24 h period studied but at a much lower extent when compared with Pcs **2**, **5**, and **6**.

The dark and phototoxicity of Pcs **2**, **3b**, **5**, and **6** were evaluated in human HEp2 cells exposed to increasing concentrations of each Pc for 24 h as shown in Figures 5 and 6, respectively. Pc **3b**, the least accumulated within cells (see Figure 4), showed no toxicity in the dark at concentrations up to 100 μM. On the other hand, Pc **2** and conjugates **5** and **6** exhibited low dark toxicity with determined IC_{50} = 70.9, 77.6, and 87.3 μM, respectively (see Figure 5). Upon exposure to a low light dose (1 J cm^{-2}), conjugates **5** and **6** were the most phototoxic to the HEp2 cells, with IC_{50} = 1.44 and 1.87 μM, respectively. Zn−Pc **3b**, bearing only one quaternary ammonium

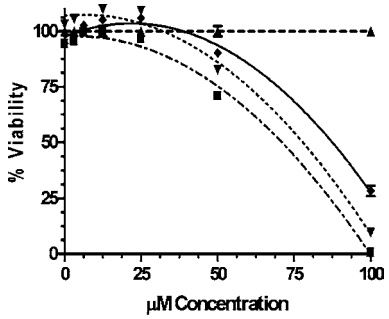


Figure 5. Dark toxicity of Pcs **2** (dash−dot−dash), **3b** (dash), conjugate **5** (dot), and conjugate **6** (full line) toward HEp2 cells using the Cell Titer Blue assay, after 24 h incubation time.

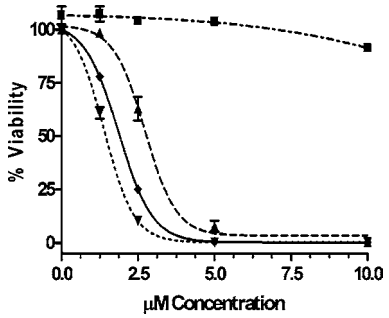


Figure 6. Phototoxicity of Pcs **2** (dash−dot−dash), **3b** (dash), conjugate **5** (dot), and conjugate **6** (full line) toward HEp2 cells using 1 J/cm^2 dose light, after 24 h incubation time.

group, also exhibited high phototoxicity, with $IC_{50} = 2.78\ \mu M$ (see Figure 6).

The subcellular localization of Pcs **3b**, **5**, and **6** was investigated in HEp2 cells using fluorescence microscopy. Figures 7−9 show the fluorescent images observed for Pcs **3b**, **5**, and **6** after 24 h incubation time, and their overlay with the organelle-specific fluorescent probes LysoSensor Green (lysosomes), Mitotracker Green (mitochondria), $DiOC_6$ (ER), and BODIPY Ceramide (Golgi). Due to the low fluorescence signal observed for Zn−Pc **2** as a result of its aggregation under the experimental conditions, the main sites of subcellular distribution of this Pc were not determined. Pcs **3b**, **5**, and **6** all showed a punctuate fluorescence pattern in the cytoplasm. While Pc **3b** was observed in both the lysosomes and the Golgi, the preferential sites of intracellular localization for Pc conjugates **5** and **6** were found to be the lysosomes.

DISCUSSION

Pc conjugates **5** and **6** were prepared from mono-amino Pc **3a** (Scheme 2) and their photophysical and cellular properties investigated and compared with those of Pcs **2** (Scheme 1) and **3b** containing, respectively, 4 and 1 quaternary ammonium groups. Conjugates **5** and **6** were designed to contain a bifunctional peptide sequence bearing NLS and cell-penetrating peptides attached to the Pc via either a short or a long (PEG-containing) linker. The conjugation of drugs to fusogenic and/or organelle-directing peptides is a strategy often used to improve their water solubility, cellular uptake, and biological efficacy (*22*−*28*, *36*). Since aggregation in aqueous media of Pc-type compounds is known to deeply influence their photosensitizing properties (*37*), we conjugated Zn−Pc **3a** to a bifunctional peptide and investigated the effect of a short (9 atom) and a long (30 atom) PEG-containing linker between the Pc and peptide moieties. The low molecular weight PEG linker was used to minimize possible intramolecular interactions between the Pc and the peptide chain, as we have previously observed with short linkers in porphyrin−peptide conjugates

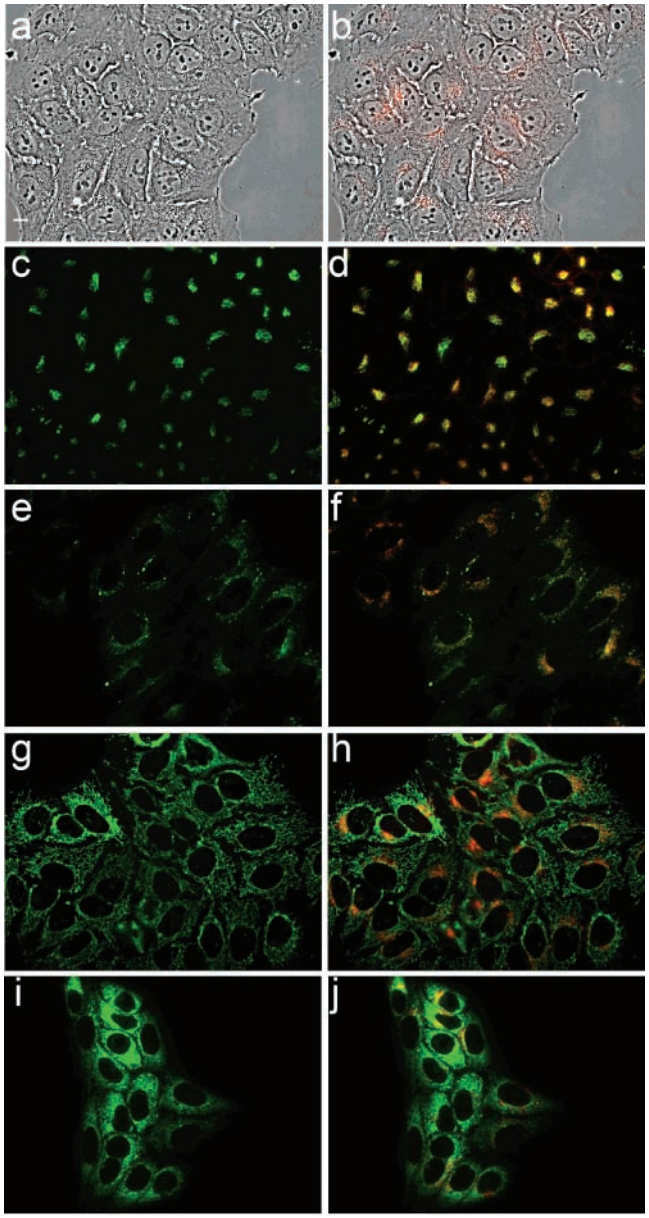


Figure 7. Subcellular localization of Pc **3b** in HEp2 cells at 10 μM after 24 h: (a) phase contrast, (b) overlay of Pc **3b** fluorescence and phase contrast, (c) BODIPY Ceramide fluorescence, (e) LysoSensor Green fluorescence, (g) MitoTracker Green fluorescence, (i) $DiOC_6$ fluorescence, (d,f,h,j) overlays of organelle tracers with Pc **3b** fluorescence. Scale bar: 10 μm.

(*38*), and to enhance the water solubility of the conjugate. The pegylation of drugs to improve their pharmacokinetic properties has been extensively used, and it is known that PEG−drug conjugates display enhanced water solubility, serum life, and tumor accumulation (*39*). A low molecular weight PEG was chosen over a high molecular weight PEG in order to avoid the formation of mixtures due to the polydispersity of the high molecular weight PEG (*40*). The synthesis of the amino−Pcs **2** and **3** followed a known methodology for the preparation of Pc macrocycles (*31*), involving the tetramerization of phthalonitriles under basic conditions.

The CD spectra for Pc conjugates **5** and **6** were obtained in aqueous TFE at pH 7.0, thus mimicking the cell membrane environment, in order to investigate the preferred conformation of the peptide chains. The peptide conformation is known to influence the mode of translocation of the Pc conjugates across membranes and their binding to biomolecules for trafficking within the cell. Our CD studies (see Figure 1) indicate that the

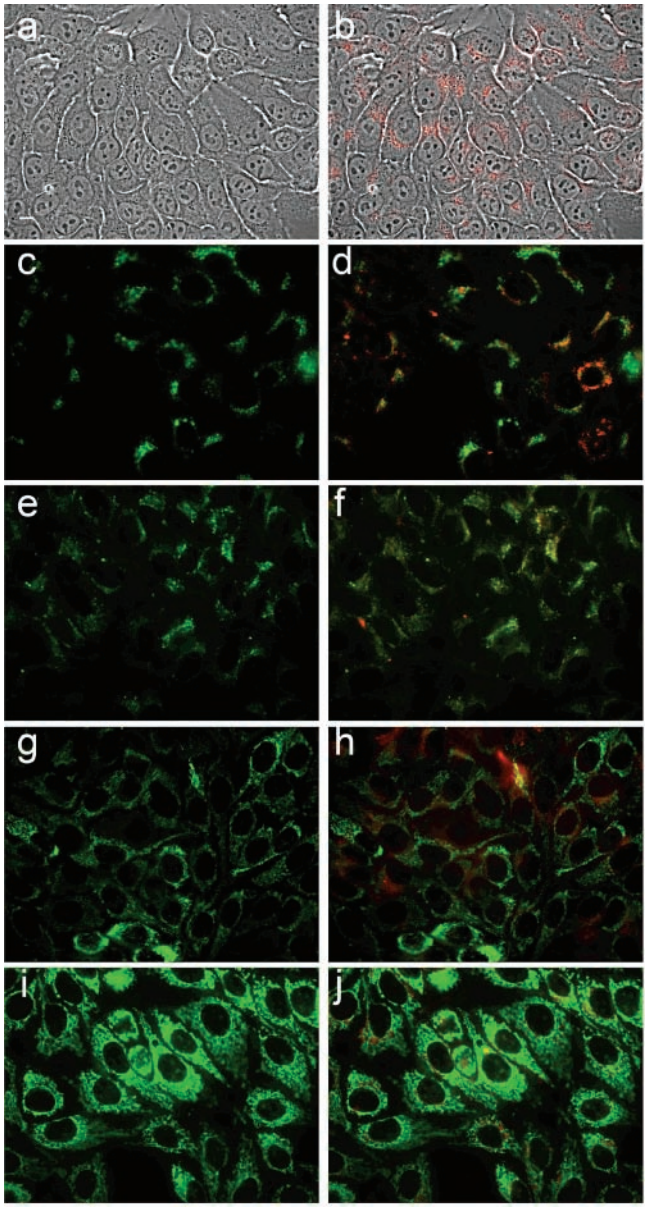


Figure 8. Subcellular localization of Pc cnjugate **5** in HEp2 cells at 10 μM after 24 h: (a) phase contrast, (b) overlay of Pc **5** fluorescence and phase contrast, (c) BODIPY Ceramide fluorescence, (e) LysoSensor Green fluorescence, (g) MitoTracker Green fluorescence, (i) $DiOC_6$ fluorescence, (d,f,h,j) overlays of organelle tracers with Pc **5** fluorescence. Scale bar: 10 μm.

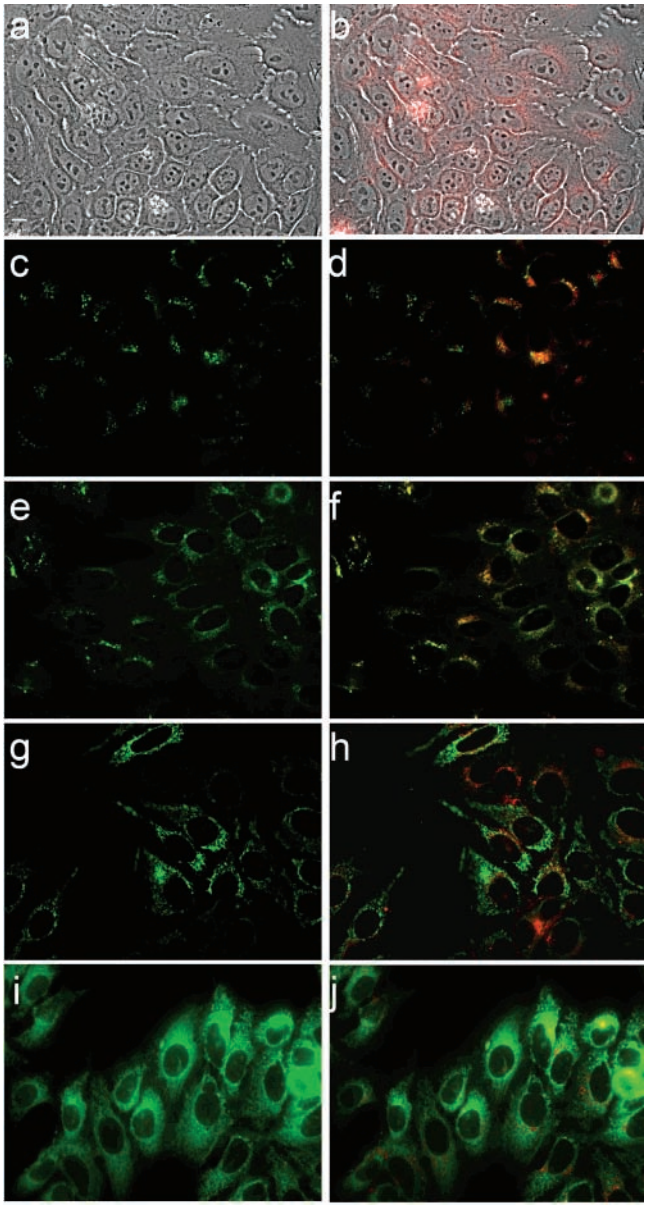


Figure 9. Subcellular localization of Pc conjugate **6** in HEp2 cells at 10 μM after 24 h: (a) phase contrast, (b) overlay of Pc **6** fluorescence and phase contrast, (c) BODIPY Ceramide fluorescence, (e) LysoSensor Green fluorescence, (g) MitoTracker Green fluorescence, (i) $DiOC_6$ fluorescence, (d,f,h,j) overlays of organelle tracers with Pc **6** fluorescence. Scale bar: 10 μm.

peptides conjugated to the Pc macrocycle in **5** and **6** adopt random coil rather than helix conformations under the conditions tested. These results are in agreement with the crystal structure reported for the complex importin α/nucleoplasmin (155−170, KRPAATKKAGQAKKKK), a protein involved in nuclear import (*41*). In this complex, the nucleoplasmin 155−170 sequence in an extended conformation binds at the minor and major binding sites of importin α. On the other hand, previous CD studies reported for the Tat protein have shown that the highly basic region from 48 to 60 (i.e., RKKRRQRRRRPPQ) forms part of the N-terminus domain of the coat protein that is located toward the interior of the virus (*42*). This stretch of basic residues adopts an extended conformation due to the electrostatic repulsion between the positively charged side groups.

The fluorescence quantum yields determined in DMSO for Zn−Pcs **2**, **3b**, and conjugates **5** and **6** (see Table 1) are in agreement with previous values reported for Zn−Pcs (*43*). Inspection of the electronic absorption spectra in aqueous solutions indicated that Pc **2** showed minimal aggregation effects at low pH due to protonation of the amino groups, while Pc **3b** and conjugates **5** and **6** did not display significant changes in their electronic spectra at different pH values, indicating no significant change in their aggregation states. Because cells display marked heterogeneity in local pH and tumor cells usually exhibit lower pH than normal cells, we investigated the pH dependence on the spectral properties of the Pcs included in this study (*44*). We observed that, while Pc **3b** did not exhibit fluorescence in any of the aqueous solutions (pH = 5.0−8.0), Pc **2** fluoresced only at pH 5.0, possibly due to reduced aggregation. This supposition is supported by the ground-state spectrum at pH = 5.0, which showed partial restoration of the Q band at this pH value. Zn−Pcs usually form aggregates in aqueous solutions, and these species typically display reduced fluorescence (*45*). Interestingly, Pc conjugates **5** and **6** showed fluorescence at all pH values with slightly higher quantum yields at pH = 5.0 even though their electronic spectra were relatively

unaffected by the solution pH. Pc conjugate **5**, bearing a short linker to the bifunctional peptide, exhibited higher fluorescence quantum yields at all pH values studied and a larger Stokes shift compared to Pc conjugate **6**. The difference in quantum yields observed for conjugates **5** and **6** may be attributed to the nature of the linker between the Pc and the peptide chain. The long PEG-containing linker is more flexible and therefore may adopt multiple conformations in aqueous solutions due to its amphiphilic character (*46*). Furthermore, the association of PEG chains to water molecules (approximately 2−3 water molecules per ethylene oxide unit) might lower the fluorescence quantum yield of conjugate **6** as compared with that of **5**.

The cellular uptake of all Pcs studied is dependent on the nature of the groups at the Pc periphery and on the overall molecular charge. Pc conjugates **5** and **6** bearing the bifunctional peptide nucleoplasmin-HIV-1 Tat 48−60 accumulated within cells to a significantly higher extent than Pcs **2** and **3b**. The high cellular uptake of the conjugates might be due to the presence of the guanidinium groups on the HIV-1 Tat sequence and the ammonium groups on the nucleoplasmin sequence, which can form hydrogen bonds with membrane phosphate groups (*26*, *47*), thus promoting endocytosis. Zn−Pc **2** bearing four quaternary ammonium groups at physiologic pH also exhibited significantly higher uptake than Pc **3b**, which only possesses one quaternary ammonium group. These results are in agreement with previous studies showing that the overall molecular charge and its distribution at the Pc periphery play an important role on the cellular uptake of these photosensitizers (*48*). Pc **3b**, the least accumulated within cells, showed no toxicity at concentrations up to 100 μM in the dark. On the other hand, Pc **2** and conjugates **5** and **6** exhibited $IC_{50} = 70.9$, 77.6, and 87.3 μM, respectively. Upon exposure to low light dose (1 J cm^{-2}), conjugates **5** and **6** bearing the peptide chain were the most phototoxic to cells ($IC_{50} = 1.4$ and 1.9 μM, respectively). Surprisingly, Pc **3b**, which showed the lowest cellular uptake and no dark cytotoxicity up to 100 μM concentration, exhibited high phototoxicity (IC_{50} of 2.8 μM). This result may be attributed to (a) its subcellular localization within more sensitive cell compartments (lysosomes and Golgi), (b) its possible relocalization after light irradiation, and/or (c) the decrease in aggregation (and consequently higher fluorescence) within the cell due to interaction with lipid membranes and/or change in pH. The reactive oxygen species produced in PDT can induce apoptosis through the Golgi network (*49*), and the cell lysosomes are also an important PDT target (*50*). Our results indicate, as has been previously reported (*4*), that not only the amount of photosensitizer within the cell, but also its subcellular distribution, determines its biological efficacy. Whereas Pc **3b** localized preferentially within the cell lysosomes and Golgi, conjugates **5** and **6** were observed mainly in the lysosomes, possibly due to their favored endocytic uptake. Although both Pc conjugates **5** and **6** contain an NLS nucleoplasmin sequence, the cell nucleus is not their main localization site; however, it is possible that after light exposure conjugates **5** and **6** could be released from the lysosomes and relocalize within more sensitive organelles, such as the nuclei, ER, and Golgi, as has been previously observed for Zn−Pcs (*7b*, *48*).

ACKNOWLEDGMENT

The authors thank Ms. Martha Juban for peptide synthesis. This work was supported by the National Science Foundation, grant numbers CHE-304833 and EPS-0346411, the State of Louisiana Board of Regents, the Spanish Government (CICYT grant no. MAT2005-07369-C03-02), and the Spanish Generalitat Valenciana (grant no. ACOMP06/054-2005).

Supporting Information Available: ^{1}H NMR of compounds synthesized, UV−vis and fluorescence spectra for all Pcs, and HPLC traces for Pc conjugates **5** and **6**. This material is available free of charge via the Internet at http://pubs.acs.org.

LITERATURE CITED

(1) Dougherty, T. J., Gomer, C. J., Henderson, B. W., Jori, G., Kessel, D., Korbelik, M., Moan, J., and Peng, Q. (1998) Photodynamic therapy. *J. Natl. Cancer Inst. 90*, 889−905.

(2) Ben-Hur, E., and Chan, W.-S. (2003) Phthalocyanines in photobiology and their medical applications. In *The Porphyrin Handbook* (Kadish, K. M., Smith, K. M., and Guilard, R., Eds.) Vol. 19, pp 1−35, Academic Press, Boston.

(3) Detty, M. R., Gibson, S. L., and Wagner, S. J. (2004) Current clinical and preclinical photosensitizers for use in photodynamic therapy. *J. Med. Chem. 47*, 3897−3915.

(4) Kessel, D. (2004) Correlation between subcellular localization and photodynamic efficacy. *J. Porphyrins Phthalocyanines 8*, 1009−1014.

(5) Rosenkranz, A. A., Jans, D. A., and Sobolev, A. S. (2002) Targeted intracellular delivery of photosensitizers to enhance photodynamic efficiency. *Immunol. Cell Biol. 78*, 452−464.

(6) Lunardi, C. N., and Tedesco, A. C. (2005) Synergic photosensitizers: A new trend in photodynamic therapy. *Curr. Org. Chem. 9*, 813−821.

(7) (a) Choi, C.-F., Tsang, P.-T., Huang, J.-D., Chan, E. Y. M., Ko, W.-H., Fong, W.-P., and Ng, D. K. P. (2004) Synthesis and in vitro photodynamic activity of new hexadeca-carboxy phthalocyanines. *Chem. Commun.* 2236−2237. (b) Liu, W., Jensen, T. J., Fronczek, F. R., Hammer, R. P., Smith, K. M., and Vicente, M. G. H. (2005) Synthesis and in vitro studies of non-aggregated water-soluble phthalocyanines. *J. Med. Chem. 48*, 1033−1041.

(8) Yang, Y.-C., Ward, J. R., and Seiders, R. P. (1985) Dimerization of cobalt(II) tetrasulfonated phthalocyanine in water and aqueous alcoholic solutions. *Inorg. Chem. 24*, 1765−176.

(9) (a) Clarkson, G. J., McKeown, N. B., and Treacher, K. E. (1995) Synthesis and characterization of some novel phthalocyanines containing both oligo(ethyleneoxy) and alkyl or alkoxy sidechains: novel unsymmetrical discotic mesogens. *J. Chem. Soc., Perkin Trans. 1* 1817−1823. (b) Toupance, T., Bassoul, P., Mineau, L., and Simon, J. (1996) Poly(oxyethylene)-substituted copper and lutetium phthalocyanines. *J. Phys. Chem. 100*, 11704−11710.

(10) (a) Li, X. Y., and Ng, D. K. P. (2001) Synthesis and spectroscopic properties of the first phthalocyanine-nucleobase conjugates. *Tetrahedron Lett. 42*, 305−309. (b) Koval, V., Chernonosov, A., Kuznetsova, A., Kuznetsov, N., Pyshnyi, D., Derkacheva, V., Lukyanets, E., and Fedorova, O. (2005) Phthalocyanine-oligonucleotide conjugates: Synthesis, thermodynamics, and DNA modification. *J. Biomol. Struct. Dyn. 22*, 822−823.

(11) (a) Chernonosov, A. A., Kuznetsov, N. A., Koval, V. V., Pyshnyi, D. V., Derkacheva, N. M., Lukyanets, E. A., and Fedorova, O. S. (2004) Thermodynamics of interaction of phthalocyanine-oligonucleotide conjugates with single- and double-stranded DNA. *Nucleosides, Nucleotides Nucleic Acids 23*, 983−987. (b) Chernonosov, A. A. (2005) Phthalocyanine conjugates of oligonucleotides as new reagents for sensitized and catalytic modification of DNA and DNA-binding proteins. *FEBS J. 272*, 542−543.

(12) Matveeva, E. G., Meerovich, I. G., and Savitsky, A. P. (1998) The synthesis of conjugates of phthalocyanines with monoclonal antibodies in AOT/n-octane reversed micelles and in water-organic mixtures. *Bioorg. Khim. 24*, 64−71.

(13) (a) Carcenac, M., Larroque, C., Langlois, R., van Lier, J. E., Artus, J. C., and Pelegrin, A. (1999) Preparation, phototoxicity and biodistribution studies of anti-carcinoembryonic antigen monoclonal antibody-phthalocyanine conjugates. *Photochem. Photobiol. 70*, 930−936. (b) Carcenac, M., Dorvillius, M., Garambois, V., Glaussel, F., Larroque, C., Langlois, R., Hynes, N. E., van Lier, J. E., and Pelegrin, A. (2001) Internalisation enhances photo-induced cytotoxicity of monoclonal antibody-phthalocyanine conjugates. *Br. J. Cancer 85*, 1787−1793.

(14) (a) Vrouenraets, M. B., Visser, G. W. M., Stigter, M., Oppelaar, H., Snow, G. B., and van Dongen, G. (2001) Targeting of aluminum (III) phthalocyanine tetrasulfonate by use of internalizing monoclonal antibodies: Improved efficacy in photodynamic therapy. *Cancer Res. 61*, 1970−1975. (b) Vrouenraets, M. B., Visser, G. W. M., Stigter, M., Oppelaar, H., Snow, G. B., and van Dongen, G. (2002)

Comparison of aluminium (III) phthalocyanine tetrasulfonate- and meta-tetrahydroxyphenylchlorin-monoclonal antibody conjugates for their efficacy in photodynamic therapy in vitro. *Int. J. Cancer 98*, 793−798.

(15) Duan, W. B., Smith, K., Savoie, H., Savoie, H., Greenman, J., and Boyle, R. W. (2005) Near IR emitting isothiocyanato-substituted fluorophores: their synthesis and bioconjugation to monoclonal antibodies. *Org. Biomol. Chem. 3*, 2384−2386.

(16) Severin, S. E., Posypanova, G. A., Katukov, V. Y., Shmyrev, I. I, Luzhkov, Y. M., Gerasimova, G. K., Zhukova, O. S., Vorozhtsov, G. N., Kaliya, O. L., Lukyanets, E. A., and Severin, E. S. (1997) Antitumor activity of conjugates of the oncofetal protein α-fetoprotein and phthalocyanines in vitro. *Biochem. Mol. Biol. Int. 43*, 873−881.

(17) Brasseur, N., Langlois, R., La Madeleine, C., Ouellet, R., and van Lier, J. E. (1999) Receptor-mediated targeting of phthalocyanines to macrophages via covalent coupling to native or maleylated bovine serum albumin. *Photochem. Photobiol. 69*, 345−352.

(18) Ogunsipe, A., and Nyokong, T. (2005) Photophysicochemical consequences of bovine serum albumin binding to non-transition metal phthalocyanine sulfonates. *Photochem. Photobiol. Sci. 4*, 510−516.

(19) (a) Huang, J. D., Lo, P. C., Chen, Y. M., Lai, J. C., Fong, W. P., and Ng, D. K. P. (2006) Preparation and in vitro photodynamic activity of novel silicon (IV) phthalocyanines conjugated to serum albumins. *J. Inorg. Biochem. 100*, 946−951. (b) Jiang, X. J., Huang, J. D., Zhu, Y. J., Tang, F. X., Ng, D. K. P., and Sun, J. C. (2006) Preparation and in vitro photodynamic activities of novel axially substituted silicon (IV) phthalocyanines and their bovine serum albumin conjugates. *Bioorg. Med. Chem. Lett. 16*, 2450−2453.

(20) Kralova, J., Synytsya, A., Pouckova, P., Koc, M., Dvorak, M., and Kral, V. (2006) Novel porphyrin conjugates with a potent photodynamic antitumor effect: Differential efficacy of mono- and bis-beta-cyclodextrin derivatives in vitro and in vivo. *Photochem. Photobiol. 82*, 432−438.

(21) (a) Lutsenko, S. V., Feldman, N. B., Finakova, G. V., Posypanova, G. A., Severin, S. E., Skryabin, K. G., Kirpichnikov, M. P., Lukyanets, E. A., and Vorozhtsov, G. N. (1999) Targeting phthalocyanines to tumor cells using epidermal growth factor conjugates. *Tumor Biol. 20*, 218−224. (b) Savitsky, A. A., Gukasova, N. V., Gumanov, S. G., Feldman, N. B., Luk'yanets, E. A., Mironov, A. F., Yakubovskaya, R. I., Lutsenko, S. V., and Severin, S. E. (2000) Cytotoxic action of conjugates of α-fetoprotein and epidermal growth factor with photoheme, chlorines, and phthalocyanines. *Biochemistry (Moscow, Russ. Fed.) 65*, 732−736.

(22) Sharman, W. M., van Lier, J. E., and Allen, C. M. (2004) Targeted photodynamic therapy via receptor mediated delivery systems. *Adv. Drug Delivery Rev. 56*, 53−76.

(23) Derossi, D., Joliot, A., Chassaing, G., and Prochiantz, A. (1994) The third helix of the Antennapedia homeodomain translocates through biological membranes. *J. Biol. Chem. 269*, 10444−10450.

(24) Vives, E. (2003) Cellular uptake of the Tat peptide: an endocytosis mechanism following ionic interactions. *J. Mol. Recog. 16*, 265−271.

(25) (a) Normand, N., van Leeuwen, H., and O'Hare, P. (2001) Particle formation by the HSV protein VP22 enabling protein and nucleic acid delivery. *J. Biol. Chem. 276*, 15042−15050. (b) Brewis, N. D., Phelan, A., Normand, N., Choolun, E., and O'Hare, P. (2003) Particle assembly incorporating a VP22-BH3 fusion protein, facilitating intracellular delivery, regulated release, and apoptosis 1. *Mol. Ther. 7*, 262−270.

(26) Rothbard, J. B., Jessop, T. C., Lewis, R. S., Murray, B. A., and Wender, P. A. (2004) Role of membrane potential and hydrogen bonding in the mechanism of translocation of guanidinium-rich peptides into cells. *J. Am. Chem. Soc. 126*, 9506−9507.

(27) (a) Sibrian-Vazquez, M., Hao, E., Jensen, T. J., and Vicente, M. G. H. (2006) Enhanced cellular uptake with a cobaltacarborane-porphyrin-HIV-1 Tat 48−60 conjugate. *Bioconjugate Chem. 17*, 928−934. (b) Sibrian-Vazquez, M., Jensen, T. J., Hammer, R. P., and Vicente, M. G. H (2006) Peptide-mediated cell transport of water-soluble porphyrin conjugates. *J. Med. Chem. 49*, 1364−1372.

(28) Boulikas, T. (1993) Nuclear localization signals. *Crit. Rev. Eukaryotic Gene Expression 3*, 193−227.

(29) Fery-Forgues, S., and Lavabre, D. (1999) Are fluorescence quantum yields so tricky to measure? A demonstration using familiar stationery products. *J. Chem. Educ. 76*, 1260−1264.

(30) Lakowicz, J. R. (1999) *Principles of Fluorescence Spectroscopy*, 2nd ed., pp 52 f, Kluwer Academic/Plenum Publishers, New York.

(31) (a) McKeown, N. B., Chambrier, I., and Cook, M. J. (1990) Synthesis and characterisation of some 1,4,8,11,15,18,22,25-octa-alkyl- and 1,4,8,11,15,18-hexa-alkyl-22,25-bis(carboxypropyl) phthalocyanines. *J. Chem. Soc., Perkin Trans. 1* 1169−1177. (b) Vacus, J., Memetzidis, G., Doppelt, P., and Simon, J. (1994) The synthesis of unsymmetrically functionalized platinum and zinc phthalocyanine complexes. *J. Chem. Soc. Chem. Commun.* 697−698.

(32) (a) Dingwall, C., Dilworth, S. M., Roberts, B., and Richardson, W. D. (1988) The nucleoplasmin nuclear localization sequence is larger and more complex than that of SV-40 large T antigen. *J. Cell. Biol. 107*, 841−849. (b) Dingwall, C., and Laskey, R. A. (1990) Nucleoplasmin: the archetypal molecular chaperone. *Semin. Cell. Biol. 1*, 11−17. (c) Prado, A., Ramos, I., Frehlick, L. J., Muga, A., and Ausio, J. (2004) Nucleoplasmin: a nuclear chaperone. *Biochem. Cell Biol. 82*, 437−445.

(33) (a) Knorr, R., Trzeciak, A., Bannwarth, W., and Gillessen, D. (1989) New coupling reagents in peptide chemistry. *Tetrahedron Lett. 30*, 1927−1930. (b) Reid, G. E., and Simpson, R. J. (1992) Automatized solid-phase peptide synthesis: Use of 2-(1*H*-benzotriazol-1-yl)-1,1,3,3,-tetramethyluronium tetrafluoroborate for coupling of tert-butyloxycarbonyl amino acids. *Anal. Biochem. 200*, 301−309.

(34) (a) Suedhem, S., Hollander, S., Shi, J., Konradsson, P., Liedberg, B., and Svensson, S. C. T. (2001) Synthesis of a series of oligo-(ethyleneglycol)-terminated alkanethiol amides designed to address structural and stability of biosensing interfaces. *J. Org. Chem. 66*, 4494−4503. (b) Wosnick, J. H., Charlene, M., Mello, C. M., and Swager, T. M. (2005) Synthesis and application of poly(phenylene ethynylene)s for bioconjugation: A conjugated polymer-based fluorogenic probe for proteases. *J. Am. Chem. Soc. 127*, 3400−3405.

(35) Greenfield, N., and Fasman, G. D. (1969) Computed circular dichroism spectra for the evaluation of protein conformation. *Biochemistry 8*, 4108−4116.

(36) (a) Lundberg, P., and Langel, U. (2003) A brief introduction to cell-penetrating peptides. *J. Mol. Recog. 16*, 227−233. (b) Richard, J. P., Melikov, K., Vives, E., Ramos, C., Verbeure, B., Gait, M. J., Chernomordik, L. V., and Lebleu, B. (2003) Cell-penetrating peptides: A reevaluation of the mechanism of cellular uptake. *J. Biol. Chem. 278*, 585−590. (c) Futaki, S., Goto, S., Suzuki, T., Nakase, I., and Sugiura, Y. (2003) Structural variety of membrane permeable peptides. *Curr. Protein Pept. Sci. 4*, 87−96. (d) Schwartz, J. J., and Zhang, S. (2000) Peptide-mediated cellular delivery. *Curr. Opin. Mol. Therapeut.* 162−167.

(37) (a) Yang, Y. C., Ward, J. R., and Seiders, R. P. (1985) Dimerization of Cobalt(II) tetrasulfonated phthalocyanine in water and aqueous alcoholic solutions. *Inorg. Chem. 24*, 1765−1769. (b) Ozoemena, K., Kuznetsova, N., and Nyokong, T. (2001) Photosensitized transformation of 4-chlorophenol in the presence of aggregated and non-aggregated metallophthalocyanines. *J. Photochem. Photobiol., A 139*, 217−224. (c) Margaron, P., Gregoire, M. J., Scasnar, V., Ali, H., and van Lier, J. E. (1996) Structure-photodynamic activity relationships of a series of 4-substituted zinc phthalocyanines. *Photochem. Photobiol. 63*, 217−223. (d) Lebedeva, N. S. (2004) Aggregation properties of water-soluble metal phthalocyanines: effect of ionic strength of solution. *Russ. Chem. Bull. 53*, 2674−2683.

(38) Sibrian-Vazquez, M., Jensen, T. J., Fronczek, F. R., Hammer, R. P., and Vicente, M. G. H. (2005) Synthesis and characterization of positively charged porphyrin−peptide conjugates. *Bioconjugate Chem. 16*, 852−863.

(39) (a) Greenwald, R. B. (2001) PEG drugs: an overview. *J. Controlled Release 74*, 159−171. (b) Hamblin, M. R., Miller, J. L., Rizvi, I., Ortel, B. Maytin, E. V., and Hasan, T. (2001) Pegylation of a chlorin(e_6) polymer conjugate increases tumor targeting of photosensitizer. *Cancer Res. 61*, 7155−7162. (c) Greenwald, R. B., Choe, Y. H., McGuire, J., and Conover, C. D. (2003) Effective drug delivery by PEGylated drug conjugates. *Adv. Drug Delivery Rev. 55*, 217−250. (d) Kim, Y. S., Song, R., Hyun Kim, D., Jun, M. J., and Sohn, Y. S. (2003) Synthesis, biodistribution and antitumor

activity of hematoporphyrin-platinum(II) conjugates. *Bioorg. Med. Chem. 11*, 1753−1760.

(40) Roberts, M. J., Bentley, M. D., and Harris, J. M. (2002) Chemistry for peptide and protein PEGylation *Adv. Drug Delivery Rev. 54*, 459−476.

(41) (a) Fontes, M. R. M., Teh, T., and Kobe, B. (2000) Structural basis of recognition of monopartite and bipartite nuclear localization sequences by mammalian importin-α. *J. Mol. Biol. 297*, 1183−1194. (b) Fontes, M. R. M., Teh, T., Jans, D., Brinkworth, R. I., and Kobe, B. (2003) Structural basis for the specificity of bipartite nuclear localization sequence binding by importin-α. *J. Biol. Chem. 278*, 27981−27987.

(42) Loret, E. P., Vives, E., Pui Shing Ho, P. S., Rochat, H., van Rietschoten, J., and Johnson, W. C., Jr. (1991) Activating region of HIV-1 Tat protein: vacuum UV circular dichroism and energy minimization. *Biochemistry 30*, 6013−6023.

(43) (a) Ogunsipe, A., Maree, D., and Nyokong, T. (2003) Solvent effects on the photochemical and fluorescence properties of zinc phthalocyanine derivatives. *J. Mol. Struct. 650*, 131−140. (b) Ogunsipe, A., Chen, J. Y., and Nyokong, T. (2004) Photophysical and photochemical studies of zinc(II) phthalocyanine derivatives - effects of substituents and solvents. *New J. Chem. 28*, 822−827. (c) Ogunsipe, A., and Nyokong, T. (2005) Photophysical and photochemical studies of sulphonated non-transition metal phthalocyanines in aqueous and non-aqueous media. *J. Photochem. Photobiol., A 173*, 211−220.

(44) Savitsky, A. P., and Lopatin, K. V. (1992) pH Dependence of fluorescence and absorbance spectra of free sulphonated aluminium phthalocyanine and its conjugate with monoclonal antibodies. *J. Photochem. Photobiol., B 13*, 327−333.

(45) (a) Dhami, S., Demello, A. J., Rumbles, G., Bishop, S. M., Phillips, D., and Beeby, A. (1995) Phthalocyanine fluorescence at high concentration - dimers or reabsorption effect. *Photochem. Photobiol. 61*, 341−346. (b) Howe, L., and Zhang, J. Z. (1997) Ultrafast studies of excited-state dynamics of phthalocyanine and zinc phthalocyanine tetrasulfonate in solution. *J. Phys. Chem. A 101*, 3207−3213.

(46) (a) Hornung, R., Fehr, M. K., Monti-Frayne, J., Tromberg, B. J., Berns, M. W., and Tadir, Y. (1999) Minimally-invasive debulking of ovarian cancer in the rat pelvis by means of photodynamic therapy using the pegylated photosensitizer PEG-m-THPC. *Br. J. Cancer 81*, 631−637. (b) Hornung, R., Fehr, M. K., Walt, H., Wyss, P., Berns, M. W., and Tadir, Y. (2000) PEG-m-THPC-mediated photodynamic effects on normal rat tissues. *Photochem. Photobiol. 72*, 696−700. (c) Kanofsky, J. R. (1990) Quenching of singlet oxygen by human plasma. *Photochem. Photobiol. 51*, 299−303.

(47) (a) Futaki, S., Suzuki, T., Ohashi, W., Yagami, T., Tanaka, S., Ueda, K., and Sugiura, Y. (2001) Arginine-rich peptides. An abundant source of membrane-permeable peptides having potential as carriers for intracellular protein delivery. *J. Biol. Chem. 276*, 5836−5840. (b) Mitchell, D. J., Kim, D. T., Steinman, L., Fathman, C. G., and Rothbard, J. B. (2000) Polyarginine enters cells more efficiently than other polycationic homopolymers. *J. Pept. Res. 56*, 318−325.

(48) (a) Wood, S. R., Holroyd, J. A., and Brown, S. B. (1997) The subcellular localization of Zn(II) phthalocyanines and their redistribution on exposure to light. *Photochem. Photobiol. 65*, 397−402. (b) Peng, Q., Farrants, G. W., Madslien, K., Bommer, J. C., Moan, J., Danielsen, H. E., and Nesland, J. M. (1991) Subcellular localization, redistribution, and photobleaching of sulfonated aluminium phthalocyanines in human melanoma cell line. *Int. J. Cancer 49*, 290−295. (c) Ruck, A., Kollner, T., Dietrich, A., Strauss, W., and Schneckenburger, H. (1992) Fluorescence formation during photodynamic therapy in the nucleus of cells incubated with cationic and anionic water-soluble photosensitizers. *J. Photochem. Photobiol., B 12*, 403−412. (d) Freeman, T. L., Cope, S. E., Stringer, M. R., Cruse-Sawyer, J. E., Brown, S. B., Batchelder, D. N., and Birbeck, K. (1998) Investigation of the subcellular localization of zinc phthalocyanines by raman mapping. *Appl. Spectrosc. 52*, 1257−1263. (e) Peng, Q. (2001) Correlation of intracellular and intratumoral photosensitizer distribution with photodynamic effect. In *Photodynamic therapy and fluorescence diagnostic in dermatology*, Comprehensive Series in Photosciences, pp 55−66.

(49) (a) Ferri, K. F., and Kroemer, G. (2001) Organelle-specific initiation of cell death pathways. *Nat. Cell Biol. 1*, E255−E263. (b) Ogata, M., Inanami, O., Nakajima, M., Nakajima, T., Hiraoka, W., and Kuwabara, M. (2003) Ca^{2+}-dependent and caspase-3−independent apoptosis caused by damage in Golgi apparatus due to 2,4,5,7-tetrabromorhodamine 123 bromide−induced photodynamic effects. *Photochem. Photobiol. 78*, 241−247. (c) Teiten, M-H., Bezdetnaya, L., Morliere, P., Santus, R., and Guillemin, F. (2003) Endoplasmic reticulum and Golgi apparatus are the preferential sites of Foscan localisation in cultured tumour cells. *Br. J. Cancer 88*, 146−152.

(50) Berg, K., and Moan, J. (1997) Lysosomes and microtubules as targets for photochemotherapy of cancer. *Photochem. Photobiol. 65*, 403−409. (b) Ricchelli, F., Franchi, L., Miotto, G., Borsetto, L., Gobbo, S., Nikolov, P., Bommer, J. C., and Reddi, E. (2005) Meso-substituted tetra-cationic porphyrins photosensitize the death of human fibrosarcoma cells via lysosomal targeting. *Int. J. Biochem. Cell Biol. 37*, 306−319.

BC060297B

Induction of RNase H Activity by Arabinose−Peptide Nucleic Acid Chimeras

Bénédicte M. Pâtureau,[†] Robert H. E. Hudson,*[,‡] and Masad J. Damha*[,†]

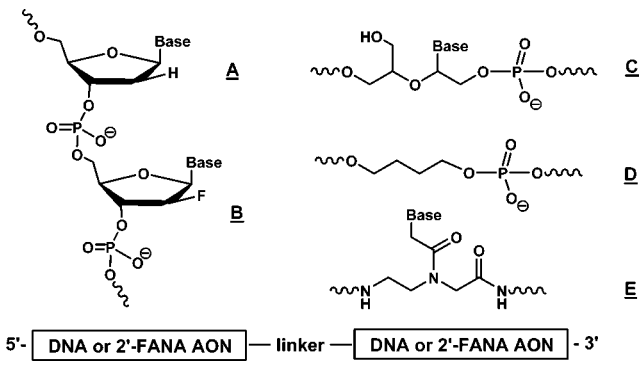
Department of Chemistry, McGill University, Montreal, Quebec, Canada H3A 2K6, and Department of Chemistry, The University of Western Ontario, Ontario, Canada N6A 5B7. Received September 25, 2006; Revised Manuscript Received November 27, 2006

We report the syntheses of chimeras of peptide nucleic acid (PNA) with DNA and 2′-deoxy 2′-fluoroarabinonucleic acid (2′-FANA). Chimeric oligomers possessing a single central PNA insert were capable of forming hybrid duplexes with complementary RNA, although with diminished thermal stability in comparison to the unmodified oligomers. We subsequently determined the ability of the DNA and 2′-FANA oligomers of mixed-base composition to elicit human RNase H1 degradation of complementary RNA that was either unstructured or as a hairpin. In the case of the more rigid FANA strand, a PNA insert led to a higher ability of the chimera to direct the degradation of both types of RNA targets. Generally, the enhancement observed was greater for a butanediol linker than for a more rigid PNA linker. Along with previous work, these studies suggest that the general flexibility associated with an acyclic insert (e.g., butyl vs PNA)—and not necessarily the presence of local structural imperfections in the heteroduplex—is beneficial for RNase H1 activity. As well, there are implications to the charge nature of non-nucleotide inserts (neutral vs negative) and their ability to maintain RNase H activity that may serve to direct further design considerations. Together, these studies support the notion that flexibility of antisense oligonucleotide (AON)/RNA hybrids is essential for high RNase H catalysis, in which an enzyme-induced altered trajectory of the bound AON/RNA substrate could facilitate optimal interaction with the catalytic site of RNase H.

INTRODUCTION

The ability of antisense oligonucleotides (AONs) to specifically bind to a single-stranded RNA via Watson−Crick complementary hybridization represents an attractive and increasingly important practical strategy for inhibition of gene expression. AONs are short, chemically modified oligonucleotide sequences designed to possess good exo- and endonuclease resistance, sufficient cell penetration, and good affinity for the target mRNA (*1*). An attractive mechanism for suppression of gene expression involves specific mRNA hydrolysis via activation of the ubiquitous intracellular enzyme RNase H (*2*). Although the origins of the substrate specificity of RNase H are not well-defined yet, structural analysis of modified AONs capable of eliciting this enzyme highlights a common feature: an O4′-*endo* sugar pucker that leads to the formation of a helical conformation intermediate between pure A- and B-forms (*3*, *4*). The discovery that [3.3.0]*bc*-ANA satisfies the conformational requirement for RNase H recognition and cleavage, without activating this enzyme, revealed the importance of flexibility within the AON strand (*3*, *5*). We therefore hypothesized that both preorganization and flexibility are two important criteria for the ability of an AON to elicit RNase H activity and thus for their therapeutic potential (*6*). This prompted us to examine the properties of known RNase H-active AONs such as DNA and 2′-FANA containing acyclic 2′,3′-secouridine (Chart 1**C**) or butanediol (**D**) linkers (*6*). 2′-FANA AONs incorporating a butyl linker showed RNase H induction with comparable efficiency to the native DNA strands, a result that is further supported by the present study. Unfortunately, a substantial decrease in the thermal stability imparted by the flexible, abasic linker, reduces its practical utility in AONs.

Chart 1[a]



[a] Top: Chemical structure of modified oligonucleotides. **A**, DNA; **B**, 2′-FANA; **C**, 2′,5′-secouridine residue; **D**, butanediol linker; **E**, peptide nucleic acid. Bottom: AON design.

Thus, we next turned our attention to a peptide nucleic acid (PNA) linker (Chart 1**E**) (*7*), which, due to the presence of an amide bond, is rendered comparably less flexible than the hydrocarbon linkers previously examined by our group (*6*), and conceivably more likely to engage in interactions with the opposing RNA residue of the formed heteroduplex. As a PNA insert also possesses an acyclic structure, and therefore some inherent flexibility relative to the native furanose framework, we surmised that its introduction in place of an aliphatic linker within the AON strand might also result in elevated RNase H activity. In the present work, we evaluate the affinity of DNA and 2′-FANA oligonucleotides containing one or three PNA inserts toward complementary DNA and RNA and compare their ability to elicit RNase H1 to native and butyl-modified AON oligonucleotides. This allowed us to assess the charge nature of non-nucleotide inserts (neutral vs negative) and their impact on RNase H activity.

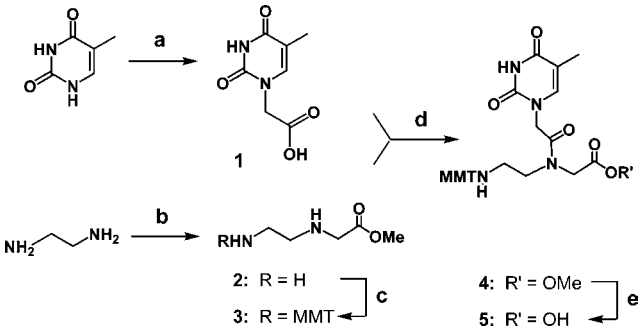
* Authors to whom correspondence should be sent: masad.damha@mcgill.ca, robert.hudson@uwo.ca.

[†] McGill University.

[‡] The University of Western Ontario.

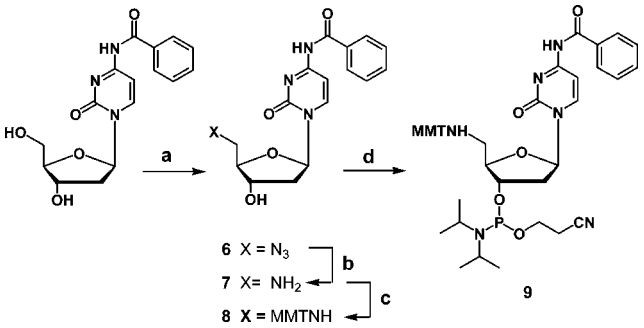
10.1021/bc060300r CCC: $37.00 © 2007 American Chemical Society
Published on Web 01/18/2007

Scheme 1[a]



[a] Reagents: (a) $ClCH_2CO_2H$, $NaOH/H_2O$, Reflux (85%); (b) $ClCH_2CO_2H$, 4 °C, (51%, 2 Steps); (c) MMT−Cl, CH_2Cl_2, $NEt(i\text{-}Pr)_2$, Overnight (50%, after Chromatography); (d) DCC, 24 h (65%); (e) 1M NaOH, 0 °C, (75%).

Scheme 2[a]



[a] Reagents: (a) PPh_3, NaN_3, CBr_4, Dry DMF, Overnight (80%); (b) PPh_3, Pyridine, H_2O, 3 h; (c) MMT−Cl, 4-DMAP Pyridine, Overnight (30% over Two Steps); (d) $Cl-P(OCE)N(i\text{-}Pr)_2$, DIPEA, THF, 2.5 h (80%).

EXPERIMENTAL PROCEDURES

Synthesis of Monomers. The *N*-(2-aminoethyl)glycine-based thymine PNA monomer was prepared according to literature precedent with minor modifications to the procedures (Scheme 1) (*8*−*12*). 2′-FANA phosphoramidites were synthesized according to established procedures (*13*) and DNA phosphoramidites purchased from ChemGenes Corp. (Ashland, MA) were used as received. The 5′-amino-dC derivative required for the PNA insertion was synthesized as described in Scheme 2). All standard 5′-*O*-dimethoxytrityl-3′-*O*-(2-cyanoethyl)-*N*,*N*-diisopropylphosphoramidites of the various 2′-deoxy- and ribonucleosides, 5′-monomethoxytritylamino-2′,5′-dideoxythymidine-3′-phosphoramidite, and the phosphitylation reagent used for derivatization [*β*-cyanoethyl-(*N*,*N*-diisopropylamino) phosphorchloridite] were purchased from ChemGenes Corp. (Ashland, MA).

Synthesis of Thymin-1-yl Acetic Acid (1). Thymin-1-yl acetic acid was prepared as previously described (*8*). Briefly, thymine (10.0 g, 79.0 mmol) was dissolved in 100 mL of water, by heating to reflux, which contained 9.0 g (160 mmol) of KOH. To this solution was slowly added chloroacetic acid (7.6 g, 80 mmol) dissolved in 25 mL of water. The pH was maintained at approximately 10 while the solution was refluxed for 2 h. Upon acidification with concd HCl, the acid (**1**) precipitated (12.4 g, 85%) and was subsequently carefully recrystallized from water. Mp 260−262 °C. EI MS: calcd 184.15, found 184 (M^+, 40%), 140 ($-CO_2$, 50%), 96 (100%).^{1}H NMR (400 MHz, DMSO-d_6): 13.10 (br s, 1H), 11.33 (s, 1H), 7.49 (s, 1H), 4.35 (s, 2H), 1.74 (s, 3H). ^{13}C NMR (100 MHz, DMSO-d_6): 169.9, 164.6, 151.3, 142.2, 142.0, 108.6, 48.7.

Methyl *N*-(2-Aminoethylglycinate)dihydrochloride (2). *N*-(2-Aminoethyl)glycine was prepared according to the method of Heimer et al. (*9*). Neat ethylenediamine (500 mL, 7.5 mol) was rapidly stirred while being cooled in an ice bath (4 °C). Solid chloroacetic acid (75 g, 0.79 mol) was added in ten portions allowing for complete dissolution between each addition. The reaction mixture was then stirred overnight at room temperature. The unreacted ethylenediamine was removed by evaporation under vacuum and later recycled. The remaining paste was triturated with DMSO and then filtered, and the solid cake was washed with DMSO and then diethyl ether. The white solid was of sufficient purity to carry on to the next step without recrystallization (51 g, 55%). Recrystallization may be done in methanol to give white plates, mp 159−161 °C. ^{1}H NMR (400 MHz, D_2O): 3.03 (s, 2H), 2.79 (app t, J = 6.5 Hz, 2H), 2.66 (app t, J = 6.5 Hz, 2H). ^{13}C NMR (100 MHz, D_2O): 177.9, 51.3, 46.2, 38.3. Compound **2** was prepared by Fischer esterification of the parent acid (*11*). *N*-(2-Aminoethyl)glycine (15.0 g, 127 mmol) was suspended in 700 mL of methanol that was saturated with gaseous, dry HCl. The mixture was refluxed for 12 h, and the product was collected at room temperature. Subsequent crops were obtained by cooling the mother liquor to −20 °C and again by reducing the volume and cooling. Yield: 24 g, 92%. Mp 190−192 °C. ^{1}H NMR (400 MHz, DMSO-d_6): 8.58 (br s, 3H), 4.05 (s, 2H), 3.68 (s, 3H), 3.26 (m, 2H), 3.18 (m, 2H). ^{13}C NMR (100 MHz, DMSO-d_6): 166.9, 52.8, 46.7, 44.0, 35.0.

Methyl *N*-(2-Monomethoxytritylaminoethylglycinate) (3) (*10*, *11*). Methyl *N*-(2-aminoethylglycinate) dihydrochloride (1.0 g, 4.9 mmol) was stirred in 20 mL of CH_2Cl_2 containing 1 mL of Hünig's base while being cooled in an ice bath (4 °C). To this slurry was dropwise added a solution of 1.2 equiv of monomethoxytrityl chloride (1.8 g, 5.8 mmol) in CH_2Cl_2. The mixture was stirred for 12 h at room temperature, after which the reaction was quenched by the addition of 5 mL CH_3OH, diluted with 100 mL of CH_2Cl_2 and was extracted (3 × 100 mL sat $NaHCO_3$, 3 × 100 mL brine), dried (anhydrous sodium sulfate), and the solvent was evaporated to yield a sticky off-white foam. TLC analysis (2:1 diethyl ether, hexanes with 1% NEt_3) was done with silica gel plates that had been pretreated with eluent and indicated the presence of monomethoxytritanol and methyl monomethoxytrityl ether, as well as unreacted started material as likely impurities. The desired product was visualized by UV shadowing, staining with HCl vapor and ninhydrin. R_f = 0.16. Isocratic silica gel column chromatography was done (60:30:1 diethyl ether/hexanes/triethylamine) to yield a viscous yellow oil (50%), as previously reported (*11*). ^{1}H NMR (400 MHz, $CDCl_3$): 7.47−6.79 (m, 14H), 3.77 (s, 3H), 3.71 (s, 3H), 3.48 (s, 2H), 2.73 (t, J = 5.6 Hz, 2H), 2.27 (t, J = 5.6 Hz, 2H), 1.89 (br s, 2H).

Methyl *N*-(2-Monomethoxytritylaminoethyl)-*N*-(thymin-1-yl) Glycinate (4). Compounds **1** and **3** were condensed to give the PNA monomer ester. Equimolar amounts of **1** (166 mg, 0.9 mmol), DCC, and HOBt were dissolved in dry DMF (3 mL) and stirred for 30 min. After the appearance of a heavy white precipitate (DCU), a solution of **3** (125 mg, 0.3 mmol) in 2 mL of DMF which contained a catalytic amount of 4-DMAP was added dropwise. The suspension was stirred for 1 h; then, 2 equiv Hünig's base was added, and stirring was continued for an additional 12 h, after which time TLC analysis (as above) indicated complete consumption of **3**. The mixture was then filtered to remove the DCU and diluted with 100 mL of CH_2Cl_2 and extracted (3 × 100 mL sat $NaHCO_3$, 2 × 100 mL brine). After drying (Na_2SO_4), removal of the solvent by evaporation gave a crude product that was purified, without chromatography, by precipitation of an ethereal solution with hexanes (65% yield). Two rotamers were observed: major (ma.) and minor (mi.). ^{1}H NMR (400 MHz, DMSO-d_6): 11.32 (br s, 1H), 7.41−6.84 (m, 15H), 4.84 (ma.) and 4.53 (mi.) (s, 2H),

4.46 (mi.) and 4.09 (ma.) (s, 2H), 3.72 (s, 3H), 3.69 (mi.) and 3.58 (ma.) (s, 3H), 3.49 (ma.) and 3.37 (mi.) (m, 2H), 2.15 (ma.) and 2.08 (mi.) (m, 2H), 1.76 (s, 3H).

***N*-(2-Monomethoxytritylaminoethyl)-*N*-(thymin-1-yl)-glycine (5)** (*12*). Compound **4** was hydrolyzed to the free acid by treatment for 1 h with equal volumes of 2 M NaOH and methanol at 4 °C. The pH of the solution was then adjusted to 4−5 by dropwise addition of aqueous NaH_2PO_4 and the title compound isolated by repeated extraction into ethyl acetate. The organic fractions were pooled, dried over anhydrous sodium sulfate, and the solvent was removed by evaporation to yield a white solid. The crude product was purified by repeated trituration with diethyl ether, and the purified product was consistent with previous reports and isolated in 75% yield (*12*). Two rotamers were observed: major (ma.) and minor (mi.). ^{1}H NMR (400 MHz, DMSO-d_6): 11.31 (s, 1H), 6.8−7.4 (m, 15H), 4.81 (ma.) and 4.50 (mi.) (s, 2H), 4.30 (mi.) and 3.92 (ma.) (s, 2H), 3.71 (s, 3H), 3.33 (ma.) and 3.15 (mi.) (m, 2H), 2.15 (ma.) and 2.09 (mi.) (m, 2H), 1.74 (s, 3H). Alternatively, the triethylammonium salt was prepared by saponification with 2 M aqueous NEt_3, 48 h at room temperature. The water was removed by evaporation under vacuum with gentle warming, and the excess triethylamine was removed by repeated coevaporation with absolute ethanol, ethyl acetate, and then dichloromethane.

Synthesis of 5′-Azido-2′,5′-dideoxy-N^4-benzoylcytidine (6) (*14*). N^4-Benzoyl-2′-deoxycytidine (1.0 g, 3.02 mmol), PPh_3 (80 mg, 3.08 mmol), NaN_3 (33 mg, 5.13 mmol), and CBr_4 (1.02 g, 3.08 mmol) were separately dried in a vacuum desiccator over P_2O_5 overnight. The following were then combined and dissolved in 15 mL of anhydrous DMF: N^4-benzoyl-2′-deoxycytidine, PPh_3, and NaN_3. CBr_4 was promptly added, and the reaction was stirred under a nitrogen atmosphere for 26 h at room temperature. The reaction was quenched by the addition of 3 mL of MeOH, and stirring was continued for 1 h. The solvent was then removed under vacuum, and the crude material was flash purified by silica gel chromatography using 5% methanol/dichloromethane to afford the desired product **1** as a white foam with a yield of 70% (0.75 g). TLC: $R_f = 0.43$ in 9:1 (v/v) dichloromethane/methanol. FAB-MS (NBA matrix): calcd [M + Na$^+$] 379.34, found 379. ^{1}H NMR (400 MHz, DMSO-d_6) of 5′-azido-2′,5′-dideoxy-N^4-benzoylcytidine: 11.3 (s, 1H, N−H), 8.2 (d, 1H, $J_{5,6} = 7.7$ Hz, H-6), 8.0 to 7.4 (m, 6H, H-5 and Bz), 6.2 (dd, 1H, $J_{1',2'} = 6.7$ Hz, $J_{1',2''} = 6.4$ Hz, H-1), 5.5 (d, 1H, $J_{OH,3'} = 4.2$ Hz, OH), 4.2 (m, 1H, H-3′), 4.0 (m, 1H, H-4′), 3.6 (m, 2H, H-5′ and H-5″), 2.3 (m, 1H, H-2′), 2.2 (m, 1H, H-2″).

Synthesis of 5′-Amino-2′,5′−dideoxy-N^4-benzoylcytidine (7) (*15*). Dry 5′-azido-2′,5′-dideoxy-N^4-benzoylcytidine (**6**; 356 mg, 1.0 mmol) was dissolved in 5 mL of anhydrous pyridine, and to the stirred solution was added 0.3 g PPh_3. After 3 h, 1 mL of water was added and stirring was continued for 2 h, at which time another 1 mL aliquot of water was added and the resulting precipitate was filtered, removing the PPh_3 and $Ph_3P{=}O$. The water/pyridine solution was extracted three times with 5 mL ethyl acetate, and the aqueous solution lyophilized to afford crude **7**. For characterization purposes, the N^4-benzoyl group was removed as follows (*16*). A small amount of **7** (220 mg, 0.6 mmol) was dissolved in a mixture containing 2.5 mL of pyridine and 2.5 mL of concentrated NH_4OH, and stirred overnight at 60 °C, after which the solution was cooled on ice and evaporated. The residue was partitioned between 15 mL of H_2O and 1.5 mL of EtOAc. The aqueous layer was extracted, washed with Et_2O (3 × 3 mL) and EtOAc/Et_2O (1:2 v/v, 2 × 5 mL), and lyophilized to afford 5′-amino-2′,5′-dideoxycytidine in 98% yield (190 mg). FAB-MS (NBA-matrix): calcd [M + Na$^+$] 249.22, found 249.0. ^{1}H NMR (270 MHz, DMSO-d_6) of 5′-amino-2′,5′-dideoxycytidine: 7.7 (d, 1H, $J_{5,6} = 7.4$ Hz, H-6), 7.15 (br s, 1H, NH_2), 6.1 (t, 1H, $J_{1',2'} = 7.17$ Hz, $J_{1',2''} = 6.43$ Hz, H-1′), 5.7(d, 1H, $J_{5,6} = 7.17$ Hz, H-5), 5.2 (br s, 3H, NH_2 and OH), 4.1 (m, 1H, H-3′), 3.7 (m, 1H, H-4′), 2.7 (m, 2H, H-5′ and H-5″), 2.1 (m, 1H, H-2′), 2.0 (m, 1H, H-2″).

Synthesis of 5′-MMTNH-2′,5′-dideoxycytidine-N^4-benzoylcytidine (8) (*8*). Compound **7** (226 mg, 1 mmol) was coevaporated twice with 20 mL dry pyridine and dissolved in 5 mL dry pyridine. MMT−Cl (460 mg, 1.5 mmol) was added and the reaction stirred overnight. When the reaction appeared complete by TLC ($R_f = 0.6$ in 1:9 v/v MeOH/CH_2Cl_2), the mixture was diluted with 50 mL dichloromethane, washed with 50 mL brine, and the organic layer dried (sodium sulfate), filtered, and evaporated to obtain the crude product. The crude product was dissolved in a minimal amount of dichloromethane and purified by flash silica gel chromatography (eluant: dichloromethane, then 19:1 (v/v) dichloromethane/methanol with 3−5 drops of TEA to prevent removal of the trityl group due to acidity of the silica) to afford the desired product **8** as white foam with a yield of 30% (180 mg). FAB-MS (NBA matrix): calcd [M + Na$^+$] 625.68, found 625.3. ^{1}H NMR (400 MHz, DMSO-d_6) of 5′-MMTNH-2′,5′-dideoxycytidine-N^4-benzoylcytidine: 11.5 (s, 1H, N−H), 8.1 to 7.1 (m, 16H, H-6, H-5 and MMTr), 6.1 (t, 1H, $J_{1',2'} = 6.4$ Hz, $J_{1',2''} = 6$ Hz, H-1′), 5.2 (d, 1H, $J_{OH,3'} = 4.8$ Hz), 4.1 (m, 1H, H-3′), 3.9 (m, 1H, H-4′), 3.7 (s, 3H, CH_3O−), 2.7 (t, 2H, $J_{NH,5'} = 8$ Hz, $J_{NH,5''} = 8$ Hz), 2.4 (m, 1H, H-5″), 2.2 (m, 2H, H-5′ and H-2″), 2.0 (m, 1H, H-2′).

Synthesis of 5′-MMTNH-2′,5′-dideoxycytidine-N^4-benzoylcytidine phosphoramidite (9). Compound **8** (73.2 mg, 0.12 mmol) was dissolved in 2 mL of anhydrous THF and the flask purged with argon. While stirring, 0.076 mL (0.44 mmol) double-distilled *N*-ethyl-*N*,*N*-diisopropylamine (DIPEA) was added, followed by the slow addition of 0.03 mL (0.14 mmol) 2-cyanoethyl-*N*,*N*-diisopropylchlorophosphoramidite. The reaction mixture was stirred until complete consumption of starting material was observed (2.5 h). The reaction progression was monitored by silica plate TLC which employed 1:19 (v/v) methanol/dichloromethane as the mobile phase. TLC: $R_f = 0.4$ and 0.47 (corresponding to two isomers). After evaporating the mixture to dryness, the crude material was dissolved in a minimum amount of dichloromethane. The chromatography column was preconditioned with 20:80 (v/v) dichloromethane/hexane and 1% TEA, and the pure compound was eluted following a stepwise gradient of dichloromethane/hexane until a 1:1 ratio was reached. The pure fractions of the two isomers were combined, concentrated on a rotatory evaporator, and dried under high vacuum to obtain a stable foam following coevaporation with diethyl ether. FAB-MS (NBA matrix): [M + Na$^+$] calcd 825.9, found 825. ^{31}P NMR (270 MHz, acetone-d_6): 153.9 and 153.8.

Oligonucleotide Synthesis. DNA and 2′-FANA oligonucleotides containing PNA inserts were prepared as previously described (*17*−*19*), purified by PAGE or anion exchange HPLC, and characterized by MALDI-TOF mass spectrometry (Kratos MS25RFA instrument) (Table 1). Sequences of all the oligonucleotides studied are listed in Table 2.

UV Thermal Denaturation Measurements. Thermal denaturation profiles were obtained on a Varian CARY 300 UV−vis spectrophotometer. Prior to experiments, equimolar solutions of AON and target DNA or RNA oligonucleotides were mixed in a buffer consisting of 140 mM KCl, 1 mM $MgCl_2$, and 5 mM Na_2HPO_4 (pH 7.2). The duplex concentration was close to 2 μM. Samples were heated at 95 °C for 10 min and then cooled slowly to room temperature and finally stored overnight at 4 °C to permit annealing. The solutions were gradually heated (0.5 °C/min) and the UV absorbance measured at 260 nm after

Table 1 [a]

entry	sequences 5′ → 3′ [b]	calcd mass (g·mol^{-1})	obsd mass (g·mol^{-1})	obsd molecular ion
I	ttt ttt ttt ttt ttt ttt	5413.6	5412.3	$(M-H)^-$
II	ttt ttt ttt ttt tPt*t ttt	5678.6	5708.3	$(M-H+Li+Na)^-$
III	ttt ttt ttP t*tt ttt ttt	5374.4	5369.0	$(M-H)^-$
VI	tta tat ttt Pt*c ttt ccc	5332.4	5350.4	$(M-H+2Li)^-$
VII	tta tat tPP Pt*c ttt ccc	5255.9	5315.8	$(M-H+K+Na)^-$
XII	att ccg tca Pc*g ctc ctc	5306.5	5307.2	$(M-H)^-$
XV	**ATT CCG TCA Pc*G CTC CTC**	5610.5	5613.3	$(M-H)^-$

[a] Matrix: 1 μL of saturated ATT/spermine solution, 1 μL fucose solution, and 1 μL autoclaved deionized water. [b] Bold uppercase, 2′-FANA nucleotides; uppercase letters, ribonucleotides; lowercase letters, deoxynucleotides; P, peptide nucleic acid; t*, 5′-amino-2′,5′-dideoxythymidine; c*, 5′-amino-2′,5′-dideoxycytidine. For characterization of oligomers XIII and XVI, see ref 6.

Table 2. Melting Temperatures (T_m) of the AON/RNA Heteroduplexes[a]

entry	sequences 5′ → 3′ [b] (composition)	T_m (°C) DNA target	T_m (°C) RNA target	ΔT_m (°C) DNA target	ΔT_m (°C) RNA target
		Homopolymeric			
I	ttt ttt ttt ttt ttt ttt	45	36.5		
II	ttt ttt ttt ttt Pt*t ttt	35.5	27	−9.5	−9.5
III	ttt ttt ttP t*tt ttt ttt	35	31	−10	−5.5
IV[c]	ttt ttt ttt Btt ttt ttt				−6
		Mixed Base			
V	tta tat ttt ttc ttt ccc	47.5	48.5		
VI	tta tat ttt Pt*c ttt ccc	34.5	38	−13	−10.5
VII	tta tat tPP Pt*c ttt ccc	15.0	38.5	−32.5	−10
VIII	tta tat ttt ctc ttt ccc	36.5	40	−11	−8.5
IX	tta tat tcc ctc ttt ccc	n.d.	28.5	n.d.	−20
X[c]	tta tat ttt Btc ttt ccc				−5
		Ha-*ras*			
XI	att ccg tca tcg ctc ctc	n.d	72		
XII	att ccg tca Pc*g ctc ctc	n.d	27.5, 55	n.d.	−17
XIII[c]	att ccg tca Bcg ctc ctc		n.d.[c]		−12
		2′-FANA			
XIV	**ATT CCG TCA TCG CTC CTC**	n.d	81		
XV	**ATT CCG TCA Pc*G CTC CTC**	n.d	71.5	n.d.	−9.5
XVI[c]	**ATT CCG TCA BCG CTC CTC**		n.d.[c]		−10

[a] Lowercase letters, deoxynucleotides; uppercase, ribonucleotides; bold uppercase, 2′-FANA nucleotides; underlined, mismatch nucleotide. Target RNA sequences correspond to rA_{18} or 5′-GGG AAA GAA AAA AUA UAA−3′ or for Ha-*ras* sequences, 5′-GAG GAG CGA UGA CGG AAU-3′; target DNA sequences correspond to dA_{18} or 5′-ggg aaa gaa aaa ata taa-3′; P, thymine peptide nucleic acid; t*, 5′-amino-2′,5′-dideoxythymidine; c*, 5′-amino-2′,5′-dideoxycytidine; B, butanediol linker. [b] Aqueous solutions of $\sim 2 \times 10^{-6}$ M of each oligonucleotide, 140 mM KCl, 1 mM $MgCl_2$, 5 mM Na_2HPO_4 buffer (pH 7.2); uncertainty of ±0.5 °C for T_m; n.d. − not determined. [c] Values taken from ref 6.

temperature stabilization. T_m values were calculated using the baseline method and have an uncertainty of ±0.5 °C.

RNase H assays. RNase H1 degradation assays were carried out to monitor the efficiencies of modified duplexes to elicit activity. The temperature at which the assays were run was usually chosen to be 10 °C lower than the determined thermal melting temperature of the least stable hybrid in the series. Whenever possible, assays were performed at 37 °C to simulate intracellular conditions. Generally, 150 pmol of antisense oligonucleotide were mixed with 50 pmol of 5′-^{32}P-labeled RNA in buffer containing 60 mM Tris-HCl (pH 7.8), 60 mM KCl, 2.5 mM $MgCl_2$, and 2 mM dithiothreitol (500 μL final volume). Samples were heated at 90 °C for 10 min and slowly cooled to room temperature to allow the duplexes to form. They were then transferred to a Plexiglass sample holder and left overnight in a freezer at −20 °C. 9 μL aliquots of the solutions were placed in sterile microtube vials and incubated at the assay temperature for at least 1 h prior to initiating enzymatic cleavage reactions.

Determination of Relative Enzyme Acceleration Profiles. Optimal conditions for enzymatic assays were evaluated from a series of preliminary RNase H dilution assays that were prepared as follows: 1 μL aliquot of purified stock enzyme solution was transferred to a microtube and diluted with varying amounts of double-distilled water. When assays were done at suboptimal temperatures (i.e., T < 37 °C), less dilution of the enzyme was necessary. Reactions were initiated in parallel at the specified temperature by addition of purified human RNase H1 (1 μL) in sterile double-distilled water. The resulting mixture was gently mixed by pipeting action and centrifuged to ensure reaction homogeneity and consistency between vials. The enzyme was handled over ice to avoid any loss of activity. Trial runs were performed on two representative test substrates, usually the first and last points (e.g., 5 and 30 min) in the presence of three enzyme dilutions. At the end of the incubation time, samples were quenched with an equal volume of denaturing loading buffer (98% deionized formamide, 10 mM EDTA, 1 mg/mL bromophenol blue (BPB), and 1 mg/mL xylene cyanole (XC)) and vortexed to mix the contents and ensure complete deactivation of the enzyme. The samples were then heated at 90 °C for 5 min to denature the strands and were subsequently loaded onto a 16% polyacrylamide sequencing gel containing 7 M ultrapure urea. Cleavage patterns were analyzed by autoradiography as described below.

Assays were done with the optimized enzyme concentration as determined above. Duplex substrate solutions were made of a 3-fold excess of AON relative to the target RNA strand. Assays were conducted in parallel for a given series. Reactions were initiated by addition of 5 μL of a freshly prepared solution of human RNase H1 in sterile water (diluted as explained above) to each test substrate (45 μL final volume: 4 time points + 1 extra = 5 × 9 μL). 9 μL of the 0 min time point were prepared in a different vial. 10 μL aliquots were taken at five defined times (0, 5, 10, 20, and 30 min) and quenched with an equal volume of loading buffer, followed by heating at 90 °C for 5

min. For Ha-*ras* sequences, reactions were initiated by the addition of 25 μL of freshly prepared human RNase H1 in sterile water (diluted as explained above) to each test substrate (30 μL final volume). 9 μL of the control solution (time = 0 min) were prepared in a different Eppendorf tube. 10 μL aliquots were taken at six defined times (0, 2, 5, 10, 20, and 30 min) and quenched with an equal volume of loading buffer, followed by heating at 90 °C for 5 min. At the completion of the experiment, the samples were heated and then quickly cooled on ice before electrophoretic analysis (16% denaturing PAGE, 1.5−2 h, 2000 V). Gels were prerun for 20 min at 1500 V before loading the samples. Degradation profiles were analyzed by autoradiography and further quantified by densitometric analysis after autoradiography. Quantification of the remaining full-length ^{32}P-RNA signal was obtained by *UN-Scan-It* digitizing software (Silk Scientific, Inc.).

RESULTS AND DISCUSSION

Duplexation Studies. For the homopolymeric sequences shown in Table 2, thermal melting experiments were performed at two wavelengths, 260 and 284 nm, corresponding to the absorbance of duplexes and triplexes, respectively. In the latter case, data obtained at the longer wavelength was primarily undertaken to rule out the existence of triple-helical species in solution (data not shown), which are favored for poly(thymine) PNA oligomers (*7*). Indeed, no transitions characteristic of triple-helical species were observed. T_m data indicative of duplex formation were thus obtained for the modified oligomers at 260 nm (**I**−**III**) and summarized in Table 2.

In assessing the thermal profiles of unmodified and PNA-containing AONs, we observed a significant drop in duplex stability for all modified oligonucleotides investigated. As expected, all oligomers (**I**, **II**, and **III**) showed greater affinity toward dA_{18} than rA_{18}. Surprisingly, we found that the stability of duplexes formed with rA_{18} appear sensitive to the site of modification, whereas the complexes formed with dA_{18} were not. For instance, whether a PNA unit substitutes a nucleotide at position 13 or 9 (numbered from the 5′-end, entries **II** and **III**, Table 2), the destabilization is the same ($\Delta T_m = \sim -10$ °C) when associating with a DNA complement. However, when hybridized with rA_{18} targets, AON **III** (substituted in the middle at position 9) is 4 °C more stable than AON **II** in which the point of substitution is closer to the 3′-end (position 13).

We next turned our attention toward mixed sequences (A/T/C) in order to do a comparative study of duplex stability of oligomers containing either a butanediol (sequence **X**, Table 2) or a PNA linker at position 10 (**VI**, Table 2). We were also interested to see if there was any beneficial additive effect upon the thermal stability of the duplex following the incorporation of three contiguous PNA residues (**VII**). In accord with the observation for homopolymeric sequence **III**, sequence **VI** showed greater destabilization with its complementary DNA target ($\Delta T_m = -13$ °C) as compared to the hybrid formed with RNA ($\Delta T_m = -10.5$ °C). Similar results have been observed by Bergman et al. (*20*). who introduced a single PNA building block in a mixed sequence DNA 13-mer. For the same RNA target, the PNA insertion (**VI**, $\Delta T_m = -10.5$ °C) was less tolerated than a butyl linker (**X**, $\Delta T_m = -5$ °C) (*6*). However, the destabilizing effect was not additive upon incorporation of three contiguous PNA residues (**VII**). In fact, the same decrease was observed for one or three insertions ($\Delta T_m \approx -10$ °C). This is not surprising since PNA−DNA chimeras are known to form stable hybrid duplexes with complementary DNA or RNA (*21*). The stability is dependent upon the overall composition and placement of DNA versus PNA (*22*), such that higher thermal stability is to be expected upon increasing the number of consecutive PNA residues. It is also interesting to note that the selectivity for the RNA complement increased with the insertion of a PNA triad. In fact, AON **VII** binds to its DNA complement very weakly at best (T_m ca. 15 °C, broad transition).

Table 3. Melting Temperatures (T_m) of (PNA)T-G Mismatch Experiments

	target strand[a]		
	RNA (ΔT_m, °C)		DNA (ΔT_m, °C)
AON strand[b]	single mismatch	triple mismatch	single mismatch
VI (single PNA insert)	39 (+1)[c]	n.a.	34 (−0.5)
VII (triple PNA insert)	n.a.	27 °C (−11.5 °C)	n.a.

[a] Target sequences correspond to RNA, in uppercase lettering, single mismatch underlined: 5′-GGG AAA GAG AAA AUA UAA-3′. RNA triple mismatch underlined: 5′- GGG AAA GAG GGA AUA UAA-3′. DNA, in lowercase, single mismatch underlined: 5′-ggg aaa gag aaa ata taa−3′. Aqueous solutions of $\sim 2 \times 10^{-6}$ M of each oligonucleotide, 140 mM KCl, 1 mM $MgCl_2$, 5 mM Na_2HPO_4 buffer (pH 7.2); uncertainty of ±0.5 °C for T_m; n.a. − not applicable. [b] See Table 2. [c] ΔT_m: the difference between the melting temperature of the perfectly matched PNA-containing AON and the hybrids containing one or three mismatches.

To gain further insight into the effect of replacing nucleotides with PNA units and the role of base pairing on the stability of the complexes, we undertook T_m studies with sequences containing one or three base mismatches either opposite or in place of PNA in the duplex (sequences **VI**−**IX**, Tables 2 and 3). First, introduction of a single mismatch in the DNA or RNA target strand opposite the PNA insert in sequence **VI** to yield a duplex with a (PNA)T-G mismatch gave a T_m which was the same as the perfectly matched sequence (Tables 2 and 3). Thus, there is no deleterious effect for a mismatch across from the single PNA insert, and both resulted in the same destabilization of the hybrid relative to the non-PNA-containing strands.

This result implies that the nucleobase of the PNA residue does not contribute to binding in this sequence context, or its base pair is worth no more energetically than the wobble pair available in (PNA)T-G mismatched strand. A possible explanation for lack of base pairing may be that the rigidity of the PNA insert does not permit it to adopt a geometry that allows interstrand hydrogen bonding with the opposing nucleobase in the complementary strand. Interestingly, a single C−A mismatch ($\Delta T_m = -11$ °C) in the mixed sequence **VIII** is less destabilizing than a putative matching PNA insert (**VI**, $\Delta T_m = -13$ °C), which supports the observation that the presence of an amide bond at the PNA−DNA junction is destabilizing (*19*, *23*). Sequence **VII**, which contains three contiguous PNA inserts, demonstrates a large destabilization when hybridized to a complement RNA to give three (PNA)T-G mismatches. The magnitude of the depression of the T_m is similar to that observed for three (DNA)C-A mismatches ($\Delta T_m = -20$ °C, Table 2), when hybridized to an RNA target. This change in T_m is much larger than when **VII** hybridizes to a matched RNA sequence ($\Delta T_m = -11.5$ °C, Table 3), thus indicating that the three PNA nucleobases partially participate to binding with the RNA target. This may be understood on the basis that the insertion of a PNA triad is sufficient to nucleate a structural perturbation that can accommodate nucleobase pairing, whereas a single residue insertion is not. This notion is supported by the similarity in CD spectra of the unmodified DNA/RNA heteroduplex (**V** and complementary RNA) to the spectra of **VI** and **VII** with the same complementary RNA. In addition, the global conformation of either the homopolymeric sequence or 2′-FANA sequence is largely unperturbed by insertion of a single PNA residue, as shown by the CD spectra of these complexes. Only the introduction of a triple PNA(T)-G mismatch showed a strong disruption of the overall morphology evidenced by a dramatic change in the CD spectra.

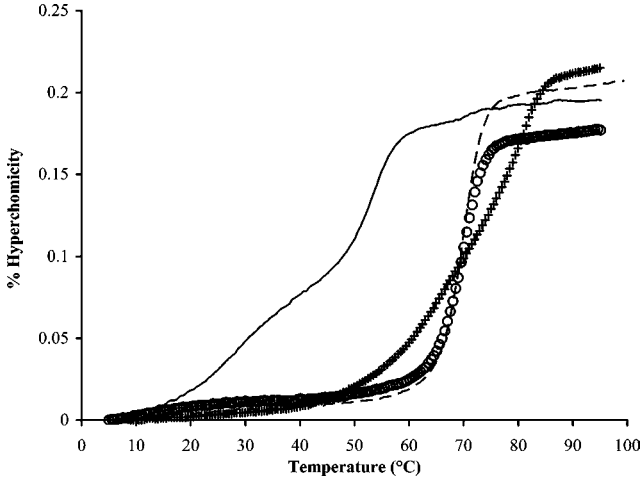


Figure 1. UV thermal melting profiles of 2′-FANA and DNA backbones containing a PNA insert complexed with Ha-*ras* 18-mer RNA. Solid line, **XII**; crosses, **XIV**; dashed line, **XI**; open circles, **XV**.

Finally, we analyzed the impact of the presence of one PNA insert in a more rigid 2′-fluoroarabinonucleic acid (2′-FANA) backbone (**XV**), using the all-DNA sequence for comparison. As expected, 2′-FANA sequence **XIV** showed a greater T_m than the unmodified DNA **XI** (Table 2) that is rationalized on the basis of greater strand preorganization that entropically favors double helix formation (*17*, *24*, *25*). The greater rigidity of the 2′-FANA scaffold may also explain the smaller destabilization that is caused ($\Delta T_m = -9.5$ °C) by a single PNA insert in the middle of the sequence (**XV**) as compared to the DNA analog **XII** ($\Delta T_m = -17$ °C). Furthermore, in contrast with the 2′-FANA counterpart, the melting curve of sequence **XII** presents two clearly distinct melting transitions (Figure 1).

The reason for the biphasic nature of this transition could lie in the fact that 2′-deoxynucleotides are more flexible than 2′-FANA residues and would be more likely to experience greater intrahelical disorder around the PNA domain. The PNA residue possibly creates distortions that prevent one-half of the strand from binding efficiently to the target. Further experiments are needed to investigate this hypothesis. Interestingly, while flanking deoxynucleotides in the AON tolerate PNA inserts poorly in comparison to a butyl linker (sequences **XII** and **XIII**, Table 2, $\Delta T_m = -17$ °C vs -12 °C), 2′-FANA sequences exhibit the same destabilization with either type of insert (**XV** and **XVI**, $\Delta T_m = -9.5$ and -10 °C).

RNase H Assays. The ability of the modified oligonucleotides to elicit human RNase H1 activity when targeted to a structured RNA (e.g., hairpin) or unstructured RNA (random coil) was next evaluated. We first examined the activity of homopolymeric AON **II** and **III** in conjunction with DNA control (**I**) and the sequence containing a butyl insert in position 10 (**IV**). The presence of a PNA linker within the AON strand increases RNase H1 activity compared to control DNA but to a smaller extent than observed with **IV**, which may be attributed to the loss of flexibility imparted by the rigid amide bond. The noted order of RNA degradation within this series is **IV** > **III** > **II** > **I** (Figure 2). Interestingly, sequences **II** and **III**—although relatively less efficient at activating RNase H with respect to central butyl-modified AON **IV**—nonetheless confer the same accelerating trends to their relevant AON−RNA substrates as those described in previous work comparing central vs 3′-terminal butyl insertions on RNase H activity (*6*).

Next, we turned our attention toward mixed sequences with DNA (**V**) as the control and the butyl-containing AON **X** for comparison. As PNA inserts induce some flexibility in the AON strand, and given the previous result with the poly(T) sequences, we expected **VI** to have greater RNase H activity than the DNA

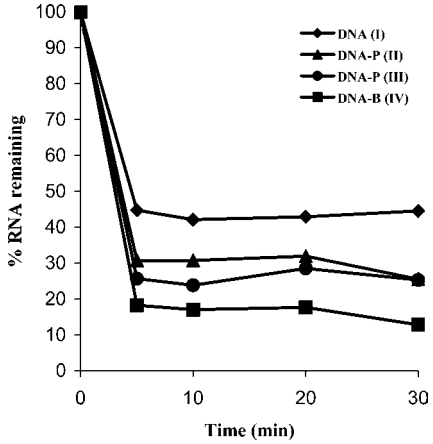


Figure 2. Time course of RNase H1-mediated cleavage of hybrids containing polypyrimidine sequences **I**−**IV** (see Table 1).

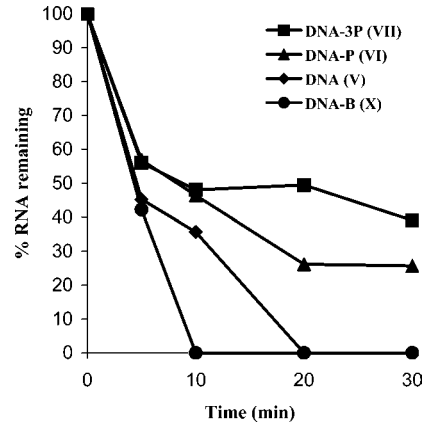


Figure 3. Time course of RNase H1-mediated cleavage of hybrids containing mixed sequences (Table 1).

control. However, hybrids of **VI** with RNA were found to be much less reactive as substrates for RNase H1 than control DNA/RNA. This effect is emphasized in comparison to the control DNA, because this sequence context is inherently a better substrate for RNase H1. Thus, for this sequence, the activity of the control DNA is enhanced by incorporation of a flexible butyl linker and diminished by incorporation of one or three PNA residues. A possible explanation may be that the PNA insert creates a greater local distortion within this duplex, as compared to the butyl linker, and becomes a less acceptable substrate for the enzyme. This idea is supported by the observation that complexes of **VI** with complementary RNA have a lower T_m than their butyl counterpart **X**. However, the thermal destabilizations associated with these two AON sequences likely have different thermodynamic origins, with diminished RNA binding likely owing to the absence of a base pairing partner in the case of butyl inserts, and to an incompatible local conformation in the case of a PNA insert. This effect may also be sequence-dependent, since it was not observed in other studies. Oligonucleotide **VII** is the least reactive of all AONs tested, which is not surprising if we consider that this oligonucleotide tends to adopt the profile of a PNA−DNA chimera, with the latter being less reactive than pure DNA, and first synthesized with the goal of introducing an RNase H-active backbone to the nonreactive PNA domain (*22*). The RNase H1 efficiency observed for each AON is the following: **X** > **V** > **VI** > **VII**; Figure 3.

Finally, we used an in vitro Ha-*ras* model system to evaluate the ability of the DNA−PNA chimera to elicit RNase H1 activity. This RNA species and its associated structure is of particular interest, since hyperactivated forms of point mutant

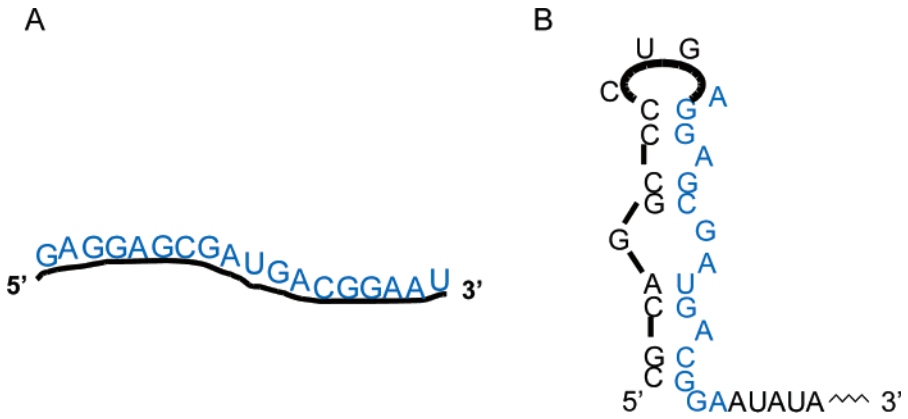


Figure 4. Secondary structures presumably adopted by (A) 18-mer and (B) 40-mer Ha-*ras* RNA. AON binding region is in blue.

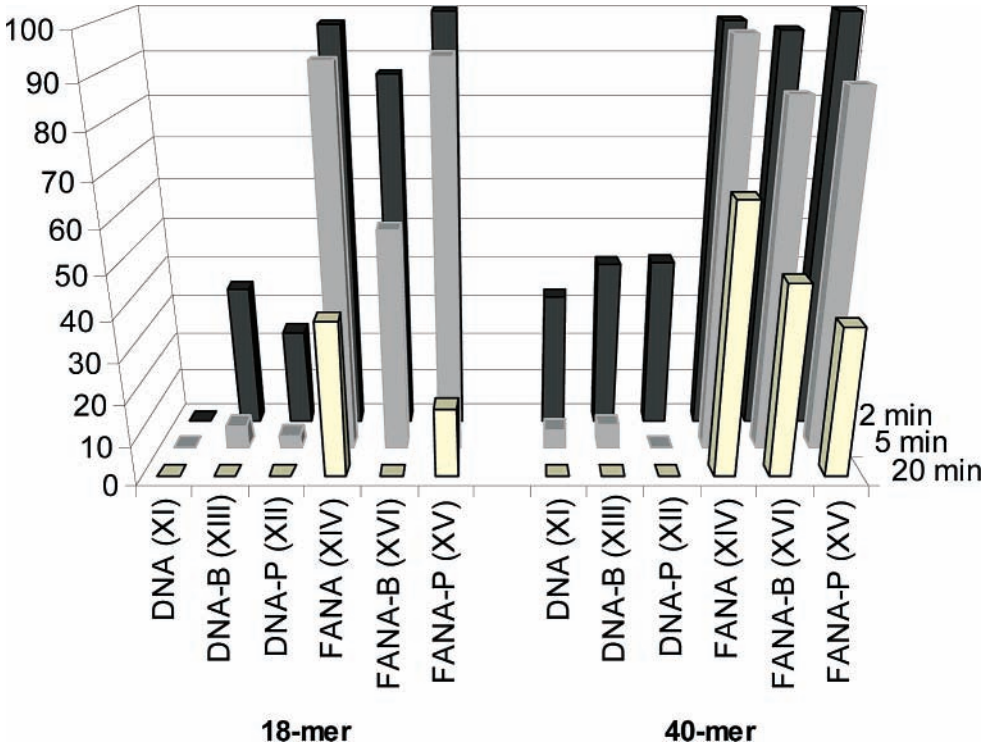


Figure 5. Quantification of the remaining full-length ^{32}P-RNA signal at two time points (20 and 30 min) for the Ha-*ras* RNA targets. For convenience, AONs are identified on the basis of the single inserts wherein B = butyl and P = peptide nucleic acid.

and nonmutated mammalian *ras* protooncogenes are responsible for various human cancers (*26*−*29*), and hence represent a potential therapeutic target. Furthermore, we wished to compare the rate and extent of reactivity of both structured and unstructured RNA targets. As is common in the antisense approach, we believe that RNA cleavage should also depend on the structure, length, and base composition of the target RNA. For this purpose, two oligomers were investigated: an 18-mer and a 40-mer, both of which are complementary to an internal nucleotide region encompassing the translation initiation site of the *ras* gene and corresponding, respectively, to residues −8 to +10 and −19 to +21 of the full-length transcript. The apparent secondary structures of both targets have previously been determined (*6*) using the MFOLD program (*30*, *31*) and supported by UV thermal profiles. No intramolecular association was observed for the 18-mer target, whereas the 40-mer was capable of self-associating into a stable 25 nucleotide hairpin structure (*6*) (Figure 4).

The ability of PNA-containing Ha-*ras* sequences (**XII**) to activate human RNase H1 was evaluated in conjunction with butyl-containing Ha-*ras*-DNA (**XIII**) and 2′-FANA sequences (**XV**, **XVI**), as well as DNA (**XI**) and 2′-FANA (**IX**) control AONs (Figure 5). The linker-containing DNA AON (**XIII**) did not enhance target degradation, which is consistent with the work of other groups (*32*, *33*).

Obviously, target accessibility is an important determinant in the ability of the AONs studied to elicit RNase-H-mediated cleavage of the RNA. For the 18-mer unstructured RNA target, complete disappearance was observed after 20 min when in the presence of complementary DNA or the butyl linker containing 2′-FANA (**XVI**), whereas the structured 40-mer target was ∼30% intact when treated with the most active oligomers **XVI** or **XV** (Figure 6). In fact, all the FANA AONs were less effective at mediating RNase H1 directed destruction of the structured RNA target as compared to the same oligomers tested against the 18-mer unstructured target. The best modified AON for the 18-mer target was the 2′-FANA possessing a butyl linker (**XVI**), whereas the PNA-containing oligomer was more efficient at eliciting the cleavage of the 40-mer target.

For 2′-FANA-based AONs, the order of enzyme efficiency is roughly the same for both the 18- and 40-mer targets: **XVI** ≈ **XV** > **XIV**. This is similar to the trend we observed earlier (**IV** > **III**, **II** > **I**) and likely correlates with a gradual decrease in the flexibility of the AON strand. In other words, the all-

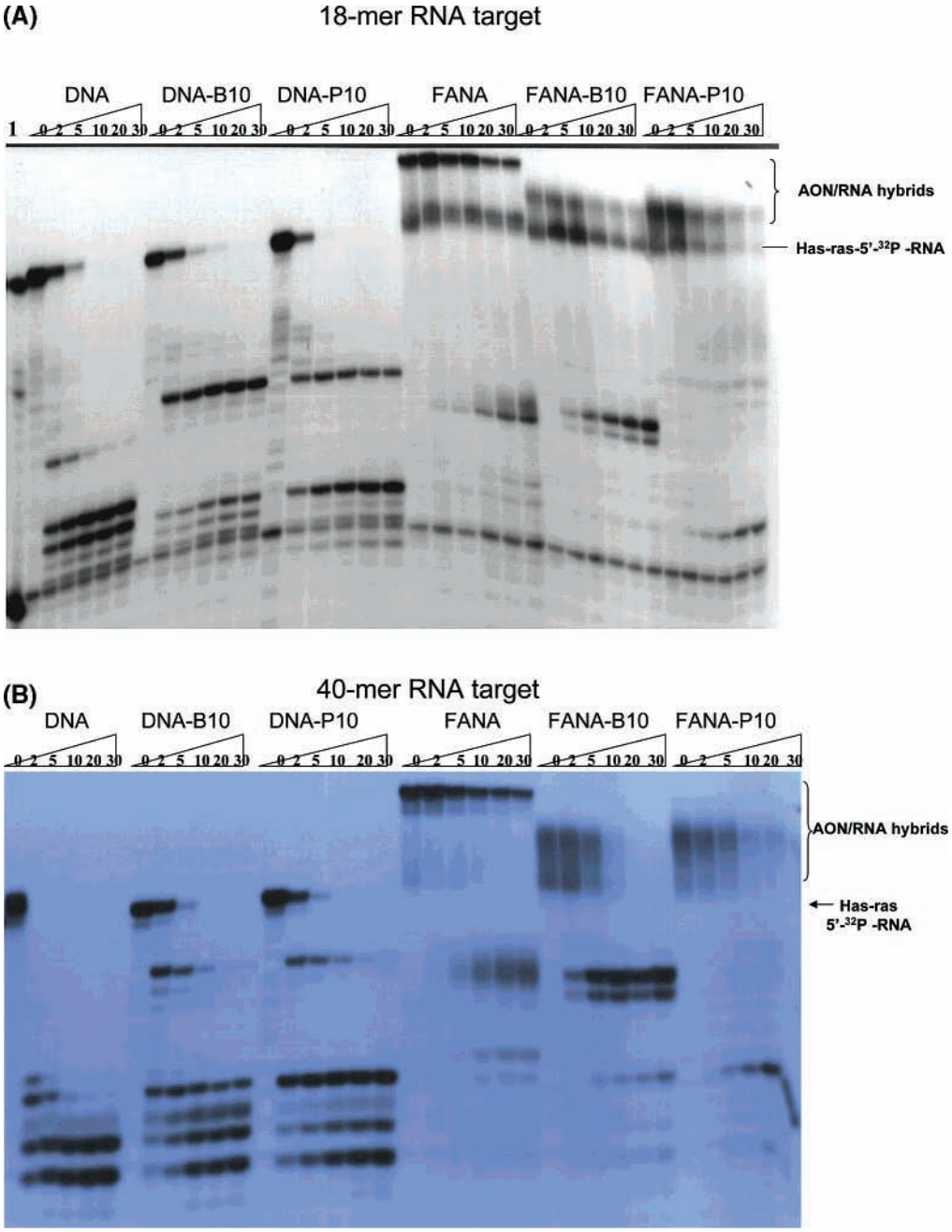


Figure 6. Degradation patterns of Ha-*ras*-RNA (A) 18-mer and (B) 40-mer hybridized with various AONs. See experimental procedures for details. $T = 37$ °C; time points: 0, 2, 5, 10, 20, and 30 min. The slowly migrating band observed for **XIV**, **XVI**, and **XV** hybridized to the 18-nt and 40-nt RNA targets corresponds to the duplexed species that does not dissociate despite heating of the sample prior to loading and the denaturing conditions of the gel electrophoresis, due to high T_m.

FANA strand **XIV** likely does not present enough flexibility to the enzyme, which would therefore require greater energy to adjust the hybrid to adopt the correct conformation for hydrolysis.

Polyacrylamide electropherograms can be inspected to qualitatively assess the effect of a non-nucleotide insert into DNA or 2′-FANA on the pattern of RNase-H-directed RNA hydrolysis. Figure 6 shows the gel from which the data presented in Figure 5 was obtained. For both the 18-mer and 40-mer targets, the DNA oligomer **XI** causes a predominance of short hydrolysis products, likely a result of multiple cleavage events. For the modified oligomers, there is a specific hydrolysis more central in the targeted RNA resulting in a slower moving band. This is clearly seen in the linker-modified DNA oligomers regardless of the identity of the linker, that is, both the butyl- and PNA-linked DNA oligomers produce similar cleavage patterns. Interestingly, the nature of the linker in a 2′-FANA sequence appears to affect the pattern of cleavage. The 2′-FANA oligomer (**XIV**) directs a central cleavage, assumed to be a primary hydrolysis event, as does the butyl linker-modified 2′-FANA (**XVI**). In contrast, the PNA-modified 2′-FANA (**XV)** presents a different cleavage pattern, with a product resulting from central hydrolysis being absent. We interpret this observation as being a result of the structural perturbation that a single PNA insert causes as well as the relative stiffness of the amide backbone, as compared to a butyl insert, which makes it a less suitable enzyme substrate.

CONCLUSIONS

Oligonucleotide analogs capable of recruiting RNase H for the destruction of mRNA have potential use as artificial regulators of gene expression. Our previous work has shown

that the ability of 2′-FANA to direct the RNase-H-mediated hydrolysis of RNA is dramatically improved by incorporation of a flexible non-nucleotide butyl linker. This modification has the deleterious effect of reducing the thermal stability of the complexes formed with complementary nucleic acids. The current study has investigated the incorporation of a neutral peptide nucleic acid linker, which we have found diminishes the thermal stability of complexes formed with complementary oligonucleotides. Although this is presumably due to some degree of structural changes at the PNA−DNA or PNA−FANA junctions in the chimeras, this was not found by comparative examination of the complexes by CD spectroscopy (data not shown).

In general, PNA-modified oligonucleotides did not lead to a substantial improvement in induction of RNase H1 activity as compared to butyl derivatized oligonucleotides. However, homopolymeric DNA sequences containing a PNA insert were more efficient at eliciting RNase H1 activity relative to the unmodified homopolymeric DNA presumably due to added flexibility. Nevertheless, the greater rigidity imparted to the oligonucleotide strand by the PNA unit as compared to the butyl linker is believed to be accountable, at least in part, for the decrease in enzymatic activity. Another effect that cannot be ruled out from the present study is a partial loss of key enzyme interactions due to the uncharged nature of the amide backbone at the insertion junction. Nonetheless, it is clear that PNA-modified substrates can still support elevated cleavage over unmodified (i.e., all-DNA or all-FANA) strands in certain sequence contexts, especially given the general inability of PNA to activate RNase H. These trends thus corroborate our previous claims on substrate flexibility as a crucial element for high RNase H activity, and also illustrate the versatility with which a non-nucleotide residue, when strategically placed in the antisense oligonucleotide, can still maintain appreciable RNase H activation. Conversely, AON sequences containing three PNA inserts were less efficient at recruiting RNase H activity due to the increasing degree of PNA character to the oligomer and associated topological consequences on overall helix architecture.

Together, these and other studies reinforce the hypothesis that local flexible sites within AON/RNA hybrids are essential for high RNase H catalysis, (*6*, *34*−*36*) in which an enzyme-induced altered trajectory of the bound substrate (*37*, *38*) could facilitate optimal interaction with the catalytic site of RNase H1.

ACKNOWLEDGMENT

The authors (M.J.D., R.H.E.H.) gratefully acknowledge the Natural Science and Engineering Research Council of Canada and the Canadian Institutes of Health Research (M.J.D.) for funding. This work was also supported by a scholarship award from the Chemical Biology Strategic Training Initiative of the Canadian Institutes of Health Research to B.P. We thank Dr. M. M. Mangos for several helpful discussions, encouragement, and assistance with the writing of this manuscript.

LITERATURE CITED

(1) Uhlmann, E., and Peyman, A. (1990) Antisense oligonucleotides: a new therapeutic principle. *Chem. Rev. 90*, 543−584.

(2) Walder, R. Y., and Walder, J. (1988) Role of RNase H in hybrid-arrested translation by antisense oligonucleotides. *Proc. Natl. Acad. Sci. U.S.A. 85*, 5011−5015.

(3) Minasov, G., Teplova, M., Nielsen, P., Wengel, J., and Egli, M. (2000) Structural basis of cleavage by RNase H of hybrids of arabinonucleic acids and RNA. *Biochemistry 39*, 3525−3532.

(4) Zamaratski, E., Pradeepkumar, P. I., and Chattopadhyaya, J. (2001) A critical survey of the structure-function of the antisense oligo/RNA heteroduplex as substrate for RNase H. *J. Biochem. Biophys. Methods 48*, 189−208.

(5) Christensen, N. K., Peterssen, M., Nielsen, P., Jacobsen, J. P., Olsen, C. E., and Wengel, J. (1998) A novel class of oligonucleotide analogs containing 2′-O,3′-C-linked [3.2.0]bicycloarabinonucleoside monomers: synthesis, thermal affinity studies, and molecular modeling. *J. Am. Chem. Soc. 120*, 5458−5463.

(6) Mangos, M. M., Min, K.-L., Viazovkina, E., Galarneau, A., Elzagheid, M. I., Parniak, M. A., and Damha, M. J. (2003) Efficient RNase H-directed cleavage of RNA promoted by antisense DNA or 2′F-ANA constructs containing acyclic nucleotide inserts. *J. Am. Chem. Soc. 125*, 654−661.

(7) Nielsen, P. E., Egholm, M., Berg, R. H., and Buchardt, O. (1991) Sequence-selective recognition of DNA by strand displacement with a thymine-substituted polyamide. *Science 254*, 1497−1500.

(8) Rabinowtiz, J. L., and Gurin, S. (1953) Some pyrimidine derivatives. *J. Am. Chem. Soc. 75*, 5758−5759.

(9) Heimer, E. P., Gallo-Torres, H. E., Felix, A. M., Ahmad, M., Lambros, T. J., Scheidl, F., and Meienhofer, J. (1984) Synthesis of analogs and oligomers of N-(2-aminoethyl)glycine and their gastrointestinal absorption in the rate. *Int. J. Pept. Res. 23*, 203−211.

(10) Will, D. W., Breipohl, G., Langner, D., Knolle, J., and Uhlmann, E. (1995) The synthesis of polyamide nucleic acids using a novel monomethoxytrityl protecting-group strategy. *Tetrahedron 51*, 12069−12082.

(11) Stetsenko, D. A., Lubyako, E. N., Potapov, V. K., Azhikina, T. L., and Sverdlov, E. D. (1996) New approach to the solid phase synthesis of polyamide nucleic acid analogues (PNA) and PNA-DNA conjugates. *Tetrahedron Lett. 37*, 3571−3576.

(12) Finn, P. J., Gibson, N. J., Fallon, R., Hamilton, A., and Brown, T. (1996) Synthesis and properties of DNA-PNA chimeric oligomers. *Nucleic Acids Res. 24*, 3357−3363.

(13) Viazovkina, E. V., Mangos, M. M., Elzagheid, M. I., and Damha, M. J. (2002). Synthesis of 2′-fluoroarabino nucleoside phosphoramidites and their use in the synthesis of 2′F-ANA. In *Current Protocols in Nucleic Acid Chemistry*, Chapter 4.15, W. J. Sons, New York.

(14) Yamamoto, I., Sekine, M., and Hata, T. (1980) One-step synthesis of 5′-azido nucleosides. *J. Chem. Soc., Perkin Trans. 1 1*, 306−310.

(15) Mag, M., and Engels, J. W. (1989) Synthesis and selective cleavage of oligodeoxyribonucleotides containing non-chiral internucleotide phosphoramidate linkages. *Nucleic Acids Res. 17*, 5973−1588.

(16) Wolfe, J. L., Kawate, T., Belenky, A., and Stanton, V., Jr. (2002) Synthesis and polymerase incorporation of 5′-amino-2′,5′-dideoxy-5′-*N*-triphosphate nucleotides. *Nucleic Acids Res. 30* (17), 3739−3747.

(17) Damha, M. J., Wilds, C. J., Noronha, A., Brukner, I., Borkow, G., Arion, D., and Parniak, M. A. (1998) Hybrids of RNA and arabinonucleic acids (ANA and 2′F-ANA) are substrates of ribonuclease H. *J. Am. Chem. Soc. 120*, 12976−12977.

(18) Wilds, C. J., and Damha, M. J. (2000) 2′-Deoxy-2′-fluoro-β-D-arabinonucleosides and oligonucleotides (2′F-ANA): synthesis and physicochemical studies. *Nucleic Acids Res. 28*, 3625−3635.

(19) van der Laan, A. C., Brill, R., Kuimelis, R. G., Kuyl-Yeheskiely, E., van Boom, J. H., Andrus, A., and Vinayak, R. (1997) A convenient automated solid-phase synthesis of PNA-(5′)-DNA-(3′)-PNA chimera. *Tetrahedron Lett. 38*, 2249−2252.

(20) Bergmann, F., Bannwarth, W., and Tam, S. (1995) Solid phase synthesis of directly linked PNA-DNA hybrids. *Tetrahedron Lett. 36*, 6823−6826.

(21) Wenninger, D., and Seliger, H. (1997) Synthesis and hybridization properties of modified oligonucleotides with PNA-DNA dimmer blocks. *Nucleosides Nucleotides 16*, 977−980.

(22) Uhlmann, E., Peyman, A., Breipohl, G., and Will, D. W. (1998) PNA: Synthetic polyamide nucleic acids with unusual binding properties. *Angew. Chem., Int. Ed. 37*, 2796−2823.

(23) van der Laan, A. C., Havenaar, P., Oosting, R. S., Kuyl-Yeheskiely, E., Uhlmann, E., and van Boom, J. H. (1998) Optimization of the binding properties of PNA-(5′)-DNA chimerae. *Bioorg. Med. Chem. Lett. 8*, 663−668.

(24) Berger, I., Tereshko, V., Ikeda, H., Marquez, V. E., and Egli, M. (1998) Crystal structures of B-DNA with incorporated 2′-deoxy-2′-

fluoro-arabino-furanosyl thymines: implications of conformational preorganization for duplex stability. *Nucleic Acids Res. 26*, 2473−2480.

(25) Denisov, A. Y., Noronha, A. M., Wilds, C. J., Trempe, J. F., Pon, R. T., Gehring, K., and Damha, M. J. (2001) Solution structure of an arabinonucleic acid (ANA)/RNA duplex in a chimeric hairpin: comparison with 2′-fluoro-ANA/RNA and DNA/RNA hybrids. *Nucleic Acids Res. 29*, 4284−4293.

(26) Chakraborty, A. K., Cichutek, K., and Duesberg, P. H. (1991) Transforming function of proto-ras genes depends on heterologous promoters and is enhanced by specific point mutations. *Proc. Natl. Acad. Sci. U.S.A. 88*, 2217−2221.

(27) Kiaris, H., and Spandidos, D. A. (1995) Mutations of Ras genes in human tumors. *Int. J. Oncol. 7*, 413−421.

(28) Kiaris, H., and Spandidos, D. A. (1995) Analysis of H-Ras, K-Ras and N-Ras genes for expression, mutation and amplification in laryngeal tumors. *Int. J. Oncol. 7*, 75−80.

(29) Hua, V. Y., Wang, W. K., and Duesberg, P. H. (1997) Dominant transformation by mutated human ras genes in vitro requires more than 100 times higher expression than is observed in cancers. *Proc. Natl. Acad. Sci. U.S.A. 94*, 9614−9619.

(30) Zuker, M., Mathews, D. H., and Turner, D. H., Eds. (1999) *Biochemistry and Biotechnology*, Kluwer Academic Publishers, Norwell, MA.

(31) Mathews, D. H., Sabina, J., Zuker, M., and Turner, D. H. (1999) Expanded sequence dependence of thermodynamic parameters improves prediction of RNA secondary structure. *J. Mol. Biol. 288*, 911−940.

(32) Vorobjev, P. E., Pyshnaya, I. A., Pyshnyi, D. V., Venyaminova, A. G., Ivanova, E. M., Zarytova, V. F., Bonora, G. M., Scalfi-Happ, C., and Seliger, H. (2001) Nuclease resistance and RNase H sensitivity of oligonucleotides bridged by oligomethylenediol and oligoethylene glycol linkers. *Antisense Nucleic Acid Drug Dev. 11*, 77−85.

(33) Vorobjev, P. E., Pyshnaya, I. A., Pyshnyi, D. V., Repkova, M. N., Venyaminova, A. G., Zenkova, M. A., Ivanova, E. M., Scalfi-Happ, C., Seliger, H., Bonora, G. M., and Zarytova, V. F. (2000) Cleavage of RNA in hybrid duplexes by the *E. coli* ribonuclease H: II. Substrate properties of oligonucleotides containing nonnucleotide linkers. *Bioorg. Khim. 26*, 758−764.

(34) Mangos, M. M., and Damha, M. J. (2002) Flexible and frozen sugar-modified nucleic acids - modulation of biological activity through furanose ring dynamics in the antisense strand. *Curr. Top. Med. Chem. (Sharjah, United Arab Emirates) 2*, 1145−1169.

(35) Lok, C.-N., Viazovkina, E., Min, K.-L., Nagy, E., Wilds, C. J., Damha, M. J., and Parniak, M. A. (2002) Potent gene-specific inhibitory properties of mixed-backbone antisense oligonucleotides comprised of 2′-deoxy-2′-fluoro-D-arabinose and 2′-deoxy nucleotides. *Biochemistry 41*, 3457−3467.

(36) Damha, M. J., Noronha, A. M., Wilds, C. J., Trempe, J.-F., Denisov, A., and Gehring, K. (2001) Properties of arabinonucleic acids (ANA & 2′F-ANA): Implications for the design of antisense therapeutics that invoke RNase H cleavage of RNA. *Nucleosides, Nucleotides Nucleic Acids 20*, 429−440.

(37) Premraj, B. J., Raja, S., and Yathindra, N. (2002) Structural basis for the unusual properties of 2′,5′ nucleic acids and their complexes with RNA and DNA. *Biophys. Chem. 95*, 253−272.

(38) Nielsen, J. T., Stein, P. C., and Petersen, M. (2003). NMR structure of an α-L-LNA:RNA hybrid: structural implications for RNase H recognition, *Nucleic Acids Res. 31*, 5858−5867.

BC060300R

Psoralen Conjugates for Visualization of Genomic Interstrand Cross-Links Localized by Laser Photoactivation

Arun Kalliat Thazhathveetil,[†] Su-Ting Liu,[†] Fred E. Indig,[‡] and Michael M. Seidman*[,†]

Laboratory of Molecular Gerontology, National Institute on Aging, 5600 Nathan Shock Drive, Baltimore, Maryland 21224, and Research Resources Branch, National Institute on Aging/NIH, 5600 Nathan Shock Drive, Baltimore, Maryland 21224
Received October 4, 2006; Revised Manuscript Received November 29, 2006

DNA interstrand cross-links are formed by chemotherapy drugs as well as by products of normal oxidative metabolism. Despite their importance, the pathways of cross-link metabolism are poorly understood. Laser confocal microscopy has become a powerful tool for studying the repair of DNA lesions that can be detected by immunofluorescent reagents. In order to apply this approach to cross-link repair, we have synthesized conjugates of 4,5′,8-trimethylpsoralen (TMP) and easily detected compounds such as Lissamine rhodamine B sulfonyl chloride (LRB-SC), biotin, and digoxigenin. These conjugates are activated by UVA, and we have analyzed the intracellular localization of DNA damage and DNA reactivity by confocal and immunofluorescence microscopy. The LRB-SC−TMP conjugate **2** appeared mainly in the mitochondria, while the biotin−TMP conjugate **4** preferentially localized in the cytoplasm. Adducts formed by UVA and digoxigenin conjugates of TMP **7a** and 4,5′-dimethylangelicin (DMA) **7b**, which forms only monoadducts, were largely localized to the nucleus. Exposure of cells incubated with **7a** and **7b** to a 364 nm UV laser directed toward defined nuclear regions of interest resulted in localized adduct formation which could be visualized by immunofluorescence. Repair-proficient cells were able to remove the photoadducts, while repair-deficient cells were unable to repair the damage. The results indicated that the digoxigenin−TMP conjugate **7a** and digoxigenin−DMA conjugate **7b** can be used for studying the repair of laser localized DNA monoadducts and cross-links.

INTRODUCTION

Genomic instability resulting from chemical or radiation damage to DNA is linked to many human disorders, including cancer. Instability is also believed to contribute to the deterioration of cellular and organ function during aging (*1*). As a consequence, the elucidation of pathways for the repair of chemical and radiation damage in DNA has been the subject of considerable research effort employing a variety of experimental approaches. In recent years, immunofluorescence microscopy has become an important tool in the study of the proteins and enzymes involved in DNA repair. One of the most powerful applications of this technology involves the introduction of localized damage by exposure of a discrete area in a cell nucleus to light from a laser. The energy from the laser activates endogenous or exogenous compounds, which in turn react with DNA. The best-known example is the activation of Hoechst dye by a 390 nm laser. Radicals released by the dye attack DNA, resulting in various damage products, including double-strand breaks. These are marked by the rapid appearance of a phosphorylated form of histone γ-H2AX in the chromatin in the vicinity of the break. Immunofluorescent staining of the phospho-histone yields a pattern that illuminates the region exposed to the laser (*2*). This approach has been used by a number of groups to characterize the dynamics of double-strand break repair (*3*, *4*). More recently, the localized laser strategy has been extended to studies on the repair of single-strand breaks and guanine oxidation products (*5*, *6*).

Although the study of localized damage has been quite productive, it is necessarily limited to the analysis of DNA lesions whose presence can be verified. This may be by the appearance of a protein specific for the DNA lesion, such as phosphorylated γ-H2AX, or by immunostaining of treated cells with antibodies against specific DNA adducts (*6*). If appropriate immunological reagents are unavailable, then it can be difficult, perhaps impossible, to verify the presence of the adduct of interest. Furthermore, it would not be possible to follow the removal of an adduct by DNA repair functions. This can be a major limitation.

We are interested in the metabolism of interstrand DNA cross-links. These are formed by lipid peroxidation products (*7*, *8*) and chemotherapy reagents such as cisplatin, nitrogen mustards, and the photoactive psoralens (*9*). They are absolute blocks to transcription and replication and cannot be accumulated in proliferating cells. In light of the clinical significance and biological implications, cross-link repair is the subject of much current research (*10*−*12*). The requirement for photoactivation would suggest that psoralens would be ideal reagents for the study of repair dynamics of localized genomic cross-links. However, there are no commercial immunological reagents available for the detection of psoralen adducts in genomic DNA. Psoralen has been chemically linked to molecular tags, such as biotin, which can be detected with fluorescent avidin or streptavidin. These have been used as hybridization probes but have not been applied to live cells. In this report, we describe the synthesis and immunofluorescence studies of 4,5′,8-trimethylpsoralen (TMP), a psoralen derivative, linked to easily detected compounds such as Lissamine rhodamine B sulfonyl chloride (LRB-SC), biotin, and digoxigenin. In live cell experiments, we find that the first two conjugates have limited utility for studies of repair of genomic interstrand cross-links, while the digoxigenin−TMP conjugate can be used to cross-link

* Correspondence to: Michael M. Seidman, Laboratory of Molecular Gerontology, National Institute on Aging, 5600 Nathan Shock Dr, Baltimore, MD 21224, Tel: 410 558 8565, Fax: 410 558 8157, seidmanm@grc.nia.nih.gov.

[†] Laboratory of Molecular Gerontology.

[‡] Research Resources Branch.

10.1021/bc060309t Not subject to U.S. Copyright. Published 2007 by American Chemical Society
Published on Web 01/09/2007

nuclear DNA in global and localized reaction protocols. Repair-proficient cells were able to remove the tagged psoralen adducts, while repair-deficient cells were not.

EXPERIMENTAL PROCEDURES

Chemicals and Reagents. LRB-SC (Acros Organics), *N*-hydroxysuccinimidyl-D-biotinyl-15-amido-4,7,10,13-tetraoxapentadecylate, biotin−NHS ester (Quanta Biodesign, Ohio), and digoxigenin-3-*O*-methylcarbonyl-ϵ-aminocaproic acid-*N*-hydroxysuccinimidyl ester, dig-NHS ester (Roche Applied Science, Indianapolis) were used as received. All other reagents were purchased from Sigma-Aldrich and used without further purification. The starting materials methylaminodiethoxyethanemethylaminomethyltrimethylpsoralen (**1**) (*13*), 4′-aminomethyl-4,5′,8-trimethylpsoralen (**3**) (mp 190−192 °C), 4′-chloromethyl-4,5′,8-trimethylpsoralen (**5a**) (mp 215−217 °C) (*14*), and 4′-chloromethyl-4,5′-dimethylangelicin (**5b**) (mp 211−213 °C) (*15*) were prepared by following the reported procedures. Thin-layer chromatography was performed on silica gel 60 F_{254} plates (0.2 mm) (E. Merck, Gibbstown, NJ), column chromatography on silica gel (100−230 mesh, Natland International Corporation, NC), and preparative thin layer chromatography on precoated silica gel (Analtech, Inc., Uniplate, layer thickness 500 μm).

Instruments. Melting points (uncorrected) were measured on a Fisher-Johns melting point apparatus. NMR was recorded on a Bruker (Bellevica, MA) AC-300 spectrometer with tetramethylsilane as an internal standard. Mass was recorded on a Micromass Q-TOF1 mass spectrometer (Micromass, Beverely, MA) in the ESI mode.

Preparation of LRB-SC−TMP Conjugate 2. To a solution of **1** (25 mg, 0.06 mmol) and triethylamine (6 μL) in 15 mL of chloroform, LRB-SC (25 mg, 0.04 mmol) was added in small portions over a period of 10 min while the reaction mixture was stirred at 0 °C. The reaction mixture was stirred at room temperature for 12 h, and the solvent was distilled off under reduced pressure to obtain a residue which was chromatographed over silica gel. Elution of the column with a mixture (1:9) of methanol and chloroform gave 34 mg (60%) of **2**, mp 145−148 °C. ^{1}H NMR (300 MHz, $CDCl_3$, 25 °C) δ ppm: 1.29 (t, J = 7.0 Hz, 12H), 2.27 (s, 3H), 2.47 (s, 3H), 2.51 (s, 3H), 2.55 (s, 3H), 2.7 (t, J = 5.3 Hz, 2H), 2.97 (s, 3H), 3.39 (t, 5.9 Hz, 2H), 3.7−3.5 (m, 18H), 6.6 (s, 2H), 6.7 (d, J = 9.4 Hz, 2H), 7.18−7.25 (m, 4H), 7.6 (s, 1H), 7.8 (d, J = 7.9 Hz, 1H), 8.7 (s, 1H). Molecular weight calculated for $C_{50}H_{60}N_4O_{11}S_2$ was 957.16, found 957.52 ($M + H^+$).

Preparation of Biotin−TMP Conjugate 4. A solution of 4′-aminomethyl-4,5′,8-trimethylpsoralen (**3**) (15 mg, 0.06 mmol) and biotin−NHS ester (25 mg, 0.04 mmol) in dichloromethane (10 mL) was stirred at room temperature for 12 h. The solvent was distilled off under reduced pressure to obtain a residue which was chromatographed over silica gel. Elution of the column with a mixture (1:9) of methanol and chloroform gave 35 mg (50%) of the conjugate **4,** mp 103−106 °C. ^{1}H NMR (300 MHz, $CDCl_3$, 25 °C) δ ppm: 1.35−1.42 (m, 2H), 1.55−1.73 (m, 4H), 2.16−2.21 (t, J = 7.4 Hz, 2H), 2.47−2.53 (m, 11H), 2.67−3.15 (m, 4H), 3.39−3.55 (m, 16 H), 3.73 (t, J = 6.0 Hz, 2H), 4.25−4.29 (m, 1H), 4.44−4.50 (m, 3H), 6.21 (d, J = 1.0 Hz, 1H), 6.28 (s, 1H), 6.8 (t, J = 5.4 Hz, 1H), 7.17 (t, J = 5.5 Hz, 1H), 7.66 (s, 1H). Molecular weight calculated for $C_{36}H_{50}N_4O_{10}S$ was 730.86, found 731.22 ($M + H^+$).

Preparation of Digoxigenin−TMP Conjugate 7a and Digoxigenin−DMA Conjugate 7b. *Preparation of 4′-[N-(13-amino-4,7,10-trioxatrideca)]aminomethyl-4,5′,8-trimethylpsoralen (**6a**).* A mixture of 4′-chloromethyl-4,5′,8-trimethylpsoralen (**5a**) (50 mg, 0.18 mmol) and 4,7,10-trioxa-1,13-tridecanediamine (590 mg, 2.7 mmol) in toluene (10 mL) was refluxed for 12 h. The solvent was removed under reduced pressure, and the residue obtained was chromatographed over silica gel. Elution of the column with a mixture of chloroform, methanol, and 28% ammonia solution (9:1:0.5) gave 50 mg (60%) of **6a** as a pale yellow viscous liquid. ^{1}H NMR (300 MHz, $CDCl_3$ + DMSO-d_6 (4:1), 25 °C) δ ppm: 1.96 (m, 2H), 2.17 (m, 2H), 2.53 (s, 3H), 2.63 (s, 6H), 3.05 (t, J = 6.4 Hz, 2H), 3.17 (t, J = 7.3 Hz, 2H), 3.55−3.64 (m, 12 H), 4.33 (s, 2H), 6.2 (s, 1H), 8.35 (s, 1H). ^{13}C NMR ($CDCl_3$ + DMSO-d_6 (4:1), 25 °C) δ ppm: 8.29, 12.80, 19.75, 25.89, 26.52, 38.46, 45.06, 67.98, 68.94, 69.45, 69.62, 69.66, 69.94, 104.67, 106.38, 108.24, 112.24, 113.95, 116.21, 123.74, 149.06, 154.19, 154.47, 158.09, 160.84. Molecular weight calculated for $C_{25}H_{36}N_2O_6$ was 460.56, found 461.29 ($M + H^+$).

*Preparation of 4′-[N-(13-amino-4,7,10-trioxatrideca)]aminomethyl-4,5′-dimethylangelicin (**6b**).* Similarly, 4′-chloromethyl-4,5′-dimethylangelicin (**5b**) (50 mg, 0.19 mmol) and 4,7,10-trioxa-1,13-tridecanediamine (612 mg, 2.8 mmol) gave 47 mg (55%) of **6b** as a pale yellow viscous liquid. ^{1}H NMR (300 MHz, $CDCl_3$, 25 °C) δ ppm: 1.73 (m, 2H), 1.85 (m, 2H), 2.47 (s, 3H), 2.48 (s, 3H), 2.76−2.85 (m, 4H), 3.51−3.59 (m, 12H), 3.99 (s, 2H), 6.23 (s, 1H), 7.33 (d, J = 8.6 Hz, 1H), 7.41 (d, J = 8.6 Hz, 1H). ^{13}C NMR ($CDCl_3$, 25 °C) δ ppm: 12.01, 19.25, 24.54, 26.22, 36.91, 38.45, 45.16, 66.58, 67.54, 68.45, 68.42, 68.32, 68.96, 108.52, 112.81, 113.51, 115.26, 115.66, 120.56, 147.76, 154.25, 155.26, 155.76, 160.31. Molecular weight calculated for $C_{24}H_{34}N_2O_6$ was 446.53, found 447.05 ($M + H^+$).

*Preparation of **7a**.* To a solution of **6a** (5.5 mg, 0.012 mmol) and dig-NHS ester (5 mg, 0.008 mmol) in anhydrous DMF (0.5 mL), triethylamine (3.4 μL) was added. The reaction was stirred at 50 °C for 18 h and the solvent removed under reduced pressure. The residue obtained was purified directly by preparative thin layer chromatography, eluting with $CHCl_3$−MeOH−28% NH_4OH (8:1:0.1) to give 3.8 mg (50%) of the conjugate **7a**, mp 68−71 °C. ^{1}H NMR (300 MHz, $CDCl_3$, 25 °C) δ ppm: 0.80 (s, 3H), 0.94 (s, 3H), 1.25−2.13 (m, 34H), 2.48 (s, 3H), 2.51 (s, 3H), 2.57 (s, 3H), 2.76 (t, 2H), 3.27−3.74 (m, 19H), 3.86 (s, 2H), 3.88 (s, 2H), 4.78−4.93 (m, 2H), 5.94 (s, 1H), 6.24−6.29 (m, 2H), 6.62 (t, 1H), 7.65 (s, 1H). Molecular weight calculated for $C_{56}H_{81}N_3O_{13}$ was 1004.25, found 1004.76 ($M + H^+$).

*Preparation of **7b**.* Similarly, **6b** (5.4 mg, 0.012 mmol) and dig-NHS ester (5 mg, 0.008 mmol) gave 4 mg (53%) of the conjugate **7b**, mp 75−78 °C. ^{1}H NMR (300 MHz, $CDCl_3$, 25 °C) δ ppm: 0.79 (s, 3H), 0.95 (s, 3H), 1.19−2.17 (m, 34H), 2.48 (s, 3H), 2.49 (s, 3H), 2.79 (t, J = 6.9 Hz, 2H), 3.26−3.67 (m, 19H), 3.87 (s, 2H), 3.99 (s, 2H), 4.77−4.92 (m, 2H), 5.92 (s, 1H), 6.23 (s, 1H), 6.40 (t, 1H), 6.62 (t, 1H), 7.34 (d, J = 8.7 Hz, 1H), 7.43 (d, J = 8.7 Hz, 1H). Molecular weight calculated for $C_{55}H_{79}N_3O_{13}$ was 990.56, found 990.62 ($M + H^+$).

Detection of Cross-Link Formation by HPLC. TMP, **7a**, and **7b** were incubated with duplex DNA and exposed to UVA (365 nm) for 10 min on ice. The irradiated samples were applied to a DIONEX DNAPac ion exchange column on a Shimadzu HPLC system (LC-10ADvp) with a dual wavelength detector (SPD-10ADvp) and an autoinjector (SIL-10AVvp). A solution of 25 mM NaOH (mobile phase A) and 1 M NaCl in 25 mM NaOH (mobile phase B) was used for the separation. A gradient of 2 min 10−50% B, 20 min 50−90% B, and 21 min 90−100% B was employed with a flow rate of 1.5 mL/min.

Cell Culture. Chinese hamster wild-type AA8 and ERCC1[1] deficient 727 cells were grown in culture dishes or glass coverslips to 80% confluency in α-MEM (Gibco) supplemented with 10% fetal bovine serum, 1 mM L-glutamine, and 1% antibiotics. HeLa cells were cultured in DMEM (Gibco), supplemented with 10% fetal bovine serum, 1 mM L-glutamine, and 1% antibotics.

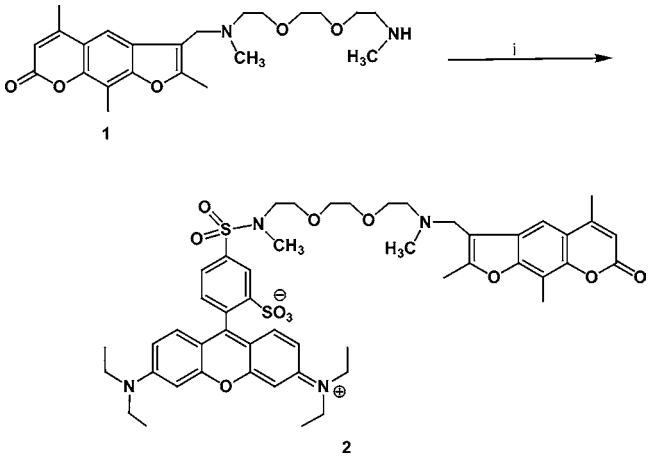
Immunofluorescence Labeling of DNA Conjugates. Cells were incubated with **7a** and **7b** at appropriate concentrations in serum and phenol red free culture medium for 30 min and then exposed to UVA for 5 min. Irradiated cells were washed three times with PBS, fixed with 4% formaldehyde at room temperature for 10 min, and lysed on ice for 15 min (1% BSA, 0.1% Triton X-100, 100 mM Glycine, 0.2 mg/mL EDTA). Cells were again rinsed three times with PBS, incubated in TE buffer (10 mM Tris base, 1 mM EDTA, pH 8) containing RNase A at 37 °C for 30 min, and blocked with PBS containing 20% fetal bovine serum at 37 °C for 1 h. The cells were then incubated with antibodies for 1 h at 37 °C and rinsed three times with washing buffer (0.05% Tween 20 in PBS), followed by incubation with secondary antibodies for 30 min at 37 °C. After washing, cells were mounted in Prolong Gold mounting medium containing DAPI as a DNA counter stain (both from Molecular Probes). Visualization of the cells treated with LRB-SC−TMP conjugate **2** did not require staining with antibodies. Cells treated with biotin−TMP conjugate **4** were stained with streptavidin−fluorescein (1 ng/mL, Vector Laboratories). Samples required for DNase I treatment were incubated with PBS containing DNase I (1 μg/mL) and $MgCl_2$ (100 μM) for 30 min at 37 °C prior to antibody staining.

Microscopy. Fluorescence images were obtained with a Zeiss Axiovert 200M microscope equipped with appropriate filters for FITC, DAPI, and Cy3/Texas red. Digital images were captured with a CCD camera and processed with the *Axio Vision* software packages (Zeiss, Germany).

Antibodies. The primary antibodies used in this study were sheep IgG polyclonal anti-digoxigenin (1.5 ng/mL, Roche Bioscience). The secondary antibody utilized in this study was donkey anti-sheep IgG conjugated with Alexa 488 (1:1000, Molecular Probes).

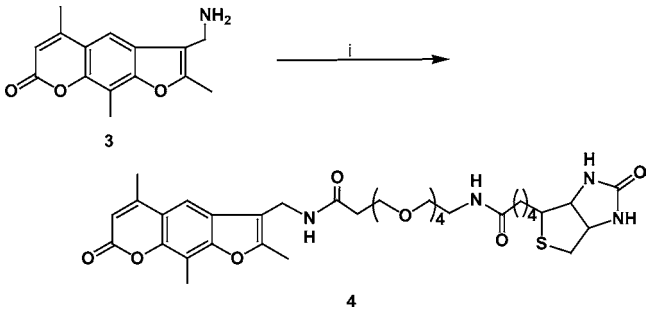
Localized Photoactivated Cross-Link Damage by UV Laser. HeLa cells or Chinese hamster AA8 cells were seeded on glass-bottom dishes (MatTek) at 2×10^5 cells per dish and incubated with 20 μM **7a** or **7b** for 1 h at 37 °C in α-MEM free of serum, antibiotics, and phenol red. Cells were kept in the dark from this point on. A Zeiss 510 Meta laser scanning confocal microscope equipped with a multiline (351 and 364 nm) 80 mW argon ion UV laser (Coherent Enterprise II) was employed in this study. We used the 364 nm emission of the UV laser at 19.8 A output to deliver a continuous beam via a quad (375/488/543/633) primary dichroic in the LSM system and through a Plan Apochromat 100X/1.4 Oil DIC objective at 20% transmission and 6.4 μs per pixel. Cell nuclei were imaged with a 633 nm HeNe laser that has no effect on the treated cells. A small region within the nucleus of each cell (6.5 μm^2 or 6 × 30 pixels) received laser energy of 80 nJ/μm^2, as measured using a light meter equipped with a 364 nm UV-optimized probe placed on the objective (International Light model IL 1400A). Laser-irradiated cells were immediately washed and incubated with complete medium at 37 °C for the times indicated and then processed for immunofluorescence imaging as described previously. Images were processed using the LSM browser software package (Zeiss).

Scheme 1. Synthesis of LRB-SC−TMP Conjugate 2[a]



[a] Reagents: (i) Lissamine rhodamine B sulfonyl chloride, triethylamine, dichloromethane, rt, 12 h.

Scheme 2. Synthesis of Biotin-TMP Conjugate 4[a]



[a] Reagents: (i) biotin−NHS ester, dichloromethane, rt, 12 h.

RESULTS

Synthesis and Cellular Localization of LRB-SC−TMP Conjugate and Biotin−TMP Conjugate. Conjugates of LRB-SC and biotin with TMP were prepared as shown in Schemes 1 and 2, respectively. Briefly, methylaminodiethoxyethanemethylaminomethyltrimethylpsoralen (**1**) was reacted with LRB-SC to give the conjugate **2,** while the reaction between the *N*-hydroxysuccinimidyl ester of a biotin derivative with 4′-aminomethyl-4,5′,8-trimethylpsoralen (**3**) afforded the biotin−TMP conjugate **4**. LRB-SC was coupled to TMP on the anticipation that it would allow direct visualization of cross-linked sites in cells. The coupling to biotin was prompted by the ready availability of reagents for detection. The cellular localization of each compound has been well-characterized. Rhodamines are known to concentrate in mitochondria (*16*), while biotin distributes throughout the cell, with a strong presence in the cytoplasm, including in the mitochondria (*17*). Psoralens are DNA intercalators which interact with all DNA, nuclear as well as mitochondrial. Thus, we were curious as to know which component of the conjugates would dominate the cellular distribution. Cells were incubated with each conjugate and exposed to UVA to photoactivate the psoralen. The cells were then washed, fixed, and either viewed directly (those treated with the conjugate **2**) or incubated with a fluorescent streptavidin prior to analysis. The results with the conjugate **2**

[1] Abbreviations: ERCC1, excision repair cross-complementing rodent repair deficiency 1; DMEM, Dulbecco's Modified Eagle's Medium; α-MEM, α-Minimum Essential Medium; PBS, phosphate buffered saline; TE, Tris base-EDTA; BSA, bovine serum albumin; EDTA, ethylenediaminetetraacetic acid; DAPI, 4′,6′-diamidino-2-phenylindole; FITC, fluorescein isothiocyanate; Cy3, sodium1-[5-(carboxyl)pent-1-yl}-2-[5-(3,3-dimethyl-1-ethyl-5-sulfonatoindolin-2-ylidene)-1-en-yl]-3,3-dimethyl-3*H*-indolium-5-sulfonate; CCD, charge-coupled device; IgG, Immunoglobulin G; XPF, xeroderma pigmentosum, complementation group F.

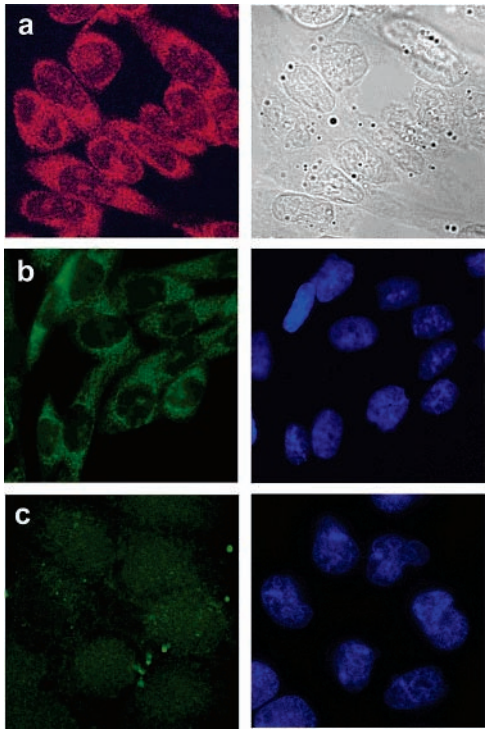
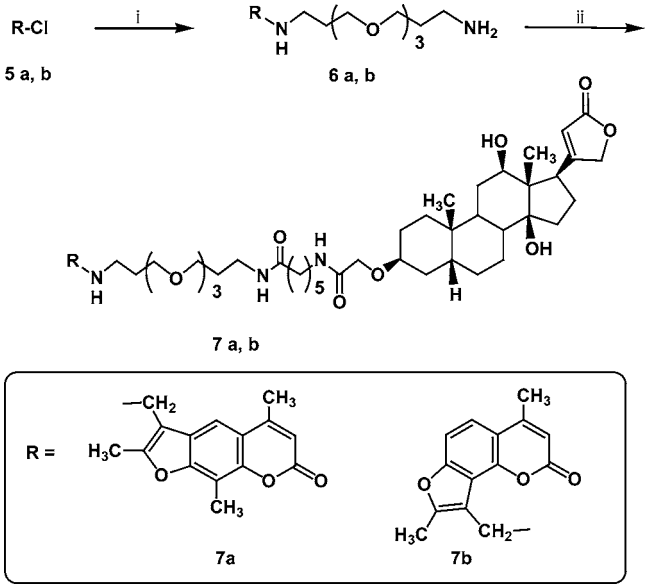


Figure 1. Fluorescence microscope images of Chinese hamster AA8 cells incubated with (a) LRB-SC−TMP conjugate **2** (30 μM), (b) biotin−TMP conjugate **4** (50 μM), (c) biotin−TMP conjugate **4** (200 μM), and free biotin (1 mM). Cells treated with conjugate **4** were stained with fluorescein−streptavidin. Corresponding bright field and DAPI images are also shown.

(Figure 1a) showed that the location of the psoralen cross-links was dictated by the properties of the LRB-SC. The adducts of conjugate **2** were found in the mitochondria. Control experiments showed the requirement for UVA treatment and that DNase I digestion of the fixed cells eliminated the LRB-SC signal (not shown). Cells incubated with conjugate **4** showed an extensive cytoplasmic presence (Figure 1b). Coincubation of cells with conjugate **4** and free biotin, to block biotin binding sites, resulted in a much greater proportion of the signal appearing in the nucleus (Figure 1c). Control experiments again showed the requirement for UVA and the sensitivity of the signal to DNase I (not shown). Although the combination of free biotin and conjugate **4** did yield a nuclear signal, high concentrations of both compounds were required. Furthermore, since biotin is a cofactor for many enzymes, we were concerned about the influence of the high levels of biotin on the cellular physiology. In light of these limitations for the LRB-SC−TMP and biotin−TMP conjugates **2** and **4**, we turned to the examination of digoxigenin as a tag for psoralen in live cell experiments.

Synthesis of Digoxigenin−TMP and −DMA Conjugates. We prepared digoxigenin conjugates of TMP and also 4,5′-dimethylangelicin (DMA), which can only form monoadducts (*18*) (Scheme 3). The latter compound was synthesized to permit analysis of cellular responses to monoadducts generated under the same conditions as the cross-links formed by TMP. Chloromethylation of TMP as well as DMA with chloromethylmethylether followed by the reaction with 4,7,10-trioxa-1,-13-tridecanediamine gave the corresponding TMP and DMA-glycol amines **6a** and **b** which were further reacted with NHS ester of digoxigenin to give the corresponding digoxigenin conjugates of TMP (**7a**) and DMA (**7b**). The poly(ethylene glycol) linker was used to enhance the water solubility of the individual conjugates.

Scheme 3. Synthesis of Digoxigenin−TMP and Digoxigenin−DMA Conjugates 7a and 7b[a]



[a] Reagents: (i) 4,7,10-trioxa-1,13-tridecanediamine, toluene, reflux, 12 h. (ii) Dig-NHS ester, DMF, 50 °C, 18 h.

Reaction of 7a and 7b with Duplex Oligonucleotides. Conjugates **7a** and **7b** were incubated with a duplex oligonucleotide containing multiple 5′ TA steps, appropriate for psoralen cross-linking. In our initial experiments with TMP, we examined the reaction products by electrophoresis on denaturing polyacrylamide gels, which resolved cross-linked from non-cross-linked oligonucleotides. However, we found that linkage to digoxigenin obscured the distinction between single-stranded and cross-linked duplex DNA (not shown). Consequently, we resolved single-strand and cross-linked duplex DNA by HPLC. Following exposure to UVA, the oligonucleotides were examined by HPLC on an ionic exchange column eluted with a NaCl gradient in 25 mM NaOH. In control reactions, the duplex oligonucleotide was incubated with varying amounts of TMP. The individual single strands had retention times of 13.3 and 13.6 min. Similarly, the non-cross-linked duplex sample showed the presence of the same two peaks (Figure 2a). In the sample incubated with the TMP, there was an additional peak of cross-linked oligonucleotide, with increased retention time (Figure 2b). Treatment of the duplex oligonucleotide with **7a** produced a peak with the same retention time as that formed in the reaction with the unconjugated TMP (Figure 2c). The samples treated with the corresponding angelicin conjugate **7b** did not show a peak in this region, although there was a broadening of the peaks in the single-strand positions (Figure 2d). We interpreted these results as demonstrating the cross-linking activity of the **7a** and the absence of that activity with the angelicin derivative **7b**. Comparison of the activity of **7a** with unconjugated TMP demonstrated that the conjugation had reduced the activity by about 10-fold.

Immunofluorescence of Cells Treated with 7a and Whole Cell UVA. Cells were grown on glass coverslips and incubated with 50 μM **7a** for 30 min, followed by exposure to UVA. The slides were fixed and incubated with sheep anti-digoxigenin antibody and then with secondary antibody covalently modified with Alexa 488. Cells treated with **7a** but no UVA showed barely detectable fluorescence (Figure 3a). However, cells treated with **7a**/UVA showed a largely nuclear fluorescence (Figure 3b). These results, which contrasted with those shown in Figure 1, indicated that the conjugate **7a** could be used to cross-link nuclear DNA in living cells.

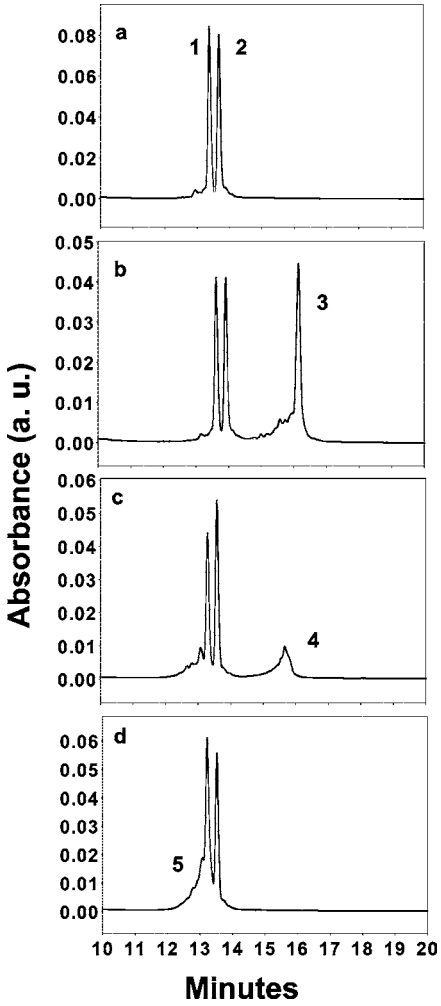


Figure 2. HPLC trace for the separation of the interstrand cross-link reaction mixtures. (a) Traces 1 and 2 represent unreacted oligos 1 and 2. (b) Trace 3 indicates the oligos 1 and 2 cross-linked by TMP. (c) Trace 4 indicates the oligos 1 and 2 cross-linked by digoxigenin−TMP conjugate **7a**. (d) Trace 5 indicates the monoadducts formed between oligos 1 and 2 and digoxigenin−DMA conjugate **7b**.

Since the intended application of the digoxigenin−TMP conjugate was to examine the repair of cross-links in treated cells, it was important to show that the cells were capable of removing the photoadducts formed between DNA and the conjugate. Accordingly, the cells were treated with **7a**/UVA, washed, returned to complete medium without **7a**, and incubated for 6 h at 37 °C. When these cells were fixed and immunostained, we observed a decline in fluorescence intensity to near-background levels (Figure 3c).

Although we interpreted the loss of the immunofluorescence signal in the cells shown in Figure 3c as due to DNA repair, it was also possible that it could have been due to a degradation of the digoxigenin tag, unrelated to DNA repair. In order to test this, we used a cell line lacking the ERCC1 gene. The protein encoded by this gene is a member of a heterodimeric protein complex (with the XPF protein) which is a component of the nucleotide excision repair pathway. It is a structure-specific endonuclease and has been shown to be critical for the repair of interstrand cross-links (*19*, *20*). ERCC1-deficient cells were treated with **7a**/UVA, fixed, and stained immediately or after 6 h of incubation at 37 °C. Figure 4 shows the fluorescent microscopy images of cells treated with **7a**/UVA. As seen from these figures, the fluorescence intensities of the cells stained immediately after treatment (Figure 4a) or after 6 h of incubation (Figure 4b) were quite similar. In a second experiment, we

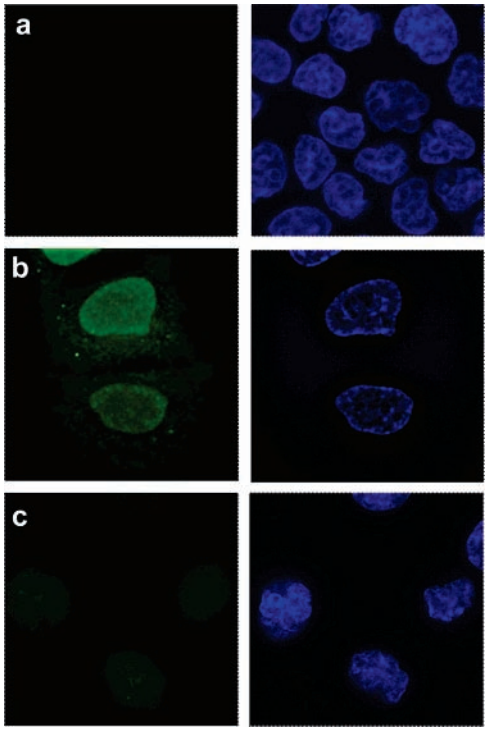


Figure 3. Fluorescence microscopy images of Chinese hamster AA8 cells incubated with digoxigenin−TMP conjugate **7a** (50 μM): (a) Cells without UVA treatment. (b) Cells irradiated with UVA and fixed immediately. (c) Cells irradiated with UVA and fixed after 6 h. Cells were stained with sheep anti-digoxigenin antibody and anti-sheep Alexa 488 antibody. Right panel shows the corresponding images of the same cells counter stained with DAPI.

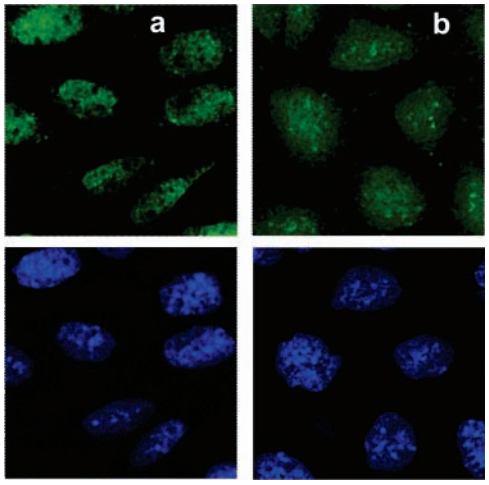


Figure 4. Fluorescence microscope images of ERCC1 (−/−) cells (727) incubated with 50 μM of digoxigenin−TMP conjugate **7a**: (a) Cells irradiated with UVA and fixed immediately. (b) Cells irradiated with UVA and fixed after 6 h. Cells were stained with sheep anti-digoxigenin antibody and anti-sheep Alexa 488 antibody. Lower panel shows the corresponding images of the same cells counter stained with DAPI.

incubated ERCC1-deficient cells overnight with **7a** prior to exposure to UVA. The signal intensity from these cells was indistinguishable from cells that were incubated for only 30 min with **7a** prior to UVA and immunostaining (not shown). These experiments demonstrated that the digoxigenin tag was stable during incubation in a cellular environment and also as part of a genomic DNA interstrand cross-link in living cells.

Localized Cross-Linking via Laser Photoactivation. In the past few years, the energy from focused laser light has been used to introduce DNA damage in defined regions of living

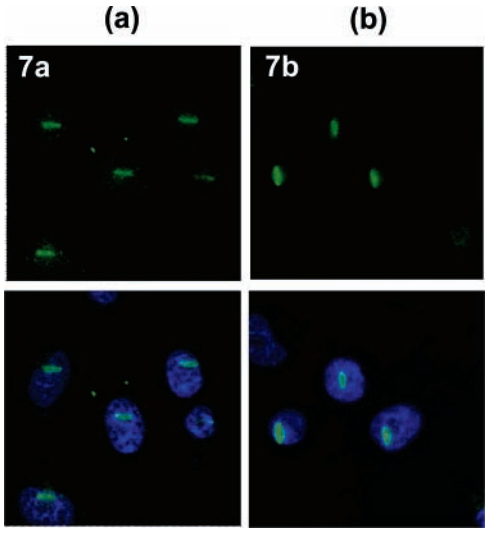


Figure 5. Confocal microscope images of HeLa cells treated with digoxigenin−TMP conjugate **7a** (20 μM) and digoxigenin−DMA conjugate **7b** (50 μM) and locally exposed to UV laser. (a) Cells with localized DNA cross-links induced by **7a** (green fluorescence). (b) Cells with localized DNA monoadducts induced by **7b** (green fluorescence). Cells were stained with sheep anti-digoxigenin antibody and anti-sheep Alexa 488 antibody. Lower panel represents the corresponding merged images of the same cells counter stained with DAPI.

cells (*3*, *6*). We applied this approach to cells incubated with digoxigenin−TMP conjugate **7a**. The cells were viewed in a confocal microscope, and **7a** was photoactivated by exposure of rectangular regions of interest (ROI) in individual cells to the 364 nm emission from a UV laser. The focus was set at the plane of the intersection of a cell nucleus and the adjacent cytoplasm. This was done to place the damage within the interior of the nucleus. The cells were then fixed and immmunostained for the covalently bound conjugate **7a**. Areas of the nucleus outside the ROI as well as cells not exposed to the localized laser served as controls for nonspecific binding of the immunodetection reagents. The results indicated that the conjugate **7a** could be used in conjunction with laser photoactivation to introduce localized genomic cross-links (Figure 5a). Similar experiments were carried out with digoxigenin−DMA conjugate **7b**, which can form only monoadducts. Figure 5b shows the immunofluorescent stripes obtained by the localized laser photoactivation of cells treated with **7b**.

The positive cells were subjected to confocal analysis to determine the extent of reaction within the nucleus. Z-stack images of multiple focal planes were capture with 0.5 μm between each section. As shown in Figure 6, the stain due to conjugate **7a** was clearly visible only in the third section (1 μm), but not in the first two sections or the last z-stack image. This result indicated that the adducts could be precisely induced in three dimensions within the nucleus.

We then asked if cells could repair the laser-induced localized cross-links. Defined regions of cross-links were introduced into repair-proficient cells with **7a**. Cells were either fixed and immunostained immediately or incubated for 6 h prior to fixing and immunostaining. The results (Figure 7) were similar to those seen in the whole-cell experiment shown in Figure 3. There was a reduction in signal to the levels seen in untreated controls. These data indicated that cells could repair the cross-links introduced by laser photoactivation of the conjugate **7a**.

DISCUSSION

Psoralens linked to detectable tags have been used for several years as hybridization probes for use on fixed cells and purified DNA (*21*, *22*). Given the current interest in repair of localized

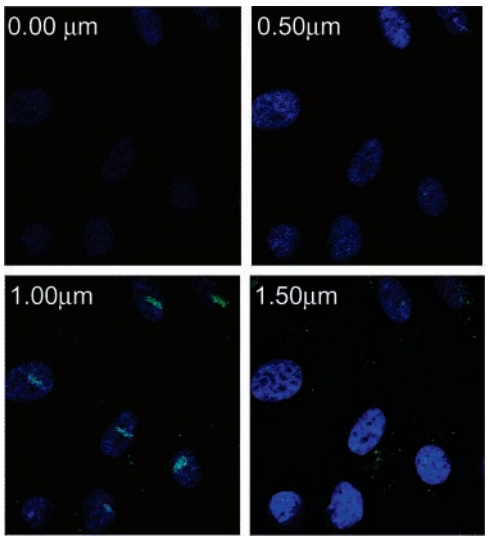


Figure 6. Merged Z stack images of HeLa cells with localized DNA cross-links induced by digoxigenin−TMP conjugate **7a** (20 μM) and UV laser. Cells were stained with sheep anti-digoxigenin antibody and anti-sheep Alexa 488 antibody and counter stained with DAPI.

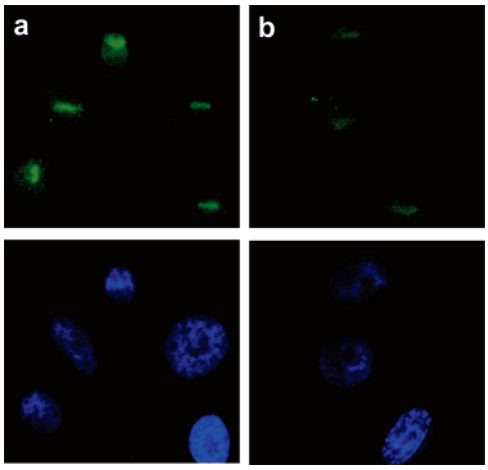


Figure 7. Confocal microscope images of repair proficient HeLa cells treated with digoxigenin−TMP conjugate **7a** (20 μM) and locally exposed to UV laser: (a) Cells with localized DNA cross-links were fixed immediately; (b) after 6 h. Cells were stained with sheep anti-digoxigenin antibody and anti-sheep Alexa 488 antibody. Lower panels represent the corresponding merged images of the same cells counter stained with DAPI.

DNA damage, it seemed reasonable to examine the utility of some of these for examining the repair of DNA cross-links in live cells. Fluorescent derivatives have an obvious appeal, however; as shown in Figure 1a, we found that conjugate **2** localized almost completely to the mitochondria. We also synthesized an Oregon Green derivative. While this compound could be used for nuclear labeling, we found that it was unstable on storage and rapidly bleached during imaging (not shown). The biotin conjugate **4** localized largely to the cytoplasm, and while nuclear labeling could be forced by coadministration of high concentrations of free biotin, we were concerned that this might influence the cellular physiology. The limitations of these compounds led us to synthesize the digoxigenin-linked psoralens. Like the other derivatives, versions of these conjugates have been used for preparing hybridization probes (*23*, *24*). However, as far as we know, they have received no application in living cells. Our results suggest that the digoxigenin−TMP conjugate can be used for studies of repair of localized cross-links in mammalian cells. The digoxigenin tag is stable in cells for extended periods prior to, and following, photoactivation.

Furthermore, we observed no cellular toxicity in the presence of these conjugates.

A key concern was that the cells survive the treatment protocol and be able to repair the DNA damage. Interpretation of repair experiments would be obviously compromised if the cells were killed by the DNA damage treatment. Our observation of repair of the cross-links, caused by conjugate **7a** activated by UVA, in repair-proficient cells appears to allay these concerns. It should now be possible to use the conjugate **7a** to follow the dynamics of repair and the recruitment of repair proteins of laser-induced localized cross-links in mammalian cells.

ACKNOWLEDGMENT

This work was supported by the intramural research program of the National Institutes of Health, National Institute on Aging.

LITERATURE CITED

(1) Mitchell, J. R., Hoeijmakers, J. H., and Niedernhofer, L. J. (2003) Divide and conquer: nucleotide excision repair battles cancer and ageing. *Curr. Opin. Cell Biol. 15*, 232−240.

(2) Rogakou, E. P., Boon, C., Redon, C., and Bonner, W. M. (1999) Megabase chromatin domains involved in DNA double-strand breaks in vivo. *J. Cell Biol. 146*, 905−916.

(3) Sedelnikova, O. A., Pilch, D. R., Redon, C., and Bonner, W. M. (2003) Histone H2AX in DNA damage and repair. *Cancer Biol. Ther. 2*, 233−235.

(4) Lan, L., Nakajima, S., Komatsu, K., Nussenzweig, A., Shimamoto, A., Oshima, J., and Yasui, A. (2005) Accumulation of Werner protein at DNA double-strand breaks in human cells. *J. Cell Sci. 118*, 4153−4162.

(5) Braithwaite, E. K., Kedar, P. S., Lan, L., Polosina, Y. Y., Asagoshi, K., Poltoratsky, V. P., Horton, J. K., Miller, H., Teebor, G. W., Yasui, A., and Wilson, S. H. (2005) DNA polymerase lambda protects mouse fibroblasts against oxidative DNA damage and is recruited to sites of DNA damage/repair. *J. Biol. Chem. 280*, 31641−31647.

(6) Lan, L., Nakajima, S., Oohata, Y., Takao, M., Okano, S., Masutani, M., Wilson, S. H., and Yasui, A. (2004) In situ analysis of repair processes for oxidative DNA damage in mammalian cells. *Proc. Natl. Acad. Sci. U.S.A. 101*, 13738−13743.

(7) Niedernhofer, L. J., Daniels, J. S., Rouzer, C. A., Greene, R. E., and Marnett, L. J. (2003) Malondialdehyde, a product of lipid peroxidation, is mutagenic in human cells. *J. Biol. Chem. 278*, 31426−31433.

(8) Marnett, L. J. (2000) Oxyradicals and DNA damage. *Carcinogenesis 21*, 361−370.

(9) Kohn, K. W. (1996) Beyond DNA cross-linking: history and prospects of DNA-targeted cancer treatment−fifteenth Bruce F. Cain Memorial Award Lecture. *Cancer Res. 56*, 5533−5546.

(10) Zhang, N., Kaur, R., Lu, X., Shen, X., Li, L., and Legerski, R. J. (2005) The Pso4 mRNA splicing and DNA repair complex interacts with WRN for processing of DNA interstrand cross-links. *J. Biol. Chem. 280*, 40559−40567.

(11) Niedernhofer, L. J., Odijk, H., Budzowska, M., van Drunen, E., Maas, A., Theil, A. F., de Wit, J., Jaspers, N. G., Beverloo, H. B., Hoeijmakers, J. H., and Kanaar, R. (2004) The structure-specific endonuclease Ercc1-Xpf is required to resolve DNA interstrand cross-link-induced double-strand breaks. *Mol. Cell Biol. 24*, 5776−5787.

(12) Sarkar, S., Davies, A. A., Ulrich, H. D., and McHugh, P. J. (2006) DNA interstrand crosslink repair during G1 involves nucleotide excision repair and DNA polymerase zeta. *EMBO J. 25*, 1285−1294.

(13) Saffran, W. A., Goldenberg, M., and Cantor, C. R. (1982) Site-directed psoralen crosslinking of DNA. *Proc. Natl. Acad. Sci. U.S.A. 79*, 4594−4598.

(14) Isaacs, S. T., Shen, C. K., Hearst, J. E., and Rapoport, H. (1977) Synthesis and characterization of new psoralen derivatives with superior photoreactivity with DNA and RNA. *Biochemistry 16*, 1058−1064.

(15) Dall'Acqua, F., Vedaldi, D., Caffieri, S., Guiotto, A., Rodighiero, P., Baccichetti, F., Carlassare, F., and Bordin, F. (1981) New monofunctional reagents for DNA as possible agents for the photochemotherapy of psoriasis: derivatives of 4,5′-dimethylangelicin. *J. Med. Chem. 24*, 178−184.

(16) Chen, L. B., Summerhayes, I. C., Johnson, L. V., Walsh, M. L., Bernal, S. D., and Lampidis, T. J. (1982) Probing mitochondria in living cells with rhodamine 123. *Cold Spring Harbor Symp. Quant. Biol. 46* (Pt 1), 141−155.

(17) Zempleni, J. (2005) Uptake, localization, and noncarboxylase roles of biotin. *Annu. Rev. Nutr. 25*, 175−196.

(18) Miolo, G., Dall'Acqua, F., Moustacchi, E., and Sage, E. (1989) Monofunctional angular furocoumarins: sequence specificity in DNA photobinding of 6,4,4′-trimethylangelicin and other angelicins. *Photochem. Photobiol. 50*, 75−84.

(19) Dronkert, M. L. and Kanaar, R. (2001) Repair of DNA interstrand cross-links. *Mutat. Res. 486*, 217−247.

(20) Gaillard, P. H. and Wood, R. D. (2001) Activity of individual ERCC1 and XPF subunits in DNA nucleotide excision repair. *Nucleic Acids Res. 29*, 872−879.

(21) Zhang, Y., Price, B. D., Tetradis, S., Chakrabarti, S., Maulik, G., and Makrigiorgos, G. M. (2001) Reproducible and inexpensive probe preparation for oligonucleotide arrays. *Nucleic Acids Res. 29*, E66.

(22) van Gijlswijk, R. P., Talman, E. G., Janssen, P. J., Snoeijers, S. S., Killian, J., Tanke, H. J., and Heetebrij, R. J. (2001) Universal linkage system: versatile nucleic acid labeling technique. *Expert Rev. Mol. Diagn. 1*, 81−91.

(23) Long, S., and Rebagliati, M. (2002) Sensitive two-color whole-mount in situ hybridizations using digoxigenin- and dinitrophenol-labeled RNA probes. *Biotechniques 32*, 494, 496, 498.

(24) Jemtland, R., Lee, K., and Segre, G. V. (1998) Heterogeneity among cells that express osteoclast-associated genes in developing bone. *Endocrinology 139*, 340−349.

BC060309T

Evaluation of a ^{99m}Tc-Labeled Cyclic RGD Tetramer for Noninvasive Imaging Integrin $\alpha_v\beta_3$-Positive Breast Cancer

Shuang Liu,*,† Wen-Yuan Hsieh,† Young Jiang,† Young-Seung Kim,† Subramanya G. Sreerama,† Xiaoyuan Chen,‡ Bing Jia,§ and Fan Wang§

School of Health Sciences, Purdue University, West Lafayette, Indiana 47907-2051, Molecular Imaging Program at Stanford, Department of Radiology & Bio-X, Stanford University, Stanford, California 94305-5344, Medical Isotopes Research Center, Peking University, Beijing 100083, China. Received October 4, 2006; Revised Manuscript Received January 10, 2007

Integrin $\alpha_v\beta_3$ plays a critical role in tumor angiogenesis and metastasis. Radiolabeled RGD peptides that are integrin $\alpha_v\beta_3$-specific are very useful for noninvasive imaging of integrin expression in rapidly growing and metastatic tumors. In this study, we determined the binding affinity of E{E[c(RGDfK)]$_2$}$_2$ (tetramer) and its 6-hydrazinonicotinamide conjugate (HYNIC-tetramer) against the binding of ^{125}I-echistatin to the integrin $\alpha_v\beta_3$-positive MDA-MB-435 breast cancer cells. The athymic nude mice bearing MDA-MB-435 xenografts were used to evaluate the potential of ternary ligand complex [^{99m}Tc(HYNIC-tetramer)(tricine)(TPPTS)] (TPPTS = trisodium triphenylphosphine-3,3′,3″-trisulfonate) as a new radiotracer for imaging breast cancer integrin $\alpha_v\beta_3$ expression by single photon emission computed tomography (SPECT). It was found that the binding affinity of tetramer ($IC_{50} = 51 \pm 11$ nM) was slightly higher than that of its dimeric analogue ($IC_{50} = 78 \pm 27$ nM) and is comparable to that of the HYNIC-tetramer conjugate ($IC_{50} = 55 \pm 11$ nM) within the experimental error. Biodistribution data showed that [^{99m}Tc(HYNIC-tetramer)(tricine)(TPPTS)] had a rapid blood clearance (4.61 ± 0.81 %ID/g at 5 min postinjection (p.i.) and 0.56 ± 0.12 %ID/g at 120 min p.i.) and was excreted mainly via the renal route. [^{99m}Tc(HYNIC-tetramer)(tricine)(TPPTS)] had high tumor uptake with a long tumor retention (5.60 ± 0.87 %ID/g and 7.30 ± 1.32 %ID/g at 5 and 120 min p.i., respectively). The integrin $\alpha_v\beta_3$-specificity was demonstrated by co-injection of excess E[c(RGDfK)]$_2$, which resulted in a significant reduction in tumor uptake of the radiotracer. The metabolic stability of [^{99m}Tc(HYNIC-tetramer)(tricine)(TPPTS)] was determined by analyzing urine and feces samples from the tumor-bearing mice at 120 min p.i. In the urine, about 20% of [^{99m}Tc(HYNIC-tetramer)(tricine)-(TPPTS)] remained intact while only ∼15% metabolized species was detected in feces. SPECT images displayed significant radiotracer localization in tumor with good contrast as early as 1 h p.i. The high tumor uptake and fast renal excretion make [^{99m}Tc(HYNIC-tetramer)(tricine)(TPPTS)] a promising radiotracer for noninvasive imaging of the integrin $\alpha_v\beta_3$-positive tumors by SPECT.

INTRODUCTION

Angiogenesis is a requirement for tumor growth and metastasis (*1*−*5*). Without the neovasculature to provide oxygen and nutrients, tumors cannot grow beyond 1−2 mm in size. Once vascularized, previously dormant tumors begin to grow rapidly and their volumes increase exponentially. Angiogenic process depends on vascular endothelial cell migration and invasion and is regulated by cell adhesion receptors. Integrins are such a family of proteins that facilitate cellular adhesion to and migration on extracellular matrix proteins found in intercellular spaces and basement membranes and regulate cellular entry and withdrawl from the cell cycle (*4*−*7*). Integrin $\alpha_v\beta_3$ is a receptor for the extracellular matrix proteins with an exposed arginine-glycine-aspartic (RGD) tripeptide sequence (*5*, *6*). Integrin $\alpha_v\beta_3$ is normally expressed at low levels on epithelial cells and mature endothelial cells but it is highly expressed on the activated endothelial cells in the neovasculature of tumors, including osteosarcomas, glioblastomas, melanomas, lung carcinomas, and breast cancer (*8*−*14*). It has been demonstrated that integrin $\alpha_v\beta_3$ is overexpressed on both endothelial and tumor cells in human breast cancer xenografts (*14*). The integrin $\alpha_v\beta_3$ expression correlates well with tumor progression and invasiveness of melanoma, glioma, and breast cancers (*8*, *9*, *13*). The highly restricted expression of integrin $\alpha_v\beta_3$ during tumor growth, invasion, and metastasis present an interesting molecular target for early detection of rapidly growing and metastatic tumors (*15*−*22*).

We and others have been using multimeric cyclic RGD peptides to develop the integrin $\alpha_v\beta_3$-targeted radiotracers to image rapidly growing and metastatic tumors (*23*−*32*). The RGD peptides serve as targeting biomolecules to carry radionuclide (e.g., ^{99m}Tc and ^{64}Cu) to the integrin $\alpha_v\beta_3$ overexpressed on tumor cells and endothelial cells of tumor neovasculature. Recently, we reported ^{64}Cu-DOTA−E{E[c(RGDfK)]$_2$}$_2$ as a positron emission tomography (PET) radiotracer to image glioma integrin $\alpha_v\beta_3$ expression (*26*). Results from the in vitro assay showed that the tetramer, E{E[c(RGDfK)]$_2$}$_2$, had a higher integrin $\alpha_v\beta_3$ binding affinity than the dimer, E[c(RGDfK)]$_2$, against ^{125}I-echistatin due to increased peptide valency. As a result, ^{64}Cu-DOTA−E{E[c(RGDfK)]$_2$}$_2$ showed very high tumor uptake and a long tumor retention (9.93 ± 1.05 %ID/g at 30 min and 4.56 ± 0.51 %ID/g at 24 h p.i.). To further illustrate the advantage of the tetramer, three DOTA conjugates (DOTA−E-c(RGDfK), DOTA−E[c(RGDfK)]$_2$, DOTA−E{E[c(RGDfK)]$_2$}$_2$) and their ^{111}In complexes were prepared (*32*). Biodistribution studies on

* To whom correspondence should be addressed. School of Health Sciences, Purdue University, 550 Stadium Mall Dr., West Lafayette, IN 47907. Phone: 765-494-0236; Fax: 765-496-1377; E-mail: lius@pharmacy.purdue.edu.

† Purdue University.

‡ Stanford University.

§ Peking University.

10.1021/bc0603081 CCC: $37.00 © 2007 American Chemical Society
Published on Web 03/07/2007

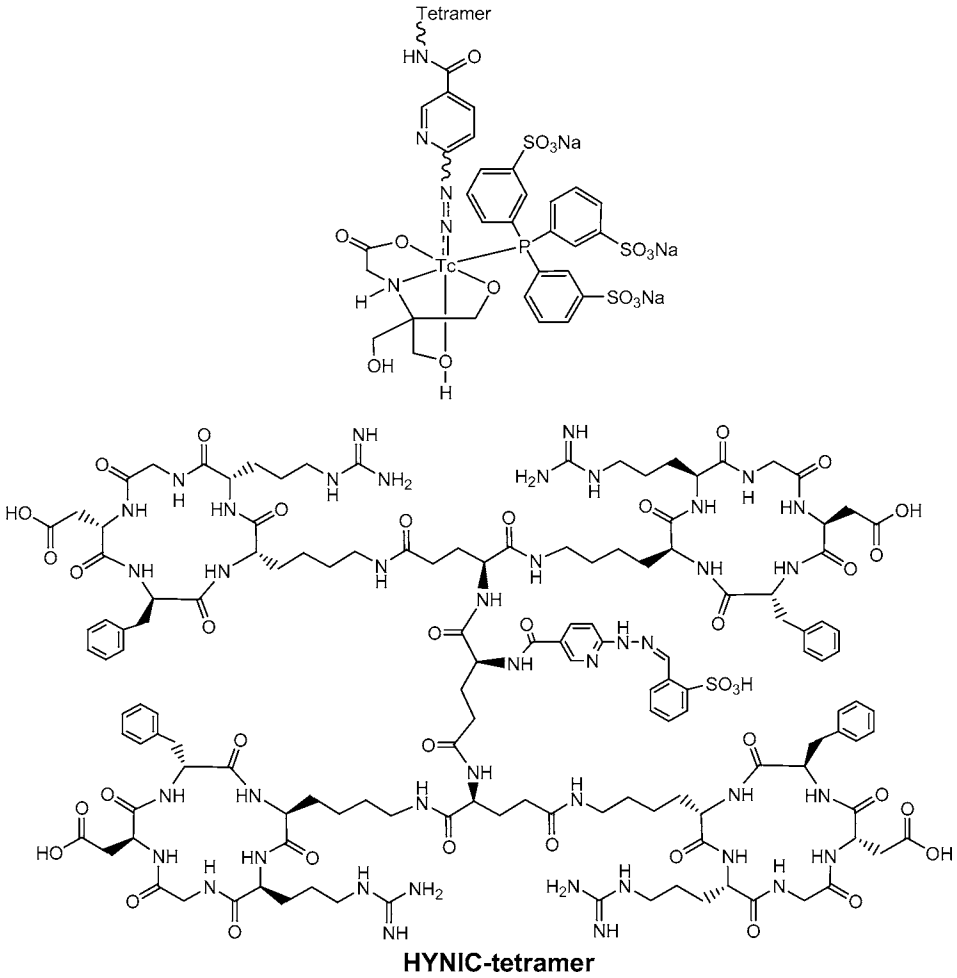


Figure 1. Schematic structure of [^{99m}Tc(HYNIC-tetramer)(tricine)(TPPTS)] (tetramer = E{E[c(RGDfK)]$_2$}$_2$; TPPTS = trisodium triphenylphosphine-3,3′,3″-trisulfonate).

^{111}In-DOTA−E-c(RGDfK), ^{111}In-DOTA−E-[c(RGDfK)]$_2$, and ^{111}In-DOTA−E{E[c(RGDfK)]$_2$}$_2$ were performed in athymic nude mice bearing subcutaneous SK-RC-52 tumors. At 8 h p.i, ^{111}In-DOTA−E{E[c(RGDfK)]$_2$}$_2$ showed a much higher tumor uptake (7.40 ± 1.12 %ID/g) than the monomer (2.30 ± 0.34 %ID/g) and the dimer (5.17 ± 1.22 %ID/g). It was concluded that the tetramer E{E[c(RGDfK)]$_2$}$_2$ is the best targeting biomolecule with respect to radiotracer tumor uptake and tumor-to-background (T/B) ratios (*32*). These promising results led us to prepare the 6-hydrazinonicotinamide-conjugated tetramer (HYNIC-tetramer) and its ^{99m}Tc complex [^{99m}Tc(HYNIC-tetramer)(tricine)(TPPTS)] (Figure 1: TPPTS = trisodium triphenylphosphine-3,3′,3″-trisulfonate). ^{99m}Tc is the ideal radionuclide for SPECT imaging due to its optimal nuclear properties ($t_{1/2}$ = 6.02 h and E_{max} = 142 KeV) and easy availability at low cost. HYNIC is used as bifunctional coupling agent for the ^{99m}Tc-labeling. TPPTS is used as the coligand because of its three negative charges and the high solution stability of its ^{99m}Tc complexes (*33*).

We now report the evaluation of [^{99m}Tc(HYNIC-tetramer)-(tricine)(TPPTS)] as a SPECT radiotracer to image the integrin $\alpha_v\beta_3$ expression in athymic nude mice bearing MDA-MB-435 human breast cancer xenografts. The objective is to explore the impact of peptide multiplicity on biodistribution characteristics and metabolism of the ^{99m}Tc-labeled multimeric cyclic RGDfK peptides. The results from this study will allow us to further demonstrate the superiority of the cyclic RGDfK tetramer over its dimeric and monomeric analogues with respect to tumor-targeting capability and in vivo kinetics.

MATERIALS AND METHODS

Trisodium triphenylphosphine-3,3′,3″-trisulfonate (TPPTS) and tricine were purchased from Sigma-Aldrich. E{E[c(RGDfK)]$_2$}$_2$ was prepared using the reported procedure (*26*). Sodium succinimidyl 6-(2-(2-sulfonatobenzaldehyde)hydrazono)-nicotinate (HYNIC-NHS) was prepared according to literature method (*34*). Na^{99m}TcO$_4$ was obtained from a commercial DuPont Pharma ^{99}Mo/^{99m}Tc generator, N. Billerica, MA. Mass spectral data were collected on a Finnigan LCQ classic mass spectrometer, School of Pharmacy, Purdue University. HPLC Method 1 used a LabAlliance semiprep HPLC system equipped with a UV−vis detector (λ = 254 nm) and Zorbax C_{18} semiprep column (9.4 mm × 250 mm, 100 Å pore size). The flow rate was 2.5 mL/min. The mobile phase was isocratic with 90% solvent A (0.1% acetic acid in water) and 10% solvent B (0.1% acetic acid in acetonitrile) at 0−5 min, followed by a gradient mobile phase going from 90% solvent A and 10% solvent B at 5 min to 60% solvent A and 40% solvent B at 20 min. The radio-HPLC method (Method 2) used the LabAlliance HPLC system equipped with a β-ram IN-US detector and Zorbax C_{18} column (4.6 mm × 250 mm, 300 Å pore size). The flow rate was 1 mL/min. The mobile phase was isocratic with 90% solvent A (25 mM ammonium acetate buffer, pH = 5.0) and 10% solvent B (acetonitrile) at 0−2 min, followed by a gradient mobile phase going from 10% solvent B at 2 min to 15% solvent B at 5 min and to 20% solvent B at 20 min.

Synthesis of HYNIC-E{E[c(RGDfK)]$_2$}$_2$ (HYNIC-tetramer). HYNIC-NHS (4.17 mg, 10 μmol) and E{E[c(RGDfK)]$_2$}$_2$

(14.0 mg, 10.6 μmol) were dissolved in a mixture of DMF and water (50:50 = v:v). The pH was adjusted to 8.5−9.0 with 0.1 N NaOH. The mixture was incubated overnight at room temperature. The product was purified by HPLC (Method 1). The peak of interest at ~14 min was collected. The collected fractions were combined, and lyophilized to give a pale yellow powder. The yield was 11 mg (~65%) with the purity >95% by HPLC. ESI-MS: $C_{136}H_{188}N_{42}O_{38}S$, calculated 3051.30, observed 3050.93 ($[M + H]^+$).

Synthesis of [^{99m}Tc(HYNIC-tetramer)(tricine)(TPPTS)]. To a vial filled with a 1.0 mL solution (pH = 4.8) containing 5 mg of TPPTS, 6.5 mg of tricine, 40 mg of mannitol, 38.5 mg of disodium succinate hexahydrate, and 12.7 mg of succinic acid were added 0.2 mL of HYNIC-tetramer solution (100 μg/mL in water) and 0.3 mL of Na[$^{99m}TcO_4$] solution (370−1850 MBq/mL). The vial was heated at 100 °C for 20−25 min in a lead-shielded water bath. After heating, the vial was placed back into the lead pig and allowed to stand at room temperature for ~10 min. A sample of the resulting solution was analyzed by the radio-HPLC. The radiochemical purity (RCP) was >95%. The HPLC retention time was ~15.5 min (Method 2). For biodistribution study, the radiotracer was first prepared and then purified by HPLC. Volatiles in the mobile phases were completely removed under vacuum. Doses were prepared by dissolving the HPLC-purified radiotracer in saline to a concentration of ~100 μCi/mL. For the blocking experiment, E[c(RGDfK)]$_2$ was dissolved in the solution containing the radiotracer (~100 μCi/mL) to give a concentration of 7.5 mg/mL. The resulting solution was filtered with a 0.20 μm Millex-LG filter to remove any particles before being injected into animals. Each tumor-bearing mouse was injected with 0.1 mL of solution.

Solution Stability. For the stability in kit matrix, samples of the reaction mixture containing the radiotracer were analyzed by HPLC at 0, 2, 4, and 6 h postlabeling. For the cysteine challenging experiment, the solution containing the radiotracer was mixed with an equal volume of a cysteine solution (1 mg/mL). Samples were analyzed by radio-HPLC at 0, 2, 4, and 6 h. For the solution stability after HPLC purification, the radiotracer was purified by HPLC (Method 2). Volatiles were removed under vacuum. The residue was dissolved in saline. Samples of the resulting solution were analyzed by HPLC at 0, 2, 4, and 6 h postlabeling.

Partition Coefficient. The log *P* value of [^{99m}Tc(HYNIC-tetramer)(tricine)(TPPTS)] was determined using the following procedure: the radiotracer was purified by HPLC. Volatiles were removed under vacuum. The residue was dissolved in a mixture of equal volume (3 mL:3 mL) n-octanol and 25 mM phosphate buffer (pH = 7.4). After being stirred vigorously for at least 20 min, the mixture was centrifuged at a speed of 8000 rpm for 5 min. Samples (in triplicates) from both n-octanol and aqueous layers were counted in a gamma counter (Beckman Gama 8000). The partition coefficients were calculated. The log *P* value was measured three different times and reported as an average of three different measurements plus the standard deviation.

Cell Integrin Receptor Binding Assay. The in vitro integrin-binding affinity and specificity of HYNIC-tetramer were assessed via displacement cell-binding assays using ^{125}I-echistatin as the integrin-specific radioligand. Experiments were performed on MDA-MB-435 human breast cancer cell line by slight modification of a method previously described (*26*). In brief, MDA-MB-435 cells were grown in Gibco's Dulbecco's medium supplemented with 10% fetal bovine serum (FBS), 100 IU/mL penicillin, and 100 μg/mL streptomycin (Invitrogen Co, Carlsbad, CA), at 37 °C in humidified atmosphere containing 5% CO_2. Filter multiscreen DV plates were seeded with 10^5 cells in binding buffer and incubated with ^{125}I-echistatin in the presence of increasing concentrations of different RGD peptide analogues. After the unlabeled ^{125}I-echistatin was removed, hydrophilic PVDF filters were collected and the radioactivity was determined using a gamma counter (Packard, Meriden, CT). The IC_{50} values were calculated by fitting the data by nonlinear regression using GraphPad Prism (GraphPad Software, Inc., San Diego, CA). Experiments were carried out twice with triplicate samples. The IC_{50} values are reported as an average of these samples plus the standard deviation.

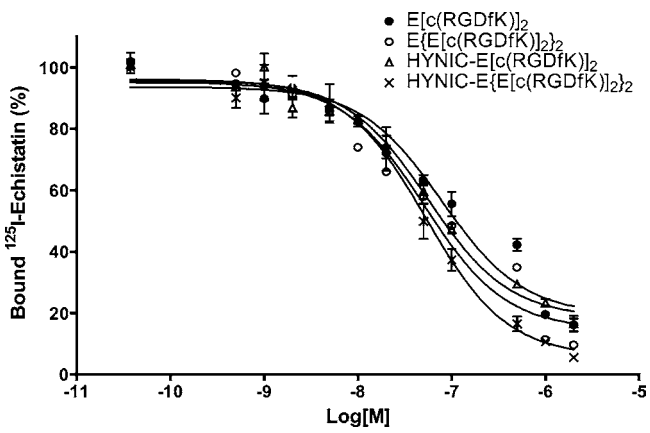


Figure 2. In vitro inhibition of ^{125}I-echistatin binding to $\alpha_v\beta_3$ integrin on MDA-MB-435 human breast cancer cells by E[c(RGDfK)]$_2$ (●), E{E[c(RGDfK)]$_2$}$_2$ (○), HYNIC-E[c(RGDfK)]$_2$ (△), and HYNIC-E{E-[c(RGDfK)]$_2$}$_2$ (×).

Breast Cancer Xenograft Model. Biodistribution, imaging, and metabolism studies were performed using athymic nude mice bearing MDA-MB-435 human breast cancer xenografts in compliance with NIH animal experiment guidelines (*Principles of Laboratory Animal Care*, NIH Publication No. 86-23, revised 1985). The animal protocols were approved by the Purdue University Animal Care and Use Committee (PACUC). Female athymic nude (nu/nu) mice were purchased from Harlan (Indianapolis, IN) at 4−5 weeks of age. The mice were implanted with 5×10^6 cells of MDA-MB-435 estrogen receptor-negative human breast cancer cells into the mammary fat pad. When tumors reached 0.4−0.6 cm in mean diameter, the tumor-bearing mice were used to biodistribution and imaging studies.

Biodistribution Protocol. Sixteen tumor-bearing mice (20−25 g) were anesthetized by intraperitoneal (i.p.) injection of ketamine (40−100 mg/kg) and xylazine (2−5 mg/kg). Once the animal was in surgical plane of anesthesia, as noted by lack of response to pain, the radiotracer (~1 μCi) dissolved in saline was administered via tail vein. Four tumor-bearing mice were sacrificed by exsanguinations and opening of the thoracic cavity at 5, 30, 60, and 120 min postinjection (p.i.). Blood was withdrawn from the heart through a syringe. Organs of interest (such as tumor, brain, eyes, heart, intestine, kidneys, liver, lungs, muscle, and spleen) were excised, washed with saline, dried with tissue, weighed, and counted on a γ-counter (Beckman RD8000). The organ uptake was calculated as a percentage of the injected dose per gram of wet tissue (%ID/g). For the blocking experiment, four tumor-bearing nude mice (20−25 g) were used, and each animal was administered 0.1 mL saline solution containing ~1 μCi of the test agent along with ~750 μg (~ 30 mg/kg) of E[c(RGDfK)]$_2$. At 1 h p.i., all four animals were sacrificed for organ biodistribution using the same procedure above.

Metabolism. Each tumor-bearing mouse was administered with the radiotracer (~100 μCi/mouse). The urine samples were collected at 2 h p.i. by manual void and were mixed with equal volume of acetonitrile. The mixture was centrifuged at 8000 rpm. The supernatant was collected and filtered through a 0.20 μm Millex-LG syringe filter unit. The filtrate was analyzed by

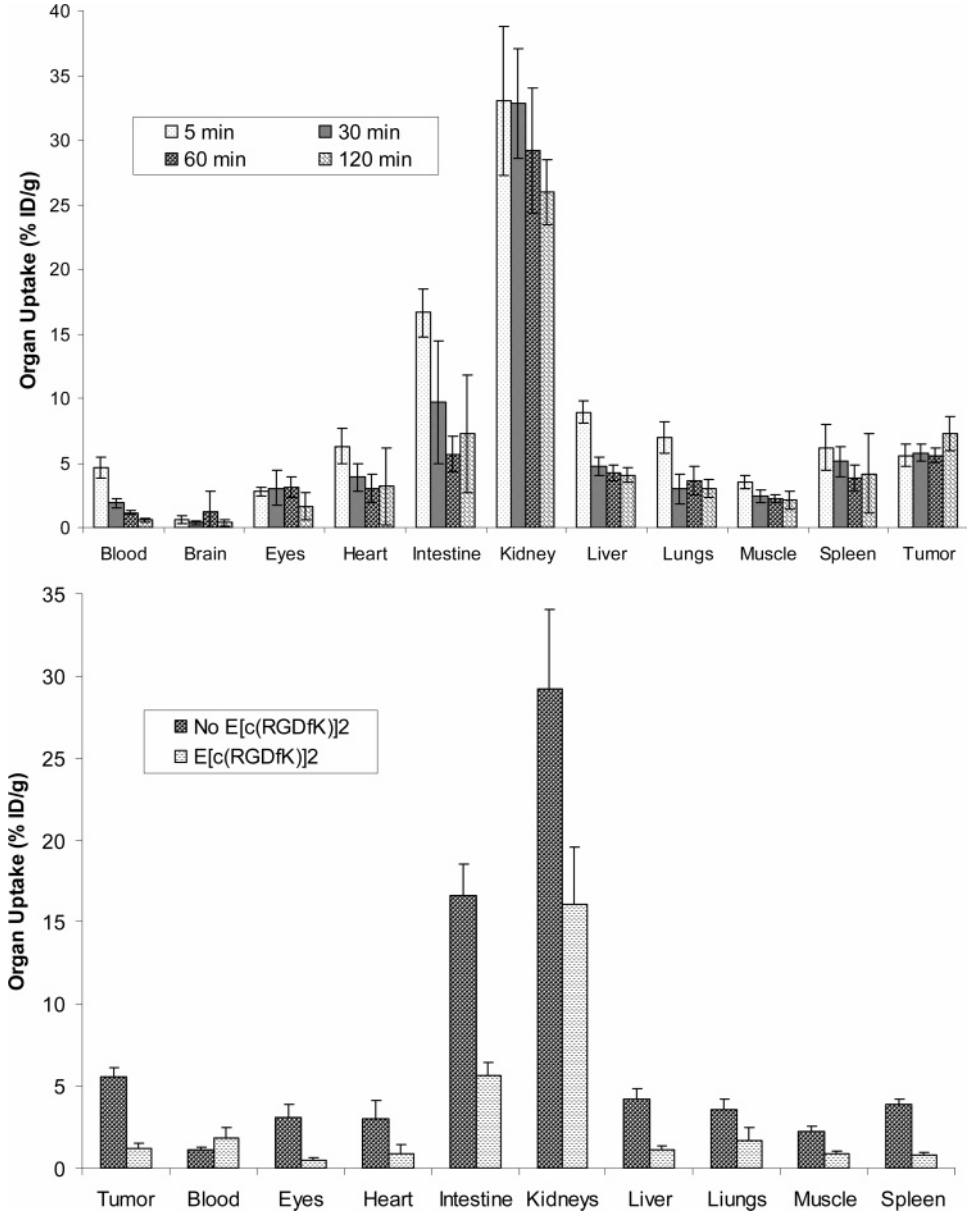


Figure 3. Top: Biodistribution data for [^{99m}Tc(HYNIC-tetramer)(tricine)(TPPTS)] at 5, 30, 60, and 120 min p.i. in nude mice bearing the MDA-MB-435 human breast cancer xenografts; Bottom: Comparison of the organ uptake (% ID/g) for [^{99m}Tc(HYNIC-tetramer)(tricine)(TPPTS)] at 60 min p.i. in the absence/presence of excess E[c(RGDfK)]$_2$. Each data point represents an average of biodistribution data in four animals.

radio-HPLC (Method 2). The feces samples were collected at 2 h p.i. and suspended in a mixture of 50% acetonitrile aqueous solution, and the resulting mixture was vortexed for 5−10 min. After centrifugation at 8000 rpm for 5 min, the supernatant was collected and passed through a 0.20 μm Millex-LG syringe driven filter unit. The filtrate was analyzed by radio-HPLC. Two tumor-bearing mice were used for the metabolism study.

SPECT Imaging. Imaging studies were performed by Dr. Wang's group using athymic nude mice bearing MDA-MB-435 breast cancer xenografts in accordance with guidelines of Peking University Health Science Center Animal Care and Use Committee. Animals were anesthetized with i.p. injection of sodium pentobarbital at a dose of 45.0 mg/kg. Each animal was administered ~400 μCi of the radiotracer in 0.2 mL of saline. Animals were placed prone on a dual head γ-camera (Siemens, E. CAM) equipped with a parallel-hole, low-energy, and high-resolution collimator. Anterior static images were acquired at 1, 2, and 4 h p.i. and were stored digitally in a 128 × 128 matrix. The acquisition count limits were set at 1000 K. After completion of imaging, animals were sacrificed by cervical dislocation.

Statistical Analysis. The biodistribution data and T/B ratios were reported as an average plus the standard variation based on the results from four animals for each time point. Comparison between two different radiotracers was also made using the one-way ANOVA test. The level of significance was set at $P < 0.05$.

RESULTS

Synthesis of HYNIC-Tetramer. The HYNIC-tetramer conjugate was prepared by coupling E{E[c(RGDfK)]$_2$}$_2$ with HYNIC-NHS under slightly basic condition (pH = 8.5−9.0) in a mixture of water and DMF (50:50 = v:v). It was purified by HPLC (Method 1). Its identity has been confirmed by ESI-MS data (m/z = 3050.93 for $[M + H]^+$ and 1526.89 for $[M + 2H]^{2+}$).

Integrin $\alpha_v\beta_3$ Binding. The integrin $\alpha_v\beta_3$-positive MDA-MB-435 breast cancer cells were used for the in vitro binding affinity studies instead of the immobilized integrin $\alpha_v\beta_3$. We compared the integrin $\alpha_v\beta_3$ binding affinity of HYNIC-tetramer, HYNIC-dimer, E[c(RGDfK)]$_2$, and E{E[c(RGDfK)]$_2$}$_2$ by

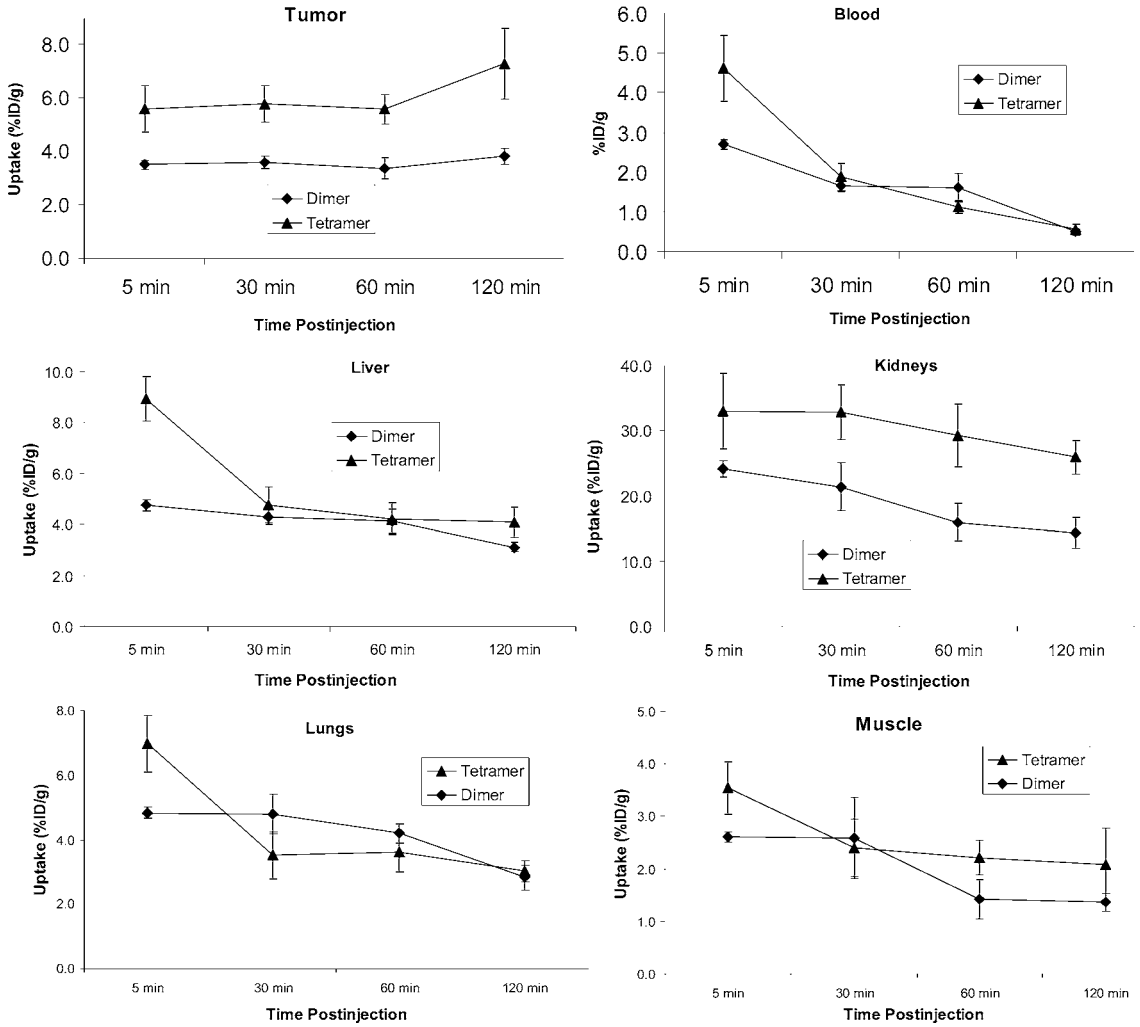


Figure 4. Direct comparison of organ uptake (% ID/g) between [^{99m}Tc(HYNIC-dimer)(tricine)(TPPTS)]) and [^{99m}Tc(HYNIC-tetramer)(tricine)-(TPPTS)]) in athymic nude mice bearing MDA-MB-435 human breast cancer xenografts.

competitive displacement of ^{125}I-echistatin. Both cyclic RGDfK peptides and their HYNIC conjugates inhibited the binding of ^{125}I-echistatin to MDA-MB-435 breast cancer cells (Figure 2). The IC_{50} values for $E\{E[c(RGDfK)]_2\}_2$ and $E[c(RGDfK)]_2$ were 51 ± 11 nM and 78 ± 27 nM, respectively. IC_{50} values for HYNIC-tetramer and HYNIC-dimer were 55 ± 11 nM and 52 ± 9 nM under the same condition. $E\{E[c(RGDfK)]_2\}_2$ has a slightly higher integrin $\alpha_v\beta_3$ binding affinity than $E[c(RGDfK)]_2$. There was no significant difference in the integrin $\alpha_v\beta_3$ binding affinity between their HYNIC conjugates within the experimental error. Attachment of HYNIC did not alter the binding affinity of the tetramer $E\{E[c(RGDfK)]_2\}_2$.

Radiochemistry. [^{99m}Tc(HYNIC-tetramer)(tricine)(TPPTS)] was prepared using a non-stannous formulation since TPPTS is a strong reducing agent for Na[$^{99m}TcO_4$] (*33*). The RCP was >95% with less than 0.5% of [^{99m}Tc]colloid. [^{99m}Tc(HYNIC-tetramer)(tricine)(TPPTS)] was analyzed using a reversed phase radio-HPLC method (Method 2). The log *P* value for [^{99m}Tc-(HYNIC-tetramer)(tricine)(TPPTS)] was −3.29 ± 0.22 in a mixture of n-octanol and 25 mM phosphate buffer, pH = 7.4. This value is lower than that (−2.66 ± 0.25) of its dimeric analogue [^{99m}Tc(HYNIC-dimer)(tricine)(TPPTS)], suggesting that increasing the peptide multiplicity decreases lipophilicity of the ^{99m}Tc-labeled cyclic RGDfK peptides. The solution stability of [^{99m}Tc(HYNIC-tetramer)(tricine)(TPPTS)] was monitored by radio-HPLC (Method 2). It was found that it remained stable in the kit matrix and in presence of cysteine challenge (1 mg/mL) for >12 h. It was also stable for >6 h after purification.

Biodistribution. [^{99m}Tc(HYNIC-tetramer)(tricine)(TPPTS)] was purified by HPLC to remove the "unlabeled" HYNIC-tetramer. Biodistribution was performed using the athymic nude mice bearing MDA-MB-435 human breast cancer xenografts. Figure 3 showed its biodistribution data in the selected organs with/without the co-injection of excess $E[c(RGDfK)]_2$. The organ uptake was expressed as %ID/g. Each data point represents an average in four animals. Figures 4 and 5 illustrate the comparison of organ uptake and T/B ratios between [^{99m}-Tc(HYNIC-tetramer)(tricine)(TPPTS)] and [^{99m}Tc(HYNIC-dimer)(tricine)(TPPTS)] in several selected organs, such as tumor, blood, liver, lungs, and kidneys. Biodistribution data and T/B ratios of [^{99m}Tc(HYNIC-dimer)(tricine)(TPPTS)] were obtained from our previous study (*24*).

In general, [^{99m}Tc(HYNIC-tetramer)(tricine)(TPPTS)] displayed a rapid clearance predominantly via renal route. The tumor uptake of [^{99m}Tc(HYNIC-tetramer)(tricine)(TPPTS)] (5.60 ± 0.87 %ID/g and 7.30 ± 1.32 %ID/g at 5 and 120 min p.i., respectively) was significantly higher than that of [^{99m}Tc-(HYNIC-dimer)(tricine)(TPPTS)] (3.50 ± 0.18 %ID/g and 3.82 ± 0.32 %ID/g at 5 and 120 min p.i., respectively) over the 2 h study period. The kidney uptake of [^{99m}Tc(HYNIC-tetramer)-(tricine)(TPPTS)] (33.05 ± 5.75 %ID/g and 25.93 ± 2.52 %ID/g at 5 and 120 min p.i., respectively) was much higher than that of [^{99m}Tc(HYNIC-dimer)(tricine)(TPPTS)] (24.15 ± 1.23 %ID/g and 14.33 ± 2.39 %ID/g at 5 and 120 min p.i., respectively) during the same study period. The blood radioactivity level for [^{99m}Tc(HYNIC-tetramer)(tricine)(TPPTS)]

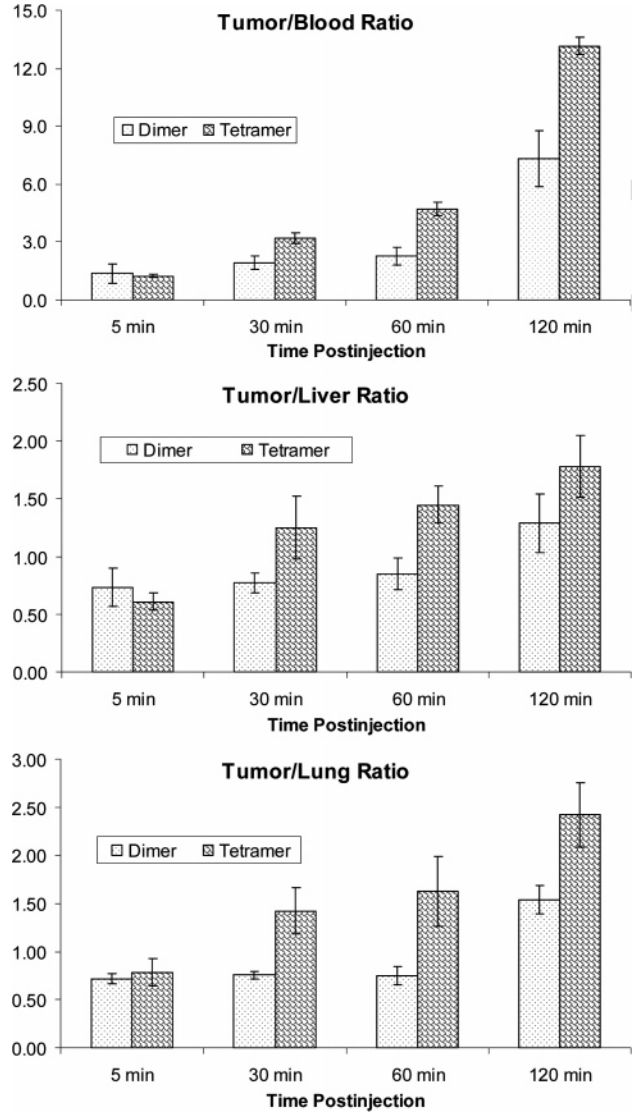


Figure 5. Direct comparison of T/B ratios between [^{99m}Tc(HYNIC-dimer)(tricine)(TPPTS)]) and [^{99m}Tc(HYNIC-tetramer)(tricine)(TPPTS)]) in athymic nude mice bearing MDA-MB-435 human breast cancer xenografts.

(4.61 ± 0.82 %ID/g) was significantly ($p < 0.01$) higher than that of [^{99m}Tc(HYNIC-dimer)(tricine)(TPPTS)] (2.70 ± 0.12 %ID/g) at 5 min p.i.; but this difference disappeared at 30−120 min p.i. (Figure 4). A similar trend was observed for their liver uptake. As a result, [^{99m}Tc(HYNIC-tetramer)-(tricine)(TPPTS)] has the tumor/blood, tumor/liver and tumor/lung ratios that are significantly better ($p < 0.05$) than those of [^{99m}Tc(HYNIC-dimer)(tricine)(TPPTS)] at 30−120 min p.i. (Figure 5).

Blocking Experiment. In this experiment, E[c(RGDfK)]$_2$ (IC_{50} = 78.27 ± 27.59 nM against ^{125}I-echistatin binding to the integrin $\alpha_v\beta_3$-positive MDA-MB-435 breast cancer cells) was used as the blocking agent at a dose of ∼30 mg/kg (∼750 μg per mouse). Such a high dose was used to make sure that the integrin $\alpha_v\beta_3$ is almost completely blocked. It was found that co-injection of a large excess of E[c(RGDfK)]$_2$ resulted in a significant reduction of the uptake of [^{99m}Tc(HYNIC-tetramer))(tricine)(TPPTS)] in the tumor. In addition, there was also substantial decrease of the uptake for [^{99m}Tc(HYNIC-tetramer))(tricine)(TPPTS)] in lungs, liver, spleen, and intestine (Figure 3). The muscle and kidney uptake was also inhibited (to a lesser degree). The blood activity in the presence of E[c(RGDfK)]$_2$ was higher than that without E[c(RGDfK)]$_2$.

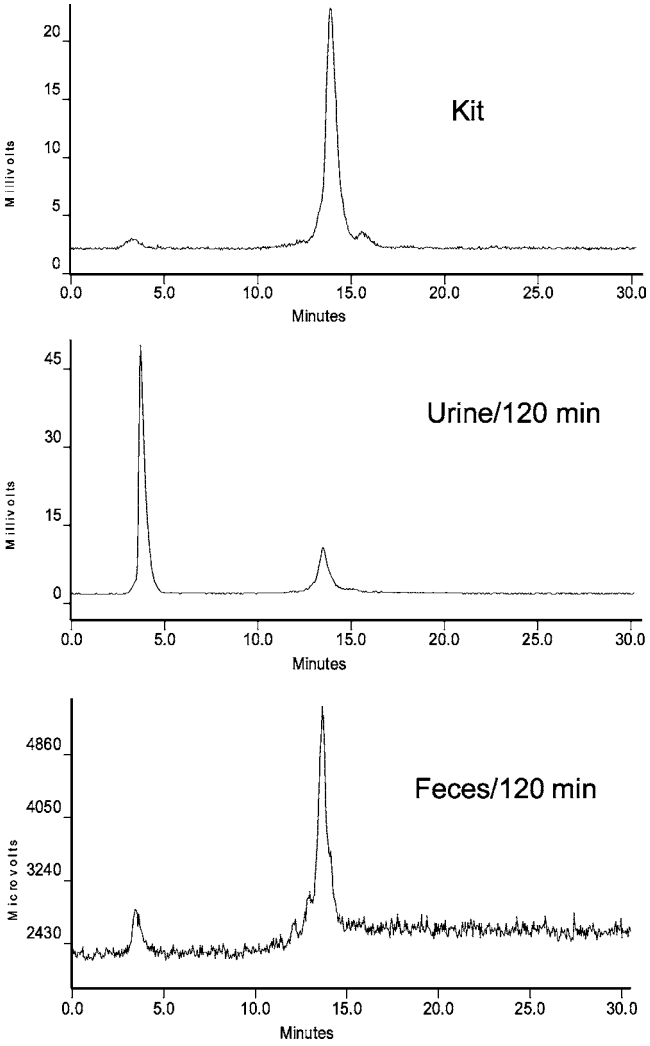


Figure 6. Radio-HPLC chromatograms of [^{99m}Tc(HYNIC-dimer)-(tricine)(TPPTS)] in the kit matrix before injection, in urine and feces at 120 min p.i. Each tumor-bearing mouse was administered with ∼3.7 MBq of radiotracer.

Metabolism. The metabolism study on [^{99m}Tc(HYNIC-tetramer)(tricine)(TPPTS)] was performed using the tumor-bearing mice. Since it is excreted via both renal and hepatobiliary routes, we collected samples from urine and feces to determine if they are able to retain their chemical integrity at 2 h postinjection. Figure 6 sowed typical radio-HPLC chromatograms of [^{99m}Tc(HYNIC-tetramer)(tricine)(TPPTS)] in the kit matrix, urine, and feces at 120 min postinjection. About 80% metabolite of [^{99m}Tc(HYNIC-tetramer)(tricine)(TPPTS)] was found in the urine while only ∼15% metabolism was detected in the feces sample at 2 h p.i. No efforts have been made to identify the metabolite(s).

SPECT Imaging. Figure 7 illustrated the selected SPECT images of tumor-bearing mice administered with ∼15 MBq of [^{99m}Tc(HYNIC-tetramer)(tricine)(TPPTS)] at 1, 2, and 4 h postinjection. Tumors were clearly visualized in all three SPECT images. The activity level in the abdominal region (particularly liver and lungs) was very low, which agreed well with the ex vivo biodistribution data at the same time point (Figure 4).

DISCUSSION

The in vivo distribution pattern of a ^{99m}Tc-based radiotracer is determined by several factors, including binding affinity of the targeting biomolecule, internalization of the radiotracer, Tc chelate, molecular charge, lipophilicity, and metabolic stability.

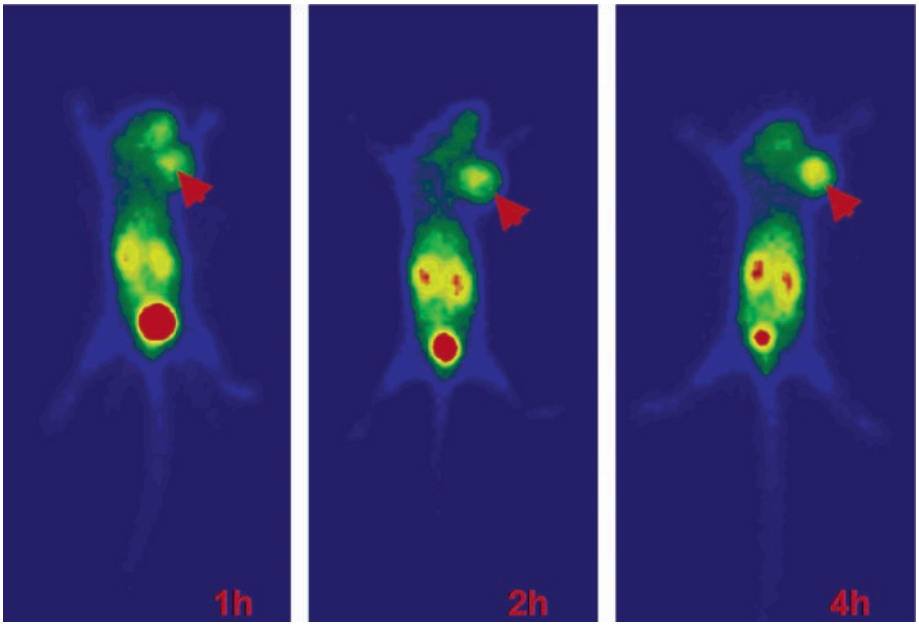


Figure 7. Representative static SPECT images of the tumor-bearing mice administered with ~15 MBq of [^{99m}Tc(HYNIC-tetramer)(tricine)-(TPPTS)] and at 1, 2, and 4 h p.i. Arrows indicate the presence of tumors.

Since the natural mode of interactions between integrin $\alpha_v\beta_3$ and RGD-containing proteins may involve multivalent binding sites, the idea to improve integrin $\alpha_v\beta_3$ binding affinity with multivalent RGD peptides could provide more effective antagonists with better targeting capability and higher cellular uptake through the integrin-dependent endocytosis pathway (*35*). Several groups applied the multivalent concept to develop integrin $\alpha_v\beta_3$-targeted radiotracers. Rajopadhye et al. were the first to use cyclic RGD peptide dimers, such as E[c(RGDfK)]$_2$, as targeting biomolecules for development of diagnostic (^{99m}Tc and ^{111}In) and therapeutic (^{90}Y) radiotracers (*37*, *38*). We also used E[c(RGDyK)]$_2$ to prepare ^{64}Cu-based PET radiotracers (*26*). Kessler et al. reported the hexaethylene glycolic acid (HEG) and poly(lysine)-tethered cyclic RGDfE dimers and tetramers with better integrin $\alpha_v\beta_3$ binding affinity than its monomeric analogues (*30*, *31*). The HEG and poly-(lysine) linkers were used to increase the distance between RGD motifs. It was found that the minimum distance is about 3.5 nm (~25 bond distances) for simultaneous binding of two RGD motifs in the immobilized integrin $\alpha_v\beta_3$ assay (*30*, *31*).

The success of E[c(RGDfK)]$_2$ and E[c(RGDyK)]$_2$ as targeting biomolecules for the integrin $\alpha_v\beta_3$ radiotracers is very intriguing. Given the short distance between two cyclic RGD motifs, it is unlikely that they would bind to the adjacent integrin $\alpha_v\beta_3$ receptors simultaneously. However, the binding of one RGD motif to integrin $\alpha_v\beta_3$ will significantly increase "local concentration" of the second RGD motif in the vicinity of receptor site. This might lead to the enhanced integrin $\alpha_v\beta_3$ binding rate or reduced dissociation rate of RGD peptide from integrin $\alpha_v\beta_3$. The high "local RGD peptide concentration" may explain the higher tumor uptake and longer tumor retention times of the radiolabeled (^{99m}Tc, ^{111}In, and ^{64}Cu) cyclic RGD dimers as compared to their monomeric analogues (*26*, *37*, *38*).

The longest distance between RGD motifs of E{E[c(RG-DfK)]$_2$}$_2$ is ~30 bond lengths. Its integrin $\alpha_v\beta_3$ binding affinity (IC_{50} = 15 ± 1 nM) is higher than that of E[c(RGDfK)]$_2$ (IC_{50} = 32 ± 2 nM) against ^{125}I-echistatin in binding to the integrin $\alpha_v\beta_3$-positive U87MG glioma cancer cells (*27*). In this study, the integrin $\alpha_v\beta_3$ binding affinity of E{E[c(RGDfK)]$_2$}$_2$ (IC_{50} = 51 ± 11 nM) is only slightly higher than that of E[c(RGDfK)]$_2$ (IC_{50} = 78 ± 27 nM) against ^{125}I-echistatin binding to the integrin $\alpha_v\beta_3$-positive MDA-MB-435 breast cancer cells. There is no significant difference in IC_{50} values between HYNIC-tetramer (55 ± 11 nM) and HYNIC-dimer (52 ± 9 nM). We believe that the different results obtained from two in vitro assays might be related to the integrin $\alpha_v\beta_3$ expression level on tumor cells (glioma versus breast cancer). Recently, we have demonstrated that the integrin $\alpha_v\beta_3$ density on MDA-MB-435 breast cancer cells was not as high as that on U87MG glioma cancer cells (*39*). Therefore, the distance between the two neighboring integrin $\alpha_v\beta_3$ receptors would be longer, which makes it more difficult for two RGD motifs in E{E[c(RGDfK)]$_2$}$_2$ and E[c(RGDfK)]$_2$ to bind to the adjacent integrin $\alpha_v\beta_3$ simultaneously. This might explain the fact that the IC_{50} of HYNIC-tetramer (55 ± 11 nM) using MDA-MB-435 breast cancer cells is more than 3-fold higher than that (15 ± 1 nM) using U87MG glioma cancer cells. This may also explain why the IC_{50} values for RGD peptides (monomers, dimers, and tetramers) obtained with the immobilized integrin $\alpha_v\beta_3$ assay (*26*−*29*) are always much lower that those obtained using the whole-cell integrin $\alpha_v\beta_3$-binding assay (*30*, *31*).

The in vivo tumor targeting capability of [^{99m}Tc(HYNIC-tetramer)(tricine)(TPPTS)] was evaluated in athymic nude mice bearing MDA-MB-435 human breast cancer xenografts. It was found to have a much higher tumor uptake than its dimeric analogue over the 2 h study period, even though HYNIC-tetramer has the IC_{50} (55 ± 11 nM) similar to that of HYNIC-dimer (52 ± 9 nM). Among the radiotracers evaluated in this animal model (*24*, *25*), [^{99m}Tc(HYNIC-tetramer)(tricine)(TPPTS)] has the highest tumor uptake (7.30 ± 1.32 %ID/g) at 2 h p.i. One might argue that the enhanced tumor uptake is related to higher molecular weight of the cyclic RGDfK tetramer, resulting in longer blood circulation time. However, there is no significant difference in the blood activity levels and the liver uptake between [^{99m}Tc(HYNIC-tetramer)(tricine)(TPPTS)] and [^{99m}Tc(HYNIC-dimer)(tricine)(TPPTS)] at 30−120 min p.i. The tumor/blood ratio of [^{99m}Tc(HYNIC-tetramer)(tricine)(TPPTS)] (13.15 ± 1.45) is almost twice of that of [^{99m}Tc(HYNIC-dimer)-(tricine)(TPPTS)] (7.32 ± 0.44) at 120 min p.i. (Figure 5). The tumor/liver and tumor/lung ratios of [^{99m}Tc(HYNIC-tetramer)-(tricine)(TPPTS)] are also significantly better ($p < 0.05$) than those of [^{99m}Tc(HYNIC-dimer)(tricine)(TPPTS)] at 30−120 min

p.i. Clearly, the tetramer E{E[c(RGDfK)]$_2$}$_2$ is a better integrin $\alpha_v\beta_3$-targeting biomolecule than its monomeric and dimeric analogues.

The kidney uptake of [^{99m}Tc(HYNIC-tetramer)(tricine)(TPPTS)] is significantly higher than that of its dimeric analogue at all four time points (Figure 4). Small peptides in blood plasma are filtered through glomerular capillaries in the kidneys and subsequently reabsorbed by proximal tubular cells by carrier-mediated endocytosis. Membranes of renal tabular cells contain negatively charged sites to which the positively charged groups, such as guanidine moieties in cyclic RGD peptides, are expected to bind. In this respect, one might suggest that different charges of E{E[c(RGDfK)]$_2$}$_2$ and E[c(RGDfK)]$_2$ could cause the difference in kidney uptake of [^{99m}Tc(HYNIC-tetramer)(tricine)-(TPPTS)] and [^{99m}Tc(HYNIC-dimer)(tricine)(TPPTS)] because E{E[c(RGDfK)]$_2$}$_2$ has more positively charged R-residues under physiological conditions. It has been shown that positively charged peptides are more efficiently reabsorbed by the proximal renal tubular cell than neutral peptides (*40*). The high kidney uptake and prolonged kidney retention has also been attributed to positively charged K residues of ^{99m}Tc-DKCK-c(RGDfK), in which one K residue is part of the Tc chelate and one is used as a linker between c(RGDfK) and the Tc chelate in addition to the K residue in c(RGDfK) (*40*). However, this explanation cannot account for the fact that the kidney uptake of [^{99m}Tc(HYNIC-tetramer)(tricine)(TPPTS)] can be partially blocked by excess E[c(RGDfK)]$_2$ (Figure 3). Therefore, the high kidney uptake and prolonged kidney retention of [^{99m}Tc-(HYNIC-tetramer)(tricine)(TPPTS)] is probably caused by several factors, including the ^{99m}Tc chelate (^{99m}Tc-HYNIC-tricine-TPPTS), presence of more R-residues, integrin $\alpha_v\beta_3$-binding, high molecular weight of E{E[c(RGDfK)]$_2$}$_2$.

The tumor-specificity of [^{99m}Tc(HYNIC-tetramer)(tricine)-(TPPTS)] was demonstrated by co-injecting excess E[c(RGD-fK)]$_2$, which resulted in significant reduction in the tumor uptake of [^{99m}Tc(HYNIC-tetramer))(tricine)(TPPTS)]. Since the integrin $\alpha_v\beta_3$ expression in lungs and liver of rats has been documented (*41*), it is not surprising to see a high uptake in liver and lungs of tumor-bearing mice. The blood activity of [^{99m}Tc(HYNIC-tetramer))(tricine)(TPPTS)] with excess E[c(RGDfK)]$_2$ was higher than that without E[c(RGDfK)]$_2$, is probably caused by its saturation effect. Similar results were obtained for [^{99m}Tc-(HYNIC-dimer)(tricine)(TPPTS)] and ^{111}In-DOTA−E[c(RGD-fK)]$_2$ in the BALB/c mice bearing ovarian carcinoma (*28*, *29*), ^{64}Cu-DOTA−E[c(RGDfK)]$_2$ in nude mice bearing the MDA-MB-435 breast cancer xenografts (*26*), and ^{64}Cu-DOTA−E{E-[c(RGDfK)]$_2$}$_2$ in nude mice bearing UG87MG glioma xenografts (*27*).

Radiolabeled cyclic RGD peptides (monomers, dimers, and tetramers) often accumulate in kidneys. Extensive metabolism has been detected for the ^{99m}Tc-labeled RGDfK monomer (*39*) and ^{64}Cu-labeled cyclic RGDfK tetramer in kidneys and urine samples (*27*). In this study, only 20% of [^{99m}Tc(HYNIC-tetramer)(tricine)(TPPTS)] remained intact in urine at 120 min p.i. Similar results were observed for [^{99m}Tc(HYNIC-dimer)-(tricine)(TPPTS)] (*24*). Surprisingly, >85% of [^{99m}Tc(HYNIC-tetramer)(tricine)(TPPTS)] remains intact in the feces sample at 2 h p.i. It is possible that the metabolized species can be reabsorbed and then excreted via renal system.

CONCLUSION

In summary, we studied biodistribution properties of the ^{99m}Tc-labeled RGD tetramer, [^{99m}Tc(HYNIC-tetramer)(tricine)-(TPPTS)], in athymic nude mice bearing MDA-MB-435 human breast cancer xenografts. The key finding of this study is that the tetramer is a much better integrin $\alpha_v\beta_3$-targeting biomolecule than its monomeric and dimeric analogues. The peptide multiplicity has a significant impact on biodistribution characteristics and metabolic patterns of ^{99m}Tc-labeled cyclic RGD peptides. On the basis of tumor uptake and T/B (particularly tumor/liver and tumor/lung) ratios, we believe that [^{99m}Tc-(HYNIC-tetramer)(tricine)(TPPTS)] is a promising new radiotracer for noninvasive imaging of the integrin $\alpha_v\beta_3$-positive tumors by SPECT.

ACKNOWLEDGMENT

The authors would like to thank Lee Ann Grote, Carol Dowell, and Cheryl Anderson from the Department of Veterinary Clinical Sciences, Purdue University, for their assistance with biodistribution studies. This work is supported in part by research grants: 1R01 CA115883-01A2 (S.L. and C.X.) from the National Cancer Institute (NCI) and BCTR0503947 (S.L.) from the Susan G. Komen Breast Cancer Foundation.

Supporting Information Available: Additional experimental data. This material is available free of charge via the Internet at http://pubs.acs.org.

LITERATURE CITED

(1) Folkman, J. (2002) Role of angiogenesis in tumor growth and metastasis. *Semim. Oncol. 29*, 15−18.
(2) Mousa, S. A. (2000) Integrins as novel drug discovery targets: potential therapeutic and diagnostic implications. *Emerg. Ther. Targets 4*, 143−153.
(3) Bögler, O., and Mikkelsen, T. (2003) Angiogenesis in Glioma: molecular mechanisms and roadblocks to translation. *Cancer J. 9*, 205−213.
(4) Hwang, R., and Varner, J. V. (2004) The role of integrins in tumor angiogenesis. *Hematol. Oncol. Clin. N. Am. 18*, 991−1006.
(5) Kumar, C. C. (2003) Integrin $\alpha_v\beta_3$ as a therapeutic target for blocking tumor-induced angiogenesis. *Curr. Drug Targets 4*, 123−131.
(6) Brooks, P. C., Clark, R. A. F., and Cheresh, D. A. (1994) Requirement of vascular integrin $\alpha_v\beta_3$ for angiogenesis. *Science 264*, 569−571.
(7) Horton, M. A. (1997) The $\alpha_v\beta_3$ integrin "vitronectin receptor". *Int. J. Biochem. Cell Biol. 29*, 721−725.
(8) Bello, L., Francolini, M., Marthyn, P., Zhang, J. P., Carroll, R. S., Nikas, D. C., Strasser, J. F., Villani, R., Cheresh, D. A., and Black, P. M. (20 $\alpha_v\beta_3$ and $\alpha_v\beta_5$ integrin expression in glioma periphery. *Neurosugery 49*, 380−389.
(9) Meitar, D., Crawford, S. E., Rademaker, A. W., and Cohn, S. L. (1996) Tumor angiogenesis correlates with metastatic disease, N-*myc*-amplification, and poor outcome in human neuroblastoma. *J. Clin. Oncol. 14*, 405−414.
(10) Gasparini, G., Brooks, P. C., Biganzoli, E., Vermeulen, P. B., Bonoldi, E., Dirix, L. Y., Ranieri, G., Miceli, R., and Cheresh, D. A. (1998) Vascular integrin $\alpha_v\beta_3$: a new prognostic indicator in breast cancer. *Clin. Cancer Res. 4*, 2625−2634.
(11) Albelda, S. M., Mette, S. A., Elder, D. E., Stewart, R. M., Damjanovich, L., Herlyn, M., and Buck, C. A. (1990) Integrin distribution in maliganant melanoma: association of the subunit with tumor progression. *Cancer Res. 50*, 6757−6764.
(12) Falcioni, R., Cimino, L., Gentileschi, M. P., D'Agnano, I., Zupi, G., Kennel, S. J., and Sacchi, A. (1994) Expression of β_1, β_3, β_4 and β_5 integrins by human lung carcinoma cells of different histotypes. *Exp. Cell Res. 210*, 113−122.
(13) Sengupta, S., Chattopadhyay, N., Mitra, A., Ray, S., Dasgupta, S., and Chatterjee, A. (2001) Role of $\alpha_v\beta_3$ integrin receptors in breast tumor. *J. Exp. Clin. Cancer Res. 20*, 585−590.
(14) Zitzmann, S., Ehemann, V., and Schwab, M. (2002) Arginine-Glycine-Aspartic acid (RGD)-peptide binds to both tumor and tumor endothelial cells in vivo. *Cancer Res. 62*, 5139−5143.
(15) Weber, W. A., Haubner, R., Vabuliene, E., Kuhnast, B., Webster, H. J., and Schwaiger, M. (2001) Tumor angiogenesis targeting using imaging agents. *Q. J. Nucl. Med. 45*, 179−182.
(16) Costouros, N. G., Diehn, F. E., and Libutti, S. K. (2002) Molecular imaging of tumor angiogenesis. *J. Cell Biol. (Suppl.) 39*, 72−78.

(17) van de Wiele, C., Oltenfreiter, R., De Winter, O., Signore, A., Slegers, G., and Dieckx, R. A. (2002) Tumor angiogenesis pathways: related clinical issues and implications for nuclear medicine imaging. *Eur. J. Nucl. Med. Mol. Imaging 29*, 699−709.

(18) Liu, S., Robinson, S. P., and Edwards, D. S. (2003) Integrin $\alpha_v\beta_3$ directed radiopharmaceuticals for tumor imaging. *Drugs Future 28*, 551−564.

(19) Liu, S., Robinson, S. P., and Edwards, D. S. (2005) Radiolabeled integrin $\alpha_v\beta_3$ antagonists as radiopharmaceuticals for tumor radiotherapy. *Topics Curr. Chem. 252*, 117−153.

(20) Haubner, R., and Wester, H. R. (2004) Radiolabeled tracers for imaging of tumor angiogenesis and evaluation of anti-angiogenic therapies. *Curr. Pharm. Des. 10*, 1439−1455.

(21) Wester, H. R., and Kessler, H. (2005) Molecular targeting with peptides or peptide-polymer conjugates: just a question of size? *J. Nucl. Med. 46*, 1940−1945.

(22) Chen, X. (2006) Multimodality imaging of tumor integrin $\alpha_v\beta_3$ expression. *Mini Rev. Med. Chem. 6*, 227−234.

(23) Liu, S., Edwards, D. S., Ziegler, M. C., Harris, A. R., Hemingway, S. J., and Barrett, J. A. (2001) ^{99m}Tc-Labeling of a hydrazinonicotinamide-conjugated vitronectin receptor antagonist useful for imaging tumors. *Bioconjugate Chem. 12*, 624−629.

(24) Liu, S., Hsieh, W. Y., Kim, Y. S., and Mohammed, S. I. (2005) Effect of coligands on biodistribution characteristics of ternary ligand ^{99m}Tc complexes of a HYNIC-conjugated cyclic RGDfK dimer. *Bioconjugate Chem. 16*, 1580−1588.

(25) Jia, B., Shi, J., Yang, Z., Xu, B., Liu, Z., Zhao, H., Liu, S., and Wang, F. (2006) ^{99m}Tc-labeled cyclic RGDfK dimer: initial evaluation for SPECT imaging of glioma integrin $\alpha_v\beta_3$ expression. *Bioconjugate Chem. 17*, 1069−1076.

(26) Chen, X., Liu, S., Hou, Y., Tohme, M., Park, R., Bading, J. R., and Conti, P. S. (2004) MicroPET imaging of breast cancer $\alpha_v\beta_3$-integrin expression with ^{64}Cu-labeled dimeric RGD peptides. *Mol. Imag. Biol. 6*, 350−359.

(27) Wu, Y., Zhang, X., Xiong, Z., Cheng, Z., Fisher, D. R., Liu, S., Gambhir, S. S., and Chen, X. (2005) MicroPET imaging of glioma α_v-integrin expression using ^{64}Cu-labeled tetrameric RGD peptide. *J. Nucl. Med. 46*, 1707−1718.

(28) Janssen, M., Oyen, W. J. G., Massuger, L. F. A. G., Frielink, C., Dijkgraaf, I., Edwards, D. S., Rajopadyhe, M., Corsten, F. H. M., and Boerman, O. C. (2002) Comparison of a monomeric and dimeric radiolabeled RGD-peptide for tumor targeting. *Cancer Biother. Radiopharm. 17*, 641−646.

(29) Janssen, M. L., Oyen, W. J. G., Dijkgraaf, I., Massuger, L. F., Frielink, C., Edwards, D. S., Rajopadyhe, M., Boonstra, H., Corsten, F. H., and Boerman, O. C. (2002) Tumor targeting with radiolabeled $\alpha_v\beta_3$ integrin binding peptides in a nude mouse model. *Cancer Res. 62*, 6146−6151.

(30) Poethko, T., Schottelius, M., Thumshirn, G., Herz, M., Haubner, R., Henriksen, G., Kessler, H., Schwaiger, M., and Wester, H.-J. (2004) Chemoselective pre-conjugate radiohalogenation of unprotected mono- and multimeric peptides via oxime formation. *Radiochim. Acta 92*, 317−327.

(31) Thumshirn, G., Hersel, U., Goodman, S. L., and Kessler, H. (2003) Multimeric cyclic RGD peptides as potential tools for tumor targeting: solid-phase peptide synthesis and chemoselective oxime ligation. *Chem. Eur. J. 9*, 2717−2725.

(32) Dijkgraaf, I., John, A. W., Kruijtzer, J. A. W., Liu, S., Soede, A., Oyen, W. J. G., Corstens, F. H. M., Liskamp, R. M. J., and Boerman, O. C. (2007) Improved targeting of $\alpha_v\beta_3$ by multimerization of RGD peptides. *Eur. J. Nucl. Med. Mol. Imaging 34*, 267−273.

(33) Liu, S. (2005) 6-Hydrazinonicotinamide derivatives as bifunctional coupling agents for ^{99m}Tc-labeling of small biomolecules. *Topics Curr. Chem. 252*, 117−153.

(34) Harris, T. D., Sworin, M., Williams, N., Rajopadhye, M., Damphousse, P. R., Glowacka, D., Poirier, M. J., and Yu, K. (1999) Synthesis of stable hydrazones of a hydrazinonicotinyl-modified peptide for the preparation of ^{99m}Tc-labeled radiopharmaceuticals. *Bioconjugate Chem. 10*, 808−814.

(35) Hynes, R. O. (2002) Integrins: bidirectional, allosteric signaling machines. *Cell 110*, 673−687.

(36) Boturyn, D., Coll, J. L., Garanger, E., Favrot, M. C., and Dumy, P. (2004) Template assembled cyclopeptides as multimeric system for integrin targeting and endocytosis. *J. Am. Chem. Soc. 126*, 5730−5739.

(37) Rajopadhye, M., Harris, A. R., Nguyen, H. M., Overoye, K. L., Bartis, J., Liu, S., Edwards, D. S., and Barrett, J. A. (2000) RP593, a ^{99m}Tc-labeled $\alpha_v\beta_3/\alpha_v\beta_5$ antagonist, rapidly detects spontaneous tumors in mice and dogs. 47th Annual Meeting of SNM, St. Louis, Missouri. *J. Nucl. Med. 41*, 34P.

(38) Janssen, M. L., Frielink, C., Dijkgraaf, I., Oyen, W. J., Edwards, D. S., Liu, S., Rajopadhye, M., Massuger, L. F., Corstens, F. H., and Boerman, O. C. (2004) Improved tumor targeting of radiolabeled RGD-peptides using rapid dose fractionation. *Cancer Biother. Radiopharm. 19*, 399−404.

(39) Zhang, X., Xiong, Z., Wu, Y., Cai, W., Tseng, J., Gambir, S. S., and Chen, X. (2006) Quantitative PET imaging of tumor integrin $\alpha_v\beta_3$ expression with ^{18}F-FRGD2. *J. Nucl. Med. 47*, 113−121.

(40) Haubner, R., Bruchertseifer, F., Bock, M., Schwaiger, M., and Wester, H. J. (2004) Synthesis and biological evaluation of ^{99m}Tc-labeled cyclic RGD peptide for imaging integrin $\alpha_v\beta_3$ expression. *Nuklearmedizin 43*, 26−32.

(41) Singh, B., Fu, C. Z., and Bhattacharya. (2000) Vascular expression of the $\alpha_v\beta_3$-integrin in lung and other organs. *Am. J. Physiol. Lung Cell Mol. Physiol. 278*, L217−L226.

BC0603081

Fusion Antibody for Alzheimer's Disease with Bidirectional Transport Across the Blood−Brain Barrier and Aβ Fibril Disaggregation

Ruben J. Boado,[†] Yufeng Zhang,[†] Yun Zhang,[†] Chun-Fang Xia,[‡] and William M. Pardridge*[,‡]

ArmaGen Technologies, Incorporated, 914 Colorado Avenue, Santa Monica, California, and Department of Medicine, University of California at Los Angeles, Los Angeles, California. Received November 7, 2006; Revised Manuscript Received December 29, 2006

Delivery of monoclonal antibody therapeutics across the blood−brain barrier is an obstacle to the diagnosis or therapy of CNS disease with antibody drugs. The immune therapy of Alzheimer's disease attempts to disaggregate the amyloid plaque of Alzheimer's disease with an anti-Aβ monoclonal antibody. The present work is based on a three-step model of immune therapy of Alzheimer's disease: (1) influx of the anti-Aβ monoclonal antibody across the blood−brain barrier in the blood to brain direction, (2) binding and disaggregation of Aβ fibrils in brain, and (3) efflux of the anti-Aβ monoclonal antibody across the blood−brain barrier in the brain to blood direction. This is accomplished with the genetic engineering of a trifunctional fusion antibody that binds (1) the human insulin receptor, which mediates the influx from blood to brain across the blood−brain barrier, (2) the Aβ fibril to disaggregate amyloid plaque, and (3) the Fc receptor, which mediates the efflux from brain to blood across the blood−brain barrier. This fusion protein is a new antibody-based therapeutic for Alzheimer's disease that is specifically engineered to cross the human blood−brain barrier in both directions.

INTRODUCTION

Monoclonal antibodies (MAb) have the potential to be new pharmaceutical agents for the diagnosis or therapy of brain disease. However, MAb's are large-molecule drugs that do not cross the blood−brain barrier (BBB). The immune therapy of Alzheimer's disease (AD) began with the active immunization of mice against the 40 amino acid amyloid Aβ peptide of AD (*1*). It was found that certain anti-Aβ antibodies could clear the brain of amyloid plaque following active immunization (*1*), which correlated with in vitro studies showing that certain anti-Aβ antibodies disaggregated preformed Aβ amyloid fibrils (*2*, *3*). The intracerebral injection of anti-Aβ antibodies in AD transgenic mice results in the rapid clearance of pre-existing plaque (*4*−*6*) and repair of dystrophic neurites (*4*, *6*). However, if anti-Aβ antibodies in the blood are to disaggregate the Aβ amyloid in the brain, there must be a mechanism for circulating antibodies to cross the BBB and enter the brain from blood. In active immunization, the mice were immunized with Complete Freund's adjuvant (*1*), which enabled circulating anti-Aβ antibodies to enter the brain from blood, because Complete Freund's adjuvant, and anti-mannan antibodies, cause BBB disruption (*7*, *8*). BBB disruption causes neuropathologic changes in the brain microvasculature (*9*) and in the brain (*10*). What is needed is an anti-Aβ MAb that is engineered to cross the BBB without the requirement for BBB disruption.

Large-molecule drugs, such as antibody therapeutics, can cross the BBB, if the molecule is able to access specific receptor-mediated transport (RMT) systems within the BBB, such as the BBB insulin receptor or BBB transferrin receptor (*11*). A protein drug that is not a ligand for a BBB RMT system can still undergo transport across the BBB, if the MAb is conjugated to a BBB molecular Trojan horse. The latter is an endogenous ligand or peptidomimetic MAb that crosses the BBB via the endogenous RMT systems. Moreover, for certain brain diseases such as AD, there must also be a mechanism for efflux from brain back to blood of the complex of the therapeutic antibody and the Aβ peptide. Otherwise, there would be no net clearance of the Aβ amyloid peptide from AD brain. Therefore, an antibody therapeutic for AD must be engineered to enable transport across the BBB in both directions.

The present work describes the genetic engineering, expression, and validation of an anti-Aβ fusion antibody that is engineered to cross the BBB in both the blood to brain and the brain to blood directions. The immune therapy of AD is viewed as a three-step process (Figure 1): (a) influx of the anti-Aβ antibody from blood to brain across the BBB, (b) binding to and disaggregation of Aβ fibrils behind the BBB, and (c) efflux of the Aβ-antibody complex from brain back to blood. The present studies describe the genetic engineering of a fusion antibody that is a trifunctional molecule. As shown in Figure 2, the "head" of the fusion antibody binds the human insulin receptor (HIR). The insulin receptor is highly expressed at the human BBB (*12*) and mediates the brain uptake of circulating insulin (*13*). In addition, the BBB insulin receptor mediates the brain uptake of certain peptidomimetic monoclonal antibodies (MAb) to the insulin receptor (*14*). The genetic engineering of either a chimeric or a humanized MAb to the HIR has been described previously (*15*, *16*), and both HIRMAbs are rapidly transported from blood to brain across the BBB of the rhesus monkey in vivo. The "tail" of the fusion antibody (Figure 2) is composed of a single-chain Fv (ScFv) antibody directed against the amino-terminal portion of the Aβ peptide. The bivalent nature of the anti-Aβ MAb is restored when each ScFv monomer is fused to the carboxyl terminus of the heavy chain of the HIRMAb, as depicted in Figure 2. The "midsection" of the fusion antibody contains the CH_2-CH_3 interface of the human IgG constant region, which is the binding site for the neonatal Fc receptor or FcRn (*17*). Unlike plasma proteins such as albumin, IgG molecules are rapidly exported unidirectionally from brain to blood across the BBB via a FcR (*18*). Confocal

* Dr. William M. Pardridge, UCLA Warren Hall 13-164, 900 Veteran Ave., Los Angeles, CA 90024. Ph: (310) 825-8858. Fax: (310) 206-5163. E-mail: wpardridge@mednet.ucla.edu.

[†] ArmaGen Technologies, Incorporated.

[‡] University of California at Los Angeles.

10.1021/bc060349x CCC: $37.00 © 2007 American Chemical Society
Published on Web 02/22/2007

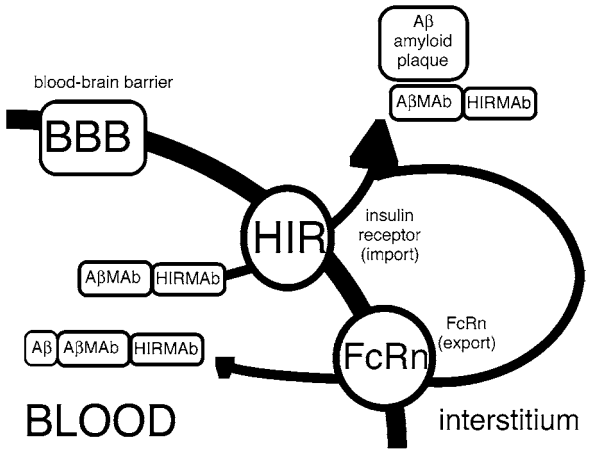


Figure 1. Import−export model of Aβ antibody therapeutics. The fusion antibody clears amyloid from brain in AD via three sequential steps, and each of these three sequential steps uses separate parts of the fusion antibody molecule. Step 1 is the influx of the fusion antibody from blood to brain across the BBB, which is mediated by binding of the fusion antibody to the BBB HIR. Step 2 is binding of the fusion antibody to the amyloid plaque in AD, which promotes disaggregation of the amyloid plaque, and this binding to the plaque is mediated by the anti-Aβ ScFv part of the fusion antibody. Step 3 is the efflux of the fusion antibody from brain to blood across the BBB, which is mediated by binding of the fusion antibody to the BBB FcRn at the CH_2-CH_3 interface of the Fc region of the fusion antibody.

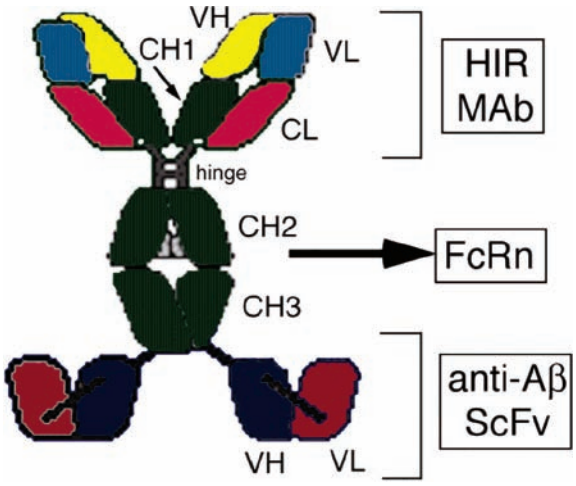


Figure 2. Antibody fusion protein with three functional domains. The first domain, the HIRMAb, binds the BBB HIR to trigger influx across the BBB. The second domain, the CH_2/CH_3 interface of the Fc region, binds to the BBB FcRn to trigger efflux from brain back to blood. The third domain, the anti-Aβ ScFv fused to the CH_3 region, binds to the Aβ amyloid peptide of AD to cause disaggregation of amyloid in brain.

microscopy studies shows the principle BBB FcR isoform is the FcRn (*19*). The FcRn is an Fc receptor that is distinct from classical Fc receptors and is responsible for transcytosis of IgG molecules in peripheral tissues (*20*). Following administration of the fusion antibody into the blood stream, the protein is enabled to cross the BBB in the blood to brain direction, bind and disaggregate Aβ fibrils in the brain of AD, and undergo efflux from brain back to blood (Figure 1).

EXPERIMENTAL PROCEDURES

Genetic Engineering. The variable region of the heavy chain (VH) and the variable region of the light chain (VL) of the murine anti-Aβ ScFv were cloned by PCR using a cDNA template derived from VH- and VL-specific primers described previously (*21*) and poly A+ RNA isolated from the murine hybridoma cell line. Following PCR and agarose gel electrophoresis, the expected major cDNA bands corresponding to the PCR amplified ~0.4 kilobase (kb) VL cDNA and ~0.4 kb VH cDNA were obtained. The VH and VL bands were isolated from the agarose gels and subcloned into a ScFv vector to link the VH and VL genes aside a gene encoding a 17 amino acid linker; the VL gene was followed by a sequence that encoded the 10 amino acid c-myc epitope (EQKLISEEDL) of the 9E10 MAb, as described previously (*21*). The anti-Aβ ScFv cDNA was subcloned into the pcDNA3.1 vector to produce the pCD−ScFv plasmid.

The engineering of the gene encoding the heavy chain of the fusion antibody was done in two steps: (a) PCR cloning of the anti-Aβ ScFv and (b) insertion of this cDNA into the universal chimeric HIRMAb heavy-chain expression vector, pCD−UHC, to form the pCD−HC−ScFv plasmid. The pCD−UHC expresses the cDNA encoding for the intronless heavy chain (HC) of the chimeric HIRMAb (*16*) and has a single HpaI site at the end of the HIRMAb HC open reading frame (orf) for insertion of genes of interest and expression of HIRMAb HC fusion proteins. For the PCR cloning of the mature anti-Aβ ScFv, the mature ScFv PCR forward oligodeoxynucleotide (ODN) was designed, so as to delete the human IgG peptide leader sequence from the anti-Aβ ScFv cDNA while maintaining the orf at the CH_3 region of the HIRMAb heavy chain of the pCD−UHC. This results in the insertion of a Ser−Ser linker between the end of the CH_3 region of the HIRMAb and the amino-terminal part of the ScFv. The anti-Aβ ScFv reverse PCR ODN was designed to delete the c-myc tag and to introduce a stop codon, TAA. Both PCR primers were 5′-phosphorylated for direct ligation into the pCD−UHC at the HpaI site. The PCR cloning of the mature anti-Aβ ScFv cDNA was done using the pCD−ScFv DNA as template. Agarose gel electrophoresis of the PCR products showed the expected single band of ~0.8 kb corresponding to the mature anti-Aβ ScFv cDNA. The engineered ScFv was ligated at the HpaI site in pCD−UHC to form the pCD−HC−ScFv expression vector. The pCD−HC−ScFv clone was validated by DNA sequencing. The deduced amino acid sequence showed that the HC of the fusion antibody was composed of 708 amino acids and included a 18 amino acid signal peptide, a 113 amino acid HIRMAb VH, a 330 amino acid human IgG1 constant region, a 2 amino acid linker, a 114 amino acid anti-Aβ ScFv VH, a 17 amino acid linker, and a 113 amino acid anti-Aβ ScFv VL. The predicted molecular weight of the fusion antibody heavy chain, minus the signal peptide, was 75 594 Da, and the predicted isoelectric point (pI) was 8.81. This pI was experimentally confirmed by isoelectric focusing.

Binding of Anti-Aβ ScFv to Aβ^{1-40} and Aβ Plaque. COS cells were transfected with the pCD−ScFv plasmid with lipofectamine 2000, and conditioned medium was tested in an ELISA. Soluble Aβ^{1-40} peptide was adsorbed to 96 well plates, and COS cell conditioned medium was added. The primary antibody was a murine 9E10 to the c-myc epitope, and 9E10 binding to the ScFv was detected with an anti-mouse IgG−peroxidase conjugate. This format was also used in Western blotting. Concentrated COS cell medium was applied to a 12% SDS-PAGE gel, and the proteins were electroblotted to nitrocellulose. The primary antibody was the 9E10 antibody, and the secondary antibody was an anti-mouse IgG−peroxidase conjugate. Frozen sections (20 um) of AD brain were incubated with COS cell medium, and ScFv binding to plaque was detected with the 9E10 antibody.

Expression of Intact Fusion Antibody in COS Cells. COS cells were dual-transfected with pCD−HC−ScFv and pCD−LC, which is the chimeric HIRMAb LC expression plasmid (*16*), and conditioned medium was collected at 3 and 6 days. The fusion antibody was purified by protein A affinity chromatog-

raphy, and the purity was assessed with both 12% SDS-PAGE followed by Coomasie blue staining and Western blotting using an anti-human IgG primary antibody.

Binding of Fusion Antibody to Aβ and to HIR. The binding of the fusion antibody to soluble Aβ^{1-40} was measured with an immunoradiometric assay described previously (*22*). The Aβ^{1-40} is plated in a 96 well format, and the binding of [^{125}I]-murine anti-Aβ MAb to the solid-phase Aβ^{1-40} is quantitated. The percent displacement of this binding is measured in the presence of increasing concentrations of either unlabeled murine anti-Aβ MAb or the fusion antibody. Binding to the HIR extracellular domain (ECD) was measured as described previously (*15*). HIR ECD was affinity purified from conditioned medium obtained from CHO cells permanently transfected with the HIR ECD. The HIR ECD was plated in a 96 well format, and binding of the HIRMAb was measured with an anti-human IgG primary antibody and a peroxidase-based ELISA. The binding of the fusion antibody or human IgG1 to the HIR ECD was measured in parallel. Binding isotherms were generated by nonlinear regression analysis using the PAR subroutine of the BMDP Statistical Software.

Blood to Brain Transport in the Primate in Vivo. The fusion antibody was iodinated with [^{125}I]-iodine and chloramine T. In parallel, the murine anti-Aβ MAb was tritiated with [^{3}H]-*N*-succinimidyl proprionate. An eight-year-old female rhesus monkey, weighing 10.2 kg, was administered by a single intravenous injection a dose of 777 μCi of [^{125}I]-fusion antibody and 888 uCi of [^{3}H]-murine anti-Aβ MAb. Serum was collected at multiple time points over a 180 min period. The serum removed from the anesthetized rhesus monkey was analyzed for total radioactivity, and expressed as a percent of injected dose (I.D.) per milliliter of serum. The ^{125}I radioactivity was counted in a γ counter, and the ^{3}H radioactivity was counted in a liquid scintillation counter; the ^{125}I isotope emits radioactivity in the ^{3}H window, and standard curves were prepared to account for ^{125}I emission in the ^{3}H channel. The serum concentration profile for the [^{125}I]-fusion antibody was fit to a two-compartment pharmacokinetic model described previously (*14*) to yield the pharmacokinetic parameters. At 180 min after drug injection, the animal was euthanized, and brain radioactivity was analyzed with the capillary depletion method, as described previously (*23*). This method separates brain homogenate into a capillary pellet and a post-vascular supernatant. If the volume of distribution (VD) of the antibody in the post-vascular supernatant is high, then this is evidence that the antibody has crossed the BBB and entered into the brain interstitial and intracellular spaces. The VD has units of μL/g brain and is the ratio of the concentration of the antibody in brain (DPM/g) divided by the concentration of the antibody in serum (DPM/uL) at the 180 min terminal time point. The primate brain was divided into frontal, midsection, and caudal parts, and coronal slabs were snap-frozen in pulverized dry ice, and 20 um frozen sections were prepared on a cryostat. The sections were exposed to Biomax X-ray film for 7−10 days, and the film was scanned, and the grayscale image was colorized with *NIH Image* software.

Brain to Blood Transport in the Rat in Vivo. Human IgG is recognized by the rat BBB Fc receptor (FcR) (*18*) and by the rodent FcRn (*24*). The [^{125}I]-fusion antibody (0.03 μCi in 0.3 μL) was injected into the cortex of the brain of the anesthetized adult rat under stereotaxic guidance per the standard protocol of the brain efflux index (BEI) technique (*18*). The fusion antibody was injected in the par2 region of the parietal cortex of brain, with the following stereotaxic coordinates: 0.2 mm anterior to bregma; 5.5 mm lateral to bregma; 4.5 mm deep from the dural surface. This region is far removed from the cerebrospinal fluid tracts, and efflux of radioactivity from the brain over time can only occur via efflux across the BBB from brain to blood. The labeled fusion antibody was injected with either 0 or 1.5 μg human Fc fragments, as described previously (*18*). The rate of efflux of the [^{125}I]-fusion antibody from rat brain was followed over 90 min.

Binding and in Vitro Disaggregation of Aβ Fibrils by Fusion Antibody. Aβ fibrils were formed after incubating Aβ^{1-40} peptide (Bachem) in an orbital shaker at 37 °C for 6 days (*25*), and the plaque was collected by centrifugation. An affinity-purified rabbit polyclonal antibody against the carboxyl terminus (CT) of the Aβ^{1-40} peptide (Signet Laboratories, catalog number 9130-005) was plated in 96 well dishes. In parallel, the preformed Aβ fibrils were incubated for either 1 or 4 h at 37 °C with the fusion antibody, human IgG1 (hIgG1), and phosphate buffered saline (PBS), or with the mouse anti-Aβ MAb and mouse IgG (mIgG), or PBS. The Aβ aggregate/fusion antibody or Aβ aggregate/mouse anti-Aβ MAb complex was then added in increasing doses (10, 30, 100 μL, which is equivalent to 100, 300, 1000 ng/mL) to the immobilized anti-CT antibody. The anti-Aβ ScFv part of the fusion antibody or the mouse anti-Aβ MAb binds an epitope on the Aβ^{1-40} peptide near the amino terminus (NT). Therefore, if Aβ fibrils are present, then a complex will form with anti-CT antibody, the Aβ fibril, the fusion antibody, and a secondary antibody coupled to peroxidase for detection of anti-Aβ antibody binding to Aβ fibril by ELISA (*2*, *3*). The secondary antibodies used for the fusion antibody and the murine anti-Aβ MAb were anti-human and anti-mouse IgG conjugates of alkaline phosphatase, respectively.

In Vivo Disaggregation of Aβ Plaque by Fusion Antibody in Transgenic Mice. APPswe/PSEN1(dE9) double transgenic (*26*) male mice were obtained from The Jackson Laboratory (Bar Harbor, ME) and investigated at 15 months of age. Following approval by the UCLA Animal Research Committee, mice were anesthetized with ketamine/xylazine, and the fusion antibody (20 pmol in 2 μL) or saline (2 μL) was injected with a mouse stereotaxis apparatus into the cortex and hippocampus on the right side of the brain with the following coordinates: 1.5 mm anterior, 2.0 mm lateral, and 2.0 mm deep relative to bregma and the dural surface for the frontal cortex; and 2.7 mm posterior, 2.5 mm lateral, and 2.5 mm deep relative to bregma and the dural surface for the hippocampus. The mice were euthanized 48 h later, and the brain was removed, and coronal slabs around the cortex and hippocampal injection sites were immersion-fixed 24 h at 4 °C in 4% paraformaldehyde in PBS, and cryoprotected successively in 10%, 20%, and 30% sucrose. The cortex or the hippocampus slab was frozen in embedding medium, and 40 consecutive 20 μm frozen sections were prepared on a Mikron cryostat at −15 °C. The slides were stained with either 4% thioflavine-S for confocal microscopy or 1% potassium ferrocyanide in 1% HCl for Prussian blue light microscopy. For examination of microhemorrhage, every eighth section was stained for Prussian blue deposits. For quantitation of amyloid plaque, every fifth section was examined by confocal microscopy using a Zeiss confocal microscope and Zeiss LSM software (*LSM 5 PASCAL*, version 3.2) for digitizing the area of amyloid plaque, relative to the field area, which was 52 642 μm^2. For each of the eight sections, eight separate fields were quantified and averaged for both the injected side and noninjected side of brain. The difference in amyloid content in the injected brain versus the contralateral, noninjected brain, for the animals injected either with fusion antibody or with saline was assessed with the Student's *t* test.

RESULTS

The cDNAs encoding the variable region of the heavy chain (VH) and variable region of the light chain (VL) were cloned following reverse transcription of RNA isolated from a mouse

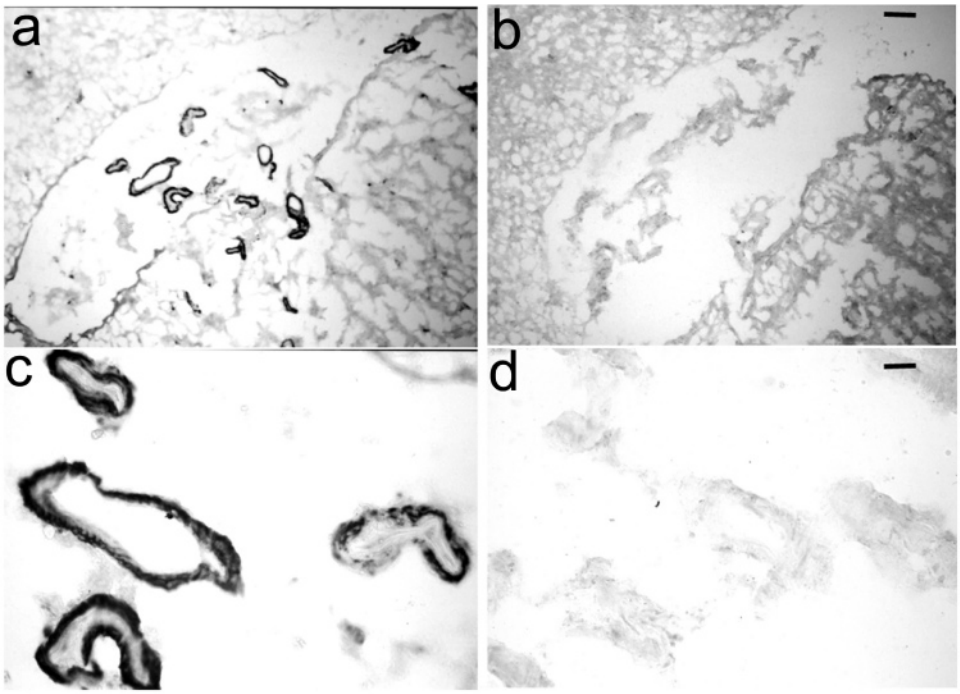


Figure 3. Immunocytochemistry of frozen sections of AD autopsy brain. The brain sections were immune stained with medium conditioned by COS cells that were transfected with pCD-ScFv (a,c), with medium conditioned by COS cells which were exposed only to lipofectamine 2000 (b), or with the mouse IgG1 isotype control antibody (d). Magnification in panels a and b is the same, and the magnification bar in panel b is 88 um; magnification in panels c and d is the same and the magnification bar in panel d is 35 um.

hybridoma secreting a MAb directed against the Aβ^{1-28} peptide. The VH and VL were joined by a 17 amino acid linker to produce a ScFv. The 10 amino acid c-myc epitope of the 9E10 MAb was fused to the carboxyl terminus of the ScFv, followed by insertion in a eukaryotic expression plasmid, designated pCD−ScFv (Methods section). Following transfection of COS cells, the reactivity of the engineered anti-Aβ ScFv against the Aβ peptide was tested with three assays: Western blot, ELISA, and immunocytochemistry of AD brain. Western blotting with the 9E10 antibody showed that a 31 kDa immunoreactive protein was selectively secreted to the medium in COS cells transfected with pCD−ScFv. The anti-Aβ ScFv secreted by transfected COS cells bound soluble Aβ^{1-40} as demonstrated with a 9E10 antibody-based ELISA (Methods section). Immunocytochemistry of frozen sections of AD autopsied brain showed the anti-Aβ ScFv specifically bound to vascular amyloid plaque (Figure 3a,c), whereas medium conditioned by COS cells exposed only to lipofectamine 2000 (Figure 3b) or the mouse IgG isotype control antibody (Figure 3d) showed no specific staining of AD brain.

The cDNA encoding the anti-Aβ ScFv was fused at the 3′ end of the cDNA encoding the heavy chain (HC) of the genetically engineered HIRMAb, and this heavy chain fusion antibody expression vector is designated pCD−HC−ScFv. A separate expression vector, designated pCD−LC, encodes the light chain of the HIRMAb (*15*, *16*). COS cells were dual transfected with pCD−HC−ScFv and pCD−LC, and the fusion antibody secreted into the medium was purified by protein A affinity chromatography. Following SDS-PAGE and Coomasie blue staining, the size of the HC of the fusion antibody was 82 kDa, whereas the size of the HC of HIRMAb was 55 kDa; the difference, 27 kDa, is equal to the size of the ScFv, minus the 9E10 epitope. The size of the light chain (LC) of either the HIRMAb or the fusion antibody is identical at 28 kDa (Figure 4a). The same sizes of the HC and LC of the fusion antibody and the HIRMAb were detected with a Western blot using a primary antibody against human IgG (Figure 4b).

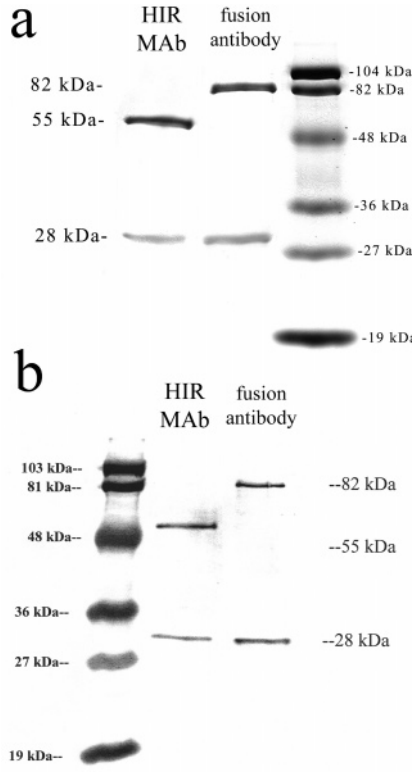


Figure 4. SDS-PAGE and Western blotting of fusion antibody. (a) SDS-PAGE and Coomasie blue staining shows correct processing of intact fusion antibody by transfected COS cells. (b) Western blotting with an anti-human IgG primary antibody. The HIRMAb and the fusion antibody are composed of the same light chain, which is 28 kDa. The size of the heavy chain of the HIRMAb is 55 kDa, whereas the size of the heavy chain of fusion antibody is 82 kDa. The heavy chain of the fusion antibody includes the 55 kDa heavy chain of the HIRMAb fused to the 27 kDa anti-Aβ ScFv.

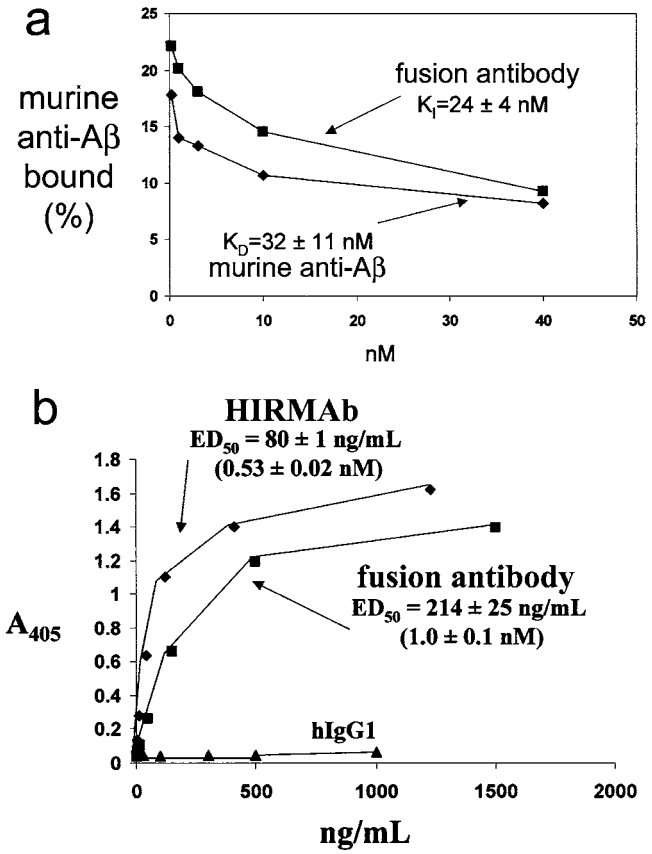


Figure 5. Bifunctional binding of fusion antibody both to Aβ and to the human insulin receptor. (a) The binding of [^{125}I]-murine anti-Aβ MAb to Aβ^{1-40} is competitively inhibited by either unlabeled murine anti-Aβ MAb or by the fusion antibody. The binding affinity of the fusion antibody is not significantly different from the affinity of the murine anti-Aβ MAb. (b) Binding of the genetically engineered HIRMAb or the fusion antibody to the HIR extracellular domain is measured with an ELISA. There is no binding of human IgG1 to the HIR ECD. The affinity of the fusion antibody for the HIR ECD is >50% of the affinity of the HIRMAb.

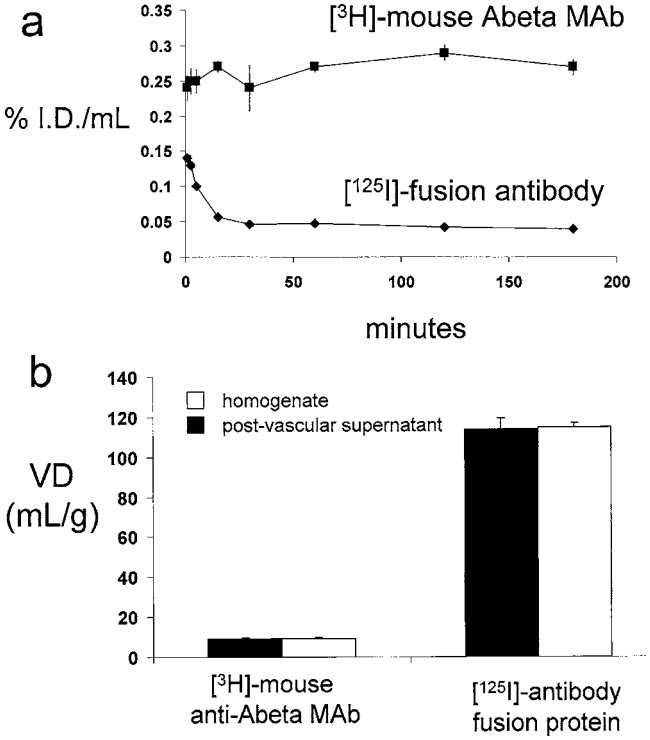


Figure 6. Blood to brain transport of fusion antibody in the primate. (a) The [^{125}I]-fusion antibody and the [^{3}H]-mouse anti-Aβ antibody were injected intravenously into the adult rhesus monkey, and serum concentrations [% of injected dose (I.D.)/mL] were determined over a 3 h period. There is no measurable clearance from blood of the [^{3}H]-mouse anti-Aβ antibody during this time period, whereas the fusion antibody is rapidly cleared from blood, owing to uptake via the insulin receptor. (b) Brain volume of distribution (VD) of the [^{3}H]-mouse anti-Aβ antibody and the [^{125}I]-fusion antibody in the rhesus monkey brain at 3 h after a single intravenous injection. The VD values for the homogenate and the post-vascular supernatant are shown. The VD for the [^{3}H]-mouse anti-Aβ antibody, 10 uL/g, is equal to the brain arterial blood volume, which indicates this antibody is not transported across the primate BBB in vivo in the blood to brain direction. The VD for the [^{125}I]-fusion antibody is >100 uL/g in both the brain homogenate and the post-vascular supernatant, which indicates the [^{125}I]-fusion antibody is transported across the BBB.

The fusion antibody bound with high affinity to soluble Aβ^{1-40}, as determined by an immunoradiometric assay (Methods section). The dissociation constant (K_D) of the original murine anti-Aβ tetrameric MAb was 32 ±11 nM, and the dissociation constant of fusion antibody binding to soluble Aβ^{1-40} was 24 ± 4 nM (Figure 5a). The fusion antibody retained high-affinity binding for the HIR based on an ELISA (Methods section) using affinity-purified HIR extracellular domain (ECD). The concentration of HIRMAb that gives 50% binding to HIR ECD is 0.53 ± 0.02 nM, whereas the ED_{50} of fusion antibody binding to the HIR ECD is 1.0 ± 0.1 nM (Figure 5b).

The fusion antibody was radiolabeled with 125-iodine, the hybridoma-derived mouse anti-Aβ MAb was tritiated, and the labeled antibodies were coinjected intravenously into an anesthetized adult female rhesus monkey. In the first 3 h after injection, there was no measurable decrease in the blood concentration of the [^{3}H]-mouse Aβ MAb, whereas there was an immediate clearance of the [^{125}I]-fusion antibody from blood in the primate (Figure 6a). The extensive distribution of the fusion antibody into the primate brain is shown by the 3 h brain scan (Figure 7). There is global uptake of the fusion antibody in all parts of the brain with a preferential uptake in gray matter relative to white matter. Brain radioactivity at 3 h after intravenous injection was measured with the capillary depletion technique, which demonstrated a high volume distribution (VD), >100 μL/g, of the [^{125}I]-fusion antibody (Figure 6b). In contrast, the brain VD for the [^{3}H]-mouse anti-Aβ MAb is 10 μL/g brain. This VD is equal to the arterial blood volume of brain (*27*) and indicates that the mouse anti-Aβ MAb does not cross the BBB in the blood to brain direction. The VD of the fusion antibody was high in the postvascular supernatant, indicating that the fusion antibody is transcytosed across the BBB into the postcapillary compartment of brain (Figure 6b).

The influx of the fusion antibody from blood to brain in vivo could not be tested in rodents, because the HIRMAb does not recognize the rodent insulin receptor. However, the rat FcRn does recognize human IgG and mediates efflux of human IgG across the BBB from brain to blood in the rat (*18*). Therefore, the transport of the fusion antibody across the BBB in the brain to blood direction was measured with the brain efflux index (BEI) method in the adult rat (Methods section). Following stereotaxic injection into the cortex of rat brain, the fusion antibody rapidly effluxed from the brain to blood and was >50% eliminated from brain at 90 min after injection. The efflux of the fusion antibody from brain was >90% blocked by human Fc fragments (Figure 8).

The binding of the fusion antibody to Aβ fibrils in vitro is demonstrated with the double-antibody ELISA outlined in Figure 9a. The fusion antibody bound to the Aβ fibrils in a dose-dependent manner following a 1 h incubation of the fusion antibody with the Aβ fibrils (Figure 9b). Following a 4 h incubation of the fusion antibody and the Aβ fibrils, most of

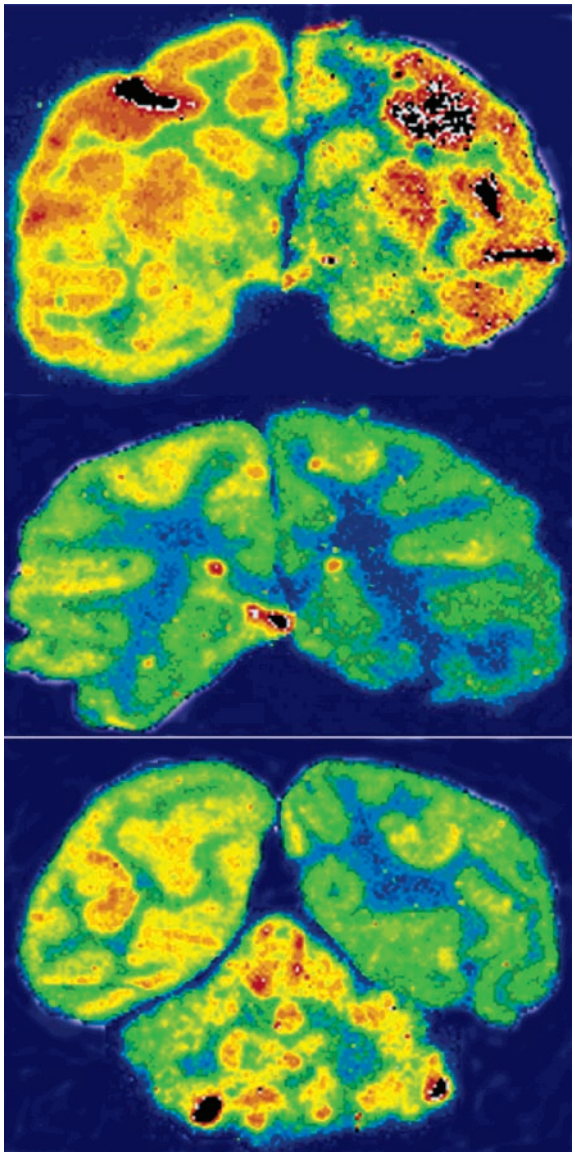


Figure 7. Global distribution of fusion antibody to primate brain. Brain scans of adult rhesus monkey at 3 h after the intravenous administration of the [^{125}I]-fusion antibody demonstrates widespread distribution of the fusion antibody into the primate brain in vivo from blood. The top scan is the most frontal part of brain, and the bottom scan is the most caudal part of brain and includes the cerebellum.

the fibrils were disaggregated (Figure 9b). A comparable binding/disaggregation of Aβ fibrils was observed with the original murine anti-Aβ MAb. The fusion antibody also disaggregates Aβ amyloid in vivo in transgenic mouse brain. The APPswe/PS1dE9 double transgenic mouse develops amyloid plaque as shown by thioflavin-S staining (Figure 9c). Quantitation of the percent of either frontal cortex or hippocampus occupied by the amyloid plaque showed that approximately 5% of the brain was amyloid. A single intracerebral injection of the fusion antibody into the hippocampus or the frontal cortex caused a 39 $\pm$ 3% and 38 $\pm$ 2% decrease, respectively, in the Aβ amyloid burden in the brain in vivo at 48 h after injection in the side ipsilateral to the injection, relative to the amyloid burden in the contralateral hippocampus or frontal cortex (Figure 9d). Conversely, the intracerebral injection of saline in either the cortex or hippocampus of the transgenic mice caused no decrease in amyloid burden in the brain (Figure 9d). Intracerebral injection of the fusion antibody caused no microhemorrhage in the brain, as demonstrated by Prussian blue staining of serial sections of cortex or hippocampus (Methods section).

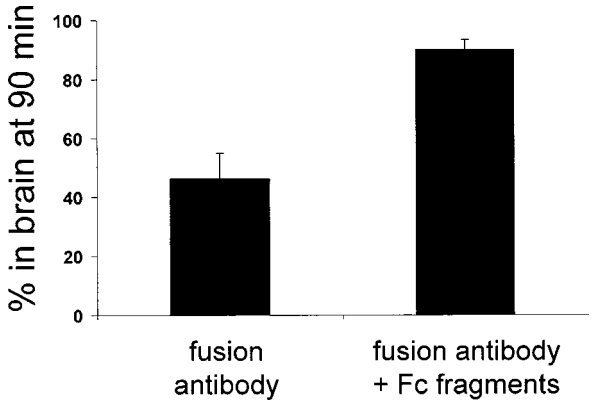


Figure 8. Brain to blood transport of fusion antibody in the rat. The [^{125}I]-fusion antibody was injected into the cortex under stereotaxic guidance, and the efflux of the fusion antibody from brain across the BBB was measured at 90 min after the injection. At this time, nearly 60% of the injected fusion antibody has effluxed from brain. This efflux was >90% blocked ($p < 0.01$) by the coinjection of human Fc fragments, which indicates that the efflux is mediated by an Fc receptor at the BBB. Data are mean $\pm$ S.E. ($n = 4$ rats per point).

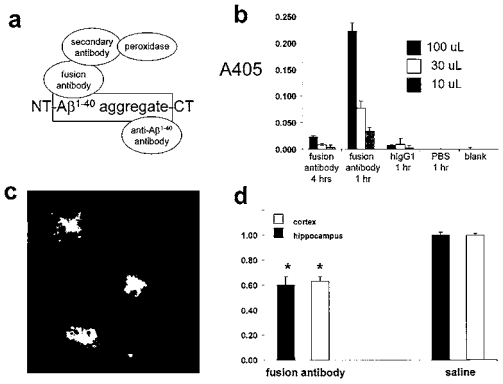


Figure 9. Fusion antibody disaggregates Aβ amyloid fibrils in vitro and in vivo. (a) Outline of Aβ plaque disaggregation assay. The Aβ fibrils are sandwiched by an anti-Aβ antibody that binds the carboxyl terminus (CT) of Aβ, and by the fusion antibody, or the murine anti-Aβ MAb, which binds the amino terminus (NT) of Aβ. (b) Disaggregation of Aβ fibrils in vitro by the fusion antibody. Aβ^{1-40} aggregates were formed over 6 days, followed by incubation with the fusion antibody, with human IgG1 (hIgG1) or with phosphate buffered saline (PBS) for either 1 or 4 h at 37 °C. The antibody that binds to the carboxyl terminal region of the Aβ^{1-40} peptide was plated in 96 well plates. The anti-Aβ ScFv portion of the fusion antibody binds to the amino terminal part of Aβ.$^{1-40}$ A positive ELISA signal is generated only if Aβ fibrils are present. The data show that the fusion antibody binds to Aβ^{1-40} plaque and that this binding causes fibril disaggregation over a 4 h period. (c) Amyloid plaque in brain of double transgenic APPswe/PS1dE9 mice stained with thioflavine-S. (d) The percent of brain occupied by amyloid plaque in either the frontal cortex or the hippocampus in the transgenic mice was quantitated with confocal microscopy. Amyloid was measured at 48 h after the intracerebral injection of 20 pmol of fusion antibody into the frontal cortex and the hippocampus on one side of the brain. The amyloid burden in the brain is expressed as a ratio of the % brain amyloid in the side ipsilateral to the injection relative to the % amyloid content in the contralateral frontal cortex or hippocampus, in the animals injected either with the fusion body or with saline. Data are mean $\pm$ SE ($n = 3$ mice for each treatment group). The decrease in amyloid content in either the frontal cortex or the hippocampus on the side of the fusion antibody injection, relative to the saline control, is statistically significant ($*p < 0.01$).

DISCUSSION

The results of these studies are consistent with the following conclusions. First, a ScFv directed against the amino-terminal portion of the Aβ peptide has been cloned, expressed, and shown to bind both soluble Aβ and Aβ fibrils (Results section and Figure 3). Second, a fusion antibody has been engineered

whereby the anti-Aβ ScFv is fused to the carboxyl terminus of the Fc region of a genetically engineered HIRMAb (Figures 2 and 4); the fusion antibody retains high-affinity binding for the HIR (Figure 5b), as well as for soluble Aβ (Figure 5a) and for Aβ fibrils (Figure 9b). Third, the fusion antibody crosses the BBB bidirectionally; the fusion antibody undergoes rapid influx from blood to brain across the rhesus monkey BBB in vivo (Figure 7); the fusion antibody undergoes receptor-mediated efflux from brain to blood across the BBB via a mechanism that is inhibited by Fc fragments (Figure 8). Fourth, the fusion antibody (Figure 2) is a trifunctional protein with three domains that are all biologically active. The first domain, which targets the HIR, enables receptor-mediated transport across the BBB in the blood to brain direction. The second domain binds to Aβ to cause disaggregation of Aβ fibrils. The third domain binds the Fc receptor to enable receptor-mediated transport of the fusion antibody from brain back to blood across the BBB.

The availability of the cDNA encoding the anti-Aβ ScFv and the cDNA encoding the heavy chain of the chimeric HIRMAb enabled the genetic engineering of a fusion antibody with dual specificities. The fusion antibody binds both the HIR and Aβ (Figure 2). There are multiple approaches to the genetic engineering of fusion antibodies (*28*−*31*). The approach taken in the present investigation was to fuse the ScFv at the carboxyl terminus of the CH_3 region of the HIRMAb heavy chain (Figure 2). Prior work has shown that the fusion of a ScFv to the carboxyl terminus of the CH_3 region of another IgG results in an approximate 10-fold reduction in binding affinity for the ScFv-targeted antigen (*28*, *32*). This was not observed in the present investigation, as the affinity of the fusion antibody for Aβ is unchanged as compared to the original murine anti-Aβ MAb (Figure 5a). The advantage of fusing the ScFv to the carboxyl terminus of the Fc region of the HIRMAb is that this configuration converts the monovalency of ScFv binding of antigen to the original bivalency of antibody binding of antigen (Figure 2).

COS cells were dual transfected with a heavy chain expression vector, pCD−HC−ScFv, and an expression vector, pCD−LC, which produces the light chain of the genetically engineered HIRMAb. Medium was concentrated, and the fusion antibody was purified by protein A affinity chromatography. SDS-PAGE and Western blotting showed that the fusion antibody was correctly processed in COS cells. The size of the light chain of the fusion antibody is identical to the size of the light chain of the HIRMAb (Figure 4), which is expected, since both the fusion antibody and the HIRMAb are composed of the same light chain. The size of the heavy chain of the fusion antibody, 82 kDa, is 27 kDa greater than the size of the heavy chain of the HIRMAb, which is 55 kDa (Figure 4). The difference between the size of the heavy chain of the fusion antibody and the size of the HIRMAb, 27 kDa, is equal to the predicted molecular weight of the ScFv. The bifunctionalilty of the fusion antibody was demonstrated by separate binding assays targeting either the HIR ECD or soluble Aβ^{1-40}. The fusion antibody binds soluble Aβ^{1-40} with a K_D of 24 $\pm$ 4 nM, and this is not significantly different from the K_D, 32 $\pm$ 11 nM, of the binding to Aβ^{1-40} of the original murine anti-Aβ MAb (Figure 5a). The 50% binding of the HIRMAb to the HIR ECD is observed at 0.53 $\pm$ 0.02 nM, and there is a > 50% retention of affinity of the fusion antibody for the HIR ECD (Figure 5b). There is no binding of human IgG1 to the HIR (Figure 5b). The fusion antibody binds soluble Aβ^{1-40} (Figure 5a) and also binds Aβ fibrils (Figure 9b). After a 4 h incubation with Aβ fibrils, the fusion antibody causes a time-dependent disaggregation of Aβ fibrils (Figure 9b). The fusion antibody also causes disaggregation of amyloid plaque in vivo in double transgenic APPswe/PS1dE9 mice (Figure 9d). A single intracerebral injection of 20 pmol of fusion antibody into either the frontal cortex or the hippocampus causes a 38−39% reduction in brain amyloid burden at 48 h after fusion antibody administration (Figure 9d). In contrast, the injection of saline into the frontal cortex or hippocampus caused no decrease in brain amyloid burden (Figure 9d). The mechanism of fusion antibody diaggregation of preformed Aβ plaque is assumed to involve binding of the antibody to amino-terminal epitopes on the Aβ peptide within the fibril, which induces progressive release of Aβ monomers and/or oligomers from the fibril (*2*, *3*).

The purpose of this investigation was to genetically engineer an anti-Aβ antibody that can also cross the BBB in both the blood to brain and brain to blood directions. Therefore, an anti-Aβ ScFv antibody was fused to the heavy chain of the genetically engineered HIRMAb to enable receptor-mediated transport in the blood to brain direction across the BBB via transport on the endogenous insulin receptor. The HIRMAb is not recognized by the rodent insulin receptor, but is recognized by the insulin receptor of Old World primates such as rhesus monkeys but not New World primates such as squirrel monkeys (*14*). The selective transport of the fusion antibody across the primate BBB relative to the murine anti-Aβ MAb is demonstrated in Figure 6b. There is no measurable clearance of the murine anti-Aβ MAb from primate blood at 3 h after intravenous administration (Figure 6a), because this antibody, which is a mouse IgG1, does not recognize any receptor that would mediate selective exodus from the blood compartment. The human FcRn, and presumably the primate FcRn, does not recognize mouse IgG1 (*24*). However, the lack of recognition of the murine anti-Aβ MAb by the primate FcRn cannot explain the lack of influx of this MAb from blood to brain. The BBB FcRn is an asymmetric transporter and mediates only the efflux of IgG from brain to blood but not the influx of IgG from blood to brain (*18*). In contrast to the slow clearance of the murine anti-Aβ MAb from the blood, the fusion antibody is rapidly removed from the blood (Figure 6a), owing to uptake via tissues such as liver, spleen, and brain that express vascular insulin receptor (*14*). This rapid removal of fusion antibody is likely mediated by the insulin receptor, since the rate of removal of the fusion antibody from the blood compartment of the rhesus monkey is virtually identical to the rate of removal of the genetically engineered HIRMAb reported previously (*15*, *16*). The systemic clearance of the [^{111}In]-chimeric HIRMAb, 0.22 $\pm$ 0.08 mL/min/kg (*15*), is not significantly different from the systemic clearance of the [^{125}I]-fusion antibody, 0.18 $\pm$ 0.05 mL/min/kg. The 3 h brain scan of the primate shows global distribution of the fusion antibody in the primate brain in vivo with a greater uptake in gray matter relative to white matter (Figure 7). This pattern of uptake reflects the approximate 3-fold greater vascular density in gray matter relative to white matter and thus 3-fold greater density of microvascular insulin receptor in gray matter as compared to white matter (*14*). The rapid transport of fusion antibody across the primate BBB in vivo is confirmed by measurements of brain VD (Figure 6b). The brain VD of the murine anti-Aβ MAb, 10 μL/g (Figure 6b), is equal to the cerebral arterial blood volume (*27*), which indicates that the murine anti-Aβ MAb does not cross the BBB in vivo in the blood to brain direction. In contrast, the brain VD for the fusion antibody is >100 μL/g brain (Figure 6b). Capillary depletion analysis shows that the fusion antibody undergoes transcytosis across the BBB and penetrates into the postvascular volume of the brain (Figure 6b). Once inside the brain, an anti-Aβ antibody may bind amyloid and cause disaggregation of the amyloid plaque.

In addition to influx from blood to brain, an Aβ antibody therapeutic must also be enabled to efflux from the brain back to blood. Otherwise, there would be no net clearance of amyloid

from the brain. Large-molecule efflux across the BBB may be quantitated with the brain efflux index method (*18*). Prior work shows that during a 90 min period after intracerebral injection, the amount of 70 kDa [^{3}H]-dextran in rat brain is 93 ± 3%, which means that the efflux from the brain via bulk flow is minimal during this time period. Therefore, the only pathway for efflux from the brain is direct transport across the BBB. Unlike other large molecules such as dextran or albumin, IgG molecules rapidly efflux from the brain to blood via a BBB Fc receptor (*18*). Previous confocal microscopy studies have shown that the neonatal FcR, also called the FcRn, is highly expressed at the brain microvascular endothelium (*19*). The FcRn binding site for IgG molecules is at the CH_2-CH_3 interface (*17*), and the FcRn binds deglycosylated IgG (*33*). Therefore, the fusion antibody was engineered to have an intact CH_2-CH_3 interface to enable binding and transport via the BBB FcRn (Figure 2). After the complex of Aβ and the fusion antibody efflux from brain to blood, the fusion antibody is rapidly cleared from blood by tissues such as liver or spleen, which express high levels of microvascular insulin receptor (*14*).

The potential immunogenicity of the fusion antibody in humans is not known until clinical trials are performed. The fusion antibody is derived from chimeric anti-HIR and anti-Aβ antibodies, and both chimeric monoclonal antibodies and antibody fusion proteins are FDA-approved products, which are given repeatedly to humans without immunologic reactions (*34*). Any underlying immunogenicity of the fusion antibody in humans could be reduced by "humanization" of either or both parts of the fusion antibody. A humanized HIRMAb has been genetically engineered and crosses the primate BBB at rates comparable to the chimeric HIRMAb (*16*).

The genetic engineering of the fusion antibody shown in Figure 2 could be replicated with other monoclonal antibody based therapeutics for multiple CNS diseases. Monoclonal antibody based therapeutics have significant potential as neurotherapeutics if the problem of BBB delivery is solved. The present work shows that antibody-based therapeutics can be delivered to brain as fusion proteins with molecular Trojan horses that cross the BBB.

ACKNOWLEDGMENT

This work was supported by NIH grant R43-NS-51857.

LITERATURE CITED

(1) Schenk, D., Barbour, R., Dunn, W., Gordon, G., Grajeda, H., Guido, T., Hu, K., Huang, J., Johnson-Wood, K., Khan, K., Kholodenko, D., Lee, M., Liao, Z., Lieberburg, I., Motter, R., Mutter, L., Soriano, F., Shopp, G., Vasquez, N., Vandevert, C., Walker, S., Wogulis, M., Yednock, T., Games, D., and Seubert, P. (1999) Immunization with amyloid-beta attenuates Alzheimer-disease-like pathology in the PDAPP mouse. *Nature (London) 400*, 173−177.

(2) Solomon, B., Koppel, R., Frankel, D., and Hanan-Aharon, E. (1997) Disaggregation of Alzheimer beta-amyloid by site-directed mAb. *Proc. Natl. Acad. Sci. U.S.A. 94*, 4109−4112.

(3) Solomon, B., Koppel, R., Hanan, E., and Katzav, T. (1996) Monoclonal antibodies inhibit in vitro fibrillar aggregation of the Alzheimer beta-amyloid peptide. *Proc. Natl. Acad. Sci. U.S.A. 93*, 452−455.

(4) Lombardo, J. A., Stern, E. A., McLellan, M. E., Kajdasz, S. T., Hickey, G. A., Bacskai, B. J., and Hyman, B. T. (2003) Amyloid-beta antibody treatment leads to rapid normalization of plaque-induced neuritic alterations. *J. Neurosci. 23*, 10879−10883.

(5) Wilcock, D. M., DeCarlo, G., Henderson, D., Jackson, J., Clarke, K., Ugen, K. E., Gordon, M. N., and Morgan, D. (2003) Intracranially administered anti-A beta antibodies reduce beta-amyloid deposition by mechanisms both independent of and associated with microglial activation. *J. Neurosci. 23*, 3745−3751.

(6) Brendza, R. P., Bacskai, B. J., Cirrito, J. R., Simmons, K. A., Skoch, J. M., Klunk, W. E., Mathis, C. A., Bales, K. R., Paul, S. M., Hyman, B. T., and Holtzman, D. M. (2005) Anti-Abeta antibody treatment promotes the rapid recovery of amyloid-associated neuritic dystrophy in PDAPP transgenic mice. *J. Clin. Invest. 115*, 428−433.

(7) Rabchevsky, A. G., Degos, J. D., and Dreyfus, P. A. (1999) Peripheral injections of Freund's adjuvant in mice provoke leakage of serum proteins through the blood-brain barrier without inducing reactive gliosis. *Brain Res. 832*, 84−96.

(8) Namer, I. J., and Steibel, J. (2000) Antibody directed against mannan of the *Mycobacterium tuberculosis* cell envelope provokes blood-brain barrier breakdown. *J. Neuroimmunol. 103*, 63−68.

(9) Lossinsky, A. S., Vorbrodt, A. W., and Wisniewski, H. M. (1995) Scanning and transmission electron microscopic studies of microvascular pathology in the osmotically impaired blood-brain barrier. *J. Neurocytol. 24*, 795−806.

(10) Salahuddin, T. S., Johansson, B. B., Kalimo, H., and Olsson, Y. (1988) Structural changes in the rat brain after carotid infusions of hyperosmolar solutions. An electron microscopic study. *Acta Neuropathol. (Berlin) 77*, 5−13.

(11) Pardridge, W. M. (2001) *Brain Drug Targeting; The Future of Brain Drug Development*, pp 1−370, Cambridge University Press, Cambridge, United Kingdom.

(12) Pardridge, W. M., Eisenberg, J., and Yang, J. (1985) Human blood-brain barrier insulin receptor. *J. Neurochem. 44*, 1771−1778.

(13) Duffy, K. R., and Pardridge, W. M. (1987) Blood-brain barrier transcytosis of insulin in developing rabbits. *Brain Res. 420*, 32−38.

(14) Pardridge, W. M., Kang, Y.-S., Buciak, J. L., and Yang, J. (1995) Human insulin receptor monoclonal antibody undergoes high affinity binding to human brain capillaries in vitro and rapid transcytosis through the blood-brain barrier in vivo in the primate. *Pharm. Res. 12*, 807−816.

(15) Coloma, M. J., Lee, H. J., Kurihara, A., Landaw, E. M., Boado, R. J., Morrison, S. L., and Pardridge, W. M. (2000) Transport across the primate blood-brain barrier of a genetically engineered chimeric monoclonal antibody to the human insulin receptor. *Pharm. Res. 17*, 266−274.

(16) Boado, R. J., Zhang, Y.-F., Zhang, Y., and Pardridge, W. M. (2007) Humanization of anti-human insulin receptor antibody for drug targeting across the human blood-brain barrier. *Biotechnol. Bioeng. 96*, 381−391.

(17) Martin, W. L., West, A. P., Jr., Gan, L., and Bjorkman, P. J. (2001) Crystal structure at 2.8 angstrom of an FcRn/heterodimeric Fc complex: mechanism of pH-dependent binding. *Mol. Cell 7*, 867−877.

(18) Zhang, Y., and Pardridge, W. M. (2001) Mediated efflux of IgG molecules from brain to blood across the blood-brain barrier. *J. Neuroimmunol. 114*, 168−172.

(19) Schlachetzki, F., Zhu, C., and Pardridge, W. M. (2002) Expression of the neonatal Fc receptor (FcRn) at the blood-brain barrier. *J. Neurochem. 81*, 203−206.

(20) Ghetie, V., and Ward, E. S. (2000) Multiple roles for the major histocompatability complex class I-related receptor FcRn. *Annu. Rev. Immunol. 18*, 739−766.

(21) Li, J. Y., Sugimura, K., Boado, R. J., Lee, H. J., Zhang, C., Duebel, S., and Pardridge, W. M. (1999) Genetically engineered brain drug delivery vectors-cloning, expression, and in vivo application of an anti-transferrin receptor single chain antibody-streptavidin fusion gene and protein. *Protein Eng. 12*, 787−796.

(22) Pardridge, W. M., Bickel, U., Buciak, J., Yang, J., Diagne, A., and Aepinus, C. (1994) Cationization of a monoclonal antibody to the human immunodeficiency virus rev protein enchances cellular uptake but does not impair antigen binding of the antibody. *Immunol. Lett. 42*, 191−195.

(23) Triguero, D., Buciak, J. B., and Pardridge, W. M. (1990) Capillary depletion method for quantifying blood-brain barrier transcytosis of circulating peptides and plasma proteins. *J. Neurochem. 54*, 1882−1888.

(24) Ober, R. J., Radu, C. G., Ghetie, V., and Ward, E. S. (2001) Differences in promiscuity for antibody-FcRn interactions across species: implications for therapeutic antibodies. *Int. Immunol. 13*, 1551−1559.

(25) Shearman, M. S., Hawtin, S. R., and Tailor, V. J. (1995) The intracellular component of cellular 3-(4,5-dimethylthiazol-2-yl)-2,5-diphenyltetrazolium bromide (MTT) reduction is specifically inhibited by beta-amyloid peptides. *J. Neurochem. 65*, 218−227.

(26) Savonenko, A., Xu, G. M., Melnikova, T., Morton, J. L., Gonzales, V., Wong, M. P., Price, D. L., Tang, F., Markowska, A. L., and Borchelt, D. R. (2005) Episodic-like memory deficits in the APPswe/PS1dE9 mouse model of Alzheimer's disease: Relationship to β-amyloid deposition and neurotransmitter abnormalities. *Neurobiol. Dis. 18*, 602−617.

(27) Ito, H., Ibaraki, M., Kanno, I., Fukuda, H., and Miura, S. (2005) Changes in the arterial fraction of human cerebral blood volume during hypercapnia and hypocapnia measured by positron emission tomography. *J. Cereb. Blood Flow Metab. 25*, 852−857.

(28) Coloma, M. J., and Morrison, S. L. (1997) Design and production of novel tetravalent bispecific antibodies. *Nature (London) 15*, 159−163.

(29) Lu, D., Jimenez, X., Zhang, H., Bohlen, P., Witte, L., and Zhu, Z. (2002) Fab-scFv fusion protein: an efficient approach to production of bispecific antibody fragments. *J. Immunol. Methods 267*, 213−226.

(30) Merchant, A. M., Zhu, Z., Yuan, J. Q., Goddard, A., Adams, C. W., Presta, L. G., and Carter, P. (2003) An efficient route to human bispecific IgG. *Nature (London) 16*, 677−681.

(31) Miller, K., Meng, G., Liu, J., Hurst, A., Hsei, V., Wong, W. L., Ekert, R., Lawrence, D., Sherwood, S., DeForge, L., Gaudreault, J., Keller, G., Sliwkowski, M., Ashkenazi, A., and Presta, L. (2003) Design, construction, and in vitro analyses of multivalent antibodies. *J. Immunol. 170*, 4854−4861.

(32) Marvin, J. S., and Zhu, Z. (2005) Recombinant approaches to IgG-like bispecific antibodies. *Acta Pharmacol. Sin. 6*, 649−658.

(33) Shields, R. L., Lai, J., Keck, R., O'Connell, L. Y., Hong, K., Meng, Y. G., Wikert, S. H., and Presta, L. G. (2002) Lack of fucose on human IgG1 N-linked oligosaccharide improves binding to human FcγRIII and antibody-dependent cellular toxicity. *J. Biol. Chem. 277*, 26733−26740.

(34) Waldmann, T. A. and Morris, J. C. (2006) Development of antibodies and chimeric molecules for cancer immunotherapy. *Adv. Immunol. 90*, 83−131.

BC060349X

Physicochemical and Biological Characterization of Targeted, Nucleic Acid-Containing Nanoparticles

Derek W. Bartlett and Mark E. Davis*

Chemical Engineering, California Institute of Technology, Pasadena, California 91125. Received November 9, 2006; Revised Manuscript Received January 11, 2007

Nucleic acid-based therapeutics have the potential to provide potent and highly specific treatments for a variety of human ailments. However, systemic delivery continues to be a significant hurdle to success. Multifunctional nanoparticles are being investigated as systemic, nonviral delivery systems, and here, we describe the physicochemical and biological characterization of cyclodextrin-containing polycations (CDP) and their nanoparticles formed with nucleic acids including plasmid DNA (pDNA) and small interfering RNA (siRNA). These polycation/nucleic acid complexes can be tuned by formulation conditions to yield particles with sizes ranging from 60 to 150 nm, ζ potentials from 10 to 30 mV, and molecular weights from $\sim 7 \times 10^7$ to 1×10^9 g mol^{-1} as determined by light scattering techniques. Inclusion complexes formed between adamantane (AD)-containing molecules and the β-cyclodextrin molecules enable the modular attachment of poly(ethylene glycol) (AD−PEG) conjugates for steric stabilization and targeting ligands (AD−PEG−transferrin) for cell-specific targeting. A 70 nm particle can contain ~10 000 CDP polymer chains, ~2000 siRNA molecules, ~4000 AD−PEG_{5000} molecules, and ~100 AD−PEG_{5000}−Tf molecules; this represents a significant payload of siRNA and a large ratio of siRNA to targeting ligand (20:1). The particles protect the nucleic acid payload from nuclease degradation, do not aggregate at physiological salt concentrations, and cause minimal erythrocyte aggregation and complement fixation at the concentrations typically used for in vivo application. Uptake of the nucleic acid-containing particles by HeLa cells is measured by flow cytometry and visualized by confocal microscopy. Competitive uptake experiments show that the transferrin-targeted particles display enhanced affinity for the transferrin receptor through avidity effects (multiligand binding). Functional efficacy of the delivered pDNA and siRNA is demonstrated through luciferase reporter protein expression and knockdown, respectively. The analysis of the CDP delivery vehicle provides insights that can be applied to the design of targeted nucleic acid delivery vehicles in general.

INTRODUCTION

Nucleic acid-based therapeutics are envisioned to play a significant role in the next generation of treatments for a variety of diseases such as cancer. In addition to the classic gene therapy approach of delivering DNA to replace mutated or absent genes, nucleic acid molecules can also be used to regulate the production of disease-associated proteins at both the transcriptional and translational levels. These nucleic acid-based drugs have received significant attention as promising new therapeutics, yet their application in vivo has been largely limited by the challenge of delivery; this has been particularly true for systemic delivery.

Naked nucleic acid molecules are rapidly degraded by ubiquitous nucleases present in the bloodstream. Double-stranded nucleic acid molecules ranging in size from small-interfering RNAs (siRNAs) to plasmids (pDNA) have a half-life of less than 1 h in serum (*1*−*3*). Selective chemical modification of nucleic acids can increase nuclease resistance and enable systemic delivery of naked siRNA molecules with functional efficacy in vivo (*1*, *4*). However, even nuclease-stabilized nucleic acids must still overcome other elimination barriers such as renal clearance that severely limit the efficacy of systemically delivered, small nucleic acid therapeutics (*5*). Attachment of specific targeting ligands can induce binding to protein carriers or uptake by the desired population of cells to be treated. Bioconjugates of the nucleic acid therapeutics covalently attached directly to targeting ligands such as cholesterol and antibodies have shown efficacy both in vitro and in vivo (*4*, *6*). While these methods for nuclease stabilization and covalent attachment of targeting ligands are promising for small nucleic acid therapeutics, the use of lipid- or polymer-based delivery vehicles is an approach for systemic delivery that can provide functions not achievable with naked nucleic acids or their covalent attachment to targeting moieties.

Carrier-mediated delivery has several advantages over the delivery of individual nucleic acid molecules. Encapsulation of the payload within a lipid bilayer or through electrostatic interactions is nonspecific, so these delivery vehicles can be used for generalized nucleic acid delivery. The use of a carrier enables delivery of many nucleic acid molecules per uptake event (this is especially important if the uptake involves highly specific cell surface receptors, since they are typically low in number), and isolation from exposure to the systemic environment can permit the use of unmodified nucleic acids (*7*). Modularly designed delivery vehicles can also take advantage of covalent or noncovalent attachment of hydrophilic polymers for steric stabilization and/or targeting ligands for cell-specific delivery, two critical features for systemic delivery (*7*, *8*). Such modifications can affect the resulting biodistribution of delivery vehicles through passive and/or active targeting (*7*−*10*).

Passive targeting occurs as a result of the intrinsic physicochemical properties of the delivery vehicle. For example, the charge and size of the delivery vehicle alone can bias its biodistribution. The charge of the delivery vehicle significantly impacts its interaction with components of the bloodstream; highly charged particles can lead to complement activation, while near-neutral particles exhibit reduced phagocytic uptake (*11*, *12*). Specifically, cationic polymers such as (poly)lysine and (poly)ethylenimine have been shown to activate the complement

* Corresponding author. Mark E. Davis, Chemical Engineering, California Institute of Technology, 1200 E. California Blvd., Pasadena, California 91125. Tel: 626-395-4251. Fax: 626-568-8743. E-mail: mdavis@cheme.caltech.edu.

10.1021/bc0603539 CCC: $37.00 © 2007 American Chemical Society
Published on Web 02/28/2007

system, and increasing polycation length and surface charge density lead to higher complement activation (*11*). Rapid binding of charged molecules by complement proteins or other opsonins can lead to immune stimulation and rapid clearance of the delivery vehicles from the bloodstream. The size of the delivery vehicle also matters for systemic delivery. On the basis of measured sieving coefficients for the glomerular capillary wall, it is estimated that the threshold for first-pass elimination by the kidneys is approximately 10 nm (diameter) (*13*), placing a lower size limit on the assembled delivery vehicles. On the other end of the size spectrum, macromolecular complexes preferentially accumulate in tumors through the enhanced permeability and retention (EPR) effect. However, large macromolecules or delivery vehicles exhibit limited diffusion in the extracellular space, such as the tumor interstitium, and in the complex intracellular environment (*14*); in both situations, restricted movement will severely limit efficacy by preventing uptake by a sufficient number of cells or hindering the ability of the delivered particles to localize to intracellular compartments such as the nucleus. Other restrictions limiting the maximum size of delivery vehicles can also be imposed by the selectivity of receptors on certain cell types. For example, a study by Rensen et al. demonstrated that particles larger than 70 nm in diameter were not recognized by the asialoglycoprotein receptor (ASGPR) (*15*), placing an upper size limit on the particles that can be delivered to hepatocytes through this receptor.

Recent efforts toward targeted delivery have focused on decorating the surface of delivery vehicles with cell surface receptor-specific targeting ligands as a means of active targeting. Hydrophilic polymers, such as poly(ethylene glycol) (PEG), can be attached to the surface of the delivery vehicles to mask surface charge and prevent nonspecific interactions, helping to prevent unwanted binding to components of the bloodstream, slow uptake by the reticuloendothelial system (RES), and alter the cellular uptake patterns (*8*, *16*). Further addition of entities that can interact with cell surface receptors such as the receptors' natural ligands, antibodies, or antibody fragments allows the delivery vehicle to target particular cell types and undergo receptor-mediated endocytosis upon binding to the surface receptor (*7*, *8*, *15*).

In light of these considerations, a successful delivery vehicle must be engineered to have the following characteristics: (i) be small enough to extravasate and exhibit adequate tissue penetration, yet avoid rapid renal clearance; (ii) minimize nonspecific interactions and opsonization while providing specific targeting to a given cell; and (iii) protect the nucleic acid from degradation, but willingly release it upon arrival at the proper site. Over the past few years, we have been developing a synthetic delivery system based on a cyclodextrin-containing polycation (CDP) that has demonstrated some success in delivering nucleic acid payloads that include pDNA, siRNA, and DNAzymes (*7*, *17*−*20*). This delivery system is the first to be de novo designed for systemic delivery of nucleic acids and completely formulated by self-assembly (*17*). Here, we describe the physicochemical and biological characterization of the cyclodextrin-containing polycation delivery system and its formulation with nucleic acids. We illustrate issues of importance when designing any polycation composite with nucleic acids through the use of the CDP and point out when the conclusions are specific to this system only.

EXPERIMENTAL PROCEDURES

Formulation of Nucleic Acid Particles. The chemical structure of the cyclodextrin-containing polycation is shown in Figure 1A. This short, linear polycation can be synthesized with (CDP−Im) or without (CDP) the imidazole groups on the terminal amines (*17*, *18*). A schematic showing particle formation using CDP−Im and nucleic acid is shown in Figure 1B; particles are formed by mixing equal volumes of CDP−Im and nucleic acid. The ratio of positive (+) charges (2 mol of positive charge per CDP−Im monomer, denoted β-CD) to negative (−) charges (1 mol of negative charge per nucleotide) is defined as the formulation charge ratio (±). Poly(ethylene glycol) (PEG) molecules containing adamantane (AD) on the proximal end and either methoxy (AD−PEG) or a targeting ligand such as transferrin (AD−PEG−Tf) on the distal end can be attached to the surface of the particles via inclusion complex formation between adamantane and the β-CD molecules on the polycation backbone (*16*, *17*). The molecular weight of the PEG chain is typically 5000 Da (PEG_{5000}).

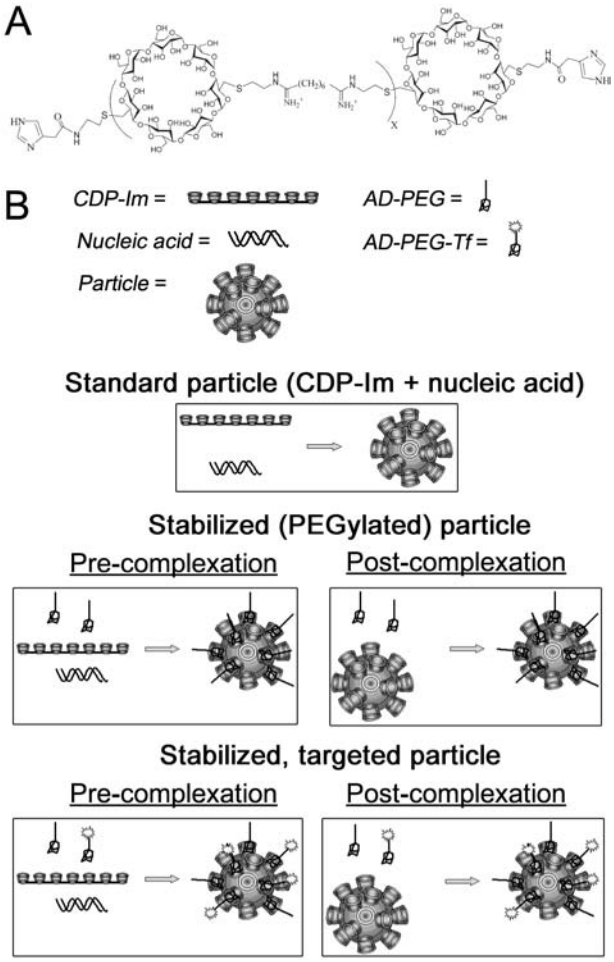


Figure 1. Formation of nucleic acid-containing particles using CDP−Im. (A) Schematic of the chemical structure of CDP−Im. (B) Schematic of particle assembly.

Formulation of PEGylated/Targeted Nucleic Acid Particles. *Pre-complexation (self-assembly).* Before addition to the nucleic acid, the CDP or CDP−Im was mixed with an AD−PEG conjugate at a 1:1 AD−PEG/β-CD (mol/mol) ratio in water. Targeted particles also require the addition of ligand-modified AD−PEG−X (e.g., AD−PEG−Tf (*7*, *19*, *20*)) as a percentage of the total AD−PEG in the mixture. For example, 1 mol % AD−PEG−Tf particles contain 0.01 mol AD−PEG−Tf for every 0.99 mol AD−PEG. The mixture of CDP (or CDP−Im), AD−PEG, and AD−PEG−ligand in water was then added to an equal volume of nucleic acid in water such that the ratio of positive charges from CDP or CDP−Im to negative charges from the nucleic acid was equal to the desired charge ratio. A schematic of this assembly process is shown in Figure 1B. Unless specified otherwise, all PEGylated or targeted nucleic acid particles used in this manuscript were prepared through the pre-complexation method.

Post-complexation. Particles were initially formulated in water by mixing equal volumes of nucleic acid and the cyclodextrin-containing polycation. After particles had formed, the AD−PEG and AD−PEG−Tf conjugates were added directly to the formulation mixture at the desired ratio of AD−PEG/β-CD (mol/mol). A schematic of this assembly process is shown in Figure 1B.

Electrophoretic Mobility Shift Assay. siRNA-containing particles were formulated at different charge ratios by changing the amount of CDP added to 1 μg of siRNA. CDP was first dissolved in 10 μL water and then added to an equal volume of water containing 1 μg of nucleic acid. After a 30 min incubation at room temperature, 10 μL of each formulation was run on a 1% agarose gel and visualized by ethidium bromide staining.

Individual Particle Charge Ratio. siRNA particles were formulated in 40 μL water at charge ratios from 5 to 30 ($\pm$). After formulation, the particles were separated from the free components by addition of 400 μL PBS, to cause particle aggregation, followed by centrifugation to pellet the aggregated particles. Since the CDP is terminated by primary amines, quantitation of polycation content was accomplished by measuring the amount of primary amines as follows. 400 μL of the supernatant was removed and combined with 200 μL of 0.01% w/v 2,4,6-trinitrobenzenesulfonic acid (Sigma). After incubating these samples for 2 h at 37 °C, 200 μL 10% sodium dodecyl sulfate (SDS) and 100 μL 1 N HCl were added to each sample before measuring the absorbance at 335 nm with a spectrophotometer. The amount of CDP in each sample was determined by comparison to a standard curve of CDP. The total positive charge present in each sample was calculated from the mass of CDP present using the fixed charge density of 0.0014 mol "+" per gram. This gave the number of unbound "+" charges present, so the number of bound "+" charges in the particles could be determined by subtracting the number unbound from the total "+" charges added during formulation. Assuming 100% incorporation of the nucleic acid into the particles at a formulation charge ratio of 3 ($\pm$) (based on the electrophoretic mobility shift assays; see Results section), the ratio of CDP to nucleic acid within each particle is equal to the number of bound "+" charges divided by the total number of "−" charges from the nucleic acid.

Serum Stability. Particles were formulated in water at a charge ratio of 3 ($\pm$) with an siRNA concentration of 0.05 g L^{-1}. 10 μL of 100% mouse serum (Sigma) were added to 10 μL of the particle formulation and subsequently incubated for 4 h at 37 °C and 5% CO_2. 0.25 μg naked siRNA in 5 μL water were added to 5 μL of 100% mouse serum and also incubated for 4 h at 37 °C and 5% CO_2. For comparison to the $t = 4$ h samples, identical amounts of naked siRNA or siRNA particles were exposed to 50% mouse serum immediately before gel loading ($t = 0$ h). 10 μL of each sample (containing 0.25 μg siRNA) were loaded per well of a 1% agarose gel. Displacement of the nucleic acid from the particles was achieved by adding 1% SDS to the sample immediately prior to gel loading. Gel electrophoresis was performed by applying 100 V for 30 min, and the bands were visualized by ethidium bromide staining.

Dynamic Light Scattering (DLS). Particle formulations were diluted to a volume of 1.4 mL, placed in a cuvette, and inserted into a ZetaPALS (Brookhaven Instruments Corporation) instrument to measure both the size and ζ potential. Reported effective hydrodynamic diameters represent the average values from a total of 5−10 runs of 30 s each, while ζ potentials represent the average of 10 runs each.

Transmission Electron Microscopy (TEM). Particles containing CDP−Im and siRNA (0.1 g L^{-1}) and PEGylated particles containing CDP−Im, AD−PEG (1:1 AD−PEG/β-CD mole ratio), and siRNA (0.5 g L^{-1}) were formulated in water at a charge ratio of 3 ($\pm$). Samples were stained with 2% uranyl acetate and then examined with an EM201C electron microscope (Philips).

Atomic Force Microscopy (AFM). Particles containing CDP−Im and siRNA (0.1 g L^{-1}) and PEGylated particles containing CDP−Im, AD−PEG (1:1 AD−PEG/β-CD mole ratio), and siRNA (0.5 g L^{-1}) were formulated in water at a charge ratio of 3 ($\pm$). 20 μL of each formulation solution were dropped on a freshly cleaved mica disc (Ted Pella, Inc.) and dried with pressurized air. Images were acquired with a Digital Instruments MultiMode AFM with a Nanoscope IV controller in tapping mode at a scan rate of 1 Hz using a BS Multi75 probe (BudgetSensors) with a resonant frequency of 75 kHz and a force constant of 3 N m^{-1}. Height images were flattened and processed for visualization with the derivative matrix convolution filter using *WSxM* scanning probe microscopy software (Nanotec Electronica).

Isothermal Titration Calorimetry (ITC). A MicroCal MCS titration calorimeter was used to investigate the thermodynamic properties of the interaction between AD−PEG conjugates and the β-cyclodextrin molecules on the CDP−Im backbone. CDP−Im (free or in particles) at 0.22 mM total β-CD in water was placed in the sample cell of the instrument. The reference cell contained water alone without CDP−Im. Small amounts of an AD−PEG stock solution at a concentration of 2.2 mM in water were titrated into the sample cell in 25 separate 10 μL increments. Titrations were performed at 30 °C. The measured parameters were δn, the number of moles of ligand (AD−PEG) added to the sample cell, and q, the amount of heat released or absorbed. The Simplex algorithm in the *Origin* data analysis software was used to determine the following parameters: K, the equilibrium binding constant; n, the number of available binding sites; and ΔH, the change in enthalpy. A more in-depth description of the thermodynamic analysis applied to ITC is provided by Blandamer et al. (*21*).

Percentage of AD−PEG$_{5000}$ Bound after Formulation. The small molecule, lactose (Lac), was attached to the end of AD−PEG$_{5000}$ to enable quantification using the Amplex Red Galactose Oxidase Assay Kit (Molecular Probes). Particles were formulated in a total volume of 100 μL water by adding a 50 μL solution containing CDP−Im and AD−PEG$_{5000}$−Lac (1:1 mole ratio of AD−PEG$_{5000}$−Lac/β-CD) in water to a 50 μL solution of siRNA in water. Control formulations were created by mixing CDP−Im and AD−PEG$_{5000}$−Lac without siRNA in 100 μL water. Particles and control formulations were filtered with Biomax (Millipore) centrifugal filtration devices with a 50 kDa MWCO to separate free and bound components. The Amplex Red Galactose Oxidase Assay Kit (Molecular Probes) was used to quantify the amount of AD−PEG$_{5000}$−Lac in the filtrate and retentate of all samples. Concentrations were determined by comparison to a standard curve of AD−PEG$_{5000}$−Lac. The percentage of AD−PEG$_{5000}$−Lac bound to the particles was determined by subtracting the fraction of recovered AD−PEG$_{5000}$−Lac in the filtrate of the particle samples from the fraction of recovered AD−PEG$_{5000}$−Lac in the filtrate of the control samples.

Percentage of AD−PEG$_{5000}$−Tf Bound after Formulation. Tf-targeted particles were formulated in a total volume of 100 μL water by adding a 50 μL solution of CDP−Im, AD−PEG$_{5000}$, and AD−PEG$_{5000}$−Tf (1:1 mole ratio of AD−PEG$_{5000}$−X/β-CD where AD−PEG$_{5000}$−X was composed of either 1 mol % or 5 mol % AD−PEG$_{5000}$−Tf and the remainder AD−PEG$_{5000}$) in water to a 50 μL solution of siRNA in water. Control formulations were created by mixing CDP−Im, AD−PEG$_{5000}$, and AD−PEG$_{5000}$−Tf without siRNA in 100 μL water. Particles and control formulations were filtered with Nanosep (Millipore) centrifugal filtration devices with a 300 kDa MWCO

to separate free and bound components. Total protein content in the filtrate (unbound AD−PEG_{5000}−Tf) and retentate (bound AD−PEG_{5000}−Tf) was determined using the BioRad DC protein assay. The percentage of AD−PEG_{5000}−Tf bound to the particles was determined by subtracting the fraction of recovered AD−PEG_{5000}−Tf in the filtrate of the particle samples from the fraction of recovered AD−PEG_{5000}−Tf in the filtrate of the control samples.

Multiangle Light Scattering (MALS). Particle formulations were loaded into a 10-mL syringe connected to a syringe pump to control the flow rate into a Dawn EOS (Wyatt Technology) multiangle light scattering instrument. The typical flow rate used was 1 mL min^{-1}. Data were fit by the *Astra* software to the Debye model with a detector fit degree of 2. The d*n*/d*c* value for the particles was determined to be 0.14 mL g^{-1}, and the mass concentration used in the calculations was determined from the total amount of CDP−Im and nucleic acid incorporated into the particles assuming an individual particle charge ratio of 1.1 (±) and complete incorporation of the nucleic acid added during formulation.

Individual Particle Stoichiometry. An estimate for the stoichiometry of each particle (i.e., number of CDP, nucleic acid, AD−PEG, and AD−PEG−Tf molecules) can be calculated from the following equations:

$$MW_{part} = \#NA \times \#bp \times MW_{bp} + \#CDP \times MW_{CDP} + \#PEG \times MW_{PEG} + \#Tf \times MW_{Tf} \quad (1)$$

$$CR = \frac{\#CDP}{\#NA \times \#bp} \quad (2)$$

$$\#PEG = f_{PEG} \times (100\% - \%Tf) \times \#CDP \times PR \times \frac{FR}{CR} \quad (3)$$

$$\#Tf = f_{Tf} \times \%Tf \times \#CDP \times PR \times \frac{FR}{CR} \quad (4)$$

where #NA is the number of nucleic acid molecules in the particle, #CDP is the number of CDP monomers (β-CD) in the particle, #PEG is the number of AD−PEG molecules in the particle, #Tf is the number of AD−PEG−Tf molecules in the particle, MW_{part} is the molecular weight of an individual particle (determined by MALS), #bp is the number of base pairs per nucleic acid molecule (e.g., 21 for siRNA), MW_{bp} is the average molecular weight of each nucleic acid base pair (~650 Da as an approximation), MW_{CDP} is the molecular weight of each CDP monomer (~1460 Da), MW_{PEG} is the molecular weight of each AD−PEG molecule (~5200 Da for AD−PEG_{5000}), MW_{Tf} is the molecular weight of each AD−PEG−Tf molecule (~85 000 Da for AD−PEG_{5000}−Tf), f_{PEG} is the fraction of the AD−PEG molecules that bind to particles during formulation, PR is the mole ratio of AD−PEG to β-CD during formulation, FR is the formulation charge ratio (±), CR is the charge ratio (± = 1.1) of each individual particle, f_{Tf} is the fraction of the AD−PEG−Tf molecules that bind to particles during formulation, and %Tf is the mole percent AD−PEG−Tf during formulation.

Salt Stability. Particle formulations were diluted to a volume of 1260 μL, placed in a cuvette, and inserted into a ZetaPALS (Brookhaven Instruments Corporation) instrument. Kinetic studies of aggregation were performed by recording the effective diameters at 1 min intervals after the addition of 1/10 volume 10× PBS to achieve a final concentration of 1× PBS, corresponding to physiological salt concentration.

Erythrocyte Aggregation. Erythrocytes were obtained from whole bovine calf blood (Rockland Immunochemicals, Inc.) by multiple rounds of centrifugation at 700 *g* and 4 °C for 10 min followed by removal of the supernatant and resuspension of the pellet of erythrocytes in cold PBS (Cellgro) until the supernatant became clear. Finally, the erythrocytes were resuspended at a concentration of 1% (v/v). The free polycations or formulated particles were added to a 24-well plate and diluted with PBS to a volume of 100 μL. Subsequently, 100 μL of the erythrocyte suspension were added to each well, and the plate was incubated for 1 h at 37 °C. Images were taken of each well using a CCD−IRIS/RGB (Sony) video camera attached to an Eclipse TE-300 (Nikon) inverted microscope to visually determine the degree of aggregation.

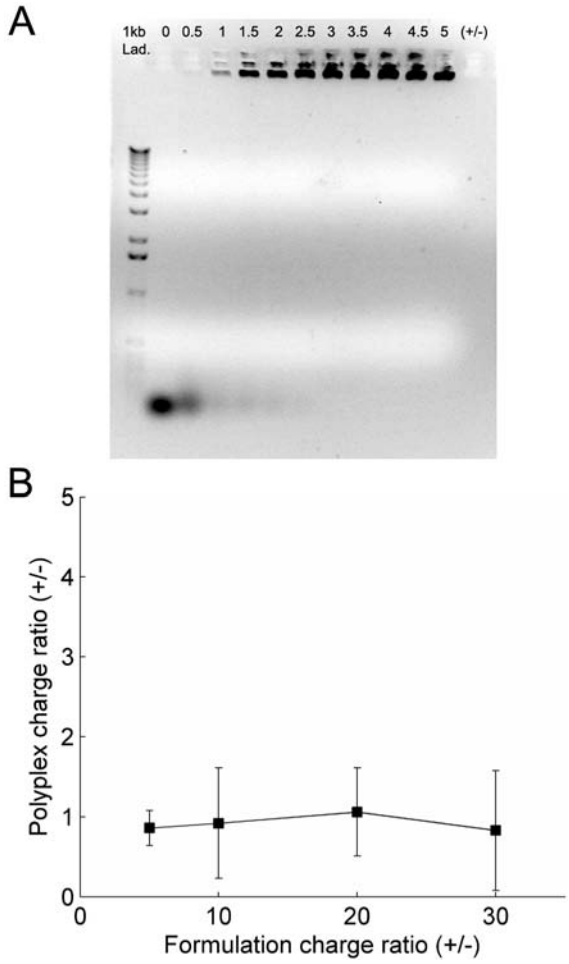


Figure 2. Effect of formulation charge ratio (±). (A) Electrophoretic gel mobility shift assay demonstrating the effect of formulation charge ratio on siRNA particle formation. (B) Individual particle charge ratio as a function of formulation charge ratio.

Complement Fixation. To test the complement fixation by polycations or CDP-based particles, antibody-sensitized sheep erythrocytes were used in a CH50 assay modified from Plank et al. (*11*). 25 μL human complement sera (Sigma) in gelatin veronal buffer (Sigma) were added in a 1:1.5 dilution series across a row of wells in a 96-well plate. To this same row of wells were added 25 μL of the desired concentration of polycation in its free form or complexed with calf thymus DNA (CT-DNA). A different concentration of the polycations or particles was added to each row of wells. After a 30-min incubation at 37 °C, 1.25×10^7 antibody-sensitized sheep erythrocytes (Sigma) were added to each well, and the plate was incubated with shaking for 1 h at 37 °C. Finally, the plate was centrifuged at 2000 rpm for 10 min, 100 μL of the supernatant from each well was transferred to a new 96-well plate, and the absorbance at 410 nm was determined using a SpectraMax 190 (Molecular Devices) microplate reader. This wavelength corresponds to an absorbance peak for the hemoglobin that is released after lysis of the erythrocytes. The CH50

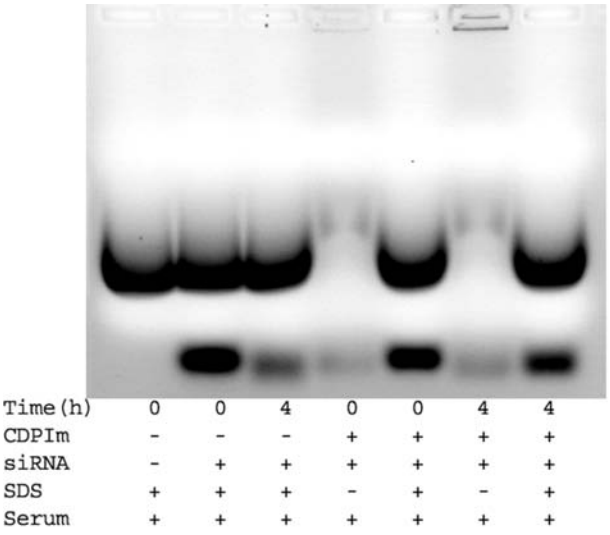


Figure 3. Nuclease stability of siRNA encapsulated within particles. For the $t = 4$ lanes, naked siRNA or siRNA within CDP−Im particles (3 (±)) was incubated in 50% mouse serum for 4 h at 37 °C and 5% CO_2. For the $t = 0$ lanes, serum was added to an equivalent amount of naked siRNA or siRNA within CDP−Im particles immediately before loading into the gel. Addition of 1% SDS was used to displace the siRNA from the particles to visualize the amount of intact siRNA remaining. The first lane demonstrates that the upper bands are nonspecific bands resulting from the interaction between SDS, serum, and the ethidium bromide stain, while the lower bands correspond to the free siRNA.

unit is used to define the serum dilution required to achieve 50% lysis of the antibody-sensitized sheep erythrocytes. If the substance being tested binds complement proteins to an appreciable degree, it will sequester these complement proteins and prevent them from binding to and lysing the erythrocytes. As a result, a lower serum dilution (CH50) will be required to achieve 50% erythrocyte lysis under these conditions. The reported %CH50max represents the ratio of the CH50 for the substance being tested to the CH50 determined for the complement sera alone (CH50max).

Cellular Uptake. *Method 1: Flow Cytometry*. A FACSCalibur (BD Biosciences) flow cytometer was used to detect the uptake of FL−siRNA (fluorescein attached to the 5′ end of the sense strand) delivered with or without the CDP−Im delivery vehicle. HeLa cells were seeded at 2×10^4 cells per well in 24-well plates 2−3 days prior to transfection and grown in medium supplemented with 10% fetal bovine serum (FBS) and antibiotics (penicillin/streptomycin). The growth medium was removed from each well and replaced with 200 μL Opti-MEM I (Invitrogen) alone, 200 μL Opti-MEM I with 100 nM FL−siRNA, or 200 μL Opti-MEM I with 100 nM FL−siRNA formulated into CDP−Im particles at a charge ratio of 3 (±). After incubation for 2 h at 37 °C and 5% CO_2, the transfection medium was removed and the cells were trypsinized and resuspended in Hanks Balanced Salt Solution (HBSS) with 1% bovine serum albumin (BSA) and 10 μg mL^{-1} propidium iodide to detect cell viability.

Method 2: Confocal Microscopy. HeLa cells were seeded at 2×10^4 cells per well in a LabTek II Chamber Slide 2 days prior to transfection and grown in medium supplemented with 10% FBS and antibiotics (penicillin/streptomycin). The growth medium was removed from each well and replaced with 200 μL Opti-MEM I containing 100 nM FL−siRNA formulated into CDP−Im particles at a charge ratio of 3 (±). After incubation for 2 h at 37 °C and 5% CO_2, cells were fixed for 15 min at room temperature using 4% paraformaldehyde in PBS. F-actin was stained with rhodamine phalloidin (Invitrogen) according to manufacturer's instructions. Cells were mounted with Biomeda Gel/Mount according to manufacturer's instructions, and the coverslips were subsequently sealed using nail polish. Fluorescent images were acquired using a Zeiss LSM 510 Meta laser scanning confocal microscope with a 40× water-immersion objective.

Competitive Uptake. Competitive uptake studies were conducted to determine the impact of free holo-transferrin (holo-

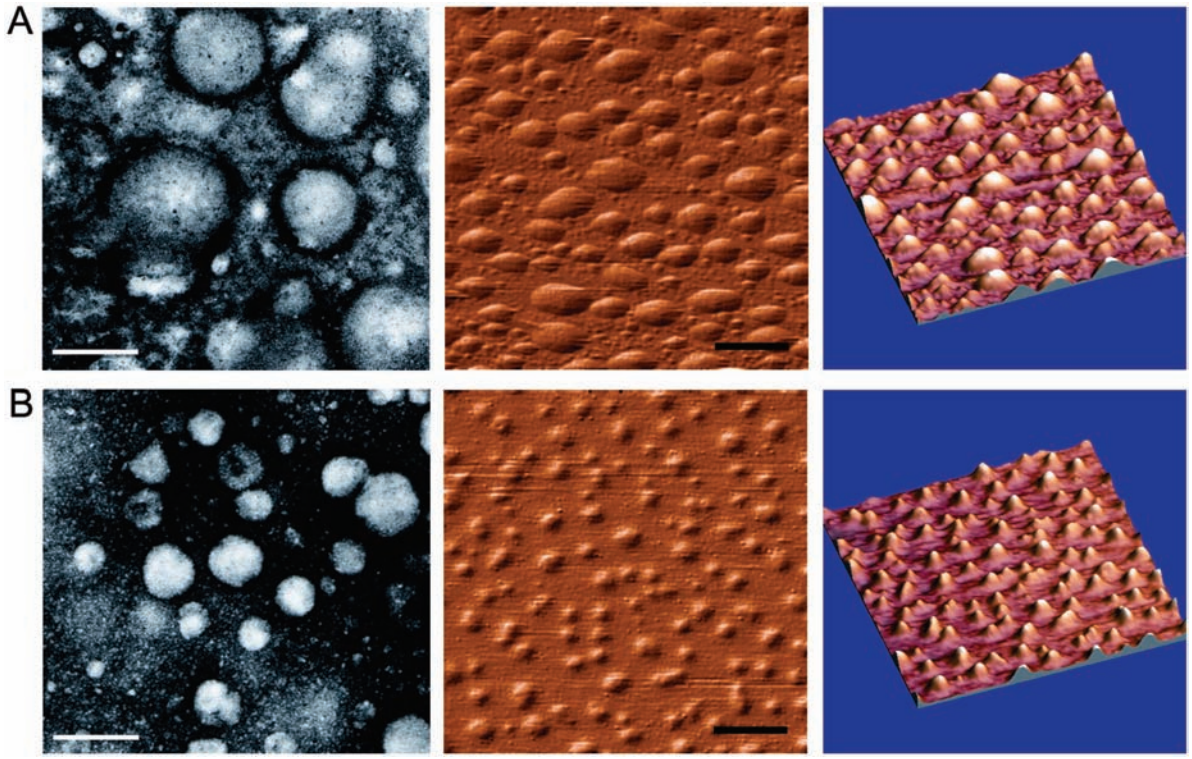


Figure 4. Transmission electron microscopy (left panels) and atomic force microscopy (center and right panels) images of (A) unPEGylated and (B) PEGylated siRNA particles formulated at a charge ratio of 3 (±). Scale bar = 100 nm (left panels) and 200 nm (center and right panels).

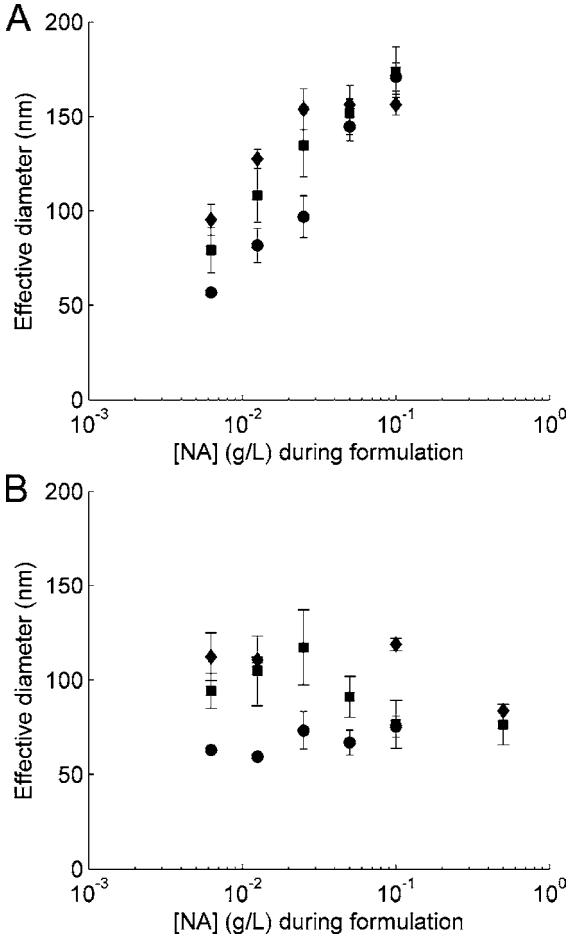


Figure 5. Effect of nucleic acid concentration ([NA]) during formulation on the size of (A) unPEGylated or (B) PEGylated particles. Particles were formulated at a charge ratio of 3 (±) using CDP−Im and either siRNA, pDNA, or CT-DNA (calf thymus DNA). PEGylated particles were formulated by adding a 1:1 mole ratio of AD−PEG_{5000}/β-CD. Particle effective diameter was determined using dynamic light scattering. Squares = CDP−Im/siRNA particles; circles = CDP−Im/pDNA particles; diamonds = CDP−Im/CT-DNA particles.

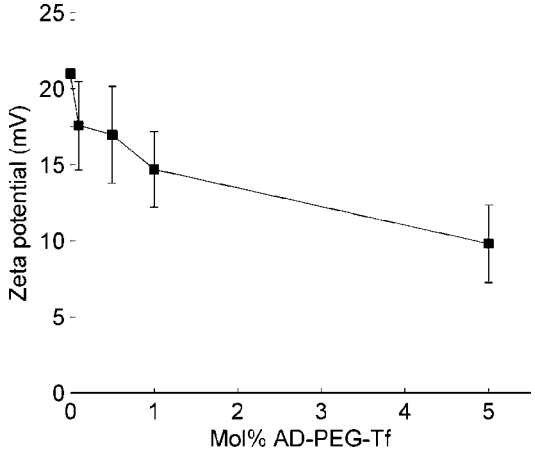


Figure 6. Particle ζ potential as a function of AD−PEG_{5000}−Tf ligand concentration during formulation. Particles were formulated at a charge ratio of 3 (±) using CDP−Im and siRNA, and the AD−PEG_{5000} or AD−PEG_{5000}−Tf molecules were added after particle formation (post-complexation). The total number of moles of AD−PEG_{5000}−X (AD−PEG_{5000} and AD−PEG_{5000}−Tf) was equal to the number of moles of β-CD, and the mixture of AD−PEG_{5000} and AD−PEG_{5000}−Tf is defined by the % AD−PEG_{5000}−Tf.

Table 1. Measured ITC Parameters for the Binding between AD−PEG_{5000} and β-CD Alone, Polycation Alone (CDP−Im), or CDP−Im/siRNA Particles Formulated at Charge Ratios from 3 (±) to 15 (±)[a]

	β-CD + Adamantane Carboxylate		
	n	*K* (M^{-1})	Δ***H*** (cal M^{-1})
β-CD	1	42000	−4440
	β-CD + AD−PEG_{5000}		
	n	*K* (M^{-1})	Δ***H*** (cal M^{-1})
β-CD	1.1	30600	−7358
	siRNA Particle + AD−PEG_{5000}		
	n	*K* (M^{-1})	Δ***H*** (cal M^{-1})
3 (±)	0.34 ± 0.09	5110 ± 730	−15200 ± 4090
5 (±)	0.38 ± 0.04	6320 ± 330	−12600 ± 570
10 (±)	0.48 ± 0.02	8090 ± 620	−10100 ± 520
15 (±)	0.49 ± 0.01	8050 ± 800	−10600 ± 450
CDP−Im	0.54 ± 0.04	8380 ± 940	−9460 ± 1490

[a] For comparison, literature values are provided for the binding between β-CD alone and adamantane carboxylate (*22*).

Tf) on the relative uptake of transferrin-targeted (containing 1 mol % AD−PEG_{5000}−Tf) or nontargeted particles. By formulating the particles with Cy3−siRNA (Cy3 attached to the 5′ end of the sense strand), a Tecan SPECTRAFluorPlus plate reader could be used to measure the total cell-associated fluorescence after transfection. Cells were seeded at 2×10^4 cells per well in 24-well plates 2−3 days prior to transfection and grown in medium supplemented with 10% FBS and antibiotics (penicillin/streptomycin). The growth medium was removed from each well and replaced with 200 μL Opti-MEM I containing 100 nM Cy3−siRNA formulated in particles. After incubation for 30 min at 37 °C and 5% CO_2, the transfection medium was removed, and the cells were lysed in 100 μL cell lysate buffer (Promega). Total fluorescence in the 100 μL lysate per well was measured with the SPECTRAFluorPlus plate reader, and the number of siRNA molecules was estimated from a standard curve of Cy3−siRNA. Cells in two wells that were not transfected were trypsinized and counted to provide an estimate for the average number of cells per well.

Avidity Effects. *Method 1: Competitive Cell Surface Transferrin Receptor (TfR) Binding Assay.* Competitive uptake experiments were performed using flow cytometry to detect the uptake of fluorescently labeled holo-Tf. Unlabeled holo-Tf, Tf conjugates (AD−PEG_{5000}−Tf), or Tf-targeted siRNA particles (1 mol % AD−PEG_{5000}−Tf) were used to compete for uptake by the transferrin receptors on the surface of HeLa cells. Cells were seeded at 2×10^4 cells per well in 24-well plates 2−3 days prior to transfection and grown in medium supplemented with 10% FBS and antibiotics (penicillin/streptomycin). The growth medium was removed from each well and replaced with 200 μL Opti-MEM I containing 1% BSA, 20 nM AlexaFluor488-labeled holo-Tf (AF488-Tf), and the desired unlabeled Tf competitor. After incubation for 1 h at 37 °C and 5% CO_2, the transfection medium was removed, and the cells were trypsinized and resuspended in HBSS with 1% BSA and 10 μg mL^{-1} propidium iodide to detect cell viability. To enable direct comparison of the effects of avidity, the total amount of Tf was kept constant whether it was in its free form, as AD−PEG_{5000}−Tf, or as AD−PEG_{5000}−Tf on the siRNA particles. The relative uptake under each condition is reported as the ratio of the mean fluorescence of the wells with unlabeled competitor to the mean fluorescence of the wells with AF488−Tf alone.

Method 2: Live-Cell Binding Assay. A live-cell binding assay was used to measure the relative binding of transferrin-targeted siRNA particles. 3×10^5 HeLa cells were resuspended in 100 μL PBS in individual microcentrifuge tubes and cooled on ice. To each microcentrifuge tube was added 100 μL PBS containing

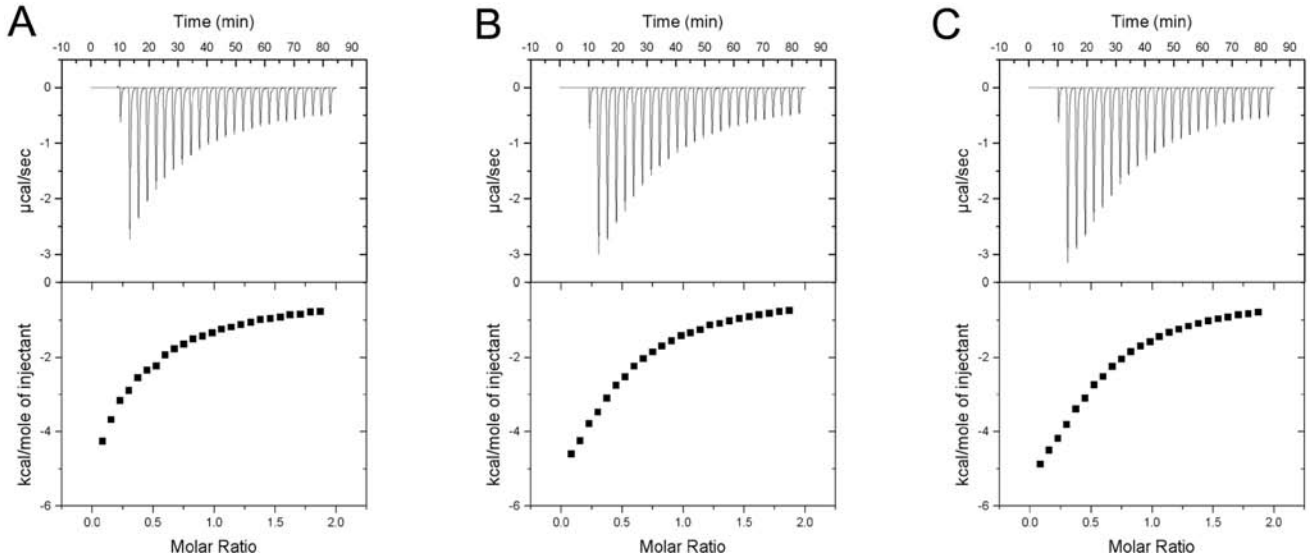


Figure 7. Isothermal titration calorimetry (ITC) plots characterizing the binding between AD−PEG_{5000} molecules and free CDP−Im or siRNA particles. (A) CDP−Im/siRNA particle (3 (±)) and AD−PEG_{5000}; (B) CDP−Im/siRNA particle (10 (±)) and AD−PEG_{5000}; (C) CDP−Im and AD−PEG_{5000}.

PEGylated or Tf-targeted particles formulated with Cy3-labeled siRNA such that the final Cy3-siRNA concentration was 100 nM. After incubating for 30 min on ice, the microcentrifuge tubes were centrifuged for 5 min at 200 *g* to pellet the cells. 100 μL of the supernatant from each microcentrifuge tube was added to a well in a black 96-well plate, and the Cy3 fluorescence was measured using a Tecan Safire plate reader. Comparison to a standard curve of Cy3−siRNA particles allowed quantification of the amount of Cy3−siRNA in each well, and the percent bound (fraction associated with the cell pellet) was determined by subtracting the fluorescence remaining in the supernatant from the initial amount added.

Luciferase Knockdown after siRNA Transfection. Functional efficacy of pDNA and siRNA delivered by CDP−Im particles was demonstrated in HeLa cells by cotransfecting the pGL3−CV vector (Promega) containing the firefly luciferase gene and a nontargeting control siRNA (siCON1) synthesized by Dharmacon or a luciferase-targeting siRNA (siLuc) synthesized by Integrated DNA Technologies. The sequence of the siCON1 siRNA is UAGCGACUAAACACAUCAAUU (sense) and UUGAUGUGUUUAGUCGCUAUU (antisense). The sequence of the siLuc siRNA is GUGCCAGAGUCCUUCGAUAdTdT (sense) and UAUCGAAGGACUCUGGCACdTdT (antisense). The Promega Luciferase Assay System was then used to quantify the relative luciferase expression in cells that had been transfected with 1 μg pGL3−CV alone, 1 μg pGL3−CV and 100 nM siCON1, or 1 μg pGL3−CV and 100 nM siLuc. HeLa cells were seeded at 2×10^4 cells per well in 24-well plates 2−3 days prior to transfection and grown in medium supplemented with 10% FBS and antibiotics (penicillin/streptomycin). CDP−Im particles were formulated to contain 1 μg pGL3−CV vector and 100 nM siRNA in 200 μL Opti-MEM I. The growth medium was removed from each well and replaced with 200 μL Opti-MEM I containing the formulated particles. After incubation for 5 h at 37 °C and 5% CO_2, 800 μL complete growth medium was added to each well. 48 h later, the cells were lysed in 100 μL 1X Luciferase Cell Culture Lysis Reagent (Promega). 10 μL of the cell lysate was added to 90 μL of the luciferase substrate, and bioluminescence was measured using a MonoLight (Pharmingen) luminometer. 5 μL of the cell lysate was used in a BioRad DC protein assay to determine the protein concentration in each lysate sample. Luciferase activities are reported as relative light units per milligram protein.

RESULTS AND DISCUSSION

Particle Formation Requires a Slight Excess of Positive Charge and Protects siRNA from Degradation in Serum. Results from an electrophoretic mobility shift assay (EMSA) demonstrate that siRNA particles completely form at charge ratios (±) greater than ~1 to 1.5 (Figure 2A). At sufficiently high charge ratios, the band corresponding to the free nucleic acid becomes undetectable, since the nucleic acid remains associated with the particles that have greatly reduced electrophoretic mobility. To determine what portion of the polycations (CDP) added during formulation actually are incorporated into the particles, the free polycations were separated from the particles after formulation. Regardless of the formulation charge ratio up to 30 (±), the charge ratio of individual particles remains ~1 (±) (Figure 2B). This is consistent with the results shown in Figure 2A where charge ratios slightly greater than 1 were required to achieve complete particle formation. A nuclease stability assay was conducted to determine if the formation of particles could protect the nucleic acid payload from degradation by nucleases present in serum. While naked siRNA degrades rapidly in serum, siRNA within particles is protected from significant degradation even after 4 h in 50% mouse serum (Figure 3). Additionally, the data given in Figure 3 show that (i) there is essentially complete encapsulation of the siRNA by the particles, and (ii) when the particles exposed to serum are disrupted with SDS, the nucleic acids released are still intact siRNA duplexes.

Formulation Conditions Affect Particle Size and ζ Potential. Transmission electron microscopy (TEM) and atomic force microscopy (AFM) were used to visualize the siRNA particles formulated at a charge ratio of 3 (±). The images in Figure 4 demonstrate that the siRNA particles assume a roughly spherical shape, but the unPEGylated particles display more variability in size and adopt a slightly oblong shape relative to the PEGylated particles when they are visualized by AFM on the mica surface. While a large fraction of the unPEGylated particles (0.1 g L^{-1} siRNA) have diameters that exceed 100 nm, PEGylated particles (0.5 g L^{-1} siRNA) formulated with a 1:1 mole ratio of AD−PEG_{5000}/β-CD consistently have diameters of <100 nm and are approximately 60−80 nm.

To further investigate the effects of formulation conditions, dynamic light scattering was used to measure the effective hydrodynamic diameter and ζ potential of the particles. Con-

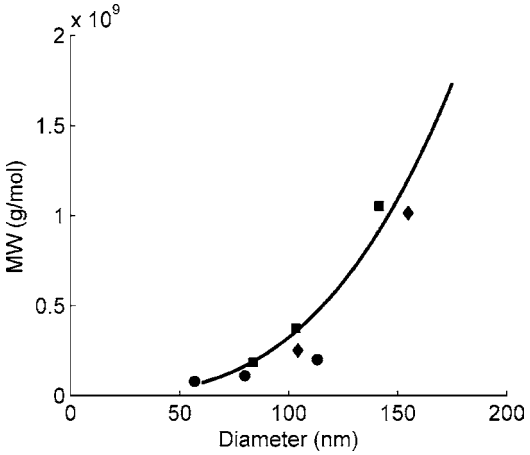


Figure 8. Relationship between particle size and molecular weight (MW) as determined by dynamic and multiangle light scattering. Particles were formulated at a charge ratio of 3 (±) using CDP−Im and either siRNA, pDNA, or CT-DNA. Effective diameters were measured using dynamic light scattering, and molecular weights were determined using multiangle light scattering. Squares = CDP−Im/siRNA particles; circles = CDP−Im/pDNA particles; diamonds = CDP−Im/CT-DNA particles; solid line = r^3 scaling dependence of the MW of particles starting with a MW of 7×10^7 g mol^{-1} for a 60 nm particle.

sistent with the TEM and AFM images, the results shown in Figure 5A reveal that the nucleic acid concentration during formulation affects the size of the particles. Particles formulated with siRNA, pDNA, and calf thymus (CT-DNA) show nearly identical trends of increased size with higher nucleic acid concentration. However, particles that are formulated in the presence of AD−PEG$_{5000}$ (PEGylated particles formed by the pre-complexation method) do not exhibit such a dependence on formulation conditions (Figure 5B). These properties allow the delivery vehicles to be fine-tuned with respect to size by altering the formulation conditions accordingly (i.e., PEGylation through the pre- or post-complexation method). The ζ potential of unPEGylated particles ranges from 10 (particles ∼60 nm in diameter) to 30 mV (particles ∼150 nm in diameter), while that of PEGylated particles ranges from 10 to 20 mV for similarly sized particles. This positive ζ potential implies that the charge ratio of the individual particles is slightly greater than 1 (±). The AD−PEG$_{5000}$ conjugates can be further modified to contain targeting ligands on the distal end of the PEG chain. For example, transferrin can be conjugated to the AD−PEG$_{5000}$ molecules to yield AD−PEG$_{5000}$−Tf (*19*). Because the transferrin protein is negatively charged, inclusion of AD−PEG$_{5000}$−Tf molecules during particle formulation reduces the ζ potential of siRNA particles in a concentration-dependent manner (Figure 6). Bellocq et al. reported a similar trend using particles made with pDNA (*19*).

AD−PEG Conjugates Bind to the Surface of Particles Through Inclusion Complex Formation. An important property of the cyclodextrin-containing polycations is their ability to form inclusion complexes with hydrophobic molecules. This provides the opportunity for modular attachment of different stabilizing molecules or targeting ligands through coupling to an adamantane (AD) molecule that forms inclusion complexes with the β-cyclodextrin molecules. Isothermal titration calorimetry was used to investigate the thermodynamics of the interaction between AD−PEG molecules and CDP−Im either in its free form or within siRNA-containing particles (Table 1). Figure 7 shows representative ITC data plots for binding between AD−PEG$_{5000}$ and CDP−Im formulated with siRNA at a charge ratio of 3 (±), CDP−Im formulated with siRNA at a charge ratio of 10 (±), and CDP−Im alone. As the charge ratio increases, the measured binding parameters approach those

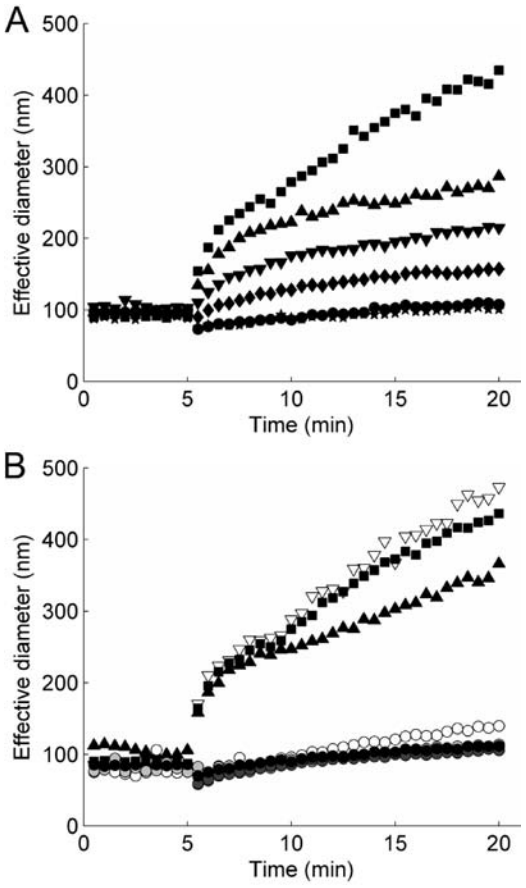


Figure 9. Aggregation of siRNA particles in physiological salt solutions. 140 μL of a 10× PBS solution were added to 1260 μL of the particles in water after 5 min, and dynamic light scattering was used to follow the formation of aggregates with time. (A) Effect of the ratio of AD−PEG$_{5000}$/β-CD on particle stability. CDP−Im/siRNA (3 (±)) particles were formulated without AD−PEG$_{5000}$ (black squares) or through the post-complexation method with an AD−PEG$_{5000}$/β-CD mole ratio of 0.25:1 (black triangles), 0.5:1 (inverted black triangles), 0.75:1 (black diamonds), 1:1 (black circles), or 2:1 (black stars). (B) Effect of PEG chain length, adamantane conjugation, and Tf targeting ligand density on particle stability. CDP−Im/siRNA (3 (±)) particles were formulated without AD−PEG$_{5000}$ (black squares), with a PEG$_{5000}$ (no adamantane)/β-CD mole ratio of 1:1 (open inverted triangles), with an AD−PEG$_{500}$/β-CD mole ratio of 1:1 (black triangles), with an AD−PEG$_{5000}$/β-CD mole ratio of 1:1 (black circles), or with a 1:1 mole ratio of AD−PEG$_{5000}$-X/β-CD where AD−PEG$_{5000}$−X was composed of 0.1 wt % AD−PEG$_{5000}$−Tf (dark gray circles), 0.1 mol % AD−PEG$_{5000}$−Tf (gray circles), 1 mol % AD−PEG$_{5000}$−Tf (light gray circles), or 5 mol % AD−PEG$_{5000}$−Tf (open circles) and the remainder AD−PEG$_{5000}$.

of free CDP−Im as expected. Given the previous results showing that the actual particle charge ratio is slightly greater than 1 (±), this is consistent with the presence of excess free CDP−Im at charge ratios of >1.

The value of *n* represents the fraction of the β-CD molecules available for inclusion complex formation with the AD−PEG molecules. Each β-CD cup can interact with a single adamantane molecule, as previous reports have shown a 1:1 binding stoichiometry between adamantane molecules and β-CD (*22*). While binding between individual β-cyclodextrins and AD−PEG$_{5000}$ conjugates gives the expected *n* value of ∼1, binding between CDP−Im and AD−PEG$_{5000}$ exhibits an *n* value of ∼0.5. When the AD−PEG$_{5000}$ molecule containing a 5000 Da PEG chain binds to a β-CD cup on the CDP−Im polymer, it likely provides steric hindrance that impedes binding between other AD−PEG$_{5000}$ molecules and nearby β-CD molecules. Support for this hypothesis comes from the observation that the *n* value for binding between CDP−Im and AD−PEG$_{500}$

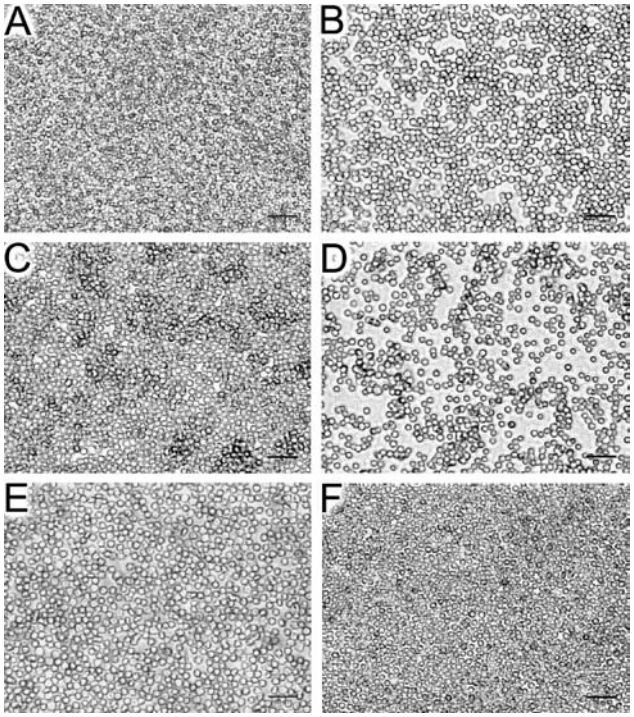


Figure 10. Erythrocyte aggregation: (A) 0.2 g L^{-1} CDP, (B) 2 g L^{-1} CDP, (C) 0.2 g L^{-1} CDP−Im, (D) 2 g L^{-1} CDP−Im, (E) CDP−Im/siRNA (3 (±)) particles at 0.2 g L^{-1} CDP−Im formulated with a 1:1 mole ratio of AD−PEG_{5000}/β-CD, (F) PBS alone. Scale bar = 20 μm.

molecules containing short 500 Da PEG chains is 0.92 ± 0.05, likely indicating that the shorter PEG chains do not interfere to as great an extent with the binding of AD−PEG_{500} to neighboring β-CD molecules.

Another interesting pattern is observed with the ΔH values, representing the change in enthalpy that results from binding between an AD−PEG molecule and a β-CD cup. These values are all negative, indicating that energy is released upon binding due to the favorable interaction between the hydrophobic adamantane and the β-CD cup. Notably, ΔH is more negative for AD−PEG_{5000} binding to the siRNA particles than it is for AD−PEG_{5000} binding to free CDP−Im. We hypothesize that this increased stabilization energy, in addition to the inclusion complex formation, is a result of favorable interactions between the PEG chains themselves when they are grouped together on the surface of an siRNA particle.

Particle Molecular Weight Can Be Used to Estimate Individual Particle Stoichiometry. Determining the individual component stoichiometry of the particles provides important insights into their functional properties. Centrifugal filtration was used to separate unbound components from those bound to the particles. As discussed previously, it was determined that the individual particle charge ratio (i.e., the ratio of positive charges from the CDP−Im to negative charges from the nucleic acid) is slightly greater than 1; we used 1.1 (±) for the calculations. The percent of the total AD−PEG_{5000} or AD−PEG_{5000}−Tf added to the formulation mixture that remains free was determined by quantifying the AD−PEG_{5000} (experiment actually used AD−PEG_{5000}−Lac, and we assumed that the value for AD−PEG_{5000} would be approximately the same) or AD−PEG_{5000}−Tf recovered in the filtrate versus the retentate after centrifugal filtration. The results of these measurements indicated that approximately 3% of the total AD−PEG_{5000} and 10% of the total AD−PEG_{5000}−Tf added during formulation remained associated with the particles. The greater degree of binding measured for the AD−PEG_{5000}−Tf conjugates may be partly due to charge interactions between the negatively charged

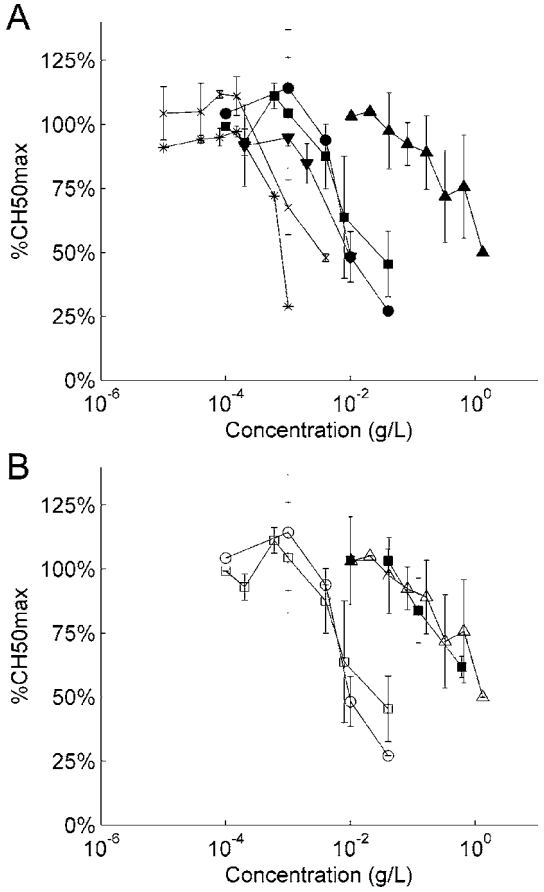


Figure 11. Complement fixation. (A) Complement fixation by free polycations. *, branched PEI; ×, linear PEI; ▲, pentalysine; ▼, polylysine (36-mer); ■, CDP; ●, CDP−Im. (B) Complement fixation by CDP/CT-DNA (3 (±)) particles formulated with a 1:1 mole ratio of AD−PEG_{5000}/β-CD (■). The curves for CDP (□), CDP-Im (○), and pentalysine (△) are shown again for comparison.

transferrin proteins and the positively charged particles. The final piece of data needed to estimate the individual particle stoichiometry is the molecular weight of the particles. This was determined using multiangle light scattering. The results in Figure 8 show that the molecular weight of particles formulated with siRNA, pDNA, or calf thymus (CT-DNA) scales approximately as r^3, where r is the radius of the particle determined by DLS. This similarity among all three types of particles is consistent with the trends observed in Figure 5, further supporting the interesting result that formulation with a variety of nucleic acids leads to particles with similar physical properties. An unPEGylated particle with a diameter of 70 nm is expected to have a molecular weight around 1×10^8 g mol^{-1} from data given in Figure 8. Inserting this molecular weight and an individual particle charge ratio of 1.1 (±) into eqs 1 and 2 yields 48 800 CDP monomers (or 9750 CDP chains with a degree of polymerization of 5) and 2110 siRNA molecules (with 21 bp per siRNA) per particle. For the sake of calculation, we can then use this value for #CDP to estimate the number of AD−PEG_{5000} and AD−PEG_{5000}−Tf molecules per particle using eqs 3 and 4. For example, a 70 nm siRNA particle with a molecular weight of 1.3×10^8 g mol^{-1} (accounting for the added mass from the PEG conjugates) formulated at a charge ratio of 3 (±) with 1 mol % AD−PEG_{5000}−Tf is calculated to contain 9750 CDP chains, 2110 siRNA molecules, 3950 AD−PEG_{5000} molecules, and 133 AD−PEG_{5000}−Tf molecules. The corresponding surface density for this number of AD−PEG_{5000} chains on a 70 nm particle is ~43 pmol cm^{-2} or 0.26 chains nm^{-2}. The calculated average distance between PEG_{5000} molecules at this surface density is ~2.0 nm, while the Flory radius is

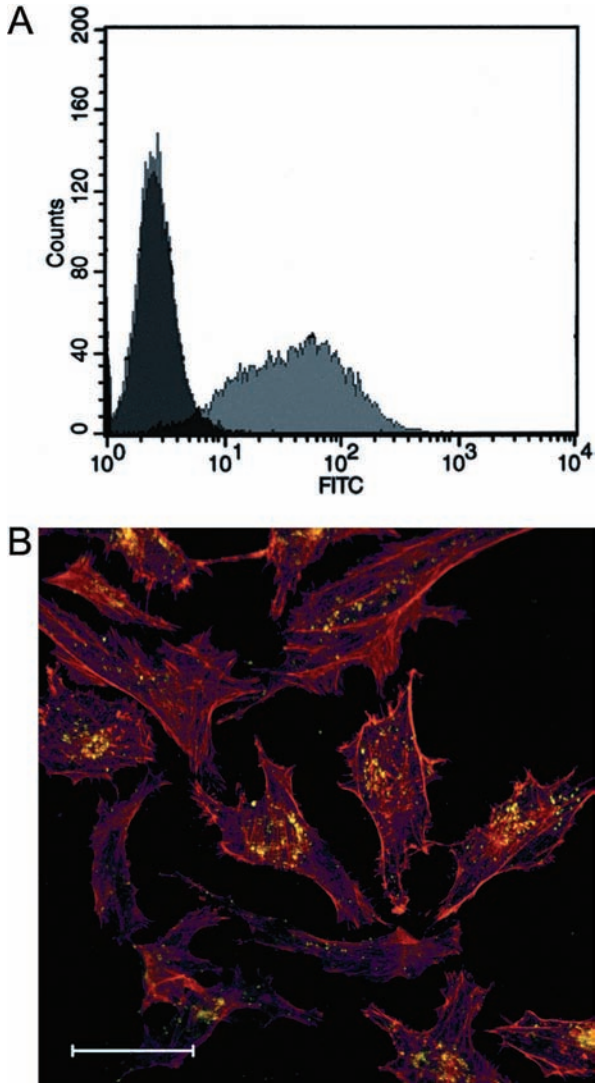


Figure 12. Uptake of CDP−Im particles containing fluorescein (FL)-labeled siRNA by HeLa cells. (A) Histogram of cell-associated fluorescence measured by flow cytometry. The left-most peaks correspond to the overlapping peaks for HeLa cells incubated with either Opti-MEM I alone or 100 nM naked FL−siRNA, while the right-most peak represents the cell-associated fluorescence after transfection with CDP−Im/FL−siRNA particles. (B) Confocal fluorescence microscopy image of HeLa cells after transfection with CDP−Im/FL−siRNA particles (green) and rhodamine phalloidin staining of F-actin (red). Scale bar = 50 μm.

~6 nm. Since the distance between PEG_{5000} molecules is much less than the Flory radius, the PEG_{5000} chains are expected to interact laterally and extend out from the surface in a dense brush layer with an estimated thickness of ~12.5 nm. Hansen et al. further examined the brush scaling laws for poly(ethylene glycol)s and predicted that PEG_{5000} solutions must have monomer volume fractions, ϕ, greater than 0.07−0.09 to be in the brush regime (*23*). This is satisfied when the PEG_{5000} surface density exceeds ~26−28 pmol cm^{-2}, again indicating that the PEG_{5000} chains on the particles are in the brush regime.

PEGylation Provides Steric Stabilization to the Particles and Reduces Nonspecific Interactions. DLS-based kinetic studies of aggregation were performed to determine whether the inclusion of AD−PEG conjugates could help to stabilize the particles against aggregation at physiological salt concentrations. First, the ratio of AD−PEG_{5000}/β-CD (mol/mol) was varied from 0 to 2 to investigate how the surface density of AD−PEG_{5000} affects the steric stability of siRNA particles formulated through the post-complexation method (Figure 9A). Particles formulated with AD−PEG_{5000}/β-CD (mol/mol) ratios of >1 do not exhibit observable aggregation after 15 min in 1× PBS. At ratios of <1, aggregation increases as the ratio of AD−PEG_{5000}/β-CD (mol/mol) decreases. These results with siRNA-containing particles are consistent with those observed by Pun et al. using particles made with pDNA (*24*). The length of the PEG molecule in the AD−PEG conjugate also impacts its ability to confer steric stabilization to the particles. As shown in Figure 9B, the stabilization effects increase with the length of the PEG chain, with AD−PEG_{500} (AD−PEG_{500}/β-CD = 1) only slightly slowing the aggregation, while AD−PEG_{5000} (AD−PEG_{5000}/β-CD = 1) prevents detectable aggregation up to 15 min after salt addition. If the AD−PEG_{500} chains, like the AD−PEG_{5000} chains, also achieve a surface density of ~43 pmol cm^{-2} (AD−PEG_{500}/β-CD = 1), then the average distance between PEG_{500} chains remains ~2.0 nm. However, since this is not less than the Flory radius for a PEG_{500} molecule (~1.5 nm), the PEG_{500} molecules are not expected to form the brushlike layer on the particle surface that is needed for steric stabilization. Furthermore, modification of up to 1 mol % of the AD−PEG_{5000} chains with Tf (AD−PEG_{5000}−Tf) leads to minimal perturbations in the salt stability of the particles. However, at 5 mol % AD−PEG_{5000}−Tf, gradual particle aggregation becomes apparent during the 15 min incubation in 1× PBS.

Besides providing steric stabilization to the particles, PEGylation can help to reduce nonspecific interactions. Specifically, experiments were performed to study the interaction between the polycations (or particles) and erythrocytes (Figure 10). Significant erythrocyte binding will lead to aggregation that can be observed by visual inspection using a light microscope. While the free CDP or CDP−Im showed negligible aggregation at 0.2 g L^{-1}, some aggregation was observed as the concentration increased to 2 g L^{-1} (Figure 10A−D). Erythrocyte aggregation was also measured after incubation with siRNA particles that were formulated with CDP−Im and a 1:1 mole ratio of AD−PEG_{5000}/CDP−Im (Figure 10E). The results demonstrate that PEGylated particles do not lead to any observable aggregation at a total CDP−Im concentration of 0.2 g L^{-1}, corresponding to the expected concentration after systemic delivery in vivo (*7*).

PEGylated Particles Show Minimal Complement Fixation. Complement fixation by poly(ethylenimine) and poly(lysine) was compared to that of CDP or CDP−Im. The CDP and CDP−Im molecules do not show as much complement fixation as PEI (branched or linear) or a 36-mer of poly(lysine), but they do exhibit higher complement fixation than a 5-mer of poly(lysine) (Figure 11A). This is consistent with the notion that polycation length and charge density can augment complement activation (*11*).

Because complement fixation was observed at the physiologically relevant concentration of 0.2 g L^{-1}, corresponding to the typical concentration of polycations in the bloodstream after delivery of nucleic acids at a dose of 2.5 mg kg^{-1} (a typical dose used for in vivo siRNA delivery (*7*)), experiments were performed to test particles formulated with calf thymus DNA and stabilized by PEGylation (Figure 11B). Notably, these formulations showed minimal complement fixation at polymer concentrations of 0.2 g L^{-1}.

Particles Achieve Intracellular Delivery of siRNA in Vitro. The uptake of particles containing fluorescently labeled siRNA was assessed using flow cytometry and confocal fluorescence microscopy. While naked siRNAs do not achieve measurable levels of cellular uptake, formulation into particles with CDP−Im dramatically increases the amount of cell-associated siRNA as measured by flow cytometry (Figure 12A). To confirm that the siRNA was being delivered to the interior of cells, confocal

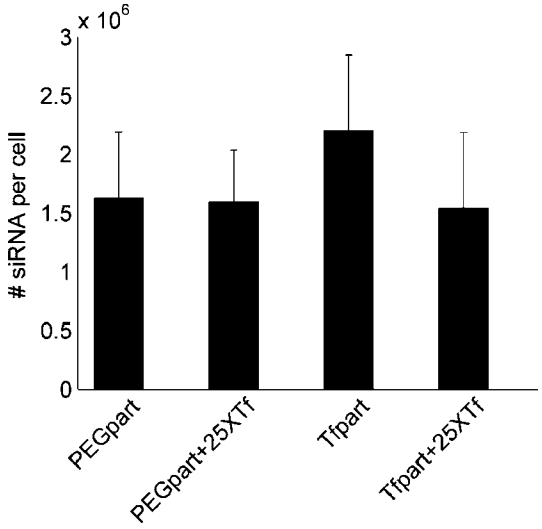


Figure 13. Uptake of PEGylated and Tf-targeted particles in the presence of holo-Tf competitor. Particles were formulated at a charge ratio of 3 (±) using CDP−Im and siRNA. PEGylated particles (PEGpart) were formulated with a 1:1 mole ratio of AD−PEG_{5000}/β-CD and Tf-targeted particles (Tfpart) were formulated with a 1:1 mole ratio of AD−PEG_{5000}−X/β-CD where AD−PEG_{5000}−X was composed of 99 mol % AD−PEG_{5000} and 1 mol % AD−PEG_{5000}−Tf. Particles containing 100 nM siRNA were added to HeLa cells in 200 μL Opti-MEM I in the absence or presence of a 25-fold (moles holo-Tf/moles AD−PEG_{5000}−Tf) excess of holo-Tf competitor.

fluorescence microscopy was used to visualize cells transfected with particles containing fluorescently labeled siRNA (Figure 12B). The internalized particles exhibited a punctate staining and were eventually observed to accumulate in the perinuclear region.

Targeting Ligands Enhance Cellular Uptake of PEGylated Particles. To verify that attachment of AD−PEG_{5000}−Tf can lead to uptake through transferrin receptor (TfR)-mediated endocytosis, the uptake of stabilized (PEGylated) particles was measured in the presence or absence of free holo-Tf. While the uptake of PEGylated particles without AD−PEG_{5000}−Tf was not affected by the presence of free holo-Tf, the uptake of Tf-targeted particles was reduced as a result of competition with free holo-Tf (Figure 13). Because the particles can be internalized simultaneously by numerous mechanisms including simple pinocytosis, there is still significant uptake even without TfR-mediated internalization under these conditions.

Targeted Particles Exhibit Increased Affinity through Avidity Effects. If multiple receptor/ligand interactions can occur simultaneously, then the effective affinity of the binding interaction can be enhanced through avidity effects. Antibodies or divalent antibody fragments are excellent examples of molecules whose binding affinities are enhanced through avidity effects. Their divalent interactions allow single antibodies to bind two separate receptors, leading to a stronger apparent affinity than exhibited by the monovalent antibody fragment (*25*). Targeted delivery vehicles that contain multiple targeting ligands on the surface should also display these avidity effects if multiple targeting ligands can simultaneously interact with the receptors. A typical cancer cell may contain thousands of receptors on its surface (*26*, *27*), and the Tf-targeted delivery vehicles can contain tens or even hundreds of Tf ligands (depending on the percent of the AD−PEG_{5000} molecules with Tf molecules attached to the distal end of the flexible PEG_{5000} chains) decorating each particle surface. This arrangement should enable multiple Tf molecules to bind to TfR on the surface of the cells. To test whether these avidity effects increase the apparent affinity of the Tf-targeted particles for the TfR on the cell surface, a competitive uptake assay was performed using

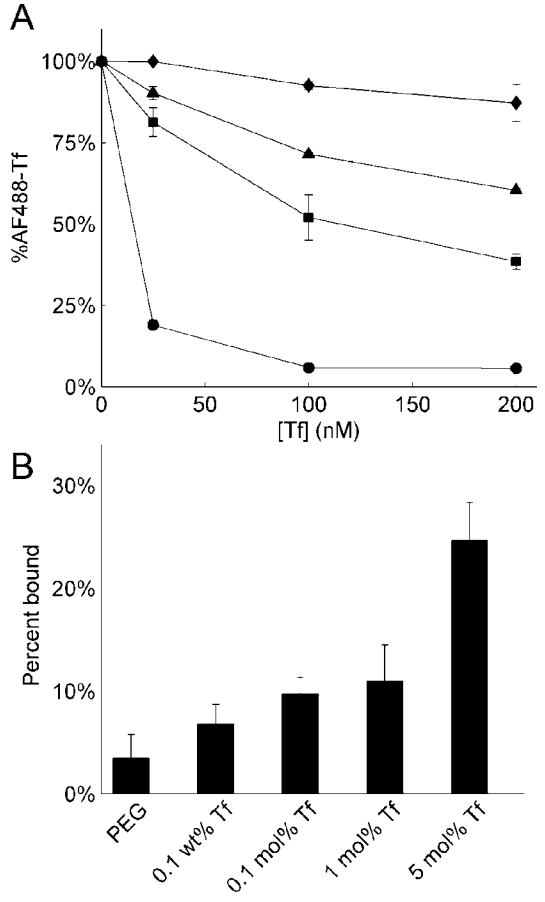


Figure 14. Effect of transferrin targeting ligand density on relative binding affinity. (A) Competitive TfR binding by free holo-Tf (circles), free AD−PEG_{5000}−Tf (triangles), Tf-targeted CDP−Im/siRNA (3 (±), 1 mol % AD−PEG_{5000}−Tf) particles (squares), and PEGylated CDP−Im/siRNA (3 (±)) particles (diamonds) in the presence of 20 nM AlexaFluor488-labeled holo-Tf. As a control, the PEGylated particles were formulated identically to the Tf-targeted particles at each concentration except without the addition of AD−PEG_{5000}−Tf during formulation. (B) Live-cell binding assay. Particles were formulated at a charge ratio of 3 (±) using CDP−Im and Cy3-labeled siRNA. PEGylated particles (PEGpart) were formulated with a 1:1 mole ratio of AD−PEG_{5000}/β-CD and Tf-targeted particles (Tfpart) were formulated with a 1:1 mole ratio of AD−PEG_{5000}−X/β-CD where AD−PEG_{5000}−X was composed of the stated % AD−PEG_{5000}−Tf and the remainder AD−PEG_{5000}. Particles containing 100 nM Cy3−siRNA were added to HeLa cells in 200 μL PBS and incubated on ice for 30 min. The "percent bound" represents the fraction of particles associated with the cell pellet after centrifugation.

flow cytometry. The results shown in Figure 14A demonstrate that the Tf-targeted particles possess enhanced affinity for the TfR relative to individual AD−PEG_{5000}−Tf molecules. Additionally, particles without the Tf targeting ligand had a minimal impact on the uptake of the fluorescently labeled holo-Tf. To determine how targeting ligand density affects particle binding to cell surface TfR, particles were incubated with HeLa cells in PBS at 4 °C to measure the amount of binding in the absence of internalization. The results shown in Figure 14B show that Tf targeting increases the amount of cell-associated particles under these conditions, and the amount of binding increases with the targeting ligand density.

Particles Deliver Functional pDNA and siRNA to Cells in Vitro. In addition to achieving intracellular delivery of the nucleic acid-containing particles, the particles need to release their nucleic acid payload intracellularly to allow it to function. Co-delivery of a luciferase-expressing plasmid and either a control or luciferase-targeting siRNA was used to demonstrate the ability of the particles to deliver functional pDNA and

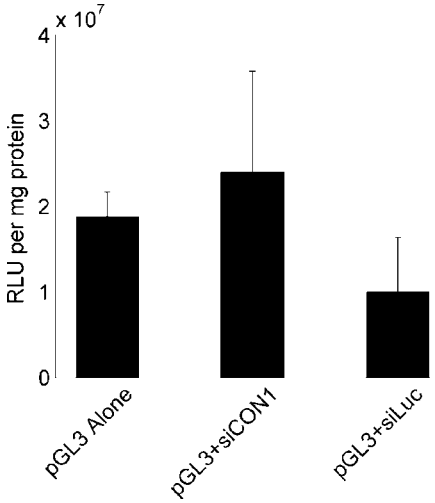


Figure 15. Luciferase expression 48 h after cotransfection of HeLa cells with particles containing pDNA and siRNA. Particles were formulated at a charge ratio of 3 (±) by combining CDP−Im with pGL3−CV (pGL3 alone), pGL3−CV and a control siRNA (pGL3+siCON1), or pGL3−CV and an siRNA against luciferase (pGL3+siLuc).

siRNA. The luciferase activity in cell lysates was quantified using a luminometer, and relative light units (RLU) were normalized to total cellular protein levels. As shown in Figure 15, cells that received CDP−Im particles containing the plasmid and siRNA against luciferase (siLuc) had luciferase activity that was ∼50% lower than cells that received CDP−Im particles with either the plasmid alone or the plasmid plus a control siRNA (siCON1).

Nanoparticles Are Multifunctional, Integrated Systems for Nucleic Acid Delivery. The results presented here highlight the importance of creating a nanoparticle that consists of multiple components that function together as a system, and control over size, surface modification, payload protection, and targeting ligand to payload ratio are key parameters to consider when designing nucleic acid delivery vehicles for in vivo systemic use. These parameters also represent some of the major advantages of nanoparticle composites for delivery of nucleic acids instead of using carrier-free delivery methods. Nucleic acid delivery vehicles can help reduce renal clearance while adding features such as stabilization against nuclease degradation, cell-specific targeting, and large payload delivery. These features make them well-suited for the systemic delivery of nucleic acids in general, and we have shown that the system investigated here can deliver pDNA, siRNA, and DNAzymes in vitro and in vivo (*7*, *17*, *19*, *20*).

The capability to fine-tune the delivery vehicle's properties combined with an understanding of how those properties affect its function in biological systems represent two key factors necessary for optimization of nucleic acid delivery vehicles. This study demonstrates the importance of a rational approach in delivery vehicle design and lays a foundation for further in vivo studies to understand the relationships between the properties of nanoparticle delivery systems and their biological function. The approach to designing nanoparticle delivery vehicles that is outlined here can be used for other synthetic materials and is thus not limited to the cyclodextrin polymer-based system illustrated.

ACKNOWLEDGMENT

We thank Nicholas Brunelli (California Institute of Technology) for performing the atomic force microscopy imaging and Patrick Koen (California Institute of Technology) for performing the transmission electron microscopy imaging. D.W.B. acknowledges support from a National Science Foundation Graduate Research Fellowship. This publication was made possible by grant number 1 R01 EB004657-01 from the National Institutes of Health (NIH). Its contents are solely the responsibility of the authors and do not necessarily represent the official views of the NIH.

LITERATURE CITED

(1) Morrissey, D. V., Blanchard, K., Shaw, L., Jensen, K., Lockridge, J. A., Dickinson, B., McSwiggen, J. A., Vargeese, C., Bowman, K., Shaffer, C. S., Polisky, B. A., and Zinnen, S. (2005) Activity of stabilized short interfering RNA in a mouse model of hepatitis B virus replication. *Hepatology 41*, 1349−1356.

(2) Layzer, J. M., McCaffrey, A. P., Tanner, A. K., Huang, Z., Kay, M. A., and Sullenger, B. A. (2004) In vivo activity of nuclease-resistant siRNAs. *RNA 10*, 766−771.

(3) Schatzlein, A. G. (2003) Targeting of synthetic gene delivery systems. *J. Biomed. Biotechnol. 2*, 149−158.

(4) Soutschek, J., Akinc, A., Bramiage, B., Charisse, K., Constien, R., Donoghue, M., Elbashir, S., Geick, A., Hadwiger, P., Harborth, J., John, M., Kesavan, V., Lavine, G., Pandey, R. K., Racie, T., Rajeev, K. G., Rohl, I., Toudjarska, I., Wang, G., Wuschko, S., Bumcrot, D., Koteliansky, V., Limmer, S., Manoharan, M., and Vornlocher, H.-P. (2004) Therapeutic silencing of an endogenous gene by systemic administration of modified siRNAs. *Nature (London) 432*, 173−178.

(5) Dykxhoorn, D. M., Palliser, D., and Lieberman, J. (2006) The silent treatment: siRNAs as small molecule drugs. *Gene Ther. 13*, 541−552.

(6) Song, E., Zhu, P., Lee, S.-K., Chowdhury, D., Kussman, S., Dykxhoorn, D. M., Feng, Y., Palliser, D., Weiner, D. B., Shankar, P., Marasco, W. A., and Lieberman, J. (2005) Antibody mediated in vivo delivery of small interfering RNAs via cell-surface receptors. *Nat. Biotechnol. 23*, 709−717.

(7) Hu-Lieskovan, S., Heidel, J. D., Bartlett, D. W., Davis, M. E., and Triche, T. J. (2005) Sequence-specific knockdown of EWS-FLI1 by targeted, nonviral delivery of small interfering RNA inhibits tumor growth in a murine model of Ewing's sarcoma. *Cancer Res. 65*, 8984−8992.

(8) Ogris, M., Brunner, S., Schuller, S., Kircheis, R., and Wagner, E. (1999) PEGylated DNA/transferrin-PEI complexes: reduced interaction with blood components, extended circulation in blood and potential for systemic gene delivery. *Gene Ther. 6*, 595−605.

(9) Morrissey, D. V., Lockridge, J. A., Shaw, L., Blanchard, K., Jensen, K., Breen, W., Hartsough, K., Machemer, L., Radka, S., Jadhav, V., Vaish, N., Zinnen, S., Vargeese, C., Bowman, K., Shaffer, C. S., Jeffs, L. B., Judge, A., MacLachlan, I., and Polisky, B. (2005) Potent and persistent in vivo anti-HBV activity of chemically modified siRNAs. *Nat. Biotechnol. 23*, 1002−1007.

(10) Zimmermann, T. S., Lee, A. C. H., Akinc, A., Bramlage, B., Bumcrot, D., Fedoruk, M. N., Harborth, J., Heyes, J. A., Jeffs, L. B., John, M., Judge, A. D., Lam, K., McClintock, K., Nechev, L. V., Palmer, L. R., Racie, T., Rohl, I., Seiffert, S., Shanmugam, S., Sood, V., Soutschek, J., Toudjarska, I., Wheat, A. J., Yaworski, E., Zedalis, W., Koteliansky, V., Manoharan, M., Vornlocher, H.-P., and MacLachlan, I. (2006) RNAi-mediated gene silencing in non-human primates. *Nature (London) 441*, 111−114.

(11) Plank, C., Mechtler, K., Szoka, F. C. J., and Wagner, E. (1996) Activation of the complement system by synthetic DNA complexes: a potential barrier for intravenous gene delivery. *Hum. Gene Ther. 7*, 1437−1446.

(12) Chonn, A., Cullis, P. R., and Devine, D. V. (1991) The role of surface charge in the activation of the classical and alternative pathways of complement by liposomes. *J. Immunol. 146*, 4234−4241.

(13) Venturoli, D., and Rippe, B. (2005) Ficoll and dextran vs. globular proteins as probes for testing glomerular permselectivity: effects of molecular size, shape, charge, and deformability. *Am. J. Physiol. Renal Physiol. 288*, F605−613.

(14) Dreher, M. R., Liu, W., Michelich, C. R., Dewhirst, M. W., Yuan, F., and Chilkoti, A. (2006) Tumor vascular permeability, accumulation, and penetration of macromolecular drug carriers. *J. Natl. Cancer Inst. 98*, 335−344.

(15) Rensen, P., Sliedregt, L., Ferns, M., Kieviet, E., van Rossenberg, S., van Leeuwen, S., van Berkel, T., and Biessen, E. (2001) Determination of the upper size limit for uptake and processing of ligands by the asialoglycoprotein receptor on hepatocytes in vitro and in vivo. *J. Biol. Chem. 276*, 37577−37584.

(16) Mishra, S., Webster, P., and Davis, M. E. (2004) PEGylation significantly affects cellular uptake and intracellular trafficking of non-viral gene delivery particles. *Eur. J. Cell Biol. 83*, 97−111.

(17) Davis, M. E., Pun, S. H., Bellocq, N. C., Reineke, T. M., Popielarski, S. R., Mishra, S., and Heidel, J. D. (2004) Self-assembling nucleic acid delivery vehicles via linear, water-soluble cyclodextrin-containing polymers. *Curr. Med. Chem. 11*, 1241−1253.

(18) Mishra, S., Heidel, J. D., Webster, P., and Davis, M. E. (2006) Imidazole groups on a linear, cyclodextrin-containing polycation produce enhanced gene delivery via multiple processes. *J. Controlled Release 116*, 179−191.

(19) Bellocq, N. C., Pun, S. H., Jensen, G. S., and Davis, M. E. (2003) Transferrin-containing polymer-based particles for tumor-targeted gene delivery. *Bioconjugate Chem. 14*, 1122−1132.

(20) Pun, S. H., Bellocq, N. C., Cheng, J., Grubbs, B. H., Jensen, G. S., Davis, M. E., Tack, F., Brewster, M., Janicot, M., Janssens, B., Floren, W., and Bakker, A. (2004) Targeted delivery of RNA-cleaving DNA enzyme (DNAzyme) to tumor tissue by transferrin-modified, cyclodextrin-based particles. *Cancer Biol. Ther. 3*, 31−40.

(21) Blandamer, M. J., Cullis, P. M. and Engberts, J. B. F. N. (1998) Titration microcalorimetry. *J. Chem. Soc., Faraday Trans. 94*, 2261−2267.

(22) Perry, C. S., Charman, S. A., Prankerd, R. J., Chiu, F. C. K., Scanlon, M. J., Chalmers, D., and Charman, W. N. (2006) The binding interaction of synthetic ozonide antimalarials with natural and modified β-cyclodextrins. *J. Pharm. Sci. 95*, 146−158.

(23) Hansen, P. L., Cohen, J. A., Podgornik, R., and Parsegian, V. A. (2003) Osmotic properties of poly(ethylene glycols): quantitative features of brush and bulk scaling laws. *Biophys. J. 84*, 350−355.

(24) Pun, S. H., and Davis, M. E. (2002) Development of a nonviral gene delivery vehicle for systemic application. *Bioconjugate Chem. 13*, 630−639.

(25) Adams, G. P., Tai, M.-S., McCartney, J. E., Marks, J. D., Stafford, W. F., III, Houston, L. L., Huston, J. S., and Weiner, L. M. (2006) Avidity-mediated enhancement of in vivo tumor targeting by single-chain Fv dimers. *Clin. Cancer Res. 12*, 1599−1605.

(26) Phillips, J., Rutledge, L., and Winters, W. (1986) Transferrin binding to two human colon carcinoma cell lines: characterization and effect of 60 Hz electromagnetic fields. *Cancer Res. 46*, 239−244.

(27) Shir, A., Ogris, M., Wagner, E., and Levitzki, A. (2006) EGF receptor-targeted synthetic double-stranded RNA eliminates glioblastoma, breast cancer, and adenocarcinoma tumors in mice. *PLoS Med. 3*, e6.

BC0603539

Sortase A as a Novel Molecular "Stapler" for Sequence-Specific Protein Conjugation

Ranganath Parthasarathy,[†] Shyamsundar Subramanian,[†] and Eric T. Boder*[,†,‡]

Departments of Chemical and Biomolecular Engineering and Bioengineering, University of Pennsylvania, Philadelphia, Pennsylvania 19104. Received October 28, 2006; Revised Manuscript Received January 6, 2007

The Sortase family of transpeptidase enzymes catalyzes sequence-specific ligation of proteins to the cell wall of Gram-positive bacteria. Here, we describe the application of recombinant *Staphylococcus aureus* Sortase A to attach a tagged model protein substrate (green fluorescent protein) to polystyrene beads chemically modified with either alkylamine or the in vivo Sortase A ligand, Gly-Gly-Gly, on their surfaces. Furthermore, we show that Sortase A can be used to sequence-specifically ligate eGFP to amino-terminated poly(ethylene glycol) and to generate protein oligomers and cyclized monomers using suitably tagged eGFP. We find that an alkylamine can substitute for the natural Gly_3 substrate, which suggests the possibility of using the enzyme in materials applications. The highly specific and mild Sortase A-catalyzed reaction, based on small recognition tags unlikely to interfere with protein expression, thus represents a useful addition to the protein immobilization and modification tool kit.

INTRODUCTION

The immobilization of proteins on surfaces continues to be an active area of research driven by widespread interest in protein−protein interactions and protein-based sensors, among others. Numerous immobilization techniques have been described in the literature (*1*−*9*). The older chemical approaches, where reactive functional groups (such as −COOH, $-NH_2$, or −S) present on a protein are covalently bonded to complementary groups on a surface, are subject to a lack of specificity (*1*); in addition, these methods can occasionally require the use of harsh reaction conditions, which may negatively impact activity of the immobilized protein. The lack of specificity stems from the presence of many solvent-accessible functional groups on a given protein that can react with a surface. This may result in multiple immobilized conformations or impaired activity due to the modification of a critical amino acid. Furthermore, several proteins may have similar functional groups, which would render chemical ligation approaches useless in selectively immobilizing a specific protein from a complex mixture (e.g., biological fluids or unpurified cellular lysates).

Another approach to immobilization is to biotinylate the protein of interest for subsequent binding to an avidin-covered surface using the strong and specific biotin−avidin interaction (*3*). The protein can be biotinylated enzymatically (which can be quite specific (*10*)) or chemically. Immobilizing a specific protein from a mixture of proteins would of course require that the target protein be biotinylated selectively.

Enzyme-directed efforts have circumvented many of these problems (*4*, *5*). In one embodiment of this concept, the protein of interest is fused to an enzyme. An irreversible inhibitor of the enzyme is covalently ligated to the target surface. Incubation of the fusion protein with the modified surface leads to specific and relatively rapid covalent bonding between the two. The disadvantages of this approach are the need to fuse relatively large proteins (22 kDa for cutinase (*5*) or O^6-alkylguanine−DNA alkyltransferase (*4*)) to the protein of interest and the need to synthesize complex substrates on an ad hoc basis (different for different enzymes) for use as surface tags. Large fusion partners can reduce yields in recombinant expression and the manipulation of reaction rates or reaction extents is not easy, since the substrate-to-enzyme stoichiometry is locked in from the outset. A further potential problem is the presence of the enzyme in the eventual fusion. This last issue is neatly avoided by the use of intein-based splicing (*1*, *8*), although this method also has the disadvantages of (a) requiring the fusion of a relatively large protein (123 residues in one case (*1*)) to the protein of interest and ligating a complementary protein to the surface with a specific orientation and (b) fixing intein−protein stoichiometry, which makes reaction conditions difficult to manipulate. However, enzyme-mediated and intein-based approaches both are very specific, which is especially relevant to the immobilization of a specific protein from a complex mixture (*1*).

An enzyme that catalyzes the ligation of two substrates through specific tags can be used to attach proteins to surfaces if the tags can be fused to the protein and surface. If the tags are small, this approach avoids the fusion of large proteins to the target protein or surface of interest while potentially retaining the specificity of enzymatic reactions. Furthermore, using the enzyme as a catalyst rather than a substrate of the immobilization reaction permits the easy optimization of reaction rates and extents by changing enzyme concentrations. High enzyme concentrations and the resulting rapid reactions could be very useful in capturing transient species or species at relatively low concentrations.

Microbial transglutaminases (mTGs) are bacterial enzymes that catalyze the formation of an amide link between the amide group of glutamine and the ϵ-NH_2 group of a lysine, thereby creating inter- or intramolecular cross-links (*11*). mTGs are also known to catalyze the reaction between an alkylamine (in place of lysine) and glutamine (*12*), but the enzymes have not been extensively investigated as a protein immobilization tool partly because specificity determinants for the reaction are not well-understood. In contrast, the bacterial transpeptidase Sortase A

* Corresponding author. E-mail: boder@seas.upenn.edu. Current Address: 220 South 33rd Street, Philadelphia, PA 19104-6393. Ph: 215-898-5658. Fax: 215-573-2093.

[†] Department of Chemical and Biomolecular Engineering.

[‡] Department of Bioengineering.

10.1021/bc060339w CCC: $37.00 © 2007 American Chemical Society
Published on Web 02/16/2007

is an extensively studied enzyme with known substrate specificity. Sortase A is used by Gram-positive bacteria to anchor surface proteins to the cell wall through a condensation reaction between a C-terminal −LPXTG tag on the former and a poly(glycine) bridge in the latter (*13*). The enzyme cleaves the LPXTG at the amide bond between the threonine and the glycine to form an acyl−enzyme intermediate. Nucleophilic attack by the amino group of the tris(Gly) on the intermediate results in the formation of an LPXT−GGG bond and the liberation of the free enzyme. It has been shown that LPETG is the optimal isoform of the tag (*14*).

In a paper highlighting the in vitro applications of Sortase A to protein conjugation, Mao and co-workers (*15*) were the first to show that this easily purified enzyme could be used to ligate model proteins (enhanced green fluorescent protein, eGFP) or peptides together if the reactants had −LPETG−COOH, or $-NH_2-$GGG, tags. In one example, a protein-transfection domain was ligated to eGFP, thereby enhancing eGFP transfer into mammalian cells (*15*). Our work furthers these in vitro applications of Sortase A by showing that (a) the tris(Gly) group can participate as a nucleophile in the reaction even when covalently bonded to a surface or a non-protein species such as poly(ethylene glycol) (PEG), and not merely in solution at a protein terminus, (b) alkylamine bound to a surface or PEG can function as a nucleophile, albeit less efficiently than tris(Gly), (c) tris(Gly) surfaces can be used to capture −LPETG-tagged proteins from crude cell lysates, and (d) the transpeptidation reaction can be used to make cyclic proteins and protein oligomers with specifically designed tagged proteins.

EXPERIMENTAL PROCEDURES

Protein Expression. Sortase A was expressed from plasmid pHTT27 (a gift from Dr. Olaf Schneewind, University of Chicago) that encodes a 159 amino acid N-terminal truncation with activity very similar to that of the full-length enzyme. eGFP variants were expressed by subcloning the gene with the desired flanking tags into the pET23-derived vector pBamUK (gift of Dr. Greg Vanduyne , University of Pennsylvania) between the *Nde I* and *Xho I* sites to add a C-terminal 6×His tag for purification. We have included the Avitag sequence GLNDIFEAQKIEWHE (*10*), which is the consensus sequence for biotinylation by bacterial biotin ligase (BirA), amino to the eGFP sequence for future use. Standard molecular biology techniques were used, and sequencing services were provided by the Central Sequencing Facility of the School of Medicine at the University of Pennsylvania. eGFP and Sortase A were expressed in BL21-DE3 *E. coli* (Invitrogen, Carlsbad, CA). Cultures were allowed to reach an OD_{600} of 0.7 before induction of expression by the addition of 1 mM isopropyl thioglucoside (IPTG, Fisher, Pittsburgh, PA). After 3 h of further growth at 37 °C, the cultures were pelleted by centrifugation and the pellets were frozen overnight at −20 °C. B-per solution (Pierce, Rockford, IL) was added to the thawed pellet to solubilize the cells, and the manufacturer's protocol was followed closely to isolate soluble protein. Nearly all of the fluorescence of the cell pellet was extracted by B-per, confirming that the eGFP remained soluble despite the presence of the added tags. Protein purification using the 6×His tag followed the procedure outlined by either Qiagen (Ni-NTA resin) or Clontech (TALON resin). Protein-enriched 0.5 mL fractions were combined and dialyzed against 50 mM Tris, 150 mM NaCl, pH 8, using a Slide-A-Lyzer dialysis cassette (Pierce) with a MWCO of 10 kDa for 48−60 h with at least one buffer change.

Conjugation of Gly_3 to Beads. Amine-terminated beads 3 μm in diameter were purchased from Polysciences (Warrington, PA). 100 μL of the beads (approximately 10^8 beads) were pelleted and washed twice in 0.1 M 2-morpholinoethane sulfonic acid (MES), pH 4.8. Fmoc-protected Gly_3 (Sigma, St Louis, MO) was dissolved in dimethylformamide and added at a final concentration of 0.8 mM to 200 μL of 0.1 M MES (pH 4.8) containing the washed beads. 1-ethyl-3-[3-dimethylaminopropyl]-carbodiimide hydrochloride (EDC, Pierce, Rockford, IL) was then added in aqueous solution to the bead slurry at a final concentration of 8 mM, and the mixture was shaken for 2 h at room temperature. After shaking, the beads were pelleted, washed once with 0.1 M MES, and twice in deionized water. They were suspended in 20% piperidine in water and shaken for 20 min, after which the beads were pelleted, washed twice in water and then twice in 50 mM Tris, 150 mM NaCl, 0.1% Tween-20, and stored in the same buffer. Except for minor, reversible aggregation, Gly_3-conjugated beads are stable for at least 7 weeks at 4 °C.

Conjugation of Gly_3 to PEGamine. Amine-terminated PEG (PEGamine) with a molecular weight of 10 kDa was obtained from Nektar Therapeutics (Huntsville, AL). The polymer terminates in $-CH_2OCH_2CH_2NH_2$. 5 mM PEGamine in 200 μL 0.1 M MES buffer (pH 4.8) was incubated with 5 mM Fmoc−Gly_3 and 25 mM EDC with shaking for 2 h at room temperature. The reaction mixture was then dialyzed against 50 mM Tris, 150 mM NaCl, pH 8, for 24 h using a 3.5 kDa MWCO dialysis cassette (Slide-A-Lyzer, Pierce, Rockford). To ensure the complete cleavage of Fmoc, the contents of the dialysis cassette were withdrawn and shaken with 20% piperidine for a half-hour. The reaction mixture was re-dialyzed for 48 h against the Tris/NaCl buffer. MALDI-TOF/TOF analysis (Proteomics Core Facility, Penn School of Medicine) was used in an effort to gauge the efficacy of polymer modification. The molecular weight of the polymer was found to have increased by 221 Da in place of the expected 172 Da. However, the peak was very broad, and the exact change in molecular weight is therefore uncertain.

Bead Reaction with Purified eGFP. Approximately 5 μL (5×10^6 beads) of a suspension of 3 μm diameter amino-terminated or Gly_3-modified beads was used per reaction. Beads were washed twice in 50 mM Tris, 150 mM NaCl, pH 8, containing 0.1% Tween-20 (the "reaction buffer") and then incubated with Sortase A and eGFP−LPETG in reaction buffer containing, in addition, 6 mM $CaCl_2$ and 3 mM β-mercaptoethanol. Addition of reagents such as BSA or NP-40 to block nonspecific binding did not alter data significantly. The concentrations of eGFP and Sortase A depended on the experiment and are mentioned in the context of specific experiments. The microcentrifuge tube containing the suspension was shaken vigorously. All of the Sortase A-mediated reactions in this work were conducted at 37 °C for 3 h unless otherwise indicated. At the end of this period, the beads were pelleted, washed three times with PBS + 0.1%BSA with careful resuspension of the beads between washes, and used for flow cytometric analysis. Flow cytometry was carried out on FACScan or FACSCalibur machines (BD Biosciences, San Diego, CA) at the Core Facility of the School of Medicine, University of Pennsylvania. Data were analyzed with *CellQuest* software (BD Biosciences, Pharmingen, San Diego, CA).

Bead Reactions with Cellular Lysate. BL21-DE3 *E. coli* cells expressing eGFP−LPETG were frozen overnight and lysed in 50 mM Tris, 150 mM NaCl, 0.1% Tween-20, at pH 8 using freeze−thaw cycles. The concentration of eGFP in the lysate was assayed by spectrophotometry at 488 nm and adjusted to 30 μM. Reaction mixtures containing 15 μM eGFP (pure or in unpurified lysate), 10 μM Sortase A, 3 mM β-mercaptoethanol, and 6 mM $CaCl_2$ were incubated at 37 °C for 3 h with an aliquot of Gly_3-conjugated beads. The beads were prepared for flow cytometric analysis as described above.

Table 1. Monomers for Sortase A-Catalyzed Ligation[a]

amino acid sequence	functional name
M***GGG***LNDIFEAQKIEWHEMVSK------***LPETG***LEHHHHHH	bifunctional eGFP
M***GGG***LNDIFEAQKIEWHEMVSK----------LEHHHHHH	monofunctional, acceptor eGFP
M--AGLNDIFEAQKIEWHEMVSK------***LPETG***LEHHHHHH	monofunctional, donor eGFP

[a] Tags relevant to Sortase A are highlighted. The dashes indicate the portion of the gene conserved among the three monomers.

Homogeneous Solution Reactions. The conditions described above were used with homogeneous reactions as well. When reactions could not be analyzed immediately, 10 mM EDTA was added to the reaction volume, and the microcentrifuge tubes were stored at 4 °C.

Reaction with PEGamine. 20 μM eGFP with a C-terminal LPETG was incubated with 30 μM Gly_3-conjugated PEGamine in the presence of 6 mM $CaCl_2$, 3 mM β-mercaptoethanol, and 10 μM Sortase A and incubated at 37 °C for 6 h.

Protein Electrophoresis and Western Blotting. Samples in LDS buffer (Invitrogen) were denatured by heating at 95 °C for 10 min in the presence of β-mercaptoethanol. Cooled samples were loaded into wells on 10% Bis-Tris NuPage gels with MES as running buffer and run using the XCell Surelock module (Invitrogen). Simply Blue reagent (Invitrogen) was used for staining the gel. For Western blotting, protein was transferred to a 0.2 μm PVDF membrane (Biorad, Hercules, CA) using the XCell II Blot Module (Invitrogen). The membrane was blocked with 5% nonfat milk in TTBS (Tris-buffered saline with 0.1% Tween-20) by shaking overnight at 4 °C, washed with TTBS, and incubated with alkaline phosphatase-conjugated anti-GFP (Rockland Immunochemicals, Gilbertsville, PA) or an anti-His_6 monoclonal antibody (Covance, Berkeley CA). An alkaline phosphatase-conjugated goat anti-mouse polyclonal antibody (Sigma, St Louis, MO) was used in the latter case. The membrane was washed again and incubated with the alkaline phosphatase substrate NBT−BCIP (Sigma, St Louis, MO). Image quantification used ImageJ. To enhance the signal-to-noise ratio for experiments involving quantification of bands, higher concentrations of Sortase A were used than in the other experiments.

RESULTS

Sortase-Mediated Conjugation of eGFP−LPETG to Gly_3-Conjugated Beads. Gly_3-conjugated beads as well as commercial amino-terminated beads were incubated with eGFP−LPETG ("donor" eGFP; Table 1) and Sortase A under conditions described below for each experiment. Flow cytometry using the intrinsic fluorescence of eGFP was employed to assess coupling to the beads. Beads that were incubated with donor eGFP and Sortase A for 3 h were visibly fluorescent to the naked eye. Flow cytograms of beads incubated with Sortase A show that they are considerably more fluorescent than those incubated without Sortase A (Figure 1a,b). The fluorescence intensity on the bead increases approximately 70-fold over the native Gly_3 beads; the ratio for nonspecifically adsorbed eGFP (reaction run in the absence of Sortase A) was about 3-fold (Figure 1b). The enzyme clearly ligates donor eGFP to the Gly_3 bead in Ca^{2+}-dependent fashion, since adding EDTA abrogates the reaction (Figure 1c). A smaller increase in fluorescence can also be seen when eGFP is coupled to amine-terminated beads by Sortase A (Figure 1d,g), with similar background binding in the absence of Sortase A and similar inhibition by EDTA (Figure 1e,f). Addition of 15 mM Gly_3 to amine-terminated bead reactions also inhibited Sortase A-mediated attachment of eGFP (data not shown). Higher concentrations of Sortase A (40 μM) were used in the experiments with the amine beads than with the Gly_3-terminated beads; comparable levels (4 μM Sortase A) yielded much lower yields of immobilized eGFP (data not shown).

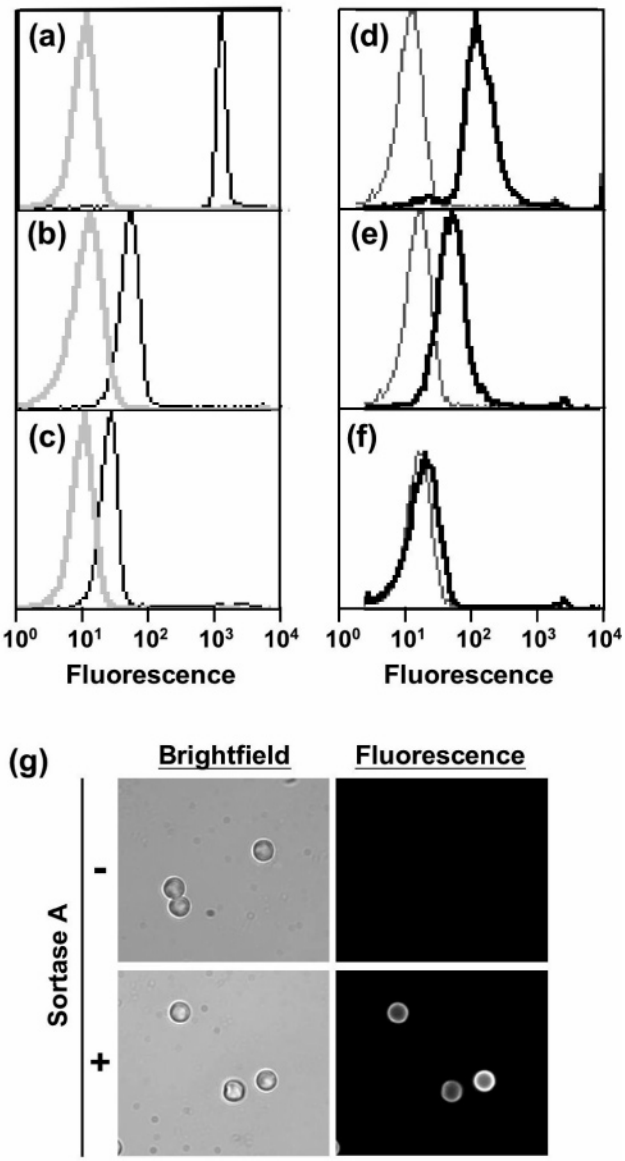


Figure 1. Characterization of GFP-conjugated polystyrene beads. (a−c) Flow cytograms of $(Gly)_3$-terminated beads before (gray lines) and after (black lines) incubation with eGFP−LPETG (a) in the presence of 4 μM Sortase A, (b) in the absence of Sortase A, or (c) in the presence of Sortase A and 10 mM EDTA. (d−f) Flow cytograms of amine-terminated beads incubated with eGFP−LPETG (d) in the presence of 40 μM Sortase A, (e) in the absence of Sortase A, or (f) in the presence of Sortase A and 10 mM EDTA. (g) Micrographs of amine-terminated beads labeled with eGFP−LPETG in the presence or absence of Sortase A.

Evidently, alkylamines can function as Sortase A substrates but with considerably reduced efficiency compared to Gly_3 conjugates.

The effect of varying the concentration of Sortase A on the reaction with the Gly_3 beads was investigated. When the enzyme is present at 40 μM, the reaction reaches steady state within 60 min; at 4 or 10 μM, the reaction reaches 90% of steady state in approximately 2 h (Figure 2a). Exponential fits, where the fluorescence of the beads at time t is given by $a_1[1 - \exp(-$

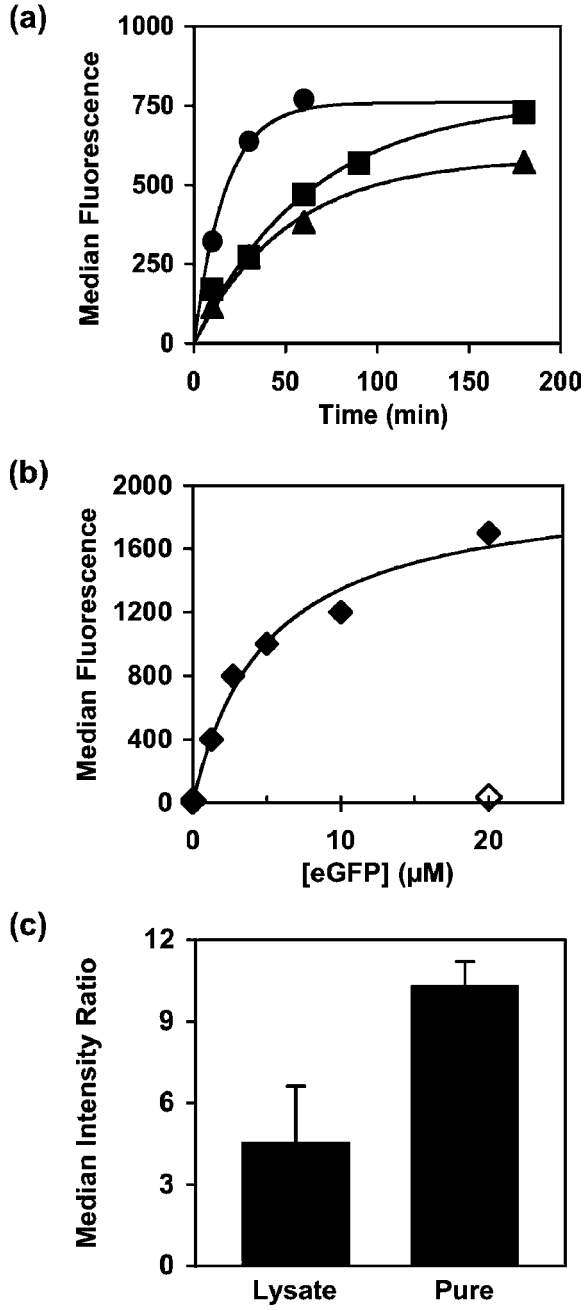


Figure 2. Reaction characteristics of Sortase A-mediated conjugation. (a) Kinetics of 20 μM eGFP coupling to Gly_3-terminated beads mediated by 40 μM (circles), 10 μM (squares), and 4 μM (triangles) Sortase A. The median fluorescence intensity of the bead population was measured by flow cytometry, and exponential functions were fit to the data. (b) eGFP concentration dependence of the median bead fluorescence after a 2 h incubation with 10 μM Sortase A. (c) Comparative activity of Sortase A (10 μM) for attachment of purified eGFP or eGFP in crude bacterial lysates. Median bead fluorescence ratio is relative to beads incubated in the absence of Sortase A.

a_2t)], yielded kinetic parameters a_2 that were very similar (0.019 and 0.016 min^{-1}) at the lowest concentrations of Sortase A, rising to 0.059 min^{-1} for the highest concentration of Sortase A tested. The reaction extent parameter, a_1, ranged from 584 at the lowest enzyme concentration to 750 for the other two concentrations tested—the difference of around 20% may not be meaningful, given that data are collected in log mode, but could arise from a slow, competitive inactivating process. The dependence of bead fluorescence at the 2 h time point on the concentration of eGFP was modeled using the equation a_3-[eGFP]/($K_{1/2}$ + [eGFP]) for a reaction run with 10 μM Sortase

Scheme 1



A, to yield a $K_{1/2}$ of 5 μM (Figure 2b). The fluorescence measured in this experiment is higher than that seen for the same conditions in Figure 2a; however, we note that the fluorescence of the Sortase control was also higher by a factor of 3 in this experiment, so a systematic offset in fluorescence values cannot be ruled out but should not affect our estimate of the half-maximal eGFP concentration. The ligation of donor eGFP to the Gly_3 beads proved to be reversible, since incubating eGFP-ligated beads with 3 mM hydroxylamine and 10 μM Sortase A for 3 h at 37 °C resulted in a 50% reduction in bead fluorescence, while beads incubated without Sortase A maintained fluorescence levels (data not shown). The ability of Sortase A to catalyze immobilization of LPETG-tagged eGFP from crude *E. coli* lysates was also investigated (Figure 2c). The fluorescence ratio of the lysate-incubated beads (+Sortase A) relative to background fluorescence of lysate-incubated beads was approximately half that of beads treated with purified eGFP−LPETG, using 15 μM eGFP (measured spectroscopically) in both cases.

Sortase A Can Engineer Protein−Protein Oligomerization. SDS-PAGE gels of an aliquot of a reaction mixture containing donor eGFP and eGFP tagged with Gly_3 at the N-terminus ("acceptor" eGFP) in the presence of Sortase A for 3 h at 37 °C (see Scheme 1) revealed a band at approximately 63 kDa (Figure 3a), as has also been reported by others (*15*). The band was not found in the absence of the enzyme or when either of the tags was absent, when the -GGG- was protected by a cleavable upstream sequence tag (data not shown), or in

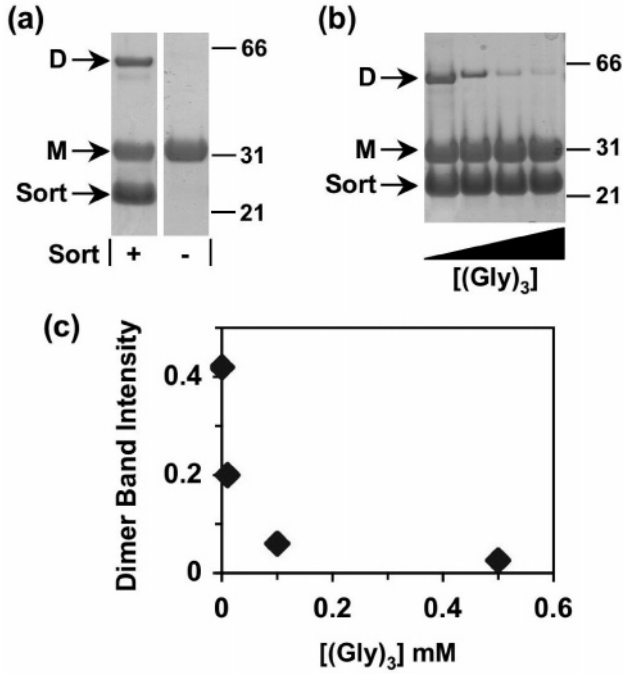


Figure 3. Sortase A-mediated protein ligation. (a) Reactions in 50 mM Tris, 150 mM NaCl, pH 8, between eGFP−LPETG (12 μM) and GGG−eGFP (36 μM) in the presence or absence of 40 μM Sortase A were analyzed by SDS-PAGE. Bands consistent in size with the monomer (M), dimer (D), and Sortase A (Sort) are labeled, and migration distances of molecular weight markers (in kDa) are indicated. (b) The same reaction in the presence of Sortase A and 0, 0.01, 0.1, and 0.5 mM soluble Gly_3. (c) The fractional intensity of the dimer band (normalized to the monomer band) as a function of the concentration of soluble Gly_3.

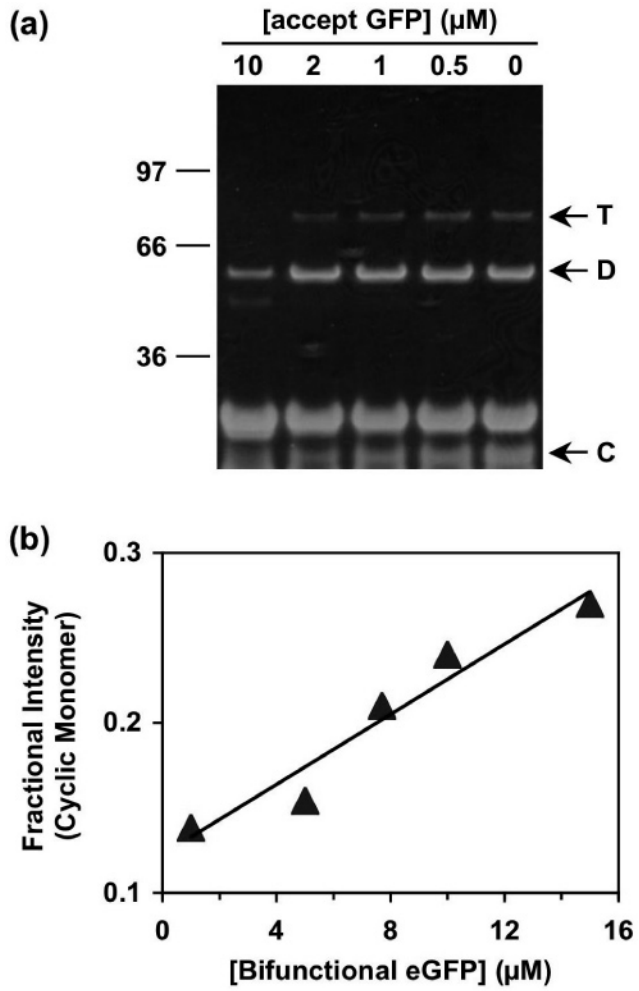
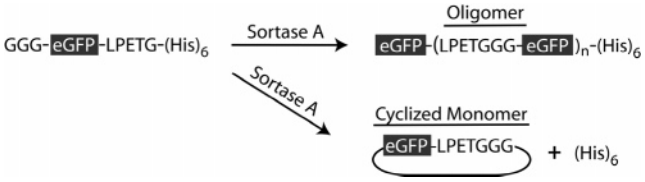


Figure 4. Oligomerization of bifunctional monomer. (a) A series of reactions containing bifunctional and acceptor eGFP in the ratios shown were analyzed by SDS-PAGE. Total amount of eGFP is constant at 15 μM. The reaction mixture included 40 μM Sortase A in 50 mM Tris−HCl and 150 mM NaCl. The scanned gel image was color-inverted for quantification. Bands consistent with expected sizes of a GFP dimer (D) and trimer (T) are marked, along with a band putatively representing a cyclized monomer (C). (b) The gel data was quantified by integrating band intensities. The integrated intensity of the cyclized monomer band relative to the monomer band is shown as a function of the concentration of bifunctional eGFP.

the presence of soluble Gly_3 concentrations above a threshold level (see below). Taking these results together, we conclude that the band represents the dimer formed between acceptor and donor GFPs. The integrated intensity of the dimer band is approximately 40% of that of the monomer band, suggesting that the reaction is approximately 30% complete at the end of 3 h or that ~30% of the monomer is competent for ligation. Increasing the concentration of soluble Gly_3 in the reaction mixture results in a steady weakening of the dimer band (Figure 3b), as the smaller molecule competes effectively with eGFP for the enzyme, confirming that the reaction is catalyzed by Sortase A. Quantification of band intensities shows that inhibition by soluble Gly_3 increases rapidly until the band falls to about one-tenth of control intensity at 0.05 mM, approximating the concentration of GFP (Figure 3c).

In contrast to the monofunctional monomers, a bifunctional monomer (Table 1) reacts in the presence of Sortase A to yield both the dimer and a species that migrates slightly faster than the monomer (Figure 4a, extreme right lane) on a polyacrylamide gel. This band is not seen with the monofunctional GFP's (Figure 3a) or in the control experiments listed above, so we

Scheme 2



conclude that it represents the cyclized monomer (see Scheme 2). The total extent of reaction at the end of 3 h in the case of the bifunctional monomer is around 40% with the putative cyclized GFP being present at 50−75% of dimer.

In a further series of reactions in the presence of Sortase A, the bifunctional eGFP was diluted with monofunctional acceptor eGFP, keeping the total concentration of the eGFP constant at 15 μM. The acceptor eGFP can be regarded as a "capping" monomer in these experiments. Aliquots of the reactions were then analyzed electrophoretically (Figure 4a). The intensity of the putative cyclized monomer band (relative to the total of all bands) increases approximately linearly with bifunctional monomer concentration (Figure 4b) as might be expected (see Discussion section), increasing our confidence in its identification. The intensity of the band representing the dimer decreases noticeably only when the (non-dimerizable) monofunctional monomer is present in substantial excess over the bifunctional monomer and the bifunctional monomer concentration is therefore significantly lower. A weak band from a putative trimer is evident, and its intensity is even more sensitive than that of the dimer band to the presence of the capping monomer.

Reactions with bi- and monofunctional eGFP monomers were also analyzed by Western blotting for eGFP (Figure 5). Considerably more detail is evident in the Western blot than in the Coomassie stained gel (Figure 4a), especially at molecular weights higher than the dimer. A densitometric trace of the lane corresponding to pure bifunctional monomer (Figure 5b) reveals major peaks at molecular weights consistent with the trimer and possibly the tetramer and pentamer (note: high molecular weight species cannot be quantitatively assigned sizes for a 10% gel under these conditions). The origin of the minor peaks in the trace (just below 91 kDa and 67 kDa) is unclear at this point, although they may represent circularized oligomers. The number of higher molecular weight bands seen decreases as the mono-to-bifunctional monomer ratio increases, as would be expected if the bands did in fact arise from higher oligomers whose formation would be limited in the presence of high concentrations of (non-polymerizable) capping monomer.

Although all of the eGFP reactants used in the ligation experiments were 6×His-tagged (Table 1), the tag is excised upon cyclization (Scheme 2). To confirm the identity of the putative cyclized monomer, we therefore used an anti-6×His antibody to probe a blot of Sortase A-mediated ligation of bifunctional eGFP (Figure 5c). The anti-6×His antibody identified bands consistent with the unreacted monomer, dimer, and trimer seen with the anti-GFP blot (Figure 5a) and stained gel (Figure 4a), but no band appears at the expected position of the cyclized monomer.

Conjugation of Donor eGFP to Amine-Terminated Poly(ethylene glycol). Amine-terminated methoxyPEG (PEGamine) with a molecular weight of 10 kDa was reacted with eGFP−LPETG in the presence or absence of Sortase A. Similar reactions were carried out in parallel between Gly_3-terminated PEG and eGFP−LPETG, with a reaction between eGFP−LPETG and GGG−eGFP as a control. Reaction mixtures were analyzed using SDS-PAGE (Figure 6). A band corresponding to a protein migrating slightly faster than the eGFP dimer is observed only in reaction mixtures containing eGFP, Sortase A, and PEGamine or Gly_3−PEG, and we attribute that to the

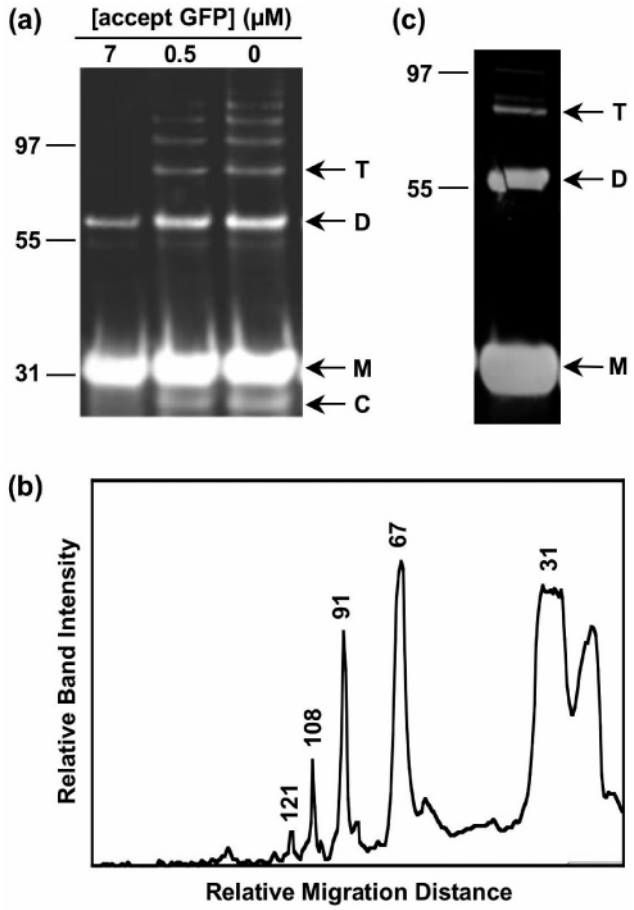


Figure 5. Verification of oligomerization and cyclization. (a) Western blot using anti-GFP antibody of a reaction mixture containing mono- and bifunctional eGFP at the mono- to- bifunctional monomer ratios shown. Bands are labeled as in Figures 3 and 4. (b) Line trace of the 0:1 mono/bifunctional lane of the blot. Peaks are labeled with apparent sizes. Molecular weight markers are shown (in kDa). Reactions contained 4 μM Sortase A and 15 μM eGFP (total). (c) Western blot using anti-His_6 antibody of a reaction mixture containing 20 μM Sortase A and 36 μM bifunctional eGFP. Bands are labeled as in (a).

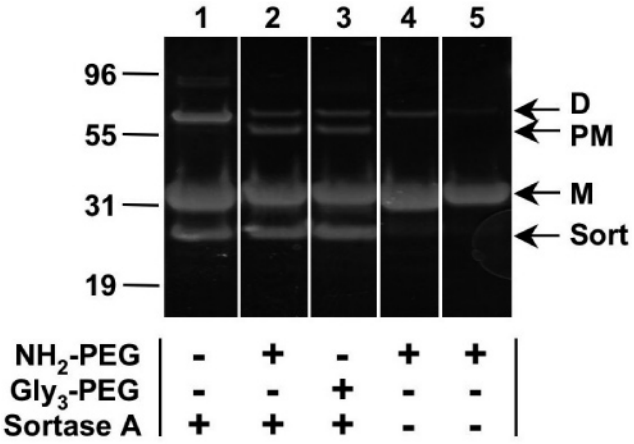


Figure 6. Ligation of PEG to eGFP. SDS-PAGE analysis of reactions between eGFP−LPETG and GGG−eGFP (lane 1) or the indicated modified PEG (lanes 2−5). Reaction mixtures contained 30 μM of each of the eGFP monomers or 30 μM of the PEG monomers, 4 μM Sortase A. The putative PEGylated eGFP monomer is indicated (PM), and molecular weight markers are shown (in kDa).

PEG−eGFP dimer. Surprisingly, both Gly_3−PEG and native PEGamine seem to form roughly similar amounts of PEG−eGFP, since the intensity of the heterodimer band is similar in both cases—approximately half that of the band corresponding to the eGFP−eGFP homodimer. Lanes 4 and 5 are control lanes without Sortase A: lane 4 contains both eGFP proteins, and lane 5 contains donor eGFP and PEGamine. A weak impurity band putatively corresponding to a small quantity of dimeric GFP in the monomer prep is evident in samples lacking Sortase A. A similar control using Gly_3−PEG and lacking Sortase A yielded similar results (data not shown).

DISCUSSION

Immobilizing proteins on surfaces presents many challenges, and development of many alternative techniques is highly desirable, since no single technique is likely to succeed with all proteins of current interest. Many recent approaches require the fusion of a large partner which may (*4*, *5*) or may not (*1*) be retained in the immobilized construct, and the fusion of a molecule (inhibitor or split-intein) to the target surface; in return for this inconvenience, the resulting immobilization is very specific. Very recent work by Neves-Petersen and colleagues (*16*) relies on the photocleavage of a disulfide bond by UV irradiation of a proximal aromatic residue. The activated cleaved bond is now available for reaction with a thiol-sensitive surface, thereby immobilizing the protein. Although this clever approach avoids the introduction of a fusion partner, the requirement that the aromatic residue be within 1 nm of the disulfide bond (and that there be only one such pair) restricts general applicability. Antibodies meet this requirement, but specifically immobilizing one protein from a complex mixture with a "tagless" approach would, in general, be a difficult task.

The approach described here promises wide applicability in that it is specific, rapid, and uses small tags that are unlikely to interfere with the function and expression of the target protein. Sortase A is easily overexpressed; it is soluble, requires no further refolding, and can be readily obtained at yields approaching 10 mg/L in simple shake flask cultures of *E. coli* with no optimization of conditions. Surface preparation for optimal Sortase A reactivity involves simple, well-understood carbodiimide chemistry with commercially available reagents. Starting with an amine-terminated bead, it is thus possible to immobilize a pure protein using Sortase A in less than 5 h.

The mechanism of Sortase A has been studied intensively. Studies on the hydrolysis of the optimal substrate, LPETG (*17*), have shown that diglycine is the optimal nucleophile, with the addition of more glycines having no effect on the reaction rate. Among dipeptide substrates, the enzyme displays a strong preference for glycine in the first position; alanine and valine can apparently substitute for glycine in the second position, although the reaction is not as efficient. However, Sortase A is not an especially efficient enzyme. Its affinity for its Gly-terminated substrates in vitro has been reported to be in the micromolar range (*17*), similar to the half-maximal eGFP concentration we find here; however, the micromolar range appears compatible with the concentrations generally used in protein immobilization work. We found that the reaction with Gly_3-terminated beads reached equilibrium in a period ranging from 30 min to 2 h, depending on Sortase A concentration, suggesting the possibility of using high concentrations of Sortase A to achieve higher reaction rates and shorter reaction times (with especially labile proteins, for example). The rapid approach to equilibrium at the highest Sortase A concentrations may reflect depletion of ligation-competent eGFP, rather than the effect of the reverse reaction, since one of the reactants (the Gly_3 on the bead) is present in considerable excess. The reaction is reversible, and GFP can be released from the bead when GFP-ligated beads are treated with Sortase A and a nucleophile such as hydroxylamine. The ability to separately manipulate enzyme and substrate concentrations to achieve desired rates distinguishes our approach from the ligand-mediated immobilization

techniques pioneered by Johanssen (*4*) and Mrksich (*5*), where the enzyme and target protein are covalently bound in a 1:1 ratio.

The similarity in length between diglycine and hexylamine and the ready availability of hexylamine-terminated surfaces to which protein ligation might be of interest motivated us to examine whether the alkylamine could function as a nucleophile with Sortase A. Schneewind and associates note that transpeptidation in the cell wall context proceeds with the glycines rather than the alkylamine side chain of a lysine (*13*, *18*). In contrast, the lysinyl side chain initiates nucleophilic attack during pilin assembly (*18*). These results can be reconciled if the enzyme−acyl intermediate is less reactive toward an alkylamine than toward Gly_n. Our work with amine-terminated and Gly_3-terminated beads shows that the latter are better substrates for ligation with eGFP−LPETG in the presence of Sortase A and therefore favors this hypothesis. A study of mTGs has also shown that alkylamines can function as surrogates for physiological nucleophiles in transamidation (*19*). Whether Sortase A can be engineered to react as facilely with the alkylamine as with its natural substrate, while retaining a high degree of specificity, will be intriguing to explore. Similar features have been found in subtiligase, which has some properties in common with Sortase A, including specifity requirements even when lysinyl side chains are present (*20*). We believe we are the first to show *direct* enzyme-catalyzed immobilization of proteins onto commercially available synthetic surfaces, certainly the first to use Sortase A for this purpose.

Mao et al. previously demonstrated that Sortase A can be used to form dimers between appropriately tagged monofunctional GFP (*15*), but the formation of oligomers and the cyclized monomer and the interplay between these species remained to be explored. When we reacted eGFP−LPETG with GGG−eGFP in the presence of Sortase A, a dimer was formed, as expected, with formation being increasingly inhibited by soluble Gly_3 at concentrations approximating that of the eGFP monomers. This substantiates the role that the Gly_3 moiety plays in the reaction and points to the specificity of the reaction. When a bifunctional eGFP (GGG−eGFP−LPETG) was incubated with Sortase A at 37 °C, we found evidence for intramolecular cyclization of the monomer: (a) the band does not react with an anti-6×His antibody, the 6×His having been excised in the course of cyclization; (b) its intensity is linearly related to the monomer concentration, consistent with a unimolecular reaction; and (c) the band is reactive with an anti-GFP antibody, confirming that it does not arise from an enzyme-related impurity. Additionally, this band was not observed in any reactions involving monofunctional eGFP, suggesting that it does not arise from cleavage of the protein. Both termini of the GFP molecule are known to lie on the same side of the protein, separated by approximately 19 Å, a distance that can be bridged by about 5−6 amino acids (*21*). The 15-member Avitag, to say nothing of the LPETG and the GGG tags, present here should bridge it readily.

Cyclic GFP has been made previously by other groups, most recently using inteins (*21*). Our approach uses far smaller tags and is therefore likely to cause less disruption should in vivo cyclization (in the presence of coexpressed Sortase A) be desired. Importantly, the approach described here also permits facile purification, since the 6×His tag present in the monomers is excised *only upon cyclization but not upon oligomerization*. One can readily envision an orthogonal purification scheme for cyclized species using a monomer with two different tags: schematically, one would pass the lysate first through, for example, a metal-affinity column to bind all of the 6×His-tagged reactants and noncyclic products. The flow-through would then be passed through an affinity column for the second tag, which would bind the cyclized species with trace amounts of the noncyclized species.

The cyclization of proteins has been suggested as a means to enhance their thermal and proteolytic stability (*22*, *23*). We anticipate that more work, perhaps with therapeutically important proteins, will be carried out if easy strategies for the protein cyclization are made available. Substantial work based on intein-mediated cyclization, oligomerization, and immobilization of proteins has been performed previously. Intein-mediated reactions require in-frame fusion of the splicing partner (at least 100 amino acids in size). These extremely specific approaches have the merit of not introducing extraneous amino acids in the course of the ligation, although a 9 amino acid linker has been intentionally introduced in circularization work (*22*) to avoid straining the protein. The range of inteins that can be used for circularization is limited, since the difficulty of isolating the circular product requires a high-affinity intein. Last, the obligatory fusion of the intein with the target protein could limit soluble expression of the protein in some cases. It certainly makes it impossible to control the reaction by independently varying reactant concentrations. In summary, intein-based approaches have enjoyed great success and are very valuable, but they may not be optimal in all cases.

Having observed that dimers formed readily between appropriately terminated monofunctional eGFP, we conducted reactions with bifunctional eGFP to determine whether higher oligomers could be formed. Small amounts of trimer were indeed found, depending on the amount of bifunctional monomer present. Factors that favor circularization (proximity of the termini, for example) probably limit oligomer formation. Western blotting with an anti-GFP antibody reveals the presence of higher molecular weight bands (putatively tetramers and pentamers), which must be present in small amounts since they are not visible in Coomassie stains (where even the trimer band is barely visible).

This result could be further generalized to amine-terminated PEG, which likewise reacted with LPETG-tagged eGFP. Adding a $(Gly)_3$ group to the amino terminus did not result in substantially different rates or outcomes. The explanation for the similar activity of these substrates, in contrast to our results with modified beads, is unclear at present, although it is possible that the terminal structure of the amine-terminated PEG sufficiently resembles di- or tris-Gly such that further substitution has no effect on the reaction. In any case, our results demonstrate that Sortase A can mediate site-specific PEGylation. The importance of being able to ligate proteins to PEG under mild conditions that would not adversely affect function is difficult to overstate. PEGylation is known to extend the circulation times of therapeutically important species in the blood stream (*24*). Additionally, PEGylated proteins with low levels of PEGylation are very useful as homing signals on drug-loaded liposomes (*25*). In this context, it may be highly desirable to mono-PEGylate proteins as over PEGylation could interfere with intercalation into the liposome. The ability of Sortase A to mono-PEGylate proteins in a manner that need not affect function nor mask a useful epitope makes it highly suited for this application.

On the basis of our results, it seems clear that Sortase A can be used to create intra- and intermolecular attachments among proteins and between proteins and surfaces. Such ligation can be reversed with small nucleophiles (e.g., hydroxylamine (*26*)); initial studies suggest that Gly_3 can also be used for this purpose (data not shown). Enzymes such as mTG's have been explored as reagents for protein ligation as well, and binding sequences needed to enhance the specificity of this enzyme are now becoming known (*27*, *28*). The advantage of Sortase A over mTGs is twofold: (a) it is more specific with a rigorously

defined specificity determinant, and (b) it is easier to overexpress and purify in *E coli*, where (unlike mTG (*29*)) it is produced solubly in large quantities. When used in its native form, Sortase A seems limited to performing ligations at chain termini, whereas mTGs can perform transamidation-based ligations at any point in the chain. This apparent limitation could be useful when only single ligations are desired (e.g., for monoPEGylation). Protein engineering approaches might yield Sortase A mutants suited for a wider range of applications and thereby enhance its usefulness as a reagent in bio- and nanotechnology, perhaps as a reagent for making multivalent inhibitors as therapeutics (*30*). The ability of Sortase A to mediate gentle protein attachment to surfaces, a feature critically important in the creation of protein arrays for proteomic applications (*31*), to mediate site-specific PEGylation, and to potentially provide a simple route to selectively label tagged cell surface proteins (an area of burgeoning interest (*32*, *33*)) underscores the promise of this versatile enzyme.

ACKNOWLEDGMENT

This work was supported by NSF NIRT 0210777 and the University of Pennsylvania Research Foundation. We thank Dr. Olaf Schneewind and Dr. Greg Vanduyne for their gift of plasmids.

LITERATURE CITED

(1) Kwon, Y., Coleman, M. A., and Camarero, J. A. (2006) Selective immobilization of proteins onto solid supports through split-intein-mediated protein trans-splicing. *Angew. Chem., Int. Ed. 45*, 1726−9.

(2) Soellner, M. B., Dickson, K. A., Nilsson, B. L., and Raines, R. T. (2003) Site-specific protein immobilization by Staudinger ligation. *J. Am. Chem. Soc. 125*, 11790−1.

(3) Yin, J., Liu, F., Li, X., and Walsh, C. T. (2004) Labeling proteins with small molecules by site-specific posttranslational modification. *J. Am. Chem. Soc. 126*, 7754−5.

(4) Kindermann, M., George, N., Johnsson, N., and Johnsson, K. (2003) Covalent and selective immobilization of fusion proteins. *J. Am. Chem. Soc. 125*, 7810−1.

(5) Hodneland, C. D., Lee, Y. S., Min, D. H., and Mrksich, M. (2002) Selective immobilization of proteins to self-assembled monolayers presenting active site-directed capture ligands. *Proc. Natl. Acad. Sci. U.S.A. 99*, 5048−52.

(6) Brueggemeier, S. B., Wu, D., Kron, S. J., and Palecek, S. P. (2005) Protein-acrylamide copolymer hydrogels for array-based detection of tyrosine kinase activity from cell lysates. *Biomacromolecules 6*, 2765−75.

(7) Danczyk, R., Krieder, B., North, A., Webster, T., HogenEsch, H., and Rundell, A. (2003) Comparison of antibody functionality using different immobilization methods. *Biotechnol. Bioeng. 84*, 215−23.

(8) Girish, A., Sun, H., Yeo, D. S., Chen, G. Y., Chua, T. K., and Yao, S. Q. (2005) Site-specific immobilization of proteins in a microarray using intein-mediated protein splicing. *Bioorg. Med. Chem. Lett. 15*, 2447−51.

(9) Sielaff, I., Arnold, A., Godin, G., Tugulu, S., Klok, H. A., and Johnsson, K. (2006) Protein function microarrays based on self-immobilizing and self-labeling fusion proteins. *Chembiochem 7*, 194−202.

(10) Cull, M. G., and Schatz, P. J. (2000) Biotinylation of proteins in vivo and in vitro using small peptide tags. *Methods Enzymol. 326*, 430−40.

(11) Folk, J. E. (1983) Mechanism and basis for specificity of transglutaminase-catalyzed epsilon-(gamma-glutamyl) lysine bond formation. *Adv. Enzymol. Relat. Areas Mol. Biol. 54*, 1−56.

(12) Ohtsuka, T., Sawa, A., Kawabata, R., Nio, N., and Motoki, M. (2000) Substrate specificities of microbial transglutaminase for primary amines. *J. Agric. Food Chem. 48*, 6230−3.

(13) Marraffini, L. A., Dedent, A. C., and Schneewind, O. (2006) Sortases and the art of anchoring proteins to the envelopes of gram-positive bacteria. *Microbiol. Mol. Biol. Rev. 70*, 192−221.

(14) Kruger, R. G., Otvos, B., Frankel, B. A., Bentley, M., Dostal, P., and McCafferty, D. G. (2004) Analysis of the substrate specificity of the *Staphylococcus aureus* sortase transpeptidase SrtA. *Biochemistry 43*, 1541−51.

(15) Mao, H., Hart, S. A., Schink, A., and Pollok, B. A. (2004) Sortase-mediated protein ligation: a new method for protein engineering. *J. Am. Chem. Soc. 126*, 2670−1.

(16) Neves-Petersen, M. T., Snabe, T., Klitgaard, S., Duroux, M., and Petersen, S. B. (2006) Photonic activation of disulfide bridges achieves oriented protein immobilization on biosensor surfaces. *Protein Sci. 15*, 343−51.

(17) Huang, X., Aulabaugh, A., Ding, W., Kapoor, B., Alksne, L., Tabei, K., and Ellestad, G. (2003) Kinetic mechanism of *Staphylococcus aureus* sortase SrtA. *Biochemistry 42*, 11307−15.

(18) Ton-That, H., and Schneewind, O. (2003) Assembly of pili on the surface of *Corynebacterium diphtheriae*. *Mol. Microbiol. 50*, 1429−38.

(19) Ohtsuka, T., Sawa, A., Kawabata, R., Nio, N., and Motoki, M. (2000) Substrate specificities of microbial transglutaminase for primary amines. *J. Agric. Food Chem. 48*, 6230−3.

(20) Chang, T. K., Jackson, D. Y., Burnier, J. P., and Wells, J. A. (1994) Subtiligase: a tool for semisynthesis of proteins. *Proc. Natl. Acad. Sci. U.S.A. 91*, 12544−8.

(21) Iwai, H., Lingel, A., and Pluckthun, A. (2001) Cyclic green fluorescent protein produced in vivo using an artificially split PI-PfuI intein from *Pyrococcus furiosus*. *J. Biol. Chem. 276*, 16548−54.

(22) Williams, N. K., Prosselkov, P., Liepinsh, E., Line, I., Sharipo, A., Littler, D. R., Curmi, P. M., Otting, G., and Dixon, N. E. (2002) In vivo protein cyclization promoted by a circularly permuted Synechocystis sp. PCC6803 DnaB mini-intein. *J. Biol. Chem. 277*, 7790−8.

(23) Iwai, H., and Pluckthun, A. (1999) Circular beta-lactamase: stability enhancement by cyclizing the backbone. *FEBS Lett. 459*, 166−72.

(24) Woodle, M. C. (1993) Surface-modified liposomes: assessment and characterization for increased stability and prolonged blood circulation. *Chem. Phys. Lipids 64*, 249−62.

(25) Ton, G. N., Fine, J. P., and Kwon, G. S. (2005) Methoxypoly-(ethylene glycol)-conjugated carboxypeptidase A for solid tumor targeting: part I: synthesis and characterization. *J. Controlled Release 104*, 129−39.

(26) Ton-That, H., Liu, G., Mazmanian, S. K., Faull, K. F., and Schneewind, O. (1999) Purification and characterization of sortase, the transpeptidase that cleaves surface proteins of *Staphylococcus aureus* at the LPXTG motif. *Proc. Natl. Acad. Sci. U.S.A. 96*, 12424−9.

(27) Tominaga, J., Kamiya, N., Doi, S., Ichinose, H., Maruyama, T., and Goto, M. (2005) Design of a specific peptide tag that affords covalent and site-specific enzyme immobilization catalyzed by microbial transglutaminase. *Biomacromolecules 6*, 2299−304.

(28) Tanaka, T., Kamiya, N., and Nagamune, T. (2005) N-terminal glycine-specific protein conjugation catalyzed by microbial transglutaminase. *FEBS Lett. 579*, 2092−6.

(29) Yokoyama, K. I., Nakamura, N., Seguro, K., and Kubota, K. (2000) Overproduction of microbial transglutaminase in *Escherichia coli*, in vitro refolding, and characterization of the refolded form. *Biosci. Biotechnol. Biochem. 64*, 1263−70.

(30) Basha, S., Rai, P., Poon, V., Saraph, A., Gujraty, K., Go, M. Y., Sadacharan, S., Frost, M., Mogridge, J., and Kane, R. S. (2006) Polyvalent inhibitors of anthrax toxin that target host receptors. *Proc. Natl. Acad. Sci. U.S.A. 103*, 13509−13.

(31) Haab, B. B. (2006) Applications of antibody array platforms. *Curr. Opin. Biotechnol. 17*, 415−21.

(32) Goldsmith, C. R., Jaworski, J., Sheng, M., and Lippard, S. J. (2006) Selective labeling of extracellular proteins containing polyhistidine sequences by a fluorescein-nitrilotriacetic acid conjugate. *J. Am. Chem. Soc. 128*, 418−9.

(33) Howarth, M., Takao, K., Hayashi, Y., and Ting, A. Y. (2005) Targeting quantum dots to surface proteins in living cells with biotin ligase. *Proc. Natl. Acad. Sci. U.S.A. 102*, 7583−8.

BC060339W

A Novel Affinity-Based Controlled Release System Involving Derivatives of Dextran with Enhanced Osmotic Activity

Jyothi Devakumar and Vijayalakshmi Mookambeswaran*

LIMTechS, Deptartment Génie Biologique, Université de Technologie de Compiègne, 60205 Compiegne, France
Received March 1, 2006; Revised Manuscript Received October 5, 2006

Dextran is a highly biocompatible molecule with osmotic activity. We synthesized histidine derivatives of dextran, DexH (dextran histidine), to test the feasibility of an IMAC-based controlled release system. DexH was synthesized by the periodate oxidation method. The effect of periodate oxidation and histidine conjugation on osmotic activity was tested. The oxidized intermediate itself exhibited higher osmotic activity than native dextran. Conjugation with histidine further increased the osmotic activity, and the resulting DexH exhibited nine times more osmotic activity than native dextran. A positive correlation was observed between the extent of derivatization with histidine and osmotic activity. Association of DexH was tested on two of the matrices, namely, Cu-IDA−Novarose and Zn-IDA−Novarose. DexH bound to both these matrices, and only partial elution was achieved with stepwise lowering of pH, and complete elution was possible only with EDTA. Interestingly, it was found that DexH in its bound state (DexH−Cu-IDA−Novarose and DexH−Zn-IDA−Novarose) exhibited lesser osmotic activity than the eluted soluble form. The IDA-Cu and IDA-Zn-based solid supports bound strongly to DexH in a species-dependent manner, as the IDA-Zn matrix selectively bound DexH with clustered histidine. Further, this DexH with clustered histidine shows higher osmotic activity. A controlled release system is proposed on the basis of this difference in the osmotic activity between the bound and eluted forms of DexH with EDTA as the external trigger to induce this transition in osmotic activity.

INTRODUCTION

Osmotically active compounds swell in the presence of aqueous solutions as they imbibe water. The rate of swelling has been studied for a large number of synthetic as well as naturally occurring substances, as these compounds find a wide range of biomedical applications that include their usage as monomers in the preparation of hydrogel networks that are used in drug delivery, entrapment of cells, and so forth (*1*−*3*). In their monomeric state, they are used as tablet disintegrants wherein they control the delivery of the pharmaceutical agent in a spatially and temporally controlled manner, resulting in what are known as controlled release systems (*4*). Molecules such as glucose, hydroxyethylcellulose, glycerol, poly(ethylene glycol)s, and dextrans of different molecular weights are extensively employed osmotic agents (*4*−*7*). In controlled release systems, the osmotic agents usually form the expandable core contained within a semipermeable compartment. They expand and bring about a large volume increase in the biological milieu, releasing the pharmaceutical agent held within.

Another interesting application solely based on the ability of these osmotically active agents to bring about large volume changes is illustrated in the patent of ref 8. In the proposed concept, the osmotically active agent forms the expandable core surrounded by a semipermeable membrane in the implanted endoprosthesis. Here, both induction and rate of expansion are controlled using a proposed affinity-based release system.

Dextran is a naturally occurring, osmotically active, high molecular weight polymer. It contains repeating glucose units comprising mainly α-(1−6)-linked D-glucose units and some short α-(1−3)-linked D-glucose branch units. It is water-soluble, inert in biological systems and does not affect cell viability, and hence highly biocompatible. Dextran has been used extensively as an osmotically active colloid in re-establishing the plasmatic volume, in postoperative prophylaxis of thromboembolic risk, for the acute treatment of ischemic cerebral attacks, for the prevention of anaphylactic reactions (*9*, *10*), for other applications.

Several derivatives of dextran, such as carboxymethyldextran, [2-(diethylamino)ethyl]dextran (*11*), dexamethasone succinate dextran (*12*), and lauroyldextran (*13*), have been synthesized and studied for their potential use in tablet formulations. Periodate oxidation is a well-known method for preparation of dextran derivatives such as streptomycin-tagged dextran (*14*), amino dextran, and protein derivation to enhance their half-life (*15*, *16*). We exploited this method to couple the amino acid histidine to dextran. Histidine-containing proteins and peptides have been extensively studied for their metal-binding ability (*17*). Poly(histidine) tags have been used to modify recombinant proteins to aid in their effective purification (*18*, *19*). In view of this, it was proposed that histidine coupled to dextran would act as an anchor that can be effectively retained on the immobilized metal affinity matrix. Also, the presence of histidine groups was found to enhance the osmotic activity of native dextran.

Here, we report the study of a novel histidine derivative of dextran with enhanced osmotic properties along with its retention and release from a metal affinity system. The dextran−histidine (DexH[1]) and its oxidized intermediate were evaluated for their osmotic activity in solution, with reference to native dextran also in solution. In parallel, the binding properties of the DexH derivative to the well-known IDA-Cu and IDA-Zn

* Corresponding author. Vijayalakshmi Mookambeswaran, LIMTechS, Dept. Génie Biologique, Université de Technologie de Compiègne, Centre de Recherche de Royallieu, BP 20529 - 60205 Compiegne. Tél.: 03 44 23 44 04. Fax: 03 44 20 39 10. viji@utc.fr; indviji@yahoo.com.

[1] Abbreviations: DexH, dextran−histidine conjugate; EDTA, ethylenediaminetetraacetic acid; Zn-IDA−Novarose, Novarose matrix coupled to IDA and in turn complexed with Zn; Cu-IDA−Novarose, Novarose matrix coupled to IDA and in turn complexed with Cu.

10.1021/bc060050e CCC: $37.00 © 2007 American Chemical Society
Published on Web 01/26/2007

matrices were exploited for retaining rather strongly the derivative to these matrices, and then eluted by dissociation with EDTA. The released DexH exhibited tremendous enhancement of osmotic activity. This was measured by the entrapment of the matrix-bound DexH as well as the free eluted form in a semipermeable membrane. On the basis of the differences between the osmotic properties of DexH in its matrix-bound form and freely soluble form, the concept of a novel controlled release system is proposed.

MATERIALS AND METHODS

Dextran, sodium meta periodate, sodium borohydride, potassium iodide, ethylene glycol, histidine, copper sulfate, zinc sulfate, IDA, MOPS, sodium acetate, sodium chloride, sodium hydroxide, and EDTA were obtained from Sigma, Dialysis tubing (10 000 MW cutoff) was from Spectrophor, and AN-69S membranes were from Biospal. Novarose High Act 100/40 was obtained from Inovata. Commercially available epoxy glue Poxymatic Rapide was used to glue the cut AN-69 membranes.

Oxidation of Dextran. The procedure was adopted from Guisan et al. (*20*). Briefly, a 25 mL solution containing 0.5 g of dextran (40 000 Da) in M/Q water was prepared. Then, 1.3 g of sodium periodate was added, and the mixture was allowed to react at room temperature. After 24 h, the solution was dialyzed against 50 volumes of distilled water to eliminate the formaldehyde produced during oxidation.

Oxidation of dextran by periodate was measured by two different methods, viz, by following the consumption of periodate in the reaction mixture and second by measuring the production of formic acid as the reaction byproduct, as a function of time (*16*).

Briefly, for the estimation of periodate, 10 μL aliquots were withdrawn from the reaction mixture at regular intervals and mixed with 500 μL of 1.5% KI solution. The volume was brought up to 1 mL with M/Q water, and absorbance of the resulting solution was measured at 400 nm. Formic acid released was measured by titrating an aliquot of the mixture against 0.1 N NaOH to pH 7.0.

Calculations were based on the hypothesis that each molecule of glucose consumes 2 molecules of periodate to produce a dialdehyde product, in turn releasing 2 molecules of formic acid.

To prepare dextrans of varying degree of oxidation, the reaction was stopped at the end of 1, 2, 3, and 24 h by the addition of ethylene glycol, and aliquots withdrawn were dialyzed to remove unreacted periodate and concentrated by lyophilization.

Synthesis of DexH. To the solution containing 95% oxidized dextran, known concentrations of histidine were added. The amount of ligand added was calculated on the basis of the assumption that each dialdehyde glucose moiety in dextran can potentially bind to one histidine. Thus, on the basis of the extent of derivatization required, histidine is added and allowed to react at 4 °C for 16 h based on the optimized experimental conditions. The pH of the resulting solution is increased to 8.5 with sodium carbonate (100 mM), followed by addition of 1 mg/mL sodium borohydride to reduce the unreacted aldehyde groups as well as to stabilize the aldehyde−amine bonds. The mixture is stirred for 15 min, and the sodium borohydride step is repeated. Finally, the reaction mixture is dialyzed extensively against M/Q water, to remove the unbound ligand and other small molecular weight reactants, and lyophilized.

Concentrations of histidine and dextran in the resulting compound were measured using Pauly's reagent and by the phenol−sulfuric acid method (*21*), respectively.

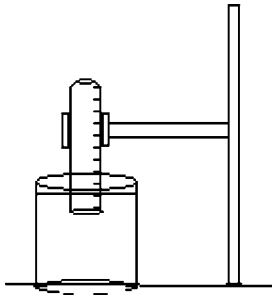


Figure 1. The AN-69 membrane setup used for measuring the osmotic activity.

Measurement of Osmotic Activity. To measure the water-absorbing capacities of different preparations the following setup was used (Figure 1). AN-69 membrane flat sheets were taken out of the hemeodialyser (Biospal, AN69S) and cut in to 5 × 5 cm^2 pieces. They were glued onto the open end of 50 mL Falcon tubes (using the epoxy glue Poxymatic Rapide). The pointed ends of the tubes were cut open to facilitate sample insertion. The tubes with the membranes were stored overnight at 4 °C, and the membrane was further secured with elastic. These tubes were then wetted in water and checked for leaks. For dialysis, the sample was inserted directly onto the membrane from the open conical end of the tube. The tubes were then weighed and positioned into a 1-L glass beaker containing water so that the membrane portion is completely immersed in water. In all the experiments, the volume of the test solution is kept to a minimum so as to maximize the membrane surface area available for exchange. The tubes were taken out at specified time intervals and weighed to measure the volume increase.

Effective volume increase is calculated using the formula

$$\text{EV (effective volume)} = \frac{\text{final weight of the setup} - \text{initial weight of the setup}}{\text{initial weight of the setup}}$$

All the experiments were carried out at least in triplicate, typically yielding an experimental error of less than 5%.

Affinity of DexH to Matrix−IDA. Novarose IDA was prepared as described earlier (*22*). 1 mL of Novarose (Novarose High Act, Inovata, 100/40) matrix coupled to IDA was saturated with Cu^{2+} or Zn^{2+} and was used as the matrix to test the affinity of DexH. The column was equilibrated with 25 mM MOPS-acetate buffer pH 7.0, and a known concentration of DexH was loaded onto the column. Elution was carried out with stepwise lowering of the pH (25 mM MOPS-acetate of pH 6.0, 5.5, 5.0, and 4.0) and finally with 100 mM EDTA. The flow rate was maintained at 0.5 mL/min, and the fractions were analyzed for histidine and dextran content.

Measurement of Water Uptake by DexH in Bound and Free Eluted Forms. A 3 mL Novarose column was packed and equilibrated with copper. From this, 1 mL was removed and kept aside as a negative control. A known concentration of DexH (of specific DexH stoichiometry) was loaded onto the remaining 2 mL column material and extensively washed until DexH was no longer detected in the wash fractions. 1 mL of this gel was used to test the osmotic activity of DexH in its bound form. The gel samples were maintained in 25 mM MOPs-acetate buffer pH 7.0. The remaining 1 mL was washed with 100 mM EDTA to elute all the bound DexH. The eluted fraction was collected and dialyzed initially against water and finally against 25 mM MOPs-acetate buffer pH 7.0 to remove copper ions and 100 mM EDTA, and then tested in comparison with the other two gel fractions for its osmotic activity in the AN-69 setup at different time intervals.

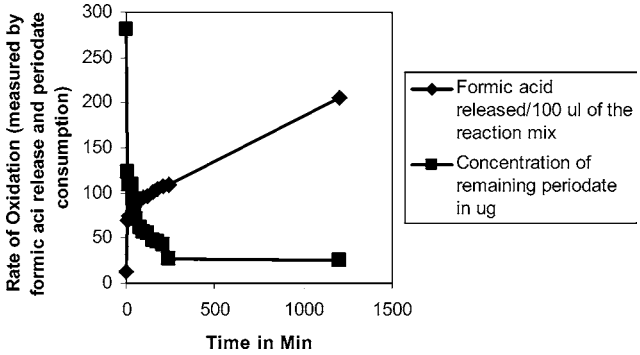


Figure 2. Time course of periodate oxidation. From the reaction mix consisting of 0.5 g of Dex-40000 and 1.3 g of periodate in a total volume of 25 mL of water, 10 and 100 μL aliquots were withdrawn and assayed for periodate consumption and release of formic acid, respectively, as described in Materials and Methods.

Table 1. Effect of Oxidation on the Osmotic Activity of Dextran

oxidation state in % (reaction time in h)	osmotic activity (effective increase in volume in mL)		
	24 h	48 h	72 h
86 (1 h)	4.5	5.5	8.0
89 (2 h)	6.6	8.2	9.0
91 (3 h)	8.1	9.1	9.9
96 (24 h)	10.8	12.0	12.4
0 (0 h)	2.7	4.5	5.0

RESULTS

Oxidation of Dextran. Oxidation of dextrans is usually carried out using the periodate method. The reaction is highly specific and results in the cleavage of the ring structure to form an acyclic backbone with intact glycosidic linkages (*23*, *24*).

The degree of oxidation is correlated to the amount of periodate used in the reaction mixture, which in turn determines the nature of the reaction end product that could be either a monoaldehyde or a dialdehyde. A dialdehyde product is ideally suited for further derivatization with an amino group-containing compound. Also, most of the oxidized dextrans reported in the literature range from 10% to 40% oxidized product based on the estimation of the liberated formic acid as well as consumption of periodate in the reaction mixture (*16*). We followed the oxidation reaction kinetics using both of these methods to obtain dextrans with different degrees of oxidation. These dextrans were tested for their osmotic activity to understand the effect of excess of OH groups generated by oxidation on the osmotic potential. On the basis of this kinetic data, we could also obtain a >90% oxidized product that was further used to obtain optimally derivatized DexH.

As indicated in Figure 2, the reaction profile obtained is in agreement with the earlier reports (*16*). All the estimations were carried out using the phenol−sulfuric acid method (*21*).

Results depicted in Figure 2 show rapid initial kinetics reaching more than 80% completion at the end of 1 h. The reaction was allowed to proceed for a total of 24 h. We could achieve a maximum of 96% oxidation under the conditions employed.

Effect of Oxidation on the Osmotic Activity. The oxidation reaction was stopped at different time intervals with the help of ethylene glycol, and the resulting product was subjected to dialysis and concentrated by lyophilization. The extent of oxidation was estimated, and the results are shown in Table 1. The various oxidized dextrans obtained were dissolved in water (1 wt %/vol) and comparatively analyzed for their osmotic activity with native dextran.

On the basis of the results obtained, it can be inferred that there is a positive correlation between the degree of oxidation and osmotic activity (Table 1). There is more than a twofold increase in the osmotic activity as measured by the increase in volume at the end of 72 h. It is possible that generation of excess OH groups is responsible for this increase. It can also be observed here that oxidation affects the swelling time. Dextrans with lower oxidation levels (<90%) exhibit an almost linear increase in osmotic activity. On the other hand, little or no increase in osmotic activity is observed after 48 h in the case of highly oxidized intermediates, indicating that swelling equilibrium is reached earlier in these intermediates (90%).

Table 2. Analysis of Osmotic Activity of DexH

derivatives tested		increase in volume (mL)		
% oxidation	% histidine derivatization	24 h	48 h	72 h
0[a]	0[a]	2.7	4.5	5.0
96[b]	0[b]	10.8	12.0	12.4
96[c]	70[c]	26.4	33.7	37.0

[a] 0% oxidation and 0% histidine derivatization represents native dextran. [b] 96% oxidation and 0% His derivatization represents the oxidized intermediate. [c] 96% oxidation and 70% derivatization represents the oxidized intermediate wherein 70% of the glucose residues were derivatized with histidine.

Table 3. Effect of Ligand Concentration on the Osmotic Activity

concn of DexH in % (wt/vol)	increase in volume in mL	
	24 h	48 h
1	24.9	32.3
2.5	27.9	34.2
5	33.2	47.8
Native Dextran		
1	2.7	4.5
2.5	4.0	5.3
5	5.2	7.3

Effect of Derivatization of Oxidized Dextran on the Osmotic Activity. It has been shown that the dialdehyde dextran can be efficiently derivatized with an amino group-containing ligand. Histidine coupling to the oxidized dextran was via the NH_2 group, leaving the imidazole free. The dextran-to-histidine ratio was varied to achieve a range of derivatized products. The resulting DexH was analyzed using histidine estimation by Pauly's and dextran estimation by the phenol−sulfuric acid method. Histidine content in the preparation is expressed as % of glucose units derivatized.

A nonoptimized DexH preparation (70% derivatized) was comparatively analyzed with native dextran as well as its oxidized intermediate (96% oxidized) for its osmotic activity.

Results shown in Table 2 indicate clearly that derivatization with histidine produces a large increase in osmotic activity of dextrans. There is about a ninefold increase in osmotic activity on derivatization at the end of 24 h.

Effect of Concentration on the Osmotic Activity of DexH. To understand the osmotic activity of DexH further, different concentrations (of 70% derivatized DexH) were tested for osmotic activity, and the results are shown in Table 3. Here, solutions of varying concentrations (expressed in wt %/vol) were prepared in M/Q water in a final volume of 1 mL and tested using the AN-69 membrane setup as described in Materials and Methods.

Data presented in Table 3 show that there is a positive correlation between concentration and volume increase with DexH. When the data are analyzed further, it can be observed that the correlation between concentration and osmotic activity is linear.

To understand this behavior, the increase was calculated by comparing the volume increase between DexH and native

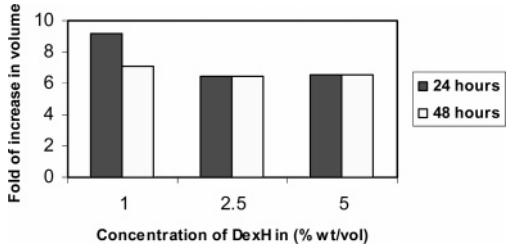


Figure 3. Comparison of increase at different concentrations. Solutions of varying concentrations of 70% derivatized DexH (expressed in wt %/vol) were prepared in M/Q water in a final volume of 1 mL and tested using the AN-69 membrane setup as described in Materials and Methods.

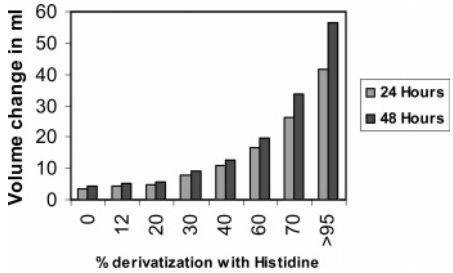


Figure 4. Effect of histidine content on the osmotic activity of DexH. 1% solutions of DexH (with varying concentrations of histidine coupled) were prepared in a final volume of 0.5 mL and tested for 24 and 48 h for their ability to induce volume changes in the AN-69 membrane setup.

Table 4. Effect of Histidine Content on the Osmotic Activity of DexH

derivatives tested		increase in volume (mL)	
% oxidation	% histidine derivatization	24 h	48 h
96	0	3.5	4.6
96	10	4.2	5.3
96	20	4.7	5.6
96	30	7.8	9.3
96	40	10.8	12.8
96	60	16.5	19.8
96	70	26.4	33.7
96	>95	41.8	56.5

dextran. At a concentration of 1%, there is about a ninefold increase, whereas at a concentration of 2.5%, only about a sixfold increase in the activity is seen (Figure 3). No increase in the activity was observed from 2.5% to 5% concentration. This discrepancy could arise from the pressure exerted in the opposite direction by the rising column of water, interfering with the in-flow in the open setup (tube of 50 mL capacity) used for testing, indicating the limitation of the system used. It is possible that the figures indicated here could represent an underestimation of the actual osmotic potential of DexH.

Effect of Concentration of Histidine on the Osmotic Activity of DexH. As can be seen from the data presented so far, the presence of histidine enhances the osmotic activity of dextran, indicating that histidine alters the osmotic property of the native dextran molecule. Thus, to understand the effect of histidine further, dextran was derivatized with varying quantities of histidine, and the volume changes of the resulting preparations were studied.

As indicated in Figure 4 and Table 4, there is a steep increase in the osmotic activity as the percent derivatization with histidine increases.

The correlation between enthalpic changes associated with periodate oxidation have been reported in literature. It is proposed that cleavage of the pyranose ring of dextran due to oxidation removes the enthalpic constraint on the elasticity of the molecule, making it shorter and stiffer (*23*). Due to these changes in the elasticity, the molecules may shift to a more extended conformation with an excess of exposed OH groups that might positively affect the osmotic activity. In conjunction with this, the presence of histidine could increase the repulsion between individual dextran molecules, enhancing the osmotic activity further. Another contributing factor could be the hydrogen-bonding abilities of excessive His groups present on dextran.

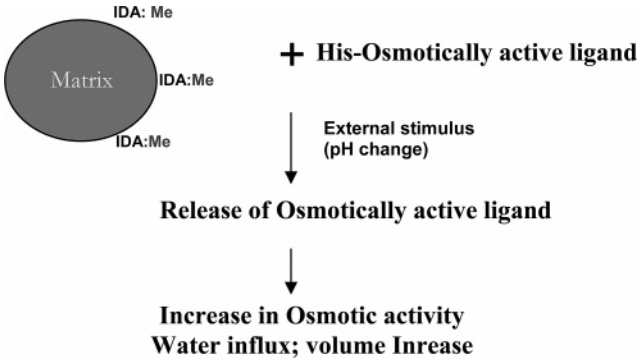


Figure 5. The envisioned affinity-based controlled release system.

Association and Dissociation of DexH to Metal Chelate Affinity Matrix. Once the histidine derivatization was successfully carried out and the resulting compound was found to exhibit a large increase in osmotic activity, due to oxidation as well as an increasing number of histidine groups on the dextran molecule, it was of interest to test the validity of the proposed controlled release systems.

The presently envisioned system would comprise a matrix capable of binding IDA that would in turn bind to the metal ion of interest at very high concentrations. This matrix would anchor DexH. The binding and release of this osmotically active DexH should be controlled by an external trigger such as changes in pH or use of EDTA. The released molecule would produce a change in osmotic activity leading to the influx of water and thereby a volume change. A schematic representation of the envisioned concept is provided below (Figure 5). Such a system would be well-suited either as a controlled release system in tablet formulations or as an affinity-based in vivo expandable system described by Cinquin et al. (*8*).

It is also required that the ligand in its bound form should be osmotically inactive or should exhibit less osmotic activity than the free form so that the system would be inert in the absence of the external trigger. After its release from the matrix in the presence of the trigger, it would bring about a large volume change and thereby behave as an ideal controlled release system. For example, the endoprosthesis would expand only in presence of an external trigger and not on immediate contact with the biological milieu, which would be the case if the osmotically active ligand alone were to be placed instead of the osmotically inactive complex. The extent of volume increase can thus be controlled in a spatial and temporal manner.

Novarose was chosen as the model matrix, as it can be coupled to high IDA and hence IDA-metal concentration. Two of the metal ions were tested for their possible affinity to DexH, viz., Cu and Zn.

Association Studies of DexH with Cu-IDA−Novarose. Association of DexH was tested on Cu-IDA−Novarose as described in Materials and Methods. Elution was initially carried out with stepwise lowering of the pH, followed by elution with 100 mM EDTA.

As indicated in Figure 6, DexH binds to the Cu-IDA matrix rather strongly. Complete elution of the bound material is possible only on treatment with 100 mM EDTA. Small peaks

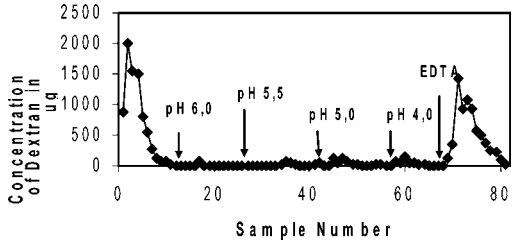


Figure 6. Chromatogram of DexH on Cu-IDA−Novarose. 1 mL of Novarose−IDA-Cu^{2+} was mixed with 25 mM MOPS−acetate buffer pH 7.0 and a known concentration of DexH was loaded onto the column. Elution was carried out with stepwise lowering of pH (25 mM MOPS acetate of pH 6.0, 5.5, 5.0, and 4.0) and finally with 100 mM EDTA. The flow rate was maintained at 0.5 mL/min, and the fractions were analyzed for histidine and dextran content.

Table 5. Chromatographic Data of DexH on Cu-IDA-Novarose

	concentration (in mg equiv of dextran)
total quantity loaded	16.824 mg
Bound	
pH 6.0	0.08
pH 5.5	0.250
pH 5.0	0.573
pH 4.0	0.575
EDTA	6.876
total bound	8.36

Table 6. Osmotic Activity of DexH in Its Bound and Free Eluted Forms

	24 h	48 h
Novarose−IDA-Cu	7.36	10.771
Novarose−IDA-Cu−DexH	10.03	14.724
eluted DexH	31.67	42.3

are visible at each of the pH values, possibly indicating heterogeneity in the polymer preparation. 1 mL of the Cu-IDA matrix was found to bind a total of 8−9 mg of DexH (dextran equivalents).

Osmotic Activity of DexH−Cu-IDA Novarose. On the basis of our initial hypothesis, DexH should bind to the matrix of interest at very high concentrations and should be effectively released only on application of an external stimulus. Also, the osmotic effect exhibited by the compound in its bound form should be less than that exhibited in its eluted free form. The following experiment was carried out to test this possibility. DexH was tested bound to Novarose−IDA-Cu as well as in its free soluble from after elution. Novarose−IDA-Cu without any bound DexH was also tested for comparison.

Data represented in Table 6 clearly indicate that DexH exhibits a large activity difference between its bound and eluted soluble form. The Novarose−IDA-Cu complex was also found to contribute to the osmotic activity. The DexH−Cu-IDA−Novarose complex exhibits osmotic activity almost equal to that exhibited by Novarose−IDA-Cu, indicating that DexH has very little osmotic activity in its bound form and fulfils one of the prerequisites of the proposed hypothesis. Also, it should be noted here that 1 mL Novarose−Cu-IDA can effectively bind and release about 8 mg of DexH preparation (Table 5), which should, in principle, exhibit osmotic activity comparable to 1% (wt/vol) DexH solution (Table 3). On the contrary, DexH in its eluted form exhibits activity equivalent to a 5% solution. It could be reasoned that Novarose−Cu-IDA is able to selectively bind DexH with high histidine content from a heterogeneous pool.

Association Studies of DexH with Zn-IDA−Novarose. Zn is relatively less toxic than Cu, and also, histidine binding to Zn-IDA is known to be less strong than that between Cu-IDA (*25*). Thus, we tested the affinity of DexH on an IDA-Zn matrix.

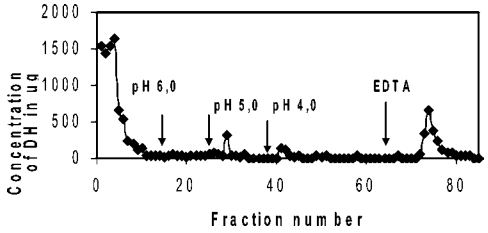


Figure 7. Chromatogram of DexH on Zn-IDA−Novarose. 1 mL of Novarose−IDA-Zn^{2+} was mixed with 25 mM MOPS-acetate buffer pH 7.0 and a known concentration of DexH was loaded onto the column. Elution was carried out with stepwise lowering of pH (25 mM MOPS acetate of pH 6.0, 5.5, 5.0, and 4.0) and finally with 100 mM EDTA. The flow rate was maintained at 0.5 mL/min, and the fractions were analyzed for histidine and dextran content.

Table 7. Chromatographic Data of DexH on Zn-IDA−Novarose

	concentration (based on dextran equivalents in mg)
load	14.000
unbound	8.250
Bound	
eluted at pH 5.0	0.728
eluted with EDTA	2.200
total bound	3.788

Table 8. Osmotic Activity of DexH in Its Bound (with Zn-IDA) and Free Eluted Form

	volume increase in mL	
matrix	24 h	48 h
Novarose−IDA-Zn	4.235	4.3
Novarose−IDA-Zn-DexH	17.2	19.4
DexH eluted	25.2	40.4

Similar chromatographic conditions were employed as in the case of the Cu-IDA matrix.

The chromatogram obtained with Zn is very similar to that of Cu (Figure 7 and Table 7), with a major elution peak only with 100 mM EDTA. It was also found that Zn exhibits a much lower binding capacity then Cu. 1 mL matrix binds to about 3.8 mg of DexH as against 8 mg in the case of Cu-IDA−Novarose (Tables 7 and 5). This could be attributed to the fact that Zn requires adjacent histidine residues for effective binding (*25*, *26*) and is thus able to bind only a small fraction of DexH molecules from the heterogeneous pool.

Osmotic Activity of DexH−Zn-IDA−Novarose. We tested the osmotic activity of DexH as a complex with Zn-IDA−Novarose under similar conditions as in the case of Cu complexes.

The results shown in Table 8 indicate that Novarose−IDA-Zn exhibits less osmotic activity than Cu-IDA−Novarose, whereas the complex of Novarose−IDA-Zn−DexH exhibits significant osmotic activity. It is of interest to note here that eluted free DexH from the Zn-IDA matrix amounts to only about 0.3% (wt/vol) solution in terms of concentration, but the osmotic activity exhibited is almost equivalent to 5% free DexH preparation. This again indicates that the ability of the Zn-IDA matrix to concentrate DexH with higher histidine content may be due to its ability to bind to adjacent histidines, which is significantly higher when compared to DexH−Cu-IDA−Novarose.

DISCUSSION

We report here a novel derivative of dextran, DexH, that exhibits enhanced osmotic properties. Oxidized intermediates of dextran are prepared using the well-known periodate method and are subsequently derivatized with histidine. An enhancement in osmotic activity is observed at the oxidized intermediate stage

itself. Significant changes are also observed with respect to the swelling time. There seems to be an inverse correlation between the degree of oxidation and the swelling time. This behavior can be explained by taking into account the structural features of native dextran as well as the changes that have been reported to occur during oxidation.

Dextran has, in its structure, a ring-oxygen atom and a bridge-oxygen atom with hydrogen-acceptor properties and a hydroxyl group with hydrogen-donor and -acceptor properties (*27*). Dextrans consists of glucose molecules bonded together mostly by α-(l−6) linkages with about 5% α-(1−3) linkages serving as branch points. The branches are short and are mainly one or two glucose monomers in length (*28*). The behavior of dextran in aqueous solution has been the subject of several investigations (*29*−*32*) Periodate-mediated oxidation is known to break the bond between the third and fourth carbon atoms, leading to formation of the dialdehyde product. This cleaves the pyranose ring, in the process generating an excess of CHO groups. This event increases the elasticity of the molecule as well as the hydrogen-bonding ability, depending on the extent of oxidation. Also, dextran solutions are known to exhibit intermolecular associations (*32*), and periodate oxidation has been shown to decrease these molecular interactions proportionally to the degree of oxidation (*33*). All these structural changes could contribute to the enhanced osmotic activity observed.

Further, the osmotic activity was found to increase on conjugation with histidine. A positive correlation was observed between the extent of derivatization and the osmotic activity. It has previously been documented that, at lower concentrations, the osmotic potential of dextran is comparable to that of albumin. But, at higher concentrations, there is a marked deviation, with dextrans exhibiting a large increase in osmotic potential with increasing concentration. This behavior is attributed to greater interaction between dextran and water, and the properties conferred by the random coil structure. Also, the coiled nature is known to change from a compact one to an expanded coil in aqueous solutions. It is possible that the introduction of a polar group such as histidine enhances the hydrogen-bonding ability of dextran, and the presence of multiple histidines can ease the conformational constraints, further enhancing the hydrodynamic interactions leading to a significant increase in osmotic activity. It would be of interest to test the effect of histidine conjugation on the intermolecular associations of dextran.

Another interesting feature observed is the selectivity observed in the case of Cu- and Zn-bound IDA matrices. When DexH preparations are loaded onto these columns, the eluted soluble fractions exhibit higher osmotic activity. It can be suggested here that the polymer preparation contains a heterogeneous pool of DexH molecules with varying degrees of derivatization with histidine, and both the IMAC systems tested could bind selectively to the DexH species with higher content of histidine. The effect is more pronounced in the case of the Zn-IDA matrix, as eluted DexH at a concentration of 0.38% exhibits a tenfold increase in osmotic activity compared to native dextran tested at a concentration of 1%. It is known that, in the case of proteins, multiplicity, density, and localization of histidine residues on the surface determines the strength of interaction with the metal-IDA matrix (*26*). Also, Cu-IDA is known to efficiently bind proteins even with a single surface histidine, whereas metals in the lower end of the series, such as Zn, bind only when multiple histidines are present on the surface. For example, as reported by Hamden et al., (*26*) myoglobin from two different species exhibits radically different affinities to the Zn-IDA matrix. Dog myoglobin with one histidine exhibits very little affinity, whereas sperm whale myoglobin with two surface histidine exhibits strong binding. Histidines separated by two amino acid residues, forming a part of an α helix, are known to be favorably positioned to form strong coordination with IDA-Zn. The same analogy can be extended to explain the behavior of DexH. Here, in DexH with a high degree of derivatization, histidines possibly exist as clusters and are readily exposed on the surface due to the expanded coil structure. The Zn-IDA matrix is able to selectively bind to these molecules with histidine clusters. Thus, the Zn-IDA matrix can be effectively used to concentrate the DexH species with high osmotic activity.

DexH with its enhanced osmotic properties would find many applications apart from the two discussed in the above sections, such as in contrast enhancers, preparation of novel hydrogels with higher swelling capacity, and so forth. Also, it would be interesting to test the effect of molecular weight on the osmotic activity. It is possible that higher molecular weight dextrans can potentially conjugate with histidine to a larger extent and thus can exhibit more osmotic activity than the one tested in this paper. This approach could also provide a method to engineer DexH with the tailor-made osmotic properties to suit specific requirements.

ACKNOWLEDGMENT

This work was carried out as a part of the project SURGETIQUE 2 within the framework of the National Network of Technology for Health (RNTS) France, from the French Ministry of Industry. We wish to thank RNTS for the financial support. We particularly thank Prof. P. Cinquin and the Societe PRAXIM, for their valuable discussions.

LITERATURE CITED

(1) Peppas, N. A., Bures, P., Leobandung, W., and Ichikawa, H. (2000) Hydrogels in pharmaceutical formulations. *Eur. J. Pharm. Biopharm. 50*, 27−46.

(2) Hoffman, A. S. (2002) Hydrogels for biomedical applications. *Adv. Drug Delivery Rev. 54*, 3−12.

(3) Drury, J. L., and Mooney, J. D. (2003) Hydrogels for tissue engineering: scaffold design variables and applications. *Biomaterials 24*, 4337−4351.

(4) Bolhuis, G. K., Van Kamp, H. V., Lerk, C. F., and Sessink, F. G. M. (1982) On the mechanism of action of modern disintegrants. *Acta Pharm. Technol. 28*, 111−114.

(5) Chang, R., Shinwari, M., Leonzio, M., Wu, L., Pang, J., and Hussain, M. A. (1998) Evaluation of the disintegrant properties for an experimental, crosslinked polyalkylammonium polymer. *Int. J. Pharm. 173*, 7−92.

(6) Santus, G., and Baker, R. W. (1995) Osmotic drug delivery: a review of the patent literature. *J. Controlled Release 35*, 1−21.

(7) Verma, R. K., Krishna, D. M., and Garg, S. (2002) Formulation aspects in the development of osmotically controlled oral drug delivery systems. *J. Controlled Release 79*, 7−27.

(8) Cinquin, P., Cinquin, O., Favier, D., Orgeas, L., Pecher, M., and Pujol, S. (2001) Micro-muscle en milieu biologique, brevet no. 01/09526, depose par l'Universite Joseph Fourier le 17 Juillet 2001.

(9) Mofenson, H. C., and Greensher, J. (1970) The nontoxic ingestion. *Pediatr. Clin. North Am. 17*, 583−90.

(10) Mofenson, H. C., Greensher, J., and Caraccio, T. R. (1984) Ingestions considered nontoxic. *Clin. Lab. Med. 4*, 587−602.

(11) Miyazaki, Y., Yakou, S., Nagai, T., and Takayama, K. (2003) The effect of polyion complex formation on in vitro/in vivo correlation of hydrophilic matrix tablets. *J. Controlled Release 91*, 315−26.

(12) Pang, Y. N., Zhang, Y., and Zhang, Z. R. (2002) Synthesis of an enzyme-dependent prodrug and evaluation of its potential for colon targeting. *World J. Gastroenterol. 8*, 913−7.

(13) Hirsch, S., Binder, V., Schehlmann, V., Kolter, K., and Bauer, K. H. (1999) Lauroyldextran and crosslinked galactomannan as coating materials for site-specific drug delivery to the colon. *Eur. J. Pharm. Biopharm. 47*, 61−71.

(14) Roseeuw, E., Coessens, V., Schacht, E., Vrooman, B., Domurado, D., and Marchal, G. (1999) Polymeric prodrugs of antibiotics with improved efficiency. *J. Mater. Sci. Mater. Med. 10*, 743−6.

(15) Betancor, L., López-Gallego, F., Hidalgo, A., Alonso-Morales, N., Fuentes, M., Fernández-Lafuente, R., and Guisán, J. M. (2004) Prevention of interfacial inactivation of enzymes by coating the enzyme surface with dextran-aldehyde. *J. Biotechnol. 110*, 201−207.

(16) Battersby, J., Clark, R., Hancock, W., Puchulu-Campanella, E., Haggarty, N., Poll, D., and Harding, H. (1996) Sustained release of recombinant human growth hormone from dextran via hydrolysis of an imine bond. *J. Controlled Release 42*, 143−156.

(17) Lu, Z., DiBlasio-Smith, E. A., Grant, K. L., Warne, N. W., LaVallie, E. R., Collins-Racie, L. A., Follettie, M. T., Williamson, M. J., and McCoy, J. M. (1996) Histidine patch thioredoxins. Mutant forms of thioredoxin with metal chelating affinity that provide for convenient purifications of thioredoxin fusion proteins. *J. Biol. Chem. 271*, 5059−5065.

(18) Mateo, C., Fernandez-Lorente, G., Pessela, B. C., Vian, A., Carrascosa, A. V., Garcia, J. L., Fernandez-Lafuente, R., and Guisan, J. M. (2001) Affinity chromatography of polyhistidine tagged enzymes. New dextran-coated immobilized metal ion affinity chromatography matrices for prevention of undesired multipoint adsorptions. *J. Chromatogr., A 915*, 97−106.

(19) Mohanty, A. K., and Wiener, M. C. (2004) Membrane protein expression and production: effects of polyhistidine tag length and position. *Protein Expr. Purif. 33*, 311−325.

(20) Guisán, J. M., Penzol, G., Armisen, P., Bastida, A., Blanco, R. M., Fernandez-Lafuente, R., and García-Junceda, E. (1997) Immobilization of enzymes acting on macromolecular substrates: reduction of steric problems. In *Immobilization of Enzymes and Cells* (Bickerstaff, G. F., Ed.) Methods in Biotechnology Series, Vol. 1, pp 261−275, The Humana Press, Totowa, NJ.

(21) Dubois, M., Gilles, K., Hamilton, J. K., Rebers, P. A., and Smith, F. (1951) A colorimetric method for the determination of sugars. *Nature (London) 168*, 167.

(22) Berna, P. P., Mrabet, N. T., Beeumen, J. V., Devreese, B., Porath, J., and Vijayalakshmi, M. A. (1997) Residue accessibility, hydrogen bonding, and molecular recognition: metal-chelate probing of active site histidines in chymotrypsins. *Biochemistry 36*, 6896−6905.

(23) Marszalek, P. E., Oberhauser, A. F., Pang, Y. P., and Fernandez, J. M. (1998) Polysaccharide elasticity governed by chair-boat transitions of the glucopyranose ring. *Nature (London) 396*, 661−664.

(24) Bobbitt, J. M. (1956) In *Advances in Carbohydrate Chemistry* (Wolfram, M. L., and Tipson, R. S., Eds.), Academic, New York.

(25) Sulkowski, E. (1989) The saga of IMAC and MIT. *BioEssays 10*, 170−175.

(26) Hemdan, E. S., Zhao, Y. J., Sulkowski, E., and Porath, J. (1989) Surface topography of histidine residues: a facile probe by immobilized metal ion affinity chromatography. *Proc. Natl. Acad. Sci. U.S.A. 86*, 1811−1815.

(27) Vinogradov, S. N., and Linnell, R. H. (1971) The hydrogen bond in biological materials. In *Hydrogen Bonding*, p 250, Von Nostrand Reinhold, New York.

(28) Larm, O., Lindberg, B., and Svensson, S. (1971) Studies on the length of the side chains of the dextran elaborated by *Leuconostoc mesenteroides* NRRL B-512. *Carbohydr. Res. 20*, 39−48.

(29) Preston, B. N., Comper, W. D., Hughes, A. E., Snook, I. K., and van Megen, W. (1982) Diffusion of dextran at intermediate concentrations. *J. Chem. Soc., Faraday Trans. 78*, 1209−1221.

(30) Laurent, T. C., Sundelof, L. O., Wik, K. V., and Warmegard, B. (1976) Diffusion of dextran in concentrated solutions. *Eur. J. Biochem. 68*, 95−102.

(31) Brown, W., Stilbs, P., and Johnsen, R. M. (1982) Self-diffusion and sedimentation of dextran in concentrated solutions. *J. Polym. Sci.: Polym. Phys. 20*, 1771−1780.

(32) Callaghan, P. T., and Pinder, D. N. (1983) A pulsed field gradient NMR study of self-diffusion in a polydisperse polymer system: dextran in water. *Macromolecules 16*, 968−973.

(33) Murphy, P. T., and Whistler, R. L. (1973) *Industrial Gums Polysaccharides and Their Derivatives*, 2nd ed. (Whistler, R. L., and De Miller, J. N., Eds.) p 513, Academic Press, New York.

(34) Uraz, H., and Giber, A. (1997) Comparison of molecular association of dextran and periodate-oxidized dextran in aqueous solutions *Carbohydr. Polym. 34*, 127−130.

BC060050E

Lipopolythioureas: A New Non-Cationic System for Gene Transfer

Jeanne Leblond, Nathalie Mignet, Céline Largeau, Maria-Vittoria Spanedda, Johanne Seguin, Daniel Scherman, and Jean Herscovici*

Inserm, U640, Paris, F-75006, CNRS, UMR8151, Paris, F-75006, Ecole Nationale Supérieure de Chimie de Paris, Paris, F-75005, Unité de Pharmacologie Chimique et Génétique, France, Université René Descartes, Faculté de Pharmacie, Paris, F-75270 France, and Chimie Moléculaire de Paris Centre, CNRS, FR 2769, Paris, F-75005. Received May 30, 2006; Revised Manuscript Received November 28, 2006

A DNA-transfection protocol has been developed that makes use of thiourea non-cationic synthetic lipid, *N*-[1,3-bis(carbamothioylamino)propan-2-yl]-2-(dialkycarbamoylmethoxy)acetamide. It was found that these new compounds could be formulated without helper lipid and that the N-decanoyl and N-lauryl derivatives transfected B16 cells in the presence of serum with an efficiency at the same level as cationic lipids, under identical conditions. In vivo transfection using intratumoral injection was also investigated. It was found that compounds **18c** and **19** showed an efficiency of the same magnitude as naked DNA and cationic lipid.

INTRODUCTION

Plasmid-based gene medicine (*1*) requires a safe and efficient delivery system to transport DNA to the cell nucleus in order to cure innate or acquired disease. Naked plasmid DNA (*2*) could be directly administrated to the muscle (*3*), liver (*4*), or tumor (*5*), but in most cases, DNA is delivered by systemic injection and, for increased efficiency, should be protected from degradation in the bloodstream. The use of cationic lipid or polymer is one of the main strategies to deliver therapeutic genes or oligonucleotides to the nucleus (*6*−*8*). As compared to viral vectors (*9*), these gene delivery technologies suffer from a lack of efficiency but offer more flexibility and safety. This lack of efficiency is particularly true for in vivo transfection, due to interaction of cationic complexes with blood proteins (*10, 11*). Several strategies have been proposed to solve this drawback, like liposome postgrafting (*12*), polymer shielding (*13, 14*), and anionic liposomal delivery system (*15*). Nonelectrostatic systems have also been worked out that might bind DNA by base stacking (*16, 17*), nucleoside interaction (*18*), or trapping into a saccharidic cluster (*19*). But in these last cases, DNA transfection was seldom observed in vitro except for the glycocluster (*19*), unless the system bore a cationic charge (*20*).

We have previously reported alternative lipids that interact with DNA in a nonelectrostatic fashion (*21*). These lipids are composed of di- or trithiourea functions that bind DNA. Unfortunately, these complexes did not transfect cells efficiently probably because of their high hydrophobic nature and their poor interaction between uncharged lipopolythiourea (LPT) liposomes and the cell membrane. Targeting LPT−DNA particles to membrane receptors seemed to represent the most suitable way to use these new DNA complexing particles for gene transfer. We recently obtained lipopolythiourea liposomes labeled with a fluorescent agent and formulated with a PEG−RGD lipid (*22*). These targeting thiourea lipoplexes were efficiently internalized by the cells displaying $\alpha_v\beta_3$ integrin receptor, as compared to the nontargeting complexes. However, no transfection was achieved by such lipoplexes. This previous study showed that modifications of the lipopolythiourea head from three linear thiourea functions to two branched thiourea functions still allowed efficient DNA compaction. Moreover, we observed that such structural element modification improved the formulation and decreased the hydrophobic properties without destabilizing the lipoplexes.

We therefore concentrated our efforts on decreasing the hydrophobicity of LPT lipids. Log *P* calculation clearly showed that hydrophilicity could be greatly improved by decreasing the length of the hydrophobic anchor. Here, we describe a general synthesis of readily available dithioureas. These derivatives interact with DNA without any helper lipid and exhibit cell transfection properties. These novel delivery agents represent a new example of nonelectrostatic nanosystem with transfecting properties.

EXPERIMENTAL PROCEDURES

Materials and Methods. All solvents were purchased from Carlo Erba-SDS (Peypin France). Dichloromethane was distilled from P_2O_5. DMF was dried over 3 Å molecular sieves and pyridine over KOH. All chemicals were purchased from Sigma-Aldrich-Fluka or Lancaster. Tosyl chloride was recrystallized in petroleum ether, and diglycolic anhydride was dehydrated (P_2O_5) prior to use. Other solvents and products were used without further purification. Reactions were monitored by thin-layer chromatography using Merck precoated 60 F254 silica gel plates. Column chromatography was performed over SDS (Peypin France) 35−70 nm silicagel according to the method of Still, Khan, and Mitra (*23*) or using small column flash chromatography (SFC) according to the following procedure: a plastic syringe was filled with silica gel (product/silica gel 1/5) and connected to a vacuum pump. The column was equilibrated with heptane, and then the sample dissolved in a minimum of dichloromethane was added to the top. The column was eluted by ten fractions of a heptane/ethyl acetate mixture. The volume was equal to the silica gel volume. For each fraction, the amount of ethyl acetate was increased (10% to 100% (v/v) heptane in ethyl acetate). Inverse-phase SPE was performed on Supelco Superclean C8 cartridge using an H_2O/CH_3CN/CH_3OH mixture. ^1H and ^{13}C NMR spectra were recorded on a Bruker Advance DRX-300 spectrometer at 300.13 MHz for ^1H and 75.47 MHz for ^{13}C. NMR spectra were processed using *Xwinnmr* (Bruker) or *SwaN-MR* (*24*). MS were carried out on a Shimazu 2010A LC-MS on ESI mode. High-resolution MS and elemental analysis were carried out by the "Service Central de Micro-analyse du CNRS" Vernaison France.

* E-mail: jean-herscovici@enscp.fr.

10.1021/bc060141b CCC: $37.00 © 2007 American Chemical Society
Published on Web 01/20/2007

Dipalmytoylphosphatidylcholine (DPPC) and phosphatidylethanolamine-lissamine rhodamine were purchased from Aventi Polar Lipids (Alabaster Alabama). Log *P* calculations were performed using *MarvinSketch* (Chemaxon, Ltd., Budapest, Hungary) (*25*).

Synthetic Procedures. *tert-Butyl 1,3-Dihydroxypropan-2-ylaminoformate (**2**).* A solution of 2-aminopropane-1,3-diol (**1**) (5 g, 55 mmol) in ethanol (200 mL) was added to a solution di-*tert*-butylcarbonate (12 g, 55 mmol) in ethanol (200 mL). The reaction mixture was stirred for 5 h, then evaporated to dryness to yield a white solid, which was recrystallized in heptane to yield 10 g of **2** (93%). Mp 82 °C. ^{1}H NMR ($CDCl_3$) δ (ppm): 1.45 (s, 9H, CH_3), 3.24 (m, 2H, OH), 3.67−3.83 (m, 5H, CH, CH_2OH), 5.34 (d, 1H, J = 6.6 Hz, NH). ^{13}C NMR ($CDCl_3$) δ (ppm): 28.44 (s, CH_3), 53.31 (s, CH), 63.45 (s, CH_2-OH), 80.07 (s, $C(CH_3)_3$), 156.14 (s, C═O). Anal. Calcd for $C_8H_{17}NO_4$ C, 49.96; H, 8.94; N, 7.32. Found C, 50.25; H, 8.96; N, 7.32.

*tert-Butyl 1,3-Bis(methoxysulfonyloxy)propan-2-ylaminoformate (**3**).* Methanesulfonyl chloride (8.3 mL, 100 mmol) and triethylamine (18.6 mL, 133 mmol) were added to a solution of diol **2** (8.5 g, 44 mmol) in dichloromethane (100 mL). The reaction mixture was stirred for 3 h; then, the solution was diluted (dichloromethane, 500 mL), washed (water, 2 × 150 mL), then dried ($MgSO_4$). After filtration and evaporation of the solvent, 15.5 g of **3** was recovered as a solid (100%). Mp 85 °C. ^{1}H NMR ($CDCl_3$) δ (ppm): 1.43 (s, 9H, CH_3), 3.06 (s, 6H, CH_3), 4.23−4.37 (m, 5H, CH, CH_2OH), 5.07 (d, 1H, J = 7.6 Hz, NH). ^{13}C NMR ($CDCl_3$) δ (ppm): 28.32 (s, CH_3), 37.54 (s, CH_3), 48.69 (s, CH), 67.02 (s, CH_2OH), 80.05 (s, $C(CH_3)_3$), 154.97 (s, C═O). MS (ESI, *m*/*z*) 370 $(M + Na)^+$, 391 $(M + HCOO)^-$. Anal. Calcd C, 34.57; H, 6.09; N, 4.03; S, 18.46. Found C, 32.86; H, 5.98; N, 4.32; S, 19.09.

*tert-Butyl 1,3-Diazidopropan-2-ylaminoformate (**4**).* A solution of dimesyl **3** (1.8 g, 5.1 mmol), sodium azide (2.0 g, 30.6 mmol), and 18-crown-6 (0.14 g, 0.5 mmol) in DMF (25 mL) was refluxed for 20 h. The mixture was coevaporated with toluene and water, then diluted in ethyl acetate, washed three times with brine, dried ($MgSO_4$), and evaporated to yield **4** as a yellow oil that was further used without any purification (1.24 g, 100%). ^{1}H NMR ($CDCl_3$) δ (ppm): 1.43 (s, 9H, CH_3), 3.40 (dd, J = 7.8 Hz, J = 16.6 Hz, CH_2), 3.51 (dd, J = 6.8 Hz, J = 16.6 Hz, CH_2), 3.85 (m, 1H, CH), 4.91 (d, 1H, J = 8.4 Hz, NH). ^{13}C NMR ($CDCl_3$) δ (ppm): 28.36 (s, CH_3), 49.61 (s, CH_2), 51.84 (s, CH), 80.05 (s, $C(CH_3)_3$), 155.19 (s, C═O).

*1,3-Diazidopropan-2-amine (**5**).* A TFA/water mixture (3:1, 80 mL) was added to a solution of diazide **4** (4.7 g, 20 mmol) in dichloromethane (20 mL). The reaction mixture was stirred for 4 h, then poured on solid $NaHCO_3$ and filtered. The aqueous phase was extracted by dichloromethane, adjusted to pH 10 (NaOH 2 N), and then extracted again with dichloromethane. The mixed organic layers were dried ($MgSO_4$), filtered, and then evaporated to dryness to give **4** (2.7 g, 96%) that was used without any purification. ^{1}H NMR ($CDCl_3$) δ (ppm): 1.45 (s, 2H, NH), 3.02 (p, 1H, J = 5.8 Hz, CH), 3.32 (dd, 2H, J = 5.8 Hz, J = 12.0 Hz, CH_2), 3.40 (dd, 2H, J = 5.8 Hz, J = 12.0 Hz, CH_2). ^{13} C NMR ($CDCl_3$) δ (ppm): 50.69 (s, CH), 55.08 (s, CH_2). MS (EI DCI) 142 $(M + H)^+$.

*N′,N′-Ditetradecylsuccinamide (**7**).* Succinic anhydride (10.7 g, 107 mmol) and 4-dimethylaminopyridine (0.48 g, 3.9 mmol) were added to a solution of ditetradecylamine (**6a**) (8g, 21.5 mmol) in a mixture of dry pyridine (32 mL) and dichloromethane (80 mL). The reaction mixture was stirred at RT for 18 h before addition of 1 N hydrochloride (20 mL). The organic layer was extracted, washed with brine, dried ($MgSO_4$), and evaporated to afford **7** as an oil (9.8 g, 98%). ^{1}H NMR ($CDCl_3$) δ (ppm): 0.85 (t, 6H, J = 6.3 Hz, CH_3), 1.23 (m, 44H, $-CH_2-$), 1.48 (m, 2H, $-CH_2-$), 2.64 (s, 4H, CH_2CO), 3.22 (m, 4H, CH_2N). ^{13}C NMR ($CDCl_3$) δ (ppm): 14.08 (s, CH_3), 22.69 (s, $-CH_2-$), 27.74 (s, $-CH_2-$), 28.10 (s, CH_2CO), 28.92 (s, $-CH_2-$), 29.67 (m, $-CH_2-$), 30.07 (s, CH_2CO), 31.96 (s, $-CH_2-$), 46.21 and 47.98 (2s, $-CH_2N$), 171.46 (s, C═O), 176.34 (s, C═O). MS (ESI, *m*/*z*) 511 $(M + H)^+$.

*N-(2-Azido-1-azidomethylethyl)-N′,N′-ditetradecylsuccinamide (**8**).* Diazide **5** (0.074 g, 0.53 mmol) was added to solution of **7** (0.26 g, 0.5 mmol) in dichloromethane (3 mL). The reaction mixture was stirred for 1 h before the addition of a solution of DCC (0.16 g, 0.75 mmol) in dichloromethane (1 mL). After overnight stirring, diethyl ether (5 mL) was added, and the resulting precipitate was filtered through a celite pad. The solvent was evaporated to yield a crude oil that was dissolved in THF (10 mL/mmol). Amberlyst-21 (0.27 g, 4 equiv) was added to remove the acid excess. The resin was removed by filtration, and then the filtrate was evaporated to yield **8** as a yellow oil (0.31 g, 93%). ^{1}H NMR ($CDCl_3$) δ (ppm): 0.87 (t, 6H, J = 6.6 Hz, CH_3), 1.25 (m, 44H, $-CH_2-$), 1.47 (m, 4H, $-CH_2-$), 2.60 (dd, 4H, J = 22 Hz, J = 8 Hz, CH_2CO), 3.23 (dt, 4H, J = 22 Hz, J = 8 Hz, CH_2N), 3.43 (dd, 4H, J = 6.0 Hz, J = 14.4 Hz, CH_2N_3), 4.15 (m, 1H, CH), 7.23 (d, 1H, J = 8 Hz, NH). ^{13}C NMR ($CDCl_3$) δ (ppm): 13.95 (s, CH_3), 22.66 (s, $-CH_2-$), 27.12 (s, $-CH_2-$), 27.84 (s, CH_2CO), 28.97 (s, $-CH_2-$), 29.66 (m, $-CH_2-$), 31.90 (m, $-CH_2-$, CH_2CO), 46.42 and 48.09 (2s, $-CH_2N$), 48.55 (s, CH), 51.62 (s, CH_2N_3), 171.39 (s, C═O), 172.87 (s, C═O). MS (ESI, *m*/*z*) 634 $(M + H)^+$.

*N-(2-Amino-1-aminomethylethyl)-N′,N′-ditetradecylsuccinamide (**9**).* A round-bottom flask equipped with a stirring bar was charged with **8** (0.30 g, 0.48 mmol), ethanol (10 mL), Pd/C (0.06 g), and hydrogen. The suspension was stirred for 19 h at RT; then, the mixture was filtered through a celite pad to yield after evaporation 0.27 g of the diamine **9** (98%) as a colorless oil. ^{1}H NMR ($CDCl_3$) δ (ppm): 0.80 (t, 6H, J = 8.4 Hz, CH_3), 1.25 (m, 44H, $-CH_2-$), 1.49 (m, 4H, $-CH_2-$), 2.43 (m, 2H, CH_2CO), 2.63 (m, 2H, CH_2CO), 2.75 (m, 4H, CH_2NH_2), 2.86 (m, 4H, NH_2), 3.25 (m, 4H, CH_2N), 3.82 (m, 1H, CH), 7.12 (d, 1H, J = 8.4 Hz, NH). ^{13}C NMR ($CDCl_3$) δ (ppm): 14.14 (s, CH_3), 22.73 (s, $-CH_2-$), 27.12 (s, $-CH_2-$), 27.82 (s, $-CH_2-$), 29.40 (s, CH_2CO), 29.66 (m, $-CH_2-$), 31.97 (m, $-CH_2-$, CH_2CO), 43.56 (s, CH_2NH_2), 46.36 and 48.10 (2s, $-CH_2N$), 53.27 (s, CH), 171.39 (s, C═O), 172.87 (s, C═O). MS (ESI, *m*/*z*) 582 $(M + H)^+$, 626 $(M + HCOO)^-$.

*N′-[1,3-Bis(methylthiocarbamoylamino)propan-2-yl]-N,N-ditetradecylbutanediamide (**10**).* Methyl isothiocyanate (11 mg, 0.15 mmol) was added to solution of diamine **9** (58 mg, 0.1 mmol) and triethylamine (14 μL, 0.1 mmol) in dichloromethane (1 mL). The solution was stirred overnight. The solvent was evaporated, and the crude was purified by SFC to yield **11** as an oil (0.046 g, 63%). ^{1}H NMR ($CDCl_3$) δ (ppm): 0.87 (t, 6H, J = 8.4 Hz, CH_3), 1.25 (m, 44H, $-CH_2-$), 1.46 (m, 4H, $-CH_2-$), 2.47 (m, 2H, CH_2CO), 2.66 (d, 2H, CH_2CO), 3.01 (s, 6H, CH_3NCS), 3.22 (m, 4H, CH_2N), 3.75−3.90 (m, 5H, CH, CH_2NCS), 7.59 (m, 5H, NH). ^{13}C NMR ($CDCl_3$) δ (ppm): 14.20 (s, CH_3), 22.79 (s, $-CH_2-$), 27.17 (s, $-CH_2-$), 28.01 (s, $-CH_2-$), 29.02 (s, CH_2CO), 29.66 (m, $-CH_2-$), 31.21 (s, CH_3 NCS), 31.78 (s, CH_2CO), 32.06 (s, $-CH_2-$), 44.75 (s, CH_2-NCS), 46.83 and 48.51 (s, $-CH_2N$), 51.99 (s, CH), 171.88 (s, C═O), 173.67 (s, C═O), 183.61 (s, C═S). HR-ESMS calcd for $C_{39}H_{78}N_6O_2NaS_2$: 749.5525. Found 749.5487.

*N-(2-Isothiocyanato-1-isothiocyanatomethylethyl)-N′,N′-ditetradecylsuccinamide (**11**).* Diisopropylethylamine (0.25 mL, 1.4 mmol) and carbon disulfide (0.11 mL, 1.9 mmol) were successively added to a solution of diamine **9** (0.28 g, 0.5 mmol) in dichloromethane (5 mL). The solution was stirred for 3 h, and then a solution of tosyl chloride (0.18 g, 0.9 mmol) in

dichloromethane was added dropwise. The mixture was stirred for 20 h at RT, diluted with dichloromethane, and washed three times with brine. The organic solution was dried ($MgSO_4$) and evaporated under vacuum. The crude was purified by SFC to yield **11** as a colorless oil (0.07 g, 22%). ^{1}H NMR ($CDCl_3$) δ (ppm): 0.88 (t, 6H, J = 6.6 Hz, CH_3), 1.25 (m, 44H, $-CH_2-$), 1.51 (m, 4H, $-CH_2-$), 2.56 (m, 2H, CH_2CO), 2.69 (m, 2H, CH_2CO), 3.25 (m, 4H, -CH_2N), 3.76 (dd, 4H, J = 6.0 Hz, J = 11.1 Hz, CH_2NCS), 4.28 (m, 1H, CH), 7.51 (d, 1H, J = 8.4 Hz, NH). ^{13}C NMR ($CDCl_3$) δ (ppm): 14.18 (s, CH_3), 22.77 (s, $-CH_2-$), 27.19 (s, $-CH_2-$), 27.87 (s, $-CH_2-$), 29.03 (s, CH_2CO), 29.74 (m, $-CH_2-$), 32.01 (m, $-CH_2-$, CH_2CO), 45.98 and 46.69 (2s, $-CH_2N$), 48.10 (s, CH), 49.04 (s, CH_2-NCS), 171.39 (s, C═O), 172.87 (s, C═O). IR (NaCl) σ (cm^{-1}): 1629 ($\nu_{N-C=O}$), 1675 ($\nu_{NH-C=O}$), 2089 ($\nu_{N=C=S}$), 2852 ($\nu_{=C-H_2}$), 2929 (ν_{CH_2}). Anal. Calcd for $C_{37}H_{68}N_4O_2S_2$: C, 66.82; H, 10.31; N, 8.42. Found C, 66.94; H, 10.70; N, 7.63.

*N′-[1,3-Bis(2,3-dihydroxypropylthiocarbamoylamino)propan-2-yl]-N,N-ditetradecylbutanediamide (**12**).* 3-Amino-1,2-propanediol (40 mg, 0.44 mmol) was added to a solution of **11** (0.073 g, 0.11 mmol) in dry DMF (1.5 mL). The solution was stirred at RT for 2 h, then heated overnight (50 °C). The solvent was evaporated, and then the resulting oil was dissolved in dichloromethane (4 mL) and washed twice with brine (1 mL). The organic layer was dried ($MgSO_4$), filtrated, and evaporated. The crude was first purified by SPE (C8, 100% H_2 O to 100% CH_3CN then to 100% CH_3OH), then by SFC to yield **12** as a colorless oil (23 mg, 25%).^{1}H NMR ($CDCl_3$) δ (ppm): 0.88 (t, 6H, J = 6.6 Hz, CH_3), 1.26 (m, 44H, $-CH_2-$), 1.55 (m, 4H, $-CH_2-$), 2.52 (t, 2H, J = 6.0 Hz, CH_2CO), 2.68 (t, 2H, J = 6.0 Hz, $-CH_2CO$), 3.11 (t, 2H, J = 7.5 Hz, $-CH_2N$), 3.18 (t, 2H, J = 7.5 Hz, $-CH_2N$), 3.21 (m, 2H, CH_2NCS), 3.39 (m, 4H, CH_2NCS), 3.53 (m, 6H, CH_2NCS, CH_2OH), 3.77 (t, 2H, J = 4.5 Hz, CHOH), 3.87 (m, 1H, CH), 6.97 (t, 1H, J = 6.0 Hz, NH). ^{13} C NMR ($CDCl_3$) δ (ppm) 14.05 (s, CH_3), 22.70 (s, $-CH_2-$), 27.02 (s, $-CH_2-$), 27.81 (s, $-CH_2-$), 28.93 (s, $-CH_2CO$), 29.66 (m, $-CH_2-$), 31.68 (s, CH_2CO), 31.91 (s, $-CH_2-$), 44.46 (s, CH_2NCS), 46.18 (s, CH_2NCS), 46.58 and 48.29 (2s, CH_2N), 53.12 (s, CH), 63.44 (s, CH_2OH), 70.93 (s, CHOH), 171.66 (s, C═O), 174.76 (s, C═O).

*Ditetradecylcarbamoylmethoxyacetic Acid (**13a**).* Glycolic anhydride (6.3 g, 53.8 mmol) was added to a solution of ditetradecylamine **6a** (8.8 g, 21.5 mmol) and DMAP (1.3 g, 10.7 mmol) in dichloromethane (200 mL). The solution was stirred for 18 h at RT; then, the reaction mixture was diluted with dichloromethane and washed successively with 1 N HCl (3 times) and brine (3 times), then dried ($MgSO_4$). Acid **13a** was isolated as a white solid after removal of the solvent (11.3 g, 100%). Mp 62 °C. ^{1}H NMR ($CDCl_3$) δ (ppm): 0.87 (t, 6H, J = 6.9 Hz, CH_3), 1.25 (m, 44H, $-CH_2-$), 1.54 (m, 2H, $-CH_2-$), 3.08 (t, 2H, J = 7.5 Hz, $-CH_2N$), 3.34 (t, 2H, J = 7.5 Hz, $-CH_2N$), 4.21 (s, 2H, CH_2CO), 4.38 (s, 2H, CH_2CO). ^{13}C NMR ($CDCl_3$) δ (ppm): 14.13 (s, CH_3), 22.72 (s, $-CH_2-$), 27.01 (s, $-CH_2-$), 28.71 (s, $-CH_2-$), 29.68 (m, $-CH_2-$), 31.97 (s, $-CH_2-$), 46.95 (s, $-CH_2N$), 71.21 (s, CH_2O), 72.87 (s, CH_2O), 170.69 (s, C═O), 172.03 (s, C═O). MS (ESI, m/z) 527 $(M + H)^+$, 95% purity by ELSD.

*Didodecylcarbamoylmethoxyacetic Acid (**13b**).* Glycolic anhydride (1.6 g, 14.1 mmol) was added to a solution of bis-dodecylamine **6b** (8.8 g, 21.5 mmol) and DMAP (0.17 g, 1.4 mmol) in dichloromethane (20 mL). The solution was stirred for 23 h and was treated as for **13a**. SFC purification gave **13b** as a white solid (1.1 g, 84%). Mp 55 °C. ^{1}H NMR ($CDCl_3$) δ (ppm): 0.88 (t, 6H, J = 6.6 Hz, CH_3), 1.26 (m, 36H, $-CH_2-$), 1.55 (t, 2H, J = 6.9 Hz, $-CH_2-$), 3.08 (t, 2H, J = 7.5 Hz, $-CH_2N$), 3.35 (t, 2H, J = 7.5 Hz, $-CH_2N$), 4.21 (s, 2H, CH_2O), 4.38 (s, 2H, CH_2O). ^{13}C NMR ($CDCl_3$) δ (ppm): 14.18 (s, CH_3), 22.76 (s, $-CH_2-$), 27.02 (s, $-CH_2-$), 27.51 (s, $-CH_2-$), 29.70 (m, $-CH_2-$), 31.98 (s, $-CH_2-$), 46.98 (s, $-CH_2N$), 71.32 (s, CH_2O), 73.15 (s, CH_2O), 170.68 (s, C═O), 174.13 (s, C═O). MS (ESI, m/z) 470 $(M + H)^+$, 100% purity by ELSD. Anal. Calcd for $C_{28}H_{56}NO_4$: C, 71.59; H, 11.80; N, 2.98. Found C, 70.26; H, 11.65; N, 2.78.

*Didecylcarbamoylmethoxyacetic Acid (**13c**).* Glycolic anhydride (4.7 g, 40 mmol) was added to a solution of didecylamine **6c** (3.0 g, 10 mmol) and DMAP (0.6 g, 5 mmol) in dichloromethane (100 mL). The solution was stirred for 20 h at RT and was treated as for **13a** to yield **13c** as a white solid (4.14 g, 100%). Mp 55 °C. ^{1}H NMR ($CDCl_3$) δ (ppm): 0.85 (t, 6H, J = 6.0 Hz, CH_3), 1.25 (m, 28H, $-CH_2-$), 1.53 (m, 4H, $-CH_2-$), 3.08 (t, 2H, J = 7.3 Hz, $-CH_2N$), 3.33 (t, 2H, J = 7.3 Hz, $-CH_2N$), 4.19 (s, 2H, CH_2O), 4.39 (s, 2H, CH_2O). ^{13}C NMR ($CDCl_3$) δ (ppm): 14.08 (s, CH_3), 22.69 (s, $-CH_2-$), 26.85 (s, $-CH_2-$), 27.45 (s, $-CH_2-$), 28.67 (s, $-CH_2-$), 29.30 (m, $-CH_2-$), 29.51 (s, $-CH_2-$), 31.89 (s, $-CH_2-$), 46.93 (s, $-CH_2N$), 71.20 (s, $-CH_2O$), 72.78 (s, $-CH_2O$), 170.7 (s, C═O), 171.1 (s, C═O). MS (ESI, m/z) 414 $(M + H)^+$. HPLC purity 100% by ELSD. Anal. Calcd for $C_{24}H_{47}NO_4$: C, 69.69; H, 11.22; N, 3.30. Found C, 69.00; H, 11.35; N, 3.39.

*N,N-Bis(azidomethyl)-2-(ditetradecylcarbamoylmethoxy)acetamide (**14a**).* A solution of DCC (0.16 g, 0.75 mmol) in dichloromethane (1 mL) was added to a solution of **13a** (4.0 g, 7.6 mmol) and **5** (1.1 g, 8 mmol) in dichloromethane (50 mL). The reaction mixture was stirred overnight, and then diethyl ether (70 mL) was added. The resulting suspension was filtered through a celite pad; then, the solvent was evaporated under reduced pressure to yield a crude oil that was first purified by SFC and then dissolved in THF (20 mL/mmol). Amberlyst-21 (4 equiv) was added to remove the acid excess. The resin was removed by filtration, and then the solvent was evaporated under reduced pressure. The amide **14a** was isolated as an oil (4.9 g, 98%). ^{1}H NMR ($CDCl_3$) δ (ppm): 0.87 (t, 6H, J = 6.6 Hz, CH_3), 1.25 (m, 44H, $-CH_2-$), 1.52 (m, 4H, $-CH_2-$), 3.06 (t, 2H, J = 7.5 Hz, $-CH_2N$), 3.31 (t, 2H, J = 7.5 Hz, $-CH_2N$), 3.47 (dd, 4H, J = 6.0 Hz, J = 12.3 Hz, CH_2N_3), 3.55 (dd, 4H, J = 5.7 Hz, J = 12.3 Hz, CH_2N_3), 4.10 (s, 2H, CH_2O), 4.17 (m, 1H, CH), 4.27 (s, 2H, CH_2O), 8.75 (d, 1H, J = 8.4 Hz, NH). ^{13}C NMR ($CDCl_3$) δ (ppm): 14.13 (s, CH_3), 22.73 (s, $-CH_2-$), 27.06 (s, $-CH_2-$), 27.64 (s, $-CH_2-$), 29.70 (m, $-CH_2-$), 31.98 (s, $-CH_2-$), 46.45 and 46.91 (2s, CH_2N), 48.44 (s, CH), 51.54 (s, CH_2N_3), 70.33 (s, CH_2O), 72.68 (s, CH_2O), 168.70 (s, C═O), 170.30 (s, C═O). MS (ESI, m/z) 650 $(M + H)^+$, 695 $(M + HCOO)^-$. HPLC purity 94% by ELSD. Anal. Calcd for $C_{35}H_{68}N_8O_3$: C, 64.78; H, 10.56; N, 17.27. Found C, 64.84; H, 10.71; N, 16.91.

*N,N-Bis(azidomethyl)-2-(didodecylcarbamoylmethoxy)acetamide (**14b**).* *N*-Hydroxysuccinimide (0.12 mg, 1.06 mmol) and DCC (0.55 g, 2.65 mmol) were added to a solution of acid **13b** (0.50 g, 1.06 mmol) in dry THF (10 mL). The reaction mixture was stirred for 2 h at RT; then, a solution of **5** (0.13 mg, 0.89 mmol) in THF (2 mL) was added, and the stirring was followed during 19 h. The suspension was evaporated under reduced pressure, diluted with ethyl acetate, and washed successively with water and brine. The organic layer was dried ($MgSO_4$) and evaporated. The crude was purified by SFC to afford **14b** as a yellow oil (0.51 g, 81%). ^{1}H NMR ($CDCl_3$) δ (ppm): 0.88 (t, 6H, J = 6.6 Hz, CH_3), 1.26 (m, 36H, $-CH_2-$), 1.50 (t, 4H, J = 6.9 Hz, $-CH_2-$), 3.04 (t, 2H, J = 7.5 Hz, $-CH_2N$), 3.30 (t, 2H, J = 7.5 Hz, $-CH_2N$), 3.45 (dd, 4H, J = 6.0 Hz, J = 12.3 Hz, CH_2N_3), 3.53 (dd, 4H, J = 6.0 Hz, J = 12.3 Hz, CH_2N_3), 4.09 (s, 2H, CH_2O), 4.20 (m, 1H, CH), 4.25 (s, 2H, CH_2O), 8.70 (d, 1H, J = 8.4 Hz, NH). ^{13}C NMR ($CDCl_3$) δ (ppm): 14.12 (s, CH_3), 22.72 (s, $-CH_2-$), 27.04 (s, $-CH_2-$), 27.62 (s, $-CH_2-$), 29.70 (m, $-CH_2-$), 31.95 (s, $-CH_2-$),

46.42 (s, $-CH_2N$), 46.89 (s, CH_2N), 48.43 (s, CH), 51.51 (s, CH_2N_3), 70.30 (s, CH_2O), 72.63 (s, CH_2O), 168.68 (s, C═O), 170.28 (s, C═O). Anal. Calcd for $C_{31}H_{60}N_8O_3$: C, 62.80; H, 10.20. Found C, 63.37; H, 10.31.

*N,N-Bis(azidomethyl)-2-(didecylcarbamoylmethoxy)acetamide (**14c**).* A solution of DCC (2.3 g, 11.1 mmol) in dichloromethane (25 mL) was added to solution of **13c** (3.0 g, 7.4 mmol) and **5** (1.1 g, 7.7 mmol) in dichloromethane (20 mL). The reaction mixture was stirred overnight, and then diethyl ether (50 mL) was added. The resulting suspension was filtered through a celite pad, and then the solvent was evaporated under reduced pressure. The crude oil that was purified by SFC to yield **14c** as an oil (2.3 g, 58%). ^{1}H NMR ($CDCl_3$) δ (ppm): 0.88 (t, 6H, J = 6.0 Hz, CH_3), 1.25 (m, 28H, $-CH_2-$), 1.51 (m, 4H, $-CH_2-$), 3.05 (t, 2H, J = 7.3 Hz, $-CH_2N$), 3.31 (t, 2H, J = 7.3 Hz, CH_2N), 3.47 (dd, 2H, J = 6.0 Hz, CH_2N_3), 3.55 (dd, 2H, J = 6.0 Hz, CH_2N_3), 4.10 (s, 2H, CH_2O), 4.22 (m, 1H, CH), 4.27 (s, 2H, CH_2O), 8.77 (d, 1H, J = 8.4 Hz, NH). ^{13}C NMR ($CDCl_3$) δ (ppm): 14.12 (s, CH_3), 22.71 (s, $-CH_2-$), 26.94 (s, $-CH_2-$), 27.63 (s, $-CH_2-$), 28.94 (s, CH_2NH_2), 29.36 (m, $-CH_2-$), 29.56 (s, $-CH_2-$), 31.92 (s, $-CH_2-$), 46.43 and 46.90 (2s, CH_2N), 48.42 (s, CH), 51.52 (s, CH_2N_3), 70.31 (s, CH_2O), 72.65 (s, CH_2O), 168.65 (s, C═O), 170.25 (s, C═O). MS (ESI, *m*/*z*) 537 $(M + H)^+$, 559 $(M + Na)^+$. Anal. Calcd for $C_{27}H_{52}N_8O_3$: C, 60.42; H, 9.76; N, 20.73. Found C, 60.64; H, 9.88; N, 20.73.

*N,N-Ditetradecyl-2-(1,3-diaminopropan-2-ylcarbamoylmethoxy)acetamide (**15a**).* A round-bottom flask was charged with **14a** (0.5 g, 0.77 mmol), ethanol (10 mL), Pd/C (0.075 g), and hydrogen. The suspension was stirred overnight at RT, and then the mixture was filtered through celite to yield after evaporation the diamine **15a** (0.45 g, 97%) as a colorless oil. ^{1}H NMR ($CDCl_3$) δ (ppm): 0.88 (t, 6H, J = 6.0 Hz, CH_3), 1.26 (m, 44H, $-CH_2-$), 1.53 (m, 4H, $-CH_2-$), 2.55 (m, 4H, NH_2), 2.71−2.87 (m, 4H, CH_2NH_2), 3.08 (t, 2H, J = 7.5 Hz, $-CH_2N$), 3.30 (t, 2H, J = 7.5 Hz, $-CH_2N$), 3.93 (m, 1H, CH), 4.09 (d, J = 7.5 Hz, CH_2O), 4.25 (d, J = 7.5 Hz, CH_2O), 8.21 (d, 1H, J = 8.4 Hz, NH). ^{13}C NMR ($CDCl_3$) δ (ppm): 14.09 (s, CH_3), 22.69 (s, $-CH_2-$), 27.02 (s, $-CH_2-$), 27.62 (s, $-CH_2-$), 29.66 (m, $-CH_2-$), 31.94 (s, $-CH_2-$), 43.69 (s, CH_2NH_2), 46.28 and 46.89 (2s, $-CH_2N$), 53.25 (s, CH), 69.63 (s, CH_2O), 72.10 (s, CH_2O), 168.70 (s, C═O), 170.30 (s, C═O). Anal. Calcd for $C_{35}H_{72}N_4O_3$: C, 66.62; H, 11.82; N, 8.88. Found C, 67.02; H, 12.03; N, 7.85.

*N,N-Didodecyl-2-(1,3-diaminopropan-2-ylcarbamoylmethoxy)acetamide (**15b**).* A round-bottom flask was charged with **14b** (0.50 g, 0.77 mmol), ethanol (10 mL), Pd/C (0.075 g), and hydrogen. The suspension was stirred overnight RT, and then the mixture was filtered through celite to yield after evaporation the diamine **15b** (0.45 g, 97%) as a colorless oil. ^{1}H NMR ($CDCl_3$) δ (ppm): 0.85 (t, 6H, J = 6.6 Hz, CH_3), 1.24 (m, 36H, $-CH_2-$), 1.49 (m, 4H, $-CH_2-$), 3.06 (m, 4H, CH_2NH_2), 3.26 (m, 4H, $-CH_2N$), 3.94 (m, 4H, CH), 4.09 (s, 2H, CH_2O), 4.26 (s, 2H, CH_2O), 8.41 (d, 1H, J = 8.4 Hz, NH). ^{13}C NMR ($CDCl_3$) δ (ppm): 14.11 (s, CH_3), 22.71 (s, $-CH_2-$), 26.99 (s, $-CH_2-$), 27.70 (s, $-CH_2-$) 29.40 (m, $-CH_2-$), 31.96 (s, $-CH_2-$), 42.42 (s, CH_2NH_2), 46.32 (s, $-CH_2N$), 46.99 (s, $-CH_2N$), 51.12 (s, CH), 69.64 (s, CH_2O), 71.82 (s, CH_2O), 168.53 (s, C═O), 170.01 (s, C═O).

*N,N-Didecyl-2-(1,3-diaminopropan-2-ylcarbamoylmethoxy)-acetamide (**15c**).* A round-bottom flask was charged with **14c** (2.3 g, 4.3 mmol), ethanol (70 mL), Pd/C (0.3 g), and hydrogen. The suspension was stirred overnight RT, and then the mixture was filtered through celite to yield after evaporation the diamine **15c** (1.5 g, 72%) as a colorless oil. ^{1}H NMR ($CDCl_3$) δ (ppm): 0.84 (t, 6H, J = 6.0 Hz, CH_3), 1.25 (m, 28H, $-CH_2-$), 1.48 (m, 4H, $-CH_2-$), 1.77 (m, 4H, NH_2), 2.54 (dd, 1H, J = 6.0 Hz, J = 12.0 Hz, CH_2NH_2), 2.71 (dd, 1H, J = 5.8 Hz, J = 12.6 Hz, CH_2NH_2), 3.05 (t, 2H, J = 7.3 Hz, $-CH_2N$), 3.26 (m, 3H, $-CH_2N$, CH), 3.39 (s, 2H, CH_2O), 4.05 (s, 2H, CH_2O), 8.20 (m, 1H, NH). ^{13}C NMR ($CDCl_3$) δ (ppm): 14.11 (s, CH_3), 22.69 (s, $-CH_2-$), 26.94 (s, $-CH_2-$), 27.66 (s, $-CH_2-$), 28.98 (s, $-CH_2-$), 29.35 (m, $-CH_2-$), 29.55 (s, $-CH_2-$), 31.90 (s, $-CH_2-$), 43.46 (s, CH_2NH_2), 46.28 and 46.90 (2s, CH_2N), 53.35 (s, CH), 69.78 (s, CH_2O), 72.15 (s, CH_2O), 168.65 (s, C═O), 170.25 (s, C═O). Anal. Calcd for $C_{27}H_{56}N_4O_3$: C, 69.37; H, 12.06; N, 8.67. Found C, 69.39; H, 11.63; N, 9.89.

*4-Isothiocyanatomethyl-2,2-dimethyl-(1,3)-dioxolane (**16**).* A solution of DCC (3.2 g, 15.5 mmol) and carbon disulfide (6.3 mL, 104 mmol) in THF (10 mL) was cooled to −5 °C by an ice/NH_4Cl (4:1, v/v) bath. Then, 2,2-dimethyl-1,2-dioxolan-4-methanamide (2.0 g, 15.5 mmol) diluted in dichloromethane (7 mL) was added dropwise. The reaction mixture was stirred for 4 h at RT. Then, the suspension was filtered, and the filtrate was concentrated and treated with diethylether. The suspension was again filtered, and the filtrate was concentrated. After purification by flash chromatography (heptane/ethyl acetate 8:2), **16** was obtained as a clear liquid (2.2 g, 85%). ^{1}H NMR ($CDCl_3$) δ (ppm): 1.31 (s, 3H, CH_3), 1.42 (s, 3H, CH_3), 3.54 (dd, 1H, J = 5.1 Hz, J = 15.0 Hz, CH_2NCS), 3.64 (dd, 1H, J = 5.1 Hz, J = 15.0 Hz, CH_2NCS), 3.80 (dd, J = 5.1 Hz, J = 8.7 Hz, CH_2O), 4.07 (dd, J = 6.3 Hz, J = 8.7 Hz, CH_2O), 4.26 (q, 1H, J = 5.3 Hz, CHO). ^{13}C NMR ($CDCl_3$) δ (ppm): 25.24 (s, CH_3), 26.85 (s, CH_3), 47.47 (s, CH_2NCS), 66.69 (s, CH_2O), 73.76 (s, CHO), 110.49 (s, $CO_2(CH_3)_3$), 133.12 (s, C═S). MS (ESI, *m*/*z*) 174 $(M + H)^+$. Anal. Calcd for $C_7H_{11}NO_2S$: C, 48.53; H, 6.40; N, 8.09; S, 18.51. Found C, 48.54; H, 6.52; N, 8.09; S, 18.51.

*2-[1,3-Bis[(2,2-dimethyl-1,3-dioxolan-4-yl)methylthiocarbamoylamino]propan-2-ylcarbamoyl-methoxy]-N,N-ditetradecylacetamide (**17a**).* Isothiocyanate **16** (0.22 g, 1.25 mmol) was added to a solution of diamine **15a** (0.24 g, 0.5 mmol) and *N,N*-diisopropylethylamine (0.87 mL, 5 mmol) in dichloromethane (4 mL). The solution was stirred overnight at RT. The solvent was evaporated under reduced pressure, and then the crude was purified by SFC (standard condition then acetone) to yield **17a** (0.37 g, 66%) as a colorless oil. ^{1}H NMR ($CDCl_3$) δ (ppm): 0.86 (t, 6H, J = 6.6 Hz, CH_3), 1.26 (m, 44H, $-CH_2-$), 1.32 (s, 6H, CH_3), 1.42 (s, 6H, CH_3), 1.50 (m, 4H, $-CH_2-$), 3.08 (t, 2H, J = 7.2 Hz, CH_2NCO), 3.20 (t, 2H, J = 7.2 Hz, CH_2N), 3.67−3.83 (m, 8H, CH_2NCS, H-8), 4.02−4.10 (m, 6H, H-3, CH_2O), 4.29 (m, 7H, CH_2O, CH, CHO), 7.7 (m, 4H, NH). ^{13}C NMR ($CDCl_3$) δ (ppm): 13.98 (s, CH_3), 22.59 (s, $-CH_2-$), 25.27 and 26.85 (2s, CH_3), 27.62 (s, $-CH_2-$), 28.91 (s, $-CH_2-$), 29.66 (m, $-CH_2-$), 31.84 (s, $-CH_2-$), 44.73 (m, CH_2NCS), 46.57 and 46.59 (2s, CH_2NCO), 54.29 (s, CH), 68.86 (s, CH_2O), 69.81 (s, CH_2O), 71.79 (s, CH_2O), 74.30 (s, CHO), 109.47 (s, $CO_2(CH_3)_3$), 168.33 (s, C═O), 171.78 (s, C═O), 183.18 (s, C═S). MS (ESI, *m*/*z*) 944 $(M + H)^+$, 966 $(M + Na)^+$. HPLC purity 96% by ELSD. Anal. Calcd for $C_{49}H_{94}N_6O_7S_2$: C, 62.38; H, 10.04; N, 8.91; S, 6.80. Found C, 61.83; H, 10.21; N, 8.64; S, 5.94.

*2-[1,3-Bis[(2,2-dimethyl-1,3-dioxolan-4-yl)methylthiocarbamoylamino]propan-2-ylcarbamoylmethoxy]-N,N-didodecylacetamide (**17b**).* Isothiocyanate **16** (0.087 g, 0.5 mmol) was added to solution of diamine **15b** (0.11 g, 0.2 mmol) and *N,N*-diisopropylethylamine (0.35 mL, 2 mmol) in dichloromethane (2 mL). The solution was stirred overnight at RT. The solvent was evaporated under reduced pressure, and then the crude was purified by SFC (standard condition then acetone) to yield **17b** (0.11 g, 62%) as a colorless oil. ^{1}H NMR ($CDCl_3$) δ (ppm): 0.87 (t, 6H, J = 6.0 Hz, CH_3), 1.26 (m, 36H, $-CH_2-$), 1.33 (s, 6H, CH_3), 1.41 (s, 6H, CH_3), 1.52 (m, 4H, $-CH_2-$), 3.09 (t, 2H, J = 7.0 Hz, $-CH_2NCO$), 3.30 (t, 2H, J = 7.0 Hz, $-CH_2NCO$), 3.67−3.80 (m, 8H, CH_2NCS), 4.08 (m, 6H, CH_2O), 4.29

(m, 7H, CH_2O, CH, CHO), 7.68 (m, 4H, NH). ^{13}C NMR ($CDCl_3$) δ (ppm): 14.15 (s, CH_3), 22.74 (s, $-CH_2-$), 25.41 and 26.98 (2s, CH_3), 27.77 (s, $-CH_2-$), 29.06 (s, $-CH_2-$), 29.68 (m, $-CH_2-$), 31.98 (s, $-CH_2-$), 40.05 (s, CH_2NCS), 46.72 and 47.17 (2s, CH_2NCO), 49.56 (s, CH), 66.97 (s, CH_2O), 70.08 (s, CH_2O), 72.06 (s, CH_2O), 74.43 (s, CHO), 109.64 (s, $CO_2(CH_3)_3$), 168.68 (s, C═O), 171.15 (s, C═O), 183.05 (s, C═S). MS (EI, *m/z*) 887 $(M + H)^+$, 886 $(M - H)^-$, 934 $(M + Cl)^-$. Anal. Calcd for $C_{45}H_{86}N_6O_7S_2$: C, 60.91; H, 9.77; N, 9.47; S, 7.23. Found C, 61.05; H, 10.21; N, 9.81; S, 6.93.

*2-[1,3-Bis[(2,2-dimethyl-1,3-dioxolan-4-yl)methylthiocarbamoylamino]propan-2-ylcarbamoylmethoxy]-N,N-didecylacetamide (**17c**).* Isothiocyanate **16** (0.22 g, 0.45 mmol) was added to solution of diamine **15c** (0.24 g, 0.5 mmol) and *N,N*-diisopropylethylamine (0.87 mL, 5 mmol) in dichloromethane (2 mL). The solution was stirred overnight. The solvent was evaporated under reduced pressure, and then the crude was purified by SFC (standard condition then acetone) to yield **17c** (0.11 g, 62%) as a colorless oil. ^1H NMR ($CDCl_3$) δ (ppm): 0.85 (t, 6H, $J = 6.6$ Hz, CH_3), 1.23 (m, 28H, $-CH_2-$), 1.30 (s, 3H, CH_3), 1.39 (s, 3H, CH_3), 1.49 (m, 4H, $-CH_2-$), 3.06 (t, 2H, $J = 7.2$ Hz, $-CH_2NCO$), 3.27 (t, 2H, $J = 7.2$ Hz, $-CH_2$-NCO), 3.68 (m, 8H, CH_2NCS), 4.04 (m, 6H, CH_2O), 4.25 (m, 7H, CH_2O, CH, CHO). ^{13}C NMR ($CDCl_3$) δ (ppm): 14.12 (s, CH_3), 22.70 (s, $-CH_2-$), 25.39 and 26.95 (2s, CH_3), 26.95 (s, $-CH_2-$), 27.72 (s, $-CH_2-$), 29.57 (m, $-CH_2-$), 31.91 (s, $-CH_2-$), 40.02 (s, CH_2NCS), 46.64 and 47.11 (2s, CH_2NCO), 51.30 (s, CH), 66.92 (s, CH_2O), 69.95 (s, CH_2O), 71.89 (s, CH_2O), 74.43 (s, CHO), 109.55 (s, $CO_2(CH_3)_3$), 168.56 (s, C═O), 171.05 (s, C═O), 182.78 (s, C═S). MS (ESI, *m/z*) 829 $(M - H)^-$, 831 $(M + H)^+$, 853 $(M + Na)^+$. Anal. Calcd for $C_{41}H_{78}N_6O_7S_2$: C, 59.24; H, 9.46; N, 10.11. Found C, 59.29; H, 9.60; N, 9.42.

*N-[1,3-Bis(2,3-dihydroxypropylthiocarbamoylamino)propan-2-yl]-2-(ditetradecylcarbamoylmethoxy)acetamide (**18a**).* 1 N Hydrochloric acid (1.3 mL) was added to a solution of **17a** (0.13 g, 0.13 mmol) in THF (1.3 mL). The reaction mixture was stirred for 3 h, and then most of the THF was evaporated under reduced pressure in a cold water bath. The resulting liquid was lyophilized to yield **18a** (0.1 g, 92%) as a white solid. Mp 50 °C. ^1H NMR ($CDCl_3$) δ (ppm): 0.86 (t, 6H, $J = 6.6$ Hz, CH_3), 1.24 (m, 44H, $-CH_2-$), 1.51 (m, 4H, $-CH_2-$), 3.06 (t, 2H, $J = 7.2$ Hz, CH_2NCO), 3.28 (m, 4H, H-1 CH_2NCO, CH_2NCS), 3.46 (m, 4H, CH_2NCS), 3.55−3.67 (m, 6H, CH_2NCS, CH_2-OH), 3.80 (m, 2H, CHOH), 4.08 (s, 2H, CH_2O), 4.17 (m, 1H, CH), 4.25 (s, 1H, CH_2O), 7.32−7.53 (m, 4H, NH), 8.29 (t, $J = 8.4$ Hz, 1H, NH). ^{13}C NMR ($CDCl_3$) δ (ppm): 14.00 (s, CH_3), 22.61 (s, $-CH_2-$), 27.00 (s, $-CH_2-$), 28.89 (s, $-CH_2-$), 29.66 (m, $-CH_2-$), 31.86 (s, $-CH_2-$), 40.31 (s, CH_2NCS), 40.81 (s, CH_2NCS), 46.73 and 46.96 (2s, CH_2NCO), 49.43 (s, CH), 64.03 (s, CH_2OH), 69.64 (s, CH_2O), 71.17 (s, CHOH), 71.85 (s, CH_2O), 168.39 (s, C═O), 170.61 (s, C═O), 183.53 (s, C═S). Anal. Calcd for $C_{43}H_{86}N_6O_7S_2$: C, 59.82; H, 10.04; N, 9.73; S, 7.43. Found C, 58.11; H, 9.64; N, 9.17; S, 6.16. HR-ESMS calcd for $C_{43}H_{86}N_6O_7NaS_2$: 885.5897. Found 885.5887.

*N-[1,3-Bis(2,3-dihydroxypropylthiocarbamoylamino)propan-2-yl]-2-(didodecylcarbamoylmethoxy)acetamide (**18b**).* 1 N Hydrochloric acid (0.5 mL) was added to a solution of **17b** (0.08 g, 0.09 mmol) in THF (0.5 mL). The reaction mixture was stirred for 2 h, and then most of the THF was evaporated under reduced pressure in a cold water bath. The resulting liquid was lyophilized to yield **18b** (0.08 g, 73%) as a colorless oil. ^1H NMR ($CDCl_3$) δ (ppm): 0.88 (t, 6H, $J = 6.0$ Hz, CH_3), 1.26 (m, 36H, $-CH_2-$), 1.53 (m, 4H, $-CH_2-$), 3.10 (m, 2H, $-CH_2$-NCO), 3.29 (m, 2H, $-CH_2NCO$), 3.62 (m, 8H, CH_2NCS), 3.92 (m, 1H, CH), 4.17 (m, 6H, CH_2O, CH_2OH), 4.34 (m, 6H, CH_2O, CHOH), 4.72 (m, 4H, OH), 7.60 (m, 4H, NH). ^{13}C NMR ($CDCl_3$) δ (ppm): 14.17 (s, CH_3), 22.76 (s, $-CH_2-$), 27.70 (s, $-CH_2-$), 28.91 (s, $-CH_2-$), 29.66 (m, $-CH_2-$), 32.00 (s, $-CH_2-$), 40.61 (s, CH_2NCS), 46.79 and 47.36 (2s, CH_2NCO), 49.94 (s, CH), 63.92 (s, CH_2OH), 69.32 (s, CH_2O), 71.13 (m, CH_2O, CHOH), 169.05 (s, C═O), 171.70 (s, C═O), 182.85 (s, C═S). Anal. Calcd for $C_{39}H_{78}N_6O_7S_2$: C, 58.03; H, 9.74. Found C, 56.13; H, 9.95. HR-ESMS calcd for $C_{39}H_{78}N_6O_7NaS_2$: 829.5271. Found 829.5245.

*N-[1,3-Bis(2,3-dihydroxypropylthiocarbamoylamino)propan-2-yl]-2-(didecylcarbamoylmethoxy)acetamide (**18c**).* 1 N Hydrochloric acid (0.5 mL) was added to a solution of **17c** (0.19 g, 0.23 mmol) in THF (2.1 mL). The reaction mixture was stirred for 3 h, and then most of the THF was evaporated under reduced pressure in a cold water bath. The resulting liquid was lyophilized to yield **18c** (0.17 g, 96%**)** as a colorless oil. ^1H NMR ($CDCl_3$) δ (ppm): 0.88 (t, 6H, $J = 6.0$ Hz, CH_3), 1.23 (m, 28H, $-CH_2-$), 1.54 (m, 4H, $-CH_2-$), 2.14 (s, 4H, OH), 3.09 (m, 2H, CH_2NCO), 3.30 (m, 2H, CH_2NCO), 3.63 (m, 8H, CH_2NCS), 3.92 (m, 1H, CH), 4.13 (m, 6H, CH_2O, CH_2OH), 4.31 (m, 7H, CH_2O, CHOH), 7.50 (m, 5H, NH). ^{13}C NMR ($CDCl_3$) δ (ppm): 14.18 (s, CH_3), 22.76 (s, $-CH_2-$), 27.02 (s, $-CH_2-$), 27.70 (s, $-CH_2-$), 29.45 (m, $-CH_2-$), 31.98 (s, $-CH_2-$), 40.36 (m, CH_2NCS), 46.83 and 47.32 (2s, $-CH_2$-NCO), 51.00 (s, CH), 63.98 (s, CH_2OH), 69.52 (s, CH_2O), 71.16 (m, CH_2O, CHOH), 169.28 (s, C═O), 171.92 (s, C═O), 183.38 (s, C═S). Anal. Calcd for $C_{35}H_{70}N_6O_7S_2$: C, 55.97; H, 9.39; N, 11.19; S, 8.54. Found C, 56.63; H, 9.59; N, 9.66; S, 5.94. HR-ESMS calcd for $C_{35}H_{70}N_6O_7NaS_2$: 773.4645. Found 773.4652.

*N′-[1,3-Bis(methylthiocarbamoylamino)propan-2-yl]-2-(didecylcarbamoylmethoxy)acetamide (**19**).* Methyl isothiocyanate (0.71 mL, 10.3 mmol) was added to solution of diamine **15c** (2.0 mg, 4.1 mmol) and triethylamine (0.58 mL, 4.13 mmol) in dichloromethane (41 mL). The solution was stirred overnight at RT. The solvent was evaporated and the crude was purified by SFC to yield **19** as an oil (2.35 g, 90%). ^1H NMR ($CDCl_3$) δ (ppm): 0.88 (t, 6H, $J = 6.0$ Hz, CH_3), 1.25 (m, 28H, $-CH_2-$), 1.52 (m, 4H, $-CH_2-$), 3.01 (s, 6H, CH_3NCS), 3.08 (t, 2H, $J = 7.3$ Hz, $-CH_2-$), 3.29 (m, 3H, $-CH_2-$), 3.40 (m, 1H, CH), 3.51−3.98 (m, 4H, CH_2NCS), 4.13 (s, 2H, CH_2O), 4.30 (s, 2H, CH_2O), 7.60 (m, 1H, NH), 8.54 (m, 4H, NH). ^{13}C NMR ($CDCl_3$) δ (ppm): 14.88 (s, CH_3), 22.79 (s, $-CH_2-$), 27.22 (s, $-CH_2-$), 27.80 (s, $-CH_2-$), 29.07 (s, $-CH_2-$), 29.44 (m, $-CH_2-$), 29.66 (s, $-CH_2-$), 32.01 (m, $-CH_2-$, CH_3NCS), 41.39 (s, CH_2NCS), 46.63 and 47.15 (2s, CH_2NCO), 50.96 (s, CH), 69.89 (s, CH_2O), 71.97 (s, CH_2O), 168.73 (s, C═O), 171.54 (s, C═O), 184.00 (s, C═S). MS (ESI, *m/z*) 631 $(M + H)^+$, 666 $(M + Cl)^-$, 676 $(M + HCOO)^-$. HPLC purity 98% by ELSD. Anal. Calcd for $C_{31}H_{62}N_6O_3S_2$: C, 59.01; H, 9.90; N, 13.32; S, 10.13. Found C, 59.85; H, 9.79; N, 13.13; S, 8.58.

Physicochemistry and Biology. *Liposome Preparation.* Lipids (and colipids if necessary) were dissolved in ethanol and were added dropwise to ten volumes of water under vigorous agitation. The mixture was stirred overnight and then evaporated under reduced pressure at RT to obtain a fairly concentrated solution of liposomes.

As an example, **18c** (5 mg, 6,4 μmol) was dissolved in 500 μL ethanol. This solution was added dropwise into 5 mL of stirred filtered water. The mixture was stirred overnight, then evaporated under reduced pressure at RT to obtain a clear suspension of **18c** (440 μL, 14.5 mM).

Size Measurement. Particle diameter was determined by dynamic light scattering on a Zeta Sizer NanoSeries Malvern (Malvern Instruments, France). Liposome concentration, 0.1 mM in H_2O, from the mean value of three runs is given (1 min equilibration, 3 min run).

Preparation of LPT−DNA Complexes. Plasmid pVax2 was used for transfection experiments. pVax2 is a derivative of the commercial plasmid pVax1 (InVitrogen), which was digested with the restriction enzymes HincII and BamHI to excise the promoter. The plasmid was then blunted with the Klenow fragment, dephosphorylated with alkaline phosphatase, pCM-Vbeta (Clontech), and was digested with EcoR1 and BamHI to excise the CMV promoter. The CMV promoter was blunted with Klenow enzyme and ligated into the blunted pVax1 to give pVax2. The plasmid pXL3031 (*26*) was digested with EcoRI and BamHI and then treated with the Klenow fragment to produce a blunted fragment containing the luciferase cDNA. This fragment was ligated into pVax2 after EcoRV digestion and phosphatase alkaline dephosphorylation to give pVax21−Luc (*27*). Plasmid (100 μL, 0.02 g/L in H_2 O) was added dropwise with constant vortexing to various amounts of LPT liposomes (in 100 μL H_2O) at RT. TU/P indicates the ratio in nanomoles of thiourea function (2 per lipid) versus nanomoles of DNA phosphates.

Gel Retardation Experiments. Samples were described as above (20 μL), and 5 μL of bromophenol blue was added. The mixture was loaded on a 0.8% agarose gel in TBE buffer (1 M Tris, 0.9 M boric acid, 0.01 EDTA) at 80 V/cm. DNA was revealed with ethidium bromide and visualized under UV light.

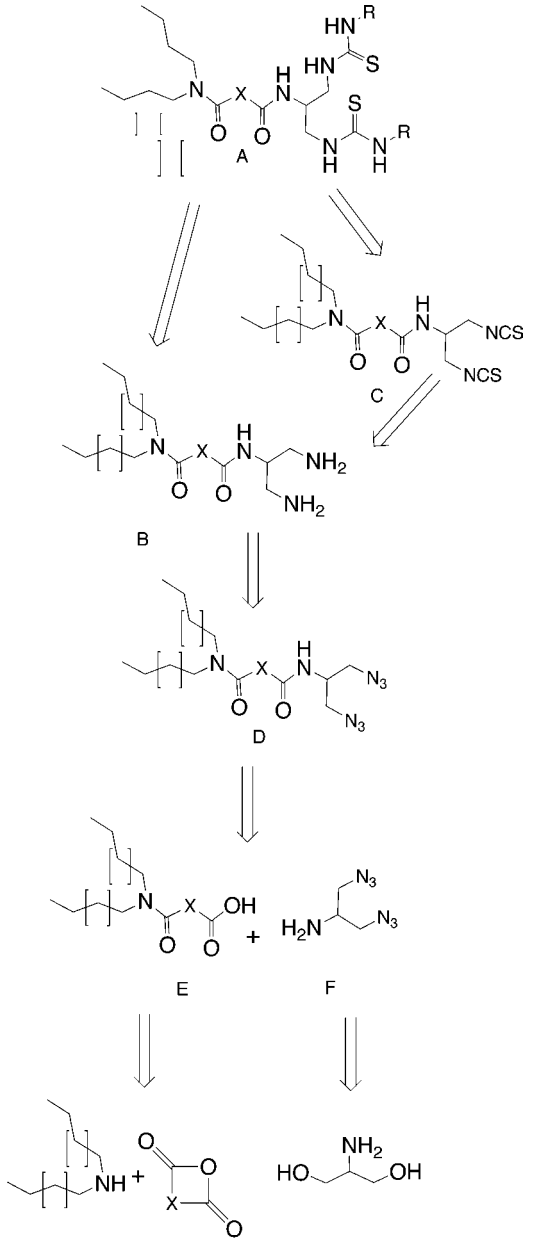
DNA Accessibility. LPT−DNA complexes (corresponding to 40 ng DNA) were loaded on a 96 well plate, and 100 μL of picogreen (diluted 200× in TBE) was added in each well. Fluorescence was measured by a Wallac Victor2 1420 Multilabel Counter Perkin-Elmer. Values are subtracted from the background and are expressed in percentage of the value of free DNA.

DNA Protection. 20 μL of culture medium (MEM with 10% or 50% murine fresh serum) were added on 20 μL of LPT−DNA complexes (0.1 g/L DNA). Samples were incubated at 37 °C. After 6 h, 10 μL of samples were frozen at −20 °C. After 24 h, all the samples were replaced at RT. SDS 2% (5 μL), EDTA (2 μL, 0.5 M), and bromophenol blue (3 μL) were added on each sample (10 μL). The mixture was loaded on agarose gel 1% containing 0.05% SDS at 80 V/cm. After 24 h washing in water, DNA was revealed with ethidium bromide and visualized under UV light.

Transfection Method. B16 murine melanoma cells were grown into DMEM supplemented with 10% fetal bovine serum, 1% antibiotics (penicillin and streptomycin), and 1% glutamine. One day before transfection, cells were treated by trypsin and deposited into 24 well plates (45 000 cells/well) and incubated 24 h at 37 °C in DMEM supplemented with 10% fetal bovine serum. 100 μL of LPT−DNA (corresponding to 0.5 μg DNA) complex was loaded on each well, and the plates were incubated at 37 °C for 48 h. Then, the cells were washed twice with PBS and treated with 200 μL of a passive lysis buffer (Promega). After 15 min, the cells were centrifuged for 5 min at 12 000 rpm. 10 μL of supernatant and 10 μL of iodoacetamide were deposited on a 96 well plate, which was incubated at 37 °C for 1 h. Protein quantification was performed with the BCA Protein Assay Kit (Pierce) and reported to the BSA taken as a reference curve. Luciferase activity was quantified using a commercial kit Luciferase Assay System (Promega). On 10 μL of the lysed cells, 50 μL of the luciferin substrate was injected via an injector, and the absorbance was read immediately at 563 nm on a Wallac Victor2 1420 Multilabel Counter from Perkin-Elmer.

Intratumoral Injection. LPT−DNA (40 μL, 10 μg DNA, 40 TU/P) was injected in the tumor of three mice C57BL6 bearing 3LL tumors. Mice were sacrificed 24 h after injection, then tumors were removed, weighed, crushed in 5 mL lysis buffer per tumor, and centrifuged for 10 min (12 000 tr/min, 4 °C). 50 μL of the supernatant was loaded on a 96 well plate, and luciferase activity was quantified using a commercial kit (Protein Assay). The luminescence was read on a Wallac Victor2 1420 Multilabel Counter from Perkin-Elmer.

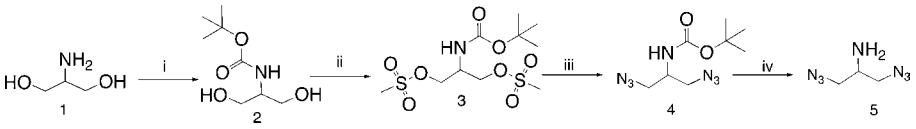
Scheme 1. Retrosynthetic Analysis of Lipopolythiourea Lipids



RESULTS AND DISCUSSION

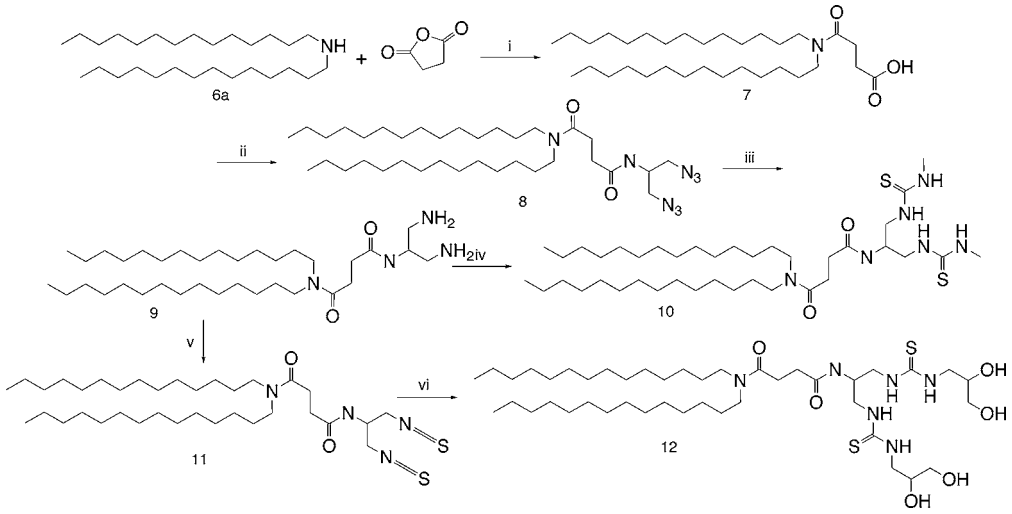
Chemistry. As we had previously established that two thiourea groups were enough for the lipid to properly interact with DNA, we kept an identical interacting lipid head, but we modified the linker and the lipid length in order to obtain lipids with a suitable hydrophilic−lipophilic balance. We chose to use a propane triamine scaffold that could be readily prepared from 2-amino-1,3-diazidopropane (*28*). The preparation of these compounds could be envisioned according to the retrosynthetic scheme shown in Scheme 1. Thiourea formation could occur either by the reaction of an isothiocyanate on diamine **B** or by the condensation of an amine on the bis-isothiocyanate **C**. Precursor **B** may be prepared by reduction of diazide **D**. The synthesis of **D** could be easily achieved by coupling acid **E**

Scheme 2 [a]



[a] (i) Boc_2O, EtOH, RT, 93%; (ii) MsCl, Et_3N, CH_2Cl_2, RT, quant.; (iii) NaN_3, DMF, 100 °C, quant.; (iv) TFA, CH_2Cl_2, RT, 96%.

Scheme 3 [a]



[a] (i) DMAP, pyridine, CH_2Cl_2, RT, 98%; (ii) DCC, **5**, CH_2Cl_2, RT, 98%; (iii) H_2, Pd/C, EtOH, RT, quant.; (iv) MeNCS, Et_3N, CH_2Cl_2, RT, 63%; (v) CS_2, DIPEA, TsCl, CH_2Cl_2, RT, 22%; (vi) 1-amino-2,3-propanediol, DMF/CH_2Cl_2, RT, 25%.

Table 1. Formulation Properties and log *P* Calculation of Lipopolythiourea

linker	terminus	LPT	anchor	log *P*	solubility	DPPC	diameter (nm)	PDI[a]
succinic	methyl	**10**	14 C	8.54	$CHCl_3$	1:1	72 ± 0.29	0.449
						1:2	205 ± 15	0.274
succinic	tetraol	**12**	14 C	6.91	$CHCl_3$	1:1	124 ± 35	0.261
glycolic	tetraol	**18a**	14 C	6.38	EtOH		89 ± 1	0.194
glycolic	tetraol	**18b**	12 C	4.79	EtOH		81 ± 16	0.237
glycolic	tetraol	**18c**	10 C	3.21	EtOH		70 ± 12	0.225
glycolic	methyl	**19**	10 C	4.84	EtOH		108 ± 1	0.158

[a] Polydispersity index.

with the amine **F**. **F** could be obtained in two steps from BOC-protected serinol via a sulfonylation/substitution protocol. Accordingly, disconnection of **E** gives the known dialkylamine and acid anhydride.

Therefore, we began the synthesis with the preparation of diazide **5** (Scheme 2), which was obtained in four steps from serinol.

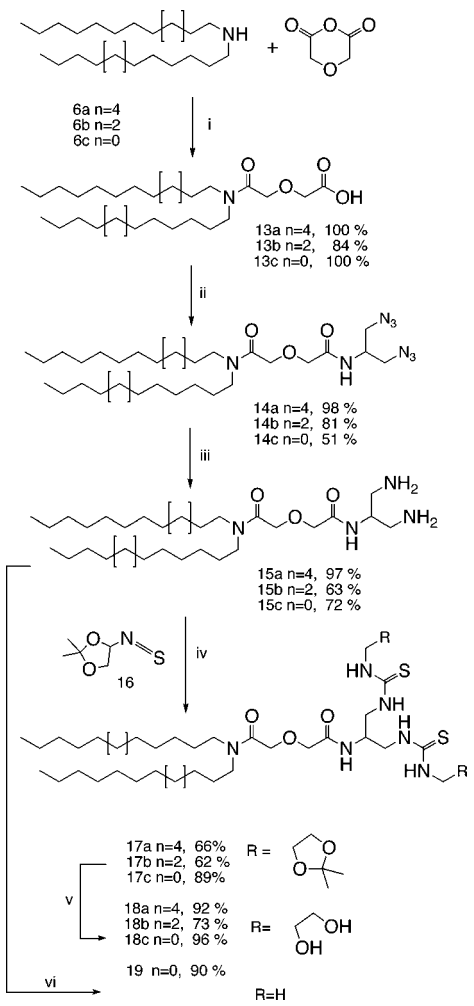
First, the amine was BOC protected; then, diol **2** was mesylated to yield **3** quantitatively. Substitution of the mesylate using sodium azide in DMF gave the diazide **4** whose BOC-protecting group was cleaved to afford **5** with an excellent global yield (89%). With the diazide **5** in hand, we turned our attention to the preparation of lipopolythioureas (Scheme 3). The synthesis started with the reaction of ditetradecylamine **6a** with succinic anhydride, which provided the acid **7** in 98% yield. Coupling **7** with the diazidoamine **5** was performed using various conditions. Both mixed-anhydride protocol using isobutyl chloroformate (*29*) and in situ preparation of the acid chloride using thionyl chloride and A-21 resin (*30*) afforded the amide **8** in 60% yield. However, DCC coupling offered higher yields (93%), and DCC/NHS was then selected for the syntheses. Catalytic hydrogenation of **8** gave the corresponding amine **9**. The first lipopolythio urea **10** was achieved by reaction of amine **9** with methyl isothiocyanate. Besides, treatment of **9** with carbon disulfide in the presence of tosyl chloride (*31*) afforded the bis-isothiocyanate **11**. The modest yield of this reaction could be explained by an intramolecular process leading to a cyclic thiourea as described by Marmillon et al. (*32*). However, no side product was isolated. Finally reaction of **11** with 1-amino 2,3-propanediol gave the lipopolythiourea **12** in 25% yield.

Concerning the preparation of the glycolic derivatives, the diamides **15a**, **15b**, and **15c** were prepared in three steps from the corresponding diamines similarly to **9** (Scheme 4). Regarding the low yields obtained in the last steps of the synthesis of **12**, a different strategy was used for the LPT formation in order to improve the reaction efficacy. **15a**, **15b**, and **15c** were treated with isothiocyanate **16** to afford the corresponding thioureas in 62% to 89% yields. Deprotection of **17a**, **17b**, and **17c** with 1 N hydrochloric acid in THF led to the tetraols **18a**, **18b**, and **18c** in good yields. In addition, the diamine **15a** was treated with methyl isothiocyanate to give the methyl thiourea **19** in 90% yield.

Formulation Characterization. The ability of lipopolythioureas (LPT) to form micellar or liposomal particles was then evaluated. Previous studies have indicated that LPT hydrophobicity prevents its solubilization in H_2O and particle formation (*22*). For this reason, phosphatidylcholine (DPPC) has been added as an amphiphilic colipid because of its high hydration potency and its zwitterionic nature.

Then, solubility of the LPT lipids in chloroform and ethanol was first evaluated. The aim of this test was to define the way for the lipid to be formulated and the necessity of adding a colipid. Data are reported in Table 1, in parallel to log *P* calculation. Both calculation and solubility were in agreement.

Scheme 4 [a]



[a] (i) DMAP, CH_2Cl_2, RT; (ii) DCC or DCC/NHS, CH_2Cl_2, RT; (iii) H_2, Pd/C, EtOH, RT; (iv) **6**, DIPEA, CH_2Cl_2, RT; (v) HCl, THF, RT; (vi) MeNCS, DIPEA, CH_2Cl_2, RT.

Indeed, the most lipophilic compounds **10** and **12**, bearing a succinic linker, exhibited a good solubility only in $CHCl_3$. Interestingly, comparison of compounds **12** and **18a** that differ only by an oxygen atom within the linker showed that this atom added interesting physicochemical properties despite the very close values of their log *P*. A more dramatic influence on log *P*, as well as solubility, was observed when the lipid length was reduced from myristyl to decanoyl, on the series of glycolic LPTs **18a**, **18b**, and **18c**. The glycolic LPT **19**, bearing a methyl group within the thiourea condensing head, clearly showed a higher log *P* as compared to its tetraol counterpart **18c**.

Next, we investigated the formulation of LPT with or without the use of the colipid DPPC. The formulations were performed using ethanolic injection, a gentle method leading spontaneously to small particles (see Material and Methods section). Data in Table 1 indicate that the formulation was also closely related to the log *P*. All the compounds under log $P = 6.4$ were soluble in ethanol and could be formulated without helper lipid. Above this value, LPT, namely, LPT with succinic linker **10** and **12**, required DPPC. A 1:1 ratio was found to be optimal for **12**, but the more lipophilic compound **10** required a higher amount of DPPC in order to obtain a homogeneous suspension as shown by the polydispersity index value (PDI). Formulation of the LPT led to liposomes with diameters ranging from 70 to 205 nm as measured by dynamic light scattering experiments. It is noteworthy that smaller particles were obtained for compounds **18a**, **18b**, and **18c**. These results clearly showed that structural changes of polar head, linker, and lipidic anchor had a real influence on the formulation properties of the resulting lipid.

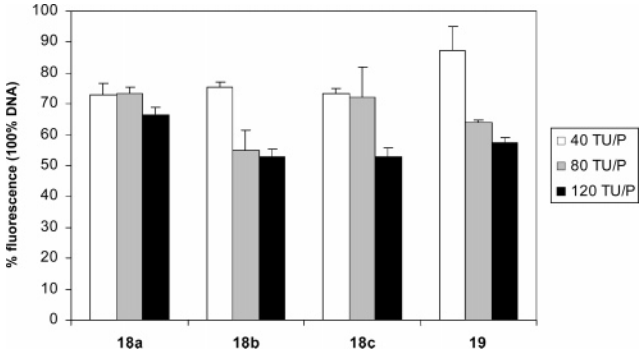


Figure 1. Accessibility of DNA in LPT/DNA complexes measured by picogreen fluorescence. Free DNA corresponds to 100% fluorescence. Measures for the free lipids were taken as the background. TU/P indicates the ratio of thiourea function per DNA phosphate.

LPT−DNA Interaction. The degree of DNA accessibility, once complexed with LPT, was assessed by the double-stranded-DNA-binding reagent picogreen. Fluorescence assays were performed using a fixed DNA amount and increasing the LPT equivalents. As observed in Figure 1, fluorescence decreased when the amount of lipids increased. However, the intensity was only half-reduced in comparison to the intensity observed with free DNA, even with a large excess of lipids (120 TU/P). This experiment means that DNA was still accessible to picogreen despite its interaction with the LPT. To evaluate if DNA was only partly associated to LPT, we loaded the complexes on an agarose gel (Figure 2). We could observe that all prepared LPT possessed the capacity to fully associate with DNA leading to LPT−DNA complexes, the required lipid amount depending on the LPT structure. Hence, lipopolythiourea **19** required more lipids to complex all DNA (40 TU/P) than compounds **18a, 18b**, and **18c**, which required a low ratio TU/P = 15 (Figure 1). From agarose gel retardation experiments, we observed that all prepared LPT totally retained DNA migration at a ratio TU/P = 15. On the other hand, DNA accessibility experiments suggested that LPT interaction with DNA led to a partially compacted structure that left free access for picogreen as previously described for sphingosine (*33*).

Lipoplex Sensitivity to Serum. DNA protection toward serum degradation was investigated in the absence and presence of LPT. After 30 min incubation at 37 °C in 10% serum containing medium, samples were treated by SDS and loaded on agarose gel containing 0.05% SDS (*34*) (Figure 3). In these conditions, free DNA was fully degraded in 24 h (lane 3), while DNA integrity was maintained in 10% serum when associated to LPT (TU/P = 40). Glycolic LPT presented the same capacity as cationic lipopolyamine RPR 209120 (*7*, *35*), taken as reference, to protect DNA (*36*). Same results have been previously found for the lipopolythiourea DTTU (*21*).

The same experiment performed with compound **18c** in 50% serum showed the ability for this lipid, as compared to free DNA, to partially protect DNA in these drastic conditions (data not shown). These data indicate that DNA is partly protected from degradation in serum-containing medium when associated to LPT. This favors the hypothesis of a strong interaction between LPT and DNA that might be mediated not only by the thiourea/phosphate interaction but also by the overall supramolecular lipid structure. These data may also suggest that the LPT−DNA complexes allow accessibility to small molecules like picogreen, but not to large ones, like DNases.

In Vitro Transfection Efficiency. We evaluated the lipids in vitro as a preliminary study for in vivo experiments. In this context, all lipids were tested in serum-containing media, which

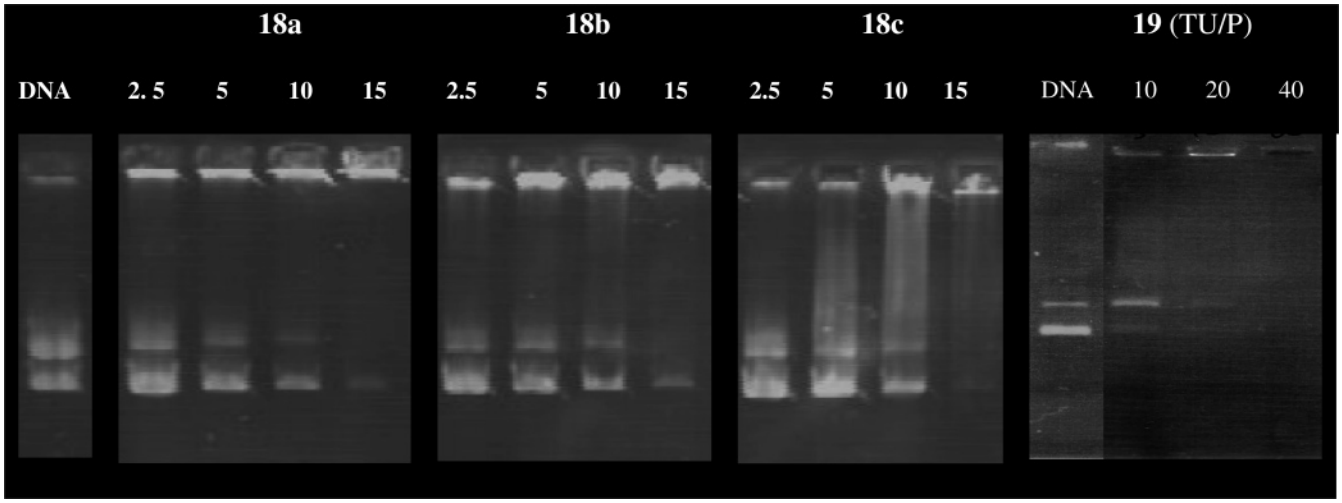


Figure 2. Migration of LPT/DNA complexes (**18a**, **18b**, **18c**, left; **19**, right) on a 0.8% agarose gel in TBE (1×). Complexes were revealed with ethidium bromide staining. From left to right, the lanes correspond to 2.5, 5, 10, and 15 TU/P.

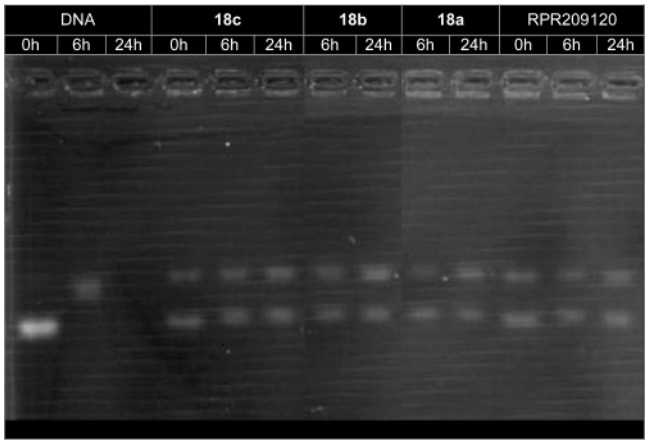


Figure 3. Complexes LPT/DNA (TU/P = 40) were incubated for 0, 6, or 24 h in 10% serum at 37 °C, then treated with SDS 2% and EDTA 0.5 M and loaded on an 1% agarose gel containing in TBE (1×) 0.05% SDS for electrophoresis (80 V/cm).

appears more appropriate (*37*). The lipopolythiourea transfection efficiency was tested on B16 cells at various TU/P ratios. The transfection efficiency of the LPT was compared to those of the cationic lipid and PEI (*38*). Results are presented in Figure 4 as well as the complex size, which might influence the result. Indeed, cationic complexes exhibit higher transfection capacity in serum when precipitated (*39*). Thus, PEI was formulated in NaCl and taken as a positive control. Although lipopolythiourea **18a** showed a poor transfection activity, compounds **18b** and **18c** led to a more significant transfection level. They proved to be comparable to the efficiency of the cationic systems of nanometric scales in these conditions, in particular, the lipoplex RPR209120/DNA, which exhibited a similar size as compared to LPT−DNA complexes. In addition, the transfection level was found to be dose-dependent. Furthermore, LPT **19** displayed the same activity as LPT **18c** with the same hydrophobic anchor. Thus, the length of the chain appeared to be decisive for transfection activity.

In Vivo Transfection Efficiency. Interestingly, intratumoral injection of the more efficient compounds as selected by in vitro experiments showed good transfection ability in vivo as compared to the lipopolyamine RPR209120 (Figure 5). No significant difference could be observed between the four samples, meaning that LPT are able to induce gene expression in vivo as well as in this cationic system.

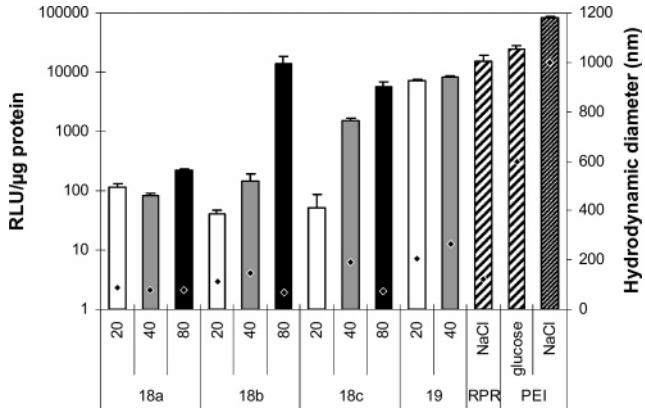


Figure 4. Hydrodynamic diameter (lozenge symbols, right scale) and gene transfection (bars, left scale) measured by luciferase activity of LPT/DNA complexes at 20, 40, and 80 TU/P ratios after 48 h incubation on B16 cells in the presence of serum. LPT/DNA complexes were prepared at 20, 40, and 80 TU/P in H_2O. RPR209120/DOPE/DNA lipoplexes was prepared N/P ratio = 8 in NaCl 150 mM. PEI/DNA polyplexes were prepared at N/P = 15 in glucose 5% or NaCl 150 mM. The complexes were then added to the cells in DMEM + 10% FBS at 37 °C. Results are expressed as the mean of an experiment performed in triplicate errors bars indicating standard error of the mean. Note: **18c** at 20TU/P was found to be precipitated (>1000 nm).

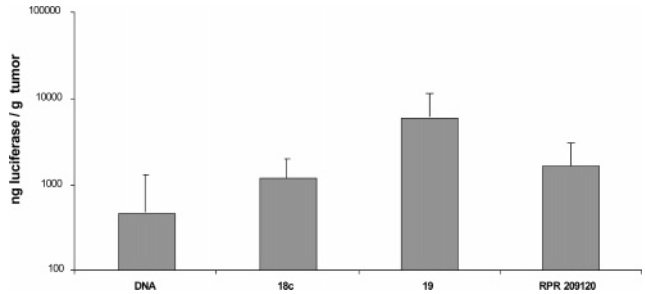


Figure 5. Luciferase activity 24 h after intratumoral injection of **18c**/DNA, **19**/DNA (40 TU/P, 10 μg DNA) and RPR209120/DOPE/DNA (ratio N/P = 5) on three mice previously injected with 3LL carcinoma cells.

CONCLUSION

The presented lipopolythioureas provided new tools for nucleic acid delivery using nonelectrostatic vectors with a transfection level comparable to cationic systems in serum-containing medium. Lipopolythioureas **18a**, **18b**, **18c**, and **19** can be formulated without the use of colipid, leading to small

stable particles. In addition, these compounds showed efficient interaction with plasmid DNA and can protect it from serum degradation during 24 h. The mechanism of LPT−DNA interaction and transfection is now under investigation.

ACKNOWLEDGMENT

This work was financially supported by INSERM, CNRS, MNERT, the Région Ile de France (SESAME, CPER), and the 6th PCRD (MOLEDA). M.−V. S. thanks the EC (MOLEDA) for a postdoctoral fellowship.

LITERATURE CITED

(1) Patil, S. D., Rhodes, D. G., and Burgess, D. J. (2005) DNA-based therapeutics and DNA delivery systems: a comprehensive review. *AAPS J. 7*, E61−77.

(2) Herweijer, H., and Wolff, J. A. (2003) Progress and prospects: naked DNA gene transfer and therapy. *Gene Ther. 10*, 453−8.

(3) Braun, S. (2004) Naked plasmid DNA for the treatment of muscular dystrophy. *Curr. Opin. Mol. Ther. 6*, 499−505.

(4) Liu, F., and Tyagi, P. (2005) Naked DNA for liver gene transfer. *Adv. Genet. 54*, 43−64.

(5) Kawase, A., Nomura, T., Yasuda, K., Kobayashi, N., Hashida, M., and Takakura, Y. (2003) Disposition and gene expression characteristics in solid tumors and skeletal muscle after direct injection of naked plasmid DNA in mice. *J. Pharm. Sci. 92*, 1295−304.

(6) Pack, D., W. Hoffman, A. S., Pun, S., and Stayton, P. S. (2005) Design and development of polymers for gene delivery. *Nat. Rev. Drug Discovery 4*, 581−593.

(7) Tranchant, I., Thompson, B., Nicolazzi, C., Mignet, N., and Scherman, D. (2004) Physicochemical optimisation of plasmid delivery by cationic lipids. *J. Gene Med. 6* (Suppl 1), S24−35.

(8) Nicolazzi, C., Garinot, M., Mignet, N., Scherman, D., and Bessodes, M. (2003) Cationic lipids for transfection. *Curr. Med. Chem. 10*, 1263−1277.

(9) Verma, I. M., and Weitzman, M. D. (2005) Gene therapy: twenty-first century medicine. *Annu. Rev. Biochem. 74*, 711−38.

(10) Wojewodzka, J., Pazdzior, G., Langner, M. (2005) A method to evaluate the effect of liposome lipid composition on its interaction with the erythrocyte plasma membrane. *Chem. Phys. Lipids 135*, 181−7.

(11) Tandia, B. M., Vandenbranden, M., Wattiez, R., Lakhdar, Z., Ruysschaert, J. M., and Elouahabi, A. (2003) Identification of human plasma proteins that bind to cationic lipid/DNA complex and analysis of their effects on transfection efficiency: implications for intravenous gene transfer. *Mol. Ther. 8*, 264−73.

(12) Thompson, B., Mignet, N., Hofland, H., Lamons, D., Seguin, J., Nicolazzi, C., de la Figuera, N., Kuen, R. L., Meng, X. Y., Scherman, D., and Bessodes, M. (2005) Neutral postgrafted colloidal particles for gene delivery. *Bioconjugate Chem. 16*, 608−14.

(13) Woodle, M. C. (1998) Controlling liposome blood clearance by surface-grafted polymers. *Adv. Drug. Delivery Rev. 32*, 139−152.

(14) Mignet, N., and Gregoriadis, G. (2006) Incorporation of PEG lipid into Lipoplexes: On-line Incorporation Assessment, and Pharmacokinetics Advantages. In *Liposome Technology*, 3rd ed., Vol. 2, Chapter 16, CRC Press: London, in press.

(15) Patil, S. D., Rhodes, D. G., and Burgess, D. J. (2005) Biophysical characterization of anionic lipoplexes. *Biochim. Biophys. Acta 1711*, 1−11.

(16) Haensler, J., and Szoka, F. C. (1993) Synthesis and characterization of a trigalactosylated bisacridine compound to target DNA to hepatocytes. *Bioconjugate Chem. 4*, 85−93.

(17) Fong, S., Heath, T., Fong, P., Liggitt, D., and Debs, R. J. (2004) Membrane-permeant, DNA-binding agents alter intracellular trafficking and increase the transfection efficiency of complexed plasmid DNA. *Mol. Ther. 10*, 706−718.

(18) Arignon, J., Prata, C. A., Grinstaff, M. W., and Barthelemy, P. (2005) Nucleic acid complexing glycosyl nucleoside-based amphiphiles. *Bioconjugate Chem. 16*, 864−872.

(19) (a) Aoyama, Y., Kanamori, T., Nakai, T., Sasaki, T., Horiuchi, S., Sando, S., and Niidome, T. (2003) Artificial viruses and their application to gene delivery. Size-controlled gene coating with glycocluster nanoparticles. *J. Am. Chem. Soc. 125*, 3455−3457. (b) Nakai, T.; Kanamori, T.; Sando, S., and Aoyama, Y. (2003) Remarkably size-regulated cell invasion by artificial viruses. Saccharide-dependent self-aggregation of glycoviruses and its consequences in glycoviral gene delivery. *J. Am. Chem. Soc. 125*, 8465−8475.

(20) (a) Moreau, L., Li, Y., Luo, D., Prata, C. A., and Grinstaff, M. W. (2005) Nucleoside phosphocholine amphiphile for in vitro DNA transfection. *Mol. Biosyst. 1*, 260−264. (b) Chabaud, P., Camplo, M., Payet, D., Moreau, L., Barthélémy, P., and Grinstaff, M. W. (2006) Cationic nucleoside lipids for gene delivery. *Bioconjugate Chem. 17*, 466−72.

(21) Tranchant, I., Mignet, N., Crozat, E., Leblond, J., Girard, C., Scherman, D., and Herscovici, J. (2004) DNA complexing lipopolythiourea.*Bioconjugate Chem. 15*, 1342−8.

(22) Leblond, J., Mignet, N., Leseurre, L., Largeau, C., Bessodes, M., Scherman, D., and Herscovici, J. (2006) Design, synthesis, and evaluation of enhanced DNA binding new lipopolythioureas. *Bioconjugate Chem. 17*, 1200−1208.

(23) Still, W. C., Kahn, M., and Mitra, A. (1978) Rapid chromatographic technique for preparative separations with moderate resolution. *J. Org. Chem. 43*, 2923−2926.

(24) Balacco, G. (1994) SwaN-NMR: A complete and expansible NMR software for the Macintosh. *J. Chem. Inf. Comput. Sci. 34*, 1235−1241.

(25) http://www.chemaxon.com/marvin.html (accessed 01/12/07).

(26) Escriou, V., Carrière, M., Bussone, F., Wils, P., and Scherman, D. (2001) Critical assessment of the nuclear import of plasmid during cationic lipid-mediated gene transfer. *J. Gene Med. 3*, 179−187.

(27) Bigey, P., and Scherman, D. Unpublished results.

(28) Benoist, E., Loussouarn, A., Remaud, P., Chatal, J-F., and Geston, J-F. (1998) Convenient and simplified approaches to N-monoprotected triaminopropane derivatives: key intermediates for bifunctionnal chelating agent synthesis. *Synthesis*, 1113−1118.

(29) Wender, P. A., Jessop, T. C., Pattabiraman, K., Pelkey, E. T., and VanDeusen, C. L. (2001) An efficient, scalable synthesis of the molecular transporter octaarginine via a segment doubling strategy. *Org. Lett. 3*, 3229−3232.

(30) Girard, C., Tranchant, I., Nioré, P-A., and Herscovici, J. (2000) A convenient method for the synthesis and one-pot reaction of acyl chlorides using a scavenging resin. *Synlett 11*, 1577−1580.

(31) Stephensen, H., and Zaragoza, F. (1997) Resin-bound isothiocyanates and their synthetic equivalents as intermediates for the solid-phase synthesis of substituted thiophenes. *J. Org. Chem. 62*, 6096−6097.

(32) Marmillon, C., Bompart, J., Calas, M., Escale, R., and Bonnet, P-A. (2000) Solution parallel synthesis of cyclic guanidines. *Heterocycles 53*, 1317−1328.

(33) Baraldo, K., Leforestier, N., Bureau, M., Mignet, N., and Scherman D. (2002). Sphingosine-based liposome as DNA vector for intramuscular gene delivery. *Pharm. Res. 19*, 1144−9.

(34) Adami, R. C., Collard, W. T., Gupta, S. A., Kwok, K. Y., Bonadio, J., and Rice, K. G. (1998) Stability of peptide-condensed DNA formulations. *J. Pharm. Sci. 87*, 678−683.

(35) Byk, G., Dubertret, C., Escriou, V., Frederic, M., Jaslin, G., Rangara, R., Pitard, B., Crouzet, J., Wils, P., Schwartz, B., and Scherman, D. (1998) Synthesis, activity and structure-activity relationship studies of novel cationic lipids for DNA transfer. *J. Med. Chem. 41*, 224−235.

(36) Xu, Y., Hui, S-W., Frederik, P., and Szoka, F. (1999) Physicochemical characterization and purification of cationic lipoplexes. *Biophys. J. 77*, 341−353.

(37) Transfecting properties of lipopolythioureas increased slightly in the absence of serum. However, the serum influence on these compounds was less important than for cationic vectors.

(38) Boussif, O., Lezoualc'h, F., Zanta, M. A., Mergny, M. D., Scherman, D., Demeneix, B., and Behr, J. P. (1995) A versatile vector for gene and oligonucleotide transfer into cells in culture and in vivo polyethylenimine. *Proc. Natl. Acad. Sci. U.S.A. 92*, 7297−7301.

(39) Escriou, V., Ciolina, C., Lacroix, F., Byk, G., Scherman, D., and Wils, P. (1998) Cationic lipid-mediated gene transfer: effect of serum on cellular uptake and intracellular fate of lipopolyamine/DNA complexes. *Biochim. Biophys. Acta 1368*, 276−88.

BC060141B

Water-Soluble Polymer Conjugates of ZnPP for Photodynamic Tumor Therapy

M. Regehly,[†] K. Greish,[‡,§] F. Rancan,[†,||] H. Maeda,*[,‡,§] F. Böhm,[||] and B. Röder*[,†]

Institut für Physik, Photobiophysik, Humboldt Universität zu Berlin, Newtonstr. 15, D-12489 Berlin, Germany, BioDynamics Research Laboratory, Cooperative Research Center, Kumamoto University 2081-7 Tabaru, Mashiki-machi, Kumamoto, 861-2202, Japan, Sojo University, Faculty of Pharmaceutical Sciences, Ikeda 4-22-1, Kumamoto 860-0082, Japan, and Universitätsklinikum Berlin, Charite, Hautklinik, Photobiologisches Labor, Ziegelstr. 5-9, D-10117 Berlin, Germany. Received June 7, 2006; Revised Manuscript Received November 12, 2006

Zn-protoporphyrin (ZnPP) is a promising candidate for cancer therapy. It is known to inhibit heme-oxygenase-1 (HO-1), resulting in suppressed biliverdin/bilirubin production accompanying lowered antioxidative capacity. As a consequence, a significant suppression of tumor growth in vivo was reported. Recent findings also showed that ZnPP efficiently generated reactive singlet oxygen under illumination of visible light. In the present report, we describe the photosensitizing capabilities of water-soluble polymer conjugates of ZnPP as novel compounds for photodynamic therapy against solid tumors. The polymer conjugation made ZnPP water-soluble, thus possible for injection for its aqueous solution. The cellular uptake and photobiological activity of ZnPP derivatives have been tested using a human T-cell leukemia cell line in vitro and demonstrated most potent phototoxic effects of SMA−ZnPP followed by PEG−ZnPP under aerobic conditions.

INTRODUCTION

Metal protoporphyrins (MePP), e.g., Zn protoporphyrin (ZnPP), exhibit many different interesting properties in terms of cancer treatment. While it is well-known that ZnPP is a strong heme oxygenase-1 (HO-1) inhibitor, it also has photosensitizing properties. It is also known that HO-1 is highly up-regulated in many cancer cells (*1*, *2*). HO-1, also known as the heat shock protein 32 (Hsp 32), is induced by various insults such as oxystress, electromagnetic irradiation (UV and X-ray), and nitric oxide, and it is also up-regulated in the inflammatory tissues; thus, it is an inducible enzyme. HO-1 catalyzes the degradation of heme in the presence of oxygen to liberate biliverdin, iron, and CO. Biliverdin is then converted to bilirubin. The hypothesis is that inhibition of HO-1 would result in the inhibition of bilirubin production, which means that suppression and depletion of HO-1 would make cells more vulnerable to oxystress or radiation, since bilirubin is a very potent antioxidative agent. Thus, such tumor cells treated with an inhibitor of HO-1 (e.g., Zn protoporphyrin) would undergo apoptosis readily (*3*).

On the other hand, ZnPP derivatives are known as efficient photosensitizers (*4*). ZnPP absorbs light in the UV−vis region and in turn changes to the first excited singlet state. In doing so, the molecules undergo intersystem crossing that leads to the population of the long-lived first excited triplet state. From this state, the energy is transferred efficiently to molecular oxygen, and thus reactive singlet molecular oxygen [$^1O_2$] (*5*) is generated, that would induce directly or indirectly cell death.

ZnPP has a very low solubility in water at neutral pH, and hence its practical use would be limited as a pharmaceutical agent. For that reason, a water-soluble form of ZnPP was prepared by conjugating it with a poly(ethylene glycol) (PEG) chain (*6*). As a result, the compound became of a macromolecular nature, i.e., apparent molecular size in solution >70Da. In our earlier studies, it was shown that macromolecules tend to accumulate in solid tumors much more extensively, e.g., a 10−30-fold higher amount than low molecular weight drugs due to unique differences in pathophysiology and architecture of tumor blood vessels, as well as overproduction of various vascular mediators at or near the tumor site that further facilitate vascular permeability. This phenomenon was coined the EPR effect (*7*, *8*). Now, the EPR (enhanced permeability and retention) effect is considered to be the key issue to achieve tumor-selective targeting of macromolecular drugs.

On the other hand, using our more recent micellar technology with poly(styrene−maleic acid) copolymer (SMA), it becomes possible to encapsulate varieties of drugs at very high loading levels, as much as 50% (w/w) in the SMA micelle, which releases free drug in a time-dependent manner, and the micellar form of drugs also exhibits this EPR effect (*9*).

The present study is focused on the comparative investigation of SMA−ZnPP micelles and PEG−ZnPP according to their photodynamic activity in vitro. Until now, an antitumor effect for PEG−ZnPP has been reported only in ref 10. In this earlier study, a hypothetical mechanism of antitumor activity of ZnPP was attributed to the inhibition of HO-1 (that suppresses bilirubin generation), and thus enhancement of vulnerability against oxystress (that derived via the host defense system such as macrophages) was envisaged.

The aim of the present study was to investigate the ability of both compounds (PEG−ZnPP and SMA−ZnPP) for intracellular generation of singlet oxygen, that causes photodynamically induced cell death. We assume that the polymer conjugates would benefit from the EPR effect driven tumor accumulation. In this context, antitumor effect is exerted both by HO-1 inhibition and singlet oxygen generated photodynamic activity. Consequently, the antitumor effect will be exhibited in a highly tumor targeted manner. Thus, it would result in a superior therapeutic effect compared to free ZnPP.

MATERIALS AND METHODS

Preparation of Polymeric Zn-Protoporphyrin. PEG−ZnPP conjugate was prepared by conjugation of succinimidyl PEG

* Corresponding authors. E-mail: roeder@physik.hu-berlin.de (B.R.), hirmaeda@ph.sojo-u.ac.jp (H.M.).
[†] Humboldt Universität zu Berlin.
[‡] Kumamoto University.
[§] Sojo University.
[||] Universitätsklinikum Berlin.

10.1021/bc060158u CCC: $37.00 © 2007 American Chemical Society
Published on Web 02/06/2007

(NOF, Tokyo) to bis(ethylenediamino) protoporphyrin and the chelation of zinc into the porphyrin ring afterward. The detailed method is described in ref 7. Poly(styrene-*co*-maleic acid) (SMA) micelles containing ZnPP were prepared similarly to the SMA−pirarubicin micelles as reported previously (*10*, *11*).

Absorption Spectra. The absorption spectra were recorded using a commercial spectrophotometer Shimadzu UV-2501 PC at room temperature. The spectrum of free ZnPP was measured after dissolving it in ethanol. Spectra of PEG−ZnPP and SMA−ZnPP were taken after dissolving in H_2O.

Time-Resolved Singlet Oxygen Luminescence Measurement. Measurements were carried out using a nanosecond Nd:YAG laser (BM Industries, Evry Cedex, France) with an attached optical parametric oscillator (BMI). The singlet oxygen emission was detected using a liquid nitrogen cooled Ge-diode (North Coast, Inc., Santa Rosa, CA). For wavelength selection, a combination of a silicon filter and an interference filter for 1270 nm was placed in front of the diode (*12*). PEG−ZnPP and SMA−ZnPP were dissolved in D_2O. The optical density was adjusted to 0.2 at the excitation wavelength of 550 nm. Rose Bengal served as a reference standard for the determination of singlet oxygen quantum yield ($Q_\Delta = 0.75$) (*13*).

Laser Flash Photolysis. The same equipment as described before was used to excite the samples for triplet−triplet absorption measurements. A continuous wave (cw) test beam was generated using an XBO lamp with the light passed through a monochromator adjusted to 480 nm. The beam traversed through the PEG− and SMA−ZnPP solutions perpendicular to the excitation beam and was detected by an avalanche Si-photodiode with an interference filter for 480 nm. Oxygen was removed by bubbling the samples with N_2 gas for approximately 40 min at room temperature (*14*).

Cell Culture and Incubation Conditions. A T-cell line of human T-lymphocytes (Jurkat cells: clone E 6−1 ATCC, human acute T-cell leukemia) were cultured in 5 mL of RPMI 1640 medium containing Glutamax-I, supplemented with 10% fetal calf serum (FCS), 100 μg/mL streptomycin, and 100 I.E./mL penicillin in 50 mL flasks. Cells were cultured at 37 °C in 100% humidity and 5% CO_2 and subcultured in new medium every 3 days. PEG−ZnPP and SMA−ZnPP were dissolved in PBS. Water-insoluble free ZnPP was dissolved in 0.1 M NaOH. Jurkat cells (2×10^5 cells/mL) were incubated in medium with four different Zn-protoporphyrin concentrations at (0.5, 1.0, 2.5, and 5 μM). All reported concentrations refer to free Zn-protoporphyrin equivalents. Cells without the studied compounds were irradiated with UVA (R/UVA) or kept in the dark (R/D) and used as a reference standard.

Intracellular Uptake. The amount of sensitizer uptaken by Jurkat cells was determined by measuring the fluorescence intensity of cell extracts. Cells were harvested 24 h after incubation, washed twice, and counted using a hemocytometer (Neubauer improved). The cell pellets were stored at −20 °C. Cells were then thawed, and the sensitizer was extracted after centrifugation using ethanol. The fluorescence intensity of cell extracts was measured with a fluorescence microplate reader Gemini EM (Molecular Devices, Germany), using $\lambda_{exc} = 420$ nm and $\lambda_{em} > 650$ nm. Concentration of the sensitizers in the cell extracts was quantified by fluorescence intensity relative to standard curves after disintegration with ethanol in the case of SMA−ZnPP.

UVA Irradiation of Cell Suspensions. Jurkat cells were washed, resuspended in PBS, and placed in a 24-well plate and covered with a quartz glass. A fluorescence lamp (type TLK 40 W, Philips) was used with 99.58% emission in the UVA region (315 and 400 nm) and 0.42% emission in the spectral range below 315 nm. The culture plate was placed under the lamp at 4 cm distance, and cells were irradiated for 5 min. At these conditions, the irradiation received by the cells in the UVA range was 10.68 W/m^2, and the received UVA dose was 0.3 J/cm^2.

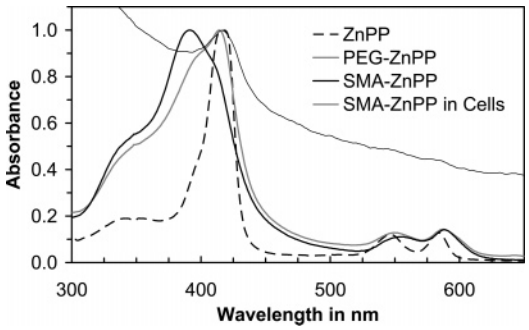


Figure 1. Normalized absorption spectra of PEG−ZnPP (solid gray line) and SMA−ZnPP (solid black line) in H_2O. The absorption of SMA−ZnPP in Jurkat cells (thin black line) exhibits a strong background due to light scattering by the cells. For comparison, the spectrum of ZnPP in ethanol is shown (dashed line).

Cell Survival after UVA Irradiation. The phototoxicity induced by PEG−ZnPP and SMA−ZnPP on Jurkat cells was determined by the XTT test (Roche Diagnostics GmbH, Mannheim, Germany). The assay is based on the conversion of the yellow tetrazolium salt XTT into an orange formazan dye by dehydrogenase in metabolically active cells, which was quantified by absorbance at 492 nm. The reference wavelength was at 650 nm, and the percentage of cell survival was determined as follows: (OD_{sample}/OD_{dark} reference) × 100 (bars; ± standard deviation, $n = 3$).

Caspase 3/7 Activity. Apoptosis was assessed using a fluorimetric assay kit (Apo-ONE Homogeneous Caspase-3/7 Assay, Promega GmbH, Germany), based on caspase 3/7 substrate (Z-DEVD-R110) as a profluorescent substrate. The cleavage and removal of the DEVD peptide by caspase 3 and 7 gives free rhodamine 110 of which the fluorescence intensity is proportional to caspase 3/7 activity. The fluorescence intensity was measured with a fluorescence microplate reader Gemini EM (Molecular Devices, Germany), using $\lambda_{exc} = 485$ nm and $\lambda_{em} > 530$ nm. Cells incubated with 1.5 μM staurosporine (St) at 37 °C were used as a positive control of apoptotic cell death. Caspase 3/7 activity was detected 3−4 h after irradiation. The caspase 3/7 activity of the samples is expressed as a percentage of the positive control values 4 h after stimulation (bars; ± standard deviation, $n = 3$).

RESULTS

In the present study, the photophysical parameters relevant for PDT of two different water-soluble polymeric forms of Zn protoporphyrin (ZnPP), poly(ethylene glycol)-conjugated ZnPP (PEG−ZnPP), and styrene−maleic acid copolymer micelles containing ZnPP (SMA−ZnPP) were compared, and their photodynamic activity was investigated in vitro in comparison with free ZnPP.

Absorption Spectra. The absorption spectrum of free ZnPP resembles that of metal-containing tetrapyrroles consisting of the Soret band and the two Q-band transitions with lower transition dipole moments and therefore lower absorbance (see Figure 1). The Soret band of PEG−ZnPP centered at 414 nm exhibits a hypsochromic shift by about 4 nm compared to that of ZnPP. For SMA−ZnPP, the blue shift is much stronger, about 27 nm. The Q-bands of PEG−ZnPP and SMA−ZnPP are red-shifted by about 3 nm with respect to ZnPP. Moreover, every absorption band is broadened. In the case of SMA−ZnPP, the spectrum is a result of aggregation of many ZnPP molecules, which are tightly enclosed, in the hydrophobic inner core of the micelles. The appearance of spectral shifts may be due to

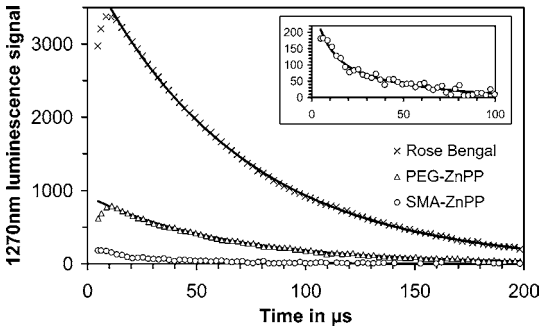


Figure 2. Time-resolved singlet oxygen emission in D_2O photosensitized by PEG−ZnPP and SMA−ZnPP. (Reference: Rose bengal) Inset: Magnification of the two-exponential kinetics of the singlet oxygen emission photosensitized by SMA−ZnPP.

interactions between individual dye (ZnPP) and styrene ring molecules. The absorption spectrum of SMA−ZnPP in Jurkat cells suspended in PBS buffered solution is an overlay of the free ZnPP absorption and a scattering background caused by the cells. Although the Q-band of ZnPP in cells treated with SMA−ZnPP cannot be clearly identified due to the low concentration of the drug in the cells, the peak of the Soret band is now located at the same wavelength as for free ZnPP seen in ethanol. From this observation, it can be concluded that the SMA micelles release free ZnPP molecules from their inner cores after being internalized by the Jurkat cells.

For PEG−ZnPP macromolecules, the situation is quite different. The red shift of the Q-band is less pronounced and is regarded as a result of the covalent attachment of the PEG chain. Attachment of PEG chain to ZnPP does not hinder relatively free rotational and vibronic motion, which corresponds to the observed broadening of the absorption spectrum, a good contrast to SMA−ZnPP.

Singlet Oxygen Measurements. It was found that PEG−ZnPP in D_2O generates singlet molecular oxygen [$^1O_2$] with a quantum yield of 17%; the lifetime was determined to be 61 μs. The last value matches the well-known lifetime of $^1O_2$ in D_2O of 60 μs (*15*). Therefore, the PEG chain does not wrap the ZnPP molecule closely enough to cause efficient quenching of singlet molecular oxygen being generated. In contrast to PEG−ZnPP, the singlet oxygen generation in the case of SMA−ZnPP is very low, and the emission decay shows a two-exponential behavior with lifetimes of 8 μs and 50 μs (see Figure 2). The longer component of the emission is attributed to singlet oxygen, which diffused out of the micelle into the D_2O environment. The shorter lifetime corresponds to singlet oxygen, which is quenched by the densely packed photosensitizer molecules within the micelle and/or the micelle-building polymers. The quantum yield of singlet oxygen generation for SMA−ZnPP was determined to be 5%.

Laser Flash Photolysis. Because of the very short lifetime of singlet oxygen in viable cells, it is very hard to follow its generation via luminescence detection directly. For this reason, we used the method of laser flash photolysis for indirect determination of singlet oxygen formation via triplet lifetime measurement. This is possible because the triplet lifetimes can be related to the singlet oxygen generation. After activation of the first excited singlet state S_1 via light absorption, a part of the molecules undergo transition to the first excited triplet state T_1 with a quantum yield Φ_T. Some of the molecules in the T_1 state are deactivated via phosphorescence (k_{phos}) or nonradiative (k_{nonrad}) transition. The fraction deactivated via interaction with molecular oxygen is referred to as f_T. The energy transfer to molecular oxygen resulting in the generation of singlet molecular oxygen is described by the yield S_Δ. For tetrapyrroles under normal air conditions, this value is nearly unity. Therefore, the

Table 1. First Excited Triplet-State Lifetimes (τ_T) of the Photosensitizers Obtained by Laser Flash Photolysis and Measured Singlet Oxygen Quantum Yield in H_2O

sample	τ_T [μs] under normal air conditions	τ_T [μs] after 40 min N_2 flushing	singlet oxygen quantum yield Φ_Δ
PEG−ZnPP in H_2O	2.5 (±0.2) μs	406 (±40) μs	0.17
PEG−ZnPP in JCS[a]	27 (±3) μs	325 (±30) μs	
SMA−ZnPP in H_2O	1.4 (±0.2) μs	484 (±40) μs	0.05
SMA−ZnPP in JCS[a]	2.4 (±0.2) μs	92 (±11) μs, 1.2 (±0.1) ms	

[a] Jurkat cell suspensions.

singlet oxygen quantum yield (Φ_Δ) can be calculated using the relation

$$\Phi_\Delta = \Phi_T \cdot f_T \cdot S_\Delta = \Phi_T \cdot \left(\frac{k_{O_2}[O_2]}{k_{phos} + k_{nonrad} + k_{O_2}[O_2]} \right) \cdot S_\Delta$$

The triplet lifetime in the presence of oxygen τ_{O_2} is given by $\tau_{O_2} = (k_{phos} + k_{nonrad} + k_{O_2}[O_2])^{-1}$. Bubbling the solution with N_2 removes oxygen and leads to an increase of the triplet lifetime. In this case, the lifetime is calculated by $\tau_{N_2} = (k_{phos} + k_{nonrad})^{-1}$. The value of the singlet oxygen quantum yield can be obtained finally by

$$\Phi_\Delta = \Phi_T \cdot \left(\frac{\tau_{N_2} - \tau_{O_2}}{\tau_{N_2}} \right) \cdot S_\Delta$$

That means that for the calculation of Φ_Δ the value of Φ_T must be known. For ZnPP in ethanol, a high Φ_T value of 0.9 was reported (*16*). In the case of SMA−ZnPP in H_2O, the aforementioned aggregate formation of ZnPP molecules located in the micellar core causes a strong decrease of the triplet quantum yield Φ_T. In cells, the free ZnPP molecules are—at least partly—released from the micelle, and because of the unknown influence of the cellular environment on the aggregation of these molecules, Φ_T is also not known. Therefore, very efficient quenching processes make it difficult to obtain the quantum yield of singlet oxygen generation in cells. On the other hand, because of the fact that S_Δ of tetrapyrroles is about 1, the triplet lifetimes measured in air-liberated and deoxygenated solutions and cell suspensions provide information on the efficiency of such dyes to generate singlet molecular oxygen. For this reason, laser flash experiments were used to compare PEG−ZnPP and SMA−ZnPP according to their ability to generate singlet oxygen.

In the presence of oxygen, the triplet lifetime of PEG−ZnPP in H_2O was measured to $\tau_T = 2.5$ μs and the lifetime of SMA−ZnPP was $\tau_T = 1.4$ μs (Table 1). In an environment with low pO_2, the triplet lifetime of the compounds dissolved in H_2O increased to 406 μs (PEG−ZnPP) and 484 μs (SMA−ZnPP) as seen in Table 1.

In comparison to these findings, the triplet-state lifetime of the two compounds accumulated in Jurkat cells under normal air conditions (aerobic) and under nitrogen (N_2) bubbling of the cell suspensions were investigated. Under normal aerobic conditions, triplet lifetimes of 27 μs (PEG−ZnPP) and 2.4 μs (SMA−ZnPP) were measured (Figure 3). In the case of PEG−ZnPP, the larger value indicates an accumulation in cellular compartments with lower oxygen concentration or a lowered diffusion rate of reactants in regions with higher viscosity (*17*), although the latter possibility is more likely in this case.

For PEG−ZnPP in cells after 40 min N_2 flushing (removing of O_2), a triplet lifetime of 325 μs was obtained (Figure 4) and a bleaching of the triplet state occurred. This can be concluded from the fact that the induced absorbance does not approach

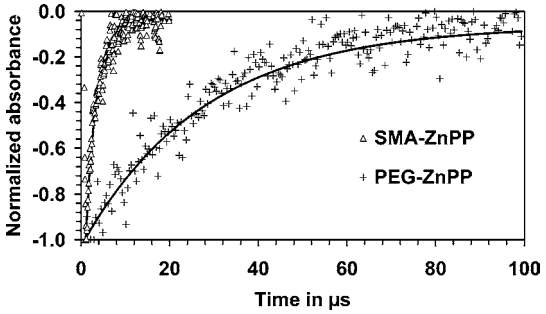


Figure 3. Laser flash photolysis of SMA−ZnPP and PEG−ZnPP in Jurkat cells under normal air conditions. For SMA−ZnPP, the triplet lifetime was obtained to 2.4 μs, whereas for PEG−ZnPP, the fit yielded a value of 27 μs.

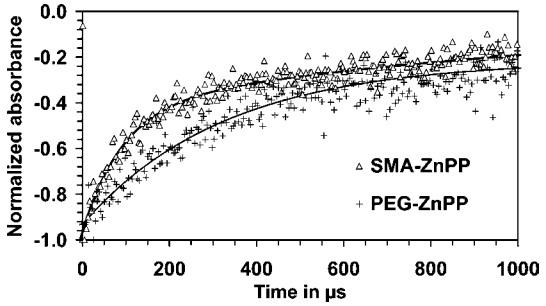


Figure 4. Laser flash photolysis of PEG−ZnPP and SMA−ZnPP in Jurkat cells after 40 min N_2 flushing. The removal of oxygen leads to an increase of the triplet lifetime. The triplet lifetime of PEG−ZnPP was determined to be 325 μs. For SMA−ZnPP, a two-exponential decay was observed consisting of a short component with 92 μs and a long one with approximately 1.2 ms.

the value before excitation. This can be treated as an indication for a chemical change of the photosensitizer, whereas an additional long-lived species could not be identified. The triplet lifetime of PEG−ZnPP is in the range of the value measured in aqueous solution. On the basis of these findings, we suggest that PEG−ZnPP is preserved primarily in its monomeric water-soluble form in cells. It generates singlet oxygen under illumination in cells but with a lower quantum yield than in aqueous solution. The interpretation is consistent with the results obtained from in vitro experiments described below.

For SMA−ZnPP after 40 min N_2 bubbling, a two-exponential triplet decay was observed. The short component with 127 μs is significantly lower than the lifetime in H_2O with oxygen removed. Such a strong reduction of the triplet lifetime may result from close association of the released ZnPP molecules. This type of situation occurs in hydrophobic environments like the lipid bilayer of cell membranes. Similar findings were reported in refs 17 and 18. This effect is due to weak interaction at high local concentrations of the photosensitizer and has to be distinguished from the aggregation of ZnPP observed in the core of SMA micelles. The latter case leads to a strong fluorescence suppression which was observed for SMA−anthracycline micelles (doxorubicin and pirarubicin) as reported previously (*10*, *11*). The longer component of the triplet decay with 1.2 ms is attributed to a bleaching process probably resulting in the formation of long-lived radicals. For SMA−ZnPP in cells, either singlet oxygen mediated phototoxicity (type II) or a free radical destruction mechanism (type I) under low oxygen concentration may occur. This result may reflect its biological effect.

Photodynamic Activity and Cell Killing. First, the intracellular uptake of the two polymeric compounds by Jurkat cells was studied in comparison with free ZnPP at different incubation concentrations (Figure 5). The intracellular uptake of the compounds increased in parallel with the concentration of the

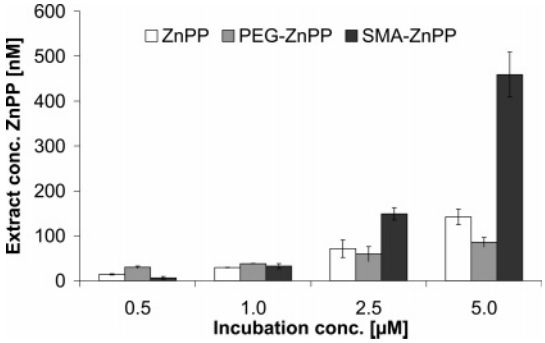


Figure 5. Intracellular uptake of sensitizers by Jurkat cells. Cells were incubated with the investigated compounds at different concentrations (expressed in ZnPP equivalents). The amount of sensitizer uptaken by Jurkat cells was determined by measuring the fluorescence intensity of cell extracts as described in Materials and Methods.

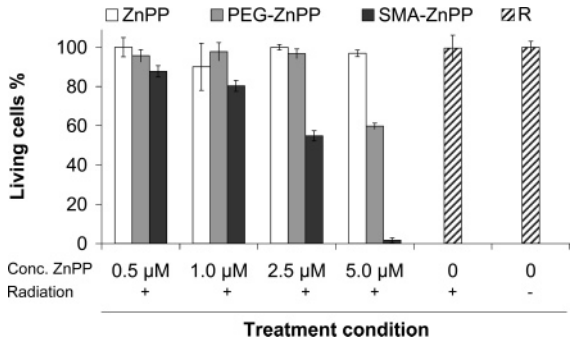


Figure 6. Phototoxicity against Jurkat cells of ZnPP, PEG−ZnPP, and SMA−ZnPP. Cell survival 24 h after irradiation (radiation, +) was measured using the XTT test. Two references (R, streaked bar) were used: cells without test compounds and kept in the dark (radiation, −) and those with radiation at the same dose of UVA.

compounds in the incubation suspension. SMA−ZnPP reached higher intracellular concentrations than PEG−ZnPP and free ZnPP (in terms of ZnPP equivalents). At an incubation concentration of 5 μM, the intracellular concentration of SMA−ZnPP was approximately 5.4 times higher than that of PEG−ZnPP and more than 3.2 times higher than that of free ZnPP. This data can be explained by the fact that the molecular concentration of ZnPP in SMA micelles is much higher (loading of >40% by weight), whereas its content in PEG−ZnPP is about 5%. Both will be internalized by endocytosis.

To investigate the photocytotoxicity of PEG−ZnPP and SMA−ZnPP in comparison with that of free ZnPP, Jurkat cells were incubated for 24 h with different concentrations of the compounds and irradiated at dose of 0.3 J/cm^2 of UVA. Cellular viabilities were estimated by XTT assay 24 h after irradiation. Less than 5% of the reference cells lost their viability after UVA exposure (Figures 6 and 7). No cytotoxic activity by ZnPP without UVA exposure alone may indicate that HO-1 inhibition does not show a significant effect at this dose range (Figure 6), although more oxystressed systems may prove this possibility in vivo. Free ZnPP does not demonstrate a phototoxic effect under illumination. As shown in Figures 6 and 7, significantly enhanced phototoxicity was observed for SMA−ZnPP at incubation concentrations higher than 1 μM. The phototoxicity increased in a concentration-dependent manner with LD_{50} of about 2.5 μM. PEG−ZnPP exerted significant phototoxic activity only at concentration of 5 μM under UVA irradiation (Figure 6).

Caspase 3 and 7 activities were measured 4 h after irradiation to answer the question regarding which cell death mechanism is induced by the uptake of ZnPP (Figure 7). Caspase 3 and 7 activity was detected when treated with both ZnPP compounds,

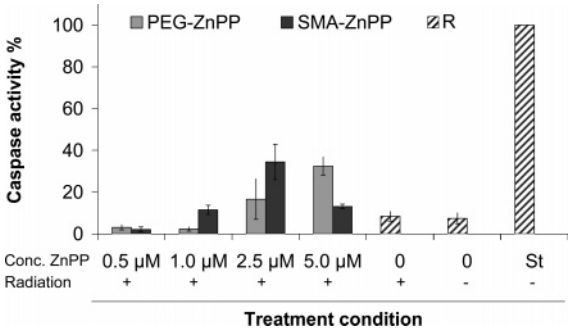


Figure 7. Photoinduction of caspase 3/7 activity on Jurkat cells. Two references (R) were used: cells without test compounds in the dark (radiation, −) and those with radiation at the same dose of UVA (radiation, +). Cells incubated for 4 h with 1.5 μM staurosporine (St) were used as a positive control for caspase activity.

even if only a low percentage of activity (about 30% of the positive control) could be measured and only at concentrations of 5 μM for PEG−ZnPP and 2.5 μM for SMA−ZnPP.

At an incubation concentration of 5 μM, only a low level of caspase activity was measured for SMA−ZnPP, whereas almost no living cells were detected with the XTT test. Thus, the caspases might have already released out of the cells. In concordance with this notion, all these cells showed Trypan blue positive staining (data not shown), indicating disruption of the integrity of cell membrane. These observations showed that cells had also undergone a necrotic cell death pathway to a considerable extent. Namely, cell viability was approximately 60% after irradiation of the cells incubated with 5 μM PEG−ZnPP, and the measurements of caspase 3 and 7 activities showed that approximately 30% of dead cells were caused by an apoptotic mechanism. These results show that SMA−ZnPP is able to initiate cell death via necrosis at higher concentrations, while PEG−ZnPP is mainly inducing the apoptotic cell death pathway.

DISCUSSION

Our experimental results obtained from in vitro studies on Jurkat cell suspensions show that both SMA−ZnPP and PEG−ZnPP exhibit photodynamic activity. SMA−ZnPP causes about five times higher phototoxicity compared to PEG−ZnPP due to the higher uptake of ZnPP by tumor cells. This fact clearly demonstrates the advantage of SMA−ZnPP over PEG−ZnPP for photodynamic therapy. In this context, the polymeric form of ZnPP is better than free ZnPP in addition to its increased water solubility.

The SMA micelle acts as a macromolecular encapsulating container for ZnPP with densely packed ZnPP molecules; it thereby seems to prevent the efficient formation of singlet oxygen to a considerable extent before delivery to tumor cells. Such dense packing of ZnPP would lead to a strong decrease of the triplet quantum yield of the photosensitizer molecules outside of cells. After incorporation into the cells via endocytosis, the SMA micelles release free ZnPP molecules in lysosomal compartments or tend to accumulate in lipophilic regions in the cells at high concentrations. The destruction of the cell membranes under UVA illumination was envisaged, as they became Trypan blue positive, indicative of a necrotic cell death pathway. The phototoxicity of SMA−ZnPP is based primarily on the generation of singlet oxygen, but probably long-lived radicals are formed additionally, especially in the case of lowered oxygen concentration, such as the lipid peroxiradical (ROO$^{\bullet}$) that can also cause DNA breakage and other damage (*19*).

Free ZnPP showed some uptake in the cells (Figure 5) though no cytotoxicity (Figure 6); this may be an arguable point that quantification of ZnPP by fluorometry after ethanol extraction would dismiss the difference of the localization of ZnPP, i.e., one bound on a cell membrane (lipid bilayer) versus endocytotic vesicle (upon endocytosis of SMA−ZnPP). Thus, free ZnPP-treated cells may not contain real intracellular ZnPP.

The comparative study of PEG−ZnPP and SMA−ZnPP shows the possibility of development of more efficient drug delivery systems for photodynamic therapy using macromolecular drug carrier systems such as SMA micelles, which exhibit tumor-selective delivery via the EPR effect, which is far better than free ZnPP or low molecular weight drugs. Moreover, by using these "intelligent" SMA micelles as a carrier system proposed in this paper, it will be possible to make a more efficient delivery system without toxicity in general. The photodynamic activity will be ideal for superficial tumors where light can penetrate, whereas on the other parts of the body, it may work by HO-1 inhibition (Hsp-32), which is considered to be one of the survival proteins of tumor cells.

In addition to the comments of polymeric ZnPP in view of singlet oxygen generation, recent reports show that Zn or ZnPP can affect the signal transduction system involving down-regulation of the oncogene on chronic myelogenous leukemic cells (*20*) or Zn transporter-mediated cytokine modulation (e.g., IL-6, etc.) (*21*). These could be the other alternative mechanisms to the EPR effect/HO-1 inhibition/increased ROS sensitivity in understanding the multiple effects after SMA−ZnPP uptake.

ACKNOWLEDGMENT

The technical assistance of Gisela Wöhlecke and the support of Anneliese Powitz, and Arun Iyer for preparing SMA micelles are greatly appreciated. H.M. thanks the Ministry of Education, Science, Culture and Sports for the Cancer Research Grant for 2005−2010. F.R. and F.B. thank the DFG for financial support (BO 1353/2−2). K.G. thanks JSPS for supporting his research in Japan.

LITERATURE CITED

(1) Doi, K., Akaike, T., Horie, H., Noguchi, Y., Fujii, S., Beppu, T., Ogawa, M., and Maeda, H. (1996) Excessive production of nitric oxide in rat solid tumor and its implication in rapid tumor growth. *Cancer 77*, 1598−1604.

(2) Doi, K., Akaike, T., Fujii, S., Tanaka, S., Ikebe, N., Beppu, T., Shibahara, S., Ogawa, M., and Maeda, H. (1999) Induction of heme oxygenase-1 by nitric oxide and ischaemia in experimental solid tumors and implications for tumor growth. *Br. J. Cancer 80*, 1945−1954.

(3) Fang, J., Sawa, T., Akaike, T., Greish, K., and Maeda, H. (2004) Enhancement of chemotherapeutic response of tumor cells by a heme oxygenase inhibitor, pegylated zinc protoporphyrin. *Int. J. Cancer 109*, 1−8.

(4) Wiehe, A., Stollberg, H., Runge, S., Paul, A., Senge, M., and Röder, B. (2001) PDT-related photophysical properties of conformationally distorted palladium(II) Porphyrins. *J. Porphyrins Phthalocyanines 5*, 853−860.

(5) Foote, C. S. (1968) Mechanisms of photosensitized oxidation. *Science 162*, 963−970.

(6) Sahoo, S. K., Sawa, T., Fang, J., Tanaka, S., Miyamoto, Y., Akaike, T., and Maeda, H. (2002) Pegylated zinc protoporphyrin: A water-soluble heme oxygenase inhibitor with tumor-targeting capacity. *Bioconjugate Chem. 13*, 1031−1038.

(7) Matsumura, Y., and Maeda, H. (1986) A new concept for macromolecular therapeutics in cancer chemotherapy: mechanism of tumoritropic accumulation of proteins and the antitumor agent smancs. *Cancer Res. 46*, 6387−6392.

(8) Maeda, H. (2001) The enhanced permeability and retention (EPR) effect in tumor vasculature: the key role of tumor-selective macromolecular drug targeting. In *Advances in Enzyme Regulation*, Vol. 41, pp 189−207, Elsevier, Oxford, U.K.

(9) Greish, K., Sawa, T., Fang, J., Akaike, T., and Maeda, H. (2004) SMA−doxorubicin, a new polymeric micellar drug for effective targeting to solid tumors. *J. Controlled Release 97*, 219−230.
(10) Fang, J., Sawa, T., Akaike, T., Akuta, T., Sahoo, S. K., Greish, K., Hamada, A., and Maeda, H. (2003) In vivo antitumor activity of pegylated zinc protoporphyrin: targeted inhibition of heme oxygenase in solid tumor. *Cancer Res. 63*, 3567−3574.
(11) Greish, K., Nagamitsu, A., Fang, J., and Maeda, H. (2005) Copoly (styrene-maleic-acid)-pirarubicin micelles: high tumor targeting efficiency with low toxicity. *Bioconjugate Chem. 16*, 230−236.
(12) Oelckers, S., Sczepan, M., Hanke, T., and Röder, B. (1997) Time-resolved detection of singlet oxygen luminescence in red ghost cell suspensions. *J. Photochem. Photobiol., B 39*, 219−223.
(13) Spiller, W., Kliesch, H., Wöhrle, D., Hackbarth, S., Röder, B., and Schnurpfeil, G. (1998) Singlet oxygen quantum yields of different photosensitizers in polar solvents and micellar solutions. *J. Porphyrins Phthalocyanines 2*, 145−158.
(14) Paul, A., Hackbarth, S., Mölich, A., Luban, C., Oelckers, S., Böhm, F., and Röder, B. Comparative study on the photosensitization of jurkat cells *in vitro* by pheophorbide-a and a pheophorbide-a diaminobutane poly-propylene-imine dendrimer complex. *Laser Phys. 13*, 22−29.
(15) Gorman, A., and Rodgers, M. (1978) Lifetime and reactivity of singlet oxygen in an aqueous micellar system: A pulsed nitrogen laser study. *Chem. Phys. Lett. 55*, 52−54.
(16) Feitelson, J., and Barboy, N. (1986) Triplet-state reactions of zinc protoporphyrins. *J. Phys. Chem. 90*, 271−274.
(17) Aveline, B., Sattler, R., and Redmond, R. (1998) Environmental effects on cellular photosensitization: correlation of phototoxicity mechanism with transient absorption spectroscopy measurements. *Photochem. Photobiol. 68*, 51−62.
(18) Aveline, B., and Redmond, B. (1998) Can cellular phototoxicity be accurately predicted on the basis of sensitizer photophysics? *Photochem. Photobiol. 69*, 306−316.
(19) Sawa, T., Akaike, T., Kida, K., Fukushima, Y., Takagi, K., and Maeda, H. (1998) Lipid peroxyl radicals from oxidized oils and heme-iron: Implication of a high-fat diet in colon carcinogenesis. *Cancer Epidemiol. Biomarkers Prev. 7*, 1007−1012.
(20) Mayerhofer, M., Florian, S., Krauth, M. T., Aichberger, K. J., Bilban, M., Marculescu, R., Printz, D., Fritsch, G., Wagner, O., Selzer, E., Sperr, W. R., Valent, P., and Sillaber, C. (2004) Identification of heme oxygenase-1 as a novel BCR/ABL-dependent survival factor in chronic myeloid leukemia, *Cancer Res. 64*, 3148−54.
(21) Yamashita, S., Miyagi, C., Fukada, T., Kagara, N., Che, Y. S., and Hirano, T. (2004) Zinc transporter LIVI controls epithelial-mesenchymal transition in zebrafish gastrula organizer. *Nature (London) 429*, 298−302.

BC060158U

Site-Specific PEGylation for High-Yield Preparation of Lys^{21}-Amine PEGylated Growth Hormone-Releasing Factor (GRF) (1−29) using a GRF(1−29) Derivative FMOC-Protected at Tyr^1 and Lys^{12}

Yu Seok Youn and Kang Choon Lee*

Drug Targeting Laboratory, College of Pharmacy, SungKyunKwan University, 300 Chonchon-dong, Jangan-ku, Suwon City 440-746, Korea. Received June 18, 2006; Revised Manuscript Received October 23, 2006

PEGylation has been viewed as an effective means of overcoming the therapeutic restriction of growth hormone-releasing factor (1−29) (GRF(1−29)) due to its short biological lifetime caused by severe proteolysis and rapid glomerular filtration. Of three isomers according to the PEGylation sites (Tyr^1, Lys^{12}, or Lys^{21}), PEGylated GRF-(1−29) at Lys^{21}-amine (Lys^{21}-PEG-GRF(1−29)) was shown to have the highest bioactivity. In this report, we propose a unique two-step site-specific PEGylation method capable of producing only Lys^{21}-PEG-GRF(1−29) with a single composition in high yield using a GRF(1−29) derivative protected at Tyr^1 and Lys^{12} and remained available at Lys^{21} ($FMOC^{1,12}$-GRF(1−29)). The first step of this reaction involved the PEG attachment to $FMOC^{1,12}$-GRF(1−29), and the second step involved the removal of FMOC moieties. This PEGylation process was optimized at the following conditions: 0.2−0.3% (v/v) triethylamine concentration, 5.0−6.0-fold molar amount of PEG, reaction temperature of 25−45 °C, and reaction time of 30 min. Under these conditions, the maximum yield of Lys^{21}-PEG-GRF(1−29) produced was ca. ∼95%, 6.3-fold higher than that by nonspecific PEGylation at pH 8.5. Significantly, this site-specific Lys^{21}-PEG-GRF(1−29) was found to have greatly increased resistance to rat plasma, liver, and kidney homogenates, with 7.0-, 25.4-, and 16.4-fold longer half-lives vs GRF(1−29), respectively. Furthermore, ^{125}I-Lys^{21}-PEG-GRF(1−29) displayed significantly reduced liver and kidney distributions and extended blood presence vs ^{125}I-GRF(1−29) in rats. Due to these benefits, Lys^{21}-PEG-GRF(1−29) displayed an enhanced initial growth hormone release in vivo despite having 15% remaining activity in vitro. This devised PEGylation method using an FMOC-protection/deprotection strategy would provide great usefulness for PEGylating bioactive peptides in terms of improved biological potency, elevated production yield, and a uniform composition.

INTRODUCTION

Growth hormone-releasing factor (GRF) is attracting growing interest because it acts as an alternative treatment to growth hormone (GH) (*1*). GRF has two beneficial therapeutic issues vs GH: first, it induces physiological GH-release mimicking the natural pattern; and second, it can be administered via non-parenteral routes (*2*−*3*) due to its small molecular size. Upon release into the circulation, however, GRF(1−29), the shortest and fully active form of GRF, is rapidly inactivated by proteolysis of dipeptidyl peptidase IV (DPP IV) (*4*) and glomerular filtration, with a short plasma half-life of 10−20 min (*5*). Accordingly, studies previously undertaken on this topic have highlighted the importance of a longer-acting GRF(1−29), and thus PEGylation has been considered to present a means of circumventing these clinical limitations by retarding the rapid turnover (*6*−*7*).

PEGylation, defined as a chemical modification with polyethylene glycol (PEG), improves therapeutic potentials of peptides and proteins by increasing proteolytic resistance, diminishing glomerular filtration, and, thus, extending biological half-life (*8*−*11*). In particular, PEGylated peptides and proteins have been shown to decrease proteolytic sensitivities due to increased steric hindrance (*12*−*14*). PEGylation of a DPP IV-sensitive peptide was found to greatly increase its resistance to this peptidase using this mechanism (*15*−*16*). Similarly, PEGylated GRF(1−29) showed a sustained in vivo GH releasing potency despite a decreased in vitro bioactivity (*6*−*7*).

The relationship between PEGylation site and bioactivity in GRF(1−29) analogs has been studied (*6*, *17*−*18*). The N-terminus region of GRF(1−29) is known to be where receptor binding takes place (*6*). In actuality, both N^{α}(Tyr^1)- and Lys^{12}-PEG_{5K}-[Ala^{15}]-GRF(1−29) analogs were found to have significantly lower bioactivities than its original species (*6*, *17*). On the contrary, PEGylation of GRF(1−29) at Lys^{21}-amine well preserved its bioactivity, tenfold higher than that at Lys^{12}-amine (*6*). Accordingly, it has been required to achieve a site-dependent PEGylation as a key consideration for its biological activity issue. Felix and co-workers developed a solid-phase PEGylation method capable of incorporating PEG into target amino acids (Tyr^1, Lys^{12}, Asp^8, Lys^{21}, or Asp^{25}) during the course of solid-phase peptide synthesis (*19*−*20*). Separately, Esposito and co-workers optimized a solution-phase Lys (Lys^{12} or Lys^{21})-amine PEGylation method of GRF(1−29) for a large laboratory-scale preparation (*6*, *21*). However, the practical use of these previous methods seems to be significantly restricted: the former accompanies the drawback of limited production because of its total synthesis character, and the latter still does not provide a uniform product because of two different compositions.

Site-specific PEGylation of bioactive peptides can be completely achieved by gaining all required factors in terms of improved therapeutic potential, uniform product composition, and increased production yield. On the basis of this, in the present study, we propose a unique site-specific PEGylation method using an FMOC-protected GRF(1−29) system that enables the high-yield production of Lys^{21}-amine PEGylated

* Correspondence to Kang Choon Lee, Drug Targeting Laboratory, College of Pharmacy, SungKyunKwan University, 300 Chonchon-dong, Jangan-ku, Suwon City 440-746, Korea. Fax: +82-31-290-7724. Tel: +82-31-290-7704. E-mail: kclee@skku.edu.

10.1021/bc060173z CCC: $37.00 © 2007 American Chemical Society
Published on Web 01/23/2007

Scheme 1

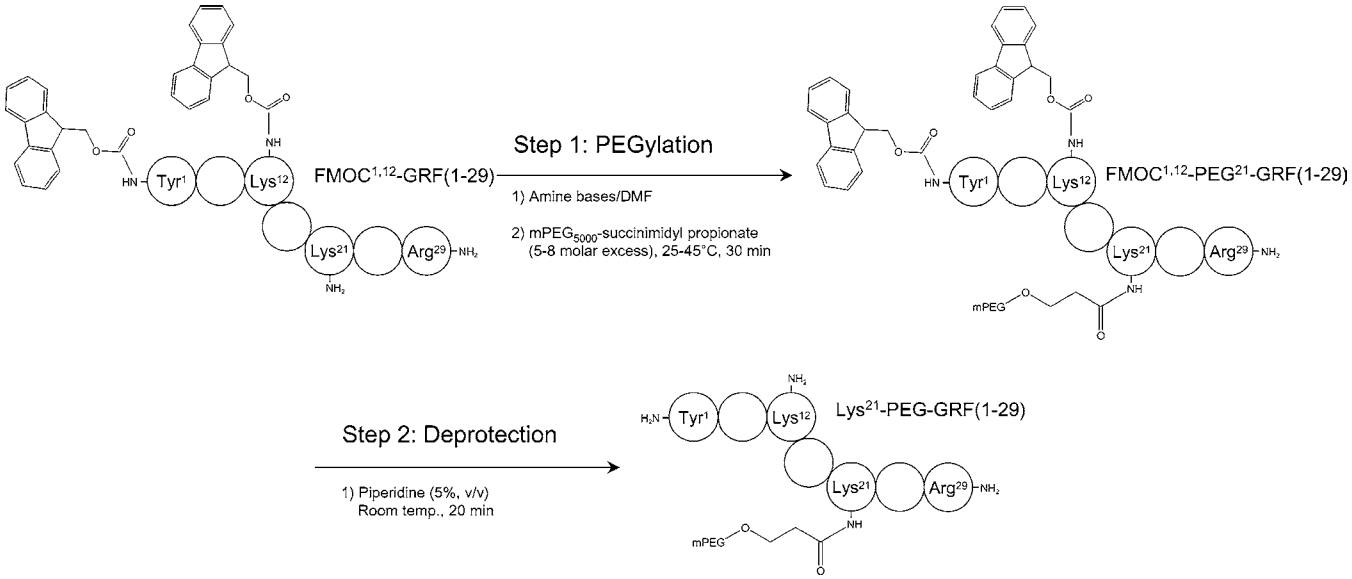


Table 1. Mass Spectrometric Characterization of GRF(1−29) Derivatives and Their Conjugation Sites[c]

	total masses (m/z[a])		endopeptidase Lys-C digested fragments masses (m/z)	
GRF(1−29) species	calculated	observed	calculated	observed
GRF(1−29)	3357.9	3358.1	Tyr^{1}∼Lys^{12}: 1448.6 Val^{13}∼Lys^{21}: 971.2 Leu^{22}∼Arg^{29}: 974.2	972.6 and 1448.2
$FMOC^{1,12}$-GRF(1−29)	3802.4	3803.5	FMOC-Tyr^{1}∼FMOC-Lys^{12}∼Lys^{21}: 2846.2 Leu^{22}∼Arg^{29}: 974.2	2845.7 and 974.2
Lys^{21}-PEG_{5K}-GRF(1−29)	8807[b]	8813[b]	Tyr^{1}∼Lys^{12}: 1448.6 Val^{13}∼PEG_{5K}-Lys^{21}∼Arg^{29}: 7377[b]	1448.1 and 7483[b]

[a] Mass/charge. [b] Number-averaged molecular mass. [c] No other significant peaks were detected in the mass range 800−10 800 m/z in every case.

GRF(1−29), which is known as an isomer with the most promising GH releasing potential.

EXPERIMENTAL PROCEDURES

Materials. GRF(1−29) and FMOC-protected GRF(1−29) at Tyr^{1}- and Lys^{12}-amines ($FMOC^{1,12}$-GRF(1−29)) were supplied by A&PEP, Inc. (Wolsan, Korea). Succinimidyl propionate monomethoxy poly(ethylene glycol) (SP-$mPEG_{5K}$, MW 5000) was purchased from Nektar Therapeutics (Huntsville, AL). Rat GH radioimmunoassay (RIA) kits were purchased from Amersham Pharmacia Biotech (Uppsala, Sweden). Male Wistar rats (150−200 g), male SD rats (180−200 g), and male ICR mice (weighing 18−22 g) were purchased from the Hanlim Experimental Animal Laboratory (Seoul). All other reagents used, unless otherwise indicated, were of the highest quality commercially available.

Stability Study of $FMOC^{1,12}$-GRF(1−29) in Various Amine Bases. $FMOC^{1,12}$-GRF(1−29) stability in various amine bases with different concentrations was evaluated. An aliquot (5 μL) from the $FMOC^{1,12}$-GRF(1−29) stock solution (5 mg/mL) was mixed with the same volume of various amine base (diisopropylethylamine, DIEA; triethylamine, TEA; 4-dimethylaminopyridine, DMAP; 2,4,6-trimethylpyridine, colidine; 2,6-dimethylpyridine, lutidine; and pyridine)/dimethyl formamide (DMF) solutions, and then left at room temperature. At predetermined times, reactions were terminated by adding 10 μL of a mixture (10:6) of 1% trifluoroacetic acid (TFA) in acetonitrile (ACN) and DMF. A 10 μL aliquot of the resulting mixture was subjected to reversed-phase high-performance liquid chromatography (RP-HPLC) using a LiChrospher 100 RP-18 column (250 × 4.0, 5 μm, Merck, Germany) at ambient temperature. Gradient elution was carried out at a flow rate of 1.0 mL/min using solvent A (0.1% TFA in deionized water (DW)) and solvent B (0.1% TFA in ACN) and a gradient profile of 35% B to 90% B over 10 min.

Site-Specific PEGylation of GRF(1−29) using $FMOC^{1,12}$-GRF(1−29). Site-specific (Lys^{21}) PEGylation of GRF(1−29) was examined by focusing on the four dominant reaction factors: (i) type of amine base; (ii) TEA concentration; (iii) PEG amount; and (iv) reaction temperature. The first part of this reaction involved the conjugation of $FMOC^{1,12}$-GRF(1−29) with PEG, and the second part involved the removal of FMOC (9-fluorenylmethoxycarbonyl) moieties from PEGylated $FMOC^{1,12}$-GRF(1−29) as described in Scheme 1. Briefly, an aliquot (5 μL) of $FMOC^{1,12}$-GRF(1−29) in DMF (10 mg/mL) was mixed with the same volume of SP-$mPEG_{5K}$ in DMF at different concentrations (1.0−8.0-folds), and reactions were initiated by adding 10 μL of various amine bases/DMF with different concentrations at reaction temperatures ranging from 25 to 65 °C. At predetermined times, FMOC was removed by adding 1 μL of piperidine at room temperature for 20 min. The overall reaction was quenched by adding 20 μL of 50% DW/ACN containing 1% TFA with thorough shaking. The resulting mixtures were analyzed by RP-HPLC (gradient profile: 34% B to 48% B over 20 min). Production yields (%) were expressed as a percentage of the peak area of Lys^{21}-PEG-GRF(1−29) produced vs the peak area of initial GRF(1−29).

Nonspecific PEGylation of GRF(1−29). Conventional nonspecific GRF(1−29) PEGylation was performed, as previously described (*22*). Briefly, 6.0 mg of SP-$mPEG_{5K}$ was added to 1 mL of GRF(1−29) (2 mg/mL) in 50 mM phosphate buffer solutions (pH 6.5, 7.0, 7.5, 8.0, and 8.5) (molar ratio of GRF-

Table 2. Residual Amounts (%) of FMOC^{1,12}-GRF(1−29) in Various Amine Bases with Different Concentrations after a 90 min Incubation at Room Temperature

	concentration (v/v or w/v %)			
amine base	0.8%	0.4%	0.2%	0.1%
diisopropylethylamine (DIEA)	97.2 ± 0.6	98.5 ± 2.5	99.8 ± 1.0	100.1 ± 0.3
triethylamine (TEA)	97.4 ± 0.9	98.8 ± 1.1	99.1 ± 0.5	99.3 ± 1.4
4-dimethylaminopyridine (DMAP)	96.9 ± 0.8	98.0 ± 0.1	98.6 ± 0.1	99.2 ± 2.3
	16%	8%	4%	2%
2,4,6-trimethylpyridine (Colidine)	99.9 ± 1.1	100.0 ± 0.8	100.4 ± 0.1	100.2 ± 0.3
2,6-dimethylpyridine (Lutidine)	99.3 ± 2.0	99.3 ± 3.1	99.7 ± 0.4	99.9 ± 0.3
pyridine	99.3 ± 0.3	100.1 ± 0.5	100.1 ± 1.5	100.0 ± 0.1

(1−29) to PEG = 1:2). Mixtures were gently shaken at room temperature for 60 min, and reactions were quenched by adjusting the pH to ∼4.0 with phosphoric acid.

Mass Characterization of GRF(1−29) Derivatives and Their Conjugation Sites. GRF(1−29) and its two derivatives together with their conjugation sites were identified using a modification of a previously described MALDI-TOF MS method (*15*, *22*). Briefly, a 5 μL aliquot of endoproteinase Lys-C solution (20 μg/mL in 50 mM Tris-HCl, pH 8.5) was added to a 10 μL of GRF(1−29) derivatives in the same buffer solution (50 μg/mL); digestion was allowed to continue at 37 °C for 30 min. Samples were subjected to MALDI-TOF MS (Voyager-RP Biospectrometry Workstation, PerSeptive Biosystems, Cambridge, MA).

Proteolytic Stability. Proteolytic stabilities of GRF(1−29) and Lys^{21}-PEG-GRF(1−29) were evaluated in rat plasma, liver, and kidney homogenate solutions using a modification of a previously described method (*12*, *23*−*24*). An aliquot (25 μL) of either GRF(1−29) or Lys^{21}-PEG-GRF(1−29) solution (400 μg/mL) was mixed with the same volume of each biological fluid (pre-incubated at 37 °C for 15 min) and then incubated until predetermined times. Incubations were stopped by adding 200 μL of ice-cold methanol. The resulting mixtures were centrifuged at 12 000 rpm for 5 min, and the supernatants were subjected to RP-HPLC (gradient elution: 34% B to 44% B over 20 min, followed by 100% B for 5 min). Degradation half-lives obtained from time vs residual amount curves were calculated by assuming first-order kinetics.

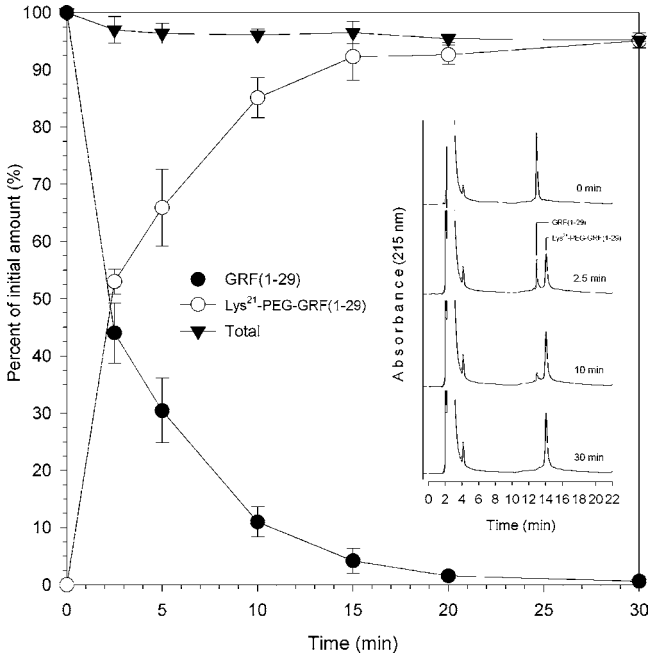


Figure 1. Stoichiometric reaction profiles of Lys^{21}-amine specific PEGylation of GRF(1−29) under optimized conditions, i.e., 0.3% TEA, a 37 °C reaction temperature, and a 5.0-fold PEG molar amount vs GRF(1−29) (inset: RP-HPLC profiles of site-specific PEGylated GRF-(1−29) mixture after FMOC deprotection at each reaction time).

Radioiodination. Radioiodinated GRF(1−29) and Lys^{21}-PEG-GRF(1−29) were prepared using the IODO-GEN method described elsewhere with slight modification (*25*). Briefly, 100 μL of an IODO-GEN (Pierce, Rockford, IL) solution in methylene chloride (1.0 mg/mL) was dispensed into a fresh tube, and the solution was then removed under a nitrogen stream. To such tubes were added 50 μL aliquots of GRF(1−29) or Lys^{21}-PEG-GRF(1−29) (0.4 mg/mL) and 50 μCi of Na^{125}I (Perkin-Elmer, Boston, MA) diluted to 100 mM with PBS (pH 7.0). After allowing reactions at room temperature for 5 min, supernatants were subjected to a C_{18} HPLC column connected to a flow-through radioisotope detector (Ramona 2000, Raytest, Straubenhardt, Germany) (gradient elution: 32% B to 64% B over 20 min). Fractions corresponding to ^{125}I-labeled samples

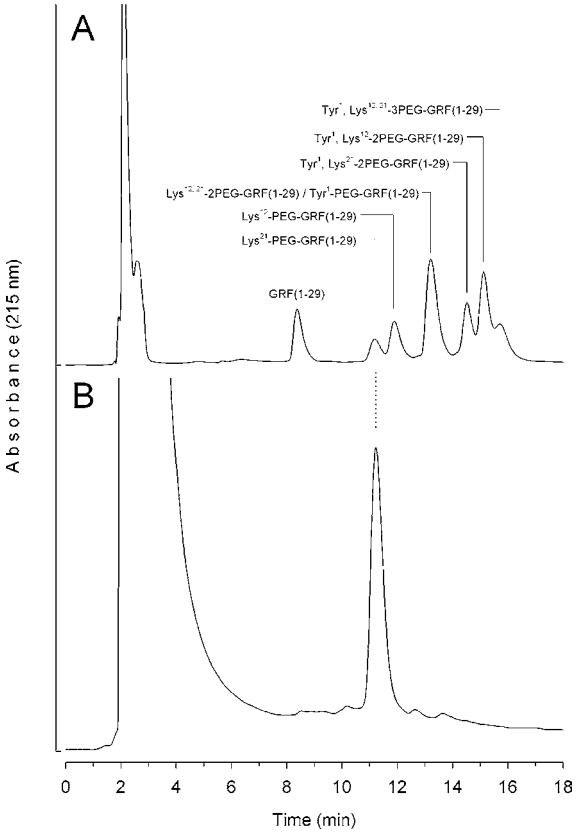


Figure 2. Chromatographic profiles of a conventional non-specific PEGylated GRF(1−29) mixture (A) and of a site-specific PEGylated GRF(1−29) mixture (B). Site-specific PEGylation of GRF(1−29) was achieved at the detailed conditions: 0.3% TEA, a molar ratio of FMOC^{1,12}-GRF(1−29) to PEG = 1:6, a reaction temperature of 37 °C, and a reaction time of 30 min. Nonspecific PEGylation of GRF(1−29) was performed with a 1:2 molar ratio of GRF(1−29) to PEG at pH 7.5 for 60 min.

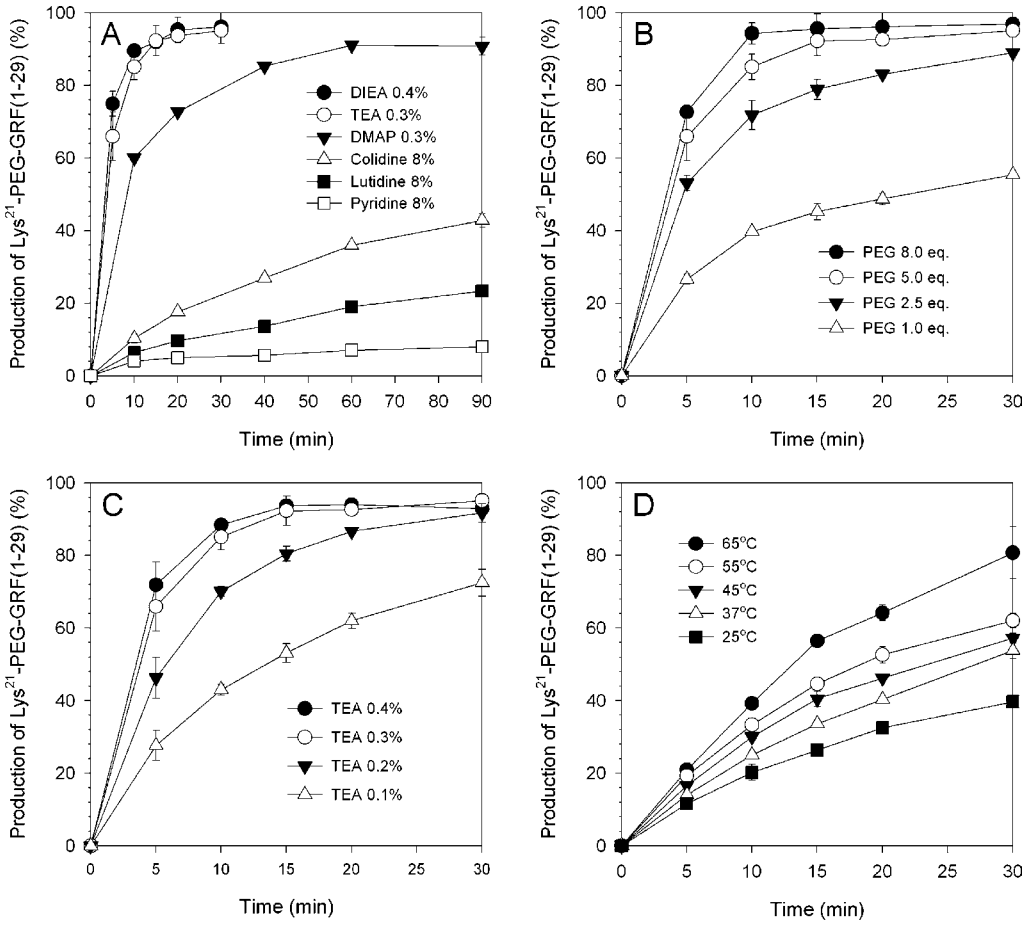


Figure 3. Reaction profiles of site-specific (Lys^{21}) PEGylation of GRF(1−29) according to various reaction factors: (A) type of amine base; (B) molar ratio of $FMOC^{1,12}$-GRF(1−29) to PEG; (C) concentration of TEA; and (D) reaction temperature. Amounts of Lys^{21}-PEG-GRF(1−29) produced were quantified by RP-HPLC, and production yields (%) were expressed as a percentage of the peak area of Lys^{21}-PEG-GRF(1−29) produced vs the peak area of initial GRF(1−29).

were collected, dried under nitrogen, and stored in 10 mM PBS solution (pH 7.4) at 4 °C until required.

Pharmacokinetic Study. Pharmacokinetic dispositions were examined using a modification of a previously described method (*26*). Radioiodinated GRF(1−29) species were administered by subcutaneous (sc) injection (approximately 0.5 μg, 4.1−4.3 × 10^4 cpm) to ICR mice. Mice were sacrificed at predetermined times. Blood samples were obtained by heart puncture, and livers and kidneys were quickly excised and rinsed three times with saline solution. Radioactivities of blood (100 μL) and whole tissue organs were measured by γ-counting (Cobra, Packard Instruments Co., Groningen, The Netherlands). Results were then used to calculate the percentage of injected dose in each organ. In the case of blood, the total blood volume on body weight of ICR mice was assumed to be 70 mL/kg, which is used to calculate the percentage of radioiodinated GRF(1−29) species in whole blood.

In Vitro GH Releasing Activity in Rat Pituitary Cells. Monolayer cultures of anterior pituitary cells obtained from Wistar rats (150−200 g) were performed using a modification of a previously described method (*27*−*28*). Pituitary cells obtained were washed twice with 1 mL of supplemented DMEM and incubated at 37 °C for 30 min. Prior to experimentation, cells were rewashed twice, and the supplemented DMEM medium was replaced with 500 μL of fresh medium containing either GRF(1−29) or Lys^{21}-PEG-GRF(1−29) with different concentrations. The cells were then incubated at 37 °C for 15 min, and media were collected and centrifuged at 10 000 rpm for 10 min. GH concentrations in response to the stimulation of GRF(1−29) species were measured using GH RIA kits (Amersham Pharmacia Biotech, Uppsala, Sweden).

In Vivo GH Releasing Potency in Rats. Male SD rats (180−200 g) were anesthetized (ketamine and xylazine (90/10 mg/kg) i.p.) and cannulated (PE tubing, 0.58 mm i.d., 0.96 mm o.d., Natsume, Tokyo) at the right jugular vein. After a 2 day recovery period, the rats were randomly divided into three groups (4 animals/group), i.e., saline, GRF(1−29), and Lys^{21}-PEG-GRF(1−29). Each sample (100 μg equiv/kg wt) was administered into rats intravenously, and blood samples were collected using the implanted cannulae. Plasma GH levels were measured using GH RIA kits.

RESULTS AND DISCUSSION

Site-specific PEGylation has been considered as an effective way of avoiding the pharmaceutical heterogeneity and pharmacological inefficiency by nonspecific PEGylation, making only biologically necessary PEGylated species (*29*−*31*). Therefore, this enables one to produce the chemically defined PEGylated species with the most bioactivity in terms of uniform composition. Furthermore, if the overall process is robust, site-specific PEGylation can greatly increase the production yield, because it is able to concentrate the reactivity on a single site. On the basis of this concept, we undertook to develop a unique high-yield PEGylation method capable of producing a uniform Lys^{21}-PEG-GRF(1−29) isomer, which has the most preserved bioactivity compared to other isomers.

Initially, we tried to increase the Lys^{21}-amine specificity in GRF(1−29) by either pH control or Lys-amine selectivity in

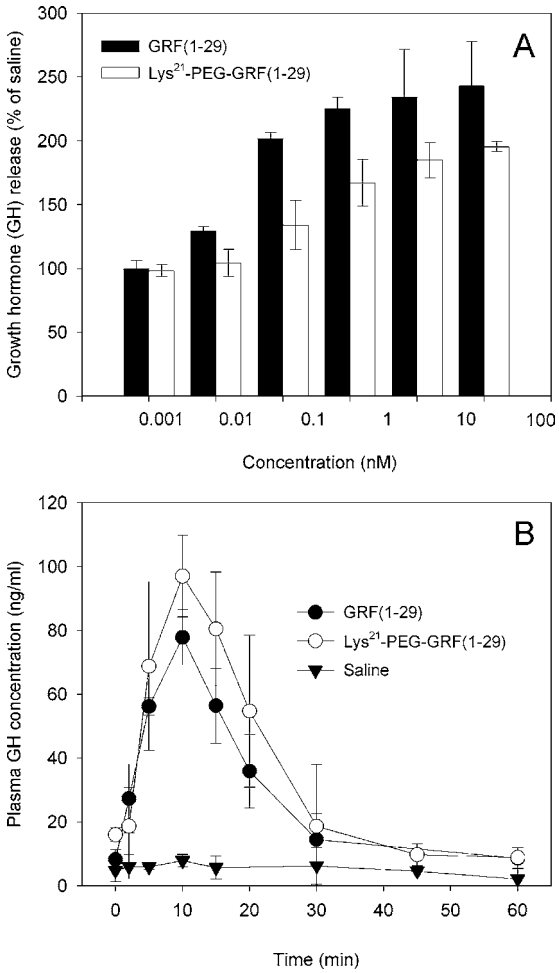


Figure 4. Dose−response curves of GRF(1−29) and Lys^{21}-PEG-GRF(1−29) in terms of stimulated GH release from rat pituitary cells (A). Data were obtained from six individual tests and are presented as means ± SDs. Changes in plasma GH levels following iv administrations of GRF(1−29) and Lys^{21}-PEG-GRF(1−29) (100 μg equiv/kg wt) in rats (B). Data are presented as means ± SDs for four rats/group. AUCs (0−60 min) for GH concentration vs time charts for each group were compared.

the organic phase. However, the Lys^{21}-PEG-GRF(1−29) production seemed to still be restricted by both cases because all GRF(1−29) amines are still open; only 5.3−15.2% (pH 6.5−8.5) and approximately 25% (0.3−1.2% TEA) of Lys^{21}-PEG-GRF(1−29) production were made, respectively (data not shown). Consequently, we confirmed that such methods are ineffective enough for the high-yield preparation of Lys^{21}-PEG-GRF(1−29). Thus, we introduced a unique GRF(1−29) derivative (FMOC^{1,12}-GRF(1−29)), which is FMOC-protected at Tys^{1}- and Lys^{12}-amines but remained available at Lys^{21}-amine.

As summarized in Table 1, this FMOC^{1,12}-GRF(1−29) derivative showed the increased mass of 3803.5 Da by its two FMOC presence (445 Da) vs the observed mass of GRF(1−29) (3358.1 Da). Furthermore, the masses of the Lys-C digested FMOC^{1,12}-GRF(1−29) fragments were determined to be 2845.7 and 974.2 Da, corresponding to the fragments of Tyr^{1}-FMOC−Lys^{12}-FMOC−Lys^{21} (calcd 2846.2) and Leu^{22}-Arg^{29} (calcd 974.2), respectively. These mass spectrometric profiles of FMOC^{1,12}-GRF(1−29) indicated that the FMOC groups are conjugated to the aimed amines (Tyr^{1} and Lys^{12}) of GRF(1−29), and that this protection would provide a much greater opportunity for Lys^{21} amine-specific PEGylation.

Prior to optimizing the site-specific PEGylation process, the stability of the FMOC moiety in FMOC^{1,12}-GRF(1−29) was assessed in DMF solutions containing amine bases. Several amine bases were inevitably added to activate the PEGylation reactivity, because this hydrophobic derivative did not show substitution activity under the aprotic condition of DMF. However, since the amine base addition can result in the potential danger that deteriorates the FMOC^{1,12}-GRF(1−29) integrity because of their strong substitution activity, its chemical stability during the course of PEGylation has become another key consideration for achieving a well-controlled site-specific (Lys^{21}) PEGylation. We tried to investigate the concentration ranges of each amine base for obtaining both good stability and PEGylation reactivity. FMOC stabilities were found to be well-maintained (96.9 ± 0.8% remaining, 37 °C, 90 min) under most conditions, particularly in 0.2−0.4% TEA range with >99.3% remaining over 30 min (Table 2).

On the basis of this stability profile, FMOC^{1,12}-GRF(1−29) could be conjugated with PEG at Lys^{21}-amine without site competition in the presence of various amine bases. After PEGylation, the FMOC moieties were removed via a typical deprotection process using piperidine (5%), and this step did not affect significantly the PEGylation reaction. In this way, Lys^{21}-PEG-GRF(1−29) was two-step produced in high yield using an FMOC protection/deprotection strategy (Scheme 1). Furthermore, this process showed a stoichiometric manner, and thus the amount of FMOC^{1,12}-GRF(1−29) reacted quantitatively matched the amount of Lys^{21}-PEG-GRF(1−29) produced, maintaining the >95.0% level of the total amount (Figure 1). This finding indicates that Lys^{21}-PEG-GRF(1−29) production is completely originated from FMOC^{1,12}-GRF(1−29) without significant side reactions. Figure 2 displays the advantage of this site-specific method in GRF(1−29) PEGylation vs the nonspecific method. The chromatogram of site-specific PEGylated GRF(1−29) mixture shows only Lys^{21}-PEG-GRF(1−29) with trace levels of other products (Figure 2B), whereas a nonspecific PEGylated GRF(1−29) mixture includes a variety of possible isomers of mono-, di-, and tri-PEGylated GRF(1−29)s as reported previously (*22*) (Figure 2A).

The next goal was to determine an optimized reaction condition capable of maximizing the Lys^{21}-PEG-GRF(1−29) production yield. To achieve this, four major reaction factors were examined as follows: (i) type of amine base, (ii) PEG amount (molar ratio of FMOC^{1,12}-GRF(1−29) to PEG), (iii) TEA concentration, and (iv) reaction temperature. First, the type of amine base was considered to be a key factor. As shown in Figure 3A, amine bases of TEA, DIEA, and DMAP displayed effective PEGylation reactivities, whereas other pyridine bases are ineffective (at PEG 5.0 equiv, 37 °C). Despite the similar PEGylation reactivity, we finally chose TEA as a candidate base because it provides an excellent FMOC stability along with a rapid reaction time. Second, the optimum molar ratio of FMOC^{1,12}-GRF(1−29) to PEG was determined to fall in the range of 1:5 to 1:6 (at 0.3% TEA, 37 °C). No significance was observed beyond this range, and no complete reactions occurred below this (Figure 3B). Third, TEA appeared to have good reactivity in the concentration range from 0.2% to 0.4% (v/v) (at PEG 2.5 equiv, 37 °C), but the reactivity was clearly decreased below 0.2% (Figure 3C). Finally, the PEGylation reaction rapidly increased with increasing reaction temperature from 25 to 65 °C (at PEG 1.5 equiv, 0.3% TEA) (Figure 3D). However, the serious instability of the FMOC moiety was observed at reaction temperatures of over 55 °C (data not shown).

Through this careful investigation, the site-specific (Lys^{21}) PEGylation of GRF(1−29) was successfully achieved using the following optimized conditions: 0.2−0.3% TEA, a reaction temperature of 25−45 °C, a reaction time of 30 min, and a 5.0−6.0-fold molar PEG amount. Under this condition, the Lys^{21}-PEG-GRF(1−29) production yield was elevated to ca. 95%,

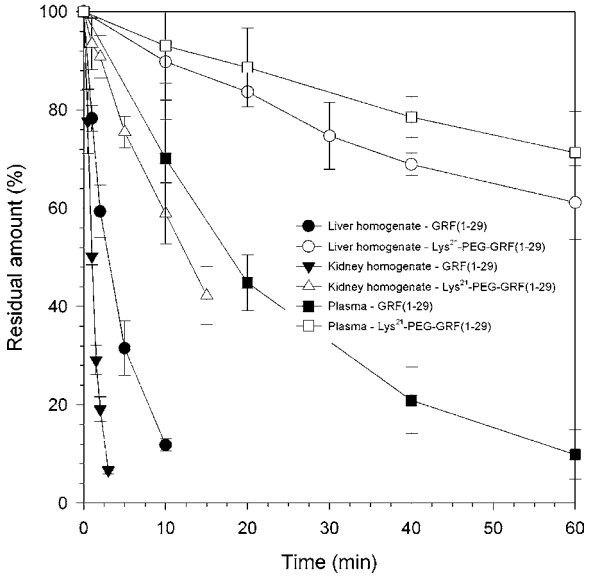


Figure 5. Degradation profiles of GRF(1−29) and Lys^{21}-PEG-GRF-(1−29) incubated with rat plasma or rat liver or kidney homogenates. Samples were analyzed by RP-HPLC. Data are presented as the means ± SDs of three determinations.

which is 6.3- and 3.8-fold greater than the yield by nonspecific PEGylation at pH 8.5 or in 0.3−1.2% TEA/DMSO, respectively. In addition, despite the high concentration (∼15.0 mg/mL) of FMOC^{1,12}-GRF(1−29), the Lys^{21}-PEG-GRF(1−29) production yields were maintained at 92.2−95.0%. Therefore, the devised site-specific PEGylation process requires only a single supporting chromatography step to isolate Lys^{21}-PEG-GRF(1−29) even at larger scale (>150 mg) due to minimal presence of other side products. Finally, the purified Lys^{21}-PEG-GRF(1−29) showed the symmetric mass peaks (M_n = 8813 Da, at a purity of >99.2% by RP-HPLC) together with the appropriate identity for Lys^{21}-amine PEGylation (Table 1).

The biological potential of this site-specific Lys^{21}-PEG-GRF-(1−29) was evaluated by examining its GH releasing activity in vitro and in vivo. First, the effect of Lys^{21}-PEG-GRF(1−29) on GH release was evaluated in rat pituitary cells. Despite the Lys^{21}-amine selection, the remaining GH releasing activity of Lys^{21}-PEG-GRF(1−29) was only 15% that of GRF(1−29) (EC_{50} = 0.219 ± 0.012 and 0.031 ± 0.002 ng/mL, respectively) (Figure 4A), consistent with the previous report (*6*). Contrary to the in vitro result, however, Lys^{21}-PEG-GRF(1−29) displayed a higher GH releasing potency than GRF(1−29) in conscious rats. In an initial GH peak analysis, plasma GH levels peaked at 77.9 ± 8.7 and 97.1 ± 12.8 ng/mL at 10 min following the iv administrations (100 μg equiv/kg wt) of GRF(1−29) and Lys^{21}-PEG-GRF(1−29), respectively (Figure 4B). The area under the curve (AUC) of GH by Lys^{21}-PEG-GRF(1−29) stimulation was greater than that of GRF(1−29) ($AUC_{0\sim60\ min}$= 1992.1 ± 449.1 vs 1626.1 ± 376.5 ng·min/mL). Despite a reduced initial GH release, Lys$^{12/21}$-PEG-GRF(1−29) was reported to have sustained long-acting in vivo GH releasing potency with additional GH release at 3 and 6 h after injection (*6*−*7*). This PEGylation effect is due to the compensation mechanism by the PEGylation advantage in terms of augmented proteolytic stability and extended plasma lifetime in vivo.

Significantly, the proteolytic stabilities of Lys^{21}-PEG-GRF-(1−29) in rat plasma, liver, and kidney homogenates, which are considered to be the representative in vivo enzyme systems containing DPP IV, were improved. GRF(1−29) was rapidly degraded in all systems, with half-lives of 18.0 ± 4.8, 3.3 ± 0.1, and 0.7 ± 0.1 min, respectively (Figure 5). On the contrary, Lys^{21}-PEG-GRF(1−29) displayed greatly increased resistance

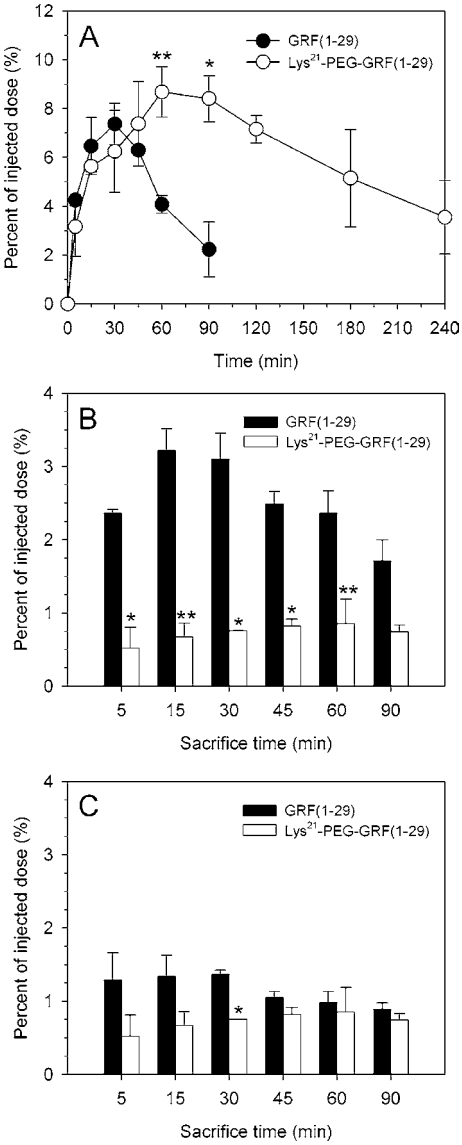


Figure 6. Pharmacokinetic dispositions of ^{125}I-GRF(1−29) and ^{125}I-Lys^{21}-PEG-GRF(1−29) in mouse (A) blood, (B) liver, and (C) kidney following sc administrations. Data are presented as the means ± SDs of three determinations. Significances were determined using the Student's *t* test (*P < 0.006 and **P < 0.03 over GRF(1−29)).

to these enzyme systems, with 7.0-, 25.4-, and 16.4-fold extended half-lives, respectively. Furthermore, the pharmacokinetic profiles of ^{125}I-Lys^{21}-PEG-GRF(1−29) in mice were clearly enhanced vs ^{125}I-GRF(1−29) (Figure 6A). ^{125}I-Lys^{21}-PEG-GRF(1−29) was found to have a 3.8-fold greater AUC_{inf} than that of ^{125}I-GRF(1−29) (2157.0 ± 523.2 vs 566.4 ± 104.5%·min, respectively) in blood (Figure 6B). In addition, PEGylation significantly reduced the liver distribution (5−90 min) of GRF(1−29) by 2.2 times (p < 0.03) and the kidney distribution (5−90 min) of ^{125}I-GRF(1−29) by about 40% (Figure 6C). Accordingly, it is clear that these improved proteolytic resistance and pharmacokinetic dispositions of Lys^{21}-PEG-GRF(1−29) resulted in the GH release potency in vivo, and these may equate to therapeutic potential for the treatment of GH-related disorders.

CONCLUSIONS

We developed a unique two-step site-specific (Lys^{21}) method of PEGylating GRF(1−29) using an FMOC-protected GRF-(1−29) derivative. This method was used to produce the uniform Lys^{21}-PEG-GRF(1−29) in high yield (∼95%), and this conju-

gate was found to have better pharmacokinetic/pharmacological profiles than GRF(1−29). Recently, site-specific PEGylation has often been achieved by using protein mutants or peptide analogs, which have the replaced amino acid sequence to confer site specificity. However, the PEGylation method described here involves no change to the native GRF(1−29) properties, because the FMOC groups are removed by a straightforward deprotection process after PEGylation. We believe that our findings suggest that PEGylation using FMOC-protected peptides has great potential for the mass production of site-specific PEGylated peptides.

ACKNOWLEDGMENT

This work was supported by a Korea Research Foundation Grant of Korea (KRF-2005-041-E00503).

LITERATURE CITED

(1) Ankersen, M., Hansen, T. K., Ahnfelt-Ronne, I., and Kappelgaard, A. M. (1999) Growth hormone secretagogues: recent advances and applications. *Drug Discovery Today 4* (11), 497−506.

(2) Jansen, M., Darby, I., Abribat, T., Dubreuil, P., Ferdinandi, E. S., and Hardy, J. G. (2004) Pulmonary delivery of TH9507, a growth hormone releasing factor analogue, in the dog. *Int. J. Pharm. 276* (1−2), 75−81.

(3) Pinski, J., Yano, T., Groot, K., Zsigo, J., Rekasi, J., Comaru-Schally, A. M., and Schally, A. V. (1993) Comparison of GH-stimulation by GH-RH(1−29)NH_2 and an agmatine29 GH-RH analog, after intravenous, subcutaneous, and intranasal administration and after pulmonary inhalation in rats. *Int. J. Pept. Protein Res. 41* (3), 246−249.

(4) Bongers, J., Lambros, T., Ahmad, M., and Heimer, E. P. (1992) Kinetics of dipeptidyl peptidase IV proteolysis of growth hormone-releasing factor and analogs. *Biochim. Biophys.* Acta *1122* (2), 147−153.

(5) Frohman, L. A., Downs, T. R., Williams, T. C., Heimer, E. P., Pan, Y. C., and Felix, A. M. (1986) Rapid enzymatic degradation of growth hormone-releasing hormone by plasma in vitro and in vivo to a biologically inactive product cleaved at the NH_2 terminus, *J. Clin. Invest. 78* (4), 906−913.

(6) Esposito, P., Barbero, L., Caccia, P., Caliceti, P., D'Antonio, M., Piguet, G., and Veronese, F. M. (2003) PEGylation of growth hormone-releasing hormone (GRF) analogues. *Adv. Drug Delivery Rev. 55* (10), 1279−1291.

(7) D'Antonio, M., Louveau, I., Esposito, P., Bertolino, M., and Canali, S. (2004) Pharmacodynamic evaluation of a PEGylated analogue of human growth hormone releasing factor in rats and pigs. *Growth Horm. IGF Res. 14* (3), 226−234.

(8) Harris, J. M., and Chess, R. B. (2003) Effect of PEGylation on pharmaceuticals. *Nat. Rev. Drug Discovery 2* (3), 214−221.

(9) Veronese, F. M., and Pasut, G. (2005) PEGylation, successful approach to drug delivery. *Drug Discovery Today 10* (21), 1451−1458.

(10) Greenwald, R. B., Choe, Y. H., Mcguire, J., and Conover, C. D. (2003) Effective drug delivery by PEGylated drug conjugates. *Adv. Drug Delivery Rev. 55* (2), 217−250.

(11) Roberts, M. J., Bentley, M. D., and Harris, J. M. (2002) Chemistry for peptide and protein PEGylation. *Adv. Drug Delivery Rev. 54* (4), 459−476.

(12) Lee, K. C., Moon, S. C., Park, M. O., Lee, J. T., Na, D. H., Yoo, S. D., Lee, H. S., and DeLuca, P. P. (1999) Isolation, characterization, and stability of positional isomers of mono-PEGylated salmon calcitonins. *Pharm. Res. 16* (6), 813−818.

(13) Caliceti, P., Salmaso, S., Walker, G., and Bernkop-Schnurch, A. (2004) Development and in vivo evaluation of an oral insulin-PEG delivery system. *Eur. J. Pharm. Sci. 22* (4), 315−323.

(14) Lee, H., Jang, I. H., Ryu, S. H., and Park, T. G. (2003) N-terminal site-specific mono-PEGylation of epidermal growth factor. *Pharm. Res. 20* (5), 818−825.

(15) Lee, S. H., Lee, S., Youn, Y. S., Na, D. H., Chae, S. Y., Byun, Y., and Lee, K. C. (2005) Synthesis, characterization, and pharmacokinetic studies of PEGylated glucagon-like peptide-1. *Bioconjugate Chem. 16* (2), 377−382.

(16) Lee, S., Youn, Y. S., Lee, S.-H., Byun, Y., and Lee, K. C. (2006) PEGylated glucagon-like peptide-1 displays preserved effects on insulin release in isolated pancreatic islets and improved biological activity in db/db mice. *Diabetologia 49* (7), 1608−1611.

(17) Felix, A. M., Lu, Y., and Campbell, R. M. (1995) Pegylated peptides IV. Enhanced biological activity of site-directed pegylated GRF analogs. *Int. J. Pept. Protein Res. 46* (3−4), 253−264.

(18) Campbell, R. M., Heimer, E. P., Ahmad, M., Eisenbeis, H. G., Lambros, T. J., Lee, Y., Miller, R. W., Stricker, P. R., and Felix, A. M. (1997) Pegylated peptides V. Carboxy-terminal PEGylated analogs of growth hormone-releasing factor (GRF) display enhanced duration of biological activity in vivo. *J. Pept. Res. 49* (6), 527−537.

(19) Lu, Y.-A., and Felix, A. M. (1994) Pegylated peptides II: Solid-phase synthesis of amino-, carboxy-, and side-chain pegylated peptides. *Int. J. Pept. Protein Res. 43* (2), 127−138.

(20) Lu, Y.-A., and Felix, A. M. (1994) Pegylated peptides III: Solid-phase synthesis with pegylating reagents of varying molecular weight: synthesis of multiply pegylated peptides. *React. Polym. 22*, 221−229.

(21) Piguet, G., Gatti, M., Barbero, L., Traversa, S., Caccia, P., and Esposito, P. (2002) Set-up of large laboratory-scale chromatographic separations of poly(ethylene glycol) derivatives of the growth hormone-releasing factor 1−29 analogue. *J. Chromatogr., A 944* (1−2), 141−148.

(22) Youn, Y. S., Na, D. H., Yoo, S. D., Song, S.-C., and Lee, K. C. (2004) Chromatographic separation and mass spectrometric identification of positional isomers of polyethylene glycol-modified growth hormone-releasing factor (1−29). *J. Chromatogr., A 1061* (1), 45−49.

(23) Na, D. H., Youn, Y. S., Park, E. J., Lee, J. M., Cho., O. R., Lee, K. R., Lee, S. D., Yoo, S. D., DeLuca, P. P., and Lee, K. C. (2004) Stability of PEGylated salmon calcitonin in nasal mucosa. *J. Pharm. Sci. 93* (2), 256−261.

(24) Youn, Y. S., Jung, J. Y., Oh, S. H., Yoo, S. D., and Lee, K. C. (2006) Improved intestinal delivery of salmon calcitonin by Lys^{18}-amine specific PEGylation: Stability, permeability, pharmacokinetic behavior and in vivo hypocalcemic efficacy. *J. Controlled Release 114* (3), 334−342.

(25) Shin, B. S., Kim, C. H., Jun, Y. S., Park, E. H., Hur, M.-W., Lee, K. C., Yoon, Y. S., Lee, M.-N., and Yoo, S. D. (2005) Dose-linear pharmacokinetics, tissue distribution, and excretion of a recombinant fusion protein ^{125}I-GST-TatdMt possessing potent anti-obesity activity. *Regul. Pept. 129* (1−3), 25−30.

(26) Youn, Y. S., Na, D. H., Yoo, S. D., Song, S.-C., and Lee, K. C. (2005) Carbohydrate-specifically polyethylene glycol-modified ricin A-chain with improved therapeutic potential. *Int. J. Biochem. Cell Biol. 37* (7), 1525−1533.

(27) Cheng, J., Wu, T.-J., Butler, B., and Cheng, K. (1997) Growth hormone releasing peptide: A comparison of the growth hormone releasing activities of GHRP-2 and GHRP-6 in rat primary pituitary cells. *Life Sci. 60* (16), 1385−1392.

(28) Giustina, A., Bonfanti, C., Licini, M., Ragni, G., and Stefana, B. (1997) Hexarelin, a novel GHRP-6 analog, stimulates growth hormone (GH) release in a GH-secreting rat cell line (GH_1) insensitive to GH-releasing hormone. *Regul. Pept. 70* (1), 49−54.

(29) Yamamoto, Y., Tsutsumi, Y., Yoshioka, Y., Nishibata, T., Kobahashi, K., Okamoto, T., Mukai, Y., Shimizu, T., Nakagawa, S., Nagata, S., and Mayumi, T. (2003) Site-specific PEGylation of a lysine-deficient TNF-α with full bioactivity. *Nat. Biotechnol. 21* (5), 546−552.

(30) Moreadith, R. W., and Collen, D. (2003) Clinical development of PEGylated recombinant staphylokinase (PEG-Sak) for bolus thrombolytic treatment of patients with acute myocardial infarction. *Adv. Drug Delivery Rev. 55* (10), 1337−1345.

(31) Rosendahl, M. S., Doherty, D. H., Smith, D. J., Carlson, S. J., Chlipala, E. A., and Cox, G. N. (2005) A long-acting, highly potent interferon α-2 conjugate created using site-specific PEGylation. *Bioconjugate Chem. 16* (1), 200−207.

BC060173Z

Synthesis and Binding Affinity of a Fluorine-Substituted Peroxisome Proliferator-Activated Gamma (PPARγ) Ligand as a Potential Positron Emission Tomography (PET) Imaging Agent

Byung Chul Lee,[†] Kyo Chul Lee,[‡] Hsiaoju Lee,[§] Robert H. Mach,[§] and John A. Katzenellenbogen*[,†]

Department of Chemistry, University of Illinois, Urbana, Illinois 61801, Laboratory of Radiopharmaceuticals, Korea Institute of Radiological and Medical Sciences, Seoul, South Korea, and Division of Radiological Sciences, Washington University School of Medicine, St. Louis, Missouri, 63110. Received June 30, 2006; Revised Manuscript Received January 12, 2007

The peroxisome proliferator-activated receptor γ (PPARγ) is an important regulator of lipid metabolism and the differentiation of pre-adipocytes. Thus, imaging PPARγ in vivo using positron-emission tomography (PET) might be useful in assessing lipid metabolism disorders and identifying tumor cell differentiation. A fluorine-substituted PPARγ ligand from tyrosine-benzophenone class, compound **1**, has a very high affinity for PPARγ receptor (K_i = 0.14 nM). To develop this compound as a PPARγ PET imaging agent, we investigated synthetic routes suitable for its labeling with the short-lived PET radionuclide fluorine-18 ($t_{1/2}$ = 110 min). To obtain the high specific activity material needed for receptor imaging with this isotope, reactions need to proceed efficiently, within a short time, starting from fluoride ion at the tracer level. The most promising approach involves introduction of fluorine into a suitable benzophenone precursor, followed by efficient coupling of this intermediate with the heterocyclic tyrosine component using a copper-catalyzed Ullmann-type condensation.

INTRODUCTION

The nuclear hormone receptor, peroxisome proliferator-activated receptor γ (PPARγ) plays critical roles in adipogenesis and insulin-mediated glucose homeostasis, and in liposarcoma, PPARγ ligands can induce cancer cells to stop proliferating, lose their malignant character, and undergo terminal differentiation to adipocytes (*1*−*10*). PPARγ is also expressed in other tumor cells, including several breast cancer cell lines, as well as in animal models for breast cancer derived from primary and metastatic tumors, and recently, a number of laboratories have shown that PPARγ activation alters the growth characteristics of breast cancer cells (*6*, *9*). Thus, PPARγ is an attractive target for in vivo imaging that might be useful in assessing lipid metabolism disorders associated with obesity, type 2 diabetes, atherogenesis, and restenosis (*11*), and in identifying small metastatic tumors.

In previous work, our group has evaluated an initial set of fluorine-18 labeled compounds based on PPARγ ligands of the phenyl propanoic acid class, such as the fluorine-substituted analog of SB 213068 (Chart 1) (*12*). These compounds showed good binding affinities for PPARγ and good binding selectivity relative to the other receptor subtypes, PPARα and PPARδ. Though respectable, the PPARγ affinities of this set of compounds were not as high as would be desirable for imaging.

Since our prior work, ligands that have much higher affinity and selectivity for both PPARγ and PPARα have been discovered, largely through the efforts of researchers at Glaxo SmithKline (GSK) (*13*−*16*). In particular, members of the novel benzophenone-tyrosine class, exemplified by farglitazar (GI 262570), have a very high affinity for PPARγ, and they have high potency in vivo. Our group also recently prepared three fluorine-substituted members of the benzophenone−tyrosine class that retain high affinity and selectivity for PPARγ and thus appear to be attractive compounds to evaluate further as agents to be labeled with the short-lived positron-emitting radionuclide fluorine-18 ($t_{1/2}$ = 110 min) for imaging PPARγ in vivo using positron-emission tomography (PET).

In this work, we have selected one fluorine-substituted analog of farglitazar, namely, compound **1**, which was also previously described by GSK (*13*−*16*), and we have investigated synthetic routes by which it might be labeled with fluorine-18 in a manner that is rapid, efficient, and suitable for starting from fluoride ion at the tracer level, as would be needed to obtain the high specific activity material needed for receptor imaging with this radioisotope.

EXPERIMENTAL SECTION

Materials and Methods. Solvents and reagents were purchased from the following commercial sources: Aldrich, Fisher, or Acros. Anhydrous THF, Et_2O, and CH_2Cl_2 were collected using a solvent dispensing system built by J. C. Meyer based on a design described by Pahgborn (*17*). TLC was performed on Merck F_{254} silica plates. The chemical shifts were reported in parts per million downfield from tetramethylsilane and were referenced to the internal solvent peaks. Coupling constants were reported in hertz. ^{1}H NMR and ^{13}C NMR spectra were recorded on Varian U400 and U500 Instruments (Palo Alto, CA). Melting points were determined using a Thomas-Hoover capillary melting point apparatus (Philadelphia, PA) and are uncorrected. Low-resolution mass spectra (MS) were recorded on a Micromass 70-VSE, Finnigan MAT CH-5 and ZAB-SE spectrometers, respectively. High-resolution mass spectra were obtained on a VG 70-SE-4E spectrometer. Mass spectra were acquired in the positive ion mode under electron impact (EI, 70 eV), fast-atom bombardment mass (FAB), and electrospray ionization (ESI) methods. Microwave-assisted reactions were performed with model 520A Resonance Instruments, Inc. (Skokie, IL). N^{α}-*tert*-Butoxycarbonyl-L--tyrosine *tert*-butyl ester, 2-(5-methyl-2-phe-

* Corresponding author. John A. Katzenellenbogen, Department of Chemistry, University of Illinois, 600 South Mathews Avenue, Urbana, Illinois 61801. Telephone: 217-333-6310. Fax: 217-333-7325. E-mail: jkatzene@uiuc.edu.

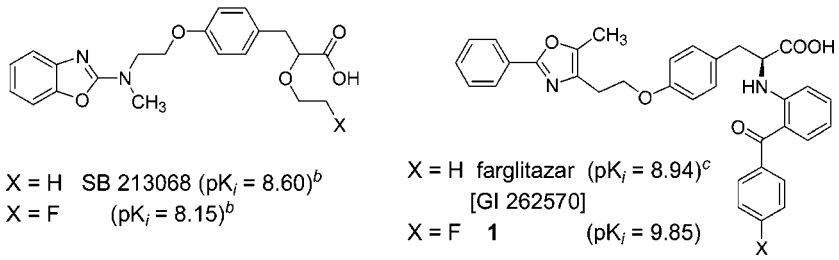
[†] University of Illinois.

[‡] Korea Institute of Radiological and Medical Sciences.

[§] Washington University School of Medicine.

10.1021/bc060190o CCC: $37.00 © 2007 American Chemical Society
Published on Web 02/20/2007

Chart 1. The Structure of PPARγ Ligands (SB 213068 and farglitazar [GI 262570]) and Fluorine-Substituted Analogs[a]



[a] pK_i: -log of the concentration of test compound required to achieve an apparent K_i value. [b] ref 12. [c] ref 14.

nyloxazol-4-yl)ethanol, and compound **11** were prepared according to the literature (*18*−*20*, respectively).

(2*S*)-[2-(4-Fluorobenzoyl)phenylamino]-3-(4-hydroxyphenyl)propionic Acid Methyl Ester (7). To a stirred solution of L--tyrosine methyl ester (1.90 g, 9.74 mmol) in toluene (10 mL) and 1,4-dioxane (10 mL) was added 2-(4-fluorobenzoyl)-cyclohexanone (2.41 g, 10.95 mmol). The reaction mixture was refluxed using a Dean−Stark trap for 12 h under nitrogen atmosphere. The resulting solution was evaporated, and anisole (20 mL) and an excess of 10% Pd/C were added. The reaction mixture was refluxed for 2 h. The resulting solution was evaporated and extracted with EtOAc (100 mL) and washed with H_2O (50 mL) and brine (50 mL). The organic layer was separated and dried with $MgSO_4$. Purification of this material by silica gel flash column chromatography using 20% EtOAc/hexane as eluant afforded 2.47 g (65%) of the title compound **7** as an orange oil: ^{1}H NMR (400 MHz, $CDCl_3$) δ 3.11 (dd, J = 14.0, 7.2 Hz, 1H), 3.18 (dd, J = 14.0, 5.6 Hz, 1H), 3.70 (s, 3H), 4.40 (t, J = 8.0 Hz, 1H), 6.59−6.70 (m, 4H), 7.07−7.13 (m, 4H), 7.33−7.38 (m, 1H), 7.42−7.45 (m, 1H), 7.59−7.63 (m, 2H); ^{13}C NMR (100 MHz, $CDCl_3$) δ 37.84, 52.38, 57.84, 111.94, 115.04, 115.26, 115.53, 118.06, 127.50, 130.31, 131.65, 135.18, 136.02, 149.94, 155.10, 163.15, 165.65, 173.14, 198.14; MS (FAB) *m*/*z* 394 (M + H). HRMS calcd for $C_{23}H_{21}FNO_4$ 394.1455, found 394.1455.

(2*S*)-[2-(4-Nitrobenzoyl)phenylamino]-3-(4-hydroxyphenyl)-propionic Acid Methyl Ester (8). Prepared from L-tyrosine methyl ester and 2-(4-nitrobenzoyl)cyclohexanone by the method used to prepare compound **7** and obtained as an orange oil (10%): ^{1}H NMR (400 MHz, $CDCl_3$) δ 3.13 (dd, J = 14.0, 7.2 Hz, 1H), 3.21 (dd, J = 13.6, 5.6 Hz, 1H), 3.73 (s, 3H), 4.43 (m, 1H), 6.57−6.66 (m, 2H), 6.72 (d, J = 8.4 Hz, 2H), 7.11 (d, J = 8.4 Hz, 2H), 7.30−7.40 (m, 2H), 7.70 (d, J = 8.8 Hz, 2H), 8.29 (d, J = 8.4 Hz, 2H); ^{13}C NMR (100 MHz, $CDCl_3$) δ 37.82, 52.46, 57.62, 112.06, 115.55, 116.95, 123.36, 127.62, 129.58, 130.39, 135.27, 136.05, 145.77, 148.78, 150.58, 154.99, 172.90, 197.13; MS (FAB) *m*/*z* 421 (M + H). HRMS calcd for $C_{23}H_{21}N_2O_6$ 421.1400, found 421.1399.

(2*S*)-[2-(4-Fluorobenzoyl)phenylamino]-3-{4-[2-(5-methyl-2-phenyloxazol-4-yl)ethoxy]phenyl}propionic Acid Methyl Ester (9). A stirred solution of compound **7** (193 mg, 0.49 mmol), 2-(5-methyl-2-phenyloxazol-4-yl)ethanol (100 mg, 0.49 mmol), and triphenylphosphine (129 mg, 0.49 mmol) in THF (30 mL) at room temperature was treated with diethyl azodicarboxylate (77 μL, 0.49 mmol) in THF (5 mL) via dropwise addition. The resulting solution was stirred for 16 h at room temperature, and then the solvent was removed in vacuo. The crude reaction mixture was purified by silica gel flash column chromatography using 30% EtOAc/hexane as eluant to afford 127 mg (45%) of the title compound **9** as a yellow oil: ^{1}H NMR (400 MHz, $CDCl_3$) δ 2.35 (s, 3H), 2.95 (t, J = 4.0 Hz, 2H), 3.11 (dd, J = 13.6, 7.2 Hz, 1H), 3.20 (dd, J = 13.6, 6.0 Hz, 1H), 3.69 (s, 3H), 4.20 (t, J = 4.0 Hz, 2H), 4.39 (m, 1H), 6.57−6.65 (m, 2H), 6.83 (d, J = 8.0 Hz, 2H), 7.10−7.18 (m, 4H), 7.31−7.35 (m, 1H), 7.40−7.45 (m, 4H), 7.61−7.65 (m, 2H), 7.98 (d, J = 8.0 Hz, 2H), 8.79 (d, J = 4.0 Hz, 1H); ^{13}C NMR (100 MHz, $CDCl_3$) δ 10.14, 26.20, 37.96, 52.16, 57.80, 66.48, 111.76, 114.53, 114.92, 115.03 (J = 21.0 Hz), 117.99, 125.80, 127.57, 128.16, 128.57, 129.70, 130.17, 131.53 (J = 8.0 Hz), 132.51, 134.86, 135.02, 136.19 (J = 4.0 Hz), 144.97, 149.97, 157.70, 159.334, 164.29 (J = 250.0 Hz), 172.87, 197.55; MS (FAB) *m*/*z* 579 (M + H). HRMS calcd for $C_{35}H_{32}FN_2O_5$ 579.2295, found 579.2295.

(2*S*)-[2-(4-Nitrobenzoyl)phenylamino]-3-{4-[2-(5-methyl-2-phenyloxazol-4-yl)ethoxy]phenyl}propionic Acid Methyl Ester (10). Prepared from **8** by the method used to prepare **9** and obtained as an orange oil (44%): ^{1}H NMR (500 MHz, $CDCl_3$) δ 2.35 (s, 3H), 2.95 (t, J = 5.0 Hz, 2H), 3.13 (dd, J = 14.0, 7.5 Hz, 1H), 3.22 (dd, J = 14.0, 6.0 Hz, 1H), 3.71 (s, 3H), 4.20 (t, J = 5.0 Hz, 2H), 4.39−4.43 (m, 1H), 6.57 (t, J = 5.0 Hz, 1H), 6.64 (d, J = 10.0 Hz, 1H), 6.84 (d, J = 10.0 Hz, 2H), 7.17 (d, J = 10.0 Hz, 2H), 7.31 (d, J = 10.0 Hz, 2H), 7.34−7.43 (m, 4H), 7.71 (d, J = 10.0 Hz, 2H), 7.97 (d, J = 5.0 Hz, 2H), 8.29 (d, J = 10.0 Hz, 2H), 9.04 (d, J = 5.0 Hz, 1H); ^{13}C NMR ($CDCl_3$, 100 MHz) δ 10.13, 26.35, 38.03, 52.21, 57.77, 66.70, 112.13, 114.77, 115.20, 117.14, 123.33, 125.92, 127.81, 128.15, 128.63, 129.62, 129.74, 130.26, 132.71, 135.10, 135.81, 144.96, 145.97, 148.93, 150.67, 158.00, 159.49, 172.65, 196.79; MS (FAB) *m*/*z* 606 (M + H). HRMS calcd for $C_{35}H_{32}N_3O_7$ 606.2240, found 606.2238.

(2*S*)-[2-(4-Fluorobenzoyl)phenylamino]-3-{4-[2-(5-methyl-2-phenyloxazol-4-yl)ethoxy]phenyl}propionic Acid (1). A stirred solution of compound **9** (50 mg, 0.086 mmol) in THF/MeOH (v/v = 3:1, 1.25 mL) was treated with 1.0 M LiOH (172 μL, 0.172 mmol). After the mixture was stirred at room temperature for 6 h, 1 N HCl (200 μL), water (1 mL), and EtOAc (5 mL) were added. The organic layer was separated and dried with sodium sulfate. The obtained organic layers were concentrated and purified by silica gel flash column chromatography using 5% MeOH/CH_2Cl_2 as eluant to afford 47 mg (96%) of the product **1** as a yellow solid: mp 140−145 °C; ^{1}H NMR (400 MHz, CD_3OD) δ 2.30 (s, 3H), 2.90 (t, J = 6.8 Hz, 2H), 3.05 (dd, J = 13.8, 7 Hz, 1H), 3.22 (dd, J = 14, 5.2 Hz, 1H), 4.15 (t, J = 6.4 Hz, 2H), 4.42 (br, 1H), 6.56 (t, J = 7.6 Hz, 1H), 6.73−6.79 (m, 3H), 7.13 (d, J = 8.4 Hz, 2H), 7.18 (t, J = 8.4 Hz, 2H), 7.33−7.37 (m, 2H), 7.44−7.47 (m, 2H), 7.58−7.61 (m 2H), 7.91−7.93 (m, 2H);^{13}C NMR (100 MHz, DMSO-d_6) δ 9.84, 14.11, 25.56, 57.66, 59.79, 65.98, 112.62, 113.96, 115.10, 115.31, 116.84, 125.41, 127.11, 129.04, 130.05, 130.43, 131.36, 131.45, 132.65, 134.40, 134.79, 136.71, 145.05, 150.06, 156.73, 158.32, 162.31, 164.78, 196.24; MS (FAB) *m*/*z* 565 (M + H). HRMS calcd for $C_{34}H_{30}FN_2O_5$ 565.2139, found 565.2139.

2-Iodo-4′-dimethylaminobenzophenone (12). To a suspension of 2-iodo-*N*-phenyl benzamide **11** in *N*,*N*-dimethylaniline (5.49 mL, 43.33 mmol) was added phosphorus oxychloride (865 μL, 9.28 mmol) dropwise over 30 min at 50 °C. On completion of the addition, the resulting dark solution was heated to 150 °C for 4 h. After the reaction mixture was cooled to room temperature, HCl (8 mL, 50% aq) was added, and the

mixture was refluxed for 2 h. The cooled solution was poured into water (200 mL) and 2 M NaOH (50 mL) and extracted with dichloromethane (50 mL × 3). The organic layer was washed with 0.2 M NaOH (25 mL), 0.2 M HCl (25 mL), and water (25 mL), respectively. The organic layer was dried with sodium sulfate, and the solvent was removed to give the crude benzophenone. Purification of the material by silica gel flash column chromatography using 30% ethyl acetate/hexane as eluant afforded 1.72 g (79%) of the product **12** as a green solid: mp 121−125 °C; ^{1}H NMR (400 MHz, $CDCl_3$) δ 3.07 (s, 6H), 6.63 (d, J = 9.2 Hz, 2H), 7.10−7.14 (m, 1H), 7.25−7.28 (m, 1H), 7.39−7.42 (m, 1H), 7.56 (d, J = 8.8 Hz, 2H), 7.88 (d, J = 8 Hz, 1H); ^{13}C NMR (100 MHz, $CDCl_3$) δ 39.99, 92.52, 110.62, 123.02, 127.64, 127.94, 130.24, 132.82, 139.23, 145.64, 153.73, 195.38; MS (ESI) *m*/*z* 352 (M + H). HRMS calcd for $C_{15}H_{14}INO$ 352.0198, found 352.0215.

2-Iodo-4′-fluorobenzophenone (13). *Method A.* The flask was charged with $AlCl_3$ (644 mg, 4.82 mmol) and cat. $FeCl_3$ (5 mg, 0.03 mmol) in fluorobenzene (3 mL). The solution was then chilled thoroughly in an ice bath under nitrogen atmosphere. To this solution was added 2-iodobenzoylchloride (1.29 g, 4.82 mmol) in fluorobenzene (3 mL). The reaction mixture was allowed to stir overnight at room temperature. At the end of the reaction, the flask was placed again in an ice bath, and water (2 mL) was slowly added. The resulting two-phase mixture was stirred vigorously for 30 min. The organic layer was dried over anhydrous sodium sulfate, and the solvent was removed in vacuo. Purification of the material by silica gel flash column chromatography using 10% ethyl acetate/hexane as eluant afforded the product **13** (1.39 g, 88%).

Method B. To a solution of compound **14** (100 mg, 0.19 mmol) in acetonirile (2 mL) was added 1 M TBAF in THF solution (210 μL, 0.21 mmol) at room temperature. The reaction mixture was heated at 90 °C for 1 h. The reaction mixture was poured into ethyl acetate (10 mL) and washed with water (10 mL) and brine (10 mL). The organic layer was dried over anhydrous sodium sulfate, and the solvent was removed in vacuo. Purification of the material by silica gel flash column chromatography using 10% ethyl acetate/hexane as eluant afforded the product **13** (59 mg, 96%) as a white solid: mp 50−52 °C; ^{1}H NMR (400 MHz, $CDCl_3$) δ 7.11−7.21 (m, 3H), 7.28 (dd, J = 7.6, 2 Hz, 1H), 7.43−7.47 (m, 1H), 7.81−7.85 (m, 2H), 7.92 (dd, J = 8.4, 2 Hz, 1H); ^{13}C NMR (100 MHz, $CDCl_3$) δ 92.05, 115.88 (d, J = 22 Hz), 127.87, 128. 29, 131.20, 131.94 (d, J = 3 Hz), 133.09 (d, J = 9.9 Hz), 139.67, 144.01, 166.07 (d, J = 254.9 Hz), 195.66; MS (EI) *m*/*z* 327 (M + H). HRMS calcd for $C_{13}H_8FIO$ 326.9682, found 326.9676. Registry Number: 138504-31-1.

2-Iodo-4′-*N*,*N*,*N*-trimethylaminobenzophenone Triflate (14). To a solution compound **12** (500 mg, 1.42 mmol) in methylene chloride (10 mL) was added methyl trifluoromethanesulfonate (193 μL, 1.70 mmol) dropwise over 10 min at room temperature under argon atmosphere. Upon completion of the addition, the resulting dark brown solution was stirred at room temperature for 12 h. The reaction mixture was poured into diethyl ether (20 mL) and washed with water (10 mL). The residue was recrystallized from diethyl ether and methylene chloride to afford 380 mg (52%) of the product **14** as a white solid: mp 163−165 °C; ^{1}H NMR (400 MHz, $CDCl_3$) δ 3.71 (s, 9H), 7.29−7.37 (m, 2H), 7.55−7.58 (m, 1H), 7.98−8.02 (m, 3H), 8.07−8.10 (m, 2H); ^{13}C NMR (100 MHz, $CDCl_3$) δ 57.68, 92.42, 122.18, 123.36, 129.42, 129.63, 132.98, 133.25, 138.45, 141.06, 144.85, 151.97, 196.91; MS (ESI) *m*/*z* 366 (M − OTf). HRMS calcd for $C_{16}H_{17}INO$ 366.0355, found 366.0346.

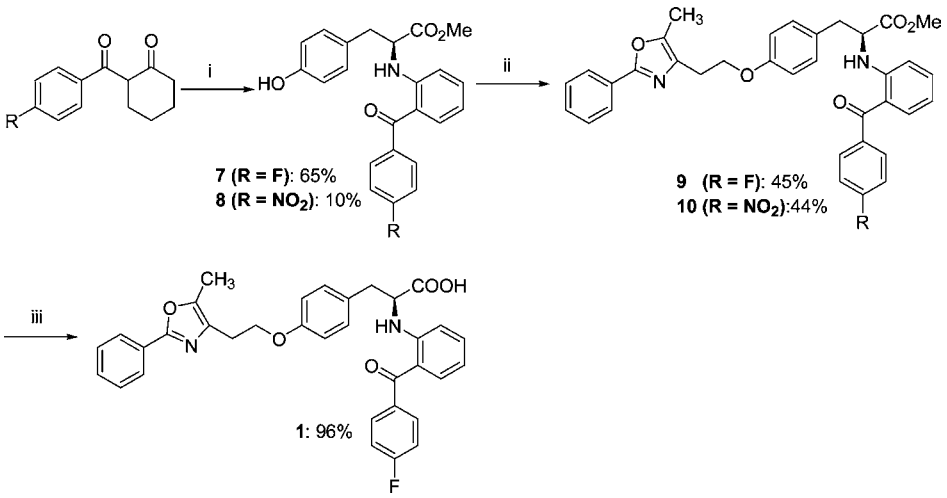
(*S*)-*tert*-Butoxycarbonylamino-3-{4-[2-(5-methyl-2-phenyloxazol-4-yl)ethoxy]-phenyl}propionic Acid *tert*-Butyl Ester (15). A stirred solution of N^{α}-*tert*-butoxycarbonyl-L-tyrosine *tert*-butyl ester (193 mg, 0.49 mmol), 2-(5-methyl-2-phenyloxazol-4-yl)ethanol (100 mg, 0.49 mmol), and triphenylphosphine (165 mg, 0.49 mmol) in tetrahydrofuran (30 mL) at room temperature was treated with diethyl azodicarboxylate (77 μL, 0.49 mmol) in tetrahydrofuran (5 mL) via dropwise addition. The resulting solution was stirred for 8 h at room temperature under nitrogen, and then the solvent was removed in vacuo. The crude reaction mixture was purified by silica gel flash column chromatography using 30% EtOAc/hexane as eluant to afford 140 mg (55%) of the product **15** as a white solid: mp 50−52 °C; ^{1}H NMR (400 MHz, $CDCl_3$) δ 1.36 (s, 9H), 1.37 (s, 9H), 2.30 (s, 3H), 2.90−3.00 (m, 4H), 4.17 (t. J = 6.6 Hz, 2H), 4.36 (q, J = 13.6 Hz, 1H), 5.04 (d, J = 8 Hz, 1H), 6.78 (d, J = 8.4 Hz, 2H), 7.02 (d, J = 8.4 Hz, 2H), 7.31−7.38 (m, 3H), 7.93 (d, J = 6.8 Hz, 2H); ^{13}C NMR (100 MHz, $CDCl_3$) δ 9.96, 26.08, 27.70, 28.07, 37.22, 54.73, 66.36, 79.22, 81.54, 114.11, 125.62, 127.47, 128.14, 128.39, 129.51, 130.24, 132.44, 144.72, 154.86, 157.46, 159.17, 170.77; MS (ESI) *m*/*z* 523 (M + H, 100%), 467 (45%). HRMS calcd for $C_{30}H_{39}N_2O_6$ 523.2808, found 523.2815.

(*S*)-Amino-3-{4-[2-(5-methyl-2-phenyloxazol-4-yl)ethoxy]-phenyl}propionic Acid (16). A solution of (*S*)-*tert*-butoxycarbonylamino-3-{4-[2-(5-methyl-2-phenyloxazol-4-yl)ethoxy]-phenyl}propionic acid *tert*-butyl ester **15** (300 mg, 0.574 mmol) in trifluoroacetic acid and CH_2Cl_2 (v/v = 1:1, 6 mL) was stirred at room temperature for 6 h. The volume was reduced by evaporation of the solvent, whereupon some crystal formation occurred; then, diethyl ether was poured into the concentrated mixture. The white solid was filtered and washed with diethyl ether (5 mL) before being dried in vacuo. The trifluoroacetate was obtained as a white solid **16** (296 mg, 97%): mp 191−193 °C; ^{1}H NMR (400 MHz, CD_3OD) δ 2.39 (s, 3H), 2.97 (t, J = 6.4, 2H), 3.01−3.25 (m, 2H), 4.10 (q, J = 8.0 Hz, 1H), 4.23 (t, J = 6.4 Hz, 2H), 6.92 (d, J = 8.4 Hz, 2H), 7.18 (d, J = 8.4 Hz, 2H), 7.46−7.49 (m, 3H), 7.93−7.96 (m, 2H); ^{13}C NMR (100 MHz, CD_3OD) δ 10.03, 26.94, 36.61, 55.48, 67.62, 116.19, 126.94, 127.65, 128.49, 130.07, 131.51, 131.62, 133.77, 147.12, 159.94, 161.17, 171.60; MS (ESI) *m*/*z* 367 (M + H). HRMS calcd for $C_{21}H_{23}N_2O_4$ 367.1658, found 367.1650.

Ullmann-Type Condensation Procedure for (2*S*)-[2-(4-Fluorobenzoyl)phenylamino]-3-{4-[2-(5-methyl-2-phenyloxazol-4-yl)ethoxy]phenyl}propionic Acid (1). *Method A.* To a solution of compound **16** (73 mg, 0.15 mmol) and 2-iodo-4′-fluorobenzophenone **13** (50 mg, 10.4 μmol) in *N*,*N*-dimethylformamide (DMF, 3 mL) were added potassium carbonate (46 mg, 0.33 mmol), and CuI (3 mg, 0.015 mmol) under a nitrogen atmosphere. After the mixture was stirred at 100 °C for 4 h, the cooled solution was concentrated in vacuo. The residue was dissolved in water and acidified to pH 5 with 1 M HCl. After extraction with ethyl acetate (5 mL), the combined organic layers were dried, concentrated, and purified by silica gel flash column chromatography using 5% MeOH/CH_2Cl_2 as eluant to afford 43 mg (51%) of the product **1**.

Method B. To a solution of trifluoroacetate salt **16** (5.0 mg, 10.4 μmol) in acetonitrile (1 mL) was added tetrabutylammonium hydroxide (40% aq solution, 13 μL, 20.6 μmol). After sonication of the mixture, the clear solution was concentrated under reduced pressure. To the tetrabutylammonium salt were added 2-iodo-4′-fluorobenzophenone **13** (3.4 mg, 10.4 μmol), CuI (1 mg), and DMF (0.5 mL) under a nitrogen atmosphere. After the mixture was stirred at 100 °C for 20 min under nitrogen atmosphere, the cooled solution was concentrated in vacuo. The residue was dissolved in water and acidified to pH 5 with 1 M HCl. After extraction with ethyl acetate (1 mL), the combined organic layers were dried, concentrated, and purified

Scheme 1 [a]



[a] Reaction conditions: (i) (a) L-tyrosine methyl ester, 1,4-dioxane/toluene, 12 h; (b) anisole, 10% Pd/C, reflux, 2 h; (ii) 2-(5-methyl-2-phenyloxazol-4-yl)ethanol, Ph_3P, DEAD, THF, 0 °C ~ rt, 12 h; (iii) **9**, LiOH, THF/MeOH (v/v = 3:1), rt, 6 h.

by short silica gel flash column chromatography using 5% MeOH/CH_2Cl_2 as eluant to afford 3.1 mg (53%) of the product **1**.

PPARγ Binding Assay. The binding of compound **1** to PPARγ was evaluated using a scintillation proximity assay (SPA) adapted from the method described by Sun et al. (*21*). Yttrium silicate (Ysi) copper His-Tag SPA beads (Amersham Biosciences, Piscataway, NJ), histidine-tagged human PPARγ ligand-binding domain (amino acids 195−477; Invitrogen, Carlsbad, CA), and the tritium ligand, [^{3}H]-rosiglitazone (American Radiolabeled Chemicals, St. Louis, MO) were obtained from the sources indicated.

[^{3}H]-Rosiglitazone and PPARγ protein were diluted to 23 μCi/mL and 50 ng/mL stock, respectively. Radioligand, protein and test compound at various concentrations (10 nM to 2 μM) were incubated at room temperature for 2 h. SPA beads were diluted and aliquoted into a clear bottom 96-well plate according to the manufacturer's specifications. Test the ligand, [^{3}H]-Rosiglitazone and protein were then added to the assay plate and incubated at room temperature for at least for 1 h before the plate was read by a Packard TopCount plate reader (Perkin-Elmer, Wellesley, MA). GW1929 (Cayman Chemical Co., Ann Arbor, MI), a potent PPARγ agonist, served as a positive control. The initial IC_{50} values of GW1929 and test compound were calculated by the *Prism* program (GraphPad Software, San Diego, CA). The reported compound IC_{50} value of the compound tested was normalized against GW1929 due to the variability of the assay (*22*). The normalized IC_{50} value is 0.14 ± 0.01 nM, which corresponds to a pK_i value of 9.85.

RESULTS AND DISCUSSION

Chemical Synthesis. We designed two synthetic routes to compound **1**, the first for preparation of an authentic sample of this compound and the second designed to proceed through precursor molecules that can be radiolabeled by fluoride ion displacement of a suitable leaving group for the eventual radiolabeling of this compound with fluorine-18.

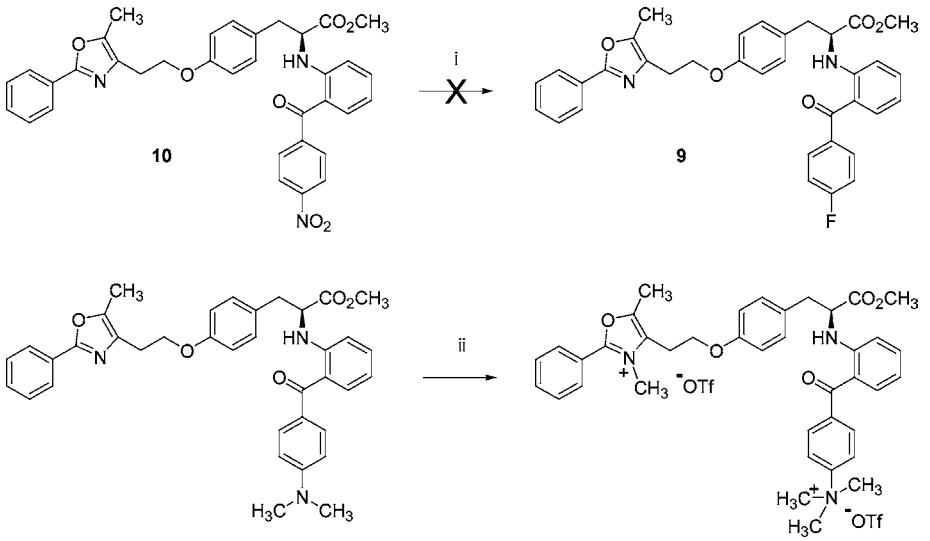
Synthesis of (2*S*)-[2-(4-fluorobenzoylphenylamino)-3-{4-[2-(5-methyl-2-phenyloxazol-4-yl)ethoxy]phenyl}propionic Acid (1). As shown in Scheme 1, an authentic sample of compound **1** was synthesized in three steps from 2-(4-fluorobenzoyl)-cyclohexanone, using a modification of known methods (*13*−*15*). 2-(4-Fluorobenzoyl)cyclohexanone (*23*) was attached to tyrosine methyl ester by an imine formation−aromatization sequence catalyzed by 10% Pd/C in anisole to produce compounds **7** and **8**. Under Mitsunobu conditions, the phenolic function in compound **7** was coupled to the known heterocyclic alcohol 2-(5-methyl-2-phenyloxazol-4-yl)ethanol (*19*) to provide compound **9**. Hydrolysis of this methyl ester with LiOH proceeded under mild conditions to give the desired fluorine-substituted PPARγ ligand **1**. Because it involves multiple steps following the introduction of the fluorine-containing component, this route is not suitable for labeling with the short-lived radionuclide fluorine-18.

An obvious approach for the direct labeling of compound **1** with fluorine would involve nucleophilic aromatic substitution by fluoride ion on a precursor of the final compound bearing a good leaving group on the para position of the benzophenone unit (i.e., compound **10**, Scheme 2). In many cases, a nitro group can function effectively as a leaving group in nucleophilic aromatic substitutions with fluoride ion, provided the system is adequately activated with electron withdrawing groups situated at ortho and/or para positions (*24*−*26*). Thus, we subjected compound **10**, the nitro analog of compound **1** that we had prepared previously, to various conditions typically used for such substitutions, but we failed to obtain any of the desired fluoro product. Although fluorine substitution of other nitrobenzophenones has been accomplished (*24*), we presume that the lack of reaction of compound **10** is due to the strongly electron donating ortho amino substituent on the other ring that can also hydrogen-bond with the benzophenone carbonyl group.

Our attempts to prepare the more reactive trimethylammonium analog of the nitro compound from the dimethyl amine analog using methyl triflate (Scheme 2) were thwarted by the dominant competitive N-methylation of the more nucleophilic oxazole ring in the tail of the molecule. Initial methylation took place on the heterocycle, so we could only obtain the bis-(ammonium) salt. Because of these difficulties with these direct fluorination approaches, we took an alternative, indirect approach to prepare target compound **1**, as outlined in Scheme 3.

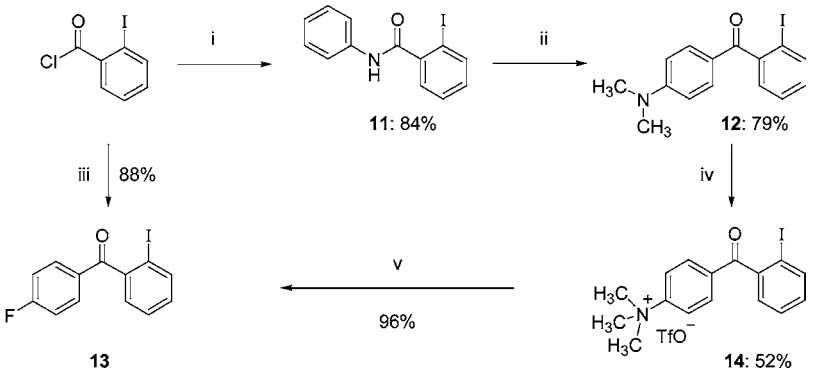
Synthesis of 2-iodo-4′-fluorobenzophenone (13). There is precedent for introducing fluoride ion by nucleophilic aromatic substitution at the para position of certain benzophenones bearing simple o,p′-substituents (*27*). We did not anticipate encountering problems in preparing the reactive p′-trimethylammonium group in the simpler benzophenone precursor **14**, because in this system this benzophenone is not attached to the nucleophilic oxazole. We imagined that fluoride ion substitution in compound **14** would proceed selectively by displacement of the more reactive p′-trimethylammonium leaving group rather

Scheme 2 [a]



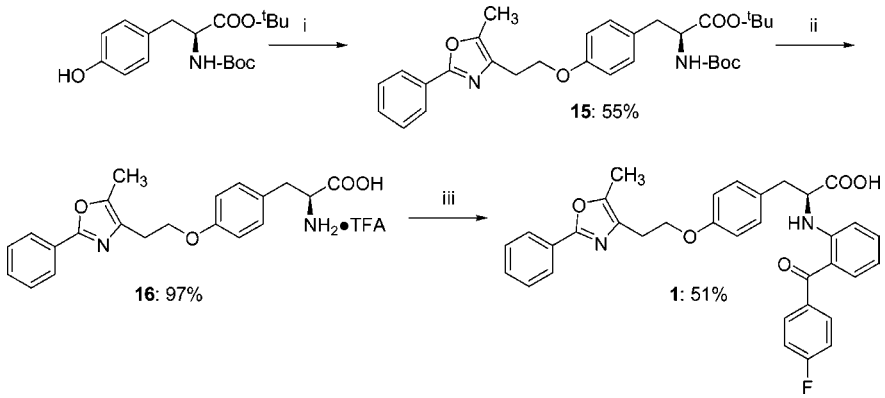
[a] Reaction conditions: (i) TBAF, DMSO, 130 °C or microwave; (ii) $CF_3SO_2OCH_3$, CH_2Cl_2, rt.

Scheme 3 [a]



[a] Reaction conditions: (i) aniline, pyridine, rt, 12 h; (ii) (1) $POCl_3$, *N*,*N*-dimethylaniline, 150 °C, 4 h, (2) 50% aq. HCl, 100 °C, 2 h; (iii) fluorobenzene, $AlCl_3$, $FeCl_3$, rt, 20 h; (iv) $CF_3SO_2OCH_3$, CH_2Cl_2, rt, 12 h; (v) TBAF, CH_3CN, 90 °C 1 h.

Scheme 4 [a]



[a] Reaction conditions: (i) 2-(5-methyl-2-phenyloxazol-4-yl)ethanol, PPh_3, DEAD, THF, 0 °C ∼ rt, 12 h; (ii) TFA/CH_2Cl_2, rt, 6 h; (iii) 13, K_2CO_3, CuI, DMF, 90 °C, 4 h.

than the o-iodo group (Scheme 3). This would leave as a final step in this approach the attachment of the *o*-iodo-*p*′-[^{18}F]-fluorobenzophenone system to the complex tyrosine unit by the displacement of the iodide using an Ullmann-type condensation (Scheme 4) (*28*, *29*). In this respect, our approach differs from earlier methods for achieving this coupling step, which involved imine formation with an *o*-benzoylcyclohexanone, followed by palladium-catalyzed aromatization (*13*, *15*).

An authentic sample of the o,p′-substituted benzophenone **13** was easily prepared by the Friedel−Crafts acylation of fluorobenzene with 2-iodobenzoyl chloride. The precursor for fluorine labeling, compound **14**, was prepared in three steps. 2-Iodo-4′-dimethylaminobenzophenone **12** was obtained in moderate yield by the Vilsmeier−Haack reaction of *N*,*N*-dimethylaniline with *N*-phenyl 2-iodo-benzamide (**11**), which was derived from the acylation of aniline with 2-iodo-

Scheme 5

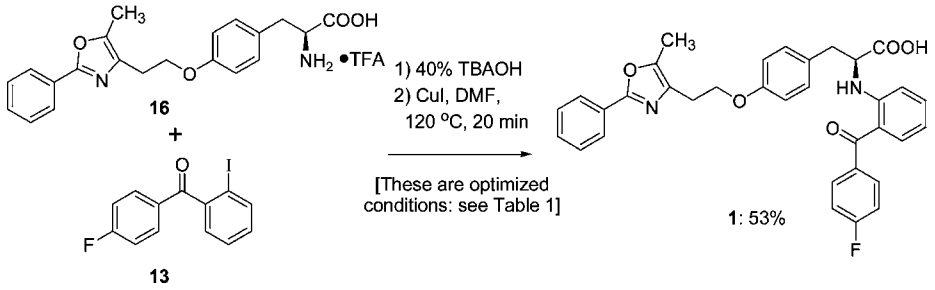


Table 1. Ullmann-Type C−N Coupling

entry	salt form	temperature	time	base	yields[f]
1[a]	TFA salt	100 °C	4 h	K_2CO_3	51%
2[b]	TFA salt	100 °C	2 h	K_2CO_3	13%
3[b]	TFA salt	120 °C	30 min	K_2CO_3	5%
4[c]	TFA salt	MW	5 min	K_2CO_3	trace
5[d]	TFA salt	MW	5 min	Cs_2CO_3 and TEA	trace
6[e]	TBA	120 °C	20 min	none	53%

[a−f] Reaction conditions: [a]Compound **16** (0.15 mmol), compound **13** (0.15 mmol), CuI (3 mg), K_2CO_3 (0.33 mmol), and DMF (3 mL); [b]Compound **16** (10.4 μmol), compound **13** (10.4 μmol), CuI (1 mg), K_2CO_3 (20.6 μmol), and DMF (500 μL); [c]Microwave irradiation (100 W, 5 min); [d]Compound **16** (10.4 μmol), compound **13** (10.4 μmol), CuI (1 mg), $Pd(Ph_3)_4$ (2 mg), Cs_2CO_3 (26.0 μmol), triethylamine (30 μL), tetrabutylammonium iodide (26.0 μmol), H_2O (10 μL), and DMF (500 μL); [e]Compound **16** (10.4 μmol), compound **13** (10.4 μmol), CuI (1 mg), tetrabutylammonium hydroxide (40% aqueous solution, 20.6 μmol), and DMF (500 μL). [f] Isolated yields.

benzoyl chloride using a catalytic amount of DMAP in pyridine (*20*, *30*, *31*). Treatment of the tertiary amine **12** with methyl trifluoromethanesulfonate produced the desired ammonium salt **14**, the key precursor for fluorine substitution. To demonstrate the effectiveness of the ammonium salt **14** as a precursor to the key intermediate **13**, we showed that the conversion of **14** to **13** occurred rapidly and in near quantitative yield when **14** was exposed to tetrabutylammonium fluoride in acetonitrile (Scheme 3).

As shown in Scheme 4, N^{α}-*tert*-butoxycarbonyl-L-tyrosine *tert*-butyl ester (*18*) was coupled to 2-[5-methyl-2-phenyloxazol-4-yl]ethanol under Mitsunobu conditions. Hydrolysis of the *tert*-butyl ester and Boc group in compound **15** with TFA in dichloromethane solution proceeded under mild conditions to give the desired phenyloxazole−tyrosine TFA salt **16**. The target compound **1** was then prepared using an Ullmann-type aryl amination of 2-iodo-4′-fluorobenzophene **13** with the amino group of the tyrosine ether **16** (Scheme 5). It is of note that this conversion can be done with the tyrosine unit **16** in its free acid form, rather than its ester derivative; this is a significant convenience for radiolabeling with short-lived isotopes, because it obviates ester hydrolysis as a final step.

Under conditions typical for Ullmann-type arylations, the conversion of **13** and **16** to **1** proceeded to only 51% yield after a 4 h reaction. We realized that this would be problematic for the synthesis of compound **1** labeled with the short-lived fluorine-18 ($t_{1/2}$ = 110 min), and thus we needed to find conditions for expediting this coupling reaction (Table 1).

While the mechanism of the Ullmann-type coupling reaction is not known, it is presumed to involve the coordination of copper ion with the aryl halide, followed by chelation with the carboxyl and/or amino groups in the coupling partner. The rate-determining step is then the intramolecular nucleophilic substitution of the aromatic ring by the amino group (*28*, *32*). Ullmann condensations typically proceed in higher yields under mild conditions, and we found the reaction yield to be strongly dependent on time. To explore how we might reduce the reaction time, we examined this reaction, when conducted on a micromolar scale (compound **16**, 5 mg, 10.4 μmol), under different conditions and using different reagents (Table 1).

When the phenyloxazole-tyrosine TFA salt **16** was reacted with the o,p′-substituted benzophenone **13** with CuI and K_2CO_3, under general Ullmann-type conditions, the reaction proceeded only slowly, with the yields of product **1** being very low at reaction times that would be applicable to labeling compound **1** with fluorine-18 (Table 1, entries 1−3). We also tried using a palladium/copper cocatalyst with microwave heating, conditions that have promoted other C−N cross couplings (*33*), but the reaction did not appear to be accelerated; yields were very low, and unknown side compounds were generated by the microwave heating (Table 1, entries 4 and 5). We noticed with interest that treatment of amino acid **16** with tetrabutylammonium hydroxide gave a TBA salt that was soluble in DMF (*34*). Interestingly, when this salt/solvent combination was used, the C−N coupling could be carried out in 20 min with 53% yield by heating to 120 °C, as shown in Table 1 (entry 6).

PPARγ Binding Affinity Determination. We retested the binding affinity of compound **1** for PPARγ in a competitive scintillation proximity radiometric binding assay, using a receptor preparation consisting of the ligand binding domain of PPARγ expressed in *E. coli* (*21*, *22*). The K_i value for compound **1** determined in this assay was 0.14 nM ($pK_i = 9.85$), consistent with the binding affinity for this compound reported earlier (*14*).

CONCLUSION

In this study, we have developed a method for introducing fluorine into a fluorine-substituted analog (compound **1**) of the high-affinity PPARγ ligand, farglitazar, that utilizes fluoride ion and that proceeds efficiently and rapidly under conditions suitable for labeling this molecule with the short-lived, positron-emitting radionuclide fluorine-18. The radiochemical synthesis of [^{18}F]compound **1** and an evaluation of its tissue distribution properties will be described in a future publication.

ACKNOWLEDGMENT

We are grateful for support of this work by grants from the Department of Energy (FG02 86ER60401 to J.A.K.) and the National Institute of Health (P01 HL13851 to M. J. Welch, P.I.).

LITERATURE CITED

(1) Brun, R. P., Kim, J. B., Hu, E., and Spiegelman, B. M. (1997) Peroxisome proliferator-activated receptor gamma and the control of adipogenesis. *Curr. Opin. Lipidol. 8*, 212−218.

(2) Kliewer, S. A., Lenhard, J. M., Willson, T. M., Patel, I., Morris, D. C., and Lehmann, J. M. (1995) A prostaglandin J2 metabolite binds peroxisome proliferator-activated receptor γ and promotes adipocyte differntiation. *Cell 83*, 813−819.

(3) Kliewer, S. A., Forman, B. M., Blumberg, B., Ong, E. S., Borgmeyer, U., Mangelsdorf, D. J., Umesono, K., and Evans, R. M. (1994) Differential expression and activation of a family of

murine peroxisome proliferator-activated receptors. *Proc. Natl. Acad. Sci. U.S.A. 91*, 7355−7359.

(4) Tontonoz, P., Hu, E., Graves, R. A., Budavari, A. I., and Spiegelman, B. M. (1994) mPPAR γ2: tissue-specific regulator of an adipocyte enhancer. *Genes Dev. 8*, 1224−1234.

(5) Mueller, E., Smith, M., Sarraf, P., Kroll, T., Aiyer, A., Kaufman, D. S., Oh, W., Demetri, G., Figg, W. D., Zhou, X. P., Eng, C., Spiegelman, B. M., and Kantoff, P. W. (2000) Effects of ligand activation of peroxisome proliferator-activated receptor gamma in human prostate cancer. *Proc. Natl. Acad. Sci. U.S.A. 97*, 10990−10995.

(6) Muller, E., Sarraf, P., Tontonoz, P., Evans, R. M., Martin, K. J., Zhang, M., Fletcher, C. D., Singer, S., and Spiegelman, B. M. (1998) Terminal differentiation of human breast cancer through PPAR gamma. *Mol. Cell 1*, 465−470.

(7) Demetri, G. D., Fletcher, C. D. M., Mueller, E., Sarraf, F., Naujoks, R., Campbell, N., Spiegelman, B. M., and Singer, S. (1999) Induction of solid tumor differentiation by the peroxisome proliferator-activated receptor-γ ligand troglitazone in patients with liposarcoma. *Proc. Natl. Acad. Sci. U.S.A. 96*, 3951−3956.

(8) Tontonoz, P., Singer, S., Froman, B. M., Sarraf, P., Fletcher, J. A., Fletcher, C. D. M., Brun, R. P., Mueller, E., Altiok, S., Oppenheim, H., Evans, R. M., and Spiegelman, B. M. (1997) Terminal differentiation of human liposarcoma cells induced by ligands for peroxisome proliferator-activated receptor γ and the retinoid X receptor. *Proc. Natl. Acad. Sci. U.S.A. 94*, 237−241.

(9) Burstein, H. J., Demetri, G. D., Muller, E., Sarraf, P., Spiegelman, B. M., and Winer, E. P. (2003) Use of the peroxisome proliferator-activated receptor (PPAR) γ ligand troglitazone as treatment for refractory breast cancer: a phase II study. *Breast Cancer Res. Treat. 79*, 391−397.

(10) Wang, X., Southard, R. C., and Kilgore, M. W. (2004) The increased expression of peroxisome proliferator-activatated receptor-γ1 in human breast cancer is mediated by selective promoter usage. *Cancer Res. 64*, 5592−5596.

(11) Berger, J. P., Akiyama, T. E., and Meinke, P. T. (2005) PPARs: therapeutic targets for metabolic disease. *Trends Pharmacol. Sci. 26*, 244−251.

(12) Kim, S-H., Jonson, S. D., Welch, M. J., and Katzenellenbogen, J. A. (2001) Fluorine-substituted ligands for the peroxisome proliferator-activated receptor gamma (PPARγ): Potential imaging agents for metastatic tumors. *Bioconjugate Chem. 12*, 439−450.

(13) Henke, B. R., Blanchard, S. G., Brackeen, M. F., Brown, K. K., Cobb, J. E., Collins, J. L., Harrington, W. W., Jr., Hashim, M. A., Hull-Ryde, E. A., Kaldor, I., Kliewer, S. A., Lake, D. H., Leesnitzer, L. M., Lehmann, J. M., Lenhard, J. M., Orband-Miller, L. A., Miller, J. F., Mook, R. A., Jr., Noble, S. A., Oliver, W., Jr., Parks, D. J., Plunket, K. D., Szewczyk, J. R., and Willson, T. M. (1998) *N*-(2-Benzoylphenyl)-L-tyrosine PPARγ agonists. 1. Discovery of a novel series of potent antihyperglycemic and antihyperlipidemic agents. *J. Med. Chem. 41*, 5020−5036.

(14) Collins, J. L., Blanchard, S. G., Boswell, E. G., Charifson, P. S., Cobb, J. E., Henke, B. R., Hull-Ryde, E. A., Kazmierski, W. M., Lake, D. H., Leesnitzer, L. M., Lehmann, J., Lenhard, J. M., Orband-Miller, L. A., Gray-Nunez, Y., Parks, D. J., Plunkett, K. D., and Tong, W. Q. (1998) *N*-(2-Benzoylphenyl)-L-tyrosine PPARγ agonists. 2. Structure−activity relationship and optimization of the phenyl alkyl ether moiety. *J. Med. Chem. 41*, 5037−5054.

(15) Cobb, J. E., Blanchard, S. G., Boswell, E. G., Brown, K. K., Charifson, P. S., Cooper, J. P., Collins, J. L., Dezube, M., Henke, B. R., Hull-Ryde, E. A., Lake, D. H., Lenhard, J. M., Oliver, W. Jr., Oplinger, J., Pentti, M., Parks, D. J., Plunket, K. D., and Tong, W. Q. (1998) *N*-(2-Benzoylphenyl)-L-tyrosine PPARγ agonists. 3. Structure−activity relationship and optimization of the N-aryl substituent. *J. Med. Chem. 41*, 5055−5069.

(16) Willson, T. M., Brown, P. J., Sternbach, D. D., and Henke, B. R. (2000) The PPARs: From orphan receptors to drug discovery. *J. Med. Chem 43*, 527−550.

(17) Pangborn, A. B., Giardello, M. A., Grubbs, R. H., Rosen, R. K., and Timmer, F. J. (1996) Safe and convenient procedure for solvent purification. *Organometallics 15*, 1518−1520.

(18) Schlienger, N., Peyrottes, S., Kassem, I., Imbach, I.-L., Gosselin, G., Aubertin, A-M., and Périgaud, C. (2000) S-Acyl-2-thioethyl aryl phosphotriester derivatives as mononucleotide prodrugs. *J. Med. Chem. 43*, 4570−4574.

(19) Hulin, B., Clark, D. A., Goldstein, S. W., McDermott, R. E., Dambek, P. J., Kappeler, W. H., Lamphere, C. H., Lewis, D. M., and Rizzi, J. P. (1992) Novel thiazolidine-2,4-diones as potent euglycemic agents. *J. Med. Chem. 35*, 1853−1864.

(20) Tuemmler, W. B., and Wildi, B. S. (1958) Polymethine dyes. I. A comparison of several vinylogous series in which the polymethine chains are terminated by aryl groups. *J. Am. Chem. Soc. 80*, 3772−3777.

(21) Sun, S., Almaden, J., Carlson, T. J., Barker, J., and Gehring, M. R. (2005) Assay development and data analysis of receptor-ligand binding based on scintillation proximity assay. *Metab. Eng. 7*, 38−44.

(22) Brown, K. K., Henke, B. R., Blanchard, S. G., Cobb, J. E., Mook, R., Kaldor, I., Kliewer, S. A., Lehmann, J. M., Lenhard, J. M., Harrington, W. W., Novak, P. J., Faison, W., Binz, J. G., Hashim, M. A., Oliver, W. O., Brown, H. R., Parks, D. J., Plunket, K. D., Tong, W. Q., Menius, J. A., Adkison, K., Noble, S. A., and Wilson, T. M. (1999) A novel N-aryl tyrosine activator of peroxisome proliferator-activated receptor-gamma reverses the diabetic phenotype of the Zucker diabetic fatty rat. *Diabetes 48*, 1415−1424.

(23) Campbell, R. D., and Gilow, H. N. (1960) β-Diketones. I. Synthesis and reactions of some 2-benzoylcyclanones. *J. Am. Chem. Soc. 82*, 2389−2393.

(24) Stone-Elander, S., and Elander, N. (1993) Fast chemistry in microwave fields: Nucleophilic ^{18}F-radiofluorinations of aromatic molecules. *Appl. Radiat. Isot. 44*, 889−893.

(25) Ludwig, T., Ermert, J., and Coenen, H. H. (2002) 4-[^{18}F]fluoroaryl alkyl ethers via an improved synthesis of n.c.a. 4-[^{18}F]fluorophenol. *Nucl. Med. Biol. 29*, 255−262.

(26) Haka, M. S., Kilbourn, M. R., Watkins, G. L., and Toorongian, S. A. (1989) Aryltrimethylammonium trifluoromethanesulfonates as precursors to aryl [^{18}F]fluorides: improved synthesis of [^{18}F]GBR-13119. *J. Label. Comp. Radiopharm. 27*, 823−833.

(27) Martin, L. L., Klioze, S. S., Worm, M., Crichlow, C. A., Geyer, H. M., III, and Kruse, H. (1979) Synthesis of spiro[isobenzofuran-1(3*H*),4′-piperidines] as potential central nervous system agents. 5. Conformationally mobile analogs derived by furan ring opening. *J. Med. Chem. 22*, 1347−1354.

(28) Ma, D., Zhang, Y., Yao, J., Wu, S., and Tao, F. (1998) Accelerating effect introduced by the structure of α-amino acid in the copper-catalyzed coupling reaction of aryl halides with α-amino acids. synthesis of benzolactam-V8. *J. Am. Chem. Soc. 120*, 12459−12467.

(29) Ma, D., Cai, Q., and Zhang, H. (2003) Mild method for ullmann coupling reaction of amines and aryl halides. *Org. Lett. 5*, 2453−2455.

(30) DoAmaral, J. R., Blanz, J. E., Jr., and French, F. A. (1969) Antimalarial activity of guanylhydrazone salts of aromatic ketones. I. Active substituent patterns. *J. Med. Chem. 12*, 21−25.

(31) Gabbutt, C. D., Heron, B., and Instone, A. C. (2003) Control of the fading properties of photochromic 3,3-diaryl-3*H*-naphtho[2,1-b]pyrans. *Heterocycles 60*, 843−855.

(32) Greenstein, J. P., and Winitz, M. (1961) *Chemistry of the Amino Acids*, Vol 1, p 569, Wiley, New York.

(33) Xu, L.-W., Xia, C.-C., Li, J.-W., Li, F.-W., and Zhou, S.-L. (2004) Efficient palladium/copper cocatalyzed C−N coupling reaction of unactivated aryl bromide of iodide with amino acid under microwave heating. *Catal. Commun. 5*, 121−123.

(34) Clement, J-B., Hayes, J. F., Sheldrake, H. M., Sheldrake, P. W., and Wells, A. S. (2001) Synthesis of SB-214857 using copper catalysed amination of arylbromides with L-aspartic acid. *Synlett 9*, 1423−1427.

BC060190O

Strategies for the Labeling of Halogen-Substituted Peroxisome Proliferator-Activated Receptor γ Ligands: Potential Positron Emission Tomography and Single Photon Emission Computed Tomography Imaging Agents

Byung Chul Lee,[†] Kyo Chul Lee,[‡] Hsiaoju Lee,[§] Robert H. Mach,[§] and John A. Katzenellenbogen*[,†]

Department of Chemistry, University of Illinois, Urbana, Illinois 61801, Laboratory of Radiopharmaceuticals, Korea Institute of Radiological and Medical Sciences, Seoul, South Korea, and Division of Radiological Sciences, Washington University School of Medicine, St. Louis, Missouri 63110. Received June 30, 2006; Revised Manuscript Received January 12, 2007

Well-known as an important regulator of lipid metabolism and adipocyte differentiation, the peroxisome proliferator-activated receptor γ (PPARγ) also has potential use as a target for antitumor therapy in certain cancers. To develop agents for radionuclide imaging PPARγ in vivo, we synthesized fluorine, bromine, and iodine-substituted analogs (**1**−**3**) of a high-affinity benzophenone−tyrosine PPARγ ligand; all three analogs retain very high affinity for the PPARγ receptor. In preparation for the synthesis of these PPARγ ligands in radiolabeled form, we have synthesized two types of precursors: (a) an aryltributylstannane (**9**), from which the bromine and iodine-substituted analogs (**2** and **3**) can readily be prepared by electrophilic destannylation, and (b) three diaryliodonium tosylate derivatives (**12a**−**c**), precursors for nucleophilic aromatic fluorination using fluoride ion. Conditions were developed whereby the thiophenyliodonium tosylate (**12c**) underwent nucleophilic aromatic substitution with fluoride ion, efficiently and in short reaction times, to produce the desired fluorine-substituted target compound **1**. These reactions laid the groundwork for producing these three PPARγ ligands in radiolabeled form; in addition, our use of diaryliodonium ion precursors for aromatic fluorination in this series provides an example that should encourage application of this approach for radiofluorination of more complicated radiopharmaceuticals.

INTRODUCTION

The peroxisome proliferator-activated receptors (PPARs) are members of the nuclear receptor superfamily, of which three subtypes are known: PPARα, PPARγ, and PPARδ (*1*−*3*). Each of these subtypes appears to regulate specific aspects of lipid metabolism, glucose homeostasis, inflammation, and cell differentiation (*4*−*6*). PPARγ can also play a critical role in certain cancers (*6*−*15*), and PPARγ ligands can induce liposarcoma cells to stop proliferating, lose their malignant character, and undergo terminal differentiation to adipocytes. In fact, in clinical trials, the PPARγ ligand troglitazone has been shown to induce differentiation of liposarcoma solid tumors in patients with advanced disease (*12*, *14*). PPARγ is also expressed in several breast cancer cell lines and in animal tumor models for breast cancer derived from primary and metastatic breast tumors, and PPARγ activation may alter the growth characteristics of breast cancer cells (*11*, *15*). Thus, PPARγ is an important target for in vivo imaging using positron emission tomography (PET) or single photon emission computed tomography (SPECT) that might be useful in assessing lipid metabolism disorders in obesity, type-2 diabetes, or vascular disease (*16*) or in identifying small metastatic tumors.

With this goal in mind, some time ago our group evaluated as PET imaging agents a set of fluorine-18 labeled PPARγ receptor ligands, based on the known compound SB 213068 (Scheme 1) (*17*). The binding of these fluorine-substituted compounds was selective for PPARγ compared to the PPARα and PPARδ subtypes; however, their affinity for PPARγ, though good, was not in the low nanomolar region as would be desirable for in vivo imaging. Also, one SB 213068 analogue (**5**), prepared in the fluorine-18 labeled form (*17*), did not show evidence of receptor-mediated uptake in tissue distribution studies in brown fat, the most receptor-rich tissue (*18*).

Since then, however, there have been a number of significant advances in the development of PPAR ligands, most notably, the discovery of systems that have much higher affinity and selectivity for both PPARγ and PPARα, largely through efforts of researchers at Glaxo SmithKline (GSK) (*19*−*22*). In particular, members of the novel benzophenone−tyrosine class (farglitazar GI 262570, **4,** Scheme 1) have particularly high affinity for PPARγ, and they show high potency in vivo. In addition, the use of the high-affinity enantiomer of this chiral compound increases its receptor binding affinity and would likely also enhance its target tissue uptake selectivity (*19*, *23*, *24*). Thus, we have selected farglitazar as a parent compound for the development of radiohalogen-labeled PPARγ-based imaging agents.

In this investigation, we have prepared three farglitazar analogues that are substituted at a tolerant aromatic ring position with fluorine, bromine, or iodine (**1**−**3**), which could be labeled, respectively, with fluorine-18, bromine-76, and iodine-124 for PET imaging or with other radionuclides for SPECT imaging. All three farglitazar derivatives retain high binding affinity for PPARγ. In model procedures for radiolabeling, we developed methods by which these three compounds can be produced from suitable precursors by reaction with simple halide species. The bromine and iodine-substituted compounds (**2** and **3**) were readily produced by electrophilic aromatic destannylation of a trialkyltin precursor. The use of electrophilic aromatic halogenation is not suitable for fluorine-18 labeling at the high specific activity needed for imaging receptors, which generally needs to be in the range of 1000 Ci/mmol for nuclear receptors such

* Corresponding author. John A. Katzenellenbogen, Department of Chemistry, University of Illinois, 600 South Mathews Avenue, Urbana, Illinois 61801, Telephone: 217-333-6310. Fax: 217-333-7325. E-mail: jkatzene@uiuc.edu.

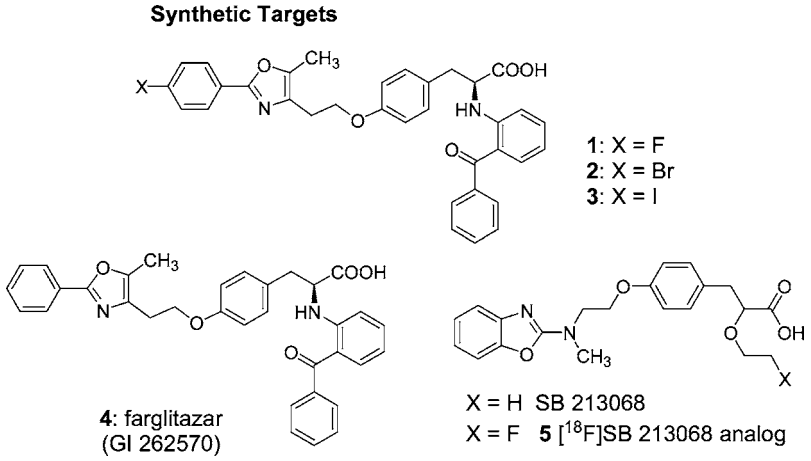
[†] University of Illinois.

[‡] Korea Institute of Radiological and Medical Sciences.

[§] Washington University School of Medicine.

10.1021/bc060191g CCC: $37.00 © 2007 American Chemical Society
Published on Web 02/23/2007

Scheme 1. Structure of Synthetic Targets and Known PPARγ Ligands in This Study



as PPARγ, because they are present at only nanomolar concentrations in target tissues (*25*). Preparation of fluorine-18 labeled radiopharmaceuticals at this specific activity level requires the use of fluoride ion as the reagent. The aromatic ring position in question is also not sufficiently activated for conventional nucleophilic aromatic substitution reactions with fluoride ion. To overcome this problem, we synthesized iodonium salts from the same trialkyltin intermediate using various hydroxyl(tosyloxy)iodoarenes (*26*−*29*). Conditions were then optimized to produce the desired fluorine-substituted compound by nucleophilic aromatic substitution by fluoride ion on this highly activated system.

The methods we have developed here lay the groundwork for the synthesis of these three halogen-substituted PPARγ ligands in iodine, bromine, and fluorine radiolabeled form. The last method, using diaryliodonium salts for fluorine labeling, in particular, demonstrates an approach that is effective for introducing fluoride ion into aromatic rings that are not sufficiently activated for conventional nucleophilic aromatic substitution reactions, and it illustrates that this approach should be applicable for the preparation of other complex fluorine-18 labeled radiopharmaceuticals.

EXPERIMENTAL SECTION

Materials and Methods. Solvents and reagents were purchased from the following commercial sources: Aldrich, Fisher, or Acros. Anhydrous THF, Et_2O, and CH_2Cl_2 were collected using a solvent dispensing system built by J. C. Meyer based on a design developed by Pahgborn (*30*). TLC was performed on Merck F_{254} silica plates. The chemical shifts were reported in parts per million downfield from TMA and were referenced to the internal solvent peaks. Coupling constants were reported in hertz. ^{1}H NMR and ^{13}C NMR spectra were recorded on Varian U400 and U500 Instruments (Palo Alto, CA). Melting points were checked using a Thomas-Hoover capillary melting point apparatus (Philadelphia, PA) and are uncorrected. Low-resolution mass spectra (MS) were recorded on a Micromass 70-VSE, Finnigan MAT CH-5, and ZAB-SE spectrometers, respectively. High-resolution mass spectra were obtained on a VG 70-SE-4E spectrometer. Mass spectra were acquired in the positive ion mode under electron impact (EI, 70 eV), fast-atom bombardment mass (FAB), and electrospray ionization (ESI) methods. Methyl 4-bromo-3-oxopentanoate and (2*S*)-2-((2-benzoylphenyl)amino)-3-(4-hydroxyphenyl)-propionic acid methyl ester were prepared according to literature methods (*19*, *20*). Koser's reagent **11a** was purchased from Aldrich. Compounds **10a**, **10b**, and **11c** were prepared according to the literature method (*31*−*33*): Diacetoxyiodo-*p*-methoxybenzene (**10a**) yield 69%, mp 131−135 °C, literature (*31*) mp 133−135 °C; 2-(diacetoxyiodo)thiophene (**10b**) yield 51%, mp 119−125 °C; literature (*32*) mp 120−122 °C (decomp); 2-[hydroxy(tosyloxy)-iodo]thiophene (**11c**) yield 95%, mp 62−66 °C (decomp), literature (*33*) mp 65−68 °C (decomp).

[2-(4-Fluorophenyl)-5-methyloxazol-4-yl]-acetic Acid Methyl Ester (6a). To a solution of 4-fluorobenzamide (1.23 g, 8.85 mmol) in 1,2-dichlorobenzene (50 mL) was added methyl 4-bromo-3-oxopentanoate (1.84 g, 8.85 mmol). The reaction mixture was refluxed using a Dean−Stark trap at 120 °C for 16 h. The resulting dark slurry was cooled to room temperature, diluted with EtOAc (100 mL), and washed with aqueous sodium bicarbonate (100 mL). The organic layer was separated and dried with sodium sulfate, and the solvents were removed in vacuo. Purification of the material by silica gel flash column chromatography using 10% EtOAc/ hexane as eluant afforded the product **6a** (683 mg, 31%) as an oil: ^{1}H NMR (400 MHz, $CDCl_3$) δ 2.35 (s, 3H), 3.56 (s, 2H), 3.73 (s, 3H), 7.10 (m, 2H), 7.97 (m, 2H); ^{13}C NMR (100 MHz, $CDCl_3$) δ 10.25, 31.91, 52.19, 115.77 (J = 22.0 Hz), 123.90 (J = 4.0 Hz), 128.09 (J = 8.4 Hz), 129.35, 145.72, 158.76, 163.77 (J = 249.6 Hz), 170.72; MS (FAB) *m*/*z* 250 (M + H). HRMS calcd for $C_{13}H_{13}FNO_3$ 250.0879, found 250.0878. Registry Number: 196810-28-3.

[2-(4-Bromophenyl)-5-methyloxazol-4-yl]acetic Acid Methyl Ester (6b). Prepared from 4-bromobenzamide by the method used to prepare compound **6a** and afforded the title compound **6b** (35%) as a white solid: mp 58−61 °C; ^{1}H NMR (500 MHz, $CDCl_3$) δ 2.33 (s, 3H), 3.55 (s, 2H), 3.71 (s, 3H), 7.52−7.54 (m, 2H), 7.81−7.83 (m, 2H); ^{13}C NMR (100 MHz, $CDCl_3$) δ 10.22, 31.84, 52.16, 124.20, 126.41, 127.42, 129.60, 131.82, 146.00, 158.64, 170.66; MS (ESI) *m*/*z* 310 (M^+). HRMS calcd for $C_{13}H_{13}BrNO_3$ 310.0079, found 310.0082. Registry N591775-29-0.

[2-(4-Iodophenyl)-5-methyloxazol-4-yl]acetic Acid Methyl Ester (6c). Prepared from 4-iodobenzamide by the method used to prepare compound **6a** and afforded the title compound **6c** (37%) as a white solid: mp 90−91 °C; ^{1}H NMR (500 MHz, $CDCl_3$) δ 2.35 (s, 3H), 3.56 (s, 2H), 3.73 (s, 3H), 7.69−7.71 (m, 2H), 7.75−7.77 (m, 2H); ^{13}C NMR (100 MHz, $CDCl_3$) δ 10.29, 31.90, 52.22, 96.21, 127.00, 127.52, 129.65, 137.81, 146.09, 158.82, 170.72; MS (ESI) *m*/*z* 358 (M^+). HRMS calcd for $C_{13}H_{13}INO_3$ 357.9940, found 357.9940.

2-[2-(4-Fluorophenyl)-5-methyloxazol-4-yl]ethanol (7a). To a stirred solution of compound **6a** (612 mg, 2.46 mmol) in tetrahydrofuran (10 mL) at 0 °C was added 1.0 M solution of $LiAlH_4$ (2.46 mL, 2.46 mmol) in tetrahydrofuran. The resulting solution was stirred at room temperature for 45 min, then cooled to 0 °C, and quenched by careful addition of a minimum volume of H_2O. The resulting heterogeneous mixture was filtered under vacuum, and the filtrate was concentrated in vacuo. Purification

of this material by silica gel flash column chromatography using 40% EtOAc/hexane as eluant afforded the product **7a** (326 mg, 60%) as a pale yellow solid: mp 102−104 °C; ^{1}H NMR (400 MHz, $CDCl_3$) δ 2.33 (s, 3H), 2.72 (t, J = 6.0 Hz, 2H), 3.41 (br, 1H), 3.92 (t, J = 6.0 Hz, 2H), 7.10−7.14 (m, 2H), 7.96−7.99 (m, 2H); ^{13}C NMR (100 MHz, $CDCl_3$) δ 10.10, 27.90, 61.77, 115.90 (J = 22.0 Hz), 128.15 (J = 4.0 Hz), 129.35 (J = 8.4 Hz), 133.66, 144.26, 158.69, 165.11 (J = 249.6 Hz); MS (EI) m/z 221 (M^+). HRMS calcd for $C_{12}H_{12}FNO_2$ 221.0852, found 221.0853. Registry Number: 853309-24-7.

2-[2-(4-Bromophenyl)-5-methyloxazol-4-yl]ethanol (7b). To a stirred solution of compound **6b** (465 mg, 1.5 mmol) in methanol (10 mL) at room temperature was added $NaBH_4$ (570 mg, 15.0 mmol) carefully and portionwise over a 3 h period using a spatula. The resulting solution was stirred at room temperature for 6 h, then cooled to 0 °C and quenched by careful addition of H_2O. Methanol was evaporated and diluted with EtOAc (15 mL) and brine (15 mL). The organic layer was separated and dried with sodium sulfate, and the solvents were removed in vacuo. Purification of the material by silica gel flash column chromatography using 40% EtOAc/hexane as eluant afforded the product **7b** (318 mg, 75%) as a white solid: mp 85−91 °C; ^{1}H NMR (400 MHz, $CDCl_3$) δ 2.29 (s, 3H), 2.70 (t, J = 6 Hz, 2H), 3.23 (br, 1H), 3.89 (t, J = 6.0 Hz, 2H), 7.65−7.68 (m, 2H), 7.73−7.77 (m, 2H); ^{13}C NMR (100 MHz, $CDCl_3$) δ 10.06, 28.12, 61.67, 124.23, 126.29, 127.34, 131.88, 134.07, 144.51, 158.58; MS (EI) m/z 283 (M^+). HRMS calcd for $C_{12}H_{12}BrNO_2$, 283.0031 found 283.0037. Registry Number: 328918-84-9.

2-[2-(4-Iodophenyl)-5-methyloxazol-4-yl]ethanol (7c). Prepared from compound **6c** by the method used to prepare compound **7b** and afforded the title compound **7c** (62%) as a white solid: mp 108−111 °C; ^{1}H NMR (400 MHz, $CDCl_3$) δ 2.32 (s, 3H), 2.70 (t, J = 6.0 Hz, 2H), 3.23 (br, 1H), 3.89 (t, J = 6.0 Hz, 2H), 7.65−7.68 (m, 2H), 7.73−7.77 (m, 2H); ^{13}C NMR (100 MHz, $CDCl_3$) δ 10.09, 28.10, 61.68, 96.18, 126.81, 127.38, 134.07, 137.81, 144.56, 158.70; MS (EI) m/z 328 (M^+). HRMS calcd for $C_{13}H_{13}INO_3$ 328.9912, found 328.9907.

(2*S*)-(2-Benzoylphenylamino)-3-(4-{2-[2-(4-fluorophenyl)-5-methyloxazol-4-yl]ethoxy}phenyl)propionic Acid Methyl Ester (8a). To a stirred solution of triphenylphosphine (165 mg, 0.49 mmol) and diethyl azodicarboxylate (77 μL, 0.49 mmol) in tetrahydrofuran (5 mL) at 0 °C was added the mixture of (2*S*)-2-((2-benzoylphenyl)amino)-3-(4-hydroxyphenyl)propionic acid methyl ester (183 mg, 0.49 mmol) and compound **7a** (108 mg, 0.49 mmol) in tetrahydrofuran (2 mL) under nitrogen atmosphere. After the mixture was stirred at 0 °C for 1 h, the resulting solution was stirred for 8 h at room temperature under nitrogen. The solvent was removed in vacuo. The crude reaction mixture was purified by silica gel flash column chromatography using 30% EtOAc/hexane as eluant to afford the product **8a** (140 mg, 55%) as a yellow oil (55%): ^{1}H NMR (400 MHz, $CDCl_3$) δ 2.34 (s, 3H), 2.94 (t, J = 6.8, 2H), 3.11 (dd, J = 13.6, 7.2 Hz, 1H), 3.20 (dd, J = 14.0, 6.0 Hz, 1H), 3.69 (s, 3H), 4.19 (t. J = 6.4 Hz, 2H), 4.38 (m, 1H), 6.56−6.64 (m, 2H), 6.82 (d, J = 8.0 Hz, 2H), 7.09 (m, 2H), 7.17 (d, J = 8.0 Hz, 2H), 7.33 (m, 1H), 7.42−7.53 (m, 4H), 7.60 (d, J = 4.0 Hz, 2H), 7.95−7.98 (m, 2H), 8.91 (d, J = 7.6 Hz, 1H); ^{13}C NMR (125 MHz, $CDCl_3$) δ 10.18, 26.28, 38.06, 52.21, 57.96, 66.52, 111.73, 114.62, 114.95, 115.79 (J = 22. 0 Hz), 118.19, 124.19 (J = 3.6 Hz), 127.95 (J = 8.3 Hz), 128.04, 128.38, 129.09, 130.29, 130.89, 132.71, 134.91, 135.55, 140.28, 145.10, 150.19, 157.80, 158.66, 163.69 (J = 249. 1 Hz), 173.05, 199.30; MS (FAB) m/z 579 (M + H). HRMS cald for $C_{35}H_{32}FN_2O_5$ 579.2295, found 579.2295.

(2*S*)-[2-Benzoylphenylamino]-3-{4-[2-(4-bromophenyloxazol 5-methyl-4-yl)ethoxy]phenyl}propionic Acid Methyl Ester (8b). Prepared from **7b** by the method used to prepare compound **8a** and obtained as a yellow oil (43%): ^{1}H NMR (500 MHz, $CDCl_3$) δ 2.34 (s, 3H), 2.94 (t, J = 6.5, 2H), 3.09−3.22 (m, 2H), 3.69 (s, 3H), 4.18 (t. J = 7.0 Hz, 2H), 4.37 (q, J = 13.5 Hz, 1H), 6.57 (t, J = 8.5 Hz, 1H), 6.63 (d, J = 8.5 Hz, 1H), 6.82 (d, J = 8.5 Hz, 2H), 7.17 (d, J = 8.5 Hz, 2H), 7.31−7.34 (m, 1H), 7.42−7.60 (m, 8H), 7.83 (d, J = 8.5 Hz, 2H), 8.90 (d, J = 7.5 Hz, 1H); ^{13}C NMR (100 MHz, $CDCl_3$) δ 10.21, 26.25, 38.01, 52.21, 57.91, 66.45, 111.70, 114.59, 114.93, 118.15, 124.03, 126.67, 127.36, 128.02, 128.36, 129.07, 130.27, 130.88, 131.87, 132.98, 134.90, 135.54, 140.24, 145.42, 150.16, 157.75, 158.55, 173.03, 199.28; MS (ESI) m/z 639 (M^+). HRMS calcd for $C_{35}H_{31}BrN_2O_5$ 639.1495, found 639.1487.

(2*S*)-[2-Benzoylphenylamino]-3-{4-[2-(4-iodophenyloxazol 5-methyl-4-yl)ethoxy]phenyl}propionic Acid Methyl Ester (8c). Prepared from **7c** by the method used to prepare compound **8a** and obtained as a yellow oil (50%): ^{1}H NMR (400 MHz, $CDCl_3$) δ 2.33 (s, 3H), 2.93 (t, J = 6.8, 2H), 3.09−3.22 (m, 2H), 3.69 (s, 3H), 4.18 (t. J = 6.4 Hz, 2H), 4.38 (q, J = 13.2 Hz, 1H), 6.55−6.59 (m, 1H), 6.63 (d, J = 8.8 Hz, 1H), 6.82 (d, J = 8.8 Hz, 2H), 7.17 (d, J = 8.8 Hz, 2H), 7.31−7.35 (m, 1H), 7.42−7.53 (m, 4H), 7.58−7.60 (m, 2H), 7.69 (d, J = 8.4 Hz, 2H), 7.75 (d, J = 8.8 Hz, 2H), 8.91 (d, J = 7.6 Hz, 1H); ^{13}C NMR (100 MHz, $CDCl_3$) δ 10.18, 26.22, 37.98, 52.17, 57.87, 66.43, 95.92, 111.68, 114.57, 114.90, 118.13, 127.17, 127.37, 127.99, 128.33, 129.04, 130.25, 130.85, 132.97, 134.86, 135.49, 137.77, 140.21, 145.42, 150.12, 157.71, 158.60, 172.98, 199.22; MS (ESI) m/z 687 (M + H). HRMS calcd for $C_{35}H_{32}IN_2O_5$ 687.1356, found 687.1358.

(2*S*)-(2-Benzoylphenylamino)-3-(4-{2-[2-(4-fluorophenyl)-5-methyloxazol-4-yl]ethoxy}phenyl)propionic Acid (1). A stirred solution of compound **8a** (50 mg, 0.086 mmol) in THF/MeOH (v/v = 3:1, 1.25 mL) was treated with 1.0 M LiOH (172 μL, 0.172 mmol). The resulting solution was stirred at room temperature for 4 h. To the reaction mixture was added 1 N HCl (200 uL), and that solution was extracted with EtOAc (5 mL). The organic layer was separated and dried with sodium sulfate. The obtained organic layers were concentrated and purified by silica gel flash column chromatography using 5% MeOH/CH_2Cl_2 as eluant to afford the product **1** (47 mg. 96%) as a yellow solid: mp 95−101 °C; ^{1}H NMR (400 MHz, CD_3OD) δ 2.29 (s, 3H), 2.89 (t, J = 6.4 Hz, 2H), 3.15 (dd, J = 13.8, 7.4 Hz, 1H), 3.23 (dd, J = 13.8, 5 Hz, 1H), 4.14 (t, J = 6.4 Hz, 2H), 4.27−4.30 (m, 1H), 6.49 (t, J = 7.6 Hz, 1H), 6.73 (d, J = 8.8 Hz, 1H), 6.77 (d, J = 8.4 Hz, 2H), 7.15−7.22 (m, 4H), 7.29−7.35 (m 2H), 7.43−7.54 (m, 4H), 7.94−7.97 (m, 2H); ^{13}C NMR (100 MHz, $CDCl_3$) δ 10.19, 26.15, 37.99, 57.90, 66.38, 111.67, 114.54, 114.90, 115.81 (J = 22.0 Hz), 118.09, 127.97, 128.01 (J = 8.0 Hz), 128.29, 129.03, 130.23, 130.85, 132.40, 134.88, 135.50, 140.17, 145.23, 150.09, 157.67, 158.61, 163.71 (J = 249.0 Hz), 172.99, 199.24; MS (FAB) m/z 565 (M + H). HRMS calcd for $C_{34}H_{30}FN_2O_5$ 565.2139, found 565.2139. Registry Number: 196808-49-8.

(2*S*)-(2-Benzoylphenylamino)-3-(4-{2-[2-(4-bromophenyl)-5-methyloxazol-4-yl]ethoxy}phenyl)propionic Acid (2). Prepared from **8b** by the method used to prepare compound **1** and obtained as a yellow solid (98%): mp 102−107 °C; ^{1}H NMR (500 MHz, DMSO-d_6) δ 2.27 (s, 3H), 2.82 (t, J = 6.5 Hz, 2H), 2.97 (dd, J = 13.5, 6.5 Hz, 1H), 3.16 (dd, J = 13.5, 5 Hz, 1H), 4.04 (t, J = 7.0 H, 2H), 4.21 (m, 1H), 6.43 (t, J = 7.0 Hz, 1H), 6.69−6.74 (m, 3H), 7.08 (d, J = 8.5 Hz, 2H), 7.24−7.25 (m, 2H), 7.46−7.55 (m, 5H), 7.66 (d, J = 8.5 Hz, 2H), 7.79 (d, J = 8.0 Hz, 2H), 8.77 (d, J = 7.5 Hz, 1H); ^{13}C NMR (100 MHz, DMSO-d_6) δ 9.84, 25.53, 36.83, 58.06, 65.96, 112.60, 113.23, 113.94, 116.77, 123.42, 126.25, 127.35, 127.84, 128.16, 128.55, 130.45, 130.76, 132.09, 132.97, 134.59, 134.68, 140.21, 145.50,

150.30, 156.66, 157.49, 175.13, 197.59; MS (ESI) *m*/*z* 625(M + H). HRMS calcd for $C_{34}H_{30}BrN_2O_5$ 625.1338, found 625.1335.

(2*S*)-(2-Benzoylphenylamino)-3-(4-{2-[2-(4-iodophenyl)-5-methyloxazol-4-yl]ethoxy}phenyl)propionic Acid (3). Prepared from **8c** by the method used to prepare compound **1** and obtained as a yellow solid (98%): mp 107−110 °C; ^{1}H NMR (500 MHz, DMSO-d_6) δ 2.29 (s, 3H), 2.85 (t, J = 6.5 Hz, 2H), 2.98 (dd, J = 13.5, 6.5 Hz, 1H), 3.13 (dd, J = 13.5, 5 Hz, 1H), 4.10 (t, J = 7.0 H, 2H), 4.42 (m, 1H), 6.54 (t, J = 7.5 Hz, 1H), 6.76 (d, J = 8.5 Hz, 2H), 6.79 (d, J = 8.5 Hz, 1H), 7.09 (d, J = 8.5 Hz, 2H), 7.31 (d, J = 8.0 Hz, 1H), 7.37 (t, J = 7.5 Hz, 1H), 7.47−7.51 (m, 4H), 7.54−7.57 (m 1H), 7.65 (d, J = 8.5 Hz, 2H), 7.84 (d, J = 8.5 Hz, 2H), 8.68 (d, J = 7.5 Hz, 1H); ^{13}C NMR (100 MHz, DMSO-d_6) δ 9.84, 25.50, 36.58, 56.80, 65.96, 96.96, 112.47, 114.14, 117.08, 126.49, 127.23, 128.20, 128.61, 129.18, 130.36, 130.94, 132.92, 134.68, 134.92, 137.88, 139.92, 145.47, 149.91, 156.93, 157.70, 162.30, 173.62, 197.99; MS (ESI) *m*/*z* 673 (M + H), 515 (80%), 257 (100%). HRMS calcd for $C_{34}H_{30}IN_2O_5$ 673.1199, found 673.1190.

(2*S*)-(2-Benzoylphenylamino)-3-(4-{2-[2-(4-tributylstannanyl)-5-methyloxazol-4-yl]ethoxy}phenyl)propionic Acid Methyl Ester (9). To a solution of tetrakis(triphenylphospine)-palladium(0) (22 mg, 5 mol %) and bis(tributyltin) (217 μL, 0.418 mmol) in dry toluene (5 mL) was added (2*S*)-[2-benzoylphenylamino]-3-{4-[2-(4-iodophenyloxazol 5-methyl-4-yl)ethoxy]phenyl}propionic acid methyl ester **8c** (258 mg, 0.38 mmol) in dry toluene (3 mL) at room temperature under nitrogen atmosphere. After addition, the reaction mixture was heated to 120 °C for 6 h. After evaporation of the solvent, the concentrate was filtered through a layer of Celite, and the residue was subjected to flash chromatography using 20% EtOAc/hexane as eluant to afford the product **9** (271 mg, 84%) as a yellow oil: ^{1}H NMR (400 MHz, $CDCl_3$) δ 0.88 (t, J = 7.2 Hz, 9H), 1.08 (t, J = 8.2, 6H), 1.30−1.36 (m, 6H), 1.50−1.58 (m, 6H), 2.35 (s, 3H), 2.95 (t, J = 6.4 Hz, 2H), 3.09−3.22 (m, 2H), 3.69 (s, 3H), 4.19 (t, J = 6.8 Hz, 2H), 4.38 (q, J = 13.2 Hz, 1H), 6.57 (t, J = 7.2 Hz, 1H), 6.63 (d, J = 8.4 Hz, 1H), 6.83 (d, J = 8.4 Hz, 2H), 7.17 (d, J = 8.4 Hz, 2H), 7.31−7.35 (m, 1H), 7.42−7.61 (m, 8H), 7.89 (d, J = 8.4 Hz, 2H), 8.91 (d, J = 7.6 Hz, 1H); ^{13}C NMR (100 MHz, $CDCl_3$) δ 9.58, 10.23, 13.66, 26.33, 27.31, 29.03, 38.09, 52.22, 57.97, 66.61, 111.72, 114.61, 114.91, 118.16, 124.95, 127.19, 128.01, 128.29, 129.07, 130.24, 130.86, 132.58, 134.87, 135.51, 136.66, 140.23, 144.83, 144.97, 150.15, 157.79, 159.73, 173.02, 199.22; MS (ESI) *m*/*z* 851 (M + H, 10%), 625 (10%), 291 (80%), 235 (100%). HRMS calcd for $C_{47}H_{59}N_2O_5Sn$ 851.3446, found 851.3486.

[(Hydroxy)(tosyloxy)iodo]-*m*-methoxybenzene (11b). To a solution of compound **10a** (2 g, 5.68 mmol) was added to solution of *p*-toluenesulfonic acid monohydrate (1.1 g, 5.7 mmol) in acetonitrile (10 mL) at room temperature under nitrogen atmosphere. The mixture was stirred for 12 h at room temperature. After the addition of diethyl ether and EtOAc (v/v = 2:1, 30 mL), the solid was filtered and dried in vacuo to give the product **11b** as a white solid (92%): mp 134−137 °C (decomp); ^{1}H NMR (400 MHz, CD_3OD) δ 1.98 (s, 3H), 3.52 (s, 3H), 6.81 (d, J = 7.5 Hz, 2H), 6.93−6.95 (m, 1H), 7.17 (d, J = 8.0 Hz, 2H), 7.22 (t, J = 8.0 Hz, 1H), 7.45 (d, J = 8.0 Hz, 2H), 7.52−7.53 (m, 1H), 9.47 (br, 1H); ^{13}C NMR (100 MHz, CD_3OD) δ 21.28, 56.53, 114.50, 120.95, 121.95, 126.89, 128.91, 129.84, 133.42, 141.92, 142.94, 162.49.

[(Hydroxy)(tosyloxy)iodo]thiophene (11c). To a solution of compound **10b** (500 mg, 1.52 mmol) was added to solution of *p*-toluenesulfonic acid monohydrate (290 mg, 1.52 mmol) in acetonitrile (10 mL) at room temperature under nitrogen atmosphere. The mixture was stirred for 1 h at room temperature. After the addition of diethyl ether and EtOAc (v/v = 2:1, 30 mL), the solid was filtered and dried in a short time under nitrogen atmosphere to give the product **11c** (95%). Because this product (**11c**) was unstable under air atmosphere and at room temperature, it was used immediately after isolation to prepare the next compound, **12c**: ^{1}H NMR (400 MHz, CD_3OD) δ 2.36 (s, 3H), 4.88 (s, 3H), 7.22 (d, J = 8.0 Hz, 2H), 7.35−7.37 (m, 1H), 7.68 (d, J = 8.4 Hz, 2H), 8.09−8.10 (m, 1H), 8.24−8.25 (m, 1H); ^{13}C NMR (100 MHz, CD_3OD) δ 21.30, 126.95, 129.83, 131.19, 141.39, 141.76, 143.29, 143.38, 145.23.

(2*S*)-[2-Benzoylphenylamino]-3-{4-[2-(4-iodophenyl(phenyl) Oxazol 5-methyl-4-yl)ethoxy]phenyl}propionic Acid Methyl Ester Iodonium Tosylate (12a). To a solution of Koser's reagent **11a** (47 mg, 0.12 mmol) in CH_3CN (3 mL) was added tin compound **9** (100 mg, 0.12 mmol) in CH_3CN (3 mL) at room temperature under nitrogen atmosphere. The reaction mixture was stirred for 12 h at room temperature under nitrogen atmosphere. The solvent was evaporated using a stream of nitrogen. The crude mixture was dissolved a small amount of EtOH (1.5 mL) and transferred to the centrifuge tube to which was added excess diethyl ether (20 mL). After centrifuging, the collected yellow oil was dried in vacuo to give the product **12a** (42 mg, 38%) as a yellow oil: ^{1}H NMR (400 MHz, CD_3OD) δ 2.32 (s, 3H), 2.34 (s, 3H), 2.91 (t, J = 6.4 Hz, 2H), 3.06−3.20 (m, 2H), 3.69 (s, 3H), 4.16 (t. J = 6.0 Hz, 2H), 4.56 (t, J = 6.0 Hz, 1H), 6.56−6.60 (m, 1H), 6.73−6.78 (m, 3H), 7.08 (d, J = 8.8 Hz, 2H), 7.21 (d, J = 8.0 Hz, 2H), 7.34−7.71 (m, 12H), 8.02 (d, J = 8.4 Hz, 2H), 8.18−8.24 (m, 4H); ^{13}C NMR (100 MHz, CD_3OD) δ 10.15, 21.29, 26.88, 38.36, 52.70, 58.29, 67.26, 113.30, 115.61, 116.13, 116.20, 116.59, 119.37, 126.94, 129.19, 129.70, 129.78, 130.00, 131.49, 132.08, 132.20, 133.24, 133.75, 135.04, 136.25, 136.38, 136.56, 137.03, 141.49, 141.59, 143.56, 148.56, 151.25, 158.68, 159.09, 174.37, 200.81; MS (ESI) *m*/*z* 763 (M^+ − OTs, 100%). HRMS calcd for $C_{41}H_{36}IN_2O_5$ 763.1669, found 763.1657.

(2*S*)-[2-Benzoylphenylamino]-3-{4-[2-(4-iodophenyl(3-methoxyphenyl) oxazol 5-methyl-4-yl)ethoxy]phenyl}propionic Acid Methyl Ester Iodonium Tosylate (12b). Prepared from tin precursor **9** and the *m*-methoxyphenyl iodonium salt **11b** by the method used to prepare iodonium salt **12a** and obtained as a yellow oil: ^{1}H NMR (400 MHz, CD_3OD) δ 2.29 (s, 3H), 2.31 (s, 3H), 2.87 (t, J = 6.0 Hz, 2H), 3.03−3.17 (m, 2H), 3.67 (s, 3H), 3.80 (s, 3H), 4.12 (t, J = 6.5 Hz, 2H), 4.53 (t, J = 6.0 Hz, 1H), 6.56 (t, J = 7.0 Hz, 1H), 6.71−6.75 (m, 3H), 7.06 (d, J = 8.5 Hz, 2H), 7.17−7.20 (m, 3H), 7.33−7.49 (m, 8H), 7.66 (d, J = 8.0 Hz, 2H), 7.69−7.71 (m, 1H), 7.79 (t, J = 2.5 Hz, 1H), 7.95 (d, J = 8.5 Hz, 2H), 8.20 (d, J = 8.5 Hz, 2H); ^{13}C NMR (100 MHz, CD_3OD) δ 10.17, 21.33, 26.87, 38.35, 52.75, 56.51, 58.34, 67.27, 113.32, 115.62, 115.95, 116.12, 116.66, 119.39, 119.68, 121.87, 126.94, 126.99, 128.38, 129.25, 129.71, 129.81, 129.85, 130.05, 131.53, 132.12, 132.24, 133.88, 135.07, 136.29, 137.04, 141.55, 141.69, 143.52, 148.62, 151.31, 158.78, 159.15, 162.83, 174.43, 200.90; MS (ESI) *m*/*z* 793 (M^+ − OTs, 100%), 752 (35%). HRMS calcd for $C_{42}H_{38}IN_2O_6$ 793.1775, found 793.1801.

(2*S*)-[2-Benzoylphenylamino]-3-{4-[2-(4-iodophenyl(2-thiophenyl) oxazol 5-methyl-4-yl)ethoxy]phenyl}propionic Acid Methyl Ester Iodonium Tosylate (12c). Prepared from tin precursor **9** and thiophene iodonium salt **11c** by the method used to prepare iodonium salt **12a** and obtained as a yellow oil: ^{1}H NMR (500 MHz, CD_3OD) δ 2.30 (s, 3H), 2.32 (s, 3H), 2.88 (t, J = 6.5 Hz, 2H), 3.04−3.17 (m, 2H), 3.67 (s, 3H), 4.13 (t, J = 6.0 Hz, 2H), 4.54 (t, J = 6.0 Hz, 1H), 6.56 (t, J = 7.5 Hz, 1H), 6.72 (d, J = 8.0 Hz, 1H), 6.75 (d, J = 9.0 Hz, 2H), 7.07 (d, J = 8.5 Hz, 2H), 7.14−7.16 (m, 1H), 7.18 (d, J = 8.0 Hz, 2H), 7.33−7.37 (m, 2H), 7.41−7.44 (m, 2H), 7.48−7.52 (m, 3H), 7.67 (d, J = 8.0 Hz, 2H), 7.86−7.87 (m, 1H), 7.95 (d, J = 9.0 Hz, 2H), 8.01−8.02 (m, 1H), 8.19 (d, J = 8.5

Hz, 2H); ^{13}C NMR (100 MHz, CD_3OD) δ 10.13, 21.29, 26.90, 38.39, 52.70, 58.33, 67.28, 99.20, 113.31, 115.63, 116.13, 119.41, 119.55, 126.95, 129.22, 129.70, 129.79, 130.01, 130.93, 131.50, 132.15, 132.22, 135.08, 136.26, 136.38, 136.41, 138.78, 141.56, 141.65, 142.39, 143.52, 148.66, 151.29, 158.73, 159.12, 174.43, 200.92; MS (ESI) *m*/*z* 769 ($M^+ - OTs$, 100%). HRMS calcd for $C_{39}H_{34}IN_2O_5S$ 769.1233, found 769.1238.

Halodestannylation Reactions with Bromine and Iodine. *Synthesis of (2S)-(2-benzoylphenylamino)-3-(4-{2-[2-(4-bromophenyl)-5-methyloxazol-4-yl]ethoxy}phenyl)propionic Acid (**2**).* To a solution of compound **9** (10 mg, 0.012 mmol) in peracetic acid (500 μL, 0.3% v/v in acetic acid) was added NH_4-Br (1.3 mg, 0.013 mmol) in H_2O (500 μL) at room temperature. The reaction mixture was stirred for 30 min at room temperature, then diluted with 0.5 N NaOH (3 mL) and EtOAc (3 mL). The organic layer was separated and dried with sodium sulfate, and the solvents were removed in vacuo. The crude mixture obtained was dissolved in THF/MeOH (v/v = 3:1, 0.5 mL) and then was treated with 0.1 M LiOH (130 μL, 0.013 mmol). The resulting solution was stirred at room temperature for 1 h. The reaction mixture was then poured into 1 N HCl (20 μL) and extracted with EtOAc. The organic layer was separated and dried with sodium sulfate. The obtained organic layers were concentrated and purified by silica gel flash column chromatography using 5% MeOH/CH_2Cl_2 as eluant to afford the product **2** (7 mg. 91%) as a yellow solid.

*Synthesis of (2S)-(2-benzoylphenylamino)-3-(4-{2-[2-(4-iodophenyl)-5-methyloxazol-4-yl]ethoxy}phenyl)propionic Acid (**3**).* To a solution of compound **9** (10 mg, 0.012 mmol) in peracetic acid (500 μL, 0.3% v/v in acetic acid) was added NaI (2 mg, 0.013 mmol) in H_2O (500 μL) at room temperature. The reaction mixture was stirred for 30 min at room temperature, then diluted with 0.5 N NaOH (3 mL) and EtOAc (3 mL). The organic layer was separated and dried with sodium sulfate, and the solvents were removed in vacuo. The hydrolysis of methyl ester was performed by the method used for **2** and obtained as a yellow solid (93%).

Fluorination of Iodonium Salts. *Synthesis of (2S)-(2-benzoylphenylamino)-3-(4-{2-[2-(4-fluorophenyl)-5-methyloxazol-4-yl]ethoxy}phenyl)propionic Acid (**1**).* To a solution of compound **12c** (10 mg, 0.011 mmol) in CH_3CN (1 mL) was added CsF (2.5 mg, 0.016 mmol). The reaction mixture was heated at 90 °C for 60 min. After cooling, the solvent was removed in vacuo. Hydrolysis of the methyl ester was performed by the method used to prepare compound **2**. The progress of the reaction and yields were analyzed by HPLC (prep silica gel column, 10 μm, 10 × 250 mm; hexane/isopropanol/methylene chloride/trifluorosulfonic acid = 70:1.5:28:0.03 (v/v): 254 nm; 4 mL/min).

PPARγ Binding Affinity Assays. The binding of compound **1** to PPARγ was evaluated using a scintillation proximity assay (SPA) adapted from the method described by Sun et al. (*34*). Briefly, only the energy emitted from the negatrons of the bead-protein-bound radioligand complex can be absorbed by scintillant-coated SPA beads to produce light, which can be detected in a liquid scintillation counter. The potency of the test compound is assessed by its displacement of a tritium-labeled ligand. Yttrium silicate (Ysi) copper His-Tag SPA beads were purchased from Amersham Biosciences (Piscataway, NJ). A histidine-tagged human PPARγ ligand-binding domain (amino acids 195−477) was acquired from Invitrogen (Carlsbad, CA). The tritium ligand, [^{3}H]-rosiglitazone, which has high affinity and high potency for PPARγ (K_d and EC_{50} ca. 15−20 nM) (*35*), was obtained from American Radiolabeled Chemicals (St. Louis, MO).

[^{3}H]-Rosiglitazone and PPARγ protein were diluted to 23 μCi/mL and 50 ng/mL stock, respectively. Radioligand, protein, and test compound at various concentrations (10 nM to 2 μM) were incubated at room temperature for 2 h. SPA beads were diluted and aliquoted into a clear-bottomed 96-well plate according to the manufacturer's specifications. Test ligand, [^{3}H]-Rosiglitazone, and protein were then added to the assay plate and incubated at room temperature for at least 1 h before the plate was read by a Packard TopCount plate reader (Perkin-Elmer, Wellesley, MA). GW1929 (Cayman Chemical Co., Ann Arbor, MI), a potent PPARγ agonist, served as a positive control. Nonspecific binding was very low. The initial IC_{50} values of GW1929 and test compound were calculated by the *Prism* program (GraphPad Software, San Diego, CA). The reported compound IC_{50} value of the compound tested was normalized against GW1929 due to the variability of the assay (*36*).

RESULTS AND DISCUSSION

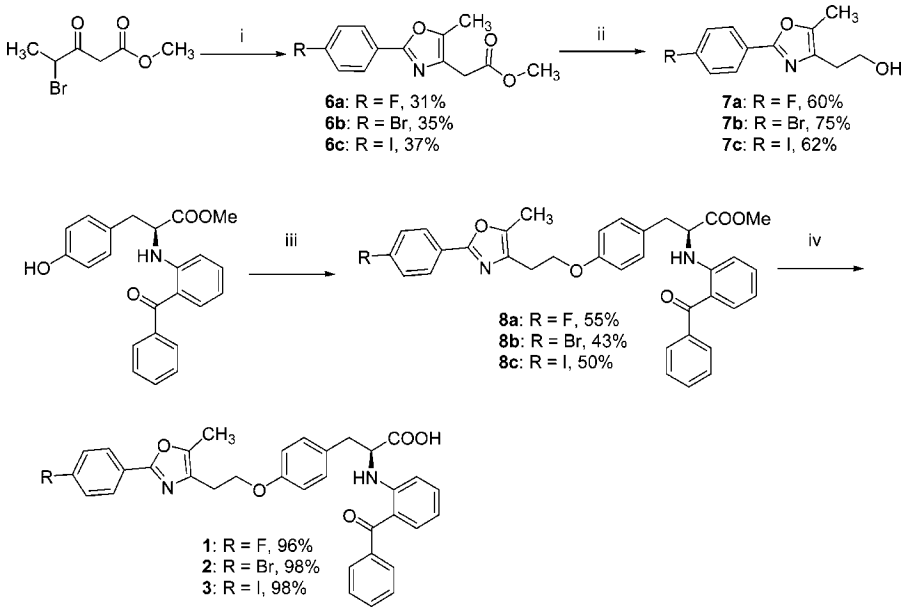
Chemical Synthesis. We prepared compounds **1**−**3** by two approaches: the first (Scheme 2) was to prepare authentic samples of these PPARγ ligands; the second proceeded through precursors from which the halogen could be introduced at a very late step, using a simple halogen reagent (Schemes 3 and 7), as would be needed for labeling these compounds with radiohalogens at high specific activity.

Synthesis of (2*S*)-(2-benzoylphenylamino)-3-(4-{2-[2-(4-halogenophenyl)-5-methyloxazol-4-yl]ethoxy}phenyl)-propionic Acid (1−3). As shown in Scheme 2, the three PPARγ ligands (**1**−**3**) were synthesized in four steps, using a modification of known methods (*19*−*21*). Three halogen-substituted phenyl oxazole rings **6a**−**c** were synthesized directly from a 4-halogen-substituted benzamide and 4-bromo-3-oxopentanoate, followed by reduction of the ester with lithium aluminum hydride or sodium borohydride in tetrahydrofuran to produce the corresponding alcohols **7a**−**c**. Using Mitsunobu conditions, alcohols **7a**−**c** were coupled to (2*S*)-2-((2-benzoylphenyl)-amino)-3-(4-hydroxyphenyl)propionic acid methyl ester. Hydrolysis of the methyl esters **8a**−**c** with LiOH solution proceeded under mild conditions to give the desired fluorine, bromine, and iodine-substituted PPARγ ligands **1**−**3**.

Synthesis of (2*S*)-(2-benzoylphenylamino)-3-(4-{2-[2-(4-tributylstannylphenyl)-5-methyloxazol-4-yl]ethoxy}phenyl)-propionic Acid Methyl Ester (9) and Iodonium Tosylates (12a−c). A different approach is needed for the synthesis of the target compounds **1**−**3** in radiolabeled form. Because the radiohalogens have relatively short half-lives (F-18, 110 min; Br-76, 16.1 h; I-124, 4.2 d), it is best if they can be introduced late in the synthesis, in a rapid and efficient manner, into appropriate precursors using simple halogenating agents that are available in radiolabeled form at high specific activity. The trialkylstannane compound **9**, which can readily be prepared from the iodo compound **8c** in the presence of bis(tributyl)tin and a catalytic quantity of tetrakis(triphenylphosphine)palladium (Scheme 3), is a precursor that could be used to prepare the bromine- and iodine-substituted PPARγ ligands **2** and **3** in labeled form by a halodestannylation reaction. These reactions proceed readily (Scheme 3).

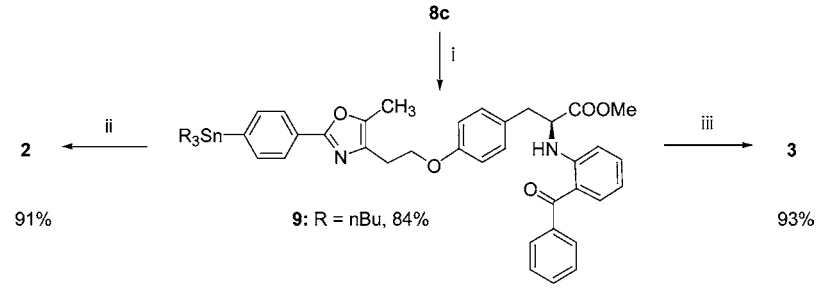
We considered a number of approaches that would be suitable for the preparation of the fluorine-substituted PPARγ ligand (**1**) in F-18 labeled form at the high specific activity required for PET imaging of nuclear receptors. For this type of tracer-level labeling, [^{18}F]fluoride ion is the only practical fluorination reagent. Fluoride ion can be introduced into certain aromatic rings by nucleophilic aromatic substitution of a suitable leaving group, such as nitro or trimethylammonium triflate, provided the ring is sufficiently activated by ortho or para electron withdrawing groups (*37*−*39*). In our system, it was not clear whether the 2-oxazolyl substituent at the para position would provide sufficient activation for fluoride ion substitution.

Scheme 2 [a]



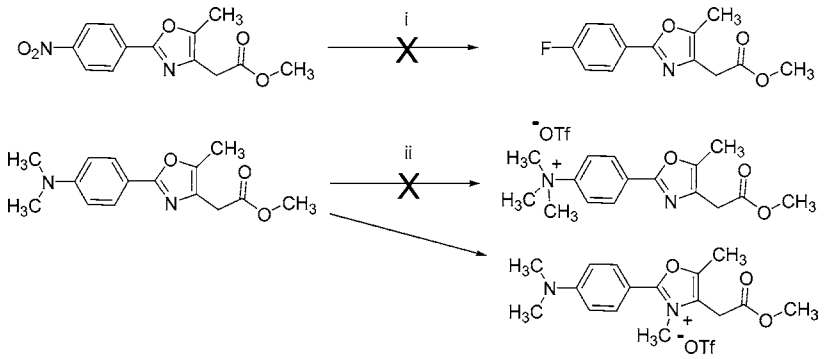
[a] Reaction conditions: (i) 4-halobenzamide, 1,2-dichlorobenzene, 130 °C, 24 h; (ii) LAH, THF, 0 °C, 1 h, or $NaBH_4$, MeOH, rt, 6 h; (iii) **7a**−**c**, PPh_3, DEAD, THF, 0 °C ∼ rt, 12 h; (iv) LiOH, THF/MeOH, rt, 6 h.

Scheme 3 [a]



[a] Reaction conditions: (i) $(PPh_3)_4Pd$, Sn_2Bu_6, toluene, 120 °C, 12 h; (ii) (a) NH_4Br, CH_3CO_3H, CH_3COOH, rt, 30 min, (b) LiOH, THF/MeOH, rt, 1 h; (iii) (a) NaI, CH_3CO_3H, CH_3COOH, rt, 30 min, (b) LiOH, THF/MeOH, rt, 1 h.

Scheme 4 [a]

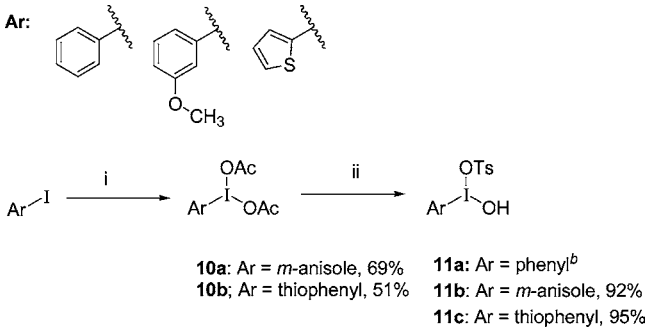


[a] Reaction conditions: (i) TMAF, DMSO, 130 °C; (ii) $CF_3SO_2OCH_3$, CH_2Cl_2, rt.

As shown in Scheme 4, in studies on a model system, we were unable to effect fluoride ion substitution on the corresponding p-nitro precursor under a variety of conditions. Curiously, we were also unable to prepare the more reactive p-trimethylammonium precursor, because in the final methylation step of the dimethylaniline precursor, the oxazole moiety became N-methylated in preference to the aromatic amine, giving the N-methyloxazolium salt as the only identifiable product. Although alternative routes to reach this precursor were considered, the uncertainty of success with this modestly activated ring system led us to consider different approaches altogether.

It was known that diaryliodonium salts can be used as precursors for fluoroarenes (*27*), and Widdowson showed that these salts are useful, as well, for the introduction of fluorine-18 into arenes (*28*). Mixed functional diaryliodonium tosylates can be prepared by the reaction of aryltrialkylstannanes with hydroxy(tosyloxy)iodobenzene (Koser's reagent, **11a**) under mild conditions (*26*−*29*). To prepare diaryliodonium precursors suitable for introducing fluorine into the PPARγ ligand **1** (Scheme 5), we reacted the tributyltin analog **9** with commercially available Koser's reagent, as well as with two other related and known hydroxy(tosyloxy)iodoarenes (**11b** and **11c**) derived, respectively, from *m*-methoxyphenyl iodide (*m*-io-

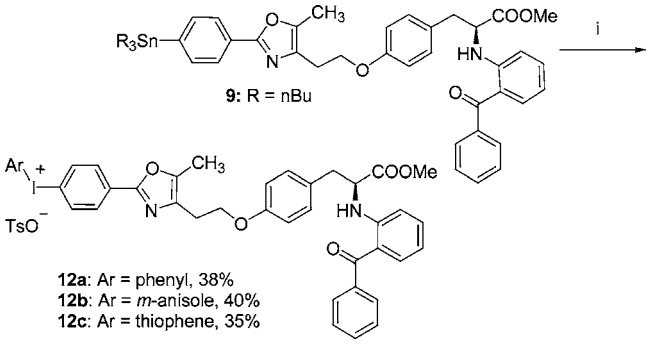
Scheme 5 [a]



10a: Ar = *m*-anisole, 69% **11a:** Ar = phenyl[b]
10b; Ar = thiophenyl, 51% **11b**: Ar = *m*-anisole, 92%
11c: Ar = thiophenyl, 95%

[a] Reaction conditions: (i) $NaIO_4$, AcONa, AcOH, Ac_2O, 120 °C, 2 h; (ii) TsOH, CH_3CN, rt, 2 h. [b] Koser's reagent **10a** was purchased from Aldrich.

Scheme 6 [a]



12a: Ar = phenyl, 38%
12b: Ar = *m*-anisole, 40%
12c: Ar = thiophene, 35%

[a] Reaction conditions: (i) **11a**−**c**, CH_2Cl_2, rt, 12 h.

doanisole) and 2-iodothiophene (*31*−*33*). These reactions proceeded readily and in good yield under mild conditions.

The diaryliodonium salts were readily prepared from the same tin precursor **9** that was used to prepare the bromo and iodoanalogs (**2** and **3**) by exposure to the three hydroxyl(tosyloxy)iodoarenes **11a**−**c** (Scheme 6). These iodonium salts are liquids that can be easily isolated, but they cannot be rigorous purified. They are sufficiently pure, however, to function as effective precursors for fluorination to produce the final compound **1** (Scheme 7).

In fluorination of mixed functional diaryliodonium salts, steric demand and/or electron deficiency of the aromatic rings determines the site of fluorine substitution (*27*, *28*, *40*, *41*). Because steric effects in the two rings of our systems are essentially equivalent, fluoride anion is expected to attack the more electron deficient ring. Thus, the three salts we have prepared present an interesting situation, where the "dispensable ring" is either phenyl or the two more electron rich rings, *m*-methoxyphenyl or 2-thiophenyl. We avoided the choice of the *p*-methoxyphenyl analog of compound **11b** series, because the reagent required, [hydroxy(tosyloxy)iodo]-*para*-methoxybenzene, is known to be unstable and to decompose violently at room temperature (*42*). The reagent to prepare the thiophene heteroaromatic iodonium salt **12c**, namely, [hydroxy(tosyloxy)iodo]thiophene **11c**, is also somewhat unstable; however, we were able to isolate it and use it immediately to prepare the PPARγ precursor **12c** (*33*).

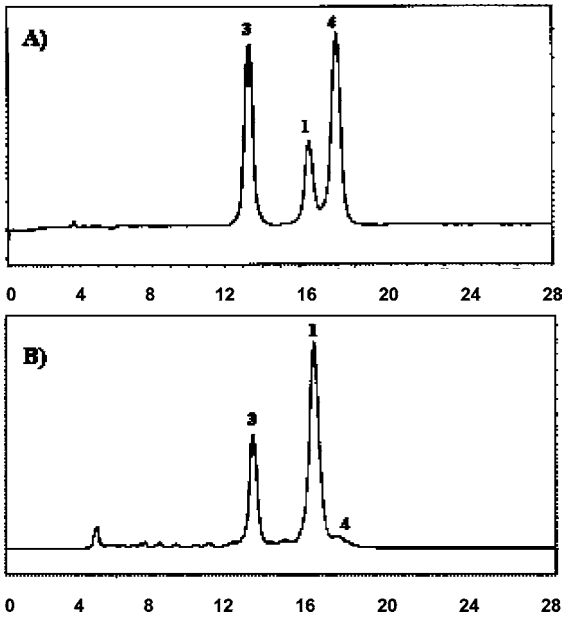


Figure 1. (A) HPLC profile of the standards. t_R = 16.7 min (**1**), 13.4 min (**3**), and 18.0 min (**4**). (B) HPLC analysis of the reaction mixture after fluorination of **12c**, followed hydrolysis.

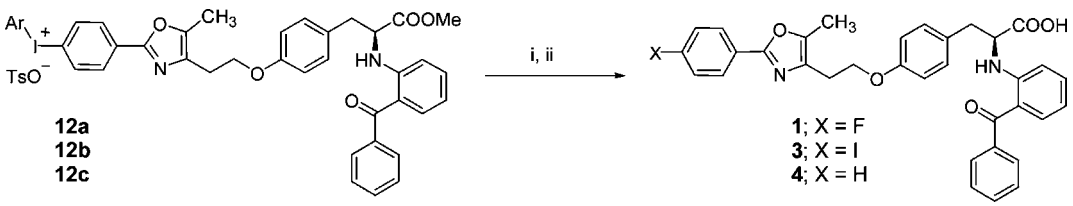
Table 1. Reaction of Fluorination with Iodonium Tosylates

		product ratio (%)[a]			
cmpd no	Ar	**1**	**3**	**4**	yields[b]
12a	phenyl	50	38	9	27%
12b	*m*-anisolyl	34	56	5	28%
12c	2-thiophenyl	68	28	1	35%

[a] Progress of the reaction and yields were analyzed by HPLC (prep. silica gel column, 10 μ, 10 × 250 mm; hexane/isopropanol/methylene chloride/trifluorosulfonic acid = 70:1.5:28.5:0.03 (v/v); 254 nm; 4 mL/min). Ratios represent the areas of the peaks associated with products **1**, **3**, and **4**; the ratios do not add to 100% because small byproduct peaks are also present. [b] Yield of isolated pure product **1**, obtained by preparative column chromatography.

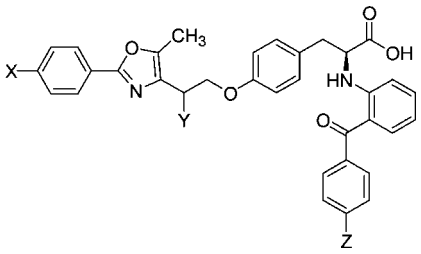
Synthesis of (2*S*)-(2-Benzoylphenylamino)-3-(4-{2-[2-(4-fluorophenyl)-5-methyloxazol-4-yl]ethoxy}phenyl)-propionic Acid (1). Various conditions were explored for the preparation of the fluoride-substituted PPARγ ligand **1** from the three precursors **12a**−**c** (Scheme 7). The results from reactions conditions optimized to give the fluorine-substituted ester (CsF in acetonitrile at 90 °C) and then mild hydrolysis to the acid with LiOH are summarized in Table 1. Reaction products were analyzed by HPLC, and the crude reaction mixture showed the presence of the desired product **1** (t_R = 16.7 min) and two side products (t_R = 13.4 and 18.0 min, Figure 1). These were identified as the iodine-substituted and reduced compounds (**3** and **4**, respectively) by comparison with authentic samples that we had prepared (cf., Scheme 2). Product ratios of **1**, **3**, and **4** were calculated from the peak areas, and the

Scheme 7 [a]



[a] Reaction conditions: (i) CsF, CH_3CN, 90 °C, 50 min; (ii) 0.5 M LiOH 80 °C, 5 min.

Table 2. Three New Fluorine-Substituted Ligands for PPARγ Receptors and Their Binding Affinities[a]



	X	Y	Z	
1	F	H	H	
2	Br	H	H	
3	I	H	H	
4	H	H	H	[farglitazar]
5	--	--	--	[see Scheme 1]
12	H	F	H	
13	H	H	F	

	pK_i [b] (nM)		
cmpd no	PPARγ	PPARα	PPARδ
1[c]	9.46 (9.42 ± 0.02)[a]	7.28	6.27
2[a]	9.61 ± 0.03	ND	ND
3[a]	9.70 ± 0.01	ND	ND
4[d]	8.93	6.31	ND
5[e]	8.15	7.60	5.55
12[c]	8.51	5.84	<5.52
13[c]	8.13 (9.85 ± 0.01)[a]	6.04	<5.52

[a] Binding affinities were determined in this study by a competitive radiometric binding assays using scintillation proximity methods; see Experimental Section. ND = not determined. [b] $pK_i = -\log$ of the concentration of test compound required to achieve an apparent K_i value. [c] K. C. Lee, unpublished.[d] ref 20. [e] ref 17.

isolated yield of compound **1** was determined after purification by preparative chromatography.

The desired product, compound **1**, was produced in highest product ratio and highest yield from the 2-thiophenyl iodonium salt (**12c**). This is consistent with the fact that, in this salt, the dispensable ring is a thiophene, the most electropositive ring of the three, and thus it is most effective in directing fluoride ion to attack the other ring, that of the complex aryl system of the PPARγ portion of the salt, as is needed to produce the desired product (**1**). The isolated yields of **1** produced from the other salts, **12a** and **12b** were only somewhat lower than that from **12c**. Notably, the unsubstituted product, **4**, potentially an undesired competitor for binding to PPARγ, is also produced in lowest amounts from the thiophenyl precursor **12c**.

As a matter of practical importance, it is also of note that in this chromatographic system the desired fluorine-substituted compound **1** elutes well behind the iodine-substituted byproduct (**3**), and it also precedes the unsubstituted compound (**4**, farglitazar itself), which in any case is produced in very small amounts. Thus, it should be possible to separate the fluorine-18 labeled product from the two reaction byproducts that have potential for competing for its binding to PPARγ, thus ensuring high effective specific activity.

Binding Affinity Determination. In previous work, we synthesized fluorine-substituted members of the benzophenone−tyrosine class (farglitazar) and demonstrated that they had very high binding affinity and selectivity for PPARγ receptor. The result of PPARγ binding measurements on compounds **1**−**4**, done using a scintillation proximity assay (*34*), and measurements of certain related ligands from other studies are shown in Table 2 (*17*, *20*, Lee, K. C., unpublished results). Fluorine substitution of the phenyl ring or alkyl chain of the 2-phenyloxazole system (compounds **1** and **13**) and fluorine substitution of benzophenone ring (compound **12)** provided higher-affinity and more selective PPARγ ligands (Lee, K. C., unpublished results) than did the fluorine-substituted analog of SB 213068 (**5**) that we prepared earlier (*17*). Among these, compound **1** appears to be an excellent ligand in terms of binding affinity and selectivity, and the pK_i value we obtained in this study is very close to that determined on this compound by a corporate laboratory (Lee, K. C., unpublished results).

In this study, we have also evaluated the effect of substitution of this phenyl ring with other halogen isotopes that could be used for PET or SPECT imaging, and both the bromine and iodine analogs (**2** and **3**) retain very high affinity for PPARγ, comparable to or greater than that of the fluorine-substituted compound **1** and the parent ligand farglitazar **4** (Table 2).

CONCLUSION

PPARγ, a nuclear receptor that plays critical roles in regulating lipid and carbohydrate metabolism and cellular differentiation and has marked effects on certain cancers, is an important target for in vivo imaging with PET. In our effort to develop radiohalogen-labeled ligands suitable for this purpose, we have prepared three homologous halogen-substituted analogues (fluorine, bromine, and iodine) of the selective and high-affinity PPARγ ligand **4** (farglitazar). All members of this benzophenone−tyrosine class retain very high affinity for PPARγ, superior to that of F-18 labeled ligands of the phenylpropanoic acid class that we investigated earlier (*17*). We have also developed methods by which the halogen can be introduced into each of these ligands (**1**−**3**) as the penultimate step: the heavy halogens are introduced by an electrophilic destannylation sequence and the fluorine by nucleophilic substitution on an optimized heteroarylarene iodonium salt. The latter reaction is an example of fluorine substitution on one of the most complex, highly functionalized systems using this approach. These strategies are easily adaptable to radiolabeling with these halogens in radiolabeled form. Further work describing the preparation of these compounds in radiolabeled form and evaluation of their in vivo tissue distribution will be described in forthcoming publications.

ACKNOWLEDGMENT

We are grateful for support of this work by grants from the Department of Energy (FG02 86ER60401 to J.A.K.) and the National Institute of Health (P01 HL13851 to M. J. Welch, P.I.).

LITERATURE CITED

(1) Issemann, I., and Green, S. (1990) Activation of a member of the steroid hormone receptor superfamily by peroxisome proliferators. *Nature (London) 347*, 645−650.

(2) Greene, M. E., Blumberg, B., McBride, O. W., Yi, H. F., Kronquist, K., Kwan, K., Hsieh, L., Greene, G., and Nimer, S. D. (1995) Isolation of the human peroxisome proliferator activated receptor gamma cDNA: Expression in hematopoietic cells and chromosomal mapping. *Gene Express. 4*, 281−289.

(3) Schmidt, A., Endo, N., Rutledge, S. J., Vogel, R., Shinar, D., and Rodan, G. A. (1992) Identification of a new member of the steroid hormone receptor superfamily that is activated by a peroxisome proliferator and fatty acids. *Mol. Endocrinol. 6*, 1634−1641.
(4) Lemberger, T., Desvergne, B., and Wahli, W. (1996) Peroxisome proliferator-activated receptors: A nuclear recepor signaling pathway in lipid physiology. *Annu. Rev. Cell Dev. Biol. 12*, 335−363.
(5) Willson, T. M., Cobb, J. E., Cowan, D. J., Wiethe, R. W., Correa, I. D., Prakash, S. R., Beck, K. D., Moore, L. B., Kliewer, S. A., and Lehmann, J. M. (1996) The structure−activity relationship between peroxisom proliferator-activated receptor gamma agonism and the antihyperglycemic activity of thiazolidinediones. *J. Med. Chem. 39*, 665−668.
(6) Brun, R. P.;, Kim, J. B., Hu, E., and Spiegelman, B. M. (1997) Peroxisome proliferator-activated receptor gamma and the control of adipogenesis. *Curr. Opin. Lipidol. 8*, 212−218.
(7) Kliewer, S. A., Lenhard, J. M., Willson, T. M., Patel, I., Morris, D. C., and Lehmann, J. M. (1995) A prostaglandin J2 metabolite binds peroxisome proliferator-activated receptor γ and promotes adipocyte differntiation. *Cell 83*, 813−819.
(8) Kliewer, S. A., Forman, B. M., Blumberg, B., Ong, E. S., Borgmeyer, U., Mangelsdorf, D. J., Umesono, K., and Evans, R. M. (1994) Differential expression and activation of a family of murine peroxisome proliferator-activated receptors. *Proc. Natl. Acad. Sci. U.S.A. 91*, 7355−7359.
(9) Tontonoz, P., Hu, E., Graves, R. A., Budavari, A. I., and Spiegelman, B. M. (1994) mPPAR γ2: Tissue-specific regulator of an adipocyte enhancer. *Genes Dev. 8*, 1224−1234.
(10) Mueller, E., Smith, M., Sarraf, P., Kroll, T., Aiyer, A., Kaufman, D. S., Oh, W., Demetri, G., Figg, W. D., Zhou, X. P., Eng, C., Spiegelman, B. M., and Kantoff, P. W. (2000) Effects of ligand activation of peroxisome proliferator-activated receptor gamma in human prostate cancer. *Proc. Natl. Acad. Sci. U.S.A. 97*, 10990−10995.
(11) Muller, E., Sarraf, P., Tontonoz, P., Evans, R. M., Martin, K. J., Zhang, M., Fletcher, C. D., Singer, S., and Spiegelman, B. M. (1998) Terminal differentiation of human breast cancer through PPAR gamma. *Mol. Cell 1*, 465−470.
(12) Demetri, G. D., Fletcher, C. D. M., Mueller, E., Sarraf, F., Naujoks, R., Campbell, N., Spiegelman, B. M., and Singer, S. (1999) Induction of solid tumor differentiation by the peroxisome proliferator-activated receptor-γ ligand troglitazone in patients with liposarcoma. *Proc. Natl. Acad. Sci. U.S.A. 96*, 3951−3956.
(13) Tontonoz, P., Singer, S., Froman, B. M., Sarraf, P., Fletcher, J. A., Fletcher, C. D. M., Brun, R. P., Mueller, E., Altiok, S., Oppenheim, H., Evans, R. M., and Spiegelman, B. M. (1997) Terminal differentiation of human liposarcoma cells induced by ligands for peroxisome proliferator-activated receptor γ and the retinoid X receptor. *Proc. Natl. Acad. Sci. U.S.A. 94*, 237−241.
(14) Burstein, H. J., Demetri, G. D., Muller, E., Sarraf, P., Spiegelman, B. M., and Winer, E. P. (2003) Use of the peroxisome proliferator-activated receptor (PPAR) γ ligand troglitazone as treatment for refractory breast cancer: a phase II study. *Breast Cancer Res. Treat. 79*, 391−397.
(15) Wang, Xin., Southard, R. C., and Kilgore, M. W. (2004) The increased expression of peroxisome proliferator-activatated receptor-γ1 in human breast cancer is mediated by selective promoter usage. *Cancer Res. 64*, 5592−5596.
(16) Berger, J P., Akiyama, T. E., and Meinke, P. T. (2005) PPARs: therapeutic targets for metabolic disease. *Trends Pharmacol. Sci. 26*, 244−251.
(17) Kim, S-H., Jonson, S. D., Welch, M. J., and Katzenellenbogen, J. A. (2001) Fluorine-Substituted ligands for the peroxisome proliferator-activated receptor gamma (PPARγ): Potential imaging agents for metastatic tumors. *Bioconjugate Chem. 12*, 439−450.
(18) Gray, S. L., Dalla Nora, E., and Vidal-Puig, A. J. (2005) Mouse models of PPAR-gamma deficiency: dissecting PPAR-gamma's role in metabolic homoeostasis. *Biochem. Soc. Trans. 33*, 1053−1058.
(19) Henke, B. R., Blanchard, S. G., Brackeen, M. F., Brown, K. K., Cobb, J. E., Collins, J. L., Harrington, W. W., Jr., Hashim, M. A., Hull-Ryde, E. A., Kaldor, I., Kliewer, S. A., Lake, D. H., Leesnitzer, L. M., Lehmann, J. M., Lenhard, J. M., Orband-Miller, L. A., Miller, J. F., Mook, R. A., Jr., Noble, S. A., Oliver, W., Jr., Parks, D. J., Plunket, K. D., Szewczyk, J. R., and Willson, T. M. (1998) *N*-(2-Benzoylphenyl)-L-tyrosine PPARγ agonists. 1. Discovery of a novel series of potent antihyperglycemic and antihyperlipidemic agents. *J. Med. Chem. 41*, 5020−5036.
(20) Collins, J. L., Blanchard, S. G., Boswell, E. G., Charifson, P. S., Cobb, J. E., Henke, B. R., Hull-Ryde, E. A., Kazmierski, W. M., Lake, D. H., Leesnitzer, L. M., Lehmann, J., Lenhard, J. M., Orband-Miller, L. A., Gray-Nunez, Y., Parks, D. J., Plunkett, K. D., and Tong, W. Q. (1998) *N*-(2-Benzoylphenyl)-L-tyrosine PPARγ agonists. 2. Structure−activity relationship and opitimization of the phenyl alkyl ether moiety. *J. Med. Chem. 41*, 5037−5054.
(21) Cobb, J. E., Blanchard, S. G., Boswell, E. G., Brown, K. K., Charifson, P. S., Cooper, J. P., Collins, J. L., Dezube, M., Henke, B. R., Hull-Ryde, E. A., Lake, D. H., Lenhard, J. M., Oliver, W., Jr., Oplinger, J., Pentti, M., Parks, D. J., Plunket, K. D., and Tong, W. Q. (1998) *N*-(2-Benzoylphenyl)-L-tyrosine PPARγ agonists. 3. Structure−activity relationship and opitimization of the N-aryl substituent. *J. Med. Chem. 41*, 5055−5069.
(22) Willson, T. M., Brown, P. J., Sternbach, D. D., and Henke, B. R. (2000) The PPARs: From orphan receptors to drug discovery. *J. Med. Chem 43*, 527−550.
(23) Haigh, D., Allen, G., Birrell, H. C., Buckle, D. R., Cantello, B. C., Eggleston, D. S., Haltiwanger, R. C., Holder, J. C., Lister, C. A., Pinto, I. L., Rami, H. K.;, Sime, J. T., Smith, S. A., and Sweeney, J. D. (1999) Nonthiazolidinedione antihyperglycaemic agents. Part 3: The effects of stereochemistry on the potency of alpha-methoxy-beta-phenylpropanoic acids. *Bioorg. Med. Chem. 7*, 821−830.
(24) Young, P. W., Buckle, D. R., Cantello, B. C., Chapman, H., Clapham, J. C., Coyle, P. J., Haigh, D., Hindley, R. M., Holder, J. C., Kallender, H., Latter, A. J., Lawrie, K. W., Mossakowska, D., Murphy, G. J., Roxbee, C. L., and Smith, S. A. (1998) Identification of high-affinity binding sites for the insulin sensitizer resiflitazone (BRL-49653) in rodent and human adipocytes using a radioiodinated ligand for peroxisomal proliferator-activated receptor gamma. *J. Pharmacol. Exp. Ther. 284*, 751−759.
(25) Katzenellenbogen, J. A., Heiman, D. F., Carlson, K. E., and Lloyd, J. E. (1982) *In vivo* and *in vitro* steroid receptor assays in the design of estrogen pharmaceuticals. In *Receptor Binding Radiotracers* (Eckelman, W. C., Ed.), Vol. 1, Chapter 6, pp 93−126, CRC Press, Boca Raton.
(26) Koser, G. F., Wettach, R. H., and Smith, C. S. (1980) New methodology in iodonium salt synthesis. Reaction of [hydoxy(tosyloxy)iodo]arenas with aryltrimethylsilanes. *J. Org. Chem. 45*, 1542−1543.
(27) van der Puy, M. (1982) Conversion of diaryliodonium salts to aryl fluorides. *J. Fluorine Chem. 21*, 385−392.
(28) Shah, A., Pike, V. W., and Widdowson, D. A. (1998) The synthesis of [^{18}F]fluoroarenes from the reaction of cyclotron-produced [^{18}F]-fluoride ion with diaryliodonium salts. *J. Chem. Soc., Perkin Trans. 1*, 2043−2046.
(29) Pike, V. W., Butt, F., Shah, A., and Widdowson, D. A. (1999) Facile synthesis of substituted diaryliodonium tosylates by treatment of aryltributylstannanes with Koser's reagent. *J. Chem. Soc., Perkin Trans. 1*, 245−248.
(30) Pangborn, A. B., Giardello, M. A., Grubbs, R. H., Rosen, R. K., and Timmer, F. J. (1996) Safe and convenient procedure for solvent purification. *Organometallics 15*, 1518−1520.
(31) Kazmierczak, P., Skulski, L., and Kraszkiewicz, L. (2001) Synthesis of (diacetoxyiodo)arenas of iodylarenes from iodoarenes, with sodium periodate as the oxidant. *Molecules 9*, 881−891.
(32) Togo, H., Nabana, T., and Yamaguchi, K. (2000) Preparation and reactivities of novel (diacetoxyiodo)arenas bearing heteroaromatics. *J. Org. Chem. 65*, 8391−8394.
(33) Nabana, T., and Togo, H. (2002) Reactivities of novel [hydoxy(tosyloxy)iodo]arenas and [hydoxy(phosphoryloxy)iodo]arenas for α-tosyloxylation and α-phosphoryloxylation of ketones. *J. Org. Chem. 67*, 4362−4365.
(34) Sun, S., Almaden, J., Carlson, T. J., Barker, J., and Gehring, M. R. (2005) Assay development and data analysis of receptor-ligand binding based on scintillation proximity assay. *Metab. Eng. 7*, 38−44.
(35) Xu, H. E., Lambert, M. H., Montana, V. G., Plunket, K. D., Moore, L. B., Collins, J. L., Oplinger, J. A., Kliewer, S. A., Gampe, R. T., Jr., McKee, D. D., Moore, J. T., and Willson, T. M. (2001) Structural determinants of ligand binding selectivity between the peroxisome proliferator-activated receptors. *Proc. Natl. Acad. Sci. U.S.A. 98*, 13919−13924.

(36) Brown, K. K., Henke, B. R., Blanchard, S. G., Cobb, J. E., Mook, R., Kaldor, I., Kliewer, S. A., Lehmann, J. M., Lenhard, J. M., Harrington, W. W., Novak, P. J., Faison, W., Binz, J. G., Hashim, M. A., Oliver, W. O., Brown, H. R., Parks, D. J., Plunket, K. D., Tong, W. Q., Menius, J. A., Adkison, K., Noble, S. A., and Wilson, T. M. (1999) A novel N-aryl tyrosine activator of peroxisome proliferator-activated receptor-gamma reverses the diabetic phenotype of the Zucker diabetic fatty rat. *Diabetes 48*, 1415−1424.

(37) Stone-Elander, S., and Elander, N. (1993) Fast chemistry in microwave fields: Nucleophilic ^{18}F-radiofluorinations of aromatic molecules. *Appl. Radiat. Isot. 44*, 889−893.

(38) Ludwig, T., Ermert, J., and Coenen, H. H. (2002) 4-[^{18}F]fluoroaryl alkyl ethers via an improved synthesis of n.c.a. 4-[^{18}F]fluorophenol. *Nucl. Med. Biol. 29*, 255−262.

(39) Haka, M. S., Kilbourn, M. R., Watkins, G. L., and Toorongian, S. A. (1989) Aryltrimethylammonium trifluoromethanesulfonates as precursors to aryl [^{18}F]fluorides: improved synthesis of [^{18}F]GBR-13119. *J. Labelled Compd. Radiopharm. 27*, 823−833.

(40) Grushin, V. V. (1992) Carboranylhalonium ions: From striking reactivity to a unified mechanistic analysis of polar reactions of diarylhalonium compounds. *Acc. Chem. Res. 25*, 529−536.

(41) Grushin, V. V., Demkina, I. I., and Tolstaya, T. P. (1992) Unified mechanistic analysis of polar reactions of diaryliodonium salts. *J. Chem. Soc., Perkin Trans. 2*, 505−511.

(42) Papoutsis, I., Spyroudis, S., Varvoglis, A., and Raptopoulou, C. P. (1997) Arylidonium derivatives of 2-amino-1,4-quinones: Preparation and reactivity. *Tetrahedron 53*, 6097−6112.

BC060191G

Covalent Attachment of Ferrocene to Soybean Peroxidase Glycans: Electron Transfer Mediation to Redox Enzymes

Neil Carolan,[†] Robert J. Forster,[‡] and Ciarán Ó'Fágáin*,[†]

School of Biotechnology, National Centre for Sensors Research, Dublin City University, Dublin 9, and School of Chemical Sciences, National Centre for Sensors Research, Dublin City University, Dublin 9, Ireland. Received July 10, 2006; Revised Manuscript Received October 26, 2006

The electrochemical properties of native soybean peroxidase (SBP) and of SBP modified with covalently attached ferrocene electron-transfer mediators within microcavities etched at the tip of 25 μm radius platinum microelectrodes are reported. The microcavities incorporate approximately 50 fmol of SBP. In the microcavity, native SBP undergoes a relatively fast reduction but a very slow oxidation. Ferrocene mediators have been attached to the SBP glycans (Fc−SBP) (approximately 1.5 ferrocene mediators per SBP molecule). Cyclic voltammetry reveals that these centers are capable of mediating the reduction of oxidized SBP and increase the rate of heterogeneous electron transfer between the enzyme and the electrode by >10-fold. Micromolar concentrations of H_2O_2 chemically oxidize the SBP and Fc−SBP systems leading to an electrocatalytic reduction at approximately −0.1 V. Successive additions of 2.5 μmol of H_2O_2 at a constant applied potential of −0.1 V gave a steady-state constant current of approximately 60 nA within 20 s. The steady-state current increased linearly with peroxide concentration for $2.5 \leq [H_2O_2] \leq 42$ μM. Ferrocene-modified SBP shows an approximately 3-fold increase in the sensitivity of the steady-state current response to successive additions of hydrogen peroxide compared to the native enzyme. This observation indicates increased turnover of the redox enzyme per unit time in the presence of the covalently attached ferrocene mediators.

INTRODUCTION

Peroxidase enzymes (donor: hydrogen peroxide oxidoreductases; EC 1.11.1.7) find widespread use in electrochemical biosensors. They act as sensitive indicators of hydrogen peroxide levels on graphite, glassy carbon, and other electrodes (*1*−*3*). They also act as coupling enzymes with oxidases (e.g., glucose or cholesterol oxidase (*4*)).

Peroxidase from the soybean plant *Glycine max* (SBP[1]; EC 1.11.1.7) has advantages over the well-known horseradish peroxidase (HRP). SBP is more thermostable, has a broader pH−activity profile, and is readily and cheaply isolated from waste soybean hulls (*5*−*7*). It is a glycoprotein of 41 kDa with four disulfides, two structural Ca^{2+} ions, and a prosthetic heme group. Cloning and expression of recombinant SBP has led to determination of its crystal structure (*7*). Its δ-meso heme edge, the site of electron transfer between reducing substrates and the catalytic intermediates compounds **I** and **II**, is much more solvent-accessible than in other plant peroxidases (*7*). Its kinetic properties have been explored using stopped-flow techniques (*8*), and the full amino acid sequence of SBP from the plant has recently been determined (*9*). Despite these key advantages over other peroxidase enzymes, there have only been a few reports on SBP-based biosensors (*1*, *4*, *10*−*13*).

Direct electron transfer from the widely studied horseradish peroxidase (HRP) to carbon-based electrodes has been observed (*14*). However, in seeking to develop enzyme-based biosensors, a key challenge is to improve the dynamics of electron transfer between the electrode and the redox enzyme (*15*). Slow dynamics frequently arise because the enzyme's redox center is encapsulated, thus significantly increasing the electrode-active site separation. A highly successful approach to increasing the electron-transfer rate is to "electrochemically wire" the enzyme by either attaching redox-active mediators, e.g., ferrocene, that have a suitable redox potential, directly to the enzyme or using a redox-conducting polymer that can shuttle electrons to and from the active site.

In this contribution, we report an SBP modification procedure that involves covalent attachment of ferrocene to the sugars of the redox enzyme (18% of its 44 kDa molecular weight), and we compare native and ferrocene-modified SBP in an amperometric microcavity biosensor, specifically, the etched tip of a 25 μm radius platinum microelectrode that is subsequently packed with native or ferrocene-modified SBP. Ferrocene attachment significantly increased the rate of electron transfer between the electrode and the active site, giving improved signal-to-noise responses, lower limits of detection, and increased dynamic range.

EXPERIMENTAL SECTION

Materials and Methods. Ethylene diamine, ferrocene carboxylic acid, *N*-hydroxysuccinimide (NHS), *N*-acetyl-L-lysine, MOPS, Sephadex G-25, sodium *meta*-periodate, $NaCNBH_3$, 3,3′,5,5′-tetramethyl benzidine (TMB), and 2,4,6-trinitrobenzene sulfonic acid (TNBS) were obtained from Sigma-Aldrich and used without further purification. BCA protein estimation kits

* Author for correspondence: School of Biotechnology, Dublin City University, Dublin 9, Ireland. E-mail ciaran.fagan@dcu.ie; Tel +353 1 7005288; Fax +353 1 7005412.

[†] School of Biotechnology.

[‡] School of Chemical Sciences.

[1] Abbreviations: AAS, atomic absorption spectrometry; BCA, bicinchoninic acid; BSA, bovine serum albumin; CV, cyclic voltammogram; DMSO, dimethyl sulfoxide; EDC, 1-(3-dimethylaminopropyl)-3-ethylcarbodiimide hydrochloride; FCA, ferrocene carboxylic acid; HRP, horseradish peroxidase; MOPS, 3-(*N*-morpholino)propane sulfonic acid; NHS, *N*-hydroxysuccinimide; PTFE, poly(tetrafluoroethylene); RZ, Reinheitzahl (purity number, A_{403}/A_{280}); SBP, soybean peroxidase; SECM, scanning electrochemical microscopy; TMB, 3,3′,5,5′-tetramethyl benzidine; TNBS, 2,4,6-trinitrobenzene sulfonic acid; Tris, tris-(hydroxymethyl)aminomethane.

10.1021/bc060206a CCC: $37.00 © 2007 American Chemical Society
Published on Web 02/16/2007

and 1-(3-dimethylaminoproypl)-3-ethylcarbodiimide hydrochloride (EDC) were from Pierce. Hydrogen peroxide (30% v/v) and $FeCl_3 \cdot 6H_2O$ were obtained from BDH.

Soybean peroxidase (SBP, food grade, batch S0103261) was a gift from Quest International, Kilnaglery, Carrigaline, County Cork, Ireland. To remove particulate matter, SBP was suspended in 25 mM MOPS pH 7.0 (2.5 mg/mL, 20 mL), mixed for 20 min at room temperature, and centrifuged for 3 min at 1800 rpm (rotor diameter 7.5 cm). The supernatant was removed and stored and the pellet discarded. The concentration of SBP solutions (typical RZ 2.7) was calculated by measuring absorbance at 403 nm (millimolar extinction coefficient 90 $mM^{-1} \cdot cm^{-1}$ (*7*).

Protein determination was via the BCA standard and micro protocols in microtiter plates according to the Pierce kit insert (*16*) using bovine serum albumin (BSA) as standard.

Buffer exchange and removal of unused materials was via overnight dialysis at 4 °C or by centrifugal gel filtration (*17*) through Sephadex G-25 at room temperature.

Catalytic activity assay (*18*): TMB (1 mg) was dissolved in 200 μL DMSO (final concentration 2%) and added to 9.8 mL of 100 mM citric acid buffer pH 5.5. Tween 20 (0.002% final concentration) was included in all buffers used in polystyrene microplates to prevent contact denaturation (*19*). Immediately prior to assay, 4 μL H_2O_2 (30% v/v) was added and mixed to give a final concentration of 0.04% H_2O_2. To a 50 μL sample or blank (buffer) in the wells of a 96 well microtiter plate, 150 μL reaction solution was added, mixed, and allowed to react for 150 s. Absorbances of all samples were read in triplicate simultaneously at 620 nm on a Labsystems Multiskan MS microplate reader.

Free amino groups were determined using 2,4,6-trinitrobenzene sulfonic acid (TNBS) (*20*) with α-*N*-acetyl-L-lysine (10−0.05 μM) as standard.

Covalent Attachment of Ferrocene Carboxylic Acid (FCA) to SBP Carbohydrates. An SBP solution (3.5 mg/mL, 20 mL) was prepared in 25 mM MOPS pH 7.0 and mixed with 400 μL 50 mM $NaIO_4$; this mixture was reacted with stirring for 2 h in the dark. Ethylene glycol (95% v/v, 0.6 mL) was added to quench the reaction, mixed, and left for 10 min. Next, 1 M ethylene diamine (0.215 mL) was added and reacted for 90 min, with stirring, at room temperature. The sample was dialyzed overnight into 25 mM MOPS pH 7.0 at 4 °C. To reduce the Schiff bases formed between ethylenediamine and the oxidized SBP carbohydrates to secondary amines, 0.2 mL $NaCNBH_3$ (100 mM in 0.1 M NaOH) was added and the reaction allowed to proceed at room temperature in the dark for 90 min with stirring before overnight dialysis into 25 mM MOPS pH 7.0 at 4 °C. To this aminated SBP preparation was added *N*-hydroxysuccinimide (NHS; 2 mM final concentration) followed 5 min later by 0.15 mL 10 mM FCA/EDC solution, in 25 mM MOPS pH 7.0. The reaction proceeded overnight with stirring at 4 °C and was followed by overnight dialysis into 25 mM MOPS pH 7.0 at 4 °C. A 0.5 mL aliquot was removed for analysis at each stage.

Atomic Absorption Spectroscopy. AAS was conducted using a Perkin-Elmer 3100 atomic absorption spectrometer with an iron hollow cathode lamp (S & J Juniper Co., Essex, England) using standard procedures. Ultrapure water was used to prepare the buffer (25 mM MOPS pH 7.0; used as blank) and standards (2.0−0.0625 mg/L $FeCl_3 \cdot 6H_2O$).

Fabrication of Etched Microelectrode. Platinum microelectrodes of 25 μm radius were fabricated and characterized using previously described procedures (*21*). The microelectrodes were etched in hot aqua regia (75 °C, for up to 20 h) to create a cavity of 2−4 μm depth, and this cavity was subsequently packed as follows. The bottom was removed from a 1.5 mL Eppendorf tube and the electrode inserted through the new bottom opening. SBP solution (0.25 mL; no external mediator) was pipetted into the tube, which was then capped. The electrode and solution were repeatedly inverted to fill the etched cavity with solution. The electrode/tube was kept at 4 °C for 5 h to allow deposition and immobilization of the SBP in the etched cavity.

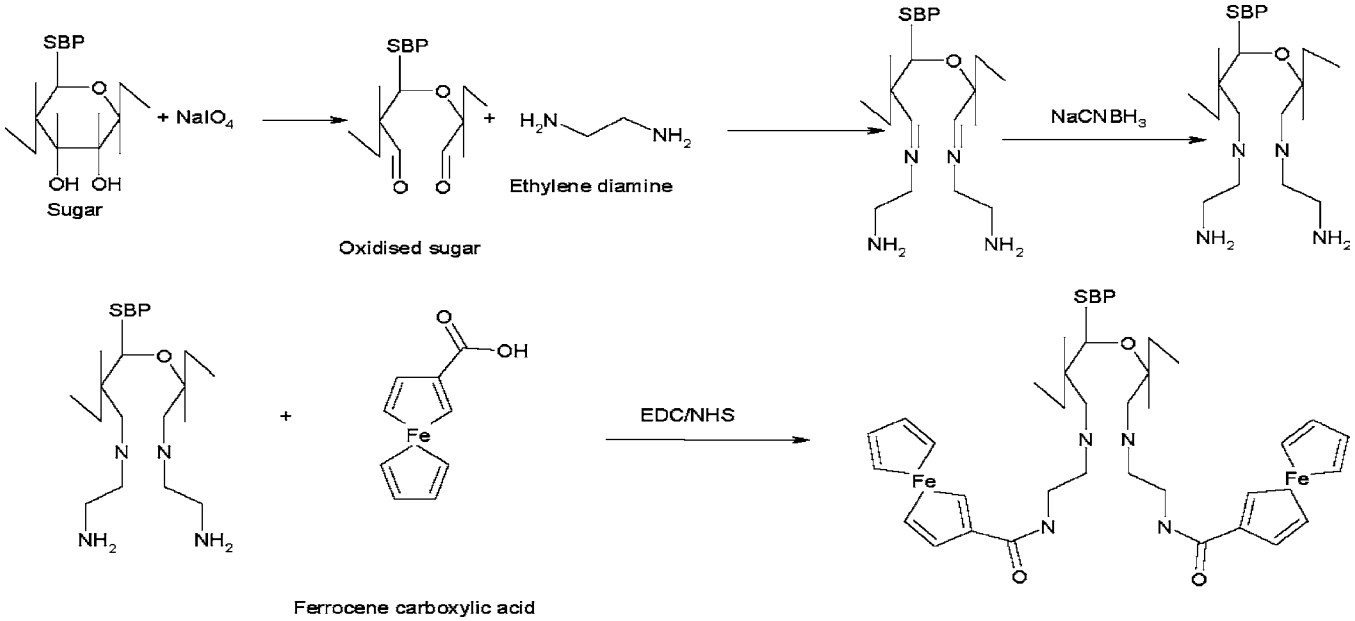
Cyclic voltammetry was performed using a CH Instruments model 660 Electrochemical Workstation and a conventional three-electrode cell. The electrochemical measurements were carried out at room temperature in a 10 mL buffer solution (25 mM MOPS/NaOH pH 7.0, 20 °C) containing the three-electrode voltammetric cell that comprised the H_2O_2 sensor. All potentials are referenced with respect to the KCl saturated Ag/AgCl reference electrode. All CVs were obtained in O_2-free buffer (*22*, *23*), achieved by purging the system with N_2 or Ar gas for at least 15 min and by maintaining a N_2 atmosphere over the buffer during all assays.

RESULTS AND DISCUSSION

Ferrocene-Modified SBP. Ideally, one would like to attach numerous ferrocenes covalently close to the SBP active site to maximize electron transfer to the underlying electrode without disrupting the catalytic function. However, SBP has few sites that can be chemically modified under mild conditions that avoid deactivation, e.g., it has no free thiol groups because its eight cysteines form disulfides. Most reported chemical modifications of the widely used horseradish peroxidase, HRP, target its glycans or lysine residues, but we have previously demonstrated that only three of HRP's six lysines are reactive under mild conditions (*24*). Comparison of SBP's and HRP's amino acid sequences (refs 9 and 25, respectively) reveals that exactly those three HRP lysines are replaced by other, less reactive residues in the SBP sequence. This leaves only SBP's glycans as potential attachment sites for FCA and necessitated a multistep approach. Scheme 1 shows the approach employed here, namely, periodate oxidation of the vicinal diols of SBP glycans to create free aldehyde groups, followed by addition of the bifunctional amine ethylenediamine. Schiff bases form between amine and the aldehydes of SBP glycans, and these Schiff bases are reduced by addition of $NaCNBH_3$. The primary amine on the opposite end of ethylenediamine is unaffected by this treatment, and the outcome is the addition of new free amino groups to the SBP molecule (aminated SBP). FCA can then be covalently coupled to aminated SBP via a further, carbodiimide-mediated reaction. Recovery of initial SBP activity (TMB assay) is high, due to the mild conditions of each of the reactions in the sequence. Initial FCA-to-SBP couplings were carried out in the presence of EDC alone, but later EDC-mediated modifications included *N*-hydroxysuccinimide (NHS), which stabilizes a reaction intermediate and aids successful FCA attachment to SBP. The procedure is successful, albeit labor-intensive. Note that covalent ferrocene coupling to SBP can be accomplished with a minimally treated commercial enzyme preparation, avoiding the added costs and delays associated with chromatographic purification. Attachment of the mediator to the external SBP glycans overcomes the problems faced by Degani and Heller (*26*) in attaching the mediator to the GO polypeptide via the ϵ-NH_2 of lysines.

Covalent attachment of ferrocene units to SBP oligosaccharides (to improve the electron-transfer dynamics) does not unduly affect the enzyme's catalytic activity. Table 1 shows that the catalytic activity increases by approximately 20%, reproducibly, following amination: this is most likely due to the removal of naturally occurring low molecular weight inhibitors from the SBP enzyme preparation by the two dialysis steps. In contrast, the protein concentration decreases by

Scheme 1. Proposed Mechanism for the Addition of Ferrocene Carboxylic Acid to SBP[a]



[a] The sugars in the SBP glycans are oxidized to produce free aldehyde groups. Next, ethylene diamine is added to the oxidized SBP. $NaCNBH_3$ reduces the Schiff bases (formed between ethylene diamine and SBP) to secondary amines without affecting the primary amine on the opposite end of the bifunctional ethylenediamine. This results in the addition of new free amino groups onto the SBP. Ferrocene carboxylic acid is then added to the aminated SBP in the presence of EDC and NHS, resulting in attachment of ferrocene units to the enzyme.

Table 1. Activity, Protein Concentration, Number of Available Amine Sites, and Iron Content of Native and Ferrocene-Modified SBP[a]

enzyme	activity[b] (%)	protein (μg/mL)	number of free $-NH_2$[c]	iron[d] (ppb)
native SBP	100	439 ± 34.0	3 ± 0.5	49 ± 8
aminated SBP	128.0 ± 14.1	234.3 ± 23.7	35 ± 6.4	52 ± 8
FCA-SBP	66.8 ± 14.3	238.0 ± 38.0	3 ± 0.9	137.5 ± 14

[a] $n = 3$. [b] SBP catalytic activity was determined at 100 μg/L protein. [c] Free $-NH_2$ groups were estimated by TNBS method (*20*). [d] Elemental iron was determined using atomic absorption spectroscopy.

approximately 50%, presumably due to the loss of low molecular weight proteins during the first dialysis step. The amination procedure yielded a 10-fold increase in the number of free amines on the SBP molecule without changing the iron content. Following the FCA−EDC−NHS modification step, catalytic activity decreased by approximately 23% compared to its initial value. The number of free amines also decreased, but the Fe concentration more than doubled, indicating successful modification of SBP by FCA. These data clearly demonstrate that the result of this procedure is the covalent binding of approximately 1.5 ferrocene centers per enzyme without significantly affecting the enzyme's catalytic activity.

Voltammetry in the Microcavity. Figure 1 shows cyclic voltammograms for the unmodified microcavity electrode as well as background corrected voltammograms for the native and ferrocene-modified SBP immobilized within the etched microcavity. The supporting electrolyte was 25 mM MOPS/NaOH, pH 7.0, and the scan rate was 0.01 V s^{-1}. In the absence of enzyme, the background charging current is flat and featureless across the whole potential range investigated. In order to quantify differences in the Faradaic current response between modified and native enzymes, the background current was modeled using a third- or fourth-order polynomial and subtracted from the overall response.

Native Enzyme. Figure 1 shows that the native SBP exhibits a well-defined, irreversible redox response with a reduction peak potential of approximately 0.05 V vs Ag/AgCl. This process corresponds to reduction of the iron center within the native

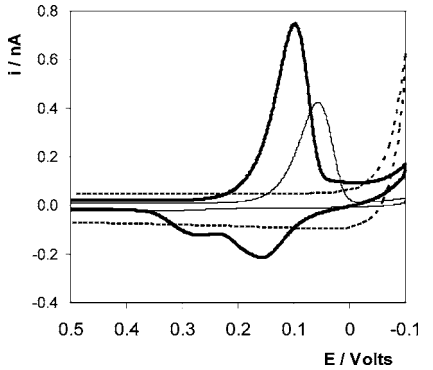


Figure 1. Cyclic voltammograms for unmodified microcavity electrode (dashed line) and native (thin line) and ferrocene-modified SBP (thick line) recorded within a platinum microcavity at a scan rate of 0.01 V s^{-1}. The supporting electrolyte is 25 mM MOPS/NaOH buffer at pH 7.0.

enzyme. No well-defined return peak is observed even at a scan rate of 0.01 V s^{-1}. This behavior could arise from very slow electrochemical reoxidation of the reduced enzyme (slow heterogeneous electron transfer) or because the reduced enzyme undergoes a subsequent chemical reaction. However, experiments involving peroxide in solution, vide infra, indicate that the reduced enzyme can be chemically reoxidized efficiently. This observation suggests that the reduced enzyme undergoes very slow electron transfer with the electrode causing an irreversible response to be observed.

Fc−SBP Response. As illustrated in Figure 1, the ferrocene-modified enzyme also shows a single, well-defined reduction peak which is centered at 0.098 V. The reduction peak potential, E_{pa}, is shifted by approximately +40 mV with respect to the native form, indicating that reduction of the native iron centers and the ferrocene mediators is thermodynamically more facile in the modified form. This behavior most likely arises because of the electron donating properties of the covalently attached ferrocene mediators. Significantly, the peak current and charge increases by a factor of approximately 2 after binding of the ferrocene moieties. While this charge most likely includes contributions from both the endogenous iron centers of the

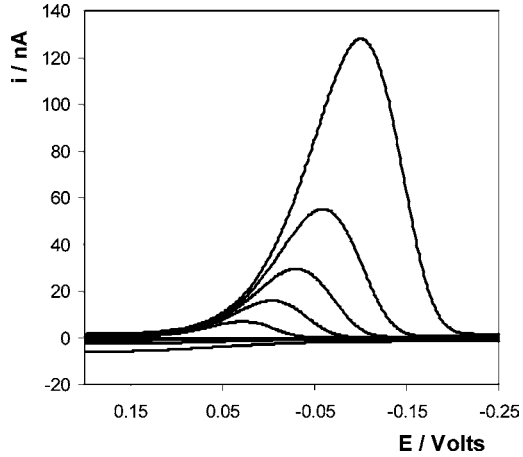


Figure 2. Effect of scan rate on the voltammetric response of native SBP packed within a microcavity electrode. From top to bottom, the scan rates are 0.2, 0.5, 1.0, 2.0, and 5.0 V s^{-1}. The supporting electrolyte is 25 mM MOPS/NaOH buffer at pH 7.0.

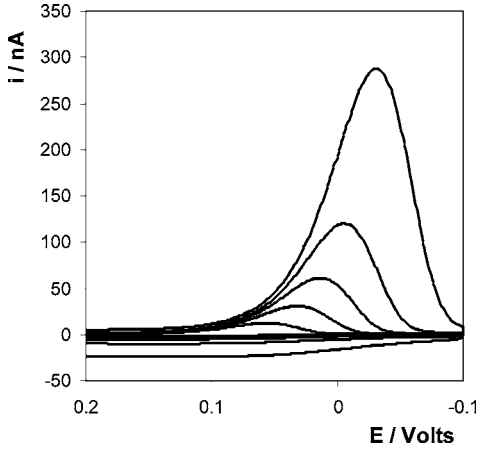


Figure 3. Effect of scan rate on the voltammetric response of ferrocene-modified SBP packed within a microcavity electrode. From top to bottom, the scan rates are 0.2, 0.5, 1.0, 2.0, and 5.0 V s^{-1}. The supporting electrolyte is 25 mM MOPS/NaOH buffer at pH 7.0.

enzyme and the tethered ferrocene centers, the magnitude of the increase in charge passed is consistent with the atomic absorption spectroscopy data presented in Table 1, which indicate that approximately 1.5 ferrocene centers become bound to each enzyme. The peak areas for the native and modified enzymes are 3.1 and 6.0 nC, respectively, and correspond to approximately 50 fmol of enzyme being immobilized within the microcavity. Given the fact that, for the Fc−SBP system, reduction of the enzyme becomes thermodynamically more facile, and the fact that the charge passed increases, it appears that, while the native SBP can undergo direct electron transfer with the electrode, reduction of the heme center within Fc−SBP is mediated by the covalently bound ferrocene centers.

In sharp contrast to the native enzyme, Fc−SBP exhibits a well-defined oxidation process with peak potentials of approximately 0.15 and 0.27 V. This process corresponds to reoxidation of the ferrocene mediators and the heme centers. The observation that the peak areas for the reduction and oxidation processes are not equivalent suggests that the ferrocene centers efficiently mediate the reduction of the heme but not its reoxidation. Significantly, the scan rate impacts dramatically on the ability to observe the ferrocene-based oxidation; e.g., even at scan rates of 0.1 V s^{-1}, the oxidation process does not give rise to a well-defined peak for ferrocene reoxidation. This observation strongly suggests that oxidation of *both* the heme and ferrocene centers at an electrode surface is kinetically very slow even in Fc−SBP.

Electron-Transfer Dynamics. Figure 2 illustrates the effect of scan rate on the voltammetry of the native SBP. A key advantage of microelectrodes is that the small currents observed eliminate any deleterious effects of ohmic drop, and the dynamics of the electrochemical processes can be explored over a wide range of time scales. This figure reveals that the peaks broaden significantly and shift in a negative potential direction with increasing scan rate. This behavior indicates that the dynamics of electron transfer between the electrode and the enzyme influences the response at high scan rate; i.e., the time constant for reduction of the enzyme and the experiment become comparable.

Figure 3 illustrates the scan rate dependence of the voltammetry for the ferrocene modified SBP packed within the microcavity. When compared to the behavior observed for the native enzyme, it is apparent that the peak potential for the ferrocene-modified enzyme is much less sensitive to the scan rate than the native form. For example, when the scan rate is increased from 0.1 to 5 V s^{-1}, E_{pc} shifts by approximately 160 mV for the native but only by 110 mV after ferrocene centers

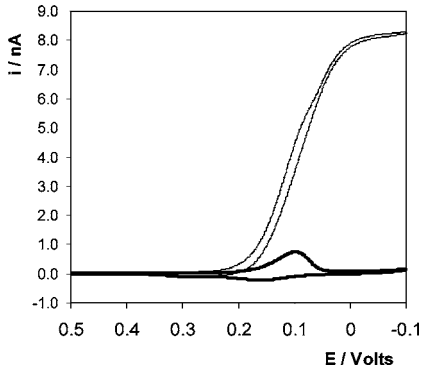


Figure 4. Cyclic voltammograms of Fc−SBP-modified microcavity electrodes at a scan rate of 0.1 V s^{-1}. The curves represent the response in the absence of H_2O_2 (thick line) and in the presence of 100 μM H_2O_2 (thin line).

are covalently bound to the enzyme. This result indicates that the ferrocene centers increase the rate of electron transfer from the electrode to the enzyme. While the results are not shown here, we have successfully simulated the electrochemical response of the native enzyme as an electrochemically irreversible reduction process (*27*). The Fc−SBP response is adequately modeled as an electrochemically irreversible reduction process for the enzyme heme, E_{irr}, and an electrochemically reversible process, E, for the bound ferrocene mediators. This analysis indicates that the rate of electron transfer from the heme centers to the electrode increases by more than an order of magnitude upon binding of the ferrocene centers. The significant increase in the electron-transfer dynamics should lead to a substantial improvement in the analytical performance of these peroxide microsensors.

Analytical Performance. Figure 4 shows cyclic voltammograms of Fc−SBP-modified microcavity electrodes before and after the addition of H_2O_2. This figure shows that adding hydrogen peroxide gives rise to an electrocatalytic reduction current at the same potential as the Fc−SBP reduction process. This result confirms that the Fc−SBP is capable of reducing H_2O_2 and that the oxidized enzyme can then be electrochemically reduced. A key objective is to assess the impact of covalently attaching the ferrocene centers on the electrocatalytic efficiency of the enzyme.

Figure 5 illustrates the microelectrode response to batch injection of 2.5 μmol injections of peroxide in 25 mM MOPS buffer at pH 7.0 (20 μL of 0.125 mol/L peroxide in buffer added to the 10 mL reaction cell) for both the native and FCA−SBP

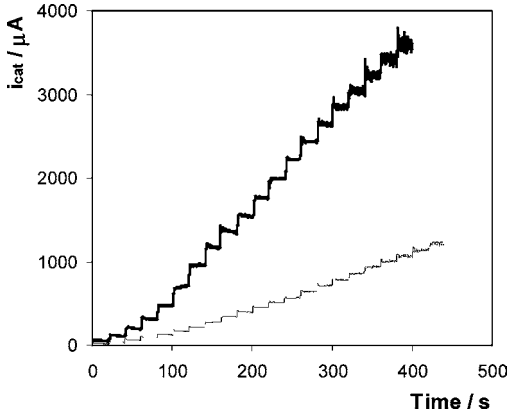


Figure 5. Current response of native (lower curve) and ferrocene-modified SBP-packed microcavity electrodes to successive injections of 2.5 μmol of peroxide. The supporting electrolyte is 25 mM MOPS/NaOH buffer at pH 7.0. The electrode is poised at −0.100 V.

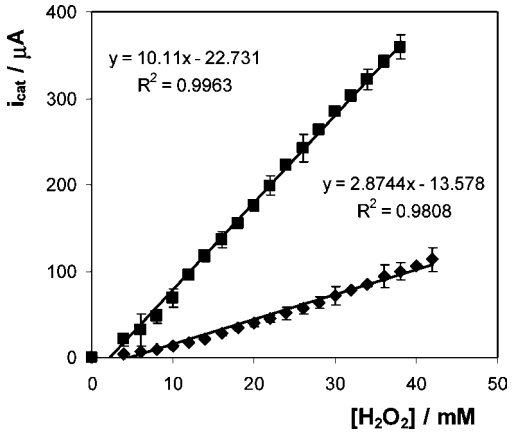


Figure 6. Calibration curve of ΔI, the change in current between successive injections, on the H_2O_2 concentration for native (lower curve) and ferrocene-modified SBP (upper curve).

microcavity biosensors. The electrode potential is poised at −0.100 V. Significantly, the fact that successive H_2O_2 additions generate measurable currents for the native SBP indicates that direct electron transfer takes place between SBP and the Pt electrode at the bottom of the microcavity. This figure shows that a steady-state response is obtained for both sensors within less than 20 s. The steady-state current arises because of the high mass transport rates that are achieved because of the radial diffusion field established at the microelectrodes. This mass transport rate is comparable to that obtained for an electrode rotated at 2500 rpm. The response time is approximately 2-fold faster than that reported by Wang et al. (*2*) based on SBP immobilized within a copolymer mix deposited on a 4 mm glassy carbon electrode. Figure 5 reveals that the response of the ferrocene-modified enzyme microsensor is significantly more sensitive than that of the native SBP with each 2.5 μmol injection of peroxide giving a 220 nA increase in current for ferrocene−SBP compared to 60 nA for the native form.

Figure 6 illustrates calibration curves for both microcavity sensors. There is a notable difference in the calibration curves for native and FCA−SBP, with the slope observed for the ferrocene derivative being approximately 3.5-fold larger. The dynamic range for both SBPs is similar with linear calibration curves being observed for $2.5 \leq [H_2O_2] \leq 42.5$ μM. We ascribe this additional activity to an increased turnover rate of the enzyme through mediated electron transfer via the ferrocene carboxylic acid units covalently attached to the SBP glycans.

CONCLUSION

We have presented a method for covalently binding ferrocene mediators to SBP glycans which is effective even with a crude SBP preparation and offers significant advantage over previously reported approaches. Approximately 1.5 ferrocene mediators are bound per enzyme site. We have also demonstrated for the first time (to the best of our knowledge) that native SBP, a heme protein, is capable of undergoing direct, mediator-free electron transfer when deposited within a microcavity etched at the tip of a platinum microelectrode. FCA−SBP gave notably improved responses over native SBP in our etched Pt electrode with the rate of electron transfer between the enzyme and the electrode increasing by more than 10-fold. The current response to peroxide injection depends linearly on peroxide concentration for both native and modified SBP sensors for $2.5 \leq [H_2O_2] \leq 42.5$ μM. However, the sensitivity of the ferrocene−SBP is approximately 3.5-fold larger than that of the native enzyme. These microcavity sensors have the potential for use in reagentless electrodes for the measurement of H_2O_2 and many other analytes that act as electron donors for peroxidases.

ACKNOWLEDGMENT

The financial support of the National Centre for Sensor Research (NCSR), the School of Biotechnology, DCU, and Science Foundation Ireland under the Biomedical Diagnostics Institute (05/CE3/B754) is deeply appreciated. Mr. Michael Woulfe (Quest International) kindly donated the soybean peroxidase and Dr. Sonia Ramírez-García is thanked for helpful advice.

LITERATURE CITED

(1) Wang, B.Q., Li, B., Cheng, G. J., and Dong, S. J. (2001) Acid-stable amperometric soybean peroxidase biosensor based on a self-gelatinizable grafting copolymer of polyvinyl alcohol and 4-vinyl pyridine. *Electroanalysis 13*, 555−558.

(2) Wang, X.-Q., Li, L. S., van der Meer, B. W., Jin, J., Tang, D., Hui, Z., Li, Y-Z., and Li, T. J. (2001) Comparison of photovoltaic behaviors for horseradish peroxidase and its mimicry by surface photovoltage spectroscopy. *Biochim. Biophys. Acta. 1544*, 333−340.

(3) Zhang, Z., Chouchane, S., Magliozzo, R. S., and Rusling, J. F. (2002) Direct voltammetry and catalysis with *Mycobacterium tuberculosis* catalysis − peroxidase, peroxidases, and catalase in lipid films. *Anal. Chem. 74*, 163−170.

(4) Kenausis, G., Chen, Q., and Heller, A. (1997) Electrochemical glucose and lactate sensors based on "wired" thermostable soybean peroxidase operating continuously and stably at 37 °C. *Anal. Chem. 69*, 1054−1060.

(5) McEldoon, J. P., and Dordick, J. S. (1996) Unusual thermal stability of soybean peroxidase. *Biotechnol. Prog. 12*, 555−558.

(6) Schmitz, N., Gijzen, M., and van Huystee, R. (1997) Characterization of anionic soybean (*Glycine max*) seed coat peroxidase. *Can. J. Bot. 75*, 1336−1341.

(7) Henriksen, A., Mirza, O., Indiani, C., Teilum, K., Smulevich, G., Welinder, K. G., and Gajhede, M. (2001) Structure of soybean seed coat peroxidase: A plant peroxidase with unusual stability and haem-apoprotein interactions. *Protein Sci. 10*, 108−115.

(8) Nissum, M., Schiødt, C. B., and Welinder, K. G. (2001) Reactions of soybean peroxidase and hydrogen peroxide pH 2.4−12.0, and veratryl alcohol at pH 2.4. *Biochim. Biophys. Acta 1545*, 339−348.

(9) Welinder, K. G., and Larsen, Y. B. (2004) Covalent structure of soybean coat peroxidase. *Biochim. Biophys. Acta. 1698*, 121−126.

(10) Vreeke, M. S., Yong, K. T., and Heller, A. (1995) A thermostable hydrogen peroxide sensor based on "wiring" of soybean peroxidase. *Anal. Chem. 67*, 4247−4249.

(11) Gaspar, S., Popescu, I. C., Gazaryan, I. G., Bautista, A. G., Sakharov, I. Y., Mattiasson, B., and Csöregi, E. (2000) Biosensors based on novel plant peroxidase: A comparative study. *Electrochim. Acta 46*, 255−264.

(12) Heller, A., and Vreeke, M. S. (E. Heller and Company) (1997) Soybean peroxidase electrochemical sensor. U.S. Patent 5,665,222.

(13) Wang, B. Q., Li, B., Wang, Z. X., Xu, G. B., Wang, Q., and Dong, S. J. (1999) Sol-gel thin film immobilized soybean peroxidase biosensor for the amperometric determination of hydrogen peroxide in acid medium. *Anal. Chem. 71*, 1935−1939.
(14) Presnova, G., Grigorenko, V., Egorov, A., Ruzgas, T., Lindgren, A., Gorton, L., and Börchers, T. (2000) Direct heterogeneous electron transfer of recombinant horseradish peroxidases on gold. *Faraday Discuss. 116*, 281−289.
(15) Dunford, H. B. (1999) *Heme Peroxidases*, p 68, Wiley VCH, Toronto.
(16) Smith, P. K., Krohn, R. I., Hermanson, G. T., Mallia, A. K., Gartner, F. H., Provenzano, M. D., Fujimoto, E. K., Goeke, N. M., Olson, B. J., and Klenk, D. C. (1985) Measurement of protein using bicinchoninic acid. *Anal. Biochem. 150*, 76−85.
(17) Helmerhorst, E., and Stokes, G. B. (1980) Microcentrifuge desalting: a rapid, quantitative method for desalting small amounts of protein. *Anal. Biochem. 104*, 130−135.
(18) Ryan, O., Smyth, M. R., and O'Fágáin, C. (1994) Thermostabilized chemical derivatives of horseradish peroxidase. *Enzyme Microb. Technol. 16*, 501−505.
(19) Berkowitz, D. B., and Webert, D. W. (1981) The inactivation of horseradish peroxidase by a polystyrene surface. *J. Immunol. Methods 47*, 121−124.
(20) Fields, R. (1971) The measurement of amino groups in proteins and peptides. *Biochem. J. 124*, 581−590.
(21) Faulkner, L. R., Walsh, M. R., and Xu, C. (1990) In *Contemporary Electroanalytical Chemistry* (Ivaska A., Ed.) p 5, Plenum Press, New York.
(22) Iwuoha, E. I., Smyth, M. R., and Vos, J. G. (1994) Amperometric glucose sensor containing nondiffusional osmium centers: Analysis of organic-phase responses. *Electroanalysis 6*, 982−989.
(23) Chattopadhyay, K., and Mazumdar, S. (2000) Direct electrochemistry of heme proteins: effect of electrode surface modification by neutral surfactants. *Bioelectrochemistry 53*, 17−24.
(24) O'Brien, A.-M., Ó Fágáin, C., Nielsen, P. F., and Welinder, K. G. (2001) Location of crosslinks in chemically stabilised horseradish peroxidase: implications for design of crosslinks. *Biotechnol. Bioeng. 76*, 277−284.
(25) Welinder, K. G. (1979) Amino acid sequence studies of horseradish peroxidase. *Eur. J. Biochem. 96*, 483−502.
(26) Degani, Y., and Heller, A. (1987) Direct electrical communications between chemically modified enzymes and metal electrodes. Electron transfer from glucose oxidase to metal electrodes via electron relays, bound covalently to the enzyme. *J. Phys. Chem. 91*, 1286−1289.
(27) Bard, A. J., and Faulkner, L. R. (2001) *Electrochemical Methods: Fundamentals and Applications*, 2nd ed., New York, J. Wiley and Sons.

BC060206A

In Vitro and In Vivo Evaluation of a Novel $^{99m}Tc(CO)_3$-Pyrazolyl Conjugate of *cyclo*-(Arg-Gly-Asp-D-Tyr-Lys)

Susana Alves,[||] João D. G. Correia,[||] Lurdes Gano,[||] Tammy L. Rold,[⊥] Adam Prasanphanich,[†] Roland Haubner,[○] Marco Rupprich,[○] Roger Alberto,[▽] Clemens Decristoforo,*[,○] Isabel Santos,[||] and Charles J. Smith*[,†,‡,#,⊥,⊗]

Department of Radiology, Department of Internal Medicine, and The Radiopharmaceutical Sciences Institute, University of Missouri-Columbia School of Medicine, Columbia, Missouri 65211, University of Missouri Research Reactor Center, University of Missouri-Columbia, Columbia, Missouri 65211, Research Division, Harry S. Truman Memorial Veterans' Hospital, Columbia, Missouri 65201, Departamento de Química, Instituto Tecnológico e Nuclear, 2686-953, Sacavém, Portugal, Department of Nuclear Medicine, University of Innsbruck, Innsbruck, Austria, and Institute of Inorganic Chemistry, University of Zurich, Winterthurer Strasse 190, CH-8057 Zurich, Switzerland. Received September 5, 2006; Revised Manuscript Received October 16, 2006

Radiolabeled peptides containing the Arg-Gly-Asp amino acid sequence (single letter code = RGD) have been studied extensively to target integrin receptors upregulated on tumor cells and neovasculature. Integrins are cell surface transmembrane glycoproteins that exist as $\alpha\beta$ heterodimers. The $\alpha_v\beta_3$ integrin is known to be overexpressed in many tumor types and is expressed at lower levels in normal tissues. Furthermore, $\alpha_v\beta_3$ and $\alpha_v\beta_5$ subtypes are expressed in neovasculature during angiogenesis. Thus, there is some impetus to image angiogenesis and tumor formation in vivo using RGD-based peptide targeting vectors. In this study, we report the design and development of a new cyclic RGD analogue *cyclo*-[Arg-Gly-Asp-D-Tyr-Lys(PZ)] (PZ = 3,5-Me_2-pz$(CH_2)_2$N$((CH_2)_3$COOH)-$(CH_2)_2NH_2$) that can be radiolabeled with the $[^{99m}Tc(CO)_3(H_2O)_3]^+$ metal aquaion. Radiochemical evaluation of this new conjugate in vitro indicated a facile radiosynthesis of the new ^{99m}Tc-RGD conjugate with high radiolabeling yields (≥95%) and high specific activities. In vitro internalization and blocking assays in $\alpha_v\beta_3$ receptor-positive, human M21 melanoma cancer cells showed the ability of this conjugate to target the integrin receptor with high specificity and selectivity. In vivo pharmacokinetic studies in normal CF-1 mice showed rapid clearance from blood with excretion primarily via/through the renal−urinary system. In vivo accumulation of radioactivity in mice bearing either $\alpha_v\beta_3$ receptor-positive or negative human melanoma tumors showed receptor specific uptake of tracer with accumulations of 2.50 ± 0.29 and 0.71 ± 0.08% ID/g in $\alpha_v\beta_3$ integrin positive (M21) and negative (M21L) tumors at 1 h postinjection (p.i.), respectively.

INTRODUCTION

Radiolabeled peptides containing the RGD amino acid sequence have been studied extensively to develop site-directed targeting vectors for integrin receptors upregulated on tumor cells and neovasculature (*1*, *2*). The RGD consensus sequence, Arg-Gly-Asp, appears in several proteins of the extracellular matrix, including vitronectin, fibronectin, fibrinogen, von Willebrand factor, thrombospondin, and osteopontin (*3*). Integrin recognition of the canonical RGD sequence plays a prominent role in many cell−cell and cell−extracellular matrix (ECM) interactions. Integrins are cell surface transmembrane glycoproteins that exist as $\alpha\beta$ heterodimers, and at least 24 different combinations of $\alpha\beta$ heterodimers are known (*4*). The integrins of most interest in cancer imaging and therapy contain the α_v subunit, particularly the $\alpha_v\beta_3$ and $\alpha_v\beta_5$ subtypes. The $\alpha_v\beta_3$ integrin is known to be overexpressed in many tumor types and expressed at lower levels in normal tissues (*5*). Both $\alpha_v\beta_3$ and $\alpha_v\beta_5$ subtypes are expressed in neovasculature during angiogenesis (*5*). Therefore, the impetus to image/treat angiogenesis and tumor formation in vivo using RGD-based peptide targeting vectors is of significant interest.

RGD peptide conjugates used to target integrin receptors are generally linear, disulfide-cyclized, or head-to-tail cyclized constructs (*6*−*18*). However, the most extensive class of RGD analogues being studied utilizes the head-to-tail cyclized RGD derivatives. These analogues represent the most promising class of RGD-based imaging agents (*2*). Early investigations into the effect of head-to-tail cyclization on RGD affinity for the $\alpha_v\beta_3$ integrin led to the identification of *cyclo*-(RGDfV) (*19*), an $\alpha_v\beta_3$ antagonist with a low nanomolar IC_{50}. Further characterization led to the observation that a bulky hydrophobic residue was required in position 4 for maximum affinity, while position 5 was tolerant of a range of substitutions (*12*). For example, the insertion of either a D- or L-tyrosine into position 4 or 5 yielded RGD peptide conjugates with available sites for radioiodination. The resulting ^{125}I-labeled peptides were tested in vitro and in vivo to examine the feasibility of using cyclic RGD peptides as in vivo imaging agents (*12*). These conjugates displayed rapid

* Corresponding authors. (C.J.S.) Harry S. Truman Memorial VA Hospital, Research Service Room A005, 800 Hospital Drive, Columbia, MO 65201. E-mail: smithcj@health.missouri.edu. Phone: (573) 814-6000 ext. 3683. Fax: (573) 882-1663. (C.D.) Department of Nuclear Medicine, University of Innsbruck, Anichstrasse 35, Innsbruck, Austria, A-6020 Innsbruck. E-mail: Clemens.decristoforo@uibk.ac.at. Phone: +435125042672. Fax: +435125042683.

[†] Department of Radiology, University of Missouri-Columbia School of Medicine.

[⊥] Department of Internal Medicine, University of Missouri-Columbia School of Medicine.

[⊗] The Radiopharmaceutical Sciences Institute, University of Missouri-Columbia School of Medicine.

[‡] University of Missouri Research Reactor Center, University of Missouri-Columbia.

[#] Harry S. Truman Memorial Veterans' Hospital.

[||] Instituto Tecnológico e Nuclear.

[○] University of Innsbruck.

[▽] University of Zurich.

10.1021/bc060234t CCC: $37.00 © 2007 American Chemical Society
Published on Web 01/13/2007

blood clearance through hepatobiliary excretion and tumor uptake at 1 h p.i. (post intravenous administration) of 1.30 ± 0.13 %ID/g in M21 melanoma human tumor xenografts (*12*). Further attempts to improve the pharmacokinetics of these RGD constructs of this type resulted in the synthesis and in vitro/in vivo evaluation of a glycosylated analogue via the attachment of a carbohydrate moiety to the ϵ amino group of Lys5 (*13*). The resulting molecule showed decreased uptake in liver and intestine and increased tumor uptake and residualization, with 2.05 ± 0.55 %ID/g in M21 melanoma human tumor xenografts. Similar results have been reported using an ^{18}F-labeled galacto-RGD analogue, an agent that has already been evaluated in human patients (*14*, *15*).

New and exciting methods of attaching radiometals to specific biomolecular targeting vectors such as RGD continue to be of significant interest. $\alpha_v\beta_3$-Targeted cyclic pentapeptides include a lysine residue in position 5 for the purpose of appending a diverse array of radiolabels. For example, PET tracers have been synthesized by appending a PEG-[^{18}F]fluorobenzoate domain (*16*). Furthermore, metal chelators such as DTPA and DOTA have also been conjugated to RGD via a Lys5 residue to coordinate a wide range of radionuclides useful for imaging and therapy (*17*, *18*). The availability of Isolink for kit preparation of the *fac*-[^{99m}Tc(CO)$_3$(H$_2$O)$_3$]$^+$ synthon (Isolink, Tyco Healthcare, St. Louis, MO) offers a new and exciting approach toward production of ^{99m}Tc-based RGD conjugates. Alberto and co-workers have well-established the macroscopic and tracer level chemistry of Tc(I) and Re(I) tricarbonyl complexes containing the *fac*-[M(CO)$_3$]$^+$ moiety (*20*−*27*). They have demonstrated the effectiveness of using ligand frameworks with a host of donor atoms (i.e., P, S, and N) to effectively stabilize the metal center to produce in vivo stable and kinetically inert complexes (*28*−*34*). Recently, Alves et al. have reported the design of a tridentate metal chelator that effectively coordinates the *fac*-[M(CO)$_3$]$^+$ metal center (M = Tc or Re) (*35*−*39*). This new ligand framework, 3,5-Me$_2$-pz(CH$_2$)$_2$N-((CH$_2$)$_3$COOH)(CH$_2$)$_2$NH$_2$ (PZ), has been shown to produce in vitro and in vivo stable complexes of ^{99m}Tc. Furthermore, ^{99m}Tc-bombesin conjugates of 3,5-Me$_2$-pz(CH$_2$)$_2$N((CH$_2$)$_3$COOH)-(CH$_2$)$_2$NH$_2$ demonstrated high selectivity and affinity for the GRP receptor, subtype 2 (*39*). As part of an International Atomic Energy Agency Co-ordinated Research Project, "Development of ^{99m}Tc-based Small Biomolecules Using Novel ^{99m}Tc Cores", there is some interest in conjugation of new ligand frameworks to Lys5 of cyclic RGD for the design and development of a novel, cyclized ^{99m}Tc-RGD analogue. The participating countries herein report the design and development of a new cyclic RGD analogue, *cyclo*-[Arg-Gly-Asp-D-Tyr-Lys(PZ)] (PZ = 3,5Me$_2$-pz(CH$_2$)$_2$N((CH2)$_3$COOH)(CH$_2$)$_2$NH$_2$), that can be radiolabeled with the *fac*-M(CO)$_3$ metal center (M = Tc or Re). In this study, we report the synthesis and radiolabeling of *cyclo*-[Arg-Gly-Asp-D-Tyr-Lys(PZ)], in vitro internalization, and blocking assays of this conjugate in $\alpha_v\beta_3$ receptor-positive, human M21 melanoma cancer cells and in vivo pharmacokinetic studies of this conjugate in normal CF-1 mice. Furthermore, in vivo evaluation of this conjugate in mice bearing either $\alpha_v\beta_3$ receptor-positive or negative human M21 melanoma tumors will be discussed.

EXPERIMENTAL PROCEDURES

Materials. *cyclo*-[Arg-Gly-Asp-D-Tyr-Lys(PZ)] was synthesized by Biosynthan (Gesellschaft fur Bioorganische Synthese mbH, Berlin, Germany). 3,5Me$_2$-pz(CH$_2$)$_2$N((CH2)$_3$COOH)-(CH$_2$)$_2$NH−BOC was synthesized as previously reported (*38*). All other reagents were purchased from either Fisher Scientific (Chicago, IL) or Sigma-Aldrich (St. Louis, MO) and used without further purification. ^{125}I-Echistatin was purchased from Amersham-Pharmacia Biotech (Vienna, Austria). $\alpha_v\beta_3$ integrin receptors were purchased from Chemicon (Temecula, CA). ^{99m}Tc, in the form of [^{99m}TcO$_4$]$^-$, was eluted from commercially available ^{99}Mo/^{99m}Tc generator systems. Isolink radiolabeling kits were provided by Tyco Healthcare International (Petten, The Netherlands).

Methods. *1. Peptide Synthesis. cyclo*-[Arg-Gly-Asp-D-Tyr-Lys(PZ-BOC)] was synthesized by the reaction of 3,5Me$_2$-pz-(CH$_2$)$_2$N((CH2)$_3$COOH)(CH$_2$)$_2$NH−BOC, (2-(5-norbornene-2,3-dicarboximido)-1,1,3,3-tetramethyluronium tetrafluoroborate (TNTU), and diisopropylethylamine (DIEA) (1:1.2:1.2) in *N*,*N*,-dimethyl formamide (DMF) for 1 h. Two equivalents of the corresponding HONB-ester (hydroxy-5-norbornene-2,3-dicarboxylimide) solution was added to 1 equiv of the unprotected cyclopeptide, *cyclo*-[Arg-Gly-Asp-D-Tyr-Lys], in DMF. The pH of the solution was adjusted to 8 by addition of *N*-methylmorpholine (NMM), and the reaction mixture was allowed to stir at room temperature for 48 h.

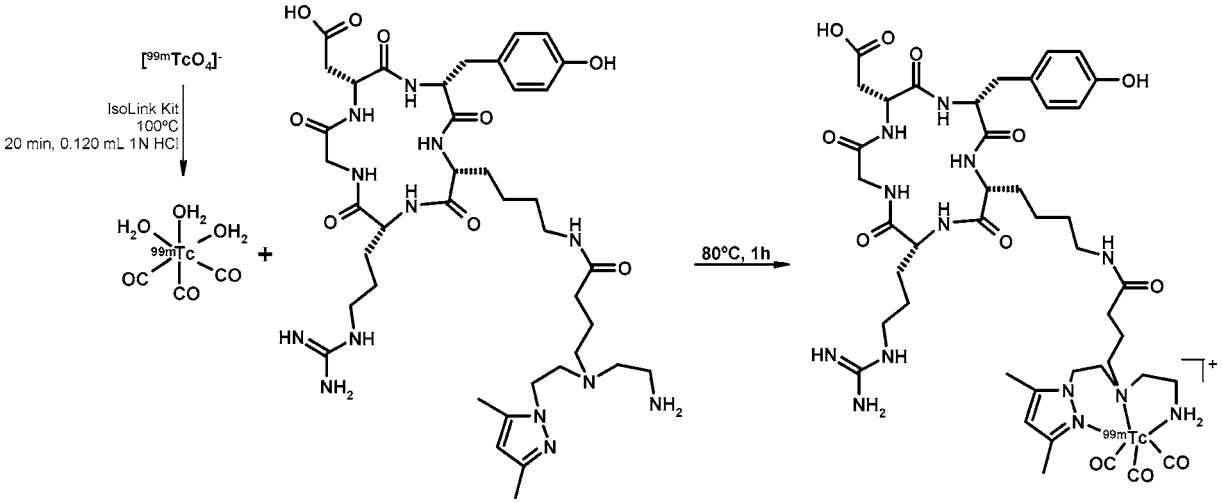
The crude, BOC-protected peptide conjugate was purified by preparative reversed phase-high performance liquid chromatography (RP-HPLC) utilizing a Shimadzu LC-8A system equipped with a SPD-6A tunable absorbance detector calibrated to 220 nm. HPLC solvents consisted of H$_2$O containing 0.05% trifluoroacetic acid (TFA, solvent A) and acetonitrile/water (80:20 containing 0.05% trifluoracetic acid (solvent B). An Ultrasep C-18 column (10.0 μm, 100 Å, 20 × 250 mm, SEPSERV GmbH, Berlin) was used with a flow rate of 15.0 mL/min. The HPLC gradient system began with a solvent composition of 95%A and 5%B and followed a linear gradient of 2.5%B/min. MALDI-MS of the BOC protected cyclic peptide was performed confirming the chemical constitution of the purified conjugate (calculated mass: 970.2; experimental mass: 970.4).

The cyclic RGD analogue, *cyclo*-[Arg-Gly-Asp-D-Tyr-Lys-(PZ)], was obtained by reaction of *cyclo*-[Arg-Gly-Asp-D-Tyr-Lys(PZ-BOC)] with TFA/water (95:2) for 1 h. Purification by preparative HPLC was performed, and the final purified analogue was analyzed by MALDI-MS (calculated mass: 870.2; experimental mass: 870.1).

2. Radiolabeling of cyclo-[Arg-Gly-Asp-D-Tyr-Lys(PZ)] Conjugate. To 0.2 mL of 2.5 × 10^{-4} M aqueous solution of *cyclo*-[Arg-Gly-Asp-D-Tyr-Lys(PZ)] was added 0.8 mL of [^{99m}Tc-(H$_2$O)$_3$(CO)$_3$]$^+$ prepared via the Isolink kit (Scheme 1). The solutions were allowed to incubate at 75 °C for 1 h. Quality control (radiochemical yield and radiochemical purity) of the products was determined by RP-HPLC. Analysis of radiolabeled and non-radiolabeled compounds was performed on a Waters 600S controller equipped with a Waters 626 pump, Waters 2487 dual wavelength absorbance detector, an Eppendorf CH-30 column heater, an in-line EG&G ORTEC NaI solid scintillation detector, and a Hewlett-Packard 3395 integrator. HPLC analysis of the new radiolabeled RGD conjugate was performed using an analytical C-18 reversed phase column (Phenomenex, 50 × 4.6 mm, 5 μm). The mobile phase consisted of a linear gradient system, with solvent A corresponding to 100% water with 0.1% trifluoroacetic acid and solvent B corresponding to 100% acetonitrile with 0.1% trifluoroacetic acid. The mobile phase began with solvent compositions of 95%A/5%B. At time = 25 min, the solvent compositions were 30%A/70%B. Solvent compositions of the mobile phase remained at 30%A/70%B for 1 min before being changed to 20%A/80%B. At time = 28 min, the solvent composition was changed to 95%A/5%B for column re-equilibration. The flow rate of the mobile phase was 1.5 mL/min. Product purification and final preparation of the labeled species were performed by collecting the samples off the chromatographic system, removal of solvent via a nitrogen stream, and reconstitution in normal saline.

3. In Vitro Stability in Human Blood. To 1 mL of whole human blood, collected in heparinized polypropylene tubes, was

Scheme 1. Radiosynthesis of [^{99m}Tc(CO)$_3$−*cyclo*-[Arg-Gly-Asp-D-Tyr-Lys(PZ)]]$^+$



added a solution of the [^{99m}Tc(CO)$_3$−*cyclo*-[Arg-Gly-Asp-D-Tyr-Lys(PZ)]]$^+$ conjugate (∼9.25 MBq). This mixture was incubated at 37 °C. Samples were taken at 5 min, 45 min, and 4 h postincubation, and centrifuged for 15 min at 2000 rpm at 4 °C. The plasma was separated and ethanol was added in a 2:1 (v/v) ratio. The samples were centrifuged at 3000 rpm (15 min, 4 °C), filtered through a Millex GV filter (0.22 μm), and the supernatant was analyzed by RP-HPLC. HPLC analyses of the ^{99m}Tc-conjugates were performed on a Shimadzu C-R4A chromatography system equipped with a Berthold - LB 505 gamma detector and a tunable absorption UV detector. Separations were achieved on an analytical C-18 reversed phase column (Nucleosil, 250 × 4.0 mm, 10 μm, 100 Å). The mobile phase consisted of a linear gradient system, with solvent A corresponding to 0.1% trifluoroacetic acid in water and solvent B corresponding to 0.1% trifluoroacetic acid in acetonitrile. The mobile phase (linear gradient) began with solvent compositions of 100%A/0%B. At time = 9 min, the solvent compositions were 75%A/25%B. Solvent compositions were changed linearly to 0%A/100%B at time = 20 min. At time = 22 min, the solvent composition was changed to 100%A/0%B for column re-equilibration. The detection wavelength was 220 nm, and the flow rate was 1 mL/min.

4. Binding Affinity of cyclo-[Arg-Gly-Asp-D-Tyr-Lys(PZ)] to $\alpha_v\beta_3$ Integrin Receptors. The in vitro binding affinity of the pyrazolyl−RGD conjugate was determined and compared directly to *cyclo*-[Arg-Gly-Asp-D-Phe-Val] using ^{125}I-echistatin as the radioligand as described by Orlando and Cheresh (*40*). Briefly, 96-well plates were coated with $\alpha_v\beta_3$ integrin receptors (Chemicon, Temecula, CA) and incubated in the presence of varying amounts of competing ligand (0.05 nM to 50 μM RGD peptide) for 3 h with 370 Bq/well (0.05 nM) ^{125}I-Echistatin (Amersham Biosciences, Piscataway, NJ). After incubation, wells were washed three times with 25 mM Tris-HCl containing 150 mM NaCl, 1 mM $CaCl_2$, 0.5 mM $MgCl_2$, 1 mM $MnCl_2$, pH 7.4, and bound ^{125}I-echistatin was solubilized with hot 2 N NaOH. Radioactivity in the resulting suspension was measured by a γ-counter (Wallac Wizard). IC_{50} values were calculated by fitting the percent inhibition values using ORIGIN software (Northhampton, MA).

5. In Vitro Internalization Analysis of [^{99m}Tc(CO)$_3$−cyclo-[Arg-Gly-Asp-D-Tyr-Lys(PZ)]]$^+$ in $\alpha_v\beta_3$ Positive M21 Melanoma Cells. $\alpha_v\beta_3$ positive M21 or $\alpha_v\beta_3$ negative M21L human melanoma cells (*41*) were grown in culture until a sufficient number of cells were available. For internalization experiments, cells were determined to be at a concentration of 2×10^6 cells/mL in RPMI 1640 containing 1% glutamine and 1% BSA. One milliliter of this solution was pipetted into each separate tube for internalization assays. [^{99m}Tc(CO)$_3$−*cyclo*-[Arg-Gly-Asp-D-Tyr-Lys(PZ)]]$^+$ conjugate (≥100000 cpm, ∼1 nM) was added to the cellular media, and the solutions were incubated at 37 °C for 90 min (n = 3) in presence of either PBS/0.5%BSA buffer (150 μL; regular assay) or 10 μM *cyclo*-[Arg-Gly-Asp-D-Tyr-Lys] (RGDyK) in PBS/0.5%BSA buffer (150 μL; nonspecific binding assay). Following the 90 min incubation period, the solutions were centrifuged, media was removed, and cells rinsed with cold TRIS buffered saline (×2). Thereafter, the cells were twice incubated at ambient temperature in 50 mM acetate buffer (pH = 4.2) for 15 min, a period sufficient to remove membrane bound radioligand. The supernatant was collected (membrane bound radioligand fraction), and the cells were washed with 50 mM acetate buffer. Cells were lysed by treatment in 1 N NaOH, and cell-associated radioactivity was collected (internalized radioligand fraction). Protein content in the NaOH fraction was determined using spectrophotometric techniques according to the Bradford method (*42*). The internalized and non-internalized fractions were determined by measuring radioactivity, and the internalized fraction was expressed as a percent of total activity per milligram of protein.

6. In Vivo Evaluation of [^{99m}Tc(CO)$_3$−cyclo-[Arg-Gly-Asp-D-Tyr-Lys(L)]] in Normal Mouse Models. All animal studies were conducted in accordance with the highest standards of care as outlined in the NIH guide for Care and Use of Laboratory Animals and the Policy and Procedures for Animal Research at the Harry S. Truman Memorial Veterans' Hospital. The animals were fed autoclaved rodent chow (Ralston Purina Company, St. Louis, MO) and water ad libitum. The biodistribution studies of [^{99m}Tc(CO)$_3$−*cyclo*-[Arg-Gly-Asp-D-Tyr-Lys-(PZ)]]$^+$ conjugate were determined in normal, CF-1 mice (female, 4−5 weeks old, ∼20 g). The mice were injected with 185 kBq (∼1×10^{-5} μg, specific activity ∼ 5.2×10^8Ci/mol) of HPLC-purified conjugate in 50 μL of isotonic saline via the tail vein. The mice were euthanized by cervical dislocation, and the tissues and organs were excised from the animals following at 1, 4, and 24 h p.i. Subsequently, the tissues and organs were weighed and counted in a NaI well counter, and the percent injected dose (%ID) and %ID/g of each organ or tissue was calculated. The %ID in whole blood was estimated assuming a whole-blood volume of 6.5% the total body weight.

In vivo stability of [^{99m}Tc(CO)$_3$−*cyclo*-[Arg-Gly-Asp-D-Tyr-Lys(PZ)]]$^+$ conjugate was determined at 1 h p.i. by assessing aliquots of urine, murine serum, and liver homogenate via RP-HPLC analysis using a method previously described herein (vide infra, in vitro serum stability). Urine: The urine was collected at the time of sacrifice and filtered through a Millex GV filter (0.22 μm), after which RP-HPLC was used to assess the degree

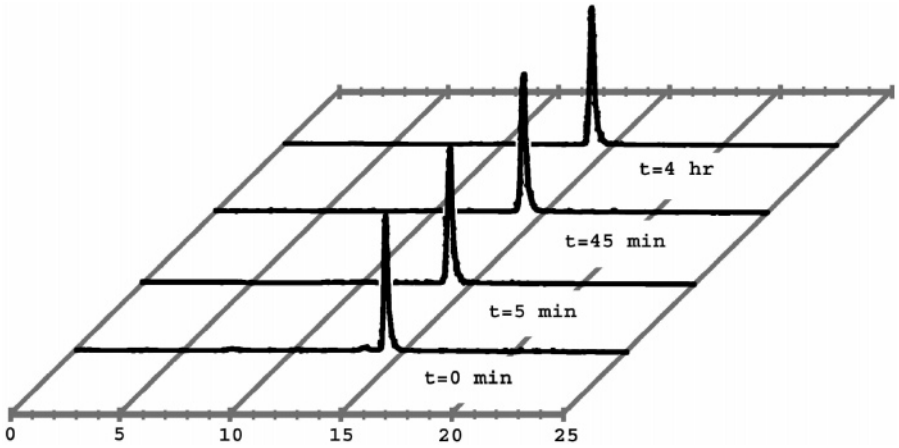


Figure 1. RP-HPLC stability profile of [^{99m}Tc(CO)$_3$−*cyclo*-[Arg-Gly-Asp-D-Tyr-Lys(PZ)]]$^+$ in whole blood (t_R = 14.2 min).

of in vivo stability. Serum: Blood collected from mice was immediately centrifuged for 15 min at 3000 rpm at 4 °C, and the serum was separated. Aliquots of 100 μL of serum were treated with 200 μL of ethanol for protein precipitation. Samples were centrifuged at 4000 rpm for 15 min at 4 °C, the supernatant was collected and passed through a Millex GV filter (0.22 μm), and the degree of in vivo stability was assessed by RP-HPLC. Liver homogenate: After radiopharmaceutical administration, animals were kept for 1 h on normal diet ad libitum. Immediately upon sacrifice, the liver was excised, rinsed, and placed in chilled 50 mM TRIS/0.2 M sucrose buffer (pH = 7.4), wherein it was homogenized. The liver homogenate was treated with ethanol in a 2:1 EtOH/homogenate v/v ratio. The sample was then centrifuged at 25 000 rpm for 15 min at 4 °C and filtered through Millex GV filter (0.22 μm), and the activity was measured. Aliquots (in duplicate) of the filtrate were analyzed by RP-HPLC as previously described. Taking into account the radionuclide decay, the recovery of the radioactivity was found to be between 70 and 80% (activity of the filtrate/total liver activity).

7. In Vivo Evaluation of [^{99m}Tc(CO)$_3$−cyclo-[Arg-Gly-Asp-D-Tyr-Lys(PZ)]]$^+$ in $\alpha_v\beta_3$ positive and $\alpha_v\beta_3$ negative M21 Human, Melanoma-Bearing, Nude Mouse Models. All animal experiments were conducted in compliance with the Austrian animal protection laws and with approval of the Austrian Ministry of Science. Tumor uptake studies were performed in nu/nu mice (female, 6−9 weeks old, ∼20 g, Charles River). For the induction of tumor xenografts, M21 and M21L cells were subcutaneously injected into the left and right flanks of the mouse at a concentration of 5×10^6 cells per mouse. Tumors were allowed to grow to sizes of ∼0.3−0.6 cm^3 prior to initiation of the study. Animals were intravenously injected with 100 μL (925 kBq, ∼1 μg of peptide conjugate, specific activity ∼2.6×10^4 Ci/mol) of [^{99m}Tc(CO)$_3$−*cyclo*-[Arg-Gly-Asp-D-Tyr-Lys(PZ)]]$^+$ conjugate via the tail vein and were maintained on normal diet ad libitum. The mice were sacrificed by cervical dislocation at 1 and 4 h p.i. Tissues and organs were collected, weighed, and counted in a gamma counter, and the percent injected dose (%ID/organ) and %ID/g of each organ or tissue was calculated. Tumor-to-organ and tumor-to-blood ratios were also determined.

RESULTS

PZ-BOC (3,5Me$_2$-pz(CH$_2$)$_2$N((CH2)$_3$COOH)(CH$_2$)$_2$NH−BOC) was synthesized as previously reported (*35*−*38*) and provided to Biosynthan for conjugation to *cyclo*-[Arg-Gly-Asp-D-Tyr-Lys]. The cyclic peptide, *cyclo*-[Arg-Gly-Asp-D-Tyr-Lys-(PZ)], was synthesized by standard solid-phase synthetic methods, purified by preparative RP-HPLC, and characterized by MALDI-MS (calculated mass: 870.2; experimental mass: 870.1).

[^{99m}Tc(CO)$_3$−*cyclo*-[Arg-Gly-Asp-D-Tyr-Lys(PZ)]]$^+$ was produced in very high yield (≥90%, specific activity ∼ 6×10^6 Ci/mol) upon addition of [^{99m}Tc(H$_2$O)$_3$(CO)$_3$]$^+$ (prepared via the Isolink radiolabeling kit) to a vial containing 2.5×10^{-4}M *cyclo*-[Arg-Gly-Asp-D-Tyr-Lys(PZ)] (Scheme 1). The radiochemical yield of the new ^{99m}Tc-conjugate was monitored by RP-HPLC. The HPLC chromatographic profile for [^{99m}Tc(CO)$_3$−*cyclo*-[Arg-Gly-Asp-D-Tyr-Lys(PZ)]]$^+$ is demonstrated in Figure 1. The chromatogram shows a single peak (t_R= 14.2 min) corresponding to the new radiometallated conjugate. Pertechnetate had a retention time of ∼2.9 min under identical HPLC conditions. Nonmetallated *cyclo*-[Arg-Gly-Asp-D-Tyr-Lys(L)] eluted as a single species with a retention time of 8.8 min. This allowed for easy separation of metalated from nonmetallated conjugate, making it possible to collect very high specific activity [^{99m}Tc(CO)$_3$−*cyclo*-[Arg-Gly-Asp-D-Tyr-Lys-(PZ)]]$^+$.

To assess the in vitro integrity of [^{99m}Tc(CO)$_3$−*cyclo*-[Arg-Gly-Asp-D-Tyr-Lys(PZ)]]$^+$ conjugate, stability assays in human blood were performed. Figure 1 shows the RP-HPLC stability profile of the new conjugate at various timepoints (0 min, 5 min, 45 min, and 4 h) postincubation with human blood. From this study, we can assess that [^{99m}Tc(CO)$_3$−*cyclo*-[Arg-Gly-Asp-D-Tyr-Lys(PZ)]]$^+$ conjugate is ≥98% stable at 4 h postincubation in whole blood.

In vitro binding affinity of cyclo[Arg-Gly-Asp-D-Tyr-Lys-(PZ)] for the $\alpha_v\beta_3$ receptor was assessed by competitive binding assays utilizing ^{125}I-Echistatin as the binding displacement ligand (*40*). *cyclo*-[Arg-Gly-Asp-D-Tyr-Lys(PZ)] showed very high binding affinity for the $\alpha_v\beta_3$ receptor with an IC$_{50}$ value of 3.01 nM (Figure 2). Comparatively, *cyclo*-[Arg-Gly-Asp-D-Phe-Val] showed an IC$_{50}$ value of 3.68 nM.

To evaluate the biological potential of [^{99m}Tc(CO)$_3$−*cyclo*-[Arg-Gly-Asp-D-Tyr-Lys(PZ)]]$^+$ conjugate, the degree of internalization in human, M21 melanoma cells was determined. This study showed approximately 1.0 ± 0.09% cellular uptake/mg of protein of [^{99m}Tc(CO)$_3$−*cyclo*-[Arg-Gly-Asp-D-Tyr-Lys-(PZ)]]$^+$ in M21 cells at 90 min postincubation. Blocking studies, in which excess *cyclo*-[Arg-Gly-Asp-D-Tyr-Lys] was incubated concurrently with [^{99m}Tc(CO)$_3$−*cyclo*-[Arg-Gly-Asp-D-Tyr-Lys-(PZ)]]$^+$, demonstrated the in vitro specificity of conjugate for $\alpha_v\beta_3$ receptor-expressing cells. The presence of 10 μM *cyclo*-[Arg-Gly-Asp-D-Tyr-Lys] reduced cellular uptake/mg of protein to 0.34 ± 0.04% for [^{99m}Tc(CO)$_3$−*cyclo*-[Arg-Gly-Asp-D-Tyr-Lys(PZ)]]$^+$ at 90 min postincubation. Comparably, cellular

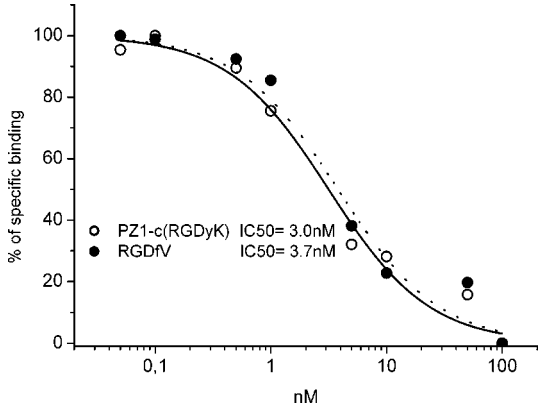


Figure 2. Competitive binding assays of *cyclo*-[Arg-Gly-Asp-D-Tyr-Lys(PZ)] and *cyclo*-[Arg-Gly-Asp-D-Phe-Val] versus ^{125}I-echistatin in $\alpha_v\beta_3$ integrin receptors. IC_{50}s = 3.01 (*cyclo*-[Arg-Gly-Asp-D-Tyr-Lys-(PZ)]) and 3.68 nM (*cyclo*-[Arg-Gly-Asp-D-Phe-Val]), respectively.

uptake/mg protein of $[^{99m}Tc(CO)_3$−*cyclo*-[Arg-Gly-Asp-D-Tyr-Lys(PZ)]]$^+$ in M21L receptor-negative cells was only 0.37 ± 0.11%.

Biodistribution studies in normal CF-1 mice are summarized in Table 1. These studies showed the $[^{99m}Tc(CO)_3$−*cyclo*-[Arg-Gly-Asp-D-Tyr-Lys(PZ)]]$^+$ conjugate to be a hydrophilic species that effectively cleared the bloodstream at 1 h p.i. For example, only 0.23 ± 0.06% ID/g of the administered dose remained in whole blood at 1 h p.i. Approximately 75% of the injected dose was excreted at 1 h p.i. via the renal−urinary pathway for this ^{99m}Tc-RGD conjugate. Hepatobiliary uptake and excretion was minimal for this conjugate. For example, only 4.25 ± 0.70 and 2.03 ± 0.20% ID/g of $[^{99m}Tc(CO)_3$−*cyclo*-[Arg-Gly-Asp-D-Tyr-Lys(PZ)]]$^+$ accumulated in intestines and liver tissue at 1 h p.i, respectively. Some residualization of radioactivity in normal kidney is evident for the $[^{99m}Tc(CO)_3$−*cyclo*-[Arg-Gly-Asp-D-Tyr-Lys(PZ)]]$^+$ conjugate (3.11 ± 0.32% ID/g, 1h p.i.). However, this radioactivity appears to wash out significantly over time. To demonstrate the effective in vivo stability or kinetic inertness of $[^{99m}Tc(CO)_3$−*cyclo*-[Arg-Gly-Asp-D-Tyr-Lys(PZ)]]$^+$ conjugate, urine, serum, and liver samples were acquired and analyzed by RP-HPLC at 1 h p.i. The samples were homogenized and reinjected onto the HPLC to verify product integrity. The conjugate showed remarkable in vivo stability as ≥98% of the conjugates were in the form of $[^{99m}Tc(CO)_3$−*cyclo*-[Arg-Gly-Asp-D-Tyr-Lys(PZ)]]$^+$ at 1 h post-intravenous administration (Figure 3).

Table 2 summarizes the results of biodistribution studies of $[^{99m}Tc(CO)_3$−*cyclo*-[Arg-Gly-Asp-D-Tyr-Lys(PZ)]]$^+$ in nude mice bearing xenografted human, M21, melanoma tumors at 1 and 4 h post-intravenous injection. High tumor uptake and retention of $[^{99m}Tc(CO)_3$−*cyclo*-[Arg-Gly-Asp-D-Tyr-Lys-(PZ)]]$^+$ in M21 melanoma tumors demonstrates effective selectivity and affinity of this new RGD conjugate for the $\alpha_v\beta_3$ receptor. For example, accumulation of radioactivity in tumor tissue was 2.50 ± 0.29 and 1.62 ± 0.44% ID/g at 1 and 4 h p.i., respectively. To demonstrate the effectiveness of $[^{99m}Tc(CO)_3$−*cyclo*-[Arg-Gly-Asp-D-Tyr-Lys(PZ)]]$^+$ for selectively targeting the $\alpha_v\beta_3$ receptor, biodistribution studies were also performed in nude mice bearing xenografted receptor-negative, M21L, melanoma tumors (Table 2). Accumulation of radioactivity in M21L tumors showed markedly less tumor uptake at 1 h p.i as compared to the receptor-positive M21 cell line. For example, tumor accumulation in this receptor-negative cell line was only 0.71 ± 0.08% ID/g at 1 h p.i. Tumor-to-blood and tumor-to-muscle ratios in the receptor-positive M21 cell line were ∼2.6 and 2.4 at 1 h p.i, respectively. Conversely, these values were only 0.78 and 0.95 in receptor-negative M21L xenografted tumors. In all of these studies (i.e., tumor-bearing and non tumor-bearing mice), there is no significant uptake or retention of radioactivity in the stomach indicating that there is minimal, if any, in vivo dissociation of the ^{99m}Tc metal center from this tridentate ligand framework to produce $[^{99m}TcO_4]^-$.

DISCUSSION

Significant effort into the design and development of specific targeting vectors for imaging angiogenesis have provided valuable insight in identifying structural features that produce kinetically inert conjugates having very high affinity and selectivity for the $\alpha_v\beta_3$ integrin, a mediator of endothelial cell migration during blood vessel formation (*1*). These studies indicate that head-to-tail cyclized derivates of the general type *cyclo*-[Arg-Gly-Asp-D-Tyr-Lys] are easily functionalized for radiolabeling at Lys5 producing antagonistic conjugates with nanomolar affinity for the $\alpha_v\beta_3$ integrin receptor (*6*−*18*). These studies have demonstrated the effectiveness of targeting angiogenesis factors for diagnosis and potential therapy of specific human tumors.

Typically, RGD peptide-based targeting vectors for integrin receptors are either linear, disulfide-cyclized, or head-to-tail cyclized constructs (*6*−*18*). However, increasing attention has recently focused on the development of dimeric or multimeric cyclic RGD peptide constructs. Multimerization is expected to increase the apparent affinity of targeting vectors for their cognate receptors due to avidity effects. In one instance, a dimeric *cyclo*-(RGDfK) construct was synthesized by bridging two lysine ϵ amino groups with a HYNIC-glutamic acid moiety (*43*). This peptide, when labeled with ^{99m}Tc, showed high receptor-mediated tumor uptake of 5.8 ± 0.7%ID/g at 1 h pi in an OVCAR-3/nude mouse in vivo model. The corresponding monomer showed tumor uptake of 5.2 ± 0.6%ID/g. However, at all timepoints, kidney retention of the dimer was significantly higher as compared to the monomer (*43*). In a second study, *cyclo*-(RGDfE) multimers were formed using variable-length PEG spacers linked to a diaminopropionic acid/lysine backbone (*44*). Monomeric, dimeric, and tetrameric forms were synthesized and labeled with ^{18}F. Biodistribution of the dimer was comparable to that of a monomeric, glycosylated ^{18}F-labeled RGD analogue (*44*).

Haubner and co-workers have used a tetrapeptide sequence (H-Asp-Lys-Cys-Lys-OH) as a chelating system for labeling a *cyclo*-RGD derivative (DKCK-RGD) with ^{99m}Tc (*45*). Gamma camera images at 4 h p.i. clearly demonstrated tumor-specific uptake of conjugate. However, there was high concentration of radioactivity in normal kidneys, possibly due to the lysine-containing tetrapeptide used as the chelating sequence (*45*).

Other attempts at targeting $\alpha_v\beta_3$ receptor expression have focused on the labeling of a disulfide-bridged undecapeptide found via a phage display library. In this study, a shortened derivative of RGD-4C ((Cys^1-Cys^9-Cys^3-Cys^7)H-Cys-Asp-Cys-Arg-Gly-Asp-Cys-Phe-Cys-OH) was coupled with HYNIC and radiolabeled with ^{99m}Tc (*11*, *46*). In two murine tumor models, only marginal tumor uptake was observed, presumably due to only modest association of this conjugate for the $\alpha_v\beta_3$ receptor ($K_a = 7 \times 10^6$ M^{-1}) (*11*, *46*).

Recent studies by Psimadas and co-workers and Line and co-workers have led to some interesting developments toward development of new $[^{99m}Tc(CO)_3$-RGD]$^+$ conjugates (*47*, *48*). For example, Psimadas et al., have conjugated picolinamine-*N*,*N*-diacetic acid (PADA) and histidine to the epsilon amine of lysine for coordination to the *fac*-$[M(CO)_3]^+$ metal center. Studies show these new conjugates can be produced in very high yields (∼98%) as single radiochemical products. Furthermore, these new conjugates were stable to histidine and cysteine challenge experiments even at 24 h postincubation with exchange ligand. In vivo evaluation of the biodistribution of

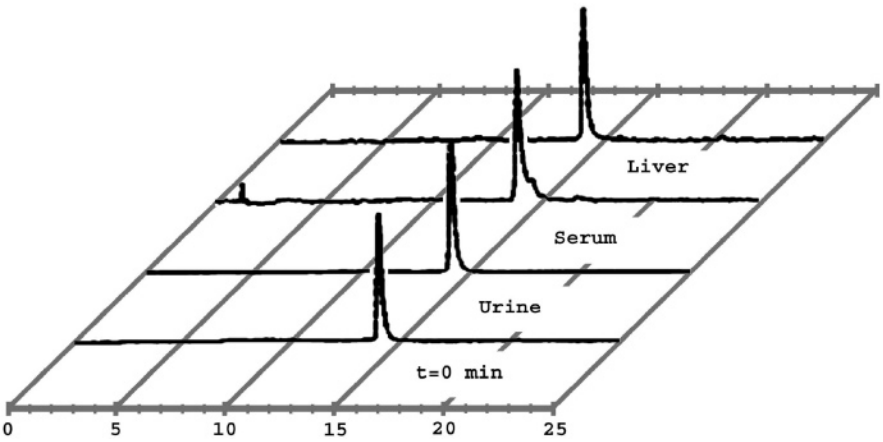


Figure 3. RP-HPLC stability profile of $[^{99m}Tc(CO)_3-$*cyclo*-[Arg-Gly-Asp-D-Tyr-Lys(PZ)]]$^+$ in murine urine, serum, and liver tissue at 1 h p.i. (t_R = 14.2 min).

Table 1. Biodistribution Studies (%ID/g(SD), $n = 5$) of $[^{99m}Tc(CO)_3-$*cyclo*-[Arg-Gly-Asp-D-Tyr-Lys(PZ)]]$^+$ Conjugate in Normal, CF-1 Mice

tissue/organ	1 h	4 h	24 h
urine[a]	74.5(3.65)	81.9(3.40)	88.5(3.63)
bladder	2.34(1.42)	1.06(0.23)	0.24(0.33)
heart	0.56(0.09)	0.31(0.11)	0.08(0.13)
lungs	1.24(0.21)	0.59(0.12)	0.19(0.09)
liver	2.03(0.20)	0.90(0.21)	0.18(0.03)
kidney	3.11(0.32)	1.75(0.27)	0.56(0.10)
spleen	1.14(0.31)	0.45(0.06)	0.42(0.60)
stomach	0.71(0.16)	0.76(0.27)	0.18(0.07)
intestines	4.25(0.70)	6.80(1.26)	0.57(0.18)
muscle	0.34(0.05)	0.26(0.05)	0.12(0.05)
bone	1.06(0.36)	0.66(0.12)	0.23(0.07)
pancreas	0.53(0.11)	0.33(0.10)	0.04(0.01)
blood	0.23(0.06)	0.03(0.01)	0.01(0.01)

[a] Calculated as percent injected dose.

Table 2. Biodistribution Studies (%ID/g(SD), $n = 5$) of $[^{99m}Tc(CO)_3-$*cyclo*-[Arg-Gly-Asp-D-Tyr-Lys(PZ)]]$^+$ Conjugate in M21 and M21L, Tumor-Bearing, Nude Mice

tissue/organ	1 h (M21)	4 h (M21)	1 h (M21L)
tumor	2.50(0.29)	1.62(0.44)	0.71(0.08)
heart	0.97(0.13)	0.51(0.09)	0.89(0.09)
lungs	2.12(1.15)	1.07(0.15)	2.34(0.40)
liver	8.89(0.71)	4.58(0.46)	10.5(1.32)
kidney	5.65(0.88)	3.12(0.22)	5.24(0.42)
spleen	2.08(0.27)	1.22(0.14)	2.30(0.33)
stomach	2.12(1.15)	1.05(0.01)	1.63(0.58)
intestines	10.1(1.30)	4.59(0.35)	10.2(1.57)
muscle	1.04(0.68)	0.32(0.08)	0.76(0.45)
bone	2.73(2.92)	0.57(0.13)	1.44(0.99)
pancreas	0.80(0.34)	0.34(0.04)	0.58(0.03)
blood	0.96(0.06)	0.48(0.11)	0.91(0.06)

these new conjugates indicated rapid clearance from the blood pool with excretion predominantly the hepatobiliary pathway (*47*, *48*). Studies by Line et al. have conjugated *fac*-$[M(CO)_3]^+$ metal chelator *N*-*ω*-bis(2-pyridyl-methyl)-L-lysine to an *N*-(2-hydroxypropyl)methacrylamide (HPMA) copolymer with side chains terminated in doubly cyclized, integrin-specific RGD derivative KACDCRGDCFCG (RGD4C) or nonreactive RGE derivative KACDCRGECFCG (RGE4C) (*49*, *50*). In this study, they were able to produce conjugates in very high yield (≥93%) with specific activities ranging from 16.8 to 19.5 MBq/nmol ($4.5-5.3 \times 10^6$ Ci/mol). $[^{99m}Tc(CO)_3$-HPMA-RGD4C] conjugate showed very high uptake in each DU145 and PC-3 prostate tumor xenografts. For example, uptake and retention of activity at 24 h p.i. was determined to be 4.60 ± 1.80% ID/g and 5.92 ± 0.41% ID/g in DU145 and PC-3 prostate tumor models, respectively. Scintigraphic images in SCID mice bearing either DU145 or PC-3 prostate tumor xenografts demonstrated the high affinity and selectivity of these conjugates for $\alpha_v\beta_3$ integrin receptors expressed in these tumor models (*49*, *50*).

In the current study, we have developed a monomeric ^{99m}Tc-radiolabeled cyclic RGD conjugate, *cyclo*-[Arg-Gly-Asp-D-Tyr-Lys(PZ)] (PZ = 3,5-Me_2-pz$(CH_2)_2$N$((CH_2)_3$COOH$)(CH_2)_2NH_2$), having high affinity for the $\alpha_v\beta_3$ integrin receptor. 3,5-Me_2-pz-$(CH_2)_2$N$((CH_2)_3$COOH$)(CH_2)_2NH_2$ coordinates technetium and rhenium metal centers in tridentate fashion through the pyrazolyl and amine nitrogen donor atoms giving the metal complexes sufficient stability for in vivo radiochemical investigations (*38*, *39*). In this study, we were able to effectively show that the new conjugate *cyclo*-[Arg-Gly-Asp-D-Tyr-Lys(PZ)] could be radiolabeled in very high yield upon simple heating with the *fac*-$^{99m}Tc(CO)_3(H_2O)_3$-synthon. Upon simple radiolabeling of conjugate, a specific activity ~ 6×10^6Ci/mol was determined for $[^{99m}Tc(CO)_3-$*cyclo*-[Arg-Gly-Asp-D-Tyr-Lys(PZ)]]$^+$. This is comparable to other $[^{99m}Tc(CO)_3$-RGD] targeting vectors having very high affinity for the $\alpha_v\beta_3$ integrin receptor. Studies indicated production of a single species even at ligand concentrations of 10^{-5} M, precluding the potential for kit development for radiolabeled conjugates of this type. The new conjugate was stable in human serum for an extended period, demonstrating the ability of the nitrogen-based pyrazolyl chelator to effectively stabilize the metal center against transmetallation reactions to serum-based proteins. For example, $[^{99m}Tc(CO)_3-$*cyclo*-[Arg-Gly-Asp-D-Tyr-Lys(PZ)]]$^+$ was ≥98% stable for periods up to 4 h postincubation as indicated by RP-HPLC.

It is essential to maximize uptake and residualization of radioactivity in human tumor tissue to optimize the diagnostic/therapeutic efficacy of the radiolabeled targeting vector. Results of internalization studies in M21 receptor-positive cells show that most of the radioactivity is not surface bound and is not lost from the cells upon incubation in pH 4.2 buffer. These studies indicate that $[^{99m}Tc(CO)_3-$*cyclo*-[Arg-Gly-Asp-D-Tyr-Lys(PZ)]]$^+$ has high specificity for $\alpha_v\beta_3$ receptor-expressing cells. For example, there was approximately 1.0 ± 0.09% cellular uptake/mg of protein of in M21 cells at 90 min postincubation. Blocking studies indicated reduced cellular uptake/mg of protein for $[^{99m}Tc(CO)_3-$*cyclo*-[Arg-Gly-Asp-D-Tyr-Lys(PZ)]]$^+$ at 90 min postincubation. Only 0.34 ± 0.04% cellular uptake/mg of protein was observed, further demonstrating the selectivity of conjugate for the integrin receptor. Cellular uptake/mg of protein of $[^{99m}Tc(CO)_3-$*cyclo*-[Arg-Gly-Asp-D-Tyr-Lys(PZ)]]$^+$ in M21L receptor-negative cells was only 0.37 ± 0.11%. Uptake of ^{125}I-radiolabeled RGD in each M21 and M21L human melanoma cells showed less than 0.25% cellular uptake/mg of protein comparatively.

In vivo evaluation of [^{99m}Tc(CO)$_3$−*cyclo*-[Arg-Gly-Asp-D-Tyr-Lys(PZ)]]$^+$ conjugate demonstrated rapid clearance from the bloodstream and excretion primarily via the renal−urinary pathway. Subsequent stability evaluation of the conjugate in human tissue showed that the conjugate was not readily metabolized in vivo, with 98% of the conjugate remaining intact upon in vivo administration. High tumor uptake and retention of [^{99m}Tc(CO)$_3$−*cyclo*-[Arg-Gly-Asp-D-Tyr-Lys(PZ)]]$^+$ in M21 melanoma tumors was observed. For example, accumulation of radioactivity in tumor tissue was 2.50 ± 0.29 and 1.62 ± 0.44% ID/g at 1 and 4 h p.i., respectively. Studies in nude mice bearing xenografted receptor-negative, M21L melanoma tumors further demonstrates high specificity and affinity of [^{99m}Tc(CO)$_3$−*cyclo*-[Arg-Gly-Asp-D-Tyr-Lys(PZ)]]$^+$ for the integrin receptor. Tumor accumulation in this receptor-negative cell line was only 0.71 ± 0.08% ID/g at 1 h p.i. These results show some similarity to those studies by Haubner and co-workers in the same tumor model (12−15). Tumor-to-blood and tumor-to-muscle ratios of [^{99m}Tc(CO)$_3$−*cyclo*-[Arg-Gly-Asp-D-Tyr-Lys(PZ)]]$^+$ in the receptor-positive M21 cell line were ∼2.6 and 2.4 at 1 h p.i, respectively. The moderately high tumor-to-blood and tumor-to-muscle ratios are a reflection of the high binding affinity of this conjugate for the integrin receptor. These ratios are maintained even at 4 h postinjection (3.3 and 5.2, respectively) demonstrating receptor-mediated transport and subsequent intracellular trapping of this conjugate in M21, $\alpha_v\beta_3$, receptor-expressing cells. Janssen and co-workers have reported $\alpha_v\beta_3$ receptor expression in murine tissues such as the liver and spleen (*51*). In fact, they were able to effectively block uptake in muscle, lung, spleen, and liver indicating localization of their ^{111}In-RGD conjugate to be $\alpha_v\beta_3$ receptor-mediated in these tissues. In the present study, we were not able to effectively block uptake in these specific tissues and therefore cannot conclude that uptake in these organs was $\alpha_v\beta_3$ receptor-mediated.

In conclusion, these studies have demonstrated the potential utility of [^{99m}Tc(CO)$_3$−*cyclo*-[Arg-Gly-Asp-D-Tyr-Lys(PZ)]]$^+$ to image angiogenesis and tumor formation in vivo. The pyrazolyl−RGD conjugate, when radiolabeled with the [^{99m}Tc(H$_2$O)$_3$(CO)$_3$]$^+$ aquaion, provided for kinetically inert complexes of very high specific activity. [^{99m}Tc(CO)$_3$−*cyclo*-[Arg-Gly-Asp-D-Tyr-Lys(PZ)]]$^+$ showed extraordinary stability in vitro and in vivo thereby retaining biological activity with high selectivity for the $\alpha_v\beta_3$ receptor.

ACKNOWLEDGMENT

This material is the result of a collaborative research project between participating countries. This work has been coordinated and partially funded by the International Atomic Energy Agency, Vienna, Austria. Special thanks go to Drs. D. V. S. Narasimhan and M. R. A. Pillai of the Department of Nuclear Sciences and Applications of the IAEA for their considerable effort into the success of this coordinated research project. We would also like to thank D. A. Cheresh, Scripps Institute, La Jolla, CA, for providing the M21 and M21L melanoma cell lines. S.A. would like to thank Fundação para a Ciência e Tecnologia for Ph.D. Grant No. BD/3052/2000. Tyco Healthcare International (Petten, The Netherlands) is also gratefully acknowledged for financial support of this project.

LITERATURE CITED

(1) Haubner, R. (2006) $\alpha_v\beta_3$-integrin imaging: A new approach to characterise angiogenesis? *Eur. J. Nucl. Med. Mol. Imaging,* in press.

(2) Haubner, R., and Wester, H. J. (2004) Radiolabeled tracers for imaging of tumor angiogenesis and evaluation of anti-angiogenic therapies. *Curr. Pharm. Des. 10,* 1439−1455.

(3) Healy, J. M., Murayama, O., Maeda, T., Yoshino, K., Sekiguchi, K., and Kikuchi, M. M. (1995) Peptide ligands for integrin $\alpha_V\beta_3$ selected from random phage display libraries. *Biochemistry 34,* 3948−3955.

(4) Reinmuth, N., Liu, W., Ahmad, S. A., Fan, F., Stoeltzing, O., Parikh, A. A., Bucana, C. D., Gallick, G. E., Nickols, M. A., Westlin, W. F., and Ellis, L. M. (2003) $\alpha_V\beta_3$ integrin antagonist S247 decreases colon cancer metastasis and angiogenesis and improves survival in mice. *Cancer Res. 63,* 2079−2087.

(5) Kerr, J. S., Slee, A. M., and Mousa, S. A. (2000) Small molecule α_V integrin antagonists: novel anticancer agents. *Exp. Opin. Invest. Drugs 9,* 1271−1279.

(6) Sivolapenko, G. B., Skarlos, D., Pectasides, D., Stathopoulou, E., Milonakis, A., Sirmalis, G., Stuttle, A., Courtenay-Luck, N. S., Konstantinides, K., and Epenetos, A. A. (1998) Imaging of metastatic melanoma utilizing a technetium-99m labelled RGD-containing synthetic peptide. *Eur. J. Nucl. Med. 25,* 1383−1389.

(7) Sutcliffe-Goulden, J. L., O'Doherty, M. J., Marsden, P. K., Hart, I. R., Marshall, J. F., and Bansal, S. S. (2002) Rapid solid phase synthesis and biodistribution of ^{18}F-labelled linear peptides. *Eur. J. Nucl. Med. 29,* 754−759.

(8) Pierschbacher, M. D., and Ruoslahti, E. (1987) Influence of stereochemistry of the sequence Arg-Gly-Asp-Xaa on binding specificity in cell adhesion. *J. Biol. Chem. 262,* 17294−17298.

(9) Gottschalk, K., and Kessler, H. (2002) The structures of integrins and integrin-ligand complexes: Implications for drug design and signal transduction. *Angew. Chem., Int. Ed. 41,* 3767−3774.

(10) Assa-Munt, N., Jia, X., Laakkonen, P., and Ruoslahti, E. (2001) Solution structures and integrin binding activities of an RGD peptide with two isomers. *Biochemistry 40,* 2373−2378.

(11) Su, Z., Liu, G., Gupta, S., Zhu, Z., Rusckowski, M., and Hnatowich, D. J. (2002) In vitro and in vivo evaluation of a technetium-99m-labeled cyclic RGD peptide as a specific marker of $\alpha_V\beta_3$ integrin for tumor imaging. *Bioconjugate Chem. 13,* 561−570.

(12) Haubner, R., Wester, H. J., Reuning, U., Senekowitsch-Schmidtke, R., Diefenbach, B., Kessler, H., Stocklin, G., and Schwaiger, M. (1999) Radiolabeled $\alpha_V\beta_3$ integrin antagonists: A new class of tracers for tumor targeting. *J. Nucl. Med. 40,* 1061−1071.

(13) Haubner, R., Wester, H. J., Burkhart, F., Senekowitsch-Schmidtke, R., Weber, W., Goodman, S. L., Kessler, H., and Schwaiger, M. (2001) Glycosylated RGD-containing peptides: Tracer for tumor targeting and angiogenesis imaging with improved biokinetics. *J. Nucl. Med. 42,* 326−336.

(14) Haubner, R., Wester, H. J., Weber, W., Mang, C., Ziegler, S. I., Goodman, S. L., Senekowitsch-Schmidtke, R., Kessler, H., and Schwaiger, M. (2001) Noninvasive imaging of $\alpha_V\beta_3$ integrin expression using ^{18}F-labeled RGD-containing glycopeptide and positron emission tomography. *Cancer Res. 61,* 1781−1785.

(15) Haubner, R., Weber, W. A., Beer, A. J., Vabuliene, E., Reim, D., Sarbia, M., Becker, K-F., Goebel, M., Hein, R., Wester, H-J., Kessler, H., and Swaiger, M. (2005) Noninvasive visualization of the activated $\alpha_V\beta_3$ integrin in cancer patients by positron emission tomography and [^{18}F]galacto-RGD. *PloS Med. 2,* 0244−0252.

(16) Chen, X., Park, R., Hou, Y., Khankaldyyan, V., Gonzales-Gomez, I., Tohme, M., Bading, J. R., Laug, W. E., and Conti, P. S. (2004) MicroPET imaging of brain tumor angiogenesis with ^{18}F-labeled PEGylated RGD Peptide. *Eur. J. Nucl. Med. Mol. Imaging 31,* 1081−1089.

(17) van Hagen, P. M., Breeman, W. A. P., Bernard, H. F., Schaar, M., Mooij, C. M., Srinivasan, A., Schmidt, M. A., Krenning, E. P., and de Jong, M. (2000) Evaluation of a radiolabelled cyclic DTPA-RGD analogue for tumor imaging and radionuclide therapy. *Int. J. Cancer 90,* 186−198.

(18) Chen, X., Park, R., Tohme, M., Shahinian, A. H., Bading, J. R., and Conti, P. S. (2004) MicroPET and autoradiographic imaging of breast cancer alpha v-integrin expression using ^{18}F- and ^{64}Cu-labeled RGD peptide. *Bioconjugate Chem. 15,* 41−49.

(19) Aumailley, M., Gurrath, M., Muller, G., Calvete, J., Timpl, R., and Kessler, H. (1991) Arg-Gly-Asp constrained within cyclic pentapeptides. Strong and selective inhibitors of cell adhesion to vitronectin and laminin fragment P1. *FEBS Lett. 291,* 50−54.

(20) Schibli, R., Schwarzbach, R., Alberto, R., Ortner, K., Schmalle, H., Dumas, C., Egli, A., and Schubiger, P. A. (2002) Steps toward specific activity labeling of biomolecules for therapeutic applica-

tion: Preparation of precursor $[^{188}Re(H_2O)_3(CO)_3]^+$ and synthesis of tailor-made bifunctional ligand systems. *Bioconjugate Chem. 13*, 750−756.
(21) Alberto, R., Schibli, R., Egli, A., Schubiger, P. A., Herrmann, W. A., Artus, G., Abram, U., and Kaden, T. A. (1995) Metal carbonyl syntheses XXII. Low pressure carbonylation of $[MOCl_4]^-$ and $[MO_4]^-$: The technetium(I) and rhenium(I) complexes $[NEt_4]_2[MCl_3(CO)_3]$. *J. Organomet. Chem. 493*, 119−127.
(22) Alberto, R., Schibli, R., Schubiger, P. A., Abram, U., Hubener, R., Berke, H, and Kaden, T. A. (1996) A simple single-step synthesis of $[^{99}Tc_3H_3(CO)_{12}]$ from $[^{99}TcO_4]^-$ and its X-ray crystal structure. Application to the production of no-carrier added $[^{99}Re_3H_3(CO)_{12}]$. *J. Chem. Soc. Chem. Commun*. 1291−1292.
(23) Abram, U., Abram, S., Alberto, R., and Schibli, R. (1996) Ligand exchange reactions starting from $[Re(CO)_3Br_3]^{2-}$. Synthesis, characterization, and structures of rhenium(I) tricarbonyl complexes with thiourea and thiourea derivatives. *Inorg. Chim. Acta 248*, 193−202.
(24) Pietzsch, H. J., Gupta, A., Reisgys, M., Drews, A., Seifert, S., Syhre, R., Spies, H., Alberto, R., Abram, U., Schubiger, P. A., and Johannsen, B. (2000) Chemical and biological characterization of technetium(I) and rhenium(I) tricarbonyl complexes with dithioether ligands serving as linkers for coupling the $Tc(CO)_3$ and $Re(CO)_3$ moieties to biologically active molecules. *Bioconjugate Chem. 11*, 414−424.
(25) Schibli, R., Katti, K. V., Higginbotham, C., Volkert, W. A., and Alberto, R. (1999) In vitro and in vivo evaluation of bidentate, water-soluble phosphine ligands as anchor groups for the organometallic fac-$[^{99m}Tc(CO)_3]^+$-core. *Nucl. Med. Biol. 26*, 711−716.
(26) Schibli, R., Katti, K. V., Volkert, W. A., and Barnes, C. L. (1998) Novel coordination behavior of fac-$[ReBr_3(CO)_3]_2^-$ with 1,3,5-triaza-7-phosphaadamantane (PTA). Systematic investigation on stepwise replacement of the halides by PTA ligand. Phase transfer studies and X-ray crystal structure of $[NEt_4][ReBr_2(PTA)(CO)_3]$, $[ReBr(PTA)_2(CO)_3]$, and $[Re(PTA)_3(CO)_3]PF_6$. *Inorg. Chem. 37*, 5306−5312.
(27) Pietzsch, H. J., Reisgys, M., Alberto, R., Hoepping, A., Scheunemann, M., Seifert, S., Wust, F., Spies, H., Schubiger, P. A., and Johannsen, B. (1999) Thioether ligands as anchor groups for coupling the "$Tc(CO)_3$" and "$Re(CO)_3$" moieties with biologically active molecules. *Technetium, Rhenium and Other Metals in Chemistry and Nuclear Medicine* (Nicolini, M., and Ulderico, M., Eds.) pp 313−316, SGE, Italy.
(28) Egli, A., Alberto, R., Tannahill, L., Schibli, R., Abram, U., Schaffland, A., Tourwe, D., and Schubiger, P. A. (1999) $[^{99m}Tc(OH_2)_3(CO)_3]^+$ labels peptide to an unprecedented high specific activity. A labelling study with amino acids and neurotensin. *Technetium, Rhenium and Other Metals in Chemistry and Nuclear Medicine* (Nicolini, M., and Ulderico, M., Eds.) pp 507−512, SGE, Italy.
(29) La Bella, R., Garcia-Garayoa, E., Langer, M., Blauestein, P., Beck-Sickinger, A. G., and Schubiger, P. A. (2002) In vitro and in vivo evaluation of a ^{99m}Tc(I)-labeled bombesin analogue for imaging of gastrin releasing peptide receptor-positive tumors. *Nucl. Med. Biol. 29*, 553−560.
(30) Alberto, R., Schibli, R., Abram, U., Egli, A., Knapp, F. F., and Schubiger, P. A. (1997) Potential of the "$[M(CO)_3]^+$" (M = Re, Tc) moiety for the labeling of biomolecules. *Radiochim. Acta 79*, 99−103.
(31) Schibli, R., La Bella, R., Alberto, R., Garcia-Garayoa, E., Ortner, K., Abram, U., and Schubiger, P. A. (2000) Influence of the denticity of ligand systems on the in vitro and in vivo behavior of ^{99m}Tc(I)-tricarbonyl complexes: A hint for the future functionalization of biomolecules. *Bioconjugate Chem. 11*, 345−351.
(32) Alberto, R., Schibli, R., and Schubiger, P. A. (1999) First application of fac-$[^{99m}Tc(OH_2)_3(CO)_3]^+$ in bioorganometallic chemistry: Design, structure, and in vitro affinity of a 5-HT_{1A} receptor ligand labeled with ^{99m}Tc. *J. Am. Chem. Soc. 121*, 6076−6077.
(33) Alberto, R., Schibli, R., Egli, A., and Schubiger, P. A. (1998) A novel organometallic aqua complex of technetium for the labeling of biomolecules: Synthesis of $[^{99m}Tc(OH_2)_3(CO)_3]^+$ from $[^{99m}TcO_4]^-$ in aqueous solution and its reaction with a bifunctional ligand. *J. Am. Chem. Soc. 120*, 7987−7988.
(34) Alberto, R., Egli, A., Schibli, R., Waibel, R., Abram, U., Kaden, T. A., Schaffland, A., Schwarzbach, R., and Schubiger, P. A. (1999) From $[TcO_4]^-$ to an organometallic aqua-ion: Synthesis and chemistry of $[^{99m}Tc(OH_2)_3(CO)_3]^+$. *Technetium, Rhenium and Other Metals in Chemistry and Nuclear Medicine* (Nicolini, M., and Ulderico, M., Eds.) pp 27−34, SGE, Italy.
(35) Alves, S., Paulo, A., Correia, J. D. G., Domingos, Â., and Santos, I. (2002) Coordination capabilities of pyrazolyl containing ligands towards the fac-$[Re(CO)_3]^+$ moiety. *J. Chem. Soc., Dalton Trans. 24*, 4714−4719.
(36) Alves, S., Paulo, A., Correia, J. D. G., Gano, L., and Santos, I. (2002) New building blocks for labeling peptides with the $[^{99m}Tc(CO)_3]^+$ core. *Technetium, Rhenium and Other Metals in Chemistry and Nuclear Medicine 6.* (Nicolini, M., and Ulderico, M., Eds.) pp 139−142; SGE, Padova.
(37) Vitor, R. F., Alves, S., Correia, J. D. G., Paulo, A., and Santos, I. (2004) Rhenium(I)- and technetium(I) tricarbonyl complexes anchored by bifunctional pyrazole-diamine and pyrazole-dithioether chelators. *J. Organomet. Chem. 689*, 4764−4774.
(38) Alves, S., Paulo, A., Correia, J. D. G., Gano, L., Smith, C. J., Hoffman, T. J., and Santos, I. (2005) Pyrazolyl derivatives as bifunctional chelators for labelling biomolecules with the fac-$[M(CO)_3]^+$ moiety (M = ^{99m}Tc, Re): Synthesis, characterization and biological behaviour. *Bioconjugate Chem. 16*, 438−449.
(39) Alves, S., Correia, J. D. G., Santos, I., Veerendra, B., Sieckman, G. L., Hoffman, T. J., Rold, T. L., Figueroa, S. D., Retzloff, L., McCrate, J., Prasanphanic, A., and Smith, C. J. (2006) Pyrazolyl conjugates of bombesin: A new tridentate ligand framework for stabilization of the fac-$M^I(CO)_3$ moiety. *Nucl. Med. Biol. 33*, 625−634.
(40) Orlando, R. A., and Cheresh, D. A. (1991) Arginine-glycine-aspartic acid binding leading to molecular stabilization between Integrin $\alpha_v\beta_3$ and its ligand. *J. Biol. Chem. 266*, 19543−19550.
(41) Taga, T., Suzuki, A., Gonzalez-Gomez, I., Gilles, F. H., Stins, M., Shimada, H., Barsky, L., Weinberg, K. I., and Laug, W. E. (2002) α_v-Integrin antagonist EMD 121974 induces apoptosis in brain tumor cells growing on vitronectin and tenascin. *Int. J. Cancer 98*, 690−697.
(42) Bradford, M. M. (1976) A rapid and sensitive method for the quantitation of microgram quantities of protein utilizing the principle of protein-dye binding. *Anal. Biochem. 72*, 248−254.
(43) Janssen, M. L., Oyen, W. J., MAuger, L. F., Frielink, C., Dijkgraaf, I., Edwards, D. S., Rajopadhye, M., Corstens, F. H., and Boerman, O. C. (2002) Comparison of a monomeric and dimeric radiolabeled RGD-peptide for tumor targeting. *Cancer Biother. Radiopharm. 17*, 641−646.
(44) Poethko, T., Schottelius, M., Thumshirn, G., Hersel, U., Herz, M., Henriksen, G., Kessler, H., Schwaiger, M., and Wester, H. J. (2004) Two-step methodology for high-yield routine radiohalogenation of peptides: ^{18}F-labeled RGD and octreotide analogs. *J. Nucl. Med. 45*, 892−902.
(45) Haubner, R., Bruchertseifer, F., Bock, M., Kessler, H., Schwaiger, M., and Wester, H. J. (2004) Synthesis and biological evaluation of a 99mTc-labeled cyclic RGD peptide for imaging the $\alpha_v\beta_3$ expression. *Nuklearmedizin 43*, 26−32.
(46) Su, Z. F., He, J., Rusckowski, M., and Hnatowich, D. J. (2003) In vitro cell studies of technetium-99m labeled RGD-HYNIC peptide, a comparison of tricine and EDDA as co-ligands. *Nucl. Med. Biol. 30*, 141−149.
(47) Psimadas, D., Fani, M., Zikos, C., Xanthopoulos, S., Archimandritis, S. C., and Varvarigou, A. D. (2006) Study of the labeling of two novel RGD-peptidic derivatives with the precursor $[^{99m}Tc(H_2O)_3(CO)_3]^+$ and evaluation for early angiogenesis detection in cancer. *Appl. Radiat. Isotopes 64*, 151−159.
(48) Fani, M., Psimadas, D., Zikos, C., Xanthopoulos, S., Loudos, G. K., Bouziotis, P., and Varvarigou, A. D. (2006) Comparative evaluation of linear and cyclic 99mTc-RGD peptides for targeting on integrins in tumor angiogenesis. *Anticancer Res. 26*, 431−434.
(49) Line, B. R., Mitra, A., Nan, A., and Hamidreza, G. (2006) Targeting tumor angiogenesis: Comparison of peptide and polymer-peptide conjugates. *J. Nucl. Med. 46*, 1552−1560.
(50) Mitra, A., Nan, A., Papadimitriou, J. C., Ghandehari, H., and Line, B. R. (2006) Polymer-peptide conjugates for angiogenesis targeted tumor radiotherapy. *Nucl. Med. Biol. 33*, 43−52.
(51) Janssen, M. L., Oyen, W. J., Dijkgraaf, I., Mauger, L. F., Frielink, C., Edwards, D. S., Rajopadhye, M., Boonstra, H., Corstens, F. H., and Boerman, O. C. (2002) Tumor targeting with radiolabeled avb3 integrin binding peptides in a nude mouse model. *Cancer Res. 36*, 6146−6151.

BC060234T

Synthesis and Biological Evaluation of N-Substituted Quinolinimides, as Potential Ligands for in Vivo Imaging Studies of δ-Opioid Receptors

Thomas Bourdier,[†,§] Géraldine Poisnel,[†,§] Martine Dhilly,[†] Jérôme Delamare,[†] Joël Henry,[‡] Danièle Debruyne,*[,†] and Louisa Barré*[,†]

Groupe de Développements Méthodologiques en Tomographie par Emission de Positons, DSV/DRM UMR CEA 2E, Université de Caen Basse Normandie, Centre Cyceron, 15 Boulevard Henri Becquerel, 14074 Caen France, and Laboratoire de Biologie et Biotechnologies Marines, UMR IFREMER 100 Physiologie et Ecophysiologie des Mollusques Marins, Université de Caen Basse-Normandie, 14032 Caen France. Received September 11, 2006; Revised Manuscript Received January 11, 2007

We report here the syntheses of *N*-substituted quinolinimide derivatives displaying sufficient affinity and high selectivity for δ-opioid receptors. Among 9-subsituted derivatives, one showed much higher selectivity for the δ receptor in binding assays than the δ antagonist methylnaltrindole (**6**: $K_i = 42$ nM; μ/δ and $\kappa/\delta > 238$ on rat brain membranes) and antagonist properties. This compound was labeled with carbon-11 ($t_{1/2} = 20.4$ min) as a potential radioligand for the noninvasive assessment of δ opioid receptors in vivo with positron emission tomography (PET). A high yielding radiosynthesis of **[^{11}C]-6**, based on the [^{11}C]methyl introduction on the pyridine moiety by a Stille reaction, was described (radiochemical yield = 60 ± 10%, specific activities = 0.8 to 1.5 Ci/μmol). The in vivo pharmacological profile in rats indicated that the radiotracer crossed the blood−brain barrier but was not stable and underwent rapid degradation in both plasma and brain. No specific binding was consequently revealed.

INTRODUCTION

Opioid receptors are classified into μ, δ, and κ subtypes and belong to the superfamily of G protein-coupled receptors (GPCRs) that produce their effects by activation of intracellular Gi/Go proteins. Most endogenous opioids and synthetic ligands do not possess absolute specificity for a given opioid receptor subtype but interact with more than one specific site. The situation is further complicated by the fact that multiple receptor subtypes coexist within cerebral regions. The molecular cloning of μ-, δ-, and κ-opioid receptors (MOP−R, DOP−R, and KOP−R, respectively) showed that they share a high degree of amino acid sequence similarity (65%), and only 35% confer selectivity (*1*−*3*).

The δ-opioid receptors play an important role in the modulation of nociceptive signaling encountered in animal models of pain (*2*). Moreover, δ agonist administration or DOP−R deficient mice studies confirmed that δ receptors are involved in emotional responses such as depressive-like behavior and anxiety. These receptors are implicated in some aspects of morphine tolerance and dependence (*4*) with limited contribution compared with μ receptors (*2*). δ-Opioid agonists do not display side effects usually observed with κ-opioid agonists such as dysphoria, diuresis, and locomotor impairment. Despite δ-opioid receptor involvement in several clinically relevant diseases and syndromes such as analgesia, addiction, Parkinson's, Alzheimer's, and seizure disorders (*1*−*8*), their precise role in humans is incompletely understood.

Positron emission tomography (PET) and single photon emission computed tomography (SPECT) are unique and complementary imaging techniques for in vivo assessment of drug distribution and interaction with biochemical target systems (*9*). They are well-adapted for the exploration of brain function in healthy and disease conditions and crucial tools for clinical research and diagnosis. PET is a quantitative and very sensitive method, but it requires high-cost facilities due to the use of tracers labeled with cyclotron-produced positron emitters (carbon-11, $t_{1/2} = 20.4$ min; florine-18, $t_{1/2} = 109.7$ min). SPECT has coarser spatial and temporal resolution, reduced sensitivity, and less quantification capability; however, it uses commercially available γ-emitter radionuclides of relatively long half-lives (iodine-123, $t_{1/2} = 13.2$ h; technetium-99m, $t_{1/2} = 6$ h) and thus is routinely employed in nuclear medicine centers.

Among opiate radioligands already available for PET imaging (*5*, *7*, *10*), only the antagonist [^{11}C]-methylnaltrindole ([^{11}C]-MeNTI) allows visualization of δ-opioid receptors in the human brain (*11*, *12*). In vitro, it displays a very high affinity for δ-opioid receptor and moderate affinities for μ and κ receptors, respectively (Chart 1) (*13*, *14*). The most recently selectivities reported by Clayson et al. (*14*) were 81 for δ over μ and 17 for δ over κ and were less attractive than values (700 for δ over μ and >3000 for δ over κ) determined by Portoghese et al. (*13*), who used a nonspecific radioligand ([^{3}H]-DADLE) associated

Chart 1. Opioid Receptor Binding of Naltrindole and Methylnaltrindole[a]

compound	Ki, nM δ	μ	κ	references
methylnaltrindole	0.02	14	65	13
	0.49	39.2	8.33	14
naltrindole	0.03	3.8	332	13
	0.15	27.5	14.3	14

[a] Opioid receptor affinities of naltrindole and methylnaltrindole were determined by displacement of radioligands from guinea pig brain membranes. In Portoghese's study (*13*), binding to δ receptors was evaluated with [^{3}H]-DADLE in the presence of 1 μM DAMGO, to μ receptors with [^{3}H]-DAMGO, and to κ receptors with [^{3}H]-EK in the presence of 1 μM DAMGO; while in Clayson's study (*14*), binding to δ receptors was evaluated with [^{3}H]-DPDPE, to μ receptors with [^{3}H]-DAMGO, and to κ receptors with [^{3}H]-U69,593.

* Corresponding author. Phone: (33)231470224. Fax: (33)-231470275. E-mail: barre@cyceron.fr; debruyne@cyceron.fr.

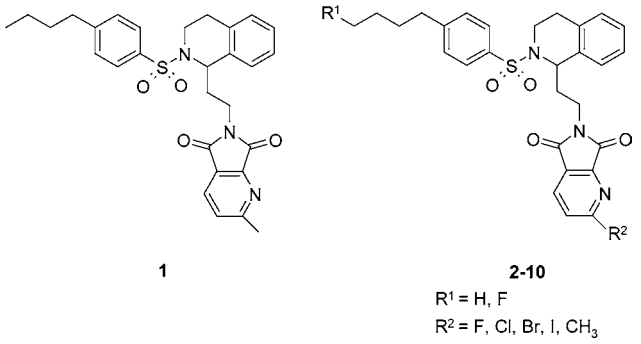
† UMR CEA 2E.

‡ UMR IFREMER 100.

§ These authors have contributed equally to this work.

10.1021/bc0602836 CCC: $37.00 © 2007 American Chemical Society
Published on Web 03/07/2007

Chart 2. Lead Compound and Target Molecules



to an excess of μ-specific ligand (DAMGO) to approach δ selectivity. In vivo, mice brain studies with [^{11}C]-MeNTI (*15*) established δ selectivity by competition with naltrindole whose binding characteristics are similar to those of MeNTI (Chart 1). Moreover, in behavior assays, the selective κ-opioid receptor antagonist, norbinaltorphimine, inhibited MeNTI antinociceptive effects significantly (*16*). Although this radioligand is metabolically stable and allows visualization of δ sites in the human brain (*5*, *7*, *10*−*12*), ligands with improved selectivity would be desirable for δ-opioid receptor imaging studies.

The development of a unique tracer for PET or SPECT requires the presence, in the same structure, of atoms (C, F, I) that can be substituted for their positron (^{11}C, ^{18}F) or γ (^{123}I)-emitting isotope.

Recently, a new series of N-substituted quinolinimide derivatives has been reported (*19*). They displayed synthetic accessibility, nanomolar affinity, and selectivity (IC_{50} μ > 10 000 and IC_{50} κ > 1000 nM) for δ-opioid receptors much higher than previous synthetic ligands (naltrindole (*13*), TAN 67 (*17*), SNC 80 (*18*)). Among them, compound **1** represents the most promising compound with an affinity of 6 nM (IC_{50} δ) for the cloned human DOP−R. From this new structural class and the associated structure−activity relationship (SAR) studies, we have investigated the incorporation of a halogen atom on the butyl chain and/or on the 2-position of the pyridine ring (Chart 2). The binding characteristics (K_i) of the new synthesized compounds **2**−**10** toward the three μ, δ, and κ receptor subtypes were determined and permitted the selection of the most promising compound **6**. Radiosynthesis of **6** was developed, its δ agonist/antagonist activity was performed using the [^{35}S]-GTPγS binding assay, and its in vivo behavior including metabolism, organ uptake, regional brain distribution, and specific binding were investigated in the rat.

EXPERIMENTAL PROCEDURES

Chemistry. *General Procedure for the Synthesis of **2**, **3**, and **6**−**8**.* A mixture of sulfonamide **13**−**14** and aldehyde **21**−**23** in trifluoroacetic acid (4 mL) was stirred at reflux for 7 h under nitrogen. The reaction mixture was quenched with ice and water (11 mL). The product was extracted with dichloromethane (3 × 10 mL). The combined organic layers were washed with saturated aqueous solution of $NaHCO_3$, dried ($MgSO_4$), and the solvents evaporated.

6-{2-[2-(4-Butylbenzenesulfonyl)-1,2,3,4-tetrahydroisoquinolin-1-yl]-ethyl}-2-chloropyrrolo[3,4-*b*]pyridine-5,7-dione (**2**). Starting from sulfonamide **13** (511 mg, 1.61 mmol) and aldehyde **21** (499 mg, 2.09 mmol), the crude compound was purified by chromatography on silica gel (7:3 heptanes/ethyl acetate) to afford a white solid; mp 84−86 °C; yield 658 mg (76%); ^{1}H NMR ($CDCl_3$) δ 8.09 (d, J = 8.0 Hz, 1H), 7.61 (d, J = 8.0 Hz, 1H), 7.54 (d, J = 8.3 Hz, 2H), 7.10−6.90 (m, 5H), 6.78 (d, J = 7.4 Hz, 1H), 5.06 (dd, J = 5.0 Hz, J = 9.6 Hz, 1H), 4.00−3.80 (m, 3H), 3.65−3.45 (m, 1H), 2.80−2.40 (m, 4H), 2.30−2.00 (m, 2H), 1.44 (qu, J = 7.6 Hz, 2H), 1.19 (sextet, J = 7.2 Hz, 2H), 0.84 (t, J = 7.2 Hz, 3H); ^{13}C NMR ($CDCl_3$) δ 165.2, 165.0, 158.0, 152.2, 148.2, 137.3, 135.4, 133.4, 132.5, 128.95, 128.8, 128.5, 127.0, 126.9, 126.7, 126.3, 126.0, 54.6, 38.9, 36.2, 35.3, 35.0, 33.0, 25.7, 22.0, 13.8; IR (KBr) 1784, 1719, 1336, and 1162 cm^{-1}; MS (EI) *m*/*z* (%) 340 (16), 329 (41), 328 (100), 197 (16), 133 (39), 91 (25); Anal. ($C_{28}H_{28}ClN_3O_4S$) C, H, N.

2-Bromo-6-{2-[2-(4-butylbenzenesulfonyl)-1,2,3,4-tetrahydroisoquinolin-1-yl]-ethyl}-pyrrolo[3,4-*b*]pyridine-5,7-dione (**3**). Starting from sulfonamide **13** (432 mg, 1.36 mmol) and aldehyde **22** (500 mg, 1.76 mmol), the crude compound was purified by chromatography on silica gel (7:3 heptanes/ethyl acetate) to afford a white solid; mp 88−90 °C; yield 607 mg (76%); ^{1}H NMR ($CDCl_3$) δ 7.99 (d, J = 8.0 Hz, 1H), 7.80 (d, J = 8.0 Hz, 1H), 7.57 (d, J = 8.3 Hz, 2H), 7.15−6.90 (m, 5H), 6.80 (d, J = 7.4 Hz, 1H), 5.08 (dd, J = 9.5 Hz, J = 5.1 Hz, 1H), 4.05−3.85 (m, 3H), 3.65−3.50 (m, 1H), 2.60−2.40 (m, 4H), 2.30−2.00 (m, 2H), 1.48 (qu, J = 7.6 Hz, 2H), 1.23 (sextet, J = 7.3 Hz, 2H), 0.87 (t, J = 7.2 Hz, 3H); ^{13}C NMR ($CDCl_3$) δ 165.3, 164.9, 152.4, 149.0, 148.2, 137.4, 135.4, 132.8, 132.6, 132.2, 128.9, 128.8, 127.0, 126.9, 126.7, 126.3, 126.2, 54.6, 38.9, 36.3, 35.3, 35.1, 33.0, 25.7, 22.0, 13.8; IR (KBr) 1784, 1717, 1331, and 1154 cm^{-1}; MS (EI) *m*/*z* (%) 386 (15), 384 (15), 330 (22), 329 (66), 328 (100), 197 (13), 133 (36), 91 (23); Anal. ($C_{28}H_{28}BrN_3O_4S$) C, H, N.

6-(2-{2-[4-(4-Fluorobutyl)-benzenesulfonyl]-1,2,3,4-tetrahydroisoquinolin-1-yl}-ethyl)-2-methyl-pyrrolo[3,4-*b*]pyridine-5,7-dione (**6**). Starting from sulfonamide **14** (187 mg, 0.55 mmol) and aldehyde **23** (165 mg, 0.75 mmol), the crude compound was purified by chromatography on silica gel (1:1 heptanes/ethyl acetate) to afford a white solid; mp 76−78 °C; yield 224 mg (76%); ^{1}H NMR ($CDCl_3$) δ 8.02 (d, J = 7.8 Hz, 1H), 7.61 (d, J = 8.3 Hz, 2H), 7.44 (d, J = 7.8 Hz, 1H), 7.15−6.95 (m, 5H), 6.81 (d, J = 7.3 Hz, 1H), 5.10 (dd, J = 9.7 Hz, J = 5.0 Hz, 1H), 4.40 (dt, J = 47.0 Hz, J = 5.5 Hz, 2H), 4.05−3.90 (m, 3H), 3.70−3.50 (m, 1H), 2.76 (s, 3H), 2.61 (t, J = 7.4 Hz, 2H), 2.55−2.45 (m, 2H), 2.30−2.05 (m, 2H), 1.75−1.50 (m, 4H); ^{19}F NMR ($CDCl_3$) δ −219.05; ^{13}C NMR ($CDCl_3$) δ 166.8, 166.5, 166.0, 151.85, 148.3, 138.0, 135.6, 132.6, 131.2, 129.0, 128.9, 127.3, 127.1, 127.0, 126.9, 126.4, 124.9, 83.8 (d, J = 165.0 Hz), 54.8, 38.9, 36.0, 35.4, 35.2, 29.6 (d, J = 19.8 Hz), 26.6 (d, J = 4.9 Hz), 25.9, 25.0; IR (KBr) 1779, 1723, 1335, and 1162 cm^{-1}; MS (EI) *m*/*z* (%) 348 (24), 347 (74), 346 (100), 321 (14), 320 (58), 215 (16), 158 (12), 151 (79), 132 (14), 131 (11), 130 (28), 109 (18), 103 (11), 92 (12), 91 (37), 90 (10); Anal. ($C_{29}H_{30}FN_3O_4S$) C, H, N.

6-(2-{2-[4-(4-Fluorobutyl)-benzenesulfonyl]-1,2,3,4-tetrahydroisoquinolin-1-yl}-ethyl)-2-chloro-pyrrolo[3,4-*b*]pyridine-5,7-dione (**7**). Starting from sulfonamide **14** (450 mg, 1.34 mmol) and aldehyde **21** (416 mg, 1.74 mmol), the crude compound was purified by chromatography on silica gel (3:2 heptanes/ethyl acetate) to afford a white solid; mp 84−86 °C; yield 618 mg (83%); ^{1}H NMR ($CDCl_3$) δ 8.09 (d, J = 8.0 Hz, 1H), 7.62 (d, J = 8.0 Hz, 1H), 7.59 (d, J = 8.3 Hz, 2H), 7.15−6.95 (m, 5H), 6.81 (d, J = 7.4 Hz, 1H), 5.08 (dd, J = 9.5 Hz, J = 5.1 Hz, 1H), 4.40 (dt, J = 47 Hz, J = 5.5 Hz, 2H), 4.05−3.85 (m, 3H), 3.70−3.50 (m, 1H), 2.60 (t, J = 7.4 Hz, 2H), 2.55−2.45 (m, 2H), 2.30−2.05 (m, 2H), 1.75−1.50 (m, 4H); ^{19}F NMR ($CDCl_3$) δ −219.06; ^{13}C NMR ($CDCl_3$) δ 165.2, 164.9, 158.1, 152.2, 148.2, 137.7, 135.4, 133.2, 132.5, 128.9, 128.8, 128.4, 127.2, 126.9, 126.7, 126.4, 126.0, 83.7 (d, J = 165.0 Hz), 54.6, 38.9, 36.2, 35.1, 29.6 (d, J = 19.7 Hz), 26.6 (d, J = 4.8 Hz), 25.8; IR (KBr) 1784, 1732, 1335, and 1161 cm^{-1}; MS (EI) *m*/*z* (%) 348 (11), 347 (34), 346 (100), 215 (10), 151 (32), 130 (11), 91 (14); Anal. ($C_{28}H_{27}ClFN_3O_4S$) C, H, N.

2-Bromo-6-(2-{2-[4-(4-fluorobutyl)-benzenesulfonyl]-1,2,3,4-tetrahydroisoquinolin-1-yl}-ethyl)-pyrrolo[3,4-*b*]pyridine-5,7-dione (**8**). Starting from sulfonamide **14** (154 mg, 0.46 mmol) and aldehyde **22** (169 mg, 0.59 mmol), the crude compound was purified by chromatography on silica gel (1:1 heptanes/ethyl acetate) to afford a white solid; mp 88−90 °C; yield 218 mg (76%); ^{1}H NMR ($CDCl_3$) δ 7.99 (d, J = 8.0 Hz, 1H), 7.80 (d, J = 8.0 Hz, 1H), 7.58 (d, J = 8.3 Hz, 2H), 7.10−6.95 (m, 5H), 6.81 (d, J = 7.4 Hz, 1H), 5.08 (dd, J = 9.5 Hz, J = 5.1 Hz, 1H), 4.40 (dt, J = 47.0 Hz, J = 5.5 Hz, 2H), 4.05−3.85 (m, 3H), 3.65−3.50 (m, 1H), 2.61 (t, J = 7.4 Hz, 2H), 2.55−2.45 (m, 2H), 2.30−2.05 (m, 2H), 1.75 (m, 4H); ^{19}F NMR ($CDCl_3$) δ −219.06; ^{13}C NMR ($CDCl_3$) δ 165.3, 164.9, 152.4, 149.1, 147.2, 137.6, 135.4, 132.7, 132.5, 132.2, 128.9, 128.8, 127.1, 127.0, 126.7, 126.4, 126.3, 83.7 (d, J = 165.0 Hz), 54.6, 38.91, 36.3, 35.2, 35.1, 29.6 (d, J = 19.7 Hz), 26.6 (d, J = 4.8 Hz), 25.8; IR (KBr) 1784, 1723, 1335, and 1162 cm^{-1}; MS (EI) *m*/*z* (%) 386 (12), 384 (12), 348 (17), 347 (51), 346 (100), 215 (12), 151 (43), 130 (16), 91 (14), 86 (11), 84 (16); Anal. ($C_{28}H_{27}BrFN_3O_4S$) C, H, N.

*General Procedure for the Synthesis of **4** and **9***. A mixture of chlorinated sulfonamide **2** or **7** (186 μmol), potassium fluoride (558 μmol), and Kryptofix 222 (186 μmol) in DMSO (820 μL) was heated at 120 °C for 3 h under nitrogen. The reaction mixture was then quenched with water (18 mL). The aqueous phase was thoroughly extracted with ethyl acetate (2 × 24 mL), and the combined organic layers were washed with water (2 × 30 mL), dried ($MgSO_4$), and the solvents evaporated. The crude compound was purified by chromatography on silica gel.

6-{2-[2-(4-Butylbenzenesulfonyl)-1,2,3,4-tetrahydroisoquinolein-1-yl]-ethyl}-2-fluoropyrrolo[3,4-*b*]pyridine-5,7-dione (**4**). Chromatography 3:2 heptanes/ethyl acetate; yield 68 mg (70%) from **2** (100 mg, 186 μmol); white solid; mp 72−74 °C; ^{1}H NMR ($CDCl_3$) δ 8.25 (dd, J = 8.2 Hz, J = 6.7 Hz, 1H), 7.57 (d, J = 8.3 Hz, 2H), 7.24 (dd, J = 8.2 Hz, J = 1.4 Hz, 1H), 7.15−6.95 (m, 5H), 6.81 (d, J = 7.3 Hz, 1H), 5.09 (dd, J = 9.6 Hz, J = 5.0 Hz, 1H), 4.05−3.80 (m, 3H), 3.70−3.50 (m, 1H), 2.60−2.40 (m, 4H), 2.30−2.00 (m, 2H), 1.48 (qu, J = 7.5 Hz, 2H), 1.22 (sextet, J = 7.3 Hz, 2H), 0.87 (t, J = 7.2 Hz, 3H); ^{19}F NMR ($CDCl_3$) δ −58.80; ^{13}C NMR ($CDCl_3$) δ 167.7 (d, J = 253.0 Hz), 165.0, 164.9, 151.4 (d, J = 15.0 Hz), 148.2, 137.4, 136.2 (d, J = 10.0 Hz), 135.4, 132.6, 128.9, 128.9, 127.0, 126.9, 126.7, 126.3, 125.5 (d, J = 4.0 Hz), 114.3 (d, J = 37.0 Hz), 54.6, 38.9, 36.3, 35.3, 35.2, 33.0, 25.8, 22.0, 13.8; IR (KBr) 1782, 1722, 1335, and 1163 cm^{-1}; MS (EI) *m*/*z* (%) 330 (20), 329 (61), 328 (100), 324 (29), 197 (18), 133 (52), 130 (13), 91 (29); Anal. ($C_{28}H_{28}FN_3O_4S$) C, H, N.

6-(2-{2-[4-(4-Fluorobutyl)-benzenesulfonyl]-1,2,3,4-tetrahydroisoquinolin-1-yl}-ethyl)-2-fluoropyrrolo[3,4-*b*]pyridine-5,7-dione (**9**). Chromatography 55:45 heptanes/ethyl acetate; yield 97 mg (68%) from **7** (100 mg, 180 μmol); white solid; mp 72−74 °C; ^{1}H NMR ($CDCl_3$) δ 8.26 (dd, J = 8.2 Hz, J = 6.7 Hz, 1H), 7.59 (d, J = 8.3 Hz, 2H), 7.24 (dd, J = 8.2 Hz, J = 1.4 Hz, 1H), 7.15−6.95 (m, 5H), 6.81 (d, J = 7.4 Hz, 1H), 5.08 (dd, J = 9.6 Hz, J = 5.0 Hz, 1H), 4.40 (dt, J = 47.0 Hz, J = 5.5 Hz, 2H), 4.05−3.85 (m, 3H), 3.70−3.50 (m, 1H), 2.60 (t, J = 7.4 Hz, 2H), 2.55−2.45 (m, 2H), 2.30−2.00 (m, 2H), 1.75−1.50 (m, 4H); ^{19}F NMR ($CDCl_3$) δ −58.80, −219.05; ^{13}C NMR ($CDCl_3$) δ 167.7 (d, J = 252.0 Hz), 165.0, 164.9, 151.4 (d, J = 16.0 Hz), 147.2, 137.7, 136.2 (d, J = 10.0 Hz), 135.4, 132.5, 129.0, 128.9, 127.1, 126.9, 126.7, 126.3, 125.5 (d, J = 4.0 Hz), 114.3 (d, J = 37.0 Hz), 83.7 (d, J = 165.0 Hz), 54.6, 38.9, 36.2, 35.2, 35.1, 29.6 (d, J = 19.7 Hz), 26.6 (d, J = 5.0 Hz), 25.8; IR (KBr) 1783, 1728, 1336, and 1162 cm^{-1}; MS (EI) *m*/*z* (%) 347 (22), 346 (100), 320 (11), 236 (15), 215 (10), 152 (13), 151 (30), 130 (11), 129 (10), 123 (12), 111 (18), 110 (13), 109 (15), 98 (15), 97 (31), 91 (15), 85 (17), 84 (16), 83 (32), 82 (19), 81 (22), 71 (25), 70 (13); Anal. ($C_{28}H_{27}F_2N_3O_4S$) C, H, N.

*General Procedure for the Synthesis of **5** and **10***. Method A: To a solution of **2** or **7** (93 μmol) and sodium iodide (279 μmol) in acetonitrile (300 μL) was added chlorotrimethylsilane (96 μmol) under nitrogen. The reaction mixture was stirred at reflux for 3 h, then was quenched with water (3 mL). The aqueous phase was thoroughly extracted with dichloromethane (3 × 3 mL). The combined organic layers were washed with a 0.4 N aqueous solution of sodium hydroxide (5 mL) and water (5 mL), dried ($MgSO_4$), and the solvents evaporated. The crude residue was purified by semipreparative HPLC (μ-BondaPak C18 column, 7.8 × 300 mm, 10 μm; flow rate, 5 mL/min; λ = 254 nm). For **5**: eluent CH_3CN/H_2O (50:50, v/v), t_R = 25.20 min; yield 33 mg, 56% from **2** (50 mg, 93 μmol). For **10**: eluent CH_3CN/H_2O (45:55, v/v) t_R = 22.10 min; yield 34 mg, 58% from **7** (50 mg, 90 μmol).

Method B: A solution of iodine in chloroform (30 mL, 0.1 N, 3 mmol) was added dropwise to a stirred solution of **24** or **25** (1.5 mmol) in chloroform (30 mL). The reaction mixture was stirred for 5 h at room temperature. The reaction mixture was quenched with saturated aqueous solution of $Na_2S_2O_3$ (100 mL), and the product was extracted with chloroform (3 × 50 mL). The combined organic layers were washed with water (100 mL), dried ($MgSO_4$), and the solvents evaporated. The crude residue was purified by chromatography on silica gel. For **5**: eluent 7:3 heptanes/ethyl acetate; yield 445 mg, 46% from **24** (1 g, 1.5 mmol); For **10**: eluent 6:4 heptanes/ethyl acetate; yield 790 mg, 52% from **25** (1.6 g, 2.34 mmol).

6-{2-[2-(4-Butylbenzenesulfonyl)-1,2,3,4-tetrahydroisoquinolin-1-yl]-ethyl}-2-iodopyrrolo[3,4-*b*]pyridine-5,7-dione (**5**). White solid; mp 94−96 °C; ^{1}H NMR ($CDCl_3$) δ 8.04 (d, J = 7.9 Hz, 1H), 7.76 (d, J = 7.9 Hz, 1H), 7.56 (d, J = 8.3 Hz, 2H), 7.10−6.90 (m, 5H), 6.80 (d, J = 7.4 Hz, 1H), 5.07 (dd, J = 9.6 Hz, J = 5.2 Hz, 1H), 4.00−3.80 (m, 3H), 3.65−3.45 (m, 1H), 2.60−2.40 (m, 4H), 2.30−2.00 (m, 2H), 1.47 (qu, J = 7.6 Hz, 2H), 1.20 (sextet, J = 7.2 Hz, 2H), 0.89 (t, J = 7.2 Hz, 3H); ^{13}C NMR ($CDCl_3$) δ 165.5, 164.9, 152.4, 148.2, 138.7, 137.3, 135.3, 132.5, 131.6, 128.9, 128.7, 126.9, 126.8, 126.6, 126.4, 126.2, 125.0, 54.5, 38.8, 36.1, 35.3, 35.0, 32.9, 25.7, 22.9, 13.8; IR (KBr) 1781, 1724, 1334, and 1161 cm^{-1}; MS (EI) *m*/*z* (%) 431 (11), 329 (22), 328 (100), 197 (8), 133 (21), 91 (16); Anal. ($C_{28}H_{28}IN_3O_4S$) C, H, N.

6-(2-{2-[4-(4-Fluorobutyl)-benzenesulfonyl]-1,2,3,4-tetrahydroisoquinolin-1-yl}-ethyl)-2-iodopyrrolo[3,4-*b*]pyridine-5,7-dione (**10**). White solid; mp 94−96 °C; ^{1}H NMR ($CDCl_3$) δ 8.05 (d, J = 7.9 Hz, 1H), 7.76 (d, J = 7.9 Hz, 1H), 7.58 (d, J = 8.3 Hz, 2H), 7.15−6.95 (m, 5H), 6.81 (d, J = 7.4 Hz, 1H), 5.08 (dd, J = 9.5 Hz, J = 5.2 Hz, 1H), 4.40 (dt, J = 47.0 Hz, J = 5.5 Hz, 2H), 4.05−3.85 (m, 3H), 3.65−3.50 (m, 1H), 2.60 (t, J = 7.4 Hz, 2H), 2.55−2.45 (m, 4H), 2.30−2.05 (m, 2H), 1.75−1.50 (m, 4H); ^{19}F NMR ($CDCl_3$) δ −219.05; ^{13}C NMR ($CDCl_3$) δ 165.9, 164.9 152.5, 147.2, 138.7, 137.7, 135.3, 132.5, 131.6, 128.9, 128.7, 127.1, 126.9, 126.7, 126.4, 126.3, 125.0, 83.6 (d, J = 165.0 Hz), 54.6, 38.9, 36.2, 35.0, 29.6 (d, J = 19.7 Hz), 26.5 (d, J = 4.9 Hz), 24.0; IR (KBr) 1781, 1719, 1334, and 1161 cm^{-1}; MS (EI) *m*/*z* (%) 347 (21), 346 (100), 320 (15), 215 (9), 151 (31), 130 (14), 109 (11), 97 (15), 96 (11), 95 (11), 91 (23), 85 (10), 84 (13), 83 (17), 82 (11), 81 (14), 71 (13); Anal. ($C_{28}H_{27}FIN_3O_4S$) C, H, N.

*General Procedure for the Synthesis of **24** and **25***. Compound **2** or **7** (1.33 mmol) and hexamethylditin (662 mg, 2 mmol) were dissolved in dry dioxane (11 mL), and a catalytic amount of tetrakis(tripheylphosphine)palladium (78 mg, 67 μmol) was added. The mixture was refluxed with stirring for 2 h under a nitrogen atmosphere. After cooling, the reaction mixture was

filtered through celite. The filtrate was concentrated under reduced pressure. The oily residue was then purified by chromatography on silica gel.

6-{2-[2-(4-Butylbenzenesulfonyl)-1,2,3,4-tetrahydroisoquinolin-1-yl]-ethyl}-2-trimethylstannanylpyrrolo[3,4-*b*]pyridine-5,7-dione (**24**). Chromatography heptanes/ethyl acetate 8:2; yield 544 mg, 61% from **2** (718 mg, 1.33 mmol); white solid; mp 86−88 °C; ^{1}H NMR ($CDCl_3$) δ 7.92 (d, J = 7.4 Hz, 1H), 7.74 (d, J = 7.4 Hz, 1H), 7.59 (d, J = 8.3 Hz, 2H), 7.15−6.95 (m, 5H), 6.81 (d, J = 7.3 Hz, 1H), 5.10 (dd, J = 9.7 Hz, J = 5.1 Hz, 1H), 4.05−3.85 (m, 3H), 3.70−3.50 (m, 1H), 2.60−2.45 (m, 4H), 2.30−2.00 (m, 2H), 1.48 (qu, J = 7.7 Hz, 2H), 1.21 (sextet, J = 7.0 Hz, 2H), 0.86 (t, J = 7.2 Hz, 3H), 0.40 (s, 9H); ^{13}C NMR ($CDCl_3$) δ 182.8, 167.1, 166.8, 151.4, 148.1, 137.4, 135.5, 134.4, 132.5, 128.9, 128.7, 127.4, 127.0, 126.8, 126.7, 126.2, 125.8, 54.6, 38.8, 35.8, 35.3, 33.0, 25.8, 22.9, 13.8, −9.0; ^{119}Sn NMR ($CDCl_3$) δ −35.4; IR (KBr) 1779, 1728, 1336, and 1162 cm^{-1}; Anal. ($C_{31}H_{37}N_3O_4SSn$) C, H, N.

6-(2-{2-[4-(4-Fluorobutyl)-benzenesulfonyl]-1,2,3,4-tetrahydroisoquinolin-1-yl}-ethyl)-2-trimethylstannanylpyrrolo[3,4-*b*]-pyridine-5,7-dione (**25**). Chromatography heptanes/ethyl acetate 7:3; yield 181 mg (69%) from **7** (213 mg, 380 μmol); white solid; mp 86−88 °C; ^{1}H NMR ($CDCl_3$) δ 7.92 (d, J = 7.4 Hz, 1H), 7.74 (d, J = 7.4 Hz, 1H), 7.60 (d, J = 8.3 Hz, 2H), 7.15−6.95 (m, 5H), 6.81 (d, J = 7.4 Hz, 1H), 5.10 (dd, J = 9.5 Hz, J = 5.1 Hz, 1H), 4.40 (dt, J = 47 Hz, J = 5.7 Hz, 2H), 4.05−3.85 (m, 3H), 3.70−3.50 (m, 1H), 2.60 (t, J = 7.3 Hz, 2H), 2.55−2.45 (m, 2H), 2.30−2.05 (m, 2H), 1.75−1.50 (m, 4H), 0.41 (s, 9H); ^{19}F NMR ($CDCl_3$) δ −218.5; ^{13}C NMR ($CDCl_3$) δ 178.1, 167.3, 167.0, 151.6, 147.3, 138.0, 135.6, 133.2, 132.7, 129.1, 128.9, 127.6, 127.3, 127.0, 126.9, 126.4, 126.04, 83.8 (d, J = 165.0 Hz), 54.8, 39.0, 36.0, 35.5, 35.2, 29.8 (d, J = 19.7 Hz), 26.7 (d, J = 5.0 Hz), 26.0, −8.8; ^{119}Sn NMR ($CDCl_3$) δ −35.3; IR (KBr) 1779, 1722, 1336, and 1162 cm^{-1}; Anal. ($C_{31}H_{36}N_3O_4FSSn$) C, H, N.

6-(2-{2-[4-(4-Fluorobutyl)-benzenesulfonyl]-1,2,3,4-tetrahydroisoquinolin-1-yl}-ethyl)-2-tributylstannanylpyrrolo[3,4-*b*]pyridine-5,7-dione (**26**). Compound **10** (675 mg, 1.04 mmol) and hexabutylditin (1.91 g, 3.12 mmol) were dissolved in dry toluene (12 mL), and a catalytic amount of tetrakis(tripheylphosphine)-palladium (91 mg, 78 μmol) was added. The mixture was refluxed with stirring for 24 h under a nitrogen atmosphere. After cooling, the reaction mixture was filtered through celite. The filtrate was concentrated under reduced pressure. The oily residue was then purified by chromatography on silica gel (8:2 heptanes/ethyl acetate) to afford **26** (340 mg, 40%) as a yellow viscous oil. ^{1}H NMR ($CDCl_3$) δ 7.89 (d, J = 7.4 Hz, 1H), 7.69 (d, J = 7.4 Hz, 1H), 7.62 (d, J = 8.2 Hz, 2H), 7.15−6.95 (m, 5H), 6.81 (d, J = 7.4 Hz, 1H), 5.10 (dd, J = 9.7 Hz, J = 5.0 Hz, 1H), 4.40 (dt, J = 47 Hz, J = 5.7 Hz, 2H), 4.05−3.85 (m, 3H), 3.70−3.50 (m, 1H), 2.60 (t, J = 7.3 Hz, 2H), 2.55−2.45 (m, 4H), 2.30−2.05 (m, 2H), 1.75−1.50 (m, 4H), 1.40−1.15 (m, 12H), 0.87 (t, J = 7.2 Hz, 9H); ^{19}F NMR ($CDCl_3$) δ −218.5; ^{13}C NMR ($CDCl_3$) δ 185.0, 167.4, 167.2, 151.5, 148.1, 138.0, 135.7, 135.1, 132.7, 129.1, 128.9, 127.3, 127.2, 127.0, 126.9, 126.4, 125.8, 83.8 (d, J = 165.0 Hz), 54.8, 39.0, 35.9, 35.5, 35.2, 29.8 (d, J = 19.8 Hz), 29.1, 27.4, 26.7 (d, J = 5.0 Hz), 26.0, 13.8, 10.5; IR (KBr) 1778, 1722, 1337 and 1162 cm^{-1}.

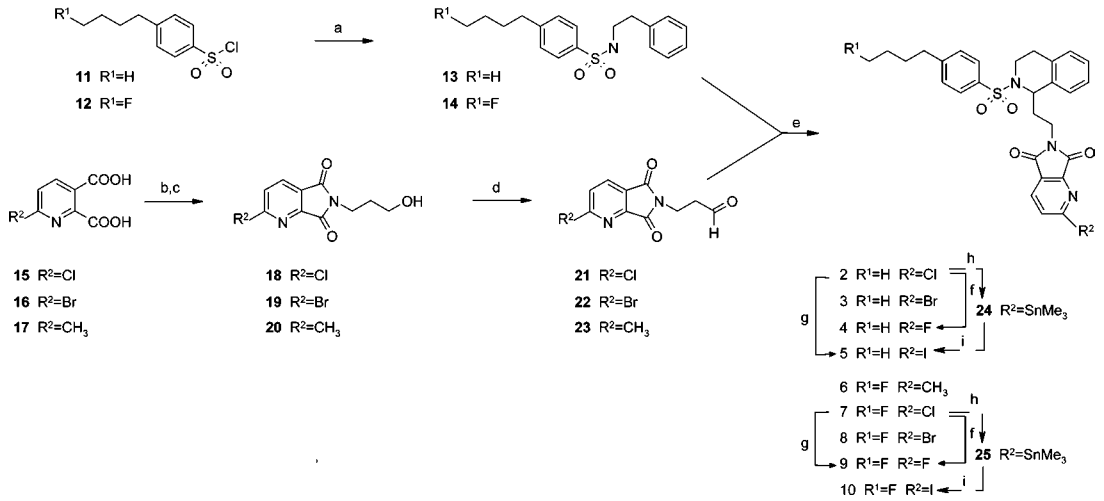
In Vitro Assays. *Membrane Preparations.* Membrane preparations and radioligand binding assays were performed according to a method previously described (*19*). Brain without cerebellum was removed from a male Wistar rat or a Hartley guinea pig and homogenized in 10 volumes (w/v) of ice-cold 50 mM Tris−HCl buffer (pH 7.4 at 4 °C) using an ultra-turax. The homogenate was centrifuged at 45 000 *g* for 15 min at 4 °C. The pellet was resuspended by homogenization in 10 volumes of ice-cold buffer (4 °C). To remove endogenous opioids that might interfere with the radioligand binding assays, the membranes were incubated at 30 °C for 30 min in a shaking water bath, recentrifuged, and resuspended in 10 volumes of ice-cold buffer. Protein concentration was measured according to the method of Bradford (*53*), using bovine serum albumin (BSA) as the standard. Membranes were stored frozen at −80 °C at a final concentration of 1 g/L with 0.1 g/L bacitracin (ICN Biomedicals, U.S.A.).

Binding Assays. Receptor binding assays were performed with crude membranes from rat (μ- and δ-opioid receptors) or guinea pig (κ-opioid receptors) brain homogenates using [^{3}H]-DAMGO as μ-selective radioligand (67 Ci/mmol, Amersham Biosciences, U.K.), [^{3}H]-deltorphin II (33.9 Ci/mmol, Perkin-Elmer Life Sciences, U.S.A.) as δ-selective radioligand and [^{3}H]-U69.593 as κ-selective radioligand (47.5 Ci/mmol, Perkin-Elmer Life Sciences, U.S.A.). The time to reach steady state was previously determined by kinetic studies and stated as 60 min for μ and κ ligands and 90 min for δ ligand. The dissociation constant (K_d) and the maximum number of binding sites (B_{max}) for each tritiated ligand were obtained using preliminary saturation binding experiments. Competitive binding experiments were then carried out on membranes (300 μg of proteins) with a constant concentration of radioligand corresponding to the dissociation rate (K_d) previously measured. Membranes were incubated with 1.9 nM [^{3}H]-DAMGO, 0.6 nM [^{3}H]-deltorphin II, or 2.6 nM [^{3}H]-U69.593 in a total volume of 1 mL incubation buffer containing 50 mM Tris−HCl, pH 7.4, 0.1 g/L bacitracin, and 1 g/L BSA. Various concentrations of test compounds 10^{-12} to 10^{-5} M (naloxone, naltrindole, deltorphin II, DAMGO, or U50.488; SIGMA RBI, U.S.A.) were added separately to incubation medium for 60 min at 25 °C. 10 mM $MgCl_2$, 5 mM EDTA, and 90 min incubation time were necessary for [^{3}H]-deltorphin II. Incubations were stopped by rapid filtration with a Filtermate Universal Harvester (Perkin-Elmer Life Sciences, U.S.A.) through Unifilter-24 GF/B Microplates that were presoaked for at least 60 min in 0.5% polyethylenimine (PEI). Membranes were washed three times with ice-cold 50 mM Tris−HCl, pH 7.4 at 4 °C, and bound radioactivity (dpm) determined using liquid scintillation counting (TopCount NXT Microplate Scintillation, Perkin-Elmer Sciences, U.S.A.). Nonspecific binding was determined for each ligand in the presence of 10 μM naloxone (Sigma RBI, U.S.A.).

Concentration−response curves for each compound were run using data of duplicate samples from at least two independent experiments using curve-fitting procedures in *SigmaPlot* (Jandel Scientific, Germany, 2001). The best nonlinear regression was obtained with a three-parameter logistic equation showing a single set of binding sites. Specific binding was determined by subtracting nonspecific binding from total binding. Percent inhibition of specific binding was determined for each concentration of compounds. The IC_{50} values, defined as the concentration required inhibiting 50% of the specific binding, were obtained from concentration−response curves. The K_i values were calculated using the following equation: $K_i = IC_{50}/(1 + [L]/K_d)$ according to Cheng and Prusoff (*54*).

[^{35}S]GTP-γ-S Functional Assay. The [^{35}S]GTP-γ-S binding assays were performed according to the methods previously described with slight modifications (*55*, *56*). Rat brain membranes (10 μg of proteins) were suspended in 1 mL of buffer containing 50 mM Tris−HCl, pH 7.4, 1 mM EGTA, 3 mM $MgCl_2$, 60 μM GDP, 0.05 nM [^{35}S]GTP-γ-S (1250 Ci/mmol, Perkin-Elmer Life Sciences, U.S.A.), and varying concentrations of naltrindole, deltorphin II, and compounds **1** and **6** (10^{-10} to 10^{-5}M). The reaction mixtures were incubated for 60 min at 30 °C (equilibrium). The reactions were terminated by rapid vacuum filtration through Unifilter-24 GF/B microplates previously soaked in ice-cold Tris−HCl, pH 7.4 at 4 °C. The filters

Scheme 1. Syntheses of 2−10[a]



[a] Reagents and conditions: (a) 2-phenylethylamine, pyridine, rt; (b) $SOCl_2$ or AcO_2, reflux; (c) 3-aminopropanol, toluene, NEt_3, reflux; (d) IBX, EtOAc, 80 °C; (e) TFA, reflux; (f) KF, K_{222}, DMSO, 120 °C; (g) TMSCl, NaI, CH_3CN, reflux; (h) Me_6Sn_2, $Pd(PPh_3)_4$, dioxane, reflux; (i) I_2, $CHCl_3$, rt.

were washed three times with ice-cold Tris−HCl, pH 7.4 at 4 °C, and then dried. The radioactivity retained on the filters was measured by liquid scintillation counting using a TopCount NXT Microplate Scintillation (Perkin-Elmer Sciences). Nonspecific binding was determined in the presence of 10 μM GTP-γ-S. Concentration−response curves for each compound were run using data of duplicate samples from at least two independent experiments using curve-fitting procedures in *SigmaPlot*. [^{35}S]-GTP-γ-S binding is expressed as percentage of basal level.

Radiosynthesis of [^{11}C]-6. In a vial (1 mL) purged with nitrogen and containing tris(dibenzylideneacetone)dipalladium-(0) (1.38 mg, 1.5 μmol) and tri-*o*-tolylphosphine (1.88 mg, 6.0 μmol) was added DMF (150 μL). The reactor was cooled at 0 °C, and [^{11}C]methyl iodide was trapped, then the mixture was stirred for 3 min at room temperature. A freshly prepared solution of tin precursor **26** (3.1 mg, 3.75 μmol), potassium carbonate (0.83 mg, 6.0 μmol), and copper(I) chloride (0.60 mg, 6.0 μmol) in DMF (100 μL) was transferred in the vial containing the radioactivity solution. The resulting mixture was stirred vigorously and was heated to 90 °C for 5 min. CH_2Cl_2 (800 μL) was added, and the radioactive solution was transferred into a cartridge (Chromabond PTS phase separation) containing 1 mL of CH_2Cl_2 and 5 mL of water. The isolated organic layer was injected onto semipreparative HPLC (Zorbax RX-SIL column 9.4 × 250 mm; mobile phase CH_2Cl_2/MeOH 99.75/0.25 v/v; flow 5 mL/min; λ = 254 nM). The fraction containing the labeled product **[^{11}C]-6** was collected at 6.30 min, the solvents were evaporated, and the residue was formulated in a sterile water/DMSO (50:50, v/v) solution. The final product was filtered through a 0.22 μm filter into a sterile vial. Routinely, **[^{11}C]-6** was ready for injection in about 40 min in batches of 70−80 mCi. The radiochemical purity and specific activity were determined by reverse-phase analytical HPLC (μ-Bondapak C18 column 4.6 × 250 mm; mobile phase CH_3CN/H_2O 70/30 v/v; flow rate 1 mL/min; λ = 254 nM).

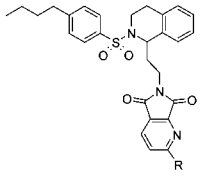
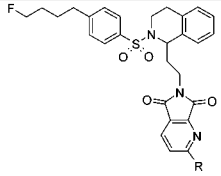
Octanol/Water Partition Coefficient. Apparent drug lipophilicity was determined by a conventional partition method between 1-octanol phase and phosphate-buffered saline (PBS), pH 7.4. Briefly, 1-octanol was mixed into PBS for 20 min, then the labeled compound was added. The tube was sealed and vigorously shaken at room temperature for 40 min. The mixture was then centrifuged at 3000 *g* for 5 min. An aliquot (100 μL) from each phase was removed, and the radioactivity was counted in a γ-counter (Cobra 2 gamma counter, Packard). The log $P_{oct/PBS}$ was calculated as follows: log $P_{oct/PBS}$ = log(radioactivity concentration in the 1-octanol phase/radioactivity concentration in the PBS phase). The reported value represents the mean of six measurements in duplicate.

Ex Vivo Experiments. *Animals.* Sprague−Dawley male rats weighing 250 to 300 g were used in all experiments. The animals were kept at constant temperature (22 °C) and humidity (50%) with 12 h light/dark cycles and were allowed free access to food and water until the time of the experiments. The anesthesia was induced with 5% isoflurane in a gas mixture of nitrous oxide/oxygen (70/30%) and maintained with 1.5−2.5% isoflurane during the entire surgical procedure. Body temperature was monitored rectally and kept close to 37 °C. Catheters were inserted into the femoral vein and artery. Animal experimental procedures were in accordance with the recommendations of the EEC (86/609/EEC), the French National Committee (decret 87/848), for the care and use of laboratory animals and were approved by the Normandy Regional Animal Ethics Committee (saisine 01/04/2005).

Biodistribution Studies. Rats were injected with **[^{11}C]-6** (0.3−0.7 mCi; 0.6−1.4 nmol) in DMSO/water solution (v/v 50/50; 200 μL) and were sacrificed at 3, 5, 10, and 30 min postinjection (n = 3 per time). Whole brain and peripheral organs were quickly dissected at 4 °C. The radioactivity of weighed tissue samples was measured in a γ-counter (Cobra 2 gamma counter, Packard). For the measurements of the cerebral distribution, the animals were decapitated at 3, 10, and 30 min (n = 3 per time) after **[^{11}C]-6** injection (0.7 ± 0.1 mCi, ∼1.4 nmol) in DMSO/water solution (v/v 70/30; 500 μL). Brains were quickly removed and dissected out on an ice-cold plate to obtain the regions of interest. These regions were weighed and counted. For blocking and competition experiments, naloxone (1 mg/ kg) or unlabeled **6** (1.3 mg/ kg) were administrated either 15 min prior to radiotracer or by coinjection, respectively. Data were expressed as the percentage of the injected dose (decay-corrected) per gram of tissue (% ID/g).

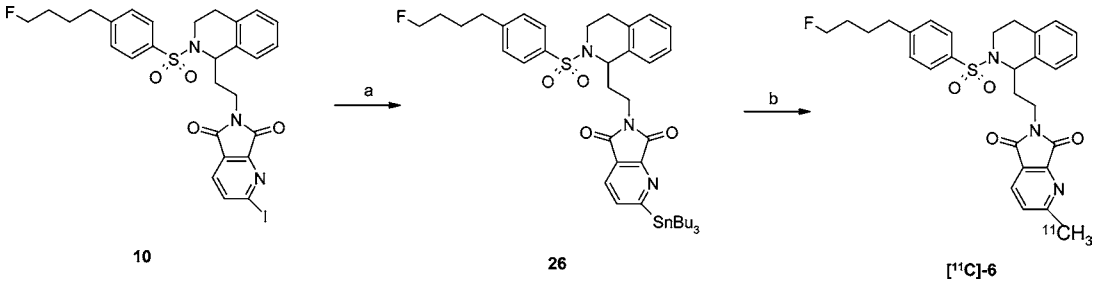
Metabolite Analysis from Brain Homogenate and Plasma. Brain radiometabolite analysis was carried out on half-brain crushed in 2.5 mL acetonitrile (UltraTurrax T25, Janke and Kunkel) after injection of **[^{11}C]6**. After centrifugation (4100 *g*, 7 min), supernatants were filtered and injected onto HPLC (reverse-phase μ-Bondapak C18 column 7.8 × 300 mm; mobile phase CH_3CN/H_2O 70:30 v/v; flow rate 5 mL/min; λ = 254 nM). Plasma metabolite analysis was carried out on intracardiac blood samples (1 mL). Following centrifugation (3000 *g*, 5 min), plasma was mixed with an equivalent volume of acetonitrile

Table 1. Opioid Receptor Binding of Target Molecules 1−10 and Reference Compounds[a]

	Compounds	N°	R	Ki ± SEM (nM)			Selectivity	
				[^{3}H]-DAMGO (μ)	[^{3}H]-deltorphin II (δ)	[^{3}H]-U69,593 (κ)	μ/δ	κ/δ
References	Naloxone			6.8 ± 0.6	72 ± 7	8.4 ± 0.8	0.1	0.1
	Naltrindole			55 ± 12	0.3 ± 0.1	17.8 ± 2.2	182	59
	Deltorphin II			2840 ± 319	1.4 ± 0.2	1943 ± 173	2029	1388
	DAMGO			6.1 ± 1.9	832 ± 26	929 ± 275	0.007	1.1
	U50,488			1508 ± 465	1241 ± 156	1.5 ± 0.4	1.2	0.001
Target molecules		**1**	CH_3	>10000	82 ± 9	>10000	>122	>122
		2	Cl	>10000	235 ± 39	>10000	>43	>43
		3	Br	>10000	322 ± 8	>10000	>31	>31
		4	F	>10000	289 ± 38	>10000	>35	>35
		5	I	>10000	192 ± 3	>10000	>52	>52
		**6**	CH_3	>10000	42 ± 8	>10000	>238	>238
		7	Cl	>10000	202 ± 14	>10000	>49	>49
		8	Br	>4000	152 ± 3	>10000	>26	>66
		9	F	>10000	131 ± 15	>10000	>76	>76
		10	I	>10000	112 ± 6	>10000	>89	>89

[a] $n = 2$ in duplicate; mean ± SEM.

Scheme 2. Radiosynthesis of [^{11}C]-6[a]



[a] Reagents and conditions: (a) Bu_6Sn_2, $Pd(PPh_3)_4$, toluene, reflux, 24 h; (b) [^{11}C]CH_3I, Pd_2dba_3:P(*o*-tol)$_3$ (1:4), K_2CO_3, CuCl, DMF, 90 °C, 5 min.

and centrifuged (3000 *g*, 7 min). Supernatants were filtered and injected onto HPLC as described above. The retention times of a [^{11}C] polar metabolite and **[^{11}C]6** were 2.5 and 5.5 min respectively. The [^{11}C] polar metabolite fraction was collected (from three experiments in competition condition) at 30 min and analyzed by a microLC-ESI-MS/MS apparatus. After evaporation of the HPLC solvents, the samples were resuspended in 10 μL of 0.1% formic acid in water and injected onto a C18 Thermo Hypersil column (50 × 0.5 mm, 3 μm) with an acetonitrile linear gradient of 4% per minute in 0.1% formic acid, from 2% to 90%. A split ratio of 30:1 was used to perfuse the column at a flow rate of 10 μL/min. The HPLC column was rinsed with 90% acetonitrile in 0.1% formic acid between each injection. The HPLC Surveyor chain was connected on-line to an orthogonal electrospray source (Deca XP MS-n Thermofinnigan) operated in the positive electrospray ionization mode (ESI+). The ions were focused into an ion trap, capable of MS and MS/MS analyses. The mass spectra were acquired over 35 ms from *m*/*z* 30 to 2000. The capillary exit of the electrospray ion source was set at 70 V, the octapole at 3 V, and the capillary temperature at 200 °C. A counterflow of nitrogen was used as a nebulizing gas. An Xcalibur data system was used to acquire the data, which were further processed with the Turbo Sequest data system.

Data Analysis. **[^{11}C]-6** uptake values in the different experimental conditions were analyzed by two-way ANOVA. When the differences between groups were greater than expected by chance, a multiple comparison Tukey's test or Fisher LSD method was used to isolate the divergent group(s); a value of $p < 0.05$ was considered statistically significant.

RESULTS AND DISCUSSION

Chemistry. Syntheses of novel analogues **2**−**10** are shown in Scheme 1. The strategy was based on the Pictet−Spengler cyclization of sulfonamides **13** and **14** with aldehydes **21**−**23**. The sulfonyl chlorides **11** and **12** were achieved by chlorosulfonation of butylbenzene and (4-fluorobutyl)benzene (*20, 21*) with chlorosulfonic acid in chloroform at room temperature (*22, 23*) and were obtained in 91% and 43% yields, respectively; the moderate yield registered for compound **12** was due to a competitive substitution reaction of the fluorine atom by the chlorine atom. The formation of the sulfonamides **13** and **14** was obtained quantitatively by the reaction of sulfonyl chlorides **11** and **12** with 2-phenylethylamine in pyridine at room temperature (*19*, *24*).

Quinolinic acids **15** and **16** were used as starting materials in the syntheses of aldehydes **21**−**23** and were synthesized by oxidation with ruthenium tetraoxide of their corresponding halogenated quinolines (*25*). Dehydration of quinolinic acids **15**−**17** with thionyl chloride (*26*) or acetic anhydride (*27*) into quinolinic anhydrides followed, without purification, by the

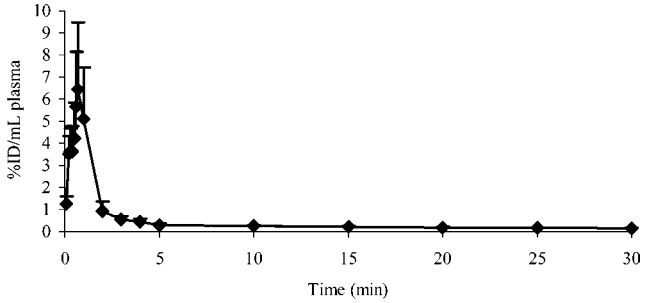


Figure 1. Radioactive kinetics in rat plasma after **[^{11}C]-6** intravenous injection; $n = 3$ at each time, mean ± SEM.

reaction with 3-aminopropanol, in the presence of triethylamine and in toluene at reflux (*28*, *29*), afforded the alcohols **18**−**20** in 46−55% yields. Initially, the aldehyde **21** was synthesized by a Swern oxidation in a poor yield (24%) and a degradation on silica gel column (*30*, *31*). To overcome this drawback, the oxidation of alcohols was performed with *o*-iodoxybenzoic acid (IBX) (*32*, *33*), a mild oxidant, in EtOAc at 80 °C, and the aldehydes **21**−**23** were isolated, without further purification, in excellent yields (95−100%). N-Substituted quinolinimides **2**, **3**, and **6**−**8** were obtained in 70−83% yields by the Pictet−Spengler reaction of sulfonamides **13** and **14** with aldehydes **21**−**23** in trifluoroacetic acid at reflux (*19*, *34*). Syntheses of N-substituted quinolinimides **4**, **5**, **9**, and **10** were undertaken by direct halogen/halogen exchange reaction from chlorinated compounds **2** and **7**. The fluorinated compounds **4** and **9** were prepared in 68−70% yields, using anhydrous potassium fluoride in the presence of Kryptofix in DMSO (*35*). Sodium iodide in acetyl chloride allowed the transformation of chlorinated compound **2** to its iodinated analogue **5** in only a poor yield (18%) (*36*). The reaction conducted with sodium iodide/chlorotrimethylsilane (*37*) was shown to be more efficient, and iodinated compounds **5** and **10** were isolated by HPLC in 56−58% yields. This method was not well adapted to obtain the compounds in large amounts; for this purpose, an alternative synthesis from chlorinated compounds **2** and **7** was used where a stannylation (*38*)/iododestannylation (*39*) reaction sequence permitted isolation of the iodinated compounds **5** and **10** in 28% and 37% overall yields.

In Vitro Studies. *Binding Assays.* In vitro binding studies of quinolinimides **1**−**10** were assessed either from rat brain membranes using [^{3}H]-DAMGO (μ) and [^{3}H]-deltorphin II (δ) or from guinea pig brain membranes using [^{3}H]-U69,593 (κ). The inhibition constants (K_i) were calculated from the IC_{50} values determined on the concentration−response curves. The results are summarized in Table 1. The values were compared with those obtained for five ligands of reference, which are as follows: naloxone, which does not really discriminate between the three opioid receptor subtypes; the selective antagonist naltrindole (δ); and the selective agonists deltorphin II (δ), DAMGO (μ), and U50,488 (κ). In the present experiments, K_i values for ligands chosen as references were found to be in agreement with previoulsy reported data (*1*, *14*, *19*, *40*−*42*).

Previously, the affinity of the lead compound **1** toward δ-opioid receptors was obtained by displacement of [^{3}H]-naltrindole from crude membranes from CHO cells stably expressing the human δ-opioid receptor cDNA (*19*) (IC_{50} δ = 6nM). We chose to evaluate the affinity and the selectivity of this compound using rat brain membranes considering our following in vivo experiment conditions. With this less selective biological material than cloned cells, the K_i value of **1** was 82 ± 9 nM, but its excellent selectivity was confirmed. Data in Table 1 show that the introduction on the lead compound **1** of a halogen instead of a methyl group in the 2-position of the pyridine ring results in a lower δ affinity and selectivity (compounds **2**−**5**). Then, we investigated the effect of the introduction of a fluorine atom on the butyl chain and observed that the affinities of compounds **6** and **8**−**10** were approximately 2-fold greater than those of compounds **1** and **3**−**5** at δ and with a slightly improved selectivity. Considering compounds **5**

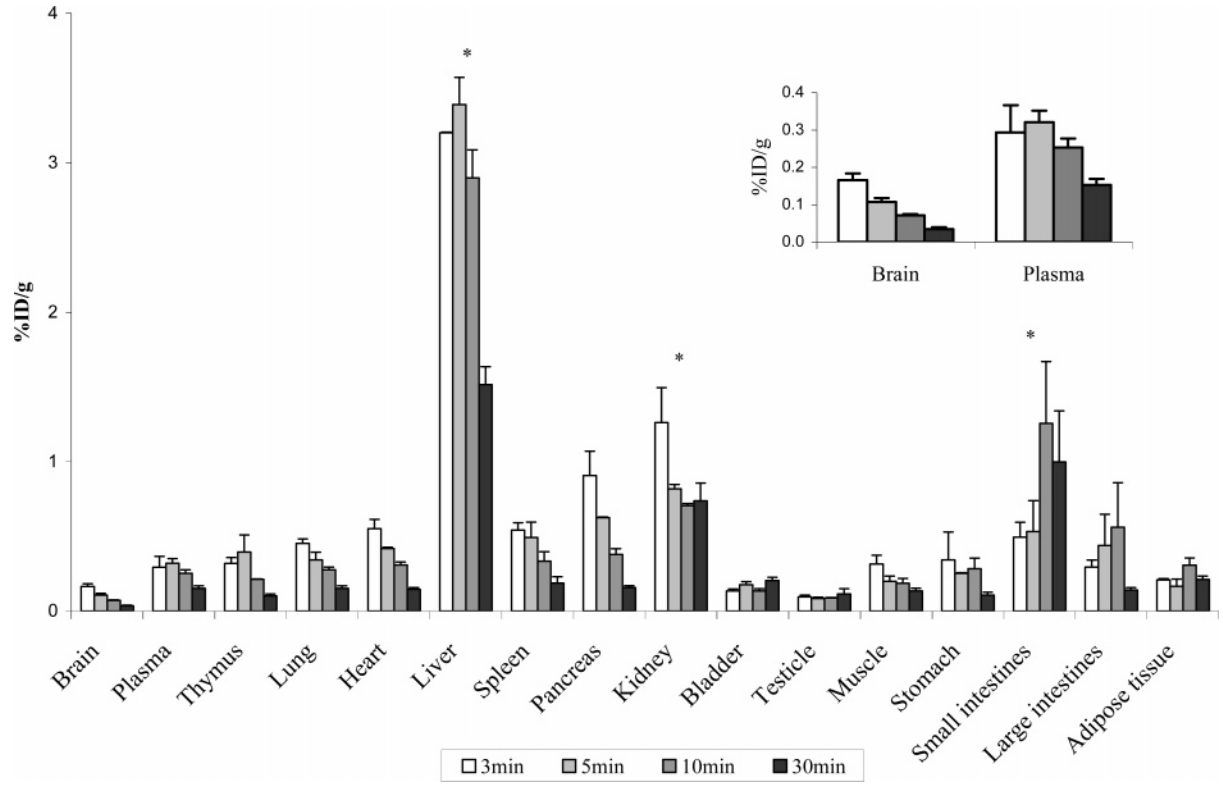


Figure 2. Radioactivity distribution in various tissues after intravenous administration of **[^{11}C]-6** in the rat; $n = 3$, mean ± SEM, * ANOVA $p < 0.001$, and post hoc Tukey's test $p < 0.001$.

Table 2. Percentage of Unchanged [^{11}C]-6 in Rat Brain and Plasma[a]

	3 min	5 min	10 min	30 min
brain	91 ± 3	71 ± 10	62 ± 4	41 ± 4
plasma	61 ± 9	40 ± 10	46 ± 8	22 ± 2

[a] Mean ± SEM; $n = 3$ for each determination.

and **10** possessing an iodine atom that could be substituted by a γ ^{123}I isotope, the low affinities registered ($K_i \approx 112-192$ nM) led us to delay the development of a radioligand for SPECT studies. Compound **6** showed a better selectivity over μ and κ receptors (μ/δ and $\kappa/\delta > 238$) than that described by Clayson (*14*) for methylnaltrindole ($\mu/\delta = 81$ and $\kappa/\delta = 17$) and the best affinity among the series ($K_i = 42 \pm 8$ nM). The lack of very specific PET radioligands for human brain δ opioid receptor imaging led us, in spite of a moderate affinity, to develop **6** as a potential tracer. We considered that a lower affinity could not be a handicap if the injected tracer dose was lower than the δ receptor density in the CNS, and the high selectivity could contribute to an increase of the signal-to-noise ratio. The introduction on this structure of either a carbon-11 isotope via [^{11}C]CH_3I on the pyridine moiety or a fluorine-18 isotope on the butyl chain could be considered.

GTP-γ-S Functional Assays. The relative efficacies of selected compound **6** and lead compound **1** were characterized using the [^{35}S]GTPγS assay. Data show the agonist and antagonist properties of these compounds, together with naltrindole ($E_{max} = 102 \pm 1\%$) and deltorphin II ($E_{max} = 129 \pm 1\%$), in stimulating [^{35}S]GTPγS binding mediated by the δ-opioid receptor on rat brain membranes. Compound **1** produced intermediate maximal stimulation of [^{35}S]GTPγS binding ($E_{max} = 110 \pm 2\%$) that confirmed the weak analgesic activity described by Barn (*19*), while compound **6** produced low maximal stimulation ($E_{max} = 104 \pm 3\%$) similar to that of the antagonist naltrindole.

Radiochemistry. Having in our hands compound **10** which could allow, via a stannane precursor, the introduction of [$^{11}CH_3$]I by a Stille reaction (*43*−*45*), we have developed the labeling of **6** with carbon-11 instead of fluorine-18 with the aim of evaluating **[^{11}C]-6** as a PET tracer (Scheme 2). The tributylstannane **26** was obtained in 40% yield from the corresponding 2-iodo derivative **10** by a palladium-catalyzed cross-coupling reaction using hexabutyltin and a catalytic amount of tetrakis(triphenylphosphine)palladium(0) in toluene (*46*). [^{11}C]Methyl iodide, obtained from the reduction of [^{11}C]-carbon dioxide, was trapped in a vial containing tris(dibenzylideneacetone)dipalladium(0) and tri-*o*-tolylphosphine in DMF; then, a freshly prepared solution of precursor **26**, potassium carbonate, and copper(I) chloride in DMF was added. The vial was heated to 90 °C for 5 min before purification on a semipreparative HPLC column. Typical syntheses provided 70−80 mCi (uncorrected) of **[^{11}C]-6** in an average decay-corrected yield of 60 ± 10% calculated from [^{11}C]methyliodide in a total synthesis time of 40 min, including radioligand formulation for intravenous administration. The radiolabeled product was over 98% radiochemically pure, determined by analytical HPLC, and the specific activity ranged from 0.8 to 1.5 Ci/μmol at EOS.

Lipophilicity. Frequently, the selection of a candidate PET radioligand has been done on the basis of the affinity value and selectivity, leading to poor results when its lipophilicity was too high. On the other hand, it is well-understood that an optimal lipophilicity (log *P* near 2) of a drug is required for good blood−brain barrier permeability. The experimental log *P* of **[^{11}C]-6** was obtained by the octanol/water partition coefficient, as detailed in the Experimental Section, and showed a good log *P* value (2.49 ± 0.03).

Ex Vivo Studies. Male Sprague−Dawley rats served for preliminary in vivo evaluation of pharmacokinetics. The injected dose calculated with the present specific radioactivity was lower than the δ-opioid receptor density described in the rat brain (*47*). Figure 1 depicts the **[^{11}C]-6** plasma kinetics where an early peak was registered (6.5% ID/mL at 1 min), followed by very short distribution ($t_{1/2} \approx 1$ min) and fast elimination ($t_{1/2} = 20$ min) phases. Figure 2 shows the organ distribution of **[^{11}C]-6** between 3 and 30 min postinjection. The accumulation was highest in liver > kidneys > small intestines and lowest in testicles and bladder; the radioactivity levels decreased in all tissues from 3 to 30 min except in small intestines.

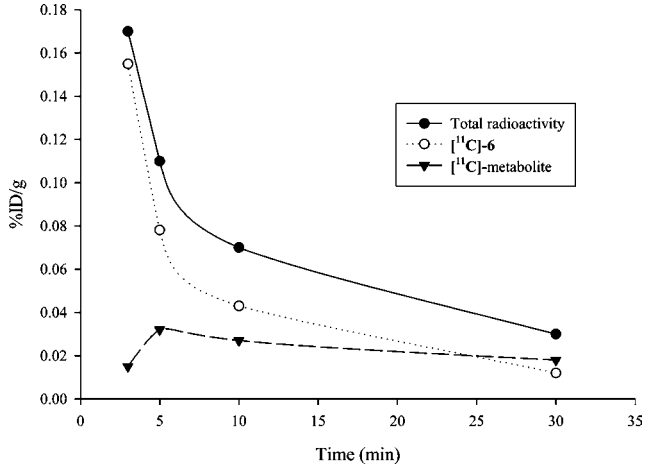


Figure 3. Time course for radioactivity expressed as % ID/g in brain after intravenous injection of **[^{11}C]-6** in rat.

The brain uptake ranged from 0.17 ± 0.02% ID/g at 3 min to 0.04 ± 0.003% ID/g at 30 min. This relatively low uptake does not correlate with the lipophilicity of **[^{11}C]-6**, which predicted a good blood−brain barrier crossing. It could be explained by a strong affinity for plasma proteins, minimizing the drug delivery to the brain. The stability of **[^{11}C]-6** was determined in brain homogenates and plasma samples. The radiochromatograms obtained from HPLC analysis exhibited two radioactive peaks, one corresponding to **[^{11}C]-6** and the other to a polar radioactive compound. Sequential studies revealed the progressive appearance of this labeled metabolite in brain and plasma (Table 2), already present at 3 min and reaching 30 min after tracer injection 59% and 88% of total radioactivity, respectively. These results led to the pharmacokinetic profiles of the parent compound and metabolite shown in Figure 3. The polar radioactive compound identified as a metabolite M1 was isolated and analyzed by LC/MS/MS. Mass spectral analysis revealed an intense protonated molecular ion at *m*/*z* 518.1 ([M + H]$^+$). The MS data tentatively assigned M1 as a structure close to either dehydrated or dehalogenated parent compound **6** (MS = 535.1), which suggested a stability of the parent compound-based structure. The MS/MS analysis of *m*/*z* 518.1 provided informative product ions at *m*/*z* 321, attributed to the phthalimido tetrahydroisoquinolinium moiety, and at *m*/*z* 356, corresponding to the benzenesulfonyl tetrahydroisoquinolinium moiety (Figure 4).

The regional brain distribution was studied at 3, 10, and 30 min. The anatomical regions of interest were selected and identified using the atlas of Paxinos and Watson (*48*), i.e., olfactory tubercles, striatum, frontal cortex, hypothalamus, cerebellum, thalamus, and hippocampus (*49*, *50*). The corpus callosum devoid of receptor was used as an indicator of the nonspecific binding. The uptake values and the region/corpus callosum ratios for selected regions are shown in Table 3. In the control condition, data indicated significant uptake of **[^{11}C]-6** at 3 min, higher in frontal cortex, olfactory tubercles, thalamus, hypothalamus, striatum ($p < 0.05$), and cerebellum ($p < 0.001$) than in corpus callosum. δ-Opioid receptors are known to be

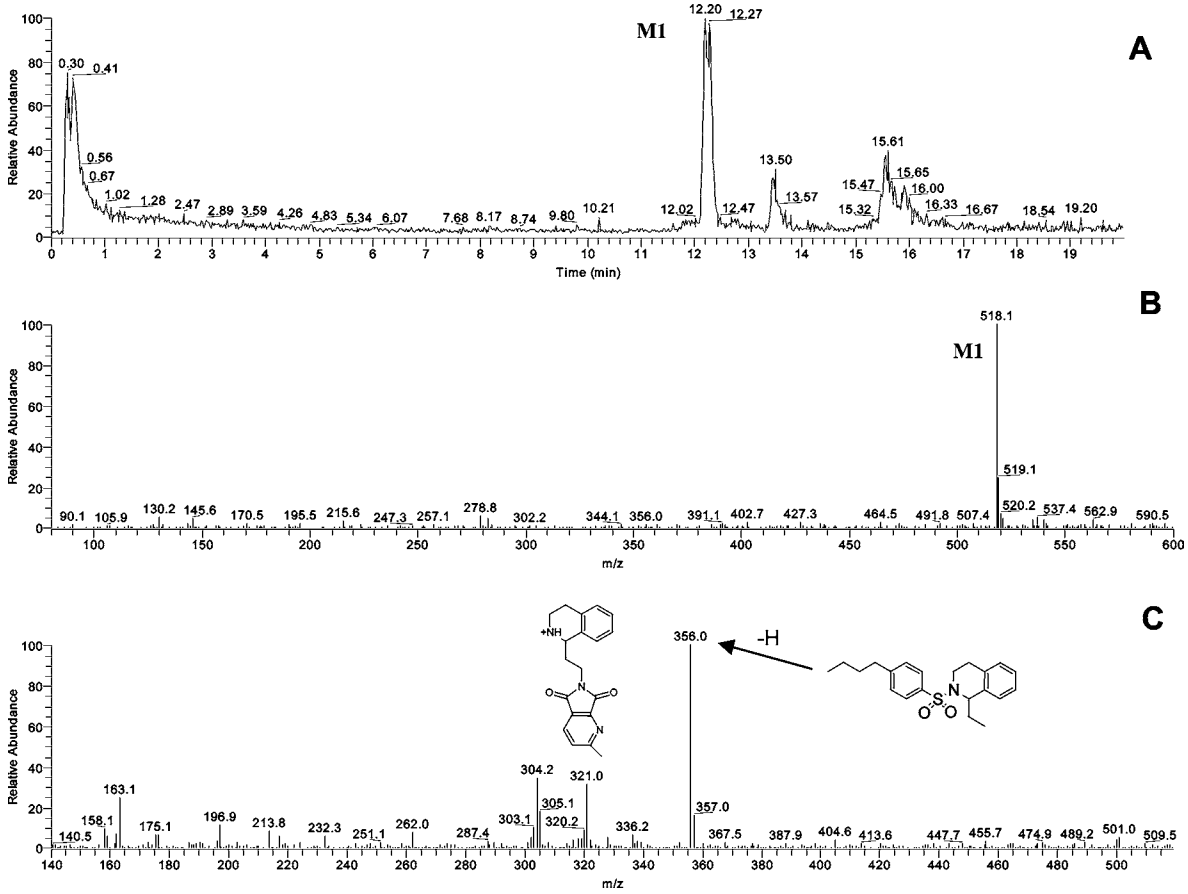


Figure 4. MicroLC-ESI-MS/MS analysis of the radiometabolite. (A) Chromatogram of the isolated radiometabolite sample revealing one main peak at 12.20 retention time. (B) MS spectrum showing the *m*/*z* 518.1 corresponding to the peak eluted at 12.20 min. (C) MS/MS spectrum of the *m*/*z* 518.1.

Table 3. [^{11}C]-6 Regional Brain Uptake in Rats[a]

	control condition			coinjection condition[b]			blocking condition[c]	
region	3 min	10 min	30 min	3 min	10 min	30 min	3 min	10 min
				Regional brain distribution (% ID/g)				
cerebellum	0.14 ± 0.01	0.09 ± 0.01	0.05 ± 0.01	0.64 ± 0.14	0.25 ± 0.06	0.05 ± 0.01	0.13 ± 0.01	0.11 ± 0.01
olfactory tubercle	0.12 ± 0.01	0.09 ± 0.01	0.05 ± 0.01	0.67 ± 0.18	0.31 ± 0.09	0.04 ± 0.01	0.11 ± 0.02	0.12 ± 0.01
hypothalamus	0.11 ± 0.01	0.10 ± 0.01	0.05 ± 0.01	0.65 ± 0.18	0.37 ± 0.13	0.05 ± 0.01	0.10 ± 0.02	0.13 ± 0.02
hippocampus	0.10 ± 0.01	0.09 ± 0.01	0.04 ± 0.01	0.54 ± 0.14	0.29 ± 0.09	0.04 ± 0.01	0.09 ± 0.01	0.12 ± 0.02
striatum	0.11 ± 0.01	0.10 ± 0.01	0.06 ± 0.01	0.62 ± 0.17	0.30 ± 0.08	0.04 ± 0.01	0.11 ± 0.02	0.12 ± 0.02
thalamus	0.12 ± 0.01	0.09 ± 0.01	0.05 ± 0.01	0.69 ± 0.19	0.31 ± 0.10	0.04 ± 0.01	0.11 ± 0.01	0.12 ± 0.01
frontal cortex	0.12 ± 0.01	0.09 ± 0.01	0.04 ± 0.01	0.62 ± 0.15	0.23 ± 0.06	0.03 ± 0.01	0.11 ± 0.02	0.10 ± 0.01
corpus callosum	0.08 ± 0.01	0.09 ± 0.01	0.07 ± 0.01	0.42 ± 0.12	0.29 ± 0.06	0.05 ± 0.01	0.06 ± 0.02	0.11 ± 0.02
				Ratio to Corpus Callosum				
cerebellum	1.82 ± 0.26	0.95 ± 0.09	0.77 ± 0.08	1.64 ± 0.20	0.88 ± 0.03	0.91 ± 0.13	2.33 ± 0.50	1.10 ± 0.12
olfactory tubercle	1.43 ± 0.05	0.98 ± 0.07	0.83 ± 0.11	1.62 ± 0.07	1.07 ± 0.08	0.71 ± 0.19	1.85 ± 0.38	1.14 ± 0.14
hypothalamus	1.42 ± 0.11	1.04 ± 0.13	0.82 ± 0.05	1.56 ± 0.04	1.20 ± 0.17	1.12 ± 0.34	1.62 ± 0.24	1.20 ± 0.10
hippocampus	1.26 ± 0.14	0.92 ± 0.08	0.67 ± 0.08	1.32 ± 0.09	0.99 ± 0.10	0.81 ± 0.19	1.66 ± 0.34	1.11 ± 0.09
striatum	1.42 ± 0.14	1.02 ± 0.09	0.92 ± 0.10	1.51 ± 0.04	1.02 ± 0.06	0.83 ± 0.21	1.79 ± 0.32	1.15 ± 0.11
thalamus	1.47 ± 0.17	0.95 ± 0.11	0.73 ± 0.08	1.66 ± 0.05	1.06 ± 0.10	0.85 ± 0.13	1.94 ± 0.44	1.15 ± 0.13
frontal cortex	1.56 ± 0.20	0.92 ± 0.07	0.59 ± 0.16	1.54 ± 0.10	0.80 ± 0.05	0.64 ± 0.22	1.97 ± 0.39	0.96 ± 0.15

[a] Results are expressed as % ID/g of tissue (mean ± SEM; $n = 3$ for each determination). [b] Coinjection with cold compound **6** (1.3 mg/ kg). [c] Blocking with naloxone (1 mg/ kg).

highly confined in olfactory tubercles, striatum, and frontal cortex (*49*). In the cerebellum, significant levels were observed only in some studies (*50*). In thalamus and hypothalamus, the present results disagreed with published data (*49*). These significant differences between cerebral regions disappeared at 10 and 30 min. These interstructural differences at 3 min could be explained by the influence of the cerebral blood flow on early radiotracer distribution. To address the nonspecific binding of **[^{11}C]-6** in vivo, displacement studies were carried out. Neither preadministration of naloxone (1 mg/kg, 15 min prior to radiotracer) nor coinjection of **[^{11}C]-6** with cold compound **6** (1.3 mg/kg) could significantly alter the tracer distribution. The coadministration of cold compound **6** caused a 5.4-fold increase in radioactivity uptake at 3 min and 3.2-fold at 10 min ($p < 0.001$) and return to baseline at 30 min. These results could be explained by the pharmacological effect of **6** characterized as a δ antagonist influencing the cerebral blood flow. Indeed, it was described that the injection of a high dose of naltrindole produced significant increases in heart rate and mean arterial pressure (*51*).

Kinetics studies of the radiotracer in the rat demonstrated a fast washout of the parent compound in blood as in the brain

mainly due to an extensive metabolism. In spite of the good selectivity of **6** for δ-opioid receptors in vitro and sufficient affinity with regard to δ-opioid receptor density in rat brain (*47*) (see recommended procedure (*52*)), significant specific binding could not be revealed. A possible interference of the [^{11}C] byproduct with other binding sites could contribute to an increase of the nonspecific binding. Further studies, using animal species more close to human relating to qualitative and/or quantitative metabolism pathways, could be envisaged.

CONCLUSION

On the basis of a series of N-substituted quinolinimide derivatives displaying nanomolar affinity on human cloned δ-opioid receptor and high selectivity for δ versus μ and κ opioid receptors, novel compounds possessing a halogen atom on the butyl chain and/or on the 2-position of the pyridine ring were synthesized in order to develop tracers for medical imaging. In vitro assays led us to consider compound **6** which displayed an affinity of 42 nM on rat brain membranes, a >238-fold selectivity for the δ over the μ and κ receptors, respectively, and antagonist properties, as a promising ligand for PET imaging. We reported a high yielding radiosynthesis of **[^{11}C]-6**, based on the [^{11}C]methyl introduction on the pyridine moiety by a Stille reaction. The radiochemical yield was 60 ± 10%, and the radiochemical purity exceeded 98%. In rats, in vivo evaluation clearly indicated that the radiotracer crossed the blood−brain barrier, but was not stable and underwent rapid metabolism in both plasma and brain. No specific binding was consequently revealed. Although the goal of identifying a new potential PET radioligand for δ-opioid receptors was not achieved, the proposed strategy is a starting point for future developments of more stable analogues.

ACKNOWLEDGMENT

This research has been supported through two grants from the CEA and the Conseil Regional de Basse Normandie. The authors wish to thank Mr. Olivier Tirel the cyclotron operator and Mr. Laurent Prieur, Mr. Laurent Chazalviel, and Mr. Ahmed Abbas who skillfully contributed to the in vivo studies.

Supporting Information Available: Additional experimental data on compounds **11**−**23**. This material is available free of charge via the Internet at http://pubs.acs.org/BC.

LITERATURE CITED

(1) Dhawan, B. N., Cesselin, F., Raghubir, R., Reisine, T., Bradley, P. B., Porthoghese, P. S., and Hamon, M. (1996) International union of pharmacology. XII. classification of opioid receptors. *Pharmacol. Rev. 48*, 567−592.

(2) Quock, R. M., Burkey, T. H., Varga, E., Hosohata, Y., Hosohata, K., Cowell, S. M., Slate, C. A., Ehlert, F. J., Roeske, W. R., and Yamamura, H. I. (1999) The δ-opioid receptor: molecular pharmacology, signal transduction, and the determination of drug efficacy. *Pharmacol. Rev. 51*, 503−532.

(3) Waldhoer, M., Bartlett, S. E., and Whistler, J. L. (2004) Opioid receptors. *Annu. Rev. Biochem. 73*, 953−990.

(4) Gavériaux-Ruff, C., and Kieffer, B. L. (2002) Opioid receptor genes inactivated in mice: the highlights. *Neuropeptides 36*, 62−71.

(5) Madar, I., Lesser, R. P., Krauss, G., Zubieta, J. K., Lever, J. R., Kinter, C. M., Ravert, H. T., Musachio, J. L., Mathews, W. B., Dannals, R. F., and Frost, J. J. (1997) Imaging of δ- and μ-opioid receptors in temporal lobe epilepsy by positron emission tomography. *Ann. Neurol. 41*, 358−367.

(6) Hudzik, T. J., Howell, A., Payza, K., and Cross, A. J. (2000) Antiparkinson potential of δ-opioid receptor agonists. *Eur. J. Pharmacol. 396*, 101−107.

(7) Koepp, M. J., and Duncan, J. S. (2000) PET: Opiate neuroreceptor mapping. *Adv. Neurol. 83*, 145−156.

(8) Mathieu-Kia, A. M., Fan, L. Q., Kreek, M. J., Simon, E. J., and Hiller, J. M. (2001) μ-, δ-, and κ-opioid receptor populations are differentially altered in distinct areas of postmortem brains of Alzheimer's disease patients. *Brain Res. 893*, 121−134.

(9) Gibson, R. E., Burns, H. D., Hamill, T. G., Eng, W. S., Francis, B. E., and Ryan, C. (2000) Non-invasive radiotracer imaging as a tool for drug development. *Curr. Pharm. Des. 6*, 973−989.

(10) Ravert, H. T., Bencherif, B., Madar, I., and Frost, J. J. (2004) PET imaging of opioid receptors in pain: progress and new directions. *Curr. Pharm. Des. 10*, 759−768.

(11) Madar, I., Lever, J. R., Kinter, C. M., Scheffel, U., Ravert, H. T., Musachio, J. L., Mathews, W. B., Dannals, R. F., and Frost, J. J. (1996) Imaging of δ opioid receptors in human brain by N1′-([^{11}C]-methyl)naltrindole and PET. *Synapse 24*, 19−28.

(12) Smith, J. S., Zubieta, J. K., Price, J. C., Flesher, J. E., Madar, I., Lever, J. R., Kinter, C. M., Dannals, R. F., and Frost, J. J. (1999) Quantification of δ-opioid receptors in human brain with N1′-([^{11}C]-methyl) naltrindole and positron emission tomography. *J. Cereb. Blood Flow Metab. 19*, 956−966.

(13) Portoghese, P. S., Sultana, M., and Takemori, A. E. (1990) Design of peptidomimetic δ opioid receptor antagonists using the message-address concept. *J. Med. Chem. 33*, 1714−1720.

(14) Clayson, J., Jales, A., Tyacke, R. J., Hudson, A. L., Nutt, D. J., Lewis, J. W., and Husbands, S. M. (2001) Selective δ-opioid receptor ligands: potential PET ligands based on naltrindole. *Bioorg. Med. Chem. Lett. 11*, 939−943.

(15) Lever, J. R., Scheffel, U., Kinter, C. M., Ravert, H. T., Dannals, R. F., Wagner, H. N., and Frost, J. J. (1992) In vivo binding of N1′-([^{11}C]methyl) naltrindole to δ-opioid receptors in mouse brain. *Eur. J. Pharmacol. 216*, 459−460.

(16) Takemori, A. E., Sultana, M., Nagase, H., and Portoghese, P. S. (1992) Agonist and antagonist activities of ligands derived from naltrexone and oxymorphone. *Life Sci. 50*, 1491−1495.

(17) Suzuki, T., Tsuji, M., Mori, T., Misawa, M., Endoh, T., and Nagase, H. (1995) Effects of a highly selective nonpeptide δ opioid receptor agonist, TAN-67, on morphine-induced antinociception in mice. *Life Sci. 57*, 155−168.

(18) Calderon, S. N., Rothman, R. B., Porreca, F., Flippen-Anderson, J. L., McNutt, R. W., Xu, H., Smith, L. E., Bilsky, E. J., Davis, P., and Rice, K. C. (1994) Probes for narcotic receptor mediated phenomena. 19. Synthesis of (+)-4-[(α R)-α-((2S,5R)-4-allyl-2,5-dimethyl-1-piperazinyl)-3- methoxybenzyl]-N,N-diethylbenzamide (SNC 80): a highly selective, nonpeptide δ opioid receptor agonist. *J. Med. Chem. 37*, 2125−2128.

(19) Barn, D. R., Caulfield, W. L., Cottney, J., McGurk, K., Morphy, J. R., Rankovic, Z., and Roberts, B. (2001) Parallel synthesis and biological activity of a new class of high affinity and selective δ-opioid ligand. *Bioorg. Med. Chem. 9*, 2609−2624.

(20) Pang, Y. P., Hong, F., Quiram, P., Jelacic, T., and Brimijion, S. (1997) Synthesis of alkylene linked bis-THA and alkylene linked benzyl-THA as highly potent and selective inhibitors and molecular probes of acetylcholinesterase. *J. Chem. Soc., Perkin Trans. 1*, 171−176.

(21) Bishop, J. E., Mathis, C. A., Gerdes, J. M., Whitney, J. M., Eaton, A. M., and Mailman, R. B. (1991) Synthesis and in vitro evaluation of 2,3-dimethoxy-5-(fluoroalkyl)-substituted benzamides: high-affinity ligands for CNS dopamine D_2 receptors. *J. Med. Chem. 34*, 1612−1624.

(22) Beauglehole, A. R., Baker, S. P., and Scammells, P. J. (2000) Fluorosulfonyl-substituted xanthines as selective irreversible antagonists for the A1-adenosine receptor. *J. Med. Chem. 43*, 4973−4980.

(23) Buckel, F., Persson, P., and Effenberger, F. (1999) Synthesis of functionalized long-chain thiols and thiophenols for the formation of self-assembled monolayers on gold. *Synthesis 6*, 953−958.

(24) Moore, J. D., Herpel, R. H., Lichtsinn, J. R., Flynn, D. L., and Hanson, P. R. (2003) ROMP-generated oligomeric sulfonyl chlorides as versatile soluble scavenging agents. *Org. Lett. 5*, 105−107.

(25) Le Bas, M. D., Guéret, C., Perrio, C., Lasne, M. C., and Barré, L. (2001) Oxidation of 2- and 3-halogenated quinolines: an easy access to 5- and 6- halogenopyridine-2,3-dicarboxylic acids. *Synthesis 16*, 2495−2499.

(26) Bagot-Guéret, C., Le Bas, M. D., Tymciu, S., Darabantu, M., Emond, P., Guilloteau, D., Lasne, M. C., Wijkhuisen, A., Barré, L., and Perrio, C. (2003) Synthesis and biological evaluation of

halogenated naphthyridone carboxamides as potential ligands for in vivo imaging studies of substance P receptors. *Bioconjugate Chem. 14*, 629−641.
(27) Cochran, J. C., and Little, W. F. (1961) Electrolytic oxidation of some substituted quinolines to quinolinic acids and acylations with substituted quinolinic anhydrides. *J. Org. Chem. 26*, 808−811.
(28) Vitry, C., Bédat, J., Prigent, Y., Levacher, V., Dupas, G., Salliot, I., Guéguiner, G., and Bourguignon, J. (2001) Chiral NADH models with restricted or blocked rotation at the amide function: attempts to interpret the mechanism of the enantioselective hydrogen transfer to methyl benzoylformate. *Tetrahedron 57*, 9101−9108.
(29) Cowan, J. C., and Sanders, J. K. M. (1985) Pyromellitimide-bridged porphyrins as model photosynthetic systems.1.Synthesis and steady state fluorescence properties. *J. Chem. Soc., Perkin Trans. 1*, 2435−2437.
(30) Blaney, P., Grigg, R., Rankovic, Z., Thornton-Pett, M., and Xu, J. (2002) Fused and bridged bi- and tri-cyclic lactams via sequential metallo-azomethine ylide cycloaddition-lactamisation. *Tetrahedron 58*, 1719−1737.
(31) Prabhakaran, P. C., Gould, S. J., Orr, G. R., and Coward, J. K. (1988) Synthesis of chirally deuteriated phthalimidopropanols and evaluation of their absolute stereochemistry. *J. Am. Soc. Chem. 110*, 5779−5784.
(32) Frigerio, M., Santagostino, M., and Sputore, S. A (1999) User entry to 2-iodoxybenzoic acid (IBX). *J. Org. Chem. 64*, 4537−4538.
(33) More, J. D., and Finney, N. S. (2002) A simple and advantageous protocol for the oxidation of alcohols with o-iodobenzoic acid (IBX). *Org. Lett. 4*, 3001−3003.
(34) Lukanov, L. K., Venkov, A. P., and Mollov, N. M. (1987) Application of the intramolecular α-amidoalkylation reaction for the synthesis of 2-arylsulfonyl-1,2,3,4-tetrahydroisoquinolines. *Synthesis 2*, 204−206.
(35) Hoyte, R. M., Zhang, J. X., Lerum, R., Oluyemi, A., Persaud, P., O'Connor, C., Labaree, D. C., and Hochberg, R. B. (2002) Synthesis of halogen-substitued pyridyl and pyrimidyl derivatives of [3,2-c]-pyrazolo corticosteroids: strategies for the development of gluco-corticoid receptor mediated imaging agents. *J. Med. Chem. 45*, 5397−5405.
(36) Corcoran, R. C., and Bang, S. H. (1990) Iodopyridines from bromo- and chloropyridines. *Tetrahedron Lett. 31*, 6757−6758.
(37) Schlosser, M., and Cottet, F. (2002) Silyl-mediated halogen/halogen displacement in pyridines and other heterocycles. *Eur. J. Org. Chem. 24*, 4181−4184.
(38) Torrado, A., and Imperiali, B. (1996) New synthetic amino acids for the design and synthesis of peptide-based metal ion sensors. *J. Org. Chem. 61*, 8940−8948.
(39) Yamamoto, Y., and Yanagi, A. (1982) Studies on organometallic compounds. II. Facile and convenient method for the synthesis of iodoazines through iododestannation of trimethylstannylazines. *Chem. Pharm. Bull. 30*, 1731−1737.
(40) Raynor, K., Kong, H., Chen, Y., Yasuda, K., Yu, L., Bell, G. I., and Reisine, T. (1994) Pharmacological characterization of the cloned κ-, δ-, and μ-opioid receptors. *Mol. Pharmacol. 45*, 330−334.
(41) Ananthan, S., Khare, N. K., Saini, S. K., Seitz, L. E., Bartlett, J. L., Davis, P., Dersch, C. M., Porreca, F., Rothman, R. B., and Bilsky, E. J. (2004) Identification of opioid ligands possessing mixed μ agonist/δ antagonist activity among pyridomorphinans derived from naloxone, oxymorphone, and hydropmorphone. *J. Med. Chem. 47*, 1400−1412.
(42) Parkhill, A. L., and Bidlack, J. M. (2002) Several δ-opioid receptor ligands display no subtype selectivity to the human δ-opioid receptor. *Eur. J. Pharmacol. 451*, 257−264.
(43) Huang, Y., Narendran, R., Bischoff, F., Guo, N., Zhu, Z., Bae, S. A., Lesage, A. S., and Laruelle, M. A. (2005) Positron emission tomography radioligand for the in vivo labelling of metabotropic glutamate 1 receptor: (3-Ethyl-2-[^{11}C]methyl-6-quinolinyl)(*cis*-4-methoxycyclohexyl)methanone. *J. Med. Chem. 48*, 5096−5099.
(44) Madsen, J., Merachtsaki, P., Davoodpour, P., Bergström, M., Långström, B., Andersen, K., Thomsen, C., Martiny, L., and Knudsen, G. M. (2003) Synthesis and biological evaluation of novel carbon-11 labelled analogues of citalopram as potential radioligands for the serotonin transporter. *Bioorg. Med. Chem. 11*, 3447−3456.
(45) Karimi, F., and Långström, B. (2002) Synthesis of 3-[(2S)-azetidin-2-ylmethoxy]-5-[^{11}C]-methypyridine, an analogue of A-85380, via a stille coupling. *J. Labelled Cmpd. Radiopharm. 45*, 423−434.
(46) Musachio, J. L., Villemagne, V. L., Scheffel, U. A., Dannals, R. F., Dogan, A. S., Yokoi, F., and Wong, D. F. (1999) Synthesis of an I-123 analog of A-85380 and preliminary SPECT imaging of nicotinic receptors in baboon. *Nucl. Med. Biol. 26*, 201−207.
(47) Quentin, T., Debruyne, D., Lelong-Boulouard, V., Poisnel, G., Barre, L., and Coquerel, A. (2005) Clorazepate affects cell surface regulation of δ and κ opioid receptors, thereby altering buprenorphine-induced adaptation in the rat brain. *Brain Res. 1063*, 84−95.
(48) Paxinos, G., and Watson, C. (1986) *The rat brain in stereotaxic coordinates*, Academic Press, New York.
(49) Mansour, A., Fox, C. A., Akil, H., and Watson, S. J. (1995) Opioid-receptor mRNA expression in the rat CNS: anatomical and functional implications. *Trends Neurosci. 18*, 22−29.
(50) Abeyta, A., Dettmer, T. S., Barnes, A., Vega, D., Carta, M., Gallegos, N., Raymond-Stintz, M., Savage, D. D., Valuenza, C. F., and Saland, L. C. (2002) Delta opioid receptor localization in the rat cerebellum. *Brain Res. 931*, 100−105.
(51) Patterson, A. B., Gordon, F. J., and Holtzman, S. G. (1997) Naltrindole, a selective δ-opioid receptor antagonist, potentiates the lethal effects of cocaine by a central mechanism of action. *Eur. J. Pharmacol. 333*, 47−54.
(52) Laruelle, M., Slifstein, M., and Huang, Y. (2003) Relationships between radiotracer properties and image quality in molecular imaging of the brain with positron emission tomography. *Mol. Imaging Biol. 5*, 363−375.
(53) Bradford, M. M. (1976) A rapid and sensitive method for the quantitation of microgram quantities of protein utilizing the principle of protein-dye binding. *Anal. Biochem. 72*, 248−254.
(54) Cheng, Y., and Prusoff, W. H. (1973) Relationship between the inhibition constant (Ki) and the concentration of inhibitor which causes 50 per cent inhibition (IC50) of an enzymatic reaction. *Biochem. Pharmacol. 22*, 3099−3108.
(55) Marki, A., Monory, K., Otvos, F., Toth, G., Krassnig, R., Schmidhammer, H., Traynor, J. R., Roques, B. P., Maldonado, R., and Borsodi, A. (1999) μ-Opioid receptor specific antagonist cyprodime: characterization by in vitro radioligand and [^{35}S]GTPγS binding assays. *Eur. J. Pharmacol. 383*, 209−214.
(56) Bozo, B., Farkas, J., Toth, G., Wollemann, M., Szucs, M., and Benyhe, S. (2000) Receptor binding and G-protein activation by new Met^5-Enkephalin-Arg^6-Phe^7 derived peptides. *Life Sci. 66*, 1241−1251.

BC0602836

In Vivo Evaluation of Cysteine-Based Chelators for Attachment of ^{99m}Tc to Tumor-Targeting Affibody Molecules

Thuy Tran,*[,†] Torun Engfeldt,[‡] Anna Orlova,[†,§] Charles Widström,[||] Alexander Bruskin,[⊥] Vladimir Tolmachev,[†,§] and Amelie Eriksson Karlström[‡]

Division of Biomedical Radiation Sciences, Rudbeck Laboratory, Uppsala University, Sweden, School of Biotechnology, Division of Molecular Biotechnology, Royal Institute of Technology, Stockholm, Sweden, Affibody AB, Bromma, Sweden, Hospital Physics, Department of Oncology, Uppsala University Hospital, Uppsala, Sweden, and Russian Research Centrum, Institute of Biophysics, Moscow, Russia. Received September 18, 2006; Revised Manuscript Received January 25, 2007

Affibody molecules present a new class of affinity proteins, which utilizes a scaffold based on a 58-amino acid domain derived from protein A. The small (7 kDa) Affibody molecule can be selected to bind to cell-surface targets with high affinity. An Affibody molecule ($Z_{HER2:342}$) with a dissociation constant (K_d) of 22 pM for binding to the HER2 receptor has been reported earlier. Preclinical and pilot clinical studies have demonstrated the utility of radiolabeled $Z_{HER2:342}$ in imaging of HER2-expressing tumors. The small size and cysteine-free structure of Affibody molecules enable complete peptide synthesis and direct incorporation of radionuclide chelators. The goal of this study was to evaluate if incorporation of the natural peptide sequences cysteine-diglycine (CGG) and cysteine-triglycine (CGGG) sequences would enable labeling of Affibody molecules with ^{99m}Tc. In a model monomeric form, the chelating sequences were incorporated by peptide synthesis. The HER2-binding affinity was 280 and 250 pM for CGG-$Z_{HER2:342}$ and CGGG-$Z_{HER2:342}$, respectively. Conjugates were directly labeled with ^{99m}Tc with 90% efficiency and preserved the capacity to bind specifically to HER2-expressing cells. The biodistribution in normal mice showed a rapid clearance from the blood and the majority of organs (except kidneys). In the mice bearing SKOV-3 xenografts, tumor uptake of ^{99m}Tc-CGG-$Z_{HER2:342}$ was HER2-specific and a tumor-to-blood ratio of 9.2 was obtained at 6 h postinjection. Gamma-camera imaging with ^{99m}Tc-CGG-$Z_{HER2:342}$ clearly visualized tumors at 6 h postinjection. The results show that the use of a cysteine-based chelator enables ^{99m}Tc-labeling of Affibody molecules for imaging.

INTRODUCTION

In recent years, progress in molecular biology has led to the identification of a number of molecular biomarkers in malignant cells, which can be used as targets for cancer treatment. For example, the elucidation of the role of tyrosine kinase receptors enabled the development of therapy directed to disruption of their signaling (*1*). Apparently, such therapy can be efficient only if a particular biomarker is present or overexpressed in a particular tumor, i.e., this therapy should be personalized. By now, the major way to determine the presence of a biomarker is a biopsy. However, heterogeneity of biomarker expression causes two problems which may lead to false-negative findings, i.e., sampling errors and discordance in the biomarker expression in primary tumors and metastases (*2*). The use of radionuclide imaging may help to avoid these problems by imaging both the whole primary tumor volume and the metastases in a single noninvasive procedure.

The use of peptide receptor ligands or their analogues as targeting agents provided excellent clinical results in the detection, e.g., of overexpression of somatostatin receptors (*3*). This was also a spectacular demonstration of a potential of small, high affinity peptides in radionuclide imaging. However, this approach cannot be applied for imaging of nonreceptor tumor markers, or for receptors for which no naturally occurring ligands have been identified, such as HER2, which signal by heterodimerization with other receptors (*4*). For this kind of target, monoclonal antibodies or their Fab or F(ab′)$_2$ fragments were mainly considered as targeting agents. Intact antibody molecules are large glycoproteins (about 150 kDa), which limits their application in molecular imaging. This is due to their relatively slow clearance from the blood circulation, which leads to a high background radioactivity and to their limited extravasation and diffusion into the tumor (*5*). The use of smaller fragments, e.g., F(ab′)$_2$, has enabled high-contrast imaging of tumors (*6*). The development of even smaller engineered antibody fragments, such as single-chain variable fragments (scFv), has become the mainstream for development of targeting agents for imaging (*7*). Still, a decrease of the targeting agent size below the size of scFv (approximately 27 kDa) would be appealing. To fulfill this goal, the use of nonimmunoglobulin scaffolds for selection of targeting proteins is promising (*8*).

Affibody molecules are an example of nonimmunoglobulin scaffolds, which have been successfully applied for *in vivo* imaging. Affibody molecules are based on a 58-amino acid residue protein domain, derived from the B-domain of staphylococcal protein A (*9*). This low-molecular weight (7 kDa) cysteine-free three-helix bundle protein has become an attractive alternative to antibody-based binding proteins in many applications in biotechnology, separomics, and analysis (see http://www.affibody.com). Recently, a new anti-HER2 targeting agent, named Affibody molecule $Z_{HER2:4}$, has been obtained by selection from an affibody library (*10*). HER2/*neu* (c-*erbB*-2) is a transmembrane receptor tyrosine kinase that mediates the growth, differentiation, and survival of cells (*11*). Overexpres-

* Corresponding author. Phone: +46 18 471 3829, fax: + 46 18 471 3432, e-mail: thuy.tran@bms.uu.se.
[†] Uppsala University.
[‡] Royal Institute of Technology.
[§] Affibody AB.
[||] Uppsala University Hospital.
[⊥] Russian Research Centrum.

10.1021/bc060291m CCC: $37.00 © 2007 American Chemical Society
Published on Web 03/02/2007

sion of HER2 receptors occurs in 25−30% of human breast and ovarian cancer, and its elevated expression is associated with poor prognosis (*12*). Herceptin (trastuzumab; Genentech), a humanized monoclonal antibody, is approved for clinical use for treatment of HER2-positive tumors. For the moment, both the American Association of Clinical Oncology and the European Group on Tumor Markers recommend an evaluation of the HER2 status of each breast cancer in order to select patients who will benefit from Herceptin therapy (*13*, *14*). In radionuclide tumor targeting, the radioiodinated (*15*, *16*) and radiobrominated (*17*) bivalent Affibody ligands $(Z_{HER2:4})_2$ have been reported to be suitable for visualization of HER2-expressing tumors. Affinity maturation of the $Z_{HER2:4}$ Affibody molecule generated a new HER-2 binding clone with a dissociation constant (K_d) of 22 pM for binding to the HER2 receptor, $Z_{HER2:342}$ (*18*). This Affibody molecule labeled with iodine or indium radioisotopes showed an excellent *in vivo* visualization of HER2-expressing tumor xenografts (*18*, *19*). The robust cysteine-free structure and the capability to quick refolding enabled synthetic production of Affibody molecules and incorporation of chelators during peptide synthesis. $Z_{HER2:342}$ with a DOTA chelator introduced at N-terminal was labeled with ^{111}In and ^{68}Ga and was successfully used in a pilot clinical study for imaging of HER2-expession in breast carcinomas (*20*, *21*).

Apparently, the radionuclide technetium-99m would be an attractive label for HER2-targeting Affibody molecules, due to its many favorable features such as low price, high availability, and optimal photon energy (140 keV) for imaging. Besides that, its short half-life ($T_{1/2}$ = 6 h) is a good match to the pharmacokinetics of Affibody molecules, which are characterized by rapid blood clearance. A site-specific technetium labeling of His_6-$(Z_{HER2:4})_2$ with Tc(I)-carbonyl chemistry was investigated (*16*). The radiolabeled conjugate provided good tumor accumulation; yet the liver uptake was too high to make it possible to detect liver metastases. For this reason, we started to investigate alternative labeling strategies. Earlier we have evaluated the incorporation of the mercaptoacetyltriglycyl-containing chelating sequence, maGGG (MAG3), for ^{99m}Tc-labeling of a synthetic variant of $Z_{HER2:342}$ (*22*). This conjugate enables imaging of HER2-expression in LS174T and SKOV-3 xenografts, both at 6 and 24 h pi. However, an appreciable part of the ^{99m}Tc-maGGG-$Z_{HER2:342}$ conjugate was excreted via bile, which might complicate the detection of HER2-expression in, e.g., ovarian carcinomas or in extrahepatic abdominal metastases of other tumors at the day of injection.

The strength of the Affibody technology lies in the capacity to generate multimeric constructs and fusion proteins in order to modify affinity/avidity, modulate *in vivo* kinetics, or introduce a peptide/protein effector function. The use of dimerization to increase apparent affinity has been mentioned above. A fusion with an albumin binding domain (ABD) to the dimeric form of $Z_{HER2:342}$ was used to prolong residence time in the blood and permit radionuclide therapy using ^{177}Lu (*23*). Obviously, such constructs are too large (more than 100 amino acids) to permit peptide synthesis in a cost-efficient way, and recombinant production is therefore required. Although it is possible to couple different chelators to recombinant proteins, this would result in a heterogeneous mixture of conjugates with different modification degree. The use of site-specific labeling would always be preferable, since it provides a more defined targeting agent. It was reported earlier that the introduction of a terminal cysteine in scFv fragments provides a chelating function for ^{99m}Tc-labeling (*24*−*26*). Recent progress in biotechnology, e.g., an introduction of TEV protease (*27*) which tolerates cysteine at +1 position of the cleavage site, has also facilitated the recombinant production of proteins with N-terminal cysteine residues.

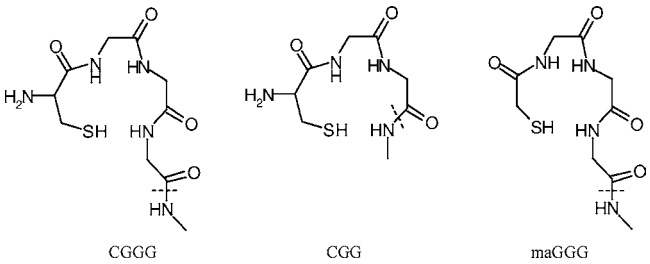


Figure 1. Chelator structures.

We hypothesized that the introduction of the ^{99m}Tc-chelating amino acid sequences cysteine-diglycine (CGG) and cysteine-triglycine (CGGG) (Figure 1) at the N-terminus of Affibody molecules would provide an attachment of ^{99m}Tc to the Affibody, which is stable enough for an *in vivo* application. The aim of the present study was to evaluate the labeling conditions and the *in vitro* and *in vivo* targeting properties of the ^{99m}Tc-labeled CGG- and CGGG-containing $Z_{HER2:342}$ Affibody conjugates.

MATERIALS AND METHODS

Materials. Fmoc-Ala-OH, Fmoc-Arg(Pbf)-OH, Fmoc-Asn-(Trt)-OH, Fmoc-Asp(*t*Bu)-OH, Fmoc-Cys(Trt)-OH, Fmoc-Gln-(Trt)-OH, Fmoc-Glu(*t*Bu)-OH, Fmoc-Gly-OH, Fmoc-Ile-OH, Fmoc-Lys(Boc)-OH, Fmoc-Met-OH, Fmoc-Phe-OH, Fmoc-Pro-OH, Fmoc-Ser(*t*Bu)-OH, Fmoc-Trp(Boc)-OH, Fmoc-Tyr(*t*Bu)-OH, and Fmoc-Val-OH were all from Applied Biosystems (Warrington, U.K.). Fmoc-Leu-OH was from Calbiochem-NovaBiochem (Läufelfingen, Switzerland).

N-Methylpyrrolidone (NMP) and acetic acid were from VWR. Dichloromethane and acetic anhydride were from Applied Biosystems (Warrington, UK). *N*-Ethyldiisopropylamine (DIEA) and piperidine were from Lancaster Synthesis (Morecambe, UK). Triisopropylsilane (TIS), trifluoroacetic acid (TFA), and *tert*-butyl methyl ether were from Merck International. Ethanedithiol (EDT) was from Aldrich Chemical Co. Inc. (Milwaukee, WI). 1-Hydroxybenzotriazole (HOBt) and 2-(1*H*-benzotriazol-1-yl)-1,1,3,3-tetramethyluronium hexafluorophosphate (HBTU) were from Advanced ChemTech (Louisville, KY).

For use in comparative biodistribution experiments, the synthetic Affibody molecule maGGG-$Z_{HER2:342}$ was labeled with ^{99m}Tc according to a previously published method (*22*). A recombinant Affibody molecule ($Z_{HER2:342}$) was indirectly radioiodinated using a succinimidyl ester of *p*-iodobenzoate according to Orlova and co-workers (*18*) and designated as ^{125}I-PIB-$Z_{HER2:342}$. An Ultra-TechneKow generator from Tyco was eluted with sterile 0.9% sodium chloride (Mallinckrodt Medical BV, Petten, The Netherlands) to obtain ^{99m}Tc as pertechnetate.

Instrumentation. An automated gamma-counter with a 3 in. NaI(Tl) detector (1480 Wizard, Wallac Oy, Turku, Finland) was used to measure the radioactivity. An instant thin layer chromatography analysis was performed using silica gel impregnated glass fiber sheets, ITLC strips (ITLC SG, from Gelman Sciences Inc). The Cyclone Storage Phosphor System and the OptiQuant image analysis software (both from Packard) were used to measure the radioactivity on the ITLC strips. The cells were counted in an electronic cell counter (Beckman Coulter, Fullerton, CA). *In vivo* imaging was performed by a dual-head e. Cam gamma camera (Siemens Medical Systems, Inc.), equipped with a low-energy, high-resolution collimator (LEHR). The acquisition of static images was performed with a 256 × 256 matrix and a zoom factor of 3.2. The energy window settings were 140 keV, 15%.

Peptide Synthesis. $Z_{HER2:342}$ was synthesized using Fmoc-chemistry on a 433A Peptide Synthesizer (Applied Biosystems, Warrington, U.K.) as previously described (*25*). Ten molar equivalents of amino acid were activated with HBTU and HOBt in NMP for each coupling reaction. Fmoc deprotection was performed by treatment with 20% piperidine−NMP. A double coupling procedure was used at 17 selected positions to increase the synthetic yield, and acetic anhydride was used to cap any remaining free amino groups. The peptide sequence is VENK FNKEMRNAYWEIALLPNLNNQQKRAFIRSLYDDPSQSAN-LLAEAKKLNDAQAPK, with double coupled amino acids underlined.

After the automatic assembly of $Z_{HER2:342}$, the N-terminal of the peptide was manually extended with the Tc-chelating sequences CGG and CGGG by coupling each amino acid with 5 mol equiv of amino acid, HBTU, and HOBt and 10 equiv of DIEA in NMP for 20 min. 20% piperidine−NMP was used for removal of the N-terminal Fmoc protecting group. Kaiser tests were performed to evaluate if the acylation and deprotection reactions were successful or had to be repeated. The manual coupling step of the chelators was used, since it is a rapid and easy way to introduce different chelating amino acid residues.

The resin-bound peptide was incubated with TFA/EDT/TIS/H2O (94:2.5:2.5:1) for 2 h to remove permanent protecting groups and liberate the peptide from the solid support. The peptide was extracted in *tert*-butyl methyl ether−H_2O (50:50), filtered, and lyophilized. The crude synthetic product was analyzed by analytical RP-HPLC using a 4.6 × 150 mm polystyrene/divinylbenzene matrix column with a particle size of 5 μm (Amersham Biosciences, Uppsala, Sweden), a 20 min gradient of 20−60% B (A: 0.1% TFA−H_2O, B: 0.1% TFA−CH_3CN) and a flow rate of 1 mL/min. All peptides were purified using a 20 min gradient of 25−45% B. The pure product was lyophilized, and the final peptide concentration was determined by amino acid analysis (Aminosyraanalyscentralen, Uppsala, Sweden). To verify the identity of the peptides, the peptide mass was analyzed on a Q-Tof II mass spectrometer fitted with an ESI source (Waters Corporation, Micromass MS Technologies, Manchester, U.K.). The Maximum Entropy 1 (MaxEnt1) algorithm was used to deconvolute the isotopic and charge state information. For the labeling experiments, the freeze-dried peptides were dissolved in degassed, deionized water to a concentration of 1 mg/mL and were stored at −20 °C

Biophysical Characterization. The melting point of each peptide was determined on a Jasco J-810 spectropolarimeter (JASCO, Tokyo, Japan). The temperature was increased from 20 to 90 °C at a rate of 5 °C/min, and the absorbance was detected at 221 nm. In addition, CD spectra were recorded from 250 to 195 nm at 20 °C before and after melting. The sample concentration was 50 μM in PBS pH 7.4 and the optical path length was 1 mm.

Biosensor Analysis. The binding kinetics of the different peptides were compared by performing a real-time biospecific interaction analysis on a Biacore 2000 instrument (Biacore, Uppsala, Sweden). HBS (10 mM HEPES, 150 mM NaCl, 3.4 mM EDTA, 0.005% Surfactant P20, pH 7.4) was used as running buffer at a flow rate of 50 μL/min, and also for dilution of the samples into the concentration range 0.3−10 nM. 500 RU (response units) of recombinant extracellular domain of HER2 (a generous gift from Prof. Gregory Adams, Fox Chase Cancer Center, Philadelphia, PA) and 900 RU of human serum albumin, HSA (KabiVitrum, Stockholm, Sweden), were immobilized onto a CM5 sensor chip (Biacore, Uppsala, Sweden) from 20 μg/mL solutions in 10 mM NaAc pH 4.5. The association time was 5 min, and the dissociation time was 10 min, followed by regeneration with 20 μL of 20 mM HCl. The BiaEval software (Biacore, Uppsala, Sweden) and the Langmuir 1:1 binding model were used for the kinetic analysis.

Labeling with ^{99m}Tc. The analysis of the labeled Affibody molecules was done by ITLC. To determine labeling yield and stability, ITLC strips were eluted with PBS. Validation experiments showed that pertechnetate, as well as tartrate, glucoheptonate, and cysteine complexes of ^{99m}Tc migrated with the eluent front, while the Affibody remained at the origin in PBS. To determine the presence of reduced hydrolyzed technetium, ITLC was eluted with pyridine:acetic acid:water (5:3:1.5). In this eluent, the technetium colloids remained at the origin, while the radiolabeled Affibody, pertechnetate, and tartrate complexes of ^{99m}Tc migrated with solvent front.

Two variants of labeling procedures were evaluated.

Indirect labeling of CGGG-$Z_{HER2:342}$ was performed according to Winnard et al. (*29*). CGGG-$Z_{HER2:342}$ (20 μL, 1 mg/mL in deionized degassed water) was mixed with 80 μL of PBS and 20 μL of a solution containing Na/K tartrate in 0.5 M $NaHCO_3$ and 0.25 M NH_4OAc. If necessary, 0.15 M NaOH was added to keep the pH of the final mixture at about 11. A fresh ^{99m}Tc-generator eluate (50−350 μL) followed by $SnCl_2 \cdot 2H_2O$ in 0.01 M HCl (10 μL, 1 mg/mL) was added, and the mixture was incubated at room temperature for 60 min.

Direct labeling: 20 μL of CGG-$Z_{HER2:342}$ or CGGG-$Z_{HER2:342}$ (1 mg/mL in deionized degassed water) was mixed with 20 μL of 0.15 M NaOH to obtain a final pH of about 11. A solution of $SnCl_2 \cdot 2H_2O$ in 0.01 M HCl (10 μL, 1 mg/mL) was added to the mixture, followed by 100−200 μL of fresh pertechnetate solution. The mixture was slightly vortexed and incubated at room temperature for 60 min.

After being labeled, ^{99m}Tc-CGG-$Z_{HER2:342}$ and ^{99m}Tc-CGGG-$Z_{HER2:342}$ were isolated from unreacted technetium and other low-molecular weight components using size-exclusion chromatography on disposable NAP-5 columns (Amersham Pharmacia Biotech AB, Uppsala, Sweden) preequilibrated with PBS. The purity of the final product was assessed by analysis with ITLC.

Stability Test. The stability of the labeled Affibody conjugates was tested in PBS and in 300 molar excess of cysteine. After purification, 100 μL of labeled conjugates was added to 500 μL of PBS. The solutions were stored at room temperature for 2 h and were analyzed using ITLC. In the cysteine challenge test, a fresh solution of cysteine was prepared (1 mg/mL in PBS, pH 7.0). The radiolabeled conjugates were added to a final molar ratio of cysteine to peptide of 300:1. The test tubes were incubated for 2 h at 37 °C, and the radiochemical purity was analyzed using ITLC. All experiments were performed in triplicate.

To analyze the serum stability, blood was collected from NMRI mice using a heparinized syringe. The blood was centrifuged at 5000*g*, and serum was collected, divided into 0.5 mL aliquots, and stored frozen before use. Serum samples were unfrozen immediately before the stability test. The test was performed in triplicate. The serum samples (240 μL) were mixed with freshly labeled ^{99m}Tc-CGG- and ^{99m}Tc-CGGG-$Z_{HER2:342}$ (10 μL) to obtain an Affibody molecule concentration similar to their concentration in blood at the moment of injection. The samples were incubated for 1 h at 37 °C. After incubation, the tested samples were analyzed by SDS-PAGE on NuPAGE 4−12% Bis-Tris Gel (Invitogen) in MES buffer (200 V constant, 35 min). To facilitate interpretation of the result, a sample of ^{99m}Tc-pertechnetate was run in parallel with the test sample on the same gel. After the analysis, the gels were dried, and radioactivity distribution along the gels was evaluated using Cyclone Storage Phosphor System.

Cell Culture. The HER2-expressing ovarian carcinoma cell line SKOV-3, displaying approximately 1.2 × 10^6 HER2

Table 1. Peptide Synthesis and Characterization Data

peptide	synthetic yield (%)	theoret mw (Da)	exptl mw (Da)	K_D (pM)	T_m (°C)
$Z_{HER2:342}$	21	6718	6718	80	64
CGG-$Z_{HER2:342}$	16	6993	6992	280	68
CGGG-$Z_{HER2:342}$	16	7050	7050	250	68

Table 2. Labeling and *in Vitro* Characterization of Radiolabeled Conjugates

	^{99m}Tc-CGGG-$Z_{HER2:342}$		^{99m}Tc-CGG-$Z_{HER2:342}$
	indirect	direct	direct
labeling yield, %	53.8 ± 10.1	90.4 ± 3.9	94.1 ± 2.6
isolated yield, %	49.3 ± 9.1	72.4 ± 5.8	69.0 ± 4.0
purity, %	98.0 ± 1.5	98.1 ± 2.0	99.0 ± 1.0
antigen binding capacity	75.0 ± 11.6	62.5 ± 13.4	57.1 ± 1.7
stability during cysteine challenge	66.9 ± 14.6	69.6 ± 6.2	70.8 ± 6.3
PBS stability	85.0 ± 17.0	82.7 ± 4.6	90.6 ± 4.6

receptors per cell, was used in this study. The cell line was cultured in McCoy's medium (Flow Irvine, UK), supplemented with 10% fetal calf serum (Sigma), 2 mM L-glutamine, and PEST (penicillin 100 U/mL and 100 μg/mL streptomycin), all from Biokrom Kg, Germany. The cells were cultured at 37 °C in a humidified incubator with 5% CO_2 and trypsinized using trypsin−EDTA solution (0.25% trypsin, 0.02% EDTA, Biokrom Kg, Germany). The SKOV-3 cells were cultivated on Petri dishes with a diameter of 3.5 cm to a cell density of 2 to 5 × 10^5 cells per dish.

Binding Specificity of ^{99m}Tc-Labeled Conjugates to HER2-Expressing Cells. Labeled conjugates were added to two groups of Petri dishes (three dishes per group) with a calculated ratio of one labeled Affibody conjugate per one HER2 receptor. One group of dishes was presaturated with a 100-fold excess of nonlabeled Affibody 10 min before the labeled conjugate was added. Cells were incubated for 1 h at 37 °C, and the incubation media was collected. The cell dishes were washed six times with cold serum-free medium and treated with 0.5 mL trypsin−EDTA for 10 min at 37 °C. When the cells were detached, 0.5 mL complete medium was added to each dish and the cells were resuspended. The cell suspension was used for radioactivity measurements.

Cellular Retention after Interrupted Incubation with ^{99m}Tc-Labeled $Z_{HER2:342}$. Labeled conjugate, 0.8 ng/10^5 cells, was added in 1 mL of complete medium to a series of Petri dishes containing SKOV-3 cells. The dishes were incubated for 2 h at 37 °C, and the incubation medium was removed. The cells were washed six times with ice-cold serum-free medium, and after addition of 1 mL of complete medium, the cell dishes were incubated further at 37 °C. At designated times of incubation (0.5, 1, 2, 4, 8, and 24 h), a group of three dishes was analyzed for cell-associated radioactivity. The media were collected in scintillation tubes, and the cells were washed six times with ice-cold serum-free medium and treated with 0.5 mL of trypsin-EDTA solution for 10 min at 37 °C. After addition of 0.5 mL of complete medium, the cells were resuspended and collected in scintillation tubes. The radioactivity content of the samples was measured on an automated gamma-counter.

Antigen Binding Capacity. The SKOV-3 cells were scraped from the surface in order to preserve the receptor expression. After resuspension of scraped cells in medium, the cells were counted in an automated cell counter, and cell pellets containing 6 × 10^6 cells were formed in Eppendorf tubes by gentle centrifugation (2 min at 2500*g*). The analysis was done in triplicate. The supernatant was removed completely, and 1 mL of medium with labeled conjugate (with a ratio of approximately one Affibody molecule per 100 HER2 receptors) was added.

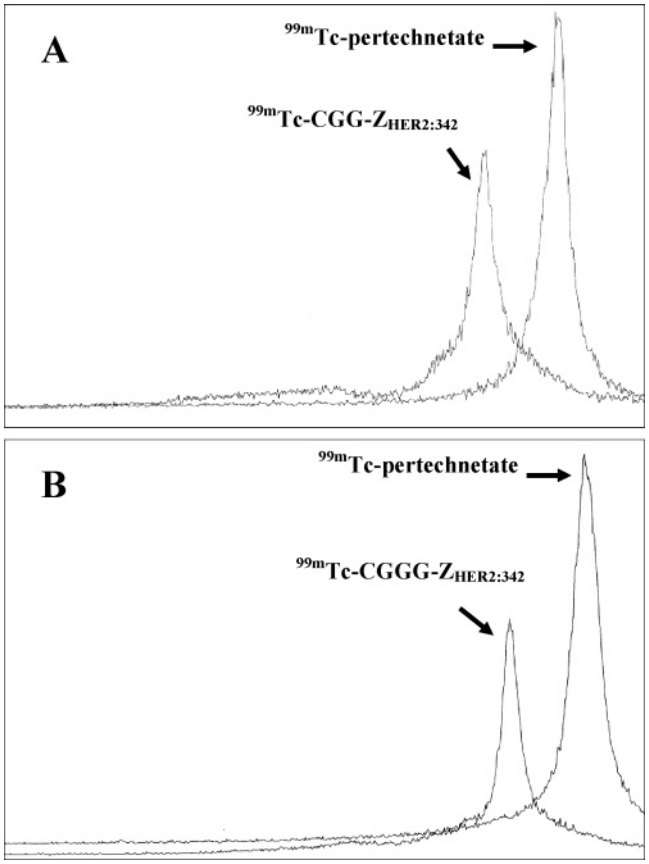


Figure 2. Analysis of ^{99m}Tc-CGG-$Z_{HER2:342}$ (A) and ^{99m}Tc-CGGG-$Z_{HER2:342}$ (B) stability in serum. A sample of each conjugate was incubated in blood serum for 1 h at 37 °C and analyzed using SDS PAGE and radioactivity distribution on the gel was measured using a PhosphorImager.

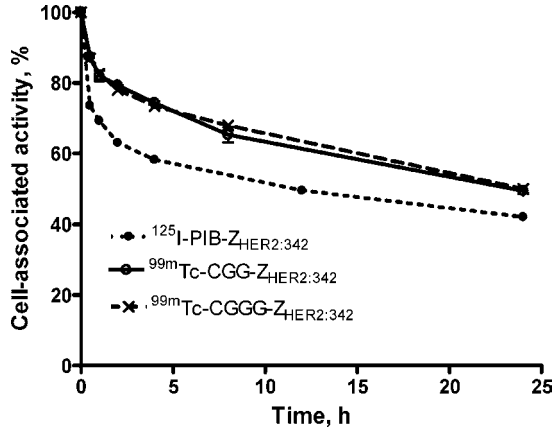


Figure 3. Cell-associated radioactivity as a function of time after interrupted incubation of SKOV-3 cells with radiolabeled $Z_{HER2:342}$. The cell-associated radioactivity at time zero after the interrupted incubation was considered as 100%. Data are presented as mean ± SD (n = 3). Error bars might not be seen, because they are smaller than point symbols.

The cells were gently resuspended and incubated for 4 h at 4 °C under slight shaking. After incubation, the cells were centrifuged (8 min at 7500*g*), and 0.5 mL supernatant medium was taken to a separate Eppendorf tube. The radioactivity was measured on both samples, and the antigen binding capacity (ABC) was calculated as ABC = (A − B)/(A + B) × 100%, where *A* is the radioactivity of the Eppendorf tube containing both the cell pellet and 0.5 mL supernatant, and *B* is the radioactivity of the Eppendorf tube containing 0.5 mL supernatant only.

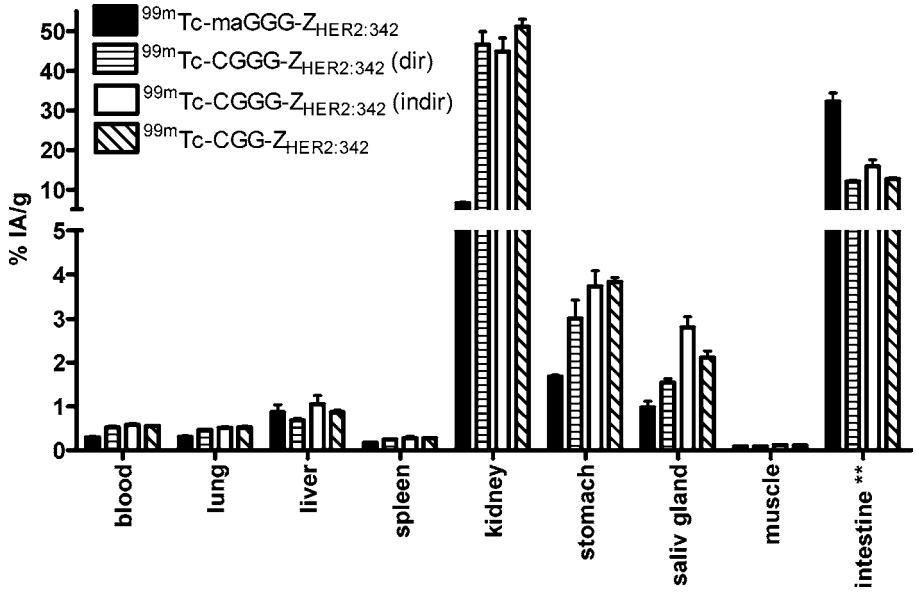


Figure 4. Biodistribution of radiolabeled Affibody molecules in NMRI normal mice 4 h pi. Data are presented as an average from four animals ± SEM. ^{99m}Tc-maGGG-$Z_{HER2:342}$ was included in the experiment for comparison. Uptake in spleen and muscle was less than 0.3% IA/g.

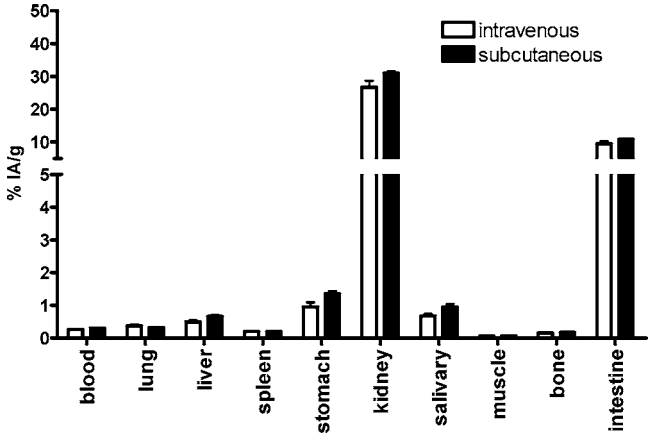


Figure 5. Biodistribution of ^{99m}Tc-CGG-$Z_{HER2:342}$ in NMRI mice after intravenous and subcutaneous injection (4 h pi). Data are presented as an average from four animals ± SEM.

Animal Model. The animal study was approved by the Local Ethics Committee for Animal Research. In comparative biodistribution studies, non-tumor-bearing NMRI mice were used. In tumor targeting and imaging experiments using ^{99m}Tc-CGG-$Z_{HER2:342}$, female Balb/c nu/nu mice were used. The animals (10−12 weeks old at arrival) were acclimatized for one week at the Rudbeck laboratory animal facility using standard diet, bedding, and environment before tumor implantation. The tumor was grafted by subcutaneous (sc) injection of ∼10^7 SKOV-3 cells in the right hind leg. Xenografts were allowed to develop during 2 months.

In all biodistribution studies, the mice were euthanized at predetermined time points with an intraperitoneal injection of Ketalar-Rompun solution (20 μL of solution per gram of body weight: Ketalar [ketamine], 10 mg/mL; Rompun [xylazin], 1 mg/mL). The mice were punctured in the heart with a 1 mL syringe rinsed with diluted heparin (5000 IE/mL, from Leo Pharma, Copenhagen, Denmark). Blood and organ samples were taken and weighed, and their radioactivity was recorded using an automatic gamma-counter with standard ^{99m}Tc protocol. The background was measured for each sample holder in the same way. The tissue uptake values were calculated as percent injected activity per gram tissue (% IA/g).

Comparative Biodistributions in Non-Tumor-Bearing NRMI Mice. Sixteen mice were randomly divided into four groups with four animals each. Each group of mice was injected subcutaneously with 1μg (∼ 100 kBq in 100 μL of PBS) of ^{99m}Tc-CGG-$Z_{HER2:342}$, ^{99m}Tc-CGGG-$Z_{HER2:342}$ (directly labeled), ^{99m}Tc-CGGG-$Z_{HER2:342}$ (indirectly labeled), or ^{99m}Tc-maGGG-$Z_{HER2:342}$, respectively. After 4 h, the mice were euthanized, and samples of blood, lung, liver, kidney, stomach, salivary glands, spleen, muscle, and intestines were collected.

In a separate study, two groups of four animals each were injected with the same batch of ^{99m}Tc-CGG-$Z_{HER2:342}$, but one group was injected intravenously and another subcutaneously. After 4 h, the mice were euthanized and the biodistribution of radioactivity was performed as described above.

Tumor Targeting in Balb/c nu/nu Mice with SKOV-3 Xenografts. Sixteen mice were randomly divided into four groups with four animals each. One group of mice was injected subcutaneously with 0.5 mg of nonlabeled recombinant $Z_{HER2:342}$ in 250 μL of PBS 1 h before radioactive injection. All mice were sc co-injected with ^{99m}Tc-CGG-$Z_{HER2:342}$ and ^{125}I-PIB-$Z_{HER2:342}$ (totally 1μg Affibody ligand, totally ∼100 kBq in 100 μL of PBS). After 1, 4, and 6 h pi, respectively, the mice were euthanized as described earlier. The mice in the blocking group were euthanized 4 h pi. Organ and tissue samples were taken, and their radioactivity uptake was determined as percent injected activity per gram tissue (%IA/g).

Gamma-Camera Imaging of HER2-Expressing Xenografts Using ^{99m}Tc-CGG-$Z_{HER2:342}$. Experimental tumor imaging was performed in two mice bearing SKOV-3 xenografts. The animals were intravenously injected through the tail with 3 MBq (10 μg) ^{99m}Tc-CGG-$Z_{HER2:342}$. Six hours after injection of ^{99m}Tc-CGG-$Z_{HER2:342}$, the animals were killed by overdosing of Rompun/Ketalar. Imaging was performed using a Siemens gamma-camera equipped with a LEHR collimator at the Department of Nuclear Medicine of Uppsala University Hospital. Static images were collected during 10 min, and the images were evaluated with a Hermes system (Nuclear Diagnostic). A quantitative analysis was done by drawing equal regions of interest (ROI) over the tumor and contralateral thigh.

RESULTS

Peptide Synthesis. The Fmoc solid-phase synthesis of $Z_{HER2:342}$ resulted in a yield of 21% of the full-length peptide, as determined by analytical RP-HPLC. The ^{99m}Tc-chelating sequences of CGG or CGGG introduced N-terminally by manual

Table 3. Biodistribution of ^{99m}Tc-CGG-$Z_{HER2:342}$ and ^{125}I-PIB-$Z_{HER2:342}$ in Balb/c nu/nu Mice Bearing SKOV-3 Xenografts. Data Are Presented as % IAg (an Average From Four Animals ± SEM)

	1 h		4 h				6 h	
organ	^{99m}Tc	^{125}I	^{99m}Tc	^{99m}Tc block	^{125}I	^{125}I block	^{99m}Tc	^{125}I
blood	2.32 ± 0.44	3.75 ± 0.61	0.84 ± 0.20	1.07 ± 0.14	0.72 ± 0.20	0.52 ± 0.10	0.62 ± 0.08	0.25 ± 0.04
lung	1.80 ± 0.36	2.96 ± 0.47	0.69 ± 0.12	0.95 ± 0.14[c]	0.71 ± 0.19	0.53 ± 0.14	0.50 ± 0.14	0.35 ± 0.14
liver	2.57 ± 0.46	5.38 ± 1.04	1.32 ± 0.16	1.33 ± 0.35	0.80 ± 0.13	0.68 ± 0.35	0.97 ± 0.09	0.27 ± 0.04
spleen	0.87 ± 0.16	2.06 ± 0.21	0.43 ± 0.19	0.58 ± 0.30	0.30 ± 0.06	0.33 ± 0.24	0.37 ± 0.15	0.12 ± 0.07
kidney	67.62 ± 12.85	34.76 ± 4.72	58.84 ± 8.76	53.96 ± 7.23	19.07 ± 4.70	11.83 ± 1.48	40.02 ± 4.00	7.75 ± 0.7
stomach	5.33 ± 1.00	2.45 ± 0.63	3.51 ± 0.39	5.44 ± 1.16[c]	0.99 ± 0.40	0.61 ± 0.05	3.36 ± 0.70	0.41 ± 0.12
salivary gland	4.95 ± 1.20	2.65 ± 0.51	4.17 ± 0.73	6.15 ± 0.90[c]	1.31 ± 0.23	0.91 ± 0.20[c]	2.52 ± 0.74	0.40 ± 0.22
thyroid[a]	0.27 ± 0.08	0.19 ± 0.07	0.19 ± 0.04	0.33 ± 0.19	0.26 ± 0.09	0.25 ± 0.15	0.16 ± 0.01	0.34 ± 0.08
tumor	3.36 ± 0.78	3.51 ± 0.62	4.23 ± 1.03	1.26 ± 0.14[c]	3.68 ± 0.98	0.84 ± 0.13[c]	5.69 ± 2.29	5.38 ± 2.14
muscle	0.34 ± 0.08	0.53 ± 0.11	0.24 ± 0.05	0.26 ± 0.05	0.18 ± 0.04	0.13 ± 0.04	0.14 ± 0.04	0.04 ± 0.03
bone	0.98 ± 0.64	0.67 ± 0.30	0.36 ± 009	0.40 ± 0.19	0.16 ± 0.09	0.17 ± 0.13	0.45 ± 0.29	0.07 ± 0.06
intestine[b]	7.77 ± 1.62	6.19 ± 0.55	17.10 ± 0.83	17.27 ± 3.88	3.72 ± 0.44	2.63 ± 0.72	9.75 ± 3.11	2.03 ± 2.30

[a] Data for thyroid are presented as % IA per organ. [b] Data for intestine with content are presented as % IA per whole sample. [c] Statistically significant difference, $p < 0.05$.

synthesis, both resulting in total synthetic yields 16% (Table 1). After purification with RP-HPLC, the purity was higher than 90%. ESI-MS was used to verify the molecular weight of the peptides. For the MS analysis, the thiol groups were capped with iodoacetamide, resulting in an additional mass of 57 Da. The data obtained correlated well with the expected masses (Table 1).

Biophysical Characterization. The stability of the secondary structure of the different proteins was studied at variable temperatures. The melting temperatures of the CGG and CGGG-modified peptides were 68 °C (Table 1). The CD spectra were recorded before and after melting of each peptide, and all generated very similar spectra, showing α-helical structure, suggesting that the proteins refold after heating to 90 °C.

Biosensor Analysis. The binding kinetics of the different Tc-chelating proteins were compared in a biospecific interaction analysis on a Biacore 2000 instrument. As shown in Table 1, both conjugates showed similar affinities to surface-immobilized HER2 receptors: 280 pM and 250 pM for CGG-$Z_{HER2:342}$ and CGGG-$Z_{HER2:342}$, respectively.

Radiolabeling. As displayed in Table 2, the efficiency of the direct labeling of cysteine-containing Affibody molecules was much higher than for the indirect labeling method (>90% vs 54%). The isolated yield from size-exclusion chromatography using NAP-5 columns was about 70% from the direct labeling and about 50% from the indirect method. Typically, the radiochemical purity of conjugates after NAP-5 separation was over 98% for both labeling methods. The presence of reduced hydrolyzed technetium was less than 2% in all experiments (data not shown).

Stability and Cell Binding of Labeled Conjugates. The *in vitro* stability of the labeled conjugates was evaluated in PBS and cysteine. The incubation of the labeled Affibody molecules for 2 h in the presence of 300 molar excess of cysteine showed a reasonably high stability. Most of the radioactivity (approximately 70%) of ^{99m}Tc-CGG-$Z_{HER2:342}$ and ^{99m}Tc-CGGG-$Z_{HER2:342}$ was still attached to the labels. The stability in PBS was even higher, especially for ^{99m}Tc-CGG-$Z_{HER2:342}$ with 90% attachment of technetium to the conjugate (Table 2).

The results of plasma stability test (Figure 2) showed that the conjugates were stable during 1 h at 37 °C. No release of radioactive low-molecular-weight products or association with serum proteins was observed. A small amount of radioactivity was associated with proteins bigger than the ^{99m}Tc-CGG-$Z_{HER2:342}$ peak (Figure 2.A), which can indicate some transchelation to blood plasma proteins.

The binding specificity of ^{99m}Tc-CGG-$Z_{HER2:342}$ and ^{99m}Tc-CGGG-$Z_{HER2:342}$ was evaluated in the HER2-expressing ovarian cancer cell line SKOV-3. The binding was specific, since it could be blocked with receptor saturation by 100-fold excess of unlabeled $Z_{HER2:342}$ (data not shown). The antigen binding capacity was estimated to be around 60% for directly labeled ^{99m}Tc-CGG-$Z_{HER2:342}$ and ^{99m}Tc-CGGG-$Z_{HER2:342}$. The difference in antigen binding capacity between directly and indirectly labeled ^{99m}Tc-CGGG-$Z_{HER2:342}$ was not statistically significant. It should be noted that the testing method used in this study provides lower value in comparison with the Lindmo analysis but is much less laborious. We use it for comparison of conjugates, not to obtain a true value for binding to an infinite excess of antigen. The cellular retention for the conjugates is illustrated in Figure 3. ^{99m}Tc-CGG-$Z_{HER2:342}$ and ^{99m}Tc-CGGG-$Z_{HER2:342}$ displayed similar patterns at all time points. For comparison, the retention of a radioiodinated Affibody via a *p*-iodobenzoate linker, ^{125}I-PIB-$Z_{HER2:342}$ (*18*), was also included, and it was found that the ^{99m}Tc-labels exhibited higher retention than the radioiodinated conjugate ($p < 0.001$), with about 50% cell-associated radioactivity 24 h after interrupted incubation, compared to 40% for iodine label.

Comparative Biodistribution in Non-Tumor-Bearing NMRI Mice. Figure 4 presents the biodistribution of the labeled conjugates in normal mice 4 h pi. For comparison, we also included the previously described ^{99m}Tc-maGGG-$Z_{HER2:342}$ (*22*) in the study. The biodistribution studies showed rapid renal excretion with about 50% IA/g trapped in the kidneys for ^{99m}Tc-CGG- and CGGG-$Z_{HER2:342}$ (both directly and indirectly labeled) 4 h pi, while the ^{99m}Tc-maGGG-$Z_{HER2:342}$ displayed much lower uptake, less than 7% IA/g. In the previous study of ^{99m}Tc-maGGG-$Z_{HER2:342}$ (*22*), we found that a high percentage of radioactivity was accumulated in the gastrointestinal tract, likely due to its excretion via the bile. In this study, we observed that the hepatobiliary excretion of the Affibody molecules was reduced with the use of CGG and CGGG chelators. The detected uptake in the intestines with their contents was about 12% IA/whole organ, an almost 3-fold reduction compared to when maGGG was used as chelator (32% IA/whole organ). Low levels of radioactivity were found in blood, lung, liver, stomach, salivary glands, spleen, and muscle for all conjugates.

The influence of injection route (intravenous or subcutaneous) on the biodistribution of ^{99m}Tc-CGG-$Z_{HER2:342}$ was also evaluated. The comparison showed that biodistribution 4 h pi was similar in both cases (Figure 5), with a small but significant increase of radioactivity in liver, stomach, and salivary gland after subcutaneous injection. These results indicate a quick drainage of Affibody-based conjugates by lymphatic system.

Tumor Targeting in Balb/c nu/nu Mice with SKOV-3 Xenografts. The *in vivo* tumor-targeting properties of ^{99m}Tc-CGG-$Z_{HER2:342}$ were evaluated through biodistribution studies on mice bearing HER2-expressing SKOV-3 xenografts, as

summarized in Table 3. In the same animals we also injected ^{125}I-PIB- $Z_{HER2:342}$ to have a reference, as this conjugate had previously demonstrated good targeting properties (*18*). The results showed that the blood level of ^{99m}Tc-CGG-$Z_{HER2:342}$ decreased rapidly, reaching 2.32 ± 0.44 %IA/g 1 h pi and 0.62 ± 0.08 %IA/g 6 h pi. The radioactivity clearance from other organs followed the same pattern. The tumor-to-kidney ratios were 0.050 ± 0.01 (1 h pi), 0.072 ± 0.017 (4 h pi), and 0.147 ± 0.074 (6 h pi) for ^{99m}Tc-CGG-$Z_{HER2:342}$. The tumor uptake of ^{99m}Tc-CGG-$Z_{HER2:342}$ did not differ significantly between the points of time.

To study the binding specificity to HER2-receptors *in vivo*, a group of mice were preinjected with a 1000-fold excess of nonlabeled Affibody molecule before injection of the labeled conjugates. As expected, the tumor uptake of both ^{99m}Tc- and ^{125}I-label in the blocked group was lower ($p < 0.005$), which verified that the uptake was receptor-specific.

An Affibody molecule radioiodinated via a *p*-iodobenzoate linker, ^{125}I-PIB-$Z_{HER2:342}$ (*18*), was used as an internal reference for comparison and was also injected into the same animals in this biodistribution study. As can be seen in Figure 6, the tumor-to-organ ratios were high for both ^{99m}Tc-CGG-$Z_{HER2:342}$ and ^{125}I-PIB-$Z_{HER2:342}$. Generally, the technetium label provided better contrast 1 h pi. The uptake was approximately equal 4 h pi, but 6 h pi, the radioiodine label provided better tumor-to-organ ratios.

Gamma-Camera Imaging of HER2-Expressing Xenografts Using ^{99m}Tc-CGG- $Z_{HER2:342}$. Gamma-camera images in BALB/c nu/nu mice bearing SKOV-3 tumors were acquired after 6 h after administration of ^{99m}Tc-CGG-$Z_{HER2:342}$. The images revealed good radioactivity accumulation in the tumors, which were clearly visualized, as shown in Figure 7. However, the uptake was high in the kidneys and in the abdomen area, which was predicted from the results of biodistribution study. Tumor-to-contralateral thigh was 29 ± 7 (average ± maximum error).

DISCUSSION

Earlier studies demonstrated that the use of solid-phase peptide synthesis can provide monomeric forms of Affibody molecules, capable for binding to target proteins and site-specific attachment of chelators for ^{111}In and ^{99m}Tc (*19*, *22*). However, the present peptide synthesis techniques would be inefficient in production of large multimeric Affibody molecules or fusion proteins. For recombinant production, which would be required in this case, an incorporation of synthetic chelators would be possible only as a separate process. A possible alternative has been proposed earlier for scFv (*24*−*26*), namely an incorporation of a terminal cysteine, which would form N3S chelator together with adjacent amino acids. Still, we had to take into account that direct translation of a labeling technique from one protein to another is not easy in the case of technetium, since the surrounding amino acids influence the stability of the chelate on one hand, and the chelator may affect the biodistribution properties of a targeting protein on the other (*30*, *31*). It is well-known that a change of chelator has a dramatic influence on the pharmacokinetics of short peptides, such as somatostatin analogues (*32*, *33*). It is also known that the biodistribution of antibodies and their fragments is relatively insensitive to the labeling method (*34*). But data concerning the biodistribution of intermediate size (5−10 kDa) molecules are rather scant.

The model Affibody molecule $Z_{HER2:342}$ was synthesized for this study by a solid-phase peptide synthesis with N-terminal extensions of the CGG or CGGG sequences. The final products showed subnanomolar affinities for the HER2 receptor, suggesting no major negative effect of CGG or CGGG attachment on binding properties of $Z_{HER2:342}$ (Table 1).

Initial experiments on labeling of CGGG-$Z_{HER2:342}$ with ^{99m}Tc were performed using tartrate as an intermediate weak chelator, i.e., by an indirect method. The labeling efficiency (Table 2) was 53.8 ± 10.1%, which is lower than obtained for maGGG-containing $Z_{HER2:342}$ conjugate (about 80%) (*22*). George and co-workers (*24*) have reported that labeling of scFv containing the GGGC sequence provided higher labeling yields (about 97%) in an alkaline condition. Alkaline pH is usually favorable for rapid ^{99m}Tc-labeling, probably because of deprotonation of sulfur and nitrogen donor atoms, which facilitates the complexation of technetium (*35*, *36*). The direct labeling method in alkaline solution (0.15 M NaOH, pH ∼ 11) provided a high radiochemical yield (90%), and a stable technetium

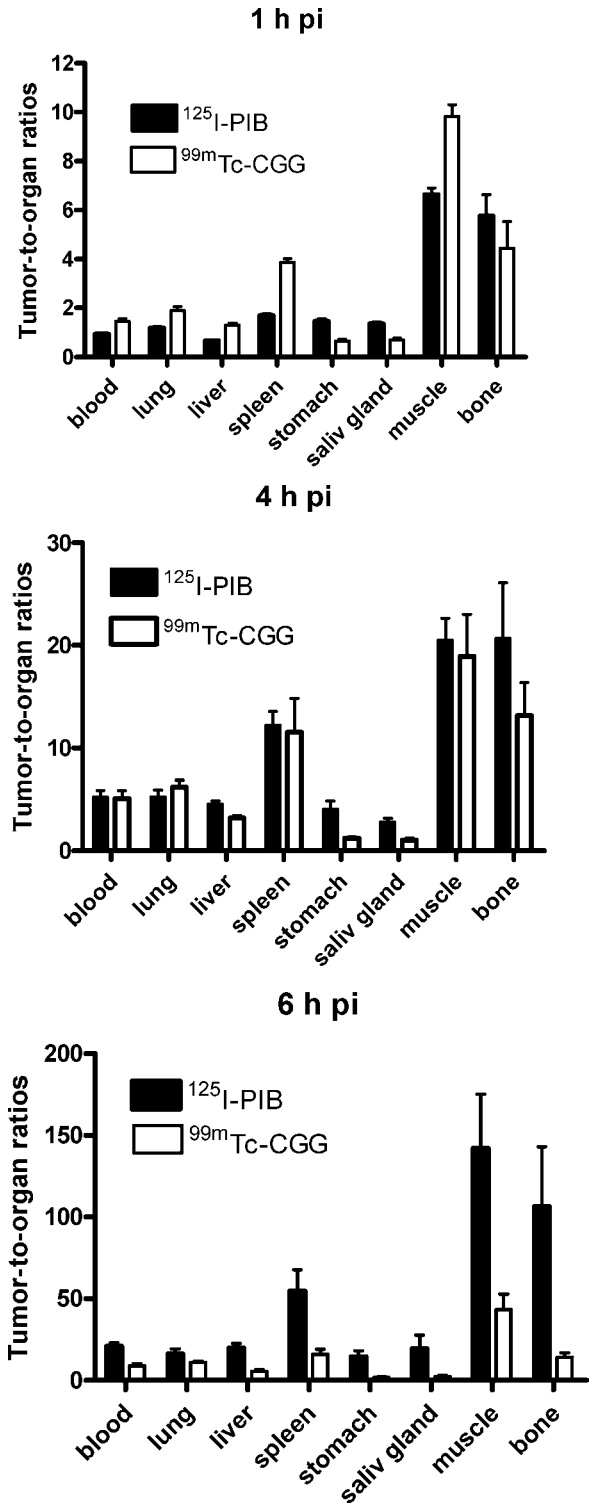


Figure 6. Tumor-to-organ ratios for ^{99m}Tc-CGG-$Z_{HER2:342}$ and ^{125}I-PIB-$Z_{HER2:342}$ in Balb/c nu/nu mice bearing SKOV3 xenografts. Data are presented as average from four animals ± SEM.

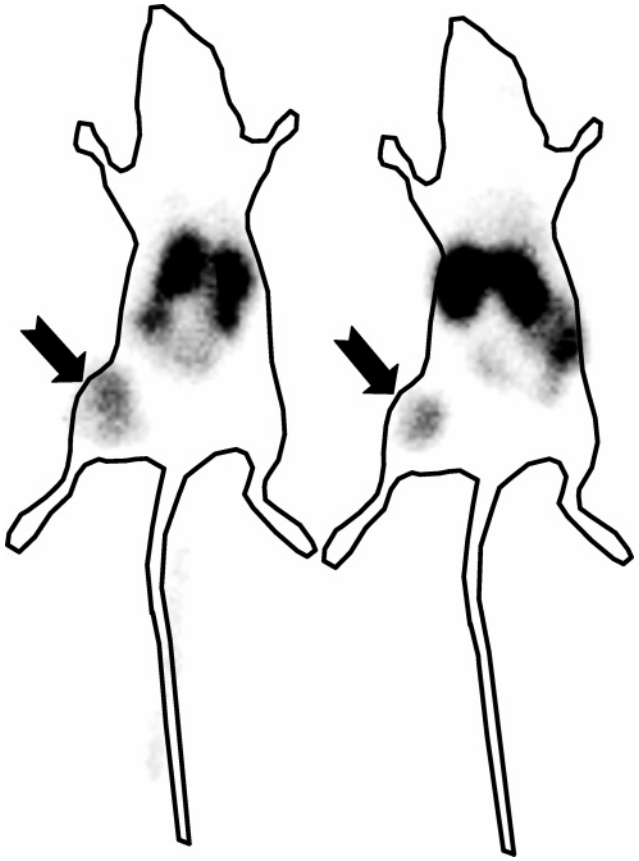


Figure 7. Gamma camera imaging of ^{99m}Tc-CGG-$Z_{HER2:342}$ in Balb/c nu/nu mice bearing SKOV3 xenografts after 6 h pi.

labeling was achieved. The specificity of binding to HER2 *in vitro* after direct labeling was preserved, and the antigen binding capacity did not differ significantly from the capacity after indirect labeling. No significant difference in biodistribution was found between directly and indirectly labeled CGGG-$Z_{HER2:342}$ (Figure 4). For this reason, direct labeling was selected for CGG-$Z_{HER2:342}$ labeling as well. The plasma stability in mouse serum indicated that the labeled conjugates were stable during 1 h. It was found that the retention of radioactivity in malignant SKOV-3 cells was better for ^{99m}Tc-labeled cysteine-containing conjugates than for a radioiodinated counterpart (Figure 3). This can be explained by better intracellular retention of radiocatabolites after internalization and lysosomal degradation of Affibody molecules.

The primary purpose of the development of an imaging agent lies in achieving high tumor-to-organ ratios, giving high contrast images. Therefore, a quick clearance from blood and unspecific compartments and quick tumor localization are essential properties of a targeting conjugate. Comparative biodistribution in normal mice (Figure 4) showed that the labeled conjugates had rather rapid blood clearance, with less than 1% IA/g at 4 h pi. This is in the same range (0.3−1.8% IA/g) as in mice for ^{99m}Tc-labeled somatostatin analogues (*37*) and lower than the blood level reported at that time for ^{99m}Tc-labeled scFv (*38*) or their multimeric constructs (*39*). The low blood radioactivity concentration suggested that, in agreement with the *in vitro* serum stability test, no considerable transchelation to blood plasma proteins occurred. Low levels of radioactivity were detected in liver and lungs, suggesting that no colloids were formed. However, a somewhat elevated radioactivity (in comparison with ^{99m}Tc-maGGG-$Z_{HER2:342}$) in stomach and salivary glands was observed, indicating some release of free pertechnetate. Since the conjugates appeared to be stable in blood plasma, it is likely that the release occurred during the catabolism of the labeled conjugates in kidney, probably due to reoxidation. Furthermore, the ^{99m}Tc-labeled cysteine-based chelators behaved similarly, while the most essential difference between these chelators and the maGGG chelator could be seen in the radioactivity accumulation in intestines. The results showed a 3-fold reduction of hepatobiliary excretion in the case of cysteine-based chelators in comparison with maGGG-$Z_{HER2:342}$. An explanation of this effect could be that the use of cysteine instead of mercaptoacetyl as a thiol group donor increases the overall hydrophilicity of the chelate due to the presence of a charged amino group and shifts excretion pathway from hepatobiliary to renal. A number of studies indicate that the use of more hydrophilic ^{99m}Tc chelates favor renal excretion (*31*, *37*, *40*, *41*). A shift to renal excretion was also indicated in this study by the increase of the kidney uptake of a factor of 7 by exchanging the maGGG chelator to cysteine-based chelators. It might be surprising that an additional charged group caused such profound difference in biodistribution of a 7-kDa protein. However, similar effects were also reported by Zhu and co-workers (*41*) for a neutrophil elastase inhibitor HNE2, which is similar in size (about 7 kDa) to the Affibody molecules. In that study, a variation of a single amino acid (phenylalanine, glycine, or glutamic acid) in the chelator modified the biodistribution of the protein in the same way as in our experiments.

The *in vitro* results showed that both ^{99m}Tc-CGG-$Z_{HER2:342}$ and ^{99m}Tc-CGGG-$Z_{HER2:342}$ provided promising characteristics as targeting agents for HER2. To further evaluate the targeting properties, one of the conjugates (^{99m}Tc-CGG-$Z_{HER2:342}$) was investigated in nude mice carrying SKOV-3 xenografts. Biodistribution data from the blocking experiment of ^{99m}Tc-CGG-$Z_{HER2:342}$ demonstrated that the binding to HER2 receptors in ovarian carcinoma tumors was receptor-specific, since the uptake was blocked by a preinjection of an excess of nonlabeled Affibody ($p < 0.005$). The *in vivo* retention in tumors was constant over time, which corresponded well with the results of the *in vitro* cellular retention study in SKOV-3 cells. Moreover, ^{99m}Tc-CGG-$Z_{HER2:342}$ had a fast blood clearance and low uptake in most organs and was mainly excreted through kidneys, thus providing a low background for imaging. At early time points (1 and 4 h pi), the technetium label provided tumor-to-organ ratios that were similar to or better than those provided by $Z_{HER2:342}$ radioiodinated using *p*-iodobenzoate. At 6 h pi, the radioiodine label was superior, probably due to a different pattern of clearance of radiocatabolites. However, the contrast level provided by the technetium label (e.g., tumor-to-blood ratio of 9.2) is acceptable. For clinical use, the ^{99m}Tc-labeled conjugate might be preferred over the ^{125}I-labeled one, due to the easy labeling (with a potential for a kit formulation), better logistics, and much lower price. Only a clinical study can answer if these factors may overweight the somewhat lower contrast in comparison with the radioiodinated counterpart.

Gamma-camera imaging with ^{99m}Tc-CGG-$Z_{HER2:342}$ at 6 h pi clearly showed the tumors in the mice. Although the accumulation in the intestines was largely reduced in comparison with the use of maGGG-chelator, the amount of radioactivity (10% IA per whole content) could still complicate the detection of extrahepatic metastases in the abdominal area on the day of injection. Nevertheless, the Affibody molecules seem to exhibit as good tumor-to-organ ratios as the other technetium-labeled anti-HER2 conjugates, if not better. For instance, ^{99m}Tc-HYNIC-trastuzumab Fab (*42*) and ^{99m}Tc-scFv barnase barstar constructs (*43*) had tumor-to-blood-ratios of 1.3 at 6 h pi and 10.8 at 24 h pi, respectively, compared to 9.2 at 6 h pi for the ^{99m}Tc-labeled Affibody molecule. This comparison would give some ideas about the *in vivo* properties but should be interpreted with care, as different HER2-xenografts and sampling techniques were used.

In summary, the Affibody molecules containing cysteine-based chelators CGG and CGGG were stably labeled with ^{99m}Tc, rapidly cleared from the blood circulation, and provided specific tumor accumulation (the latter case was for ^{99m}Tc-CGG-$Z_{HER2:342}$). It was evident that ^{99m}Tc-CGG-$Z_{HER2:342}$ clearly showed tumors in mice in the gamma-camera study. Thus, incorporation of cysteine into recombinant Affibody molecules would provide an efficient way for site-specific labeling of these proteins.

ACKNOWLEDGMENT

The authors thank Dr. Lars Abrahmsén, Dr. Joachim Feldwish, and Dr. Anders Wennborg from Affibody AB for intellectual discussions. Thanks to Mrs. Aseel Cherif for providing us with Tc-generator eluate, Mrs. Veronika Eriksson for keeping the cell lab in excellent working conditions, and the staff of the animal department at Rudbeck laboratory. We thank Gustav Sundqvist at KTH for running the ESI-MS analyses. Financial support was provided by the Swedish Cancer Society (Cancerfonden) and the Swedish Research Council (Vetenskapsrådet).

LITERATURE CITED

(1) Baselga, J. (2006) Targeting tyrosine kinases in cancer: the second wave. *Science 312*, 1175−1178.

(2) Zidan, J., Dashkovsky, I., Stayerman, C., Basher, W., Cozacov, C., and Hadary, A. (2005) Comparison of HER-2 overexpression in primary breast cancer and metastatic sites and its effect on biological targeting therapy of metastatic disease. *Br. J. Cancer. 93*, 552−556.

(3) Heppeler, A., Froidevaux, S., Eberle, A. N., and Maecke, H. R. (2000) Receptor targeting for tumor localisation and therapy with radiopeptides. *Curr. Med. Chem. 94*, 971−994.

(4) Mosesson, Y., and Yarden, Y. (2004) Oncogenic growth factor receptors: implications for signal transduction therapy. *Semin. Cancer Biol. 14*, 262−270.

(5) Jain, R. K. (1987) Transport of molecules across tumor vasculature. *Cancer Metastasis Rev. 6*, 559−593.

(6) Smith-Jones, P. M., Solit, D. B., Akhurst, T., Afroze, F., Rosen, N., and Larson, S. M. (2004) Imaging the pharmacodynamics of HER2 degradation in response to Hsp90 inhibitors. *Nat. Biotechnol. 22*, 701−706.

(7) Weiner, M. L. and Adams, G. P. (2000) New approaches to antibody therapy. *Oncogene 19*, 6144−6151.

(8) Van, de Wiele, C., Revets, H., and Mertens, N. (2004) Radioimmunoimaging. Advances and prospects. *Q. J. Nucl. Med. Mol. Imaging 48*, 317−325.

(9) Nord, K., Gunneriusson, E., Ringdahl, J., Stahl, S., Uhlen, M., and Nygren, P-A. (1997) Binding proteins selected from combinatorial libraries of an alpha-helical bacterial receptor domain. *Nat. Biochechnol. 15*, 772−777.

(10) Wikman, M., Steffen, A-C., Gunneriusson, E., Tolmachev, V., Adams, G. P., Carlsson, J., and Stahl, S. (2004) Selection and characterisation of HER2/neu-binding affibody ligands. *Protein Eng., Des. Sel. 17*, 455−462.

(11) Stern, D. F., Heffernan, P. A., and Weinberg, R. A. (1986) p185, a product of the neu proto-oncogene, is a receptorlike protein associated with tyrosine kinase activity. *Mol. Cell. Biol. 6*, 1729−1740.

(12) Slamon, D. J., Clark, G. M., Wong, S. G., Levin, W. J., Ullrich, A., and McGuire, W. L. (1987) Human breast cancer: correlation of relapse and survival with amplification of the HER-2/neu oncogene. *Science 235*, 177−182.

(13) Bast, R. C., Jr., Ravdin, P., Hayes, D. F., Bates, S., Fritsche, H., Jessup, J. M., Kemeny, N., Locker, G. Y., Mennel, R. G., and Somerfield, M. R. American Society of Clinical Oncology Tumor Markers Expert Panel. (2001) 2000 update of recommendations for the use of tumor markers in breast and colorectal cancer: clinical practice guidelines of the American Society of Clinical Oncology. *J. Clin. Oncol. 19*, 1865−1878.

(14) Molina, R., Barak, V., van Dalen, A., Duffy, M. J., Einarsson, R., Gion, M., Goike, H., Lamerz, R., Nap, M., Sölétormos, G., and Stieber, P. (2005) Tumor markers in breast cancer- European Group on Tumor Markers recommendations. *Tumor Biol. 26*, 281−293.

(15) Steffen, A-C., Orlova, A., Wikman, M., Gunneriusson, E., Nilsson, F. Y., Adams, G. P., Tolmachev, V., and Carlsson, J. (2006) Affibody mediated tumor targeting of HER-2 expressing xenografts in mice. *Eur. J. Nucl. Med. Mol. Imaging 33*, 631−638.

(16) Orlova, A., Nilsson, F. Y., Wikman, M., Ståhl, S., Carlsson, J., and Tolmachev, V. (2006) Comparative in vivo evaluation of iodine and technetium labels on anti-HER2 affibody for single-photon imaging of HER2 expression in tumors. *J. Nucl. Med. 47*, 512−519.

(17) Mume, E., Orlova, A., Nilsson, F. Y., Larsson, B., Nilsson, A. S., Sjöberg, S., and Tolmachev, V. (2005) Evaluation of ((4-hydroxyphenyl)ethyl)maleimide for site-specific radiobromination of anti-HER2 affibody. *Bioconjugate Chem. 16*, 1547−1555.

(18) Orlova, A., Magnusson, M., Eriksson, T., Nilsson, M., Larsson, B., Höiden-Guthenberg, I., Widstrom, C., Carlsson, J., Tolmachev, V., Stahl, S., and Nilsson, F. Y. (2006) Tumor imaging using a picomolar affinity HER-2 binding affibody molecules. *Cancer Res. 66*, 4339−4348.

(19) Tolmachev, V., Nilsson, F. Y., Widstrom, C., Andersson, K., Rosik, D., Gedda, L., Wennborg, A., and Orlova, A. (2006) ^{111}In-benzyl-DTPA-$Z_{HER2:342,}$ an Affibody-based conjugate for *in vivo* imaging of HER2 expression in malignant tumors. *J. Nucl. Med. 47*, 846−853.

(20) Orlova, A., Tolmachev, V., Pehrson, R., Lindborg, M., Tran, T., Sandström, M, Nilsson, F.Y., Wennborg, A., Abrahmsén, L., and Feldwisch, J. (2007) Synthetic Affibody molecules: A novel class of affinity ligands for molecular imaging of HER2 expressing malignant tumors. *Cancer Res.*, in press.

(21) Baum, R. P., Orlova, A., Tolmachev, V., and Feldwisch, J. (2006) Receptor PET/CT and SPECT using an Affibody molecule for targeting and molecular imaging of HER2 positive cancer in animal xenografts and human breast cancer patients. *J. Nucl. Med. 47*, 108.

(22) Engfeldt, T., Orlova, A., Tran, T., Bruskin, A., Widstrom, C., Eriksson Karlstrom, A., and Tolmachev, V. (2006) Imaging of HER2-expressing tumors using a synthetic affibody containing ^{99m}Tc-chelating mercaptoacetyl-GGG sequence. *Eur. J. Nucl. Med. Mol. Imaging*, [Epub ahead of print] PMID 17146656.

(23) Tolmachev, V., Orlova, A., Pehrson, R., Galli, J., Baastrup, B., Andersson, K., Sandström, M., Rosik, D., Carlsson, J., Lundqvist, H., Wennborg, A., and Nilsson, F. Y. (2007) Radionuclide therapy of HER2-positive microxenografts using a ^{177}Lu-labeled HER2-specific Affibody molecule. *Cancer Res. 67 (6).*

(24) George, A. J., Jamar, F., Tai, M. S., Heelan, B. T., Adams, G. P., McCartney, J. E., Houston, L. L., Weiner, L. M., Opperman, H., and Peters, A. M. (1995) Radiometal labeling of recombinant proteins by a genetically engineered minimal chelation site: Technetium-99m coordination by single-chain Fv antibody fusion proteins through a C-terminal cysteinyl peptide. *Proc. Natl. Acad. Sci. U.S.A. 92*, 8358−8362.

(25) Tolbert, T. J., and Wong, C. H. (2002) New methods for proteomic research: Preparation of proteins with N-terminal cysteines for labeling and conjugation. *Angew. Chem., Int. Ed. 41*, 2111−2174.

(26) Liberatore, M., Neri, D., Neri, G., Pini, A., Iurilli, A. P., Ponzo, F., Spampinato, G., Padula, F., Pala, A., and Colella, A. C. (1995) Efficient one-step direct labelling of recombinant antibodies with technetium-99m. *Eur. J. Nucl. Med. 22*, 1326−1329.

(27) Verhaar, M. J., Keep, P. A., Hawkins, R. E., Robson, L., Casey, J. L., Pedley, B., Boden, J. A., Begent, R. H., and Chester, K. A. (1996) Technetium-99m radiolabeling using a phage-derived single-chain Fv with a C-terminal cysteine. *J. Nucl. Med. 37*, 868−872.

(28) Engfeldt, T., Renberg, B., Brumer, H., Nygren, P-A., and Eriksson Karlstrom, A. (2005) Chemical synthesis of triple-labeled three-helix bundle binding proteins for specific fluorescent detection of unlabeled protein. *ChemBioChem 6*, 1043−1050.

(29) Winnard, P. Jr., Chang, F., Rusckowski, M., Mardirossian, G., and Hnatowich, D. J. (1997) Preparation and use of NHS-MAG3 for technetium-99m labeling of DNA. *Nucl. Med. Biol. 24*, 425−432.

(30) Vanderheyden, J. L., Liu, G., He, J., Patel, B., Tait, J. F., and Hnatowich, D. J. (2006) Evaluation of ^{99m}Tc-MAG3-annexin V: influence of the chelate on *in vitro* and *in vivo* properties in mice. *Nucl. Med. Biol*. *33*, 135−144.

(31) Qu, T., Wang, Y., Zhu, Z., Rusckowski, M., and Hnatowich, D. J. (2001) Different chelators and different peptides together influence the *in vitro* and mouse *in vivo* properties of ^{99}Tc^{m}. *Nucl. Med. Commun. 22*, 203−215.

(32) Froidevaux, S., Heppeler, A., Eberle, A. N., Meier, A. M., Hausler, M., Beglinger, C., Behe, M., Powell, P., and Macke, H. R. (2000) Preclinical comparison in AR4−2. J tumor-bearing mice of four radiolabeled 1,4,7,10-tetraazacyclododecane-1,4,7,10-tetraacetic acid-somatostatin analogs for tumor diagnosis and internal radiotherapy. *Endocrinology 141*, 3304−3312.

(33) Eisenwiener, K. P., Prata, M. I., Buschmann, I., Zhang, H. W., Santos, A. C., Wenger, S., Reubi, J. C., and Macke, H. R. (2002) NODAGATOC, a new chelator-coupled somatostatin analogue labeled with [$^{67/68}$Ga] and [^{111}In] for SPECT, PET, and targeted therapeutic applications of somatostatin receptor (hsst2) expressing tumors. *Bioconjugate Chem. 13*, 530−541.

(34) Liu, S. and Edwards, D. S. (1999) ^{99m}Tc-labeled small peptides as diagnostic radiopharmaceuticals. *Chem. Rev. 9*, 2235−2268.

(35) Bormans, G., Cleynhens, B., Adriaens, P., Vanbilloen, H., De Roo, M., and Verbruggen, A. (1995) Investigation of the labeling characteristics of ^{99m}Tc-mercaptoacetyltriglycine. *Nucl. Med. Biol. 22*, 339−349.

(36) Thakur, M. L., Pallela, V. R., Consigny, P. M., Rao, P. S., Vessileva-Belnikolovska, D., and Shi, R. (2000) Imaging vascular thrombosis with ^{99m}Tc-labeled fibrin alpha-chain peptide. *J. Nucl. Med. 41*, 161−168.

(37) Decristoforo, C., and Mather, J. S. (1999) Technetium-99m somatostatin analogues: effect of labeling methods and peptide sequence. *Eur. J. Nucl. Med. 26*, 869−876.

(38) Pietersz, G. A., Patrick, M. R., and Chester, K. A. (1998) Preclinical characterization and *in vivo* imaging studies of an engineered recombinant technetium-99m-labeled metallothionein-containing anti-carcinoembryonic antigen single-chain antibody. *J. Nucl. Med. 39*, 47−56.

(39) Goel, A., Baranowska-Kortylewicz, J., Hinrichs, S. H., Wisecarver, J., Pavlinkova, G., Augustine, S., Colcher, D., Booth, B. J., and Batra, S. K. (2001) ^{99m}Tc-labeled divalent and tetravalent CC49 single-chain Fv's: novel imaging agents for rapid in vivo localization of human colon carcinoma. *J. Nucl. Med. 42*, 1519−1527.

(40) Verbeke, K., Snauwaert, K., Cleynhens, B., Scheer, W., and Verbruggen, A. (2000) Influence of the bifuncational chelate on the biological behavior of ^{99m}Tc-labeled chemotactic peptide conjugates. *Nucl. Med. Biol. 27*, 769−779.

(41) Zhu, Z., Wang, Y., Zhang, Y., Liu, G., Liu, N., Rusckowski, M., and Hnatowich, D. J. (2001) A novel and simplified route to the synthesis of N3S chelators for ^{99m}Tc labeling. *Nucl. Med. Biol. 28*, 703−708.

(42) Tang, Y., Scollard, D., Chen, P., Wang, J., Holloway, C., and Reilly, M. R. (2005) Imaging of HER2/neu expression in BT-373 human breast cancer xenografts in athymic mice using (^{99m}Tc)-HYNIC-trastuzumab (Herceptin) Fab fragments. *Nucl. Med. Commun. 26*, 427−432.

(43) Deyev, S. M., Waibel, R., Lebedenko, E. N., Schubiger, A. P., and Plückthun, A. (2003) Design of multivalent complexes using barnase*barstar module. *Nat. Biotechnol. 21*, 1486−1492.

BC060291M

Synthesis and Application of a Novel Ligand for Affinity Chromatography Based Removal of Endotoxin from Antibodies

Laura A. McAllister, Mark S. Hixon, Roberta Schwartz, Diane S. Kubitz, and Kim D. Janda*

Departments of Chemistry and Immunology, The Skaggs Institute for Chemical Biology, and Worm Institute for Research and Medicine (WIRM), The Scripps Research Institute, 10550 N. Torrey Pines Road, La Jolla, California 92037
Received September 22, 2006; Revised Manuscript Received December 22, 2006

Endotoxin or lipopolysaccharide (LPS) contamination in proteins expressed by Gram-negative bacteria is a major drawback associated with protein expression. Endotoxin intoxication in humans and animals above a certain threshold level can result in a fatal immune response. Reduction in endotoxin levels is therefore essential before proteins can be used in in vivo studies or sold as pharmaceutical products. Affinity chromatography employing the peptide Polymyxin B (PMB) as an affinity ligand is one way in which endotoxin contamination has been addressed; this is, however, a costly process. We describe the synthesis of a novel affinity ligand based on the structure of the drug pentamidine, which can be applied effectively in endotoxin removal. The synthetic route to this ligand is straightforward and inexpensive, while the ligand can be readily immobilized onto activated sepharose beads. Thus, we demonstrate that these pentamidine affinity beads bind endotoxin/LPS with comparable capacity to PMB affinity systems, that the beads can be recycled efficiently and economically without loss of binding capacity, and application of the functionalized beads for endotoxin removal in an authentic contaminated antibody sample.

INTRODUCTION

Endotoxin or lipopolysaccharide (LPS) (Figure 1) is the major constituent of the outer membrane of Gram-negative bacteria, composed of a nontoxic polysaccharide portion and the biologically active portion known as lipid A (*1*). Lipid A is a bisphosphorylated disaccharide bearing several hydrophobic acyl chains (Figure 2). The presence of endotoxin in blood, known as Gram-negative sepsis, is the leading cause of death in intensive care units (*2*). Endotoxin/LPS induces an exaggerated response by the immune system resulting in uncontrolled production of inflammatory mediators, which can lead to fatal shock syndrome and eventually multiple organ failure (*3*).

Proteins expressed by Gram-negative bacteria are often contaminated with endotoxin; this contamination must be reduced sufficiently before a protein can be used in in vivo studies within animal models or sold as pharmaceutical products, for human use, such as vaccines. The FDA recommends that no more than 5.0 EU per kilogram of body weight be introduced parenterally into a human or an animal (10 EU is approximately 1 ng of *E. coli* LPS). Endotoxin removal is an expensive, time-consuming, and laborious part of the protein purification process, which often results in poor recovery of the protein (*4*). Affinity chromatography, whereby a ligand with a high binding affinity for LPS is immobilized on a solid support, is the gold standard for endotoxin removal. Polymyxin B (PMB) is a cyclic lipopeptide produced by *Bacillus polymyxa* that binds LPS with high affinity. Agarose-supported Polymyxin B is used in affinity chromatography for endotoxin removal (Pierce, product no. 20344, Detoxi-Gel AffinityPak Prepacked Columns (5 × 1 mL, currently $95); however, we note that, while this ligand-support system is exceptional for LPS removal, it is also prohibitively expensive. Furthermore, Polymyxin B is a synthetically challenging molecule and is therefore obtained exclusively by bacterial expression.

* Corresponding author. K. D. Janda. E-mail: kdjanda@scripps.edu. Tel: 858 784 2516. Fax 858 784 2595.

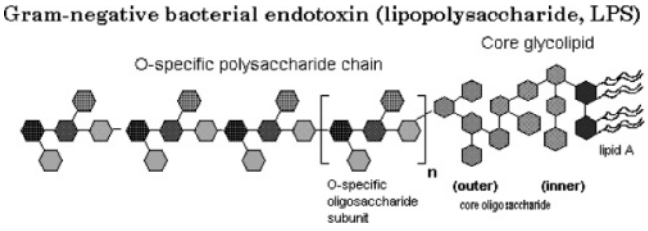


Figure 1. Schematic representation of the structure of bacterial endotoxin/LPS.

The anti-*Pneumocystis carinii* drug, pentamidine (Figure 2), has been reported to bind to lipid A (the toxic constituent of LPS) with a comparable affinity to PMB (*5*, *6*). The high affinity of this drug for lipid A has been attributed to the terminal amidine groups of the drug being an optimal distance apart for their simultaneous interaction with the two anionic phosphate groups of lipid A. We reasoned that a ligand based on the structure of pentamidine could be applied to affinity-based removal of endotoxins. We sought to unveil an economical, synthetically accessible alternative to Polymyxin B which displays similar endotoxin binding ability. Such a molecule could be readily synthesized on a large scale at low cost and would offer a less expensive alternative to the use of PMB in the endotoxin removal process. Herein, we report an efficient, facile synthesis of a tethered derivative of pentamidine that can be immobilized onto a sepharose support. Chemical synthesis of this ligand is straightforward and inexpensive, and we demonstrate that this support can remove endotoxin with comparable effectiveness to PMB affinity systems. The pentamidine-based affinity system can be recycled repeatedly using inexpensive reagents with no significant reduction in performance and results in greater protein recovery than the PMB system.

10.1021/bc0602984 CCC: $37.00 © 2007 American Chemical Society
Published on Web 02/22/2007

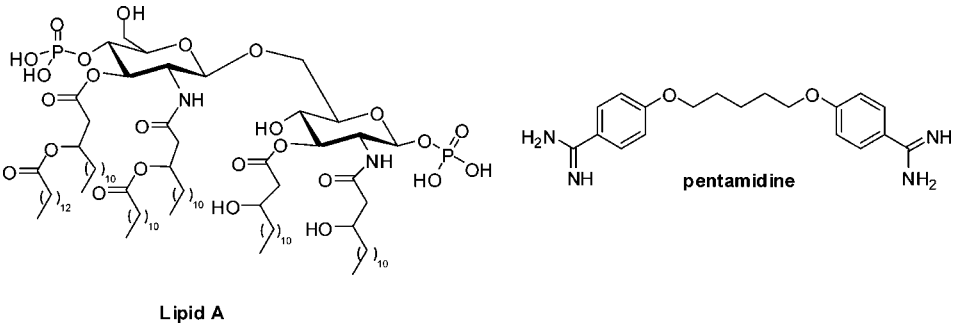


Figure 2. Structure of lipid A and the anti-*Pneumocystis carinii* drug, pentamidine.

EXPERIMENTAL PROCEDURES

General Considerations. All synthetic reactions were performed under an atmosphere of Ar or N_2, using anhydrous solvents unless otherwise stated. Reactions were carried out using oven-dried glassware. THF was distilled from sodium/benzophenone, and CH_2Cl_2 and MeOH were distilled from CaH_2. Anydrous DMF, toluene, and ethanol were purchased from Aldrich. Reagents were purchased from commercial sources and used without further purification. ^{1}H NMR and ^{13}C NMR were recorded on Bruker AMX-400, Bruker DRX-500, or Bruker DRX-600 instruments, with chemical shift values being reported in parts per million relative to residual chloroform (δH = 7.27 or δC = 77.2) as an internal standard. High-resolution mass spectrometry was carried out at The Scripps Research Institute using an IonSpec Ultima high-resolution FTMS instrument. Reactions were monitored by thin-layer chromatography (TLC) carried out on 0.25 mm E. Merck silicagel plates (60F-254) visualizing by UV light and $KMnO_4$ stain. Flash chromatography was carried out using Merck silica gel 60 (230−400 mesh). Reagent-grade solvents for chromatography were obtained from Fisher Scientific.

A BODIPY−TR cadaverine probe was purchased from Invitrogen. LPS from *E. coli* 0111:B4, LPS from *E. coli* 0111:B4 FITC conjugate, pentamidine isethionate, Polymyxin B, and agarose-supported Polymyxin B were all purchased from Sigma. The Reacti-Gel CDI support was purchased from Pierce. Fluorescence measurements were carried out on a SpectraMax GeminiEM fluorescence plate reader. Corning nonbinding surface 96-well plates obtained from Fischer were used for all fluorescence assays. 1 mL Detoxi-Gel columns were obtained from Pierce. The *Limulus* Amebocyte Lysate (LAL) QCL-1000 assay kit was purchased from Cambrex bioscience.

Dimethyl 3-(*tert*-Butyldimethylsilyloxy)pentanedioate (1b). To a solution of dimethyl 3-hydroxy-glutarate (**1a**) (2.92 g, 16.6 mmol, 1 equiv) in DMF (10 mL) was added imidazole (1.24 g, 18.3 mmol, 1.1 equiv) and TBSCl (2.74 g, 18.3 mmol, 1.1 equiv). The reaction was allowed to stir at room temperature (rt) for 16 h. The reaction was diluted with 50% EtOAc/Hx and the organic layer washed with H_2O. The organic layer was then dried ($MgSO_4$) and concentrated in vacuo to give dimethyl 3-(*tert*-butyldimethylsilyloxy)pentanedioate (**1b**) (4.80 g, 16.5 mmol, 99.5%) as a clear oil which was used without further purification.

^{1}H NMR ($CDCl_3$, 500 MHz) δ 0.06 (6H, s, (CH_3)$_2$Si), 0.84 (9H, s, (CH_3)$_3$Si)), 2.55 (4H, d, J = 7.0 Hz, 2 × CH_2), 3.69 (6H, s, 2 × CH_3O), 4.55 (1H, t, C*H*O).

^{13}C NMR ($CDCl_3$, 125 MHz) δ −5.00 (2 × *C*H$_3$), 17.9 (*C*(CH$_3$)$_3$), 25.6 (*C*H$_3$)$_3$C), 42.4 (2 × *C*H$_2$), 51.5 (2 × *C*H$_3$O), 66.3 (*C*HO), 171.3 (*C*═O).

MS (ESI-TOF): [M + H]$^+$, $C_{13}H_{27}O_5Si$ requires 291.1622, found 291.1620.

3-(*tert*-Butyldimethylsilyloxy)pentane-1,5-diol (2). To a solution of dimethyl 3-(*tert*-butyldimethylsilyloxy)pentanedioate (**1b**) (7.75 g, 26.7 mmol, 1 equiv) in CH_2Cl_2 (150 mL) at 0 °C was added DIBALH (71 mL of 1.5 M solution in toluene, 106.8 mmol, 4 equiv). The reaction was allowed to stir at 0 °C for 3 h and then quenched with an aq sat solution of potassium sodium tartrate and allowed to stir overnight. The reaction mixture was then extracted several times with $CHCl_3$. Combined organic layers were dried ($MgSO_4$) and concentrated in vacuo to give 3-(*tert*-butyldimethylsilyloxy)pentane-1,5-diol (**2**) (5.78 g, 24.7 mmol, 93%) as a clear oil which was used without further purification.

^{1}H NMR ($CDCl_3$, 600 MHz) δ 0.09 (6H, s, (CH_3)$_2$Si), 0.88 (9H, s, (CH_3)$_3$Si)), 1.57 (2H, broad s, 2 × O*H*), 1.75 (2H, m, CH_2), 1.83 (2H, m, CH_2), 3.71 (2H, m, CH_2O), 3.79 (2H, m, CH_2O), 4.14 (1H, m, C*H*O).

^{13}C NMR ($CDCl_3$, 150 MHz) δ −4.70 (2 × *C*H$_3$), 17.9 (*C*(CH$_3$)$_3$), 25.8((*C*H$_3$)$_3$C), 38.4 (2 × *C*H$_2$), 59.8 (2 × *C*H$_2$O), 69.6 (*C*HO).

MS (ESI-TOF): [M + H]$^+$, $C_{11}H_{27}O_3Si$ requires 235.1724, found 235.1721.

4,4′-(3-(Tert-butyldimethylsilyloxy)pentane-1,5-diyl)bis-(oxy)dibenzonitrile (3a). To a solution of 3-(*tert*-butyldimethylsilyloxy)pentane-1,5-diol (**2**) (5.78 g, 24.7 mmol, 1 equiv) in THF (150 mL) was added 4-hydroxybenzonitrile (8.8 g, 74.1 mmol, 3 equiv), DIAD (19.1 mL, 98.8 mmol, 4 equiv), and PPh_3 (25.8 g, 98.8 g, 4 equiv). The reaction was allowed to stir at rt for 18 h. EtOAc was added, and the reaction mixture was washed with 1 M NaOH, dried ($MgSO_4$), and concentrated in vacuo. The crude product mixture was purified by flash chromatography on silica gel (30% EtOAc/Hx) to give 4,4′-(3-(tert-butyldimethylsilyloxy)pentane-1,5-diyl)bis(oxy)dibenzonitrile (**3a**) together with an impurity derived from DIAD. This mixture was used in the next step without further purification.

^{1}H NMR ($CDCl_3$, 600 MHz) δ −0.01 (6H, s, 2 × CH_3Si), 0.88 (9H, s, (CH_3)$_3$Si), 2.01 (4H, m, 2 × CH_2), 4.10 (4H, t, J = 6.6 Hz, 2 × CH_2O), 4.20 (1H, m, C*H*O), 6.93 (4H, d, J = 9.0 Hz, 4 × Ar*H*), 7.58 (4H, d, J = 9.0 Hz, 4 × Ar*H*).

^{13}C NMR ($CDCl_3$, 150 MHz) δ −4.65 (*C*H$_3$)$_2$Si, 17.9 (*C*(CH$_3$)$_3$), 21.6 (2 × *C*H$_2$), 25.8 ((*C*H$_3$)$_3$Si), 64.5 (*C*H$_2$O), 65.8 (*C*HO), 103.9 (2 × Ar*C*), 115.1 (4 × Ar*C*H), 119.2 (2 × *C*N), 134.0 (4 × Ar*C*H), 162.1 (2 × Ar*C*O).

MS (ESI-TOF): [M + H]$^+$, $C_{25}H_{33}N_2O_3Si$ requires 437.2255, found 437.2255.

4,4′-(3-Hydroxypentane-1,5-diyl)bis(oxy)dibenzonitrile (3b). 4,4′-(3-(tert-butyldimethylsilyloxy)pentane-1,5-diyl)bis(oxy)-dibenzonitrile (**3a**) from the previous step was dissolved in MeOH (250 mL). Conc HCl (6 drops) was added and the reaction allowed to stir at rt for 1 h. The reaction mixture was concentrated in vacuo, and the crude product mixture was purified by flash chromatography on silica gel (30% EtOAc/Hx) to give 4,4′-(3-hydroxypentane-1,5-diyl)bis(oxy)dibenzonitrile (**3b**) (3 g, 9.3 mmol, 38% over 2 steps) as a white solid.

^{1}H NMR ($CDCl_3$, 600 MHz) δ 2.00 (2H, m, CH_2), 2.06 (2H. m, CH_2), 4.18 (3H, m, C*H*O and CH_2O), 4.26 (2H, m, CH_2O), 6.96 (4H, d, J = 9.0 Hz, 4 × Ar*H*), 7.57 (4H, d, J = 9.0 Hz, 4 × Ar*H*).

^{13}C NMR ($CDCl_3$, 150 MHz) δ 36.5 (*C*H_2), 65.5 (*C*H_2O), 66.6 (*C*HO), 104.1 (2 × Ar*C*), 115.1 (4 × Ar*C*H), 119.1 (2 × *C*N), 134.0 (4 × Ar*C*H), 161.9 (2 × Ar*C*O).

MS (ESI-TOF): $[M + H]^+$, $C_{19}H_{19}N_2O_3$ requires 322.1390, found 322.1395.

***tert*-Butyl 2-(1,5-Bis(4-cyanophenoxy)pentan-3-yloxy)acetate (*4*).** To a solution of 4′-(3-hydroxypentane-1,5-diyl)bis(oxy)dibenzonitrile (**3b**) (32 mg, 0.10 mmol, 1 equiv) in toluene (2 mL) was added 25% aq NaOH and tetrabutylammonium hydrogen sulfate (4 mg). The reaction was allowed to stir vigorously at rt for 4 h. The reaction mixture was then extracted with CH_2Cl_2. The combined organic layers were dried ($MgSO_4$) and concentrated in vacuo. The crude product mixture was purified by flash chromatography on silica gel (30% EtOAc/Hx) to give *tert*-butyl 2-(1,5-bis(4-cyanophenoxy)pentan-3-yloxy)acetate (**4**) (34 mg, 0.08 mmol, 77%) as a clear oil.

^{1}H NMR ($CDCl_3$, 600 MHz) δ 1.39 (9H, s, (CH_3)$_3$C), 2.07 (4H, q, J = 7.2 Hz, 2 × CH_2), 3.84 (1H, t, J = 7.2 Hz, C*H*O), 3.97 (2H, s CH_2CO$_2$*t*Bu), 4.14 (2H, m, CH_2O), 4.24 (2H, m, CH_2O), 6.94 (4H, d, J = 8.5 Hz, 4 × Ar*H*), 7.56 (4H, d, J = 9.0 Hz, 4 × Ar*H*).

^{13}C NMR ($CDCl_3$, 150 MHz) δ 28.0 (*C*H_3)$_3$C), 33.7 (2 × *C*H_2), 64.6 (2 × *C*H_2O), 67.7 (*C*HO), 74.8 (*C*H_2CO$_2$*t*Bu), 81.7 (*C*(CH$_3$)$_3$), 104.0 (2 × Ar*C*), 115.2 (4 × Ar*C*H), 119.2 (2 × *C*N), 133.9 (4 × Ar*C*H), 162.0 (2 × Ar*C*O), 169.3 (*C*═O).

MS (ESI-TOF): $[M + Na]^+$, $C_{25}H_{28}N_2O_5Na$ requires 459.1890, found 459.1883.

***tert*-Butyl 6-(2-(1,5-Bis(4-cyanophenoxy)pentan-3-yloxy)-acetamido)hexylcarbamate (5).** To a solution of *tert*-butyl 2-(1,5-bis(4-cyanophenoxy)pentan-3-yloxy)acetate (**4**) (262 mg, 0.61 mmol, 1 equiv) in CH_2Cl_2 (20 mL) was added TFA (4 mL), and the reaction was allowed to stir at rt for 1 h. The reaction was then concentrated in vacuo to give *tert*-butyl 6-(2-(1,5-bis(4-cyanophenoxy)pentan-3-yloxy)acetamido)hexylcarbamate which was used without further purification. *tert*-Butyl 6-(2-(1,5-bis(4-cyanophenoxy)pentan-3-yloxy)acetamido)hexylcarbamate (0.61 mmol, 1 equiv) was dissolved in CH_2Cl_2 (20 mL). NEt_3 (0.43 mL, 3.05 mmol, 5 equiv), BOP (322 mg, 0.73 mmol, 1.2 equiv), and *N*-Boc-1,6-diaminohexane (158 mg, 0.73 mmol, 1.2 equiv) were added and the reaction allowed to stir at rt for 4 h. The reaction mixture was washed with aq sat NaCl, dried ($MgSO_4$), and concentrated in vacuo. The crude product mixture was purified by flash chromatography on silica gel (EtOAc) to give *tert*-butyl 6-(2-(1,5-bis(4-cyanophenoxy)pentan-3-yloxy)acetamido)hexylcarbamate (**5**) (264 mg, 0.46 mmol, 75% over 2 steps).

^{1}H NMR (MeOD, 600 MHz) δ 1.26 (4H, m, 2 × CH_2), 1.41 (13H, s and m, 2 × CH_2 and (CH$_3$)$_3$C of NHBoc), 2.11 (4H, m, 2 × CH_2), 2.99 (2H, m, CH_2N), 3.15 (2H, m, CH_2N), 3.92 (1H, t, J = 6.0 Hz, C*H*O), 3.99 (2H, s, CH_2), 4.21 (4H, m, 2 × CH_2O), 7.05 (4H, d, J = 9.0 Hz, 4 × ArC*H*), 7.63 (4H, d, J = 8.4 Hz, 4 × ArC*H*).

^{13}C NMR (MeOD, 150 MHz) δ 27.5 (2 × *C*H$_2$), 28.8 ((*C*H$_3$)$_3$C), 30.5 (*C*H$_2$), 30.9 (*C*H$_2$), 34.6 (2 × *C*H$_2$), 39.9 (*C*H$_2$N), 41.4 (*C*H$_2$N), 66.1 (2 × *C*H$_2$O), 69.7 (*C*H$_2$O), 76.4 (*C*HO), 79.5 (C_{quat} of NHBoc), 104.8 (2 × Ar*C*), 116.6 (4 × Ar*C*H), 120.1 (2 × *C*N), 135.2 (4 × Ar*C*H), 158.6 (*C*═O), 163.8 (2 × Ar*C*O), 172.3 (*C*═O).

MS (ESI-TOF): $[M + Na]^+$, $C_{35}H_{42}N_4O_6Na$ requires 601.2996, found 601.2298.

***N*-(6-Aminohexyl)-2-(1,5-bis(4-carbamimidoylphenoxy)-pentan-3-yloxy)acetamide (6).** To a solution of *tert*-butyl 6-(2-(1,5-bis(4-cyanophenoxy)pentan-3-yloxy)acetamido)hexylcarbamate (**5**) (70.6 mg, 0.12 mmol, 1 equiv) in anhydrous ethanol was added NEt_3 (0.14 mL, 0.98 mmol, 8 equiv) and anhydrous NH_2OH (68 mg, 0.98 mmol, 8 equiv). The reaction mixture was placed in a sealed tube and heated overnight at 90 °C. The reaction mixture was then concentrated in vacuo to remove the ethanol solvent. The residue was dissolved in EtOAc and washed with water. The organic layer was then dried ($MgSO_4$) and concentrated to give the bis-aldoxime. A solution of the bis-aldoxime in MeOH (30 mL) was placed under an argon atmosphere. 10% Pd/C (10 mg) was added and the reaction mixture placed under an atmosphere of hydrogen at balloon pressure. After 18 h, the hydrogen atmosphere was removed, and the reaction mixture was filtered through celite and concentrated in vacuo to give *tert*-butyl 6-(2-(1,5-bis(4-cyanophenoxy)pentan-3-yloxy)acetamido)hexylcarbamate (62 mg, 0.10 mmol, 84% over 2 steps). Finally, *tert*-butyl 6-(2-(1,5-bis-(4-cyanophenoxy)pentan-3-yloxy)acetamido)hexylcarbamate was treated with 25% TFA in CH_2Cl_2 (20 mL). The reaction was allowed to stir at rt for 4 h and then concentrated in vacuo to give the *N*-(6-aminohexyl)-2-(1,5-bis(4-carbamimidoylphenoxy-)pentan-3-yloxy)acetamide (**6**) in quantitative yield, which was used in the immobilization step without further purification.

^{1}H NMR (MeOD, 600 MHz) δ 1.33 (4H, m, 2 × CH_2), 1.47 (2H, m, CH_2), 1.60 (2H, m, CH_2), 2.11 (4H, m, 2 × CH_2), 2.87 (2H, t, J = 7.5 Hz, CH_2N), 3.16 (2H, t, J = 7.2 Hz, CH_2N), 3.92 (1H, m, C*H*O), 3.98 (2H, s, CH_2O), 4.22 (4H, m, 2 × CH_2O), 7.11 (4H, d, J = 8.4 Hz, 4 × Ar*H*), 7.76 (4H, d, J = 9.0 Hz, 4 × Ar*H*).

^{13}C NMR (MeOD, 150 MHz) δ 27.0 (*C*H$_2$), 27.4 (*C*H$_2$), 28.5 (*C*H$_2$), 30.4 (*C*H$_2$), 34.8 (2 × *C*H$_2$), 39.8 (*C*H$_2$N), 40.7 (*C*H$_2$N), 66.2 (2 × *C*H$_2$O), 69.9 (*C*H$_2$O), 76.4 (*C*HO), 116.3 (4 × Ar*C*H), 121.2 (2 × Ar*C*), 131.1 (4 × Ar*C*H), 165.1 (2 × Ar*C*O), 167.6 (*C*═NH), 172.5 (*C*═O).

MS (ESI-TOF): $[M + H]^+$, $C_{27}H_{41}N_6O_4$ requires 513.3184, found 513.3187.

Immobilization of Ligand (6) onto Activated Sepharose Beads. Endotoxin-binding ligand *N*-(6-aminohexyl)-2-(1,5-bis-(4-carbamimidoylphenoxy)pentan-3-yloxy)acetamide (**6**) was attached to carbonyldiimidazole-activated Sepharose beads (Reacti-Gel CDI support, Pierce) according to the manufacturer's directions. Briefly, a 5 mg/mL solution of ligand *N*-(6-aminohexyl)-2-(1,5-bis(4-carbamimidoylphenoxy)pentan-3-yloxy)-acetamide in 100 mM borate buffer, pH 9, was prepared. Reacti-Gel beads were added to a polypropylene cartridge, acetone solvent was drained off, and 1 mL of 5 mg/mL ligand solution was added to the cartridge per milliliter of Reacti-Gel beads. The mixture was allowed to shake for 24 h at rt. The solution of ligand was then drained from the beads. 50 mM Tris buffer, pH 9.2, was added (1 mL of buffer per mL of bead volume) and the mixture allowed to shake overnight in order to quench unreacted CDI groups. Finally, excess Tris buffer was drained, and the beads were washed with PBS buffer (pH 7.4) and stored in a suspension of PBS until use. Control beads were prepared analogously by treatment of Reacti-Gel beads with 100 mM borate buffer containing no ligand, followed by blocking reactive groups with Tris buffer.

Fluorescein Displacement Assay for Quantifying Binding Affinity to LPS. The BODIPY-cadaverine (BC) displacement assay was used to quantify the binding affinity of ligand **6** to LPS. This assay was performed according to a published procedure (*7*). Briefly, 10 mM stock of ligand in 50 mM Tris (pH 7.4) was prepared. A stock solution of 5 mg/mL LPS from *E. coli* 0111:B4 (Sigma) in 50 mM Tris (pH 7.4) and a stock solution of 500 μM BC (BODIPY−TR cadaverine, obtained from Invitrogen)−50 mM Tris (pH 7.4) were prepared. 0.1 mL of each of the LPS and BC stocks were mixed and the mixture diluted to a final volume of 10 mL using 50 mM Tris buffer to

give an LPS−BC mixture composed of 50 μg/mL LPS and 5 μM BC. Corning nonbinding surface 96 well plates were used in this assay.

To the first well of a 96 well plate was added 40 μL of 10 mM ligand stock solution and 40 μL of 50 mM Tris buffer. Twofold serial dilution across the plate was carried out, and then 40 μL of Tris was added to each well to give 80 μL volume in each well. 80 μL of LPS−BC (50 μg/mL−5μM) mixture was added to each well. Each experiment was repeated in triplicate. Fluorescence measurements were made at 25 °C on a SpectraMAX GeminiEM fluorescence plate reader. BC excitation wavelength of 580 nm was used; emission was measured at 620 nm.

The K_d(app) values for interaction of ligand **6**, PMB, and pentamidine with LPS were calculated. Curves were fitted to the function $F = F_{max}[L]/(K_d + [L]) + c$ using *WinCurveFit* software. In the case of ligand **6** and pentamidine, fluorescence measurement values used in the curve fit were corrected to account for a concentration-dependent linear background fluorescence effect.

Binding Assays of Sepharose−Ligand 6 Beads with FITC-Labeled LPS. Sepharose−ligand **6** beads were tested for the ability to bind endotoxin using FITC-labeled LPS. A 50 mg/mL concentrated stock solution of *E. coli* 0111:B4 FITC conjugate (purchased from Sigma) in 50 mM Tris buffer, pH 7.4, was prepared. A standard curve of fluorescence at various concentrations of LPS−FITC was prepared (excitation at 495 nm, emission at 525 nm).

Sepharose−ligand **6** beads, control beads, and commercially available agarose-supported Polymyxin B (purchased from Sigma) were tested concurrently for ability to bind LPS−FITC. The experiments were carried out as follows.

100 mg of dried beads was weighed into an Eppendorf tube, and 400 μL of 50 mM Tris buffer, pH 7.4, was added to the tube. A known quantity of concentrated LPS−FITC stock (50 mg/mL) was added to each tube, and the tubes were allowed to shake 30 min. The mixtures were then centrifuged; and 100 μL of the supernatant was removed and placed in a microplate well, and the fluorescence (ex 495 nm, em 525 nm) was measured. Following the fluorescence measurement, the sample was returned to the appropriate Eppendorf tube, and a further aliquot of concentrated LPS−FITC stock was added. This process was repeated until a final LPS−FITC concentration of 8000 μg/mL had been reached. [LPS−FITC] free in the supernatant after incubation was calculated and plotted against the original [LPS−FITC] in the tube.

Curves were fitted to the following function using *Kaleidagraph*:

$$LPS_{free} = LPS_{total} - \left[\frac{(LPS_{total} + M_1 + M_2 - \sqrt{(LPS_{total} + M_1 + M_2)^2 - 4LPS_{total}M_2})}{2}\right]$$

where $M_1 = K_d$ and M_2 = total binding sites.

Endotoxin Removal and Protein Loss Following Purification of Samples of Endotoxin-Contaminated Antibody. Sepharose−ligand **6**, control beads, and Pierce Detoxigel beads (agarose-bound PMB) were poured into columns of 1 mL volume. Using pyrogen-free solutions, each column was equilibrated with 3× column volume washes of 1% sodium deoxycholate soln, followed by 5× the column volume of nanopure, filtered water. Solutions of antibody (of known concentration, volume, and endotoxin content) buffered with 0.1−0.5 M NaCl were loaded onto each column. Columns were capped off and allowed to incubate for 1 h. Samples were then eluted from the columns, and the columns were then rinsed with an addition 1 mL of water to clear the void space. Samples were collected, the OD at 280 nm was measured, and the protein concentration was calculated. Endotoxin levels in each sample were then tested using the LAL (*Limulus* Amebocyte Lysate) endotoxin test kit, purchased from Cambrex Bioscience (cat. no. 50-647U).

The LAL endotoxin test uses modified *Limulus* amebocyte lysate and a chromogenic peptide substrate. Bacterial endotoxin catalyzes the conversion of a pro-enzyme in the *Limulus* amebocyte lysate to an active enzyme. The active enzyme then catalyzes the release of *p*-nitroaniline from a colorless peptide substrate. After a given time period, the reaction is stopped by addition of acid, and the *p*-nitroaniline released can be quantitated photometrically by measuring absorbance at 405−410 nm. The amount of *p*-nitroaniline released is proportional to the endotoxin concentration present and can be calculated from a standard curve.

The LAL assay was carried out according to the manufacturer's directions as described in the instruction manual. Briefly, samples were diluted to various strengths, mixed with the lysate reagent supplied in the kit, and incubated at 37 °C for 10 min. The chromogenic peptide substrate was then added and the samples allowed to incubate for a further 6 min. Finally, the reaction was stopped by the addition of 25% glacial acetic acid. Absorbance at 405−410 nm was measured, and these values were used to calculate endotoxin content in the samples.

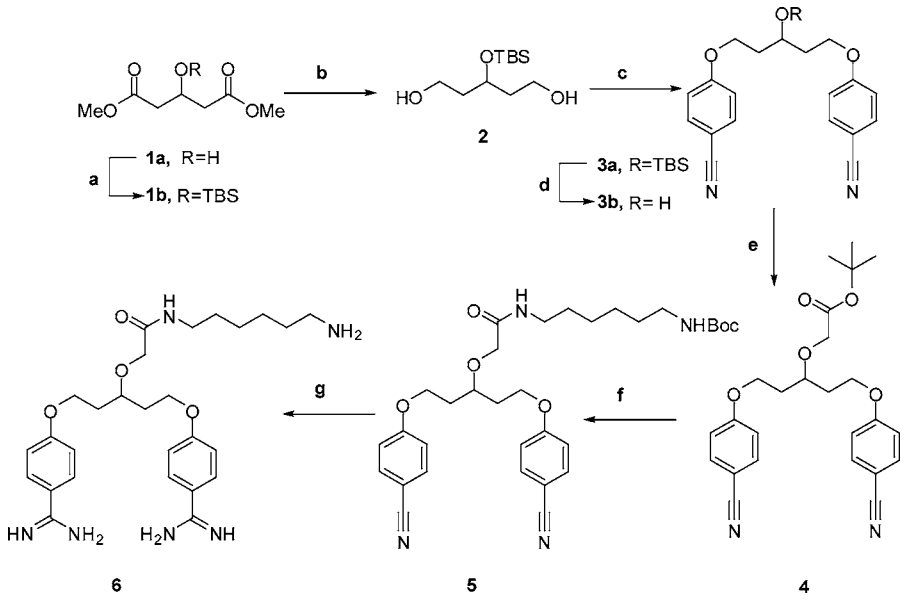
RESULTS AND DISCUSSION

Synthetic Route to Tethered Pentamidine-Derived Ligand. Synthesis of tethered pentamidine ligand **6** is shown in Scheme 1. The alcohol functionality of commercially available dimethyl 3-hydroxyglutarate **1a** was protected as the TBS ether and the terminal ester groups were subsequently reduced with DIBALH to give diol **2** in good yield. Mitsonobu reaction of diol **2** with 4-hydroxybenzonitrile followed by removal of the silicon protecting group afforded bis-nitrile **3b**. Alkylation of the secondary alcohol in **3b** with *tert*-butyl bromoacetate was achieved under mild conditions using a biphasic system of THF/H_2O in the presence of 25% NaOH and a phase-transfer catalyst to give *tert*-butyl ester **4**. Deprotection of ester **4** by treatment with TFA, followed by BOP coupling of the resulting acid with *N*-Boc-1,6-diaminohexane provided amide **5**. Finally, the nitrile groups were converted into amidines in a two-step process. Bis-nitrile **5** was first treated with hydroxylamine, which had been dried by azeotroping with toluene prior to the reaction. If hydrated hydroxylamine is used in this step, then a significant amount of the nitrile is converted to the corresponding amide. This unwanted byproduct is difficult to separate from the desired bis-amidine **6**, such that HPLC purification is required. However, use of anhydrous hydroxylamine results exclusively in the formation of the desired bis-aldoxime intermediate, which can then be converted to pure bis-amidine in good yield by catalytic hydrogenation. Ultimately, removal of the Boc group from the terminal nitrogen gave pentamidine-derived ligand **6**.

Binding Affinity of Pentamidine-Derived Ligand (6) to LPS. Prior to immobilization of ligand **6** onto sepharose support, we examined its binding affinity to an LPS solution. Although pentamidine itself is reported to bind strongly to lipid A, we felt it was important to confirm that incorporation of a tether functionality did not have a detrimental effect on binding affinity. It has been postulated that modifying the structure of pentamidine such that it incorporates a hydrophobic chain at an appropriate position may indeed improve its affinity for LPS/lipid A due to stabilizing interactions with the acyl chains of lipid A (*6*).

A fluorescent probe displacement assay employing BODIPY−TR cadaverine (BC) was used to test the binding affinity of ligand **6** with LPS, and for comparison, pentamidine and Polymyxin B were also examined (*7*). BC interacts strongly with

Scheme 1. Synthetic Route to Ligand 6[a]



[a] (a) TBSCl, imdazole, DMF, rt, 100%; (b) DIBALH, CH_2Cl_2, 0 °C, 93%; (c) 4-hydroxybenzonitrile, PPh_3, DIAD, THF; (d) HCl, MeOH, 38% over 2 steps; (e) *tert*-butyl-2-bromoacetate, $NaHSO_4$, 25% NaOH, toluene, rt, 77%; (f) 1. 25% TFA in CH_2Cl_2; 2. *N*-Boc-1,6-diaminohexane, BOP, NEt_3, CH_2Cl_2, 75%; (g) 1. $NH_2OH{\cdot}HCl$ (anhydrous), NEt_3, EtOH, sealed tube; 2. H_2, Pd/C, AcOH, MeOH, 84% over 2 steps; 3. 25% TFA in CH_2Cl_2.

LPS, and upon binding, its fluorescence emission intensity at 620 nm is significantly reduced. In the presence of compounds which bind LPS, BC is displaced, and an increase in emission intensity at 620 nm is observed. This assay provides a convenient method of calculating apparent dissociation constants for the binding of molecules to LPS.

The BODIPY fluorescent displacement assay curves for ligand **6** and for PMB are shown in Figure 3. It was found that ligand **6** binds to LPS with K_d(app) of 180 μM (±60), which is similar to the affinity of pentamidine at 190 μM (±40) (curve not shown). Therefore, it could be concluded that incorporation of a tether group at this position in the molecule does not adversely affect the binding affinity. In our control, K_d(app) of Polymyxin B was found to be 2 μM (±0.6), which is consistent with published results (*8*). It is noteworthy that David et al. have reported PMB and pentamidine to bind lipid A with similar affinities, having K_d(apps) of 0.37 and 0.12 μM, respectively (*5*). In our studies, where we examined relative affinities to LPS, we discovered that PMB has an appreciably greater affinity for LPS than pentamidine. However, the affinity of pentamidine and its derivatives, such as ligand **6**, is still significant in view of the simplicity of their molecular structures.

Immobilization of Ligand 6 onto CDI-Activated Sepharose, Reacti-Gel. Ligand **6** was immobilized onto commercially available carbonyldiimidazole-activated sepharose beads (Reacti-Gel, Pierce) as shown in Scheme 2. Reacti-Gel is an activated form of sepharose particularly suitable for immobilizing small organic molecules and peptides bearing free amino groups. A solution of the ligand in basic aqueous buffer was allowed to react with the Reacti-Gel beads to form a carbamate linkage to the support; unreacted groups were then blocked by incubation with Tris buffer.

Binding Studies of FITC-Labeled LPS with Sepharose-Supported Ligand 6. The ability of our affinity beads to remove LPS from solutions was assessed using LPS from *E. coli* 0111: B4, which had been labeled with fluorescein (LPS−FITC). The change in fluorescence of a solution after incubation with the beads was measured. Thus, modified sepharose beads **7** were filtered to remove excess buffer, and 100 mg samples of **7** were weighed for use. 50 mM Tris buffer (400 μL) was added to **7**, and aliquots of a concentrated LPS−FITC stock (50 mg/mL)

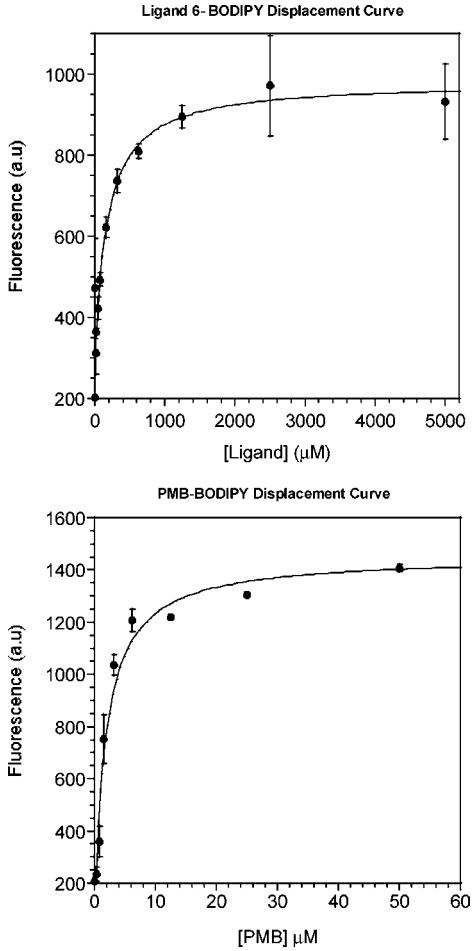
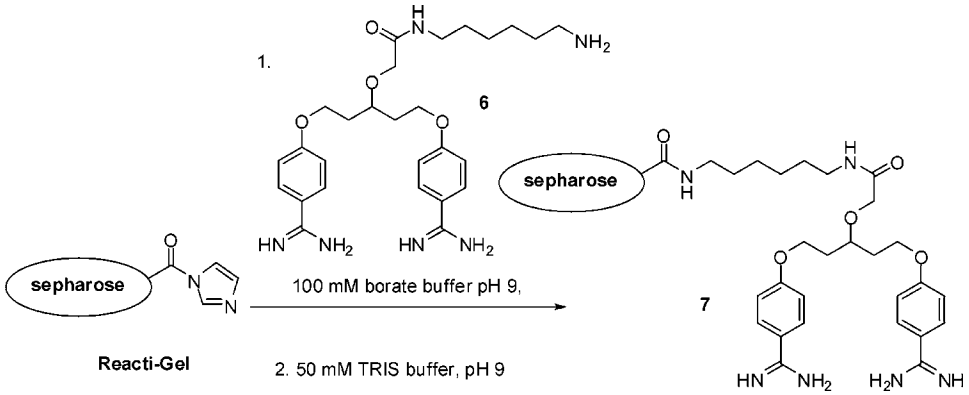


Figure 3. Displacement of LPS bound BC by ligand **6** (top). Displacement of LPS bound BC by Polymyxin B (bottom).

were added successively to the suspension of beads. After the addition of each aliquot, the mixture was allowed to shake for 30 min. Following centrifuging to separate **7** from the LPS−FITC solution, a 100 μL aliquot from the supernatant was

Scheme 2. Immobilization of Ligand 6 onto Reacti-Gel Beads



removed and its fluorescence measured. This experiment was also performed concurrently on control beads (Reacti-Gel which had not been treated with ligand **6** but had been treated with Tris buffer to block reactive groups) and on commercially available agarose-supported Polymyxin B. A standard curve of fluorescence versus concentration of FITC−LPS was prepared ($\lambda_{ex} = 496$ nm and $\lambda_{em} = 525$ nm) and used to calculated free LPS concentration in the supernatant following incubation with each type of bead. Free [LPS−FITC] in the supernatant was plotted against the total [LPS−FITC] for both **7** and agarose−PMB beads and curves fitted to the following function:

$$\mathrm{LPS_{free}} = \mathrm{LPS_{total}} - \left[\frac{(\mathrm{LPS_{total}} + M_1 + M_2 - \sqrt{(\mathrm{LPS_{total}} + M_1 + M_2)^2 - 4\mathrm{LPS_{total}}M_2})}{2}\right]$$

where $M_1 = K_d$ and $M_2 =$ total binding sites. Figure 4 shows the relationships between $[\mathrm{LPS-FITC}]_{free}$ and $[\mathrm{LPS-FITC}]_{total}$. We were surprised to find that both **7** and agarose−PMB beads performed similarly, particularly at lower [LPS−FITC] concentrations. However, we note that the K_d values for both ligands appear to be significantly greater when they are attached to the support than their K_d values in solution. Sepharose-bound ligand **6** displays a K_d of 596 μM ± 120 and agarose-bound PMB shows a K_d of 948 μM ± 340, indicating that the resin-bound versions of both these ligands do not interact as strongly with endotoxin as they do in solution. However, both systems can effectively reduce endotoxin concentration by approximately 50% at the lower concentrations. From this data, we were also able to estimate a maximal binding capacity for both affinity beads. Agarose−PMB resin had a maximal binding capacity of 24 ± 5 μg [LPS−FITC]/mg resin, while resin **7** had a maximal binding capacity of 17 ± 2 μg [LPS−FITC]/mg resin. The apparently higher maximal binding capacity for the agarose−PMB system may account for its improved performance in reducing [LPS−FITC] levels at higher concentrations.

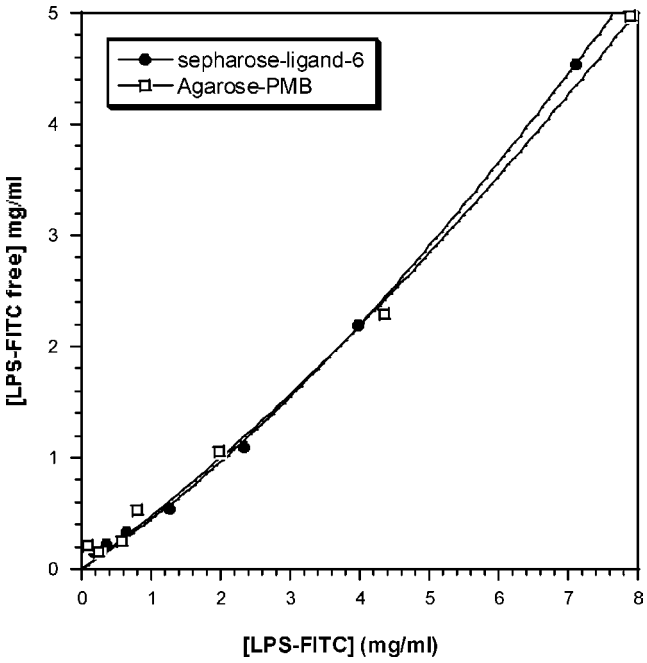


Figure 4. Binding of LPS-FITC by sepharose−ligand **6** and agarose PMB affinity beads.

These results suggested that our affinity system can effectively remove LPS from contaminated solutions. Subsequently, we wanted to assess if this support could be successfully recycled. Table 1 shows the results of recycling with various reagents. Following the incubation of each sample of beads with 500 μg/mL LPS−FITC solution, the beads were washed with a solution of the recycling reagent. The beads were then reincubated with a 500 μg/mL solution of LPS−FITC, and the reduction in LPS−FITC concentration was measured by the fluorescence method described (vide supra). In most cases, the beads could be recycled with only a slight reduction in LPS binding capability after the first round of recycling. We found that 2% Triton X-100 was very effective at restoring LPS binding capability of the beads even after the third round of recycling.

Application of Sepharose-Bound Ligand 6 Beads in Affinity Chromatographic Purification of Endotoxin-Contaminated Antibodies. Finally, we have applied affinity beads **7** in the chromatographic purification of endotoxin-contaminated samples of several different antibody samples of various protein contamination levels and endotoxin contamination levels. Protein loss during affinity-based purification procedures is a significant shortcoming associated with endotoxin removal. We therefore wanted to ensure that our system could effectively reduce endotoxin levels without resulting in unacceptable levels of protein loss. The antibody samples were each passed through a 1 mL column of affinity beads **7**, Pierce Detoxi-Gel beads (i.e.,

Table 1. Recycling of Affinity Beads

recycling reagent	sepharose−ligand **6** (% reduction in concn of LPS-FITC soln)	agarose−PMB (% reduction in concn of LPS−FITC soln)
before recycling	43 (±3)	57 (±1)
1% sodium deoxycholate	34 (±1)	46 (±4)
methanol	1st round: 39 (±8)	1st round: 45 (±1)
	2nd round: 25 (±4)	2nd round: 45 (±1)
1 M NaOH then methanol	35 (±3)	47 (±3)
2% Triton X-100	1st round: 37 (±6)	1st round: 60 (±2)
	2nd round: 27 (±1)	2nd round: 60 (±1)
	3rd round: 34 (±4)	3rd round: 55 (±4)

Table 2. Endotoxin Removal from Antibody Samples

	Results of LAL Endotoxin Test (EU/ml) affinity column		
antibody	sepharose−ligand **6**	control	agarose−PMB
1 mL of 2.7 mg/mL A7R34 (10-25 EU/mL)[a]	ND[b]	>10	ND[b]
4 mL of 2.7 mg/mL A7R34 (10-25 EU/mL)[a]	ND[b]	>10	ND[b]
4 mL of 3.48 mg/mL KA 417F4 (1.25 EU/mL)[a]	ND[b]	5−10	ND[b]
1.5 mL of 10 mg/mL GNL 23A6 (125-250 EU/mL)[a]	250−500	500−1000	5−10
2 mL of 11 mg/mL FTB 8E9 (500−1000 EU/mL)[a]	50	125−250	25−50

[a] Values in paretheses indicate initial endotoxin contamination level prior to affinity chromatography. [b] ND indicates that endotoxin was not detected; levels were below sensitivity of detection in LAL assay, i.e., ≤0.1 EU/mL.

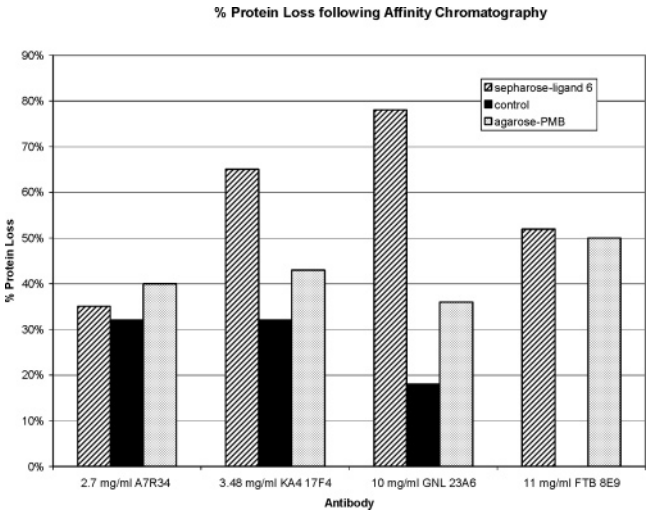


Figure 5. Graph representing % protein loss from samples of antibody following affinity chromatography.

agarose-bound PMB), and control beads. Following elution from the column, the samples were tested for endotoxin concentration using the LAL (*Limulus* Amebocyte Lysate) assay (*9*) and for protein content. The results of the endotoxin testing and protein content tests are shown in Table 2 and Figure 5, respectively.

Table 2 displays the results of LAL endotoxin testing on the antibody samples following affinity chromatography. Antibody A7R34 was contaminated with 10−25 EU/mL prior to affinity chromatography. When a sample loading of 1 mL of A7R34 was applied to 1 mL chromatography columns, both sepharose−ligand **6** and agarose−PMB columns reduced endotoxin levels to a level lower than the detection limit of the LAL assay, while the control column did not reduce endotoxin content. At a higher sample loading volume of 4 mL of A7R34 (and therefore higher endotoxin load), the sepharose−ligand **6** column was also effective in reducing endotoxin level completely. Each affinity column was regenerated, and antibody KA 417F4 contaminated with 1.25 EU/mL was applied. Gratifyingly, the endotoxin level in KA 417F4 was also reduced to a negligible level by the sepharose−ligand **6** affinity system. ELISA studies on purified KA 417F4 against the original BSA−hapten conjugate to which it was raised confirmed that the antigen binding capability of the antibody had not been diminished during the purification process and that no cross contamination had occurred (i.e., that KA 417F4 had not become contaminated with A7R34). Antibodies GNL 23A6 and FTB 8E9 both had considerably higher protein concentrations and endotoxin contamination levels. In both cases, affinity chromatography with the agarose−PMB system was slightly more effective at reducing endotoxin levels. This is possibly due to a greater number of binding sites; however, affinity beads **7** did give a significant reduction in endotoxin level in the case of both antibodies. These results confirmed that sepharose−ligand **6** beads could reduce endotoxin levels as effectively as the agarose−PMB systems at lower endotoxin loadings and that regeneration of the columns was effective and did not result in cross contamination between protein samples.

Figure 5 shows the percentage of protein loss from different antibody samples following chromatography using each type of affinity system. With the exception of antibody GNL 23A6, protein loss following chromatography with the sepharose−ligand **6** system was comparable to that found with the PMB systems. There does not appear to be a strong correlation between antibody concentration and protein loss; for example, 2.7 mg/mL AR734 and 11 mg/mL FTB 8E9 have the most comparable protein loss of any of the antibodies tested despite a large difference in antibody concentration. The differences in percentage of protein loss between the different antibodies may be attributed to the differences in charge on the protein itself. Ansprach (*4*) has reported significant differences between protein recoveries of negatively charged BSA and positively charged lysozyme when endotoxin-contaminated solutions of each of these proteins were subjected to identical endotoxin removal affinity columns. Ansprach proposed that the negatively charged protein competes with endotoxin for ligand binding sites on the affinity column, and thus protein recovery is reduced. It was also observed that different affinity sorbents displayed different degrees of protein loss depending on the degree of specificity of the ligand for endotoxin over the negatively charged protein. The high protein loss on GNL 23A6 for the sepharose−ligand **6** column may be attributed to the charge of the antibody.

CONCLUSION

In conclusion, we have described a simple synthetic route to a novel ligand which binds endotoxin. We have demonstrated that sepharose beads bearing this ligand can be used in affinity chromatography for the removal of endotoxin from contaminated solutions. These affinity beads can be recycled using a variety of simple reagents. In addition, we have verified that this inexpensive system does not result in any greater loss in protein than more expensive commercially available PMB systems. By acknowledging the crucial role of endotoxin removal in protein purification, this system provides an efficient, economical alternative to the PMB systems.

ACKNOWLEDGMENT

This work was supported by The Skaggs Institute for Chemical Biology.

LITERATURE CITED

(1) David, S. A. (2001) Towards a rational development of anti-endotoxin agents: novel approaches to sequestration of bacterial endotoxins with small molecules. *J. Mol. Recognit. 14*, 370−387.

(2) Gashe, Y., Pittet, D., and Sutter, P. (1995) Outcome and prognosis factors in bacteremic sepsis. In *Clinical trials for treatment of sepsis*, pp 35−51, Springer-Verlag, Berlin.

(3) Bone, R. C. (1993) Gram-negative sepsis: a dilemma of modern medicine. *Clin. Microbiol. Rev. 6*, 57−68.

(4) Anspach, F. B., and Hilbeck, O. (1995) Removal of endotoxins by affinity sorbents. *J. Chromatogr., A 711*, 81−92.

(5) David, S. A., Bechtel, B., Annaiah, C., Mathan, V. I., and Balaram, P. (1994) Interaction of cationic amphiphilic drugs with lipid A:

implications for development of endotoxin antagonists. *Biochim. Biophys. Acta 1212*, 167−175.
(6) David, S. A., Mathan, V. I., and Balaram, P. (1995) Interactions of linear dicationic molecules with lipid A: structural requisites for optimal binding affinity. *J. Endotoxin Res. 2*, 325−336.
(7) Wood, S. J., Miller, K. A., and David, S. A. (2004) Anti-endotoxin agents. 1. Development of a fluorescent probe displacement method optimized for the rapid identification of lipopolysaccharide-binding agents. *Comb. Chem. High Throughput Screening 7*, 239−249.
(8) Wood, S. J., Miller, K. A., and David, S. A. (2004) Anti-endotoxin agents. 2. Pilot high-throughput screening for novel lipopolysaccharide-recognizing motifs in small molecules. *Comb. Chem. High Throughput Screening 7*, 733−747.
(9) *Limulus* Amebocyte Lysate QCL-1000 instruction manual, cat. no. 50-647.U, Cambrex Bioscience, Walkersville, MD.

BC0602984

Efficient Sequence-Directed Psoralen Targeting Using Pseudocomplementary Peptide Nucleic Acids

Ki-Hyun Kim,† Xue-Jun Fan, and Peter E. Nielsen*

Department of Cellular and Molecular Medicine, University of Copenhagen, The Panum Institute, Blegdamsvej 3c, 2200 Copenhagen N, Denmark. Received October 14, 2006; Revised Manuscript Received November 21, 2006

A pair of decameric pseudocomplementary PNAs which bind to their mixed purine−pyrimidine sequence target in duplex DNA by double duplex invasion has been synthesized with a derivative of 8-methoxypsoralen conjugated to one of the PNAs. It is shown that this pair of psoralen-conjugated pseudocomplementary PNA oligomers, which target a site in the pBluescriptKS+ vector, upon irradiation with long-wavelength UV light (UVA) with high efficiency and specificity form photoadducts to an adjacent 5′-TA site, and more than 50% of these adducts are DNA interstrand cross-links. Transcription elongation by T7 or T3 RNA polymerase is specifically arrested at the psoralen cross-linking site, yielding more than 90% arrested product. These results emphasize the potential of pseudocomplementary PNA oligomers for highly specific gene targeting, in particular, with respect to sequence-directed psoralen photomodification of double-stranded DNA. Thus, such psoralen−PNA conjugates could be very useful in a range of biology and drug discovery applications.

INTRODUCTION

Design and discovery of chemical agents capable of sequence-specific DNA modification is a challenge with a wide potential for the development of gene knockdown and gene repair technologies in molecular biology and medicine. Many examples of such agents based on DNA minor groove binders (*1*), triple helix forming oligonucleotides (*2*), or zinc-finger DNA binding proteins (*3*) in combination with DNA alkylating reagents (*4*, *5*), photoreactive psoralens (*6*−*9*), or nucleases (*10*, *11*) have been described.

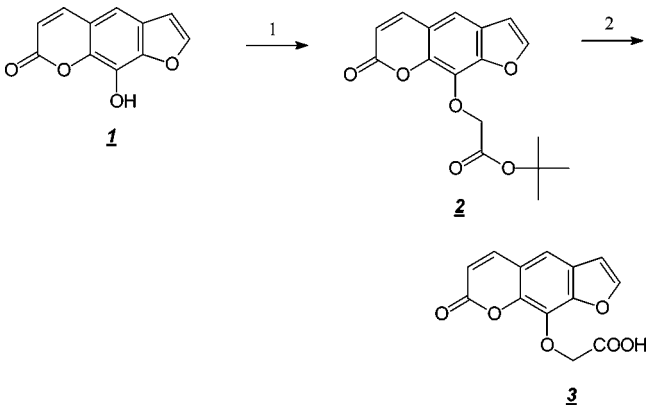
Such reagents may guide the discovery and development of highly specific antigene anticancer drugs and may lead to new techniques for highly specific site-directed mutagenesis in vivo. In particular, sequence-specific repair of targeted genes in somatic cells could eventually have a very significant impact on modalities for the treatment of genetically based diseases. State of the art techniques for the latter typically result in a low percentage (<2%) of repair (*12*−*14*). However, a recent study using Zn-finger−nuclease conjugates indicates that repair efficiencies approaching 20% may be reached when double-stranded DNA breaks are specifically introduced into the target domain (*10*).

We have introduced pseudocomplementary peptide nucleic acids (pcPNAs) as duplex DNA binding agents with only limited sequence constraints (≥50% AT content of the target) (*15*). In these PNAs, adenines and thymines are exchanged with diaminopurine and thiouracil, respectively, thereby strongly reducing the duplex formation of two (pseudo)complementary PNA oligomers (pcPNAs) but essentially not compromising their affinity for a complementary DNA target. Therefore, a pair of such pcPNAs can bind a duplex DNA target by double duplex invasion in which each PNA binds its complementary DNA strand.

It is well-established that psoralen DNA photolesions, in particular interstrand DNA cross-links, cause double-strand breaks in eukaryotic cells (*16*−*19*), and that such cross-links are mutagenic. Therefore, agents that target specifically induce psoralen cross-linking of double-stranded DNA could be of major interest in molecular biology and drug discovery for target-specific mutagenesis and somatic gene repair.

We now report the synthesis of psoralen-conjugated pseudocomplementary PNA oligomers which target a mixed purine−pyrimidine sequence and upon irradiation with long-wavelength UV light (UVA) with high efficiency form photoadducts to an adjacent 5′-TA site.

Scheme 1. Synthesis of the Psoralen Carboxylic Acid Derivative 3[a]



1 *2* *3*

[a] 1: *t*-butyl-2-bromoacatate/K_2CO_3 (92% yield). 2: Trifluoroacetic acid (95% yield).

EXPERIMENTAL SECTION

The psoralen carboxylic acid derivative was synthesized as shown in Scheme 1 (see also ref 20 reporting a psoralen "PNA monomer").

8-(*tert*-Butoxycarbonylmethyleneoxy)psoralen (3). A solution of 8-hydroxypsoralen (*21*) (333 mg, 1.64 mmol), *tert*-butyl-2-bromoacetate (1.28 g, 6.59 mmol), and K_2CO_3 (1.67 g) in dry acetone (50 mL) was refluxed for 2 h. The solid was removed by filtration and the acetone removed in vacuo. The residue was purified by column chromatography (silica gel, CH_2-

* Corresponding author. pen@imbg.ku.dk.

† Present address: Departments of Therapeutic Radiology and Genetics, Yale University School of Medicine, P.O Box 208040, New Haven, CT 06520-8040, USA.

10.1021/bc0603236 CCC: $37.00 © 2007 American Chemical Society
Published on Web 01/26/2007

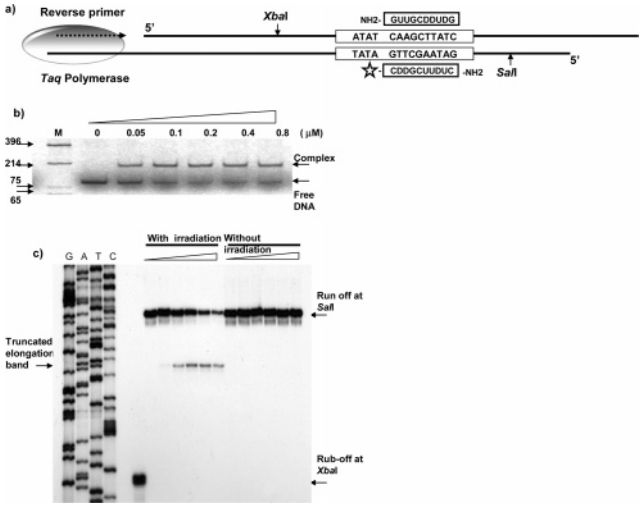


Figure 1. Analysis of photoadducts formed by pseudocomplementary PNA−psoralen conjugates. (A) Schematic drawing of the PNAs, the PNA target DNA, and the position of the primer. (B) Analysis of PNA 2222/2300 binding to *Sal*I-digested linear p260 by gel shift assay. An equimolar mixture of PNA 2222 and PNA 2300 at the indicated concentrations was incubated with *Sal*I-digested p260 in TE buffer in the presence of 10 mM KCl for 4 h at 37 °C. Subsequently, the sample was treated with restriction enzyme *Xba*I and analyzed by electrophoresis in a 10% nondenaturing polyacrylamide gel in TBE buffer. DNA bands were visualized by silver staining. (C) Determination of photoadduct formation site by PCR-based primer extension. PNA 2222/2300−p260 samples incubated as described above were UV-irradiated at 365 nm for 20 min on ice and subjected to PCR-based primer extension analysis. The DNA products were separated on a 10% denaturing polyacrylamide gel containing 7 M urea in TBE buffer and detected by radiography. Nonirradiated controls were also analyzed as well as a primer extension control of *Xba*I-digested p260.

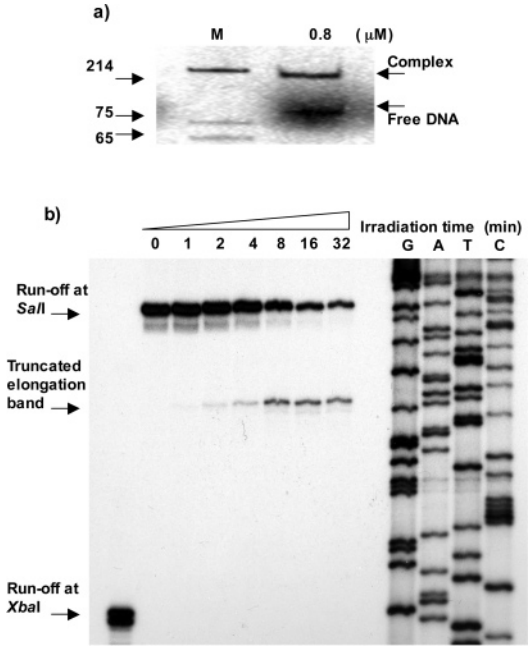


Figure 2. UV irradiation dependence of photoadduct formation. (A) Gel shift analysis of PNA binding to *Sal*I-digested p260 as described in Figure 1. (B) Primer extension-PCR analysis of the pcPNA−p260 complex described in (A) after UV irradiation. Conditions as in Figure 1C.

$C1_2$) to afford a white solid (474 mg, 92%). ^{1}H NMR (DMSO, 250 MHz) δ: 8.40 (d, J = 9.6 Hz, 1H), 8.10 (d, J = 2.2 Hz, 1H), 7.63 (s, 1H), 7.08 (d, J = 2.2 Hz, 1H), 6.44 (d, J = 9.6 Hz, 1H), 5.08 (s, 2H), 1.36 (s, 9H). ^{13}C NMR (DMSO, 62.9 MHz) δ: 167.67, 159.68, 147.78, 145.68, 15.28, 141.42, 130.37, 125.93, 116.37, 114.27, 113.32, 107.04, 81.56, 68.67, 27.63. Mass FAB+ found 316.10 (calcd. 316.24). R_f O.75 (MeOH/CH_2C1_2).

8-(Carboxymethyleneoxy)psoralen (3). Compound *2* (474 mg, 1.5 mmol) in neat TFA was refluxed for 2 h, after which the TFA was removed in vacuo and the product was coevaporated twice from acetonitrile to afford a white foam (330 mg, 95%). mp 204−206 °C. ^{1}H NMR (DMSO, 250 MHz) δ: 8.12 (d, J = 9.6 Hz, 1H), 8.10 (d, J = 2.0 Hz, 1H), 7.62 (s, l H), 7.07 (d, J = 2.0 Hz, 1H), 6.43 (d, J = 9.6 Hz, 1H), 5.12 (s, 2H). ^{13}C NMR (DMSO, 62.9 MHz) δ: 170.15, 159.85, 147.88, 145.89, 145.36, 141.61, 130.52, 126.06, 116.48, 114.36, 113.42, 107.09, 68.33. R_f 0.6 (1-butanol/AcOH/$H_2$0 2:1:1).

Pseudocomplementary PNA Synthesis. In this study, the following pseudocomplementary PNAs were used.

PNA 2222: H-$(Lys)_2$-GDU_S DDG CU_SU_S G-Lys-NH_2.

PNA 2225: Pso-$(eg1)_2$-$(Lys)_2$-CDD CGU_S U_SDU_S C-Lys-NH_2.

PNA 2300: Pso-$(eg1)_2$-$(Lys)_2$-CDD GCU_S U_SDU_S C-Lys-NH_2.

D designates 2.6-diaminopurine and U_s designates 2-thiouracil. Three lysine amino acids were attached for increasing the solubility and the binding affinity to DNA. 8-(carboxymethyleneoxy)psoralen (Pso) was attached to the N-terminal of PNA via two eg1 (8-amino-2,6-dioxaoctanoic acid) flexible linkers on the solid support using standard coupling conditions. The pseudocomplementary PNAs were synthesized and purified as described previously (*16*). The PNAs were homogeneous by HPLC and exhibited one major peak at the expected mass as analyzed by MALDI-TOF mass spectroscopy: PNA 2222 M_w = 3199 (calcd. 3202); PNA 2225 M_w = 3655 (calcd. 3655); PNA 2300 M_w = 3652 (calcd. 3656).

Plasmid Construct. Three plasmids, pBluescriptII SK+ (Stratagene), p206, and pSK1Xpso, were used in this study. Plasmids pSK1Xpso and P206 are simple derivatives of the pBluescriptII KS+ phagemid cloning vector (Stratagene), produced by cloning a synthetic duplex oligonucleotide (5′-GATCTTTCTTTTAAAATTA-3′ and 5′-GATCTAATTTTAA-AAGAAA-3′, or 5′-GATCCGTAGATCACT-3′ and 5′-GATC-CAGTGATCTACG-3′, respectively) into the *Bam*HI site of the polylinker between the promoters for T3 and T7 phage RNA polymerase (neither of these inserts are directly relevant for the experiments described in this paper, as the PNA target is part of the original pBluescriptII SK+ vector). These three plasmids behaved essentially identically with respect to PNA binding and psoralen targeting using the pcPNAs.

Double Duplex Invasion Complex Formation. For the formation of double duplex invasion complexes, a 1:1 mixture of PNA 2222 and PNA 2300 was incubated with 200 ng of *Sal*I-digested pBluescriptII SK+ or p206 (as indicated) in TE buffer (pH 7.4) with 10 mM KCl for 4 h at 37 °C.

Gel Shift Assay for Binding Efficiency of Pseudocomplementary PNA. Double duplex invasion complex was (following desired restriction enzyme treatment) analyzed by gel electrophoresis in 10% native polyacrylamide gels (30:1 acrylamide to bisacrylamide) using TBE buffer (90 mM Tris pH 8.0, 90 mM boric acid, and 2 mM EDTA). DNA bands were visualized by silver staining.

Analysis of Photoadduct Formation by PCR-Based Primer Extension. PNA double duplex invasion complexes were irradiated with long-wavelength UV light (365 nm, 13 J/m^2) for 20 min (or as indicated) on ice. Linear PCR primer extension analysis was performed by incubation in 30 μL PCR mixture (0.4 mM $MgCl_2$, 0.5 mM dNTP (each), 2 pmol ^{32}P-labled M13 reverse primer, and 2.5 unit *Taq* polymerase) for 30 cycles (45 s at 95 °C; 45 s at 56 °C; 80 s at 72 °C), followed by electrophoresis in 10% denaturing polyacrylamide (20:1 acrylamide to bisacrylamide) gels containing 7 M urea in TBE buffer.

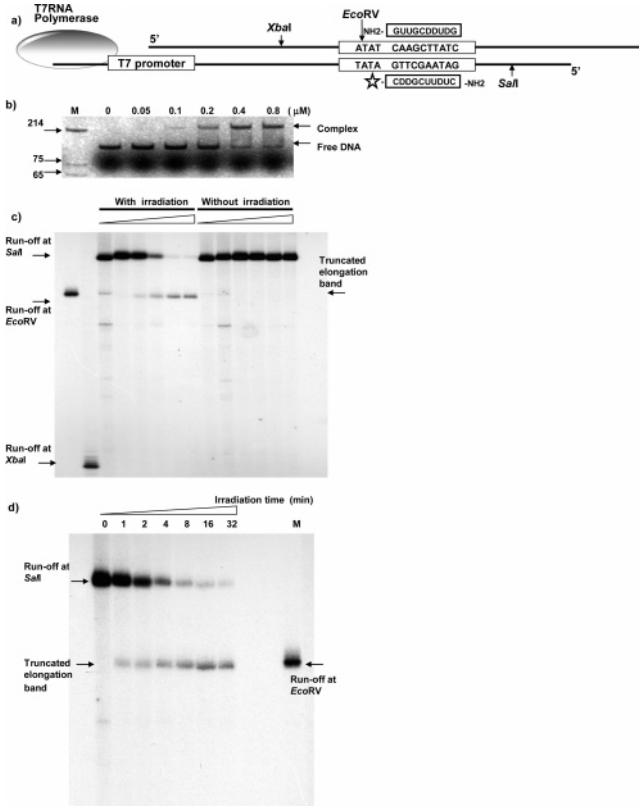


Figure 3. Concentration and UV-dose dependence of transcription elongation inhibition by pseudocomplementary PNA−psoralen conjugates. (A) Schematic drawing of the PNAs, the PNA target DNA, and the position of the T7 promoter. (B) Analysis of the binding of PNA 2222/2300 to *Sal*I-digested linear p206. As in Figure 1B, (C) Concentration dependence (0−0.8 μM as in (B)) of transcription elongation inhibition by photoadduct formation. The T7 RNA polymerase transcription products were analyzed by electrophoresis in 10% denaturing polyacrylamide gel containing 7 M urea in TBE buffer, and autoradiography. As RNA size marker, the runoff products of *Eco*RV- and *Xba*I-digested p206 were included. (D) UV-dose dependence of transcription elongation inhibition by photoadduct formation. The transcription reaction products were analyzed as described in (C).

As a marker, a DNA-sequencing reaction ladder of p260 was used. In parallel, PCR-based primer extension with nonirradiated PNA−plasmid mixture was done as a control. Radioactive bands were visualized by autoradiography using amplifying screen and Agfa Curix RP1 X-ray films exposed at −80 °C for 16 h.

Analysis of Photoadduct Formation by Transcription Elongation Arrest Assay Using T7 or T3 Phage RNA Polymerase. Transcription elongation arrest assay was performed in 30 μL transcription reaction mixture (0.5 mM NTP (except UTP), 0.1 mM UTP, 0.1 MBq [α-^{32}P]-UTP, 5 mM DTT, and 10 unit T7 or T3 RNA polymerase). After incubation at 37 °C for 20 min, the reaction was terminated by adding stop buffer (95% formamide, 20 mM EDTA, 0.05% bromophenol blue, 0.05% xylene cyanol), and the mixture was analyzed by electrophoresis in 10% denaturating polyacrylamide (20:1 acrylamide to bisacrylamide) gel containing 7 M urea in TBE buffer. As a size marker, the reaction mixture of transcription with *Eco*RV-digested and *Xba*I-digested linear p206 was used. Radioactive bands were visualized by autoradiography exposed at −80 °C for 16 h.

Analysis for Psoralen Interstrand Cross-Linking. Double duplex invasion complex was formed by incubating a 3′-^{32}P end-labeled *Xba*I/*Pvu*II DNA fragment of pBluescriptKS+ with PNA 2222 and PNA 2300 (20 nM each) in 120 μL 20 mM sodium phosphate, 1 mM EDTA, pH 6.5, overnight at 37 °C. Subsequently, the samples were UV-irradiated at 365 nm.

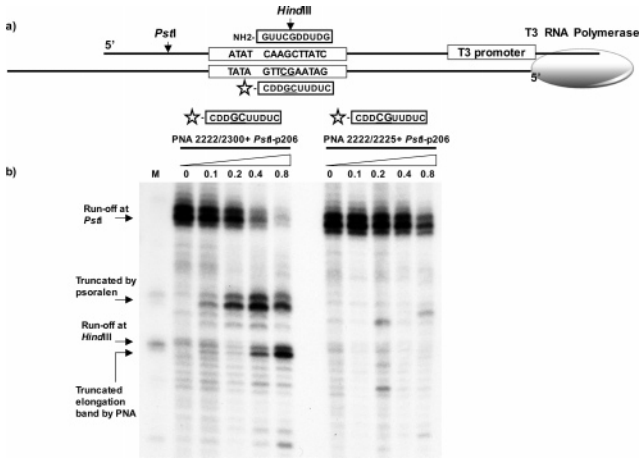


Figure 4. Effect of mismatches on duplex invasion complex formation. (A) Schematic drawing of the PNAs, the PNA target DNA, and the position of the T3 promoter. (B) Analysis of the effect of double duplex invasion complex formation and psoralen cross-linking on transcription elongation using T3 RNA polymerase. Double duplex invasion complex was formed by incubating a mixture of PNA 2222/2300 or PNA 2222/2225 (0 to 0.8 μM) with *Pst*I-cleaved p206 (PNA 2225 is a double mismatch control of PNA 2300). After UV-irradiation at 365 nm for 20 min, transcription was performed, and the transcription products were analyzed by electrophoresis in 10% denaturing polyacrylamide gel containing 7 M urea in TBE buffer. As an RNA size marker, the transcription runoff product of *Hind*III-digested linear p206 was included.

Immediately prior to gel analysis, the samples were heated to 100 °C by boiling (in order to denature the DNA duplexes) and then analyzed by electrophoresis on a 10% native polyacrylamide gel in TBE. Radioactive bands were visualized by autoradiography.

RESULTS AND DISCUSSION

Pseudocomplementary PNAs require 50% AT content for optimal binding to a 10 bp target site (*15*), and 5′-TA sites are optimal for psoralen photoadduct and interstrand cross-link formation (*22*). A combination of these requirements are statistically quite frequent in DNA, and we identified a suitable target (5′-*ATAT*CAAGCTTATC) containing 60% AT at the *Hind*III site in the poly linker of the cloning vector pBluescript SK.

For this target, we synthesized a set of pseudocomplementary PNAs (H-Lys$_2$-GDU$_S$DDGCU$_S$U$_S$G-LysNH$_2$ (PNA 2222) and pso-(eg1)$_2$-Lys$_2$-CDDCGU$_S$U$_S$DU$_S$C-LysNH$_2$ (PNA 2300)) each containing three lysines for improved binding and one of them conjugated to 8-(carboxymethyleneoxy)psoralen through an 18-atom ethylene glycol type linker. Upon binding to the designated target, the psoralen should be positioned optimally for photoreaction with the ATAT target (Figure 1a). Using a gel shift assay, we first demonstrated efficient binding of this set of PNAs at sub-micromolar concentrations (Figure 1b), and by *Taq* DNA−polymerase primer extension runoff analysis (Figure 1c), we observed one and only one premature arrest of the polymerase (for the irradiated samples only) giving rise to a truncated elongation product of a length that corresponds to arrest at the 5′-TA at the psoralen sequence target (Figure 1c). These results clearly demonstrate that the pcPNAs bind their designated target and position the psoralen for photoreaction with the 5′-A*TA*T site. By employing fixed PNA concentration (0.8 μM), a clear irradiation dose response is demonstrated by the experiments presented in Figure 2. From these results, we may also estimate that the efficiency of the photoreaction is close to 100%, as ca. 80% PNA saturation of the binding site (Figure 2a) gives rise to an 80% reduction in the intensity of the runoff elongation product (Figure 2b) after 30 min irradiation.

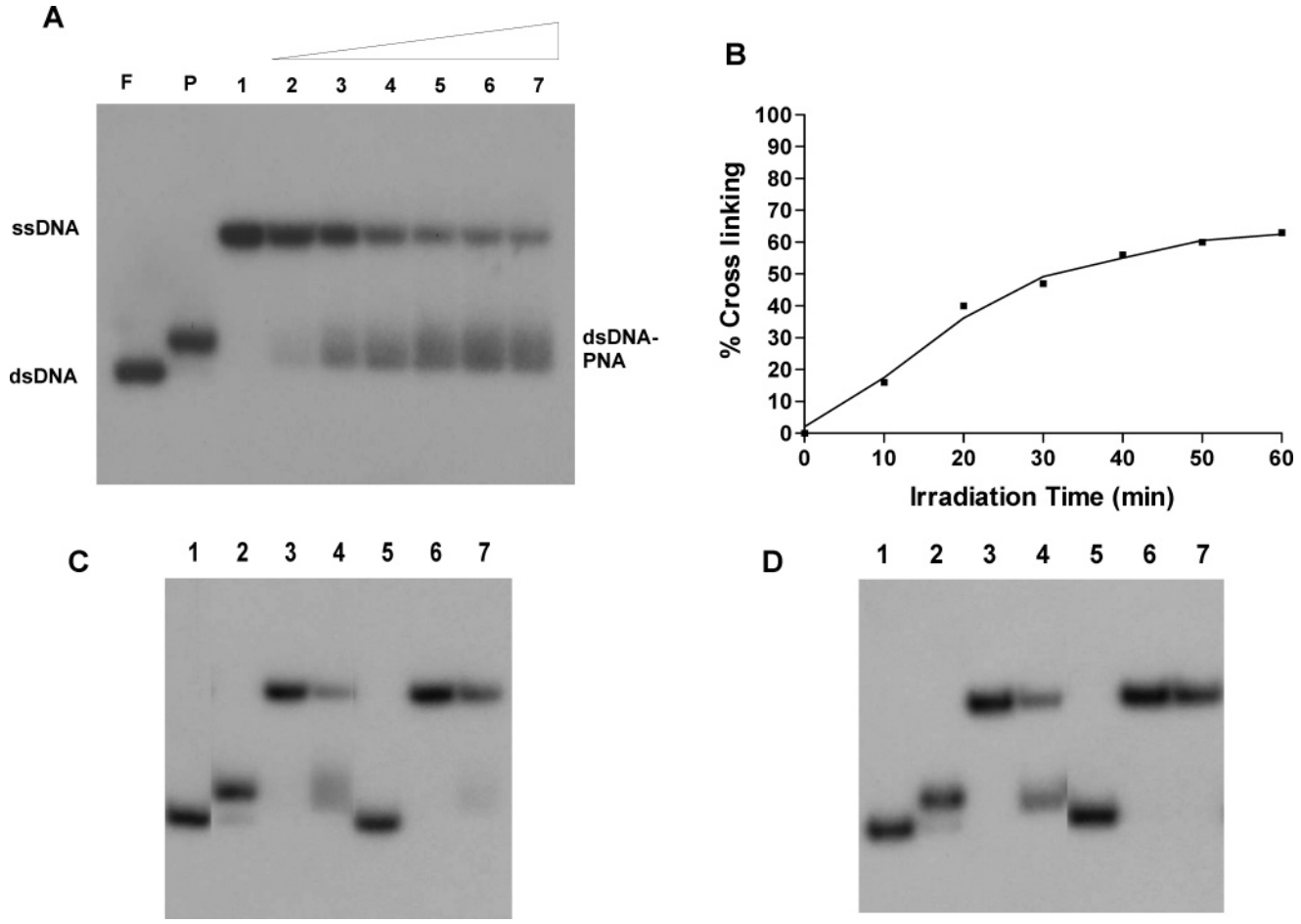


Figure 5. Determination of psoralen interstrand cross-link formation by renaturation analysis. (A) Double duplex invasion complex was formed by incubating PNA 2222/2300 (20 nM each) and a 3′-^{32}P end-labeled *Xba*I/*Pvu*II DNA fragment of pBluescriptKS+ overnight at 37 °C. Subsequently, the samples were UV-irradiated at 365 nm, heated to 100 °C by boiling (in order to denature the DNA duplexes), and analyzed by electrophoresis on a 10% native polyacrylamide gel in TBE (F, free DNA without PNA (without denaturation); P, DNA fragment with bound PNA without denaturation; lanes 1−7: 0, 10, 20, 30, 40, 50, or 60 min irradiation (with subsequent deaturation). (B) The results were quantified by phosphorimager scanning and the relative cross-linking determined as the relative fraction of the dsDNA−PNA band to total amount of DNA. (C) Interstrand cross-linking control using only PNA 2300. Lane 1: control without PNA. Lanes 2−4: PNA 2222 + PNA 2300. Lanes 5−7: PNA 2300. Irradiation was for 30 min (lanes 4 and 7). The samples of lanes 1, 2, and 5 were not denatured prior to gel loading. (D) Same as (C), but the irradiation was performed after addition of KCl to a final concentration of 140 mM.

We have shown that double duplex invasion complexes by decameric pcPNAs do not arrest elongating phage RNA polymerases, such as T7 or T3 RNA polymerases (*15*). The experiment presented in Figure 3 confirms this conclusion using this new set of pcPNAs. However, upon irradiation, the amount of full-length runoff product decreases drastically and a shorter transcript appears, the length of which corresponds to transcription elongation arrest at the psoralen−PNA cross-linking site (Figure 3c). Furthermore, as demonstrated by the experiment presented in Figure 3d, the formation of the truncated transcript (and concomitant disappearance of the full-length transcript) is irradiation dose-dependent and corresponds to practically a 100% yield relative to the PNA binding.

In order to address the target/sequence specificity of the psoralen photoreaction, we introduced a two-base mismatch in the psoralen-conjugated pcPNA by reversing a GC base step (PNA 2225: pso-$(eg1)_2$-Lys_2-CDDCGU$_S$U$_S$DU$_S$C-LysNH_2). This conjugate in combination with PNA 2222 did not photoreact with the target when analyzed by T3 RNA polymerase transcription, whereas the RNA polymerase was arrested by adducts formed by the fully matched set of psoralen−pcPNAs (Figure 4b). Interestingly, in this case as the transcribing polymerase is approaching from the PNA side, the polymerase is also arrested or paused within the PNA target, indicating that the PNA held in place by the psoralen is interfering with transcription elongation.

We also determined the extent of interstrand cross-linking (as opposed to psoralen monoadducts) produced in the system. DNA fragments containing interstrand cross-links will readily renature to a double-stranded structure after heat denaturation, whereas for non-cross-linked fragments, this is a much slower process. The results presented in Figure 5 show that under the conditions used full binding of the PNA is achieved as indicated by migration shifting of the DNA fragment (compare lanes F and P). Upon heat denaturation, the double-stranded fragment (with bound PNA) disappears, and a new band of much slower migration appears (compare lane P and lane 1: 0 min), which is ascribed to the single-stranded product. Upon irradiation of the PNA−dsDNA complex and subsequent denaturation, a (broad) band corresponding to the double-stranded fragment reappears (compare lane 0 min with lanes 2−7: 5−60 min). From the ratio between the amounts of single-stranded and double-stranded DNA molecules, we estimate that the interstrand cross-linking efficiency is over 60% (Figure 5b). As a control, we also made an analogous experiment including only the psoralen-bearing PNA (2300) but not the corresponding pseudocomplementary PNA (2222). The results (Figure 5c, lane 5) show that as expected no complex with dsDNA was formed (as opposed to the situationen when both PNAs were present

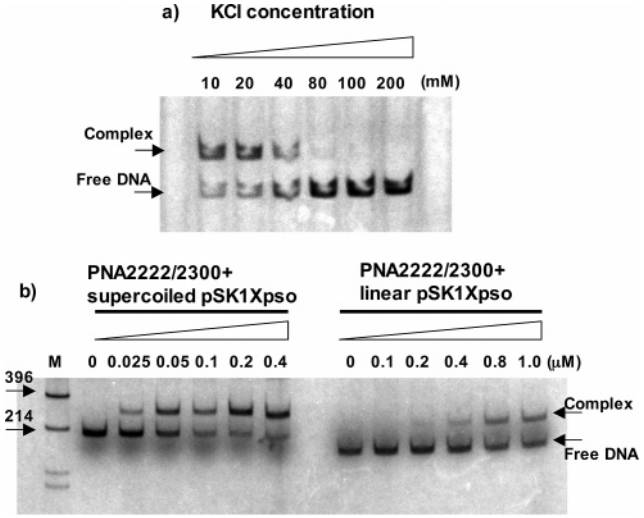


Figure 6. Effect of ionic strength and superhelical density on double duplex invasion complex formation. (A) Effect of KCl on double duplex invasion complex formation. Double duplex invasion complexes were formed by incubating PNA 2222/2300 (0.4 μM) and supercoiled pSK1Xpso in TE buffer (pH 7.4) in the presence of varying KCl concentrations (10 to 200 mM) at 37 °C for 2 h. Subsequently, the samples were treated restriction enzymes *Xba*I and *Sal*I and analyzed by electrophoresis in 10% nondenaturing polyacrylamide gel in TBE buffer (M: DNA size marker). DNA bands were visualized by silver staining. (B) Comparison of the binding efficiency of PNA 2222/2300 to supercoiled and *Xba*I linearized pSK1Xpso. Subsequently, the samples were treated with restriction enzymes *Xba*I and *Sal*I, or *Sal*I only, respectively, and analyzed as described in (A).

(lane 2), which resulted in >90% complex). However, a significant amount of DNA cross-linking took place upon irradiation (Figure 5c, lane 7) in the presence of only PNA 2300. It was noted that the band in the gel was more diffuse, and the cross-linking is ascribed to random cross-linking in the DNA fragment of TA sites by the psoralen−PNA conjugate, which due to the positive charge (+4) has unspecific DNA affinity. This conclusion was supported by the results of a similar experiment performed in 140 mM K^+ (Figure 5d) showing that the cross-linking by PNA 2300 alone is not seen under these conditions (lane 7), while the cross-linking in the presence of both PNAs (2222 and 2300) persists (lane 4), and in addition, the cross-linked band is sharper under these conditions, consistent with target-specific cross-linking. Quantification of the results presented in Figure 5d, lanes 2 and 4) shows that, at 80% binding of the PNA to the target, 47% cross-linking is achieved, giving a cross-linking efficiency of 58%.

It is well-established that helix invasion by PNA oligomers is significantly inhibited by increasing ionic strength (*23*, *24*) and accelerated by DNA negative supercoiling (*25*). The present system exhibits very similar behavior, as binding is negatively affected by 40 mM K^+. However, binding to a supercoiled DNA target is 20-fold more efficient than to a relaxed target (Figure 6b). Therefore, in analogy to dsDNA targeting via triplex invasion complexes (*25*), in vivo dsDNA targeting based on double duplex invasion may also be facilitated by the topological and dynamic state of DNA in vivo.

CONCLUSIONS

The present results clearly emphasize the potential of pseudocomplementary PNA oligomers for highly specific gene targeting, in particular, with respect to sequence-directed psoralen photomodification of double-stranded DNA. It is noteworthy that (at least in the present system) the yield of photomodification is almost stoichiometric and that transcription elongation is effectively arrested by the adducts (while not by the double duplex invasion complexes per se). Thus, such psoralen−PNA conjugates could be very useful in a range of biology and drug discovery applications as already illustrated by the properties of psoralen−TFO conjugates (e.g., *6*−*9*, *26*). Likewise, triplex-forming homopyrimidine bisPNAs−psoralen conjugates have already successfully been used to induce site-directed mutations in cells in culture (*27*). Attempts to exploit pcPNA-directed psoralen photomodification of double-stranded DNA for biological and medically relevant applications are in progress.

ACKNOWLEDGMENT

This work was supported by the EU Commission (contracts no LSHC-CT-2004-005204 (SNIPER) and LSHC-CT-2004-503569 (EMIL)).

LITERATURE CITED

(1) White, S., Szewczyk, J., Turner, J., Barid, E., and Dervan, P. (1998) Recognition of the four Watson-Crick base pairs in the DNA monir groove by the synthetic ligands. *Nature (London) 391*, 468−471.
(2) Kuan, J. Y., and Glazer, P. M. (2004) Targeted gene modification using triplex-forming oligonucleotides. *Methods Mol. Biol. 262*, 173−194.
(3) Klug, A. (1999) Zinc finger peptides for the regulation of gene expression. *J. Mol. Biol. 293*, 215−218.
(4) Brazier, J. A., Shibata, T., Townsley, J., Taylor, B. F., Frary, E., Williams, N. H., and Williams, D. M. (2005) Amino-functionalized DNA: the properties of C5-amino-alkyl substituted 2′-deoxyuridines and their application in DNA triplex formation. *Nucleic Acids Res. 33*, 1362−1371.
(5) Ziemba, A., Derosier, L. C., Methvin, R., Song, C. Y., Clary, E., Kahn, W., Milesi, D., Gorn, V., Reed, M., and Ebbinghaus, S. (2001) Repair of triplex-directed DNA alkylation by nucleotide excision repair. *Nucleic Acids Res. 29*, 4257−4263.
(6) Vasquez, K. M., Dagle, J. M., Weeks, D. L., and Glazer, P. M. (2001) Chromosome targeting at short polypurine sites by cationic triplex-forming oligonucleotides. *J. Biol. Chem. 276*, 38536−38541.
(7) Lacroix, L., Lacoste, J., Reddoch, J. F., Mergny, J. L., Levy, D. D., Seidman, M. M., Matteucci, M. D., and Glazer, P. M. (1999) Triplex formation by oligonucleotides containing 5-(1-propynyl)-2′-deoxyuridine: decreased magnesium dependence and improved intracellular gene targeting. *Biochemistry 38*, 1893−1901.
(8) Takasugi, M., Guendouz, A., Chassignol, M., Decout J. L., L'homme, J., Thuong, N. T., and Helene, C. (1991) Sequence-specific photo-induced cross-linking of the two strands of double-helical DNA by a psoralen covalently linked to a triple helix-forming oligonucleotide. *Proc. Natl. Acad. Sci. U.S.A. 88*, 5602−6.
(9) Diviacco, S., Rapozzi, V., Xodo, L., Helene, C., Quadrifoglio, F., and Giovannangeli, C. (2001) Site-directed inhibition of DNA replication by triple helix formation. *FASEB J. 15*, 2660−8.
(10) Urnov, F. D., Miller, J. C., Lee, Y. L., Beausejour, C. M., Rock, J. M., Augustus, S., Jamieson, A. C., Porteus, M. H., Gregory, P. D., and Holmes, M. C. (2005) Highly efficient endogenous human gene correction using designed zinc-finger nucleases. *Nature (London) 435*, 646−651.
(11) Nakatsukasa, T., Shiraishi, Y., Negi, S., Imanishi, M., Futaki, S., and Sugiura, Y. (2005) Site-specific DNA cleavage by artificial zinc finger-type nuclease with cerium-binding peptide. *Biochem. Biophys. Res. Commun. 330*, 247−252.
(12) Igoucheva, O., Alexeev, V., and Yoon, K. (2004) Oligonucleotide-directed mutagenesis and targeted gene correction: a mechanistic point of view. *Curr. Mol. Med. 4*, 445−463.
(13) Knauert, M. P., Lloyd, J. A., Rogers, F. A., Datta, H. J., Bennett, M. L., Weeks, D. L., and Glazer, P. M. (2005) Distance and affinity dependence of triplex-induced recombination. *Biochemistry 44*, 3856−3864.
(14) Chan, P. P., Lin, M., Faruqi, A. F., Powell, J., Seidman, M. M., and Glazer, P. M. (1999) Targeted correction of an episomal gene in mammalian cells by a short DNA fragment tethered to a triplex-forming oligonucleotide. *J. Biol. Chem. 274*, 11541−11548.
(15) Lohse, J., Dahl, O., and Nielsen, P. E. (1999) Double duplex invasion by peptide nucleic acid: a general principle for sequence-

specific targeting of double-stranded DNA. *Proc. Natl. Acad. Sci. U.S.A. 96*, 11804−11808.

(16) Majumdar, A., Khorlin, A., Dyatkina, N., Lin, F. L., Powell, J., Liu, J., Fei, Z., Khripine, Y., Watanabe, K. A., George, J., Glazer, P. M., and Seidman, M. M. (1998) Targeted gene knockout mediated by triple helix forming oligonucleotides. *Nat. Genet. 20*, 212−214.

(17) Puri, N., Majumdar, A., Cuenoud, B., Natt, F., Martin, P., Boyd, A., Miller, P. S., and Seidman, M. M. (2001) Targeted gene knockout by 2′-O-aminoethyl modified triplex forming oligonucleotides. *J. Biol. Chem. 276*, 28991−28998.

(18) Raha, M., Wang, G., Seidman, M. M., and Glazer, P. M. (1996) Mutagenesis by third-strand-directed psoralen adducts in repair-deficient human cells: high frequency and altered spectrum in a xeroderma pigmentosum variant. *Proc. Natl. Acad. Sci. U.S.A. 93*, 2941−2946.

(19) Barre, F. X., Ait-Si-Ali, S., Giovannangeli, C., Luis, R., Robin, P., Pritchard, L. L., Helene, C., and Harel-Bellan, A. (2000) Unambiguous demonstration of triple-helix-directed gene modification. *Proc. Natl. Acad. Sci. U.S.A. 97*, 3084−3088.

(20) Okamoto A., Tanabe, K., and Saito, I. (2001) Synthesis and properties of peptide nucleic acids containing a psoralen unit. *Org. Lett. 3*, 925−927.

(21) Antonello, C., Magno, S. M., Gia, O., Carlessare, F., Baccichetti, F., and Bordin, F. (1979) *Farmaco, Ed. Sci. 34*, 139.

(22) Cimino, G., Shi, Y., and Hearst, J. (1985) Psoralens as photoactive probes of nucleic acid structure and function: organic chemistry, photochemistry, and biochemistry. *Annu. Rev. Biochem. 54*, 1151−1193.

(23) Kurakin, A., Larsen, H., and Nielsen, P. (1998) Cooperative strand displacement by peptide nucleic acid (PNA). *Chem. Biol. 5*, 81−89.

(24) Peffer, N., Hanvey, J., Bisi, J., Thomson, S., Hassman, C., Noble, S., and Babiss, L. (1993) Strand-invasion of duplex DNA by peptide nucleic acid oligomers. *Proc. Natl. Acad. Sci. U.S.A. 90*, 10648−10652.

(25) Bentin, T., and Nielsen, P. (1996) Enhanced peptide nucleic acid binding to supercoiled DNA: possible implications for DNA "breathing" dynamics. *Biochemistry 35*, 8863−8869.

(26) Besch, R., Giovannangeli, C., Schuh, T., Kammerbauer, C., and Degitz, K. (2004) Characterization and quantification of triple helix formation in chromosomal DNA. *J. Mol. Biol. 341*, 979−89.

(27) Kim, K. H., Nielsen, P. E., and Glazer, P. M. (2006) Site-specific gene modification by PNAs conjugated to psoralen. *Biochemistry 45*, 314−323.

BC0603236

TECHNICAL NOTES

Synthesis of a Fluorescent Ganglioside G_{M1} Derivative and Screening of a Synthetic Peptide Library for G_{M1} Binding Sequence Motifs

Niels Röckendorf,[†] Steffen Bade,[†] Timothy R. Hirst,[‡] Hans H. Gorris,[†] and Andreas Frey*[,†]

Division of Mucosal Immunology, Department of Clinical Medicine, Research Center Borstel, Borstel, Germany, and John Curtin School of Medical Research, The Australian National University, Canberra, Australia. Received August 1, 2006; Revised Manuscript Received December 18, 2006

A ganglioside G_{M1} probe bearing a dark-red fluorescent dye at the sphingosine moiety of the molecule was prepared by a convenient one-pot synthesis. The labeled G_{M1} permitted the detection of the natural ganglioside G_{M1} ligand *Escherichia coli* heat-labile enterotoxin subunit B (EtxB) in picomole quantities on a solid support. When an epitope mapping of several ganglioside binding proteins and protein fragments was performed by screening a cellulose membrane-bound synthetic library of 64 16mer peptides with the new probe, several peptides displaying ganglioside G_{M1} affinity could be identified. We consider the labeled glycolipid described herein a versatile tool for manifold biochemical investigations.

INTRODUCTION

Carbohydrate structures are abundant on cell surfaces and occur in a wide variety, reflecting the diverse functions they exert in biological systems. Carbohydrate moieties have been shown to protect cells, to mediate cell attachment, and to participate in signal transduction pathways (*1*, *2*). Among other possibilities, they can be attached to cell surfaces via linkage to sphingolipids (*3*), thereby forming glycosphingolipids, such as gangliosides.

Glycosphingolipids are composed of two functional units. Their lipid moiety, named ceramide, is responsible for anchoring the molecule in the outer leaflet of the lipid bilayer of the cell membrane. The glycosyl moiety of glycosphingolipids consists of a branched saccharide chain that extends from the membrane surface. The carbohydrate antenna acts as a receptor in intercellular communication processes but may also be exploited by microbial pathogens in order to infect the cells or to manipulate them (*4*). Bacterial toxins of the AB_5-type such as cholera toxin or heat-labile enterotoxin from *Escherichia coli* enter their target cells by binding to ganglioside G_{M1} followed by endocytosis of the complex formed. Once inside, the toxins induce a profound electrolyte and water release which in turn may improve the habitat of the bacteria or facilitate their spread (*5*, *6*).

The multiple and important roles glycosphingolipids are recognized to play has sparked interest in both the development of traceable glycosphingolipid derivatives for studying their cell biology and the use of glycosphingolipid ligands for drug and vaccine targeting purposes. Several ganglioside derivatives carrying fluorescent labels either on their sphingosine or saccharide moiety have been described and used for various applications (*7*−*9*). Their biological behavior seems to be strongly dependent on the site of fluorophore attachment as well as on the structure of the fluorophore itself (*10*), which limits their use in basic studies of glycosphingolipid function. Moreover, none of the fluorescent ganglioside derivatives described so far operates beyond the spectral range where autofluorescence of eukaryotic tissue or membrane supports is observed. Such autofluorescence not only hampers detection of the dye in live cells but may also interfere with fluorescence-based solid-phase assays. Consequently, assays with fluorophore-labeled glycolipids that involve the use of membrane supports or tissue material call for fluorescent dyes which emit light in the far-red to near-infrared region (650−1100 nm), since at these wavelengths, little background fluorescence is usually observed (*11*).

In order to exploit ganglioside G_{M1} as a gateway for drug or vaccine delivery, soluble as well as particulate ganglioside G_{M1} targeting systems have been developed (*12*−*14*). These systems are based on the B subunits of cholera toxin (CTB) or *Escherichia coli* heat-labile enterotoxin (EtxB) and were used, e.g., in mucosal immunizations to target antigens to epithelial cells of the mucosa-associated lymphoid tissue (*13*) or to investigate the accessibility of cell membranes of different intestinal cell types (*15*, *16*). Importantly, the ganglioside binding capability of these proteinaceous ligands may be compromised when they are attached to particulate carriers for use in drug delivery systems (*14*). Thus, small peptides or peptoid structures with high binding affinity to gangliosides would be preferable for these purposes. The identification of such ganglioside ligands, however, requires traceable ganglioside G_{M1} derivatives that can be used without background problems for the screening of solid-phase bound substance libraries and thus must be superior to the currently available compounds.

In the present study, a new fluorescent ganglioside G_{M1} derivative is introduced which meets these requirements. The new probe is characterized regarding its EtxB binding behavior and utilized to identify short ganglioside G_{M1} binding peptides

* Corresponding author. Dr. Andreas Frey, Division of Mucosal Immunology, Research Center Borstel, Parkallee 22, D-23845 Borstel, Germany. Phone: +49-4537-188-562; Fax: +49-4537-188-693; E-mail: afrey@fz-borstel.de.

[†] Research Center Borstel.

[‡] The Australian National University.

10.1021/bc0602376 CCC: $37.00 © 2007 American Chemical Society
Published on Web 02/27/2007

by screening a solid-phase synthesized library of peptides derived from G_{M1} binding proteins and protein fragments.

EXPERIMENTAL PROCEDURES

Materials. Heat-labile enterotoxin subunit B (EtxB) from *Escherichia coli* was isolated according to a procedure described earlier (*17*). Casein (Hammarsten grade) was obtained from BDH (via VWR International, Darmstadt, Germany), Lyso-ganglioside G_{M1} was from Sigma-Aldrich (Taufkirchen, Germany), and DY650-NHS was from Dyomics (Jena, Germany). PVDF membranes (Westran clear signal membranes, 0.45 μm pore size), nitrocellulose membranes (0.2 μm pore size), cellulose membrane supports (Whatman 540), and a Minifold I 96-well blotting device were from Whatman International (Dassel, Germany). Fmoc amino acid building blocks with side chain protecting groups if required (*t*Bu (serine, threonine, and tyrosine); O*t*Bu (aspartic and glutamic acid); Boc (lysine and tryptophane); Acm (cysteine); Trt (histidine, asparagine, and glutamine), Pbf (arginine)) were obtained from Merck Biosciences (Bad Soden, Germany). Anhydrous hydroxybenzotriazole (HOBt) was from Dojindo Laboratories (Kumamoto, Japan) and dimethylformamide (DMF) from Promochem (Wesel, Germany). *N*-Methylpyrrolidone (NMP; Fluka, Taufkirchen, Germany) was deionized by treatment with ion-exchange mixed bed resin AG501-X8 (Bio Rad Laboratories, München, Germany). All other chemicals and solvents were of analytical grade and purchased from Sigma-Aldrich; they were used without further purification.

HPLC was performed using an Äkta Purifier (GE Healthcare, Freiburg, Germany). Purifications were carried out on a Jupiter (C18, 300 Å, 5 μm, 4.6 × 250 mm) reversed-phase (RP) column (solvents ratio v/v reported) (Phenomenex, Aschaffenburg, Germany). Fourier transform ion cyclotron resonance mass spectrometry was carried out on a Bruker Daltonics (Bremen, Germany) Apex II ESI-FT-MS instrument equipped with a 7 T activity-shielded magnet and an Apollo electrospray ion source in negative detection mode. Fluorescence intensities were quantitated with an Odyssey Infrared Imager running software version 1.2.15 (LI-COR Biosciences, Bad Homburg, Germany). Spatially addressable multiple peptide synthesis was carried out using a pipetting robot ASP 222 (Intavis Bioanalytical Instruments, Köln, Germany).

Synthesis. For preparation of lysoG$_{M1}$-DY650 conjugates (**1**/**2**), lyso-ganglioside G_{M1} was dissolved in dry DMF at a concentration of 2 mg/mL (1.03 mM). 200 μL of this solution was mixed with a solution of DY650-NHS in dry DMF (225 μL, 2 mg/mL), diisopropylethylamine (DIPEA, 7 μL) was added, and the mixture was incubated with shaking under an argon atmosphere at 30 °C. After 36 h, the reaction mixture was analyzed by ESI-MS, the solvent was removed in vacuo, and the residue was redissolved in acetonitrile/water (500 μL, 20% (v/v)). The resulting solution was subjected to HPLC purification on RP-18 silica gel (A = water, B = acetonitrile, 20% B to 100% B, 1 mL/min, 90 mL, retention volume 67 mL), and product fractions were collected. ESI-MS (m/z): fraction 1 1947.95 [M^+] (1947.94 calcd for $C_{95}H_{145}N_5O_{35}S$); fraction 2 1975.98 [M^+] (1975.98 calcd for $C_{97}H_{149}N_5O_{35}S$) (see also Supporting Information).

Peptide libraries were synthesized on cellulose membrane supports following the procedure of Frank (*18*). The cellulose membranes were derivatized with Fmoc-protected β-alanine in DMF (2.5 mL (0.02 mL/cm^2 membrane), 0.2 M Fmoc-β-alanine, 0.2 M methylimidazol, 0.26 M diisopropylcarbodiimide (DIC), 24 h, room temperature (RT)). Excess hydroxyl groups were blocked (capped) with acetic anhydride in DMF (15 mL (0.13 mL/cm^2 membrane), 2% (v/v), 24 h, RT, rocking), and the membranes were washed 3× with DMF (15 mL (0.13 mL/cm^2 membrane)). Fmoc cleavage was performed by incubating the membranes twice with piperidine in DMF (10 mL (0.09 mL/cm^2 membrane), 20% (v/v), 5 min each, RT, rocking). Presence of free amino functions on the cellulose membranes was confirmed with bromophenol blue. For that, membranes were washed 5× with DMF (15 mL (0.13 mL/cm^2 membrane)), stained with bromophenol blue in DMF (15 mL (0.13 mL/cm^2 membrane), 0.01% (w/v), 10 min, RT, rocking), washed 3× with 100% ethanol (15 mL (0.13 mL/cm^2 membrane)), and air-dried.

Table 1. Ganglioside G_{M1}-Binding Proteins and Peptides

set	protein/source	motif[a] [aa−aa]	peptide no.[b]	ref
I	cholera toxin B subunit	50−75	A1−A6	25
II	cholera toxin B subunit	50−75	A7−B4	26
III	*E. coli* enterotoxin B subunit	26−45	B5−B7	27
IV	amyloid β protein	1−40	B8−D4	28
V	phage display peptides	n.a.[c]	D5−D7	21
VI	saposin B	52−69	D8−E1	29
VII	saposin C	8−29	E2−E5	29
VIII	myelin basic protein	1−44	E6−G4	30
IX	*Staphylococcus aureus* leukocidin	270−287	G5−G6	31
X	cholera toxin B subunit	rational[d]	G7−H4	this study
XI	random peptides	n.a.	H5−H8	this study

[a] Linear sequence motif proposed to be responsible for ganglioside G_{M1} binding. Numbering refers to the amino acid positions published in the respective reference. [b] Alphanumeric numbering of the 16mer peptides covering the motif indicated. The numbering refers to their position on the membrane (see Figure 2). [c] Not applicable. [d] Motifs designed rationally from crystal structure data ("linearized discontinuous motif").

The above capping, washing, Fmoc-cleavage and staining steps were repeated between all synthesis cycles from the definition of the synthesis areas (spots) onward, but capping was reduced to 20 min after the third cycle.

For definition of the synthesis areas, 0.1 μL of Fmoc-β-alanine-pentafluorophenyl (Pfp) ester (0.2 M Fmoc-β-alanine-Pfp-ester in NMP) was applied by a pipetting robot on defined membrane areas.

For subsequent synthesis cycles, the amino acids were converted into their corresponding HOBt esters immediately before use by adding 1.25 mol DIC per mole amino acid to a solution containing 0.4 M N-α-Fmoc-protected amino acid and 0.7 M HOBt in NMP (final concentration: 0.2 M amino acid, 0.35 M HOBt, 0.25 M DIC) and allowing the mixture to react for 30 min at RT. Precipitates were removed by a short centrifugation step, and 0.2 μL of these N-α-Fmoc-protected amino acid active esters were applied to the respective synthesis areas. Coupling of each amino acid was repeated three times, and a minimum of 40 min reaction time was allowed in each synthesis cycle. After the last cycle, the peptides were N-terminally acetylated with acetic anhydride in DMF (15 mL (0.13 mL/cm^2 membrane) 2% (v/v), 20 min, RT, rocking).

Side chain protecting groups (except Acm) were removed by immersing the membranes twice in a cleavage cocktail (50% (v/v) trifluoroacetic acid, 3% (v/v) triisobutylsilane, and 2% (v/v) water in dichloromethane (DCM), 10 mL (0.09 mL/cm^2 membrane), 1 h each, RT, rocking). Subsequently, membranes were washed 4× with DCM (15 mL (0.13 mL/cm^2 membrane)), 3× with DMF (15 mL (0.13 mL/cm^2 membrane)), 4× with 1 M acetic acid (15 mL (0.13 mL/cm^2 membrane)), and finally 3× with 100% ethanol (15 mL (0.13 mL/cm^2 membrane)). Membranes were air-dried and desiccated overnight in vacuo and stored in the presence of desiccant at −20 °C. The sequences of the peptides synthesized are compiled in Table 2. The library was prepared in six replicas on a single cellulose membrane.

LysoG$_{M1}$−DY650 Binding to EtxB. EtxB was dissolved in physiological phosphate buffer (10 mM sodium phosphate buffer, 150 mM NaCl, pH 7.5) at a concentration of 5 mg/mL

Table 2. Peptide Sequences Synthesized on Cellulose Membrane Supports for Screening of G_{M1}-Binding Capacity[a]

No.	Sequence	No.	Sequence
A1	VEVPGQHIDSQKK	E1	YSEIAIQMMMHMQ
A2	VPGQHIDSQKKAI	E2	CEFLVKEVTKLID
A3	GQHIDSQKKAIER	E3	FLVKEVTKLIDNN
A4	HIDSQKKAIERMK	E4	VKEVTKLIDNNKT
A5	DSQKKAIERMKNT	E5	EVTKLIDNNKTEK
A6	SQKKAIERMKNTL	E6	ASQKRPSQRHGSK
A7	VEVPGSQHIDSQK	E7	QKRPSQRHGSKYL
A8	VPGSQHIDSQKKA	E8	RPSQRHGSKYLAT
B1	GSQHIDSQKKAIE	F1	SQRHGSKYLATAS
B2	QHIDSQKKAIERM	F2	RHGSKYLATASTM
B3	IDSQKKAIERMKD	F3	GSKYLATASTMDH
B4	SQKKAIERMKDTL	F4	KYLATASTMDHARHGF
B5	SYTESMAGKREMV	F5	LATASTMDHARHG
B6	TESMAGKREMVII	F6	TASTMDHARHGFL
B7	SMAGKREMVIITF	F7	STMDHARHGFLPR
B8	LEVPTDGNAGLLA	F8	MDHARHGFLPRHR
C1	VPTDGNAGLLAEP	G1	HARHGFLPRHRDT
C2	TDGNAGLLAEPQI	G2	RHGFLPRHRDTGI
C3	GNAGLLAEPQIAM	G3	GFLPRHRDTGILD
C4	AGLLAEPQIAMFC	G4	LPRHRDTGILDSI
C5	LLAEPQIAMFCGR	G5	KYEVNWKTHEIKV
C6	AEPQIAMFCGRLN	G6	YEVNWKTHEIKVK
C7	PQIAMFCGRLNMH	G7	AEYHNTQIHTLND
C8	IAMFCGRLNMHMN	G8	ATFQVEVPGSQHI
D1	MFCGRLNMHMNVQ	H1	AKVEKLCVWNNKT
D2	CGRLNMHMNVQNG	H2	GALSETYSFIKEY
D3	RLNMHMNVQNGKW	H3	ESLAGKREQSDIH
D4	NMHMNVQNGKWDS	H4	ASDWYDEMLTWNI
D5	DFRRLPGAFWQLR	H5	DGTVSTHECRLEY
D6	GWWYKGRARPVSA	H6	FSHSGEGDMIWER
D7	VWRLLAPPFSNRL	H7	HHCSILKEVWHVK
D8	SQYSEIAIQMMMH	H8	PDQDGVVTAMHGF

[a] No. indicates the alphanumeric numbering of the respective peptide and refers to its position on the membrane (see Figure 2).

(86 μM), twofold serial dilutions were prepared (concentration range: 5 mg/mL to 80 μg/mL), and 1 μL of each dilution was mixed with 100 μL Dulbecco's phosphate buffered saline (D-PBS; 2.7 mM KCl, 1.5 mM KH_2PO_4, 136 mM NaCl, 8.1 mM Na_2HPO_4, pH 7.4). PVDF membranes were soaked in ethanol for 10 min, washed with water and PBS, and transferred to a 96-well blotting device in the wet state. The EtxB solutions diluted in D-PBS were applied to the membranes under gentle vacuum. Then, the membranes were incubated for 4 h at RT in blocking solution (0.1% (w/v) Tween 20 in D-PBS (PBST)) followed by overnight incubation at RT in a solution of **2** (approximately 10 ng/mL (approximately 5 nM), in 10 mL PBST). They were washed 6× for 10 min with PBST and 2× for 10 min with D-PBS. Fluorescence was measured with an Odyssey infrared imager at 700 nm. Measurements were performed in triplicate; signals are reported as mean fluorescence intensities ± SEM above cutoff. The cutoff was determined according to a method described earlier (*19*).

LysoG_{M1}−DY650 Binding to Peptide Libraries. The cellulose membrane-bound peptide libraries were blocked with casein/PBS (1% casein in D-PBS) for 3 h at RT and incubated overnight at RT with a solution of **2** (approximately 10 ng/mL (approximately 5 nM) in 10 mL casein/PBS). They were washed 6× for 10 min with 10 mL PBST and 2× for 10 min with 10 mL D-PBS, and the bound lysoG_{M1}−DY650 was quantitated on the wet membranes in the Odyssey infrared imager at 700 nm. The experiment was performed in quintuplicate using five identical libraries that had been synthesized in parallel. Signals are reported as mean fluorescence intensities ± SEM above average background outside the spot areas. For all spots, an "average signal" was calculated as the mean of the fluorescence intensities of all spots. From this average signal, the upper and lower cutoff values to classify true binders (signals above upper cutoff) and nonbinders (signals below lower cutoff) was determined using *t*-statistics according to a method described earlier (*19*).

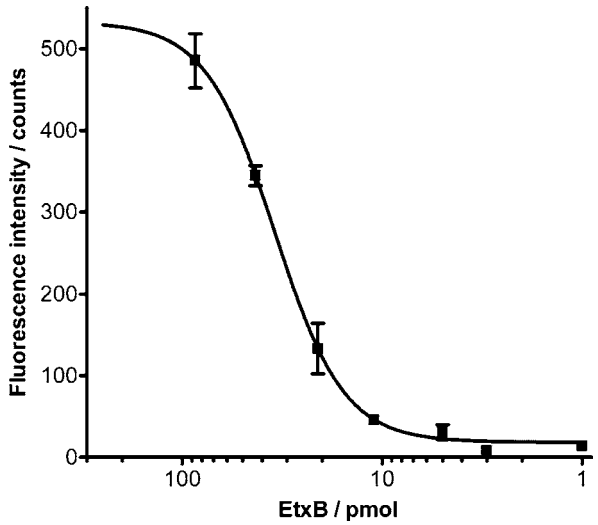


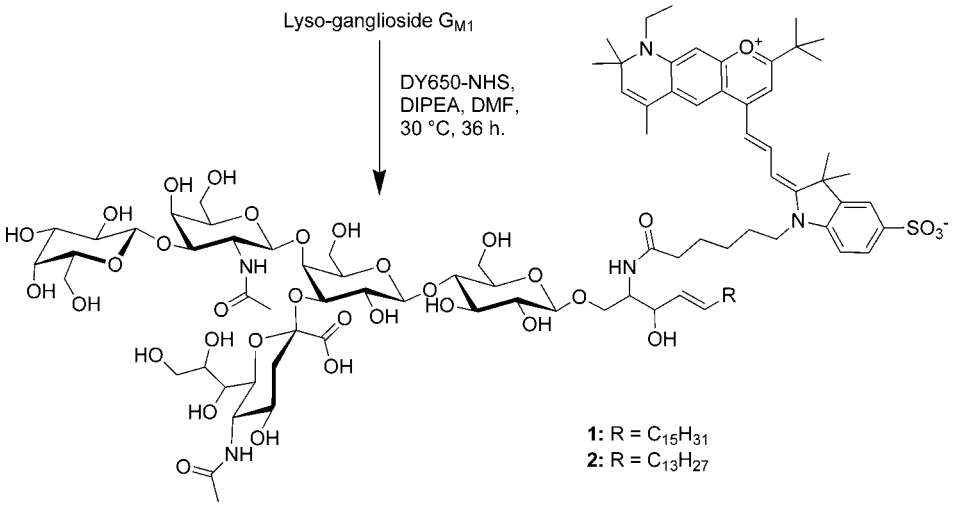
Figure 1. Detection of heat-labile enterotoxin B subunit (EtxB) from *Escherichia coli* by lysoG_{M1}-DY650. Decreasing amounts of EtxB were immobilized on a PVDF membrane and detected with lysoG_{M1}-DY650. Fluorescence emission intensities of bound lysoG_{M1}-DY650 at 700 nm are given in arbitrary units (mean ± SEM of triplicate experiments).

RESULTS AND DISCUSSION

Preparation of a LysoG_{M1}−DY650 Derivative. Since the carbohydrate part of ganglioside G_{M1} is essential for ligand binding, one runs the risk of inactivating the molecule when a bulky group, such as a fluorophore, is attached. The only locale that may be permissive to modification or replacement seems to be the generic fatty acid moiety residing on the amino group of sphingosine. We thus decided to substitute the fatty acid with a dark red fluorescent dye in order to obtain a traceable probe. A G_{M1} derivative that already lacks the fatty acid moiety and contains a free amino function instead is lysoganglioside G_{M1} (lysoG_{M1}) (*20*). Consequently, lysoG_{M1} was chosen as starting material.

As a fluorophore, we selected DY650, a member of the cyanine dye family that carries a lipophilic C-6 spacer and fluoresces at 674 nm after excitation at 653 nm. Due to its emission in the dark red, DY650 should be especially useful in all experiments where autofluorescence is to be expected. Autofluorescence of crude biological samples or organic membrane materials peaks around 550 nm and thus coincides with the emission spectra of popular fluorophores such as Bodipy-FL, which is often used as a label for glycosphingolipids (*10*). In comparison to Bodipy-FL, the DY650 fluorophore shows a twofold higher absorption as well as a doubled Stokes shift, and it is suitable for readout with a variety of fluorescence imagers using red to near-infrared excitation sources. Besides its favorable optical properties, DY650 offers chemical advan-

Scheme 1. Synthesis of Fluorescent Probes 1 and 2



tages, too. The molecular structure of this dye contains no net charge, since the dye's negatively charged sulfo group is compensated by its positively charged aromatic oxonium substructure. Coulomb interactions and hence unspecific binding of DY650 conjugates to charged residues in sample materials should therefore be reduced in comparison to other dyes, which often carry multiple ionic groups in order to increase their solubility in aqueous media.

The preparation of the lysoG$_{M1}$−DY650 conjugate was designed as a one-pot synthesis in which lysoG$_{M1}$ was deprotonated by the sterically hindered base diisopropylethylamine (DIPEA) and reacted with DY650−NHS in dimethylformamide (DMF) in the dark at 30 °C. The reaction was monitored by ESI-MS. It revealed that product formation was slow and came to completion after 36 h only. We attribute this rather low reactivity of the NHS-ester to the fact that the reacting amino function is located at a sterically hindered secondary carbon. Purification of the crude lysoG$_{M1}$−DY650 conjugate was achieved by RP-HPLC, and two product fractions containing the fluorescent glycoconjugates **1** and **2** with molecular weights of 1948 and 1976 were collected (Scheme 1). The occurrence of two different product molecules is due to the fact that the lysoG$_{M1}$, which we used as starting material in the synthesis, is a mixture of two compounds which differ solely in the length of their alkyl chain. The fluorescent G$_{M1}$ derivative **1** carries a C_{15} alkyl chain in its sphingosine moiety, while derivative **2** has a C_{13} alkyl chain in this position. Since fluorescent probe **2** could be enriched to higher purity than **1**, derivative **2** was used in all further experiments.

Binding of LysoG$_{M1}$−DY650 to a G$_{M1}$ Ligand. We first investigated the probe's binding behavior toward a natural G$_{M1}$ binding partner, heat-labile enterotoxin subunit B (EtxB) from *Escherichia coli*, in a dot blot-type assay. Using this setup, a detection limit of 10 pmol EtxB per dot was reached (Figure 1), despite the fact that the probe was excited at a suboptimal wavelength (680 nm) because no laser source for the dye's excitation maximum was available. Even higher sensitivities may be achievable if excitation of the probe is performed at 653 nm, the excitation maximum of DY650. Thus, lysoG$_{M1}$−DY650 was able to bind with high affinity to the natural G$_{M1}$ ligand EtxB, demonstrating that the binding properties of the pentasaccharide moiety were retained in the labeled molecule.

Binding of LysoG$_{M1}$−DY650 to Putative G$_{M1}$ Binding Peptides. We finally wanted to validate the newly developed lysoG$_{M1}$−DY650 derivative as a tool for the detection of molecules which display a high affinity to ganglioside G$_{M1}$. Our ultimate goal is the identification of small ganglioside G$_{M1}$ binding peptides that might be used for drug targeting.

We accomplished an epitope mapping by designing a peptide library consisting of candidate sequences that were taken from known or alleged G$_{M1}$ binding proteins or protein fragments (Table 1) by breaking down the respective sequence motifs into overlapping 16mer peptides (12 to 15 amino acids overlap). We also included three 15mer peptides which had been identified previously as potential G$_{M1}$ ligands in phage display experiments (*21*) and thus could serve as controls. For the sake of comparability, they were extended to 16mers by addition of a C-terminal alanine.

Last, we completed our peptide library with peptides that we deduced from the crystal structure of cholera toxin B-pentamer cocrystallized with bound G$_{M1}$ (*22*). Amino acids that are part of the G$_{M1}$ binding pocket and are involved in G$_{M1}$ binding were selected and assembled sequentially by linear arrangement.

This way, 64 different 16mer peptide sequences were obtained (Table 2) and synthesized on a cellulose membrane support using the SPOT technique (*18*, *23*). With this method, such a high peptide density in each spot of the membrane can be achieved that even weak ligand−peptide interactions are detectable due to multivalency effects. This advantage of SPOT-synthesized peptide libraries is of particular value in our case, as we aimed to detect a carbohydrate−peptide interaction, and this type of interaction is notoriously weak.

Identification of short ganglioside G$_{M1}$ binding peptides was performed by incubating the cellulose membrane-bound library with lysoG$_{M1}$−DY650 and quantitating the fluorescence intensities of the single peptide spots after excitation at 680 nm (Figure 2). Background fluorescence of the membrane support was very low due to the long excitation wavelength used and the blocking of the cellulose membrane with 1% (w/v) casein/PBS. The entire procedure proved highly reproducible, as indicated by the low coefficient of variation that 5 independent screening experiments yielded for each single peptide (mean coefficient of variation for 64 peptides: 11.6%).

The peptides were classified according to their fluorescence intensities into two groups, nonbinders and binders. A peptide was defined as nonbinder if the fluorescence intensity of the respective spot was significantly lower than the "average signal" calculated from the mean fluorescence of all 64 spots (one-tailed t test, $P < 0.05$). Likewise, an upper cutoff value as threshold for significantly higher than average signals was determined. Peptide spots with a fluorescence intensity above this cutoff display better than "average" binding with a probability of ≥99.5% and were hence defined as true binders.

With these discrimination criteria, 25 peptides were classified as nonbinders (Figure 2B, open bars), 15 peptides could not be assigned to either group (Figure 2B, hatched bars), and 24

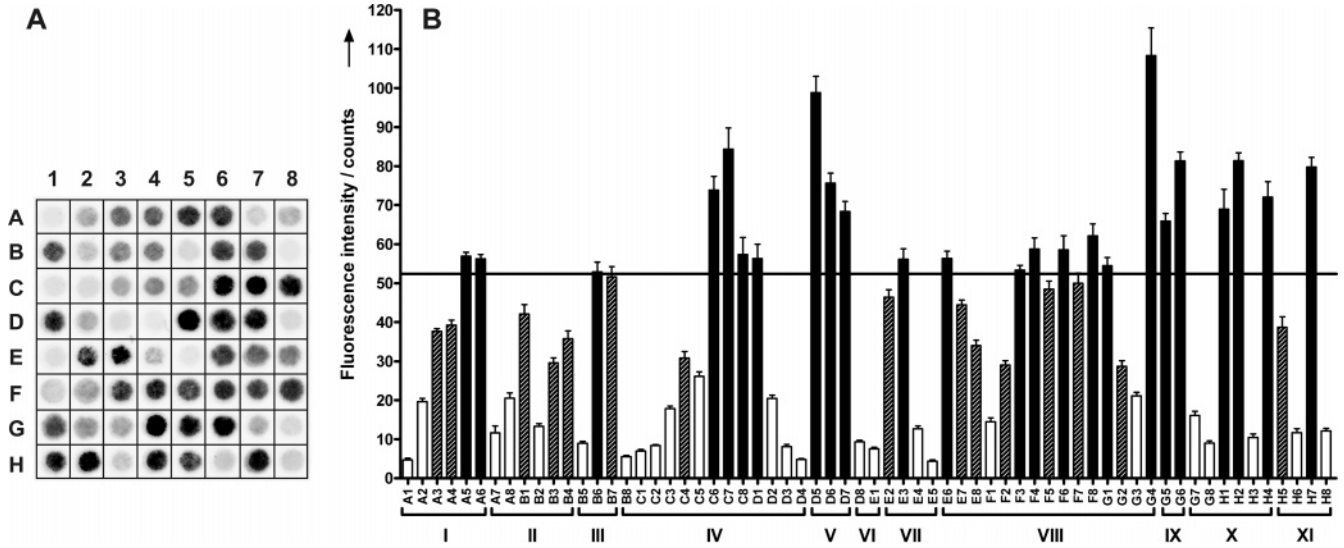


Figure 2. Detection of peptides capable of binding lysoG$_{M1}$-DY650. A library of 64 different peptides was synthesized onto a cellulose membrane support. After blocking, the membrane was incubated with lysoG$_{M1}$-DY650 and fluorescence was measured at 700 nm. (A) Image of the peptide library as generated by the infrared imager depicting the fluorescence signals obtained after incubation of the membrane with lysoG$_{M1}$-DY650. (B) Quantitation of G$_{M1}$ binding to single peptide spots. Filled bars represent signal intensities of peptides assigned to the group of binders; open bars represent nonbinders; hatched bars represent peptides which could not be assigned to either group. Roman numerals indicate the respective set to which the peptides belong (see Table 1). Individual peptides are numbered alphanumerically according to their position on the membrane (for sequences, see Table 2). Fluorescence emission intensities determined for each single spot at 700 nm are shown (mean ± SEM of five experiments). The horizontal line indicates the upper cutoff value used to define true G$_{M1}$ binders.

peptides were found to be binders (Figure 2B, filled bars). All three phage-display-derived, alanine-extended peptides that had been shown to interact with G$_{M1}$ in previous experiments (*24*) (peptide spots D5, D6, and D7 in Figure 2A) belong to the latter group, a finding that we consider a promising preliminary result pertaining to the validation of our screening system. In our assay setup, lysoG$_{M1}$−DY650 showed a stronger interaction with peptide D5 than with peptides D6 and D7 (Figure 2B). This is in conflict with the original report (*21*) where peptide D7 showed the highest inhibition of CTB binding to G$_{M1}$. We reason that these discrepancies are due to the different assay formats used. Originally, the G$_{M1}$ binding performance of the three peptides had been determined in solution, whereas our screening system measures the binding behavior of peptides attached to a solid phase.

The highest fluorescence intensity achieved in our assay resulted from binding of lysoG$_{M1}$−DY650 to peptide G4, which encompasses the C-terminal part of the myelin basic protein fragment. For peptides B8−D4 derived from amyloid β protein, signal intensity peaks at candidate C7, which indicates that the sequence motif of C7 is mainly responsible for the interaction between ganglioside G$_{M1}$ and amyloid β protein (Table 1).

Two linear CTB-derived motifs could be assigned to the group of binders. These peptides, A4 and A5, vary by only one amino acid, an asparagine instead of an aspartic acid, from peptides B3 and B4, but exhibit a much higher fluorescence intensity than the latter. This point mutation originates from a discrepancy in the reported parent sequences (*25*, *26*) and illustrates nicely that the exchange of a single amino acid alone is able to alter the affinity of a peptide ligand to its target. Apparently, a negative charge is highly unfavorable at the respective position. This assumption is supported by the fact that peptide B1 which shares a major part of its sequence with its "neighboring" peptides, B2−B4, but lacks their aspartic acid—and hence the negative charge—displays a similar signal intensity as the other "uncharged" candidate peptides A3−A6. Regardless of the underlying reason for this charge effect, the example emphasizes the value of our assay, which is evidently capable of accurately reflecting the differences in the G$_{M1}$ binding affinities of these closely related peptides.

The peptides derived from the other G$_{M1}$ binding protein fragments exhibited little or no binding to lysoG$_{M1}$−DY650, which suggests that the G$_{M1}$ binding properties of those proteins mainly reside in their three-dimensional structure.

Intriguingly, some of the candidate sequences which we designed on the basis of the structural data of the CTB−G$_{M1}$ complex show rather high fluorescence signals, rendering them true binders (peptides H1, H2, and H4). This demonstrates that rational design may constitute a worthwhile route toward the identification of peptidic ganglioside G$_{M1}$ ligands.

ACKNOWLEDGMENT

We thank Dr. Buko Lindner for performing the mass spectrometrical analyses. This work was funded by the German Federal Ministry of Education and Research (BMBF, grants 13N8473 and 01KO113) and by the German Research Foundation (DFG, grant FR 958/4-1).

Supporting Information Available: ESI-MS spectra and HPLC profile of ganglioside−dye conjugates. This material is available free of charge via the Internet at http://pubs.acs.org/BC.

LITERATURE CITED

(1) Murrell, M. P., Yarema, K. J., and Levchenko, A. (2004) The systems biology of glycosylation. *Chembiochem 5*, 1311−1313.
(2) Hakomori, S. I., and Igarashi, Y. (1995) Functional role of glycosphingolipids in cell recognition and signaling. *J. Biochem. 118*, 1091−1103.
(3) Futerman, A. H., and Hannun, Y. A. (2004) The complex life of simple sphingolipids. *EMBO Rep. 5*, 777−782.
(4) Yates, A. J., and Rampersaud, A. (1998) Sphingolipids as receptor modulators. An overview. *Ann. N. Y. Acad. Sci. 845*, 57−71.
(5) Spangler, B. D. (1992) Structure and function of cholera toxin and the related *Escherichia coli* heat-labile enterotoxin. *Microbiol. Rev. 56*, 622−647.
(6) De Haan, L., and Hirst, T. R. (2004) Cholera toxin: a paradigm for multi-functional engagement of cellular mechanisms. *Mol. Membr. Biol. 21*, 77−92.
(7) Nakagawa, T., Tani, M., Kita, K., and Ito, M. (1999) Preparation of fluorescence-labeled G$_{M1}$ and sphingomyelin by the reverse

hydrolysis reaction of sphingolipid ceramide N-deacylase as substrates for assay of sphingolipid-degrading enzymes and for detection of sphingolipid-binding proteins. *J. Biochem. 126*, 604−611.

(8) Schwarzmann, G., Wendeler, M., and Sandhoff, K. (2005) Synthesis of novel NBD-G_{M1} and NBD-G_{M2} for the transfer activity of G_{M2}-activator protein by a FRET-based assay system. *Glycobiology 15*, 1302−1311.

(9) Song, X., and Swanson, B. I. (1999) Direct, ultrasensitive, and selective optical detection of protein toxins using multivalent interactions. *Anal. Chem. 71*, 2097−2107.

(10) Burns, A. R., Frankel, D. J., and Buranda, T. (2005) Local mobility in lipid domains of supported bilayers characterized by atomic force microscopy and fluorescence correlation spectroscopy. *Biophys. J. 89*, 1081−1093.

(11) Williams, R. J., Narajanan, N., Casay, G. A., Lipowska, M., Strekowski, L., Patonay, G., Peralta, J. M., and Tsang, V. C. W. (1994) Instrument to detect near-infrared fluorescence in solid-phase immunoassay. *Anal. Chem. 66*, 3102−3107.

(12) Asou, H. (1990) Localisation of ganglioside G_{M1} with biotinylated choleragen. *Methods Enzymol. 184*, 405−408.

(13) O'Dowd, A. M., Botting, C. H., Precious, B., Shawcross, R., and Randall, R. E. (1999) Novel modification to the C-terminus of LTB that facilitate site-directed chemical coupling of antigens and the development of LTB as a carrier for mucosal vaccines. *Vaccine 17*, 1442−1453.

(14) Olivier, V., Meisen, I., Meckelein, B., Hirst, T. R., Peter-Katalinic, J., Schmidt, M. A., and Frey, A. (2003) Influence of targeting ligand flexibility on receptor binding of particulate drug delivery systems. *Bioconjugate Chem. 14*, 1203−1208.

(15) Frey, A., Giannasca, K. T., Weltzin, R., Giannasca, P. J., Reggio, H., Lencer, W. I., and Neutra, M. R. (1996) Role of the glycocalyx in regulating access of microparticles to apical plasma membranes of intestinal epithelial cells: implications for microbial attachment and oral vaccine targeting. *J. Exp. Med. 184*, 1045−1059.

(16) Mantis, N. J., Frey, A., and Neutra, M. R. (2000) Accessibility of glycolipid and oligosaccharide epitopes on rabbit villus and follicle-associated epithelium. *Am. J. Physiol. 278*, G915−G923.

(17) Amin, T., and Hirst, T. R. (1994) Purification of the B-subunit oligomer of *Escherichia coli* heat-labile enterotoxin by heterologous expression and secretion in a marine vibrio. *Protein Expression Purif. 5*, 198−204.

(18) Frank, R. (1992) Spot-synthesis: an easy technique for the positionally addressable, parallel chemical synthesis on a membrane support. *Tetrahedron 48*, 9217−9232.

(19) Frey, A., Di Canzio, J., and Zurakovski, D. (1998) A statistically defined endpoint titer determination method for immunoassays. *J. Immunol. Methods 221*, 35−41.

(20) Sonnino, S., Acquotti, D., Kirschner, G., Uguaglianza, A., Zecca, L., Rubino, F., and Tettamanti, G. (1992) Preparation of lyso-G_{M1} ($Il_3Neu_5AcGgOse_4$-long chain bases) by a one-pot reaction. *J. Lipid Res. 33*, 1221−1226.

(21) Matsubara, T., Ishikawa, D., Taki, T., Okahata, Y., and Sato, T. (1999) Selection of ganglioside G_{M1}-binding peptides by using a phage library. *FEBS Lett. 456*, 253−256.

(22) Merritt, E. A., Sarfaty, S., van den Akker, F., L'Hoir, C., Martial, J. R., and Hol, W. G. J. (1994) Crystal structure of cholera toxin B-pentamer bound to receptor G_{M1} pentasaccharide. *Protein Sci. 3*, 166−175.

(23) Wenschuh, H., Gausepohl, H., Germeroth, L., Ulbricht, M., Matuschewski, H., Kramer, A., Volkmer-Engert, R., Heine, N., Ast, T., Scharn, D., and Schneider-Mergener J. (2000) Positionally addressable parallel synthesis on continuous membranes. In *Combinatorial Chemistry: A Practical Approach* (Ferrini, H., Ed.) pp 95−116, Oxford University Press, Oxford, U.K.

(24) Siebert, H. C., Born, K., Andre, S., Frank, M., Kaltner, H., von der Lieth, C. W., Heck, A. J. R., Jimenez-Barbero, J. J., Kopitz, J., and Gabius, H. J. (2005) Carbohydrate chain of ganglioside G_{M1} as a ligand: identification of the binding strategies of three 15 mer peptides and their divergence from the binding modes of growth-regulatory galectin-1 and cholera toxin. *Chem.—Eur. J. 12*, 388−402.

(25) Delmas, A., and Partidos, C. D. (1996) The binding of chimeric peptides to G_{M1} ganglioside enables induction of antibody responses after intranasal immunization. *Vaccine 14*, 1077−1082.

(26) Kurosky, A., Markel, D. E., and Peterson, J. W. (1977) Covalent structure of the β chain of cholera enterotoxin. *J. Biol. Chem. 252*, 7257−7264.

(27) Matkovic-Calogovic, D., Loregian, A., D'Acunto, M. R., Battistutta, R., Tossi, A., Palu, G., and Zanotti, G. (1999) Crystal structure of the B subunit of *Escherichia coli* heat labile enterotoxin carrying peptides with anti-Herpes simplex virus type 1 activity. *J. Biol. Chem. 274*, 8764−8769.

(28) Kakio, A., Nishimoto, S., Yanagisava, K., Kozutsumi, Y., and Matzuzaki, K. (2002) Interaction of amyloid β-protein with various gangliosides in raft-like membranes: importance of G_{M1} ganglioside-bound form as an endogenous seed for alzheimer amyloid. *Biochemistry 41*, 7385−7390.

(29) Champagne, M. J., Lamontagne, S., and Potier, M. (1994) Binding of G_{M1}-ganglioside to a synthetic peptide derived from the lysosomal sphingolipid-activator-protein saposin B. *FEBS Lett. 347*, 265−267.

(30) Tseng, S. F., Deibler, G. E., and DeVries, G. H. (1999) Myelin basic protein and myelin basic protein peptides induce the proliferation of schwann cells via ganglioside G_{M1} and the FGF receptor. *Neurochem. Res. 24*, 255−260.

(31) Nariya, H., Izaki, K., and Kamio, Y. (1993) The C-terminal region of the S component of staphylococcal leukocidin is essential for the biological activity of the toxin. *FEBS Lett. 329*, 219−222.

BC0602376

Synthesis of Symmetrical and Unsymmetrical PAMAM Dendrimers by Fusion between Azide- and Alkyne-Functionalized PAMAM Dendrons

Jae Wook Lee,[†,*] Jung Hwan Kim,[†] Hee Joo Kim,[†] Seung Choul Han,[†] Ji Hyeon Kim,[‡] Won Suk Shin,[§] and Sung-Ho Jin[§,*]

Department of Chemistry, Dong-A University, Hadan-2-dong, Busan 604-714, Korea, Department of Chemical & Biochemical Engineering, Dongguk University, Seoul 100-715, Korea, and Department of Chemistry Education & Center for Plastic Information System, Pusan National University, Busan 609-735, Korea . Received August 17, 2006; Revised Manuscript Received January 25, 2007

A new convergent synthetic method for the synthesis of PAMAM dendrimers has been developed. The fusion between propargyl-functionalized PAMAM dendrons and azido-functionalized PAMAM dendrons via the Cu(I)-catalyzed Huisgen [2 + 3] dipolar cycloaddition reaction (click chemistry) of an alkyne and an azide leads to the formation of symmetric PAMAM dendrimers in high yields. Furthermore, the coupling reactions between the different generation dendrons afford the size-differentiated unsymmetrical PAMAM dendrimers.

INTRODUCTION

Dendrimers, which are prepared by repetition of a given set of reactions using either divergent or convergent strategies, are highly branched and regular macromolecules with well-defined structures and have served as functional objects in nanotechnology and nanoscience (*1*, *2*). Recent advances in nanomedicine showed that dendrimers are a novel class of nanoscale carriers that can be multifunctionally used for targeting, imaging, and treatment of biological systems (*3*). Especially PAMAM dendrimers, which are nanoscopic spherical macromolecules composed of polyamidoamino units with repeating dendritic branching, have been extensively studied in many fields such as drug, drug and gene delivery, and in magnetic resonance imaging. The interior cavities of PAMAMs are often used to encapsulate hydrophobic or hydrophilic drugs (*4*, *5*). In order to better control the release rate, imaging, and targeting properties of drugs, the terminal groups of PAMAMs have been functionalized with various moieties, such as drugs, biospecific ligands, and fluorescent tags (*6*, *7*). These dendrimer-based nanodevices hold great promise for various biomedical applications. In the future, more expanded applications of PAMAM dendrimers rely on efficient and practical synthetic procedures.

The early synthetic efforts in PAMAM dendrimer synthesis applied the divergent synthesis procedure building the dendrimers from the core by an iterative synthetic procedure (*8*). The convergent approach of dendrimer synthesis introduced by Fréchet and co-workers revolutionized the synthetic approaches to develop monodisperse dendrimers (*9*, *10*). The convergent methodology installs the core in the final step, enabling the incorporation of various functionalities. It provides greater structural control than the divergent approach due to its relatively low number of coupling reactions at each growth step. The ability to prepare well-defined (un)symmetrical dendrimers is the most attractive feature of the convergent synthesis method. Therefore, the synthesis of PAMAM dendrimers via the convergent approach is a significant challenge. However, an example in the convergent synthesis of PAMAM dendrimers by the amide coupling between carboxylic acid and amine is reported (*11*). In continuation of our efforts in the convergent synthesis of dendrimers, we here report the efficient synthesis of symmetric and unsymmetric PAMAM dendrimers by 1,3-dipolar cycloaddition of azide- and alkyne-functionalized PAMAM dendrons.

The reactions employed in the synthesis of dendrimers should be high yielding without any side reactions. Well-known processes, such as Michael reaction, Williamson ether synthesis, amidations, and reductions have been used extensively in the synthesis of dendrimers (*10*). The Cu(I)-catalyzed Huisgen [2 + 3] dipolar cycloaddition reaction between an organic azide and an alkyne (*12*, *13*), the best example of click chemistry (*14*, *15*), is clearly a breakthrough in the synthesis of dendrimers (*16*, *17*). The reaction is characterized by mild and simple reaction conditions, reliable 1,4-regiospecific 1,2,3-triazole formations, and tolerance toward water as well as a wide range of functionalities (*18*). Although many reports have been found in the synthesis of the triazole-mediated dendritic materials using click chemistry (*19*−*26*), there are a few reports that demonstrate the synthesis of the PAMAM dendrimer in spite of its importance for new material design (*27*−*29*).

EXPERIMENTAL PROCEDURES

General. ^{1}H NMR spectra were recorded on a 300 or 500 MHz NMR spectrometer using the residual proton resonance of the solvent as the internal standard. Chemical shifts are reported in parts per million (ppm). When peak multiplicities are given, the following abbreviations are used: s, singlet; d, doublet; t, triplet; q, quartet; quin, quintet; d of d, doublet of a doublet; m, multiplet; br, broad. ^{13}C NMR spectra were proton decoupled and recorded on a 75 or 125 MHz NMR spectrometer using the carbon signal of deuterated solvent as the internal standard. FAB and MALDI mass spectra were obtained from Korea Basic Science Institute (KBSI) in Daegu or Daejeon and POSTECH. Flash chromatography was performed with 37−75 μm silica gel. Analytical thin layer chromatography was performed on silica plates with F_{254} indicator, and the visualization was accomplished by UV lamp or using an iodine chamber. Polydispersity (PDI) of dendrimers was determined by gel permeation chromatography (GPC) analysis relative to polystyrene calibration (Agilent 1100 series GPC, Plgel 5μm

* Corresponding authors. E-mail: jlee@donga.ac.kr; E-mail: shjin@pusan.ac.kr.
[†] Dong-A University.
[‡] Dongguk University.
[§] Pusan National University.

10.1021/bc060256f CCC: $37.00 © 2007 American Chemical Society
Published on Web 03/03/2007

MIXED-C, refractive index detector) in THF solution. All chemicals were obtained from commercial sources and used as received, unless otherwise mentioned. THF was distilled over Na/Ph_2CO ketyl.

General Procedure for the Preparation of Dendrimers 3-Gmn from Propargyl-PAMAM Dendrons 1-Dm and Azido-PAMAM Dendrons 2-Dn. A mixture of propargyl-dendrons **1-Dm** (0.10 mmol) and azido-dendrons **2-Dn** (0.11 mmol) in THF−H_2O (4:1, 1 mL) in the presence of 5 mol % $CuSO_4 \cdot 5H_2O$ with 10 mol % sodium ascorbate was stirred at room temperature for ∼4 h. The reaction mixture was poured into brine (20 mL), and the resulting solution was extracted with EtOAc (20 mL × 4). The combined organic phase was dried with sodium sulfate, concentrated, and purified by column chromatography (EtOAc/methanol system) to afford the desired product.

3-G11. 95% yield; IR 2955, 2840, 1734, 1437, 1258, 1199, 1174, 1044 cm^{-1}; ^1H NMR (500 MHz, $CDCl_3$): δ = 2.02 (quintet, J = 6.6 Hz, 2H), 2.39 (t, J = 6.7 Hz, 6H), 2.47 (t, J = 7.0 Hz, 4H), 2.71 (t, J = 6.8 Hz, 4H), 2.77 (t, J = 7.0 Hz, 4H), 3.62 (s, 6H), 3.64 (s, 6H), 3.78 (s, 2H), 4.31 (t, J = 7.0 Hz, 2H), 7.55 (s, 1H); ^{13}C NMR (75 MHz, $CDCl_3$): δ = 173.3, 173.2, 144.6, 123.4, 52.0, 51.9, 50.8, 49.5, 49.3, 48.9, 48.2, 33.0, 32.8, 28.5; MS (FAB): m/z = 500 [M^+ + H]; HRMS (FAB) calcd for $C_{22}H_{37}N_5O_8$: 499.2642. found: 500.2837 [M^+ + H]. PDI = 1.01.

3-G22. 97% yield; IR 3314, 2952, 2828, 1734, 1663, 1533, 1437, 1357, 1257, 1198, 1176, 1046 cm^{-1}; ^1H NMR (500 MHz, $CDCl_3$): δ = 2.02 (m, 2H), 2.34 (m, 4H), 2.41−2.44 (m, 30H), 2.54−2.55(m, 8H), 2.73−2.77 (m, 16H), 3.28 (t, J = 4.7 Hz, 8H), 3.66 (s, 24H), 3.84 (s, 2H), 4.36 (t, J = 6.4 Hz, 2H), 6.97 (br s, 2H), 7.15 (br s, 2H), 7.67 (s, 1H); ^{13}C NMR (75 MHz, $CDCl_3$): δ = 173.4, 172.7, 172.4, 143.8, 123.5, 53.3, 52.0, 50.2, 50.0, 49.6, 49.6, 48.2, 47.8, 37.5, 37.5, 34.2, 33.9, 33.4, 33.0, 28.4; MS (FAB): m/z = 1301 [M^+ + H]; HRMS (FAB) calcd for $C_{58}H_{101}N_{13}O_{20}$: 1299.7286. found: 1300.7364 [M^+ + H]. PDI = 1.02.

3-G33. 94% yield; IR 3294, 2954, 2918, 2848, 1737, 1658, 1649, 1542, 1437, 1257, 1200, 1177, 1046 cm^{-1}; ^1H NMR (500 MHz, $CDCl_3$): δ = 2.02 (m, 2H), 2.34−2.36 (m, 10H), 2.42 (t, J = 6.5 Hz, 48H), 2.53 (t, J = 5.7 Hz, 24H), 2.57 (m, 8H), 2.74 (t, J = 6.6 Hz, 32H), 2.79 (t, J = 6.3 Hz, 16H), 3.26−3.27 (m, 24H), 3.65 (s, 48H), 3.82 (s, 2H), 4.35 (t, J = 6.4 Hz, 2H), 7.07−7.09 (m, 8H), 7.59 (br, 2H), 7.73 (s, 1H), 7.77 (br, 2H); ^{13}C NMR (125 MHz, $CDCl_3$): δ = 173.3, 173.2, 144.8, 123.3, 52.0, 51.9, 50.8, 49.5, 49.3, 49.0, 48.2, 33.1, 32.8, 28.5; MS (MALDI): m/z calcd for $C_{130}H_{229}N_{29}O_{44}$: 2900.6573. found: 2901.6875 [M^+ + H].

3-G31. 92% yield; IR 3303, 2952, 2827, 1735, 1664, 1651, 1539, 1436, 1257, 1198, 1176, 1043 cm^{-1}; ^1H NMR (500 MHz, $CDCl_3$): δ = 2.04 (m, 2H), 2.36 (t, J = 6.5 Hz, 6H), 2.42 (t, J = 6.6 Hz, 24H), 2.53 (t, J = 5.8 Hz, 12H), 2.58 (t, J = 5.5 Hz, 4H), 2.74 (t, J = 6.6 Hz, 20H), 2.78−2.82 (m, 12H), 3.28 (t, J = 5.4 Hz, 12H), 3.66 (s, 24H), 3.67 (s, 6H), 3.84 (s, 2H), 4.33 (t, J = 6.9 Hz, 2H), 7.04 (br s, 4H), 7.66 (s, 1H), 7.73 (br s, 2H); ^{13}C NMR (75 MHz, $CDCl_3$): δ = 172.9, 172.8, 172.13, 172.06, 143.0, 123.1, 52.7, 52.3, 51.5, 50.2, 49.7, 49.0, 48.9, 47.7, 47.0, 37.2, 37.0, 33.6, 33.3, 32.5, 32.2, 27.9; MS (FAB): m/z = 1701 [M^+ + H]; HRMS (FAB) calcd for $C_{76}H_{133}N_{17}O_{26}$: 1699.9608. found: 1700.9686 [M^+ + H]. PDI = 1.03.

3-G32. 92% yield; IR 3310, 2952, 2827, 1735, 1664, 1651, 1537, 1437, 1257, 1197, 1177, 1045 cm^{-1}; ^1H NMR (500 MHz, $CDCl_3$): δ = 2.02 (m, 2H), 2.33−2.36 (m, 2H), 2.41−2.43 (m, 36H), 2.53, (m, 12H), 2.59 (m, 4H), 2.73−2.75 (m, 24H), 2.81 (m, 16H), 3.26−3.27 (m, 16H), 3.66 (s, 36H), 3.83 (s, 2H), 4.35 (t, J = 6.9 Hz, 2H), 6.98 (br s, 2H), 7.05 (br s, 4H), 7.66 (s, 1H), 7.74 (br s, 2H); ^{13}C NMR (75 MHz, $CDCl_3$): δ = 172.9, 172.1, 143.2, 123.0, 52.7, 52.3, 51.5, 49.7, 49.4, 49.0, 47.7, 47.1, 37.2, 376.0, 33.7, 33.5, 33.3, 32.5, 32.1, 27.9; MS (FAB): m/z = 2101 [M^+ + H]; HRMS (FAB) calcd for $C_{94}H_{165}N_{21}O_{32}$: 2100.1930. found: 2101.2008 [M^+ + H]. PDI = 1.03.

3-G41. 95% yield; IR 3295, 2952, 2829, 1737, 1649, 1539, 1436, 1257, 1198, 1176, 1045 cm^{-1}; ^1H NMR (500 MHz, $CDCl_3$): δ = 2.03 (m, 2H), 2.35 (m, 18H), 2.42 (m, 48H), 2.53 (m, 24H), 2.57 (m, 4H), 2.74 (m, 36H), 2.79 (m, 28H), 3.27 (m, 28H), 3.65 (s, 54H), 3.83 (s, 2H), 4.33 (t, J = 6.9 Hz, 2H), 7.05 (br s, 8H), 7.63 (br s, 4H), 7.69 (s, 1H), 7.83 (br s, 2H); ^{13}C NMR (125 MHz, $CDCl_3$): δ = 173.4, 173.2, 173.1, 172.8, 172.7, 143.7, 123.8, 53.3, 52.9, 52.5, 52.0, 50.9, 50.5, 50.3, 49.7, 49.5, 48.3, 47.6, 37.9, 37.6, 37.2, 34.2, 33.9, 33.1, 32.8, 32.4, 30.1, 28.6; MS (MALDI): calcd for $C_{148}H_{261}N_{33}O_{50}$: 3300.8895. found: 3323.7861 [M^+ + Na].

3-G42. 88% yield; IR 3290, 2952, 2828, 1734, 1648, 1545, 1436, 1257, 1199, 1177, 1043 cm^{-1}; ^1H NMR (500 MHz, $CDCl_3$): δ = 2.05 (m, 2H), 2.34 (m, 18H), 2.41 (m, 60H), 2.52 (m, 28H), 2.73 (m, 72H), 3.26 (m, 32H), 3.64 (s, 60H), 3.79 (s, 2H), 4.34 (m, 2H), 7.01 (br s, 2H), 7.07 (br s, 8H), 7.63 (br s, 4H), 7.71 (s, 1H), 7.83 (br s, 2H); ^{13}C NMR (125 MHz, $CDCl_3$): δ = 173.43, 173.39, 172.9, 172.8, 143.0, 124.4, 53.7, 53.3, 52.9, 52.0, 51.9, 50.5, 50.2, 49.7, 48.4, 47.4, 37.9, 37.6, 34.8, 34.2, 33.1, 32.9, 30.1, 28.6; MS (FAB): m/z = 3702.2 [M^+ + H]; MS (MALDI): calcd for $C_{166}H_{293}N_{37}O_{56}$: 3701.1701. found: 3702.2282 [M^+ + H].

3-G43. 76% yield; IR 3286, 2952, 2827, 1734, 1651, 1539, 1437, 1257, 1195, 1177, 1043 cm^{-1}; ^1H NMR (500 MHz, $CDCl_3$): δ = 2.01 (m, 2H), 2.35 (m, 28H + 6), 2.41−2.44 (m, 56H), 2.53−2.57 (m, 40H), 2.73−2.76 (m, 56H), 2.80 (m, 32H), 3.27 (m, 40H), 3.66 (s, 72H), 3.80 (s, 2H), 4.36 (m, 2H), 7.07 (br s, 12H), 7.59 (br s, 2H), 7.65 (br s, 4H), 7.73 (s, 1H), 7.84 (br s, 2H); ^{13}C NMR (125 MHz, $CDCl_3$): δ = 173.4, 172.9, 172.82, 172.75, 143.2, 124.2, 53.3, 52.9, 52.0, 50.5, 50.3, 49.7, 46.0, 37.9, 37.6, 34.5, 34.2, 33.1, 32.7, 30.0, 28.5; MS (MALDI): calcd for $C_{202}H_{357}N_{45}O_{68}$: 4501.5861. found: 4524.6025 [M^+ + Na].

RESULTS AND DISCUSSION

In the convergent synthesis of the dendrimers, two feasible methods are the fusion of two dendrons and the stitch of multifunctional group with dendrons. We have developed the stitching method for the synthesis of symmetric dendrimers using click chemistry between an alkyne and an azide (*17*, *21*, *22*, *26*). At this time, we are fascinated to utilize the fusion method of two dendrons for the synthesis of symmetric and unsymmetric PAMAM dendrimers. The synthetic strategy for the PAMAM dendrimers **3-Gmn** utilized a fusion of the propargyl-functionalized PAMAM dendrons **1-Dm** and the azido-functionalized PAMAM dendrons **2-Dn** (Figure 1). The propargyl-functionalized PAMAM dendrons **1-Dm** (**m** = 1−4: generation of dendron) and azido-functionalized PAMAM dendrons **2-Dn** (**n** = 1−3: generation of dendron) are synthesized by the divergent approach using propargylamine and azidopropylamine as a focal point, respectively (*27*, *28*). This methodology involves typical stepwise and iterative two-step reaction sequences, consisting of amidation of methyl ester groups with a large excess of ethylenediamine and Michael addition of primary amines with methyl acrylate to produce methyl ester terminal groups.

Stitching together different dendrons effectively and efficiently without any ensuing problems in isolation and purification is a major challenge. The clue was provided by click chemistry due to the high yields and lack of byproducts. Building dendrimers via the fusion approach of dendrons

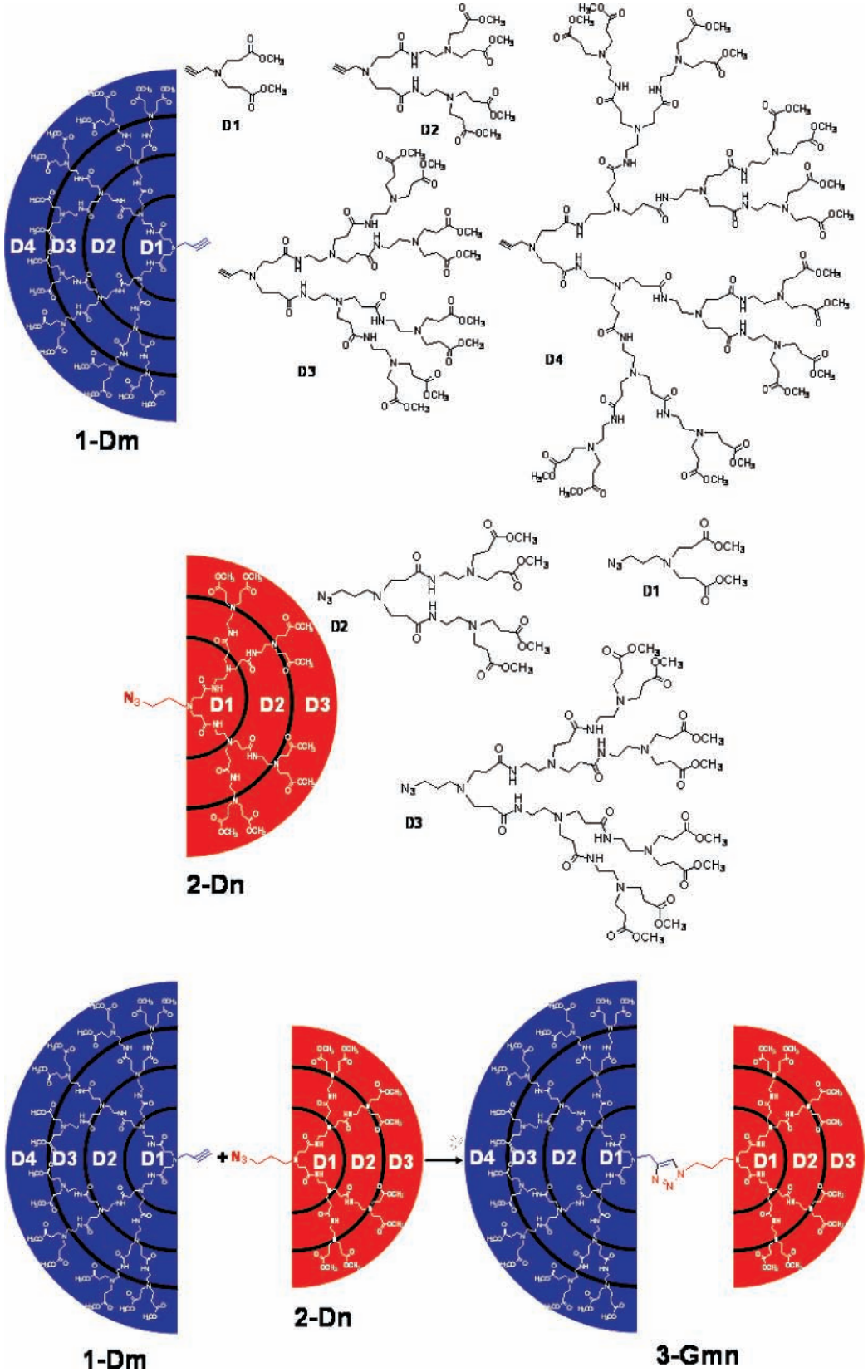


Figure 1. Structures of dendrons **1-Dm** and **2-Dn** and synthetic strategy for PAMAM dendrimers **3-Gmn**.

together allows the synthesis of symmetric and unsymmetrical dendrimers. To efficiently connect the propargyl focal point PAMAM dendrons **1-Dm** with azide-PAMAM dendrons **2-Dn** for the synthesis of PAMAM dendrimer, the click condition using Cu(I) species was selected as synthetic method. The substrate-specificity in the copper-catalyzed cycloaddition reaction between an azide and an alkyne was found to influence at the reaction time. The click reaction of alkyne-PAMAM dendrons **1-Dm**, conducted from the conditions of 5 mol % of $CuSO_4 \cdot 5H_2O$ with 10 mol % of sodium ascorbate, was completed at room temperature within a short time which may potentially be explained by anchimeric assistance due to the amine moiety presented in dendrons (*27*, *30*).

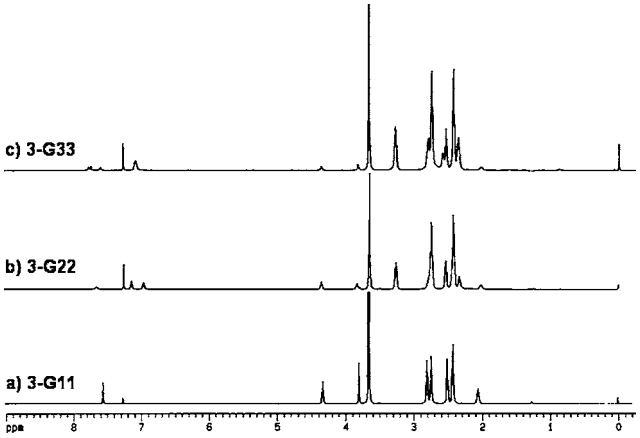


Figure 2. ^{1}H NMR spectra of PAMAM dendrimers (a) **3-G11**, (b) **3-G22**, and (c) **3-G33**.

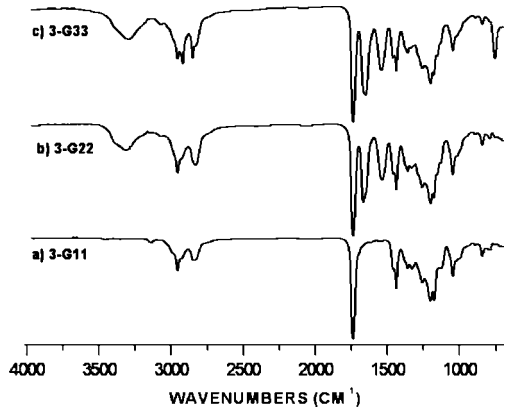


Figure 3. IR spectra of PAMAM dendrimers (a) **3-G11**, (b) **3-G22**, and (c) **3-G33**.

Thus, the reaction of alkyne-dendron **1-D1** and azido-dendrons **2-D1** in 5 mol % $CuSO_4 \cdot 5H_2O$ with 10 mol % sodium ascorbate in a 4:1 solvent ratio of THF to H_2O for 1.5 h at room temperature afforded the desired product **3-G11** in 98% yield. The generation of product and disappearance of the dendrons were monitored by TLC runs of the reaction mixture. Given the success in the synthesis of first generation dendrimer **3-G11**, we expanded this reaction to get higher generation dendrimers. The reactions of **1-D2** with **2-D2** and of **1-D3** with **2-D3** afforded the PAMAM dendrimers **3-G22** and **3-G33** in yields of 97% and 94%, respectively, after 2.5 and 4 h. For completion of the reaction between two dendrons, the higher generation dendrons take slightly longer time than the lower generation dendrons which can be imagined by the simple steric hindrance of dendrons. This result showed that the formation of triazole can be regarded as a new connector to construct the symmetric PAMAM dendrimers from dendrons. The symmetric PAMAM dendrimers were purified by column chromatography, and the structures were confirmed by ^{1}H and ^{13}C NMR spectroscopy, IR spectroscopy, and FAB or MALDI mass spectra.

From the ^{1}H NMR spectra ($CDCl_3$), peaks of the methylene protons adjacent to the carbon of triazole, the triazole proton, and the methylene protons adjacent to the nitrogen of triazole in dendrimers **3-Gmn** were found at 3.78, 7.55, and 4.31 ppm for **3-G11**, 3.84, 7.67, and 4.36 ppm for **3-G22**, 3.82, 7.73, and 4.35 ppm for **3-G33**, respectively (Figure 2). As the dendrimer generation increased, peaks of the triazole proton shifted gradually to downfield which may be influenced by the dendritic effect (*31*). The IR spectra also shows the disappearance of acetylene peak at ~3277 cm^{-1} and the azide peak at ~2096 cm^{-1} in the final dendrimers (Figure 3) while the ^{1}H NMR

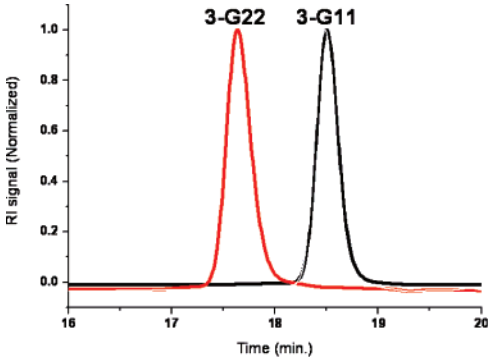


Figure 4. GPC diagrams of dendrimers **3-G11** and **3-G22** obtained from THF eluent.

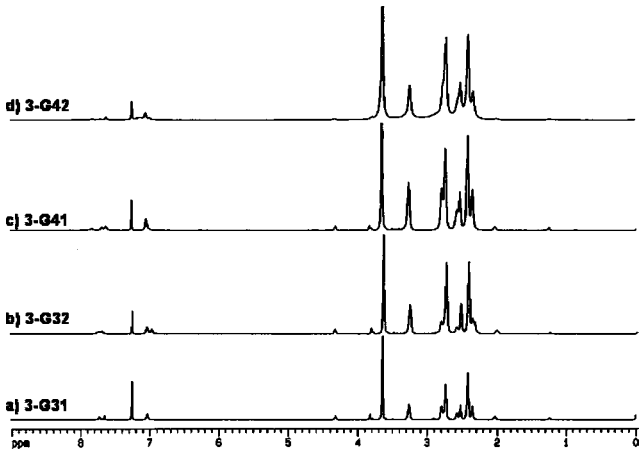


Figure 5. ^{1}H NMR spectra of PAMAM dendrimers (a) **3-G31**, (b) **3-G32**, (c) **3-G41**, and (d) **3-G42**.

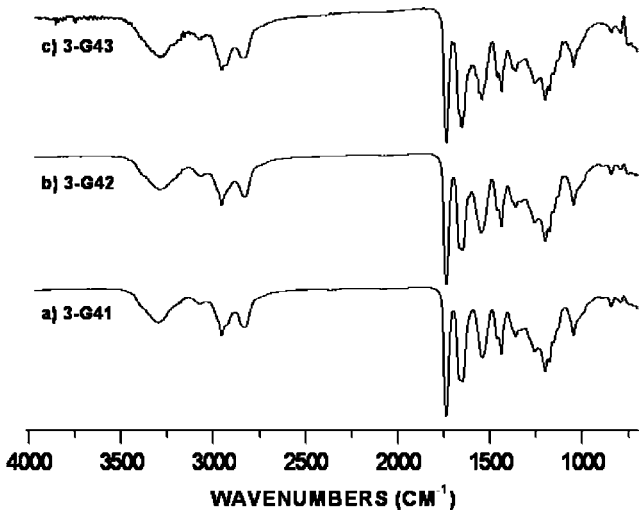


Figure 6. IR spectra of PAMAM dendrimers (a) **3-G41**, (b) **3-G42**, and (c) **3-G43**.

revealed no alkyne peak at around δ 2.46 ppm. Their mass spectra were exhibited very good correlation with the calculated molecular masses. Analysis of the dendrimers by gel-permeation chromatography (GPC) from THF eluent shows very low polydispersity values, PDI = 1.01 and 1.02 for **3-G11** and **3-G22**, respectively (Figure 4). Unfortunately, the PDI value by GPC analysis of **3-G33** could not be obtained due to their poor solubility and aggregation property in THF.

To probe the viability of our approach, we next turned our attention toward the construction of unsymmetrical PAMAM dendrimers. Unsymmetric dendrimers were assembled through the click reactions between different generations of dendrons.

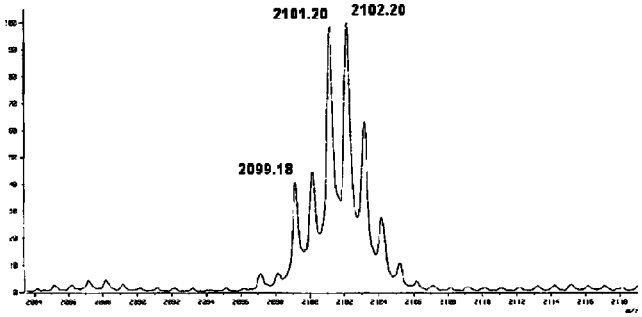


Figure 7. FAB mass spectrum of dendrimer **3-G32**.

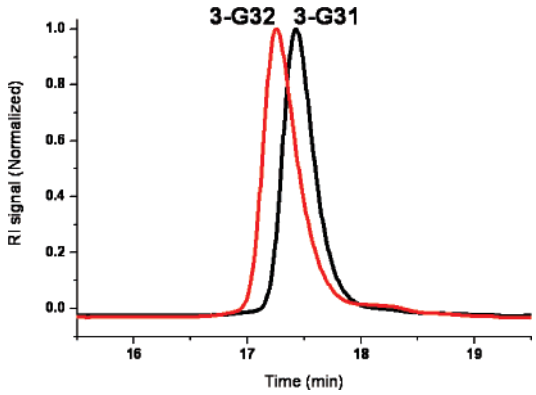


Figure 8. GPC diagrams of dendrimers **3-G31** and **3-G32** obtained from THF eluent.

We used **1-D3** and **1-D4** dendrons as higher generation dendrons for developing unsymmetric dendrimers. The reaction of third generation alkyne-focal dendron **1-D3** with **2-D1** and **2-D2** in the presence of 5 mol % $CuSO_4 \cdot 5H_2O$ with 10 mol % sodium ascorbate in a 4:1 solvent ratio of THF to H_2O afforded the unsymmetrical PAMAM dendrimers **3-G31** and **3-G32** in yields of 92% and 91%, respectively, after 2 h. The reaction of fourth generation alkyne-focal dendron **1-D4** with **2-D1**, **2-D2**, and **2-D3** provided the unsymmetrical PAMAM dendrimers **3-G41**, **3-G42**, and **3-G43** in yields of 95%, 88%, and 76%, respectively, after 2, 2.5, and 4 h. The products were separated by column chromatography. The low yield of **3-G43**, in the absence of any side product(s) as observed by TLC, could be due to significant retention of the polar dendrimer in silica column. To improve the isolated yield of dendrimers, the membrane dialysis could be applied. Therefore, the results showed that the formation of triazole between alkyne-dendrons and azide-dendrons are found to be an efficient connector to construct various unsymmetric dendrimers and may be applied for the synthesis of functional materials. We are currently investigating the synthesis of functional unsymmetric dendrimers using the dendrons peripherally modified with various substituents.

The structures of all unsymmetric PAMAM dendrimers were also confirmed by ^1H and ^{13}C NMR spectroscopy and mass spectra. From the ^1H NMR spectra ($CDCl_3$), we observed that the chemical shifts of the methylene protons adjacent to the carbon of triazole, the triazole proton, and the methylene protons adjacent to the nitrogen of triazole in unsymmetric dendrimers were similar to those in the corresponding dendron(s) of symmetric dendrimers (Figure 5). IR data also confirmed that neither alkyne ($\sim$3277 cm^{-1}) nor azide (2096 cm^{-1}) residues remain in the final dendrimer (Figure 6). Their mass spectra were exhibited very good correlation with the calculated molecular masses (Figure 7). Analysis of the dendrimers by gel-permeation chromatography (GPC) from THF eluent shows very low polydispersity value, PDI = 1.03 for both **3-G31** and **3-G32** (Figure 8). Unfortunately, the PDI value by GPC analysis of other dendrimers also could not be obtained due to their poor solubility and/or aggregation properties in THF.

CONCLUSION

We have demonstrated for the first time that click reaction between the propargyl-functionalized PAMAM dendrons and the azido-functionalized PAMAM dendrons lead to the formation of symmetric PAMAM dendrimers in high yields. Furthermore, the coupling reactions between the different generation dendrons afforded the size-differentiated unsymmetrical PAMAM dendrimers. This method may then provide an insight into designing various (un)symmetrical dendrimers such as amphiphilic dendrimers. We are currently working toward synthesis of various functional dendrimers using this strategy for various applications.

ACKNOWLEDGMENT

This research was supported by the University IT Research Center (ITRC) Project of the Ministry of Information and Communication (J.W.L) and by the Korea Science and Engineering Foundation (KOSEF) grant funded by the Korea government (MOST) (No. M10600000157-06J0000-15710) (S.H.J). We also thank the Korean Ministry of Education (BK 21 Program) for graduate studentships.

LITERATURE CITED

(1) Grimsdale, A. C., and Müllen, K. (2005) The chemistry of organic nanomaterials. *Angew. Chem., Int. Ed. 44*, 5592−5629.
(2) Tomalia, D. A. (2005) Birth of a new macromolecular architecture: dendrimers as quantized building blocks for nanoscale synthetic polymer chemistry. *Prog. Polym. Sci. 30*, 294−324.
(3) Moghimi, S. M., Hunter, A. C., and Murry, J. C. (2005) Nanomedicine: current status and future prospects. *FASEB J. 19*, 311−330.
(4) Esfand, R., and Tomalia, D. A. (2001) Poly(amidoamine) (PAMAM) dendrimers: from biomimicry to drug delivery and biomedical applications. *Drug Discovery Today 6*, 427−436.
(5) Beezer, A. E., King, A. S. H., Martin, I. K., Mitchel, J. C., Twyman, L. J., and Wain, C. F. (2003) Dendrimers as potential drug carriers; encapsulation of acidic hydrophobes within water soluble PAMAM derivatives. *Tetrahedron 59*, 3873−3880.
(6) Patri, A. K., Majoros, I., and Baker, J. R., Jr. (2002) Dendritic polymer macromolecular carriers for drug delivery. *Curr. Opin. Chem. Biol. 6*, 466−471.
(7) Quintana, A., Raczka, E., Piehler, L., Lee, I., Myc, A., Majoros, I., Patri, A. K., Thomas, T., Mule, J., and Baker, J. R., Jr. (2002) Design and function of a dendrimer-based therapeutic nanodevice targeted to tumor cells through the folate receptor. *Pharm. Res. 19*, 1310−1316.
(8) Tomalia, D. A., Baker, H., Dewald, J. R., Hall, M., Kallos, G., Martin, S., Roeck, J., Ryder, J., and Smith, P. (1985) A new class of polymers: starburst-dendritic macromolecules. *Polym. J. 17*, 117.
(9) Hawker, C. J., and Fréchet, J. M. J. (1990) Preparation of polymers with controlled molecular architecture. a new convergent approach to dendritic macromolecules. *J. Am. Chem. Soc. 112*, 7638−7647.
(10) Grayson, S. M., and Fréchet, J. M. J. (2001) Convergent dendrons and dendrimers: from synthesis to applications. *Chem. Rev. 101*, 3819−3867.
(11) Pittelkow, M., and Christensen, J. B. (2005) Convergent synthesis of internally branched PAMAM dendrimers. *Org. Lett. 7*, 1295−1298.
(12) Rostovtsev, V. V., Green, L. G., Fokin, V. V., and Sharpless, K. B. (2002) A stepwise huisgen cycloaddition process: copper(I)-catalyzed regioselective "ligation" of azides and terminal alkynes. *Angew. Chem., Int. Ed. 41*, 2596−2599.
(13) Tornøe, C. W., Christensen, C., and Meldal, M. (2002) Peptidotriazoles on solid phase: [1,2,3]-triazoles by regiospecific copper(I)-catalyzed 1,3-dipolar cycloadditions of terminal alkynes to azides. *J. Org. Chem. 67*, 3057−3064.

(14) Kolb, H. C., Finn, M. G., and Sharpless, K. B. (2001) Click chemistry: diverse chemical function from a few good reactions. *Angew. Chem., Int. Ed. 40*, 2004−2021.
(15) Kolb, H. C., and Sharpless, K. B. (2003) The growing impact of click chemistry on drug discovery. *Drug Discovery Today 8*, 1128−1137.
(16) Wu, P., Feldman, A. K., Nugent, A. K., Hawker, C. J., Scheel, A., Voit, B., Pyun, J., Fréchet, J. M. J., Sharpless, K. B., and Fokin, V. V. (2004) Efficiency and fidelity in a click-chemistry route to triazole dendrimers by the copper(I)-catalyzed ligation of azides and alkynes. *Angew. Chem., Int. Ed. 43*, 3928−3932.
(17) Lee, J. W., and Kim, B. K. (2005) A facile route to triazole dendrimers via click chemistry linking tripodal acetylene and dendrons. *Bull. Korean Chem. Soc. 26*, 658−660.
(18) Bock, V. D., Hiemstra, H., and van Maarseveen, J. H. (2006) Cu^{I}-catalyzed alkyne−azide "click" cycloadditions from a mechanistic and synthetic perspective. *Eur. J. Org. Chem.* 51−68.
(19) Malkoch, M., Schleicher, K., Drockenmuller, E., Hawker, C. J., Russell, T. P., Wu, P., and Fokin, V. V. (2005) Structurally diverse dendritic libraries: a highly efficient functionalization approach using click chemistry. *Macromolecules 38*, 3663−3678.
(20) Joralemon, M. J., O'Reilly, R. K., Matson, J. B., Nugent, A. K., Hawker, C. J., and Wooley, K. L. (2005) Dendrimers clicked together divergently. *Macromolecules 38*, 5436−5443.
(21) Lee, J. W., Kim, B. K., and Jin, S. H. (2005) Convergent synthesis of triazole dendrimers via click chemistry using tripodal core. *Bull. Korean Chem. Soc. 26*, 833−836.
(22) Lee, J. W., Kim, B. K., Kim, J. H., Shin, W. S., and Jin, S. H. (2005) Facile synthesis of Fréchet type dendritic benzyl azides and dendrimer via cycloaddition reaction with tripodal core. *Bull. Korean Chem. Soc. 26*, 1790−1794.
(23) Rijkers, D. T. S., van Esse, G. W., Merkx, R., Brouwer, A. J., Jacobs, H. J. F., Pieters, R. J., and Liskamp, R. M. J. (2005) Efficient microwave-assisted synthesis of multivalent dendrimeric peptides using cycloaddition reaction (click) chemistry. *Chem. Commun.* 4581−4583.
(24) Wu, P., Malkoch, M., Hunt, J. N., Vestberg, R., Kaltgrad, E., Finn, M. G., Fokin, V. V., Sharpless, K. B., and Hawker, C. J. (2005) Multivalent, bifunctional dendrimers prepared by click chemistry. *Chem. Commun.* 5775−5777.
(25) Lee, J. W., and Kim, B. K. (2006) Synthesis of symmetric and unsymmetric triazole dendrimers via dipolar cycloaddition reaction. *Synthesis* 615−618.
(26) Lee, J. W., Kim, J. H., Kim, B. K., Shin, W. S., and Jin, S. H. (2006) Synthesis of Fréchet type dendritic benzyl propargyl ether and Fréchet type triazole dendrimer. *Tetrahedron 62*, 894−900.
(27) Lee, J. W., Kim, B. K., Kim, H. J., Han, S. C., Shin, W. S., and Jin, S. H. (2006) Convergent synthesis of symmetrical and unsymmetrical PAMAM dendrimers. *Macromolecules* **2006**, *39*, 2418−2422.
(28) Lee, J. W., Kim, J. H., and Kim, B. K. (2006) Synthesis of azide-functionalized PAMAM dendrons at the focal point and their application for synthesis of PAMAM-like dendrimers. *Tetrahedron Lett.* **2006**, *47*, 2683−2686.
(29) Lee, J. W., Kim, J. H., Kim, B. K., Kim, J. H., Shin, W. S., Jin, S. H. and Kim, M. (2006) Convergent Synthesis of PAMAM-like Dendrimers from Azide-functionalized PAMAM Dendrons. *Bull. Korean Chem. Soc. 27*, 1795−1800.
(30) Lee, J. W., Kim, B. K., Kim, J. H., Shin, W. S., and Jin, S. H. (2006) Facile approach for diblock codendrimers by fusion between Fréchet dendrons and PAMAM dendrons. *J. Org. Chem. 71*, 4988−4991.
(31) Wong, C.-H., Chow, H.-F., Hui, S.-K., and Sze, K.-H. (2006) Generation-independent dimerization behavior of quadruple hydrogen-bond-containing oligoether dendrons. *Org. Lett. 8*, 1811−1814.

BC060256F

Polyhistidine Fusion Proteins Can Nucleate the Growth of CdSe Nanoparticles

Baikuntha P. Aryal and David E. Benson*

Department of Chemistry, Wayne State University, Detroit, Michigan 48202. Received September 6, 2006; Revised Manuscript Received November 7, 2006

A $(His\text{-}Asn)_6$ domain fused to fatty acid binding protein provides the low-temperature assembly of CdSe nanoparticles starting with common inorganic salt precursors. This observation is significant, since fusion proteins with this protein domain are common for affinity purification. While not optimized, this domain readily provides CdSe nanoparticles from room-temperature solutions. The nanoparticles are soluble and do not precipitate during standard biochemical purification procedures. High-resolution transmission electron microscopy demonstrates that the CdSe nanoparticles are crystalline. Surface defects on these nanoparticles are presumed, as weak emission was observed. This report presents a straightforward method to produce protein-attached semiconducting nanoparticles that can be used for biological assays.

INTRODUCTION

Biomolecular conjugates of nanoparticles are an emerging class of functional smart materials (*1*). Semiconducting nanoparticles have provided visible to near-infrared fluorescence (*2*) and photocatalysis (*3*) to the functions of the attached biomolecules. Semiconducting nanoparticles are typically synthesized through high-temperature synthetic routes to control the distribution of nanoparticle sizes (*4*), followed by biomolecule attachment. Low-temperature biosynthetic routes (*5, 6*) have also been reported. These methods have used peptides (*7*, *8*) or proteins (*9*) known to generate CdS or Fe_3O_4 nanoparticles in vivo. Additional nanoparticulate materials can be generated through using different ionic precursors (*10*) or metathesis reactions (*11*). Nanoparticle diameters can be controlled using protein cages with larger (*12*) or smaller (*13*) diameters. Alternatively, phage-displayed peptides have been selected to bind specific material faces that can also nucleate nanoparticle formation (*5*). The nanomaterials generated by these methods are typically crystalline, but the narrow band gap semiconductor materials do not all have intense fluorescence emission (*14*). Fluorescence of semiconducting nanoparticles is quenched by lattice defects on the nanoparticle surface (*15*), which high-temperature routes (*4*, *16*) minimize by Ostwald ripening (*17*). Low-temperature synthetic methods are currently being developed that maximize nanoparticle surface crystallinity and fluorescence (*18*, *19*). A low-temperature route to protein-semiconducting nanoparticle formation using common inorganic salts and a common fusion protein domain would provide a highly accessible synthetic method. Such a synthetic method would remove the need for high-temperature methods and decrease the high cost currently associated with these bioconjugates. Here, we demonstrate that a NH_3^+-Met-$(His\text{-}Asn)_6$ fusion protein provides CdSe nanoparticle nucleation and attachment at room temperature (Scheme 1). This finding is important, since polyhistidine fusion domains are routinely attached to proteins and used for affinity purification. Such a low-temperature route to semiconducting nanoparticle formation would circumvent high-temperature methods and allow protein-directed growth of nanoparticulate materials. A similar report has just appeared where Au nanoparticles were nucleated by a His_6 fusion domain (*20*). Reduction with $NaBH_4$ was necessary for Au nanoparticle formation, but also degrades many proteins. The significance of the current article is that a low-temperature route that does not require reactive precursors is reported. Polyhistidine domains also bind metal ions, in a coordinatively unsaturated mono- or binuclear fashion (*21*, *22*), and could nucleate CdS or CdSe nanoparticles. Addition of lattice-forming anions (S^{2-} or Se^{2-}) and divalent metal cations for charge neutralization facilitates the nucleation and growth of the nanoparticulate material (*8*). With advances in low-temperature semiconducting nanoparticle synthetic methods (*18*, *19*), this report demonstrates a method for routine biomolecule−nanoparticle assembly from room-temperature aqueous solutions.

EXPERIMENTAL PROCEDURES

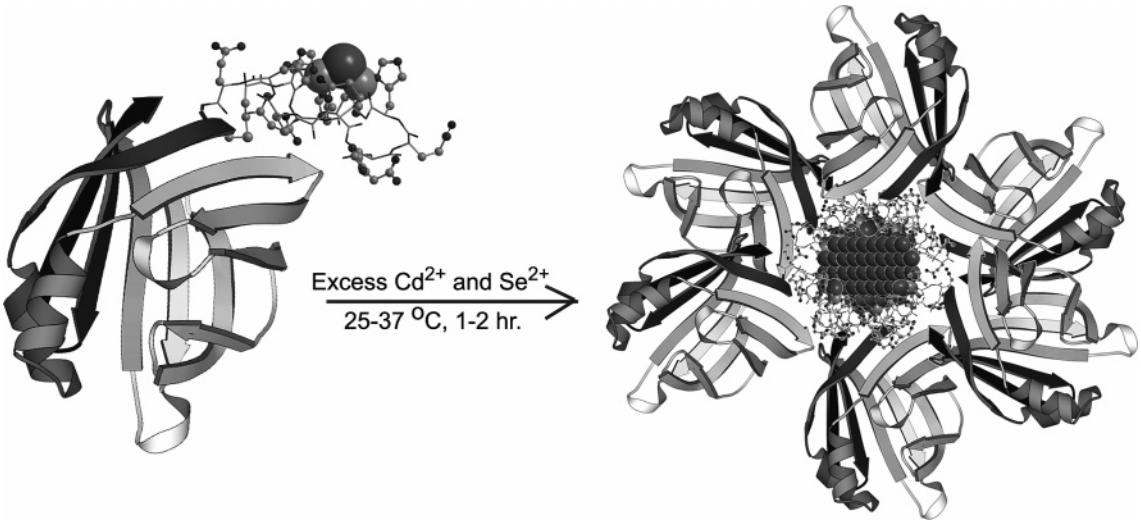
All chemicals were purchased from Aldrich and used without further purification, unless otherwise noted. Plasmid DNA encoding rat intestinal fatty acid binding protein (FABP) was a generous gift from Professor Carl Frieden (Washington University, St. Louis). The FABP coding sequence was ligated into the pPROTet expression vector (ClonTech) that encodes a NH_3^+-Met-$(His\text{-}Asn)_6$- domain and an enterokinase binding sequence before the inserted, encoded protein. The FABP conjugate from the pPROTet expression vector is termed $(HN)_6$−FABP. This protein was purified by immobilized metal affinity chromatography to homogeneity, chelated, and desalted. FABP was produced by cleaving the $(HN)_6$ peptide with enterokinase (New England Biolabs 64 pg/μg (protein), 25 °C, 16 h) followed by repurification. Protein concentrations were determined by absorbance ($\epsilon_{280} = 16\,500\ M^{-1}\ cm^{-1}$) or using the Bradford method (*23*).

$(HN)_6$−FABP Mediated Growth of Nanoparticles. $CdCl_2$ and Na_2Se (1 mM each) were added to a 50 μM $(HN)_6$−FABP or bovine serum albumin (BSA, Sigma) in anaerobic aqueous solution (20 mM *N*-morpholinosulfonate [MOPS], pH 7.5). The anaerobicity of solutions was maintained by standard O_2-sensitive techniques for aqueous solutions, and most manipulations were performed in a Coy Laboratories (Grass Lake, MI) inert atmosphere bag. After the reaction, the $(HN)_6$−FABP and BSA solutions were subjected to gel filtration chromatography (molecular weight cut off = 6000 Da, Pharmacia, 10-DG). Protein concentrations after purification were estimated using the Bradford assay (*23*). Centrifugal ultrafiltration (YM-30 or YM 100, Millipore) was performed to estimate protein dissociation from the CdSe nanoparticle surface. Dissociated

* Corresponding author. Phone: (313) 577-6914. Fax: (313) 577-8822. E-mail: dbenson@chem.wayne.edu.

10.1021/bc060277+ CCC: $37.00 © 2007 American Chemical Society
Published on Web 02/22/2007

Scheme 1. Proposed Method for Protein-Templated CdSe Nanoparticle Synthesis[a]



[a] Left: A $(His\text{-}Asn)_6$ peptide domain modeled to coordinate a $[Cd_2Se]^{2+}$ complex (see experimental, stick only, polypeptide backbone; ball and stick, amino acid side chains; light gray spheres, Cd^{2+} ions; dark gray spheres, Se^{2-} ions) attached to the amino terminus of IFABP (PDB code, 1IFC). Right: a suggested model of CdSe nanoparticle coated with multiple proteins whose stability is maintained through the $(His\text{-}Asn)_6$ domain.

protein was collected in the filtrate and determined by the Bradford assay (*23*). Absorbance and fluorescence spectra were recorded for samples within cuvettes loaded and sealed within the anaerobic bag. Fluorescence emission spectra were recorded with a Horiba Fluoromax-3 (10 nm slit width, 0.8 s integration). Samples were also dried for 36 h at 37 °C on carbon-coated grids and examined by high-resolution transmission electron microscopy (TEM, JEOL FastEM 2010, 200 kV). Formation of $O_2^{\bullet-}$ by nanoparticle photoexcitation was determined by illuminating aerobic nanoparticle-containing solutions, with 100 μM 5,5-dimethyl-1-pyrroline-*N*-oxide (DMPO) as a radical trap, in quartz cuvettes with a Xe arc lamp (150 W; water and $\lambda >$ 310 nm filters) for 20 min (*24*). These solutions were loaded into an EPR capillary flow cell (Bruker), and radical production was examined with a Bruker ESP-300 EPR spectrometer (microwave frequency, 9.856 GHz; microwave power, 20 mW; modulation amplitude, 1 G; modulation frequency, 100 kHz). Spectra of the photoilluminated samples were compared with 2,2,6,6-tetramethyl-1-piperidine-1-oxyl (TEMPO) solutions for frequency calibration and spin quantization.

Molecular Modeling of Initial $[Cd_2Se]^{2+}$ Complex. The NH_2-Met-$(His\text{-}Asn)_6$-COOH was modeled in *Chem Draw/Chem 3D* (Cambridge Soft) using the MM2 force field (*25*). The MM2 force field was selected due to the parametrization for both Cd^{2+} and Se^{2-} ions. Initial models of Cd^{2+} ion coordinated conformations were imposed by generating the N,N′,N″-methine (three-coordinate) or N,N′-methylene (two-coordinate) derivatives of the histidine side chains. The stronger C−N bond length force constants, relative to the Cd−N force constants, allowed a pseudo-tetrahedral Cd^{2+} ion coordination geometry to be enforced during geometry minimization by *Chem3D*. Geometry-minimized conformations were examined for maximal solvent exposure and minimal cross-threading of the polypeptide backbone. Once a collection of candidate metal−histidine linkages was selected, the thioether derivative of the N-methylene(ine) groups was formed to constrain the conformation for the $[Cd_2Se]^{2+}$ complex. The bond lengths to the N-methyl groups were elongated to typical $Cd\text{-}N_{imidazole}$ (2.28 Å, Cd-substituted carboxypeptidase) or Cd-(μ-Se) (2.26 Å, from Wurtzite CdSe unit cell parameters) bond lengths and geometry-minimized. The carbon and sulfur atoms were then substituted with trigonal pyramidal or tetrahedral Cd^{2+} ions and bridging Se^{2-} ions and subjected to a final round of geometry minimization. This modeled structure is shown in Scheme 1; Cd_1 coordinated to His2 ($N_{\epsilon 2}$) and His4 ($N_{\epsilon 2}$), Cd_2 coordinated to His8 ($N_{\delta 1}$), His10 ($N_{\delta 1}$), and His12 ($N_{\delta 1}$). Once the $[Cd_2Se]^{2+}$ complex was removed, geometry minimization showed only small backbone movements, suggesting this complex is conformationally accessible.

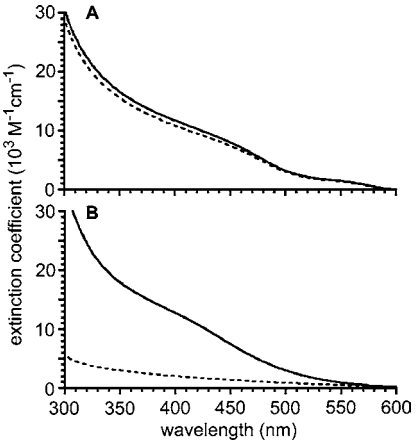


Figure 1. UV−vis spectra of 24 h, 25 °C $CdCl_2/Na_2Se$ (1 mM each) reactions with proteins before (solid line) and after (dashed line) purification by gel filtration: (A) $(HN)_6$-FABP; (B) BSA. Extinction coefficients are calculated on the basis of the protein concentration (50 μM, before purification; 32 μM, after purification).

RESULTS AND DISCUSSION

$(HN)_6$−FABP was used to demonstrate polyhistidine-domain-mediated CdSe nanoparticle nucleation. FABP is a monomeric protein with a mass of 16 KDa that nonspecifically binds hydrophobic molecules. The stability of FABP ($T_M \approx 70$ °C) is high and makes a stable scaffold for developing a biosynthetic method for CdSe nanoparticle production (*26*−*29*). Addition of a 20-fold molar excess $CdCl_2$ and Na_2Se to $(HN)_6$−FABP, FABP, or BSA under anaerobic aqueous conditions at room temperature produced brown solutions. For reactions with $(HN)_6$−FABP, the brown color changed to a red-orange color over a 24 h period (Figure 1A). Reactions with FABP that did not contain the $(HN)_6$ peptide domain produced a brown precipitate after 12 h. This control reaction was important, due to the promiscuous ligand binding of FABP. The brown color persisted for 24 h, with no precipitate, for reactions containing

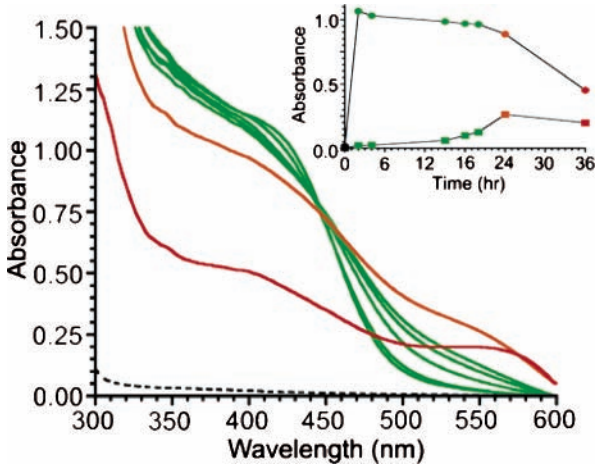


Figure 2. Time-dependent growth of $(HN)_6$-FABP capped CdSe nanoparticles. Absorbance spectra of a 50 μM $(HN)_6$-FABP solution were recorded before (dotted line) and after (solid green lines, 2 h, 4 h, 14 h, 16 h; solid orange line, 24 h; and solid red line, 36 h) the addition of $CdCl_2$ and Na_2Se (1 mM each) under anaerobic conditions (pH 7.5, 20 mM MOPS). Inset: absorbance at 425 nm (circles) and 550 nm (squares) as a function of time (symbol colors refer to line color of main figure).

BSA (Figure 1B). BSA is also known for promiscuous ligand binding (e.g., metal ions, hydrophobic molecules), where the weak Cd^{2+}/Se^{2-} ion-mediated chromophore formation is reflective of these binding events. The colored soluble species in the $(HN)_6$−FABP and BSA reactions were assumed to be due to Cd^{2+} ions and Se^{2-} ions forming a distribution of CdSe nanoparticles. On the basis of absorbance spectra (*30*), the average diameter of the CdSe nanoparticles formed by $(HN)_6$−FABP ranged from 2 to 3 nm. After 24 h at room temperature, the $(HN)_6$−FABP and BSA formed CdSe nanoparticles were isolated by gel filtration chromatography (6000 MW cutoff). Only the isolated $(HN)_6$−FABP fractions maintained the color (red-orange) after gel filtration (Figure 1). Ultrafiltration (30 000 or 100 000 MW cutoff) of the $(HN)_6$−FABP and BSA nucleated CdSe nanoparticle samples, before chromatography, yielded less than 1 μM $(HN)_6$−FABP in the filtrate as opposed to 40 μM BSA in the filtrate. Maltose-binding protein with a C-terminal His_5 domain (MBP−His_5) (*31*, *32*) was used for CdSe nucleation reactions and produced similar spectral and isolation properties to those observed with the $(HN)_6$−FABP samples (Supporting Information). BSA, while functioning as a polyelectrolyte to facilitate CdSe nanoparticle nucleation, had a weak nanoparticle affinity for purification. BSA has been reported previously to nucleate Ag_2S nanoparticles and nanorods (*33*); however, no purification was reported. This finding suggested that $(HN)_6$−FABP and MBP−His_5 can nucleate *and* form a tightly associated complex with CdSe nanoparticles. Such a distinction is important for generating biomolecule-adsorbed nanoparticles for use as soluble fluorophores for biological analysis.

Reactions at 37 °C were examined to decrease the polydispersity of $(HN)_6$−FABP-mediated CdSe nanoparticle sizes. Absorbance measurements (Figure 2) showed the initial formation of a shoulder at 425 nm (average diameter ∼2.0 nm). Weak emission spectra were observed for samples purified after 2 h of reaction (Figure 3) with broad emission maxima observed around 450 nm. The emission maxima shifted ∼5 nm as the excitation wavelengths were varied from 330 to 360 nm, indicating some polydispersity. On the basis of the extinction coefficients for CdSe nanoparticle band gap absorbances (*34*), we estimate that one CdSe nanoparticle is formed per 4−7 $(HN)_6$−FABP (assuming a yield near unity). Using the absorbance-derived CdSe nanoparticle concentration, the quantum

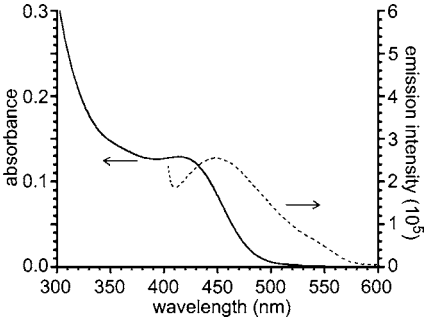


Figure 3. Absorbance (left axis/arrow) and fluorescence emission (right axis/arrow) spectra of $(HN)_6$-FABP-capped CdSe nanoparticles (2 h, 37 °C reaction: $(HN)_6$-FABP (50 μM) with $CdCl_2/Na_2Se$ (1 mM each), purified by gel filtration, diluted 1:10): absorbance, solid line; emission spectrum, dotted line, excited at 340 nm.

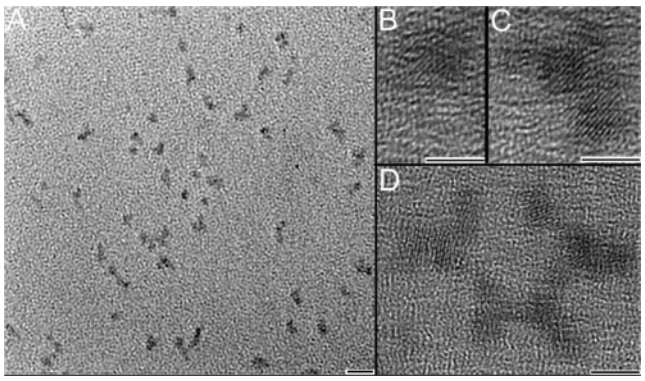


Figure 4. $(HN)_6$-FABP-mediated CdSe nanoparticle nucleation and aggregation: (A) medium resolution transmission electron micrograph (20 nm scale bar) of $(HN)_6$-FABP in the presence of $CdCl_2$ and Na_2Se for 24 h at 37 °C dried on a carbon-coated TEM grid for 36 h; (B−D) High-resolution micrographs (5 nm scale bar) of representative particles/aggregates. Panels B−D were used for lattice spacing determination (d = 3.72 Å). Multiple lines were drawn perpendicular to the lattice fringes and the average d spacing was derived across 10 to 15 lattice fringes per line. A line in panel B is shown as an example which is 52.5 Å over 14 lattice planes (d = 3.75 Å).

yield was estimated as 0.005% compared to 1% for CdSe nanoparticles formed by high-temperature methods. As time progressed, the 425 nm shoulder decreased in intensity (Figure 2 inset), followed by the growth of a shoulder at 550 nm (average diameter ∼3.1 nm). Between 2 and 16 h, the spectra exhibited an isobestic point at 450 nm, suggesting that the small nanoparticles form larger nanoparticles in a concerted fashion. After 40 h, these reactions had a detectable amount of precipitation. The spectral evolution and precipitation suggested initial CdSe nanoparticle nucleation (425 nm shoulder), followed by nanoparticle aggregation (550 nm shoulder), that eventually leads to CdSe precipitation. In contrast, the room-temperature reactions showed both the 425 and 550 nm shoulders, while no precipitation was observed. FABP is thermally stable ($T_M \approx$ 70 °C); however, a reversible transition between 35 and 50 °C has been reported (*35*). The FABP domain with low thermal stability is thought to be the helix−turn−helix mouth of the fatty acid binding pocket (*36*). The conversion of the 425 nm absorbing species to the 550 nm absorbing species, supposedly from nanoparticle aggregation, could be facilitated by thermal denaturation of the FABP helix−turn−helix domain.

TEM analysis confirmed formation and aggregation of hexagonal CdSe nanoparticles. Figure 4 shows a $(HN)_6$−FABP-nucleated, chromatographically purified sample after 24 h at 37 °C that was dried (∼36 h) on a carbon TEM grid. Lower-resolution micrographs showed minimal CdSe macrocrystallite formation, suggesting that the aggregated nucleated CdSe particles were nucleated by $(HN)_6$−FABP. The average nano-

particle diameter was 3.5 nm with a 0.7 nm size distribution (Supporting Information). The broad size distribution by TEM was consistent with the observed broad absorbances (Figures 1−3) and broad emission spectra (Figure 3). However, there were a large number of dimeric and multimeric assemblies of nanoparticles observed (Figure 4). The putative precursor nanoparticle diameters ranged from 2 to 3 nm, consistent with the initial optical nanoparticle size estimates. The majority of nanoparticle interactions were observed as dimeric interactions (Figure 4C). The weak and broad emission observed by these nanoparticles is due to the surface defects from the low-temperature growth conditions. Lattice fringes with *d* spacings of 3.72 Å were observed (Figure 4B−D) for the larger/aggregated particles showing overall that the nucleated CdSe nanoparticles are crystaline. The observed *d* spacing is consistent with the 100 face of hexagonal CdSe. After 72 h at 37 °C, Cd^{2+}/Se^{2-} incubations with $(HN)_6$−FABP showed coalescence of these small nanocrystallites into spherical 60−80 nm hexagonal CdSe nanocrystallites (Supporting Information).

Despite the TEM detected crystalinity of the $(HN)_6$−FABP-nucleated CdSe nanoparticles, the emission quantum yield is low (∼0.005%). Surface defect sites are typically invoked to describe low-emission quantum yields. These defect sites have reduction potentials ranging from the reduction potential of the conduction band ($E° \approx -500$ mV vs NHE (*37*), Se-rich) to the reduction potential of the valence band ($E° \approx +1.7$ V vs NHE (*37*), Cd-rich) (*38*). Defect sites with reduction potentials between the conduction and valence bands can undergo radiative relaxation and cause emission at long wavelengths (deep trap emission). No deep trap emission was observed with the $(HN)_6$−FABP-nucleated CdSe nanoparticles. Se-rich trap states have been suggested as producing superoxide radicals upon prolonged photoillumination (*24*, *39*), which has been suggested to confer CdSe nanoparticle toxicity (*40*). No significant EPR-detected $O_2^{\bullet-}$ production (<0.5 μM) from aerobic O_2 was observed in DMPO-spin-trapped, $(HN)_6$−FABP nucleated CdSe nanoparticle samples that were photoilluminated for 20 min. Under the same conditions, mercaptohexadecanoate-capped CdSe nanoparticles formed from high-temperature methods produced 5 μM $O_2^{\bullet-}$ (*24*). It should be noted that the majority of CdSe materials that are soluble in solution exhibit quantum confinement effects (absorbances at higher energy than bulk CdSe) from estimates of 4−7 proteins per CdSe nanoparticle. The conclusion is that a small number of microcrystallites can be excluded by this statement and suggests that Cd-rich defect sites are responsible for the diminished emission quantum yield of $(HN)_6$−FABP-nuclated CdSe nanoparticles. Such Cd-rich defects could be expected since the role of the $(HN)_6$ domain is to bind Cd^{2+} ions, not Se^{2-} ions. The role of the protein in this process is to arrest CdSe precipitation at a specific size regime, where proteins of different sizes should change the optimal CdSe nanoparticle diameter. Since a common peptide domain used for affinity purification provides this activity, such a correlation could be readily explored.

These observations have two important implications. This finding demonstrates that a protein domain routinely fused to proteins and used for affinity purification provides the ability to bind and nucleate metallic (*20*) and metal sulfide or selenide (chalcogenide) nanoparticles. Due to the similar synthetic preparations of low molecular weight Fe- and Cd-containing chalcogenide clusters (*41*), formation of CdSe nanoparticles could be similar to heterogeneous iron sulfide species formed by low-affinity ferredoxin mimetic peptides (*42*). The work with ferredoxin mimetic peptides has shown that specific conformations must be formed to generate $[Fe_4S_4]^{2+/+}$ clusters. If the proper conformation of ligand side chains are provided, then discrete $[Fe_4S_4]^{2+/+}$ clusters are observed (*43*). In the absence of the proper peptide conformation, a brown and hard-to-purify species forms, more than likely due to a heterogeneous mixture of iron sulfur clusters attached to proteins (*42*). Phytochelatin peptides $(\gamma\text{-Glu-Cys})_n$-Gly are used by bacteria to nucleate CdS nanoparticle growth by coordinating Cd^{2+} ions without sequestering the ions from solvent (*8*). Biogenic sulfide anions assist in forming nanoparticulate CdS materials that are removed from the cell (*7*). The CdSe/$(HN)_6$ domain chemistry could be similar to CdS/phytochelatin chemistry, where peptides that coordinate Cd^{2+} ions with bridging Se^{2-} ligands facilitate the nucleation and growth of CdSe nanoparticles with multiple $(HN)_6$ fusion proteins attached (Scheme 1). The peptide drawn in Scheme 1 is a molecular model of such an initial complex (geometry-minimized, MM2 force field; see Experimental Procedures). This model shows that a conformation of the $(HN)_6$ domain is accessible for coordination and formation of a $[Cd_2Se]^{2+}$ complex ion but does not attempt to address all equilibrium conformations or energetics of the $(HN)_6$ domain. It should be noted that a low molecular weight precursor method has already been reported with $(NMe_4)_4[Cd_{10}Se_4(SPh)_{16}]$-mediated CdSe nanoparticle synthesis (*44*). An important point is that polyhistidine fusion domains both nucleate and stabilize CdSe nanoparticles so that these bioconjugates can be purified by gel filtration chromatography. Toward the rational design of proteins that nucleate and stabilize metal chalcogenide nanoparticles, this report represents a zeroth-order rational design. As low-temperature synthetic methods for crystalline metal chalcogenide nanoparticles are further developed (*18*, *19*), polyhistidine fusion proteins could be used to nucleate, functionalize, and solubilize semiconducting nanoparticles for biological assays. Thus, reagents for fluorescence imaging of small molecule concentrations could be generated by incubating the sensing protein with inorganic salt precursors.

ACKNOWLEDGMENT

The authors acknowledge funding from the National Institutes of Environmental Health Sciences (ES06639) and the National Science Foundation (DBI-0508134). We also acknowledge training and help in collecting the TEM images from Dr. Palaniappan Arumugam.

Supporting Information Available: Distribution of nanoparticle diameters from Figure 4, TEM/electron diffraction images of large CdSe crystallites formed after 72 h at 37 °C, and EPR data from DMPO spin trapping experiments, and spectra from MBP-His_5 experiments. This material is available free of charge via the Internet at http://pubs.acs.org.

LITERATURE CITED

(1) Katz, E., and Willner, I. (2004) Integrated nanoparticle-biomolecule hybrid systems: Synthesis, properties, and applications. *Angew. Chem., Int. Ed. 43*, 6042−6108.

(2) Medintz, I. L., Uyeda, H. T., Goldman, E. R., and Mattoussi, H. (2005) Quantum dot bioconjugates for imaging, labelling and sensing. *Nat. Mater. 4*, 435−446.

(3) Katz, E., Zayats, M., Willner, I., and Lisdat, F. (2006) Controlling the direction of photocurrents by means of CdS nanoparticles and cytochrome c-mediated biocatalytic cascades. *Chem. Commun.* 1395−1397.

(4) Peng, Z. A., and Peng, X. (2001) Formation of high-quality CdTe, CdSe, and CdS nanocrystals using CdO as precursor. *J. Am. Chem. Soc. 123*, 183−184.

(5) Merzlyak, A., and Lee, S.-W. (2006) Phage as templates for hybrid materials and mediators for nanomaterial synthesis. *Curr. Opin. Chem. Biol. 10*, 246−252.

(6) Vriezema, D. M., Comellas-Aragones, M., Elemans, J. A. A. W., Cornelissen, J. J. L. M., Rowan, A. E., and Nolte, R. J. M. (2005) Self-assembled nanoreactors. *Chem. Rev. 105*, 1445−1490.
(7) Dameron, C. T., Reese, R. N., Mehra, R. K., Kortan, A. R., Carroll, P. J., Steigerwald, M. L., Brus, L. E., and Winge, D. R. (1989) Biosynthesis of cadmium sulfide quantum semiconductor crystallites. *Nature (London) 338*, 596−7.
(8) Dameron, C. T., and Dance, I. G. (1996) Biogenic cadmium sulfide semiconductors, In *Biomimietic Mateials Chemistry* (Mann, S., Ed.) pp 69−90, Wiley, New York.
(9) Liu, X., and Theil, E. C. (2005) Ferritins: Dynamic management of biological iron and oxygen chemistry. *Acc. Chem. Res. 38*, 167−175.
(10) Bontidean, I., Ahlqvist, J., Mulchandani, A., Chen, W., Bae, W., Mehra Rajesh, K., Mortari, A., and Csoregi, E. (2003) Novel synthetic phytochelatin-based capacitive biosensor for heavy metal ion detection. *Biosens. Bioelectron. 18*, 547−53.
(11) Douglas, T., Dickson, D. P. E., Betteridge, S., Charnock, J., Garner, C. D., and Mann, S. (1995) Synthesis and structure of an iron(III) sulfide-ferritin bioinorganic nanocomposite. *Science 269*, 54−7.
(12) Douglas, T., Strable, E., Willits, D., Aitouchen, A., Libera, M., and Young, M. (2002) Protein engineering of a viral cage for constrained nanomaterials synthesis. *Adv. Mater. 14*, 415−418.
(13) Flenniken, M. L., Willits, D. A., Brumfield, S., Young, M. J., and Douglas, T. (2003) The small heat shock protein cage from *Methanococcus jannaschii* is a versatile nanoscale platform for genetic and chemical modification. *Nano Lett. 3*, 1573−1576.
(14) Banerjee, I. A., Yu, L., and Matsui, H. (2005) Room-temperature wurtzite ZnS nanocrystal growth on Zn finger-like peptide nanotubes by controlling their unfolding peptide structures. *J. Am. Chem. Soc. 127*, 16002−16003.
(15) Nirmal, M., and Brus, L. (1999) Luminescence photophysics in semiconductor nanocrystals. *Acc. Chem. Res. 32*, 407−414.
(16) Murray, C. B., Norris, D. J., and Bawendi, M. G. (1993) Synthesis and characterization of nearly monodisperse CdE (E = sulfur, selenium, tellurium) semiconductor nanocrystallites. *J. Am. Chem. Soc. 115*, 8706−15.
(17) Peng, X., Wickham, J., and Alivisatos, A. P. (1998) Kinetics of II-VI and III-V colloidal semiconductor nanocrystal growth: "Focusing" of size distributions. *J. Am. Chem. Soc. 120*, 5343−5344.
(18) Li, R., Lee, J., Kang, D., Luo, Z., Aindow, M., and Papadimitrakopoulos, F. (2006) Band-edge photoluminescence recovery from zinc-blende CdSe nanocrystals synthesized at room temperature. *Adv. Funct. Mater. 16*, 345−350.
(19) Tong, H., and Zhu, Y.-J. (2006) Synthesis of CdS nanocrystals based on low-temperature thermolysis of one single-source organometallic precursor. *Nanotechnology 17*, 845−851.
(20) Ueno, T., Koshiyama, T., Tsuruga, T., Goto, T., Kanamaru, S., Arisaka, F., and Watanabe, Y. (2006) Bionanotube tetrapod assembly by in situ synthesis of a gold nanocluster with (Gp5-His6)3 from bacteriophage T4. *Angew. Chem., Int. Ed. 45*, 4508−4512.
(21) Conti, M., Falini, G., and Samori, B. (2000) How strong is the coordination bond between a histidine tag and Ni-nitrilotriacetate? An experiment of mechanochemistry on single molecules. *Angew. Chem., Int. Ed. 39*, 215−218.
(22) Yang, T. T., Nelson, P. S., Bush, G. L., Meyer, D. I., and Kain, S. R. (1997) An immobilized Co^{2+} affinity matrix for purification of 6′-histidine-tagged proteins. *Am. Biotechnol. Lab. 15*, 12−14.
(23) Bradford, M. M. (1976) A rapid and sensitive method for the quantitation of microgram quantities of protein utilizing the principle of protein-dye binding. *Anal. Biochem. 72*, 248−252.
(24) Aryal, B. P., and Benson, D. E. (2006) Metallothioneins initiate semiconducting nanoparticle cellular toxicity. *Small 2*, 1158−1163.
(25) Lii, J. H., Gallion, S., Bender, C., Wikstroem, H., Allinger, N. L., Flurchick, K. M., and Teeter, M. M. (1989) Molecular mechanics (MM2) calculations on peptides and on the protein Crambin using the CYBER 205. *J. Comput. Chem. 10*, 503−13.
(26) Wu, F., Corsico, B., Flach, C. R., Cistola, D. P., Storch, J., and Mendelsohn, R. (2001) Deletion of the helical motif in the intestinal fatty acid-binding protein reduces its interactions with membrane monolayers: Brewster angle microscopy, IR reflection-absorption spectroscopy, and surface pressure studies. *Biochemistry 40*, 1976−1983.
(27) Rajabzadeh, M., Kao, J., and Frieden, C. (2003) Consequences of single-site mutations in the intestinal fatty acid binding protein. *Biochemistry 42*, 12192−12199.
(28) Chattopadhyay, K., Saffarian, S., Elson, E. L., and Frieden, C. (2002) Measurement of microsecond dynamic motion in the intestinal fatty acid binding protein by using fluorescence correlation spectroscopy. *Proc. Natl. Acad. Sci. U.S.A. 99*, 14171−14176.
(29) Chattopadhyay, K., Zhong, S., Yeh, S.-R., Rousseau, D. L., and Frieden, C. (2002) The intestinal fatty acid binding protein: The role of turns in fast and slow folding processes. *Biochemistry 41*, 4040−4047.
(30) Steigerwald, M. L., and Brus, L. E. (1990) Semiconductor crystallites: A class of large molecules. *Acc. Chem. Res. 23*, 183−8.
(31) Sandros, M. G., Gao, D., Gokdemir, C., and Benson, D. E. (2005) General, high-affinity approach for the synthesis of fluorophore appended protein nanoparticle assemblies. *Chem. Commun.* 2832−2834.
(32) Medintz, I. L., Clapp, A. R., Mattoussi, H., Goldman, E. R., Fisher, B., and Mauro, J. M. (2003) Self-assembled nanoscale biosensors based on quantum dot FRET donors. *Nat. Mater. 2*, 630−638.
(33) Yang, L., Xing, R., Shen, Q., Jiang, K., Ye, F., Wang, J., and Ren, Q. (2006) Fabrication of protein-conjugated silver sulfide nanorods in the bovine serum albumin solution. *J. Phys. Chem. B 110*, 10534−10539.
(34) Yu, W. W., Qu, L., Guo, W., and Peng, X. (2003) Experimental determination of the extinction coefficient of CdTe, CdSe, and CdS nanocrystals. *Chem. Mater. 15*, 2854−2860.
(35) Arighi, C. N., Rossi, J. P. F. C., and Delfino, J. M. (1998) Temperature-induced conformational transition of intestinal fatty acid binding protein enhancing ligand binding: A functional, spectroscopic, and molecular modeling study. *Biochemistry 37*, 16802−16814.
(36) Arighi, C. N., Rossi, J. P. F. C., and Delfino, J. M. (2003) Temperature-induced conformational switch in intestinal fatty acid binding protein (IFABP) revealing an alternative mode for ligand binding. *Biochemistry 42*, 7539−7551.
(37) Hagfeldt, A., and Graetzel, M. (1995) Light-induced redox reactions in nanocrystalline systems. *Chem. Rev. 95*, 49−68.
(38) Houtepen, A. J., and Vanmaekelbergh, D. (2005) Orbital occupation in electron-charged CdSe quantum-dot solids. *J. Phys. Chem. B 109*, 19634−19642.
(39) Ipe, B. I., Lehnig, M., and Niemeyer, C. M. (2005) On the generation of free radical species from quantum dots. *Small 1*, 706−709.
(40) Derfus, A. M., Chan, W. C. W., and Bhatia, S. N. (2004) Probing the cytotoxicity of semiconductor quantum dots *Nano Lett. 4*, 11−18.
(41) Dance, I. G., Choy, A., and Scudder, M. L. (1984) Syntheses, properties, and molecular and crystal structures of $(Me_4N)_4[E_4M_{10}(SPh)_{16}]$ (E = sulfur, selenium; M = zinc, cadmium): Molecular supertetrahedral fragments of the cubic metal chalcogenide lattice. *J. Am. Chem. Soc. 106*, 6285−6295.
(42) Mulholland, S. E., Gibney, B. R., Rabanal, F., and Dutton, P. L. (1999) Determination of nonligand amino acids critical to $[4Fe-4S]^{2+/+}$ assembly in ferredoxin maquettes. *Biochemistry 38*, 10442−10448.
(43) Kennedy, M. L., and Gibney, B. R. (2002) Proton coupling to $[4Fe-4S]^{2+/+}$ and $[4Fe-4Se]^{2+/+}$ oxidation and reduction in a designed protein. *J. Am. Chem. Soc. 124*, 6826−6827.
(44) Cumberland, S. L., Hanif, K. M., Javier, A., Khitrov, G. A., Strouse, G. F., Woessner, S. M., and Yun, C. S. (2002) Inorganic clusters as single-source precursors for preparation of CdSe, ZnSe, and CdSe/ZnS nanomaterials. *Chem. Mater. 14*, 1576−1584.

BC060277+

Protein−Liposome Conjugates Using Cysteine-Lipids And Native Chemical Ligation

Sanne W. A. Reulen,[†,||] Wilco W. T. Brusselaars,[†,||] Sander Langereis,[‡] Willem J. M. Mulder,[§] Monica Breurken,[†] and Maarten Merkx*[,†]

Laboratory of Macromolecular and Organic Chemistry, and Biomedical NMR, Department of Biomedical Engineering, Eindhoven University of Technology, and SyMO-Chem BV, P.O. Box 513, 5600 MB Eindhoven, The Netherlands.
Received September 7, 2006; Revised Manuscript Received December 19, 2006

Liposomes have become popular drug delivery vehicles and have more recently also been applied as contrast agents for molecular imaging. Most current methods for functionalization of liposomes with targeting proteins rely on reactions of amine or thiol groups at the protein exterior, which generally result in nonspecific conjugation at multiple sites on the protein. In this study, we present native chemical ligation (NCL) as a general method to covalently couple recombinant proteins in a highly specific and chemoselective way to liposomes containing cysteine-functionalized phospholipids. A cysteine-functionalized phospholipid (Cys−PEG−DSPE) was prepared and shown to readily react with the MESNA thioester of EYFP, which was used as a model protein. Characterization of the EYFP−liposomes using fluorescence spectroscopy showed full retention of the fluorescent properties of conjugated EYFP and provides a lower limit of 120 proteins per liposome. The general applicability of NCL was further tested using CNA35, a collagen-binding protein recently applied in fluorescent imaging of collagen. NCL of CNA35 thioester yielded liposomes containing ∼100 copies of CNA35 per liposome. The CNA35−liposomes were shown to be fully functional and bind collagen with a 150-fold higher affinity compared to CNA35. Our results show that NCL is an attractive addition to existing conjugation methods that allows direct, covalent, and highly specific coupling of recombinant proteins to liposomes and other lipid-based assemblies.

INTRODUCTION

Liposomes and micelles have attracted a lot of interest as drug delivery vehicles (*1*, *2*) and more recently as carriers of contrast agents (MRI, ultrasound) in molecular imaging (*3*−*5*). An important development in these fields has been the introduction of "sterically stabilized" or "stealth" liposomes that have an increased circulation time and altered biodistributions (*6*). These liposomes typically contain ∼5% PEGylated phospholipids resulting in a liposome surface with low immunogenicity and increased liposome stability (*7*−*9*). For applications in molecular imaging and targeted drug delivery, the liposomes also need to be functionalized with targeting ligands, which in most cases are proteins (e.g., antibodies) or peptides. Most current synthetic strategies to covalently couple proteins to liposomes involve either amine or thiol groups at the exterior of the protein (*10*, *11*). Although methods for direct coupling to liposomes have been reported (*12*), amine groups are commonly converted to thiol groups, which are subsequently reacted with phospholipids containing thiol reactive groups such as maleimides, activated disulfides, or iodoacetyl groups (*2*). All of these conjugation methods are nonspecific and result in conjugation at multiple sites on the protein, which sometimes also results in protein inactivation. Due to this lack of control over the conjugation site, protein conjugation is still, to some extent, a process of trial and error. An approach to circumvent the nonspecific modification of proteins is the use of so-called docking proteins as intermediates between the liposome and the targeting protein. Examples include the use of protein G as a docking site for IgG (*13*) and the use of RNase I as a docking site of proteins with a C-peptide tag (*14*−*16*). Although these approaches result in a more homogeneous presentation of targeting ligands on the liposomes, they require additional conjugation steps and depend on a noncovalent bond between targeting ligand and docking protein. To date, no general strategy is available that allows the direct covalent conjugation of liposomes to a single, precisely defined site on a recombinant protein.

Native chemical ligation (NCL) was first reported by Dawson et al. as a unique method to ligate two unprotected peptide fragments to form a native peptide bond, thereby allowing the complete chemical synthesis of large proteins (*17*, *18*). NCL is a chemoselective reaction that occurs spontaneously between a peptide with a C-terminal thioester and a peptide with an N-terminal cysteine under aqueous conditions at neutral pH. The possibilities of NCL have been extended by the development of expression systems that use self-cleavable intein domains to generate recombinant proteins with C-terminal thioester groups (*19*). NCL has been applied to attach synthetic moieties such as fluorescent dyes, biotin, isoprenyl groups, and dendrimers to recombinant proteins, and has also been used in the site-specific immobilization of proteins to surfaces (*20*−*23*). Here, we report on the application of NCL as a method to covalently couple recombinantly expressed proteins in a highly specific and chemoselective way to liposomes containing cysteine-functionalized phospholipids. While this work was in progress, Bertozzi and co-workers reported the novel synthesis of cysteine-functionalized phospholipids for the lipidation of green fluorescent protein (GFP) and subsequent incorporation of the lipidated GFP in supported lipid bilayers (*24*). The focus of our work was to explore the suitability of NCL in the

* Corresponding author. E-mail: m.merkx@tue.nl. Fax: (+31) 40-245-1036.

[†] Laboratory of Macromolecular and Organic Chemistry, Department of Biomedical Engineering, Eindhoven University of Technology.

[‡] SyMO-Chem BV.

[§] Biomedical NMR, Department of Biomedical Engineering, Eindhoven University of Technology.

[||] Both authors contributed equally to the work presented.

10.1021/bc0602782 CCC: $37.00 © 2007 American Chemical Society
Published on Web 02/22/2007

synthesis of protein−liposome conjugates, however, demonstrating for the first time that protein thioesters can be directly conjugated to cysteine-functionalized phospholipids embedded in liposomes.

EXPERIMENTAL PROCEDURES

General. Unless stated otherwise, all reagents and chemicals were obtained from commercial sources and used without further purification. Dichloromethane (DCM) was obtained by distillation from P_2O_5. 1,2-distearoyl-*sn*-glycero-3-phosphoethanolamine-*N*-[amino(poly(ethylene glycol))2000] (NH_2−PEG−DSPE), 1,2-distearoyl-*sn*-glycero-3-phosphocholine (DSPC), 1,2-distearoyl-*sn*-glycero-3-phosphoethanolamine-*N*-[methoxy-(poly(ethylene glycol))2000] (PEG−DSPE), and 1,2-dipalmitoyl-*sn*-glycero-3-phosphoethanolamine-*N*-(lissamine rhodamine B sulfonyl) (rhodamine−DPPE) were purchased from Avanti Polar Lipids (Albaster, U.S.A.). Gd−DTPA−bis(stearylamide) was purchased from Gateway Chemical Technology (St. Louis, MO). Trityl-protected cysteine (Tr-Cys(Tr)-OH) was obtained from Bachem (Bubendorf, Switzerland). Trityl-protected succinimidyl-activated cysteine (Tr-Cys(Tr)-OSu) was prepared according to a literature procedure (*20*). UV−vis spectra were recorded on a Shimadzu Multispec 1501 spectrophotometer. Fluorescence spectra were obtained on an Edinburgh Instruments FS920 double-monochromator spectrophotometer. Primers used for all the cloning procedures were supplied by MWG (Ebersberg, Germany).

Synthesis of Cysteine-Functionalized 1,2-Distearoyl-*sn*-glycero-3-phosphoethanolamine-*N*-[amino(poly(ethylene glycol))2000] (Cys−PEG−DSPE). NH_2−PEG−DSPE (**1**) (100 mg, 35.8 μmol) was dissolved in DCM (1 mL) under an atmosphere of argon. Tr-Cys(Tr)-OSu (30 mg, 43 μmol) and triethylamine (10 μL, 71 μmol) were added to the solution. The reaction proceeded overnight at room temperature. The solution was concentrated under reduced pressure, and the crude product was dissolved in $CHCl_3$ (0.5 mL). The crude product was purified by column chromatography (silica, $CHCl_3$/MeOH, 19:1 v/v → 9:1 v/v), and trityl-protected Cys−PEG−DSPE (**2**) (44 mg, 13 μmol) was obtained in 36% yield. Compound **2** was dissolved in triethyl silane (25 μL, 158 mmol). Subsequently, a solution of trifluoroacetic acid (1 mL) and DCM (1 mL) was added. The obtained solution was stirred for 2 h at room temperature. The solution was concentrated under reduced pressure, and the crude product was precipitated in diethyl ether. The product was filtrated and dried under reduced pressure to give Cys−PEG−DSPE lipid (**3**) (34 mg, 12 μmol, 92%). Compounds **1**−**3** were analyzed in detail with RP-HPLC and MALDI-TOF (see Supporting Information).

Plasmid Constructs. The EYFP gene was amplified by PCR from vector pEYFP-N1 (Clontech) using the primers 5′-GTG GTC ATA TGG TGA GCA AGG GCG AG-3′ and 5′-GTG GTG AAT TCC TTG TAC AGC TCG TCC ATG C-3′. The CNA35 gene was amplified from pQE30CNA35 (a kind gift from Dr. Magnus Höök, Texas A & M University, U.S.A. (*25*)) using the primers 5′-GTG GTC ATA TGG GAT CCG CAC GAG ATA TTT C-3′ and 5′-GTG GTT GCT CTT CCG CAT GCC TTG GTA TCT TTA TCC TGT TTT AAA AC-3′. The PCR products and the pTXB1 vector (IMPACT system, New England Biolabs) were double-digested with the restriction endonucleases *Nde* I and *Sap* I (CNA35) or *Nde* I and *Eco*R I (EYFP) followed by ligation of the amplified DNA fragments in the open plasmids to yield pTXB1−CNA35 and pTXB1−EYFP, respectively. DNA sequencing using T7 promoter and intein-specific reversed primers (New England Biolabs) confirmed the correct in-frame fusion of the proteins with the intein sequence.

Protein Expression and Purification. The expression plasmids pTXB1−CNA35 and pTXB1−EYFP were transformed into *E. coli* BL21 (DE3) cells. The same expression conditions were used for both proteins. Bacteria were grown in LB medium containing 100 μg/mL ampicillin at 37 °C and 250 rpm to an optical density (OD_{600nm}) between 0.6 and 0.8. Protein expression was induced with 0.5 mM IPTG, and the cultures were incubated overnight at 15 °C. Cells were harvested by centrifugation for 30 min at 8000 *g* at 4 °C. The supernatant was removed, and the cell pellet was resuspended using the BugBuster protocol (Novagen). After incubation for 20 min at room temperature, the cell suspension was centrifuged at 16 000 *g* for 20 min at 4 °C. The supernatant was directly applied to a column of chitin beads and equilibrated with 10 column volumes of column buffer (20 mM sodium phosphate, 0.1 mM EDTA, 0.5 M NaCl, pH 8). The column was washed with 10 volumes of column buffer after which the column was quickly flushed with 3 column volumes of cleavage buffer (20 mM sodium phosphate, 0.1 mM EDTA, 0.5 M NaCl, pH 6) containing 50 mM sodium 2-mercaptoethanesulfonate (MESNA) and incubated overnight at room temperature. Elution fractions were collected and pooled, after which the cleavage step was repeated to gain more thioester-terminated proteins. The proteins were buffer-exchanged into 10 mM HEPES, 135 mM NaCl, pH 8.0 (HBS) using Amicon ultracentrifuge tubes (MWCO 10 kDa). The concentrations of EYFP protein with a C-terminal MESNA thioester (EYFP−MESNA) and CNA35 protein with a C-terminal MESNA thioester (CNA35−MESNA) were determined by UV−vis using $\epsilon_{514nm} = 84\ 000\ M^{-1}\ cm^{-1}$ (*26*) and $\epsilon_{280nm} = 33\ 167\ M^{-1}\ cm^{-1}$, respectively. 1 L *E. coli* culture typically yielded 20 mg of EYFP−MESNA and 40 mg of CNA35−MESNA.

Ligation of EYFP to Pure Cysteine-Functionalized Phospholipids. Cys−PEG−DSPE lipid **3** was dissolved in buffer containing 200 mM sodium phosphate, 200 mM NaCl, pH 7.2. Native chemical ligation reactions were performed in 200 μL with a final concentration of EYFP−COSR of 87 μM. A 10-fold molar excess of compound **3** (final concentration 870 μM) was used. 1% (v/v) benzyl mercaptan and 1% (v/v) thiophenol, or 100 mM MESNA, were added to the ligation mixtures. After overnight incubation at room temperature, the samples were centrifuged to remove precipitate, and the supernatant was analyzed using SDS-PAGE.

Liposome Preparation. Liposomes were prepared by lipid film hydration as described previously (*27*). A mixture of DSPC (37 μmol), Gd−DTPA−bis(stearylamide) (25 μmol), cholesterol (33 μmol), PEG−DSPE (2.5 μmol), rhodamine−DPPE (0.1 μmol), and Cys−PEG−DSPE (2.5 μmol) was dissolved in $CHCl_3$/MeOH 1:1 (v/v) and concentrated under reduced pressure at room temperature. The obtained lipid film was hydrated in HBS buffer (4 mL). This dispersion was extruded five times at 65 °C through polycarbonate membrane filters with pores of 100 or 200 nm. Phospholipid concentrations were determined by phosphate analysis according to Rouser (*28*). The amount of lipids per liposome was calculated using a lipid surface area of 0.6 nm^2 (*29*) and assuming unilamellar liposomes.

Ligation of EYFP to Cysteine−Liposomes. Native chemical ligation of cysteine−liposomes (450 μM Cys−PEG−DSPE) with EYFP−MESNA (33 μM) was performed for 48 h at 20 °C in HBS, pH 8, containing either 100 mM MESNA or 1% (v/v) thiophenol and 1% (v/v) benzyl mercaptan. The coupling efficiency was monitored via SDS-PAGE analysis. The amount of lipidated EYFP was calculated by scanning of the SDS-PAGE gel and integration of the bands of unreacted and reacted protein. The liposome concentration was calculated from the lipid concentration that was determined via phosphate analysis using the assumption of unilamellar liposomes. The number of EYFP proteins per liposome was then obtained by dividing the concentration of lipidated EYFP by the liposome concentration.

The EYFP−liposomes were ultracentrifuged in a Kontron Centrikon T-2060 ultracentrifuge with a TFT 70.38 rotor for 1 h at 270 000 *g* and 20 °C, after which the liposomal pellet was resuspended in HBS. Pellet and supernatant were analyzed using SDS-PAGE to confirm the separation between reacted and unreacted protein. The incorporation of EYFP was also established using fluorescence spectroscopy. Emission spectra of EYFP−liposomes were measured using an excitation wavelength of 490 nm. The ratio of the EYFP (527 nm) and rhodamine (590 nm) peaks in the emission spectrum was compared to a calibration curve with known molar ratios of EYFP to rhodamine, thus providing an alternative method to determine the amount of EYFP per liposome.

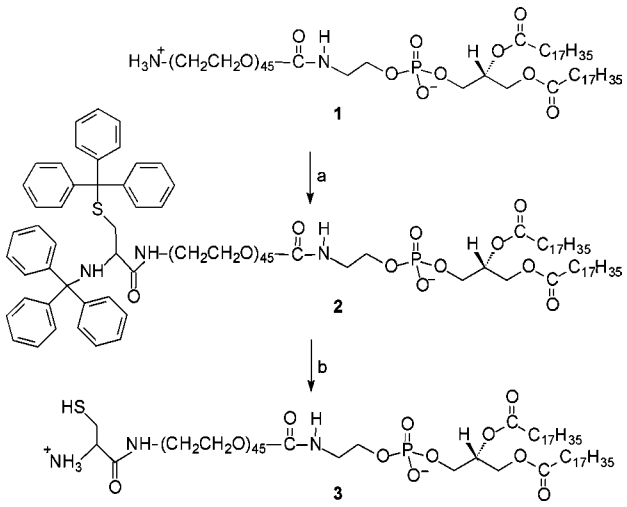
Ligation of CNA35 to Cysteine−Liposomes. Native chemical ligation of cysteine−liposomes (180 μM Cys−PEG−DSPE) with CNA35 thioester (50 μM) was performed for 24 h at 20 °C in HBS, pH 8, containing 100 mM MESNA. The amount of lipidated CNA35 was calculated by scanning the SDS-PAGE gel and integrating the bands of unreacted and reacted protein. The liposome concentration was calculated from the lipid concentration that was determined via phosphate analysis using the assumption of unilamellar liposomes. The amount of lipidated CNA35 was divided over the liposome concentration to determine the number of CNA35 proteins per liposome. Ultracentrifugation of CNA35−liposomes was performed in a Kontron Centrikon T-2060 ultracentrifuge with a TFT 70.38 rotor for 1 h at 270 000 *g* and 20 °C. The obtained liposomal pellet was resuspended in HBS. Pellet and supernatant were analyzed using SDS-PAGE to confirm the separation between reacted and unreacted protein. The concentration of CNA35 in the liposome fraction was determined with the Quant-iT Protein Assay Kit (Invitrogen) according to manufacturer instructions. This amount of lipidated CNA35 was divided by the liposome concentration to determine the number of CNA35 proteins per liposome.

Collagen Binding Assay. 96 well Corning EIA/RIA microplates were coated overnight at 4 °C with 1.4 μg/well (45 μL) rat tail collagen type I (Sigma, C7661) in TBS (50 mM Tris, 150 mM NaCl, pH 7.5). After overnight incubation, the plates were blocked with 100 μL TBS containing 5% (w/v) skim milk powder for 2 h at room temperature. After washing the plates 3 times with 300 μL TBS, the plates were incubated with CNA35−liposomes or nonmodified liposomes in HBS supplemented with 5% (w/v) skim milk powder for 3 h at room temperature. Plates were washed 5 times with 50 mM Tris, 500 mM NaCl, pH 7.5, and subsequently washed 2 times with TBS. The fluorescence of the rhodamine-containing liposomes was measured at 620 nm in triplicate on a Thermo Fluoroskan Ascent FL plate reader after excitation at 578 nm.

RESULTS AND DISCUSSION

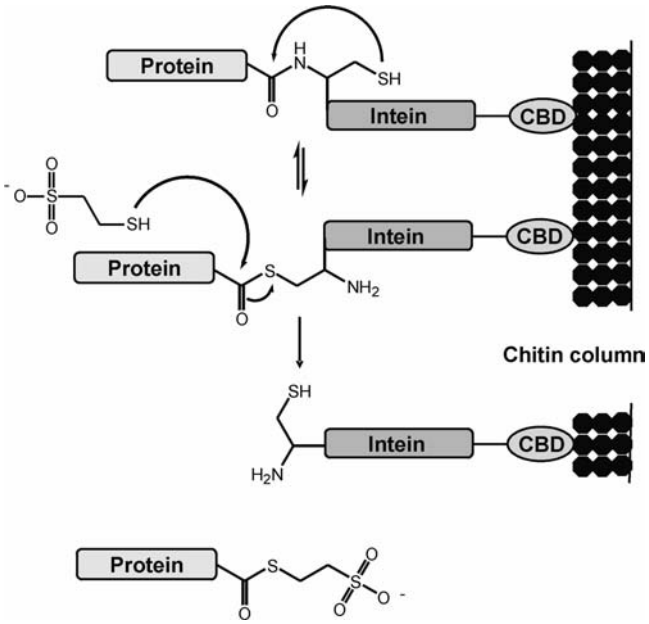
In order to use native chemical ligation as a site-specific method to prepare protein−liposomes, the PEG terminus of PEG−DSPE was functionalized with a cysteine containing a free amine group. The introduction of the reactive group at the end of the PEG chain (far removed from the lipid tail) has been reported to enhance ligation efficiencies (*30*) and was also applied in previous work using maleimide-functionalized phospholipids (*27*, *31*). Cys−PEG−DSPE (**3**) was obtained in a two-step synthesis starting from the commercially available 1,2-distearoyl-*sn*-glycero-3-phosphoethanolamine-*N*-[amino(poly(ethylene glycol))2000] (**1**) (Scheme 1). In the first step, the amine end group of **1** was reacted with succinimidyl-activated trityl-protected cysteine to yield intermediate **2** in 36% yield. The second step involved deprotection of the cysteine using trifluoroacetic acid (TFA) to give Cys−PEG−DSPE **3** in 92% yield, which was confirmed using RP-HPLC and MALDI-TOF (see Supporting Information).

Scheme 1. Synthesis of Cys−PEG−DSPE (3)[a]



[a] (a) DCM, triethylamine, Tr-Cys(Tr)-OSu; (b) triethylsilane, TFA, DCM.

Scheme 2. Synthesis of Thioester-Terminated Proteins Using Self-Cleavable Intein Domains



Enhanced yellow fluorescent protein (EYFP) was chosen as a model protein to study the performance of Cys−PEG−DSPE in native chemical ligation reactions. The fluorescence of EYFP depends on proper folding of the protein and can thus be used to assess protein stability after ligation. In addition, fluorescence can be used to determine the amount of proteins conjugated per liposome. A C-terminal fusion protein of EYFP with intein and chitin binding domains was expressed in *E. coli* using the IMPACT system. The fusion protein was purified on a chitin resin and treated with 50 mM MESNA to induce the intein-catalyzed cleavage of the fusion protein and the formation of EYFP with a C-terminal MESNA thioester (EYFP−MESNA) (Scheme 2). SDS-PAGE and ESI-MS analysis (see Supporting Information) showed the presence of a single protein with a mass of 27 849 Da that corresponds to the calculated mass of EYFP−MESNA (theoretical mass: 27845.2 Da). We first studied the reaction of pure Cys−PEG−DSPE (not incorporated in a liposome) with EYFP−MESNA in the presence of two different thiol catalysts, thiophenol/benzyl mercaptan and MESNA. Since ligation of Cys−PEG−DSPE to EYFP increases its molecular weight by approximately 3 kDa, the ligation reaction could be monitored

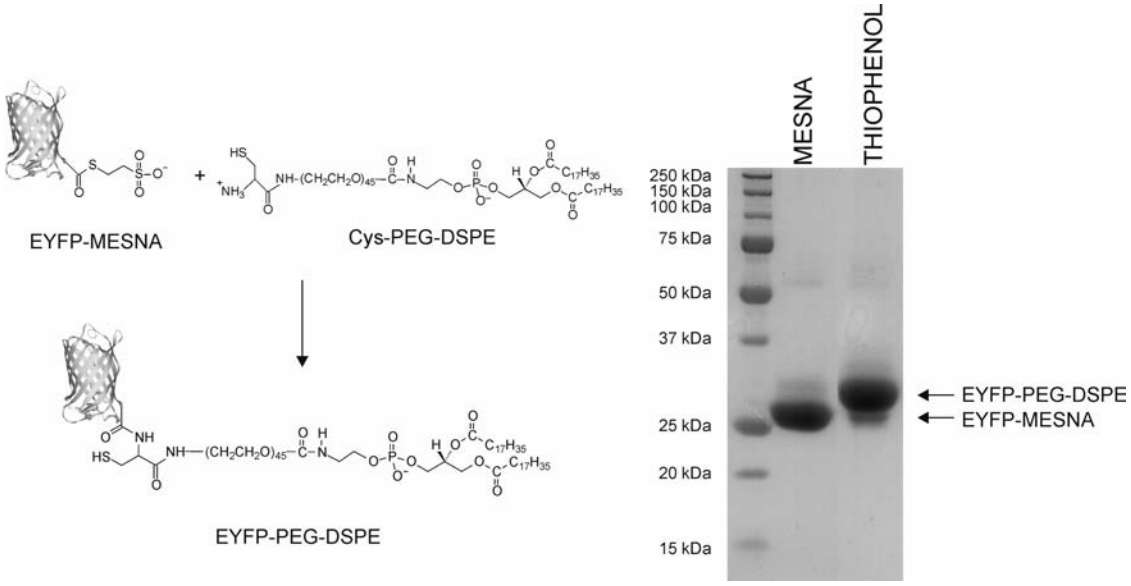


Figure 1. Native chemical ligation of Cys−PEG−DSPE **3** (870 μM) with EYFP−MESNA (87 μM) in 0.2 M sodium phosphate pH 7.2 with either 100 mM MESNA or 1% (v/v) thiophenol + 1% benzyl mercaptan (THIOPHENOL).

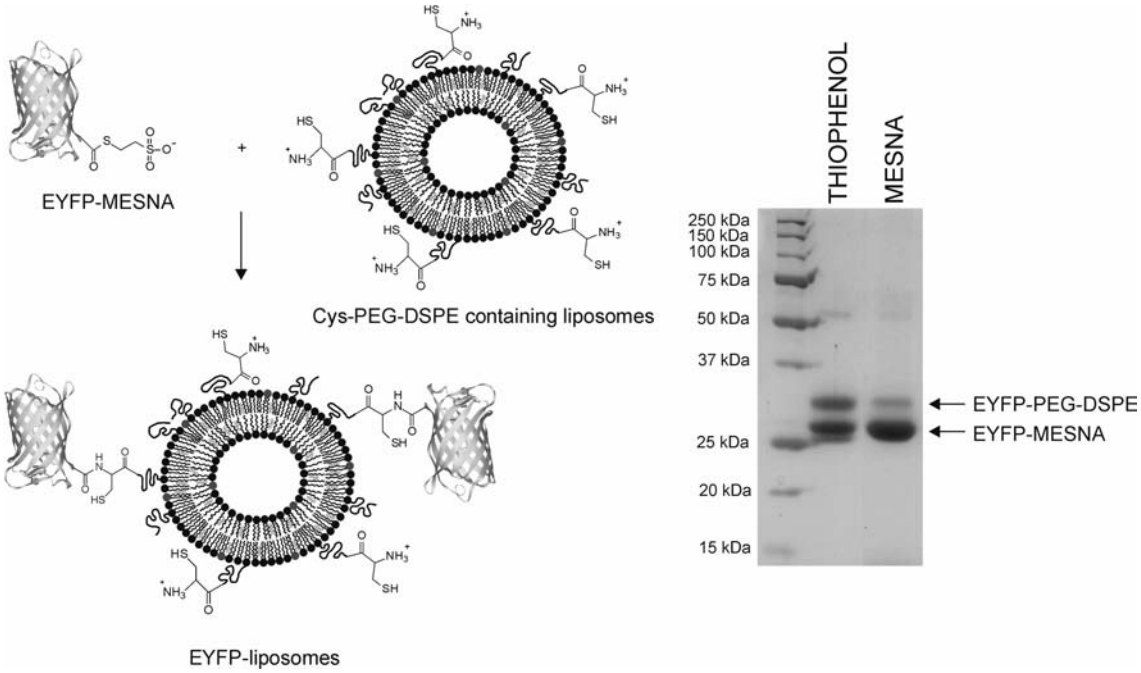


Figure 2. Native chemical ligation of liposomes containing Cys−PEG−DSPE (450 μM cysteine−lipid) with EYFP−MESNA (33 μM) in HBS pH 8 with either 100 mM MESNA or 1% (v/v) thiophenol + 1% benzyl mercaptan (THIOPHENOL).

using SDS-PAGE. Nearly quantitative reaction of EYFP to the lipidated form of EYFP (EYFP−PEG−DSPE) was observed in the presence of thiophenol, whereas a much lower conversion (∼5%) was obtained using MESNA as the catalyst (Figure 1). Since PEGylated phospholipids such as Cys−PEG−DSPE are known to form relatively stable micelles (*32*), the ligation reaction probably resulted in the formation of EYFP micelles. We are currently characterizing the properties of these putative protein micelles.

Having established the suitability of Cys−PEG−DSPE in native chemical ligation reactions, we next tested whether the same native chemical ligation can also be performed when Cys−PEG−DSPE is incorporated into liposomes. Liposomes containing 2.5% of Cys−PEG−DSPE, Gd−DTPA−bis(stearylamide) lipids, and rhodamine-functionalized lipids were prepared by lipid film hydration as described previously (*27*). We again compared thiophenol/benzyl mercaptan and MESNA as catalysts and monitored the reaction using SDS-PAGE. Figure 2 clearly shows the presence of lipidated EYFP proteins upon reaction of 33 μM EYFP−thioester with 450 μM liposome-embedded Cys−PEG−DSPE. To the best of our knowledge, this is the first report that describes the direct coupling of proteins to liposomes via native chemical ligation. Although the ligation reaction is more efficient in the presence of thiophenol/benzyl mercaptan (conversion ≈ 30%) than in the presence of MESNA (conversion ≈ 10%), the use of MESNA has important advantages, in particular, when working with lipid-based systems. Thiophenol and benzyl mercaptan are poorly water soluble and are likely to accumulate in the phospholipid bilayer of liposomes, making it almost impossible to remove these toxic compounds after the ligation reaction. MESNA is a water-soluble thiol with a nonoffensive odor compared to thiophenol and benzyl mercaptan, and is easily removed after ligation via centrifugation.

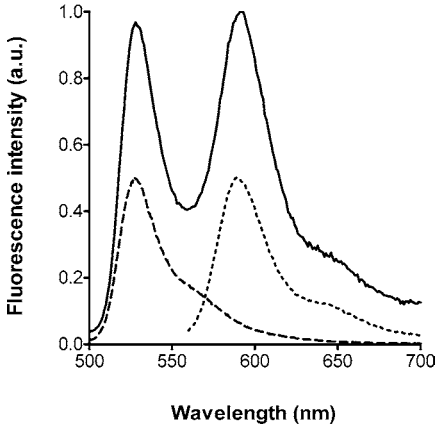


Figure 3. Emission spectrum of EYFP−liposome conjugates using an excitation wavelength of 490 nm (solid line). The emission spectra of EYFP−MESNA (dashed line) and nonmodified rhodamine-containing liposomes (dotted line) are also shown for comparison.

To prove that the lipidated EYFP observed in SDS-PAGE was still attached to the liposomes, liposomes were separated from unreacted EYFP via ultracentrifugation. SDS-PAGE analysis showed that all of the unreacted EYFP was present in the supernatant, whereas most of the lipidated EYFP was found associated with the liposomal pellet (see Supporting Information). Fluorescence spectroscopy was used to determine the number and proper folding of the conjugated EYFP proteins. The fluorescence emission spectrum of the EYFP−liposomes showed peaks at 527 and 590 nm, corresponding to EYFP and rhodamine, respectively (Figure 3). The observation of EYFP fluorescence not only demonstrates that the protein kept its native fold after ligation, but the relative intensity of the EYFP fluorescence compared to the rhodamine fluorescence can also be used to estimate the number of EYFP proteins per liposome. The ratio of EYFP to rhodamine was compared to a calibration curve with known molar ratios of EYFP to rhodamine, yielding approximately 120 proteins per 200 nm liposome. Another method to estimate the number of proteins per liposome is to calculate the amount of lipidated protein from the relative intensities of lipidated and non-lipidated protein bands on the SDS-PAGE gel obtained after NCL, and divide this number by the original liposome concentration. This calculation assumes that all lipidated protein is incorporated into liposomes and yielded 180 EYFP per 200 nm liposome.

Although EYFP is a good model protein to prove that proteins can be conjugated to liposomes via native chemical ligation, we also wanted to use a biomedically relevant protein with a specific binding function. We recently developed a collagen-specific fluorescent probe based on a collagen-binding protein domain (CNA35) from the bacterial adhesion protein of *Staphylococcus aureus* (*33*). Solid-phase binding assays showed a dissociation constant of approximately 0.5 μM for collagen type I. In addition to providing an example of a targeted liposomal contrast agent, we were also interested to see whether attachment of multiple CNA35 proteins to a liposomal scaffold would yield a probe with a higher affinity for collagen due to multivalent interactions between CNA35 and collagen.

The IMPACT expression vector pTXB1 was again used to obtain recombinant CNA35 with a C-terminal MESNA thioester (Scheme 2). An alanine residue was added to the C-terminus of CNA35 during cloning, as this residue is known to enhance the rate of native chemical ligation reactions (*18*). Affinity purification on a chitin column and subsequent cleavage with MESNA yielded CNA35−MESNA in excellent yield. SDS-PAGE analysis typically showed the presence of several smaller bands besides the major band at 35 kDa, which are probably degradation products of CNA35 (Figure 4). ESI-MS showed a single protein peak with a mass of 34 757 Da (theoretical mass: 34774 Da). Collagen-binding assays using fluorescently labeled CNA35−MESNA showed that the modified C-terminus did not affect the collagen-binding properties.

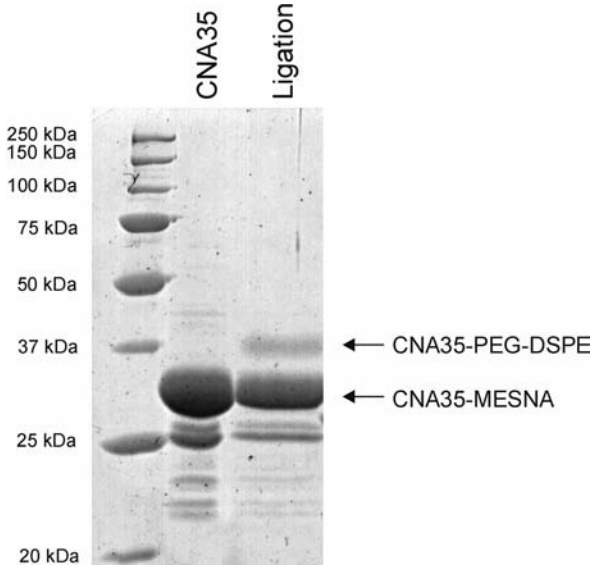


Figure 4. SDS-PAGE analysis of CNA35−MESNA before and after native chemical ligation to liposomes containing Cys−PEG−DSPE.

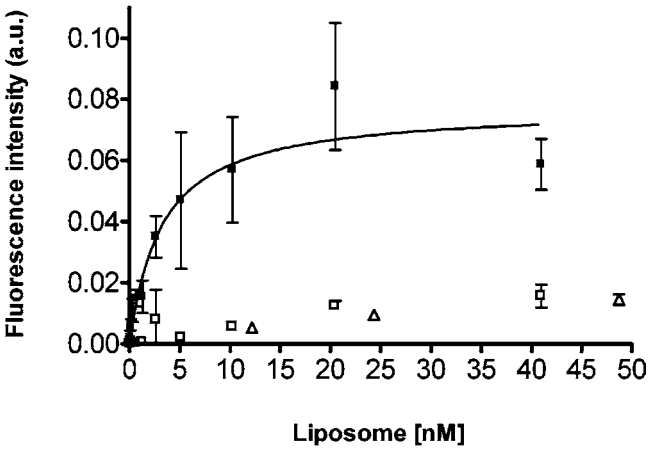


Figure 5. Solid-phase binding assay of CNA35−liposomes to rat tail collagen type I (solid squares). Liposome binding was monitored by measuring the fluorescence of the rhodamine lipids at 620 nm using an excitation of 578 nm. Control experiments using nonmodified liposomes incubated on rat tail collagen type I (open triangle) and CNA35−liposomes incubated on milk-powder blocked well without collagen (open squares) are also shown for comparison. The solid line represents a fit to a 1:1 binding model using a K_d of 3 nM.

CNA35−MESNA was ligated to liposomes using the same procedure as described for EYFP using MESNA as a catalyst. SDS-PAGE analysis again indicated the formation of lipidated protein by the appearance of a new band at approximately 38 kDa (Figure 4). CNA35-modified liposomes were separated from MESNA and unreacted CNA35 by two ultracentrifugation steps (see Supporting Information). A protein quantification assay was used to determine the amount of protein in the liposome fraction. This protein concentration was divided by the known liposome concentration, yielding ~100 proteins per 100 nm liposome. This number is in reasonable agreement with the amount of lipidated CNA35 that was detected by SDS-PAGE analysis immediately after ligation, which gave ~80 CNA35 proteins per 100 nm liposome. The rhodamine fluorescence of the CNA35-functionalized liposomes was used to study their binding to a collagen-coated 96 well plate. Figure 5 shows specific binding of these liposomes to rat tail collagen type I at

low nanomolar concentrations. Control experiments using nonfunctionalized liposomes or plates without collagen did not show a similar signal. A fit of the binding curve using a simple 1:1 binding model yielded a K_d of 3 ± 1 nM, representing a 150-fold increase in affinity compared to the protein itself. These results show that CNA35 conjugated to liposomes via native chemical ligation is fully active in binding collagen. Whether the observed increase in collagen affinity is due to multiple, simultaneous interactions between probe and collagen or mainly a statistical effect due to the presence of ~100 copies of protein per liposome remains to be investigated.

In summary, we have demonstrated that native chemical ligation is an attractive method to directly conjugate recombinantly expressed proteins to sterically stabilized poly(ethylene glycol) liposomes via cysteine-functionalized phospholipids. In contrast to other conjugation methods such as thiol−maleimide reactions, NCL is highly specific and exclusively occurs at the protein's C-terminus, which in most proteins is not important for binding activity. An additional advantage of NCL is that only a single site in the protein is available for conjugation, whereas cross-linking is sometimes observed between liposomes and proteins using classical thiol/amine chemistries (*34*). The strategy reported here for liposomes should be readily applicable to other lipid-based imaging agents such as immunomicelles (*35*), iron oxide nanoparticles (*31*, *36*), and quantum dots with a lipid coating (*37*−*40*).

ACKNOWLEDGMENT

This study was funded by the BSIK program entitled Molecular Imaging of Ischemic Heart Disease (project number BSIK03033). The authors thank Anouk Dirksen for help with the synthesis of the cysteine-functionalized lipid, Marieke Rensen for constructing pTXB1-EYFP, Ingrid van Baal for supplying trityl-protected succinimidyl-activated cysteine, Erik Sanders for providing assistance with liposome preparation and characterization, and Bert Meijer, Klaas Nicolay, and Gustav Strijkers for general support.

Supporting Information Available: Experimental details including the RP-HPLC and MALDI-TOF analysis of the synthesized phospholipids, ESI-MS spectra of EYFP-MESNA and CNA35-MESNA, and SDS-PAGE analysis of the purification of EYFP-MESNA, CNA35-MESNA, EYFP-liposomes, and CNA35-liposomes. This material is available free of charge via the Internet at http://pubs.acs.org/BC.

LITERATURE CITED

(1) Allen, T. M., and Cullis, P. R. (2004) Drug delivery systems: entering the mainstream. *Science 303*, 1818−1822.

(2) Torchilin, V. P. (2005) Recent advances with liposomes as pharmaceutical carriers. *Nat. Rev. Drug Discovery 4*, 145−160.

(3) Massoud, T. F., and Gambhir, S. S. (2003) Molecular imaging in living subjects: seeing fundamental biological processes in a new light. *Genes Dev. 17*, 545−580.

(4) Weissleder, R., and Mahmood, U. (2001) Molecular imaging. *Radiology 219*, 316−333.

(5) Mulder, W. J., Strijkers, G. J., van Tilborg, G. A., Griffioen, A. W., and Nicolay, K. (2006) Lipid-based nanoparticles for contrast-enhanced MRI and molecular imaging. *NMR Biomed. 19*, 142−164.

(6) Allen, T. M., and Hansen, C. (1991) Pharmacokinetics of stealth versus conventional liposomes: effect of dose. *Biochim. Biophys. Acta 1068*, 133−141.

(7) Allen, T. M., Hansen, C., Martin, F., Redemann, C., and Yau-Young, A. (1991) Liposomes containing synthetic lipid derivatives of poly(ethylene glycol) show prolonged circulation half-lives in vivo. *Biochim. Biophys. Acta 1066*, 29−36.

(8) Klibanov, A. L., Maruyama, K., Torchilin, V. P., and Huang, L. (1990) Amphipathic polyethyleneglycols effectively prolong the circulation time of liposomes. *FEBS Lett. 268*, 235−237.

(9) Papahadjopoulos, D., Allen, T. M., Gabizon, A., Mayhew, E., Matthay, K., Huang, S. K., Lee, K. D., Woodle, M. C., Lasic, D. D., Redemann, C., and Martin, F. J. (1991) Sterically stabilized liposomes: improvements in pharmacokinetics and antitumor therapeutic efficacy. *Proc. Natl. Acad. Sci. U.S.A. 88*, 11460−11464.

(10) Nobs, L., Buchegger, F., Gurny, R., and Allemann, E. (2004) Current methods for attaching targeting ligands to liposomes and nanoparticles. *J. Pharm. Sci. 93*, 1980−1992.

(11) Hermanson, G. T. (1995) *Bioconjugate Techniques.* pp 556−569, Chapter 12, Academic Press, Inc., San Diego.

(12) Weissig, V., Lasch, J., Klibanov, A. L., and Torchilin, V. P. (1986) A new hydrophobic anchor for the attachment of proteins to liposomal membranes. *FEBS Lett. 202*, 86−90.

(13) Chen, C. S., Baeumner, A. J., and Durst, R. A. (2005) Protein G-liposomal nanovesicles as universal reagents for immunoassays. *Talanta 67*, 205−211.

(14) Backer, M. V., Patel, V., Jehning, B. T., and Backer, J. M. (2006) Self-assembled "dock and lock" system for linking payloads to targeting proteins. *Bioconjugate Chem. 17*, 912−919.

(15) Backer, M. V., Gaynutdinov, T. I., Gorshkova, I. I., Crouch, R. J., Hu, T., Aloise, R., Arab, M., Przekop, K., and Backer, J. M. (2003) Humanized docking system for assembly of targeting drug delivery complexes. *J. Controlled Release 89*, 499−511.

(16) Blankenberg, F. G., Mandl, S., Cao, Y. A., O'Connell-Rodwell, C., Contag, C., Mari, C., Gaynutdinov, T. I., Vanderheyden, J. L., Backer, M. V., and Backer, J. M. (2004) Tumor imaging using a standardized radiolabeled adapter protein docked to vascular endothelial growth factor. *J. Nucl. Med. 45*, 1373−1380.

(17) Dawson, P. E., Muir, T. W., Clark-Lewis, I., and Kent, S. B. (1994) Synthesis of proteins by native chemical ligation. *Science 266*, 776−779.

(18) Hackeng, T. M., Griffin, J. H., and Dawson, P. E. (1999) Protein synthesis by native chemical ligation: expanded scope by using straightforward methodology. *Proc. Natl. Acad. Sci. U.S.A. 96*, 10068−10073.

(19) Muir, T. W., Sondhi, D., and Cole, P. A. (1998) Expressed protein ligation: a general method for protein engineering. *Proc. Natl. Acad. Sci. U.S.A. 95*, 6705−6710.

(20) van Baal, I., Malda, H., Synowsky, S. A., van Dongen, J. L., Hackeng, T. M., Merkx, M., and Meijer, E. W. (2005) Multivalent peptide and protein dendrimers using native chemical ligation. *Angew. Chem., Int. Ed. Engl. 44*, 5052−5057.

(21) Lesaicherre, M. L., Lue, R. Y., Chen, G. Y., Zhu, Q., and Yao, S. Q. (2002) Intein-mediated biotinylation of proteins and its application in a protein microarray. *J. Am. Chem. Soc. 124*, 8768−8769.

(22) Lue, R. Y., Chen, G. Y., Hu, Y., Zhu, Q., and Yao, S. Q. (2004) Versatile protein biotinylation strategies for potential high-throughput proteomics. *J. Am. Chem. Soc. 126*, 1055−1062.

(23) Gottlieb, D., Grunwald, C., Nowak, C., Kuhlmann, J., and Waldmann, H. (2006) Intein-mediated in vitro synthesis of lipidated Ras proteins. *Chem. Commun.* 260−262.

(24) Grogan, M. J., Kaizuka, Y., Conrad, R. M., Groves, J. T., and Bertozzi, C. R. (2005) Synthesis of lipidated green fluorescent protein and its incorporation in supported lipid bilayers. *J. Am. Chem. Soc. 127*, 14383−14387.

(25) Xu, Y., Rivas, J. M., Brown, E. L., Liang, X., and Höök, M. (2004) Virulence potential of the staphylococcal adhesin CNA in experimental arthritis is determined by its affinity for collagen. *J. Infect. Dis. 189*, 2323−2333.

(26) Patterson, G., Day, R. N., and Piston, D. (2001) Fluorescent protein spectra. *J. Cell Sci. 114*, 837−838.

(27) Mulder, W. J., Strijkers, G. J., Griffioen, A. W., van Bloois, L., Molema, G., Storm, G., Koning, G. A., and Nicolay, K. (2004) A liposomal system for contrast-enhanced magnetic resonance imaging of molecular targets. *Bioconjugate Chem. 15*, 799−806.

(28) Rouser, G., Fkeischer, S., and Yamamoto, A. (1970) Two dimensional then layer chromatographic separation of polar lipids and determination of phospholipids by phosphorus analysis of spots. *Lipids 5*, 494−496.

(29) Strijkers, G. J., Mulder, W. J., van Heeswijk, R. B., Frederik, P. M., Bomans, P., Magusin, P. C., and Nicolay, K. (2005) Relaxivity of liposomal paramagnetic MRI contrast agents. *Magma 18*, 186−192.
(30) Hansen, C. B., Kao, G. Y., Moase, E. H., Zalipsky, S., and Allen, T. M. (1995) Attachment of antibodies to sterically stabilized liposomes: evaluation, comparison and optimization of coupling procedures. *Biochim. Biophys. Acta. 1239*, 133−144.
(31) van Tilborg, G. A., Mulder, W. J., Deckers, N., Storm, G., Reutelingsperger, C. P., Strijkers, G. J., and Nicolay, K. (2006) Annexin A5-functionalized bimodal lipid-based contrast agents for the detection of apoptosis. *Bioconjugate Chem. 17*, 741−749.
(32) Ashok, B., Arleth, L., Hjelm, R. P., Rubinstein, I., and Onyuksel, H. (2004) In vitro characterization of PEGylated phospholipid micelles for improved drug solubilization: effects of PEG chain length and PC incorporation. *J. Pharm. Sci. 93*, 2476−2487.
(33) Krahn, K. N., Bouten, C. V., van Tuijl, S., van Zandvoort, M. A., and Merkx, M. (2006) Fluorescently labeled collagen binding proteins allow specific visualization of collagen in tissues and live cell culture. *Anal. Biochem. 350*, 177−185.
(34) Takasaki, J., and Ansell, S. M. (2006) Micelles as intermediates in the preparation of protein−liposome conjugates. *Bioconjugate Chem. 17*, 438−450.
(35) Torchilin, V. P., Lukyanov, A. N., Gao, Z., and Papahadjopoulos-Sternberg, B. (2003) Immunomicelles: targeted pharmaceutical carriers for poorly soluble drugs. *Proc. Natl. Acad. Sci. U.S.A. 100*, 6039−6044.
(36) Nitin, N., LaConte, L. E., Zurkiya, O., Hu, X., and Bao, G. (2004) Functionalization and peptide-based delivery of magnetic nanoparticles as an intracellular MRI contrast agent. *J. Biol. Inorg. Chem. 9*, 706−712.
(37) Michalet, X., Pinaud, F. F., Bentolila, L. A., Tsay, J. M., Doose, S., Li, J. J., Sundaresan, G., Wu, A. M., Gambhir, S. S., and Weiss, S. (2005) Quantum dots for live cells, in vivo imaging, and diagnostics. *Science 307*, 538−544.
(38) Mulder, W. J., Koole, R., Brandwijk, R. J., Storm, G., Chin, P. T., Strijkers, G. J., de Mello Donega, C., Nicolay, K., and Griffioen, A. W. (2006) Quantum dots with a paramagnetic coating as a bimodal molecular imaging probe. *Nano Lett. 6*, 1−6.
(39) Dubertret, B., Skourides, P., Norris, D. J., Noireaux, V., Brivanlou, A. H., and Libchaber, A. (2002) In vivo imaging of quantum dots encapsulated in phospholipid micelles. *Science 298*, 1759−1762.
(40) van Tilborg, G. A., Mulder, W. J., Chin, P. T., Storm, G., Reutelingsperger, C. P., Nicolay, K., and Strijkers, G. J. (2006) Annexin A5-conjugated quantum dots with a paramagnetic lipidic coating for the multimodal detection of apoptotic cells. *Bioconjugate Chem. 17*, 865−868.

BC0602782

Convenient Synthesis of Maleimido-Derivatized Lanthanide(III) Chelates and Their Use in Mercapto Group Conjugation

Jari Hovinen

PerkinElmer Life and Analytical Sciences, Turku Site, POB 10, FIN-20101 Turku, Finland. Received September 11, 2006; Revised Manuscript Received December 18, 2006

Simple synthesis of luminescent europium(III) and terbium(III) chelates tethered to a maleimido function (**7**, **8**) is described. The method is based on the following: (i) synthesis of protected ligands tethered to a maleimido function and their purification on silica gel; (ii) deprotection by acidolysis; (iii) conversion of the deprotected ligands to the corresponding lanthanide(III) chelates by passing them through a column of strong cation exchange resin loaded with the appropriate lanthanide(III) ions. According to this procedure, large quantities of mercapto-selective biomolecule-labeling reactants of high purity can be prepared.

The unique fluorescence properties of lanthanide(III) chelates, such as the long fluorescence delay after excitation of these molecules, very sharp emission lines, and large Stokes shift (i.e., the difference in the chelate's excitation and emission lines) have been widely exploited in assays based on time-resolved fluorescence (*1*−*4*). Indeed, lanthanide(III) chelates have been used in *in vitro* diagnostics over two decades. The excellent fluorescence properties of luminescent lanthanide(III) chelates can be exploited particularily in homogeneous assays, where the use of conventional chromophores causes a very high background signal. The different photochemical properties of europium, terbium, dysprosium, and samarium chelates enable development of multiparametric homogeneous assays. Accordingly, numerous highly luminescent lanthanide(III) chelates have been synthesized and used especially in assays based on fluorescence resonance energy transfer and fluorescence quenching (*5*−*11*).

In order to exploit lanthanide(III) chelates in bioaffinity assays, these molecules have to be linked covalently to bioactive molecules. This can be done in solution by allowing the appropriately activated chelates to react with functional groups of the bioactive molecules (*12*−*16*). Alternatively, the bioactive molecules can be labeled on solid phase using appropriately derivatized building blocks which can be introduced to the biomolecule structure using oligonucleotide (*17*−*19*) and oligopeptide (*20*, *21*) synthesizers.

Although solid-phase labeling has several advantages, solution-phase labeling of large biomolecules such as proteins cannot be avoided. In these cases the labeling reaction has to be as effective and selective as possible.

Thiols are known to react with haloacetamides, maleimides, disulfides and their analogues, mercurials, vinyl sulfones, aryl halides, aziridines, and oxiranes (*22*). For the coupling purposes, the reactions of haloacetamides, maleimides, and disulfides are the most commonly employed. Several mercapto-selective labels are currently commercially available. From them, the haloacetyl derivatives display a wide range of other reactivities, while disulfides are practically completely specific to thiols. The reactivity of maleimides is between them. The problem of the use of disulfides is the lability of the bioconjugate in the presence of reducing agents which are often present in the conjugation reaction. Because of the high reactivity of haloacetamides, the pH of the conjugation reaction has to be carefully controlled. At too low pH, the reaction is slow, while at too high pH, amino functions, often abundantly present in the bioactive molecule to be labeled, compete with the target mercapto function for the label. Furthermore, to avoid oxidation of the mercapto function to be labeled, the labeling reaction has to be performed in the presence of a reducing agent, most commonly tris(carboxyethyl)phosphine (TCEP). The reducing agent, in turn, reacts with the haloacetamido chelate, markedly decreasing the yield of the desired biomolecule conjugate. Accordingly, labeling using maleimido chemistry might be the method of choice.

The known mercapto-selective luminescent lanthanide(III) chelates are haloacetamido or maleimido derivatives (*23*−*25*). They have been synthesized by allowing the corresponding amino chelates or ligands to react with the appropriate activating agents. Since lanthanide(III) chelates are highly hydrophilic molecules, their purification is rather laborious, often including HPLC purifications and various precipitation procedures. Here is described an alternative method for the preparation of lanthanide(III) chelates tethered to a maleimido group. Also their suitability to biomolecule derivation is demonstrated.

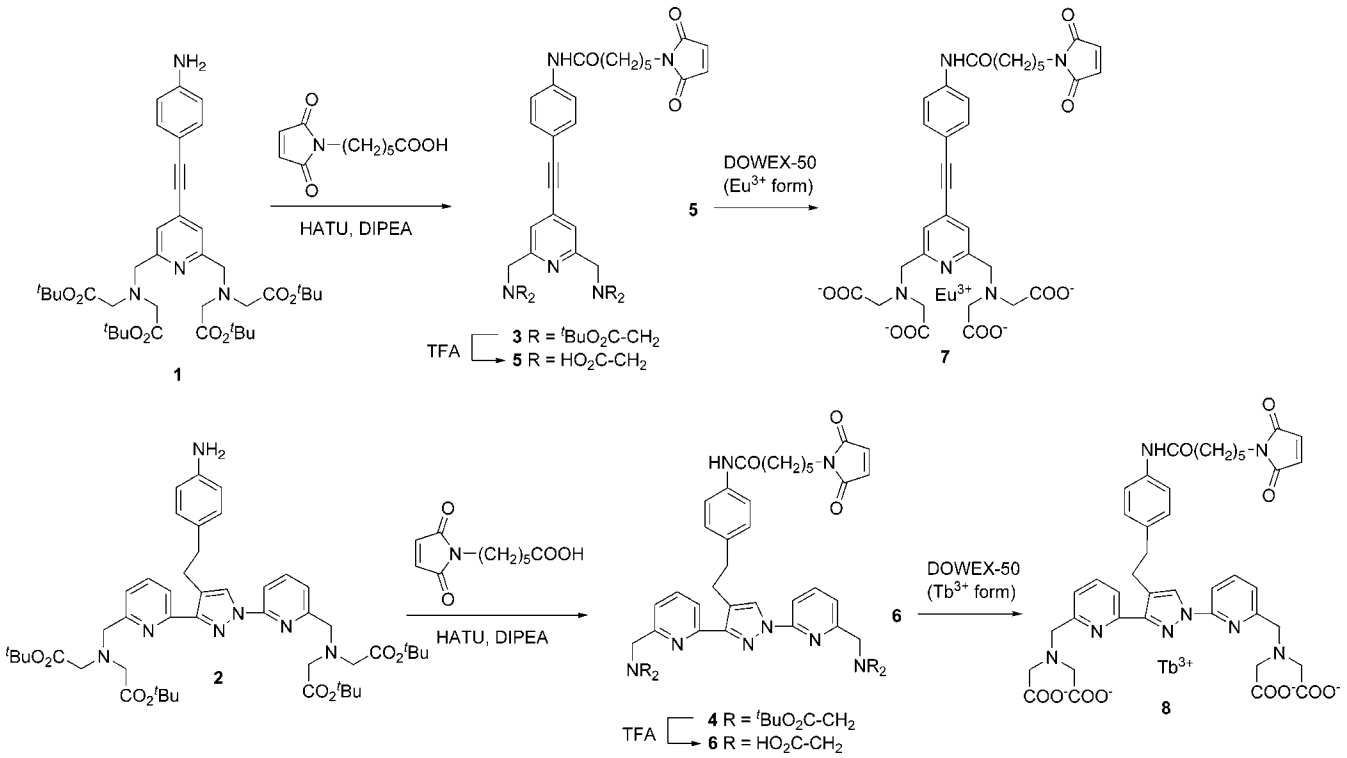
EXPERIMENTAL PROCEDURES

General Methods. Adsorption column chromatography was performed on columns packed with silica gel 60 (Merck). HPLC purifications were performed using a Shimadzu LC 10 AT instrument equipped with a diode array detector, a fraction collector, and a reversed phase column (LiChrocart 125-3 Purospher RP-18e 5 μm). Mobile phase (Buffer A): 0.02 M triethylammonium acetate (pH 7.0); (Buffer B): A in 50% (v/v) acetonitrile. Gradient: from 0 to 1 min 95% A, from 1 to 21 min from 95% A to 100% B. Flow rate was 0.6 mL min^{-1}. The cation exchange resin (Dowex 50 × 8, 20−50 mesh, H^+ form) was converted to the Ln^{3+} form by treatment with the approriate lanthanide(III) chloride followed by washing with distilled water until pH of the eluent was neutral. 6-Maleimidocaproic acid and the model peptide (CVEIDK) were purchased from Fluka and Sigma-Genosys, respectively. NMR spectra were recorded on a Bruker 250 spectrometer operating at 250.13 MHz for ^{1}H. TMS was used as an internal reference. Coupling constants are given in hertz. ESI-TOF mass spectra were recorded on an Applied Biosystems Mariner instrument.

* Corresponding author. Dr. Jari Hovinen, Tel + 358 2 2678 513; fax + 358 2 2678 380; jari.hovinen@perkinelmer.com.

10.1021/bc060282d CCC: $37.00 © 2007 American Chemical Society
Published on Web 03/07/2007

Scheme 1



Tetra-*tert*-butyl 2,2′,2″,2‴-{[4-[(4-(6-Maleimidohexylcarboxamido)phenyl)ethynyl]pyridine-2, 6-diyl]bis(methylenenitrilo)}tetrakis(acetate), 3. 6-Maleimidocaproic acid (60 mg, 0.28 mmol), *O*-(7-azabenzotriazol-1-yl)-1,1,3,3-tetramethyluronium hexafluorophosphate (106 mg, 0.28 mmol), and DIPEA (98 μL, 0.56 mmol) were dissolved in dry DMF (3 mL), and the mixture was strirred for 30 min at RT. Tetra-*tert*-butyl 2,2′,2″,2‴-{[4-[(4-aminophenyl)ethynyl]pyridine-2,6-diyl]bis-(methylenenitrilo)}tetrakis(acetate) (**1** (*26*; 100 mg, 0.14 mmol)) was added, and the reaction was allowed to proceed overnight at RT. The reaction mixture was diluted with dichloromethane (50 mL) and washed with 10% aq citric acid. The organic layer was dried over Na_2SO_4 and concentrated. Purification on silica gel (eluent: methanol/dichloromethane, 5:95, v/v) yielded 0.12 g (92%) of compound **3** as an oil. ^{1}H NMR ($CDCl_3$): 7.62 (d, J = 8.5, 2H); 7.49 (d, J = 8.5, 2H); 7.17 (s, 2H); 6.70 (d, J = 15.5, 2H); 3.91 (s, 4H); 3.54 (t, J = 7.3, 2H); 3.43 (s, 8H); 2.40 (t, J = 7.3, 2H); 1.78 (m, 2H); 1.65 (m, 2H); 1.47 (s, 36H); 1.39 (m, 4H). ESI-TOF MS for $C_{49}H_{68}N_5O_{11}(M + H)^+$ calcd, 902.49; obsd, 902.53.

Tetra-*tert*-butyl 2,2′,2″,2‴-{{6,6′-{4″-[2-(4-(6-Maleimidohexylcarboxamido)phenyl)ethyl]pyrazole-1″,3″-diyl}bis-(pyridine)-2,2′-diyl}bis(methylenenitrilo)}tetrakis-(acetate), 4. The title compound was prepared as desribed above for compound **3** but using tetra-*tert*-butyl 2,2′,2″,2‴-{{6,6′-{4″-[2-(4-aminophenyl)ethyl]pyrazole 1″,3″-diyl}bis(pyridine)-2,2′-diyl}bis(methylenenitrilo)}tetrakis(acetate) (**2**) (*27*). The reaction was complete in 2 h at RT. Yield was 87% (an oil). ^{1}H NMR ($CDCl_3$): 8.35 (s, 1H); 7.94 (d, J = 6.8, 1H); 7.91 (d, J = 6.8, 1H); 7.78 (t, J = 7.6, 1H); 7.74 (t, J = 7.8, 1H,); 7.62 (d, J = 7.6, 1H); 7.47 (d, J = 7.4, 1H); 7.41 (d, J = 8.3, 2H); 7.17 (d, J = 8.3, 2H); 6.69 (d, J = 8.3, 2H), 4.10 (s, 2H); 4.05 (s, 2H); 3.53 (s, 4H); 3.51 (s, 4H); 3.49 (m, 2H); 3.25 (m, 2H); 2.87 (m, 2H); 2.34 (t, J = 7.5, 2H); 1.78 (m, 2H); 1.76−1.35 (m, 8H); 1.47 (s, 18H); 1.44 (s, 18H). ESI-TOF MS for $C_{49}H_{68}N_5O_{11}$-$(M + H)^+$ calcd, 1049.57; obsd, 1049.55.

2,2′,2″,2‴-{4-(4-(6-Maleimidohexylcarboxamido)phenylethynyl)pyridine-2,6-diyl]bis(methylenenitrilo)}tetrakis-(acetic acid) Europium(III), 7. Compound **3** (50 mg, 0.055 mmol) was dissolved in trifluoroacetic acid (1 mL) and stirred for 2 h at RT before being concentrated *in vacuo*. The residue was triturated with diethyl ether, and the solid material was collected by filtration, washed with diethyl ether, and dried *in vacuo*. It was then dissolved in water (pH adjusted to ca. 7 with Na_2CO_3), and passed through a Dowex-50 resin (Eu^{3+} form) using distilled water as the eluent. Fractions containing the desired chelate were pooled and concentrated to ca. half volume. Precipitation from acetone afforded the title compound as a powder. ESI TOF MS for $C_{33}H_{31}EuN_5O_{11}$ $(M)^-$ calcd, 826,12; obsd, 826.12

2,2′,2″,2‴-{{6,6′-{4″-2-[4-(6-(2,5-Dioxo-2*H*-pyrrol-1(5*H*)-yl)hexyl)carboxamidophenyl)ethyl]pyrazole-1″,3″-diyl}-bis(pyridine)-2,2′-diyl}bis(methylenenitrilo)}tetrakis(acetic acid) Terbium(III), 8. Compound **4** was converted to the title compound as described above but using Dowex 50-resin loaded with Tb^{3+}. ESI TOF MS for $C_{41}H_{40}$ $N_8O_{11}Tb^-$ $(M)^-$ calcd, 979.21, obsd, 979.22.

Labeling of the Oligopeptide with the Europium Chelate 7. The model peptide (Ac-CVEIDK-$CONH_2$) (1 mg, 1.3 μmol) was dissolved in Tris-HCl buffer (1 mL; pH 7). Compound **7** (1 equiv) was added, and the reaction was allowed to proceed for 1 h at RT. Purification on HPLC yielded the desired oligopeptide conjugate. t_R 18.14 min. ESI TOF MS for $C_{64}H_{85}$ $EuN_{13}O_{22}S$ $(M)^-$, calcd, 1572.49; obsd, 1572.67.

RESULTS AND DISCUSSION

Preparation of maleimido-functionalized europium(III) and terbium (III) chelates is shown in Scheme 1. Accordingly, reaction of the amines (**1**, **2**) with preactivated 6-maleimidocaproic acid gave the protected ligands (**3**, **4**) in excellent yield. Purification was easily performed on silica gel column chromatography. It is worth noting that preparation of **3** requires the use of a powerful activator such as *O*-(7-azabenzotriazol-1-yl)-1,1,3,3-tetramethyluronium hexafluorophosphate (HATU) due to the low nucleophilicity of the aromatic amino function of **2**. Treatment of the protected ligands (**3**, **4**) with trifluoroacetic acid yielded the corresponding iminoacetic acid derivatives (**5**,

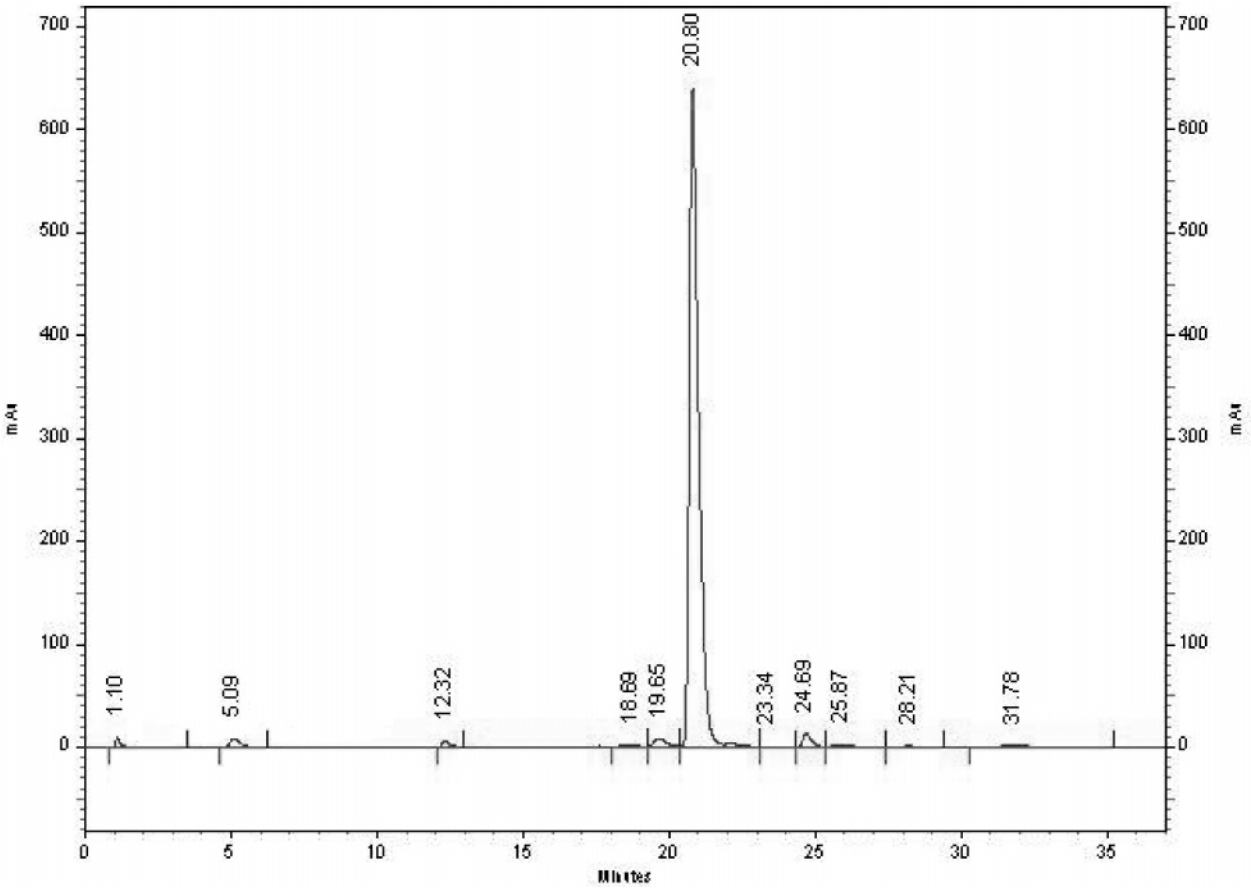


Figure 1. A reversed phase HPLC trace of a luminescent europium(III) chelate tethered to a maleimido group (**7**) synthesized according to the method described, detected at 300 nm. The peak at t_R 20.80 min is the desired product as jugded on ESI-TOF MS. For chromatographic conditions, see Experimental Procedures.

6). As expected (*28*), the maleimido function was completely stable during cleavage of the *tert*-butyl groups.

Lanthanide(III) chelates are most commonly prepared by treatment of the free ligands with a slight excess of lanthanide chloride at pH 6−7. When the chelation is completed, the excess of lanthanide is conveniently removed by increasing pH of the reaction mixture to ca. 11 where the uncomplexed lanthanide precipitates as lanthanide(III) hydroxide. However, this procedure cannot be used in the present case, since the maleimido function is known to hydrolyze in basic conditions (*29*). Here, the ligands were conveniently converted to the corresponding lanthanide(III) chelates (**6**, **7**) simply by passing through a strong cation exchange resin loaded with Eu^{3+} and Tb^{3+} ions for **4** and **5**, respectively. The chelates were analyzed on mass spectrometry, and the observed molecular weights were in accordance with the proposed structures.[1] A typical HPLC trace of the maleimido chelate after treatment with Dowex-50 resin is shown in Figure 1.

In order to demonstrate the suitability of the maleimido-derivatized lanthanide(III) chelates to biomolecule derivatization **7** was allowed to react with Caspase-6 subtrate at pH 6.5. The reaction was completed in a few minutes at ambient temperature. The reaction was clean, and the desired peptide conjugate was purified on reversed-phase HPLC and characterized by ESI-TOF mass spectrometry.

[1]For photophysical properties of lanthanide(III) chelates based on phenylethynylpyridine and (pyrazole-1,3-diyl)bis(pyridine) ligands, see Latva, M., Takalo, H., Mukkala, V.-M., Matachescu, C., Rodriques-Ubis, J., and Kankare, J. (1997) *J. Luminescence*, *75*, 149−169, and references 13, 19, 25 and 26.

CONCLUSIONS

Here is presented a convenient method for the preparation of maleimido-derivatized lanthanide(III) chelates. The maleimido tether is coupled to protected ligands giving rise to hydrophobic, stable intermediates which can be synthesized in large scale and purified on classical silica gel column chromatography. When desired, the protecting groups can be removed with acidolysis, and the free ligands can be converted to the corresponding lanthanide(III) chelates simply by passing through a cation exchange resin loaded with the appropriate lanthanide(III) ions.

LITERATURE CITED

(1) Hemmilä, I., and Mukkala, V.-M. (2001) Time-resolution in fluorometry technologies, labels, and applications in bioanalytical assays. *Crit. Rev. Clin. Lab. Sci. 38*, 441−519.

(2) Hemmilä, I. (1991) Applications of Fluorescence in Immunoassays. In *Chemical Analysis: A Series of Monographs on Analytical Chemistry and Its Applications*, Vol. 117, John Wiley & Sons, Inc., New York.

(3) Hemmilä, I., and Laitala, V. (2005) Progress in lanthanides as luminescent probes. *J. Fluoresc. 15*, 529−542.

(4) Selvin, P. R. (1996) Lanthanide-based resonance energy transfer. *IEEE J. Sel. Top. Quantum Electron. 2*, 1077−1087.

(5) Karvinen, J., Hurskainen, P., Gopalakrishnan, S., Burns, D., Warrior, U., and Hemmilä, I. (2002) Homogeneous time-resolved fluorescence quenching assay (LANCE) for caspase-3. *J. Biomol. Screen. 7*, 223−231.

(6) Gopalakrishnan, S., Karvinen, J., Kofron, J., Burns, D., and Warrior, U. (2002) Application of micro arrayed compound screening (pcARCS) to identify inhibitors of caspase-3. *J. Biomol. Screen. 7*, 317−323.

(7) Karvinen, J., Laitala, V., Mäkinen, M.-L., Mulari, O., Tamminen, J., Hermonen, J., Hurskainen, P., and Hemmilä, I. (2004) Fluorescence quenching-based assays for hydrolyzing enzymes. Application of time-resolved fluorometry in assays for caspase, helicase, and phosphatase. *Anal. Chem. 76*, 1429−1436.

(8) Karvinen, J., Elomaa, A., Mäkinen, M.-L., Hakala, H., Mukkala, V.-M., Peuralahti, J., Hurskainen, P., Hovinen, J., and Hemmilä, I. (2004) Caspase multiplexing: simultaneous homogeneous time-resolved quenching assay (TruPoint) for caspases 1, 3, and 6. *Anal. Biochem. 325*, 317−325.

(9) Wang, G., Yan, J., Hai, X., Matsumoto, K. (2006) Homogenous time-resolved fluoroimmunoassay of 3,5,3′-triiodo-L-thyronine in hyman serum by using europium fluorescence energy transfer *Talanta 70*, 133−138.

(10) Ge, P., and Selvin, P. R. (2004) Carbostyril Derivatives as Antenna Molecules for Luminescent Lanthanide Chelates. *Bioconjugate Chem. 15*, 1088.

(11) Ylikoski, A., Elomaa, A., Ollikka, P., Hakala, H., Mukkala, V.-M., Hovinen, J., and Hemmilä, I. (2004) A Homogenous time-resolved fluorescence quenching assay (TruPointTM) for genotyping. *Clin. Chem. 50*, 1943−1947.

(12) Mukkala, V.-M., Helenius, M., Hemmilä, I., Kankare, J., and Takalo, H. (1993) Development of luminescent europium(III) and terbium(III) chelates of 2,2′:6′,2″-terpyridine derivatives for protein labelling. *Helv. Chim. Acta 76*, 1361−1378.

(13) Takalo, H., Mukkala, V.-M., Mikola, H., Liitti, P., and Hemmilä, I. (1994) Synthesis of europium(III) chelates suitable for labeling of bioactive molecules. *Bioconjugate Chem. 5*, 278−282.

(14) Cooper, M. E., and Sammes, P. G. (2000) Synthesis and spectral properties of a new luminescent europium(III) terpyridyl chelate. *J. Chem. Soc., Perkin Trans. 2* 1695−1700.

(15) Peuralahti, J., Puukka, K., Hakala, H., Mukkala, V.-M., Mulari, O., Hurskainen, P., and Hovinen, J. Synthesis of nonluminescent lanthanide(III) chelates tethered to an aminooxy function and their applicability to biomolecule derivatization. *Bioconjugate Chem. 13*, 876−880.

(16) Hovinen, J. (2006) Synthesis of aminooxy chelates and their use in carbonyl group conjugation. *Chem. Biodivers. 3*, 296−303.

(17) Hovinen, J. and Hakala, H. (2001) Versatile strategy for oligonucleotide derivatization. Introduction of lanthanide(III) chelates to oligonucleotides. *Org. Lett. 3*, 2473−2476.

(18) Hakala, H., Ollikka, P., Degerholm, J., and Hovinen, J. (2002) Oligonucletide conjugates based on acyclonucleotides and their use in DNA hybridization assays. *Tetrahedron 58*, 8771−8777.

(19) Jaakkola, L., Peuralahti, J., Hakala, H., Kunttu, J., Tallqvist, P., Mukkala, V.-M., Ylikoski, A., and Hovinen, J. (2005) Solid phase synthesis of oligonucleotides labeled with luminescent lanthanide-(III) chelates. *Bioconjugate Chem. 16*, 700−709.

(20) Peuralahti, J., Hakala, H., Mukkala, V.-M., Hurskainen, P., Mulari, O., and Hovinen, J. (2002) Introduction of lanthanide(III) chelates to oligopeptides on solid phase. *Bioconjugate Chem. 13*, 870−875.

(21) Jaakkola, L., Peuralahti, J., Hakala, H., Mukkala, V.-M., Hurskainen, P., Hovinen, J. (2006) Labeling of oligopeptides and proteins with luminescent lanthanide(III) chelates. *J. Pept. Sci. 19*, 199−205.

(22) Aslam, M., and Dent, A. *Bioconjugation. Protein Coupling Techniques for the Biomedical Sciences*, Macmillan Reference Ltd, London, G.B., 1998.

(23) Chen, J., and Selvin, P. R. (1999) Thiol-reactive luminescent chelates of terbium and europium. *Bioconjugate Chem., 10*, 311−315.

(24) Ge, P., and Selvin, P. R. (2003) Thiol-Reactive Luminescent Lanthanide Chelates: Part 2. *Bioconjugate Chem. 14*, 870−876.

(25) Takalo, H., Hänninen, E., and Kankare, J. (1993) Luminescence of europium(III) chelates with 4-(arylethynyl)pyridines as ligands. *Helv. Chim. Acta 76*, 877−883.

(26) Rodrìques-Ubis, H., Takalo, H., and Mukkala, V.-M. (1999) Biospecific binding reactants labeled with luminescent lanthanide chelates. US Patent 5 859, 215.

(27) Marchán, V. In *Peptide-oligonucleotide conjugates: synthetic approaches and applications*, Conference, Chemiedozententagung, Hamburg, Germany, March 19−22, 2006; A26.

(28) Schelte, P., Boeckler, C., Frisch, B., and Schuber, F. (2000) Differential reactivity of maleimide and bromoacetyl functions with thiols: application to the preparation of liposomal diepitope constructs. *Bioconjugate Chem. 11*, 118−123.

BC060282D

On the Unusual Stability of Succinimidyl Esters in pNIPAm-AAc Microgels

Justin D. Debord and L. Andrew Lyon*

School of Chemistry and Biochemistry & Petit Institute for Bioengineering and Bioscience, Georgia Institute of Technology, Atlanta, Georgia 30332-0400 . Received August 9, 2006; Revised Manuscript Received October 5, 2006

In this contribution, we describe the effects of amide coupling reactions on the physical properties of thermoresponsive hydrogel microparticles (microgels). These microgels, when treated *via* aqueous carbodiimide/sulfo-succinimide coupling protocols, displayed a dramatic modulation of the microgel phase transition thermodynamics. UV spectrophotometry was used to determine that this modulation was due to remarkably stable hydrogel conjugates of sulfo-NHS that resisted degradation under standard hydrolysis protocols. These intermediates result in a shift of the phase transition, along with a large increase in equilibrium microgel swelling degree, due to an increase in chain−chain Coulombic repulsion. Only aggressive hydrolysis protocols resulted in the recovery of the native microgel phase transition, suggesting that an unusually stable succinimidyl ester is formed in the microgel during coupling.

INTRODUCTION

Protein−polymer hybrid materials have been of great interest for some time, especially in the areas of drug delivery (*1*), the modulation of protein:ligand binding (*2*), biosensing (*3*, *4*), and chromatography (*5*). Awareness has also been increasing in the use of thermoresponsive polymers for responsive biomaterials (*6*). Our group has worked extensively on bioconjugates of hydrogel microparticles and nanoparticles (microgels) (*3*, *4*, *6*−*8*) and through the course of these studies has observed unusual phenomena when "standard" amide bond-forming conjugation protocols are used. Therefore, a series of investigations was initiated to more completely study these phenomena. In the course of this investigation it was discovered that the use of *N*-hydroxysulfosuccinimide (sulfo-NHS) in a carbodiimide coupling scheme (*9*) resulted in a dramatic modulation of the microgel phase transition thermodynamics. We report that these effects are due to unusually stable polymer-conjugated succinimidyl ester moieties that persist for many months in aqueous media and are resistant to standard methods of NHS ester hydrolysis. These results may have significant implications for how bioconjugation strategies are developed for complex nanomaterials such as porous, amphiphilic hydrogel particles.

Thermoresponsive microgels such as those composed of poly(*N*-isopropylacrylamide) (pNIPAm) and acrylic acid (AAc) are discussed extensively elsewhere (*10*−*12*). The presence of acrylic acid monomers in the microgels provides a means to form an amide bond with an amine (*9*). Specifically, the water-soluble carbodiimide reagent 1-[3-(dimethylamino)propyl]-3-ethylcarbodiimide HCl (EDC) is useful in that it allows for the formation of amide linkages between amine substituents on a molecule (e.g., protein, ligand, fluorescent tag, etc.) and the carboxylic acid incorporated via the acrylic acid in the microgel (*3*, *13*, *14*).

This coupling procedure is essentially the aqueous phase version of the standard amide coupling reaction used for peptide synthesis in organic media. The aqueous phase reaction suffers from significant drawbacks relative to its organic solvent counterpart. Most importantly, the isoacylurea formed by the reaction of EDC and carboxylic acid is quite labile, as water attacks it to regenerate the carboxylic acid (*15*). In order to increase the conjugation efficiency, sulfo-NHS is frequently used, as shown in Scheme 1. This reagent replaces the isoacylurea to form a succinimidyl ester that hydrolyzes at a slower rate (*9*, *16*). The hydrolysis of the NHS ester is shown in Scheme 2. Conjugations such as these are essentially complete after several hours. It is generally accepted that the pH can be raised to quickly hydrolyze any remaining active esters, thereby quenching the reaction (*13*). Alternatively, the conjugated materials can be incubated overnight in PBS buffer (0.01 M, pH 7.4), which will result in hydrolysis of the ester bond.

EXPERIMENTAL PROCEDURES

Materials. All chemicals were obtained from Aldrich unless otherwise noted. The coupling reagents 1-[3-(dimethylamino)-propyl]-3-ethylcarbodiimide HCl (EDC) and *N*-hydroxysulfo-succinimide (sulfo-NHS), as well as phosphate-buffered saline (PBS) were used as received. The buffer component 2-[*N*-morpholino]ethanesulfonic acid (MES) was purchased from Sigma and used as received. Water used in all syntheses was distilled and then purified using a Barnstead E-Pure system. A 0.2 μm filter incorporated into this system removed particulate matter.

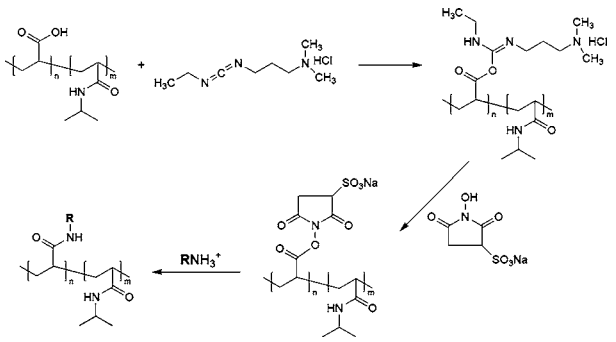
Conjugate Preparation. Aqueous carbodiimide coupling is a well-known cross-linking technique (*9*, *13*). Here, 100-μL of pNIPAm-AAc microgel solution (15 g/L) was mixed with 500 μL of MES buffer (0.1 M, pH 5.5). The coupling reagents EDC (4.4 mM final concentration) and sulfo-NHS (7 mM final concentration) are added to the microgel solution. and the prepared microgels are allowed to mix on a shaker table for at least 48−72 h. The microgels are then cleaned of excess reagents and spent reactants by successive centrifugation (5× at 14000*g*) and resuspension in PBS buffer (0.01 M, pH 7.4). Efforts to hydrolyze the active esters included addition of hydroxylamine (0.1 M, 25 μL), as well as various concentrations of NH_4OH. None of these resulted in significant loss of sulfo-NHS over the incubation period. Cleaned microgel conjugate solutions were then stored at 5 °C.

Photon Correlation Spectroscopy (PCS). The radii of the native and EDC/sNHS-treated pNIPAM-AAc microgels were determined in aqueous solution by PCS (Protein Solutions, Inc.). The temperature of the microgel samples was controlled via a Peltier device (±0.1 °C) integrated into the sample holder.

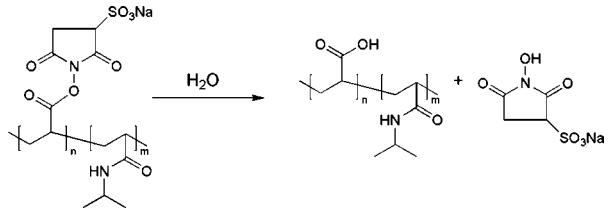
* Corresponding author. E-mail: LL62@mail.gatech.edu.

10.1021/bc060248z CCC: $37.00 © 2007 American Chemical Society
Published on Web 02/27/2007

Scheme 1. EDC-NHS Coupling of a Primary Amine to the pNIPAm-AAc Copolymer



Scheme 2. Hydrolysis of the NHS-ester



Microgel samples were thermally equilibrated for 10 min before measurements were taken. The hydrodynamic radii of the particles were calculated from diffusion coefficients using the Stokes−Einstein equation. All correlogram analyses were performed with manufacturer-supplied software (Dynamics v.5.25.44, Protein Solutions, Inc.). The data presented are the averaged values of 20 measurements, with a 10 s integration time for each.

Phase Transition (Cloud-Point) Experiments. Phase transition curves of scattering intensity versus temperature were constructed from experiments performed on a steady-state fluorescence spectrophotometer (Photon Technology International) equipped with a Model 814 PMT photon-counting detector. The instrument was controlled by manufacturer-supplied software (Felix v.1.41, Photon Technology International). In the experimental setup, the λ_{ex} and λ_{em} were set to the same value and the band-pass was adjusted to 2 nm. Light from the instrument impinged on the experimental sample, and the scattered light was collected at a 90° angle. The programmable temperature controller (Linkam Scientific Instruments model PE 60) provides real-time solution temperature data via a temperature probe with accuracy of ±0.1 °C.

UV Analysis. UV data was collected on a Shimadzu UV1601 spectrophotometer. Samples were analyzed by pipetting 100 μL of the centrifuged microgel supernatant into 1 mL of PBS (0.01 M, pH 7.4)

RESULTS AND DISCUSSION

In this study, we treated pNIPAm-co-AAc microgels with EDC and sulfo-NHS under standard conditions (*13*), and the resultant behavior of the treated microgels was investigated. Microgels treated under these conditions were analyzed via light scattering in order to ascertain any change in the phase transition behavior of the microgels. The light scattering data in Figure 1a show a typical phase transition curve for pNIPAm-AAc microgels at pH 3.5 (open circles). The solution scattering intensity increases at the phase transition temperature due to water expulsion from the microgels and concomitant polymer phase separation. The adjacent curve (filled circles) was obtained from microgels that had been treated with EDC and sulfo-NHS, followed by rigorous cleaning by repeated centrifugation/resuspension steps. This sample does not display any evidence of a normal phase transition. Rather, the scattering stays at a

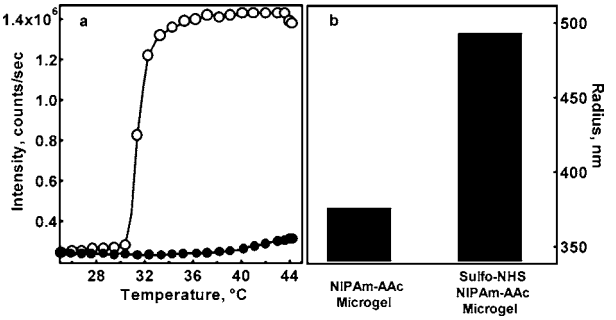


Figure 1. (a) Scattering intensity as a function of temperature for 0.11 mg/mL solutions of native pNIPAm-AAc microgels (open circles) and EDC/sulfo-NHS-treated pNIPAm-AAc microgels (filled circles) in water at pH 3.5. (b) Radii of native and EDC/sulfo-NHS-treated microgels as determined by photon correlation spectroscopy at 25 °C.

relatively low level until ~38 °C at which point the scattering intensity begins to increase gradually. Samples of microgels that were reacted with only EDC or only sulfo-NHS did not show a modulation of the phase transition temperature (see Supporting Information). It has been shown that hydrogels synthesized with anionic monomers exhibit phase transitions at higher temperatures due to Coulombic repulsion between polymer chains (*10*−*12*). The shifted phase transition in Figure 1a may similarly be the result of charge repulsion between sulfo-succinimidyl moieties attached to the microgel via the active ester. Hence, this implies that these active esters conjugated to the microgels are less susceptible to hydrolysis than what is typically observed, where the half-life for the NHS-ester is typically on the order of a few hours (*13*). The photon correlation spectroscopy (PCS) data shown in Figure 1b support the conjecture that sulfo-NHS is still bound to the microgels. At pH 3.5, the microgels treated with EDC and sulfo-NHS show a much larger radius than that of the native microgels. The treated microgels show a size monodispersity similar to the native microgels, ruling out aggregation as a factor in the increased radius. On the other hand, Coulombic repulsion of neighboring charged sulfonate groups would account for this effect, as an expanded polymer network results in larger microgel radii (*17*).

To confirm the presence of sulfo-NHS on the treated microgels, more extreme hydrolysis conditions than that found in simple aqueous media were employed. Such a hydrolysis condition can be achieved via a solution of 95% ethanol−5% PBS (0.01 M, pH 7.4). A small amount of freeze-dried polymer previously treated with EDC/sNHS was added to the solution and heated to 40 °C. The polymer solution was incubated for several hours, cooled to room temperature, and allowed to equilibrate on a shaker table for 72 h. To serve as a control, a microgel sample was mixed with an aliquot of sulfo-NHS (no EDC), cleaned by centrifugation, and carried through the same hydrolysis protocols. Both sets of microgels were then separated from solution via centrifugation. Supernatant was collected before and after hydrolysis treatment and analyzed via UV spectroscopy. Sulfo-NHS ($\epsilon \sim 8500\ M^{-1}\ cm^{-1}$) has a peak in the UV at approximately 268 nm in PBS (0.01 M, pH 7.4). Supernatant from treated microgels preceding the EtOH-PBS treatment resulted in no detectable loss of sulfo-NHS (Figure 2, open circles). However, supernatant from treated microgels incubated in EtOH−PBS showed a small release of sulfo-NHS. No release of sulfo-NHS was detectable from the supernatants of the control sample (data not shown). These data serve to confirm the presence of sulfo-NHS esters on the microgels and also reveal that the ester is hydrolyzing, but apparently at a very slow rate. Following the procedure outlined above, the treated microgels exhibited modestly shifted phase transition temperatures. This shift to a lower phase transition temperature is most likely due to the hydrolysis of a small amount of sulfo-NHS

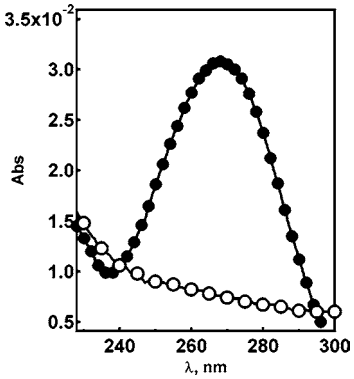


Figure 2. UV spectra of supernatant solutions recovered from EDC-sulfoNHS-modified microgels before EtOH−PBS incubation (open circles) and after 72 h incubation in EtOH−PBS (filled circles). λ_{max} = 268 nm.

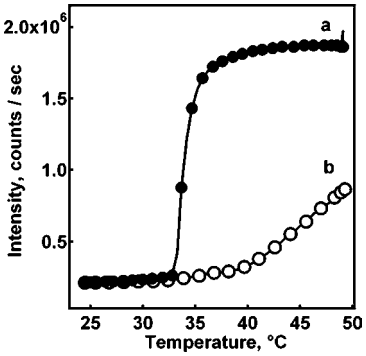


Figure 3. Scattering intensity as a function of temperature for 0.11 mg/mL solutions of (a, filled circles) ethanol−aq NaOH-incubated EDC and sulfo-NHS NIPAm-AAc microgels and (b, open circles) EDC and sulfo-NHS-treated pNIPAm-AAc microgels in water at pH 3.5.

and a resultant decrease in Coulombic repulsion between chains (Supporting Information).

In an effort to completely hydrolyze the succinimidyl ester and recover the native phase transition behavior of the microgels, EDC/sulfo-NHS-treated microgels were dispersed in a more basic solution of EtOH and aq NaOH. The polymer dispersion was heated to 50 °C for 15 min, cooled to room temperature and heated again to 50 °C for 15 min before being incubated for 24−48 h at room temperature. The microgels were separated from the reaction medium by centrifugation and redispersed in water. The results from light scattering experiments on these microgels (Figure 3) reveal that the phase transition temperature changed dramatically. Before incubation (open circles), the microgels exhibited phase transitions around 45−50 °C. The incubated microgels (filled circles) show a phase transition at ∼34 °C. The highly basic ethanolic solution allows for greater hydrolysis of the sulfo-NHS ester moieties and regenerates the original acid sites, resulting in the regeneration of a phase transition typical for native pNIPAm-AAc microgels at pH 3.5. Note that under these conditions, sulfo-NHS itself degrades and is not detectable *via* UV spectroscopy. The above data suggest that the environment of the microgel interior is such that much harsher conditions are necessary for the hydrolysis of sulfo-NHS esters than would be typically expected. The consequence is the long-lived stable esters that affect the solution properties of the microgels themselves.

In addition to the changes in physical properties, these long-lived esters appear to be responsible for decreasing the efficiency of amine conjugation. Experiments with protein, ligand, and fluorophore coupling have resulted in peculiar results, namely, *higher* coupling yields when sulfo-NHS is omitted from the EDC coupling protocols. The data in Figure 4 show an example

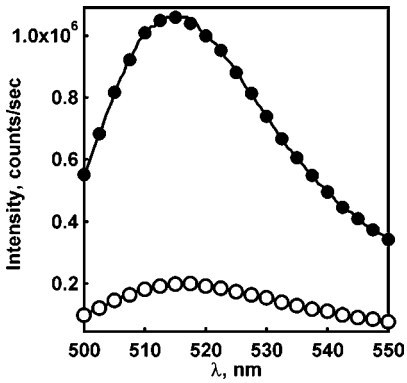


Figure 4. Fluorescence intensity of from a dispersion of microgels conjugated with 1 μL of fluoresceinamine (5.0 mg/mL) *via* EDC (4.4 mM) coupling (filled circles) and microgels conjugated with 1 μL fluoresceinamine (5.0 mg/mL) *via* EDC (4.4 mM) and sulfo-NHS (0.77 mM) coupling (open circles). All microgel solutions conjugated with sulfo-NHS result in lower fluorescence intensity proportional to the amount of sulfo-NHS added, suggesting that the sulfo-NHS competes for sites with the fluorophore by forming a stable ester.

of this effect. Here, the fluorophore fluoresceinamine was EDC coupled to pNIPAM-AAc microgels both with and without sulfo-NHS. When sulfo-NHS is included in the reaction, a dramatically lower yield of fluorophore coupling is observed relative to the EDC-only reaction. Effects such as this have been observed in our lab for proteins (avidin, streptavidin, and various IgGs), ligands (biotin, peptides), and other amine-containing fluorophores. We interpret these results as being due to competition for the chemoligation sites. That is, acid groups that react with sulfo-NHS are not as available for amide coupling as those that do not react with sulfo-NHS.

CONCLUSIONS

In summary, we have shown that treatment of pNIPAm-AAc microgels with the carbodiimide coupling reagents EDC and sulfo-NHS results in microgels containing 'long-lived' sulfo-NHS intermediates, despite the use of standard hydrolysis protocols. These intermediates result in a shift of the phase transition of the microgels to higher temperatures, along with a large increase in equilibrium microgel swelling degree, due to an increase in chain−chain Coulombic repulsion. Despite the typically labile nature of the ester bond in aqueous media, no hydrolysis of the sulfo-NHS ester is observed in standard aqueous solutions, while water/ethanol mixtures allow for hydrolysis rates that are detectable by UV spectroscopy. Extremely aggressive hydrolysis in basic ethanol affords almost complete removal of the sulfo-NHS moieties, thus regenerating the normal microgel phase transition behavior.

While the mechanistic origins of these unusual reactivities are not clear from these studies, it is perhaps not surprising that hydrolysis rates would be perturbed in hydrogel phases, given previous observations of differences in water mobility in microgel networks (*18, 19*). However, the susceptibility of the NHS ester to nucleophilic attack should not necessarily be sensitive to the behavior of water in the network, as water does not directly participate in that reaction. To address this issue, we are currently undertaking more detailed mechanistic studies on model polymers. Regardless of the mechanisms involved in the present study, these results point to the dramatically different reactivity that may be present in complex macromolecular materials such as hydrogels and other novel nanostructures, a point that should be acknowledged when applying "standard" chemoligation strategies to nonstandard materials. In light of the enhanced stabilities of the NHS esters, our group now performs acid−amine chemoligation reactions using EDC only,

as the NHS step obviously decreases the overall yield of the desired coupling reaction.

ACKNOWLEDGMENT

Financial support from an NSF-CAREER award (CHE-9984012) is gratefully acknowledged.

Supporting Information Available: Phase transition curves of microgels exposed to various EDC, EDC/sulfo-NHS, and hydrolysis treatments. This material is available free of charge *via* the Internet at http://pubs.acs.org/BC.

LITERATURE CITED

(1) Lu, Z.-R., Kopeckova, P., and Kopecek, J. (1999) Polymerizable Fab′ antibody fragments for targeting of anticancer drugs. *Nat. Biotechnol. 17*, 1101−1104.

(2) Ding, Z., Fong, R. B., Long, C. J., Stayton, P. S., and Hoffman, A. S. (2001) Size-dependent control of the binding of biotinylated proteins to streptavidin using a polymer shield. *Nature 411*, 59−62.

(3) Kim, J., Singh, N., and Lyon, L. A. (2006) Label-Free Biosensing with Hydrogel Microlenses. *Angew. Chem., Int. Ed. 45*, 1446−1449.

(4) Kim, J., Nayak, S., and Lyon, L. A. (2005) Bioresponsive Hydrogel Microlenses. *J. Am. Chem. Soc. 127*, 9588−9592.

(5) Fong, R. B., Ding, Z., Long, C. J., Hoffman, A. S., and Stayton, P. S. (1999) Thermoprecipitation of Streptavidin via Oligonucleotide-Mediated Self-Assembly with Poly(*N*-isopropylacrylamide). *Bioconjugate Chem. 10*, 720−725.

(6) Nayak, S., and Lyon, L. A. (2005) Soft Nanotechnology with Soft Nanoparticles (Invited Review). *Angew. Chem., Int. Ed. 44*, 7686−7708.

(7) Nayak, S., and Lyon, L. A. (2004) Ligand-Functionalized Core/Shell Microgels with Permselective Shells. *Angew. Chem., Int. Ed. 43*, 6706−6709.

(8) Nayak, S., Lee, H., Chmielewski, J., and Lyon, L. A. (2004) Folate-Mediated Cell Targeting and Cytotoxicity Using Thermoresponsive Microgels. *J. Am. Chem. Soc. 126*, 10258−10259.

(9) Grabarek, Z., and Gergely, J. (1990) Zero-Length Crosslinking Procedure with the Use of Active Esters. *Anal. Biochem. 185*, 131−135.

(10) Pelton, R. H. (2000) Temperature-sensitive aqueous microgels. *Adv. Colloid Interface Sci. 85*, 1−33.

(11) Saunders, B. R., and Vincent, B. (1999) Microgel particles as model colloids: theory, properties and applications. *Adv. Colloid Interface Sci. 80*, 1−25.

(12) Jones, C. D., and Lyon, L. A. (2000) Synthesis and Characterization of Multiresponsive Core-Shell Microgels. *Macromolecules 33*, 8301−8306.

(13) Hermanson, G. T. (1996) *Bioconjugate Techniques*, 1st ed., Vol. 1, Academic Press, San Diego.

(14) Kawaguchi, H., Fujimoto, K., Nakazawa, Y., Sakagawa, M., Ariyoshi, Y., Shidara, M., Okazaki, H., and Ebisawa, Y. (1996) Modification and functionalization of hydrogel microspheres. *Colloid Surf. A-Physicochem. Eng. Asp. 109*, 147−154.

(15) Hoare, D. G., and Koshland, D. E. J. (1967) *J. Biol. Chem. 242*, 2447−2453.

(16) Anjaneyulu, P. S. R., and Staros, J. V. (1987) *Int. J. Pept. Res. 30*, 117−124.

(17) Fernandez-Nieves, A., Fernandez-Barbero, A., Vincent, B., and de las Nieves, F. J. (2000) Charge controlled swelling of microgel particles. *Macromolecules 33*, 2114−2118.

(18) Guillermo, A., Addad, J. P. C., Bazile, J. P., Duracher, D., Elaissari, A., and Pichot, C. (2000) NMR investigations into heterogeneous structures of thermosensitive microgel particles. *J. Polym. Sci. Pt. B-Polym. Phys. 38*, 889−898.

(19) Griffiths, P. C., Stilbs, P., Chowdhry, B. Z., and Snowden, M. J. (1995) PGSE-NMR studies of solvent diffusion in poly(N-isopropylacrylamide) colloidal microgels. *Colloid Polym. Sci. 273*, 405−11.

BC060248Z

CORRECTIONS

Volume 17, Number 6, November/December 2006.

Maoliang Wang, Amartya Basu, Thomas Palm, Jack Hua, Stephen Youngster, Lisa Hwang, Hsien-Ching Liu, Xiguang Li, Ping Peng, Yue Zhang, Hong Zhao, Zhihua Zhang, Clifford Longley, Mary Mehlig, Virna Borowski, Prakash Sai, Manickam Viswanathan, Eun Jang, Gerald Petti, Sam Liu, Karen Yang, and David Filpula*

ENGINEERING AN ARGININE CATABOLIZING BIOCONJUGATE: BIOCHEMICAL AND PHARMACOLOGICAL CHARACTERIZATION OF PEGYLATED DERIVATIVES OF ARGININE DEIMINASE FROM *MYCOPLASMA ARTHRITIDIS*

The original publication (*1*) contained an error in Figure 3. The correct figure is below.

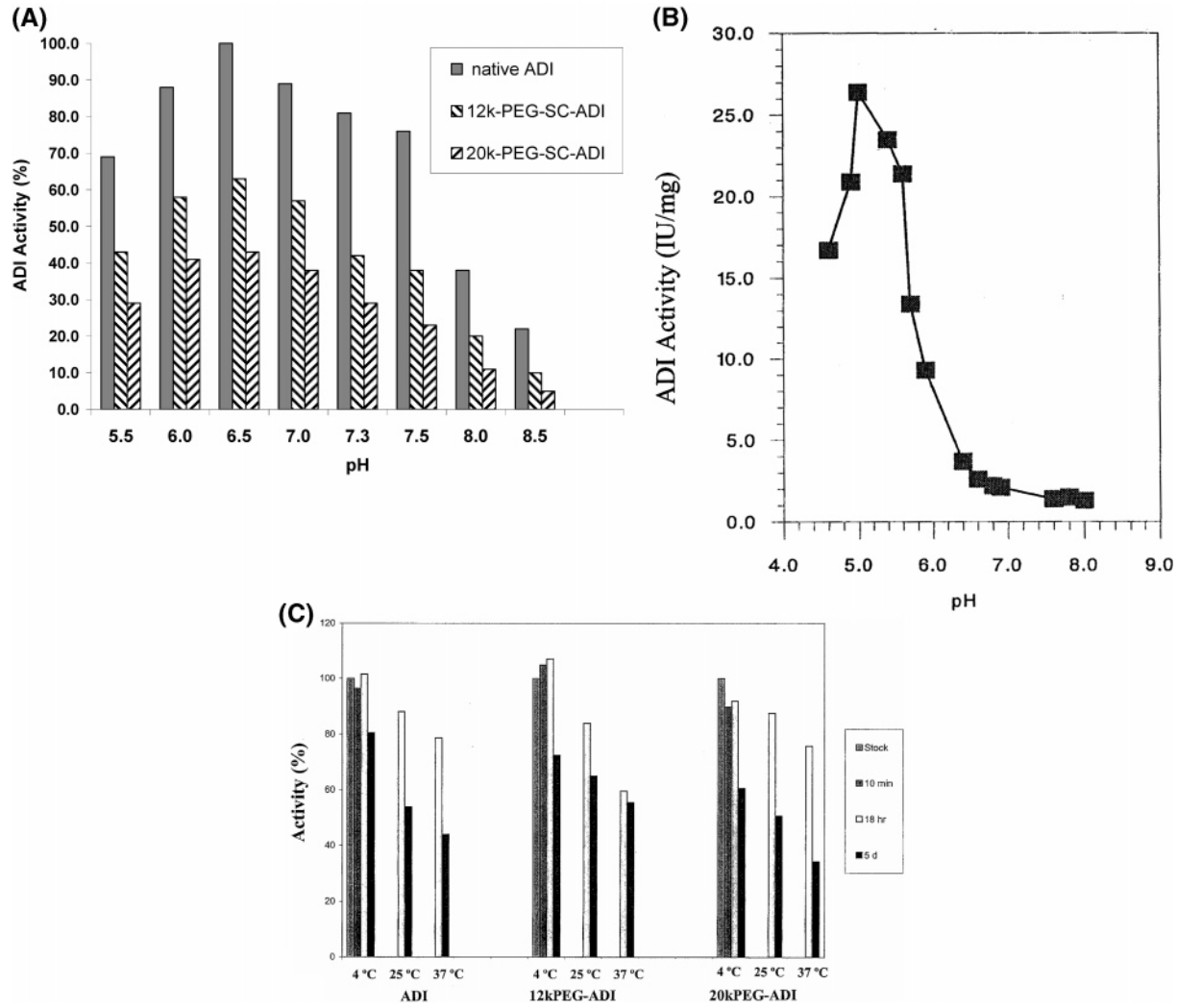


Figure 3. pH dependence of *M. arthritidis* ADI and PEG−ADI activity. (A) ADI, 12 kDa PEG−ADI, and 20 kDa PEG−ADI activity are measured at eight pH values. Values (%) are shown relative to native ADI at pH = 6.5 (100%). (B) pH profile of specific activity of *P. putida* ADI. (C) Stability studies in rat plasma for *M. arthritidis* ADI, 12 kDa PEG−ADI, and 20 kDa PEG−ADI stored at 4, 25, and 37 °C, and assayed at 10 min, 18 h, or 5 days. Relative activity is shown with 100% corresponding to the 4 °C stock solution.

BC060380Z

10.1021/bc060380z
Published on Web 03/03/2007

MAY/JUNE 2007
Volume 18, Number 3

© Copyright 2007 by the American Chemical Society

Bioconjugate Chemistry

COMMUNICATIONS

Peptide Beacons: A New Design for Polypeptide-Based Optical Biosensors

Kenneth J. Oh,[†] Kevin J. Cash,[‡] Verena Hugenberg,[†] and Kevin W. Plaxco*[,†,§]

Department of Chemistry and Biochemistry, Department of Chemical Engineering, and Interdepartmental Program in Biomolecular Science and Engineering, University of California, Santa Barbara, Santa Barbara, California 93106. Received October 11, 2006; Revised Manuscript Received April 3, 2007

Both epitope mapping and other *in vitro* selection techniques produce short polypeptides that tightly and specifically bind to any of a wide range of macromolecular targets. Here, we demonstrate a potentially general means of converting such polypeptides into optical biosensors. The sensing architecture we have developed, termed peptide beacons, is based on the observation that, whereas short peptides are almost invariably unfolded and highly dynamic, they become rigid when complexed to a macromolecular target. Using this effect to segregate a long-lived fluorophore from an electron transfer based, contact quencher (both covalently attached to the peptide), we have produced a robust optical sensor for anti-HIV antibodies. The binding-induced segregation of the fluorophore-quencher pair produces a 6-fold increase in sensor emission, thus allowing us to readily detect as low as ~250 pM of the target antibody. Because the sensor is based on binding-induced folding and a visible-light fluorophore, it is sufficiently selective to work directly in complex, contaminant-ridden samples such as saliva and blood.

INTRODUCTION

Molecular beacons (*1*) (MBs[1]), stem-loop DNAs that undergo a conformational change upon target binding, have proven useful for the optical (*2*) and electronic (*3*) detection of oligonucleotides. In the absence of target, the MB stem holds terminally attached quencher and fluorophore moieties in proximity, reducing emission. Upon target binding, the stem is disrupted, segregating the termini and producing a large, readily measured increase in fluorescence emission (*4*). While sensitive and convenient, however, the generality of the MB approach has proven limited, with only the detection of oligonucleotide-binding targets reported to date. Given the number of analytes, such as antibodies (*5*), better recognized by polypeptides, the development of polypeptide-based MB analogues could thus significantly extend the utility of this promising approach.

The development of polypeptide-based MB analogues has been hampered by the fact that polypeptides do not form stable stem−loop structures (*6*). We have, however, recently demonstrated a solution to this problem in a new class of sensors, termed peptide beacons (PB), that exploit the observation that, while unbound polypeptides are highly dynamic, their structure becomes fixed upon binding to a macromolecular target. Using this effect to segregate pyrene excimers attached to the termini of sensing polypeptides, we have recently extended the MB approach to polypeptide-based detection (*7*).

Pyrene excimer-based peptide beacons achieve sub-nanomolar detection limits and excellent specificity when tested in con-

* kwp@chem.ucsb.edu.
[†] Department of Chemistry and Biochemistry.
[‡] Department of Chemical Engineering.
[§] Interdepartmental Program in Biomolecular Science and Engineering.

[1] Abbreviations: HIV, human immunodeficiency virus; MB, molecular beacon; PB, peptide beacon; ELISA, enzyme-linked immunosorbent assay.

10.1021/bc060319u CCC: $37.00 © 2007 American Chemical Society
Published on Web 04/27/2007

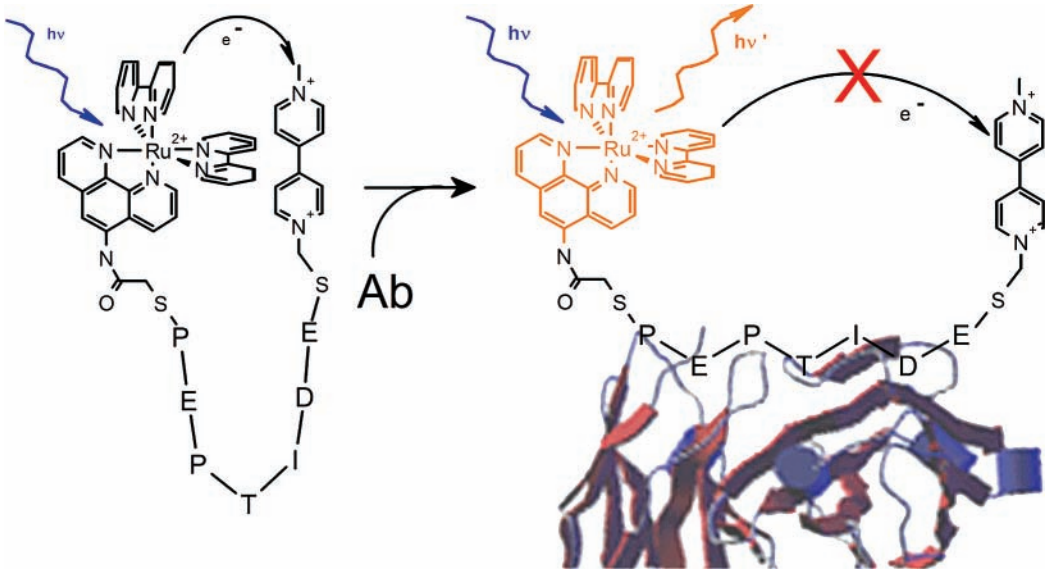


Figure 1. The PB architecture comprises a long-lived fluorophore, an electron-accepting quencher, and a recognition peptide. In the absence of target (left), intramolecular collisions allow for fluorescence quenching. Upon target binding (right), the fluorophore is segregated from the quencher, preventing electron transfer and enhancing fluorescence.

taminant-free buffer. They largely fail, however, when deployed in complex, contaminant ridden samples due to the relatively poor optical characteristics of pyrene: pyrene excitation occurs in the UV, which results in significant background fluorescence, and the signal gain of pyrene-based PBs is only 2-fold (*7*). Here, we describe an alternative PB architecture that, in contrast, is characterized by visible-light excitation and significantly improved signal gain (Figure 1).

RESULTS

We have synthesized a new PB architecture based on a highly antigenic (*8*), six-residue epitope from the HIV protein p17. As is true with almost all unstructured polypeptides, the two ends of the unbound epitope collide on a time scale of <100 ns (*9*). When bound to its target antibody, however, the epitope adopts a rigid, modestly extended conformation (*10*). We also employed a fluorophore, ruthenium(II) bisbipyridine−phenanthroline, that exhibits a ∼800 ns lifetime, exciting in the visible, and exhibiting a 160 nm Stokes shift (*11*). Optimization of the PB signal change upon binding requires that quenching be efficiently halted upon even the smallest binding-induced segregation, requiring in turn that we employ an electron transfer based mechanism that decreases exponentially with distance. To this end, we employed the electron accepting quencher methyl viologen. Our new PB thus consists of a ruthenium/viologen pair conjugated to the termini of the p17 epitope via cysteine linkers (Figure 1).

The emission of our new PB architecture is enhanced 6-fold upon addition of its target antibody (Figure 2). The signal gain and emissivity of the PB allow us to readily quantify the target antibody at concentrations as low as ∼250 pM, close to the 200 pM dissociation constant reported for the unmodified polypeptide (*12*). Finally, the gain of the PB is independent of its concentration (data not shown), indicating that the observed quenching is intramolecular.

The PB mechanism is linked to a binding-specific conformational change, and thus, the sensor should be selective against contaminants. Nevertheless, the background fluorescence present in realistically complex samples generally limits the sensitivity of optical sensors. This problem is minimized here by the use of a visible-light fluorophore with a 160 nm Stokes shift, attributes that allow us to detect the target antibody even in complex, contaminant-ridden samples (such as serum and saliva;

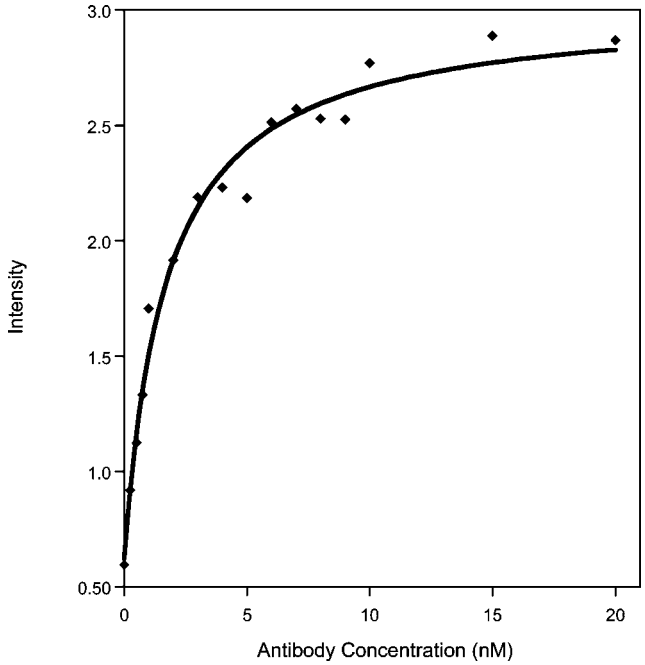


Figure 2. The emission of the PB increases approximately 6-fold upon target binding. Shown are data collected in buffer at a PB concentration of 1 nM.

Figure 3), albeit with poorer detection limits than observed in buffer. Of note, the signal gain observed in serum is similar to that observed in buffer, confirming that the sensor is unaffected by any of the hundreds of proteins contaminating these materials (*13*).

DISCUSSION

Here, we have demonstrated a novel biosensor that is sensitive, operationally convenient, and selective enough to be employed directly in complex, contaminant-ridden samples. The sensitivity of PBs is competitive with absorption-based, label-free sensing approaches, such as surface plasmon resonance and quartz crystal microbalances (*14*). In contrast to these approaches, however, the PB architecture combines this sensitivity with excellent selectivity: because signaling is linked to a specific, binding-induced conformational change, the PB ap-

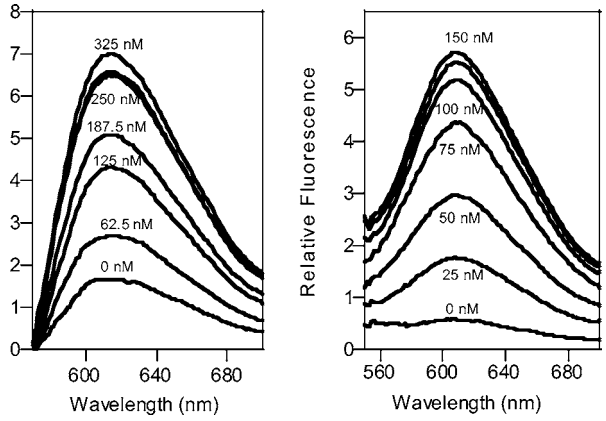


Figure 3. The PB approach is selective to work even in grossly contaminated samples in the background-subtracted spectra of (left) 250 nM PB in 50% serum and (right) 100 nM PB in saliva.

proach is relatively insensitive to the nonspecific binding that typically complicates adsorption-based sensing schemes (*15*). Additionally, the fluorophore we have employed excites in the visible and exhibits a large Stokes shift, reducing background fluorescence and allowing for deployment in clinical samples. The described PB approach also appears to be a more general platform than previous peptide-based optical sensing approaches (*16*, *17*) in that PBs neither require that binding specifically sequester a quencher (*18*) nor rely upon tryptophan fluorescence, which is difficult to monitor in the presence of typical contaminants (*19*). (Of note, we do not observe any significant quenching when tryptophan is titrated against a model ruthenium complex, suggesting that the approach is not limited to tryptophan-free polypeptides—data not shown.) Last, while the described PB does not exhibit the low picomolar-to-femtomolar sensitivities reported for the most highly optimized Western Blot and ELISA assays (*20*, *21*), the approach does not require the cumbersome equipment and batch processing employed by these techniques.

The PB sensing strategy may be general, as its only requirements are that intramolecular collisions in the unbound polypeptide are rapid and intermolecular collisions in the bound state are slow relative to the excited-state lifetime of the fluorophore, that the bound state of the peptide segregates the fluorophore/quencher pair by at least a few ångströms, and that the fluorophore and quencher do not disrupt binding. Given that the majority of small peptides are highly dynamic relative to the lifetime of our ruthenium fluorophore (*9*, *11*), and given the ready elucidation of novel polypeptide-based recognition elements by phage and bacterial display techniques (*22*), it appears that the PB approach described here will be applicable to a wide range of macromolecular targets.

ACKNOWLEDGMENT

This work was supported by the NIH Grant EB002046 and the UCBioSTAR program. This work made use of MRL Central Facilities supported by the MRSEC Program of the NSF under award no. DMR05-20415.

Supporting Information Available: Experimental procedures. This material is available free of charge via the Internet at http://pubs.acs.org.

LITERATURE CITED

(1) Tyagi, S., and Kramer, F. R. (1996) Molecular beacons: probes that fluoresce upon hybridization. *Nat. Biotechnol. 14*, 303−308.
(2) Kuhn, H., Demidov, V. V., Coull, J. M., Fiandaca, M. J., Gildea, B. D., and Frank-Kamenetskii, M. D. (2002) Hybridization of DNA and PNA molecular beacons to single-stranded and double-stranded DNA targets. *J. Am. Chem. Soc. 124*, 1097−1103.
(3) Fan, C., Plaxco, K. W., and Heeger, A. J. (2003) Electrochemical interrogation of conformational changes as a reagentless method for the sequence-specific detection of DNA. *Proc. Natl. Acad. Sci. U.S.A. 100*, 9134−9137.
(4) Fang, X., Liu, X., Schuster, S., and Tan, W. (1999) Designing a novel molecular beacon for surface-immobilized DNA hybridization studies. *J. Am. Chem. Soc. 121*, 2921−2922.
(5) Winter, G., Griffiths, A. D., Hawkins, R. E., and Hoogenboom, H. R. (1994) Making antibodies by phage display technology. *Annu. Rev. Immunol. 12*, 433−455.
(6) Pincus, M. R. (1992) Identification of structured peptide segments in folding proteins. *Biopolymers 32*, 347−351.
(7) Oh, K. J., Cash, K. J., and Plaxco, K. W. (2006) Excimer-based peptide beacons: a convenient experimental approach for monitoring polypeptide-protein and polypeptide-oligonucleotide interactions. *J. Am. Chem. Soc. 128*, 14018−14019.
(8) Papsidero, L. D., Sheu, M., and Ruscetti, F. W. (1989) Human immunodeficiency virus type 1-neutralizing monoclonal antibodies which react with p17 core protein: characterization and epitope mapping. *J. Virol. 63*, 267−272.
(9) Lapidus, L. J., Eaton, W. A., and Hofrichter, J. (2000) Measuring the rate of intramolecular contact formation in polypeptides. *Proc. Natl. Acad. Sci. U.S.A. 97*, 7220−7225.
(10) Massiah, M. A., Starich, M. R., Paschall, C., Summers, M. F., Christensen, A. M., and Sundquist, W. I. (1994) Three-dimensional structure of the human immunodeficiency virus type 1 matrix protein. *J. Mol. Biol. 244*, 198−223.
(11) Castellano, F. N., Dattelbaum, J. D., and Lakowicz, J. R. (1998) Long-lifetime Ru(II) complexes as labeling reagents for sulfhydryl groups. *Anal. Biochem. 255*, 165−170.
(12) Ota, A., and Ueda, S. (1998) Evaluation of the affinity measurement of anti-HIV-1 p17 monoclonal antibody by BIAcore. *Hybridoma 17*, 471−477.
(13) Adkins, J. N., Varnum, S. M., Auberry, K. J., Moore, R. J., Angell, N. H., Smith, R. D., Springer, D. L., and Pounds, J. G. (2002) Toward a human blood serum proteome: analysis by multidimensional separation coupled with mass spectrometry. *Mol. Cell. Proteom. 1*, 947−955.
(14) Kösslinger, C., Uttenthaler, E., Drost, S., Aberl, F., Wolf, H., Brink, G., Stanglmaier, A., and Sackmann, E. (1995) Comparison of the QCM and the SPR method for surface studies and immunological applications. *Sens. Actuators, B 24*, 107−112.
(15) Asanov, A. N., Wilson, W. W., and Oldham, P. B. (1998) Regenerable biosensor platform: a total internal reflection fluorescence cell with electrochemical control. *Anal. Chem. 70*, 1156−1163.
(16) Kohn, J. E., and Plaxco, K. W. (2005) Engineering a signal transduction mechanism for protein-based biosensors. *Proc. Natl. Acad. Sci. U.S.A. 102*, 10841−10845.
(17) Neuweiler, H., Schultz, A., Vaiana, A. C., Smith, J. C., Kaul, S., Wolfrum, J., and Sauer, M. (2002) Detection of individual p53-autoantibodies by using quenched peptide-based molecular probes. *Angew. Chem., Int. Ed. 41*, 4769−4773.
(18) Jean, J. M., Clerte, C., and Hall, K. B. (1999) Global and local dynamics of the human U1A protein determined by tryptophan fluorescence. *Protein Sci. 8*, 2110−2120.
(19) Lotte, K., Plessow, R., and Brockhinke, A. (2004) Static and time-resolved fluorescence investigations of tryptophan analogues − a solvent study. *Photochem. Photobiol. Sci. 3*, 348−359.
(20) Regnault, V., Arvieux, J., Vallar, L., and Lecompte, T. (1998) Immunopurification of human β2-glycoprotein I with a monoclonal antibody selected for its binding kinetics using a surface plasmon resonance biosensor. *J. Immunol. Methods 211*, 191−197.
(21) Rayevskaya, G., Pilipenko, V. G., Tkacikova, L., Spivak, N. Y., Mikula, I., and Chumak, R. M. (2000) Characterization of the third generation enzyme immunoassay IEA HIV1/2 III for the detection of anti HIV specific antibodies in human sera. *Folia Microbiol. 45*, 577−580.
(22) Bessette, P. H., Rice, J. J., and Daugherty, P. S. (2004) Rapid isolation of high-affinity protein binding peptides using bacterial display. *Protein Eng., Des. Sel. 17*, 731−739.

BC060319U

Supporting Information

Peptide Beacons: A New Design for Polypeptide-Based Optical Biosensors.

*Kenneth J. Oh[1], Kevin J. Cash[2], Verena Hugenberg[1], Kevin W. Plaxco[1,3]**

[1]Department of Chemistry and Biochemistry, [2]Department of Chemical Engineering, and [3]Interdepartmental Program in Biomolecular Science and Engineering, University of California, Santa Barbara, Santa Barbara, CA 93106.

*kwp@chem.ucsb.edu

Materials and Methods

Synthesis of the Peptide Beacon.

Synthesis of N-methyl-N'-(2)bromoethyl-4,4'-bipyridinium. To produce N-methyl-4,4'-bipyridinium, 10 g of 4,4'-bipyridine was dissolved in 500 mL of chloroform. Twenty-five mL of iodomethane was added to the reaction, and was allowed to react at room temperature for 48 hours. The product was separated from the starting materials by performing phase extractions with H_2O, three times at 25 mL each. The starting material remained in the chloroform layer. The product was then further purified via HPLC using a gradient of 5% to 25% acetonitrile in H_2O and 0.1% trifluoroacetic acid, and the product eluted at 14 minutes. The product in solution was then lyophilized to a dry powder, and stored at –20˚ C. The product was verified on an Applied Biosystems PE Sciex QSTAR-Pulsar quadrupole orthogonal time-of-flight mass spectrometer fitted with an electrospray source (ESI-MS), m/z = 171. Five g of the product was dissolved in 100 mL acetonitrile and 10 mL of THF to which 15 mL of 1,2-dibromoethane was added. The solution was then allowed to reflux for 8 hours. The solvent mixture was then removed by rotary evaporation. The product was purified from the starting material by reverse-phase HPLC on a Waters Xterra MSC18 column, using gradient of 5% to 25% acetonitrile in H_2O and 0.1% trifluoroacetic acid, and the product eluted at 12 minutes. The reverse-phase mobile phase solvent was then removed by lyophilization, and the dry powder was stored at –20˚ C. The product was verified by ESI-MS, m/z = 278.

Synthesis of Ru(bipy)$_2$phen-5-iodoacetamide (adapted from *11*). Five mg of Ru(bipy)$_2$phen-5-amine (Fluka; diastereomers not determined), was dissolved in 100 mL of acetonitrile followed by the addition

of 100 mg of iodoacetic anhydride (Sigma-Aldrich). The solution was allowed to react for 8 hours at 4˚ C. The solvent was removed by rotary evaporation. The product was separated by reverse-phase HPLC on a 10% to 50% acetonitrile gradient over 60 minutes, the product elutes at 36 minutes. The product was then verified by ESI-MS, m/z = 777.

Conjugation of p17 peptide epitope to Ru(bipy)$_2$phen-5-iodoacetamide. Twenty mg (17 μmol) of the p17 peptide (sequence CEKIRLRC; from Biopeptide, San Diego) was treated with a 10x excess TCEP to reduce any disulfide cross linkages in 100mM TRIS-HCl buffer, pH = 7.5. The peptide was then purified via reverse-phase HPLC, lyophilized, and subsequently resuspended in a 200 mM of argon-degassed TRIS-HCl buffer, pH 7.8. Thirteen mg of Ru(bipy)$_2$phen-5-iodoacetamide was dissolved in the above buffer. The two solutions were mixed and allowed to react for 24 hours at room temperature under argon. The solution was then lyophilized, and purified via reverse-phase HPLC on a 10% to 50% acetonitrile gradient in H_2O and 0.1% trifluoroacetic acid over 60 minutes. The product elutes at 34 minutes. The product was verified using electrospray mass spectrometry, m/z = 1711. Ten mg of the p17 peptide-Ru(bipy)$_2$phen conjugate in 10 mL of 100 mM TRIS-HCl buffer, pH 7.5 was then treated with a 10x excess of TECP to reduce any disulfide cross-links and purified via reverse-phase HPLC to separate it from any unreacted TECP. The reduced p17 peptide-Ru(bipy)$_2$phen conjugate was then lyophilized to a powder, resuspended in 10 mL of 200 mM TRIS-HCl buffer, pH 7.5, degassed with argon. Twenty mg of N-methyl-N'-2-bromoethyl-4,4'-bipyridinium, dissolved in 4 mL of the same buffer, was added and the resulting solution and was allowed to react for 48 hours at room temperature under argon. The solution was then lyophilized, and purified via reverse-phase HPLC on a 10% to 50% acetonitrile gradient in H_2O and 0.1% TFA over 60 minutes. The product elutes at 28 minutes. The product was verified by ESI-MS, m/z = 1910. The resultant product was stored at –20˚ C and exhibits stability over long periods of time as a lyophilized powder. Of note, our PBs are a mixture of constructs in which the fluorophore is on either the amino- or carboxy-end of the

polypeptide, thus simplifying synthesis. Because electron-transfer is highly distance dependent, the orientation of the fluorophore and quencher does not affect the PB signaling.

Spectral Interrogation

Fluorescence Measurements were performed on a Varian Cary Eclipse Fluorimeter. Samples were excited at 450 nm. Titrations were performed with a fixed concentration of PB in a 1 mL quartz cuvette, in 100 mM TRIS buffer, pH 7.8. The anti-p17 antibody (Zeptometrix, Buffalo, New York) clone 32/1.24.89 was aliquoted for the three different titrations of buffer, saliva, and blood serum in increments of 0.25, 0.25 and 0.25 normal equivalents, respectively. After each addition, the solution was allowed to stand for two minutes at 28˚C, and then a measurement was acquired. The reported spectra represent the mean of multiple measurements. All of the reported experiments were conducted in the presence of dissolved oxygen. Experiments with oxygen-free buffers (obtained via purging with argon for 40 minutes) produce only slightly increased fluorescence intensity (data not shown)

Using Luminescent Nanoparticles as Staining Probes for Affymetrix GeneChips

Lin Wang, Charles Lofton, Michael Popp, and Weihong Tan*

Center for Research at the Bio/Nano Interface, Department of Chemistry, Shands Cancer Center and UF Genetics Institute, University of Florida, Gainesville, Florida 32611-7200. Received November 22, 2006; Revised Manuscript Received March 14, 2007

Microarray technology provides efficient access to genetic information using miniaturized, high-density arrays of DNA probes. We investigated the application of luminescent nanoparticles as probes for Affymetrix GeneChips detection without the need for signal amplification. Our goal is to investigate the feasibility of using luminescent nanoparticles as probes in a commercial microarray system without changing its configurations. With the present imaging modality and existing optical excitation and detection systems of the Affymetrix GeneChips, our early results indicate that nanoparticles not only can be used for GeneChip labeling but also are superior to the traditional fluorescent protein streptavidin-phycoerythrin (SAPE). The advantage of the particles lies in a simplified staining procedure, higher photobleaching threshold, and enhanced luminescence signal. The nanoparticles can be used for detection of low-abundance targets without any amplification step. A concentration detection limit of 50 fM has been achieved. This work demonstrates the feasibility of using luminescent nanoparticles as probes for commercial microarray systems, making them less costly, more reproducible, and potentially quantitative.

DNA and oligonucleotide microarrays have revolutionized gene expression profiling by allowing highly parallel and quantitative monitoring of thousands, and in some cases all, of the gene transcripts from an organism (*1*). This greatly increased scale with DNA microarrays has made it possible to tackle qualitatively different questions in biology and medicine. However, despite their extensive profiling and genotyping capability, using microarrays for the assessment of transcripts at low abundance levels remains elusive due to the insufficient detection sensitivity. This can be improved by significant pre-amplification of the starting material (*2*−*3*) which is most often done using a two-round T7/aRNA method. This method, however, has increased noise over the more conventional one-round amplification procedures (*4*−*5*).

Alternatively, microarray sensitivity can potentially be improved by increasing the fluorescence signal of the gene target. Unfortunately, although the new generation of fluorophores such as the Alexa series generate greater signal, their limited sensitivity for microarrays as well as their photostability need further improvement. The rapidly evolving field of bionanotechnology has opened up a promising era in new probe development (*6*−*8*). Gold nanoparticle (NP)-promoted reduction of silver was reported to detect target DNA at a concentration of 50 fM (*6*). The detection, however, relied on coating the gold NP with silver, a complicated process which caused reduced reproducibility. Two-color microarray-based detection has also been demonstrated by using Cy3- and Cy5-doped gold-core/silica-shell NPs in a sandwich hybridization (*7*). Each NP was embedded with ∼100 dye molecules, and the study revealed a detection limit of 1 pM for target DNA. Quantum dots have similarly been used for DNA microarray and achieved a detection limit of 2 nM for target DNA (*8*). So far, however, NP probes have been tested only in proof-of-concept experiments where allele-specific surface-immobilized capture probes and gene-specific oligonucleotide-functionalized NP probes are hybridized to the target sequentially. Under these conditions, only a few genetic markers can be simultaneously detected. Thus far, the use of NPs to analyze genetic information has not yet been demonstrated in a real commercial system.

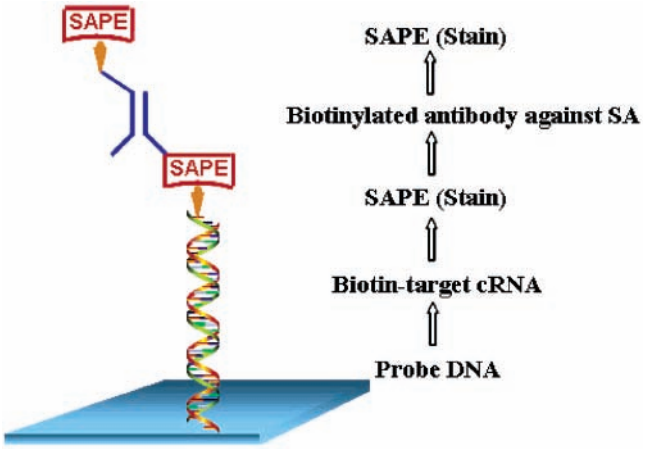


Figure 1. Signal amplification scheme in the Affymetrix system.

Herein, we report the first study using dye-doped silica NPs to visualize the hybridization signal of target RNA binding to probes on Affymetrix GeneChips. Due to their extensive genetic content and the fact that they are supplied ready for use, Affymetrix GeneChip arrays are quickly gaining acceptance as the optimal method for determining transcription profiles. An integral component of the Affymetrix GeneChip technology is probe redundancy. Multiple probes homologous to different regions of the target RNA are designed. This improves the signal-to-noise ratio, increases the dynamic range of detection, and minimizes cross-hybridization effects. An additional level of redundancy comes from the use of mismatch (MM) probes identical to the perfect match (PM) probes except in a single base located in a central position. In the conventional GeneChip labeling strategy (Figure 1), the biotinylated cRNA is fragmented and hybridized to the GeneChip array. After hybridization, the arrays are washed and stained with streptavidin−phycoerythrin (SAPE). The signal is then amplifed by first washing with a solution containing biotinylated anti-streptavidin (goat) antibody

* 352-846-2410 (phone and fax), E-mail: tan@chem.ufl.edu.

10.1021/bc060365u CCC: $37.00 © 2007 American Chemical Society
Published on Web 04/21/2007

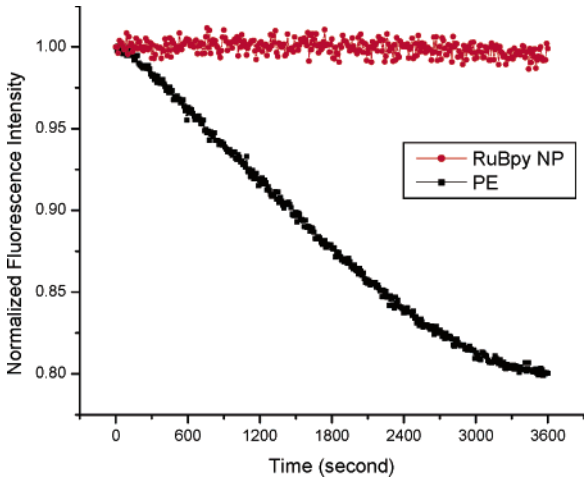


Figure 2. Photostability test of RuBpy-doped silica NPs (top) and PE (bottom) in solution phase under the exposure of a 150 W xenon lamp.

and then a final staining with SAPE. Comparisons of gene expression levels are generated on the basis of the detection of the fluorescence signal emitted from each element on the array. This signal amplification strategy, however, is time-consuming, may generate amplification bias, and disturb the abundance levels of the original transcripts.

Our efforts focused on replacing the conventional SAPE with dye-doped silica NPs (*9*) in an attempt to increase the fluorescence signal and thereby the sensitivity. Each of our dye-doped silica NPs contains a large number of dye molecules, emitting a fluorescence signal more than 10 000 times that of a fluorophore (*10*). This extreme brightness facilitates ultrasensitive determination of trace analytes that are undetectable with existing fluorescence labeling techniques. We aim to investigate whether this new NP reporter technology enhances the commercial microarray performance without either introducing additional amplification bias or requiring a change in the configuration of the commercial system.

The RuBpy dye-doped NPs were spherically uniform with an average diameter of 60 ± 3 nm (RSD = 5%, n = 200). Fluorescence intensity of these NPs was measured, and the effective fluorescence intensity of each particle is equivalent to that of 30 000 RuBpy dye molecules (Supporting Information). Moreover, the silica matrix of the NPs serves as a protective shell or dye isolator; it limits the effect of the outside environment on dye molecules which are otherwise susceptible to photobleaching due to their inherent molecular nature. To compare the photobleaching thresholds of SAPE and NPs, photostability tests were performed on both RuBpy NPs and the PE solutions. Within 1 h of continuous Xenon lamp excitation, no noticeable photobleaching was observed for NPs. However, a significant decrease in fluorescence intensity was observed for the PE solution during the same time period (Figure 2). This observation suggests that the silica matrix isolates the dye molecules from the outside environment and thereby prevents photo-oxidation by oxygen (*11*). Unlike SAPE, which should be kept in the dark either wrapped in foil or stored in an amber tube, the dye-doped NPs can be exposed to room light without interfering with their signaling properties; they are more robust tools for microarray staining. Indeed, after scanning a NP-stained microarray ten times successively, only negligible signal variation was observed. More importantly, the remarkably high photochemical stability of dye-doped NPs allows them to withstand numerous illumination cycles and permits several microarray measurements to be taken at different times. This enables experiment optimization or verification of the measurements by different researchers. Furthermore, this improved photostability would possibly allow for extended integration time, improved signal-to-noise ratios and sensitivity, resulting in overall increased assay reliability.

In order to integrate the dye-doped NPs into the microarray system, our initial idea was to replace the SAPE with streptavidin-labeled NPs. However, considering the effects of strong steric hindrance between the rigid NP and the solid-phase surface, different NP labeling strategies were designed. In addition to direct labeling of SA onto NPs, NHS-PEG-biotin molecules were immobilized onto amine-modified NPs (*13*). These PEG linkers allowed the conjugated biotin molecules to extend out from the NP surface in order to increase binding efficiency. PEG linkers are also well-known for their ability to prevent nonspecific interactions and act as hydrophilic spacers, minimizing any detrimental interactions between the attached biomolecule and the solid surface. To demonstrate the successful immobilization of biotin molecules on the NPs, streptavidin-coated microspheres and biotin-PEG-labeled NPs were mixed (*12*−*13*). The confocal images of the resultant microsphere−NP complexes prove the successful biotinylation of the NPs (Supporting Information).

The Affymetrix GeneChip Test3 arrays (T3 array) were used to compare the performance of different NP staining strategies. The T3 array contains a limited number of probe sets representing genes from various organisms including mammals, plants, and eubacteria. The array also has two inbuilt controls—the B2 oligo, which serves as a positive hybridization control, and four bacterial genes involved in biotin metabolism (bioB, bioC, bioD, creX). These four genes are spiked into the hybridization cocktail in varying molar ratios and are used to evaluate hybridization efficiency. Biotin-labeled cRNA samples from a human lung cancer cell line (A549) were hybridized on the arrays and stained with NPs using three different strategies (Figure 3). The first array was stained with streptavidin-directly labeled NPs (NP-SA); the second array was stained with PEG-biotin-streptavidin-labeled NPs (NP-PEG-biotin-SA); and the third array was first incubated with 1 mg/mL streptavidin, then washed and stained with PEG-biotin-labeled NPs (SA+NP-PEG-biotin) (Figure 4). In this last case, the streptavidin is first bound with biotin tags on the cRNA. Because each streptavidin has four biotin binding sites, it can further bind to biotin tags on the NPs. We found the binding efficiency of the three types of particles as follows: NP-SA < NP-PEG-biotin-SA < SA + NP-PEG-biotin.

This result demonstrates that the PEG linkers improved biomolecule recognition efficiency and reduced NP nonspecific binding. The superiority of the third strategy over the second may be due to better stability and smaller size of biotin-labeled NPs than protein-attached NPs, and the additional washing step. The third strategy was used in all further studies. Using NPs as the staining probe, we found the percentage of genes present on the T3 array to be 21.8%, which is within the range obtained with the normal double SAPE staining (16−25%). The background noise using NP staining probe is at a similar level to the SAPE staining, illustrating minimal nonspecfic binding of NPs on the microarrays.

To demonstrate whether bioconjugated NPs could improve the Affymetrix gene expression analysis by increasing its signal and thereby achieving higher sensitivity, we diluted the stock solution containing four bacterial hybridization control genes (bioB, bioC, bioD, creX) by 100-fold. (It is worth noting that only the concentrations of the commercial stock solutions of these four genes are available, while those in the biological sample (cRNA samples from the cell line) are unknown.) An aliquot of the three diluted hybridization cocktails was hybridized on three arrays in parallel and then stained with different methods. The first was single-stained with SAPE; the second was stained with SAPE, followed by antibody amplification and

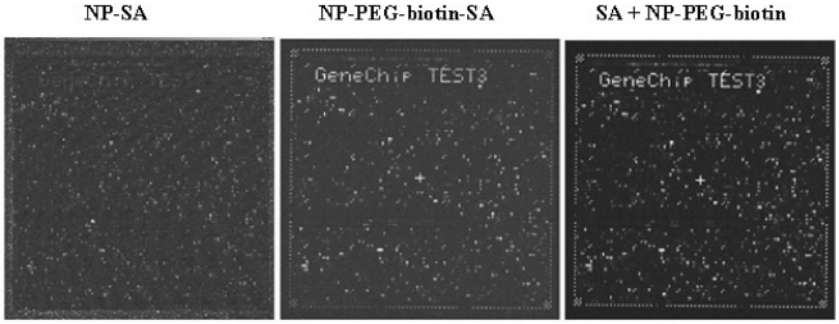


Figure 3. Test3 array images using different NP staining strategies.

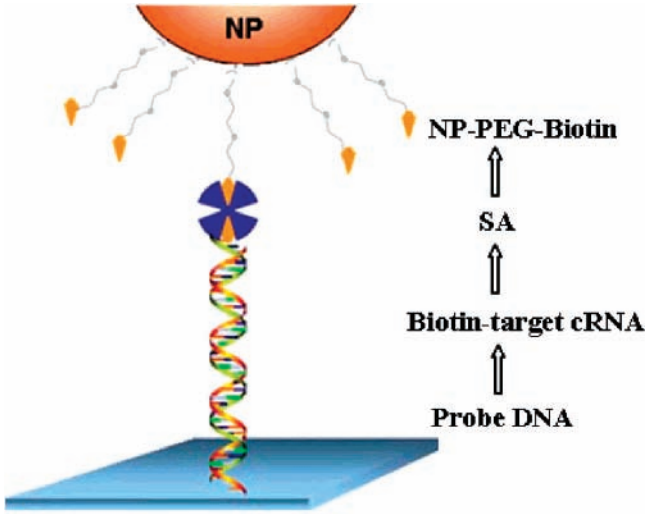


Figure 4. Strategy of NP-based labeling for microarray technology.

Table 1. Control Gene Expression on Test3 Arrays after 100-fold Dilution[a]

final concentrations of control cRNAs	bioB (15 fM)	bioC (50 fM)	bioD (0.25 pM)	Cre (1 pM)
SAPE (one staining)	A	A	A	P
SAPE (two staining)	A	P	P	P
NP (one staining)	A	P	P	P

[a] A = absent; P = present.

second SAPE staining; the third was incubated with streptavidin followed by NP-PEG-biotin staining. After the washing and scanning steps, we found that the detection limit of gene expression with one SAPE staining was 1 pM, with two SAPE stainings, it was 50 fM, and with one RuBpy NP staining, it was 50 fM (Table 1). The NP single staining probe exhibited sensitivity which is 20× higher than the SAPE single staining probe, and comparable to two SAPE stainings.

It should be noted that all the chip signals were scanned on the Affymetrix GC3000 scanner using the optimal excitation/emission wavelengths for PE (Ex 532 nm; Em 570 nm) but not for RuBpy (Ex 460 nm; Em 600 nm). By comparison, the emission signal of RuBpy NPs excited at 532 nm is only 5% as intense as when excited at 460 nm. Even under such unfavorable conditions, the NPs were still more sensitive than one SAPE staining and comparable to two SAPE stainings. Changing the laser excitation diode and scanner filters or synthesizing dye-doped NPs matching the configuration of the scanner would possibly lead to a major enhancement in the signal from the NP-stained microarrays. Another noteworthy issue is the steric crowding effects due to the physical size of the NPs. Each feature (size 11 μm) of the array consists of more than 1 million copies of oligonucleotide probes. Therefore, each probe occupies a square of 11 μm on each side. The NP is around 60 nm in diameter (several times larger than streptavidin−phycoerythrin). This large and bulky size may block some biological binding sites in close proximity. Therefore, some biomolecules were not signaled, leading to lower sensitivity. Reduction of the particle size may address this problem. However, this is not a critical issue at a low target concentration because the distance between hybridized targets will be nearly as large or larger than the diameter of a NP. In that case, the ratio of target molecule to NP will be close to 1.

In conclusion, we used luminescent NPs as staining probes for Affymetrix Genechips and found that they simplified the staining procedure as well as showed enhanced detection sensitivity and photostability when compared to SAPE. As NPs can be used for detection of low-abundance targets without the amplification step, the method is potentially less costly and more quantitative, and the NP probe itself is less photolabile. In order to further improve the performance of dye-doped NPs for gene chips, a few modifications need to be implemented. The single-wavelength laser diodes and the Axon scanner optics need to be optimized for our luminescent NPs or we need to sythesize dye-doped NPs matching the Ex/Em wavelength of PE. The NP size also needs to be optimized to reduce the steric crowding effect. If dye-doped NPs and the optical setup are optimized in the Affymetrix GeneChip array, NP probe could be expected to be more sensitive, less costly, and potentially more reproducible and quantitative, and thereby greatly increses the scope for precise molecular diagnosis in single gene and genetically complex diseases.

ACKNOWLEDGMENT

We thank Dr. Sheng Zhong and Dr. Keith Robertson at UF Medical School for providing us with the biological sample. This work was supported by NSF NIRT and NIH grants. L.W. receives support as an ACS Division of Analytical Chemistry Graduate Student Fellow sponsored by GlaxoSmithKline.

Supporting Information Available: Reagents, instruments, and experimental details. This material is available free of charge via the Internet at http://pubs.acs.org.

LITERATURE CITED

(1) Hardiman, G. (2003) Microarray technologies 2003—an overview. *Pharmacogenomics 4,* 251−256.

(2) Che, S. L., and Ginsberg, S. D. (2004) Amplification of RNA transcripts using terminal continuation. *Lab. Invest. 84,* 131−137.

(3) Eberwine, J., Yeh, H., Miyashiro, K., Cao, Y. X., Nair, S., Finnell, R., Zettel, M., and Coleman, P. (1992) Analysis of gene expression in single live neurons. *Proc. Natl. Acad. Sci. U.S.A. 89,* 3010−3014.

(4) Mirnics, K., and Pevsner, J. (2004) Progress in the use of microarray technology to study the neurobiology of disease. *Nat. Neurosci. 7,* 434−439.

(5) Mirnics, K., Middleton, F. A., Lewis, D. A., and Levitt, P. (2001) Analysis of complex brain disorders with gene expression microarrays: schizophrenia as a disease of the synapse. *Trends Neurosci. 24*, 479−486.
(6) Taton, T. A., Mirkin, C. A., and Letsinger, R. L. (2000) Scanometric DNA array detection with nanoparticle probes. *Science 289*, 1757−1760.
(7) Zhou, X. C., and Zhou, J. Z. (2004) Improving the signal sensitivity and photostability of DNA hybridizations on microarrays by using dye-doped core-shell silica nanoparticles. *Anal. Chem. 76*, 5302−5312.
(8) Gerion, D., Chen, F. Q., Kannan, B., Fu, A. H., Parak, W. J., Chen, D. J., Majumdar, A., and Alivisatos, A. P. (2003) Room-temperature single-nucleotide polymorphism and multiallele DNA detection using fluorescent nanocrystals and microarrays. *Anal. Chem. 75*, 4766−4772.
(9) Tan, W. H., Wang, K. M., He, X. X., Zhao, X. J., Drake, T., Wang, L., and Bagwe, R. P. (2004) Bionanotechnology based on silica nanoparticles. *Med. Res. Rev. 24*, 621−638.
(10) Zhao, X. J., Bagwe, R. P., and Tan, W. H. (2004) Development of organic-dye-doped silica nanoparticles in a reverse microemulsion. *Adv. Mater. 16*, 173−176. Zhao, X. J., Tapec, R., and Tan, W. H. (2003) Ultrasensitive DNA detection using highly fluoresecent bioconjugated nanoparticles. *J. Am. Chem. Soc. 125*, 11474−11475.
(11) Santra, S., Wang, K. M., Tapec, R., and Tan, W. H. (2001) Development of novel dye-doped silica nanoparticles for biomarker application. *J. Biomed. Opt. 6*, 160−166. Santra, S., Zhang, P., Wang, K. M., Tapec, R., and Tan, W. H. (2001) Conjugation of biomolecules with luminophore-doped silica nanoparticles for photostable biomarkers. *Anal. Chem. 73*, 4988−4993.
(12) Wang, L., Yang, C. Y., and Tan, W. H. (2005) Dual-luminophore-doped silica nanoparticles for multiplexed signaling. *Nano Lett. 5*, 37−43.
(13) Wang, L., and Tan, W. H. (2006) Multicolor FRET silica nanoparticles by single wavelength excitation. *Nano Lett. 6*, 84−88.

BC060365U

ARTICLES

High-Throughput System for Analyzing Ligand-Induced Cofactor Recruitment by Vitamin D Receptor

Midori A. Arai,[†,⊥] Ken-ichi Takeyama,[‡] Saya Ito,[‡] Shigeaki Kato,[‡] Tai C. Chen,[§] and Atsushi Kittaka*[,†]

Faculty of Pharmaceutical Sciences, Teikyo University, Sagamiko, Kanagawa 199-0195, Japan, Institute of Molecular and Cellular Bioscience, The University of Tokyo, Yayoi, Tokyo 113-0032, Japan, and Boston University School of Medicine, Boston, Massachusetts 02118. Received April 30, 2006; Revised Manuscript Received February 4, 2007

A high-throughput screening system for analyzing small molecule-induced coactivator (CoA) recruitment by the vitamin D receptor (VDR) has been developed. The vitamin D-induced protein−protein interactions between VDR and fluorophore (Cy3 or Cy5)-labeled TIF2 or SRC-1 were successfully detected by using a new HCHO fixing method of the protein complex on microplates. The results obtained from this screening of our synthetic vitamin D analogues suggest that the CoA-recruiting activities play an important role in determining the biological activity of various vitamin D analogues and explain the discrepancies between the VDR binding affinity and their biological activity.

INTRODUCTION

The superfamily of nuclear receptors (NRs) activates transcription by recruiting coactivators in a ligand-dependent manner to assemble regulatory complexes on target genes (*1*, *2*). The structure of a NR comprises four regions (A/B, C, D, and E/F) including a highly conserved DNA-binding domain and a C-terminal ligand-binding domain (LBD). This C-terminal E/F region contains the activation function-2 (AF-2) motif that mediates ligand-dependent transcriptional activation. The steroid hormones, thyroid hormone, retinoic acids, and 1α,25-dihydroxyvitamin D_3 [1α,25$(OH)_2D_3$] all bind to their respective NRs, which include the androgen receptor, estrogen receptors, retinoic acid receptors, retinoid X receptors, and the vitamin D receptor (VDR). 1α,25$(OH)_2D_3$ (Figure 1A, **1**), the active form of vitamin D, binds specifically to VDR and plays a vital role in calcium homeostasis (*3*, *4*), osteoclastogenesis (*5*, *6*), keratinocyte differentiation (*7*, *8*), phosphate homeostasis (*9*), immune response, cellular proliferation, differentiation, and apoptosis (*10*, *11*).

Crystal structures of the VDR-LBD, alone and in complex with its ligands (*12*), with coactivator peptides (*13*), or as heterodimers, have been reported (*14*). The LBD is generally a three-layered α-helical sandwich of α-helices (H1−H12). When the ligand binds to LBD, H12 moves to seal the ligand-binding cavity, creating the AF-2 motif and a hydrophobic cleft (Figure 1B). This hydrophobic region, together with other surface residues, accommodates the receptor interaction domain (RID) of coactivators (*15*, *16*), such as transcriptional factor 2 (TIF2) (*17*), steroid receptor coactivating factor 1 (SRC-1) (*18*), TRAP220 (*19*), and AIB-1 (*20*) (Figure 1C). The RID includes short helical regions called "NR boxes", which contain the consensus sequence LXXLL (where X is any amino acid). The resulting conformational changes in the VDR lead to the removal of corepressors and the recruitment of various coactivators followed by histone acetylation and target gene promoter activation (*21*).

The active form of vitamin D or its analogues have been used clinically for treating psoriasis (*22*), osteoporosis (*23*, *24*), and secondary hyperparathyroidism (*25*). Furthermore, 1α,25-$(OH)_2D_3$ or its analogues have been shown to inhibit the proliferation of breast, colon, and prostate cancer cells in cultures and tumor cell growth in animal models and stimulate HL-60 cell differentiation. However, the mechanism of interaction between ligand-inducible NRs and cofactor proteins (coactivator, coregulator, and corepressor) remains unknown except in a few cases (*26*, *27*). Such ligand-induced cofactor recruitment has been investigated in cells using a two-hybrid assay and transactivation activity under the expression of a specific coactivator. For direct detection of the complex, a gel shift assay using radio-labeled vitamin D response element and a pull-down assay of radiolabeled coactivator have been used. Other methods using flow cytometry (*28*) and fluorescence resonance energy transfer (*29*, *30*) have also been reported.

A high-throughput system would be extremely useful for examining the correlation between molecular mechanisms and the phenotypes induced by small ligands. Despite the growing success in forward and reverse chemical genetics studies, including protein microarrays, small-molecule microarrays, and cell-based high-throughput assays (*31*, *32*), it remains a key challenge to develop such a system for analyzing ligand-induced interactions between NRs and cofactors. Nishikawa and coworkers reported excellent pioneering work on a high-throughput detection system that used alkaline phosphatase-fused TIF2 on the microplate (*33*). Here we describe a rapid in vitro high-throughput system to examine ligand-induced coactivator (CoA) recruitment using fluorophore-labeled cofactors and a formaldehyde (HCHO)-based fixing method (Figure 2). Moreover, using this system, we are able to explain some of the discrep-

* Corresponding author. akittaka@pharm.teikyo-u.ac.jp.
[†] Teikyo University.
[‡] The University of Tokyo.
[§] Boston University School of Medicine.
[⊥] Current address: Chiba University, Inage, Chiba, 263-8522, Japan.

10.1021/bc0601121 CCC: $37.00 © 2007 American Chemical Society
Published on Web 04/05/2007

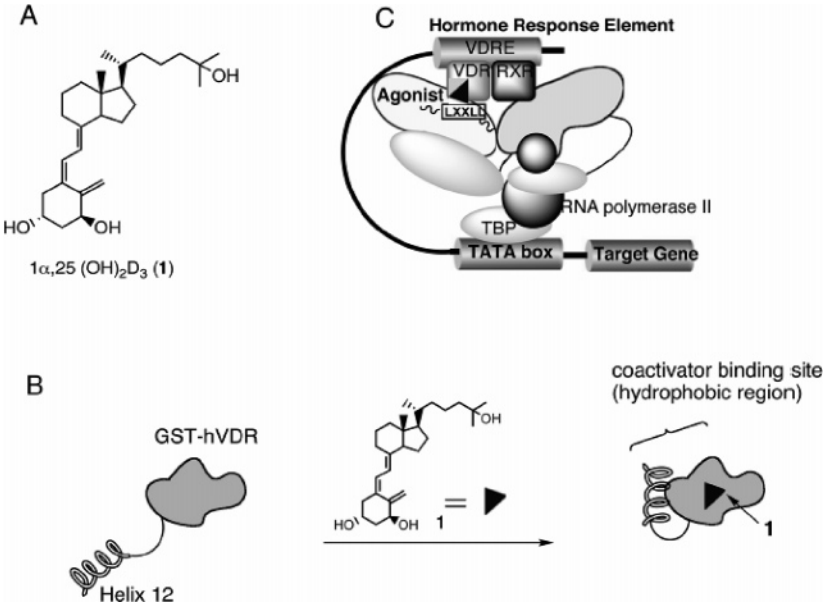


Figure 1. Models for the mechanism of action of vitamin D_3 derivatives on VDR. (A) Structure of the natural active hormone 1α,25 $(OH)_2D_3$ (**1**). (B) Conformational change on VDR induced by ligand binding. (C) Model for **1**-induced assembly of transcriptionally active regulatory complexes on target genes.

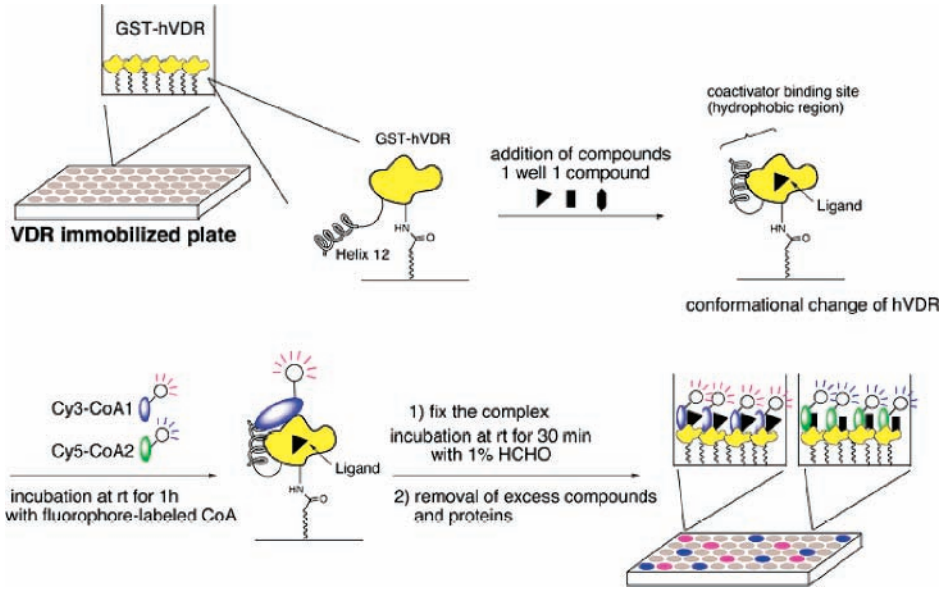


Figure 2. A diagram for the high-throughput detection of VDR-fluorophore-labeled CoA with small molecules on the microplate.

ancies between VDR binding affinity and the biological activity of our original vitamin D_3 analogues.

EXPERIMENTAL PROCEDURES

Preparation of Plasmids. pGEXhVDR$_{4-427}$, which contains GST fused human VDR, was provided by Prof. S. Kato. pGEXhTIF2$_{609-907}$; GST fused at N-terminal a human TIF2 fragment (RID) containing amino acids 609−907 was prepared by subcloning pcDNA3-hTIF2 (full length) plasmid as a template by PCR. This protein also has a flag tag between GST and TIF2 (RID). The primers for PCR are as follows: forward-primer, 5′-GGGGGATCCATGGACTACAAGGACGATGATGACAAGAAGGAAACAAATGAC-3′, reverse-primer, 5′-GGGGAATTCTCAGTTTCTGATTGGTGG-3′. The PCR-amplified DNA fragment was digested with *Bam*HI and *Eco*RI and ligated with pGEX4T-1 expression vector (Pharmacia) digested with *Bam*HI and *Eco*RI to generate pGEXhTIF2$_{609-907}$. pGEXhSRC-1$_{290-567}$; GST fused at N-terminal a human SRC-1 fragment (RID) containing amino acids 290−567 was prepared by subcloning pcDNA3-hSRC-1 plasmid as a template by PCR. This protein also has a flag tag between GST and SRC-1 (RID). The primers for PCR are as follows: forward-primer, 5′-GGGGAATTCATGGACTACAAGGACGATGATGACAAGTCTTCAGGAGGTTCT-3′, reverse-primer, 5′-AGGGCTCGAGTGATCAGTTTCATCTTT-3′. The PCR-amplified DNA fragment was digested with *Eco*RI and *Xho*I and ligated with pGEX4T-1 expression vector (Pharmacia) digested with *Eco*RI and *Xho*I to generate pGEXhSRC-1$_{290-567}$.

Expression and Purification of Recombinant GST-Proteins. *E. coli* strain DH5α serves as a host for pGEXhVDR$_{4-427}$, or pGEXhTIF2$_{609-907}$ and pGEXhSRC-1$_{290-567}$. An overnight plateau phase culture of DH5α was used to inoculate fresh LB medium (Q-BIO gene) containing 50 μg/L ampicillin. Cells were grown at 25 °C to a density of OD_{600} of 0.4−0.6 and induced by 0.1 mM IPTG (isopropyl-1-thio-β-D-galactopyranoside) followed by incubation for an additional 3

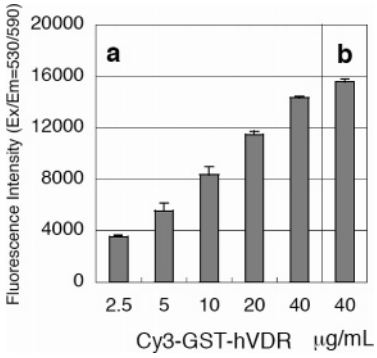


Figure 3. Immobilization of GST-hVDR on the microplate. The relationship between immobilized Cy3-GST-hVDR (Cy3/protein = 2.1) and protein concentration added. a: 2 h incubation, b: overnight incubation. After incubation of various concentrations of Cy3-GST-hVDR, wells were washed and fluorescence intensity was determined.

h at 18 °C. The cells were harvested and were lysed by sonication. The lysate was centrifuged at 37 000 rpm for 30 min at 4 °C. The resulting supernatant was added to prewashed glutathione sepharose 4B beads (Amersham Biosciences) and gentry mixed at 4 °C for 30 min. The beads obtained after centrifugation (3200 rpm, 5 min, at 4 °C) were washed 5 times (1000 rpm, 1 min, at 4 °C) with PBS-Triton X-100 buffer (PBS plus 1% Triton X-100). The recombinant proteins (GST-VDR_{4-427}, GST-$hTIF2_{609-907}$, and GST-$hSRC\text{-}1_{290-567}$) were eluted with 30 mM gluthatione buffer (50 mM Tris·HCl pH 8.8) and then dialyzed against PBS buffer using Slide-A-Lyzer^R Dialysis Cassette (Extra Strength, 10 000 MWCO, 0.5−3 mL capacity; Pierce). The recombinant proteins were estimated to be greater than 90% pure by SDS-PAGE.

Preparation of GST-hVDR Bound Microplate. Typical procedure: Nunc Immobilizer Amino 96 well Plate, white (Nalge Nunc Int., New York) was used for immobilizing GST-hVDR. The microplate wells were incubated with 100 μL of GST-hVDR (100 μg/mL, PBS, or PBS plus 100 mM Na_2CO_3 pH 9.6 buffer) 2 h to overnight at 4 °C. The protein solution was removed, and then each well was washed twice with 200 μL of PBS-Tween buffer (PBST; PBS plus 0.05% Tween 20). To block remaining activated succinimidyl ester units on the well, the wells were incubated for 2 h at room temperature with 100 μL of 10 mM ethanolamine (in 100 mM Na_2CO_3 pH 9.6 buffer) and then washed two times with 200 μL of PBST. The microplate wells were incubated with 100 μL of Cy3-labeled-GST-hVDR in PBS (40 μg/mL, dye/protein = 2.1) overnight at 4 °C. After removal of protein solution, each well was washed twice with 200 μL of PBST and then dried under reduced pressure 2 h to overnight in the dark. For the experiments described in the left five bars of Figure 3A, the microplate wells were incubated with 50 μL of Cy3-GST-hVDR (5, 10, 20, 40 μg/mL, dye/protein = 2.1) for 2 h on ice, whereas b bar in the same panel depicts the wells incubated overnight at 4 °C. The protein solution was removed, and each well was washed twice with 200 μL of PBST followed by drying under reduced pressure overnight. Microplate Reader: Powerscan HT, Dainippon Pharmaceutical Co., LTD, or Fluoroskan Ascent, Thermo Electron Corporation. Cy3; excitation 530 nm, emission 590 nm. Cy5; excitation 590 nm, emission 645 nm.

Detection of GST-hVDR in the Microplate by Anti-hVDR Antibody. We checked immobilized GST-hVDR (without Cy dye) on a well by hVDR antibody (rat monoclonal antibody, NeoMerkers) and Cy3-conjugated secondary antibody (Cy3-anti-rat IgG, Jackson ImmunoResearch Lab. Inc.). After immobilizing GST-hVDR (100 μL of 100 μg/mL, overnight, 4 °C) to a Nunc Immobilizer Amino 96 well Black Plate (Nalge Nunc Int., New York), wells were washed three times with 200 μL of PBST. To block remaining activated surface on the well, wells were incubated for 2 h at room temperature with 200 μL of 10 mM ethanolamine (in 100 mM Na_2CO_3 pH 9.6 buffer). After washing three times with 200 μL of PBST, hVDR antibody in PBS was added to wells and incubated for 1 h at room temperature. After washing three times with 200 μL of PBST, Cy3-conjugated secondary antibody in PBS was added to wells, incubated for 1 h at room temperature, and then washed three times with 200 μL of PBST, dried, and detected by a microplate reader.

Preparation of Cy-Dye-Labeled GST-hVDR (full) or GST-hCoA (RID). The Cy dye-labeled proteins were prepared by mixing of protein in PBS solution with Cy3 or Cy5 bisfunctional dye reagents (succinimidyl ester type; Amersham Biosciences) in DMSO for 1h at 4 °C in the dark. Cy dye solution was made by adding 100 μL of DMSO to 1 vial of Cy dye reagent (Amersham Biosciences) and stored at −20 °C. Usually, 2−4 μL of DMSO solution was added to 1 mL of protein solution (0.4−0.5 mg/mL) in PBS. After incubation, the mixture was directly dialyzed with PBS at 4 °C to remove excess unreacted dye reagents using Slide-A-Lyzer Dialysis Cassette (Extra Strength, 10 000 MWCO, 0.5−3 mL capacity; Pierce). After overnight dialysis, PBS was replaced with fresh PBS and dialyzed for an additional 3 h. The ratio of dye/protein was obtained after the absorption for Cys3 (ϵ 150 000 M^{-1} cm^{-1}), Cys5 (ϵ 250 000 M^{-1} cm^{-1}), and protein were determined at the wavelength 552, 650, and 280 nm, respectively. For Cy dye-labeled CoAs, the buffer was changed to NET-N buffer (20 mM Tris·HCl pH 7.5, 200 mM NaCl, 1 mM EDTA, 0.05% Nonidet P-40) by using Microcon YM-10 (Millipore), before the assay.

Detection of Ligand-Dependent Interaction between VDR and the Cy-Dye-Labeled CoA (RID) on Microplates. To GST-VDR immobilized wells (after ethanolamine blocking) were added 50 μL of Cy3-GST-hTIF2 (RID) or Cy5-GST-hSRC-1 (RID) (100 μg/mL) and 2 μL of 2 mM vitamin D_3 derivative in EtOH solution (final concn 16−160 μM). For background, 2 μL of EtOH was added. After 1 h incubation at room temperature, the VDR-CoA complex with a ligand was fixed by adding 10 μL of 8% formaldehyde (HCHO) aq (final concn 1.3%) and incubated 30 min at room temperature. After removal of the mixture, the wells were washed once with 200 μL of NET-N buffer gently and dried under reduced pressure in the dark 1 h to overnight. The fluorescence intensity was detected by a microplate reader. Usually, the assays were carried out in three individual wells, and the mean value and SD were calculated.

Transactivation Assay. Human MCF-7 breast cancer cells were maintained in Dulbecco's modified Eagle's medium without phenol red (Sigma-Aldrich), supplemented with 5% FBS which had been stripped with dextran-coated charcoal. Cells were transfected with plasmids using Polyfect (QIAGEN) and OPTI-MEM (GIBCO) in 12-well Petri dishes. The following plasmids were used for transfection: a reporter plasmid (2 μg) containing the *GAL4* upstream activation sequence (17-mer [×2], β-globlin promoter, and chloramphenicol acetyltransferase gene [CAT]) was cotransfected with 0.5 μg of pM(GAL4-DBD)-rVDR(DEF) (*26*). As a reference plasmid for normalization, 24 ng of pRL-CMV plasmid (Promega) was used. $1\alpha,25(OH)_2D_3$ (**1**) or vitamin D analogues (**2**α−**4**β) were added to the medium at 6 h after transfection (ligand final concentration: 10^{-8} M). After 18 h, luciferase activity was determined using the Luciferase Assay System (Promega). The mean value and SD of three individual wells were calculated.

Antiproliferative Activity on Prostate Cells. Tritiated thymidine incorporation into DNA was used to determine the effect of vitamin D_3 analogues on the proliferation of PZ-HPV-7 cells, obtained from ATCC (ATCC, Manassas, VA). PZ-HPV-7

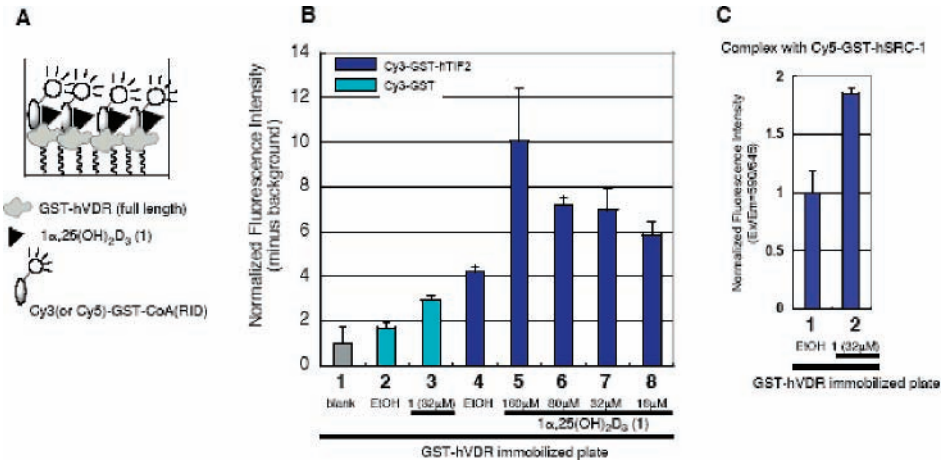


Figure 4. Detection of the ligand-dependent interaction between hVDR (full) and the fluorescent-labeled CoA (RID) on the microplate. (A) Model of the VDR complex with fluorescent labeled-CoA induced by 1α,25(OH)$_2$D$_3$ (**1**). (B) Detection of the complex between GST-hVDR and Cy3-GST-hTIF2 (RID) induced by 1α,25(OH)$_2$D$_3$ (**1**). All experiments were performed in a GST-hVDR immobilized plate. Excitation 530 nm, emission 590 nm. The value of background (without GST-hVDR) was subtracted. Fluorescence intensity of blank was normalized to 1. **1**; without Cy3-protein (blank). **2**; EtOH with Cy3-GST. **3**; 1α,25(OH)$_2$D$_3$ (**1**) with Cy3-GST. **4**; EtOH with Cy3-TIF2 (RID). **5**; 160 μM 1α,25(OH)$_2$D$_3$ (**1**) with Cy3-TIF2 (RID). **6**; 80 μM 1α,25(OH)$_2$D$_3$ (**1**) with Cy3-TIF2 (RID). **7**; 32 μM 1α,25(OH)$_2$D$_3$ (**1**) with Cy3-TIF2 (RID). **8**; 16 μM 1α,25(OH)$_2$D$_3$ (**1**) with Cy3-TIF2 (RID). (C) Detection of the complex between GST-hVDR and Cy5-GST-hSRC-1 induced by 1α,25(OH)$_2$D$_3$ (**1**). Excitation 590 nm, emission 645 nm. The value of background (without GST-hVDR) was subtracted. Fluorescence intensity with EtOH was normalized to 1. **1**; EtOH with Cy5-SRC-1 (RID). **2**; 32 μM 1α,25(OH)$_2$D$_3$ (**1**) with Cy5-SRC-1 (RID).

cells were grown on 24-well plates to 70% confluency in normal growth medium (*39*). Cells were then grown in the absence of growth factors for 24 h prior to the treatment with either ethanol vehicle (control), analogues, or 1α,25(OH)$_2$D$_3$ for 18 h (*39*). At the end of incubation, the medium was replaced with 0.5 mL of fresh basal medium containing 1 μCi of [methyl-^{3}H]-thymidine and incubated for 3h at 37 °C. ^{3}H-Thymidine incorporation into DNA was stopped by placing the 24-well plate on ice; unincorporated ^{3}H-thymidine then was removed and cells were washed three times with ice-cold PBS. DNA labeled with ^{3}H-thymidine was extracted by perchloric acid method as previously described (*39*) and counted using a beta-counter.

RESULTS

For preparing the VDR-microplates, glutathione-*S*-transferase-fused-hVDR (GST-hVDR) (full length) was first expressed in *Escherichia coli*, purified with glutathione sepharose 4B (Amersham Biosciences), and then immobilized to a microplate by a chemical linkage (*34*). To optimize a immobilize condition of GST-hVDR proteins, we applied increasing concentrations of Cy3-tagged GST-hVDR to a 96-well microplate (Nunc Immobilizer Amino Plate, Nalge Nunc Int.) (Figure 3) and incubated on ice for 2 h. After the incubation, the plates were washed with buffer and the fluorescence intensity of Cy3 was measured (Figure 3, left five bars). We further compared the length of incubation time. We found that overnight incubation at 4 °C increased immobilization (Figure 3, bar b) and generated more reproducible coating of the proteins (data not shown). We also monitored immobilized GST-hVDR (without Cy dye) by hVDR antibody and Cy3-conjugated secondary antibody. Although an immobilizing method using gluthatione-GST interaction principle was also investigated (*34*), the chemical immobilization method was shown to achieve better reproducibility.

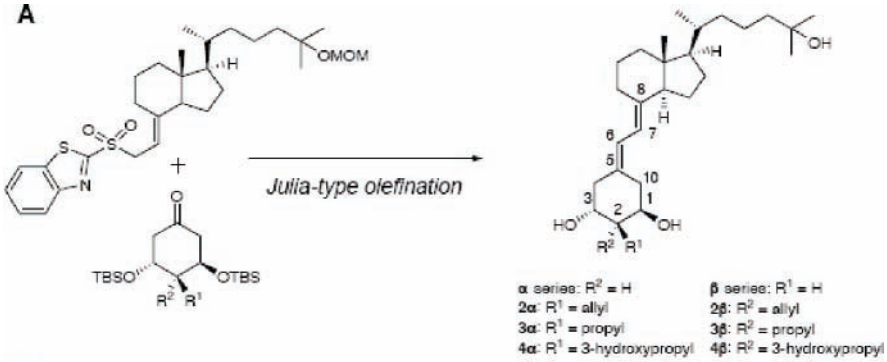
The Cy-dye-labeled CoAs (receptor interaction domain: RID) were prepared by incubating GST-CoAs (RID) with dye reagents (Amersham Biosciences) for 1 h at 4 °C. The buffer, incubation time, temperature, and concentration of CoA for the optimal ligand-induced VDR-CoA interaction were also investigated. It was found that NET-N buffer (20 mM Tris·HCl pH 7.5, 200 mM NaCl, 1 mM EDTA, 0.05% Nonidet P-40), which was used in the pull-down assay, generated a better VDR-CoA interaction. To detect the ligand-induced CoA recruitment by VDR, the dye-labeled GST-CoA (RID) was added to a GST-hVDR-immobilized well with natural hormone 1α,25(OH)$_2$D$_3$ (**1**). After 1 h incubation at room temperature, 10 μL of 8% HCHO (aq) solution (final concn 1.3%) was added to fix the VDR-CoA complex, which was then removed after 30 min incubation. The microplate was washed gently once with 200 μL of NET-N buffer and dried at room temperature under reduced pressure for 1 h in the dark. The fluorescence intensity was then measured using a microplate reader. This assay can also be accomplished with 2 h VDR immobilization. Although the fluorescence intensity of the complex was detectable without HCHO-fixation, the addition of HCHO greatly improved the reproducibility of the fluorescence intensity. HCHO is commonly used to fix animal tissues, presumably by making methylene bridges between proteins.

After Cy3-labeled GST was prepared, we checked the nonspecific interaction between the immobilized GST-hVDR and Cy3-GST under formaldehyde condition. As shown in Figure 4B (**1**−**3**), Cy3-GST did not bind to GST-hVDR specifically. The fluorescence value of **1** (nontreatment with Cy3-protein; blank value), **2** (EtOH), and **3** (1α,25(OH)$_2$D$_3$) were not significantly changed. On the other hand, when Cy3-GST-TIF2 (RID) was used, the significant increasing value was obtained (Figure 4B, **4**−**8**). The complex between GST-hVDR and Cy3-GST-TIF2 (RID), induced by 1α,25(OH)$_2$D$_3$ (**1**), was detected successfully. Because the ligands were prepared as ethanol solution, the solvent effect was investigated in **2** or **4**. Moreover, the relationships between the fluorescence intensity and concentration of 1α,25(OH)$_2$D$_3$ (**1**) was obtained (**5**−**8**). The complex between GST-hVDR and Cy5-GST-SRC-1 (RID), induced by 1α,25(OH)$_2$D$_3$ (**1**), was also detected successfully (Figure 4C).

DISCUSSION

Because vitamin D analogues have many biological properties, a selective activity profile is very important in the development of pharmacological agents. Many vitamin D analogues have been synthesized and their biological activities reported. Among them, 19-nor A-ring derivatives showed a selective activity profile, e.g., a high potency in inducing differentiation of malignant cells with very low or no bone

A



B

Compound	VDR binding affinity[a,b,c]	HL-60 cell differentiation[a,c,d]	Anti-proliferative activity on prostate cells [a,e]	Transactivation activity [a,f]
1	100	100	100	100
2α (allyl)	3	54	102	161
3α (propyl)	3	84	164	151
4α (hydroxypropyl)	100	3563	100000	157
2β (allyl)	0.15	20	338	187
3β (propyl)	0.3	32	165	142
4β (hydroxypropyl)	3	667	70115	156

[a] The potency of **1** was normalized to 100. [b] Bovine thymus VDR. [c] ref. 37. [d] Dtermined by NBT assay; relative activity was calculated at EC_{50}. [e]Cell type: PZ-HPV-7 cells, an immortalized normal prostate cell line (Ligand; 10^{-6}M). [f] Relative luciferase activity (Ligand; 10^{-5}M)

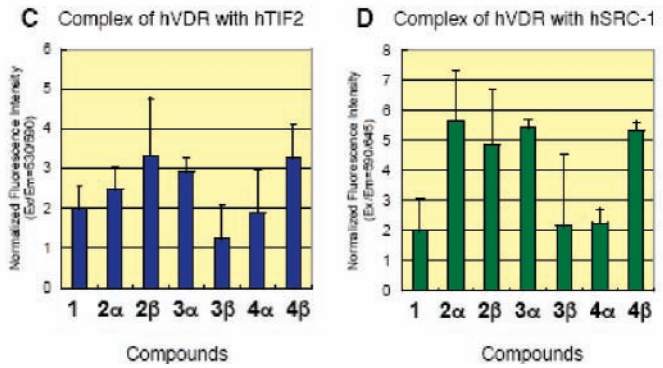


Figure 5. Synthesis and evaluation of 2-substituted-19-norvitamin D_3 derivatives (**2**α-**4**β). (A) Synthesis of 2-substituted-19-norvitamin D_3 derivatives (**2**α−**4**β) by Julia-type olefination (*37*). (B) Relative binding affinity and biological activities of **2**α−**4**β. (C) The recruitment of Cy3-GST-hTIF2 (RID) on GST-hVDR (full) by **2**α−**4**β. (D) The recruitment of Cy3-GST-hSRC-1 (RID) on GST-hVDR (full) by **2**α−**4**β. Cy3-GST-hTIF2 (RID) or Cy5-GST-hSRC-1 (RID) was added to a GST-hVDR (full) immobilized microplate well in the presence of vitamin D ligand (final 32 μM). After incubation at room temperature for 1 h, the GST-VDR (full):GST-CoA (RID) complex was fixed with 1.3% formaldehyde and washed. Background (EtOH) value was subtracted, and fluorescence intensity with 1α,25$(OH)_2D_3$ (**1**) was normalized to 2.

calcification activity (*35*, *36*). Kato et al. have reported the different selectivity of recruiting coactivators with vitamin D derivatives (*26*); however, in most cases, the relationship between biological activity and selectivity is unknown. A high-throughput system would be useful in analyzing this relationship.

We have previously reported efficient syntheses and biological evaluation of new 2-substituted-1α,25-dihydroxy-19-norvitamin D_3 analogues, 2α-allyl- (**2**α), 2β-allyl- (**2**β), 2α-propyl- (**3**α), 2β-propyl- (**3**β), 2α-(3-hydroxypropyl)- (**4**α), and 2β-(3-hydroypropyl)-1α,25-dihydroxy-19-norvitamin D_3 (**4**β), shown in Figure 5A (*37*). The A-ring precursor synthesized from (−)-quinic acid and CD-ring precursor were coupled by using Julia-type olefination to synthesize 19-norvitamin D_3 analogues in high yields. Previously, we have reported that **2**α, **3**α, **2**β, **3**β 19-norvitamin D_3 compounds had negligible VDR binding affinity compared to **1** but showed significant prodifferentiation activity in HL-60 cells. We also reported that **4**α and **4**β had either equivalent or 3% of VDR binding affinity as **1**, however, they respectively showed either 36- or 7-fold higher activity in HL-60 prodifferentiation assay (*37*). Similar discrepancy between VDR binding and antiproliferative activity was observed in prostate cells. For example, **2**α, **3**α, and **3**β had slightly higher antiproliferative activity than **1**, and **2**β, **4**α, and **4**β were 3-, 1000-, and 700-fold more active than **1** in inhibiting prostate cell proliferation (Figure 5B). Furthermore, these analogues were shown to have significantly higher VDR transactivation activity than that induced by the natural hormone **1** (Figure 5B).

Recently, Eelen et al. reported that the superagonists, 14-epi-analogues of 1α,25-dihydroxyvitamin D_3, are more potent inducers of VDR-CoA interactions (*27*). It is likely that our synthetic 19-norvitamin D_3 analogues (**2**α−**4**β) might be more effective inducers of CoAs recruitment by VDR. Therefore, we applied our novel high throughput analyzing system to evaluate the effects of 19-norvitamin D_3 analogues (**2**α−**4**β) on ligand-induced cofactor recruitment by VDR. As shown in Figure 5C, compounds **2**α, **2**β, **3**α, and **4**β showed stronger hTIF-2 recruitment than **1**. Compounds **2**α, **2**β, **3**α, and **4**β showed 2−3-fold stronger hSRC-1 recruitment than **1** (Figure 5D).

Interestingly, even when these derivatives showed low VDR-binding affinity, they had strong CoAs recruitment abilities. This

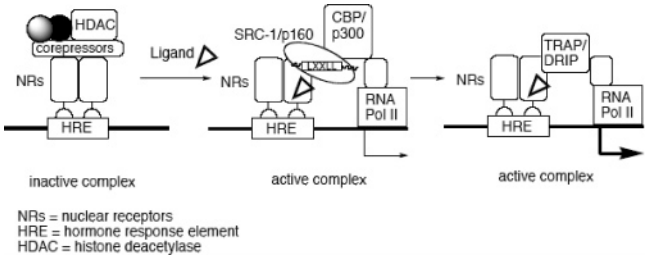


Figure 6. Combinatorial control of gene expression by NRs: Initial binding of ligand causes dissociation of corepressors. Conformational change of NRs makes binding site for SRCs and CBP. SRC and CBP complex results in local acetyltransferase activity and disruption of local nucleosomal structure. TRAP/DRIP directly interacts on the basal transcription machinery to effect transcriptional initiation.

suggests that CoAs recruitment is sensitive to the three-dimensional structure of the VDR; a small difference in conformation caused by change in ligand, and/or differences in the stability of protein−protein interactions, would be sufficient to affect CoAs recruitment ability. Compound **4**α was about 36-fold more potent in the induction of HL-60 cell differentiation than **1**, and even the weaker VDR binding ligand **4**β showed 7-fold higher cell differentiation activity than **1**. Many other cofactors, such as corepressors, HDACs, CBP/p300, and TRAP/DRIP, affect transactivation and combinatorial transcriptional initiation occurs (38 and Figure 6), so the precise molecular mechanism cannot be defined without additional data. However, it is obvious that the biological activity of vitamin D ligands must be influenced not only by VDR-binding activity but also by CoA-recruiting activity and selectivity. We believe that this high-throughput screening system for analyzing small molecule-induced CoA recruitment by VDR has great potential to become a powerful technique for examining the molecular mechanism of biological activities by small molecules.

In this study, we have developed a novel rapid system for analyzing ligand-induced cofactor recruitment by VDR using fluorophore-labeled CoA and HCHO fixation method. The high-throughput screening of small molecules can be utilized to differentiate different ligands that cause NR conformation changes. Moreover, since several different fluorophores (Cy3, Cy5 etc.) can be used, in principle, it will be possible to analyze simultaneously the interactions between the NR and several cofactors, and the cofactor selectivity of each ligand−NR complex. We believe that this method will have broad application for investigating ligand-based cofactor recruitment of NRs in vitro.

ACKNOWLEDGMENT

This study was supported by a Grant-in-Aid for Young Scientists (B) from the Ministry of Education, Culture, Sports, Science and Technology, Japan, (No. 16790027 and 18790012 to M.A.A.) and in part by Grants-in-Aid for Scientific Research (C) from Japan Society for the Promotion of Science (No. 15590021 and 17590012 to A.K.). A.K. also gratefully acknowledges Uehara Memorial Foundation for financial support. This work was also supported in part by a grant from US Army DAMD17-01-0025 (to T.C. Chen). We thank Dr. Yamashita and Dr. Maruyama (Teikyo University) for discussions.

LITERATURE CITED

(1) Chambon, P. (2005) The nuclear receptor superfamily: a personal retrospect on the first two decades. *Mol. Endocrinol. 19*, 1418−1428.

(2) Pike, J. W. and Shevde, N. K. (2005) The vitamin D receptor. In *Vitamin D* (Feldman, D., Pike, J. W., and Glorieux, F. H., Eds.) 2nd ed., pp 167−191, Elsevier Academic Press, San Diego.

(3) Wasserman, R. H. (2005) Vitamin D and the intestinal absorption of calcium: a view and overview. In *Vitamin D* (Feldman, D., Pike, J. W., and Glorieux, F. H., Eds.) 2nd ed., pp 412−451, Elsevier Academic Press, San Diego.

(4) Heaney, R. P. (2005) The vitamin D requirement in health and disease. *J. Steroid Biochem. Mol. Biol. 97*, 13−19.

(5) Harada, S. -I. and Rodan, G. A. (2003) Control of osteoblast function and regulation of bone mass. *Nature 423*, 349−355.

(6) Yasuda, H., Higashio, K., and Suda, T. (2005) Vitamin D and osteoclastogenesis. In *Vitamin D* (Feldman, D., Pike, J. W., and Glorieux, F. H., Eds.) 2nd ed., pp 665−685, Elsevier Academic Press, San Diego.

(7) Hosomi, J., Hosoi, J., Abe, E., Suda, T., and Kuroki, T. (1983) Regulation of terminal differentiation of cultured mouse epidermal cells by 1α,25-dihydroxyvitamin D_3. *Endocrinology 113*, 1950−1957.

(8) Bikle, D. D. (2005) Vitamin D: role in skin and hair. In *Vitamin D* (Feldman, D., Pike, J. W., and Glorieux, F. H., Eds.) 2nd ed., pp 609−630, Elsevier Academic Press, San Diego.

(9) Tenenhouse, H. S. and Portale, A. A. Phospate homeostasis. (2005). In *Vitamin D* (Feldman, D., Pike, J. W., and Glorieux, F. H., Eds.) 2nd ed., pp 453−475, Elsevier Academic Press, San Diego.

(10) van Leeuwen, J. P. T. M. and Pols, H. A. P. (2005) Vitamin D: cancer and differentiation. In *Vitamin D* (Feldman, D., Pike, J. W., and Glorieux, F. H., Eds.) 2nd ed., pp 1571−1597, Elsevier Academic Press, San Diego.

(11) DeLuca, H. F. (2004) Overview of general physiologic features and functions of vitamin D. *Am. J. Clin. Nutr. 80*, 1689S-1696S.

(12) Rochel, N., Wurtz, J. M., Mitschler, A., Klaholz, B., and Moras, D. (2000) The crystal structure of the nuclear receptor for vitamin D bound to its natural ligand. *Mol. Cell 5*, 173−179.

(13) Vanhooke, J. L., Benning, M. M., Bauer, C. B., Pike, J. W., and DeLuca, H. F. (2004) Molecular structure of the rat vitamin D receptor ligand binding domain complexed with 2-carbon-substituted vitamin D_3 hormone analogues and a LXXLL-containing coactivator peptide. *Biochemistry 43*, 4101−4110.

(14) Rochel, N., and Moras, D. (2005) VDR LBD crystal structures. In *Vitamin D* (Feldman, D., Pike, J. W., and Glorieux, F. H., Eds.) 2nd ed., pp 279−289, Elsevier Academic Press, San Diego.

(15) Nolte, R. T., Wisely, G. B., Westin, S., Cobb, J. E., Lambert, M. H., Kurokawa, R., Rosenfeld, M. G., Willson, T. M., Glass, C. K., and Miburn, M. V. (1998) Ligand binding and co-activator assembly of the peroxisome proliferator-activated receptor-γ. *Nature 395*, 137−143.

(16) Shiau, A. K., Barstad, D., Loria, P. M., Cheng, L., Kushner, P. J., Agard, D. A., and Greene, G. L. (1998) The structural basis of estrogen receptor/coactivator recognition and the antagonism of this interaction by tamoxifen. *Cell 95*, 927−937.

(17) Voegel, J. J., Heine, M. J. S., Zechel, C., Chambon, P., and Gronemeyer, H. (1996) TIF2, a 160 kDa transcriptional mediator for the ligand-dependent activation function AF-2 of nuclear receptors. *EMBO J. 15*, 3667−3675.

(18) Onate, S. A., Tsai, S. Y., Tsai, M. -J., and O'Mally, B. W. (1995) Sequence and characterization of a coactivator for the steroid hormone receptor superfamily. *Science 270*, 1354−1357.

(19) Ren, Y., Behre, E., Ren, Z., Zhang, J., Wang, Q., and Fondell, J. D. Specific structural motifs determine TRAP220 interactions with nuclear hormone receptors. (2000) *Mol. Cell Biol. 20*, 5433−5446.

(20) Anzick, S. L., Kononen, J., Walker, R. L., Azorsa, D. O., Tanner, M. M., Guan, X. -Y., Sauter, G., Kallioniemi, O. -P., Trent, J. M., and Meltzer, P. S. (1997) AIB1, a steroid receptor coactivator amplified in breast and ovarian cancer. *Science 277*, 965−968.

(21) Freedman, L. P. and Reszka, A. A. (2005) Vitamin D receptor cofactors: function, regulation, and selectivity. In *Vitamin D* (Feldman, D., Pike, J. W., and Glorieux, F. H., Eds.) 2nd ed., pp 263−277, Elsevier Academic Press, San Diego.

(22) Reichrath, J. and Holick, M. F. (2005) Psoriasis and other skin diseases. In *Vitamin D* (Feldman, D., Pike, J. W., and Glorieux, F. H., Eds.) 2nd ed., pp 1791−1804, Elsevier Academic Press, San Diego.

(23) Nishii, Y. and Okano, T. (2001) History of the development of new vitamin D analogs: studies on 22-oxacalcitriol (OCT) and 2β-(3-hydroxypropoxy)calcitriol (ED-71). *Steroids 66*, 137−146.

(24) Eastell, R. and Riggs, B. L. (2005) Vitamin D and osteoporosis. In *Vitamin D* (Feldman, D., Pike, J. W., and Glorieux, F. H., Eds.) 2nd ed., pp 1101−1120, Elsevier Academic Press, San Diego.

(25) Fukagawa, M. and Kurokawa, K. (2005) Renal failure and secondary hyperparathyroidism. In *Vitamin D* (Feldman, D., Pike, J. W., and Glorieux, F. H., Eds.) 2nd ed., pp 1821−1831, Elsevier Academic Press, San Diego.

(26) Takeyama, K. -I., Masuhiro, Y., Fuse, H., Endoh, H., Murayama, A., Kitanaka, S., Suzawa, M., Yanagisawa, J., and Kato, S. (1999) Selective interaction of vitamin D receptor with transcriptional coactivators by a vitamin D analog. *Mol. Cell. Biol. 19*, 1049−1055.

(27) Eelen, G., Verlinden, L., Rochel, N., Claessens, F., Clercq, P. D., Vandewalle, M., Tocchini-Valentini, G., Moras, D., Bouillon, R., and Verstuyf, A. (2005) Superagonistic action of 14-epi-analogs of 1,25-dihydroxyvitamin D explained by vitamin D receptor-coactivator interaction. *Mol. Pharmacol. 67*, 1566−1573.

(28) Iannone, M. A., Simmons, C. A., Kadwell, S. H., Svoboda, D. L., Vanderwall, D. E., Deng, S. -J., Consler, T. G., Shearin, J., Gray, J. G., and Pearce, K. H. (2004) Correlation between in vitro peptide binding profiles and cellular activities for estrogen receptor-modulating compounds. *Mol. Endocrinol. 18*, 1064−1081.

(29) Zhou, G., Cummings, R., Li, Y., Mitra, S., Wilkinson, H. A., Elbrecht, A., Hermes, J. D., Schaeffer, J. M., Smith, R. G., and Moller, D. E. (1998) Nuclear receptors have distinct affinities for coactivators: characterization by fluorescence resonance energy transfer. *Mol. Endocrinol. 12*, 1594−1604.

(30) Llopis, J., Westin, S., Ricote, M., Wang, J., Cho, C. Y., Kurokawa, R., Mullen, T. -M., Rose, D. W., Rosenfeld, M. G., Tsien, R. Y., and Glass, C. K. (2000) Ligand-dependent interactions of coactivators steroid receptor coactivator-1 and peroxisome proliferator-activated receptor binding protein with nuclear hormone receptors can be imaged in live cells and are required for transcription. *Proc. Natl. Acad. Sci. U.S.A. 97*, 4363−4368.

(31) Kim, Y. -K., Arai, M. A., Arai, T., Lamenzo, J. O., Dean, E. F., III, Patterson, N., Clemons, P. A., and Schreiber, S. L. (2004) Relationship of stereochemical and skeletal diversity to cellular measurement space. *J. Am. Chem. Soc. 126*, 14740−14745.

(32) Kanoh, N., Honda, K., Simizu, S., Muroi, M., and Osada, H. (2005) Photo-cross-linked small-molecule affinity matrix for facilitating forward and reverse chemical genetics. *Angew. Chem., Int. Ed. 44*, 3559−3562.

(33) Kanayama, T., Mamiya, S., Nishihara, T., and Nishikawa, J. -I. (2003) Basis of a high-throughput method for nuclear receptor ligands. *J. Biochem. 133*, 791−797.

(34) LaBaer, J. and Ramachandran, N. (2005) Protein microarrays as tools for functional proteomics. *Curr. Opin. Chem. Biol. 9*, 14−19.

(35) Sicinski, R. R., Rotkiewics, P., Kolinski, A., Sicinska, W., Prahl, J. M., Smith, C. M., and DeLuca, H. F. (2002) 2-Ethyl and 2-ethylidene analogues of 1,25-dihydroxy-19-norvitamin D_3: Synthesis, conformational analysis, biological activities, and docking to the modeled rVDR ligand binding domain. *J. Med. Chem. 45*, 3366−3380.

(36) DeLuca, H. F., Plum, L. A., Clagett-Dame, M., Shevde, N. K., Pike, J. W., and Sicinski, R. R. (2005) 2-Carbon-modified analogs of 19-nor-1α,25-dihydroxyvitamin D_3. In *Vitamin D* (Feldman, D., Pike, J. W., and Glorieux, F. H., Eds.) 2nd ed., pp 1543−1555, Elsevier Academic Press, San Diego.

(37) Ono, K., Yoshida, A., Saito, N., Fujishima, T., Honzawa, S., Suhara, Y., Kishimoto, S., Sugiura, T., Waku, K., Takayama, H., and Kittaka, A. (2003) Efficient synthesis of 2-modified 1α,25-dihydroxy-19-norvitamin D_3 with Julia Olefination: high potency in induction of differentiation on HL-60 cells. *J. Org. Chem. 68*, 7407−7415.

(38) McKenna, N. J. and O'Malley, B. W. (2002) Combinatorial control of gene expression by nuclear receptors and coregulators. *Cell 108*, 465−474.

(39) Chen, T. C., Persons, K., Liu, W. W., Chen, M. L., and Holick, M. F. (1995) The antiproliferative and differentiative activities of 1,25-dihydroxyvitamin D_3 are potentiated by epidermal growth factor and attenuated by insulin in cultured human keratinocytes. *J. Invest. Dermatol. 104*, 113−117.

BC0601121

DNA-Directed Assembly of Supramolecular Fluorescent Protein Energy Transfer Systems

Florian Kukolka,[†] Oliver Schoeps,[‡] Ulrike Woggon,*[,‡] and Christof M. Niemeyer*[,†]

Fachbereich Chemie Biologisch-Chemische Mikrostrukturtechnik and Fachbereich Physik, Universität Dortmund, Otto-Hahn Str. 6, D-44227 Dortmund, Germany. Received May 31, 2006; Revised Manuscript Received January 16, 2007

Fluorescent proteins with a wide variety of physicochemical properties have evolved in the past few years. The use of these proteins for applications in biomolecular nanosciences requires their precise positioning at the nanometer length scale. To address this challenge, we report here on the self-organization of DNA-tagged fluorescent probes to construct a set of photofunctional supramolecular complexes which include the enhanced yellow fluorescent protein (EYFP). The optical functionality is based on the strongly distance dependent fluorescence resonance energy transfer (FRET), occurring between the donor (EYFP) and an acceptor fluorophore, i.e., the fluorescent dye Atto647. The photophysical properties of four bimolecular FRET complexes, each possessing a well-defined donor−acceptor distance defined by the length of the interconnecting DNA backbone, are investigated by two-dimensional photoluminescence excitation spectroscopy (2D-PLE).

INTRODUCTION

The major goal of the development and investigation of artificial light-harvesting systems concerns the mimicry of the initial steps of incredibly efficient photon energy uptake and funneling toward a reaction center during photosynthesis. In addition to the general understanding of the fundamental principles of such complex reaction cascades, there is currently also a great interest in the development of photonic energy transfer systems, because such devices hold promise for applications in several research areas of nanotechnology, such as molecular photonics and bioelectronics (*1*). Several organic chromophores have already been used for photon energy uptake in artificial light-harvesting complexes, such as porphyrin derivatives (*2*), polypyridine complexes of d^6 metal ions (*2, 3*), or perylenes (*5*−*8*).

However, in order to fabricate well-defined arrangements of different chromophores, one major problem in the realization of complex superstructures concerns the precise control of the spatial arrangement of the various components within the functional unit (*1*). To address this problem, the biomimetic self-assembly of the individual compounds appears to be straightforward. For example, the extraordinary specific molecular recognition of complementary ssDNA sequences has already been utilized for the spatially defined organization of DNA-tagged molecular and colloidal components (*9*−*14*). The photophysical characterization of such arrangements of synthetic fluorophores assembled along short double-stranded (ds)DNA molecules has been the subject of current research. For example, up to five different organic fluorophores have been organized at the nanometer length scale by means of DNA hybridization to form a photonic wire (*15*−*19*). These systems revealed a unidirectional energy transport based on fluorescence resonance energy transfer (FRET) along an energy cascade.

* Prof. Dr. U. Woggon, Universität Dortmund, Fachbereich Physik, Otto-Hahn Str. 6, D-44227 Dortmund (Germany). E-mail: ulrike.woggon@uni-dortmund.de. Prof. Dr. C. M. Niemeyer, Universität Dortmund, Fachbereich Chemie, Biologisch-Chemische Mikrostrukturtechnik, Otto-Hahn Str. 6, D-44227 Dortmund (Germany). Telefax: Int. + 49 (0)231/755 7082. E-mail: christof.niemeyer@uni-dortmund.de.

[†] Fachbereich Chemie Biologisch-Chemische Mikrostrukturtechnik.

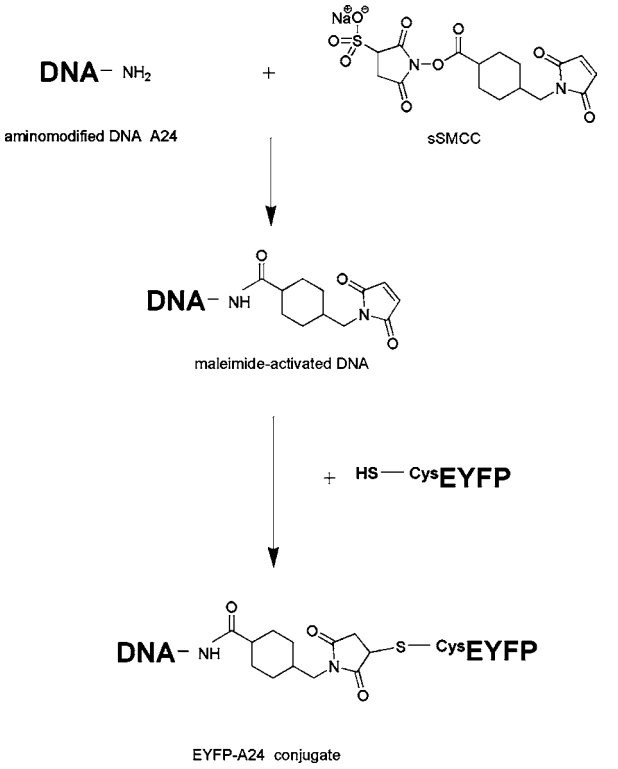
[‡] Fachbereich Physik.

We have recently suggested utilizing fluorescent proteins for the synthesis and investigation of artificial light-harvesting antennae systems (*20*). The most prominent example of fluorescent proteins is the naturally occurring green fluorescent protein from the north Pacific jellyfish *Aequorea victoria* (*av*GFP), which has been used extensively as a biological marker (*21*). A full range of fluorescent proteins with emission maxima ranging from blue to red are nowadays available. These are either mutants of the *av*GFP or derivatives of similar proteins from other marine organisms (*22*−*25*), and the ongoing discovery of novel proteins with different physicochemical characteristics suggests that the range of these interesting proteins is by far not fully exhausted yet. For example, fluorescent proteins with the ability of being reversibly photoswitched between a fluorescent and a nonfluorescent state have recently attracted attention (*26*−*28*). In addition, proteins, in general, can be tailored with a large variety of synthetic moieties, such as non-natural amino acids (*29*), to modulate their spectral properties and binding capabilities. Hence, one may anticipate that this panel of natural fluorophores should be well-suited as building blocks for artifical supramolecular antennae systems or as components of nanoscaled optical data storage devices. To initiate this novel approach, we recently reported on the synthesis of a semisynthetic covalent DNA−fluorescent protein conjugate, as a first step to the DNA-directed assembly of supramolecular fluorescent protein FRET systems (*20*).

We report here on the assembly and spectroscopic characterization of various unique FRET systems (FS), which were constructed by means of DNA hybridization using the enhanced yellow fluorescent protein (EYFP) as the donor (D) and the organic fluorescent dye Atto647 as the acceptor (A) for energy transfer. In these systems, the interchromophore distance of donor and acceptor can be conveniently changed by variation of the binding sites of the fluorophores at the DNA "carrier" helix. In contrast to another study based on single-molecule spectroscopy, in which donor and acceptor were assembled by hybridization of a DNA−dye and DNA−EYFP conjugate along a complementary DNA scaffold (*30*) to obtain two different complexes, we report here on the assembly of four different FRET systems in a more direct, bimolecular hybridization, thus allowing us to gradually change the distance between A and D.

10.1021/bc060143w CCC: $37.00 © 2007 American Chemical Society
Published on Web 03/23/2007

Scheme 1



The different FRET systems were characterized by two-dimensional photoluminescence excitation spectroscopy (2D-PLE). 2D-PLE is a powerful method to study electronic couplings and energy transfer between donor and acceptor states in FRET systems. The emission is monitored over a whole range of wavelengths instead of a narrow detection window, as in conventional, one-dimensional PLE. This enables one to display the full landscape of photoluminescence (PL) intensity as a function of the excitation energy and to analyze energy transfer within a multicomponent system. The mutual correlations between donor and acceptor states can be qualitatively identified from the magnitude of the corresponding off-diagonal signal in the spectrally resolved 2D intensity maps. From the experimental 2D contour plots, we were able to derive energy transfer efficiencies and to calculate the Förster radius R_0 for the EYFP−Atto647 system.

EXPERIMENTAL PROCEDURES

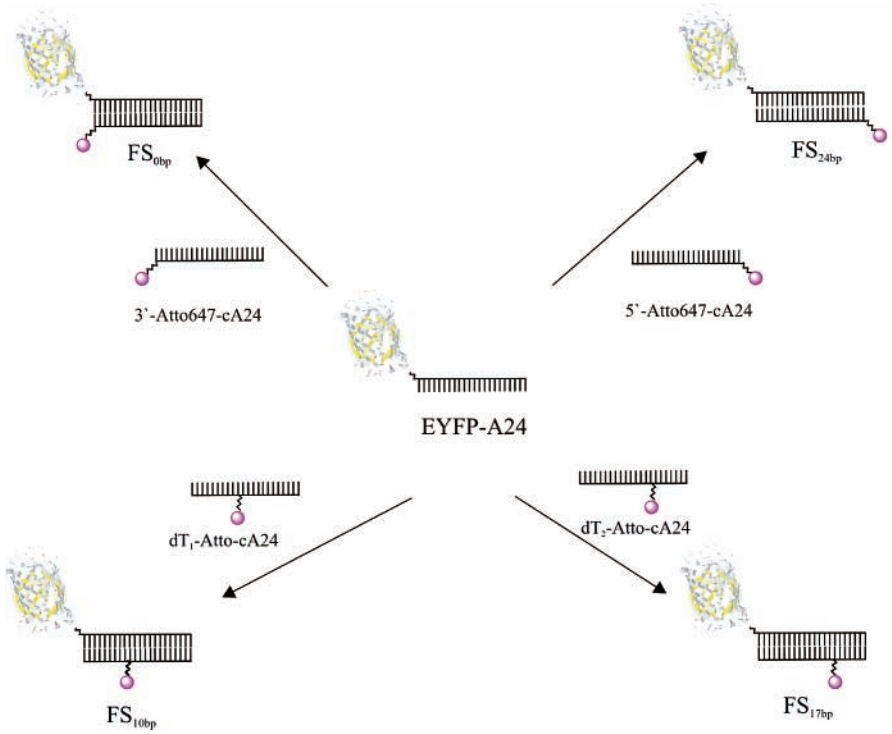
DNA−Chromophore Conjugates. Recombinant ^{Cys}EYFP was covalently coupled to the 5′-end of a 24mer oligonucleotide (sequence A24: 5′-TCC TGT GTG AAA TTG TTA TCC GCT-3′) yielding conjugate ^{Cys}EYFP−A24 similar to the method previously described (*20*). Because the two cystein groups of the native EYFP are not accessible for covalent coupling with DNA oligomers (*20*), a ^{Cys}EYFP mutant was created by site-directed mutagenesis bearing an extra cysteine residue at the C-terminal end, which is located at the protein's surface. The protein was expressed in *E. coli* and purified by affinity chromatography. The amino-modified oligonucleotides were first derivatized with the heterobifunctional cross-linker sulfo-succinimidyl-4-[*N*-maleimidomethyl]-cyclohexane-1-carboxylate (sSMCC), which comprises a maleimide and a N-hydroxy-succinimide (NHS) ester group, that are reactive toward thiols and primary amines, respectively (Scheme 1). The maleimide-containing DNA oligomers were then reacted with the ^{Cys}EYFP, and the conjugates were purified by anion-exchange chromatography and analyzed by UV/vis spectroscopy. The ratio of absorbances measured at 260 and 280 nm, respectively, was found to be 1.50, and this value was in good aggreement with a control solution comprising equimolar amounts of DNA A24 and the EYFP (1.53). In contrast, control samples containing either of the two components in a 2-fold excess, i.e., DNA/EYFP = 2:1 or DNA/EYFP = 1:2, revealed values of 1.61 and 1.41, respectively, thus confirming the 1:1 stoichiometric ration of DNA/EYFP in the ^{Cys}EYFP−A24 conjugate. Moreover, analysis of the ^{Cys}EYFP−A24 conjugate by SDS-PAGE showed a single band with a molecular weight of approximately 39 kDa, which is in good aggreement with the expected mass of a 1:1 conjugate (data not shown). The conjugates were stored in TETBS buffer (20 mM Tris-buffered saline containing 150 mM NaCl, 5 mM EDTA, 0.005% Tween-20, pH 7.5).

Atto647−DNA conjugates were purchased lyophilized from TIB MOLBIOL (Berlin, Germany), dissolved in H_2O at a concentration of 100 μM, and stored at −20 °C until use. In these conjugates, the Atto647−fluorophore is attached through a C_6-linker to the 3′-end, through a C_7-linker to the 5′-end, or through a C_2-linker at two different thymine bases dT (italicized) of the 24mer oligonucleotide cA24 (sequence: 5′-AGC GGA *T*AA CAA T*T*T CAC ACA GGA-3′), which is fully complementary to sequence A24, leading to four different conjugates: 3′-Atto−cA24, 5′-Atto−cA24, dT_1-Atto−cA24, and dT_2-Atto−cA24 (Scheme 2). According to manufacturer's information, the DNA oligomers contained one Atto647 dye per DNA oligomer. Analysis of the Atto-labeled oligonucleotides by MALDI-TOF mass spectrometry indicated the expected molecular weights with slight deviations of less than 2%. The 1:1 stoichiometric ratio was additionally confirmed, on one hand, by quantifying the absorbances of the Atto647−cA24 conjugates at both 260 and 649 nm and the independent calculation of conjugate concentrations. On the other hand, the Atto647−cA24 conjugates were titrated in the course of the assembly of the FRET system with the complementary ^{Cys}EYFP−A24. These titrations showed a maximum in the quenching of the EYFP fluorescence as well as in the FRET-based Atto647 emission at the stoichiometric ratio of 1:1, thus confirming the 1:1 stoichiometry of both conjugates (data not shown).

Assembly of FRET Systems. The four different supramolecular FRET systems with differing numbers of base pair separations ($FS_{0bp-24bp}$, Scheme 2) were assembled by hybridization of ^{Cys}EYFP−A24 with the Atto647-labeled oligomers, such that the variation in donor and acceptor distance should be reflected in different FRET efficiencies. To this end, the ^{Cys}EYFP−A24 conjugate and Atto−oligomers were mixed in TETBS at a final concentration of 0.5 μM. For higher hybridization efficiencies, the samples were heated up to 50 °C for 5 min, slowly cooled to room temperature, and then stored at 4 °C until used in PLE measurements. As controls, the single fluorophore DNA conjugates were hybridized with complementary unlabeled DNA, and an EYFP−DNA conjugate (^{Cys}EYFP−cA24) containing the same DNA sequence as the Atto647−DNA conjugates was incubated with the Atto−oligomer species.

2D-PLE Measurements. For measuring the PLE spectra, the sample was illuminated using a 150 W xenon lamp spectrally filtered by a 1 m monochromator. The collected luminescence was spectrally dispersed in a 0.25 m spectrometer and recorded with an optical multichannel analyzer, yielding spectra over the full visible wavelength range. These spectra were then normalized to the photon flux at the excitation wavelength, which was monitored by a photodiode. The excitation wavelength was scanned over 240 nm with a step size of 1 nm. All signals were corrected with respect to the spectral sensitivity of both the excitation monitoring and the fluorescence detection systems.

Scheme 2



We present the PLE signals of the individual samples as two-dimensional, color-coded plots of the emission intensity, spectrally dispersed along the *x*-axis, while the *y*-axis represents the different excitation wavelengths. The diagonal line, stemming from scattered excitation light, indicates the resonance case of excitation energy being equal to the detection energy.

2D-PLE of the Fluorescent Protein EYFP. In order to establish the major constituent of our FRET system, we initially investigated the internal energy relaxation pathway of the EYFP. An ideal donor system, in general, should emit at a single, homogeneously broadened ground-state energy with intensities proportional to the density and oscillator strength of the absorbing states of the corresponding donor absorption spectrum. The photoluminescence (PL) line width of the emitting state should not be influenced by an internal fine structure of the optical ground state, which would cause inhomogeneous broadening by a superposition of several optically allowed and dark states. Figure 1 shows the measured 2D-PLE intensity map of solely the EYFP−A24 donor conjugate. The excitation wavelength was tuned from short excitation wavelengths/high energies (460 nm/2.694 eV) toward longer wavelengths/lower energies (535 nm/2.316 eV) in steps of 1 nm while recording for each excitation the corresponding emission spectrum within a detection range between 500 and 620 nm. As shown in Figure 1 (left), the EYFP emission has a maximum at 528 nm with an asymmetric line shape showing a long spectral tail toward longer wavelengths, reaching the zero level around 650 nm. The signal on the upper left side of the diagonal line might indicate the presence of excited vibrational degrees of freedom in the sample, that contribute to the complete energy balance for radiative recombination. This observation is not affected by DNA, since it is observed in samples consisting of the fluorophores only. To analyze the PL line shape as a function of excitation energy, we normalized the full emission spectra with respect to the number of exciting photons derived from the absorption strength at the corresponding wavelength measured before in the same experimental setup. The result is shown in Figure 1 (right). It confirms that the shape of the emission spectrum is independent of the excitation energy, thereby ruling out a fine structure that may interfere with an energy transfer signature in the 2D-PLE plot of the combined donor−acceptor system.

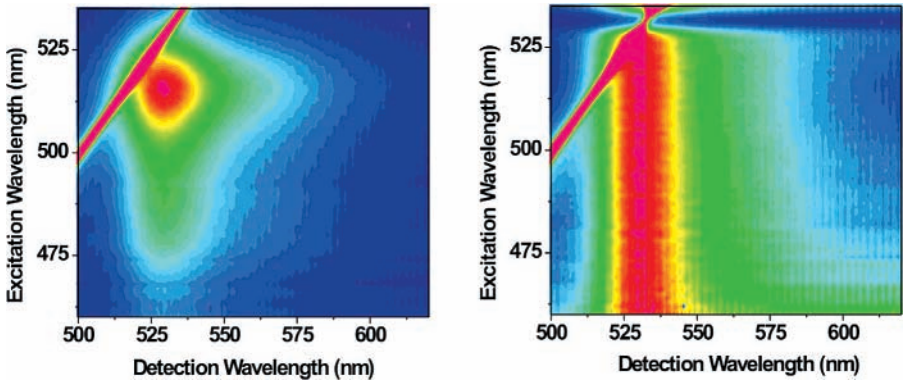


Figure 1. Left: 2D-PLE of the EYFP donor in color-coded (linear) intensities covering a range from 0 (blue) to 50 000 (red) counts. Right: 2D-PLE of the EYFP donor normalized with respect to the number of absorbing states showing an excitation-independent emission line shape and emission maximum. The color-coded (linear) intensity covers a range from 0 (blue) to 1 (red). The intensity which is recorded as the diagonal signal arises from scattered excitation light.

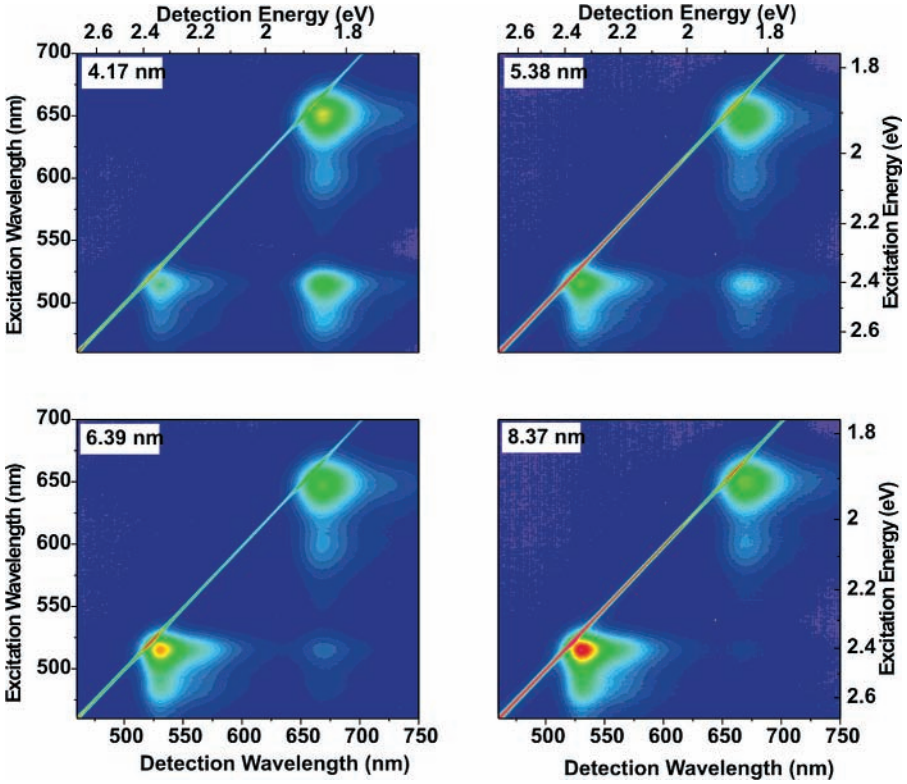


Figure 2. 2D-PLE signals of the different FRET systems FS_{0bp}, FS_{10bp}, FS_{17bp}, and FS_{24bp} with the corresponding donor−acceptor distances. The signature at the upper right corner of each graph arises from the Atto647 acceptor, and the signature at the lower left corner from the EYFP donor. The off-diagonal signature at the acceptor emission energy (lower right corner) shows the emission due to transfer. A distance-dependent quenching of the donor emission is accompanied by an enhanced acceptor PL.

RESULTS AND DISCUSSION

2D-PLE of the Donor−Acceptor System EYFP−Atto647. In the four different supramolecular FRET systems ($FS_{0bp-24bp}$; for a schematic representation of the structures, see Scheme 2), the donor and acceptor distance was increased stepwise from 0 over 10, 17, to 24 base pairs (bp), by varying the binding site of the Atto dye on the DNA in the corresponding Atto647−DNA conjugates. As will be discussed below, these variations in the number of base pairs leads to donor−acceptor distances of 4.17, 5.38, 6.39, and 8.37 nm, respectively. The 2D-PLE spectra of these four different supramolecular FRET systems are shown in Figure 2. In case of a too large donor−acceptor distance, no transfer was expected, and the 2D-PLE signals of donor and acceptor should appear as two independent features, namely, the above-discussed 2D-PLE of the control EYFP−A24 in addition to a similar spectral feature of the acceptor Atto647. Indeed, such a pattern was clearly observed for FS_{24bp}, with a donor−acceptor separation of 8.37 nm. If the donor−acceptor pair is separated by a distance that allows for significant FRET, a third feature should be visible in the PLE plot. It appears as PL intensity at the spectral position of the acceptor's preferential recombination wavelength, while exciting the system at the wavelength of maximum donor absorption (see the 2D-PLE plot for FS_{0bp}; Figure 2). The strength of that off-diagonal signal is considered to be the fingerprint of energy transfer. For a quantitative analysis, the transfer efficiency is extracted from the luminescence intensity F of both emitting species, analyzing either the intensity at the peak positions or the volume under the curve down to 50% of the maximum. The transfer efficiency E is then extracted as $E = [1 + (F_D\eta_A/F_A\eta_D)]^{-1}$. For the FRET systems shown in Figure 2, we obtained values for E of 0.79, 0.53, 0.26, and 0.074 for FS_{0bp}, FS_{10bp}, FS_{17bp}, and FS_{24bp}, respectively.

More obvious information about the energy transfer pathways and the absolute transfer efficiency can be obtained by transforming the PLE signals into a loss/gain statistic by subtracting the intensities of the control samples, i.e., the hybridized samples of the individual fluorophores ^{Cys}EYFP−A24 + bcA24 and Atto647−cA24 + bA24 (see Figure 3).

Figure 3 shows the spectral window of the differential 2D-PLE around the donor absorption. The violet color code indicates fluorescence quenching, while the red color code corresponds to absolute gain. With increasing donor−acceptor distance, the donor emission becomes less quenched while the acceptor gain decreases until the transfer is completely hindered by a too large donor−acceptor separation. In case the EYFP was quenched via another competitive channel without significant transfer to the Atto647 acceptor, we would expect a strong negative (violet) signal at the donor emission in the differential 2D-PLE plot but no (or weak) positive (red) signal at the acceptor energy. Since such a feature and also a significant gain at another spectral position was not observed, we again concluded that the energy of the EYFP donor is directly transferred to the Atto647 acceptor in the FRET systems FS_{0bp}, FS_{10bp}, and FS_{17bp}.

FRET Efficiencies and Determination of the Donor−Acceptor Distance. To estimate the distance between the donor and the acceptor, one has to take into account the helical nature of double-stranded DNA. Under the conditions used in our experiments, we expect the DNA to adopt the regular conformation of the right-handed B-DNA helix. In this conformation, the DNA has a diameter of 2 nm, the increase in height per base pair is 0.34 nm, and ten base pairs comprise one entire helical turn. To confirm the assumption that the DNA in the FRET systems is indeed in the B-form conformation, we measured CD spectra of FS_{0bp} and a sample containing an equimolar mixture of unlabeled A24 and cA24 (Figure 5). Both curves display strong negative and positive cotton effects around 250 and 280 nm, respectively. This pattern is characteristic for B-form DNA and is in agreement with previously reported similar systems (*16*). Since the persistence length of duplex

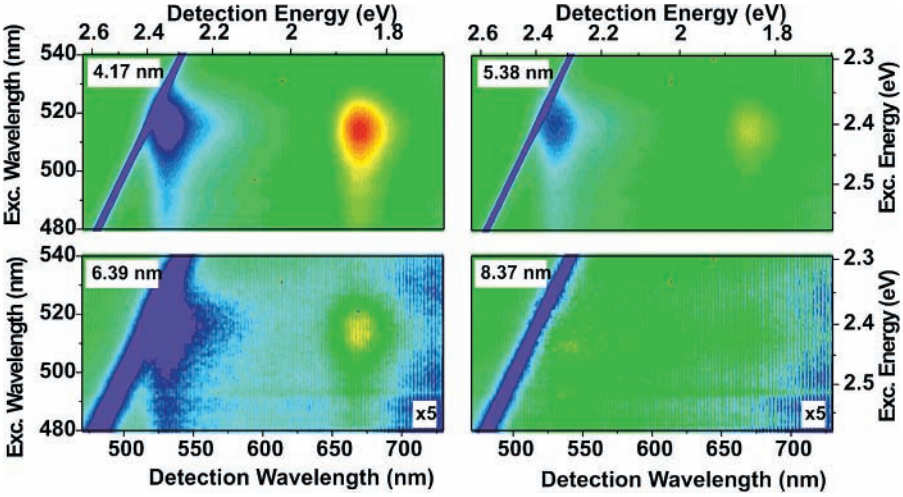


Figure 3. Differential 2D-PLE spectra obtained by subtracting the PLE signals of the control samples (isolated, hybridized donor and acceptor) from the PLE of the FRET systems. The linear color scale shows quenching (violet), enhancement (red), and constancy (green) of the emission intensities on a scale corresponding to −50% to +50% for the top row and −10% to +10% for the bottom row.

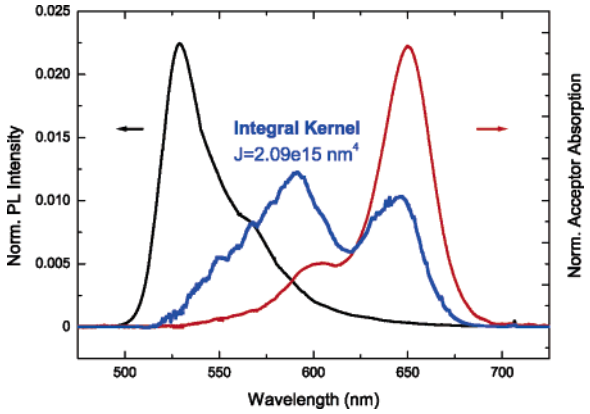


Figure 4. Measured donor emission spectrum (black) and acceptor absorbance (red). The blue curve shows the resulting overlap integral kernel yielding $J = 2.09 \cdot 10^{15}$ nm^4.

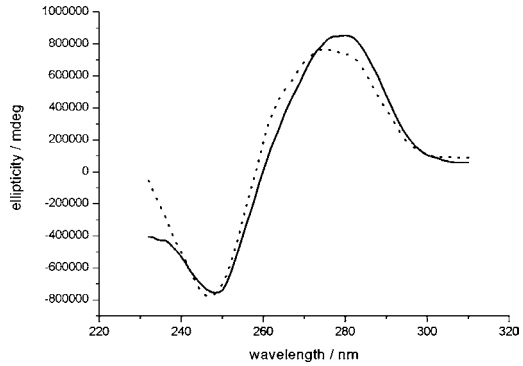


Figure 5. CD spectra of FRET system FS_{0bp} (solid curve) and an equimolar mixture of unlabeled A24 and cA24 (dotted line).

DNA is about 50 nm (*31*), the 24 bp dsDNA system with a nominal length of 8.16 nm studied here can be regarded as a rigid-rod linear system. Donor and acceptor positions were therefore represented as vectors in a cylindrical coordinate system (*32*) with the symmetry axis of the DNA as the *z*-axis and the DNA−donor link defining the direction of the *x*-axis (see schematic representation in Figure 6). The absolute value of the donor and acceptor connecting vector then represents the distance. To calculate the values R_D and R_A for the distances between the *z*-axis and the donor and acceptor, respectively, one first needs to estimate the Förster distance for the donor and acceptor pair. According to Förster theory, the Förster radius R_0 can be calculated by

$$R_0^{\,6} = 8.79 \cdot 10^{-5} \cdot [Q_D \kappa^2 n^{-4} J]$$

yielding R_0 in Å with J in M^{-1} cm^{-1}(nm) (*4*). Q_D is the quantum efficiency of the donor, $\kappa^2 = {}^2/_3$ of the orientational factor, and $n = 1.33$ is the refractive index of the medium. J is the spectral overlap integral, which can be derived from the experimentally obtained absorption and emission spectra. The Förster radius R_0 is the distance at which the energy transfer efficiency is 50%. For the calculation of J, the measured donor emission spectrum was normalized to an area of 1 on a wavelength scale (see Figure 4). It was multiplied by the measured acceptor's extinction, taking into account the optical path length within the cuvette as well as the concentration. After multiplication with the fourth power of the wavelength, the result was numerically integrated to obtain $J = \int f_{Don}(\lambda) \epsilon_{Acc}(\lambda) \lambda^4 \, d\lambda$. Using the experimentally determined J, we find $R_0 = 5.38$ nm as a first estimate for the Förster radius.

Correlation of the cylindrical model with the data measured for the FRET efficiencies (Figure 2) and the calculated R_0 allows one to calculate the values of $R_D = 2.8$ nm and $R_A = 1.38$ nm and to translate the number of base pairs between donor and acceptor into metric values of 4.17, 5.38, 6.39, and 8.37 nm for the $FS_{0bp-24bp}$. To calculate the transfer efficiencies from the maximal emission intensities of donor and acceptor upon donor excitation F_D and F_A, respectively, we took quantum efficiencies of 20% for the Atto647 (according to information of the manufacturer) and 62% for the EYFP (*33*) into account via $E = [1 + (F_D \eta_A / F_A \eta_D)]^{-1}$. The independence of the PL line shape from the excitation wavelength ensures equal results when using peak intensities or volumes under the 2D-PLE intensity plots (not shown).

Figure 6 illustrates the derived change in donor−acceptor distance when increasing the number of base pairs (bp). The closest distance is found for a distance of approximately 5 bp. In this FRET system, the donor would just sit on top of the acceptor, having the same angular coordinates. The minimum distance for 0 bp separation is determined by the diameter of the DNA cylinder and the approximate length of the linking molecules, as well as the distance from the EYFP chromophore inside of the protein structure to the surface. The measured transfer efficiencies in dependence of the donor−acceptor distance is displayed in Figure 7. The data points are in very good agreement with a Förster-type curve for a distance-

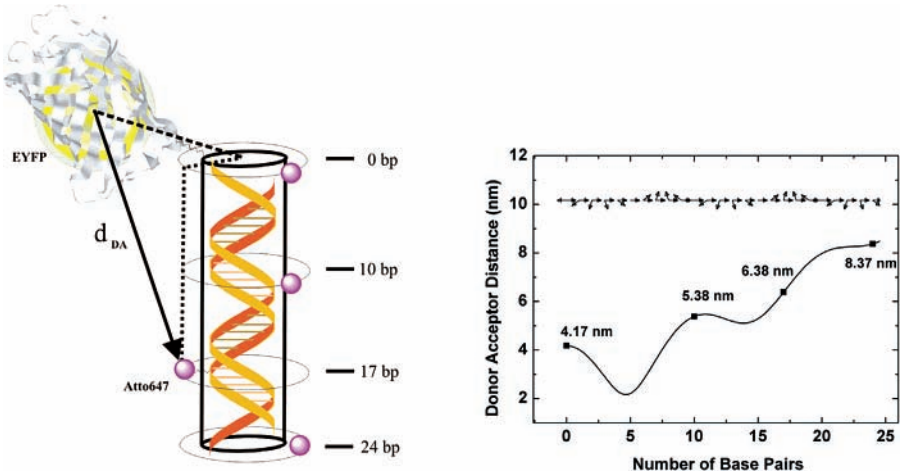


Figure 6. Cylindrical model of the FRET systems and translation of base pair separation into metric distances. Left: Scheme of the different arrangements of donor and acceptor in the four FRET systems depending on the attachment site of the Atto dye on the DNA. Right: The donor−acceptor distance as a function of the number of base pair separation between the two fluorophores. The vectors on top sketch the angular orientation.

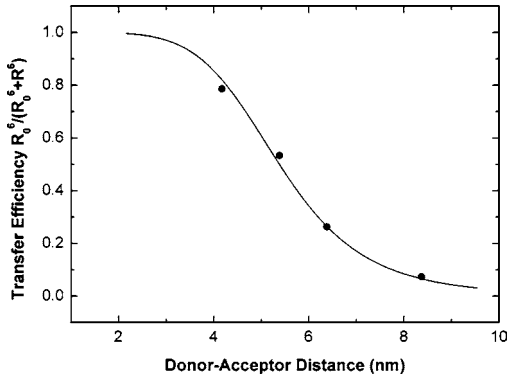


Figure 7. Transfer efficiencies deduced from PL intensities as a function of donor−acceptor distance (black dots) and expected transfer efficiencies calculated from Förster theory (red curve).

dependent energy transfer, proving that DNA−fluorescent protein based supramolecular FRET systems can be rationally designed for generating energy transfer systems with predictable optical properties.

CONCLUSION

We reported here on four supramolecular FRET systems which were obtained by hybridizing the ^{Cys}EYFP−DNA conjugates with the complementary Atto647−cDNA conjugates. The donor−acceptor distance was altered in a controlled way by variation of the number of base pairs separating the donor EYFP and the acceptor dye Atto647. The interchromophore distances were calculated within a cylinder model of the DNA helix yielding 4.17, 5.38, 6.38, and 8.37 nm for the used separations of 0, 10, 17, and 24 base pairs, respectively. For these donor−acceptor distances, the energy transfer was evidenced in 2D-PLE spectra which clearly showed the loss/gain statistics. The calculated values for the FRET efficiencies and the Förster radius are in good agreement with the experimentally obtained values. We anticipate that the molecular construction approach reported here should allow one to rationally assemble more complex, nanoscaled optical systems by taking advantage of the incredibly diverse physicochemical properties of fluorescent proteins.

ACKNOWLEDGMENT

This work was supported by Deutsche Forschungsgemeinschaft (DFG, grants Ni-399/6-1/6-2) and by funding of the PROTEOMICS project by the Ministry of Innovation and Research of the state Northrhine Westfalia.

LITERATURE CITED

(1) Garcia-Parajo, M. F., Hernando, J., Sanchez, Mosteiro, G., Hoogenboom, J. P., van Dijk, E. M., and van Hulst, N. F. (2005) Energy transfer in single-molecule photonic wires. *Chemphyschem 6*, 819−827.

(2) Choi, M. S., Yamazaki, T., Yamazaki, I., and Aida, T. (2004) Bioinspired molecular design of light-harvesting multiporphyrin arrays. *Angew. Chem. Int. Ed. 43*, 150−158.

(3) Hammarstrom, L. (2003) Towards artificial photosynthesis: ruthenium-manganese chemistry mimicking photosystem II reactions. *Curr. Opin. Chem. Biol. 7*, 666−673.

(4) Sykora, M., Maxwell, K. A., DeSimone, J. M., and Meyer, T. J. (2000) Mimicking the antenna-electron transfer properties of photosynthesis. *Proc. Natl. Acad. Sci. U.S.A. 97*, 7687−7691.

(5) Hofkens, J., Cotlet, M., Vosch, T., Tinnefeld, P., Weston, K. D., Ego, C., Grimsdale, A., Müllen, K., Beljonne, D., and Brédas, J.-L. Jordens, S., Schweiter, G., Sauer, M., De Schryver, F. (2003) Revealing competitive Forster-type resonance energy-transfer pathways in single bichromophoric molecules. *Proc. Natl. Acad. Sci. U.S.A. 100*, 13146−13151.

(6) Jordens, S., De Belder, G., Lor, M., Schweitzer, G., Van der Auweraer, M., Weil, T., Reuther, E., Mullen, K., and De Schryver, F. C. (2003) Energy transfer within perylene-terrylene dendrimers evidenced by polychromatic transient absorption measurements. *Photochem. Photobiol. Sci. 2*, 177−186.

(7) Qu, J., Pschirer, N. G., Liu, D., Stefan, A., De Schryver, F. C., and Mullen, K. (2004) Dendronized perylenetetracarboxdiimides with peripheral triphenylamines for intramolecular energy and electron transfer. *Chemistry 10*, 528−537.

(8) Weil, T., Reuther, E., Beer, C., and Mullen, K. (2004) Synthesis and characterization of dendritic multichromophores based on rylene dyes for vectorial transduction of excitation energy. *Chemistry 10*, 1398−1414.

(9) Niemeyer, C. M., Sano, T., Smith, C. L., and Cantor, C. R. (1994) Oligonucleotide-directed self-assembly of proteins: Semisynthetic DNA-streptavidin hybrid molecules as connectors for the generation of macroscopic arrays and the construction of supramolecular bioconjugates. *Nucl. Acids Res. 22*, 5530−5539.

(10) Alivisatos, A. P., Johnsson, K. P., Peng, X., Wilson, T. E., Loweth, C. J., Bruchez, M. P., Jr., and Schultz, P. G. (1996) Organization of 'nanocrystal molecules' using DNA. *Nature (London) 382*, 609−611.

(11) Mirkin, C. A., Letsinger, R. L., Mucic, R. C., and Storhoff, J. J. (1996) A DNA-based method for rationally assembling nanoparticles into macroscopic materials. *Nature (London) 382*, 607−609.

(12) Niemeyer, C. M. (2001) Nanoparticles, proteins, and nucleic acids: biotechnology meets materials science. *Angew. Chem., Int. Ed. 40*, 4128−4158.

(13) Niemeyer, C. M., Koehler, J., and Wuerdemann, C. (2002) DNA-directed assembly of bienzymic complexes from in-vivo biotinylated NAD(P)H:FMN oxidoreductase and luciferase. *ChemBioChem 3*, 242−245.
(14) Rosi, N. L., and Mirkin, C. A. (2005) Nanostructures in biodiagnostics. *Chem. Rev. 105*, 1547−1562.
(15) Kawahara, S.-i., Uchimaru, T., and Murata, S. (1999) Sequential multistep energy transfer: enhancement of efficiency of long-range fluorescence resonance energy transfer. *Chem. Commun*. 563−564.
(16) Ohya, Y., Yabuki, K., Hashimoto, M., Nakajima, A., and Ouchi, T. (2003) Multistep fluorescence resonance energy transfer in sequential chromophore array constructed on oligo-DNA assemblies. *Bioconjugate Chem. 14*, 1057−1066.
(17) Ohya, Y., Nakajima, A., and Ouchi, T. (2005) Time-resolved laser spectroscopic analysis of multi-step fluorescence resonance energy transfer on chromophore array constructed oby oligo-DNA assembly. *Supramol. Chem. 17*, 283−289.
(18) Heilemann, M., Tinnefeld, P., Sanchez Mosteiro, G., Garcia Parajo, M., Van Hulst, N. F., and Sauer, M. (2004) Multistep energy transfer in single molecular photonic wires. *J. Am. Chem. Soc. 126*, 6514−6515.
(19) Vyawahare, S., Eyal, S., Mathews, K. D., and Quake, S. R. (2004) Nanometer-scale fluorescence resonance optical waveguides. *Nano Lett. 4*, 1035−1039.
(20) Kukolka, F., and Niemeyer, C. M. (2004) Synthesis of fluorescent oligonucleotide−EYFP conjugate: towards supramolecular construction of semisynthetic biomolecular antennae. *Org. Biomol. Chem. 2*, 2203−2206.
(21) Heim, R. (1999) Green fluorescent protein forms for energy transfer. *Methods Enzymol. 302*, 408−423.
(22) Wiedenmann, J., Schenk, A., Rocker, C., Girod, A., Spindler, K. D., and Nienhaus, G. U. (2002) A far-red fluorescent protein with fast maturation and reduced oligomerization tendency from *Entacmaea quadricolor* (Anthozoa, Actinaria). *Proc. Natl. Acad. Sci. U.S.A. 99*, 11646−11651.
(23) Fradkov, A. F., Chen, Y., Ding, L., Barsova, E. V., Matz, M. V., and Lukyanov, S. A. (2000) Novel fluorescent protein from *Discosoma* coral and its mutants possesses a unique far-red fluorescence. *FEBS Lett. 479*, 127−130.
(24) Labas, Y. A., Gurskaya, N. G., Yanushevich, Y. G., Fradkov, A. F., Lukyanov, K. A., Lukyanov, S. A., and Matz, M. V. (2002) Diversity and evolution of the green fluorescent protein family. *Proc. Natl. Acad. Sci. U.S.A. 99*, 4256−4261.
(25) Verkhusha, V. V., and Lukyanov, K. A. (2004) The molecular properties and applications of Anthozoa fluorescent proteins and chromoproteins. *Nat. Biotechnol. 22*, 289−296.
(26) Cinelli, R. A. G., Pellegrini, V., Ferrari, A., Faraci, P., Nifosì, R., Tyagi, M., Giacca, M., and Beltram, F. (2001) Green fluorescent proteins as optically controllable elements in bioelectronics. *Appl. Phys. Lett. 79*, 3353−3355.
(27) Ando, R., Mizuno, H., and Miyawaki, A. (2004) Regulated fast nucleocytoplasmic shuttling observed by reversible protein highlighting. *Science 306*, 1370−1373.
(28) Dickson, R. M., Cubitt, A. B., Tsien, R. Y., and Moerner, W. E. (1997) On/off blinking and switching behaviour of single molecules of green fluorescent protein. *Nature (London) 388*, 355−358.
(29) Mendel, D., Cornish, V. W., and Schultz, P. G. (1995) Site-directed mutagenesis with an expanded genetic code. *Annu. Rev. Biophys. Biomol. Struct. 24*, 435−462.
(30) Kukolka, F., Mueller, B. K., Paternoster, S., Arndt, A., Niemeyer, C. M., Braeuchle, C., and Lamb, D. C. (2006) A single molecule FRET Analysis of fluorescent DNA-protein conjugates for nanobiotechnology. *Small 2*, 1083−1089.
(31) Hagerman, P. J. (1988) Flexibility of DNA. *Annu. Rev. Biophys. Chem. 17*, 265−286.
(32) Clegg, R. M., Murchie, A. I., Zechel, A., and Lilley, D. M. (1993) Observing the helical geometry of double-stranded DNA in solution by fluorescence resonance energy transfer. *Proc. Natl. Acad. Sci. U.S.A. 90*, 2994−2998.
(33) Ormo, M., Cubitt, A. B., Kallio, K., Gross, L. A., Tsien, R. Y., and Remington, S. J. (1996) Crystal structure of the *Aequorea victoria* green fluorescent protein. *Science 273*, 1392−1395.

BC060143W

Fluorescent Fructose Derivatives for Imaging Breast Cancer Cells

Jelena Levi, Zhen Cheng, Olivier Gheysens, Manish Patel, Carmel T. Chan, Yingbing Wang, Mohammad Namavari, and Sanjiv Sam Gambhir*

Molecular Imaging Program at Stanford (MIPS), Departments of Radiology and Bioengineering, Bio-X Program, Stanford University, Stanford, California 94305. Received June 26, 2006; Revised Manuscript Received March 5, 2007

Breast cancer cells are known to overexpress Glut5, a sugar transporter responsible for the transfer of fructose across the cell membrane. Since Glut5 transporter is not significantly expressed in normal breast cells, fructose uptake can potentially be used to differentiate between normal and cancerous cells. Fructose was labeled with two fluorophores at the C-1 position: 7-nitro-1,2,3-benzadiazole (NBD) and Cy5.5. The labeling site was chosen on the basis of the presence and substrate specificity of the key proteins involved in the first steps of fructose metabolism. Using fluorescence microscopy, the uptake of the probes was studied in three breast cancer cell lines: MCF 7, MDA-MB-435, and MDA-MB-231. Both fluorescent fructose derivatives showed a very good uptake in all tested cell lines. The level of uptake was comparable to that of the corresponding glucose analogs, 2-NBDG and Cy5.5-DG. Significant uptake of 1-NBDF derivative was not observed in cells lacking Glut5 transporter, while the uptake of the 1-Cy5.5-DF derivative was independent of the presence of a fructose-specific transporter. While 1-NBDF showed Glut5-specific accumulation, the coupling of a large fluorophore such as Cy5.5 likely introduces big structural and electronic changes, leading to a fructose derivative that does not accurately describe the uptake of fructose in cells.

INTRODUCTION

With an estimated 211 240 diagnosed cases and 40 870 deaths in 2005, breast cancer represents the second leading cause of cancer deaths and one of the most frequently diagnosed malignancies among U.S. women (*1*). When it is detected early, breast cancer patients have a survival rate of 98% (*1*). Despite its limitations (*2*, *3*), screening mammography is still the most widely used method for early detection. Mammography relies on anatomical differences between normal and cancerous tissues, and as such does not provide specific information about the molecular processes and changes at the cellular level. Modalities that offer functional imaging (*4*), such as positron emission tomography (PET[1]), single photon emission computed tomography (SPECT), and magnetic resonance imaging (MRI), are increasingly gaining importance in breast cancer detection (*5*−*8*). Detection using probes that differentiate between cancerous and normal breast cells at a molecular level provides specific information that can potentially be utilized for earlier detection, therapy response assessment, and overall better management of patients, ultimately leading to a better survival rate.

The most common, best-studied example of imaging molecular processes at a cellular level is the use of the glucose analog, 2-[^{18}F] fluoro-2-deoxy glucose (FDG) with PET (*9*). Most cancers overexpress Glut1, a high-affinity glucose transporter, and therefore have an increased capacity for glucose uptake when compared to normal cells (*10*, *11*). Once inside the cell, FDG undergoes the first step of metabolism, phosphorylation by hexokinase. Phosphorylated FDG cannot be further metabolized because it is not a substrate for aldolase, an enzyme involved in the second step of metabolism, nor can it leave the cell due to the charged phosphate. The accumulation of FDG thus describes specific molecular processes: transport by Glut1 and phosphorylation with hexokinase.

Glut transporters are transmembrane proteins responsible for transporting sugars such as glucose, fructose, and galactose through the cell membrane. To date, 13 members of the Glut family have been identified, all having a similar sequence but different tissue expression and substrate specificity (*11*, *12*). To satisfy high-energy needs associated with increased proliferation, cancers commonly overexpress one or more Glut transporters. Breast cancer cells are found to have high levels of Glut5, a fructose-specific transporter, not significantly expressed in normal breast cells (*13*). Fructose can be transported by another member of the Glut family, Glut2, a low-affinity transporter that can also transport glucose. Glut2 is not found to be differentially expressed in normal and breast tumor cells (*13*) and as such does not likely represent a relevant target for detecting molecular changes in breast cancer cells. A recent study (*14*) reported 85% of the 33 tested breast cancer tissues expressing Glut 5. The same study done on 215 different tumor samples has found that, besides the ubiquitous glucose transporter, Glut1, the most commonly expressed transporters in cancer tissues are Glut2 and Glut5, both fructose transporters, suggesting the importance of fructose metabolism not only in breast but also in other cancers.

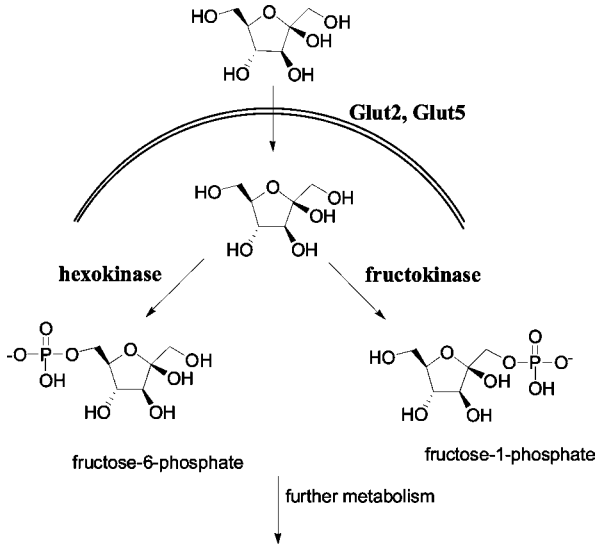
Molecules tagged with fluorescent labels have found a broad application in imaging as a cheaper and safer alternative to radioactive probes (*15*). Although poor light penetration through tissues makes their utilization in humans difficult, they are successfully applied in preclinical, small animal research (*15*−*18*). For the purpose of developing more specific imaging probes for breast cancer, we have synthesized fructose-based optical probes using two fluorophores as labels: 7-nitro-1,2,3-benzoxadiazole, NBD, and cyanine dye, Cy5.5. NBD fluorophore has

* Author to whom correspondence should be addressed. Sanjiv Sam Gambhir M.D., Ph.D., Molecular Imaging Program at Stanford, Department of Radiology and Bio-X Program, 318 Campus Dr., Clark Center, E-150, Stanford University, Stanford, CA 94305, 650-725-2309 (V), 650-724-4948 (Fax), E-mail: sgambhir@stanford.edu.

[1] Abbreviations: NIR, near-infrared; NBD, 7-nitro-1,2,3-benzoxadiazole; Cy5.5-DG, Cy5.5-D-glucosamine; Cy5.5-NHS, Cy5.5 *N*-hydroxysuccinimide ester; MRI, magnetic resonance imaging; PET, positron emission tomography; [^{18}F]FDG, 2-deoxy-2-[^{18}F]fluoro-D-glucose; HPLC, high-performance liquid chromatography; eGFP, enhanced green fluorescent protein.

10.1021/bc060184s CCC: $37.00 © 2007 American Chemical Society
Published on Web 04/20/2007

Scheme 1. Transport and Phosphorylation of Fructose[a]



[a] Fructose is transported by Glut2 and Glut5 transporters across the cell membrane. While Glut2 can transport both glucose and fructose, Glut5 is a fructose-specific transporter. Fructose can be phosphorylated by two enzymes: hexokinase that phopsphorylates fructose in C-6 position and fructokinase (ketohexokinase) that phosphorylates fructose in C-6 position.

been used to label glucose at two positions, C-2 and C-6. Fluorescent glucose analog, 2-[*N*-(7-nitrobenz-2-oxa-1,3-diazol-4-yl)amino]-2-deoxy-D-glucose (2-NBDG) was developed for the viability assessment of *E. coli* (*19*). It has already been shown that it is transported through the cell membrane using the same mechanism as glucose, and that it is a substrate for hexokinase (*19*−*21*). Although transported by the same mechanism, 6-NBDG has a fluorophore at the phosphorylation site and is, therefore, not a substrate for hexokinase (*22*). Cy5.5 dye has better spectral characteristics than NBD, emitting light in the NIR region where there is minimal spectral interference from biological tissues (*23*). In preclinical settings, Cy5.5-labeled tracers have found broad application in tumor detection and drug treatment assessment (*24*−*27*).

In order to choose the labeling position that would allow transport and phosphorylation by the same proteins used by fructose, we looked into substrate specificity of the Glut5 transporter and kinases that can phosphorylate fructose. Fructose can be phosphorylated by two enzymes: hexokinase (HK) and fructokinase (ketohexokinase, KHK). Hexokinase phosphorylates fructose at the C-6 position, while fructokinase phosphorylates it at the C-1 position (Scheme 1). Ideally, we would like to label fructose in such a way to keep both C-1 and C-6 positions available for whichever of the two enzymes might be involved in phosphorylation. However, studies on substrate specificity of Glut5 show bulky groups being tolerated only at C-1 and C-6 positions (*28*, *29*). Furthermore, for fructokinase, C-2, C-3, and C-4 seem to be important for binding and enzyme activity, while groups at C-6 are well-tolerated (*30*, *31*). Similarly, hexokinase allows modification of structure at the C-1 position, the site furthest away from the site of phosphorylation, while hydroxyls at C-3 and C-4 are needed for the productive binding to the enzyme and the subsequent turnover (*32*). Because derivatization at either the C-1 or C-6 position allows phosphorylation by only one of the kinases but prevents enzyme activity of the other, we first wanted to determine the metabolic pathway that fructose takes once inside the cell by looking into the presence and the levels of the two kinases in the breast cancer cell lines. On the basis of the results of the Western analysis and considering substrate specificity of proteins involved in the first steps of fructose metabolism, we chose to label fructose in the C-1 position. Fructose has been labeled at the C-1 position with ^{18}F and evaluated as a PET imaging agent for fibrosarcoma (*33*). Possibly due to the use of fibrosarcoma as a tumor model, for which levels of Glut5 have not been determined, 1-deoxy-1-[^{18}F]fluoro-D-fructose did not show good imaging potential.

Here, we wish to present the syntheses of two fluorescent fructose derivatives, 1-[*N*-(7-nitrobenz-2-oxa-1,3-diazol-4-yl)-amino]-1-deoxy-D-fructose (1-NBDF) and 1-Cy5.5-1-deoxy-D-fructose (1-Cy5.5-DF), and evaluation of their possible application as breast cancer imaging probes.

MATERIALS AND METHODS

General. Ketohexokinase (fructokinase) rabbit polyclonal antibody was purchased from Abnova corporation (Taipei, Taiwan). Hexokinase I rabbit polyclonal antibody was purchased from Abgent (San Diego, CA). Hexokinase II rabbit polyclonal antibody was purchased from Chemicon International, Inc. (Temecula, CA). Peroxidase conjugated goat anti-mouse IgG and goat anti-rabbit IgG were purchased from Sigma-Aldrich Chemical Co. (St. Louis, MO). Enhanced chemiluminescence (ECL) reagents and Cy5.5 *N*-hydroxysuccinimide ester (Cy5.5-NHS) were purchased from Amersham Biosciences (Piscataway, NJ). 2-NBDG was obtained from Molecular Probes (Eugene, OR). 2-Cy5.5-2-deoxy-D-glucose (Cy5.5-DG) was synthesized using the procedure reported earlier (*34*). All other chemicals were purchased from Sigma-Aldrich Chemical Co. (St. Louis, MO) and were used without further purification. Glass-bottomed tissue culture dishes were acquired from MatTek Corporation (Ashland, MA). Purification and analysis of the products was performed using the Dionex Summit high-performance liquid chromatography (HPLC) system (Dionex Corporation, Sunnyvale, CA), equipped with a 340U four-channel UV−vis absorbance detector. For the analysis of the products, reverse-phase HPLC column Dionex Acclaim120 (C18, 4.6 mm × 250 mm) was used. Reverse-phase semipreparative HPLC column Zorbax SB (C18, 9.4 mm × 250 mm) was used for purification and isolation of products. The mobile phase was 0.1% trifluoroacetic acid (TFA) in water and 0.1% TFA in acetonitrile (CH_3CN). The flow was 1 mL/min with gradient starting at 5% CH_3CN and ending at 80% CH_3CN at 42 min. UV wavelengths used for detection of NBD-labeled fructose were 218 and 475 nm. For Cy5.5-labeled fructose, detection wavelengths were 218, 280, and 590 nm. Electron spray ionization (ESI) mass spectrometry was done by Vincent Coates Foundation Mass Spectrometry Laboratory, Stanford University. Matrix-assisted laser desorption/ionization time-of-flight mass spectrometry (MALDI-TOF-MS) was performed by the Protein and Nucleic Acid Biotechnology Facility, Stanford University. All NMR spectra were obtained on a Varian XL-400 (Varian, Palo Alto, CA) at 400 MHz ^1H (100 MHz ^{13}C) .

Cell Lines. Human breast cancer cell lines MCF-7, MDA-MB-435, MDA-MB-231 and human hepatocellular carcinoma cells, HepG2, were obtained from American Type Culture Collection (Manassas, VA). MCF-7 cells were grown in minimum essential medium (Eagle) (MEM, Invitrogen, Carlsbad, CA) supplemented with 0.1 mM nonessential amino acids, 1 mM sodium pyruvate, 1.5 g/L sodium bicarbonate, 0.01 mg/mL bovine insulin, 10% fetal bovine serum (FBS), and 1% penicillin−streptomycin. MDA-MB-435 cells were cultured in Leibovitz's L-15 medium (Invitrogen, Carlsbad, CA) supplemented with 0.01 mg/mL insulin, 10% FBS, and 1% penicillin−streptomycin. MDA-MB-231 cells were cultured in Dulbecco's modified Eagle high glucose medium (DMEM, Invitrogen, Carlsbad, CA) supplemented with 10% FBS and 1% penicillin−streptomycin. HepG2 cells were grown in MEM supplemented with 10% FBS and 1% penicillin−streptomycin.

Ketohexokinase and Hexokinase Western Analysis. Cells were washed with ice-cold phosphate buffered saline (PBS) once and lysed in 1× passive lysis buffer (Promega, Madison, WI) for 10 min on ice. After centrifugation at 13 500 rpm for 15 min at 4 °C, protein content was determined using Bradford assay (Biorad, Hercules, CA). 75 μg of total protein were resolved using the 4−12% NU-PAGE gradient gel (Invitrogen, Carlsbad, CA) and electroblotted onto nitrocellulose membrane (Schleicher & Schuell, Keene, NH). The membrane was first incubated with blocking buffer (5% nonfat dry milk in Tris-buffered saline containing 0.01% Tween 20 (TBST)) for 1 h, and then overnight at 4 °C with an appropriate primary antibody diluted in blocking buffer according to manufacturer's recommendations. The membrane was washed three times with TBST and incubated with appropriate secondary antibodies: peroxidase-conjugated anti-mouse IgG (1:3000 dilution in the blocking buffer) or peroxidase-conjugated anti-rabbit IgG (1:3000 dilution in the blocking buffer) for 1 h. As a loading control, the membrane was incubated with the monoclonal anti-human α-tubulin antibody (1:5000 dilution in the blocking buffer). Enhanced chemiluminescent method was used for visualization of protein bands.

The extraction of mouse liver was performed according to a protocol approved by the Stanford University Administrative Panels on Laboratory Animal Care (A-PLAC). Normal mouse liver was harvested and immediately frozen in dry ice. SDS lysis buffer (50 mM Tris pH 7.4, 2% SDS) containing Complete Mini protease inhibitor (Roche, Palo Alto, CA) was used to lyse the liver. After freezing at −80 °C and thawing at 37 °C three times, liver lysate was centrifuged, and supernatant used for protein detection as described above.

Chemical Syntheses. *1-(Benzylamino)-1-deoxy-D-fructose (**2**).* 1-(Benzylamino)-1-deoxy-D-fructose was synthesized following the published procedure (*35*). Our synthesis starts with D-glucose instead of the D-mannose used in the paper. Briefly, D-glucose (1.8 g, 10 mmol, 1 equiv) was reacted with benzylamine (1.1 mL, 10 mmol, 1 equiv) in boiling absolute ethanol for 5 min. After cooling, the solid was collected and used in the next step without further purification. *N*-Benzyl-β-glucopyranosylamine (1 g, 3.7 mmol, 1 equiv) was heated at 80 °C in the 10:3 mixture of 1,4-dioxane and methanol, in the presence of 0.5 g (5.5 mmol, 1.5 equiv) of oxalic acid for 10 min. The product was collected and recrystallized from isopropanol. ^{1}H NMR (400 MHz, D_2O): 7.28 (5H, m), 4.10 (2H, s), 3.77 (2H, m), 3.66 (1H, dd, J = 3.35 Hz, J = 9.76 Hz), 3.53−3.46 (2H, m), 3.08 (2H, s). ^{13}C NMR (100 MHz, D_2O): 165.55, 130.29, 130.084, 129.88, 129.37, 95.53, 69.69, 69.34, 68.97, 63.97, 52.13, 51.72. ESI$^+$ 270.1. The calculated molecular weight is 269.1 g/mol.

*1-Amino-1-deoxy-D-fructose Oxalate Salt (**3**).* 1-(Benzylamino)-1-deoxy-D-fructose oxalate salt (1 g) was dissolved in 30 mL water. 1 g of Pd/C (10 wt %) was added and the mixture hydrogenated overnight. The catalyst was filtered off and the solvent removed in vacuo. ^{1}H NMR (400 MHz, D_2O): 3.74 (m, 2H), 3.62 (m, 1H), 3.48 (m, 2H), 2.97 (m, 2H). ^{13}C NMR (100 MHz, D_2O): 95.45, 69.62, 69.38, 68.97, 63.91, 45.16. ESI$^+$ 179.9. The calculated molecular weight is 179.1 g/mol.

1-NBDF. 10 mg amino fructose was dissolved in 200 μL 0.3 M $NaHCO_3$ and added to the solution of 10 mg 4-chloro-7-nitrobenzofurazan (NBD chloride) in 400 μL methanol. The mixture was stirred at room temperature for 20 h. Solvents were removed in vacuo, water (400 μL) was added, and the precipitate removed by centrifugation. The filtrate was injected onto the HPLC column. Two major isomers are observed with retention times of 11.5 min and 12.05 min. Both peaks show the same molecular ion in negative ESI 341. Isomers were combined for subsequent uptake studies.

1-Cy5.5-DF. 1 mg Cy5.5-NHS ester was dissolved in 300 μL sodium phosphate buffer (pH 8.5−9). To this solution was added a solution of ∼0.5 mg of 1-amino-1-deoxy-D-fructose in 100 μL phosphate buffer. The mixture was kept at room temperature for 4 h and then directly injected onto HPLC. The 1-Cy5.5-DF fraction was eluted from the column at 15.8 min. MALDI-MS analysis of the collected fraction shows a molecular ion peak of 1077.82. The calculated Mw is found to be 1078.24 g/mol.

Cell Uptake Studies. 1×10^5 MCF-7, MDA-MB-435, MDA-MB-231, and HepG2 cells were plated in 35 mm MatTek glass-bottomed culture dishes 1 day ahead of the imaging study. Cells were washed once with PBS right before incubation with 10 μM probes at 37 °C or 4 °C for 15 min. For the staining of nuclei, after the incubation with 1-Cy5.5-DF, MDA-MB-231 cells were incubated with a solution of Sytox Green (Molecular Probe, Eugene, OR) in 95% ethanol for 15 min. To assess the effect of D-fructose and D-glucose on the uptake of fluorescent-labeled fructose, 1×10^5 MDA-MB-435 cells were coincubated with 10 μM labeled probe and 50 mM D-fructose or 50 mM D-glucose for 15 min at 37 °C. After the incubation, cells were washed three times with cold PBS and imaged using a microscope.

The uptake of 1-NBDF in MCF7 cells was also followed by flow cytometry. Cells (0.1 million) were incubated for 1 h with four different concentrations of 1-NBDF: 10 μM, 7 μM, 5 μM, and 3 μM. After washing two times with 0.5 mL cold PBS, the cells were suspended in 200 μL PBS and analyzed on FACS-Calibur (Becton Dickinson, Franklin Lakes, NJ) using FL-2 channel. The samples were done in triplicate.

Fluorescence Microscopy Studies. Cells were imaged using an Axiovert 200M fluorescence microscope (Carl Zeiss MicroImaging, Inc., Thornwood, NY). To image 1-NBDF in cells and Sytox Green stained nuclei, the eGFP filter set (excitation 450/490 nm, emission 515/565 nm) was used, while for Cy5.5-labeled fructose, the fluorescent signal was recorded using the Cy5 filter set (exciter 640/30 nm; emitter 700/50 nm). An AttoArc HBO 100 W microscopic illuminator was used as a light source. Images were recorded using a thermoelectrically cooled charged-coupled device (CCD) (Micromax, model RTE/CCD-576, Princeton Instruments, Inc., Trenton, NJ) and analyzed using *MetaMorph* software version 6.2r4 (Molecular Devices Corporation, Downingtown, PA).

RESULTS AND DISCUSSION

Fructose can be metabolized via two pathways, one that involves phosphorylation at the C-6 position by hexokinase and the other that starts with phosphorylation at C-1 by fructokinase. Since substrate specificity studies of the proteins involved in transport and phosphorylation point to substitutions at C-1 and C-6 positions as the only ones permissible, the fluorophore labeling site had to be chosen on the basis of the presence and levels of the two kinases that can phosphorylate fructose. That is why we first investigated the expression of hexokinase and fructokinase in the breast cancer cell lines. There are four hexokinase isoforms in mammalian cells. Of those four, two isoforms, hexokinase I and II, are found overexpressed in many cancer cells, hexokinase II being recognized as the key isoform associated with high glycolytic rates (*36*). Among the three breast cancer cell lines studied, MCF7 cell line shows the highest levels of both hexokinase I and II (Figure 1), whereas the other two cell lines, MDA-MB-435 and MDA-MB-231, show considerably lower expression. While Western analysis shows the presence of fructokinase in the liver, the main organ of fructose metabolism, no fructokinase is detected in any of the breast cancer cell lines tested (Figure 1). This suggests that, because only hexokinase is detected in these breast cancer cells, fructose,

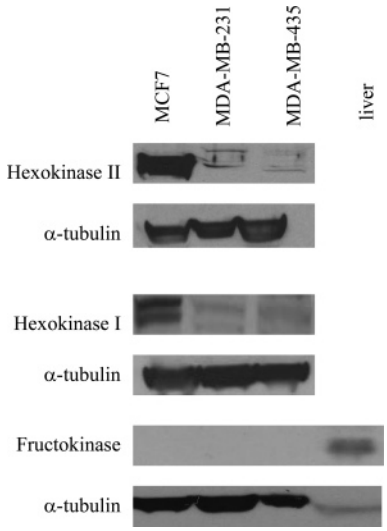


Figure 1. Western blot analysis of hexokinase and fructokinase levels in breast cancer cells and liver. The highest levels of both hexokinase I and II are found in MCF7 cells. Fructokinase was not observed in any of the breast cancer cell lines tested.

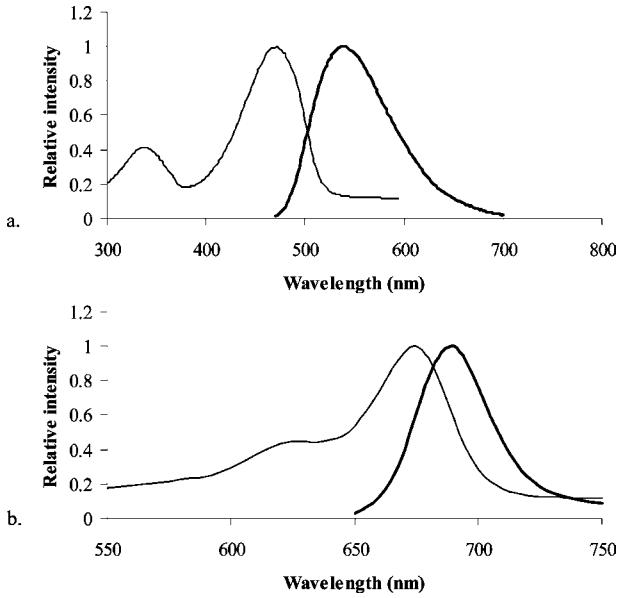


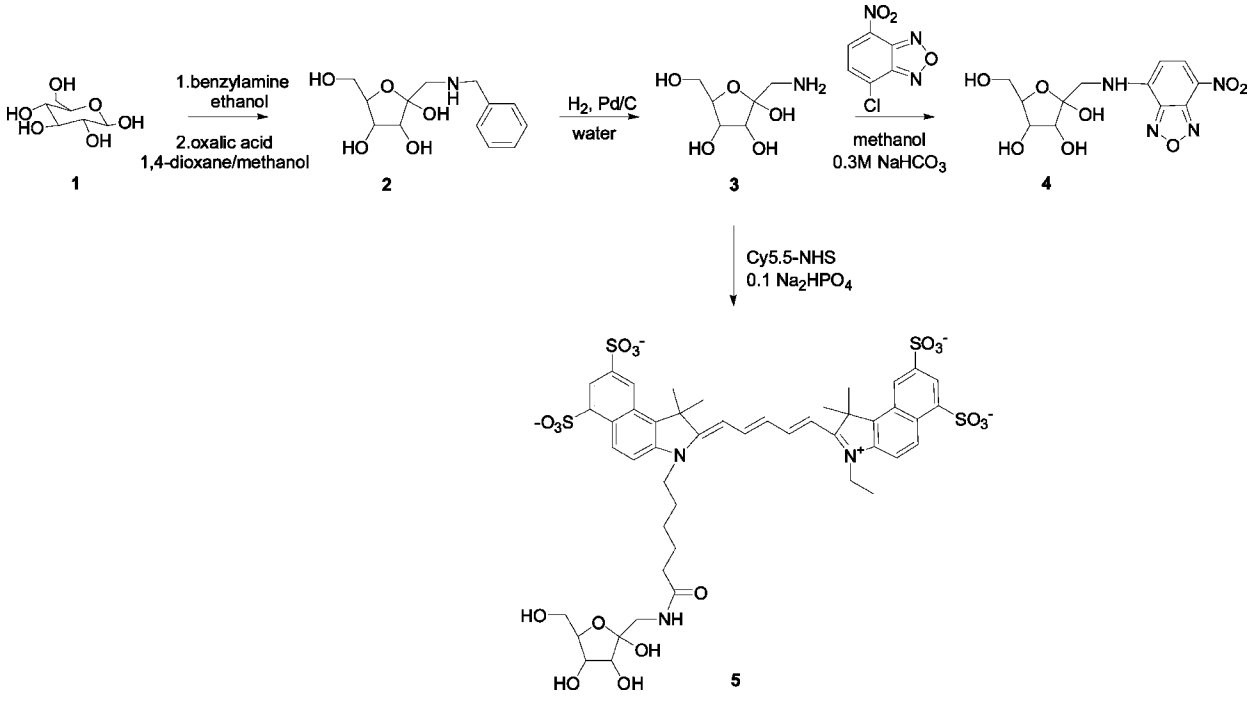
Figure 2. Absorbance (thin line) and fluorescence (thick line) spectra for 1-NBDF (a) and 1-Cy5.5-fructose (b).

once inside the cell, is phosphorylated in the C-6 position. In view of these results, and considering Glut5 and hexokinase substrate specificity, only fructose labeled in the C-1 position should be considered a possible imaging probe—it is expected to be transported by the Glut 5 transporter and trapped in the cells by hexokinase.

Two fluorescent labels were conjugated to fructose in the C-1 position: NBD and Cy5.5. The syntheses of the fluorescent fructose derivatives are shown in Scheme 2. Both syntheses required 1-amino-1-deoxy-D-fructose (**3**), which was prepared by hydrogenation of the Amadori rearrangement product (**2**). 1-NBDF was synthesized by reacting 1-amino-1-deoxy-D-fructose with NBD chloride under basic conditions. The coupling reaction is not very efficient and has a typical yield of only 5%. Two peaks were observed in the HPLC chromatogram, corresponding to different isomers of 1-NBDF. For uptake studies, these isomers were combined, since the Glut5 transporter seems to be accepting all of the four possible fructose isomers, α/*β* fructopyranose and α/*β* fructofuranose (*28*). 1-Cy5.5-DF was synthesized by coupling 1-amino-1-deoxy-D-fructose with Cy5.5-NHS ester. Only one broad peak was observed in the HPLC chromatogram, suggesting closely running 1-Cy5.5-DF isomers.

NBD-chloride is nonfluorescent, but when coupled to the amine group of amino fructose, the NBD group shows fluorescence with the excitation maximum at 472 nm and the emission maximum at 538 nm (Figure 2a). For 1-Cy5.5-DF, the maximum excitation wavelength was found to be 675 nm, while the maximum emission wavelength was at 695 nm (Figure 4b). Cy5.5 dye shows the same spectral characteristics as its fructose conjugate (data not shown). Since the NBD group

Scheme 2. Synthesis of 1-NBDF and 1-Cy5.5-F[a]



[a] Note that fructose exists as a mixture of pyranose and furanose forms but is represented here in the *β*-furanose form for simplicity.

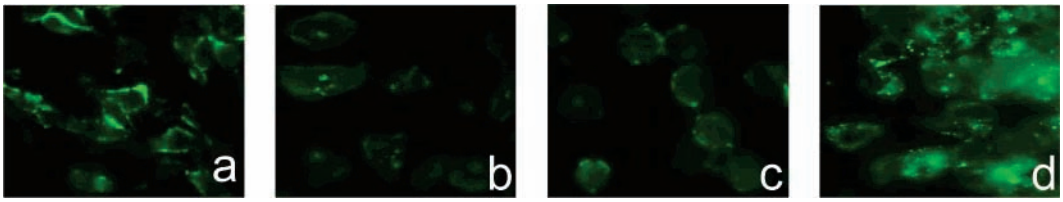


Figure 3. Autofluorescence of MDA-MB-435 (a), MDA-MB-231 (b), MCF7(c), and HepG2 cells (d). Cells were imaged using eGFP filter set, λ_{ex} 450/490 nm, λ_{em} 515/565 nm. All cells showed autofluorescence of low intensity, mostly localized on the cell membrane.

absorbs and emits light in the region where the interference from endogenous fluorophores is expected, it is important to determine the degree of intrinsic fluorescence of the cells. The extent of autofluorescence of different cell lines was investigated by imaging cells, using a fluorescent microscope and appropriate filter sets. Autofluorescence was detected only when using eGFP filter set (λ_{ex} 450/490 nm, λ_{em} 515/565 nm) (Figure 3a−d), while no significant autofluorescence was observed in the NIR region (data not shown). All imaged cell lines showed autofluorescence of very low intensity. Since the observed autofluorescence was limited to the cell membrane and was of relatively small intensity, it is not expected to present a problem in studying the uptake of the 1-NBDF in cell culture.

In order to investigate the tumor targeting ability of the two fluorescent fructose derivatives in cell culture, breast cancer cell lines (MDA-MB-435, MDA-MB-231, and MCF7) were incubated with the probes at 37 °C and imaged using a fluorescent microscope. As a positive control, cells were incubated with the corresponding fluorescent glucose analogs, 2-NBDG and Cy5.5-DG. Good uptake in cancer cells for those two glucose analogs has been previously established (*34*, *37*). Both fructose derivatives were taken up by the breast cancer cells (Figure 4a−f). The level of uptake, as judged by the fluorescence intensity, was comparable to the uptake of the positive probes, 2-NBDG and Cy5.5-DG (Figure 4 g,h). The images suggest a difference in accumulation of the two fructose derivatives. While incubation with 1-NBDF resulted in uniform cell fluorescence, incubation with 1-Cy5.5-DF led to more localized accumulation. In order to investigate localization of 1-Cy5.5-DF, after incubation with the probe, cell nuclei were stained with Sytox Green. The overlay of the images showed cytoplasmic localization of 1-Cy5.5-DF clearly separated from the nucleus (Figure 4i). For the purpose of comparison, cells were also incubated with the Cy5.5-NHS ester. As mentioned earlier, the NBD chloride is nonfluorescent, and as such, its uptake cannot be investigated using the fluorescent microscope. Incubation of cells with the Cy5.5 dye resulted in a cell-associated fluorescence signal (Figure 4j). Although the fluorescence was mostly localized on the cell surface, the uptake of the dye was also observed. Staining of the cell membrane with the Cy5.5 dye alone could be explained by the likely reaction of amine-reactive Cy5.5-NHS ester with many amino groups present on the cell surface. The observed uptake of the dye was likely due to the subsequent endocytosis. The nature of the transport mechanism was investigated by incubating cells with the probes at 4 °C. At low temperature, the uptake of the probes was not observed, indicating an energy-dependent transport (Figure 4k,l).

The uptake of 1-NBDF in MCF 7 cells was further analyzed and quantified using flow cytometry. The amount of probe accumulated clearly correlated with the concentration of the probes that the cells were exposed to (data not shown).

Seeking to explore whether fluorescent fructose probes are specific for the Glut5-expressing cells, we studied their uptake in hepatocarcinoma cells, HepG2, a cell line expressing glucose transporters Glut1−3, while no significant levels of Glut5 transporter are detected (*38*, *39*). The uptake of fructose

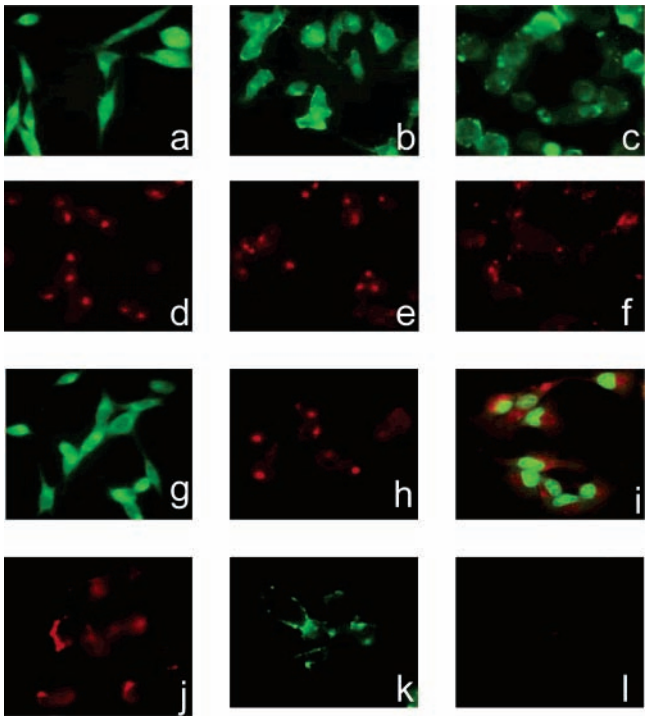


Figure 4. Uptake of fluorescent fructose derivatives in MDA-MB-435 (a,d), MDA-MB-231 (b,e), and MCF-7 cells (c,f). MDA-MB-435 cells incubated with 2-NBDG (g) showed comparable fluorescence intensities to cells incubated with 1-NBDF. Fluorescence of MDA-MB-435 cells incubated with Cy5.5-DG (h) was similar to the fluorescence of cells incubated with 1-Cy5.5-F. Incubation of MDA-MB-231 and MCF7 cells with Cy5.5-DG and NBDG resulted in similar fluorescence intensities as the ones observed after uptake of fluorescent fructose derivatives (data not shown). 1-Cy5.5-DF showed cytoplasmic rather than nuclear accumulation in MDA-MB-435 cells (i). Incubation with Cy5.5-NHS ester results in the staining of MDA-MB-435 cells (j). Incubation of MDA-MB-435 cells with C-1 fructose derivatives at low temperature results in minimal uptake of the probes (k,l).

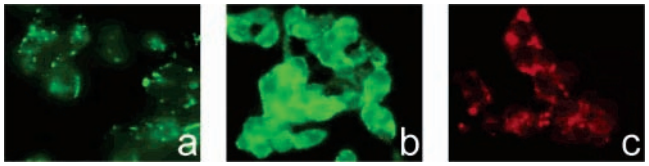


Figure 5. Uptake of 1-NBDF, 2-NBDG, and 1-Cy5.5-DF in HepG2 cells. HepG2 cells lacking Glut5 transporter showed fluorescence of low intensity after incubation with 1-NBDF (a), indicating the absence of the probe transport. 2-NBDG and 1-Cy5.5-F, transported through a different mechanism, were readily taken up by HepG2 cells (b,c).

analogues is not expected in these cells due to the lack of transporter. No significant uptake of 1-NBDF was observed, while glucose analog, 2-NBDG, transported by glucose transporters, showed accumulation in HepG2 cells (Figure 5). These results imply that the uptake of 1-NBDF depends on the presence of the Glut5 transporter and can thus be used to distinguish between the cells expressing and the cells lacking this transporter. In contrast, 1-Cy5.5-DF derivative accumulated

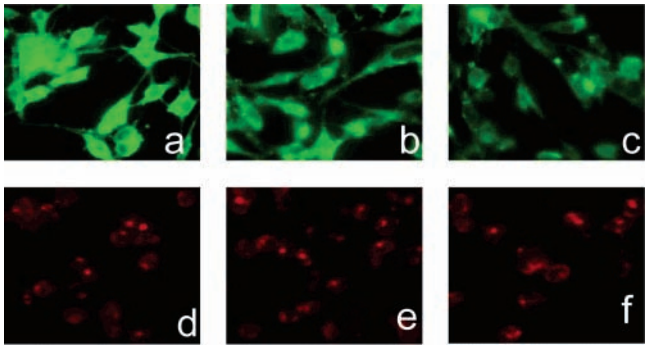


Figure 6. The effect of coincubation with D-fructose and D-glucose on the uptake of the probes in MDA-MB-435 cells. Addition of 50 mM D-fructose (b), as well as addition of 50 mM D-glucose (c) to the incubation medium containing 10 μm 1-NBDF, resulted in decreased fluorescence compared to the cells that have been incubated with 1-NBDF only (a). No effect on the uptake of Cy 5.5-labeled fructose was observed (d,e,f). Analysis of the inhibition by flow cytometry did not show blocking of the transport, indicating that the observed decrease in fluorescence in the cells coincubated with unlabeled fructose and glucose cannot be explained by the inhibitory effect of the sugars on the uptake of 1-NBDF, but rather by the qualitative effect that high concentration of the sugars might have on the fructose transport.

in HepG2 cells, showing that its uptake was not associated with the presence of the Glut 5 transporter.

To further examine the mechanism of transport, MDA-MB-435 cells were coincubated with fluorescent fructose derivatives and unlabeled D-fructose. As judged by the decrease in fluorescence intensity (Figure 6), the uptake of 1-NBDF seems to be diminished by coincubation with D-fructose. The addition of D-glucose has a similar effect, suggesting the inhibition of uptake through the Glut2 transporter, which can transfer both fructose and glucose across the cell membrane. On the other hand, the uptake of 1-Cy5.5-DF was not affected by the addition of either D-fructose or D-glucose, implying that 1-Cy5.5-DF does not use Glut transporters to enter the cell. However, the investigation of the uptake inhibition by flow cytometry failed to show decreased uptake in the cells coincubated with various concentrations of fructose and glucose. The observed decrease in cell fluorescence (Figure 6) could be due to the qualitative rather than quantitative changes that unlabeled fructose and glucose introduce. Other studies report uptake of D-[U-^{14}C]-fructose in cells coincubated with excess cold fructose suggesting that transport is not blocked by cold substrate (*13*, *40*). For the purpose of blocking the transport, the most suitable agents would be substances that bind to the transporter and prevent their function. Cytochalasin B is known to prevent glucose transport by binding to glucose transporters (*41*), but to the best of our knowledge, a molecule preventing the function of Glut5 has not been reported. Fused-ring glyco-1,3-oxazolidin-2-thiones and glyco-1,3-oxazolidin-2-ones have been reported to inhibit the Glut5 transporter, but their specificity and mechanism of action has not been fully evaluated, which limits their current use (*42*).

Although this study suggests uptake of 1-NBDF through Glut5, it remains to be determined whether 1-NBDF gets phosphorylated by hexokinase and at what relative rate compared to glucose. It will also be important for future studies to determine if there is efflux of the probes out of cells, since Glut5 is a bidirectional transporter. On the basis of its behavior in cell culture, it would be interesting to explore the possibility of using 1-NBDF for in vivo studies in small animals. As discussed earlier, 1-NBDF does not have optimal spectral characteristics, but using instruments with multispectral imaging techniques might minimize interference caused by autofluorescence.

In summary, two fluorescent fructose derivatives were synthesized and evaluated in cell culture for their Glut5-detecting ability in breast cancer. Both derivatives show good uptake in breast cancer cells tested. Importantly, we found that the uptake of 1-NBDF appears to correspond with the uptake of fructose in cells. The NBD group is small in size and does not seem to perturb the structure of the fructose to the point at which the labeled analogue is no longer recognized by the Glut5 transporter. In contrast, the coupling of fructose with a very bulky fluorophore such as Cy5.5 results in a derivative that shows nonspecific uptake in breast cancer cells, and as such cannot likely be used in breast cancer imaging.

ACKNOWLEDGMENT

We would like to thank the NCI ICMIC P50 CA114747 (SSG) for funding support.

LITERATURE CITED

(1) *American Cancer Society: Fact Sheets: Breast Cancer* (2005) American Cancer Society, Atlanta.
(2) Buist, D. S., Porter, P. L., Lehman, C., Taplin, S. H., and White, E. (2004) Factors contributing to mammography failure in women aged 40−49 years. *J. Natl. Cancer Inst. 96*, 1432−1440.
(3) Berlin, L. (2001) The missed breast cancer redux: time for educating the public about the limitations of mammography? *AJR Am. J. Roentgenol. 176*, 1131−1134.
(4) Massoud, T. F., and Gambhir, S. S. (2003) Molecular imaging in living subjects: seeing fundamental biological processes in a new light. *Gen. Dev. 17* (5), 545−580.
(5) Koomen, M., Pissano, E. D., Kuzmiak, C., Pavic, D., and McLelland, R. (2005) Future directions in breast imaging. *J. Clin. Oncol. 23* (8), 1674−1677.
(6) Lehman, C. D., and Schnall, M. D. (2005) Imaging in breast cancer: magnetic resonance imaging. *Breast Cancer Res. 7*, 215−219.
(7) Quon A., and Gambhir S. S. (2005) FDG-PET and beyond: molecular breast cancer imaging. *J. Clin. Oncol. 23* (8) 1664−1673.
(8) Benard, F., and Turcotte, E. (2005) Imaging in breast cancer: single-photon emission computed tomography and positron emission tomography. *Breast Cancer Res. 7*, 153−162.
(9) Gambhir, S. S. (2002) Molecular imaging of cancer with positron emission tomography. *Nat. Rev. Cancer 2* (9), 683−693.
(10) Younes, M., Lechago, L. V., Somoano, J. R., Mosharaf, M., and Lechago, J. (1996) Wide expression of the human erythrocyte glucose transporter Glut1 in human cancers. *Cancer Res. 56*, 1164−1167.
(11) Medina, R. A., and Owen, G. I. (2002) Glucose transporters: expression, regulation and cancer. *Biol. Res. 35*, 9−26.
(12) Joost, H. G., and Thorens, B. (2001) The extended GLUT-family of sugar/polyol transport facilitators: nomenclature, sequence characteristics, and potential function of its novel members. *Mol. Membr. Biol. 18* (4), 247−256.
(13) Zamora-León, P., Golde, D. W., Concha, I. I., Rivas, C. I., Delgado-López, F., Baselga, J., Nualart, F., and Vera, J C. (1996) Expression of the fructose transporter Glut5 in human breast cancer. *Proc. Natl. Acad. Sci. U.S.A. 93*, 1847−1852.
(14) Godoy, A., Ulloa, V., Rodriguez, F., Reinicke, K., Yanez, A., De Los Angeles, Garcia, M., Medina, R., Carrasco, M., Barberis, S., Castro, T., Martinez, F., Koch, H., Vera, J. C., Poblete, M. T., Figureoa, C. D., Peruzzo, B., Perez, F., and Nualart, F. (2006) Differential subcellular distribution of glucose transporters Glut1−6, and Glut9 in human cancer: ultrastructural localization of Glut1 and Glut5 in breast tumor tissues. *J. Cell. Physiol. 207*, 614−627.
(15) Weissleder, R., and Ntziachristos, V. (2003) Shedding light onto live molecular targets. *Nat. Med. 2* (2), 123−31.
(16) Kim, S., Lim, Y. T., Soltesz, E. G., De Grand, A. M., Lee, J., Nakayama, A., Parker, J. A., Mihaljevic, T., Laurence, R. G., Dor, D. M., Cohn, L. H., Bawendi, M. G., and Frangioni, J. V. (2004) Near infrared fluorescent type II quantum dots for sentinel lymph node mapping. *Nat. Biotechnol. 22*, 93−97.
(17) Graves, E. E., Weissleder, R., and Ntziachristos, V. (2004) Fluorescence molecular imaging of small animal tumor model. *Curr. Mol. Med. 4*, 419−430.

(18) Choy, G., Choyke, P., and Libutti, S. K. (2003) Current advances in molecular imaging: non-invasive in vivo bioluminescent and fluorescent optical imaging in cancer research optical imaging in cancer research. *Mol. Imaging 2*, 303−312.
(19) Yoshioka, K., Takahashi, H., Homma, T., Saito, M., Oh, K.-B., Nemoto, Y., and Matsuoka, H. (1996) A Novel fluorescent derivative of glucose applicable to the assessment of glucose uptake activity of *Escherichia coli*. *Biochim. Biophys. Acta 1289*, 5−9.
(20) Yoshioka, K., Oh, K.-B., Saito, M., Nemoto, Y., and Matsuoka, H. (1996) Evaluation of 2-[N-(7-nitrobenz-2-oxa-1,3-diazol-4-yl)-amino]-2-deoxy-D-glucose, a new fluorescent derivative of glucose, for viability assessment of yeast *Candida albicans*. *Appl. Microbiol. Biotechnol. 46*, 400−404.
(21) Yoshioka, K., Saito, M., Oh, K.-B., Nemoto, Y., Matsuoka, H., Natsume, M., and Abe, H. (1996) Intracellular fate of 2-NBDG, a fluorescent probe for glucose uptake activity in *Escherichia coli* cells. *Biosci. Biotechnol. Biochem. 60*, 1899−1901.
(22) Speizer, L., Haugland, R., and Kutchai, H. (1985) Assymetric transport of a fluorescent glucose analogue by human erythrocytes. *Biochim. Biophys. Acta*. *815*, 75−84.
(23) Richards-Kortum, R., and Sevick-Muraca, E. (1996) Quantitative optical spectroscopy for tissue diagnostics. *Annu. Rev. Phys. Chem. 47*, 555−606.
(24) Ke, S., Wen, X., Gurfinkel, M., Charnsangavej, C., Wallace, S., Sevick-Muraca, E. M., and Li, C. (2003) Near-infrared optical imaging of epidermal growth factor receptor in breast cancer xenografts. *Cancer Res. 63*, 7870−7875.
(25) Veiseh, O., Sun, C., Gunn, J., Kohler, N., Gabikian, P., Lee, D., Bhattarai, N., Ellenbogen, R., Sze, R., Hallahan, A., Olson, J., and Zhang, M. (2005) Optical and MRI multifunctional nanoprobe for targeting gliomas. *Nano Lett. 5*, 1003−1008.
(26) Pham, W., Choi, Y., Weissleder, R., and Tung, C.-H. (2004) Developing a peptide-based near-infrared molecular probe for protease sensing. *Bioconjugate Chem. 15*, 1403−1407.
(27) Ntziachristos, V., Schellenberger, E. A., Ripoll, J., Yessayan, D., Graves, E., Bogdanov, A., Jr., Josephson, L., and Weissleder, R. (2004) Visualization of antitumor treatment by means of fluorescence molecular tomography with annexin V-Cy 5.5 conjugate. *Proc. Natl. Acad. Sci. U.S.A. 101*, 12294−12299.
(28) Tatibuet, A., Yang, J., Morrin, C., and Holman, G. D. (2000) Synthesis and evaluation of fructose analogs as inhibitors of the D-fructose transporter Glut5. *Bioorg. Med. Chem. 8*, 1825−1833.
(29) Yang, J., Dowden, J., Tatibuet, A., Hatanaka, Y., and Holman, G. D. (2002) Development of high-affinity ligands and photoaffinity labels for the D-fructose transporter. *Biochem. J. 367*, 533−539.
(30) Raushel, F. M., and Cleland, W. W. (1973) The substrate and anomeric specificity of fructokinase. *J. Biol. Chem. 248*, 8174.
(31) Raushel, F. M., and Cleland, W. W. (1977) Bovine liver fructokinase: purification and kinetic properties. *Biochemistry 16*, 2169−2175.
(32) Chenault, H. K., Mandes, R. F., and Hornberger, K. R. (1997) Synthetic utility of yeast hexokinase. Substrate specificity, cofactor regeneration, and product isolation. *J. Org. Chem. 62*, 331−336.
(33) Haradahira, T., Tanaka, A., Maeda, M., Kanazawa, Y., Ichiya, Y.-I., and Masuda, K. (1995) Radiosynthesis, rodent biodistribution, and metabolism of 1-deoxy-1-[^{18}F]fluoro-D-fructose. *Nucl. Med. Biol. 22*, 719−725.
(34) Cheng, Z., Levi, J., Xiong, Z., Gheysens, O., Keren, S., Chen, X., and Gambhir, S. S. (2006) Near-infrared fluorescent glucose analog and cyanin dye for tumor optical imaging in cell culture and in living mice. *Bioconjugate Chem. 17*, 662−669.
(35) Ponpipom, M. M., Bugianesi, R. L., and Shen, T. Y. (1980) Synthesis of N-substituted D-mannosylamines and 1-(benzylamino)-1-deoxy-alditols for biological evaluation. *Carbohydr. Res. 82*, 135−140.
(36) Aloj, L., Caraco, C., Jagoda, E., Eckelman, W. C., and Neumann, R. D. (1999) Glut-1 and hexokinase expression: relationship with 2-fluoro-2-deoxy-D-glucose uptake in A431 and T47D cells in culture. *Cancer Res. 59*, 4709−4714.
(37) O' Neil, R. G., Wu, L., and Mullani, N. (2005) Uptake of a fluorescent deoxyglucose analog (2-NBDG) in tumor cells. *Mol. Imaging Biol. 7*, 388−392.
(38) Yamamoto, T., Seino, Y., Fukumoto, H., Koh, G., Yano, H., Inagaki, N., Yamada, Y., Inoue, K., Manabe, T., and Imura, H. (1990) Over-expression of facilitative glucose transporter genes in human cancer. *Biochem. Biophys. Res. Commun. 170*, 223−230.
(39) Chan, K. K., Chan, J. Y. W., Chang, K. K. W., and Fung, K.-P. (2004) Inhibition of cell proliferation in human breast tumor cells by antisense oligonucleotides against facilitative glucose transporter 5. *J. Cell. Biochem. 93*, 1134−1142.
(40) Concha, I. I., Velasquez, F. V., Martinez, J. M., Angulo, C., Droppelmann, A., Reyes, A. M., Slebe, J. C., Vera, J. C., and Golde, D. W. (1997) Human erythrocytes express Glut5 and transport fructose. *Blood 89*, 4190−4195.
(41) Bell, G. I., Burant, C. F., Takeda J., and Gould, G. W. (1993) Structure and function of mammalian facilitative sugar transporters. *J. Biol. Chem. 268*, 19161−19164.
(42) Girniene, J., Tatibuet, A., Sackus, A., Yang, J., Holman, G. D., and Rollin, P. (2003) Inhibition of the D-fructose transporter protein Glut5 by fused-glyco-1,3-oxazolidin-2-thiones and -oxazolidin-2-ones. *Carbohydr. Res. 338*, 711−719.

BC060184S

D-Mannose-Modified Iron Oxide Nanoparticles for Stem Cell Labeling

Daniel Horák,*[,†,‡] Michal Babič,[†,‡] Pavla Jendelová,[‡,§] Vít Herynek,[‡,||] Miroslava Trchová,[†] Zbyněk Pientka,[†] Emil Pollert,[⊥] Milan Hájek,[‡,||] and Eva Syková[‡,§]

Institute of Macromolecular Chemistry AS CR, Heyrovský Sq. 2, 162 06 Prague 6, Czech Republic, Center for Cell Therapy and Tissue Repair, Charles University, V Úvalu 84, 150 06 Prague 5, Czech Republic, Institute of Experimental Medicine AS CR, Víděnská 1083, 142 20 Prague 4, Czech Republic, Institute of Clinical and Experimental Medicine, Víděnská 1958/9, 140 21 Prague 4, Czech Republic, and Institute of Physics AS CR, Cukrovarnická 10, 162 53 Prague 6, Czech Republic
Received June 28, 2006; Revised Manuscript Received December 12, 2006

New surface-modified iron oxide nanoparticles were developed by precipitation of Fe(II) and Fe(III) salts with ammonium hydroxide according to two methods. In the first method, precipitation was done in the presence of D-mannose solution (in situ coating); the second method involved oxidation of precipitated magnetite with sodium hypochlorite followed by addition of D-mannose solution (postsynthesis coating). Selected nanoparticles were characterized by transmission electron microscopy (TEM), atomic force microscopy (AFM), elemental analysis, dynamic light scattering, infrared (IR), X-ray powder analysis, and ultrasonic spectrometry. While the first preparation method produced very fine nanoparticles ca. 2 nm in diameter, the second one yielded ca. 6 nm particles. Addition of D-mannose after synthesis did not affect the iron oxide particle size. UV−vis spectroscopy suggested that D-mannose suppresses the nonspecific sorption of serum proteins from DMEM culture medium on magnetic nanoparticles. Rat bone marrow stromal cells (rMSCs) were labeled with uncoated and D-mannose-modified iron oxide nanoparticles and with Endorem (Guerbet, France; control). Optical and transmission electron microscopy confirmed the presence of D-mannose-modified iron oxide nanoparticles inside the cells. D-Mannose-modified nanoparticles crossed the cell membranes and were internalized well by the cells. Relaxivity measurements of labeled cells in gelatin revealed very high relaxivities only for postsynthesis D-mannose-coated iron oxide nanoparticles.

INTRODUCTION

Regenerative medicine is a new field in which new treatment strategies are employed. One of the most promising approaches in preclinical research into brain or spinal cord injuries involves the use of cell therapies. After transplantation, the cells integrate into the host environment and respond to intrinsic signals (*1*). Stem cells administered via intravenous infusion migrate to the site of the injury and enter the nervous tissue through a more permeable or opened blood−brain barrier (*2*, *3*).

In the majority of experiments the donor cells are labeled before transplantation (retroviral labeling, bromodeoxyuridine, red fluorescent "cell tracker" PKH 26, green fluorescent protein [GFP]). After a certain time the host organism is sacrificed and evaluation of the position of the transplanted cells is carried out by microscopic analysis. This method, however, does not give data about the dynamics of the process or the movements of the transplanted stem cells in the host organism and requires sacrificing the host organism.

Initial findings confirmed that nanoparticles based on microcrystals of iron oxides could be observed by magnetic resonance imaging (MRI) in brain cells. The first reports (*4*, *5*) of imaging cell transplants labeled by superparamagnetic contrast agents in rat brains appeared in 1992. Different iron oxide nanoparticles coated by dextran were tested, and it was shown that MRI could be used for the dynamic in vivo tracking of labeled cells (*6*, *7*). The greatest progress was achieved with dextran-coated monocrystalline iron oxide nanoparticles (MION) (*8*, *9*), and the migration of MION-labeled oligodendrocyte progenitors was shown (*10*). Dendrimer-encapsulated superparamagnetic iron oxides were used for labeling and in vivo tracking of stem cells (*11*). Recently, immortalized cells from the MHP36 hippocampal cell line labeled in vitro with gadolinium rhodamine dextran were tracked in ischemia-damaged rat hippocampus in perfused brains ex vivo (*12*). Study of embryonic stem cells labeled in vitro with the magnetic resonance (MR) contrast agent Sinerem using a lipofection procedure successfully showed migration of labeled cells into focal cerebral ischemic lesions evoked by middle cerebral artery occlusion (*13*). Another suitable contrast agent for mesenchymal and embryonic stem cells is a commercially available contrast agent based on dextran-coated iron oxide nanoparticles, Endorem (Guerbet, France), which has also been approved as a blood pool agent for human use. Endorem-labeled cells migrated to a cortical photochemical lesion or a spinal cord compression lesion in rats (*14*−*16*).

Our aim is to design new iron oxide nanoparticles for stem cell labeling and investigate and control their surface and morphological characteristics. Surface modification of iron oxide is a key issue for enhancing its permeability through the cell membrane. Biocompatible polymers and targeting agents are therefore attached to the nanoparticle surface to prevent the nanoparticles from agglomeration, make them more biocompatible, and increase their nonspecific intracellular uptake (*17*). Our preliminary experiments with cationic (perchloric acid-stabilized) or anionic (tetramethylammonium hydroxide-stabilized) iron oxides showed that the colloids were unstable in the medium required for cell cultivation and that the particles aggregated. Similarly, dextran-coated iron oxide tended to adhere on the cell surface, while (diethylaminoethyl)dextran-

* To whom correspondence should be addressed. Phone: +420-296-809-260. Fax: +420-296-809-410. E-mail: horak@imc.cas.cz.
† Institute of Macromolecular Chemistry AS CR.
‡ Charles University.
§ Institute of Experimental Medicine AS CR.
|| Institute of Clinical and Experimental Medicine.
⊥ Institute of Physics AS CR.

10.1021/bc060186c CCC: $37.00 © 2007 American Chemical Society
Published on Web 03/20/2007

coated particles hindered cell proliferation. Uptake of (carboxymethyl)dextran-coated ferrofluid by endocytosing cells was too low. In a continuation of the search for a suitable surface modification to enhance nanoparticle transport into the cells, D-mannose was selected as the cell surface is known to possess receptors for this molecule (*18*). Moreover, D-mannose-bound poly(2-hydroxyethyl methacrylate) hydrogels were found to support adhesion of keratinocytes (epidermal cells) and their subsequent cultivation without the presence of feeder cells (*19*).

EXPERIMENTAL SECTION

Materials. $FeCl_2 \cdot 4H_2O$, $FeCl_3 \cdot 6H_2O$, and D-mannose were purchased from Fluka (Buchs, Switzerland), sodium hypochlorite solution (NaClO) from Bochemie (Bohumín, Czech Republic), and sodium citrate dihydrate from Lachema (Brno, Czech Republic). All other reagent-grade chemicals were purchased from Aldrich (Milwaukee, WI) and used as received. The commercial contrast agent Endorem was provided by Guerbet (Roissy, France). Ultrapure Q water ultrafiltered on a Milli-Q Gradient A10 system (Millipore, Molsheim, France) was used for preparation of solutions.

In Situ Precipitation of Iron Oxide in D-Mannose Solution. Molday's procedure (*20*) for coating iron oxide nanoparticles with dextran was modified to prepare iron oxide nanoparticles in D-mannose solution. Briefly, 10 mL of 50 wt % D-mannose aqueous solution was mixed under stirring with 10 mL of a water solution containing 1.51 g of $FeCl_3 \cdot 6\ H_2O$ and 0.64 g of $FeCl_2 \cdot 4\ H_2O$; 15 mL of 7.5% NH_4OH solution was slowly added until pH 12 was reached, and the mixture was heated to 60 °C for 15 min. Large aggregates were destroyed by sonication (Ultrasonic Homogenizer 4710 Series, Cole-Palmer Instruments, at 40% output) for 5 min. To remove unreacted water-soluble salts and excessive D-mannose, particles were washed by dialysis using a Visking membrane (molecular weight cutoff 14 000; Carl Roth GmbH, Karlsruhe, Germany) against 2 L of water for 24 h at room temperature (the water was changed 5 times, 2 L each time) until pH 6 was reached. The volume of water was reduced by evaporation—dry residue: 80 mg of iron oxide/mL of colloid.

Preparation of Iron Oxide Nanoparticles and Postsynthesis Coating with D-Mannose. A solution of $FeCl_2$ (0.2 mol/L) and $FeCl_3$ (0.2 mol/L) in a 1:2 molar ratio was coprecipitated in an excess of 0.5 mol/L NH_4OH. After 15 min, the product was repeatedly separated in a magnetic field and washed with Q-water to reach peptization. The colloid was subsequently sonicated for 5 min (Ultrasonic Homogenizer 4710 Series, Cole-Palmer Instruments, 40% output) and oxidized with 5 wt % NaClO aqueous solution in the presence of 0.1 M sodium citrate solution. Washing and sonication procedures were then repeated. Finally, 20 wt % aqueous D-mannose solution was added to colloidal iron oxide (maghemite, γ-Fe_2O_3). The resulting product was washed three times with 10 mL of water after centrifugation at 14 000 rpm for 3 min (the colloid was so stable that it did not permit magnetic separation).

Characterization. The particle morphology and particle size distribution were examined by transmission electron microscopy (TEM; JEOL JEM 200 CX). An iron oxide nanoparticle dispersion in water was sprayed onto a grid with a carbon membrane. The number-average diameter was determined by measurement of at least 500 particles for each batch from microphotographs using the Atlas program (Tescan, Digital Microscopy Imaging, Brno, Czech Republic). The number-average (D_n) particle diameter was calculated as $D_n = \Sigma N_i D_i / \Sigma N_i$, where N_i is the number of particles with diameter D_i. Polydispersity PDI $= D_w/D_n$, where D_w is the weight-average particle diameter, $D_w = \Sigma N_i D_i^4 / \Sigma N_i D_i^3$. A multimode AFM Nanoscope IIIa (Digital Instruments, Santa Barbara, CA) was used to observe the nanoparticles in situ in tapping mode using OTESPA silicon cantilevers (Veeco Instruments, Dourdan, France) with a radius of 5 nm and oscillating at 245 kHz.

D-Mannose and iron oxide content was calculated from elemental analysis (Perkin-Elmer 2400 CHN) and from the iron content analyzed by atomic adsorption spectrometry (AAS Perkin-Elmer 3110) of an extract from a sample obtained with dilute HCl (1:1) at 80 °C for 1 h.

The hydrodynamic diameter (*z* average) and polydispersity as a measure of the distribution width were obtained by dynamic light scattering (DLS) with an Autosizer Lo-C (Malvern Instruments Ltd., Malvern, Great Britain).

The coating of D-mannose on the surface of the magnetic nanoparticles was investigated using a Fourier transformation infrared (FTIR) spectrometer (NICOLET IMPACT 400) in an H_2O-purged environment with a doped triglycine sulfate (DTGS) detector. The Golden Gate single attenuated total reflection (ATR) system (Specac Ltd., Orpington, Great Britain) was used to measure the spectra of powdered samples by an ATR spectroscopic technique over a wavelength range of 400−4000 cm^{-1}. Typical parameters used were as follows: 256 sample scans, resolution 4 cm^{-1}, Happ-Genzel apodization, KBr beamsplitter.

Differences in ultrasonic velocity between reference (water) and iron oxide colloid were monitored under the slow addition of various concentrations of D-mannose using an Ultrasound Spectrometer HR-US 102 (Ultrasonic Scientific, Dublin, Ireland). In a typical experiment, 1 mL of iron oxide colloid (18 mg of γ-Fe_2O_3/mL) was in the first cell and 1 mL of Q-water in the second cell. D-Mannose solution (1 mg of D-mannose/mL) was then simultaneously added in 10 μL aliquots to both cells with a Hamilton syringe.

X-ray powder diffraction using a Bruker D8 diffractometer (Cu Kα, Sol-X energy-dispersive detector) was used to determine the magnetite phase composition.

In protein adsorption experiments, 1 mL of the colloid with a concentration of 22 mg of iron oxide/mL was mixed with 1 mL of DMEM (Dulbecco's modified Eagle's medium)/10% FBS (fetal bovine serum) medium on a Vortex-T Genie-2 (Scientific Industries, Bohemia, USA) for 1 h; the liquid was separated from the solid by centrifugation and measured on a Perkin-Elmer Lambda 20 UV/vis spectrophotometer. An aqueous solution of DMEM/10% FBS medium (1/1 v/v) served as a standard.

Cell Cultures. To isolate rat bone marrow stromal cells (rMSCs), femurs were dissected from 4-week-old Wistar rats. The ends of the bones were cut, and the marrow was extruded with 5 mL of DMEM with L-glutamine (PAA, Pasching, Austria) using a needle and syringe. Marrow cells were plated in 80 cm^2 tissue culture flasks in DMEM/10% FBS with 100 U/mL penicillin and 100 U/mL streptomycin. After 24 h, the nonadherent cells were removed by replacing the medium. The medium was changed every 2−3 days as the cells grew to confluence. The cells were lifted by incubation with 0.25 wt % trypsin.

Transmission Electron Microscopy of Labeled Cells. For electron microscopic examination, rMSCs were fixed at 4 °C in 2.5% buffered glutaraldehyde for 1 h followed by 1% osmium tetroxide for 2 h. The cells were dehydrated in ascending concentrations of ethanol, immersed in propylene oxide, and embedded in Epon 812 resin (Agar Scientific Ltd., Standsted, England). The samples were cut in ultrathin sections (~60 nm), contrasted with 4% uranyl acetate and Reynold's lead citrate, and examined in a Philips Morgagni 268 electron microscope.

Quantitative Analysis of Labeled Cells. rMSCs were plated in duplicate on uncoated 6-well culture plates at a density of 10^5 cells/mm^2. Endorem or D-mannose-modified nanoparticles

Table 1. Cell Labeling with Surface-Modified and Unmodified Iron Oxide Nanoparticles and Their Characterization

run	D-mannose/γ-Fe_2O_3	D_n (nm)	PDI	percentage of labeled cells[a] (%)
Endorem				58.6
1[b]	7.3[d]	1.6	1.07	51.2[e]/82.3[f]
2	0	6.05	1.46	27.9
3[c]	1.3	5.9	1.39	49.1
4[c]	2.6	6.6	1.33	80.6
5[c]	4.1	6.4	1.26	51.3

[a] Average of 10 measurements. [b] In situ coating. [c] Postsynthesis coating. [d] D-Mannose/Fe_3O_4. [e] Diluted (0.02 mg of iron oxide/mL). [f] Undiluted (0.2 mg of iron oxide/mL) colloid.

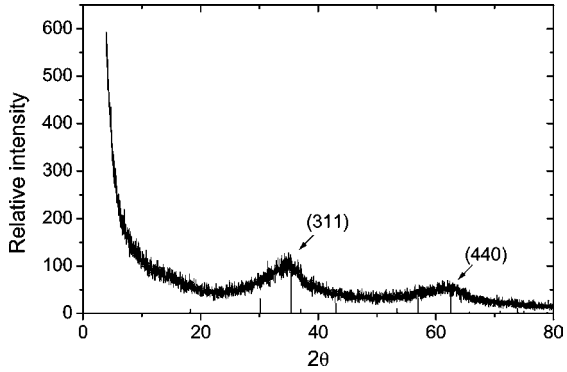


Figure 1. X-ray powder analysis of in situ D-mannose-coated magnetite nanoparticles No. 1. Vertical bars: Fe_3O_4 standard.

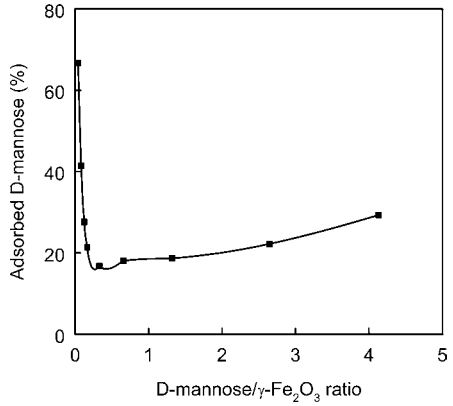


Figure 2. Dependence of the amount of D-mannose adsorbed from solution on the D-mannose/γ-Fe_2O_3 ratio.

were added to the culture medium (10 μL/mL) for 72 h. After the Endorem was washed out of the culture medium, the cells were fixed with 4% paraformaldehyde in 0.1 M PBS (phosphate-buffered saline) and stained for iron to produce ferric ferrocyanide (Prussian blue). Labeled and unlabeled cells were quantified using an inverted light microscope (Axiovert 200, Zeiss, Jena, Germany) by counting randomly five fields per well and two wells per each run. The cells captured on each image were manually labeled as Prussian blue positive or negative; the labeled cells were then counted, and the staining intensity of Prussian blue positive cells was evaluated using the Image analysis toolbox in Matlab 6.1 (The MathWorks, Natick, USA). Histograms of the intensity of the cytoplasmic staining were constructed.

MR Relaxometry and MR Imaging. Suspensions of contrast agents were prepared together with suspensions of cells labeled by Endorem or D-mannose-modified nanoparticles in 4% gelatin (Sigma, Czech Republic) and subjected to MR relaxometry. T_1 and T_2 relaxation times (which are responsible for contrast in T_1- and T_2-weighted MR images) were measured on a 0.5 T Bruker Minispec relaxometer. Relaxation time values were

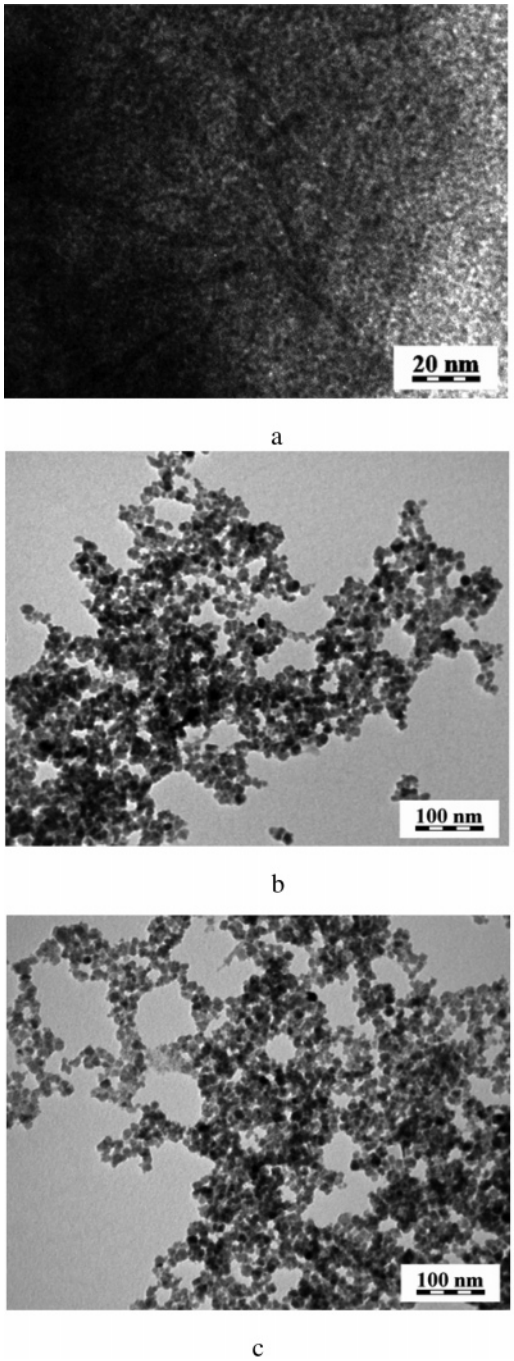


Figure 3. TEM images of in situ D-mannose-coated Fe_3O_4 particles (a; No. 1) and γ-Fe_2O_3 particles before (b; No. 2) and after modification with D-mannose (c; No. 3).

converted to relaxivities and, after deducting the contribution of pure gelatin, related to the actual iron concentration c, i.e., $r_1 = (1/T_1 - 1/T_{1gel})/c$ or $r_2 = (1/T_2 - 1/T_{2gel})/c$ in the case of contrast agent suspensions. In the case of samples containing labeled cells, the relaxivity was related, after deducting the contribution of unlabeled cells, to 10^6 cells in 1 mL.

Samples containing labeled cells (31 100 or 62 200 cells suspended in 0.5 mL of 4% gelatin) underwent MR imaging using a standard T_2-weighted turbospin echo sequence (effective echo time $T_E = 62.7$ ms, repetition time $T_R = 3000$ ms, matrix 256×256, slice thickness 1 mm, FOV = 35 mm). As a control, 62 000 unlabeled cells were suspended in 0.5 mL of 4% gelatin.

Iron Analysis. The amount of iron in the cells after mineralization was determined by spectrophotometry. Cell-containing samples were mineralized by addition of 5 mL of

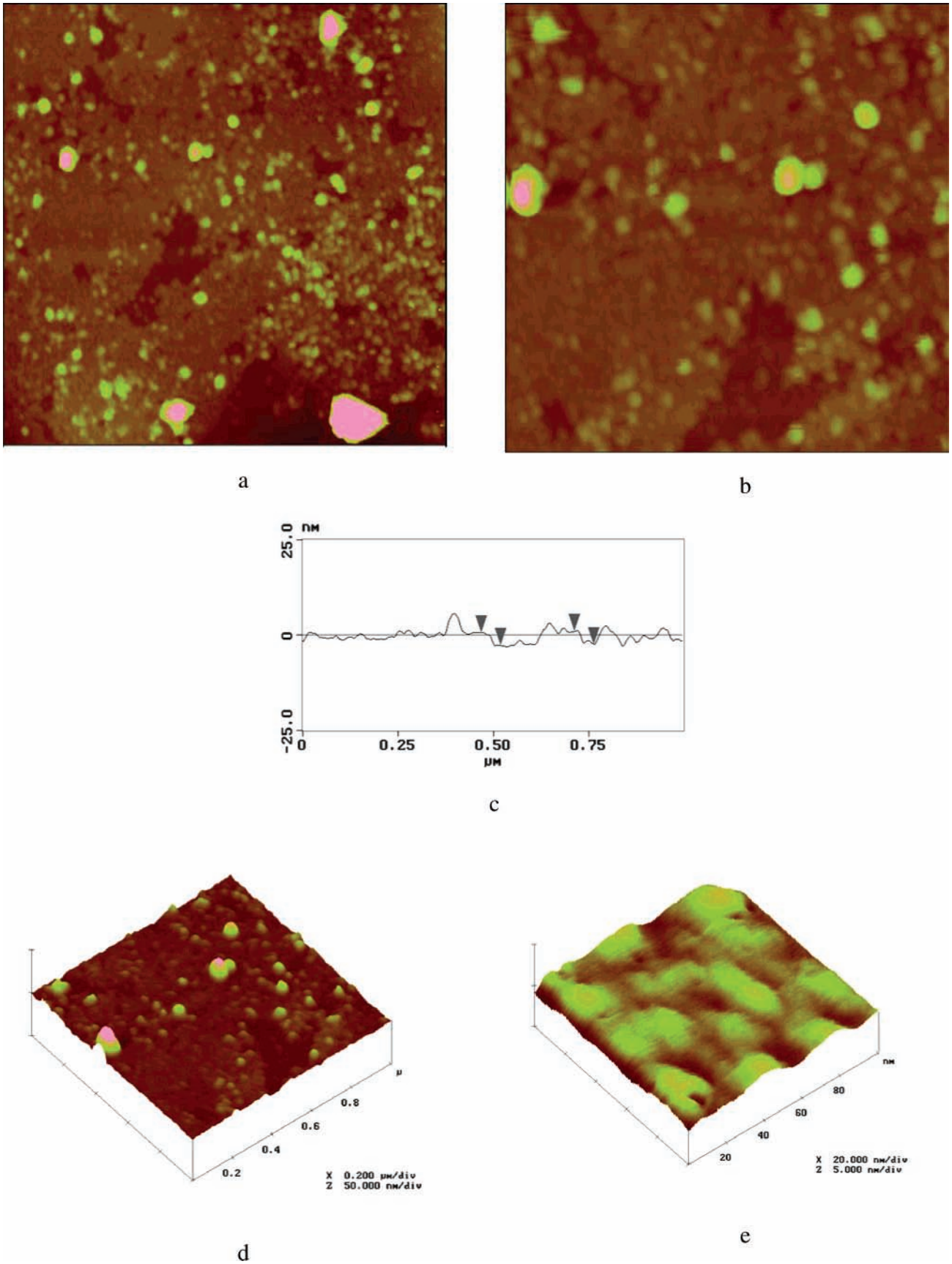


Figure 4. AFM images of D-mannose-stabilized magnetite particles No. 1: (a) overview and (b) detailed micrograph of the layer of magnetite particles on the thin carbon film on the TEM grid; (c) section analysis of the location shown in the micrograph—the cross-section line was horizontal and taken 150 nm from the bottom; (d) 3D image of the surface of the sample; (e) detailed 3D image of a location where no large particles were present. Scan size was (a) 2 or (b) 1 μm; the grayscale covers 50 nm.

HNO_3 and 1 mL of H_2O_2 in an ETHOS 900 microwave mineralizator (Millestone, Sydney, Australia). Deionized water was added to reach a total volume of 100 mL. The iron content was determined using a Spectroflame M120S apparatus (Spec-

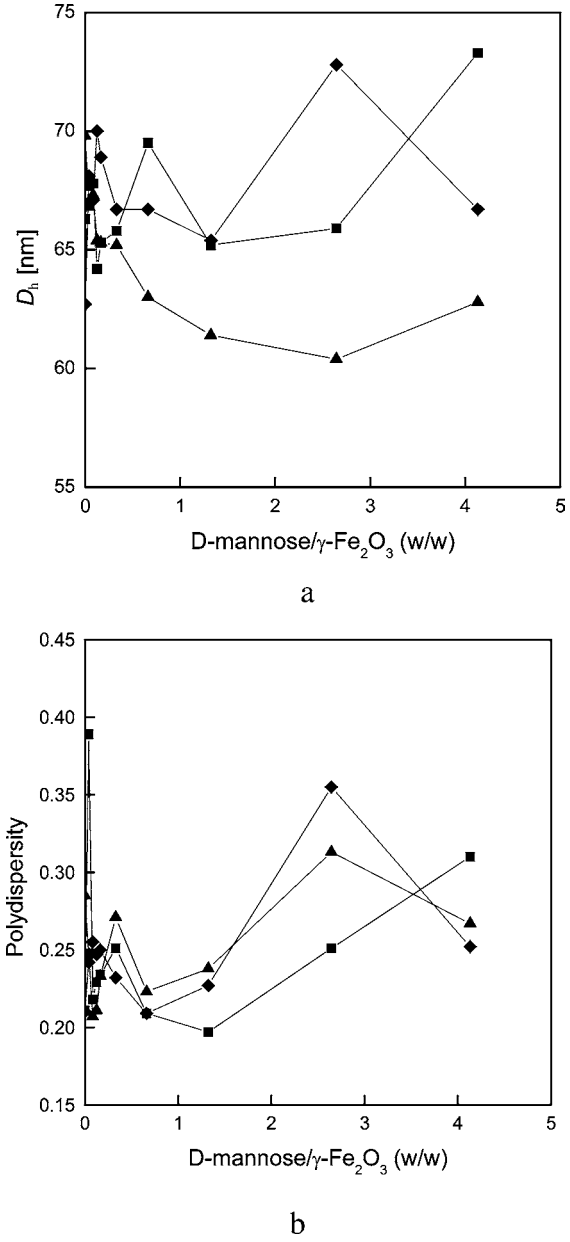


Figure 5. Dependence of (a) hydrodynamic particle diameter D_h and (b) polydispersity on the D-mannose/γ-Fe_2O_3 ratio, measured from dynamic light scattering experiments at three time points: day 1 (◆), 16 (■), and 51 (▲).

tro, Littleton, USA) calibrated with a standard Astasol solution (Analytika, Prague, Czech Republic). The measurements were repeated four times, and the average mean value was determined.

RESULTS AND DISCUSSION

Iron oxide colloids were prepared by two methods: (i) coprecipitation of Fe(II) and Fe(III) salts by ammonium in concentrated D-mannose solution (in situ coating) and (ii) precipitation followed by oxidation to maghemite (*21*) and slow addition of D-mannose solution (postsynthesis coating).

In Situ Precipitation of Iron Oxide in D-Mannose Solution. Magnetite was synthesized in a one-step process by alkaline coprecipitation of iron(II) and iron(III) precursors in an aqueous solution of D-mannose. This in situ coating, based on a modified Molday's procedure (*20*), is the easiest way to obtain surface-modified magnetic nanoparticles (run 1 in Table 1). The coating prevents particle aggregation. Elemental analysis of the resulting particles after washing revealed 58.9 wt % iron, 9.3 wt % carbon, and 2.6 wt % hydrogen, suggesting the conjugate contained about 30 wt % of D-mannose. D-Mannose is thought to be bound to the nanoparticles via a well-known coordination bond (chelate) formed between D-mannose and Fe(II) or Fe(III) on the surface of magnetite (*22*). The presence of magnetite

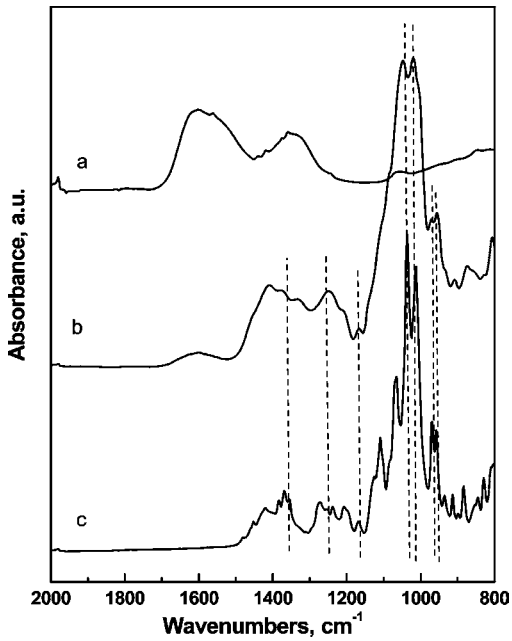


Figure 6. ATR FTIR spectra of magnetic particles before and after surface modification: spectrum of iron oxide (a) before modification and (b) after coating with D-mannose (run No. 4) and (c) spectrum of pure D-mannose.

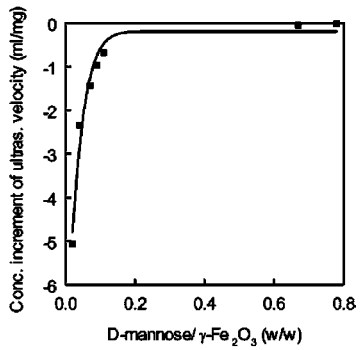


Figure 7. Dependence of the concentration increment of the ultrasonic velocity on the D-mannose/γ-Fe_2O_3 ratio.

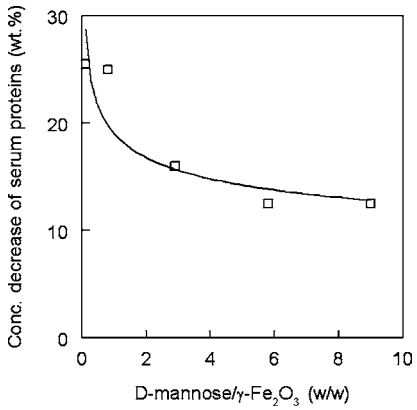


Figure 8. Effect of the D-mannose/iron oxide ratio on the decrease in serum protein concentration in culture medium, related to a standard (initial DMEM medium diluted with water 1/1 v/v), after protein sorption with D-mannose-modified iron oxide nanoparticles, as determined by UV spectrometry at 274 nm.

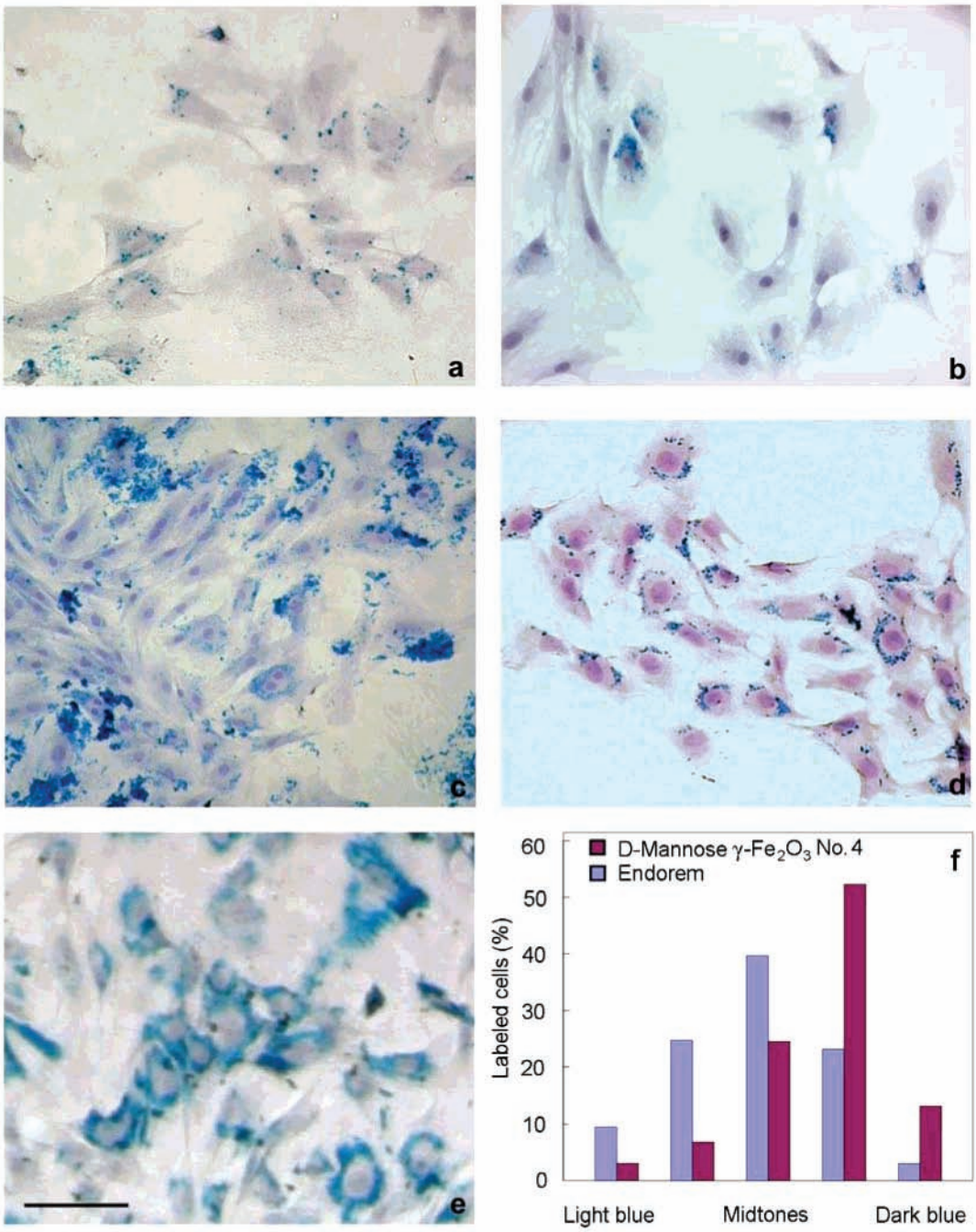


Figure 9. Microscopic observation of bone marrow stromal cells labeled with (a) Endorem (control experiment), (b) primary uncoated iron oxide nanoparticles No. 2, (c) undiluted (0.2 mg of iron oxide/mL) and (d) diluted (0.02 mg of iron oxide/mL) D-mannose-modified iron oxide nanoparticles No. 1, and (e) D-mannose-modified iron oxide nanoparticles No. 4. Scale bar: 50 μm. (f) Histograms showing the distribution of the intensity of Prussian blue staining in rMSCs labeled with Endorem or D-mannose-modified iron oxide nanoparticles No. 4.

spinel phase was confirmed by X-ray powder analysis (Figure 1). Due to the coating, only the most intense reflections (311 and 440) were observed. Significant broadening of the reflections indicates a very small particle size, in agreement with the TEM and AFM data.

Postsynthesis Iron Oxide Coating with D-Mannose. An iron oxide colloid was also obtained by a two-step procedure involving preparation of iron oxide cores in the first step (run 2 in Table 1) followed by addition of a stabilizer protecting them from aggregation and ensuring other necessary properties. Iron oxide cores were prepared by precipitation of iron salts, in particular $FeCl_2$ and $FeCl_3$, by increasing the pH followed by oxidation of the resulting magnetite with sodium hypochlorite. Oxidation resulted in maghemite (γ-Fe_2O_3), which is chemically stable and does not change its properties. This is in contrast to magnetite, which undergoes uncontrolled oxidation in the presence of oxygen. The conformation of the maghemite phase by Mössbauer spectroscopy and other magnetic properties were described in our previous report (*21*). D-Mannose was used as a stabilizer added to the primary iron oxide nanoparticles. The resulting particles were washed with water and freeze-dried to determine iron content and C and H content. Figure 2 summarizes the adsorption of D-mannose on the particles. At low D-mannose/γ-Fe_2O_3 ratios, the majority of D-mannose adsorbed to the particle surface; with increasing ratios, however, the efficiency of D-mannose adsorption initially decreased, then reached a plateau, and did not change further. It is interesting to note that after freeze drying, the product was rather voluminous without obvious agglomerates, indicating that D-mannose was attached to the iron oxide. Other supporting

evidence for such a claim is presented in the following sections; see the light scattering data, IR, and ultrasonic spectroscopy.

Nanoparticle Size Measurement by TEM, AFM, and DLS. The shapes and sizes of the magnetic nanoparticles obtained both in situ and by postsynthesis coating were observed using TEM. TEM images of the synthesized magnetic particles showed relatively high uniformity in terms of size and spherical shape. The presence of D-mannose during colloid preparation had a profound effect on the precipitation process. A TEM image of the iron oxide nanoparticles from run 1 (Figure 3a), precipitated in a concentrated D-mannose solution, shows their extremely fine size, ca. 2 nm (Table 1). This small size is due to the presence of D-mannose during precipitation, which interferes with the nucleation step of iron oxide formation, resulting in a smaller size compared with the postsynthesis method in which the coating is applied to the existing particles. The orientation of the magnetic particles is visible in Figure 3a. To confirm the TEM results, these particles were also studied by atomic force microscopy (AFM; Figure 4). A D-mannose layer containing iron oxide nanoparticles and many rounded, elevated structures (5−50 nm high) were noticeable in an AFM micrograph of magnetite particles spread across the carbon film on the TEM grid (Figure 4a). The surface structure is even more discernible at double magnification (Figure 4b), especially in the section analysis (Figure 4c). A plane lying 3.4−3.5 nm under the "surface" level can be distinguished in several places in Figure 4b. This plane is thought to be the surface of the carbon film, which is completely smooth as shown by AFM observation. The topography is illustrated in a 3D image of separated magnetite particles (Figure 4d) and in a detailed 3D image of a location where no large particles are present (Figure 4e). It can thus be concluded that the carbon film was covered with a 3.5-nm-thick layer of magnetite nanoparticles, which is in agreement with the TEM results. The layer contained rounded particle clusters 10−80 nm in size and many smaller particles (see the wrinkled surface in Figure 4e), which were otherwise not easily distinguishable. Some spots on the carbon film were not covered by the layer. Individual magnetite particles were not observed, indicating that all the iron oxide nanoparticles were stabilized with D-mannose. The iron oxide crystal growth was obviously retarded due to the unique structure of D-mannose present during precipitation. This is in contrast to the nanoparticles from run 3 (Table 1) obtained by postsynthesis coating of the primary bare colloid with D-mannose. TEM images of such particles (Figure 3c) showed no marked differences in either shape or size from uncoated iron oxide particles (2, Figure 3b). Their average diameter was 6−7 nm, and their polydispersity was PDI 1.3−1.5.

Iron oxide nanoparticle colloids obtained by postsynthesis coating were also investigated by dynamic light scattering measurements. The size calculated from DLS was ca. 10 times larger than that from TEM, mainly due to the effect of large particles on the hydrodynamic diameter. DLS provides the *z* average of the diameter, while TEM gives the number average. Figure 5 shows the dependence of hydrodynamic particle diameter and polydispersity on the D-mannose/γ-Fe_2O_3 ratio at three time points. D-Mannose-modified iron oxide particles were moderately larger than those that were uncoated due to the presence of a D-mannose hydrated shell. Moreover, Figure 5 documents the aging of the samples. Both the size and notably the polydispersity of uncoated iron oxide particles increased with storage time. This indicates aggregation of the particles without D-mannose protection. In contrast, the size and polydispersity of D-mannose-coated iron oxide nanoparticles did not dramatically change with time, implying that the particles do not aggregate (Figure 5). D-Mannose can thus be considered to be an effective stabilizer, preventing particle aggregation.

FTIR Spectra. The surface structure of the magnetic nanoparticles obtained by postsynthesis coating was analyzed by ATR FTIR spectroscopy. The infrared spectra of iron oxide before modification (run No. 2) and after coating with D-mannose (run 4) as well as the spectrum of pure D-mannose are shown in Figure 6a−c. Two broad bands of iron oxide dominate in the spectrum of the magnetic particles before modification (Figure 6a). The typical peaks of the C−H, C−O−H, and C−O−C vibrations of D-mannose (Figure 6c) are clearly distinguishable in the spectrum of the coated magnetic particles (Figure 6b). This indicates that the surface of the γ-Fe_2O_3 nanoparticles is covered with D-mannose (Figure 6). D-Mannose can be attached to iron oxide nanoparticles by the hydroxy group located on the C2 carbon in the axial position (*23*). This is a configuration specific to D-mannose, in contrast to, e.g., glucose and other common sugars that have this hydroxy group only in the equatorial position.

High-Resolution Ultrasonic Spectroscopy. Both uncoated and D-mannose-modified iron oxide nanoparticles were also characterized using high-resolution ultrasonic spectroscopy. Figure 7 shows the dependence of the concentration increment of the ultrasonic velocity on the amount of D-mannose added to the iron oxide. At low D-mannose/γ-Fe_2O_3 ratios, the ultrasonic velocity increased steeply with addition of D-mannose, which results from formation of a more ordered structure than in solution. After exceeding the critical D-mannose concentration, i.e., at a D-mannose/γ-Fe_2O_3 ratio > 0.065, the ultrasonic velocity almost did not change; that is, the excess D-mannose remained in solution. This indicates that until the critical D-mannose/γ-Fe_2O_3 ratio is reached, D-mannose molecules preferentially adsorb on the surface of iron oxide nanoparticles, forming a coat. Binding is obviously achieved via the D-mannose hydroxy group (*23*) at the carbon atom in position C2, possibly C3 and C4.

Protein Adsorption from Culture Medium. Adsorption of proteins from culture medium onto the iron oxide nanoparticles is an important tool for elucidating the transport of iron oxide in cells and also for nanoparticle coagulation. Iron oxide nanoparticles were thus mixed with serum-containing DMEM medium, the liquid separated by centrifugation, and the UV spectra of the supernatant recorded against a standard. The relative concentration decrease of serum proteins was correlated with the D-mannose/iron oxide ratio. Figure 8 indicates that even uncoated iron oxide nanoparticles adsorbed some serum proteins from the culture medium. With increasing D-mannose/iron oxide ratios used in the preparation of the nanoparticles, the amount of adsorbed serum proteins decreased. This is in agreement with published data on suppression of protein adsorption on saccharide-covered surfaces (*24*). The fact that D-mannose suppressed the nonspecific sorption of serum proteins on magnetic nanoparticles provides indirect evidence that the iron oxide particles were indeed coated with D-mannose. Moreover, it indicates that the cellular uptake mechanism of D-mannose-modified nanoparticles differs from that of PLL-modified ones (*25*).

Cell Labeling. Cell labeling with magnetic substances is an increasingly common method for in vivo cell monitoring and separation (*26*), as the labeled cells can be detected by magnetic resonance imaging. First, rat bone marrow stromal cells (rMSCs) labeled with either uncoated or surface-modified iron oxide nanoparticles were observed using an optical microscope. Cell labeling with Endorem served as a control (Figure 9a). Endorem has, however, a tendency to adhere to the surface of the cells, and it also sticks to the bottom of a vessel. Using the Prussian blue reaction, the cellular iron content was measured in rMSCs exposed to the nanoparticles.

Uncoated Iron Oxide. Uncoated iron oxide nanoparticles (No. 2) were used to label cells in order to elucidate the

importance of iron oxide modification/coating in subsequent experiments. Observation using an optical microscope with phase contrast revealed the iron oxide nanoparticles in rMSCs as dark dots. Cells in contact with the nanoparticles proliferated to some extent, and approximately 10% of the cells endocytosed the iron oxide (Figure 9b). Endocytosis might be explained by adsorption of proteins from the culture medium onto the iron oxide surface, subsequently inducing an undesirable partial coagulation of the particles. As the resulting coagulates were of a broad size distribution, only the smaller ones could penetrate the cells, whereas the larger ones were not internalized into the cells. In an attempt to increase the cell labeling, the iron oxide surface was modified with D-mannose.

D-Mannose-Modified Colloid. Modification of the colloid with D-mannose made the situation more complex, and differences were noted when the iron oxide was precipitated in a D-mannose solution compared to adding saccharide to the uncoated iron oxide nanoparticles. Cells in contact with D-mannose-modified nanoparticles No. 1 (prepared by precipitation in a concentrated D-mannose solution) proliferated well. If 10 μL of undiluted D-mannose-modified nanoparticles No. 1 was added to 1 mL of medium containing bone marrow stromal cells (to achieve a concentration of 0.2 mg of iron oxide/mL of medium), the nanoparticles were taken up by the cells (Figure 9c). A large percentage of cells was labeled (more than 80%; Table 1). However, some clumps of particles adhered to the surface of the cells and were difficult to wash out (Figure 9c). Thus, surface-bound iron oxide was indistinguishable from that internalized by the cells when observed by optical microscopy. The colloid was therefore diluted to concentrations of 0.1, 0.05, and 0.02 mg of iron oxide/mL of media. Improved results were already obtained at a concentration of 0.05 mg of iron oxide/mL, and at a concentration of 0.02 mg of iron oxide/mL, the cells were labeled with the nanoparticles without any iron oxide clusters adhering to the cell surface (Figure 9d); the percentage of labeled cells was still greater than 50% (Table 1). Compared with Endorem (0.11 mg of Fe_3O_4/mL), a lower concentration of D-mannose-modified iron oxide nanoparticles No. 1 was sufficient to label the cells. The very good ability of the cells to internalize the colloid can be explained by the extremely small size of the particles. Minimizing particle size was important for the ease of cellular internalization, but it reduced magnetic susceptibility at the same time. Moreover, colloid No. 1 was sensitive to aging; the particles coagulated within several days of storage. Modification by the postsynthesis coating of iron oxide nanoparticles with D-mannose was therefore developed. Table 1 summarizes the results of cell labeling experiments indicating that the degree of cell labeling depended on the D-mannose/γ-Fe_2O_3 ratio. The ratio 2.6/1 (colloid No. 4) can be considered as optimal, with ca. 80% of the cells being labeled. At a higher ratio (4.1/1; run 5) the particles adhered to the cell surface and the uptake of the nanoparticles did not significantly increase. This correlates with the results presented in Figure 2, which also documents that there is a limit to the ability of γ-Fe_2O_3 particles to adsorb D-mannose. Moreover, a high concentration of D-mannose results in an increased viscosity, promoting particle aggregation and adhesion to the cell surface. The mechanism responsible for the cellular internalization of ca. 10 nm nanoparticles is thought to be receptor-mediated endocytosis and/or diffusion through the cell membrane (*27*).

Image analysis tools were used to evaluate not only the percentage of labeled cells but also the intensity of Prussian blue staining. The resulting histograms (Figure 9f) show the distribution of the intensity of Prussian blue staining in rMSCs. In Endorem-labeled cells, the majority of cells (88%) were moderately stained, while in D-mannose-coated iron oxide No. 4 labeled cells, the staining intensity generally (90%) ranged from moderate to strong. These results confirm that the cells labeled with D-mannose-coated nanoparticles No. 4 contained a higher amount of iron per cell than did the cells with dextran-coated iron oxide.

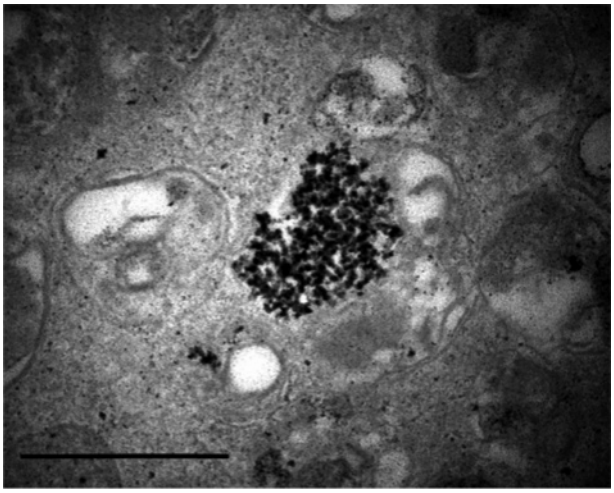


Figure 10. TEM micrograph of rMSCs labeled with D-mannose-modified iron oxide nanoparticles No. 4. Scale bar: 500 nm.

Table 2. r_1 and r_2 Relaxivities of D-mannose-coated Iron Oxide Nanoparticles No. 4 and Endorem and of rMSCs Labeled by These Contrast Agents

	phantoms containing a suspension of pure contrast agent (s^{-1}/mM Fe)		phantoms containing labeled cells (s^{-1}/million of cells/mL)	
	r_1	r_2	r_1	r_2
D-mannose-coated iron oxide nanoparticles	7.31 ± 0.11	140.4 ± 1.4	0.32 ± 0.04	12.1 ± 0.9
Endorem	19.8 ± 1.5	127 ± 9	0.18 ± 0.06	1.24 ± 0.15

Transmission Electron Microscopy of Labeled Cells. Light microscopy revealed that D-mannose-modified nanoparticles were distributed rather randomly in the cytoplasm. To further confirm that D-mannose-coated iron oxide nanoparticles were internalized by the cells rather than simply bound to the surface of the cells and visualize the location of the nanoparticles inside the cells after internalization, TEM images were taken. A TEM image (Figure 10) shows clusters of nanoparticles (No. 4) as black dots scattered in the cell cytoplasm. Cell membrane-bound nanoparticle clusters — as a result of endocytosis — were not detected. Since a highly D-mannose-specific and energy-independent transporter has been found on the surface of the majority of mammalian cells, D-mannose-coated nanoparticles are most likely transported into the cells via this mannose transporter.

MR Relaxometry. MR relaxometry enables quantification of relaxation times (and relaxivities), which are responsible for contrast enhancement in T_1- and T_2-weighted MR images. Table 2 compares the relaxivities of gelatin samples containing suspensions of two contrast agents, D-mannose-coated iron oxide nanoparticles No. 4 and commercially available Endorem, and the relaxivities of gelatin samples containing cells labeled by these contrast agents. A higher r_1 relaxivity was observed for Endorem and a higher r_2 relaxivity for D-mannose-coated iron oxide nanoparticles. Both r_1 and r_2 were higher in the case of D-mannose-coated iron oxide-labeled cells (in the case of r_2 almost 10-fold) than for Endorem-labeled cells. We hypothesize that the higher relaxivity of the D-mannose-coated iron oxide nanoparticles is responsible for not only such a huge increase in relaxivity but also the substantially higher internalization of D-mannose-coated iron oxide nanoparticles as the r_1 relaxivity

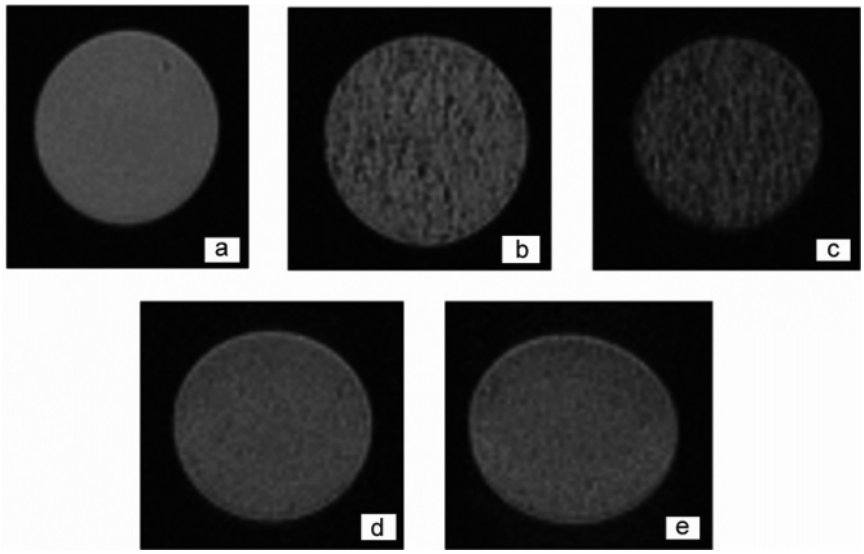


Figure 11. T_2-weighted MR images of gelatin phantoms containing (a) unlabeled cells, (b) 31 100 or (c) 62 200 cells labeled with D-mannose-coated iron oxide nanoparticles, and, for comparison, (d) 31 100 and (e) 62 200 cells labeled with Endorem.

of the D-mannose-coated iron oxide-labeled cells is also higher than the r_1 of Endorem-labeled cells, although D-mannose-coated iron oxide displayed a lower r_1 relaxivity than did Endorem. This hypothesis was confirmed by iron analysis of cell suspensions; the average amount of iron as determined by spectrophotometry after mineralization was 51.7 pg of iron per cell for D-mannose-coated iron oxide nanoparticles and 14.6 pg of iron per cell for Endorem-labeled cells.

These highly promising results were obtained with iron oxide nanoparticles coated by the postsynthesis method. Particles precipitated in situ in D-mannose solution did not display improved relaxivity, probably because they were too small, as reflected by the very low relaxivity of gelatin samples containing labeled cells: $r_2 = 0.114 \pm 0.006\ s^{-1}/10^6$ cells/mL. To mimic signal behavior in the tissue, in vitro imaging of labeled cells was performed. Phantoms with different numbers of rat MSCs labeled by Endorem or by D-mannose-coated iron oxide nanoparticles were prepared and suspended in gelatin. Unlabeled cells (Figure 11a) did not change the signal at all. Cells labeled with D-mannose-coated nanoparticles (Figure 11b,c) produced a visibly greater signal decrease than did Endorem-labeled cells (Figure 11d,e). These detectable changes in the MR signal correspond to 1.17 (Figure 11b,d) or 2.34 (Figure 11c,e) cells per image voxel, depending on the concentration of cells in the phantom. Since it was shown (*14*) that MSCs (300 000 cells in 5 μL) labeled with Endorem and implanted into the rat brain were clearly visible on T_2-weighted images, we believe that use of this novel cellular contrast agent would enable detection of very small numbers of labeled cells.

CONCLUSION

Iron oxide nanoparticles were produced by coprecipitation of Fe(II) and Fe(III) salts in an alkaline medium. The surface of the magnetic nanoparticles was modified by D-mannose, and the particles were characterized by several methods to confirm that D-mannose successfully coated the particles. The intracellular uptake of the D-mannose-coated nanoparticles by rMSCs was confirmed by both optical and transmission electron microscopy. Relaxometric measurements revealed that only postsynthesis-coated nanoparticles possessed very high r_2 relaxivity. D-Mannose-modified iron oxide nanoparticles are a promising tool for labeling living cells, particularly stem cells, for diagnostic and therapeutic applications in cell-based therapies due to their high relaxivities, which are responsible for contrast in MR imaging, and their easy internalization by cells. They can prove useful in human and veterinary medicine, biology, and microbiology for monitoring the fate of cells transplanted into a host organism, including their in vivo migration, localization, and differentiation, by means of noninvasive magnetic resonance.

ACKNOWLEDGMENT

The authors gratefully acknowledge support from the Grant Agency of the Czech Republic (grants 525/05/0311 and 309/06/1594), the Center for Cell Therapy and Tissue Repair (grant 1M0021620803), the Grant Agency of AS CR (grant KAN201110651), and the EC-FP6 project DiMI (LSHB-CT-2005-512146).

LITERATURE CITED

(1) Rosario, C. M., Yandava, B. D., Kosaras, B., Zurakowski, D., Sidman, R. L., and Snyder, E. Y. (1997) Differentiation of engrafted multipotent neural progenitors towards replacement of missing granule neurons in meander tail cerebellum may help determine the locus of mutant gene action. *Development 124*, 4213−24.

(2) Lu, D., Mahmood, A., Wang, L., Li, Y., Lu, M., and Chopp, M. (2001) Adult bone marrow stromal cells administered intravenously to rats after traumatic brain injury migrate into brain and improve neurological outcome. *NeuroReport 12*, 559−63.

(3) Nakano, K., Migita, M., Mochizuki, H., and Shimada, T. (2001) Differentiation of transplanted bone marrow cells in the adult mouse brain. *Transplantation 71*, 1735−40.

(4) Hawrylak, N., Ghosh, P., Broadus, J., Schlueter, C., Greenough, W. T., and Lauterbur, P. C. (1993) Nuclear magnetic resonance (NMR) imaging of iron oxide-labeled neural transplants. *Exp. Neurol. 121*, 81−92.

(5) Norman, A. B., Thomas, S. R., Pratt, R. G., Lu, S. Y., and Norgren, R. B. (1992) Magnetic resonance imaging of neural transplants in rat brain using a superparamagnetic contrast agent. *Brain Res. 594*, 279−83.

(6) Yeh, T., Zhang, W., Ildstad, S. T., and Ho, C. (1993) Intracellular labeling of T-cells with superparamagnetic contrast agents. *Magn. Reson. Med. 30*, 617−25.

(7) Yeh, T., Zhang, W., Ildstad, S. T., and Ho, C. (1995) In vivo dynamic MRI tracking of rat T-cells labeled with superparamagnetic iron-oxide particles. *Magn. Reson. Med. 33*, 200−208.

(8) Bulte, J. W., Brooks, R. A., Moskowitz, B. M., Bryant, L. H. J., and Frank, J. A. (1999) Relaxometry and magnetometry of the MR contrast agent MION-46L. *Magn. Reson. Med. 42*, 379−84.

(9) Shen, T., Weissleder, R., Papisov, M., Bogdanov, A. J., and Brady, T. J. (1993) Monocrystalline iron oxide nanocompounds (MION): physicochemical properties. *Magn. Reson. Med. 29*, 599−604.

(10) Bulte, J. W., Zhang, S. C., van Gelderen, P., Herynek, V., Jordan, E. K., Duncan, I. D., and Frank, J. A. (1999) Neurotransplantation of magnetically labeled oligodendrocyte progenitors: magnetic resonance tracking of cell migration and myelination. *Proc. Natl. Acad. Sci. U.S.A. 96*, 15256−61.

(11) Bulte, J. W., Douglas, T., Witwer, B., Zhang, S. C., Strable, E., Lewis, B. K., Zywicke, H., Miller, B., van Gelderen, P., Moskowitz, B. M., Duncan, I. D., and Frank, J. A. (2001) Magnetodendrimers allow endosomal magnetic labeling and in vivo tracking of stem cells. *Nat. Biotechnol. 19*, 1141−7.

(12) Modo, M., Cash, D., Mellodew, K., Williams, S. C. R., Fraser, S. E., Meade, T. J., Price, J., and Hodges, H. (2002) Tracking transplanted stem cell migration using bifunctional, contrast agent-enhanced, magnetic resonance imaging. *Neuroimage 17*, 803−811.

(13) Hoehn, M., Kustermann, E., Blunk, J., Wiedermann, D., Trapp, T., Wecker, S., Focking, M., Arnold, H., Hescheler, J., Fleischmann, B. K., Schwindt, W., and Buhrle, C. (2002) Monitoring of implanted stem cell migration in vivo: A highly resolved in vivo magnetic resonance imaging investigation of experimental stroke in rat. *Proc. Natl. Acad. Sci. U.S.A. 99*, 16267−72.

(14) Jendelová, P., Herynek, V., De Croos, J., Glogarová, K., Andersson, B., Hájek, M., and Syková, E. (2003) Imaging the fate of implanted bone marrow stromal cells labeled with superparamagnetic nanoparticles. *Magn. Reson. Med. 50*, 767−76.

(15) Jendelová, P., Herynek, V., Urdzikova, L., Glogarová, K., Kroupová, J., Bryja, V., Burian, M., Hájek, M., and Syková, E. (2004) MR tracking of transplanted bone marrow and embryonic stem cells labeled by iron oxide nanoparticles in rat brain and spinal cord. *J. Neurosci. Res. 76*, 232−43.

(16) Syková, E., Urdziková, L., Jendelová, P., Burian, M., Glogarová, K., and Hájek, M. (2005) Bone marrow cells - a tool for spinal cord injury repair. *Exp. Neurol. 193*, 261−2.

(17) Zhang, Y., and Zhang, J. (2005) Surface modification of monodisperse magnetite nanoparticle for improved intracellular uptake to breast cancer cells. *J. Colloid Interface Sci. 283*, 352−7.

(18) Zhang, J., Zhu, J., Bu, X., Cushion, M., Kinane, T. B., Avraham, H., and Koziel, H. (2005) Cdc42 and RhoB activation are required for mannose receptor-mediated phagocytosis by human alveolar macrophages. *Mol. Biol. Cell 16*, 824−34.

(19) Labský, J. (2003) Binding of D-mannose to poly(2-hydroxyethyl methacrylate) hydrogels by azo coupling. *Biomaterials 24*, 4031−6.

(20) Molday, R. S. (1984) Magnetic iron-dextran microspheres. U.S. Patent 4,452,773.

(21) Pollert, E., Knížek, K., Maryšsko, M., Závěta, K., Lančok, A., Boháček, J., Horák, D., and Babič, M. (2006) Magnetic poly(glycidyl methacrylate) microspheres containing maghemite prepared by emulsion polymerization. *J. Magn. Magn. Mater. 306*, 241−247.

(22) Geetha, K., Raghavan, M. S. S., Kulshreshtha, S. K., Sasikala, R., and Rao, C. P. (1995) Transition-metal saccharide chemistry-synthesis, spectroscopy, electrochemistry and magnetic-susceptibility studies of iron(III) complexes of monosaccharides and disaccharides. *Carbohydr. Res. 271*, 163−175.

(23) Koshikawa, M. K., and Hori, T. (2000) Adsorption selectivity of sugars toward hydrous zirconium(IV) and hydrous iron(III) oxide surfaces. *Phys. Chem. Chem. Phys. 2*, 1497−502.

(24) Zhu, J., and Marchard, R. E. (2006) Dendritic saccharide surfactant polymers as antifouling interface materials to reduce platelet adhesion. *Biomacromolecules 7*, 1036−41.

(25) Horák, D., Babič, M., Trchová, M., Jendelová, P., Glogarová, K., Lesný, P., Herynek, V., Hájek, M., and Syková, E. Poly(L-lysine)-modified iron oxide nanoparticles for stem cell labeling. *Bioconjugate Chem.*, in preparation.

(26) Olsvik, O., Popovic, T., Skjerve, E., Cudjoe, K. S., Hornes, E., Ugelstad, J., and Uhlen, M. (1994) Magnetic separation techniques in diagnostic microbiology. *Clin. Microbiol. Rev. 7*, 43−54.

(27) Dormer, K., Seeney, C., Lewelling, K., Lian, G., Gibson, D., and Johnson, M. (2005) Epithelial internalization of superparamagnetic nanoparticles and response to external magnetic field. *Biomaterials 24*, 2061−72.

BC060186C

A Human Antibody Fragment with High Affinity for Biodegradable Polymer Film

Hideki Watanabe,[†] Kouhei Tsumoto,[†,||] Seiichi Taguchi,[‡,⊥] Koichi Yamashita,[‡] Yoshiharu Doi,[‡] Yoshiyuki Nishimiya,[§] Hidemasa Kondo,[§] Mitsuo Umetsu,[†] and Izumi Kumagai*[,†]

Department of Biomolecular Engineering, Graduate School of Engineering, Tohoku University, Aoba-yama 6-6-11-606, Sendai 980-8579, Japan, Polymer Chemistry Laboratory, RIKEN Institute, 2-1 Hirosawa, Wako-shi, Saitama 351-0198, Japan, and Functional Protein Research Group, Research Institute of Genome-based Biofactory (RIGB), National Institute of Advanced Industrial Science and Technology (AIST), 2-17-2-1 Tsukisamu-Higashi, Toyohira, Sapporo 062-8517, Japan. Received July 8, 2006; Revised Manuscript Received December 9, 2006

Antibodies with high affinity for the surface of a solid material would be advantageous in biomaterial science as a protein device. A human antibody fragment that binds to poly(hydroxybutyrate) (PHB), a biodegradable polymer matter, was generated by a phage display system. Clone PH7-3d3 was isolated after several rounds of selection and prepared as a fragment of immunoglobulin variable regions (Fv). The quartz crystal microbalance technique showed that PH7-3d3 Fv completely inhibited PHB enzymatic degradation by competing with PHB depolymerase. Kinetic analysis based on surface plasmon resonance demonstrated that PH7-3d3 Fv bound to the PHB film with an equilibrium dissociation constant of 14 nM. The three-dimensional structure of PH7-3d3 Fv was resolved to 1.7 Å, revealing that the complementarity determining regions (CDRs) in the Fv fragment form a relatively flat surface on which uncharged polar and aromatic amino acids are distributed in clusters. The structure of PH7-3d3 Fv was similar to that of PHB depolymerase in the orientation of aromatic residues in the binding sites. Alanine scanning mutagenesis demonstrated that these aromatic residues, especially tryptophan residues in CDRs, were critical in the interaction between PH7-3d3 Fv and PHB. Our results suggest the possible selection of an antibody fragment that binds a material surface in a manner similar to protein−ligand interaction.

INTRODUCTION

Although most globular proteins target soluble molecules, some enzymes such as cellulose, chitinase, and PHB[1] depolymerase recognize and bind to a solid-phase biopolymer. Many researchers in the interdisciplinary fields like nanobiotechnology have attempted to exploit these proteins as a specific molecule to solid phase, because they can specifically immobilize the molecules of interest on the support material (*1*, *2*). For technological applications in which proteins serve as recognition devices, understanding the mechanism of recognition between solid surface and protein is necessary. To date, however, only limited information on the molecular recognition mechanism is available for three reasons: (i) few naturally occurring biomolecules that target solid surfaces are available, (ii) there are few efforts to generate such novel proteins de novo, and (iii) the methods for the analysis of the solid surface recognition mechanism are not well developed.

The antibody, which plays a key role in the immune system, is a naturally occurring recognition device that shows excellent binding ability and specificity. To our knowledge, although many antibodies against various antigens, including proteins, haptens, and carbohydrates, have been prepared by means of hybridoma technology, attempts to prepare the antibodies against solid surfaces have been unsuccessful, except the monoclonal antibody against amino acid crystals, because of the poor immunogenic potential of materials and the difficulty in sensitization of the vertebrate immune system by materials.

In contrast, immunization is not required in antibody production based on the in vitro selection method such as the phage display system, thus allowing the preparation of antibodies that recognizes various material surfaces. Although some peptides bound to solid surfaces such as gold (*4*), GaAs (*5*), and ZnS (*6*) were selected using phage display (*1*, *7*, *8*), few studies involve the binding of an antibody to a solid surface, which is capable of showing higher affinity compared with a low molecular weight peptide and being a model for studying the mechanism of molecular recognition between a material surface and a biomacromolecule.

The aim of the present study is to select a human antibody fragment that binds to a solid surface by phage display and to analyze the mechanism of the interaction between the antibody and the solid surface in detail. We use poly(hydroxybutyrate) (PHB), a biodegradable polymer, as a model material surface. PHB, which was found as an insoluble granule in bacteria (*9*), is a polyester of hydroxybutyric acid. The PHB granule serves as a reservoir of non-nitrogenous material under the conditions of insufficient nourishment; therefore, the host bacteria also carry the catabolic enzyme PHB depolymerase. PHB granules are produced in many bacteria, including *Bacillus megaterium* and *Alcaligenes eutrophus*, but also on the plasma membranes of *Escherichia coli* (*10*) and human erythrocytes (*11*). From a practical point of view, the effective combination of a human antibody fragment and a naturally occurring biomaterial would lead to material and medical engineering applications as well

* Izumi Kumagai, tel: +81-22-795-7274; fax: +81-22-795-6164; kmiz@mail.tains.tohoku.ac.jp.

[†] Tohoku University.

[‡] RIKEN Institute.

[§] AIST.

[||] Present address: Department of Medical Genome Sciences, Graduate School of Frontier Sciences, The University of Tokyo, 5-1-5 Kashiwanoha, Kashiwa 277-8562, Japan.

[⊥] Present address: Division of Molecular Chemistry, Graduate School of Engineering, Hokkaido University, Sapporo 060-8628, Japan.

[1] Abbreviations: Fv, fragment of immunoglobulin variable regions; VH, variable region of immunoglobulin heavy chain; VL, variable region of immunoglobulin light chain; CDR, complementarity determining region; QCM, quartz crystal microbalance; SPR, surface plasmon resonance; PHB, polyhydroxybutyrate; SBD, substrate binding domain.

10.1021/bc060203y CCC: $37.00 © 2007 American Chemical Society
Published on Web 03/27/2007

as providing a model for studying specific interactions between proteins and solid-phase surfaces.

EXPERIMENTAL PROCEDURES

Selection of Antibody Fragments. Human antibody fragment libraries were subjected to selection on the basis of Fv fragment stabilization under coexistent antigens as described previously (*12*). Variable regions of light and heavy chains (VL and VH, respectively) were displayed on the filamentous bacteriophage M13. The phage viruses displaying VL chain with affinity for PHB, were first selected from the VL chain library, and then the selection and assay of the phage virus with the VH chain was carried out in the presence of the selected VL chain for stabilizing the VH chain.

PHB purchased from ICI, Inc., was dissolved in chloroform and then dispersed in an amount of hexane to form refined PHB precipitates. Approximately 10^9 phages were mixed with 3 mg of the prepared PHB matter in 1 mL of PBS and 0.1% Tween 20 detergent. The mixture was incubated at room temperature with gentle agitation for 1 h. The residual phage viruses on PHB matter were amplified by directly adding the PHB matter into *E. coli* media after the exclusion of the unbound phage from the phage−PHB solution. After three rounds of selection, random clones were isolated, expressed as soluble fragments, and tested in enzyme-linked immunosorbent assay (ELISA).

ELISA Analysis. PHB was adsorbed on 96-well microtiter plates. Antibody fragments were applied to the plates after nonspecific binding to the plates was blocked by using Super Blocking Buffer (Pierce), and the plates were incubated for 1 h at room temperature. After five washes with PBS, the binding of antibody fragments was detected with Fluoroskan Ascent FL (Labsystems), using ECL Western Blotting Detection Reagent (Amersham Biosciences).

Preparation of Antibody Fragments. The VH and VL genes were inserted into the secretory coexpression vector pRA2; the resulting plasmid was named pRA2FHL. *E. coli* strain BL21 (DE3) was transformed with pRA2FHL and cultured at 28 °C for 18 h in 2 × YT medium containing 100 μg/mL ampicillin. Expression of the Fv fragment under the control of the T7 promoter was induced by adding 1 mM isopropyl β-D-thiogalactopyranoside (IPTG). The harvested cells were centrifuged and suspended in 50 mM Tris−HCl (pH 8.0) buffer with 200 mM NaCl. After sonication, the suspension was centrifuged at 5800 *g* for 30 min at 4 °C. The gene products in the supernatant were refined by means of a metal-chelate chromatography column that interacted with the histidine tag in the expressed VH and VL, after salting out with ammonium sulfate.

Quartz Crystal Microbalance (QCM) Analysis. The apparatus and experimental procedure for QCM analysis were essentially the same as those described previously (*13*). The QCM oscillator in a QCA-917 (SEIKO EG&G) was washed with a freshly prepared piranha solution (H_2SO_4/H_2O_2 = 3/1, v/v), and it was rinsed with distilled water several times. Dissolved PHB in chloroform (1.5 wt %) was cast on one side of the oscillator placed on a spin-coater (MOC Co., Ltd., ME-300) at 4000 rpm under dry air, and then the film was kept at 110 °C for 1 day after the melting treatment at 210 °C for 30 s on a hot stage (Linkam LK-600PM). After stabilization of QCM in a 0.01 M phosphate buffer solution (pH 7.4) for 1 day, the selected Fv fragment was injected into the QCM cell. For the inhibition assay for PHB enzymatic degradation, the selected Fv fragment was injected 4.5 h after the replacement from an enzyme-free solution to a 0.02 μM enzyme solution.

Surface Plasmon Resonance (SPR) Analysis. For the SPR analysis, a sensor chip of Au (Biacore) was ultrasonically cleaned in acetone, soaked in a freshly prepared piranha solution, and rinsed with double-distilled water in advance. PHB dissolved in chloroform (0.25% w/v) was spin-cast onto the chip at 6000 rpm. The chip was melted at 210 °C for 30 s and then kept at 110 °C for 24 h. The SPR resonance angle was confirmed to be within the range needed to detect binding. SPR measurements were performed using Biacore 2000 (Biacore). The running buffer for the experiments was PBS. Kinetic parameters were determined on the basis of a 1:1 Langmuir model by using the data from association phases.

Table 1. Adsorption Equilibrium Constants for PH7-3d3 and Naturally Occurring Depolymerases[a]

protein	substrate	K_e [mL/μg]	organism
PH7-3d3	PHB	2.9	human
SBD_{Cac}	PHB	1.0	*Comamonas acidovorans* (*18*)
SBD_{Cte}	PHB	1.1	*Comamonas testosterone* (*18*)
SBD_{Afa}	PHB	0.8	*Alcaligenes faecalis* (*18*)
SBD_{I}	PHB	0.26	*Pseudomonas stutzeri* (*19*)
SBD_{II}	PHB	0.07	*Pseudomonas stutzeri* (*19*)
SBD_{II-I}	PHB	0.4	*Pseudomonas stutzeri* (*19*)
CenA	cellulose (BMCC)	0.041	*Cellulomonas fimi* (*35, 39*)
Cex	cellulose (BMCC)	0.033	*Cellulomonas fimi* (*35, 39*)
EndoIII	cellulose (Avicel)	0.012	*Trichoderma viride* (*36, 39*)
E3	cellulose (Avicel)	0.0003	*Thermobifida fusca* (*37, 39*)
CBHI	cellulose (Avicel)	0.00054	*Trichoderma reesei* (*38, 39*)

[a] The K_e value of PH7-3d3 was calculated from the K_D determined by SPR analysis. Reported values for substrate binding domain (SBD) of PHB depolymerases and for cellulases were listed as references.

Table 2. Crystallographic Data for PH7-3d3 Fv

space group	*I*222
unit cell dimensions	$a = 63.4$, $b = 73.6$, $c = 103.3$
V_M (Å^3)	2.4 ($Z = 8$)
wavelength (Å)	0.979
resolution (Å)	1.7
completeness (%)	99.3
resolution range	20−1.7
R factor	19.0
free *R* factor	21.4

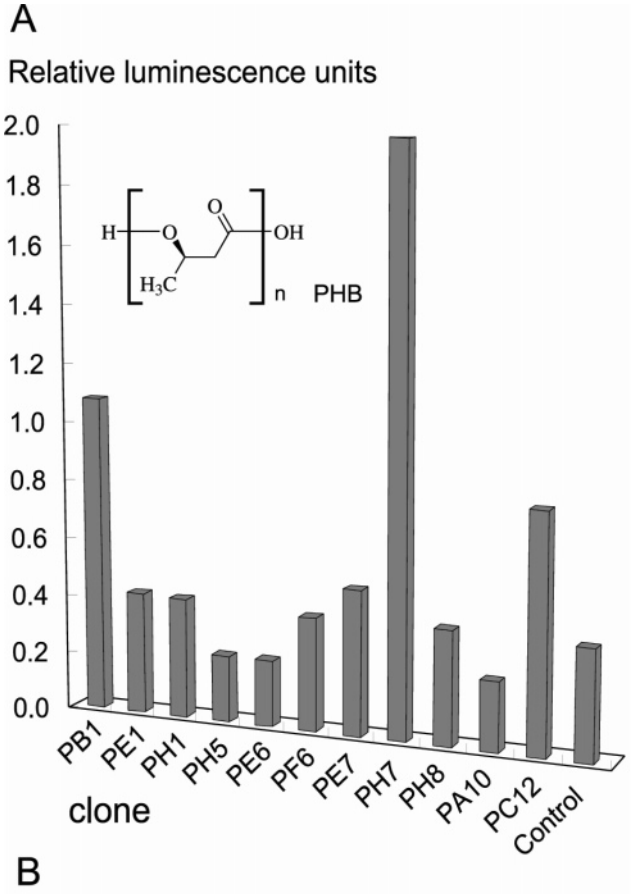
X-ray Crystallography. The soluble Fv was concentrated to 10 mg/mL by using Centricon YM-10 (Millipore). Fv was crystallized in 20% PEG 8000, 100 mM CHES (pH = 9.3). Diffraction data to 1.7 Å were collected at 100 K by using synchrotron radiation on beamline 6A of the Photon Factory (Tsukuba, Japan). The diffraction images were integrated with the *hkl* program *DENZO*, and the intensity data were processed with SCALA in the CCP4 suite (*14*). The crystallographic data and statistics are summarized in Table 2. The structure was determined by a molecular replacement method with the program *Molrep* (*15*) in the CCP4 suite. The coordinates were refined using the programs *REFMAC* (*16*) and *CNS* (*17*). The atomic coordinates and structure factors were deposited in the Protein Data Bank (entry code 2D7T).

Alanine Scanning Mutagenesis. The solvent-exposed amino acid residues in the complementarity determining regions (CDRs) were chosen for mutagenesis analysis. Each site-directed Fv mutant in which an amino acid in CDRs was mutated to alanine residue was performed by overlap extension PCR (Supporting Information). All the Fv mutants were prepared as described in the section of preparation of antibody fragments, and their binding to PHB surfaces were analyzed using SPR.

RESULTS

Selection of a Human Antibody Fragment on PHB Surface. Using a phage-displayed antibody library, the antibody fragments with affinity for PHB were selected. After three rounds of selection, ELISA was used to test the randomly isolated clones for their binding to PHB (Figure 1A). Clone PH7-3d3 showed tight binding to PHB as indicated by its high

A



B

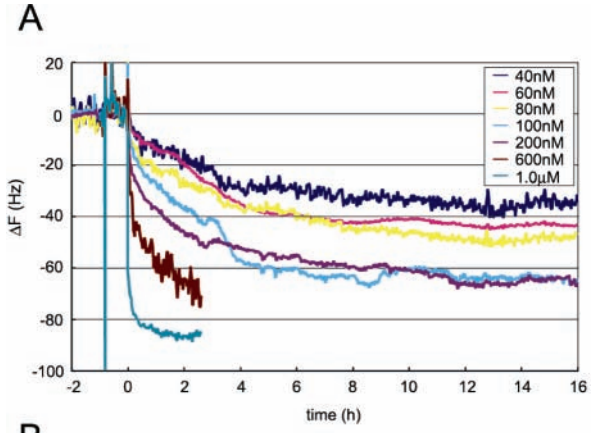
CDR H1	NYMH
CDR H2	WINPKSGDTNYAQKFQG
CDR H3	GWWGMDV
CDR L1	RASQNINNYLH
CDR L2	AASNLQG
CDR L3	LQTHAYPLT

Figure 1. Screening of antibody fragments bound to PHB. A. ELISA analysis of VH clones selected after the three rounds of selection. The binding of clones was detected as chemiluminescence intensity. The inset shows structural formula of poly(hydroxybutyrate) (PHB). B. The CDR amino acid sequences of the clone PH7-3d3.

chemiluminescence value. The amino acid sequences of the complementary determining regions (CDRs) of the selected clone PH7-3d3 are shown in Figure 1B. The tip of the CDR-H3 loop is composed of four amino acid residues—Gly, Trp, Trp, and Gly—that lie in series, which seems to be the distinctive feature of CDR-H3. The roles of these residues are discussed later. For further analysis, the clone PH7-3d3 was prepared as soluble Fv. SDS polyacrylamide gel electrophoresis verified the purity of samples and confirmed that both chains of the Fv existed in a 1:1 molar ratio. The final yield of Fv was 40 mg per 1 L culture of *E. coli* (data not shown).

QCM Analysis. We assessed the ability of PH7-3d3 Fv to bind to a PHB film by using the QCM technique (*13*). QCM analysis showed that the PH7-3d3 Fv bound tightly to the PHB film, and its binding was detected at the concentration of approximately 40 nM (Figure 2A). We also measured the QCM sensorgram of other Fv fragment with higher chemiluminescence

A



B

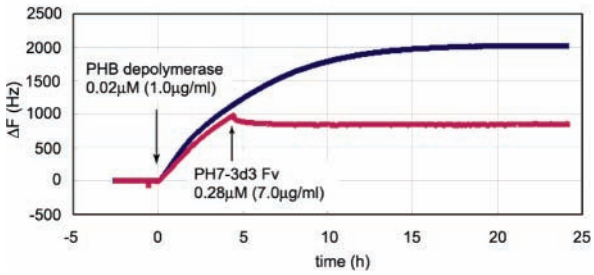


Figure 2. QCM analysis for the binding of Fv to PHB. A. Dependency of dose on the concentration of the injected Fv. B. PHB enzymatic degradation in the presence (red) and absence (blue) of PH7-3d3 Fv. Arrows indicate the injection of PHB depolymerase and Fv.

in ELISA assay than that of the background; however, no frequency changes were observed (data not shown), indicating that only the clone PH7-3d3 has the binding function to the PHB film.

PHB, which is derived from storage materials of bacteria, can be hydrolyzed by PHB depolymerase. Using QCM, we then analyzed how PH7-3d3 Fv altered the biodegradability catalyzed by PHB depolymerase derived from *Alcaligenes faecalis* T1 (Figure 2B). A frequency shift corresponds to a mass change caused by PHB hydrolysis. Enzymatic hydrolysis of PHB film by the depolymerase was completely inhibited by the addition of the Fv (Figure 2B, arrow). A rapid frequency decrease of 80 Hz occurred on the injection of PH7-3d3 Fv, and then the value of this frequency change is nearly equivalent to the shift caused by the Fv binding. The inhibition of hydrolysis is, therefore, attributed to the specific coating of the Fv onto the PHB surface.

Kinetic Study Based on Surface Plasmon Resonance (SPR) Analysis. We then analyzed the binding of PH7-3d3 Fv to the spin-coated PHB film by SPR (Figure 3A). The binding of PH7-3d3 Fv was confirmed, whereas there were no noteworthy responses upon the addition of hen egg-white lysozyme (HEL) and anti-HEL antibody HyHEL10 Fv to the PHB film. PHB, as seen from the structural formula, contains more oxygen atoms than other hydrophobic polymers such as polystyrene, and it is assumed to hydrophobically adsorb less globular protein. The binding of PH7-3d3 Fv to the dextran layer was not detected (Figure 3A).

To examine the recognition mechanism in detail, quantitative analysis from the aspect of kinetics is necessary. Although the kinetic studies based on SPR have been performed for protein−protein interaction to gain insight at the molecular level, we have obtained limited information regarding protein−material surface interaction to date. This difference may be due to protein denaturation on the surface, which influences the dissociation of adsorbed proteins and complicates the fitting analysis using a particular model. Here, we measured the binding affinity of

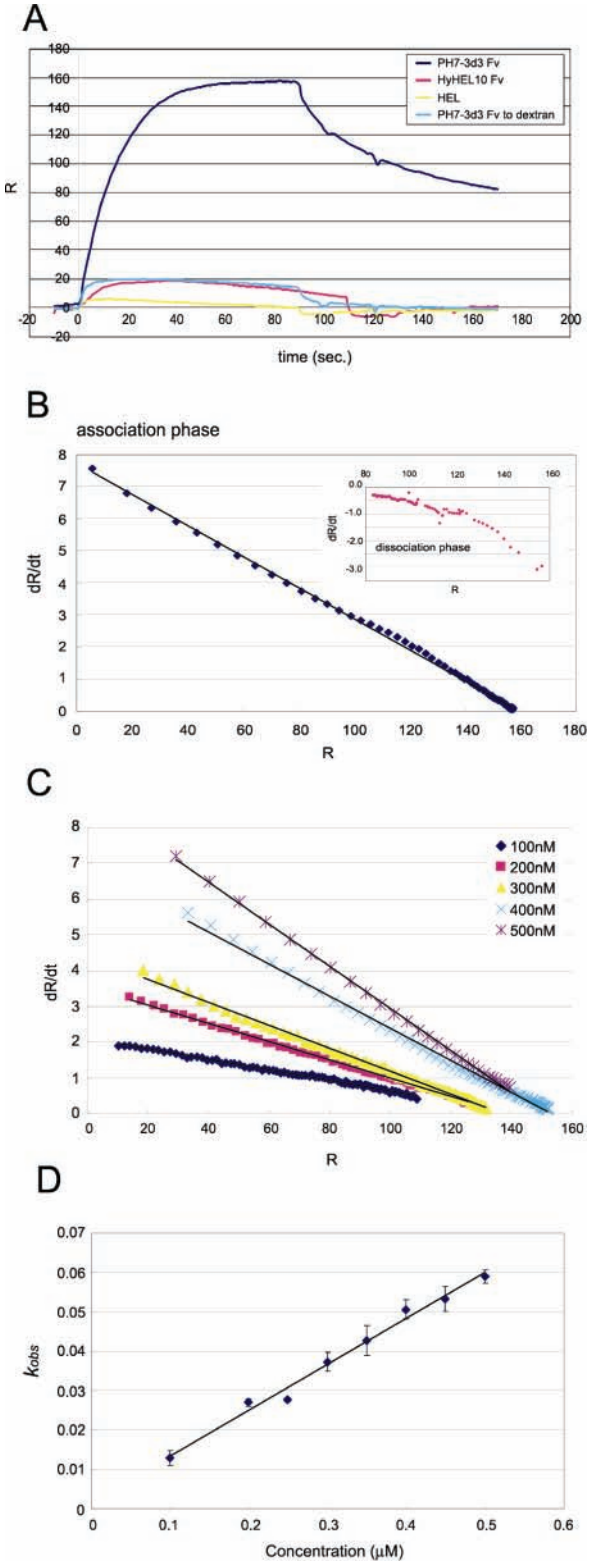


Figure 3. SPR analysis of the binding of PH7-3d3 to the PHB surface. A. Binding behavior of several kinds of protein on the PHB surface. Hen egg-white lysozyme (HEL) and the anti-HEL antibody fragment HyHEL10 Fv were used as control proteins. The binding of PH7-3d3 Fv to a layer of dextran also is shown. The concentration of all samples used in the observation was 200 nM. B. dR/dt vs R plots of the association and dissociation (inset) phases. C. Dose dependency of dR/dt vs R plots. D. The apparent association rate constant (k_{obs}) vs concentration plots. The association rate constant (k_{on}) and dissociation rate constant (k_{off}) were determined from the slope and intercept of the line. The value of the dissociation constant (K_D) was calculated as k_{off}/k_{on}.

PH7-3d3 Fv to the PHB surface according to a 1:1 Langmuir model using only the association phase. As shown in Figure 3B, dR/dt versus R plots for the dissociation phase did not yield a straight line, whereas the association phase showed good agreement with the model.

Figure 3D shows a plot of the apparent association rate constant, k_{obs}, versus concentration and the line's slope and intercept, which are equal to k_{on} and k_{off}, respectively. From these results, the kinetic parameters k_{on}, k_{off}, and K_D were determined to be 1.2×10^5 s^{-1} M^{-1}, 1.7×10^{-3} s^{-1}, and 1.4×10^{-8} M, respectively. The adsorption equilibrium constant of PH7-3d3 was calculated to be $K_e = 2.9$ mL/μg, which is comparable to or larger than those of the substrate binding domains (SBD) of PHB depolymerases as reported by Kasuya et al. (*18*) and Ohura et al. (*19*). In comparison to other depolymerases including cellulases, PH7-3d3 Fv showed a substantially higher affinity for the substrate (Table 1). These results indicate the possibility that in vitro selection enables us to generate human antibody fragments with higher affinities than those of the naturally occurring substrate binding domains.

X-ray Crystallography. Little information on the mechanism of molecular recognition between protein and the material surface is available at the amino acid level. To date, molecular dynamics (MD) simulation or docking studies have been performed for the interactions between solid surfaces and gold binding protein (*20*), carbon nanotube binding peptide (*21*), and amino acid crystal binding antibody (*22*). To gain insight into the interaction between PH7-3d3 and the PHB film surface, we performed X-ray structural analysis of PH7-3d3 Fv. Structural determination of PH7-3d3 Fv was based on the molecular replacement method using various search models (pdb codes 1AD9 for VH, 1DEE for VL) and was refined to an R value of 19.0% ($R_{free} = 21.4\%$).

Figure 4A shows the overall structure of the Fv. The CDR loops, which in general build an antigen binding site, formed a relatively flat surface that resembled those of antibodies against macromolecular antigens like proteins (*23*). Note that the putative antigen binding site lacks a cavity or groove, which typically is seen in those of antibodies for low molecular weight haptens and peptide or carbohydrate antigens (*23*). Although we have not obtained the structural data for any anti-plastic antibodies other than PH7-3d3, a flat binding site is likely to generate a highly complementary binding interface with the planar polymer surface. In addition, we examined the amino acid residues in the binding site for PHB. Polar amino acid residues such as Asn are juxtaposed around a cluster of aromatic amino acid residues (Trp and Tyr). Using *ICM-REBEL* (Molsoft), we calculated the electrostatic potential of the molecular surface around the CDRs (Figure 4B). The molecular surface formed from the CDRs is mainly a noncharged polar surface, which we anticipate is favored in the binding to uncharged plastic.

Alanine Scanning Mutagenesis. On the basis of the three-dimensional structure of PH7-3d3 Fv, we used alanine scanning mutagenesis to identify the amino acid residues critical for interaction. All the solvent-exposed amino acid residues in the CDRs were chosen as target residues for mutation (Figure 4B). We determined the equilibrium dissociation constant (K_D) of the mutants by SPR, and then their Gibbs free energy changes were calculated. The involvement of solvent-exposed residues in antigen binding was represented as relative Gibbs energy changes (Figure 5). Each loss of the binding free energy ($\Delta\Delta G$) due to the point mutation was illustrated in color on a space-filling model of Fv (Figure 4C).

Figure 5 shows that the mutation of aromatic residues to alanine residue tended to affect the interaction more than did the mutation of polar residues. Of all the solvent-exposed residues in the CDRs, the mutation of HN32, HW50, HW100, HW101, and LH92, which are localized in the center of the

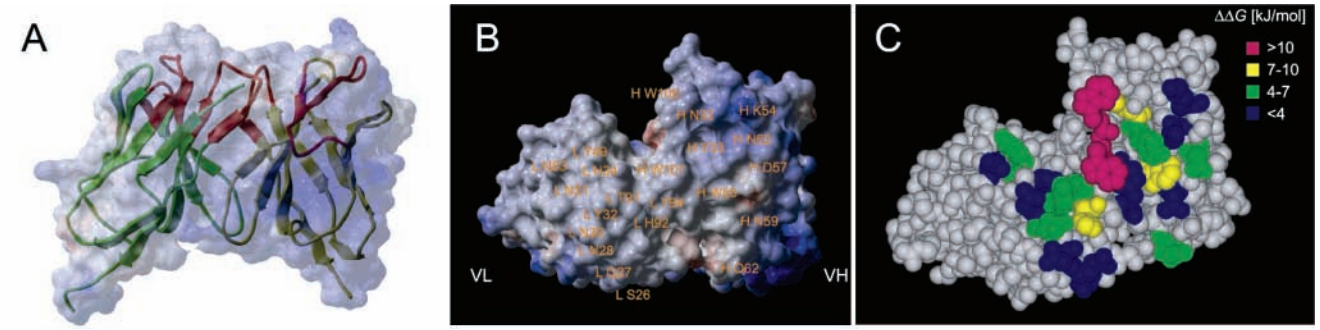


Figure 4. Structural analysis of PH7-3d3 Fv. A. Molecular surface as viewed from the side. The VH domain is shown in yellow; VL is in green. The CDR loops are colored in red in both chains. B. The molecular surface around the CDRs, as viewed from the top. Solvent-exposed amino acid residues in CDRs are annotated. C. Mapping of the amino acid residues critical for the binding of PH7-3d3 to the PHB surface. The resulting decrease in the binding due to alanine substitution was converted to $\Delta\Delta G$ (see Figure 5). The value of $\Delta\Delta G$ in each solvent-exposed residue is color-coded on the model.

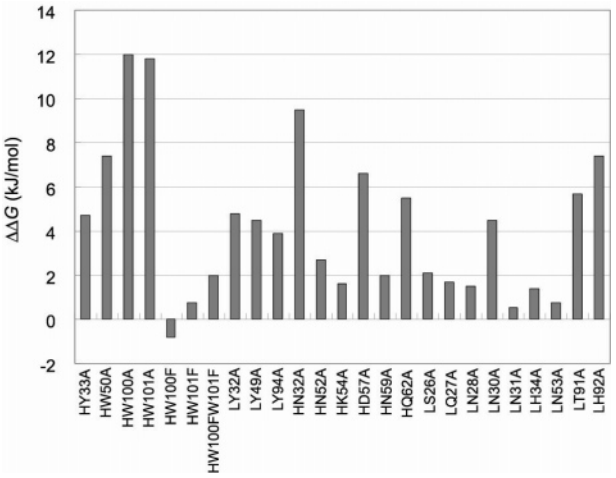


Figure 5. The relative Gibbs free energy changes of the alanine-substituted mutants. The equilibrium dissociation constants (K_D) of each mutant were determined by the same method described in the case of wild type (WT). The Gibbs free energy ΔG was calculated by the equation $\Delta G = RT \ln K_D$. The change in the Gibbs free energy $\Delta\Delta G$ of each mutant was obtained by the subtraction of ΔG of wild type from those of mutants.

CDRs (Figure 4B), resulted in the marked reduction of affinity. Note that the two tryptophan residues HW100 and HW101, which are adjacent to each other in the CDR-H3 loop, have pronounced effects on binding.

Tryptophan residues are known to frequently occur in the binding site critical for protein−protein interactions (*24*). To assess the roles of the tryptophan residues, we made three mutants—HW100F, HW101F, and HW100FW101F—where the tryptophan residues were mutated to phenylalanine. Interestingly, all three mutants bound to the PHB surface with nearly equal affinity (Figure 5), indicating that the binding tolerates the mutation of tryptophan to another aromatic residue.

Three amino acid residues—HN32, HW50, and LH92— were also shown to affect the binding to PHB film. In comparison with HW50 and LH92, the side chain of HN32 is buried and seems to be unable to contact the antigen. The location of HN32 beneath HW100 suggests that HN32 might sustain the orientation of HW100 and stabilize the conformation of the CDR H3 loop to optimally allow it to contact the antigen.

DISCUSSION

PHB, which has been developed as a biodegradable material, is a naturally occurring plastic, and its depolymerases have been isolated from several kinds of bacteria (*18*, *19*). We considered that the comparison of the naturally occurring depolymerases with the in vitro selected antibody and the analogical approach to the antibody−antigen interaction mechanism would contribute to the analysis of the protein−material surface interaction. Yamashita et al. analyzed protein adsorption to PHB film and used QCM to analyze the hydrolysis mechanism (*25*). They reported that PHB hydrolysis was not inhibited by the addition of bovine serum albumin or cellulase, which showed minimal binding of the proteins to PHB. In contrast, a PHB depolymerase mutant entirely lacking the catalytic site completely blocked PHB biodegradation. Therefore, the authors suggested that specific interactions were needed for biodegradation inhibition caused by the exchange of depolymerase for other proteins.

Exchange of proteins on the surface depends not only on the binding site, but also on the binding affinity. Our SPR analysis revealed that PH7-3d3 Fv bound to the PHB surface with higher affinity than PHB depolymerase (Table 1). Therefore, PH7-3d3 Fv is capable of competing with PHB depolymerase, which was also supported by QCM assay (Figure 2B). Kasuya et al. aligned amino acid sequences of substrate binding domains in PHB depolymerases derived from *Alcaligenes faecalis* T1, *Comamonas testosteroni*, *Comamonas* sp., *Streptomyces exfoliates*, *Psuedomonas pickettii*, and *Pseudomonas lemoignei* (*18*). They identified tyrosine and phenylalanine (aromatic residues) and serine, threonine, glutamine, and asparagine (polar residues) as conserved residues in the depolymerases. The driving force for the binding to the PHB surface is not electrically charged, but may be hydrogen bonding, van der Waals contact, or hydrophobic effect; therefore, it is reasonable to consider that all of these residues may be involved in binding. Except for phenylalanine, which does not occur in the tip of CDR loops frequently according to germline gene sequence (*26*), all of the listed residues appear in the CDRs.

The crystal structure of PHB depolymerase from *Penicillium funiculosum* was recently determined by Hisano et al. (*27*). The comparison of the structure of PH7-3d3 Fv with that of the depolymerase revealed that they had some similarities, especially in the distribution of solvent-exposed amino acid residues on the putative binding sites. In the two models, a number of hydrophobic residues on the molecular surface, which contribute to the adsorption to the PHB surface via hydrophobic interaction, and some polar residues around them were aligned in a plane. Some tyrosine and tryptophan residues located in the antigen binding site of PH7-3d3 and the tyrosine residues in the PHB adsorption site of the depolymerase had the same orientation in a way that allowed the aromatic rings to be in face-to-face contact with the PHB surface. The orientation could be effective in adsorption to the surface. The sequential and structural similarities suggest that PH7-3d3 Fv and PHB depolymerases might bind to PHB surface in a similar manner, which is consistent with the results of kinetic analysis and inhibition assay using SPR and QCM.

The alanine scanning mutagenesis studies showed that HN32, HW50, LH92, and especially HW100 and HW101, were critical for the interaction between PH7-3d3 Fv and the PHB film (Figure 5). On the other hand, mutants HW100F, HW101F, and HW100FHW101F, in which tryptophan residues in CDR-H3 were mutated to phenylalanine, have no decrease of binding affinity (Figure 5). This finding indicates that the aromatic ring can compensate for the key interaction between PH7-3d3 and PHB film via the indole ring of Trp, and it strongly suggests that the driving force of the binding is not due to hydrogen bonding but results from other factors such as van der Waals contacts, π electron donors, or hydrophobic effect. Complementarity at the molecular interface becomes particularly important when binding depends on these factors. The planar molecular surface formed by the CDRs of PH7-3d3 Fv suggests that the deletion of the bulky aromatic ring leads to decreased complementarity between binding interfaces.

Bogan et al. statistically identified tryptophan, tyrosine, and arginine as the residues that are apt to be "hot spots" (i.e., that various specific residues play a key role in protein−protein interaction) (*24*). In contrast, the mutation of polar residues surrounding these aromatic residues had less influence on binding. They subsequently proposed a mechanism in which the residues in the center of the binding surface are important as hot spots, and this role originates from being shielded from solvent by the surrounding polar residues. In the case in which those polar residues work as a solvent-shielding ring (referred to as the "O-ring"), single mutation is incapable of decreasing the binding ability. Then, our results (Figure 4) can be discussed in analogy with the concept of hot spots that has been applied to a number of protein−protein interactions, suggesting the possibility of in vitro selection of an antibody that recognizes a material surface in a similar manner to protein−ligand interaction.

CONCLUSION

Few works regarding the proteins that function at the solid−liquid interface have been reported, because only a few natural examples of these kinds of proteins have ever been identified and characterized. The specific mechanism underlying the interaction between a protein and a material surface remains to be revealed. In this study, we focused on a natural antibody repertoire and selected an antibody fragment that binds to PHB from a human antibody library. This is the first report of generating a human antibody fragment with high affinity for a given material surface based on phage display system. Protein engineering of antibodies (i.e., antibody engineering) has generated vast amounts of information and knowledge, including that of macro- and microscopic interaction analysis (*28*−*31*), improvement of functional properties based on site-directed mutagenesis analysis (*32*) or evolutionary engineering approaches (*33*), and construction of multivalent antibody fragments (*34*). The methodology we show here links the knowledge of material engineering with that of antibody engineering. From this practical viewpoint, our current work can be viewed as the generation of a highly regulated protein device that functions on the surface of a material and leads to self-assembly of materials via antibodies targeting solid surfaces.

ACKNOWLEDGMENT

We thank Dr. K. Makabe for helpful discussions. This work was supported in part by the Grant-in-aid for Scientific Research (S) from JSPS, Japan.

Supporting Information Available: The list of the oligonucleotide primer pairs for the alanine scanning mutagenesis of Fv fragment. This material is available free of charge via the Internet at http://pubs.acs.org.

LITERATURE CITED

(1) Sarikaya, M., Tamerler, C., Jen, A. K., Schulten, K., and Baneyx, F. (2003) Molecular biomimetics: nanotechnology through biology. *Nat. Mater. 2*, 577−585.
(2) Ji, Q., Vincken, J. P., Suurs, L. C., and Visser, R. G. (2003) Microbial starch-binding domains as a tool for targeting proteins to granules during starch biosynthesis. *Plant Mol. Biol. 51*, 789−801.
(3) Geva, M., Frolow, F., Eisenstein, M., and Addadi, L. (2003) Antibody recognition of chiral surfaces. Enantiomorphous crystals of leucine-leucine-tyrosine. *J. Am. Chem. Soc. 125*, 696−704.
(4) Brown, S. (1997) Metal-recognition by repeating polypeptides. *Nat. Biotechnol. 15*, 269−272.
(5) Whaley, S. R., English, D. S., Hu, E. L., Barbara, P. F., and Belcher, A. M. (2000) Selection of peptides with semiconductor binding specificity for directed nanocrystal assembly. *Nature (London) 405*, 665−668.
(6) Lee, S. W., Mao, C., Flynn, C. E., and Belcher, A. M. (2002) Ordering of quantum dots using genetically engineered viruses. *Science 296*, 892−895.
(7) Naik, R. R., Stringer, S. J., Agarwal, G., Jones, S. E., and Stone, M. O. (2002) Biomimetic synthesis and patterning of silver nanoparticles. *Nat. Mater. 1*, 169−172.
(8) Wang, S., Humphreys, E. S., Chung, S. Y., Delduco, D. F., Lustig, S. R., Wang, H., Parker, K. N., Rizzo, N. W., Subramoney, S., Chiang, Y. M., and Jagota, A. (2003) Peptides with selective affinity for carbon nanotubes. *Nat. Mater. 2*, 196−200.
(9) Lemoigne, M. (1927) Microbial autolysis and the autolytic origin of β-hydroxybutyric acid. *Ann. Inst. Pasteur 41*, 148.
(10) Huang, R., and Reusch, R. N. (1996) Poly(3-hydroxybutyrate) is associated with specific proteins in the cytoplasm and membranes of *Escherichia coli*. *J. Biol. Chem. 271*, 22196−22202.
(11) Reusch, R. N., Huang, R., and Kosk-Kosicka, D. (1997) Novel components and enzymatic activities of the human erythrocyte plasma membrane calcium pump. *FEBS Lett. 412*, 592−596.
(12) Watanabe, H., Tsumoto, K., Asano, R., Nishimiya, Y., and Kumagai, I. (2002) Selection of human antibody fragments on the basis of stabilization of the variable domain in the presence of target antigens. *Biochem. Biophys. Res. Commun. 295*, 31−36.
(13) Yamashita, K., Aoyagi, Y., Abe, H., and Doi, Y. (2001) Analysis of adsorption function of polyhydroxybutyrate depolymerase from *Alcaligenes faecalis* T1 by using a quartz crystal microbalance. *Biomacromolecules 2*, 25−28.
(14) Collaborative Computational Project, No. 4. (1994) The CCP4 suite: programs for protein crystallography. *Acta Crystallogr., Sect. D: Biol. Crystallogr. 50*, 760−763.
(15) Vagin, A., and Teplyakov, A. (1997) MOLREP: an automated program for molecular replacement. *J. Appl. Cryst. 30*, 1022−1025.
(16) Murshudov, G. N., Vagin, A. A., and Dodson, E. J. (1997) Refinement of macromolecular structures by the maximum-likelihood method. *Acta Crystallogr., Sect. D: Biol. Crystallogr. 53*, 240−255.
(17) Brünger, A. T., Adams, P. D., Clore, G. M., DeLano, W. L., Gros, P., Grosse-Kunstleve, R. W., Jiang, J. S., Kuszewski, J., Nilges, M., Pannu, N. S., Read, R. J., Rice, L. M., Simonson, T., and Warren, G. L. (1998) Crystallography & NMR system: A new software suite for macromolecular structure determination. *Acta Crystallogr., Sect. D: Biol. Crystallogr. 54*, 905−921.
(18) Kasuya, K., Ohura, T., Masuda, K., and Doi, Y. (1999) Substrate and binding specificities of bacterial polyhydroxybutyrate depolymerases. *Int. J. Biol. Macromol. 24*, 329−336.
(19) Ohura, T., Kasuya, K. I., and Doi, Y. (1999) Cloning and characterization of the polyhydroxybutyrate depolymerase gene of *Pseudomonas stutzeri* and analysis of the function of substrate-binding domains. *Appl. Environ. Microbiol. 65*, 189−197.
(20) Braun, R., Sarikaya, M., and Schulten, K. (2002) Genetically engineered gold-binding polypeptides: structure prediction and molecular dynamics. *J. Biomater. Sci., Polym. Ed. 13*, 747−757.
(21) Wang, S., Humphreys, E. S., Chung, S. Y., Delduco, D. F., Lustig, S. R., Wang, H., Parker, K. N., Rizzo, N. W., Subramoney, S., Chiang, Y. M., and Jagota, A. (2003) Peptides with selective affinity for carbon nanotubes. *Nat. Mater. 2*, 196−200.

(22) Geva, M., Eisenstein, M., and Addadi, L. (2004) Antibody recognition of chiral surfaces. Structural models of antibody complexes with leucine-leucine-tyrosine crystal surfaces. *Proteins 55*, 862−873.
(23) MacCallum, R. M., Martin, A. C., and Thornton, J. M. (1996) Antibody-antigen interactions: contact analysis and binding site topography. *J. Mol. Biol. 262*, 732−745.
(24) Bogan, A. A., and Thorn, K. S. (1998) Anatomy of hot spots in protein interfaces. *J. Mol. Biol. 280*, 1−9.
(25) Yamashita, K., Funato, T., Suzuki, Y., Teramachi, S., and Doi, Y. (2003) Characteristic interactions between poly(hydroxybutyrate) depolymerase and poly[(R)-3-hydroxybutyrate] film studied by a quartz crystal microbalance. *Macromol. Biosci. 3*, 694−702.
(26) Zemlin, M., Klinger, M., Link, J., Zemlin, C., Bauer, K., Engler, J. A., Schroeder, H. W., Jr., and Kirkham, P. M. (2003) Expressed murine and human CDR-H3 intervals of equal length exhibit distinct repertoires that differ in their amino acid composition and predicted range of structures. *J. Mol. Biol. 334*, 733−749.
(27) Hisano, T., Kasuya, K., Tezuka, Y., Ishii, N., Kobayashi, T., Shiraki, M., Oroudjev, E., Hansma, H., Iwata, T., Doi, Y., Saito, T., and Miki, K. (2006) The crystal structure of polyhydroxybutyrate depolymerase from *Penicillium funiculosum* provides insights into the recognition and degradation of biopolyesters. *J. Mol. Biol. 356*, 993−1004.
(28) Braden, B. C., Goldman, E. R., Mariuzza, R. A., and Poljak, R. J. (1998) Anatomy of an antibody molecule: structure, kinetics, thermodynamics and mutational studies of the antilysozyme antibody D1.3. *Immunol. Rev. 163*, 45−57.
(29) van Oss, C. J. (1997) Kinetics and energetics of specific intermolecular interactions. *J. Mol. Recognit. 10*, 203−216.
(30) Livingstone, J. R. (1996) Antibody characterization by isothermal titration calorimetry. *Nature (London) 384*, 491−492.
(31) Tsumoto, K., Ueda, Y., Maenaka, K., Watanabe, K., Ogasahara, K., Yutani, K., and Kumagai, I. (1994) Contribution to antibody-antigen interaction of structurally perturbed antigenic residues upon antibody binding. *J. Biol. Chem. 269*, 28777−28782.
(32) Papanastasiou, D., Mamalaki, A., Eliopoulos, E., Poulas, K., Liolitsas, C., and Tzartos, S. J. (1999) Construction and characterization of a humanized single chain Fv antibody fragment against the main immunogenic region of the acetylcholine receptor. *J. Neuroimmunol. 94*, 182−195.
(33) Wörn, A., and Plückthun, A. (2001) Stability engineering of antibody single-chain Fv fragments. *J. Mol. Biol. 305*, 989−1010.
(34) Todorovska, A., Roovers, R. C., Dolezal, O., Kortt, A. A., Hoogenboom, H. R., and Hudson, P. J. (2001) Design and application of diabodies, triabodies and tetrabodies for cancer targeting. *J. Immunol. Methods 248*, 47−66.
(35) Gilkes, N. R., Jervis, E., Henrissat, B., Tekant, B., Miller, R. C., Warren, R. A., and Kilburn, D. G. (1992) The adsorption of a bacterial cellulase and its two isolated domains to crystalline cellulose. *J. Biol. Chem. 267*, 6743−6749.
(36) Beldman, G., Voragen, A. G. J., Rombouts, F. M., Searle-van Leeuwen, M. F., and Pilnik, W. (1987) Adsorption and kinetic behavior of purified endoglucanases and exoglucanases from *Trichoderma viride*. *Biotechnol. Bioeng. 30*, 251−257.
(37) Bothwell, M. K., Daughhetee, S. D., Chaua, G. Y., Wilson, D. B., and Walker, L. P. (1997) Binding capacities for *Thermomonospora fusca* E3, E4 and E5, the E3 binding domain, and *Trichoderma reesei* CBHI on Avicel and bacterial microcrystalline cellulose. *Biores. Technol. 60*, 169−178.
(38) Ståhlberg, J., Johansson, G., and Petterson, G. (1991) A new model for enzymatic hydrolysis of cellulose based on the two-domain structure of cellobiohydrolase-1. *Bio/Technology 9*, 286−290.
(39) Lynd, L. R., Weimer, P. J., van Zyl, W. H., and Pretorius, I. S. (2002) Microbial cellulose utilization: fundamentals and biotechnology. *Microbiol. Mol. Biol. Rev. 66*, 506−577.

BC060203Y

Ultrasound-Mediated Gene Delivery: Influence of Contrast Agent on Transfection

Sophie Mehier-Humbert,[†,‡] Feng Yan,[‡] Peter Frinking,[‡] Michel Schneider,[‡] Richard H. Guy,[†,§] and Thierry Bettinger*[,‡]

University of Geneva, Department of Pharmacy and Biopharmacy, 30 quai Ansermet, 1211 Geneva 4, Switzerland, Bracco Research SA, 31 route de la Galaise, 1228 Plan-les Ouates, Switzerland, and Department of Pharmacy and Pharmacology, University of Bath, Claverton Down, Bath, BA2 7AY, U.K. Received August 7, 2006; Revised Manuscript Received October 20, 2006

MAT B III cells were insonified at ultrasound frequencies of 1.15 and 2.25 MHz in the presence of different ultrasound contrast agents (UCA) and a plasmid encoding for the green fluorescent protein. The transfection efficiency was assessed by flow cytometry, while contrast agent destruction by ultrasound was evaluated using optical and scanning electronic microscopies. It was found that the gas and shell properties of the UCA have an important influence on cell transfection. A good correlation was observed between bubble destruction and transfection rate, and it was demonstrated, for the first time, that hard-shelled contrast agents (gas microcapsules) are promising candidates for ultrasound-mediated gene delivery.

INTRODUCTION

Ultrasound contrast agents (UCA) are widely used in diagnostic applications in medical research and clinical practice. Recently, they have been exploited in ultrasound-mediated gene delivery (*1*−*3*). This new approach uses acoustic cavitation effects of gas microbubbles to induce transient membrane permeabilization (sonoporation) at the cellular level, thereby facilitating the transfer of genetic materials. In comparison to other transfection techniques (viral or nonviral), sonoporation may allow in vivo gene transfer more specifically with high spatial and temporal control, since the site and levels of transfection can be precisely localized and controlled by ultrasound (*4*, *5*). This approach has been applied in vitro (*6*−*9*) and in vivo (*3*, *10*−*12*). It is thought that sonoporation is induced by acoustic cavitation (*13*), which generates microstreaming or microjets in the surrounding medium (*14*−*16*), resulting in permeabilization of the cell membrane.

Most UCA are made of gas microbubbles and are referred to as "soft-shelled" agents, e.g., Albunex, Optison, and Definity (*17*). These UCA have been used in sonoporation as cavitation nuclei (*9*, *18*−*20*). Agents specially designed for gene delivery have also been reported (*21*, *22*), and are generally soft-shelled, comprising phospholipids or proteins with a plasmid-bearing surface and a perfluorocarbon gas core. Hard-shelled UCA (i.e., containing a rigid lipid or polymeric shell) may also be used for ultrasound-mediated gene delivery. These agents, although not yet commercially available, have been extensively studied for diagnostic imaging (*23*−*25*), drug delivery (*26*), acoustic properties (*27*, *28*), and other biophysical applications (*29*). While it is generally believed that UCA destruction at high acoustic pressure is the main cause of sonoporation, there have been few studies in which cell transfection and UCA destruction have been assessed at the same time and then related to the formulation properties of the contrast agent. In the present work, it was hypothesized that the physicochemical parameters of UCA, including bubble size, shell properties, and encapsulated gas, may be modulated to improve the efficiency of gene transfection in sonoporation. Two types of experimental UCA were investigated for in vitro transfection: gas microbubbles, stabilized with phospholipids, and gas-filled microcapsules with a rigid shell made of either triglyceride or polystyrene. Contrast agent destruction was also evaluated and correlated with transfection.

EXPERIMENTAL PROCEDURES

Cell Culture. Rat mammary carcinoma cells (MAT B III) were incubated at 37 °C under 5% CO_2 in 225 cm^2 tissue culture flasks, in a MacCoy's 5A medium containing Glutamax-I (Life Technologie, Switzerland), supplemented with 10% v/v heat-inactivated fetal calf serum (FCS) and 1% v/v antibiotics (initial concentration: 10 000 IU/mL penicillin, 10 000 μg/mL streptomycin, 25 μg/mL fungizone).

Ultrasound Contrast Agents (UCA). UCA were formulated with various shell materials and gases (Table 1). The particle concentration and average number diameter of each agent were determined using a Coulter Multisizer II (Coulter Electronics Limited, Luton, Bedfordshire, England). Table 1 includes the resistance of each UCA to hydrostatic pressure (Pc50, expressed in mmHg), a critical value at which 50% of UCA are destroyed/collapsed. This pressure was determined as described elsewhere (*30*). BR14 and the commercial agent SonoVue are both phospholipid-stabilized gas microbubbles containing, respectively, C_4F_{10} and SF_6. These microbubbles were prepared accordingly to published procedure (*31*). Studies performed using Coulter counter and HPLC analyses confirm that BR14 microbubbles are coated with a monolayer of phospholipid molecules (unpublished results). It is well-known that the thickness of a monolayer of mixed phospholipids spread at a gas−liquid interface is about 2−3 nm (e.g., determined by Langmuir through or Langmuir−Blodgett) (*32*). Figure 1A depicts BR14 microbubbles. Gas-filled microcapsules were prepared by an emulsification procedure according to published protocol (*33*). The characteristics of similar gas-filled microcapsules (also called microballoons) were already reported by Schneider et al. (*23*, *34*, *35*). A comparative study on the behavior of lipid- and polymer-shelled agents (the two agents

* Corresponding author. Dr. T. Bettinger, Bracco Research SA, 31 route de la Galaise, 1228 Plan-les Ouates, Switzerland; thierry.bettinger@brg.bracco.com; fax# 0041 22 884 88 85.

[†] University of Geneva, Department of Pharmacy and Biopharmacy.

[‡] Bracco Research SA.

[§] Department of Pharmacy and Pharmacology, University of Bath.

10.1021/bc0602432 CCC: $37.00 © 2007 American Chemical Society
Published on Web 04/10/2007

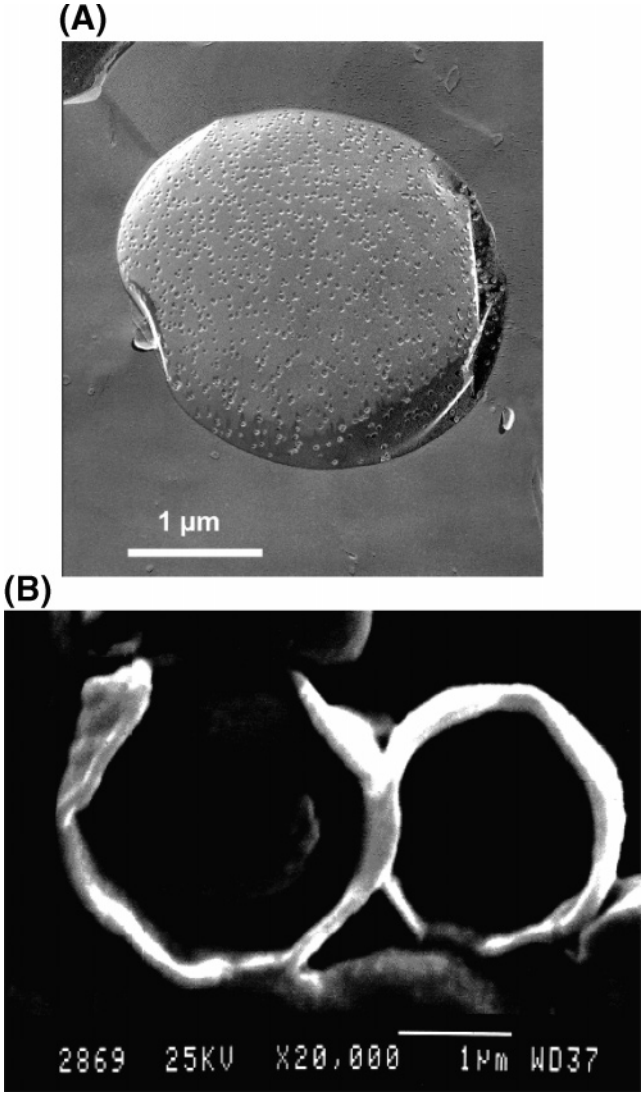


Figure 1. (A) Freeze−fracture electron micrograph of a microbubble (BR14) stabilized by a thin phospholipid film. (B) Scanning electronic micrograph of microcapsules (BG1768)—the shell is made of polystyrene (100 kDa) and has a thickness of about 50−200 nm. The open-shelled structure was obtained after ultrasound exposure of the microcapsules.

used in the present study) in response to acoustic exposure was performed by Bloch et al. (*36*).

For hard-shelled agents, formulated with either triglyceride (Figure 1B) or polystyrene, the estimated shell thickness was 50−200 nm. The soft-shelled agents are hereafter referred to as microbubbles, and the rigid-shelled UCA as microcapsules.

Ultrasound Exposure. A 3 mL polystyrene round-bottom tube was used as an exposure chamber. 500 μL of a cell suspension, at a final concentration of 1×10^6 cells/mL, was mixed with culture medium containing the plasmid gWiz-GFP (5757 base pairs; Aldevron, Fargo, ND), encoding for the green fluorescent protein (GFP). Most sonoporation experiments (except those studying the effects of bubble concentration and size) were performed with a final plasmid concentration of 10 μg/mL and a bubble-to-cell ratio of 30. The tube was mounted in a rotating exposure system and immersed in a water bath at 37 °C. The distance between the transducer and the tube was 7.6 cm. MAT B III cells were insonified for 10 s, using two different transducers (Figure 2). Peak-negative pressures were measured with a membrane hydrophone (Precision Acoustics, Ltd.) for each transducer at a distance of 76 mm (near-field distance for both transducers). The polystyrene tube was cut in half along its axis and was positioned in front of the membrane hydrophone to account for attenuation of the ultrasound beam by the tube. A duty cycle of 20% and a pulse repetition frequency of 100 Hz were applied for all experiments.

After insonification, the mixture was placed in 12-well plates and supplemented with 2 mL of medium containing 10% FCS. Finally, the cells were incubated at 37 °C under a 5% CO_2 atmosphere for 24 h.

Assay of Reporter Gene. GFP-positive cells were analyzed 24 h after ultrasound exposure by flow cytometry (FACS Calibur, Becton Dickinson AG, Switzerland). The cell suspension was placed in 5 mL polystyrene round-bottom tubes and washed twice with phosphate-buffered saline (PBS). The pellet was resuspended with 250−300 μL of PBS, and 20 μL of a propidium iodide (PI) solution (40 μg/mL, Sigma-Aldrich Chemie GmbH, Schnelldorf, Germany) was added to assess cell viability. Results are expressed as a percentage of GFP-positive cells and relative fluorescence intensity (arbitrary units, au), using the software *CellQuest Pro* (Becton Dickinson Bioscience, Binninggerstrasse 94, CH-4123 Allschwill, Switzerland). The percentage of positive cells is calculated on the basis of the total number of cells, including dead cells.

Microbubble Destruction. Microbubbles (12.5×10^6 BR14 bubbles, corresponding to a bubble-to-cell ratio of 25) were suspended in 500 μL of a MAT B III cell suspension (final concentration 1×10^6 cells/mL in medium without FCS) in the sample tube. The suspensions were then exposed to ultrasound using identical parameters to those employed in the transfection experiments. Microbubbles were counted before and after insonification using computer-assisted microscopic analysis (Leica - Program Routine BR20.Q5R, Leica Microsystem AG, Glattbrugg, Switzerland). The percentage of intact bubbles and the bubble size distribution were determined.

Scanning Electron Microscopy (SEM). Microcapsule destruction was assessed using scanning electron microscopy (LEO S470; experiments were performed at Surcotec SA, Plan-les-Ouates, Switzerland). Briefly, 15×10^6 particles were suspended in 500 μL of PBS in a sample tube and exposed to ultrasound as before. After insonification, the suspensions of ten tubes were pooled in a 15 mL polystyrene tube. The microcapsules were then washed twice in distilled water by centrifugation (10 min, 800 g), and the pellet comprising the ruptured microcapsules was collected to be freeze-dried. The washed capsules were then stuck onto an adhesive tape, fitted onto the metal stand of the microscope, and placed under vacuum at room temperature overnight. After gold sputtering, the samples were analyzed at 20 kV acceleration voltages. Microcapsules nonexposed to ultrasound were used as control.

Statistical Analysis. All results are reported and displayed as mean ± standard deviation ($n \geq 6$). Tests of significance were performed using a one-way analysis of variance (*Minitab* software v 13.20, Minitab, Inc., Paris, France), with $p < 0.05$ considered to be statistically significant.

RESULTS

Transfection Efficiency and Cell Viability. Transfection efficiency was assessed as (i) the percentage of transfected cells calculated from the ratio of GFP-positive cells to the total number (including dead cells); (ii) the fluorescence intensity of the cells determined by flow cytometery, relative to average amount of GFP produced per transfected cell; and (iii) the cell viability, expressed as viable cells/total cells and determined by propidium iodide exclusion.

Effect of UCA Concentration and Size. MAT B III cells (1×10^6/mL) were sonoporated using the 1.15 or 2.25 MHz transducer at acoustic pressures of 570 and 207 kPa (peak

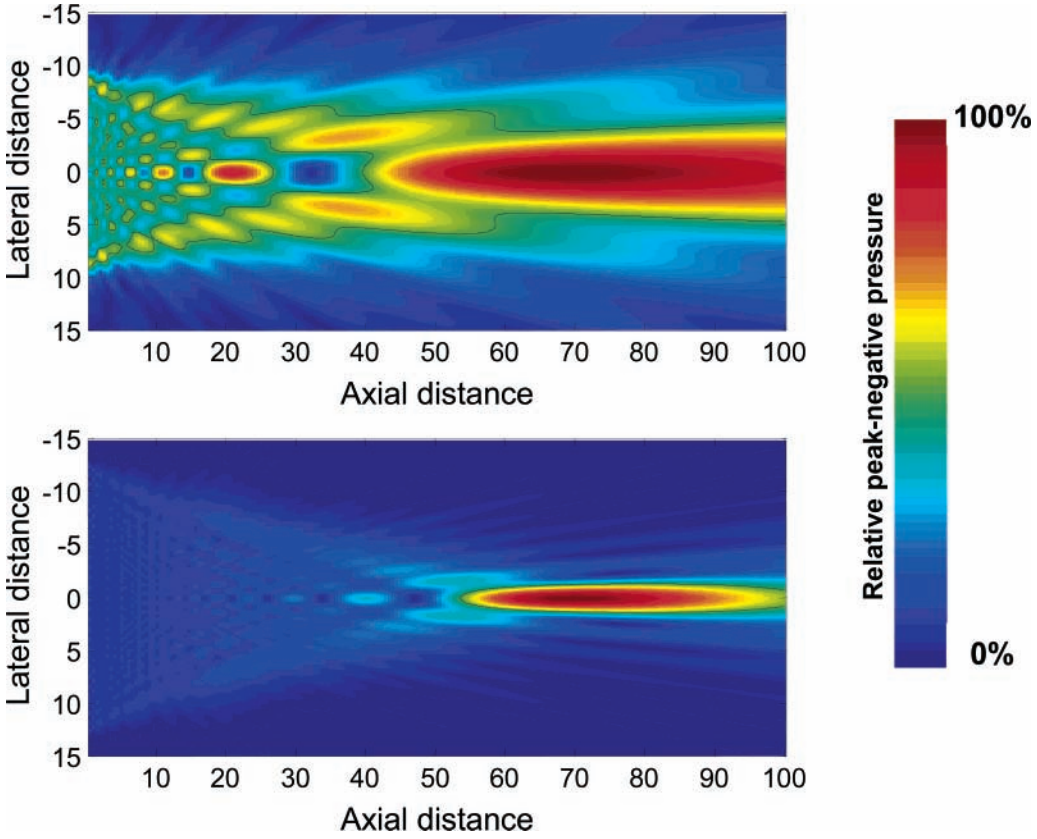


Figure 2. Ultrasound beam simulation for single-element transducers. Upper panel: 1.15 MHz unfocused transducer (Valpey Fisher; Hopkinton, MA); aperture = 0.75 in, narrow band excitation. Lower panel: 2.25 MHz focused transducer (Panametrics; Waltham, MA) (3 in); aperture = 1 in, narrow band excitation. Both plots are normalized to their maximum peak negative pressure in the field. The contours indicate the −6 dB values relative to the maximum.

Table 1. Physicochemical Characteristics of UCA Studied

formulation	shell composition	gas	mean diameter (μm)	concentration (part/mL)	Pc50 (mmHg)
		Microbubbles; Soft-Shelled (2−3 nm)			
1A009	phospholipid monolayer	C_4F_{10}	2.0	3.0×10^8	630
1A009-like	phospholipid monolayer	air	2.0	2.0×10^8	40−50
1A009-like	phospholipid monolayer	C_3F_8	2.0	3.0×10^8	580
BG1126 (1A009-like)	phospholipid monolayer	C_4F_{10}	1.0	1.5×10^9	450
BG1127 (1A009-like)	phospholipid monolayer	C_4F_{10}	2.1	5.7×10^8	700
		Microcapsules; Hard-Shelled (~100 nm)			
BG1382; BG1766	triacylglyceride	air	1.6	$2.1-2.6 \times 10^9$	>1200
BG1431	triacylglyceride	C_4F_{10}	1.6	1.2×10^9	>1200
BG1767; BG1768; BG1769	polystyrene(30; 100; 300 kDa)	air	1.7	$1.3-2.6 \times 10^9$	>1200

negative pressure, *P*_), respectively. The exposure duration was 10 s. Perfluorobutane gas microbubbles (BR14) were used as UCA, and the bubble-to-cell ratio was varied from 0 to 150. As shown in Figure 3A, the transfection rate first increased with the bubble-to-cell ratio, peaked at 30 bubbles/cell, and then decreased progressively at higher bubble concentrations. A transfection rate of 8−17% (expressed in % of GFP-positive cells) was obtained depending on the transducer frequency and bubble concentration, with a cell viability varying between 60% and 80% (Figure 3B). Cell viability decreased with bubble-to-cell ratio and reached a plateau at 30 bubbles/cells. Interestingly, both transducers gave similar trends for transfection and cell viability.

Suspensions of BR14-like phospholipid-stabilized microbubbles were fractioned into two narrow-sized populations by decantation. One had a median number diameter, Dn_{50}, of 0.99 μm (BG1126), and for the other, Dn_{50} was 1.9 μm (BG1127). Transfection was performed with these bubble fractions and with the original BR14 bubbles, using different bubble-to-cell ratios. The results are summarized in Table 3 and show that, under the experimental conditions considered, bubble size appeared to have little effect on transfection efficiency (no statistically significant difference between the two decanted samples at $p < 0.05$). The study focused therefore on UCA shell and gas properties.

Effect of UCA Shell Properties. *Microbubbles vs Microcapsules.* The effect of UCA shell properties on MAT B III transfection was first studied using the 2.25 MHz transducer, with an ultrasound exposure of 10 s and an applied peak negative pressure varying from 0 to 800 kPa. MAT B III cells were sonoporated in the presence of plasmid and either soft-shelled microbubbles (BR14) or hard-shelled microcapsules (BG1382) made of triglycerides. Air was the encapsulated gas for both agents.

As shown in Figure 4A, the percentage of GFP-positive cells increased with acoustic pressure and reached a plateau of 16% and 25% at 570 kPa, respectively, for the two agents. An important difference in the cell transfection rate was observed below 570 kPa between the soft-shelled and hard-shelled agents ($p < 0.05$). For instance, at a pressure of 247 kPa, 10% of GFP-

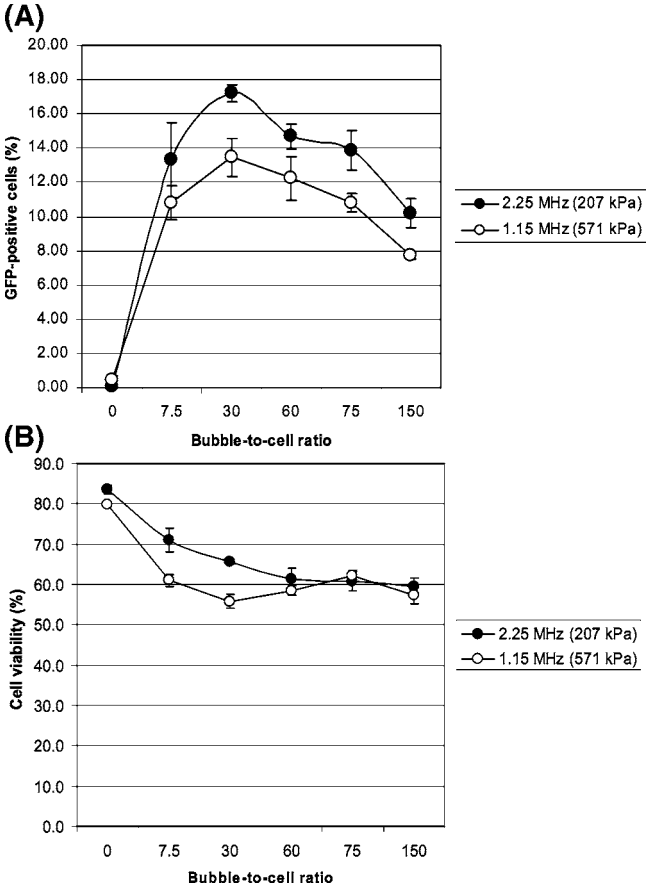


Figure 3. Effect of bubble concentration (bubble-to-cell ratio) on transfection efficiency. MAT B III cells were insonified using C_4F_{10} microbubbles (BR14) at either 1.15 MHz at 571 kPa (−●−) or 2.25 MHz at 207 kPa (−○−). (A) Percentage of transfected cells. (B) Cell viability (%).

Table 2. Effect of Bubble Size on Transfection (viability and % GFP-positive cells)

frequency [MHz]	transducer type	aperture [mm]	near field distance [mm]	manufacturer
1.15	unfocused/air-backed	19.1	76	Valpey Fisher
2.25	focused	25.4	76	Panametrics V304

Table 3

			viability		% GFP positive cells	
UCA	median diameter (μm)	bubble-to-cell ratio	mean	sd	mean	sd
1A009	$Dn_{50} = 1.4$; $Dv_{50} = 8.9$	0	91.9	0.0	0.02	0.0
		25	77.3	2.8	23.1	1.5
BG1126	$Dn_{50} = 0.99$; $Dv_{50} = 1.6$	0.12	83.2	4.0	15.5	1.5
		12	76.2	2.2	17.7	3.9
		25	79.4	0.4	21.0	4.5
BG1127	$Dn_{50} = 1.9$; $Dv_{50} = 3.9$	0.12	85.8	1.0	13.1	1.3
		12	78.9	0.9	20.7	0.3
		25	80.3	0.3	26.5	2.2

positive cells were obtained for microbubbles vs only 0.4% for microcapsules. These results suggest that soft-shelled microbubbles made of phospholipids require a lower pressure to induce acoustic cavitation than microcapsules to facilitate DNA delivery into cells. Microcapsules, being more pressure-resistant, appeared to have a higher cavitation threshold (400−600 kPa for 2.25 MHz), below which only few cells were sonoporated.

The GFP fluorescence from transfected cells is plotted in Figure 4B as a function of ultrasound pressure. Surprisingly, the microcapsules, although showing a lower transfection rate over the entire range of acoustic pressures, gave significantly higher fluorescence (by a factor about 1.5). This means that more plasmid copies per cell were delivered into the cell nucleus in the presence of the hard-shelled agent. Cell viability decreased with increasing ultrasound pressure for both agents with a viability varying from 93% to 72%. The microcapsules resulted in generally lower cell viability as compared to the microbubbles (about 10−15%; data not shown).

A similar experiment was performed using the air-backed transducer with a center frequency of 1.15 MHz and at acoustic pressures varying from 0 to 480 kPa (Figure 4C,D). The same UCAs were compared, except that the encapsulated gas, in this case, was a perfluorocarbon (C_4F_{10}). Transfection rates increased steadily with ultrasound pressure for the two agents. The ultrasound pressure required for maximum transfection was much lower for this frequency; i.e., only about 50% of that required with the 2.25 MHz transducer. This difference in pressure threshold could be due to the beam profile of the two transducers: the 1.15 MHz transducer is unfocused, providing a more homogeneous and a larger insonification field than the 2.25 MHz focused transducer (see Figure 2). In comparison to sonoporation at 2.25 MHz, even higher levels of fluorescence were obtained with the microcapsules (Figure 4D). However, cell viability was 15−25% lower with the capsules (60−79%) than with the microbubbles (85−94%) for the same applied pressure (data not shown).

Microcapsules Made of Different MW Polystyrenes. The shell properties of microcapsules are generally determined by the nature and amount of the materials employed. Three formulations of hard-shelled microcapsules, made with polystyrene of different molecular weights (30, 100, and 300 kDa), were compared. A constant amount of polymer was used in the three preparations, and air was the encapsulated gas core. It was expected that using a polymer, such as polystyrene, would provide a much more rigid shell than that obtained with triglycerides (BG1382, BG1431; see Table 1), particularly when using a high molecular weight polymer of 300 kDa.

MAT B III cells were sonoporated in the presence of polystyrene microcapsules using the focused 2.25 MHz transducer with ultrasound pressure varying from 0 to 809 kPa. The results are summarized in Figure 5. For all three formulations, transfection increased with increasing acoustic pressure from 360 to 570 kPa and reached a plateau of 14−18% GFP-positive cells (Figure 5A). Interestingly, at a pressure of 360 kPa, the transfection rate obtained was significantly higher with the low MW polystyrene: 8% of GFP-positive cells for 30 kDa vs only 2% for the 100 and 300 kDa polymers. The low MW microcapsules also showed a lower acoustic cavitation threshold, similar to that of microbubbles (see Figure 4A). In contrast, the results in Figure 5B showed that the 100 and 300 kDa microcapsules gave significantly higher fluorescence intensities. For example at 364 kPa, these microcapsules, despite their 4-fold lower transfection rates, resulted in 60% more GFP produced per transfected cell as compared to the 30 kDa microcapsules.

Effect of UCA Encapsulated Gas. MAT B III cells were insonified using the 2.25 MHz-focused transducer. Microbubbles used in this experiment were filled with air, perfluoropropane (C_3F_8), or perfluorobutane (C_4F_{10}). As shown in Figure 6A, similar transfection rates were obtained for UCA filled with C_3F_8 and C_4F_{10} and were significantly higher than those for the air-filled microbubbles at all applied acoustic pressures. A small

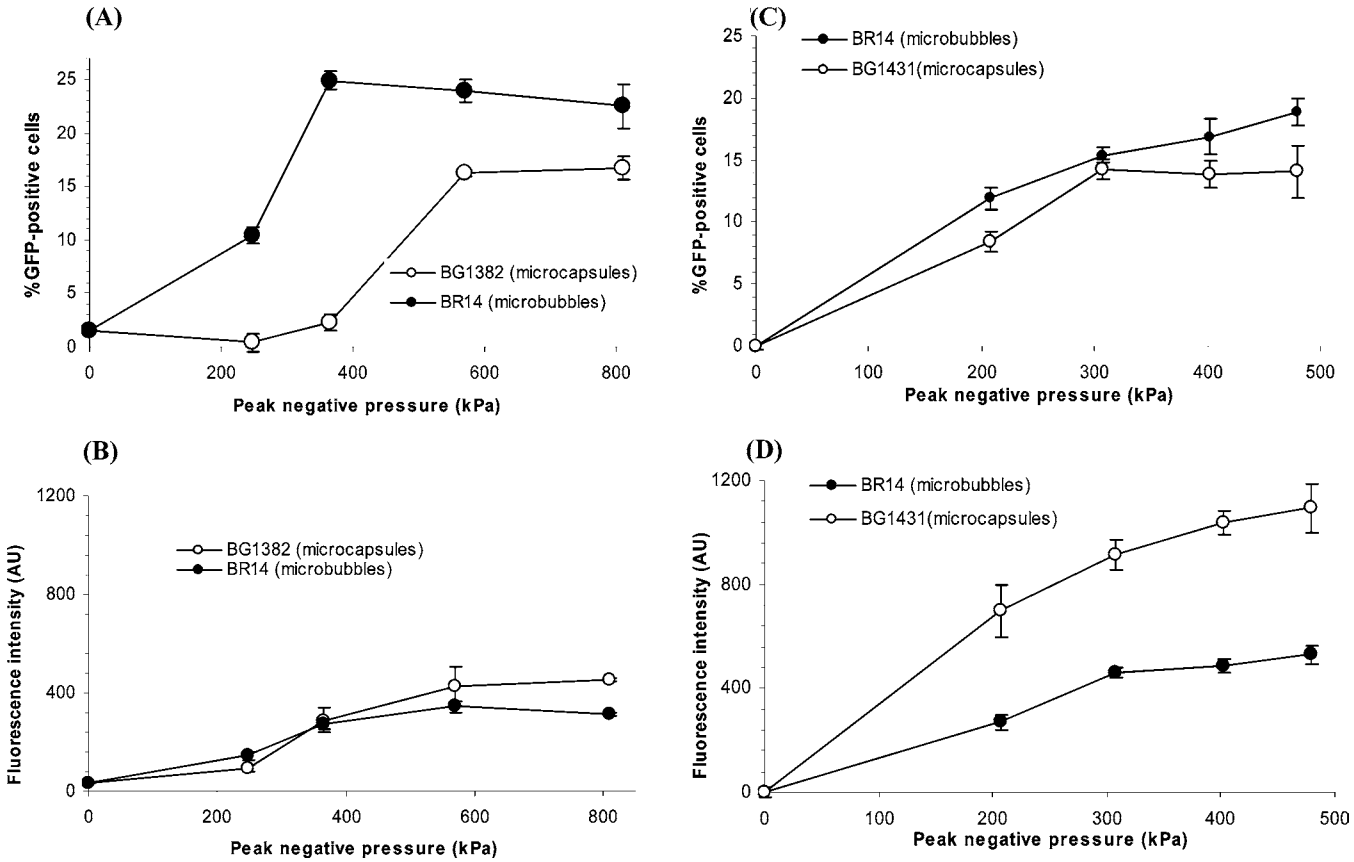


Figure 4. Effect of UCA shell properties on transfection efficiency. MAT B III cells were insonified at various peak negative pressures at 2.25 MHz (A and B) and 1.15 MHz (C and D), in the presence of either a soft-shelled agent, BR14 (−●−), or a hard-shelled agent, BG1766 or BG1382 (−○−). (A,C) Percentage of transfected cells. (B,D) Fluorescence intensity (expressed in arbitrary units (au)). Both UCA contained air as the encapsulated gas.

increase of fluorescence intensity was also observed for the perfluorocarbon gases (Figure 6B).

A similar study was performed with hard-shelled agents (BG1382, 1431) using the 1.15 MHz transducer. The results are in Figure 6. In this case, the encapsulated gas had no impact on transfection (Figure 6A) but significantly improved GFP production (Figure 6B): at pressures above 300 kPa, the fluorescence intensity was almost 2-fold higher with C_4F_{10} compared to air. These results clearly show that, in addition to shell properties, the gas encapsulated in UCA may also play an important role in sonoporation.

Contrast Agent Destruction. It is generally believed that acoustic cavitation and subsequent sonoporation can be enhanced by UCA destruction. It is still unclear, however, whether microbubble or microcapsule destruction is a prerequisite for successful sonoporation and whether there is a relationship between bubble destruction and transfection efficiency. To address these points, microbubbles and microcapsules were insonified using the same ultrasound exposure conditions as described above with the 1.15 and 2.25 MHz transducers. Bubble size distribution was analyzed by optical microscopy before and after ultrasound exposure. As microcapsule destruction could not be directly assessed by optical microscopy or Coulter analysis due to their rigid shells, scanning electron microscopy (SEM) was used to evaluate these agents.

Microbubbles. After a 10 s ultrasound exposure at 1.15 MHz and 402 kPa, more than 90% of gas microbubbles were destroyed (determined using computer-assisted microscopic analysis; data not shown). Figure 7A shows that the bubble size distribution was significantly modified by ultrasound exposure. The bubbles of 4−7 μm seemed to be most sensitive. An increase from 12% to 38% in the large bubble fraction was noted upon ultrasound exposure. This could be explained by the fact that large bubbles (>8 μm) are generally more persistent and less easily destroyed than small ones. The 6 μm bubbles showed the lowest count after insonification; interestingly enough, this diameter roughly corresponds to the calculated resonance diameter for ultrasound at 1.15 MHz.

Bubble destruction and transfection experiments were further performed in parallel using BR14 microbubbles and the focused 2.25 MHz transducer with the acoustic pressure varying from 0 to 809 kPa. As shown in Figure 7B, the 3 μm bubbles appeared most sensitive, and this again correlated well with the calculated resonance diameter of microbubbles for this frequency. Size distribution analysis indicated that 63% to 74% of the bubbles were destroyed during exposure, depending on applied pressure with the 2.25 MHz transducer (Figure 7B). There was a good correlation between transfection rate and bubble destruction as a function of the applied pressure: the higher the pressure, the larger the bubble destruction and the better the transfection (Figure 7C).

Microcapsules. Microcapsules of polystyrene 100 kDa were exposed to 570 kPa ultrasound insonification at 2.25 MHz. Scanning electron microscopy (SEM) revealed the morphology of the microcapsules before (Figure 8A) and after (Figure 8B) ultrasound exposure. Although sample preparation for SEM could alter the appearance of hollow microcapsules (the control microcapsules seemed to be flat rather than spherical in Figure 8A), differences were evident between insonified and control samples. Most ultrasound-treated microcapsules showed an open or deflated structure with a folded shell. In contrast, the control microcapsules presented a regular shape with smooth surfaces

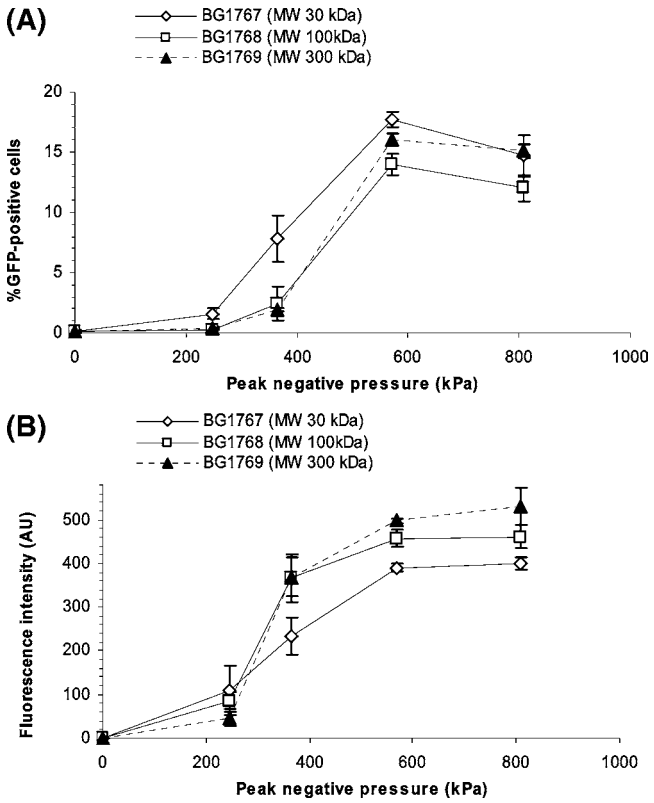


Figure 5. Effect of UCA shell properties on transfection efficiency. Microcapsule shell(s) were polystyrene of different molecular weights: 30 kDa (−×−), 100 kDa (−□−), and 300 kDa (−▲−). MAT B III cells were insonified at various peak negative pressures at 2.25 MHz, in the presence of 30 capsules/cell. (A) Percentage of transfected cells. (B) Fluorescence intensity (expressed in arbitrary units (au)). Both agents contained air as the encapsulated gas.

(Figure 8A). The open or deflated structures were observed for both small and large microcapsules, suggesting that shell properties such as stiffness, thickness, and surface homogeneity may play a more important role in microcapsule destruction than size. The SEM in Figure 8B shows that some microcapsules remained intact (a few had a small hole on the shell surface), but many were broken as a result of ultrasound exposure.

Similar experiments were also performed with the microcapsules of polystyrene 30 and 300 kDa under the same exposure conditions. Generally, the 300 kDa microcapsules were less altered, in terms of their number and shape, than those of 30 kDa (data not shown). It seemed that the shells made of high MW polystyrene were more stable to ultrasound exposure; however, upon destruction, these capsules may collapse more violently, projecting DNA molecules directly toward the cell nucleus. This may explain why fluorescent intensity (GFP production) was higher for these high MW agents (Figure 4D).

DISCUSSION

In vitro sonoporation has been widely investigated. It has been shown that ultrasound exposure parameters, such as acoustic pressure or intensity (*18*, *37*), frequency (*9*, *38*), duration of exposure, pulse-repetition frequency and duty cycle (*37*, *39*), and temperature (*40*, *41*) are important for transfection and delivery of small molecules into cells. Effects of contrast agents and bubble concentration have been also studied (*39*, *42*, *43*). In vitro gene transfection has equally been demonstrated with various cell types, such as rat fibroblasts, chondrocytes (*6*) and cultured Chinese hamster ovary cells (*9*), human cancer cells HeLa, NIH/3T3 C127I (*44*), and prostate cancer cells DU145 (*41*). Other aspects involved in sonoporation have also been evaluated, such as bubble-to-cell ratio or distance (*19*), cell-to-cell heterogeneity of molecular uptake (*37*), ultrasound modalities (*43*), DNA integrity (*41*), and plasmid-attached microbubbles (*21*, *22*, *45*, *46*).

On the other hand, UCA destruction has been evaluated initially for diagnostic imaging purposes (*47*−*51*), before being extended to UCA-induced bioeffects (*52*−*55*) and therapeutic applications (*5*, *56*−*58*). There have been very few studies in which the influence of UCA properties on gene/drug delivery has been systematically assessed, and UCA formulations dedicated to this application have not been optimized in any way. The present study aimed at addressing this issue by assessing, in particular, the effect of UCA size, shell, and gas composition on transfection efficiency. These parameters have been shown to be important in both contrast agent destruction and enhanced acoustic cavitation.

Bubble Concentration and Size. UCA bioeffects on cell lysis appear to decrease with the cubic power of the distance between microbubbles and cells (*19*). A high bubble concentration generally favors cell transfection, but it may also induce strong acoustic attenuation in vitro and in vivo, thereby reducing transfection efficiency. High bubble concentration may also lead to more cell damage, reducing in vitro cell viability and inducing in vivo side effects. For a given sonoporation sample volume, bubble-to-cell distance decreases with both bubble-to-cell ratio and cell density. It was thought that the bubble/cell ratio would be more relevant to assess the effect of UCA concentration on transfection, rather than the number of microbubbles (or microcapsules) alone. In the literature, the use of a UCA dilution factor has also been reported; however, this parameter is meaningful only for a given contrast agent with a defined bubble concentration.

The in vitro results showed a maximum transfection rate with a ratio of 30 bubbles per cell for the two different transducers used in the present study. At this ratio, the bubble/cell distance was ca. 30 μm (*19*). A further increase of the bubble-to-cell ratio tended to reduce transfection rate (Figure 3A). Since the high bubble-to-cell ratios (60, 75, and 150) did not induce more cell damage, this would suggest that the lower percentage of GFP-positive cells obtained was only due to a strong acoustic attenuation caused by microbubbles. These observations are consistent with other studies (*13*, *37*). The high concentration used in this study might yield to secondary effect, such as Bjerknes forces, by which aggregates of bubbles are formed (*59*). Aggregates of bubbles might interact differently with cells compared to individual bubbles. This possible interaction was not taken into account in the study.

It is well-known that bubble size is an important parameter for UCA stability and acoustic response. For instance, contrast agent destruction and its mechanism depend on acoustic pressure and bubble size (*60*). The results obtained in the present study showed little influence of microbubble size on transfection efficiency (Table 3). This lack of effect may be due to heterogeneity of bubble size; indeed, the three bubble samples all had relatively large size distributions: while the median diameters of three preparations were quite different (1.6, 3.9, and 8.9 μm), their Dn values were rather similar: 1.0, 1.4, and 1.9 μm, respectively. Bubbles smaller than 3 μm were predominant: 85% for BR14, 84% for BG1126 (large bubbles), and 99% for BG1127 (small bubbles). The bubble destruction experiment performed at the same frequency and pressure showed that more than 70% of microbubbles were destroyed, in particular, the smaller ones between 1 and 4 μm (see Figure 7A). This is in agreement with a previous report (*50*) which showed that, at a frequency of 2.25 MHz and a peak negative

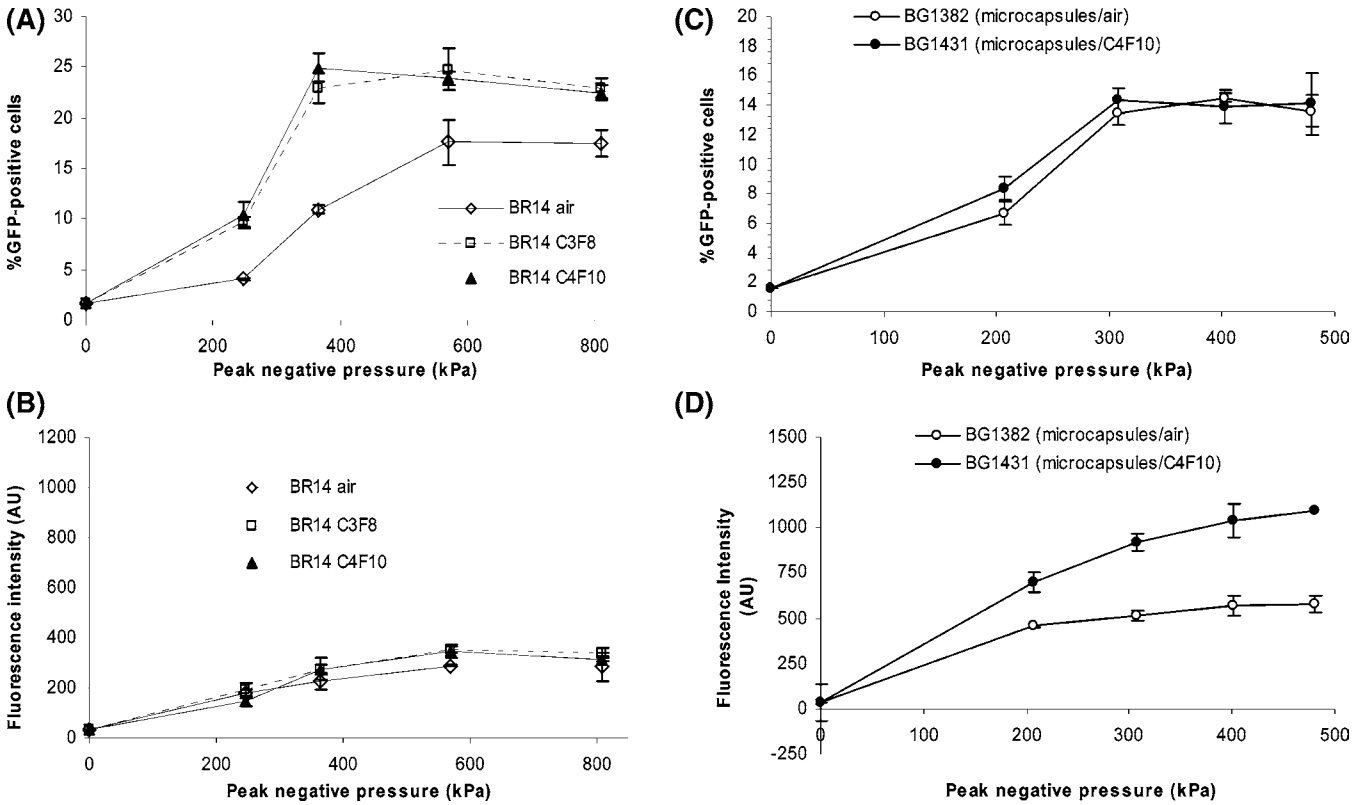


Figure 6. Effect of the encapsulated gas on transfection efficiency. Microbubbles (BR14) were filled with air (−×−), C_3F_8 (−□−), or C_4F_{10} (−▲−) (A,B); and microcapsules were filled with air (−○−) or C_4F_{10} (−●−) (C,D). MAT B III cells were insonified at various peak negative pressures at 2.25 MHz (A,B) or 1.15 MHz (C,D), in the presence of 30 bubbles/cell. (A,C) Percentage of transfected cells. (B,D) Fluorescence intensity (expressed in arbitrary units (au)).

pressure of 800 kPa, small microbubbles (<3 μm) were particularly susceptible to strong size expansion and fragmentation.

These results do not, however, prove that small bubbles are more efficient than large ones in sonoporation. It was not possible to deduce whether transfection was principally induced by stable or inertial (transient) cavitation. It is well-known that very large bubbles (100 μm) can steadily oscillate, inducing microstreaming effects yet remaining intact (*61*). Moreover, small bubbles can also coalesce into larger ones capable of stable cavitation. This raises the following questions. Is stable cavitation sufficient for cell transfection? Is microbubble destruction for a soft-shelled agent necessary to deliver plasmid/drug molecules into cells? When and how does sonoporation occur: below or above the inertial cavitation threshold? A direct and real-time observation of transfection using a high-speed camera would be very useful to clarify these points. To further study the size effect of UCA, microbubbles with a narrow size distribution and low bubble-to-cell ratio should be used to avoid interference from bubbles of different sizes and acoustic attenuation.

Shell Properties. The effects of UCA shell properties on transfection are particularly interesting. Both microbubbles and microcapsules efficiently transfected MAT B III cells at comparable rates. However, the acoustic pressure threshold for transfection was significantly different for these two agents. Higher pressures were required for hard-shelled microcapsules: For example, at 2.25 MHz, an acoustic pressure of 300 kPa was sufficient for microbubbles to transfect 5−10% of the total cells, whereas 400−600 kPa was necessary for microcapsules. This suggests that the cavitation mechanism may not be the same for the two types of agents. On the basis of in-house acoustic characterization (attenuation and backscatter measurements), the triglyceride-based agent is considered as capsules when compared to lipid-shelled microbubbles (e.g., SonoVue) (unpublished data). Bloch et al. (*36*) showed that BR14-like phospholipid-stabilized microbubbles, when insonified at 2.25 MHz, oscillated in response to ultrasound at 180 kPa; in contrast, the polymer-shelled microcapsules remained largely intact at pressures up to 1.5 MPa, and there was no evidence of significant oscillation. However, depending on the molecular weight of the polymer used for the preparation of the microcapsules, they might respond at low acoustic pressure conditions, but in terms of relative wall excursion, it is still substantially lower compared to phospholipid-based agents. Moreover, for destruction, the phospholipid agents are destroyed through fragmentation, whereas for capsules, as used in this study, typically the shell breaks and the contained gas will be released.

Sonoporation with microcapsules resulted in much higher plasmid uptake than with microbubbles. Microcapsule destruction and subsequent gas/shell fragmentation may result in more violent and effective microstreaming or microjets, propelling DNA molecules close to the cell nucleus and thus reducing their cytosolic transfer and degradation (*62*). Higher GFP production obtained with hard-shelled agents could be the result of more intact plasmid being successfully transferred. While the two types of UCA gave similar transfection rates, the microcapsules were destroyed to a lesser extent than the microbubbles (data not shown). This would suggest that, for in vivo applications, where the bubble-to-cell ratio is generally very low, the use of hard-shelled agents and high acoustic intensity would be more effective. However, cell viability was generally 10% lower for rigid microcapsules than for microbubbles; that is, high acoustic pressure with hard-shelled agents might induce more side effects.

The mechanical properties of polymers (including stiffness and shear strength) generally depend upon molecular weight.

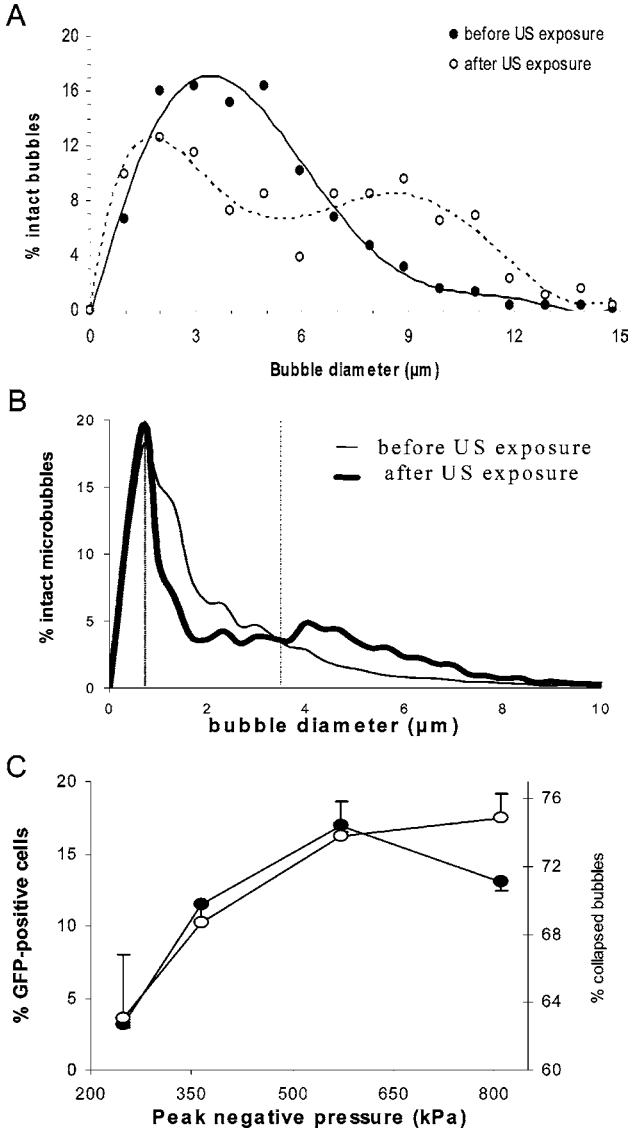


Figure 7. Size distribution of BR14 bubbles before and after insonification. C_4F_{10} microbubbles (BR14, at a concentration of 25 bubbles/cell) were insonified at 1.15 MHz at P_- = 402 kPa (A) 2.25 MHz at a peak negative pressure of 570 kPa (B). (C) Correlation between ultrasound-induced bubble destruction (−○−) and transfection efficiency (−●−). C_4F_{10} microbubbles (BR14, at a concentration of 25 bubbles/cell) were insonified at 2.25 MHz at acoustic pressures varying from 247 to 809 kPa. Size of the microbubbles was determined by computer-assisted microscopy analysis.

It would appear that sonoporation with polymer-shelled agents may be optimized by adjusting this physicochemical parameter. Low MW (30 kDa) polystyrene microcapsules transfected more efficiently at low acoustic pressures, similarly to microbubbles (Figure 5A), but resulted in a lower amount of GFP per cell (low fluorescence intensity). On the other hand, the high MW microcapsules (100 and 300 kDa) required a higher acoustic pressure for transfection, yet resulted in a higher level of GFP per cell.

Encapsulated Gas. The most important difference between first- and second-generation UCA is the encapsulated gas. For example, Albunex, Optison, and PESDA all have shells made of denatured human serum albumin, but Optison and PESDA contain C_3F_8 and perform better than air-filled Albunex, both in diagnostic imaging and in sonoporation (*52, 63, 64*).

This study confirmed that the encapsulated gas can play an important role in sonoporation. For microbubbles, the use of water-insoluble gases, such as C_3F_8 and C_4F_{10}, significantly improved transfection rates compared to air (Figure 6); while for rigid microcapsules, the substitution of air by C_4F_{10} increased the amount of GFP/cell but not the percentage of transfected cells. For microbubbles, destruction and collapse may occur via two distinct mechanisms: (i) acoustically driven gas diffusion at low acoustic pressure and (ii) bubble fragmentation at high pressure (*36, 60*). Dissolution of a free gas bubble of 2 μm in gas-saturated water by static diffusion requires about 8 ms for air, 90 ms for C_3F_8, and 900 ms for C_4F_{10} (*50*). Under ultrasound exposure, the dissolution of a shelled-gas bubble by fragmentation could be very fast, within a few milliseconds. Similar transfection behaviors observed for C_3F_8 and C_4F_{10} microbubbles (Figure 6A) suggest that the destruction of these gas bubbles was essentially driven by acoustic diffusion or fragmentation. Lower transfection with air microbubbles could be due to their instability. These microbubbles have a very low resistance to pressure with a Pc_{50} of only 40−50 mmHg as compared to about 600 mm Hg for C_3F_8 and C_4F_{10} microbubbles (see Table 1).

The effect of the encapsulated gas in microcapsules is rather complex; the pressure stability of microcapsules is primarily determined by the properties of the shell rather than the gas encapsulated inside (Table 1). Since hard-shelled agents do not significantly oscillate in ultrasound, effective microstreaming only occurs when the shell is broken at high acoustic pressure (*36*). This means that the gas cannot have any effect before its release and that the cavitation threshold of microcapsules is determined only by the properties of the shell. The effect of encapsulated gas within the microcapsules on fluorescence intensity was surprising: a twofold increase was obtained with C_4F_{10} compared to air (Figure 6D). After shell rupture, the gas released from hard-shelled microcapsules may generate large, free gas bubbles, which persist for a few milliseconds before dissolving in the surrounding liquid (*28, 29*). The persistence of free gas bubbles depends on bubble size, the gas, and the acoustic intensity. The dissolution rate of free gas bubbles may be important for the uptake of plasmid by sonoporated cells. Longer persistence (or lower dissolution rate) of free C_4F_{10} bubbles may provide more stable cavitation nuclei and stronger microstreaming effects than air. It is quite possible that microcapsule rupture only results in free gas bubbles, whereas that of phospholipid-shelled microbubbles may generate both free and stabilized gas microbubbles. This is due to the unique properties of phospholipids in aqueous media: that is, their capability to instantaneously self-assemble and to repair membrane structure (similar to that occurring at the plasma membrane during sonoporation). As a consequence, the bubble dissolution rate after fragmentation will be determined by the properties of both the shell and the encapsulated gas, and this may explain the lower, and relatively constant, fluorescence intensity obtained for different types of gas microbubbles (Figure 6B).

In summary, the effect of the encapsulated gas on transfection is related to the shell properties of the UCA. For microbubbles, a gas with low water solubility improves bubble cavitation/microstreaming effects and subsequent transfection both before and after bubble fragmentation; in contrast, for microcapsules, the gas properties affect the persistence of the released, free bubbles, only after UCA destruction (shell rupture).

Correlation with UCA Destruction. A good correlation is observed between transfection at 2.25 MHz and UCA destruction (Figure 7C). Recent studies (*36, 50, 65*) showed that bubble destruction, involving initially fast bubble expansion, followed by fragmentation and gas dissolution, can generate very high bubble fragment velocities (about 30 m/s). Even though stable bubble oscillation at low acoustic pressures (e.g., 200 kPa) may be sufficient to induce cell transfection, the high shear stress caused by violent microstreaming or microjets from bubble destruction/fragmentation may explain the maximum transfec-

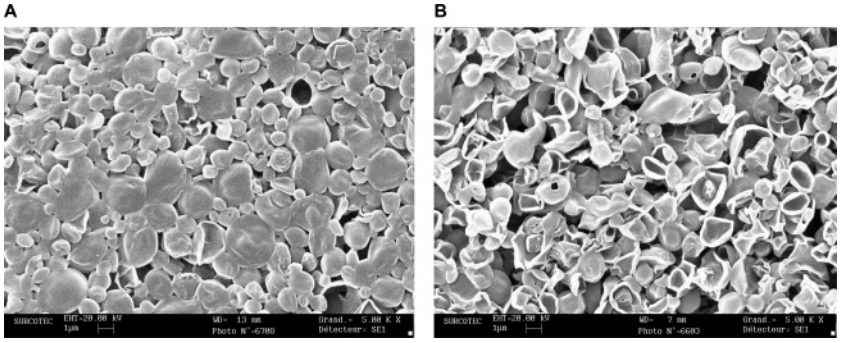


Figure 8. Scanning electron microscopy images of 100 kDa polystyrene (A) before and (B) after ultrasound exposure at 2.25 MHz and $P_- = 570$ kPa.

tion and lowest cell viability obtained at high ultrasound pressure (≥570 kPa at 2.25 MHz) (*15*, *16*).

CONCLUSIONS

The effects of UCA properties on in vitro cell transfection and related contrast agent destruction were investigated. Among different formulation parameters, the shell seemed to play a critical role. Gas bubbles stabilized by a soft shell, a monolayer of phospholipids (BR14), may steadily oscillate under low acoustic pressure and generate cell sonoporation. At a pressure of 200 kPa, significant transfection was obtained (5−10% of total cells) with a cell viability of 80−90%. At higher pressures (>300 kPa, 2.25 MHz), bubble destruction became significant, resulting in a maximum transfection rate (15−25% of GFP-positive cells/total cells) and a lower cell viability (∼70%). Microcapsules, on the other hand, showed only a negligible transfection at this pressure due to the stiffness of their shell. Hard-shelled agents do not significantly respond to ultrasound pressure waves until the shell is destabilized. Consequently, microstreaming effects will be negligible before UCA destruction. This is especially true for microcapsules made of high molecular weight polystyrene (100 and 300 kDa), for which destruction and gene transfection only occurred at pressures approaching 600 kPa (with the 2.25 MHz focused transducer). Transfection rates with microcapsules improved by using the unfocused air-backed transducer at lower frequency (1.15 MHz). The requirement of UCA agent destruction to induce transfection implies that only inertial (transient) cavitation is effective for these agents.

The results in this study also showed that rigid microcapsules generally delivered more DNA molecules into the cell, and subsequently into the cell nucleus, and produced more GFP per cell than microbubbles (by a factor of 1.5 to 2). The exact mechanism involved remains unknown; it is possible that microstreaming/microjets, and subsequent shear stress, caused by destruction/fragmentation of microcapsules, are much stronger due to the large expansion and rapid collapse of the released free gas bubbles. It is interesting to note that the level of GFP/cell can be further improved by combining a hard-shelled agent and a gas with low water solubility such as perfluorobutane (C_4F_{10}). By contrast, for microbubbles, the nature of the entrapped gas had little effect.

While significant progress has been made in both the mechanistic understanding and experimental optimization of sonoporation, more research is required to improve efficacy for in vivo applications. Gene or drug delivery in vivo will be limited by the extremely unfavorable bubble-to-cell ratio, low plasmid concentration, low or nondividing properties of targeted cells, and the accessibility of the cells to the UCA. For instance, at diagnostic imaging doses of UCA, the bubble-to-cell ratio may be lower than 1 ppm. Different approaches have been proposed to tackle these problems (including optimization of ultrasound exposure parameters and settings, exploring new ultrasound modalities, designing novel and dedicated transducers, use of plasmid-loaded microbubbles, targeted UCA and radiation force-assisted targeting, combination of lipofection and sonoporation, etc.). The optimization of UCA formulation parameters will no doubt contribute to the development of this exciting technology.

ACKNOWLEDGMENT

We would like to thank Philippe Bussat for the preparation of the hard-shelled agents.

LITERATURE CITED

(1) Bekeredjian, R., Chen, S., Frenkel, P. A., Grayburn, P. A., and Shohet, R. V. (2003) Ultrasound-targeted microbubble destruction can repeatedly direct highly specific plasmid expression to the heart. *Circulation 108* (8), 1022−1026.

(2) Bekeredjian, R., Chen, S., Pan, W., Grayburn, P. A., and Shohet, R. V. (2004) Effects of ultrasound-targeted microbubble destruction on cardiac gene expression. *Ultrasound Med. Biol. 30* (4), 539−543.

(3) Lu, Q. L., Liang, H. D., Partridge, T., and Blomley, M. J. (2003) Microbubble ultrasound improves the efficiency of gene transduction in skeletal muscle in vivo with reduced tissue damage. *Gene Ther. 10* (5), 396−405.

(4) Unger, E. C., Hersh, E., Vannan, M., and McCreery, T. (2001) Gene delivery using ultrasound contrast agents. *Echocardiography 18* (4), 355−361.

(5) May, D., Allen, J. S., and Ferrara, K. (2002) Dynamics and fragmentation of thick-shelled microbubbles. *IEEE Transactions on Ultrasonics, Ferroelectrics, and Frequency Control 49* (10), 1400−1410.

(6) Kim, H. J., Greenleaf, J. F., Kinnick, R. R., Bronk, J. T., and Bolander, M. E. (1996) Ultrasound-mediated transfection of mammalian cells. *Hum. Gene Ther. 7* (11), 1339−1346.

(7) Lawrie, A., Brisken, A. F., Francis, S. E., Tayler, D. I., Chamberlain, J., Crossman, D. C., Cumberland, D. C., and Newman, C. M. (1999) Ultrasound enhances reporter gene expression after transfection of vascular cells in vitro. *Circulation 99* (20), 2617−2620.

(8) Miller, D. L., and Gies, R. A. (2000) The influence of ultrasound frequency and gas-body composition on the contrast agent-mediated enhancement of vascular bioeffects in mouse intestine. *Ultrasound Med. Biol. 26* (2), 307−313.

(9) Miller, D. L., Bao, S., and Morris, J. E. (1999) Sonoporation of cultured cells in the rotating tube exposure system. *Ultrasound Med. Biol. 25* (1), 143−149.

(10) Lawrie, A., Brisken, A. F., Francis, S. E., Cumberland, D. C., Crossman, D. C., and Newman, C. M. (2000) Microbubble-enhanced ultrasound for vascular gene delivery. *Gene Ther. 7* (23), 2023−2027.

(11) Anwer, K., Kao, G., Proctor, B., Anscombe, I., Florack, V., Earls, R., Wilson, E., McCreery, T., Unger, E., Rolland, A., and Sullivan, S. M. (2000) Ultrasound enhancement of cationic lipid-mediated gene transfer to primary tumors following systemic administration. *Gene Ther. 7* (21), 1833−1839.

(12) Miller, D. L., and Song, J. (2003) Tumor growth reduction and DNA transfer by cavitation-enhanced high-intensity focused ultrasound in vivo. *Ultrasound Med. Biol. 29* (6), 887−893.
(13) Greenleaf, W. J., Bolander, M. E., Sarkar, G., Goldring, M. B., and Greenleaf, J. F. (1998) Artificial cavitation nuclei significantly enhance acoustically induced cell transfection. *Ultrasound Med. Biol. 24* (4), 587−595.
(14) Koch, S., Pohl, P., Cobet, U., and Rainov, N. G. (2000) Ultrasound enhancement of liposome-mediated cell transfection is caused by cavitation effects. *Ultrasound Med. Biol. 26* (5), 897−903.
(15) Wu, J. (2002) Theoretical study on shear stress generated by microstreaming surrounding contrast agents attached to living cells. *Ultrasound Med. Biol. 28* (1), 125−129.
(16) Wu, J., Ross, J. P., and Chiu, J. F. (2002) Reparable sonoporation generated by microstreaming. *J. Acoust. Soc. Am. 111* (3), 1460−1464.
(17) Miller, A. P., and Nanda, N. C. (2004) Contrast echocardiography: new agents. *Ultrasound Med. Biol. 30* (4), 425−434.
(18) Bao, S., Thrall, B. D., and Miller, D. L. (1997) Transfection of a reporter plasmid into cultured cells by sonoporation in vitro. *Ultrasound Med. Biol. 23* (6), 953−959.
(19) Ward, M., Wu, J., and Chiu, J. F. (2000) Experimental study of the effects of Optison concentration on sonoporation in vitro. *Ultrasound Med. Biol. 26* (7), 1169−1175.
(20) Danialou, G., Comtois, A. S., Dudley, R. W., Nalbantoglu, J., Gilbert, R., Karpati, G., Jones, D. H., and Petrof, B. J. (2002) Ultrasound increases plasmid-mediated gene transfer to dystrophic muscles without collateral damage. *Mol. Ther. 6* (5), 687−693.
(21) Unger, E. C., Hersh, E., Vannan, M., Matsunaga, T. O., and McCreery, T. (2001) Local drug and gene delivery through microbubbles. *Prog. Cardiovasc. Dis. 44* (1), 45−54.
(22) Christiansen, J. P., French, B. A., Klibanov, A. L., Kaul, S., and Lindner, J. R. (2003) Targeted tissue transfection with ultrasound destruction of plasmid-bearing cationic microbubbles. *Ultrasound Med. Biol. 29* (12), 1759−1767.
(23) Schneider, M., Bussat, P., Barrau, M. B., Bodino, F., Gotti, C., Hybl, E., Pelaprat, M. L., and Yan, F. (1991) A new ultrasound contrast agent based on biodegradable polymeric microballoons. *Invest. Radiol. 26 Suppl. 1*, S190−S191.
(24) Bauer, A., Blomley, M., Leen, E., Cosgrove, D., and Schlief, R. (1999) Liver-specific imaging with SHU 563A: diagnostic potential of a new class of ultrasound contrast media. *Eur. Radiol. 9 Suppl. 3*, S349−S352.
(25) Schlosser, T., Pohl, C., Kuntz-Hehner, S., Omran, H., Becher, H., and Tiemann, K. (2003) Echoscintigraphy: a new imaging modality for the reduction of color blooming and acoustic shadowing in contrast sonography. *Ultrasound Med. Biol. 29* (7), 985−991.
(26) Frinking, P. J., Bouakaz, A., de Jong, N., Ten Cate, F. J., and Keating, S. (1998) Effect of ultrasound on the release of microencapsulated drugs. *Ultrasonics 36* (1−5), 709−712.
(27) Hoff, L., Sontum, P. C., and Hovem, J. M. (2000) Oscillations of polymeric microbubbles: effect of the encapsulating shell. *J. Acoust. Soc. Am. 107* (4), 2272−2280.
(28) Frinking, P. J., and de Jong, N. (1998) Acoustic modeling of shell-encapsulated gas bubbles. *Ultrasound Med. Biol. 24* (4), 523−533.
(29) Bouakaz, A., Frinking, P. J., de Jong, N., and Bom, N. (1999) Noninvasive measurement of the hydrostatic pressure in a fluid-filled cavity based on the disappearance time of micrometer-sized free gas bubbles. *Ultrasound Med. Biol. 25* (9), 1407−1415.
(30) Schneider, M., Arditi, M., Barrau, M. B., Brochot, J., Broillet, A., Ventrone, R., and Yan, F. (1995) BR1: a new ultrasonographic contrast agent based on sulfur hexafluoride-filled microbubbles. *Invest. Radiol. 30* (8), 451−457.
(31) Schneider, M., Bichon, D., Bussat, P., Puginier, J., and Hybl, E. (1991) Patent WO 91/15244.
(32) Dufrene, Y., Barger, W., Green, J., and Lee, G. (1997) Nanometer-scale surface properties of mixed phospholipid monolayers and bilayers. *Langmiur 13*, 4779−4784.
(33) Bichon, D., Bussat, P., and Schneider, M. (1991) Eur. Patent EU 0,458,745 A1.
(34) Schneider, M., Broillet, A., Bussat, P., and Ventrone, R. (1994) The use of polymeric microballoons as ultrasound contrast agents for liver imaging. *Invest. Radiol. 29 Suppl. 2*, S149−S151.
(35) Schneider, M., Bussat, P., Barrau, M. B., Arditi, M., Yan, F., and Hybl, E. (1992) Polymeric microballoons as ultrasound contrast agents. Physical and ultrasonic properties compared with sonicated albumin. *Invest. Radiol. 27* (2), 134−139.
(36) Bloch, S. H., Wan, M., Dayton, P. A., and Ferrara, K. W. (2004) Optical observation of lipid- and polymer-shelled ultrasound microbubble contrast agents. *Appl. Phys. Lett. 84* (4), 631−633.
(37) Guzman, H. R., Nguyen, D. X., Khan, S., and Prausnitz, M. R. (2001) Ultrasound-mediated disruption of cell membranes. II. Heterogeneous effects on cells. *J. Acoust. Soc. Am. 110* (1), 597−606.
(38) Huber, P. E., Jenne, J., Debus, J., Wannenmacher, M. F., and Pfisterer, P. (1999) A comparison of shock wave and sinusoidal-focused ultrasound-induced localized transfection of HeLa cells. *Ultrasound Med. Biol. 25* (9), 1451−1457.
(39) Miller, D. L., and Quddus, J. (2000) Sonoporation of monolayer cells by diagnostic ultrasound activation of contrast-agent gas bodies. *Ultrasound Med. Biol. 26* (4), 661−667.
(40) Nozaki, T., Ogawa, R., Loreto, F. B., Jr., Kagiya, G., Fuse, H., and Kondo, T. (2003) Enhancement of ultrasound-mediated gene transfection by membrane modification. *J. Gene. Med. 5* (12), 1046−1055.
(41) Zarnitsyn, V. G., and Prausnitz, M. R. (2004) Physical parameters influencing optimization of ultrasound-mediated DNA transfection. *Ultrasound Med. Biol. 30* (4), 527−538.
(42) Guzman, H. R., McNamara, A. J., Nguyen, D. X., and Prausnitz, M. R. (2003) Bioeffects caused by changes in acoustic cavitation bubble density and cell concentration: a unified explanation based on cell-to-bubble ratio and blast radius. *Ultrasound Med. Biol. 29* (8), 1211−1222.
(43) Pislaru, S. V., Pislaru, C., Kinnick, R. R., Singh, R., Gulati, R., Greenleaf, J. F., and Simari, R. D. (2003) Optimization of ultrasound-mediated gene transfer: comparison of contrast agents and ultrasound modalities(1). *Eur. Heart J. 24* (18), 1690−1698.
(44) Unger, E. C., McCreery, T., and Sweitzer, R. H. (1997) Ultrasound enhances gene expression of liposomal transfection. *Invest. Radiol. 32* (12), 723−727.
(45) Frenkel, P. A., Chen, S., Thai, T., Shohet, R. V., and Grayburn, P. A. (2002) DNA-loaded albumin microbubbles enhance ultrasound-mediated transfection in vitro. *Ultrasound Med. Biol. 28* (6), 817−822.
(46) Guo, X., and Szoka, F. C., Jr. (2003) Chemical approaches to triggerable lipid vesicles for drug and gene delivery. *Acc. Chem. Res. 36* (5), 335−341.
(47) Wei, K., Skyba, D. M., Firschke, C., Jayaweera, A. R., Lindner, J. R., and Kaul, S. (1997) Interactions between microbubbles and ultrasound: in vitro and in vivo observations. *J. Am. Coll. Cardiol. 29* (5), 1081−1088.
(48) Moran, C. M., Anderson, T., Pye, S. D., Sboros, V., and McDicken, W. N. (2000) Quantification of microbubble destruction of three fluorocarbon-filled ultrasonic contrast agents. *Ultrasound Med. Biol. 26* (4), 629−639.
(49) Shi, W. T., Forsberg, F., Tornes, A., Ostensen, J., and Goldberg, B. B. (2000) Destruction of contrast microbubbles and the association with inertial cavitation. *Ultrasound Med. Biol. 26* (6), 1009−1019.
(50) Chomas, J. E., Dayton, P., Allen, J., Morgan, K., and Ferrara, K. W. (2001) Mechanisms of contrast agent destruction. *IEEE Transactions on Ultrasonics, Ferroelectrics, and Frequency Control 48* (1), 232−248.
(51) Chen, Q., Zagzebski, J., Wilson, T., and Stiles, T. (2002) Pressure-dependent attenuation in ultrasound contrast agents. *Ultrasound Med. Biol. 28* (8), 1041−1051.
(52) Ward, M., Wu, J., and Chiu, J. F. (1999) Ultrasound-induced cell lysis and sonoporation enhanced by contrast agents. *J. Acoust. Soc. Am. 105* (5), 2951−2957.
(53) Miller, M. W., Miller, D. L., and Brayman, A. A. (1996) A review of in vitro bioeffects of inertial ultrasonic cavitation from a mechanistic perspective. *Ultrasound Med. Biol. 22* (9), 1131−1154.
(54) Dalecki, D., Child, S. Z., Raeman, C. H., Xing, C., Gracewski, S., and Carstensen, E. L. (2000) Bioeffects of positive and negative acoustic pressures in mice infused with microbubbles. *Ultrasound Med. Biol. 26* (8), 1327−1332.
(55) Dalecki, D. (2004) Mechanical bioeffects of ultrasound. *Annu. Rev. Biomed. Eng 6*, 229−248.
(56) Lindner, J. R., and Kaul, S. (2001) Delivery of drugs with ultrasound. *Echocardiography 18* (4), 329−337.

(57) Stride, E., and Saffari, N. (2003) On the destruction of microbubble ultrasound contrast agents. *Ultrasound Med. Biol. 29* (4), 563−573.
(58) Dijkmans, P. A., Juffermans, L. J., Musters, R. J., van Wamel, A., Ten, Cate, F. J., van Gilst, W., Visser, C. A., de Jong, N., and Kamp, O. (2004) Microbubbles and ultrasound: from diagnosis to therapy. *Eur. J. Echocardiogr. 5* (4), 245−256.
(59) Dayton, P. A., Morgan, K., Klibanov, A. L., Brandenburger, G. H., Nightingale, K., and Ferrara, K. (1997) A preliminary evaluation of the effects of primary and secondary radiation forces on acoustic contrast agents. *IEEE Transactions on Ultrasonics, Ferroelectrics, and Frequency Control 44* (6), 1264−1277.
(60) Chomas, J. E., Dayton, P., May, D., and Ferrara, K. (2001) Threshold of fragmentation for ultrasonic contrast agents. *J. Biomed. Opt. 6* (2), 141−150.
(61) Marmottant, P., and Hilgenfeldt, S. (2003) Controlled vesicle deformation and lysis by single oscillating bubbles. *Nature (London) 423* (6936), 153−156.
(62) Lechardeur, D., Sohn, K. J., Haardt, M., Joshi, P. B., Monck, M., Graham, R. W., Beatty, B., Squire, J., O'Brodovich, H., and Lukacs, G. L. (1999) Metabolic instability of plasmid DNA in the cytosol: a potential barrier to gene transfer. *Gene Ther. 6* (4), 482−497.
(63) Li, T., Tachibana, K., Kuroki, M., and Kuroki, M. (2003) Gene transfer with echo-enhanced contrast agents: comparison between Albunex, Optison, and Levovist in mice−initial results. *Radiology 229* (2), 423−428.
(64) Dolan, M. S., El Shafei, A., Puri, S., Tamirisa, K., St. Vrain, J., Flanagan, J., Havens, E., and Labovitz, A. J. (2001) For left ventricular opacification and endocardial border definition: is it really important which contrast agent we use, or is it the imaging modality we choose? *Eur. J. Echocardiogr. 2* (3), 154−162.
(65) Dayton, P. A., Chomas, J. E., Lum, A. F., Allen, J. S., Lindner, J. R., Simon, S. I., and Ferrara, K. W. (2001) Optical and acoustical dynamics of microbubble contrast agents inside neutrophils. *Biophys. J. 80* (3), 1547−1556.

BC0602432

Preparation of Poly(ethylene glycol)-Attached Dendrimers Encapsulating Photosensitizers for Application to Photodynamic Therapy

Chie Kojima, Yoko Toi, Atsushi Harada, and Kenji Kono*

Graduate School of Engineering, Osaka Prefecture University, Osaka, Japan. Received August 7, 2006; Revised Manuscript Received January 25, 2007

Photodynamic therapy (PDT) is a noninvasive treatment of some diseases including cancer. We have developed poly(ethylene glycol) (PEG)-attached dendrimers as a drug-carrier candidate. In this study, we prepared nanocapsules of photosensitizers using PEG-attached dendrimers for application to PDT. Two PEG-attached dendrimers derived from poly(amido amine) (PAMAM) and poly(propylene imine) (PPI) dendrimers (PEG−PAMAM and PEG−PPI) were synthesized, and rose bengal (RB) and protoporphyrin IX (PpIX) were used as photosensitizers. Results showed that fewer PpIX molecules were encapsulated by both PEG-attached dendrimers than RB, but the complexes were more stable under physiological conditions. Furthermore, we demonstrated that PEG−PPI held photosensitizers in a more stable manner than PEG−PAMAM because of their inner hydrophobicity. We described the cytotoxicity of the complexes of photosensitizers induced by light irradiation in vitro. The complex of PpIX with PEG−PPI exhibited efficient cytotoxicity, compared with free PpIX. It was suggested that the cytotoxicity was caused by the high level of singlet oxygen production and the efficient delivery to mitochondria. Our results suggest that these PEG-attached dendrimers are a promising vehicle for PDT.

INTRODUCTION

Photodynamic therapy (PDT) is a new clinical treatment of superficial tumors and age-related muscular degeneration. This technique involves the systemic administration of a photosensitive drug, by which singlet oxygen is generated after light irradiation, to engender oxidative damage to cells (*1*). This PDT affects only the irradiated areas because singlet oxygen is short-lived, thereby realizing a site-specific and noninvasive treatment. Photosensitizers play a crucial role in generating singlet oxygen in PDT. Porphyrin derivatives have been studied for decades as powerful photosensitizers. One of them, Photofrin, has already been approved for clinical application (*2*). A second generation of photosensitizers for accumulation at affected areas has also been prepared to enhance the potential of PDT, which is achieved using a drug carrier. Liposomes, with their high loading capacity and long circulation properties, are classically used as a drug vehicle that provides less adverse effects. In fact, a liposomal drug for PDT, Visudyne, has been marketed (*3*).

Recently, many researchers have applied dendrimers to drug delivery systems (DDSs). Dendrimers have monodispersed molecular weight, well-defined morphology, and inner space to hold drug molecules. It has been suggested that dendrimer uniformity, along with their chemical and biological reproducibility, is useful for passive targeting to tissues involved in angiogenesis (*4*). Novel photosensitizers made from dendrimers have been reported by some groups. Kataoka et al. studied poly(aryl ether) dendrimers with a porphyrin core: so-called dendrimer porphyrins. They also prepared complexes of dendrimer porphyrins with block polymers containing poly(ethylene glycol) (PEG) as photosensitive biocompatible nanoparticles (*5*). As other types of photosensitive dendrimers, pheophorbide-a and a precursor of porphyrin, 5-aminolevulinic acid (ALA), were bound to the dendrimers in the periphery (*6*). It has also been reported that water-soluble dendrimers having a porphyrin core and other dyes in the periphery create two-photon excitation during low-energy light illumination (*7*). These dendrimers are attached covalently to photosensitizers, so that their photosensitive properties must change from their intrinsic ones. In addition, time and effort are required for synthesis of photosensitive dendrimers. Noncovalent encapsulation of photosensitizers by dendrimers can overcome these obstacles: photosensitizer-encapsulating nanoparticles are applicable to a variety of photosensitizers and are also easily prepared.

We have studied PEG-attached poly(amido amine) (PAMAM) dendrimers (PEG−PAMAM) as drug capsules of anticancer drugs such as adriamycin and methotrexate (*8*, *9*). This kind of dendrimer cannot be removed from blood immediately, because it has been reported that PEG-modified macromolecules and liposomes are efficient at maintaining circulation in blood (*10*). These are applicable as vehicles against diseases involved in angiogenesis because of the enhanced permeability of macromolecules (*4*, *11*). In our previous study, we synthesized several PAMAM dendrimers with different generations of dendrimer and different molecular weights of PEG. Results of that study showed that these dendrimers can encapsulate anticancer drugs. However, the drugs were easily dissociated from PEG-attached dendrimers under isotonic conditions (*8*). Anticancer drugs must be retained until they reach the tumor tissues and must be released to exhibit their action. Therefore, we prepared controlled-release PEG-attached dendrimers (*9*).

In this study, we prepared PEG-attached dendrimers encapsulating photosensitizers on PDT. They can act without release from carriers because reactive oxygen species generated from them, inside dendrimers, can injure cells. Therefore, photosensitizers are good candidates as guest molecules of PEG-attached dendrimers. We synthesized PEG-attached poly(propylene imine) (PPI) dendrimers (PEG−PPI) in addition to PEG−PAMAM, both of which contain many inner tertiary amino groups. Two photosensitizers, rose bengal (RB) and protoporphyrin IX (PpIX), were used because they have acidic moieties

* To whom correspondence should be addressed: Department of Applied Chemistry, Graduate School of Engineering, Osaka Prefecture University, 1-1 Gakuen-cho, Naka-ku, Sakai, Osaka 599-8531, Japan. Tel.: +81 72 254 9330; Fax: +81 72 254 9330; E-mail: kono@chem.osakafu-u.ac.jp.

10.1021/bc060244u CCC: $37.00 © 2007 American Chemical Society
Published on Web 03/22/2007

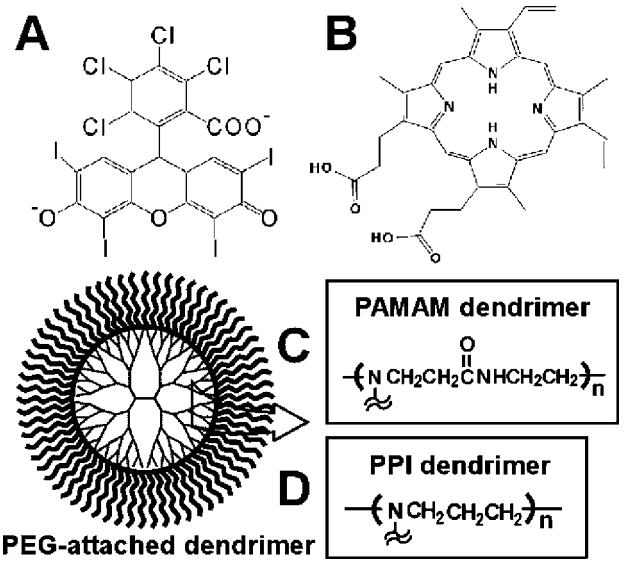


Figure 1. Structures of RB (A), PpIX (B), and PEG-attached PAMAM (C) and PPI (D) dendrimers.

to facilitate interaction with amino groups of dendrimers (Figure 1). We investigated interaction of a couple of photosensitizers with these two PEG-attached dendrimers and compared the complexes' chemical properties for PDT. We examined cytotoxicity of PEG-attached dendrimers encapsulating these photosensitive drugs after irradiation to evaluate the performance of a carrier of photosensitizers. Efficiency of singlet oxygen production by light irradiation and subcellular localization of photosensitizers influence the phototoxicity. Our results suggest that phototoxicity was affected by the stability, singlet oxygen generation, and the cytological behavior of the complex of PEG-modified dendrimers with photosensitizers.

EXPERIMENTAL PROCEDURES

Materials. The PAMAM and PPI dendrimers, poly(ethylene glycol) monomethyl ether, 9,10-anthracene dipropionic acid (ADPA), and PpIX were purchased from Sigma-Aldrich Corp. (St. Louis, MO). From Wako Pure Chemical Industries, Ltd. (Osaka, Japan), RB, 3-(4,5-dimethyl-2-thiazoryl)-2,5-diphenyl-2*H*-tetrazolium bromide (MTT) and paraformaldehyde were purchased. Also, 4-nitrophenyl chloroformate and 5-(dimethylamino)-1-naphthalenesulfonic acid (DNS) were obtained, respectively, from Tokyo Chemical Industry Co., Ltd. (Tokyo, Japan), and Kanto Chemical Co., Inc. (Tokyo, Japan). MitoTracker Green FM was obtained from Invitrogen Corp. (Carlsbad, CA).

Synthesis of PEG-Attached Dendrimers. We synthesized PEG−PAMAM as described in our previous report (*8*); PEG−PPI was prepared according to our previous report, except the starting material. Briefly, poly(ethylene glycol) monomethyl ether with molecular weight of 2000 was reacted with 4-nitrophenyl chloroformate. It was then bound to PPI dendrimer of generation 5 (G5) with 64 amino groups at the periphery. Also, PEG−PPI was purified using a Sephadex G-75 column (Pharmacia) and dialysis. Yield: 577 mg (57.3%). σ_H (400 MHz, D_2O): 1.68 (br, $CH_2CH_2CH_2N$), 2.83 (br, $CH_2CH_2CH_2N$, $CH_2CH_2CH_2N$), 3.03 (br, $CH_2CH_2CH_2NHCOO$), 3.22 (s, OCH_3), 3.55 (m, CH_2CH_2O), 4.04 (br, $NHCOOCH_2$).

Gel Permeation Chromatography (GPC). The GPC system (Shodex SB-2004; Showa Denko K.K., Japan) had differential refractive index detection (RI-930; Jasco, Inc., Japan). Both PEG−PAMAM and PEG−PPI were eluted with 10 mM phosphate buffer containing 0.2 M sodium sulfate (pH 7.4) at 1.0 mL·min^{-1} at 25 °C.

For complex stability assay, we modified the system except the eluent buffer. The system was equipped with three columns, Shodex SB-803HQ, SB-804HQ (Showa Denko K.K., Japan), and TSK-gel G3000PW (Toso Co., Ltd., Japan), and two detectors, differential refractive index detector (RI-930; Jasco Inc., Japan) and fluorescence detector (λ_{ex} = 400 nm, λ_{em} = 630 nm; FR-2020Plus; Jasco, Inc., Japan). Samples (10 μL) were injected and eluted at 0.5 mL·min^{-1} at 30 °C.

Hydrophobicity of PEG-Attached Dendrimers. PEG−PAMAM or PEG−PPI was added to 1 μM of DNS dissolved in distilled water. The emission spectra excited at 310 nm were examined (*12*).

Encapsulation of Photosensitive Drugs. Encapsulation assay was done according to our previous report (*8*). RB and PEG-attached dendrimers were dissolved in water (first solvent) and incubated for 30 min at 27 °C. The solutions were lyophilized to remove water; then, chloroform (second solvent) was added. After 6 h incubation, the mixtures were centrifuged to remove free RB aggregation. The supernatants were evaporated and dried under vacuum; then, the residues were dissolved in 10 mM phosphate buffer containing 100 mM NaCl (third solvent). The absorbance was measured at 557 nm, an isosbestic point (*9*).

In the case of PpIX, the treatment was almost identical, except for the solvents and UV−vis measurement. The first, second, and third solvents were replaced, respectively, by *N*,*N*′-dimethylformamide (DMF), water, and DMF. The absorbance was measured at 407 nm, the maximum wavelength of PpIX absorption spectra. We confirmed that the spectra in the absence and presence of dendrimers were the same above 350 nm.

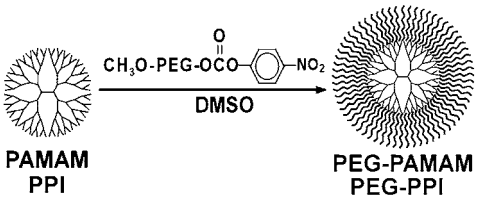
Complex Stability with PEG-Attached Dendrimers. The release of photosensitizers from PEG-attached dendrimers was estimated according to our previous report (*8*). Briefly, PEG-attached dendrimers encapsulating RB or PpIX at 10 equiv per dendrimer were dissolved in phosphate buffer saline (PBS) and dialyzed (pore size: 120−140 kDa). The residues in the dialysis bag were monitored by measuring the absorbance at 557 nm (RB) or 407 nm (PpIX). The PpIX solutions sampled in the bag were diluted 20 times by DMF to measure the absorbance. The external solution was changed every 3 h. Free RB solution was analyzed as a control, but free PpIX was not attainable because of its poor water solubility.

For complex stability assay in the presence of fetal bovine serum (FBS), the complexes of PpIX with PEG-attached dendrimers at 1 equiv per dendrimer were incubated in PBS containing various amounts of FBS for 3 h, and the solutions were centrifuged at 21 800 *g* for 20 min. The supernatants were used as samples for GPC analysis.

Generation of Singlet Oxygen. We prepared PBS solutions containing 36 μM of ADPA and 10 μM of RB or PpIX in the absence or presence of PEG-attached dendrimers. These solutions were irradiated using a Xe lamp (400 W·m^{-2}, XEF-152S; San-Ei Electric Co., Ltd.) with a 530 nm filter. Then, the time-dependent absorbance of ADPA was measured at 379 nm (*7*).

Phototoxicity of PEG-Attached Dendrimers Loading PpIX. The HeLa cells (5×10^4 cells) incubated for 1 day in a 24-well plate were added to free photosensitizers and PEG−PAMAM and PEG−PPI loading them at different equivalents at a wide range of concentrations. After 3 h incubation, cells were washed twice with PBS and irradiated using a Xe lamp (400 W·m^{-2}, XEF-152S; San-Ei Electric Co., Ltd.) for 10 min, followed by 24 h incubation (*6b*). Then, surviving cells were evaluated using MTT assay (*13*). Photosensitizers in the absence and presence of dendrimers were dissolved in PBS, except free PpIX. Free PpIX was dissolved in distilled dimethylsulfoxide (DMSO). Under our conditions, neither DMSO nor light irradiation without photosensitive drugs influenced cell viability.

Scheme 1



Subcellular Localization of PpIX with and without PEG-Attached Dendrimers. The HeLa cells (1×10^5 cells) incubated for 1 day in 35 mm glass-bottom dishes were added to 1 μM of free PpIX and PpIX-loading PEG−PAMAM and PEG−PPI at 10 equiv per dendrimer. After 3 h incubation, cells were washed with PBS, fixed with 3.7% paraformaldehyde, and analyzed using laser confocal microscopy with the attached computer software (*LSM 510* v 2.5; Carl Zeiss, Inc.) according to a procedure described in a previous report (*14*).

RESULTS

Synthesis and Characterization of PEG-Attached PAMAM and PPI Dendrimers. PAMAM dendrimer of G4 and PPI dendrimer of G5, each with 64 termini, were reacted with PEG chain (molecular weight: 2000) according to Scheme 1. PEG−PAMAM was already reported (*8*). As for PEG−PPI, the integral ratio of a typical signal of PEG chain (OCH_3) to PPI dendrimer ($NCH_2CH_2CH_2$) of the ^{1}H NMR spectrum indicated that every terminal amino group was attached to PEG chains. In addition, a ninhydrin test of PEG−PPI was negative, indicating that these dendrimers have no primary amino groups.

These dendrimers were characterized by GPC. Figure 2 showed a single peak, suggesting no contamination of noncovalent PEG chains. The elution volumes of PEG−PAMAM and PEG−PPI were almost equal, indicating that the hydrodynamic sizes are similar, even though intact PAMAM dendrimer of G4 was larger than PPI dendrimer of G5 (*15*). This fact suggested that these dendrimers extend to similar sizes because of steric hindrance and PEG chain solubility.

We analyzed emission spectra of DNS to examine the hydrophobicity of the dendrimer interior (*12*). Emission spectrum of DNS is affected by the hydrophobicity of the surroundings. The blue shift of the emission maximum and the increase of fluorescence intensity are observed in the hydrophobic environment. The emission maximum of PEG−PPI was blue-shifted to a greater extent, although that of PEG−PAMAM was blue-shifted only slightly, as shown in Figure 3A. The fluorescence intensity in the presence of PEG−PPI was also higher than that in PEG−PAMAM (Figure 3B). These facts indicate that PPI dendrimer is more hydrophobic than PAMAM dendrimer, as reported previously (*16*). Both PAMAM and PPI dendrimers have equal amounts of amino groups, but PAMAM dendrimer has amide groups. Amide groups of PAMAM dendrimer are expected to contribute to the interior hydrophilicity.

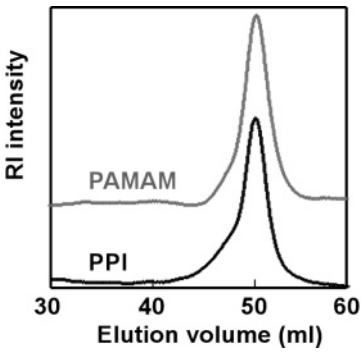


Figure 2. GPC profiles of PEG-attached PAMAM (top) and PPI (bottom) dendrimers. A peak of PEG with 2 kDa is apparent at 58.5 mL.

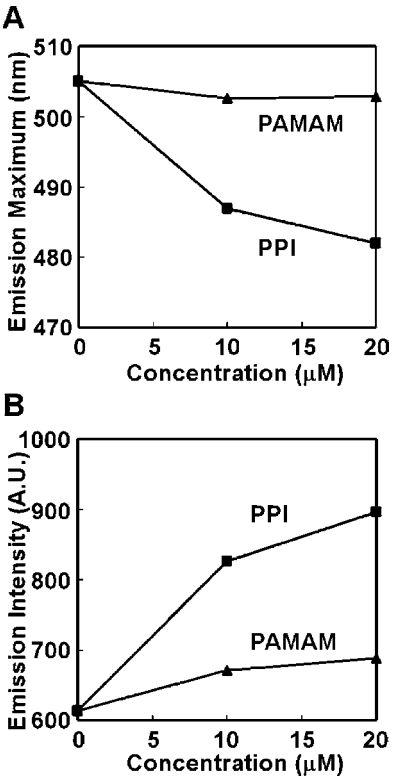


Figure 3. Comparison of the hydrophobicity of PEG−PAMAM (triangles) with that of PEG−PPI (squares). (A) Emission maximum. (B) Fluorescence intensity.

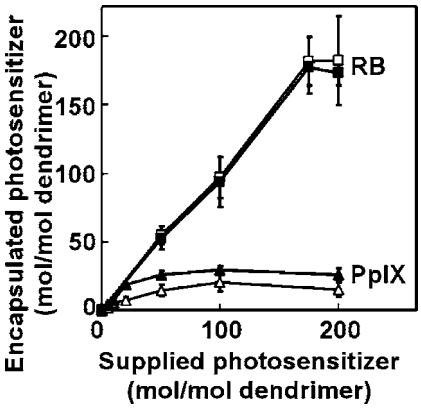


Figure 4. Encapsulation of RB (square) and PpIX (triangles) by PEG−PAMAM (open) and PEG−PPI (closed) dendrimers.

Complex of Photosensitive Drugs with PEG-Attached Dendrimers. To evaluate PEG-attached dendrimers as a drug carrier of photosensitizers, we examined the binding property to photosensitizers such as RB and PpIX. Photosensitizers can be soluble even in a poor solvent, through complexation with dendrimers. We extracted complexes from poor solvents to estimate the numbers of photosensitizers bound to a dendrimer (*8*). We found that 182 and 177 molecules of RB and 20 and 30 molecules of PpIX were bound, respectively, per PEG−PAMAM and PEG−PPI at the maximum (Figure 4). We reported that an important driving force of that binding is the electrostatic interaction between inner amino groups of dendrimers and carboxyl groups of guest molecules (*8*). This fact suggested that carboxyl groups of RB and PpIX interacted with inner tertiary amino groups of PEG−PPI and PEG−PAMAM via electrostatic interaction. Our results indicated that more RB molecules were encapsulated by PEG-attached dendrimers than

by PpIX. Experimental conditions might contribute to this phenomenon: The complexes with RB were extracted using chloroform; PpIX was extracted using water. In a hydrophobic environment, electrostatic interaction between dendrimers and guest molecules is more effective: RB was complexed easily with dendrimers. In water, on the other hand, hydrophobic interaction among guest molecules is efficient; consequently, hydrophobic PpIX tends to interact with other PpIX molecules to engender their aggregation. We also found that PEG−PPI encapsulated more PpIX molecules than PEG−PAMAM. This result suggests that the association of PpIX with dendrimers in water is driven by hydrophobic interaction, consistent with the difference of hydrophobicity of PEG-attached dendrimers (Figure 3).

We next investigated the release behavior of photosensitizers from these dendrimers by dialysis. Free drug molecules are permeable through a dialysis bag, but the complexes are not. Residual photosensitizers in the dialysis bag were detected using UV−vis absorbance (*8*). The RB complexes showed similar profiles to those of free RB, indicating that water-soluble RB molecules were released immediately in PBS solution (Figure 5A). In contrast, more than 50% of hydrophobic PpIX remained in PEG-attached dendrimers after 24 h (Figure 5B). Dialysis assay of PpIX did not obviate the possibility that aggregates of released PpIX remained in the dialysis bag. We performed another release assay to validate this release behavior of PpIX. Absorption of the supernatant of PpIX-loading PEG-attached dendrimers after centrifugation was measured at different time incubations because free PpIX molecules aggregate easily for removal. These results were almost identical to those of the dialysis assay (see Supporting Information). These release experiments suggest that the complexes of PpIX with PEG-attached dendrimers were stable.

Our results indicate that hydrophilic RB was released more rapidly from PEG-attached dendrimers in PBS than hydrophobic PpIX. As described previously, the complex formation was involved in electrostatic and hydrophobic interaction. Electrostatic interaction is suppressed under isotonic conditions. Therefore, hydrophobicity might influence the complexes' stability. Figure 5 also shows that photosensitizers were released more easily from PEG−PAMAM than from PEG−PPI. That result is consistent with our results, which indicated that PEG−PPI is more hydrophobic than PEG−PAMAM (Figure 3). The complex of PpIX with PEG−PPI was the most stable one assessed in this study. Therefore, we suggest that the hydrophobicity of host and guest molecules mainly influenced the complex stability in PBS.

The influence of serum proteins on the complex stability is indispensable for application to PDT. We investigated the complex stability in the presence of serum proteins. The complexes were incubated in the serum-containing PBS for 3 h. Since it is well-known that PpIX molecule binds to serum proteins (*17*), PEG-attached dendrimers were separated from serum proteins using GPC, and then fluorescence intensity of PpIX associated with the PEG-attached dendrimer was measured. We found that serum proteins hardly promoted the dissociation of PpIX from PEG−PPI in the presence of 10% serum. A large fraction of PpIX molecules were still retained in the dendrimer after 3 h incubation in 50% serum. In contrast, PpIX molecules were readily released from the PEG−PAMAM even in the presence of 10% serum (Figure 5C). These results suggest that the complexes with PEG−PPI were much more stable than those with PEG−PAMAM in the presence of serum proteins. This stability difference might be related to the hydrophobicity of their interior: binding of PpIX to PEG−PAMAM was too weak to maintain the complex due to its relatively hydrophilic interior. Therefore, we established stable

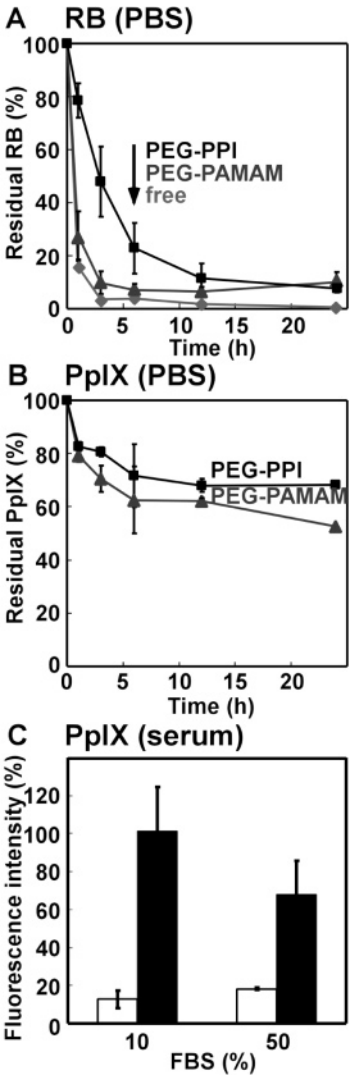


Figure 5. Release of RB (A) and PpIX (B) from PEG−PAMAM (triangles) and PEG−PPI (squares) dendrimers in PBS. Residual photosensitizer (%) was calculated from absorbance of the complex solution in the dialysis bag. Profile for dendrimer-free RB is also shown (rhombi). (C) Effect of serum on release of PpIX from PEG−PAMAM (open) or PEG−PPI (closed). The complexes were incubated in PBS containing 0%, 10%, or 50% FBS for 3 h and were separated using GPC. Relative fluorescence intensity (%) of the complex was calculated by comparison with fluorescence intensity of the complex incubated in serum-free PBS.

complexes under physiological conditions using the combination of hydrophobic PpIX and PEG−PPI with hydrophobic interiors.

Generation of Singlet Oxygen Induced by Light Irradiation. Photosensitive drugs generate singlet oxygen after light irradiation. We examined whether the complex formation affected the photosensitive properties of RB and PpIX using ADPA as a chemical trap. Photobleaching of anthracene moiety of ADPA is useful to monitor singlet oxygen generation (*7*, *18a*). We found that RB encapsulated by PEG-attached dendrimers suppressed the decrease of the absorbance, indicating that the complex formation inhibited the production of singlet oxygen (Figure 6A). RB molecules might be quenched because of high local concentration inside dendrimers (*6a*).

In contrast, free PpIX and the complex with PEG−PAMAM generated less singlet oxygen than the complex with PEG−PPI (Figure 6B). Free PpIX molecules readily aggregate in PBS to impair the ability of photosensitizers, as described in previous reports (*18*). PpIX molecules in the complexes with PEG−PPI, however, are dispersible at the molecular level to maintain the

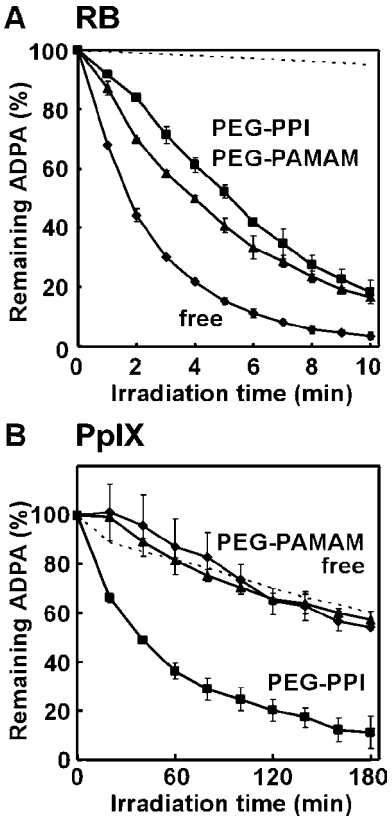


Figure 6. Generation of singlet oxygen induced by RB (A) and PpIX (B) at various irradiation times. The free photosensitizer (rhombi) data and those of complexes with PEG−PAMAM (triangles) or PEG−PPI (squares) at 10 equiv per dendrimer are shown. Degradation of ADPA alone by irradiation is also shown as dotted lines.

photosensitive activity. Figure 6B might indicate that small PpIX aggregates existed in the presence of PEG−PAMAM. It is inferred that PpIX molecules interact with each other, even inside, because PAMAM dendrimers are more hydrophilic than PPI dendrimers (Figure 3). This suggestion is supported by some reports that porphyrin derivatives can aggregate in the complex with PAMAM dendrimers (*19*). We also performed ADPA analysis, by which PEG-attached dendrimers encapsulating PpIX at different equivalents were used. The result showed that greater amounts of PpIX per dendrimer generated less singlet oxygen, which might be attributable to quenching of the PpIX molecules inside dendrimers (see Supporting Information).

Cytotoxicity of the Photosensitizers Encapsulated by PEG-Attached Dendrimers. As an in vitro model of PDT, we examined the cytotoxicity of HeLa cells induced by photosensitizers after light irradiation (*20*). The HeLa cells were treated with photosensitizers encapsulated by PEG-attached PAMAM or PPI dendrimer as well as free ones for 3 h. Both PEG-attached dendrimers themselves exhibited no cytotoxicity under our conditions (data not shown). We found that free RB and the complex with PEG-attached dendrimers exhibited almost equal cytotoxicity to HeLa cells (see Supporting Information). These results are explained using the release profiles that RB molecules were easily released from PEG-attached dendrimers (Figure 5A).

We also examined the cytotoxicity of PpIX in the absence and presence of PEG-attached dendrimers. First, we optimized the equivalent of PpIX molecules per dendrimer for cytotoxicity after light irradiation. As shown in panels A and B of Figure 7, the most effective phototoxicity was obtained for 10 molecules of PpIX encapsulated for each PEG−PAMAM and for each PEG−PPI. That result suggests that the balance of positive and negative factors on complex formation is important to exhibit efficient phototoxicity. The PEG-attached dendrimers with more

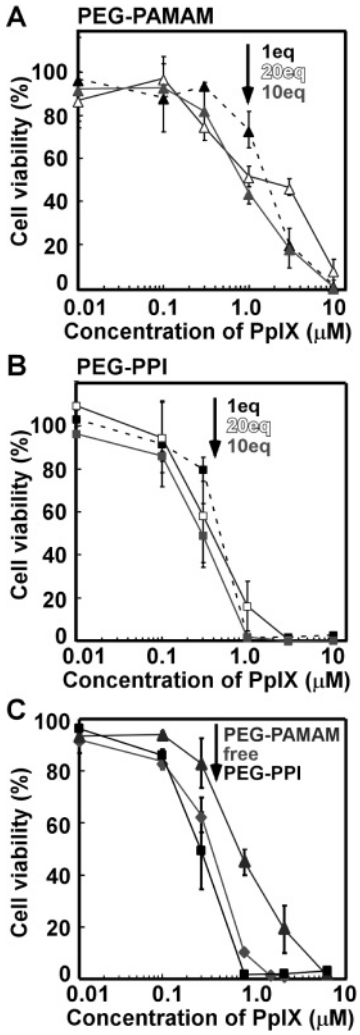


Figure 7. Phototoxicity of PpIX in HeLa cells. The complexes of PpIX with PEG−PAMAM (A) or PEG−PPI (B) were prepared at different equivalents (1 equiv (dash line), 10 equiv (closed), and 20 equiv (open)). The most effective complex with PEG−PAMAM (triangles) or PEG−PPI (squares) dendrimers are shown in panel C. Free photosensitizer (rhombi) was also shown as a control. Cell viability was expressed as the percentage of the untreated control cells.

PpIX were best for the efficient delivery of PpIX into cells. On the other hand, more PpIX per dendrimer induced quenching of PpIX inside dendrimers, thereby suppressing the generation of singlet oxygen (see Supporting Information). Our data indicated that the complex at 10 equiv generated the greatest amount of singlet oxygen in cells.

The most effective PpIX complexes with PEG−PAMAM and PEG−PPI were compared with free PpIX (Figure 7C). Results showed that free PpIX and the complex with PEG−PPI were more cytotoxic than the complex with PEG−PAMAM. The PpIX molecules were complexed stably with PEG-attached dendrimers, different from RB. Especially, 80% of PpIX molecules were still associated with PEG−PPI after 3 h (Figure 5B,C). In addition, PpIX molecules with PEG−PPI can generate more singlet oxygen (Figure 6B), suggesting that the complex with PEG−PPI can function as a photosensitive drug without releasing PpIX.

Toxicity in the dark was also investigated. Without irradiation, 10 μM of RB solutions with and without PEG-attached dendrimers exhibited no toxicity (data not shown). However, PpIX exhibits some cytotoxicity (Table 1) even in the presence of PEG-attached dendrimers, consistent with previous reports (*5a*). For PDT, it is important to reduce cytotoxicity in dark conditions.

Table 1. Viability (%) of Cells Treated with PpIX in the Dark

		complex	
PpIX	free	PEG−PAMAM	PEG−PPI
1 μM	66.1 (±3.9)	75.9 (±5.0)	48.2 (±4.8)
10 μM	27.4 (±1.1)	40.1 (±0.1)	30.5 (±2.4)

Subcellular Localization of PpIX. Intracellular localization of PpIX is a crucial feature of PDT. Singlet oxygen at mitochondria is known to induce apoptotic cell death (*21*). We observed localization to mitochondria in HeLa cells by staining with MitoTracker. As shown in Figure 8, PpIX molecules complexed with PEG−PPI were mostly merged in MitoTracker-positive dots. On the other hand, for free molecules and the complex with PEG−PAMAM, PpIX molecules were partially localized at mitochondria. These data suggest that PpIX was localized to mitochondria efficiently by PEG−PPI.

PpIX, a precursor of heme, is known to localize at mitochondria. However, it was reported that fewer exogenous PpIX molecules localize there in comparison to ALA-mediated endogenous PpIX (*22*). Moreover, few exogenous PpIX were accumulated at mitochondria after 3 h (*23*). It has also been reported that pegylation of a photosensitizer can be efficient for targeting mitochondria (*24*). These observations suggest that stable PpIX complexes with PEG-attached dendrimers were localized to mitochondria, but that free or released PpIX were not. The PpIX molecules complexed with PEG−PPI were more stable than with PEG−PAMAM, as shown in Figure 5B,C. Therefore, PEG−PPI can contribute to localization of PpIX molecules to mitochondria.

DISCUSSION

We used two types of photosensitizers (RB and PpIX) and PEG-attached dendrimers (PEG−PAMAM and PEG−PPI) to produce complexes to apply to PDT. For RB, the complexes with PEG-attached PAMAM and PPI dendrimers were unstable under isotonic conditions. Figure 6A indicated that high local concentrations inside both PEG-attached dendrimers provide less singlet oxygen, suggesting that the photosensitive action is controllable by regulating the release behavior of RB from dendrimers. Therefore, PEG-attached dendrimers with the ability of controlled release by bearing a disulfide and polymer network can be more useful as vehicles of RB for PDT (*9*).

In the case of PpIX, we observed different phototoxicity of free dye from that of the complexes. Figure 7C indicated that the PpIX complex with PEG−PPI is more toxic after light irradiation than the complex with PEG−PAMAM. These results probably arose from the complex stability in serum-containing solutions, the productive rate of singlet oxygen and the subcellular localization of photosensitizers. As shown in Figure 5C, the complexes with PEG−PPI were much more stable than those with PEG−PAMAM in the presence of FBS. Because PpIX molecules were released from PEG−PAMAM during the incubation with cells, encapsulation of PpIX in PEG−PAMAM might not be effective for PDT. Demonstrably, encapsulation in PEG−PPI enhanced the generation of singlet oxygen (Figure 6B) and the localization of PpIX molecules at mitochondria (Figure 8) to engender effective phototoxicity. Although these dendrimers have the same numbers of primary and tertiary amino groups, their properties such as hydrophobicity and complex formation are different. Differences of their properties such as hydrophobicity and pK_a might be attributable to the efficiency for PDT, which remains to be investigated in detail.

The complex with PEG−PPI exhibited almost equal phototoxicity to that of free PpIX. It has already been reported that association of photosensitizers with cells is enhanced by hydrophobicity (*23*). In addition, it is well-understood that PEG chains abrogate the association with many biomolecules. These reports suggest that PEGylation negatively affects association with cells (*10*). Consistent with this notion, we found that the fluorescence intensity of free PpIX in HeLa cells was approximately 2-fold higher than that of the complex with PEG-PPI (data not shown). However, free PpIX molecules generated less singlet oxygen than the complex with PEG−PPI (Figure 6B). In addition, they were not localized efficiently at mito-

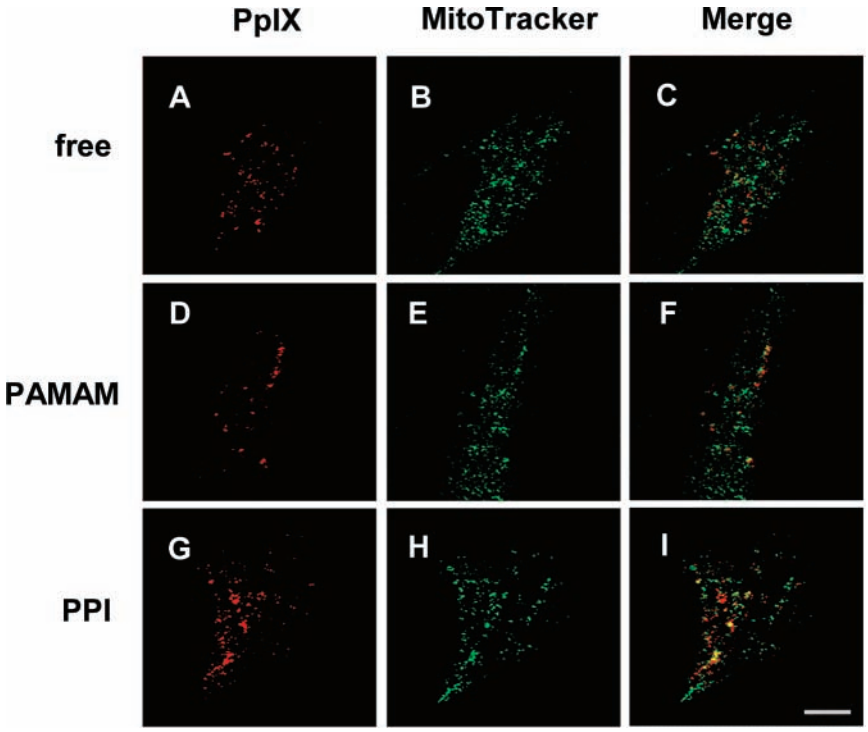


Figure 8. Subcellular localization of free PpIX (A−C) and complexes of PpIX with PEG−PAMAM (D−F) or PEG−PPI (G−I). Here, PpIX is a red fluorescent dye (A,D,G), and mitochondria are labeled using MitoTracker green (B,E,H). Merged images of the left two columns are shown (C,F,I). These are representative images from more than 50 cells examined in each experiment. Bar, 10 μm.

chondria (Figure 8). Taken together, these results suggested that PpIX molecules complexed with PEG−PPI have phototoxicity attributable to the localization at mitochondria, along with more singlet oxygen, in spite of lower amounts of PpIX associated with cells. Although the cytotoxicity of PpIX in dark conditions was observed, toxicity might be reduced using ALA instead of PpIX (*2*, *6b*, *22*, *25*), which remains to be improved.

In conclusion, we synthesized and characterized two PEG-attached dendrimers: PEG−PAMAM and PEG−PPI. We prepared complexes using those dendrimers and photosensitizers such as RB and PpIX. Results showed that PEG−PPI can encapsulate more photosensitizers and hold them inside under physiological conditions. Results also indicated that a hydrophobic photosensitizer, PpIX, can form a stable complex with PEG−PPI under physiological conditions, which suggests that the stable complexes were obtained through hydrophobic interaction rather than electrostatic interaction. Properties of complexes influenced the generation of singlet oxygen, subcellular localization, and the cytotoxic effect. Especially, we demonstrated the efficient phototoxicity of PpIX complexed with PEG−PPI via effective production of singlet oxygen and delivery to mitochondria. We demonstrated photosensitive activity of the complex of PpIX with PEG-attached dendrimers at the same level of free PpIX in vitro. This behavior is important for in vivo application because this kind of nanocapsule can be targeted to the affected tissues. Therefore, we propose that our PEG-attached dendrimers are a promising carrier for PDT.

ACKNOWLEDGMENT

We are grateful to Hisataka Sabe (Osaka Bioscience Institute, Japan) for generous support in microscopic analysis. We thank Yasuhiro Haba for support in synthesis. This work was supported in part by Grants-in-aid from the Ministry of Education, Science, Sports and Culture of Japan, and Grants from Iketani Science and Technology Foundation and Saneyoshi Scholarship Foundation.

Supporting Information Available: Additional experimental information. This material is available free of charge via the Internet at http://pubs.acs.org/BC.

LITERATURE CITED

(1) (a) Moan, J., and Peng, Q. (2003) An outline of the hundred-year history of PDT. *Anticancer Res. 23*, 3591−3600. (b) Dolmans, D. E., Fukumura, D., and Jain, R. K. (2003) Photodynamic therapy for cancer. *Nat. Rev. Cancer 3*, 380−387.

(2) Detty, M. R., Gibson, S. L., and Wagner, S. J. (2004) Current clinical and preclinical photosensitizers for use in photodynamic therapy. *J. Med. Chem. 47*, 3897−3915.

(3) Derycke, A. S., and de Witte, P. A. (2004) Liposomes for photodynamic therapy. *Adv. Drug Delivery Rev. 56*, 17−30.

(4) (a) Lee, C. C., MacKay, J. A., Frechet, J. M., and Szoka, F. C. (2005) Designing dendrimers for biological applications. *Nat. Biotechnol. 12*, 1517−1526. (b) D'Emanuele, A., and Attwood, D. (2005) Dendrimer-drug interactions. *Adv. Drug Delivery Rev. 57*, 2147−2162. (c) Gillies, E. R., and Frechet, J. M. (2005) Dendrimers and dendritic polymers in drug delivery. *Drug Discovery Today 10*, 35−43. (d) Boas, U., and Heegaard, P. M. (2004) Dendrimers in drug research. *Chem. Soc. Rev. 33*, 43−63.

(5) (a) Nishiyama, N., Stapert, H. R., Zhang, G. D., Takasu, D., Jiang, D. L., Nagano, T., Aida, T., and Kataoka, K. (2003) Light-harvesting ionic dendrimer porphyrins as new photosensitizers for photodynamic therapy. *Bioconjugate Chem. 14*, 58−66. (b) Zhang, G. D., Harada, A., Nishiyama, N., Jiang, D. L., Koyama, H., Aida, T., and Kataoka, K. (2003) Polyion complex micelles entrapping cationic dendrimer porphyrin: effective photosensitizer for photodynamic therapy of cancer. *J. Controlled Release 93*, 141−150. (c) Jang, W. D., Nishiyama, N., Zhang, G. D., Harada, A., Jiang, D. L., Kawauchi, S., Morimoto, Y., Kikuchi, M., Koyama, H., Aida, T., and Kataoka, K. (2005) Supramolecular nanocarrier of anionic dendrimer porphyrins with cationic block copolymers modified with polyethylene glycol to enhance intracellular photodynamic efficacy. *Angew. Chem., Int. Ed. 44*, 419−423. (d) Ideta, R., Tasaka, F., Jang, W. D., Nishiyama, N., Zhang, G. D., Harada, A., Yanagi, Y., Tamaki, Y., Aida, T., and Kataoka, K. (2005) Nanotechnology-based photodynamic therapy for neovascular disease using a supramolecular nanocarrier loaded with a dendritic photosensitizer. *Nano Lett. 5*, 2426−2431. (e) Usui, T., Sugisaki, K., Amano, S., Jang, W. D., Nishiyama, N., and Kataoka, K. (2005) New drug delivery for corneal neovascularization using polyion complex micelles. *Cornea 24*, S39−S42.

(6) (a) Hackbarth, S., Horneffer, V., Wiehe, A., Hillekamp, F., and Roder, B. (2001) Photophysical properties of pheophorbide-*a*-substituted diaminobutane poly-propylene-imine dendrimer. *Chem. Phys. 269*, 339−346. (b) Battah, S., Chee, C. E., Nakanishi, H., Gersher, S., MacRober, A. J., and Edwards, C. (2001) Synthesis and biological studies of 5-Aminolevulinic acid-containing dendrimers for photodynamic therapy. *Bioconjugate Chem. 12*, 980−988. (c) Battah, S., O'Neill, S., Edwards, C., Balaratnam, S., Dobbin, P., and MacRober, A. J. (2006) Enhanced porphyrin accumulation using dendritic derivatives of 5-aminolaevulinic acid for photodynamic therapy: an in vitro study. *Int. J. Biochem. Cell Biol. 38*, 1382−1392.

(7) Oar, M. A., Serin, J. M., Dichtel, W. R., Frechet, J. M., Ohulchanskyy, T. Y., and Prasad, P. N. (2005) Photosensitization of singlet oxygen via two-photon-excited fluorescence resonance energy transfer in a water-soluble dendrimer. *Chem. Mater. 17*, 2267−2275.

(8) Kojima, C., Kono, K., Maruyama, K., and Takagishi, T. (2000) Synthesis of polyamidoamine dendrimers having poly(ethylene glycol) grafts and their ability to encapsulate anticancer drugs. *Bioconjugate Chem. 11*, 910−917.

(9) (a) Kojima, C., Haba, Y., Fukui, T., Kono, K., and Takagishi, T. (2003) Design of biocompatible dendrimers with environment sensitivity. *Macromolecules 36*, 2183−2186. (b) Haba, Y., Harada, A., Takagishi, T., and Kono, K. (2005) Synthesis of biocompatible dendrimers with a peripheral network formed by linking of polymerizable groups. *Polymer 46*, 1813−1820.

(10) Greenwald, R. B., Conover, C. D., and Choe, Y. H. (2000) Poly(ethylene glycol) conjugated drugs and prodrugs: a comprehensive review. *Crit. Rev. Ther. Drug Carrier Syst. 17*, 101−161.

(11) Shimizu, K., and Oku, N. (2004) Cancer anti-angiogenic therapy. *Biol. Pharm. Bull. 27*, 599−605.

(12) Chen, W., Tomalia, D. A., and Thomas, J. L. (2000) Unusual pH-dependent polarity changes in PAMAM dendrimers: evidence for pH-responsive conformational changes. *Macromolecules 33*, 9169−9172.

(13) Takahashi, T., Kono, K., Itoh, T., Emi, N., and Takagishi, T. (2003) Synthesis of novel cationic lipids having polyamidoamine dendrons and their transfection activity. *Bioconjugate Chem. 14*, 764−773.

(14) Kojima, C., Hashimoto, A., Yabuta, I., Hirose, M., Hashimoto, S., Kanaho, Y., Sumimoto, H., Ikegami, T., and Sabe, H. (2004) Regulation of Bin1 SH3 domain binding by phosphoinositides. *EMBO J. 23*, 4413−4422.

(15) (a) Scherrenberg, R., Coussens, B., van Vliet, P., Edouard, G., Brackman, J., de Brabander, E., and Mortensen, K. (1998) The molecular characteristics of poly(propyleneimine) dendrimers as studied with small-angle neutron scattering, viscosimetry, and molecular dynamics. *Macromolecules 31*, 456−461. (b) Tomalia, D. A., Naylor, A. M., and Goddard, W. A., III (1990) Starburst dendrimers: molecular-level control of size, shape, surface-chemistry, topology, and flexibility from atoms to macroscopic matter. *Angew. Chem., Int. Ed. Engl. 29*, 138−175.

(16) Richter-Egger, D. L., Tesfai, A., and Tucker, S. A. (2001) Spectroscopic investigations of poly(propyleneimine) dendrimers using the solvatochromic probe phenol blue and comparisons to poly(amidoamine) dendrimers. *Anal. Chem. 73*, 5743−5751.

(17) (a) Seery, V. L., and Muller-Eberhard, U. (1973) Binding of porphyrins to rabbit hemopexin and albumin. *J. Biol. Chem. 248*, 3796−3800. (b) Cohen, S., and Margalit, R. (1990) Binding of porphyrin to human serum albumin. *Biochem. J. 270*, 325−330.

(18) (a) Hoebeke, M., and Damoiseau, X. (2002) Determination of the singlet oxygen quantum yield of bacteriochlorin *a*: a comparative study in phosphate buffer and aqueous dispersion of dimiristoyl-L-α-phosphatidylcholine liposomes. *Photochem. Photobiol. Sci. 1*, 283−287. (b) Damoiseau, X., Tfibel, F., Hoebeke, M., and Fontaine-Aupart, M. P. (2002) Effect of aggregation on bacteriochlorin *a* triplet-state formation: a laser flash photolysis study. *Photochem. Photobiol. 76*, 480−485.

(19) (a) Kubat, P., Lang, K., Janda, P., and Anzenbacher, P., Jr. (2005) Interaction of porphyrins with a dendrimer template: self-aggregation controlled by pH. *Langmuir 21*, 9714−9720. (b) Paulo, P. M., and Costa, S. M. (2003) Non-covalent dendrimer-porphyrin interactions: the intermediacy of H-aggregates? *Photochem. Photobiol. Sci. 2*, 597−604.

(20) Ding, X., Xu, Q., Liu, F., Zhou, P., Gu, Y., Zeng, J., An, J., Dai, W., and Li, X. (2004) Hematoporphyrin monomethyl ether photodynamic damage on HeLa cells by means of reactive oxygen species production and cytosolic free calcium concentration elevation. *Cancer Lett. 216*, 43−54.

(21) (a) Plaetzer, K., Kiesslich, T., Oberdanner, C. B., and Krammer, B. (2005) Apoptosis following photodynamic tumor therapy: induction, mechanism and detection. *Curr. Pharm. Des. 11*, 1151−1165. (b) Almeida, R. D., Manadas, B. J., Carvalho, A. P., and Duarte, C. B. (2004) Intracellular signaling mechanisms in photodynamic therapy. *Biochim. Biophys. Acta 1704*, 59−86.

(22) Ji, Z., Yang, G., Vasovic, V., Cunderlikova, B., Suo, Z., Nesland, J. M., and Peng, Q. (2006) Subcellular localization pattern of protoporphyrin IX is an important determinant for its photodynamic efficiency of human carcinoma and normal cell lines. *J. Photochem. Photobiol., B 84*, 213−220.

(23) Yee, K. K., Soo, K. C., Bay, B. H., and Olivo, M. (2002) A comparison of protoporphyrin IX and protoporphyrin IX dimethyl ester as a photosensitizer in poorly differentiated human nasopharyngeal carcinoma cells. *Photochem. Photobiol. 76*, 678−682.

(24) Hamblin, M. R., Miller, J. L., Rizvi, I., Ortel, B., Maytin, E. V., and Hasan, T. (2001) Pegylation of a chlorine$_{e6}$ polymer conjugate increases tumor targeting of photosensitizer. *Cancer Res. 61*, 7155−7162.

(25) Uehlinger, P., Zellweger, M., Wagnieres, G., Juillerat-Jeanneret, L., van den Bergh, H., and Lange, N. (2000) 5-Aminolevulinic acid and its derivatives: physical chemical properties and protoporphyrin IX formation in cultured cells. *J. Photochem. Photobiol., B 54*, 72−80.

BC060244U

Efficient Surface Patterning of Oligonucleotides Inside a Glass Capillary through Oxime Bond Formation

Nabil Dendane,[#,†] Antoine Hoang,[#] Ludovic Guillard,[†] Eric Defrancq,[†,*] Françoise Vinet,[#] and Pascal Dumy[†]

Département de Chimie Moléculaire - UMR CNRS 5250, ICMG FR2607, Université Joseph Fourier, BP 53, 38041 Grenoble Cedex 9, France, and LETI-CEA, 17 rue des Martyrs, 38054 Grenoble Cedex 9, France. Received August 16, 2006; Revised Manuscript Received December 5, 2006

The efficient surface patterning of oligonucleotides was accomplished onto the inner wall of fused-silica capillary tubes as well as on the surface of glass slides through oxime bond formation. The robustness of the method was demonstrated by achieving the surface immobilization of up to three different oligonucleotide sequences inside the same capillary tube. The method involves the preparation of surfaces grafted with reactive aminooxy functionalities masked with the photocleavable protecting group, 2-(2-nitrophenyl) propyloxycarbonyl group (NPPOC). Briefly, NPPOC-aminooxy silane **1** was prepared and used to silanize the glass surfaces. The NPPOC group was cleaved under brief irradiation to unmask the reactive aminooxy group on surfaces. These reactive aminooxy groups were allowed to react with aldehyde-containing oligonucleotides to achieve an efficient surface immobilization. The advantage associated with the present approach is that it combines the high-coupling efficiency of oxime bond formation with the convenience associated with the use of photolabile groups. The present strategy thus offers an alternative approach for the immobilization of biomolecules in the microchannels of "labs on a chip" devices.

INTRODUCTION

The miniaturization of biological assays represents an intensive domain of research especially for the design of high-throughput screening systems. In this context, the microarrays of biomolecules such as DNA, carbohydrates, and peptides have emerged as versatile tools with diverse applications in the areas of genetic analysis, molecular diagnostics, and drug discovery. Similarly, there is a significant interest in the design of microfluidic systems with an objective to achieve integration of synthesis, purification, and analysis steps on a chip. The "lab on a chip" device along with the microarrays technologies would indeed revolutionize the diagnostic field by permitting more rapid, economical, and multiparametric analysis with minimum volumes of samples (*1*, *2*).

The critical step in the preparation of microarrays and/or "lab on a chip" device is the control of surface chemistry. One challenging task is to carry out the surface immobilization of biomolecules (DNA, proteins) without affecting their intrinsic properties. Two major strategies are being currently used for the patterning of biomolecules on planar arrays. The first approach involves surface synthesis (in situ synthesis) whereas the second approach implicates the deposition of prefabricated biomolecules on the surface. The in-situ synthesis, pioneered by Fodor and Coll (*3*) for the preparation of DNA arrays, takes advantage of the photolithography technique for the photochemical addressing of the oligonucleotides on the surface and provides high-density arrays. While very promising, the method suffers from the fact that only short-length oligonucleotide sequences can be synthesized on the surface and the costs incurred are relatively high. Moreover, the procedure becomes arduous when used for the preparation of other microarrays (carbohydrates and peptides for example). On the other hand, the deposition technology involves the attachment (covalent or noncovalent) of prefabricated biomolecules to the surface (*4*). This approach utilizes "spotting techniques" and benefits from the fact that automated robots can be used to immobilize biomolecules on the surface. The major advantage is the fact that biomolecules prepared by chemical or enzymatic methods can be fully purified and characterized prior to spotting. This spotting technology is limited to low complexity arrays only but allows more flexibility. The surface immobilization is mostly achieved by chemical reaction between surface-bound reactive groups and prefunctionalized biomolecules. A large number of combinations of surface/biomolecule functions have been used for this purpose and mostly include maleimide/thiol (*5*), "click chemistry" involving alkyne/azide (*6*, *7*), hydrazide/aldehyde (*8*, *9*), etc. The patterning of biomolecules inside the microchannels used in the design of "lab on a chip" is more complicated due to the closed geometry of this format. To our knowledge, only two methods have been reported to date. The first method involves the photogeneration of surface-bound aldehyde groups for the immobilization of proteins via the formation of a Schiff base (*10*). The second method is based on the photo-cross-linking of surface-bound benzophenone derivatives with biomolecules via C−H insertion (*11*). Consequently, the design and development of alternative chemical approaches for surface immobilization of biomolecules inside the closed space (microchannels) have assumed significant research interest.

The paper describes a new method that allows an efficient immobilization of oligonucleotides (as an example of biomolecules) onto the surface of inner wall of fused-silica capillary tubes as well as of glass slides by utilizing the oxime chemistry. The present approach involves the grafting of aminooxy functionalities protected with a photolabile group on the surface. The photolabile group is then removed by irradiation thereby generating reactive aminooxy functions at predefined positions. This is followed by the deposition of the biomolecule functionalized with an aldehyde group, which reacts with the

* Corresponding author. Fax: +33(0)4.76.51.49.46, E-mail: Eric.Defrancq@ujf-grenoble.fr.

† University J. Fourier.

LETI-CEA.

10.1021/bc060254v CCC: $37.00 © 2007 American Chemical Society
Published on Web 03/10/2007

aminooxy functions and thus gets immobilized onto the surfaces due to the formation of oxime bond. In order to prove the concept, we have used oligonucleotides as biomolecule and we have first studied all the steps required for the immobilization of oligonucleotides on a planar format. The sensitivity of the arrays prepared by this method for detecting the target sequence was evaluated, and a reasonably high sensitivity of detection (1 nM) was achieved. The potential utility of the present approach for the surface functionalization and immobilization inside the microchannel for "lab on a chip" devices has been further demonstrated by carrying out surface immobilization of three different oligonucleotides sequences onto the inner wall of a same capillary tube and simultaneously monitoring the three hybridization events.

EXPERIMENTAL PROCEDURES

Materials and Methods. All solvents and reagents used were of highest purity available. The complementary labeled oligonucleotides were purchased from MWG Biotech and the hybridization solution from Sigma. Flexible fused-silica capillaries with UV-transparent coating (interior diameter: 100 μm) were obtained from Polymicro Technologies (Phoenix, AZ). The oligonucleotides were characterized by ESI mass spectra on an Esquire 3000 (Bruker) spectrometer. The analysis was performed in negative mode using 50% aqueous acetonitrile as eluent. The oligonucleotides were dissolved in 50% aqueous acetonitrile containing 2% of NEt_3. ^1H, ^{29}Si, and ^{13}C NMR spectra were recorded on Bruker AC 200 and Avance 300 spectrometers. The irradiation experiment on capillaries were performed on an Olympus inverted microscope model IX60, equipped with a 100 W mercury lamp and a 365 nm interference filter. The patterning was performed by irradiation of the focus zone. Hybridization experiments were carried out using a Gentac Scanner (Genomic Solution). The excitation and emission wavelengths employed for different probes are as follows: Fluorescein ($\lambda_{Exc.}$ = 494 nm, $\lambda_{Em.}$ = 518 nm), Cy3 ($\lambda_{Exc.}$ = 550 nm, $\lambda_{Em.}$ = 570 nm), Cy5 ($\lambda_{Exc.}$ = 649 nm, $\lambda_{Em.}$ = 670 nm), Texas Red ($\lambda_{Exc.}$ = 595 nm, $\lambda_{Em.}$ = 615 nm).

Synthesis. The 5′-aldehyde oligonucleotides were prepared as previously reported (*12*). The oligonucleotide sequences employed in the present work are 5′-d-XTTTTTGATAAACCCACTCTA-3′ (**Seq1)**, 5′-d-XTTTTTTGATCATGTTGTTGCTTG-3′ (**Seq2**), 5′-d-XTTTTTTCGGATACCCAAGGA-3′ **(Seq3**) respectively, where X represents the 5′-aldehyde linker.

Compound 2. A solution of *N*-hydroxyphthalimide (3.50 g, 21 mmol) and potassium carbonate (8 g, 41 mmol) in DMF (250 mL) was heated for 1 h at 50 °C under argon. 11-Bromoundecene (5.0 g, 21 mmol) was added, and the reaction mixture was stirred for 3 h at 50 °C. Then the reaction mixture was filtered, and the filtrate was evaporated under vacuum. The residue so obtained was redissolved in CH_2Cl_2 and successively washed with 0.1 N aq NaOH and brine. The organic layer was dried over Na_2SO_4 and evaporated to give compound **2** as a white powder (6.45 g, 97%). Mp 38−40 °C; ^1H NMR ($CDCl_3$) δ 1.20−1.50 (m, 12H; $6CH_2$), 1.78 (m, 2H; CH_2CH_2O), 2.02 (m, 2H; $CH_2CH{=}CH_2$), 4.18 (t, 2H; CH_2O), 4.95 (m, 2H; $CH_2{=}CH$), 5.79 (m, 1H; $CH_2{=}CH$), 7.70−7.85 (m, 4H; Ar−H); ^{13}C NMR ($CDCl_3$) δ 25.66 (CH_2), 28.27 (CH_2), 29.03 (CH_2), 29.20 (CH_2), 29.39 (CH_2), 29.49 (CH_2), 29.52 (CH_2), 33.90 (CH_2), 78.72 (CH_2), 114.22 (CH_2), 123.56 (CH), 129.14 (Cquat), 134.52 (CH), 139.30 (Cquat), 163.75 (Cquat); MS (ESI): M_{calcd} = 315 ($C_{19}H_{25}NO_3$), found (*m/z*): 338 $(M + Na)^+$; Anal. calcd C 72.36 H 7.99 N 4.45, found C 72.21 H 8.13 N 4.40.

Compound 3. Compound **2** (3 g, 9.5 mmol) was dissolved in CH_2Cl_2 (30 mL), and hydrazine hydrate (0,966 g, 19.3 mmol) was added. The solution was refluxed for 2 h and then filtered. The filtrate was evaporated under vacuum. The crude product was purified by silica gel column chromatography using EtOAc/cyclohexane as eluent (1/2, v/v) to obtain **3** as white oil (1.65 g, 94%). ^1H NMR ($CDCl_3$) δ 1.20−1.40 (m, 12H; $6CH_2$), 1.56 (m, 2H; CH_2), 2.03 (m, 2H; CH_2), 3.65 (t, 2H; CH_2O), 4.90−5.02 (m, 2H; $CH{=}CH_2$), 5.74−5.87 (m, 1H; $CH{=}CH_2$); ^{13}C ($CDCl_3$) δ 26.11 (CH_2), 28.51 (CH_2), 29.02 (CH_2), 29.20 (CH_2), 29.51 (CH_2), 29.58 (CH_2), 29.61 (CH_2), 33.89 (CH_2), 76.26 (CH_2), 114.20 (CH_2), 139.25 (CH); MS (ESI): M_{calcd} = 185 ($C_{11}H_{23}NO$), found (*m/z*): 186 $(M + H)^+$.

Compound 4. A solution of 2-(2-nitrophenyl)propyl chloroformate (740 mg, 3 mmol) in CH_2Cl_2 (3 mL) was added dropwise to the solution of compound **3** (470 mg, 2.54 mmol) in pyridine (2 mL). The solution was stirred for 2 h in darkness and filtered, and the filtrate was evaporated under vacuum. The residue so obtained was redissolved in CH_2Cl_2, and the organic layer was washed successively with 10% aq sodium carbonate, 1 N aq HCl, and brine. The organic layer was dried (Na_2SO_4) and evaporated under vacuum. The crude product was purified by silica gel column chromatography using EtOAc/cyclohexane (1/4, v/v) as eluent to obtain compound **4** as an orange oil (873 mg, 87%). ^1H NMR ($CDCl_3$) δ 1.20−1.40 (m, 12H; $6CH_2$), 1.35 (d, 3H; CH_3), 1.56 (m, 2H; CH_2), 2.03 (m, 2H; CH_2), 3.69−3,78 (m, 3H; $CH + CH_2O$), 4.21−4.35 (m, 2H; CH_2OCO), 4.90−5.01 (m, 2H; $CH{=}CH_2$), 5.74−5.87 (m, 1H; $CH{=}CH_2$), 7.34−7.56 (m, 4H, Ar−H); ^{13}C NMR ($CDCl_3$) δ 17.64 (CH_3), 25.86 (CH_2), 27.96 (CH_2), 29.01 (CH_2), 29.19 (CH_2), 29.49 (CH_2), 33.37 (CH), 33.89 (CH_2), 69.35 (CH_2), 77.14 (CH_2), 114.22 (CH_2), 124.20 (CH), 127.57 (CH), 128.21 (CH), 132.74 (CH), 137.14 (Cquat), 139.28 (CH), 150.66 (Cquat), 157.28 (Cquat); MS (ESI): M_{calcd} = 392 ($C_{21}H_{32}N_2O_5$), found (*m/z*): 415 $(M + Na)^+$; Anal. calcd C 64.27 H 8.22 N 7.14, found C 64.16 H 8.48 N 6.88.

Compound 1. Karstedt catalyst (0.1 M platinum(0)-1,3-divinyl-1,1,3,3-tetramethyldisiloxane complex dissolved in poly-(dimethylsiloxane), 15 μL, 0.02 equiv) was added to a solution of compound **4** (663 mg, 1.69 mmol) in triethoxysilane (1.5 mL). The reaction mixture was stirred for 4 h at 60 °C. The solvent was evaporated next under vacuum to obtain compound **1**. This was used in next step without further purification. ^1H NMR (200 MHz, $CDCl_3$) δ 0.6 (m, 2H; $CH_2{-}Si$), 1.10−1.30 (m, 16H; $CH_3 + CH_2$), 1.35 (d, 3H; CH_3), 1.56 (m, 2H; CH_2), 3.65−3.90 (m, 9H; $CH + 4CH_2O$), 4.28 (m, 2H; CH_2OCO), 7.20 (br s, 1H; NH), 7.35−7.75 (m, 4H, Ar−H); ^{13}C NMR (75 MHz, $CDCl_3$) δ 10.9 (CH_2), 18.0 (CH_3), 18.8 (CH_3), 23.2 (CH_2), 23.3 (CH_2), 26.3 (CH_2), 28.4 (CH_2), 29.8 (CH_2), 29.9 (CH_2), 30.0 (CH_2), 30.1 (CH_2), 33.8 (CH), 58.8 (CH_2O), 69.8 (CH_2O), 77.6 (CH_2), 124.6 (CH), 128.0 (CH), 128.6 (CH), 132.2 (CH), 137.0 (Cquat), 150.1 (Cquat), 157.1 (Cquat); ^{29}Si NMR (59 MHz, $CDCl_3$) δ −21.7. IR (NaCl): 3279 (br), 2975, 2926, 2855, 1752, 1728, 1528, 1082 cm^{-1}. MS (ESI): M_{calcd} = 556 ($C_{27}H_{48}N_2O_8Si$), found (*m/z*): 579 $(M + Na)^+$, 595 $(M + K)^+$. Anal. calcd C 58.25 H 8.69 N 5.03, found C 58.62 H 8.57 N 5.05.

Functionalization and Oligonucleotide Immobilization on Glass Surfaces. *Step 1. Hydratation of the Surface:* The glass slides were dipped in an aq ethanolic solution of NaOH (1 g NaOH, 4 mL H_2O, 3 mL EtOH) for 1 h and washed successively with ultrapure H_2O, 0.2 N aq HCl, and H_2O again. The glass slides were then dried under nitrogen.

Step 2. Silanization with 1: The glass slides were dipped in a 5 mM solution of compound **1** in toluene/NEt_3 (97/3, v/v) for overnight storage at room temperature. The slides were washed with toluene followed by EtOH and finally dried under nitrogen. The glass slides were then cured at 110 °C for 3 h.

Step 3. Photodeprotection: An aq pyridine solution (from 5% to 50%) was deposited on the glass slides, and a mask

(containing holes of diameter: 80 μm) was applied on the surface. Irradiation for different time span was carried out by using a mercury lamp (100 W, 24 mW/cm^2). After removal of the mask, the glass slides were washed with H_2O and dried under nitrogen.

Step 4. Immobilization: The glass slides were dipped in a solution of 0.4 M ammonium acetate buffer containing oligonucleotide-5′-aldehyde (**Seq1**, 2−20 μM) for different time durations (30 s−12 h). The glass slides were then successively washed with H_2O, 1% aq SDS solution, and H_2O and finally dried under nitrogen.

Step 5. Hybridization: The glass slides were dipped in the hybridization solution of Cy3 labeled complementary oligonucleotide at different concentrations (0.1−100 nM) for 1 h at 39 °C. The glass slides were washed with 2X SSC buffer and dried under nitrogen. The glass slides were then scanned on a Gentac Scanner (Genomic Solution).

Functionalization and Oligonucleotide Immobilization on Glass Surfaces Inside the Capillary Tubes. *Step 1. Hydratation of the Capillary Tube:* The capillary tube was filled with an aq ethanolic solution of NaOH (1 g NaOH, 4 mL H_2O, 3 mL EtOH) for 1 h and washed successively with ultrapure H_2O, 0.2 N aq HCl, and H_2O. The capillary tube was then dried under nitrogen.

*Step 2. Silanization with **1**:* The capillary tube was filled with a 10 mM solution of compound **1** in trichloroethylene and incubated for overnight at room temperature. The capillary was then washed with trichloroethylene followed by EtOH and dried under nitrogen. Finally, the capillary tube was cured at 110 °C for 3 h.

Step 3. Photodeprotection: The capillary tube was filled with a 5% aq pyridine solution and was mounted on the microscope stage. Irradiation for different time span was carried out by using a mercury lamp (100 W, 24 mW/cm^2). The irradiations were focused at different positions on the capillary. Each irradiation thus corresponded to a separate spot on the capillary array. The capillary was then washed with H_2O and dried under nitrogen.

Step 4. Immobilization: The capillary was filled with a 0.4 M ammonium acetate buffer solution containing oligonucleotide-5′-aldehyde (**Seq1**, 20 μM) for 2 min. A constant reagent flow (0.1−10 μL min^{-1}) was applied by using a syringe pump. The capillary was successively washed with H_2O, 1% aq SDS solution, and H_2O and finally dried under nitrogen.

Step 5. Hybridization: The capillary was filled with the hybridization solution of Cy3 labeled complementary oligonucleotide at different concentrations (10−100 nM) for 1 h at 39 °C. A constant flow of hybridization solution (0.1−10 μL.min^{-1}) was maintened by using a syringe pump. The capillary was washed with 2X SSC buffer and then scanned by using a four-color microarray GeneTAC Scanner (Genomic Solutions).

The same procedure as described above was further applied for surface immobilization of three different oligonucleotides inside the same capillary tube (multiple functionalization) by using oligonucleotides **Seq1**, **Seq2**, and **Seq3**. Each immobilization corresponded to a separate spot inside the capillary. The complementary sequences for **Seq1**, **Seq2**, and **Seq3** were labeled with Fluorescein, Cy5, and Texas Red, respectively. These three complementary sequences were used as a mixture in the present case to carry out hybridization experiments.

Specificity of Immobilization Chemistry. In order to investigate the site specificity of the approach, two control experiments were performed: the first one consisted of quenching the aminooxy group liberated during the photodeprotection, the second involved the use during the immobilization step of oligonucleotides, which do not contain the complementary aldehyde reactive group. The first control was carried out in a capillary tube as follows: the first three steps of the functionalization were carried out as before and the capillary tube was then washed with an acetone aqueous solution for 20 min. In this case, the liberated aminooxy functions on the glass surface should be quenched by the acetone by oxime bond formation. Subsequently, the oligonucleotide immobilization and hybridization steps were performed as before and the capillary tube was subjected to laser scanning. For the second control, the immobilization step was carried out by using a 0.4 M ammonium acetate buffer solution containing oligonucleotide-5′-diol (20 μM) for 2 min. Hybridization was then performed using the complementary labeled strand as usual, and the capillary tube was scanned by using a four-color microarray GeneTAC Scanner (Genomic Solutions).

Characterization of the Glass Surfaces. *Contact Angle (θ) Measurements*: The measurements of the contact angle θ of the NPPOC-modified glass surfaces were performed on a Digidrop (GBX) apparatus by using water and diiodomethane solvents. The analysis was done several times by using a series of different slides, and average values of 79° and 42° were found for water and diiodomethane, respectively. By comparison, the contact angle θ of unmodified glass slides was found to be less than 10° using water.

Multireflexion IR (MIR method): 2920 (υ_{CH}), 1725 (υ_{CO}), 1550 (υ_{NO2}) cm^{-1}. The measurements were carried out using a homemade setup placed in the sample compartment of a FTIR Bruker IFS55 spectrometer.

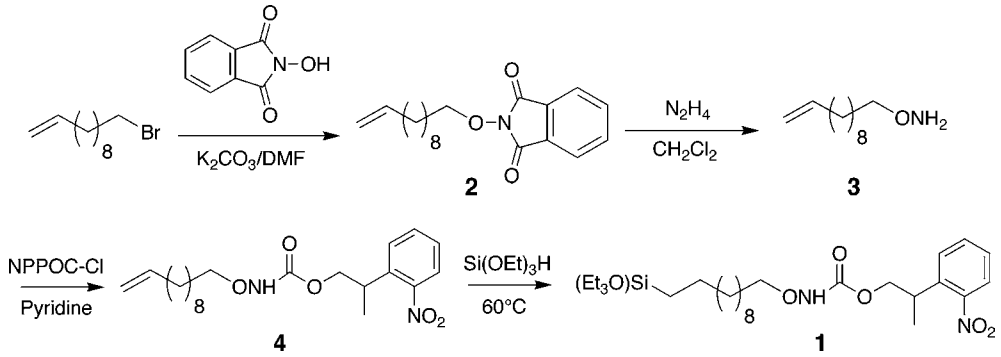
Atomic Force Microscopy: The measurements were carried out on an AFM PicoPlus system (Molecular Imaging) by using acoustic mode (MAC mode). A roughness (rms) of 4 nm was found.

Ellipsometry: Ellipsometric measurements were performed using an imaging ellipsometer EP3-SE from Nanofilm Technology GmbH (Germany). Vase experiments were performed ex situ under air conditions at 20 different wavelengths ranging from 366.3 to 1001.9 nm and at variable angles of incidence ranging from 50° to 80° by steps of 2°. Optical modeling was performed using the EP3View software from Nanofilm Technology GmbH. A four-layer model, Si/SiO_2/Silane/ambient air, was used to fit the data. The optical properties of the bare silicon wafer were previously measured using a three-layer model, Si/SiO_2/ambient air.

RESULTS AND DISCUSSION

An alternative approach for surface patterning of biomolecules was envisioned. The key features of the present approach were the preparation of surfaces grafted with the aminooxy functionality masked with a photocleavable protecting group and surface immobilization of aldehyde-containing oligonucleotides through the formation of oxime bonds. The possibility of a photolabile protecting group was explored because it is more convenient to use. The photolabile group can easily be removed by simple irradiation with light and thus excludes exhaustive deprotection chemistries from the protocol and subsequently associated side-reactions. The oxime bond formation was selected for the surface immobilization because it has been successfully utilized for the preparation of oligonucleotide (*12*−*14*), peptide (*15*), and carbohydrates conjugates (*16*). The advantages associated with the use of oxime bonds are that the reaction is chemoselective and proceeds with high coupling efficiency without any additive. This bond is stable over a large range of pH. Last but not the least, these linkages have been used earlier for the preparation of oligonucleotides (*17*, *18*) and carbohydrates arrays (*19*). It was therefore expected that the present approach would combine the high coupling efficiency of the oxime bond formation with the convenience associated with the use of photolabile protecting groups and will thus aid in achieving an efficient surface patterning.

Scheme 1



The most documented photolabile-protecting group for an amine functionality is undoubtedly the nitroveratryloxycarbonyl group (NVOC). However, the NVOC photocleavage leads to the formation of an aldehyde byproduct that can react with the liberated aminooxy function. Hence, the NVOC was not found to be suitable for the present purpose. It was therefore decided to use the 2-(2-nitrophenyl)propyloxycarbonyl group (NPPOC) instead of NVOC to mask the aminooxy moieties. The NPPOC group has been used earlier for the protection of amines and alcohols for the preparation of peptides and DNA microarrays by in situ synthesis approach (*20*, *21*). It is cleaved under illumination faster than the corresponding NVOC-protected compounds. More importantly, the photocleavage of the NPPOC group leads to an alkene that cannot react with the aminooxy moiety. Thus, NPPOC was thought suitable for the present investigation.

1. Synthesis of the Triethoxysilane Derivative 1. The triethoxysilane derivative **1** was prepared from commercially available 11-bromo-1-undecene in a few simple steps (Scheme 1). The aminooxy group was introduced first by using the dicarboximide derivative in basic conditions, followed by the cleavage of the protecting group with hydrazine. The free aminooxy functionality was protected next by using the photolabile NPPOC chloride derivative. Hydrosilylation was finally carried out using triethoxysilane in presence of Kärstedt's catalyst to obtain silane **1**. The derivatives **1**−**4**, prepared herein, were characterized by satisfactory ^{1}H and ^{13}C NMR and mass spectrometry data.

2. Oligonucleotide Surface Immobilization on Glass Slides. The glass slides were used as a model surface to carefully investigate and standardize the procedure involved in oligonucleotide immobilization before employing it for closed surfaces inside the capillary tubes. The crucial steps involved in the process and evaluated herein were the silanization of surfaces with **1**, the photocleavage of the NPPOC to unmask the aminooxy functionalities, and the immobilization of the aldehyde-containing oligonucleotides and their hybridization with the complementary sequences.

The glass slides were pretreated with sodium hydroxide before silanization. The silane **1** was then chemisorbed from a toluene/NEt_3 solution (97/3) onto the glass slides for overnight storage at room temperature. The silanization step was followed by a curing at 110 °C for 3 h to stabilize the silane layer. This silane coating was found to be stable at least for several months. The characterization of the modified surface was achieved using different techniques. The presence of carbamate function of NPPOC group was detected on the glass slide by multireflexion IR (MIR method). A strong signal for the carbonyl band of the carbamate at 1725 cm^{-1} was observed. Contact angle θ was measured for the modified glass slides using water, and the hydrophobic diiodomethane and θ values of 79° and 42° were found, respectively. On the other hand, the θ value of unmodified glass surfaces was found to be less than 10° using water. These measurements thereby strongly reflect the large increase in the hydrophobicity of the surfaces modified with NPPOC. Last, the thickness of the modified silane layer was evaluated at 5−6 nm by ellipsometry study and the roughness of this silane's layer on the surface was measured at about 4 nm by AFM method (see the Supporting Information).

Following silanization, three crucial steps were performed next to demonstrate the efficiency of the present approach. This included the photocleavage of the protecting group, coupling reaction with oligonucleotide-5′-aldehyde and hybridization with the complementary fluorescent probe. The photocleavage reaction on the glass slide was carried out by irradiation at 365 nm through a mask containing holes with a diameter of 80 μm. The time of irradiation (2−20 s) and solvents (water, water/pyridine, water/ammonia) were varied. It was found that presence of base is required for the photolysis to proceed, as the process in water alone was sluggish. The immobilization of the prefunctionalized oligonucleotides was achieved by dipping the glass slide in a 0.4 M ammonium acetate buffer solution (30 s−12 h) containing the oligonucleotide-5′-aldehyde (**Seq1**) at different concentrations (2−20 μM). The pH of the buffer was adjusted to 4.6 because slightly acidic conditions are known to be conductive for the formation of oxime bonds. As a matter of fact, the use of water alone resulted in lower immobilization efficiencies. Finally, the ability of the surface-bound oligonucleotide arrays to hybridize with the complementary sequence was investigated. The complementary sequences were labeled with Cy3. After hybridization and subsequent washings, the glass slides were scanned under a fluorescent scanner. The signal intensity obtained in this manner directly reflected the efficiency of the method. When the glass slides were irradiated through the mask, a pattern of fluorescent and nonfluorescent areas with the shape of the mask were revealed (Figure 1 shows a representative scanned image from the hybridization experiments). Of the several conditions tested, the best results were achieved using the following conditions: irradiation at 365 nm for 5 s in a 5% aqueous pyridine solution, deposition using a 20 μM solution of aldehydic oligonucleotide in 0.4 M ammonium acetate buffer for 2 min. These conditions mentioned herein represent the best compromise obtained between the times of irradiation and coupling and the quantity of oligonucleotide-5′-aldehyde to be used. The crucial issue of sensitivity was also evaluated. The concentration of the Cy3-labeled complementary sequence was varied (0.1−100 nM) by using the conditions described earlier (Figure 1B). The sensitivity of detection was found to be reasonably high at 1 nM (with a ratio signal/noise S/N close to 6).

3. Oligonucleotide Surface Immobilization Inside the Capillary Tubes. The strategy developed herein was employed for the surface immobilization of oligonucleotides onto the inner wall of capillary tube. The surface immobilization of biomolecules inside the tube is more challenging, and this study has great significance because it may have potential utility in the

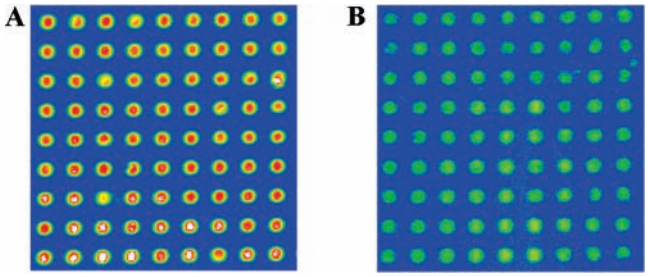


Figure 1. Scanned images of the oligonucleotide arrayed glass slides. The arraying was carrying out by irradiation through a mask (hole diameter: 80 μm) at 365 nm for 5 s in a 5% aqueous pyridine solution, followed by the deposition of a 20 μM solution of aldehydic oligonucleotide (**Seq1**) in 0.4 M ammonium acetate buffer for 2 min. Hybridization was carried out at 39 °C for 1 h using a solution of Cy3-labeled complementary oligonucleotide sequence at different concentrations (0.1−100 nM). A. concentration of the complementary sequence is 100 nM. B. concentration of the complementary sequence is 1 nM. The fluorescence intensities are color-coded, varying from blue (low) to green, yellow, red, and then white (saturation); the gain of the detector was kept constant for comparison of the fluorescence intensity.

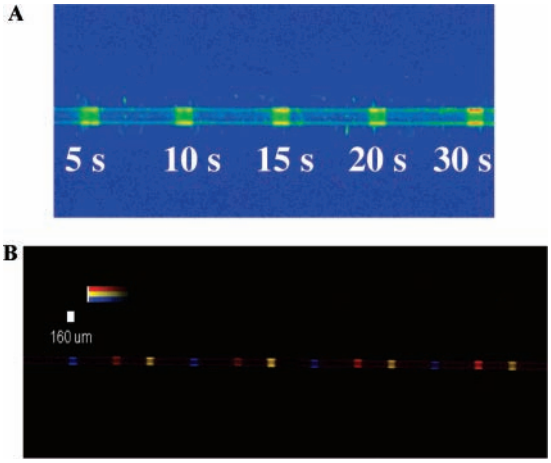


Figure 2. Scanned images of the oligonucleotides arrayed capillary tube. A. Irradiation at 365 nm for various time periods in a 5% aqueous pyridine solution, deposition of a 20 μM solution of aldehydic oligonucleotide (**Seq1**) in 0.4 M ammonium acetate buffer for 2 min and hybridization with the complementary strand labeled with Cy3. B. Multiple deposition of the three oligonucleotides **Seq1**, **Seq2**, and **Seq3** and hybridization with the mixture of corresponding complementary sequences labeled with Fluorescein, Cy5, and Texas Red, respectively. The fluorescence is color-coded: blue for fluorescein, yellow for Cy5, and red for Texas Red.

design of "labs on a chip". Besides, the microfluidic capillary format offers a number of advantages over the planar format, including smaller sample volume and higher surface-to-volume ratio.

The glass capillary tube was silanized with **1** by adapting the procedure described above. Trichloroethylene was used instead of toluene, as the latter caused the degradation of the fused-capillary. The photocleavage of NPPOC was carried out by irradiation at 365 nm for varying time periods on an inverted microscope equipped with a mercury lamp (100 W) and a 365 nm interference filter. The length of the irradiated zone was adjusted at 150 μm by a slit aperture. In this way, irradiation to liberate the surface-bound aminooxy group was performed only at the preselected portions of the tube. The surface immobilization was carried out by dipping the extremity of the capillary tube in a 0.4 M ammonium acetate buffer solution containing the oligonucleotide-5′-aldehyde (**Seq1**). The capillary tube containing the surface-immobilized oligonucleotides was then dipped in the hybridization solution containing the Cy3-labeled complementary sequence for **Seq1**. After several washings with SSC buffer to remove the unhybridized complementary sequences, the capillary tubes were scanned using a fluorescent scanner (Figure 2A). The results from hybridization experiments clearly showed the fluorescence spot localized at the irradiated portion of the capillary tube. The photodeprotection was found to be rapid, as an irradiation time of 2 s was sufficient to give measurable response. It was noted that prolonged irradiation times resulted in some enlargement of the zone compared to the size of the irradiated zone due to light scattering. Two control experiments were performed by using a quencher (acetone) of the aminooxy group liberated during the photodeprotection as well as by using for the immobilization step an oligonucleotide, which does not contain the complementary aldehyde reactive group for oxime bond formation. In these two cases, no significant signal was clearly observed at the irradiated position, thus demonstrating the specificity of the method. Thus, site-selective immobilization of DNA was accomplished even in the closed environment of a capillary tube.

The efficiency and robustness of the process developed herein was next investigated by achieving sequential surface immobilization of three different oligonucleotide sequences inside the same capillary tube. A set of three different aldehyde-containing oligonucleotide sequences, **Seq1**, **Seq2**, and **Seq3**, respectively, were arrayed inside the same capillary tube by repeating the protocol described in the present work. Briefly, the capillary tube was silanized with **1**. The silanized tube was irradiated at certain preselected positions, and this was followed by the surface immobilization of the **Seq1** oligonucleotide sequence. After subsequent washing to remove free oligonucleotides, the process was repeated at certain other preselected positions of the same capillary tube to carry out surface immobilization of oligonucleotide sequences **Seq2** and **Seq3**, respectively. Thus, the surface immobilization of three different oligonucleotides was accomplished inside the same capillary tube. Then a mixture of the three oligonucleotide sequences complementary to **Seq1**, **Seq2**, and **Seq3** was run through the arrayed capillary tube. The three sequences complementary to **Seq1**, **Seq2**, and **Seq3** were labeled with Fluorescein, Cy5, and Texas Red, respectively. The complementary sequences labeled with different fluorescent probes were used to facilitate the simultaneous detection of three hybridization events inside the same capillary tube. The tube was next scanned at different wavelengths corresponding to the three labels on the complementary strand (Figure 2B). The results showed that the complementary labeled sequences were able to hybridize with their targets, as evident from the probe-specific fluorescence emission at predetermined immobilization sites inside the capillary tube (Figure 2B, also see the Supporting Information). These hybridization experiments thus unambiguously demonstrated the selective surface immobilization of different oligonucleotides **Seq1**, **Seq2**, and **Seq3** at the predefined position inside the tube. No side reactions were observed during the repetitive flow of aldehyde-containing oligonucleotide through the capillary tube.

CONCLUSION

Thus, an efficient protocol for surface patterning of oligonucleotides was developed. The efficiency of the present method was demonstrated by carrying out the surface immobilization of oligonucleotides on surfaces of glass slides and inside the capillary tubes. The robustness of the process was further demonstrated by achieving the surface immobilization of up to three different oligonucleotide sequences at predetermined positions inside the same capillary tube. The present method reported herein is simple and convenient. It involves the preparation of surfaces grafted with aminooxy moieties masked with a photocleavable protecting group. A short irradiation at

365 nm cleaves the photocleavable protecting group thereby unmasking the aminooxy functions at preselected positions on the surface. Deposition of aldehyde-containing oligonucleotides on surfaces results in the formation of oxime bonds between aldehyde functionality of the oligonucleotide and the surface-bound aminooxy moieties, thereby leading to an efficient surface immobilization of oligonucleotides. Since the oxime ligation has been used for the preparation of oligonucleotide, peptide, and carbohydrate bioconjugates, it should be possible to extend the present strategy to the preparation of carbohydrate and peptide arrays. Finally, the immobilization protocol reported herein could also be explored as an efficient and alternative approach to design "lab on a chip" devices.

ACKNOWLEDGMENT

This work was supported by the "Centre National de la Recherche Scientifique" (CNRS) and the "Commissariat à l'Energie Atomique" (CEA). We are grateful to NanoBio program for the facilities of the Synthesis and Surface Characterization platforms. We thank Dr. Y. Singh for careful reading of this manuscript and Prof. P. Labbé for help with the surface characterization.

Supporting Information Available: Experimental details. This material is available free of charge via the Internet at http://pubs.acs.org.

LITERATURE CITED

(1) Ismagilov, R. F. (2003) Integrated microfluidic systems. *Angew. Chem., Int. Ed. 42*, 4130−4132.
(2) Kumar, A., Goel, G., Fehrenbach, E., Puniya, A. K., and Singh, K. (2005) Microarrays: the technology, analysis and application. *Eng. Life Sci. 5*, 215−222.
(3) Fodor, S. P. A., Read, J. L., Pirrung, M. C., Stryer, L., Lu, A. T., and Solas, D. (1991) Light-directed, spatially addressable parallel chemical synthesis. *Science 251*, 767−773.
(4) Thibault, C., Le, Berre, V., Casimirius, S., Trévisiol, E., François, J., and Vieu, C. (2005) Direct microcontact printing of oligonucleotides for biochip applications. *J. Nanobiotechnol. 3*, 1−12.
(5) Brun, M. A., Disney, M. D., and. Seeberger, P. H. (2006) Miniaturization of microwave-assisted carbohydrate functionalization to create oligosaccharide microarrays. *ChemBioChem 7*, 421−424.
(6) Sun, X.-L., Stabler, C. L., Cazalis, C. S., and Chaikof, E. L. (2006) Carbohydrate and protein immobilization onto solid surfaces by sequential diels-alder and azide-alkyne cycloadditions. *Bioconjugate Chem. 17*, 52−57.
(7) Duckworth, B. P., Xu, J., Taton, T. A., Guo, A., and Mark D. Distefano, M. D. (2006) Site-specific, covalent attachment of proteins to a solid surface. *Bioconjugate Chem. 17*, 967−974.
(8) Olivier, C., Hot, D., Huot, L., Ollivier, N., El-Mahdi, O., Gouyette, C., Huynh-Dinh, T., Gras-Masse, H., Lemoine, Y., and Melnyk, O. (2003) α-Oxo semicarbazone peptide or oligodeoxynucleotide microarrays. *Bioconjugate Chem. 14*, 430−439.
(9) Lee, M.-R., and Shin, I. (2005) Facile preparation of carbohydrate microarrays by site-specific, covalent immobilization of unmodified carbohydrates on hydrazide-coated glass slides. *Org. Lett. 7*, 4269−4272.
(10) Ligler, F. S., Breimer, M., Golden, J. P., Nivens, D. A., Dodson, J. P., Green, T. M., Haders, D. P., and Sadik, O. A. (2002) Integrating waveguide biosensor. *Anal. Chem. 74*, 713−719.
(11) Balakirev, M. Y., Porte, S., Vernaz-Gris, M., Berger, M., Arié, J.-P., Fouqué, B., and Chatelain, F. (2005) Photochemical patterning of biological molecules inside a glass capillary. *Anal. Chem. 77*, 5474−5479.
(12) Forget, D., Boturyn, D., Defrancq, E., Lhomme, J., and Dumy, P. (2001) Highly efficient synthesis of peptide-oligonucleotide conjugates: chemoselective oxime and thiazolidine formation. *Chem. Eur. J. 7*, 3976−3984.
(13) Katajisto, J., Virta, P., and Lönnberg, H. (2004) Solid-phase synthesis of multiantennary oligonucleotide glycoconjugates utilizing on-support oximation. *Bioconjugate Chem. 15*, 890−896.
(14) Zatsepin, T. S., Stetsenko, D. A., Gait, M. J., and Oretskaya, T. S. (2005) Use of carbonyl group addition-elimination reactions for synthesis of nucleic acid conjugates. *Bioconjugate Chem. 16*, 471−489.
(15) Rose, K. (1994) Facile synthesis of homogeneous artificial protein. *J. Am. Chem. Soc. 116*, 30−33.
(16) Hang, H. C., and Bertozzi, C. R. (2001) Chemoselective approaches to glycoprotein assembly. *Acc. Chem. Res. 34*, 727−736.
(17) Boncheva, M., Scheibler, L., Lincoln, P., Vogel, H., and Akerman, B. (1999) Design of oligonucleotide arrays at interfaces. *Langmuir 15*, 4317−4320.
(18) Defrancq, E., Hoang, A., Vinet, F., and Dumy, P. (2003) Oxime bond formation for the covalent attachment of oligonucleotides on glass support. *Bioorg. Med. Chem. Lett. 13*, 2683−2686.
(19) Tully, S. E., Rawat, M., and Hsieh-Wilson, L. C. (2006) Discovery of a TNFα antagonist using chondroitin sulfate microarrays. *J. Am. Chem. Soc. 128*, 7740−7741.
(20) Bhushan, K. R. (2006) Light-directed maskless synthesis of peptide arrays using photolabile amino acid monomers. *Org. Biomol. Chem. 4*, 1857−1859.
(21) Beier, M., and Hoheisel, J. D. (2000) Production by quantitative photolithographic synthesis of individually quality checked DNA microarrays. *Nucleic Acids Res. 28*, e11.

BC060254V

Construction and Evaluation of the Tumor Imaging Properties of ^{123}I-Labeled Recombinant and Enzymatically Generated Fab Fragments of the TAG-72 Monoclonal Antibody CC49

Ying Tang,[†,‡,⊥] Shaoxian Yang,[§] Jean Gariépy,[§] Deborah A. Scollard,[‡] and Raymond M. Reilly*[,†,‡,∥]

Department of Pharmaceutical Sciences, University of Toronto, Toronto, ON, Canada, Toronto General Research Institute, University Health Network, Toronto, ON, Canada, Department of Medical Biophysics, University of Toronto, Toronto, ON, Canada, and Department of Medical Imaging, University of Toronto, Toronto, ON, Canada. Received August 21, 2006; Revised Manuscript Received December 7, 2006

Tumor-associated glycoprotein-72 (TAG-72) is overexpressed in a high percentage of epithelial cancers and has proven useful as a target for imaging and targeted radiotherapy. Our goal was to express a recombinant Fab (rFab) of the TAG-72 monoclonal antibody CC49 in *Pichia pastoris* and directly compare its tumor and normal tissue uptake and imaging properties with enzymatically generated Fab (eFab). In this study, the genes coding for CC49 Fab were cloned from hybridoma cells and expressed in *P. pastoris*. Fab was purified to homogeneity and its immunoreactivity toward bovine submaxillary mucin (TAG-72) confirmed by ELISA. The tumor and normal tissue localization of ^{123}I-CC49 rFab and eFab were compared in athymic mice bearing s.c. LS174T colon cancer or TAG-72-negative A375 melanoma xenografts. Results showed that pure and immunoreactive rFab of CC49 was produced and labeled with ^{123}I. At 24 h post i.v. injection (p.i.), tumor uptake for ^{123}I-rFab in LS174T xenografts was 6.0% ID/g which was 18-fold higher than in A375 tumors. Tumor-to-normal tissue ratios increased between 2 and 24 h and exceeded 5:1 at 24 h p.i. of ^{123}I-rFab. ^{123}I-rFab exhibited significantly lower liver uptake at 12 h p.i. and lower kidney uptake at 2 h p.i. than ^{123}I-eFab. LS174T tumors were imaged as early as 2 h after administration of ^{123}I-rFab. We conclude that CC49 rFab can be produced in a *P. pastoris* host system and accumulated at comparable levels as eFab in LS174T colon cancer xenografts in mice. The lower liver uptake of ^{123}I-rFab as compared with eFab suggests that it may be more useful for imaging liver lesions. No major effect, except for kidneys and liver, was observed on tumor and normal tissue uptake due to introduction of hexahistidine and FLAG affinity tags or peptide linkers in the scaffold of rFab.

INTRODUCTION

Monoclonal antibodies (mAbs) directed against tumor-associated antigens overexpressed on the surface of tumor cells can deliver radionuclides to tumors for imaging. Small antibody fragments such as Fab or scFv are particularly suitable for this purpose because these fragments extravasate more efficiently, penetrate more deeply into tumor nodules, and clear more rapidly from the body compared with intact IgG, leading to higher tumor-to-normal tissue uptake ratios at early times (*1*−*3*). The utility of antibody fragments in tumor imaging is exemplified by anti-carcinoembryonic antigen (CEA) arcitumomab (CEA-Scan, Immunomedics Inc, Morris Plains NJ), which consists of Fab′ of murine anti-CEA IgG labeled with ^{99m}Tc (*4*). ^{99m}Tc-labeled arcitumomab has been used for imaging colorectal and breast cancers (*5*−*7*).

Tumor-associated glycoprotein-72 (TAG-72) (*8*) is an epithelial mucin overexpressed in a high percentage of colorectal, ovarian, gastric, and breast cancers (*9*). CC49 is a murine high-affinity, second-generation TAG-72 mAb which has been conjugated to radionuclides for radioimmunodetection and radioimmunotherapy in patients with primary and metastatic TAG-72-positive cancers (*10*−*16*). Engineered scFv-based antibody fragments of CC49 have been reported (*17*−*19*). The very fast clearance of these CC49 scFvs from the blood suggested that small antibody fragments are attractive agents for imaging TAG-72-positive tumors. Recombinant scFv-based antibody fragments are technically favored over fragments containing interchain disulfide bonds such as Fab in part because the heterologous expression of scFv is more convenient and the yield is higher. In comparison with scFvs however, Fab is thermodynamically more stable because of the interchain disulfide bond and mutual stabilization between the V_H/V_L and C_H1/C_L interface. In addition, Fab is kinetically more stable than scFv as manifested by a slow unfolding rate, which renders Fab more resistant to denaturation (*20*, *21*). Although murine Fab has the potential to be immunogenic in humans, the incidence of human anti-mouse antibody (HAMA) response reported from several studies in practice is very low (less than 2%) (*2*, *22*).

In this study, we report for the first time the synthesis of recombinant Fab (rFab) of monoclonal antibody CC49 in a heterologous *Pichia pastoris* expression system and their tumor targeting properties compared to enzymatically generated Fab (eFab) produced by proteolytic digestion of CC49 IgG. Our rationale for producing the rFab was several fold. First, we were interested in evaluating the ability of the *P. pastoris* expression system to produce rFab of antitumor antibodies. Second, we were interested in evaluating the effects of affinity tags that are often incorporated into recombinant antibodies (including the

* Address correspondence and requests for reprints to Raymond M. Reilly, Ph.D., Leslie Dan Faculty of Pharmacy, University of Toronto, 144 College St., Toronto, Ontario M5S 3M2. Tel.: (416) 946-5522, fax: (416) 978-8511, e-mail: raymond.reilly@utoronto.ca.

† Department of Pharmaceutical Sciences, University of Toronto.

‡ Toronto General Research Institute.

§ Department of Medical Biophysics, University of Toronto.

∥ Department of Medical Imaging, University of Toronto.

⊥ Current address: Ying Tang, Ph.D., postdoctoral fellow, Radiation Oncology Branch, NIH/NCI, Bldg. 10, Rm. 3B42, 10 Center Dr., Bethesda, MD 20892. E-mail: tangyi@mail.nih.gov.

10.1021/bc060260r CCC: $37.00 © 2007 American Chemical Society
Published on Web 03/16/2007

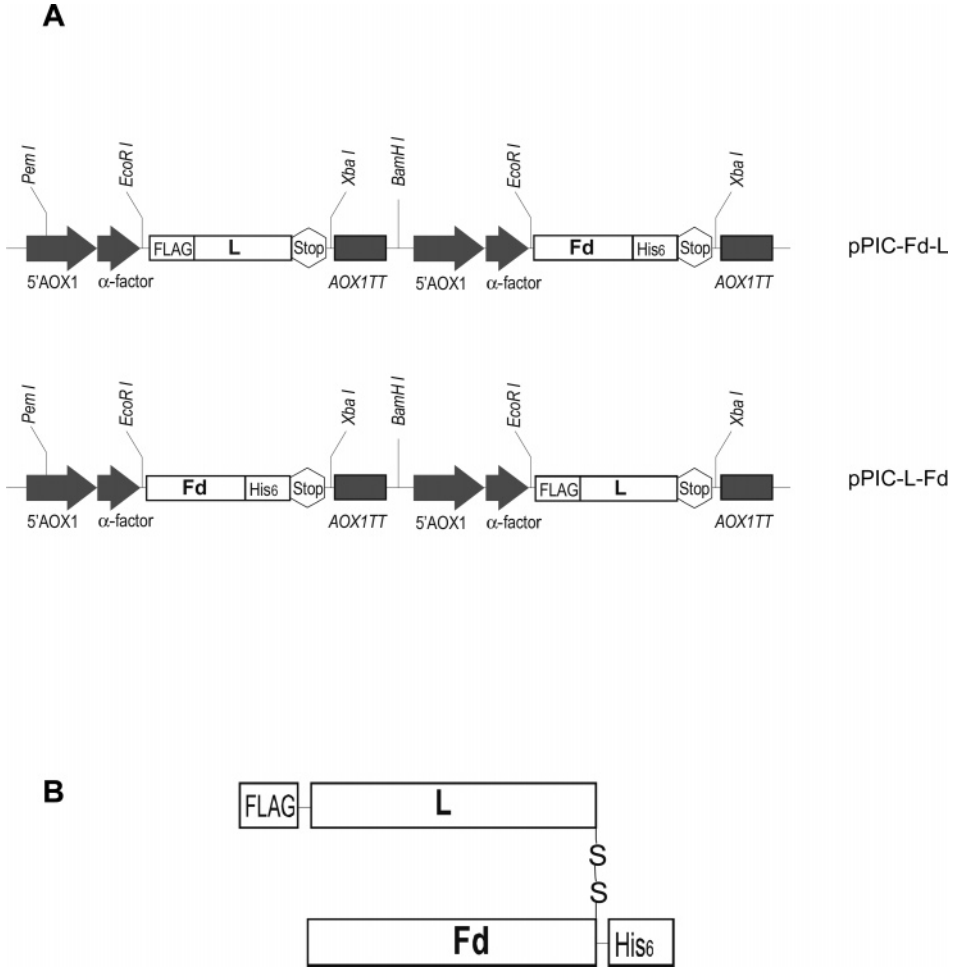


Figure 1. (A) Linear representation of coexpression plasmids pPIC-Fd-L and pPIC-L-Fd. **(B)** Schematic representation of rFab. A FLAG tag (amino acid sequence DYKDDDDK) is fused to the N-terminus of L through a linker sequence (GGGGS); A His_6 tag (amino acid sequence HHHHHH) was fused to the C-terminus of Fd through a GGGGS linker. L and Fd are covalently linked by a disulfide bond.

rFab) on their tumor and normal tissue localization. Third, we were interested in designing a method of producing Fab fragments of CC49 that would be more reproducible than that of enzymatic digestion of IgG, which is fraught with risk for heterogeneous generation of Fab with low molecular weight contaminating peptides as well as smaller fragments and residual intact IgG. Finally, although in the current study the rFab and eFab were radiolabeled with ^{123}I, we speculated that the generation of rFab of CC49 with an incorporated His_6 tag may allow radiolabeling in the future with ^{99m}Tc(I)carbonyl complexes as described by Waibel et al. (*23*).

EXPERIMENTAL PROCEDURES

Materials. The CC49 hybridoma cell line was provided by Dr. J. Schlom at the U.S. National Cancer Institute (Bethesda MD). The hybridoma secretes murine CC49 $IgG_{1,\kappa}$. *E. coli* TOP10F′ (Invitrogen, San Diego, CA) was used for cloning, subcloning, and propagation of plasmids. KM71H (*aox1::ARG4, arg4*) strain of *P. pastoris* was used as the host for protein expression. The pCR 2.1 vector (Invitrogen) was used for cloning the genes encoding the light chain (L) and Fd of the heavy chain from the hybridoma cells; the pPICZαA (Invitrogen) vector containing an α-factor secretion-signal peptide was used to construct coexpression plasmids for rFab expression. *Taq* and *Pfx* DNA polymerases (Invitrogen) were used for polymerase chain reaction (PCR). Restriction enzymes and ligases were from New England Biolabs Ltd. (Beverly, MA). Nickel-nitrilotriacetic acid (Ni-NTA) agarose was from Qiagen Inc. (Valencia, CA). Immobilized Protein-A was from Pierce (Rockford, IL). All oligonucleotide primers for PCR were synthesized by ACGT Corporation (Toronto, ON).

Expression of rFab in *P. pastoris* and Purification. The pPIC-Fd-L or pPIC-L-Fd plasmids (supplemental experimental procedures and Figure S1 in Supporting Information) were linearized at the unique *Pme I* site in the first 5′*AOX1* promoter region before electrotransforming *P. pastoris* KM71H cells using a MicroPulser electroporator (Bio-Rad, Hercules, CA). The transformed KM71H cells were selected for resistance to Zeocin (100 μg/mL) on YPD agar plates (1% yeast extract, 2% peptone, 2% dextrose, and 2% agar). Transformed clones were grown at 30 °C in buffered glycerol-complex medium to an optical density of $OD_{600} = 10$ and then were transferred to buffered methanol-complex medium at a cell density of 15% (w/w, wet cell weight) to induce protein expression. The methanol concentration and induction time were optimized. At the time point of maximum rFab yield determined by ELISA (see Supporting Information), the culture was centrifuged at 3000*g* for 15 min at 4 °C to isolate the supernatant containing secreted rFab.

rFab was precipitated from the culture supernatant by adding ammonium sulfate to 50% saturation at 25 °C (31.3 g ammonium sulfate per 100 mL of supernatant). rFab was purified by affinity chromatography on a Ni-NTA agarose (Qiagen) column. Protein bound to the column was eluted with 100 mM imidazole in 20 mM Tris-HCl and 0.5 M NaCl, pH 8.0. The eluate was buffer-exchanged into PBS, pH 7.0, using Centricon YM-30 ultrafiltration devices (Amicon, Billerica, MA; M_r cutoff 30 kDa).

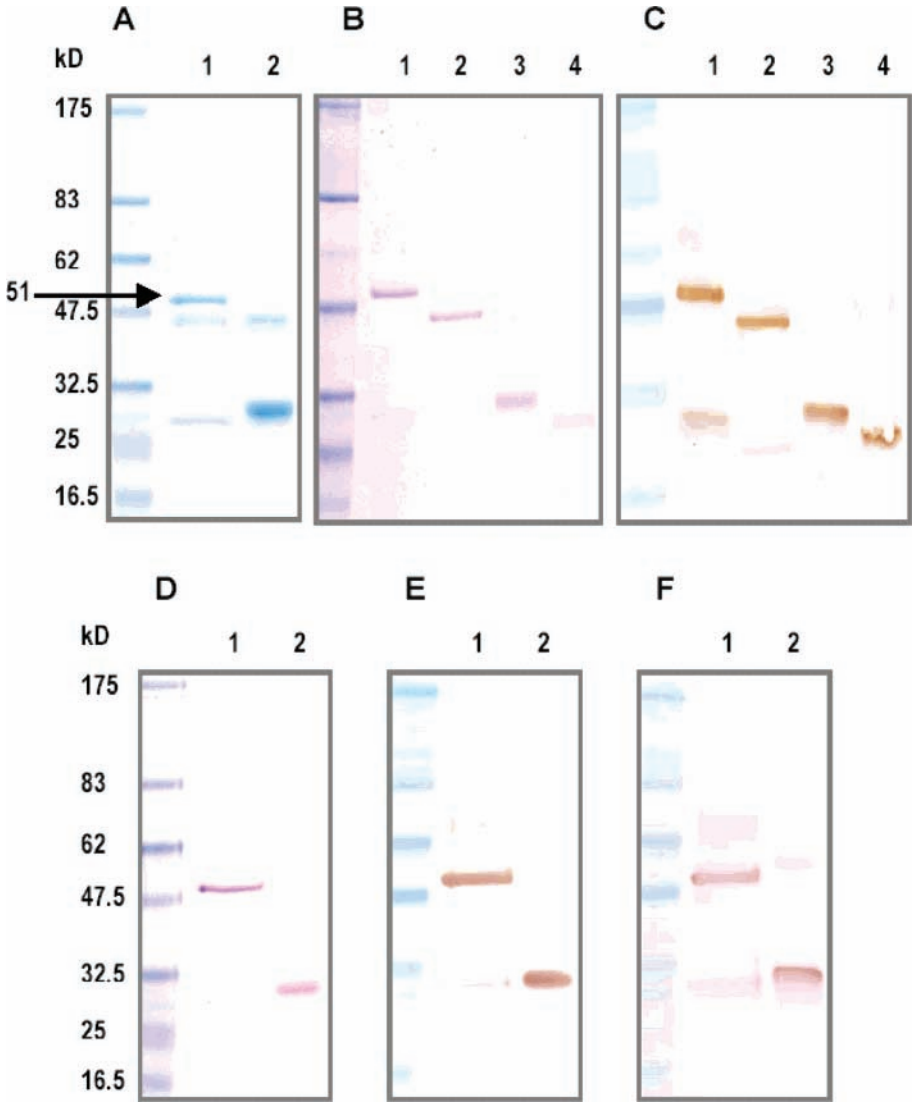


Figure 2. (A) Coomassie-stained SDS-PAGE gel of the crude culture supernatant collected at 48 h after methanol induction. The unpurified sample was concentrated five times and electrophoresed under nonreducing (lane 1) and reducing (β-mercaptoethanol, lane 2) conditions on a 4−20% Tris-HCl gradient gel. **(**B**)** SDS-PAGE comparison of purified rFab (lanes 1 and 3) and papain-produced Fab (lanes 2 and 4) of CC49 under nonreducing (lanes 1 and 2) and reducing (lanes 3 and 4) conditions. **(**C**)** Western blot of purified rFab (lanes 1 and 3) and papain-produced Fab (lanes 2 and 4) of CC49 under nonreducing (lanes 1 and 2) and reducing (lanes 3 and 4) conditions. The proteins were probed with a goat-anti mouse Fab. **(**D**)** Coomassie-stained SDS-PAGE gel of rFab under nonreducing (lane 1) and reducing (lane 2) conditions. **(**E**)** Western blot of purified rFab under nonreducing (lane 1) and reducing (lane 2) conditions. Proteins were probed with tetra-histidine antibody. **(**F**)** Western blot of purified rFab under nonreducing (lane 1) and reducing (lane 2) conditions. Proteins were probed with FLAG M2 antibody.

Enzymatic Preparation of CC49 Fab. Fab fragments of CC49 were prepared by proteolysis of CC49 IgG using immobilized papain (Pierce). After digestion, the supernatant was purified on immobilized Protein-A (Pierce). Purified enzymatically produced Fab (eFab) was buffer-exchanged into PBS, pH 7.0, using Centricon YM-30 ultrafiltration devices.

Analysis of the Purity of rFab. The identity and purity of CC49 rFab was assessed by SDS-PAGE, Western blot, and size-exclusion high performance liquid chromatography (HPLC). For SDS-PAGE, rFab (1−2 μg) was electrophoresed under reducing (β-mercaptoethanol) and nonreducing conditions on a 4−20% Tris-HCl gradient mini-gel (Bio-Rad, Mississauga, ON) stained with Coomassie brilliant blue R-250 (Bio-Rad). Western blot was performed using a panel of horseradish peroxidase (HRP)-conjugated antibodies as probes, including goat anti-mouse Fab (Sigma), anti-tetra-histidine (Qiagen), and anti-FLAG M2 (Sigma). Each antibody was diluted at 1:2000 in PBS/0.5% Tween-20. rFab was also analyzed by size-exclusion HPLC on a BioSep SEC-S2000 column (Phenomenex Inc, Torrance, CA) eluted with 100 mM NaH_2PO_4 buffer, pH 7.0, at a flow rate of 0.8 mL/min using a System Gold Model 125 HPLC interfaced with a Model 166 UV detector (Beckman-Coulter, Mississauga, ON) set at 280 nm.

Protein Concentration. The molar extinction coefficient for rFab at 280 nm [$\epsilon = 75\,560$ cm^{-1} M^{-1}, equivalent to $E = 1.49$ cm^{-1} (mg/mL)$^{-1}$] was calculated (*24*) based on the amino acid sequence for CC49 Fab (*25*−*28*). The protein concentration was measured spectrophotometrically at 280 nm.

Immunoreactivity of CC49 rFab with TAG-72. The ability of rFab or eFab to displace the binding of ^{111}In-labeled CC49 IgG to bovine submaxillary mucin (BSM), a source of TAG-72 (*29*), was measured. CC49 IgG was labeled with ^{111}In (MDS-Nordion, Kanata, ON) to a specific activity of 237 kBq/μg (6.4 μCi/μg) following derivatization with diethylenetriaminepentaacetic acid (DTPA) as previously reported (*30*). Each well of Immulon2 HB strips (Dynex Technologies Inc., Chantilly, VA) was coated with 20 ng of BSM in 100 μL of PBS, pH 7.0, at 4 °C overnight. Nonspecific binding was blocked by 5% BSA in PBS, pH 7.0. rFab or eFab (1.0 or 2.5 μM) in 40 μL of PBS containing 1% BSA was added in duplicate, then ^{111}In-CC49

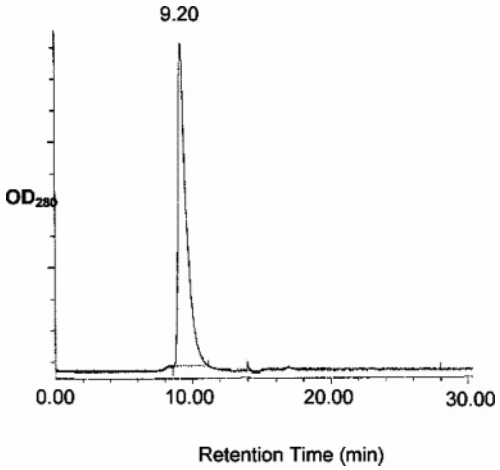


Figure 3. Size-exclusion HPLC of purified rFab of CC49. The solid line represents UV absorbance at 280 nm. rFab was detected as a single peak with a retention time of t_R 9.2 min.

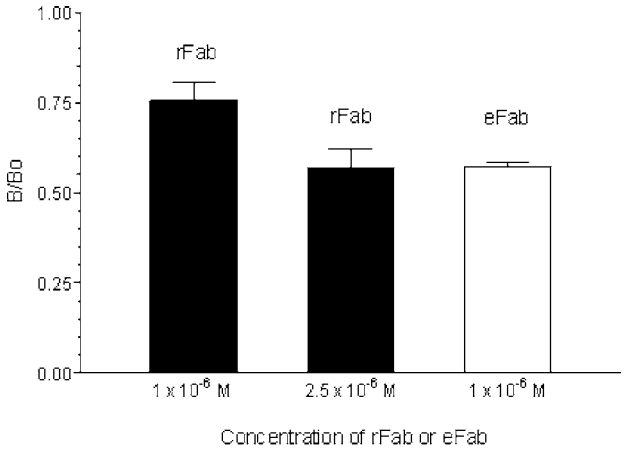


Figure 4. Comparison of the displacement of the binding of ^{111}In-labeled CC49 IgG to bovine submaxillary mucin (a source of TAG-72 antigen) coated onto wells in a microELISA plate by 1.0 or 2.5 $\times$ 10^{-6} M rFab or eFab. B/B_o represents the ratio of radioactivity bound in the presence compared to absence of rFab or eFab

IgG (50 000 CPM) at a final concentration of 5 nM in 40 μL of PBS was added in each well. After incubation at room temperature for 2 h, the wells were rinsed with PBS and the radioactivity bound measured in a γ-counter.

Tissue Distribution and Imaging of TAG-72-Positive Xenografts in Mice. The tumor and normal tissue distribution of ^{123}I-labeled rFab or eFab were evaluated in female athymic mice bearing s.c. LS174T human colon cancer (TAG-72 positive) and A375 human melanoma (TAG-72 negative) xenografts (*17*). Four-week-old BALB/c nu/nu athymic mice (Charles River, Wilmington, MA) were injected s.c. with 1 $\times$ 10^6 LS174T cells in the right flank and with 2 $\times$ 10^6 A375 cells in the left flank. rFab and eFab were labeled with ^{123}I using the Iodogen method (*31*) and then purified on a protein desalting spin column (Pierce). The radiochemical purity (RCP) of ^{123}I-rFab or eFab was >98% by paper chromatography (Whatman No. 1, Maidstone, England) developed in 85% methanol (R_f ^{123}I-Fab: 0.0; R_f ^{123}I- iodide). The specific activity of ^{123}I-rFab and eFab were 37 kBq/μg. At 10−14 days when the implanted tumors reached 5−8 mm in diameter, the mice were injected i.v. (tail vein) with 15 μg of ^{123}I-rFab or eFab (0.5 MBq). The mice received Lugol's iodine solution in their drinking water 2 days prior to radiopharmaceutical injection to attempt to block thyroid accumulation of radioiodine. Groups of three mice were sacrificed at 2, 6, 12, and 24 h postinjection (p.i.). Tumors and samples of normal tissues were collected and weighed, and their radioactivity content was measured in a γ-counter. Radioactivity uptake was expressed as percent injected dose per gram (% ID/g) and as tumor-to-normal tissue (T/NT) ratios. In a separate study, tumor-bearing mice were injected i.v. with 3 MBq (15 μg) of ^{123}I-rFab. Posterior whole body images were obtained up to 24 h p.i. using a small field-of-view gamma-camera fitted with a 4-mm pinhole collimator (ADAC Model TransCam, ADAC Laboratories Inc., Milpitas, CA). The principles of Laboratory Animal Care (NIH Publication No. 86-23, revised 1985) were followed, and animal studies were conducted under a protocol approved by the Animal Care Committee at the University Health Network (No. TG: 00-026) following Canadian Council on Animal Care (CCAC) guidelines.

Statistical Comparisons. Statistical significance was assessed using an unpaired, two-tailed Student's *t*-test or one-way ANOVA ($P < 0.05$).

RESULTS

Construction of Coexpression Plasmids To Express rFab of CC49. The genes coding for the L chain and the Fd chain up to the first cysteine residue in the hinge region of the heavy chain that forms the disulfide bond with the L chain were cloned (supplemental experimental procedures in Supporting Information). A coexpression plasmid based on the *P. pastoris* secretion vector pPICZαA was constructed to coexpress the L and Fd chains of CC49 (Figure 1). In the plasmid (pPIC-L-Fd or pPIC-Fd-L, Figure 1A), the expression of the L and Fd chains was driven individually by a methanol-inducible 5′*AOX1* promoter.

Expression of CC49 rFab in *P. pastoris* in a Shake Flask. CC49 rFab was expressed in *P. pastoris* strain KM71H transformed with plasmid pPIC-L-Fd or pPIC-Fd-L. L and Fd chains were expressed as separate polypeptides, assembled into rFab in the cells through the formation of a disulfide bond between L and Fd peptide chains and then secreted into the culture medium as folded rFab (Figure 1B). Two transformants Clone #24-5 (pPIC-Fd-L) and Clone #5-3 (pPIC-L-Fd) resulted in the greatest rFab expression as measured by ELISA, and a large-scale expression was carried out in a 500 mL Erlenmeyer flask over 48 h induced with 1% methanol added to the culture medium every 12 h. The yield of purified rFab in shake-flask expression was 1−2 mg/L determined by measuring the OD_{280}.

Purity of CC49 rFab. The crude culture supernatant containing expressed rFab was collected after methanol induction. The supernatant was concentrated five times before being electrophoresed under nonreducing (Figure 2A, lane 1) and reducing (β-mercaptoethanol, Figure 2A, lane 2) conditions on a 4−20% Tris-HCl gradient gel. After purification, the SDS-PAGE gel revealed a single band at M_r 51 kDa (Figure 2B, lane 1). This apparent molecular weight (M_r) was consistent with the calculated M_r based on the amino acid sequence of CC49 rFab (*25*−*28*). This band at M_r 51 kDa dissociated into a single band at 30 kDa under reducing conditions (Figure 2B, lane 3). Western blot revealed that both the 51 kDa and 30 kDa bands were reactive with goat anti-mouse Fab antibodies (Figure 2C, lanes 1 and 3). The 51 kDa and 30 kDa bands (Figure 2D) were also reactive with antibodies directed against tetra-histidine (Figure 2E) identifying the His_6 tag at the C-terminus of the Fd chain and were reactive with anti-FLAG antibodies (Figure 2F) identifying the FLAG tag at the N-terminus of the L chain. These results confirmed that the 51 kDa protein was rFab and contained an intermolecular disulfide bond covalently linking the L and Fd chains. For comparison, SDS-PAGE analysis (Figure 2B, lanes 2 and 4) and Western blot (Figure 2C, lanes 2 and 4) of eFab prepared by proteolytic digestion of CC49 IgG using immobilized papain are shown. The slightly greater M_r for rFab compared with eFab (M_r 51 kDa vs 48 kDa) was

Table 1. Biodistribution of ^{123}I-rFab in Athymic Mice Bearing s.c. TAG-72-Positive LS174T Human Colon Cancer Xenografts and TAG-72-Negative A375 Human Melanoma Xenografts[a]

	2 h, p.i.		6 h, p.i.		12 h, p.i.		24 h, p.i.	
tissue	%ID/g	T/NT	%ID/g	T/NT	%ID/g	T/NT	%ID/g	T/NT
blood	14.7 ± 1.73	0.9 ± 0.14	5.3 ± 0.24	1.9 ± 0.41	3.0 ± 0.24	2.4 ± 0.19	1.1 ± 0.07	5.2 ± 0.10
heart	6.5 ± 1.06	2.1 ± 0.44	2.1 ± 0.13	4.8 ± 0.82	1.0 ± 0.07	7.6 ± 0.42	0.4 ± 0.07	14.1 ± 1.99
lung	6.6 ± 0.70	1.9 ± 0.20	2.8 ± 0.32	3.4 ± 0.40	1.6 ± 0.09	4.8 ± 0.34	0.6 ± 0.05	9.4 ± 0.38
liver	3.8 ± 0.29	3.4 ± 0.34	1.5 ± 0.30	6.7 ± 1.26	0.8 ± 0.18	9.5 ± 0.83	0.4 ± 0.06	14.7 ± 1.55
kidneys	32.3 ± 4.96	0.4 ± 0.05	7.9 ± 0.40	1.3 ± 0.28	3.8 ± 0.58	2.1 ± 0.36	1.2 ± 0.14	5.0 ± 0.39
spleen	3.5 ± 0.24	3.6 ± 0.40	1.5 ± 0.23	6.8 ± 0.81	0.8 ± 0.15	9.0 ± 0.68	0.4 ± 0.03	15.9 ± 0.82
stomach	13.3 ± 1.99	1.0 ± 0.06	6.5 ± 2.74	2.0 ± 0.76	3.6 ± 1.62	2.7 ± 0.82	1.0 ± 0.12	6.4 ± 0.56
intestines	2.8 ± 0.20	4.5 ± 0.43	1.4 ± 0.30	7.4 ± 1.31	0.7 ± 0.16	11.1 ± 1.42	0.2 ± 0.02	25.1 ± 1.09
muscle	1.9 ± 0.32	6.9 ± 0.26	0.9 ± 0.07	11.6 ± 2.33	0.5 ± 0.05	15.4 ± 1.39	0.2 ± 0.06	32.0 ± 9.31
A375	4.8 ± 0.97	2.7 ± 0.21	1.8 ± 0.22	5.7 ± 1.07	0.9 ± 0.07	8.2 ± 0.64	0.3 ± 0.02	18.0 ± 1.24
LS174T	12.9 ± 2.21		10.1 ± 2.14		7.4 ± 0.93		6.0 ± 0.27	

[a] Tissue distribution was expressed as % ID /g. T/NT: Tumor (LS174T)-to-normal tissue ratios. Values are mean ± SE ($n = 3$ mice/time point).

Table 2. Biodistribution of ^{123}I-eFab in Athymic Mice Bearing s.c. TAG-72-Positive LS174T Human Colon Cancer Xenografts and TAG-72-Negative A375 Human Melanoma Xenografts[a]

	2 h		6 h		12 h	
tissue	%ID/g	T/NT	%ID/g	T/NT	%ID/g	T/NT
blood	10.0 ± 1.28	1.2 ± 0.22	7.3 ± 1.60	1.2 ± 0.23	2.1 ± 0.17	2.8 ± 0.50
heart	4.4 ± 0.71	2.7 ± 0.59	2.9 ± 0.94	3.6 ± 1.07	0.8 ± 0.03	6.9 ± 1.20
lung	6.8 ± 0.65	1.7 ± 0.29	4.0 ± 1.22	2.5 ± 0.61	1.1 ± 0.10	5.1 ± 0.41
liver	5.4 ± 0.64	2.1 ± 0.40	3.2 ± 0.96	3.4 ± 1.37	2.1 ± 0.26	2.7 ± 0.10
kidneys	89.1 ± 4.77	0.1 ± 0.02	9.9 ± 1.11	0.9 ± 0.12	3.6 ± 0.48	1.6 ± 0.12
spleen	4.9 ± 1.01	2.5 ± 0.66	2.9 ± 0.97	3.6 ± 0.94	1.0 ± 0.07	5.8 ± 0.52
stomach	30.1 ± 9.79	0.5 ± 0.19	15.8 ± 4.97	0.6 ± 0.20	2.4 ± 0.36	2.4 ± 0.21
intestines	5.1 ± 0.97	2.4 ± 0.55	2.6 ± 0.78	3.9 ± 1.16	0.6 ± 0.06	10.1 ± 0.46
muscle	2.8 ± 0.23	4.0 ± 0.61	1.3 ± 0.21	6.9 ± 1.02	0.2 ± 0.03	23.0 ± 3.38
A375	3.9 ± 0.30	3.3 ± 0.62	2.1 ± 0.67	4.9 ± 1.47	0.5 ± 0.03	10.4 ± 1.60
LS174T	11.1 ± 1.19		8.4 ± 0.20		5.7 ± 0.78	

[a] Tissue distribution was expressed as % ID /g. T/NT: Tumor (LS174T)-to-normal tissue ratios. Values are mean ± SE ($n = 3$ mice/time point).

expected because the rFab included a His_6 tag, a FLAG tag, and the GGGGS linker (Figure 1B), which contributed 2.8 kDa to the molecular mass. Size-exclusion HPLC (Figure 3) showed a single peak with a retention time (t_R) of 9.2 min corresponding to rFab.

Immunoreactivity of CC49 rFab with TAG-72. rFab competed with ^{111}In-CC49 IgG for binding to BSM, a source of TAG-72 antigen (Figure 4). The specific binding of ^{111}In-CC49 IgG to TAG-72 was reduced to 76 ± 5.1% by 1.0×10^{-6} M rFab and to 57 ± 5.2% by 2.5×10^{-6} M rFab. A 2.5-fold lower concentration of eFab (1.0×10^{-6} M) was required to reduce the binding of ^{111}In-CC49 IgG to 57 ± 1.4% (Figure 4), indicating that the affinity of rFab for TAG-72 was 2- to 3-fold lower than that of rFab.

Tissue Distribution and Imaging of TAG-72-Positive Xenografts in Mice. ^{123}I-rFab accumulated in LS174T xenografts reaching a level of 12.9 ± 2.2% ID/g at 2 h p.i. (Table 1). Tumor retention of ^{123}I-rFab decreased from 10.1 ± 2.1% ID/g at 6 h to 7.4 ± 0.9% ID/g at 12 h p.i. ($P > 0.05$ compared with that at 2 h) and to 6.0 ± 0.3% ID/g at 24 h p.i. ($P = 0.04$ compared with that at 2 h). In contrast, the retention of ^{123}I-rFab in control TAG-72-negative A375 tumors was significantly lower at all time points ($P < 0.05$) and decreased more than 16 fold between 2 and 24 h p.i. ^{123}I-rFab was rapidly eliminated from the blood. By 24 h p.i., the blood concentration decreased 13 fold compared to that at 2 h p.i. (1.1 ± 0.07 vs 14.7 ± 1.73, $P < 0.01$). The greatest tissue uptake occurred in the kidneys at 2 h p.i. (32.3 ± 4.9% ID/g). The specific accumulation of ^{123}I-rFab in LS174T tumors was reflected in the T/NT ratios (Table 1). The ratios of tumor (LS174T) to all tissues including the TAG-72-negative A375 tumors increased from 2 to 24 h p.i. For example, the tumor/blood (T/B) ratio increased from 0.9 ± 0.1 at 2 h p.i. to 5.2 ± 0.1 at 24 h ($P < 0.0001$). At 24 h p.i. the ratio of radioactivity in LS174T to that in A375 tumors was 18.0 ± 1.2. Uptake of ^{123}I-rFab in LS174T tumors (Table 1) was not significantly different than that of ^{123}I-eFab (Table 2; $P > 0.05$). Interestingly, the uptake of ^{123}I-eFab in the kidneys was significantly greater at 2 h than that of ^{123}I-rFab (89.1 ± 4.8 vs 32.3 ± 4.9 %ID/g, $P < 0.01$) but was similar to that of ^{123}I-rFab at later times ($P > 0.05$). T/NT ratios were similar for ^{123}I-rFab and ^{123}I-eFab except for a much higher tumor/kidney ratio at 2 h ($P < 0.001$) as well as greater tumor/liver and tumor/spleen ratios at 12 h after injection ($P < 0.05$) for ^{123}I-rFab. LS174T xenografts were clearly imaged as early as 2 h after injection of ^{123}I-rFab, whereas similarly sized A375 tumor could not be differentiated from the body background (Figure 5).

DISCUSSION

The second-generation, high-affinity TAG-72 monoclonal antibody CC49 has proven to be one of the most clinically useful antitumor antibodies for radioimmunoimaging and radioimmunotherapy of solid tumors (*10*−*17*). In this study, we generated rFab of CC49 using a *P. pastoris* expression system and directly compared its tumor and normal tissue localization properties with those of enzymatically generated CC49 Fab (eFab) in athymic mice implanted s.c. with LS174T human colon cancer xenografts. To our knowledge, such a direct comparison of eFab and rFab of an antitumor monoclonal antibody has never been reported, despite the potential that genetically engineered antibodies may demonstrate altered binding affinities and tissue distribution due to their incorporated affinity tags (e.g., polyhistidine) or other modifications. The CC49 rFab differs from eFab in that rFab contains a His_6 tag, a FLAG tag, and the GGGGS peptide linkers. Despite a 2-to-3-fold lower TAG-72-binding affinity for rFab *in vitro*, both rFab and eFab exhibited a similar pattern of tumor retention and tissue distribution in tumor-bearing mice except in the liver and kidneys.

Kidney retention of ^{123}I-rFab was significantly lower than that of ^{123}I-eFab (32.3 ± 4.9 vs 89.1 ± 4.8% ID/g, $P < 0.01$)

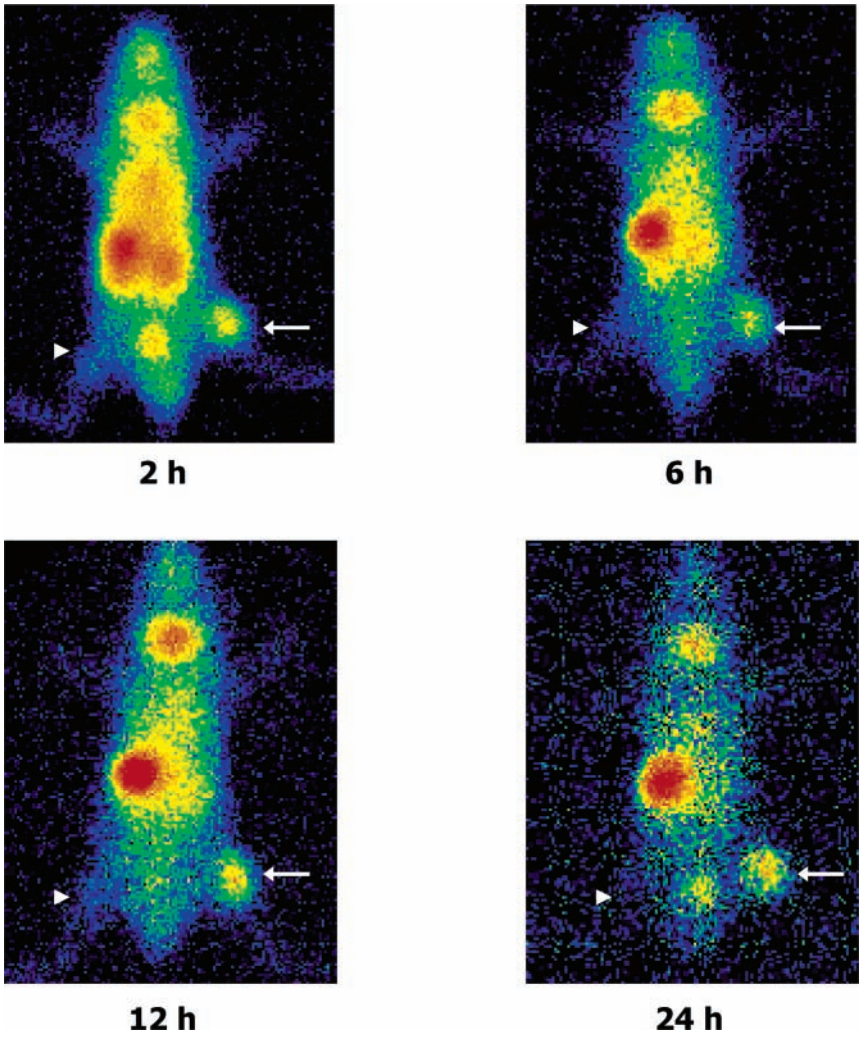


Figure 5. Posterior whole body image of a representative athymic mouse bearing a s.c. TAG-72-overexpressing LS174T human colon cancer xenograft on the right flank (white arrow). A s.c. TAG-72-negative A375 human melanoma xenograft on the left flank (arrowhead only) served as the negative control tumor. Each mouse was injected i.v. with 15 μg of ^{123}I-rFab (3 MBq) and imaged at 2, 6, 12, and 24 h p.i. The series of images were obtained from the same mouse. 250 000, 100 000, 100 000, and 50 000 counts were collected at 2, 6, 12, and 24 h p.i., respectively.

at 2 h p.i., but the difference was not significant at later times, i.e., 6 and 12 h ($P > 0.05$). The reason for the lower initial kidney uptake of ^{123}I-rFab may be related to the net negative charges introduced by the FLAG tag. It was previously reported that introduction of three negatively charged amino acids reduced the kidney retention of radioiodinated CC49 scFv fragments at early time points after administration to mice bearing s.c. LS174T xenografts (*32*). It was proposed that changes in the isoelectric point (pI) could affect kidney uptake. However, the difference in kidney uptake among three CC49 scFv variants, i.e., scFv[pI 8.1], scFv[pI 5.8], and scFv[pI 5.2], was not statistically significant except at 0.5 h p.i. At this time, the scFv with the lowest pI [pI 5.2] showed the highest kidney uptake, whereas scFv with intermediate pI [pI 5.8] had the lowest uptake (*32*). It appears, therefore, that pI did not correlate directly with kidney uptake among the three scFv variants that were studied. The pI values of eFab and rFab were not measured in our study, but the theoretical pI values were calculated using the Swiss-Prot database (*33*) based on the amino acid sequences. These pI values were 6.3 for eFab and 7.6 for rFab. His_6 was also reported to affect the blood clearance and kidney retention of a radioiodinated $(scFv)_2$ of CC49. The blood clearance for the His_6-tagged $(scFv)_2$ was slightly slower while the kidney retention was lower at early time points (20.0 and 14.8 %ID/g at 0.5 and 1 h p.i., respectively) than that for $(scFv)_2$ (41.2 and 24.7 %ID/g at 0.5 and 1 h p.i., respectively) (*18*). In our study, the liver retention of ^{123}I-rFab was lower than that of ^{123}I-eFab and the tumor-to-liver ratio was higher for ^{123}I-rFab at all times examined. The reason for the lower liver uptake of ^{123}I-rFab is not known, but this finding suggests that it could be more useful than ^{123}I-eFab for scintigraphic detection of hepatic lesions.

The blood concentration of ^{123}I-rFab at 12 h was higher than that of ^{123}I-eFab (3.0 ± 0.2 vs 2.1 ± 0.2% ID/g, $P < 0.05$). However, this did not significantly lower the T/B ratio for ^{123}I-rFab compared to ^{123}I-eFab (2.4 ± 0.2 vs 2.8 ± 0.5, respectively, $P > 0.05$) because the tumor uptake for ^{123}I-rFab was higher. In short, the 3-fold lower TAG-72 binding affinity for rFab than eFab *in vitro* failed to translate into any significant difference in tumor accumulation. Consistent with this finding, it was previously noted that a 320-fold decrease in K_d of an anti-HER2/neu scFv resulted in only a 7-fold increase in tumor accumulation in mice (*34*). These and other observations indicate that *in vitro* receptor-binding affinity is not the sole determinant of the accumulation of antibody fragments in tumors (*35*, *36*). Nevertheless, it has been reported that increased avidity by means of engineering bivalent, dimeric $(scFv)_2$ (M_r 54 000) improved tumor retention 2 to 36-fold at 24 h p.i. compared to monovalent scFv (M_r 27 000) in mice (*37*, *38*). T/B ratios between divalent $(scFv)_2$ and monovalent scFv, however, were similar (*37*, *38*). The enhanced tumor retention of divalent

$(scFv)_2$ was likely a combined result of higher avidity, and prolonged residence time as a result of the larger molecular size (*37*, *38*).

Schlom's group and others studied the tumor retention and tissue distribution in mice bearing LS174T xenografts of radioiodinated Fab′ produced by pepsin digestion of CC49 IgG. The tumor retention of radioiodinated Fab′ was 3.9 to 6.2% ID/g at 6 h p.i.; it was 2.9 to 3.7% ID/g at 24 h (*17*, *19*). This level of tumor retention is lower than that observed in our study for ^{123}I-rFab (10.1 ± 2.1% ID/g at 6 h; 6.0 ± 0.3% ID/g at 24 h) or ^{123}I-eFab (8.4 ± 0.2% ID/g at 6 h). It was noted that the size of LS174T tumor xenografts in our study was similar to that previously used by Schlom's group (0.5−0.8 cm diameter) to evaluate the tumor uptake of CC49 Fab′. The blood concentration was also much lower for radioiodinated Fab′ (0.9−1.68 and 0.1 %ID/g at 6 and 24 h, respectively) than observed in our study for ^{123}I-rFab (5.3 and 1.1 %ID/g at 6 and 24 h, respectively) (*17*, *19*). It is unclear whether the slight differences in amino acid sequences between Fab′ and rFab, or between Fab′ and eFab, may be responsible for these disparities in biodistribution and blood clearance, because in our study, mice were injected with a higher dose of rFab or eFab (15 μg/mouse) than previously examined for Fab′ (<10 μg/mouse) (*17*, *19*). Nonlinear, dose-dependent pharmacokinetics have been reported clinically for the HER2/neu monoclonal antibody, trastuzumab (Herceptin). In these studies, there was a decreased rate of serum clearance with increasing doses (*39*).

It has been generally assumed that small affinity tags do not have a major effect on the biological/immunological properties of a biomolecule (*40*). The affinity tags, i.e., His_6 and FLAG, did not appear to yield major differences in the tumor and normal tissue distribution and imaging properties of ^{123}I-labeled CC49 rFab compared to eFab. The safety of the FLAG tag in patients is unknown, but the His_6 tag has been shown to be safe for human administration (*1*). Besides its usefulness for affinity chromatographic purification of rFab, the His_6 tag also presents a site for labeling the rFab with the ^{99m}Tc (I)-tricarbonyl complex (*23*) or with ^{94m}Tc for positron-emission tomography (PET) (*41*). It would also be possible to label the rFab with ^{124}I instead of ^{123}I for PET (*42*, *43*).

CONCLUSIONS

In summary, pure and immunoreactive rFab fragments of the second-generation, high-affinity TAG-72 monoclonal antibody CC49 were generated in *P. pastoris* that have excellent tumor-targeting properties. The specific accumulation of ^{123}I-labeled CC49 rFab in TAG-72-positive LS174T human colon cancer xenografts and its rapid clearance from the blood and most normal tissues suggest that it would be useful for imaging colorectal cancer and other tumors expressing TAG-72. The significantly lower liver accumulation of CC49 rFab compared to eFab observed in this study suggests that CC49 rFab may provide greater sensitivity for the detection of liver lesions. Incorporation of His_6 and FLAG affinity tags did not intefere with tumor targeting, although rFab exhibited a 2−3 fold lower binding affinity for TAG-72.

ACKNOWLEDGMENT

This study was funded by a grant from a Diagnostic and Surgical Breast Imaging award (DAMD17-00-1-0595) to R.M.R., by a predoctoral fellowship (DAMD17-03-1-0372) to Y.T. from the U.S. Army Breast Cancer Research Program, and by a grant from the Ontario Research and Development Challenge Fund. J.G. is supported by the Canadian Breast Cancer Research Alliance. The authors wish to thank Dr. Jeffery Schlom at the U.S. National Cancer Institute (Bethesda, MD) for providing the CC49 hybridoma.

Supporting Information Available: Experimental details on the cloning of the CC49 Fab expression plasmids and the ELISA used to monitor Fab expression. This material is available free of charge via the Internet at http://pubs.acs.org.

LITERATURE CITED

(1) Begent, R. H., Verhaar, M. J., Chester, K. A., Casey, J. L., Green, A. J., Napier, M. P., Hope-Stone, L. D., Cushen, N., Keep, P. A., Johnson, C. J., Hawkins, R. E., Hilson, A. J., and Robson, L. (1996) Clinical evidence of efficient tumor targeting based on single-chain Fv antibody selected from a combinatorial library. *Nat. Med. 2*, 979−984.

(2) Goldenberg, D. M., Abdel-Nabi, H., Sullivan, C. L., Serafini, A., Seldin, D., Barron, B., Lamki, L., Line, B., and Wegener, W. A. (2000) Carcinoembryonic antigen immunoscintigraphy complements mammography in the diagnosis of breast carcinoma. *Cancer 89*, 104−115.

(3) Sanidas, E. E., Koukouraki, S., Velidaki, A., Manios, A., Stathopoulos, E., De, Bree, E., Kafousi, M., Kodogiannis, E., Karkavitsas, N., and Tsiftsis, D. D. (2003) Contribution of 99mTc-anti-carcinoembryonic antigen antibody and 99mTc-sestamibi scintimammography in the evaluation of high risk palpable breast lesions. *Nucl. Med. Commun. 24*, 291−296.

(4) Hansen, H. J., Jones, A. L., Sharkey, R. M., Grebenau, R., Blazejewski, N., Kunz, A., Buckley, M. J., Newman, E. S., Ostella, F., and Goldenberg, D. M. (1990) Preclinical evaluation of an "instant" 99mTc-labeling kit for antibody imaging. *Cancer Res. 50*, 794s−798s.

(5) Moffat, F. L., Jr., Pinsky, C. M., Hammershaimb, L., Petrelli, N. J., Patt, Y. Z., Whaley, F. S., and Goldenberg, D. M. (1996) Clinical utility of external immunoscintigraphy with the IMMU-4 technetium-99m Fab' antibody fragment in patients undergoing surgery for carcinoma of the colon and rectum: results of a pivotal, phase III trial. The Immunomedics Study Group. *J. Clin. Oncol. 14*, 2295−2305.

(6) Goldenberg, D. M., and Wegener, W. (1997) Studies of breast cancer imaging with radiolabeled antibodies to carcinoembryonic antigen. Immunomedics Breast Cancer Study Group. *Acta Med. Aust. 24*, 55−59.

(7) Goldenberg, D. M. (1997) Perspectives on oncologic imaging with radiolabeled antibodies. *Cancer 80*, 2431−2435.

(8) Johnson, V. G., Schlom, J., Paterson, A. J., Bennett, J., Magnani, J. L., and Colcher, D. (1986) Analysis of a human tumor-associated glycoprotein (TAG-72) identified by monoclonal antibody B72.3. *Cancer Res. 46*, 850−857.

(9) Sheer, D. G., Schlom, J., and Cooper, H. L. (1988) Purification and composition of the human tumor-associated glycoprotein (TAG-72) defined by monoclonal antibodies CC49 and B72.3. *Cancer Res. 48*, 6811−6818.

(10) Alvarez, R. D., Huh, W. K., Khazaeli, M. B., Meredith, R. F., Partridge, E. E., Kilgore, L. C., Grizzle, W. E., Shen, S., Austin, J. M., Barnes, M. N., Carey, D., Schlom, J., and LoBuglio, A. F. (2002) A Phase I study of combined modality (90)Yttrium-CC49 intraperitoneal radioimmunotherapy for ovarian cancer. *Clin. Cancer Res. 8*, 2806−2811.

(11) Meredith, R. F., Alvarez, R. D., Partridge, E. E., Khazaeli, M. B., Lin, C. Y., Macey, D. J., Austin, J. M., Jr., Kilgore, L. C., Grizzle, W. E., Schlom, J., and LoBuglio, A. F. (2001) Intraperitoneal radioimmunochemotherapy of ovarian cancer: a phase I study. *Cancer Biother. Radiopharm. 16*, 305−315.

(12) Tempero, M., Leichner, P., Baranowska-Kortylewicz, J., Harrison, K., Augustine, S., Schlom, J., Anderson, J., Wisecarver, J., and Colcher, D. (2000) High-dose therapy with 90Yttrium-labeled monoclonal antibody CC49: a phase I trial. *Clin. Cancer Res. 6*, 3095−3102.

(13) Liu, T., Meredith, R. F., Saleh, M. N., Wheeler, R. H., Khazaeli, M. B., Plott, W. E., Schlom, J., and LoBuglio, A. F. (1997) Correlation of toxicity with treatment parameters for 131I-CC49 radioimmunotherapy in three phase II clinical trials. *Cancer Biother. Radiopharm. 12*, 79−87.

(14) Meredith, R. F., Khazaeli, M. B., Macey, D. J., Grizzle, W. E., Mayo, M., Schlom, J., Russell, C. D., and LoBuglio, A. F. (1999) Phase II study of interferon-enhanced 131I-labeled high affinity

CC49 monoclonal antibody therapy in patients with metastatic prostate cancer. *Clin Cancer Res. 5*, 3254s-3258s.
(15) Mulligan, T., Carrasquillo, J. A., Chung, Y., Milenic, D. E., Schlom, J., Feuerstein, I., Paik, C., Perentesis, P., Reynolds, J., and Curt, G. (1995) Phase I study of intravenous Lu-labeled CC49 murine monoclonal antibody in patients with advanced adenocarcinoma. *Clin. Cancer Res. 1*, 1447−1454.
(16) Macey, D. J., Grant, E. J., Kasi, L., Rosenblum, M. G., Zhang, H. Z., Katz, R. L., Rieger, P. T., LeBherz, D., South, M., Greiner, J. W., Schlom, J., Podoloff, D. A., and Murray, J. L. (1997) Effect of recombinant alpha-interferon on pharmacokinetics, biodistribution, toxicity, and efficacy of 131I-labeled monoclonal antibody CC49 in breast cancer: a phase II trial. *Clin. Cancer Res. 3*, 1547−1555.
(17) Milenic, D. E., Yokota, T., Filpula, D. R., Finkelman, M. A., Dodd, S. W., Wood, J. F., Whitlow, M., Snoy, P., and Schlom, J. (1991) Construction, binding properties, metabolism, and tumor targeting of a single-chain Fv derived from the pancarcinoma monoclonal antibody CC49. *Cancer Res. 51*, 6363−6371.
(18) Goel, A., Beresford, G. W., Colcher, D., Pavlinkova, G., Booth, B. J., Baranowska-Kortylewicz, J., and Batra, S. K. (2000) Divalent forms of CC49 single-chain antibody constructs in Pichia pastoris: expression, purification, and characterization. *J. Biochem. (Tokyo) 127*, 829−836.
(19) Pavlinkova, G., Beresford, G. W., Booth, B. J., Batra, S. K., and Colcher, D. (1999) Pharmacokinetics and biodistribution of engineered single-chain antibody constructs of MAb CC49 in colon carcinoma xenografts. *J. Nucl. Med. 40*, 1536−1546.
(20) Rothlisberger, D., Honegger, A., and Pluckthun, A. (2005) Domain interactions in the Fab fragment: a comparative evaluation of the single-chain Fv and Fab format engineered with variable domains of different stability. *J. Mol. Biol. 347*, 773−789.
(21) Shimba, N., Torigoe, H., Takahashi, H., Masuda, K., Shimada, I., Arata, Y., and Sarai, A. (1995) Comparative thermodynamic analyses of the Fv, Fab* and Fab fragments of anti-dansyl mouse monoclonal antibody. *FEBS Lett. 360*, 247−250.
(22) Kuus-Reichel, K., Grauer, L. S., Karavodin, L. M., Knott, C., Krusemeier, M., and Kay, N. E. (1994) Will immunogenicity limit the use, efficacy, and future development of therapeutic monoclonal antibodies? *Clin. Diagn. Lab. Immunol. 1*, 365−372.
(23) Waibel, R., Alberto, R., Willuda, J., Finnern, R., Schibli, R., Stichelberger, A., Egli, A., Abram, U., Mach, J. P., Pluckthun, A., and Schubiger, P. A. (1999) Stable one-step technetium-99m labeling of His-tagged recombinant proteins with a novel Tc(I)-carbonyl complex. *Nat. Biotechnol. 17*, 897−901.
(24) Gill, S. C., and von Hippel, P. H. (1989) Calculation of protein extinction coefficients from amino acid sequence data. *Anal. Biochem. 182*, 319−326.
(25) Hamlyn, P. H., Browniee, G. G., Cheng, C. C., Gait, M. J., and Milstein, C. (1978) Complete sequence of constant and 3′ noncoding regions of an immunoglobulin mRNA using the dideoxynucleotide method of RNA sequencing. *Cell 15*, 1067−1075.
(26) Honjo, T., Obata, M., Yamawaki-Katoaka, Y., Kataoka, T., Kawakami, T., Takahashi, N., and Mano, Y. (1979) Cloning and complete nucleotide sequence of mouse immunoglobulin gamma 1 chain gene. *Cell 18*, 559−568.
(27) Sakano, H., Rogers, J. H., Huppi, K., Brack, C., Traunecker, A., Maki, R., Wall, R., and Tonegawa, S. (1979) Domains and the hinge region of an immunoglobulin heavy chain are encoded in separate DNA segments. *Nature 277*, 627−633.
(28) Rixon, M. W., Gourlie, B. B., Kaplan, D. A., Schlom, J., and Mezes, P. S. (1993) Preferential use of a H chain V region in antitumor-associated glycoprotein-72 monoclonal antibodies. *J. Immunol. 151*, 6559−6568.
(29) Gonzales, N. R., Padlan, E. A., De, Pascalis, R., Schuck, P., Schlom, J., and Kashmiri, S. V. (2003) Minimizing immunogenicity of the SDR-grafted humanized antibody CC49 by genetic manipulation of the framework residues. *Mol. Immunol. 40*, 337−349.
(30) Reilly, R., Lee, N., Houle, S., Law, J., and Marks, A. (1992) In vitro stability of EDTA and DTPA immunoconjugates of monoclonal antibody 2G3 labeled with indium-111. *Int. J. Radiat. Appl. Instrum. Part A 43*, 961−967.
(31) Fraker, P. J., and Speck, J. C., Jr. (1978) Protein and cell membrane iodinations with a sparingly soluble chloroamide, 1,3,4,6-tetrachloro-3a,6a-diphrenylglycoluril. *Biochem. Biophys. Res. Commun. 80*, 849−857.
(32) Pavlinkova, G., Beresford, G., Booth, B. J., Batra, S. K., and Colcher, D. (1999) Charge-modified single chain antibody constructs of monoclonal antibody CC49: generation, characterization, pharmacokinetics, and biodistribution analysis. *Nucl. Med. Biol. 26*, 27−34.
(33) Swiss-Prot. http://ca.expasy.org/tools/pi_tool.html. 2006.
(34) Adams, G. P., Schier, R., Marshall, K., Wolf, E. J., McCall, A. M., Marks, J. D., and Weiner, L. M. (1998) Increased affinity leads to improved selective tumor delivery of single-chain Fv antibodies. *Cancer Res. 58*, 485−490.
(35) Gallinger, S., Reilly, R. M., Kirsh, J. C., Odze, R. D., Schmocker, B. J., Hay, K., Polihronis, J., Damani, M. T., Shpitz, B., and Stern, H. S. (1993) Comparative dual label study of first and second generation antitumor-associated glycoprotein-72 monoclonal antibodies in colorectal cancer patients. *Cancer Res. 53*, 271−278.
(36) Reilly, R. (2004) The immunoreactivity of radiolabeled antibodies−its impact on tumor targeting and strategies for preservation. *Cancer Biother. Radiopharm. 19*, 669−672.
(37) Nielsen, U. B., Adams, G. P., Weiner, L. M., and Marks, J. D. (2000) Targeting of bivalent anti-ErbB2 diabody antibody fragments to tumor cells is independent of the intrinsic antibody affinity. *Cancer Res. 60*, 6434−6440.
(38) Viti, F., Tarli, L., Giovannoni, L., Zardi, L., and Neri, D. (1999) Increased binding affinity and valence of recombinant antibody fragments lead to improved targeting of tumoral angiogenesis. *Cancer Res. 59*, 347−352.
(39) Baselga, J. (2001) Phase I and II clinical trials of trastuzumab. *Ann. Oncol. 12 Suppl 1*, S49−S55.
(40) Casey, J. L., Keep, P. A., Chester, K. A., Robson, L., Hawkins, R. E., and Begent, R. H. (1995) Purification of bacterially expressed single chain Fv antibodies for clinical applications using metal chelate chromatography. *J. Immunol. Methods. 179*, 105−116.
(41) Reilly R. M. (2007) The radiopharmaceutical science of monoclonal antibodies and peptides for imaging and targeted in situ radiotherapy of cancer. In *Handbook of Biopharmaceutical Technology* (Gad, S. C., Ed.) John Wiley and Sons, New York (in press).
(42) Robinson, M. K., Doss, M., Shaller, C., Narayanan, D., Marks, J. D., Adler, L. P., Gonzalez, Trotter, D. E., and Adams, G. P. (2005) Quantitative immuno-positron emission tomography imaging of HER2-positive tumor xenografts with an iodine-124 labeled anti-HER2 diabody. *Cancer Res. 65*, 1471−1478.
(43) Sundaresan, G., Yazaki, P. J., Shively, J. E., Finn, R. D., Larson, S. M., Raubitschek, A. A., Williams, L. E., Chatziioannou, A. F., Gambhir, S. S., and Wu, A. M. (2003) 124I-labeled engineered anti-CEA minibodies and diabodies allow high-contrast, antigen-specific small-animal PET imaging of xenografts in athymic mice. *J. Nucl. Med. 44*, 1962−1969

BC060260R

A Fluorescent Photoprobe for the Imaging of Endothelin Receptors

Carsten Höltke,[†,‡,*] Angelika von Wallbrunn,[‡,§] Klaus Kopka,[†,§] Otmar Schober,[†] Walter Heindel,[‡] Michael Schäfers,[†,§] and Christoph Bremer[‡,§]

Department of Clinical Radiology, Albert-Schweitzer-Strasse 33, University Hospital Münster, 48149 Münster, Germany, Department of Nuclear Medicine, Albert-Schweitzer-Strasse 33, University Hospital Münster, 48149 Münster, Germany, and Interdisciplinary Center for Clinical Research (IZKF Münster), Domagkstrasse 3, University of Münster, 48149 Münster, Germany. Received August 24, 2006; Revised Manuscript Received January 9, 2007

A novel fluorescent photoprobe for the imaging of endothelin A receptors (ET_AR) was developed. Based on the nonpeptidyl, high-affinity, and selective ET_AR antagonist 3-benzo[1,3]dioxol-5-yl-5-hydroxy-5-(4-methoxyphenyl)-4-(3,4,5-trimethoxybenzyl)-5*H*-furan-2-one (PD 156707), a modification of the lead structure with a PEG-spacer containing an amino moiety was performed. Labeling of this precursor with the fluorescent marker Cy 5.5 NHS-ester was accomplished by adaption of common peptide labeling procedures. The affinity of the Cy 5.5-labeled receptor antagonist was evaluated using human carcinoma cell lines with different degrees of ET_AR expression. Fluorescence microscopy revealed that ET_AR-positive MCF-7 human breast adenocarcinoma and HT-1080 human fibrosarcoma cells effectively bind the photoprobe at very low doses (nM), while ET_AR-negative MDA-MB-435 human breast cancer cells showed no fluorescence signal. Binding specificity of the probe could be demonstrated by predosing with a specific ET_AR antibody or the parent antagonist PD 156707 as a competing inhibitor. The results suggest that the modified photoprobe tightly binds to ET_A receptors and thus may be a possible candidate for the imaging of ET_AR-overexpressing tissues *in vivo*.

INTRODUCTION

Endothelin (ET) was first described by Hickey et al. (*1*) and subsequently isolated by Yanagisawa et al. (*2*) as a 21-amino acid peptide with vasoactive potency. Since their discovery, the role of the endothelins in several diseases, including cardiovascular, inflammatory, and renal diseases, has increasingly been investigated (*3*−*8*). More recently, the role of endothelin as a progression factor in human tumor cell lines has been discussed (*9*−*11*).

ETs and their receptors have been found to contribute to tumorigenesis and tumor progression through autocrine and paracrine pathways. Of the three ET isoforms, ET-1 has been the most extensively studied, and appears to be the most important isoform in cancer pathophysiology. Increased expression of ET-1 has been demonstrated in several human malignancies (*12*−*14*) including breast carcinoma (*15*, *16*). The most important ET-1 binding receptor, the endothelin A receptor (ET_AR), mediates tumorigenesis and tumor progression by activation of tumor proliferation (*13*), invasion (*17*), angiogenesis (*18*), and inhibition of apoptosis (*19*, *20*).

Accordingly, increased ET_AR expression has been demonstrated in various cancers, whereas in normal tissue the endothelin B receptor (ET_BR) subtype predominates (*13*, *14*, *21*). In view of these data, ET_AR has been suggested as a novel target for anticancer therapy in several malignancies with ET dysregulation including breast cancer. In preclinical studies, pharmacological blockade of the ET_A receptor has been shown to inhibit the growth of ovarian and cervix carcinoma cell xenografts (*22*, *23*). Atrasentan (ABT-627, Abbott Laboratories, IL), an orally bioavailable ET_AR antagonist, has been shown to be effective in patients with advanced androgen-refractory prostate carcinoma (*24*, *25*). Moreover, in breast cancer an altered ET system has been described (*15*, *26*) including an overexpression of ET-1, ET_AR, and ET_BR in human breast carcinomas (*16*, *27*), where expression of ET_AR indicated a poor outcome (*16*) as well as chemotherapy resistance (*28*).

In this context, a method for the visualization of ET receptor density in affected tissue would be invaluable for clinical diagnosis and the evaluation of therapy. While radiolabeling of ET receptor agonists and antagonists for the use in single photon emission computed tomography (SPECT) or positron emission tomography (PET) has been reported (*29*−*34*) none of the approaches have been utilized for the imaging of ET receptors in humans *in vivo*.

Varying the labeling strategy to fluorochrome-based molecules is an alternative to scintigraphic imaging techniques since it is relatively inexpensive, free of ionizing radiation and isotope decay, and applicable for tomographic (e.g., fluorescence-mediated tomography, FMT) and surface-weighted (e.g., fluorescence reflectance imaging, FRI) imaging techniques. Optical imaging techniques allow the detection of molecules in picomolar (10^{-12} M) concentrations, which is comparable to conventional scintigraphic imaging techniques and about 6 orders of magnitude more sensitive than MRI. Besides high signal-to-noise ratios (SNRs) imaging in the near-infrared (λ = 650 nm to 950 nm) shows very efficient tissue penetration as the absorption by water and hemoglobin is relatively low ('diagnostic window') (*35*, *36*).

In this study we describe the synthesis of an ET_AR ligand based on PD 156707 (Figure 1, *37*). A polyethylene glycol (PEG) spacer group containing an amino functionality was inserted to enable labeling with fluorescent dyes without changing the ET_A binding domain. The conjugation of the fluorescent dye Cy 5.5 was accomplished by using a recommended labeling procedure (Amersham Biosciences UK Limited, Buckinghamshire, UK). A model compound with a shorter PEG spacer and a phthalimidoyl-protecting group was synthe-

* Corresponding author. E-mail: carsten.hoeltke@uni-muenster.de, tel.: +49-251-8347362, fax: +49-251-8347363.

‡ Department of Clinical Radiology, University Hospital Münster.

† Department of Nuclear Medicine, University Hospital Münster.

§ Interdisciplinary Center for Clinical Research (IZKF), University of Münster.

10.1021/bc060264w CCC: $37.00 © 2007 American Chemical Society
Published on Web 04/07/2007

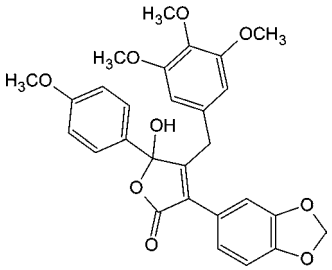


Figure 1. Structure of lead compound PD 156707.

sized and used in a biochemical affinity assay to evaluate the binding potencies of such modified compounds toward ET receptors. PD 156707 was also synthesized and used as a competing ligand and for comparison of the affinity values. The Cy 5.5-labeled ligand was used in *in vitro* binding assays with ET_A-positive MCF-7 human breast adenocarcinoma cells and HT-1080 human fibrosarcoma cells as well as with ET_A-negative MDA-MB-435 human breast cancer cells. An ET_AR-specific antibody and PD 156707 were used to test specific binding of the ET_AR-selective photoprobe.

EXPERIMENTAL SECTION

Materials and Methods. All chemicals, reagents, and solvents for the synthesis of the compounds were analytical grade and purchased from commercial sources. PD 156707 and 2-(1,3-benzodioxol-5-yl)-1-(4-benzyloxyphenyl)-4-oxobutyric acid methyl ester **3** were synthesized as reported (*37*). 2-{2-[2-(2-Azidoethoxy)ethoxy]ethoxy)ethyl methanesulfonate **7** was prepared according to the procedure described by Tahtaoui et al. for the PEG_3 derivative (*38*). Melting points (uncorrected) were determined on a Stuart Scientific SMP3 capillary melting point apparatus. ^{1}H NMR and ^{13}C NMR spectra were recorded on a Bruker ARX 300 or AMX 400 (Bruker BioSpin GmbH, Rheinstetten, Germany) or a Varian 500 MHz INOVA spectrometer (Varian Deutschland GmbH, Darmstadt, Germany), respectively. Mass spectrometry was performed using a Varian MAT 212 (EI = 70 eV, Varian Deutschland GmbH, Darmstadt, Germany), a Bruker MALDI-TOF-MS Reflex IV (matrix: DHB, Bruker Daltonics GmbH, Bremen, Germany), or a QUATTRO LCZ (Waters Micromass, Manchester, UK) spectrometer with a nanospray capillary inlet. Elemental analysis was realized by a Vario EL III analyzer (Elementar Analysensysteme GmbH, Hanau, Germany).

Cell Lines and Reagents. Human breast adenocarcinoma cell line MCF-7 (ATCC-No. HTB-22), MDA-MB-435 human breast carcinoma cells (ATCC-No. HTB-123), and HT-1080 human fibrosarcoma cells (ATCC-No. CCL-121) were cultured in RPMI 1640 (Invitrogen Corporation, San Diego, CA) supplemented with 10% fetal calf serum, penicillin, and streptomycin. Cells were grown routinely in a monolayer culture at 37 °C in a 5% CO_2 humidified air atmosphere. Polyclonal ET_AR antibody (N-15) was purchased from Santa Cruz (Santa Cruz Biotechnology, Santa Cruz, CA).

Synthetic Organic Chemistry. *4,5-Dimethoxy-3-{2-[2-(2-phthalimidoylethoxy)ethoxy]ethoxy}benzaldehyde **2**.* A solution of 500 mg (2.75 mmol) of 4,5-dimethoxy-3-hydroxybenzaldehyde **1** and 860 μL (1.03 g, 5.50 mmol) of 1,2-bis(2-chloroethoxy)ethane in 20 mL of DMF was treated with 2.24 g (6.88 mmol) of cesium carbonate and heated to 55 °C for 20 h. After cooling, the mixture was poured into 100 mL of ice−water and extracted with chloroform. The organic extracts were washed twice with 50 mL water and with brine, dried over sodium sulfate, and evaporated. The resulting yellow oil was flash-chromatographed (petroleum ether/ethyl acetate 2/1) to yield 3-{2-[2-(2-chloroethoxy)ethoxy]ethoxy}-4,5-dimethoxybenzaldehyde (730 mg, 2.20 mmol, 80%), which was directly used for the next synthesis step.

The residue from the above step and 414 mg (2.20 mmol) of phthalimide potassium salt were dissolved in 25 mL of DMF and stirred at 50 °C for 68 h. After hydrolysis with 50 mL of ice−water, the mixture was extracted with chloroform, and the combined organic phases were washed with water and brine and dried over sodium sulfate. Evaporation of the solvent yielded 932 mg of a yellow oil, which was purified by silica gel column chromatography (petroleum ether/ethyl acetate 1/1). The desired product accrued as a colorless oil (595 mg, 1.34 mmol, 61%). ^{1}H NMR ($CDCl_3$) δ = 9.85 (s, 1H), 7.83 (m, 2H), 7.69 (m, 2H), 7.12 (m, 2H), 4.16 (m, 2H), 3.93 (s, 3H), 3.92 (s, 3H), 3.89 (m, 2H), 3.83 (m, 2H), 3.75 (m, 2H), 3.67 (m, 4H) ppm. ^{13}C NMR δ = 190.9, 168.2, 153.8, 152.9, 144.4, 133.9, 132.2, 131.6, 123.2, 109.3, 106.6, 70.8, 70.3, 69.7, 69.0, 68.0, 61.0, 56.4, 37.3 ppm. MS: m/z = 466 $[M + Na]^+$, 443 $[M]^+$. Anal. calcd for $C_{23}H_{25}NO_8$: C 62.30, H 5.68, N 3.16. Found C 61.97, H 5.76, N 3.10.

*3-Benzo[1,3]dioxol-5-yl-4-(4,5-dimethoxy-3-{2-[2-(2-phthalimidoylethoxy)ethoxy]ethoxy}benzyl)-5-hydroxy-5-(4-methoxyphenyl)-5H-furan-2-one **4**.* A mixture of 887 mg (2.00 mmol) of 4,5-dimethoxy-3-{2-[2-(2-phthalimidoylethoxy)ethoxy]ethoxy}-benzaldehyde **2**, 689 mg (2.10 mmol) 2-(1,3-benzodioxol-5-yl)-1-(4-methyoxyphenyl)-4-oxobutyric acid methyl ester **3** and 120 mg (2.20 mmol) of sodium methoxide were dissolved in 20 mL of methanol at 0 °C and then heated to reflux for 12 h under an argon atmosphere. Acetic acid was added (1.0 mL), and the mixture was heated to reflux for another 6 h. After cooling to room temperature, the mixture was poured into 50 mL of water and extracted with ethyl acetate. The combined organic extracts were successively washed with water and brine and dried over sodium sulfate. After evaporation of the solvent, a yellow oil remained which was purified by silica gel column chromatography (petroleum ether/ethyl acetate 2/1 > 1/1 > 1/2). Yield: 800 mg (1.06 mmol, 53%). ^{1}H NMR ($CDCl_3$) δ = 7.80 (m, 2H), 7.67 (m, 2H), 7.38 (m, 2H), 6.92 (m, 2H), 6.79 (m, 3H), 6.13 (d, 1H, J = 2.0 Hz), 5.98 (d, 1H, J = 2.0 Hz), 5.94 (s, 2H), 3.87 (m, 4H), 3.77 (s, 3H), 3.73 (m, 2H), 3.71 (s, 3H), 3.69 (m, 2H), 3.64 (m, 2H), 3.62 (s, 3H), 3.61 (s, 4H) ppm. The proton of the butenolide hydroxy group was not detected. ^{13}C NMR δ = 171.1, 168.4, 160.4, 160.3, 153.0, 152.2, 148.1, 147.7, 143.7, 137.3, 134.0, 132.1, 131.8, 129.0, 128.2, 127.5, 123.3, 123.2, 123.1, 113.9, 109.5, 108.4, 108.2, 106.4, 101.3, 70.7, 70.2, 69.8, 68.6, 67.9, 60.7, 55.9, 55.3, 37.4, 32.1 ppm. MS: m/z = 792 $[M + K]^+$, 776 $[M + Na]^+$, 753 $[M]^+$, 736 $[M - OH]^+$. HRMS: Calcd. for $C_{41}H_{39}NO_{13}Na^+$ 776.2314, found 776.2303.

*3-{2-[2-(2-{2-Azidoethoxy}ethoxy)ethoxy]ethoxy}-4,5-dimethoxybenzaldehyde **8**.* A mixture of 5.22 g (17.55 mmol) of 2-{2-[2-(2-azidoethoxy)ethoxy]ethoxy}ethyl methanesulfonate **7**, 3.20 g (17.55 mmol) of 3,4-dimethoxy-5-hydroxybenzaldehyde **1**, and 11.5 g (35.20 mmol) of cesium carbonate in 120 mL of DMF was heated at 50 °C for 17 h. The mixture was poured into 100 mL of saturated aqueous ammonium chloride solution and extracted with methylene chloride. The combined organic layers were washed with water and brine, dried over $MgSO_4$, and evaporated. The residue was purified by silica gel column chromatography (toluene/ethyl acetate 1/1), yielding 4.58 g (11.95 mmol, 68%) of the product as a clear yellow oil. ^{1}H NMR ($CDCl_3$) δ = 9.77 (s, 1H), 7.09 (d, 1H, J = 2.2 Hz), 7.06 (d, 1H, J = 2.2 Hz), 4.17 (m, 2H), 3.88 (s, 3H), 3.85 (s, 3H), 3.83 (m, 2H), 3.66 (m, 2H), 3.60 (m, 8H), 3.30 (t, 2H, J = 5.4 Hz) ppm. ^{13}C NMR δ = 190.7, 153.6, 152.7, 144.2, 131.5, 109.0, 106.4, 70.7, 70.6, 70.5 (2 signals), 69.8, 69.5, 68.8, 60.8,

56.1, 50.5 ppm. MS: m/z = 383 $[M]^+$. Anal. calcd for $C_{17}H_{25}N_3O_7$: C 53.26, H 6.57, N 10.96. Found C 53.15, H 6.66, N 10.99.

3-Benzo[1,3]dioxol-5-yl-4-(3-(2-{2-[2-(2-azidoethoxy)ethoxy]-ethoxy}ethoxy)-4,5-dimethoxybenzyl)-5-hydroxy-5-(4-methoxy-phenyl)-5H-furan-2-one ***9***. A mixture of 1.16 g (3.00 mmol) of 3-(2-{2-[2-(2-azidoethoxy)ethoxy]ethoxy}ethoxy)-4,5-dimethoxy-benzaldehyde **8**, 1.10 g (3.20 mmol) of 2-(1,3-benzodioxol-5-yl)-1-(4-methoxyphenyl)-4-oxobutyric acid methyl ester **3**, and 216 mg (4.00 mmol) of sodium methoxide in 20 mL of methanol was heated to reflux for 15 h under an argon atmosphere. Acetic acid was added (1.5 mL), and the mixture was heated to reflux for further 5 h. After cooling, the mixture was poured into 50 mL of water and extracted with ethyl acetate. The combined organic extracts were successively washed with water and brine and dried over sodium sulfate. After evaporation of the solvent, a yellow oil remained, which was purified by silica gel column chromatography (diisopropyl ether/acetone 3/1). Yield: 1.49 g (2.15 mmol, 72%). ^{1}H NMR ($CDCl_3$) δ = 7.60 (m, 2H), 7.13, (m, 2H), 7.03 (m, 3H), 6.25 (s, 1H), 6.22 (s, 1H), 6.17 (s, 2H), 4.17 (m, 2H), 4.00 (s, 3H), 3.96 (s, 3H), 3.94−3.80 (m, 17H), 3.57 (m, 2H) ppm. The proton of the butenolide hydroxy group was not detected. ^{13}C NMR δ = 171.0, 160.4, 160.3, 153.0, 152.1, 148.1, 147.7, 137.2, 131.7, 128.9, 128.1, 127.4, 123.1, 123.0, 113.9, 109.4, 108.3, 108.1, 106.3, 105.7, 101.3, 70.6 (2 signals), 70.5, 69.9, 69.7, 68.6, 68.4, 60.7, 55.9, 55.3, 50.6, 32.0 ppm. MS: m/z = 732 $[M + K]^+$, 716 $[M + Na]^+$, 693 $[M]^+$, 676 $[M - OH]^+$, 668 $[M - N_2]^+$. Anal. calcd for $C_{35}H_{39}N_3O_{12}$: C 60.60, H 5.67, N 6.06. Found C 60.50, H 5.90, N 5.69.

3-Benzo[1,3]dioxol-5-yl-4-(3-(2-{2-[2-(2-aminoethoxy)ethoxy]-ethoxy}ethoxy)-4,5-dimethoxybenzyl)-5-hydroxy-5-(4-methoxy-phenyl)-5H-furan-2-one ***10***. A mixture of 1.49 g (2.15 mmol) of 3-benzo[1,3]dioxol-5-yl-4-(3-(2-{2-[2-(2-azidoethoxy)ethoxy]-ethoxy}ethoxy)-4,5-dimethoxybenzyl)-5-hydroxy-5-(4-methoxy-phenyl)-5*H*-furan-2-one **9** and 1.00 g (3.00 mmol) of polymer-bound PPh_3 (polystyrene, 2% DVB, Fluka) was suspended in 10 mL of THF and stirred at room temperature overnight. Water was added (200 μL, ≈10 mmol) and stirring was continued for 3 days. The polymer was removed by filtration and the filtrate was evaporated in vacuo. The remaining oil was purified by silica gel column chromatography (EtOAc/MeOH/NEt_3 5/1/0.3), yielding 246 mg of the product (0.37 mmol, 17%). ^{1}H NMR ($CDCl_3$) δ = 7.32 (d, 2H, J = 8.1 Hz), 6.83, (m, 2H), 6.75 (d, 2H, J = 8.1 Hz), 6.68 (d, 1H, J = 7.7 Hz), 6.14 (s, 1H), 5.91 (s, 1H), 5.85 (s, 2H), 3.88 (m, 2H), 3.70 (s, 4H), 3.64 (s, 3H), 3.59 (m, 4H), 3.54 (s, 3H), 3.48 (m, 4H) 3.37 (m, 2H), 3.15 (m, 2H) ppm. The protons of the butenolide hydroxy group and the amino function were not detected. ^{13}C NMR δ = 171.2, 160.8, 160.1, 152.8, 151.9, 147.9, 147.5, 137.2, 131.8, 129.2, 127.8, 127.4, 123.2, 123.1, 113.7, 109.4, 108.5, 108.2, 106.6, 106.0, 101.2, 70.6, 70.4, 70.3, 70.2, 69.8, 69.7, 68.6, 60.6, 55.8, 55.2, 40.0, 32.0 ppm. MS: m/z = 690 $[M + Na]^+$, 668 $[M + H]^+$. Elemental or HRMS analysis could not be obtained from this product.

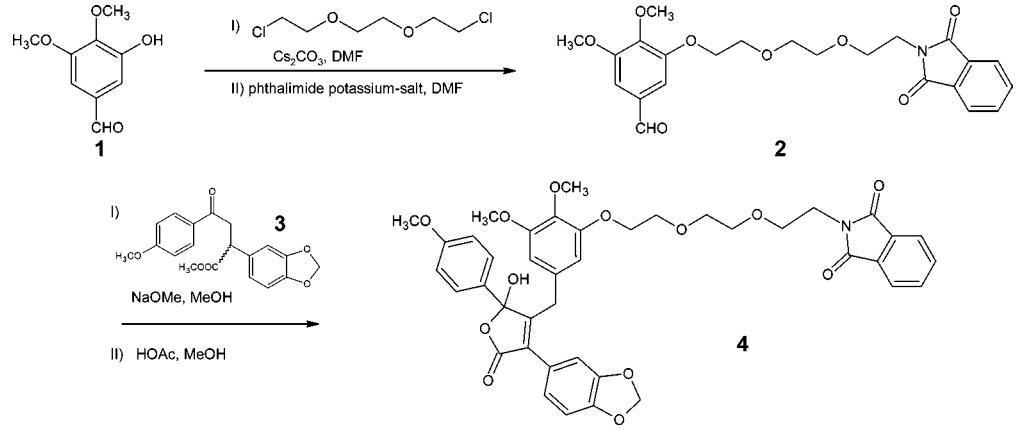
2-(3-{2-[2-(2-{2-Azidoethoxy}ethoxy)ethoxy]ethoxy}-4,5-dimethoxyphenyl)-1,3-dioxolane ***11***. A mixture of 4.95 g (12.91 mmol) of 3-{2-[2-(2-{2-azidoethoxy}ethoxy)ethoxy]ethoxy}-4,5-dimethoxybenzaldehyde **8**, 5 mL (5.57 g, 90 mmol) of ethylene glycol, and 200 mg (1.0 mmol) of *p*-toluene sulfonic acid monohydrate was refluxed in 120 mL of toluene for 8 h using a Dean−Stark trap. After cooling to room temperature, the reaction mixture was poured into 200 mL of diluted sodium bicarbonate solution, washed with water and brine, and dried over magnesium sulfate. After removal of the solvent, the residue was purified by silica gel column chromatography (cyclohexane/ethyl acetate 1/1), giving 4.43 g (10.8 mmol, 80%) of the product as a clear oil. ^{1}H NMR ($CDCl_3$) δ = 6.73 (dd, 2H, J = 5.0 Hz, J = 1.8 Hz), 5.72 (s, 1H), 4.19 (m, 2H), 4.11 (m, 2H), 4.03 (m, 2H), 3.87 (s, 3H), 3.84 (s, 3H), 3.76−3.71 (m, 4H), 3.70−3.64 (m, 8H), 3.37 (m, 2H) ppm. ^{13}C NMR δ = 153.3, 152.4, 139.2, 133.1, 105.4, 103.6, 103.4, 70.7, 70.6, 70.5 (2 signals), 69.9, 69.6, 68.7, 65.1, 60.6, 56.0, 50.6 ppm. MS: m/z = 427 $[M]^+$. Anal. calcd for $C_{19}H_{29}N_3O_8$: C 53.39, H 6.84, N 9.83. Found C 52.30, H 6.89, N 9.72.

2-(3-{2-[2-(2-{2-Aminoethoxy}ethoxy)ethoxy]ethoxy}-4,5-dimethoxyphenyl)-1,3-dioxolane ***12***. Fifty milligrams of Pd/C were added to a solution of 7.18 g (16.8 mmol) of 2-(3-{2-[2-(2-{2-azidoethoxy}ethoxy)ethoxy]ethoxy}-4,5-dimethoxyphe-nyl)-1,3-dioxolane **11** in 100 mL of ethanol. The mixture was stirred at ambient temperature under a hydrogen atmosphere overnight, filtered, and purified by silica gel column chroma-tography to give 5.69 g (14.2 mmol, 84%) of the product as a clear oil. ^{1}H NMR ($CDCl_3$) δ = 6.73 (dd, 2H, J = 5.2 Hz, J = 1.7 Hz), 5.72 (s, 1H), 4.19 (m, 2H), 4.11 (m, 2H), 4.02 (m, 2H), 3.86 (s, 3H), 3.84 (s, 3H), 3.87−3.85 (m, 2H), 3.75−3.69 (m, 2H), 3.69−3.59 (m, 6H), 3.57 (t, 1H, J = 5.4 Hz), 3.49 (t, 1H, J = 5.4 Hz), 2.84 (t, 1H, J = 5.2 Hz), 2.79 (t, 1H, J = 5.2 Hz), 1,74 (br, 2H) ppm. ^{13}C NMR δ = 153.2, 152.3, 139.1, 133.0, 105.3, 103.5, 103.3, 73.2, 70.6, 70.5, 70.4, 70.1, 69.5, 68.6, 65.0, 60.5, 55.9, 41.6 ppm. MS: m/z = 424 $[M + Na]^+$, 402 $[M + H]^+$. HRMS: Calcd for $C_{19}H_{32}NO_8^+$ 402.2122, found 402.2122.

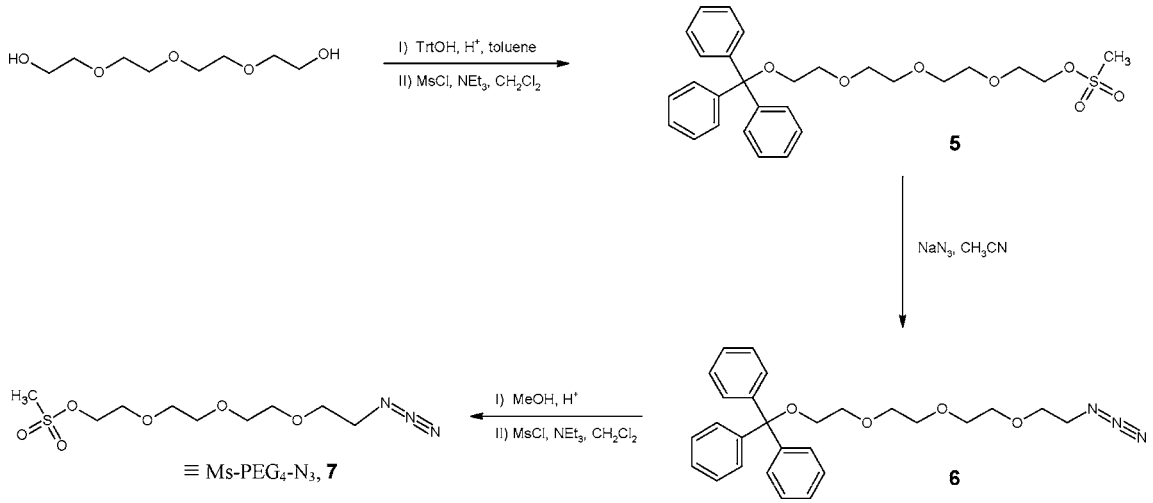
N-Boc-2-(3-{2-[2-(2-{2-Aminoethoxy}ethoxy)ethoxy]ethoxy}-4,5-dimethoxyphenyl)-1,3-dioxolane ***13***. A solution of 4.27 g (10.0 mmol) of 2-(3-{2-[2-(2-{2-aminoethoxy}ethoxy)ethoxy]-ethoxy}-4,5-dimethoxyphenyl)-1,3-dioxolane **12** and 1.66 mL (12.0 mmol) of triethylamine in 50 mL of methylene chloride was cooled in an ice bath. A 2.40 g (11.0 mmol) amount of di-*tert*-butyl dicarbonate was dissolved in 20 mL of methylene chloride and added dropwise. The mixture was warmed to room temperature and stirred overnight. After evaporation of the solvent, the residue was purified by silica gel column chroma-tography (cyclohexane/ethyl acetate 1/2), yielding 2.51 g (5.0 mmol, 50%) of the product as a clear oil. ^{1}H NMR ($CDCl_3$) δ = 6.73 (dd, 2H, J = 4.3 Hz, J = 1.7 Hz), 5.73 (s, 1H), 5.07 (br, 1H), 4.20 (m, 2H), 4.12 (m, 2H), 4.03 (m, 2H), 3.87 (s, 3H), 3.84 (s, 3H), 3.74 (m, 2H), 3.70−3.60 (m, 8H), 3.53 (t, 2H, J = 5.3 Hz), 3.30 (m, 2H), 1.44 (s, 9H) ppm. ^{13}C NMR δ = 153.9, 153.2, 152.3, 139.0, 133.0, 105.1, 103.6, 103.4, 79.0, 70.7, 70.5, 70.4, 70.1, 70.0, 69.6, 68.6, 65.1, 60.6, 56.0, 40.3, 28.3 ppm. MS: m/z = 501 $[M]^+$, 444 $[M - C_4H_9]^+$. Anal. calcd for $C_{24}H_{39}NO_{10}$: C 57.47, H 7.84, N 2.79. Found C 57.25, H 7.94, N 2.79.

N-Boc-3-{2-[2-(2-{2-Aminoethoxy}ethoxy)ethoxy]ethoxy}-4,5-dimethoxybenzaldehyde ***14***. A solution of 2.00 g (3.99 mmol) of *N*-Boc-2-(3-{2-[2-(2-{2-aminoethoxy}ethoxy)ethoxy]-ethoxy}-4,5-dimethoxyphenyl)-1,3-dioxolane **13** in 50 mL of acetone was treated with iodine (100 mg, 10% n/n) and stirred at room temperature for 60 min. Acetone was removed and replaced by ethyl acetate. The organic phase was washed with diluted sodium thiosulfate solution, water, and brine and dried over magnesium sulfate. After removal of the solvent, 1.17 g (3.74 mmol, 94%) of a slightly yellow oil remained. ^{1}H NMR ($CDCl_3$) δ = 9.85 (s, 1H), 7.16 (d, 1H, J = 1.8 Hz), 7.13 (d, 1H, J = 1.8 Hz), 5.00 (br, 1H), 4.25 (m, 2H), 3.95 (s, 3H), 3.92 (s, 3H), 3.89 (m, 2H), 3.74 (m, 2H), 3.70−3.59 (m, 6H), 3.53 (t, 2H, J = 5.0 Hz), 3.30 (t, 2H, J = 5.0 Hz), 1.44 (s, 9H) ppm. ^{13}C NMR δ = 190.9, 155.9, 153.7, 152.8, 144.3, 131.6, 109.1, 106.6, 79.1, 70.8, 70.6, 70.5, 70.2, 70.1, 69.6, 69.0, 60.9, 56.2, 40.5, 28.3 ppm. MS: m/z = 480 $[M + Na]^+$, 358 $[M - (COO^tBuH_2)]^+$. HRMS: Calcd. for $C_{22}H_{35}NO_9Na^+$ 480.2204, found 480.2203.

Scheme 1. Preparation of Model Compound 4



Scheme 2. Preparation of PEG Derivative MsO-PEG$_4$-N$_3$, 7 (adapted from Tahtaoui (*38*))

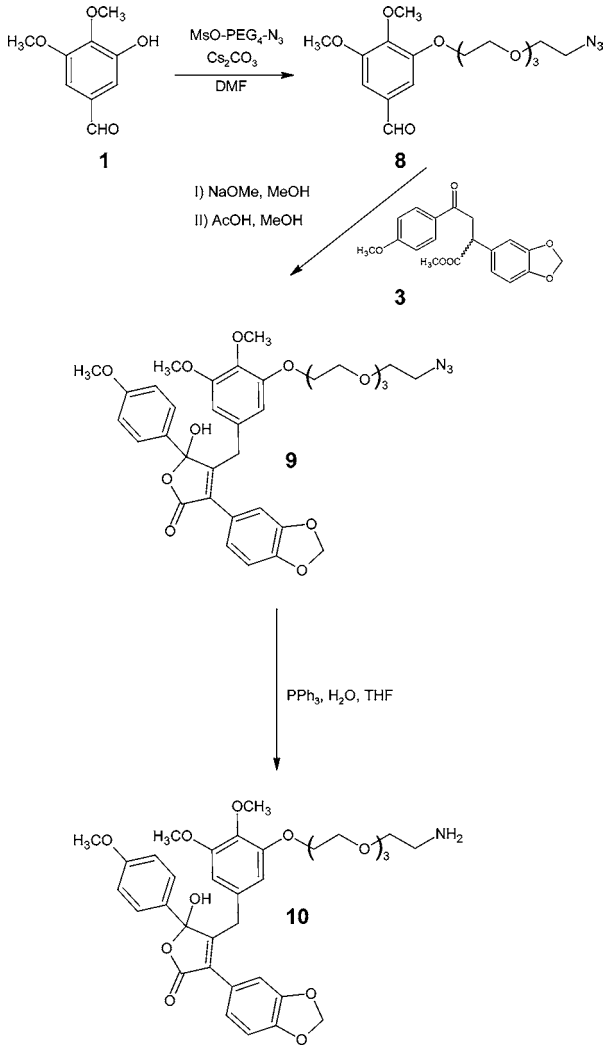


N-Boc-3-Benzo[1,3]dioxol-5-yl-3-(2-{2-[2-(2-aminoethoxy)-ethoxy]ethoxy}ethoxy)-4,5-dimethoxybenzyl)-5-hydroxy-5-(4-methoxyphenyl)-5H-furan-2-one ***15***. A solution of 5.76 g (12.6 mmol) of 3-(2-{2-[2-(2-aminoethoxy)ethoxy]ethoxy}ethoxy)-4,5-dimethoxybenzaldehyde **14**, 4.31 g (12.6 mmol) of 2-(1,3-benzodioxol-5-yl)-1-(4-methoxyphenyl)-4-oxobutyric acid methyl ester **3**, and 756 mg (14.00 mmol) of sodium methoxide were dissolved in 120 mL of methanol at 0 °C and then heated to reflux for 72 h under an argon atmosphere. Acetic acid was added (2.0 mL), and the mixture was heated to reflux for a further 7 h. After evaporation of the solvent, the residue was partitioned between water and ethyl acetate. The organic layer was successively washed with water and brine and dried over sodium sulfate. After evaporation of the solvent a yellow oil remained which was purified by silica gel column chromatography (cyclohexane/ethyl acetate 1/2). Yield: 7.21 g (9.39 mmol, 75%). ^{1}H NMR ($CDCl_3$) δ = 7.74 (d, 2H, J = 8.8 Hz), 6.96−6.91 (m, 2H), 6.83 (d, 2H, J = 8.8 Hz), 6.79 (d, 1H, J = 7.5 Hz), 6.15 (s, 1H), 5.99 (s, 1H), 5.96 (s, 2H), 5.67 (br, 1H), 5.11 (br, 1H), 3.96−3.92 (m, 2H), 3.85−3.80 (m, 2H), 3.79 (s, 3H), 3.74 (s, 3H), 3.71−3.68 (m, 2H), 3.67−3.57 (m, 8H), 3.62 (s, 3H), 3.50 (t, 2H, J = 5.1 Hz), 3.30−3.22 (m, 2H), 1.41 (s, 9H) ppm. ^{13}C NMR δ = 171.0, 160.5, 160.1, 156.1, 152.8, 152.0, 148.0, 147.6, 137.0, 131.8, 129.0, 127.9, 127.4, 123.1, 123.0, 113.8, 109.4, 108.3, 107.9, 106.1, 105.8, 101.2, 79.2, 70.6, 70.5, 70.4, 70.1 (2 signals), 69.7, 68.5, 60.7, 60.4, 55.8, 55.3, 32.1, 28.4 ppm. MS: m/z = 790 [M + Na]$^+$, 668 [M − (COO*t*BuH_2)]$^+$. HRMS: Calcd for $C_{40}H_{49}NO_{14}Na^+$ 790.3045, found 790.3032. Anal. calcd for $C_{40}H_{49}NO_{14}$: C 62.57, H 6.43, N 1.82. Found C 62.48, H 6.55, N 1.80.

3-Benzo[1,3]dioxol-5-yl-3-(2-{2-[2-(2-aminoethoxy)ethoxy]-ethoxy}ethoxy)-4,5-dimethoxybenzyl)-5-hydroxy-5-(4-methoxy-phenyl)-5H-furan-2-one (TFA salt, ***16****).* A solution of 4.59 g (5.98 mmol) of the Boc-protected butenolide **15** in 25 mL of methylene chloride was cooled in an ice bath. Trifluoroacetic acid (TFA, 8.0 mL, dissolved in 10.0 mL of methylene chloride) was added dropwise over a period of 30 min. Stirring was continued for 30 min at 0 °C and another 60 min at room temperature. The solvent and excess TFA was removed under vacuum. The remaining viscous oil was treated with methanol and water (10 mL, 2/1) and again evaporated to dryness. An off-white foam remained which did not deliquesce if cooled to 4 °C. Yield: 4.66 g (5.97 mmol, 99%). ^{1}H NMR (DMSO-d_6) δ = 8.04 (br, 3H), 7.55 (d, 2H, J = 8.8 Hz), 7.12−7.08 (m, 3H), 7.07 (d, 2H, J = 8.8 Hz), 6.18 (d, 2H, J = 1.5 Hz), 6.15 (s, 1H), 6.13 (s, 1H), 4.00−3.93 (m, 2H), 3.91 (s, 3H), 3.88−3.80 (m, 4H), 3.79−3.74 (m, 6H), 3.73 (s, 3H), 3.70 (s, 3H), 3.64 (s, 4H), 3.15 (q, 2H, J = 5.5 Hz) ppm (the protons of the ammonium and hydroxy functions were not detected). ^{13}C NMR δ = 170.7, 161.4, 159.6, 158.3 (q, $J_{C,F}$ = −35 Hz), 152.2, 151.3, 147.3, 146.9, 135.9, 131.7, 129.1, 127.6, 126.6, 123.3, 123.0, 116.2 (q, $J_{C,F}$ = −295 Hz), 113.6, 109.3, 108.1, 107.2, 106.3, 105.7, 101.2, 69.9, 69.8, 69.7, 69.6, 68.8, 67.8, 66.7, 59.8, 55.4, 55.1, 38.6, 31.4 ppm. ^{19}F NMR δ = −74.4 ppm. HRMS: Calcd. for $C_{35}H_{42}NO_{12}^+$ 668.2702, found 668.2707.

Fluorochrome Conjugation, Compound **17**. The amino-functionalized derivative **16** (1.0 mg, 1.3 μmol) was dissolved in 600 μL of a bicarbonate buffer (0.1 M $NaHCO_3$, pH 8.6). To this was added a solution of Cy 5.5 NHS ester (1.5 mg, 1.3 μmol) in 400 μL of DMSO. The solution was vortexed for 1 h

Scheme 3. Preparation of Amino-Functionalized Target Compound 10 by Staudinger Reaction



at room temperature in the dark. Purification of the Cy 5.5-labeled derivative **17** was performed by gradient HPLC using a Knauer system with two K-1800 pumps, an S-2500 UV detector, and a RP-HPLC Nucleosil 100-5 C18 column (250 mm × 4.6 mm). Eluent A: water (0.1% TFA). Eluent B: Acetonitrile (0.1% TFA). Gradient from 90% A to 40% A over 40 min at a flow rate of 1.5 mL/min, detection at $\lambda = 254$ nm. The appropriate fractions ($t_R = 31$ min) were collected, lyophilized, redissolved in PBS, and finally stored at −20 °C. The average content of **17** was 0.8 ± 0.3 μmol/mL (≈60%) as determined by fluorometer measurements with $\lambda_{abs} = 678$ nm and $\epsilon_{678} = 250000\ M^{-1}\ cm^{-1}$. MS: $m/z = 521.0\ [M]^{3-}$ (100%), 781.9 $[M + H]^{2-}$, 792.8 $[M + Na]^{2-}$, 1564.6 $[M + 2H]^{-}$, 1586.5 $[M + H + Na]^{-}$, 1608.5 $[M + 2Na]^{-}$, 1630.5 $[M - H + 3Na]^{-}$, 1652.5 $[M\text{-}2H + 4Na]^{-}$.

Biology. *Tissue Preparation.* Microsomes were prepared by homogenizing cardiac ventricles from DBA mice at 4 °C for 90 s in 1 mL of buffer A (10 mM EDTA, 10 mM HEPES, 0.1 mM benzamidine, pH 7.4), using a Polytron PT 3000 (Kinematica, Lucerne, Switzerland). Homogenates were centrifuged at $45.000g_{max}$ for 15 min at 4 °C. The pellets were resuspended in 1 mL of buffer B (1 mM EDTA, 10 mM HEPES, 0.1 mM benzamidine, pH 7.4) and recentrifuged at $45.000g_{max}$ for 15 min at 4 °C. The pellets were resuspended in 1 mL of buffer B and centrifuged at $10.000g_{max}$ for 10 min at 4 °C. The supernatants were recentrifuged at $45.000g_{max}$ for 15 min at 4 °C. The pellets, partially enriched ventricular membranes, were resuspended in buffer C (50 mM Tris·HCl, 5 mM $MgCl_2$, pH 7.4) and stored frozen at −80 °C.

Competition Experiments. For competition binding studies, the prepared membranes were resuspended in buffer D (10 mM Tris·HCl, 154 mM NaCl, 0.1 mM ascorbic acid, pH 7.4) at 0 °C. Ten microgram amounts of membranes were incubated with a constant concentration of [^{125}I]ET-1 (Perkin-Elmer Live Sciences Inc., Billerica, MA, 40 pM) and with varying concentrations (10 pM to 100 μM) of ET antagonist **4** and PD 156707 at 37 °C for 4 h. Reactions were stopped by filtering onto Whatman GF/B filters and washed with 0.9% NaCl at 4 °C. The membrane-bound radioactivity was determined in a γ-scintillation counter. Values for the maximum number of binding sites (B_{max}) and the dissociation constant (K_D) were determined using the Scatchard method as described in previous papers (*30*, *39*). Competition binding curves were analyzed by nonlinear regression analysis using the *XMGRACE* program (Linux software).

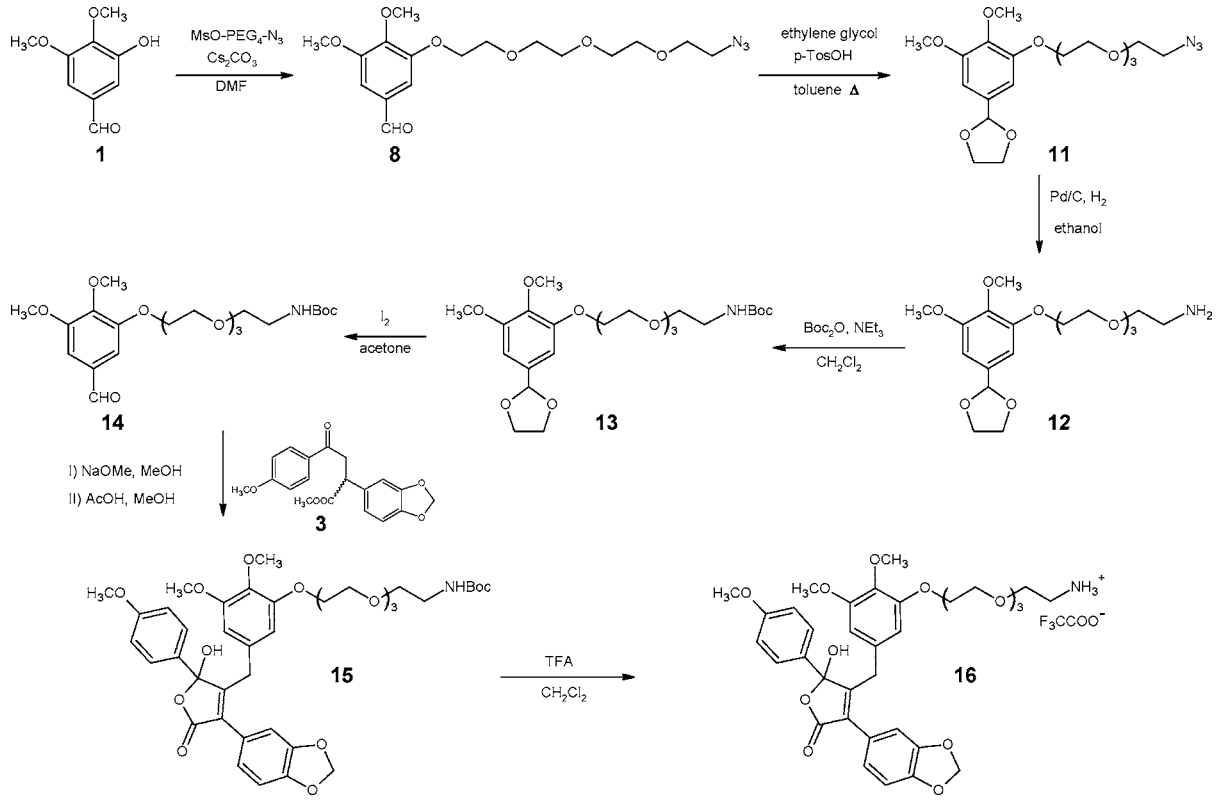
Cell Binding Assays. Cells (HT-1080 fibrosarcomas, MDA-MB-435 ductal carcinomas, MCF-7 adenocarcinomas, 5×10^4 each) were seeded in four-well plates (Nunc GmbH & Co. KG, Wiesbaden, Germany) and incubated in culture medium (0.5 mL/well) overnight. For binding studies, cells were washed twice with PBS and resuspended in 150 μL of binding buffer (20 mM HEPES in PBS with Ca^{2+}/Mg^{2+}, 0.2% BSA, 0.1% glucose, pH 7.4). Cy 5.5 (final amount 5.0 nmol, 33.3 μM) or Cy 5.5 conjugate **17** (5.0 nmol, 33.3 μM) was added into each well. After an incubation period of 45 min at 4 °C, cells were washed twice with PBS and were resuspended in binding buffer. For competition assays, the parent ET_AR antagonist PD 156707 (final amount 50 nmol, 333 μM) or ET_AR antibody (1.3 μg) was added to each well for 45 min at 4 °C. Cells could be directly visualized by fluorescence microscopy (40× objective, Nikon TE 2000-S, Nikon-Düsseldorf, Germany). The microscope was equipped with a mercury vapor lamp (100 W), 620/775 nm and 545/675 nm (excitation/emission) filters (AHF Analysentechnik, Tübingen, Germany), a Nikon DXM1200F camera, and ACT1/DXM1200F software (Nikon, Japan).

Western Blot Analysis. Confluent (80−100%) HT-1080, MDA-MB-435, and MCF-7 cells were treated with 0.5 mL of trypsin and harvested by scraping in cold PBS. After two centrifugation steps (1500 rpm, 5 min, 4 °C) cells were resuspended in lysis buffer (0.5% Tween 20, 50 mM Tris-HCl pH 8, 250 mM NaCl, 5 mM EDTA pH 8, 50 mM NaF, 0.5 mM Na_3VO_4, 0.9 mg/mL protease inhibitor cocktail, Sigma, St. Louis, MO), and the protein concentration of each sample was determined (Lowry protein assay, total amount 40 μg). To concentrate the protein, a 2-fold volume of cold acetone was added to each sample and placed in −20 °C for 16 h, followed by centrifugation at $10.000g_{max}$ at 4 °C for 30 min. Protein pellets were dissolved in 100 μL of 6× sodium dodecyl sulfate (SDS) sample buffer (New England Biolabs, Beverley, MA). Following precipitation, proteins were electrophoretically separated in nonreducing 10% SDS-PAGE and transferred to PVDF membranes (Millipore Corporation, Bedford, MA). After blocking, immunoblots were incubated with ET_AR polyclonal antibody (N-15, Santa Cruz Biotechnology, Santa Cruz, CA) and with peroxidase-conjugated donkey anti-goat IgG secondary antibody (Sigma, St. Louis, MO). Peroxidase activity was revealed using ECL chemiluminescence (Amersham Biosciences, Freiburg, Germany) and X-ray film, as described by the manufacturers. Human endothelial cell lysate (5 μg, BD Bioscience, San Diego, CA) was used as a positive control.

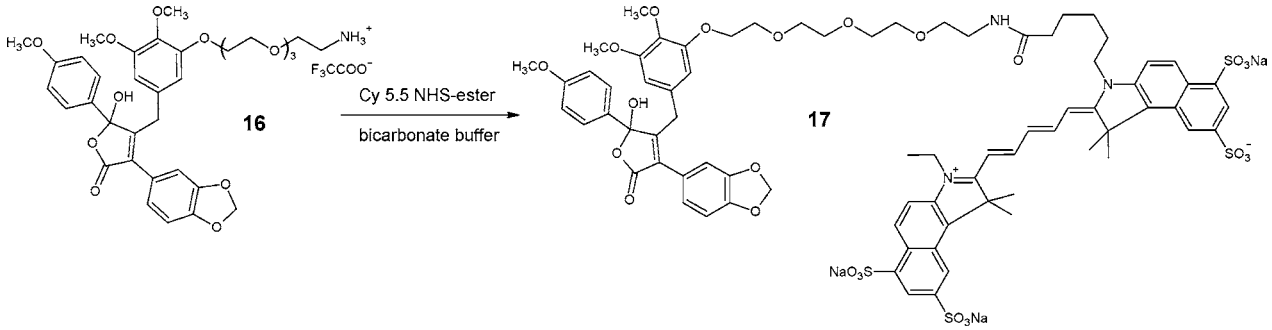
RESULTS AND DISCUSSION

The objective of this work was the modification of an existing lead structure (PD 156707) with a fluorescent dye, to allow for

Scheme 4. Preparation of Target Compound 16



Scheme 5. Synthesis of Conjugate 17



near-infrared detection of target receptors. Taking into account the size of the dye molecule compared to that of the parent antagonist, we chose a short polyethylene glycol spacer to displace the dye from the ET_AR-binding site and preserve the desired affinity and selectivity.

Chemistry. We synthesized the butenolide compound **4** via the route outlined in Scheme 1. Ketoester **3** was synthesized starting from 4′-methoxyacetophenone and piperonal as described by Doherty et al. (*37*). Benzaldehyde **2** was prepared by reaction of 3,4-dimethoxy-5-hydroxybenzaldehyde **1** with 1,2-bis(2-chloroethoxy)ethane and cesium carbonate in DMF. We found that the use of cesium carbonate instead of potassium carbonate allows us to perform the substitution reactions of these phenolic alcohols with nucleophiles at lower temperature and in shorter reaction times. Reaction with potassium phthalimide in DMF at elevated temperature gives the product **2** in 61% overall yield. To obtain butenolide **4**, condensation of the benzaldehyde with ketoester **3** was arranged. This is carried out by subsequently adding ketoester **3** and aldehyde **2** to a solution of sodium methoxide in methanol at 0 °C and then refluxing the mixture for 12−15 h under an inert atmosphere (argon). Finally, the addition of acetic acid and another 5−6 h reflux is required to obtain the ring-closed butenolide product **4**.

The attempt to obtain amino-functionalized products by hydrazinolysis of phthalimidoyl-modified butenolide derivatives such as **4** failed. The hydrazine not only reacted with the phthalimidoyl group but also inserted into the butenolide ring, giving a pyridazine derivative (data not shown).

The synthesis of benzaldehyde **8** (Schemes 3, 4) began with the preparation of the PEG-spacer. This was achieved in accordance with the procedure described by Tahtaoui et al. for the corresponding PEG_3 derivative and is outlined in Scheme 2 (*38*). Subsequent reaction of triphenylmethanol and methanesulfonyl chloride with tetraethylene glycol yields the trityl-protected, activated PEG derivative **5**, which is converted to the azide **6** by reaction with sodium azide in acetonitrile at reflux. The trityl group is then removed by reaction with *p*-toluenesulfonic acid in methanol, and the free hydroxy function is activated with methanesulfonyl chloride, giving 2-{2-[2-(2-azidoethoxy)ethoxy]ethoxy}ethyl methanesulfonate (MsO-PEG_4-N_3, **7**) in 50% overall yield. The coupling of the so-modified PEG spacer to 3,4-dimethoxy-5-hydroxybenzaldehyde **1** is conducted by reaction of the compounds and cesium carbonate in DMF at 80 °C for 4 h. The final step is the reaction of the ketoester **3** with the corresponding aldehyde **8** to yield butenolide **9**. This is carried out as described above for benzaldehyde **2** (Scheme 1).

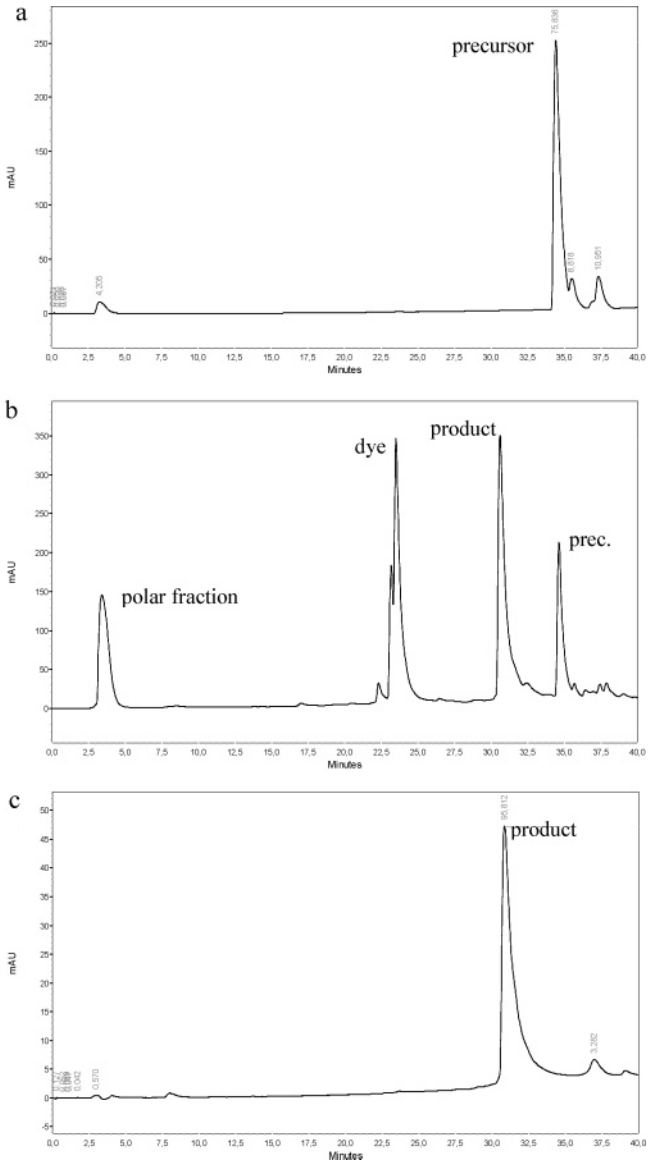


Figure 2. HPLC-chromatograms of precursor **16** (a), a reaction mixture with Cy 5.5 NHS-ester, bicarbonate buffer, and DMSO (b) and the purified sample of conjugate **17** (c).

Compound **9** is then converted to the free amine **10** by Staudinger reaction with triphenylphosphine and water in THF (Scheme 3). Regrettably, the yields in this step were disappointing (<20%), and several byproducts made the purification rather difficult. This was probably due to reaction of the phosphine with one of the oxygen-containing moieties of the butenolide ring structure. To circumvent these difficulties, a second reaction sequence was chosen, in which the amine was generated earlier and then protected for further conversion. This second sequence (Scheme 4) also begins with the reaction of 3,4-dimethoxy-5-hydroxybenzaldehyde **1** with PEG-derivative **7**. The aldehyde function of azide **8** is then protected with ethylene glycol, giving dioxolane **11** in 80% yield after purification. This kind of protection allows subsequent reduction of the azide and BOC protection of the generated amine **12** without the risk of intermolecular imine formation. The dioxolane protecting group of **13** can easily be destroyed by reaction with catalytic amounts of iodine in acetone without affecting the BOC protecting group. The product benzaldehyde **14** and ketoester **3** are then converted to the desired butenolide derivative by the same procedure as described above for the azide functionalized aldehyde **8** (Scheme 3). The product of this rection is the PEG-modified, *N*-Boc-protected butenolide

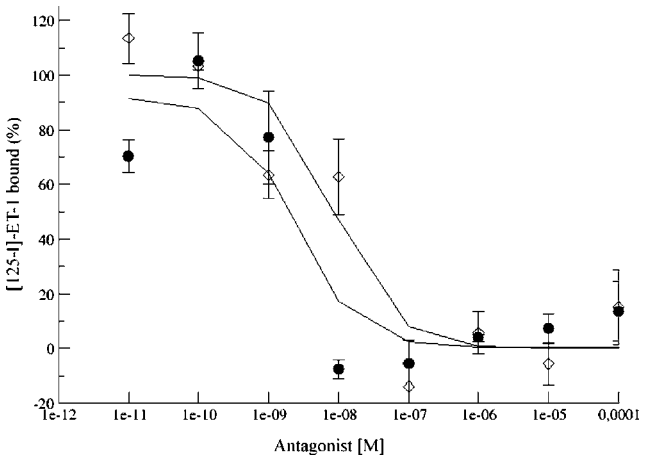


Figure 3. Competition binding study with model compound **4** in comparison to lead structure PD 156707 (● PD 156707, IC_{50} = 2.0 nM, ◇ Compd. **4**, IC_{50} = 9.0 nM).

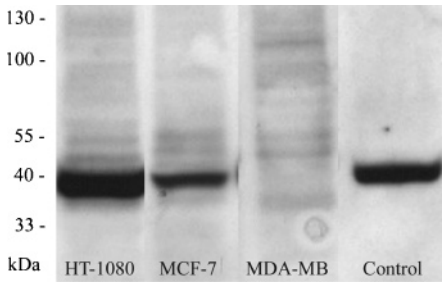


Figure 4. Western blot analysis of the three cell lines HT-1080, MCF-7, and MDA-MB-435 and human endothelial cell lysate as positive control (from left to right). ET_A receptor expression (→ 39 kDa band) was revealed by N15 polyclonal antibody (Santa Cruz) and peroxidase-conjugated donkey anti-goat secondary antibody (Sigma). HT-1080 fibrosarcoma cell show the highes expression level of ET_AR while MCF-7 adenocarcinomas only moderately express the target structure and MDA-MB-435 cells are devoid of the ET_A receptor.

15, which in the final step is deprotected by treatment with trifluoroacetic acid (TFA) in methylene chloride. The final product **16** can be isolated as the TFA salt which can be handled and stored easily at 4 °C.

Fluorochrome Conjugation. The amino-functionalized compound **16** was used for the conjugation of cyanine dye Cy 5.5 (used as the corresponding NHS-ester). The reactions were carried out in accordance with recommended peptide labeling procedures (Amersham Biosciences UK Limited, Buckinghamshire, UK), using an aqueous bicarbonate buffer and DMSO as solvents and reaction conditions of 1 h at room temperature. The conjugate **17** (Scheme 5) was purified by reversed phase HPLC on an analytical column by collection of the appropriate fractions. After lyophilization and redissolving in PBS, the sample showed a purity of >95% (Figure 2). The identification of the labeled ligand was possible by mass spectrometry with the triply negatively charged ion emerging at 100% intensity.

In Vitro Competition Studies. The affinity of the prepared butenolide derivative **4** (Scheme 1) toward ET receptors was determined by competition binding studies using [^{125}I]ET-1 and mouse cardiac ventricular membrane preparations. The binding of [^{125}I]ET-1 to ventricular membranes was specific, saturable, and of high affinity. Scatchard (*39*−*41*) transformation of the saturation data yielded values for the dissociation constant (K_D = 208 ± 2 pM) and the maximum number of binding sites (B_{max} = 300 ± 3 fmol/mg protein). The receptor affinity of butenolide **4** was compared to that of the lead compound PD 156707. We found an IC_{50} value of 8.4 ± 1.7 nM for the

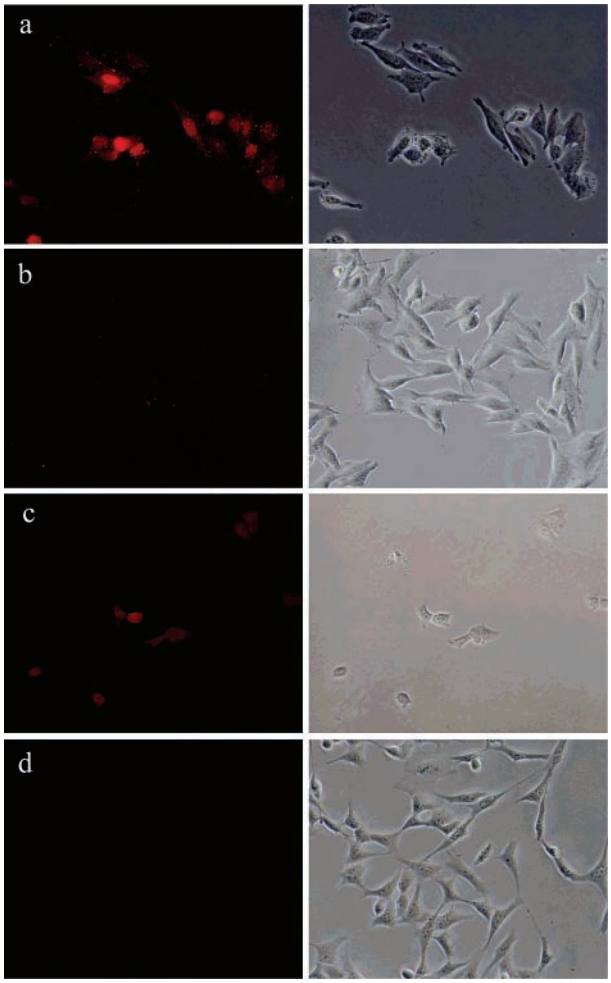


Figure 5. Fluorescence microscopic (left) and phase contrast (right) images of HT-1080 (a), MCF-7 (c), and MDA-MB-435 (d) cells. All cells were incubated with conjugate **17** and subsequently washed with PBS. Note that HT-1080 cells reveal the highest cellular fluorescence (a) while MCF-7 cells show only moderate cellular fluorescence (c) and MDA-MB-435 do not bind the tracer (d). Moreover, predosing of HT-1080 cells with an ET_AR specific antibody resulted in a significant reduction of cellular binding of the probe (b), confirming the binding specificity of Cy 5.5 conjugate **17** (40× objective magnification).

model compound **4** and a value of 2.2 ± 0.5 nM for the lead compound PD 156707 (*37*, 0.3 nM, Figure 3). This result shows that it is possible to modify this small-molecule receptor antagonist with an appropriate spacer group and a relatively large signaling molecule without affecting its receptor binding potencies.

Western Blot Analysis. The cellular expression level of the ET_A receptor was determined by western blot analysis (Figure 4). Using the Santa Cruz polyclonal antibody revealed a low molecular weight band at 39 kDa which corresponds to a proteolytic fragment of the high molecular weight (49 kDa) protein still possessing the ligand binding properties of the receptor (*42*, *43*). The highest amount of protein was found in human fibrosarcoma cells HT-1080, indicated by an intense major band at 39 kDa. A weaker band was found for the human adenocarcinoma cell line MCF-7, indicating a lower amount of ET_A receptor protein while the absence of the 39 kDa band for MDA-MB-435 cells confirmed that these cells were not expressing the ET_A receptor. Therefore, these cell lines providing different levels of target expression were ideally suited to test the conjugate **17** for receptor targeting efficiacy. Human endothelial cell lysate, which shows an intense band at 39 kDa, was used as a positive control (Figure 4).

In Vitro Cell Binding Assays. We tested the specificity of the fluorochrome conjugated ligand **17** for the ET_A receptor using ET_AR-positive MCF-7 human breast adenocarcinoma and HT-1080 human fibrosarcoma cells and ET_AR-negative MDA-MB-435 human breast carcinoma cells. Binding of the labeled antagonist could be directly analyzed by fluorescence microscopy. Negligible signals were detected from the cells when incubated with Cy 5.5 dye alone (5 nmol, data not shown). Incubation of the cells with 2 nmol (33.3 μM) of **17** allowed visualization of the ET_A receptor. The signal was distributed over the cell surface and was membrane-associated (Figure 5). Blocking of the signal was possible with 1.3 μg of the ET_A receptor-specific antibody (Figure 5B) or with a tenfold excess of the unlabeled antagonist PD 156707 (data not shown). The ET_A receptor expressing human fibrosarcoma cells HT-1080 showed a higher fluorescence signal than human breast cancer cell line MCF-7 (Figures 5A,C), while ET_A-negative MDA-MB-435 human breast carcinoma cells showed no accumulation of the ligand (Figure 5D). Thus, these results nicely correlate with the western blot analysis (Figure 4) and confirm target specific binding of the probe.

CONCLUSION

The aim of this work was to develop a nonpeptide, high-affinity ET_A receptor antagonist which is applicable for optical imaging of ET_AR expression. We chose 3-benzo[1,3]dioxol-5-yl-5-hydroxy-5-(4-methoxyphenyl)-4-(3,4,5-trimethoxybenzyl)-5*H*-furan-2-one (PD 156707) as the lead structure and developed a route for the synthesis of an amino-PEG-derivatized compound which can be used for the conjugation of common amino-reactive fluorescent markers. We used Cy 5.5 for conjugation, thus obtaining a near-infrared fluorescent photoprobe for the selective imaging of ET_ARs. The specificity of binding to ET_AR was shown by western blot analysis and *in vitro* cell binding assays. Incubation of human cancer cells with the conjugate lead to the specific visualization of the ET_AR positive cell lines HT-1080 and MCF-7. The signal was distributed over the cell surface and was membrane-associated. Blocking of the signal was possible with the unlabeled ET_AR antagonist PD 156707 or with an ET_AR specific antibody, verifying specific binding to cell surface sites. The ET_AR negative cell line MDA-MB-435 did not show any accumulation of the ligand. The results suggest that the modified photoprobe **17** tightly binds to ET_A receptors, thus representing a potential candidate for the *in vivo* imaging of ET_AR-overexpressing tissues in scientific research and medical diagnosis.

ACKNOWLEDGMENT

Financial support of the Deutsche Forschungsgemeinschaft (SFB 656 A1/A4, Scha 758/5-1) is gratefully acknowledged. We would like to thank Sandra Schröer for the *in vitro* competition experiments and Dr. H. Luftmann at the Organic Chemistry Department of the WWU Münster for mass spectrometry.

LITERATURE CITED

(1) Hickey, K. A., Rubanyi, G., Paul, R. J., and Highsmith, R. F. (1985) Characterization of a coronary vasoconstrictor produced by cultured endothelial cells. *Am. J. Physiol. 248*, C550−6.

(2) Yanagisawa, M., Kurihara, H., Kimura, S., Tomobe, Y., Kobayashi, M., Mitsui, Y., Yazaki, Y., Goto, K., and Masaki, T. (1988) A novel potent vasoconstrictor peptide produced by vascular endothelial cells. *Nature 332*, 411−5.

(3) Dhaun, N., Goddard, J., and Webb, D. J. (2006) The endothelin system and its antagonism in chronic kidney disease. *J. Am. Soc. Nephrol. 17*, 943−55.

(4) Giaid, A., Yanagisawa, M., Langleben, D., Michel, R. P., Levy, R., Shennib, H., Kimura, S., Masaki, T., Duguid, W. P., and Stewart, D. J. (1993) Expression of endothelin-1 in the lungs of patients with pulmonary hypertension. *N. Engl. J. Med. 328*, 1732−9.
(5) Pittman, Q. J. (2006) Endothelin-an emerging role in proinflammatory pathways in brain. *Am. J. Physiol. Regul. Integr. Comp. Physiol. 290*, R162−3.
(6) Plusczyk, T., Witzel, B., Menger, M. D., and Schilling, M. (2003) ETA and ETB receptor function in pancreatitis-associated microcirculatory failure, inflammation, and parenchymal injury. *Am. J. Physiol. Gastrointest. Liver Physiol. 285*, G145−53.
(7) Saito, Y., Nakao, K., Mukoyama, M., and Imura, H. (1990) Increased plasma endothelin level in patients with essential hypertension. *N. Engl. J. Med. 322*, 205.
(8) Teerlink, J. R., Loffler, B. M., Hess, P., Maire, J. P., Clozel, M., and Clozel, J. P. (1994) Role of endothelin in the maintenance of blood pressure in conscious rats with chronic heart failure. Acute effects of the endothelin receptor antagonist Ro 47−0203. (bosentan). *Circulation 90*, 2510−8.
(9) Grant, K., Loizidou, M., and Taylor, I. (2003) Endothelin-1: a multifunctional molecule in cancer. *Br. J. Cancer 88*, 163−6.
(10) Levin, E. R. (1995) Endothelins. *N. Engl. J. Med. 333*, 356−63.
(11) Nelson, J., Bagnato, A., Battistini, B., and Nisen, P. (2003) The endothelin axis: emerging role in cancer. *Nat. Rev. Cancer 3*, 110−6.
(12) Asham, E., Shankar, A., Loizidou, M., Fredericks, S., Miller, K., Boulos, P. B., Burnstock, G., and Taylor, I. (2001) Increased endothelin-1 in colorectal cancer and reduction of tumour growth by ET(A) receptor antagonism. *Br. J. Cancer 85*, 1759−63.
(13) Bagnato, A., Salani, D., Di Castro, V., Wu-Wong, J. R., Tecce, R., Nicotra, M. R., Venuti, A., and Natali, P. G. (1999) Expression of endothelin 1 and endothelin A receptor in ovarian carcinoma: evidence for an autocrine role in tumor growth. *Cancer Res. 59*, 720−7.
(14) Nelson, J. B., Chan-Tack, K., Hedican, S. P., Magnuson, S. R., Opgenorth, T. J., Bova, G. S., and Simons, J. W. (1996) Endothelin-1 production and decreased endothelin B receptor expression in advanced prostate cancer. *Cancer Res. 56*, 663−8.
(15) Alanen, K., Deng, D. X., and Chakrabarti, S. (2000) Augmented expression of endothelin-1, endothelin-3 and the endothelin-B receptor in breast carcinoma. *Histopathology 36*, 161−7.
(16) Wülfing, P., Diallo, R., Kersting, C., Wülfing, C., Poremba, C., Rody, A., Greb, R. R., Boecker, W., and Kiesel, L. (2003) Expression of endothelin-1, endothelin-A, and endothelin-B receptor in human breast cancer and correlation with long-term follow-up. *Clin. Cancer Res. 9*, 4125−31.
(17) Rosano, L., Varmi, M., Salani, D., Di Castro, V., Spinella, F., Natali, P. G., and Bagnato, A. (2001) Endothelin-1 induces tumor proteinase activation and invasiveness of ovarian carcinoma cells. *Cancer Res. 61*, 8340−6.
(18) Salani, D., Di Castro, V., Nicotra, M. R., Rosano, L., Tecce, R., Venuti, A., Natali, P. G., and Bagnato, A. (2000) Role of endothelin-1 in neovascularization of ovarian carcinoma. *Am. J. Pathol. 157*, 1537−47.
(19) Del Bufalo, D., Di Castro, V., Biroccio, A., Varmi, M., Salani, D., Rosano, L., Trisciuoglio, D., Spinella, F., and Bagnato, A. (2002) Endothelin-1 protects ovarian carcinoma cells against paclitaxel-induced apoptosis: requirement for Akt activation. *Mol. Pharmacol. 61*, 524−32.
(20) Eberl, L. P., Egidy, G., Pinet, F., and Juillerat-Jeanneret, L. (2000) Endothelin receptor blockade potentiates FasL-induced apoptosis in colon carcinoma cells via the protein kinase C-pathway. *J. Cardiovasc. Pharmacol. 36*, S354−6.
(21) Ali, H., Dashwood, M., Dawas, K., Loizidou, M., Savage, F., and Taylor, I. (2000) Endothelin receptor expression in colorectal cancer. *J. Cardiovasc. Pharmacol. 36*, S69−71.
(22) Bagnato, A., Cirilli, A., Salani, D., Simeone, P., Muller, A., Nicotra, M. R., Natali, P. G., and Venuti, A. (2002) Growth inhibition of cervix carcinoma cells in vivo by endothelin A receptor blockade. *Cancer Res. 62*, 6381−4.
(23) Rosano, L., Spinella, F., Salani, D., Di Castro, V., Venuti, A., Nicotra, M. R., Natali, P. G., and Bagnato, A. (2003) Therapeutic targeting of the endothelin a receptor in human ovarian carcinoma. *Cancer Res. 63*, 2447−53.
(24) Carducci, M. A., Nelson, J. B., Bowling, M. K., Rogers, T., Eisenberger, M. A., Sinibaldi, V., Donehower, R., Leahy, T. L., Carr, R. A., Isaacson, J. D., Janus, T. J., Andre, A., Hosmane, B. S., and Padley, R. J. (2002) Atrasentan, an endothelin-receptor antagonist for refractory adenocarcinomas: safety and pharmacokinetics. *J. Clin. Oncol. 20*, 2171−80.
(25) Carducci, M. A., Padley, R. J., Breul, J., Vogelzang, N. J., Zonnenberg, B. A., Daliani, D. D., Schulman, C. C., Nabulsi, A. A., Humerickhouse, R. A., Weinberg, M. A., Schmitt, J. L., and Nelson, J. B. (2003) Effect of endothelin-A receptor blockade with atrasentan on tumor progression in men with hormone-refractory prostate cancer: a randomized, phase II, placebo-controlled trial. *J. Clin. Oncol. 21*, 679−89.
(26) Yamashita, J., Ogawa, M., Inada, K., Yamashita, S., Matsuo, S., and Takano, S. (1991) A large amount of endothelin-1 is present in human breast cancer tissues. *Res. Commun. Chem. Pathol. Pharmacol. 74*, 363−9.
(27) Wülfing, P., Götte, M., Sonntag, B., Kersting, C., Schmidt, H., Wülfing, C., Buerger, H., Greb, R., Boecker, W., and Kiesel, L. (2005) Overexpression of Endothelin-A-receptor in breast cancer: regulation by estradiol and cobalt-chloride induced hypoxia. *Int. J. Oncol. 26*, 951−60.
(28) Wülfing, P., Tio, J., Kersting, C., Sonntag, B., Buerger, H., Wülfing, C., Euler, U., Boecker, W., Tulusan, A. H., and Kiesel, L. (2004) Expression of endothelin-A-receptor predicts unfavourable response to neoadjuvant chemotherapy in locally advanced breast cancer. *Br. J. Cancer 91*, 434−40.
(29) Davenport, A. P., Kuc, R. E., Fitzgerald, F., Maguire, J. J., Berryman, K., and Doherty, A. M. (1994) [125I]-PD151242: a selective radioligand for human ETA receptors. *Br. J. Pharmacol. 111*, 4−6.
(30) Höltke, C., Law, M. P., Wagner, S., Breyholz, H. J., Kopka, K., Bremer, C., Levkau, B., Schober, O., and Schäfers, M. (2006) Synthesis, in vitro pharmacology and biodistribution studies of new PD 156707-derived ET(A) receptor radioligands. *Bioorg. Med. Chem. 14*, 1910−7.
(31) Johnström, P., Aigbirhio, F. I., Clark, J. C., Downey, S. P., Pickard, J. D., and Davenport, A. P. (2000) Syntheses of the first endothelin-A- and -B-selective radioligands for positron emission tomography. *J. Cardiovasc. Pharmacol. 36*, S58−60.
(32) Johnström, P., Fryer, T. D., Richards, H. K., Barret, O., Clark, J. C., Ohlstein, E. H., Pickard, J. D., and Davenport, A. P. (2004) In Vivo Imaging of Cardiovascular Endothelin Receptors Using the Novel Radiolabelled Antagonist [18F]-SB209670 and Positron Emission Tomography (microPET). *J. Cardiovasc. Pharmacol. 44*, S34−S38.
(33) Mathews, W. B., Zober, T. G., Ravert, H. T., Scheffel, U., Hilton, J., Sleep, D., Dannals, R. F., and Szabo, Z. (2006) Synthesis and in vivo evaluation of a PET radioligand for imaging the endothelin-A receptor. *Nucl. Med. Biol. 33*, 15−9.
(34) Ravert, H. T., Mathews, W. B., Hamill, T. G., Burns, H. D., and Dannals, R. F. (2000) Radiosynthesis of a potent endothelin receptor antagonist: [11C]-L753037. *J. Labelled Compd. Radiopharm.* 1205−1210.
(35) Bremer, C., Ntziachristos, V., Weitkamp, B., Theilmeier, G., Heindel, W., and Weissleder, R. (2005) Optical imaging of spontaneous breast tumors using protease sensing 'smart' optical probes. *Invest. Radiol. 40*, 321−7.
(36) Ntziachristos, V., Bremer, C., Graves, E. E., Ripoll, J., and Weissleder, R. (2002) In vivo tomographic imaging of near-infrared fluorescent probes. *Mol. Imaging 1*, 82−8.
(37) Doherty, A. M., Patt, W. C., Edmunds, J. J., Berryman, K. A., Reisdorph, B. R., Plummer, M. S., Shahripour, A., Lee, C., Cheng, X. M., and Walker, D. M., and et al. (1995) Discovery of a novel series of orally active non-peptide endothelin-A (ETA) receptor-selective antagonists. *J. Med. Chem. 38*, 1259−63.
(38) Tahtaoui, C., Parrot, I., Klotz, P., Guillier, F., Galzi, J. L., Hibert, M., and Ilien, B. (2004) Fluorescent pirenzepine derivatives as potential bitopic ligands of the human M1 muscarinic receptor. *J. Med. Chem. 47*, 4300−15.
(39) Kopka, K., Wagner, S., Riemann, B., Law, M. P., Puke, C., Luthra, S. K., Pike, V. W., Wichter, T., Schmitz, W., Schober, O., and Schafers, M. (2003) Design of new beta1-selective adrenoceptor ligands as potential radioligands for in vivo imaging. *Bioorg. Med. Chem. 11*, 3513−27.

(40) McGonigle, P., and Molinoff, P. B. (1989) Quantitative aspects of drug-receptor interactions. In *Basic Neurochemistry* (Siegel, G., Agranoff, B., Albers, R. W., Molinoff, P. B., Eds.) pp 183−201, Raven Press, New York.
(41) Scatchard, G. (1949) The attractions of proteins for small molecules and ions. *Ann. N. Y. Acad. Sci.* 660−672.
(42) Hughes, S. J., Wall, N., Scholfield, C. N., McGeown, J. G., Gardiner, T. A., Stitt, A. W., and Curtis, T. M. (2004) Advanced glycation endproduct modified basement membrane attenuates endothelin-1 induced [Ca2+]i signalling and contraction in retinal microvascular pericytes. *Mol. Vis. 10*, 996−1004.
(43) Kozuka, M., Ito, T., Hirose, S., Lodhi, K. M., and Hagiwara, H. (1991) Purification and characterization of bovine lung endothelin receptor. *J. Biol. Chem. 266*, 16892−6.

BC060264W

Immobilization of Aprotinin to Fibrinogen as a Novel Method for Controlling Degradation of Fibrin Gels

Jason D. Smith,[†,‡] Andrew Chen,[†] Lauren A. Ernst,[‡] Alan S. Waggoner,[‡] and Phil G. Campbell*[,†,‡]

Institute for Complex Engineered Systems and Molecular Biosensor and Imaging Center, Carnegie Mellon University, Pittsburgh, Pennsylvania. Received August 29, 2006; Revised Manuscript Received January 23, 2007

The goal of this work was to demonstrate that aprotinin conjugated to fibrinogen could (1) maintain its function and (2) control fibrin degradation. Using the chick chorioallantoic membrane (CAM) assay, we found that blood vessels did not directly invade fibrin constructs containing immobilized fibroblast growth factor-2. Because the fibrin quickly degraded within approximately 5 days, we hypothesized that controlling fibrinolysis may improve direct blood vessel invasion. Aprotinin, a protease inhibitor typically added to slow fibrinolysis, is a small protein and can diffuse out of the gel resulting in the loss of fibrinolysis protection. Therefore, using a novel synthesis strategy, aprotinin and a fluorescent reporter, Cy3, were chemically conjugated to fibrinogen. In vitro microplate absorbance assays showed that the conjugated aprotinin was able to inhibit plasmin-mediated fibrin degradation and that its activity was comparable to equimolar levels of soluble, nonconjugated aprotinin. Additionally, we found that fibrinolysis rates could be tuned by varying the level of conjugated aprotinin within the gel. The conjugated aprotinin also demonstrated functionality in vivo. In the chick CAM assay, fibrin gels containing conjugated aprotinin were approximately 5 times larger than gels containing soluble aprotinin after 4 days. Also, in support of our hypothesis, we found that immobilized aprotinin within fibrin gels demonstrated substantial blood vessel invasion.

INTRODUCTION

Our laboratory studies the use of fibrin-based constructs for bone tissue engineering applications. Fibrin is the primary provisional extracellular matrix (ECM) protein in wound healing (*1*). Fibrin supports cell adhesion and proliferation (*2*, *3*), can bind a number of growth factors, such as fibroblast growth factor-2 (FGF-2), with high specificity (*4*, *5*), and can be actively remodeled and degraded by cells (*6*−*8*). For these reasons, fibrin is an attractive scaffolding material for tissue engineering applications (*9*−*17*).

One of our laboratory's focus areas is to develop strategies to induce blood vessel ingrowth into such fibrin-based constructs for translation to tissue engineering applications. Our basic in vivo model is the chick chorioallantoic membrane (CAM) assay, a commonly used in vivo angiogenesis assay to study blood vessel development as well as the angiogenic nature of tissue engineered constructs (*9*, *10*, *18*−*28*). However, our initial experiments indicated that the fibrin was completely degraded at the construct/CAM interface as the CAM is invading the construct. Therefore, it appears that vascularization does not directly occur into the construct but is secondary to the invading CAM. Therefore, we asked the following question: Could direct angiogenic invasion be induced into the construct by controlling fibrin degradation?

In vivo, fibrin degradation, or fibrinolysis, occurs primarily through the serine protease plasmin (*8*, *18*, *19*). Aprotinin is a small (58 amino acids), potent competitive inhibitor for the active site of plasmin and is typically added to commercial fibrin glues to slow fibrinolysis (*7*, *20*−*22*). Because of its small size, however, aprotinin can freely diffuse out of the fibrin gel in vivo and is therefore no longer able to protect fibrin from degradation.

To circumvent this problem, we engineered a fused construct, directly linking aprotinin to fibrinogen, to immobilize aprotinin within the construct. Fibrinolysis would still be plasmin-mediated (and thus cell-mediated), but conjugated inhibitor levels would control the degradation rate. In this work, we conjugated aprotinin and a Cy3 fluorescent dye to fibrinogen through the use of a cysteine-based trifunctional cross-linker. Aprotinin was chosen due to its small size (<2% the molecular weight of fibrinogen) and potent plasmin inhibition. The Cy3 fluorescent dye served for quantitation of the conjugated aprotinin as well as a reporter of its localization. The conjugated aprotinin was tested in vitro and in vivo and found to be active in both venues. Additionally, the CAM assay showed that slowing fibrin degradation results in improved direct vascularization within the fibrin construct.

MATERIALS AND METHODS

Reagents. Cystine, diisopropylethylamine (DIPEA), tris(2-carboxyethyl)phosphine hydrochloride (TCEP), recombinant bovine lung aprotinin, EDTA, and sodium *meta*-periodate were obtained from Sigma (St. Louis, MO). Tetraethylammonium hydroxide and *O*-(*N*-succinimidyl)-*N*,*N*,*N*′,*N*′-tetramethyluronium tetrafluoroborate (TSTU) were purchased from Fluka (Seelze, Germany). Human fibrinogen was purchased from diaPharma (West Chester, OH). C-18 column media was purchased from Separation Methods Technologies (Newark, DE) and the BioGel P-4 from BioRad (Hercules, CA). 4-(4-*N*-Maleimidophenyl)butyric acid hydrazide hydrochloride (MPBH) was obtained from Pierce (Rockford, IL).

Synthesis Strategy of Aprotinin−Fibrinogen Conjugate Molecule. Cystine was neutralized with tetraethylammonium hydroxide and dried by rotary evaporation. The cystine tetraethylammonium salt (0.7 mg) and 7 mg of monofuctional NHS-

* To whom correspondence should be addressed. Phil G. Campbell, Carnegie Mellon University, 5000 Forbes Ave., 1201 Hamburg Hall, Pittsburgh, PA 15213; E-mail: pcampbel@cs.cmu.edu.

[†] Institute for Complex Engineered Systems.

[‡] Molecular Biosensor and Imaging Center.

10.1021/bc060265o CCC: $37.00 © 2007 American Chemical Society
Published on Web 04/14/2007

ester Cy3 (synthesized in-house) were dissolved in 1 mL DMF, incubated at room temperature on a rotating rack, and followed by HPLC. Reaction progression ceased after 6 days resulting in a 50% yield. The reaction mixture was diluted with 6 mL ethyl acetate and the precipitate collected by centrifugation and redissolved in 1 mL of 20 mM potassium acetate in methanol. This process was repeated two additional times after which the precipitated material was vacuum-dried at 50 °C for 3 h followed by storage in a desiccator. The dried reaction material was dissolved in 5 mL ddH_2O, loaded on a 10 mL C-18 column, and washed with 20 mL ddH_2O wash. A 2.5% step gradient in acetonitrile was performed (10 mL/step). The 10% acetonitrile step was increased to 20 mL total to collect the band of interest. Appropriate fractions were combined and then dried by rotary evaporation. The bisCy3−cystine product (Figure 1, species I) was shown to be ∼98% pure by HPLC and the structure confirmed by ^{1}H NMR and MALDI mass spectroscopy.

BisCy3−cystine (4.6 mg) and TSTU (3.1 mg) were dissolved in 500 μL DMF containing 0.1% DIPEA. The activation reaction was protected from light and proceeded for 3 days at room temperature with stirring. The dye was precipitated with ethyl acetate, vacuum-dried as above, and stored in a desiccator. Approximately 2.8 mg of activated bisCy3−cystine was recovered (∼60% yield).

Recombinant bovine lung aprotinin (23.4 mg, Sigma) was dissolved in 400 μL deionized formamide + 0.1% DIPEA, added to the activated bisCy3−cystine, and transferred to a round-bottom flask containing a stir bar. The reaction proceeded for 48 h at room temperature, under argon, and protected from light. Progress of the coupling reaction was monitored by the incorporation of Cy3 label into the aprotinin band by SDS-PAGE (Figure 1, species II). The reaction mixture was diluted with 500 μL 200 mM HEPES, pH 7.0, 240 μL 1 mM TCEP, and 660 μL ddH_2O. Disulfide concentration was estimated by the Cy3 concentration (ϵ_{552} = 150 000). EDTA was added to a final concentration of 2 mM. Disulfide reduction was performed for 2 h at room temperature with stirring. MPBH was added to the flask at a 6-fold excess over Cy3 (ϵ_{552} = 150 000) and reacted for an additional 3 h. The product was purified on a 10 mL column containing BioGel P-4 prepared in 20 mM HEPES, 150 mM NaCl, pH 7.4 (Figure 1, species III). Fractions of interest were concentrated using Centricon C3 centrifugation tubes (MWCO ≈ 3000 Da). The final retentate was lyophilized.

Equal volumes of 18.7 mg/mL human fibrinogen and 20 mM sodium *meta*-periodate were mixed and reacted for 30 min at room temperature. The reaction was dialyzed overnight against 20 mM HEPES, pH 7.4, using Pierce Slide-A-Lyzer kits (3500 MWCO). Cy3−cysteine−aprotinin−MPBH was added to the fibrinogen at a 7:1 molar labeling ratio and reacted for 2 h at room temperature followed by separation on a BioGel P-30 size exclusion column equilibrated with 20 mM HEPES, 150 mM NaCl, pH 7.4 (Figure 1, species IV). Fractions were combined, aliquoted, and frozen at −80 °C. Fibrinogen concentration as measured by the Coomassie Plus Assay Kit (Pierce) was 1 mg/mL (2.94 μM), and Cy3 concentration (ϵ_{552} = 150 000) was 14 μM. Since one aprotinin is expected for every Cy3, the theoretical aprotinin concentration was also 14 μM (91 μg/mL), giving an aprotinin/fibrinogen labeling ratio of 4.8:1.

In Vitro Degradation Assay. Microplate-based experiments were similar to those performed by Wolberg et al. (*23*). Solution A contained human fibrinogen, either soluble or fibrinogen-conjugated aprotinin, and HEPES buffer. Solution B contained thrombin (Enzyme Research Labs, South Bend, IN), plasmin (Haematologic Technologies, Inc., Essex Junction, VT), calcium chloride (Sigma), and deionized water. Solutions A and B were mixed directly in the 96 well plate to a total volume of 200 μL/well. The final concentrations were as follows: 1 mg/mL fibrinogen, 5 nM thrombin, 100 nM plasmin, and 5 mM calcium chloride in 20 mM HEPES, 150 mM NaCl, pH 7.4. The concentration of aprotinin varied from 5 nM to 50 nM. Fibrinogen added as a result of the conjugated molecule was less than 0.1% of the gel fibrinogen concentration. Gel absorbance was followed over time at 405 nm and 37 °C at 2.5 min intervals using a Wallac Microplate Reader (Gaithersburg, MD).

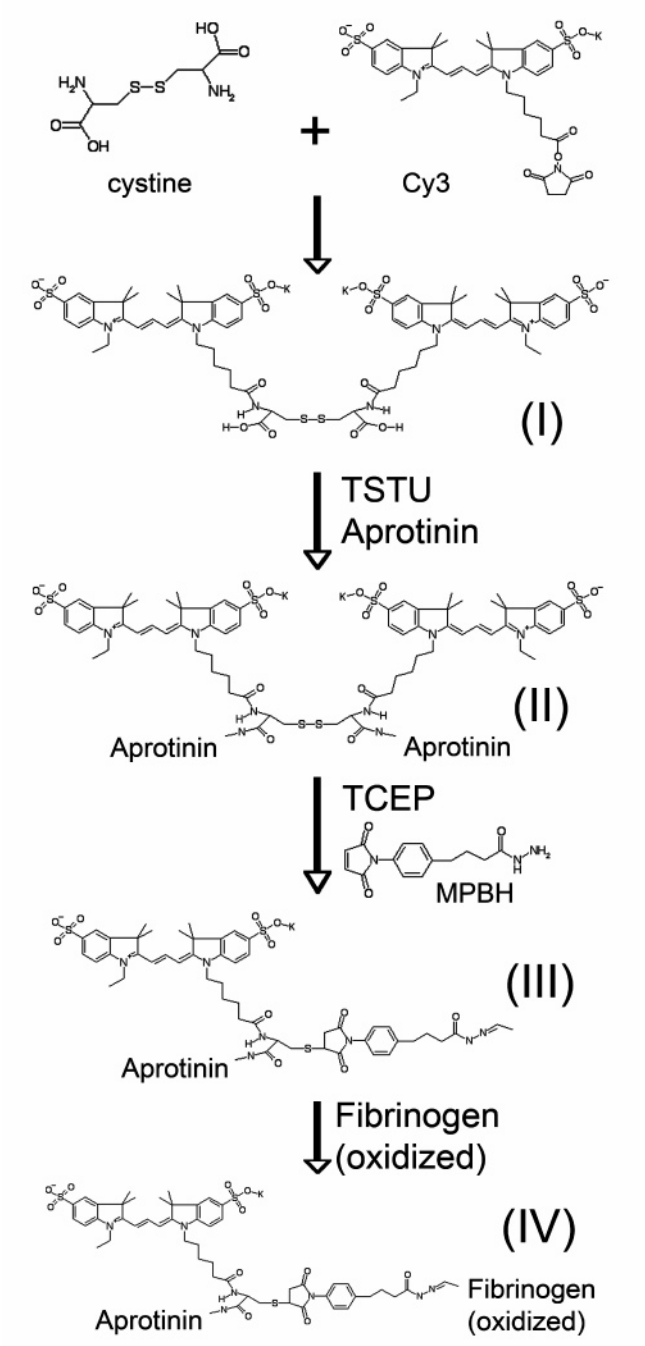


Figure 1. Schematic of aprotinin-fibrinogen conjugate. Cystine was reacted with activated Cy3 dye in DMF and reverse phase column purified. The bisCy3−cystine product (species I) was reacted with TSTU in DMF + 0.1% DIPEA to activate the cystine's carboxylic acid groups. Aprotinin was dissolved in formamide + 0.1% DIPEA and added to the activated bisCy3−cystine compound (species II). In HEPES-buffered saline (HBSS) TCEP was added to species II to reduce cystine disulfide bonds and was followed by the addition of MPBH heterobifunctional crosslinker. The product (species III) was purified by size exclusion chromatography and lyophilized. The product was added to periodate activated fibrinogen to produce the final aprotinin−fibrinogen conjugate (species IV) which was purified by size exclusion using HBSS.

Ex Ovo Chick CAM Assay. Fibrin gels were made in 8 mm × 1 mm cylindrical molds. Final concentrations within the gel are 17 mg/mL fibrinogen, 10 ng/mL fibroblast growth factor-2 (FGF-2) (PeproTech, Inc., Rocky Hill, NJ), 61.7 nM thrombin, and 1 μg/mL of either soluble aprotinin or aprotinin conjugated to fibrinogen. Additional fibrinogen levels due to aprotinin−fibrinogen conjugate addition were less than 0.1% of final fibrinogen levels. White Leghorn eggs were purchased from a local farm and incubated at 38 °C and 70% humidity in a rotating circulated air incubator (G.Q.F. Manufacturing Co., Savanna, GA). On day 3, eggs were cracked into Petri dishes containing 4 mL Dulbecco's Modified Eagles Medium (DMEM) (Gibco, Carslbad, CA) and placed in a 37 °C incubator (Forma Scientific, Waltham, MA). Fibrin gels were placed on the CAM of 10 day old embryos. One gel of each type (soluble and conjugated aprotinin) was placed on each embryo. Fibrin gel images were acquired every 24 h using a M2BIO stereomicroscope (Kramer Scientific, Valley Cottage, NY) with a 1.6× objective (0.075 NA), 0.6× zoom, a Retiga Exi cooled CCD camera (QImaging, Burnaby, BC, Canada), and *QED In Vivo* imaging software v 2.0.39 (Media Cybernetics, Silver Springs, MD). Fibrin gel diameters were measured (in pixels) using *Image J* software (NIH, Bethesda, MD). The relative areas of gels containing conjugated aprotinin to soluble aprotinin were calculated for 12 sets of gels and are reported as the mean ± SEM at each day post-placement on the chick CAM. Using *SYSTAT 9* software (Point Richmond, CA), means were compared using a one-way analysis of variance followed by Tukey's post hoc test. $P \leq 0.05$ was considered significant.

Fluorescence Visualization/Histological Processing. Poly(ethylene glycol)−amino conjugated 705 nm emitting quantum dots (QDs) were sonicated for 10 min prior to injection. Superficial CAM veins were injected with 20−25 μL QDs using an aspirator tube assembly (Sigma) and borosilicate capillaries (Sutter Instruments, Novato, CA) that were pulled into microneedles using a model P-87 micropipette puller (Sutter Instruments, Novato, CA).

After QD injection, the fibrin construct and surrounding CAM were excised and fixed in 1% glutaraldehyde and 3% paraformaldehyde (Electron Microscopy Sciences, Hatfield, PA) in PBS for 3 h at room temperature followed by three 5 min washes in PBS. Samples were sectioned in the perpendicular plane in relation to their original orientation on the CAM at 300 μm thicknesses using a vibratome VT 1000S (Leica, Wetzlar, Germany). Each resulting section is a cross section containing the fibrin construct and underlying CAM. Sections were mounted on glass microslides including a coverslip and imaged for QD fluorescence using a Zeiss Axioplan 2 (Thornwood, NY) epifluorescence microscope with a 2.5× objective (0.12NA), Zeiss AxioCam MRm CCD camera, and Zeiss *AxioVision* acquisition software v 4.3. Cy3 and 705 nm QDs were imaged using Ex:Em 540/25:620/60 and 460spuv:705/40 filter sets (Chroma, Rockingham, VT), respectively.

Vibratomed sections of interest were prepared for transmission electron microscopy (TEM) analysis. The section was washed with three changes of PBS followed by fixation with 1% OsO_4 buffered with PBS for 30 min at room temperature. After osmium fixation, sections were washed with three changes of dH_2O and dehydrated with an ascending series of ethanol (50%, 70%, 80%, 90%, and 100%). Propylene oxide was used as a transitional solvent, and the specimens infiltrated with LR White (London Resin Company, Reading, Berkshire, England). The LR White was polymerized at 60 °C for 48 h. Thin (100 nm) sections were cut using a diamond knife on a Reichert-Jung Ultracut E ulatramicrotome (Leica, Wetzlar, Germany), picked up using copper grids, and stained with uranyl acetate and lead citrate. The grids were viewed on a Hitachi H-7100 transmission electron microscope (Pleasanton, CA) operating at 50 kV. Digital images were obtained using an AMT Advantage 10 CCD Camera System (Advanced Microscopy Techniques Corporation, Danvers, MA) and NIH *Image* software.

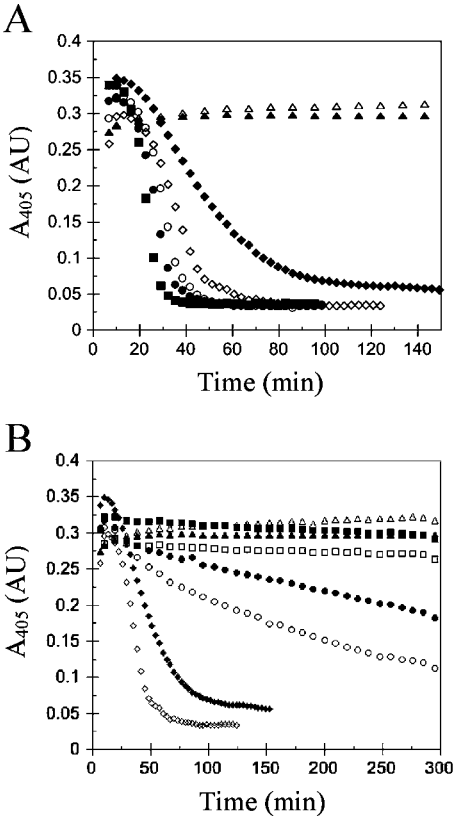


Figure 2. Plasmin degradation of fibrin gels. Fibrin gels containing indicated levels of aprotinin and plasmin in 96 well plates were followed over time by absorbance at 405 nm. The experiment was performed in triplicate. A representative data set was split into two panels for clarity. A: Fibrin gels (1 mg/mL) subjected to 100 nM plasmin containing 5 (circles) and 10 (diamonds) nM soluble (● and ◆) or fibrinogen-conjugated (○ and ◇) aprotinin. Fibrin (▲) and aprotinin-conjugated (30 nM) fibrin (△) controls were not subjected to plasmin, and the plasmin control (■) contained no aprotinin. B: Data from the same experiment as in panel A showing fibrin gels subjected to 100 nM plasmin containing 10 (diamonds), 30 (circles), and 50 (squares) nM soluble (◆, ●, and ■) or fibrinogen-conjugated (◇, ○, and □) aprotinin. The same fibrin controls from A are also shown.

Scanning Electron Microscopy. Gels were made in the same manner as for the ex ovo CAM assay: 17 mg/mL fibrinogen, 10 ng/mL FGF-2, and 61.7 nM thrombin containing 0, 5, 10, 30, 50, and 150 nM of either soluble aprotinin or aprotinin conjugated to fibrinogen. Gels were fixed overnight in 1% glutaraldehyde and 3% paraformaldehyde in PBS followed by three 5 min washes in PBS. Samples were then fixed in 1% OsO_4 buffered with PBS. The OsO_4 was removed with three 5 min washes with dH_2O, followed by dehydration in an ascending series of ethanol (50%, 70%, 80%, 90%, and three changes of 100%). The samples were held in each ethanol wash for 10 min and then held in 100% ethanol overnight. Samples were dried in a Pelco CPD2 critical point dryer (Clovis, CA) and using CO_2 at 1200 psi and 42 °C. Dried samples were attached to SEM stubs using double-sided tape and coated with gold using a Pelco SC-6 sputter coater. Specimens were examined using a Hitachi 2460N scanning electron microscope (Pleasanton, CA). Digital images were obtained using *Quartz PCI* software (Vancouver, BC, Canada).

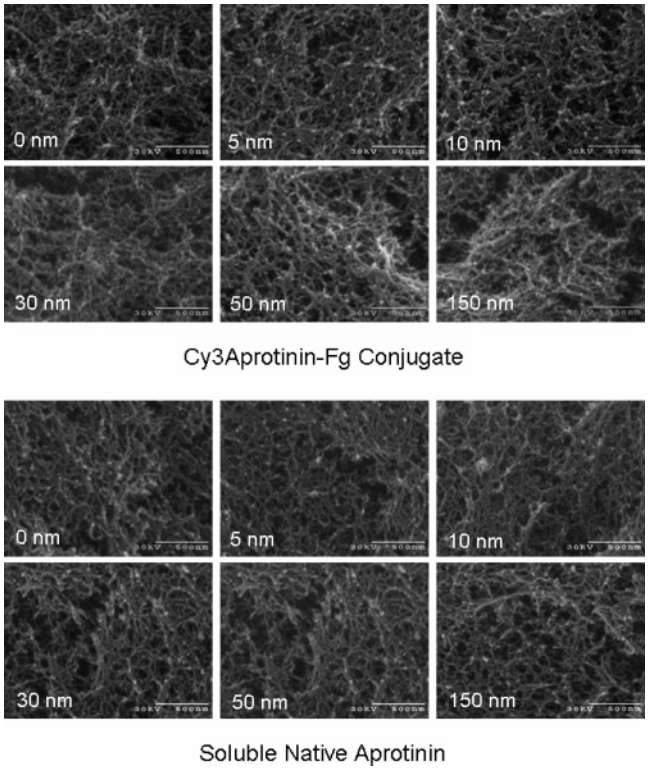


Figure 3. Aprotinin does not affect fibrin structure. 17 mg/mL fibrin gels containing 0, 5, 10, 30, 50, and 150 nM of either fibrinogen-conjugated aprotinin (top panel) or soluble aprotinin (bottom panel) were analyzed by SEM. No significant differences were seen within a sample group or between the soluble aprotinin-containing gels and the conjugated aprotinin-containing gels.

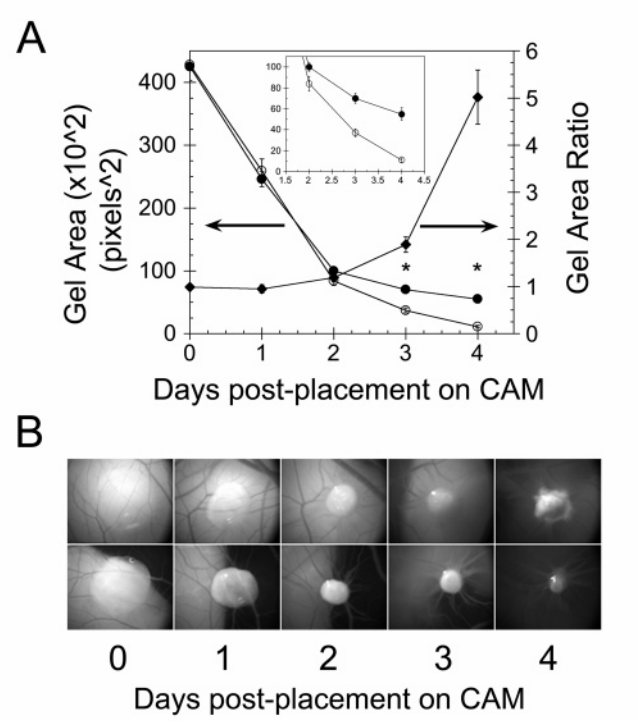


Figure 4. Degradation of conjugated and nonconjugated aprotinin fibrin in the chick CAM assay. A: Fibrin gels containing 10 ng/mL FGF-2 and either 1 μg/mL conjugated or nonconjugated aprotinin were placed on the CAM of 10 day old embryos. Images of the gels were obtained over 4 days using bright field microscopy, and gel areas were calculated using *Image J* software. Data represent the average area over time ± SEM ($n = 12$ each, aprotinin-conjugated and nonconjugated gels). B: A representative image set of the data shown in panel A. Images in the top and bottom rows are of gels containing conjugated and nonconjugated aprotinin, respectively. Asterisks indicate statistical significance ($P \leq 0.05$).

RESULTS

Fibrin concentrations used in these experiments were on the same order as those used in clinical fibrin glues (*22*, *24*). These constructs, however, typically degraded within 5 days post-placement on the CAM. We hypothesized that blood vessels did not invade the fibrin because it was degraded too quickly. Aprotinin was added to our constructs to slow degradation but due to its small size quickly diffused out of the construct and no longer conferred protection. In fact, constructs containing no aprotinin demonstrated the same residence time on the CAM as constructs containing 1 μg/mL of aprotinin, a typical concentration used in clinical settings (data not shown). In an effort to retain plasmin inhibition, and thus inhibit fibrin degradation, we chemically conjugated aprotinin to fibrinogen (Figure 1).

Aprotinin was conjugated to fibrinogen using a cysteine-based trifunctional cross-linker (Figure 1). Cy3 was co-conjugated as a reporter of construct localization as well as a tool for quantitating conjugated aprotinin levels. To minimize possible interference with aprotinin activity, the Cy3 was not linked directly to the aprotinin. Similarly, aprotinin's N-terminus was chosen as the cysteine conjugation site due to its location opposite the plasmin binding site. The conjugate molecule was linked to fibrinogen's glycosylation sites for two reasons: (*1*) these sites serve to limit the number of linkages that can occur and (*2*) the antenna-like structure of the sugar moieties may possibly serve to better display the aprotinin to "intercept" plasmin. At this point, the construct has been successfully synthesized three out of five times. For this work, the construct aprotinin/fibrinogen molar ratio was approximately 5:1.

The aprotinin-conjugated fibrinogen was first tested in an in vitro microplate absorbance assay. Absorbance-based assays have been extensively used to study fibrin structure, gelation, and fibrinolysis (*23*, *25*, *26*). Fibrin gels containing plasmin were made with varying levels of soluble aprotinin and compared to gels containing conjugated aprotinin to theoretically equal levels. Variable aprotinin addition, both soluble and conjugated, was able to tune fibrin degradation times from just a few minutes to many hours (Figure 2A,B). The data also show that at equal concentrations the immobilized aprotinin has a lower (approximately 2-fold) but comparable activity to its soluble-form counterpart. As controls, cysteine, Cy3, and the MPBH cross-linker were assayed at concentrations equivalent to the 30 nM conjugated aprotinin test case. None were found to significantly inhibit degradation over the plasmin-only control (data not shown).

The effect of soluble vs conjugated aprotinin on fibrin structure was further examined by scanning electron microscopy (Figure 3). 17 mg/mL gels containing the indicated aprotinin levels were examined, and aprotinin levels were not shown to significantly alter fibrin structure. More importantly, there was no difference seen between soluble and conjugated aprotinin-containing samples. Therefore, these results would indicate that the effects of the conjugated aprotinin were due to aprotinin's anti-proteolytic activity rather than an indirect effect due to fibrin structural changes.

We next tested the aprotinin-conjugated fibrinogen in an in vivo setting—the chick CAM assay. Fibrin gels containing either soluble or conjugated aprotinin at 1 μg/mL (154 nM), a concentration typically used in clinical application, were placed on the CAMs of ten day old embryos. FGF-2 was added to induce an angiogenic response and along with it fibrin degradation. Images of the gels were acquired every 24 h for 4 days

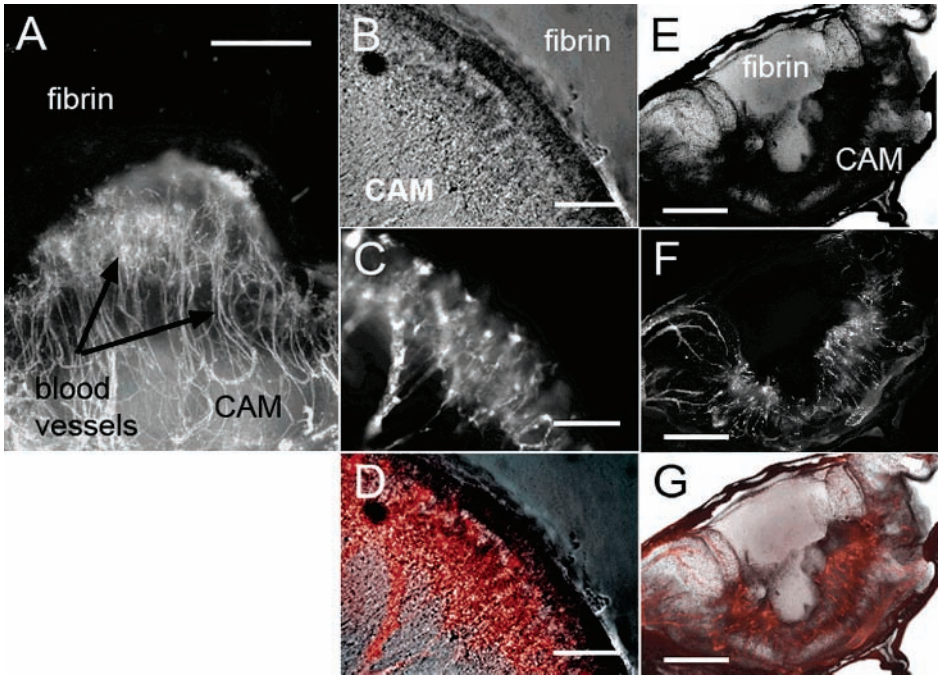


Figure 5. Blood vessel response to fibrin containing soluble aprotinin. Fibrin gels containing 10 ng/mL FGF-2 and 154 nM aprotinin were placed on the CAM of 10-day old embryos. Three (A−D) or four (E−G) days post-placement 705 nm emitting quantum dots were intravitally injected. Fibrin and connected CAM were excised, fixed in 3% paraformaldehyde in PBS, vibratomed to 300 μm thickness, and imaged on a Zeiss Axioplan 2 epifluorescence microscope. A: Fibrin and underlying CAM showing blood vessel fluorescence. B−D: Interfacial area between CAM and fibrin construct. B,C: Bright field (E) and QD-labeled blood vessel fluorescence (F) images. G: Overlay of images in E and F with QD fluorescence artificially colored red. Overlay shows blood vessels follow invasion front. E−G: Bright field (D) and QD-labeled blood vessel fluorescence (E). F: Overlay of images in D and E with QD fluorescence artificially colored red. Overlay shows blood vessels do not invade the construct. Scale bars are 200 μm in A−D and 50 μm in E−G.

using a stereomicroscope. Because we could not determine fibrin volumes from these images, we estimated fibrin size from measured fibrin areas (Figure 4).

Two distinct modes of area loss are seen. Gel area is greatly reduced during the first 48 h where CAM adhesion and CAM-mediated fibrin gel contraction take place. Both sets of fibrin gels were affected equally. After the initial 48 h, degradation becomes the driving force. At this point, the immobilized aprotinin gels degraded more slowly than the soluble aprotinin gels, and after 4 days were approximately 5 times larger than fibrin-containing soluble aprotinin. Unlike fibrin-containing immobilized aprotinin, by day 5 soluble aprotinin gels were completely degraded.

Finally, we examined the blood vessel response to fibrin gels containing either soluble or conjugated aprotinin. As in the time course, in vivo experiment fibrin gels (17 mg/mL) containing FGF-2 and either soluble or conjugated aprotinin were placed on the CAMs of ten day old chick embryos. Three or four days later, 705 nm emission quantum dots were intravitally injected, and the fibrin and connected CAM were excised, fixed, and vibratomed as described in the Materials and Methods. Fibrin gels containing soluble aprotinin demonstrated no direct blood vessel invasion into the construct (Figure 5). At three days post-placement on the CAM, blood vessels can be seen moving vertically toward the fibrin and then becoming a dense network of vessels at the fibrin interface (Figure 5A). This is most likely due to the effect of FGF-2 being released from the fibrin/CAM interface as the fibrin is degraded. A closeup of the interfacial region in Figure 5A shows that a non-vascularized cellularized zone precedes vascular invasion into the fibrin construct (Figure 5B−D). Additionally, examination of gels at four days post-placement, a time when the gels are almost completely degraded, shows a lack of vessel invasion (Figure 5E−G).

Fibrin gels containing 1 μg/mL conjugated aprotinin were also examined in the same manner. In these experiments, we have the added benefit of a fluorescent fibrin marker, Cy3, to visualize its localization. Samples examined four days post-placement on the CAM showed large-scale vessel invasion into the fibrin construct as visualized by the overlap of blood vessel and fibrin label fluorescence (Figure 6A−C, D−F). Although these samples still maintain substantial amounts of fibrin (Figure 4B), the more slowly degrading fibrin allowed for fibrin degradation and remodeling without complete destruction of the original construct. Interestingly, the rate of fibrin degradation may be important for blood vessel invasion, since areas of low fibrinolysis demonstrated poorer vascularization (Figure 6D,E arrows).

Closer examination of these samples by TEM shows the fibrin degradation and replacement by newly forming CAM-derived tissue. Blood vessels were confirmed by TEM analysis (Figure 6G); however, most of the vessels examined failed to have recruited pericytes or smooth muscle cells, an indication of their immaturity. Additionally, we observed multiple cell types as well as the production of new collagen fibers (Figure 6H,I).

DISCUSSION

In this work, we created a novel synthesis strategy for protein conjugation. This method is somewhat complex and not without its difficulties. The initial linkage of cysteine to Cy3 is quite straightforward (Figure 1, species I). On the other hand, the reaction to create species II (Figure 1) was a slow process and suffered from lower yields. Also, monitoring of the reaction by SDS-PAGE was difficult due to the small molecular weight differences between the reaction products. Most importantly, the synthesis was troubled by a lack of confirmation of aprotinin conjugation with MPBH. The two reported synthesis failures were due to this problem. Current work is focusing on improving synthesis speed and efficiency with positive results.

In the in vitro assay, the conjugated aprotinin had comparable activity to the soluble form (Figure 2). Due to the high aprotinin

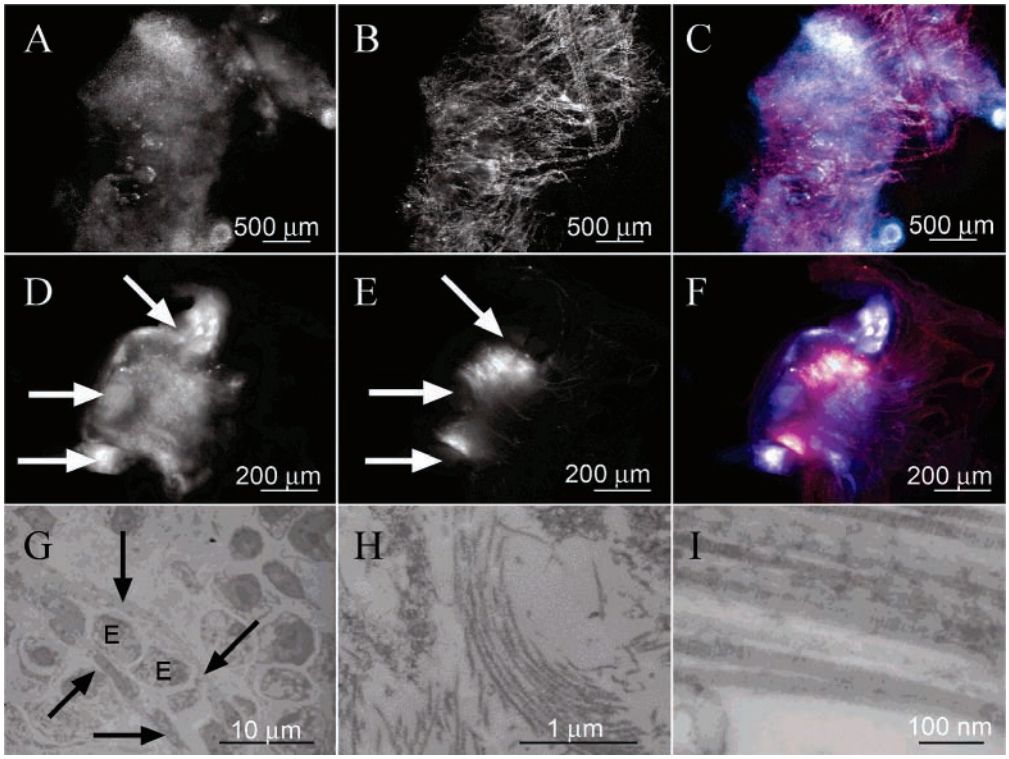


Figure 6. Blood vessel response to fibrin containing conjugated aprotinin. Fibrin gels containing 10 ng/mL FGF-2 and 154 nM conjugated aprotinin were placed on the CAM of 10 day old embryos. Four days post-placement, 705 nm emitting quantum dots were intravitally injected. Fibrin and connected CAM were excised, fixed in 3% paraformaldehyde in PBS, vibratomed to 300 μm thickness, and imaged on the Zeiss Axioplan 2. Cy3 fibrin label (A,C,D,F) and QD blood vessel label (B,C,E,F) fluorescence images of two sections from individual fibrin constructs (A−C and D−F). Fluorescence overlays (C,F) show the blood vessels (red) have invaded the fibrin construct (blue). Sections shown are derived from the central region of each sample. Arrows in D,E indicate higher-density fibrin areas. The sample shown in D−F was processed for TEM analysis revealing immature blood vessels (G) and collagen fiber production (H,I). G: Arrows indicate capillary endothelial cells. Erythrocytes (E) are seen within the vessel. H: Collagen fiber production and remodeling. I: The banding pattern distinctive of collagen fibers is clearly seen.

labeling ratio, there was only one aprotinin-conjugated fibrinogen for every 50 or 150 unconjugated fibrinogen for the 10 nM and 30 nM aprotinin gels, respectively. It is quite interesting that highly localized and immobilized aprotinin inhibited plasmin with similar efficiency as freely diffusing aprotinin. The small difference in conjugated and soluble aprotinin activity could be due to a number of factors including steric hindrance (i.e., burial of the immobilized aprotinin within fibrin fibrils), inactivation during synthesis, or the inability of the immobilized aprotinins to uniformly protect the fibrin. We are currently examining methods to address the contributions of these factors to conjugated aprotinin activity.

Experiments performed in vitro indicate that not only can varying levels of aprotinin-conjugated fibrinogen control degradation rate but also the conjugated aprotinin does not significantly alter the properties of the gel. Microplate assays demonstrate that gelation and gel absorbance (a measure of fibrin structure) is not significantly impacted by the presence of conjugated aprotinin over soluble aprotinin (Figure 2). Also, SEM analysis shows that, indeed, the fibrillar architecture of gels containing soluble or conjugated aprotinin was not significantly different (Figure 3). SEM-analyzed samples were those of identical composition to the in vivo assay. Lower concentrations, such as those tested in the in vitro microplate assay, were not able to be tested due to the fragile nature of those gels and their collapse upon dehydration during SEM sample preparation.

The ratio of aprotinin to fibrinogen molecules is expected to impact cell mediated fibrin degradation. At 1 μg/mL aprotinin with a 4.8:1 aprotinin/fibrinogen labeling ratio, there was only 1 conjugated fibrinogen molecule per 1600 native fibrinogens. These small regions of protease protection within the larger gel space resulted in non-homogeneous globular degradation fragments of fibrin. This can be seen to some degree with the large and small globular patterns of Cy3-fibrin fluorescence in the images in Figures 4 and 6. Lower aprotinin labeling ratios would be expected to create a more homogeneous degradation pattern whose affect on the CAM response has yet to be determined. Thus, varying the inhibitor level or its distribution may represent a method for modulating regenerative responses within tissue engineering applications.

There are differences in the degradation times seen in Figures 2 and 4. Low fibrin concentrations (1 mg/mL) were utilized for the in vitro experiments due to the need to keep low gel absorbances. High concentrations (17 mg/mL) were used for the ex ovo CAM experiments in order to obtain sufficient residence times. The in vitro tests were purely to demonstrate proof of concept and were not meant to be directly translatable into the CAM experiment. Besides, the presence of cells, additional proteases, and other factors make prediction of degradation time a priori impossible. Higher aprotinin concentrations were used in the ex ovo experiments to be comparable to aprotinin levels used in clinical fibrin applications. However, these results do show that the conjugated aprotinin works over a range of fibrin concentrations.

The conjugated aprotinin has at least two potential applications. Because tissue regeneration occurs over different time frames for different tissues, the conjugated aprotinin could be used to optimally tune fibrin degradation over a particular time frame. Additionally, complex constructs could be created with solid free-form fabrication (SFF) (*27*) techniques to specifically control degradation within the construct. This may possibly allow for architectural control of the regenerating tissue, all with the use of fibrin.

The conjugated aprotinin might also be used for temporal growth factor delivery. For example, Richardson et al. (*28*) showed that delivery of vascular endothelial growth factor (VEGF) followed by platelet-derived growth factor (PDGF-BB) from synthetic constructs improved angiogenesis when compared to delivering either growth factor alone or simultaneously. If aprotinin-conjugated fibrin can be patterned (by SFF techniques for example) to degrade more slowly than neighboring, unaltered fibrin, then it is possible that growth factors bound to the aprotinin-conjugated fibrin would be seen by cells after growth factors within nonconjugated fibrin. We tended to see immature vessels within the fibrin construct when using only FGF-2 (Figure 6G); therefore, temporal delivery of PDGF-BB may lead to improved vessel maturity, similar to that seen by Richardson et al. (*28*).

We have presented an approach to engineer fibrin degradation within fibrin constructs, which allows us to better tune degradation rates independent of simply increasing fibrin density, as this may be undesireable or impossible for the particular application. Control remains critical as the presence of too much aprotinin may have deleterious effects in fibrin-glue applications (*29*). The ability to control fibrin degradation, the possibility of temporal growth factor delivery, and/or the manipulation of structural features within a constant fibrin density construct (*27*) is quite intriguing and worth further examination.

ACKNOWLEDGMENT

This work was supported by grants from the National Science Foundation (CTS-0210238), National Institutes of Health (1 R01 EB00 364-01 and 1 T32 EB00424-03), and Pennsylvania Infrastructure Technology Alliance. The authors would like to thank Joe Suhan at Carnegie Mellon for his SEM and TEM work and Marcel Bruchez at Quantum Dot Corporation (Hayward, CA) for their generous gift of quantum dots.

LITERATURE CITED

(1) Clark, R. A. (2001) Fibrin and wound healing. *Ann. N. Y. Acad. Sci. 936*, 355−67.
(2) Bunce, L. A., Sporn, L. A., and Francis, C. W. (1992) Endothelial cell spreading on fibrin requires fibrinopeptide B cleavage and amino acid residues 15−42 of the beta chain. *J. Clin. Invest. 89*, 842−50.
(3) Sporn, L. A., Bunce, L. A., and Francis, C. W. (1995) Cell proliferation on fibrin: modulation by fibrinopeptide cleavage. *Blood 86*, 1802−10.
(4) Sahni, A., Odrljin, T., and Francis, C. W. (1998) Binding of basic fibroblast growth factor to fibrinogen and fibrin. *J. Biol. Chem. 273*, 7554−9.
(5) Sahni, A., Sporn, L. A., and Francis, C. W. (1999) Potentiation of endothelial cell proliferation by fibrin(ogen)-bound fibroblast growth factor-2. *J. Biol. Chem. 274*, 14936−41.
(6) Meh, D. A., Mosesson, M. W., DiOrio, J. P., Siebenlist, K. R., Hernandez, I., Amrani, D. L., and Stojanovich, L. (2001) Disintegration and reorganization of fibrin networks during tissue-type plasminogen activator-induced clot lysis. *Blood Coagulation Fibrinolysis 12*, 627−37.
(7) Sierra, D. H. (1993) Fibrin sealant adhesive systems: a review of their chemistry, material properties and clinical applications. *J. Biomater. Appl. 7*, 309−52.
(8) Walker, J. B., and Nesheim, M. E. (1999) The molecular weights, mass distribution, chain composition, and structure of soluble fibrin degradation products released from a fibrin clot perfused with plasmin. *J. Biol. Chem. 274*, 5201−12.
(9) Borges, J., Mueller, M. C., Padron, N. T., Tegtmeier, F., Lang, E. M., and Stark, G. B. (2003) Engineered adipose tissue supplied by functional microvessels. *Tissue Eng. 9*, 1263−70.
(10) Borges, J., Tegtmeier, F. T., Padron, N. T., Mueller, M. C., Lang, E. M., and Stark, G. B. (2003) Chorioallantoic membrane angiogenesis model for tissue engineering: a new twist on a classic model. *Tissue Eng. 9*, 441−50.
(11) Brey, E. M., King, T. W., Johnston, C., McIntire, L. V., Reece, G. P., and Patrick, C. W., Jr. (2002) A technique for quantitative three-dimensional analysis of microvascular structure. *Microvasc. Res. 63*, 279−94.
(12) Clark, R. A. (2003) Fibrin glue for wound repair: facts and fancy. *Thromb. Haemostasis 90*, 1003−6.
(13) Cummings, C. L., Gawlitta, D., Nerem, R. M., and Stegemann, J. P. (2004) Properties of engineered vascular constructs made from collagen, fibrin, and collagen-fibrin mixtures. *Biomaterials 25*, 3699−706.
(14) Hokugo, A., Kubo, Y., Takahashi, Y., Fukuda, A., Horiuchi, K., Mushimoto, K., Morita, S., and Tabata, Y. (2004) Prefabrication of vascularized bone graft using guided bone regeneration. *Tissue Eng. 10*, 978−86.
(15) Sakiyama-Elbert, S. E., and Hubbell, J. A. (2000) Development of fibrin derivatives for controlled release of heparin-binding growth factors. *J. Controlled Release 65*, 389−402.
(16) Urech, L., Bittermann, A. G., Hubbell, J. A., and Hall, H. (2005) Mechanical properties, proteolytic degradability and biological modifications affect angiogenic process extension into native and modified fibrin matrices in vitro. *Biomaterials 26*, 1369−79.
(17) Wong, C., Inman, E., Spaethe, R., and Helgerson, S. (2003) Fibrin-based biomaterials to deliver human growth factors. *Thromb. Haemostasis 89*, 573−82.
(18) Francis, C. W., and Marder, V. J. (1986) Concepts of clot lysis. *Annu. Rev. Med. 37*, 187−204.
(19) Turner, R. B., Liu, L., Sazonova, I. Y., and Reed, G. L. (2002) Structural elements that govern the substrate specificity of the clot-dissolving enzyme plasmin. *J. Biol. Chem. 277*, 33068−74.
(20) Fritz, H., and Wunderer, G. (1983) Biochemistry and applications of aprotinin, the kallikrein inhibitor from bovine organs. *Arzneimittelforschung 33*, 479−94.
(21) Le Guehennec, L., Layrolle, P., and Daculsi, G. (2004) A review of bioceramics and fibrin sealant. *Eur. Cell Mater. 8*, 1−11; discussion 1−11.
(22) Marx, G., and Mou, X. (2002) Characterizing fibrin glue performance as modulated by heparin, aprotinin, and factor XIII. *J. Lab. Clin. Med. 140*, 152−60.
(23) Wolberg, A. S., Gabriel, D. A., and Hoffman, M. (2002) Analyzing fibrin clot structure using a microplate reader. *Blood Coagulation Fibrinolysis 13*, 533−9.
(24) Byrne, D. J., Hardy, J., Wood, R. A., McIntosh, R., and Cuschieri, A. (1991) Effect of fibrin glues on the mechanical properties of healing wounds. *Br. J. Surg. 78*, 841−3.
(25) Carr, M. E., and Gabriel, D. A. (1980) The effect of dextran 70 on the structure of plasma-derived fibrin gels. *J. Lab. Clin. Med. 96*, 985−93.
(26) Shah, G. A., Nair, C. H., and Dhall, D. P. (1987) Comparison of fibrin networks in plasma and fibrinogen solution. *Thromb. Res. 45*, 257−64.
(27) Weiss, L. E., Amon, C. H., Finger, S., Miller, E. D., Romero, D., Verdinelli, I., Walker, L. M., and Campbell, P. G. (2005) Bayesian computer-aided experimental design of heterogenous scaffolds for tissue engineering. *Comput.-Aided Des. 37*, 1127−1139.
(28) Richardson, T. P., Peters, M. C., Ennett, A. B., and Mooney, D. J. (2001) Polymeric system for dual growth factor delivery. *Nat. Biotechnol. 19*, 1029−34.
(29) Krishnan, L. K., Vijayan Lal, A., Uma Shankar, P. R., and Mohanty, M. (2003) Fibrinolysis inhibitors adversely affect remodeling of tissues sealed with fibrin glue. *Biomaterials 24*, 321−7.

BC060265O

Albumin-Binding Prodrugs of Camptothecin and Doxorubicin with an Ala-Leu-Ala-Leu-Linker That Are Cleaved by Cathepsin B: Synthesis and Antitumor Efficacy

Björn Schmid,[†,§] Da-Eun Chung,[†,§] André Warnecke,[†] Iduna Fichtner,[‡] and Felix Kratz*[,†]

Tumor Biology Center, Breisacher Strasse 117, 79106 Freiburg, Germany, and Max-Delbrück Centrum, Robert-Rössle-Strasse 10, 13122 Berlin, Germany. Received September 5, 2006; Revised Manuscript Received November 20, 2006

We have recently validated a macromolecular prodrug strategy for improved cancer chemotherapy based on two features: (a) rapid and selective binding of thiol-reactive prodrugs to the cysteine-34 position of endogenous albumin and (b) acid-sensitive promoted or enzymatic release of the drug at the tumor site [Kratz, F., Warnecke, A., Scheuemann, K., Stockmar, C., Schwab, J., Lazar, P., Druckes, P., Esser, N., Drevs, J., Rognan, D., Bissantz, C., Hinderling, C., Folkers, G., Fichtner, I., and Unger, C. (2002) *J. Med. Chem. 45*, 5523−33]. In the present work, we developed water-soluble camptothecin (CPT) and doxorubicin (DOXO) prodrugs that incorporate the peptide linker Ala-Leu-Ala-Leu that serves as a substrate for the tumor-associated protease, cathepsin B, which is overexpressed in several solid tumors. Consequently, two albumin-binding prodrugs were synthesized [EMC-Arg-Arg-Ala-Leu-Ala-Leu-Ala-CPT (**1**) and EMC-Arg-Arg-Ala-Leu-Ala-Leu-DOXO (**2**) (EMC = 6-maleimidocaproic acid)]. Both prodrugs exhibited excellent water-solubility and bound rapidly and selectively to the cysteine-34 position of endogenous albumin. Further in vitro studies showed that the albumin-bound form of the prodrugs was cleaved specifically by cathepsin B as well as in human tumor homogenates. Major cleavage products were CPT−peptide derivatives and CPT for the CPT prodrug and H-Leu-Ala-Leu-DOXO, H-Leu-DOXO, and DOXO for the doxorubicin prodrug. In vivo, **1** was superior to free camptothecin in an HT-29 human colon xenograft model; the antitumor efficacy of prodrug **2** was comparable to that of free doxorubicin in the M-3366 mamma carcinoma xenograft model at equimolar doses.

INTRODUCTION

Both anticancer agents camptothecin (CPT) and doxorubicin (DOXO) are DNA-damaging drugs, which act by inhibiting the progression of the enzymes topoisomerase I (CPT) and II (DOXO), which unwind DNA for transcription. Doxorubicin is one of the most active antineoplastic agents developed to date and shows a broad spectrum of antitumor efficacy against hematological and solid cancers (*1*). Camptothecin gained clinical importance with the development of water-soluble topotecan and irinotecan that have meanwhile been approved for the therapy of colorectal, ovarian, and lung cancer (*2*, *3*).

Even though both agents show significant antitumor activity, their clinical potential is limited by severe side effects, such as myelosuppression, nausea, vomiting, and especially cardiotoxicity with DOXO and gastrointestinal disorders and stomatitis with topotecan and irinotecan. In order to circumvent these limitations and to improve the therapeutic potential of anticancer drugs, several synthetic polymers and proteins have been investigated as drug carriers (*4*−*6*).

We have recently described maleimide-bearing prodrugs of CPT and DOXO that bind in situ to the cysteine-34 position of circulating albumin after intravenous administration and release the drug at the tumor site (*7*, *8*). Albumin is a promising drug carrier because of its passive accumulation in solid tumors due to their high metabolic turnover, angiogenesis, hypervasculature, defective vascular architecture, and impaired lymphatic drainage (*9*). An acid-sensitive prodrug of doxorubicin, i.e., the 6-maleimidocaproyl hydrazone derivative (DOXO-EMCH), demonstrated superior antitumor efficacy compared to the parent compound doxorubicin in several preclinical models. In a recently completed clinical phase I study, DOXO-EMCH exhibited a good safety profile and antitumor efficacy (*10*, *11*).

In our present work, we set out to develop albumin-binding prodrugs of CPT and DOXO that incorporate the cathepsin-sensitive peptide linker Ala-Leu-Ala-Leu. This peptide sequence has been used as an inactivating moiety in several low-molecular-weight DOXO prodrugs, in particular, (CPI-0004Na) by Trouet et al. (*12*) releasing the derivative *N*-(L-leucyl)-doxorubicin that diffuses inside cells where it is cleaved to DOXO as the final product. In addition, Trouet et al. (*13*) have shown that an Ala-Leu-Ala-Leu-linker is cleaved by lysosomal enzymes in vitro. This linker has been integrated in several other conjugates, i.e., in MTX immunoconjugates by Umemoto et al. (*14*) and in human serum albumin (HSA) conjugates of MTX by Fitzpatrick et al. (*15*) to liberate the anticancer agent at the tumor site by unspecific lysosomal enzymes.

Furthermore, Struder et al. (*16*) used this linker to prepare an antibody conjugate with benzyl-EDTA that was efficiently cleaved by cathepsin B and to a lesser degree by cathepsin D. In the work by Michejda et al. (*17*), a pentapeptide Ala-Leu-Ala-Leu-Ala linker was used in a receptor-targeted drug derivative of ellipticine (an ellipticine-peptide conjugate). This linker was cleaved by the aspartate protease cathepsin D between the Ala-Leu bonds releasing Ala- and Ala-Leu-Ala derivatives of ellipticine. Both cathepsins B and D are localized in lysosomes (*18*, *19*), and overexpression in various malignant tumors has been shown, especially in breast cancer (*19*−*21*),

* To whom correspondence should be addressed. Dr. Felix Kratz, Tumor Biology Center, Department of Medical Oncology, Clinical Research, Breisacher Strasse 117, D-79106 Freiburg, Federal Republic of Germany; Tel.: +49-761-2062930; Fax.: +49-761-2062905; e-mail: felix@tumorbio.uni-freiburg.de.

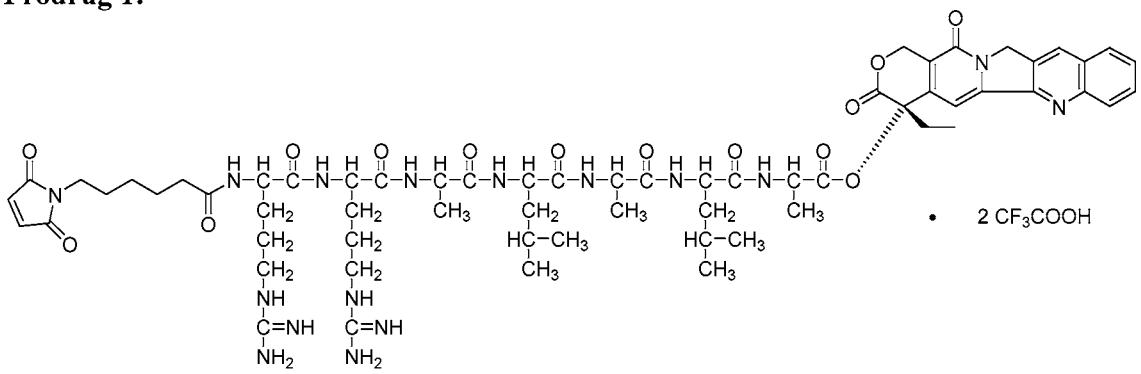
† Tumor Biology Center.

‡ Max-Delbrück Centrum.

§ Both authors contributed equally to this work.

10.1021/bc0602735 CCC: $37.00 © 2007 American Chemical Society
Published on Web 03/23/2007

Prodrug 1:



Prodrug 2:

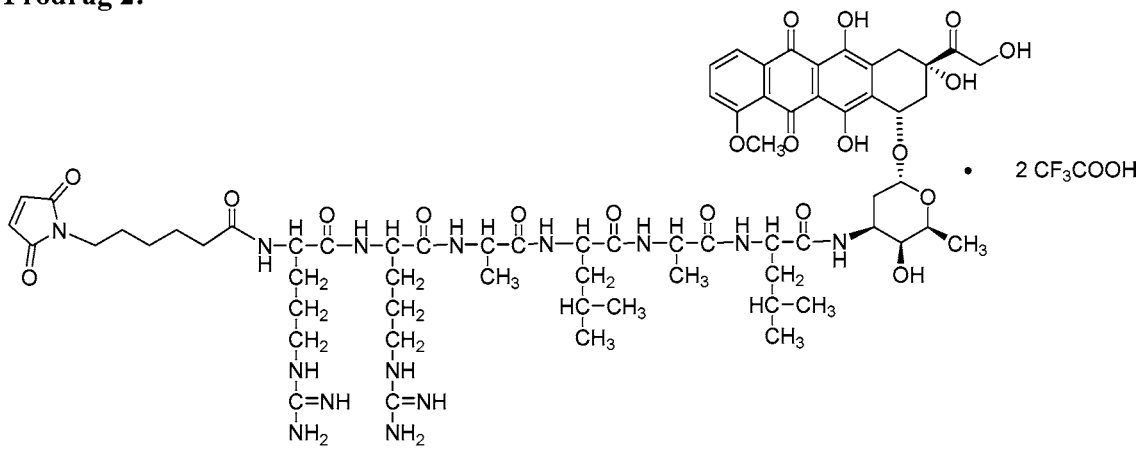


Figure 1. Structures of the albumin-binding prodrugs **1** and **2** containing a cathepsin B specific substrate.

and for cathepsin B also in melanoma (*22*), lung (*23*, *24*), and colon (*25*) carcinoma.

Inspired by this work, we developed albumin-binding prodrugs with DOXO and CPT of the general formula EMC-Arg-Arg-Ala-Leu-Ala-Leu-Ala-CPT and EMC-Arg-Arg-Ala-Leu-Ala-Leu-DOXO [EMC = 6-maleimidocaproic acid] (see Figure 1). Two arginine residues were introduced in the prodrugs to render water solubility, an important prerequisite for intravenous application and in situ coupling to endogenous albumin.

The aim of this work was to assess in detail the pH-dependent cleavage profile of the prodrugs in the presence of cathepsins B and D, as well as in biological fluids, i.e., blood plasma and tumor homogenates, and to evaluate the antitumor efficacy in vivo in comparison to free CPT and DOXO, respectively. Our cleavage studies with the Ala-Leu-Ala-Leu prodrugs showed that they exhibited a distinct cleavage pattern for cathepsin B but not for cathepsin D.

EXPERIMENTAL PROCEDURES

General. Chemicals and solvents were purchased from Sigma-Aldrich, Fluka, Merck, KMF, LGC Promochem, and Roth and were used without further purification. Camptothecin was purchased from Hande Tech Development, Inc. (U.S.A.). Doxorubicin hydrochloride was purchased from Yick-Vic Chemicals & Pharmaceuticals (HK), China. EMC-Arg-Arg-Ala-Leu-Ala-Leu-OH was custom-made by JPT Peptide Technologies GmbH (FRG). Human serum albumin (5% solution) was purchased from Octapharma GmbH. The protein contained approximately 60% free thiol groups as assessed with the Ellmann's test. The buffers used were vacuum-filtered through a 0.2 μm membrane (Sartorius, FRG) and thoroughly degassed with ultrasound prior to use. Enzymatically active cathepsins B and D were purchased from Calbiochem (Bad Soden, FRG). Xenograft tumors were gratefully received from Dr. I. Fichtner (Experimental Pharmacology and Oncology GmbH, Berlin). Lyophilization was performed with a lyophilizator Alpha 2-4 (Christ, FRG).

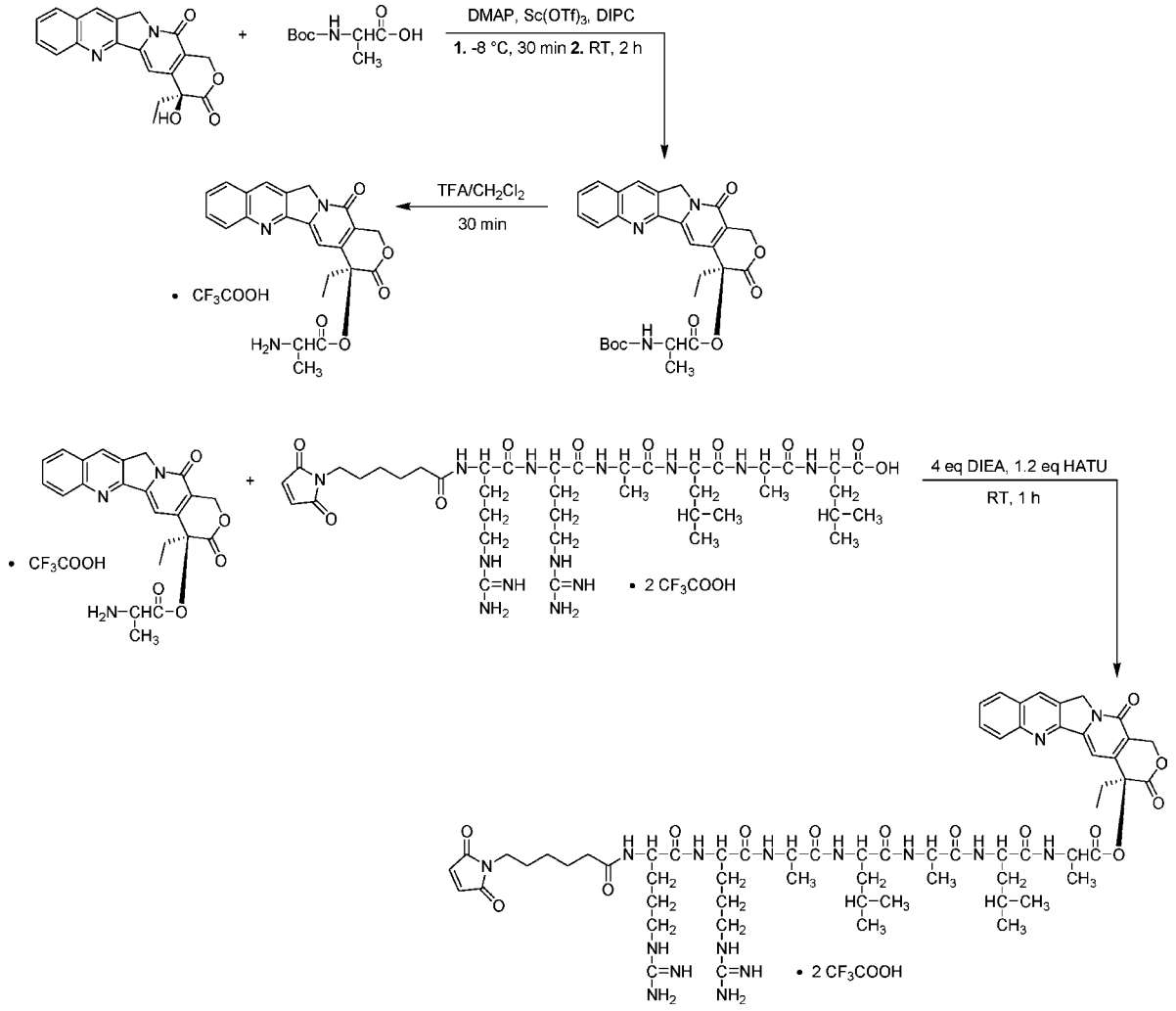
Spectral Analyses. Mass spectra were obtained on a Thermo Electron LCQ Advantage with associated MAT SS 200 data system using electron spray ionization. UV/vis spectrophotometry was carried out with a double-beam spectrophotometer U-2000 from Hitachi. LC-MS-ESI spectrometry was carried out on a Finnigan LCQ Advantage mass spectrometer (capillary temperature, 300 °C; source-induced dissociation voltage, 25 V; Thermo Electron, Dreieich, FRG) coupled to a Finnigan Surveyor HPLC system (Thermo Electron, Dreieich, FRG) with a Jupiter C_4 column (300-5, 150 × 2 mm, Phenomenex, Aschaffenburg, FRG). Chromatographic conditions: flow, 300 μL/min; mobile phase A, 1% MeCN, 99% H_2O demin, 0.06% TFA; mobile phase B, 100% MeCN, 0.06% TFA; gradient, 15−20 min increase from 10% mobile phase B to 50% mobile phase B; injection volume, 15 μL.

Chromatography. Details of the chromatographic conditions are available as Supporting Information.

Synthesis of Camptothecin-20-*O*-(L-alaninate) × TFA. The compound was synthesized according to a published procedure (*26*) and subsequent BOC cleavage with TFA/CH_2Cl_2.

Synthesis of EMC-Arg-Arg-Ala-Leu-Ala-Leu-Ala-CPT × 2 TFA (1). To a solution of camptothecin-20-*O*-(L-alaninate) trifluoroacetate (32.5 mg, 0.061 mmol), EMC-Arg-Arg-Ala-Leu-Ala-Leu-OH × 2 TFA (75 mg, 0.067 mmol), and *N*-ethyldiisopropylamine (DIEA) (42 μL, 0.240 mmol) in 1 mL *N*,*N*-dimethylformamide (DMF) was added *O*-(azabenzotriazol-1-yl)-*N*,*N*,*N*',*N*'-tetramethyluronium hexafluorophosphate (HATU)

Scheme 1. Synthesis of the Albumin-Binding CPT Prodrug 1



(25.5 mg, 0.067 mmol) under a nitrogen atmosphere. The solution was stirred for 1 h at room temperature. Subsequently, the product was precipitated with diethyl ether, and the crude product was purified by preparative chromatography on a Nucleosil C18 column (100-7, 250 × 21 mm) with precolumn (100-7, 50 × 21 mm) from Macherey-Nagel. Chromatographic conditions: flow, 10.0 mL/min; mobile phase A, 30% MeCN, 70% demin H_2O, 0.1% TFA; mobile phase B, 50% MeCN, 50% demin H_2O, 0.1% TFA; gradient, 1−43 min 0% to 100% mobile phase B; 43−53 min 100% mobile phase B isocrat; 53−63 min 0% to 100% mobile phase A; injection volume, 500−1000 μL. After lyophilization, 34 mg (36%) of **1** was obtained as a bright yellow solid.

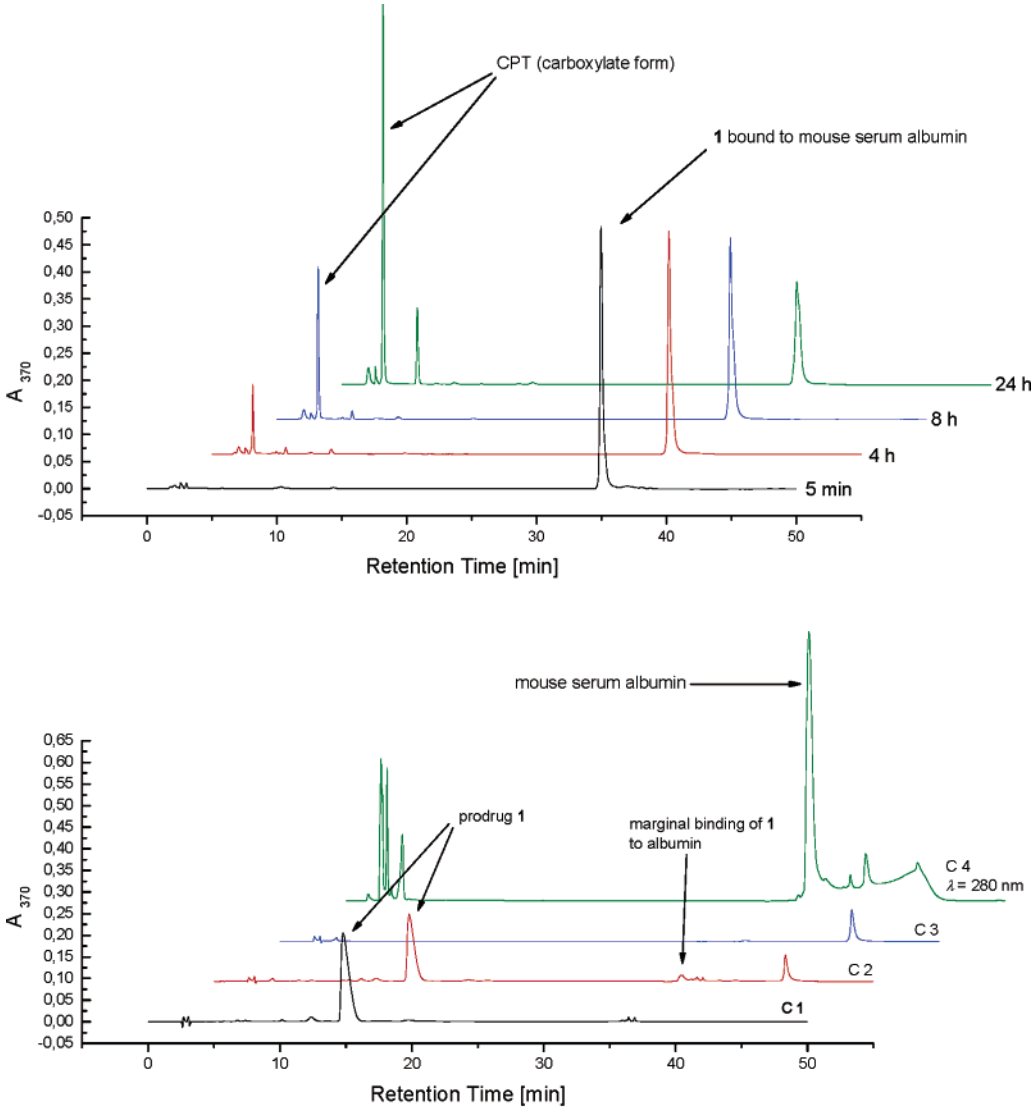
ESI-MS dir-pos (4.0 kV, 30% MeCN, 0.2% triethylammonium acetate (TEAA)): *m/z* (%) 1293.4 ($[M]^+$, 100), 1294.5 ($[M + H]^+$, 66). HPLC purity (λ = 370 nm): >95%.

Synthesis and Characterization of EMC-Arg-Arg-Ala-Leu-Ala-Leu-Doxo × 2 TFA (2). Doxorubicin hydrochloride (10.6 mg, 0.017 mmol), EMC-Arg-Arg-Ala-Leu-Ala-Leu-OH × 2 TFA (21.6 mg, 0.019 mmol), and DIEA (10 μL, 0.060 mmol) were dissolved in 5 mL of anhydrous DMF. After stirring at room temperature for 15 min, HATU (6.5 mg, 0.017 mmol) was added, and the mixture was stirred at room temperature for 2 h. The product was precipitated with anhydrous diethyl ether, washed three times, and the solvent removed by centrifugation. The crude product was then purified by flash chromatography using reverse-phase Lichroprep RP-C18 from Merck with a particle size of 0.040−0.063 mm and acetonitrile/water 30:70 to afford 20 mg (83%) of product as a red powder after lyophilization. Mass (ESI-MS 5.0 kV, MeCN, 0.05% TFA): *m/z* (%) 1417.7 ($[M]^+$, 100), 1418.7 ($[M + H]^+$, 68). HPLC purity (495 nm): >95%.

Synthesis and Characterization of H-Leu-DOXO. Doxorubicin hydrochloride (696 mg, 1.20 mmol), Fmoc-Leu-OH (424 mg, 1.20 mmol), 1-hydroxybenzotriazole hydrate (162 mg, 1.20 mmol), and 4-methylmorpholine (264 μL, 2.40 mmol) were suspended in 20 mL of DMF. After stirring for 2 h, the solution became clear, and *N,N′*-diisopropylcarbodiimide (DIPC) (223 μL, 1.44 mmol) was added. After stirring at +5 °C for 4 days, DMF was removed in high vacuum. The doxorubicin amino acid derivative Fmoc-Leu-DOXO was purified through chromatography on silica gel using chloroform/methanol 10:1, affording 650 mg (62%) product as a red powder.

The protecting group was removed by dissolving Fmoc-Leu-DOXO (400 mg, 0.45 mmol) in 16 mL tetrahydrofuran and subsequent addition of 1,8-diazabicyclo[5.4.0]-undec-7-ene (98%) [(DBU, 400 μL)]. The blue mixture was stirred for 5 min and the product precipitated with diethyl ether. The crude solid was dried in high vacuum and then purified through chromatography on silica gel using chloroform/methanol 5:1 to afford 69 mg (23%) of H-Leu-DOXO as a red powder. Mass (ESI-MS, 4.0 kV, MeOH): *m/z* 657.1 $[M]^+$. HPLC purity (495 nm): >95%.

Synthesis of the Albumin Conjugates of 1 and 2 (HSA-1 and HSA-2). *For 1:* 1.5 mg of **1** were dissolved in 2 mL of human serum albumin (HSA) and were incubated under stirring at 37 °C for 1 h, after which no free **1** was detectable. The



C 1	**1** in glucose-phosphate buffer pH 5.8
C 2	**1** + mouse plasma blocked with EMC after 10 min
C 3	mouse plasma blocked with EMC
C 4	mouse plasma blocked with EMC at λ = 280 nm

Figure 2. Chromatograms of incubation studies of mouse plasma after 5 min, 4 h, 8 h, and 24 h with **1** at 37 °C and chromatograms of incubation studies of mouse plasma preincubated with an excess of 6-maleimidocaproic acid (EMC) for 2 h and subsequent incubation with **1** after 10 min at 37 °C. Chromatographic conditions: see Experimental Section. The peak in the blocking study with EMC at ~ 43 min results from a compound in the mouse plasma absorbing at 370 nm.

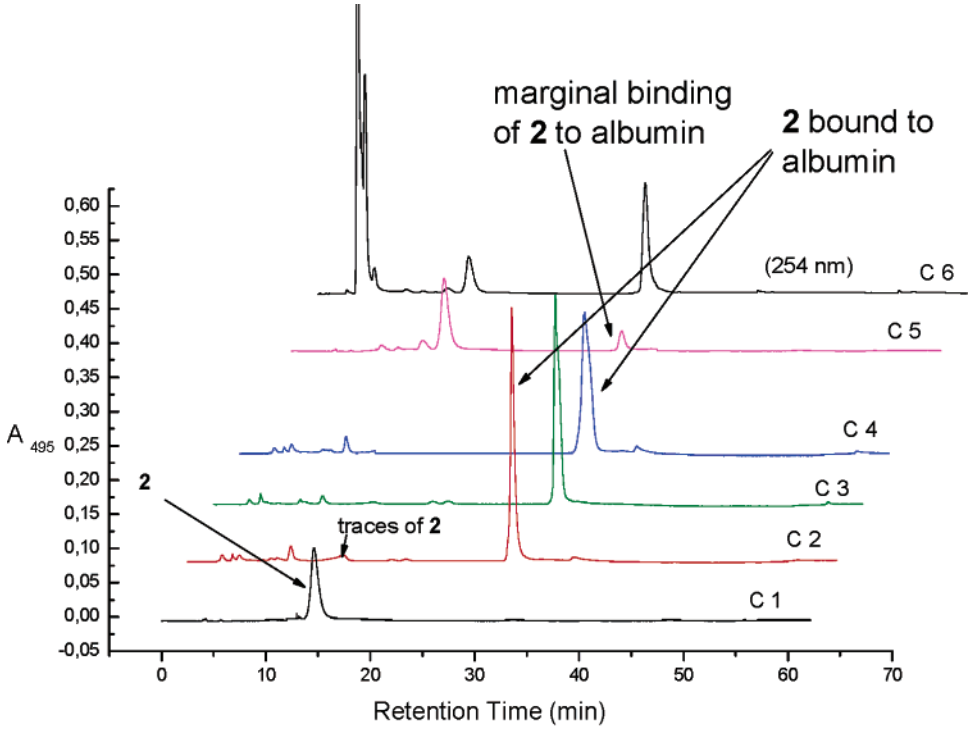
concentration was adjusted to 500 μM. The sample was kept frozen at −20 °C and thawed prior to use.

*For **2**:* 1.7 mg of **2** was dissolved in 2 mL HSA, and the solution was incubated at room temperature for 2 h. The albumin conjugate was obtained after subsequent size-exclusion chromatography (sephacryl S-100; Tris buffer: 50 mM Tris-HCl pH 7.4 or 50 mM sodium acetate buffer pH 5.0). The content of anthracycline in the sample was determined using the ϵ-value for doxorubicin [ϵ_{495} (pH 7.4) = 10 650 M^{-1} cm^{-1}]. The concentration of **2** in the conjugate was adjusted to 600 ± 50 μM by concentrating the sample with CENTRIPREP-10 concentrators (Amicon, FRG) (4 °C and 4500 rpm). Samples were kept frozen at −20 °C and thawed prior to use.

Incubation Studies of 1 and 2 with Mouse Blood Plasma. 0.75 mg of **1** or **2** was dissolved in 100 μL of sterile-filtered glucose-phosphate buffer (10 mM sodium phosphate/5% D-glucose buffer, pH 5.8). 30 μL aliquots of these solutions were added immediately to 570 μL of mouse plasma (gratefully received from Dr. N. Esser, Tumor Biology Center, Freiburg, FRG) and incubated at 37 °C. Samples were collected after 5 min, 4 h, 8 h, and 24 h and analyzed by HPLC. The decrease in the peak area of the conjugate at 370 nm for **1** and at 495 nm for **2** with time was used to determine the half-lives.

Incubation Studies of HSA-1 and HSA-2 with Cathepsin B. *For **1**:* 300 μL of the **HSA-1** stock solution (500 μM) were mixed with 290 μL of TEAA buffer (20 mM, pH 7.4 and pH 5.0) containing L-cysteine (8 mM) and 10 μL of a cathepsin B solution (71.7 μg/mL, 110 mU). The samples were incubated at 37 °C for 5 min, 2 h, and 24 h, and were analyzed by HPLC. Each 150 μL aliquot of the 2 and 24 h samples was kept frozen at −20 °C for subsequent analysis by LC-MS spectrometry.

*For **2**:* 150 μL of the **HSA-2** stock solution (600 μM) was mixed with 6 μL cathepsin B (71.7 μg/mL, 110 mU) and 204 μL of buffer (Tris buffer pH 7.4 and sodium acetate buffer pH



C 1	**2** in glucose-phosphate buffer pH 6.4
C 2	**2** + mouse plasma after 5 min
C 3	**2** + mouse plasma after 4 h
C 4	**2** + mouse plasma after 24 h
C 5/C 6	**2** + mouse plasma blocked with EMC after 10 min, **C 6**: λ = 254 nm

Figure 3. Chromatograms of incubation studies of mouse plasma after 5 min, 4 h, 8 h, and 24 h with **2** at 37 °C and chromatograms of incubation studies of mouse plasma preincubated with an excess of 6-maleimidocaproic acid (EMC) for 2 h and subsequent incubation with **2** after 10 min at 37 °C. Chromatographic conditions: see Experimental Section.

5.0) containing cysteine (8 mM). The samples at each pH (7.4 and 5.0) were incubated at 37 °C and were collected after 5 min, 1.5 h, 3 h, and 24 h. 60 μL of each sample was diluted with 40 μL of buffer to a final concentration of 150 μM and analyzed by HPLC with fluorescence detection.

Incubation Studies of HSA-1 and HSA-2 with Cathepsin D. *For **1**:* 150 μL of the **HSA-2** stock solution (500 μM) was mixed with 100 μL of cathepsin D (110.3 μg/mL, 15 U) and 50 μL of TEAA buffer pH 5 or pH 7.4. The samples were incubated at 37 °C for 5 min, 2 h, and 24 h and were analyzed by HPLC.

*For **2**:* 150 μL of the **HSA-2** stock solution (600 μM) was mixed with 150 μL cathepsin D (110.3 μg/mL, 15 U) and 150 μL of buffer (sodium acetate buffer pH 5.0) containing cysteine (8 mM). The samples were incubated at 37 °C for 5 min, 1.5 h, 3 h, and 24 h and were analyzed by HPLC.

Incubation Studies of HSA-1 and HSA-2 with Tumor Tissue Homogenates. For preparing the tumor homogenates, two protocols were used, the first at pH 5.0 that primarily liberates intracellular proteases (*27*) and the second at pH 7.4 that is used for extracting extracellular proteases (*28*). All following steps were carried out on ice. Tissues of colon HT-29 and mamma 3366 (M-3366) xenografts were cut into small pieces, and 200 mg samples were transferred into a 2 mL Eppendorf tube to which was added 800 μL of buffer (50 mM Tris−HCl buffer, pH 7.4, containing 1 mM monothioglycerol; or 50 mM sodium acetate buffer, pH 5.0, containing 100 mM sodium chloride, 4 mM EDTA Na_2, and 0.1% Brij 35). Homogenization was carried out with a micro-dissmemberator at 3000 rpm for 3 min with the aid of glass balls. Afterward, the samples were centrifuged at 5000 rpm for 10 min at 4 °C. The supernatant was aliquoted and kept frozen at −78 °C prior to use.

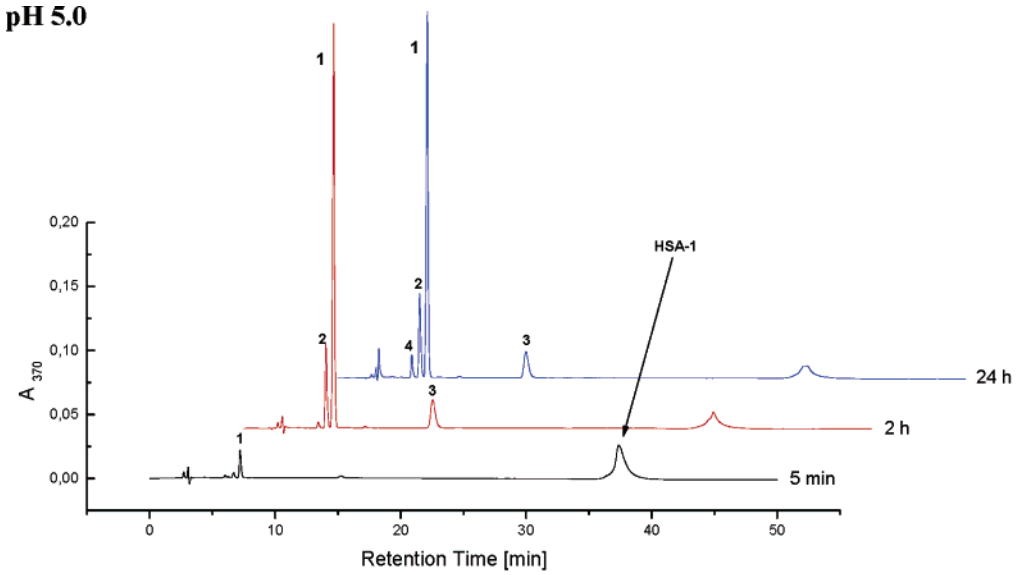
*For **1**:* 300 μL of the **HSA-1** stock solution (500 μM) was mixed with 150 μL of TEAA buffer (20 mM, pH 7.4 and pH 5.0) and 150 μL of HT-29 colon tumor tissue homogenate (pH 7.4 and pH 5.0). The samples were incubated at 37 °C for 5 min, 4 h, 8 h, and 24 h and were analyzed by HPLC. 150 μL of the 4 and 24 h samples were kept frozen at −20 °C and thawed prior to analysis by LC-MS spectrometry.

*For **2**:* 100 μL of the **HSA-2** stock solution (600 μM) was incubated with 100 μL of M-3366 tumor tissue homogenate (pH 7.4 and pH 5.0) at 37 °C for 5 min, 2 h, 5 h, and 24 h. At the mentioned times, 50 μL of each sample was diluted 1:1 to a final concentration of 150 μM and analyzed by HPLC.

Additionally, the HT-29 and M-3366 tumor homogenates were preincubated for 30 min with a 100 μM solution of the cathepsin B inhibitor CA074 (*29*) at a ratio of 10:1 (v/v), and cleavage properties were evaluated as described above.

In Vivo Efficacy of 1 and 2. For the in vivo testing of **1** and **2** in comparison with their parent compounds, female NMRI: nu/nu mice (in-house breeding) were used. The mice were held in individually ventilaged cages under sterile and standardized environmental conditions (25 ± 2 °C room temperature, 50 ± 10% relative humidity, 12 h light-dark rhythm). They received autoclaved food and bedding (ssniff, Soest, Germany) and acidified (pH 4.0) drinking water ad libitum. All animal experiments were performed under the auspices of the German Animal Protection Law.

Ten million cells of HT-29 and fragments of M-3366 tumor



Peak number	Retention time [min]	Observed fragment ions [*m/z*]	Peak assignment
1	7.20	555.1 $[M + Na]^+$	H-Leu-Ala-CPT
2	6.54	626.0 $[M + Na]^+$	H-Ala-Leu-Ala-CPT
3	15.04	739.1 $[M + Na]^+$, 717.0 $[M + 2H]^+$	H-Leu-Ala-Leu-Ala-CPT
4	5.88	349.1 $[M + H]^+$	CPT lactone

Figure 4. Chromatograms of incubation studies with **HSA-1** in the presence of cathepsin B (71.7 μg/mL, 110 mU) at pH 5.0 at 37 °C after 5 min, 2 h, and 24 h.

tissue were transplanted subcutaneously (s.c.) into the left flank region of anesthetized (40 mg/kg i.p. Radenarkon, Asta Medica, Frankfurt, Germany) mice on day zero. Mice were randomly distributed to the experimental groups (six mice per group). When the tumors were grown to a palpable size (90−130 mm^3), treatment was initiated. HT-29 xenografted mice were treated intravenously at days 6, 13, and 20 with 10 mM sodium phosphate/5% D-glucose buffer pH 5.8, camptothecin, or **1** (compound was administered as a solution in 10 mM sodium phosphate/5% D-glucose buffer pH 5.8); for doses, see corresponding tables and figures. The volume of administration was 0.23 mL/25 g body weight. M-3366 xenografted mice were treated intravenously at days 19 and 26 with 10 mM sodium phosphate/5% D-glucose buffer pH 7.0, doxorubicin, or **2** (compound was administered as a solution in 10 mM sodium phosphate/5% D-glucose buffer pH 7.0). The volume of administration was 0.2 mL/20 g body weight.

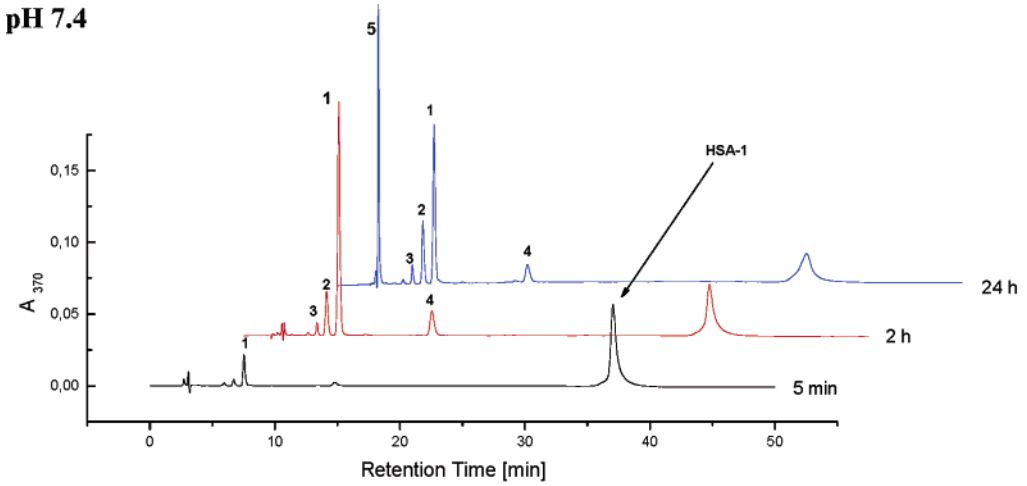
Tumor size was measured twice weekly with a caliper-like instrument in two dimensions. Individual tumor volumes (V) were calculated by the formula $V = (\text{length} + [\text{width}]^2)/2$ and related to the values on the first day of treatment (relative tumor volume, RTV). At each measurement day, treated/control values (T/C) were calculated as a percentage for each experimental group; the optimum (lowest) values obtained within four weeks after treatment were used for evaluating the efficacy of the compounds, and optimum T/C values are presented in the respective tables. Statistical analysis was performed with the U-test (Mann and Whitney) with $p < 0.05$. The body weights of mice were determined every 3 to 4 days.

RESULTS AND DISCUSSION

Chemistry. For the synthesis of the albumin-binding prodrug **1**, EMC-Arg-Arg-Ala-Leu-Ala-Leu-OH was reacted with H-Ala-CPT × TFA, prepared according to a two-step procedure in which the first step is a stereoselective acylation of 20-(*S*)-camptothecin (*26*). Treatment of H-Ala-CPT × TFA with EMC-Arg-Arg-Ala-Leu-Ala-Leu-OH × 2 TFA in the presence of HATU and DIEA afforded a quantitative reaction in a short time (Scheme 1). Purification of the crude product was achieved by preparative HPLC with a considerable loss in yield. The bright yellow solid was characterized by mass spectrometry, and purity was determined by HPLC (see Experimental Section). The incorporation of two arginines into the peptide linker of the prodrug **1** resulted in superior water solubility in buffer solution (>7 mg/mL) compared to the almost insoluble CPT (2.5 μg/mL).

For the synthesis of the albumin-binding prodrug **2**, EMC-Arg-Arg-Ala-Leu-Ala-Leu-OH × 2TFA was coupled to the 3′-NH_2 position of doxorubicin in anhydrous DMF in the presence of HATU and DIEA as a one-step procedure. The crude product was purified through chromatography on a reverse-phase RP-C18 column. Prodrug **2** showed excellent water solubility with up to 10 mg/mL being dissolved in buffer solution in the pH range of 6.0 to 7.0.

Albumin-Binding Properties and Stability of 1 and 2. In order to show that prodrugs **1** and **2** bind rapidly and selectively to the cysteine-34 group of endogenous serum albumin, HPLC studies were performed in which mouse plasma was incubated with the prodrugs. Figures 2 and 3 show the chromatographic profiles of **1** and **2** incubated with mouse blood plasma after 5 min (λ = 370 nm for CPT derivatives, and λ = 495 nm for DOXO derivatives). While the free prodrugs elute at ∼15 min (**1**) and ∼14 min (**2**), the signals disappeared almost completely after incubation with mouse plasma, and a single peak eluting



Peak number	Retention time [min]	Observed fragment ions [*m/z*]	Peak assignment
1	7.54	555.1 $[M + Na]^+$	H-Leu-Ala-CPT
2	6.87	626.0 $[M + Na]^+$	H-Ala-Leu-Ala-CPT
3	5.88	349.1 $[M + H]^+$	CPT lactone
4	15.04	739.1 $[M + Na]^+$, 717.0 $[M + 2H]^+$	H-Leu-Ala-Leu-Ala-CPT
5	3.37	349.1 $[M + H]^+$, 305.2 $[M + H - CO_2]^+$	CPT carboxylate

Figure 5. Chromatograms of incubation studies with **HSA-1** in the presence of cathepsin B (71.7 μg/mL, 110 mU) at pH 7.4 at 37 °C after 5 min, 2 h, and 24 h.

at the retention time of mouse serum albumin (MSA) (33−37 min) was observed.

In order to prove the fast binding results from a Michael addition of the sulfhydryl group of MSA with the maleimide group of the prodrugs, analogous HPLC experiments were carried out in which the cysteine-34 position of MSA was blocked with an excess of EMC prior to incubation with **1** and **2** (see Figures 2 and 3). In this case, marginal binding (**1**, ∼8%; **2**, <10%) to MSA was observed after incubating plasma with **1** and **2** for 10 min.

In order to determine the plasma stability of **1,** the respective albumin conjugate was generated by incubation of the CPT derivative with mouse blood plasma at 37 °C and subsequently analyzing samples after 3 min, 4 h, 8 h, 24 h, and 28 h through HPLC. From the decrease of the peak areas, the half-life of the conjugate of **1** was calculated as $t_{1/2} = 32$ h. Additionally, buffer stability of the albumin conjugate of **1** at pH 7.4 and pH 5.0 over 24 h was tested with the following results: degradation at pH 7.4, ∼15%; degradation at pH 5.0, <5% (chromatograms available as Supporting Information).

The stability of albumin-bound **2** in mouse blood plasma was assessed after **2** had been incubated at 37 °C with plasma for 4 and 24 h. HPLC showed that the albumin conjugate is highly stable over 24 h (∼5% degradation) (see Figure 3).

Cleavage Profiles of the Albumin Conjugate of 1. The ratio of the carboxylate form and the lactone form of released CPT is essential for the antitumor activity of the prodrug. It is known that the carboxylate form of CPT is inactive and even toxic, whereas the lactone form of CPT is the active agent. At more acidic pH, the equilibrium between the carboxylate and lactone forms generally shifts to the lactone form of CPT.

The cleavage properties of compound **1** were evaluated using enzymatically active cathepsin B, cathepsin D, and HT-29 colon tumor tissue homogenates at both pH 7.4 and pH 5.0. After incubation with cathepsin D, no cleavage of **HSA-1** could be detected (data not shown). In contrast, incubation with cathepsin B and HT-29 colon tissue homogenate resulted in a fast and almost complete cleavage over a period of 24 h, especially at pH 5.0 (see Figures 4, 5, 7, and 8). The different cleavage products were identified by LC-MS and by the use of CPT and H-Ala-CPT standards. Unfortunately, the HPLC method used for incubation studies could not be transferred one-to-one to the LC-MS investigations. Therefore, the cleavage products could not be assigned by retention times but by their peak areas and by the use of the reference substances (mass spectra of the individual peaks are available as Supporting Information). For cleavage with cathepsin B (see Figures 4 and 5), the following products were identified: H-Leu-Ala-Leu-Ala-CPT, H-Ala-Leu-Ala-CPT, H-Leu-Ala-CPT as the major product, CPT (lactone form), and additionally at pH 7.4, CPT in the carboxylate form. Cleavage in HT-29 colon tumor homogenate (see Figures 7 and 8) at pH 5.0 resulted in a more pronounced degradation of the albumin conjugate over 24 h than that observed at pH 7.4. Interestingly, the cleavage profile with tumor homogenate additionally showed the formation of H-Ala-CPT, which could not be observed after cleavage with cathepsin B. The identified cleavage products at pH 5.0 were H-Ala-Leu-Ala-CPT, H-Leu-Ala-CPT, H-Ala-CPT, and CPT (lactone form). After 4 h of incubation, the main products were H-Leu-Ala-CPT and H-Ala-CPT, changing after 24 h of incubation to H-Ala-CPT and CPT in the carboxylate form. At pH 7.4, H-Leu-Ala-CPT, H-Ala-CPT, CPT (lactone form), and CPT in the carboxylate form were found. Cleavage at pH 7.4 to CPT in the carboxylate form is also attributed to unspecific hydrolysis, although cleavage in pH 7.4 buffer solution after 24 h was not as

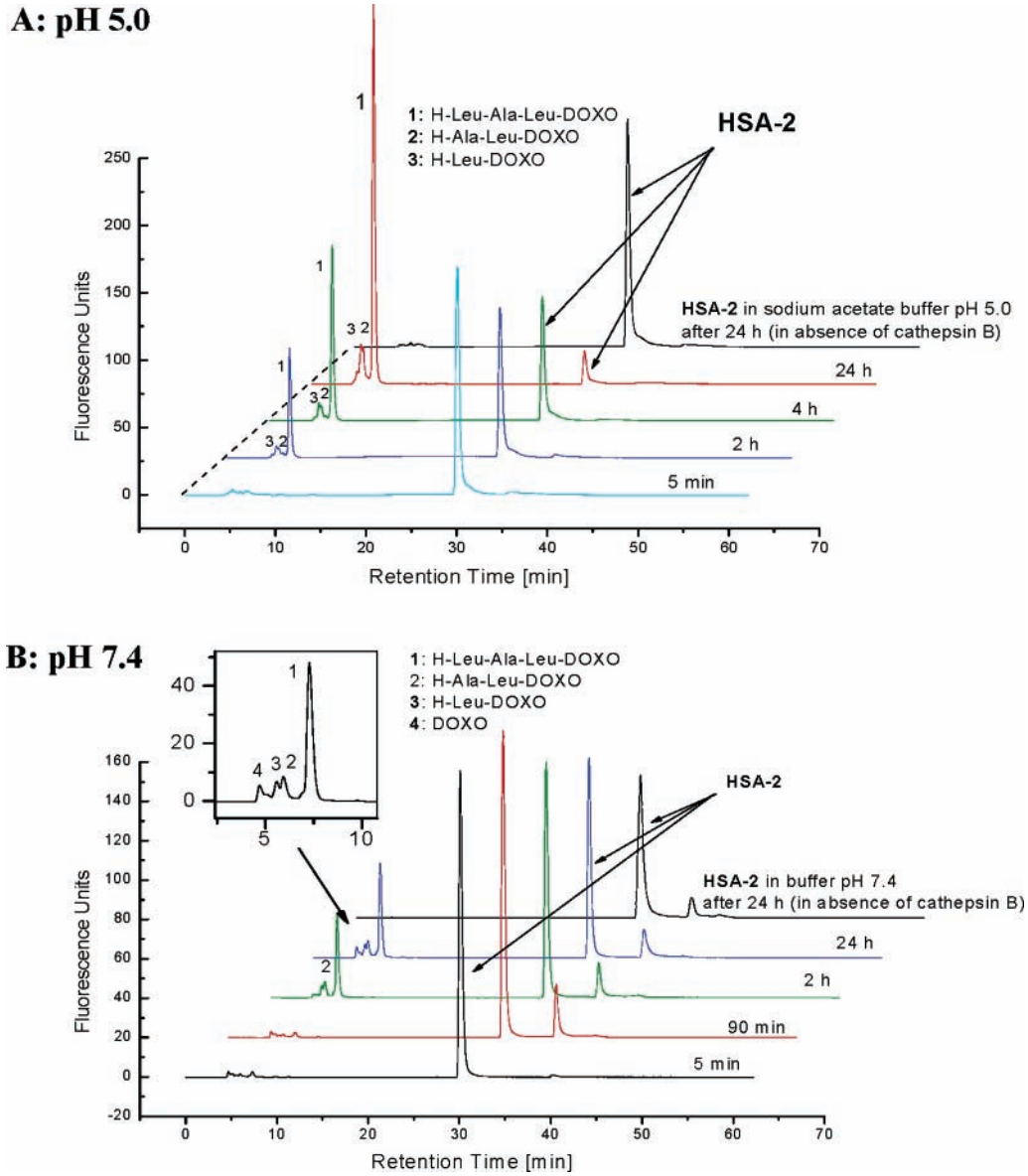


Figure 6. Chromatograms of incubation studies with **HSA-2** in the presence of cathepsin B (71.7 μg/mL, 110 mU) at pH 5.0 (A) and pH 7.4 (B) at 37 °C after 5 min, 2 h, 24 h and 5 min, 90 min, 2 h, 24 h respectively.

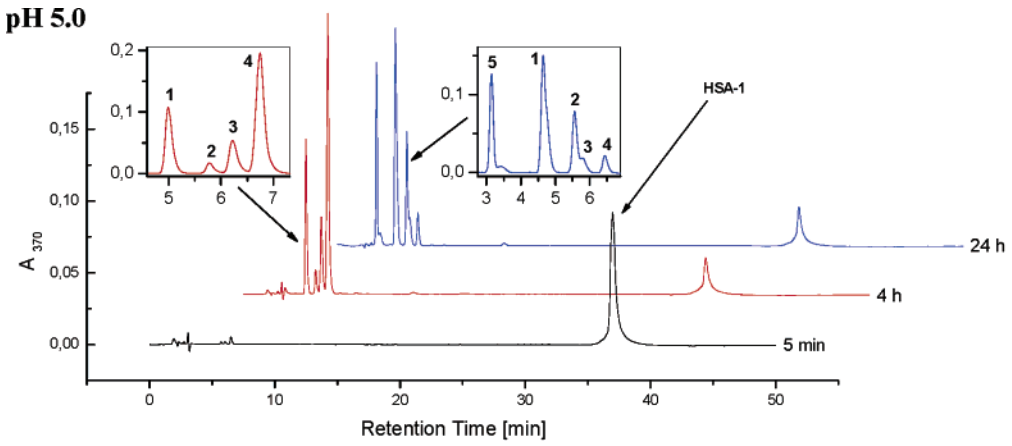
pronounced as with tumor tissue homogenate or cathepsin B. Additionally, the cleavage properties of the HT-29 tumor homogenate preincubated with the cathepsin B inhibitor CA074 (*29*) at pH 5.0 were investigated to determine if cathepsin B is the major protease responsible for the cleavage of the peptide sequence. The corresponding chromatograms (see Figure 9) recorded after 5 min, 4 h, and 24 h show that the cleavage of prodrug **1** was notably inhibited with respect to the cleavage products H-Leu-Ala-CPT, H-Ala-Leu-Ala-CPT, and CPT (carboxylate form).

The appearance of the carboxylate form of CPT at pH 7.4 in several studies, especially in the mouse plasma stability study (Figure 2) and the study with tumor homogenate (Figure 8), might be related to the fact that proteins, primarily albumin, switch the equilibrium to the carboxylate form due to interaction with the binding domain IIA (*30*−*35*).

The incubation study at pH 5 with **HSA-1** in the presence of cathepsin B (Figure 4) showed no generation of CPT in the carboxylate form, in contrast to the incubation study with HT-29 tumor homogenate at the same pH value (Figure 7). Two reasons could explain this difference: (a) preferential binding of the carboxylate form to proteins in the tumor tissue homogenate, and (b) in the presence of cathepsin B, no H-Ala-CPT was generated, which readily releases free CPT; di-, tri-, and tetrapeptide derivatives of CPT are reported to be more stable than amino acid derivatives of CPT (*36*).

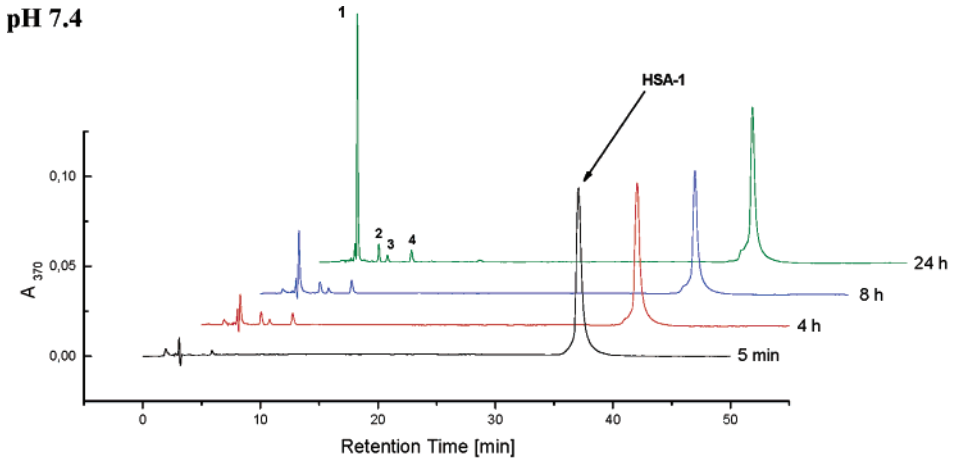
Cleavage Profiles of the Albumin Conjugate of 2. In order to investigate whether and how fast **HSA-2** is cleaved by cathepsin B at pH 5.0 and pH 7.4 as well as by cathepsin D at pH 5.0, **HSA-2** was incubated with the enzymes and chromatograms recorded with fluorescence spectrophotometer using reverse-phase HPLC.

Rapid cleavage to a main product eluting at 6.3 min (see Figure 6A) was observed after incubating **HSA-2** with cathepsin B at pH 5.0. After 24 h of incubation, cleavage was almost complete. In order to characterize this cleavage product, 1000 μL [1100 μM] **HSA-2** and 300 μL of cathepsin B were incubated, and the cleavage product was isolated through size exclusion chromatography (sephadex G-25) using demineralized water. Mass spectrometry of the lyophilized sample showed a distinct mass peak at 840.8 $[M]^+$ and its Na^+ adduct at 863.1 $[M + Na]^+$ corresponding to [H-Leu-Ala-Leu-DOXO] (mass spectrum available as Supporting Information). Small amounts



Peak number	Retention time [min]	Observed fragment ions [*m/z*]	Peak assignment
1	5.05	331.2 [– alanine]$^+$, 303.2 [– alanine – CO]$^+$	H-Ala-CPT
2	5.71	349.1 [M + H]$^+$	CPT lactone
3	6.21	626.1 [M + Na]$^+$	H-Ala-Leu-Ala-CPT
4	6.75	555.0 [M + Na]$^+$	H-Leu-Ala-CPT
5	3.20	349.1 [M + H]$^+$, 305.2 [M + H – CO_2]$^+$	CPT carboxylate

Figure 7. Chromatograms of incubation studies with **HSA-1** and HT-29 tissue homogenate after 5 min, 4 h, (8 h), and 24 h at pH 5.0 at 37 °C.



Peak number	Retention time [min]	Observed fragment ions [*m/z*]	Peak assignment
1	3.22	349.1 [M + H]$^+$, 305.2 [M + H – CO_2]$^+$	CPT carboxylate
2	5.05	331.2 [– alanine]$^+$, 303.2 [– alanine – CO]$^+$	H-Ala-CPT
3	5.88	349.1 [M + H]$^+$	CPT lactone
4	7.88	555.0 [M + Na]$^+$	H-Leu-Ala-CPT

Figure 8. Chromatograms of incubation studies with **HSA-1** and HT-29 tissue homogenate after 5 min, 4 h, (8 h), and 24 h at pH 7.4 at 37 °C.

of the cleavage products H-Leu-DOXO and H-Ala-Leu-DOXO were also observed, which were identified by an additional LC-MS experiment (mass spectra available as Supporting Information).

The cleavage of **HSA-2** by cathepsin B at pH 7.4 showed the same cleavage products, especially [H-Leu-Ala-Leu-DOXO] at pH 5.0, but cleavage at pH 7.4 proved to be less effective and much slower; therefore, the cathepsin B concentration for the incubation study at pH 7.4 was increased (see Figure 6B). Incubation studies at pH 7.4 with **HSA-2** also show a sparse degradation to an unidentified product eluting at ~37 min only visible with fluorescence detection.

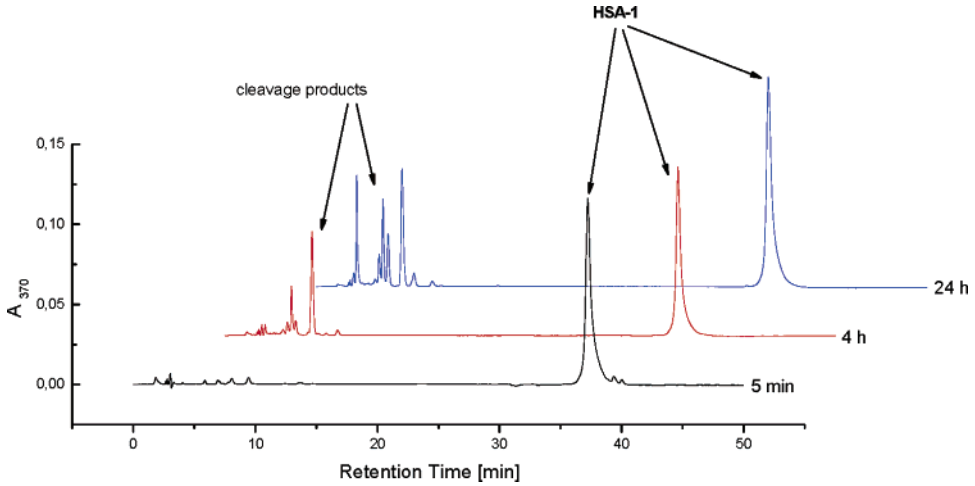


Figure 9. Chromatograms of incubation studies with **HSA-1** and HT-29 tissue homogenate preincubated with the cathepsin B inhibitor CA-074 after 5 min, 4 h, and 24 h at pH 5.0 and 37 °C. Chromatographic conditions: see Experimental Section.

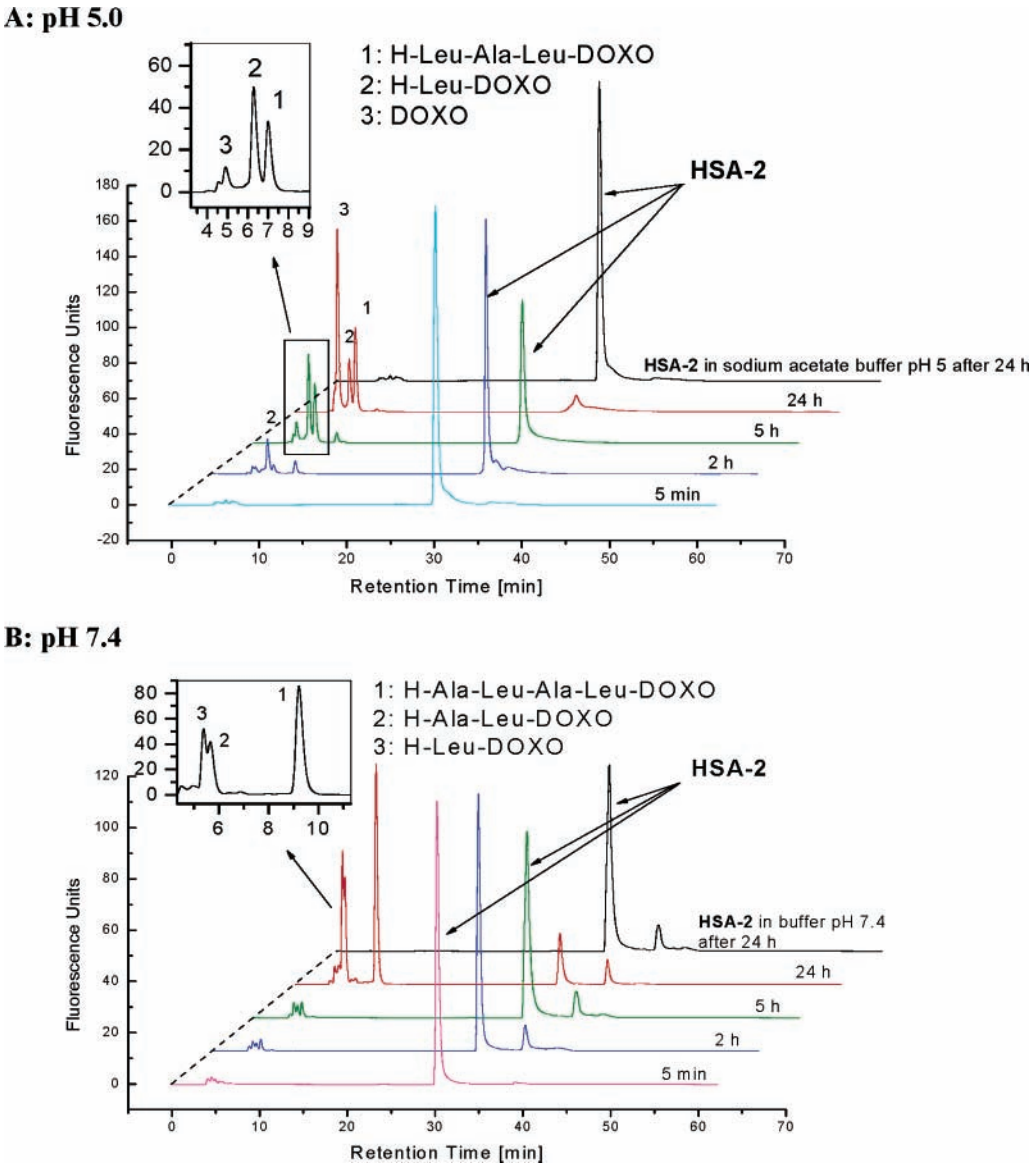


Figure 10. Chromatograms of incubation studies with **HSA-2** and M-3366 tissue homogenate after 5 min, 2 h, and 5 h at pH 5.0 (A) and pH 7.4 (B) at 37 °C.

Incubation studies with **HSA-2** and cathepsin D showed only marginal cleavage (data not shown).

In order to obtain a picture of the cleavage profile in biological samples, we incubated both **HSA-2** and the cleaved

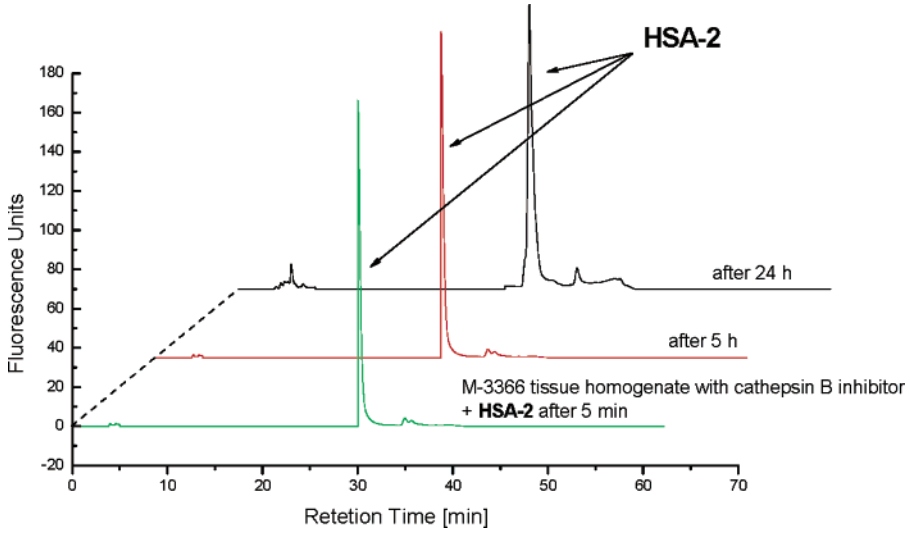


Figure 11. Chromatograms of incubation studies with **HSA-2** and M-3366 tissue homogenate preincubated with the cathepsin B inhibitor CA-074 after 5 min, 5 h, and 24 h at pH 5.0 and 37 °C.

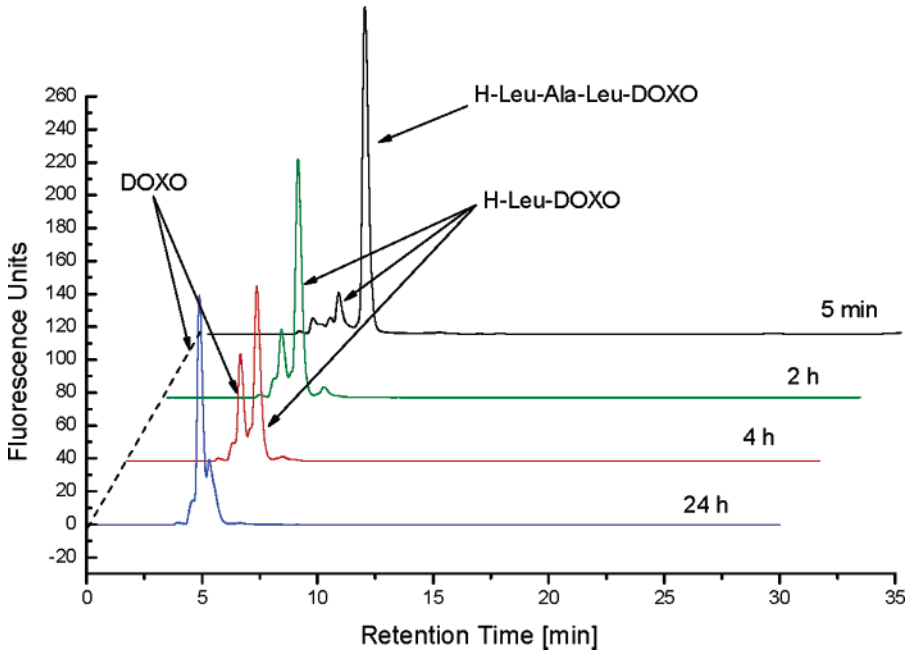


Figure 12. Chromatograms of incubation studies with the cleavage product [H-Leu-Ala-Leu-DOXO] and M-3366 tissue homogenate after 5 min, 2 h, 4 h, and 24 h at 37 °C. Concentration of [H-Leu-Ala-Leu-DOXO] was 125 μM. Chromatographic conditions: see Experimental Section.

Table 1. Antitumor Activity of CPT Prodrug 1 against Human Colorectal Xenografts (HT-29) in Vivo

compound	dose[a] [mg/kg]	total mortality	body weight change [%] (day 6−9)	*T/C* [%] maximal
CPT	3 × 12.5	0/6	−2	40[b] (day 22)
1	3 × 12.5	1/6 (on day 20)	−1	17[b,c] (day 29)

[a] Dose refers to CPT equivalents. [b] Significant to buffer solution. [c] Significant to camptothecin.

doxorubicin tripeptide [H-Leu-Ala-Leu-DOXO] with M-3366 tissue homogenates and analyzed the cleavage products over 24 h (see Figures 10and 12). The cleavage products were identified by "peak spiking" with H-Leu-DOXO, H-Leu-Ala-Leu-DOXO, and DOXO references, which were added to the incubated samples. An increase of the peak area at the corresponding retention time confirmed the identification of the respective cleavage product.

Incubation with **HSA-2** at pH 5.0 showed two cleavage products, H-Leu-Ala-Leu-DOXO and H-Leu-DOXO after 2 h. After 5 h, the main cleavage product was H-Leu-DOXO and small amounts of DOXO were observed, which increased over 24 h (see Figure 10A). Incubation with **HSA-2** at pH 7.4 showed a different cleavage profile than at pH 5.0. Only after 24 h were the cleavage products H-Leu-DOXO, H-Ala-Leu-DOXO, and the tetrapeptide derivative H-Ala-Leu-Ala-Leu-DOXO eluting at 9 min observed that were obviously produced by enzymes in M-3366 tissue homogenate other than cathepsin B (see Figure 10B). Identification of these cleavage products was performed by LC-MS (mass spectra of the individual peaks are available as Supporting Information).

In a further experiment, we preincubated the M-3366 tissue homogenate with the cathepsin B inhibitor CA-074 at pH 5.0 in order to elucidate whether cathepsin B is responsible for cleaving the peptide sequence to the cleavage products H-Leu-Ala-Leu-DOXO and H-Leu-DOXO. As shown in Figure 11, no cleavage was observed after 5 and 24 h, confirming that

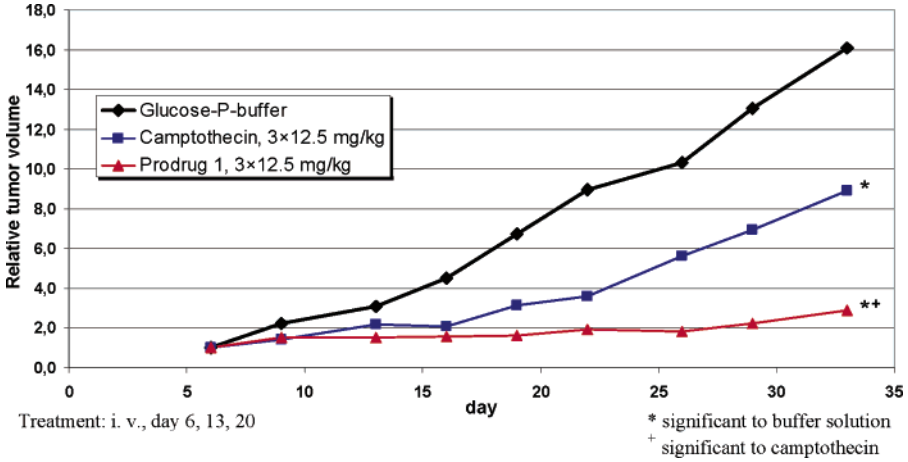


Figure 13. Curves depicting tumor growth inhibition of subcutaneously HT-29 xenografts under therapy with CPT and prodrug **1**.

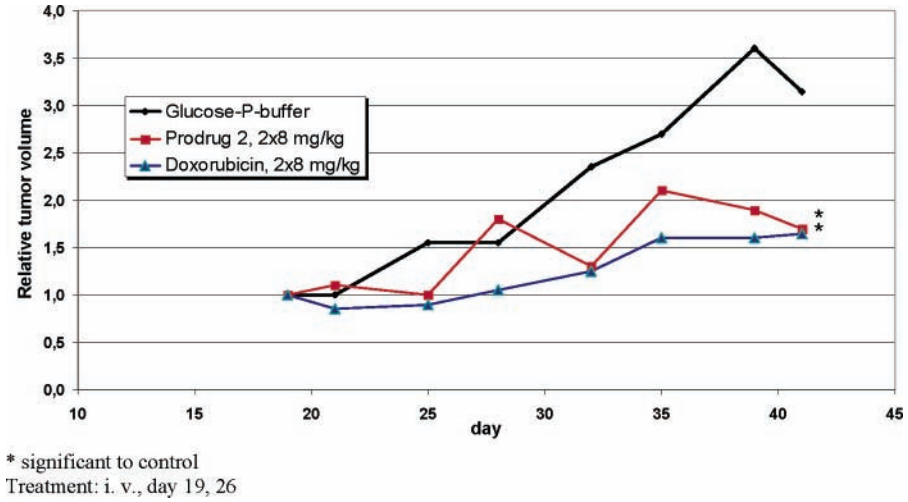


Figure 14. Curves depicting tumor growth inhibition of subcutaneous M-3366 xenografts under therapy with doxorubicin and prodrug **2**.

cathepsin B is the major enzyme responsible for the cleavage in M-3366 tissue homogenate at pH 5.0.

H-Leu-Ala-Leu-DOXO was cleaved primarily to H-Leu-DOXO in M-3366 tissue homogenate after 2 h, and almost complete degradation to DOXO over 24 h was observed (see Figure 12).

H-Leu-DOXO is known to have activity against several human tumor cell lines, e.g., MCF-7 (breast carcinoma) (*37*, *38*), HT-1080 (fibrosarcoma) (*39*), and LNCaP (prostate carcinoma) (*40*−*46*); it was also shown to have less cardiac toxicity than DOXO in animal models (*40*, *41*).

In Vivo Activity of 1 and 2 Compared to the Free Drug. The in vivo efficacy of **1** and CPT was assessed in xenografted nude mice using a human HT-29 colorectal cell line. CPT was evaluated at a dose of 3 × 12.5 mg/kg (i.v.), which was reported to be the maximum tolerated dose (MTD) for camptothecin in nude mice (*47*). Prodrug **1** was tested at the same dose of 3 × 12.5 mg/kg (i.v.) CPT equivalents. Table 1 and Figure 13 show the results of this experiment. In general, although one animal died, therapy with **1** produced no significant body weight loss (see Table 1 and curves depicting body weight change, available as Supporting Information). Whereas CPT (3 × 12.5 mg/kg) was moderately active (*T*/*C* max: 40%), **1** exhibited superior antitumor activity at the same dose, and mice treated with **1** showed a good antitumor response (*T*/*C* max: 17%).

The antitumor efficacy of **2** was evaluated in nude mice using a breast carcinoma 3366 (M-3366) xenograft in a strict comparison to free doxorubicin. A preliminary toxicity study in two healthy mice showed that the MTD of **2** was 1 × 24 mg/kg doxorubicin equivalents and thus ∼3-fold higher than for free doxorubicin. Consequently, **2** was compared with doxorubicin at the following doses: doxorubicin at a dose of 2 × 8 mg/kg corresponding to the MTD of doxorubicin in nude mice and **2** at doses of 2 × 8 mg/kg doxorubicin equivalents and 1 × 24 mg/kg doxorubicin equivalents. The results of these in vivo experiments are shown in Table 2 and Figure 14.

Table 2. Antitumor Activity of DOXO Prodrug 2 Against Human Mamma Carcinoma Xenografts (M-3366) in Vivo

compound	dose[a] [mg/kg]	total mortality	body weight change [%] (day 6−9)	*T*/*C* [%] maximal
DOXO	2 × 8	0/6	−9	44[b] (day 39)
2	2 × 8	1/6 (on day 20)	0	53[b] (day 39)
2	1 × 24	5/6 (on day 20)	−14	n.e.[c]

[a] Dose refers to DOXO equivalents. [b] Significant to buffer solution [c] n.e.: not evaluatable.

Table 2 and Figure 14.

Doxorubicin at its optimal dose of 2 × 8 mg/kg produced a moderate inhibition in tumor growth with a body weight loss of up to −9% with a slow recovery thereafter. The efficacy of **2** at 2 × 8 mg/kg was comparable with the therapeutic results of doxorubicin at 2 × 8 mg/kg, but no body weight loss was observed (see curves depicting body weight change, available as Supporting Information). After the first application of **2** at the dose of 2 × 8 mg/kg, one animal died due to an acute reaction. After application, all mice showed a mild ataxia and red flushing prolonging for 20 min. The in vivo testing of **2** at the dose of 1 × 24 mg/kg was aborted after the first application

due to acute toxicity (5 of 6 mice died), an observation that was not made in preliminary toxicity studies in healthy nude mice.

CONCLUSIONS

In the past 30 years, cysteine proteases have been known to be involved in a number of steps in tumor progression, such as tumor growth, invasion, migration, and the formation of metastasis (*48*). Especially, the cysteine proteases of the papain family such as cathepsins B, L, H, and S have been investigated intensively in the past. Cathepsins are known to digest and cleave a number of tissues such as collagen and proteoglycane (*49*). The cysteine protease cathepsin B is mostly localized in lysosomes (*18*), and overexpression of cathepsin B has been found in various malignant tumors, especially in melanoma (*22*), breast (*20*), lung (*23*, *24*), and colon (*25*) carcinoma. The overexpressed levels of cathepsin B in tumors as well as in some extracellular fluids are associated with tumor progression and with disease-free and overall survival and may therefore serve as a prognostic factor for cancer patients.

Thus, we developed two albumin-binding prodrugs incorporating a peptide sequence which can be specifically cleaved by cathepsin B, releasing an amino acid derivative of doxorubicin or camptothecin, which subsequently is cleaved to free doxorubicin and camptothecin as the final product.

In the past few years, several low- and high-molecular-weight prodrugs of doxorubicin have been developed that were designed to be activated by cathepsin B. The HPMA copolymer-Gly-Phe-Leu-Gly-doxorubicin conjugate PK1 incorporating a cathepsin B cleavable linker has been evaluated clinically (*50*). Furthermore, two immunoconjugates of doxorubicin, in which DOXO is linked to the chimeric BR96 antibody through lysosomally cleavable dipeptides Phe-Lys or Val-Cit (BR96-Phe-Lys-PABC-DOXO and BR96-Val-Cit-PABC-DOXO; PABC = *para*-aminobenzyloxycarbonyl) (*51*) have been developed. Both conjugates showed rapid and nearly quantitative drug release with cathepsin B.

To date, three polymeric derivatives of camptothecin have entered clinical trials: two HPMA copolymer-bound camptothecin drugs (*47*, *52*) and Prothecan, a PEG-based CPT-Ala prodrug (*53*). In all cases, binding CPT to polymers leads to highly water-soluble formulations which release the drug in a controlled fashion due to the incorporation of a hydrolyzable or enzymatically degradable amino acid spacer. Especially, cleavage by cathepsin B was described for the following CPT prodrugs: a camptothecin analogue-carboxymethyl dextran conjugate bearing a Gly-Gly-Gly linker (*54*), an immunoconjugate of CPT containing a Phe-Lys linker (*55*), a poly(ethylene glycol) conjugate of 10-amino-7-ethylcamptothecin (*56*), and recently a folate receptor-targeted PEG-peptide conjugate of CPT (*57*).

In the present work, we could show that cathepsin B cleaves the Ala-Leu-Ala-Leu linker in the albumin-bound form of the CPT prodrug **1** and the DOXO prodrug **2** in all of the peptide bonds adjacent to the EMC-Arg-Arg-Ala residue. Cleavage was more efficient at pH 5.0 than at pH 7.4. In tumor homogenates, the cleavage pattern was similar, but a pronounced cleavage to CPT (and the CPT carboxylate form) and to DOXO was observed. Although the extent of cleavage for both prodrugs was similar in the HT-29 and M-3366 tumor xenografts, **1** was significantly more active than CPT in contrast to **2**, which was as effective as doxorubicin. A possible explanation for this difference could be differences in the EPR (enhanced permeation and retention) effect for these tumors.

In summary, we have prepared albumin-binding prodrugs with the anticancer drug camptothecin and doxorubicin that are water-soluble, bind rapidly and selectively to the cysteine-34 position of endogenous serum albumin, and are cleaved specifically by cathepsin B. Further studies of **1** in a larger panel of human tumor xenografts should reveal the potential of this CPT prodrug.

ACKNOWLEDGMENT

The support of the Dr. Mildred-Scheel Stiftung der Deutschen Krebshilfe is gratefully acknowledged. We thank Christoph Warth for carrying out the LC-MS experiments.

Supporting Information Available: Chromatography; curves depicting body weight change; chromatograms of the albumin conjugate of prodrug **1** (250 μM) depicting the buffer stability; mass spectra of the cleavage products of **1** and mass spectra of the cleavage products of **2**. This material is available free of charge via the Internet at http://pubs.acs.org/BC.

LITERATURE CITED

(1) Gianni, L., Grasselli, G., Cresta, S., Locatelli, A., Vigano, L., and Minotti, G. (2003) Anthracyclines. *Cancer Chemother. Biol. Response Modif. 21*, 29−40.

(2) Kollmannsberger, C., Mross, K., Jakob, A., Kanz, L., and Bokemeyer, C. (1999) Topotecan - a novel topoisomerase I inhibitor: pharmacology and clinical experience. *Oncology 56*, 1−12.

(3) Rothenberg, M. L. (2001) Irinotecan (CPT-11): recent developments and future directions - colorectal cancer and beyond. *Oncologist 6*, 66−80.

(4) Kratz, F., Warnecke, A., Rodrigues, P. C. A., and Riebeseel, K. (2001) In *Polymeric Biomaterials* (Dumitriu, S., Ed.) pp 851−894, Marcel Dekker, New York.

(5) Putnam, D., and Kopecek, J. (1995) Polymer conjugates with anticancer activity. *Adv. Polym. Sci. 122*, 55−123.

(6) Haag, R., and Kratz, F. (2006) Polymer therapeutics: concepts and applications. *Angew. Chem., Int. Ed. 45*, 1198−215.

(7) Warnecke, A., and Kratz, F. (2003) Maleimide-oligo(ethylene glycol) derivatives of camptothecin as albumin-binding prodrugs: synthesis and antitumor efficacy. *Bioconjugate Chem. 14*, 377−387.

(8) Kratz, F., Warnecke, A., Scheuermann, K., Stockmar, C., Schwab, J., Lazar, P., Drückes, P., Esser, N., Drevs, J., Rognan, D., Bissantz, C., Hinderling, C., Folkers, G., Fichtner, I., and Unger, C. (2002) Probing the cysteine-34 position of endogenous serum albumin with thiol-binding doxorubicin derivatives. Improved efficacy of an acid-sensitive doxorubicin derivative with specific albumin-binding properties compared to that of the parent compound. *J. Med. Chem. 45*, 5523−5533.

(9) Kratz, F., and Beyer, U. (1998) Serum proteins as drug carriers of anticancer agents: a review. *Drug Delivery 5*, 281−299.

(10) Unger, C., Medinger, M., Steinbild, S., Drevs, J., and Häring, B. (2006) Phase I dose-escalation and pharmacokinetic (PK) study of a (6-maleimidocaproyl) hydrazone derivative of doxorubicin (DOXO-EMCH) in patients with advanced cancers. German Cancer Congress, Berlin, March 22−26, 2006.

(11) Gmehling, D., Medinger, M., Kratz, F., Mross, K., Haering, B., Unger, C., and Drevs, J. (2005) Phase I dose-escalation and pharmacokinetic (PK) study of a (6-maleimidocaproyl)hydrazone derivative of doxorubicin (DOXO-EMCH) in patients with advanced cancers. *Proc. Am. Assoc. Cancer Res. 46*, 3987.

(12) Dubois, V., Dasnois, L., Lebtahi, K., Collot, F., Heylen, N., Havaux, N., Fernandez, A. M., Lobl, T. J., Oliyai, C., Nieder, M., Shochat, D., Yarranton, G. T., and Trouet, A. (2002) CPI-0004Na, a new extracellularly tumor-activated prodrug of doxorubicin: in vivo toxicity, activity, and tissue distribution confirm tumor cell selectivity. *Cancer Res. 62*, 2327−2331.

(13) Trouet, A., Masquelier, M., Baurain, R., and Deprez-De Campeneere, D. (1982) A covalent linkage between daunorubicin and proteins that is stable in serum and reversible by lysosomal hydrolases, as required for a lysosomotropic drug-carrier conjugate: *in vitro* and *in vivo* studies. *Proc. Natl. Acad. Sci. U.S.A. 79*, 626−629.

(14) Umemoto, N., Kato, Y., Endo, N., Takeda, Y., and Hara, T. (1989) Preparation and in vitro cytotoxicity of a methotrexate-anti-MM46

monoclonal antibody conjugate via an oligopeptide spacer. *Int. J. Cancer 43*, 677−684.
(15) Fitzpatrick, J. J., and Garnett, M. C. (1995) Studies on the mechanism of action of an MTX-HSA-MoAb conjugate. *Anticancer Drug Des. 10*, 11−24.
(16) Studer, M., Kroger, L. A., DeNardo, S. J., Kukis, D. L., and Meares, C. F. (1992) Influence of a peptide linker on biodistribution and metabolism of antibody-conjugated benzyl-EDTA. Comparison of enzymatic digestion in vitro and in vivo. *Bioconjugate Chem. 3*, 424−429.
(17) Czerwinski, G., Tarasova, N. I., and Michejda, C. J. (1998) Cytotoxic agents directed to peptide hormone receptors: defining the requirements for a successful drug. *Proc. Natl. Acad. Sci. U.S.A. 95*, 11520−11525.
(18) Kos, J., and Lah, T. T. (1998) Cysteine proteinases and their endogenous inhibitors: target proteins for prognosis, diagnosis and therapy in cancer (review). *Oncol. Rep. 5*, 1349−1361.
(19) Rochefort, H., Capony, F., and Garcia, M. (1990) Cathepsin D: a protease involved in breast cancer metastasis. *Cancer Metastasis Rev. 9*, 321−331.
(20) Thomssen, C., Schmitt, M., Goretzki, L., Oppelt, P., Pache, L., Dettmar, P., Janicke, F., and Graeff, H. (1995) Prognostic value of the cysteine proteases cathepsins B and cathepsin L in human breast cancer. *Clin. Cancer Res. 1*, 741−746.
(21) Goel, A., and Chauhan, S. S. (1997) Role of proteases in tumor invasion and metastasis. *Indian J. Exp. Biol. 35*, 553−564.
(22) Kos, J., Stabuc, B., Schweiger, A., Krasovec, M., Cimerman, N., Kopitar-Jerala, N., and Vrhovec, I. (1997) Cathepsins B, H, and L and their inhibitors stefin A and cystatin C in sera of melanoma patients. *Clin. Cancer Res. 3*, 1815−1822.
(23) Ebert, W., Knoch, H., Werle, B., Trefz, G., Muley, T., and Spiess, E. (1994) Prognostic value of increased lung tumor tissue cathepsin B. *Anticancer Res. 14*, 895−899.
(24) Werle, B., Julke, B., Lah, T., Spiess, E., and Ebert, W. (1997) Cathepsin B fraction active at physiological pH of 7.5 is of prognostic significance in squamous cell carcinoma of human lung. *Br. J. Cancer. 75*, 1137−1143.
(25) Campo, E., Munoz, J., Miquel, R., Palacin, A., Cardesa, A., Sloane, B. F., and Emmert-Buck, M. R. (1994) Cathepsin B expression in colorectal carcinomas correlates with tumor progression and shortened patient survival. *Am. J. Pathol. 145*, 301−309.
(26) Greenwald, R. B., Pendri, A., and Zhao, H. (1998) Stereoselective acylation of 20-(S)-camptothecin with amino acid derivatives using scandium triflate/DMAP. *Tetrahedron: Asymmetry 9*, 915−918.
(27) Werle, B., Ebert, W., Klein, W., and Spiess, E. (1994) Cathepsin B in tumors, normal tissue and isolated cells from the human lung. *Anticancer Res. 14*, 1169−1176.
(28) Duffy, M. J., Blaser, J., Duggan, C., McDermott, E., O'Higgins, N., Fennelly, J. J., and Tschesche, H. (1995) Assay of matrix metalloproteases types 8 and 9 by ELISA in human breast cancer. *Br. J. Cancer 71*, 1025−1028.
(29) Buttle, D. J., Murata, M., Knight, C. G., and Barrett, A. J. (1992) CA074 methyl ester: a proinhibitor for intracellular cathepsin B. *Arch. Biochem. Biophys. 299*, 377−380.
(30) Burke, T. G., and Mi, Z. (1993) Preferential binding of the carboxylate form of camptothecin by human serum albumin. *Anal. Biochem. 212*, 285−287.
(31) Burke, T. G., and Mi, Z. (1994) The structural basis of camptothecin interactions with serum albumin: impact on drug stability. *J. Med. Chem. 37*, 40−46.
(32) Burke, T. G., Munshi, C. B., Mi, Z., and Jiang, Y. (1995) The important role of albumin in determining the relative human blood stabilities of the camptothecin anticancer drugs. *J. Pharm. Sci. 84*, 518−519.
(33) Mi, Z., and Burke, T. G. (1994) Differential interactions of camptothecin lactone and carboxylate forms with human blood components. *Biochemistry 33*, 10325−10336.
(34) Fleury, F., Ianoul, A., Berjot, M., Feofanov, A., Alix, A. J., and Nabiev, I. (1997) Camptothecin-binding site in human serum albumin and protein transformations induced by drug binding. *FEBS Lett. 411*, 215−220.
(35) Fleury, F., Kudelina, I., and Nabiev, I. (1997) Interactions of lactone, carboxylate and self-aggregated forms of camptothecin with human and bovine serum albumins. *FEBS Lett. 406*, 151−156.
(36) Greenwald, R. B., Pendri, A., Conover, C. D., Lee, C., Choe, Y. H., Gilbert, C., Martinez, A., Xia, Y., Wu, D., and Hsue, M. (1998) Camptothecin-20-PEG ester transport forms: the effect of spacer groups on antitumor activity. *Bioorg. Med. Chem. 6*, 551−562.
(37) Fernandez, A. M., Van Derpoorten, K., Dasnois, L., Lebtahi, K., Dubois, V., Lobl, T. J., Gangwar, S., Oliyai, C., Lewis, E. R., Shochat, D., and Trouet, A. (2001) N-Succinyl-(β-alanyl-L-leucyl-L-alanyl-L-leucyl)doxorubicin: an extracellularly tumor-activated prodrug devoid of intravenous acute toxicity. *J. Med. Chem. 44*, 3750−3753.
(38) Trouet, A., Passioukov, A., Van derpoorten, K., Fernandez, A. M., Abarca-Quinones, J., Baurain, R., Lobl, T. J., Oliyai, C., Shochat, D., and Dubois, V. (2001) Extracellularly tumor-activated prodrugs for the selective chemotherapy of cancer: application to doxorubicin and preliminary in vitro and in vivo studies. *Cancer Res. 61*, 2843−2846.
(39) Kline, T., Torgov, M. Y., Mendelsohn, B. A., Cerveny, C. G., and Senter, P. D. (2004) Novel antitumor prodrugs designed for activation by matrix metalloproteinases-2 and -9. *Mol. Pharm. 1*, 9−22.
(40) Deprez-DeCampeneere, D., Jaenke, R., and Trouet, A. (1982) Comparative cardiac and renal toxicity of daunorubicin in the rat and rabbit. *Cancer Treat. Rep. 66*, 395−397.
(41) de Jong, J., Geijssen, G. J., Munniksma, C. N., Vermorken, J. B., and van der Vijgh, W. J. (1992) Plasma pharmacokinetics and pharmacodynamics of a new prodrug N-L-leucyldoxorubicin and its metabolites in a phase I clinical trial. *J. Clin. Oncol. 10*, 1897−1906.
(42) de Jong, J., Klein, I., Bast, A., and van der Vijgh, W. J. (1992) Analysis and pharmacokinetics of N-L-leucyldoxorubucin and metabolites in tissues of tumor-bearing BALB/c mice. *Cancer Chemother. Pharmacol. 31*, 156−160.
(43) de Jong, J., Vermorken, J. B., and van der Vijgh, W. J. (1992) Analysis and pharmacokinetics of a new prodrug N-L-leucyldoxorubicin and its metabolites in plasma using HPLC with fluorescence detection. *J. Pharm. Biomed. Anal. 10*, 309−314.
(44) DeFeo-Jones, D., Garsky, V. M., Wong, B. K., Feng, D. M., Bolyar, T., Haskell, K., Kiefer, D. M., Leander, K., McAvoy, E., Lumma, P., Wai, J., Senderak, E. T., Motzel, S. L., Keenan, K., Van Zwieten, M., Lin, J. H., Freidinger, R., Huff, J., Oliff, A., and Jones, R. E. (2000) A peptide-doxorubicin 'prodrug' activated by prostate-specific antigen selectively kills prostate tumor cells positive for prostate-specific antigen in vivo. *Nat. Med. 6*, 1248−1252.
(45) Garsky, V. M., Lumma, P. K., Feng, D. M., Wai, J., Ramjit, H. G., Sardana, M. K., Oliff, A., Jones, R. E., DeFeo-Jones, D., and Freidinger, R. M. (2001) The synthesis of a prodrug of doxorubicin designed to provide reduced systemic toxicity and greater target efficacy. *J. Med. Chem. 44*, 4216−4224.
(46) Wong, B. K., DeFeo-Jones, D., Jones, R. E., Garsky, V. M., Feng, D. M., Oliff, A., Chiba, M., Ellis, J. D., and Lin, J. H. (2001) PSA-specific and non-PSA-specific conversion of a PSA-targeted peptide conjugate of doxorubicin to its active metabolites. *Drug Metab. Dispos. 29*, 313−318.
(47) Caiolfa, V. R., Zamai, M., Fiorino, A., Frigerio, E., Pellizzoni, C., d'Argy, R., Ghiglieri, A., Castelli, M. G., Farao, M., Pesenti, E., Gigli, M., Angelucci, F., and Suarato, A. (2000) Polymer-bound camptothecin: initial biodistribution and antitumour activity studies. *J. Controlled Release 65*, 105−119.
(48) Koblinski, J. E., Ahram, M., and Sloane, B. F. (2000) Unraveling the role of proteases in cancer. *Clin. Chim. Acta 291*, 113−135.
(49) Barrett, A. J., and Kirschke, H. (1981) Cathepsin B, cathepsin H, and cathepsin L. *Methods Enzymol. 80 Pt C*, 535−561.
(50) Vasey, P. A., Kaye, S. B., Morrison, R., Twelves, C., Wilson, P., Duncan, R., Thomson, A. H., Murray, L. S., Hilditch, T. E., Murray, T., Burtles, S., Fraier, D., Frigerio, E., and Cassidy, J. (1999) Phase I clinical and pharmacokinetic study of PK1 [*N*-(2-hydroxypropyl)-methacrylamide copolymer doxorubicin]: first member of a new class of chemotherapeutic agents-drug-polymer conjugates. *Clin. Cancer Res. 5*, 83−94.
(51) Dubowchik, G. M., Firestone, R. A., Padilla, L., Willner, D., Hofstead, S. J., Mosure, K., Knipe, J. O., Lasch, S. J., and Trail, P. A. (2002) Cathepsin B-labile dipeptide linkers for lysosomal release of doxorubicin from internalizing immunoconjugates: model studies

of enzymatic drug release and antigen-specific in vitro anticancer activity. *Bioconjugate Chem. 13*, 855−869.

(52) Schoemaker, N. E., van Kesteren, C., Rosing, H., Jansen, S., Swart, M., Lieverst, J., Fraier, D., Breda, M., Pellizzoni, C., Spinelli, R., Grazia, Porro, M., Beijnen, J. H., Schellens, J. H., and ten Bokkel Huinink, W. W. (2002) A phase I and pharmacokinetic study of MAG-CPT, a water-soluble polymer conjugate of camptothecin. *Br. J. Cancer. 87*, 608−614.

(53) Greenwald, R. B. (2001) PEG drugs: an overview. *J. Controlled Release 74*, 159−171.

(54) Harada, M., Sakakibara, H., Yano, T., Suzuki, T., and Okuno, S. (2000) Determinants for the drug release from T-0128, camptothecin analogue-carboxymethyl dextran conjugate. *J. Controlled Release 69*, 399−412.

(55) Walker, M. A., Dubowchik, G. M., Hofstead, S. J., Trail, P. A., and Firestone, R. A. (2002) Synthesis of an immunoconjugate of camptothecin. *Bioorg. Med. Chem. Lett. 12*, 217−219.

(56) Guiotto, A., Canevari, M., Orsolini, P., Lavanchy, O., Deuschel, C., Kaneda, N., Kurita, A., Matsuzaki, T., Yaegashi, T., Sawada, S., and Veronese, F. M. (2004) Synthesis, characterization, and preliminary in vivo tests of new poly(ethylene glycol) conjugates of the antitumor agent 10-amino-7-ethylcamptothecin. *J. Med. Chem. 47*, 1280−1289.

(57) Paranjpe, P. V., Stein, S., and Sinko, P. J. (2005) Tumor-targeted and activated bioconjugates for improved camptothecin delivery. *Anticancer Drugs 16*, 763−775.

BC0602735

Biotinylated Photocleavable Polyethylenimine: Capture and Triggered Release of Nucleic Acids from Solid Supports

Rachel G. Handwerger[†] and Scott L. Diamond[†,‡,*]

Institute for Medicine and Engineering, 1024 Vagelos Laboratories, University of Pennsylvania, Philadelphia, Pennsylvania 19104. Received September 8, 2006; Revised Manuscript Received January 2, 2007

A *b*iotinylated *p*hotoc*l*eavable *p*oly*e*thylen*i*mine (B-PC-PEI) was designed and synthesized for the capture and controlled release of nucleic acids from solid supports. B-PC-PEI was synthesized via a three-step reaction process and verified by ^{1}H NMR and mass spectrometry. In aqueous solution, the *o*-nitrobenzyl group within B-PC-PEI was efficiently cleaved by 5 min of 365 nm light exposure from a distance of 20 cm (9 mW/cm^2). When coupled to streptavidin-coated beads, the PEI domain of Cy5-labeled B-PC-PEI was released by 365 nm light exposure. In contrast, a Cy5-labeled biotinylated PEI (B-PEI) was used as a control and negligible fluorescence loss was observed. Cy5-labeled siRNA was electrostatically captured to streptavidin-coated beads preabsorbed with B-PC-PEI or B-PEI, and flow cytometry demonstrated significant loss of fluorescence from the bead surface after 5 min of light exposure only for B-PC-PEI, demonstrating controlled release of siRNA from the bead surface. Finally, the release of the Cy5-labeled siRNA into the supernatant was quantified. The release of Cy5-siRNA into the supernatant was significantly greater after 5 min of light exposure for B-PC-PEI/streptavidin beads compared to 0 min exposure and remained unchanged for B-PEI/streptavidin beads. B-PC-PEI facilitates capture and triggered release of surface-tethered nucleic acids with light exposure and is fully compatible with streptavidin-based applications.

INTRODUCTION

Photolabile protecting groups function by rendering a molecule of interest inert until photolysis and have been used extensively since their introduction in 1962 (*1*) for controlled release and kinetic studies (*2*−*13*). For biological systems, this approach allows control of concentration, location, and timing of the compound's release into a system. Furthermore, this technology, when applied to biomedical release applications, may mitigate problems such as off-target effects of a therapeutic agent. The potential to use photolytic release for gene delivery was first described by Monroe et al., who synthesized a 1-(4,5-dimethoxy-2-nitrophenyl)diazoethane caged plasmid DNA (pDNA) for light-activated gene delivery. However, the caging group limited transcription of pDNA because of direct modification of the pDNA backbone, and photolysis caused pDNA nicking. Also the caged pDNA had to be formulated with liposomes or precipitated onto gold beads for transfection (*8*).

Spatially controlled delivery of nucleic acids often involves substrate-mediated delivery or encapsulation within a polymeric scaffold. For substrate-mediated delivery of DNA, biotinylated polymers such as polyethylenimine (PEI)[1] and polylysine (PLL) have been attached to avidin-coated supports and provided for increased and positionally controlled transfection compared to polymer/DNA polyplexes absorbed nonspecifically onto the surface (*14*, *15*) or delivered via standard transfection methods (*14*). The increased function of surface-tethered polyplexes could be due to inhibition of aggregation and consequent intracellular sequestration (*15*) or to elevated local concentration of nucleic acids at the cell surface, which can increase transfection efficiency (*16*). Nucleic acids have also been immobilized in degradable scaffolds for localized delivery. There are many examples of both biological and synthetic scaffolds in the literature (as reviewed by Pannier and Shea (*17*)). The delivery of pDNA to cells from polymer scaffolds is controlled by the polymer degradation rate, a property that can be engineered (*18*).

2-Nitrobenzyl groups for photolability have been commonly used for biomedical applications. While the exact mechanisms and chemical intermediates leading to photolability are not fully resolved, light exposure does cause an intramolecular H-atom transfer which leads to an *aci*-nitro tautomer followed by nitroso group formation. This process is discussed in detail in McCray and Trentham (*7*), Pillai (*19*), Il'ichev et al. (*20*), and Schwörer and Wirz (*21*). In particular, α-substituted 2-nitrobenzyl esters exhibit highly efficient cleavage and are stable in biological systems (*4*, *6*, *22*, *23*) and under synthetic conditions for biomolecules such as peptide synthesis (*19*). Moreover, the near-UV light used to activate the photolysis is not harmful to many biomolecules and biological systems (*24*).

Photocleavable biotin molecules (B-PC) have been previously developed to combine both photolability and high affinity capture (*25*). The biotin−avidin association is essentially irreversible ($K_a = 10^{15}$ M^{-1}) and commonly used. Subsequent release of the biomolecule after isolation remains a challenge, as the association is relatively unaffected by pH, temperature, and 8 M guanidine-HCl at neutral pH. Typically, harsh conditions (e.g., detergents in combination with high temperature) succeed in dissociating the biotin−avidin interaction. B-PCs eliminate this shortcoming because exposure to light at specific wavelengths can cleave the biomolecule from the biotin. B-PCs have been used for several applications, including isolation and release of small peptides (*25*) and nucleotides for DNA extension products (*22*), and phosphorylation and purification of oligonucleotides (*26*).

* Corresponding author. Tel: 215-573-5702; Fax: 215-573-6815; Email: sld@seas.upenn.edu.

† Department of Bioengineering.

‡ Department of Chemical and Biomolecular Engineering.

[1] Abbreviations: B, biotin; PC, photocleavable; PEI, polyethylenimine; PLL polylysine; siRNA, small interfering RNA.

10.1021/bc060280t CCC: $37.00 © 2007 American Chemical Society
Published on Web 04/14/2007

In this report, we present a new approach that combines photolability and surface-tethering technology for the capture and controlled release of nucleic acids without covalent modification of the nucleic acids. PEI was covalently modified with a photolabile biotin group. This new compound was attached to the surface of streptavidin-coated beads and then mixed with siRNA to form tethered polyplexes. Exposure at 365 nm to the functionalized beads caused the release of PEI/siRNA complexes from the surface of the bead into the supernatant. Spatially and temporally controlled release of metered doses of nucleic acids from a solid surface can be potentially useful for biomedical applications, determination of rate-limiting factors for gene delivery, and for screening studies where temporally and spatially controlled release could offer insight into cellular processes.

EXPERIMENTAL PROCEDURES

Synthesis of Biotin−PC-PEI. All chemicals were purchased from Sigma-Aldrich (St. Louis, MO) unless otherwise specified. All experiments were performed under dimmed light conditions and with foil coverings.

Biotin−PC-Linker **3** was synthesized as previously described in Bai et al. (*22*). Briefly, 1-[5-(aminomethyl)-2-nitro]phenylethanol **1** (0.045 g, 0.23 mmol), a generous gift from Dr. Jingyue Ju of Columbia University, was dissolved in 1.5 mL of DMF. A volume of 0.325 mL of 1 M $NaHCO_3$ was added to the solution and stirred. To the mixture, biotin-NHS ester **2** (0.045 g, 0.10 mmol, Invitrogen, Carlsbad, CA) in 1.5 mL of DMF was slowly added while stirring. The reaction solution was stirred for 5 h (RT). The final product, **3** (0.048 g, 0.090 mmol, 90% yield), was purified using a silica gel column (80% CH_2Cl_2:20% MeOH (v:v)). ^{1}H NMR (300 MHz, MeOH-*d*) δ 7.89 (d, 1H), 7.80 (s, 1H), 7.34 (d, 1H), 5.35 (q, 1H), 4.52−4.48 (m, 3H), 4.33−4.29 (m, 1H), 3.23−3.18 (m, 3H), 2.95 (d, 1H), 2.70 (d, 1H), 2.30 (t, 2H), 2.20 (t, 2H), 1.78−1.47 (m, 16H).

Biotin−PC-NHS ester **4** was synthesized as previously described in Bai et al. (*22*). Briefly, **3** (0.011 g, 0.021 mmol) and *N*,*N*′-disuccinimidyl carbonate (0.0092 g, 0.036 mmol) were dissolved in 0.3 mL of anhydrous DMF. Triethylamine (0.008 mL, 0.057 mmol) was added, and the reaction mixture was stirred under Ar for 6 h (RT). The solvent was evaporated and the product dissolved in 1 mL of 1 M $NaHCO_3$. The solution was extracted 3× with EtOAc and concentrated in vacuo. The product mixture was dissolved in DMF and purified by preparative TLC (85% CH_2Cl_2:15% MeOH (v:v)). The product band was isolated from the TLC plate and soaked in DMF for 4.5 h (RT), after which it was centrifuged to separate the product from the silica. The solvent was removed in vacuo to yield **4** (0.0022 mg, 0.0032 mmol, 16% yield). ^{1}H NMR (300 MHz, DMSO-d_6) δ 8.74 (s, 1H), 8.02 (d, 1H), 7.75 (t, 1H), 7.66 (s, 1H), 7,47 (s, 1H), 6.42 (s, 1H), 6.36 (s, 1H), 6.28 (q, 1H), 4.40 (d, 2H), 4.35−4.28 (m, 1H), 4.12 (m, 1H), 3.09−3.01 (m, 1H), 2.99 (s, 2H), 2.89−2.78 (m, 6H), 2.56 (s, 1H), 2.16 (t, 2H). 2.03 (t, 3H), 1.72 (d, 2H), 1.50−1.24 (m, 12H).

Biotin−PC-PEI (B-PC-PEI) **5**. Polyethylenimine (PEI, 800 Da, 0.0006 g, 0.00075 mmol) was dissolved in 0.3 mL of H_2O, to which 0.07 mL of 1 M $NaHCO_3$ was added dropwise. The reaction mixture was allowed to equilibrate and **4** (0.0011 g, 0.0016 mmol) in 0.3 mL of DMSO was slowly added. The reaction was stirred for 5 h and then concentrated in vacuo to yield **5**.

Synthesis of Biotin−PEI. PEI (800 Da, 0.0083 g, 0.010 mmol) was dissolved in 0.2 M $NaHCO_3$ (1 mL) and stirred to equilibrate. To the mixture was slowly added biotin-NHS ester **2** (0.010 g, 0.022 mmol) in anhydrous DMSO (1 mL). The reaction was stirred for 5.5 h and concentrated in vacuo to yield Biotin−PEI (B-PEI).

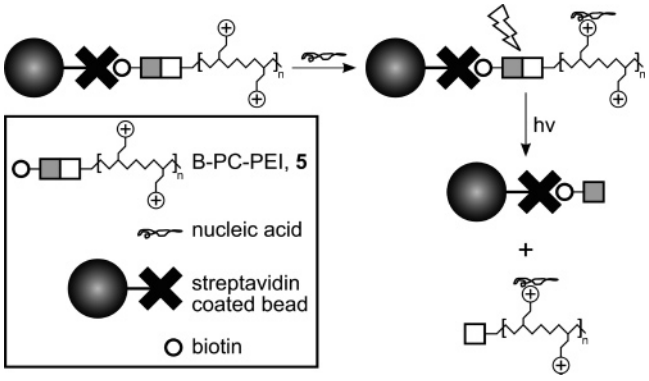


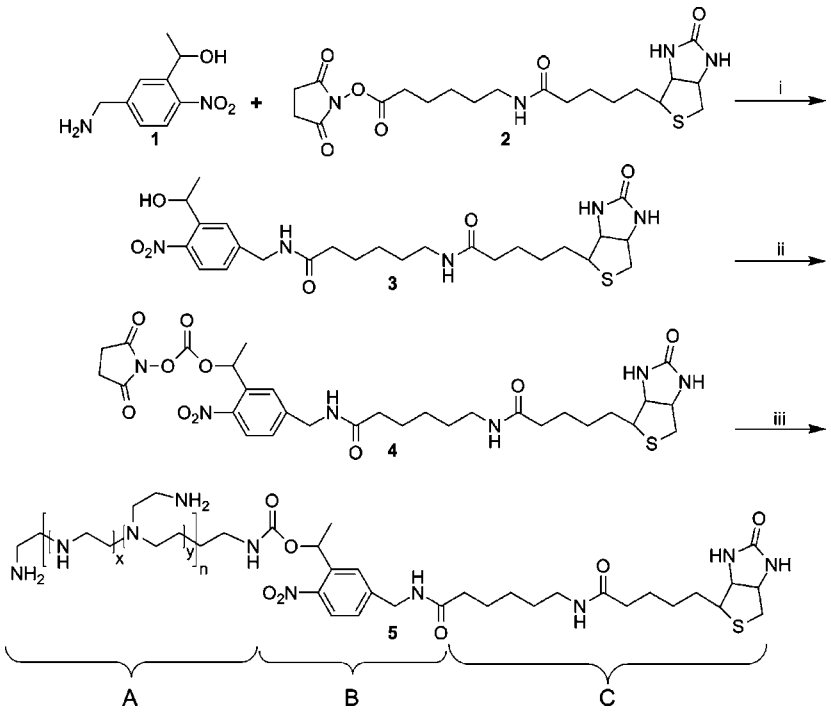
Figure 1. Schematic of B-PC-PEI bead formulation with nucleic acids and release with light exposure.

Testing for Photocleavability. UV irradiation was performed with a Model B-100A Hi Intensity UV Lamp (UVP Inc., Upland, CA) at a distance of 20 cm (emission peak at 365 nm, 9 mW/cm^2). B-PC-PEI, B-PEI, and PEI (0.01 mM) in H_2O receiving either 0, 5, or 10 min of 365 nm light exposure were analyzed by mass spectrometry on a 4700 Proteomics Analyzer with TOF/TOF optics (Applied Biosystems, Foster City, CA) at the University of Pennsylvania's Proteomics Core Facility.

Measuring Release of PEI from Streptavidin Microbeads. UV irradiation was performed, as described previously. For tracer studies, B-PC-PEI and B-PEI were covalently labeled with Cy5 NHS ester (Amersham Biosciences, Piscataway, NJ) according to the manufacturer's protocol using the ratio 1 mol Cy5 per 1 mol PEI primary amine. Streptavidin-coated magnetic beads (600 000 beads, Dynabeads M-280 streptavidin beads, Invitrogen) in 0.92 μL of phosphate-buffered saline (PBS, pH 7.4, Invitrogen) were added to 0.92 μL of 4.96 pmol/μL Cy5-labeled B-PEI or B-PC-PEI. A volume of 1.86 μL PBS was added, and the beads were allowed to incubate for 2 h (RT). The volume was brought to 300 μL, and 100 μL aliquots received either 0, 5, or 10 min of 365 nm light exposure. The samples were analyzed in a total volume of 400 μL of PBS on a BD FACSCalibur system (BD Biosciences, Franklin Lakes, NJ) at the University of Pennsylvania's Flow Cytometry and Cell Sorting Facility; 10 000 events were recorded per sample. The machine was calibrated to a negative control of unmodified streptavidin beads and a positive control of streptavidin beads directly labeled with Cy5 NHS ester. Flow cytometry data was analyzed with a custom Matlab (Mathworks Inc., Natick, MA) script designed to calculate the *x*-distance of the weighted maximum peak height for each sample. The fluorescence remaining on the bead after light exposure was calculated as a ratio comparing the *x*-distance of the maximum peak height at the specified time of 365 nm exposure to the *x*-distance of the maximum peak height for 0 min of 365 nm exposure.

Measuring Release of siRNA/PEI Polyplexes from Streptavidin Microbeads. Small interfering RNAs (siRNA) for lysosomal DNase II (siRNA ID = 121319, Ambion, Austin, TX) were labeled with Cy5 using a Label IT Nucleic Acid Labeling Kit (Mirus Bio Corporation, Madison, WI) according to the manufacturer's protocol and purified by ethanol precipitation. B-PC-PEI and B-PEI (unlabeled) were incubated with the streptavidin beads, as above, except for 1.5 h. The coated beads were diluted 10× with HEPES-buffered saline (HBS, 15 mM HEPES, 150 mM NaCl, pH 7.2) and added to the Cy5-labeled siRNA in HBS at varying N/P ratios. The polyplexes were allowed to form for 15 min (RT), and then the volume was adjusted to 300 μL with HBS. Aliquots (100 μL) were exposed to either 0, 5, or 10 min of 365 nm light (Figure 1). The samples

Scheme 1. Three-Step Synthesis of B-PC-PEI 5[a]



[a] Reagents and conditions: (i) $NaHCO_3$, DMF for 5 h; (ii) *N*,*N*′-disuccinimidyl carbonate, anhydrous DMF, Et_3N for 6 h; (iii) polyethylenimine, $NaHCO_3$, DMSO for 5 h.

were analyzed in a total volume of 400 μL of HBS on a BD FACSCalibur.

Quantifying the Amount of siRNA Released into the Supernatant. Streptavidin beads were prepared as above for siRNA/PEI polyplexes except after incubation with the Cy5-labeled siRNA the volume was brought to 100 μL with HBS. The samples were then placed on a Dynal MPC magnet (Invitrogen), and the supernatant was removed to remove any unbound siRNA/PEI polyplexes. The beads were then dissolved in 200 μL of HBS, and 100 μL aliquots received either 0, 5, or 10 min of 365 nm exposure. After exposure, the samples were placed on the magnet, the supernatant was separated from the beads, and the fluorescence of each was measured in 100 μL of HBS. The measurements were taken in a black 96-well plate (Nunc, Rochester, NY) on an EnVision Multilabel Plate Reader (Perkin-Elmer, Wellesley, MA). The fluorescence intensity (FI) data was used to calculate percent release [$100 \times FI_{supernatant}/(FI_{supernatant} + FI_{beads})$].

siRNA Stability. Negative control siRNA (0.4 μg, #4611G, Ambion) was tested alone, complexed with B-PC-PEI (N/P = 0.4), and complexed with B-PC-PEI attached to streptavidin beads (as described above). Each of these conditions received either 0 or 5 min of 365 nm light exposure, after which 2 μL of 6x loading dye (Promega, Madison, WI) was added. The samples (10 μL) were loaded into the wells of a 1% agarose gel in 1x TAE with SYBR Safe gel stain (Molecular Probes, Carlsbad, CA). The gel was run at 100 V for 30 min. Positive and negative controls were naked siRNA and B-PC-PEI, respectively.

RESULTS

Design, Synthesis, and Validation of Biotin−PC-PEI. Biotin−PC-PEI (B-PC-PEI) was designed to consist of three functional domains: (1) a cationic polymer domain (A in Scheme 1), in this case PEI, to electrostatically interact with and condense nucleic acids; (2) a photolabile domain (B in Scheme 1) to selectively release the polyplexes; (3) a biotin domain (C in Scheme 1) used to tether the compound to a streptavidin-coated surface or interact with free streptavidin. B-PC-PEI was synthesized via a three-step reaction process (Scheme 1) and was verified by ^{1}H NMR (Figure 2) and mass spectrometry (Figure 3A). By comparing mass spectrometry data from B-PC-PEI (Figure 3A) and unmodified PEI (not shown), it is estimated that the majority of the PEI received, on average, one photolabile-biotin arm (domains B and C, peaks centered around m/z = 966.62) and a smaller percentage received two photolabile-biotin arms (peaks centered around m/z = 1527.86).

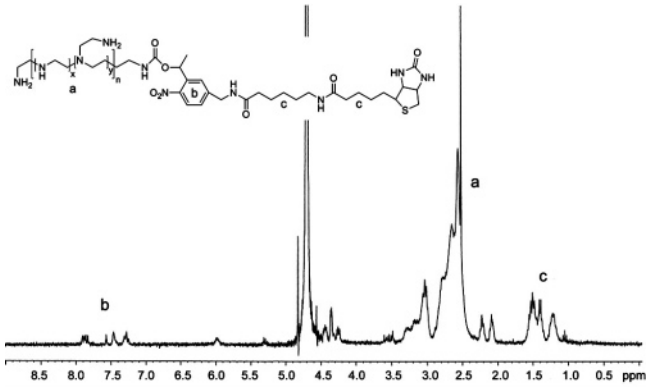


Figure 2. ^{1}H NMR of B-PC-PEI.

After validation of its formation, B-PC-PEI was analyzed for the ability to breakdown after exposure to 365 nm light. B-PC-PEI was analyzed by mass spectrometry before and after 5 min of 365 nm light exposure (Figures 3A and 3B, respectively). After 5 min of light exposure, the peaks centered around m/z = 1527.86 completely disappeared and the peaks centered around m/z = 966.62 shifted to a lower m/z value, indicating that the photolabile biotin arms were cleaved from the PEI. Increasing the duration of light exposure to 10 min did not further increase the breakdown of B-PC-PEI (not shown). As a control, Biotin−PEI (B-PEI) was synthesized to have

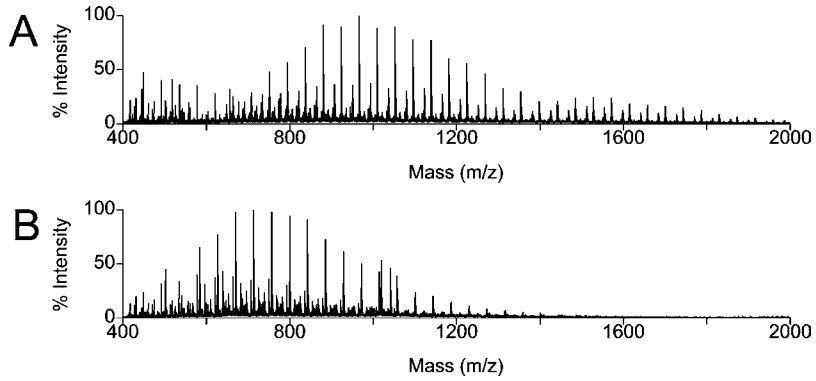


Figure 3. Mass spectrometry for B-PC-PEI without light exposure (A) and with 5 min of 365 nm light exposure (B).

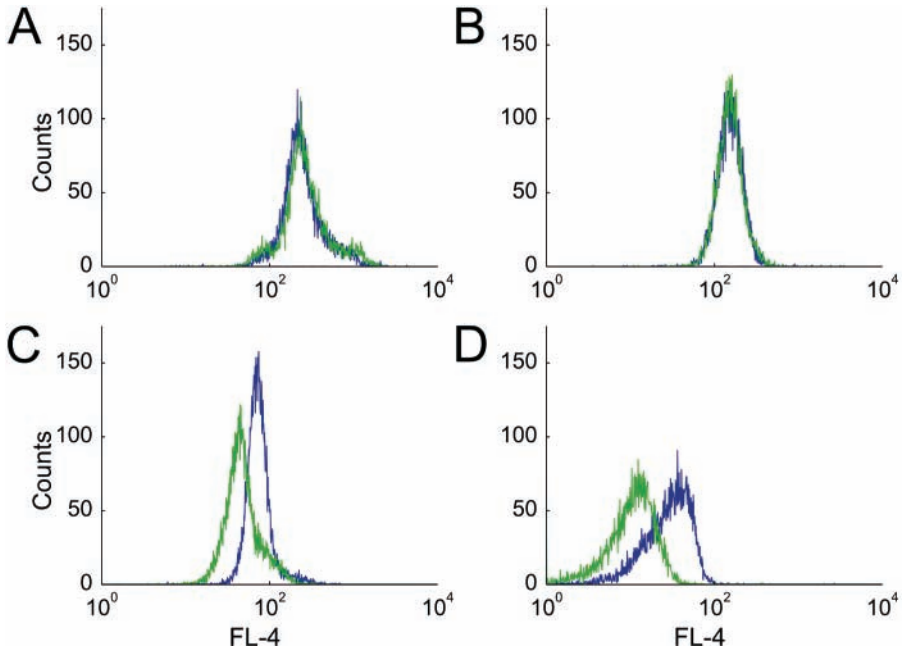


Figure 4. Flow cytometry data showing the fluorescence shifts of B-PEI/streptavidin beads without (A) or with (B) siRNA, and of B-PC-PEI/streptavidin beads without (C) or with (D) siRNA due to light exposure (green line, 10 min (A and C) or 5 min (B and D) of 365 nm exposure; blue line, 0 min exposure).

domains A and C of B-PC-PEI (i.e., no photolabile domain B, see Scheme 1 for designations). Mass spectrometry validated the formation of this compound and showed no change in the spectra with exposure to 5 or 10 min of 365 nm light (not shown).

Release of PEI from Streptavidin Beads. B-PC-PEI was immobilized to the surface of streptavidin-coated beads as depicted in Figure 1. To determine release of the PEI domain from the streptavidin beads, the PEI primary amines of B-PC-PEI were labeled with Cy5 NHS ester prior to immobilization. The streptavidin beads bound with Cy5-labeled B-PC-PEI were then exposed to 0, 5, or 10 min of 365 nm light and analyzed by flow cytometry for fluorescence loss. As a control, B-PEI, labeled with Cy5, was subjected to the same procedure to differentiate between fluorescence loss due to photobleaching from the 365 nm light exposure and fluorescence loss due to actual release of the Cy5-labeled PEI domain from the surface of the bead.

As can be seen in Figure 4A and 4C, after 10 min of 365 nm exposure, there was a negligible loss of fluorescence due to photobleaching (Figure 4A, B-PEI) and a much larger shift (fluorescence loss) due to actual cleavage of the Cy5-labeled PEI domain from the surface of the bead (Figure 4C, B-PC-PEI). This data when looked at numerically as the fraction of remaining fluorescence associated with the bead (see Experimental Procedures for details of the calculations) translates to values of 0.78 ± 0.15 and 0.90 ± 0.09 ($n = 6$, $p < 0.07$) for B-PC-PEI and B-PEI, respectively, after 5 min of light exposure, and 0.51 ± 0.12 and 0.97 ± 0.23 ($n = 6$, $p < 0.0008$) for B-PC-PEI and B-PEI, respectively, after 10 min of light exposure.

Release of siRNA from Streptavidin Beads. To quantify the release of nucleic acids from streptavidin beads, unlabeled B-PC-PEI was immobilized to streptavidin beads, as described above, and added to Cy5-labeled siRNA at an N/P ratio = 0.16 (Figure 1). The immobilized siRNA/B-PC-PEI polyplexes received either 0, 5, or 10 min of 365 light exposure and were analyzed by flow cytometry for fluorescence loss. As with the experiments measuring the loss of PEI from the surface of the streptavidin beads, B-PEI in place of B-PC-PEI was used as a control. As seen in Figure 4B and 4D, after 5 min of 365 nm light exposure, there was negligible fluorescence loss due to photobleaching (Figure 4B, B-PEI/siRNA), and significant fluorescence loss due to release of siRNA from the surface of the bead (Figure 4D, B-PC-PEI/siRNA). Quantitatively, the fraction of remaining fluorescence was 0.52 ± 0.14 and 0.94 ± 0.10 ($n = 3$, $p < 0.007$) for B-PC-PEI/siRNA and B-PEI/siRNA polyplexes, respectively. Increasing the light exposure to 10 min further increased the release of the B-PC-PEI/siRNA polyplexes with the fraction remaining reduced to 0.27 ± 0.13

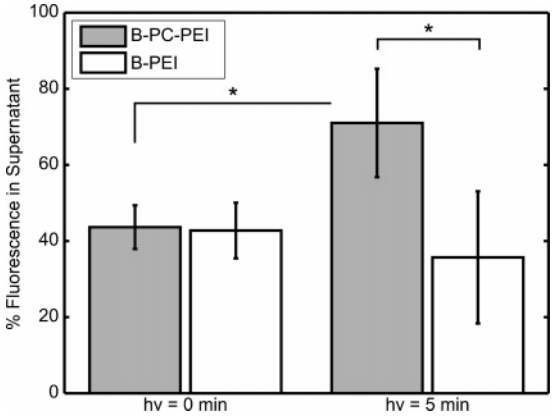


Figure 5. Release of surface bound siRNA/PEI complexes into the supernatant (* = $p < 0.03$).

($p < 0.05$ comparing B-PC-PEI/siRNA at 5 and 10 min light exposure). This data was consistent at N/P ratios of 1.6 and 4.8 for B-PC-PEI, but N/P = 0.16 showed optimal fluorescence readings for flow cytometry.

As an additional test, siRNA was immobilized to the streptavidin beads as above, but the fluorescence in both the supernatant and on the bead were measured. Fluorescence was measured as relative fluorescence units on a plate reader and converted into percent fluorescence in the supernatant (as described in the Experimental Procedures). After 0 min of 365 nm light exposure, both B-PC-PEI and B-PEI immobilized polyplexes (N/P = 0.4) released a similar amount of fluorescence in the supernatant (Figure 5). With 5 min of 365 nm light exposure, the amount of fluorescence in the supernatant was significantly higher for B-PC-PEI than for B-PEI immobilized polyplexes ($p < 0.03$, Figure 5). Increasing light exposure to 10 min did not enhance release of siRNA from B-PC-PEI polyplexes (71.03 ± 14.24% and 78.34 ± 7.59% at 5 and 10 min of light exposure, respectively ($p > 0.05$)). Using these measurements, it is estimated that about 7 μg siRNA/mg bead is immobilized.

Finally, agarose gel electrophoresis was used to assess the integrity of the siRNA after exposure to the light-activated release conditions. The gels showed no difference in mobility between naked siRNA before or after light exposure, B-PC-PEI/siRNA polyplexes before or after light exposure, and B-PC-PEI/siRNA polyplexes released from streptavidin beads before or after light exposure (not shown).

DISCUSSION

Spatially and temporally controlled release of nucleic acids has many potential applications, including disease treatment and discovery of molecular processes involved in gene delivery. For nonviral gene therapy applications, spatial targeting has been attempted though inclusion of receptor targeting ligands to facilitate vector uptake into specific cells populations (*27*−*30*) and through the use of biotinylated cationic polymers for substrate-mediated delivery (*14*, *15*).

We developed a novel compound, B-PC-PEI, that combines surface-mediated delivery with photolabile technology for capture and light-activated controlled release of nucleic acids from solid supports. B-PC-PEI consists of three functional domains designed to tether the compound to a surface, interact with nucleic acids, and release the nucleic acids from the surface through exposure to 365 nm light. This represents the first time this type of compound has been used for the controlled release of noncovalently modified nucleic acids from streptavidin-coated solid supports.

The use of biotinylated PEI for substrate-mediated delivery of pDNA can result in positive transfection (*15*). The retention of nucleic acids within a PEI polyplex depends on the molecular weight of the polymer used (*31*), the characteristics of the polymer (e.g., linear versus branched (*32*)), and the N/P ratio (*33*). Additionally, the extent of biotinylation will also affect the electrostatic interactions between PEI and nucleic acids because each biotin added should remove one free primary amine. The amount of release for a biotinylated PEI should be tunable by adjusting each of these properties, and therefore it should be easy to design the system to have negligible nucleic acid release from the polymer unless the whole polyplex is released from the substrate with light, as with B-PC-PEI. Further validating this point, the use of biotinylated PLL did not show enhanced transfection unless the majority of the polyplex was formed with a non-biotinylated PLL (*15*).

For B-PC-PEI, photolysis of the PEI domain from the remaining molecule occurred within 5 min when in free solution (Figure 3) and 10 min when attached to streptavidin beads (Figure 4C). It is possible that increased light exposure was necessary to release the Cy5-labeled PEI domain from the streptavidin beads because the beads or the Cy5 attenuated some of the light. Also, PEI has been thought to form nonspecific interactions with streptavidin (*15*) so it is possible that for this experiment, those forces needed to be overcome as well. Comparing the fluorescence loss from the Cy5-labeled B-PC-PEI (Figure 4C) and B-PEI (Figure 4A) beads upon light exposure shows clearly that the loss is due to actual cleavage of the PEI domain from the bead and not photobleaching.

In addition to the two causes of fluorescence loss described previously, for the siRNA there could also be loss due to release of weakly associated siRNA from the bead. Similar to the results with the Cy5-labeled biotin-compounds, there was negligible fluorescence loss due to photobleaching or diffusion after 5 min of 365 nm light exposure (B-PEI polyplexes, Figure 4B). For polyplexes made with B-PC-PEI there was a significant loss of bead-associated fluorescence after only 5 min of light exposure (Figure 4D). As with the PEI domain, increasing the duration of light exposure further increased polyplex loss; however, the majority of siRNA was released in the first 5 min. This differs from the PEI results possibly because PEI is less able to nonspecifically interact with the streptavidin when it is electrostatically condensing the siRNA.

The loss of siRNA fluorescence from the bead was further validated by a gain in fluorescence in the supernatant (Figure 5). At 0 min of 365 nm light exposure both B-PC-PEI and B-PEI polyplexes have a similar percent fluorescence in the supernatant (presumably due to diffusion), but by 5 min of light exposure the B-PC-PEI/siRNA polyplexes had released 71.03 ± 14.24% of the polyplexes into the supernatant while the B-PEI polyplexes remained unchanged from the 0 min time point. Additionally, increasing the duration of light to 10 min did not significantly enhance the release of the B-PC-PEI polyplexes. It is important to note that release of siRNA at 0 min for both B-PC-PEI and B-PEI polyplexes is most likely due to the low N/P ratio. Increasing the N/P ratio would cause greater retention of the siRNA within the polyplex; however, N/P = 0.4 gave optimal fluorescence readings. Additionally, since it is the PEI and not the siRNA that is directly coupled to the beads and the light-activated mechanism, any released siRNA should be released as polyplexes with the PEI.

Finally, the integrity of the siRNA was tested with agarose gel electrophoresis, and under all conditions tested, light exposure did not change the mobility or noticeably degrade the siRNA. This result is expected, as experiments conducted by Quick and Anseth showed negligible change in pDNA integrity after 365 nm light exposure (*34*). Additionally, Quick and

Anseth showed retained pDNA activity after light exposure at 365 nm (*34*).

While polymers have been previously engineered for the controlled release of nucleic acids (*35*−*39*), the release has largely relied on cellular process. In this report, we have demonstrated the synthesis and functionality of a compound, B-PC-PEI, that is able to selectively release nucleic acids from a solid support after light application and which has many potential applications ranging from biological studies to therapeutic applications.

ACKNOWLEDGMENT

Drs. Xiaopeng Bai and Jingyue Ju of Columbia University for their help with chemical synthesis. This research was funded by NIH grants HL64388 and HL66565 (S.L.D.).

LITERATURE CITED

(1) Barltrop, J. A., and Schofield, P. (1962) Photosensitive Protecting Groups. *Tetrahedron Lett. 16* 3(16), 697−699.

(2) Sugi, H., Iwamoto, H., Akimoto, T., and Ushitani, H. (1998) Evidence for the load-dependent mechanical efficiency of individual myosin heads in skeletal muscle fibers activated by laser flash photolysis of caged calcium in the presence of a limited amount of ATP. *Proc. Natl. Acad. Sci. U.S.A. 95*, 2273−8.

(3) Meldrum, R. A., Shall, S., Trentham, D. R., and Wharton, C. W. (1990) Kinetics and mechanism of DNA repair. Preparation, purification and some properties of caged dideoxynucleoside triphosphates. *Biochem. J. 266*, 885−90.

(4) Kaplan, J. H., Forbush, B., 3rd, and Hoffman, J. F. (1978) Rapid photolytic release of adenosine 5′-triphosphate from a protected analogue: utilization by the Na:K pump of human red blood cell ghosts. *Biochemistry 17*, 1929−35.

(5) Walker, J. W., Reid, G. P., McCray, J. A., and Trentham, D. R. (1988) Photolabile 1-(2-Nitrophenyl)ethyl Phosphate Esters of Adenine Nucleotide Analogues. Synthesis and Mechanism of Photolysis. *J. Am. Chem. Soc. 110*, 7170−7177.

(6) Walker, J. W., McCray, J. A., and Hess, G. P. (1986) Photolabile protecting groups for an acetylcholine receptor ligand. Synthesis and photochemistry of a new class of *o*-nitrobenzyl derivatives and their effects on receptor function. *Biochemistry 25*, 1799−805.

(7) McCray, J. A., and Trentham, D. R. (1989) Properties and uses of photoreactive caged compounds. *Annu. Rev. Biophys. Biophys. Chem. 18*, 239−70.

(8) Monroe, W. T., McQuain, M. M., Chang, M. S., Alexander, J. S., and Haselton, F. R. (1999) Targeting expression with light using caged DNA. *J. Biol. Chem. 274*, 20895−900.

(9) Murphy, K. P., and Bliss, T. V. (1999) Photolytically released nitric oxide produces a delayed but persistent suppression of LTP in area CA1 of the rat hippocampal slice. *J. Physiol. 515* (*Pt 2*), 453−62.

(10) Perdicakis, B., Montgomery, H. J., Abbott, G. L., Fishlock, D., Lajoie, G. A., Guillemette, J. G., and Jervis, E. (2005) Photocontrol of nitric oxide production in cell culture using a caged isoform selective inhibitor. *Bioorg. Med. Chem. 13*, 47−57.

(11) Yip, K. P. (2005) Flash photolysis of caged nitric oxide inhibits proximal tubular fluid reabsorption in free-flow nephron. *Am. J. Physiol.: Regul. Integr. Comp. Physiol. 289*, R620−R626.

(12) Banerjee, A., Grewer, C., Ramakrishnan, L., Jager, J., Gameiro, A., Breitinger, H. G., Gee, K. R., Carpenter, B. K., and Hess, G. P. (2003) Toward the development of new photolabile protecting groups that can rapidly release bioactive compounds upon photolysis with visible light. *J. Org. Chem. 68*, 8361−7.

(13) McCarron, J. G., MacMillan, D., Bradley, K. N., Chalmers, S., and Muir, T. C. (2004) Origin and mechanisms of Ca2+ waves in smooth muscle as revealed by localized photolysis of caged inositol 1,4,5-trisphosphate. *J. Biol. Chem. 279*, 8417−27.

(14) Segura, T., and Shea, L. D. (2002) Surface-tethered DNA complexes for enhanced gene delivery. *Bioconjugate Chem. 13*, 621−9.

(15) Segura, T., Volk, M. J., and Shea, L. D. (2003) Substrate-mediated DNA delivery: role of the cationic polymer structure and extent of modification. *J. Controlled Release 93*, 69−84.

(16) Luo, D., and Saltzman, W. M. (2000) Enhancement of transfection by physical concentration of DNA at the cell surface. *Nat. Biotechnol. 18*, 893−5.

(17) Pannier, A. K., and Shea, L. D. (2004) Controlled release systems for DNA delivery. *Mol. Ther. 10*, 19−26.

(18) Quick, D. J., and Anseth, K. S. (2004) DNA delivery from photocrosslinked PEG hydrogels: encapsulation efficiency, release profiles, and DNA quality. *J. Controlled Release 96*, 341−51.

(19) Pillai, V. N. R. (1980) Photoremovable Protecting Groups in Organic Synthesis. *Synthesis 1980*, 1−26.

(20) Il'ichev, Y. V., Schworer, M. A., and Wirz, J. (2004) Photochemical reaction mechanisms of 2-nitrobenzyl compounds: methyl ethers and caged ATP. *J. Am. Chem. Soc. 126*, 4581−95.

(21) Schworer, M. A., and Wirz, J. (2001) Photochemical Reaction Mechanisms of 2-Nitrobenzyl Compounds in Solution. I. 2-Nitrotoluene: Thermodynamic and Kinetic Parameters of the aci-Nitro Tautomer. *Helv. Chim. Acta 81* 84(6), 1441−1458.

(22) Bai, X., Kim, S., Li, Z., Turro, N. J., and Ju, J. (2004) Design and synthesis of a photocleavable biotinylated nucleotide for DNA analysis by mass spectrometry. *Nucleic Acids Res. 32*, 535−41.

(23) Bai, X., Li, Z., Jockusch, S., Turro, N. J., and Ju, J. (2003) Photocleavage of a 2-nitrobenzyl linker bridging a fluorophore to the 5′ end of DNA. *Proc. Natl. Acad. Sci. U.S.A. 100*, 409−13.

(24) Holmes, C. P. (1997) Model Studies for New o-Nitrobenzyl Photolabile Linkers: Substituent Effects on the Rates of Photochemical Cleavage. *J. Org. Chem. 62*, 2370−2380.

(25) Olejnik, J., Sonar, S., Krzymanska-Olejnik, E., and Rothschild, K. J. (1995) Photocleavable biotin derivatives: a versatile approach for the isolation of biomolecules. *Proc. Natl. Acad. Sci. U.S.A. 92*, 7590−4.

(26) Olejnik, J., Krzymanska-Olejnik, E., and Rothschild, K. J. (1996) Photocleavable biotin phosphoramidite for 5-end-labeling, affinity purification and phosphorylation of synthetic oligonucleotides. *Nucleic Acids Res. 24*, 361−6.

(27) Erbacher, P., Remy, J. S., and Behr, J. P. (1999) Gene transfer with synthetic virus-like particles via the integrin-mediated endocytosis pathway. *Gene Ther. 6*, 138−45.

(28) Ogris, M., Steinlein, P., Carotta, S., Brunner, S., and Wagner, E. (2001) DNA/polyethylenimine transfection particles: influence of ligands, polymer size, and PEGylation on internalization and gene expression. *AAPS Pharmsci. 3*, E21.

(29) Remy, J. S., Kichler, A., Mordvinov, V., Schuber, F., and Behr, J. P. (1995) Targeted gene transfer into hepatoma cells with lipopolyamine-condensed DNA particles presenting galactose ligands: a stage toward artificial viruses. *Proc. Natl. Acad. Sci. U.S.A. 92*, 1744−8.

(30) Simoes, S., Slepushkin, V., Gaspar, R., de Lima, M. C., and Duzgunes, N. (1998) Gene delivery by negatively charged ternary complexes of DNA, cationic liposomes and transferrin or fusigenic peptides. *Gene Ther. 5*, 955−64.

(31) Godbey, W. T., Wu, K. K., and Mikos, A. G. (1999) Size matters: molecular weight affects the efficiency of poly(ethylenimine) as a gene delivery vehicle. *J. Biomed. Mat. Res. 45*, 268−75.

(32) Dunlap, D. D., Maggi, A., Soria, M. R., and Monaco, L. (1997) Nanoscopic structure of DNA condensed for gene delivery. *Nucleic Acids Res. 25*, 3095−101.

(33) Boussif, O., Lezoualc'h, F., Zanta, M. A., Mergny, M. D., Scherman, D., Demeneix, B., and Behr, J. P. (1995) A versatile vector for gene and oligonucleotide transfer into cells in culture and in vivo: polyethylenimine. *Proc. Natl. Acad. Sci. U.S.A. 92*, 7297−301.

(34) Quick, D. J., and Anseth, K. S. (2003) Gene delivery in tissue engineering: a photopolymer platform to coencapsulate cells and plasmid DNA. *Pharm. Res. 20*, 1730−7.

(35) Oupicky, D., Carlisle, R. C., and Seymour, L. W. (2001) Triggered intracellular activation of disulfide crosslinked polyelectrolyte gene delivery complexes with extended systemic circulation in vivo. *Gene Ther. 8*, 713−24.

(36) Trubetskoy, V. S., Loomis, A., Slattum, P. M., Hagstrom, J. E., Budker, V. G., and Wolff, J. A. (1999) Caged DNA does not aggregate in high ionic strength solutions. *Bioconjugate Chem. 10*, 624−8.

(37) Funhoff, A. M., van Nostrum, C. F., Janssen, A. P., Fens, M. H., Crommelin, D. J., and Hennink, W. E. (2004) Polymer side-chain degradation as a tool to control the destabilization of polyplexes. *Pharm. Res. 21*, 170−6.

(38) Petersen, H., Merdan, T., Kunath, K., Fischer, D., and Kissel, T. (2002) Poly(ethylenimine-co-L-lactamide-co-succinamide): a biodegradable polyethylenimine derivative with an advantageous pH-dependent hydrolytic degradation for gene delivery. *Bioconjugate Chem. 13*, 812−21.

(39) Hirosue, S., Muller, B. G., Mulligan, R. C., and Langer, R. (2001) Plasmid DNA encapsulation and release from solvent diffusion nanospheres. *J. Controlled Release 70*, 231−42.

BC060280T

Molecular Imaging of Gastrin-Releasing Peptide Receptor-Positive Tumors in Mice Using ^{64}Cu- and ^{86}Y-DOTA−(Pro^1,Tyr^4)-Bombesin(1−14)

Gráinne B. Biddlecombe,[†] Buck E. Rogers,[§,‡] Monique de Visser,[#] Jesse J. Parry,[§] Marion de Jong,[#] Jack L. Erion,[||] and Jason S. Lewis[†,‡,*]

Mallinckrodt Institute of Radiology, Department of Radiation Oncology, and the Alvin J. Siteman Cancer Center, Washington University School of Medicine, St. Louis, Missouri 63110, Department of Nuclear Medicine, Erasmus MC, Rotterdam, The Netherlands, and BioSynthema Inc., St. Louis, Missouri 63108. Received September 8, 2006; Revised Manuscript Received February 5, 2007

Bombesin is a tetradecapeptide neurohormone that binds to gastrin-releasing peptide receptors (GRPR). GRPRs have been found in a variety of cancers including invasive breast and prostate tumors. The peptide MP2346 (DOTA−(Pro^1,Tyr^4)-bombesin(1−14)) was designed to bind to these GRP receptors. This study was undertaken to evaluate radiolabeled MP2346 as a positron emission tomography (PET) imaging agent. MP2346 was radiolabeled, in high radiochemical purity, with the positron-emitting nuclides ^{64}Cu ($t_{1/2}$ = 12.7 h, β^+ = 19.3%, E_{avg} = 278 keV) and ^{86}Y ($t_{1/2}$ = 14.7 h, β^+ = 33%, E_{avg} = 664 keV). ^{64}Cu-MP2346 and ^{86}Y-MP2346 were studied *in vitro* for cellular internalization by GRPR-expressing PC-3 (human prostate adenocarcinoma) cells. Both ^{64}Cu- and ^{86}Y-MP2346 were studied *in vivo* for tissue distribution in nude mice with PC-3 tumors. Biodistribution in PC3 tumor-bearing mice demonstrated higher tumor uptake, but lower liver retention, in animals injected with ^{86}Y-MP2346 compared to ^{64}Cu-MP2346. Receptor-mediated uptake was confirmed by a significant reduction in uptake in the PC-3 tumor and other receptor-rich tissues by coinjection of a blockade. Small animal PET/CT imaging was carried out in mice bearing PC-3 tumors and rats bearing AR42J tumors. It was possible to delineate PC-3 tumors *in vivo* with ^{64}Cu-MP2346, but superior ^{86}Y-MP2346-PET images were obtained due to lower uptake in clearance organs and lower background activity. The ^{86}Y analogue demonstrated excellent PET image quality in models of prostate cancer for the delineation of the GRPR-rich tumors and warrants further investigation.

INTRODUCTION

Gastrin-releasing peptide (GRP), a 27-amino acid mammalian peptide, is responsible for the release of gastrin from stomach cells. The receptor for GRP (GRPR) has been found in a variety of cancers including ovarian, lung, gastrointestinal, and colon (*1*−*6*). GRPRs have also been shown to be present on invasive breast and prostate tumors (*7*, *8*). Bombesin (BN) is a 14-amino acid neuropeptide that was originally isolated from the skin of the Bombina frog and binds with high affinity to GRPR (*9*). A noninvasive method of detecting (by imaging) and treating GRPR-positive tumors has been achieved by the radiolabeling of BN analogues with diagnostic and therapeutic radionuclides (*10*−*12*).

Indium-111- and ^{99m}Tc-labeled BN analogues have been studied as potential single-photon emission computed tomography (SPECT) radiopharmaceuticals (*13*−*20*). BN analogues radiolabeled with ^{131}I, ^{188}Re, and ^{177}Lu (*21*−*23*) have been evaluated for potential radiotherapy applications. Positron emission tomography (PET) is a more quantitative imaging method compared to SPECT with better spatial resolution and image contrast. Animal studies have been carried out using ^{68}Ga-, ^{18}F-, and ^{64}Cu-labeled BN analogues utilizing PET and have shown good tumor localization and visualization (*24*−*28*).

Copper-64 ($t_{1/2}$ = 12.7 h, β^+ = 19.3%, E_{avg} = 278 keV) and ^{86}Y ($t_{1/2}$ = 14.7 h, β^+ = 33%, E_{avg} = 664 keV) can both be prepared on small cyclotrons utilizing the ^{64}Ni(p,n)^{64}Cu and ^{86}Sr(p,n)^{86}Y reactions, respectively (*29*, *30*). Because of the decay scheme of ^{64}Cu (17.4% β^+, 41% EC, 40% β^-), it has the potential to be used both for diagnostic and therapeutic applications (*31*). Yttrium-86 is a PET-emitting nuclide and can act as an imaging surrogate for ^{90}Y, which has been used extensively in nuclear medicine as a therapeutic nuclide. DOTA−(Pro^1, Tyr^4)-bombesin(1−14) (MP2346), where DOTA = 1,4,7,10-tetraazacyclododecan-*N*,*N*′,*N*″,*N*‴ tetraacetic acid (Figure 1) was previously synthesized and demonstrated promise for scintigraphic imaging of GRPR-expressing tumors after radiolabeling with ^{111}In (*13*). The goal of this study was to evaluate both ^{64}Cu- and ^{86}Y-radiolabeled MP2346 as candidates for the noninvasive detection of GRPR-positive tumors using PET.

EXPERIMENTAL PROCEDURES

General Methods and Materials. All chemicals unless otherwise stated were purchased from the Sigma-Aldrich Chemical Co. (St. Louis, MO). Water was distilled and then deionized (18 MΩ/cm^2) by passing through a milli-Q water filtration system (Millipore Corp., Milford, MA). Copper-64 and ^{86}Y were produced on a CS-15 biomedical cyclotron at Washington University School of Medicine, using published methods (*29*, *30*). PC-3 (human prostate adenocarcinoma) cells were obtained from American Type Culture Collection (ATCC) (Manassas, VA) and maintained in our laboratories by serial cell culture. Radioactivity was counted with a Beckman Gamma

* Address for correspondence: Jason S. Lewis, Ph.D., Mallinckrodt Institute of Radiology, Washington University School of Medicine, 510 South Kingshighway Blvd., Campus Box 8225, St. Louis, MO 63110. Phone: (314) 362-4696; fax: (314) 362-9940, e-mail: j.s.lewis@wustl.edu.

[†] Mallinckrodt Institute of Radiology, Washington University School of Medicine.

[§] Department of Radiation Oncology, Washington University School of Medicine.

[‡] Alvin J. Siteman Cancer Center, Washington University School of Medicine.

[#] Erasmus MC.

[||] BioSynthema Inc.

10.1021/bc060281l CCC: $37.00 © 2007 American Chemical Society
Published on Web 03/23/2007

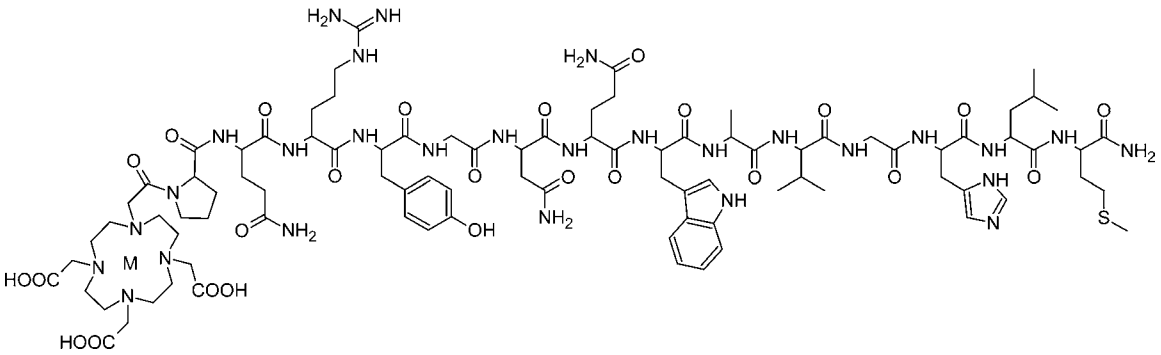


Figure 1. Structure of MP2346 (DOTA−Pro-Gln-Arg-Tyr-Gly-Asn-Gln-Trp-Ala-Val-Gly-His-Leu-Met-NH_2) with M corresponding to the chelated ^{64}Cu or ^{86}Y metal.

8000 counter containing a NaI crystal (Beckman Instruments, Inc., Irvine, CA).

Radiolabeling of MP2346. The GRPR binding peptide MP2346 (CAS 593287-40-2) was synthesized by a solid-phase method as described, and its purity was confirmed with HPLC and mass spectrometry (*14*). Labeling of MP2346 (10 μg) with $^{64}CuCl_2$ (11.15 mCi) took place in a 100 μL aliquot of 0.5 M NH_4OAc (pH 5.5) incubated at 80 °C for 30 min. Quality control of the product was performed using radio thin-layer chromatography on $MKC_{18}F$ silica gel plates using NH_4OAc/methanol (30:70) as the mobile phase ($^{64}CuCl_2$ $R_f = 0$; ^{64}Cu-MP2346 $R_f = 0.7$). The reaction between MP2346 (1.8 μg) with $^{86}YCl_3$ (2.1 mCi) took place in 0.5M NH_4OAc (pH 6.5) incubated at 80 °C for 30 min. Quality control was performed using the same TLC conditions as with the ^{64}Cu analogue ($^{86}YCl_3$ $R_f = 0$; ^{86}Y-MP2346 $R_f = 0.5$). Reaction progress and purity were also monitored by analytical reversed-phase HPLC, which was performed on an Waters Alliance 2695 Separations Module (Milford, MA) with a Waters 996 photodiode array detector (PDA) and an Carroll & Ramsey 105-S1 radioactivity detector (Berkeley, CA) with a Waters XTerra MS C_{18} 3.5 μm (2.1 × 50 mm) column. The mobile phase was H_2O (0.1% formic acid) and CH_3CN (solvent B). The gradient consisted of 15% B to 85% A in 60 min (0.5 mL/min flow rate) (^{64}Cu-MP2346, $t_R =$ 5.8 min; ^{86}Y-MP2346, $t_R = 6.9$ min; unreacted ^{64}Cu or ^{86}Y were eluted in the void volume, $t_R < 1.0$ min; uncomplexed MP2346, $t_R = 16.4$ min).

Internalization Studies. PC-3 cells were harvested and seeded into six-well plates at 5×10^5 cells per well. On the following day, the cells were washed with Hanks balanced salt solution (HBSS), and 1 mL of internalization media (DMEM plus 30 mM HEPES, 2 mM L-glutamine, 1 mM sodium pyruvate, and 1% BSA) was added to each well. The ^{64}Cu-MP2346 or ^{86}Y-MP2346 was then added such that the final concentration of peptide was approximately 1 nM. To three of the six wells per plate was added an excess (10 μg) of [Tyr^4]-bombesin (Sigma Chemical Co., St. Louis, MO) to act as an inhibitor. The plates (one per time point) were then incubated at 37 °C for 15, 30, 60, 120, 240, or 1200 min. At each time point, the corresponding plate was removed, the radioactive media was aspirated, and the cells were washed with cold HBSS. This was followed by an acid wash (HBSS plus 20 mM sodium acetate, pH 4.0), which was collected for the determination of surface-bound radioactivity. Immediately after collection of the acid wash, 1 mL of 10 mM sodium borate/1.0% SDS was added to the wells and allowed to incubate for 2−3 min at room temperature to facilitate cell lysis. The lysates were collected and, along with the surface fractions, were counted on a gamma counter. Protein amounts were determined using the Pierce BCA Protein Assay Kit (Rockford, IL) in a separate set of plates in which all of the steps were followed, but no radioactivity was added. The data are presented as fmol of internalized radioactivity normalized to protein amount. Maximum internalizations were determined from nonlinear curve fitting using Prism software and the one site binding hyperbola equation provided.

Biodistribution Studies. All animal experiments were conducted in compliance with the Guidelines for the Care and Use of Research Animals established by Washington University's Animal Studies Committee. Biodistribution studies were carried out on male athymic nude mice (Charles River Laboratories, Wilmington, MA) that had been implanted with 3×10^6 PC-3 cells into either the upper-right or lower-left flank of the animal. Tumors were allowed to grow for 36 days after implantation, at which time the animals received either 8−10 μCi of ^{64}Cu-MP2346 or ^{86}Y-MP2346 (7−10 ng) in 50 μL of saline via lateral tail vein injection. Animals were then euthanized at desired time points (1, 4, and 24 h, $n = 5$ per group). Two additional groups of mice (1 h time point only) were preinjected with unlabeled peptide to act as a receptor-blockade (100 μg of [Tyr^4]-bombesin) immediately prior to administering ^{64}Cu-MP2346 or ^{86}Y-MP2346. This constitutes a 10 000- or 15 000-fold increase over the mass of peptide injected with ^{64}Cu-MP2346 or ^{86}Y-MP2346, respectively. Following sacrifice, selected tissues and organs of interest were then removed and weighed and radioactivity measured in a gamma counter. The percent dose per gram (%ID/g) was then calculated.

Imaging Studies. Small animal PET images were obtained on a microPET-FOCUS 220 (Siemens Medical Solutions USA, Inc.) (*32*) and were coregistered with CT images from a MicroCAT II System (ImTek Inc., Knoxville, TN). Mice were anesthetized with 1−2% isoflurane prior to scanning, positioned supine, and immobilized in a custom prepared cradle. To reduce scattering caused by the prompt gammas of ^{86}Y, the energy window of the small animal PET (typically 250−750 keV) was narrowed to 470−580 keV and the data obtained normalized to a ^{86}Y cylinder phantom. The image registration between microCT and PET images was accomplished by using a landmark registration technique with AMIRA image display software (AMIRA, TGS Inc, San Diego, CA.). The registration method proceeds by rigid transformation of the microCT images from landmarks provided by fiducial markers directly attached to the animal bed. Images were obtained of male athymic nude mice (Charles River Laboratories, Wilmington, MA) that had been implanted with 3×10^6 PC-3 cells into the right flank. Images of male Lewis rats (Charles River Laboratories, Wilmington, MA) that had been implanted with AR42J tumor pieces in the left flank of the rat 10 days before the study were also obtained. In these studies, the mice received either ^{64}Cu-MP2346 ($n = 3$, 125 μCi, 125 ng) or ^{86}Y-MP2346 ($n = 3$, 200 μCi, 200 ng). These mice were imaged side by side with mice ($n = 3$ per group) that had been coadministered with 100 μg of [Tyr^4]-bombesin along with the radiolabeled peptide. The Lewis rats in the ^{86}Y-MP2346 PET study were imaged individually. One group ($n = 3$) was given ^{86}Y-MP2346 (200 μCi, 200 ng) and

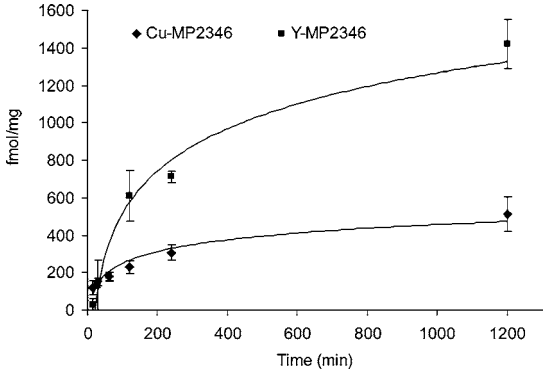


Figure 2. Internalization of ^{64}Cu-MP2346 and ^{86}Y-MP2346 into PC-3 cells. ^{64}Cu-MP2346 or ^{86}Y-MP2346 was added to the cells and incubated at 37 °C. At various time points, the media was removed and the cells were acid-washed to remove surface-bound radioactivity and harvested. The cell pellets (internalized) and acid wash (surface-bound) were counted. The data are presented as fmol of internalized radioactivity normalized to protein amount against time. The data are shown as the mean of three experiments ± SD with each experiment being performed in triplicate.

another group ($n = 3$) was coadministered 100 μg of [Tyr^4]-bombesin. For imaging studies tumor, kidney, and liver standard uptake values (SUV, defined as the ratio of activity in tissue per milliliter to the activity in the injected dose per subject body weight; (nCi/mL) × [weigh (g)/injected dose (nCi)]) of ^{64}Cu- or ^{86}Y-activity were generated by measuring regions of interest that encompassed the entire organ from the small animal PET images.

Statistical Methods. All of the data are presented as mean ± SD. For statistical classification, a Student's t test was performed using GraphPad PRISM (San Diego, CA). Differences at the 95% confidence level ($p < 0.05$) were considered significant.

RESULTS

Radiolabeling of MP2346. Radiolabeling of MP2346 with ^{64}Cu and ^{86}Y was performed over a range of temperatures, incubation times, and buffer pHs. The optimal conditions for labeling MP2346 with $^{64}CuCl_2$ in 0.5M NH_4OAc (pH 5.5) were found to be 80 °C for 30 min. Radiochemical yields >99% at a specific activity of 0.99 mCi/μg (1958 mCi/μmol) were achieved. The ^{86}Y analog was labeled with $^{86}YCl_3$ in 0.5 M NH_4OAc (pH 6.5) at 80 °C over 30 min. Radiochemical yields >94% (1.0 mCi/μg; 2000 mCi/μmol) were obtained by this method.

Internalization Studies. The internalization of ^{64}Cu-MP2346 and ^{86}Y-MP2346 into PC-3 (human prostate adenocarcinoma) cells is shown in Figure 2. The internalization of ^{64}Cu-MP2346 and ^{86}Y-MP2346 were monitored over a 20 h period. The amount of specifically internalized peptide normalized to the protein content of the cells was 121.83 ± 33.74 fmol/mg for ^{64}Cu-MP2346 and 28.09 ± 30.76 fmol/mg for ^{86}Y-MP2346 after 15 min incubation. Internalization increased steadily for both compounds and after 20 h of incubation, 512.04 ± 83.41 fmol/mg of ^{64}Cu-MP2346 and 1420.419 ± 129.94 fmol/mg of ^{86}Y-MP2346 were internalized into the PC-3 cells. The amount of surface-bound radioactivity was <100 fmol/mg for all time points (data not shown). Nonlinear curve fitting showed that the maximum internalization was 535 fmol/mg for ^{64}Cu-MP2346 and 1945 fmol/mg for ^{86}Y-MP2346.

Biodistribution Studies. Biodistribution studies were carried out on male athymic nude mice that had been implanted with PC-3 tumors into the right flank of the animals. Tumors were allowed to grow for 36 days, at which time the animals either received 8−10 μCi (~8−10 ng) of ^{64}Cu-MP2346 or 8−10 μCi (~8−10 ng) of ^{86}Y-MP2346 via tail vein injection. The mass of the injected peptide was the same for the two radiocompounds, and therefore differences between the biodistribution profiles are not due to the mass of the peptide administered. Table 1 shows the summary of the biodistribution data of ^{64}Cu-MP2346 and ^{86}Y-MP2346 in male nude mice bearing PC-3 tumors at 1, 4 and 24 h. Table 2 gives selected tumor/organ ratios for ^{64}Cu-MP2346 and ^{86}Y-MP2346.

Table 1. Biodistribution of ^{64}Cu-MP2346 and ^{86}Y-MP2346 in Male Nude Mice Bearing Day-36 PC-3 Tumors (%ID/g ± Standard Deviation, $n = 5$) at 1, 4, and 24 h[a]

tissue	1 h	4 h	24 h
	^{64}Cu-MP2346		
blood	0.128 ± 0.015	0.076 ± 0.024	0.069 ± 0.007
lung	0.426 ± 0.117	0.409 ± 0.166	0.218 ± 0.043
liver (all)	1.329 ± 0.304	1.412 ± 0.345	1.089 ± 0.429
spleen	0.278 ± 0.098	0.332 ± 0.135	0.175 ± 0.049
kidney	6.148 ± 1.067	4.936 ± 0.810	1.222 ± 0.296
muscle	0.316 ± 0.255	0.084 ± 0.120	0.034 ± 0.013
fat	0.071 ± 0.038	0.045 ± 0.046	0.012 ± 0.017
heart	0.160 ± 0.048	0.121 ± 0.038	0.185 ± 0.024
bone	0.885 ± 0.928	0.131 ± 0.101	0.038 ± 0.026
pancreas	4.387 ± 1.090	3.339 ± 0.463	1.155 ± 0.327
PC-3 tumor	0.793 ± 0.181	0.421 ± 0.214	0.309 ± 0.199
pancreas[a]	0.464 ± 0.259		
PC-3 tumor[a]	0.099 ± 0.134		
	^{86}Y-MP2346		
blood	0.219 ± 0.098	0.009 ± 0.002	0.001 ± 0.001
lung	0.302 ± 0.062	0.097 ± 0.060	0.030 ± 0.020
liver (all)	0.170 ± 0.027	0.145 ± 0.048	0.152 ± 0.069
spleen	0.742 ± 0.296	0.803 ± 0.241	0.463 ± 0.105
kidney	8.309 ± 2.412	8.789 ± 2.106	2.623 ± 0.391
muscle	0.089 ± 0.010	0.016 ± 0.002	0.005 ± 0.004
fat	0.059 ± 0.007	0.006 ± 0.006	0.003 ± 0.002
heart	0.091 ± 0.030	0.022 ± 0.010	0.002 ± 0.002
bone	0.336 ± 0.228	0.087 ± 0.025	0.044 ± 0.012
pancreas	14.456 ± 5.719	13.358 ± 2.954	12.965 ± 2.229
PC-3 tumor	2.646 ± 1.228	1.243 ± 0.658	1.405 ± 0.222
pancreas[a]	0.304 ± 0.018		
PC-3 tumor[a]	0.667 ± 0.179		

[a] Two additional groups were preadministered blockade (100 μg of [Tyr^4]-bombesin) immediately prior to administering ^{64}Cu-MP2346 or ^{86}Y-MP2346. Similar trends were also observed for the other receptor-rich tissues, the stomach and intestines, where uptake of the two radiocompounds was significantly reduced by administration of blockade.

Table 2. Selected Tumor/Organ Ratios for ^{64}Cu- and ^{86}Y-MP2346 in Male Nude Mice Bearing Day-36 PC-3 Tumors (%ID/g ± Standard Deviation, $n = 5$) at 1, 4, and 24 h

	^{64}Cu (1 h)	^{86}Y (1 h)	^{64}Cu (4 h)	^{86}Y (4 h)	^{64}Cu (24 h)	^{86}Y (24 h)
tumor/blood	6.192	12.074	5.511	134.3	4.487	1680
tumor/muscle	2.718	29.89	4.996	79.20	9.056	271.4
tumor/liver	0.597	15.60	0.298	8.590	0.284	9.223
tumor/kidney	0.129	0.318	0.085	0.141	0.253	0.536

Both ^{64}Cu-MP2346 and ^{86}Y-MP2346 demonstrated rapid clearance of radioactivity from the blood over the 24 h period. Although blood levels of ^{86}Y-MP2346 were initially higher at 1 h compared to the ^{64}Cu analog (0.219 ± 0.098 vs 0.128 ± 0.015 %ID/g, $p < 0.005$), by 24 h there was a significant reduction in the blood levels of ^{86}Y-MP2346 compared to ^{64}Cu-MP2346 (0.001 ± 0.001 vs 0.069 ± 0.007 %ID/g, $p < 0.0001$). This combined with the increased uptake of ^{86}Y-MP2346 in the tumor resulted in over a 300-fold increase in the tumor/blood ratio for ^{86}Y-MP2346 compared to ^{64}Cu-MP2346 at 24 h.

The liver activity of ^{64}Cu-MP2346 is consistently higher at all time points (1 h, 1.329 ± 0.304 %ID/g; 4 h, 1.412 ± 0.345 %ID/g; 24 h, 1.089 ± 0.429 %ID/g) compared to ^{86}Y-MP2346 (1 h, 0.170 ± 0.027 %ID/g; 4 h, 0.145 ± 0.048 %ID/g; 24 h, 0.152 ± 0.069 %ID/g). These data result in superior tumor/liver ratios for the ^{86}Y-MP2346 (Table 2). It is also important

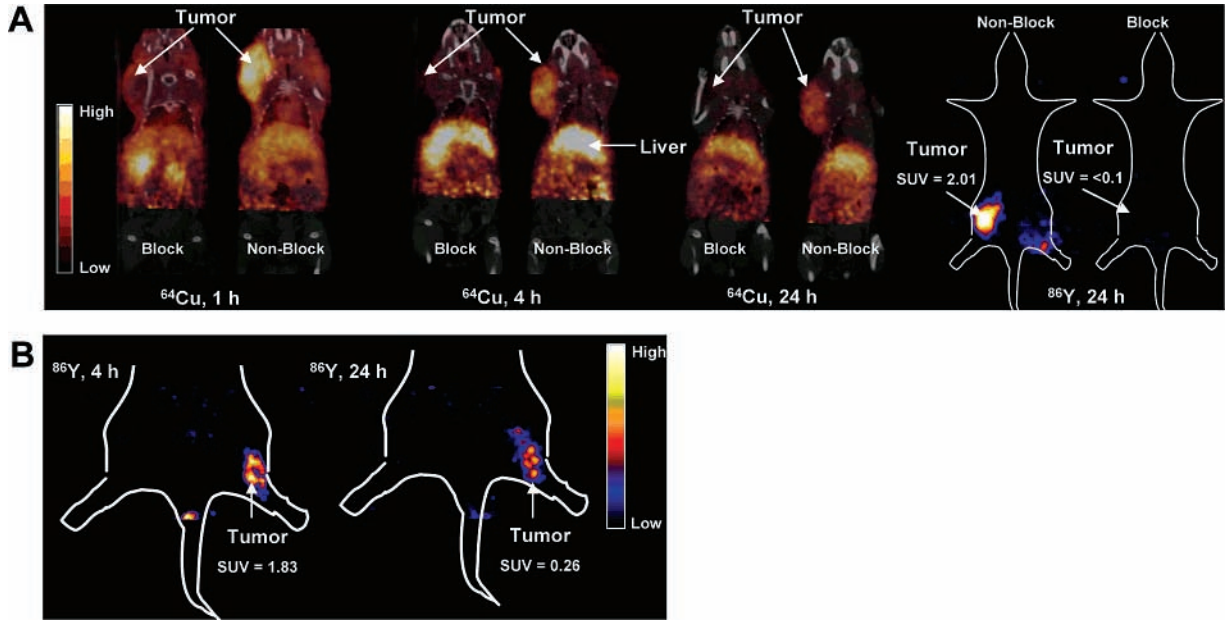


Figure 3. (A) ^{64}Cu-MP2346 PET with coregistered CT at 1, 4, and 24 h in nude mice with PC-3 tumors in the right neck (SUV values not shown on figure). At each time point, a mouse that received blockade (left) was coimaged with a mouse that did not receive blockade (right). Also shown is ^{86}Y-MP2346 PET (without CT coregistration) in nude mice with PC-3 tumors in right flank At each time point, a mouse that received blockade (right) was coimaged with a mouse that did not receive blockade (left). The PET images also show that the administration of a blockade dose substantially reduces tumor uptake of both agents by such an extent that the tumor cannot be delineated for either compound at any time point. (B) ^{86}Y-MP2346 PET at 4 and 24 h postinjection in male Lewis Rats with AR42J tumors in left leg. In both the mice and rats PET imaging it is evident from the ^{86}Y images that background accumulation is very low (i.e., low nontarget tissue uptake) and that in the nonblockade mouse very little tumor tracer accumulation is noted.

to note that for both agents, there is very little liver clearance of activity over 24 h. Kidney uptake of ^{64}Cu-MP2346 was initially high but reduced ~5-fold by 24 h (1 h, 6.148 ± 1.067 %ID/g; 4 h, 4.936 ± 0.810 %ID/g; 24 h, 1.222 ± 0.296 %ID/g). In contrast ^{86}Y-MP2346 showed slightly higher kidney retention at 1 h (8.309 ± 2.412 %ID/g), which remained constant over 4 h (8.789 ± 2.106 %ID/g) and then only showed a 3-fold decrease by 24 h (2.623 ± 0.391 %ID/g).

The GRPR-rich pancreas demonstrated uptake of ^{64}Cu-MP2346 (1 h, 4.387 ± 1.090 %ID/g; 4 h, 3.339 ± 0.463 %ID/g; 24 h, 1.155 ± 0.327 %ID/g) which was significantly lower ($p < 0.001$) than values obtained for ^{86}Y-MP2346 at all time points (1 h, 14.456 ± 5.719 %ID/g; 4 h, 13.358 ± 2.954 %ID/g; 24 h, 12.965 ± 2.229 %ID/g). To demonstrate receptor-mediated targeting of the agents two additional groups were preadministered blockade (100 μg of [Tyr^4]-bombesin) immediately prior to administering ^{64}Cu-MP2346 or ^{86}Y-MP2346 and were sacrificed at 1 h postinjection. In these animals, the pancreas demonstrated receptor-mediated blocking with a significant decease in tissue retention of the tracers in the receptor-rich pancreas compared to the nonblocked animals (^{64}Cu-MP2346, 0.464 ± 0.259 vs 4.387 ± 1.090 %ID/g, $p < 0.0005$; ^{86}Y-MP2346, 0.304 ± 0.018 vs 14.456 ± 5.719 %ID/g, $p < 0.0005$). Similar trends were also observed for the other receptor-rich tissues, the stomach and the intestines, where uptake of the tracers was significantly reduced by administration of blockade (data not shown).

Uptake of ^{86}Y-MP2346 into the GRPR-rich PC-3 tumor was significantly higher at all time points compared to ^{64}Cu-MP2346 (1 h, 2.646 ± 1.228 vs 0.793 ± 0.181 %ID/g, $p < 0.0005$; 4 h, 1.243 ± 0.658 vs 0.421 ± 0.214 %ID/g, $p < 0.0005$; 24 h, 1.405 ± 0.222 vs 0.309 ± 0.199 %ID/g, $p < 0.0005$), resulting in superior tumor/blood, tumor/muscle and tumor/liver ratios for ^{86}Y-MP2346 compared to ^{64}Cu-MP2346 (Table 2). Administration of blockade (100 μg of [Tyr^4]-bombesin) immediately prior to administering ^{64}Cu-MP2346 or ^{86}Y-MP2346 resulted in significant reduction in PC-3 tumor accumulation for both agents (^{64}Cu-MP2346, 0.099 ± 0.134 vs 0.793 ± 0.181 %ID/g, $p < 0.0005$; ^{86}Y-MP2346, 0.667 ± 0.179 vs 2.646 ± 1.228 %ID/g, $p < 0.0005$) confirming receptor-mediated accumulation of the compounds into the tumor.

Imaging Studies. Small animal PET/CT images of ^{64}Cu-MP2346 and ^{86}Y-MP2346 in PC-3 tumor-bearing mice and ^{86}Y-MP2346 in AR42J-bearing rats are shown in Figure 3A and 3B. SUV data for ^{64}Cu-MP2346 over 24 h is shown in Figure 4. Small animal PET/CT images of ^{64}Cu-MP2346 in the PC-3 model allows for clear delineation of the PC-3 tumor in the upper-right flank of the animal after 1 h and as far out as 24 h postinjection (Figure 3A). Also noted in these images is the accumulated activity in the liver of the mice consistent with the data obtained from the acute biodistribution data (Table 1). In the ^{86}Y-MP2346 images, low background accumulation is observed (i.e., low nontarget tissue accumulation), and this is consistent with the biodistribution data and the tumor/tissue ratios reported (Tables 1 and 2). In all cases the ^{86}Y-MP2346 images in the PC-3-bearing mice are superior to the ^{64}Cu-MP2346 images because of the high tumor/tissues ratios reported from the biodistribution data (Table 2). Because of the excellent image quality obtained with ^{86}Y-MP2346 in the PC-3-bearing mice, we wanted to confirm this in a second rodent model and therefore undertook imaging in Lewis rats bearing AR42J tumors. The low tumor/background ratio associated with ^{86}Y-MP2346 also allows for excellent tumor visualization in the AR42J rats (Figure 3B), where the tumor is easily delineated in the lower-left flank of the rat at 4 and 24 h postinjection.

In Figure 3A the significant reduction in tumor accumulation in the blocked animals confirmed specific uptake of the ^{64}Cu-MP2346 and ^{86}Y-MP2346 in the receptor-rich tumor tissue. SUV data were calculated for the tumors in both blocked and nonblocked animals (Figure 3 and Figure 4). This analysis showed that there were statistical differences ($p < 0.001$) between tumor concentration of mice that did and did not receive a coinjection of blockade at all time points examined and that

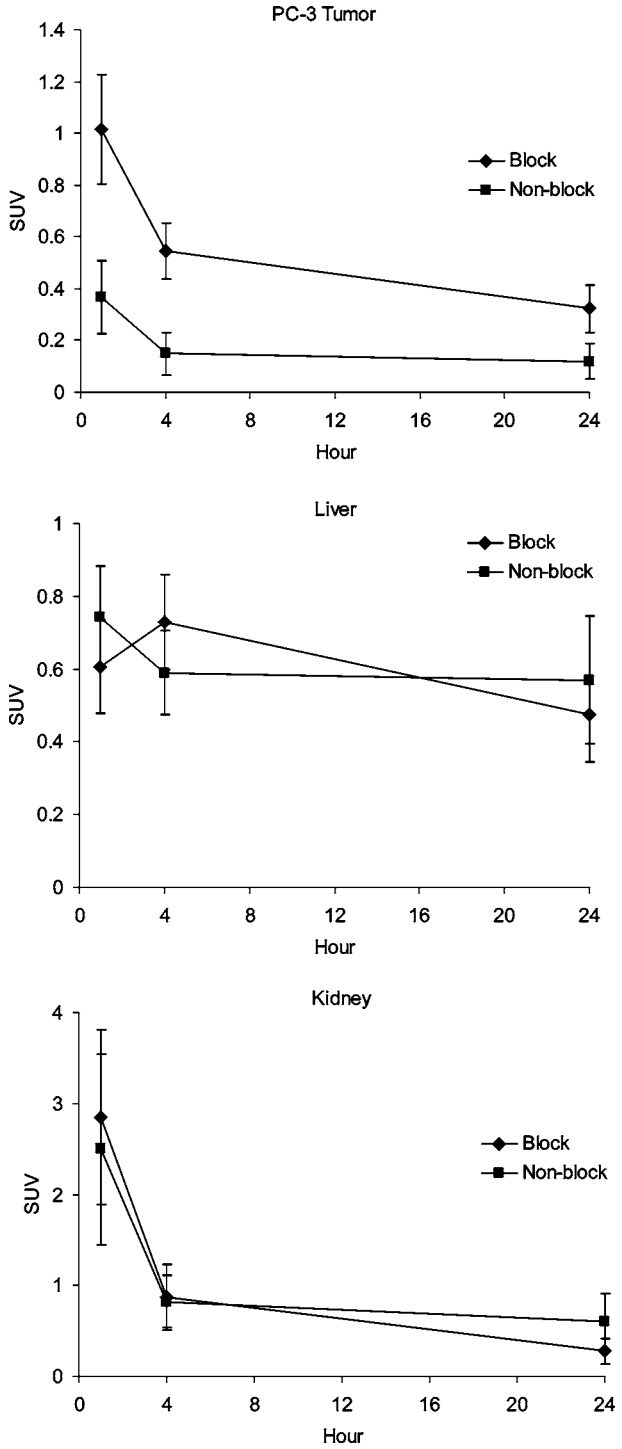


Figure 4. SUV data obtained for PET analysis of ^{64}Cu-MP2346 in mice implanted with PC-3 tumors. In these studies, the mice received ^{64}Cu-MP2346 ($n = 3$, 125 μCi, 125 ng). These mice were imaged side by side with mice ($n = 3$ per group) that had been coadministered with 100 μg of [Tyr^4]-bombesin along with the radiolabeled peptide.

the PET data were consistent with the trends and relationships observed with the acute biodistribution data.

DISCUSSION

Peptide-based agents targeting the GRPRs on tumors have been developed and studied in animals and humans for diagnostic and therapeutic applications (*10*−*26*). The breadth of work undertaken on GRPR-targeting radiopharmaceuticals has been comprehensively reviewed by Smith et al. in 2003 and 2005 (*11*, *12*). Multiple BN analogs have been explored and compared (*11*, *12*) and have demonstrated the potential of these systems for use in humans. In this current report we evaluated both ^{64}Cu- and ^{86}Y-radiolabeled MP2346 [DOTA−(Pro^1, Tyr^4)-bombesin(1−14)] as candidates for the noninvasive detection of GRPR-positive tumors using PET. DOTA is able to chelate a variety of β-, β+, or α-particle-emitting radiometals, remaining stable under a variety of physiologic conditions.

Both agents were radiolabeled in high specific activity by the addition of the radionuclides of choice to the peptide in ammonium acetate buffer. The specific activities obtained (∼1 mCi/μg) are high, but higher values are achievable, especially if the HPLC conditions used are utilized for an additional purification step, removing unlabeled peptide from labeled peptide. Figure 2 shows that the ^{64}Cu-peptide, ^{64}Cu-MP2346, internalized into PC-3 cells with ∼34% of the maximum internalized reached by 1 h. This is similar to the 1 h internalization of ^{111}In-MP2346 into CA20948 and AR42J cells (*13*). ^{86}Y-MP2346 internalized into PC-3 cells with only ∼13% of the maximum internalized reached by 1 h. However, after 20 h of incubation, nearly a 3-fold higher level of internalization is noted for the ^{86}Y-MP2346 analogue compared with ^{64}Cu-MP2346. It has been reported that the level of peptide internalization is crucial for *in vivo* targeting with radiolabeled peptides (*33*, *34*). For example, in the well-defined model of somatostatin receptor targeting, a significant correlation exists between the level of somatostatin peptide internalization into receptor positive tissues and the *in vivo* uptake (*35*). It is reasonable to assume that the bombesin receptor-targeting peptides discussed in this current work will follow similar patterns to those reported for somatostatin peptides, and therefore the higher level of internalization of the ^{86}Y analogue explains in part the superior *in vivo* properties of ^{86}Y-MP2346 compared to ^{64}Cu-MP2346.

The biodistribution data presented in Table 1 for ^{64}Cu-MP2346 and ^{86}Y-MP2346 show distinct differences in the kinetics of the two compounds in both receptor-rich and nontarget organs. This can be attributed to inherent differences in the physical and chemical properties of the individual agents (e.g., overall charge, pK_a) due to the different metals incorporated into MP2346, and not the mass of the peptide administered since this was identical in the comparative experiments. As discussed above, it is likely that cellular internalization is the most influential factor in the uptake and retention of the agents in the tumor and other receptor-positive tissues. In other nontarget tissues, the ^{86}Y analogue in general showed a more favorable biodistribution compared with ^{64}Cu-MP2346. This was most notable in the higher tumor uptake and lower nontarget tissue (in particular the liver) accumulation resulting in superior tumor/tissue ratios (Table 2). The reasons for these differences are not due to cellular internalization but are consequences of the different chemical and physical properties of ^{86}Y-MP2346 and ^{64}Cu-MP2346.

The kidney uptake of ^{86}Y-MP2346 is not optimal and is higher than ^{64}Cu-MP2346 and could be a problem in the translation of this agent to the clinic due to high absorbed doses. Although these kidney values are lower than those found for the ^{18}F-labeled peptides, ^{18}F-FB[Lys^3]BBN (1 h, ∼16 %ID/g) and ^{18}F-FB-Aca-BBN(7−14) (1 h, ∼8 %ID/g) (*27*), they are comparable to those found with other ^{64}Cu-BN systems (*24*−*26*). The uptake of ^{86}Y-MP2346 and subsequent retention, compared to the uptake and washout noted with the ^{64}Cu analogue could be attributed to the net charge of the compound. It has been reported that the renal retention of ^{64}Cu- and ^{111}In-labeled chelates was higher for positively charged peptides and lower for neutral and negatively charged ones (*36*−*38*). Given the expected charge of ^{86}Y-MP2346 is +1 and ^{64}Cu-MP2346 is neutral (at slightly acid pH), this could account for the difference in renal uptake and clearance. Subtle alteration

of ^{86}Y-MP2346 to present an overall neutral or negative charge could reduce renal uptake and improve clearance. If this strategy does not work tracer accumulation could possibly be tempered by the use of D-lysine or a similar agent to decrease this retention (*39*).

The liver burden associated with ^{64}Cu-MP2346 (1 h, 1.329 %ID/g), although significantly lower than that found with other ^{64}Cu-BN peptide systems, (^{64}Cu-DOTA−[Lys^3]BBN, ∼4.5 %ID/g (*26*); ^{64}Cu-DOTA−Aca-BBN(7−14), ∼13 %ID/g (*25*); ^{64}Cu-DOTA−Aoc-BN(7−14), ∼13 %ID/g (*24*)) could still hinder the delineation of GRPR-positive tumors in anatomical regions in close proximity to the liver and could also lead to high radiation-absorbed doses. Although DOTA is a promiscuous chelator for many 2+ and 3+ charged metals, ^{64}Cu has been shown to dissociate *in vivo* from DOTA and DOTA conjugates (*40*). Copper-64 then undergoes metabolism and transchelation to superoxide dismutase and other proteins causing increased blood and liver accumulation (*41*, *42*). The cross-bridged cyclam chelator, CBTE2A, has demonstrated improved *in vivo* stability and consequently a reduction in transchelation (*40*−*43*). CBTE2A has been conjugated to the somatostatin peptide analogue Tyr^3-octreotate (Y3-TATE) and ^{64}Cu-CBTE2A−Y3-TATE showed improved nontarget organ clearance and higher tumor ratios compared with ^{64}Cu-TETA anolog (*42*). By incorporation of the CBTE2A moiety (replacing DOTA) onto the peptide system used in this study, an improved biodistribution would be anticipated.

The tumor uptake of ^{86}Y-MP2346 at all time points is superior to that found with ^{64}Cu-MP2346 (Table 1) and can be attributed to the superior cellular internalization of this agent (Figure 2). These values compare well with those found for other analogs in the same tumor model; for example, La Bella et al. showed with two ^{99m}Tc-labeled BN analogues showed 0.3−0.6 %ID/g at 24 h postinjection in the PC-3 tumor (*17*, *20*). These values are similar to that found with ^{64}Cu-MP2346 but ∼2−6-fold lower than those for ^{86}Y-MP2346. The PET agents ^{18}F-FB[Lys^3]-BBN and ^{18}F-FB-Aca-BBN(7−14) showed PC-3 uptake values at 1 h of 5.94 ± 0.78 %ID/g and 0.43 ± 0.18 %ID/g, respectively (*27*). ^{177}Lu-DOTA−Aoc-BN(7−14) was reported to have 4.2 %ID/g in the PC-3 tumor with a tumor/blood ratio of 11.1 at 1 h, an uptake value slightly higher than that found with ^{86}Y-MP2346 but resulting in a similar tumor/blood ratio (Table 2) (*23*). The ^{64}Cu analogue of DOTA−Aoc-BN(7−14) was shown to have 5.5 %ID/g at 2 h in the PC-3 tumor, a value much higher than that found with ^{64}Cu-MP2346, but only ∼2-fold higher than that determined with ^{86}Y-MP2346. However, on comparison of the tumor/blood ratios, ^{64}Cu-DOTA−Aoc-BN(7−14) had a tumor/blood ratio of 4.2, a value lower than that for ^{64}Cu-MP2346 (6.192 at 1 h, Table 2) and 3-fold lower than that for ^{86}Y-MP2346 (12.074 at 1 h, Table 2). ^{64}Cu-DOTA−[Lys^3]BBN demonstrated 3.97 ± 0.15 %ID/g in the PC-3 tumor (*26*) with the truncated analog showing ∼3.0 %ID/g (*25*). These values are comparable to those found for ^{86}Y-MP2346 but higher than those for ^{64}Cu-MP2346, but as discussed above, the liver burden, with the other analogs, is significantly higher. In all of these studies nontarget tissue accumulation differed again presumably because of peptide affinity, overall charge, and metal−chelate stability. Overall differences in tumor accumulation could also be attributed to the amount of peptide mass administered to the animals, the tumor volume and the status of the PC-3 cells maintained within each laboratory so care must be taken in the comparison of the current studies with those previously reported.

The PET imaging confirms the data obtained in the biodistribution studies. The less than optimal biodistribution of ^{64}Cu-MP2346 results in high background and liver accumulation. ^{86}Y-MP2346 produces high quality PET images (Figure 2 and 3) in PC-3-bearing mice and this excellent image quality was confirmed in AR42J-bearing rats where tumor activity is high even after 1 h against very low background activity. The liver shows very low accumulation of the ^{86}Y-labeled peptide, suggesting that the Y-DOTA chelate is more stable that the Cu analog and is not susceptible to transchelation *in vivo*. It is important to note that these images have been produced following the administration of larger amounts of peptide due to the higher dose (∼20 fold) than that given in the biodistribution studies. Nevertheless, the observed tissue distribution in the rat images is consistent with the biodistribution found in sampled tissues in mice. Additionally, in both studies, animals that were preinjected with a large quantity of [Tyr^4]-bombesin had significantly reduced uptake of the agents in the receptor positive tumors with little change in uptake in receptor negative tissue. This further confirms the receptor-mediated uptake of the agents *in vivo*.

CONCLUSION

In conclusion, ^{64}Cu-MP2346 and ^{86}Y-MP2346 were evaluated as agents for the PET imaging of the GRP receptor. In particular ^{86}Y-MP2346 due to its good tumor concentration and low nontarget tissue accumulation allows for the excellent delineation of the GRPR-positive PC-3 tumor and warrants further evaluation for diagnostic purposes as a GRPR PET imaging agent.

ACKNOWLEDGMENT

We are very grateful for the technical assistance of Lori Strong, Nicole Fettig, Jerrel R. Rutlin, Laura Meyer, Susan Adams, Rebecca Andrews, Todd Perkins, and Dr. Jeongsoo Yoo. This work was supported by the National Cancer Institute (R24 CA86307). Small animal PET imaging is supported by an NIH/NCI SAIRP grant (R24 CA83060) with additional support from the Small Animal Imaging Core of the Alvin J. Siteman Cancer Center at Washington University and Barnes-Jewish Hospital. The SAIC Core is supported by an NCI Cancer Center Support Grant no. 1 P30 CA91842.

LITERATURE CITED

(1) Carroll, R. E., Matkowskyj, K. A., Chakrabarti, S., McDonald, T. J., and Benya, R. V. (1999) Aberrant expression of gastrin-releasing peptide and its receptor by well-differentiated colon cancers in humans. *Am. J. Physiol. 276*, G655−65.

(2) Chave, H. S., Gough, A. C., Palmer, K., Preston, S. R., and Primrose, J. N. (2000) Bombesin family receptor and ligand gene expression in human colorectal cancer and normal mucosa. *Br. J. Cancer 82*, 124−30.

(3) Corjay, M. H., Dobrzanski, D. J., Way, J. M., Viallet, J., Shapira, H., Worland, P., Sausville, E. A., and Battey, J. F. (1991) Two distinct bombesin receptor subtypes are expressed and functional in human lung carcinoma cells. *J. Biol. Chem. 266*, 18771−9.

(4) Ferris, H. A., Carroll, R. E., Lorimer, D. L., and Benya, R. V. (1997) Location and characterization of the human GRP receptor expressed by gastrointestinal epithelial cells. *Peptides 18*, 663−72.

(5) Reubi, J. C., Wenger, S., Schmuckli-Maurer, J., Schaer, J. C., and Gugger, M. (2002) Bombesin receptor subtypes in human cancers: detection with the universal radioligand ^{125}I-[D-TYR(6), beta-ALA-(11), PHE(13), NLE(14)] bombesin(6−14). *Clin. Cancer Res. 8*, 1139−46.

(6) Sun, B., Schally, A. V., and Halmos, G. (2000) The presence of receptors for bombesin/GRP and mRNA for three receptor subtypes in human ovarian epithelial cancers. *Regul. Pept. 90*, 77−84.

(7) Gugger, M., and Reubi, J. C. (1999) Gastrin-releasing peptide receptors in non-neoplastic and neoplastic human breast. *Am. J. Pathol. 155*, 2067−76.

(8) Markwalder, R., and Reubi, J. C. (1999) Gastrin-releasing peptide receptors in the human prostate: relation to neoplastic transformation. *Cancer Res. 59*, 1152−9.

(9) Anastasi, A., Erspamer, V., and Bucci, M. (1972) Isolation and amino acid sequences of alytesin and bombesin, two analogous active tetradecapeptides from the skin of European discoglossid frogs. *Arch. Biochem. Biophys. 148*, 443−6.

(10) Varvarigou, A., Bouziotis, P., Zikos, C., Scopinaro, F., and De Vincentis, G. (2004) Gastrin-releasing peptide (GRP) analogues for cancer imaging. *Cancer Biother. Radiopharm 19*, 219−29.

(11) Smith, C. J., Volkert, W. A., and Hoffman, T. J. (2003) Gastrin releasing peptide (GRP) receptor targeted radiopharmaceuticals: A concise update. *Nucl. Med. Biol. 30*, 861−868.

(12) Smith, C. J., Volkert, W. A., and Hoffman, T. J. (2005) Radiolabeled peptide conjugates for targeting of the bombesin receptor superfamily subtypes. *Nucl. Med. Biol. 32*, 733−40.

(13) Breeman, W. A., de Jong, M., Erion, J. L., Bugaj, J. E., Srinivasan, A., Bernard, B. F., Kwekkeboom, D. J., Visser, T. J., and Krenning, E. P. (2002) Preclinical comparison of ^{111}In-labeled DTPA- or DOTA-bombesin analogs for receptor-targeted scintigraphy and radionuclide therapy. *J. Nucl. Med. 43*, 1650−6.

(14) Breeman, W. A., Hofland, L. J., de Jong, M., Bernard, B. F., Srinivasan, A., Kwekkeboom, D. J., Visser, T. J., and Krenning, E. P. (1999) Evaluation of radiolabelled bombesin analogues for receptor-targeted scintigraphy and radiotherapy. *Int. J. Cancer 81*, 658−65.

(15) Breeman, W. A. P., de Jong, M., Bernard, B. F., Kwekkeboom, D. J., Srinivasan, A., van der Pluijm, M. E., Hofland, L. J., Visser, T. J., and Krenning, E. P. (1999) Pre-clinical evaluation of [^{111}In-DTPA-Pro^1, Tyr^4]bombesin, a new radioligand for bombesin-receptor scintigraphy. *Int. J. Cancer 83*, 657−663.

(16) Karra, S., Schibli, R., Gali, H., Katti, K., Hoffman, T., Higginbotham, C., Sieckman, G., and Volkert, W. (1999) ^{99m}Tc-labeling and in vivo studies of a bombesin analogue with a novel water-soluble dithiadiphosphine-based bifunctional chelating agent. *Bioconjugate Chem. 10*, 254−260.

(17) La Bella, R., Garcia-Garayoa, E., Bahler, M., Blauenstein, P., Schibli, R., Conrath, P., Tourwe, D., and Schubiger, P. A. (2002) A ^{99m}Tc-postlabeled high affinity bombesin analogue as a potential tumor imaging agent. *Bioconjugate Chem. 13*, 599−604.

(18) Van de Wiele, C., Dumont, F., Dierckx, R. A., Peers, S. H., Thornback, J. R., Slegers, G., and Thierens, H. (2001) Biodistribution and dosimetry of ^{99m}Tc-RP527, a gastrin-releasing peptide (GRP) agonist for the visualization of GRP receptor-expressing malignancies. *J. Nucl. Med. 42*, 1722−1727.

(19) Van de Wiele, C., Dumont, F., Broecke, R. V., Oosterlinck, W., Cocquyt, V., Serreyn, R., Peers, S., Thornback, J., Slegers, G., and Dierckx, R. A. (2000) Technetium-99m RP527, a GRP analogue for visualization of GRP receptor-expressing malignancies: a feasibility study. *Eur. J. Nucl. Med. 27*, 1694−1699.

(20) La Bella, R., Garcia-Garayoa, E., Langer, M., Blauenstein, P., Beck-Sickinger, A. G., and Schubiger, P. A. (2002) In vitro and in vivo evaluation of a ^{99m}Tc(I)-labeled bombesin analogue for imaging of gastrin releasing peptide receptor-positive tumors. *Nucl. Med. Biol. 29*, 553−560.

(21) Rogers, B. E., Curiel, D. T., Mayo, M. S., Laffoon, K. K., Bright, S. J., and Buchsbaum, D. J. (1997) Tumor localization of a radiolabeled bombesin analogue in mice bearing human ovarian tumors induced to express the gastrin releasing peptide receptor by an adenoviral vector. *Cancer 80*, 2419−2424.

(22) Safavy, A., Khazaeli, M. B., Qin, H., and Buchsbaum, D. J. (1997) Synthesis of bombesin analogues for radiolabeling with Rhenium-188. *Cancer (Suppl) 80*, 2354−2359.

(23) Smith, C. J., Hoffman, T. J., Hayes, D. L., Owen, N. K., Sieckman, G. L., and Volkert, W. A. (2001) Radiochemical investigations of ^{177}Lu-DOTA-8-Aoc-BBN[7−14]NH_2: A new gastrin releasing peptide receptor (GRPr) targeting radiopharmaceutical. *J. Label. Compd. Radiopharm. 44*, S706−S708.

(24) Rogers, B. E., Bigott, H. M., McCarthy, D. W., Della Manna, D., Kim, J., Sharp, T. L., and Welch, M. J. (2003) MicroPET imaging of a gastrin-releasing peptide receptor-positive tumor in a mouse model of human prostate cancer using a ^{64}Cu-labeled bombesin analogue. *Bioconjugate Chem. 14*, 756−63.

(25) Yang, Y.-S., Zhang, X., Xiong, Z., and Chen, X. (2006) Comparative in vitro and in vivo evaluation of two ^{64}Cu-labeled bombesin analogs in a mouse model of human prostate adenocarcinoma. *Nucl. Med. Biol. 33*, 371−380.

(26) Chen, X., Park, R., Hou, Y., Tohme, M., Shahinian, A. H., Bading, J. R., and Conto, P. S. (2004) microPET and Autoradiographic Imaging of GRP Receptor Expression with ^{64}Cu-DOTA-[Lys^3]-Bombesin in Human Prostate Adenocarcinoma Xenografts. *J. Nucl. Med. 45*, 1390−1397.

(27) Zhang, X., Cai, W., Cao, F., Schreibmann, E., Wu, Y., Wu, J. C., Xing, L., and Chen, X. (2006) ^{18}F-labeled bombesin analogs for targeting GRP receptor-expressing prostate cancer. *J. Nucl. Med. 47*, 492−501.

(28) Breeman, W. A., de Jong, M., de Blois, E., Bernard, B. F., Konijnenberg, M., and Krenning, E. P. (2005) Radiolabelling DOTA-peptides with ^{68}Ga. *Eur. J. Nucl. Med. Mol. Imaging 32*, 478−85.

(29) McCarthy, D. W., Shefer, R. E., Klinkowstein, R. E., Bass, L. A., Margeneau, W. H., Cutler, C. S., Anderson, C. J., and Welch, M. J. (1997) Efficient production of high specific activity ^{64}Cu using a biomedical cyclotron. *Nucl. Med. Biol. 24*, 35−43.

(30) Yoo, J., Tang, L., Perkins, T. A., Rowland, D. J., Laforest, R., Lewis, J. S., and Welch, M. J. (2005) Preparation of high specific activity ^{86}Y using a small biomedical cyclotron. *Nucl. Med. Biol. 32*, 891−7.

(31) Blower, P. J., Lewis, J. S., and Zweit, J. (1996) Copper radionuclides and radiopharmaceuticals in nuclear medicine. *Nucl. Med. Biol. 23*, 957−980.

(32) Tai, Y. C., Ruangma, A., Rowland, D. J., Siegel, S., Newport, D. F., Chow, P. L., and Laforest, R. (2005) Performance evaluation of the microPET Focus: A third-generation microPET scanner dedicated to animal imaging. *J. Nucl. Med. 46*, 455−463.

(33) Hofland, L. J., and Lamberts, S. W. J. (2003) The pathophysiological consequences of somatostatin receptor internalization and resistance. *Endocr. Rev. 24*, 28−47.

(34) Reubi, J. C. (2003) Peptide receptors as molecular targets for cancer diagnosis and Therapy. *Endocr. Rev. 24*, 389−427.

(35) Storch, D., Béhé, M., Walter, M. A., Chen, J., Powell, P., Mikolajczak, R., and Mäcke, H. R. (2005) Evaluation of [^{99m}Tc/EDDA/HYNIC0]Octreotide derivatives compared with [^{111}In-DOTA0,-Tyr^3, Thr^8]Octreotide and [^{111}In-DTPA0]Octreotide: Does tumor or pancreas uptake correlate with the rate of internalization? *J. Nucl. Med. 46*, 1561−1569.

(36) Akizawa, H., Arano, Y., Mifune, M., Iwado, A., Saito, Y., Mukai, T., Uehara, T., Ono, M., Fujioka, Y., Ogawa, K., Kiso, Y., and Saji, H. (2001) Effect of molecular charges on renal uptake of ^{111}In-DTPA-conjugated peptides. *Nucl. Med. Biol. 28*, 761−8.

(37) Jones-Wilson, T. M., Deal, K. A., Anderson, C. J., McCarthy, D. W., Kovacs, Z., Motekaitis, R. J., Sherry, A. D., Martell, A. E., and Welch, M. J. (1998) The in vivo behavior of copper-64-labeled azamacrocyclic complexes. *Nucl. Med. Biol. 25*, 523−30.

(38) Rogers, B. E., Anderson, C. J., Connett, J. M., Guo, L. W., Edwards, W. B., Sherman, E. L., Zinn, K. R., and Welch, M. J. (1996) Comparison of four bifunctional chelates for radiolabeling monoclonal antibodies with copper radioisotopes: biodistribution and metabolism. *Bioconjugate Chem. 7*, 511−22.

(39) de Jong, M., Bakker, W. H., Breeman, W. A. P., Bernard, W. H., Hofland, L. J., Visser, T. J., Srinivasan, A., Schmidt, M., Béhé, M., Mäcke, H. R., and Krenning, E. P. (1998) Preclinical comparison of [DTPA^0]octreotide, [DTPA^0,Tyr^3]-octreotide and [DOTA^0,Tyr^3]-octreotide as carriers for somatostatin receptor-targeted scintigraphy and radionuclide therapy. *Int. J. Cancer 75*, 406−411.

(40) Wadas, T. J., Wong, E. H., Weisman, G. R., and Anderson, C. J. (in press) Copper chelation chemistry and its role in copper radiopharmaceuticals. *Curr. Pharm. Des.*

(41) Boswell, C. A., Sun, X., Niu, W., Weisman, G. R., Wong, E. H., Rheingold, A. L., and Anderson, C. J. (2004) Comparative in vivo stability of copper-64-labeled cross-bridged and conventional tetraazamacrocyclic complexes. *J. Med. Chem. 47*, 1465−74.

(42) Sprague, J. E., Peng, Y., Sun, X., Weisman, G. R., Wong, E. H., Achilefu, S., and Anderson, C. J. (2004) Preparation and biological evaluation of copper-64-labeled Tyr^3-octreotate using a cross-bridged macrocyclic chelator. *Clin. Cancer Res. 10*, 8674−8682.

(43) Sun, X., Wuest, M., Weisman, G. R., Wong, E. H., Reed, D. P., Boswell, C. A., Motekaitis, R., Martell, A. E., Welch, M. J., and Anderson, C. J. (2002) Radiolabeling and in vivo behavior of copper-64-labeled cross-bridged cyclam ligands. *J. Med. Chem. 45*, 469−77.

BC060281L

N,N-Dimethylsphingosine−Coumarin: Synthesis, Chemical Characterization, and Biological Evaluation

Sukhen C. Ghosh,[†] Edmond Auzenne,[‡] David Farquhar,[†] and Jim Klostergaard*[,‡]

Departments of Experimental Therapeutics and Molecular and Cellular Oncology, The University of Texas M. D. Anderson Cancer Center, 1515 Holcombe Boulevard, Houston, Texas 77030. Received September 11, 2006; Revised Manuscript Received February 1, 2007

Coumarin derivatives of *N,N*-dimethylsphingosine (DMSP) were prepared and chemically characterized. They were apparently biologically equivalent to DMSP in terms of tumor cell cytotoxicity and were used to establish the rapid mitochondrial localization of this sphingolipid in tumor cells, followed closely by its marked reduction of mitochondrial membrane potential.

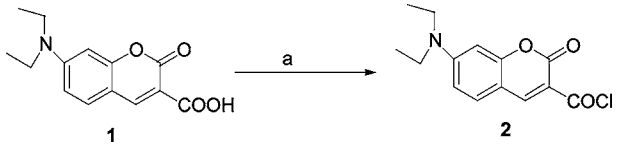
INTRODUCTION

Sphingolipids (SLs) and their metabolic pathways are increasingly recognized as promising targets for cancer therapy. Of particular focus in these pathways is the conversion of pro-apoptotic sphingosine (Sp) to anti-apoptotic sphingosine-1-phosphate (Sp-1-P) by the enzyme sphingosine kinase (SpK) (*1*). Since Sp is derived by deacylation of ceramide (Cer), a SL or Cer/Sp-1-P rheostat has been hypothesized to determine cellular fate; the relative cellular concentrations of Cer and Sp vs Sp-1-P determine whether a cell proliferates or undergoes apoptosis (*2*). SpK is itself oncogenic (*3*), governed by growth factors (*4*) and protein kinases (*5*).

Dimethylsphingosine (DMSP) is a competitive inhibitor of SpK (*6*) and is a useful tool to elucidate the role of Sp-1-P as an intracellular second messenger. DMSP is also a promising compound for the chemotherapeutic management of various types of malignancies (*7*). Aside from inhibition of SpK, some evidence indicates that mitochondria are a target of Sp, the parent compound (*8*). Since DMSP lacks a significant spectroscopic signature and in order to facilitate mechanistic studies of this SL, we incorporated a fluorescent probe into it and conducted chemical and biological characterization of the fluorescenated DMSP.

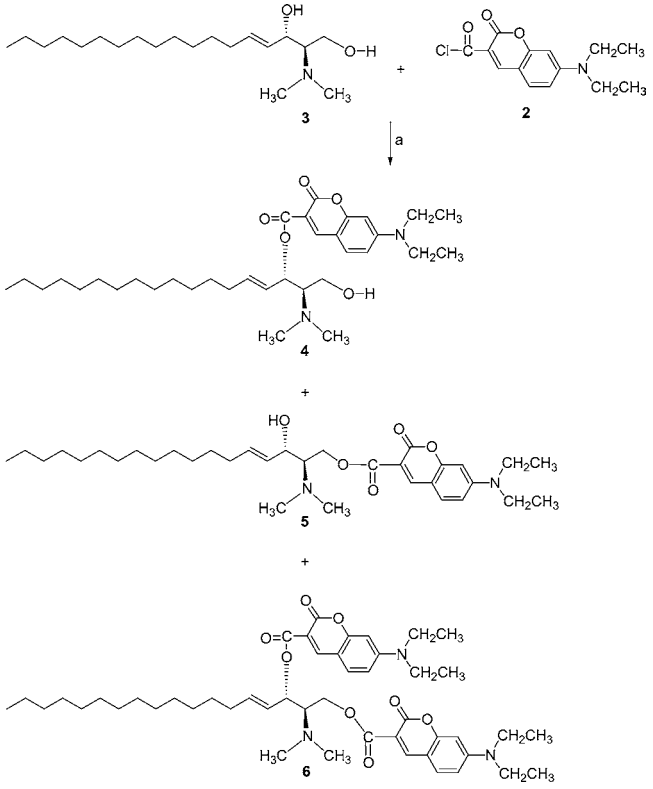
7-(Diethylamino)coumarin-3-carboxylic acid, **1**, was converted to the corresponding acid chloride, **2**, by reaction with oxalyl chloride in dichloromethane (Scheme 1). Compound **2** was then reacted with DMSP, **3**, to give a mixture of the isomeric esters, **4** and **5**, together with a trace amount of the diester **6** (Scheme 2). These products were separated by column chromatography on silica gel. No differences in cytotoxic activity against three tumor cell lines were observed among compounds **4**, **5**, and DMSP, indicating that these substitutions were without significant effect on the biological activity of DMSP. Time-lapse fluorescence microscopy studies with **4** and **5** indicated that they were rapidly accumulated intracellularly and localized in mitochondria. This localization was associated with a rapid and marked reduction in mitochondrial membrane potential.

Scheme 1 [a]



[a] Reagents and conditions: (a) oxalyl chloride, CH_2Cl_2, catalytic amount of DMF, rt for 12 h.

Scheme 2 [a]



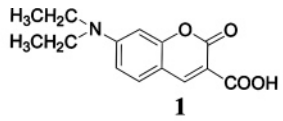
[a] Reagents and conditions: (a) 2,4,6-collidine, CH_2Cl_2, −40 °C for 4 h, then 25 °C for 12 h.

EXPERIMENTAL PROCEDURES

Chemistry. All chemicals and reagents were purchased either from Sigma-Aldrich Company (St. Louis, MO) or from Molecular Probes, Inc. (Carlsbad, CA). Nuclear magnetic resonance spectra (^{1}H NMR and ^{13}C NMR) were recorded at ambient temperature on Bruker Advance model 300 or 500 MHz spectrometers. Samples were dissolved in an appropriate deuterated solvent ($CDCl_3$ or D_2O). The ^{1}H chemical shifts are

* Author to whom correspondence should be addressed.
[†] Department of Experimental Therapeutics.
[‡] Department of Molecular and Cellular Oncology.

10.1021/bc060285q CCC: $37.00 © 2007 American Chemical Society
Published on Web 04/14/2007



1

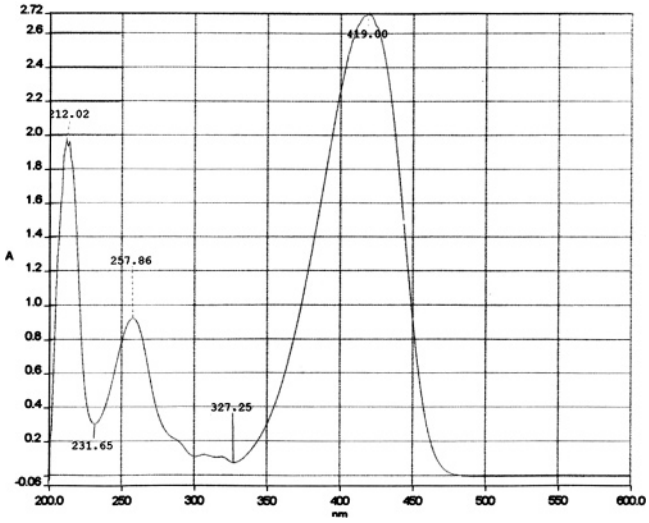
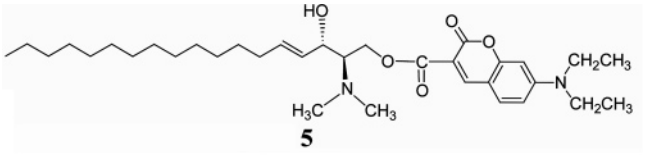


Figure 1. Absorption spectrum of compound **1** in methanol solution (UV cutoff 205 nm).



5

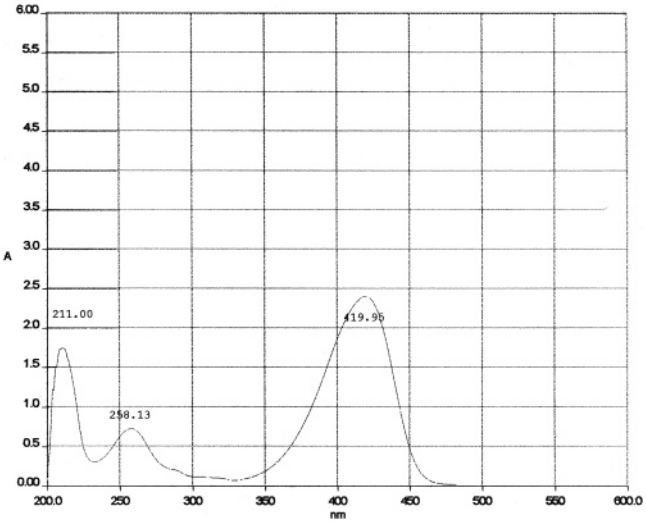


Figure 2. Absorption spectrum of compound **5** in methanol solution (UV cutoff 205 nm).

reported as parts per million (δ ppm) relative to tetramethylsilane (Me_4Si, $\delta = 0.00$) as an internal standard. Chemical shifts for ^{13}C are reported as δ relative to deuterated chloroform ($CDCl_3$, central peak $\delta = 77.0$ ppm) as an internal standard. Column chromatography was performed on silica gel (Merck, 230−400 mesh). UV spectra were obtained on a Perkin-Elmer spectrophotometer. Mass spectra analyses were performed by the analytical services section of the Department of Experimental Therapeutics, M. D. Anderson Cancer Center, Houston, TX. All reactions were carried out in dry glassware and protected from atmospheric moisture. Solvents were dried over freshly activated (300 °C, 1 h) molecular sieves (type 4A). Evaporations were carried out on a rotary evaporator under aspirator vacuum at a bath temperature of 30−40 °C.

Synthesis of 7-(Diethylamino)-2-oxo-2*H*-chromene-3-carboxylic Acid Chloride (2). Oxalyl chloride (150 μL, 240 mg, 1.9 mmol) was added, under a dry argon atmosphere, to a solution of 7-(diethylamino)coumarin-3-carboxylic acid, **1** (100 mg, 0.38 mmol), in anhydrous CH_2Cl_2 (20 mL), followed by DMF (20 μL) as a catalyst. Gas evolution ensued for about 5 min during which time the solution darkened. After 12 h at room temperature, the solvent was evaporated under vacuum to give a red solid. ^1H NMR ($CDCl_3$): δ 8.68 (s, 1H), 7.45 (d, 1H, $J = 9.0$ Hz), 6.69 (dd, 1H, $J_1 = 9.0$ Hz and $J_2 = 3.9$ Hz), 6.48 (d, 1H, $J = 3.0$ Hz), 3.50 (q, 4H), 1.35 (t, 6H, $J = 6.0$ Hz). The UV spectrum of the starting compound **1** is shown in Figure 1.

Syntheses of 2-*N*,*N*-Dimethylamino-3-[7-(diethylamino)-2-oxo-2*H*-chromone-3-carboxyl]-octadec-4-ene-1-ol (4), 2-*N*,*N*-Dimethylamino-1-[7-(diethylamino)-2-oxo-2*H*-chromone-3-carboxyl]-octadec-4-ene-3-ol (5), and 2-*N*,*N*-Dimethylamino-1,3-bis[7-(diethylamino)-2-oxo-2*H*-chromone-3-carboxyl]-octadec-4-ene (6). *N*,*N*-Dimethylsphingosine (**3**, 100 mg, 0.30 mmol) was added under a dry argon atmosphere to a solution of **2** (80 mg, 0.30 mmol) in anhydrous CH_2Cl_2 maintained at −40 °C. 2,4,6-Collidine (75 mg, 0.60 mmol) was added, and the reaction mixture was maintained at −40 °C for 4 h and then at 25 °C for a further 12 h. It was washed several times with an equal volume of saturated sodium bicarbonate solution, dried, and evaporated. The crude reaction product was separated into its individual components, **4**, **5**, and **6**, by column chromatography on silica gel using CH_2Cl_2 and CH_3OH (9:1) as eluent.

*Compound **4***. Yield 18%. $R_f = 0.5$ (CH_2Cl_2/MeOH, 9:1). ^1H NMR ($CDCl_3$): δ 8.42 (s, 1H), 7.36 (d, 1H, $J = 8.7$ Hz), 6.61 (dd,1H, $J_1 = 9.0$ Hz and $J_2 = 2.4$ Hz), 6.45(d,1H, J= 2.4 Hz), 5.86−5.76 (m,1H), 5.71 (t, 1H, $J = 6.6$ Hz), 5.53 (dd, 1H, $J_1 = 15.3$ Hz and $J_2 = 6.9$ Hz), 3.81 (m, 2H), 3.48 (q, 4H), 2.80 (m, 1H), 2.41 (s, 6H), 2.02 (q, 2H), 1.26 (m, 28H), 0.9(t, 3H, $J = 6.0$ Hz). ^{13} C NMR ($CDCl_3$): δ 163.44, 158.59, 158.49, 153.06,149.77, 135.57, 131.20, 126.98, 109.64, 108.46, 107.79, 96.67, 72.87, 68.19, 58.22, 45.13, 41.44, 32.28, 31.93, 29.68, 29.66, 29.61, 29.45, 29.36, 29.21, 28.80, 22.69, 14.13, 12.43.

*Compound **5***. Yield 50%. $R_f = 0.4$ (CH_2Cl_2/MeOH, 9:1). ^1H NMR ($CDCl_3$): δ 8.44 (s, 1H), 7.37 (d, 1H, $J = 8.7$ Hz), 6.62 (dd, 1H, $J_1 = 9.0$ Hz and $J_2 = 2.4$ Hz), 6.45 (d, 1H, $J = 2.1$ Hz), 5.79 (m, 1H), 5.54 (dd, 1H, $J_1 = 15.45$ Hz and $J_2 = 6.0$ Hz), 4.51 (m, 2H), 4.38 (t, 1H, $J = 5.4$ Hz), 3.66 (d, 1H, $J = 5.7$ Hz), 3.47 (q, 4H), 2.88 (q, 1H), 2.50 (s, 6H), 2.03 (q, 2H), 1.26 (m, 28 H), 0.9 (t, 3H, $J = 6.3$ Hz). ^{13} C NMR ($CDCl_3$): δ 164.40, 158.61, 158.36, 153.06, 149.71, 132.59, 131.21, 129.78, 109.63, 108.28, 107.76, 96.70, 70.76, 66.26, 62.06, 45.13, 43.05, 32.37, 31.93, 29.69, 29.66, 29.64, 29.52, 29.36, 29.25, 29.22, 22.69, 14.13, 12.43.

The UV spectrum and the MALDI-TOF mass spectrogram of compound **5** are shown in Figures 2 and 3, respectively.

*Compound **6***. Yield 2% ($R_f = 0.7$, CH_2Cl_2/MeOH, 9:1). ^{1} H NMR ($CDCl_3$): δ 8.42 (s, 1H), 8.41 (s, 1H), 7.38 (d, 1H, $J = 4.2$ Hz), 7.36 (d, 1H, $J = 4.2$ Hz), 6.60 (t, 1H, $J = 2.4$ Hz), 6.57 (t, 1H, $J = 2.4$ Hz), 6.41 (t, 2H, $J = 3.0$ Hz), 5.8 (m, 2H), 5.64 (dd, 1H, $J_1 = 4.2$ Hz and $J_2 = 8.7$ Hz), 4.64 (m, 2H), 3.45 (q, 8H), 3.20 (q, 1H), 2.43 (s, 3H), 2.07 (q, 2H), 1.61 (s, 3H), 1.23 (m, 28 H), 0.88 (t, 3H, $J = 6.0$ Hz). ^{13} C NMR: δ 164.02, 163.12, 158.86, 158.81, 158.60, 158.44, 153.28, 149.68, 149.52, 135.88, 131.69, 126.97, 109.86, 109.04, 108.07, 97.01, 73.34, 65.80, 61.79, 45.46, 42.28, 32.75, 32.31, 30.08, 30.05, 29.85, 29.74, 29.61, 29.27, 23.07, 14.51, 12.82.

Cytotoxicity Assays. Human PC-3 prostatic carcinoma cells were cultured in DMEM/F-12 medium (GIBCO, Grand Island,

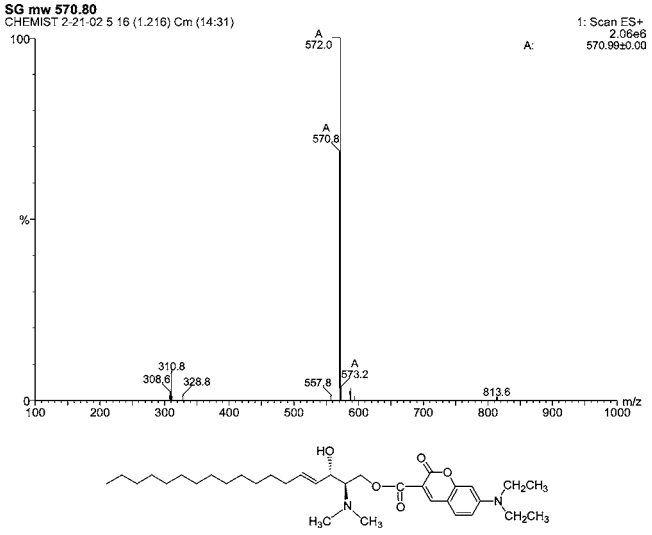


Figure 3. ESI mass spectrogram of compound **5**.

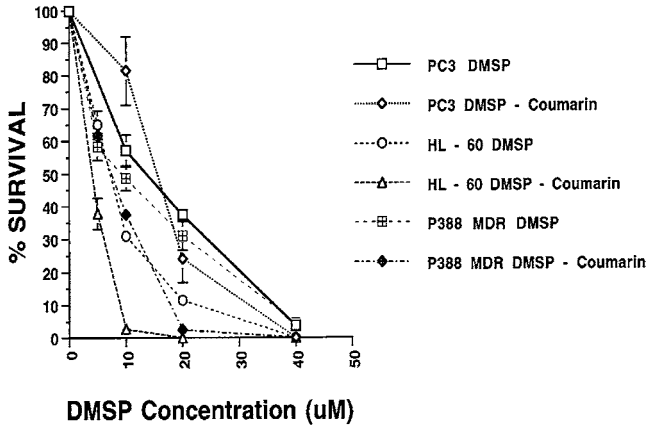


Figure 4. Dose–response effects of DMSP and DMSP–coumarin on viability (24 h MTT assay) of human PC-3 prostatic carcinoma, human HL60 acute myelogenous leukemia, and mouse P388 multidrug-resistant lymphocyte leumemia cell lines.

NY) supplemented with 5% fetal calf serum (GIBCO) at 37 °C in an incubator supplied with 5% CO_2/95% air, as previously described (*9*). The murine P388 acute myelogenous leukemia (AML) MDR-expressing subline P388MDR, and HL60, a human promyelocytic-like AML line, were cultured similarly. The P388MDR line had been selected from the parental cells by growth in the presence of increasing concentrations of doxorubicin (Dox) and displayed a stable resistance phenotype in the absence of further selection pressure. To ensure that the leukemia cells were in the logarithmic phase of growth for the cytotoxicity assays, they were allowed to grow to a density of 10^6 cells/mL before experimental manipulation.

Tumor cells were plated at (1.5−2.0) × 10^4 cells in 100 μL of medium per triplicate cell in flat-bottom 96-well microwell plates (Corning Glass Works, Corning, NY). Thereafter, they were incubated with known concentrations of DMSP or coumarin-tagged DMSP for 24 h. Since preliminary studies had revealed that the cytotoxic activity of compounds **4** and **5** were indistinguishable, their admixture was used in these cytotoxicity assays, as well as in the time-lapse fluorescence studies (see below). Remaining viable cells were stained with MTT. Resolubilized dye (MTT−formazan) was quantified by measurement of optical density at 570 nm in a microplate reader. The viability of treated cells was determined as a percentage of the optical density of dye in control cultures.

Time-Lapse Fluorescence Microscopy. Digital time lapse acquisition of PC-3 cells was performed using the Cell Observer function of a Zeiss Axiovert 200M motorized inverted microscope. Cells growing in a 12-well tissue culture plate were placed in a chamber on a temperature-controlled stage and maintained in a heated, humidified, 5% CO_2 atmosphere. The Axiovision Software was used to program the motorized stage to move sequentially from well-to-well and to acquire phase contrast as well as fluorescent color images at preselected time points. Phase images and fluorescent images, using appropriate excitation and emission settings for DMSP−coumarin (490/515 nm), were acquired.

Mitochondrial Membrane Potential (MMP) Plate-Based Fluorescence Assay. PC-3 cells were plated in triplicate in flat-bottom 96-well microwell plates (CoStar), essentially as described above for the cytotoxicity assays. After overnight incubation, DMSP (20 μM), DMSP−coumarin (20 μM), or control media was added and incubation was continued for 2 h. Thereafter, the protocol of the vendor (Cell Technology, Mountain View, CA) was followed for the addition of the fluorescent cationic dye to detect MMP. MMP-linked fluorescence in untreated control and treated (DMSP or DMSP−coumarin) cells was detected by excitation at 530 nm and emission at 590 nm. Background fluorescence was determined in untreated control cells that did not have the cationic dye added.

The percentage of MMP in treated cells was compared with that in untreated control cells by the expression Percentage of control MMP = (fluorescence in treated cells − background fluorescence) ÷ (fluorescence in untreated control cells − background fluorescence).

RESULTS AND DISCUSSION

Cytotoxicity Assays. The results are shown in Figure 4. PC-3 cells were essentially all killed by the highest concentration (40 μM) of either DMSP or DMSP−coumarin, whereas the IC_{50} was reached between 10 and 20 μM of either agent, indicating that substitution with coumarin did not cause significant effects on DMSP functions associated with induction of cell death. Similar results were obtained with these reagents on HL-60 cells, although both of the IC_{50}'s were lower: ∼5−10 μM for DMSP and 5 μM slightly exceeded 50% killing of HL60 cells for DMSP−coumarin. With the P388MDR targets, again there was minimal distinction between DMSP and DMSP−coumarin, and the IC_{50}'s were ∼10 μM for DMSP and ∼5−10 μM for DMSP−coumarin. Overall, based on the cytotoxicity assays in the prostatic as well as the leukemia models, substitution of DMSP with coumarin was well-tolerated.

Time-Lapse Fluorescence Microscopy. The results in Figure 5 demonstrate the uptake of DMSP−coumarin in PC-3 cells, tracking its green fluorescence. PC-3 cells viewed prior to or immediately after introduction of DMSP−coumarin (20 μM) were clearly evident by phase contrast but not by fluorescence microscopy (data not shown). However, already after 60 min of further incubation (panel A), initial intracellular accumulation and localization to perinuclear mitochondria was apparent. This localization became increasingly pronounced and more clearly punctate after 2 h (panel B) and 4 h (panel C). (In related studies, we have shown that this accumulation is closely linked with loss of inner mitochondrial membrane potential, release of cytochrome *c*, and caspase activation).

Effects of DMSP−Coumarin on MMP. PC-3 cells were treated with DMSP or DMSP−coumarin (20 μM) for 2 h prior to assaying mitochondrial membrane potential in control and treated cells. The results are shown in Table 1. DMSP rapidly and dramatically reduced the MMP of PC-3 cells to only background levels; similarly, the effect of DMSP−coumarin was

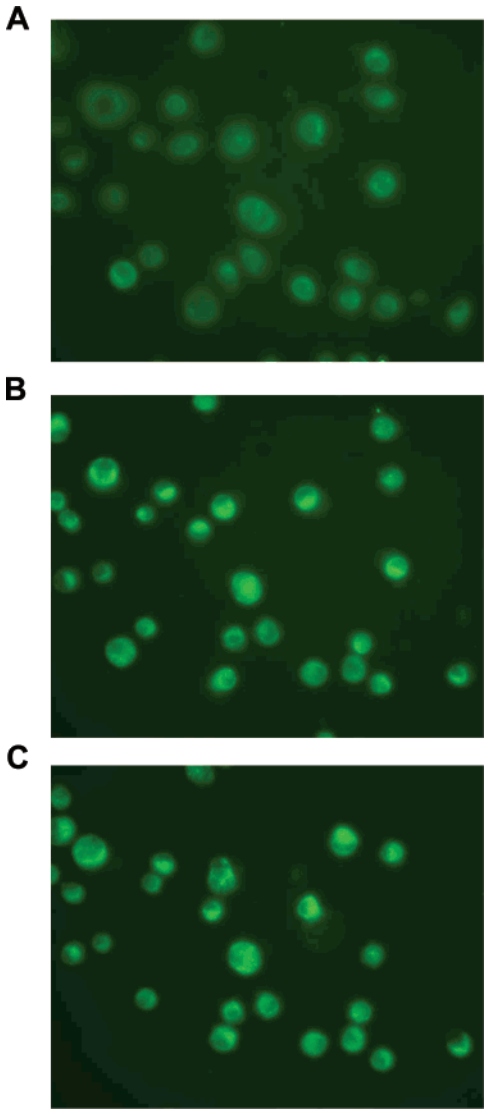


Figure 5. Time-lapse fluorescence microscopy of uptake of DMSP−coumarin in PC-3 cells. Green fluorescence is evident after 60 min of incubation (A) as intracellular accumulation and localization to perinuclear mitochondria; localization became increasingly pronounced after 2 h (B) and 4 h (C).

Table 1. Effect of DMSP and DMSP−coumarin on MMP in PC-3 Cells[a]

treatment	% MMP[b,c]
DMSP	−3.0 ± 8.8
DMSP−coumarin	7.1 ± 6.4

[a] PC-3 cells were treated with DMSP or DMSP−coumarin (both at 20 μM) for 2 h prior to addition of fluorescent cationic dye to detect MMP. MMP-linked fluorescence was detected by excitation at 530 nm and emission at 590 nm. [b] Percentage of MMP in DMSP- or DMSP−coumarin-treated cells compared with that in untreated control PC-3 cells. Calculated as (fluorescence in treated cells − background fluorescence) ÷ (fluorescence in untreated control cells − background fluorescence). [c] Mean ± SEM from six determinations.

also pronounced, causing reduction to 7.1% ± 6.4% of control MMP. Thus, when considered together, the kinetics of localization and subsequent loss of MMP indicate that a very rapid depolarization is induced by DMSP in PC-3 targets once it reaches the mitochondria.

Recent studies have revealed pharmacological tools with which to perturb the SL rheostat, *in vitro* and *in vivo*. For example, chemical library screening has defined inhibitors of SpK that are reportedly more specific and potent than DMSP, for example, SKI II (*10*, *11*). In our hands, SKI II causes a much more protracted effect against human prostatic cancer and leukemic target cell lines than does DMSP and, particularly, lacks the rapid effect on MMP observed with DMSP (Klostergaard et al., in preparation). The fungal metabolite FTY720 has been shown to down-regulate G-protein-coupled receptors through which extracellular Sp-1-P exerts its effects; further, FTY720 is endowed with a modified sphingoid backbone and also displays rapid homing to mitochondria and the ability to disrupt MMP (*12*, *13*), suggesting that the latter property might be inherent in this backbone structure. The identification of mitochondrial domains with which the sphingoid backbone interacts might be illuminating with regard to its mechanism of induction of the intrinsic apoptotic pathway: for example, by conducting experiments using fluorescenated sphingosine(s) and mitochondria prelabeled with suitable fluorescent dyes appropriate for a donor−acceptor interaction for fluorescence resonance energy transfer (*14*).

In summary, the availability of a fluorescent, biologically equivalent DMSP will advance studies both *in vitro* and *in vivo*, such as of its subcellular localization, mechanism of action, biodistribution, and pharmacology.

ACKNOWLEDGMENT

We thank Mr. William Spohn for assistance with the time-lapse fluorescence microscopy studies and Dr. Jaw-Ching Liu for assistance with manuscript preparation.

LITERATURE CITED

(1) Spiegel, S., and Milstien, S. (2003) Sphingosine-1-phosphate: an enigmatic signalling lipid. *Nat. Rev. Mol. Cell Biol. 4*, 397−407.

(2) Cuvillier, O., Pirianov, G., Kleuser, B., Vanek, P. G., Coso, O. A., Gutkind, S., and Spiegel, S. (1996) Suppression of ceramide-mediated programmed cell death by sphingosine-1-phosphate. *Nature 381*, 800−803.

(3) Xia, P., Gamble, J. R., Wang, L., Pitson, S. M., Moretti, P. A., Wattenberg, B. W., D'Andrea, R. J., and Vadas, M. A. (2000) An oncogenic role of sphingosine kinase. *Curr. Biol. 10*, 1527−1530.

(4) Olivera, A., and Spiegel, S. (1993) Sphingosine-1-phosphate as second messenger in cell proliferation induced by PDGF and FCS mitogens. *Nature 365*, 557−560.

(5) Shu, X., Wu, W., Mosteller, R. D., and Broek, D. (2002) Sphingosine kinase mediates vascular endothelial growth factor-induced activation of ras and mitogen-activated protein kinases. *Mol. Cell. Biol. 22*, 7758−7768.

(6) Edsall, L. C., Van Brocklyn, J. R., Cuvillier, O., Kleuser, B., and Spiegel, S. (1998) *N*,*N*-Dimethylsphingosine is a potent competitive inhibitor of sphingosine kinase but not of protein kinase C: modulation of cellular levels of sphingosine 1-phosphate and ceramide. *Biochemistry 37*, 12892−12898.

(7) Shirahama, T., Sweeney, E. A., Sakakura, C., Singhal, A. K., Nishiyama, K., Akiyama, S., Hakomori, S., and Igarashi. Y. (1997) In vitro and in vivo induction of apoptosis by sphingosine and N, N-dimethylsphingosine in human epidermoid carcinoma KB-3−1 and its multidrug-resistant cells. *Clin. Cancer Res. 3*, 265−272.

(8) Taha, T. A., Kitatani, K., El-Alwani, M., Bielawski, J., Hannun, Y. A., and Obeid, L. M. (2006) Loss of sphingosine kinase-1 activates the intrinsic pathway of programmed cell death: modulation of sphingolipid levels and the induction of apoptosis. *FASEB J. 20*, 482−484.

(9) Klostergaard, J., Auzenne, E., and Leroux, E. (1998) Characterization of cytotoxicity induced by sphingolipids in multidrug-resistant leukemia cells. *Leuk. Res. 22*, 1049−1056.

(10) French, K, J., Schrecengost, R. S., Lee, B. D., Zhuang, Y., Smith, S. N., Eberly, J. L., Yun, J. K., and Smith, C. D. (2003) Discovery and evaluation of inhibitors of human sphingosine kinase. *Cancer Res. 63*, 5962−5969.

(11) French, K. J., Upson, J. J., Keller, S. N., Zhuang, Y., Yun, J. K., and Smith, C. D. (2006) Antitumor activity of sphingosine kinase inhibitors. *J. Pharmacol. Exp. Ther. 318*, 596−603.

(12) Nagahara, Y., Ikekita, M., and Shinomiya, T. (2000) Immunosuppressant FTY720 induces apoptosis by direct induction of permeability transition and release of cytochrome c from mitochondria. *J. Immunol. 165*, 3250−3259.

(13) Solary, E., Bettaieb, A., Dubrez-Daloz, L., and Corcos, L. (2003) Mitochondria as a target for inducing death of malignant hematopoietic cells. *Leuk. Lymphoma 44*, 563−574.

(14) Periasamy, A., Day, R. N., and Masters, B. R. (2006) Molecular Imaging, FRET Microscopy and Spectroscopy. *J. Biomed. Opt. 11*, 69−90.

BC060285Q

Synthesis and in Vitro Characterization of an ABC Triblock Copolymer for siRNA Delivery

Tatiana Segura[†,‡] and Jeffrey A. Hubbell*[,†]

Ecole Polytechnique Fédérale de Lausanne (EPFL), Institute of Bioengineering and Institute of Chemical Sciences and Engineering, CH-1015, Lausanne, Switzerland, and University of California, Los Angeles, Chemical and Biomolecular Engineering Department, Los Angeles, California. Received September 11, 2006; Revised Manuscript Received December 18, 2006

The ability to specifically down-regulate gene expression using the RNAi pathway in mammalian cells has tremendous potential in therapy and in basic science. However, delivery systems capable of efficient and biocompatible delivery of siRNA to target cells are not yet satisfactory. Here, we report the synthesis and in vitro characterization of ABC triblock copolymers that self-assemble with siRNA based on electrostatics and with each other by hydrophobic interactions. The ABC triblock copolymer is based on poly(ethylene glycol) (PEG), poly(propylene sulfide) (PPS), and a positively charged peptide (PEG−PPS−peptide). The diblock copolymer PEG_{45}−$PPS_{5,10}$ was synthesized using anionic polymerization of propylene sulfide upon a PEG macroinitiator, and the peptide domain was coupled to the PPS terminus using a disulfide exchange reaction with an N-terminal cysteine residue on the peptide. The peptides were designed to interact electrostatically with siRNA, selecting the TAT peptide domain of HIV (RKKRRQRRR) and an oligolysine (Lys_9). The resulting triblock copolymers were able to self-assemble with siRNA as demonstrated by dynamic light scattering and gel electrophoresis. Complex size was found to be dependent on the amount of polymer used (charge ratio) and the length of the hydrophobic PPS block, achieving sizes ranging from 171 nm to 601 nm. Cell internalization and gene expression down-regulation studies showed that the triblock copolymers are able to transport siRNA inside the cell and mediate gene expression down-regulation, with the amount of internalization and gene transfer affected by charge ratio, PPS length, and the presence of serum. The proposed triblock was able to mediate gene expression down-regulation of GAPDH, achieving up to 90.5% ± 0.02% down-regulation.

INTRODUCTION

In 2001, Elhashir and co-workers (*1*) demonstrated that incorporation of double-stranded, 21-nucleotide-long pieces of RNA results in activation of the RNA interference (RNAi) pathway and the specific down-regulation of genes with sequences that are homologous to the double-stranded RNA. This RNAi pathway activation did not result in the activation of the interferon response, which was seen with longer double-stranded RNAs (*1*, *2*). They called the double-stranded RNA small interfering RNA or siRNA. Since this finding, the idea of using siRNAs as a genetic therapeutic and as a basic science tool has been investigated by many groups (*3*). In the area of basic science, decreasing the expression level of a gene within a cell has the power to reveal or confirm the roles of specific components of signaling pathways and can lead to a mechanistic understanding of cell behavior, disease pathogenesis, and drug action (*4*, *5*). Therapeutic strategies using siRNA are also under development and have recently shown promise to reduce of tumor growth (*6*, *7*), reduce neovascularization in the eye (*8*), reduce viral infection (*9*), and reduce postoperative adhesions (*10*). However, the lack of an efficient delivery system that can efficiently target and deliver the siRNA to the desired cell population is limiting the full therapeutic potential of this approach.

Nonviral siRNA delivery suffers from many of the same limitations as other gene delivery approaches, including packaging efficiency, colloidal stability, targeted internalization, endosomal escape, and vector decomplexation, for which a delivery system has yet to be found that is as efficient as viral vectors. Nevertheless, current strategies for siRNA delivery employ the same delivery vectors as used for nonviral gene delivery such as cationic polymers (*7*, *11*, *12*), lipids (*13*, *14*), and peptides (*15*), which self-assemble with siRNA electrostatically.

In the field of drug delivery, there is extensive interest in amphiphilic block copolymers that can self-assemble in aqueous environments into stable supermolecular structures. A variety of such structures can be generated, such as micellar and vesicular assemblies, both of which can be important for pharmacological applications. Extensive investigation has been conducted in poly(ethylene glycol) (PEG)-containing block copolymers, such as copolymers with poly(propylene glycol) (*16*−*18*), and poly(ethylene) (*19*). In our laboratory, a novel class of amphiphilic triblock copolymers (ABA) composed of hydrophilic PEG (A) and hydrophobic poly(propylene sulfide) (PPS) (B) polymer domains has been synthesized using mild polymerization conditions that do not require extremely anhydrous conditions and allow for incorporation of biological molecules such as peptides (*20*). When these triblock copolymers contain a substantial hydrophobic portion (as determined by PPS block length), they have been found to self-assemble into vesicular polymersomes of ca. 100 nm size that have a watery core, which could be used for encapsulating drugs (*21*). Other supermolecular structures, such as spherical and cylindrical micelles, have also been observed, being obtained by

* Corresponding author. Jeffrey A. Hubbell, EPFL SV-LMRP, Station 15, CH-1015 Lausanne, Switzerland, Phone +41 21 693 9681, Fax + 41 21 693 9665, E-mail jeffrey.hubbell@epfl.ch.

† Institute of Bioengineering and Institute of Chemical Sciences and Engineering.

‡ University of California, Los Angeles.

10.1021/bc060284y CCC: $37.00 © 2007 American Chemical Society
Published on Web 03/15/2007

modifying the length of the hydrophobic and hydrophilic polymer domains (*22*). The presence of PEG in the surface of these supermolecular structures also makes them ideal for biological applications, given that their surface would be relatively protein-resistant.

Here, we report the synthesis and in vitro characterization of ABC triblock copolymers that self-assembles with siRNA based on electrostatics and with each other by hydrophobic interactions. The ABC triblock copolymer is based on PEG (A), PPS (B), and a peptide (C). The peptide was designed to interact electrostatically with siRNA: two peptide sequences were investigated, namely, the HIV-1 TAT sequence (CGGWRK-KRRQRRR, the terminal C being used for block conjugation, the W for detection at 280 nm, and the intervening GG being used as a linker) or a Lys_9 sequence (K_9, CGGWKKKKKKKKK, likewise, the C, W, and GG residues being used for block conjugation, detection, and linking). The proposed triblock copolymer was able to form condensed structures with siRNA and mediate gene down-regulation of GAPDH, achieving up to 90.5% ± 0.02% down-regulation.

MATERIALS AND METHODS

Materials. Peptides were purchased from NeoMPS (Strasburg, France) at >95% purity by HPLC. All synthesis reagents were purchased from Fluka (Buchs, Switzerland). siGlo (siL-amin A/C-Cy3) was purchased from Perbio (Lausanne, Switzerland). KDarlet GAPDH enzymatic activity assay, siRNA GAPDH, siRNA NEG were purchased from Ambion (Austin, TX). All other reagents were purchased from VWR (Dietikon, Switzerland) unless otherwise noted.

PEG−Allyl Ether Synthesis. PEG_{45} monomethyl ether (PEG_{45}) was modified with allyl bromide as previously described (*20*) with modifications. In short, PEG_{45} (20 g, 10 mmol) was dissolved in tetrahydrofuran (THF, 300 mL) under inert atmosphere and heated to reflux for 3 to 4 h in a Soxhlet apparatus filled with molecular sieves. The solution was allowed to cool to the touch, and 2.5 equiv of NaH (0.6 g, 25 mmol) was added. The solution was stirred and allowed to react for 15 min before 1.4 mL (3.46 g, 40 mmol) of allyl bromide was added to the solution under stirring and allowed to react for 24 h. The reaction mixture was passed through a filter to remove the NaBr salt formed during the reaction. The volume of the solution was reduced to about 20 mL by evaporation and precipitated two times in diethyl ether. A white solid polymer was obtained (16.68 g, 83.4% yield, conversion 100%). ^{1}H NMR ($CDCl_3$): δ 3.56−3.7 (broad, PEG polymer protons), 3.41 (s, 3H, $-OC\mathbf{H}_3$), 4.01−4.04 (dd, 2H, $-CH_2OC\mathbf{H}_2CH{=}CH_2$), 5.15−5.30 (m, 2H, $-CH_2OCH_2CH{=}C\mathbf{H}_2$), 5.85−5.98 (m, 1H, $-CH_2OCH_2C\mathbf{H}{=}CH_2$).

PEG−Thioacetate Synthesis. PEG−allyl ether was modified with thioacetic acid to form PEG−thioacetate as previously described (*20*) with modifications. PEG−allyl ether (8 g, 4 mmol) was introduced to a Schlenck tube in toluene (64 mL). The toluene was degassed with sonication for 20 min and bubbling with argon gas for 30 min. The PEG/toluene solution was further degassed with pump evacuation and filling the Sclenck tube with argon. This procedure was repeated five times. The reaction mixture was then warmed to 60 °C, and the first of five AIBN aliquots were added (1.3 g × 5, 0.8 mmol × 5), followed by the first of five thioacetic acid aliquots (0.456 mL × 5, 6.4 mmol × 5). The five aliquots were added over an 8−10 h period. The reaction was allowed to continue for 18 h at 60 °C and an additional 24 h at room temperature. The reaction mixture was mixed with activated DOWEX 1/8−100 (Cl) resin and incubated for 1 h. After filtration, the volume of the solution was reduced to about 20 mL by evaporation and then precipitated three times with diethyl ether. Dichloromethane was used to redissolve the precipitate. A slightly pale yellow solid was obtained (5.26 g, 65.7% yield, conversion 90%). ^{1}H NMR ($CDCl_3$): δ 1.81−1.90 (q, 2H, $-OCH_2C\mathbf{H}_2CH_2S-$), 2.35 (s, 3H, $-SCOC\mathbf{H}_3$), 2.92−2.97 (t, 2H, $-OCH_2CH_2C\mathbf{H}_2S-$), 3.39−3.89 (broad, PEG chain protons), 3.41 (s, 3H, $-OC\mathbf{H}_3$).

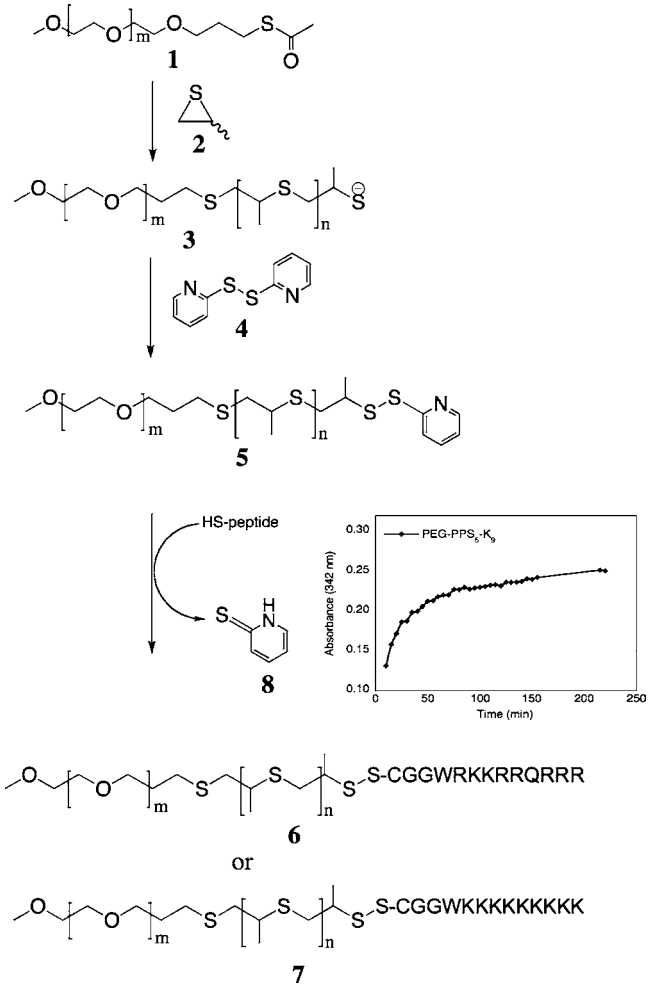


Figure 1. Synthetic scheme of poly(ethylene glycol)−poly(propylene sulfide)−peptide (PEG−PPS−peptide). PEG−thioacetate **1** is activated by sodium methoxylate to form a sulfide that can initiate the anionic polymerization of propylene sulfide **2** to form the AB block copolymer PEG−PPS **3**. 2,2-Dipyridine dithione **4** was used as the end-capping agent to generate the AB diblock copolymer terminated with a mixed disulfide **5**. The peptides TAT (CGWRKKRRQRRR) and K_9 (CGG-WKKKKKKKKK) reacted with **5** via a disulfide exchange reaction to generate the ABC triblock copolymers shown, **6** and **7**. The formation of the triblock copolymer was monitored by recording the absorbance at 342 nm, which corresponded to the release of pyridine thione, **8** (graphical insert).

PEG−PPS Diblock Copolymer Synthesis. The polymer $PEG_{45}-PPS_x$−pyridyldithione was synthesized using anionic polymerization of propylene sulfide (PS) with 2,2-dipyridine dithione as the end-capping agent to form PEG−PPS−pyridyldithione (Figure 1). PEG−thioacetic acid (1 g, 0.5 mmol) was dissolved in dry THF (23 mL). Sodium methoxylate (NaMeOH, 1.1 mL, 0.55 mmol) was added to the solution and allowed to react for 30 min. Propylene sulfide (0.394 mL, 5 mmol or 0.196 mL, 2.5 mmol) was added via syringe and allowed to react for 1.5 h. Dipyridine dithione (0.44 mg, 2 mmol) was dissolved in THF and added to the reaction mixture via syringe. The progress of the reaction can be easily followed by the appearance of an intense yellow color. After filtration and solvent evaporation, the product was precipitated in diethyl ether. A pale yellow solid was obtained (336.2 mg, 33.6% yield for $n = 5$; and 284 mg, 28.41% yield for $n = 10$). ^{1}H NMR

($CDCl_3$): δ 1.35−1.45 (d, C**H**$_3$ in PPS chain), 1.81−1.90 (broad q, 2H, −OC**H**$_2$CH$_2$CH$_2$S), 3.6−3.7 (broad PEG chain protons), 7.8−7.83 (m, 1H pyridine group). The degree of polymerization of the PPS block was determined by taking the ratio of PEG protons to PPS protons, resulting in polymers with $n = 5.06$ and $n = 10.71$. The polydispersity index (PDI) of the polymers was determined by GPC with PDI = 1.15 and PDI = 1.26, respectively.

PEG−PPS−Peptide Triblock Polymer Synthesis. The peptides Ac-CGGWRKKRRQRRR-NH_2 (TAT) and Ac-CGG-WKKKKKKKKK-NH_2 (K_9) were bound to the PEG_{45}−PPS−pyridyldithione polymers using a disulfide exchange reaction between the disulfide end-capping PEG−PPS and the cysteine group of the peptide. The course of the reaction was monitored following the release of 2-pyridinethione at 342 nm (see inset in Figure 1). Upon dilution in D_2O at 12 mg/mL, the solution turned cloudy, indicating the formation of aggregates. Furthermore, upon dilution in $CDCl_3$ at 12 mg/mL, the solution again turned cloudy with a green color indicating the formation of aggregates and the strong amphiphilic nature of the molecule. ^{1}H NMR in water: δ 1.35−1.45 (broad d, C**H**$_3$ in PPS chain), 1.81−1.90 (broad peak no q visible and signal integration reduced, 2H, −OC**H**$_2$CH$_2$CH$_2$S), 3.6−3.7 (broad PEG chain protons unchanged). Protons from the peptide were not observed. ^{1}H NMR in $CDCl_3$: δ 1.35−1.45 (broad no d visible, C**H**$_3$ in PPS chain), 1.81−1.90 (q, 2H, −OC**H**$_2$CH$_2$CH$_2$S), 3.6−3.7 (broad PEG chain protons), 7.08−7.13 and 7.2−7.24 (t, tryptophan amino acid residue), and 7.5−7.54 and 7.6−7.64 (d, tryptophan amino acid residue).

Fluorescence Reduction Assay. The ability of PEG−PPS−peptide to form complexes with siRNA was tested using an ethidium bromide (EtBr) fluorescence reduction assay. siRNA (15 pmol, 100 μL) was mixed with EtBr, and the resulting fluorescence emission was measured using a fluorescence microplate reader (Tecan, Männedorf, Switzerland). The reduction of fluorescence emission was measured as triblock copolymer was added to generate the indicated charge ratio.

Dynamic Light Scattering Analysis. The ability of PEG−PPS−peptide alone or in solution with siRNA to form nanosized aggregates was studied using dynamic light scattering (DLS) in a nanozetasizer (Malvern, U.K.). Size measurements of triblock copolymers alone were measured dissolving the individual polymers in Tris-buffer saline (TBS) at a 10 mg/mL and using the standard settings in the instrument. For PEG−PPS−peptide/siRNA size measurements, complexes were formed by adding the triblock copolymer solution (150 μL) to an siRNA solution (150 pmol, in 150 μL TBS) at different charge ratios. 100 μL of the solution was used to measure size, and the other was dissolved in MiliQ water to 1000 μL and used to measure ζ-potential of the complexes.

Cellular Internalization in Vitro. Cell internalization studies were assessed via fluorescence microscopy (Zeiss, Feldbach, Switzerland) and fluorescence-activated cell sorting (FACS). HeLa cells (40 000 cells/well, 24-well plate) were seeded the day before adding complexes with siRNA labeled with Cy3 (microscopy) or Cy5 (FACS). The day of transfection, siRNA/polymer complexes (25 pmol siRNA) were formed at charge ratios of ±6 for the microscopy studies and ±3 or ±6 for the FACS studies, were added to the cells, and were incubated with the cells for either 24 or 4 h for the microscopy experiments and FACS experiments, respectively. After incubation, the cells were washed three times with PBS and either visualized using a fluorescence microscope or trypsinized, centrifuged, and resuspended in 1% FBS in PBS and analyzed via FACS. The cells were not fixed. Untreated cells were used to determine the native background of the cells and to adjust the gates. The live cell gate was adjusted so that 10 000 events were read. The positive cell gate was defined as having less than 0.5% positive cells for untreated cells (a 95% confidence interval).

Cell Proliferation Assay. The toxicity of the triblock copolymer/siRNA complexes was assessed using the MTT assay (Promega Corp, Madison, Wisconsin). HeLa cells (7000 cells/well) were plated on a 96-well plate the day before they were exposed to the triblock copolymers/siRNA complexes. To determine the effect of complex concentration on toxicity, different siRNA concentrations were delivered with complexes at a charge ratio of ±6. Complexes were incubated with the cells for 24 h, then removed, and new media added. The MTT solution (20 μL) was added to each well and incubated for 2 h. Absorbance readings were measured at 490 nm. Untreated cells were used as the 100% cell proliferation control and siRNA complexed with Lipofectamine 2000 (LF2000, Invitrogen, Basel, Switzerland) was used as a comparative control using a 20 pmol siRNA/μL LF2000.

GAPDH Gene Expression Down-Regulation. The efficacy of the delivery strategy was studies using a GAPDH enzyme activity assay (Ambion, Austin, Texas). HeLa cells (7000 cells/well) were plated in 96-well plates the day before transfection and transfected with 10 pmol siRNA at a charge ratio of ±6. The transfections were done both in the presence and absence of FBS (0% or 10%) and in the presence and absence of chloroquine (Sigma, Lyon, France, 100 μM). Before transfection, the cell culture medium was replaced with transfection medium. For complexation, siRNA (30 pmol, 60 μL Optim-Mem) was mixed with the triblock copolymer or unmodified peptide (60 μL, TBS) and mixed by vortexing for 10 s. The complex was allowed to form undisturbed for 10 min. The extent of gene expression down-regulation was assessed 48 h post-transfection. LF2000 complexes were formed using a 1 μL of LF2000 to 20 pmol of siRNA. To determine if the transfection procedure affected GAPDH expression, a nontargeting sequence of siRNA was used (siNEG). GAPDH activity was only significantly reduced when LF2000 was used as the delivery vector for siNEG. The remaining GAPDH activity was measured as described by the manufacturer using the kinetic fluorescence increase method over 5 min and was calculated according to the following equation: % remaining expression = $\Delta_{\text{fluorescence,GAPDH}}/\Delta_{\text{fluorescence,siNEG}}$, where $\Delta_{\text{fluorescence}} = \text{fluorescence}_{1\text{min}} - \text{fluorescence}_{5\text{min}}$ for either transfected (GAPDH), mock transfected (siNEG), or untransfected cells. Untransfected cells are cells that are exposed to serum or serum-free media for the 4 h of transfection and then replaced with cMEM. For LF2000, the control is a mock transfection using siNEG to determine the level of down-regulation that occurs due to the transfection procedure.

Statistics. All statistical analyses were performed using the computer program *Prism* (GraphPad, San Diego, CA). Experiments were statistically analyzed using a one-way analysis of variance using the Tukey test, which compares all pairs of columns, using a 95% confidence interval. When only two groups were compared, the Student *t* test was used as indicated in the figure legends.

RESULTS

Polymer Synthesis and Characterization. The ABC triblock copolymer PEG−PPS−peptide was synthesized using anionic polymerization of propylene sulfide upon the terminus of an activated PEG−thiol under an inert atmosphere, followed by peptide grafting using a disulfide exchange reaction (see Figure 1 and Material and Methods). The peptide coupling reaction was monitored using the release of 2-pyridine dithione at 342 nm, which demonstrated that the reaction reached a plateau after 2 h (see inset in Figure 1). After each step of the synthesis and purification, the intermediate product was characterized with

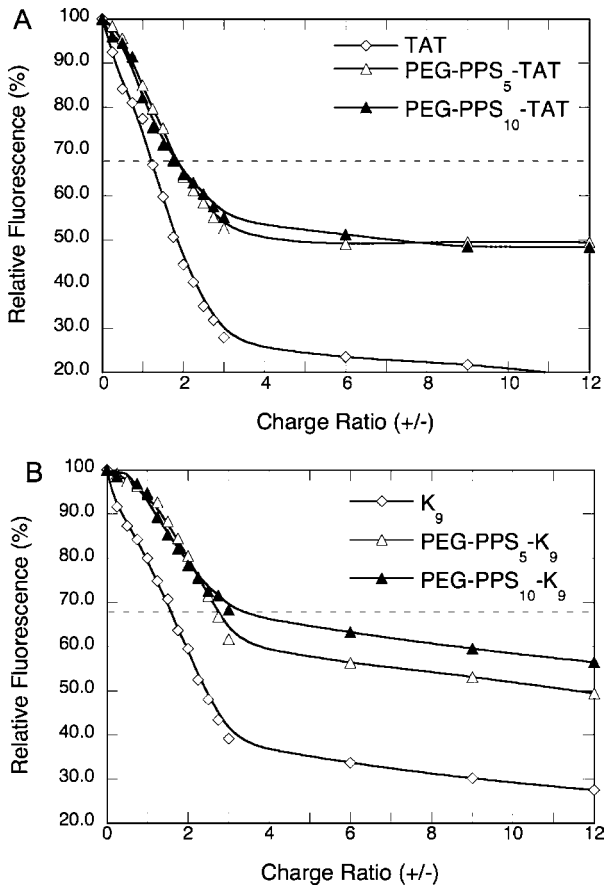


Figure 2. Relative fluorescence intensity of siRNA−EtBr complexes with PEG−PPS_n−TAT (A) and PEG−PPS_n−K_9 (B) at different charge ratios. The florescence intensity decreases as more polymer is added until a plateau is reached, indicating that particles have formed. The dotted line indicates the charge ratio at which complex migration in agarose gel electrophoresis is stopped.

^{1}H NMR to confirm that the correct product was achieved and that there were not remaining impurities. At the concentrations required for ^{1}H NMR analysis, however, the triblock copolymer formed aggregates, presumably micelles, both in an aqueous environment (D_2O) or in deuterated chloroform, due to its strong amphiphilic nature. ^{1}H NMR of the triblock thus contained broad peaks that were difficult to integrate. On the basis of the characterization performed, the polymers PEG_{45}−PPS_5−peptide and PEG_{45}−PPS_{10}−peptide were obtained, where the subscripted numbers indicate the degree of polymerization of the respective blocks.

EtBr Exclusion Assay. The ability of the triblock polymer to form condensed structures with siRNA was studied using an EtBr dye exclusion assay (Figure 2). All polymers were able to exclude EtBr from the siRNA as more polymer was added (higher charge ratios), indicating that condensed particles were forming. Both the TAT and K_9 peptides when used alone resulted in the highest condensation, reaching up to an 80% decrease in fluorescence intensity. Triblock copolymers based on TAT (Figure 2A) showed little dependence on the PPS degree of polymerization in their ability to form condensed particles with siRNA, with the maximum fluorescence decrease being reached at a charge ratio of 3, showing a 50% decrease. Triblock copolymers based on K_9 (Figure 2B), on the other hand, showed more of an effect of PPS length, with PPS_5 resulting in more condensed structures than PPS_{10}. The maximum fluorescence decrease was also 50%.

Size and ζ-Potential Characterization. In the absence of siRNA, the triblock polymers PEG−PPS_5−TAT, PEG−PPS_{10}−TAT, PEG−PPS_5−K_9, and PEG−PPS_{10}−K_9 each formed aggregates in solution at a concentration of 10 mg/mL, with sizes of 11.3 ± 0.4, 16.0 ± 0.3, 13.1 ± 0.1, and 16.0 ± 0.6 nm, respectively (Figure 3A,D). These measurements are consistent with a nanostructure morphology of spherical micelles. There was a statistical significance between the sizes of PEG−PPS_5−peptide and PEG−PPS_{10}−peptide aggregates for both TAT and K_9 peptides ($p < 0.001$), indicating that the degree of polymerization of the PPS domain affects the overall size of the particles formed. Furthermore, for triblock copolymers with PPS degree of polymerization of 5, there was a statistical difference of the size of aggregates formed between TAT and K_9 peptides ($p < 0.01$), indicating that the character of the peptide also affects the size of the resulting micellar aggregates.

Size and surface charge of the aggregates formed between siRNA and PEG−PPS_5−TAT, PEG−PPS_{10}−TAT, PEG−PPS_5−K_9, and PEG−PPS_{10}−K_9, as well as the TAT and K_9 peptides not associated to the block copolymer, were measured using DLS and ζ-potential (Figure 3). Complex size was found to be dependent on the amount of polymer used (charge ratio) and the length of the hydrophobic domain (PPS degree of polymerization). For PEG−PPS_5−TAT triblock polymers, the size of the particles formed decreased as the amount of polymer increased, with sizes ranging from 199.0 ± 79.3 to 160.2 ± 1.5 nm (Figure 3B, open triangles). However, for the triblock polymers where the PPS unit was longer (PPS_{10}), the trend was reversed, such that increasing the amount of polymer from a charge ratio of ±3 to ±24 increased the size of the particles, with particle size ranging from 222.2 ± 0.8 to 601.2 ± 72.8 nm and 182.4 ± 6.5 to 312.3 ± 42.7 nm for PEG−PPS_{10}−TAT (Figure 3B, closed triangles) and PEG−PPS_{10}−K_9 (Figure 3E, closed triangles), respectively. ζ-Potential measurement for particles formed with TAT-containing polymers increased from ∼−20 mV to ∼0 mV (Figure 3C) and for K_9-containing polymers from ∼0 mV and to ∼+10 mV (Figure 3F) as charge ratio was increased from ±3 to ±24.

PEG−PPS−Peptide/siRNA Internalization Studies. HeLa cell internalization of PEG−PPS−peptide complexes with siRNA was assessed by FACS and confirmed with fluorescence microscopy. FACS data were analyzed by determining the number of cells in the positive gate and the total mean fluorescence intensity (MFI) of the cell population (Figures 4 and 5). Cellular internalization of PEG−PPS−peptide complexes was greatly affected by the presence of serum as well as the length of the PPS domain and the charge ratio of the complex. For the TAT-containing polymers, maximal internalization in the presence of serum was only 38.2 ± 0.1%, whereas in the absence of serum, 99.9 ± 0.1% of the cells had internalized the polymer complex with siRNA (Figure 4A compared to C). Polymers formed with the K_9 peptide were also sensitive to the presence of serum (Figure 5A compared to C); however, polymer structure could somehow overcome this difference. For example, 93.3 ± 1.6% of the cells treated with PEG−PPS_{10}−K_9 at a charge ratio ±6 were positive for internalization in the presence of serum, compared with 99.0 ± 0.3% in the absence of serum. For these polymers, charge ratio was important: the PEG−PPS_{10}−K_9 polymer at a charge ratio of ±3 were internalized by only 63.4 ± 3.1% and 94.7 ± 0.6% of the cells in the presence and absence of serum, respectively, compared to the above-mentioned 93.3% and 99.00% for ±6 ($p < 0.001$). In contrast, internalization by TAT-containing polymers was not affected by the charge ratio used.

The mean fluorescence intensity (MFI) of the cells was also affected by the presence of serum, the length of the PPS domain, and the charge ratio of the complexes (Figures 4 and 5, panels B,D). In general, longer PPS domains and higher charge ratio achieved more particle internalization (higher MFI) than shorter

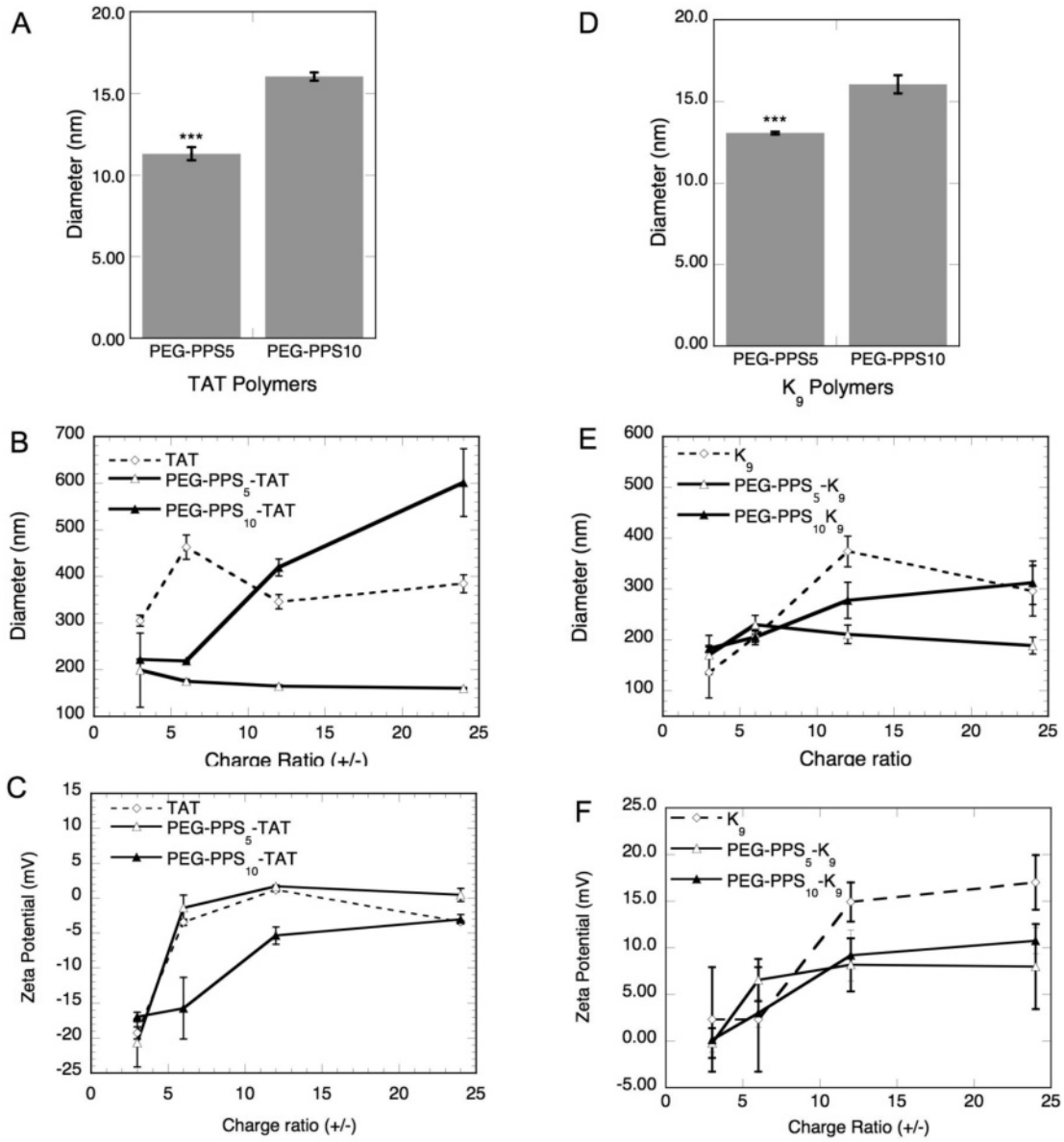


Figure 3. Mean diameter of micelles forming in 1% w/v solutions of PEG−PPS_n−TAT (A) and PEG−PPS_n−K_9 (D) in the absence of siRNA. Size and ζ-potential measurements as a function of charge ratio for TAT peptide-based polymers (B,C) and K_9-based polymers (E,F). The siRNA complexes with copolymers are much larger than the copolymer micelles that form without siRNA. Statistical analyses were done using the Student *t* test. The symbol *** indicates statistical significance at a level of $p < 0.001$.

PPS domains or lower charge ratio. Interestingly, the MFI was also affected by the type of peptide used, with the polymers formed with the K_9 peptide (Figure 5B,D) being less adversely affected by serum than the polymers formed with the TAT peptide (Figure 4B,D). In the presence of serum, the maximum MFI observed with PEG−PPS_{10}−K_9 was 12.4 ± 0.1 (at a charge ratio of ±6), compared to 22.4 ± 1.6 in the absence of serum (Figure 5, B vs D). The effect for the polymers formed with the TAT peptide was stronger: in the presence of serum, the maximum MFI observed with PEG−PPS_{10}−K_9 was 4.7 ± 0.01 (at a charge ratio of ±6), compared to 263.3 ± 63.8 in the absence of serum (Figure 4, B vs D). Fluorescence microscopy of complexes formed with Cy3-labeled siRNA corroborate the data found in FACS analysis. Figures 4E and 5E show fluorescence images for internalization of PEG−PPS_5−TAT and PEG−PPS_5−K_9 complexes, respectively, which show substantially more internalization than those complexes formed with TAT or K_9 (Figures 4F and 5F).

Comparisons with LF2000 were also made, and in all cases evaluated at the same siRNA dose (as in Figures 4 and 5), complex uptake was less with the polymer vectors than with the cationic lipid vector.

Toxicity of PEG−PPS−Peptide/siRNA Complexes. A cellular proliferation assay was used as an indirect measure of the toxicity caused by exposure to the triblock copolymer/siRNA complexes (Figure 6). None of the concentrations used for the different triblock copolymer/siRNA transfections resulted in a statistically significant reduction of cell proliferation, indicating that no toxicity occurred as a result of treatment with the complexes. In contrast, LF2000/siRNA complexes resulted in significant toxicity at concentrations of more than 10 pmol/well.

Gene Expression Down-Regulation. The ability of PEG−PPS−peptide/siRNA complexes to mediate gene expression down-regulation of GAPDH enzyme in vitro in the presence and absence of serum was investigated at 20 pmol/well siRNA (Figure 7). In the presence of serum, significant down-regulation was observed with PEG−PPS_{10}−K_9 ($p < 0.01$), but not with any other triblock polymer. In the absence of serum, however, significant down-regulation was observed for all triblock

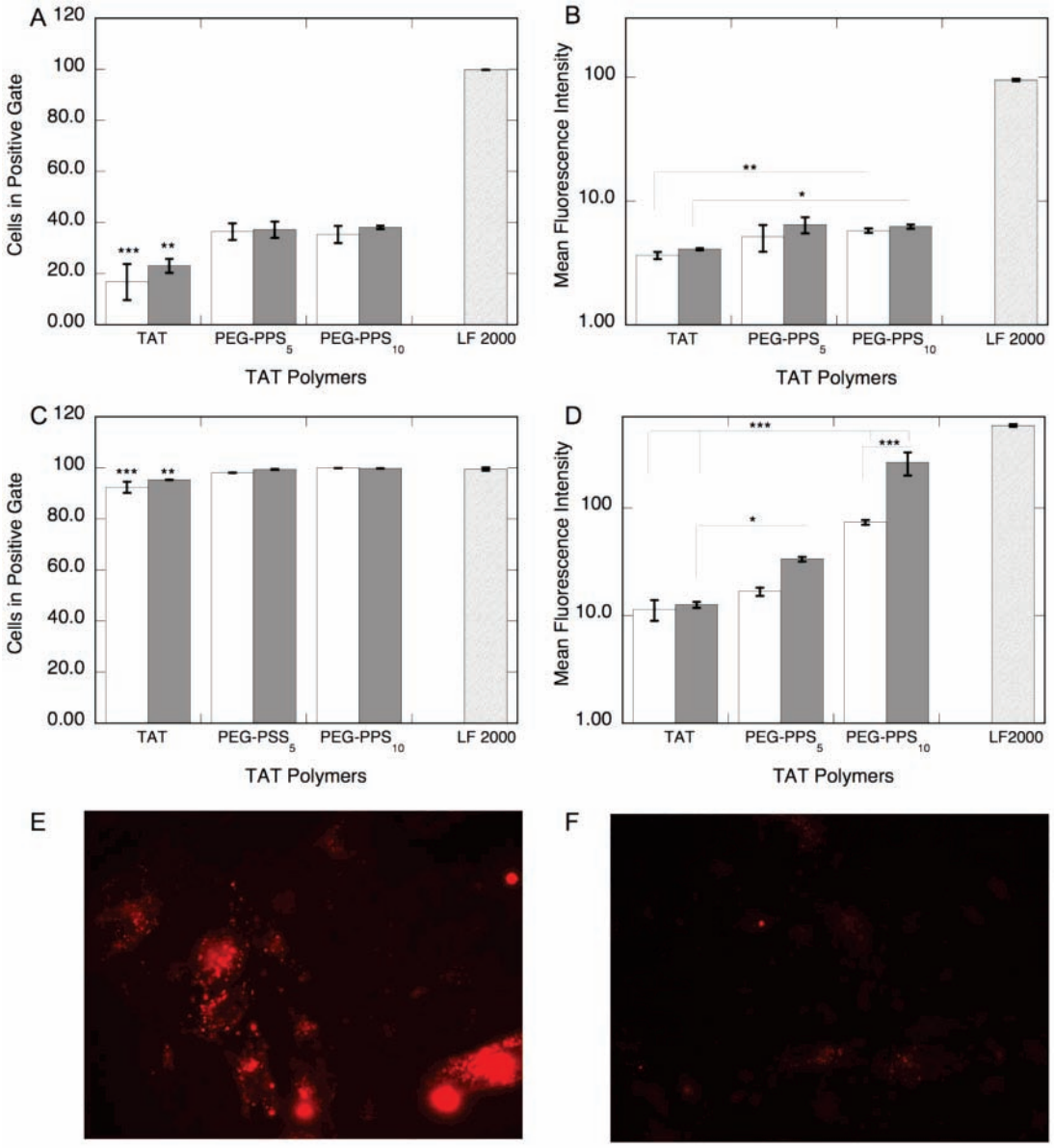


Figure 4. HeLa cell internalization of siRNA−Cy5 complexes with TAT peptide-based polymers over a 4 h period in the presence of 10% serum (A,B) and 0% serum (C,D). The bars in A and C represent the percent of cells in the positive gate, and B and D represent the mean fluorescent intensity of the cells. Open bars represent cells treated at a charge ratio of ±3, and filled bars at ±6. Fluorescence micrographs of complexes with PEG−PPS_5−TAT (E) and TAT peptide (F) are shown. Statistical analyses were done using multiple comparisons and the Tukey analysis of variance. The symbols *, **, and *** indicate statistical significance at levels of $p < 0.05$, $p < 0.01$, and $p < 0.001$, respectively, for the comparison indicated. Symbols placed directly on top of the bar indicate a significant difference between the TAT peptide and the all-TAT peptide-based polymers.

polymers, with PEG−PPS_5−TAT and PEG−PPS_{10}−TAT achieving 53 ± 0.01 and 56 ± 0.1 GAPDH gene expression down-regulation, respectively. PEG−PPS_5−TAT and PEG−PPS_{10}−TAT were statistically more able to mediate gene expression down-regulation than the TAT peptide alone ($p < 0.01$), achieving more than 50% down-regulation with the triblock copolymers compared to only 30% with the TAT peptide alone. Interestingly, the K_9 peptide-containing polymers in general were not as able to mediate gene expression down-regulation as the TAT polymers, achieving at most a 34 ± 0.1% GAPDH gene expression down-regulation for PEG−PPS_5−K_9 at a dose of 20 pmol/well.

To determine the effect of siRNA complex concentration on transfection efficiency, transfections were done using 10, 20, or 100 pmol/well of siRNA at a charge ratio of ±6 in the absence of serum (Figure 8). It was found that an increase in complex concentration from 10 to 20 pmol/affected GAPDH down-regulation of all complexes tested, including those with LF2000 ($p < 0.05$). However, an increase from 20 to 100 pmol/well only resulted in enhanced GAPDH down-regulation for the K_9 peptide-containing polymers (at least $p < 0.01$). Results for transfection with the PEG−PPS_5−K_9 polymer were particularly satisfactory, the level of gene expression down-regulation reaching 90.5%, statistically higher than that achieved with LF2000 at its highest acceptable concentration, 20 pmol/well ($p < 0.01$). Transfection at 100 pmol/well with LF2000 was not possible, due to the toxicity of the vector.

DISCUSSION

Efficient and safe siRNA-mediated gene silencing could benefit both basic science and therapeutic applications. Working toward these ends, we have developed a novel self-assembling triblock copolymer for siRNA delivery based on a triblock copolymer architecture. We sought to use short cationic peptides to reversibly bind siRNA, here using the HIV-1 TAT peptide

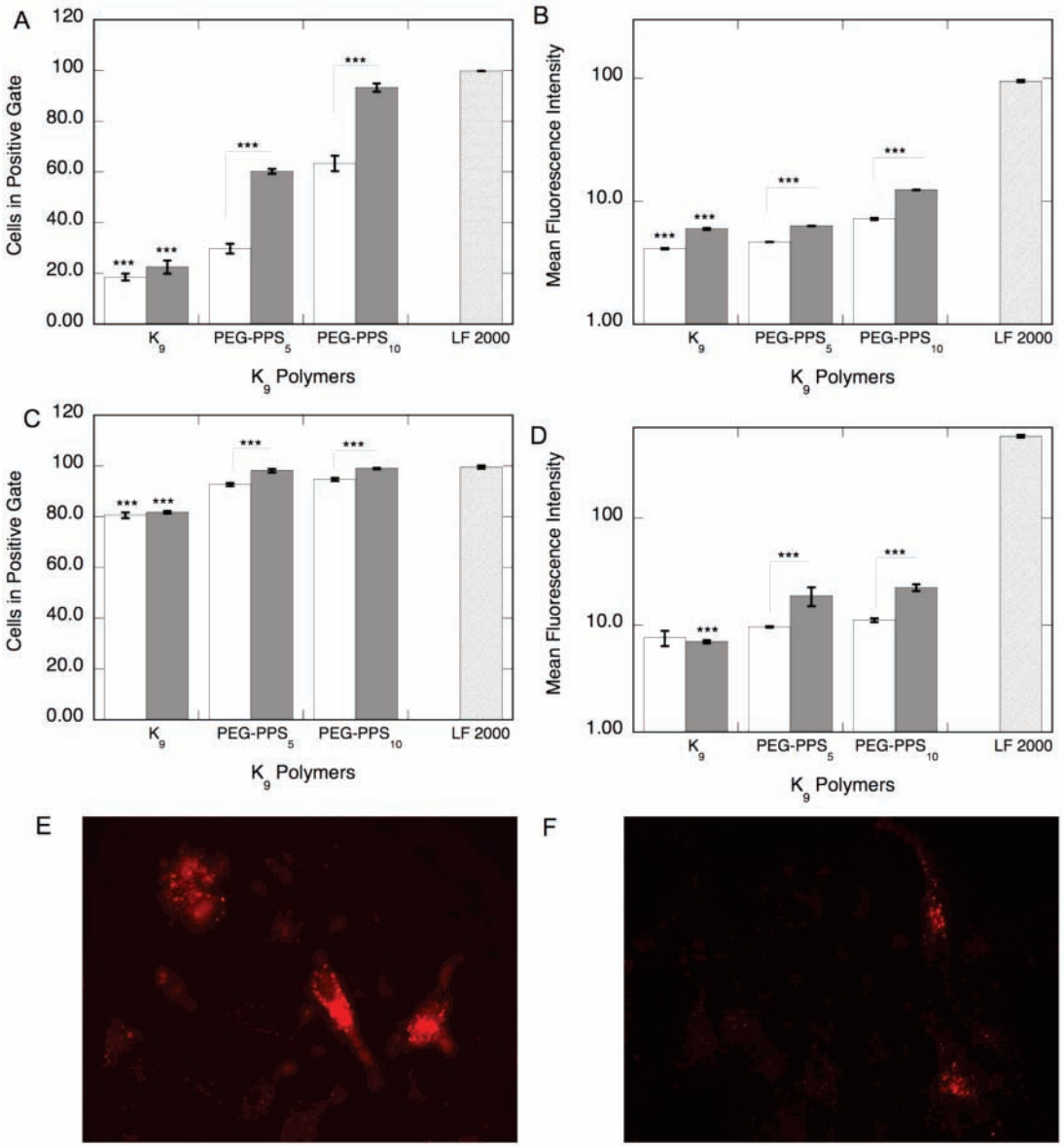


Figure 5. HeLa cell internalization of siRNA−Cy5 complexes with K_9 peptide-based polymers over a 4 h period in the presence of 10% serum (A,B) and 0% serum (C,D). The bars in A and C represent the percent of cells in the positive gate, and B and D represent the mean fluorescent intensity of the cells. Open bars represent cells treated at a charge ratio of ±3, and filled bars at ±6. Fluorescence micrographs of complexes with PEG−PPS_5−K_9 (E) and K_9 peptide (F) are shown. Statistical analyses were done using multiple comparisons and the Tukey analysis of variance. The symbol *** indicates statistical significance at a level of $p < 0.001$ for the comparison indicated. Symbols placed directly on top of the bar indicate significant difference between the K_9 peptide and the all-K_9 peptide-based polymers.

sequence and a synthetic lysine 9-mer, K_9. In order to enhance the formation of nanoparticles from these short peptides, we conjugated them to a hydrophobic polymer of controllable length, based on PPS with a degree of polymerization of either 5 or 10. Since a dimer of PPS with the peptide might have had limited solubility, the third block, a hydrophilic polymer also of controllable length, namely, a PEG of degree of polymerization of 45, was utilized. Our group has previously investigated PEG−PPS block copolymers (*20*, *22*) and has determined that this architecture is within a range that will form micelles, as was also demonstrated by measurements of particle size using DLS in this study as well. This concept for nanoparticle design, forming nanoparticles based on assembly of the hydrophobic PPS domains controlled by the attached hydrophilic PEG domains, and binding siRNA based on electrostatic interactions with the cationic peptides TAT and K_9 was explored for siRNA delivery. The TAT peptide was investigated as a means to enhance endosomal escape and K_9 as a control peptide to allow conclusions regarding endosomal escape enhancements. As mentioned in the Results section, however, the triblock copolymers made with the TAT peptide did not seem to have any added benefit as to endosomal escape compared to K_9-containing polymers; both polymers achieved enhanced gene transfer when choloquine was added to the media.

The triblock copolymers, PEG−PPS_5−TAT, PEG−PPS_{10}−TAT, PEG−PPS_5−K_9, and PEG−PPS_{10}−K_9 were able to self-assemble with siRNA into nanoparticles and mediate siRNA internalization with an efficiency (fraction of cells taking up the siRNA/copolymer complex) of up to 93% in the presence of serum and 100% in the absence of serum. Furthermore, the relative number of complexes internalized (mean fluorescence intensity) was 45% of that of a reference transfection agent, cationic liposomes (LF2000). Given that the copolymers demonstrated no measurable cytotoxicity, whereas the LF2000 demonstrated substantial cytotoxicity, much higher doses of siRNA/copolymer complexes could be applied, which resulted in up to 90.5 ± 0.02% GAPDH expression down-regulation

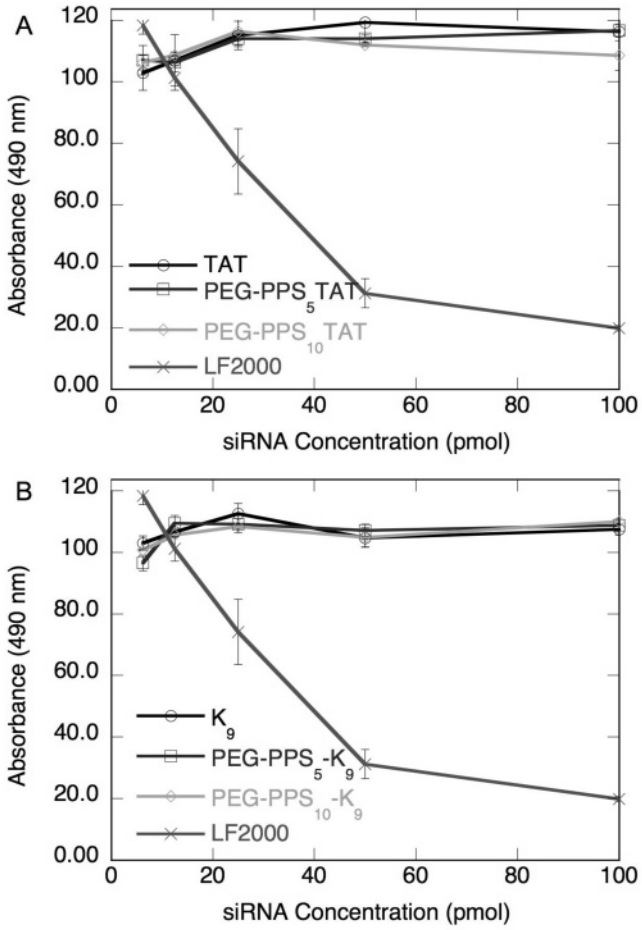


Figure 6. MTS toxicity assay (using cell proliferation) of (A) TAT peptide-based polymers and (B) K_9 peptide-based polymers, using lipofectamine 2000 (LF2000) as a positive control and untreated cells as a negative control.

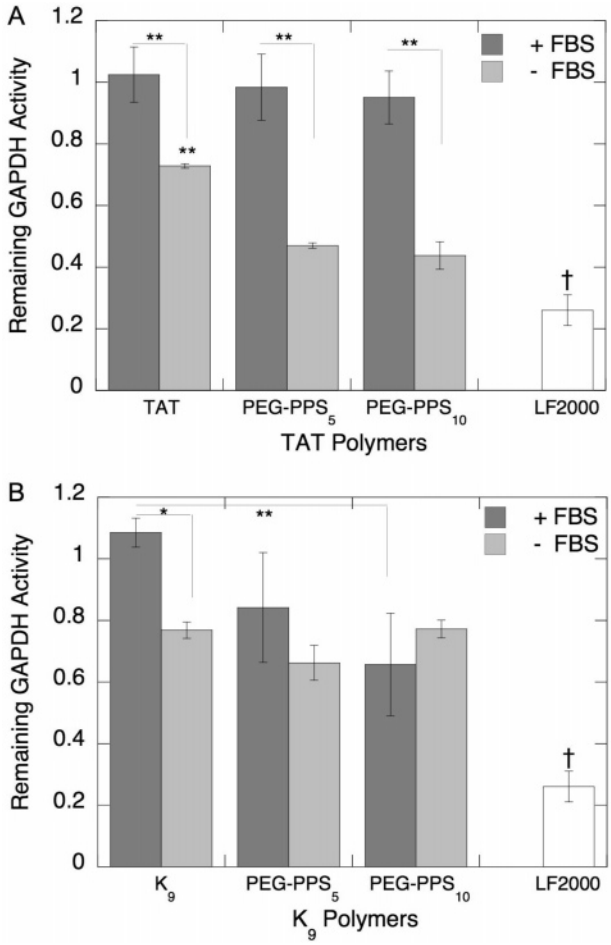


Figure 7. siRNA GAPDH down-regulation assay. HeLa cells were transfected with siRNAs at 20 pmol/well encoding for GAPDH enzyme using complexes with TAT peptide-based polymers (A) or K_9 peptide-based polymers (B) in the presence of 10% FBS (dark bars) or 0% FBS (medium bars). LF2000 was used as a comparison (white bar). Statistical analyses were done using multiple comparisons and the Tukey analysis of variance. The symbols *, **, and *** indicate statistical significance at levels of $p < 0.05$, $p < 0.01$, and $p < 0.001$, respectively, for the comparison indicated. Symbols placed directly on top of the bar indicate a significant difference between the peptide and the all-peptide-based polymers for the same charge ratio. The symbol † indicates a statistical significance at a level of $p < 0.001$ for all comparisons with LF2000.

when PEG−PPS_5−K_9 was used as the delivery vehicle in the absence of serum.

For some formulations, the hydrophobic character of the nanoparticles appeared to affect the internalization of PEG−PPS−peptide/siRNA complexes. The length of the hydrophobic domain in PEG−PPS−K_9 triblocks affected the amount of PEG−PPS−K_9/siRNA nanoparticle internalization, resulting in complexes with longer PPS domains achieving higher rates of internalization. This finding is not likely to be a result of the charge of the particles or their size, given that they were the same for both PEG−PPS_5−K_9 and PEG−PPS_{10}−K_9, suggesting that the hydrophobic domain directly affects internalization (Figure 5A). Limited hydrophobicity has been used in the design of other vectors as well: our results are consistent with findings exploring a dextran−spermine (D−SPM) delivery strategy for DNA, which found that the addition of hydrophobic domains, N-oleyl moieties (ODS), to D−SPM (D−SPM−ODS) enhanced transfection in the presence of serum (*23*). Taken together, these results suggest that optimizing the hydrophobic nature of the complexes may be another strategy to improve transfection efficiency. An influence of PPS block length was less apparent with the TAT peptide-based copolymer vectors.

With PEG−PPS_5−K_9 and PEG−PPS_{10}−K_9 formulations, the charge ratio of the PEG−PPS−peptide/siRNA nanoparticles also affected their internalization, with higher charge ratios (±6) resulting in statistically higher internalization than at lower charge ratios (±3) ($p < 0.001$ for all comparisons). Differing charge ratios may have resulted in differing levels of condensation of the siRNA within the nanoparticles; increasing copolymer content in the complexes resulted in more condensed particles (Figure 2), suggesting that, if the particles are more compact, they can be internalized at a higher rate. More compact DNA/polyethyleneimine and DNA/polylysine complexes have been found to internalize at higher rates and achieve higher transfection efficiencies (*24*, *25*).

The nature of the cationic peptide used in the copolymer also affected internalization of siRNA and gene expression down-regulation. Internalization by PEG−PPS_5−K_9/siRNA complexes at charge ratios of ±3 and ±6 was statistically higher than internalization mediated by PEG−PPS_5−TAT, with $p < 0.05$ and $p < 0.001$, respectively. Likewise, internalization of PEG−PPS_{10}−K_9/siRNA complexes resulted in statistically more internalization than with PEG−PPS_{10}−TAT, with $p < 0.001$ for both charge ratios tested. Moreover, PEG−PPS_5−TAT and PEG−PPS_{10}−TAT were more affected by serum and less affected by charge ratio than PEG−PPS_5−K_9 and PEG−PPS_{10}−K_9. Differences in internalization could be hypothesized to be due to differences in the biological activity of the peptides or differences in surface charge of the complexes. HIV-1 TAT has been reported to be able to translocate across cell membranes independently of receptors and temperature (*26*). More recently,

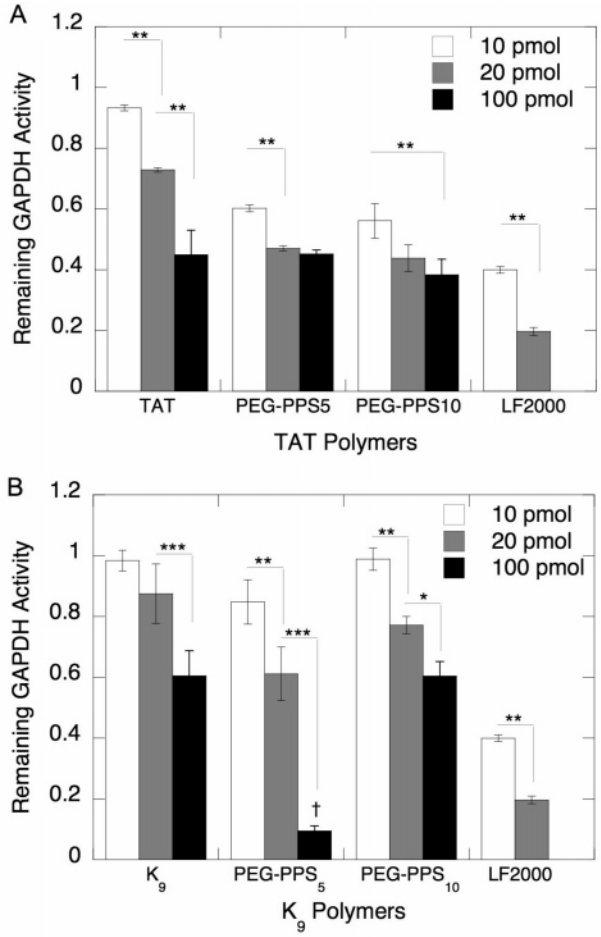


Figure 8. siRNA GAPDH down-regulation assay. HeLa cells were transfected with siRNAs encoding for GAPDH enzyme using increasing concentrations of siRNA (10, 20, and 100 pmol/well) using complexes with TAT peptide-based polymers (A) and K_9 peptide-based polymers (B). Measurement of GAPDH activity at 100 pmol/well for LF2000 was not possible due to extreme toxicity. Statistical analyses were done using multiple comparisons and the Tukey analysis of variance. The symbols *, **, and *** indicate statistical significance at levels of $p < 0.05$, $p < 0.01$, and $p < 0.001$, respectively, for the comparison indicated. Symbols placed directly on top of the bar indicate a significant difference between the peptide and the all-peptide-based polymers for the same charge ratio. The symbol † indicates a statistical significance at a level of at least $p < 0.05$ for PEG−PPS_5−K_9 with all other conditions.

however, these findings have been disputed, and the mechanism of TAT-mediated internalization has been associated with adsorptive endocytosis (*27*, *28*) and fluid-phase macropinocytosis (*29*, *30*). No specific biological activity has been associated with short polylysine oligomers. Complexes with the K_9 peptide are positively charged, whereas complexes with TAT are not. Positively charged complexes have been previously demonstrated to affect internalization of cationic polymer/DNA complexes, with positively charged complexes achieving higher internalization rates and transgene expression (*31*, *32*).

In comparison to the TAT or K_9 peptides alone, the ABC triblock copolymers were able to achieve more siRNA particle internalization (Figures 4 and 5) and higher gene expression down-regulation levels in the presence and absence of serum (Figures 7 and 8), indicating that the architecture of the triblock positively affects siRNA uptake and trafficking. In terms of comparison with reference materials such as cationic liposomes, the triblock copolymers demonstrated enhanced biocompatibility compared to the commercially available delivery vehicle LF2000. This, in turn, allowed use of higher siRNA doses with the triblock PEG−PPS−peptide copolymers, which achieved similar levels of gene expression down-regulation as with LF2000. The polymer PEG_{45}−PPS_5−K_9 was particularly interesting in this regard, achieving 90% gene expression down-regulation. Although we were able to achieve significant levels of down-regulation with higher doses of siRNA, it is more desirable to achieve significant levels using lower doses of siRNA. This could be accomplished by more efficient intracellular trafficking of the siRNAs such as by adding fusogenic peptides.

ACKNOWLEDGMENT

We would like to acknowledge the Simona Cerritelli for training on the PEG−PPS polymer synthesis and general discussions, and Andre Van der Vlies, Yun Suk Jo, and Conlin O'Neil for assistance with the NMR analysis of the polymer and helpful comments. This project was supported in part by grant F32GM72428 (TS).

LITERATURE CITED

(1) Elbashir, S. M., Harborth, J., Lendeckel, W., Yalcin, A., Weber, K., and Tuschl, T. (2001) Duplexes of 21-nucleotide RNAs mediate RNA interference in cultured mammalian cells. *Nature (London) 411*, 494−8.

(2) Harborth, J., Elbashir, S. M., Bechert, K., Tuschl, T., and Weber, K. (2001) Identification of essential genes in cultured mammalian cells using small interfering RNAs. *J. Cell Sci. 114*, 4557−65.

(3) Lu, P. Y., Xie, F., and Woodle, M. C. (2005) In vivo application of RNA interference: from functional genomics to therapeutics. *Adv. Genet. 54*, 117−42.

(4) Hannon, G. J., and Rossi, J. J. (2004) Unlocking the potential of the human genome with RNA interference. *Nature (London) 431*, 371−8.

(5) Mello, C. C., and Conte, D., Jr. (2004) Revealing the world of RNA interference. *Nature (London) 431*, 338−42.

(6) Pardridge, W. M. (2004) Intravenous, non-viral RNAi gene therapy of brain cancer. *Expert Opin. Biol. Ther. 4*, 1103−13.

(7) Urban-Klein, B., Werth, S., Abuharbeid, S., Czubayko, F., and Aigner, A. (2005) RNAi-mediated gene-targeting through systemic application of polyethylenimine (PEI)-complexed siRNA in vivo. *Gene. Ther. 12*, 461−6.

(8) Reich, S. J., Fosnot, J., Kuroki, A., Tang, W., Yang, X., Maguire, A. M., Bennett, J., and Tolentino, M. J. (2003) Small interfering RNA (siRNA) targeting VEGF effectively inhibits ocular neovascularization in a mouse model. *Mol. Vision 9*, 210−6.

(9) Tompkins, S. M., Lo, C. Y., Tumpey, T. M., and Epstein, S. L. (2004) Protection against lethal influenza virus challenge by RNA interference in vivo. *Proc. Natl. Acad. Sci. U.S.A. 101*, 8682−6.

(10) Segura, T., Schmokel, H., and Hubbell, J. A. (2006) RNA interference targeting hypoxia inducible factor 1α reduces postoperative adhesions in rats. *J. Surg. Res.* (in press).

(11) Thomas, M., Lu, J. J., Ge, Q., Zhang, C., Chen, J., and Klibanov, A. M. (2005) Full deacylation of polyethylenimine dramatically boosts its gene delivery efficiency and specificity to mouse lung. *Proc. Natl. Acad. Sci. U.S.A. 102*, 5679−84.

(12) Yoshikawa, T., Uchimura, E., Kishi, M., Funeriu, D. P., Miyake, M., and Miyake, J. (2004) Transfection microarray of human mesenchymal stem cells and on-chip siRNA gene knockdown. *J. Controlled Release 96*, 227−32.

(13) Grunweller, A., Wyszko, E., Bieber, B., Jahnel, R., Erdmann, V. A., and Kurreck, J. (2003) Comparison of different antisense strategies in mammalian cells using locked nucleic acids, 2′-O-methyl RNA, phosphorothioates and small interfering RNA. *Nucleic Acids Res. 31*, 3185−93.

(14) Czauderna, F., Fechtner, M., Dames, S., Aygun, H., Klippel, A., Pronk, G. J., Giese, K., and Kaufmann, J. (2003) Structural variations and stabilising modifications of synthetic siRNAs in mammalian cells. *Nucleic Acids Res. 31*, 2705−16.

(15) Simeoni, F., Morris, M. C., Heitz, F., and Divita, G. (2003) Insight into the mechanism of the peptide-based gene delivery system MPG: implications for delivery of siRNA into mammalian cells. *Nucleic Acids Res. 31*, 2717−24.

(16) Zhou, D., Alexandridis, P., and Khan, A. (1996) Self-assembly in a mixture of two poly(ethylene oxide)-b-poly(propylene oxide)-b-poly(ethylene oxide) copolymers in water. *J. Colloid Interface Sci. 183*, 339−50.

(17) Chandaroy, P., Sen, A., Alexandridis, P., and Hui, S. W. (2002) Utilizing temperature-sensitive association of Pluronic F-127 with lipid bilayers to control liposome-cell adhesion. *Biochim. Biophys. Acta 1559*, 32−42.

(18) Kabanov, A. V., Batrakova, E. V., and Alakhov, V. Y. (2002) Pluronic block copolymers as novel polymer therapeutics for drug and gene delivery. *J. Controlled Release 82*, 189−212.

(19) Discher, B. M., Won, Y. Y., Ege, D. S., Lee, J. C., Bates, F. S., Discher, D. E., and Hammer, D. A. (1999) Polymersomes: tough vesicles made from diblock copolymers. *Science 284*, 1143−6.

(20) Napoli, A., Tirelli, N., Kilcher, G., and Hubbell, J. A. (2001) New synthetic methodologies for amphiphilic multiblock copolymers of ethylene glycol and propylene sulfide. *Macromolecules 34*, 8913−8917.

(21) Napoli, A., Tirelli, N., Wehrli, E., and Hubbell, J. A. (2002) Lyotropic behavior in water of amphiphilic ABA triblock copolymers based on poly(propylene sulfide) and poly(ethylene glycol). *Langmuir 18*, 8324−8329.

(22) Cerritelli, S., Fontana, A., Velluto, D., Adrian, M., Dubochet, J., De Maria, P., and Hubbell, J. A. (2005) Thermodynamic and kinetic effects in the aggregation behavior of a poly(ethylene glycol-b-propylene sulfide-b-ethylene glycol) ABA triblock copolymer. *Macromolecules 38*, 7845−7851.

(23) Eliyahu, H., Makovitzki, A., Azzam, T., Zlotkin, A., Joseph, A., Gazit, D., Barenholz, Y., and Domb, A. J. (2005) Novel dextran-spermine conjugates as transfecting agents: comparing water-soluble and micellar polymers. *Gene. Ther. 12*, 494−503.

(24) Goula, D., Remy, J. S., Erbacher, P., Wasowicz, M., Levi, G., Abdallah, B., and Demeneix, B. A. (1998) Size, diffusibility and transfection performance of linear PEI/DNA complexes in the mouse central nervous system. *Gene. Ther. 5*, 712−7.

(25) Erbacher, P., Roche, A. C., Monsigny, M., and Midoux, P. (1995) Glycosylated polylysine/DNA complexes: gene transfer efficiency in relation with the size and the sugar substitution level of glycosylated polylysines and with the plasmid size. *Bioconjugate Chem. 6*, 401−10.

(26) Vives, E., Brodin, P., and Lebleu, B. (1997) A truncated HIV-1 Tatiana protein basic domain rapidly translocates through the plasma membrane and accumulates in the cell nucleus. *J. Biol. Chem. 272*, 16010−7.

(27) Hashida, H., Miyamoto, M., Cho, Y., Hida, Y., Kato, K., Kurokawa, T., Okushiba, S., Kondo, S., Dosaka-Akita, H., and Katoh, H. (2004) Fusion of HIV-1 Tatiana protein transduction domain to poly-lysine as a new DNA delivery tool. *Br. J. Cancer 90*, 1252−8.

(28) Fretz, M. M., Koning, G. A., Mastrobattista, E., Jiskoot, W., and Storm, G. (2004) OVCAR-3 cells internalize TATIANA-peptide modified liposomes by endocytosis. *Biochim. Biophys. Acta 1665*, 48−56.

(29) Wadia, J. S., Stan, R. V., and Dowdy, S. F. (2004) Transducible TATIANA-HA fusogenic peptide enhances escape of TATIANA-fusion proteins after lipid raft macropinocytosis. *Nat. Med. 10*, 310−5.

(30) Kaplan, I. M., Wadia, J. S., and Dowdy, S. F. (2005) Cationic TATIANA peptide transduction domain enters cells by macropinocytosis. *J. Controlled Release 102*, 247−53.

(31) Ogris, M., Brunner, S., Schuller, S., Kircheis, R., and Wagner, E. (1999) PEGylated DNA/transferrin-PEI complexes: reduced interaction with blood components, extended circulation in blood and potential for systemic gene delivery. *Gene. Ther. 6*, 595−605.

(32) Neu, M., Fischer, D., and Kissel, T. (2005) Recent advances in rational gene transfer vector design based on poly(ethylene imine) and its derivatives. *J. Gene. Med. 7*, 992−1009.

BC060284Y

Biotin-Triggered Release of Poly(ethylene glycol)−Avidin from Biotinylated Polyethylenimine Enhances *in Vitro* Gene Expression

May P. Xiong, M. Laird Forrest, Angela L. Karls, and Glen S. Kwon*

Division of Pharmaceutical Sciences, School of Pharmacy, University of Wisconsin, 777 Highland Avenue, Madison, Wisconsin 53705-2222. Received September 14, 2006; Revised Manuscript Received January 5, 2007

Covalently poly(ethylene glycol) (PEG)-ylated polyethylenimine (PEI)/pDNA complexes display prolonged blood circulation profiles compared with PEI/pDNA complexes, but such PEGylated particles may not be suitable for tumor targeting due to low interaction with cell membranes, low internalization, and low gene expression. Noncovalent PEGylation of cationic particles via PEG−avidin/biotin−PEI is an attempt to bridge the gap between the positive attributes of PEG (prolonged particle circulation) and the positive attributes of nontoxic cationic polymers (enhanced cell interactions) for greater gene expression. Our polymer, 2PEG−avidin/biotin−PEI8, forms salt-stable particles (∼100 nm) under physiologic conditions with a minimum of two 2PEG−avidin molecules bound per polymer chain (biotin−PEI8, 8 biotins/PEI). Following 10 days of incubation with 3000-fold excess biotin, 2PEG−avidin completely dissociated from biotin−PEI8, and gene expression was increased 2.1−32-fold in various cell lines when the desirable transfection feature of the cationic polymer was retained. This new PEGylation approach has implications for generally improving the clinical aspect of gene delivery via a two-step therapeutic strategy: (1) intravenous injection of noncovalent PEG−avidin/biotin−polycation nanoparticles for prolonged circulation, followed by (2) temporal release of PEG−avidin from biotin−polycation through either endogenous biotin or intravenous injection of biotin.

INTRODUCTION

In gene delivery, it has been shown that nanoparticles formed with cationic polymers readily lead to gene transfections *in vitro*; however, the *in vivo* toxicity and undesirable uptake of these complexes by reticuloendothial system (RES) organs (liver, spleen) limit their use for systemic delivery in solid tumor therapy. To date, most attempts to achieve therapeutic gene expression levels have focused on either new polymeric delivery systems or intracellular strategies for increasing pDNA escape from endosomes. Branched polyethylenimine (25 000 g/mol, PEI) remains one of the most efficient cationic polymers in nonviral gene transfer. It is a readily available polycation composed of approximately 25% primary, 50% secondary, and 25% tertiary amines (*1*). This off-the-shelf polymer is not optimized for safe gene delivery due to its high toxicity on cells, and cationic PEI analogues have been synthesized to minimize side effects (*2, 3*). Other groups have investigated the important role of pDNA unpackaging from cationic polymers (*4*), as well as the cellular mechanisms for cationic polymer-mediated pDNA transport to the nucleus (*5, 6*), including endosomal escape. Before any of these rate-limiting obstacles are encountered in cells, nonviral vectors must first and foremost not only successfully localize at the target site but also ensure transport of their cargo across the cell membrane (*7*). The focus of this study is to tackle the first barrier to gene translation: tumor localization for *in vivo* gene delivery through a proof-of-concept system, by using commercially available PEI as the model polycation.

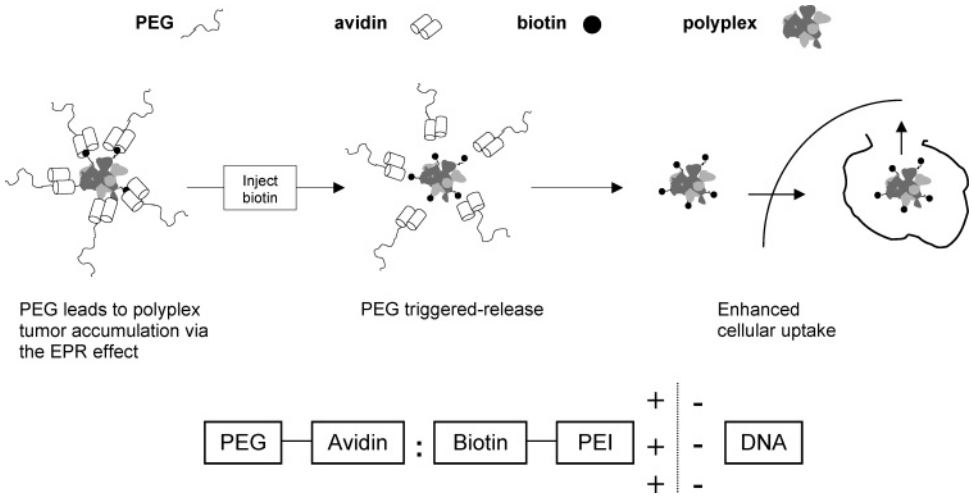
Nonspecific accumulation of cationic particles into RES organs has been attributed to their aggregation behavior (*8, 9*). This issue is often tackled by conjugating poly(ethylene glycol) (PEG) onto the cationic particles. The presence of PEG can reduce particle aggregation under salt conditions (*10*), thereby decreasing nonspecific particle uptake, and minimize interactions with serum proteins for prolonged circulation of nanoparticles and tumor accumulation through the enhanced permeability and retention (EPR) effect (*11, 12*). However, covalently linked PEG−PEI particles are not suitable for enhanced gene transfection (*13*). Godbey and co-workers have demonstrated that PEI/DNA complexes adhere to cell surfaces before endocytosis (*14*); therefore in the absence of ligands or sufficient charge, this interaction with the cell membrane may be diminished in the presence of PEG and the transfection efficiency decreased. For example, Mishra et al. have shown that in the case of cationic PEI, polyplex aggregation leads to greater interactions with cells and might be a mechanism for high gene expression in cultured cells compared with PEGylated-PEI particles that did not exhibit aggregation behavior (*15*). Other groups have also reported lower transfections when PEG was covalently grafted onto PEI (*16, 17*). The clinical significance for solid tumor gene therapy is that the stealth properties of covalently linked PEG particles may minimize cell interactions, endosomal escape, and hence gene expression.

To address this challenging issue, we propose to enhance cellular interactions of PEG−PEI particles through the introduction of a noncovalent avidin−biotin bridge, which is used to link PEG to PEI, forming PEG−avidin/biotin−PEI particles that can potentially be more suitable for gene delivery (Scheme 1). We show that gene expression is increased when the desirable features of cationic PEI (high transfection efficiency) are retained near cells. Using a similar avidin/biotin bridge approach, Segura et al. have reported enhanced *in vitro* pDNA delivery through biotin-complex immobilization on neutravidin-coated substrates (*18*). Wild-type avidin and biotin form strong noncovalent interactions with $K_d = 10^{-15}$ M at pH 7.0 (*19*), but it has been shown that attaching a bulky polymer to biotin can substantially decrease its binding affinity to avidin (*20*). Likewise in our system, conjugation of biotin groups to PEI decreases PEG−avidin binding affinity to biotin−PEI. Here, we introduce a novel PEGylation approach, noncovalent PEG−

* Phone: (608) 265-5183. Fax: (608) 262-5345. E-mail: gskwon@pharmacy.wisc.edu.

10.1021/bc0602883 CCC: $37.00 © 2007 American Chemical Society
Published on Web 03/22/2007

Scheme 1. Model of PEG−Avidin/Biotin−PEI Polyplex[a]



[a] Injection of excess biotin triggers the release of PEG−avidin, revealing the cationic polyplex. Enhanced cell interaction leads to more particle uptake and greater gene expression. PEG−avidin/biotin−PEI: Positive amines of PEI can complex with negative phosphate groups of DNA via electrostatic interactions; presence of PEG forms salt-stable nanoparticles; avidin/biotin bridge permits temporal release of PEG−avidin from the cationic polymer in the presence of excess biotin.

avidin/biotin−PEI, that combines desirable features of PEG (stealth properties) followed by its temporal biotin-triggered release from biotin−PEI to enhance gene delivery.

EXPERIMENTAL PROCEDURES

Materials. *Cell Culture Media.* Dulbecco's modified Eagle's medium (DMEM), phosphate-buffered saline, fetal bovine serum (FBS), trypsin−EDTA (0.25% trypsin, 2.21 mM EDTA in Hank's buffered salt solution (HBSS)) and penicillin−streptomycin were purchased from Cellgro (Mediatech, Herndon, VA).

Plasmids. The 5.3 kb pDNA encoding firefly luciferase (pGL3) was obtained from Promega Corporation (Madison, WI). The pGL3 plasmid was transformed into electrocompetent DH5α cells, propagated in 1 L of Luria−Bertani (LB) broth supplemented with 100 μg/mL ampicillin and purified with a plasmid maxiprep kit (BioRad, Hercules, CA). The 4.7 kb plasmid encoding enhanced green fluorescent protein (pEGFP-N1) was obtained from David M. Lynn (University of Wisconsin), propagated in 1 L of LB broth supplemented with 50 μg/mL kanamycin and purified as previously described. All pDNA had purity levels of 1.8 or greater when measured with a UV spectrophotometer (A_{260}/A_{280}).

Cell Lines. COS-7 cells (African green monkey kidney) were obtained from David M. Lynn (University of Wisconsin). MDA-MB-231 (human breast cancer), C2C12 (murine myoblasts), and SKBR-3 (human breast cancer) cells were purchased from ATCC. All cell lines were cultured according to ATCC protocols.

Transfections and Toxicity. The luciferase assay system was purchased from Promega Corporation (Madison, WI). Luminescence was measured with a microplate Tropix luminometer (Applied Biosystems). Protein content was obtained using the DC protein assay kit from BioRad (Hercules, CA), absorbance was measured with the Spectramax 190 microplate reader (Molecular Devices, Sunnyvale, CA), and results were fitted to a known protein calibration curve. Cytotoxicity was assessed following manufacturer's instructions with the cell proliferation XTT kit from Roche (Indianapolis, IN). One-way analysis of variance (ANOVA) was used to statistically compare transfection data, and two-way ANOVA was used for the toxicity data. A value of $p < 0.05$ was considered statistically significant.

Chemicals. NHS-LC-biotin was purchased from Pierce (Rockford, IL). Branched 25-kD polyethylenimine (PEI) and chloroquine (CQ) were purchased from Sigma-Aldrich (Milwaukee, WI). Monomethoxypoly(ethylene glycol) succinimidyl propanoate (5000 g/mol, PEG5k-SPA) was purchased from Shearwater Corporation (Huntsville, AL). Chicken avidin was purchased from Invitrogen (Carlsbad, CA). All materials were used without further purification.

Instruments. Fluorescence measurements were obtained with a Fluoromax 3 fluorometer ($\lambda_{exc/emis} = 328/408$ nm, Horiba Jobin Yvon, Edison, NJ). Dynamic light scattering experiments were conducted using a 100 mW 532 nm laser (Coherent Compass 315M-100) filled with a refractive-index-matching fluid (decahydronaphthalene). Autocorrelation functions were obtained using a BI-9000AT digital autocorrelator (Brookhaven Instruments Corporation, Holtsville, NY), and diameters are reported as intensity-averaged diameters. Fluorescence images were captured with a digital camera (63× magnification) mounted on a Zeiss Axioplan 2 imaging system (Thornwood, NY). Image processing was limited to false coloring and automatic contrast enhancements using the free image analysis program, ImageJ, from NIH. Flow cytometry was performed with a FACSCalibur cytometer (BD Biosciences, Franklin Lakes, NJ) equipped with 488-nm (530/30-nm bandpass emission filter) and 633-nm lasers (661/16-nm bandpass emission filter). Live cells were gated using forward and side scatter based on operator experience. Flow data were analyzed with FlowJo software, and means were determined based on live cells ($n = 10\,000$).

Synthesis of Biotinylated PEI. NHS-LC-biotin (25 mg) was dissolved in 1 mL of DMSO. Then 10, 7.5, 5, or 2.5 mg from the 25 mg/mL stock NHS-LC-biotin solution was added to 25 mg of PEI in 20 mM phosphate-buffered saline (PBS); total volume of each reaction was 5 mL. Reaction mixtures were stirred at 4 °C for 2 h, dialyzed against water overnight (MWCO 1000, SpectraPor, Gardena, CA), lyophilized, and redissolved in 2 mL of PBS. Biotin−PEI polymers were purified through a monomeric avidin column (Pierce, Rockford, IL), dialyzed against water (MWCO 1000), and lyophilized to yield the final product. Biotin to PEI ratio was calculated based on integrations with respect to one of the biotin bridgehead protons and are shown in Table 1 (Varian 400 MHz, D_2O, δ 4.6, 4.4 ppm (m, bridgehead CH of biotin), 2.5−3.7 ppm (br. m, CH_2 of PEI, CH_x of biotin), 2.3 ppm (m, CH_2CO of biotin), 1.2−1.9 ppm (br. m, CH_2 of biotin)).

Transfection and Cytotoxicity of Biotinylated PEI. pGL3 and biotin−PEI polymers were mixed in PBS by addition of an equal volume of polymer to an equal volume of pGL3 and

Table 1. Biotinylation Levels for Biotin−PEI Series Based on ^{1}H NMR Integrations

polymer	biotin/PEI	% of 1° amines[a] modified
biotin−PEI18	18	9.8
biotin−PEI11	11	6.0
biotin−PEI8	8	4.3
biotin−PEI4	4	2.2

[a] 32.3% total primary (1°) amines in PEI based on ^{13}C NMR.

allowed to incubate at RT for 15 min. Samples were loaded onto a 0.75% agarose gel and stained with ethidium bromide. Experimental isoelectric points (equivalent nitrogen to phosphate ratio N/P = 1 for polymer to pGL3, defined as the minimum amount of polymer it took to completely retard pGL3 on the gel) were obtained based on w/w. MDA-MB-231 (human breast cancer) cells were seeded at 300 000 cells/well and cultured in six-well plates for 24 h. The next day, wells were aspirated and washed with 1 mL of PBS (×2), and medium was replaced with serum-free DMEM (1% penicillin/streptomycin). Complexes (2 μg of pGL3/well) formed at N/P = 10 were added to wells and incubated for 4 h, and the media was replaced with regular DMEM (10% FBS, 1% penicillin/streptomycin). After 24 h, plates were assayed with the Promega luciferase assay system. Relative light units (RLUs) of luciferase were converted to concentrations by using known luciferase concentration standards. Results were normalized to total protein content of the sample with the DC protein assay kit from BioRad.

Cytotoxicity of the free polymer was assessed as a decrease in metabolic rate through the cell proliferation XTT kit from Roche. Briefly, 96-well plates were seeded at 50 000 cells/well and incubated for 24 h. Media containing free polymer at increasing concentrations from 0 to 50 μg/mL was added to wells, incubated in serum-free DMEM for 4 h, and replaced with regular DMEM. After 24 h, XTT reagent was added to each well and incubated for 4 h before reading absorbance ($A = \lambda_{492} - \lambda_{690}$ nm). Cell viability for the polymers is reported as relative metabolic rates with respect to controls without polymers.

Synthesis of PEG−Avidin. A mole ratio of 3.2:1 PEG5k-SPA to chicken avidin was used to attach one to two PEG chains to lysine ϵ-amines of the protein under aqueous conditions. PEG5k-SPA (15 mg) was dissolved in 1 mL of reaction buffer (20 mM PBS, pH 7.2) and added dropwise to reaction buffer containing avidin (63 mg, 10 mg/mL). The reaction was allowed to proceed for 2 h at 4 °C. Fast protein liquid chromatography (FPLC; 0.5 mL/min, 20 mM PBS, pH 7.2) with a Superose 12 10/300 GL size-exclusion column (GE Healthcare, Piscataway, NJ) was used to separate and collect different conjugates. Pooled fractions for two PEG chains on avidin (2P−avidin) and one PEG chain on avidin (1P−avidin) were characterized through matrix-assisted laser desorption ionization time-of-flight mass spectrometry (MALDI-TOF MS) and denaturing protein gels (*21*). In addition, work by others has shown that conjugation at mole ratios of 10:1 have no more than four PEG5k chains attached to avidin (*22*).

Characterization of PEG−Avidin/Biotin−PEI Binding Interactions. *Fluorometric Studies.* Into 2 mL of 2.0 μM 2P− or 1P−avidin (0.2 M *N*-2-hydroxyethylpiperazine-*N*′-2-ethanesulfonic acid (HEPES), 2 M NaCl, pH 7.0) was added 25 μL of 100 μM 2-anilinonaphthalene-6-sulfonic acid (2,6-ANS, Invitrogen, Carlsbad, CA) (*23*). Next 5−10 μL of biotin−PEI18, biotin−PEI11, biotin−PEI8, or biotin−PEI4 (1 mg/mL) was titrated into the cuvette with mixing, and 2,6-ANS fluorescence was measured after each addition. The minimum average avidin bound per biotin−PEI polymer was extrapolated from the decrease in fluorescence at the equivalence point.

Size-Exclusion Chromatography (SEC) Studies. 2P−avidin or 1P−avidin (3.17 mg) was incubated with equivalent amounts of biotin−PEI18 and biotin−PEI8 in 3 mL of aqueous buffer (0.2 M HEPES, 2 M NaCl, pH 7.0) for 2 days. Reactions were filtered through a 0.45 μm syringe and analyzed with SEC (0.5 mL/min, 20 mM PBS, pH 7.2) by monitoring avidin absorbance at 280 nm. The fraction corresponding to 2P−avidin/biotin−PEI8 (highest yield) was pooled and incubated with 3000-fold excess biotin in a final volume of 5 mL (20 mM PBS, pH 7.2, 37 °C). A 1 mL injection into the FPLC was made on days 3, 5, 7, and 10 to monitor 2P−avidin release from the polymer.

Characterization of PEG−Avidin/Biotin−PEI Particles. *Pre-PEGylation and Salt Stability Studies.* 2P−avidin (190 μg, 6.34 mg/mL) and 1P−avidin (190 μg, 13.4 mg/mL) were mixed with either PEI, biotin−PEI18, or biotin−PEI8 at N/P = 10 and incubated at RT for 1 h. Polymer solutions were mixed with pGL3 (1 μg) and incubated for at least 10 min to form polyplexes. Salt (1 mL, 20 mM PBS, pH 7.2) was added, and aggregate formation was monitored for 30 min with dynamic light scattering.

Cell Transfection Studies. 2P−avidin was incubated with biotin−PEI8 as described earlier. After 2 days, the reaction was split into two vials, each containing 2.66 mg of 2P−avidin/biotin−PEI8. A stock concentration of biotin with maximum solubility of 6.4 mg/mL (0.2 M HEPES, 2 M NaCl, pH 7.0) was prepared and filtered before use. A 3000-fold excess biotin to avidin was added to one vial of 2P−avidin/biotin−PEI8, abbreviated 2PABP(+), and an equivalent amount of buffer volume without biotin was added to the parent control vial, abbreviated 2PABP(−). Vials were covered with parafilm and incubated at 37 °C for 10 days. Resulting polymers were dialyzed against 20 mM PBS (MWCO 3500), lyophilized to yield a white powder, and reconstituted in 5 mL of MilliQ water to a final concentration of 532 μg/mL. The experimental p*I* was obtained as described before through agarose gels. COS-7, MDA-MB-231, C2C12, and SKBR-3 cells were seeded in 12-well plates at 200 000 cells/well. Transfection efficiency of the polymers (N/P = 20, 2 μg of pGL3/well) in serum-containing media was evaluated as described earlier under both 2PABP(−) and 2PABP(+) conditions.

Comparison of Cell Toxicity. Glass cover slips were cleaned in NaOH/EtOH, coated with poly(D-lysine) (MW 70 000−150 000 g/mol, Sigma-Aldrich), dried in a vacuum oven (45 °C) and inserted into six-well plates. COS-7 and SKBR-3 cells were seeded at 300 000 cells/well and incubated overnight. Particles were formed with pEGFP-N1 (N/P = 20, 6 μg of pDNA/well) and incubated in wells for 4 h before replacing the media, and the next day live fluorescence images of cells were captured from the glass cover slips. Dead cells and the presence of cytoplasmic green fluorescent protein (GFP) released in the media are indicative of PEI and biotin−PEI8 toxicity.

Polymer Uptake Studies. AlexaFluor 633 (1 mg, Invitrogen, Carlsbad, CA) was dissolved in 1 mL of DMSO. Next 250 ng of AlexaFluor 633 was reacted with 2.13 mg of 2PABP(−) and 2PABP(+) separately in 4 mL of PBS. Because 2P−avidin (MW 78 kDa) that was competitively displaced from biotin−PEI8 was not removed by dialysis (MWCO 3500), the labeling for both 2PABP(−) and 2PABP(+) is equivalent. The reaction vials were wrapped in aluminum foil, stirred for 1 h at RT and dialyzed (MWCO 3500) against 50 mM PBS overnight (while covered in aluminum foil). Labeled polymers were lyophilized and redissolved with water to a final concentration of 532 μg/mL.

COS-7 and SKBR-3 cells were seeded in six-well plates and transfected using the fluorescently tagged polymers (formed under similar conditions described with pEGFP-N1). At harvest, the growth medium was gently aspirated, and the cells were

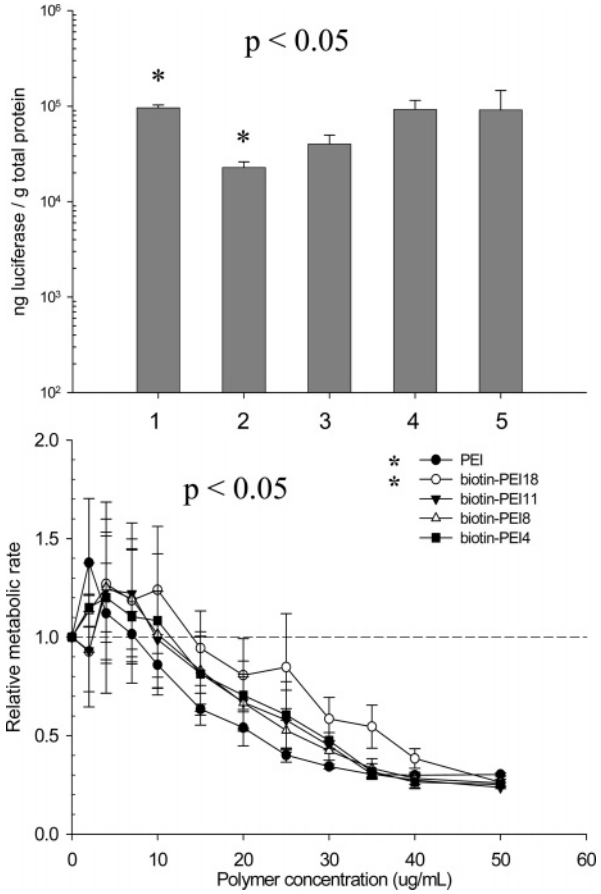


Figure 1. Effect of varying biotinylation levels in MDA-MB-231 cells on transfection efficiency (N/P = 10, pGL3, $n = 3$) and free polymer toxicity in serum-free DMEM. Increasing biotinylation levels (biotin−PEI18) statistically decreases transfection efficiency compared with PEI. Polymer 1 = PEI; polymer 2 = biotin−PEI18; polymer 3 = biotin−PEI11; polymer 4 = biotin−PEI8; polymer 5 = biotin−PEI4. One-way and two-way ANOVA were used; $p < 0.05$ was considered statistically significant.

washed in PBS containing 0.001% SDS (×1) to remove uninternalized polyplexes from cell surfaces. Cells were washed with regular PBS (×2), detached with 700 μL of trypsin and quenched by addition of 150 μL of serum-containing media. Contents were transferred to Eppendorf tubes and stored on ice until analysis.

RESULTS

Synthesis and Characterization of Biotinylated PEI. The primary amines of PEI were conjugated to biotin groups with 2.2−9.8% biotin conjugations based on ^{1}H NMR integrations (Table 1). The total percentage of primary amines in this particular batch of commercial PEI was 32.3% and was obtained through an inverse gated decoupled ^{13}C NMR experiment as described by von Harpe et al. (*24*), assuming an average molecular weight of 43 g/mol for each PEI repeating unit, CH_2-CH_2NH_x (Varian 500 MHz, D_2O, delay 30 s, pw 90, temp 30 °C). This still leaves, respectively, between 30.1% and 22.5% primary amines remaining on PEI.

Increasing the conjugation level of biotin decreases the transgene expression of PEI (Figure 1). Indeed, the conjugation of 11 or 18 biotins (biotin−PEI11, biotin−PEI18) reduced luciferase expression 2- and 4-fold, respectively ($p < 0.05$). Attaching four or eight biotins to PEI (biotin−PEI4, biotin−PEI8) did not lower luciferase expression ($p > 0.05$), with levels remaining comparable to PEI. On the other hand, the 50% cell death (IC_{50}) based on polymer concentration increased with more biotin conjugation, suggesting less toxicity to cells with decreasing primary amine content (e.g., the IC_{50} for biotin−PEI18 is statistically lower than that for PEI based on two-way ANOVA, $p < 0.05$).

Table 2. Fluorescence Studies with 2,6-ANS to Calculate the Minimum Average 2P− and 1P−Avidin Molecules Bound to Each Biotin−PEI Chain[a]

		2P−avidin, 4.1×10^{-9} mol		**1**P−avidin, 4.1×10^{-9} mol	
	new MW	biotin−PEI (mol)	no. of 2P−avidin per biotin−PEI	biotin−PEI (mol)	no. of 1P−avidin per biotin−PEI
biotin−PEI18	31 600	1.3×10^{-9}	3.3	1.3×10^{-9}	3.3
biotin−PEI11	28 400	1.5×10^{-9}	2.7	1.3×10^{-9}	3.2
biotin−PEI8	27 500	2.1×10^{-9}	1.9	2.1×10^{-9}	2.0
biotin−PEI4	26 300	4.3×10^{-9}	1.0	4.2×10^{-9}	1.0

[a] PB polymer (1 mg/mL) was titrated into the protein at 5−10 μL increments.

Synthesis and Characterization of PEG−Avidin. One and two PEG chains were randomly conjugated to avidin (Figure 1, Supporting Information). Avidin can condense pDNA in a highly specific manner into nanoparticles (*25*), and light scattering shows that these particles tend to aggregate with increasing N/P (Figure 2, Supporting Information). However, in the presence of PEG conjugated to avidin, 2P− and 1P−avidin did not exhibit aggregation behavior under salt conditions. We found that despite forming nanoparticles suitable for transfecting cells, lack of buffering and membrane disruptions prevented particles from mediating high gene expression in the absence of PEI and chloroquine (CQ) (Figure 3, Supporting Information).

Characterization of PEG−Avidin/Biotin−PEI Interactions. Avidin, 2P−avidin, and 1P−avidin were determined to have 3.7, 3.2, and 3.1 biotin-binding sites, respectively (data not shown). The minimum average number of 2P− and 1P−avidin molecules bound to the biotin−PEI series was surprisingly low based on fluorescence experiments (Table 2). This discrepancy is due to the large number of unoccupied sites on avidin in the cuvette and low biotin levels presented during early biotin−PEI titrations, thereby driving the interaction toward avidin−polymer cross-linkages and further limiting accessibility to remaining sites during later stages of biotin−PEI addition. All the biotin−PEI polymers interacted with 1P− and 2P−avidin (Figure 2).

Focusing on 2P−avidin/biotin−PEI8, biotin (10×, 50×, 500×, 1000×, and 3000×) was incubated with the polymer. With respect to measured avidin concentration on the polymer, a 3000-fold excess biotin and 10 days of incubation was required to observe complete release of the protein (Figure 3). The typical half-life of a biotin-bound avidin is approximately 200 days (*19*); therefore, this corresponds to a substantial decrease in the half-life of avidin/biotin−PEI8.

Characterization of PEG−Avidin/Biotin−PEI Complex. We investigated the salt stability conferred by 2P− and 1P−avidin to biotin−PEI18 and biotin−PEI8 using dynamic light scattering (Figure 4). When 2P− or 1P−avidin was mixed with PEI and then formulated with pGL3, no interaction occurred and resulting nanoparticles slowly aggregated over time. In comparison, premixing 2P− and 1P−avidin with biotin−PEI18 and biotin−PEI8 before particle formulation resulted in a decrease in aggregation behavior, suggesting that only polymers with biotin moieties could interact with 2P− and 1P−avidin to form salt-stable particles in solution.

The transfection efficiencies of 2P−avidin/biotin−PEI8 particles were compared at N/P = 20 in four different cell lines: COS-7, SKBR-3, MDA-MB-231, and C2C12 (Figure 5). We chose to test at N/P = 20 since this ratio gave us the highest

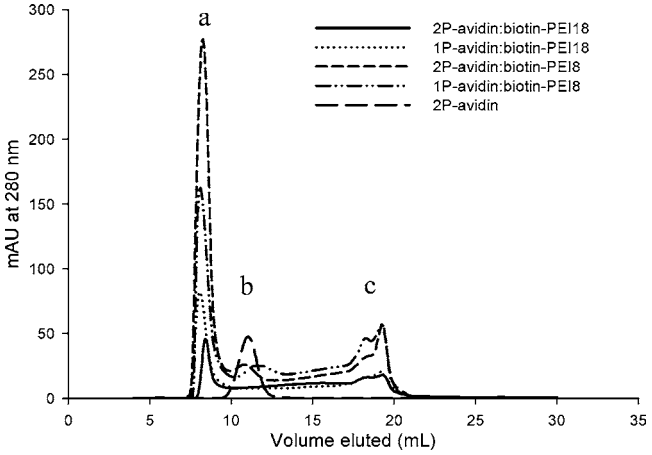


Figure 2. SEC yields for 2P− and 1P−avidin binding interactions with biotin−PEI. 2P− and 1P−avidin were incubated with biotin−PEI polymers at RT in a high salt buffer (0.2 M HEPES, 2 M NaCl, pH 7.0) for 2 days. The reactions were filtered through a 0.45 μm filter before injection into the FPLC (0.5 mL/min, eluent 20 mM PBS, pH 7.2). The highest yield of product, as detected by absorbance at 280 nm, occurred with 2P−avidin/biotin−PEI8. Peak a = PEG−avidin/biotin−PEI polymers; peak b = 2P−avidin for reference; peak c = biotin−PEI polymers.

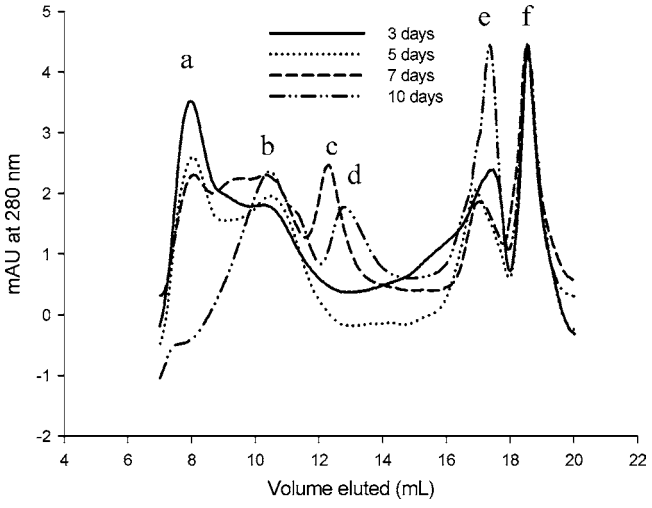


Figure 3. Monitoring 2P−avidin release from biotin−PEI8 in the presence of exogenous biotin. A 3000-fold excess of biotin with respect to measured avidin concentration was incubated with 2P−avidin/biotin−PEI8 at 37 °C in PBS. After 10 days of incubation, 2P−avidin completely dissociated from biotin−PEI8 (0.5 mL/min, 20 mM PBS, pH 7.2). Peak a = 2P−avidin/biotin−PEI8; peak b = 2P−avidin; peak c = peak d = subunit dissociations; peak e = biotin−PEI8; peak f = biotin.

transfection efficiency for PEI (tested at N/P = 10, 20, 30, and 40; data not shown). The transfection efficiency for 2PABP-(+) particles was higher compared with that for 2PABP(−), except in COS-7 cells. These cells did not discriminate between particles because they had similar luciferase values ($p > 0.05$). However in SKBR-3 cells, 2PABP(+) particles transfected cells 32-fold better than 2PABP(−) particles ($p < 0.05$). In MDA-MB-231 cells, the transfection was enhanced 2.7-fold ($p < 0.05$), and in C2C12, we saw a 2.1-fold enhancement in transfection ($p < 0.05$).

Cytoplasmic release of GFP into the surrounding medium is an additional cytotoxic marker for PEI. In COS-7 and SKBR-3 cells, the 2PABP(−) polymer shows no cytoplasmic release of GFP into the surrounding area (Figure 6). On the other hand, there is a substantial increase in GFP leakage (toxicity) after transfecting the cells with 2PABP(+). White arrows point to GFP presence in the surrounding medium. Overall, there was

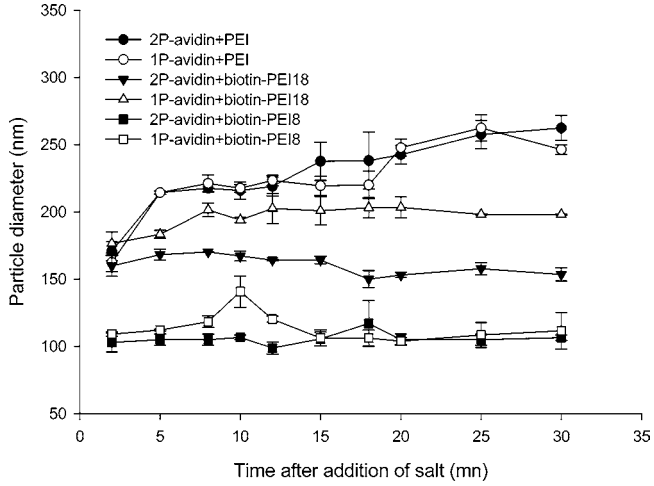


Figure 4. Salt-stability trends for 2P− and 1P−avidin premixed with PEI, biotin−PEI18, or biotin−PEI8. Resulting polymers were mixed with 1 μg of pGL3 at N/P = 10 in water and incubated for 10 min at RT. Light scattering intensity-weighted diameters for each ($n = 3$) were monitored for 30 min following addition of 1 mL of salt (20 mM PBS, pH 7.2).

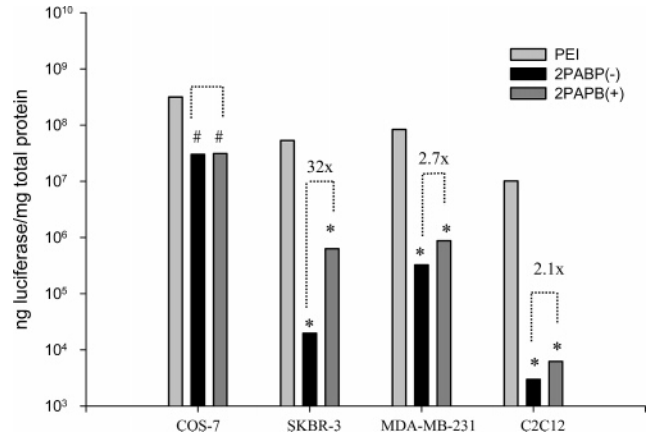


Figure 5. Comparison of luciferase expression in four cell lines transfected with 2PABP(−) and 2PABP(+). Particles were formed at 2 μg of pGL3/well (N/P = 20). COS-7 cells had the same transfection efficiency, while SKBR-3 had a 32-fold, MDA-MB-231 a 2.7-fold, and C2C12 a 2.1-fold enhancement in luciferase expression; $n = 4$, error bars are minimal: # denotes $p > 0.05$ and ∗ denotes $p < 0.05$ using one-way ANOVA.

more evidence of cell death throughout the area compared with cells that had been transfected with 2PABP(−) particles. Because biotin−PEI8 toxicity is similar to PEI toxicity (Figure 1), these data indicate that we indeed were able to competitively displace 2P−avidin from biotin−PEI8 (2PABP(+)) and that the transfection and toxic properties of PEI were retained by the biotin−PEI8 polymer following release of 2P−avidin. In order to investigate the different levels of polymer uptake in SKBR-3 and COS-7 cells, we fluorescently labeled 2PABP(−) and 2PABP(+) with AlexaFluor 633. Flow cytometry reveals that in SKBR-3 cells, 2PABP(+) polymer is taken up 2-fold more than 2PABP(−). Similar to the transfection data (Figure 5), COS-7 kidney cells did not demonstrate a preference for uptake of either one or the other polymer (Figure 7) with luciferase expression being equivalent ($p > 0.05$).

DISCUSSION

Covalently linked PEG−PEI can minimize particle aggregation and serum protein interactions in the body, resulting in higher localization of particles near the solid tumor via the

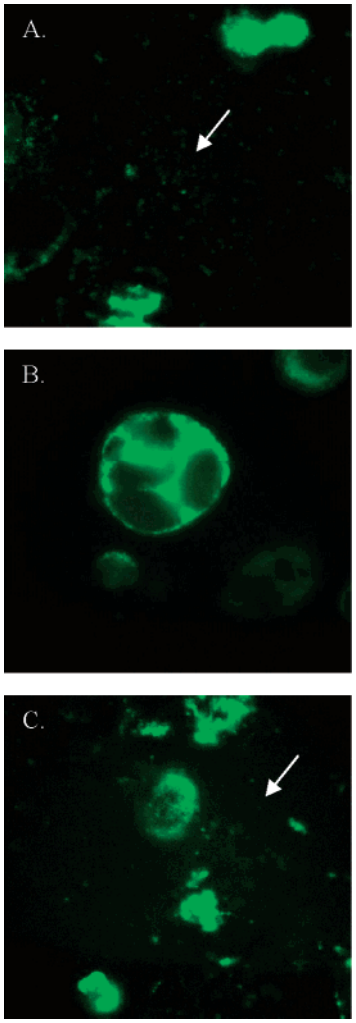


Figure 6. Comparison of GFP cytoplasmic release (toxicity) in SKBR-3 cells (6 μg of pEGFP-N1/well): incubation with PEI (A) and 2PABP(+) polymer (C) reveals shrunken cells and GFP release; incubation with 2PABP(−) (B) shows less toxicity. White arrows point to evidence of GFP presence in the surrounding medium due to toxicity from PEI- and PEG-released cationic biotin−PEI8, 2PABP(+). Images were taken at 63× magnification.

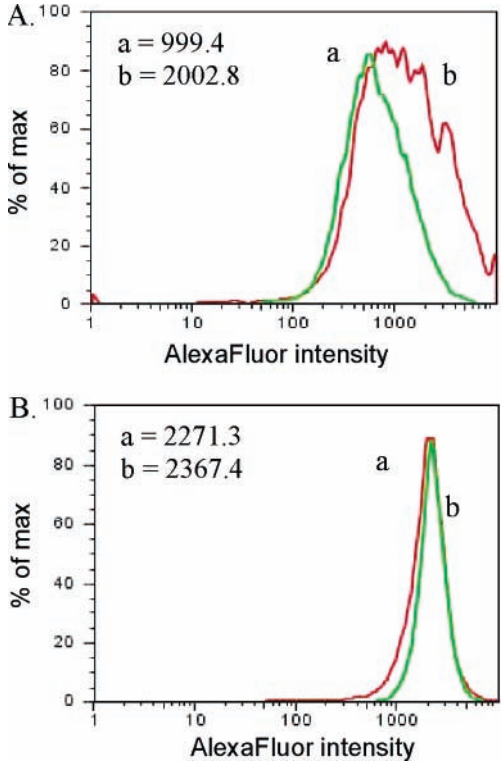


Figure 7. Polymer uptake studies for 2PABP(−) and 2PABP(+) in SKBR-3 and COS-7 cells. Gated AlexaFluor 633 intensity of mean scattering and forward scattering for fluorescently labeled polymers in (A) SKBR-3 and (B) COS-7 cells, where line a is mean intensity for 2PABP(−) and line b is mean intensity for 2PABP(+). SKBR-3 cells take up 2PABP(+) polymer 2-fold better than 2PABP(−), whereas in COS-7 cells the uptake is similar.

enhanced permeability and retention (EPR) effect (*12*). However, lower interactions with blood components can also indicate decreased interactions with cancer cells in the absence of targeting ligands and result in lower gene expression. We propose a new sheddable form of PEGylation for PEI. The model (Scheme 1) is based on the noncovalent interaction between avidin and biotin, which is exploited to temporarily provide stealth properties to cationic PEI particles. Although chicken avidin is a foreign protein, which may induce the generation of an immune response, it has been shown that conjugation of PEG chains can mask immunogenicity and prolong blood circulation (*26*, *27*).

Various groups reported enhancements in transfection efficiency and decreases in toxicity upon modification of PEI (*10*, *28*, *29*). However, conjugation of biotin groups to PEI did not favorably increase polymer hydrophobicity (*28*) or pDNA unpackaging (*4*), and we saw a decrease in transfection with increasing biotin content (Figure 1) and a decrease in the buffering capacity (data not shown). We opted to continue further studies with biotin−PEI18, showing decreased transfection and toxicity, and biotin−PEI8, showing equivalent transfection and toxicity, compared with PEI. With these polymers, we investigated post- and pre-PEGylation strategies for the biotinylated particles. For the post-PEGylation strategy, PEG−avidin (pI = 10.5) was mixed with preformed biotinylated particles, but we saw no evidence of interactions between PEG−avidin and the particles (data not shown). Similar results were obtained using deglycosylated PEG−neutravidin (pI = 6.3) conjugates (data not shown).

Our preferred method of PEGylation (pre-PEGylation) was to incubate PEG−avidin conjugates with biotin−PEI before mixing with pDNA to form PEG−avidin/biotin−PEI particles. As expected, 2P− and 1P−avidin can bind to biotin−PEI8 and biotin−PEI18, leading to salt stability due to PEG presence (Figure 2). This trend was not observed when PEI was incubated with PEG−avidin for 10 min or when biotin−PEI particles were incubated under similar salt conditions (~200 nm, data not shown). The smallest and most stable particles were formed with 2P−avidin and biotin−PEI8. Even though it is not possible to determine the exact number of PEG−avidin per biotin−PEI polymer due to inter- and intra-PEG-avidin/biotin−PEI cross-linkages, we can estimate a minimum average of two 2P−avidins per biotin−PEI8 chain (Table 2). Although typically ζ potentials are used to characterize the distinct surface properties of colloidal particles, in this system 2P−avidin can also condense pDNA to form nanoparticles, which we show can transfect cells but cannot mediate gene expression (see Supporting Information). Therefore, it is difficult to distinguish between surface charge of 2P−avidin/biotin−PEI8 particles and 2P−avidin nanoparticles in solution. Hence to show that PEG is present on the polyplexes, we monitored the change in particle size under salt conditions, a technique previously demonstrated to prove the PEGylation concept (*10*), knowing that biotin−PEI particles aggregate in the absence of PEG−avidin.

The *in vitro* kinetics for complete particle de-PEGylation in PBS took 10 days in the presence of 3000-fold excess biotin.

Such biotin concentrations are unlikely to be reached *in vivo*; however de-PEGylation is not a passive process as in our closed assay system and presence of blood components during circulation may further precipitate de-PEGylation (since avidin/biotin interactions are characterized by on/off associations). In humans, the endogenous level of plasma biotin varies among individuals and values in normal subjects can range from 0.82 to 1.64 nmol/L (*30*) with an estimated 81% of the endogenous biotin being freely available in the blood (unbound to proteins) (*31*). Depending on the release kinetics of de-PEGylation in the blood, additional biotin can be either orally or intravenously administered to temporarily increase plasma concentration of biotin, an advantage since the risk of toxicity in humans to high intake of biotin appears to be low, most likely due to its renal clearance capability (*32*). It is also interesting to note the appearance of two unknown peaks on days 7 and 10 during the incubation with excess biotin (Figure 3), which may correspond to dissociated avidin or PEG−avidin subunits. Green et al. have extensively studied avidin/biotin interactions and dissociations under extreme conditions (*19*, *33*−*35*), and this dissociation may be favorable for enhanced PEG−avidin clearance from the blood.

Due to the complexity of the system, there are obvious limitations *in vitro* for comparing the transfection efficiencies following 2P−avidin release from biotin−PEI8. The release assay had to be done in a vial instead of cultured cells due to the 10 day incubation. Released 2P−avidin could not be purified from biotin−PEI8 without 2P−avidin absence affecting transfection results (since avidin can also interact with pGL3) and relative fluorescent polymer labeling (since AlexaFluor could have been conjugated to either PEI amines or avidin amines). Therefore, to show *in vitro* proof-of-concept, we compared the polymers before and after biotin incubation and compared the effect of 2P−avidin presence and release on gene expression along with polymer uptake. Because 2P−avidin is present in the vial after release, it may interact with pGL3 during particle formulation. However, we have shown that the presence of avidin in solution plays no role in mediating gene delivery in the absence of both PEI and chloroquine (CQ) (Figure 3, Supporting Information). Therefore the expectation for the assay is that the transfection efficiency of 2PABP(+) should be higher than that of 2PABP(−), regardless of transfection magnitude.

We found that the transfection efficiencies were diverse in the cell lines studied but overall followed similar trends (Figure 5). The COS-7 kidney cells expressed the same levels of luciferase for 2PABP(−) and 2PABP(+) particles ($p > 0.05$). These cells are not very sensitive to charge and size, since they have been reported to take up particles as large as 3000 nm (*36*). On the other hand, luciferase expression was 32-fold higher in SKBR-3, 2.7-fold higher in MDA-MB-231, and 2.1-fold higher in C2C12 cells when transfected with just 2 μg of pGL3/well. Currently, there is no clear correlation between polymer charge and extracellular (membrane disruption) toxicity since cationic PEI analogues that are degradable under low pH conditions are less toxic to cells than nondegradable commercial PEI (*2*). Despite the high toxicity of PEI, the greater gene expression of cationic polymers may be explained by greater cell membrane interactions and the ability to use the cell's trafficking machinery to transport pDNA from the cytoplasm to the nucleus (*6*). Our flow cytometry analysis concurs with the transfection data and reveals that in SKBR-3 cells, 2PABP(+) polymer is taken up 2-fold better than 2PABP(−) with a 32-fold increase in gene expression, whereas in COS-7 cells, the uptake was indiscriminate (similar gene expression levels). Although 2PABP(−) uptake and gene expression was lower than its cationic counterpart, the polymer was favorably less toxic to cells (Figure 6) and could still mediate gene expression. Similar studies with covalently grafted PEG−PEI show less toxicity with a high degree of PEG shielding but also less transfection when the level and length of PEG grafting began to impede with pDNA complexation, and PEG−PEI complexes with high positive surface charge and less degree of grafting proved to be the most efficient for *in vitro* gene transfer (*16*). Nevertheless, there is still some contradiction in the literature when it comes to the transfection properties of PEG. Kataoka et al. reported less toxicity and higher transfections with PEGylated complexes (*37*, *38*) compared with their un-PEGylated counterparts, but their results might be cell line dependent and affected by amounts of pDNA used and ultimately polymer properties.

In conclusion, we have shown that the interaction between avidin and biotin can be exploited in gene delivery to noncovalently link PEG to PEI. 2P−avidin/biotin−PEI8 (2PABP(−)) internalization might lower gene expression due to decreased interactions with cell components, but this property may also explain the favorable decrease in intracellular toxicity observed with the polymer. Therefore, it does appear that greater cellular interactions may lead to enhanced gene expression but that polycations less toxic than PEI will probably make the most use of this new noncovalent PEGylation approach in gene delivery applications. This new PEGylation concept via avidin/biotin interactions has potential implications for improving clinical gene delivery via a two-step therapeutic approach: (1) injection of noncovalent PEG−avidin/biotin−polycation nanoparticles for prolonged systemic circulation, followed by (2) endogenous biotin-based competition (or supplemental biotin injection) for PEG−avidin release from nanoparticles to enhance tumor localization and gene expression.

ACKNOWLEDGMENT

This work was partially supported by NIH Grant R01 AI-43346-08. The author acknowledges the PhRMA foundation for a predoctoral fellowship in pharmaceutics.

Supporting Information Available: Additional information about the synthesis and characterization of 2P−avidin and 1P−avidin. This material is available free of charge via the Internet at http://pubs.acs.org.

LITERATURE CITED

(1) Boussif, O., Lezoualc'h, F., Zanta, M. A., Mergny, M. D., Scherman, D., Demeneix, B., and Behr, J. P. (1995) A versatile vector for gene and oligonucleotide transfer into cells in culture and in vivo: polyethylenimine. *Proc. Natl. Acad. Sci. U.S.A. 92* (16), 7297−7301.

(2) Forrest, M. L., Koerber, J. T., and Pack, D. W. (2003) A degradable polyethylenimine derivative with low toxicity for highly efficient gene delivery. *Bioconjugate Chem. 14*, 934−940.

(3) Kunath, K., von Harpe, A., Fischer, D., Petersen, H., Bickel, U., Voigt, K., and Kissel, T. (2003) Low-molecular-weight polyethylenimine as a non-viral vector for DNA delivery: comparison of physicochemical properties, transfection efficiency and in vivo distribution with high-molecular-weight polyethylenimine. *J. Controlled Release 89* (1), 113−125.

(4) Gabrielson, N. P., and Pack, D. W. (2006) Acetylation of Polyethylenimine Enhances Gene Delivery via Weakened Polymer/DNA Interactions. *Biomacromolecules 7* (8), 2427−2435.

(5) Suh, J., Wirtz, D., and Hanes, J. (2003) Efficient active transport of gene nanocarriers to the cell nucleus. *Proc. Natl. Acad. Sci. U.S.A. 100* (7), 3878−3882.

(6) Vaughan, E. E., and Dean, D. A. (2006) Intracellular trafficking of plasmids during transfection is mediated by microtubules. *Mol. Ther. 13* (2), 422−428.

(7) Mastrobattista, E., van der Aa, M. A., Hennink, W. E., and Crommelin, D. J. (2006) Artificial viruses: a nanotechnological approach to gene delivery. *Nat. Rev. Drug Discovery 5* (2), 115−121.

(8) Fischer, D., Osburg, B., Petersen, H., Kissel, T., and Bickel, U. (2004) Effect of poly(ethylene imine) molecular weight and pegylation on organ distribution and pharmacokinetics of polyplexes with oligodeoxynucleotides in mice. *Drug Metab. Dispos. 32* (9), 983−992.
(9) Chollet, P., Favrot, M. C., Hurbin, A., and Coll, J. L. (2002) Side-effects of a systemic injection of linear polyethylenimine-DNA complexes. *J. Gene Med. 4* (1), 84−91.
(10) Pun, S. H., Bellocq, N. C., Liu, A., Jensen, G., Machemer, T., Quijano, E., Schluep, T., Wen, S., Engler, H., Heidel, J., and Davis, M. E. (2004) Cyclodextrin-modified polyethylenimine polymers for gene delivery. *Bioconjugate Chem. 15* (4), 831−840.
(11) Maeda, H., Wu, J., Sawa, T., Matsumura, Y., and Hori, K. (2000) Tumor vascular permeability and the EPR effect in macromolecular therapeutics: a review. *J. Controlled Release 65* (1−2), 271−284.
(12) Matsumura, Y., and Maeda, H. (1986) A new concept for macromolecular therapeutics in cancer chemotherapy: mechanism of tumoritropic accumulation of proteins and the antitumor agent smancs. *Cancer Res. 46* (12, Part 1), 6387−6392.
(13) Merdan, T., Kunath, K., Petersen, H., Bakowsky, U., Voigt, K. H., Kopecek, J., and Kissel, T. (2005) PEGylation of poly(ethylene imine) affects stability of complexes with plasmid DNA under in vivo conditions in a dose-dependent manner after intravenous injection into mice. *Bioconjugate Chem. 16* (4), 785−792.
(14) Godbey, W. T., Wu, K. K., and Mikos, A. G. (1999) Tracking the intracellular path of poly(ethylenimine)/DNA complexes for gene delivery. *Proc. Natl. Acad. Sci. U.S.A. 96* (9), 5177−5181.
(15) Mishra, S., Webster, P., and Davis, M. E. (2004) PEGylation significantly affects cellular uptake and intracellular trafficking of nonviral gene delivery particles. *Eur. J. Cell Biol. 83*, 1−15.
(16) Petersen, H., Fechner, P. M., Martin, A. L., Kunath, K., Stolnik, S., Roberts, C. J., Fischer, D., Davies, M. C., and Kissel, T. (2002) Polyethylenimine-*graft*-poly(ethylene glycol) copolymers: influence of copolymer block structure on DNA complexation and biological activities as gene delivery system. *Bioconjugate Chem. 13* (4), 845−854.
(17) Sung, S. J., Min, S. H., Cho, K. Y., Lee, S., Min, Y. J., Yeom, Y. I., and Park, J. K. (2003) Effect of polyethylene glycol on gene delivery of polyethylenimine. *Biol. Pharm. Bull. 26* (4), 492−500.
(18) Segura, T., and Shea, L. D. (2002) Surface-tethered DNA complexes for enhanced gene delivery. *Bioconjugate Chem. 13* (3), 621−629.
(19) Green, N. M. (1990) Avidin and streptavidin. *Methods Enzymol. 184*, 51−67.
(20) Kaiser, K., Marek, M., Haselgrubler, T., Schindler, H., and Gruber, H. J. (1997) Basic studies on heterobifunctional biotin−PEG conjugates with a 3-(4-pyridyldithio)propionyl marker on the second terminus. *Bioconjugate Chem. 8* (4), 545−551.
(21) Xiong, M. P., and Kwon, G. S. (2005) PEGylation of yeast cytosine deaminase for pretargeting. *J. Pharm. Sci. 94* (6), 1249−1258.
(22) Caliceti, P., Chinol, M., Roldo, M., Veronese, F. M., Semenzato, A., Salmaso, S., and Paganelli, G. (2002) Poly(ethylene glycol)-avidin bioconjugates: suitable candidates for tumor pretargeting. *J. Controlled Release 83* (1), 97−108.
(23) Green, N. M. (1965) A spectrophotometric assay for avidin and biotin based on binding of dyes by avidin. *Biochem. J. 94*, 23C−24C.
(24) von Harpe, A., Petersen, H., Li, Y., and Kissel, T. (2000) Characterization of commercially available and synthesized polyethylenimines for gene delivery. *J. Controlled Release 69* (2), 309−322.
(25) Morpurgo, M., Radu, A., Bayer, E. A., and Wilchek, M. (2004) DNA condensation by high-affinity interaction with avidin. *J. Mol. Recognit. 17* (6), 558−566.
(26) Abuchowski, A., van Es, T., Palczuk, N. C., and Davis, F. F. (1977) Alteration of immunological properties of bovine serum albumin by covalent attachment of polyethylene glycol. *J. Biol. Chem. 252* (11), 3578−3581.
(27) Ton, G. N., Weichert, J. P., Longino, M. A., Fine, J. P., and Kwon, G. S. (2005) Methoxypoly(ethylene glycol)-conjugated carboxypeptidase A for solid tumor targeting: part II: pharmacokinetics and biodistribution in normal and tumor-bearing rodents. *J. Controlled Release 104* (1), 155−166.
(28) Forrest, M. L., Meister, G. E., Koerber, J. T., and Pack, D. W. (2004) Partial acetylation of polyethylenimine enhances in vitro gene delivery. *Pharm. Res. 21* (2), 365−371.
(29) Chen, D. J., Majors, B. S., Zelikin, A., and Putnam, D. (2005) Structure-function relationships of gene delivery vectors in a limited polycation library. *J. Controlled Release 103* (1), 273−283.
(30) Harthe, C., and Claustrat, B. (2003) A sensitive and practical competitive radioassay for plasma biotin. *Ann. Clin. Biochem. 40* (Pt 3), 259−263.
(31) Mock, D. M., and Malik, M. I. (1992) Distribution of biotin in human plasma: most of the biotin is not bound to protein. *Am. J. Clin. Nutr. 56* (2), 427−432.
(32) Mock, N. I., Malik, M. I., Stumbo, P. J., Bishop, W. P., and Mock, D. M. (1997) Increased urinary excretion of 3-hydroxyisovaleric acid and decreased urinary excretion of biotin are sensitive early indicators of decreased biotin status in experimental biotin deficiency. *Am. J. Clin. Nutr. 65* (4), 951−958.
(33) Green, N. M., and Toms, E. J. (1972) The dissociation of avidin-biotin complexes by guanidinium chloride. *Biochem. J. 130* (3), 707−711.
(34) Green, N. M. (1963) Avidin. 4. Stability at extremes of pH and dissociation into sub-units by guanidine hydrochloride. *Biochem. J. 89*, 609−620.
(35) Green, N. M. (1975) Avidin. *Adv. Protein Chem. 29*, 85−133.
(36) Jewell, C. M., Hays, M. E., Kondo, Y., Abbott, N. L., and Lynn, D. M. (2006) Ferrocene-containing cationic lipids for the delivery of DNA: oxidation state determines transfection activity. *J. Controlled Release 112*, 129−138.
(37) Fukushima, S., Miyata, K., Nishiyama, N., Kanayama, N., Yamasaki, Y., and Kataoka, K. (2005) PEGylated polyplex micelles from triblock catiomers with spatially ordered layering of condensed pDNA and buffering units for enhanced intracellular gene delivery. *J. Am. Chem. Soc. 127* (9), 2810−2811.
(38) Itaka, K., Yamauchi, K., Harada, A., Nakamura, K., Kawaguchi, H., and Kataoka, K. (2003) Polyion complex micelles from plasmid DNA and poly(ethylene glycol)-poly(L-lysine) block copolymer as serum-tolerable polyplex system: physicochemical properties of micelles relevant to gene transfection efficiency. *Biomaterials 24* (24), 4495−4506.

BC0602883

Evaluation of Chemical, Physical, and Biologic Properties of Tumor-Targeting Radioiodinated Quinazolinone Derivative

Ketai Wang, Agop M. Kirichian, Ayman F. Al Aowad, S. James Adelstein, and Amin I. Kassis*

Harvard Medical School, Department of Radiology, 200 Longwood Avenue, Boston, Massachusetts 02115. Received September 18, 2006; Revised Manuscript Received November 28, 2006

Our group is developing a novel technology, enzyme-mediated cancer imaging and therapy (EMCIT), that aims to entrap radioiodinated compounds within solid tumors for noninvasive tumor detection and therapy. In this approach, a water-soluble, radioiodinated prodrug is hydrolyzed in vivo to a highly water-insoluble compound by an enzyme overexpressed extracellularly by tumor cells. We have synthesized and characterized the water-soluble prodrug, 2-(2′-phosphoryloxyphenyl)-6-[^{125}I]iodo-4-(3*H*)-quinazolinone **[^{125}I]5**, which is readily hydrolyzed by alkaline phosphatase, an enzyme expressed by many tumor cell lines, to a water-insoluble drug, 2-(2′-hydroxyphenyl)-6-[^{125}I]iodo-4-(3*H*)-quinazolinone **[^{125}I]1**. In the course of our study, we discovered that ammonium 2-(2′-phosphoryloxyphenyl)-6-tributylstannyl-4-(3*H*)-quinazolinone, an intermediate in the radioiodination of the prodrug, exists as two isomers (**3** and **4**) whose radioiodination leads, respectively, to **[^{125}I]6** and **[^{125}I]5**. These prodrugs have different in vitro and in vivo biologic activities. Compound **6** is not hydrolyzed by alkaline phosphatase (ALP), whereas **5** is highly soluble (mg/mL) in aqueous solution and is rapidly dephosphorylated in the presence of ALP to **1**, a water-insoluble molecule (ng/mL). Mouse biodistribution studies indicate that **[^{125}I]6** has high uptake in kidney and liver and **[^{125}I]5** has very low uptake in all normal organs. Compounds **3** and **6** are converted, respectively, to **4** and **5** after incubation in DMSO. The stability of **5** in human serum is high. The minimum ALP concentration needed to hydrolyze **5** is much greater than the ALP level in the blood of patients with cancer, and the latter should not affect the pharmacokinetics of the compound. Incubation of **5** with viable human and mouse tumor-cell lines—but not with normal human cells and mouse tissues—leads to its hydrolysis and the formation of large crystals of **1**. We expect that **5** will also be hydrolyzed in vivo by tumor cells that express phosphatase activity extracellularly and anticipate the specific precipitation of radioiodinated **1** within tumor cell clusters. This should lead to high tumor-to-normal-tissue ratios and enable imaging (SPECT/PET) and radionuclide therapy of solid tumors.

INTRODUCTION

We are developing a novel strategy called enzyme-mediated cancer imaging and therapy (EMCIT), which is a method for enzyme-dependent, site-specific, in vivo precipitation of a water-soluble radioactive molecule (prodrug) within the extracellular space of solid tumors (*1*). The radiolabeled prodrug is hydrolyzed to its water-insoluble form by a hydrolase overexpressed on the extracellular surface of tumor cells, and the resulting water-insoluble drug is expected to be trapped within the extracellular spaces of the targeted solid tumor. Following tumor targeting and clearance from normal tissues and organs, the entrapped radioactive compound should lead to high tumor-to-normal-tissue ratios and enable the imaging (SPECT/PET) and radiotherapy of solid tumors.

Alkaline phosphatase (ALP) was investigated to ascertain the validity of the proposed approach, since this hydrolase (i) is known to be minimally expressed on the plasma membrane of normal cells and overexpressed on the membrane of many human tumor cells (*2*−*9*), (ii) is post-translationally modified with two *N*-glycosylation sites and a glycosylphosphatidylinositol (GPI) anchor by which it is tethered to the cell membrane, (iii) has a reasonably high second-order rate constant ($k_{cat}/K_m = 5 \times 10^7\ M^{-1}\ s^{-1}$), and (iv) has already been used to hydrolyze several chemotherapeutic prodrugs in vitro and in tumor-bearing animals in vivo (*10*−*14*). Additionally, (i) a high-resolution structure of the human placental isoform (PLAP) has been determined at 1.8 Å resolution and is available from the Protein Data Bank (code 1EW2) for analysis (*15*), and (ii) ALP-expressing tumors in cancer patients and tumor-bearing mice have been successfully imaged with radiolabeled antiALP antibodies (*16*−*20*). Consequently, we have been carrying out in silico molecular modeling to systematically investigate the structure−activity relationships of phosphorylated quinazolinone derivatives with PLAP.

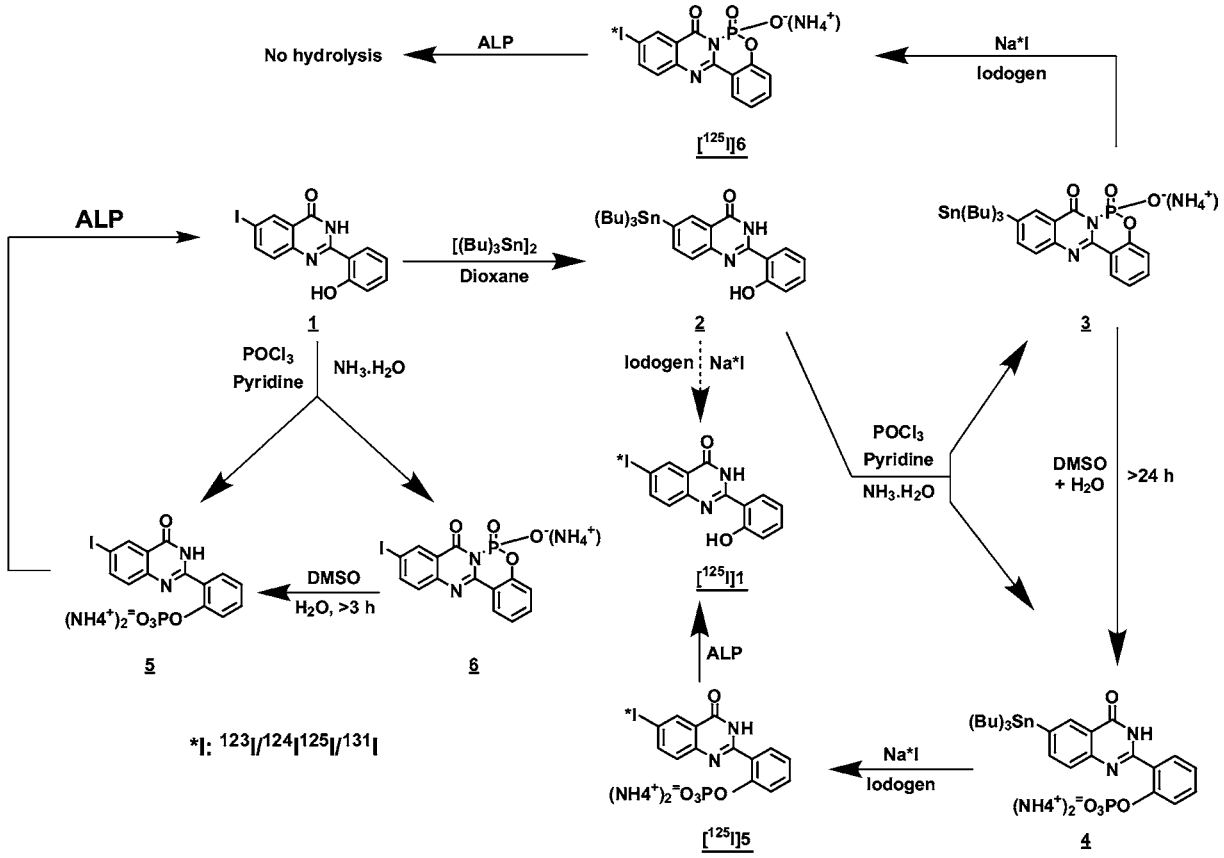
In 2002, we reported the synthesis and characterization of ammonium 2-(2′-phosphoryloxyphenyl)-6-iodo-4-(3*H*)-quinazolinone (**5**) and 2-(2′-hydroxyphenyl)-6-iodo-4-(3*H*)-quinazolinone (**1**) (*1*). In these studies, we demonstrated that nonfluorescent and water-soluble **5** is hydrolyzed by alkaline phosphatase to water-insoluble and highly fluorescent **1**. We also synthesized ammonium 2-(2′-phosphoryloxyphenyl)-6-tributylstannyl-4-(3*H*)-quinazolinone (**4**) (Scheme 1), a precursor for the synthesis of **5**, and found that the intravenous injection of **[^{125}I]5** in normal mice leads to high activity (∼5%−7% ID/g) in normal liver and kidneys (*1*).

Having observed that the pharmacokinetics of **[^{125}I]5** in mice are very different when the prodrug is radioiodinated using **4** that has been dissolved in DMSO, we have been reevaluating the findings and interpretation of some of our earlier studies. It has become evident that the tin precursor of **5** is a mixture of two compounds—**3** (MW 590) and **4** (MW 608)—whose radioiodination results in the formation of a mixture of **[^{125}I]6** (MW 426) and **[^{125}I]5** (MW 444). We describe herein the

* To whom correspondence should be addressed at Harvard Medical School, Armenise Building, Room D2-137, 200 Longwood Avenue, Boston, Massachusetts 02115. Telephone: (617) 432-7777. Fax: (617) 432-2419. E-mail: amin_kassis@hms.harvard.edu.

10.1021/bc0602937 CCC: $37.00 © 2007 American Chemical Society
Published on Web 03/27/2007

Scheme 1. Pathway for Synthesis of Tributyltin and $^{125}I/^{127}I$ Quinazolinone Derivatives



syntheses of the derivatives and their chemical and biologic characterization.

EXPERIMENTAL PROCEDURES

General Remarks. Alkaline phosphatase (bovine intestinal mucosa, calf intestinal mucosa, human placental type XXIV, porcine kidney) and all other chemicals were obtained from Sigma-Aldrich Incorporated. Carrier-free sodium [^{125}I]iodide was purchased from Amersham Corporation. HPLC separations (Waters) were performed on a reversed-phase Zorbax SB-C_{18} column, 9.4 × 250 mm (Agilent Technology), with UV absorption (Waters 486 detector) and γ-ray detection (gamma-ram, IN/US Systems) used to analyze the eluates.

Syntheses (Scheme 1) and Chemical and Biophysical Characterization. *Ammonium 2-(2′-Phosphoryloxyphenyl)-6-tributylstannyl-4-(3H)-quinazolinone (**3** and **4**).* 2-(2′-Hydroxyphenyl)-6-iodo-4-(3*H*)-quinazolinone (**1**) and 2-(2′-hydroxyphenyl)-6-tributylstannyl-4-(3*H*)-quinazolinone (**2**) were synthesized as previously reported (*1*). To phosphorylate the tin derivative, phosphorus oxychloride (5 μL, 53.6 μmol) in dry pyridine (0.5 mL) was added dropwise to a stirred solution of **2** (25 mg, 47.5 μmol) in dry pyridine (0.4 mL) cooled to 0 °C. The solution turned yellow. The reaction mixture was stirred for 1 h at 0 °C and then was neutralized by adding ammonium hydroxide (0.5 mL diluted from 15 μL 28% ammonium hydroxide solution). The solvent was evaporated under reduced pressure (rotary evaporator), and a light-yellow solid was produced. HPLC and ^{31}P NMR showed two peaks, **3** and **4** (Figure 1A,C). When a mixture of **3** and **4** (0.5 mg) was dissolved in DMSO (100 μL) and left overnight, a solution containing only **4** was obtained (Figure 1B,D). ESI-HRMS: calcd for **3** $[M - H]^-$ 589.1296, found 589.1296; calcd for **4** $[M + H]^+$ 609.1540, found 609.1539. ^{31}P NMR for **3** and **4**: −16.922 ppm and −2.958 ppm, respectively.

Ammonium 2-(2′-Phosphoryloxyphenyl)-6-[^{125}I]iodo-4-(3H)-quinazolinone ([^{125}I]5 and [^{125}I]6). Ammonium 2-(2′-phosphoryloxyphenyl)-6-tributylstannyl-4-(3*H*)-quinazolinone (mixture of **3** and **4**, 0.5 mg) was dissolved in DMSO (100 μL) for 1 min, 3 h, or overnight; and 1 μL (5 μg/μL DMSO solution) was added to a reaction vial coated with 1,3,4,6-tetrachloro-3α,6α-diphenylglycouril (Iodogen, 10 μg), along with phosphate buffer (12 μL, 0.1 M, pH 7.4) and the desired quantity of Na^{125}I (0.2−2.0 mCi, 400 μCi/μL). After vortex mixing at ambient temperature for 5 min, the solution was analyzed by HPLC (linear gradient from 10% disodium hydrogen phosphate, 0.05 M, pH 2.5, to 100% methanol for 6 min; flow rate of 3 mL/min) for the presence of **[^{125}I]5** and **[^{125}I]6**.

2-(2′-Hydroxyphenyl)-6-[^{125}I]iodo-4-(3H)-quinazolinone ([^{125}I]1). Compound **[^{125}I]5** (5 μL, 200 μCi) was incubated with ALP (10 U/2 μL) at 37 °C for 5 min. The product **[^{125}I]1** was identified by HPLC against a 2-(2′-hydroxyphenyl)-6-[^{125}I]iodo-4-(3*H*)-quinazolinone standard. In addition, **2**, incubated for 5 min in DMSO, was radioiodinated using Iodogen and Na^{125}I as described above, and the solution was analyzed by C_{18} HPLC.

*Ammonium 2-(2′-Phosphoryloxyphenyl)-6-iodo-4-(3H)-quinazolinone (**5** and **6**).* Compound **1** (25 mg, 47.4 μmol) was added to dried pyridine (0.5 mL) at 0 °C, followed by phosphorus oxychloride (5 μL, 53 μmol) dissolved in dried pyridine (0.5 mL) under argon gas. The reaction was complete within 1 h, as indicated by silica gel TLC. The solution was cleared and neutralized to pH 7 by adding ammonium hydroxide (0.5 mL diluted from 15 μL 28% ammonium hydroxide solution). At the end of neutralization, the solution turned light yellow. The solvent was evaporated, and a mixture of yellow solids including **5** and **6** was obtained. After an overnight incubation of the mixture in DMSO, **6** was converted to **5**, as indicated by HPLC and ^{31}P NMR with one peak present at −2.897. ESI-HRMS: calcd for **5** $[M + H]^+$ 444.9451, found

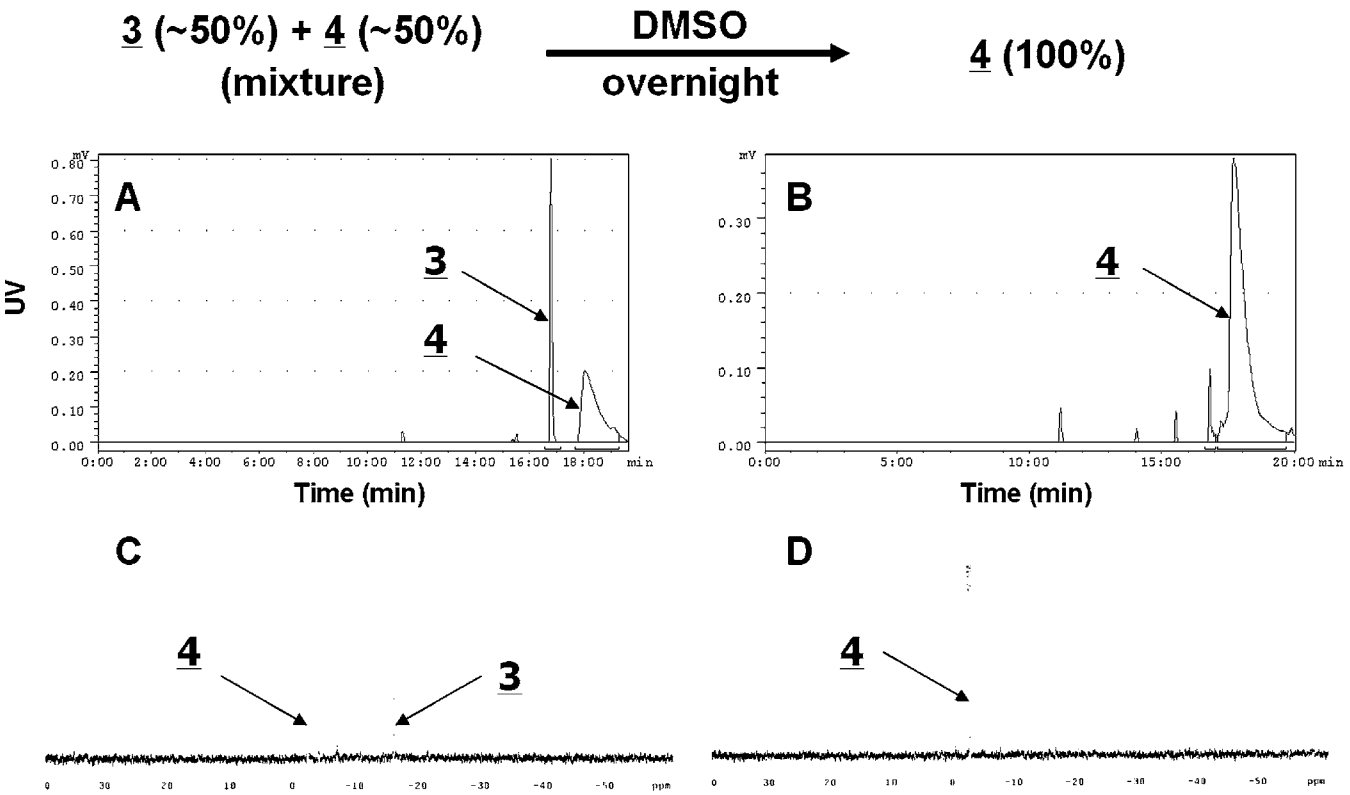


Figure 1. HPLC (A and B) and ^{31}P NMR (C and D) of stannylated intermediates **3** and **4**, demonstrating conversion of **3** to **4** upon incubation in DMSO.

444.9443; calcd for **6** $[M - H]^-$ 424.9175, found 424.9188. ^{31}P NMR for **5** and **6**: −2.897 ppm and −16.568 ppm, respectively.

*Water Solubility of 2-(2′-Hydroxyphenyl)-6-[^{125}I]iodo-4-(3H)-quinazolinone ([**^{125}I**]**1**) and 2-(2′-Phosphoryloxyphenyl)-6-[^{125}I]-iodo-4-(3H)-quinazolinone ([**^{125}I**]**5**).* Since **1** is highly water-insoluble, a novel radiotracer method was developed to determine its solubility (*21*). In this approach, various volumes of a saturated solution of ^{127}I-labeled **1**, spiked with ^{125}I-labeled **1**, in DMSO are placed in centrifuge tubes, and sufficient deionized water is added to make the final volumes equivalent. After vortex mixing, the tubes are centrifuged. Since (i) the ^{127}I- and ^{125}I-labeled compounds have the same solubilities and are, therefore, equally distributed in the DMSO−water solution, and (ii) the amount of nonradioactive compound (added in the DMSO solution) is known, the concentration of the compound in solution can be calculated and plotted as a function of the DMSO-to-water ratio. The water solubility of the compound is then determined by extrapolation of the linear fit of the data points to zero DMSO, i.e., the *y*-axis intercept when $x = 0$ (*Origin 7.0*, OriginLab Corporation, Northampton, MA). The water solubility of prodrug **5** was assessed by the conventional UV spectrophotometry method.

*Kinetics of 2-(2′-Phosphoryloxyphenyl)-6-[^{125}I]iodo-4-(3H)-quinazolinone ([**^{125}I**]**5**) Hydrolysis by Alkaline Phosphatase.* Compound **5** (4 μg) was incubated with bovine ALP (10 U/mL) at 37 °C for 8 min. The kinetics of hydrolysis of nonfluorescent, water-soluble **5** to fluorescent, water-insoluble **1** were followed with a luminescence spectrometer (Perkin-Elmer S50B, excitation at 340 nm, emission at 504 nm). To assess the kinetics of the hydrolysis, the Michaelis−Menten constant of the enzyme (K_m) and the maximum velocity of the reaction (V_{max}) were determined by a Lineweaver-Burke straight-line plot with a slope equal to K_m/V_{max}, where the *y*-intercept of the line is $1/V_{max}$ and the *x*-intercept is $-1/K_m$.

To determine the minimum concentration of ALP required to hydrolyze **[^{125}I]5** to **[^{125}I]1**, **[^{125}I]5** was incubated with various concentrations of human, bovine, porcine, and calf ALP (between 0.0001 and 1 U/μL PBS) for 5 min, and the formation of **[^{125}I]1** was assessed by HPLC. After integrating the peak area of **[^{125}I]1**, the percentage conversions of **[^{125}I]5** to **[^{125}I]1** were determined. The mean (±sem) values of **[^{125}I]1** (at the same ALP concentration for all four phosphatases) were calculated and plotted versus each ALP concentration. A fit of the data points furnished a sigmoidal line from which the IC_{50} value as well as the minimum concentration of ALP needed for hydrolysis was calculated.

Compound **[^{125}I]5** (2 μL, 0.1 mCi/μL) was also incubated at 37 °C with various human ALP concentrations (0.000 01, 0.0001, 0.001, 0.01, and 0.1 U/μL PBS) for 5 min, 1 h, 12 h, 24 h, and 48 h. At each of these incubation times, the concentration of ALP needed to convert 50% **[^{125}I]5** to **[^{125}I]1** was determined (IC_{50}) and plotted against time.

*Stability of Radiolabeled Prodrug ([**^{125}I**]**5**) in Serum.* Compound **[^{125}I]5** (2 μL, 0.2 mCi/μL) was incubated at 37 °C with human and other animal sera (18 μL) for 48 h. The percentage of **[^{125}I]5** remaining in the serum solution was measured at multiple times by HPLC, and the breakdown products of the prodrug were analyzed by HPLC. Alkaline phosphatase (10 U/20 μL) was also added to human serum−**[^{125}I]5** mixtures, and the ability of the hydrolase to dephosphorylate the quinazolinone was determined 5 min later.

Biologic Studies. *Mammalian-Cell-Mediated Hydrolysis of 2-(2′-Phosphoryloxyphenyl)-6-[^{125}I/^{127}I]iodo-4-(3H)-quinazolinone ([**^{125}I**]**5**/5) to 2-(2′-Hydroxyphenyl)-6-[^{125}I/^{127}I]iodo-4-(3H)-quinazolinone ([**^{125}I**]**1**/1).* The cell-mediated hydrolysis of the nonfluorescent, water-soluble prodrug (**5**) to the fluorescent, water-insoluble drug (**1**) was assessed in the presence of human and mouse tumor cells, including human breast cell lines (BT-474 and MCF7), human ovarian carcinoma (SKOV-3, OVCAR-

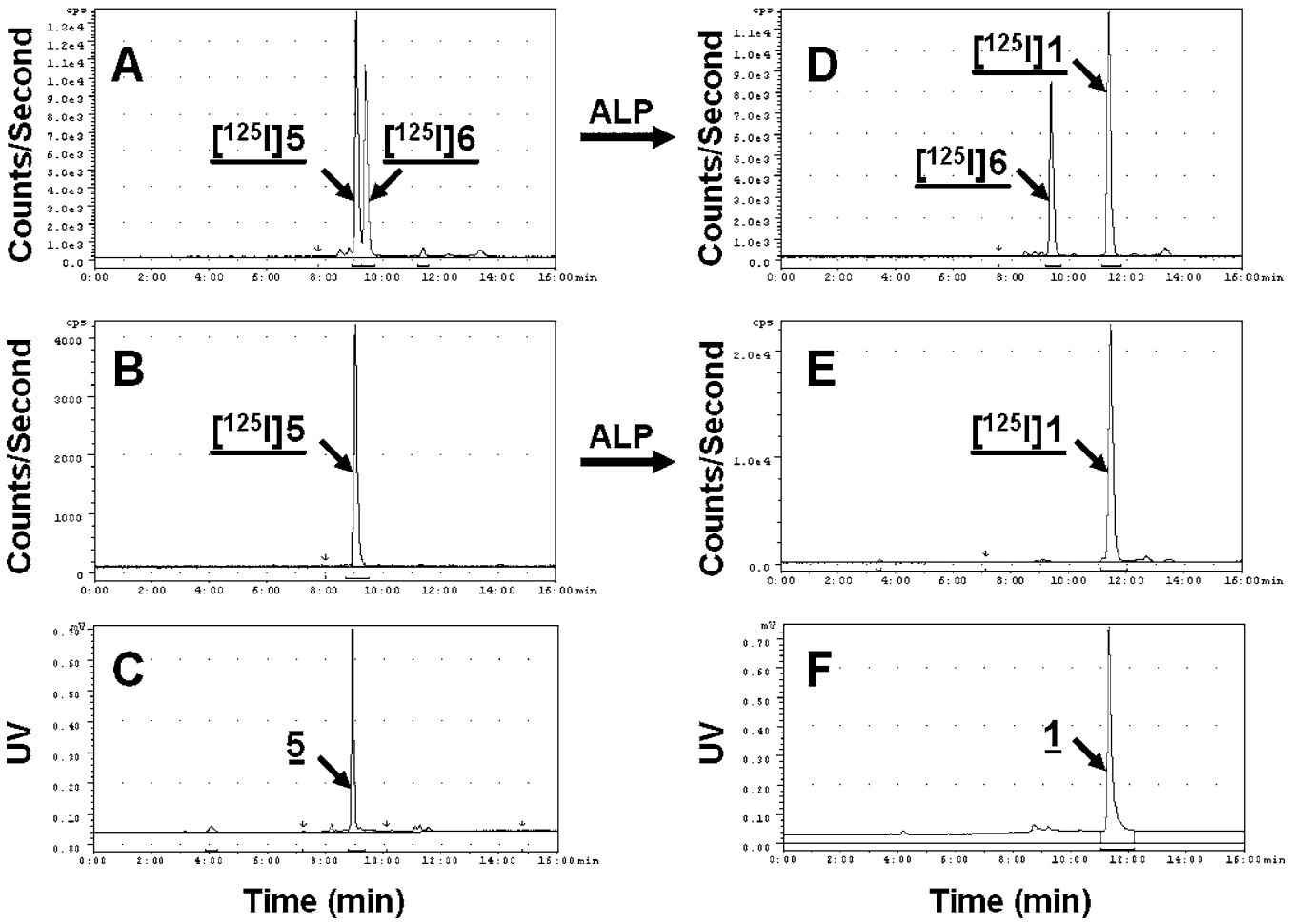


Figure 2. HPLC profiles of **[^{125}I]1**, **1**, **[^{125}I]5**, **5**, and **[^{125}I]6**, demonstrating (i) time-dependent conversion of **3** to **4** upon preincubation of mixture in DMSO for <1 min (A) and 24 h (B); (ii) selective hydrolysis of **[^{125}I]5** to **[^{125}I]1** following 5 min incubation in ALP (A and D) (note absence of hydrolysis of **[^{125}I]6**); and (iii) hydrolysis of **[^{125}I]5** to **[^{125}I]1** following 5 min incubation in ALP (B and E). HPLC profiles of authentic **5** (C) and **1** (F).

3), human small-cell lung carcinoma (HTB-173), mouse Lewis lung carcinoma (LLC1), and human mammary endothelial cells (HMEC), and mouse kidney, liver, and spleen tissues. For cultured cells, logarithmically growing cells were trypsinized and suspended in medium, and 5×10^4 cells (in 0.2 mL DMEM, pH 7.4) were seeded onto slides (Lab-Tek II Chamber Slide, Nalge Nunc International Company) and allowed to adhere by an overnight incubation at 37 °C. They were then washed with medium, and **5** (1 mg/mL medium, pH 7.4) was added. The slides were incubated an additional 24 h, washed with PBS, and fixed in ice-cold ethanol, and the cell nuclei were stained with DAPI. The slides were observed under a light/fluorescence microscope. Similarly, normal mouse tissues (liver, kidney, and spleen) were dissected and incubated for 24 h in **5** (1 mg/mL medium, pH 7.4), washed in PBS, and cut into ~1 mm^3 fragments that were then pressed between two glass slides and observed under the fluorescence microscope.

To ascertain that the cell-mediated hydrolysis occurs through ALP, OVCAR-3 cells were incubated with **5** (24 h, 37 °C, pH 7.4) in the presence or absence of levamisole (10 mM), a specific inhibitor of alkaline phosphatase (*22*, *23*). The cells were then observed and photographed under a fluorescence microscope (before and after being washed with PBS).

Logarithmically growing viable human squamous-cell lung carcinoma cells (HTB-182) were also seeded onto Lab-Tek chamber slides. After an overnight incubation at 37 °C, the medium was removed, **[^{125}I]5** (~20 μCi, 0.2 mL DMEM, pH 7.4) was added, and the cells were reincubated for 24 h. The slides were then washed in PBS (0.01 M, pH 7.4), and the cells were fixed in ice-cold ethanol (−20 °C) for 10 min. After the slides were dried, they were dipped vertically into Kodak NTB-2 emulsion, melted at 45 °C, withdrawn, and left to drain and gel. They were stored at 4 °C in a black box containing Drierite (anhydrous $CaSO_4$). After exposure (3 days to 1 week), the emulsion-coated slides were dipped at room temperature in Kodak developer D-19 for 5 min, washed in distilled water, immersed in Kodak Fixer for 5 min, and rinsed again in distilled water. Finally, the nuclei were stained with Vecta-Shield Mounting Medium with DAPI (Vector Laboratories), and the slides were viewed under a light (ARG grains)/fluorescence (DAPI-stained nuclei) microscope.

*Ex Vivo Conversion of 2-(2′-Phosphoryloxyphenyl)-6-iodo-4-(3H)-quinazolinone (**5**) to 2-(2′-Hydroxyphenyl)-6-iodo-4-(3H)-quinazolinone (**1**) by Solid Tumors Grown in Vivo.* The ability of tumor cells grown as solid tumors in vivo to hydrolyze **5** to **1** in vitro was examined. Balb/c nude female mice were injected intraperitoneally (i.p.) with 2×10^6 SKOV-3 cells. When the tumors became palpable, the animals were killed and the tumors were dissected and incubated with **5** (1 mg/mL) for 3 h. The tumors were then washed, pressed between two glass slides, and observed under the light/fluorescence microscope. Similarly, C57BL/6 mice were injected i.p. with 2×10^6 mouse metastatic B16F10 melanoma cells and were killed when the abdomen became distended. The tumor-laden spleens were dissected and incubated with **5** for 3 h before being washed and observed under the fluorescence microscope.

*Biodistribution of 2-(2′-Phosphoryloxyphenyl)-6-[^{125}I]iodo-4-(3H)-quinazolinone (**[^{125}I]5**) and **[^{125}I]6** in Mice.* C57BL/6

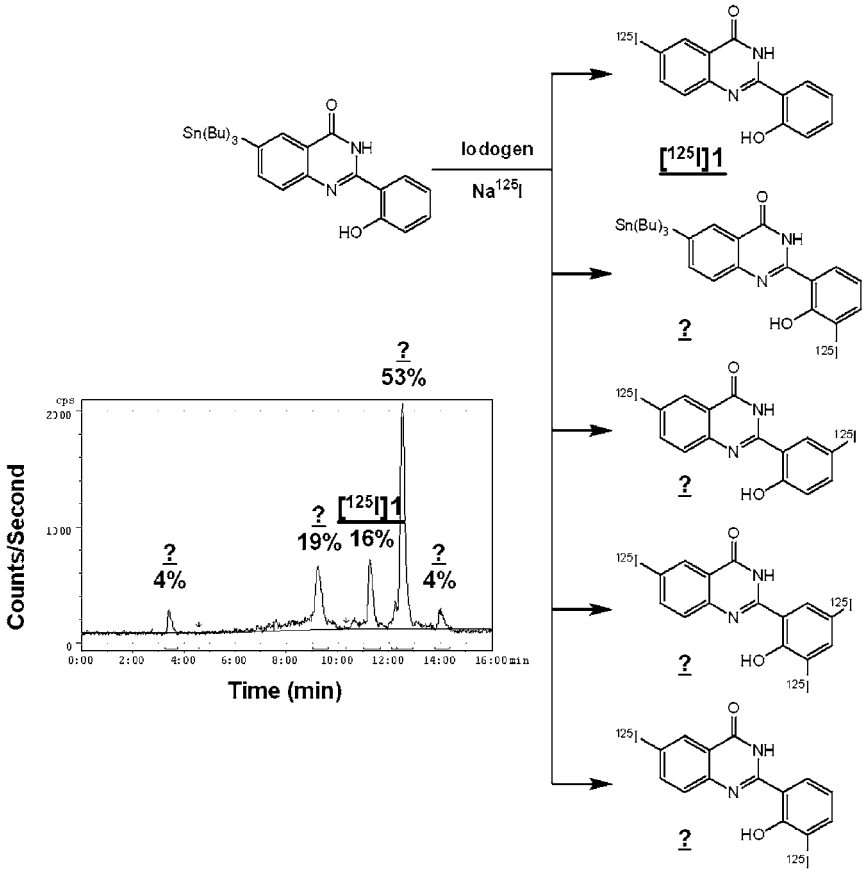


Figure 3. HPLC profile after radioiodination of **2**, demonstrating multiproduct formation including **[^{125}I]1** in low yield. Other possible derivatives (?) are shown.

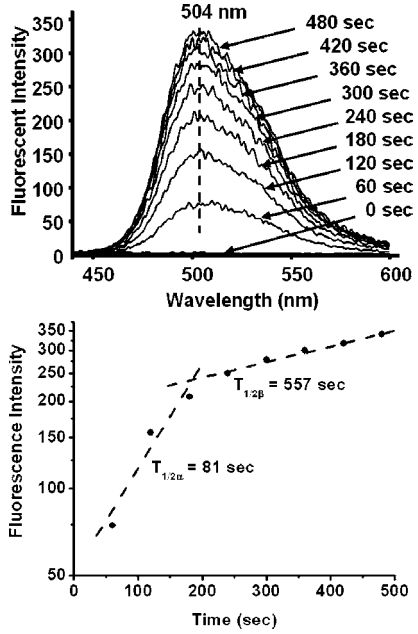


Figure 4. Kinetics of ALP-mediated hydrolysis of **5** to **1** at 37 °C (excitation at 340 nm, emission at 504 nm). Top: change in UV fluorescence spectra of **1** after incubation of **5** (4 μg) with ALP (10 U/mL water) as function of time. Bottom: change in fluorescence intensity of **1** at 504 nm as function of time.

mice ($n = 5$) were injected i.v. with **[^{125}I]5** or a mixture of **[^{125}I]5** and **[^{125}I]6** (5−10 μCi/0.1 mL) synthesized either following a 24 h incubation in DMSO or in the absence of DMSO. The animals were killed 1 and 24 h later, and radioactivity present in various tissues was assayed in a γ counter. On the basis of the injected activity and the weight of these organs, the percentage injected dose per gram (% ID/g) was calculated. Blood clearance was also followed over a 24 h period by counting 10 μL aliquots of blood, obtained from five mice each injected intravenously with **[^{125}I]5** (100 μCi /0.1 mL), in a γ counter. Whole-body clearance was also determined in these mice using a Capintec counter.

RESULTS

Syntheses (Scheme 1) and Chemical and Biophysical Characterization. *Syntheses and Radioiodination.* The key precursor for synthesizing radioiodinated prodrug **5** is ammonium 2-(2′-phosphoryloxyphenyl)-6-tributylstannyl-4-(3*H*)-quinazolinone (**4**) (*1*). In the current studies, we show that this stannylated derivative exists as two isomers, **3** and **4** (Scheme 1, Figure 1), that are readily radioiodinated to **6** and **5**, respectively. The data also demonstrate that, in the presence of DMSO, **3** is converted to **4** over time, and this process can be followed with HPLC and ^{31}P NMR (Figure 1). Consequently, when the tin precursor mixture of **3** and **4** is kept in DMSO for less than 1 min before radioiodination, the HPLC profile shows two peaks that correspond to **6** (∼44%) and **5** (∼55%) (Figure 2A) even though the radioiodination yield of both compounds is >99%. After the mixture of **3** and **4** is incubated at room temperature in DMSO overnight and then radioiodinated, the radiolabeled yield is ∼100% **5** (Figure 2B). Similarly, the incubation of a mixture of **6** and **5** in DMSO for 1 h also results in the complete conversion of **6** to **5**. Why the conversion of **6** to **5** occurs faster (within 2 h) than that of **3** to **4** (within 24 h) is unclear.

Unlike the quantitative yield that occurs when **4** is radioiodinated (Figure 2B), the treatment of **2** with Iodogen and Na^{125}I leads to the formation of a complex mixture of radioiodinated products that includes **[^{125}I]1** (∼16% yield) and several yet-to-

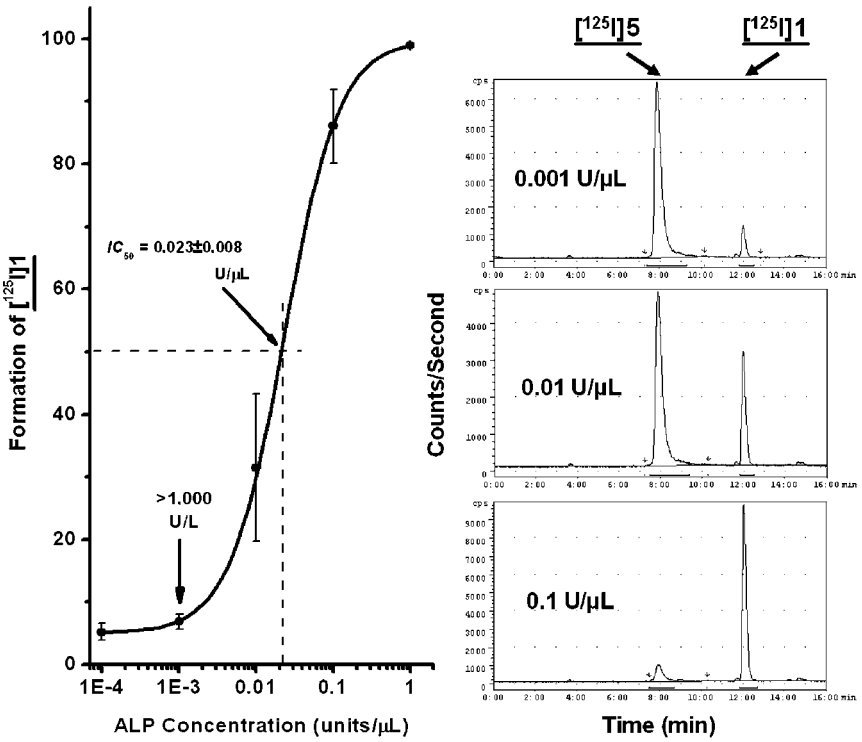


Figure 5. Kinetics of hydrolysis (HPLC quantitative analysis) of **[125I]5** to **[125I]1** determined after 5 min incubation in various concentrations of human, bovine, porcine, and calf ALP (PBS, pH 7.4), demonstrating that >1000 U/L is necessary to initiate hydrolysis. Sample HPLC profiles (with human ALP) are shown on right.

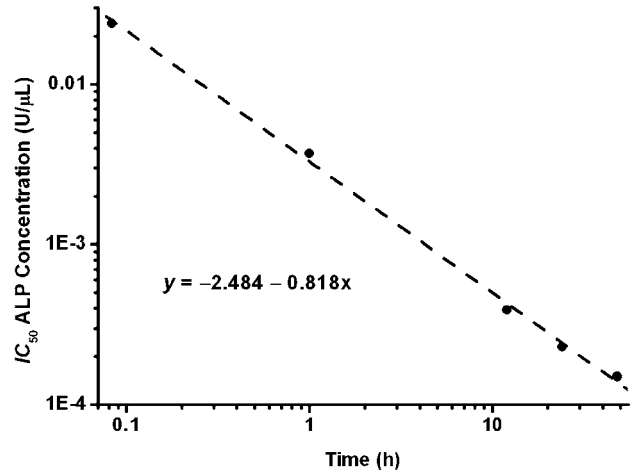


Figure 6. IC_{50} of ALP (bovine intestinal mucosa)-mediated hydrolysis of **[125I]5** as function of time (0.1 M PBS, 37 °C, pH 7.4).

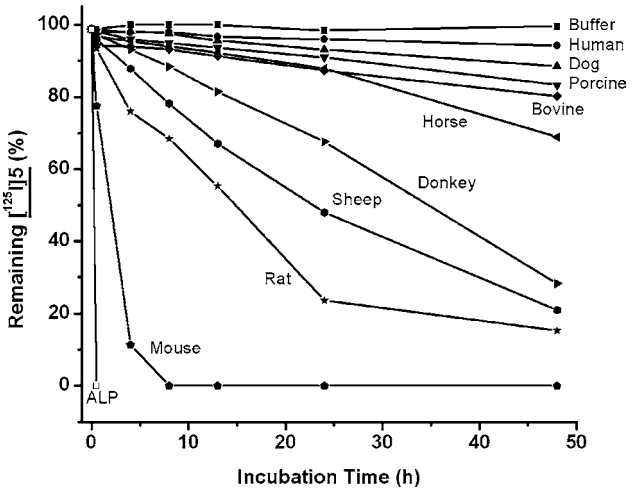


Figure 7. Stability of **[125I]5** in various types of mammalian serum (at 37 °C). $T_{1/2\alpha}$ in mouse serum = 2.0 h; $T_{1/2\alpha}$ in rat serum = 15.6 h; $T_{1/2\alpha}$ in human serum = several months. Complete hydrolysis of **[125I]-5** is seen upon 5 min incubation in ALP (□).

be identified ^{125}I-labeled products (Figure 3). Our current approach for the synthesis of pure **[125I]1** is via the ALP-mediated dephosphorylation of **[125I]5**.

*Water Solubility of 2-(2′-Hydroxyphenyl)-6-iodo-4-(3H)-quinazolinone (**1**) and 2-(2′-Phosphoryloxyphenyl)-6-iodo-4-(3H)-quinazolinone (**5**).* The solubility of **1**, as measured by the radiotracer method (*21*), is 1.9 ng/mL. The solubility of **5**, determined by spectrophotometry, is 7.8 mg/mL. Therefore, **5** is 4.18×10^6 times more soluble than **1**.

*Kinetics of 2-(2′-Phosphoryloxyphenyl)-6-iodo-4-(3H)-quinazolinone (**5**) Hydrolysis by Alkaline Phosphatase.* The ALP conversion of water-soluble, nonfluorescent prodrug **5** to water-insoluble, fluorescent drug **1** was determined spectroscopically. The fluorescence intensity at 504 nm increases with time (Figure 4). Further analysis of the data indicates that the enzyme-dependent appearance of **1** is biphasic with $T_{1/2\alpha}$ of 81 s and $T_{1/2\beta}$ of 557 s.

HPLC analysis has been utilized to determine the minimum concentration of ALP necessary for the hydrolysis of **[125I]5**. In these studies, **[125I]5** was incubated (room temperature, 5 min) with various concentrations (U/μL) of ALP (human, bovine, porcine, and calf), and the appearance of dephosphorylated **[125I]-1** was quantified. The HPLC peak corresponding to that of substrate **[125I]5** ($t_R \approx 8$ min) disappears as a function of increasing ALP concentration (Figure 5). Simultaneously, a new peak appears at $t_R \approx 12$ min that matches the retention-time value of nonradiolabeled **1**. Complete conversion of **[125I]5** to **[125I]1** occurs when the ALP concentration is $>10^6$ U/L. A plot of formation of **[125I]1** versus ALP concentration furnishes a sigmoidal curve (IC_{50} = 23 000 U/L) indicating that the minimum ALP concentration needed to hydrolyze **[125I]5** is ≥1000 U/L (Figure 5).

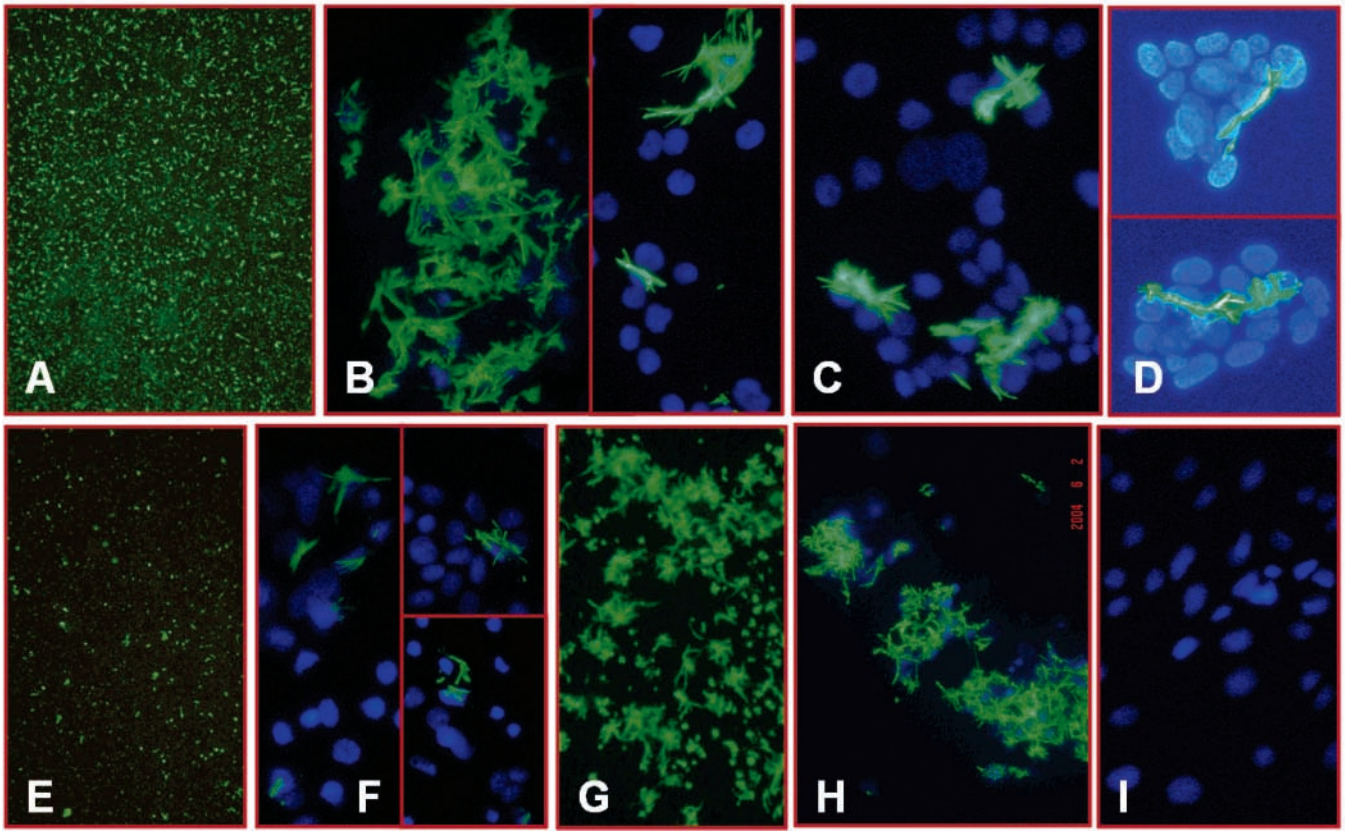


Figure 8. Fluorescence microscopy of viable human (A−G) and mouse (H) tumor cell lines incubated in vitro for 24 h with **5** showing its hydrolysis and crystallization of **1** (green). OVCAR-3 (A,B) and SKOV-3 (C) ovarian carcinoma cells; BT-474 (D) and MCF7 (E,F) breast cancer cells; HTB-173 small-cell lung carcinoma cells (G); and LLC1 Lewis lung carcinoma cells (H). Incubation of **5** with viable normal human mammary epithelial cells (HMEC) does not induce any observable hydrolysis (I). A and E: cells not washed, low power; B−D and F−I: cells washed, and counterstained with DAPI (blue nuclei), high power.

When **[^{125}I]5** is incubated with ALP (≥1 U/μL) for 5 min at room temperature, the compound is rapidly hydrolyzed, and a new peak appears on HPLC whose retention time is identical to that of **[^{125}I]1** (Figure 2B,E). However, when a mixture of **[^{125}I]5** and **[^{125}I]6** is incubated with ALP, only **[^{125}I]5** is converted to **[^{125}I]1** (55% of mixture) (Figure 2A,D).

HPLC has also been used to determine the IC_{50} when the incubation time of **[^{125}I]5** in varying ALP concentrations is changed. When the log IC_{50} is plotted as a function of log time, a linear relationship is obtained (Figure 6).

*Stability of Radiolabeled 2-(2′-Phosphoryloxyphenyl)-6-[^{125}I]-iodo-4-(3H)-quinazolinone (**[^{125}I]5**) in Animal and Human Serum.* Pure **[^{125}I]5** (20 mCi/mL) kept in buffer for a week is still 100% radiochemically unadulterated. However, this compound has very different stabilities in animal and human serum (Figure 7). In mouse serum, its half-life is 2.0 h, whereas in human serum, even after 48 h, 94% of **[^{125}I]5** is unchanged radiochemically. HPLC analysis indicates that the product of decomposition is the same in various types of serum and has the same retention-time peak as **[^{125}I]1**. That the observed stability of **[^{125}I]5** in human serum is not due to the presence of alkaline phosphatase inhibitors is demonstrated by the quantitative and rapid hydrolysis of **[^{125}I]5** to **[^{125}I]-1** upon the addition of alkaline phosphatase to the serum samples.

Biologic Studies. *Mammalian-Cell-Mediated Hydrolysis of 2-(2′-Phosphoryloxyphenyl)-6-iodo-4-(3H)-quinazolinone (**5**) to 2-(2′-Hydroxyphenyl)-6-iodo-4-(3H)-quinazolinone (**1**).* We determined the ability of human ovarian carcinoma cells (OVCAR-3 and SKOV-3), human breast cancer cells (BT-474 and MCF7), human small-cell lung carcinoma cells (HTB-173), and mouse Lewis lung carcinoma (LLC1) to hydrolyze water-soluble **5** to fluorescent, water-insoluble **1**. The in vitro incubation (37 °C, pH 7.4) of all these tumor cell lines with **5** leads to the formation of very large (≤20 μm) fluorescent crystals (Figure 8A−H), many of which are irreversibly bound to the cells (Figure 8B−D and 8F−H). Furthermore, autoradiography of viable human squamous-cell lung carcinoma cells (HTB-182) incubated with **[^{125}I]5** shows the presence of intense grains (Figure 9), consistent with the dephosphorylation of this radioiodinated analog and the formation of water-insoluble **[^{125}I]1**.

To ascertain that the hydrolysis of **5** by tumor cells is ALP-mediated, human tumor cells (OVCAR-3) cells were incubated with the quinazolinone derivative in the presence and absence of levamisole. The presence of this specific inhibitor of alkaline phosphatase (*22*, *23*) completely inhibits **5** dephosphorylation, as exemplified by the absence of any fluorescent crystal formation (Figure 10B). As expected, **1** is formed in the absence of levamisole (Figure 10A).

We also assessed the ability of normal human cells and mouse tissues to hydrolyze **5**. No hydrolysis (no fluorescent **1** crystal formation) is observed when human mammary epithelial cells (HMEC) are incubated with **5** (Figure 8I) or when this derivative is incubated in medium (in the absence of cells). Similar results (minimal fluorescence or its absence) have also been obtained following a 24 h incubation of normal mouse tissues (kidneys, liver, and spleen) with **5** (Figure 11A−C).

Finally, the incubation of mammalian cells up to 48 h with **5** (1 mg/mL) does not lead to any microscopic alterations in their appearance and in their attachment to the incubation flasks.

*Ex Vivo Conversion of 2-(2′-Phosphoryloxyphenyl)-6-iodo-4-(3H)-quinazolinone (**5**) to 2-(2′-Hydroxyphenyl)-6-iodo-4-(3H)-quinazolinone (**1**) by Solid Tumors Grown in Vivo.* Human ovarian SKOV-3 tumors grown in the peritoneal cavity of nude

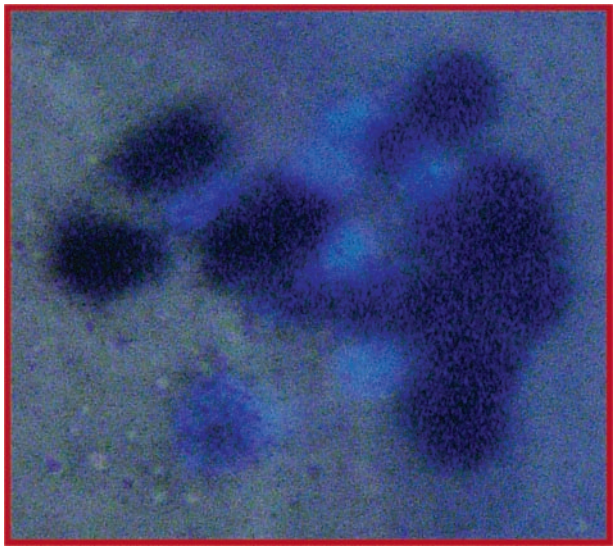


Figure 9. Autoradiography of viable human squamous-cell lung carcinoma cells (HTB-182) after 24 h, in vitro incubation (37 °C, pH 7.4) with **[^{125}I]5**, demonstrating its hydrolysis and formation of intense black grains where **[^{125}I]1** is formed. Cells counterstained with DAPI (blue nuclei).

mice and mouse B16F10 melanoma tumor metastases present within the spleen of mice were dissected and incubated ex vivo with **5**. Under both circumstances, fluorescence microscopy indicates the presence of fluorescent crystals (**1**) that are associated with the SKOV-3 solid tumors (Figure 11D) and within the B16F10 melanoma-infiltrated spleens (Figure 11E).

Biodistribution of 2-(2′-Phosphoryloxyphenyl)-6-iodo-4-(3H)-quinazolinone [^{125}I]5 and [^{125}I]6 in Mice. Table 1 contains the biodistribution data obtained 1 and 24 h after the i.v. injection of **[^{125}I]5** and **[^{125}I]6** into mice. Compound **[^{125}I]5** has minimal uptake in all normal organs and tissues with less than 0.2% ID/g remaining by 24 h. On the other hand, the i.v. injection of **[^{125}I]6** (mixed with [^{125}I]**5**, ∼50:50) demonstrates substantially higher uptake in the kidneys, liver, lungs, and blood (∼2%−12% ID/g). Since the % ID/g values for **[^{125}I]5** are all very low, the values obtained for the mixture of **[^{125}I]5** and **[^{125}I]6**, in fact, reflect those of **[^{125}I]6**. The blood clearance of **[^{125}I]5** is triphasic with $T_{1/2\alpha}$ of 13 min, $T_{1/2\beta}$ of 1.3 h, and $T_{1/2\gamma}$ of 18.1 h, whereas the whole body clearance has a $T_{1/2}$ of 5.3 h (Figure 12).

DISCUSSION

Ideally, radiolabeled agents for cancer imaging and therapy must (i) be stable in blood following their administration in an animal, (ii) be taken up rapidly by tumors ($T_{1/2}$ in circulation much shorter than physical $T_{1/2}$ of the radionuclide), (iii) be retained for long periods of time within tumors ($T_{1/2}$ in tumor much longer than physical $T_{1/2}$ of the radionuclide), (iv) be concentrated efficiently by tumors (i.e., high % ID/g), (v) be taken up minimally by normal tissue cells, (vi) have a short residence in normal tissues, (vii) achieve high tumor-to-normal-tissue uptake ratios, and (viii) be labeled with an emitter whose decay characteristics are suitable for imaging (SPECT or PET) or therapy. We believe that the EMCIT strategy meets many of these requirements. First, being molecules of low molecular weight (MW <500), the administered phosphorylated quinazolinone derivatives (e.g., **5**/**[^{125}I]5**) have very short residence times within the blood and are rapidly cleared from the circulation and the body (Figure 12). Additionally, **[^{125}I]5** is not taken up or retained by normal tissues (Table 1), i.e., the compound has minimal affinity for normal cells and is not significantly hydrolyzed by them. Second, the high stability of **5** in human serum is very promising (Figure 7). However, the unexpected variable (and lower) stability of such quinazolinone derivatives in the sera from other animal species may, from a practical point

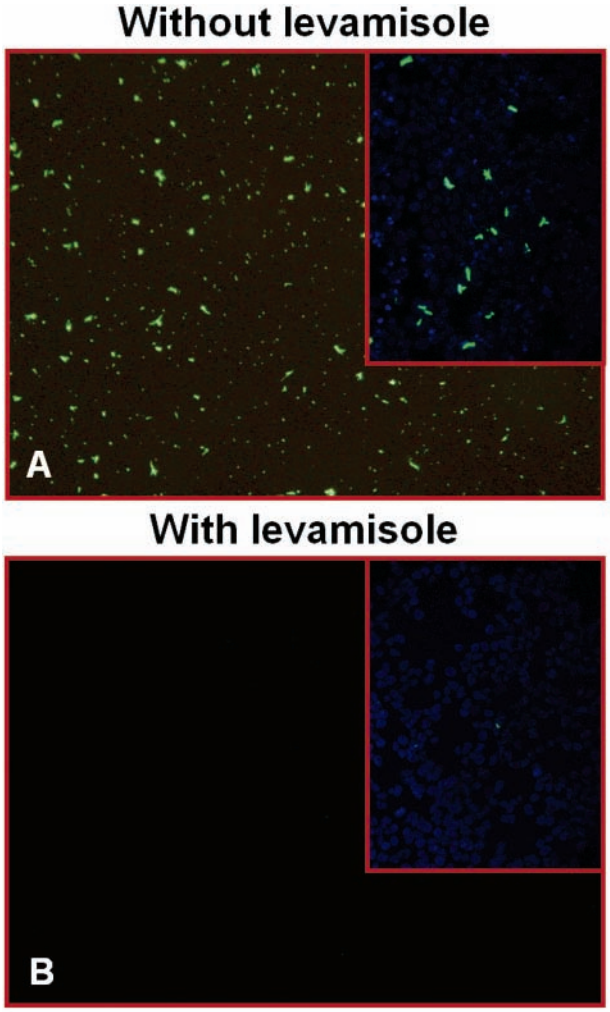


Figure 10. Fluorescence microscopy of human OVCAR-3 ovarian carcinoma cells after 24 h, in vitro incubation (37 °C, pH 7.4) with **5** ±10 mM levamisole, showing absence of hydrolysis and lack of crystallization to **1** (green) in presence of ALP-specific inhibitor levamisole. Inserts: cells washed and counterstained with DAPI, high power.

Table 1. Biodistribution of [^{125}I]5 and [^{125}I]6 Following Intravenous Injection into C57BL/6 Mice[a]

	[^{125}I]5		**[^{125}I]5−[^{125}I]6** mixture (∼**50:50**)
	1 h	24 h	24 h
blood	1.07 ± 0.62[a]	0.070 ± 0.061	1.86 ± 0.18
heart	0.32 ± 0.16	0.17 ± 0.25	0.59 ± 0.070
thyroid	1.31 ± 0.41	3.37 ± 3.96	2.34 ± 0.40
muscle	0.095 ± 0.025	0.021 ± 0.014	0.21 ± 0.030
bone	0.25 ± 0.070	0.10 ± 0.15	0.21 ± 0.015
lungs	0.97 ± 0.20	0.44 ± 0.27	1.84 ± 0.12
stomach	0.71 ± 0.25	0.086 ± 0.088	0.34 ± 0.030
S.I. + cont.	1.56 ± 0.92	0.090 ± 0.076	0.38 ± 0.040
L.I. + cont.	12.15 ± 5.77	0.18 ± 0.22	0.42 ± 0.070
spleen	1.40 ± 0.49	0.20 ± 0.27	0.33 ± 0.030
liver	2.32 ± 0.69	0.13 ± 0.11	9.45 ± 1.80
kidneys	1.76 ± 0.39	0.13 ± 0.12	13.59 ± 2.27
bladder	102.87 ± 50.23	0.41 ± 0.53	0.89 ± 0.26
urine	0.13 ± 0.040	0.81 ± 1.19	9.37 ± 0.44
testis	0.12 ± 0.12	0.19 ± 0.62	0.44 ± 0.050
fat	0.31 ± 0.10	0.015 ± 0.011	0.14 ± 0.020
skin	0.77 ± 0.39	0.040 ± 0.032	0.35 ± 0.010

[a] % ID/g.

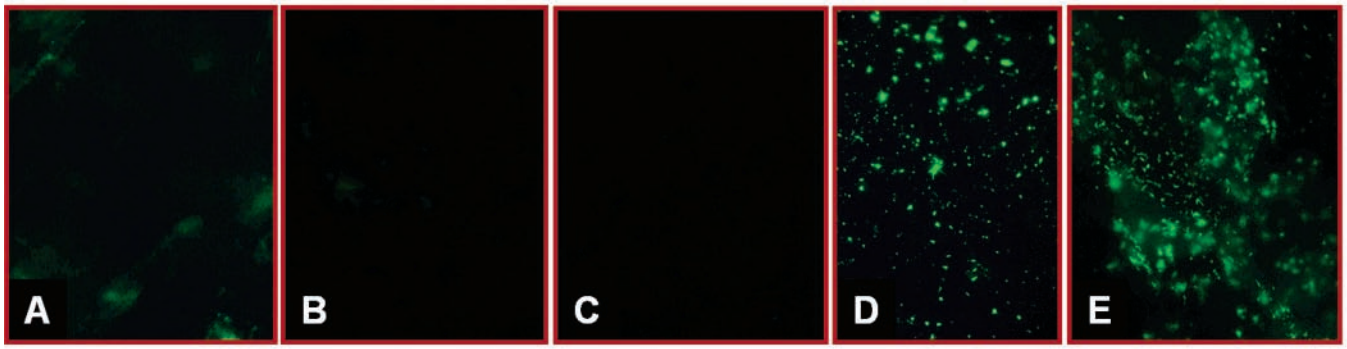


Figure 11. Fluorescence microscopy of (i) three normal mouse tissues (A, kidneys; B, liver; and C, spleen) after 24 h, in vitro incubation with **5**, showing absence of **5** hydrolysis (lack of green crystals); (ii) spleen tissue from mouse injected (i.p.) earlier with B16F10 melanoma cells (D) after 3 h, in vitro incubation with **5** (nonfluorescent), demonstrating its hydrolysis to **1** (fluorescent) by tumor cell metastases present within spleen; (iii) SKOV-3 tumor mass grown i.p. in nude mouse (E) after 20 h, in vitro incubation with **5** (nonfluorescent), demonstrating its hydrolysis to **1** (fluorescent).

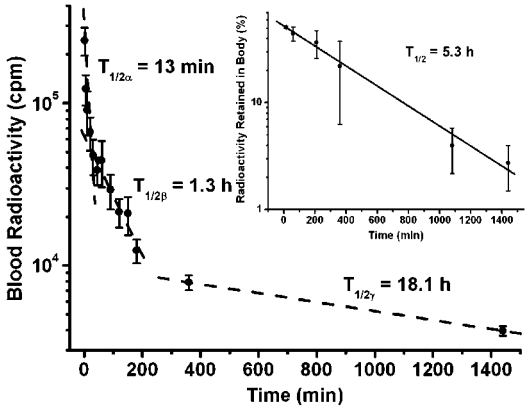


Figure 12. Blood clearance of radioactivity in mice after i.v. injection of **[^{125}I]5**. Insert: whole-body clearance of radioactivity in mice after i.v. injection of **[^{125}I]5**.

of view, create a problem in assessing the full potential of the EMCIT technology in small-animal (e.g., mouse) tumor models. Third, the molecule is an excellent enzyme substrate, hydrolyzed very efficiently and specifically to **1** by those tumor cells overexpressing ALP extracellularly and not by normal cells (Figures 8−11). Fourth, the EMCIT approach provides a repetitive hydrolysis machine, i.e., the enzyme enables the continuous hydrolysis of its water-soluble substrate (e.g., **[^{123}I]-5**, **[^{124}I]5**, **[^{131}I]5**), an event that leads to the formation and concentration of radioimaging (e.g., **[^{123}I]1** or **[^{124}I]1**) or radiotherapeutic (e.g., **[^{131}I]1**) precipitates within targeted tumors and metastases. Moreover, previous experimental in vivo data had shown that (i) the intravenous injection of **[^{125}I]5** into mice preinjected subcutaneously with ALP leads to the efficient uptake of radioactivity (i.e., **[^{125}I]1**) within the ALP-rich regions (*1*), and (ii) once formed, the water-insoluble radiolabeled **[^{125}I]-1** molecules (>6-fold less soluble than **5**) do not transit through the tissues and are therefore indefinitely entrapped (*1*).

Our current results indicate the direct radioiodination of the stannylated quinazolinone derivative **2** produces a mixture of products (Figure 3) and the yield of **[^{125}I]1** among these products is only 16%. This mixture of radioiodinated products may be a consequence of the presence of the hydroxyl group on the benzene ring, an activating group that permits introduction at its neighboring 3-position of a second group by electrophilic substitution. When the hydroxyl group within stannylated **2** is phosphorylated to stannylated prodrugs **3** and **4** and this mixture is left in DMSO for >24 h, all of **3** converts to **4** (Figure 1). Since the reactivity of the various positions on the phosphorylated benzene ring to halogenation is now lost, the radioiodination of **4** leads to the production of a single radioiodinated quinazolinone derivative **5** in greater than 99% yield (Figure 2B). The hydrolase ALP is then used to quantitatively and rapidly (<5 min) dephosphorylate the intermediate **5** to **1** (Figure 2E).

In an earlier publication (*1*), we had reported the synthesis and in vitro and in vivo characterization of what we believed to be pure **[^{125}I]5**. We have since come to realize that the tributyltin quinazolinone precursor used to synthesize the radioiodinated product exists as two isomers, **3** (MW 590) and **4** (MW 608) (Scheme 1 and Figure 1), and that, in the presence of DMSO, **3** is completely converted to **4** over a 24 h period (Figure 1A,B). The ^{31}P NMR spectrum indicates that the conversion process occurs at the phosphorus atoms (Figure 1C,D). This characteristic of the ^{31}P NMR spectrum is observed with similar compounds reported in the literature (*24*). Mass spectrum analysis shows that the molecular weights of 590 for **3** and 608 for **4** have an 18 unit difference—a value that equals a water molecule. This is consistent with the structures of **3** and **4** in Scheme 1. Consequently, the radioiodination of this mixture led to the synthesis of what is now known to be a mixture of **[^{125}I]5** and **[^{125}I]6**, two isomers of the same phosphorylated iodoquinazolinone derivative that differ substantially. Specifically, the retention times of the two derivatives on C_{18} HPLC separation are different (Figure 2A). In addition, while **5** is an excellent substrate for ALP (Figure 2B,E), as well as for prostatic acid phosphatase (*25*), **[^{125}I]6** is not hydrolyzed by either enzyme (Figure 2A,D). In another set of studies (*26*), the structural differences of the two iodoquinazolinone isoforms were examined using in silico molecular modeling techniques and docking methods to model the interaction/binding between the isoforms and ALP. The docking results demonstrate that **5** fits the active binding site of ALP favorably and interacts with the catalytic amino acid Ser92, which plays an important role in the hydrolysis process, whereas **6** does not. Finally, the uptake and retention of the two isomers by various normal tissues following their intravenous injection into mice is different (Table 1). The observations that **[^{125}I]5** are (i) minimally hydrolyzed by normal tissues (Figure 11A−C), (ii) not taken up or retained by any normal tissue (Table 1), (iii) an excellent substrate for ALP (Figure 2B,E), (iv) specifically hydrolyzed by ALP-expressing tumor cells (Figures 8−10 and 11D,E), and (v) not toxic to cells emphasize the suitability of this compound for the EMCIT approach.

Phosphatases, such as ALP, are often elevated in the sera of patients with various cancers and certain other diseases (*27*−*41*). To ascertain that these phosphatases will not lead to significant hydrolysis of the radioiodinated quinazolinone derivatives during the transit/sojourn of the latter through the blood and normal tissues of an animal, i.e., prior to their specific hydrolysis by the ALP-overexpressing tumor cells, HPLC was used to determine the minimum ALP concentration necessary

to initiate the hydrolysis of **5** to **1**. The data show that (i) complete conversion of **5** to **1** occurs when the ALP concentration is $>10^6$ U/L, and (ii) the minimum ALP concentration needed to hydrolyze **[^{125}I]5** is ≥1000 U/L, a value that is 2-fold higher than the 500 U/L found in the blood of cancer patients (*29*, *42*−*48*). Consequently, such radioiodinated quinazolinone analogues are not expected to be hydrolyzed en route following their intravenous injection into cancer patients.

CONCLUSIONS

The prodrug ammonium 2-(2′-phosphoryloxyphenyl)-6-iodo-4-(3*H*)-quinazolinone exists in two forms, **5** (MW 444) and **6** (MW 426). Compound **6** is not hydrolyzed by alkaline phosphatase and has a high uptake in key nontargeted organs; its presence needs to be avoided during preparation of the radiopharmaceutical, and this can be accomplished by leaving the mixture of **3** and **4** in DMSO for at least 24 h. Compound **6** is also readily converted to **5** in the presence of DMSO. Compound **5** is stable in human serum and is completely (>99%) and rapidly (<5 min) hydrolyzed by alkaline phosphatase (1 U/μL). The concentration of ALP present in the sera of patients with cancer and/or other disease is insufficient to hydrolyze **5**. The very low uptake of **[^{125}I]5** in almost all normal organs (<0.2% ID/g) and the efficient hydrolysis by various human and mouse tumor cells indicate that the tumor-to-normal-tissue uptake ratios will be favorable. Compound **5** is highly soluble in water (7.8 mg/mL), and its hydrolysis product **1** is very insoluble in water (1.9 ng/mL), which is advantageous for trapping the precipitated drug within the interstitial spaces of solid tumors. On the basis of these in vitro cell and ex vivo tumor studies, we anticipate that radiolabeled **5** will be hydrolyzed by tumor cells and water-insoluble **1** will be retained indefinitely within solid tumors in vivo. We believe that these quinazolinone-based radiopharmaceuticals will eventually lead to the development of a novel noninvasive approach for imaging (^{123}I—SPECT; ^{124}I—PET) and treating (^{131}I) solid tumors and their metastases.

ACKNOWLEDGMENT

This work was supported in part by the U.S. Department of Defense Grants W81XWH-04-1-0499—Radiodetection and Radiotherapy of Breast Cancer (to A.I.K.) and W81XWH-06-1-0204—Radiodiagnosis and Radiotherapy of Ovarian Cancer (to A.I.K.).

LITERATURE CITED

(1) Ho, N., Harapanhalli, R. S., Dahman, B. A., Chen, K., Wang, K., Adelstein, S. J., and Kassis, A. I. (2002) Synthesis and biologic evaluation of a radioiodinated quinazolinone derivative for enzyme-mediated insolubilization therapy. *Bioconjugate Chem. 13*, 357−364.

(2) Higashino, K., Ohtani, R., Kudo, S., Hashinotsume, M., Hada, T., Kang, K.-Y., Ohkochi, T., Takahashi, Y., and Yamamura, Y. (1975) Hepatocellular carcinoma and a variant alkaline phosphatase. *Ann. Intern. Med. 83*, 74−78.

(3) Miyayama, H., Doellgast, G. J., Memoli, V., Gandbhir, L., and Fishman, W. H. (1976) Direct immunoperoxidase staining for Regan isoenzyme of alkaline phosphatase in human tumor tissues. *Cancer 38*, 1237−1246.

(4) Benham, F. J., Povey, M. S., and Harris, H. (1978) Placental-like alkaline phosphatase in malignant and benign ovarian tumors. *Clin. Chim. Acta 86*, 201−215.

(5) Dempo, K., Elliott, K. A. C., Desmond, W., and Fishman, W. H. (1981) Demonstration of gamma-glutamyl transferase, alkaline phosphatase, CEA and HCG in human lung cancer. *Oncodev. Biol. Med. 2*, 21−37.

(6) van Nagell, J. R., Jr., Donaldson, E. S., Hanson, M. B., Gay, E. C., and Pavlik, E. J. (1981) Biochemical markers in the plasma and tumors of patients with gynecologic malignancies. *Cancer 48*, 495−503.

(7) Nouwen, E. J., Pollet, D. E., Eerdekens, M. W., Hendrix, P. G., Briers, T. W., and De Broe, M. E. (1986) Immunohistochemical localization of placental alkaline phosphatase, carcinoembryonic antigen, and cancer antigen 125 in normal and neoplastic human lung. *Cancer Res. 46*, 866−876.

(8) Nouwen, E. J., Hendrix, P. G., Dauwe, S., Eerdekens, M. W., and De Broe, M. E. (1987) Tumor markers in the human ovary and its neoplasms: a comparative immunohistochemical study. *Am. J. Pathol. 126*, 230−242.

(9) Wick, M. R., Swanson, P. E., and Manivel, J. C. (1987) Placental-like alkaline phosphatase reactivity in human tumors: an immunohistochemical study of 520 cases. *Hum. Pathol. 18*, 946−954.

(10) Senter, P. D., Schreiber, G. J., Hirschberg, D. L., Ashe, S. A., Hellström, K. E., and Hellström, I. (1989) Enhancement of the *in vitro* and *in vivo* antitumor activities of phosphorylated mitomycin C and etoposide derivatives by monoclonal antibody−alkaline phosphatase conjugates. *Cancer Res. 49*, 5789−5792.

(11) Sahin, U., Hartmann, F., Senter, P., Pohl, C., Engert, A., Diehl, V., and Pfreundschuh, M. (1990) Specific activation of the prodrug mitomycin phosphate by a bispecific anti-CD30/anti-alkaline phosphatase monoclonal antibody. *Cancer Res. 50*, 6944−6948.

(12) Wallace, P. M., and Senter, P. D. (1991) In vitro and in vivo activities of monoclonal antibody−alkaline phosphatase conjugates in combination with phenol mustard phosphate. *Bioconjugate Chem. 2*, 349−352.

(13) Senter, P. D., Wallace, P. M., Svensson, H. P., Vrudhula, V. M., Kerr, D. E., Hellström, I., and Hellström, K. E. (1993) Generation of cytotoxic agents by targeted enzymes. *Bioconjugate Chem. 4*, 3−9.

(14) Mamber, S. W., Mikkilineni, A. B., Pack, E. J., Rosser, M. P., Wong, H., Ueda, Y., and Forenza, S. (1995) Tubulin polymerization by paclitaxel (taxol) phosphate prodrugs after metabolic activation with alkaline phosphatase. *J. Pharmacol. Exp. Ther. 274*, 877−883.

(15) Le Du, M. H., Stigbrand, T., Taussig, M. J., Ménez, A., and Stura, E. A. (2001) Crystal structure of alkaline phosphatase from human placenta at 1.8 Å resolution: implication for a substrate specificity. *J. Biol. Chem. 276*, 9158−9165.

(16) Jemmerson, R., Takeya, M., Shah, N., and Fishman, W. H. (1984) Tumor immunolocalization using monoclonal antibodies which bind placental alkaline phosphatase. *Prog. Clin. Biol. Res. 166*, 245−256.

(17) Davies, J. O., Davies, E. R., Howe, K., Jackson, P. C., Pitcher, E. M., Sadowski, C. S., Stirrat, G. M., and Sunderland, C. A. (1985) Radionuclide imaging of ovarian tumours with ^{123}I-labelled monoclonal antibody (NDOG2) directed against placental alkaline phosphatase. *Br. J. Obstet. Gynaecol. 92*, 277−286.

(18) Critchley, M., Brownless, S., Patten, M., McLaughlin, P. J., Tromans, P. M., McDicken, I. W., and Johnson, P. M. (1986) Radionuclide imaging of epithelial ovarian tumours with ^{123}I-labelled monoclonal antibody (H317) specific for placental-type alkaline phosphatase. *Clin. Radiol. 37*, 107−112.

(19) Epenetos, A. A., Carr, D., Johnson, P. M., Bodmer, W. F., and Lavender, J. P. (1986) Antibody-guided radiolocalisation of tumours in patients with testicular or ovarian cancer using two radioiodinated monoclonal antibodies to placental alkaline phosphatase. *Br. J. Radiol. 59*, 117−125.

(20) Kalofonos, H. P., Kosmas, C., Hird, V., Snook, D. E., and Epenetos, A. A. (1994) Targeting of tumours with murine and reshaped human monoclonal antibodies against placental alkaline phosphatase: immunolocalisation, pharmacokinetics and immune response. *Eur. J. Cancer 30A*, 1842−1850.

(21) Wang, K., Adelstein, S. J., and Kassis, A. I. (2006) Radiotracer-based method for determining water solubility of highly insoluble compounds. *J. Labelled Compd. Radiopharm. 49*, 773−788.

(22) Van Belle, H. (1976) Alkaline phosphatase. I. Kinetics and inhibition by levamisole of purified isoenzymes from humans. *Clin. Chem. 22*, 972−976.

(23) Garba, M.-T., and Marie, P. J. (1986) Alkaline phosphatase inhibition by levamisole prevents 1,25-dihydroxyvitamin D_3-stimulated bone mineralization in the mouse. *Calcif. Tissue Int. 38*, 296−302.

(24) Tobias, S. C., and Borch, R. F. (2004) Synthesis and biological evaluation of a cytarabine phosphoramidate prodrug. *Mol. Pharm. 1*, 112−116.

(25) Pospisil, P., Wang, K., Al Aowad, A. F., Iyer, L. K., Adelstein, S. J., and Kassis, A. I. (2007) Computational modeling and

experimental evaluation of a novel prodrug for targeting the extracellular space of prostate tumors. *Cancer Res. 67*, 2197−2205.
(26) Chen, K., Wang, K., Kirichian, A. M., Al Aowad, A. F., Iyer, L. K., Adelstein, S. J., and Kassis, A. I. (2006) *In silico* design, synthesis, and biological evaluation of radioiodinated quinazolinone derivatives for alkaline phosphatase-mediated cancer diagnosis and therapy. *Mol. Cancer Ther. 5*, 3001−3013.
(27) Brenckman, W. D., Jr., Lastinger, L. B., and Sedor, F. (1981) Unpredictable fluctuations in serum acid phosphatase activity in prostatic cancer. *JAMA 245*, 2501−2504.
(28) Loor, R., Wang, M. C., Valenzuela, L., and Chu, T. M. (1981) Expression of prostatic acid phosphatase in human prostate cancer. *Cancer Lett. 14*, 63−69.
(29) Eerdekens, M. W., Nouwen, E. J., Pollet, D. E., Briers, T. W., and De Broe, M. E. (1985) Placental alkaline phosphatase and cancer antigen 125 in sera of patients with benign and malignant diseases. *Clin. Chem. 31*, 687−690.
(30) Moss, D. W. (1987) Fetal intestinal alkaline phosphatase in serum and amniotic fluid. *Clin. Biochem. 20*, 393−398.
(31) Moss, D. W. (1992) Perspectives in alkaline phosphatase research. *Clin. Chem. 38*, 2486−2492.
(32) Mulders, P. F. A., Fernandez del Moral, P., Theeuwes, A. G. M., Oosterhof, G. O. N., van Berkel, H. T. H., and Debruyne, F. M. J. (1992) Value of biochemical markers in the management of disseminated prostatic cancer. *Eur. Urol. 21*, 2−5.
(33) Shih, W.-J., Gross, K., Mitchell, B., Collins, J., Wierzbinski, B., Magoun, S., and Ryo, U. Y. (1992) Prostate adenocarcinoma using Gleason scores correlates with prostate-specific antigen and prostate acid phosphatase measurements. *J. Natl. Med. Assoc. 84*, 1049−1050.
(34) Wirth, M. P., and Frohmüller, H. G. W. (1992) Prostate-specific antigen and prostatic acid phosphatase in the detection of early prostate cancer and in the prediction of regional lymph node metastases. *Eur. Urol. 21*, 263−268.
(35) Vitali, A., Ardoino, S., Durante, P., Ferro, M. A., Li Causi, F., Parodi, C., Sanguineti, G., Gaffuri, M., Paerachino, M., and Salvadori, R. P. (1994) Correlation between immunohistochemical patterns and serum levels of PSA and PSAP in prostatic pathology: evaluation of 198 prostatic fine needle biopsies. *Anticancer Res. 14*, 1503−1507.
(36) Moss, D. W., Raymond, F. D., and Wile, D. B. (1995) Clinical and biological aspects of acid phosphatase. *Crit. Rev. Clin. Lab. Sci. 32*, 431−467.
(37) Fontana, A., and Delmas, P. D. (2000) Markers of bone turnover in bone metastases. *Cancer 88*, 2952−2960.
(38) Alatas, F., Alatas, Ö., Metintas, M., Çolak, Ö., Erginel, S., and Harmanci, E. (2002) Usefulness of bone markers for detection of bone metastases in lung cancer patients. *Clin. Biochem. 35*, 293−296.
(39) Huggins, C., and Hodges, C. V. (2002) Studies on prostatic cancer I. The effect of castration, of estrogen and of androgen injection on serum phosphatases in metastatic carcinoma of the prostate. *J. Urol. 167*, 948−951.
(40) San Francisco, I. F., Olumi, A. F., Yoon, J. H., Regan, M. M., and DeWolf, W. C. (2003) Preoperative serum acid phosphatase and alkaline phosphatase are not predictors of pathological stage and prostate-specific antigen failure after radical prostatectomy. *BJU Int. 92*, 924−928.
(41) Shih, L.-Y., Shih, H.-N., and Chen, T.-H. (2004) Bone resorption activity of osteolytic metastatic lung and breast cancers. *J. Orthop. Res. 22*, 1161−1167.
(42) McComb, R. B., Bowers, G. N., Jr., and Posen, S. (1979) *Alkaline Phosphatase*, Plenum Press, New York, pp 229−287.
(43) Nouwen, E. J., Pollet, D. E., Schelstraete, J. B., Eerdekens, M. W., Hänsch, C., Van de Voorde, A., and De Broe, M. E. (1985) Human placental alkaline phosphatase in benign and malignant ovarian neoplasia. *Cancer Res. 45*, 892−902.
(44) Doellgast, G. J., and Homesley, H. D. (1984) Placental-type alkaline phosphatase in ovarian cancer fluids and tissues. *Obstet. Gynecol. 63*, 324−329.
(45) Vergote, I., Onsrud, M., and Nustad, K. (1987) Placental alkaline phosphatase as a tumor marker in ovarian cancer. *Obstet. Gynecol. 69*, 228−232.
(46) Kaplan, M. M. (1986) Serum alkaline phosphatase—another piece is added to the puzzle. *Hepatology 6*, 526−528.
(47) De Broe, M. E., and Pollet, D. E., for the hPLAP Study Group (1988) Multicenter evaluation of human placental alkaline phosphatase as a possible tumor-associated antigen in serum. *Clin. Chem. 34*, 1995−1999.
(48) Fishman, W. H. (1995) The 1993 ISOBM Abbott Award Lecture. Isozymes, tumor markers and oncodevelopmental biology. *Tumor Biol. 16*, 394−402.

BC0602937

^{64}Cu-Labeled Alpha-Melanocyte-Stimulating Hormone Analog for MicroPET Imaging of Melanocortin 1 Receptor Expression

Zhen Cheng,*,† Zhengming Xiong,†,‡ Murugesan Subbarayan,† Xiaoyuan Chen,† and Sanjiv Sam Gambhir†

Molecular Imaging Program at Stanford (MIPS), Departments of Radiology and Bioengineering, Bio-X Program, Stanford University, Stanford, California 94305-5344 and Department of Pediatrics, Tongji Medical College, Huazhong University of Science and Technology & Tongji Hospital, Wuhan, China 430030. Received October 3, 2006; Revised Manuscript Received January 3, 2007

The alpha-melanocyte-stimulating hormone (α-MSH) receptor (melanocortin type 1 receptor, or MC1R) plays an important role in the development and growth of melanoma cells. It was found that MC1R was overexpressed on most murine and human melanoma, making it a promising molecular target for melanoma imaging and therapy. Radiolabeled α-MSH peptide and its analogs that can specifically bind with MC1R have been extensively explored for developing novel agents for melanoma detection and radionuclide therapy. The goal of this study was to evaluate a ^{64}Cu-labeled α-MSH analog, Ac-Nle-Asp-His-D-Phe-Arg-Trp-Gly-Lys(DOTA)-NH_2 (DOTA−NAPamide), as a potential molecular probe for microPET imaging of melanoma and MC1R expression in melanoma xenografted mouse models. 1,4,7,10-tetraazacyclododecane-1,4,7,10-tetraacetic acid (DOTA) conjugated NAPamide was synthesized and radiolabeled with ^{64}Cu ($t_{1/2}$=12 h) in NH_4OAc (0.1 M; pH 5.5) buffered solution for 60 min at 50 °C. Cell culture studies reveal rapid and high uptake and internalization of ^{64}Cu−DOTA−NAPamide in B16F10 cells. Over 90% of receptor-bound tracer is internalized at 3 h incubation. A cellular retention study demonstrates that the receptor-bound ^{64}Cu−DOTA−NAPamide is slowly released from the B16F10 cells into the medium; 66% of the radioactivity is still associated with the cells even after 3 h incubation. The biodistribution of ^{64}Cu−DOTA−NAPamide was then investigated in C57BL/6 mice bearing subcutaneous murine B16F10 melanoma tumors with high capacity of MC1R and Fox Chase Scid mice bearing human A375M melanoma with a relatively low number of MC1R receptors. Tumor uptake values of ^{64}Cu−DOTA−NAPamide are found to be 4.63 ± 0.45% and 2.49 ± 0.31% ID/g in B16F10 and A375M xenografted melanoma at 2 h postinjection (pi), respectively. The B16F10 tumor uptake at 2 h pi is further inhibited to 2.29 ± 0.24% ID/g, while A375M tumor uptake at 2 h pi remains 2.20 ± 0.41% ID/g with a coinjection of excess α-MSH peptide. MicroPET imaging of ^{64}Cu−DOTA−NAPamide in B16F10 tumor mice clearly shows good tumor localization. However, low A375M tumor uptake and poor tumor to normal tissue contrast were observed. This study demonstrates that ^{64}Cu−DOTA−NAPamide is a promising molecular probe for α-MSH receptor positive melanoma PET imaging as well as MC1R expression imaging in living mice.

INTRODUCTION

Malignant melanoma has emerged as a significant public health problem in western countries (*1*). Currently, effective therapies are not available for treatment of metastatic melanoma. Extensive efforts have been spent to develop novel strategies for melanoma systemic treatment. For example, immunotherapy, chemotherapy, and biological therapy have been investigated intensively; however, little success has been achieved. The most important approach responsible for the improvement of survival rate of melanoma still remains early diagnosis (*2*).

Recently, peptide receptor-targeted radionuclide therapy (PRRT) has been shown to be an attractive approach for treatment of receptor-expressing tumors in preclinical and clinical settings (*3*, *4*). It was shown that the somatostatin analog, [tetraazacyclododecane-tetraacetic acid (DOTA[1]), Tyr^3] octreotide radiolabeled with ^{90}Y could effectively inhibit tumor growth in a rat subcutaneous tumor model (*5*). Complete or partial remissions were also achieved in a study using ^{177}Lu-labeled [DOTA,Tyr^3] octreotate for treating patients with gastroenteropancreatic neuroendocrine tumors (*6*). The success of using radiolabeled somatostatin analogs for tumor radiotherapy has inspired researchers to develop other radiolabeled peptides for treatment of different tumors.

It has been reported that most murine and human melanoma metastases bear up-regulated alpha-melanocyte-stimulating hormone (α-MSH) receptors (melanocortin type 1 receptor, or MC1R) (*7*, *8*). This suggests that α-MSH peptides may serve as vehicles for delivering radionuclides, fluorescent molecules, or chemotherapeutic drugs for targeting melanoma. Novel radiolabeled α-MSH analogs for melanoma imaging or therapy have been investigated, and significant progress has been achieved in this field. For example, a library of α-MSH analogs radiolabeled with ^{99m}Tc (*9*, *10*), ^{111}In (*11*−*14*, *26*, *27*), ^{125}I (*15*), ^{67}Ga (*16*), ^{86}Y (*17*), and ^{64}Cu (*17*, *18*) exhibited excellent tumor-targeting abilities and pharmacokinetic properties in xenografted or metastastic melanoma models, suggesting the potential application of these radiometals or radiohalogens labeled α-MSH peptides for melanoma detection. Most importantly, it was reported that an α-MSH peptide ReCCMSH(Arg^{11}) radiolabeled with therapeutic radionuclide, either ^{188}Re or ^{212}Pb, showed promising therapeutic effects in mice bearing either

* To whom correspondence should be addressed. Phone: 650-724-3642. Fax: 650-724-4948. E-mail: zcheng@stanford.edu.

† Stanford University.

‡ Huazhong University of Science and Technology & Tongji Hospital.

[1] Abbreviations: α-MSH, alpha-melanocyte-stimulating hormone; melanocortin type 1 receptor, MC1R; DOTA, 1,4,7,10-tetraazacyclododecane-1,4,7,10-tetraacetic acid; PET, positron emission tomography; SPECT, single-photon emission spectroscopy; HPLC, high-performance liquid chromatography; 2-deoxy-2-[^{18}F]fluoro-D-glucose ([^{18}F]FDG); pi, postinjection.

10.1021/bc060306g CCC: $37.00 © 2007 American Chemical Society
Published on Web 03/10/2007

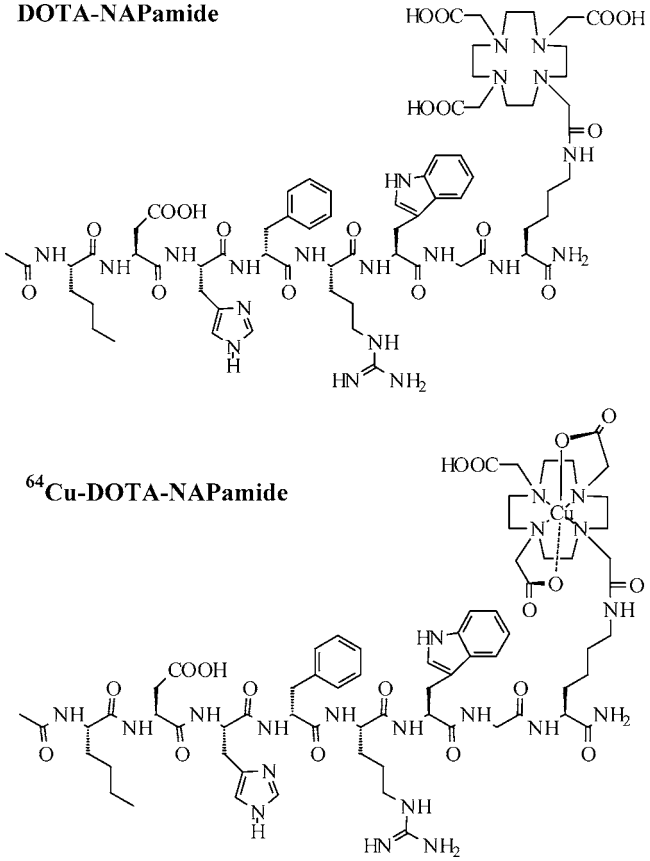


Figure 1. Schematic structures of DOTA−NAPamide and ^{64}Cu−DOTA−NAPamide.

B16F1 murine or TXM13 human xenografted melanoma (*19*, *20*). These results highlight the possibility of using α-MSH peptide tagged with therapeutic radionuclides for metastatic melanoma therapy.

However, it was found that on different human and murine melanoma cell lines the receptor number of MC1R ranged from as low as undetectable to around 10 000 (*7*). Considering the density of MC1R is one of the major factors that ultimately determine the uptake of the MC1R ligand in melanoma, to develop a noninvasive imaging tool with an ability to visualize the MC1R expression in living subjects will be very useful. This type of molecular probe may eventually render us the power to not only diagnose melanoma early but also screen patients suitable for PRRT strategy. To this end, an α-MSH analog, Ac-Nle-Asp-His-D-Phe-Arg-Trp-Gly-Lys(DOTA)-NH_2 (DOTA−NAPamide, *16*), was radiolabeled with a positron emitter ^{64}Cu ($t_{1/2}$ = 12.7 h, $E_{\beta^+\text{max}}$ = 656 keV, 19%) (Figure 1). The ability of ^{64}Cu−DOTA−NAPamide to image the MC1R expression using micropositron emission tomography (microPET) was further evaluated on two melanoma mice models with different MC1R densities.

MATERIALS AND METHODS

General. DOTA was obtained from Macrocyclics Inc. (Richardson, TX). NAPamide was synthesized with over 95% purity by the Stanford Protein and Nucleic Acid Biotechnology Facility using standard 9-fluorenylmethyloxycarbonyl (Fmoc)/*O*-benzotriazolyl-tetramethyluronium hexafluorophosphate (HBTU) chemistry on rink amide MBHA resin. All other chemicals were obtained from Sigma-Aldrich Chemical Co. (St. Louis, MO). ^{64}Cu was provided by the Washington University School of Medicine (St. Louis, MO). A CRC-15R PET dose calibrator (Capintec Inc., Ramsey, NJ) was used for all radioactivity measurements. Reverse-phase high-performance liquid chromatography (RP-HPLC) was performed on a Dionex Summit HPLC system (Dionex Corp., Sunnyvale, CA) equipped with a 170U 4-Channel UV−vis absorbance detector and radioactive detector (Carroll & Ramsey Associates, model 105S, Berkeley, CA). UV detection wavelengths were 218, 254, and 280 nm for all experiments. Both semipreparative (Zorbax SB-C18, 9.4 mm × 250 mm) and analytical (Dionex Acclaim120 C18, 4.6 mm × 250 mm) RP-HPLC columns were used. The mobile phase was solvent A, 0.1% trifluoroacetic acid (TFA)/H_2O, and solvent B, 0.1% TFA/acetonitrile. Matrix-assisted laser desorption/ionization time-of-flight mass spectrometry (MALDI-TOF-MS) was performed on a Perseptive Voyager-DE RP Biospectrometry instrument (Framingham, MA) by the Stanford Protein and Nucleic Acid Biotechnology Facility. Alpha-cyano-4-hydroxy-cinnamic acid (α-CHCA, prepared as 10 g/L in 33.3% CH_3CN:33.3% EtOH:33.3% H_2O:0.1% TFA) was used as solid matrix. A375M cell line was a generous gift from Dr. M. Kolodny; University of California, Los Angeles, CA, and B16/F10 murine melanoma cells were obtained from the American Type Tissue Culture Collection. C57BL/6 and Fox chase scid mice were purchased from Charles River Laboratories (Boston, MA).

Chemistry and Radiochemistry. DOTA was conjugated with NAPamide in a manner similar to that described before (*21*). Briefly, DOTA, 1-ethyl-3-[3-(dimethylamino)propyl]carbodiimide (EDC), and *N*-hydroxysulfonosuccinimide (SNHS) at a molar ratio of 1:1:0.8 were mixed and incubated at 4 °C for 30 min (pH = 5.5). NAPamide was then added to the in-situ-prepared sulfosuccinimidyl ester of DOTA (DOTA−OSSu) in a theoretical stoichiometry of 5:1. The reaction solution was mixed and reacted at 4 °C overnight (pH 8.5−9.0). The resulting DOTA−NAPamide conjugate was then purified by HPLC on a semipreparative C-18 column. The flow rate was 3 mL/min, with the mobile phase starting from 95% solvent A and 5% solvent B (0−3 min) to 35% solvent A and 65% solvent B at 33 min, then going to 85% solvent B and 15% solvent A (33−36 min), maintaining this solvent composition for another 3 min (36−39 min), and returning to initial solvent composition by 42 min. Fractions were collected and lyophilized. The target product was characterized by MALDI-TOF-MS and ready for use in the radiolabeling reactions. Analytic HPLC was performed on the same HPLC system using a C-18 analytical column and flow rate of 1 mL/min.

The DOTA−NAPamide was radiolabeled with ^{64}Cu by addition of 185 MBq (5 mCi) $^{64}CuCl_2$ (2 μg of peptide per 37 MBq ^{64}Cu) in 0.1 N NaOAc (pH 5.5) buffer followed by a 1 h incubation at 50 °C. The reaction was then terminated by adding 5 μL of TFA, and radiolabeled complex was purified by analytical radio-HPLC. The flow rate was 1 mL/min, with the mobile phase starting from 80% solvent A and 20% solvent B (0−3 min) to 70% solvent A and 30% solvent B at 33 min, then going to 85% solvent B and 15% solvent A (33−36 min), maintaining this solvent composition for another 3 min (36−39 min), and returning to initial solvent composition by 42 min. Purified radiolabeled peptide was dried by a rotary evaporator. The radiolabeled compound was reconstituted in phosphate-buffered saline (PBS) and passed through a 0.22 μm Millipore filter into a sterile vial for in vitro and animal experiments.

The nonradioactive ^{nat}Cu−DOTA−NAPamide was also synthesized by mixing DOTA−NAPamide (400 μg, 0.269 μmol) with high-purity natural copper chloride ($CuCl_2$, 55 μg, 0.409 μmol) in 0.1 N NaOAc (pH 5.5) buffer followed by 2 h incubation at 70 °C. The product was purified by HPLC and confirmed by MALDI-TOF−MS.

Octanol/Water Partition Coefficient. To determine the lipophilicity of ^{64}Cu−DOTA−NAPamide, approximately 370

kBq of ^{64}Cu-labeled complex in 500 μL of PBS (pH 7.4) was added to 500 μL of octanol in an Eppendorf microcentrifuge tube. The resulting biphasic system was mixed vigorously for 10 min and left at room temperature for another 60 min. The two phases were then separated by centrifugation at 2000 *g* for 5 min (model 5415R Eppendorf microcentrifuge; Brinkman, Westbury, NY). From each layer an aliquot of 100 μL was removed and counted in a γ-counter (Packard Instruments). The partition coefficient (log *P*) was then calculated as a ratio of counts in the octanol fraction to the counts in the water fraction. The experiment was repeated 3 times.

In Vitro Cell Assays. B16F10 murine and A375M human melanoma cells were cultured in Dulbecco's Modified Eagle Medium (DMEM) high glucose medium, which was supplemented with 10% heat-inactivated fetal bovine serum (FBS), 2 mM L-glutamine, and 48 mg of gentamicin. The cells were expanded in 75-cm^2 tissue culture flasks and kept in a humidified atmosphere of 5% CO_2 at 37 °C, with the medium changed every other day. A confluent monolayer was detached with trypsin and dissociated into a single-cell suspension for further cell culture.

The in vitro cell binding assays were performed with the murine melanoma cell line B16F10 as previously described (*7*−*9*). Briefly, cells were seeded at a density of 0.2 million/well in 24-well tissue culture plates and allowed to attach overnight. Following a wash with the binding medium [Modified Eagle's Media with 25 mM HEPES, 0.2% bovine serum albumin (BSA), and 0.3 mM 1,10-phenanthroline], the cells were incubated at 25 °C for 2 h with either DOTA−NAPamide or ^{nat}Cu−DOTA−NAPamide (peptide concentration varying from 10^{-12} to 10^{-6} M) and approximately 50 000 counts per minute (cpm) of ^{125}I-(Tyr^2)- [Nle,^{4}D-Phe^7]-α-MSH [^{125}I-(Tyr^2)-NDP] in 0.5 mL of binding media. The cells were rinsed twice with 0.01 M PBS (pH 7.4)/0.2% BSA and lysed in 0.5 mL of 1.0 M NaOH for 5 min, and the radioactivity of the cells was measured. The data was analyzed using the ORIGIN6.0 computer program (Northampton, MA), and the IC_{50} values, the concentration of competitor required to inhibit 50% of radioligand binding, of the DOTA−NAPamide and ^{nat}Cu−DOTA−NAPamide were calculated.

A typical saturation binding experiment was performed to determine the MC1R densities on the A375M and B16F10 melanoma cells. The cells (1×10^6) were incubated in 0.15 mL of binding medium in the presence of ^{125}I-(Tyr^2)-NDP ranging from approximately 2×10^3 to 2×10^6 cpm per tube with and without 10^{-6} M NDP for 2 h at 37 °C. The radioactivity of bound and free radioligand was counted. The data were analyzed by ORIGIN6.0, and the binding capacities of the B16F10 and A375M were calculated.

Cell uptake, internalization, and cellular retention of the ^{64}Cu−DOTA−NAPamide were examined in B16F10 cells using the method described previously (*15*). Briefly, in 24-well tissue plates prepared as described above, approximately 170 000 dpm of ^{64}Cu-labeled peptide (76.5 nCi, 0.283 ng, 0.38 nM) in 0.5 mL of binding media were added to each well containing cells and incubated at 37 °C for 5 min to 3 h. The nonspecific binding was determined by coincubation with nonradiolabeled NDP at a final concentration of 10 μM. Internalization of the radiolabeled peptide was determined by washing the cells with acidic buffer [40 mM sodium acetate (pH 4.5) containing 0.9% NaCl and 0.2% BSA] to remove the membrane-bound radiocomplex and then measuring the remaining internalized radioactivity. The cellular retention properties of the membrane-bound and internalized ^{64}Cu-labeled peptides were determined by incubating B16F10 cells in binding media at 37 °C with the radiolabeled complexes for 3 h. The binding media were then removed, the cells were washed twice with cold 0.01 M PBS (pH 7.4)/0.2% BSA, 0.5 mL of culture media was added, and radioactivity released into the media was monitored at various time points over a 3-h incubation period.

Animal Biodistribution Studies. All animal studies were carried out in compliance with Federal and local institutional rules for the conduct of animal experimentation. C57 BL/6 female mice, 7−8 weeks old, were inoculated subcutaneously in the right shoulder with 1×10^6 cultured B16/F10 murine melanoma cells. Nine to ten days postinoculation, the tumors grew to a weight of ∼500 mg and the tumor-bearing mice were subject to in vivo biodistribution and imaging studies, while 6 week old Fox chase ICR Scid mice were inoculated with 4×10^6 A375M human melanoma cells. Three to four weeks postinoculation, the mice bearing A375M tumors were ready for further studies.

For biodistribution studies the C57 BL/6 mice bearing B16F10 mouse melanoma and Fox chase mice bearing A375M human melanoma ($n = 4$ for each group) were injected with 703−777 KBq (19−21 μCi, 70−78 ng) of ^{64}Cu−DOTA−NAPamide with (blocking group, $n = 3$) or without coinjection of 200 μg of NDP through the tail vein and sacrificed at different time points from 30 min to 24 h postinjection (pi). Tumor and normal tissues of interest were removed and weighed, and their radioactivity was measured in a gamma counter. The radioactivity uptake in the tumor and normal tissues was expressed as a percent of the injected radioactive dose per gram of tissue (% ID/g).

MicroPET Imaging. PET imaging of tumor-bearing mice was performed on a microPET R4 rodent model scanner (Concorde Microsystems Inc., Knoxville, TN). The mice bearing B16F10 and A375M melanoma were injected with about 4.44 MBq (120 μCi) of ^{64}Cu−DOTA−NAPamide via the tail vein. At 120 min postinjection, the mice were anesthetized with 2% isoflurane and placed in the prone position and near the center of the field of view of microPET. The 10-min static scans were obtained, and the images were reconstructed by a two-dimensional ordered subsets expectation maximum (OSEM) algorithm. Regions of interest (ROIs) were then drawn over the tumor on decay-corrected whole-body coronal images. The counts per pixel per minute were obtained from the ROI and converted to counts per milliliter per minute using a calibration constant. By assuming a tissue density of 1 g/mL, the ROIs were converted to counts/g/min. An image ROI-derived % ID/g of tissue was then determined by dividing counts per gram per minute with injected dose (ID).

Statistical Method. Statistical analysis was performed using the Student's *t*-test for unpaired data. A 95% confidence level was chosen to determine the significance between groups, with $P < 0.05$ being significantly different.

RESULTS

Chemistry and Radiochemistry. Synthesis of DOTA−NAPamide conjugate (Figure 1) was achieved through coupling of in-situ-prepared DOTA−OSSu ester with the ϵ-amino group of the lysine residue in the NAPamide. The desired product was purified by semipreparative HPLC, and the purity of the target compound was generally obtained in 70% yield with over 95% purity. The retention time on analytical HPLC for DOTA−NAPamide was found to be 19.1 min. The purified DOTA−NAPamide was characterized by MALDI-TOF-MS. The measured molecular weight (MW) was consistent with the expected MW: $m/z = 1485.97$ for $[M + H]^+$ ($C_{68}H_{101}N_{20}O_{18}$, calcd MW = 1485.75). For ^{nat}Cu−DOTA−NAPamide, MW was measured as 1546.36 for $[M + H]^+$ ($C_{68}H_{99}CuN_{20}O_{18}$, calcd MW = 1546.67).

DOTA−NAPamide conjugate was then successfully labeled with ^{64}Cu at 50 °C for 1 h incubation. The purification of radiolabeling solution using RP-HPLC afforded ^{64}Cu−DOTA−

NAPamide with >95% radiochemical purity. Under several of HPLC conditions tested in this study, separation of ^{64}Cu−DOTA−NAPamide and unlabeled DOTA−NAPamide was not achieved. A modest specific activity of 0.4 Ci/μmol (14.8 MBq/nmol, 270 μCi/μg) ^{64}Cu−DOTA−NAPamide was obtained as determined by analytic HPLC (decay corrected). The specific activity of the tracer prepared in this research is very close to that of another ^{64}Cu-labeled α-MSH analog, ^{64}Cu−DOTA−ReCCMSH(Arg^{11}) (300 μCi/μg) which was reported recently (*17*). From the octanol−water partition coefficient measurements the log *P* value of tracer was determined to be −1.15 ± 0.01, indicating intermediate hydrophilicity of this compound.

In Vitro Receptor-Binding Assay and Biological Activity. A typical saturation binding experiment was performed to determine the MC1R densities on A375M and B16F10 melanoma cells. The cells (1×10^6) were incubated in 0.15 mL of binding medium in the presence of ^{125}I-(Tyr^2)-NDP ranging from approximately 2×10^3 to 2×10^6 cpm per tube with and without 10^{-6} M NDP for 2 h at 37 °C. The radioactivity of bound and free radioligand was counted. The data were analyzed by ORIGIN6.0, and the binding capacity of B16F10 and A375M were calculated to be 21 687 ± 4171 and 400 ± 93 (sites/cell ± SD), respectively.

The receptor-binding affinity study of peptides for MC1R was performed using B16F10 cells. The IC_{50} values of DOTA−NAPamide and ^{nat}Cu−DOTA−NAPamide were determined to be 2.67 ± 0.23 and 3.66 ± 0.29 nM, respectively, from the competitive receptor binding assay (Figure 2A). The IC_{50} value of DOTA−NAPamide is very close to what is reported in the literature (1.19 ± 0.19 nM, determined by using B16F1 cells) (*14*). Furthermore, the binding affinity of DOTA−NAPamide is only slightly reduced by chelation with Cu. Figure 2B shows the cell binding and internalization of ^{64}Cu−DOTA−NAPamide in B16F10 cells at 37 °C over a 3 h incubation period. The cell binding observed for the radiolabeled peptide steadily increased over the 3-h incubation time, and it reached a plateau 4.7% at 3 h. The ^{64}Cu−DOTA−NAPamide showed rapid internalization with approximately 73% internalization of the receptor-bound radiolabeled complexes within 5 min of incubation, while around 94% of receptor-bound tracer was internalized at 3-h incubation. Cellular retention of the radiolabeled complex as a function of time is shown in Figure 2C. The receptor-bound ^{64}Cu−DOTA−NAPamide slowly released from the cells into the medium, with 66% of the radioactivity still associated with the cells even after 3 h incubation.

Biodistribution Studies. The in vivo biodistribution of ^{64}Cu−DOTA−NAPamide was examined with both the B16F10 mouse melanoma and the A375M human melanoma tumor-bearing mouse model. Biodistribution of the radiolabeled peptide at 1, 2, 4, and 24 h was obtained in the B16F10 mouse model (Figure 3A), while 2 and 24 h biodistribution data was obtained in the A375M melanoma model (Figure 3B). In both tumor models the radiolabeled complex displayed rapid blood clearance; 0.97 ± 0.47% and 1.33 ± 0.34% ID/g blood uptake was observed at 2 h pi for B16F10 and A375M tumor bearing mice, respectively. Rapid and moderate activity accumulation in the high MC1R expressing B16F10 tumors was observed at early time points (3.69 ± 0.28% ID/g at 1 h pi). Tumor uptake slowly increased to 4.63 ± 0.45% ID/g at 2 h pi and 4.43 ± 0.94% ID/g at 4 h pi, then the activity was slowly washed out from the tumor, and uptake dropped to 1.67 ± 0.58% ID/g over 24 h (Figure 3A). While for the A375M tumor with low MC1R expression, tumor uptake was 2.49 ± 0.31% ID/g at 2 h pi (Figure 3B), which was significantly lower than the uptake of ^{64}Cu−DOTA−NAPamide in the B16F10 tumor model ($P < 0.05$). Furthermore, the in vivo specificity of ^{64}Cu−DOTA−NAPamide tumor uptake was investigated by coinjection of 200 μg of nonradiolabeled NDP with the radiolabeled peptide complex to the A375M melanoma-bearing Fox Chase ICR Scid mice and B16F10 melanoma-bearing C57 mice at 2 h. In the B16F10 tumor model, coinjection of NDP specifically reduced the tumor uptake of ^{64}Cu−DOTA−NAPamide from 4.63 ± 0.45 to 2.29 ± 0.24 (% ID/g; $P < 0.05$) without changing the distribution of ^{64}Cu−DOTA−NAPamide in most of the normal tissues studied (Figure 4). However, coinjection of NDP with radiolabeled peptide did not reduce uptake of ^{64}Cu−DOTA−NAPamide in the A375M tumor (2.49 ± 0.31% ID/g for nonblocking versus 2.20 ± 0.41% ID/g for blocking) at 2 h pi.

For both tumor models ^{64}Cu−DOTA−NAPamide displayed high accumulation and retention in the liver. It was observed that 12.17 ± 2.00% and 4.53 ± 1.19% ID/g remaining was still in the liver at 24 h pi for A375M and B16F10 tumor mice model, respectively. High renal activity accumulation was also observed at all times in both tumor models (Figure 3A and B).

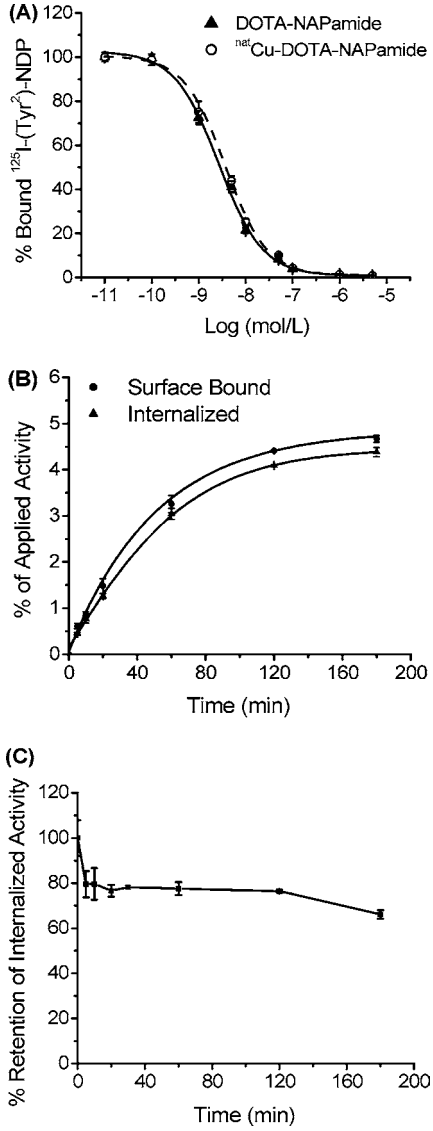


Figure 2. (A) In vitro inhibition of ^{125}I-(Tyr^2)-NDP binding to MC1R on murine B16F10 melanoma cell line by DOTA−NAPamide (IC_{50} = 2.67 ± 0.23 nmol/L) and ^{nat}Cu−DOTA−NAPamide (IC_{50} = 3.66 ± 0.29 nmol/L). Results expressed as percent of binding are mean of triplicate measurement ± standard deviation. (B) Cell binding and internalization over time for ^{64}Cu−DOTA−NAPamide with B16/F10 cells at 37 °C. Surface-bound radioactivity and internalized activity are expressed as a percent of total applied activity. (C) Percent retention of internalized ^{64}Cu−DOTA−NAPamide radioactivity in B16/F10 cells over time at 37 °C.

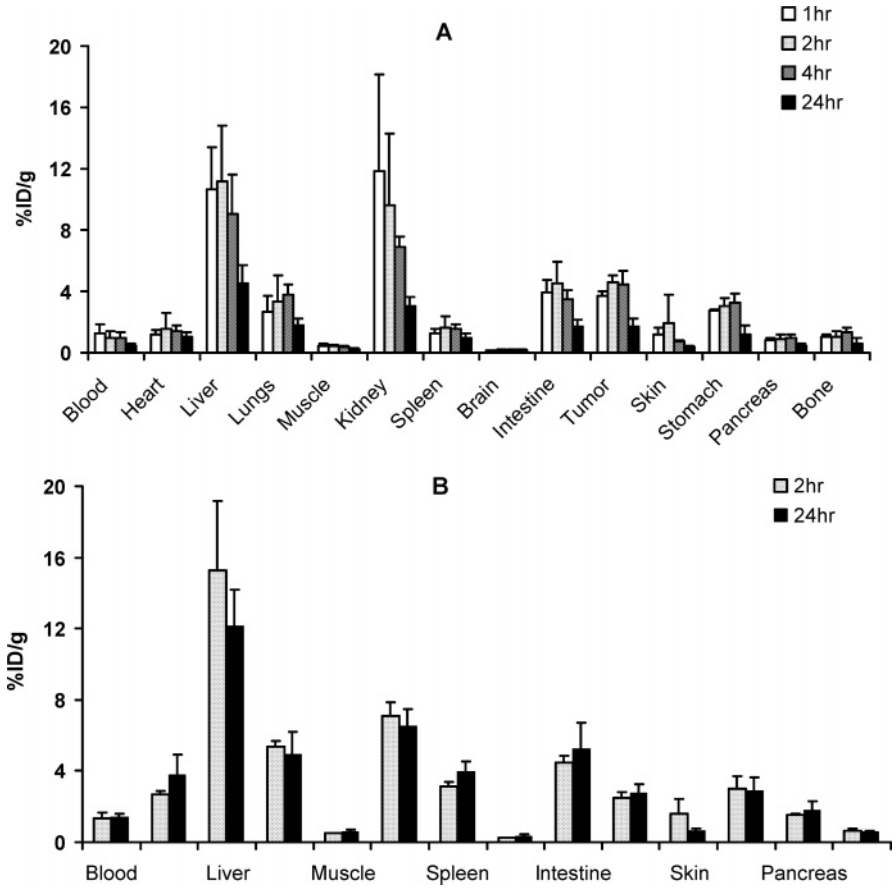


Figure 3. (A) Biodistribution data for ^{64}Cu−DOTA−NAPamide in C57 mice bearing subcutaneously xenotransplanted B16F10 murine melanoma (A) and Fox Chase ICR Scid mice bearing A375M human melanoma (B). Data are expressed as the percent administered activity (injected dose) per gram of tissue (% ID/g) ($n = 4$). ^{64}Cu−DOTA−NAPamide exhibited significantly higher uptake in B16F10 at 2 h postinjection than in A375M ($P < 0.05$).

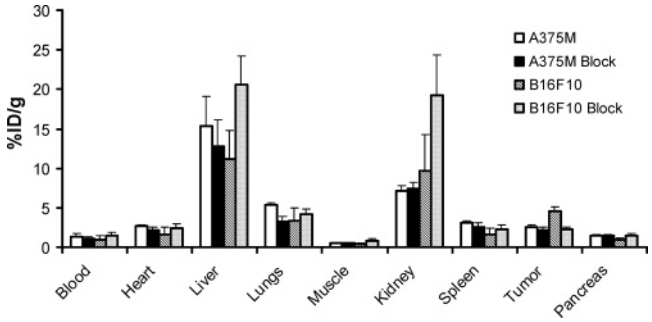


Figure 4. Receptor-blocking study: biodistributions of ^{64}Cu−DOTA−NAPamide in A375M melanoma-bearing Fox Chase ICR Scid mice and B16F10 melanoma-bearing C57 mice at 2 h with and without coinjection of 200 μg of NDP as a blocking agent. Significant inhibition of uptake in B16F10 melanoma ($P < 0.0015$), while not in A375M melanoma ($P > 0.05$), was observed. Data are expressed as normalized accumulation of activity in % ID/g ± SD ($n = 3$ for each group).

MicroPET Imaging. Decay-corrected coronal (top) and transaxial (bottom) microPET images of mouse bearing A375M tumor on the right shoulder and mouse bearing B16F10 tumor at 1, 2, and 4 h after tail veil injection of 4.44 MBq (120 μCi) ^{64}Cu−DOTA−NAPamide are shown in the Figure 5A and C, respectively. Although the radioactivity accumulation in the liver and kidney are quite high, the B16F10 tumor is still clearly visualized with good tumor to contralateral background contrast at 1−4 h pi. However, lower uptake in A375M tumor was observed, resulting in poor tumor to normal tissue contrast. Quantification of activity accumulation in the A375M and B16F10 melanoma and major organs (Figure 5B and D) agreed well with the biodistribution results.

DISCUSSION

Molecular imaging of cancer is a fast-growing research field (*22*). Molecular imaging technologies have demonstrated great benefits for better understanding cancer biology as well as facilitating cancer drug development and cancer early detection (*22, 23*). Development of novel imaging methods and molecularly targeted probes will allow us to not only locate a tumor but also visualize the expression and activity of specific molecular targets and biological processes in a tumor. Currently, 2-deoxy-2-[^{18}F]fluoro-D-glucose ([^{18}F]FDG) is widely used in malignant melanoma diagnosis and staging in clinic. The molecular targets for [^{18}F]FDG are glucose transporters (e.g., GLUT1), and hexokinase. [^{18}F]FDG only provides the glucose metabolic activity of a tumor (*24*). MC1R plays an important role in the proliferation and differentiation of melanocytes as well as in the development and growth of melanoma cells. It is also considered as a genetic linker to skin cancer (*25*). Overexpression of MC1R in melanoma cells makes it a promising molecular target for melanoma imaging and therapy. Thus, it is important to develop a PET molecular probe for imaging MC1R expression in living subjects.

Several α-MSH analogs which can recognize the MC1R have been labeled with different radionuclides for melanoma detection and radiotherapy (*9*−*20*, *26*−*28*). The most promising melanoma-targeting peptides are linear peptide NAPamide (*16*) and rhenium-cyclized CCMSH peptides (*9*, *11*, *15*). NAPamide is a short peptide with only eight amino acid residues. It can be easily synthesized in high yield and purity using the conventional solid-phase peptide synthesis and Fmoc/HBTU chemistry. Conjugating the peptide with metal chelate, DOTA, can also be easily achieved through reaction between the Lys^8 ϵ-amino

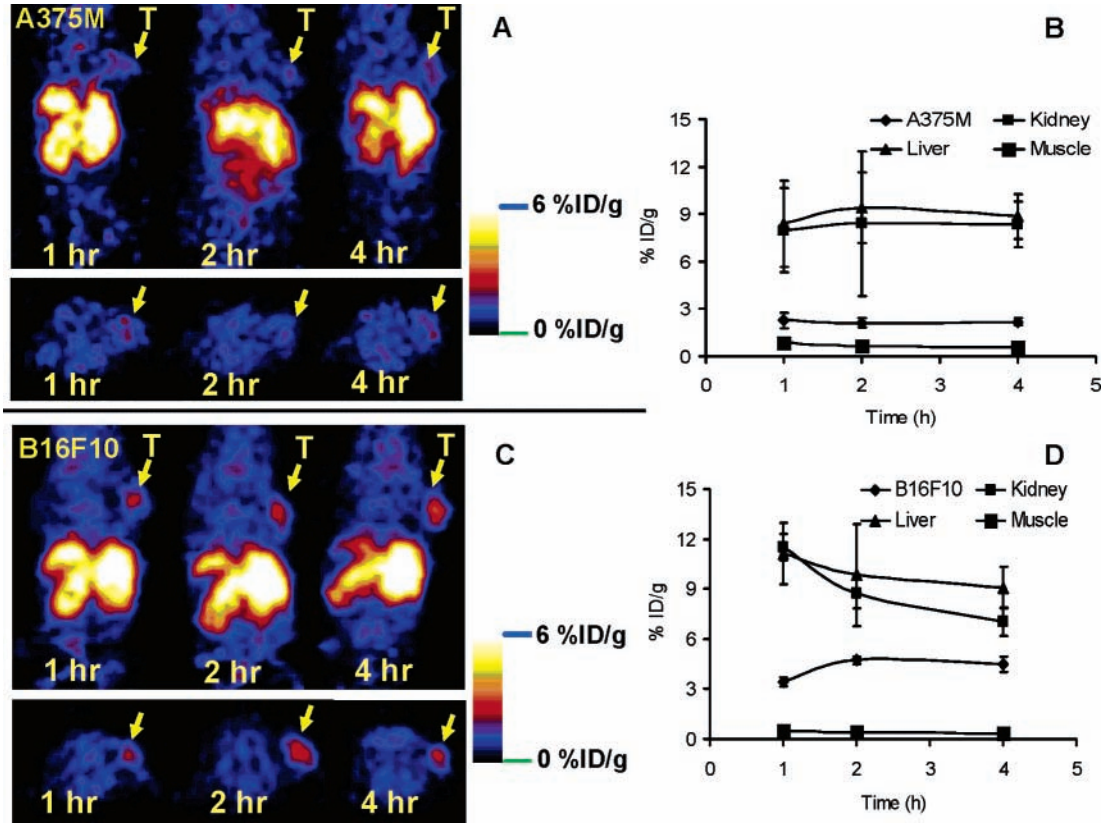


Figure 5. Decay-corrected coronal (top) and transaxial (bottom) microPET images of Fox Chase ICR Scid mouse bearing A375M tumor on the right shoulder (A) and C57 mouse bearing B16F10 tumor (C) at 1, 2, and 4 h after tail veil injection of (4.44 MBq, 120 μCi) ^{64}Cu−DOTA−NAPamide. Arrows indicate location of tumors (T). Time activity curves derived from the multitime point microPET imaging of mice bearing A375M (B) and B16F10 (D) melanoma. The regions of interest (ROIs) are shown as mean % ID/g ± SD ($n = 3$).

group in the NAPamide and in-situ-activated DOTA in buffered solution. The resulting DOTA−NAPamide conjugate as well as Cu-coordinated ligand (^{nat}Cu−DOTA−NAPamide) displays high binding affinity to MC1R (Figure 2A). ^{111}In- and ^{67}Ga-labeled DOTA−NAPamide exhibit high tumor, moderate kidney, and low blood uptake at 4 h pi (*16*). ^{64}Cu is a positron emitter that can be readily produced using a medical cyclotron. Its intermediate half-life makes it suitable for small peptide radiolabeling (*29*−*33*). Considering all of these advantages, we hypothesized that radiolabeling DOTA−NAPamide with ^{64}Cu would generate a novel molecular probe for routine PET imaging of melanoma and MC1R expression.

Subsequently, ^{64}Cu−DOTA−NAPamide was prepared and its MC1R targeting ability evaluated in cell culture and in vivo. Murine melanoma cell line B16F10 and human melanoma cell line A375M were then used in biological studies because they express different levels of MC1R ($B_{max} = 2.2 \times 10^4$ and 400 receptors/cell for B16F10 and A375M, respectively). In vitro B16F10 cell studies show that ^{64}Cu−DOTA−NAPamide specifically binds to MC1R and reaches a plateau at 3 h incubation. The majority of receptor-bound radiolabeled complexes are rapidly internalized from 5 min to 3 h incubation (Figure 2B). A cellular retention study demonstrates that the receptor-bound ^{64}Cu−DOTA−NAPamide is slowly washed out from cells, with 66% of the radioactivity still associated with the cells even after 3 h incubation. These results are quite similar to the results of cell uptake, internalization, and retention of ^{99m}Tc−CCMSH reported previously (*9*). The high MC1R binding and internalization property of ^{64}Cu−DOTA−NAPamide in cell culture justifies its further evaluation in animal models.

In vivo biodistribution studies show that ^{64}Cu−DOTA−NAPamide possesses reasonable uptake in high MC1R expression B16F10 melanoma at 1−24 h pi (Figure 3A) and that the maximum uptake of 4.63 ± 0.45% ID/g is achieved at 2 h pi. When coinjected with a large amount of NDP peptide, accumulation of the tracer at 2 h pi is reduced by 50% (Figure 4), demonstrating the specific accumulation of the tracer. More interestingly, the tracer uptake in low MC1R expression A375M tumor at 2 h pi is around 50% uptake of B16F10 tumor. Coinjection of NDP cannot inhibit tracer uptake in A375M tumor. These data indicate that the 2.49% ID/g uptake of A375M at 2 h pi is likely nonspecific accumulation. We also observe increased liver and kidney uptake values in the B16F10 blocked mice group compared to B16F10 group in this research. It is possible that the large amount of NDP peptide used in this study (200 vs 20 μg used in ref *17*) may play a role in altering the biodistribution of the tracer in the kidney and liver. Further studies are needed to confirm and elucidate this phenomenon.

High accumulation and retention of ^{64}Cu−DOTA−NAPamide in the liver is observed in both B16F10 and A375M tumor models (Figure 3A and B). This can be explained by the release of uncoordinated ^{64}Cu from radiolabeled peptide by decomposition in the blood or transchelation in the liver. Better chelation systems for ^{64}Cu such as TETA (1,4,8,11-tetraazacyclotetradecane-*N*,*N*′,*N*″,*N*‴-tetraacetic acid) or cross-bridged cyclam ligands may improve the metal−chelate stability and subsequently improving the biodistribution (*34*−*35*). Similar to other radiometal-labeled peptides (*9*, *11*, *17*, *21*, *30*), high renal activity accumulation and retention of ^{64}Cu−DOTA−NAPamide is also observed in both tumor models (Figure 3A and B). This could possibly be decreased by the use of L- or D-lysine without affecting tumor attention (*9*, *15*) in order to achieve a better kidney to normal tissue ratio and reduce radiation dose to the tested subject.

The biodistribution of ^{111}In- and ^{67}Ga-labeled DOTA−NAPamide was evaluated in the study using B6D2F1 mice

bearing B16F1 melanoma (*16*). Both ^{111}In- and ^{67}Ga-labeled DOTA−NAPamide exhibit high tumor uptake and rapid clearance from normal tissue. For example, ^{111}In- and ^{67}Ga-labeled DOTA−NAPamide display 7.56 ± 0.51 and 9.43 ± 1.06% ID/g tumor uptake at 4 h pi, respectively. The uptake values for normal tissues such as liver, lung, spleen, and muscle are all below 0.45% ID/g at 4 h pi (*16*). In contrast, ^{64}Cu-labeled DOTA−NAPamide shows lower B16F10 tumor uptake (for example, 4.43 ± 0.94% ID/g at 4 h pi) but higher uptake and retention in normal tissues when used in C57 BL/6 mice bearing B16F10 murine melanoma. The observation that the α-MSH peptide labeled with different radiometals can change their in vivo properties has been reported before (*17*). It is generally believed that the charge of the radiopeptide and the in vivo stability of the metal−chelate are responsible for their different in vivo behaviors. Our results reported here further highlight the importance of selecting the appropriate radiometal for peptide labeling so that the best tracer can be developed for molecular target imaging.

MicroPET imaging and quantification analysis of ^{64}Cu−DOTA−NAPamide in mice bearing A375M or B16F10 tumor 1, 2, and 4 h after tail veil injection reveal moderate B16F10 tumor-to-background, while the A375M tumor-to-background ratio is low (Figure 5). These results are consistent with the finding obtained from the biodistribution studies. Therefore, in addition to early detection of α-MSH receptor positive melanoma, it is also possible to differentiate melanoma with different MC1R densities in living subjects using the molecular probe ^{64}Cu−DOTA−NAPamide in conjunction with quantitative PET imaging technology. Future research is needed to further evaluate whether this tracer can help in selection of patients for anti-MC1R treatment.

In conclusion, ^{64}Cu−DOTA−NAPamide demonstrates high cell uptake, internalization, and retention in MC1R high expression melanoma. Biodistribution and microPET imaging studies show moderate specific uptake in a B16F10 melanoma model with high MC1R density while a low uptake in A375M melanoma with low MC1R capacity. ^{64}Cu−DOTA−NAPamide is a promising molecular probe for PET imaging MC1R expression in living subjects.

ACKNOWLEDGMENT

This work was supported, in part, by the National Cancer Institute (NCI) Small Animal Imaging Resource Program (SAIRP) (grant R24 CA93862) and NCI In Vivo Cellular Molecular Imaging Center (ICMIC) (grant P50 CA114747, S.S.G.). Production of ^{64}Cu at the Washington University School of Medicine is supported by the NCI (grant R24 CA86307).

LITERATURE CITED

(1) Jemal, A., Murray, T., Ward, E., Samuels, A., Tiwari, R. C., Ghafoor, A., Feuer, E. J., and Thun, M. J. (2005) Cancer statistics, 2005. *CA Cancer J. Clin. 55*, 10−30.

(2) Thompson, J. F., Scolyer, R. A., and Kefford, R. F. (2005) Cutaneous melanoma. *Lancet 365*, 687−701.

(3) Krenning, E. P., Kwekkeboom, D. J., Valkema, R., Pauwels, S., Kvols, L. K., and De Jong, M. (2004) Peptide receptor radionuclide therapy. *Ann. N.Y. Acad. Sci. 1014*, 234−45.

(4) Reubi, J. C., Macke, H. R., and Krenning, E. P. (2005) Candidates for peptide receptor radiotherapy today and in the future. *J. Nucl. Med. 46* (Suppl 1), 67S−75S.

(5) de Jong, M., Breeman, W. A., Bernard, B. F., Bakker, W. H., Visser, T. J., Kooij, P. P., van Gameren, A., and Krenning, E. P. (2001) Tumor response after [^{90}Y-DOTA(0),Tyr^3] octreotide radionuclide therapy in a transplantable rat tumor model is dependent on tumor size. *J. Nucl. Med. 42*, 1841−6.

(6) Kwekkeboom, D. J., Bakker, W. H., Kam, B. L., Teunissen, J. J., Kooij, P. P., de Herder, W. W., Feelders, R. A., van Eijck, C. H., de Jong, M., Srinivasan, A., Erion, J. L., and Krenning, E. P. (2003) Treatment of patients with gastro-entero-pancreatic (GEP) tumours with the novel radiolabelled somatostatin analogue [^{177}Lu-DOTA-(0),Tyr^3]octreotate. *Eur. J. Nucl. Med. Mol. Imaging 30*, 417−22.

(7) Siegrist, W., Solca, F., Stutz, S., Giuffre, L., Carrel, S., Girard, J., and Eberle, A. N. (1989) Characterization of receptors for alpha-melanocyte-stimulating hormone on human melanoma cells. *Cancer Res. 49*, 6352−8.

(8) Siegrist, W., Stutz, S., and Eberle, A. N. (1994) Homologous and heterologous regulation of alpha-melanocyte-stimulating hormone receptors in human and mouse melanoma cell lines. *Cancer Res. 54*, 2604−10.

(9) Chen, J., Cheng, Z., Hoffman, T. J., Jurisson, S. S., and Quinn, T. P. (2000) Melanoma-targeting properties of ^{99m}technetium-labeled cyclic alpha-melanocyte-stimulating hormone peptide analogues. *Cancer Res. 60*, 5649−58.

(10) Chen, J., Giblin, M. F., Wang, N., Jurisson, S. S., and Quinn, T. P. (1999) In vivo evaluation of ^{99m}Tc/^{188}Re-labeled linear alpha-melanocyte stimulating hormone analogs for specific melanoma targeting. *Nucl. Med. Biol. 26*, 687−93.

(11) Cheng, Z., Chen, J., Miao, Y., Owen, N. K., Quinn, T. P., and Jurisson, S. S. (2002) Modification of the structure of a metallopeptide: synthesis and biological evaluation of ^{111}In-labeled DOTA-conjugated rhenium-cyclized alpha-MSH analogues. *J. Med. Chem. 45*, 3048−56.

(12) Chen, J., Cheng, Z., Owen, N. K., Hoffman, T. J., Miao, Y., Jurisson, S. S., and Quinn, T. P. (2001) Evaluation of an ^{111}In-DOTA-rhenium cyclized alpha-MSH analog: a novel cyclic-peptide analog with improved tumor-targeting properties. *J. Nucl. Med. 42*, 1847−55.

(13) Froidevaux, S., Calame-Christe, M., Tanner, H., Sumanovski, L., and Eberle, A. N. (2002) A novel DOTA-alpha-melanocyte-stimulating hormone analog for metastatic melanoma diagnosis. *J. Nucl. Med. 43*, 1699−706.

(14) Froidevaux, S., Calame-Christe, M., Tanner, H., and Eberle, A. N. (2005) Melanoma targeting with DOTA-alpha-melanocyte-stimulating hormone analogs: structural parameters affecting tumor uptake and kidney uptake. *J. Nucl. Med. 46*, 887−95.

(15) Cheng, Z., Chen, J., Quinn, T. P., and Jurisson, S. S. (2004) Radioiodination of rhenium cyclized alpha-melanocyte-stimulating hormone resulting in enhanced radioactivity localization and retention in melanoma. *Cancer Res. 64*, 1411−8.

(16) Froidevaux, S., Calame-Christe, M., Schuhmacher, J., Tanner, H., Saffrich, R., Henze, M., and Eberle, A. N. (2004) A gallium-labeled DOTA-alpha-melanocyte- stimulating hormone analog for PET imaging of melanoma metastases. *J. Nucl. Med. 45*, 116−23.

(17) McQuade, P., Miao, Y., Yoo, J., Quinn, T. P., Welch, M. J., and Lewis, J. S. (2005) Imaging of melanoma using ^{64}Cu- and ^{86}Y-DOTA-ReCCMSH(Arg^{11}), a cyclized peptide analogue of alpha-MSH. *J. Med. Chem. 48*, 2985−92.

(18) Cheng, Z., Xiong, Z. M., Wu, Y., Zhang, X., Chen, X., and Gambhir, S. S. (2005) MicroPET Imaging of Melanoma Using Cu-64 Labeled alpha-Melanocyte Stimulating Hormone Peptide Analogue. *Mol. Imaging Biol. 7*, 126.

(19) Miao, Y., Owen, N. K., Fisher, D. R., Hoffman, T. J., and Quinn, T. P. (2005) Therapeutic efficacy of a ^{188}Re-labeled alpha-melanocyte-stimulating hormone peptide analog in murine and human melanoma-bearing mouse models. *J. Nucl. Med. 46*, 121−9.

(20) Miao, Y., Hylarides, M., Fisher, D. R., Shelton, T., Moore, H., Wester, D. W., Fritzberg, A. R., Winkelmann, C. T., Hoffman, T., and Quinn, T. P. (2005) Melanoma therapy via peptide-targeted α-radiation. *Clin. Cancer Res. 11*, 5616−21.

(21) Wu, Y., Zhang, X., Xiong, Z., Cheng, Z., Fisher, D. R., Liu, S., Gambhir, S. S., and Chen, X. (2005) microPET Imaging of Glioma Integrin $\alpha_v\beta_3$ Expression Using ^{64}Cu-Labeled Tetrameric RGD Peptide. *J. Nucl. Med. 46*, 1707−18.

(22) Gambhir, S. S. (2002) Molecular imaging of cancer with positron emission tomography. *Nat. Rev. Cancer 2*, 683−93.

(23) Weissleder, R. (2006) Molecular imaging in cancer. *Science 312*, 1168−71.

(24) Belhocine, T. Z., Scott, A. M., Even-Sapir, E., Urbain, J. L., and Essner, R. (2006) Role of nuclear medicine in the management of cutaneous malignant melanoma. *J. Nucl. Med.* 47, 957−67.

(25) Sturm, R. A. (2002) Skin colour and skin cancer − MC1R, the genetic link. *Melanoma Res. 12*, 405−16.
(26) Bagutti, C., Stolz, B., Albert, R., Bruns, C., Pless, J., and Eberle, A. N. (1994) [^{111}In]-DTPA-labeled analogues of alpha-melanocyte-stimulating hormone for melanoma targeting: receptor binding in vitro and in vivo. *Int. J. Cancer 58*, 749−55.
(27) Bard, D. R. (1995) An improved imaging agent for malignant melanoma, based on [Nle^4,D-Phe^7]alpha-melanocyte stimulating hormone. *Nucl. Med. Commun. 16*, 860−6.
(28) Vaidyanathan, G., and Zalutsky, M. R. (1997) Fluorine-18-labeled [Nle^4,D-Phe^7]-alpha-MSH, an alpha-melanocyte stimulating hormone analogue. *Nucl. Med. Biol. 24*, 171−8.
(29) Anderson, C. J., Dehdashti, F., Cutler, P. D., Schwarz, S. W., Laforest, R., Bass, L. A., Lewis, J. S., and McCarthy, D. W. (2001) ^{64}Cu-TETA-octreotide as a PET imaging agent for patients with neuroendocrine tumors. *J. Nucl. Med. 42*, 213−21.
(30) Rogers, B. E., Bigott, H. M., McCarthy, D. W., Della Manna, D., Kim, J., Sharp, T. L., and Welch, M. J. (2003) MicroPET imaging of a gastrin-releasing peptide receptor-positive tumor in a mouse model of human prostate cancer using a ^{64}Cu-labeled bombesin analogue. *Bioconjugate Chem. 14*, 756−63.
(31) Chen, X., Hou, Y., Tohme, M., Park, R., Khankaldyyan, V., Gonzales-Gomez, I., Bading, J. R., Laug, W. E., and Conti, P. S. (2004) Pegylated Arg-Gly-Asp peptide: ^{64}Cu labeling and PET imaging of brain tumor $\alpha_v\beta_3$-integrin expression. *J. Nucl. Med. 45*, 1776−83.
(32) Sprague, J. E., Peng, Y., Sun, X., Weisman, G. R., Wong, E. H., Achilefu, S., and Anderson, C. J. (2004) Preparation and biological evaluation of copper-64-labeled tyr^3-octreotate using a cross-bridged macrocyclic chelator. *Clin. Cancer Res. 10*, 8674−82.
(33) Lewis, J. S., Lewis, M. R., Cutler, P. D., Srinivasan, A., Schmidt, M. A., Schwarz, S. W., Morris, M. M., Miller, J. P., and Anderson, C. J. (1999) Radiotherapy and dosimetry of ^{64}Cu-TETA-Tyr^3-octreotate in a somatostatin receptor-positive, tumor-bearing rat model. *Clin. Cancer Res. 5*, 3608−16.
(34) Boswell, C. A., Sun, X., Niu, W., Weisman, G. R., Wong, E. H., Rheingold, A. L., and Anderson, C. J. (2004) Comparative in vivo stability of copper-64-labeled cross-bridged and conventional tetraazamacrocyclic complexes. *J. Med. Chem. 47*, 1465−74.
(35) Sun, X., Wuest, M., Weisman, G. R., Wong, E. H., Reed, D. P., Boswell, C. A., Motekaitis, R., Martell, A. E., Welch, M. J., and Anderson, C. J. (2002) Radiolabeling and in vivo behavior of copper-64-labeled cross-bridged cyclam ligands. *J. Med. Chem. 45*, 469−77.

BC060306G

Releasable PEGylation of Mesothelin Targeted Immunotoxin SS1P Achieves Single Dosage Complete Regression of a Human Carcinoma in Mice

David Filpula,*,† Karen Yang,† Amartya Basu,† Raffit Hassan,‡ Laiman Xiang,‡ Zhenfan Zhang,† Maoliang Wang,† Qing-cheng Wang,‡ Mitchell Ho,‡ Richard Beers,‡ Hong Zhao,† Ping Peng,† John Zhou,† Xiguang Li,† Gerald Petti,† Ahsen Janjua,† Jun Liu,† Dechun Wu,† Deshan Yu,† Zhihua Zhang,† Clifford Longley,† David FitzGerald,‡ Robert J. Kreitman,‡ and Ira Pastan‡

Enzon Pharmaceuticals, Incorporated, 20 Kingsbridge Road, Piscataway, New Jersey 08854, and Laboratory of Molecular Biology, National Cancer Institute, NIH, Bethesda, Maryland 20892. Received October 7, 2006; Revised Manuscript Received January 20, 2007

Recombinant immunotoxins exhibit targeting and cytotoxic functions needed for cell-specific destruction. However, antitumor efficacy, safety, and pharmacokinetics of these therapeutics might be improved by further macromolecular engineering. SS1P is a recombinant anti-mesothelin immunotoxin in clinical trials in patients with mesothelin-expressing tumors. We have modified this immunotoxin using several PEGylation strategies employing releasable linkages between the protein and the PEG polymers, and observed superior performance of these bioconjugates when compared to similar PEG derivatives bearing permanent linkages to the polymers. PEGylated derivatives displayed markedly diminished cytotoxicity on cultured mesothelin-overexpressing A431-K5 cells; however, the releasable PEGylated immunotoxins exhibited increased antitumor activity in A431-K5 xenografts in mice, with a diminished animal toxicity. Most significantly, complete tumor regressions were achievable with single dose administration of the bioconjugates but not the native immunotoxin. Pharmacokinetic analysis of the releasable PEGylated derivatives in mice demonstrated an over 80-fold expansion of the area under the curve exposure of bioactive protein when compared to native immunotoxin. A correlation in degree of derivatization, release kinetics, and polymer size with potency was observed in vivo, whereas in vitro cytotoxicity was not predictive of efficacy in animal models. The potent antitumor efficacy of the releasable PEGylated mesothelin-targeted immunotoxins was not exhibited by similar untargeted PEG immunotoxins in this model. Since the bioconjugates can also exhibit the attributes of passive targeting via enhanced permeability and retention, this is the first demonstration of a pivotal role of active targeting for immunotoxin bioconjugate efficacy.

INTRODUCTION

Mesothelin is an attractive target for tumor-specific therapy due to its high expression on several cancers and limited expression on normal tissues. The 40 kDa glycosylphosphatidyl inositol-linked cell surface glycoprotein is overexpressed in pancreatic carcinoma, ovarian cancer, and malignant mesotheliomas, whereas normal pleura, pericardium, and peritoneum exhibit detectable mesothelin expression in the surrounding mesothelial cells (*1*−*15*). The biological function of mesothelin is not established; although it is not essential for normal mouse development (*16*−*21*), recent studies suggest that mesothelin binds to the mucin glycoprotein CA125 and that this interaction mediates cell adhesion (*22*).

An anti-mesothelin mAb[1] was generated by immunizing mice with a mesothelin expression plasmid and library screening of splenic RNA variable domains using scFv phage display technology. Affinity maturation was conducted using site-selected mutagenesis and screening (*6*, *12*−*15*, *23*). The isolated SS1 Fv exhibited high affinity for mesothelin (K_d = 0.7 nM) and was stabilized by a disulfide bond between the light and heavy variable domains of the Fv (*24*−*26*). The SS1 Fv was employed in the construction of an immunotoxin SS1P via genetic fusion to a truncated *Pseudomonas* exotoxin A (PE) (*27*−*30*). SS1P is highly cytotoxic to mesothelin-expressing cells in culture and demonstrates antitumor effects against the human epidermoid carcinoma cell line, A-431, that is stably transfected with a mesothelin cDNA expression vector (A431-K5) and subcutaneously implanted in mouse xenografts. SS1P [SS1-(dsFv)PE38] has recently been investigated in clinical trials (*1*, *7*, *9*).

Several recombinant immunotoxins composed of an antibody Fv targeting moiety and a PE cytotoxic moiety have been evaluated in animal models and clinical studies (*31*, *32*). These immunotoxins have produced potent antitumor responses in human cancer xenografts in nude mice (*33*, *34*), and major clinical responses to recombinant immunotoxins were observed in hematologic malignancies (*35*, *36*). However, these chimeric proteins also exhibit side effects that limit the dose and frequency of administration. The PE domain of the immunotoxin may exhibit nonspecific binding to normal tissues, while

* To whom correspondence should be addressed. Tel # 732-980-4941; FAX # 732-885-2950; E-mail: david.filpula@enzon.com.

† Enzon Pharmaceuticals, Inc.

‡ National Cancer Institute.

[1] Abbreviations: ALD, aldehyde; AUC, area under the curve; B-SS1P, bicin-SS1P; Bicin, bis-*N*-2-hydroxyethylglycine, dsFv, disulfide stabilized Fv; C_{max}, maximal concentration; D-SS1P, DGA2-SS1P; DGA2, diglycolic acid; ELISA, enzyme-linked immunosorbent assay; EPR, enhanced permeability and retention; HRP, horseradish peroxidase; i.v., intravenous; LD_{50}, lethal dose with 50% mortality; mAb, monoclonal antibody; mPEG, monomethoxy-PEG; MRT, mean retention time; MW, molecular weight; NHS, *N*-hydroxysuccinimide; PBS, phosphate-buffered saline; PE, *Pseudomonas* exotoxin A; PEG, poly(ethylene glycol); PEG_2, branched PEG; RP, reversed phase; rPEGylation, releasable PEGylation; RNL, reversible nitrogen linker; SC, succinimidyl carbonate; SE-HPLC, size exclusion high performance liquid chromatography; $t_{1/2}$, serum half-life; T_{max}, time of maximal concentration.

10.1021/bc060314x CCC: $37.00 © 2007 American Chemical Society
Published on Web 03/09/2007

neutralizing human anti-PE antibodies, and less frequently, anti-mouse Fv antibodies, are formed in patients treated with these therapeutics, resulting in either dose-limiting toxicity or diminished therapeutic potency. In addition, recombinant immunotoxins (~63 kDa) do not exhibit prolonged blood residency, in contrast to mAbs, leading to increased distribution in both tumors and normal tissues, including kidneys and liver. Although a prolonged blood residency might be achieved via continuous infusion, it would be desirable to construct an immunotoxin with intrinsically improved pharmacokinetics, reduced toxicity, and diminished antigenicity/immunogenicity.

PEGylation is a well-developed technology that has shown the capacity to address each of the above concerns. Bioconjugation of proteins with PEG via permanent linkages is employed in at least six marketed protein therapeutics (*37*). We previously reported an improvement in serum half-life, a reduction in immunogenicity and toxicity, and enhanced antitumor efficacy in a PEGylated chimeric toxin composed of transforming growth factor-α and PE (*28*). However, these positive attributes came at the expense of a marked loss of specific cytotoxic activity. Site-specific PEGylation of anti-Tac(Fv)-PE immunotoxin LMB-2 also improved antitumor activity and diminished toxicity and immunogenicity (*29, 38*). In this case, the engineered protein design of the bioconjugate employed a free thiol in the connector peptide of the immunotoxin. In practice, this approach may be limited by the inefficiency of protein refolding due to incorrectly disulfide-linked, misfolded protein impurities, and also by the inefficiency of conjugation and purification of the conjugates. It would be desirable to develop a bioconjugate strategy wherein no special polypeptide alterations are required and whereby nearly quantitative yields of bioconjugate from native protein are achieved. Designing the optimal immunotoxin through the combination of protein engineering and bioconjugation approaches is a challenging undertaking. Recombinant immunotoxins, such as SS1P, are multifunctional proteins that exhibit biological activity only after intracellular processing. Chemical modification strategies must consider the preservation of antigen-binding, translocation, and ADP-ribosylation functions, while enhancing composite pharmacological properties, including avoidance of rapid clearance from renal filtration, antibody or cellular clearance, or physical degradation.

Although conventional PEGylation utilizes stable linkages between the polymers and the protein, recent research has investigated the potential of releasable PEGylation (rPEGylation), wherein the designed covalent linkages of the PEG strands are chemically unstable within a physiological environment and the attached polymers are detached via a controlled release mechanism (*30, 39*−*44*). This unconventional prodrug-based PEGylation approach might have an appropriate application in immunotoxin engineering. Immunotoxins are themselves biological prodrugs that are activated by a designed intracellular release mechanism. Further engineering of the immunotoxin as a double prodrug bioconjugate offers several hypothetical advantages. rPEGylation could provide multiple PEG attachments over the protein surface and allow optimized pharmacokinetics and biodistribution, with diminished immunogenicity and antigenicity. Although the rPEGylated immunotoxin may have severely compromised cytotoxic activity in its prodrug form, a designed incremental release in vivo of the unmodified immunotoxin protein from the attached polymers may provide a superior distribution of fully active protein at the target sites. Underlying this hypothesis is a requirement for a beneficial shift in the balance between the counteracting forces of clearance of the released protein and retention of the PEG modified protein. Furthermore, rPEGylated immunotoxins might accrue additional tumor targeting benefits from the enhanced permeability and retention (EPR) phenomenon (*45, 46*). In the first investigations to examine the in vitro and in vivo performance of immunotoxins modified with rPEGylation, we have studied several rPEGylated bioconjugates composed of SS1P and designed rPEG polymers of varying release kinetics, polymer size, and degree of modification.

EXPERIMENTAL PROCEDURES

Materials. PEG_2-40 kDa-NHS was obtained from Nektar Therapeutics (Huntsville, AL). All other activated PEG polymers were supplied by Enzon Pharmaceuticals, Inc. (Piscataway, NJ). Hiload Superdex 75 or 200, Q Sepharose Fast Flow, and HiTrap Q-XL were supplied by GE Healthcare (Piscataway, NJ).

Production of Recombinant SS1P. The subunits of SS1P were expressed in *Escherichia coli* BL21(λDE3) and purified as previously described for other immunotoxins (*23*, *25*, *31*). Active monomeric protein was purified from the refolding solution by ion exchange and size exclusion chromatography. LC-MS analysis confirmed the predicted 62 591 mass of SS1P.

Linker Synthesis. The Bicin3, DGA2, and RNL-8a linkers were synthesized as previously described (*39*−*41, 44*).

Preparation of Releasable PEG−SS1P Conjugates. In PEGylation reactions employing releasable linkers such as DGA2, RNL-8a, and Bicin3, SS1P at 1.5−2.5 mg/mL was PEGylated in 0.05−0.1 M sodium phosphate, pH 7.6, 25 °C, and purified by reported procedures (*40, 44*). With fast stirring without creating foam, the PEG powder at 10:1 to 50:1 reaction molar ratio of PEG to SS1P was added to the SS1P solution at 1 g/min. The reaction was continued at 25 °C for 1 h and quenched by adding glycine. Immediately after quenching, the solution pH was lowered to 6.5 with monobasic sodium phosphate and the conjugate was purified on a size exclusion column (Superdex 200 or 75 Hiload) equilibrated in 20 mM sodium phosphate, pH 6.5, 140 mM NaCl. Alternatively, the conjugate was purified on an anion exchange column (Q Sepharose Fast Flow) using either 10 mM sodium phosphate, pH 7.4, as the equilibration buffer, with 0.3 M NaCl in 10 mM sodium phosphate, pH 7.4, as the gradient elution buffer, or 10 mM Tris−HCl, pH 7.6, as the equilibration buffer, and 0.3 M NaCl in 10 mM Tris−HCl, pH 7.6, as the gradient elution buffer. The column fractions containing the peak were combined and dialyzed against PBS, pH 6.5. The sample was concentrated to about 1 mg/mL using Centriplus 30k (Millipore, MA) and passed through a sterile filter (Acrodisc Syringe Filter, 0.2 μm HT Tuffyn membrane, Pall, MI). The number of PEG polymers per SS1P molecule was initially estimated by SDS-PAGE prior to further analysis. The release of SS1P from releasable PEG−SS1P was conducted by incubation in a PBS pH 8.5 buffer, at 37 °C or 25 °C. The purity of the product was analyzed on a TSK gel filtration column equilibrated in 50 mM sodium phosphate, pH 6.5, 150 mM NaCl (G4000SWXL, 7.8 × 30 cm, 8 μm, Tosoh Biosciences). The peak area was calculated at 220 nm. Since the conventional TNBS and fluorescamine assay methods for measurement of percent PEG modification require a basic pH which is not suitable for rPEG−SS1P, we used the ammonium ferrothiocyanate colorimetric method to analyze free and protein-coupled PEG (*47*).

Preparation of Permanent PEG−SS1P Conjugates. For PEGylation reactions that employed permanent linkers such as SC and NHS, SS1P at 1.5−2.5 mg/mL was PEGylated in 0.05 M sodium phosphate, pH 6.0−9.0, at 25 °C and purified as previously described (*29, 30, 37*−*41*). With fast stirring without creating foam, the PEG powder at 3:1 to 15:1 reaction molar ratio of PEG to SS1P was added to SS1P solution at 1 g/min. The reaction was continued at 25 °C for 1−2 h for the pH 7.4−9.0 reactions and 4 h for pH 6.0−7.0 reactions. The reaction was quenched by adding glycine. The conjugate was purified by an anion exchange column (Q Fast Flow Sepharose) where

the equilibration buffer was 10 mM Tris−HCl, pH 7.6, and the gradient elution buffer contained 0.3 M NaCl in 10 mM Tris−HCl, pH 7.6. Alternatively, a size exclusion column (Superdex 200 or 75 Hiload) was used for purification with a pH 7.4 PBS equilibration buffer. The sample was concentrated to about 1 mg/mL using Centriplus 30k and passed through an Acrodisc sterile filter.

Preparation of ALD−PEG−SS1P. For N-terminal selective PEGylation, SS1P at 2 mg/mL was incubated with aldehyde-PEG-20k (ALD-PEG-20k) at a 10:1 reaction molar ratio (PEG/SS1P) in 100 mM sodium phosphate, pH 6.5, 25 °C, for 3 h. The reduction of Schiff base was completed in 15 mM sodium cyanoborohydride at 25 °C, 16 h. Mono-PEGylated and di-PEGylated conjugates were isolated on HiTrap Q-XL at pH 7.5. SDS-PAGE analysis showed that the PEG attachment in mono PEG-SS1P was selectively located on the heavy chain (V_H-PE) and the PEG in di-PEG-SS1P was found on both the heavy and light chains (V_L) of SS1P.

Cell Lines and Cytotoxicity Assay. A431-K5, a cell line established by transfection of an expressible cDNA encoding mesothelin into human epidermoid cancer A431 cells (American Type Culture Collection, Manassas, VA), was used in cytotoxicity assays in vitro and in vivo. A431-K5 has a stable and uniform expression of mesothelin (33 000 mesothelin sites per cell; Raffit Hassan, NCI, unpublished data), which is similar to that observed with tumor specimens obtained from patients (*9, 10, 17, 18, 20*). The specific cytotoxicity of SS1P and PEGylated SS1P compounds was assessed by protein synthesis inhibition assays in 96-well plates, by a modified nonradioactive assay (*10, 34*).

Antitumor Activity of SS1P and PEGylated SS1P. The antitumor activity of SS1P and PEG−SS1P compounds was determined in nude mice bearing A431-K5 human cancer cells that express mesothelin. Starting on day 7, animals were treated with i.v. injections of each of the immunotoxin compounds diluted in 0.2 mL of phosphate buffered saline (PBS)/0.2% mouse serum albumin (MSA).

Pharmacokinetics. BALB/c mice (6−8 week old females) were supplied by Sprague Dawley Harlan (Madison, WI). Mice (3/group) were injected i.v. with 100 μL per mouse of SS1P (0.125 or 0.4 mg/kg) or its PEGylated conjugates (0.5 or 1.5 mg/kg). Mice were terminally bled by cardiac puncture at 0.17, 0.5, 1, 3, 6, 24, 48, and 120 h. The concentrations of the compounds were analyzed by in vitro cytotoxicity with A431-K5 cells, and data were modeled using *WinNonlin* software to determine pharmacokinetic parameters.

Flow Cytometry. Flow cytometry studies with A431-K5 cells were used to analyze SS1P and PEG−SS1P compounds binding to mesothelin cell receptors. Cells were resuspended (10^6 cells/mL) in D-MEM, 5% FBS. SS1P compounds (0.1, 1, 10, or 100 ng) in 100 μL of FACS medium were added to each tube and incubated for 30 min on ice, and 100 μL of mouse anti-PE-40 mAb (1 μg/mL) was added and incubated 30 min on ice. Phycoerythrin-conjugated goat anti-mouse polyclonal antibody (10 μg/mL; 100 μL) was added, and analysis was conducted on FACS Calibur (BD Biosciences, San Jose, CA).

Surface Plasmon Resonance Analysis. Surface plasmon resonance techniques were performed using a Biacore X instrument (Biacore, Inc., Piscataway, NJ). Recombinant mesothelin-maltose binding protein (MBP) was prepared using the pMAL protein fusion and purification system (New England BioLabs, Beverly, MA). Anti-MBP mAb was immobilized on a CM5 chip and subjected to ligand stability analysis for six cycles with 500 nM mesothelin-MBP. For each kinetic experiment, equal amounts of mesothelin-MBP were allowed to be captured by the surface-immobilized anti-MBP mAb. The SS1P or PEG−SS1P proteins served as analytes. Over the stable mAb-MBP-mesothelin surface, different concentrations of SS1P or PEG−SS1P were examined. The data were analyzed using Biacore *BiaEvaluation* software (version 3.0).

Analysis of Anti-SS1P Antibodies in Human Sera by Competition ELISA. Microtiter wells were coated with 1 μg SS1P/50μL in 20 mM Tris−HCl, pH 8.0. Diluted human antisera, combined with serial dilutions of either SS1P or PEG−SS1P, were added (100 μL total volume) and incubated at 25 °C for 1.5 h. The wells were washed and HRP conjugated rabbit anti-human Ig (1:40 000 dilution), 50 μL/well, was added and incubated at 25 °C for 45 min. Following washing, 100 μL of TMB-E substrate was added, and the plates were read at 450 nm.

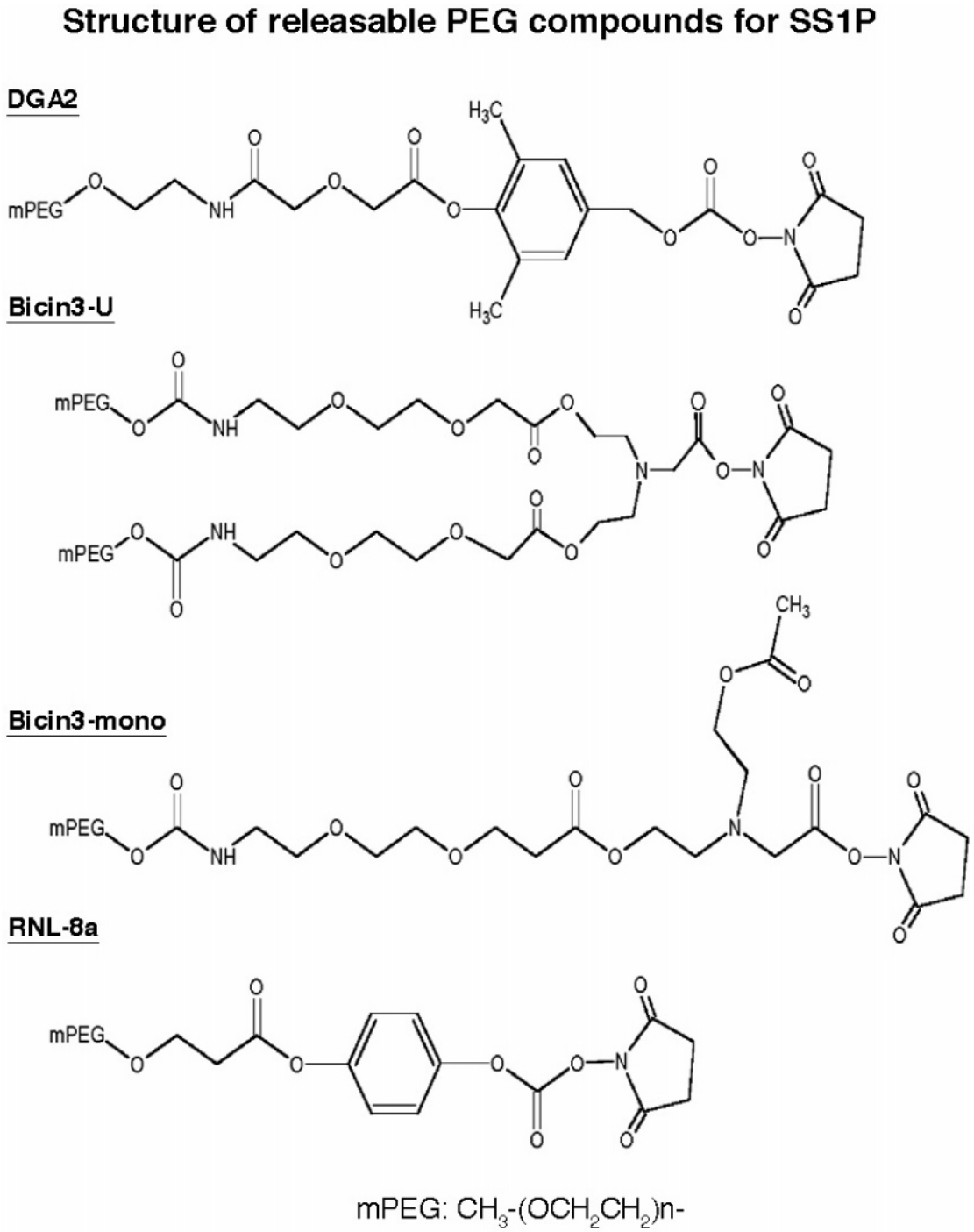
RESULTS

Preparation and Characterization of PEG−SS1P Compounds. Seven amine-reactive, NHS-activated PEG polymers were employed in the construction of PEGylated bioconjugates of the immunotoxin SS1P. As shown in Chart 1, four unconventional releasable linker designs were evaluated. The bis-*N*-2-hydroxyethylglycine (Bicin3), diglycolic acid (DGA2), and reversible nitrogen linker (RNL-8a) linker chemistries have been recently described with regard to their mechanism of controlled release from PEGylated proteins (*39−41*, *44*). The DGA2 (fast release) and RNL-8a (slow release) linkers are both aromatic designs wherein an initial ester cleavage triggers a classical 1,6-benzyl elimination reaction which releases the original amine and results in linker degradation. In contrast, the Bicin3 linker employs a wholly aliphatic design. Following the hydrolysis of the exposed ester group of the linker, a cyclization event promotes linker self-immolation and release of the original amine (lysine) group. The Bicin3 linker was employed as a release linkage to either mono (linear) PEG or to branched (U) PEG in our studies such that examination of the influence of PEG geometry could also be included in our investigations. Release kinetics for either type of linker may be tailored by the inclusion of side chain groups strategically designed in the linker to provide either steric interference (for slower release) or anchimeric assistance (for faster release) to the degradation pathway, and we chose representative linkers from the two structural types that include a range of release kinetics.

For example, Scheme 1 depicts the linkage chemistry of the Bicin3-mono version and its proposed mechanism of release. The NHS-activated PEG (**1**) is conjugated to SS1P protein to form the bioconjugate (**2**). Decapping is very rapid in vivo to produce **3**, and the ester hydrolysis reaction proceeds at a rate determined by the molecular design of the linker side chains to produce **4**. Cyclization occurs via participation of both hydroxyethyl side chains, and linker detachment releases the original lysine(s) of SS1P plus the morpholinolactone (**5**). DGA2 and RNL-8a linker characteristics and release mechanisms have also been described (*40, 41*).

Protein bioconjugates with these rPEG polymers bonded to lysine residues are stable at pH <7 and release the original unmodified protein with release kinetics in the therapeutically useful range of hours to days, depending on linker design, polymer size, total number of PEG attachment sites, and pH of release medium. Figure 1 and Table 1 show the effects of pH on release kinetics. Following conjugation reactions, unmodified SS1P protein and free PEG polymers are removed from the PEGylated SS1P compounds by ion exchange chromatography and size exclusion chromatography. Both aromatic and aliphatic linker designs allow recovery of multi-PEGylated bioconjugates in >90% yields and provide the option of tailoring the number of PEG attachments through adjustments of reaction stoichiometry and purification protocols. Since both types of linkers have been successfully employed in reversible protein conjuga-

Chart 1. Structure of Activated PEG Polymers Composed Of Poly(ethylene glycol) Polymer, Releasable Linker, and *N*-Hydroxysuccinimide (NHS) Leaving Group[a]

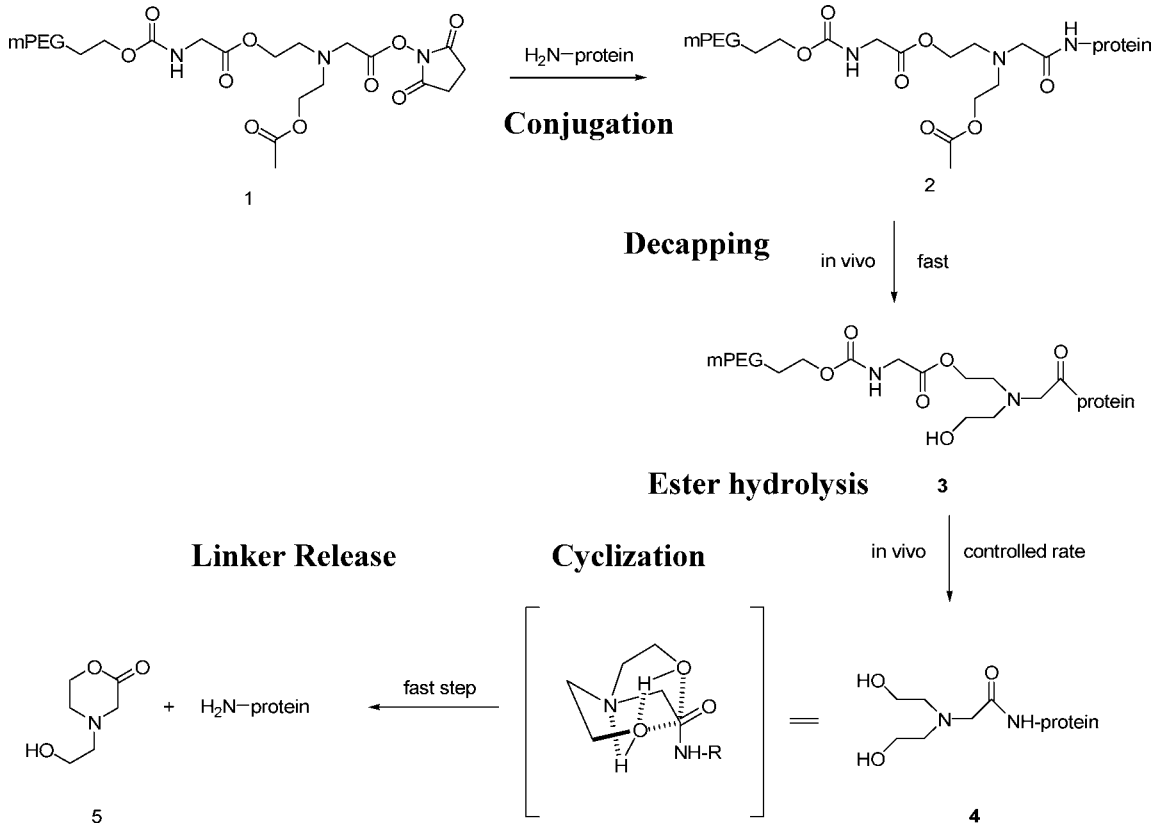


[a] Amide or carbamate linkages to primary amines in conjugates of SS1P are formed at the linker carbonyl group proximal to the NHS ester. The mechanisms of controlled release of authentic native protein from the linker and PEG have been described for both the aromatic-based DGA2 and RNL-8a linkers (*40*, *41*) and the aliphatic Bicin3 linker (*39*, *44*).

tion, further comparative studies in animal models may be instructive to evaluate these individual chemistries.

We chose to focus our investigations on SS1P with an intermediate degree of rPEGylation, such that the number of PEG attachments and total PEG mass of most of the test compounds were comparable. In the design of the PEG−SS1P conjugates, a molecular mass mainly in the 40−60 kDa range was selected, since this strategy provided a practical compromise between optimizing the compound's pharmacokinetics and ensuring release of the SS1P before systemic clearance of the intact bioconjugate. Bioconjugates of this size will not exhibit rapid renal clearance, due to their sufficient total polymer mass. Therefore, the total numbers of PEG attachments were fewer for the large (40 kDa) PEG polymers than for smaller (12 kDa) PEG polymers. In addition, the use of branched linkers for PEG attachments allowed fewer total attachment sites for 12 kDa or 20 kDa linear PEGs, since the branched 40 kDa design tethers two 20 kDa linear PEGs to a common linker; similarly, the branched 24 kDa design contains two linear 12 kDa PEGs per linker. Multiple analytical methods were employed to characterize the composition of the multi-PEGylated SS1P compounds and confirmed batch consistency, as summarized in Table 1, using capillary electrophoresis, size-exclusion chromatography, chemical analysis of PEG, and SDS-PAGE. SS1P bioconjugates

Scheme 1. Example of the Chemistry of Conjugation and the Linker Decomposition in Vivo for the Bicin3-Mono Linker[a]



[a] Reaction of an activated PEG of the bicin linker type (**1**) with a protein amine forms the bioconjugate (**2**). In vivo, the acetyl group is rapidly lost, while the elimination reaction to release the PEG segment from (**3**) occurs at a controllable rate to produce (**4**). The final release of the original protein and morpholinolactone (**5**) is predicted to occur via a cyclization intermediate.

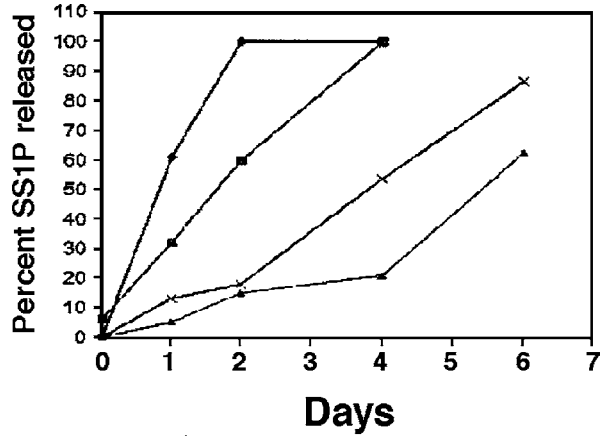


Figure 1. Comparison of release kinetics of four rPEG−SS1P compounds in PBS at pH 8.5, 25 °C: DGA2-12 kDa-PEG-SS1P (◆), Bicin3-U-24 kDa-PEG-SS1P (■), Bicin3-mono-30 kDa-PEG-SS1P (▲), and RNL-8a-12 kDa-PEG-SS1P (×). Release was monitored at 220 nm on SE chromatography on a TSK-gel, G4000SWXL column with a mobile phase of 50 mM sodium phosphate, pH 6.5, 140 mM NaCl, 0.5 mL/min. See Table 1 for release rates at pH 7.4.

with conventional permanent PEG polymers (SC-12k, ALD-20k, PEG_2-40k) (*48*) were further analyzed by MALDI-TOF, LC-MS, and reversed-phase chromatography.

Cytotoxic Activity of PEG−SS1P. A modified nonradioactive cytotoxicity assay was used for the SS1P immunotoxin and its PEGylated counterparts. The specific cytotoxicity (IC_{50}) of the immunotoxins was determined on A431-K5 cells, which highly express the target mesothelin surface protein (*4*, *23*). As shown in Table 1, the in vitro potency of the SS1P immunotoxin was markedly compromised by the random PEGylation strategies used in this study. SS1P conjugates bearing three or more permanent PEG attachments exhibited marginal or no activity in this bioassay. With conjugates derived from the site-selective PEG−aldehyde linkage, a single PEG attachment at one of the N-termini of the Fv subunits virtually eliminates in vitro bioactivity. Although releasable compounds such as DGA2-12 kDa-PEG-SS1P and Bicin3-24 kDa-PEG-SS1P, which also contain about 3−6 PEGs, retained some cytotoxic activity, this is attributed to the partial release of PEG during the incubation in cell culture. However, it is not uncommon for highly effective PEGylated protein therapeutics to exhibit fractional activity in vitro (*37*, *41*, *48*).

Pharmacokinetics of PEG−SS1P. BALB/c mice were injected i.v. at 100 μL per mouse with SS1P (0.125 or 0.4 mg/kg) or its PEGylated conjugates (0.5 or 1.5 mg/kg). Plasma concentration profiles of unmodified SS1P exhibited a rapid elimination with a half-life of about 26 min. In contrast, the plasma concentration profiles of DGA2-12 kDa-PEG and Bicin3-U-24 kDa-PEG bioconjugates demonstrated more complex elimination kinetics, as expected for these rPEG−SS1P compounds. As shown in Table 2, the plasma half-life, maximal concentration, and mean retention time of these two PEG−SS1P proteins were extended over 10-fold, while the time of maximal concentration was delayed from 30 min for SS1P to 2 h for the bioconjugates. Most significantly, the area under the plasma concentration curve (AUC) exposure of both rPEG−SS1P derivatives was increased about 80-fold compared to native SS1P. The PEG_2-40 kDa-PEG-SS1P compound contained a permanent amide linkage of only one PEG per SS1P. In comparison to native SS1P, prolonged blood residency was achieved, although not to the extent exhibited by the first three rPEG−SS1P derivatives (Table 2).

Animal Toxicity Studies. The nonspecific toxicity of the PEGylated immunotoxins in mice was examined by i.v.

Table 1. Features and Analysis of PEGylated SS1P and αCD22 Bioconjugates

compound	linker[a]	PEG mass on linker (kDa)	PEG # (AFTC/TNBS)[b]	PEG # (SEC/CE)	PEG # (PAGE)	SS1P release in vitro $t_{1/2}$[c](h)	IC_{50} (ng/mL)	flow cyt[d] (% of SS1P)
SS1P	none	none	none	none	none	n.a.[f]	0.7	100
DGA2-12k-SS1P	R	12	4−5	4, 5, 6	4, 5, 6	125	2.1	33
Bicin3-U-24k-SS1P	R	24	2−3	2, 3, 4	3	90	3.7	39
Bicin3-mono-30k-SS1P	R	30	3−5	4, 5	4, 5	140	16.5	11
RNL-8a-12k-SS1P	R	12	4−5	4, 5, 6	4, 5, 6	>300	>100	6
SC-12k-SS1P	P	12	5−6	4, 5, 6	4, 5, 6	n.r.[e]	>100	19
ALD-20k-SS1P	P	20	1−2	1	1	n.r.	39	23
PEG_2-40k-SS1P	P	40	1	1	1	n.r.	8.8	63
DGA2-12k-αCD22	R	12	4−5	4, 5, 6	4, 5, 6	125	n.a.	n.a.
Bicin3-U-24k-αCD22	R	24	2−3	2, 3	2, 3	90	n.a.	n.a.

[a] R, releasable; P, permanent. [b] PEG # is the number of attached PEGs per SS1P determined by ammonium ferrothiocyanate (AFTC), trinitrobenzene sulfonic acid (TNBS), capillary electrophoresis (CE), size exclusion chromatography (SEC), and SDS-PAGE. [c] Half-life of SS1P release from PEG at pH 7.4, 25 °C, in PBS. [d] Flow cytometric analysis of % bound PEG-SS1P compound relative to unmodified SS1P on A431-K5 cells (native SS1P = 100% bound). [e] n.r. = no release. [f] n.a. = not applicable.

Table 2. Pharmacokinetics of PEGylated SS1P Bioconjugates

compound	linker[a]	$t_{1/2}$ [b](h) in vivo	MRT[b] (min)	AUC[b] (min mg/mL)	T_{max}[b] (min)	C_{max}[b] (μg/mL)
SS1P	none	0.44	0.64	0.36	30	3.4
DGA2-12k-SS1P	R	4.8	4.7	28.6	120	51.5
Bicin3-U-24k-SS1P	R	4.8	5.2	31.3	120	47.0
Bicin3-mono-30k-SS1P	R	5.0	6.5	18.8	180	20.9
RNL-8a-12k-SS1P	R	4.4	5.5	0.77	60	1.1
PEG_2-40k-SS1P	P	2.5	3.6	2.0	10	8.7

[a] R, releasable; P, permanent. [b] Pharmacokinetic parameters are $t_{1/2}$, biological half-life; MRT, mean residence time; AUC, area under the plasma concentration curve; T_{max}, time of maximal concentration; C_{max}, maximal concentration.

administration of 2.0, 3.0, 4.0, or 6.0 mg/kg. Almost all deaths occurred within 4 days of treatment. The enormous increase in drug exposure provided by the rPEGylated derivatives did not, however, correspond to an increase in animal toxicity. The LD_{50} of native SS1P was found to be about 1.0 mg/kg; in contrast, the PEG−SS1P compounds were much better tolerated. The LD_{50} values (mg SS1P protein/kg) for DGA2-12kDa-SS1P, Bicin3-U-24kDa-SS1P, and RNL-8a-12kDa-SS1P were 3.0, 3.0, and 4.0 mg/kg, respectively. For the antitumor studies, we employed one or two dose levels below the dose that produced sickness or death.

Antitumor Activity of Permanent or rPEG−SS1P. Antitumor activity of SS1P and PEG−SS1P compounds was determined in nude mice bearing A431-K5 human cancer cells that express mesothelin. Cells (3×10^6) were injected s.c. into nude mice on day 0. Tumors of ~140 mm^3 in size developed in animals by day 7 after tumor implantation, after which animals were treated with i.v. injections of each of the immunotoxin compounds. In most experiments, therapy with native SS1P or with the PEG−SS1P compounds was given only once on day 7. In some experiments, animals received PEG−SS1P twice on days 7 and 11 or SS1P three times on days 7, 9, and 11. The control groups received vehicle only. It was previously determined that SS1P inhibited tumor growth in a dose-dependent manner and that at least three doses of SS1P (0.5 mg/kg) were required to achieve regression in this mouse xenograft model (*4*, *23*). Usually three independent studies were conducted with each of the PEGylated compounds using two different preparations of the SS1P conjugates.

As shown in Figure 2A, DGA2-12 kDa-PEG-SS1P (D−SS1P) was extremely active. A single dose of 2.0 mg/kg produced 90% tumor shrinkage on day 14 and 3/6 mice showed complete tumor regression. Mice receiving two doses of D-SS1P also showed a profound antitumor response with 4/8 mice showing complete response and an average tumor size regression of 90% (Table 3).

As shown in Figure 2B, Bicin3-U-24 kDa-PEG-SS1P (B−SS1P) was also very active. Complete regression was achieved in 1/4 mice receiving 2.0 mg/kg and 3/4 mice receiving 3.0 mg/kg. In mice receiving two doses of 2.0 mg/kg, 4/8 mice showed complete regression of the tumors.

Figure 2C shows the antitumor effects of the Bicin3-mono-30 kDa-PEG-SS1P; it appeared to be somewhat less active than the first two compounds tested. At 3 mg/kg, a single dose caused a maximal decrease in tumor size of 68%, whereas two doses of 2.0 mg/kg caused an average decrease in size of 92% with 1/5 complete remission.

The other compound with a slowly reversible linkage that showed significant antitumor activity in a small pilot study is RNL-8a-12 kDa-PEG-SS1P. However, as shown in Table 3, it is less active than the other compounds.

Further antitumor investigations were carried out with permanent PEG derivatives, multi-PEGylated SC-12 kDa-PEG-SS1P and mono-PEGylated PEG_2-40 kDa-PEG-SS1P. Only the latter compound produced sustained regression with 1/4 of the mice showing complete regression at a dose of 3.0 mg/kg (Figure 3 and Table 3).

PEGylated proteins have also been reported to accumulate in tumor xenografts via passive targeting by the EPR effect due to the leaky vasculature and deficient lymphatic drainage exhibited by tumors (*45*, *46*). To investigate the capability of nontargeted rPEGylated immunotoxins to demonstrate antitumor effects, we generated analogous rPEGylated immunotoxins targeting CD22, which is not present on A431-K5 cells. These compounds showed no antitumor activity, confirming that the antitumor activities of the PEG−SS1P derivatives are specific.

Immunogenicity and Immunoreactivity of PEG−SS1P. Since the immune response of patients to immunotoxins may limit their duration of efficacy, we assessed the immunoreactivity of PEG−SS1P compounds relative to unmodified SS1P. Figure 4A shows the results of sandwich ELISA analysis of SS1P and several PEG−SS1P derivatives, in which plates coated with a mAb reacting with PE38 were exposed to increasing amounts of each conjugate and the amount of immunotoxin bound was detected with a rabbit polyclonal antibody to PE38. Cross-reactivity of the PEG−SS1P compounds to the rabbit anti-PE antibodies is diminished compared to native SS1P. Two independent preparations of SS1P exhibited equivalent strong immunoreactivity, while the two independent preparations of heavily PEGylated Bicin3-mono-30 kDa-PEG-SS1P demonstrated the weakest cross-reactivity. The N-terminally mono-PEGylated ALD-20 kDa-PEG-SS1P was strongly reactive with the anti-PE antibodies as expected due to PEG attachment on the Fv portion of the Fv-PE toxin. Other rPEGylated derivatives were intermediate in signal. This suggests a possible strategy for evading the rapid drug clearance in patients due to existing neutralizing antibodies.

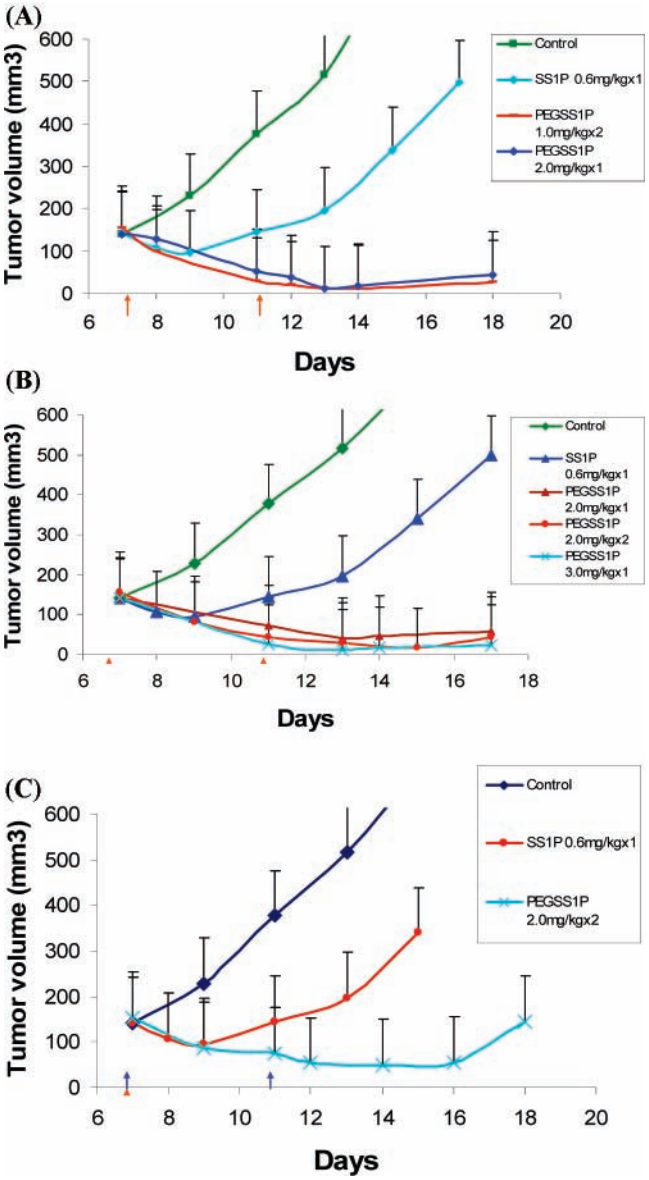


Figure 2. Antitumor effects of rPEG−SS1P and SS1P on A431-K5 solid tumors. Cells (3×10^6) were injected s.c. into nude mice on day 0. Starting on day 7 (tumor volume = ~140 mm^3), animals were treated with i.v. injections of each of the immunotoxin compounds at the indicated doses. Therapy with native SS1P or PEG−SS1P was given once on day 7. In an additional group, therapy with the PEG−SS1P compounds was given on days 7 and 11 (arrows). Control mice received vehicle only. All PEG−SS1P compounds are compared to SS1P (0.6 mg/kg × 1) administration and tumor volumes (mm^3) are shown (mean ± SD). (A) DGA2-12 kDa-PEG-SS1P (1.0 mg/kg × 2, or 2.0 mg/kg × 1). (B) Bicin3-U-24 kDa-PEG-SS1P (2.0 mg/kg × 1, 2.0 mg/kg × 2, or 3.0 mg/kg × 1). (C) Bicin3-mono-30 kDa-PEG-SS1P (2.0 mg/kg × 2).

To assess the immunogenicity of the PEG−SS1P compounds, BALB/c mice were immunized i.v. once per week with SS1P (2.5 μg/mouse) or PEG−SS1P (10 μg/mouse) for four weeks. Higher doses of unmodified SS1P could not be administered due to toxicity of the native toxin. Blood samples were collected every 7 days before subsequent immunization. The specific IgG and IgM levels were determined by capture ELISA. At day 28, IgM antibody levels were similar for SS1P and two rPEGylated derivatives; IgG antibody levels were also similar at day 28 for these compounds (data not shown). The mouse antisera were also investigated in cytotoxicity assays, and both the anti-SS1P and anti-PEG−SS1P antisera were determined to contain neutralizing antibodies. Although immunogenicity in mice does not predict human immunogenicity, these data do suggest that an immune response is not precluded in the current rPEG−SS1P compounds. The great increase in blood residency time of the PEG−SS1P compounds in mice might provide an increased opportunity for development of an immune response.

Table 3. Antitumor Effects of PEGylated SS1P Bioconjugates

compound	dose	day of best response	% decrease in size	CR	mice/ group
DGA2-12k-SS1P	1.0 mg/kg × 2	13	92%	4/8	8
DGA2-12k-SS1P	2.0 mg/kg × 1	13	92%	3/6	6
Bicin3-U-24k-SS1P	2.0 mg/kg × 1	13	78%	1/4	4
Bicin3-U-24k-SS1P	2.0 mg/kg × 2	13	92%	4/8	8
Bicin3-U-24k-SS1P	3.0 mg/kg × 1	11	92%	3/4	4
Bicin3-mono-30k-SS1P	2.0 mg/kg × 2	13	68%	1/5	5
Bicin3-mono-30k-SS1P	3.0 mg/kg × 1	13	68%	0/2	2
RNL-8a-12k-SS1P	2.0 mg/kg × 1	14	73%	0/2	2
RNL-8a-12k-SS1P	4.0 mg/kg × 1	14	89%	1/2	2
SC-12k-SS1P	1.0 mg/kg × 1	4	51%	0/2	2
SC-12k-SS1P	2.0 mg/kg × 1	5	38%	0/2	2
PEG_2-40k-SS1P	2.0 mg/kg × 1	12	64%	0/4	4
PEG_2-40k-SS1P	3.0 mg/kg × 1	14	86%	1/4	4
positive control: SS1P	0.6 mg/kg × 1	9	32%	0/5	5
negative control: no SS1P	none	none	none	0/20	20

To assess the cross-reactivity of PEG-SS1P and native SS1P to human antibodies versus SS1P, antisera were collected from two patients undergoing SS1P therapy and analyzed in competition ELISA as shown in Figure 4B. Human antisera were mixed with dilutions of either SS1P or PEG−SS1P and then added to SS1P coated plates. The detection reagent was rabbit anti-human IgG (HRP conjugate). The permanent or rPEG−SS1P compounds demonstrated cross-reactivity to the anti-SS1P human antibodies, although the PEG−SS1P compounds exhibited a one- to two-log reduced binding efficiency in this competition immunoassay when compared to native SS1P. These data support the hypothesis that PEG−SS1P may be less prone to rapid clearance in patients with existing antibodies to the SS1P protein.

Target Binding and Uptake of PEG−SS1P. To assess the bioactivity of the PEG−SS1P derivatives in (1) mesothelin binding, (2) cell surface mesothelin binding, and (3) cell uptake and processing, we performed several studies. For the DGA2-12 kDa-PEG-SS1P (D−SS1P) and Bicin3-U-24 kDa-PEG-SS1P (B−SS1P), a determination of K_D, k_{on}, and k_{off} were performed

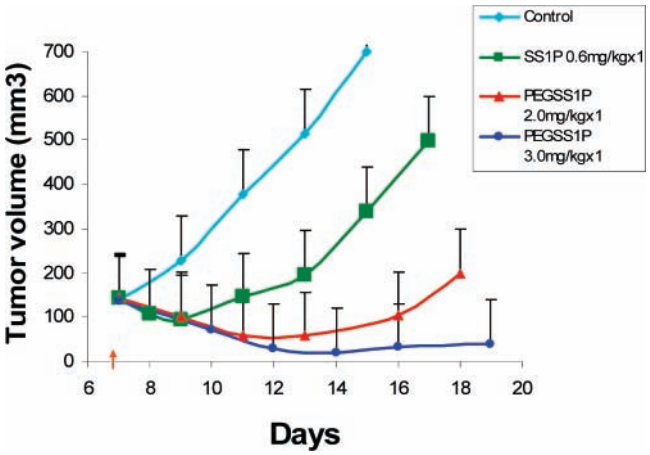


Figure 3. Antitumor effects of PEGylated SS1P with a nonreleasable linker on A431-K5 solid tumors. Cells (3×10^6) were injected s.c. into nude mice on day 0. Starting on day 7, animals were treated with i.v. injections of the immunotoxin compounds (arrow). Therapy with native SS1P (0.6 mg/kg × 1) was given once on day 7; therapy with the PEG_2-40 kDa-PEG-SS1P compound was given once at day 7 (2.0 mg/kg or 3.0 mg/kg). Control mice received vehicle only. Tumor volumes (mm^3) are shown (mean ± SD).

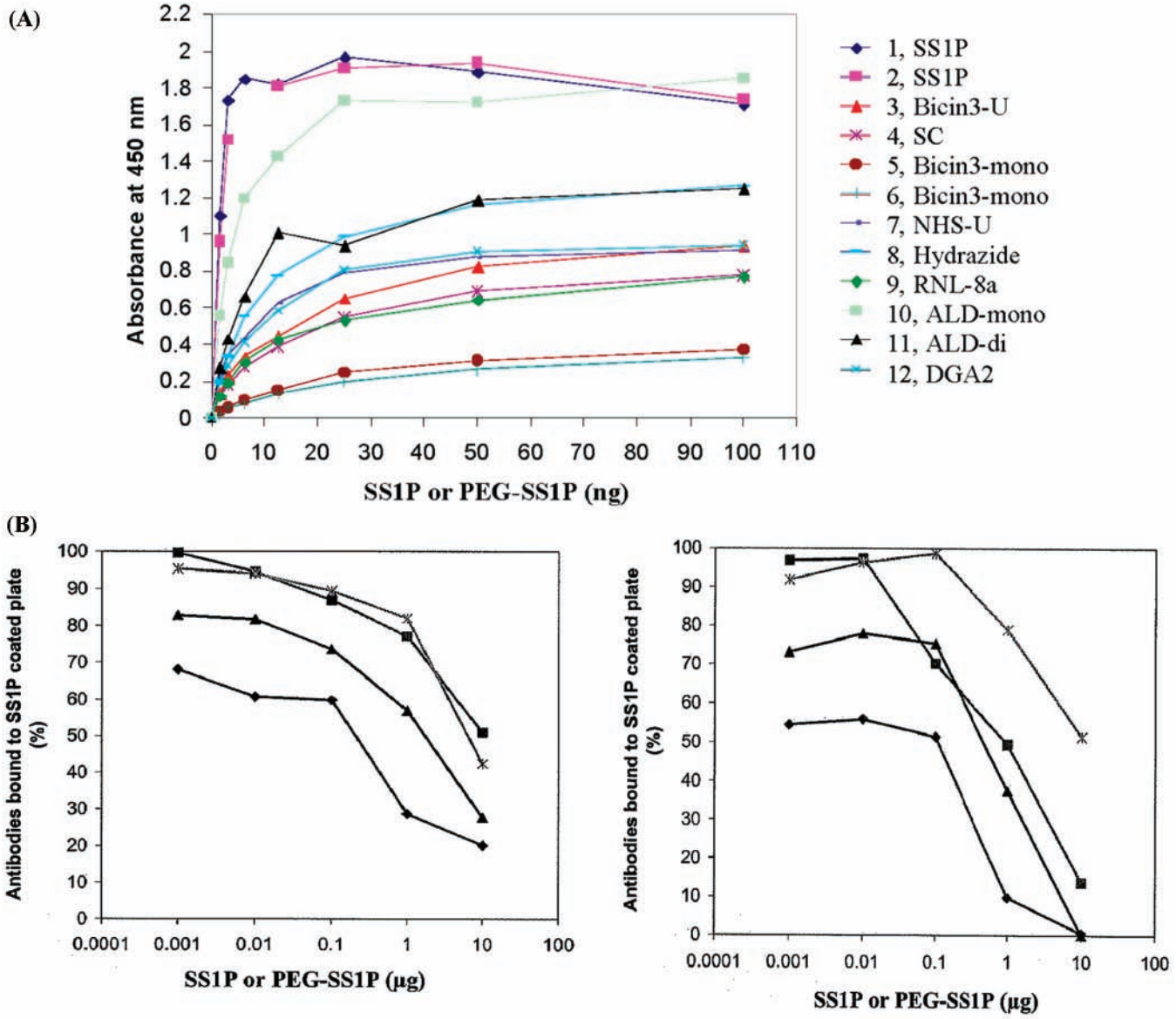


Figure 4. Immunoreactivity of PEG−SS1P. (A) Antigenicity of PEG−SS1P compounds was evaluated by sandwich ELISA. The ELISA plate was coated with mouse monoclonal anti-PE antibody. Different concentrations of SS1P or PEG−SS1P conjugate were added, and rabbit polyclonal anti-PE antiserum (1:40 000 dilution) was added as the primary antibody reagent, while HRP conjugated goat anti-rabbit IgG (1:5000 dilution) and TMB were the secondary reagents. Absorbance was read at 450 nm. The 12 compounds are numbered: (1) native SS1P, lot #1; (2) native SS1P, lot #2; (3) Bicin3-24 kDa-PEG-SS1P; (4) SC-12 kDa-PEG-SS1P; (5) Bicin3-mono-30 kDa-PEG-SS1P, lot #1; (6) Bicin3-mono-30 kDa-PEG-SS1P, lot #2; (7) PEG_2-40 kDa-PEG-SS1P; (8) hydrazide-12 kDa-PEG-SS1P; (9) RNL-8a-12 kDa-PEG-SS1P; (10) ALD-mono-20 kDa-PEG-SS1P; (11) ALD-di-20 kDa-PEG-SS1P; and (12) DGA2-12 kDa-PEG-SS1P. (B) (left) Cross-reactivity of human anti-SS1P serum to PEG−SS1P (patient #1). Plates were coated with 1 μg SS1P/50 μL per well. Human antiserum (1:40 000 dilution) versus SS1P was mixed with serial dilutions of SS1P or PEG−SS1P compounds (based on μg protein) and added to the wells (25 °C, 1.5 h). Following incubation and washing, HRP conjugated rabbit anti-human Ig was added to each well. Following incubation and washing, 100 μL TMB-E substrate were added, and the plates were read immediately at 450 nm. Native SS1P (◆), DGA2-12 kDa-PEG-SS1P (■), PEG_2-40 kDa-PEG-SS1P (▲), and SC-12 kDa-PEG-SS1P (∗) were included in the analysis. (right) Cross-reactivity of human anti-SS1P serum to PEG-SS1P (patient #2, 1:4000 dilution).

by Biacore analysis. The high-affinity SS1P (K_d = 0.7 nM) demonstrated diminished affinity in the D−SS1P (K_d = 39.5 nM) and B−SS1P (K_d = 8.1 nM) derivatives. In agreement with prior studies on PEGylated Fv compounds (*49*, *50*), this was largely the consequence of a reduction in association rate. For SS1P, $k_{on} = 1.1 \times 10^6$ M^{-1} s^{-1}, while the D−SS1P and B−SS1P derivatives have k_{on} rates of 6.3×10^3 M^{-1} s^{-1} and 6.4×10^4 M^{-1} s^{-1}, respectively. Dissociation rates (k_{off}) were relatively conserved among the compounds, SS1P (8.3×10^{-4} s^{-1}), D−SS1P (2.5×10^{-4} s^{-1}), and B−SS1P (5.1×10^{-4} s^{-1}). It is noteworthy that on-rates of a binding molecule are concentration-dependent, whereas off-rates are not. Hence, the attached PEG strands may in effect diminish the dynamic concentration of binding competent molecules available for association with their target.

Flow cytometry investigations were conducted with the PEG−SS1P compounds to evaluate their cell surface binding to A431-K5 cells. SS1P and PEG−SS1P compounds at equimolarity were incubated with the cells, and mouse anti-PE mAb was added, followed by phycoerythrin-conjugated goat anti-mouse polyclonal antibody. A shift toward low fluorescence intensity indicates reduced binding of PEG−SS1P to the cells. These flow cytometry results (Figure 5) correlate with the determined IC_{50} values from the cytotoxicity analysis (see Table 1). For example, SS1P demonstrated maximal cell binding and maximal cytotoxicity (IC_{50} = 0.7 ng/mL) in these analyses,

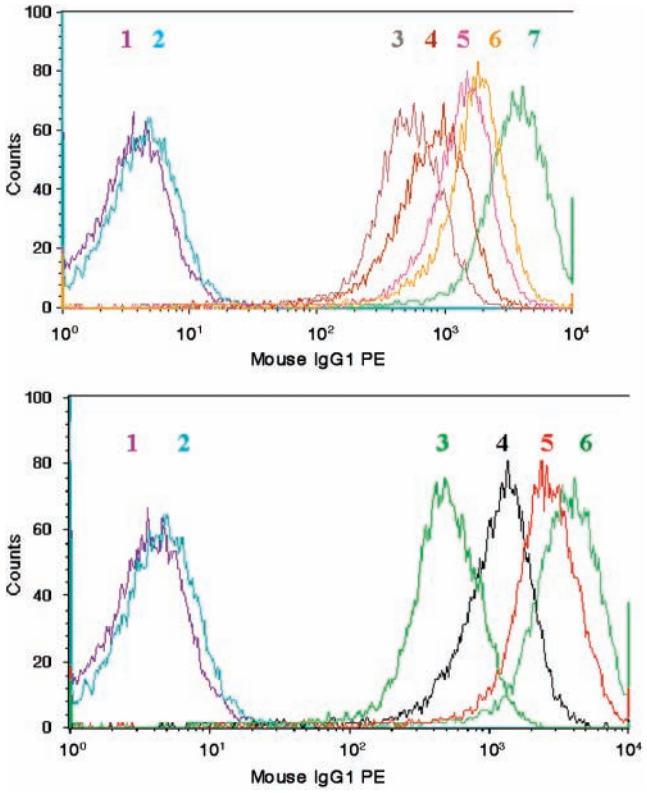


Figure 5. Flow cytometry analysis following PEG−SS1P binding to A431-K5 cells. In flow cytometry studies, A431-K5 cells were incubated with PEG−SS1P compounds prior to addition of mouse anti-PE mAb and phycoerythrin-conjugated goat anti-mouse polyclonal antibody for analysis on FACS Calibur. A shift toward low fluorescence intensity indicates reduced binding of PEG−SS1P to the cells. Cell populations are shown (upper graph): (1) cells without anti-mouse Ab fluorescence labeling, (2) without SS1P, with labeled anti-mouse Ab, (3) with di-PEGylated ALD-20 kDa-PEG-SS1P, (4) with mono-PEGylated ALD-20 kDa-PEG-SS1P, (5) with mono-PEGylated NHS-40 kDa-PEG-SS1P, (6) with mono-PEGylated SC-20 kDa-PEG-SS1P, and (7) with native SS1P; or (lower graph): (1) as above, (2) as above, (3) with DGA2-12 kDa-PEG-SS1P, after 16 h in vitro PEG release, (4) with DGA2-12 kDa-PEG-SS1P, before PEG release, (5) with DGA2-12 kDa-PEG-SS1P, after 4 h in vitro PEG release, and (6) with native SS1P.

whereas the mono-PEGylated ALD−PEG−SS1P (IC_{50} = 39 ng/mL) and di-PEGylated ALD−PEG−SS1P (IC_{50} = 310 ng/mL) demonstrated decreasing cell binding with PEG attachments. Two independent preparations of PEG_2-40 kDa-SS1P compounds were intermediate in IC_{50} and in cell binding in this comparison. As shown in Figure 5 (lower graph), SS1P exhibited maximal binding, while DGA2-12 kDa-PEG-SS1P (IC_{50} = 2.1 ng/mL) showed reduced cell binding. Upon 4 h of in vitro pH 8.5 hydrolysis of the PEG linkage and release of native SS1P, both the cytotoxicity (IC_{50} = 0.93 ng/mL) and the degree of cell binding increase together. However, following prolonged hydrolysis at pH 8.5, the immunotoxin partially denatures as revealed by both a decrease in cytotoxicity (IC_{50} = 30.2) and diminished cell binding by flow cytometry.

Overall activity is a function of the efficiency of intracellular processing of the PEG−SS1P compounds as well. To investigate the immunotoxin processing of PEG−SS1P from binding through subcellular localization, we used a fluorescein-linked 5 kDa NHS−PEG, which forms a permanent amide linkage in conjugation with SS1P. Mono-PEGylated conjugates were purified and characterized. Although the fluorescein−PEG conjugated SS1P exhibited stronger cell binding by flow cytometry than any of the rPEG−SS1P compounds (data not shown), it demonstrated essentially no in vitro cytotoxicity (IC_{50} >1000 ng/mL). We used fluorescence microscopy (Figure 6) and differential interference contrast (DIC) microscopy (data not shown) to investigate the subcellular localization of this fluorescein-labeled PEG−SS1P compound after incubation with A431-K5 cells in vitro. Figure 6 shows phase contrast, fluorescence, and merged microscopic analysis of cellular uptake and subcellular localization. The images revealed an efficient uptake of the compound by A431-K5 cells and localization mainly in the endosomal/lysosomal compartment in the perinuclear area of the cytoplasm, probably as a consequence of the interference of the dye moiety in correct protein processing and trafficking. Control cells (A431), which do not exhibit cell surface expression of mesothelin, demonstrated no cellular uptake of the fluorescein-labeled PEG−SS1P compound. Therefore, as expected, SS1P bioconjugates must maintain at least two general biological functions for efficacy, both cell binding and intracellular processing.

DISCUSSION

We describe macromolecular engineering of recombinant immunotoxin SS1P through employment of rPEGylation. Four rPEGylated designs were investigated wherein three to five large PEG polymers were linked to SS1P via releasable linkers. The rPEG−SS1P compounds exhibited prolonged blood residency time and greatly expanded AUC therapeutic exposure while reducing the nonspecific toxicity of the immunotoxin. A major achievement of this program was a substantial improvement in antitumor efficacy demonstrated by the rPEG−SS1P compounds. For the first time, complete remissions of established mesothelin-expressing tumor xenografts were observed in mice with single-dose administration of rPEG−SS1P conjugates. The significant increase in a therapeutic window for rPEG−SS1P may offer clinical advantages for the use of immunotoxins in cancer patients.

Bioconjugation of proteins with PEG via permanent linkages is a well-developed technology employed in marketed PEGylated protein therapeutics and numerous experimental compounds (*37*, *48*). PEG attachments to proteins have significant benefits in prolonging the in vivo activity of proteins by impeding the rapid clearance of proteins from renal filtration, antibody or cellular recognition, or physical degradation. Although an extensive surface modification of proteins, especially foreign proteins, by multiple PEG strands is often preferred in development of PEGylated protein drugs, this strategy can be limited by the reduction or elimination of biological activity of the PEG protein. Recent methods in PEGylation technology have focused on designing a composite bioconjugate using both protein engineering and improved chemical linkages (*13*, *36*, *42*). Site-specific attachments of PEG polymer strands may afford better retention of bioactivity, while minimizing the heterogeneity of the conjugates. However, some unwanted polymer-derived effects may still be encountered either in formulation or in pharmacological outcomes. Therefore, our recent research has examined the potential development of rPEGylation, wherein covalent attachments of strands of PEG polymers are shed via a controlled release mechanism derived from a degradable linkage at the attachment site on the protein surface (*39*, *40*, *44*).

The immunotoxin SS1P must maintain target binding, protein translocation/processing, and enzymatic ADP-ribosylating activities to be an effective therapeutic. These requirements challenge conventional PEGylation approaches. First, random permanent attachment of one large polymer (or a few small polymers) to the protein will likely compromise one or more of these functions while providing suboptimal surface shielding from antibodies. Second, permanent site-specific attachments of PEG will also reduce biological activity and may drastically reduce yields during manufacturing. In contrast, employment

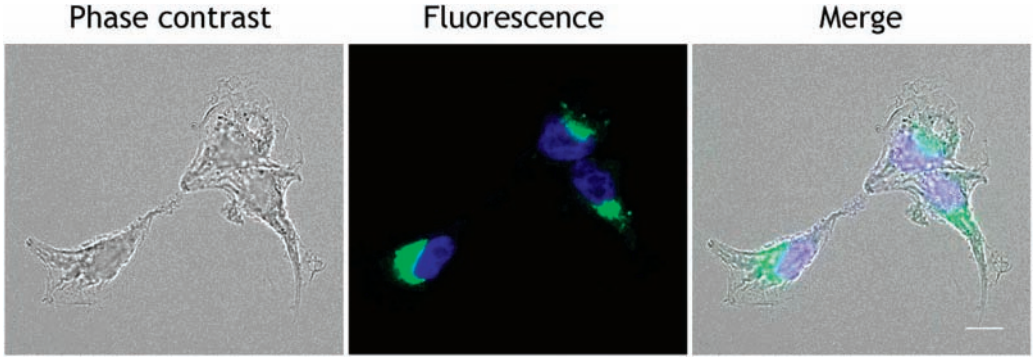


Figure 6. A431-K5 cellular internalization studies with 20 nM fluorescein labeled 5 kDa-PEG-SS1P in vitro (16 h). Phase contrast, fluorescence, and merged microscopic images are shown with 10 μm scale bar (lower right) with fluorescein in green and the nucleus stained blue with DAPI.

of rPEGylation may allow widespread modification of the protein while actually simplifying purification, since the heavily PEGylated proteins are readily purified from native protein. While such formulations of SS1P are heterogeneous, the end product is homogeneous and corresponds to the original unmodified SS1P, which is regenerated in vivo. Although this strategy does add complexity to the analysis of in vivo biodistribution, pharmacokinetics, and pharmacodynamics, the overall benefits in increased antitumor efficacy and diminished toxicity, suggested by our present work, support rPEGylation as an important new platform technology for immunotoxins and related therapeutics. Further studies on the biodistribution of the PEG−SS1P compounds may provide insight into the differential deposition of the immunotoxin in tumors and major organs. However, the design of these labeled conjugates may be more complex than the recently reported biodistribution study of ^{111}In-labeled SS1P, which also used a conjugation method for the radioisotope complex (*51*).

Immunogenicity is a central concern in the development and drug monitoring of protein therapeutics, including PEGylated proteins. Binding antibodies and neutralizing antibodies are commonly encountered. Clinical experience with SS1P has revealed the eventual development of neutralizing antibodies in most patients. It is uncertain whether our current rPEG−SS1P can completely overcome this problem. Immunized mice did develop neutralizing antibodies against SS1P following prolonged administration of rPEG−SS1P compounds. While these animal results are not predictive of outcomes in patients, it may be challenging to completely abolish the immune response to the SS1P conjugates in humans. In this context, however, two PEGylated nonhuman protein drugs, ADAGEN and ONCASPAR, have been administered to patients successfully over multiple cycles, despite the occurrence of antibody responses in several of these patients. Either animal or human antisera against SS1P bind much less efficiently to the PEG−SS1P compounds, suggesting that PEG−SS1P compounds will have a lower in vivo clearance in patients as a result of binding or neutralizing antibodies.

We also utilized multiple physical and functional assays to evaluate the composition, stability, and activities of the rPEG−SS1P conjugates. From flow cytometry and cytotoxicity investigations, we established a correlation between the efficiency of target binding by the SS1P derivatives and their in vitro IC_{50} values. However, using fluorescence and DIC microscopy, we also demonstrated that uptake alone of a fluorescein labeled PEG−SS1P conjugate does not guarantee correct intracellular processing. In this instance, it is proposed that the PEG−dye moiety, while permitting internalization, interferes with the biological release mechanism of the toxin. We further observed that in vitro binding or activity assays are inadequate to predict efficacy in vivo of the rPEG−SS1P, since the controlled release of the active drug is not fully revealed in vitro. rPEG−SS1P may acquire full bioactivity in vivo following programmed release.

An intrinsic feature of recombinant immunotoxins is target-specific delivery. In juxtaposition to active targeting, the phenomenon of passive targeting of drugs via the EPR effect has been shown to offer significant drug accumulation in tumors (*45*, *46*). PEG modification is one common approach to exploiting the EPR effect (*45*). Therefore, we wished to determine the extent to which an analogous nontargeted immunotoxin would produce antitumor responses in the mesothelin-expressing xenografts. An rPEGylated dsFv-PE immunotoxin, which binds CD22, was prepared with equivalent linkers and PEG attachments and investigated in the A431-K5 xenograft model. No antitumor effects were observed. These results suggest a pivotal role of active targeting via mesothelin binding and internalization for the antitumor effects of the PEG−SS1P bioconjugates.

In summary, rPEGylation of mesothelin-targeted immunotoxin SS1P greatly improves antitumor efficacy while decreasing nonspecific toxicity. The further co-development of protein engineering and bioconjugate technologies may provide superior immunotoxins with tailored pharmacological properties.

ACKNOWLEDGMENT

This research was supported in part by the Intramural Research Program of the NIH, National Cancer Institute, Center for Cancer Research. We thank Steve Youngster, Diane Chang, Qing Dong, and Michelle Boro for performance of SE-HPLC, RP-HPLC, and endotoxin analysis. We are grateful to Mary Mehlig and Virna Borowski for performance of mouse PK and immunogenicity studies. We are also grateful to Jack Lipman and Ivan Horak for critical review of the manuscript.

LITERATURE CITED

(1) Hassan, R., Bera, T., and Pastan, I. (2004) Mesothelin: a new target for immunotherapy. *Clin. Cancer Res. 10*, 3937−3942.

(2) Sato, N., Hassan, R., Axworthy, D. B., Wong, K. J., Yu, S., Theodore, L. J., Lin, Y., Park, L., Brechbiel, M. W., Pastan, I., Paik, C. H., and Carrasquillo, J. A. (2005) Pretargeted radioimmunotherapy of mesothelin-expressing cancer using a tetravalent single-chain Fv-streptavidin fusion protein. *J. Nucl. Med. 46*, 1201−1209.

(3) Fan, D., Yano, S., Shinohara, H., Solorzano, C., Van Arsdall, M., Bucana, C. D., Pathak, S., Kruzel, E., Herbst, R. S., Onn, A., Roach, J. S., Onda, M., Wang, Q. C., Pastan, I., and Fidler, I. J. (2002) Targeted therapy against human lung cancer in nude mice by high-affinity recombinant antimesothelin single-chain immunotoxin. *Mol. Cancer Ther. 1*, 595−600.

(4) Hassan, R., Lerner, M. R., Benbrook, D., Lightfoot, S. A., Brackett, D. J., Wang, Q. C., and Pastan, I. (2002) Antitumor activity of SS-(dsFv)PE38 and SS1(dsFv)PE38, recombinant antimesothelin im-

munotoxins against human gynecologic cancers grown in organotypic culture in vitro. *Clin. Cancer Res. 8*, 3520−3526.
(5) Hassan, R., Wu, C., Brechbiel, M. W., Margulies, I., Kreitman, R. J., and Pastan, I. (1999) ^{111}Indium-labeled monoclonal antibody K1: biodistribution study in nude mice bearing a human carcinoma xenograft expressing mesothelin. *Int. J. Cancer 80*, 559−563.
(6) Chowdhury, P. S., Viner, J. L., Beers, R., and Pastan, I. (1998) Isolation of a high-affinity stable single-chain Fv specific for mesothelin from DNA-immunized mice by phage display and construction of a recombinant immunotoxin with anti-tumor activity. *Proc. Natl. Acad. Sci. U.S.A. 95*, 669−674.
(7) Ho, M., Hassan, R., Zhang, J., Wang, Q. C., Onda, M., Bera, T., and Pastan, I. (2005) Humoral immune response to mesothelin in mesothelioma and ovarian cancer patients. *Clin. Cancer Res. 11*, 3814−3820.
(8) Bera, T. K., Williams-Gould, J., Beers, R., Chowdhury, P., and Pastan, I. (2001) Bivalent disulfide-stabilized fragment variable immunotoxin directed against mesotheliomas and ovarian cancer. *Mol. Cancer Ther. 1*, 79−84.
(9) Hassan, R., Kreitman, R. J., Pastan, I., and Willingham, M. C. (2005) Localization of mesothelin in epithelial ovarian cancer. *Appl. Immunohistochem. Mol. Morphol. 13*, 243−247.
(10) Li, Q., Verschraegen, C. F., Mendoza, J., and Hassan, R. (2004) Cytotoxic activity of the recombinant anti-mesothelin immunotoxin, SS1(dsFv)PE38, towards tumor cell lines established from ascites of patients with peritoneal mesotheliomas. *Anticancer Res. 24*, 1327−1335.
(11) Hassan, R., Viner, J. L., Wang, Q. C., Margulies, I., Kreitman, R. J., and Pastan, I. (2000) Anti-tumor activity of K1-LysPE38QQR, an immunotoxin targeting mesothelin, a cell-surface antigen overexpressed in ovarian cancer and malignant mesothelioma. *J. Immunother. 23*, 473−479.
(12) Brinkmann, U., Webber, K., Di Carlo, A., Beers, R., Chowdhury, P., Chang, K., Chaudhary, V., Gallo, M., and Pastan, I. (1997) Cloning and expression of the recombinant Fab fragment of monoclonal antibody K1 that reacts with mesothelin present on mesotheliomas and ovarian cancers. *Int. J. Cancer 71*, 638−644.
(13) Chowdhury, P. S., Chang, K., and Pastan, I. (1997) Isolation of anti-mesothelin antibodies from a phage display library. *Mol. Immunol. 34*, 9−20.
(14) Chang, K., and Pastan, I. (1996) Molecular cloning of mesothelin, a differentiation antigen present on mesothelium, mesotheliomas, and ovarian cancers. *Proc. Natl. Acad. Sci. U.S.A. 93*, 136−40.
(15) Chang, K., and Pastan, I. (1994) Molecular cloning and expression of a cDNA encoding a protein detected by the K1 antibody from an ovarian carcinoma (OVCAR-3) cell line. *Int. J. Cancer 57*, 90−97.
(16) Bera, T. K., and Pastan, I. (2000) Mesothelin is not required for normal mouse development or reproduction. *Mol. Cell Biol. 20*, 2902−2906.
(17) Muminova, Z. E., Strong, T. V., and Shaw, D. R. (2004) Characterization of human mesothelin transcripts in ovarian and pancreatic cancer. *BMC Cancer 4*, 19.
(18) Robinson, B. W., Creaney, J., Lake, R., Nowak, A., Musk, A. W., de Klerk, N., Winzell, P., Hellstrom, K. E., and Hellstrom, I. (2003) Mesothelin-family proteins and diagnosis of mesothelioma. *Lancet 362*, 1612−1616.
(19) Ordonez, N. G. (2003) Application of mesothelin immunostaining in tumor diagnosis. *Am. J. Surg. Pathol. 27*, 1418−1428.
(20) Argani, P., Iacobuzio-Donahue, C., Ryu, B., Rosty, C., Goggins, M., Wilentz, R. E., Murugesan, S. R., Leach, S. D., Jaffee, E., Yeo, C. J., Cameron, J. L., Kern, S. E., and Hruban, R. H. (2001) Mesothelin is overexpressed in the vast majority of ductal adenocarcinomas of the pancreas: identification of a new pancreatic cancer marker by serial analysis of gene expression (SAGE). *Clin. Cancer Res. 7*, 3862−3868.
(21) Onda, M., Willingham, M., Nagata, S., Bera, T. K., Beers, R., Ho, M., Hassan, R., Kreitman, R. J., and Pastan, I. (2005) New monoclonal antibodies to mesothelin useful for immunohistochemistry, fluorescence-activated cell sorting, Western blotting, and ELISA. *Clin. Cancer Res. 11*, 5840−5846.
(22) Rump, A., Morikawa, Y., Tanaka, M., Minami, S., Umesaki, N., Takeuchi, M., and Miyajima, A. (2004) Binding of ovarian cancer antigen CA125/MUC16 to mesothelin mediates cell adhesion. *J. Biol. Chem. 279*, 9190−9198.
(23) Chowdhury, P. S., and Pastan, I. (1999) Improving antibody affinity by mimicking somatic hypermutation in vitro. *Nat. Biotechnol. 17*, 568−572.
(24) Brinkmann, U., Reiter, Y., Jung, S. H., Lee, B., and Pastan, I. (1993) A recombinant immunotoxin containing a disulfide-stabilized Fv fragment. *Proc. Natl. Acad. Sci. U.S.A. 90*, 7538−7542.
(25) Reiter, Y., Brinkmann, U., Kreitman, R. J., Jung, S. H., Lee, B., and Pastan, I. (1994) Stabilization of the Fv fragments in recombinant immunotoxins by disulfide bonds engineered into conserved framework regions. *Biochemistry 33*, 5451−5459.
(26) Reiter, Y., Brinkmann, U., Lee, B., and Pastan, I. (1996) Engineering antibody Fv fragments for cancer detection and therapy: disulfide-stabilized Fv fragments. *Nat. Biotechnol. 14*, 1239−1245.
(27) Allured, V. S., Collier, R. J., Carroll, S. F., and McKay, D. B. (1986) Structure of exotoxin A of *Pseudomonas aeruginosa* at 3.0-Ångstrom resolution. *Proc. Natl. Acad. Sci. U.S.A. 83*, 1320−1324.
(28) Wang, Q. C., Pai, L. H., Debinski, W., FitzGerald, D. J., and Pastan, I. (1993) Polyethylene glycol-modified chimeric toxin composed of transforming growth factor α and *Pseudomonas* exotoxin. *Cancer Res. 53*, 4588−4594.
(29) Tsutsumi, Y., Onda, M., Nagata, S., Lee, B., Kreitman, R. J., and Pastan, I. (2000) Site-specific chemical modification with polyethylene glycol of recombinant immunotoxin anti-Tac(Fv)-PE38 (LMB-2) improves antitumor activity and reduces animal toxicity and immunogenicity. *Proc. Natl. Acad. Sci. U.S.A. 97*, 8548−8553.
(30) Roberts, M. J., and Harris, J. M. (1998) Attachment of degradable poly(ethylene glycol) to proteins has the potential to increase therapeutic efficacy. *J. Pharm. Sci. 87*, 1440−1445.
(31) Brinkmann, U., Pai, L. H., FitzGerald, D. J., Willingham, M., and Pastan, I. (1991) B3(Fv)-PE38KDEL, a single-chain immunotoxin that causes complete regression of a human carcinoma in mice. *Proc. Natl. Acad. Sci. U.S.A. 88*, 8616−8620.
(32) Pastan, I., and FitzGerald, D. (1991) Recombinant toxins for cancer treatment. *Science 254*, 1173−1177.
(33) Bang, S., Nagata, S., Onda, M., Kreitman, R. J., and Pastan, I. (2005) HA22 (R490A) is a recombinant immunotoxin with increased antitumor activity without an increase in animal toxicity. *Clin. Cancer Res. 11*, 1545−1550.
(34) Kreitman, R. J., and Pastan, I. (1998) Accumulation of a recombinant immunotoxin in a tumor *in vivo*: fewer than 1000 molecules per cell are sufficient for complete responses. *Cancer Res. 58*, 968−975.
(35) Kreitman, R. J., Wilson, W. H., Robbins, D., Margulies, I., Stetler-Stevenson, M., Waldmann, T. A., and Pastan, I. (1999) Responses in refractory hairy cell leukemia to a recombinant immunotoxin. *Blood 94*, 3340−3348.
(36) Kreitman, R. J., Wilson, W. H., Bergeron, K., Raggio, M., Stetler-Stevenson, M., FitzGerald, D. J., and Pastan, I. (2001) Efficacy of the anti-CD22 recombinant immunotoxin BL22 in chemotherapy-resistant hairy-cell leukemia. *N. Engl. J. Med. 345*, 241−247.
(37) Harris, J. M., and Chess, R. B. (2003) Effect of PEGylation on pharmaceuticals. *Nat. Rev. Drug Discovery 2*, 214−221.
(38) Benhar, I., Wang, Q. C., FitzGerald, D., and Pastan, I. (1994) *Pseudomonas* exotoxin A mutants: replacement of surface-exposed residues in domain III with cysteine residues that can be modified with polyethylene glycol in a site-specific manner. *J. Biol. Chem. 269*, 13398−404.
(39) Zhao, H., Yang, K., Martinez, A., Basu, A., Chintala, R., Liu, H. C., Janjua, A., Wang, M., and Filpula, D. (2006) Linear and branched bicin linkers for releasable PEGylation of macromolecules: controlled release in vivo and in vitro from mono- and multi-PEGylated proteins. *Bioconjugate Chem. 17*, 341−351.
(40) Greenwald, R. B., Yang, K., Zhao, H., Conover, C. D., Lee, S., and Filpula, D. (2003) Controlled release of proteins from their poly(ethylene glycol) conjugates: drug delivery systems employing 1,6-elimination. *Bioconjugate Chem. 14*, 395−403.
(41) Greenwald, R. B., Choe, Y. H., McGuire, J., and Conover, C. D. (2003) Effective drug delivery by PEGylated drug conjugates. *Adv. Drug Delivery Rev. 55*, 217−250.
(42) Zalipsky, S., Qazen, M., Walker, J. A., II, Mullah, N., Quinn, Y. P., and Huang, S. K. (1999) New detachable poly(ethylene glycol) conjugates: cysteine-cleavable lipopolymers regenerating natural phospholipid, diacyl phosphatidylethanolamine. *Bioconjugate Chem. 10*, 703−707.

(43) Tsubery, H., Mironchik, M., Fridkin, M., and Shechter, Y. (2004) Prolonging the action of protein and peptide drugs by a novel approach of reversible polyethylene glycol modification. *J. Biol. Chem. 279*, 38118−38124.

(44) Greenwald, R. B., Zhao, H., Yang, K., Reddy, P., and Martinez, A. (2004) A new aliphatic amino prodrug system for the delivery of small molecules and proteins utilizing novel PEG derivatives. *J. Med. Chem. 47*, 726−734.

(45) Yu, D., Peng, P., Dharap, S. S., Wang, Y., Mehlig, M., Chandna, P., Zhao, H., Filpula, D., Yang, K., Borowski, V., Borchard, G., Zhang, Z., and Minko, T. (2005) Antitumor activity of poly(ethylene glycol)-camptothecin conjugate: the inhibition of tumor growth in vivo. *J. Controlled Release 110*, 90−102.

(46) Maeda, H., Sawa, T., and Konno, T. (2001) Mechanism of tumor-targeted delivery of macromolecular drugs, including the EPR effect in solid tumor and clinical overview of the prototype polymeric drug SMANCS. *J. Controlled Release 74*, 47−61.

(47) Li, S., Yang, Z., Sun, X., Tan, Y., Yagi, S., and Hoffman, R. M. (2003) A simultaneous colorimetric assay of free and protein-coupled polyethylene glycol. *Anal. Biochem. 313*, 335−337.

(48) Roberts, M. J., Bentley, M. D., and Harris, J. M. (2002) Chemistry for peptide and protein PEGylation. *Adv. Drug Delivery Rev. 54*, 459−476.

(49) Yang, K., Basu, A., Wang, M., Chintala, R., Hsieh, M. C., Liu, S., Hua, J., Zhang, Z., Zhou, J., Li, M., Phyu, H., Petti, G., Mendez, M., Janjua, H., Peng, P., Longley, C., Borowski, V., Mehlig, M., and Filpula, D. (2003) Tailoring structure-function and pharmacokinetic properties of single-chain Fv proteins by site-specific PEGylation. *Protein Eng. 16*, 761−770.

(50) Kubetzko, S., Sarkar, C. A., and Pluckthun, A. (2005) Protein PEGylation decreases observed target association rates via a dual blocking mechanism. *Mol. Pharmacol. 68*, 1439−1454.

(51) Zhang, Y., Xiang, L., Hassan, R., Paik, C. H., Carrasquillo, J. A., Jang, B. S., Le, N., Ho, M., and Pastan, I. (2006) Synergistic antitumor activity of taxol and immunotoxin SS1P in tumor-bearing mice. *Clin. Cancer Res. 12*, 4695−4701.

BC060314X

Anginex-Conjugated Liposomes for Targeting of Angiogenic Endothelial Cells

Ricardo J. M. G. E. Brandwijk,[#] Willem J. M. Mulder,[§] Klaas Nicolay,[§] Kevin H. Mayo,[†] Victor L. J. L. Thijssen,[#] and Arjan W. Griffioen[#,*]

Angiogenesis Laboratory, Research Institute Growth and Development (GROW), Department of Pathology, Maastricht University & University Hospital, Maastricht, The Netherlands; Biomedical NMR, Department of Biomedical Engineering, Eindhoven University of Technology, Eindhoven, The Netherlands, and Department of Biochemistry, Molecular Biology and Biophysics, University of Minnesota, Minneapolis, Minnesota 55455. Received October 9, 2006; Revised Manuscript Received February 1, 2007

Identification of a tumor angiogenesis specific ligand would allow targeting of tumor vasculature. Lipidic vehicles can be used to deliver therapeutic agents for treatment of disease or contrast agents for molecular imaging. A targeting ligand would allow specific delivery of such formulations to angiogenic sites, thereby reducing side effects and gaining efficiency. Anginex, a synthetic 33-mer angiostatic peptide, has been described to home angiogenically activated endothelium, suggesting an ideal candidate as targeting ligand. To investigate this application of anginex, fluorescently labeled paramagnetic liposomes were conjugated with anginex. Using phase contrast and fluorescence microscopy as well as magnetic resonance imaging (MRI), we demonstrate that anginex-conjugated liposomes bind specifically to activated endothelial cells, suggesting application as an angiogenesis targeting agent for molecular targeting and molecular imaging of angiogenesis-dependent disease.

INTRODUCTION

Lipid-based vesicles, such as liposomes, can be used as therapeutic vehicles for transport, e.g., drugs, DNA, proteins/peptides, and antibodies (*1*, *2*), or for diagnostic purposes such as the delivery of MRI contrast agents (*3*). However, liposomes have a relatively short circulation time because they are taken up by the mononuclear phagocyte system (MPS) (*4*−*6*). In order to increase their circulation time, hydrophilic carbohydrates or polymers (e.g., PEG) can be included in the lipidic formulation which prevents rapid clearance and uptake by MPS (*7*). Moreover, the use of pegylated lipids with distal functional moieties such as maleimide allows the conjugation of targeting ligands to the liposomes. Targeted liposomes enhance the specificity and efficiency of treatment which may result in a higher therapeutic success rate and in reduction of undesirable side effects (*8*). An important requirement for successful targeted delivery is the specificity of the ligand/receptor pair for the site of interest. For example, we have previously demonstrated that a RGD−peptide functions as a targeting ligand for integrin $\alpha v\beta 3$ which can be used to target liposomes specifically to angiogenically activated endothelial cells (*9*).

Angiogenesis, i.e., the outgrowth of new vessels from pre-existing vasculature, is a prerequisite for tumor growth and metastasis (*10*, *11*). The tumors' dependence on this process, together with the observation that the endothelial cells that mediate the vessel growth change the expression of specific cell surface-related molecules (*12*), makes tumor angiogenesis receptive for targeted treatment strategies. We have previously described the (33-mer) synthetic angiostatic peptide anginex that inhibits migration and proliferation of activated EC *in vitro* (*13*, *14*) and exerts a strong antitumor response *in vivo* without affecting physiological angiogenesis (*15*). It has been demonstrated that fluorescently labeled anginex specifically homes to tumor vasculature (*15*, *16*). Recently, we identified galectin-1 as the main receptor of anginex on activated endothelial cells (*17*).

In the clinical oncology field there is a need for targeting ligands that allow more specific therapy and can be used for noninvasive imaging techniques (*18*). Using tumor angiogenesis markers for targeting, noninvasive imaging would allow more accurate diagnosis and monitoring of angiogenic development and the effect of angiostatic treatment (*19*, *20*). On the basis of our observations, we hypothesized that anginex is an excellent ligand for targeting of therapeutic or diagnostic liposomes to activated endothelial cells in the tumor vasculature. To test this hypothesis, we conjugated anginex to fluorescently labeled and paramagnetic liposomes. The endothelial cell specificity of the anginex−liposome conjugates was confirmed on human umbilical vein endothelial cells (HUVEC) and an immortalized endothelial cell line (EVL-C2). In addition, we were able to demonstrate, by microscopic analysis and by MR imaging, that anginex-conjugated liposomes specifically bind to and are taken up by activated endothelial cells, making them attractive vehicles for targeted delivery or diagnostic use in the treatment of disease.

MATERIALS AND METHODS

Materials. 1,2-Distearoyl-*sn*-glycero-3-phosphocholine (DSPC), cholesterol (Chol), 1,2-distearoyl-*sn*-glycero-3-phosphoethanolamine-*N*-[methoxy(polyethylene glycol)-2000] (PEG2000−DSPE), 1,2-distearoyl-*sn*-glycero-3-phosphoethanolamine-*N*-[maleimide(polyethylene glycol)2000] (Mal-PEG2000−DSPE), and 1,2-dipalmitoyl-*sn*-glycero-3-phosphoethanolamine-*N*-(lissamine rhodamine B sulfonyl) (rhodamine-PE) were obtained from Avanti Polar Lipids (Albaster, AL). Gd-DTPA−bis(stearylamide) (Gd-DTPA−BSA) was purchased from Gateway Chemical Technology (St.Louis, MO). HEPES was obtained from Merck (Darmstadt, Germany). All other chemicals were of analytic grade or the best grade available. Polycarbonate filters for liposome extrusion were from Costar (Cambridge, MA).

* Corresponding author: Arjan W. Griffioen, Ph.D., Department of Pathology, Maastricht University & University Hospital Maastricht, P.O. Box 5800, 6202 AZ Maastricht, The Netherlands, phone: +31-43-3874630, fax: +31-43-3876613, e-mail: aw.griffioen@path.unimaas.nl.

[#] Maastricht University & University Hospital.

[§] Eindhoven University of Technology.

[†] University of Minnesota.

10.1021/bc060316h CCC: $37.00 © 2007 American Chemical Society
Published on Web 03/23/2007

Peptide Synthesis. Anginex with an additional cysteine at the N-terminal site was synthesized using a Milligen/Biosearch 9600 peptide solid-phase synthesizer using Fmoc chemistry. Lyophilized peptides were purified by preparative reversed-phase HPLC on a C18 column with an elution gradient of 0−60% (v/v) acetonitrile with 0.1% (v/v) trifluoroacetic acid in water. Purity and composition of the peptides were verified by HPLC (Beckman Model 6300) analysis of amino acid composition of hydrolysates prepared by treating the peptides under argon in 6 N HCl for 24 h at 110 °C. The amino acid sequences of peptides were confirmed by N-terminal sequencing and mass spectometry. As described before, the cyclic 5-mer RGD peptide (c(RGDf(-S-acetylthioacetyl)K)) was synthesized at a purity of 95% by Ansynth Service BV (*9*).

Liposome Preparation. Liposomes were prepared by lipid film hydration. A mixture of the appropriate amounts of lipids (typically 100−200 μmol of total lipid) was dissolved in chloroform/methanol 1:1 (v/v) and evaporated to dryness by rotary evaporation at 40 °C. For the paramagnetic PEG liposomes that were used to couple RGD or anginex peptides covalently to the distal end of the PEG chains, Gd-BSA, DSPC, cholesterol, PEG2000−DSPE, and Mal-PEG2000−DSPE were mixed at a molar ratio of 0.75/1.10/1/0.075/0.075. For fluorescence microscopy, 0.1 mol % of rhodamine−PE was added. The lipid film was subsequently hydrated in 3 mL of HEPES-buffered saline (HBS), containing 20 mM HEPES and 135 mM NaCl (pH 6.5). The resulting lipid dispersion was extruded sequentially six times through polycarbonate membrane filters with a pore diameter of 400 nm and subsequently 10 times through filters with a pore diameter of 200 nm using a Lipofast Extruder (Avestin, Canada). The temperature during extrusion was 65 °C.

Peptide Coupling to Liposomes. The cyclic 5mer RGD (c(RGDf(-S-acetylthioacetyl)K)) and anginex were conjugated to the liposomes by sulfhydryl-maleimide coupling maleimide-PEG−DSPE. Acetyl-protected RGD−peptide was deacetylated in 0.05 M HEPES/0.05 M hydroxylamine-HCl/0.03 mM ethylenediamine tetraacetic acid (pH 7.0) for 1 h at room temperature (*21*). The activated peptide was added to the Mal-PEG2000−DSPE-containing liposomes in a 3 μg peptide/μmol lipid ratio. Anginex, synthesized with a C-terminal cysteine, was dissolved in water and added to the liposomal solution (10 μg peptide/1 μmol lipid). Coupling of both peptides was allowed overnight at 4 °C, and uncoupled peptide was separated from the liposomes by centrifugating at 200 000*g* with a Beckman OptimaTM LE-80K ultracentrifuge and a Ti70 fixed angle rotor for 60 min. The liposomes were respectively conjugated with ~700 cyclic RGD moieties and ~125 anginex moieties per particle. The supernatant was removed, and an appropriate amount of buffer, typically 1.5 mL, was added to the pellet to obtain a lipid suspension with a lipid concentration of ~40 mM (10 mM gadolinium). The final liposomal suspension was stored at 4 °C under N_2.

Cell Culture. HUVECs were isolated as described before (*22*). Isolated cells were cultured in gelatin-coated culture flasks (Costar) with RPMI1640 (Gibco) supplemented with 20% human serum, 2 mM L-glutamine (Gibco) and 50 U/mL penicillin/streptomycin (Life sciences). Immortalized endothelial cell line EVL-*C2* (*23*) was cultured under the same culture conditions as HUVEC. Cultures were incubated at 37 °C in the presence of 5% CO_2.

***In Vitro* Targeting of Endothelial Cells.** For all tested applications the initial steps were similar. Endothelial cells were cultured in gelatin-coated flasks to approximately 75% confluency (appoximately 1.5×10^6 cells) using standard culture conditions. Flasks were washed once with PBS before 4 mL of fresh culture medium was added. Anginex-conjugated, RGD-conjugated, and nonconjugated liposomes (150 μL of liposomes; total amount anginex 60 μg) were added to the cells and incubated in the CO_2 incubator at 37 °C for 3 h. Subsequently, liposome-containing medium was removed, the cells were washed with 14 mL of PBS, and fresh medium was added. The final wash step was skipped for the control cells. Finally, the association of the targeted and nontargeted liposomes with endothelial cells was assessed under a phase contrast fluorescence microscope (Leica), at 20× and 40× magnification. Experiments were carried out in triplicate. Competition experiments were performed with free anginex. To that end, anginex (3 mg/mL in MQ) was added to the medium to a final concentration of respectively 10 or 30 μg/mL (total anginex concentration respectively 60 and 180 μg) immediately before addition of the liposome solution.

Magnetic Resonance Imaging of Cell Pellets. For MRI imaging, cells were harvested using trypsine digestion and centrifuged for 5 min at 400*g*. The obtained cell pellet was washed with approximately 5 mL of culture medium. After a second centrifugation step, the cell pellet was fixed with 1% paraformaldehyde and put in small 200 μL tubes. MRI experiments were performed on fixed cell pellets using a 6.3 T horizontal bore magnet (Oxford Instruments Superconductivity, Eynsham, Oxon, England) interfaced to a Varian (Varian, Palo Alto, CA) VXR-S MRI console. A 3 cm quadrature-driven birdcage coil was used. The cups containing cell pellets were placed in a custom-made sample holder, capable of carrying four Eppendorf cups. Quantification of $T1$ was done with an inversion recovery spin−echo sequence with 13 different inversion times, ranging from 10 to 3100 ms in an exponential fashion. The MRI data analysis was performed using Mathematica 5.0 (Wolfram Research, Inc., Champaign, IL). $T1$ maps of HUVEC pellets were calculated in one slice through the pellet on a pixel-by-pixel basis. The $T1$ is reported as mean ± SD of the pixels in a circular region of interest (ROI) defined by the contour of the pellet. In Student's t tests, $P < 0.05$ was considered statistically significant.

RESULTS

We set out to test the applicability of anginex as a ligand to target liposomes to activated endothelial cells. To that end, fluorescent paramagnetic liposomes were prepared to allow parallel detection of the liposomes with optical methods as well as with MR imaging. Targeting specificity was introduced by covalently linking anginex containing a free cysteine via the thiol group to the maleimide group of the lipid Mal-PEG−DSPE (*24*). As a control, cyclic RGD was coupled as described previously (*9*). A schematic presentation of the ligand-conjugated liposomes is given in Figure 1.

To demonstrate specific binding to endothelial cells, cultured human umbilical vein endothelial cells (HUVEC) were incubated for 3 h with either anginex-conjugated liposomes or with bare liposomes. After liposome incubation and extensive washing, phase contrast microscopy revealed that only anginex-conjugated liposomes efficiently bound to the cell surface (data not shown). RGD-conjugated liposomes, used as a positive control, also bound the endothelial monolayer. Using fluorescence microscopy, the liposomes were visualized and were found to bind throughout the endothelial surface (Figure 2a, left and middle panel). Cells incubated with bare liposomes did marginally or did not show fluorescence signal (Figure 2a, right panel). Although small differences in morphology were visible between the three independent experiments due to different passage numbers, the binding or presence of the liposomes did not induce obvious changes in EC morphology or signs of apoptosis. At higher magnification, internalization of part of the conjugated liposomes was visible in vesicles (Figure 2b,

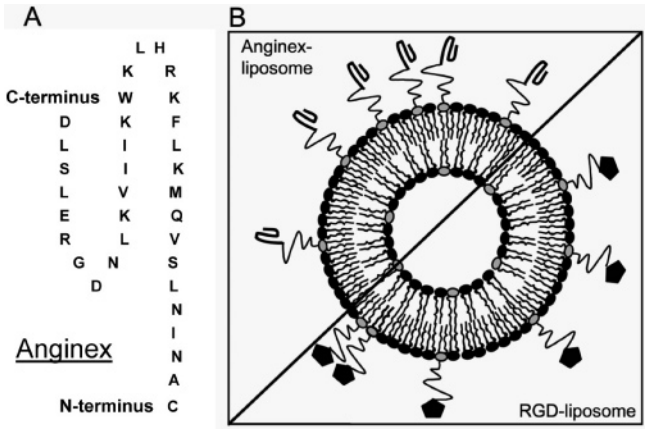


Figure 1. Schematic representation of (A) anginex and (B) paramagnetic liposomes conjugated to the peptides anginex and cyclic-RGD respectively. The black lipids represent Gd-DTPA-BSA and the gray lipids PEG−DSPE. Peptides are covalently conjugated to the maleimide group of Mal-PEG−DSPE.

middle panel). Addition of the nuclear stain 4,6-diamidino-2-phenylindole (DAPI) demonstrated that the liposomes did not enter the nucleus. Similar results were obtained with the RGD−liposome conjugates (data not shown)

To demonstrate that the interaction of the anginex−liposome conjugates with the HUVEC was mediated through anginex, a competition assay with free anginex was performed by adding anginex prior to incubation with the anginex−liposome conjugates. There was a clear concentration dependent inhibition of anginex−liposome binding following addition of free anginex (Figure 2c). At a concentration of 10 μg/mL, reduced fluorescence signal from the anginex−liposome conjugates was observed as compared to the situation in which no free anginex was added to HUVEC (Figure 2c, middle panel). In the case where cells were preincubated with 30 μg/mL anginex, almost no association of anginex−liposome conjugates with HUVEC was observed (Figure 2c, right panel). Comparable results were obtained with the endothelial cell line EVL-c2 (data not shown).

To test the applicability of anginex-targeted contrast agents, magnetic resonance imaging was applied to HUVEC incubated with paramagnetic conjugated liposomes. After 3 h of incubation with either anginex, RGD, or bare liposomes, HUVEC were washed twice and pelleted in small cups. As control nontreated cells were used. Visible inspection of the pelleted cells revealed an intense pink color in only anginex− and RGD−liposome-treated cells. Before imaging, all cells were fixed with 1% paraformaldehyde. MR imaging was performed on approximately 1.5×10^6 cells (Figure 3a). A quantitative *T*1-map, in which cells with a high concentration of contrast liposomes have a lower *T*1 than cells with a low concentration of contrast liposomes, was made of the various cell pellets. The *T*1-values of cell pellets that were incubated with anginex− and RGD−liposome conjugates had comparable values, which were significantly lower than the controls (Figure 3b). The *T*1 of the anginex pellet was 862 ± 41 ms and for RGD 1287 ± 33 ms, whereas control HUVEC and nonligand liposomes were respectively 2363 ± 88 ms and 1766 ± 30 ms. These data show that the level of association of the anginex−liposome conjugates, like that of the control RGD−liposome conjugates, is sufficient to be detected by MRI.

DISCUSSION

We hypothesized that anginex is an excellent ligand for targeted delivery of lipidic vehicles with therapeutic and/or contrast agents to activated endothelial cells in the tumor vasculature. In this study, we demonstrate that anginex can be conjugated to liposomes, and these conjugated liposomes indeed target to activated endothelial cells. Furthermore, we show that anginex-targeted paramagnetic liposomes can be used for MR imaging of activated endothelial cells *in vitro*.

To develop improved and new antitumor therapies, specific targets are needed to deliver drugs or contrast agents for imaging to the tumor without introducing toxic side effects or background signals. Tumor angiogenesis is a very suitable process for targeting because tumor growth and metastasis are dependent on angiogenesis. Furthermore, activated endothelial cell, which are the key players in this process, have a unique expression profile, are easily accessible, and are less prone to develop resistance against treatment. We previously described anginex, a *de novo*-designed small 33 amino acid angiostatic peptide, which is capable of inhibition of angiogenic endothelial cell migration and proliferation, subsequently leading to apoptosis. Additionally, anginex was shown to home specifically to tumor vasculature in a mouse model. To confirm the targeting qualities of anginex, we coupled the peptide covalently to maleimide moieties exposed at the distal end of PEG chains of liposomes. The applicability of these contrast-enhancing paramagnetic liposomes has already been demonstrated for the use of molecular MR imaging of endothelial cells *in vitro* using an E-selectin specific antibody and *in vivo* by using cyclic RGD−peptide as targeting unit (*9*, *24*). Similar to that for RGD, we observed binding of anginex−liposome conjugates to activated endothelial cells *in vitro*. Conjugated liposomes seemed to bind to all available endothelial cells, whereas using unconjugated liposomes hardly any binding was observed. This indicates a specific binding of the liposomes due to conjugation of the ligand, supporting the hypothesis of the applicability of anginex as a potent targeting ligand. Apparently, adding an additional cysteine to the N-terminus of anginex and linking it to a lipidic vehicle does not affect the binding of anginex to its receptor. This was expected since recombinant anginex, which has an extra N-terminal methionine is also fully active and retains the required β-sheet structure (*25*). Furthermore, addition of human serum albumin also has no influence on the *in vitro* activity of anginex (*26*). This is most likely due to the fact that the N-terminus is flexible and that the N-terminal amino acids are not required for the function of anginex (*14*, *27*).

An important prerequisite for targeting is the presence of a site-specific interaction molecule for the targeting ligand. For the RGD−liposome conjugates, this is the $\alpha v\beta 3$-integrin receptor (*28*). We recently identified galectin-1 as the main tumor endothelial cell-specific receptor for anginex (*17*). Galectin-1 expression is rapidly upregulated upon endothelial cell activation, and expression levels have been shown to be increased in the vasculature of different human tumors (*17*, *29*, *30*). This renders anginex/galectin-1 an excellent pair for targeting of liposomes to tumor vessels, which makes it an attractive target that can be used for diagnostic purposes in imaging.

Fluorescence microscopy revealed that a substantial part of the anginex-conjugated liposomes is internalized into the cell in perinuclear vesicles. This is consistent with galectin-1-mediated uptake of free anginex (*17*). This was confirmed in our competition experiment where increasing amounts of free anginex were able to inhibit binding and internalization of anginex−liposome conjugates , indicating an anginex-dependent binding of the anginex−liposome conjugates to HUVEC. The concentrations of free anginex in the competition experiments were based on the concentration needed to reach maximum therapeutic effect (40 μg/mL) (*13*). Considering that not all anginex molecules conjugated to the liposomes will be available for binding to the cell, we expected that the used concentrations

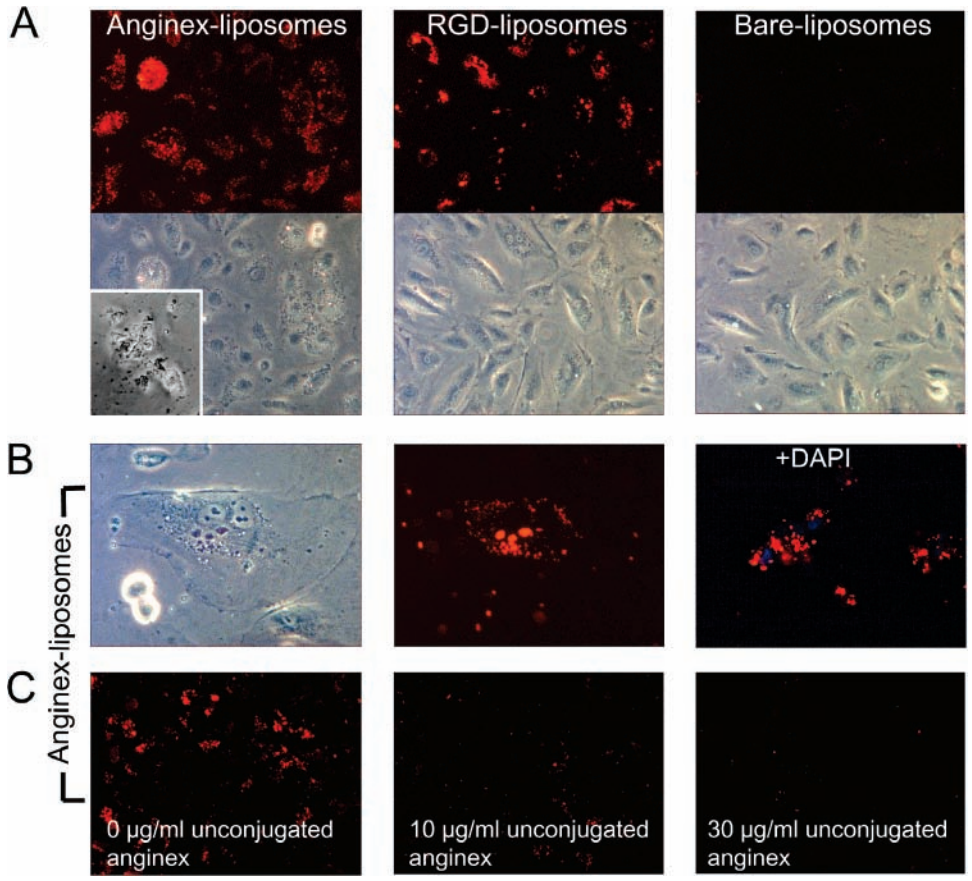
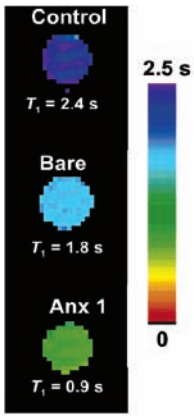


Figure 2. Fluorescence microscopy of HUVEC incubated with fluorescently labeled paramagnetic liposomes. Pictures are representative for all experiments. (A) HUVEC were incubated for 3 h with respectively anginex, RGD, and nontargeted liposomes. Insert: HUVEC undergoing apoptosis as a result of anginex treatment. (B) Perinuclear localization of anginex−liposome conjugates in one HUVEC cell shown by phase contrast and fluorescence image. Anginex−liposome conjugates do not enter the nucleus as shown by blue DAPI counter staining. (C) Competition of anginex−liposome conjugates with respectively 0, 10, 30 μg/mL free anginex.



HUVEC incubated with (n=2)	T_1(ms)
Control	2363 ± 88
Bare liposomes	1766 ± 30
RGD-liposomes	1287 ± 33
Anginex-liposomes	862 ± 41

Figure 3. *T*-1 weighted image of cells incubated with anginex, bare liposomes, or without liposomes. The *T*1 relaxation times of the different cell pellets are presented on the right.

would be sufficient to attain partial or complete blocking of anginex−liposome binding. Ultimate proof for receptor-mediated uptake of the anginex−liposome conjugates would be obtained in galectin-1 knockout endothelial cells. Indeed, tumors in galectin-1 knockout mice no longer respond to anginex treatment, suggesting that the binding of the anginex−liposome conjugates to HUVEC is anginex- and galectin-1-dependent.

To evaluate if anginex is also suitable as targeting ligand for MRI contrast agents, a quantitative *T*1-measurement was made of HUVEC pellets incubated with anginex-conjugated paramagnetic liposomes. As a positive control, RGD−liposome conjugates were used (*9*), and as negative control, bare paramagnetic liposomes or no liposomes were applied. Both conjugated paramagnetic liposomes were shown to bind specifically to endothelial cells. Furthermore, a clear difference in contrast was seen between ligand-conjugated liposomes and the controls leading to a significant difference in *T*1 values. The fact that the conjugated liposomes were internalized might also be a benefit for imaging. By internalizing the contrast agent, the concentration per cell can be elevated, revealing a brighter signal (*31*).

Besides diagnostic applications, anginex-targeted liposomes might be used as drug carrier. Therefore, water soluble drugs (e.g., doxorubicin) or even DNA constructs for gene therapy can be put inside the liposomal lumen (*32*, *33*). Thus, anginex-mediated targeting to tumor vasculature might be used to combine diagnosis and local therapy of cancer. However, for imaging, stabilization of liposomes is useful with drug delivery because the stability causes a slow release of the drugs. Another problem is the measurement of the amount of drugs released in the tissue. This can be solved by combining the drug and the contrast agent instead of loading drugs into liposomes with contrast-enhancing components in their bilayer (*34*, *35*). Nevertheless, preliminary data with contrast-enhancing liposomes loaded with doxorubicin show promising results *in vivo* (unpublished data).

Anginex is a potent angiostatic agent, and one of the main angiostatic characteristics of anginex is induction of apoptosis in activated EC. Although this might interfere with targeting, we have demonstrated that the induction of apoptosis by anginex occurs more than 48 h after administration (*13*). This is far beyond the time frame of targeting, suggesting that the induction

of apoptosis will not affect targeting. This is supported by the fact that other vascular targeting ligands, such as RGD−peptides, also induce endothelial cell apoptosis (*36*−*38*) without affecting their applicability as a targeting ligand (*39*, *40*).

Similar to that for apoptosis, the time frame of the experiments in this study did not allow us to investigate the effects of conjugated anginex on migration and proliferation (*41*). However, for imaging purposes, a possible effect will not influence the targeting ability and its function as a contrast agent.

In conclusion, we have demonstrated that the angiostatic peptide anginex is a potent ligand for the targeting of liposomes to activated endothelial cells. In addition, the *in vitro* results show a high specificity of the anginex-conjugated paramagnetic liposomes for endothelial cells that was confirmed by MRI. Therefore, anginex might serve as a targeting ligand for drug and gene therapy applications and for imaging of tumor vasculature in order to diagnose, treat, and monitor cancer.

ACKNOWLEDGMENT

This study was supported by a generous research grant from the Technology Foundation STW, applied science division of NWO and the technology program of the Ministry of Economic Affairs (MPG 5465 to A.W.G.)

LITERATURE CITED

(1) Brandwijk, R. J. M. G. E., Griffioen, A. W., and Thijssen, V. L. J. L. (2007) Targeted gene delivery strategies for angiostatic cancer treatment. *Trends Mol. Med.*, in press.
(2) Koning, G. A., Schiffelers, R. M., and Storm, G. (2002) Endothelial cells at inflammatory sites as target for therapeutic intervention. *Endothelium 9*, 161−71.
(3) Torchilin, V. P. (2005) Recent advances with liposomes as pharmaceutical carriers. *Nat. Rev. Drug Discovery 4*, 145−60.
(4) Lasic, D. (1993) *Liposomes: from physics to applications*, Chapter 11, Elsevier Science Publishing Company, Amsterdam.
(5) Papahadjopoulos, D., and Gabizon, A. (1990) Liposomes designed to avoid the reticuloendothelial system. *Prog. Clin. Biol. Res. 343*, 85−93.
(6) Allen, T. M. (1994) The use of glycolipids and hydrophilic polymers in avoiding rapid uptake of liposomes by the mononuclear phagocyte system *Adv. Drug Delivery Rev. 13*, 285−309.
(7) Allen, T. M., and Hansen, C. (1991) Pharmacokinetics of stealth versus conventional liposomes: effect of dose. *Biochim. Biophys. Acta 1068*, 133−41.
(8) Backer, M. V., Aloise, R., Przekop, K., Stoletov, K., and Backer, J. M. (2002) Molecular vehicles for targeted drug delivery. *Bioconjugate Chem. 13*, 462−7.
(9) Mulder, W. J., Strijkers, G. J., Habets, J. W., Bleeker, E. J., van der Schaft, D. W., Storm, G., Koning, G. A., Griffioen, A. W., and Nicolay, K. (2005) MR molecular imaging and fluorescence microscopy for identification of activated tumor endothelium using a bimodal lipidic nanoparticle. *FASEB J. 19*, 2008−10.
(10) Folkman, J. (1995) Angiogenesis in cancer, vascular, rheumatoid and other disease. *Nat. Med. 1*, 27−31.
(11) Molema, G., and Griffioen, A. W. (1998) Rocking the foundations of solid tumor growth by attacking the tumor's blood supply. *Immunol. Today 19*, 392−4.
(12) Bergers, G., and Benjamin, L. E. (2003) Tumorigenesis and the angiogenic switch. *Nat. Rev. Cancer 3*, 401−10.
(13) Griffioen, A. W., van der Schaft, D. W., Barendsz-Janson, A. F., Cox, A., Struijker Boudier, H. A., Hillen, H. F., and Mayo, K. H. (2001) Anginex, a designed peptide that inhibits angiogenesis. *Biochem. J. 354*, 233−42.
(14) Dings, R. P., Arroyo, M. M., Lockwood, N. A., van Eijk, L. I., Haseman, J. R., Griffioen, A. W., and Mayo, K. H. (2003) Beta-sheet is the bioactive conformation of the anti-angiogenic anginex peptide. *Biochem. J. 373*, 281−8.
(15) van der Schaft, D. W., Dings, R. P., de Lussanet, Q. G., van Eijk, L. I., Nap, A. W., Beets-Tan, R. G., Bouma-Ter Steege, J. C., Wagstaff, J., Mayo, K. H., and Griffioen, A. W. (2002) The designer anti-angiogenic peptide anginex targets tumor endothelial cells and inhibits tumor growth in animal models. *FASEB J. 16*, 1991−3.
(16) Akerman, M. E., Pilch, J., Peters, D., and Ruoslahti, E. (2005) Angiostatic peptides use plasma fibronectin to home to angiogenic vasculature. *Proc. Natl. Acad. Sci. U.S.A. 102*, 2040−5.
(17) Thijssen, V. L., Postel, R., Brandwijk, R. J., Dings, R. P., Nesmelova, I., Satijn, S. A., Verhofstad, N., Nakabeppu, Y., Baum, L. G., Bakkers, J., Mayo, K. H., Poirier, F., and Griffioen, A. W. (2006) Galectin-1 is essential in angiogenesis and is a target for anti-angiogenesis therapy. *Proc. Natl. Acad. Sci. U.S.A., 103*, 15975−15980.
(18) McDonald, D. M., and Choyke, P. L. (2003) Imaging of angiogenesis: from microscope to clinic. *Nat. Med. 9*, 713−25.
(19) moseley, M. (2004) Multimodality Imaging: Introduction. *Stroke 35*, 2632−2634.
(20) Doubrovin, M., Serganova, I., Mayer-Kuckuk, P., Ponomarev, V., and Blasberg, R. G. (2004) Multimodality in vivo molecular-genetic imaging. *Bioconjugate Chem. 15*, 1376−88.
(21) Kok, R. J., Schraa, A. J., and Bos, E. J. (2002) Preparation and functional evaluation of RGD-modified proteins as $\alpha_v\beta_3$ integrin directed therapeutics. *Bioconjugate Chem. 13*, 128−135.
(22) van der Schaft, D. W., Toebes, E. A., Haseman, J. R., Mayo, K. H., and Griffioen, A. W. (2000) Bactericidal/permeability-increasing protein (BPI) inhibits angiogenesis via induction of apoptosis in vascular endothelial cells. *Blood 96*, 176−81.
(23) van Leeuwen, E. B., Veenstra, R., van Wijk, R., Molema, G., Hoekstra, A., Ruiters, M. H., and van der Meer, J. (2000) Characterization of immortalized human umbilical and iliac vein endothelial cell lines after transfection with SV40 large T-antigen. *Blood Coagul. Fibrinol. 11*, 15−25.
(24) Mulder, W. J., Strijkers, G. J., Griffioen, A. W., van Bloois, L., Molema, G., Storm, G., Koning, G. A., and Nicolay, K. (2004) A liposomal system for contrast-enhanced magnetic resonance imaging of molecular targets. *Bioconjugate Chem. 15*, 799−806.
(25) Brandwijk, R. J., Dings, R. P., van der Linden, E., Mayo, K. H., Thijssen, V. L., and Griffioen, A. W. (2006) Anti-angiogenesis and anti-tumor activity of recombinant anginex. *Biochem. Biophys. Res. Commun. 349*, 1073−8.
(26) Dings, R. P., van der Schaft, D. W., Hargittai, B., Haseman, J., Griffioen, A. W., and Mayo, K. H. (2003) Anti-tumor activity of the novel angiogenesis inhibitor anginex. *Cancer Lett. 194*, 55−66.
(27) Mayo, K. H., Dings, R. P., Flader, C., Nesmelova, I., Hargittai, B., van der Schaft, D. W., van Eijk, L. I., Walek, D., Haseman, J., Hoye, T. R., and Griffioen, A. W. (2003) Design of a partial peptide mimetic of anginex with antiangiogenic and anticancer activity. *J. Biol. Chem. 278*, 45746−52.
(28) Ruoslahti, E., and Pierschbacher, M. D. (1986) Arg-Gly-Asp: a versatile cell recognition signal. *Cell 44*, 517−8.
(29) Clausse, N., van den Brule, F., Waltregny, D., Garnier, F., and Castronovo, V. (1999) Galectin-1 expression in prostate tumor-associated capillary endothelial cells is increased by prostate carcinoma cells and modulates heterotypic cell-cell adhesion. *Angiogenesis 3*, 317−25.
(30) Lotan, R., Belloni, P. N., Tressler, R. J., Lotan, D., Xu, X. C., and Nicolson, G. L. (1994) Expression of galectins on microvessel endothelial cells and their involvement in tumour cell adhesion. *Glycoconjugate J. 11*, 462−8.
(31) van Tilborg, G. A., Mulder, W. J., Deckers, N., Storm, G., Reutelingsperger, C. P., Strijkers, G. J., and Nicolay, K. (2006) Annexin A5-functionalized bimodal lipid-based contrast agents for the detection of apoptosis. *Bioconjugate Chem. 17*, 741−9.
(32) Allen, T. M. (1997) Liposomes. Opportunities in drug delivery. *Drugs 54 Suppl 4*, 8−14.
(33) Drummond, D. C., Meyer, O., Hong, K., Kirpotin, D. B., and Papahadjopoulos, D. (1999) Optimizing liposomes for delivery of chemotherapeutic agents to solid tumors. *Pharmacol. Rev. 51*, 691−743.
(34) Ponce, A. M., Viglianti, B. L., Yu, D., Yarmolenko, P. S., Michelich, C. R., Woo, J., Bally, M. B., and Dewhirst, M. W. (2007) Magnetic resonance imaging of temperature-sensitive liposome release: drug dose painting and antitumor effects. *J. Natl. Cancer Inst. 99*, 53−63.
(35) Viglianti, B. L., Ponce, A. M., Michelich, C. R., Yu, D., Abraham, S. A., Sanders, L., Yarmolenko, P. S., Schroeder, T., MacFall, J.

R., Barboriak, D. P., Colvin, O. M., Bally, M. B., and Dewhirst, M. W. (2006) Chemodosimetry of in vivo tumor liposomal drug concentration using MRI. *Magn. Reson. Med. 56*, 1011−8.

(36) Meerovitch, K., Bergeron, F., Leblond, L., Grouix, B., Poirier, C., Bubenik, M., Chan, L., Gourdeau, H., Bowlin, T., and Attardo, G. (2003) A novel RGD antagonist that targets both alphavbeta3 and alpha5beta1 induces apoptosis of angiogenic endothelial cells on type I collagen. *Vascul. Pharmacol. 40*, 77−89.

(37) Modlich, U., Kaup, F. J., and Augustin, H. G. (1996) Cyclic angiogenesis and blood vessel regression in the ovary: blood vessel regression during luteolysis involves endothelial cell detachment and vessel occlusion. *Lab. Invest. 74*, 771−80.

(38) Westlin, W. F. (2001) Integrins as targets of angiogenesis inhibition. *Cancer J. 7 Suppl 3*, S139−43.

(39) Meyer, A., Auernheimer, J., Modlinger, A., and Kessler, H. (2006) Targeting RGD recognizing integrins: drug development, biomaterial research, tumor imaging and targeting. *Curr. Pharm. Des. 12*, 2723−47.

(40) Temming, K., Schiffelers, R. M., Molema, G., and Kok, R. J. (2005) RGD-based strategies for selective delivery of therapeutics and imaging agents to the tumour vasculature. *Drug Resist. Updates 8*, 381−402.

(41) Brandwijk, R. J., Nesmelova, I., Dings, R. P., Mayo, K. H., Thijssen, V. L., and Griffioen, A. W. (2005) Cloning an artificial gene encoding angiostatic anginex: From designed peptide to functional recombinant protein. *Biochem. Biophys. Res. Commun. 333*, 1261−8.

BC060316H

Synthesis, Characterization, and *in Vitro* Activity of Dendrimer−Streptokinase Conjugates

Xiangtao Wang,[†,§] Rajyalakshmi Inapagolla,[‡] Sujatha Kannan,*[,†] Mary Lieh-Lai,[†] and Rangaramanujam M. Kannan[‡]

Critical Care Medicine, Department of Pediatrics, Children's Hospital of Michigan/Wayne State University, Detroit, Michigan 48201, and Department of Chemical Engineering and Materials Science, Wayne State University, Detroit, Michigan 48202. Received October 13, 2006; Revised Manuscript Received January 30, 2007

Dendrimer conjugation with low molecular weight drugs has been of increasing interest recently for improving pharmacokinetics, targeting drugs to specific sites, and facilitating cellular uptake. Opportunities for increasing the performance of relatively large therapeutic proteins such as streptokinase (SK) using dendrimers are being explored in this study. Using the active ester method, a series of streptokinase−poly(amido amine) (PAMAM) G3.5 conjugates were synthesized with varying amounts of dendrimer-to-protein molar ratios. Characterization of these conjugates by GPC, IEC, and native-PAGE suggested that the conjugation reaction was successful, resulting in relatively pure SK−dendrimer conjugates. The conjugate made with an equimolar ratio of dendrimer to streptokinase (1:1) exhibited the highest enzymatic activity retention (∼80% retained) that has been reported so far for conjugated streptokinase with macromolecules such as PEG or dextran. SK conjugates with higher streptokinase-to-dendrimer molar ratios (1:10 and 1:20) exhibited lower initial enzymatic activities. However, these conjugates showed sustained thrombolytic activity in plasma, perhaps due to the release of SK from the conjugate. All of the SK conjugates displayed significantly improved stability in phosphate buffer solution, compared to free SK. The high coupling reaction efficiencies and the resulting high enzymatic activity retention achieved in this study could enable a desirable way for modifying many bioactive macromolecules with dendrimers.

INTRODUCTION

Acute thromboembolic events such as stroke, myocardial ischemia, pulmonary embolism, and deep vein thrombosis are major causes of increased morbidity. Of these, coronary artery disease and stroke account for 40% of all annual deaths in the U.S.A. Timely therapy is crucial for achieving adequate reperfusion to salvage the affected organ. Local or systemic infusion of thrombolytic agents is the most common treatment for clot dissolution. A number of clinical trials have demonstrated the benefits of thrombolytic treatment, especially in myocardial ischemia and stroke. Streptokinase (SK), a 47 kDa single-chain protein, was one of the first clinically used intravenous thrombolytic agents. The initial studies comparing streptokinase to a placebo in the 1980s were extremely influential in proving the benefits of the use of thrombolytic agents in myocardial ischemia. Streptokinase interacts with the circulating or clot-bound plasminogen to form a noncovalent, 1:1 stoichiometric complex capable of converting another plasminogen molecule to active plasmin (*1*−*4*). The latter degrades fibrin, the main component and skeleton of a clot network, leading to rapid lysis of intravascular clots. Though SK is a relatively inexpensive and effective thrombolytic agent, its clinical use is limited by its short *in vivo* half-life, immunogenicity, and high incidence of systemic bleeding, undermining its therapeutic efficacy (*5*). Due to the short plasma half-life of SK (30 min) (*6*), higher doses and continuous infusion of SK are often required for clinical treatment; this in turn increases the risk of bleeding and immune reactions. Over the past decade, a number of studies have concentrated on improving the efficacy, potency, ease of administration, and duration of action of thrombolytic agents, while trying to decrease the side effects. Development of new or modified thrombolytic agents with higher clot specificity, longer circulation time, and lower antigenicity still remains a challenge.

Strategies that have been attempted to improve the therapeutic efficacy of thrombolytic agents include attachment of polymers such as poly(ethylene glycol) (PEG) or polysaccharides (dextran) (*7*−*9*) and encapsulation in liposomes or microsomes (*10*). Attachment of SK to PEG appeared to decrease SK's antigenicity, thereby increasing its circulation time, but resulted in a 67% loss in its enzymatic activity. Conjugation of SK with dextran (MW 35−50 kDa) increased its circulation time to over 3 days, with a reduction in the hemorrhagic complications and allergic reactions associated with SK use (*8*, *11*, *12*). This conjugate had a 50% loss in enzymatic activity (*8*) and was less efficient than free SK in achieving fibrinolysis (*13*). Liposomal entrapment suffered from drawbacks such as poor stability, low entrapment efficiency (30% to small liposomes and up to 60% to large liposomes) (*14*, *15*), and a great loss in protein activity (5−15% activity retained), thus limiting its further application.

Recently, there has been a significant thrust to explore dendrimers as potential drug delivery vehicles. Dendrimers are monodisperse, branched polymers with highly reactive end functionalities (Figure 1) that can be used for covalent conjugation of drugs, ligands, and/or antibodies for targeted delivery of the drug to the site of action (*16*−*27*). Dendrimers have predominantly been conjugated to small molecules, rather than biological macromolecules. The few previous attempts to conjugate dendrimers with proteins have mostly focused on antibodies (*28*−*36*) using an amine-terminated dendrimer and relatively lengthy coupling procedures to introduce sulfhydryl

* Corresponding author. Dr Sujatha Kannan, Department of Pediatrics, Critical Care Medicine, Children's Hospital of Michigan, 3901 Beaubien Detroit, Michigan, Detroit, MI-48201 (USA). Phone: 313-745-6109. Fax: 313-966-0105. E-mail: skannan@med.wayne.edu.

† Department of Pediatrics.

‡ Department of Chemical Engineering and Materials Science.

§ Currently with the Institute for Medicinal Plant Development, Chinese Academy of Medical Sciences, Republic of China.

10.1021/bc060322d CCC: $37.00 © 2007 American Chemical Society
Published on Web 04/13/2007

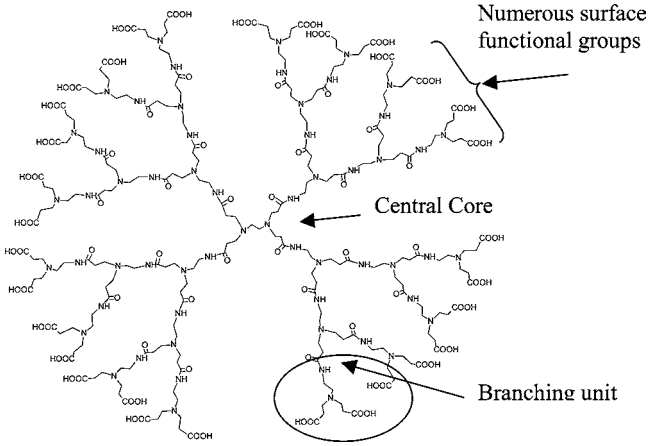


Figure 1. Dendritic structure with the core and branching units.

groups onto the dendrimer/protein. Nearly all of the conjugates maintained, to varying degrees, the binding specificity of the original antibody (*28*).

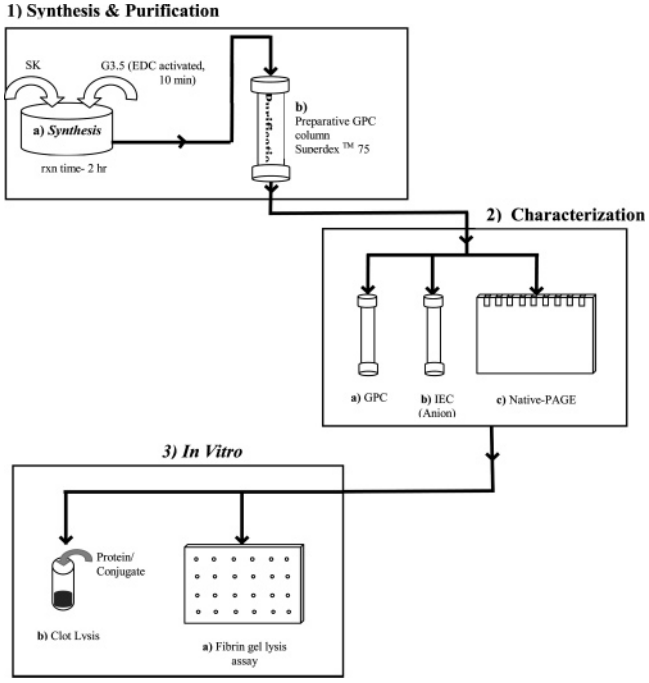
Unlike linear polymers such as PEG, we hypothesize that dendrimers, with their compact structure, may not wrap around proteins to mask the enzyme's active sites but might still increase the protein stability by occupying the antigen recognition sites. Therefore, conjugating SK with dendrimer may not only retain the enzymatic activity of the drug but also improve its stability by increasing its circulation time. Anionic dendrimers have been shown to have lower toxicity with a longer clearance time from the blood than cationic dendrimers (*37*−*40*). Hence, the commercially available starburst poly(amidoamine) (PAMAM) dendrimer of generation G3.5 (Figure 1) with an ethylenediamine core and peripheral carboxyl groups was used to attach SK (30). Our long-term goal is to utilize this novel dendritic nanodevice to achieve effective clot lysis while minimizing immunogenicity and the risk of bleeding. As a first step toward this goal, dendrimer−SK conjugates with varying SK−dendrimer molar ratios were prepared and characterized to determine coupling efficiency, and *in vitro* enzymatic activity was tested and compared against free streptokinase.

EXPERIMENTAL PROCEDURES

Materials. 1-[3-(Dimethylamino)propyl]-3-ethylcarbodiimide methiodide (EDC-methiodide), *N*-hydroxysulfosuccinimide sodium salt (sulfo-NHS), tris (hydroxymethyl)aminomethane hydrochloride, and agarose (for routine use, gelling temperature 36 ± 1.5 °C) were purchased from Sigma. Generation 3.5 PAMAM COOH dendrimer was purchased from Dendritech, Inc., MI, and dialysis membranes (MWCO 3500 Da) from Spectra Pore, CA. Recombinant streptokinase and SK activity assay kit were purchased from Shanghai SIIC−SMU Biotech Com, Ltd. (Shanghai, PR China). ^{125}I-fibrinogen was obtained from Amersham Corp. (Arlington Heights, IL). Ultracel YM-3, YM-10, and YM-30 Centricon centrifugal filters (regenerated cellulose 3000 Da MWCO, 10 000 Da MWCO, and 30 000 Da MWCO) were purchased from Millipore Corporation (Bedford, MA). Superdex 75 prep grade (34 μm), Superdex G-25 PD-10 Column, and Mono QTM 4.6/100 PE column were purchased from Amersham Bioscience AB (SE-751 84 Uppsala Sweden). 4−20% Tris−glycine gradient precast polyacrylamide minigels were purchased from ISC BioExpress (Kaysville, UT). All other reagents were of analytical grade or HPLC grade.

Purification of PAMAM G3.5 Dendrimer. A BioSuite 250 HR SEC column (5 μm, 7.8 × 300 mm) connected to a Waters HPLC system was used for PAMAM dendrimer purification. The column was eluted with orthophosphate buffer (0.1 M, pH 7.00) at a flow rate of 0.5 mL/min. UV absorbance of the eluent was detected at both 280 and 210 nm. Fractions containing pure G3.5 peak were collected, concentrated by Ultracel YM-3 Centricon centrifugal filter (MWCO 3000 Da), dialyzed against water for 24 h (dialysis membrane MWCO 3500 Da, under perfect sink conditions), and lyophilized to obtain solid purified G3.5 (50−60% in yield).

Scheme 1. Schematic Representation of the Experimental Protocol[a]



[a] Three major steps: 1. Synthesis (1a) of the protein−dendrimer conjugates (EDC as coupling agent) and purification using a Superdex 75 preparative column (1b). 2. Characterization of the conjugates using GPC (2a), Anion exchange column (2b), and native-PAGE (2c). 3. *In vitro* performance of the conjugates using a fibrin gel (3a) and clot (3b) lysis assays.

SK−G 3.5 Conjugation. SK (13.5 mg, lyophilized powder) containing mannitol as the stabilizing agent was reconstituted with deionized water. A PD-10 column was used to remove mannitol from the reconstituted SK by eluting with borate buffer (0.1 M, pH 8.50). The carboxyl groups of PAMAM G3.5 dendrimer were activated in aqueous solution (pH 2.0) at ambient temperature for 10 min using EDC-methiodide and s-NHS as the coupling reagents (G3.5/EDC/sulfo-NHS = 1:64:64 molar ratio). The activated dendrimer solution was added to SK solution (in borate buffer, 0.1 M, pH 8.50) at different SK/G3.5 molar ratios (1:1, 1:5, 1:10, and 1:20) and gently stirred at ambient temperature for 2 h (Scheme 1).

Purification of SK−G3.5 Conjugates. The experimental protocol followed in this study is depicted in Scheme 1. The reaction solution was initially purified by gel permeation chromatography (GPC) using a Superdex 75 column (40 × 1.6 cm i.d.; 50 mL Superdex 75, preparative grade, 34 μm) connected to a Waters HPLC system. The column was eluted with orthophosphate buffer (0.1 M, pH 7.00) as the mobile phase (flow rate 0.6 mL/min), and UV absorbance was measured at 210 and 280 nm. Fractions containing SK conjugate and possibly free SK were collected and concentrated by Ultracel YM-30 Centricon centrifugal filter (MWCO 30 000 Da). The concentrated fractions were further purified by ion exchange chromatography (IEC) to remove free protein from the conjugate.

Chromatographic Characterization of SK−G3.5 Conjugates by GPC and IEC. Analytical gel permeation chromatography (GPC) was used to analyze the obtained SK−G3.5 conjugates using a BioSuite 250 HR SEC column and ortho-

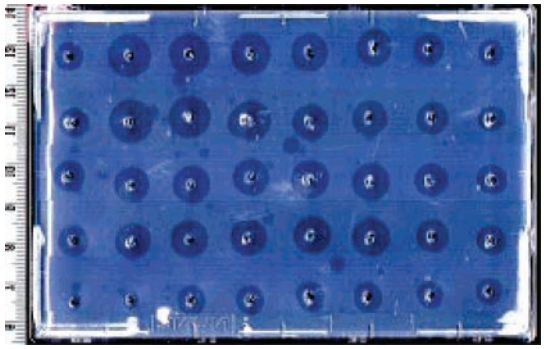


Figure 2. Agar gel plate and the fibrin lysis cycles, scanned against black background.

phosphate buffer (0.1 M, pH 7.00) as eluent at 0.6 mL/min. The progress of the coupling reaction was monitored by analyzing the diluted reaction solution using GPC. For IEC examination, a prepacked Mono Q 4.6/100 PE column was pre-equilibrated with Tris−HCl buffer (20 mM, pH 6.50) containing 0.15 M sodium chloride. After sample injection, the column was eluted at 0.9 mL/min with a gradient pattern: 0−4 min, Tris−HCl buffer (20 mM, pH 6.50) containing 0.15 M NaCl; 4−16 min, Tris−HCl buffer with NaCl concentration (from 0.15 to 1 M). UV absorbance was measured at 210 and 280 nm.

Native PAGE. Native PAGE conditions used for the analysis of SK−dendrimer conjugates were similar to those described previously for dendrimers (*41*, *42*). The free protein, free dendrimer, and protein−dendrimer conjugates (1:1, 1:5, 1:10, and 1:20; SK/G3.5 molar ratio) were analyzed using 4−20% Tris−glycine gradient express gel under native conditions. The running buffer used was Tris−glycine native buffer (2.5 mM Tris, 19.2 mM glycine, pH 8.3). A sample buffer containing 50% sucrose and 1% methylene blue was mixed with an equal volume of salt-free sample solution, and 10 μL of the mixture was loaded into each well. The gel was run at low voltage on a Bio-Rad Mini PROTEAN III vertical gel electrophoresis system at 4 °C and then stained overnight with 2.5% Coomassie Blue−R250 solution (in 10% acetic acid and 50% methanol). The destaining solution used was a 10% acetic acid solution with 50% methanol. Both staining and destaining were performed at 4 °C.

Activity Assay Based on Fibrin Gel Lysis. A modified fibrinolytic activity assay method based on that described by Li (*43*) was used to determine the *in vitro* biological activity of SK. 250 mg of agarose was dissolved in 20 mL normal saline at 60 °C and mixed with human fibrinogen (100 mg, in 10 mL normal saline), thrombin (0.1 mL, 10 U/mL), and plasminogen (120 μg, 1.2 μg/mL). This mixture was then quickly poured into a 12.5 × 8 × 0.5 cm^3 plastic plate to form an even, solidified, fibrin gel. Wells of 2 mm in diameter were made in the solidified fibrin gel, and 10 μL of free SK or conjugates (400 IU/mL of SK calculated from the amount used for the conjugation reaction) were loaded in each well in triplicate. The plate was then sealed and incubated at 37 °C. Streptokinase loaded into the wells converted plasminogen in the gel to plasmin, which lyses the fibrin, leading to a transparent ring around the well. After 8 h, the plate was scanned to record the size of the lytic ring (Figure 2). The area and the diameter of the lytic rings in the gel were measured using *Image J* software. The regression of the average diameter of the lytic rings against the logarithm of the activity was calculated to get a calibration curve from standard SK. The activities of the test samples were determined from this calibration curve based on the average diameter of the corresponding rings.

Lysis of ^{125}I-Fibrinogen Clots in Plasma. ^{125}I-labeled clots were prepared from human plasma as previously described (*44*, *45*). ^{125}I-fibrinogen containing plasma (0.68 μCi/mL) was quickly mixed with $CaCl_2$ (20 mM) and thrombin (1 U/mL). The mixture was aliquoted (100 μL each) into 1.5 mL Eppendorf tubes to form clots and then incubated at 37 °C for 2 h. The obtained clots were washed four times with PBS to remove free ^{125}I or unconverted ^{125}I-fibrinogen. The clots were then suspended in 1 mL of plasma containing free SK or SK−G3.5 conjugates (400 U/mL) and incubated at 37 °C. The negative control sample contained clot suspended in plasma without SK. At different time intervals, 25 μL of supernatant was collected with a corresponding amount of plasma supplementation. The radioactivity was measured using Packard Cobra II Auto Gamma Counters (Canberra Packard, Meriden, CT 06450, U.S.A.). The overall radioactivity in the supernatant was calculated and divided by the original radioactivity of the clot after accounting for time decay in radioactivity to obtain the percent clot lysis.

RESULTS AND DISCUSSION

Purification of PAMAM G3.5 Dendrimer and SK. The GPC analysis of commercially available PAMAM G3.5 displayed a single peak at 210 nm and three to four peaks at 280 nm, indicating some impurities (Figure 3). After purification, the dendrimer displayed a single peak at both 210 and 280 nm (Figure 3). BSA, glutamine, glycine, and mannitol are the widely used stabilizing agents for SK to maintain its enzymatic activity during lyophilization and storage (*46*, *47*). However, the functional groups (amine and hydroxyl groups) on these additives can compete with SK for reacting with the carboxyl groups of PAMAM G3.5 dendrimer, leading to reduced coupling efficiency, heterogeneous conjugates, or conjugation failure. Therefore, SK needs to be purified before reaction. The mannitol in the received SK product was removed using a PD-10 column.

Preparation of SK−G3.5 Conjugates. Water-soluble EDC−methiodide and sulfo-NHS were used to activate the carboxyl groups of PAMAM G3.5 dendrimer in aqueous solution. The activated ester of the dendrimer would be expected to react with the amine groups of SK to form an amide bond. We found that the activation step played a key role in the bioconjugation. Since active ester is unstable and can be easily hydrolyzed by water, the activated dendrimer should be reacted immediately with SK. However, if the activation time is too short, the active coupling reagents may cause SK cross-linking. Activation times of 10, 30, and 60 min were tried, and a 10 min activation time was found to be optimal, resulting in high coupling efficiency. Also, no obvious protein cross-linking was suggested by chromatographic analysis (data not shown). Therefore, a 10 min activation time was used for all the conjugates. Since carboxyl groups are easily activated in neutral to slightly acidic conditions, the purified G3.5 dendrimer was dissolved in water (pH 2) to reach a final pH of 4.0 activation (*48*). After activation, SK in borate buffer (0.1 M, pH 8.5) was immediately added, and the final pH of the reaction solution ranged between 8.2 and 8.5, at which SK is stable.

Several reaction times (2, 4, and 6 h) and SK/G3.5 molar ratios (1:1, 1:5, 1:10, and 1:20) were investigated. The conjugates synthesized with reaction times of 4−6 h displayed nearly identical chromatographic profiles to those synthesized in 2 h (Figure 4). Since shorter reaction times are desirable to preserve the stability of protein, we used a 2 h reaction time for all the conjugates. We have shown here that relatively mild conjugation conditions involving dendrimer activation at a pH of 4.0 for 10 min, followed by a 2 h reaction with SK in borate buffer, were effective in achieving PAMAM G3.5−SK conjugates.

Purification and Characterization of SK−G3.5 Conjugates. Purification of protein−dendrimer conjugates is challenging because attaching a polymer usually widens the protein peak, thus reducing the separation resolution (*49*). For this

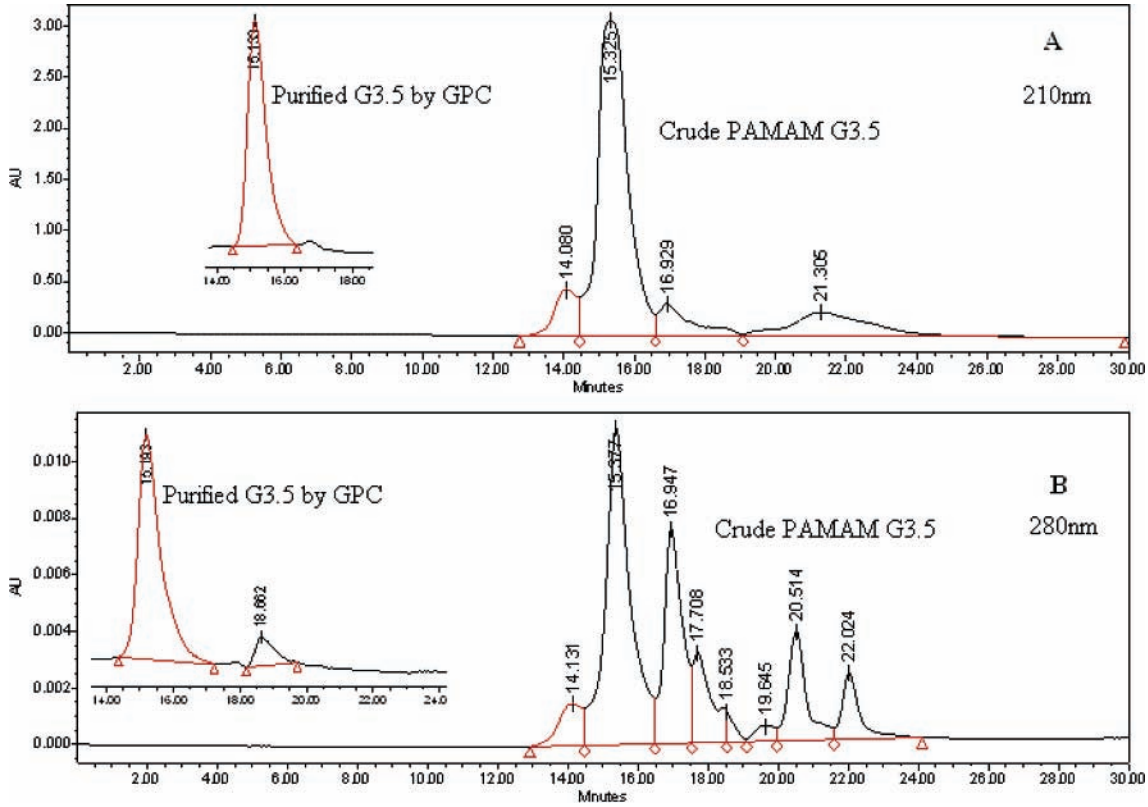


Figure 3. Comparison of GPC profiles of crude PAMAM G3.5 dendrimer and purified PAMAM G3.5 dendrimers (A, 210 nm; B, 280 nm). After purification by GPC, the PAMAM dendrimer displayed as single peaks at both 210 nm and 280 nm.

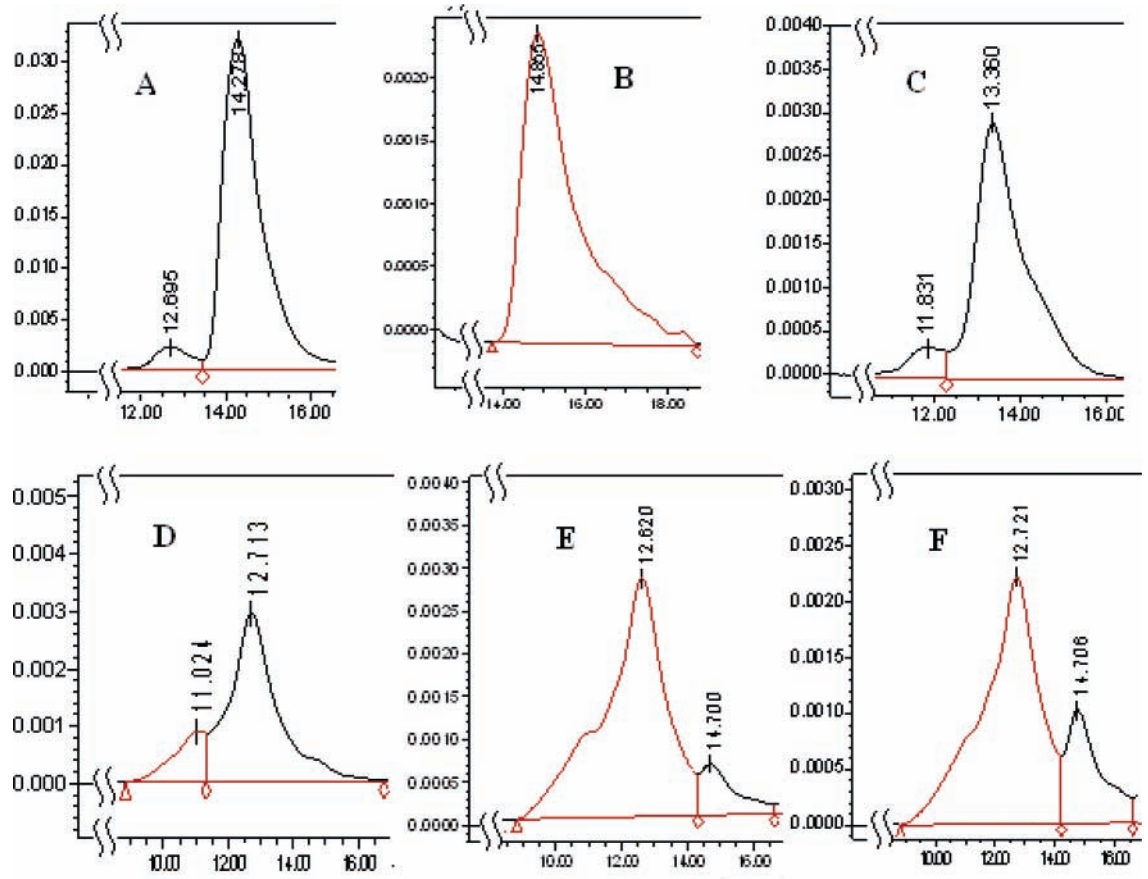


Figure 4. GPC comparisons of SK−G3.5 conjugation solutions of different starting SK−G3.5 molecular ratios (reaction solution, 2 h, at 280 nm): A for free SK, B for free PAMAM, C for SK−G3.5 (1:1), D for SK−G3.5 (1:5), E for SK−G3.5 (1:10), F for SK−G3.5 (1:20).

purpose, a preparative GPC column was used with Superdex 75 (34 μm) as packing material. This column has a M_r fractionation range of 3×10^3 to 7×10^4 Da, suitable for separating SK−G3.5 conjugates (theoretical MW > 6×10^4

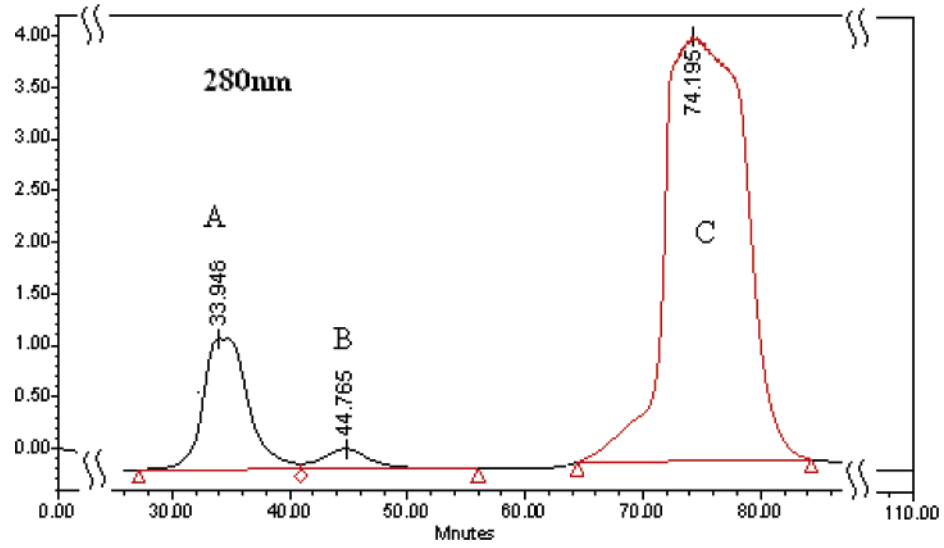


Figure 5. Chromatographic profile of separation of SK−G3.5 (1:5) conjugate using Superdex 75 column. Peak A: conjugate (plus free SK if there was some left in the reaction solution). Peak B: unreacted PAMAM G3.5 dendrimer. Peak C: coupling reagents.

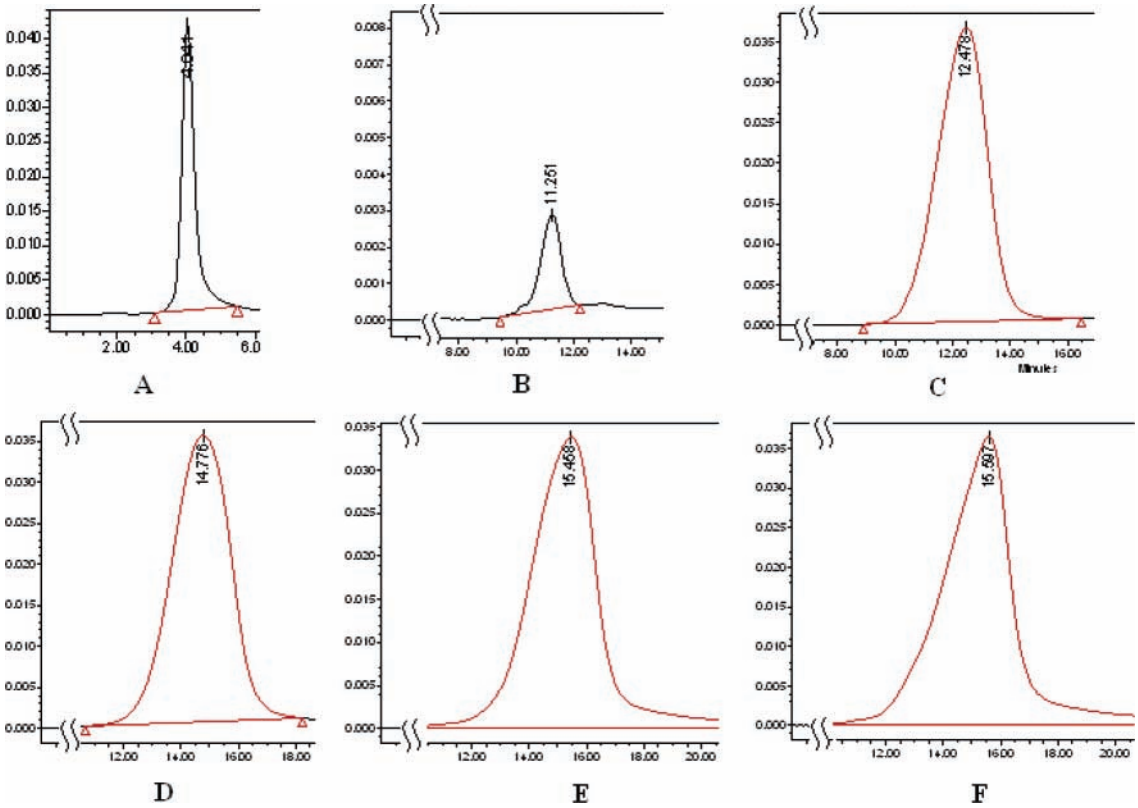


Figure 6. IEC comparison (280 nm) of SK−G3.5 (1:1, 1:5, 1:10, 1:20, molar ratio) conjugates with free SK and free dendrimer: A for free SK (RT = 4.041 min), B forfree PAMAM G3.5 dendrimer (RT = 11.323 min), C for SK−G3.5 (1:1), D for SK−G3.5 (1:5), E for SK−G3.5 (1:10), and F for SK−G3.5 (1:20). (Only the sections of the original IEC chromatograms containing the SK−G3.5 conjugate peak are shown here; however, the complete IEC profiles were similar to those presented in Figure 7, with no free SK or free dendrimer observed.)

Da) from unreacted PAMAM G3.5 dendrimer (MW 12 931 Da) and coupling reagents (EDC−methiodide and sulfo-NHS, MW < 400). Figure 5 depicts the chromatographic profile of SK−G3.5 conjugate solution, where the dendrimer−SK conjugate along with possibly free SK was separated from unreacted dendrimer and coupling agents (retention times around 34, 45, and 74 min, respectively). Fractions containing SK conjugate and possibly some free SK (peak at 34 min in Figure 5) were collected.

Free SK in the reaction solution cannot be clearly separated from the conjugate by GPC. However, using IEC, a separation technique based on surface charge density of molecules, a clear separation of free SK (RT = 4.0 min) and free dendrimer (RT = 11.3 min) from SK conjugates (RT = 12.5 to 15.6 min) was achieved (Figure 6 and Table 1). PAMAM G3.5 is a highly branched polymer with 64 carboxyl groups on the surface carrying a high density of negative charge. When conjugated to SK, the high negative charge of the dendrimer will lead to a significant change in the surface charge density of SK. We expect that attaching more dendrimer molecules leads to a greater negative charge and hence longer IEC retention time for the conjugates. Thus, desirable separation was achieved using anion IEC. We observed no free SK peak in IEC analysis of the SK conjugates (Figure 7), suggesting that the conjugation

Table 1. Comparison of IEC Retention Time of SK−G3.5 Conjugates with That of Free PAMAM G3.5 Dendrimer (280 nm)

	RT (min)	ΔRT[a] (min)
free SK	4.041	
purified G3.5	11.340	
SK−G3.5 (1:1)-2 h	12.478	1.138
SK−G3.5 (1:5)-2 h	14.776	3.436
SK−G3.5 (1:10)-2 h	15.458	4.118
SK−G3.5 (1:20)-2 h	15.597	4.257

[a] ΔRT was the retention time shift using free dendrimer as reference.

reaction was effective. We would expect the retention time of the conjugate to increase with an increase in the molar ratios of dendrimer used (1:1 < 1:5 < 1:10 < 1:20), as the charge of the conjugate becomes more negative when more dendrimer molecules are attached to SK (Figure 6 and Table 1). However, it was observed that the increase in retention time of the 1:20 conjugate was not appreciably different from that of the 1:10 conjugate. This may be ascribed to the steric hindrance of the attached dendrimer that prevents more dendrimer molecules from approaching the amine groups of the SK molecule, leading to saturation in the number of dendrimer molecules that could be attached to SK.

After purification by GPC, the product displayed a single peak for the SK conjugate. There was no peak observed at retention times less than 5 min, indicating the absence of unreacted or cross-linked SK in the final product (Figures 6 and 7). This also suggests that our coupling efficiency was high. These purified conjugates were then used for the *in vitro* studies. The possibility of formation of the SK−G3.5 complex was excluded on the basis of the observation that a physical mixture of PAMAM G3.5 and SK (at similar molar ratios in borate buffer) demonstrated only individual peaks for dendrimer and SK, by both GPC and IEC.

The conjugates were also characterized by native PAGE, where the SK conjugates migrated differently from that of free SK (Figure 9). The migration distance in native PAGE is dependent upon the charge and molecular weight of the protein. The attachment of a negatively charged dendrimer to SK results in a conjugate that is more negatively charged than free SK and thus has a longer migration distance (Figure 9). The purified conjugates did not demonstrate any bands in the regions corresponding to either free SK or free dendrimer.

The dendrimer−protein conjugations that have been previously attempted used high amounts of NH_2-terminated dendrimer with expensive heterobifunctional cross-linking agents and lengthy procedures of introducing sulfhydryl groups on the dendrimer or protein before conjugation, leading to reduced overall yield and loss of protein activity (*33*−*35*, *40*). This is the first study reporting conjugation of a therapeutic protein with dendrimer with high coupling efficiency. The inherent properties of this negatively charged PAMAM dendrimer, such as low cytotoxicity and longer blood circulation times, together with mild reaction conditions and high coupling efficiency as demonstrated here, makes it suitable for conjugating dendrimer to various biologically active proteins and polypeptides.

Previous attempts at conjugating polymers such as PEG to SK have involved long reaction times and use of large amounts of polymer, resulting in low yield of conjugates (*9*, *50*). However, in this study, even at a molar ratio of 1:1 (SK/G3.5), most of the SK was attached to PAMAM G3.5 dendrimer within 2 h. This may be because of the remarkably higher reactivity of the dendrimer functional groups (*36*, *51*). This unusual

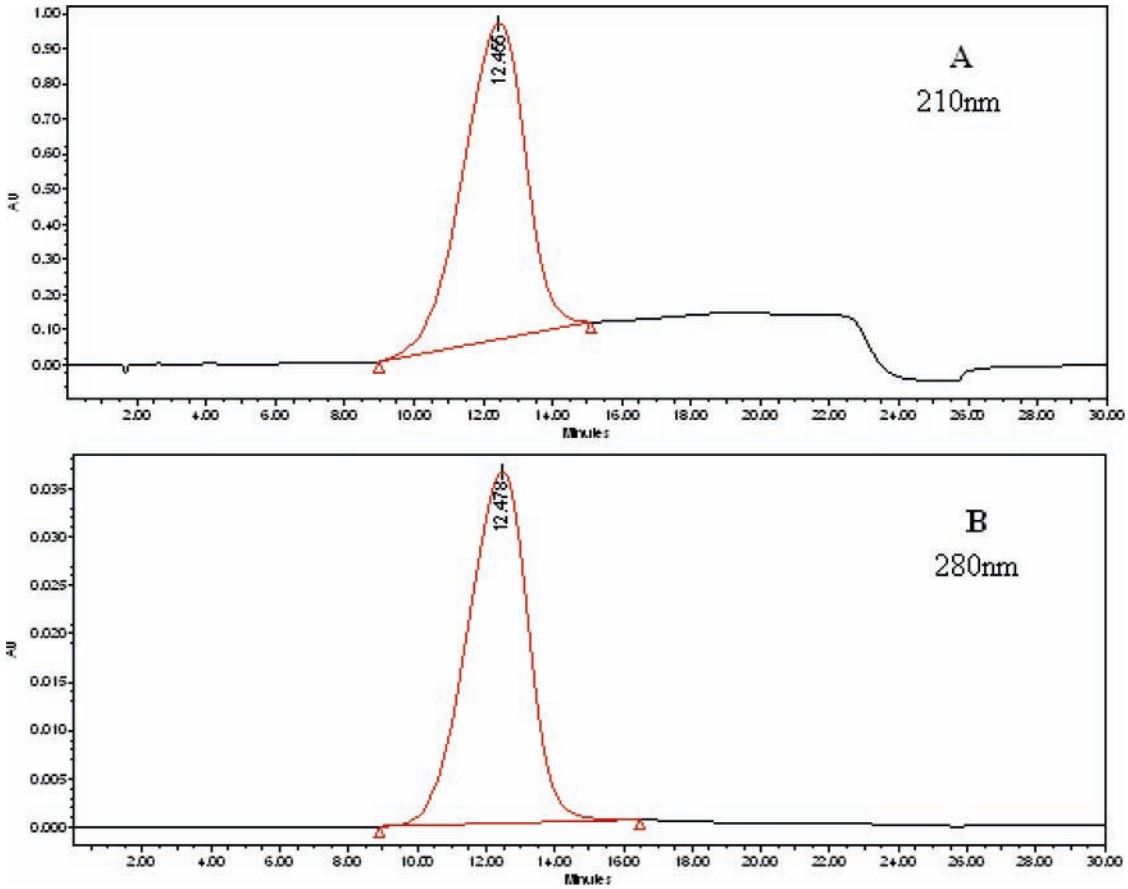


Figure 7. IEC examination of the purity of the SK−G3.5 (1:1)-2 h conjugate (A, 210 nm; B, 280 nm) fraction collected from GPC. Free SK was usually eluted out at about 4 min under the same condition, and free dendrimer around 11.2 min. IEC chromatograms of other conjugates were similar, with no peak observed between 0 and 10 min (also see Figure 6).

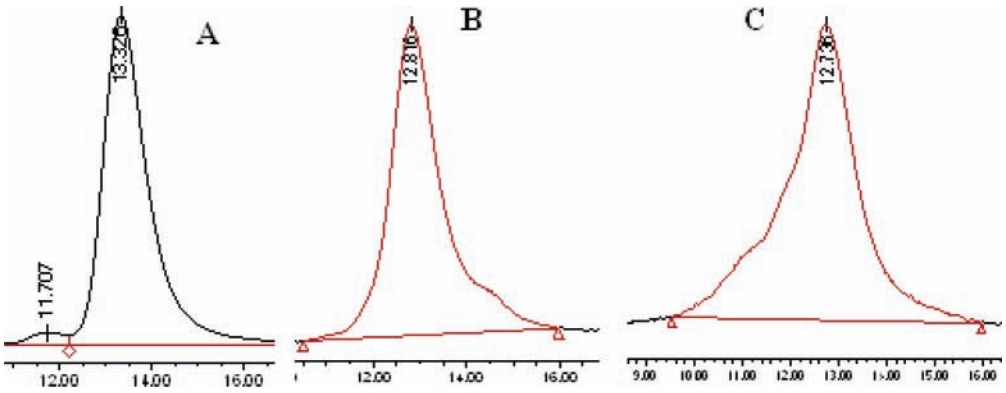


Figure 8. GPC of purified SK−G3.5 conjugates (A for SK−G3.5 (1:1), B for SK−G3.5 (1:10), C for SK−G3.5 (1:20).

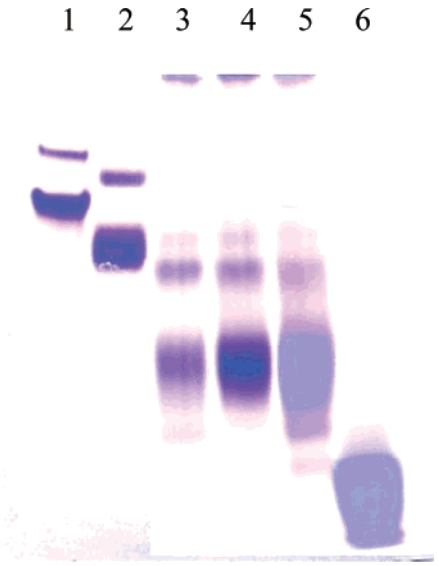


Figure 9. Native-PAGE of SK−G3.5 conjugates. Lane 1 for free SK, lane 2 for SK−G3.5 (1:1), lane 3 for SK−G3.5 (1:5), lane 4 for SK−G3.5 (1:10), lane 5 for SK−G3.5 (1:20), lane 6 for free dendrimer.

Table 2. SK Activity Measured for Different Conjugates (mean ± SD) ($n = 3$)[a]

SK−G3.5 conjugate	average activity (U/mL)	% activity retention
1:1-2 h	319.40 ± 2.73	79.8 ± 0.7
1:5-2 h	94.52 ± 2.38	23.6 ± 0.6
1:10-2 h	62.66 ± 0.75	15.7 ± 0.2
1:20-2 h	40.55 ± 1.63	10.14 ± 0.4

[a] Theoretical activity of all the SK conjugates was 400 IU/mL based on calculation.

reactivity appears to allow coupling reactions under mild reaction conditions and with high efficiency.

Fibrin Gel Lysis. The activity of the SK−dendrimer conjugates, as measured by fibrin gel lysis, decreased as the molar ratio of dendrimer used for conjugation increased (Table 2). The 1:1 conjugate (molar ratio, SK/dendrimer) retained almost 80% of the original activity, while the 1:5, 1:10, and 1:20 conjugates retained only 24%, 16%, and 10% respectively. Similar results have also been recently reported for SK−polyglycerol conjugates (*52*).

The problem of significant loss (sometimes even 95%) in biological activity during conjugation is one of the major concerns with protein modification (*53*). Attaching a polymer conveys many advantages to proteins, e.g., increased blood circulation, improved stability, and reduced immunogenicity. However, the same mechanism that prevents the approach of proteolytic enzymes or antibodies to modified protein can also hinder a substrate from approaching the active site of the protein,

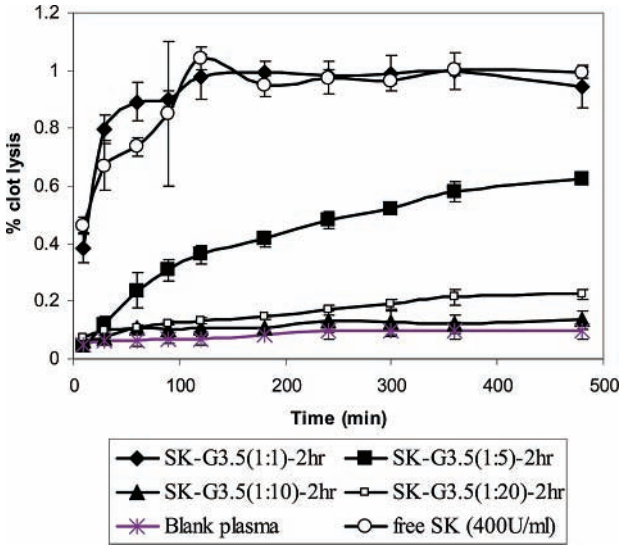


Figure 10. Radiation clot lysis of SK conjugates of different SK−G3.5 molar ratios in comparison with free SK (within 8 h).

especially when the substrate has high molecular weight. It is also possible that any nonspecific attachment of polymer to SK may directly occupy or shield SK's active sites, especially when a large amount of polymer is used. Hence, less modification would lead to higher activity in the SK conjugates. However, for SK conjugates with a higher degree of modification, the activity may be recovered once the dendrimers are detached, which could result in sustained release of SK and a longer duration of action. This is further detailed in the *in vitro* clot lysis assay.

Lysis of ^{125}I-Fibrinogen Clots. The thrombolytic activity of the conjugates compared to that of free SK over 8 h is depicted in Figure 10. The activities of free SK and SK−G3.5 (1:1) conjugate were similar to each other with 100% clot lysis within 3 h, whereas SK−G3.5 (1:5), SK−G3.5 (1:10), and SK−G3.5 (1:20) conjugates showed much less activity (62%, 22%, and 13% clot lysis, respectively) even at 8 h. However, when thrombolytic activities of the conjugates were compared over a prolonged period of time (Figure 11, up to nearly 48 h), a rapid increase in the rate of clot lysis was noted for SK−G3.5 (1:10) and SK−G3.5 (1:20) conjugates after the initial slow phase of thrombolysis. This variation in the thrombolytic profiles of the conjugates with greater protein modification may be due to a difference in the release of SK or active SK fragments from the conjugates over time. Although amide bonds between SK and dendrimer are generally considered to be stable in plasma (*12*), it is possible that proteolytic enzymes in plasma may cause degradation of the SK conjugate with prolonged incubation, leading to a release of free SK and/or of active SK fragments. Since SK has to bind to plasminogen to form the activator

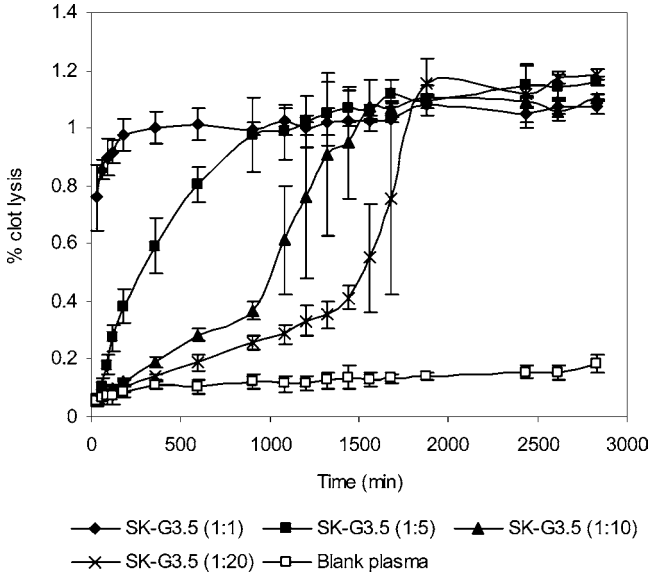


Figure 11. Radiation clot lysis of SK conjugates of different SK−G3.5 molar ratios over 48 h and the possible activity release.

complex, it is possible that the plasminogen binding sites are not readily accessible in the SK conjugates containing more dendrimer molecules. As the dendrimer gets released over time, the SK molecule may become more accessible. Once plasminogen binds with SK to form the activator complex, the thrombolytic activity rapidly increases leading to 100% clot lysis.

In order to assess the release of SK and SK fragments from the conjugates, the stability of these conjugates was studied in PBS at 37 °C. While free SK was completely degraded at 34 h, the SK−G3.5 conjugates degraded slowly, with only 4% of the 1:1 conjugate, 11% of the 1:5, 15% of the 1:10, and 34% of the 1:20 conjugate remaining intact even at 94 h. This indicates that attaching dendrimer greatly improved SK stability, and this improvement was dependent on the degree of modification of SK conjugates, with higher modification leading to higher stability.

The thrombolytic action regained from the SK−G3.5 (1:10) and SK−G3.5 (1:20) conjugates demonstrated that their initial reduced activity was not completely due to the real activity loss during conjugation but at least partly due to temporary coverage of the SK active sites by dendrimers. Through careful tailoring of the linkage between SK and dendrimer (for example, ester bond, Schiff base bond, or stimuli-sensitive spacer), the highly modified SK conjugates could offer a prodrug model to provide a sustained release or long-term effectiveness for a large number of bioactive proteins.

CONCLUSIONS

Dendrimers are being used for drug targeting, imaging, and many other biomedical applications. This paper describes a useful method for effective attachment of dendrimer to various proteins, peptides, and other amine-containing hydrophilic molecules. Through a simple active ester reaction, carboxyl groups of the PAMAM G3.5 dendrimer were reacted with the amino groups of SK under mild aqueous conditions. A series of conjugates with increasing amounts of dendrimer to protein molar ratios have been synthesized. Optimal activation conditions (pH and activation time) led to rapid conjugation (2 h) with high coupling efficiency, as verified by GPC, IEC, and PAGE. The SK−dendrimer molar ratio had a major effect on the activity retention of SK conjugates. With an increase in the number of dendrimer molecules attached to SK, the activity (at shorter time points) decreases for the conjugate. This is possibly due to the masking of active sites of SK by dendrimer. The SK−G3.5 (1:1) conjugate retained up to 80% of protein activity and exhibited quick *in vitro* clot lysis (comparable to that of free SK). The *in vitro* stability study indicates that attachment of dendrimer improved SK stability. Along with the increasing dendrimer/SK ratio, the stability increased. Hence, it could be expected that all of the SK conjugates would have much better stability and longer circulation times than free SK *in vivo*. SK−G3.5 (1:1) conjugate could also be further conjugated to thrombus-specific antibodies or ligands to realize thrombus-targeted SK delivery and targeted thrombolysis.

ACKNOWLEDGMENT

Financial support from the Children's Research Center of Michigan, Wayne State University Presidential Research Enhancement Fund, Pfizer Scholars grant, and NIH−Pediatric Pharmacologic Research Unit supplemental funding (NIH 3U01HD-37261-04SI) are gratefully acknowledged.

LITERATURE CITED

(1) McClintock, D. K., and Bell, P. H. (1971) The mechanism of activation of human plasminogen by streptokinase. *Biochem. Biophys. Res. Commun. 43*, 694−702.

(2) Summaria, L., Arzadon, L., Bernabe, P., and Robbins, K. C. (1974) The interaction of streptokinase with human, cat, dog, and rabbit plasminogens. The fragmentation of streptokinase in the equimolar plasminogen-streptokinase complexes. *J. Biol. Chem. 249*, 4760−9.

(3) Bajaj, A. P., and Castellino, F. J. (1977) Activation of human plasminogen by equimolar levels of streptokinase. *J. Biol. Chem. 252*, 492−8.

(4) Boxrud, P. D., Fay, W. P., and Bock, P. E. (2000) Streptokinase binds to human plasmin with high affinity, perturbs the plasmin active site, and induces expression of a substrate recognition exosite for plasminogen. *J. Biol. Chem. 275*, 14579−89.

(5) Wu, X. C., Ye, R., Duan, Y., and Wong, S. L. (1998) Engineering of plasmin-resistant forms of streptokinase and their production in *Bacillus subtilis*: streptokinase with longer functional half-life. *Appl. Environ. Microbiol. 64*, 824−9.

(6) Houng, A., Quen, S., Jean, L.-F., and Reed, G. L. (1995) Construction of a recombinant streptokinase that resists cleavage and inactivation by plasmin. *Thromb. Haemostasis 73*, 1130.

(7) Ginger, L. G., and Mather, A. N. (1976) (Baxter Laboratories, Inc.) U.S. Patent 3.628,218.

(8) Cazov, E. I., Smirnov, V. N., Torchilin, V. P., Tereshilin, I. M., and Moskvich, B. V. (1981) (All-Union Cardiological Research Center, USSR) Ger. Offen. Application DE 80−3032606.

(9) Brucato, F. H., and Pizzo, S. V. (1990) Catabolism of streptokinase and polyethylene glycol-streptokinase: evidence for transport of intact forms through the biliary system in the mouse. *Blood 76*, 73−9.

(10) Kim, I. S., Choi, H. G., Choi, H. S., Kim, B. K., and Kim, C. K. (1998) Prolonged systemic delivery of streptokinase using liposome. *Arch. Pharm. Res. 21*, 248−52.

(11) Kim, Y.-W., and Kim, D.-C. (1999) Evaluation of thrombolytic effect of streptokinase-dextran conjugate in a rat model of arterial thrombosis. *Yakche Hakhoechi 29*, 211−216.

(12) Veronese, F. M., and Morpurgo, M. (1999) Bioconjugation in pharmaceutical chemistry. *Farmaco 54*, 497−516.

(13) Mikhailets, G. A., Kashkin, A. P., and Sonina, S. I. (1982) Preclinical study of the pharmacological and toxic properties of Streptodecase. *Immobilizovannye Fermenty Med. Med. Prom-sti. 1982*, 37−51.

(14) Perkins, W. R., Vaughan, D. E., Plavin, S. R., Daley, W. L., Rauch, J., Lee, L., and Janoff, A. S. (1997) Streptokinase entrapment in interdigitation-fusion liposomes improves thrombolysis in an experimental rabbit model. *Thromb. Haemostasis 77*, 1174−8.

(15) Leach, J. K., O'Rear Edgar, A., Patterson, E., Miao, Y., and Johnson Arthur, E. (2003) Accelerated thrombolysis in a rabbit model of carotid artery thrombosis with liposome-encapsulated and microencapsulated streptokinase. *Thromb. Haemostasis 90*, 64−70.

(16) Malik, N., and Duncan, R. (2002) (The Dow Chemical Company, U.K.) U.S. Patent Application 2001−881126.
(17) Padilla De Jesus Omayra, L., Ihre Henrik, R., Gagne, L., Frechet Jean, M. J., and Szoka Francis, C., Jr. (2002) Polyester dendritic systems for drug delivery applications: *in vitro* and *in vivo* evaluation. *Bioconjugate Chem. 13*, 453−61.
(18) Quintana, A., Raczka, E., Piehler, L., Lee, I., Myc, A., Majoros, I., Patri Anil, K., Thomas, T., Mule, J., and Baker James, R., Jr. (2002) Design and function of a dendrimer-based therapeutic nanodevice targeted to tumor cells through the folate receptor. *Pharm. Res. 19*, 1310−6.
(19) Kolhe, P., Misra, E., Kannan Rangaramanujam, M., Kannan, S., and Lieh-Lai, M. (2003) Drug complexation, *in vitro* release and cellular entry of dendrimers and hyperbranched polymers. *Int. J. Pharm. 259*, 143−60.
(20) Malik, N., Duncan, R., Tomalia, D. A., and Esfand, R. (2003) (Dendritic Nanotechnologies, Inc., U.S.A.) U.S. Patent Application 2001−16733.
(21) Nakanishi, H., Mazda, O., Satoh, E., Asada, H., Morioka, H., Kishida, T., Nakao, M., Mizutani, Y., Kawauchi, A., Kita, M., Imanishi, J., and Miki, T. (2003) Nonviral genetic transfer of Fas ligand induced significant growth suppression and apoptotic tumor cell death in prostate cancer *in vivo*. *Gene Ther. 10*, 434−42.
(22) Kannan, S., Kolhe, P., Raykova, V., Glibatec, M., Kannan Rangaramanujam, M., Lieh-Lai, M., and Bassett, D. (2004) Dynamics of cellular entry and drug delivery by dendritic polymers into human lung epithelial carcinoma cells. *J. Biomater. Sci., Polym. Ed. 15*, 311−30.
(23) Khandare, J., Kolhe, P., Pillai, O., Kannan, S., Lieh-Lai, M., and Kannan Rangaramanujam, M. (2005) Synthesis, cellular transport, and activity of polyamidoamine dendrimer−methylprednisolone conjugates. *Bioconjugate Chem. 16*, 330−7.
(24) Kukowska-Latallo Jolanta, F., Candido Kimberly, A., Cao, Z., Nigavekar Shraddha, S., Majoros Istvan, J., Thomas Thommey, P., Balogh Lajos, P., Khan Mohamed, K., and Baker James, R., Jr. (2005) Nanoparticle targeting of anticancer drug improves therapeutic response in animal model of human epithelial cancer. *Cancer Res. 65*, 5317−24.
(25) Patri Anil, K., Kukowska-Latallo Jolanta, F., and Baker James, R., Jr. (2005) Targeted drug delivery with dendrimers: comparison of the release kinetics of covalently conjugated drug and non-covalent drug inclusion complex. *Adv. Drug Delivery Rev. 57*, 2203−14.
(26) Thomas Thommey, P., Majoros Istvan, J., Kotlyar, A., Kukowska-Latallo Jolanta, F., Bielinska, A., Myc, A., and Baker James, R., Jr. (2005) Targeting and inhibition of cell growth by an engineered dendritic nanodevice. *J. Med. Chem. 48*, 3729−35.
(27) Kolhe, P., Khandare, J., Pillai, O., Kannan, S., Lieh-Lai, M., and Kannan Rangaramanujam, M. (2006) Preparation, cellular transport, and activity of polyamidoamine-based dendritic nanodevices with a high drug payload. *Biomaterials 27*, 660−9.
(28) Roberts, J. C., Adams, Y. E., Tomalia, D., Mercer-Smith, J. A., and Lavallee, D. K. (1990) Using starburst dendrimers as linker molecules to radiolabel antibodies. *Bioconjugate Chem. 1*, 305−8.
(29) Barth, R. F., Adams, D. M., Soloway, A. H., Alam, F., and Darby, M. V. (1994) Boronated starburst dendrimer-monoclonal antibody immunoconjugates: evaluation as a potential delivery system for neutron capture therapy. *Bioconjugate Chem. 5*, 58−66.
(30) Singh, P., Moll, F., III, Lin, S. H., Ferzli, C., Yu, K. S., Koski, R. K., Saul, R. G., and Cronin, P. (1994) Starburst dendrimers: enhanced performance and flexibility for immunoassays. *Clin. Chem. 40*, 1845−9.
(31) Kobayashi, H., Sato, N., Saga, T., Nakamoto, Y., Ishimori, T., Toyama, S., Togashi, K., Konishi, J., and Brechbiel, M. W. (2000) Monoclonal antibody-dendrimer conjugates enable radiolabeling of antibody with markedly high specific activity with minimal loss of immunoreactivity. *Eur. J. Nucl. Med. 27*, 1334−9.
(32) Cordova, A., and Janda, K. D. (2001) Synthesis and catalytic antibody functionalization of dendrimers. *J. Am. Chem. Soc. 123*, 8248−59.
(33) Lee, S. C., Parthasarathy, R., Botwin, K., Kunneman, D., Rowold, E., Lange, G., Klover, J., Abegg, A., Zobel, J., Beck, T., Miller, T., Hood, W., Monahan, J., McKearn, J. P., Jansson, R., and Voliva, C. F. (2004) Biochemical and immunological properties of cytokines conjugated to dendritic polymers. *Biomed. Microdevices 6*, 191−202.
(34) Patri Anil, K., Myc, A., Beals, J., Thomas Thommey, P., Bander Neil, H., and Baker James, R., Jr. (2004) Synthesis and *in vitro* testing of J591 antibody−dendrimer conjugates for targeted prostate cancer therapy. *Bioconjugate Chem. 15*, 1174−81.
(35) Thomas Thommey, P., Patri Anil, K., Myc, A., Myaing Mon, T., Ye Jing, Y., Norris Theodore, B., and Baker James, R., Jr. (2004) In vitro targeting of synthesized antibody-conjugated dendrimer nanoparticles. *Biomacromolecules 5*, 2269−74.
(36) Singh, P. (1998) Terminal groups in Starburst dendrimers: activation and reactions with proteins. *Bioconjugate Chem. 9*, 54−63.
(37) Jevprasesphant, R., Penny, J., Jalal, R., Attwood, D., McKeown, N. B., and D'Emanuele, A. (2003) The influence of surface modification on the cytotoxicity of PAMAM dendrimers. *Int. J. Pharm. 252*, 263−6.
(38) Malik, N., Wiwattanapatapee, R., Klopsch, R., Lorenz, K., Frey, H., Weener, J. W., Meijer, E. W., Paulus, W., and Duncan, R. (2000) Dendrimers: relationship between structure and biocompatibility *in vitro*, and preliminary studies on the biodistribution of 125I-labelled polyamidoamine dendrimers *in vivo*. *J. Controlled Release 65*, 133−48.
(39) Duncan, R., and Izzo, L. (2005) Dendrimer biocompatibility and toxicity. *Adv. Drug Delivery Rev. 57*, 2215−37.
(40) Svenson, S., and Tomalia Donald, A. (2005) Dendrimers in biomedical applications−reflections on the field. *Adv. Drug Delivery Rev. 57*, 2106−29.
(41) Sharma, A., Desai, A., Ali, R., and Tomalia, D. (2005) Polyacrylamide gel electrophoresis separation and detection of polyamidoamine dendrimers possessing various cores and terminal groups. *J. Chromatogr., A 1081*, 238−44.
(42) Shi, X., Patri Anil, K., Lesniak, W., Islam Mohammad, T., Zhang, C., Baker James, R., Jr., and Balogh Lajos, P. (2005) Analysis of poly(amidoamine)-succinamic acid dendrimers by slab-gel electrophoresis and capillary zone electrophoresis. *Electrophoresis 26*, 2960−7.
(43) Li, C., Huang, J., Shao, Z., Wang, W., Yang, G., and Huang, P. (2004) Study on pharmacokinetics of native r-SAK in a thrombosis model of the femoral artery in rabbits. *Zhongguo Linchuang Kangfu 8*, 466−468.
(44) Gurewich, V., Pannell, R., Louie, S., Kelley, P., Suddith, R. L., and Greenlee, R. (1984) Effective and fibrin-specific clot lysis by a zymogen precursor form of urokinase (pro-urokinase). A study *in vitro* and in two animal species. *J. Clin. Invest. 73*, 1731−9.
(45) Lopez, M., Ojeda, A., and Arocha-Pinango, C. L. (2000) In vitro clot lysis: a comparative study of two methods. *Thromb. Res. 97*, 85−7.
(46) Mihara, H, S. H., Matsuura, A., and Inukai, T. (1986), U.S. Patent Application 06/508,163.
(47) Lopez, M., Gonzalez, L. R., Reyes, N., Sotolongo, J., and Pujol, V. (2004) Stabilization of a freeze-dried recombinant streptokinase formulation without serum albumin. *J. Clin. Pharm. Ther. 29*, 367−73.
(48) Hermanson, G. T. (1996) *Bioconjugate Techniques*, 1st ed., Academic Press, New York.
(49) Smith, R. A., Dupe, R. J., English, P. D., and Green, J. (1981) Fibrinolysis with acyl-enzymes: a new approach to thrombolytic therapy. *Nature (London) 290*, 505−8.
(50) Koide, A., Suzuki, S., and Kobayashi, S. (1982) Preparation of polyethylene glycol-modified streptokinase with disappearance of binding ability towards anti-serum and retention of activity. *FEBS Lett. 143*, 73−6.
(51) Frechet, J. M. (1994) Functional polymers and dendrimers: reactivity, molecular architecture, and interfacial energy. *Science 263*, 1710−5.
(52) Fernandes Edson Giuliani, R., de Queiroz Alvaro Antonio, A., Abraham Gustavo, A., and San Roman, J. (2006) Antithrombogenic properties of bioconjugate streptokinase-polyglycerol dendrimers. *J. Mater. Sci. Mater. Med. 17*, 105−11.
(53) Roberts, M. J., and Harris, J. M. (1998) Attachment of degradable poly(ethylene glycol) to proteins has the potential to increase therapeutic efficacy. *J. Pharm. Sci. 87*, 1440−5.

BC060322D

Single Cell Fluorescence Imaging Using Metal Plasmon-Coupled Probe

Jian Zhang, Yi Fu, and Joseph R. Lakowicz*

Center for Fluorescence Spectroscopy, University of Maryland School of Medicine, Department of Biochemistry and Molecular Biology, 725 West Lombard Street, Baltimore, Maryland 21201. Received October 27, 2006; Revised Manuscript Received February 5, 2007

This work constitutes the first fluorescent imaging of cells using metal plasmon-coupled probes (PCPs) at single cell resolution. *N*-(2-Mercapto-propionyl)glycine-coated silver nanoparticles were synthesized by reduction of silver nitrate using sodium borohyride and then succinimidylated via ligand exchange. Alexa Fluor 647-labeled concanavalin A (con A) was chemically bound to the silver particles to make the fluorescent metal plasmon-coupled probes. The fluorescence images were collected using a scanning confocal microscopy. The fluorescence intensity was observed to enhance 7-fold when binding the labeled con A on a single silver particle. PCPs were conjugated on HEK 293 A cells. Imaging results demonstrate that cells labeled by PCPs were 20-fold brighter than those by free labeled con A.

INTRODUCTION

Molecular fluorescence imaging techniques play critical roles in the early detection, diagnosis, and treatment of disease, as well as aid in the studies of biological and biochemical mechanisms, immunology, and neuroscience on single cells (*1*−*4*). Generally, an imaging agent consists of an organic fluorophore moiety and a targeting functionality, such as an antibody, peptide, DNA, or a special ligand (*5*−*7*). However, most imaging agents have several limitations: complicated preparation, strong signal background, fast photobleaching, and single color.

Recently, the use of fluorescently labeled metal particles has become attractive due to near-field interaction of the fluorophore with metal particles (*8*−*17*). The metal particle with the subwavelength size usually displays an energy resonance arising from the collective oscillation of migrated electrons on its surfaces (*18*, *19*), which is defined as plasmon resonance. The wavelength of plasmon resonance is closely relevant to the metal core including metal species, core size, and core shape as well as the dielectric properties of coating layer (*19*−*21*). The fluorophore can be described as an oscillating dipole to radiate energy during fluorescence occurrence (*22*). When it is localized near the metal particle, the radiating energy is dramatically altered through coupling with the metal plasmon resonance to cause a change of the emission properties, which is defined as radiative decay engineering (RDE) (*23*−*25*). Generally, RDE can lead to an enhancement of intensity to be 10^1 to 10^3 times depending upon both the fluorophore and metal core factors as well as the distance between them. Besides the intensity enhancement, the near field interaction of fluorophore with the metal particle can also result in its shorter lifetime (*26*), which leads to less time for the photochemistry while in the excited-state and thus more excitation−emission cycles prior to photobleaching. Hence, the fluorophore usually displays a better photostability near the metal particle (*27*).

The metal particle is known to have large surface area, good chemical stability, and homogeneous dispersion in solution (*28*−*30*). The development of surface chemistry can enable versatile decoration of fluorophores as well as provide targeting functionalities on the metal particle (*31*, *32*). Hence, we can use the dye-labeled metal particle as a novel fluorescence imaging agent to satisfy our specific requirements in the measurements. Because the optical properties of dye-labeled metal particles can be controlled well by the metal plasmon resonance as discussed above, we define it as metal plasmon-coupled probe (PCP). PCP is suggested to be able to offer easier preparation, higher brightness, better photostability, and multiple colors as a new generation of fluorescence imaging agent (*22*, *23*). In this paper, we are concerned with developing a method to make PCPs and label cells using these PCPs. The fluorescence images by PCPs were collected using scanning confocal microscopy at the single cell level and compared with those by unmodified fluorophores.

Dye-labeled concanavalin A (abbreviated as con A) can bind to sugars residing on the cell membrane (*33*−*35*), so it is commonly used in cell labeling in culture (*36*, *37*). In this study, the dye-labeled con A was chemically bound to the silver particle to generate PCP (Scheme 1). The silver particle was synthesized in a typical protocol by reduction of silver salt (*28*). In order to bind con A, the metal particle was functionalized by succinimidyl ester at a terminal position via ligand exchange (*30*, *38*). The con A was bound to the succinimidylated particle by condensation between the succinimidyl ester on the metal particle and the lysine residual on the protein molecule. Alexa Fluor 647-labeled con A was used in the study because of its efficient enhancement as a near-infrared fluorophore near the metal substrate (*39*). HEK 293 A cell line, which is originally derived from human embryonic kidney and utilized frequently in *in vivo* imaging (*40*, *41*), was conjugated by PCPs, and the fluorescence imaging was monitored using confocal microscopy.

EXPERIMENTAL PROCEDURES

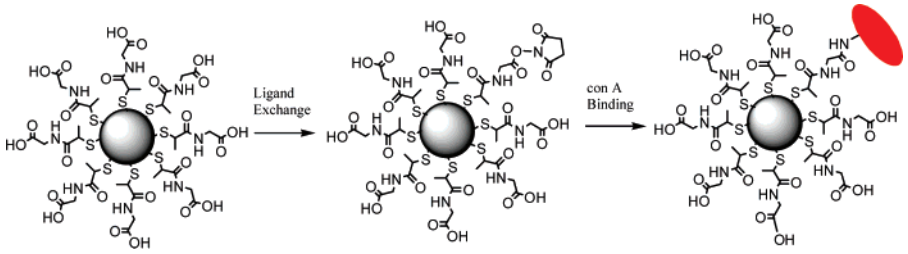
All reagents and spectroscopic grade solvents were used as received from Fisher or Aldrich. Alexa Fluor 647-labeled concanavalin A (con A) was commercially available from Molecule Probes. HEK293 A cell line was from Invitrogen. RC dialysis membrane (MWCO 50 000) was purchased from Spectrum Laboratories, Inc. Nanopure water (>18.0 MΩ cm) purified using Millipore Milli-Q gradient system was used in all experiments.

Preparation of Tiopronin-Coated Silver Nanoparticles. *N*-(2-Mercaptopropionyl)glycine (abbreviated as tiopronin)-

* Corresponding author. E-mail: lakowicz@cfs.umbi.umd.edu.

10.1021/bc0603384 CCC: $37.00 © 2007 American Chemical Society
Published on Web 03/22/2007

Scheme 1. Tiopronin-Coated Silver Particles Were Succinimidylated via Ligand Exchange and Then Chemically Bound by Alexa Fluor 647-Labeled Con A via Condensation



coated silver nanoparticles were prepared using a modified Brust reaction with a mole ratio of tiopronin/silver nitrate = 1/6 in methanol using an excess amount of sodium borohydride as reducing agent (*42*−*44*). Removal of the solution by filtration, the residual precipitated solid was washed with methanol and acetone, respectively, to obtain the metal particles. The particles (1 mg/mL) and tiopronin (10 mM) were codissolved in water, and the solution was stirred for 24 h to anneal the particles (*45*, *46*). The water was removed under vacuum and the residue was washed thoroughly with methanol and acetone. The solid tiopronin-coated particles were further purified through dialysis against water (MWCO 50 000).

Functionalization of Silver Particles. (2-Mercapto-propionylamino)acetic acid 2,5-dioxo-pyrrolidin-1-yl ester was synthesized as previously reported (*47*). A 4×10^{-8} mol amount of this compound was codissolved with a 4×10^{-8} mol amount of tiopronin-coated silver particles in water and stirred for 72 h at room temperature for ligand exchange. Some tiopronin molecules were expected to be displaced by the succinimidyl ester molecules on the metal cores in a mole ratio of 1/1 (*38*). Unbound compounds were removed by dialysis against water (MWCO 50 000), and the resultant metal particles were obtained under vacuum.

Binding con A onto Silver Particles. Alexa Fluor 647-labeled concanavalin A (con A) was chemically bound on the succinimidylated metal particle by condensation between the terminal succinimidyl ester on the metal particle and the lysine residue on the con A (*35*, *36*). The metal particles (2×10^{-8} M) and dye-labeled con A (2×10^{-8} M) were codissolved in molar ratio of 1/1 in water and stirred for 2 h at room temperature. One drop of ammonia was added to the solution to block the nonreacting succinimidyl ester on the metal particle. The solution was centrifuged at 5000 rpm/s to remove the aggregates in the reaction and then dialyzed against 10 mM glucose−BAS buffer solution to remove the impurities.

Conjugating Dye-Labeled con A and PCPs on Cell Lines. HEK293 A cell lines were suspended in 500 μL aliquots of 250 g/mL con A solutions made in 0.01 M PBS buffer (pH = 7.2) and agitated for 1 h at room temperature (*37*). PCPs were incubated with the cells at the same fluorophore concentration and for the same incubation time as the unmodified dye-labeled con A. All cell samples were washed three times with PBS buffer solution before using imaging measurements.

Spectra and Imaging Measurements. Absorption spectra were monitored with a Hewlett-Packard 8453 spectrophotometer. Ensemble fluorescence spectra were recorded with a Cary Eclipse Fluorescence Spectrophotometer. Transmission electron micrographs (TEM) were taken with side-entry Philips electron microscopy at 120 keV. Samples were cast from water solutions onto standard carbon-coated (200−300 Å) Formvar films on copper grids (200 mesh) by placing a droplet of a 10-fold diluted aqueous sample solution on the grids. The size distribution of the metal core was analyzed with Scion Image Beta Release 2 counting at least 200 particles. For fluorescence imaging measurements, the diluted samples were dispersed on a pre-cleaned glass coverslip. The coverslips (18×18 μm, Corning) were first soaked in a 10:1 (v:v) mixture of concentrated H_2SO_4 and 30% H_2O_2 overnight, thoroughly rinsed with water, sonicated in absolute ethanol, and dried with an air stream. All the single-molecule measurements were performed using time-resolved confocal microscopy (MicroTime 200, PicoQuant). Briefly, it consists of an inverted confocal microscope coupled to a high-sensitivity detection setup. A single mode pulsed laser diode (635 nm, 100 ps, 40 MHz) (PDL800, PicoQuant) was used as the excitation light. An oil immersion objective (Olympus, 100×, 1.3NA) was used both for focusing laser light onto the sample and collecting fluorescence emission from the sample. The fluorescence that passed a dichroic mirror (Q655LP, Chroma) was focused onto a 75 μm pinhole for spatial filtering to reject out-of-focus signals. The emission signals were discretely focused onto single photon avalanche diodes (SPAD) (SPCM-AQR-14, Perkin-Elmer Inc). The data collected using the TimeHarp 200 board was stored in the time-tagged time-resolved mode (TTTR), recording every detected photon with its individual timing, which is the basis for the following single-molecule analysis.

RESULTS AND DISCUSSION

The tiopronin-coated silver particles displayed a typical silver plasmon absorbance at 405 nm in water (Figure 1) (*43*). The average diameter of the metal cores was 20 nm as measured from 200 transmission electron micrographs images (TEM, Figure 2a), and their *average* chemical compositions were estimated to be ca. $(Ag)_{2.5\times105}(Tio)_{5.0\times103}$. The silver particles were succinimidylated via ligand exchange using (2-mercapto-propionylamino)acetic acid 2,5-dioxo-pyrrolidin-1-yl ester. Typically, such ligand exchange occurs in a molar ratio of 1/1 on the surface of metal particles according to Murray et al. (*38*), so we suggest that there exists average one succinimidyl ligand on each metal particle even though the ligand exchange is completely accomplished. The reason for one succinimidyl ester ligand/per particle is to compare the cell imaging by PCPs and unmodified con A at the same quantity of fluorophore. In future work, we can conjugate more dye-labeled con A molecules to

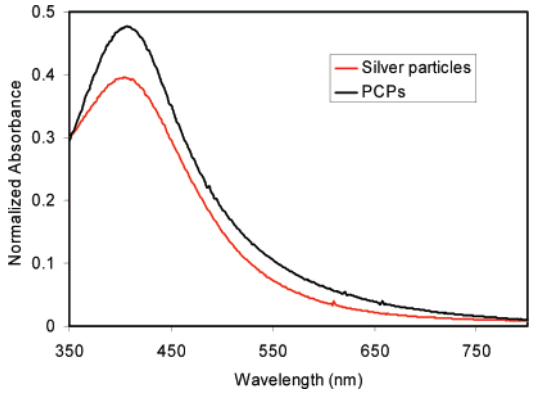


Figure 1. Normalized absorbance spectra of tiopronin-coated silver particle and con A-bound silver particles in water.

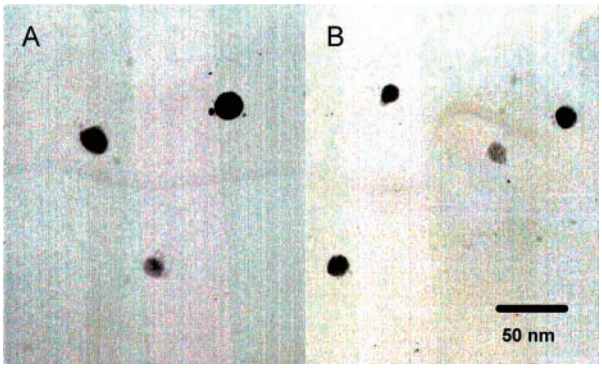


Figure 2. Transmission electron micrographs (TEM) images of (A) tiopronin-coated silver particles and (B) con A-bound particles.

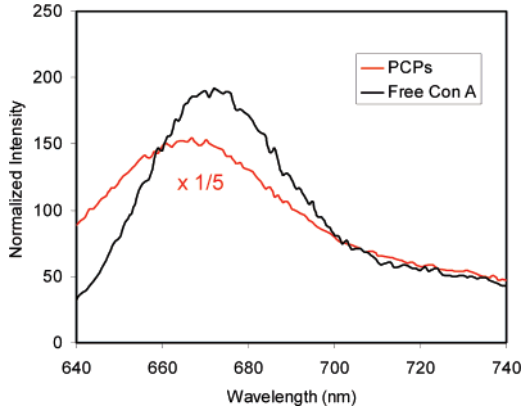


Figure 3. Ensemble fluorescence spectra of Alexa 647-labeled con A and con A-bound silver particle in water.

get PCPs with higher brightness and more capability to capture on the membranes of cells.

Alexa Fluor 647-labeled con A was chemically bound to the silver particle via condensation reaction (Scheme 1). Because only one succinimidyl ester was expected to bind per metal particle, each metal particle was bound maximally by one con A molecule. No significant cross-linking was observed from TEM images (Figure 2b). Even if cross-linking had occurred in the con A binding, the aggregate was removed by the centrifugation. The con A-bound silver particles, so-called PCPs, displayed a blue-shifting of fluorescence wavelength from 672 to 667 nm with the binding, accompanied by simultaneous band broadening (Figure 3). However, the binding did not alter the metal plasmon absorbance (Figure 1), which was principally due to the limitation of the con A amount on each metal particle. This result is consistent with what we require for PCPs in this case.

In order to obtain the exact amount of con A on each metal particle, the metal cores of PCPs (1×10^{-6} M) were removed by adding dropwise sodium cyanide (*32*). The concentration of con A in the residual solution was measured to be 8×10^{-7} M according to the fluorescence intensity. Hence, the molar ratio of bound con A/metal particle was estimated to be 0.8, showing that one metal particle was bound by less than one con A. TEM images of PCPs (Figure 2b) displayed an insignificant change from the tiopronin-coated particles (Figure 2a), indicating that the above surface reactions did not obviously influence the metal core. Furthermore, TEM results also confirmed that there was not significant cross-linking between the metal particles and con A molecules as described earlier.

Fluorescence images were collected by scanning confocal microscopy. Tiopronin-coated silver particles displayed light-scattering images with typical photoblinking behavior, which take on 'streaky" appearances and the spots no longer appear as full and round shapes (Figure 4a). The streaks are not noise, having intensity levels significantly greater than the background. The strong blinking behavior may arise from temporal variations in the emission rate during illumination, most likely from strong "nondestructive" silver blinking as confirmed by our previous result (*48*). Contrarily, full and round spots were observed from the unmodified con A with an average intensity at 50 kHz (Figure 4b). A representative time trace was given as gradual intensity decay (Figure 5), indicating that each con A molecule consists of multiple dye molecules. After binding con A to the silver particle, the fluorescence of PCPs became more intense (Figure 4c), about 7 fold brighter than that of unmodified con A. This enhancement efficiency is in good agreement with the value obtained from the ensemble spectra in solution (6 fold). Most of the unmodified con A molecules were bleached away within 15 s (Figure 5), while at least half of the PCPs were monitored indefinitely without photobleaching, implying that the fluorophores on the metal particles became more photostable. Enhanced brightness and lengthened photostability are typical properties of metal-enhanced fluorescence as in our previous description (*24*, *25*).

HEK293 A cell lines were conjugated with either unmodified con A or PCPs. The imaging was monitored with confocal microscopy at the single cell level (Figure 6). At least 50 images were collected for each sample. Although the cells were measured under dry conditions, the averaged size of the HEK293 A cells was in the range of 5−10 μm, close to those of living cells on a glass substrate, reported by Zeng, et al. (*49*). It was difficult to distinguish the individual bright spots on the cells, implying that the probes were packed densely on the cell membranes in both situations. The brightness was analyzed on the basis of the average value of the cell images. It is shown that the image brightness of cells by unmodified con A (Figure 6d,e) is identical to that of free unmodified con A (Figure 4b), implying that the conjugation cannot significantly alter the brightness of the probe on the cell. However, the image brightness of cells labeled by PCPs (Figure 6a−c) is 20-fold greater than that of free unmodified con A. Theses images by PCPs are even 4-fold brighter than those by unconjugated PCPs, which is most likely attributed to the coupling effect of PCPs on the cell membrane (*42*).

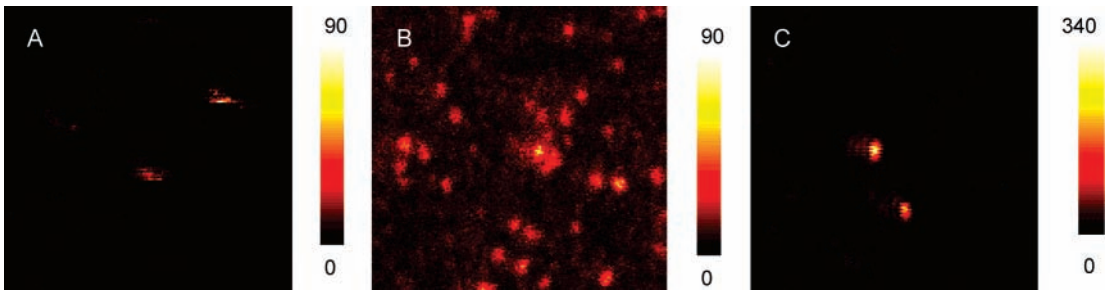


Figure 4. Scattering/fluorescence images (a) tiopronin-coated silver particles, (b)Alexa Fluor 647 labeled con A, and (c) con A-bound silver particles.

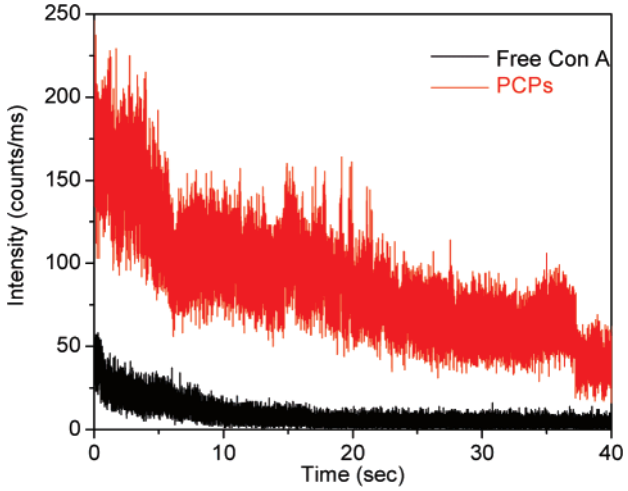


Figure 5. Respective time traces of unmodified con A and bound silver particles.

In order to understand the possible interactions between the metal particles and cells, we utilized the tiopronin-coated metal particles instead of PCPs in the incubation experiment. The metal particles were hardly observed near the cells after washing, implying that PCPs were conjugated on thee cultured cell basically through the interaction of bound con A instead of the silver particles. However, bulky PCPs may meet stronger steric hindrance when being proximate to and conjugating to the cells. The quantity of PCP on the cell surface must be less than that of unmodified con A. Because there is only one con A on each PCP, the quantity of fluorophore by PCP is proposed to be less than that by unmodified con A on the cell membrane. Therefore, the intensity enhancement of fluorescence on the cell images by PCPs is most probably attributed to the coupling effect among PCPs (*24*). In fact, when the metal particles are in close proximity to each other, the electric fields have been estimated to become more intensive due to overlapping from the individual fields (*50*), and the fluorophore localized in these overlapped fields is enhanced more efficiently (*43*). This result reveals that the signal intensity on the cell membrane can be enhanced not only as individually but more efficiently as coupled when PCPs are conjugated.

The coupling effect of PCPs also displays a better photostability on the cell membrane. Real-time intensity traces illustrate that almost half of the unmodified con A molecules on cells were bleached out in 5 s, while intensities of PCPs decay more gradually (Figure 7). If the fluorophores are supposed to be bleached proportionally with time as shown in the decay curves, we can propose that the photostability of PCPs on the cell membrane is at least 10 times longer than that of unmodified con A.

The coupling mechanism of fluorophore with metal particles can be discussed by lifetimes. It is known that the interaction between the fluorophore and metal particles can result in a dramatic change of radiating energy that is expressed as an apparent increase of intrinsic decay rate (*25*). Such an increase of intrinsic decay rate can be monitored by the lifetime of a fluorophore. In this study, the lifetime data were collected from the time traces using single molecule time-corrected single photon counting (TCSPC). The lifetime of unmodified con A was estimated to be 2.5 ns and furthermore shortened to be 1.2 ns when bound to the metal particles, affirming the existence of interaction between fluorophores and metal particles. When the fluorophore was associated on the cells as an unmodified state or PCP, the intensity was observed to decay differently in which the decay by PCP was more rapid than that by unmodified con A (Figure 8), and the lifetimes were estimated to be 1.1 ns (PCPs) and 2.4 ns (unmodified con A), respectively. It is uncertain why the lifetime did not further shorten when associating PCPs on the cells membrane. Many factors including the distance between the PCPs and environmental changes for the fluorophore, etc., may be partially responsible.

The tiopronin-coated metal particles with an average diameter of 20 nm were decorated quantitatively by Alexa Fluor 647-labeled con A in a molar ratio of 1:1 to generate metal plasmon-coupled probes (PCPs) as fluorescence imaging agents. HEK293 A cells were conjugated by PCPs and unmodified dye-labeled con A, respectively, and fluorescently imaged using scanning

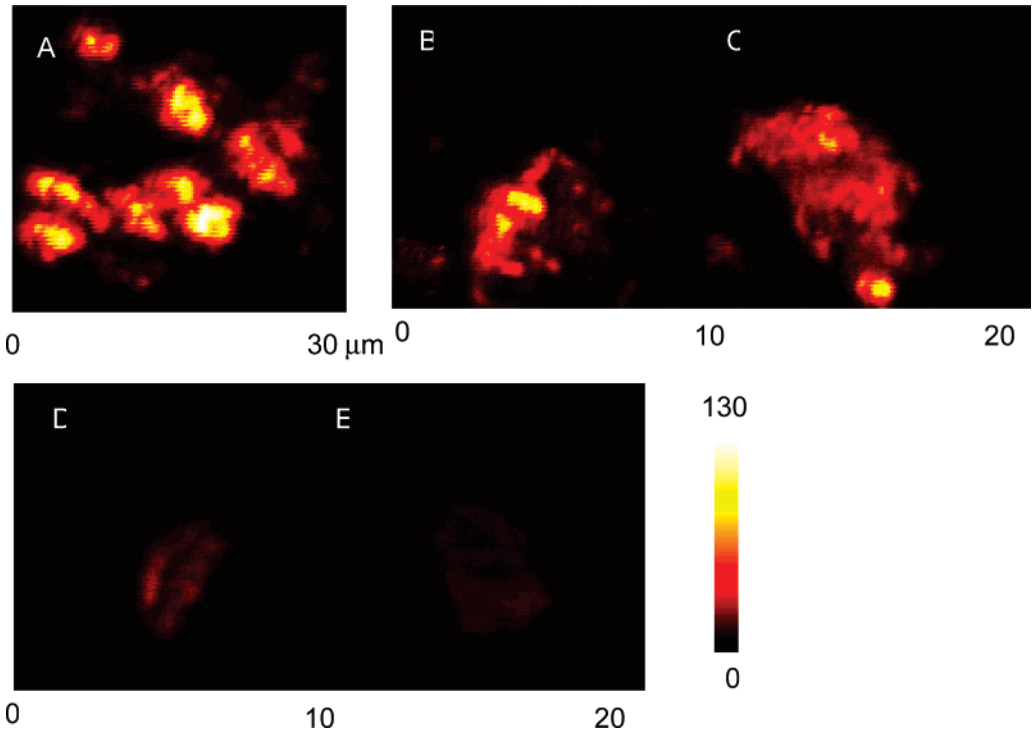


Figure 6. Representative fluorescent images of HEK 293 A cell lines (a−c) labeled by PCPs, and (d and e) labeled by unmodified con A.

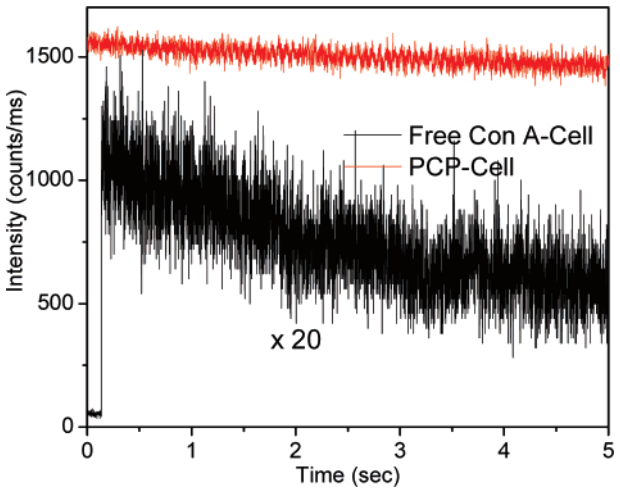


Figure 7. Respective time traces from fluorescent images labeled by con A and PCPs on the cell membrane.

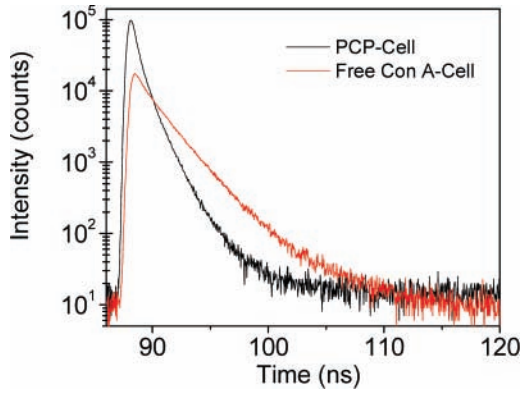


Figure 8. Respective TCSPC curves from fluorescent images labeled by unmodified con A and PCPs on the cell membrane.

confocal microscopy at the single cell level. The fluorescence images of cell lines by PCPs were 20 times brighter than those by unmodified con A, and the photostability was 10 times longer. These results reveal that the PCPs can work efficiently as brighter and more photostable imaging agents. In this case, the dye-labeled con A is only bound to the silver particles in a molar ratio of 1:1 for research convenience. Actually, with increasing the binding number of con A on each metal particle to an optimal value, PCP is supposed to be brighter up to hundreds of times than unmodified con A. The high number of con A on PCP can increase its capability to catch the target on the cell membrane. One metal particle can also be decorated readily by more than one kind of fluorophore, so multicolor PCP will be investigated in further work. In addition, PCP displays a longer photostability, so it can be utilized in long-range diagnosis and treatment of disease.

ACKNOWLEDGMENT

This research was supported by a grant from NIH, EB-00682, HG-02655, and NCRR, RR-08119. We greatly appreciate the discussion with Dr. Hali Hartmann in Medical Biotechnology Center and the University of Maryland Biotechnology Institute.

LITERATURE CITED

(1) Weissleder, R., Tung, C. H., Mahmood, U., and Bogdanov, A. (1999) In vivo imaging of tumors with protease-activated near-infrared fluorescent probes. *Nature Biotechnol. 17*, 375−378.

(2) Ntziachristos, V., and Chance, B. (2001) Probing physiology and molecular function using optical imaging: applications to breast cancer. *Breast Cancer Res. 3*, 41−46.

(3) Chen, I., and Ting, A. Y. (2005) Site-specific labeling of proteins with small molecules in live cells. *Curr. Opin. Biotechnol. 16*, 35−40.

(4) Howarth, M., Takao, K., Hayashi, Y., and Ting, A. Y. (2005) Targeting quantum dots to surface proteins in living cells with biotin ligase. *Proc. Nat. Acad. Sci. U.S.A. 102*, 7583−7588.

(5) Rosenthal, S. J., Tomlinson, I., Adkins, E. M., Schroeter, S., Adams, S., Swafford, L., McBride, J., Wang, Y., DeFelice, L. J., and Blakely, R. D. (2002) Targeting Cell Surface Receptors with Ligand-Conjugated Nanocrystals. *J. Am. Chem. Soc. 124*, 4586−4594.

(6) Vivero-Pol, L., George, N., Krumm, H., Johnsson, K., and Johnsson, N. (2005) Multicolor Imaging of Cell Surface Proteins. *J. Am. Chem. Soc. 127*, 12770−12271.

(7) Van Dijk, M. A., Lippitz, M., and Orrit, M. (2005) Far-Field Optical Microscopy of Single Metal Nanoparticles. *Acc. Chem. Res. 38*, 594−601.

(8) Shen, Y., Swiatkiewicz, J., Lin, T.-C., Markowicz, P., and Prasad, P. N. (2002) Near-Field Probing Surface Plasmon Enhancement Effect on Two-Photon Emission. *J. Phys. Chem. B 106*, 4040−4042.

(9) Yonzon, C. R., Jeoung, E., Zou, S., Schatz, G. C., Mrksich, M., and Van Duyne, R. P. (2004) A Comparative Analysis of Localized and Propagating Surface Plasmon Resonance Sensors: The Binding of Concanavalin A to a Monosaccharide Functionalized Self-Assembled Monolayer. *J. Am. Chem. Soc. 126*, 12669−12676.

(10) Yu, F., Persson, B., Lofas, S., and Knoll, W. **(**2004) Attomolar Sensitivity in Bioassays Based on Surface Plasmon Fluorescence Spectroscopy. *J. Am. Chem. Soc. 126*, 8902−8903.

(11) Lee, I.-Y. S., Suzuki, H., Ito, K., and Yasuda, Y. (2004) Surface-Enhanced Fluorescence and Reverse Saturable Absorption on Silver Nanoparticles. *J. Phys. Chem. B 108*, 19368−19372.

(12) Ekgasit, S., Thammacharoen, C., Yu, F., and Knoll, W. (2004) Evanescent Field in Surface Plasmon Resonance and Surface Plasmon Field-Enhanced Fluorescence Spectroscopies. *Anal. Chem. 76*, 2210−2219.

(13) Song, J.-H., Atay, T., Shi, S., Urabe, H., and Nurmikko, A. V. (2005) Large Enhancement of Fluorescence Efficiency from CdSe/ZnS Quantum Dots Induced by Resonant Coupling to Spatially Controlled Surface Plasmons. *Nano Lett. 5*, 1557−1561.

(14) Baluschev, S., Yu, F., Miteva, T., Ahl, S., Yasuda, A., Nelles, G., Knoll, W., and Wegner, G. (2005) Metal-Enhanced Up-Conversion Fluorescence: Effective Triplet-Triplet Annihilation near Silver Surface. *Nano Lett. 5*, 2482−2484.

(15) Kawasaki, M., and Mine, S. (2005) Enhanced Molecular Fluorescence near Thick Ag Island Film of Large Pseudotabular Nanoparticles. *J. Phys. Chem. B 109*, 17254−17261.

(16) Malicka, J., Gryczynski, I., Gryczynski, Z., and Lakowicz, J. R. (2003) Effects of Fluorophore-to-silver Distance on the Emission of Cyanine-dye-labeled Oligonucleotides. *Anal. Biochem. 315*, 57−66.

(17) Aslan, K., Huang, J., Wilson, G. M., and Geddes, C. D. (2006) Metal-Enhanced Fluorescence-Based RNA Sensing. *J. Am. Chem. Soc. 128*, 4206−4207.

(18) Antunes, P. A., Constantino, C. J. L., Aroca, R. F., and Duff, J. (2001) Langmuir and Langmuir-Blodgett Films of Perylene Tetracarboxylic Derivatives with Varying Alkyl Chain Length: Film Packing and Surface-Enhanced Fluorescence Studies. *Langmuir 17*, 2958−2964.

(19) Kumbhar, A. S., Kinnan, M. K., and Chumanov, G. (2005) Multipole Plasmon Resonances of Submicron Silver Particles. *J. Am. Chem. Soc. 127*, 12444−12445.

(20) Bruzzone, S., Malvaldi, M., Arrighini, G. P., and Guidotti, C. (2005) Theoretical Study of Electromagnetic Scattering by Metal Nanoparticles. *J. Phys. Chem. B 109*, 3807−3812.

(21) Hubert, C., Rumyantseva, A., Lerondel, G., Grand, J., Kostcheev, S., Billot, L., Vial, A., Bachelot, R., Royer, P., Chang, S.-h., Gray, S. K., Wiederrecht, G. P., and Schatz, G. C. (2005) Near-Field Photochemical Imaging of Noble Metal Nanostructures. *Nano Lett. 5*, 615−619.

(22) Kreibig, U., and Vollmer, M. (1995) *Optical Properties of Metal Clusters*, Springer Series in Materials Science, Vol. 25, Springer-Verlag, Berlin and Heidelberg, Germany.

(23) Lakowicz, J. R. (2006) *Principles of Fluorescence Spectroscopy*, 3rd ed., Kluwer Academic/Plenum Publishers, New York.

(24) Lakowicz, J. R. (2005) Radiative Decay Engineering 5: Metal-Enhanced Fluorescence and Plasmon Emission. *Anal. Biochem. 337*, 171−194.
(25) Lakowicz, J. R. (2001) Radiative Decay Engineering: Biophysical and Biomedical Applications. *Anal. Biochem. 298*, 1−24.
(26) Drexhage, K. H. (1974) *Progress in Optics XII* (Wolf, E., Eds.) North Holland: Amsterdam.
(27) Gryczynski, I., Malicka, J., Shen, Y., Gryczynski, Z., and Lakowicz, J. R. (2002) Multiphoton Excitation of Fluorescence near Metallic Particles: Enhanced and Localized Excitation. *J. Phys. Chem. B 106*, 2191−2195.
(28) Hayat, M. A. Ed. (1991) *Colloidal Gold: Principles, Methods, and Applications*; Academic Press, San Diego.
(29) Feldheim, D. L., and Foss, C. A. (2002) *Metal Nanoparticles. Synthesis, Characterization and Applications*, Marcel Dekker, Inc., New York.
(30) Templeton, A. C., Wuelfing, W. P., and Murray, R. W. (2000) Monolayer-Protected Cluster Molecules. *Acc. Chem. Res. 33*, 27−36.
(31) Kamat, P. V. (2002) Photophysical, Photochemical and Photocatalytic Aspects of Metal Nanoparticles. *J. Phys. Chem. B 106*, 7729−7744.
(32) Rosi, N. L., and Mirkin, C. A. (2005) Nanostructures in Biodiagnostics. *Chem. Rev. 105*, 1547−1562.
(33) Osella, D., Pollone, P., Ravera, M., Salmain, M., and Jaouen, G. (1999) Use of Heavy-Metal Clusters in the Design of N-Succinimidyl Ester Acylation Reagents for Side-Chain-Specific Labeling of Proteins. *Bioconjugate Chem. 10*, 607−612.
(34) Schuler, B., and Pannell, L. K. (2002) Specific Labeling of Polypeptides at Amino-Terminal Cysteine Residues Using Cy5-benzyl Thioester. *Bioconjugate Chem. 13*, 1039−1043.
(35) Barbarella, G., Zambianchi, M., Ventola, A., Fabiano, E., Della Sala, F., Gigli, G., Anni, M., Bolognesi, A., Polito, L., Naldi, M., and Capobianco, M. (2006) Bright Oligothiophene *N*-Succinimidyl Esters for Efficient Fluorescent Labeling of Proteins and Oligonucleotides. *Bioconjugate Chem. 17*, 58−67.
(36) Biran, I., and Walt, D. R. (2002) Optical Imaging Fiber-Based Single Live Cell Arrays: A High-Density Cell Assay Platform. *Anal. Chem. 74*, 3046−3054.
(37) Kelly, T. L., Lam, M. C. W., and Wolf, M. O. (2006) Carbohydrate-Labeled Fluorescent Microparticles and Their Binding to Lectins. *Bioconjugate Chem. 17*, 575−578.
(38) Ingram, R. S., Hostetler, M. J., and Murray, R. W. (1997) Poly-hetero-ω-functionalized Alkanethiolate-Stabilized Gold Cluster Compounds. *J. Am. Chem. Soc. 119*, 9175−9178.
(39) Zhang, J., Matveeva, E., Gryczynski, I., Leonenko, Z., and Lakowicz, J. R. (2005) Metal-Enhanced Fluoroimmunoassay on a Silver Film by Vapor Deposition. *J. Phys. Chem. B 109*, 7969−7975.
(40) Zhao, H.-F., Kiyota, T., Chowdhury, S., Purisima, E., Banville, D., Konishi, Y., and Shen, S.-H. (2004) A Mammalian Genetic System To Screen for Small Molecules Capable of Disrupting Protein-Protein Interactions. *Anal. Chem. 76*, 2922−2927.
(41) Mikolajczyk, J., Scott, F. L., Krajewski, S., Sutherlin, D. P., and Salvesen, G. S. (2004) Activation and Substrate Specificity of Caspase-14. *Biochemistry 43*, 10560−10569.
(42) Brust, M., Walker, M., Bethell, D., Schiffrin, D. J., Whyman, R. J. (1994) Synthesis of Thiol Derivatised Gold Nanoparticles in a Two-Phase Liquid/Liquid System. *J. Chem. Soc., Chem. Commun*. 801−802.
(43) Zhang, J., Malicka, J., Gryczynski, I., and Lakowicz, J. R. (2005) Surface-Enhanced Fluorescence of Fluorescein-Labeled Oligonucleotides Capped on Silver Nanoparticles. *J. Phys. Chem. B 109*, 7643−7648.
(44) Huang, T., and Murray, R. W. (2002) Quenching of $[Ru(bpy)_3]^{2+}$ Fluorescence by Binding to Au Nanoparticles. *Langmuir 18*, 7077−7081.
(45) Hicks, J. F., Miles, D. T., and Murray, R. W. (2002) Quantized Double-Layer Charging of Highly Monodisperse Metal Nanoparticles. *J. Am. Chem. Soc. 124*, 13322−13328.
(46) Schaaff, T. G., Shafigullin, M. N., Khoury, J. T., Vezmar, I., and Whetten, R. I. (2001) Properties of a Ubiquitous 29 kDa Au:SR Cluster Compound. *J. Phys. Chem. B 105*, 8785−8796.
(47) Zhang, J., Roll, D., Geddes, C. D., and Lakowicz, J. R. (2004) Aggregation of Silver Nanoparticle-Dextran Adducts with Concanavalin A and Competitive Complexation with Glucose. *J. Phys. Chem. B 108*, 12210−12214.
(48) Geddes, C. D., Parfenov, A., Gryczynski, I., and Lakowicz, J. R. (2003) Luminescent Blinking from Silver Nanostructures. *J. Phys. Chem. B 107*, 9989−9993.
(49) Zeng, L., Miller, E. W., Pralle, A., Isacoff, E. Y., and Chang, C. J. (2006) A Selective Turn-On Fluorescent Sensor for Imaging Copper in Living Cells. *J. Am. Chem. Soc. 128*, 10−11.
(50) Storhoff, J. J., Lazarides, A. A., Mirkin, C. A., Letsinger, R. L., Mucic, R. C., and Schatz, G. C. (2000) What Controls the Optical Properties of DNA-Linked Gold Nanoparticle Assemblies? *J. Am. Chem. Soc. 122*, 4640−4650.

BC0603384

Direct Identification of Nonreducing GlcNAc Residues on N-Glycans of Glycoproteins Using a Novel Chemoenzymatic Method

Elizabeth Boeggeman,[†,‡] Boopathy Ramakrishnan,[†,‡] Charlton Kilgore,[†] Nelly Khidekel,[⊥] Linda C. Hsieh-Wilson,[⊥] John T. Simpson,[§] and Pradman K. Qasba*[,†]

Structural Glycobiology Section, CCR-Nanobiology Program, Center for Cancer Research, NCI-Frederick, and Protein Chemistry Laboratory, SAIC-Inc. NCI-Frederick, Frederick, Maryland 21702, and Division of Chemistry and Chemical Engineering and Howard Hughes Medical Institute, California Institute of Technology, Pasadena, California 91125 Received November 1, 2006 ; Revised Manuscript Received January 8, 2007

The mutant β1,4-galactosyltransferase (β4Gal-T1), β4Gal-T1-Y289L, in contrast to wild-type β4Gal-T1, can transfer GalNAc from the sugar donor UDP-GalNAc to the acceptor, GlcNAc, with efficiency as good as that of galactose from UDP-Gal. Furthermore, the mutant can also transfer a modified sugar, C2 keto galactose, from its UDP derivative to *O*-GlcNAc modification on proteins that provided a functional handle for developing a highly sensitive chemoenzymatic method for detecting *O*-GlcNAc post-translational modification on proteins. We report herein that the modified sugar, C2 keto galactose, can be transferred to free GlcNAc residues on N-linked glycoproteins, such as ovalbumin or asialo-agalacto IgG1. The transfer is strictly dependent on the presence of both the mutant enzyme and the ketone derivative of the galactose. Moreover, the PNGase F treatment of the glycoproteins, which cleaves the N-linked oligosaccharide chain, shows that the modified sugar has been transferred to the N-glycan chains of the glycoproteins and not to the protein portion. The application of the mutant galactosyltransferase, β4Gal-T1-Y289L, to produce glycoconjugates carrying sugar moieties with reactive groups, is demonstrated. We envision a broad potential for this technology such as the possibilities to link cargo molecules to glycoproteins, such as monoclonal antibodies, via glycan chains, thereby assisting in the glycotargeting of drugs to the site of action or used as biological probes.

INTRODUCTION

In recent years, it has become evident that a number of biological processes, such as cell adhesion (*1*, *2*), cell−cell recognition (*3*), formation of glycosynapses (*4*, *5*), immune defense (*6*), targeting, and signaling, appear to be modulated by the glycan moieties of glycoproteins and glycolipids, where they serve as ligands in the specific protein−carbohydrate (*7*), lipid−carbohydrate, and carbohydrate−carbohydrate interactions (*5*, *8*). They also serve as recognition targets for their complementary binding proteins, the lectins (*7*). Because of the molecular diversity of glycans, and being specific recognition ligands in various biological processes, they are also used to design drugs that target various diseases (*9*).

Glycans can be classified as linear or branched sugars. The linear sugars are the glycosaminoglycans comprising polymers of sulfated disaccharide repeat units that are O-linked to a core protein, forming a proteoglycan aggregate (*10*). The branched glycans are found as N-linked and O-linked sugars on glycoproteins or on glycolipids (*11*). These carbohydrate moieties of the linear and branched glycans are synthesized by a super family of enzymes, the glycosyltransferases, which transfer a sugar moiety from a sugar donor to an acceptor molecule.

X-ray crystal structures of the catalytic domain of many glycosyltransferases have been determined in recent years. These studies show that the specificity of the sugar donor is determined by a few residues in the sugar−nucleotide binding pocket of glycosyltransferases, which are conserved among family members from different species (*12*). This structural information has made it possible to reengineer the existing glycosyltransferases. For example, the β1,4-galactosyltranferase family in vertebrates (β4Gal-T1 to T7) is responsible for the transfer of galactose from the donor UDP-galactose (UDP-Gal) to various glycans in a β1−4 linkage (*13*, *14*). The residue Tyr289 (or Phe) in the catalytic pocket of β4Gal-T1, determines the sugar donor substrate specificity of the enzyme toward UDP-Gal (*12*, *15*). Mutation of Tyr289 to Leu or Ile enlarges the binding pocket such that the mutant enzyme, β4Gal-T1-Y289L, has β1,4-*N*-acetylgalactosaminyltransferase (β4GalNAc-T) activity, which is as efficient as its β1,4-galactosyltransferase (β4Gal-T) activity (*15*, *16*). Similarly, in blood group A GalNAc-transferase, the residues Leu266 and Gly268, and in blood group B Gal-transferase, the residues Met266 and Ala268 determine the specificities toward their respective sugar donors, UDP-GalNAc and UDP-Gal (*17*). Mutation of Met266 to Leu266 in blood group B Gal-transferase changes the enzyme sugar donor specificity toward UDP−GalNAc. Furthermore, in β1,3-glucuronyltransferase-1 (GlcA-T1), His 308 (His 311 in GlcAT-P) (*18*, *19*) determines the enzyme specificity toward the sugar donor UDP−GlcUA. Mutation of His308 to Arg308 changes the specificity of the sugar donor to UDP−Glc, UDP−Man, or UDP−GlcNAc.

The *O*-GlcNAc modification on proteins is the dynamic posttranslational modification in which the β-*N*-acetylglucosamine is covalently attached to serine or threonine residues in proteins. Several methods have been reported for the identification of *O*-GlcNAc modification on proteins. One of the detection methods involves the enzymatic labeling by β4Gal-

* Corresponding author: Structural Glycobiology Section, CCR, Nanobiology Program, NCI-Frederick, Building 469, Room 221, Frederick, Maryland 21702. E-mail: qasba@helix.nih.gov. Phone: (301) 846-1934. Fax: (301) 846-7149.

[†] Structural Glycobiology Section, CCR-Nanobiology Program, NCI-Frederick.

[‡] SAIC-Inc. NCI-Frederick, Frederick.

[§] Protein Chemistry Laboratory, SAIC-Inc. NCI-Frederick.

[⊥] California Institute of Technology.

10.1021/bc060341n Not subject to U.S. Copyright. Published 2007 by American Chemical Society
Published on Web 03/20/2007

Table 1. Transfer of GalNAc from UDP-GalNAc by β4Gal-T1-Y289L to Oligosaccharide Acceptors[a]

sugar acceptor	nmoles of available substrate	nmoles of available GlcNAc residues	nmoles of GalNAc transferred	% acceptor converted to product
GlcNAc	24.90	24.90	24.09 ± 0.07	96.74
β-benzyl-GlcNAc	25.00	25.00	24.50 ± 0.22	98.00
chitobiose	25.00	25.00	24.78 ± 0.21	99.12
chitotriose	25.00	25.00	24.90 ± 0.05	99.60
chitotetraose	25.00	25.00	24.88 ± 0.02	99.52
pentasaccharide[b]	25.00	50.00	24.50 ± 0.5	49.00[c]
heptasaccharide[b]	25.00	50.00	24.68 ± 0.04	49.36[c]
ovalbumin	24.00	variable[d]	9.00 ± 14	37.50[e]

[a] Galactosyltransferase assays with GalNAc were performed as described in the Materials and Methods section. The mutant β4Gal-T1-Y289L was assayed at a final concentration of 24 μg/mL. Assays were done at 30 °C with overnight incubations using 1.5 mM of UDP-GalNAc and 1 mM of acceptors. [b] The pentasaccharide substrate, GlcNAcβ1,2-Manα1,6(GlcNAcβ1,2-Manα1,3)Man, and the heptasaccharide tetrapeptide substrate, Arg-[GlcNAcβ1,2-Manα1,6-(GlcNAcβ1,2-Manα1,3)-Manβ1,4-GlcNAcβ1,4-GlcNAcβ]-Asn-Glu-Gly, are branched structures which have 2 mol of GlcNAc per mole of substrate available for the transfer reaction. [c] GalNAc is transferred to only 50% of the available GlcNAc residues in the branched substrate structures. [d] Ovalbumin also has a branched N-linked glycan. The amount of GlcNAc available for transfer is variable. [e] Percentage of the acceptor converted to product has been calculated on the basis of the amount of ovalbumin used in the assay.

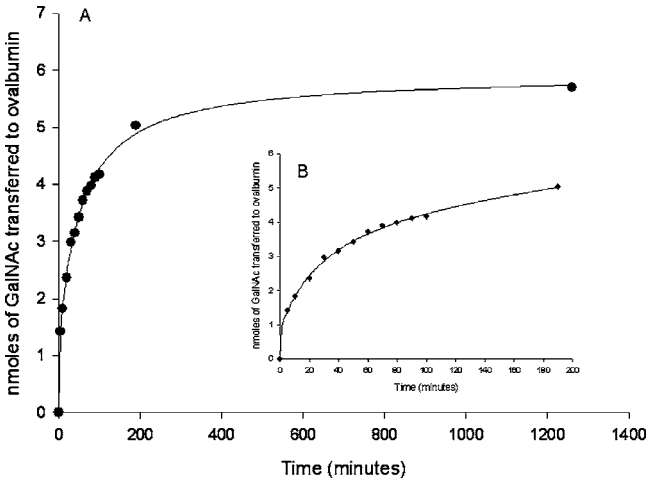


Figure 1. (A) Enzyme kinetics activity of the mutant enzyme, β4Gal-T1-Y289L, with UDP−GalNAc as a donor substrate and ovalbumin as a glycoprotein acceptor substrate. GalNAc-T activity was measured using 500 μM UDP−GalNAc and 0.5 mg of ovalbumin in 100 μL incubation mix containing Mn^{2+} and Tris pH 8.0 (Material and Methods section). The mutant enzyme was used at a final concentration of 40 μg/mL, and activity was measured at the indicated times. For MS analysis, the reaction was carried out for a period of 20 h at 30 °C. (B) The insert shows the results of the kinetic analysis between zero and 200 min of incubation time.

T1 of *O*-GlcNAc using UDP-^{3}H galactose (*20*). However, this method is time-consuming and expensive. The engineered β4Gal-T1-Y289L was shown to transfer from a UDP derivative, a galactose moiety that has a ketone substitution at the C2 position of the galactose ring (*21*). The introduced ketone was then used as a functional handle that allowed the development of a highly sensitive and rapid chemoenzymatic method to detect *O*-GlcNAc modification on proteins (*21*).

Here, we show that the C2 keto galactose moiety can also be transferred from its UDP derivative to only free GlcNAc residues on the N-linked glycan chains of ovalbumin or on asialo-agalacto IgG1 molecules. That the modified galactose is transferred only to the GlcNAc residues on the N-glycan chains was confirmed by the PNGase F treatment of the glycoprotein that cleaves the N-linked glycan chains. As previously described (*21*), the transfer was followed by coupling the C2 keto galactose moiety on the glycan chain to an aminooxy biotin which was then detected by a sensitive chemiluminescence assay. Using this strategy, one can couple two glycoproteins that have modified glycan chains, with each having reactive functional groups with heterobifunctional linkers (*22*). The advantage of this methodology is that the modification occurs in a site-directed manner, only where the carbohydrate is attached to the glycoprotein. This specificity permits the use of site-directed immunotherapy without affecting the antigen binding affinity of the immunoglobulin. The advantages and potential use of this approach in developing a drug delivery system or a biological probe are discussed.

EXPERIMENTAL PROCEDURES

Preparation and Purification of Wild-Type β4Gal-T1 and Mutant β4Gal-T1-Y289L. The β4Gal-T1 that has a Cys342 mutated to Thr342 was used as wild-type β4Gal-T1. This mutation does not affect the enzymatic properties of β4Gal-T1, and it makes the protein stable at room temperature (*15*). This wild-type β4Gal-T1 and the mutant β4Gal-T1-Y289L, derived from the wild type, were constructed in the pET23a vector (Novagen, Inc.) as described previously (*15*, *23*, *24*). The *E. coli* strain BL21(DE3)pLysS, containing these plasmids, was used for the expression of these proteins (Novagen, Inc). The recombinant proteins were expressed in the inclusion body fraction and purified according to the published method (*25*). From a liter of induced bacterial culture, the yield of purified inclusion bodies is generally 80−100 mg. However, the presence of PEG-400 and L-arginine during folding of the inclusion bodies increases the yields of the native protein, resulting in an overall folding efficiency of ∼60% (*25*).

Supply of Reagents. The oligosaccharide acceptors, *N*-acetylglucosamine (GlcNAc), chitobiose (GlcNAcβ1,4-GlcNAc), and chitotriose (GlcNAcβ1,4-GlcNAcβ1,4-GlcNAc) were obtained from Sigma Chemicals, U.S.A.; chitotetrose (GlcNAcβ1,4-GlcNAcβ1,4-GlcNAcβ1,4-GlcNAc) and the pentasaccharide GlcNAcβ1,2-Mana1,6-(GlcNAcβ1,2-Mana1,3)-Man were purchased from Dextra-labs, U.K. The heptasaccharide tetrapeptide, Arg-[GlcNAcβ1,2-Manα1,6-(GlcNAcβ1,2-Mana1,3)-Manβ1,4-GlcNAcβ1,4-GlcNAcβ]-Asn-Glu-Gly, which carries both 1,2−1,6-arm and 1,2−1,3-arm linked to core mannose, was purchased from Calbiochem, U.S.A. The UDP derivative of C2 keto galactose was synthesized as described earlier (*21*). The *N*′-aminooxymethylcarbonylhydrazino-D-biotin (ARP) was purchased from Dojindo Laboratories. Peptide *N*-glycosidase F (PNGase F) was obtained from New England Labs. Albumin from chicken egg white grade VI was purchased from Sigma, and IgG1 was provided by Drs. Mei-Yun Zhang and Yang Feng from Dr. Dimiter S. Dimitrov's laboratory at the Nanobiology program, CCR, NCI.

GalNAc-T Enzyme Assays. The protein concentrations were measured using the Bio-Rad Protein Assay kit on the basis of the method of Bradford and further verified by SDS-PAGE electrophoresis. An enzymatic assay procedure for β4Gal-T1 has been reported previously (*26*). The enzyme activities of the β4Gal-T1-Y289L mutant were measured using UDP−GalNAc as the sugar nucleotide donor, and at various concentrations of the acceptors, GlcNAc, chitobiose, chitotriose, chitotetrose, the mono, di-, tri-, tetrasaccharides, respectively, and the N-linked branched oligosaccharide structures. For the specific activity measurements, a 100 μL incubation mixture containing 10 mM $MnCl_2$, 25 mM Tris−HCl, pH 8.0, 500 μM of UDP−GalNAc, 20 ng of the mutant β4Gal-T1-Y289L, and 0.5 μCi ^{3}H-UDP−GalNAc was used for the GalNAc-T reaction. The reaction was terminated by adding 200 μL of cold water, and the mixture

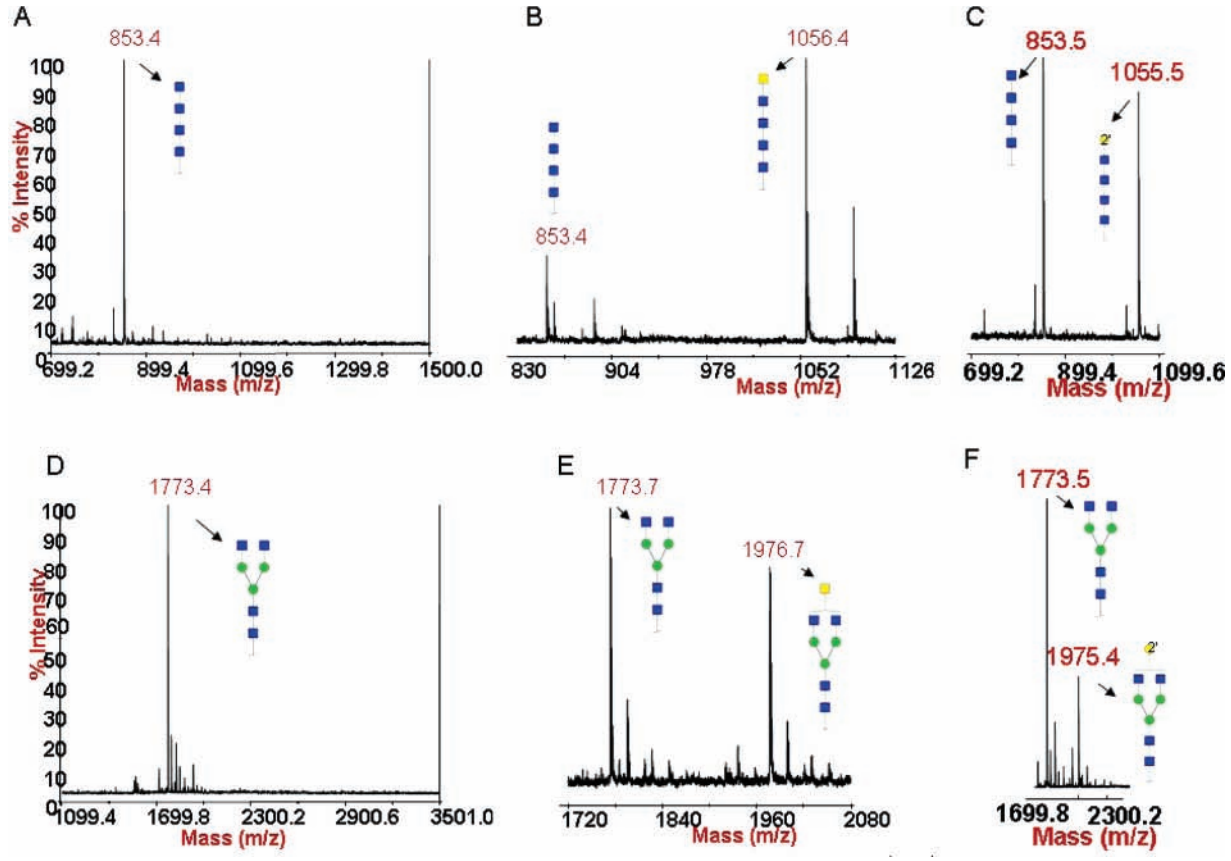


Figure 2. MALDI mass spectra of glycans after the transfer of GalNAc to the sugar acceptors chitotetrose GlcNAcβ1,4-GlcNAcβ1,4-GlcNAcβ1,4-GlcNAcβ (A,B,C) and a heptasaccharide tetrapeptide Arg-[GlcNAcβ1,2-Manα1,6-(GlcNAcβ1,2-Manα1,3)-Manβ1,4-GlcNAcβ1,4-GlcNAcβ]-Asn-Glu-Gly (D,E,F). Major peaks are annotated with the carbohydrate structure shown in the symbols for monosaccharides, according to the nomenclature adopted by the consortium for functional glycomics, http://www.functionalglycomics.org/static/consortium/. GlcNAc (blue squares), mannose (green spheres), GalNac (yellow squares), and C2 keto galactose (yellow sphere). The symbols were drawn using the GlycoWorkbench program found in the eurocarb database http://www.eurocarbdb.org/. The transferred C2 keto galactose moiety in panels C and F is shown. Panel A shows a peak at 853.4 *m*/*z* corresponding to the linear glycan structure chitotetrose. Panel B shows a shift in the molecular mass from the starting ion at 853.4 *m*/*z* to a peak of 1056.4 *m*/*z* after addition of a GalNAc moiety (Material and Methods section). Panel C shows chitotetrose with the transferred C2 keto galactose moiety to the terminal GlcNAc residue. Panel D shows a peak at 1773.4 *m*/*z* corresponding to the starting branched heptasaccharide peptide structure, Arg-[GlcNAcβ1,2-Manα1,6-(GlcNAcβ1,2-Manα1,3)-Manβ1,4-GlcNAcβ1,4-GlcNAcβ]-Asn-Glu-Gly. Panel E shows a peak at 1976.7 *m*/*z* that corresponds to a heptasaccharide peptide having one added GalNAc moiety. Panel F shows the peak at 1975.4 *m*/*z* that corresponds to a heptasaccharide to which one C2-keto galactose moiety has been transferred to one of the available terminal GlcNAc moieties.

was passed through a 0.5 mL bed volume column of AG 1-X8 cation resin (Bio-Rad) to remove any unreacted ^{3}H-UDP−GalNAc. The column was washed successively with 300, 400, and 500 μL of water, and the column flowthrough was diluted to 20 mL with Biosafe scintillation fluid; radioactivity was measured with a Beckman counter LS-3801. A reaction without the acceptor sugar was used as a control.

Transfer of C2 Keto Galactose from its UDP Derivative to Free GlcNAc Residues on Glycoacceptors Using the Mutant of β4Gal-T1-Y289L. Albumin from chicken egg white grade VI (40 μg) and recombinant IgG1 (2−5 μg) were incubated with 1 mM UDP-C2 keto galactose and 500 ng of the mutant β4Gal-T1-Y289L or 488 ng of wild-type β4Gal-T1 in a 10 μL final incubation mixture containing 10 mM $MnCl_2$ and 25 mM Tris−HCl (pH 8.0). Reactions were incubated at 30 °C for 3 h.

Biotinylation of Ovalbumin and IgG1. The ketone-labeled proteins were subsequently diluted to 30 μL in a mixture containing 50 mM NaOAc (pH 3.9) and *N*-aminooxymethylcarbonylhydrazino-D-biotin (ARP). The biotinylation reactions were incubated with gentle shaking for 12−16 h at 25 °C. The reactions were stopped by boiling in Tris-glycine-SDS sample buffer containing β-mercaptoethanol and analyzed as described (*21*).

Western Blotting of Ovalbumin and Asialo-Agalacto-IgG1. Proteins were resolved in 14% Tris−glycine gel (Invitrogen) and then transferred by electrophoresis to nitrocellulose (0.45 μm pore size) for 2 h at 25 V, and biotinylated protein bands identified as described previously (*21*). Briefly, the nitrocellulose blots were blocked for 1 h at room temperature with shaking in a solution containing 5% dry milk in 0.02% Tween-20. Blots were rinsed thoroughly with water and probed with streptavidin conjugated with horseradish peroxidase (HRP) (Amersham Biosciences) (1:4000) in 1× PBS pH 7.4, 0.02% Tween-20 containing 3% BSA for 1 h at 25 °C. After probing with the conjugated streptavidin, the nitrocellulose membranes were washed 4× for 10 min in 5% dry milk containing 0.02% Tween-20. The streptavidin−HRP signal was visualized by chemiluminescence after 2 min exposure to ECL detection reagents (Amersham) and exposure to Kodak Biomax XAR film.

Peptide: *N*-Glycosidase F Treatment. Ovalbumin and asialo-agalacto-IgG1 samples, approximately 3 μg each, were boiled for 10 min in 1% SDS and 1% β-mercaptoethanol. Samples were then incubated in the presence or absence of PNGase F (2500 units) for 16 h at 37 °C in a buffer containing 5 mM sodium phosphate and 1% NP-40. Samples were then

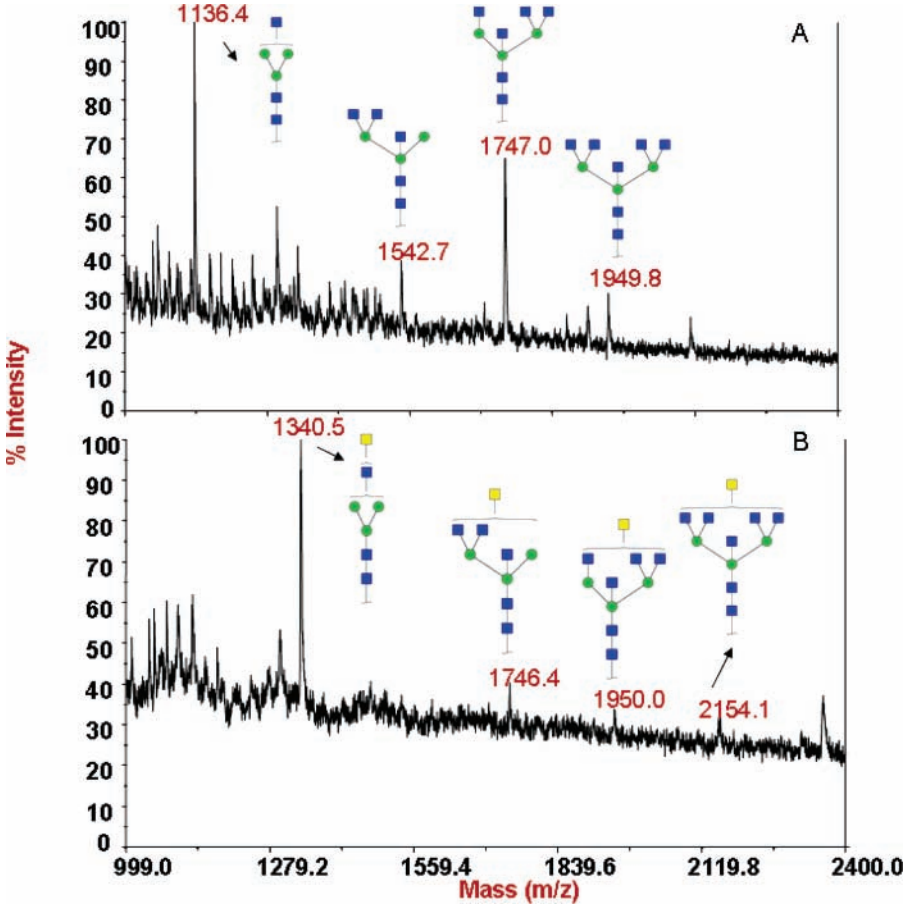


Figure 3. MALDI mass spectra of the glycans released from chicken ovalbumin. After PNGase F treatment of chicken ovalbumin, the released oligosaccharides were passed through the microcon YM-10 columns and analyzed by MALDI mass spectrometry. Only the peaks of interest are annotated, showing their molecular mass and possible structures. Carbohydrate structures are shown in symbol form, as described in the Figure 2 legend. (A) Glycans released from the commercial sample (Sigma) of chicken ovalbumin before GalNAc transfer. Ions at 1136.4, 1542.7, 1747.0, and 1949.8 *m*/*z* are assigned to ovalbumin structures reported (*29*). (B) Glycan structures released from chicken ovalbumin after the transfer of GalNAc from UDP−GalNAc with the mutant enzyme β4Gal-T1-Y289L. Ions at 1340.5, 1746.4, 1950.0, and 2154.1 *m*/*z* are assigned to structures in the ovalbumin preparation onto which GalNAc moieties have been transferred.

boiled in SDS-PAGE loading buffer and then resolved by SDS-PAGE.

MALDI Mass Spectrometric Analyses of Oligosaccharides. An Applied Biosystems Voyager-DE Pro time-of-flight mass spectrometer was utilized for analyses. The accelerating voltage was 20 kV, guide wire 0.05%, and grid voltage 94%. The instrument was operated in linear mode under positive ion conditions. A nitrogen laser was used at 337 nm with 150 laser shots averaged per spectrum. 2,5-Dihydroxybenzoic acid (Aldrich Chemicals, St. Louis, MO) was used as the matrix for all experiments. The matrix concentration was 20 mg/mL in water. Sample preparation was a modified "dried droplet" procedure, whereby 0.3 μL of sample was spotted onto the MALDI target, followed by 0.3 μL of matrix. The mixture was then allowed to air-dry prior to analysis. Calibration was performed using instrument default settings, and data analysis was carried out using Data Explorer software residing on the Voyager mass spectrometer.

MALDI Mass Spectrometric Analyses of the N-Glycans of Ovalbumin. Albumin from chicken egg white (grade VI), 1 mg in 100 μL deionized water, was washed in a microcon YM-10 centrifugal filter device with 1.5 mL of deionized water to remove free oligosaccharide chains. The washed sample was concentrated and incubated at 30 °C for 18 h in a 100 μL final incubation mixture containing 0.5 mM UDP−GalNAc, 2 μg of the mutant β4Gal-T1-Y289L, 10 mM $MnCl_2$, and 25 mM Tris−HCl (pH 8.0). The samples were then digested for 18 h at 37 °C with 2500 units of PNGase F (NEB) in 50 mM sodium phosphate buffer. The digested samples were applied onto a Microcon YM-10 filter device, and the filtrate containing the released N-glycans was analyzed by mass spectrometry as described above.

RESULTS

Sugar Donor Specificity of β4Gal-T1. Our laboratory previously showed that the sugar donor specificity of β4Gal-T1 toward UDP−Gal is determined by a single amino acid, Tyr, at position 289 (*15*). When Tyr289 is mutated to Leu, the sugar donor specificity of β4Gal-T1 is broadened in a way that, in contrast to the wild-type enzyme which lacks GalNAc-T activity, the mutant β4Gal-T1-Y289L exhibits both β4Gal-T and β4GalNAc-T activities (*15*). The Tyr289 mutant can also transfer from the UDP derivatives the galactose moiety that has, at the C2 position, substitutions other than the 2-N-acetyl group (−NH−CO−CH_3 in GalNAc) (*21*). Here, we first investigated the transfer of GalNAc to N-glycans of glycoproteins by the mutant enzyme, β4Gal-T1-Y289L.

Transfer Preferences of β4Gal-T1-Y289L to oligosaccharide acceptors. In a previous study from our laboratory, we had shown by double substrate kinetics that the true K_m for both chitobiose and chitotriose was nearly the same (*27*), suggesting that the presence of an additional GlcNAc residue in chitotriose, not present in chitobiose, did not affect the ground-state binding of these acceptor substrates to the enzyme. Moreover, the apparent K_m values for chitobiose and chitotriose were similar

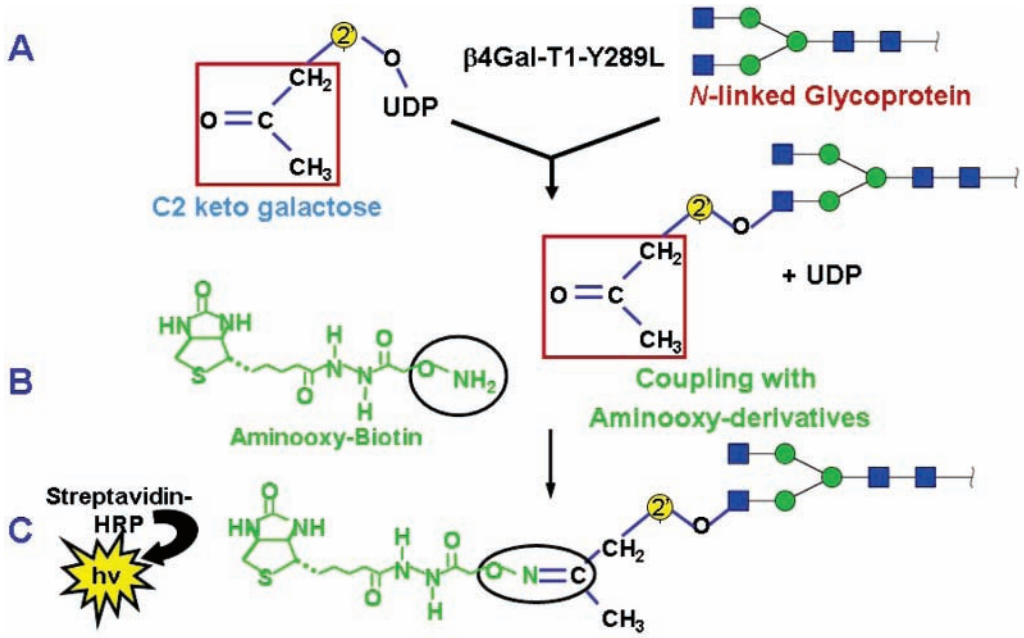


Figure 4. Detection of GlcNAc glycosylated proteins by β4Gal-T1-Y289L. Strategy for the detection of a terminal GlcNAc residue in the N-linked glycoprotein by the mutant β4Gal-T1-Y289L. (A) In contrast to the wild-type β4Gal-T1, the mutant enzyme β4Gal-T1-Y289L transfers to the GlcNAc residues of the N-linked glycoprotein a Gal moiety, from the UDP derivative, that has modifications located at the C2 position of galactose, such as the N-acetyl moiety (GalNAc) (*15*) or a ketone moiety (*21*). (B) The C2 ketone moiety of the substituting group in galactose can then be coupled with aminooxy derivatives under mild conditions (*21*). (C) When aminooxy biotin (*N*-(aminooxyacetyl)-*N*′-(D-biotinoyl) hydrazine) is used as the coupling agent, the product can be labeled by streptavidin conjugated to horseradish peroxidase (HRP) and detected by a sensitive chemiluminescence method.

to the true K_m values obtained by double substrate kinetics. In this study, we tested the amount of acceptor converted to product for various linear and branched structures (Table 1). In the linear structures, 25 nmol of the acceptor GlcNAc was available in the reaction, and in the branched structures with two terminal GlcNAc residues, 50 nmol of the acceptor GlcNAc was available in the reaction mixture. The linear acceptors, mono-, di-, tri- and tetrasaccharides, all showed 97% to 100% conversion of the acceptor to product (Table 1). Both chitobiose and chitotriose showed 99% conversion. In the pentasaccharide, GlcNAcβ1,2-Manα1,6-(GlcNAcβ1,2-Manα1,3)-Man, and the heptasaccharide tetrapeptide, Arg-[GlcNAcβ1,2-Manα1,6-(GlcNAcβ1,2-Mana1,3)-Manβ1,4-GlcNAcβ1,4-GlcNAcβ]-Asn-Glu-Gly (which carries GlcNAc on both the 1,2−1,6-arm and the 1,2−1,3-arm linked to core mannose), GalNAc is only transferred to 50% of the available GlcNAc residues on these acceptor substrates (Table 1).

Transfer of GalNAc Residue to N-Linked Glycoproteins. Over 20 years ago, it was shown β4Gal-T1 could transfer galactose from UDP−Gal to ovalbumin in the absence of α-lactalbumin (*28*). Only recently, the permissive mutant β4Gal-T1-Y289L was shown to transfer GalNAc from UDP−GalNAc to GlcNAc residues (*15*). Galactosyltransferase and *N*-acetylgalactosaminyltransferase assays with the β4Gal-T1-Y289L mutant, using ovalbumin as the acceptor, were performed by a radiochemical assay as described previously (*15*, *25*). The kinetics of transfer of GalNAc to ovalbumin was analyzed over a period of 20 h as described in the Materials and Methods section (Figure 1). Due to the heterogeneity observed with commercial ovalbumin preparations (*29*), the amount of available acceptor substrate is variable, and we show that, after overnight incubation, only 37% of acceptor is converted into product (Table 1).

MALDI Mass Spectra Determination of Glycans before and after Treatment with UDP−GalNAc and UDP-C2 Keto-Modified Galactose. The transfer of GalNAc and C2 keto-modified galactose from their respective UDP derivatives was followed by MALDI mass profiling (Figure 2). In the MALDI profile, in the range between *m*/*z* 700 and 1500, a unique peak at *m*/*z* 853.4 corresponds to the chitotetrose, prior to the transfer of the donor sugar (Figure 2A). Transfers of GalNAc (Figure 2B) and C2 keto-modified galactose (Figure 2C) are observed as peaks at *m*/*z* 1056.4 and 1055.5, respectively. The MALDI profile in a range between *m*/*z* 1099.4 and 3501.0 (Figure 2D) shows a major peak at *m*/*z* 1773.4 corresponding to the heptasaccharide tetrapeptide, Arg-[GlcNAcβ1,2-Manα1,6-(GlcNAcβ1,2-Manα1,3)-Manβ1,4-GlcNAcβ1,4-GlcNAcβ]-Asn-Glu-Gly. The addition of GalNAc (Figure 2E) and C2-keto galactose (Figure 2F) to either antenna of the heptasaccharide is observed as peaks at *m*/*z* 1976.7 and 1975.4, respectively. Under the conditions used in this experiment (Materials and Methods section), the transfer of GalNAc to the GlcNAc residue on one of the antenna of the biantennary structure was observed.

MALDI Mass Spectra Determination of N-Linked Carbohydrates from Ovalbumin. To determine the nature of the N-glycans attached to ovalbumin, glycans were released with PNGase F, purified on amicon filters, and analyzed by MALDI. In the MALDI profile, obtained from the released N-glycan chains of ovalbumin, peaks in the range between *m*/*z* 999.0 and 2400.0 were observed. Four major peaks were found at *m*/*z* 1136.4, 1542.7, 1747.0, and 1949.8 (Figure 3A). These are mainly bi- to penta-antennary structures which lack the terminal sialic acid and galactose present on N-glycans of mammalian proteins. Upon transfer of GalNAc to one antenna of the penta-antennary structures, the peaks observed at *m*/*z* 1340.5, 1746.4, 1950.0, and 2154.1 correspond to structures with one additional monosaccharide unit, the GalNAc residue that has been transferred from UDP−GalNAc by the mutant enzyme β4Gal-T1-Y289L (Figure 3B).

Detection of GlcNAc Residue on Glycosylated Proteins by β4Gal-T1-Y289L. Figure 4 shows the schematics of the transfer of C2 keto galactose to the N-glycan moiety of a glycoprotein. The ketone moiety at the C2 position of galactose

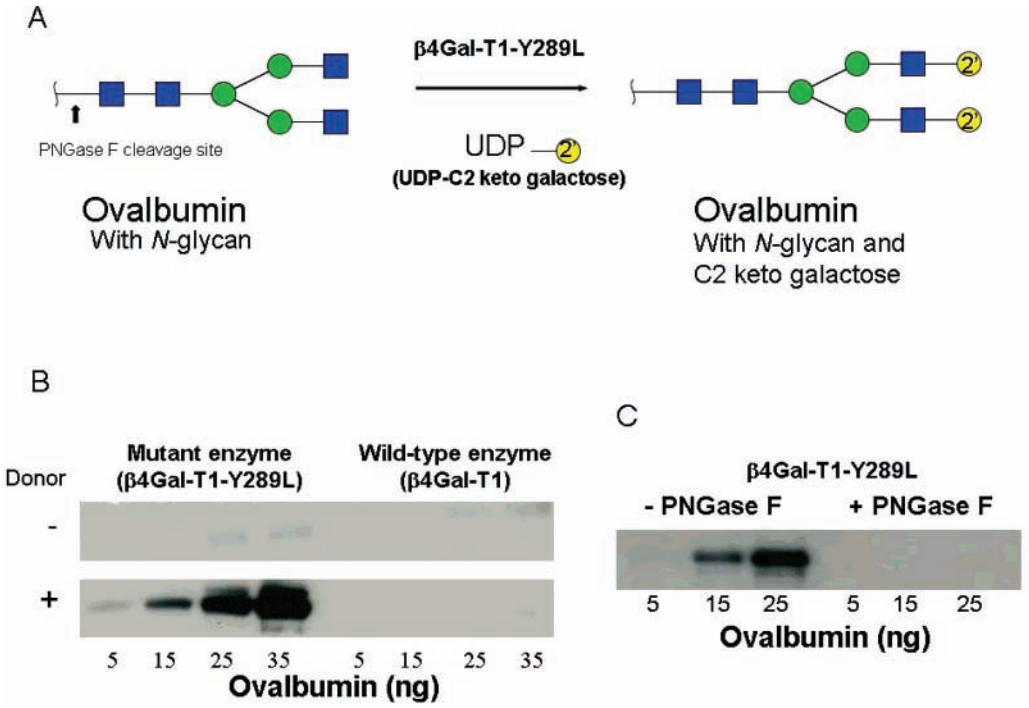


Figure 5. Transfer of the C2 keto derivative of galactose to free GlcNAc residues on the N-glycan chains of ovalbumin by the mutant enzyme β4Gal-T1-Y289L and the chemoenzymatic detection of the transferred C2 keto derivative. (A) N-Glycan chain, attached to ovalbumin, has been shown using the symbols for monosaccharides as described in Figure 2. The C2 keto galactose (yellow spheres) is transferred to the GlcNAc residues (blue squares) at the nonreducing end of the glycan chain, by the mutant enzyme β4Gal-T1-Y289L. The mannose residues in ovalbumin are shown as the green spheres. An arrow shows the cleavage site for PNGase F. (B) Detection of the transferred C2 keto galactose is accomplished by linking with the aminooxy biotin, followed by the chemiluminescence technique. After the transfer of the sugar moiety by the transferase enzyme and subsequent linking to the aminooxy biotin, the mixtures were resolved by SDS-PAGE, transferred by Western blot to nitrocellulose membranes, and probed with streptavidin−HRP. In the absence of the sugar donor substrate (−), little signal was detected using either the wild-type enzyme β4Gal-T1 or the mutant enzyme β4Gal-T1-Y289L. The chemiluminescence was detected only in the samples that contained UDP-C2 keto galactose, mutant enzyme (+), and at least 5 ng of ovalbumin. The wild-type enzyme, β4Gal-T1, having Tyr at position 289, cannot transfer the modified C2 keto galactose. (C) PNGase F treatment of the biotinylated ovalbumin. Ovalbumin samples, after the transfer of the modified C2 keto galactose, were treated with PNGase F (Materials and Methods section), which removes the N-glycan chains from the protein. In contrast to untreated samples (−), in the PNGase F-treated samples (+) no chemiluminescence was detected, showing that the transfer of the modified C2 keto galactose is selective for the glycan portion of ovalbumin.

is a flexible chemical handle, which under mild conditions can be coupled to aminooxy-containing ligands (Figure 4B). When a biotinylated derivative of the aminooxy-containing ligand (*N*-(aminooxyacetyl)-*N*′-(D-biotinoyl) hydrazine) was used as a coupling agent, the transfer and coupling reaction could be followed by detecting the biotinylated product by chemiluminescence with streptavidin conjugated to horseradish peroxidase (HRP) (Figure 4C).

Transfer of C2 Keto Galactose from its UDP Derivative to GlcNAc Residues on the Glycan Chains of Ovalbumin and Asialo-Agalacto-IgG1 by the Mutant Enzyme *β*4Gal-T1-Y289L and Coupling of Aminooxy biotin to the Modified Sugar. The mutant enzyme, β4Gal-T1-Y289L, can transfer the C2 keto galactose from its UDP derivative to the GlcNAc residue on the N-glycan chain of ovalbumin (Figure 5A) or to an asialo-agalacto-IgG1 molecule (Figure 6A). The transfer of the modified sugar by the mutant enzyme is carried out at 30 °C for 3 h. Reactions were also performed in the absence of UDP donor (Figure 5B). The transfer has been followed by coupling to the ketone group at the C2 position of galactose, the biotinylated aminooxy ligand, followed by resolving proteins by SDS-PAGE analysis, transfer of proteins to nitrocellulose filters by Western blotting, and probing by streptavidin−HRP techniques. The transfer is strictly dependent on the presence of the donor and the mutant enzyme, as observed by the strong chemiluminescence of the transferred material (Figure 5B). The wild-type enzyme cannot utilize the C2 ketone derivative of the galactose (Figure 5B).

Peptide: *N*-Glycosidase F (PNGase F) Treatment Removes N-Glycan Chains with Modified Sugar on Glycoproteins. The biotinylated aminooxy ligand is linked only to the N-glycan chain of ovalbumin or IgG1, as shown by PNGase F treatment, which removes N-glycan chains from the protein. No chemiluminescence was detected at ovalbumin or IgG1 protein bands in the Western blot analysis, suggesting that the transferred C2 keto-modified galactose was linked only to the released carbohydrate moiety (Figures 5C and 6B).

DISCUSSION

This study has shown that it is possible to modify free GlcNAc residues on two N-linked glycoproteins, ovalbumin and immunoglobulin, by enzymatic methods. These modifications have only been possible due to the availability of the structural information of glycosyltransferases which helped to design mutant enzymes that can transfer unnatural sugar donors (*15*, *21*, *30*). Here, we show that the transfer is strictly dependent on the presence of both the mutant enzyme β4Gal-T1-Y289L and the ketone derivative of the galactose, while the wild-type enzyme cannot transfer the galactose with the C2 ketone moiety. We also show that the modifications occur only at the N-glycan chains of the glycoproteins, as indicated by PNGase F treatment.

The results of the transfer of ^{3}H-labeled GalNAc by β4Gal-T1-Y289L to several linear and N-linked branched oligosaccharides concur with the results obtained by the MALDI mass spectral analysis. Also, the results obtained by the chemoenzymatic method are consistent with the MALDI mass spectral analysis. The efficiency of transfer of GalNAc to various linear

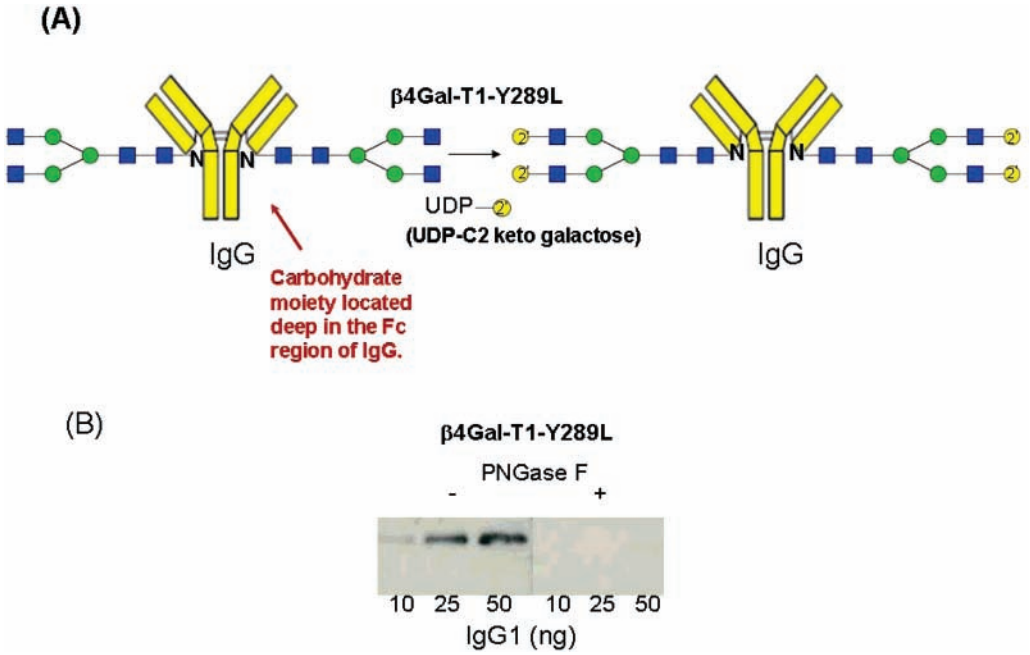


Figure 6. Coupling to IgG via N-glycan chains. Selective labeling of the asialo- IgG1 molecule confirmed by PNGase F treatment. (A) Schematic diagram of an IgG molecule with the N-glycan structures attached at the Fc region. (B) The C2 keto galactose moiety was transferred to the carbohydrate in the Fc region of IgG1, using the mutant enzyme β4Gal-T1-Y289L. Mixtures were either treated without PNGase F (−) or with PNGase F (+) containing NP-40, prior to the coupling to aminooxy biotin. The mixtures were resolved by SDS-PAGE, transferred by Western blot to nitrocellulose membranes, and probed with streptavidin−HRP. No chemiluminescence was detected in PNGase F treated sample (+), showing that the transfer of the modified C2 keto galactose moiety is selective for the glycan portion of IgG1 and glycosylation has occurred in the heavy chain of IgG1 at the free GlcNAc residues (10, 25, and 50 ng).

oligosaccharide acceptors was nearly 100%. The length of the oligosaccharide acceptor did not affect the transfer efficiency of GalNAc. However, when branched oligosaccharide acceptors are used in the enzymatic assay, the efficiency of transfer of GalNAc is reduced. Comparison of the MALDI profiles before and after addition of GalNAc and C2 keto galactose indicated that only one molecule of GalNAc is transferred to one of the two GlcNAc residues available for the transfer on the pentasaccharide, GlcNAcβ1,2-Manα1,6-(GlcNAcβ1,2-Manα1,3)-Man and the heptasaccharide tetrapeptide, Arg-[GlcNAcβ1,2-Manα1,6-(GlcNAcβ1,2-Manα1,3)-Manβ1,4-GlcNAcβ1,4-GlcNAcβ]-Asn-Glu-Gly. Both enzymatic and MALDI analysis showed that GalNAc is transferred to only 50% of the available GlcNAc residues in the branched structures. This may be explained by the results of a previous work from our laboratory using kinetic and crystallographic analysis, which showed that, at lower concentrations, the 1,2−1,6-arm of a biantennary N-glycan is a preferred antenna for galactosylation by β4Gal-T1 (*27*). In contrast, at higher concentrations, the 1,2−1,3-arm of a biantennary N-glycan is a preferred antenna for galactosylation (unpublished results).

When the acceptor is ovalbumin, the transfer efficiency is reduced to 37%. This can be explained by the known structural variability of N-glycans on ovalbumin preparations as has been previously observed (*29*). The largest ovalbumin structure found by MALDI mass spectral analysis was a galactosylated hybrid glycan of composition $(Man)_3(GlcNAc)_7(GalNAc)_1$ (2154.1 *m*/*z*; see Figure 3B).

Having demonstrated the labeling of ovalbumin by enzymatic and MALDI mass analysis, we explored the sensitivity of the chemoenzymatic approach for the detection of N-linked modifications on ovalbumin. This chemoenzymatic method enabled the detection of N-linked modifications within minutes using as little as 5 ng of ovalbumin and 10 ng of IgG1. This study also shows the possibility of modifying the single N-linked glycosylation site at Asn297 on the Fc domain of IgG1. Although some glycosylation may occur outside the Fc domain, this is usually a rare event (*31*). The glycans that are linked to Asn297 of IgG1 have been characterized on the basis of the number of terminal galactoses into three groups, IgG1-G2, IgG1-G1, and IgG1-G0 (*32*). In the IgG1-G0, the glycans do not have terminal galactose residues, but instead have terminal GlcNAc residues, as in the heptasaccharide tetrapeptide used in this study. Only 5% to 14% of the total serum IgG1 is fully sialylated (*32*, *33*), and generally, IgG1-G2, IgG1-G1, and IgG1-G0 fractions are present in 16%, 35%, and 35% of the total IgG glycan pool, respectively (*32*). Here, we show that the C2 keto galactose moiety can be transferred from its UDP derivative to the free GlcNAc residues on the N-linked glycan chains of the IgG1 molecules. The transfer was followed by coupling the ketone handle to an aminooxy biotin, which was then detected by a sensitive chemiluminescence assay (*21*).

The method of coupling a target agent to a carrier protein via glycan chains, as described here using ovalbumin and IgG1 as model systems, offers an advantage over other cross-linking methods. Here, the target agent is linked in a site-directed manner, only where the carbohydrate is attached to the glycoprotein, as in the IgG1 molecule at the Fc domain, away from the antigen binding site. The problem common to previous approaches using monoclonal antibodies for immunotherapy is the lack of specificity of the reactions, resulting in heterologous labeling and a decrease in the antibody affinity for the antigen.

The currently described method also represents a sensitive and effective approach to monitor the glycosylation of therapeutic glycoproteins and monoclonal antibodies. The potential of glycosyltransferase mutants to produce glycoconjugates carrying sugar moieties with reactive groups may be a benefit to the glycotargeting of drugs to their site of action. The role of glycotargeting in the internalization of drugs has been established by numerous studies (*34*, *35*) since the discovery of the asialoglycoprotein receptor (*36*); however, much of its potential remains unexplored. Although a great number of pharmaceutical agents are discovered each year, the clinical

application of these is many times hindered because of failure to reach the site of action. Our approach using mutant glycosyltransferases to transfer chemically reactive sugar residues for linking of other molecules via specific glycan chains has the potential for development of an efficient drug delivery system. A word of caution is that there is still the challenge to up-scale the production of chimeric proteins needed in pharmaceutical settings.

ACKNOWLEDGMENT

We thank Drs. Dimiter S. Dimitrov, Mei-Yun Zhang, and Yang Feng from the Nanobiology program, CCR, NCI, for providing IgG1samples, and Dr. Maria Manzoni from the Structural Glycobiology Section, CCR, NCI, for the critical reading of the manuscript. This project has been funded in whole or in part with federal funds from the National Cancer Institute, National Institutes of Health, under contract N01-CO-12400. The content of this publication does not necessarily reflect the views or policies of the Department of Health and Human Services, nor does mention of trade names, commercial products or organizations imply endorsement by the U.S. Government. This Research was supported in part by the Intramural Research Program of the NIH, National Cancer Institute, Center for Cancer Research.

LITERATURE CITED

(1) Lowe, J. B. (2003) Glycan-dependent leukocyte adhesion and recruitment in inflammation. *Curr. Opin. Cell. Biol. 15*, 531−538.

(2) Talbot, P., Shur, B. D., and Myles, D. G. (2003) Cell adhesion and fertilization: steps in oocyte transport, sperm-zona pellucida interactions, and sperm-egg fusion. *Biol. Reprod. 68*, 1−9.

(3) Roth, S., McGuire, E. J., and Roseman, S. (1971) Evidence for cell-surface glycosyltransferases. Their potential role in cellular recognition. *J. Cell Biol. 51*, 536−547.

(4) Hakamori, S. The glycosynapse. (2002) *Proc. Natl. Acad. Sci. U.S.A. 99*, 225−232.

(5) Hakomori, S. (2004) Carbohydrate-to carbohydrate interaction, through glycosynapse, as a basis of cell recognition and membrane organization. *Glycoconjugate J. 21*, 125−137.

(6) Rudd, P. M., Elliott, T., Cresswell, P., Wilson, I. A., and Dwek, R. A. (2001) Glycosylation and the immune system. *Science 291*, 2370−2376.

(7) Sharon, N., and Lis, H. (2004) History of lectins: from hemagglutinins to biological recognition molecules. *Glycobiology 14*, 53R−62R.

(8) Bucior, I., and Burger, M. M. (2004) Carbohydrate-carbohydrate interaction as a major force initiating cell-cell recognition. *Glycoconjugate J. 21*, 111−123.

(9) Gornik, O., Dumic, J., Flogel, M., and Lauc, G. (2006) Glycoscience: a new frontier in rational drug design. *Acta Pharm. 56*, 19−30.

(10) Raman, R., Sasisekharan, V., and Sasisekharan, R. (2005) Structural insights into biological roles of protein-glycosaminoglycan interactions. *Chem. Biol. 12*, 267−277.

(11) Lowe, J. B., and Marth, J. D. (2003) A genetic approach to mammalian glycan function. *Annu. Rev. Biochem. 72*, 643−691.

(12) Qasba, P. K., Ramakrishnan, B., and Boeggeman, E. (2005) Substrate-induced conformational changes in glycosyltransferases. *Trends Biochem. Sci. 30*, 53−62.

(13) Amado, M., Almeida, R., Schwientek, T., and Clausen, H. (1999) Identification and characterization of large galactosyltransferase gene families: galactosyltransferases for all functions. *Biochim. Biophys. Acta 1473*, 35−53.

(14) Hennet, T. (2002) The galactosyltransferase family. *Cell. Mol. Life Sci. 59*, 1081−1095.

(15) Ramakrishnan, B., and Qasba, P. K. (2002) Structure-based design of beta-1,4-galactosyltransferase-I (beta 4Gal-T1) with equally efficient N-acetylgalactosaminyltransferase activity: point mutation broadens beta 4Gal-T1 donor specificity. *J. Biol. Chem. 277*, 20833−20839.

(16) Ramakrishnan, B., Boeggeman, E., Ramasamy, V., and Qasba, P. K. (2004) Structure and catalytic cycle of beta-1,4-galactosyltransferrase. *Curr. Opin. Struct. Biol. 14*, 593−600.

(17) Marcus, S. L., Polakowski, R., Seto, N. O. L., Leinala, E., Borisova, S., Blancher, A., Roubinet, F., Evans, S. V., and Palcic, M. M. (2003) A single point mutation reverses the donor specificity of human blood group B-synthesizing galactosyltransferase. *J. Biol. Chem. 278*, 12403−12405.

(18) Pedersen, L. C., Darden, T. A., and Negishi, M. (2002) Crystal structure of β1,3 glucuronyltransferase I in complex with active donor substrate UDP-GlcUA. *J. Biol. Chem. 277*, 21869−21873.

(19) Kakuda, S., Shiba, T., Ishiguro, M., Tagawa, H., Oka, S., Kajihara, Y., Kawasaki, T., Wakatsuki, S., and Kato, R. (2004) Structural basis for acceptor substrate recognition of a human glucuronyltransferase, GlcAT-P, an enzyme critical in the biosynthesis of the carbohydrate epitope HNK-1. *J. Biol. Chem. 279*, 22693−22703.

(20) Torres, C. R., and Hart, G. W. (1984) Topography and polypeptide distribution of terminal N-acetylglucosamine residues on the surfaces of intact lymphocytes. *J. Biol. Chem. 259*, 3308−3317.

(21) Khidekel, N., Arndt, S., Lamarre-Vincent, N., Lippert, A., Poulin-Kerstien, K. G., Ramakrishnan, B., Qasba, P. K., and Hsieh-Wilson, L. C. (2003) A chemoenzymatic approach toward the rapid and sensitive detection of O-GlcNAc posttranslational modifications. *J. Am. Chem. Soc. 125*, 16162−16163.

(22) Qasba, P. K., Ramakrishnan, B., and Boeggeman, E. (2006) Mutant glycosyltransferases assist in the development of a targeted drug delivery system and contrast agents for MRI. *AAPS J. 8*, E190−195.

(23) Boeggeman, E. E., Balaji, P. V., Sethi, N., Masibay, A. S., and Qasba, P. K. (1993) Expression of deletion constructs of bovine β1,4-galactosyltransferase in *Escherichia coli*: importance of Cys134 for its activity. *Protein Eng. 6*, 779−785.

(24) Ramakrishnan, B., Shah, P. S., and Qasba, P. K. (2001) Alpha-Lactalbumin (α-LA stimulates milk beta-1,4-galactosyltransferase I (beta 4Gal-T1) to transfer glucose from UDP-glucose to N-acetylglucosamine. Crystal structure of beta 4Gal-T1 × α-LA complex with UDP-Glc. *J. Biol. Chem. 276*, 37665−37671.

(25) Boeggeman, E., Ramakrishnan, B., and Qasba, P. K. (2003) The *N*-terminal stem region of bovine and human β1,4-galactosyltransferase I increases the in vitro folding efficiency of their catalytic domain from inclusion bodies. *Protein Expression Purif. 30*, 219−220.

(26) Boeggeman, E., and Qasba, P. K. (2002) Studies on the metal binding sites in the catalytic domain of β1,4-galactosyltransferase. *Glycobiology 12*, 395−407.

(27) Ramasamy, V., Ramakrishnan, B., Boeggeman, E., Ratner, D. M., Seeberger, P. H., and Qasba, P. K. (2005) Oligosaccharide preferences of beta1,4-galactosyltransferase-I: crystal structures of Met340His mutant of human beta1,4-galactosyltransferase-I with a pentasaccharide and trisaccharides of the N-glycan moiety. *J. Mol. Biol. 353*, 53−67.

(28) Powell, J. T., and Brew, K. (1976) A comparison of the interactions of galactosyltransferase with a glycopropein substrate (ovalbumin) and with α-lactalbumin. *J. Biol. Chem. 251*, 3653−3663.

(29) Harvey, D. J., Wing, D. R., Kuster, B., and Wilson, I. B. H. (2000) Composition of N-linked carbohydrates from ovalbumin and co-purified glycoproteins. *J. Am. Soc. Mass Spectrom. 11*, 654−571.

(30) Ramakrishnan, B., Boeggeman, E., and Qasba, P. K. (2005) Mutation of arginine 228 to lysine enhances the glucosyltransferase activity of bovine beta-1,4-galactosyltransferase I. *Biochemistry 44*, 3202−3210.

(31) Parekh, R. B., Dwek, R. A., Sutton, B. J., Fernandes, D. L., Leung, A., Stanworth, D., Rademacher, T. W., Mizuochi, T., Taniguchi, T., Matsuta, K., Takeuchi, F., Nagano, Y., Miyamoto, T., and Kobata, A. (1985) Association of rheumatoid arthritis and primary osteoarthritis with changes in the glycosylation pattern of total serum IgG. *Nature (London) 316*, 452−457.

(32) Arnold, J. N., Dwek, R. A., Rudd, P. M., and Sim, R. B. (2006) Mannan binding lectin and its interaction with immunogloblulins in health and in disease. *Immunol. Lett. 106*, 103−110.

(33) Kaneko, Y., Nimmerjahn, F., and Ravetch, J. V. (2006) Anti-inflammatory activity of immunoglobulin G resulting from Fc sialylation. *Science 313*, 670−673.
(34) Rogers, J. C., and Kornfeld, S. (1971) Hepatic uptake of proteins coupled to fetuin glycopeptide. *Biochem. Biophys. Res. Commun. 45*, 1461−1467.
(35) Hangeland, J. J., Levis, J. T., Lee, Y. C., and Tso, P. O. P. (1995) Cell-type specific and ligand specific enhancement of cellular uptake of oligodeoxynucleoside methylphosphonates covalently linked with a neoglycopeptide, YEE (ah-GalNAc). *Bioconjugate Chem. 6*, 695−701.
(36) Tanabe, T., Pricer, W. E., Jr., and Ashwell, G. (1979) Subcellular membrane topology and turnover of a rat hepatic binding protein specific for asialoglycoproteins. *J. Biol. Chem. 254*, 1038−1043.

BC060341N

Use of a Folate−PPE Conjugate To Image Cancer Cells *in Vitro*

Ik-Bum Kim,[†,§] Heungsoo Shin,[‡,§] Andres J. Garcia,[⊥] and Uwe H. F. Bunz[†,*]

School of Chemistry and Biochemistry, 770 State Street, Georgia Institute of Technology, Atlanta, Georgia 30332, Department of Bioengineering, Division of Applied Chemical Engineering and Bioengineering, Hanyang University, 17 Haengdang-dong, Seongdong-gu, Seoul, 133-791, Korea, and Woodruff School of Mechanical Engineering, Petit Institute for Bioengineering and Bioscience, Georgia Institute of Technology, Atlanta, Georgia 30332-0363. Received November 2, 2006; Revised Manuscript Received January 24, 2007

We have demonstrated synthesis and application of a water-soluble, folate-substituted poly(*p*-phenyleneethynylene) (PPE) as a fluorescent contrast agent to image cancer cells. This fluorescent polymer targets and images KB cancer cells *in vitro* with high selectivity. To deliver PPE to the cells, folate ligands have been attached to an amine-functionalized PPE via an amide coupling agent. The hydrolysis of the ester groups gave a water-soluble PPE, **5**. The PPE **5** is minimally cytotoxic at concentrations of 1−10 μg/mL, which is sufficient to stain KB cancer cells efficiently. PPE **6**, devoid of folate ligands, did not stain KB cells. As a low folic acid (−) receptor control group, NIH 3T3 fibroblast cells were incubated with **5** and did not show fluorescent labeling. The folate receptor-mediated endocytosis of KB cells was evidenced by laser scanning confocal microscopy and fluorescence microscopy. The photochemical stability and ability to sustain multivalency provide advantages of PPEs over other fluorescent contrast agents. Their minimal cytotoxicity makes the PPE superior to the cytotoxic CdSe quantum dots.

INTRODUCTION

Molecular imaging with small fluorescent molecules or with inorganic II−VI semiconductor quantum dots (CdS, CdSe, CdTe) is pervasive in biomedical applications, including in the detection of cancer cells (*1*−*3*). Although organic dyes have a long history in biological applications, their limitations are their susceptibility to often rapid photobleaching and their general inability to sustain multivalent interactions (*4*). Inorganic semiconductor nanoparticles (quantum dots) have been intensively studied in *in vitro* and *in vivo* to image cancer cells, as they overcome the limitations of conventional dyes, i.e., attachment of multiple binding elements combined with often low fluorescence quantum yield in water (*5*−*7*). However, the popular CdSe-core quantum dots are composed of individually cytotoxic ions. Due to residual leaching such nanoparticles are cytotoxic (*8*, *9*).

Poly(*p*-phenyleneethynylene)s are fluorescent, photostable, and easily functionalized and can be made in water soluble form for bioanalytical applications (*10*−*12*). They have been used in the detection of heavy metal ions, lectins, proteases, and bacteria, playing out the intrinsic strengths of polymeric, i.e., multivalent, yet fluorescent scaffolds (*13*−*17*). We expected that grafting of folic acid onto a PPE could selectively deliver the polymer to folate-receptor-overexpressing KB cells because of the high binding affinity ($K_d \sim 100$ pM) of folic acid for the folate-receptor proteins. Folic acid and its conjugate enter into the intracellular cytoplasm via endocytosis and are widely used for the targeted delivery of anticancer drugs to folate-receptor-positive cancer cells such as ovarian, prostate, and breast cancers, where the folate receptors are overexpressed while having limited expression in normal cells (*18*−*22*). Despite several promising results in cancer cell targeting, the design of folate-mediated delivery systems remains challenging due to several constraints of commonly used materials such as cytotoxicity, complexity of conjugation processes, immunogenicity, and limited endocytotic permeability. For the fluorescent staining of FR-overexpressing cancer cells, it would be beneficial to use the fluorescent water-soluble polymers, acting as not only the delivery vehicles but also the fluorescent imaging agents. Here, we report synthesis of a folate−PPE conjugate **5** and its selective uptake by and imaging of cancer cells with minimal cytotoxicity to normal cells.

EXPERIMENTAL PROCEDURES

Synthesis of Monomers (1−3). Synthesis of **1**, **2**, and **3** were described in our previous reports (*10*, *12*).

Synthesis of Polymer (4). Monomer **1** (222 mg, 0.300 mmol), **2** (160 mg, 0.300 mmol), and **3** (218 mg, 0.660 mmol) were dissolved in a mixture of triethylamine (1 mL) and DMF (5 mL) in a Schlenk flask (25 mL) under a flow of nitrogen with magnetic stirring. $(Ph_3P)_2PdCl_2$ (2.0 mg, 2.8 μmol) CuI (0.5 mg, 2.8 μmol) were added to the flask. The reaction mixture was stirred at room temperature for 24 h. The solution was slowly added to ether (200 mL). The precipitate was washed with ether and water. A yellow solid was obtained in 99% yield (421 mg). PPE **4** shows an absorption maximum at 436 nm and an emission maximum at 470 nm in chloroform, typical for a dialkoxy-PPE. ^{1}H NMR (DMSO-d_6): δ 7.14, 4.92, 4.19, 3.56, 3.49, 3.09, 1.21.

Synthesis of Polymer (5). Polymer **4** (100 mg, 0.0715 mmol) was dissolved in DMF (10 mL) in a flask (50 mL) under a flow of nitrogen under magnetic stirring. Folic acid (74 mg, 0.17 mmol), 2,4,6-Trimethylpyridine (20 mg, 0.17 mmol), and EDC·HCl (33 mg, 0.17 mmol) were added to the flask in an ice bath. The reaction mixture was stirred at the room temperature for 24 h. The solvent was evaporated under a reduced pressure.

* Corresponding author. E-mail: uwe.bunz@chemistry.gatech.edu, Fax: + int. 1(404)385-1795.

[†] School of Chemistry and Biochemistry, Georgia Institute of Technology.

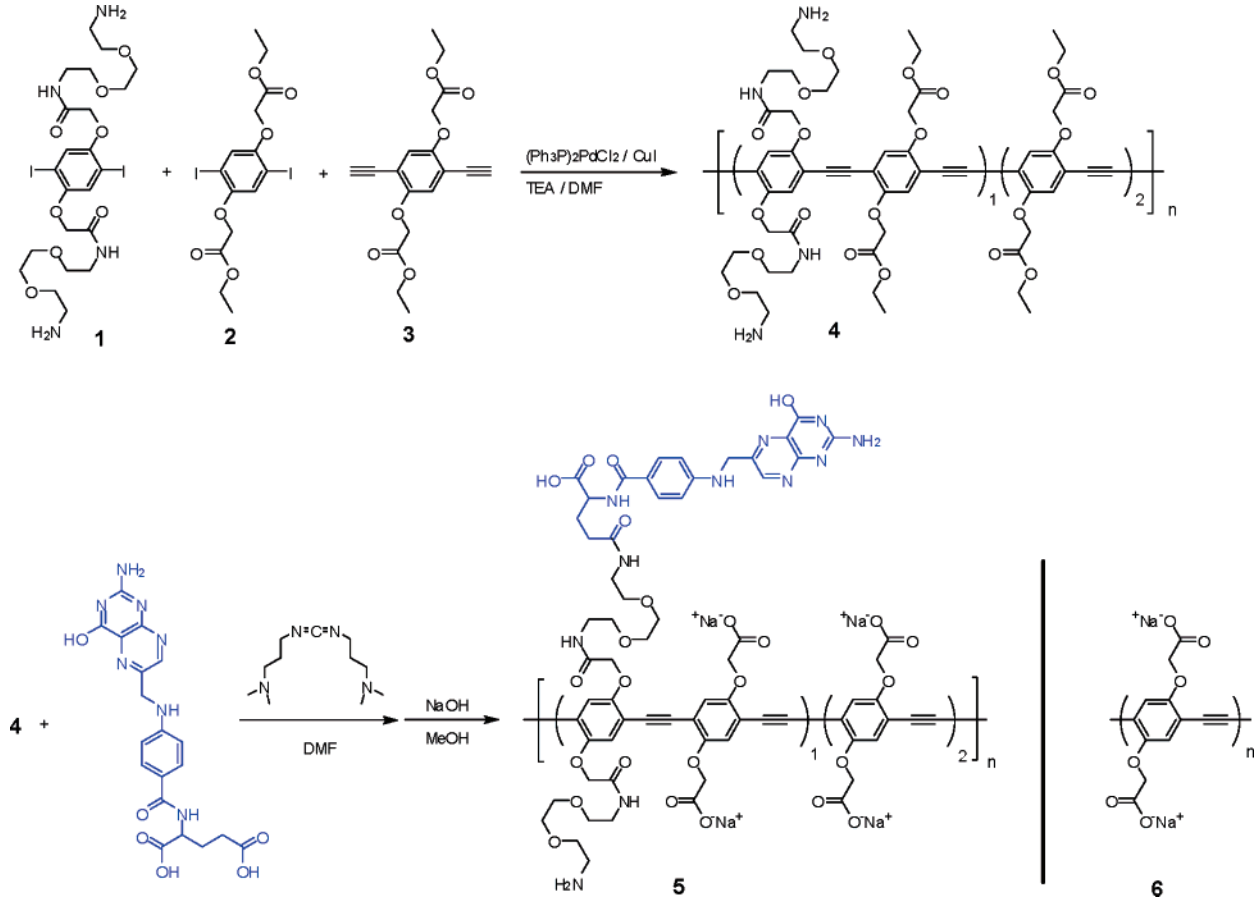
[‡] Department of Bioengineering, Hanyang University.

[⊥] Woodruff School of Mechanical Engineering, Petit Institute for Bioengineering and Bioscience, Georgia Institute of Technology.

[§] The authors contributed to this work equally

10.1021/bc0603440 CCC: $37.00 © 2007 American Chemical Society
Published on Web 03/21/2007

Scheme 1. Synthesis and Structures of PPEs Used in This Work



Methanol (20 mL) and NaOH (400 mg, 10.0 mmol) were added to the reaction mixture, and the temperature was increased to 40 °C. The mixture was stirred for 24 h. The precipitate was collected in a glass funnel and washed with methanol and acetone. An orange solid (94 mg, 74% yield) was obtained. ^{1}H NMR (D_2O): δ 7.40, 6.97, 6.88, 6.50, 4.44, 3.78, 3.29, 2.10.

Cell Culture. A frozen vial of KB cells (passage number: 17) in MEM-EBSS media (Hyclone, UT) containing 10% FBS and 1% penicillin−streptomycin (pen/strep) was thawed, immediately resuspended with RPMI 1640 folate-free media with 10% FBS (Hyclone, UT) and 1% pen/strep (herein referred to folate-free RPMI 1640), and inoculated onto a cell culture treated Petri dish (100 mm in diameter). The cells were cultured for 10 days before use at 37 °C, 95% relative humidity, and 5% CO_2 with repetitive change of the media every 3 days. NIH 3T3 fibroblasts were obtained from ATCC (American Type Culture Collection, Manassas, VA) and maintained in Delbecco's Modified Eagles Media (DMEM) supplemented with 10% FBS and 1% pen/strep.

Cytotoxicity and Proliferation Assay. The cytotoxicity of **5** was examined as previously described (*23*). Briefly, 24 h prior to the cytotoxicity test, KB cells cultured on the Petri dish were enzymatically lifted by using a trypsin−EDTA solution (0.5%), resuspended with folate-free RPMI 1640 media, and replated on 96-well plates at 500 000 cells/mL media. The cells were allowed to attach to the plate overnight. On the day of the assay, the yellowish colored powder of **5** was dissolved in phosphate-buffered saline (PBS, pH 7.4) (Invitrogen) solution. The conditioned media was prepared by mixing the solution of **5** with folate-free RPMI 1640 media. The concentration of **5** in the conditioned media varied from 1 μg/mL media to 100 μg/mL. The media of KB cells cultured for 24 h were evaporated, replenished with the conditioned media containing **5**, and cultured for additional 4 and 24 h. On the specified time point, the media was aspirated and the plates were washed three times with serum-free, folate-free RPMI 1640 media. The LIVE/DEAD viability cytotoxicity assay reagents were prepared (combination of 4 μM ethidium homodimer-1 and 2 μM calcein AM), added to the 96-well samples, wrapped with aluminum foil, and incubated for 30 min. The positive control was KB cells only, without **5**, and the negative control was to expose KB cells to 70% (v/v) methanol for 30 min. Following the incubation for 30 min, the fluorescence intensity of each sample was measured using a microplate reader and then was normalized by the value for the positive control (cell viability). The live/dead cell population following the treatment with LIVE/DEAD reagents was visualized by fluorescence microscopy to corroborate the quantitative results. We also investigated the effect of **5** on the metabolic activity of KB cells. At each time point of cell culture (4 and 24 h) following exposure to **5**, the number of cells was measured using a PicoGreen DNA kit (Molecular Probes, Eugene, OR). PicoGreen binds to double stranded DNA in cells and the fluorescence intensity of each sample was obtained using a microplate reader.

Folate-Receptor-Mediated Targeting. The intercellular uptake of **5** was investigated with KB cells and NIH 3T3 fibroblasts. On the day before the experiment, KB cells were lifted from the plate and resuspended with folate-free RPMI 1640 media. Approximately 100 000 cells/mL were seeded on Lab-Tek chamber slides (Nalge Nunc, Naperville, IL) and incubated overnight; **6** and **5** were dissolved in folate-free RPMI 1640 media to prepare a series of concentrations ranging from 0.001 mg/mL to 0.1 mg/mL. KB cells cultured for 24 h on the chamber slides were rinsed with serum-free, folate-free RPMI 1640 media and a solution of either **5** or **6** was then added to the chamber slides. The slides were incubated for 4 and 24 h at

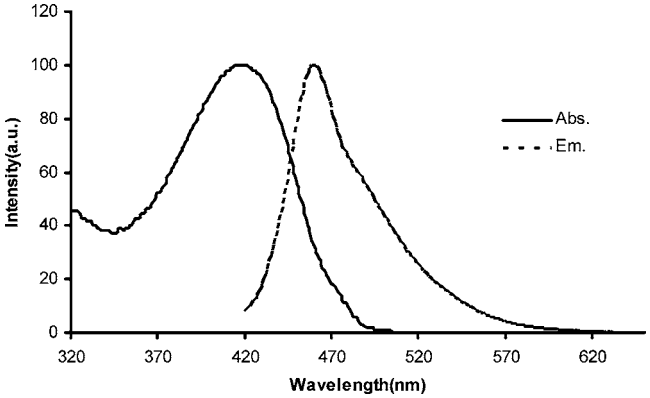


Figure 1. Normalized absorption and emission spectra of PPE **5** in water. $\lambda_{max\ abs} = 421$ nm, $\lambda_{max\ emiss} = 460$ nm. The emission spectrum of **5** is typical for a dialkoxy PPE. The shoulder near 490 nm is of vibronic origin.

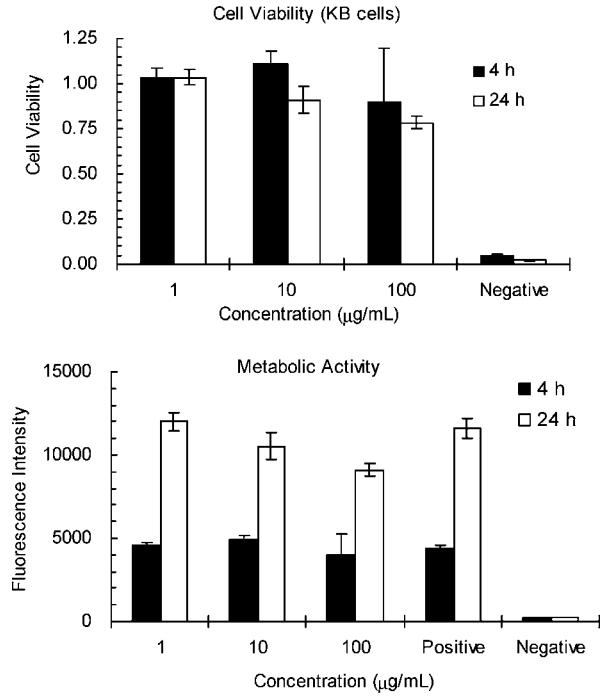


Figure 2. KB cell viability upon different concentrations of PPE **5** after 4 and 24 h incubation (viability = 1 means that 100% of cells in the condition were viable). The negative control was the group in which cells were treated with 70% methanol for 30 min before treatment with each dye (LIVE/DEAD reagent or PicoGreen), and the positive control was the cells cultured without exposure to PPE **5**. The concentration of PPE **5** in the media was varied from 1 to 100 μg/mL. At 4 and 24 h after incubation with PPE **5**, LIVE/DEAD reagents were added to each sample, and the fluorescence intensity was measured. Cell viability was calculated by normalization of the fluorescence intensity from each sample with that of the control that was under no treatment. The metabolic assay measures change in DNA content produced by cells, which is indicative of proliferation capability. The metabolic assay, combined with the cell viability assay, supports that KB cells exposed to PPE **5** are not only viable but also are capable of proliferating under the concentrations tested in this study.

37 °C. At each time point, the media were aspirated completely and the cells were rinsed with folate-free RPMI 1640 media and PBS three times, fixed with 3.7% formaldehyde for 10 min, rinsed with PBS twice, and blocked in 5% FBS for 1 h. For microscopic analysis, a coverslip was mounted on the slide with a drop of VECTRASHIELD mounting media (Vector Laboratories, Inc., CA). The samples were cured overnight, preventing exposure to light sources. The intercellular distribution of the conjugated polymers **5** and **6** was visualized by normal

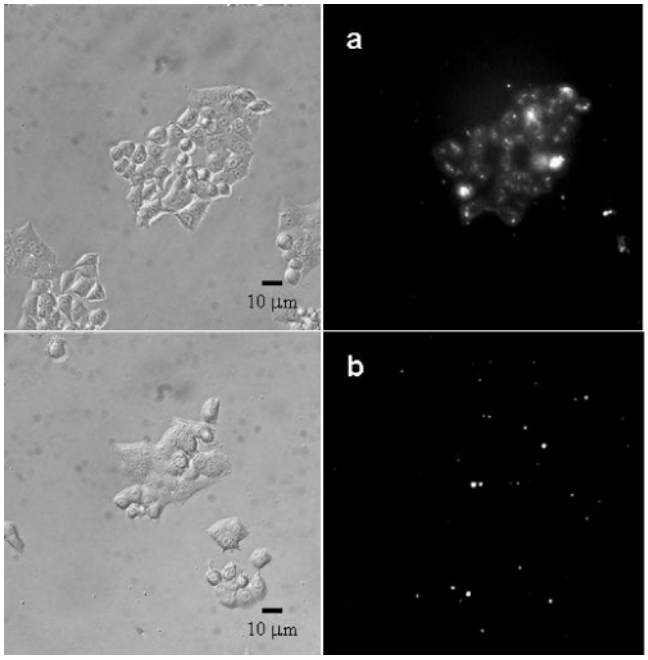


Figure 3. Fluorescence microscopy images (10×) of KB cells after incubated with (a) PPE **5**, and (b) PPE **6** for 24 h. Transmittance images (left) and fluorescence images (right). Punctuate staining has appeared (b) after KB cells were incubated with **6** and washed with PBS buffer several times, indicating some nonspecific interactions between KB cells and **6**. The normal fluorescence microscopy allows visualization of localized PPE **5** on KB cells; however, it does not provide the information whether the dye was permeablized through the cellular membrane and placed within the cytoplasm. This figure shows that **5** was colocalized on KB cells while PPE **6** only had little nonspecific binding to KB cells or the tissue culture plate.

fluorescence microscopy and two-photon confocal microscopy at excitation and emission wavelength of approximately 480 and 540 nm, respectively. The same procedure was applied to NIH 3T3 fibroblasts except using normal DMEM supplemented with 10% FBS.

RESULTS AND DISCUSSION

Synthesis of **5** is accomplished by the postfunctionalization of the random copolymer, PPE **4** (Scheme 1), which was synthesized from **1**−**3** in the presence of $(Ph_3P)_2PdCl_2$/CuI and a triethylamine/DMF mixture as solvent. This approach allows controlling the molar ratio of amine monomer **1** and diester monomers **2** and **3** to 1:1:2. The PPE **4** is well soluble in THF, CH_2Cl_2, and DMF. The number average molecular weight (M_n) of **4** is 8.3×10^3 with a polydispersity index of 1.70 (GPC, polystyrene standard). The coupling reaction of folic acid with **4** was carried out in the presence of the carbodiimide EDC (1-ethyl-3-(3′-(dimethylamino)propyl)carbodiimide) (*24*) in anhydrous DMF. PPE **5** was obtained after hydrolysis of the ester groups by NaOH in methanol. Based on the molecular weight of PPE **4**, the length of one extended PPE chain of **4** (and therefore **5**) is 12 nm. It is well soluble in water and shows an absorption maximum at 420 nm and an emission maximum at 460 nm (*25*−*27*). Even though the peak fluorescence of **5** in water is in the blue, which can interfere with autofluorescence of tissues and proteins, **5** has a broad emission that tails into the green (Figure 1). Using a green fluorescence filter, the KB cells are easily visualized after staining with **5**.

The fluorescence quantum yield of dialkoxy PPEs in organic solvents is high, up to 0.86; the quantum yields of PPEs **5** and **6**, however, were only 0.02 and 0.08 in water, respectively. The decrease in the quantum yield of PPE **5** compared to that of PPE **6** is probably due to the presence of the electron-accepting

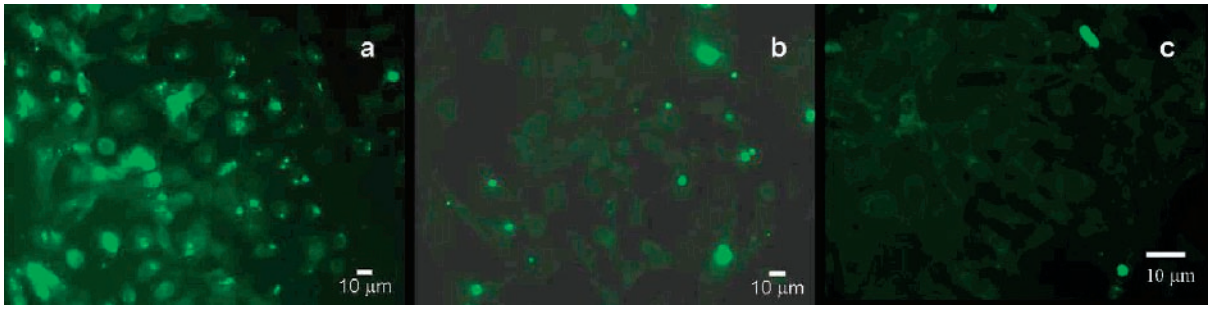


Figure 4. Fluorescence microscopy images (40×) of (a) KB cells after incubation with PPE **5**, (b) KB cells after incubation with PPE **6**. The KB cells are slightly stained by **6** due to nonspecific interactions, (c) NIH 3T3 fibroblast cells after incubation with PPE **5** for 4 h. The fluorescence microscopy images were obtained from KB cells incubated for 4 h.

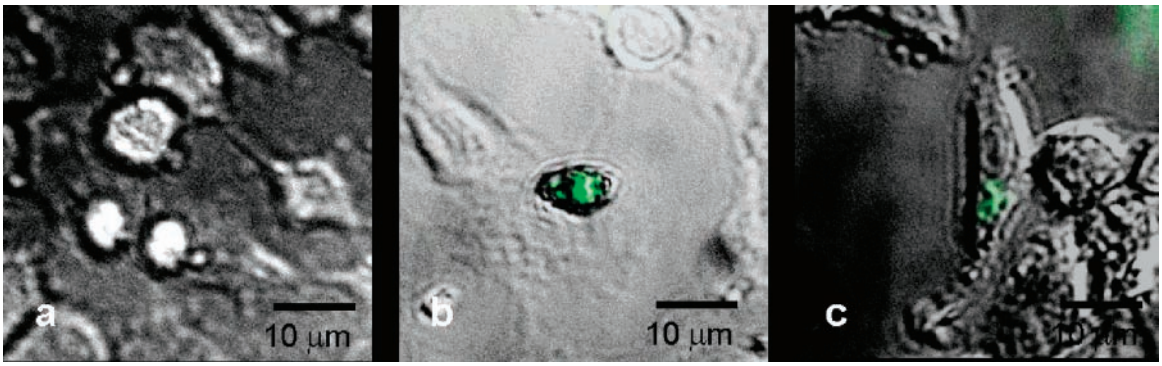


Figure 5. Confocal microscopy images (63×) of KB cells after incubation with (a) PPE **6** for 4 h, (b and c) PPE **5** for 4 h. The features highlighted in green show the fluorescence. Confocal microscopy allowed us to obtain figures at the interface where the KB cells had contact with the tissue culture plate. When we analyzed the image according to layer-by-layer z scanning, no fluorescence from PPE **5** was observed at the membrane while the fluorescence intensity was increased as we focused down to the cell-culture plate interface, confirming that PPE **5** was internalized and emitted measurable amounts of fluorescence within KB cells.

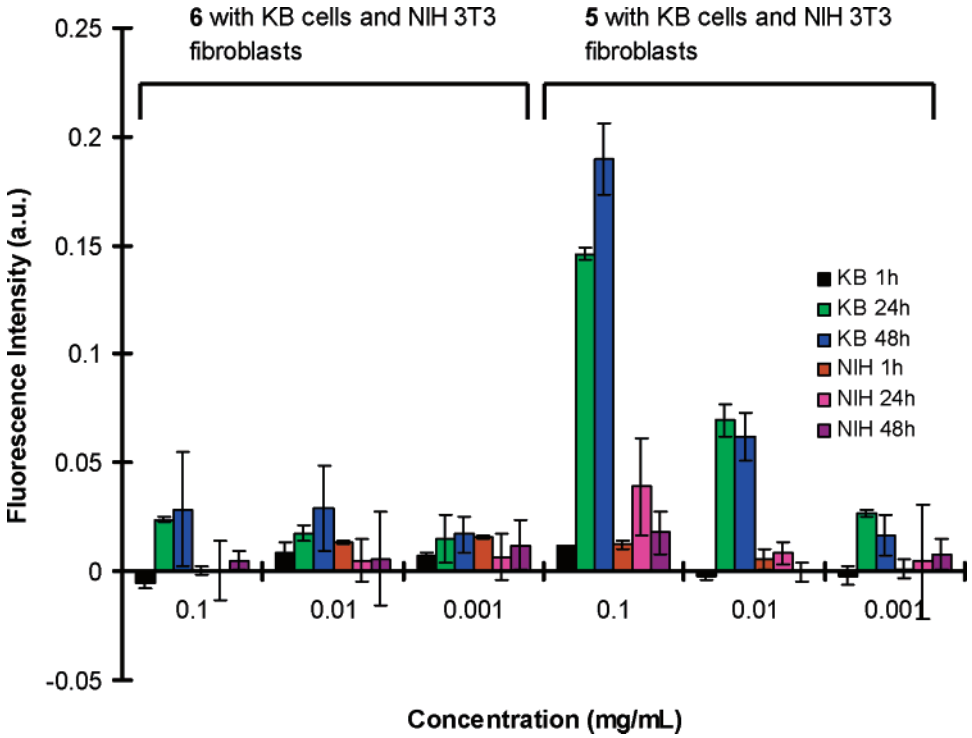


Figure 6. Fluorescence intensity of KB cells and NIH 3T3 fibroblasts after incubation with PPE **5** and PPE **6** for 1, 24, and 48 h.

folate substituent that will act as an intrinsic energy transfer fluorescence quencher. We were concerned about the low quantum yield, but we expected that a more hydrophobic environment would increase the quantum yield. In the presence of bovine serum albumin (5 μM), the most abundant protein in serum, the quantum yield of **5** increased from 0.02 to 0.15 due to the significant decrease in polarity of the formed complex of BSA and **5** (*11*), suggesting that **5** would function well as fluorescent beacon in a hydrophobic environment.

The cytotoxic effects of PPE **5** and PPE **6** on KB cells were investigated (Figure 2) (*28*). Cell viability decreased slightly at a concentration of >10 μg/mL of **5**. KB cells incubated with

PPE **5** showed no enhanced rate of cell death relative to PPE **6** or to a control without added PPE. A functional assay was conducted to evaluate the cytotoxic effects of PPE **5** on KB cells in more detail. The total number of metabolically active (active mitochondrial dehydrogenase enzyme) cells increased approximately 2-fold after the exposure of the cell culture to **5**. At a concentration of >1 μg/mL, PPE **5** exhibits sufficient fluorescent intensity to be detected inside the intracellular domain, yet at this concentration the cytotoxic effects of **5** are minimal, suggesting that the endocytosis of **5** by KB cells is facile and that there is probably fluorescence enhancement of **5** in the cells. We attribute the fluorescence enhancement to a decrease in polarity and/or the complexation of the folate ligand, leading to its spatial separation from the main chain.

To visualize the receptor-mediated uptake, separate samples of KB cells were incubated for 4 h with both PPE **5** and PPE **6**. Spatial distribution of the PPEs was examined by fluorescence microscopy (Figure 3). KB cells treated with **5** displayed cellular localization of the fluorescence, while **6** showed negligible fluorescent labeling of KB cells but some punctuate staining, due to nonspecific interactions between the KB cells and **6**. The magnified image suggests that endocytosed PPE **5** is primarily localized in the cytoplasm, not in the cell nucleus (Figure 5), and although the nucleus was not counterstained, it was easily recognizable after uptake of **5**. A concentration of 10 μg/mL **5** is sufficient to image targeted KB cells *in vitro*. Interestingly enough, the microscopy experiments were not disturbed by the blue autofluorescence of the cells. As a low folic acid (−) receptor control group, NIH 3T3 fibroblast cells were incubated with both PPE **5** and PPE **6** for 4 h. Compared to KB cells incubated with **5**, we observed no fluorescent labeling of the NIH 3T3 cells (Figure 4). Although there is some nonspecific binding of PPE **6** to KB cells, only PPE **5** was internalized by the folate receptor-mediated endocytosis pathway. The quantification of endocytosis-mediated PPE inside the cells was done by fluorescence microreader, showing that only **5** was significantly incorporated inside KB cells (Figure 6). A time-dependent increase of fluorescence intensity was only observed in KB cells incubated with **5**, but not in any of the controls (**6** and NIH 3T3 fibroblasts). The cell culture under low temperature (4 °C) showed significantly decreased uptake of **5** by KB cells, suggesting that ATP-consuming endocytosis is the mechanism for the PPE uptake.

In conclusion, **5** is of low cytotoxicity, making it promising as an imaging agent for biological applications at concentrations <10 μg/mL. The photochemical stability of PPE allowed imaging the cells after 48 h without any loss in fluorescence intensity. The folate−PPE conjugate **5** shows specific targeting and imaging of KB cancer cells *in vitro* by folate receptor-mediated endocytosis. The endocytosed PPE is localized in the cytoplasm. The combination of photochemical stability and low cytotoxicity suggests **5** as a potentially useful *in vivo* imaging agent for folate-receptor overexpressing cancer cells. Multivalency (*29*) and chemical versatility of PPEs are their advantages over conventional organic dyes. We will construct multitasking PPEs containing targeting agents and small molecule therapeutics.

ACKNOWLEDGMENT

U.B. and I.K. thank the DOE (DE-FG02-04ER46141) for generous support.

LITERATURE CITED

(1) Chan, W. C. W., and Nie, S. (1998) Quantum dot bioconjugates for ultrasensitive nonisotopic detection. *Science 281*, 2016−2018.

(2) Bruchez, M., Moronne, M., Peter, G., Weiss, S., and Alivisatos, A. P. (1998) Semiconductor nanocrystals as fluorescent biological labels. *Science 281*, 2013−2016.

(3) Han, M., Gao, X., Su, J. Z., and Nie, S. (2001) Quantum-dot-tagged microbeads for multiplexed optical coding of biomolecules. *Nat. Biotechnol. 19*, 631−635.

(4) Frangioni, J. V. (2003) In vivo near-infrared fluorescence imaging. *Curr. Opin. Chem. Biol. 7*, 626−634.

(5) Green, M. (2004) Semiconductor quantum dots as biological imaging agents. *Angew. Chem., Int. Ed. 43*, 4129−4131.

(6) Gao, X., Cui, Y., Levenson, R. M., Chung, L. W. K., and Nie, S. (2004) In vivo cancer targeting and imaging with semiconductor quantum dots. *Nat. Biotechnol. 22*, 969−976.

(7) Kim, S., Lim, Y. T., Soltesz, E. G., De Grand, A. M., Lee, J., Nakayama, A., Parker, J. A., Mihaljevic, T., Laurence, R. G., Dor, D. M., Cohn, L. H., Bawendi, M. G., and Frangioni, J. V. (2004) Near-infrared fluorescent type II quantum dots for sentinel lymph node mapping. *Nat. Biotechnol. 22*, 93−97.

(8) Derfus, A. M., Chan, W. C. W., and Bhatia, S. N. (2004) Probing the cytotoxicity of semiconductor quantum dots. *Nano. Lett. 4*, 11−18.

(9) Alivisatos, A. P., Gu, W., and Larabell, C. (2005) Quantum dots as cellular probes. *Annu. Rev. Biomed. Eng. 7*, 55−76.

(10) Kim, I.-B., and Bunz, U. H. F. (2006) Modulating the sensory response of a conjugated polymer by proteins: An agglutination assay for mercury ions in water. *J. Am. Chem. Soc. 128*, 2818−2819.

(11) Kim, I.-B., Dunkhorst, A., and Bunz, U. H. F. (2005) Nonspecific interactions of a carboxylate-substituted PPE with proteins. A cautionary tale for biosensor applications. *Langmuir 21*, 7985−7989.

(12) Kim, I.-B., Dunkhorst, A., Gilbert, J., and Bunz, U. H. F. (2005) Sensing of lead ions by a carboxylate-substituted PPE: Multivalency effects. *Macromolecules 38*, 4560−4562.

(13) Kim, I.-B., Erdogan, B., Wilson, J. N., and Bunz, U. H. F. (2004) Sugar-poly(para-phenylene ethynylene) conjugates as sensory materials: Efficient quenching by Hg^{2+} and Pb^{2+} ions. *Chem. Eur. J. 10*, 6247−6254.

(14) Pinto, M. R., Schanze, K. S. (2004) Amplified fluorescence sensing of protease activity with conjugated polyelectrolytes. *Proc. Nat. Acad. Sci. U.S.A. 101*, 7505−7510.

(15) Disney, M. D., Zheng, J., Swager, T. M. and Seeberger, P. H. (2004) Detection of bacteria with carbohydrate-functionalized fluorescent polymers. *J. Am. Chem. Soc. 126*, 13343−13346.

(16) Kim, I.-B., Wilson, J. N., and Bunz, U. H. F. (2005) Mannose-substituted PPEs detect lectins: A model for Ricin sensing. *Chem. Commun.* 1273−1275.

(17) Cairo, C. W., Gestwicki, J. E., Kanai, M., and Kiessling, L. L. (2002) Control of multivalent interactions by binding epitope density. *J. Am. Chem. Soc. 124*, 1615−1619.

(18) Hilgenbrink, A. R., and Low, P. S. (2005) Folate receptor-mediated drug targeting: from therapeutics to diagnostics. *J. Pharm. Sci. 94*, 2135−2146.

(19) Sudimack, J., and Lee, R. J. (2000) Targeted drug delivery via the folate receptor. *Adv. Drug Delivery Rev. 41*, 147−162.

(20) leamon, C. P., and Reddy, J. A. (2004) Folate-targeted chemotherapy. *Adv. Drug Delivery Rev. 56*, 1127−1141.

(21) Dixit, V., Bossche, J. V., Sherman, D. M., Thompson, D. H., and Andres, R. P. (2006) Synthesis and grafting of thioctic acid-PEG-folate conjugates onto Au nanoparticles for selective targeting of folate receptor-positive tumor cells. *Bioconjugate Chem. 17*, 603−609.

(22) Pan, D., Turner J. L., and Wooley, K. L. (2003) Folic acid-conjugated nanostructured materials designed for cancer cell targeting. *Chem. Commun.* 2400−2401.

(23) Shin, H., Temenoff, J. S., and Mikos, A. G. (2003) In vitro cytotoxicity of unsaturated oligo[poly(ethyleneglycol) fumarate] macromers and their cross-linked hydrogels. *Biomacromolecules 4*, 552−560.

(24) Carpino, L. A., and El-Faham, A. (1995) Efficiency in peptide coupling: 1-Hydroxy-7-azabenzotriazole vs 3,4-Dihydro-3-hydroxy-4-oxo-1,2,3-benzotriazine. *J. Org. Chem. 60*, 3561−3564.

(25) Bunz, U. H. F. (2000) Poly(aryleneethynylene)s: Syntheses, properties, structures, and applications. *Chem. Rev. 100*, 1605−1644.
(26) Bunz, U. H. F. (2005) Synthesis and structure of PAEs. *Adv. Polym. Sci. 177*, 1−52.
(27) Halkyard, C. E., Rampey, M. E., Kloppenburg, L., Studer-Martinez, S. L., and Bunz, U. H. F. (1998) Evidence of aggregate-formation for 2,5-Dialkylpoly(p-phenyleneethynylenes) in solution and thin films. *Marcromolecules 31*, 8655−8659.
(28) KB cells, employed as a model system, originate from human nasopharyngeal cells that overexpress the folic acid receptor, especially when cultured in folate-free media.
(29) Mammen, M., Choi, S. K., and Whitesides, G. M. (1998) Polyvalent interactions in biological systems: Implications for design and use of multivalent ligands and inhibitors. *Angew. Chem. 37*, 2755−2794.

BC0603440

Use of Antibody as Carrier of Oligomers of Peptidomimetic $\alpha_v\beta_3$ Antagonist to Target Tumor-Induced Neovasculature

In Soo Shin,[†] Beom-Su Jang,[†] S. Narasimhan Danthi,[‡] Jianwu Xie,[‡] Sarah Yu,[†] Nhat Le,[†] Jin-Soo Maeng,[†] In Sook Hwang,[†] King C. P. Li,[‡,§] Jorge A. Carrasquillo,[†,||] and Chang H. Paik*[,†]

Department of Nuclear Medicine and Department of Radiology, Warren G. Magnuson Clinical Center, National Institutes of Health, Bethesda, Maryland 20892. Received November 7, 2006; Revised Manuscript Received January 19, 2007

Sulfhydryl selective reactions were explored to conjugate oligomers of a peptidomimetic integrin $\alpha_v\beta_3$ antagonist, 4-[2-(3,4,5,6-tetrahydropyrimidine-2-ylamino)ethyloxy]benzoyl-2-(*S*)-aminoethylsulfonylamino-β-alanine (IA) to monoclonal antibody (MoAb) to increase integrin $\alpha_v\beta_3$ receptor-binding avidity. To generate sulfhydryl groups, *N*-succinimidyl-*S*-acetylthioacetate (SATA) was conjugated to both MoAb and IA. Sulfhydryl groups were then generated upon the deacetylation of the protecting acetyl group from the *S*-acetylthioacetato (ATA) moiety of MoAb−$(ATA)_n$ or IA−ATA with 0.02 M hydroxylamine in the presence of 1 mM EDTA at pH 7.2. The major focus was on optimizing the reaction concentrations, molar ratios, and reaction pH to conjugate high levels of IA−(A-SH) to MoAb−$(A\text{-}SH)_n$ without causing the inter- and intramolecular cross-linking of MoAb. Stepwise reactions of MoAb−$(A\text{-}SH)_n$ (15 μM MoAb) with a homobifunctional cross-linker, 1,8-bis(maleimido)diethylene glycol (BM$[PEO]_2$) at a >50× molar excess to the −SH, followed by the reaction of the purified product MoAb−$(A\text{-}S\text{-succinimidomaleimido-}[PEO]_2)_n$ with IA−(A-SH) at pH 7.2 afforded monomeric MoAb−(A-*S*-succinimido-$[PEO]_2$-succinimido-*S*-A-IA)$_n$ with <10% high molecular weight oligomeric MoAb. Monomeric MoAb−(A-*S*-S-$[PEO]_2$-S-*S*-A-IA)$_{10}$ (MoAb−IA_{10}) radiolabeled with ^{111}In using 2-(*p*-isothiocyanatobenzyl)cyclohexyl−DTPA and with ^{125}I using the Iodogen method showed >70% bindability to 0.4 μM $\alpha_v\beta_3$. When injected iv to nude mice with the receptor-positive M21 tumor, MoAb−IA_{10} radiolabeled with both ^{111}In and ^{125}I accumulated rapidly and was retained in the tumor for a 44 h period while the radioactivity cleared rapidly from the blood, thereby resulting in increasing tumor-to-blood ratios over time. The tumor uptake was similar between the ^{125}I label and the ^{111}In label for a 44 h period. In contrast, the blood radioactivity was lower, but liver and other organ uptakes were much higher for the ^{111}In label than for the ^{125}I. The ^{111}In label produced higher tumor-to-blood ratios but much lower tumor-to-organ ratios than the ^{125}I. The rapid blood clearance, a short peak tumor uptake time, and a low peak tumor uptake value with prolonged tumor retention of this macromolecule appear to support a hypothesis that MoAb−IA_{10} primarily binds to $\alpha_v\beta_3$ receptors on angiogenic vessels, but not on the tumor. This hypothesis was substantiated by the fluorescence microscopic analysis of FITC−MoAb−IA_{10}, which showed that FITC−MoAb−IA_{10} outlined neovasculatures but not tumor cells at 4 and 21 h ex vivo. Additional proof was observed when blood vessels outlined with rhodamine−lectin, which specifically binds to blood vessels, were superimposable on neovasculatures outlined with FITC−MoAb−IA_{10}.

1. INTRODUCTION

Angiogenesis is the physiological process in which new blood vessels are formed from pre-existing blood vessels. This process is essential for a tumor to receive nutrients and oxygen for survival (*1*). Since tumor angiogenesis precedes the anatomical change of tumor size and the newly formed vessels are readily accessible, the detection of tumor angiogenesis should be a sensitive means of assessing the status of tumors. Antiangiogenesis therapy using cytotoxic α- and β-emitters may be an effective approach, because damaged endothelial cells and adjacent tumor cells can block blood flow to tumors, thereby killing a wide variety of solid tumors.

Integrins are a family of heterodimeric endothelial transmembrane glycoproteins composed of α and β subunits (*2*). Integrins expressed on activated endothelial cells regulate cell migration, differentiation, and proliferation during angiogenesis (*3*). One of these integrins, integrin $\alpha_v\beta_3$, is overexpressed in tumor-induced angiogenic vessels, various malignant human tumors, and diseases such as osteoporosis, rheumatoid arthritis, and macular degeneration, whereas it is not expressed in blood vessels of normal mature tissues (*4*, *5*). Integrin $\alpha_v\beta_3$ is a receptor for extracellular proteins including vitronectin, fibronectin, and fibrinogen, which contain an arginine-glycine-aspartic acid (RGD) sequence (*6*). Recently, RGD peptides and peptidomimetic antagonists (IA) specific for the integrin receptors have been synthesized and labeled with various γ and positron emitters (*7*−*13*) for scintigraphic detection, and γ- and β-emitters for radiotherapy of tumors (*10*, *14*−*24*). Steady progress has been reported in optimizing the radiolabeling methods of RGD peptides to improve the receptor-binding and tumor-targeting pharmacokinetics (*18*, *25*, *26*). Recently, RGD peptides were conjugated to antibodies to increase the receptor-binding affinity (*27*). It was also reported that RGD-conjugated Fc fragments (*26*) and RGD-conjugated anti-CD3 antibodies (*28*) inhibited angiogenesis in the tumor and redirected the cytolytic property of cytotoxic T lymphocytes to $\alpha_v\beta_3$-expressing endothelial cells, respectively.

* Corresponding author. Tel.: +1 301 496 1426. Fax: +1 301 402 4548. E-mail address: cpaik@mail.nih.gov.

[†] Department of Nuclear Medicine.

[‡] Department of Radiology.

[||] Current address: Memorial Sloan-Kettering Cancer Center, Nuclear Medicine Service Mail Box 77, 1275 York Avenue, New York, NY 10021.

[§] Current address: The Methodist Hospital, Department of Radiology, 6565 Fannin Street, MB1−066, Houston, TX 77030.

10.1021/bc0603485 Not subject to U.S. Copyright. Published 2007 by American Chemical Society
Published on Web 03/22/2007

To increase the affinity, Burnett et al. (*29*) modified the ethylamine terminus of IA to a series of the corresponding carbamate derivatives and reported that the hydrophobic carbamate-linked appendages improved the $\alpha_v\beta_3$ receptor-binding affinity of the parent compound IA by 2 to 20 times. The affinity of IA was also improved by coupling to a cationic polymerized lipid-based nanoparticle that was successfully used to deliver a gene (*30*) or ^{90}Y (*20*) to neovasculature for tumor regression.

We have undertaken the conjugation of high levels of IA molecules to monoclonal antibody T101 to improve the affinity of IA and to test a possibility of targeting $\alpha_v\beta_3$ receptors on neovasculature. T101 (MoAb) is a murine anti-CD5 monoclonal antibody of IgG_{2a} isotype and is nonspecific to $\alpha_v\beta_3$ receptor. We used whole IgG as a carrier because this IgG has a large number (>60) of lysine residues, each of which contains a reactive ϵ-amino group. Thus, intact MoAb can be conjugated at the lysine residues with a large number of antagonists to increase receptor-binding avidity, and sequentially conjugated with other molecules such as pendant groups to radiolabel with γ or positron emitters for scintigraphic imaging or β-emitters for cancer therapy and fluorescein for optical imaging. We also used intact MoAb instead of antibody fragments, because we were interested in assessing the status of tumor-induced angiogenesis and because IgG does not readily cross the endothelial tight junctions due to its large molecular size (150 kDa), thus more suitable for specific imaging of tumor-induced neovasculature than antibody fragments. Another advantage of using antibody as a carrier is that it would also provide an opportunity to diversify into a pretargeting approach using an antibody specific for radiometal chelates as a carrier described initially by Meares et al. (*31*−*36*) or a three-step pretargeting approach involving injection of three components: MoAb conjugated with both IA and biotin, avidin, and radiolabeled biotin (*37*−*42*). These pretargeting approaches could potentially amplify tumor-to-nontumor background ratios. This paper describes the conjugation of IA molecules to MoAb; the labeling of IA-conjugated MoAb with FITC, ^{125}I, and ^{111}In; in vitro binding study with $\alpha_v\beta_3$ receptor; and biodistribution and histochemistry studies using nude mice with the receptor-positive M21 tumor to demonstrate the accumulation of the IA-conjugated MoAb on tumor-induced neovasculature.

2. EXPERIMENTAL PROCEDURES

2.1. Conjugation of SATA to MoAb. A heterofunctional cross-linker, *N*-succinimidyl-*S*-acetylthioacetate (SATA; Pierce, Rockford, IL) at a concentration ranging from 0.135 to 13 mM was reacted with MoAb (27 μM) in 0.1 M phosphate buffer, pH 7.2, at room temperature for 1 h. MoAb conjugated with several different levels of *S*-acetylthioacetyl moieties (ATA) was purified with size exclusion Zeba Desalt Spin Columns (Pierce, Rockford, IL). To determine the level of the *S*-acetylthioacetato moiety per MoAb, the S-acetyl protecting group was deacetylated with hydroxylamine (0.02 M) at room temperature in the presence of 1 mM EDTA to generate the mercaptoacetyl (A-SH) group. The concentration of the sulfhydryl group was then titrated with Ellman's reagent (Pierce, Rockford, IL) following manufacturer's instructions. The MoAb concentration was determined by measuring the absorbance at 280 nm (ϵ = 1.4 mL/mg) or by Bradford assay with Coomassie plus protein assay reagent (Pierce, Rockford, IL) according to manufacturer's instructions (*43*).

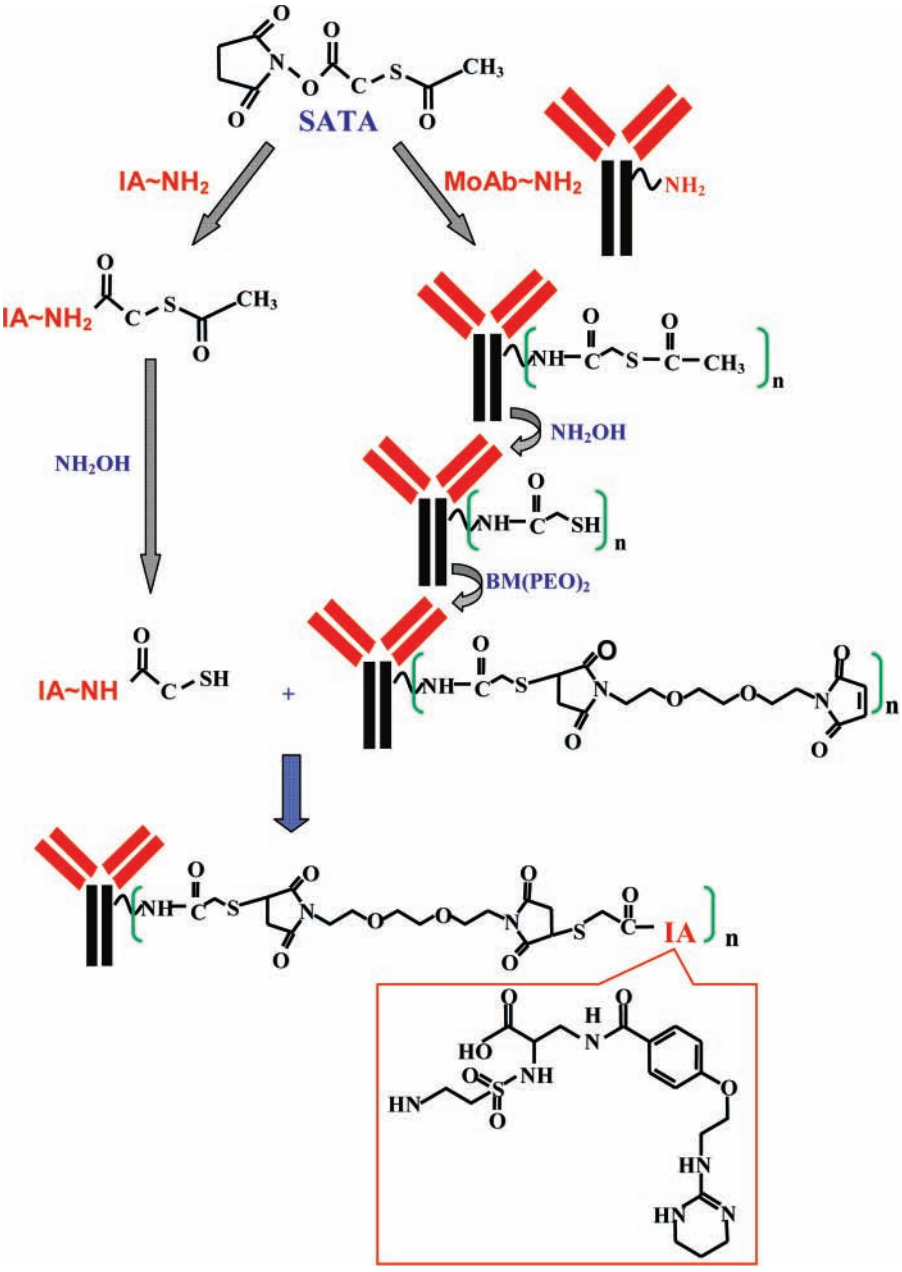
***2.2.* Preparation of *S*-Acetylthioaceto−IA.** The synthesis of IA was previously reported (*29*). The amino terminus of IA (0.02 M) was reacted with SATA (0.2 M) in 0.1 M sodium phosphate buffer, pH 7.2, at room temperature for 1 h to modify IA with a moiety containing an ATA. The product mixture was loaded on a Sep-Pak C18 cartridge (Pierce, Rockford, IL) and eluted with a stepwise gradient of acetonitrile solution from 0% to 50% acetonitrile in water. The product IA−ATA was collected with 50% acetonitrile. The chemical purity of IA−ATA was confirmed by HPLC (Gilson, Middleton, WI) equipped with a reverse-phase ACE 5C-18 column (4.6 × 100 mm, 5 μm, MAC-MOD Analytical Inc., Chadds Ford, PA) and a UV monitor. The HPLC system was operated under the following gradient elution conditions: eluent A, 50 mM triethylammonium phosphate in water; eluent B, 100% acetonitrile; gradient, 0−2 min with 100% eluent A, 2−5 min with 100%−80% eluent A, 5−12 min with 80%−65% eluent A, and 12−20 min with 65%−0% eluent A; flow rate, 1.0 mL/min. The concentration of IA−SATA was determined by the Ellman's reagent as described above.

2.3. Conjugation of IA−ATA to MoAb−$(ATA)_n$. IA−ATA was conjugated to MoAb−$(ATA)_n$ using a homobifunctional cross-linker, 1,8-bis(maleimido)diethylene glycol ($BM[PEO]_2$). MoAb−$(ATA)_n$ (20 μM) was reacted with $BM[PEO]_2$ at a molar excess in the presence of hydroxylamine (0.02 M) and 1 mM EDTA in 0.1 M sodium phosphate, pH 7.2, at room temperature for 30 min. To ensure MoAb−$(ATA)_n$ (n = 5 and 10) conjugation to only one maleimido group of the homobifunctional $BM[PEO]_2$ and prevent the inter- and intramolecular cross-linking of MoAb caused by $BM[PEO]_2$, MoAb−$(A\text{-}SH)_n$ (n = 5 and 10) was reacted with $BM[PEO]_2$ at ≥50× molar excess to the concentration of A-SH. The resulting product, MoAb−(acetyl-*S*-succinimidomaleimido$[PEO]_2)_n$, was purified using a size exclusion Zeba Desalt Spin Columns (Pierce, Rockford, IL). The purified product was immediately reacted with IA-A-SH at a 4× molar excess to the concentration of the maleimido$[PEO]_2$. The level of IA-(A-SH) conjugated per MoAb was determined by titrating the concentration of IA-(A-SH) before and after the conjugation reaction with the Ellman's reagent as describe above. The product MoAb−(acetyl-*S*-succinimido-$[PEO]_2$-succinimido-*S*-acetyl-$IA)_n$ (MoAb−(A-*S*-$S[PEO]_2$S-*S*-A-$IA)_n$) was purified with a size exclusion Zeba Desalt. The protein concentration was determined as described above.

2.4. Radiolabeling. The final products MoAb−(A-*S*-$S[PEO]_2$S-*S*-A-$IA)_n$ with n = 5 and 10 were conjugated with 2-(*p*-isothiocyanatobenzyl)cyclohexyl−DTPA (CHX-A″; Macrocyclic, Dallas, TX) and labeled with $^{111}InCl_3$ (Perkin-Elmer, Boston, MA) as described previously (*44*, *45*). The product was purified with a size exclusion Zeba Desalt Spin column (Pierce, Rockford, IL) or a microcon filter with a 30 kDa cutoff (Millipore, Bedford, MA). The purified product was labeled with ^{111}In chloride in 0.2 M sodium acetate, pH 4.5, at room temperature for 1 h. DTPA (0.2 mM) was then added to the reaction solution to bind possible free ^{111}In ion. The labeled product was purified with a size exclusion PD-10 column (GE Healthcare Bio-Sciences AB, Uppsala, Sweden). The radiochemical purity was assessed by HPLC (Gilson, Middleton, WI) equipped with a size exclusion TSK gel $G3000SW_{XL}$ column (7.8 × 300 mm, 5 μm, TOSOH Bioscience, Japan; 0.067 M sodium phosphate/0.15 M sodium chloride, pH 6.8; 1.0 mL/min), a UV monitor, and an on-line flow radioactivity detector (Bioscan Inc., Washington, DD).

2.5. Fluorescein Labeling. MoAb−(A-*S*-$S[PEO]_2$S-*S*-A-$IA)_{10}$ (12 μM) was reacted with FITC (0.18−1.6 mM) in 0.1 M sodium bicarbonate buffer, pH 8.4, for 18 h at room temperature. The labeled product with four fluorescein molecules per MoAb (10 μM) was purified with a size exclusion Zeba Desalt Spin column (Pierce, Rockford, IL) or by HPLC equipped with a size exclusion TSK $G3000SW_{XL}$ column, and the fluorescein-labeled product with a molecular weight similar to monomeric MoAb was collected.

Scheme 1. Synthesis of IA-Conjugated MoAb



2.6. SDS-PAGE Analysis. To estimate the extent of the inter- and intramolecular cross-linking caused by the conjugation reaction with $BM(PEO)_2$, electrophoresis was performed with 14% Tris−glycine gel (Invitrogen, Carlsbad, CA) in a running buffer containing 25 mM Tris, 192 mM glycine, pH 8.3, and 0.1% (w/v) SDS (Bio-Rad, Hercules, CA). The MoAb conjugates from the reactions of MoAb−$(acetylthiol)_{10}$ with $BM(PEO)_2$ at a molar ratio of $BM(PEO)_2$ to thiol ranging from 50 to 200 were treated with 5% β-mercaptoethanol (ICN Biomedicals Inc., Aurora, OH) at 90 °C for 5 min to reduce the interchain disulfide bonds. The samples were loaded on the gel together with a mixture of molecular weight standards (SeeBluePlus2, Invitrogen, Carlsbad, CA; the standards include myosin, phosphorylase B, BSA, glutamic dehydrogenase, alcohol dehydrogenase, carbonic anhydrase, myoglobin lysozyme, aprotinin, and insulin B chain). The runned gel was stained for proteins with colloidal Coomassie blue (Invitrogen, Carlsbad, CA).

2.7. Receptor-Binding Assay. To assess the receptor-binding ability of the ^{111}In labeled MoAb−$(A\text{-}S\text{-}S[PEO]_2S\text{-}S\text{-}A\text{-}IA)_n$, ^{111}In-labeled MoAb with $n = 10$ (2.2×10^6 cpm, 0.04 μM) was incubated with human integrin $\alpha_v\beta_3$ (M_w 237 000; Chemicon, Temecula, CA) at a concentration ranging from 0.1 to 0.4 μM in 32 μL PBS at 37 °C for 3 h. To assess the percentage of nonspecific binding, the binding assay was performed in the presence of a 20× molar excess of cold MoAb−$(A\text{-}S\text{-}S[PEO]_2S\text{-}S\text{-}A\text{-}IA)_{10}$ to integrin $\alpha_v\beta_3$. In a separate experiment, ^{111}In-labeled MoAb−$(A\text{-}S\text{-}S[PEO]_2S\text{-}S\text{-}A\text{-}IA)_n$ with $n = 5$ and 10 (2.2×10^6 cpm, 0.04 μM MoAb) were incubated with 0.4 μM $\alpha_v\beta_3$ to determine the effect of the level of IA conjugation on the receptor binding. The percent binding to the integrin $\alpha_v\beta_3$ was analyzed by size exclusion HPLC. The binding of the ^{111}In-labeled MoAb to $\alpha_v\beta_3$ shifted the HPLC peak (9.5 min) for the ^{111}In-labeled MoAb to a higher molecular weight peak (6.8 min). The addition of the molar excess of MoAb−$(A\text{-}S\text{-}S[PEO]_2S\text{-}S\text{-}A\text{-}IA)_{10}$ completely blocked the formation of the higher molecular weight complex.

2.8. Tumor Model. A human M21 melanoma cell line that expresses $\alpha_v\beta_3$ was used to make an in vivo tumor model. Human M21 melanoma cells initially received from Dr. David Cheresh (Scripps Research Institutes, La Jolla, CA) were

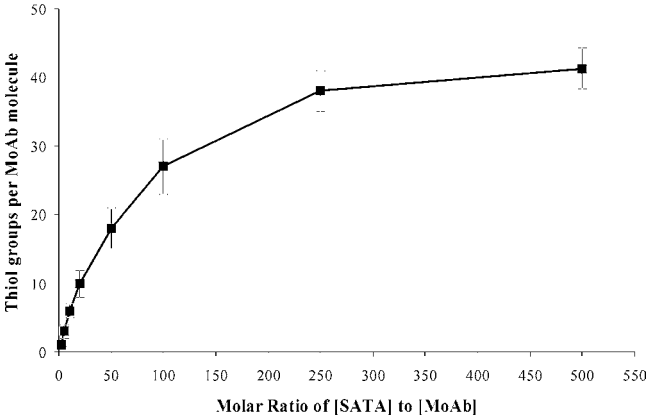


Figure 1. Relationship between level of SATA conjugation to MoAb and SATA to MoAb reaction molar ratios. [MoAb] = 27 μM. The number of SATA conjugated per MoAb increased up to 40 as the reaction concentration of SATA was increased. The values represent means and standard deviations. $N = 5$.

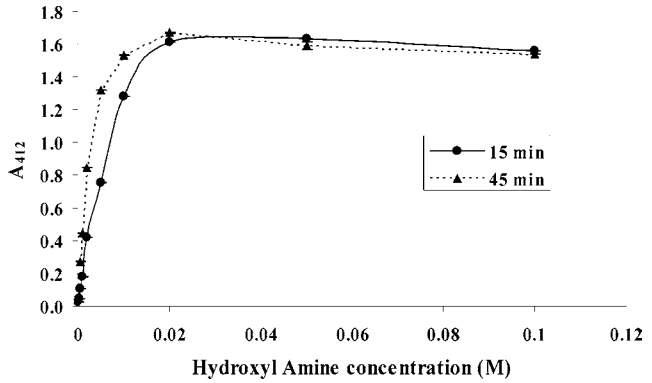


Figure 2. Relationship between hydroxylamine concentration and deacylation level of the S-acetyl protecting group of MoAb−(SATA). [SATA] in MoAb−$(SATA)_n$ = 0.21 mM. The concentration of hydroxylamine ranged from 0.5 to 100 mM. The reaction was performed at pH 7.2 at room temperature for 15 or 45 min. The optimal concentration of hydroxylamine was determined to be 0.02 M for these reaction times. [−SH] was titrated with Ellman's reagent. The absorbance at 412 nm was plotted vs hydroxylamine concentration. The values represent means and standard deviations. $N = 3$.

cultured in RPMI 1640 supplemented with 10% FBS and 1% penicillin−streptomycin under a humidified atmosphere with 5% CO_2. The cell culture medium was then exchanged with PBS. Tumor xenografts were established by inoculation of 3×10^6 cells subcutaneously into the right flank of athymic mice (NCI−DCT, Frederick, MD).

2.9. Biodistribution Studies. Animal experiments were performed under a protocol approved by the NIH Animal Care and Use Committee. Biodistribution was performed when the tumor size reached approximately 0.5 cm^3. Groups of five mice with M21 tumor were injected iv with the ^{111}In-labeled MoAb−(A-*S*-S[PEO]$_2$S-*S*-A-IA)$_{10}$ (MoAb−IA_{10}) (2 μCi/0.2 μg) with or without coinjection of 240 μg IA in 0.2 mL PBS containing 1% BSA. Similarly, nude mice with tumor were injected with the ^{125}I-labeled MoAb−IA_{10} (2 μCi/0.5 μg). The ^{111}In product and the ^{125}I product with >70% binding ability to $\alpha_v\beta_3$ at 0.4 μM were used for the biodistribution studies. The animals were euthanized at 4, 21, and 44 h by CO_2 inhalation and exsanguinated by cardiac puncture before dissection. Blood and various organs were removed and weighed, and their decay-corrected radioactivity counts were measured with a γ-counter (Wallac, Inc., Perkin-Elmer, Inc., Boston, MA). The percentage of injected dose per gram (% ID/g) of the blood or each organ was calculated and was normalized to a 20 g mouse. The whole-body (WB) radioactivity count was obtained by adding the

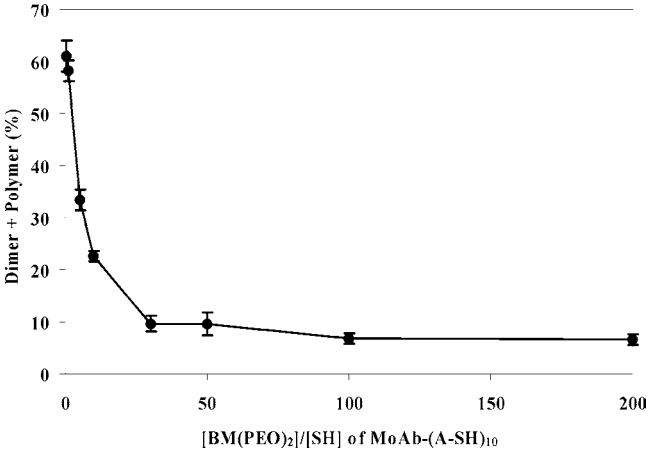


Figure 3. Relationship between formation of MoAb dimer plus polymer and $BM(PEO)_2$ to MoAb−$(A\text{-}SH)_{10}$ reaction molar ratios. MoAb−$(A\text{-}SH)_{10}$ at 15 μM MoAb was reacted with $BM(PEO)_2$ in sodium phosphate buffer, pH 7.2, at room temperature for 0.5 h. The products were analyzed by size exclusion HPLC. The formation of higher molecular weight MoAb due to the intermolecular cross-linking decreased as the concentration of the homobifunctional cross-linker $BM(PEO)_2$ was increased. The formation of the higher molecular weight MoAb became <10% when a 50× molar excess of $BM(PEO)_2$ to the A-SH concentration was reacted with MoAb−$(A\text{-}SH)_{10}$. The values are means and standard deviations. $N = 3$.

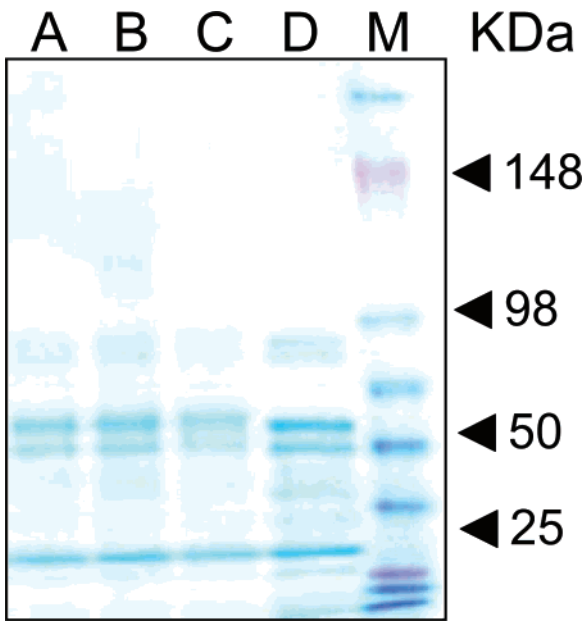


Figure 4. SDS PAGE analysis of MoAb−$(COCH_2\text{-}S\text{-}SM[PEO]_2)_{10}$. MoAb−$(COCH_2SH)_{10}$ (15 μM MoAb) was reacted with $BM(PEO)_2$ in sodium phosphate buffer, pH 7.2, at room temperature for 30 min. The products were treated with 2-mercaptoethanol before the SDS PAGE analysis to reduce the interchain disulfide bridges. Lanes: (A) [BM-$(PEO)_2$]/[-SH] = 50; (B) [$BM(PEO)_2$]/[-SH] = 100; (C) [$BM(PEO)_2$]/[-SH] = 200; (D) MoAb; (M) molecular weight markers. All three samples showed bands corresponding to 25 and 50 kDa fragments indicating that the homobifunctional cross-linker $BM(PEO)_2$ reacted at a [$BM(PEO)_2$]/[-SH] ratio higher than 50 did not cause the inter- and intramolecular cross-linking of MoAb.

radioactivity of all organs and that of the carcass measured by the γ-counter, and the whole-body radioactivity was expressed as the percentage of the injected dose (% ID).

2.10. Ex Vivo Fluorescence Microscopy. Mice with M21 tumor were injected iv with the fluorescein-labeled MoAb−IA_{10} (200 μg) in 0.2 mL PBS, pH 7.2, containing 1% BSA. The animals were euthanized at 4 and 21 h by CO_2 inhalation and exsanguinated by cardiac puncture before dissection. The animals were injected iv with rhodamine−lectin (1 mg) in 0.2

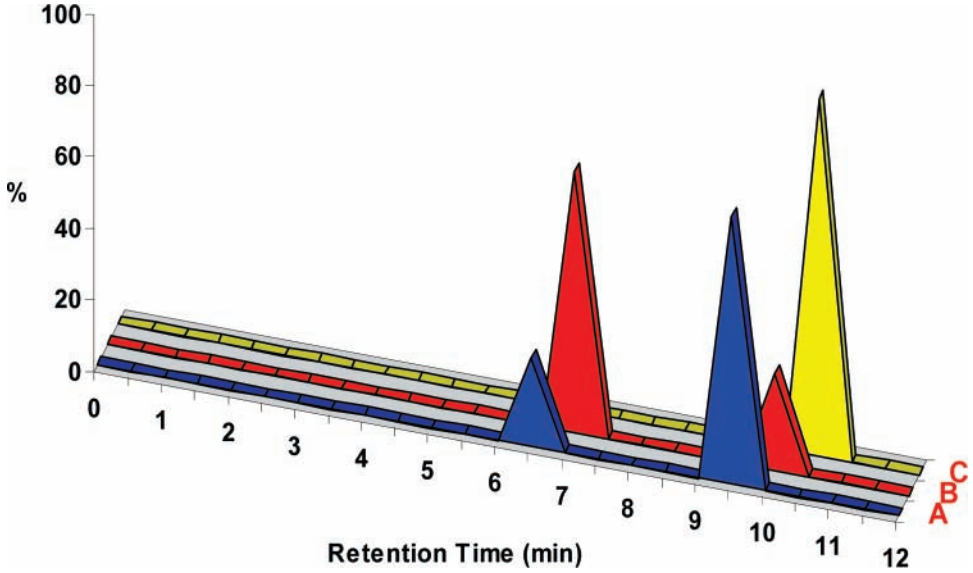


Figure 5. Size exclusion HPLC profile for binding of ^{111}In-labeled MoAb−IA$_n$ to integrin $\alpha_v\beta_3$. (A) 25% of the total ^{111}In-labeled MoAb−IA$_5$ was bound to the receptor at 0.4 μM, whereas (B) 73% of the total ^{111}In-labeled MoAb−IA$_{10}$ was bound. (C) The receptor binding was completely blocked when ^{111}In-labeled MoAb−IA$_n$ was incubated with 0.4 μM $\alpha_v\beta_3$ in the presence of 8 μM cold MoAb−IA$_{10}$.

mL PBS 5 min before the animals were euthanized to delineate vessels during observation with fluorescence microscopy (Olympus, Melville, NY). Tumors were dissected, mounted, and counterstained with 4,6-diamidino-2-phenylindole (DAPI).

2.11. Statistical Analysis. Statistical analysis was performed using ANOVA for comparing multiple groups, and the Student's *t* test was performed for unpaired data between two groups. All tests were two-sided, and a probability value (*P*) of less than 0.05 was considered significant.

3. RESULTS AND DISCUSSION

3.1. Chemistry. This research was undertaken to explore the use of antibody as a carrier of peptidomimetic antagonists specific for integrin $\alpha_v\beta_3$ receptor to improve its receptor-binding affinity and to target $\alpha_v\beta_3$ receptor on neovasculature. To achieve this goal, T101, an irrelevant MoAb to $\alpha_v\beta_3$ receptor, was used as a carrier of a peptidomimetic integrin $\alpha_v\beta_3$ antagonist, 4-[2-(3,4,5,6-tetrahydropyrimidine-2-ylamino)ethyloxy]benzoyl-2-(*S*)-aminoethylsulfonylamino-β-alanine (IA). Sulfhydryl selective reactions were used to conjugate IA to MoAb, because the sulfhydryl group could be readily quantified with Ellman's reagent. High levels of IA molecules were conjugated to MoAb in three steps (Scheme 1). In the first step, a large number of *S*-acetylthioacetato (ATA) moieties were conjugated to MoAb upon the reaction with *N*-succinimidyl-*S*-acetylthioacetate (SATA) at a molar excess. The number of ATA molecules conjugated per MoAb increased proportionally to the concentration of SATA, and the conjugation was then leveled off at approximately 40 ATA molecules conjugated per MoAb (Figure 1). The products MoAb−(ATA)$_n$ with $n = 5$ and 10 were used for the further reactions. In a separate reaction, the *S*-acetylthioaceto moiety was conjugated to IA. The concentration of the *S*-acetylthioaceto moiety was estimated by titrating the sulfhydryl group by the Ellman's reagent following removal of the protecting acetyl group from the *S*-acetylthioaceto moiety. Hydroxylamine was used for this deacetylation reaction. The optimum concentration of hydroxylamine to complete the deacetylation was determined to be 0.02 M (Figure 2). Hydroxylamine at 0.02 M in phosphate buffer, pH 7.2, completed the deacetylation within 15 min at room temperature without interfering with the addition of the mercaptoacetyl (A-SH) of MoAb−(A-SH)$_n$ with $n = 5$ or 10 to the maleimido group of BM[PEO]$_2$. Then, the MoAb−(A-SH)$_n$ and IA−(A-SH) were coupled via stepwise reactions with a homobifunctional reagent, BM[PEO]$_2$. We used BM[PEO]$_2$ with an eight-atom water-soluble polyether spacer arm to minimize the insolubility of the products and keep IA molecules away from MoAb to achieve more effective binding of IA to the $\alpha_v\beta_3$ receptor.

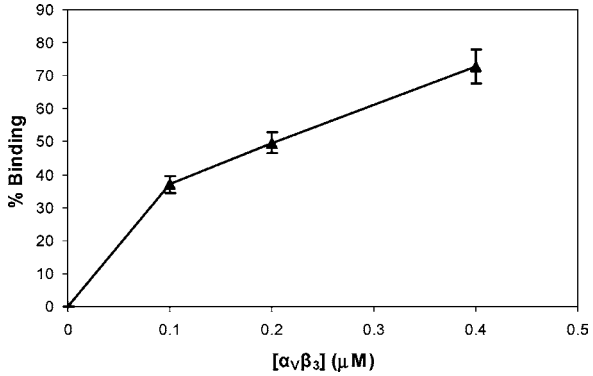


Figure 6. Percent binding of ^{111}In-labeled MoAb−IA$_{10}$ to $\alpha_v\beta_3$. ^{111}In-labeled MoAb−IA$_{10}$ (<0.04 μM MoAb) was incubated with $\alpha_v\beta_3$ integrin (M_w 237 KDa) at 0.1, 0.2, and 0.4 μM at 37 °C for 3 h and analyzed with size exclusion HPLC. The percent binding increased proportionally to the concentration of $\alpha_v\beta_3$. The percent binding increased to 73% when $\alpha_v\beta_3$ concentration was 0.4 μM.

The major focus was on optimizing the reaction concentrations, molar ratios, and the reaction pH to conjugate high levels of IA to MoAb without causing the inter- and intramolecular cross-linking of MoAb. First, an SH group was generated in the presence of 1 mM EDTA at pH <7.2 when the acetyl-protecting group of ATA of MoAb−(ATA)$_n$ was deacetylated by hydroxylamine. Second, we used MoAb−(A-SH)$_n$ with the MoAb concentration of <15 μM when conjugated with (BM-[PEO]$_2$). Finally, we used a molar excess of a homobifunctional cross-linker, BM[PEO]$_2$, to the sulfhyryl group of MoAb−(A-SH)$_n$ to minimize the inter- and intramolecular cross-linking of MoAb. Consequently, we synthesized the final product MoAb−(A-*S*-S[PEO]$_2$S-*S*-A-IA)$_n$ with $n = 5$ and 10. The results of size exclusion HPLC analysis (Figure 3) and SDS PAGE electrophoresis profile (Figure 4) indicated that the formation of dimeric and polymeric forms of MoAb was less than 9.6% of the total when MoAb−(A-SH)$_n$ was reacted with ≥50× molar excess of BM−[PEO]$_2$ to the sulfhydryl and the resulting MoAb−(COCH$_2$-*S*-SM[PEO]$_2$)$_n$ was reacted with a 4× molar

Table 1. Biodistribution of ^{111}In- and ^{125}I-Labeled MoAb−IA$_{10}$ in M21 Tumor-Bearing Mice (% ID/g, mean ± S.D, $N = 5$)

	4 h		21 h		44 h	
	^{111}In	^{125}I	^{111}In	^{125}I	^{111}In	^{125}I
blood	6.67 ± 1.00[a]	11.41 ± 1.26	0.49 ± 0.12[a]	4.83 ± 0.36	0.16 ± 0.05[a]	2.69 ± 0.62
spleen	36.95 ± 3.66[a]	4.91 ± 1.97	42.41 ± 9.57[a]	1.65 ± 0.08	25.05 ± 4.16[a]	0.76 ± 0.22
liver	49.74 ± 5.54[a]	5.09 ± 1.06	49.06 ± 8.24[a]	1.48 ± 0.18	31.85 ± 4.74[a]	0.78 ± 0.15
stomach	0.84 ± 0.16[a]	10.83 ± 0.27	0.74 ± 0.23[a]	2.39 ± 0.62	1.07 ± 1.83[c]	0.77 ± 0.15
intestine	2.91 ± 0.56[c]	2.21 ± 0.55	1.82 ± 0.47[a]	0.72 ± 0.19	0.98 ± 0.27[a]	0.31 ± 0.06
kidney	13.39 ± 1.23[a]	3.76 ± 0.38	8.62 ± 1.49[a]	0.93 ± 0.06	7.99 ± 1.22[a]	0.59 ± 0.14
heart	2.03 ± 0.63[a]	3.63 ± 0.58	1.01 ± 0.39[a]	1.71 ± 0.42	0.73 ± 0.24[c]	0.75 ± 0.13
lung	5.21 ± 0.86[c]	5.77 ± 0.37	2.63 ± 1.07[c]	2.31 ± 0.05	1.09 ± 0.44[c]	1.35 ± 0.41
muscle	0.37 ± 0.07[a]	0.60 ± 0.11	0.19 ± 0.05[c]	0.29 ± 0.08	0.14 ± 0.05[c]	0.19 ± 0.00
bone	4.78 ± 0.60[a]	1.79 ± 0.23	4.98 ± 2.15[a]	0.66 ± 0.15	2.50 ± 0.54[a]	0.36 ± 0.07
tumor	1.49 ± 0.15[c]	1.81 ± 0.41	0.96 ± 0.40[b]	1.53 ± 0.50	0.63 ± 0.03[c]	0.80 ± 0.20
whole body (% ID)	88.24 ± 1.24[a]	48.16 ± 4.07	76.80 ± 2.87[a]	20.57 ± 1.14	63.71 ± 2.01[a]	11.67 ± 3.01

[a] $P < 0.01$. [b] $P < 0.05$. [c] $P > 0.05$.

excess of IA−(A-SH). To investigate the receptor binding activity, the products MoAb−(A-*S*-S[PEO]$_2$S-*S*-A-IA)$_n$ with $n = 5$ and 10 IA molecules were conjugated with 2-(*p*-isothiocyanatobenzyl)cyclohexyl−DTPA, labeled with ^{111}In, and purified by size exclusion HPLC to obtain monomeric MoAb products. Comparing ^{111}In-labeled MoAb−(A-*S*-S[PEO]$_2$S-*S*-A-IA)$_n$ with $n = 5$ and 10, the product with $n = 10$ showed a higher percent binding (72.9%) to 0.4 μM $\alpha_v\beta_3$ than that (25.0%) with $n = 5$ (Figure 5). The percent binding also increased proportionally to the concentration of $\alpha_v\beta_3$ up to 0.4 μM, which was the highest concentration available (Figure 6). The binding was blocked by adding a 20× molar excess of cold MoAb−(A-*S*-S[PEO]$_2$S-*S*-A-IA)$_{10}$ to $\alpha_v\beta_3$ (Figure 5). Since MoAb−(A-*S*-S[PEO]$_2$S-*S*-A-IA)$_n$ with $n = 10$ showed higher affinity to $\alpha_v\beta_3$ than that with $n = 5$, MoAb−(A-*S*-S[PEO]$_2$S-*S*-A-IA)$_{10}$ (MoAb−IA$_{10}$) was radiolabeled with ^{111}In and ^{125}I for biodistribution studies.

3.2. Animal Studies. We performed comparative biodistribution studies between the ^{125}I-labeled MoAb−IA$_{10}$ and the ^{111}In-labeled MoAb−IA$_{10}$, because these two radiolabels often show large differences in organ retention due to the differences in their metabolism and the structure of the catabolites. Thus, comparative biodistribution studies between these two radiolabels would provide useful information in developing radiopharmaceuticals for tumor detection. The comparative biodistribution studies showed similar tumor uptake between the ^{125}I-labeled MoAb−IA$_{10}$ and the ^{111}In-labeled MoAb−IA$_{10}$ for a 44 h period. A slightly higher concentration of the ^{125}I-labeled MoAb−IA$_{10}$ in tumor could be accounted for by the contribution from the higher blood ^{125}I concentration, assuming that about 10% of radioactivity in the tumor is contributed from the radioactivity in blood (Table 1). In contrast to the similarity shown in tumor uptake, there were large differences in blood and organ concentrations between the ^{125}I-labeled MoAb−IA$_{10}$ and the ^{111}In-labeled MoAb−IA$_{10}$ for a 44 h period. The ^{111}In label resulted in lower radioactivity in the blood but much higher radioactivity in most organs including the liver, spleen, kidney, and bone than the ^{125}I label. The ^{125}I concentration was especially low in the liver, but high in the thyroid and the stomach, indicating that the ^{125}I label was rapidly catabolized in the liver and the ^{125}I catabolite re-entered the circulation. The ^{125}I catabolite in the circulation was either taken up by the thyroid and the stomach or excreted through the renal system as shown by low whole-body retention (12% ID at 44 h) of the ^{125}I label (Table 1). The ^{111}In label was taken up primarily by the liver, spleen, and kidney. However, only a little ^{111}In activity was cleared from those organs during a 44 h period (Table 1), indicating that the ^{111}In product is catabolized more slowly or the ^{111}In catabolites are eliminated more slowly from those organs. This slow organ clearance was reflected in high whole-body retention of the ^{111}In label with 64% ID retained at 44 h. The ^{111}In-labeled MoAb−IA$_{10}$ also showed much higher liver uptake but lower blood retention than ^{111}In-labeled MoAb without IA conjugation that we previously reported (*44*). The coinjection of the ^{111}In label with cold IA (240 μg) drastically decreased the liver uptake at 21 h ($P < 0.01$), whereas it substantially increased the ^{111}In in the blood ($P < 0.01$), tumor, and all organs except spleen and bone compared to the ^{111}In without the IA coinjection (Table 2). The mechanism of liver uptake of the radioabeled MoAb−IA$_{10}$ was not investigated, but it may be that the modified MoAb was taken up in large part by reticuloendothelial cells and in some portions by receptor-mediated uptake. High liver uptake is the major drawback for the use of MoAb−IA$_{10}$ as a carrier of the γ-emitter ^{111}In for scintigraphic imaging of tumor-induced neovasulature. Nevertheless, the rapid blood clearance, short peak tumor uptake time, and low peak tumor uptake value with prolonged tumor retention of this macromolecule appear to indicate that it was localized on angiogenic vessels mediated by binding to $\alpha_v\beta_3$ receptors. To substantiate a hypothesis that MoAb−IA$_{10}$ accumulated on angiogenic vessels but not on the tumor, the receptor-positive M21 tumors excised from the tumor-bearing nude mice 4 and 21 h after receiving FITC-labeled MoAb−IA$_{10}$ were analyzed by a fluorescence microscope. The fluorescence microscopic analysis showed that FITC−MoAb−IA$_{10}$ outlined neovasculatures but not tumor cells at 4 and 21 h (Figure 7). The neovasculatures outlined with FITC−MoAb−IA$_{10}$ were superimposed with blood vessels outlined with rhodamine−lectin. This fluorescence microscopic analysis supports the hypothesis that the ^{111}In-labeled MoAb−IA$_{10}$ accumulated on the neovasculatures via binding to $\alpha_v\beta_3$ receptors. In conclusion, MoAb−IA$_{10}$, which clears rapidly from the circulation and accumulates in tumor-induced blood vessels without accumulating in $\alpha_v\beta_3$-expressing tumors, was synthesized. High retention in the liver and kidney was shown to be a drawback for the use of the ^{111}In-labeled MoAb−IA$_{10}$ in scintigraphic detection of tumors near the abdomen, although

Table 2. Biodistribution of ^{111}In-Labeled MoAb−IA$_{10}$ with and without 240 μg IA Coinjection in M21 Tumor-Bearing Mice at 21 h (% ID/g, mean ± S.D, $N = 5$)

organ	without IA coinjection	with 240 μg IA coinjection
blood	0.49 ± 0.12[a]	2.27 ± 1.30
spleen	42.41 ± 9.57[c]	39.24 ± 8.14
liver	49.06 ± 8.24[a]	28.90 ± 2.76
stomach	0.74 ± 0.23[a]	1.27 ± 0.30
intestine	1.82 ± 0.47[a]	3.37 ± 0.25
kidney	8.62 ± 1.49[c]	9.26 ± 1.58
heart	1.01 ± 0.39[a]	1.67 ± 0.14
lung	2.63 ± 1.07[b]	3.71 ± 0.59
muscle	0.19 ± 0.05[a]	0.37 ± 0.10
bone	4.98 ± 2.15[c]	5.11 ± 0.85
tumor	0.96 ± 0.40[b]	1.64 ± 0.57
whole body (% ID)	76.80 ± 2.87[b]	71.53 ± 3.91

[a] $P < 0.01$. [b] $P < 0.05$. [c] $P > 0.05$.

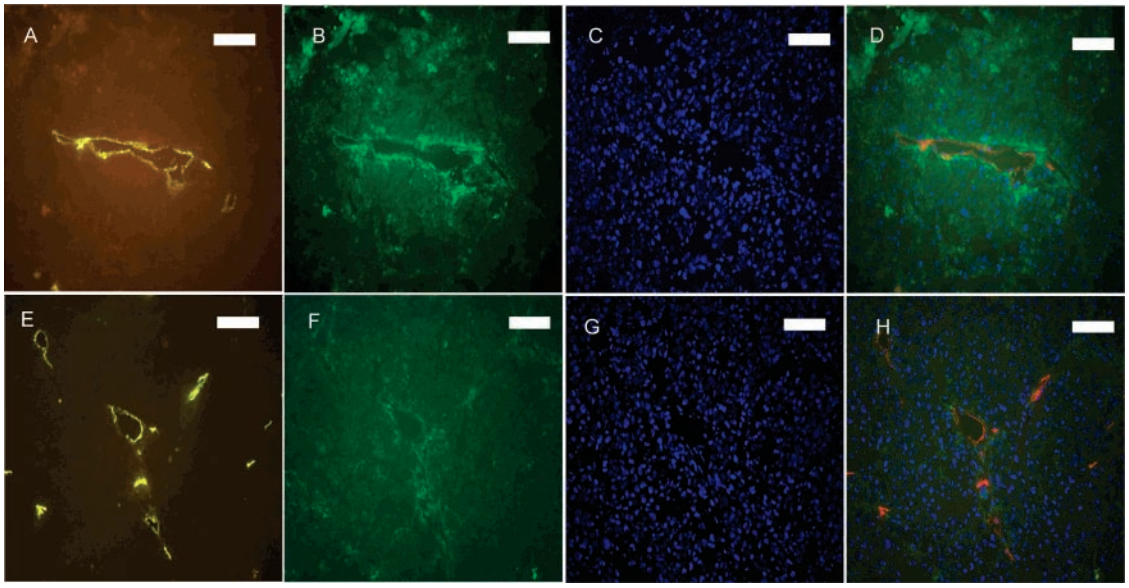


Figure 7. Fluorescence microscopy of $\alpha_v\beta_3$-expressing M21 tumors. Mice with M21 tumor were injected iv with the fluorescein-labeled MoAb−IA_{10} (200 μg) in 0.2 mL PBS, pH 7.2, containing with 1% BSA. The animals were euthanized at 4 h (A−D) and 21 h (E−H) by CO_2 inhalation and exsanguinated by cardiac puncture before dissection. The animals were injected iv with rhodamine−lectin (1 mg) in 0.2 mL PBS 5 min before they were euthanized to delineate vessels during observation with fluorescence microscope. (A,E) rhodamine−lectin; (B,F) FITC-labeled MoAb−IA_{10}; (C,G) DAPI; (D,H) merge. Bar represents 100 μm.

the tumor-to-blood ratio reached 3.9 at 43 h postinjection. In contrast, the tumor-to-liver and tumor-to-kidney ratios became ≥1 at 43 h for the ^{125}I-labeled MoAb−IA_{10}, but slow clearance from blood was the drawback for the ^{125}I-labeled MoAb−IA_{10} because this slow blood clearance would delay imaging time substantially (Table 1). Further optimization of tumor targeting methods is needed to improve angiogenesis detection agents. We are currently investigating a pretargeting approach using an avidin−biotin system to amplify tumor-to-background ratios to image tumor-induced neovasculature.

ACKNOWLEDGMENT

We thank Colleen Henrichsen for editorial assistance and Dr. Gouri S. Jas for reviewing this manuscript.

LITERATURE CITED

(1) Risau, W. (1995) Differentiation of endothelium. *FASEB J. 9*, 926−933.
(2) Takagi, J., and Springer, T. A. (2002) Integrin activation and structural rearrangement. *Immunol. Rev. 186*, 141−163.
(3) Clezardin, P. (1998) Recent insights into the role of integrins in cancer metastasis. *Cell. Mol. Life Sci. 54*, 541−548.
(4) Folkman, J. (1995) Angiogenesis in cancer, vascular, rheumatoid and other disease. *Nat. Med. 1*, 27−31.
(5) Stromblad, S., and Cheresh, D. A. (1996) Integrins, angiogenesis and vascular cell survival. *Chem. Biol. 3*, 881−885.
(6) Ruoslahti, E., and Pierschbacher, M. D. (1986) Arg-Gly-Asp: a versatile cell recognition signal. *Cell 44*, 517−518.
(7) Haubner, R., Wester, H. J., Reuning, U., Senekowitsch-Schmidtke, R., Diefenbach, B., Kessler, H., Stocklin, G., and Schwaiger, M. (1999) Radiolabeled $\alpha_v\beta_3$ integrin antagonists: a new class of tracers for tumor targeting. *J. Nucl. Med. 40*, 1061−1071.
(8) van Hagen, P. M., Breeman, W. A., Bernard, H. F., Schaar, M., Mooij, C. M., Srinivasan, A., Schmidt, M. A., Krenning, E. P., and de Jong, M. (2000) Evaluation of a radiolabelled cyclic DTPA-RGD analogue for tumour imaging and radionuclide therapy. *Int. J. Cancer 90*, 186−198.
(9) Harris, T. D., Kalogeropoulos, S., Nguyen, T., Liu, S., Bartis, J., Ellars, C., Edwards, S., Onthank, D., Silva, P., Yalamanchili, P., Robinson, S., Lazewatsky, J., Barrett, J., and Bozarth, J. (2003) Design, synthesis, and evaluation of radiolabeled integrin $\alpha_v\beta_3$ receptor antagonists for tumor imaging and radiotherapy. *Cancer Biother. Radiopharm. 18*, 627−641.
(10) Chen, X., Park, R., Tohme, M., Shahinian, A. H., Bading, J. R., and Conti, P. S. (2004) MicroPET and autoradiographic imaging of breast cancer α_v-integrin expression using 18F- and 64Cu-labeled RGD peptide. *Bioconjugate Chem. 15*, 41−49.
(11) Haubner, R., Bruchertseifer, F., Bock, M., Kessler, H., Schwaiger, M., and Wester, H. J. (2004) Synthesis and biological evaluation of a (99m)Tc-labelled cyclic RGD peptide for imaging the $\alpha_v\beta_3$ expression. *Nuklearmedizin 43*, 26−32.
(12) Chen, X., Sievers, E., Hou, Y., Park, R., Tohme, M., Bart, R., Bremner, R., Bading, J. R., and Conti, P. S. (2005) Integrin $\alpha_v\beta_3$-targeted imaging of lung cancer. *Neoplasia 7*, 271−279.
(13) Naimushin, Y. A., and Mazurov, A. V. (2005) Ability of different glycoprotein IIb-IIIa ligands to support platelet aggregation induced by activating antibody CRC54. *Biochemistry (Moscow, Russ. Fed.) 70*, 782−789.
(14) DeNardo, S. J., Burke, P. A., Leigh, B. R., O'Donnell, R. T., Miers, L. A., Kroger, L. A., Goodman, S. L., Matzku, S., Jonczyk, A., Lamborn, K. R., and DeNardo, G. L. (2000) Neovascular targeting with cyclic RGD peptide (cRGDf-ACHA) to enhance delivery of radioimmunotherapy. *Cancer Biother. Radiopharm. 15*, 71−79.
(15) Burke, P. A., DeNardo, S. J., Miers, L. A., Kukis, D. L., and DeNardo, G. L. (2002) Combined modality radioimmunotherapy. Promise and peril. *Cancer 94*, 1320−1331.
(16) Bernard, B., Capello, A., van Hagen, M., Breeman, W., Srinivasan, A., Schmidt, M., Erion, J., van Gameren, A., Krenning, E., and de Jong, M. (2004) Radiolabeled RGD-DTPA-Tyr3-octreotate for receptor-targeted radionuclide therapy. *Cancer Biother. Radiopharm. 19*, 173−180.
(17) Capello, A., Krenning, E. P., Bernard, B. F., Breeman, W. A., van Hagen, M. P., and de Jong, M. (2004) Increased cell death after therapy with an Arg-Gly-Asp-linked somatostatin analog. *J. Nucl. Med. 45*, 1716−1720.
(18) Chen, X., Hou, Y., Tohme, M., Park, R., Khankaldyyan, V., Gonzales-Gomez, I., Bading, J. R., Laug, W. E., and Conti, P. S. (2004) Pegylated Arg-Gly-Asp peptide: 64Cu labeling and PET imaging of brain tumor $\alpha_v\beta_3$-integrin expression. *J. Nucl. Med. 45*, 1776−1783.
(19) Chen, X., Liu, S., Hou, Y., Tohme, M., Park, R., Bading, J. R., and Conti, P. S. (2004) MicroPET imaging of breast cancer α_v-integrin expression with 64Cu-labeled dimeric RGD peptides. *Mol. Imaging Biol. 6*, 350−359.
(20) Li, L., Wartchow, C. A., Danthi, S. N., Shen, Z., Dechene, N., Pease, J., Choi, H. S., Doede, T., Chu, P., Ning, S., Lee, D. Y., Bednarski, M. D., and Knox, S. J. (2004) A novel antiangiogenesis

therapy using an integrin antagonist or anti-Flk-1 antibody coated 90Y-labeled nanoparticles. *Int. J. Radiat. Oncol. Biol. Phys. 58*, 1215−1227.

(21) Janssen, M., Frielink, C., Dijkgraaf, I., Oyen, W., Edwards, D. S., Liu, S., Rajopadhye, M., Massuger, L., Corstens, F., and Boerman, O. (2004) Improved tumor targeting of radiolabeled RGD peptides using rapid dose fractionation. *Cancer Biother. Radiopharm. 19*, 399−404.

(22) Onthank, D. C., Liu, S., Silva, P. J., Barrett, J. A., Harris, T. D., Robinson, S. P., and Edwards, D. S. (2004) ^{90}Y and ^{111}In complexes of a DOTA-conjugated integrin $\alpha_v\beta_3$ receptor antagonist: different but biologically equivalent. *Bioconjugate Chem. 15*, 235−241.

(23) Wu, Y., Zhang, X., Xiong, Z., Cheng, Z., Fisher, D. R., Liu, S., Gambhir, S. S., and Chen, X. (2005) MicroPET imaging of glioma integrin $\alpha_v\beta_3$ expression using (64)Cu-labeled tetrameric RGD peptide. *J. Nucl. Med. 46*, 1707−1718.

(24) Capello, A., Krenning, E. P., Bernard, B. F., Breeman, W. A., Erion, J. L., and de Jong, M. (2006) Anticancer activity of targeted proapoptotic peptides. *J. Nucl. Med. 47*, 122−129.

(25) Haubner, R., Wester, H. J., Burkhart, F., Senekowitsch-Schmidtke, R., Weber, W., Goodman, S. L., Kessler, H., and Schwaiger, M. (2001) Glycosylated RGD-containing peptides: tracer for tumor targeting and angiogenesis imaging with improved biokinetics. *J. Nucl. Med. 42*, 326−336.

(26) Li, J., Ji, J., Holmes, L. M., Burgin, K. E., Barton, L. B., Yu, X., Wagner, T. E., and Wei, Y. (2004) Fusion protein from RGD peptide and Fc fragment of mouse immunoglobulin G inhibits angiogenesis in tumor. *Cancer Gene Ther. 11*, 363−370.

(27) Kok, R. J., Schraa, A. J., Bos, E. J., Moorlag, H. E., Asgeirsdottir, S. A., Everts, M., Meijer, D. K., and Molema, G. (2002) Preparation and functional evaluation of RGD-modified proteins as $\alpha_v\beta_3$ integrin directed therapeutics. *Bioconjugate Chem. 13*, 128−135.

(28) Schraa, A. J., Kok, R. J., Botter, S. M., Withoff, S., Meijer, D. K., de Leij, L. F., and Molema, G. (2004) RGD-modified anti-CD3 antibodies redirect cytolytic capacity of cytotoxic T lymphocytes toward $\alpha_v\beta_3$-expressing endothelial cells. *Int. J. Cancer 112*, 279−285.

(29) Burnett, C. A., Xie, J., Quijano, J., Shen, Z., Hunter, F., Bur, M., Li, K. C., and Danthi, S. N. (2005) Synthesis, in vitro, and in vivo characterization of an integrin $\alpha_v\beta_3$-targeted molecular probe for optical imaging of tumor. *Bioorg. Med. Chem. 13*, 3763−3771.

(30) Hood, J. D., Bednarski, M., Frausto, R., Guccione, S., Reisfeld, R. A., Xiang, R., and Cheresh, D. A. (2002) Tumor regression by targeted gene delivery to the neovasculature. *Science 296*, 2404−2407.

(31) Reardan, D. T., Meares, C. F., Goodwin, D. A., McTigue, M., David, G. S., Stone, M. R., Leung, J. P., Bartholomew, R. M., and Frincke, J. M. (1985) Antibodies against metal chelates. *Nature (London) 316*, 265−268.

(32) Goodwin, D. A., Meares, C. F., McCall, M. J., McTigue, M., and Chaovapong, W. (1988) Pre-targeted immunoscintigraphy of murine tumors with indium-111-labeled bifunctional haptens. *J. Nucl. Med. 29*, 226−234.

(33) Barbet, J., Peltier, P., Bardet, S., Vuillez, J. P., Bachelot, I., Denet, S., Olivier, P., Leccia, F., Corcuff, B., Huglo, D., Proye, C., Rouvier, E., Meyer, P., and Chatal, J. F. (1998) Radioimmunodetection of medullary thyroid carcinoma using indium-111 bivalent hapten and anti-CEA x anti-DTPA-indium bispecific antibody. *J. Nucl. Med. 39*, 1172−1178.

(34) Corneillie, T. M., Whetstone, P. A., Lee, K. C., Wong, J. P., and Meares, C. F. (2004) Converting weak binders into infinite binders. *Bioconjugate Chem. 15*, 1389−1391.

(35) Corneillie, T. M., Lee, K. C., Whetstone, P. A., Wong, J. P., and Meares, C. F. (2004) Irreversible engineering of the multielement-binding antibody 2D12.5 and its complementary ligands. *Bioconjugate Chem. 15*, 1392−1402.

(36) Sharkey, R. M., Cardillo, T. M., Rossi, E. A., Chang, C. H., Karacay, H., McBride, W. J., Hansen, H. J., Horak, I. D., and Goldenberg, D. M. (2005) Signal amplification in molecular imaging by pretargeting a multivalent, bispecific antibody. *Nat. Med. 11*, 1250−1255.

(37) Hnatowich, D. J., Virzi, F., and Rusckowski, M. (1987) Investigations of avidin and biotin for imaging applications. *J. Nucl. Med. 28*, 1294−1302.

(38) Paganelli, G., Magnani, P., Zito, F., Villa, E., Sudati, F., Lopalco, L., Rossetti, C., Malcovati, M., Chiolerio, F., and Seccamani, E. (1991) Three-step monoclonal antibody tumor targeting in carcino-embryonic antigen-positive patients. *Cancer Res. 51*, 5960−5966.

(39) Axworthy, D. B., Fritzberg, A. R., Hylarides, M. D., Mallett, R. W., Theodore, L. J., Gustavson, L. M., Su, F.-M., Beaumier, P. L., and Reno, J. M. (1994) Preclinical evaluation of an antitumor monoclonal antibody/streptavidin conjugate for pretargeted ^{90}Y radioimmunotherapy in a mouse xenograft model. *J. Immunother. 16*, 158.

(40) Cremonesi, M., Ferrari, M., Chinol, M., Stabin, M. G., Grana, C., Prisco, G., Robertson, C., Tosi, G., and Paganelli, G. (1999) Three-step radioimmunotherapy with yttrium-90 biotin: dosimetry and pharmacokinetics in cancer patients. *Eur. J. Nucl. Med. 26*, 110−120.

(41) Sato, N., Hassan, R., Axworthy, D. B., Wong, K. J., Yu, S., Theodore, L. J., Lin, Y., Park, L., Brechbiel, M. W., Pastan, I., Paik, C. H., and Carrasquillo, J. A. (2005) Pretargeted radioimmunotherapy of mesothelin-expressing cancer using a tetravalent single-chain Fv-streptavidin fusion protein. *J. Nucl. Med. 46*, 1201−1209.

(42) Goldenberg, D. M., Sharkey, R. M., Paganelli, G., Barbet, J., and Chatal, J. F. (2006) Antibody pretargeting advances cancer radioimmunodetection and radioimmunotherapy. *J. Clin. Oncol. 24*, 823−834.

(43) Bradford, M. M. (1976) A rapid and sensitive method for the quantitation of microgram quantities of protein utilizing the principle of protein-dye binding. *Anal. Biochem. 72*, 248−254.

(44) Kinuya, S., Jeong, J. M., Garmestani, K., Saga, T., Camera, L., Brechbiel, M. W., Gansow, O. A., Carrasquillo, J. A., Neumann, R. D., and Paik, C. H. (1994) Effect of metabolism on retention of indium-111-labeled monoclonal antibody in liver and blood. *J. Nucl. Med. 35*, 1851−1857.

(45) Camera, L., Kinuya, S., Garmestani, K., Wu, C., Brechbiel, M. W., Pai, L. H., McMurry, T. J., Gansow, O. A., Pastan, I., Paik, C. H., Carrasquillo, J. A. (1994) Evaluation of the serum stability and in vivo biodistribution of CHX-DTPA and other ligands for yttrium labeling of monoclonal antibodies. *J. Nucl. Med. 35*, 882−889.

BC0603485

Synthesis and Biological Assay of GSH Functionalized Fluorescent Quantum Dots for Staining *Hydra vulgaris*

Claudia Tortiglione,[†] Alessandra Quarta,[‡] Angela Tino,[†] Liberato Manna,[‡] Roberto Cingolani,[‡] and Teresa Pellegrino*[,‡]

CNR, Istituto di Cibernetica "E Caianiello", Via Campi Flegrei, 34, 80078 Pozzuoli, Italy, and National Nanotechnology Laboratory of CNR-INFM, Unità di ricerca IIT and Scuola Superiore ISUFI, Via per Arnesano, 73100 Lecce, Italy Received November 12, 2006; Revised Manuscript Received January 31, 2007

Quantum dots (QDs) have been used extensively as fluorescent markers in several studies on living cells. Here, we report the synthesis of conjugates based on glutathione (GSH) and QDs (GSH−QDs) and we prove how these functionalized fluorescent probes can be used for staining a freshwater invertebrate called *Hydra vulgaris*. GSH is known to promote *Hydra* feeding response by inducing mouth opening. We demonstrate that GSH−QDs as well are able to elicit biological activity in such an animal, which results in the fluorescent staining of *Hydra*. GSH−QDs, once they reach the gastric region, are internalized by endodermal cells. The efficiency of GSH−QD internalization increases significantly when nanoparticles are coadministrated with free GSH. We also compared the behavior of bare QDs to that of GSH−QDs both in the presence and in the absence of free GSH. The conclusions from these series of experiments point to the presence of GSH binding proteins in the endodermal cell layer and uncover a novel role played by glutathione in this organism.

INTRODUCTION

Colloidal semiconductor nanocrystals, also known as quantum dots (QDs), are emerging as a new class of inorganic fluorophores for imaging living and fixed cells in fluorescence microscopy (*1*). The QD probes have unique photophysical properties, such as size-tunable emission spectrum, narrow emission peak, broad absorption profile, and high brightness. In addition, QDs are much more stable to the permanent loss of fluorescence than conventional organic fluorophores (*2*, *3*). Therefore, they offer several advantages over standard organic dyes for multicolor, long-term, and high-sensitivity fluorescence imaging.

Recently, several strategies have been developed to deliver stable, water-soluble quantum dots (*4*). These procedures allow also to introduce on the outmost shell of the QDs specific anchoring points by which biomolecules can be conjugated to the nanoparticles. In the latest years, it has been demonstrated that these new bioconjugates are useful for applications in many of the classical immunocytochemistry protocols, as well as for *in vivo* staining of living cells on higher vertebrates (*5*). On the other hand, no studies of cell tracking, migration, or physiological response using QD functionalized with bioactive molecules have been reported on less-evolved organisms.

The tripeptide glutathione (γ-L-glutamyl-L-cysteinylglycine, GSH) has been well-known to biochemists for generations. Both the reduced form (GSH) and its oxidized dimer (GSSG) have been implicated in a variety of molecular reactions throughout the animal kingdom. Although it is best known for its role as a free radical scavenger, GSH also performs a number of other functions in cell survival and metabolism, including amino acid transport, detoxification of xenobiotics, maintenance of protein redox state, neuromodulation, and neurotransmission (*6*). Almost 50 years ago, Loomis and Lenhoff (*7*) suggested a role of GSH in signal transduction in the coelenterate *Hydra*. Hydra, together with coral, sea anemones, and jellyfish, are members of the primitive phylum Cnidaria. It is shaped as a "two-ply hollow tube", made up of both outer (ectodermal) and inner (endodermal) epithelial layers. The mesoglea, an extracellular matrix, separates the two epithelia. At the posterior end of the tube, there is a basal disk with which the *Hydra* usually attaches to a surface, whereas at the anterior end, there is a mouth surrounded by a ring of tentacles (Figure SI1, Supporting Information). The tentacles are armed with many nematocytes, which contain nematocysts (stinging capsules). The latter start the feeding process by reverting a coiled tube, which pierces and wounds the prey. In the absence of prey, GSH is the physiological stimulator of the feeding behavior (*8*), by inducing tentacle contraction and mouth opening. Grosvenor et al. (*9*) and Bellis et al. (*10*) described a class of binding sites for GSH in *Hydra* that provides the basis for the behavioral response.

Hydra is a model organism that offers several potential advantages as an investigation target by means of QDs, such as (i) the simplicity of the body structure, which allows easy detection of fluorescent probes; (ii) the dynamics of the two epithelia, as *Hydra* cells, which continuously divide, migrate and are eliminated at the apical and basal ends of the polyp, allow cell migration and tracking studies; and (iii) the regenerating capability, involving extensive remodeling and plasticity phenomena, whose temporal dynamics can be best approached by using photostable fluorescent probes. Finally, and most importantly, *Hydra* allows us to validate by a reliable assay the biological activity of GSH-conjugated QDs.

In this report, we describe the synthesis and the characterization of core−shell CdSe/ZnS QDs conjugated to glutathione for the staining of *Hydra*. The biological activity evoked by GSH−QDs in living *Hydra* animals was also studied. We found that cells lining the gastric cavity were able to internalize the bare QDs in the presence of reduced GSH in the media bath, as intense fluorescence was present in this cell type. Interestingly, in the same conditions, the efficacy of the internalization

* To whom correspondence should be addressed. teresa.pellegrino@unile.it.

[†] Istituto di Cibernetica "E Caianiello".

[‡] National Nanotechnology Laboratory of CNR-INFM, Unità di ricerca IIT and Scuola Superiore ISUFI.

10.1021/bc060355t CCC: $37.00 © 2007 American Chemical Society
Published on Web 04/19/2007

doubled in the presence of GSH-coated QDs. These results demonstrate the involvement and the activation of GSH-specific endodermal cell uptake mechanisms in *Hydra*, such as those mediated by carriers, specific receptors, or membrane metabolic enzymes into any type of living cells. GSH-functionalized nanoparticles represent the first example of fluorescent and bioactive GSH adduct suitable for specific staining of one type of tissue on *Hydra*.

MATERIALS AND METHODS

Chemicals. (1-Ethyl-3-(3-dimethylaminopropyl)carbodiimide hydrochloride) (EDC), γ-L-glutamyl-L-cysteinylglycine (GSH), 5,5′-dithiobis(2-nitrobenzoic acid) (Ellman's reagent), and 4′,6-diamidino-2-phenylindole dihydrochloride (DAPI) were purchased from Aldrich. *O*,*O*′-Bis(2-aminoethyl)octadecaethylene glycol, diamino-PEG-897) was purchased from Fluka. DL-Dithiothreitol (DTT) was purchased from Biochemika. *N*-Hydroxysuccinimide (NHS) was purchased from Pierce. Agarose gel EEO was purchased from Eppendorf. All solvents that we used had purity of analytical grade.

Synthesis of Water-Soluble Quantum Dots. TOP/TOPO-capped CdSe/ZnS core/shell QDs were prepared by following standard colloidal synthesis procedures (*11*, *12*). For fluorescence imaging, given the *Hydra* autofluorescence, we found it more convenient to work with QD samples with an emission band peaked at wavelengths longer than 590 nm. As-synthesized QDs are hydrophobic, and therefore, they were transferred into water by means of a standard procedure based on wrapping them within an amphiphilic polymer shell, which had been developed in a previous work by our group (*13*). The resulting polymer-coated particles (PC-QDs) were purified twice by high-performance liquid chromatography HPLC (Agilent1100 on a Sephacryl S-300 HR column, using 150 mM NaCl in 50 mM phosphate buffer at pH 7.0 as mobile phase). These purified PC-QDs have carboxyl groups dangling at the outer surface of the polymer layer. The concentration of the quantum dots was determined by measuring their optical absorption spectra, as their molar extinction coefficient is know from the literature (*14*). As an example, the extinction coefficient of a quantum dot sample with the first exciton peak centered at 590 nm was estimated as 258 050 cm^{-1} M^{-1} by extrapolation from the published curve (*14*).

Functionalization of Quantum Dots with Diamino-PEG 897 ($NH_2-PEG-NH_2$). The buffer of the HPLC-purified, PC-QDs was exchanged with 50 mM sodium borate buffer (pH 9.0) by using a centrifuge tube (MWCO 30 000). The same buffer was used to dissolve diamino-PEG ($NH_2-PEG-NH_2$) with molecular weight equal to 897.10. For the coupling experiments, one of the two amine groups of the diamino-PEG molecules was linked to one of the carboxyl groups present on the PC-QDs. This was achieved by using EDC as cross-linker, which induced amide bond formation (*15*). Interparticle cross-linking, due to the bridging of one or more diamino-PEG molecules between two PC-QDs via both terminal amine groups, was negligible at ratios of diamino-PEG molecules to PC-QDs equal to 500:1 or lower. Therefore, a 500:1 ratio was used in all experiments.

In a typical procedure, a buffer solution of 6 μM PC-QDs and a solution of 3 mM diamino-PEG were mixed together, after which a solution of 600 mM EDC was added to reach an excess molar ratio of EDC to PC-QDs equal to 10^5:1. The resulting solution was incubated for 3 h under vigorous stirring. To remove the excess of unreacted diamino-PEG, the solution was filtered several times through centrifuge tubes (MWCO 30 000). Diamino-PEG-functionalized QDs (PEG−QDs) were resuspended in water at a 6 μM final concentration.

Conjugation of GSH to Quantum Dots. GSH has two free carboxyl groups and a free thiol group. The COOH groups can be exploited to link the GSH to the PEG−QDs via formation of an amide bond with the free amino groups of the diamino-PEG molecules bound to the polymer shell that encases the PC-QDs. In detail, to a 6 μM solution of PEG−QDs dissolved in sodium borate buffer (pH 9.0), a 10 mM GSH solution dissolved in the same buffer was added, to reach a molar excess of GSH per PEG−QD equal to 1700:1. Borate buffer solutions containing EDC 100 mM and NHS 75 mM, respectively, were then added. The resulting solution was incubated at room temperature for 3 h under vigorous stirring. To remove the unreacted GSH, the sample was washed five times on 20 mL centrifuge filters (30 000 MWCO). In general, for the experiments carried out on *Hydra*, the sample was then reconcentrated on the filter to reach a final concentration equal to 6 μM.

Characterization by Gel Electrophoresis. Prior to gel electrophoresis, to each sample a solution containing Orange G and 30% glycerol in gel-loading buffer corresponding to 20% of the sample volume was added. 2% agarose gels were prepared in 0.5× TBE buffer. The electrophoretic run was carried out for 60 min at 100 V. After the run, the gel was observed under UV light.

Ellman's Test and DTT Treatment. To assess the amount of GSH bound to the PEG−QDs, Ellman's assays were carried out (*16*). This procedure allowed us to quantify the SH groups of the glutathione. The Ellman's reagent, namely, 5,5′-dithiobis(2-nitrobenzoic acid), reacts with free thiol groups (SH) and releases a chromogenic compound (5-thio-2-nitrobenzoic acid) that can be detected easily by means of its optical absorption band peaked at 412 nm. The absorbance at this wavelength is therefore directly proportional to the concentration of −SH groups in solution. Due to the broad optical absorption spectrum of the QDs, the absorption region of the 5-thio-2-nitrobenzoic acid is covered and the absorbance of this chromogen could not be read directly in the presence of GSH−QD. In order to overcome this inconvenience, after the Ellman's reaction the sample solution was centrifuged in cutoff filters in order to separate the yellow chromogen (which passed easily through the membrane) from the GSH−QD conjugates (which did not pass through the pore membrane).

The concentration of thiol groups in solutions of GSH−QDs was determined by extrapolation from a calibration curve that was built by carrying out the Ellman's test on free GSH solutions at known concentrations. Ellman's tests were actually carried out both on solutions of GSH−QDs conjugates and on the same solutions after they had been treated with a 10 mM solution of dithiothreitol (DTT). DTT is able to cleave the disulfide bonds to form free −SH groups (*17*). The DTT treatment was applied routinely to both PEG−QDs and GSH−QDs samples immediately prior to the *in vivo* experiments. In a typical procedure, a solution of 10 mM DTT was added to a 6 μM solution of GSH−QDs. The resulting mixture was left under stirring for 3 h, after which the sample was centrifuged in 30 000 MWCO centrifuge filters in order to remove the excess of free DTT. At least five washes were carried out before redissolving the sample in *Hydra* physiological solution (Hy Sol: $CaCl_2$, 1 mM; and $NaHCO_3$, 0.1 mM).

Growth and Maintenance of *Hydra*. *Hydra vulgaris* (strain Zurich, originally obtained by P. Tardent) were asexually cultured in physiological solution by the method of Loomis and Lenhoff (*7*) with minor modifications. The animals were kept at 18 ± 1 °C and fed three times per week with freshly hatched *Artemia salina nauplii*. All animals were starved 24 h prior to the experiments.

***In Vivo* Experiments.** Groups of 20 animals were collected in plastic multiwells, allowed to equilibrate at room temperature in physiological solution (Hy Sol) buffered with 1 mM Tris−HCl (pH 7.4). The test was initiated by adding 300 μL of Hy

Sol containing either PEG−QDs or GSH−QDs at different concentrations (ranging from 3 to 300 nanomolar) to each well containing 20 polyps. One hour after incubation, the final volume was brought to 1 mL and the animals were kept at 18 °C for 24 h. For each QD concentration tested, a parallel trial was performed by adding GSH 10 μM. 24 h after incubation, the samples were rinsed in Hy solution several times before observation by fluorescence microscopy.

Fluorescence Microscopy. *In vivo* experiments were monitored for the first hour under a fluorescence stereomicroscope (Olympus ZSX-RFL2) equipped with a GFP filter set (BP460−490/DM505/LP510). In vivo fluorescence imaging of the whole animals and dissociated cells, along with imaging of fixed tissue sections, was accomplished by using an inverted microscope (Axiovert 100, Zeiss) equipped with a digital color camera (Olympus, DP70) and fluorescence filter sets (BP450−490/FT510/LP515). For imaging acquisition and analysis, the software system *Cell F* (Olympus) was used.

***Hydra* Tissue Dissociation and Cryosectioning.** *Hydra* polyps were dissociated according to Flick and Bode (*18*) with minor modifications. This procedure allows dissociation of *Hydra* tissue into a suspension of viable cells. Briefly, test animals were rinsed with Hy Sol and soaked in the dissociation solution for 60 min at 0 °C. Following a mechanic dissociation by a narrow glass pipet, the suspensions containing dissociated cells were transferred on microscope slides for fluorescence microscopy.

For tissue sectioning, test animals were fixed in 4% paraformaldeyde, pH = 7.4, at 4 °C, rinsed three times in phosphate saline buffer (PBS: 8 g/L NaCl; 0.2 g/L KCl; 1.44 g/L $Na_2HPO_4 \bullet 7H_20$; 0.24 g/L KH_2PO_4), soaked overnight in 30% saccharose in PBS and then embedded in the frozen section medium Neg-50 (Richard-Allan Scientific). Cryosections of 10 μm thickness were obtained by a cryostat (Leitz, digital 1760), collected on gelatin-coated slides (Superfrost microscope slides, Menzel), and mounted with Aquatex mounting medium (Merk) before imaging. For cell nuclei detection, sections were stained with 4′,6-diamidino-2-phenylindole dihydrochloride (DAPI) 1 mg/L before mounting.

RESULTS

Synthesis of Glutathione−Quantum Dots Conjugates. In Figure 1A, a sketch of the GSH−QDs conjugates is shown. We transfer hydrophobic TOP/TOPO capped CdSe−ZnS nanocrystals into water by wrapping the QDs in an amphiphilic polymer (poly(maleic anhydride-*alt*-1-tetradecene)) and then by cross-linking this polymer shell using bis(6-aminohexyl)amine (*13*). The resulting water-soluble polymer-coated quantum dots have a negatively charged surface, due to the hydrolyzed carboxyl groups present at the surface of the polymer shell. Therefore, these nanoparticles migrate from the negative pole toward the positive pole in the gel electrophoresis run (Figure 1B, lane 1). The carboxyl groups are then used to link diamino-PEG molecules through amide bond formations via the cross-linker EDC. The diamino-PEG molecules are introduced because they stabilize more effectively the nanoparticles in the *Hydra* solution and also because they introduce amino groups at the surface of the QDs. These amino groups in turn are used to link the tripeptide glutathione (GSH) through an additional amide bond formation. In a previous study, it was demonstrated by some of us that it is possible to tune the number of PEG molecules attached per nanoparticle by varying the length of the PEG molecule and the ratio of EDC added per molecule (*19*). In the present case, to achieve a dense surface of glutathione molecules attached per QDs, we have chosen PEG molecules of molecular weight equal to 897. At this length, it is possible to pack the surface of the quantum dots with a saturated number of PEG molecules (*19*). This prevents the nanoparticles from precipitating (as they become highly stable), and in addition, it ensures a saturated number of amino groups attached per PC-QDs. To verify the linkage of the PEG molecules to the QDs, we used gel electrophoresis. The PEG−QDs still move toward to the positive pole, although they are visibly retarded with respect to the original polymer-coated QDs (Figure 1B, lane 2). Once the glutathione is attached to the PEG−QDs, these dots have almost the same mobility on the gel as the starting PEG−QDs, although the front edge of the band is slightly retarded with respect to the latter (Figure 1B, lane 3), a behavior that can be attributed to the attachment of the small gluthatione tripeptide to the PEG−QDs.

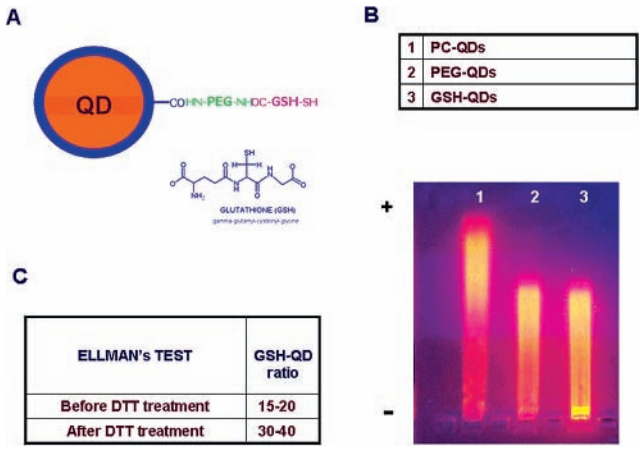


Figure 1. (A) Schematic representation of a GSH−QD conjugate. Polymer-coated quantum dots were first conjugated to diamino-modified PEG molecules and then to GSH through amide bond formation. (B) Characterization of the GSH−QD conjugates by means of gel electrophoresis. The samples loaded on the bottom part of the gel move through the gel from the negative to the positive pole. Lane 1 represents the migration of the polymer-coated quantum dot (PC-QD). Lane 2 corresponds to the migration of polymer-coated quantum dot functionalized with diamino PEG molecules having a molecular weight of 897 (PEG−QD). Lane 3 corresponds to the migration of PEG-coated quantum dots bound to GSH molecules (GSH−QD). (C) Evaluation of the number of GSH attached per nanoparticle. Ellman's test allows one to detect the number of thiol groups and therefore the cysteine groups attached per quantum dot. The measure was repeated on GSH−QD samples before and after DTT addition.

Furthermore, the GSH−QD band also shows a partial precipitation in the loading well. This behavior is very likely due to the formation of interparticle S−S bridges that could form among some GSH−QDs. This hypothesis is supported by the Ellman's test performed on GSH−QD samples before and after treatment with a reducing agent such as DTT. Statistically, the number of free thiol groups and therefore of reduced GSH molecules attached per QD doubles after treatment with DTT (Figure 1C).

We have also characterized the various steps of the conjugation reaction by FT−IR measurements. By checking the absorption spectra of the polymer-coated QDs, the PEG−QDs, and the GSH−QDs, respectively, a significant change of the corresponding profiles was observed. In the spectra corresponding to the GSH−QDs, a new peak appeared at 1776 cm^{-1}. While the assignment of this new peak is not obvious, we believe that it can be ascribed to the formation of a new amide bond between the carboxy group of the GSH and the amino group of a PEG molecule present on the surface of the PC-QDs (see Supporting Information, Figure SI2).

One critical aspect of the linking reaction is that it must ensure that the thiol groups of the cysteine are still present in the reduced form after the attachment to the dots. Lenhoff and Bovaird (*20*) showed in fact that *Hydra* recognizes the specific

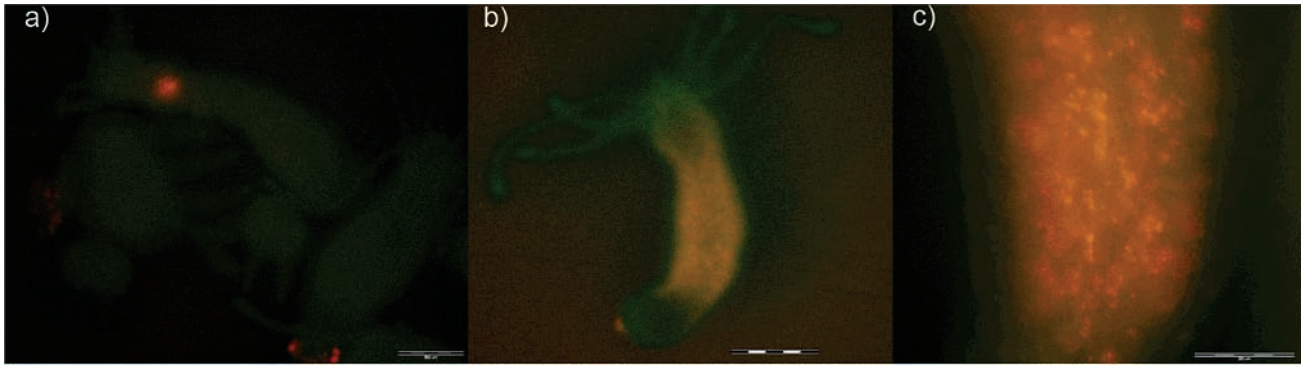


Figure 2. *In vivo* fluorescence imaging of *Hydra* polyps treated with 300 nM GSH−QDs (emission max: 610 nm). (a) Image taken 1 h after treatment. A fluorescent stain is located inside the body and can move along it. (b) 24 h after treatment, an intense fluorescence is distributed all along the gastric region. (c) Enlargement of the body column showing clearly the signal inside the body of the animal. The plane of focus lies close to the outer body surface. Scale bars: 500 μm (a,b) and 200 μm (c). The same results where observed when the feeding activator GSH (10 μM) was added to the bathing solution, stimulating mouth opening and allowing the nanoparticles to reach the gastrovascular cavity.

structure of the intact tripeptide backbone of glutathione, while tripeptide analogues with large and charged substituents at the sulfydryl group of glutathione competitively inhibit glutathione action. It is worth noting that the conversion of the oxidized form of gluthatione (GSSG) to its reduced form is crucial not only to ensure the activation of the feeding response but also because GSSG is actually known to act as an inhibitor of the feeding response (*20*). Therefore, before studying the interaction of GSH−QDs with *Hydra*, we always carried out a treatment of the GSH−QD sample with a reducing agent, in this specific case, DTT.

Activity of GSH−QDs on Living *Hydra*. The biological activity exerted by GSH−QDs and the putative cell targets were assayed in living *Hydra* by incubation of groups of animals separately with either polymer-coated QDs (PC-QDs) or PEG−QDs or with GSH−QDs. In a first series of experiments, the hydra bath was exposed only to quantum dot samples (either PEG−QDs or GSH−QDs), while in a second series of experiments, 10 μM GSH was also added together with the nanoparticles. At this concentration, the feeding response (i.e., tentacle writhing and mouth opening) was induced, allowing the medium that bathes the polyps to enter the body cavity. This assay, modified from Lenhoff (*21*) by Pierobon (*22*), and used as a reliable and quantifiable assay for study of aminoacid neurotransmitters in *Hydra*, allowed us to investigate the putative effect of the functionalized nanoparticles on the endodermal cells.

When the *Hydra* bath contained GSH−QDs, after incubation for 1 h at room temperature, fluorescence was detected in a small number of animals inside the body, as shown in Figure 2a. After 24 h of incubation at 18 °C, this fluorescent signal was spread inside the whole animal body (Figure 2b). By zooming in on the *Hydra* body, as shown in Figure 2c, the fluorescent regions always appeared out of focus, indicating that the fluorescent material was located inside the body cavity. At this stage, it was not possible to determine whether internalization of the nanoparticles from endodermal cells had occurred or whether the fluorescent material had simply filled the body cavity. The percentage of animals showing this phenotype was equal to 15% when using GSH−QDs, while no animals showed a similar phenotype when using differently coated QDs (PC-QDs and PEG−QDs) (see below). The percentage of *Hydras* able to stably internalize the nanoparticles increased up to 71% when in a parallel experiment 10 μM GSH was added together with the GSH−QDs to the *Hydra* bathing solution (Figure 2). In both cases, in fact, the fluorescence pattern and intensity lasted unaltered until the animals were fed again, after which the signal started to face slowly and was diluted throughout the emerging buds. To investigate the possible uptake mechanisms of QDs from endodermal cells, the same experiment was repeated at the same conditions, but the incubation was carried out at 4 °C, when endocytosis mechanisms, among all, are inhibited. After a 24 h incubation time, no spreading of the fluorescence inside the *Hydra* body was observed and the quantum dots remained localized in large aggregation spots inside the animal body (data not shown). To establish whether there was any concentration dependence in the uptake, GSH−QD conjugates were tested at different concentrations, ranging from 3 to 400 nM. Higher concentrations (up to 0.8−1 μM) were shown to affect animal vitality, as they induced irreversible death. It was observed that the optimal concentration of GSH−QDs required to stain the highest percentage of *Hydra* was 300 nM. When 10 μM GSH was also added to the bath, the concentration of GSH−QDs was kept constant at 300 nM.

Selective Uptake of GSH−QDs. In order to study more in detail the cellular localization of the nanoparticles that had entered into the body cavity, two types of experiments were performed. A first type of experiment is based on the fluorescence microscopy analysis of *Hydra* tissue slices obtained by standard cryosectioning of whole, stained animals. Figure 3a shows an optical image of the Hydra transverse section. In the image a thin cell spacer, called mesoglea (forming a line in the middle of the section) clearly separates two types of tissues: the endodermal cell layer (in Figure 3a is the region above the mesoglea, on the upper left region of the figure) and the ectodermal layer (on the right edge of the same figure). In Figure 3b, DAPI staining defines the position of the nuclei of the same cross sections, while in Figure 3c, the corresponding fluorescence derived from the QDs is shown. Figure 3d, obtained by merging Figure 3b with Figure 3c, shows the locations of both the nuclei and the QDs and confirms that the fluorescence from the QDs is located in the endodermal cells, probably in the cytoplasm. A subcellular location of QDs was not possible with this procedure. A second proof of the cell internalization of the GSH−QDs was provided by fluorescence imaging of the stained polyps after tissue dissociation. By applying the procedure of Flick and Bode (*18*) (see Materials and Methods section), stained *Hydra* were dissociated into single cells or clusters of cells and immediately observed under a fluorescence microscope. This procedure, although it does not allow us to define the cell type, confirmed the location of the QDs fluorescence inside the cells, as shown in Figure 4.

PC-QDs and PEG−QDs are not active on Living *Hydra*. As control experiments, bare PC-QDs and PEG−QDs were tested on living *Hydra* as described above. No animals showed a fluorescence phenotype similar to that observed with GSH−QDs. Instead, a more localized fluorescence was detected on the basal disk confined on the foot of the animal, as shown in

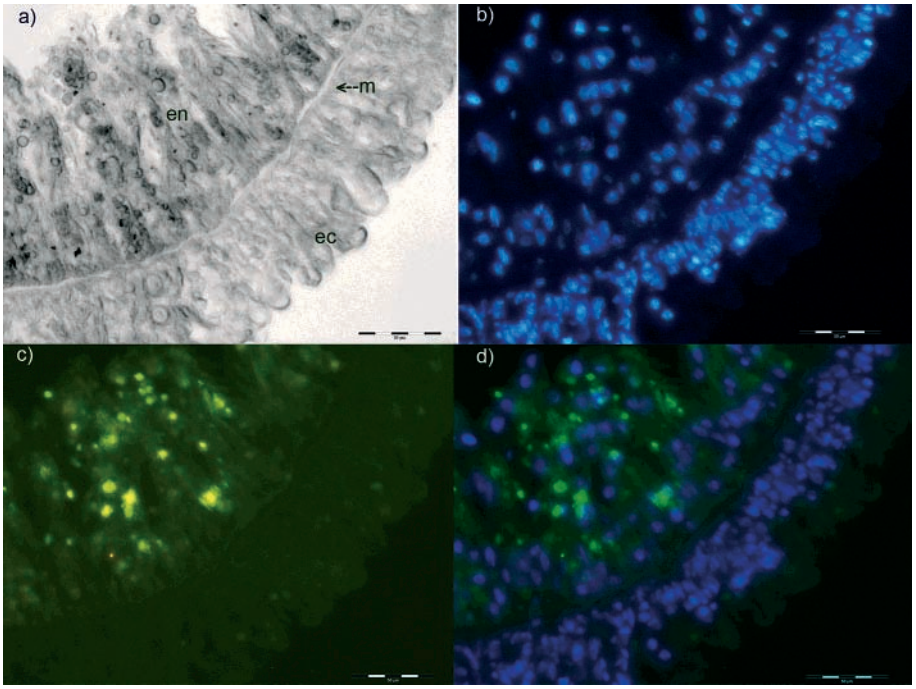


Figure 3. Cellular localization of QDs in *Hydra* cross sections. The whole *Hydra* was treated with 300 nM GSH−QDs for 24 h, fixed in 4% paraformaldehyde, and included for cryosectioning as described in the Materials and Methods section. Images were collected using an inverted microscope (Axiovert, 100, Zeiss) equipped with fluorescence filter sets. (a) Nomarski-DIC picture of 10 mM transversal section. Endodermal cells (en) are separated from ectodermal cells (ec) by an extracellular matrix, the mesoglea (m), indicated by the arrow. (b) DAPI staining of the same section to aim at the localization of the cell nuclei (blue color). (c) Fluorescence imaging under BP450−490/FT510/LP515 filter sets. Nanoparticles are located into endodermal cells. (d) Picture merged from parts b and c showing both DAPI (blue color) and nanoparticle (green color) fluorescence. QDs did not colocalize with nuclei.

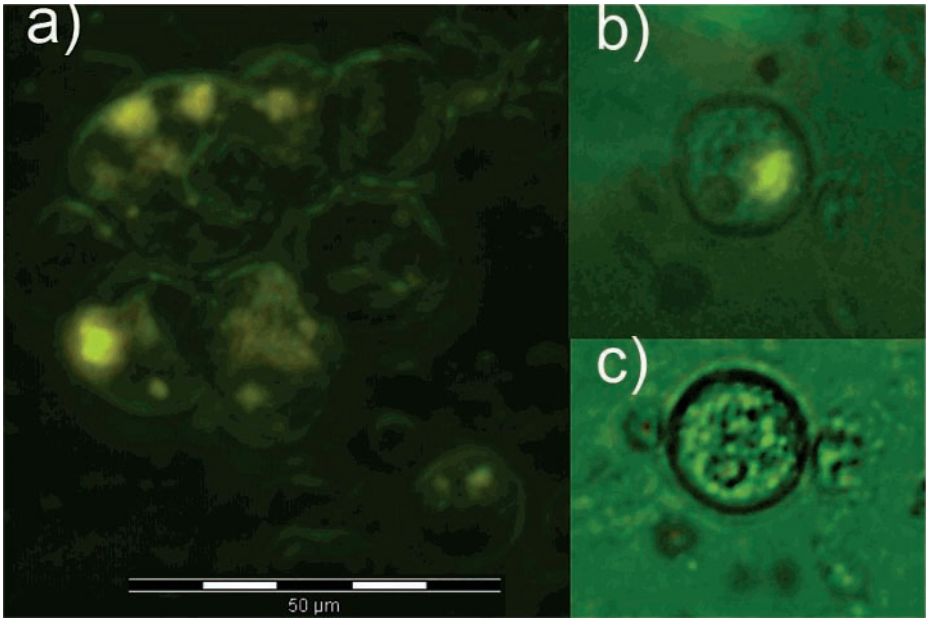


Figure 4. Dissociated cells from whole *Hydra* polyps treated with 300 nM GSH−QDs for 24 h. Single and clustered cells show nanoparticle fluorescence (yellow) inside the cytoplasm. The picture is merged from Nomarski-DIC and fluorescence images. Scale bar = 50 μm.

Figure 5a, 5b. These figures report bright-field and fluorescence images of a *Hydra* treated with PC-QDs. The same phenotype was still observed on *Hydra* treated with PEG−QDs, as shown in Figure 5c. QDs binding to the basal disk might depend on the sticky properties of the mucous secreted in this region, which serves to anchor the animal to a substrate. A further control experiment was carried out in parallel to evaluate the effect of PC-QDs and PEG−QDs on the endodermal cells. 10 μM GSH was added to the *Hydra* bathing medium together with the QDs in order to induce mouth opening and to allow QDs to enter the body cavity. No internalization was observed in the case of PC−QDs, while an effect similar to that observed with GSH−QDs was found with PEG−QDs. In fact, after 1 h of incubation, fluorescent material was detected in the body lumen, and it spread inside the animal body over the following 24 h. However, the fluorescence lasted only 48 h, after which it became weaker until it almost faded completely. In this set of experiments, only 27% of the *Hydra* showed fluorescence signal. Table 1 reports a summary of the different trials that were performed.

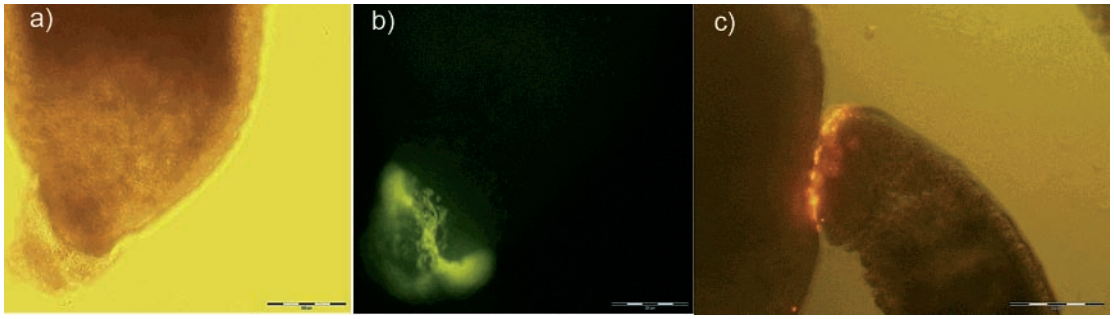


Figure 5. *In vivo* fluorescent imaging of *Hydra* polyps treated with different QDs (a) bright-field image of the *Hydra* peduncle and basal disc. (b) Fluorescence microscopy of the same region as in part a. Polyps were treated with PC-QDs (max emission = 510 nm). Fluorescence is present in the basal disk. (c) Image merge from bright-field and fluorescence images of *Hydra* treated with PEG−QDs (max emission = 610 nm). Fluorescence is present at the basal disk of a budding *Hydra.* Scale bar = 200 mm.

Table 1. Number of animals, expressed as a percentage of 20 treated animals, showing endodermal fluorescent signal after 24 h incubation with the indicated type of QDs, with or without addition of 10 μM GSH[a]

	free GSH added	no free GSH added
PEG−QDs	27%	0%
GSH−QDs	71%	15%

[a] The data shown are averaged over three independent experiments.

DISCUSSION

Overall, the results reported here suggest several interesting conclusions about the behavior of the *Hydra* when exposed to quantum dots. In the case of GSH−QDs, a fluorescent signal inside the body of the animal was observed. Because no ectodermal cells but only endodermal cells were stained by using GSH−QDs, a delivery of QDs inside the animal body must have occurred. This means that a response that culminated in mouth opening was promoted by GSH−QDs. The activity induced by GSH−QDs appeared different from the feeding behavior evoked by unbound GSH, as in fact tentacle writhing and wide mouth opening were not observed. However, such activity appears specific for GSH−QDs, as it was not induced in any of the observed cases by bare polymer-coated QDs (PC-QDs) or by diamino-PEG-functionalized quantum dots (PEG−QDs). Both PC-QDs and PEG−QDs were adsorbed to the mucous-producing ectodermal cells in the basal disk of living animals, but were unable to induce any behavioral response. This foot fluorescence was rapidly lost, due to the continuous cell displacement at the animal basal end. These data show that GSH−QDs alone can stimulate a response, although in a small percentage (15%) of the treated animals. Possible reasons for this low percentage could be a low concentration of the GSH molecules conjugated to the QD surface or the modified stereochemical conformation of the bound GSH molecules, which does not allow for correct interaction with the protein target. From Lenhoff's studies (*20*) of the kinetics of the *Hydra* GSH-activated feeding response, it was shown that the duration of the feeding response increased with increasing GSH concentration, in a range from 1 to 10 μM. In the present work, under the experimental condition at which biological activity was observed, the concentration of GSH molecules bound to the nanoparticles was estimated to be around 5 μM, thus falling into the "active" GSH concentration range. Therefore, the low level of evoked activity of the GSH−QDs might be due to the fact that, once GSH is bound to the QDs, its active site either is not accessible or is not properly oriented to bind to the protein target effectively. In addition, it must be noted that, when a GSH−QD binds to the protein target via a GSH molecule, all the remaining GSH molecules located on that specific QD will no longer be available to other protein targets. Therefore, this should also account for the low level of activity observed for GSH−QDs.

Upon addition of unbound GSH to the treated animals, which allowed the nanoparticles to reach the gastric cavity, the functionalized QDs were unexpectedly taken up by the endodermal cells.

An important consideration raised by this internalization concerns the specificity of this process. Is there a specific uptake or is there a GSH-receptor-mediated process occurring in the gastric cavity? One way to address this point is by considering that, once the QDs are driven into the gastric cavity, there is a substantial difference regarding whether they carry GSH bound to their surface or not. The first difference concerns the percentage of the stained animals, which is 71% for GSH−QDs and only 27% in the case of PEG−QDs. The second important difference concerns the fate of the nanoparticles taken up by the endodermal cells. Bare PEG−QDs driven into the *Hydra* body by free GSH are taken up by endodermal cells within 24 h. However, 48 h later the fluorescence is weaker, and it becomes hard to detect a few days later. This suggests the presence of a nonspecific uptake process, probably due to endocytosis operated by endodermal cells. On the other hand, GSH−QDs, no matter how they are driven into the gastric cavity (with or without addition of free GSH), once they are taken up by the endodermal cells, show no signs of weakening over time, as they last up to a new animal feeding. These results suggest that GSH−QDs might follow a different path as compared to that followed by PEG−QDs. Furthermore, it appears likely that the GSH-mediated pathway preserves the QDs from photodegradation, as opposed to the fate of PEG−QDs, whose fluorescence is rapidly degraded.

Apart from previous studies on radioligand binding of GSH to its putative receptors in a crude membrane preparation, including membranes coming from whole *Hydra vulgaris* homogenates (*10*, *23*), no studies of *in vivo* imaging of the GSH binding sites had been reported so far. Recently, Shaw et al. (*24*), while attempting to synthesize a fluorescent probe to study GSH receptor localization, produced a ligand that binds and antagonizes the NMDA receptor in cultured mammalian neuronal cells. To the best of our knowledge, the present study is the first one which allows localization *in vivo* of a GSH binding site, and we are confident that future investigations might shed light on the nature of this molecule as GSH-carrier, -receptor, or -membrane bound metabolic enzyme. Considering the multiple roles played by glutathione in metabolic functions, and in particular in the nervous system of higher vertebrates, GSH-functionalized nanocrystals prepared and tested in this work represent promising tools for a wide variety of investigations, such as the elucidation of the role played by GSH in neurotransmission and the identification of its putative receptor. Finally,

considering the more conventional and best-known antioxidant and free radical scavenging action of glutathione, GSH−QDs represent potentially useful redox-sensitive probes which could be used to label living cells or subcellular components according to their redox state.

CONCLUSIONS

In conclusion, we have designed and prepared GSH-functionalized quantum dot conjugates which allowed us to study the behavior of a small freshwater invertebrate called *Hydra*. We have tested and shown the biological activity of GSH molecules linked to fluorescent quantum dots by assaying the behavior of *Hydra vulgaris*.

Furthermore, by comparing the behavior of PEG−QDs in presence of free GSH to that of GSH−QDs both in the case of free GSH addition and in the absence of free GSH, we could suggest the presence of at least two mechanisms of internalization of particles of endodermal and not ectodermal cells, one relying upon particle size, charge, and surface composition, and the other, GSH-mediated, highly specific, which indicates the presence of GSH binding proteins in the endodermal cell layer. Considering the plasticity of *Hydra* tissues and the extensive remodeling that underlies the regeneration mechanism in this model organism, we can conclude that these photostable fluorophores represent suitable probes for this type of investigation.

ACKNOWLEDGMENT

We thank Vittorio Guglielmotti and Luigia Cristino for help with the cryostat sections and for discussion on fluorescent patterns, and Luigi Carbone, Angela Fiore, and Riccardo Di Corato for supplying QD samples. We thank also Giuseppe Ciccarella and Andrea Ragusa for helpful discussion on the characterization of samples. The authors are especially grateful to P. Pierobon for many inspiring discussions. This work was partially supported by the Italian Ministry of Research (FIRB grants RBN01KJHT-007 and RBIN048TSE, RBLA03ER38) and by the European STREP project SA-NANO (contract number 013698).

Supporting Information Available: Additional information as mentioned in the text. This material is available free of charge via the Internet at http://pubs.acs.org.

LITERATURE CITED

(1) Medintz, I. L., Uyeda, H. T., Goldman, E. R., and Mattoussi, H. (2005) Quantum dot bioconjugates for imaging, labelling and sensing. *Nat. Mater. 4*, 435−446.

(2) Parak, W. J., Pellegrino, T., and Plank, C. (2005) Labelling of cells with quantum dots. *Nanotechnology 16*, R9−R25.

(3) Michalet, X., Pinaud, F., Lacoste, T. D., Dahan, M., Bruchez, M. P., Alivisatos, A. P., and Weiss, S. (2001) Properties of fluorescent semiconductor nanocrystals and their application to biological labeling. *Single Molecules 2*, 261−276.

(4) Michalet, X., Pinaud, F. F., Bentolila, L. A., Tsay, J. M., Doose, S., Li, J. J., Sundaresan, G., Wu, A. M., Gambhir, S. S., and Weiss, S. (2005) Quantum dots for live cells, in vivo imaging, and diagnostics. *Science 307*, 538−544.

(5) Klostranec, J. M., and Chan, W. C. W. (2006) Quantum dots in biological and biomedical research: Recent progress and present challenges. *Adv. Mater. 18*, 1953−1964.

(6) Shaw C. A. (1998) Multiple roles of glutathione in the nervous system. *Glutathione in the nervous system.* (Shaw C. A., Ed.) pp 3−22, Chapter 1, Taylor & Francis, Washington DC.

(7) Loomis, W. F., and Lenhoff, H. M. (1956) Growth and sexual differentiation of Hydra in mass culture. *J. Exp. Zool. 132*, 555−574.

(8) Loomis, W. F. (1955) Glutathione control of the specific feeding reactions of Hydra. *Ann. N. Y. Acad. Sci. 62*, 208−209.

(9) Grosvenor, W., Bellis, S. L., Kass-Simon, G., and Rhoads, D. E. (1992) Chemoreception in hydra - specific binding of glutathione to a membrane-fraction. *Biochim. Biophys. Acta 1117*, 120−125.

(10) Bellis, S. L., Laux, D. C., and Rhoads, D. E. (1994) Affinity purification of hydra glutathione binding-proteins. *FEBS Lett. 354*, 320−324.

(11) Peng, Z. A., and Peng, X. G. (2001) Formation of high-quality CdTe, CdSe, and CdS nanocrystals using CdO as precursor. *J. Am. Chem. Soc. 123*, 183−184.

(12) Dabbousi, B. O., Rodriguez-Viejo, J., Mikulec, F. V., Heine, J. R., Mattoussi, H., Ober, R., Jensen, K. F., and Bawendi, M. G. (1997) (CdSe)ZnS core-shell quantum dots: Synthesis and characterization of a size series of highly luminescent nanocrystallites. *J. Phys. Chem. B 101*, 9463−9475.

(13) Pellegrino, T., Manna, L., Kudera, S., Liedl, T., Koktysh, D., Rogach, A. L., Keller, S., Radler, J., Natile, G., and Parak, W. J. (2004) Hydrophobic nanocrystals coated with an amphiphilic polymer shell: A general route to water soluble nanocrystals. *Nano Lett. 4*, 703−707.

(14) Yu, W. W., Qu, L. H., Guo, W. Z., and Peng, X. G. (2003) Experimental determination of the extinction coefficient of CdTe, CdSe, and CdS nanocrystals. *Chem. Mater. 15*, 2854−2860.

(15) Williams, A., and Ibrahim, I. T. (1981) Carbodiimide chemistry: recent advances. *Chem. Rev. 81*, 589−636.

(16) Riddles, P. W., Blakeley, R. L., and Zerner, B. (1979) Ellman's reagent: 5,5′-dithiobis(2 nitrobenzoic acid)- a reexamination. *Anal. Chem. 94*, 75−81.

(17) Hermanson, G.-T. (1996) Bioconjugate Techniques. *Modification of Nucleic acids and oligonucleotides.* (Hermanson, G.-T., Ed.) pp 77−79, Chapter 3, Academic Press, San Diego.

(18) Flick, K. M., and Bode, H. R. (1983) Dissociating tissues into cells and the development of Hydra from aggregated cells. *Hydra: research methods.* (Lenhoff, H. M., Ed.) pp 251−259 Chapter 32, Plenum Press, New York.

(19) Sperling, R. A., Pellegrino, T., Li, J. K., Chang, W. H., and Parak, W. J. (2006) Electrophoretic separation of nanoparticles with a discrete number of functional groups. *Adv. Funct. Mater. 16*, 943−948.

(20) Lenhoff, H. M., and Bovaird, J. (1961) Action of glutamic acid and glutathione analogs on the Hydra glutathione receptor. *Nature (London) 189*, 486−487.

(21) Lenhoff, H. M. (1961) Activation of the feeding reflex in *Hydra litoralis*. I. Role played by reduced glutathione and quantitative assays of the feeding reflex. *J. Gen. Physiol. 45*, 331−344.

(22) Pierobon, P., Sogliano, C., Minei, R., Tino, A., Porcu, P., Marino, G., Tortiglione, C., and Concas, A. (2004) Putative NMDA receptors in Hydra: a biochemical and functional study. *Eur. J. Neurosci. 20*, 2598−2604.

(23) Bellis, S. L., Kasssimon, G., and Rhoads, D. E. (1992) Partial characterization and detergent solubilization of the putative glutathione chemoreceptor from hydra. *Biochemistry 31*, 9838−9843.

(24) Shaw, C. A., Pasqualotto, B. A., Curry, K., Kim, S. U., LeCompte, K. A., and Langmuir, M. E. (1999) A novel fluorescent GSH-adduct binds to the NMDA receptor. *J. Neurosci. Methods 93*, 21−26.

BC060355T

Folic Acid-Conjugated Protein Cages of a Plant Virus: A Novel Delivery Platform for Doxorubicin

Yupeng Ren,[†] Sek Man Wong,[‡,§] and Lee-Yong Lim[†,||,*]

Department of Pharmacy and Department of Biological Sciences, National University of Singapore, Science Drive 4, Singapore 117543, Temasek Life Sciences Laboratory, 1 Research Link, Singapore, 117604, and Pharmacy, School of Biomedical, Biomolecular and Chemical Sciences, University of Western Australia, Crawley, WA 6009, Australia. Received November 20, 2006; Revised Manuscript Received January 22, 2007

The protein cage of a plant virus may provide a template for monodispersed nanosized systems for drug delivery. Using the Hibiscus chlorotic ringspot virus (HCRSV) as a model plant virus, we have prepared nanosized protein cages (30 nm) capable of encapsulating the anticancer drug, doxorubicin. The technique utilized the simultaneous encapsulation of a polyprotic acid of mw 200 kDa to produce an encapsulation efficiency for doxorubicin of about 7.5%. Folic acid was conjugated onto the capsids to impart cancer-targeting capability. The resultant nanosized systems improved the uptake and cytotoxicity of doxorubicin in the ovarian cancer cells, OVCAR-3, with statistical significance. Plant virus capsids may therefore provide viable templates for targeted drug delivery in cancer chemotherapy.

INTRODUCTION

Plant viruses which have genomic materials encapsidated within protein cages may provide viable delivery platforms for drugs (*1*). Unlike viruses isolated from animal origins, plant viruses are less pathogenic (*2*, *3*) and may avoid the immunogenicity response in animals (*4*). The protein cages, or capsids, offer versatility for drug loading. Compounds can either be physically encapsulated within the capsids following the removal of native RNA, or chemically conjugated onto the capsid. As the capsids are assembled from identical coat protein units, they are exact in molecular weight (mw), uniform in size, and precise in structure (*5*). This homogeneity in size and shape is an advantage over most nanoscale drug delivery systems prepared from random aggregation of macromolecules such as lipids or polymers (*6*).

Plant viral capsids provide other advantages for drug delivery. Amino acids in the coat protein are potential chemical conjugation sites for ligand attachment to develop stealth and/or targeting drug delivery platforms. Both macromolecules, such as polyethylene glycol or entire proteins (*4*, *7*), and small inorganic atoms, such as gold (*8*), have been conjugated onto the surface of viral protein cages to yield novel properties. The insertion of foreign peptides by recombinant DNA technology can further entitle the capsids to specific bioactivity (*9*, *10*).

Of the wide variety of plant viruses known to man, the icosahedral plant viruses are to date the most researched as vessels for foreign material loading. By adjusting the environmental pH and ion content, the capsids of these viruses can be transformed from assembled to swollen to disassembled states (*11*). This permits the removal of native viral RNA from the coat proteins, which are then purified and reassembled into protein cages for cargo loading. Proof of concept was first demonstrated with the Cowpea chlorotic mottle virus (CCMV)[1] (*12*, *13*). The protein cages of CCMV could host foreign ions as well as polyacids (*12*), the capacity to host different ions being made possible by modulating the inner surface charges of the protein cage through gene mutation (*13*). More recently, gold nanoparticles of appropriate size were also encapsidated within the CCMV-derived protein cages (*14*, *15*). Success in these experiments has prompted an interest in using the plant viral protein cages as platforms for drug delivery. Loading of cargo has been achieved through chemical conjugation of the molecules with specific amino acid groups presenting on the interior surface of the viral protein cages (*16*, *17*). In another development, the anticancer drug, doxorubicin, was covalently attached to the interior surface of small heat-shocked viral protein cages (*18*).

To date, there is no report on the loading of small chemotherapeutic drugs into plant viral protein cages by physical encapsulation, although this method has proven effective for the loading of crystals (*12*, *13*), polymers (*12*), and gold nanoparticles (*14*, *15*). Our previous research on another plant virus, the HCRSV, has established two prerequisites for the successful loading and retention of exogenous material in the viral protein cages (*19*). First, the material should possess a negative charge so that it will bind with the coat protein and initiate the reassembly of the icosahedral capsid structure. Second, the material should have an adequately high mw to

* Corresponding author. E-mail: limly@cyllene.uwa.edu.au; telephone: 61-8-64884413; fax: 61-8-64881025.

[†] Department of Pharmacy, National University of Singapore.

[‡] Department of Biological Sciences, National University of Singapore.

[§] Temasek Life Sciences Laboratory.

[||] Pharmacy, School of Biomedical, Bimolecular and Chemical Sciences, University of Western Australia.

[1] Abbreviations: HCRSV, Hibiscus chlorotic ringspot virus; CCMV, Cowpea chlorotic mottle virus; PSA, polystyrenesulfonic acid; PC−Dox, doxorubicin-loaded capsids; fPC−Dox, folic acid-conjugated, doxorubicin-loaded capsids; FR, folic acid receptor; EDTA, ethylenediamine-*N*,*N*,*N*′,*N*′-tetraacetic acid; DTT, dithiothreitol; PMSF, phenylmethanesulfonyl fluoride; EDAC, 1-ethyl-3-[3-dimethylaminopropyl]-carbodiimide hydrochloride; NHS, *N*-hydroxysuccinimide; TEM, transmission electron microscope; Dox−PSA, doxorubicin complexed with PSA; Dox−CP, doxorubicin incubated with empty viral capsids; PSA−PC, preformed PSA-loaded capsids; LE, loading efficiency, EE, encapsulation efficiency; RE, reassembly efficiency; *N*, the number of doxorubicin molecules encapsidated within each capsid; fPC−Dox + f, fPC−Dox in the presence of 1 mM of folic acid; MTT, 3-(4,5-dimethylthiazol-2-yl)-2,5-diphenyltetrazolium bromide; OD, optical density.

10.1021/bc060361p CCC: $37.00 © 2007 American Chemical Society
Published on Web 04/04/2007

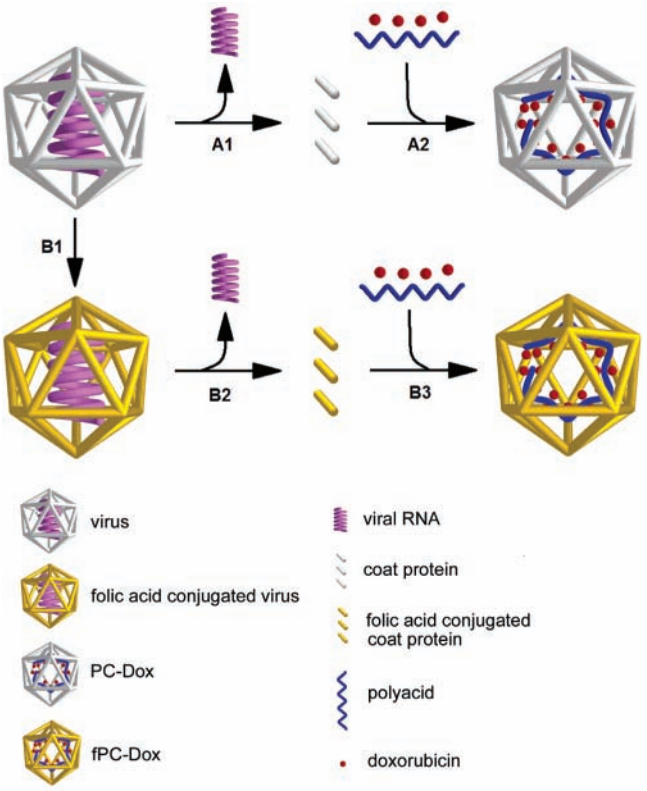


Figure 1. Schematic illustration of the preparation of doxorubicin-loaded viral protein cage without (PC−Dox) and with folic acid conjugation (fPC−Dox). Steps A1 and B2 are indicative of the removal of viral RNA from the plant virus and purification of coat proteins. Steps A2 and B3 involve the encapsulation of polyacid and doxorubicin during the reassembly of protein cage. Step B1 refers to the conjugation of folic acid onto the viral protein coat.

avoid excessive leaching of encapsidated material through the cavities present on the capsid surface upon dilution.

Doxorubicin, like many other anticancer drugs, is a small molecule (mw = 545 Da), and it is positively charged (pK_a = 8.4) in physiological fluids as well as under the conditions for reassembling of plant virus capsids (*20*). These properties made it difficult to load and retain doxorubicin within the plant virus capsid by simple encapsulation during the reassembly of the protein cage.

To impart the requisite size and charge to the anticancer agent, we employed the aid of a polyacid. This method, which we termed "polyacid association", involved the simultaneous loading of doxorubicin with polystyrenesulfonic acid (PSA) of mw 200 kDa into the capsid of the HCRSV. The 3:1 (PSA:drug) w/w ratio of mixing ensures the attraction of doxorubicin molecules to the polyacid by electrostatic forces, and a net negative charge for the resultant complex. The complex thus provided the nucleus for binding with, and initiation of, the final reassembly of coat proteins into the viral capsids (Figure 1). The resultant system was denoted as PC−Dox.

We also prepared folic acid-conjugated equivalents, denoted as fPC−Dox, where the HCRSV viruses were conjugated with folic acid before they were disassembled for doxorubicin−PSA encapsulation. Folic acid has been widely studied as a small molecule−ligand for targeting drug delivery systems to cancer cells. The principle of this application is based on the differential expression of folic acid receptor (FR) on normal and cancer cells. FR expression is elevated in malignant cancer cells, e.g., cancer cells of ovary, uterus, and mesothelium (*21, 22*), while most normal cells express low levels of FR. Proof of concept of the folic acid-mediated targeting systems have been shown with the delivery of drugs and liposomes to a variety of cancer cells (*22, 23*). In this study, folic acid was conjugated on the protein cages to promote the cellular uptake of drug by cancer cells.

EXPERIMENTAL PROCEDURES

Materials. HCRSV was purified from infected kenaf leaves (*24*). RPMI 1640 medium and folic acid-deficient RPMI 1640 medium were purchased from Sigma Chemical Co. (Steinheim, Germany) and supplemented with 10% fetal bovine serum (Gibco BRL Life Technologies, Grand Island, NY). OVCAR-3 cell line (Passage 22 to 32) was obtained from ATCC (Manassas, VA) and maintained in folic acid-deficient RPMI 1640 medium for 2 months before use (*25*). CCL-186 cell line (Passage 15 to 25) was obtained from ATCC and cultured in RPMI 1640 medium. Polystyrenesulfonic acid and folic acid were from Sigma (St. Louis, MO). Doxorubicin was purchased from Pharmacia (Bentley, WA, Australia).

Preparation of Doxorubicin-Loaded Capsids (PC−Dox). The coat protein of HCRSV was purified by dialysis against 1000 mL of pH 8.0 Tris buffer (50 mM Tris/base, 5 mM EDTA, 2 mM DTT, 0.2 mM PMSF, pH 8.0) for 12 h followed by centrifugation to remove viral RNA as described previously (*19*). After further dialysis against 1000 mL of pH 7.0 Tris buffer (50 mM Tris/base, 5 mM EDTA, 2 mM DTT, 0.2 mM PMSF, 1 M NaCl, pH 7.0) for 4 h, 1 mL of the coat protein solution (1 mg/mL) was incubated with 0.5 mL of doxorubicin−PSA solution (0.2 mg/mL of doxorubicin, 0.6 mg/mL of PSA (mw = 200 kDa) in pH 7.0 Tris buffer) for 8 h at 4 °C. The solution was adjusted to pH 5 with sodium acetate buffer (1 M sodium acetate, pH 5.0), and $CaCl_2$ was added to a final concentration of 5 mM to reassemble the protein cages. The solution was centrifuged under 15 000*g* for 10 min, and the supernatant was put on a 15% sucrose cushion and ultracentrifuged at 100 000*g* (SW41 rotor) for 1 h to sediment the protein cages. The pelleted PC−Dox was suspended in 0.1 mL of resuspension buffer (50 mM sodium acetate, 20 mM NaCl, 5 mM EDTA, 20 mM $CaCl_2$, pH 5.0) and stored at 4 °C until use.

Preparation of Folic Acid-Conjugated, Doxorubicin-Loaded Capsids (fPC−Dox). The carbodiimide coupling method was used to conjugate folic acid onto the capsids (*26−30*). Five milligrams of folic acid, 50 mg of 1-ethyl-3-[3-dimethylaminopropyl]carbodiimide hydrochloride (EDAC), and 50 mg of *N*-hydroxysuccinimide (NHS) were dissolved in 50 mL of bicarbonate buffer (50 mM $NaHCO_3$, pH 6) at ambient temperature. Five milligrams of HCRSV was then incubated with the reaction mix at 4 °C for 8 h**.** The solution was concentrated to about 0.5 mL by ultrafiltration and washed thrice with 10 mL of resuspension buffer to remove the unreacted materials. Dialysis against Tris buffers as described above was employed to remove the viral RNA and purify the coat protein. To determine the conjugation efficiency of a sample, the conjugated folic acid was quantified based on OD_{360nm} using an extinction coefficient of 5312 mol^{-1} cm^{-1} (Beckman Du 640B spectrometer, CA) (*28−32*), while the protein content was determined by the bis-cinchoninic acid assay (TECAN SpectraFluor, MA) (*33*). Reassembly of the purified folic acid-conjugated coat protein into protein cages, with simultaneous loading of doxorubicin and polystyrenesulfonic acid, were also conducted using methods similar to those described for the unconjugated protein coats.

Characterization of PC−Dox and fPC−Dox. The morphology of HCRSV, PC−Dox, and fPC−Dox were observed under a transmission electron microscope (TEM) (CM10, Philips Electronic Instruments Co, NJ) after staining with 1% of phosphotungstic acid. Sucrose gradient centrifugation was performed to confirm the existence of the drug-loaded protein cages. About 0.5 mL of PC−Dox and fPC−Dox in resuspension

buffer was centrifuged on 10−40% sucrose gradient at 100 000*g* for 3 h. Fractions of the sucrose gradient were collected for OD_{485nm} measurement to detect for doxorubicin. Control samples, including free doxorubicin, doxorubicin complexed with PSA at a weight ratio of 3:1 (Dox−PSA), doxorubicin incubated with empty viral capsids under reassembly conditions (Dox-CP), and doxorubicin incubated with preformed PSA-loaded capsids (PSA-PC) (*19*), were also subjected to the sucrose gradient centrifugation.

Native electrophoresis of PC−Dox and fPC−Dox was performed on 1% agarose gel under 5 V/cm for 1 h (Bio-Rad Sub-Cell electrophoresis system). Bands of coat protein were visualized by Coomassie blue staining, while the doxorubicin bands were visualized under ultraviolet light. Loading efficiency (LE), encapsulation efficiency (EE), reassembly efficiency (RE), and the number of doxorubicin molecules encapsidated within each capsid (*N*) were calculated using eqs 1−4. The amount of doxorubicin was calculated by comparing the $OD_{485\ nm}$ of sample and standard solutions, both of which were diluted with resuspension buffer (pH 5). The amount of reassembled coat protein (protein cage) was quantified by the BCA assay after the encapsidated doxorubicin was removed via a 6-day dialysis against PBS (pH 7.4). Drug release experiments were performed by the dialysis method (*34*). Fifty microliters of PC−Dox and fPC−Dox suspensions, with an equivalent doxorubicin concentration of 100 μg/mL, were placed in separate dialysis tubes (mw cutoff 12 400, Sigma-Aldrich) and dialyzed against 25 mL of PBS (pH 7.4) at 37 °C. At specified time points, 0.2 mL of the dialysis buffer was sampled for fluorescence measurements (Ex 480 nm, Em 535 nm) to quantify the released doxorubicin.

$$\text{LE}\ (\%) = \text{weight}_{\text{doxorubicin loaded}}/\text{weight}_{\text{protein cage}} \times 100\% \quad (1)$$

$$\text{EE} = \text{weight}_{\text{doxorubicin loaded}}/\text{weight}_{\text{total doxorubicin used}} \times 100\% \quad (2)$$

$$\text{RE} = \text{weight}_{\text{protein cage}}/\text{weight}_{\text{total coat protein used}} \times 100\% \quad (3)$$

$$N = \text{LE}/\text{mw}_{\text{doxorubicin}} \times (\text{mw}_{\text{coat protein}} \times 180) \quad (4)$$

The $mw_{doxorubicin}$ and $mw_{coat\ protein}$ values were 545 and 37 000, respectively.

Cellular Uptake of Doxorubicin. OVCAR-3 and CCL-186 cells were subcultured in six-well plates at concentrations of 100 000 cells/well. After 24 h, the cells were incubated with doxorubicin, PC−Dox, and fPC−Dox at equivalent doxorubicin concentration of 5 μg/mL. In the case of fPC−Dox, the incubation was also conducted in the presence of 1 mM of folic acid (fPC−Dox + f). The cells were washed thrice in ice-cold PBS to remove the samples, then lyzed with 0.5 mL of lysis buffer (50 mM Tris, 0.8% Triton, 0.2% SDS, pH 7.4). Cell-associated doxorubicin was determined by measuring the fluorescence of the lysate using a microplate reader (TECAN SpectraFluor, MA, Ex 485 nm and Em 535 nm) (*35*).

Confocal Microscopy. Cells were cultured in Lab-Tek chambered glass system and incubated for 1 h with samples of doxorubicin, PC−Dox, fPC−Dox and fPC−Dox + f, at a doxorubicin concentration of 5 μg/mL. The cells were washed thrice with PBS and the intracellular doxorubicin was visualized under a confocal microscope (CSLM, Zeiss Axiovert 200M, Oberkochen, Germany, Ex_{480nm} and Em_{540nm}) (*36*).

MTT Assay. PC−Dox, fPC−Dox and fPC−Dox + f samples were diluted with folic acid-deficient RPMI 1640 medium to give doxorubicin concentration in the range of 0.005 to 30 μg/mL. OVCAR-3 and CCL-186 cells were subcultured in 96-well plates at a density of 20 000 and 5000 cells/well, respectively. After 24 h, the culture medium was aspirated, and the cells were incubated with 0.1 mL of doxorubicin, PC−Dox, fPC−Dox, or fPC−Dox + f samples for 2 h. The cells were then washed thrice in ice-cold PBS and incubated with 0.2 mL of fresh cell culture medium for 3 days. Cell viability was determined by the MTT assay, and IC_{50} values were calculated using the nonlinear regression sigmoidal dose−response equation (Prism Version 3.00) (*25, 37−39*).

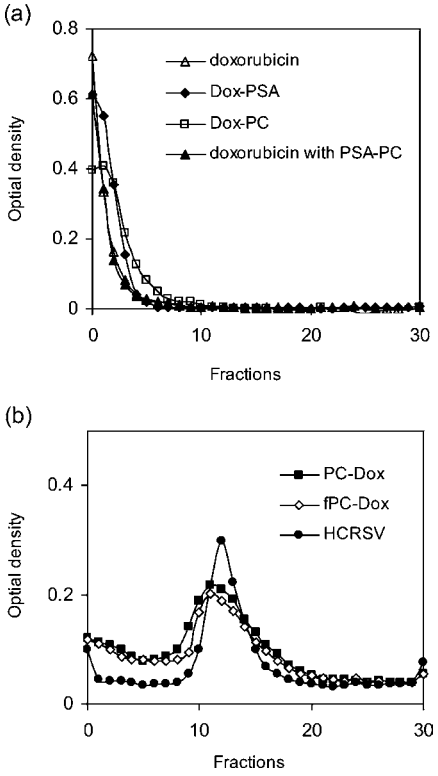


Figure 2. Optical density of fractions obtained from sucrose gradients. HCRSV was detected at 260 nm while other samples were detected at 485 nm. (a) Doxorubicin in control samples stayed at the top of the sucrose gradient after centrifugation. (b) Doxorubicin in PC−Dox and fPC−Dox showed greater propensity to sediment after centrifugation.

RESULTS AND DISCUSSION

Fractions isolated from the sucrose gradient centrifugation and subjected to optical density (OD) measurements indicated that the free doxorubicin, Dox−PSA, Dox-CP, and doxorubicin incubated with preformed PSA-PC were retained at the top (Figure 2, a), while native HCRSV were retained in fraction 13 of the sucrose gradient. In contrast, sucrose gradient centrifugation analysis of PC−Dox and fPC−Dox showed high doxorubicin content in fractions 11−15, with peak doxorubicin content noted in fraction 12 (Figure 2, b). The sedimentation rate of doxorubicin in these samples is higher than that of free doxorubicin, indicating that the drug had been loaded into the viral capsids. Interestingly, the sedimentation rates of PC−Dox and fPC−Dox were comparable with that of native HCRSV, suggesting similar cargo loads in the viral capsids of these samples. It may therefore be concluded that successful drug encapsulation was achieved in the PC−Dox and fPC−Dox samples but not in the Dox-CP and preformed PSA-PC samples. The failure to load doxorubicin into the preformed PSA-PC suggests that the drug could only be encapsulated during protein cage reassembly. The implication is that doxorubicin loaded in the PC−Dox and fPC−Dox samples was not likely to result from physical or chemical binding onto the surface of the protein cages but was contained within the HCRSV capsids.

Native agarose gel electrophoresis was applied to analyze the electrostatic properties of the samples. As shown in Figure 3 a,

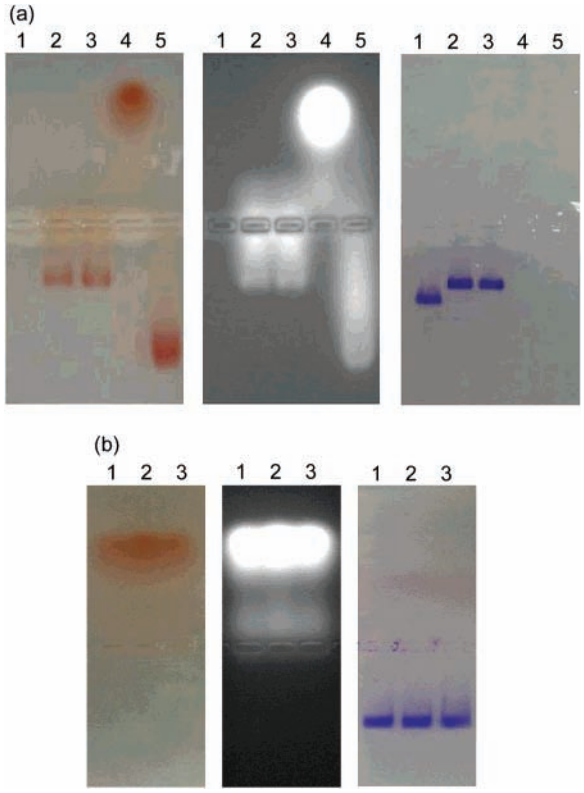


Figure 3. Native agarose gel electrophoresis. (a) Lanes 1−5 contain HCRSV, fPC−Dox, PC−Dox, doxorubicin, and doxorubicin−PSA complex. (b) Lanes 1−3 contain doxorubicin incubated with HCRSV, preformed PSA-PC, and PSA-fPC. The photos were taken by a digital camera, under ultraviolet light and after staining with coomassie blue, respectively.

free doxorubicin had migrated to the cathode, while PC−Dox, fPC−Dox, and the doxorubicin−PSA complex had moved in the opposite direction toward the anode. The relative positions of the bands indicate the opposing polarity of the samples and confirmed that the PSA−doxorubicin complex possessed a strong net negative charge. A comparison of the gels following coomassie blue staining showed that the doxorubicin band colocalized with the protein bands in the PC−Dox and fPC−Dox samples, once more underscoring the successful encapsulation of the drug in the viral capsids. Compared with the native HCRSV, the PC−Dox and fPC−Dox possessed a slightly lower charge density. In our previous study, HCRSV capsids loaded with PSA alone were determined to have the same negative charge density as the native HCRSV (*19*). Therefore, the lower charge density of PC−Dox and fPC−Dox could be attributed to the loaded doxorubicin. Samples in which doxorubicin was incubated with the preformed polyacid-loaded protein cages showed an absence of drug-loaded capsids (Figure 3, b). This negative control, together with that the results obtained from the sucrose gradient analysis, further confirms the encapsulation of doxorubicin during the process of capsid reassembly.

Both PC−Dox and fPC−Dox appeared as spherical particles with a diameter of about 30 nm and were indistinguishable from the native HCRSV when viewed under the TEM (Figure 4). The "polyacid association" method was found to be efficient for capsid reassembly and drug loading. As shown in Table 1, doxorubicin loaded into PC−Dox and fPC−Dox amounted to 59 and 49%, respectively, of the initial doxorubicin load used to prepare the samples, while more than 60% of the coat protein was found to have reassembled into capsids in these two samples. Measured against the coat protein content, the drug loading efficiency (LE) was 7.5%, amounting to about 900 doxorubicin molecules encapsulated in each protein cage. The encapsulated doxorubicin concentration would be in the vicinity of 300 mM, given that the inner diameter of the HCRSV protein cage was about 110 Å (*40*).

Folic acid conjugation efficiency ($\text{weight}_{\text{folic acid}}/\text{weight}_{\text{coat protein}}$) for fPC−Dox was 1.9% (SD = 0.1%, $n = 3$), which translated to about two folic acid molecules conjugated to each coat protein. The folic acid is postulated to bind with the Lys amino acids on the exposed protruding domain of the coat proteins. Since the icosahedral HCRSV capsid is made up of 180 coat protein units (*24*, *40*), the implication is that each fPC−Dox particle would have 360 conjugated folic acid molecules.

The release of doxorubicin from PC−Dox and fPC−Dox following dilution was evident during sucrose gradient centrifugation and agarose gel electrophoresis. Fractions obtained from the sucrose gradient showed increasing doxorubicin concentration from fractions 0 to 10. Since the viral capsids were retained in fraction 12, this suggests that doxorubicin was released from the capsids as they sediment along the centrifugation path. Observation of the agarose gel also showed a strong trail of doxorubicin associated with the bands for PC−Dox and fPC−Dox (Figure 3, a). As the protein bands of PC−Dox and fPC−Dox (Figure 3, a) did not exhibit degradation trails, the protein cages were probably stable under the experimental conditions. The orange color trails and fluorescence trails might therefore be attributed to the doxorubicin which had been released from the capsids and had migrated toward the cathode.

In vitro drug release experiments were conducted under simulated physiological conditions (pH 7.4, 37 °C) (*34*). Sustained release was evident when the drug release profiles of PC−Dox and fPC−Dox were compared with that of free doxorubicin (Figure 5). More than 80% of the drug load was released from the free doxorubicin into the receptor chamber after 5 h, whereas the drug-loaded capsids yielded the same amount of doxorubicin only after 24 h. Drug release from the PC−Dox and fPC−Dox did not, however, occur at a constant rate. There was a fairly rapid release of doxorubicin in the initial phase, where 40% of the drug load was released in 4 h, followed by a slower pace of release of the remaining drug load from the capsids. The mechanisms that effect drug release upon dilution were probably similar to those that allowed doxorubicin to be loaded into the viral capsids in the first place, i.e., reversible electrostatic attraction with the polyacid and physical entrapment by the viral protein cage. The sustained-release profile, coupled with the almost complete release of the entire drug load, rendered the HCRSV protein cages as attractive platforms for controlled release drug delivery. However, to reduce drug release during storage, the samples should be stored in small volumes of resuspension buffer at low temperature (4 °C).

In vitro cellular uptake and cytotoxicity experiments were conducted on the ovarian epithelial adenocarcinoma OVCAR-3 cell line, and the CCL-186 cells, a human diploid fibroblast. The OVCAR-3 cells have been used to evaluate folic acid-targeting drug delivery systems because of the presence of overexpressed folic acid receptors in these cells (*41*−*43*). The CCL-186, on the other hand, served as a representative human normal cell and was used as a control to evaluate the capacity of the delivery systems to selectively deliver doxorubicin to cancer cells.

Cellular uptake of doxorubicin was visualized by confocal microscopy and quantified by fluorimetry. Quantitative data showed a 2-fold higher cellular uptake of doxorubicin from fPC−Dox than from PC−Dox by the OVCAR-3 cells (Figure 6). Uptake of doxorubicin from PC−Dox was in fact no different from that of free doxorubicin, suggesting that the encapsulation of doxorubicin within the HCRSV capsids could not by itself aid in the intracellular accumulation of the drug in the

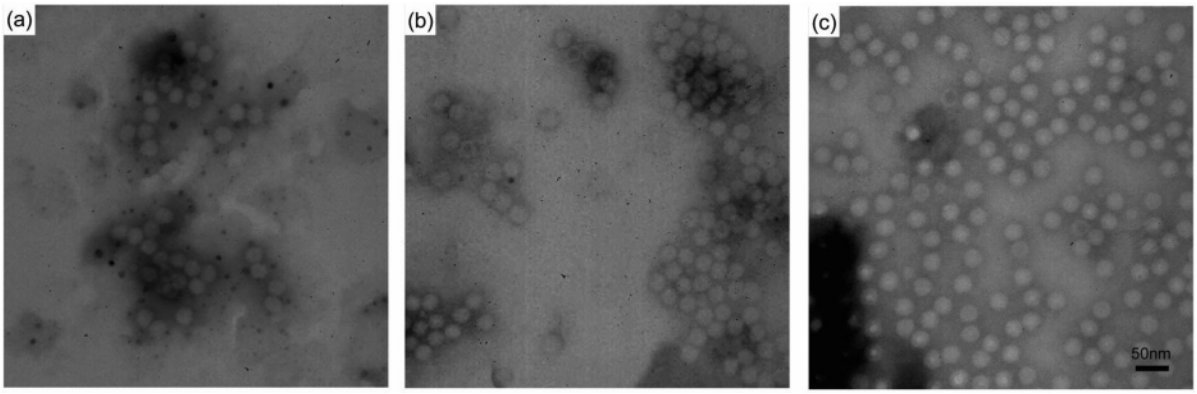


Figure 4. TEM micrographs of (a) PC−Dox, (b) fPC−Dox, and (c) native HCRSV without modifications. The two drug-loaded viral protein cage particles were comparable in morphology and size with the native HCRSV.

Table 1. PC−Dox and fPC−Dox Samples: Efficiency of Doxorubicin Loading and Reassembly of Coat Proteins into Capsids. Data Represent Mean ± SD, $n = 3$.

samples	EE (%)[a]	RE (%)[b]	LE (%)[c]	N^d
PC−Dox	59.3 ± 13.7	74.7 ± 12.1	7.8 ± 0.5	953
fPC−Dox	48.7 ± 4.7	63.8 ± 5.1	7.5 ± 0.3	916

[a] $\text{weight}_{\text{doxorubicin}}/\text{weight}_{\text{coat protein}}$ expressed as a percentage. [b] $\text{weight}_{\text{doxorubicin loaded}}/\text{weight}_{\text{doxorubicin used for preparation}}$ expressed as a percentage. [c] $\text{weight}_{\text{capsids}}/\text{weight}_{\text{coat protein used for preparation}}$ expressed as a percentage. [d] Number of doxorubicin molecules encapsidated within each capsid.

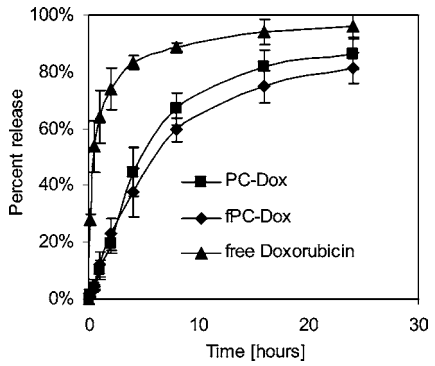


Figure 5. Doxorubicin release profile of PC−Dox, fPC−Dox, and free doxorubicin. More than 80% of free doxorubicin was released into the receptor chamber after 5 h whereas the drug-loaded capsids yielded the same amount of doxorubicin after 24 h.

OVCAR-3 cells. Coincubation of fPC−Dox with folic acid negated the higher cellular uptake of doxorubicin from this sample, implicating a folic acid-mediated uptake mechanism in the OVCAR-3 cells. Enhanced uptake of doxorubicin from fPC−Dox was not observed in the CCL-186 cells, which showed comparable drug uptake from the free doxorubicin, PC−Dox, and fPC−Dox samples.

Confocal micrographs provided supporting evidence for the folic acid-mediated preferential uptake of fPC−Dox by the OVCAR-3 cells (Figure 7). OVCAR-3 cells incubated with fPC−Dox showed more intense fluorescence compared to cells incubated with free doxorubicin or PC−Dox. Upon the addition of folic acid to the fPC−Dox sample, however, the fluorescence exhibited by the cells was reduced to a level similar to those observed in cells incubated with PC−Dox or free doxorubicin. Doxorubicin typically accumulates in the nuclei of cells. However, for the fPC−Dox, which increased the intracellular fluorescence of doxorubicin, the fluorescence was not concentrated in the nuclei but in many bright small spots in the cytoplasm (Figure 7, c). The phenomenon was consistent with a FR-mediated uptake, whereby the drug-loaded capsids following endocytosis would be directed to the endosomes (*44*).

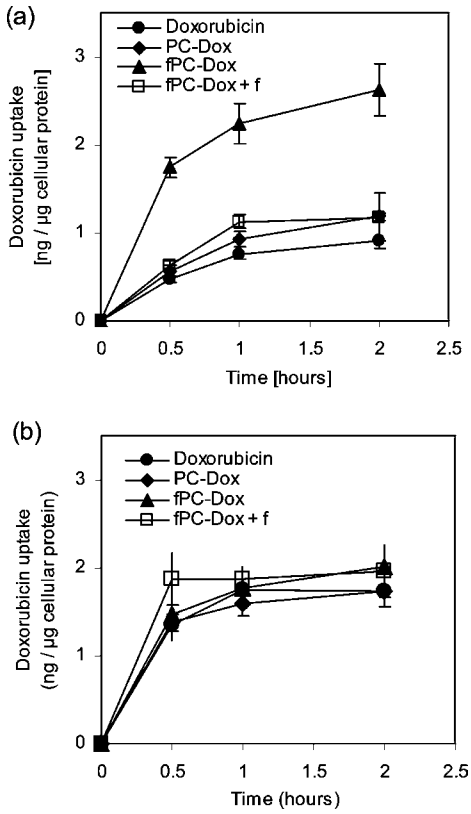


Figure 6. Cellular uptake of doxorubicin by (a) OVCAR-3 and (b) CCL-186 cells incubated with free doxorubicin, PC−Dox, and fPC−Dox. Uptake of fPC−Dox was also undertaken in the presence of folic acid (fPC−Dox + f). Data represent mean ± SD ($n = 3$).

For the CCL-186 cells, slightly stronger fluorescence was observed in cells incubated with free doxorubicin than in cells incubated with PC−Dox or fPC−Dox. These observations are therefore in good agreement with the quantitative uptake data.

Cytotoxicity of the various doxorubicin formulations against the OVCAR-3 and CCL-186 cells was assessed via the MTT assay after 2 h of exposure. The log *C* vs viability curves of OVCAR-3 cells showed that the fPC−Dox had higher cytotoxicity against this cell line compared with the other formulations (Figure 8). The PC−Dox formulation did not decrease the $IC_{50\text{doxorubicin}}$, again affirming that the encapsulation of the drug alone did not confer additional benefits to its delivery to cancer cells. The $IC_{50\text{doxorubicin}}$ of fPC−Dox formulation (0.11 μg/mL) was observed to decrease 4-fold compared with the $IC_{50\text{doxorubicin}}$ of free doxorubicin (0.48 μg/mL). This enhancement of kill was again mediated by the folic acid conjugation on the capsid surface, for the addition of free folic acid

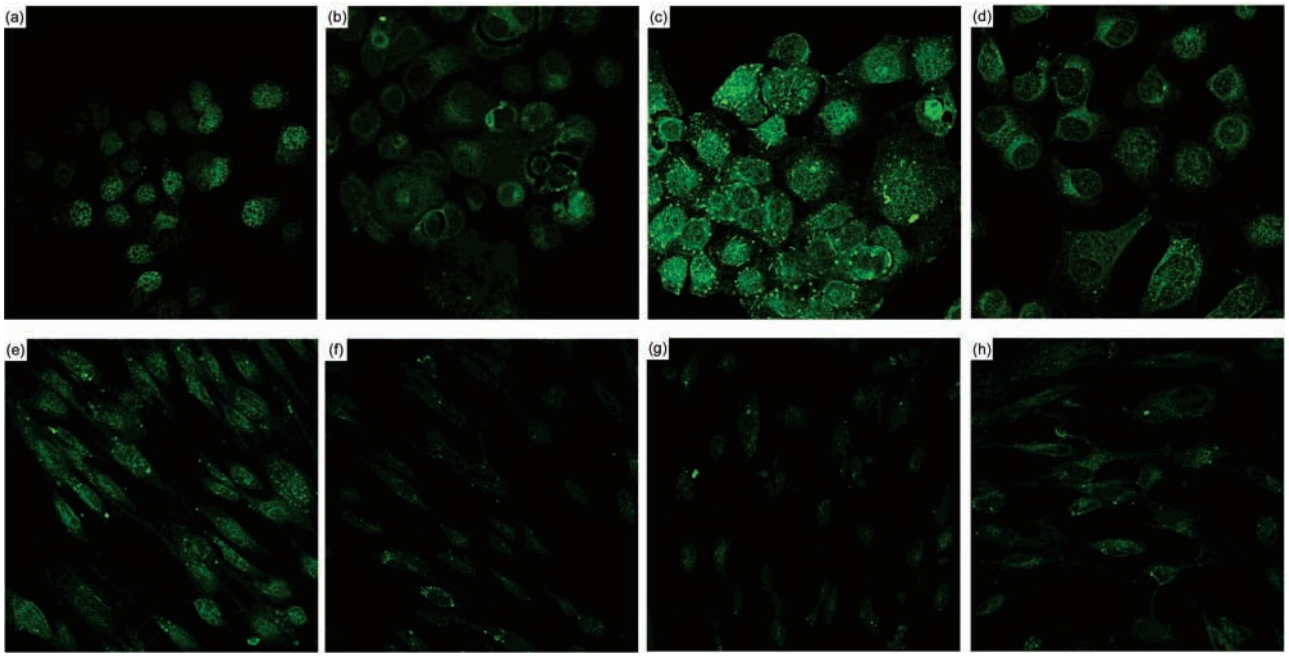


Figure 7. Confocal micrographs of OVCAR-3 cells incubated for 1 h with free doxorubicin (a), PC−Dox (b), fPC−Dox (c), and fPC−Dox in the presence of folic acid (d), and of CCL-186 cells incubated for 1 h with free doxorubicin (e), PC−Dox (f), fPC−Dox (g), and fPC−Dox in the presence of folic acid (h).

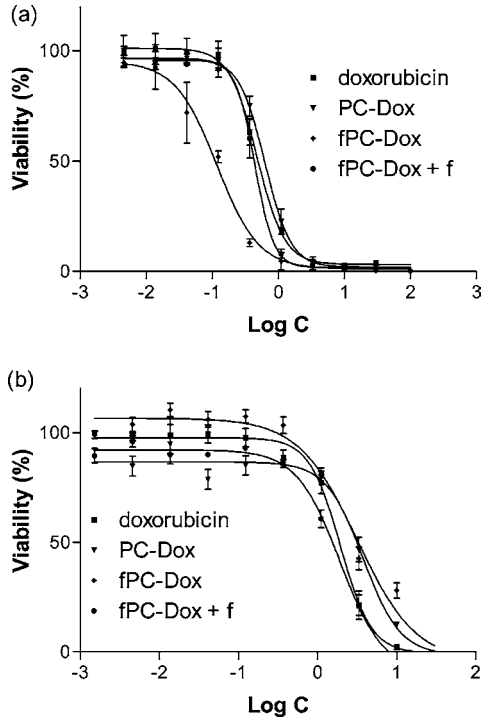


Figure 8. Viability of cells after treated by different formulations. (a) Cell viability of OVCAR-3. (b) Cell viability of CCL-186. The fPC−Dox was more efficient in inhibiting the growth of OVCAR-3 cells than other formulations while there was no such difference between the formulations in CCL-186 cells.

effectively abolished the added effect. A comparison of the $IC_{50doxorubicin}$ across cell types indicates that the CCL-186 cells, with the $IC_{50doxorubicin}$ of 1.95 μg/mL, were about 4-fold more resistant to the cytotoxicity of the drug than the OVCAR-3 cells. Interestingly, the encapsulation of doxorubicin in either the PC−Dox or fPC−Dox led to increased $IC_{50doxorubicin}$ of 3.4 μg/mL and 3.2 μg/mL against the CCL-186 cells, alluding to a conferred protection of the cells against the drug.

The selective higher uptake rate and cytotoxicity of fPC−Dox in cancer cells relative to normal cells may be explained by the up-regulation of folic acid receptors, in some cases approaching 2 orders of magnitude, in many cancer cell types (*22*, *45*). To confirm a folic acid-mediated mechanism, the uptake and cytotoxicity experiments for fPC−Dox were conducted in the presence of high concentration of free folic acid, which was found to negate the benefits of fPC−Dox. This suggested the uptake of fPC−Dox by folic acid-mediated endocytosis in the OVCAR-3 cells. The preferential uptake of fPC−Dox led to its stronger cytotoxic effect, as denoted by the lower $IC_{50doxorubicin}$ value, in cancer cells.

On the other hand, the uptake and cytotoxicity data suggest that the PC−Dox was not an efficient delivery system for cancer chemotherapy. This is reasonable considering the current lack of evidence to support cytoinvasive and cytotoxicity properties of plant viruses in animal cells. PC−Dox could, however, be useful in clinical applications where sustained drug release and/or protection against cytotoxic drugs are desired.

To conclude, a new "polyacid association" method was established to physically encapsulate the anticancer drug, doxorubicin, inside the protein cage of HCRSV at high loading efficiency. The conjugation of folic acid allows the viral capsids to selectively increase the uptake and cytotoxicity of doxorubicin in the ovarian cancer cells OVCAR-3. This indicates that the folic acid-conjugated, doxorubicin-loaded HCRSV capsid has potential for the targeted delivery of cancer chemotherapeutics. However, much work remains to be done to develop the protein cages of plant viruses into feasible drug delivery systems. For the fPC−Dox, further work on the immune response and *in vivo* efficacy of the formulation will be required to assess its potential for clinical applications.

ACKNOWLEDGMENT

This work was supported by the ARF grants R-148-000-045-112 and R-154-000-252-112 from National University of Singapore (NUS). Ren Yupeng is a recipient of the NUS graduate research scholarship.

LITERATURE CITED

(1) Douglas, T., and Young, M. (2006) Viruses: Making Friends with Old Foes. *Science 312*, 873−875.

(2) Nicholas, B. L., Brennan, F. R., Martinez-Torrecuadrada, J. L., Casal, J. I., Hamilton, W. D., and Wakelin, D. (2002) Characterization of the immune response to canine parvovirus induced by vaccination with chimaeric plant viruses. *Vaccine 20*, 2727−2734.
(3) Rae, C. S., Khor, I. W., Wang, Q., Destito, G., Gonzalez, M. J., Singh, P., Thomas, D. M., Estrada, M. N., Powell, E., Finn, M. G., and Manchester, M. (2005) Systemic trafficking of plant virus nanoparticles in mice via the oral route. *Virology 343*, 224−235.
(4) Raja, K. S., Wang, Q., Gonzalez, M. J., Manchester, M., Johnson, J. E., and Finn, M. G. (2003) Hybrid virus-polymer materials. 1. Synthesis and properties of PEG-decorated cowpea mosaic virus. *Biomacromolecules 4*, 472−476.
(5) Phelps, D. K., Speelman, B., and Post, C. B. (2000) Theoretical studies of viral capsid proteins. *Curr. Opin. Struct. Biol. 10*, 170−173.
(6) Huang, Y. Z., Gao, J. Q., Liang, W. Q., and Nakagawa, S. (2005) Preparation and characterization of liposomes encapsulating chitosan nanoparticles. *Biol. Pharm. Bull. 28*, 387−390.
(7) Chatterji, A., Ochoa, W., Shamieh, L., Salakian, S. P., Wong, S. M., Clinton, G., Ghosh, P., Lin, T., and Johnson, J. E. (2004) Chemical conjugation of heterologous proteins on the surface of Cowpea mosaic virus. *Bioconjugate Chem. 15*, 807−813.
(8) Soto, C. M., Blum, A. S., Wilson, C. D., Lazorcik, J., Kim, M., Gnade, B., and Ratna, B. R. (2004) Separation and recovery of intact gold-virus complex by agarose electrophoresis and electroelution: application to the purification of cowpea mosaic virus and colloidal gold complex. *Electrophoresis 25*, 2901−2906.
(9) Khor, I. W., Lin, T., Langedijk, J. P., Johnson, J. E., and Manchester, M. (2002) Novel strategy for inhibiting viral entry by use of a cellular receptor-plant virus chimera. *J. Virol. 76*, 4412−4419.
(10) Brown, W. L., Mastico, R. A., Wu, M., Heal, G., Adams, C. J., Murray, J. B., Simpson, J. C., Lord, J. M., Taylor-Robinson, A. W., and Stockley, P. G. (2002) RNA bacteriophage capsid-mediated drug delivery and epitope presentation. *Intervirology 45*, 371−380.
(11) Fox, J. M., Wang, G., Speir, J. A., Olson, N. H., Johnson, J. E., Baker, T. S., and Young, M. J. (1998) Comparison of the native CCMV virion with in vitro assembled CCMV virions by cryoelectron microscopy and image reconstruction. *Virology 244*, 212−218.
(12) Douglas, T., and Young, M. (1998) Host-guest encapsulation of materials by assembled virus protein cages. *Nature 393*, 152−155.
(13) Douglas, T., Strable, E., Willits, D., Aitouchen, A., Libera, M., and Young, M. (2002) Protein Engineering of a Viral Cage for Constrained Nanomaterials Synthesis. *Adv. Mater. 14*, 415−418.
(14) Chen, C., Daniel, M. C., Quinkert, Z. T., De, M., Stein, B., Bowman, V. D., Chipman, P. R., Rotello, V. M., Kao, C. C., and Dragnea, B. (2006) Nanoparticle-Templated Assembly of Viral Protein Cages. *Nano Lett. 6*, 611−615.
(15) Loo, L., Guenther, R. H., Basnayake, V. R., Lommel, S. A., and Franzen, S. (2006) Controlled Encapsidation of Gold Nanoparticles by a Viral Protein Shell. *J. Am. Chem. Soc. 128*, 4502−4503.
(16) Hooker, J. M., Kovacs, E. W., and Francis, M. B. (2004) Interior Surface Modification of Bacteriophage MS2. *J. Am. Chem. Soc. 126*, 3718−3719.
(17) Schlick, T. L., Ding, Z., Kovacs, E. W., and Francis, M. B. (2005) Dual-surface modification of the tobacco mosaic virus. *J. Am. Chem. Soc. 127*, 3718−3723.
(18) Flenniken, M. L., Liepold, L. O., Crowley, B. E., Willits, D. A., Young, M. J., and Douglas, T. (2005) Selective attachment and release of a chemotherapeutic agent from the interior of a protein cage architecture. *Chem. Commun. (Camb.) 28*, 447−449.
(19) Ren, Y, Wong, S. M., and Lim, L. Y. (2006) In vitro-reassembled plant virus-like particles for loading of polyacids. *J. Gen. Virol. 87*, 2749−2754.
(20) Gallois, L., Fiallo, M., and Garnier-Suillerot, A. (1998) Comparison of the interaction of doxorubicin, daunorubicin, idarubicin and idarubicinol with large unilamellar vesicles. Circular dichroism study. *Biochim. Biophys. Acta 1370*, 31−40.
(21) Lu, Y., and Low, P. S. (2002) Folate-mediated delivery of macromolecular anticancer therapeutic agents. *Adv. Drug. Delivery Rev. 54*, 675−693.
(22) Ross, J. F., Chaudhuri, P. K., and Ratnam, M. (1994) Differential regulation of folate receptor isoforms in normal and malignant tissues in vivo and in established cell lines. Physiologic and clinical implications. *Cancer 73*, 2432−2443.
(23) Leamon, C. P., and Low, P. S. (1991) Delivery of macromolecules into living cells: a method that exploits folate receptor endocytosis. *Proc. Natl. Acad. Sci. U.S.A. 88*, 5572−5576.
(24) Lee, K. C., Lim, D., Wong, S. M., and Dokland, T. (2003) Purification, crystallization and X-ray analysis of Hibiscus chlorotic ringspot virus. *Acta Crystallogr. D: Biol. Crystallogr. 59*, 1481−1483.
(25) Lee, R. J., and Low, P. S. (1995) Folate-mediated tumor cell targeting of liposome-entrapped doxorubicin in vitro. *Biochim. Biophys. Acta 1233*, 134−44.
(26) Reddy, J. A., Clapp, D. W., and Low, P. S. (2001) Retargeting of viral vectors to the folate receptor endocytic pathway. *J. Controlled Release 74*, 77−82.
(27) Drabick, J. J., Bhattacharjee, A. K., Hoover, D. L., Siber, G. E., Morales, V. E., Young, L. D., Brown, S. L., and Cross, A. S. (1998) Covalent polymyxin B conjugate with human immunoglobulin G as an antiendotoxin reagent. *Antimicrob. Agents Chemother. 42*, 583−588.
(28) Stella, B., Arpicco, S., Peracchia, M. T., Desmaele, D., Hoebeke, J., Renoir, M., D'Angelo, J., Cattel, L., and Couvreur, P. (2000) Design of folic acid-conjugated nanoparticles for drug targeting. *J. Pharm. Sci. 89*, 1452−1464.
(29) Zhang, L., Hou, S., Mao, S., Wei, D., Song, X., and Lu, Y. (2004) Uptake of folate-conjugated albumin nanoparticles to the SKOV3 cells. *Int. J. Pharm. 287*, 155−162.
(30) Bharali, D. J., Lucey, D. W., Jayakumar, H., Pudavar, H. E., and Prasad, P. N. (2005) Folate-receptor-mediated delivery of InP quantum dots for bioimaging using confocal and two-photon microscopy. *J. Am. Chem. Soc. 127*, 11364−11371.
(31) Shinoda, T., Takagi, A., Maeda, A., Kagatani, S., Konno, Y., and Hashida, M. (1998) In vivo fate of folate−BSA in non-tumor- and tumor-bearing mice. *J. Pharm. Sci. 87*, 1521−1526.
(32) Dube, D., Francis, M., Leroux, J. C., and Winnik, F. M. (2002) Preparation and tumor cell uptake of poly(*N*-isopropylacrylamide) folate conjugates. *Bioconjugate Chem. 13*, 685−692.
(33) Smith, P. K., Krohn, R. I., Hermanson, G. T., Mallia, A. K., Gartner, F. H., Provenzano, M. D., Fujimoto, E. K., Goeke, N. M., Olson, B. J., and Klenk, D. C. (1985) Measurement of protein using bicinchoninic acid. *Anal. Biochem. 150*, 76−85.
(34) Liu, S. Q., Tong, Y. W., and Yang, Y. Y. (2005) Incorporation and in vitro release of doxorubicin in thermally sensitive micelles made from poly(N-isopropylacrylamide-co-N,N-dimethylacrylamide)-β-poly(D,L-lactide-co-glycolide) with varying compositions. *Biomaterials 26*, 5064−5074.
(35) Veldman, R. J., Koning, G. A., van Hell, A., Zerp, S., Vink, S. R., Storm, G., Verheij, M., and van Blitterswijk, W. J. (2005) Coformulated N-octanoyl-glucosylceramide improves cellular delivery and cytotoxicity of liposomal doxorubicin. *J. Pharmacol. Exp. Ther. 315*, 704−710.
(36) Xiong, X. B., Huang, Y., Lu, W. L., Zhang, X., Zhang, H., Nagai, T., and Zhang, Q. (2005) Intracellular delivery of doxorubicin with RGD-modified sterically stabilized liposomes for an improved antitumor efficacy: in vitro and in vivo. *J. Pharm. Sci. 94*, 1782−1793.
(37) Saul, J. M., Annapragada, A., Natarajan, J. V., and Bellamkonda, R. V. (2003) Controlled targeting of liposomal doxorubicin via the folate receptor in vitro. *J. Controlled Release 92*, 49−67.
(38) Pan, X. Q., Zheng, X., Shi, G., Wang, H., Ratnam, M., and Lee, R. J. (2002) Strategy for the treatment of acute myelogenous leukemia based on folate receptor beta-targeted liposomal doxorubicin combined with receptor induction using all-trans retinoic acid. *Blood 100*, 594−602.
(39) Yang, L., Li, J., Zhou, W., Yuan, X., and Li, S. (2004) Targeted delivery of antisense oligodeoxynucleotides to folate receptor-overexpressing tumor cells. *J. Controlled Release 95*, 321−331.
(40) Doan, D. N., Lee, K. C., Laurinmaki, P., Butcher, S., Wong, S. M., and Dokland, T. (2003) Three-dimensional reconstruction of hibiscus chlorotic ringspot virus. *J. Struct. Biol. 144*, 253−261.
(41) Verbaan, F. J., Klouwenberg, P. K., van Steenis, J. H., Snel, C. J., Boerman, O., Hennink, W. E., and Storm, G. (2005) Application of poly(2-(dimethylamino)ethyl methacrylate)-based polyplexes for gene transfer into human ovarian carcinoma cells. *Int. J. Pharm. 304*, 185−192.
(42) van Steenis, J. H., van Maarseveen, E. M., Verbaan, F. J., Verrijk, R., Crommelin, D. J., Storm, G., and Hennink, W. E. (2003)

Preparation and characterization of folate-targeted pEG-coated pDMAEMA-based polyplexes. *J. Controlled Release 87*, 167−176.
(43) Corona, G., Giannini, F., Fabris, M., Toffoli, G., and Boiocchi, M. (1998) Role of folate receptor and reduced folate carrier in the transport of 5-methyltetrahydrofolic acid in human ovarian carcinoma cells. *Int. J. Cancer 75*, 125−133.
(44) Chatterjee, S., Smith, E. R., Hanada, K., Stevens, V. L., and Mayor, S. (2001) GPI anchoring leads to sphingolipid-dependent retention of endocytosed proteins in the recycling endosomal compartment. *EMBO J. 20*, 1583−92.
(45) Miotti, S., Bagnoli, M., Ottone, F., Tomassetti, A., Colnaghi, M. I., and Canevari, S. (1997) Simultaneous activity of two different mechanisms of folate transport in ovarian carcinoma cell lines. *J. Cell Biochem. 65*, 479−491.

BC060361P

Conjugation of a New Two-Photon Fluorophore to Poly(ethylenimine) for Gene Delivery Imaging

Ali Hayek,[†] Sebnem Ercelen,[‡] Xin Zhang,[‡] Frédéric Bolze,[†] Jean-François Nicoud,*[,†] Emmanuel Schaub,[‡] Patrice L. Baldeck,[§] and Yves Mély*[,‡]

Groupe des Matériaux Organiques, Institut de Physique et Chimie des Matériaux de Strasbourg, Université Louis Pasteur (CNRS, UMR 7504), BP 43 23 rue du Loess, F-67034 Strasbourg, France, Photophysique des Interactions Biomoléculaires, (CNRS, UMR 7175), Institut Gilbert Laustriat, Faculté de Pharmacie, 74, route du Rhin - BP 60024 F-67401 Illkirch-Graffenstaden, France, and Laboratoire de Spectrométrie Physique, Université Joseph Fourier, (CNRS, UMR 5588), BP 87 F-38402 Saint Martin d'Hères, France. Received November 21, 2006; Revised Manuscript Received January 30, 2007

We report herein the molecular engineering of an efficient two-photon absorbing (TPA) chromophore based on a donor−donor bis-stilbenyl entity to allow conjugation with biologically relevant molecules. The dye has been functionalized using an isothiocyanate moiety to conjugate it with the amine functions of poly(ethylenimine) (PEI), which is a cationic polymer commonly used for nonviral gene delivery. Upon conjugation, the basic architecture and photophysical properties of the active TPA chromophore remain unchanged. At the usual N/P ratio (ratio of the PEI positive charges to the DNA negative charges) of 10 used for transfection, the transfection efficiency and cytotoxicity of the labeled PEI/DNA complexes were found to be comparable to those of the unlabeled PEI/DNA complexes. Moreover, when used in combination with unlabeled PEI (at a ratio of 1 labeled PEI to 3 unlabeled PEI), the labeled PEI does not affect the size of the complexes with DNA. The labeled PEI was successfully used in two-photon fluorescence correlation spectroscopy measurements, showing that at N/P = 10 most PEI molecules are free and the diffusion coefficient of the complexes is consistent with the 360 nm size measured by quasielastic light scattering. Finally, two-photon images of the labeled PEI/DNA complexes confirmed that the complexes enter into the cytoplasm of HeLa cells by endocytosis and hardly escape from the endosomes. As a consequence, the functionalized TPA chromophore appears to be an adequate tool to label the numerous polyamines used in nonviral gene delivery and characterize their complexes with DNA in two-photon applications.

INTRODUCTION

During the past decade, two-photon fluorescence imaging has evolved as a powerful technique for three-dimensional scanning microscopy in biological research (*1*, *2*). This technique offers many advantages over conventional confocal microscopy. First of all, the two-photon absorption only occurs at the laser focus where the laser light intensity is maximum, so that dye bleaching and fluorescence above and below the focused spot are avoided. Furthermore, the excitation source is generally an IR laser, which takes advantage of the transparency window of biological tissues. In addition, the IR light is more penetrating and less damaging to cells than the more energetic UV−vis light, enabling observation of thicker samples and during more extended periods without degradation (*3*). Furthermore, two-photon excitation was found to be ideally suited for fluorescence correlation spectroscopy (FCS), allowing the determination of the local concentrations and diffusion coefficients of fluorescently labeled molecules in cells (*4*, *5*). However, the use of two-photon microscopy and FCS is still hampered by the availability of appropriate two-photon dyes. Indeed, classical one-photon dyes, well-known in epifluorescence or confocal microscopy, are still largely used in two-photon applications, though they exhibit only low two-photon cross sections. Consequently, the development of new water-soluble dyes, specifically engineered for their multiphoton absorption and fluorescence, is strongly required. Recently, we reported the synthesis of water-soluble efficient blue TPA fluorophores (*6*). These compounds present a D-π-rigid core-π-D symmetric architecture, where D = donor group(s), π = conjugated spacer, and rigid core = biaryl system (Figure 1a). By introducing oligo(ethylene glycol) moieties, we obtained good water solubility (up to 100 g.L^{-1} for the fluorophore shown in Figure 1b), which enables the use of these dyes for cellular imaging (*7*). To go one step further in the validation and application of these water-soluble dyes, our aim in this work was to prepare functionalized TPA fluorophores in order to label biologically relevant molecules and monitor them in cells by two-photon microscopy and FCS. For this purpose, we selected poly(ethylenimine)s (PEIs) that are among the most efficient nonviral gene delivery agents (*8*, *9*). PEIs are rich in amino groups and positively charged at neutral pH. Due to their high cationic charge density, PEIs are proficient condensing agents for DNA that lead to the formation of small particles (<100 nm) at high nitrogen-to-phosphate ratios (N/P > 5) (*10*). These DNA/PEI complexes exhibit good transfection efficiency in vitro and in various in vivo applications (*11*). To conjugate the amine functions of PEI, we synthesized the isothiocyanate-functionalized TPA chromophore **1** (Figure 2). This dye was conjugated to PEI at a ratio of 1 dye per 40 amine functions. The corresponding conjugate PEI derivative was shown to substitute nonconjugated PEIs in their complexes with DNA and can be used to monitor the intracellular pathway of the complexes in cells by two-photon microscopy.

* Corresponding authors. Pr. J.-F. Nicoud (chemistry): Fax 33 (0)3 88 10 72 46; Tel 33 (0)3 88 10 71 55, E-mail: nicoud@ipcms.u-strasbg.fr. Pr. Y. Mély (transfection): Fax 33(0)3 90 24 43 13; Tel 33 (0)3 90 24 42 63, E-mail: yves.mely@pharma.u-strasbg.fr.

[†] Université Louis Pasteur.

[‡] Institut Gilbert Laustriat.

[§] Université Joseph Fourier.

10.1021/bc060362h CCC: $37.00 © 2007 American Chemical Society
Published on Web 04/03/2007

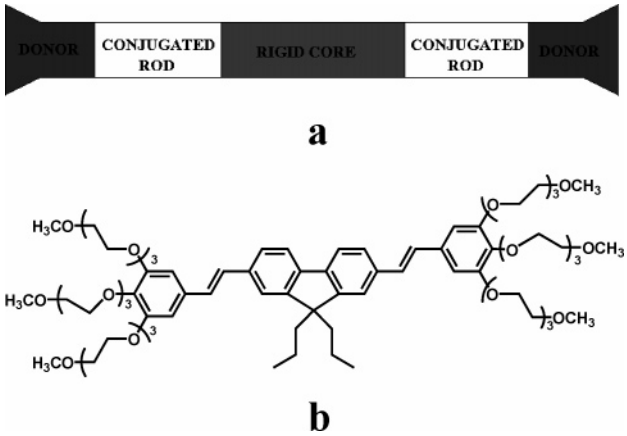


Figure 1. General architecture of a 1D two-photon absorbing chromophore (a) and chemical structure of a symmetrical water-soluble chromophore (b) (*8*).

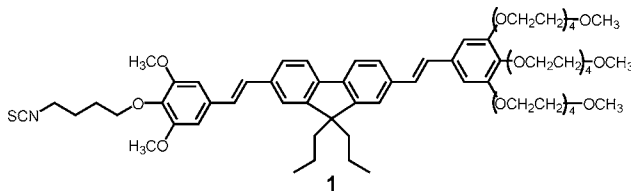


Figure 2. Amine-reactive TPEF chromophore **1**.

EXPERIMENTAL PROCEDURES

Materials. Branched PEI (25 kDa) was purchased from Aldrich. Lysis reagent was from Promega. All other chemicals and reagents were purchased from Aldrich or Acros Organics and were used as received unless specified otherwise. THF was distilled over sodium under argon atmosphere prior to use. Compounds **3**, **4**, and **7** were prepared as previously described (*6*).

Synthesis. ^{1}H and ^{13}C NMR spectra were recorded with a 300 MHz Brucker Advance 300 instrument in $CDCl_3$ (Aldrich) with $CHCl_3$ as an internal standard (7.24 ppm for ^{1}H and 77 ppm, middle of the three peaks, for ^{13}C spectra). High-resolution ESI mass spectra were recorded with a Microtof instrument at Service de spectrométrie de masse de l'Institut de chimie LC3-ULP- Strasbourg. TLC was run on Merck precoated aluminum plates (Si 60 F254). Column chromatographies were run on Merck silica gel (60−120 mesh) or neutral alumina (Merck) 70−230 mesh.

*4-(t-Butyldimethylsilanyloxy)-3,5-dimethoxybenzaldehyde (**5**).* Under argon, in a 250 mL two-necked flask, 4.6 g of *t*-butyldimethylsilylchloride (30 mmol) and 2.1 g of imidazole (30 mmol) were dissolved in 120 mL of a dimethylformamide/dichloromethane mixture (1/1 v/v). When the solution became homogeneous, 5 g of syringaldehyde (27 mmol) was added and the mixture was heated at 80 °C overnight. Then, the solvents were evaporated under vacuum. The yellow solid was dissolved in 200 mL of CH_2Cl_2, washed with water (150 mL), dried on $MgSO_4$, and evaporated under reduced pressure to give a yellow oil. The oil was solubilized in ethanol (40 mL) and cooled down in the freezer overnight. The white precipitate was filtered and dried to give 4.96 g of the desired protected product **5** in 62% yield. ^{1}H NMR (300 MHz, $CDCl_3$, δ ppm): 9.82 (s, 1H), 7.10 (s, 2H), 3.87 (s, 6H), 1.01 (s, 9H), 0.16 (s, 6H). ^{13}C NMR (75.75 MHz, $CDCl_3$, δ ppm): 191.98, 151.92, 140.98, 129.3, 106.66, 55.75, 25.62, 18.73, 4.58. HRMS calculated *m*/*z* for $C_{15}H_{24}O_4SiLi$, 303.1604; found, 303.1599.

*4-{2-[4-(t-Butyldimethylsilanyloxy)-3,5-dimethoxy]styryl}-4′-(diethoxyphosphinylmethyl)-9,9′-di-n-propylfluorene (**6**).* To a solution of 4,4′-bis(diethoxyphosphinylmethyl)-9,9′-dipropylfluorene **4** (3.34 g, 6.08 mmol, 1 equiv) in 50 mL of anhydrous THF was added 0.73 g of NaH (30.4 mmol, 5 equiv, 60% in mineral oil). After the effervescence ceased, the suspension was stirred for 1 h at room temperature under an argon atmosphere. After cooling at 0 °C, a solution of 1.80 g of **5** (6.08 mmol, 1 equiv) in anhydrous THF (50 mL) was added slowly. The mixture was stirred for 24 h and neutralized by ethanol (10 mL). The solvents were evaporated under vacuum giving an oil, which was dissolved in CH_2Cl_2 and washed with brine (50 mL) and water (50 mL). The crude product was purified by column chromatography on silica gel with dichloromethane/methanol as eluant (97/3 in vol). The desired product **6** was obtained as a yellow oil (m = 1.47 g, 35% yield). ^{1}H NMR (300 MHz, $CDCl_3$, δ ppm): 7.65−7.60 (m, 2H), 7.48−7.45 (m, 2H), 7.29−7.26 (m, 2H), 7.07 (s, 2H), 6.76 (s, 2H), 4.09−3.98 (m, 4H), 3.87 (s, 6H), 3.24 (d, 2H, J = 21.49 Hz), 2.20−1.97 (m, 4H), 1.23 (t, 6H, J = 7.02 Hz), 1.03 (s, 9H), 0.67 (s, 10H), 0.16 (s, 6H). ^{13}C NMR (75.75 MHz, $CDCl_3$, δ ppm): 151.27, 151.27, 151.22, 151.11, 140.23, 104.20, 139.69, 139.64, 136.41, 136.39, 134.42, 130.29, 130.25, 130.17, 128.55, 128.46, 128.27, 127.50, 125.37, 124.28, 124.19, 120.45, 119.75, 119.61, 119.56, 103.61, 62.13, 62.04, 55.74, 55.10, 42.78, 35.00, 33.18, 25.76, 18.76, 17.12, 16.38, 16.30, 14.37, −4.66. HRMS calculated *m*/*z* for $C_{40}H_{57}O_6PSi$, 692.3662; found, 692.3664.

*4-{2-[4-(t-Butyldimethylsilanyloxy)-3,5-dimethoxy]styryl}-4′-{2-[3,4,5-tris(1,4,7,10,13-pentaoxotetradecyl)]styryl}-9,9′-di-n-propylfluorene (**2**).* This product was prepared as described for **6** using 500 mg of **6** (0.72 mmol, 1 equiv), 144 mg of NaH (3.6 mmol, 5 equiv), and 523 mg of aldehyde **7** (0.72 mmol, 1 equiv). Product **2** was obtained as a yellow oil (m = 909.80 mg, 85% yield). ^{1}H NMR (300 MHz, $CDCl_3$, δ ppm): 7.64 (d, 2H J = 8.33 Hz), 7.48−7.46 (m, 4H), 7.08 (s, 2H), 7.05 (d, J = 1.32 Hz), 6.80 (s, 2H), 6.76 (s, 2H), 4.25−4.16 (m, 6H), 3.89 (t, 4H, J = 5.26 Hz), 3.87 (s, 6H), 3.81 (t, 2H, J = 5.26 Hz), 3.77−3.61 (m, 24H), 3.57−3.53 (m, 6H), 3.38 (s, 3H), 3.37 (s, 6H), 2.02−1.97 (m, 4H), 1.03 (s, 9H), 0.70 (s, 10H), 0.16 (s, 6H). ^{13}C NMR (75.75 MHz, $CDCl_3$, δ ppm): 152.74, 151.72, 151.45, 140.58, 140.23, 138.26, 136.46, 136.04, 134.42, 133.10, 130.26, 128.72, 128.31, 127.64, 127.50, 125.59, 125.44, 120.60, 120.46, 119.81, 119.77, 106.13, 103.62, 71.88, 70.79, 70.65, 70.62, 70.57, 70.54, 70.47, 69.73, 68.81, 58.97, 55.73, 55.10, 53.39, 42.86, 25.76, 18.71, 17.15, 14.45, −4.65.

*4-{2-[4-(2,6-Dimethoxy-4-vinylphenoxy)butyl]isoindolin-1,3-dione-4′-[3,4,5-tris-(1,4,7,10,13-pentaoxotetradecyl)]styryl}-9,9′-di-n-propylfluorene (**9**).* (a) Deprotection of the phenol moiety: In a 100 mL two-necked flask, under an argon atmosphere, 550 mg of **2** (0.43 mmol, 1 equiv) was dissolved in 50 mL anhydrous THF. A solution of TBAF (0.19 g, 0.65 mmol, 1.5 equiv) in THF (1 mL) was introduced dropwise into the flask. The mixture was stirred at room temperature for 2 h and put in 100 mL of 1 M phosphoric acid. The aqueous phase was extracted with diethyl ether, washed with water, and dried on magnesium sulfate. The solvent was removed under reduced pressure, and the crude product was purified by column chromatography on silica gel (ethyl acetate/hexane mixture as eluant 50/50 in vol). The phenolic product was obtained as a yellow oil (m = 1.02 g, 90% yield). ^{1}H NMR (300 MHz, $CDCl_3$, δ ppm): 7.64 (d, 2H J = 8.33 Hz), 7.48−7.46 (m, 4H), 7.08 (d, 2H, J = 2.20 Hz), 7.05 (d, 2H, J = 1.09 Hz), 6.809 (s, 2H), 6.801 (s, 2H), 5.58 (s, 1H), 4.23 (t, 4H, J = 4.83 Hz), 4.18 (t, 2H, J = 4.83 Hz), 3.97 (s, 6H), 3.89 (t, 4H, J = 5.26 Hz), 3.81 (t, 2H, J = 5.26 Hz), 3.77−3.61 (m, 24H), 3.57−3.53 (m, 6H), 3.38 (s, 3H), 3.37 (s, 6H), 2.02−1.97 (m, 4H), 0.70 (s, 10H). ^{13}C NMR (75.75 MHz, $CDCl_3$, δ ppm): 152.72, 151.51, 151.45, 147.19, 140.55, 140.31, 138.30, 136.34, 136.09, 134.68, 133.08, 129.14, 128.71, 128.09, 127.67, 127.40, 125.59, 125.43, 120.61, 120.44, 119.83, 106.15, 103.21, 77.16, 72.38, 71.90, 70.81,

70.65, 70.57, 70.54, 70.51, 70.49, 69.73, 68.83, 59.10, 58.99, 56.27, 55.11, 42.86, 29.66, 24.20, 19.76, 17.15, 14.45, 13.65.

(b) Product **9**. In a 100 mL three-necked flask were introduced DMF (50 mL), 340 mg of the previous deprotected phenolic compound (0.29 mmol, 1 equiv), 204 mg of K_2CO_3 (1.48 mol, 5 equiv), and 100.15 mg of *N*-(4-bromobutyl)phthalimide (0.35 mmol, 1.20 equiv). The mixture was then heated at 80 °C for 4 days under an argon atmosphere. The solvent was removed under vacuum, and the residue dissolved in dichloromethane, washed with water, and dried over magnesium sulfate. After evaporation of the dichloromethane, the crude product was purified by column chromatography on silica gel, with dichloromethane as eluant to give the desired product **9** as a yellow oil (m = 333 mg, 85% yield). ^{1}H NMR (300 MHz, $CDCl_3$, δ ppm): 7.86−7.83 (m, 2H), 7.72−7.69 (m, 2H), 7.65 (d, 2H J = 8.33 Hz), 7.50−7.46 (m, 4H), 7.09 (s, 2H), 7.05 (d, 2H, J = 0.87 Hz), 6.80 (s, 2H), 6.76 (s, 2H), 4.23 (t, 4H, J = 4.83 Hz), 4.18 (t, 2H, J = 4.83 Hz), 4.03 (t, 2H, J = 6.35 Hz), 3.91 (s, 6H), 3.89 (t, 4H, J = 5.26 Hz), 3.81 (t, 2H, J = 5.26 Hz), 3.77−3.61 (m, 24H), 3.57−3.53 (m, 6H), 3.38 (s, 3H), 3.37 (s, 6H), 2.02−1.76 (m, 8H), 0.70 (s, 10H). ^{13}C NMR (75.75 MHz, $CDCl_3$, δ ppm): 168.40, 153.59, 152.74, 151.51, 140.49, 140.31, 138.29, 136.83, 136.18, 136.14, 133.78, 133.11, 133.08, 132.15, 128.70, 128.57, 127.98, 127.70, 125.57, 123.09, 120.61, 120.44, 119.84, 106.16, 103.49, 77.17, 72.55, 72.38, 71.89, 70.79, 70.65, 70.62, 70.58, 70.57, 70.54, 70.52, 70.48, 69.74, 68.82, 58.98, 56.07, 55.13, 42.86, 37.78, 27.44, 25.22, 17.15, 14.45. HRMS m/z calculated for $C_{76}H_{103}NO_{20}Na$, 1372.6971; found, 1372.7004.

*4-{2-[4-(4-Aminobutyloxy)-3,5-dimethoxy]styryl}-4′-{2-[3,4,5-tris(1,4,7,10,13-pentaoxotetradecyl)]styryl}-9,9′-di-n-propylfluorene (**10**).* In a 250 mL two-necked flask, 240 mg of **9** (0.2 mmol, 1 equiv) was dissolved in absolute ethanol (30 mL) under argon atmosphere. Hydrazine hydrate (0.2 mL, 0.802 mmol) was then added. The mixture was refluxed for 5 h, then cooled to room temperature, after which aqueous 1 M HCl (5 mL) was added slowly. Then, the reaction mixture was neutralized with dilute sodium carbonate solution to pH = 7. The aqueous phase was extracted with dichloromethane, the organic phase was dried on $MgSO_4$, and the solvent was removed under vacuum. The crude product was purified by column chromatography on silica gel with methanol/dichloromethane mixture (5/95 in vol) as eluant to give 163 mg of the free amine **10** as a yellow oil (75% yield). ^{1}H NMR (300 MHz, $CDCl_3$, δ ppm): 7.65 (d, 2H J = 8.33 Hz), 7.50−7.46 (m, 4H), 7.10 (s, 2H), 7.05 (s, 2H), 6.80 (s, 2H), 6.78 (s, 2H), 4.23 (t, 4H, J = 4.83 Hz), 4.18 (t, 2H, J = 4.83 Hz), 4.02 (t, 2H, J = 6.35 Hz), 3.92 (s. 6H), 3.89 (t, 4H, J = 5.26 Hz), 3.81 (t, 2H, J = 5.26 Hz), 3.77−3.61 (m, 22H), 3.57−3.53 (m, 6H), 3.38 (s, 3H), 3.37 (s, 6H), 2.80 (t, 2H, J = 7.01 Hz), 2.02−1.65 (m, 8H), 0.70 (s, 10H). ^{13}C NMR (75.75 MHz, $CDCl_3$) δ (ppm): 153.54, 153.13, 152.73, 152.35, 151.49, 151.23, 140.52, 138.26, 137.00, 136.15, 133.09, 128.65, 127.92, 127.71, 125.57, 122.80, 120.62, 119.84, 119.55, 111.27, 108.05, 106.13, 105.47, 103.57, 77.17, 73.23, 73.08, 72.38, 71.88, 70.78, 70.73, 70.63, 70.61, 70.56, 70.46, 69.73, 68.81, 68.70, 58.97, 56.11, 55.98, 55.13, 55.02, 42.85, 41.87, 38.19, 29.97, 27.45, 17.16, 14.45. HRMS calculated m/z for $C_{68}H_{102}NO_{18}$, 1220.7096; found, 1220.7090.

*4-{2-[4-(4-Isothiocyanatobutyloxy)-3,5-dimethoxy]styryl}-4′-{2-[3,4,5-tris(1,4,7,10,13-pentaoxotetradecyl)]styryl}-9,9′-di-n-propylfluorene (**1**).* In a 100 mL two-necked flask, 350 mg of the amine derivative **10** (0.28 mmol, 1 equiv) was dissolved in 5 mL of anhydrous dichloromethane under argon atmosphere. The resulting solution was cooled at −20 °C. Then, 169 mg of 4-*N*,*N*-dimethylaminopyridine (1.29 mmol, 4.50 equiv) and 0.13 mL of thiophosgene (0.46 mmol, 1.60 equiv) were added. The reaction progress was monitored by TLC (silica, CH_2Cl_2/MeOH 85/15 in vol as eluant). After the disappearance of the starting materials, the solvent was removed under vacuum, and the crude product was chromatographed on silica gel, with CH_2Cl_2/MeOH 90/10 in vol as eluant. The desired amine-reactive chromophore **1** was obtained as a yellow oil (m = 346 mg, 99% yield). ^{1}H NMR (300 MHz, $CDCl_3$, δ ppm): 7.65 (d, 2H, J = 8.33 Hz), 7.53−7.44 (m, 4H), 7.11 (s, 2H), 7.05 (s, 2H), 6.80 (s, 2H), 6.78 (s, 2H), 4.23 (t, 4H, J = 4.83 Hz), 4.18 (t, 2H, J = 4.83 Hz), 4.02 (t, 2H, J = 6.35 Hz), 3.92 (s, 6H), 3.89 (t, 4H, J = 5.26 Hz), 3.81 (t, 2H, J = 5.26 Hz), 3.77−3.61 (m, 24H), 3.57−3.53 (m, 6H), 3.38 (s, 3H), 3.37 (s, 6H), 2.03−1.85 (m, 8H), 0.70 (s, 10H). ^{13}C NMR (75.75 MHz, $CDCl_3$, δ ppm): 153.50, 152.74, 151.52, 140.58, 140.47, 136.68, 136.18, 136.10, 133.34, 133.08, 128.79, 128.69, 127.86, 127.73, 125.60, 120.63, 119.85, 106.15, 103.43, 77.17, 72.38, 72.07, 71.89, 70.79,70.74, 70.65, 70.62, 70.57, 70.48, 69.73, 68.81, 58.98, 56.06, 55.93, 55.13, 44.79, 42.85, 26.99, 26.84, 17.15, 14.45. HRMS calculated m/z for $C_{69}H_{99}NO_{18}S$, 1262.5853; found, 1262.5827.

Two-Photon Absorption Properties. The TPA cross section spectra were obtained by up-conversion fluorescence using a Nd:YAG pumped optical parametric oscillator that produces 2.6 ns [full width at half-maximum (fwhm)] pulses in the 450−650 nm spectral range and using a Ti:sapphire femtosecond laser in the range 700−900 nm. This setup does not allow TPA measurements between 650 and 700 nm. The excitation beam is collimated over the cell length (10 mm). The fluorescence, collected at 90° of the excitation beam, was focused into an optical fiber connected to a spectrometer. The incident beam intensity was adjusted to ensure an intensity-squared dependence of the fluorescence over the whole spectral range. Calibration of the spectra was performed by comparison with *p*-bis(*o*-methylstyryl)benzene, for which σ_2 = 70 GM (Göppert-Mayer) at 570 nm (1 GM = 10^{-50} cm^4.s.photon^{-1}) and with the published 700−900 nm Rhodamine B two-photon absorption spectrum (*12*).

PEI−Dye Conjugation. In all experiments, we used a fresh stock solution of branched PEI (Mw = 25 kDa) with 100 mmol/L of primary amino groups (determination by the TNBS method, using spermine for the calibration curve (*13*)). Conjugation was achieved in microcentrifuge tubes by adding 50 μL of a solution of dye **1** in water (5 mg/mL) and 450 μL of borate buffer (pH = 9.4) to 500 μL of the PEI solution. PEI was incubated with dye **1** for 1 h with continuous stirring at room temperature. The mixture was allowed to stand overnight, and the unreacted dye was removed by gel chromatography (Sephadex G-25, Pharmacia, Freiburg Germany). The dye concentration of the PEI−**1** conjugate was then determined by absorption spectroscopy, using an extinction coefficient of 3.8 × 10^4 M^{-1} cm^{-1} at 354 nm.

Preparation of PEI/DNA Complexes. Complexes of DNA with PEI or PEI−**1** were prepared as described previously (*8*). Briefly, the indicated amounts of plasmid DNA (expressed in phosphate groups) and PEI−**1** (expressed in amine groups) prepared in 250 μL HEPES 20 mM, pH 7.4, were briefly mixed and incubated at room temperature. PEI/DNA complexes were formed at molar ratios of PEI nitrogen to DNA phosphate (N/P) ranging from 0.5 to 10.

Spectroscopic Measurements and Particle Size Measurements. One-photon absorption and fluorescence spectra were recorded on a Cary 400 spectrophotometer and a Fluorolog (Jobin-Yvon) spectrofluorimeter, respectively. The condensation of DNA by PEI−**1** was monitored by using the fluorescence of the DNA bis-intercalator YOYO-1. Plasmid DNA−YOYO-1 complexes were obtained by mixing equal volumes of solutions of DNA and YOYO-1 in 20 mM HEPES, 150 mM NaCl, pH 7.4. To ensure a uniform distribution of YOYO-1, the solution was incubated overnight at 4 °C under continuous stirring. The sizes of the PEI−**1**/DNA complexes were determined using a

Zetamaster 3000 (Malvern Instruments, Paris, France) with the following specifications: sampling time, 30 s; medium viscosity, 1.054 cP; refractive index (RI) medium, 1.34; RI particle, 1.45; scattering angle, 90°; temperature, 25 °C. Data were analyzed using the multimodal number distribution software of the instrument.

Two-Photon Imaging and FCS Measurements. Two-photon FCS and microscopy were performed on a home-built setup. Two-photon excitation (TPE) is provided by a Tsunami Ti:sapphire laser pumped with a Millennia V solid-state laser (Spectra-Physics, Mountain View, CA). Pulses of ~100 fs are produced with a 80 MHz frequency at 760 nm. After a beam expander, the infrared light is focused into the sample by a water-immersion Olympus objective (60×, NA = 1.2) mounted on an Olympus IX70 inverted microscope. The back aperture of the objective is slightly overfilled, creating a diffraction-limited focal spot. Samples were placed in eight wells of a Lab-Tek chambered cover glass (Nalge Nunc International, Rochester, NY) positioned in the *X* and *Y* directions by a motorized stage (Märzhäuser, Germany). The fluorescence from the samples was collected through the same objective and directed by a COWL750 dichroic mirror (Coherent, Orsay, France) toward a 50 μm diameter optical fiber coupled to an avalanche photodiode (SPCM 200 FC, EG&G, Canada). The residual infrared light was rejected by a BG39 Filter (Coherent). For FCS measurements, the normalized autocorrelation function (ACF), $G(\tau)$, of the fluorescence intensity fluctuations was calculated online by an ALV5000E digital correlator card (ALV, Langen, Germany). Calibration of the system was performed with a 50 nM tetramethylrhodamine (TMR) solution. Assuming a diffusion constant of 2.8×10^{-10} m^2 s^{-1} (*14*), the equatorial (r_0) and axial (z_0) radii of the focal volume were, respectively, 0.29 and 1.3 μm, giving an effective volume of 0.2 fL. Assuming a three-dimensional Gaussian distributed excitation intensity, the ACF curves were fitted with eqs 1 and 2 of Clamme et al. (*15*).

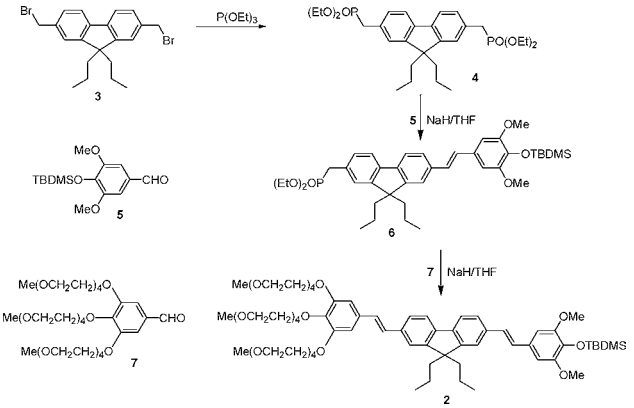
The imaging system on the same setup is based on the use of two galvo mirrors (model 6210, Cambridge Technology), in the so-called descanned detection mode. The two mirrors are used to deflect the beam along the *X*-axis and *Y*-axis, respectively. Each axis is driven by a closed-loop power amplifier, and the position of the mirrors is controlled through two ADC electronic boards (PCI6711, National Instruments). The photons were counted using a counter/timer board (PCI6602, National Instruments), synchronized with the scan of the galvo-mirrors. Nominally, one picture is 512 × 512 in size, and the dwelling time for each pixel is 4 μs (about 1 s per scan).

PEI−**1**/DNA complexes for two-photon imaging were prepared in 20 mM HEPES, 150 mM NaCl, pH 7.4, buffer. Equal volumes of 5 mM PEI−**1** (expressed in amine groups) and 1.4 mM DNA (expressed in phosphate groups) were mixed to reach a 60 μM final concentration of DNA and a N/P ratio of 10. Solutions were briefly vortexed and left for equilibration for 20 min before cell transfection. Prior to transfection, cells were seeded for 24 h in two wells of a Lab-Tek chambered coverglass at 10^5 cells per well in order to reach 70% confluence. After 24 h, the cells were rinsed and supplemented with 1.5 mL 10% FBS DMEM and 200 μL of complexes in order to deliver 4 μg of plasmid to the cells. After 2 h incubation, the cells were rinsed three times and covered with Hank's balanced salt solution (HBSS) for two-photon imaging.

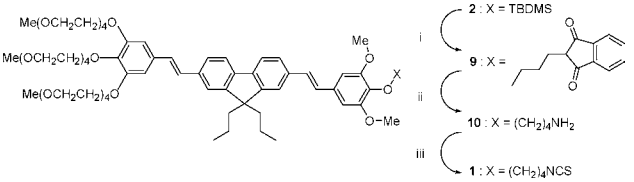
Cell Transfection and Cytotoxicity. HeLa cells were incubated in serum-free Opti-MEM with pCMVLuc plasmid (2 μg/well) complexed with PEI−**1** at N/P ratios ranging from 0.5 to 10. After 3 h 30 min, the transfection medium was replaced with fresh complete medium, and cells were cultured for an additional 24 h. Then, cells were lysed for luciferase activity quantization. Luciferase expression was recorded over 10 s using a Lumat LB9501/16 instrument (Berthold, Bad Wildbad, Germany) from an aliquot of the supernatant (5−10 μL) and expressed as RLU/mg of protein (luciferase activity per mg of protein in cell lysates).

Cytotoxicity of the PEI−**1**/DNA complexes was evaluated by quantification of the cellular content in proteins. The cells were transfected with PEI−**1**/DNA complexes in serum-free Opti-MEM. Twenty-four hours after the addition of the transfection solution, the cells were washed three times in PBS and lysed by the addition of 100 μL of cell culture lysis reagent (Promega). The cellular proteins were measured using the bicinchoninic acid assay (Interchim, Montlucon, France) following an incubation time of 30 min at 60 °C. The absorbance was read at 562 nm (*16*).

Scheme 1. Synthetic Pathway for the Preparation of the Key Intermediate 2



Scheme 2. Preparation of the Isothiocyanate Amine Reactive Chromophore 1[a]



[a] (i) (a) Bu_4NF, THF, (b) **8**, Na_2CO_3; (ii) H_2N-NH_2, EtOH; (iii) $CSCl_2$, CH_2Cl_2/DMAP.

RESULTS AND DISCUSSION

Synthesis and Characterization of the Isothiocyanate-Functionalized Two-Photon Fluorophore. The reactive group chosen in this study is an isothiocyanate moiety for its versatility in bioconjugation with amines. The basic architecture of the target isothiocyanate fluorophore is identical to our previously described active two-photon excited fluorescent (TPEF) chromophores (*6*). On one side of this fluorophore, three identical oligo(ethylene glycol) chains are used to provide good water solubility. On the opposite side, we opted for a syringaldehyde derivative (three ether functions, two as methyl ether, one as linker for further conjugation) in order to keep three O-alkyl groups (Figure 2). To prepare the chromophore **1**, the key intermediate is the protected phenol **2**. To get this intermediate, we prepared first the TBDMS-protected syringaldehyde derivative **5** and followed then the synthetic pathway shown in Scheme 1. The bisphosphonate **4** was reacted with 1 equiv of TBDMS-protected syringaldehyde **5** in basic conditions at 0 °C, and the pure dissymmetric compound **6** was isolated in 35% yield from the reaction mixture containing the monophosphonate compound **6**, the unreacted bis-phosphonate **4**, and the bis-coupled symmetric molecule. Compound **6** was then reacted at room

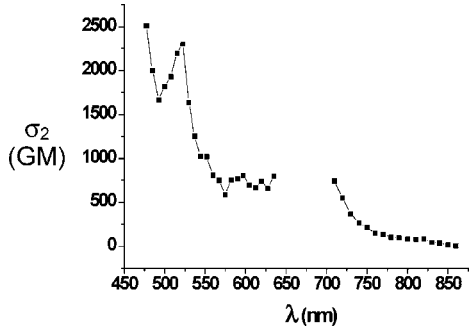


Figure 3. TPA spectra of **1** in water.

Table 1. Spectroscopic Properties of the Isothiocyanate-Functionalized Fluorophore 1

solvent	λ_{max}abs (nm)	ϵ ($M^{-1}\,cm^{-1}$)	λ_{max}ex (nm)	λ_{max}em (nm)	Φ (%)
CH_2Cl_2	365	6.9×10^4	365	435	83
H_2O	354	3.8×10^4	354	450	15

temperature with 1 equiv of aldehyde **7** to give the protected phenol derivative **2** in 44% yield. Chromophore **1** was finally obtained following the synthetic way described in Scheme 2. Fluoride deprotection of the TBDMS group affords the reactive phenolic moiety, which is etherified in situ with the commercially available *N*-(4-bromobutyl)phtalimide **8** according to Williamson conditions, to give the protected amine **9**. The amino group is then deprotected by hydrazine in ethanol to yield the free amine **10**. The isothiocyanate reactive group was finally obtained by reaction of the primary amine in **10** with thiophosgene. The targeted functionalized dye **1** was obtained in 95% yield. Structures of all new compounds have been confirmed by ^1H and ^{13}C NMR, and high-resolution mass spectrometry. Dye **1** has been designed to exhibit good water solubility to allow efficient conjugation in buffered aqueous media. Its solubility is over 10 $g.L^{-1}$ in saline physiological solution (turbidimetric method). The linear photophysical properties of this novel functionalized dye are similar to those of the parent symmetrical chromophore previously described (*6*), since the basic photoactive structure remains unchanged. The absorption and emission characteristics of **1** in dichloromethane and water solutions are described in Table 1. This fluorophore presents an intense absorption band in the 365 nm region in dichloromethane and 354 nm in water. This dye also exhibits an intense blue fluorescence in both methylene chloride (435 nm) and water (450 nm).

The nonlinear photophysical properties of **1** have been determined in water and methylene chloride from 480 to 650 nm in the visible, and from 700 to 900 nm in the IR (Figure 3). This chromophore exhibits a large TPA absorption in the red-IR region over 250 GM at 700 nm and a good resistance to photobleaching. Both the one- and two-photon properties of this blue fluorescent dye are promising for two-photon applications in biology.

PEI Conjugation and Spectroscopic Characterization of the Conjugated PEI. To show the potency of the isothiocyanate-functionalized chromophore to be used for two-photon microscopy applications, we conjugated PEI with derivative **1** (Figure 4). Conjugation was performed in borate buffer, pH 9.4, and unreacted dye was removed by gel chromatography. A conjugation of 2.6% of the primary amines of the PEI molecule, corresponding to an average number of 15 fluorophores per PEI molecule, was achieved. The absorption properties of the free chromophore **1** and PEI−**1** are compared in Figure 5. Conjugation to PEI slightly affects the vibronic structure of the absorption spectrum of **1**. In fact, the most pronounced change is the slight blue shift and relative increase of the vibronic peak

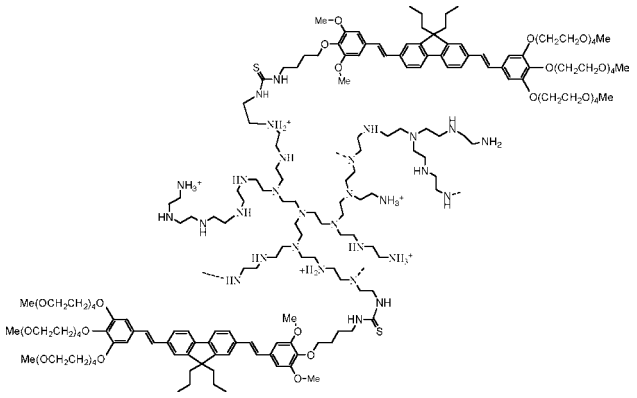


Figure 4. Schematic structure of the conjugate PEI−**1**.

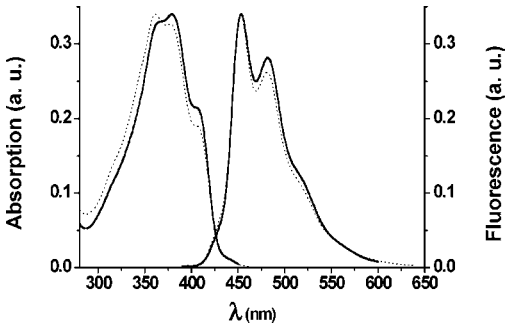


Figure 5. Absorption and fluorescence emission spectra of **1** and PEI−**1**. Both compounds are in 20 mM HEPES and 150 mM NaCl buffer, pH 7.4. $\lambda_{ex} = 354$ nm.

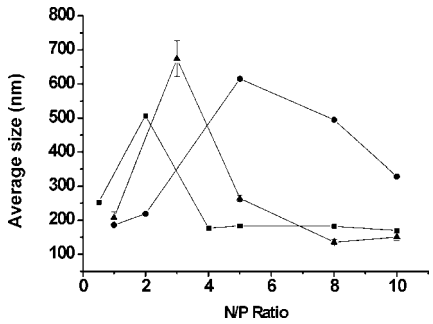


Figure 6. Average size of the PEI−**1**/DNA binary complexes as a function of the N/P ratio. The complexes are in 20 mM HEPES and 150 mM NaCl buffer, pH 7.4. PEI/DNA (■); PEI−**1**/DNA (●); DNA complexes with a mixture of labeled and unlabeled PEI added at a 1:3 ratio (▲).

at 361 nm, which becomes the strongest absorption peak of **1** in the conjugate. In the emission spectrum, no shift of the maximum emission accompanies the coupling of **1** to PEI, but only a slight relative increase of the emission shoulder at 480 nm. The quantum yield of fluorescence is not significantly affected by the conjugation of chromophore **1** with PEI (12% for PEI−**1** compared to 15% for free dye). It thus appears that conjugation of **1** to PEI only marginally modifies the electronic properties of **1**.

Size of the PEI−1/DNA Complexes and Condensation of DNA in These Complexes. The size of the complexes of calf thymus DNA with PEI−**1** at various N/P ratios was measured by light scattering and compared with the corresponding complexes obtained with nonlabeled PEI (Figure 6). In the case of nonlabeled PEI/DNA complexes, the size of the complexes increases with N/P, reaches a maximum at N/P = 2, and then decreases at higher N/P ratio. At N/P = 2, the complexes are neutral and thus have a strong tendency to aggregate, explaining the large size at this N/P ratio (*17*). In contrast, the smallest sizes are obtained at N/P ≥ 5 when the complexes are strongly

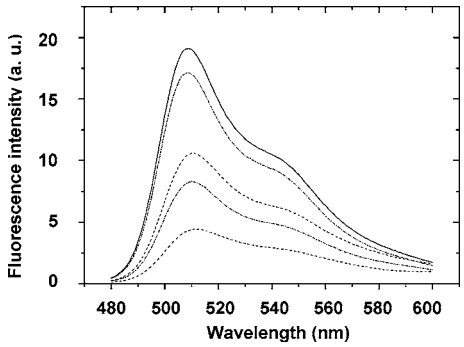


Figure 7. Fluorescence spectra of YOYO-1-labeled DNA complexed with PEI and PEI−**1**. The concentrations of DNA (phosphate) and YOYO-1 were 60 and 1.2 μM, respectively, to ensure a ratio of 1 YOYO-1 molecule per 50 bases. Spectra were recorded in the absence (solid line) or presence of PEI (dashed line) or PEI−**1** (dash−dotted line) at N/P ratios of 2 (top spectra) and 5 (bottom spectra). Samples were prepared as described in Figure 4. Excitation was at 470 nm.

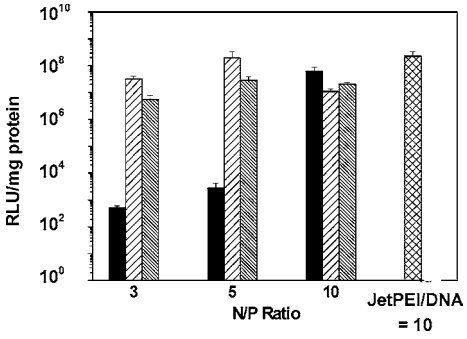


Figure 8. Transfection efficiency of PEI−**1**/DNA complexes. HeLa cells were incubated with pCMVLuc plasmid (2 μg/well) complexed to PEI−**1** (left), unlabeled PEI (center), or a mixture of PEI−**1** and unlabeled PEI (at a 1:3 ratio, right) in serum-free Opti-MEM. After 3 h 30 min, the transfection medium was replaced with fresh complete medium, and cells were cultured for an additional 24 h, before lysis. Gene expression was determined by the luciferase assay and expressed as RLU/mg of protein (luciferase activity per mg of protein in cell lysates). JetPEI was used as a control.

positively charged (*8*) and have thus no tendency to aggregate, due to electrostatic repulsions. A similar qualitative dependence of the size of the complexes as a function of N/P is obtained when PEI is substituted by PEI−**1**. However, two major differences are immediately apparent. The first one is the significant shift of the N/P ratio (from 2 to 5) at which the complexes are probably neutral and exhibit a size maximum. The second difference is the larger size of the complexes obtained with PEI−**1**, not only at the size maximum (650 nm vs 500 nm) but also at higher N/P ratios. Indeed, even at N/P = 10, the DNA/PEI−**1** complexes are about 350 nm and, thus, more than two times bigger than the complexes with unlabeled PEI. Both differences may be partly attributed to the decrease of the amine content of PEI−**1** due to labeling. This decreases the charge density of PEI and, thus, its ability to condense DNA, since condensation is strongly dependent on the extent of charge neutralization (*18*). The second and probably most important reason for the differences between labeled and unlabeled complexes may be related to the large size of dye **1** that may sterically hinder the proper neutralization of DNA charges by the labeled PEI and, consequently, the optimal compaction of the bound DNA. These drawbacks could be partially avoided if the complexes are obtained by adding labeled PEI together with unlabeled PEI at a ratio of 1:3 to the DNA. In these conditions, the complexes at N/P $\geq$ 8 are the same size as the complexes with unlabeled PEI, and the size maximum is shifted to N/P = 3. Importantly, both the larger maximum size of the latter complexes and the systematic shift of their sizes at N/P < 8 with respect to the unlabeled complexes suggest that both labeled and unlabeled PEI molecules are bound in the complexes with DNA. It may thus be inferred that, in these complexes, unlabeled PEI largely compensates for the defects of DNA compaction induced by the labeled PEI. To further investigate the condensation level of DNA in its complexes with PEI and PEI−**1**, we used the fluorescent DNA bis-intercalator YOYO-1 (*19*). This compound is characterized by a very high affinity for DNA (*20*) and remains bound to DNA during condensation by PEI (*19*). Moreover, the fluorescence intensity of free YOYO-1 is 3200 times lower than that of the bound form and could thus be neglected. When the level of DNA-bound YOYO-1 is sufficiently large (1 YOYO-1 for 50 bases), condensation by PEI was shown to induce a dramatic fluorescence decrease due to electronic interaction among YOYO-1 molecules bound on the same DNA molecule (*19*). Fluorescence spectra of YOYO-1 bound to DNA complexed with PEI and PEI−**1** at different N/P ratios are given in Figure 7. In excellent agreement with our conclusions above, the fluorescence of YOYO-1 in complexes with PEI−**1** was significantly higher than in complexes with unlabeled PEI at N/P ratios of 2 and 5, indicating that PEI−**1** less efficiently condenses DNA than unlabeled PEI.

Transfection Efficiency and Cytotoxicity of DNA/PEI−1 Complexes. PEI−**1**/DNA complexes were assessed for their in vitro transfection efficiency by monitoring the transient expression of the luciferase reporter gene in Hela cells. At N/P $\leq$ 5, the complexes gave luciferase signals (10^3 RLU/mg protein, Figure 8) that were 3 to 4 orders of magnitude lower than those obtained with unlabeled PEI but comparable to that of naked DNA (data not shown). This indicates that complexes with PEI−**1** are unable to transfect cells at these ratios. In sharp contrast, PEI−**1**/DNA complexes and PEI/DNA complexes show comparable transfection efficiencies at N/P > 5. Moreover, complexes obtained by mixing DNA with PEI−**1** and PEI at a 1:3 ratio were found to be as active as PEI/DNA complexes at all N/P ratios. These data show that by analogy to a large variety of compounds (poly(ethylene glycol), sugars, peptides, etc.; for a review, see Godbey et al. (*9*, *21*, *22*)), the conjugation of **1** does not compromise the transfection properties of PEI. In fact, the poor transfection observed with PEI−**1**/DNA complexes at N/P $\leq$ 5 may be rationalized by the size measurements, which suggest that the complexes may be negatively charged or neutral at these ratios and thus cannot efficiently interact with the cell membrane and be internalized by the cells (*8*, *23*). Finally, cell viability experiments using the bicinchoninic acid assay showed that only 10% of dead cells were observed after transfection with PEI−**1**/DNA or PEI/DNA complexes at N/P = 10 (data not shown), indicating that conjugation with **1** does not increase the cytotoxicity of PEI.

Two-Photon FCS and Microscopy of PEI−1/DNA Complexes. To demonstrate the validity of PEI−**1** in two-photon applications, we first performed two-photon FCS measurements of PEI−**1** either in its free form or bound to DNA. Two-photon excitation of the dye was provided by a tunable Ti:sapphire laser. Due to the optical specifications of our setup, it was not possible to excite the sample at wavelengths lower than 760 nm. Unfortunately, the TPA cross section of **1** at 760 nm is far from its maximum (below 700 nm, Figure 3). As a consequence, the brightness per molecule did no exceed 0.5 kHz/molecule and the signal-to-noise ratio was fair in the FCS measurements. Nevertheless, the fit of the FCS curves of free PEI−**1** (Figure 9) provided an observed diffusion constant of 1.6×10^{-10} $m^2.s^{-1}$ that is consistent with the previously reported diffusion constant of Rhodamine-labeled PEI (*15*). Moreover, in further agreement with the Rhodamine-labeled PEI data, a population with a slower diffusion constant ($(3.8 \pm 0.3) \times 10^{-11}$ $m^2.s^{-1}$) was detected

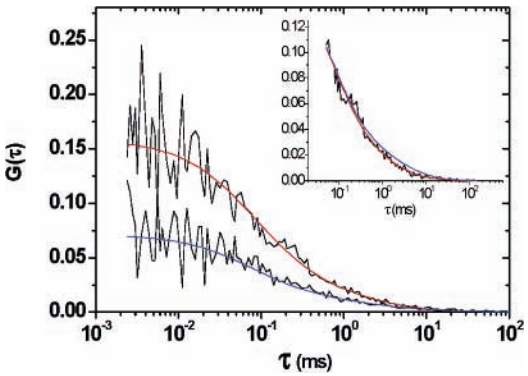


Figure 9. Autocorrelation curves of free PEI−**1** and PEI−**1**/DNA complexes. The concentration of PEI−**1** was 600 μM for both curves. The complexes were obtained at N/P = 10. The red and blue lines correspond to the best fits of the autocorrelation curves of PEI−**1** and PEI−**1**/DNA complexes, according to eq 2 of Clamme et al. (2003) with the diffusion coefficients given in the text. In the inset, the fitted curves were normalized and their bottom part was highlighted to show their differences.

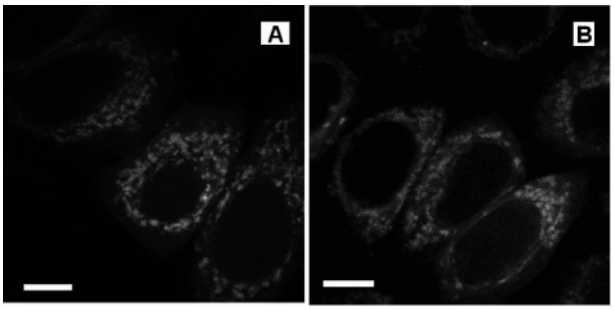


Figure 10. Two-photon microscopy of free PEI−**1** (A) and PEI−**1**/DNA complexes (B) in HeLa cells. Free PEI−**1** (600 μM) and PEI−**1**/DNA complexes (60 μM DNA, N/P = 10) were incubated for 2 h with HeLa cells, as described in Materials and Methods. Images were taken 30 min, post-transfection. Each bar represents 10 μm.

in some autocorrelation curves. However, since this diffusion constant is significantly different from that associated with the complexes and since its contribution to the autocorrelation curve is limited, this population corresponds to a minor species that cannot interfere with PEI−**1**/DNA measurements. Next, the FCS curve of the PEI−**1**/DNA complexes at N/P = 10 was recorded. In full agreement with our previous data using rhodamine-labeled PEI (*15*), the autocorrelation curves of PEI−**1**/DNA complexes were similar to the curves obtained with free PEI−**1** and, thus, were largely dominated by the contribution of free PEI. This confirms that a large proportion of PEI remains free when PEI is mixed with DNA. In fact, the only difference with free PEI is the presence of a small shoulder at long times in the autocorrelation curve of the complexes. The autocorrelation curves could be adequately fitted with a two-population model. If the correlation times of the two populations were allowed to float, the short correlation time was typical of that of free PEI. According to its small contribution, the correlation time (which is inversely related to the diffusion constant) of the complexes fluctuates in a larger range than that of free PEI. Nevertheless, if we assume that complexes are spherical, we obtained from their diffusion constant ($(1.2 \pm 0.6) \times 10^{-12}$ m^2.s^{-1}) a diameter of 360 nm that is in excellent agreement with that determined by light scattering (Figure 6).

In a next step, two-photon imaging of HeLa cells incubated with free PEI−**1** or transfected with PEI−**1** complexes at N/P = 10 was performed with the same setup as for FCS. In excellent agreement with previous studies (*15*, *24*), both free PEI−**1** and PEI−**1**/DNA complexes were found in discrete fluorescence patches that accumulate around the nucleus (Figure 10). This shows that conjugation of PEI by the chromophore does not compromise the efficient internalization of free and bound PEI by the cells and their accumulation in perinuclear compartments, identified as endosomes.

CONCLUSION

We described herein the synthesis and characterization of a functionalized two-photon absorbing chromophore with blue emission. This chromophore was successfully conjugated to PEI and was found to substitute unlabeled PEI, without compromising the transfection properties of PEI. In spite of a nonoptimized excitation wavelength, the labeled PEI was successfully used in two-photon FCS and imaging. The obtained results were close to those previously reported for Rhodamine-labeled PEI. However, due to its rather large size, the dye decreases to some extent the condensing properties of PEI, affecting the size of the PEI/DNA complexes. Thus, it is recommended to use them in a mixture with unlabeled PEI, since complexes obtained with a 3:1 ratio of unlabeled to labeled PEI were found to be highly similar to the unlabeled PEI/DNA complexes.

ACKNOWLEDGMENT

Part of this work was supported by the CNRS and University Louis Pasteur of Strasbourg. A.H. is grateful to the French ministry of research for a fellowship. Other part of this work and S.E. have been supported by the Agence Française contre les Myopathies (AFM) and CNRS.

LITERATURE CITED

(1) Abbotto, A., Baldini, G., Beverina, L., Chirico, G., Collini, M., D'Alfonso, L., Diaspro, A., Magrassi, R., Nardo, L., and Pagani, G. A. (2005) Dimethyl-pepep: a DNA probe in two-photon excitation cellular imaging. *Biophys. Chem. 114*, 35−41.

(2) Krishna, T. R., Parent, M., Werts, M. H., Moreaux, L., Gmouh, S., Charpak, S., Caminade, A. M., Majoral, J. P., and Blanchard-Desce, M. (2006) Water-soluble dendrimeric two-photon tracers for in vivo imaging. *Angew. Chem., Int. Ed. 45*, 4645−4648.

(3) Squirrell, J. M., Wokosin, D. L., White, J. G., and Bavister, B. D. (1999) Long-term two-photon fluorescence imaging of mammalian embryos without compromising viability. *Nat. Biotechnol. 17*, 763−767.

(4) Berland, K. M., So, P. T., and Gratton, E. (1995) Two-photon fluorescence correlation spectroscopy: method and application to the intracellular environment. *Biophys. J. 68*, 694−701.

(5) Medina, M. A., and Schwille, P. (2002) Fluorescence correlation spectroscopy for the detection and study of single molecules in biology. *Bio-essays 24*, 758−764.

(6) Hayek, A., Bolze, F., Nicoud, J.-F., Baldeck, P. L., and Mély, Y. (2006) Synthesis and characterization of water-soluble two-photon excited blue fluorescent chromophores for bioimaging. *Photochem. Photobiol. Sci. 5*, 102−106.

(7) Hayek, A., Bolze, F., Nicoud, J.-F., Dupperay, A., Grichine, A., Baldeck, P., and Vial, J.-C. (2006) Two-photon water-soluble dyes and their amine reactive derivatives for two-photon bio-imaging applications. *Nonlinear Opt., Quantum Opt. 35*, 155−164.

(8) Boussif, O., Lezoualc'h, F., Zanta, M. A., Mergny, M. D., Scherman, D., Demeneix, B., and Behr, J.-P. (1995) A versatile vector for gene and oligonucleotide transfer into cells in culture and in vivo: polyethylenimine. *Proc. Natl. Acad. Sci. U.S.A. 92*, 7297−7301.

(9) Godbey, W. T., Wu, K. K., and Mikos, A. G. (1999) Poly-(ethylenimine) and its role in gene delivery. *J. Controlled Release 60*, 149−160.

(10) Baker, A., Saltik, M., Lehrmann, H., Killisch, I., Mautner, V., Lamm, G., Christofori, G., and Cotten, M. (1997) Polyethylenimine (PEI) is a simple, inexpensive and effective reagent for condensing and linking plasmid DNA to adenovirus for gene delivery. *Gene Ther. 4*, 773−782.

(11) Wightman, L., Kircheis, R., Rossler, V., Carotta, S., Ruzicka, R., Kursa, M., and Wagner, E. (2001) Different behavior of branched and linear polyethylenimine for gene delivery in vitro and in vivo. *J. Gene Med. 3*, 362−372.
(12) Xu, C., and Webb, W. W. (1996) Measurement of two-photon excitation cross sections of molecular fluorophores with data from 690 to 1050 nm. *J. Opt. Soc. Am. B 13*, 481−491.
(13) Snyder, S. L., and Sobocinski, P. Z. (1975) An improved 2,4,6-trinitobenzenesulfonic acid method for the determination of amines. *Anal. Biochem. 64*, 284−288.
(14) Egele, C., Schaub, E., Piémont, E., de Rocquigny, H., and Mély, Y. (2005) Investigation by fluorescence correlation spectroscopy of the chaperoning interactions of HIV-1 nucleocapsid protein with the viral DNA initiation sequences. *C. R. Biol. 328*, 1041−1051.
(15) Clamme, J. P., Krishnamoorthy, G., and Mély, Y. (2003) Intracellular dynamics of the gene delivery vehicle polyethylenimine during transfection: investigation by two-photon fluorescence correlation spectroscopy. *Biochim. Biophys. Acta 1617*, 52−61.
(16) Zaric, V., Weltin, D., Erbacher, P., Rémy, J. S., Behr, J.-P., and Stephan, D. (2004) Effective polyethylenimine-mediated gene transfer into human endothelial cells. *J. Gene Med. 6* (2), 176−184.
(17) Choosakoonkriang, S., Lobo, B. A., Koe, G. S., Koe, J. G., and Middaugh, C. R. (2003) Biophysical characterization of PEI/DNA complexes. *J. Pharm. Sci. 92*, 1710−1722.
(18) Arscott, P., Li, A., and Bloomfield, V. A. (1990) Condensation of DNA by trivalent cations 1: effect of DNA length and topology on the size and shape of condensed particles. *Biopolymers 30*, 619−630.
(19) Krishnamoorthy, G., Duportail, G., and Mély, Y. (2002) Structure and dynamics of condensed DNA probed by 1,1′-(4,4,8,8-tetramethyl-4,8-diazaundecamethylene)bis[4-[[3- methylbenz-1,3-oxazol-2-yl]methylidine]-1,4-dihydroquinolinium] tetraiodide fluorescence. *Biochemistry 41*, 15277−15287.
(20) Hirons, G. T., Fawcett, J. J., and Crissman, H. A. (1994) TOTO and YOYO: new very bright fluorochromes for DNA content analyses by flow cytometry. *Cytometry 15*, 129−140.
(21) Lungwitz, U., Breunig, M., Blunk, T., and Gopferich, A. (2005) Polyethylenimine-based non-viral gene delivery systems. *Eur. J. Pharm. Biopharm. 60*, 247−266.
(22) Kichler, A. (2004) Gene transfer with modified polyethylenimines. *J. Gene Med. 6 Suppl. 1*, S3−10.
(23) Behr, J.-P. (1994) Gene transfer with synthetic cationic amphiphiles: prospects for gene therapy. *Bioconjugate Chem. 5*, 382−389.
(24) Remy-Kristensen, A., Clamme, J.-P., Vuilleumier, C., Kuhry, J. G., and Mély, Y. (2001) Role of endocytosis in the transfection of L929 fibroblasts by polyethylenimine/DNA complexes. *Biochim. Biophys. Acta 1514*, 21−32.

BC060362H

Turnip Yellow Mosaic Virus as a Chemoaddressable Bionanoparticle

Hannah N. Barnhill,[†] Rachel Reuther,[†] P. Lee Ferguson,[†] Theo Dreher,[‡] and Qian Wang*,[†]

Department of Chemistry and Biochemistry and Nanocenter, University of South Carolina, 631 Sumter Street, Columbia, South Carolina 29208, and Department of Microbiology, Oregon State University, Corvallis, Oregon 97331. Received December 18, 2006; Revised Manuscript Received February 2, 2007

Viruses and virus-like particles (VLPs) have been demonstrated to be robust scaffolds for the construction of nanomaterials. In order to develop new nanoprobes for time-resolved fluoroimmuno assays as well as to investigate the two-dimensional self-assembly of viruses and VLPs, the icosahedral turnip yellow mosaic virus (TYMV) was investigated as a potential building block in our study. TYMV is an icosahedral plant virus with an average diameter of 28 nm that can be isolated inexpensively in gram quantities from turnips or Chinese cabbage. There are 180 coat protein subunits per TYMV capsid. The conventional *N*-hydroxysuccinimide-mediated amidation reaction was employed for the chemical modification of the viral capsid. Tryptic digestion with sequential MALDI-TOF MS analysis identified that the amino groups of K32 of the flexible N-terminus made the major contribution for the reactivity of TYMV toward *N*-hydroxysuccinimide ester (NHS) reagents. The reactivity was also monitored with UV−vis absorbance and fluorescence, which revealed that approximately 60 lysines per particle could be addressed. We hypothesized that the flexible A chain contains the reactive lysine because the crystal structure of TYMV has shown that chain A is much more flexible compared to B and C, especially at the N-terminal region where the Lys-32 located. In addition, about 90 to 120 carboxyl groups, located in the most exposed sequence, could be modified with amines catalyzed with 1-(3-dimethylaminopropyl-3-ethylcarbodiimide) hydrochloride (EDC) and sulfo-NHS. TYMV was stable to a wide range of reaction conditions and maintained its integrity after the chemical conjugations. Therefore, it can potentially be employed as a reactive scaffold for the display of a variety of materials for applications in many areas of nanoscience.

INTRODUCTION

Viruses and virus-like particles (VLPs), also known as bionanoparticles, have recently emerged as promising building blocks for nanomaterials (*1*−*7*). For example, it has already been shown that semiconductive or conductive nanowires can be prepared with rod-like tobacco mosaic virus (TMV) as the template (*2*, *7*−*14*). Spherical nanoparticles were produced using the hollow protein shell of icosahedral cowpea chlorotic mottle virus (CCMV) as a nanoreactor (*4*, *15*). With genetically modified filamentous bacteriophage M13 as a template, inorganic, organic, and biological nanosized materials have been aligned into nanowires (*16*, *17*), nanorings (*18*), nanofibers (*19*), films (*20*, *21*), and other nanostructures (*22*−*24*).

Because of increasing interest in using bionanoparticles for drug delivery and other biomedical applications (*1*, *25*−*27*), it is of particular demand to develop methods to anchor functional groups on viral particles. Cowpea mosaic virus (CPMV) was the first virus to be demonstrated as a robust platform for the conjugation with a variety of molecules, ranging from small molecules such as fluorescent dyes (*5*, *28*−*31*) to larger particles such as quantum dots (*32*). In addition, polymers (*33*, *34*), stilbene derivatives (*30*), biotin (*28*, *29*), DNA (*35*), peptides and proteins (*36*−*38*), and carbohydrates (*34*, *39*) have been successfully conjugated to CPMV in an ordered and predictable manner. Following CPMV, the chemical reactivities of many other viruses have been studied, including CCMV (*40*), *Nudaurelia capensis omega* virus (*41*), TMV (*42*, *43*), and bacteriophage MS2 (*44*). Moreover, it is possible to engineer multiple orthogonal reactive sites on the viral capsid using conventional bioconjugation techniques or newly developed chemistries (*5*, *42*, *44*).

In order to develop new nanoprobes for time-resolved fluoroimmuno assays as well as to investigate the two-dimensional self-assembly of bionanoparticles (*6*, *45*, *46*), the icosahedral turnip yellow mosaic virus (TYMV) was explored as a potential building block in our study. As a member of the tymovirus group, TYMV is a plant virus with an average diameter of 28 nm and made of a single-stranded RNA of 1.9 $\times$ 10^6 Da and 180 chemically identical protein subunits of 20 133 Da. The subunits arrange into 60 trimeric asymmetric units loosely assembled in a $T = 3$ icosahedral symmetry as shown in Figure 1 (*47*−*49*). The structure of TYMV has been exhaustively studied by X-ray crystallographic analysis (*47*, *48*) and electron microscopy using negative staining (*50*). It can be isolated from the infected leaves of either the turnip or Chinese cabbage in gram quantities. Comparing with other plant viruses, TYMV has some unique advantages in chemistry, biomedical applications, and materials development. First, empty capsids can be isolated naturally from the host plant or generated artificially by treating under pressure (*51*), basic environment (*52*), or repeated freeze−thaw process (*53*). Second, some of these methods result in a hole in the otherwise intact capsid, which may provide a route for the introduction of useful materials, such as quantum dots or drugs, and opens the possibility of interior modification of the capsid. Third, TYMV is stable from 4 °C to RT for months and 60 °C for several hours. It can withstand, for a wide pH range (4−10), up to 50% organic solvent and a variety of reaction conditions. Finally, the capsid of TYMV represents a very rigid spherical assembly; therefore, we can predict the conformation of the coat proteins and attached molecules based on the X-ray structural data (*48*). In this paper, we will report the chemoselective modification of native TYMV at the lysine residues and carboxyl groups.

* Corresponding author. Phone: ++001-803-777-8436. Fax: ++001-803-777-9521. E-mail: wang@mail.chem.sc.edu.

[†] University of South Carolina.

[‡] Oregon State University.

10.1021/bc060391s CCC: $37.00 © 2007 American Chemical Society
Published on Web 04/12/2007

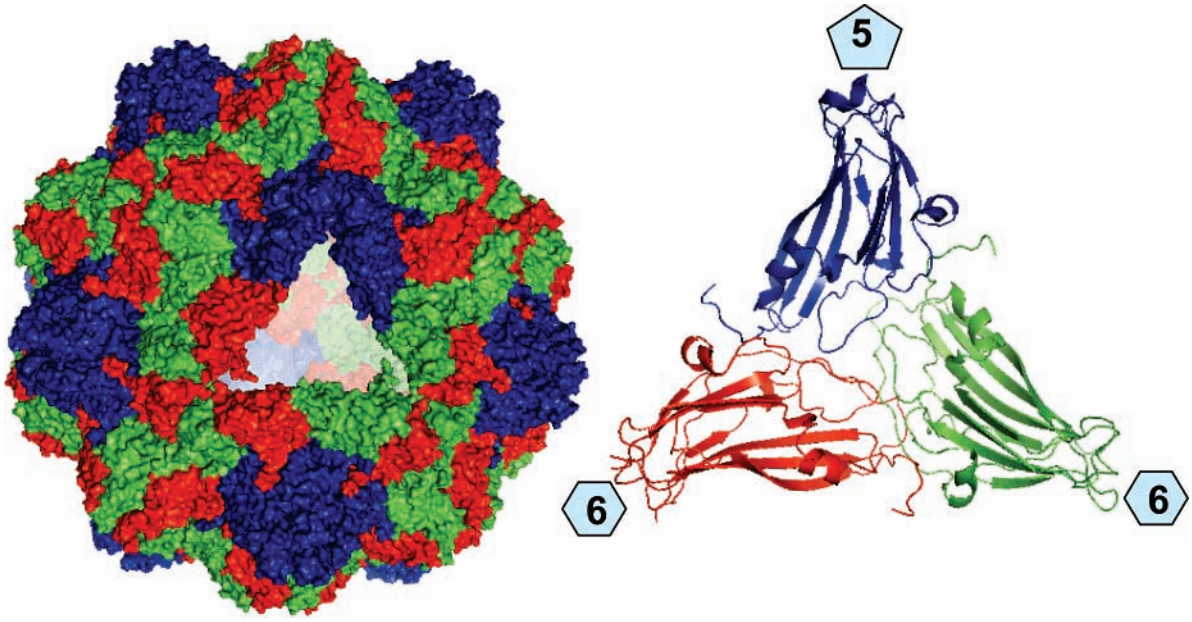
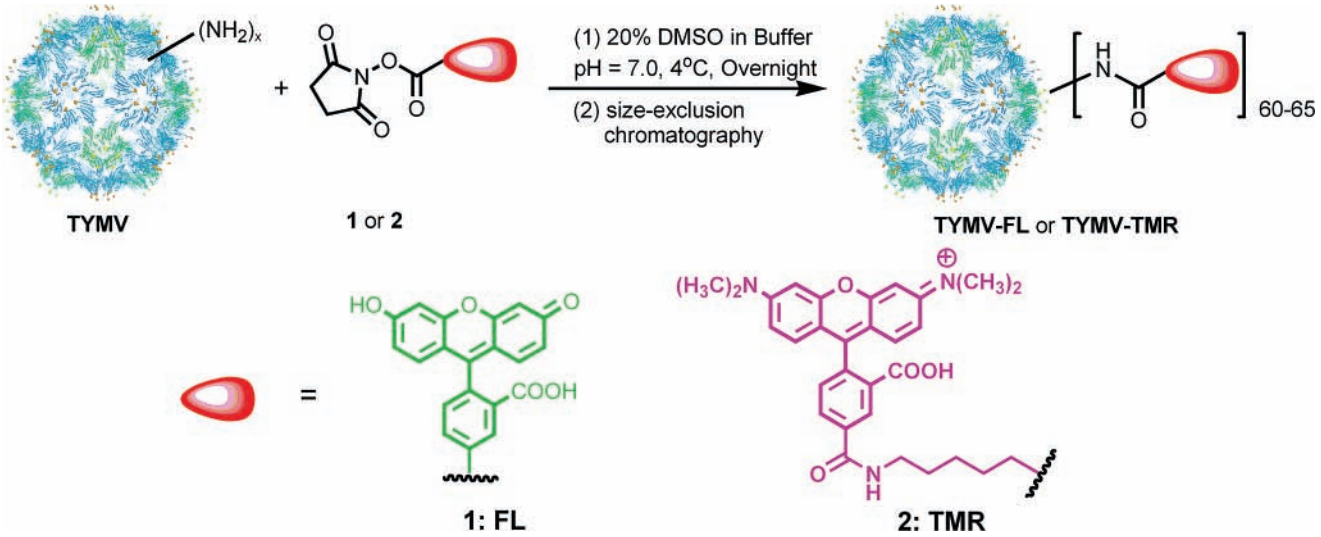


Figure 1. (Left) Structure of TYMV protein capsid with an asymmetric unit cut out. Protein subunits are colored as blue (chain A), red (chain B), and green (chain C) (*49*). (Right) Enlarged ribbon diagram of TYMV asymmetric unit, which includes three subunits. The 5- and 6-fold axes are labeled where they form on the intact capsid (*48*).

Scheme 1



EXPERIMENTAL PROCEDURES

General. Most bioreagents were purchased from Bio-Rad or Fisher and used without further purification. Anti-TYMV antibody was raised in rabbits. Reactive dyes were purchased from Molecular Probes and used without further purification. Unless otherwise indicated, "buffer" refers to 10 mM potassium phosphate at pH 7.8. Size exclusion columns for purification of virus-containing reaction mixtures were prepared by pre-swelling 23 g of Bio-Gel P-100 (Bio-Rad) in 400 mL of buffer and loading the gel into Bio-Spin disposable chromatography columns (Bio-Rad). The columns were allowed to drain upon standing and were then further dried by centrifugation (3 min at 800 *g*). For 80 μL of virus solution (1 mg/mL), approximately 1 mL of prepared gel is required. Ultracentrifugation was performed at the indicated rpm values using a Beckman Optima L-90K Ultracentrifuge equipped with either SW41 or 50.2 Ti rotors. TEM analyses were carried out by depositing 20 μL aliquots of each sample at a concentration of 0.1 to 0.3 mg/mL onto 100-mesh carbon-coated copper grids for 2 min. The grids were then stained with 20 μL of 2% uranyl acetate and viewed with a Hitachi H-8000 TEM electron microscope. FPLC analyses were performed on an AKTA Explorer (GE Biotech) using a Superose-6 size-exclusion column. Potassium phosphate buffer (0.05 M, pH 7.0) with 0.15 M NaCl was used as eluent, and the intact virions show retention volume of approximately 10 mL at an elution rate of 0.4 mL/min, whereas broken particles and individual subunit proteins elute after more than 20 mL. Western Blot analysis was carried out using a Bio-Rad Mini Trans-Blot Electrophoretic Transfer Cell with a 15% polyacrylamide gel.

Purification of TYMV. Chinese cabbage was grown for 3 weeks after which it was inoculated with TYMV. After one week leaves began showing symptoms. After an additional 2 weeks, the leaves were picked and subjected to purification. Infected leaves were blended with 3× volume of buffer and 0.1% β-mercaptoethanol. The mixture was filtered and the filtrate subjected to centrifugation to remove bulk plant material. The supernatant was collected and clarified by adding an equal volume of $CHCl_3$/1-butanol (v/v = 1:1). The aqueous layer was collected, and the virus was precipitated with 8%

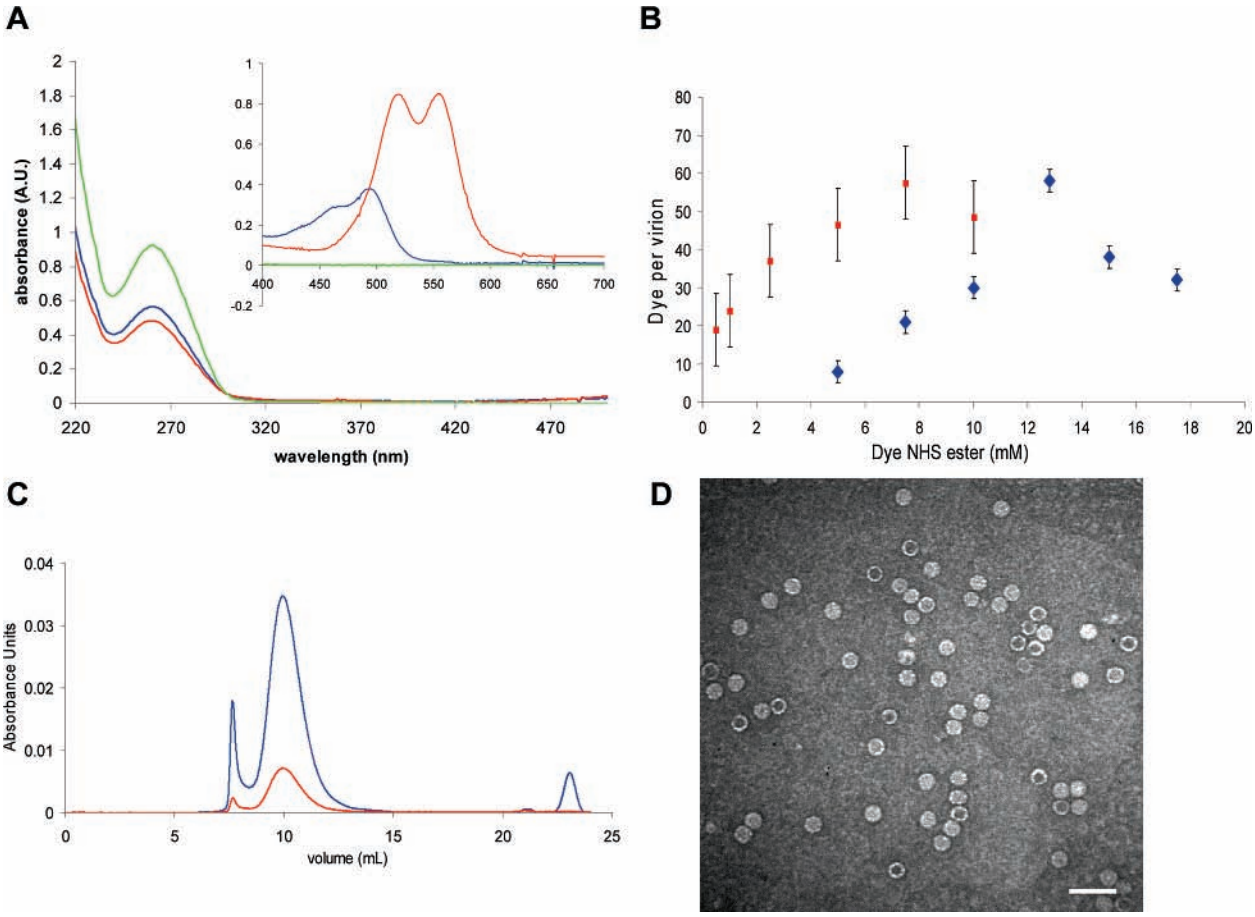


Figure 2. (A) UV−vis spectra show virus absorbance of WT−TYMV (green line) and TYMV after modification with **1** (blue line) and **2** (red line) after purification and a 20-fold dilution. UV−vis absorbances of the dyes on TYMV directly after purification with no dilution are shown in the inset. (B) Loading of **1** (blue) and **2** (red) on TYMV related to concentration of reagents in the reaction mixture. (C) Size exclusion FPLC analysis of **2**-modified TYMV: intact particles elute at 10 mL, denatured protein at 23.5 mL, and aggregated TYMV at 8 mL. Blue line is absorbance at 260 nm and red line is absorbance at 555 nm, indicating that **2** is attached to the intact particles. (D) TEM image of **1**-modified TYMV, the scale bar = 100 nm.

PEG 8K and 0.2 M NaCl. The pellet was centrifuged, resuspended in buffer, and purified by centrifuging over a sucrose gradient which showed two bands, one for the filled particle and one for the empty particle. In general, the virus was stored in buffer at a concentration of 10 mg/mL at 4 °C and stable for months.

SDS-PAGE Analysis. Polyacrylamide gel electrophoresis was carried out in Bio-Rad MiniPROTEAN 3 gel electrophoresis cell. For analysis by coomassie blue staining, 1 μg of TYMV was denatured by heating at 95 °C for 5 min with Tris-HCl buffer containing β-mercaptoethanol, bromophenol blue, and glycerol. The proteins were then resolved on a 15% polyacrylamide gel at 200V for 1 h and stained with Bio-Rad Biosafe Coomassie Blue stain for 1 h and destained with distilled water. Fluorescently labeled TYMV was visualized with a UVP Epi Chemi II imager before staining.

MALDI-TOF MS of TYMV Subunit. A solution of TYMV (1 mg/mL, 26 μL) was treated with guanidinium-HCl (6.0 M, 4 μL) for 5 min at RT. The denatured protein was spotted onto a MALDI plate using Millipore ZipTip $_{\mu-C18}$ tips to remove the salts. The samples were analyzed using a Bruker Ultra-Flex I TOF/TOF mass spectrometer with MS grade sinapinic acid in 70% acetonitrile and 0.1% TFA as the matrix.

Trypsin in-Gel Digestion and MALDI Study. Pure viral protein (1 mg) was resuspended in Tris−HCl buffer (pH 7.4, 100 mM, 26 μL). Urea (6.0 M, 100 μL) and DTT (200 mM, 5 μL) were added, and the solution was incubated for 1 h at RT. Then the solution was diluted ten times and incubated with sequencing-grade modified trypsin (protein:enzyme = 50:1) for 18 h at 37 °C. The pH was then adjusted to slightly below 6 to quench the reaction. Tryptic digests were then analyzed by MALDI-TOF MS and MALDI-TOF-TOF MS-MS using a Bruker Ultra-Flex I TOF/TOF mass spectrometer and mass spectroscopy grade trypsin in 70% acetonitrile and 0.1% TFA as the matrix.

Reactivity Screening of TYMV. The reactivity of the lysine residues of TYMV was screened by incubating with varying concentrations of fluorescein *N*-hydroxysuccinimidyl (NHS) ester **1** or *N*,*N*,*N*′,*N*′-tetramethylrhodamine NHS ester **2** at a virus concentration of 1.0 mg/mL in a mixed solution of buffer and DMSO (v/v = 80:20). Reactions were purified by size-exclusion chromatography using Bio-Gel P-100 (Bio-Rad) in Bio-Spin disposable chromatography columns as described above. The carboxylic acid residues of TYMV were screened for reactivity by incubating with varying concentrations of fluoresceinamine **3**, EDC (10 mM), and sulf-NHS (5.0 mM) in buffer and purified by size exclusion chromatography. The loading of dyes per virion was determined by UV−visible spectroscopy. Virus concentrations were determined by measuring the absorbance at 260 nm; virus at 1.0 mg/mL gives a standard absorbance of 8.3. The average molecular weight of the TYMV capsid is 3.6 $\times$ 10^6. Dye concentrations were obtained by measurement of absorbance at λ_{max} (495 nm for **1** and 555 nm for **2**), with molar absorbtivity calibrated for each use by mixing known quantities of dye with TYMV (1.0 mg/mL). The integrity of the modified TYMV was determined by TEM, FPLC, and SDS-PAGE. Reactive residues were identified using tryptic digestion of

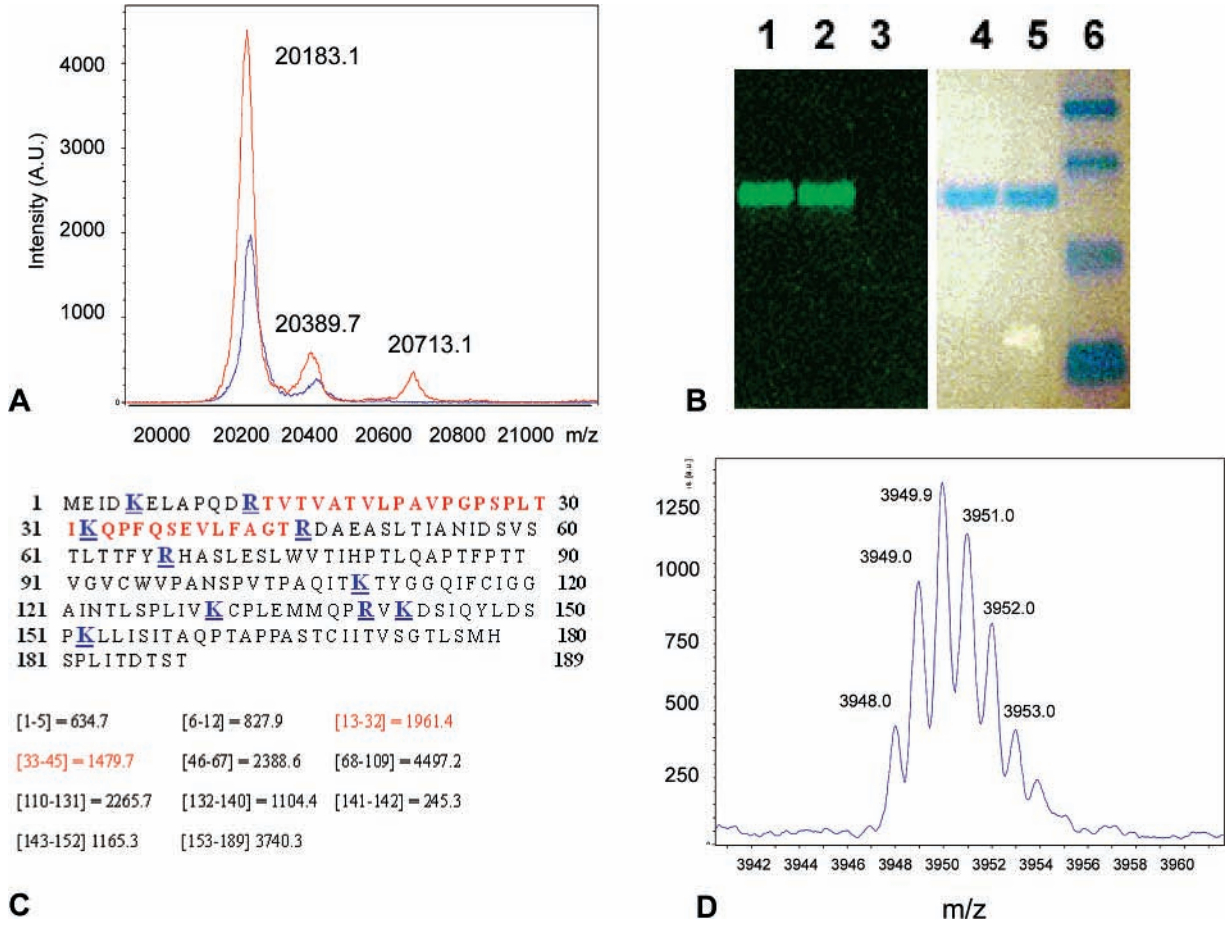


Figure 3. (A) MALDI-TOF MS of whole subunit of WT−TYMV (blue line) and TYMV after modification with **2** (red line). WT peak = 20 183 *m/z*, modified peak = 20 713 *m/z* (the mass of modification with **2** = 527 Da). Peak at 20 389 *m/z* is a matrix adduct. (B) SDS-PAGE of fluorescein-modified TYMV visualized under UV irradiation (left) or upon Coomassie Blue staining (right). (C) Tryptic digestion map of the coat protein of TYMV with the tryptic residues (K and R) highlighted in blue and the peptide sequence including reactive Lys-32 highlighted in red. (D) MALDI-TOF MS spectrum of tryptic digest, highlighting the peak corresponding to **2**-modified peptide containing residues T13−R45. Theoretical *m/z* = 3950.1, measured *m/z* = 3949.9 indicating Lys-32 as the reactive residue on the basis that the dye adduct suppresses tryptic cleavage at K32.

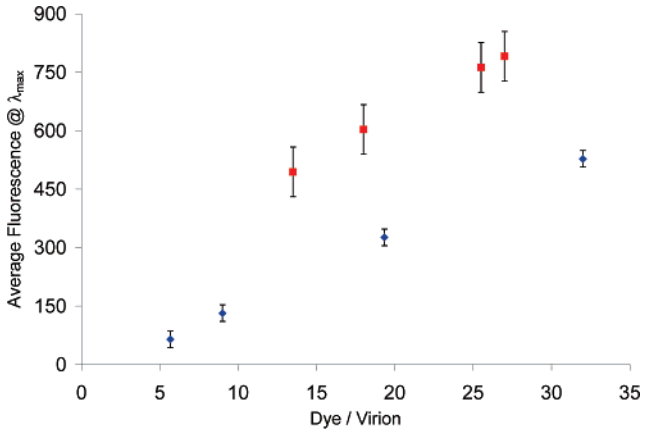


Figure 4. Fluorescence vs dye loading for **1** modified (blue) and **2** modified (red) TYMV.

modified particles and MALDI-TOF mass spectrometry as described above.

RESULTS AND DISCUSSION

TYMV was able to be purified in high yield from Chinese cabbage, i.e., about 0.5 mg of pure virus per gram of wet leaves. Purification yields from turnips were slightly lower, i.e., 0.2 mg of virus per gram of wet leaves. The integrity of virus through the purification was confirmed by FPLC, TEM, SDS-PAGE, and Western-blot analysis. Fluorescein (FL) *N*-hydroxysuccinimidyl (NHS) ester **1** and *N*,*N*,*N*′,*N*′-tetramethylrhodamine (TMR) NHS ester **2**, which are selective for reactions with amino groups of proteins, were utilized to screen the reactivity of TYMV at pH 7.8 to give TYMV−FL and TYMV−TMR (Scheme 1).

The reactions were purified over size exclusion chromatography and analyzed by UV−vis absorbance. As shown in Figure 2A, the absorbance of the virus, taken after a 20-fold dilution, gives the absorbance of viral genome and capsid proteins at 260 and 280 nm together with the absorbance of the dyes on TYMV. The UV−vis measurements were used to calculate the dye/virion ratios based on the molar absorbtivity of the dye and of the virus. When different concentrations of reagent **1** were used, up to 60 fluorescein molecules were attached on TYMV (see Figure 2B) although a loading of 40 dye molecules per virion was more typical. A consistent loading of 60 TMR were anchored on TYMV using dye **2** (Figure 2B). The different reactivities are likely due to the accessibility of the dyes to the reactive sites. Dye **2** has an additional five-carbon spacer between the bulky dye moiety and the NHS group, which makes it easier to access the reactive sites. The TYMV particles were stable to the reactions and remained intact as shown by FPLC and TEM (Figure 2C and 2D).

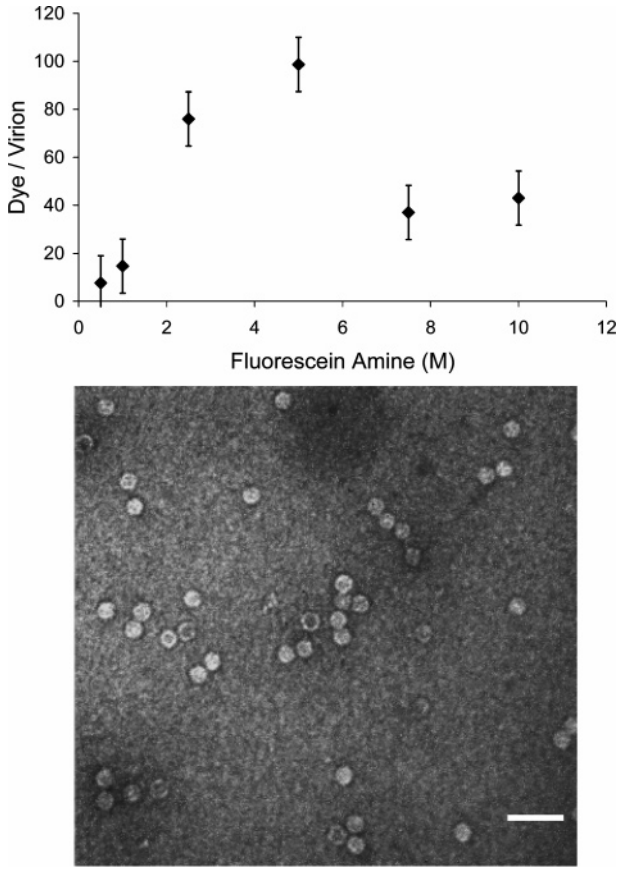


Figure 5. (Top) Reactivity of the carboxylic acid residues of TYMV with **3** activated with EDC and sulfo-NHS. (Bottom) TEM analysis of **3**-modified TYMV (scale bar = 100 nm).

MALDI-TOF MS analysis of the subunit of TYMV (before and after the modification) confirmed a partial single modification (Figure 3A). The addition of dye motifs will alter the ionization efficiency of the protein in MALDI due to capping of basic residues; however, the presence of the peak at m/z = 20713.1 corresponds to the addition of one TMR unit on the TYMV coat protein and is only present in the mass spectrum of the modified TYMV [The peak at m/z = 20389.7 corresponds to a matrix adduct commonly seen in MALDI-TOF mass spectra of proteins and is present in both the WT−TYMV and the modified TYMV (*54*)]. Therefore, the absolute signal intensity could not precisely reflect the relative ratio of modified vs unmodified protein. SDS-PAGE of the fluorescein-modified particles also showed the covalent attachment of dyes to the TYMV subunit (Figure 3B). Figure 3C shows tryptic map of the TYMV coat protein, with the reactive peptide highlighted in red and K32 underlined. Upon in-solution digestion of the protein bands with trypsin, the digested fragments were analyzed by MALDI-TOF MS and confirmed that K32 is the reactive residue as shown by appearance of the peak m/z = 3949.9, indicating K32 as the reactive residue. This mass was calculated based on the attachment of the dye and on the fact that the dye adduct suppresses tryptic cleavage at K32 (Figure 3D). Using trypsin alone, we were able to achieve 88.8% to 93.7% sequence coverage for the WT protein; however, using V8 protease digestion in addition to trypsin gave us between 95.2% and 100% sequence coverage.

Within each asymmetric unit of TYMV capsid, there are three different subunits chains termed A, B, and C as shown in Figure 1. Although they are chemically identical proteins, each subunit is located in a different microenvironment and adapts a slightly different configuration. While chains B and C make up hexameric structures on the virus, chain A makes up the pentameric units. Studies on the crystal structure of TYMV have shown that chain A is much more flexible compared to B and C, especially at the *N*-terminal region where the K32 located (*55*, *56*). It is possible that the flexibility of A chain allows the access of NHS reagents; therefore, only about one-third of the K32 residues are chemically addressable. Other than trace amount of modification at K142, forced reaction conditions (longer reaction time or more concentrated starting reagents) could not accomplish quantitative modification of K32, as demonstrated by the existence of the unmodified peptide peak containing K32 at m/z = 1961.4 in the tryptic digestion of modified TYMV.

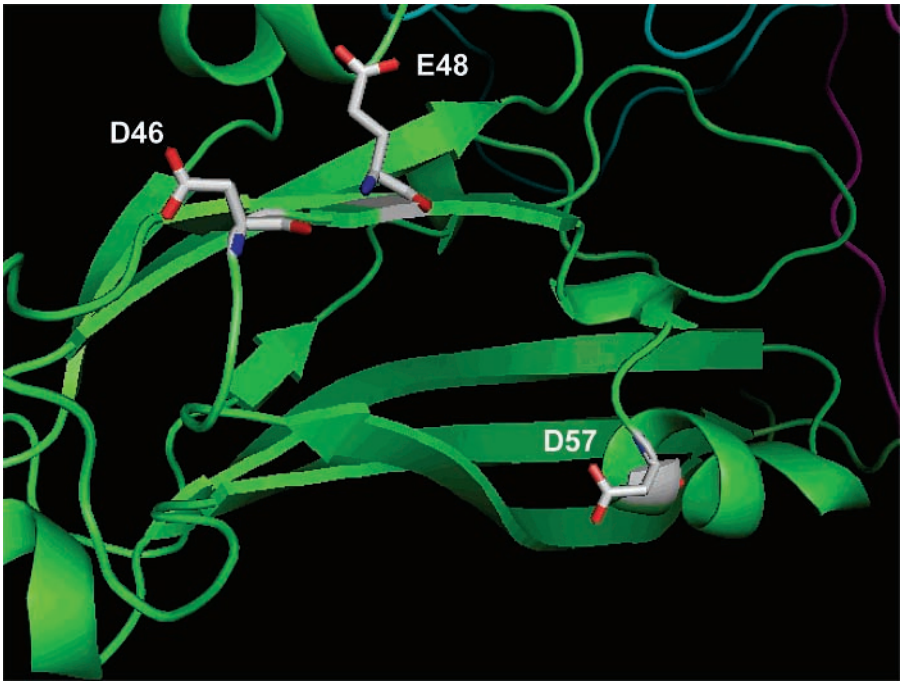
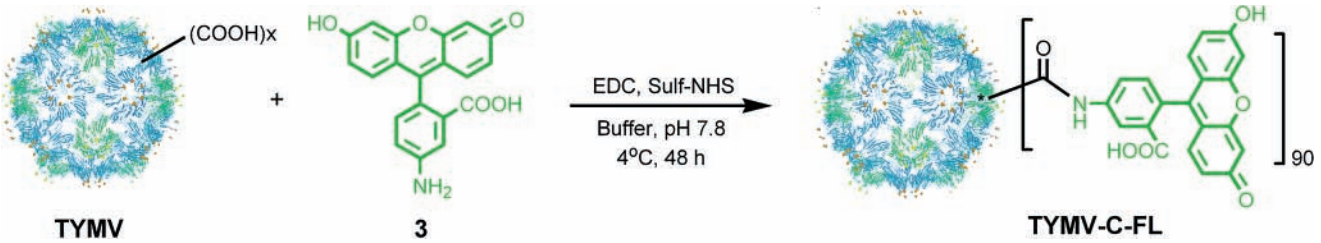


Figure 6. TYMV coat protein highlighting reactive peptide sequence (D46 to R67). Aspartate and glutamate residues (D46, E48, and D57) are highlighted as wire models. The figure is generated with PyMol software.

Scheme 2



Since the fluorescent dyes were covalently linked to the viral capsid at the defined position, they were isolated by the protein scaffold which prohibited the possible concentration quenching. As shown in Figure 4, for both **1** and **2**, the fluorescence signals increased linearly over a wide range of dye-per-virus ratios, suggesting negligible quenching in the virus conjugates even at dye loadings up to ca. 40 dye/virion (a local concentration of dye equal to 4.6 mM considering TYMV occupies a space of 1.4×10^{-23} m^3). This result is very similar to the recent report from Ratna, Soto, and co-workers (*31*), that fluorescent dyes can be anchored on CPMV with controlled distance which prevented the formation of nonfluorescent dimers and subsequent quenching and afforded highly fluorescent viral nanoparticles (*31*). Such kind of engineered viral particles can potentially be used as probes in microarray-based genotyping assays and sandwich immunoassays with improved sensitivities (*31*, *38*).

Many studies have shown that the carboxyl residues of various viral capsids are amenable to reaction with primary amines under activation (*40*, *42*, *57*). Besides the C-terminus of the protein, there are 13 carboxylic acid residues per TYMV subunit which belong to Asp and Glu side chains. As shown in Scheme 2, upon treating with fluorescein amine **3** under activation with 1-(3-dimethylaminopropyl-3-ethylcarbodiimide) hydrochloride (EDC) and sulf-NHS, about 90 carboxyl groups were derivatized after 24 h incubation. Under forcing conditions, i.e., longer reaction time, up to 120 units of **3** could be attached to TYMV without affecting the integrity of the capsid (Figure 5). The reactivity drops sharply at higher concentrations of **3** as the dye precipitates out of solution. In general, the reactivity of carboxyl groups greatly depends on their accessibility to solvent, and the modification often takes place at the most exposed residues or the most flexible loops. Proteomic studies have shown that the most exposed loop containing residues D46 through R67 is the reactive peptide. Shown in Figure 6 is the loop highlighting all the aspartate and glutamate residues. Work is ongoing to determine the exact position of the carboxylic acid modification, although fluorescent resonance energy transfer studies suggested the energy transfer takes place in a single environment, indicating a single reactive site (*58*).

CONCLUSION

The bionanoparticle TYMV was purified in high yield from infected plant tissue and was shown to be stable to a variety of reaction conditions. On the basis of orthogonal chemical reactions, specific sites on the virion surface can be labeled selectively. Amine-targeted chemistry afforded functionalization at the Lys-32 lysine residue, as confirmed by the proteomic analysis. The use of dyes showed no self-quenching of fluorescence even at high labeling values. Targeting the chemical reaction toward carboxylate residues pointed to three possible reactive sites, Asp-46, Glu-48, and Asp-57. This could lead to dual-modified particles with multiple functionalities for the application of TYMV as a fluorescent biological probe (*58*). Studies are underway toward the genetic manipulation of the TYMV scaffold, as well as the application of dual-modified TYMV nanoparticles in the development of new functional materials.

ACKNOWLEDGMENT

This work was supported by USA NSF-NER program, DOD-DURIP, and the W. M. Keck Foundation. We are grateful to Alex McPherson for the TYMV inocula, Lisa Alexander and Venkata S. Kotakadi for the assistance of TYMV production, Mike Walla for the assistance of the proteomics study, and Loic Charbonnière for helpful discussions about the manuscript.

LITERATURE CITED

(1) Lee, L. A., and Wang, Q. (2006) Adaptations of nanoscale viruses and other protein cages for medical applications. *Nanomedicine 2*, 137−149.

(2) Douglas, T., and Young, M. (1999) Virus particles as templates for materials synthesis. *Adv. Mater. 11*, 679−681.

(3) Douglas, T., and Young, M. (2006) Viruses: Making friends with old foes. *Science 312*, 873−875.

(4) Douglas, T., and Young, M. (1998) Host-guest encapsulation of materials by assembled virus protein cages. *Nature 393*, 152−155.

(5) Wang, Q., Lin, T., Tang, L., Johnson, J. E., and Finn, M. G. (2002) Icosahedral virus particles as addressable nanoscale building blocks. *Angew. Chem., Int. Ed. 41*, 459−462.

(6) Russell, J. T., Lin, Y., Böker, A., Long, S., Carl, P., Zettl, H., He, J., Sill, K., Tangiraia, R., Emrick, T., Littrell, K., Thiyagarajan, P., Cookson, D., Fery, A., Wang, Q., and Russell, T. P. (2005) Self-assembly and cross-linking of bionanoparticles at liquid-liquid interfaces. *Angew. Chem., Int. Ed. 44*, 2420−2426.

(7) Flynn, C. E., Lee, S.-W., Peelle, B. R., and Belcher, A. M. (2003) Viruses as vehicles for growth, organization and assembly of materials. *Acta Mater. 51*, 5867−5880.

(8) Royston, E., Lee, S. Y., Culver, J. N., and Harris, M. T. (2006) Characterization of silica-coated tobacco mosaic virus. *J. Colloid Interface Sci. 298*, 706−712.

(9) Lee, S. Y., Choi, J. W., Royston, E., Janes, D. B., Culver, J. N., and Harris, M. T. (2006) Deposition of platinum clusters on surface-modified tobacco mosaic virus. *J. Nanosci. Nanotechnol. 6*, 974−981.

(10) Slocik, J. M. N. R., Stone, M. O., and Wright, D. W. (2005) Viral templates for gold nanoparticle synthesis. *J. Mater. Chem. 15*, 749−753.

(11) Fonoberov, V. A., and Balandin, A. A. (2005) Phonon confinement effects in hybrid virus-inorganic nanotubes for nanoelectronic applications. *Nano Lett. 5*, 1920−1923.

(12) Knez, M., Sumser, M., Bittner, A. M., Wege, C., Jeske, H., Martin, T. P., and Kern, K. (2004) Spatially selective nucleation of metal clusters on the tobacco mosaic virus. *Adv. Funct. Mater. 14*, 116−124.

(13) Dujardin, E., Peet, C., Stubbs, G., Culver, J. N., and Mann, S. (2003) Organization of metallic nanoparticles using tobacco mosaic virus templates. *Nano Lett. 3*, 413−417.

(14) Fowler, C. E., Shenton, W., Stubbs, G., and Mann, S. (2001) Tobacco mosaic virus liquid crystals as templates for the interior design of silica mesophases and nanoparticles. *Adv. Mater. 13*, 1266−1269.

(15) Douglas, T., Strable, E., Willits, D., Aitouchen, A., Libera, M., and Young, M. (2002) Protein engineering of a viral cage for constrained nanomaterials synthesis. *Adv. Mater. 14*, 405−418.

(16) Mao, C., Solis, D. J., Reiss, B. D., Kottmann, S. T., Sweeney, R. Y., Hayhurst, A., Georgiou, G., Iverson, B., and Belcher, A. M. (2004) Virus-based toolkit for the directed synthesis of magnetic and semiconducting nanowires. *Science 303*, 213−217.

(17) Mao, C., Flynn, C. E., Hayhurst, A., Sweeney, R., Qi, J., Georgiou, G., Iverson, B., and Belcher, A. M. (2003) Viral assembly of oriented quantum dot nanowires. *Proc. Nat. Acad. Sci. U.S.A. 100*, 6946−6951.

(18) Nam, K. T., Peelle, B. R., Lee, S.-W., and Belcher, A. M. (2004) Genetically driven assembly of nanorings based on the M13 virus. *Nano Lett. 4*, 23−27.

(19) Lee, S.-W., and Belcher, A. M. (2004) Virus-based fabrication of micro- and nanofibers using electrospinning. *Nano Lett. 4*, 387−390.

(20) Lee, S.-W., Wood, B. M., and Belcher, A. M. (2003) Chiral smectic C structures of virus-based films. *Langmuir 19*, 1592−1598.

(21) Lee, S.-W., Mao, C., Flynn, C. E., and Belcher, A. M. (2002) Ordering of quantum dots using genetically engineered viruses. *Science 296*, 892−895.

(22) Lee, S.-W., Lee, S. K., and Belcher, A. M. (2003) Virus-based alignment of inorganic, organic, and biological nanosized materials. *Adv. Mater. 15*, 689−692.

(23) Flynn, C. E., Mao, C., Hayhurst, A., Williams, J. L., Georgiou, G., Iverson, B., and Belcher, A. M. (2003) Synthesis and organization of nanoscale II-VI semiconductor materials using evolved peptide specificity and viral capsid assembly. *J. Mater. Chem. 13*, 2414−2421.

(24) Reiss, B. D., Mao, C., Solis, D. J., Ryan, K. S., Thomson, T., and Belcher, A. M. (2004) Biological routes to metal alloy ferromagnetic nanostructures. *Nano Lett. 4*, 1127−1132.

(25) Khor, I. W., Lin, T., Langedijk, J. P. M., Johnson, J. E., and Manchester, M. (2002) Novel strategy for inhibiting viral entry by use of a cellular receptor-plant virus chimera. *J. Virol. 76*, 4412−4419.

(26) Rae, C. S., Wei Khor, I., Wang, Q., Destito, G., Gonzalez, M. J., Singh, P., Thomas, D. M., Estrada, M. N., Powell, E., Finn, M. G., and Manchester, M. (2005) Systemic trafficking of plant virus nanoparticles in mice via the oral route. *Virology 343*, 224−35.

(27) Singh, P., Gonzalez, M. J., and Manchester, M. (2006) Viruses and their uses in nanotechnology. *Drug Dev. Res. 67*, 23−41.

(28) Wang, Q., Kaltgrad, E., Lin, T., Johnson, J. E., and Finn, M. G. (2002) Natural supramolecular building blocks: Wild-type cowpea mosaic virus. *Chem. Biol. 9*, 805−811.

(29) Wang, Q., Lin, T., Johnson, J. E., and Finn, M. G. (2002) Natural supramolecular building blocks: Cysteine-added mutants of cowpea mosaic virus. *Chem. Biol. 9*, 813−819.

(30) Wang, Q., Raja, K. S., Janda, K. D., Lin, T., and Finn, M. G. (2003) Blue fluorescent antibodies as reporters of steric accessibility in virus conjugates. *Bioconjugate Chem. 14*, 38−43.

(31) Soto, C. M., Blum, A. S., Vora, G. J., Lebedev, N., Meador, C. E., Won, A. P., Chatterji, A., Johnson, J. E., and Ratna, B. R. (2006) Fluorescent signal amplification of carbocyanine dyes using engineered viral nanoparticles. *J. Am. Chem. Soc. 128*, 5184−5189.

(32) Medintz, I. L., Sapsford, K. E., Konnert, J. H., Chatterji, A., Lin, T., Johnson, J. E., and Mattoussi, H. (2005) Decoration of discretely immobilized cowpea mosaic virus with luminescent quantum dots. *Langmuir 21*, 5501−5510.

(33) Raja, K. S., Wang, Q., Gonzalez, M., Manchester, M., Johnson John, E., and Finn, M. G. (2003) Hybrid virus-polymer materials. 1. Synthesis and properties of PEG-decorated cowpea mosaic virus. *Biomacromolecules 4*, 472−476.

(34) Sen Gupta, S., Raja, K. S., Kaltgrad, E., Strable, E., and Finn, M. G. (2005) Virus-glycopolymer conjugates by copper(I) catalysis of atom transfer radical polymerization and azide-alkyne cycloaddition. *Chem. Commun.* 4315−4317.

(35) Strable, E., Johnson John, E., and Finn, M. G. (2004) Natural nanochemical building blocks: icosahedral virus particles organized by attached oligonucleotides. *Nano Lett. 4*, 1385−1389.

(36) Chatterji, A., Ochoa, W., Shamieh, L., Salakian, S. P., Wong, S. M., Clinton, G., Ghosh, P., Lin, T., and Johnson, J. E. (2004) Chemical conjugation of heterologous proteins on the surface of Cowpea mosaic virus. *Bioconjugate Chem. 15*, 807−813.

(37) Chatterji, A., Burns, L. L., Taylor, S. S., Lomonossoff, G. P., Johnson, J. E., Lin, T., and Porta, C. (2002) Cowpea mosaic virus: from the presentation of antigenic peptides to the display of active biomaterials. *Intervirology 45*, 362−370.

(38) Sapsford, K. E., Soto, C. M., Blum, A. S., Chatterji, A., Lin, T. W., Johnson, J. E., Ligler, F. S., and Ratna, B. R. (2006) A cowpea mosaic virus nanoscaffold for multiplexed antibody conjugation: Application as an immunoassay tracer. *Biosens. Bioelectron. 21*, 1668−1673.

(39) Raja, K. S., Wang, Q., and Finn, M. G. (2003) "Sweet" viruses: artificial carbohydrate-decorated virus particles. *ChemBioChem 4*, 1348−1351.

(40) Gillitzer, E., Willits, D., Young, M., and Douglas, T. (2002) Chemical modification of a viral cage for multivalent presentation. *Chem. Commun.*, 2390−2391.

(41) Taylor, D., Wang, Q., Bothner, B., Natarajan, P., Finn, M. G., and Johnson, J. E. (2003) Correlation of chemical reactivity of Nudaurelia capensis omega virus with a pH-induced conformational change. *Chem. Commun.*, 2770−2771.

(42) Schlick, T. L., Ding, Z., Kovacs, E. W., and Francis, M. B. (2005) Dual-surface modification of the tobacco mosaic virus. *J. Am. Chem. Soc. 127*, 3718−3723.

(43) Endo, M., Wang, H., Fujitsuka, M., and Majima, T. (2006) Pyrene-stacked nanostructures constructed in the recombinant tobacco mosaic virus rod scaffold. *Chem. Eur. J. 12*, 3735−3740.

(44) Hooker, J. M., Kovacs, E. W., and Francis, M. B. (2004) Interior surface modification of bacteriophage MS2. *J. Am. Chem. Soc. 126*, 3718−3719.

(45) Barnhill, H. N., Kotakadi, V. S., Ziessel, R., Charbonniere, L., and Wang, Q. (2006) Dual modification of turnip yellow mosaic virus: synthesis of a biotinylated luminescent nanoparticle. *Am. Chem. Soc., Div. Polym. Mater. Sci. Eng., Proc. 94*, 379−380.

(46) Lin, Y., Boker, A., He, J., Sill, K., Xiang, H., Abetz, C., Li, X., Wang, J., Emrick, T., Long, S., Wang, Q., Balazs, A., and Russell, T. P. (2005) Self-directed self-assembly of nanoparticle/copolymer mixtures. *Nature 434*, 55−59.

(47) Klug, A., Finch, J. T., and Franklin, R. E. (1957) Structure of turnip yellow mosaic virus. *Nature 179*, 683−684.

(48) Canady, M. A., Larson, S. B., Day, J., and McPherson, A. (1996) Crystal structure of turnip yellow mosaic virus. *Nat. Struct. Biol. 3*, 771−781.

(49) Reddy, V. S., Natarajan, P., Okerberg, B., Li, K., Damodaran, K. V., Morton, R. T., Brooks, C. L., III, and Johnson, J. E. (2001) Virus Particle Explorer (VIPER), a website for virus capsid structures and their computational analyses. *J. Virol. 75*, 11943−11947.

(50) Brenner, S., and Horne, R. W. (1959) A negative staining method for high resolution electron microscopy of viruses. *Biochim. Biophys. Acta 34*, 103−110.

(51) Leimkühler, M., Goldbeck, A., Lechner, M. D., Adrian, M., Michels, B., and Witz, J. (2001) The formation of empty shells upon pressure induced decapsidation of turnip yellow mosaic virus. *Arch. Virol. 146*, 653−667.

(52) Kaper, J. M. (1964) Alkaline degradation of turnip yellow mosaic virus. I. The controlled formation of empty protein shells. *Biochemistry 3*, 486−493.

(53) Katouzian-Safadi, M., Favre, A., and Haenni, A. L. (1980) Effect of freezing and thawing on the structure of turnip yellow mosaic virus. *Eur. J. Biochem. 112*, 479−486.

(54) Pimenta, A. M. C., Stocklin, R., Favreau, P., Bougis, P. E., and Martin-Eauclaire, M. F. (2001) Moving pieces in a proteomic puzzle: Mass fingerprinting of toxic fractions from the venom of *Tityus Serrulatus*. *Rapid Commun. Mass Spectrom. 15*, 1562−1572.

(55) van Roon, A. M., Bink, H. H., Plaisier, J. R., Pleij, C. W., Abrahams, J. P., and Pannu, N. S. (2004) Crystal structure of an empty capsid of turnip yellow mosaic virus. *J. Mol. Biol. 341*, 1205−1214.
(56) Larson, S. B., Lucas, R. W., Greenwood, A., and McPherson, A. (2005) The RNA of turnip yellow mosaic virus exhibits icosahedral order. *Virology 334*, 245−254.
(57) Steinmetz, N. F., Lomonossoff, G. P., and Evans, D. J. (2006) Cowpea mosaic virus for material fabrication: Addressable carboxylate groups on a programmable nanoscaffold. *Langmuir 22*, 3488−3490.
(58) Barnhill, H. N., Claudel-Gillet, S., Ziessel, R., Charbonniére, L. J., and Wang, Q. (2007) A prototype protein assembly as scaffold for time-resolved fluoroimmuno assays. Unpublished results.

BC060391S

An Enzyme-Labeled Protein Polymer Bearing Pendent Haptens

Jo Tominaga,[†] Noriho Kamiya,[†,‡,*] and Masahiro Goto[†,‡]

Department of Applied Chemistry, Graduate School of Engineering, and Center for Future Chemistry, Kyushu University, 744 Motooka, Fukuoka 819-0395, Japan. Received June 9, 2006; Revised Manuscript Received December 1, 2006

A new methodology for the preparation of enzyme-labeled protein polymers bearing pendent haptens was developed through the combination of chemical modification and posttranslational protein modification catalyzed by microbial transglutaminase (MTG). As a model hapten, trinitrobenzene (TNB) was chosen and chemically conjugated with the accessible Lys residues of β-casein. The resultant trinitrophenylated β-casein was further modified with formaldehyde to render the residual Lys residues inert toward self-cross-linking by MTG. *Escherichia coli* alkaline phosphatase (AP), comprising a specific peptide tag carrying a MTG-reactive Lys residue, was then conjugated to the Gln residues in β-casein−TNB conjugates. The resultant AP-labeled β-casein-bearing pendent TNB moieties (AP-βCT) showed comparable specific activity with native AP. It was found that only the AP-βCT with a sufficient number of pendent TNBs are capable of binding to a surface adsorbed with anti-TNP and anti-TNT antibodies, indicating the presence of polyvalent interactions. The utility of AP-βCT was demonstrated by competitive immunoassays for trinitrophenol (TNP) and trinitrotoluene (TNT), with detection limits of 0.99 μg/L and 0.18 μg/L, respectively. The present study demonstrates the potential of dual labeling of protein scaffolds by chemical and enzymatic protein manipulation to create a new proteinaceous architecture.

1. INTRODUCTION

Enzyme−antigen conjugates hold great promise as versatile molecular tools for biotechnological applications. These conjugates have found notable usage in the oriented immobilization of enzymes via the specific interaction between antigen and antibody (*1*−*3*), and in enzyme-linked immunosolvent assays (ELISAs) for the detection and quantitative analysis of target substances (*4*−*8*). In general, the chemical conjugation of antigens to enzymes is conducted using cross-linking reagents such as glutaraldehyde and bifunctional protein cross-linkers (*9*). However, depending on the number of reactive amino groups available on the enzyme molecules, the conjugates often represent heterogeneous molecular species due to the uncontrollable and unpredictable chemical attachment of labeling molecules, which could lead to partial or complete inactivation of the target functionality. Site-specific conjugation between enzymes and antigens can alleviate such obstacles.

Recent advances in recombinant DNA technology have facilitated genetic approaches to conduct the site-specific labeling of an enzyme with an antigen. For instance, the affinity peptide tag, Asp-Try-Lys-Asp-Asp-Asp-Asp-Lys (FLAG), was genetically fused to an enzyme, and the FLAG-labeled recombinant enzyme was subsequently immobilized on a support displaying anti-FLAG antibodies (*1*−*3*). With respect to ELISA applications, the C-terminal fusion of horseradish peroxidase (HRP) with a human heart fatty acid binding protein (hFABP) was prepared, and the HRP-hFABP fusion protein was applied to competitive ELISA for the detection of hFABP (*10*). However, it should be noted that by genetic manipulation, site-specific enzyme−antigen conjugation was basically limited to the N- or C-terminus of the target enzymes. Moreover, the site-specific labeling of low-molecular-weight antigens (i.e., haptens) with enzymes is difficult to perform through genetic approaches. Here, we report on a new methodology for linking enzymes with multiple antigens while retaining perfect orientation for optimal enzymatic activity.

To avoid inactivation of the enzymes through modification, we turned our focus to site-specific protein modification using enzymes that perform posttranslational modifications on proteins. Microbial transglutaminase (MTG) from *Streptomyces mobaraensis* is a unique enzyme that catalyzes the acyl transfer reaction between a primary amine and the γ-carboxyamide group of Gln residues in peptides and proteins (*11*). When the ϵ-amino groups of certain Lys residues act as acyl-acceptors, proteins are site-specifically conjugated through the formation of covalent ϵ-(γ-Gln)Lys bonds (*12*−*14*). Toward a variety of applications, the *direct* incorporation of primary amine-derivatized organic molecules into proteins through the use of MTG has been investigated so far. For instance, polyethylene glycol−protein conjugates (*15*), hapten−protein conjugates (*16*), biotin−antibody conjugates (*17*), and trypsin−cyclodextrin conjugates (*18*) were successfully obtained using MTG as a protein modifier. In the present study, we explored the *indirect* introduction of small organic molecules into enzymes using a template protein polymer.

β-Casein is a major component of milk proteins and is basically a flexible, nonglobular protein whose precise secondary structure has still yet to be assigned (*19*). Since our previous research (*20*−*22*), which showed that β-casein is an excellent proteinaceous substrate possessing reactive Gln and Lys residues toward MTG, we are now looking to employ β-casein as a template protein polymer. Our concept is thus based on the targeted modification of either Lys or Gln residues in β-casein, in which chemical and enzymatic modifications are combined. To demonstrate this idea, the stepwise labeling of haptens and enzymes to β-casein was conducted in order to create an enzyme-labeled polymer-bearing pendent haptens. We selected trinitrophenol (TNP) and trinitrotoluene (TNT) as targets, because the ϵ-amino groups of proteins are known to be easily trinitrophenylated by the chemical protein modifier, trinitrobenzene sulfonic acid (TNBS) (*23*). Since TNT serves as an indicator for environmental contamination with nitroaromatic

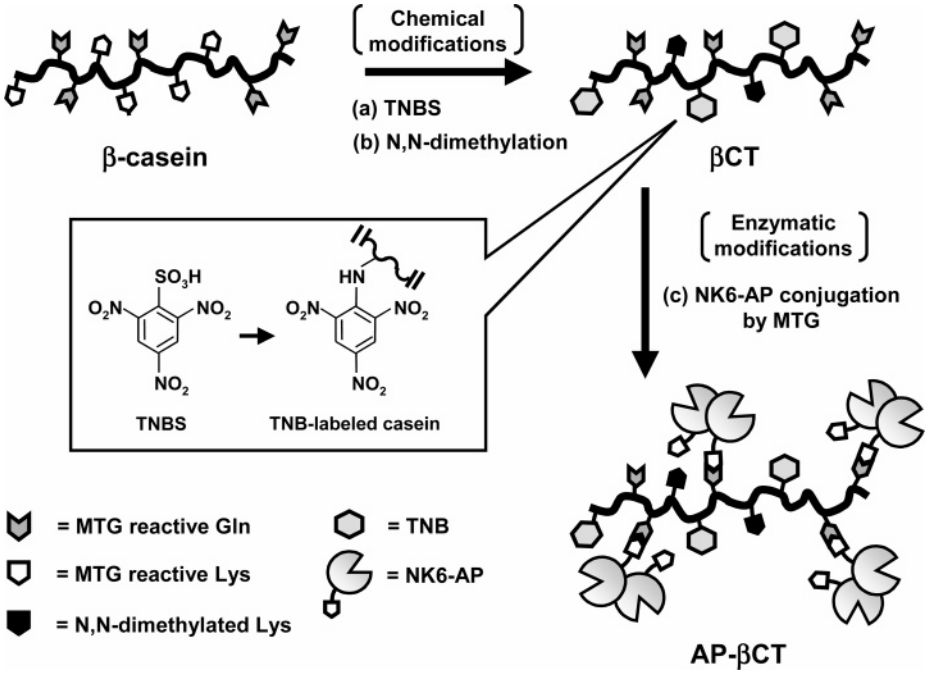
* To whom correspondence should be addressed. Tel/Fax. +81-92-802-2806 / +81-92-802-2810. E-mail: noritcm@mbox.nc.kyushu-u.ac.jp.

[†] Department of Applied Chemistry.

[‡] Center for Future Chemistry.

10.1021/bc060161d CCC: $37.00 © 2007 American Chemical Society
Published on Web 03/01/2007

Scheme 1



compounds, a number of immunological detection methods for TNP/TNT were developed (*24*−*28*). Here, *Escherichia coli* alkaline phosphatase (AP), a widely used enzyme in ELISA (*29*, *30*), was employed a model enzyme. A recombinant AP tagged with a specific peptide linker bearing a MTG-reactive Lys residue was prepared. The MTG-mediated labeling of the recombinant AP with multi-trinitrophenylated β-casein and its immobilization and potential in competitive ELISA for TNP/TNT detection were discussed.

2. EXPERIMENTAL PROCEDURES

2.1. Materials. MTG was provided by Ajinomoto Co. Inc. (Japan), and its activity was measured using the colorimetric hydroxamate procedure with N-carbobenzyloxy-glutaminyl-glycine (Sigma), as previously described (*31*). One unit (U) of activity was defined as the amount of enzyme that catalyzes the formation of 1 μmol of the hydroxamate per minute using L-glutamic acid γ-monohydroxamate (Sigma) as standard. Bovine β-casein was purchased from Sigma and used without further purification. A fluorescent substrate of AP, ECF substrate, was purchased from Amersham Biosciences. Prior to use, the ECF substrates were dissolved in ECF detection buffer provided by the manufacturer and then 10-fold diluted by deionized water prior to use. TNP was purchased from Kishida Chemical Co. (Japan). A dilute solution of TNT was purchased from Chugokukayaku Co. (Hiroshima, Japan). Anti-TNP goat polyclonal IgG antibodies were purchased from Biomeda (Foster City, CA). Anti-TNT mouse monoclonal IgG antibody was purchased from Strategic Diagnostics Inc. (Newark, DE). All other reagents were of analytical grade and commercially available.

2.2. Preparation of Recombinant AP Tagged with Specific Peptide Linker for MTG. A specific peptide consisting of six amino acids (MKHKGS) was genetically attached to the N-terminus of AP. The resultant recombinant AP was abbreviated as NK6-AP. The plasmid vector construction, protein expression in *E. coli* strain BL21(DE3) (Novagen), and purification procedures of NK6-AP were described in our previous report in detail (*20*).

2.3. Measurement of AP Activity. The catalytic activity of AP was measured with *p*-nitrophenylphosphate (*p*-NPP) as a substrate. The hydrolysis of *p*-NPP (1 mM) was initiated by the addition of each AP formulation to 1 mL of 1 M Tris-HCl buffer (pH 8.0) at 25 °C under vigorous stirring. The initial activity was determined by detecting the increase in the absorbance at 410 nm (derived from *p*-nitrophenol (*p*-NP)). The molar extinction coefficient of *p*-NP under experimental conditions was determined to be 1.69×10^4 using UV−vis spectrophotometry (Jasco V-570, Japan). One unit (U) of AP activity was defined as the amount of enzyme that catalyzes the formation of 1 μmol of *p*-NP per minute.

2.4. Preparation of a β-Casein−TNB Conjugate. β-Casein (5 mg/mL) was dissolved in 100 mM borate buffer at pH 9.2. Preparation of the β-casein−TNB conjugate (abbreviated as βCT) was initiated by the addition of TNBS (dissolved in the same buffer to a final concentration of 0.2 mM or 10 mM), and the reaction mixture was stirred overnight at 25 °C (Scheme 1a). The remaining TNBS was removed by repeated dialysis against deionized water (three times) and more thoroughly by gel chromatography on a PD-10 column (Amersham Biosciences) using deionized water as eluent. N,N-Dimethylation of the remaining Lys residues (Scheme 1b) was conducted as follows. The reaction was initiated by the addition of $NaBH_4$ (2 mg), followed by the five-times addition of formaldehyde (2 μL) to the βCT solutions (4 mL) at 5-min intervals. The remaining formaldehyde was removed from the reaction mixture by repeated dialysis against deionized water (three times), and more thoroughly by gel chromatography on a PD-10 column using deionized water as eluent. The overall procedure for N,N-dimethylation was conducted twice. Trinitrophenylated amino groups in β-casein was calculated by the absorbance at 344 nm ($\epsilon_{344} = 1.1 \times 10^4\ M^{-1}\ cm^{-1}$) derived from trinitrophenylamino groups (*23*). The susceptibly of βCT to MTG-mediated cross-linking was analyzed by SDS-PAGE after incubating MTG (1.1 U) and βCT (0.8 mg/mL) for 3 h.

2.5. Site-Specific Conjugation of NK6-AP to βCT by MTG. As preliminary experiments to test the reactivity of NK6-AP to βCT, the conjugation of NK6-AP (0.17 mg/mL) and βCT (0.8 mg/mL) was investigated in the presence of MTG (1.1 U/mL) in 100 mM Tris-HCl buffer (pH 8.0). After incubation overnight at 25 °C, SDS-PAGE analysis of the reaction products was conducted. When preparing the final construct (Scheme

1c), an excess amount of NK6-AP (0.75 mg/mL) compared to βCTs (0.04 mg/mL) was reacted with MTG (1.1 U/mL) for 24 h to modify as much MTG-reactive Gln residues as possible. The resultant NK6-AP-βCT conjugate (abbreviated as AP-βCT) was purified by gel filtration chromatography using a HiLoad 16/60 Superdex 200 pg column (Amersham Biosciences) with 100 mM Tris-HCl buffer (pH 8.0) as eluent, at a flow rate of 1 mL/min. The fractions of AP-βCT were collected by measuring the AP activity of each fraction. The molecular weight distribution of AP-βCT was estimated using a Gel Filtration LMW Calibration Kit and a Gel Filtration HMW Calibration Kit (Amersham Biosciences).

2.6. Competitive Immunoassay of TNP and TNT with AP-βCT. ELISA experiments were carried out with Nunc Maxi Sorp microtiter plates (Nalge Nunc, Germany) with the aid of an ELISA washer, Model 1575 (Bio-Rad, Hercules, CA) and a microplate reader, LS-55KG (Perkin-Elmer, Wellesley, MA). The washing buffer solution (TBST) employed was prepared from TBS (Tris buffered saline, comprising 25 mM Tris, 137 mM sodium chloride, 2.68 mM potassium chloride, pH 7.4) by adding 0.05% (v/v) polyoxyethylene sorbitan monolaurate (Tween 20). Commercial stock solutions of the anti-TNP and anti-TNT antibodies were diluted to 2 μg/mL in 50 mM carbonate buffer, pH 9.6, and incubated at room temperature for 1 h (100 μL/ well). After the microtiter plate was washed three times with TBST, each well was blocked with 200 μL of TBS containing 0.5% BSA for 1 h and washed again. A mixture of AP-βCT and TNP or TNT (0−1 mg/L) in TBS (100 μL/ well) was incubated for 1 h at room temperature, and the plate was washed again three times. Finally, 150 μL of the ECF substrate solution was added to each well and left to incubate for 30 min. The fluorescence intensity of each well was measured using a microplate reader (excitation: 430 nm, emission: 560 nm). The data obtained were fitted to the following four-parameter logistic plot:

$$y = (a - d)/[1 + (x/c)^b] + d$$

where y represents the fluorescence intensity, x is the concentration of analyte, a and d are the upper and lower asymptotes, b is the slope, and c is the midpoint of the liner portion of the curve. The detection limit was defined as the concentration of analyte yielding 15% inhibition of the maximum.

3. RESULTS AND DISCUSSION

3.1. Lys-Specific Labeling of β-Casein with TNB: Preparation of βCT. TNBS, a well-known amine modification reagent, was used to label the Lys residues in β-casein, thus leaving the remaining Gln residues for the subsequent MTG-mediated conjugation with NK6-AP. In the present study, we prepared two types of enzyme-labeled protein polymers, of which a different number of haptens are formed to establish the preparation procedures, as well as to investigate the basic characteristics of the resultant conjugates. The two types of βCTs possessing different numbers of TNB moieties were prepared by changing the molar ratio of TNBS to β-casein in the preparation of βCTs. From the spectroscopic measurement of βCTs, it was found that about 1 or 12 Lys residues of β-casein were trinitrophenylated. Since β-casein has twelve amine groups (eleven ε-amino groups of Lys residues and one N-terminal α-amine (*32*)), it was suggested that all the amino groups were substantially labeled with TNBs in the latter construct. Since the residual Lys residues are capable of participating in the self-cross-linking of βCTs in the presence of MTG, they were further modified with formaldehyde. The resultant β-caseins bearing either 1 or 12 TNB moieties are abbreviated as βCT1 and βCT12, respectively. To confirm whether all of the MTG-reactive Lys residues were modified with TNBS or formaldehyde, two types of βCTs were treated with MTG. SDS-PAGE analyses showed that the self-cross-linking of βCT1 and βCT12 by MTG was virtually suppressed (data not shown), suggesting that both βCTs were suitable for the subsequent MTG-mediated conjugation with NK6-AP.

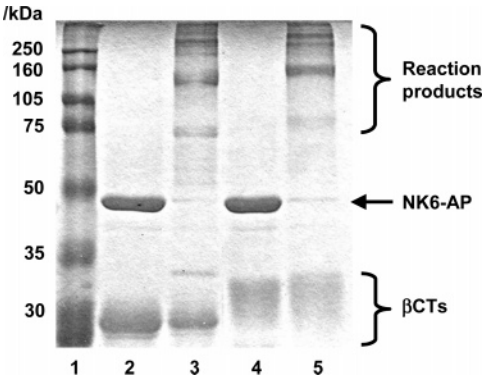


Figure 1. SDS-PAGE analysis of MTG-mediated conjugation of NK6-AP to βCTs (lane 1, molecular weight markers; lane 2, NK6-AP and βCT1; lane 3, NK6-AP and βCT1 treated with MTG; lane 4, NK6-AP and βCT12; lane 5, NK6-AP and βCT12 treated with MTG;). The protein band observed around 50 kDa was of NK6-AP (lanes 2 and 4). The concentrations of NK6-AP and βCTs were 0.17 mg/mL and 0.8 mg/mL, respectively.

3.2. Gln-Specific Conjugation of NK6-AP with βCT by MTG. We first tested if MTG-mediated labeling of NK6-AP directing to MTG-reactive Gln residues in βCTs is possible. Figure 1 shows the SDS-PAGE analysis of the cross-linking reaction in the presence of an excess amount of βCTs compared to NK6-AP. Under the experimental conditions, the protein bands of NK6-AP had almost disappeared in both cases, while new bands were evident in the high-molecular-weight range (lanes 3 and 5 in Figure 1). This suggests that the Gln residues in β-casein could also be recognized by MTG even after modification of the Lys residues. Note that the catalytic activity of NK6-AP was perfectly retained after the treatment of both βCTs with MTG (data not shown), which can be explained by the fact that the active site of AP is located at the opposite side of its N-terminus (*33*).

Next, AP-βCTs were prepared in the presence of an excess amount of NK6-AP as compared to βCTs, in order to modify as much MTG-reactive Gln residues as possible. Figure 2 shows the gel filtration chromatograms of NK6-AP and AP-βCTs. With respect to the conjugation of NK6-AP with βCT1, the major fraction of reaction products was distributed to the molecular weight markers ranging from 232 to 440 kDa, which corresponds to about 4−8 NK6-AP molecules (i.e., 2−4 NK6-AP dimers) per βCT1. On the other hand, the apparent molecular weight of the conjugate prepared with NK-AP and βCT12 was estimated to be about 440−669 kDa, which corresponds to about 8−12 NK6-AP molecules (i.e., 4−6 NK6-AP dimers) per βCT12. The results imply that βCT12 is more reactive toward MTG than βCT1. Since MTG-reactive Gln residues are often located close to the bulky and hydrophobic amino acids, such as Val and Phe residues (*34*), increasing the hydrophobicity of β-casein by trinitrophenylation and N,N-dimethylation may increase the reactivity of the Gln residues in MTG-mediated protein conjugation. The resultant NK6-AP-βCT1 and NK6-AP-βCT12 conjugates (abbreviated as AP-βCT1 and AP-βCT12, respectively) corresponding to the major fraction of reaction products were employed in the subsequent experiments.

3.3. Immobilization of AP-βCTs on a Surface via Antigen−Antibody Interaction. Figure 3 shows the result of immobilization of both AP-βCTs on a microtiter plate via antigen−antibody interactions. Here, the concentrations of AP-βCTs applied to

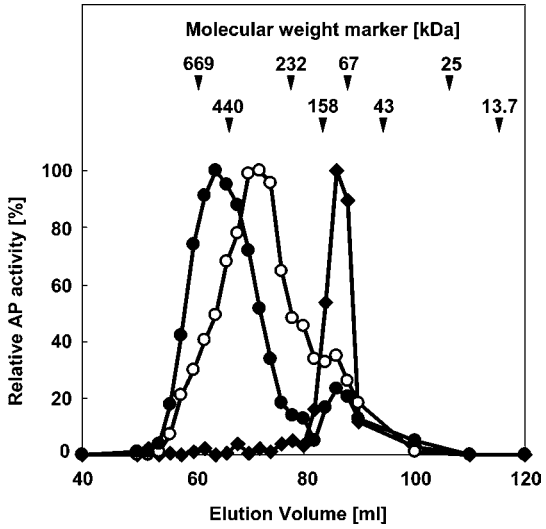


Figure 2. Gel filtration chromatograms of free NK6-AP (closed diamonds), NK6-AP after MTG conjugation with βCT1 (open circles), and NK6-AP after MTG conjugation with βCT12 (closed circles). The concentrations of NK6-AP and βCTs in the cross-linking reaction were 0.75 mg/mL and 0.04 mg/mL, respectively.

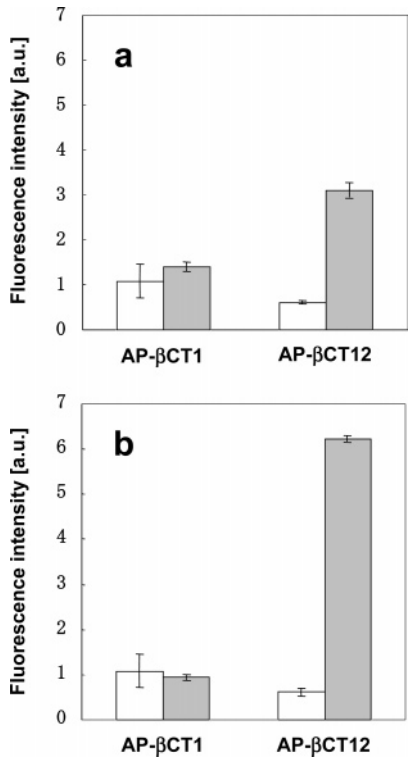


Figure 3. Comparison of the immobilization efficacy of AP-βCTs to (a) anti-TNP antibody- and (b) anti-TNT antibody-immobilized surfaces evaluated by the fluorescence intensity of AP-catalyzed reaction products at 560 nm. Nonspecific adsorption to a surface without antibodies (open bars) and adsorption to a surface displaying antibodies (dark bars) are shown. The mean values and standard deviations (error bars) are depicted in the figure.

the wells were adjusted by the TNB basis, which means that approximately 10-fold higher amount of AP-βCT1 (1.8 mU/mL) than AP-βCT12 (0.18 mU/mL) was applied to the wells. The difference in the applied concentration may be attributed to the higher background signal of AP-βCT1 compared to AP-βCT12 (white bars in Figure 3a and 3b) due to the increase in nonspecific adsorption of AP-βCT1. Interestingly, only AP-βCT12 was efficiently immobilized on a surface displaying anti-TNP antibodies (Figure 3a) and anti-TNT antibodies (Figure

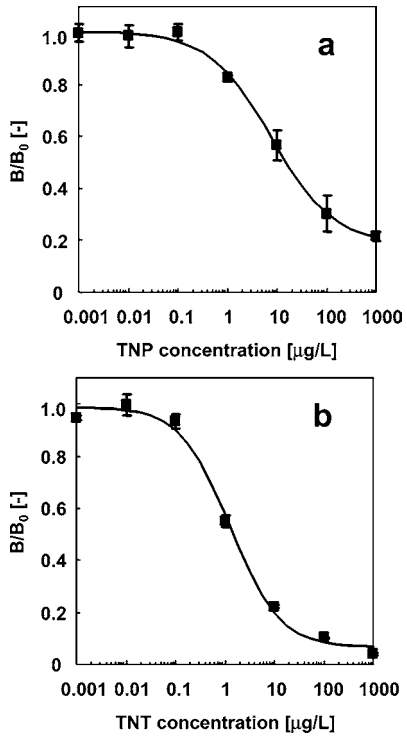
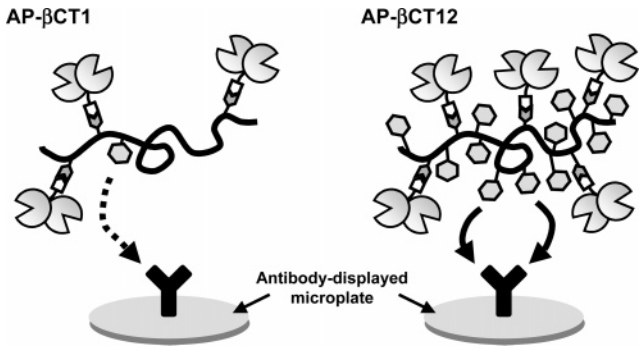


Figure 4. Calibration curves of the competitive ELISA for (a) TNP and (b) TNT detection obtained with AP-βCT12. The results are expressed in terms of B/B_0, where B and B_0 represent the fluorescent intensity in the presence and absence of TNT, respectively. The mean values and standard deviations (error bars) are depicted in the figure.

Scheme 2



3b), whereas limited immobilization was observed with AP-βCT1 in both cases. The results suggest that the accessibility of TNB moieties in AP-βCT1 was lower than that in AP-βCT12, which leads to the inhibition of hapten-antibody interactions on the microplate surface, possibly due to steric hindrance. On the other hand, AP-βCT12 with a sufficient number of TNB moieties is likely to facilitate interactions with the surface-bound antibodies. Moreover, the distinct immobilization behaviors of the AP-βCTs could also be explained by the higher apparent affinity (i.e., avidity) of AP-βCT12 due to divalent binding to the antibodies (Scheme 2). Therefore, it was suggested that the multiple labeling of a template protein polymer with antigens is particularly helpful for the stable capture of recombinant proteins on the same template via antigen−antibody interactions.

3.4. Competitive ELISA for TNP and TNT Detection by AP-βCT12. To explore the potential of an enzyme-labeled protein polymer bearing pendent haptens, TNP and TNT detection by competitive ELISA was conducted with AP-βCT12 showing a capability for binding to the immobilized antibodies. The calibration curves obtained with AP-βCT12 are shown in Figure 4. The fluorescence intensity detected in each well decreased in response to the concentration of TNP (Figure 4a)

and TNT (Figure 4b), and concentrations over 0.99 μg/L and 0.18 μg/L were detected for TNP and TNT, respectively. With respect to TNP detection, relatively lower signal-to-noise ratio observed in AP-βCT12 immobilization against anti-TNP antibodies compared with anti-TNT antibodies (Figure 3) is likely to increase the background signal in the presence of 1000 μg/L TNP (Figure 4a). In terms of TNT, the detection limit is slightly higher than the reported value using the same antibody (0.06 μg/L), in which the competitive ELISA was conducted with HRP directly labeled with TNB (*35*). This suggests that a nonglobular protein polymer labeled with multiple TNBs exhibits a higher affinity for the anti-TNT antibody, compared to its globular counterpart labeled with the same hapten, possibly due to the presence of polyvalent interactions.

In closing, we have demonstrated the dual labeling of a protein polymer by targeting the different side chains of amino acids through a combination of chemical, genetic, and enzymatic approaches. We found that multiple labeling of a protein polymer with haptens can add polyvalency that could be useful for increasing the affinity to a target receptor (*36*). Since β-casein can be replaced by native (*37*) and synthetic (*38*) protein polymers, the MTG-mediated site-specific and multiple labeling of recombinant proteins on a protein polymer can expand the possibility of designing a novel proteinaceous architecture.

ACKNOWLEDGMENT

We thank Prof. Yoshihiko Imato and Mr. Masahiro Sato of Kyushu University for helpful discussions on designing competitive ELISA. We are grateful to Ajinomoto Co., Inc. (Japan) for providing MTG samples. The present work was supported by the 21st Century COE Program, "Functional Innovation of Molecular Informatics" from the MEXT of Japan (to M.G.) and Industrial Technology Research Grant Program in '06 from New Energy and Industrial Technology Development Organization (NEDO) of Japan (to N.K.). J.T. was supported by Research Fellowships of the Japan Society for the Promotion of Science (JSPS) for Young Scientists.

LITERATURE CITED

(1) Vishiwanath, S. K., Watson, C. R., Huang, W., Bachas, L. G., and Bhattacharyya, D. (1997) Kinetic studies of site-specifically and randomly immobilized alkaline phosphatase on functionalized membranes. *J. Chem. Technol. Biotechnol. 68*, 294−302.

(2) Liu, J., Wang, J., Bachas, L. G., and Bhattacharyya, D. (2001) Activity studies of immobilized subtilisin on functionalized pure cellulose-based membranes. *Biotechnol. Prog. 17*, 866−871.

(3) Wang, J., Bhattacharyya, D., and Bachas, L. G. (2001) Orientation specific immobilization of organophosphorus hydrolase on magnetic particles through gene fusion. *BioMacromolecules 2*, 700−705.

(4) Daie, J., and Wyse, R. (1982) Adaptation of the enzyme-linked immunosorbent assay (ELISA) to the quantitative analysis of abscisic acid. *Anal. Biochem. 119*, 365−371.

(5) Hahnau, S., and Weiler, E. W. (1991) Determination of the mycotoxin cyclopiazonic acid by enzyme immunoassay. *J. Agric. Food. Chem. 39*, 1887−1891.

(6) Dzgoev, A. B., Gazaryan, I. G., Lagrimini, L. M., Ramanathan, K., and Danielsson, B. (1999) High-sensitivity assay for pesticide using a peroxidase as chemiluminescent label. *Anal. Chem. 71*, 5258−5261.

(7) Zeravik, J., Skryjova, K., Nevorankova, Z., and Franek, M. (2004) Development of direct ELISA for the determination of 4-nonylphenol and octylphenol. *Anal. Chem. 76*, 1021−1027.

(8) Wang, J., Wang, X., Chen, F., Wan, P. J., He, G., and Li, Z. (2005) Development of competitive direct ELISA for gossypol analysis. *J. Agric. Food. Chem. 53*, 5513−5517.

(9) Hermanson, G. T., Ed. (1996) *Bioconjugate Techniques*, Academic Press, San Diego, CA.

(10) Grigorenko, V., Andreeva, I., Borchers, T., Spener, F., and Egorov, A. (2001) A genetically engineered fusion protein with horseradish peroxidase as a marker enzyme for use in competitive immunoassays. *Anal. Chem. 73*, 1134−1139.

(11) Yokoyama, K., Nio, N., and Kikuchi, Y. (2004) Properties and applications of microbial transglutaminase. *Appl. Microbiol. Biotechnol. 65*, 447−454.

(12) Kamiya, N., Tanaka, T., Suzuki, T., Takazawa, T., Takeda, S., Watanabe, K., and Nagamune, T. (2003) S-peptide as a potent peptidyl linker for protein cross-linking by microbial transglutaminase from Streptomyces mobaraensis. *Bioconjugate Chem. 14*, 351−357.

(13) Kamiya, N., Takazawa, T., Tanaka, T., Ueda, H., and Nagamune, T. (2003) Site-specific cross-linking of functional proteins by transglutamination. *Enzyme Microb. Technol. 33*, 492−496.

(14) Tanaka, T., Kamiya, N., and Nagamune, T. (2005) N-terminal glycine-specific protein conjugation catalyzed by microbial transglutaminase. *FEBS Lett. 579*, 2092−2096.

(15) Sato, H., Hayashi, E., Yamada, N., Yatagai, M., and Takahara, Y. (2001) Further studies on the site-specific protein modification by microbial transglutaminase. *Bioconjugate Chem. 12*, 701−710.

(16) Josten, A., Meusel, M., and Spener, F. (1998) Microbial transglutaminase-mediated synthesis of hapten protein conjugates for immunoassay. *Anal. Biochem. 258*, 202−208.

(17) Josten, A., Haalck, L., Spener, F., and Meusel, M. (2000) Use of microbial transglutaminase for the enzyme biotinylation of antibodies. *J. Immunol. Methods 240*, 47−54.

(18) Villalonga, R., Fernandez, M., Fragoso, A., Cao, R., Pierro, P. D., Mariniello, L., and Porta, R. (2003) Transglutaminase-catalyzed synthesis of trypsin-cyclodextrin conjugates: kinetics and stability properties. *Biotechnol. Bioeng. 81*, 732−737.

(19) Horne, D. S. (2002) Casein structure, self-assembly and gelation. *Curr. Opin. Colloid Interface Sci. 7*, 456−461.

(20) Tominaga, J., Kamiya, N., Doi, S., Ichinose, H., and Goto, M. An enzymatic strategy for site-specific immobilization of functional proteins using microbial transglutaminase. *Enzyme Microb. Technol. 35*, 613−618.

(21) Kamiya, N., Doi, S., Tominaga, J., Ichinose, H., and Goto, M. (2005) Transglutaminase-mediated protein immobilization to casein nanolayers created on a plastic surface. *BioMacromolecules 6*, 35−38.

(22) Tominaga, J., Kamiya, N., Doi, S., Ichinose, H., Maruyama, T., and Goto, M. (2005) Design of a specific peptide tag that affords covalent and site-specific enzyme immobilization catalyzed by microbial transglutaminase. *BioMacromolecules 6*, 2299−2304.

(23) Haynes, R., Osuga, D. T., and Feeney, R. E. (1967) Modification of amino groups inhibitors of proteolytic enzyme. *Biochemistry 6*, 541−547.

(24) Heiss, C., Weller, M. G., and Niessner, R. (1999) Dip-and-read test strips for the determination of trinitrotoluene (TNT) in drinking water. *Anal. Chim. Acta 396*, 309−316.

(25) Green, T. M., Charles, P. T., and Anderson, G. P. (2002) Detection of 2,4,6-trinitrotoluene in seawater using a reversed-displacement immunosensor. *Anal. Biochem. 310*, 36−41.

(26) Goldman, E. R., Cohill, T. J., Patterson, C. H., Anderson, G. P., Kusterbeck, A. W., and Mauro, J. M. (2003) Detection of 2,4,6-trinitrotoluene in environmental samples using a homogeneous fluoroimmunoassay. *Environ. Sci. Technol. 37*, 4733−4736.

(27) Sakai, T., Torimaru, A., Shinahara, K., Miura, N., Imato, T., Toko, K., and Matsumoto, K. (2003) Preparation of a polyclonal antibody and a bioassay for nitroaromatic compounds by an enzyme-linked immunosorbent assay technique and a surface plasmon resonance biosensor. *Sens. Mater. 15*, 439−452.

(28) Shankaran, D. R., Gobi, K. V., Matsumoto, K., Imato, T., Toko, K., and Miura, N. (2004) Highly sensitive surface plasmon resonance immunosensor for parts-per-trillion level detection of 2,4,6-trinitrophenol. *Sensor. Actuat. B-Chem. 100*, 450−454.

(29) Wright, R. M., Dudas, D., Gavin, B., Dottavio, D., Hexham, J. M., and Lake, P. (2001) A high-capacity alkaline phosphatase reporter system for the rapid analysis of specificity and relative affinity of peptides from phage-display libraries. *J. Immunol. Methods 253*, 223−232.

(30) Takazawa, T., Kamiya, N., Ueda, H., and Nagamune, T. (2004) Enzymatic labeling of a single chain variable fragment of an antibodywith alkaline phosphatase by microbial transglutaminase. *Biotechnol. Bioeng. 86*, 399−404.

(31) Folk, J. E., and Cole, P. W. (1965) Structural requirements of specific substrates for guinea pig liver transglutaminase. *J. Biol. Chem. 240*, 2951−2960.

(32) Girardet, J. M., Courthaudon, J. L., Campagna, S., Puyjalon, V., Lorient, D., and Linden, G. (1999) Proteolysis of milk casein micelle and sodium caseinate in oil-in-water emulsions. *Int. Dairy J. 9*, 409−410.

(33) Kim, E. E., and Wyckoff, H. W. (1991) Reaction mechanism of alkaline phosphatase based on crystal structures. *J. Mol. Biol. 218*, 449−464.

(34) Ohtsuka, T., Ota, M., Nio, N., and Motoki, M. (2000) Comparison of substrate specificities of transglutaminases using synthetic peptide as acyl donor. *Biosci. Biotechnol. Biochem. 64*, 2608−2613.

(35) Zeck, A., Weller, M. G., and Niessner, R. (1999) Characterization of a monoclonal TNT-antibody by measurement of the cross-reactivities of nitroaromatic compounds. *Fresenius J. Anal. Chem. 364*, 113−120.

(36) Mammen, M., Choi, S. K., and Whitesides, G. M. (1998) Polyvalent interactions in biological systems: implications for design and use of multivalent ligands and inhibitors. *Angew. Chem., Int. Ed. 37*, 2754−2794.

(37) Yang, J., Gitlin, I., Krishnamurthy, V. M., Vazquez, J. A., Costello, C. E., and Whitesides, G. M. (2003) Synthesis of monodisperse polymers from proteins. *J. Am. Chem. Soc. 125*, 12392−12393.

(38) Sperinde, J. J., and Griffith, L. G. (1997) Synthesis and characterization of enzymatically-cross-linked poly(ethylene glycol) hydrogels. *Macromolecules 30*, 5255−5264.

BC060161D

Synthesis of Amphiphilic Derivatives of Rose Bengal and Their Tumor Accumulation

Nami Sugita,*,† Ken-ichi Kawabata,† Kazuaki Sasaki,† Isao Sakata,‡ and Shin-ichiro Umemura§

Central Research Laboratory, Hitachi, Ltd., 1-280 Higashi-koigakubo, Kokubunji-shi, Tokyo 185-8601, Japan, Photochemical Co., Ltd., Okayama 701-1221, Japan, and School of Health Sciences, Faculty of Medicine, Kyoto University, Kyoto 606-8507, Japan. Received June 30, 2006; Revised Manuscript Received January 18, 2007

It is known that the combination of laser light and its sensitizer is effective for noninvasive tumor treatment, referred to as photodynamic therapy. Using the combination of ultrasound and its sensitizer has also been suggested for a similar kind of tumor treatment, referred to as sonodynamic therapy. The purpose of this paper is to obtain such sensitizers accumulating selectively in tumors. Amphiphilic derivatives of rose bengal (RB) were synthesized to add a tumor-accumulating property to RB. One type of the synthesized RB derivatives (RBD3), having an alkyl chain with a branching carboxyl group, was found to be superior in amphiphilicity to the other types. Tumor tissue distribution of the synthesized derivatives in mice bearing colon 26 carcinoma was evaluated. It was found that RBD3s with carbon chain lengths of 12, 14, and 16 had higher concentrations in the tumor tissue than RB by more than 1 order of magnitude, several hours after administration. The concentrations correlated well with their water/1-octanol partition coefficients. Since RB is known to induce *in vitro* cell damage in combination with either laser light or ultrasound, the newly synthesized amphiphilic RB derivatives may be potentially useful as a tumor-selective sensitizer for both light and ultrasound.

INTRODUCTION

Photodynamic therapy (PDT) is known as a non- or less-invasive tumor treatment (*1*, *2*). The key components of PDT are a photosensitizer and laser light. The light activates a photosensitizer to react with oxygen, forming singlet oxygen that kills tumor cells. PDT may have some advantages: it can target the tissue to be treated very precisely, and can be repeated multiple times targeting the same tissue. However, it can treat only superficial regions because of the poor penetration of light into tissue.

Similar to laser light, ultrasound can enhance the bioeffect of some chemicals (*3*, *4*) and can even activate its sensitizers through the collapses of cavitation bubbles (*5*). Furthermore, it has a unique feature of penetrating deeply into tissue. The thermal bioeffect of ultrasound alone has already been used clinically for tumor treatment, known as high-intensity focused ultrasound (HIFU) treatment (*6*−*8*). It was found that some photosensitizers such as hematoporphyrin, protoporphyrin, a gallium-deutroporphyrin complex, ATX-70, and a chlorine derivative, ATX-S10, also showed an ultrasonically induced antitumor effect on tumor cells (*9*−*13*), based on which sonodynamic therapy (SDT) was proposed. From the effect of active oxygen scavengers on the ultrasonically induced *in vitro* cell damage, it was hypothesized that active oxygen generated by ultrasonically activated porphyrins was the most important mediator for the porphyrin-enhanced ultrasonically induced cell damage (*10*, *11*, *13*). *In vivo* animal experiments strongly suggested the potential effectiveness of SDT with such porphyrins (*13*−*15*).

Some xanthene photosensitizers have been found not only to be ultrasonically activated (*16*) but also to reduce both *in vitro* and *in vivo* cavitation thresholds, the acoustic intensity needed to induce cavitation, by more than 1 order of magnitude (*17*−*19*). Therefore, their potential as a sonosensitizer for SDT can be even higher than porphyrins. Rose bengal (3′,4′,5′,6′-tetrachloro-2′-(2,4,5,7-tetraiodo-6-hydroxy-3-oxo-3*H*-xanthen-9-yl)benzoic acid, bis(sodium salt), RB (**1**), Scheme 1) is one such xanthene photosensitizer, known to produce singlet oxygen with a quantum yield of nearly 100% on illumination (*19*). RB is reported to induce plasma membrane damage on illumination at 514 nm (*21*) and may have potential as a sensitizer for PDT. RB is also reported to induce *in vitro* cell damage when activated with ultrasound (*20*). The reason why both sensitizing effects of RB were shown in only *in vitro* experiments and not *in vivo* experiments with solid tumors is because RB cannot accumulate in tumor tissue. When RB is introduced into a living body, it is excreted immediately after accumulation in the liver (*22*). Although RB has high potential to be a sensitizer for both PDT and SDT, it cannot be used to treat solid tumors as is. To obtain a RB derivative (RBD) useful for PDT and SDT of solid tumors, its tumor-accumulative derivatives were newly synthesized and the process is described in this paper.

As a guide to adding a tumor-accumulative property to the xanthene dye, we referred to the cases where porphyrin dyes were used. Dougherty et al. reported that amphiphilicity was an important factor in tumor accumulation of porphyrin dyes (*23*). Since RB dissolves well in water but not well in nonpolar solvents, a lipophilic property needed to be added to obtain its amphiphilic derivatives. An alkyl group was used to add the lipophilic property, while a carboxyl group was used as the hydrophilic group to obtain the hydrophilic−lipophilic balance as an amphiphilic compound. To examine the amphiphilicity of the newly synthesized derivatives, their solubility in both polar and nonpolar solvents and their partition coefficients between polar and nonpolar phases were measured. Furthermore, their accumulation in murine tumor tissue was studied. It was quantified by measuring fluorescence from the compound in a slice of excised tissue (*24*).

* To whom correspondence should be addressed. Phone: +81-42-323-1111 ext. 3923, fax: +81-42-327-3347. E-mail: nami.sugita.mg@hitachi.com.

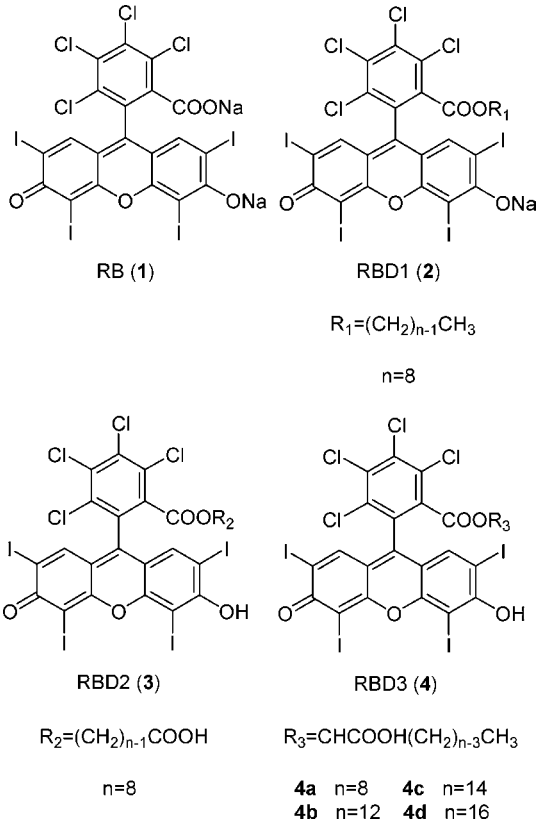
† Hitachi, Ltd.

‡ Photochemical Co., Ltd.

§ Kyoto University.

10.1021/bc060189p CCC: $37.00 © 2007 American Chemical Society
Published on Web 03/17/2007

Scheme 1. Structure of Rose Bengal and Derivatives



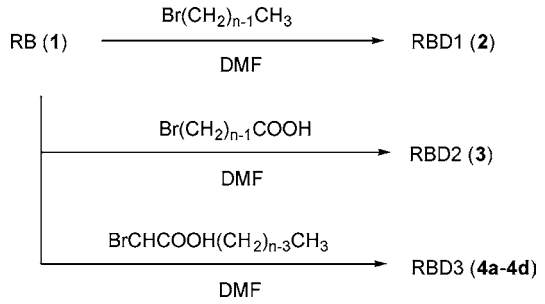
EXPERIMENTAL PROCEDURES

Chemicals. RB (**1**), 90% dye content, was purchased from Sigma Chemical Co. (St. Louis, MO), and ATX-70 was supplied by Photochemical Co. (Okayama, Japan). All bromides used in the esterification reactions can be obtained from Kanto Chemical Co. (Tokyo, Japan), Wako Pure Chemical Industries (Osaka, Japan), Aldrich (Milwaukee, WI), or Lancaster Synthesis UK (Lancashire, UK). Phosphate-buffered saline (PBS) solution (pH = 7.4) was prepared in water using powder purchased from Sigma Chemical Co. (St. Louis, MO). Tetraborate pH standard solution (pH = 9.18) was purchased from Wako Pure Chemical Industries (Osaka, Japan). All products were used without prior purification. Deionized and distilled water was used throughout the experiments.

General Procedures. ^{1}H and ^{13}C nuclear magnetic resonance (NMR) spectra were measured on a Bruker AMX-500 spectrometer in dimethyl sulfoxide (DMSO)-d_6, and tetramethylsilane was used as external standard. Chemical shifts were reported in δ (ppm) and J values in hertz. Infrared (IR) spectra were obtained using a Hitachi I-3000 spectrophotometer, visible absorption spectra were obtained on a Hitachi U-3400 spectrophotometer, and fluorescence spectra were measured with a Hitachi F-4500 spectrofluorometer. High-resolution mass spectrometry (HRMS) was performed by Toray Research Central, Inc.

Synthetic Procedures. Three types of derivatives were synthesized (Scheme 1). RBD1 (**2**, RB, C-2′ alkyl ester, C-6 sodium salt) was synthesized with a method described by Lamberts et al. for the preparation of the C-2′ benzyl ester, C-6 sodium salt (*25*, *26*). Syntheses of RBD2 (**3**, RB, C-2′ ω-carboxyalkyl ester, C-6 molecular form) and RBD3 (**4**, RB, C-2′ α-carboxyalkyl ester, C-6 molecular form) consisted of the same basic procedure as the synthesis of RBD1, except ω-carboxyalkyl bromide was used in RBD2 and α-carboxyalkyl bromide was used in RBD3 in place of the alkyl bromide. The synthetic route to RBDs is shown in Scheme 2.

Scheme 2. Synthesis of Rose Bengal Derivatives



*Synthesis of Rose Bengal Octyl Ester, Monosodium Salt (**2**).* RB (**1**) (1.0 g; 1.0 mmol) was dissolved in *N*,*N*-dimethylformamide (DMF, 10 mL), and 1-bromooctane (0.5 g; 2.7 mmol) was added. This solution was magnetically stirred and heated for 6 h at 80 °C. The excess 1-bromooctane and DMF were distilled off *in vacuo*, and the residue was stirred with diethyl ether overnight. After filtration and thorough diethyl ether washing, in order to remove excess **1** and inorganic species, the residue was stirred with water overnight and was filtered to afford a deep purple powder which had no distinct mp. The isolated yield of **2** was 1.0 g (95%). IR (KBr) 1736 cm^{-1} (ester C═O). ^{1}H NMR (DMSO-d_6) δ (ppm): 0.84 (t, CH_3, 3H, J = 7.3 Hz), 0.88 (m, CH_2, 2H, J = 7.7 Hz), 1.01 (m, CH_2, 2H, J = 7.3 Hz), 1.09 (m, CH_2, 4H, J = 7.0 Hz), 1.16 (m, CH_2, 2H, J = 7.1 Hz), 1.24 (m, CH_2, 2H, J = 7.1 Hz), 3.93 (t, OCH_2, 2H, J = 6.8 Hz) 7.47 (s, ArH, 2H). ^{13}C NMR (DMSO-d_6) δ (ppm): 14.1(CH_3), 22.1, 25.0, 27.7, 28.4, 28.5, 31.3 (CH_2), 66.2 (OCH_2), 76.0 (C-2,7), 97.2 (C-4,5), 110.4 (C-8a,8b), 128.8, 129.9, 131.9, 133.8, 134.4, 134.9, 139.3, (C-1′, 2′, 3′, 4′, 5′, 6′, 9) 136.1 (C-1,8), 157.0 (C-4a,4b), 163.2 (C═O), 171.8 (C-3,5). HRMS Calculated for $C_{28}H_{21}O_5Cl_4I_4$: $(M + H)^+$, *m*/*z* 1084.6322 Found: *m*/*z* 1084.6309.

*Synthesis of Rose Bengal ω-Carboxyheptyl Ester, Molecular Form (**3**).* RB (**1**) (1.0 g; 1.0 mmol) was dissolved in DMF (10 mL), and 8-bromooctanoic acid (0.68 g; 3.1 mmol) was added. This solution was magnetically stirred and heated for 7 h at 80 °C. DMF was distilled off *in vacuo* and the residue was stirred with diethyl ether overnight. After filtration and thorough diethyl ether washing the residue was stirred with water overnight, in order to remove excess **1** and inorganic species. After filtration, it was recrystallized from ethanol, yielding 0.54 g (49%) of reddish purple powder, which had no distinct mp. IR (KBr) 1736 cm^{-1} (ester C═O). ^{1}H NMR (DMSO-d_6) δ (ppm): 0.89 (m, CH_2, 2H, J = 7.3 Hz), 1.03 (m, CH_2, 2H, J = 7.7 Hz), 1.09 (m, CH_2, 4H, J = 6.8 Hz), 1.43 (m, CH_2, 2H, J = 7.5 Hz), 2.18 (t, CH_2COOH, 2H, J = 7.8 Hz), 3.93 (t, OCH_2, 2H, J = 6.3 Hz), 7.48 (s, ArH, 2H), 8.17 (br.s, ArOH), 11.9 (br.s, COOH). ^{13}C NMR (DMSO-d_6) δ (ppm): 24.6, 25.0, 27.7, 28.4, 28.4 (CH_2), 33.7 (CH_2COOH), 66.2 (OCH_2), 76.0 (C-2,7), 97.3 (C-4,5), 110.3 (C-8a,8b), 128.8, 129.9, 131.9, 133.8, 134.4, 134.9, 139.4, (C-1′, 2′, 3′, 4′, 5′, 6′, 9) 136.2 (C-1,8), 157.0 (C-4a,4b), 163.2 (C═O), 171.8 (C-3,6), 174.5 (COOH). HRMS Calculated for $C_{28}H_{19}O_7Cl_4I_4$: $(M + H)^+$, *m*/*z* 1114.6064 Found: *m*/*z* 1114.6083

*Synthesis of Rose Bengal α-Carboxyheptyl (**4a**), Undecyl (**4b**), Tridecyl (**4c**), and Pentadecyl (**4d**) Ester, Molecular Form.* RB (**1**) (1.0 g; 1.0 mmol) was dissolved in DMF (10 mL), and 2-bromooctanoic acid, 2-bromododecanoic acid, 2-bromotetradecanoic acid, and 2-bromohexadecanoic acid (ca. 3 mmol) were added, respectively. This solution was magnetically stirred and heated for 6 days at 30 °C. DMF was distilled off *in vacuo*, and the residue was stirred with diethyl ether overnight. After filtration and thorough diethyl ether washing, the residue was stirred with water overnight to remove excess **1** and inorganic species. After filtration, recrystallization of them from ethanol

yielded **4a** 0.21 g (19%), **4b** 0.20 g (17%), **4c** 0.24 g (20%), and **4d** 0.38 g (31%) of reddish purple powder, which had no distinct mp.

4a. IR (KBr) 1756 cm^{-1} (ester C═O). ^1H NMR (DMSO-d_6) δ (ppm): 0.83 (t, CH_3, 3H, J = 7.0 Hz), 0.91 (m, CH_2, 2H, J = 7.3 Hz), 0.99−1.13 (m, CH_2, 4H), 1.18 (m, CH_2, 2H, J = 7.0 Hz), 1.25−1.42 (m, CH_2, 2H), 4.67 (dd, OCH, 1H, J = 4.5 Hz, 7.5 Hz), 7.46, 7.47 (s, ArH, 2H), 8.19 (br.s, ArOH,), 13.05 (br.s, COOH). ^{13}C NMR (DMSO-d_6) δ (ppm): 14.0 (CH_3), 22.2, 24.1, 28.2, 30.3, 30.9 (CH_2), 74.1 (OCH), 75.9, 76.1 (C-2,7), 97.0, 97.3 (C-4,5), 111.1, 111.2 (C-8a,8b), 129.2, 130.2, 132.0, 132.9, 134.6, 135.3, 139.4, (C-1′, 2′, 3′, 4′, 5′, 6′, 9) 136.0, 136.4 (C-1,8), 157.3, 157.5 (C-4a,4b), 162.7 (C═O), 169.5 (COOH) 171.7, 171.8 (C−3,6). HRMS Calculated for $C_{28}H_{19}O_7Cl_4I_4$: $(M + H)^+$, m/z 1114.6064 Found: m/z 1114.6083

4b. IR (KBr) 1742 cm^{-1} (ester C═O). ^1H NMR (DMSO-d_6) δ (ppm): 0.85 (t, CH_3, 3H, J = 6.8 Hz), 0.88−0.97 (m, CH_2, 2H), 0.97−1.06 (m, CH_2, 2H), 0.97−1.06 (m, CH_2, 2H), 1.06−1.13 (m, CH_2, 2H),1.13−1.43 (m, CH_2, 12H), 4.64 (dd, OCH, 1H, J = 4.5 Hz, 7.5 Hz), 7.44, 7.45 (s, ArH, 2H), 8.48 (br.s, ArOH), 13.03 (br.s, COOH). ^{13}C NMR (DMSO-d_6) δ (ppm): 14.0 (CH_3), 22.1, 24.2, 28.4, 28.6, 28.7, 28.9, 29.0, 30.2, 31.3 (CH_2), 74.2 (OCH), 75.7, 75.9 (C-2,7), 97.0, 97.2 (C-4,5), 110.7, 110.9 (C-8a,8b), 129.1, 130.2, 131.9, 133.0, 134.4, 135.1, 139.2, (C-1′, 2′, 3′, 4′, 5′, 6′, 9) 135.8, 136.2 (C-1,8), 157.2, 157.4 (C-4a,4b), 162.5 (C═O), 169.5 (COOH) 171.7, 171.8 (C−3,6). HRMS Calculated for $C_{32}H_{27}O_7Cl_4I_4$: $(M + H)^+$, m/z 1170.6690 Found: m/z 1170.6711.

4c. IR (KBr) 1742 cm^{-1} (ester C═O). ^1H NMR (DMSO-d_6) δ (ppm): 0.85 (t, CH_3, 3H, J = 6.8 Hz), 0.90−0.99 (m, CH_2, 2H), 0.99−1.07 (m, CH_2, 2H), 1.07−1.13 (m, CH_2, 2H), 1.13−1.44 (m, CH_2, 16H), 4.66 (dd, OCH, 1H, J = 4.3 Hz, 7.8 Hz), 7.43, 7.45 (s, ArH, 2H), 8.21 (br.s, ArOH), 13.04 (br.s, COOH). ^{13}C NMR (DMSO-d_6) δ (ppm): 14.0 (CH_3), 22.1, 24.1, 28.4, 28.6, 28.7, 28.9, 29.0, 29.0, 29.1, 30.1, 31.3 (CH_2), 74.0 (OCH), 75.7, 76.0 (C-2,7), 97.0, 97.3 (C-4,5), 110.7, 111.0 (C-8a,8b), 129.1, 130.2, 132.0, 132.9, 134.5, 135.2, 139.2, (C-1′, 2′, 3′, 4′, 5′, 6′, 9) 135.9, 136.3 (C-1,8), 157.3, 157.4 (C-4a,4b), 162.6 (C═O), 169.4 (COOH) 171.7, 171.8 (C−3,6). HRMS Calculated for $C_{34}H_{31}O_7Cl_4I_4$: $(M + H)^+$, m/z 1198.7003 Found: m/z 1198.6973.

4d. IR (KBr) 1720 cm^{-1} (ester C═O). ^1H NMR (DMSO-d_6) δ (ppm): 0.85 (t, CH_3, 3H, J = 6.9 Hz), 0.89−0.98 (m, CH_2, 2H), 0.98−1.06 (m, CH_2, 2H), 1.06−1.13 (m, CH_2, 2H),1.13−1.42 (m, CH_2, 20H), 4.64 (dd, OCH, 1H, J = 4.2 Hz, 7.6 Hz), 7.43, 7.45 (s, ArH, 2H), 8.29 (br.s, ArOH), 13.02 (br.s, COOH). ^{13}C NMR (DMSO-d_6) δ (ppm): 13.9 (CH_3), 22.1, 24.2, 28.4, 28.6, 28.7, 28.9, 28.9, 29.0, 30.2, 31.3 (CH_2), 74.2 (OCH), 75.7, 75.9 (C-2,7), 97.0, 97.2 (C-4,5), 110.7, 110.9 (C-8a,8b), 129.1, 130.2, 131.9, 133.0, 134.4, 135.1, 139.2, (C-1′, 2′, 3′, 4′, 5′, 6′, 9) 135.8, 136.2 (C-1,8), 157.2, 157.4 (C-4a,4b), 162.5 (C═O), 169.5 (COOH) 171.7, 171.7 (C−3,6). HRMS Calculated for $C_{36}H_{35}O_7Cl_4I_4$: $(M + H)^+$, m/z 1226.7316 Found: m/z 1226.7365.

Measurement of Solubility. In these experiments, 1-octanol was used as the nonpolar solvent, and PBS solution (pH7.4) and tetraborate pH standard solution (pH = 9.18) were used as the polar solvents. One milliliter of an appropriate solvent was added to excess dye in a centrifuge tube. The tube was covered and sonicated for 15 min. After that, it was heated for 2 h in a hot water bath (80−90 °C). Then it was sonicated for another 15 min. After allowing the mixtures to stand overnight at 25 °C, they were centrifuged. Then the supernatant was centrifuged again. The dye contents of each solvent were determined by UV−vis absorbance. Each measurement was performed at least three times.

Measurement of Partition Coefficient. The partition coefficient (P) values of RB and RBDs were measured using 1-octanol and tetraborate pH standard solution (pH = 9.18). Dyes were dissolved at a final concentration of 50 μM in 1.5 mL of 1-octanol and 1.5 mL of tetraborate solution (pH = 9.18). The phases were mixed for 10 min (200 rpm). Samples were centrifuged at 1077g for 10 min, and the dye contents of the organic and aqueous phases were determined by UV−vis absorbance. Each measurement was performed at least three times.

Tumor Cells and Animals. Colon 26 adenocarcinoma used in our research was supplied by the Cancer Institute (Tokyo, Japan). The cell lines were passed weekly through male BALB/c mice (five weeks old). Transplanted tumors were initiated with a subcutaneous trocar injection of approximately 1 mm^3 pieces of fresh tumor into the left dorsal scapula region of male five-week-old CDF_1 mice. When the tumor grew to a diameter of about 10 mm approximately 14 days after implantation, the drug-accumulation study was started.

Preparation of Injections. RB and ATX-70 were dissolved in PBS solution. RBD2 was dissolved in 0.1 N sodium hydroxide aqueous solution. After that, pH of the solution was adjusted to about 7.5 by adding hydrochloric acid, and then it was added to the PBS solution. RBD1 was dissolved in DMSO, which had a volume of about 40% of the solution and then was handled in the same way as described for RBD2. RBD3s were dissolved in DMSO, which accounted for about 20% of the total volume of the solution and then was handled in the same way as described for RBD2 and RBD1. The dye concentration was 2 mg/mL.

Preparation of Tissue Sample. The injections described in the previous section were administered to tumor-bearing CDF_1 mice at doses of 10 mg/kg, by intravenous injections into the caudal vein. The tumor and liver were immediately taken from the animals after sacrificing them at arranged times after injection. The tissue were softly washed with saline and divided into several pieces about 1 mm in thickness.

Measurement of Fluorescence Index. Accumulation of dyes in tissue was quantified referring to a method described by Nakajima et al. (*24*), in which they directly measured the fluorescence spectra of porphyrin dyes in solid tissue samples. It is known that both tissues and porphyrin dyes emit fluorescence when excited at around 350 nm. They excited the tissue samples at 337 nm and observed the fluorescence emissions at around 470 nm as well as 650 nm. The former arose solely from the biological tissue itself (autofluorescence), and the latter mainly from the porphyrin dye. The fluorescence index of the dye was obtained by subtracting the autofluorescence from the peak intensity of the latter and dividing it by the peak intensity of the former. They confirmed that the fluorescence indices of the porphyrin dyes in the tissue samples were proportional to the administered doses.

RB and its derivatives emit fluorescence when excited at 530 nm while tissues alone do not, and tissues emit fluorescence when excited at 337 nm while neither RB nor its derivatives do. Therefore we modified Nakajima's method using two excitation wavelengths: one to excite the dye and the other to excite the tissue itself. The experimental setup is shown in Figure 1. To avoid direct interference of the excitation light with the photon detector, a tissue sample was placed at an angle of 45° to the light path. It was affixed to the inner wall of a 1-cm quartz cell and placed in a solid specimen holder (Hitachi 650-0161).

The autofluorescence intensity was obtained as the peak fluorescence intensity observed at around 460 nm when the tissue taken from a mouse was excited at 337 nm. The dye fluorescence intensity was obtained as the peak fluorescence intensity observed at around 580 nm when the tissue was excited

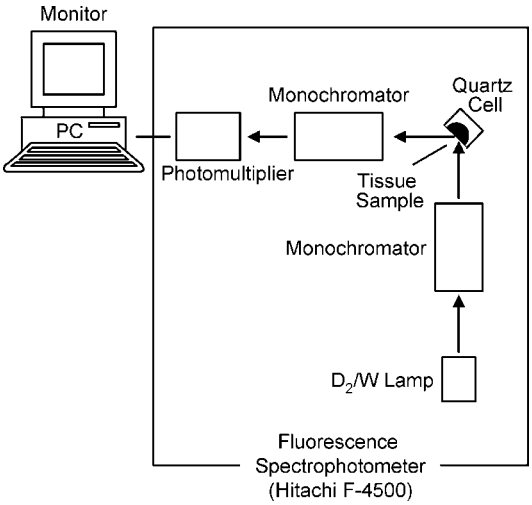


Figure 1. Experimental setup for quantification of tissue accumulation of dyes.

at 530 nm. Dividing the dye fluorescence intensity by the autofluorescence intensity obtained the fluorescence index of the dye.

ATX-70 emits fluorescence when excited at 410 nm while tissues alone do not, and it does not emit fluorescence at around 460 nm when excited at 337 nm. The fluorescence intensity of ATX 70 was therefore obtained as the peak fluorescence intensity observed at around 580 nm when the tissue was excited at 410 nm. The autofluorescence intensity was obtained, and the fluorescence index of the dye was calculated in the same way as for RB and RBDs.

RESULTS

Pursuit of Reaction to Rose Bengal Derivatives. RB was completely consumed in the synthesis of RBD1 and RBD2 at 80 °C. No existence of RB in reaction solvent was checked by thin layer chromatography. However, the conversion rate of RB to RBD3s did not improve sufficiently at 80 °C even when the reaction time was extended.

We followed the reactions of RB to RBD3s by ^{1}H NMR. At more than 35 °C, before the peak of RB at 7.3 ppm disappeared, a peak of side product appeared at around 2.5 ppm. On the other hand, at not more than 30 °C, although the reaction time was greatly extended from several hours to several days, RB was completely converted to RBD3s. The peak of RB completely disappeared and the peak of side product was not observed.

Identification. The structures of the synthesized RBDs were confirmed by IR, NMR, and HRMS. IR and NMR experiments showed the presence of an ester bond in RBDs. The results of the IR analysis of RBDs indicated the band at around 1720−1760 nm^{-1}, typical of C═O stretching of an ester carbonyl group. This was not found in the parent RB spectrum. The ^{13}C NMR spectra showed the peak attributed to a carbonyl carbon in RB that shifted to higher magnetic field from 164.8 ppm in RB to around 162.5−163.2 ppm in RBDs.

The NMR experiments showed the presence of an alkyl chain in RBDs. The results of the ^{1}H NMR analysis of RBDs indicated peaks at around 0.8−1.5 ppm, typical of methylene groups, and the results of the ^{13}C NMR analysis indicated peaks at around 22−31 ppm, also typical of methylene groups. The NMR analysis of RB, which was the starting material, indicated peaks only in low magnetic field, typical of aromatic groups. The results of the ^{1}H NMR analysis of RBD1 and RBD2 indicated a triplet peak at 3.93 ppm, a typical situation where CH_2 is next to the ester carbonyl group. In contrast, the results for RBD3s indicated the double doublet peak at around 4.7 ppm, which is typical of a CH found next to an ester carbonyl group. The results of the ^{1}H NMR analysis of RBD1 and RBD3s indicated a triplet peak at around 0.85 ppm, which is typical of a terminal CH_3 of an alkyl chain. For RBD2 no such peak was indicated at this position. In the ^{1}H NMR spectra of RBD2 and RBD3s, peaks attributed to the hydrogen of a carboxyl group around 13 ppm and a hydroxyl group around 8.3 ppm were observed.

The HRMS experiments showed chemical formulas and molecular weights that supported the estimated structures of RBDs. The results of the HRMS analysis of RBD1 and RBD2 indicated a Na adduct ion $(M + 23)^+$.

Table 1. Solubility and Partition Coefficient for Rose Bengal and Derivatives

	solubility (mM) (25 °C)			
		water		
compound code	1-octanol	pH 7.4	pH 9.18	1-octanol/water (pH 9.18) partition coefficient
RB	3.64	197	313	1.5
RBD1 ($n = 8$)	8.9	<0.013	<0.009	-
RBD2 ($n = 8$)	0.23	0.7	2.1	155
RBD3 ($n = 8$)	0.53	1.0	4.43	48.7
RBD3 ($n = 12$)	7	0.019	0.6	30.1
RBD3 ($n = 14$)	7	0.011	1.6	17.3
RBD3 ($n = 16$)	6.9	0.034	1.4	45.4

Solubility. The solubility of RB and RBDs in nonpolar and polar solvents was measured, and the results are listed in Table 1. In these measurements, 1-octanol was used as the nonpolar solvent, and PBS solution (pH = 7.4) and tetraborate solution (pH = 9.18) were used as the polar solvents. Regarding polar solvents, the solubility of RB and RBDs at pH 9.18 was higher than those at pH 7.4.

RB dissolved greatly in polar solvents, but the solubility in 1-octanol was 2 orders of magnitude lower than that in the polar solvents. The solubility of RBD1 with a carbon chain length of eight in 1-octanol was about twice as high as that of RB. In contrast, RBD1 hardly dissolved at all in polar solvents. RBD2 and RBD3 with a carbon chain length of eight both dissolved slightly in polar solvents, but their solubility in 1-octanol was lower than that of RB. The solubility of RBD3 was twice as high as that of RBD2. Therefore, we chose RBD3 for a more detailed investigation, and synthesized RBD3s with several carbon chain lengths. The solubility of RBD3s with carbon chain lengths of 12, 14, and 16 in 1-octanol was almost the same. It was a little lower than that of RBD1 with a carbon chain length of eight, but about twice as high as that of RB. The solubility of RBD3s with carbon chain lengths of 12, 14 and 16 in polar solvents varied a little. It was 2 orders of magnitude lower than that of RBD3 with a carbon chain length of eight at pH 7.4, but the difference was reduced to less than an order of magnitude at pH 9.18.

Partition Coefficient. *P* of RB and RBDs between polar and nonpolar phases was measured, and the results are also listed in Table 1. Here, 1-octanol and tetraborate solution (pH = 9.18) were used as the partition solvent. *P* of RB was the lowest. *P* of RBD1 could not be calculated because the tetraborate solution phase was too dilute to find UV−vis absorbance. If *P* of RBD1 had been calculated, it would have been the highest. Among the results of finite numbers, *P* of RBD2 was the highest and it was 2 orders of magnitude higher than that of RB. Among the RBD3s, there was no simple relation between the carbon chain lengths and the values of *P*.

Accumulation in Tissues. Figures 2 and 3 plot the fluorescence indices of RBDs with a carbon chain length of eight after administration in the murine liver tissue and in the tumor tissue, respectively. Those of the starting material, RB, and a tumor-selective porphyrin dye, ATX-70, are also shown for compari-

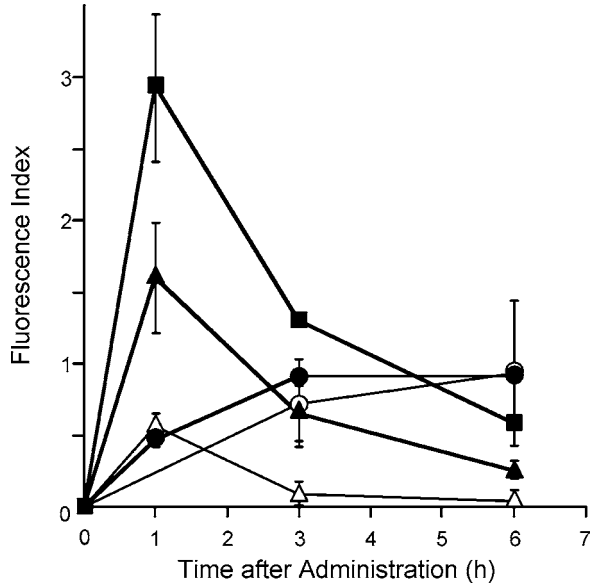


Figure 2. Fluorescence index of various RBDs ($n = 8$) in liver tissue. Solid circles are RBD1, solid triangles are RBD2, and solid squares are RBD3. For reference, the data of RB (open triangles) and ATX-70 (open circles) are also shown. These are the mean values ± SD of three mice.

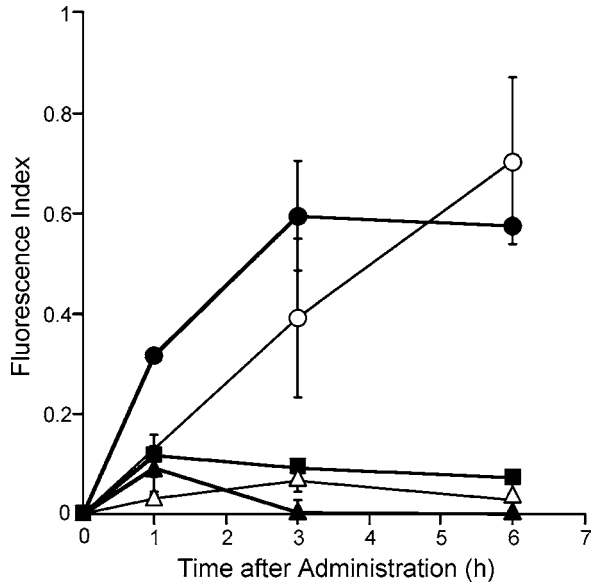


Figure 3. Fluorescence index of various RBDs ($n = 8$) in tumor tissue. Solid circles are RBD1, solid triangles are RBD2, and solid squares are RBD3. For reference, the data of RB (open triangles) and ATX-70 (open circles) are also shown. These are the mean values ± SD of three mice.

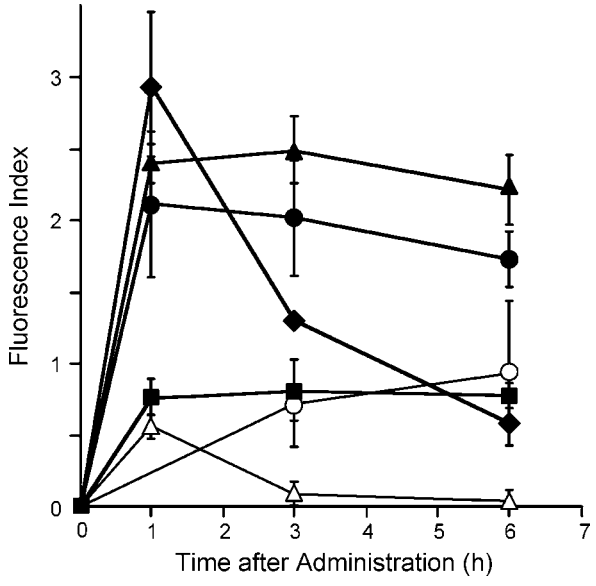


Figure 4. Fluorescence index of RBD3 with various carbon chain lengths in liver tissue. Solid diamonds are $n = 8$, solid triangles are $n = 12$, solid circles are $n = 14$, and solid squares are $n = 16$. For reference, the data of RB (open triangles) and ATX-70 (open circles) are also shown. These are the mean values ± SD of three mice.

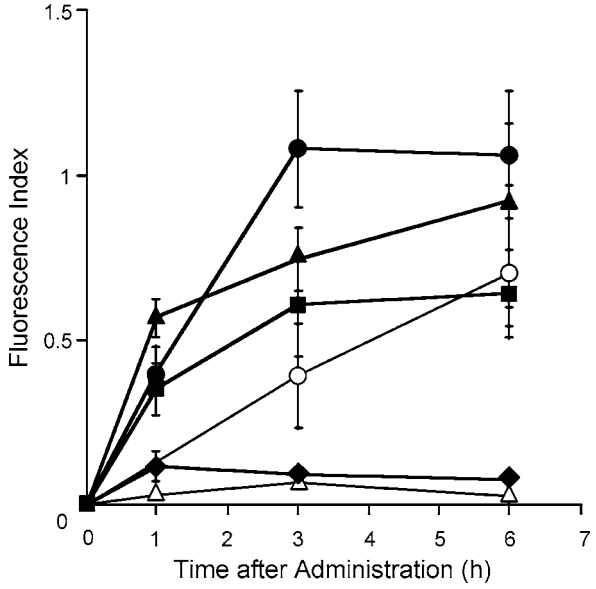


Figure 5. Fluorescence index of RBD3 with various carbon chain lengths in tumor tissue. Solid diamond are $n = 8$, solid triangles are $n = 12$, solid circles are $n = 14$, and solid squares are $n = 16$. For reference, the data of RB (open triangles) and ATX-70 (open circles) are also shown. These are the mean values ± SD of three mice.

son. RB suddenly accumulated in liver tissue after administration and then was excreted. In contrast, ATX-70 accumulated in both liver and tumor tissues, and both fluorescence indices increased as time proceeded. RBD1 behaved similarly to ATX-70 in both liver and tumor tissues. However, RBD2 and RBD3 showed the same tendency as RB.

Figures 4 and 5 plot the fluorescence indices of RBD3s with different carbon chain lengths after administration in the murine liver tissue and in the tumor tissue, respectively. The behavior of the RBD3 fluorescence indices in liver tissue changed from being similar to RB to being similar to ATX-70 as the chain length increased. In tumor tissue, the fluorescence indices of RBD3 with a chain length of eight were as low as those of RB. However, with longer chain lengths, a remarkable accumulation in tumor tissue was observed. It reached a level similar to or even higher than that of ATX-70. The optimum carbon chain length was found to be 14. The fluorescence index of RBD3 with a carbon chain length of 14 in the murine tumor tissue 6 h after administration was not only approximately 40 times higher than that of RB but also about 1.5 times higher than that of ATX-70.

Relationship between Amphiphilicity and Accumulation in Tumor Tissue. Figure 6 shows the relationship between the solubility in 1-octanol of RBDs and their fluorescence index in the tumor 6 h after administration. The dyes are divided into two groups. One group (solid circles), with relatively high solubility in 1-octanol, higher than 6 mM, showed relatively high accumulation in tumor tissue. The other group (open circles), with relatively low solubility in the nonpolar solvent, showed very low accumulation in tumor tissue.

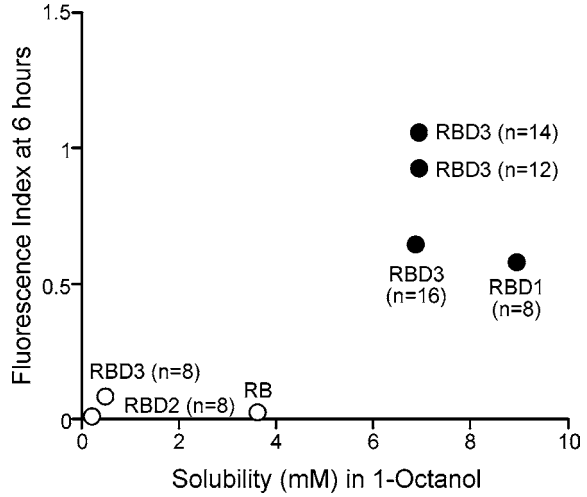


Figure 6. Relationship between lipophilicity (solubility in 1-octanol) of RBDs and their 6-h fluorescence index in tumor tissue. For reference, RB data are also shown.

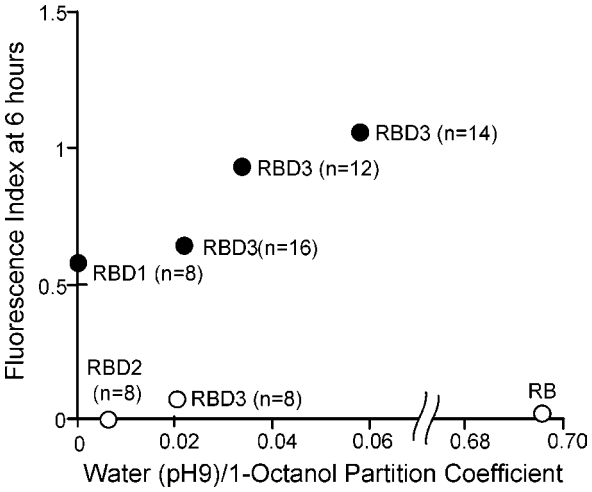


Figure 7. Relationship between amphiphilicity (partition coefficient) of RBDs and their 6-h fluorescence index in tumor tissue.

Figure 7 shows the relationship between the water (pH 9.18)/1-octanol partition coefficient, *P*wo, of RBDs and their fluorescence index in the tumor 6 h after administration. Here, we chose to use P_{wo} instead of P_{ow}, the 1-octanol partition coefficient/water, as an indicator of amphiphilic property. For the group of solid circles, a good correlation between P_{wo} and the fluorescence index in tumor tissue, with a correlation coefficient of 0.95, is observed.

DISCUSSION

As the method to synthesize RBDs, esterification of a carboxylate anion and an alkyl bromide was chosen. RB has two nucleophiles. One is the carboxylate anion at the C-2′ position and the other is the phenolate anion at the C-6 position. However, because of the sterically imposing iodines ortho to the phenoxide at the C-6 position, a nucleophilic substitution occurs selectively at the C-2′ position (*27*). Lamberts et al. synthesized various RBDs with various substituents at the C-2′ position (*25*−*27*).

From the spectroscopic results, it was confirmed that the couplings of RB and the three types of bromide were accomplished (Scheme 2). Regarding the C-6 position, it was found that the sodium salt was retained in RBD1, but the sodium was substituted by the hydrogen in RBD2 and RBD3s. We think this difference between RBD1 and the other derivatives is due to the difference in the reaction condition. The bromide used in the syntheses of RBD2 and RBD3s had a carboxyl group in them, so the reaction environment may have become acidic. Lamberts et al. used DMF as a reaction solvent to synthesize sodium salt-type derivatives of RB, on the other hand they used water and acetone to synthesize its molecular form derivatives (*25*, *26*).

Two kinds of reaction should have competed with each other in the syntheses of RBD2 and RBD3s. One is the desired esterification of the carboxylate anion in RB and the carbocation in the bromide. The other is an unexpected coupling of the bromides, between the carboxyl group and the carbocation both in the bromides. In the bromides used in the syntheses of RBD3s, a carboxyl group is bonded to the carbon next to the bromine. In the syntheses of RBD3s, the reaction point of desirable esterification between RB and the bromide is crowded. We think this is the reason why the reaction was difficult to run in the syntheses of RBD3s especially.

The yield of RBD2 and RBD3s was considerably low in comparison with that of RBD1 though RB was mostly converted to RBD2 and RBD3s. The purification of RBD2 and RBD3s was difficult because of their amphiphilicity. We think this is the reason for their low yield. A better method of purification should be developed in the future.

We modified Nakajima's method (*24*) and used it to evaluate the accumulation of dyes in tissues. Since the fluorescence indices of dyes in tissues, obtained by their method, were confirmed to be proportional to the doses, they should be proportional to the concentrations of the dyes in tissues.

In what follows, we discuss the relationship between the amphiphilicity of the synthesized derivatives and their accumulation in tumor tissue. From Figures 6 and 7, the balance between lipophilicity and hydrophilicity of a compound is confirmed to be an important factor for its tumor accumulation. Furthermore, the regiochemical arrangement of lipophilic and hydrophilic substituents in the compound's structure is speculated to have contributed to its amphiphilicity.

It is known that RB is excreted rapidly into the bile by carrier-mediated hepatobiliary transport (*22*, *28*). Our results for RB in Figures 2 and 3 are consistent with this knowledge. RB was quickly excreted from the body before it could be accumulated in tumor tissue. Among the RBDs with a carbon chain length of eight, RBD1 showed the most drastic improvement from RB in tumor accumulation, while RBD2 and RBD3 showed much less improvement. The solubility of RBD1 in 1-octanol was about twice as high as that of RB (Table 1). This increment in the lipophilicity seems to have been sufficiently effective for RBD1 not to bind to the carriers and be excreted by the transport mediated by them. The level and the time course of concentration of RBD1 in both liver and tumor tissues were similar to those of ATX-70, an amphiphilic porphyrin dye known to accumulate well in tumor tissue (*14*).

However, the water solubility of RBD1 may be too low to be delivered intravenously as a stable aqueous solution in a practical case. The hydrophilicity that RB originally had was lost because a part of the carboxylate anion, one of the two hydrophilic groups in RB, was converted to the ester when the alkyl chain was added to RB. To solve this problem, not only a lipophilic group but also a hydrophilic group was introduced in the synthesis of RBD2 and RBD3 (Scheme 1). Of these two, RBD3 accumulated in the tumor tissue significantly better than both RBD2 and RB (Figure 3), although its solubility in 1-octanol was reduced to less than that of RB (Table 1). Therefore, we chose RBD3 and synthesized RBD3s with longer carbon chains in order to improve its lipophilicity.

As shown in Figure 5, RBD3s with carbon chain lengths of 12, 14, and 16 accumulated in the tumor tissue at a concentration

level similar to or even higher than ATX-70. The improvement in the tumor accumulation from RBD3 with a carbon chain length of eight and RB was dramatic. RBD3s with longer carbon chain lengths also accumulated in liver tissue in a similar way to ATX-70, and very differently from RBD3 with a carbon chain length of eight and RB (Figure 4).

A distinct relationship between the lipophilicity and the tumor accumulation of RBDs was seen in Figure 6. This is consistent with reports on photosensitizing agents for PDT stating that the agents with lipophilicity tend to localize in tumor tissue because they are bound to lipoproteins and are transported (*23*). The tumor accumulation of RB itself was too low to correlate well with the other RBDs because of its carrier-mediated rapid excretion from the body.

Amphiphilicity is also known to be a key factor for tumor-targeting agents as reported for porphyrin dyes (*29*, *30*). Zhang et al. reported that a homologous series of 2-nitroimidazoles with similar lipophilicity showed significantly different *in vivo* tumor uptake depending on their amphiphilicity, and that the octanol-to-water partition coefficient, P_{ow}, of 1 was optimal to achieve their renal excretion and high target-to-background distribution ratios (*31*).

It is interesting that a good correlation between the tumor accumulation and the water-to-octanol partition coefficient, P_{wo}, rather than P_{ow}, is seen for the group of solid circles in Figure 7. Since their P_{wo} are much less than 1, this result is consistent with the report by Zhang et al. in spite of the significant difference in the structure (*31*).

It is even more interesting that the hydrophilicity to lipophilicity ratio, P_{wo}, of RBD3s increased as the length of their alkyl chain increased from 8 to 14. It started decreasing only after the chain length exceeded 14. In other words, both hydrophilicity and lipophilicity increased at the same time when the chain length increased from 8 to 14. In RBD3s, the hydrophilic carboxyl group and lipophilic alkyl chain branch locate right next to each other. We would speculate that the alkyl chain may change its three-dimensional conformation in relation to the carboxyl group according to the hydrophilicity and lipophilicity of the environment, and that the advantage in the degree of freedom of a long chain may overcome the potential increase in hydrophobicity up to a certain chain length. Kim et al. also mentioned that the regiochemical arrangement of lipophilic and hydrophilic substituents in the structure is needed for amphiphilicity (*30*).

In measuring of the partition coefficient, we used tetraborate pH standard solution of pH 9.18 rather than PBS of pH 7.4, which is normally used, because of its closeness to plasma in pH. It was much easier to perform reproducible measurements at pH 9.18 than pH 7.4. The dissociation of RBD2 and RBD3s may not be stable at pH 7.4, which is close to their pK_a.

In this study, the importance of amphiphilicity with a balance between lipophilicity and hydrophilicity to obtain tumor-accumulative agents was shown. Among the RBDs we synthesized, RBD3, which has an alkyl chain and a branching carboxyl group located next to each other, showed the highest potential as such an agent. By optimizing the length of the alkyl chain, we were able to obtain RBDs, that accumulated in tumor tissue at a concentration level similar to or even better than the known tumor-accumulative porphyrin dye. The poor tumor accumulation of RB has been its greatest drawback as a potential agent for tumor treatment. This paper would eliminate this drawback by proposing the tumor-accumulative RBDs. Further *in vitro* and *in vivo* experiments are currently underway to confirm whether the obtained RBDs maintain the excellent photo- and sono-sensitizing abilities of RB.

ACKNOWLEDGMENT

The authors thank Dr. N. Yumita for his advice on the animal experiments and Dr. B. Choi for his advice on the synthetic procedures. Part of this work was supported by the New Energy and Industrial Technology Development Organization (NEDO), Japan.

LITERATURE CITED

(1) Dougherty, T. J., Kaufman, J. E., Goldfarb, A., Weishaupt, K. R., Boyle, D., and Mittleman, A. (1978) Photoradiation therapy for the treatment of malignant tumors. *Cancer Res. 38*, 2628−2635.

(2) Hayata, Y., Kato, H., Konaka, C., Ono, J., and Takizawa, N. (1982) Hematoporphyrin derivative and laser photoradiation in the treatment of lung cancer. *Chest 81*, 269−277.

(3) Kremkau, F. W., Kaufmann, J. S., Walker, M. M., Burch, P. G., and Spurr, C. L. (1976) Ultrasonic enhancement of nitrogen mustard cytotoxicity in mouse leukemia. *Cancer 37*, 1643−1647.

(4) Akimoto, R. (1985) An experimental study on enhancement of the effect of anti-cancer drug by ultrasound. *J. Jpn. Soc. Cancer Ther. 20*, 562−570.

(5) Yumita, N., Okumura, A., Nishigaki, R., Umemura, K., and Umemura, S. (1987) The combination treatment of ultrasound and antitumor drugs on Yoshida sarcoma. *Jpn. J. Hypertherm. Oncol. 3*, 175−182.

(6) Lynn, J. G., Zwemer, R. L., Chick, A. J., and Miller, A. F. (1942) A new method for the generation and use of focused ultrasound in experimental biology. *J. Gen. Physiol. 26*, 179−193.

(7) Fry, W. J., Barnard, J. W., Fry, F. J., and Brennan, J. F. (1955) Ultrasonically produced localized selective lesions in the central nervous system. *Am. J. Phys. Med. 34*, 413−423.

(8) Sanghvi, N. T., and Hawes, R. H. (1994) High-intensity focused ultrasound. *Gastrointest. Endosc. Clin. N. Am. 4*, 383−395.

(9) Yumita, N., Nishigaki, R., Umemura, K., and Umemura, S. (1989) Hematoporphyrin as a sensitizer of cell-damaging effect of ultrasound. *Jpn. J. Cancer Res. 80*, 219−222.

(10) Umemura, S., Yumita, N., Nishigaki, R., and Umemura, K. (1990) Mechanism of cell damage by ultrasound in combination with Hematoporphyrin. *Jpn. J. Cancer Res. 81*, 962−966.

(11) Umemura, S., Yumita, N., and Nishigaki, R. (1993) Enhancement of ultrasonically induced cell damage by a gallium-porphyrin complex, ATX-70. *Jpn. J. Cancer Res. 84*, 582−588.

(12) Umemura, S., Kawabata, K., Sasaki, K., Yumita, N., Umemura, K., and Nishigaki, R. (1996) Recent advances in sonodynamic approach to cancer therapy. *Ultrason. Sonochem. 3*, S187−S191.

(13) Yumita, N., Nishigaki, R., Sakata, I., Nakajima, S., and Umemura, S. (2000) Sonodynamically induced antitumor effect of 4-formyloximethylidene-3-hydroxy-2-vinyl-deuterio-porphynyl(IX)-6,7-di aspatric acid (ATX-S10). *Jpn. J. Cancer Res. 91*, 255−260.

(14) Yumita, N., Sasaki, K., Umemura, S., and Nishigaki, R. (1996) Sonodynamically induced antitumor effect of a gallium-porphyrin complex, ATX-70. *Jpn. J. Cancer Res. 87*, 310−316.

(15) Sasaki, K., Yumita, N., Nishigaki, R., and Umemura, S. (1998) Antitumor effect sonodynamically induced by focused ultrasound in combination with Ga-porphyrin complex. *Jpn. J. Cancer Res. 89*, 452−456.

(16) Umemura, S., Kawabata, K., and Sasaki, K. (1996) Enhancement of sonodynamic tissue damage production by second-harmonic superimposition: Theoretical analysis of its mechanism. *IEEE Trans. Ultrason. Ferroelect. Freq. Contr. 43*, 1054−1062.

(17) Umemura, S., Kawabata, K., and Sasaki, K. (1997) *In vitro* and *in vivo* enhancement of sonodynamically active cavitation by second-harmonic superimposition. *J. Acoust. Soc. Am. 101*, 569−577.

(18) Kawabata, K., and Umemura, S. (1997) Xanthene dyes for reducing acoustic cavitation threshold in aqueous solution. *Ultrasonics 35*, 469−474.

(19) Gandin, E., Lion, Y., and Van de Vorst, A. (1983) Quantum yield of singlet oxygen production by xanthene derivatives. *Photochem. Photobiol. 37*, 271−278.

(20) Umemura, S., Yumita, N., Umemura, K., and Nishigaki, R. (1999) Sonodynamically induced effect of rose bengal on isolated sarcoma 180 cells. *Cancer Chemother. Pharmacol. 43*, 389−393.

(21) Kochevar, I. E., Bouvier, J., Lynch, M., and Lin, C. (1994) Influence of dye and protein location on photosensitization of the plasma membrane. *Biochim. Biophys. Acta 1196*, 172−180.

(22) Fischer, E., and Varga, F. (1979) Hepatic storage and biliary excretion of rose bengal in the rat. *Acta Physiol. Acad. Sci. Hung. 54*, 89−94.

(23) Dougherty, T. J. (1987) Photosensitizers: Therapy and detection of malignant tumors. *Photocem. Photobiol. 45*, 879−889.

(24) Nakajima, S., Hayashi, H., Omote, Y., Yamazaki, Y., Hirata, S., Maeda, T., Kubo, Y., Takemura, T., Kakiuchi, Y., Shindo, Y., Koshimizu, K., and Sakata, I. (1990) The tumor-localizing properties of porphyrin derivatives. *J. Photochem. Photobiol. B: Biol. 7*, 189−198.

(25) Lamberts, J. J. M., and Neckers, D. C. (1984) Rose bengal and non-polar derivatives: The birth of dye sensitizers for photooxidation. *Z. Naturforsch. 39b*, 474−484.

(26) Lamberts, J. J. M., and Neckers, D. C. (1985) Rose bengal derivatives as singlet oxygen sensitizers. *Tetrahedron 41*, 2183−2190.

(27) Neckers, D. C., and Valdes-Aguilera, O. M. (1993) Photochemistry of the xanthene dyes. *Advances in Photochemistry* (Volman D., Hammond G. S., and Neckers, D. C., Eds.) pp 316−394, Volume 18, John Wiley & Sons, Inc., Hoboken, NJ.

(28) Wang, H. K., Miyachi, S., Yamazaki, M., Sawada, Y., Chung, Y. B., Iga, T., Hanano, M., and Sugiyama, Y. (1992) Nonlinear pharmacokinetics of hepatobiliary transport of rose bengal in rats after iv bolus administration with varying doses. *Biopharm. Drug Dispos. 13*, 647−662.

(29) Zheng, G., Potter, W. R., Camacho, S. H., Missert, J. R., Wang, G., Bellnier, D. A., Henderson, B. W., Rodgers, M. A., Dougherty, T. J., and Pandey, R. K. (2001) Synthesis, photophysical properties, tumor uptake, and preliminary in vivo photosensitizing efficacy of a homologous series of 3-(1′-alkyloxy)ethyl-3-devinylpurpurin-18-*N*-alkylimides with variable lipophilicity. *J. Med. Chem. 44*, 1540−1559.

(30) Kim, Y., Song, R., Kim, D. H., Jun, M. J., and Sohn, Y. S. (2003) Synthesis, biodistribution and antitumor activity of hematoporphyrin-platinum (II) conjugates. *Bioorg. Med. Chem. 11*, 1753−1760.

(31) Zhang, X., Su, Z., Ballinger, J. R., Rauth, A. M., Pollak, A., and Thornback, J. R. (2000) Targeting hypoxia in tumors using 2-nitroimidazoles with peptidic chelators for technetium-99m: Effect of lipophilicity. *Bioconjugate Chem. 11*, 401−407.

BC060189P

Synthesis of Enzyme-Degradable, Peptide-Cross-Linked Dextran Hydrogels

Stéphane G. Lévesque[†,§] and Molly S. Shoichet[†,‡,§,*]

Department of Chemical Engineering and Applied Chemistry, University of Toronto, 200 College Street, Toronto, Ontario M5S 3E5, Department of Chemistry, University of Toronto, 80 St. George St., Toronto, Ontario M5S 3H6, and Institute of Biomaterials and Biomedical Engineering, 164 College Street, Toronto, Ontario M5S 3G9, University of Toronto
Received July 12, 2006; Revised Manuscript Received December 20, 2006

Hydrogels derived from synthetic polymers have been previously engineered to degrade under the activity of matrix metalloproteinases (MMPs). It is believed that these systems can act as extracellular-matrix (ECM) equivalents mimicking the degradation and remodeling of the ECM through the activity of cell-secreted enzymes. In this study, MMP-sensitive hydrogels derived from dextran were developed. In order to avoid the incorporation of hydrolyzable esters often introduced in dextran modification strategies, the polysaccharide was modified with *p*-maleimidophenyl isocyanate (PMPI) thereby introducing maleimide functionalities in the backbone and resulting in dextran derivatized with *p*-maleimidophenyl isocyanate (Dex-PMPI). This strategy was favored to separate out the effects of random hydrolysis and enzymatic digestion in the degradation of the dextran hydrogels. A peptide cross-linker, derived from collagen and susceptible to gelatinase A (MMP-2) digestion, was synthesized with bifunctional cysteine termini and used to cross-link the Dex-PMPI. These hydrogels were found to be hydrolytically stable for more than 200 days yet degraded either within 30 h when exposed to bacterial collagenase or within 16 days when exposed to human MMP-2, demonstrating enzymatic-mediated digestion of the peptide cross-links. Further modification of the cross-linked hydrogels with laminin-derived peptides enhanced cell adhesion and survival, demonstrating the potential of these materials for use in tissue engineering applications.

INTRODUCTION

One aspect of tissue engineering is the development of multicomponent scaffolds that can elicit specific biological functions. Ideally, these scaffolds would act as extracellular-matrix (ECM) equivalents, mimicking the cellular environment as closely as possible. The natural ECM is not only a physical support for the cells but also plays a key role in signal transduction by presenting adhesion molecules and serving as a reservoir for other molecules, such as cytokines, that influence growth and cell function. The dynamic interactions between cell and ECM have been mimicked in scaffold design where both physical and chemical stimuli have been incorporated to guide tissue regeneration both spatially and temporally (*1*−*4*); however, these scaffolds have not been optimized for nerve repair strategies.

Most biodegradable synthetic polymers studied for tissue-engineering applications, such as polycaprolactone, polylactide, polyglycolide, and poly(lactide-*co*-glycolide), rely on random ester hydrolysis of the backbone chain instead of tailoring the degradation to specific cellular activity. Over the years, advances in molecular biology have provided a better understanding of the cellular environment which has been used to design scaffolds that mimic the degradation and the remodeling of the ECM. In this environment, growth, repair, and development are controlled by cell-secreted and cell-activated enzymes, such as matrix metalloproteinases (MMPs) and plasmin. These processes are regulated through enzymatic degradation and *de novo* synthesis of ECM components, making the degradation of this natural support dynamic. Due to their involvement in tissue remodeling, the activity of these enzymes is highly localized in the cellular periphery and is tightly regulated.

MMPs, which are calcium-requiring and zinc-dependent endopeptidases, constitute one of the major families of proteinases playing key roles in the responses of cells to their environment (*5*). They have the ability to hydrolyze one or several components of the ECM, as well as nonmatrix proteins thereby influencing cell migration, proliferation, differentiation, and death by both modifying the cellular microenvironment and regulating the activity of biological molecules. MMPs are secreted as inactive zymogens, and their activity is highly regulated at the transcriptional and posttranscriptional level. Expressed during development (*6*, *7*), most MMPs have been found to be produced at very low or undetectable levels in the adult central nervous system (CNS); however, they are up-regulated following spinal cord injury (*8*, *9*) and may play a beneficial role in CNS repair strategies (*5*, *9*). MMPs are expressed in the growth cones of numerous vertebrate neurons (*10*−*12*) and may regulate axonal guidance (*13*−*15*). Muir and co-workers previously reported that MMP-2 activity facilitated neurite extension of dorsal root ganglia (DRG) neurons within a reconstituted ECM (*11*) and promoted axonal growth by degrading inhibitory chondroitin sulfate proteoglycans (*15*). MMP-2 is therefore highly relevant to the enzymatic degradation of ECM analogues designed for neuronal applications.

Hubbell and West introduced the concept of mimicking the dynamic remodeling of the ECM through the development of telechelic peptide-poly(ethylene glycol) (PEG)-peptide block copolymers which were degraded either by plasmin or bacterial collagenase (*16*). Different hydrogels sensitive to proteases such as MMPs (*3*, *4*, *17*) and plasmins (*17*, *18*) have been developed for various tissue engineering applications, mimicking some fundamental aspects of cell−ECM interactions by taking advantage of the time- and location-dependent ECM degradation activity exhibited during cellular outgrowth.

* To whom correspondence should be addressed: Molly Shoichet, Terrence Donnelly Centre for Cellular and Biomolecular Research, University of Toronto, 160 College St., Rm. 514, Toronto, Ontario, M5S 3E1. Phone: 416-978-1460; fax: 416-9784317; e-mail: molly@ecf.utoronto.ca.

† Department of Chemical Engineering and Applied Chemistry.

‡ Department of Chemistry.

§ Institute of Biomaterials and Biomedical Engineering.

10.1021/bc0602127 CCC: $37.00 © 2007 American Chemical Society
Published on Web 04/03/2007

Dextran is a natural polysaccharide which consists mainly of linear chains of α-1,6 linked D-glucopyranose residues. It has been widely used in biotechnology applications (*19*−*22*), studied as a drug delivery vehicle (*23*−*26*), and more recently has been investigated as a biomaterial (*27*−*30*). Dextran hydrogels are particularly compelling as scaffolds for soft tissue-engineering applications because dextran is resistant to both protein adsorption (*31*, *32*) and cell adhesion (*27*, *33*, *34*), allowing specific cellular behavior, such as adhesion (*34*, *35*), to be dialed into the hydrogel design. Unlike PEG, which has modifiable groups only at the termini, dextran has three hydroxyl groups on each glucopyranose repeat unit that are available for chemical modification with either cross-linking agents for hydrogel formation (*36*, *37*) or bioactive molecules (*38*−*41*).

In previous studies, we have reported methods to create macroporous, interconnected dextran scaffolds for tissue-engineering applications using glycidyl-methacrylate derivatized dextran (Dex-MA) (*36*) and to render these hydrogels cell-adhesive by covalently immobilizing ECM-derived peptides (*42*). To create biodegradable hydrogels, we cross-linked the dextran with MMP-2-labile oligopeptides and characterized it for degradation and cytocompatibility *in vitro*. Specifically, dextran was first modified with *p*-maleimidophenyl isocyanate (PMPI), a sulfhydryl- and hydroxyl-reactive heterobifunctional cross-linker. The isocyanate terminus of PMPI reacts with the dextran hydroxyl functional group forming a hydrolytically stable carbamate linkage and provides a maleimide moiety on the other terminus, which reacts by Michael-type addition with a sulfhydryl functionalized cross-linker to form a thioether cross-linked hydrogel. The peptide cross-linker was specifically designed to be susceptible to MMP-2 degradation and to have a cysteine residue at each terminus, allowing conjugate addition to dextran derivatized with *p*-maleimidophenyl isocyanate (Dex-PMPI). To gain greater insight into the specificity of the protease activity, dicysteine peptides with high and low MMP-2-sensitive peptide sequences, GCRD**GPQGIASQ**DRCG and GCRD**GPQGPAGQ**DRCG, were used to create the cross-linked gels and compared in terms of enzymatic degradation. Moreover, to explore these materials for tissue engineering applications, these dextran cross-linked hydrogels were modified with cell-adhesive peptides, CGDPG*YIGSR* and CQAAS*IKVAV*, and compared in terms of neural cell adhesion.

EXPERIMENTAL PROCEDURES

Materials and Methods. All chemicals were purchased from Sigma-Aldrich Canada Ltd. (Oakville, ON) and used as received, unless otherwise noted. Water was distilled and deionized using Millipore Milli-RO 10 Plus at 18 MΩ resistance.

Synthesis of Functionalized Dextran. *Synthesis of Dex-PMPI.* Dextran 40 kDa (*Leuconostoc mesenteroides*) was dried under vacuum and dissolved under nitrogen in 12 mL of anhydrous dimethyl sulfoxide (DMSO) at predetermined reaction temperatures (25 °C or 45 °C), after which dibutylin dilaurate (DBTDL) was added. A range of catalyst concentrations from 0 to 5.4 mM was examined. PMPI (50 mg; Pierce Chemical Co., Rockford, IL) was dissolved in 3 mL of DMSO and then added to the dextran solution. The amount of dextran used varied from a molar ratio of 0.1 to 0.4 of PMPI to dextran glucopyranose residue. The reaction was conducted in the dark for 4 and 24 h. The solution was precipitated in 70 mL of cold ethanol, washed several times with ethanol to remove any residual traces of DMSO and catalyst, dried at room temperature under nitrogen, and stored as a yellow powder at −20 °C. Proton nuclear magnetic resonance (^{1}H NMR) spectra were collected on a Gemini 300 MHz spectrometer (Varian Associates, Inc. NMR Instruments, Palo Alto, CA) using HOD (4.8 ppm) as the reference. ^{1}H NMR (D_2O): δ 7.6 ppm (d, 2H, Ar−H ortho to maleimide), 7.4 ppm (d, 2H, Ar−H ortho to carbamate), 7.0 ppm (s, 2H, maleimide vinyl), 5.0 ppm (s, 1H, anomeric proton), 5.3 ppm (s, 1H, α-1,3 linkage) 3.3−4.2 ppm (br m, 6H, glucopyranosyl ring). The degree of modification (DS) was determined according to eq 1

$$DS = \frac{I_B}{I_A} \times 100 \quad (1)$$

where I_B is the integrated region of PMPI around δ 7.0−7.6 ppm (6H) and I_A is the integrated area of the glucopyranosyl ring of dextran at δ 3.3−4.2 ppm (6H).

Fourier transform infrared spectroscopy (FTIR) spectra were obtained on a Nicolet Avatar E.S.P. spectrometer (Thermo Electron Co., Waltham, MA). Samples of dextran and Dex-PMPI were ground separately with KBr powder (10-fold excess relative to sample mass) and pressed into pellets for FTIR examination. OMNIC software (Thermo Electron Co., Waltham, MA) was used for data acquisition and analysis. FTIR (KBr, in cm^{-1}): dextran 3398 (s, ν_{O-H}), 2915 (s, $\nu_{C-H/C-H2}$), 1013 (s, ν_{C-OH}); PMPI 3120 (s, $\nu_{sym\ maleimide\ C-H}$), 3088 (s, $\nu_{asym\ maleimide\ C-H}$), 3073 (s, $\nu_{aromatic\ C-H}$), 2275 (s, $\nu_{asym\ N=C=O}$), 1776 (w, $\nu_{sym\ maleimide\ C=O}$), 1719 (s, $\nu_{asym\ maleimide\ C=O}$), 1583 (w, $\nu_{maleimide\ C=C}$), 1529 (s, $\nu_{sym\ aromatic\ C-C}$), 1447 (w, $\nu_{asym\ aromatic\ C-C}$), 1386 (s, $\nu_{sym\ maleimide\ C-N-C}$), 1145 (s, $\nu_{asym\ maleimide\ C-N-C}$), Dex-PMPI 1714 (s, $\nu_{carbamate\ C=O}$), 1519 (s, ν_{N-H}), 1232 (s, $\nu_{carbamate\ =C-O-C-}$).

Typical Synthesis of Dex-PMPI DS 10. Dextran 40 kDa (378 mg) was dissolved under nitrogen in 12 mL of anhydrous DMSO at 45 °C after which 45 μL of DBTDL was added. PMPI (50 mg) was dissolved in DMSO (17 mg/mL) and then added to the dextran solution in order to obtain a DS of 10. The reaction mixture was stirred overnight under nitrogen and in the dark. Dex-PMPI was purified as reported previously and stored at −20 °C (recovery yield: 87%, DS: 10; based on ^{1}H NMR).

Peptide Synthesis. Two collagen-derived peptides containing octapeptide sequences cleavable by MMP (in **bold** and \ indicates the cleavage point) and capped by a tetrapeptide containing a cysteine residue at opposite ends were used as peptide cross-linkers: Ac-Gly-Cys-Arg-Asp-**Gly-Pro-Gln-Gly-Ile-Ala-Ser-Gln**-Asp-Arg-Cys-Gly-COOH (GCRD**GPQG\IASQ**-DRCG) and Ac-Gly-Cys-Arg-Asp-**Gly-Pro-Gln-Gly\Pro-Ala-Gly-Gln**-Asp-Arg-Cys-Gly-COOH (GCRD**GPQG\PAGQ**DRCG). **GPQGIASQ** was selected as a highly MMP-2 sensitive sequence while **GPQGPAGQ** was chosen for its very low sensitivity to MMP-2 (*43*, *44*). The GCRD sequence capping the peptides was used to improve peptide solubility and to introduce thiols as previously described by Lutolf et al. (*3*).

For the studies of hydrogel degradation, three peptides with fluororescent labels were synthesized. Two mono-cysteine collagen-derived peptides with sequences similar to the peptide cross-linkers but containing a fluorescent 5-carboxyfluorescein (5-FAM)-L-lysine residue were synthesized: Ac-Gly-Cys-Arg-Asp-**Gly-Pro-Gln-Gly\Ile-Ala-Ser-Gln**-Asp-Arg-Gly-Lys(5-FA M)-$CONH_2$ (GCRD-**GPQG\IASQ**DRGK-FAM) and Ac-Gly-Cys-Arg-Asp-**Gly-Pro-Gln-Gly\Pro-Ala-Gly-Gln**-Asp-Arg-Gly-Lys(5-FAM)-$CONH_2$ (GCRD**GPQG\PAGQ**DRGK-FAM). A nonfunctional monothiol peptide terminated by a fluorescent 7-methoxycoumarin (Mca)-L-lysine residue, Cys-Gly-Lys(Mca) (CGK-Mca), was also synthesized.

Finally, two laminin-derived peptides containing respectively the Tyr-Ile-Gly-Ser-Arg and Ile-Lys-Val-Ala-Val motifs (in italic) were synthesized to promote cellular adhesion and neurite outgrowth: H_2N-Cys-Asp-Pro-Gly-*Tyr-Ile-Gly-Ser-Arg*-COOH (CDPG*YIGSR*) and H_2N-Cys-Gln-Ala-Ala-Ser-*Ile-Lys-Val-Ala-*

Val-COOH (CQAAS*IKVAV*), where the spacer group results in a more biomimetic conformation (*45*).

All peptides were synthesized by solid-phase synthesis using a Pioneer Peptide Synthesis System (Applied Biosystems, Foster City, CA) with standard Fmoc/ HATU chemistry. Amino acids including Fmoc-Lys(Mca)-OH were purchased from Novabiochem (EMD Biosciences, Inc., La Jolla, CA). Fmoc-Lys(5-FAM)-OH was from AnaSpec, Inc. (San Jose, CA). Activators and resins were purchased from Applied Biosystems and *N*,*N*-dimethylformamide (DMF) was from Caledon Laboratories Ltd. (Georgetown, ON). Laminin-derived peptides and fluorophore-labeled peptides were cleaved and deprotected from the resin for 2 h, and the peptide cross-linkers were treated for 4 h as previously described (*42*). The sulfhydryl content of peptide cross-linkers was determined photometrically using Ellman's reagent (5,5′-dithio-bis(2-nitrobenzoic acid). Peptide cross-linkers with free thiol content higher or equal to 80% were used for the experiments.

Degradation of Soluble Peptide Cross-Linkers. The substrate specificity of MMP-2 toward the cross-linkers was determined using a previously published fluorometric assay (*46*). Briefly, peptides were prepared as 540 mM stock solution in degradation buffer (50 mM Tricine, pH 7.5, 200 mM NaCl, 10 mM $CaCl_2$, 0.05% Brij-35). Digestion assays were carried out in degradation buffer by incubating a range of substrate concentrations (40, 80, 125, 160, 250, and 340 μM) with 40 nM MMP-2 at 30 °C. At predetermined time points, 20-μL aliquots of the degradation assay solution were withdrawn and added to 30 μL of *o*-phenanthroline (20 mM) to quench the enzymatic reaction. Rates of hydrolysis were monitored through the formation of free amines resulting from the peptide cleavage by active human MMP-2 (recombinant MMP-2; Calbiochem, San Diego, CA). Fluorescamine solution (200 μL, 5 mM in degradation buffer solution minus Brij-35) was added to the aliquots. The formation of fluorophores by the reaction of fluorescamine with the free amino groups was quantifed by fluorimetric measurement ($\lambda_{excitation} = 387$ nm, $\lambda_{emission} = 480$ nm) using a Gemini EM microplate spectrofluorometer (Molecular Devices Corp., Sunnyvale, Ca). The kinetic parameters of the peptides were determined by Michaelis−Menten analysis as reported in Supporting Information.

Hydrogel Formation. Hydrogels were formed by the conjugate addition of the sulfhydryl groups on PEG-dithiol or peptide cross-linkers to the maleimides of derivatized dextran. Dex-PMPI was dissolved in 100 mM phosphate buffered saline (PBS) pH 6.5 to give a final desired concentration (2.5, 5, 10, or 20 wt %). For example, 2.5 mg of Dex-PMPI was dissolved in 12.5 μL PBS buffer and mixed with 1.6 mg of peptide cross-linker dissolved in 12.5 μL of PBS buffer to make 10 wt % dextran hydrogel. The reaction solution was quickly vortexed, transferred into a mold, and placed in an incubator at 37 °C overnight.

Hydrolytic Stability of Hydrogels. *Dextran Hydrogels Cross-Linked with PEG-Dithiol.* Hydrogel samples (100 μL) of 2.5% dextran cross-linked with PEG-dithiol were immersed in 100 mM PBS solution (pH 7.4, 0.02% sodium azide) and incubated at 37 °C with buffer exchange every 2 days. The hydrolytic stability was determined by measuring the hydrogel water content (WC) according to eq 2. The hydrogels were weighed daily to determine the hydrated mass (W_h). The dry mass (W_d) was obtained for each hydrogel by freeze-drying the hydrogels and subsequently measuring the mass.

$$\mathrm{WC} = \frac{W_h - W_d}{W_h} \times 100\% \qquad (2)$$

Dex-Peptide Hydrogels. Hydrogel samples (50 μL) of 20% Dex-PMPI cross-linked with GCRD**GPQGIASQ**DRCG were immersed in 100 mM PBS solution (pH 7.4, 0.02% sodium azide), incubated at 37 °C with weekly buffer exchanges. Dex-MA (*36*) was also cross-linked with the peptide cross-linker through Michael-type reaction to form a 20% hydrogel and was used as comparison for stability. The hydrogels were weighed periodically to determine the normalized hydrogel weight (NW_h; eq 3) in the buffer.

$$\mathrm{NW}_h = \frac{W_t}{W_o} \qquad (3)$$

where W_t is the hydrated mass at time t and W_o the initial mass of the hydrogel after gelation.

Enzymatic Degradation. *Collagenase Degradation.* Hydrogel samples (50 μL) of 20% Dex-PMPI cross-linked with GCRD**GPQGIASQ**DRCG were placed in PBS, pH 7.4, 100 mM with 0.2 mg/mL of sodium azide and 1 mM $CaCl_2$ at 37 °C for 24 h at which time their hydrated mass was measured. Methacrylated dextran hydrogels obtained by redox polymerization of Dex-MA were prepared as previously described (*36*) and were used as controls. Each sample was then immersed into 1 mL of PBS solution with 0.2 mg/mL of sodium azide and either without enzyme or with 2 ng/mL of bacterial collagenase (from *Clostridium histolyticum*) and incubated at 37 °C. At predetermined time points, the hydrogels were removed from the medium and their NW_h was determined.

MMP-2 Degradation. The degradation of hydrogels was followed with both bacterial collagenase (as described above) and with MMP-2. With bacterial collagenase, degradation was followed by measuring hydrogel wet mass, which is suitable when the enzyme concentration is maintained by the use of a large volume of degradation media. For practical reasons, with MMP-2, degradation was monitored by measuring the release of fluorescent peptides in the media, which is suitable for maintaining the enzyme concentration when small degradation-media volumes are required. To study the degradation of the hydrogel through the activity of MMP-2, two mono-cysteine fluorescent peptides, CGK-Mca and either GCRD**GPQGIASQ**DRGK-FAM or GCRD**GPQGPAGQ**DRGK-FAM, were covalently immobilized to Dex-PMPI followed by its cross-linking using either GCRD**GPQGIASQ**DRCG or GCRD**GPQGPAGQ**DRCG peptides, respectively. Dex-PMPI (2.5 mg) was dissolved in 25 μL of a solution of fluorescent peptides (0.4 mM/peptide). After 10 min, 25 μL of peptide cross-linker (27 mg/mL) was added. The solution was vortexed and transferred to a mold and incubated overnight. Hydrogels were washed for 1 week in degradation buffer to remove any unreacted fluorescent peptides. They were then placed in 1 mL of degradation buffer containing 40 nM of MMP-2. The enzymatic activity was correlated to the release of the dextran-CGK-Mca ($\lambda_{excitation} = 340$ nm, $\lambda_{emission} = 405$ nm) and the fluorescein-labeled peptide fragment ($\lambda_{excitation} = 494$ nm, $\lambda_{emission} = 521$ nm), **IASQ**DRGK-FAM or **PAGQ**DRGK-FAM, into the degradation buffer solution. At predetermined time points, the release of the fluorophore was quantified by transferring 100-μL aliquots of supernatant to a 96-multiwell opaque plate and measuring the sample fluorescence. The aliquots were returned back to the degradation buffer solution. The degradation solution was refreshed daily until complete degradation of the hydrogel.

Cytotoxicity Assay. *Macromer Cytotoxicity.* The cytotoxity of Dex-PMPI was investigated. Cells were incubated in presence of soluble dextran or Dex-PMPI in the medium solution. NIH-3T3 fibroblast cells were cultured at 37 °C in culture medium (Dulbecco's Modified Eagle Medium (DMEM) supplemented with 2 mM L-glutamine, 10% fetal bovine serum (FBS), 50 units/mL penicillin/50 mg/mL streptomycin; all from Invitrogen Corp., Grand Island, NY).

Dextran and Dex-PMPI DS 10 with Mw of 6 kDa and 40 kDa were added to medium at the following concentrations: 10, 1, 0.1, 0.01, 0,001, and 0 mg/mL dextran and 10, 1, 0.1, 0.01, 0,001, 0.0001, and 0 mg/mL Dex-PMPI. Cells were plated on collagen-coated 96-multiwell black-wall clear-bottom Costar plate (Corning Inc. Acton, MA) and cultured for 2 days. Samples were prepared in sextuplicate. To test for cell viability, a luminescent cell proliferation assay using CellTiter-Glo (Promega Corp., Madison, WI) was used. The CellTiter-Glo assay quantif the amount of ATP present, indicating presence of metabolically active cells. The amount of ATP is directly proportional to the number of cells present in culture (*47*).

Hydrogel Cytotoxicity. The toxicity was also investigated on hydrogel extracts. Dex-PMPI hydrogels cross-linked with GCRD**GPQGIASQ**DRCG only or also containing CDPG*YIGSR* and CQAAS*IKVAV* were prepared. Similar hydrogels with grafted laminin-derived peptides were used in the next section to briefly investigate cell adhesion on the dextran-peptide hydrogels. Dex-PMPI (1.25 mg) was dissolved in 25 μL of a solution of laminin-derived peptides (0.8 mM/peptide). After 10 min, the solution was sterilized via centrifugation filtration using an Ultrafree MC sterile centrifugal filter (0.22 μm; Millipore, Billerica, MA) and 25 μL of filter-sterilized peptide cross-linker (27 mg/mL) was added. The solution was vortexed, transferred to a mold and incubated overnight at 37 °C.

Hydrogels were washed for 1 week with daily changes with DMEM supplemented with 10% FBS, 2 mM L-glutamine, and 50 units/mL penicillin/50 mg/mL streptomycin at 37 °C to remove any unreacted laminin-derived peptides or any leachables. The medium collected daily was pooled together and store at 4 °C. The collected medium was mixed with fresh culture medium (DMEM supplemented with 10% FBS, 2 mM L-glutamine, and 50 units/mL penicillin/50 mg/mL streptomycin) in order to have sufficient volume for cell culture (25% diluted in DMEM).

Embryonic day (E)15 dissociated rat DRG neurons were isolated from embryonic day 15 (E15) rats as reported in Supporting Information. NIH-3T3 fibroblast cells and DRGs were exposed to the tested gel extracts at 37 °C (50 ng/ mL nerve growth factor (NGF; Invitrogen Corp.) was added for DRGs), plated on collagen-coated 96-multiwell black-wall clear-bottom plate, and cultured up to 3 days (1 plate/day) at 37 °C. Cells were also cultured into medium without extract as control. Samples were prepared in dodecaplicate. Once a day, cell culture was terminated and cell viability was assessed using the CellTiter-Glo assay.

Cell Adhesion. On the basis of previous results (*42*), cell adhesion was briefly investigated using laminin-derived peptides, CDPG*YIGSR* and CQAAS*IKVAV*. The cell-adhesive peptides were introduced into the hydrogel to promote cellular adhesion. Dex-PMPI (0.88 mg) was dissolved in 17.5 μL of a solution of cell-adhesive peptides (0.8 mM/ peptide). The solution was vortexed for 10 min and sterilized via centrifugation filtration, and 17.5 μL of filter-sterilized peptide cross-linker (27 mg/mL) was added. The solution was vortexed and transferred to the bottom of well of a 96-multiwell half-area plate and incubated overnight. Hydrogels were washed for 1 week with culture medium (DMEM supplemented with 10% FBS, 2 mM L-glutamine, and 50 units/mL penicillin/50 mg/mL streptomycin) at 37 °C to remove any unreacted laminin-derived peptides.

NIH-3T3 fibroblast cells and DRGs were cultured separately at 37 °C in culture medium. NGF (50 ng/mL) was added to the culture medium used for DRGs. Cells were plated onto the gels at a cell density of 3200 cells/gel. Cells were incubated at 37 °C for 2 days and then fixed in 3.7% formaldehyde for 20 min, rinsed with HBSS, and incubated in 0.1% Triton X-100 for 90 s. Finally, each well was rinsed with HBSS and incubated for 20 min in Alexa Fluor 488 phalloidin (Molecular Probes, Burlington, ON) solution (5 μL in 200 μL of HBSS). The phalloidin solution was replaced with HBSS, and the samples were stored at 4 °C until viewed under fluorescent microscopy. Samples were visualized with a Ziess Axiovert 100 inverted microscope (Carl Zeiss Canada Ltd., Toronto, ON), and images were captured using a digital camera.

Statistics. The statistics were performed with commercially available software program SigmaStat 3.11 (Systat Software Inc., Richmond, CA). All experimental results are reported as mean ± 95% confidence interval. For multiple comparisons, one-way ANOVA was performed using Bonferroni *t*-test as posthoc test. Student's *t*-test was used to make pairwise comparisons. In all tests a *p*-value of <0.05 was regarded as significant.

RESULTS

Synthesis of PMPI-Derivatized Dextran. The heterobifunctional linker PMPI, introduced by Annunziato et al. (*48*), has been used to modify biomolecules (*48*) and PEG (*49*−*51*). In this project, it was used to derivatize natural polymers such as dextran for the purpose of forming hydrogels. Here, dextran reacts with PMPI in DMSO in the presence of the DBTDL as catalyst (Figure 1A). The successful conjugation of PMPI to dextran was confirmed by the FTIR spectrum of the Dex-PMPI adduct, which indicated the formation of carbamate linkages (1714, 1519, and 1232 cm^{-1}) and the disappearance of the isocyanate peak (2275 cm^{-1}). The ^1H NMR spectrum for Dex-PMPI showed distinctive peaks: the anomeric proton of the dextran glucopyranosyl ring at δ 5.0 ppm (singlet), the PMPI group at 7.0 ppm (singlet) for the maleimide carbon−carbon double bond, and at 7.4 ppm (doublet) and 7.6 ppm (doublet) for the aromatic protons. The DS of PMPI coupled to dextran was quantitatively determined using the integrated areas of the relevant chemical shifts, according to eq 1.

The coupling reaction between dextran and PMPI was studied in the presence of different amounts of DBTDL at either 25 °C or 45 °C for 4 h or 24 h. As shown in Table 1, successful coupling required the DBDTL catalyst, without which no or little product formation was observed. Under identical reaction conditions at 4 h and 25 °C, the coupling yield of 0% without DBTDL increased to 15% with 30 μL of DBTDL. The importance of DBTDL was further confirmed when the reaction was repeated at 45 °C; the yield increased from 14% to 58% in the presence of 15 μL of DBTDL. At a temperature of 25 °C and in presence of 30 μL of DBTDL, the coupling yield increased from 15% to 33% when the reaction time was extended from 4 to 24 h. The optimum coupling yield was obtained after reaction for 24 h at 45 °C in the presence of a minimum of 30 μL of DBTDL, which yielded DEX-PMPI with a DS of 10 or 20 depending on the initial amount of PMPI used. These reaction conditions were used to synthesize DEX-PMPI DS10 (hereafter referred as Dex-PMPI), which was used for the remaining studies.

Hydrogel Formation and Hydrolytic Stability. Dextran hydrogels were first formed by cross-linking Dex-PMPI with PEG-dithiol via Michael-type addition. The PEG-dithiol was a useful model system to test the cross-linking system and the hydrolytic stability of the resulting hydrogels. The concentration of polymeric precursors was found to affect the rate of gelation: 20% Dex-PMPI gelled within seconds, whereas 2.5% Dex-PMPI only gelled after several minutes. The hydrogels were allowed to swell in PBS, and their WC was followed over 15 days (according to eq 2) during which time the WC was found to be constant at 94.9 ± 0.2%. No excessive swelling was observed, suggesting that the cross-linked gels were hydrolytically stable.

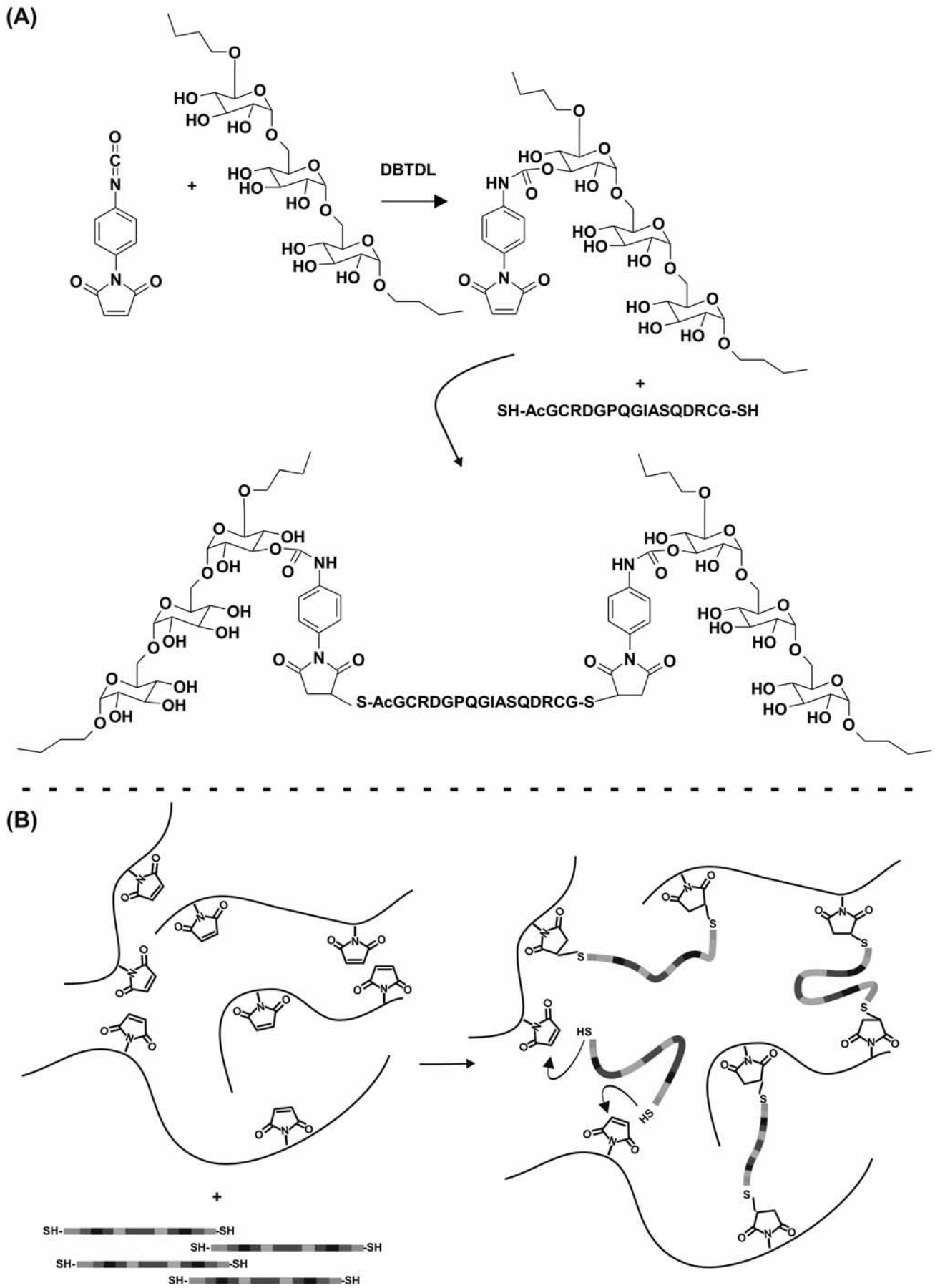


Figure 1. (A) Reaction of dextran with *p*-maleimidophenyl isocynate (PMPI) and (B) preparation of dextran-peptide hydrogel through the Michael-type reaction of peptide cross-linker to Dex-PMPI.

Table 1. Reaction Conditions for the Coupling of PMPI to Dextran

theoretical DS (%)	exptl DS (%)	DBTDL (mL)	time (h)	*T*, °C	coupling yield (%)
10	0	0	4	25	0
37	5	0	4	45	14
38	22	15	4	45	58
38	6	30	4	25	15
15	5	30	24	25	33
15	15	30	24	45	100
10	10	45	24	45	100
20	20	45	24	45	100

Table 2. Degradation Kinetics of Soluble Peptides by MMP-2

peptide	k_{cat}/K_M, $M^{-1}\,S^{-1}$	k_{cat}, S^{-1}	K_M, μM
GPQGIASQ	583[a]	2[a]	3400[a]
GPQGPAGQ	<9[a]	ND[b]	ND[b]
GCRD**GPQGIASQ**DRCG	2591 ± 570[c]	0.47 ± 0.21[c]	189 ± 106[c]
GCRD**GPQGPAGQ**DRCG	20 ± 13[c]	ND[c]	ND[c]

[a] ND, not determined. [b] Netzel-Arnett, S., Sang, Q.-X., Moore, W., et al. (1993) *Biochemistry 32*, 6427−6432. [c] ±95% confidence interval (n = 3).

The hydrolytic stability of the dextran hydrogel cross-linked with dithiol peptides was similarly analyzed by evaluating the NW_h of 20% Dex-MA or Dex-PMPI hydrogels cross-linked with the peptide GCRD**GPQGIASQ**DRCG over a 200-day period (Figure 2). The Dex-PMPI-peptide hydrogel swelled to 2.25 times its original mass within the first 20 days and then did not change appreciably for the remaining 200 days, demonstrating the hydrolytic stability of these hydrogels. Both the thioether obtained by the conjugate addition of the thiol to the maleimide and the carbamate formed by coupling PMPI to dextran were resistant to hydrolysis. In contrast, Dex-MA-peptide hydrogel swelled to 3.25 times of their original mass within the first 8 days and then completely dissolved on day 9 due to the hydrolysis of glycidyl-methacrylate esters in Dex-MA.

Degradation of Soluble Peptide Cross-Links. As reported by Netzel-Arnett et al. (*43*), the **GPQGIASQ** sequence, derived from the calf and chick α1 (I) collagen chain, is highly sensitive to hydrolysis by MMP-2, whereas **GPQGPAGQ**, with Ile and Ser substituted by Pro and Gly, respectively, has low sensitivity (Table 2). Both peptides were extended on each terminus with the tetrapeptide sequence GCRD to improve solubility and to introduce the thiol groups required for cross-linking (*3*). The kinetic parameters for MMP-2 degradation of the peptides with and without GCRD were determined by Michaelis−Menten analysis. Substrate degradation was followed by measuring the fluorescence of fluorescamine adduct fragments of the peptide cleavage reaction ($\lambda_{excitation}$ = 387 nm, $\lambda_{emission}$ = 480 nm) and the kinetic parameters k_{cat}, K_m and k_{cat}/K_M were obtained using Lineweaver−Burk plots (eq 2S, Supporting Information) and by plotting the initial rate versus the product between the enzyme and substrate concentrations (eq 3S, Supporting Information). As it was previously reported (*3*), elongating the peptide sequence up to the P8 position changed the kinetic parameters and improved both the catalytic efficiency (i.e., higher k_{cat}/K_M) and the substrate affinity (i.e., lower K_M). As shown in Table 2, elongation of the peptide sequences with GCRD fragments led to a greater than fourfold increase in k_{cat}/K_M for GCRD**GPQGIASQ**DRCG and more than doubled the k_{cat}/K_M for GCRD**GPQGPAGQ**DRCG. Despite the increase in k_{cat}/K_M values, the higher MMP-2 cleavage efficiency for **GPQGIASQ** relative to **GPQGPAGQ** was maintained, with GCRD**GPQGIASQ**DRCG having a k_{cat}/K_M 2 orders of magnitude larger than that for GCRD**GPQGPAGQ**DRCG.

Enzymatic Degradation. *Collagenase Degradation.* Collagenase-mediated degradation of 20% Dex-PMPI-GCRDGPQGIASQDRCG cross-linked hydrogels was followed by monitoring the hydrated mass of the hydrogel over time and compared to two controls: (1) identical hydrogels without collagenase and (2) a redox-polymerized poly(Dex-MA) hydrogel exposed to the same amount (2 ng/mL) of bacterial collagenase. As shown in Figure 3, dextran-peptide hydrogels degraded completely after 30 h of incubation with collagenase whereas without collagenase, the mass increased to a NW_h of 1.2, demonstrating swelling but no degradation. These data demonstrate that the dextran-peptide hydrogels degraded only by an enzymatic process. Moreover, poly(Dex-MA) hydrogels obtained by redox polymerization did not degrade when exposed to collagenase, demonstrating that dextran-peptide hydrogels degrade by collagenase cleavage of the peptide cross-link and not the dextran backbone.

MMP-2 Degradation. MMP2-mediated degradation of the dextran-peptide hydrogels was assessed using a fluorimetric assay. Hydrogels were synthesized with 5% Dex-PMPI cross-

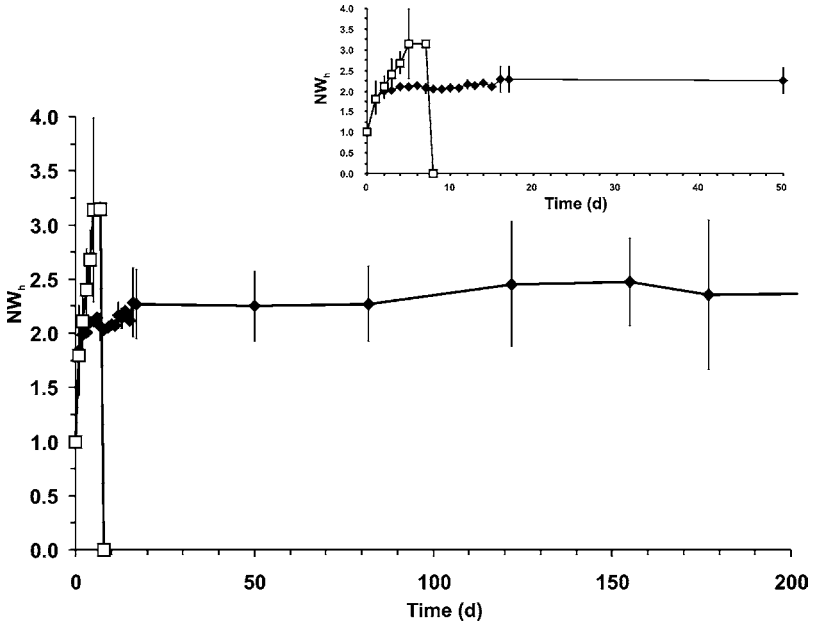


Figure 2. Hydrolytic stability of water dextran-peptide hydrogels; normalized hydrogel weight (NW_h) of 20% dextran-peptide hydrogels cross-linked through conjugate addition **GPQGIASQ** peptides to (□) Dex-MA and (◆) Dex-PMPI (n = 3, mean ± 95% confidence interval).

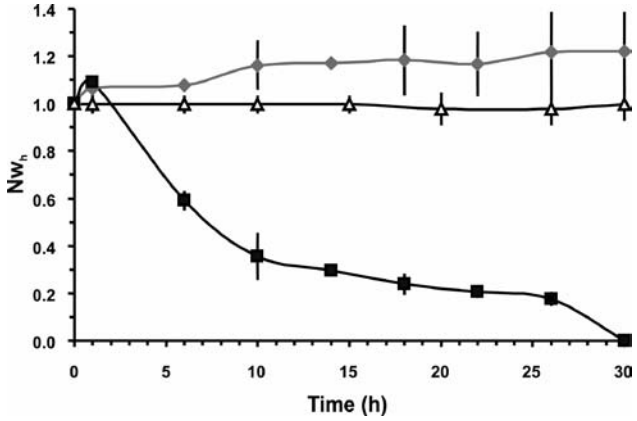


Figure 3. Bacterial collagenase degradation of dextran-peptide hydrogels; normalized hydrogel weight (NW_h) of (grey diamond) 20% dextran-peptide, no collagenase, (■) 20% dextran-peptide, 2 ng/mL collagenase, (△) 20% poly(Dex-MA) by redox polymerization, 2 ng/mL collagenase (peptide = GCRD**GPQGIASQ**DRCG, $n = 3$, mean ± 95% confidence interval).

linked with GCRD**GPQGIASQ**DRCG. During hydrogel preparation, CGK-Mca and GCRD**GPQGIASQ**DRGK-FAM peptides were added in order to follow hydrogel degradation/dissolution by Mca fluorescence ($\lambda_{excitation} = 340$ nm, $\lambda_{emission} = 405$ nm) independently of cross-link cleavage (measured by FAM fluorescence; $\lambda_{excitation} = 494$ nm, $\lambda_{emission} = 521$ nm) in the supernatant, assuming that the cross-link peptides and FAM-modified peptides degrade at similar rates. Hydrogels were incubated with 40 nM MMP-2, and the fluorescence of the supernatant was followed overtime. As shown in Figure 4, there was 100% release of both fluorophores and complete dissolution of the hydrogels after 16 days of incubation, which corresponds to the plateau observed in Figure 4. There was a near-linear increase in the release of the fluorescent **IASQ**DRGK-FAM fragment into the degradation medium from dextran-peptide hydrogels due to MMP-2 digestion. Fluorescent dextran-CGK-Mca was released at a slower rate until close to the end of the incubation period, indicating that a substantial amount of cross-links must be digested prior to dextran dissolution. The dextran-peptide hydrogels appeared to decrease in size during degradation, suggesting a surface erosion process. The same experiment was repeated with dextran hydrogels cross-linked with GCRD**GPQGPAGQ**DRCG, the peptide with low sensitivity to MMP-2, and modified with GCRD**GPQGPAGQ**DRGK-FAM to examine MMP-2 susceptibility (Figure 5). The degradation experiment with GCRD**GPQGPAGQ**DRCG was pursued for 7 days due to the low enzyme sensitivity of the cross-links. As shown in Figure 6, the release of the fluorescent **PAGQ**DRGK-FAM fragment was significantly slower than that of **IASQ**DRGK-FAM, confirming the higher sensitivity to cleavage by MMP-2 for GCRD**GPQGIASQ**DRCG compared to GCRD**GPQGPAGQ**DRCG in the cross-linked hydrogel. Moreover, this demonstrates that the rate of peptide-cross-linked dextran hydrogel degradation can be controlled by the choice of peptide cross-link and enzyme affinity.

Cytotoxicity Assay. The cytotoxicity of dextran and Dex-PMPI DS 10 with Mw of 6 kDa and 40 kDa was investigated by incubating cells in presence of soluble polysaccharides in the medium solution. Dextran and Dex-PMPI solutions were incubated with fibroblast cultures for 2 days at concentrations up to 10 mg/mL (Figure 7). The cytotoxicity was assessed by determining the presence of metabolically active cells by quantifying the amounts of ATP present. It was previously reported that the amount of ATP is directly proportional to the number of cells present in culture (*47*). As shown in Figure 7A, the presence of dextran 6 kDa and 40 kDa in the medium did not significantly impede the metabolic activity of the cultured fibroblasts. These results suggest that the polysaccharide, under its natural form, is not cytotoxic for the molecular weights and concentrations investigated. By contrast, as shown in Figure 7B, increasing the concentration of Dex-PMPI 6 kDa or 40 kDa in the culture medium to 1 mg/mL and 10 mg/mL resulted in a significant decrease in the production of ATP ($p < 0.001$ and $p = 0.049$ for 1 mg/mL and $p < 0.001$ for 10 mg/mL). This indicates that, above a Dex-PMPI concentration

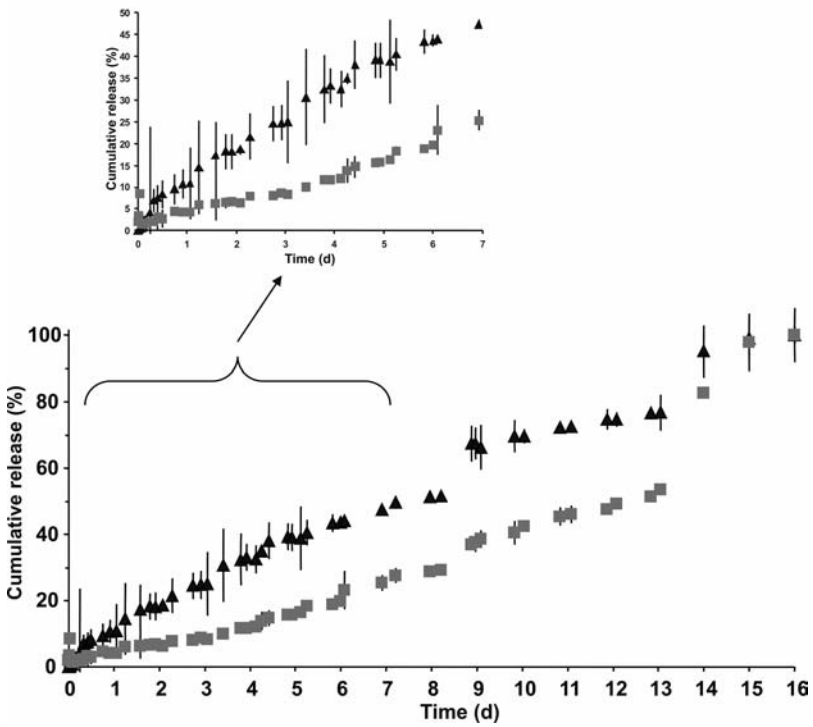


Figure 4. MMP-2 degradation of dextran-peptide hydrogels; cumulative release of fluorophores from 20% dextran-peptide hydrogels exposed to 40 nM MMP-2: (▲) **IASQ**DRGK-FAM and (grey square) dextran-CGK-Mca ($n = 3$, mean ± 95% confidence interval).

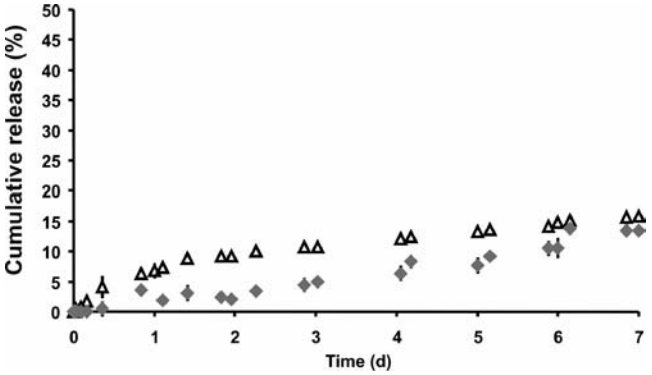


Figure 5. MMP-2 degradation of dextran-peptide hydrogels; cumulative release of fluorophores from 20% dextran-peptide hydrogels exposed to 40 nM MMP-2: (△) **PAGQ**DRGK-FAM and (grey diamond) dextran-CGK-Mca ($n = 3$, mean ± 95% confidence interval).

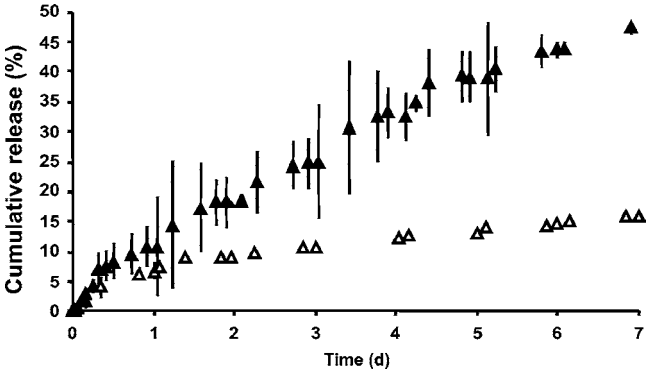


Figure 6. MMP-2 degradation of dextran-peptide hydrogels; cumulative release of fluorophores from 20% dextran-peptide hydrogels exposed to 40 nM MMP-2: (▲) **IASQ**DRGK-FAM and (△) **PAGQ**DRGK-FAM ($n = 3$, mean ± 95% confidence interval).

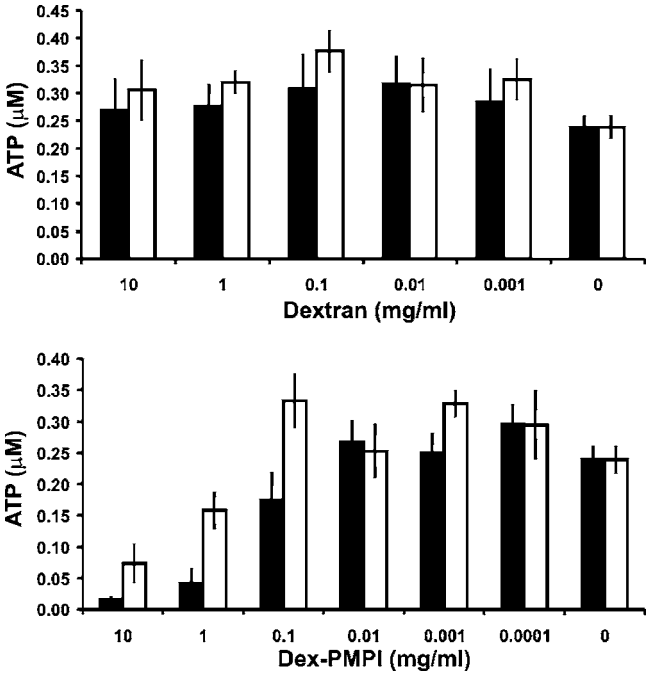


Figure 7. Cell viability of 3T3 cells exposed to soluble dextran and Dex-PMPI in culture medium: (A) Dextran, (B) Dex-PMPI; ■ 6 kDa, □ 40 kDa; cell viability is expressed in ATP production ($n = 6$, mean ± 95% confidence interval).

of 1 mg/ mL, the maleimide functionalities covalently immobilized to the dextran backbone can affect the cellular activity and even lead to some cytoxicity.

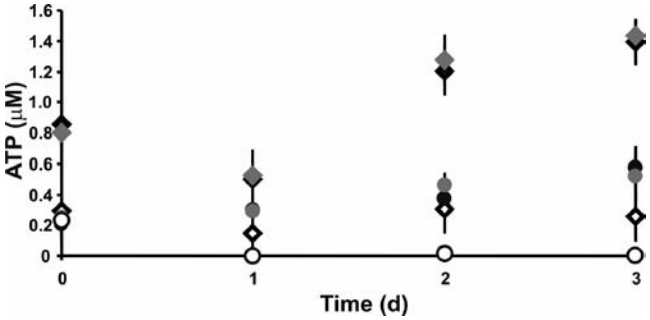


Figure 8. Cell viability of 3T3 cells and DRG neurons exposed to hydrogel extracts; control: ◆ 3T3, ● DRG, extracts from Dex-PMPI cross-linked with GCRD**GPQGIASQ**DRCG: (tilted gray square) 3T3, (gray circle), extracts from Dex-PMPI cross-linked with GCRD**GPQGIASQ**DRCG and immobilized CDPG*YIGSR* and CQAAS*IKVAV*: (grey square) 3T3, (grey circle) DRG (cell viability is expressed in ATP production) ($n = 12$, mean ± 95% confidence interval).

The cytotoxicity of polysaccharide-based hydrogels was studied by exposing fibroblasts and DRGs respectively to culture medium containing extracts of Dex-PMPI hydrogels cross-linked with GCRD**GPQGIASQ**DRCG. Two sets of hydrogels were used for the extraction assay; in one set, the hydrogels were simply Dex-PMPI cross-linked with GCRD**GPQGIASQ**DRCG, and in the second set, the hydrogels were cross-linked with the same peptide but also contained CDPG*YIGSR* and CQAAS*IKVAV* as cell-adhesive peptides. Both sets of hydrogels were extracted in cell culture medium for 7 days at 37 °C, and the extracts were incubated with fibroblast and DRG cultures for 3 days. Again the cytotoxicity was assessed by quantifying the amounts of ATP present. As seen in Figure 8, when compared to the controls, no cytotoxicity was detected from Dex-PMPI hydrogel extract, indicating that an insufficient amount of unreacted Dex-PMPI or peptide cross-linkers diffused from the hydrogels to cause any significant cytotoxicity to the fibroblasts or DRGs. The metabolic activity of 3T3 cells and DRG neurons significantly decreased when exposed to extracts obtained from hydrogels containing laminin-derived peptides. These results indicate that the cytotoxicity was probably caused by unreacted laminin-derived peptides binding and saturating the cell-surface receptors, thus interfering with the cell adhesion mechanism required for survival of these anchorage-dependent cells. These results are important because they underline the importance of thoroughly washing the hydrogels prior to cell culture.

Cell Culture. Cell adhesion of NIH-3T3 fibroblast cells and primary chick DRG neurons was investigated on MMP-degradable dextran hydrogels. Dex-PMPI hydrogels were modified with laminin-derived peptides CDPG*YIGSR* and CQAAS*IKVAV* to provide a cell-adhesive substrate to the cells and cross-linked with GCRD**GPQGIASQ**DRCG. As shown in Figure 9, both fibroblasts and DRGs adhered, respectively, to dextran-peptide hydrogels containing the laminin-derived peptides but did not adhere to hydrogels lacking cell-adhesive peptides. This was not surprising given the high water content of dextran hydrogels, which are known to be non-cell adhesives (*27*, *33*, *34*) and based on the results previously (*42*). Imaging was difficult due to the uneven surface of the hydrogels.

DISCUSSION

Since the first MMP-sensitive telechelic peptide-PEG-peptide block copolymers were developed by West and Hubbell (*16*), polymers such as PEG and poly-*N*-isopropylacrylamide have been used to develop other MMP-degradable hydrogels (*3*, *4*, *17*). In the present study, a MMP-degradable dextran was synthesized and characterized. Dextran is the first naturally derived polymer to be tested for this type of application and is particularly compelling because it is inherently nonadhesive to

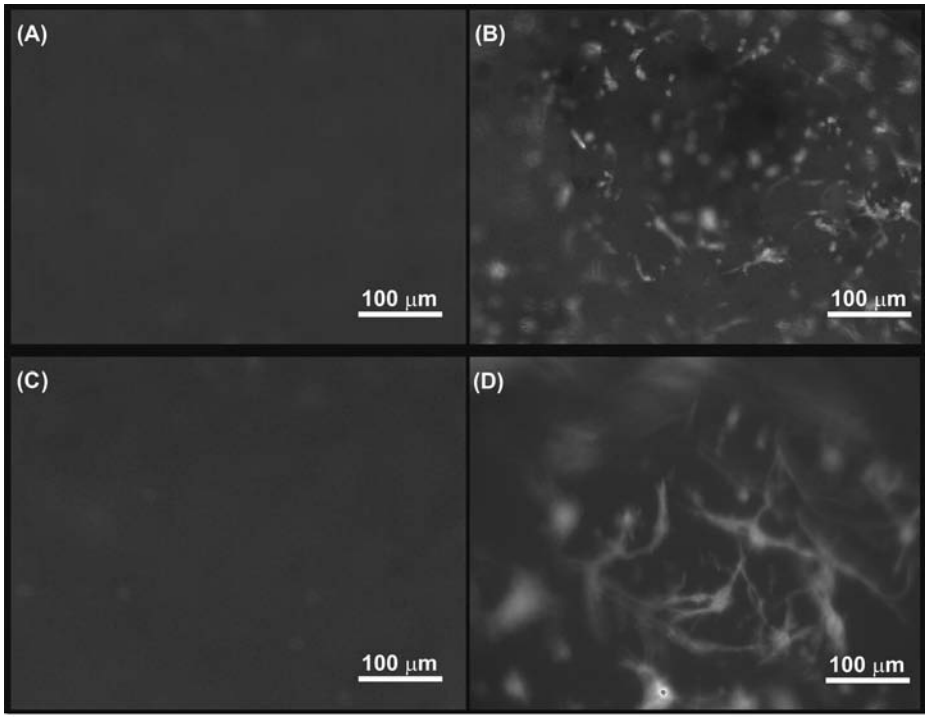


Figure 9. Cellular adhesion of NIH-3T3 fibroblast cells and DRG neurons to dextran-peptide hydrogels. Representative images of (A) NIH 3T3 fibroblasts cultured on unmodified dextran-peptide hydrogel demonstrates no visible adherent cells, (B) NIH 3T3 fibroblasts cultured on dextran-peptide hydrogel containing laminin-derived peptides after 2 days in vitro (2×10^5 cells/cm^2 were plated), (C) DRGs plated on unmodified dextran-peptide hydrogel demonstrate no visible adherent cells, and (D) DRGs cultured on dextran-peptide hydrogels containing laminin-derived peptides after 2 days of culture (2×10^5 cells/cm^2 were plated).

proteins (*31*, *32*) and cells (*27*, *33*, *34*), allowing cell adhesion to be "dialed-in" with peptide modification. In addition, dextran has multiple functional hydroxyl groups available for derivatization and conjugation. For example, there are significantly more reactive functional groups on dextran than on a multiarm PEG. Dextran 40 kDa derivatized to a DS of 10 has approximately 25 modified hydroxyls per polysaccharide molecule, whereas commercially available modified four-arm PEG has 4 reactive hydroxyls per molecule. These multiple sites allow efficient covalent modification with ECM-derived peptides to promote cellular adhesion or to immobilize bioactive molecules, such as growth factors, without having a significant impact on the degree of cross-linking required for gelation.

There have been several studies on dextran bioconjugation. However, most of these methods are either two-step conjugation procedures, such as carboxymethylation followed by carbodiimide conjugation (*52*) or periodate oxidation followed by Schiff base reaction (*53*, *54*), or introduce hydrolyzable esters, such as meth(acrylates) (*55*−*57*). The dextran derivatization method described here with PMPI is a one-step reaction which introduces a stable carbamate bond and a maleimide group for Michael-type addition.

Prior to this work, PMPI had been primarily used to modify bioactive molecules (*48*) and PEG (*49*−*51*) or to immobilize biomolecules such as proteins (*48*), DNA (*58*), or oligonucleotides (*51*) on surfaces. In unpublished work, we have also extended the utility of this cross-linking agent to other polymers, including four-armed PEG-PMPI and PMPI-derivatized methylcellulose, demonstrating broad applicability as a heterobifunctional agent for hydrogel applications through Michael-type addition. Moreover, by using the DBTDL catalyst common in the polyurethane literature (*59*, *60*), we were able to achieve high yield for PMPI modification of dextran (Table 1). The Dex-PMPI cross-linked hydrogels were shown to be hydrolytically stable, demonstrating that the peptide dictates the degradation rate.

GPQGIASQ, an eight-amino-acid sequence derived from the α1 (I) collagen chain of calf and chick, was selected as the MMP substrate (*43*, *44*). Many MMPs, such as MMP-1, MMP-2, MMP-3, MMP-7 MMP-8, and MMP-9, can cleave this peptide at the Gly-Ile bond; however, MMP-2 has the greatest digestive efficiency (*43*, *44*). **GPQGPAGQ** was selected as a control because it has been reported to have little degradation sensitivity to most MMPs (*43*, *44*). Nagase et al., in studying the human MMP specificity using collagen-derived synthetic peptides, have assembled a database of more than 45 peptide sequences that have different degrees of sensitivity to MMP digestion (*44*). They reported that the efficiency of peptide hydrolysis varied for different MMPs, giving sequences that were more or less susceptible to cleavage by collagenases, gelatinases, matrilysins, or stromelysins. The kinetic characteristics of the 16-amino-acid GCRD-capped sequence used in this study follow the trend of their respective 8-amino-acid sequences (Table 2). On the basis of these data and on the synthetic peptide database built by Nagase et al., MMP-sensitive hydrogels can be designed to have higher affinity for one or more specific MMPs and this can be used, in turn, to control hydrogel degradation.

MMPs are highly involved in ECM remodeling processes such as tissue morphogenesis and wound healing. They are expressed following spinal cord injury and recent data suggest a beneficial role for MMP activity following SCI (*5*, *9*). Enzyme-degradable hydrogels susceptible to MMP digestion have been previously investigated for bone, cartilage, and vascular applications where they are postulated to provide greater control over tissue regeneration. The MMP-sensitive hydrogels described in this report were designed for neural tissue-engineering applications and may be useful for investigating the mechanisms of cell migration and/or axonal outgrowth.

The Dex-PMPI-peptide hydrogel was found to degrade under the actions of both bacterial collagenase and MMP-2, as shown through the wet mass variation and the release of fluorophores

into solution, respectively. Although hydrogels were exposed to lower concentration of bacterial collagenase than MMP-2, they degraded significantly more rapidly. This faster rate of degradation when exposed to bacterial collagenase likely reflects the fact that bacterial collagenases, unlike mammalian collagenases, are more active and less specific in cleaving collagen (*61*). As reported previously by Hennink and co-workers, the swelling behavior of dextran hydrogels degrading through bulk degradation is characterized by hydrogel swelling followed by rapid dissolution (*62*). It is believed that during bulk degradation, the cross-links are cleaved throughout the hydrogel to a point where the dextran chains only bear about two cross-links per chain, and further degradation of the cross-links results in the rapid disintegration of the hydrogel to soluble products. Similar observations were reported with MMP-degradable PEG hydrogels (*3*). In this study, hydrogels degraded by bacterial collagenase were characterized by an absence of significant swelling and a progressive mass loss (Figure 3). In addition, as shown in Figure 4, hydrogel degradation mediated by the activity of MMP-2 is accompanied by a continuous and progressive release of soluble dextran. These observations suggest proteolytic degradation of dextran-peptide hydrogels by a predominantly surface-erosion mechanism rather than by bulk degradation, which has been reported for MMP-degradable PEG hydrogels.

Interestingly, the activity of MMP-2 toward the **GPQGIASQ** sequence is 2 orders of magnitude greater than toward the **GPQGPAGQ** sequence for soluble peptides (Table 2). The difference in rates of hydrogel degradation by MMP-2 appear to be much closer for the respective dextran-peptide hydrogels (Figure 6). Under their soluble form, the peptides are very mobile and can adopt a conformation that will facilitate binding and cleavage by MMP-2. Once immobilized within the hydrogel, they likely lose some of this mobility. Moreover, the hydrogel degradation seems to be predominantly driven by surface erosion, thus limiting the access of MMP-2 to the surface of the hydrogel.

This study focused on preparing a new type of MMP-sensitive dextran-based hydrogel which could be used in neural tissue engineering. Although, many MMPs have been reported to be present following spinal cord injury and are believed to have a beneficial role in the healing process, MMP-2 was selected as a model enzyme. Along with previous observations reported by other groups (*3*, *4*, *63*−*65*) and our results, the degradation rate of the hydrogel can be tailored by enzyme specificity to the peptide sequence.

As reported, the gelation of Dex-PMPI hydrogels through Michael-type reaction is very fast, which may be advantageous for *in situ* gelation. Dex-PMPI was found to be non-cytotoxic as monomers at concentrations lower than 1 mg/mL. In addition, following gelation, the amount of un-cross-linked Dex-PMPI leaching out of the hydrogel was insufficient to cause any cytotoxicity. As shown in Figure 8, unreacted peptides leaching out of the Dex-PMPI hydrogel impeded cell viability. To pursue the *in situ* gelation use, peptide purification techniques have to be refined in order to improve the purity of peptides containing reactive thiols and optimized peptide immobilization.

Given that neural cells produce MMP-2 after injury and that MMP-2 degrades the dextran-peptide scaffolds, we were interested in cellular activity on the hydrogels and specifically cell adhesion. MMP-degradable hydrogels require the presence of cell-adhesive peptides for cell adhesion, survival, and ultimately invasion into the network (*17*, *65*, *66*). These data, coupled with previous reports, prompted us to explore modification of dextran-cross-linked hydrogels with laminin-derived peptides. Results reported previously showed that dextran hydrogels modified with CQAAS*IKVAV* and CDPG*YIGSR* promote greater adhesion of DRG neurons than those hydrogels modified with CG*RGD*S (*42*). Interestingly, both NIH-3T3 and DRG cells adhered and survived when plated on dextran-peptide hydrogels modified with these laminin-derived peptides. Just as the cross-link density influenced the cell invasion (*3*), the ECM-peptide modification for cell adhesion must be optimized for cell migration (*3*, *17*) and neurite outgrowth (*67*, *68*). Interestingly, ECM peptides may also be manipulated to promote the expression of the MMPs (*69*).

CONCLUSIONS

MMP-sensitive dextran hydrogel systems were synthesized using peptide cross-linkers to control the rate of MMP-2 degradation and susceptibility to proteolytic remodeling. We have reported a new method to conjugate dextran through the use of the heterobifunctional PMPI molecule. Dextran-peptide hydrogels synthesized with Dex-PMPI degraded when incubated in the presence of bacterial collagenase or MMP-2 through enzymatic digestion of the peptide cross-links. Laminin-derived peptide-modified dextran hydrogels promoted cell adhesion and survival, allowing questions of cell-mediated expression of MMP for cell-based degradation to be pursued.

ACKNOWLEDGMENT

We are grateful to Ying Fang Chen for the cell culture experiments, to Dr. Nam-Chiang Wang for his advice on peptide synthesis (Advanced Protein Technology Centre, The Hospital for Sick Children, Toronto), and to Dr. Ying Yang and Dr. Ling Xu for the mass spectrometer analyses (Proteomics and Mass Spectrometry Centre, Medical Sciences Building, University of Toronto, Toronto, ON). We thank the Natural Sciences and Engineering Research Council of Canada (MSS), the Advanced Regenerative Tissue Engineering Center (an ORDCF-funded center), Matregen Corp., and the Fonds québécois de la recherche sur la nature et les technologies (SGL) for financial support.

Supporting Information Available: Degradation kinetics of soluble peptide cross-linkers and isolation of rat DRG neurons. This material is available free of charge via the Internet at http://pubs.acs.org/BC.

LITERATURE CITED

(1) Zisch, A. H., Lutolf, M. P., Ehrbar, M., Raeber, G. P., Rizzi, S. C., Davies, N., Schmokel, H., Bezuidenhout, D., Djonov, V., Zilla, P., and Hubbell, J. A. (2003) Cell-demanded release of VEGF from synthetic, biointeractive cell ingrowth matrices for vascularized tissue growth. *FASEB J. 17*, 2260−2262.

(2) Seliktar, D., Zisch, A. H., Lutolf, M. P., Wrana, J. L., and Hubbell, J. A. (2004) MMP-2 sensitive, VEGF-bearing bioactive hydrogels for promotion of vascular healing. *J. Biomed. Mater. Res. A 68*, 704−716.

(3) Lutolf, M. P., Lauer-Fields, J. L., Schmoekel, H. G., Metters, A. T., Weber, F. E., Fields, G. B., and Hubbell, J. A. (2003) Synthetic matrix metalloproteinase-sensitive hydrogels for the conduction of tissue regeneration: engineering cell-invasion characteristics. *Proc. Natl. Acad. Sci. U.S.A. 100*, 5413−5418.

(4) Kim, S., Chung, E. H., Gilbert, M., and Healy, K. E. (2005) Synthetic MMP-13 degradable ECMs based on poly(N-isopropylacrylamide-co-acrylic acid) semi-interpenetrating polymer networks. I. Degradation and cell migration. *J. Biomed. Mater. Res. A 75*, 73−88.

(5) Yong, V. W., Power, C., Forsyth, P., and Edwards, D. R. (2001) Metalloproteinases in biology and pathology of the nervous system. *Nat. Rev. Neurosci. 2*, 502−511.

(6) Ulrich, R., Gerhauser, I., Seeliger, F., Baumgartner, W., and Alldinger, S. (2005) Matrix metalloproteinases and their inhibitors in the developing mouse brain and spinal cord: a reverse transcription quantitative polymerase chain reaction study. *Dev. Neurosci. 27*, 408−418.

(7) Vaillant, C., Didier-Bazes, M., Hutter, A., Belin, M. F., and Thomasset, N. (1999) Spatiotemporal expression patterns of metalloproteinases and their inhibitors in the postnatal developing rat cerebellum. *J. Neurosci. 19*, 4994−5004.
(8) Chernoff, E. A., O'Hara, C. M., Bauerle, D., and Bowling, M. (2000) Matrix metalloproteinase production in regenerating axolotl spinal cord. *Wound Repair Regen. 8*, 282−291.
(9) Duchossoy, Y., Horvat, J. C., and Stettler, O. (2001) MMP-related gelatinase activity is strongly induced in scar tissue of injured adult spinal cord and forms pathways for ingrowing neurites. *Mol. Cell Neurosci. 17*, 945−956.
(10) Zuo, J., Ferguson, T. A., Hernandez, Y. J., Stetler-Stevenson, W. G., and Muir, D. (1998) Neuronal matrix metalloproteinase-2 degrades and inactivates a neurite-inhibiting chondroitin sulfate proteoglycan. *J. Neurosci. 18*, 5203−5211.
(11) Muir, D. (1994) Metalloproteinase-dependent neurite outgrowth within a synthetic extracellular matric is induced by nerve growth factor. *Exp. Cell Res. 210*, 243−252.
(12) Nordstrom, L. A., Lochner, J., Yeung, W., and Ciment, G. (1995) The metalloproteinase Stromelysin-1 (Transin) mediates PC12 cell growth cone invasiveness through basal laminae. *Mol. Cell Neurosci. 6*, 56−68.
(13) Webber, C. A., Hocking, J. C., Yong, V. W., Stange, C. L., and McFarlane, S. (2002) Metalloproteases and guidance of retinal axons in the developing visual system. *J. Neurosci. 22*, 8091−8100.
(14) Hubschmann, M. V., Skladchikova, G., Bock, E., and Berezin, V. (2005) Neural cell adhesion molecule function is regulated by metalloproteinase-mediated ectodomain release. *J. Neurosci. Res 80*, 826−837.
(15) Ferguson, T. A., and Muir, D. (2000) MMP-2 and MMP-9 increase the neurite-promoting potential of schwann cell basal laminae and are upregulated in degenerated nerve. *Mol. Cell Neurosci. 16*, 157−167.
(16) West, J. L., and Hubbell, J. A. (1999) Polymeric biomaterials with degradation sites for proteases involved in cell migration. *Macromolecules 32*, 241−244.
(17) Gobin, A. S., and West, J. L. (2002) Cell migration through defined, synthetic extracellular matrix analogues. *FASEB J. 16*, 751−753.
(18) Halstenberg, S., Panitch, A., Rizzi, S., Hall, H., and Hubbell, J. A. (2002) Biologically engineered protein-graft-poly(ethylene glycol) hydrogels: a cell adhesive and plasmin degradable biosynthetic material for tissue repair. *Biomacromolecules 3*, 710−723.
(19) Bollag, D. M. (1994) Gel-filtration chromatography. *Methods Mol. Biol. 36*, 1−9.
(20) Shibusawa, Y. (1999) Surface affinity chromatography of human peripheral blood cells. *J. Chromatogr. B. Biomed. Sci. Appl. 722*, 71−88.
(21) Pawlowski, R., Szigeti, V., Loyd, R., and Przybylski, R. J. (1984) Primary culture of chick embryo skeletal muscle on dextran microcarrier. *Eur. J. Cell Biol. 35*, 296−303.
(22) Hirtenstein, M., Clark, J., Lindgren, G., and Vretblad, P. (1980) Microcarriers for animal cell culture: a brief review of theory and practice. *Dev. Biol. Stand. 46*, 109−116.
(23) Kim, S. H., and Chu, C. C. (2000) In vitro release behavior of dextran-methacrylate hydrogels using doxorubicin and other model compounds. *J. Biomater. Appl. 15*, 23−46.
(24) Saxena, B. B., Singh, M., Gospin, R. M., Chu, C. C., and Ledger, W. J. (2004) Efficacy of nonhormonal vaginal contraceptives from a hydrogel delivery system. *Contraception 70*, 213−219.
(25) Brondsted, H., Andersen, C., and Hovgaard, L. (1998) Crosslinked dextran-a new capsule material for colon targeting of drugs. *J. Controlled Release 53*, 7−13.
(26) Cortesi, R., Esposito, E., Osti, M., Squarzoni, G., Menegatti, E., Davis, S. S., and Nastruzzi, C. (1999) Dextran cross-linked gelatin microsphere as a drug delivery. *Eur. J. Pharm. Biopharm. 47*, 153−160.
(27) Ferreira, L., Rafael, A., Lamghari, M., Barbosa, M. A., Gil, M. H., Cabrita, A. M., and Dordick, J. S. (2004) Biocompatibility of chemoenzymatically derived dextran-acrylate hydrogels. *J. Biomed. Mater. Res. A 68*, 584−596.
(28) Cadee, J. A., van Luyn, M. J. A., Brouwer, L. A., Plantinga, J. A., van Wachem, P. B., de Groot, C. J., den Otter, W., and Hennink, W. E. (2000) In vivo biocompatibility of dextran-based hydrogels. *J. Biomed. Mater. Res. 50*, 397−404.
(29) Trudel, J., and Massia, S. P. (2002) Assessment of the cytotoxicity of photocross-linked dextran and hyaluronan-based hydrogels to vascular smooth muscle cells. *Biomaterials 23*, 3299−3307.
(30) Kosmala, J., Henthorn, D., and Brannon-Peppas, L. (2000) Preparation of interpenetrating networks of gelatin and dextran as degradable biomaterials. *Biomaterials 21*, 2019−2023.
(31) Osterberg, E., Bergstrom, K., Holmberg, K., Riggs, J. A., Vanalstine, J. M., Schuman, T. P., Burns, N. L., and Harris, J. M. (1993) Comparison of polysaccharide and poly(ethylene glycol) coatings for reduction of protein adsorption on polystyrene surfaces. *Colloids Surfaces A: Physicochem. Eng. Aspects 77*, 159−169.
(32) Frazie, R. A., Matthijs, G., Davies, M. C., Roberts, C. J., Schacht, E., and Tendler, S. J. (2000) Characterization of protein-resistant dextran monolayers. *Biomaterials 21*, 957−966.
(33) Massia, S. P., Stark, J., and Letbetter, D. S. (2000) Surface-immobilized dextran limits cell adhesion and spreading. *Biomaterials 21*, 2253−2261.
(34) Massia, S. P., and Stark, J. (2001) Immobilized RGD peptides on surfaces-grafted dextran promote biospecific cell attachment. *J. Biomed. Mater. Res. 56*, 390−399.
(35) Massia, S. P., Holecko, M. M., and Ehteshami, G. R. (2004) In vitro assessment of bioactive coatings for neural implant applications. *J. Biomed. Mater. Res. 68A*, 177−186.
(36) Levesque, S. G., Lim, R. M., and Shoichet, M. S. (2005) Macroporous interconnected dextran scaffolds of controlled porosity for tissue-engineering applications. *Biomaterials 26*, 7436−7446.
(37) van Dijk-Wolthuis, W. N. E., Tsang, S. K. Y., Kettenes-van, den Bosch, J. J., and Hennink, W. E. (1997) A new class of polymerizable dextrans with hydrolyzable groups: hydroxyethyl methacrylated dextran with and without oligolactate spacer. *Polymer 38*, 6235−6242.
(38) Chau, Y., Tan, F. E., and Langer, R. (2004) Synthesis and characterization of dextran-peptide-methotrexate conjugates for tumor targeting via mediation by matrix metalloproteinase II and matrix metalloproteinase IX. *Bioconjugate Chem. 15*, 931−941.
(39) Sugahara, S., Kajiki, M., Kuriyama, H., and Kobayashi, T. R. (2002) Paclitaxel delivery systems: the use of amino acid linkers in the conjugation of paclitaxel with carboxymethyldextran to create prodrugs. *Biol. Pharm. Bull. 25*, 632−641.
(40) Baudys, M., Letourneur, D., Liu, F., Mix, D., Jozefonvicz, J., and Kim, S. W. (1998) Extending insulin action in vivo by conjugation to carboxymethyl dextran. *Bioconjugate Chem. 9*, 176−183.
(41) Gedda, L., Olsson, P., Ponten, J., and Carlsson, J. (1996) Development and in vitro studies of epidermal growth factor-dextran conjugates for boron neutron capture therapy. *Bioconjugate Chem. 7*, 584−591.
(42) Levesque, S. G., and Shoichet, M. S. (2006) Synthesis of cell-adhesive dextran hydrogels and macroporous scaffolds. *Biomaterials 27*, 5277−5285.
(43) Netzel-Arnett, S., Sang, Q.-X., Moore, W. G. I., Navre, M., Birkedal-Hansen, H., and Van Wart, H. E. (1993) Comparative sequence specificities of human 72- and 92 kDa gelatinases (type IV collagenases) and PUMP (matrilysin). *Biochemistry 32*, 6427−6432.
(44) Nagase, H., and Fields, G. B. (1996) Human matrix metalloproteinase specificity studies using collagen sequence-based synthetic peptides. *Biopolymers 40*, 399−416.
(45) Shaw, D., and Shoichet, M. S. (2003) Toward spinal cord injury repair strategies: peptide surface modification of expanded poly(tetrafluoroethylene) fibers for guided neurite outgrowth in vitro. *J. Craniofac. Surg. 14*, 308−316.
(46) Lauer-Fields, J. L., Tuzinski, K. A., Shimokawa, K., Nagase, H., and Fields, G. B. (2000) Hydrolysis of triple-helical collagen peptide models by matrix metalloproteinases. *J. Biol. Chem. 275*, 13282−13290.
(47) Crouch, S. P., Kozlowski, R., Slater, K. J., and Fletcher, J. (1993) The use of ATP bioluminescence as a measure of cell proliferation and cytotoxicity. *J. Immunol. Methods 160*, 81−88.
(48) Annunziato, M. E., Patel, U. S., Ranade, M., and Palumbo, P. S. (1993) p-maleimidophenyl isocyanate: a novel heterobifunctional linker for hydroxyl to thiol coupling. *Bioconjugate Chem. 4*, 212−218.
(49) Manjula, B. N., Tsai, A., Upadhya, R., Perumalsamy, K., Smith, P. K., Malavalli, A., Vandegriff, K., Winslow, R. M., Intaglietta, M., Prabhakaran, M., Friedman, J. M., and Acharya, A. S. (2003)

Site-specific PEGylation of Hemoglobin at Cys-93 (β): correlation between the colligative properties of the PEGylated protein and the length of the conjugated PEG chain. *Bioconjugate Chem. 14*, 464−472.

(50) Manjula, B. N., Malavalli, A., Smith, P. K., Chan, N. L., Arnone, A., Friedman, J. M., and Acharya, A. S. (2000) Cys-93-betabeta-succinimidophenyl polyethylene glycol 2000 hemoglobin A. Intramolecular cross-bridging of hemoglobin outside the central cavity. *J. Biol. Chem. 275*, 5527−5534.

(51) Cha, T. W., Boiadjiev, V., Lozano, J., Yang, H., and Zhu, X. Y. (2002) Immobilization of oligonucleotides on poly(ethylene glycol) brush-coated Si surfaces. *Anal. Biochem. 311*, 27−32.

(52) Brunswick, M., Finkelman, F. D., Highet, P. F., Inman, J. K., Dintzis, H. M., and Mond, J. J. (1988) Picogram quantities of anti-Ig antibodies coupled to dextran induce B cell proliferation. *J. Immunol. 140*, 3364−3372.

(53) Heindel, N. D., Zhao, H. R., Egolf, R. A., Chang, C. H., Schray, K. J., Emrich, J. G., McLaughlin, J. P., and Woo, D. V. (1991) A novel heterobifunctional linker for formyl to thiol coupling. *Bioconjugate Chem.* 427−430.

(54) Hermanson, G. (1996) *Bioconjugate techniques*, Academic Press, San Diego.

(55) Ferreira, L., Gil, M. H., and Dordick, J. S. (2002) Enzymatic synthesis of dextran-containing hydrogel. *Biomaterials 23*, 3957−3967.

(56) Hennink, W. E., and van Nostrum, C. F. (2002) Novel cross-linking methods to design hydrogels. *Adv. Drug Delivery Rev. 54*, 13−36.

(57) Kim, S. H., Won, C. Y., and Chu, C. C. (1999) Synthesis and characterization of dextran-maleic acid based hydrogel. *J. Biomed. Mater. Res. 46*, 160−170.

(58) Jin, L., Horgan, A., and Levicky. (2003) Preparation of end-tethered DNA monolayers on siliceous surfaces using heterobifunctional cross-linkers. *Langmuir 19*, 6968−6975.

(59) Lipatova, T. E., Bakalo, L. A., Sirotinskaya, A. L., and Lopatina, V. S. (1970) Mechanism of polyurethane synthesis in the presence of dibutyltin dilaurate. *Vysokomol. Soedin. Ser. A 12*, 911−916.

(60) Yang, M., and Santerre, J. P. (2001) Utilization of quinolone drugs as monomers: characterization of the synthesis reaction products for poly(norfloxacin diisocyanatododecane polycaprolactone). *Biomacromolecules 2*, 131−141.

(61) French, M. F., Mookhtiar, K. A., and E, V. W. H. (1987) Limited proteolysis of type I collagen at hyperreactive sites by class I and II Clostridium histolyticum collagenases: complementary digestion patterns. *Biochemistry 26*, 681−687.

(62) van Dijk-Wolthuis, W. N. E., Hoogeboom, J. A. M., van Steenbergen, M. J., Tsang, S. K. Y., and Hennink, W. E. (1997) Degradation and release behavior of dextran-based hydrogels. *Macromolecules 30*, 4639−4645.

(63) Kim, S., and Healy, K. E. (2003) Synthesis and characterization of injectable poly(*N*-isopropylacrylamide-co-acrylic acid) hydrogels with proteolytically degradable cross-links. *Biomacromolecules 4*, 1214−1223.

(64) Mann, B. K., Gobin, A. S., Tsai, A. T., Schmedlen, R. H., and West, J. L. (2001) Smooth muscle cell growth in photopolymerized hydrogels with cell adhesive and proteolytically degradable domains: synthetic ECM analogs for tissue engineering. *Biomaterials 22*, 3045−51.

(65) Lutolf, M. P., Raeber, G. P., Zisch, A. H., Tirelli, N., and Hubbell, J. A. (2003) Cell-responsive synthetic hydrogels. *Adv. Mater. 15*, 888−892.

(66) Lutolf, M. P., Weber, F. E., Schomoekel, H. G., Schense, J. C., Kohler, T., Muller, R., and Hubbell, J. A. (2003) Repair of bone defects using synthetic mimetics of collagenous extracellular matrices. *Nat. Biotechnol. 21*, 513−518.

(67) Schense, J., Bloch, J., Aebisher, P., and Hubbell, J. A. (2000) Enzymatic incorporation of bioactive peptides into fibrin matrices enhances neurite extension. *Nat. Biotechnol. 18*, 415−419.

(68) Schense, J., and Hubbell, J. A. (2000) Three-dimensional migration of neurites is mediated by adhesion site density and affinity. *J. Biol. Chem. 275*, 6813−6818.

(69) Weeks, B. S., Nomizu, M., Ramchandran, R. S., Yamada, Y., and Kleinman, H. K. (1998) Laminin-1 and the RKRLQVQLSIRT laminin-1 α1 globular domain peptide stimulate matrix metalloproteinase secretion by PC12 cells. *Exp. Cell Res. 243*, 375−382.

BC0602127

New Triphosphate Conjugates Bearing Reporter Groups: Labeling of DNA Fragments for Microarray Analysis

Ludmila A. Alexandrova, Maxim V. Jasko, Elena E. Belobritskaya, Alexander V. Chudinov, Olga N. Mityaeva, Tatyana V. Nasedkina, Alexander S. Zasedatelev, and Marina K. Kukhanova*

Engelhardt Institute of Molecular Biology, Russian Academy of Sciences, 32 Vavilov Street, Moscow 119991, Russian Federation. Received July 14, 2006; Revised Manuscript Received January 17, 2007

A simple and convenient method for incorporation of fluorescent or ligand groups into 3′-termini of DNA fragments is proposed. A set of triphosphoric acid monoesters bearing fluorescent groups or biotin attached to the triphosphate fragment through linkers of different lengths and structures was synthesized. All the compounds were substrates for calf thymus terminal deoxynucleotidyltransferase and were used for incorporation of marker groups into 3′-termini of DNA fragments. The compounds were successfully applied for DNA labeling during post-PCR target preparation for microarray analysis.

INTRODUCTION

Non-radioactive labeled DNA and deoxyoligomers bearing different marker groups such as fluorescent dyes, biotin, or photo-cross-linking reagents are widely applied in molecular biology, biotechnology, and medicine. They are used as hybridization probes in medical diagnostics of hereditary diseases, detection of infectious agents, identification of individuals in forensic testing, and for high throughput genetic analysis. DNA fragments joined to marker groups can be synthesized by either enzymatic or chemical methods (*1*−*7*). Chemical methods yield as a rule oligomers with functional groups easily modified with markers, but they can neither guarantee regiospecificity nor high efficacy. Efficient and base-specific DNA labeling can be ensured by using dNTP analogues bearing marker groups in the reactions catalyzed by either template-dependent DNA polymerases or template-independent calf thymus TdT[1] [EC 2.7.7.31] (*1*, *2*). However, a set of labeled and biologically active dNTP analogues that display substrate properties for these enzymes is very limited. Recently it was shown that monoesters of triphosphoric acid bearing bulky substituents were substrates for both template-independent calf thymus TdT (*8*−*10*) and template-instructed DNA polymerses (*11*). The efficacy of incorporation of such triphosphates into the oligomer 3′-ends depends on the nature of substituents and the length of linker between the triphosphate residue and the marker group.

Herein, we developed a simple and convenient method for the introduction of fluorescent groups or biotin into DNA fragments during post-PCR target preparation for microarray analysis. We synthesized triphosphates bearing different marker groups attached to the triphosphate moiety through different linkers and showed that they are effective substrates for TdT and could be used for DNA labeling.

* Corresponding author. Tel: 7-495 135-2255; fax: 7-495-135-1405; e-mail: kukhan86@hotmail.com.

[1] Abbreviations: Bio, biotinyl; Bio-dUTP, 5-(3-*N*-biotinylaminopropen-1-yl)-2′-deoxyuridine 5′-triphosphate; CDI, 1,1′-carbonyldiimidazole; Cy5-dUTP, 5-aminopropargyl-2′-deoxyuridine 5′-triphosphate coupled to Cy5 fluorescent dye; DBI, 3-(4,4-difluoro-1,3,5,7-tetramethyl-4-bora-3a,4a-diaza-*s*-indacene-2-yl)propionyl; DNP, 2,4-dinitrophenyl; DNS, 5-*N*,*N*-dimethylamino-1-naphthalenesulfonyl (dansyl); DSC, *N*,*N*′-disuccinimidyl carbonate; Fmoc, 9-fluorenylmethoxycarbonyl; Flu, fluoresceinyl; RdB, rhodaminyl; TdT, terminal deoxynucleotidyltransferase; PAAG, polyacrylamide gel.

EXPERIMENTAL PROCEDURES

Chemicals. 2-Aminoethyl dihydrogen phosphate, dansyl chloride, 2,4-dinitrofluorobenzene, fluorescein isothiocyanate (isomer I), rhodamine B isothiocyanate (mixture of isomers), and *N*-(9-fluorenylmethoxycarbonyloxy)succinimide were purchased from Aldrich; 4-amino-1-butanol, $POCl_3$, CDI, and Dowex 50 Wx8 were obtained from Fluka; LiChroprep RP-18 (23−40 μm) and LiChroprep RP-8 (40−63 μm) were obtained from Merck; DEAE-cellulose DE 32 was from Whatman, Cy5-dUTP and streptavidin conjugated with Cy5 were purchased from Amersham Biosciences. 5-(3-*N*-Biotinylaminopropen-1-yl)-2′-deoxyuridine 5′-triphosphate (Bio-dUTP) was prepared according to the reported procedure (*12*). *N*-(9-Fluorenylmethoxycarbonyl)-8-amino-3,6-dioxaoctanoic and 4-amino-1-butylic esters of triphosphoric acid were obtained similarly to (*8*, *9*). 6-*N*-(5-*N*,*N*-Dimethylamino-1-naphthalenesulfonyl)aminohexanoic acid and 6-*N*-(2,4-dinitrophenyl)aminohexanoic acid were prepared according to the reported procedures (*13*, *14*), respectively.

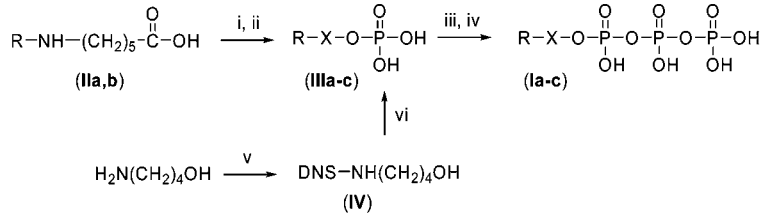
[γ-^{32}P]ATP (6000 Ci/mmol) was from "Isotop" (Russia); T4 polynucleotide kinase and TdT were purchased from Fermentas (Lithuania). The 18-mer oligonucleotide primer CCGTCAATTCCTGTAGTC was from "Litech" (Russia). The primer was labeled at the 5′-end with T4 polynucleotide kinase using [γ-^{32}P]-ATP (*15*), purified on a Sephadex-G50 spin-column (Amersham Biosciences) and used for elongation reactions. All solvents were purchased from Fluka.

Spectroscopic Analysis. UV spectra were measured in water at pH 7.0 on a UV-vis-2401 P (Shimadzu, Japan) spectrophotometer. ^{1}H NMR spectra were recorded on an AMX III-400 (Bruker) SY spectrometer (Billerica, MA, USA) at 400 MHz with Me_4Si and sodium 3-(trimethylsilyl)propane-1-sulfonate as internal standards for $CDCl_3$ and D_2O solutions, respectively. ^{31}P NMR spectra were recorded at 162 MHz with ^{1}H-decoupling in D_2O if not stated otherwise and 85% H_3PO_4 as an external standard. Chemical shifts (δ) are in ppm and coupling constants (J) are in hertz. MALDI-TOF MS (matrix-assisted laser desorption ionization−time-of-flight mass spectra) were measured using Kompact MALDI 4 (Kratos Analytical, Manchester, U.K.). The fluorescence spectra were registered by a Photon

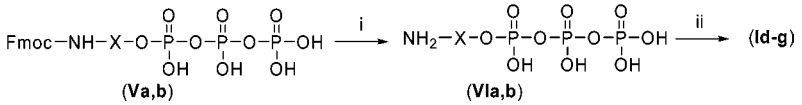
10.1021/bc060213z CCC: $37.00 © 2007 American Chemical Society
Published on Web 03/13/2007

Scheme 1[a]

Method A

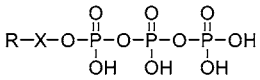


Method B



[a] Method A: X = $NH(CH_2)_5C(O)NH(CH_2)_2$, a. R = DNS, b. R = DNP. c. X = $NH(CH_2)_4$, R = DNS; (i) CDI, DMF, 20 °C, 1 h; (ii) $NH_2C_2H_4OP(O)(OH)_2$, Et_3N, H_2O, 20 °C, 18 h; (iii) CDI, DMF, 20 °C, 1 h; (iv) $(Bu_3NH)_2H_2P_2O_7$, DMF, 20 °C, 20 h; (v) DNS-Cl, dioxane, 20 °C, 18 h; (vi) $POCl_3$, $(EtO)_3PO$, 20 °C, 20 h. Method B: **V**, **VI**: a. X = $(CH_2)_4$, b. X = $CH_2CH_2[O(CH_2)_2]_2$; (i) 25% aqueous ammonia, 16 h, 5 °C; (ii) Et_3N, MeIm, DMF, H_2O, RdB isothiocyanate (for **Id**), BDI *N*-hydroxysuccinimide ester (for **Ie**), Flu isothiocyanate (for **Ig**), or Bio *N*-hydroxysuccinimide ester (for **If**), 20 °C, 18 h.

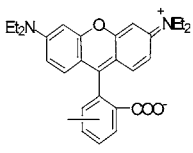
Table 1. Structures of Alkyl Triphosphates



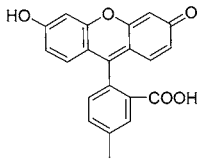
I: **R -** fluorescent groups or biotin;

X – linker

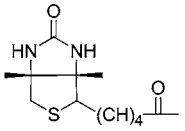
Compound	R	X
Ia	DNS	$NH(CH_2)_5C(O)NH(CH_2)_2$
Ib	DNP	$NH(CH_2)_5C(O)NH(CH_2)_2$
Ic	DNS	$NH(CH_2)_4$
Id	RdB	$NH(CH_2)_4$
Ie	DBI	$NH(CH_2)_4$
If	Bio	$NH(CH_2)_4$
Ig	Flu	$NHCH_2CH_2[O(CH_2)_2]_2$



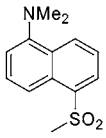
RdB



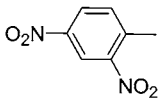
Flu



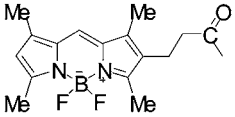
Bio



DNS



DNP



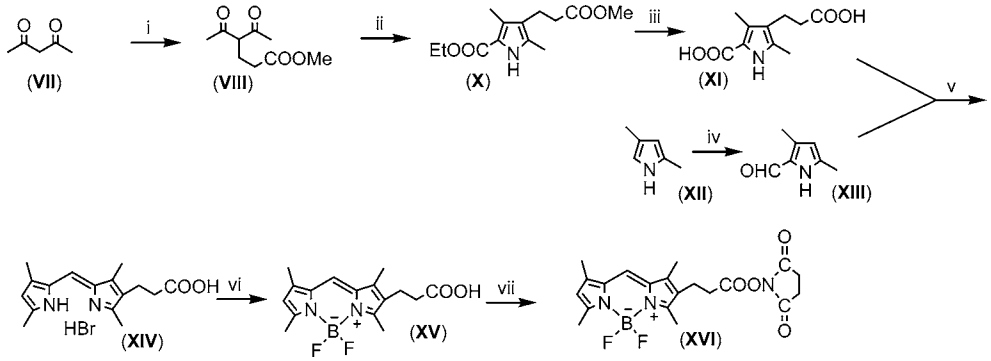
DBI

Technology International spectrofluorimeter (PTI, Canada). Melting points were determined on a Koffler bloc (Dresden, Germany) and uncorrected.

The compounds (Table 1) were synthesized by the methods similar to described previously (*8*−*10*) (Scheme 1, 2).

Synthesis. 2-*N*-[6-*N*-(5-*N*,*N*-Dimethylamino-1-naphthalenesulfonyl)aminohexanoyl]aminoethyl Phosphoric Acid IIIa and 2-*N*-[6-*N*-(2,4-Dinitrophenyl)aminohexanoyl]aminoethyl Phosphoric Acid IIIb. CDI (48 mg, 0.3 mmol) was added to solutions of 6-*N*-(5-*N*,*N*-dimethylamino-1-naphthalenesulfonyl)-aminohexanoic acid **IIa** (55 mg, 0.15 mmol) or 6-*N*-(2,4-dinitrophenyl)aminohexanoic acid **IIb** (44 mg, 0.15 mmol) in dry DMF (3 mL). The reaction mixture was stirred for 1 h at 20 °C and added to a solution of 2-aminoethyl dihydrogen phosphate (28 mg, 0.2 mmol) in water (3 mL) containing Et_3N (20 μL), and the mixture was stirred at 20 °C for 18 h. After dilution with water (50 mL), the mixture was loaded on a DEAE-cellulose (HCO_3^-) column (2 × 9 cm). The column was washed with 20% aqueous MeOH (100 mL) and eluted in a linear gradient of NH_4HCO_3 (0 → 0.3 M) in 20% aqueous MeOH (pH 7.5, total volume 0.6 L). The target fractions were collected, evaporated, and coevaporated with water, and the residues were dissolved in water (1 mL) and purified on a LiChroprep RP-8 column (1.5 × 20 cm) in a linear gradient of

Scheme 2[a]



[a] (i) CH_2═$CHCOOCH_3$, K_2CO_3; (ii) 1. $CH_3C(O)CH_2COOEt$ (**IX**), $NaNO_2$, CH_3COOH, 2. Zn; (iii) NaOH; (iv) $POCl_3$, DMF; (v) HBr, CH_3COOH; (vi) BF_3·OEt_2, iPr_2EtN, THF; (vii) DSC, Py, CH_3CN.

MeOH (0 → 20%, total volume 0.6 L) in 0.01 M NH_4HCO_3 under UV control. The target fractions were freeze-dried to give **IIIa** (28 mg, 53%) or **IIIb** (30 mg, 67%).

2-*N*-[6-*N*-(5-*N*,*N*-Dimethylamino-1-naphthalenesulfonyl)-aminohexanoyl]aminoethyl phosphoric acid IIIa: UV−vis (H_2O, pH 7.0): λ_{max} 333 nm (ϵ = 2500 M^{-1} cm^{-1}), 245 nm (ϵ = 8670 M^{-1} cm^{-1}), λ_{max} 216 nm (ϵ = 21700 M^{-1} cm^{-1}). ^1H NMR (D_2O): δ 8.47 (d, 1H, J = 8.72 Hz, H-2 (DNS)), 8.24 (d, 1H, J = 8.72 Hz, H-4 (DNS)), 8.22 (d, 1 H, J = 6.54, H-8 (DNS)), 7.66 (m, 2H, H-3 + H-7 (DNS)), 7.39 (d, 1H, J = 7.79 Hz, H-6 (DNS)), 3.51 (m, 2H, CH_2O), 3.20 (t, 2H J = 7.17 Hz, CH_2NHCO), 2.89 (t, 2H, J = 6.53 Hz, CH_2NH(DNS)), 2.84 (s, 6H, $(H_3)_2$), 1.80 (t, 2H, J = 7.5 Hz, CH_2CO), 1.08 (m, 6H, $(CH_2)_3$-central). ^{31}P NMR (D_2O): δ 4.50 s.

2-*N*-[6-*N*-(2,4-Dinitrophenyl)aminohexanoyl]aminoethyl phosphoric acid IIIb: UV−vis (H_2O, pH 7.0): λ_{max} 363 nm (ϵ = 17500 M^{-1} cm^{-1}), 265 nm (ϵ = 8340). ^1H NMR (D_2O): δ 8.70 (d, 1H, J = 2.18 Hz, H-3 (DNP)), 7.97 (dd, 1H, J = 2.18 Hz, J = 9.65, H-5 (DNP)), 6.85 (d, 1H, J = 9.65 Hz, H-6 (DNP)), 3.72 (m, 2H, CH_2O), 3.25 (m, 4H, 2 NCH_2), 2.13 (m, 2H, t, J = 7.16 Hz, CH_2CO), 1.51 (m, 4H, $(CH_2)_2$), 1.26 (m, 2H, CH_2-central). ^{31}P NMR (D_2O): δ 2.12 s.

4-*N*-(5-*N*,*N*-Dimethylamino-1-naphthalenesulfonyl)amino-1-butanol IV. A mixture of 4-amino-1-butanol (178 mg, 2 mmol) and dansyl chloride (135 mg, 0.5 mmol) in 1,4-dioxane (3 mL) was kept overnight at 20 °C. The solution was evaporated, and the residue was dissolved in $CHCl_3$ (1 mL) and loaded on a silica gel column (2 × 17 cm). The column was washed with $CHCl_3$ (50 mL), and the product was eluted with 4% MeOH in $CHCl_3$. The target fractions were combined and evaporated to yield **IV** (67 mg, 41%) as light-yellow solid residue. UV−vis (MeOH): λ_{max} 337 nm (ϵ = 2500 M^{-1} cm^{-1}), 250 nm (ϵ = 8670 M^{-1} cm^{-1}), λ_{max} 219 nm (ϵ = 21700 M^{-1} cm^{-1}). ^1H NMR ($CDCl_3$): δ 8.29 (d, 1H, J = 8.4 Hz, H-2), 8.23 (d, 1H, J = 8.41 Hz, H-4 (DNS)), 8.21 (d, 1H, J = 7.16 Hz, H-8 (DNS)), 7.53 (m, 2H, H-3 + H-7), 7.17 (d, 1H, J = 7.48 Hz, H-6 (DNS)), 5.21 (t, 1H, J = 5.9 Hz, NH), 3.50 (t, 2H, J = 5.9 Hz, CH_2O), 2.91 (m, 8H, CH_2N+$(CH_3)_2$), 1.40 (m, 4H, $(CH_2)_2$-central).

4-*N*-(5-*N*,*N*-Dimethylamino-1-naphthalenesulfonyl)aminobutyl Phosphoric Acid IIIc. Phosphorus oxychloride (16 μL, 0.17 mmol) was added dropwise to a precooled (0 °C) solution of 4-*N*-(5-*N*,*N*-dimethylamino-1-naphthalenesulfonyl)amino-1-butanol **IV** (18 mg, 0.057 mmol) in triethyl phosphate (1 mL), and the reaction mixture was kept at 0 °C for 20 h and diluted with water (50 mL). The target product was purified as described above for **IIIa**,**b** to give 12 mg (50%) of **IIIc** as ammonium salt. UV−vis (H_2O, pH 7.0): λ_{max} 333 nm (ϵ = 2500 M^{-1} cm^{-1}), 245 nm (ϵ = 8670 M^{-1} cm^{-1}), λ_{max} 216 nm (ϵ = 21700 M^{-1} cm^{-1}). ^1H NMR (D_2O): δ 8.34 (d, 1H, J = 8.4 Hz, H-2 (DNS)), 8.29 (d, 1H, J = 8.41 Hz, H-4 (DNS)), 8.14 (d, 1H, J = 7.16 Hz, H-8 (DNS)), 7.58 (m, 2H, H-3 + H-7 (DNS)), 7.43 (d, 1H, J = 7.78 Hz, H-6 (DNS)), 3.50 (m, 2H, CH_2O), 3.03 (m, 6H, $(CH_3)_2$), 2.87 (m, 2H, CH_2N), 1.14 (m, 4H, $(CH_2)_2$-central). ^{31}P NMR (D_2O): δ 2.10 s.

Synthesis of Triphosphoric Acid Monoesters Ia−c (Scheme 1A). 1,1′-Carbonyldiimidazole (32 mg, 0.2 mmol) was added to a solution of tri-*n*-butylammonium salt of phosphate ester (**IIIa**, **IIIb**, or **IIIc**, 50 μM) in dry DMF (3 mL), and the reaction mixture was stirred for 1 h at 20 °C. Anhydrous MeOH (0.33 mL, 8 mmol) was added, the solvents were evaporated after 40-min stirring, and the residue was dissolved in dry DMF (5 mL) followed by the addition of bis(tri-*n*-butylammonium) pyrophosphate (0.5 mL, 0.15 mmol). The mixture was stirred at 20 °C overnight. After dilution with water (50 mL), the mixture was loaded on a DEAE-cellulose (HCO_3^-) column (2 × 9 cm). The column was washed with 20% aqueous MeOH (100 mL), and the products were eluted in a linear gradient of NH_4HCO_3 (0 → 0.4 M) in 20% aqueous MeOH (pH 7.5, total volume 0.6 L). The target fractions were collected, evaporated, and coevaporated with water, and the residues were dissolved in water (1 mL). The product was purified on a LiChroprep RP-8 column (1.5 × 20 cm). The target fractions were eluted in a linear gradient of MeOH (0 → 20%, total volume 0.6 L) in 0.01 M NH_4HCO_3 under the UV control, and freeze-dried to give 4.7 mg (27%) of **Ia**, 5.5 mg (35%) of **Ib**, and 5.9 mg (37%) of **Ic** as ammonium salts.

2-*N*-[6-*N*-(5-*N*,*N*-Dimethylamino-1-naphthalenesulfonyl)-aminohexanoyl]aminoethyl triphosphoric acid Ia: UV−vis (H_2O, pH 7.0): λ_{max} 333 nm (ϵ = 2500 M^{-1} cm^{-1}), 245 nm (ϵ = 8670 M^{-1} cm^{-1}), λ_{max} 216 nm (ϵ = 21700 M^{-1} cm^{-1}). ^1H NMR (D_2O): δ 8.47 (d, 1H, J = 8.72 Hz, H-2 (DNS)), 8.24 (d, 1H, J = 8.72 Hz, H-4 (DNS)), 8.22 (d, 1H, J = 6.54 Hz, H-8 (DNS)), 7.66 (m, 2H, H-3 + H-7 (DNS)), 7.39 (d, 1H, J = 7.79 Hz, H-6 (DNS)), 3.85 (m, 2H, CH_2O), 3.24 (t, 2H, J = 4.78 Hz, CH_2NHCO), 2.87−2.71 (m, 8H, CH_2NH(DNS) + $(CH_3)_2$), 1.70 (t, 2H, J = 7.5, CH_2CO) 1.08 (m, 6H, $(CH_2)_3$-central). ^{31}P NMR (D_2O): δ −8.42 (d, 1P, J = 21.3 Hz, P_γ), −10.35 (d, 1P, J = 19.3 Hz, P_α), −21.80 (dd, 1P, P_β).

2-*N*-[6-*N*-(2,4-Dinitrophenyl)aminohexanoyl]aminoethyl triphosphoric acid Ib: UV−vis (H_2O, pH 7.0): λ_{max} 363 nm (ϵ = 17500 M^{-1} cm^{-1}), 265 nm (ϵ = 8340 M^{-1} cm^{-1}). ^1H NMR (D_2O): δ 8.93 (d, 1H, H-3 (DNP)), 8.10 (dd, 1H, J = 2.8 Hz, H-5 (DNP)), 6.97 (d, 1H, J = 9.65 Hz, H-6 (DNP)), 3.88 (m, 2H, CH_2OP), 3.34 (t, 1H, J = 7.16 Hz, CH_2NH (DNP)), 3.27 (t, 1H, J = 4.98 Hz, CH_2NHCO), 2.13 (t, 2H, J = 7.47 Hz, CH_2CO), 1.55 (q, 2H, J = 6.48 Hz, CH_2), 1.46 (q, 2H, J = 6.48 Hz, CH_2), 1.28 (m, 2H, CH_2-central). ^{31}P NMR (D_2O): δ −7.88 (d, 1P, J = 21.4 Hz, P_γ), −10.32 (d, 1P, J = 19.3 Hz, P_α), −21.77 (dd, 1P, P_β).

4-*N*-(5-*N*,*N*-Dimethylamino-1-naphthalenesulfonyl)aminobutyl triphosphoric acid Ic: UV−vis (H_2O, pH 7.0): λ_{max}

333 nm ($\epsilon = 2500\ M^{-1}\ cm^{-1}$), 245 nm ($\epsilon = 8670\ M^{-1}\ cm^{-1}$), λ_{max} 216 nm ($\epsilon = 21700\ M^{-1}\ cm^{-1}$). ^{1}H NMR ($D_2O$): δ 8.37 (d, 1H, $J = 8.4$ Hz, H-2), 8.33 (d,1H, $J = 8.41$ Hz, H-4), 8.12 (d, 1H, $J = 7.16$ Hz, H-8), 7.56 (m, 2H, H-3 + H-7), 7.29 (d, 1H, $J = 7.78$ Hz, H-6), 3.59 (m, 2H, CH_2O), 2.81 (m, 2H, CH_2N), 2.74 (s, 6H, $(CH_3)_2$), 1.27 (m, 4H, $(CH_2)_2$-central). ^{31}P NMR (D_2O): δ −8.74 (d, 1P, $J = 19.5$ Hz, P_γ), −10.6 (d, 1P, $J = 20.3$ Hz, P_α), −22.2 (dd, 1P, P_β).

Synthesis of Triphosphoric Acid Monoesters Id−f (Scheme 1B). 9-Fluorenylmethoxycarbonyl)aminobutyl triphosphoric acid **Va** (44 mg, 0.08 mmol) was dissolved in 25% aqueous ammonia (2 mL) and kept for 16 h at 5 °C. The reaction mixture was filtered, the filtrate was evaporated and coevaporated with water, and the residue was dissolved in water (1 mL) and purified on a LiChroprep RP-18 column (2 × 16 cm) in 0.01 M NH_4HCO_3 as an eluent. The target fractions were collected, evaporated, coevaporated with water, and freeze-dried to give **VIa** (24 mg, 97%). To the solution of **VIa** (12 mg, 0.04 mmol) in a mixture of H_2O (1 mL) and DMF (5 mL) was added Et_3N (0.5 mL), and the solvents were evaporated to a volume of approximately 2 mL. Rhodamine B isothiocyanate (21.4 mg, 0.04 mmol), BDI *N*-hydroxysuccinimide ester (16.7 mg, 0.04 mmol), or biotin *N*-hydroxysuccinimide ester (13.6 mg, 0.04 mmol), Et_3N (0.08 mL), and *N*-methylimidazole (0.04 mL) were added, and the mixture was stirred at 20 °C overnight. The reaction mixture was evaporated, and the residue was dissolved in water (10 mL) and extracted with CCl_4 (3 mL) and *n*-butanol (2 × 3 mL). The aqueous solution was diluted with water (50 mL). The target products were purified as described above for **Ia−c** to give **Id** (25 mg, 75%), **Ie** (4.4 mg, 12%), or **If** (2.3 mg, 11%) as ammonium salts.

Aminobutyl triphosphoric acid VIa: ^{1}H NMR (D_2O): δ 3.8 (m, 2H, CH_2O), 2.89 (m, 2H, CH_2N), 1.53 (m, 4H, $(CH_2)_2$). ^{31}P NMR (D_2O): δ −8.92 (d, 1P, $J = 18.3$ Hz, P_γ), −10.41 (d, 1P, $J = 19.4$ Hz, P_α), −22.07 (dd, 1P, P_β).

4-*N*-(Rhodaminylaminothiocarbonyl)aminobutyl triphosphoric acid Id: UV−vis (H_2O, pH 7.0): λ_{max} 556 nm ($\epsilon = 59000\ M^{-1}\ cm^{-1}$), 355 nm ($\epsilon = 4700\ M^{-1}\ cm^{-1}$), 284 nm ($\epsilon = 13100\ M^{-1}\ cm^{-1}$), 258 nm ($\epsilon = 18100$). ^{1}H NMR ($D_2O$): δ 7.75 m, 6.87 m, 6.54 m, 6.38 m, 6.25 m (9H, aryl), 3.87 (m, 2H, CH_2O), 3.21 (m, 10H, CH_2N and $(CH_2CH_3)_4$), 1.63 (m, 4H, $(CH_2)_2$), 0.91 (m, 12H, $(CH_2CH_3)_4$). ^{31}P NMR (D_2O): δ −10.07 (d, 1P, $J = 18.3$ Hz, P_γ), −10.34 (d, 1P, $J = 19.3$ Hz, P_α), −21.94 (dd, 1P, P_β).

4-*N*-[3-(4,4-Difluoro-1,3,5,7-tetramethyl-4-bora-3a,4a-diaza-*s*-indacene-2-yl)propionyl]aminobutyl triphosphoric acid Ie: UV−vis (H_2O, pH 7.0): λ_{max} 517 nm ($\epsilon = 72000\ M^{-1}\ cm^{-1}$). ^{1}H NMR ($D_2O$): δ 7.35 (s, 1H, H-8), 6.14 (s, 1H, H-6), 3.85 (m, 2H, CH_2O), 2.89 (m, 2H, CH_2N), 2.72 (t, 2H, $J = 8.0$ Hz, CH_2CH_2CO), 2.49 (t, 2H, CH_2CH_2CO), 2.45 and 2.44 (2 × s, 6H, 3-CH_3 and 5-CH_3), 2.23 and 2.25 (2 × s, 6H, 1-CH_3 and 7-CH_3), 1.63 (m, 4H, $(CH_2)_2$). ^{31}P NMR (D_2O): δ −10.05 (d, 1P, $J = 18.3$ Hz, P_γ), −10.38 (d, 1P, $J = 19.5$ Hz, P_α), −22.21 (dd, 1P, P_β).

4-*N*-(Biotinyl)aminobutyl triphosphoric acid If: UV (H_2O, pH 7.0): λ_{max} 195 nm (ϵ 2220 $M^{-1}\ cm^{-1}$). ^{1}H NMR (D_2O): δ 4.25 and 4.05 (2 m, 2H, 2 CHN (Bio)), 3.85 (m, 2H, CH_2O), 3.15 (m, 1H, CHS (Bio)), 3.02 (t, 2H, $J = 6.3$ Hz, CH_2N), 2.83 (dd, 1H, $J = 13.5$ Hz, CH_aS), 2.61 (d, 1H, CH_bS), 2.23 (t, 2H, $J = 7$ Hz, CH_2CO), 1.62 and 1.41 (m, 10H, 5 × CH_2). ^{31}P NMR (D_2O): δ −9.72 (d, 1P, $J = 19.1$ Hz, P_γ), −10.42 (d, 1P, $J = 20.1$ Hz, P_α), −21.9 (dd, 1P, P_β).

***N*-(Fluoresceinylaminothiocarbonyl)-8-amino-3,6-dioxaoctanoic Triphosphoric Acid Ig.** *N*-(9-Fluorenylmethoxycarbonyl)-8-amino-3,6-dioxaoctanoic triphosphoric acid **Vb** (20 mg, 0.03 mmol) was dissolved in 25% aqueous ammonia (2 mL), and the reaction mixture was kept for 16 h at 5 °C and filtered. The filtrate was evaporated to a volume of approximately 1 mL, and DMF (1 mL), Et_3N (0.02 mL), and fluorescein isothiocyanate (20 mg, 0.05 mmol) were added. The mixture was stirred at 20 °C overnight, evaporated, and coevaporated with water (3 × 10 mL), and the residue was dissolved in 1 mL of water. The products were purified on a LiChroprep RP-8 column (2 × 18 cm) in 0.05 M NH_4HCO_3 as an eluent. The target fractions were collected, evaporated, coevaporated with water, and freeze-dried to give **Ig** (1 mg, 5%) as the ammonium salt.

Ig: UV−vis (H_2O, pH 9.0): λ_{max} 492 nm ($\epsilon = 65000\ M^{-1}\ cm^{-1}$), 320 nm ($\epsilon = 7000\ M^{-1}\ cm^{-1}$), 293 nm ($\epsilon = 42100\ M^{-1}\ cm^{-1}$), 207 nm ($\epsilon = 36000\ M^{-1}\ cm^{-1}$). ^{1}H NMR ($D_2O$): 6.94 m, 7.50 m, 7.76 m, 7.92s (9H, Flu), 4.25 (m, 2H, CH_2-OP), 3.89 (m, 10H, $(CH_2)_5$). ^{31}P NMR (D_2O): δ −9.84 (d, 1P, $J = 18.3$ Hz, P_γ), −10.49 (d, 1P, $J = 19.3$ Hz, P_α), −22.59 (dd, 1P, P_β).

Methyl 4-acetyl-5-oxo-hexanoate VIII. Methyl acrylate (86.1 g, 1.0 mol) was added dropwise during 30 min to a mixture of acetylacetone **VII** (110.1 g, 1.1 mol) and potassium carbonate (7.0 g, 50.6 mmol) under stirring at 100 °C. The mixture was stirred for 3 h at 100 °C and filtered, and the residue was washed with acetone (10 mL). The combined filtrates were concentrated in vacuum to give a viscous oil (117 g, 63%). ^{1}H NMR ($CDCl_3$): δ 3.68 (t, 1H, $J = 7.1$ Hz, CH), 3.61 (s, 3H, $COOCH_3$), 2.52 (t, 2H, $J = 7.1$ Hz, $CH_2CH_2COOCH_3$), 2.14 (s, 6H, 2 $C(O)CH_3$), 2.07 (m, 2H, $CH_2CH_2COOCH_3$). Bp 140−143 °C/12 mm.

4-(2′-Methoxycarbonylethyl)-2-ethoxycarbonyl-3,5-dimethylpyrrole X. A solution of ethyl acetoacetate **IX** (61.2 g; 0.47 mol) in acetic acid (180 mL) was treated with sodium nitrite (37.4 g; 0.23 mol) in water (61 mL) under stirring at 4−7 °C. The mixture was stirred for 1 h at 5−7 °C and 24 h at ambient temperature. Methyl 4-acetyl-5-oxo-hexanoate **VIII** (98.5 g; 0.53 mol), acetic acid (100 mL), and then zinc dust (68.5 g; 1.05 mol) were gradually added under stirring. The mixture was heated at 80 °C for 1 h and refluxed for additional 2 h. The hot solution was poured onto ice (800 g) and filtered off, zinc powder was washed with the hot acetic acid, and the filtrates were combined. The oil layer was separated, and product was allowed to crystallize under storage. The product was filtered off, washed with water, and recrystallized from ethanol:water mixture (2:1) to give pale yellow plates (56.0 g, 47%). ^{1}H NMR ($CDCl_3$): δ 8.72 (s, 1H, NH), 4.27 (q, 2H, $J = 7.0$ Hz, OCH_2-CH_3), 3.65 (s, 3H, OCH_3), 2.69 (dd, 2H, $J = 6.5$ Hz, $J = 8.0$ Hz, $CH_2CH_2COOCH_3$), 2.42 (dd, 2H, $J = 7.5$ Hz, $J = 8.0$ Hz, $CH_2CH_2COOCH_3$), 2.26 (s, 3H, 5-CH_3), 2.20 (s, 3H, 3-CH_3), 1.35 (t, 3H, $J = 7.0$ Hz, OCH_2CH_3). Mp 103−104 °C.

4-(2′-Carboxyethyl)-2-carboxy-3,5-dimethylpyrrole XI. 4-(2′-Methoxycarbonylethyl)-2-ethoxycarbonyl-3,5-dimethylpyrrole **X** (1.79 g, 7.1 mmol) was added to a solution of NaOH (1.4 g; 35 mmol) in H_2O (7 mL) and ethanol (20 mL), and the mixture was refluxed for 2 h. Ethanol was removed in vacuum, and the mixture was neutralized with 10% HNO_3 under stirring at 0−4 °C. The precipitate was filtered, washed with ice−water, and vacuum-dried to give a pink powder (0.97 g, 65%). ^{1}H NMR ($CDCl_3$): δ 11.80 (s, 2H, 2 COOH), 10.91 (s, 1H, NH), 2.53 (t, 2H, $J = 7.5$ Hz, CH_2CH_2COOH), 2.26 (t, 2H, $J = 7.5$ Hz, CH_2CH_2COOH), 2.16 (s, 3H, 5-CH_3), 2.11 (s, 3H, 3-CH_3).

2-Formyl-3,5-dimethylpyrrole XIII. Phosphorus oxychloride (2.0 g; 13 mmol) was added dropwise during 15 min to DMF (0.96 g; 13 mmol) under stirring at 10 °C. After stirring for 15 min at ambient temperature, the solution was deluted with 1,2-dichloroethane (3 mL) and cooled to 5 °C and a solution of 2,4-dimethylpyrrole **XII** (1.12 g; 11.8 mmol) in 1,2-dichloroethane (3 mL) was added dropwise at 5 °C during 1 h. The mixture was refluxed for 15 min and cooled to room temperature, and sodium acetate (8.83 g; 65 mmol) in water

(12 mL) was added. The reaction mixture was refluxed for 15 min and cooled to room temperature, and the organic layer was separated. The water layer was extracted with diethyl ether (3 × 50 mL), and organic liquids were combined, washed with saturated aqueous solution of Na_2CO_3, and dried over anhydrous Na_2CO_3. The solvents were evaporated, and the solid residue was crystallized from water to give white crystals (1.2 g, 83%). ^{1}H NMR ($CDCl_3$): δ 9.97 (s, 1H, NH), 9.45 (s, 1H, CHO), 5.84 (s, 1H, H-4), 2.31 (s, 3H, 5-CH_3), 2.29 (s, 3H, 3-CH_3). Mp 89−90 °C.

4-(2″-Carboxyethyl)-3,3′,5,5′-tetramethylpyrromethene Hydrobromide XIV. A solution of 33% HBr in acetic acid (0.27 mL) was added to a solution of 2-carboxy-4-(2′-carboxyethyl)-3,5-dimethylpyrrole **XI** (105.6 mg; 0.5 mmol) and 3,5-dimethyl-2-formylpyrrole **XIII** (61.5 mg, 0.5 mmol) in acetic acid (2.5 mL) under stirring at 4−7 °C. The mixture was heated on a water bath for 10 min, cooled to room temperature and poured into diethyl ether (25 mL). After 12 h at 0 °C, the precipitate was filtered, washed with diethyl ether, and vacuum-dried to give a yellow-red powder (173 mg, 98%). UV−vis (MeOH): λ_{max} 474 nm (ϵ = 22000 M^{-1} cm^{-1}). ^{1}H NMR ($CDCl_3$): δ 13.08 (s, 2H, NH), 7.06 (s, 1H, H-6), 6.14 (s, 1H, H-4′), 2.75 (t, 2H, J = 7.5 Hz, CH_2CH_2COOH), 2.66 and 2.67 (2 × s, 6H, 5-CH_3 and 5′-CH_3), 2.51 (t, 2H, J = 7.0 Hz, CH_2CH_2COOH), 2.34 (s, 3H, 3-CH_3), 2.29 (s, 3H, 3′-CH_3).

3-(4,4-Difluoro-1,3,5,7-tetramethyl-4-bora-3a,4a-diaza-*s*-indacene-2-yl)pro pionic Acid XV. Boron trifluoride diethyl etherate (1.52 g, 1.35 mL, 10.7 mmol) was added to a solution of **XIV** (90 mg; 0.255 mmol) and *N*-ethyldiisopropylamine (130 mg; 1.0 mmol) in THF (9.0 mL). The mixture was stirred at 60 °C for 2 h, cooled to room temperature, and extracted with toluene (2 × 20 mL). The solvents were evaporated in vacuum at 35−40 °C. The residue was dissolved in cold toluene (100 mL), and the solution was washed with cold water (3 × 10 mL) and brine (10 mL), dried over Na_2SO_4, and filtered. The products were separated by flash chromatography on a silica gel column (20 × 90 mm). The column was washed subsequently with toluene (50 mL), toluene−acetic acid (30:2:60 mL), and toluene−acetic acid−THF (30:2, 60 mL). The solvents were evaporated at 30−35 °C and reevaporated with toluene to remove acetic acid. The title compound **XV** was obtained as a purple precipitate and was crystallized from toluene (64.5 mg; 79%). UV−vis (MeOH): λ_{max} 517 nm (ϵ = 72000 M^{-1} cm^{-1}). Fluorescence: λ_{max} 520 nm; ^{1}H NMR ($CDCl_3$): δ 7.01 (s, 1H, H-8), 6.02 (s, 1H, H-6), 2.72 (t, 2H, J = 8.0 Hz, CH_2CH_2-COOH), 2.69 (s, 6H, 3-CH_3, 5-CH_3), 2.49 (t, 2H, J = 8.0 Hz, CH_2CH_2COOH), 2.23 and 2.19 (s, 6H, 1-CH_3, 7-CH_3). Mp 167−168 °C; MALDI-TOF-MS: calcd for $C_{16}H_{19}BF_2N_2O_2$ (M^+) 320.14, found (M^+) 319.5, (M^+-19) 300.7.

***N*-Hydroxysuccinimide Ester of 3-(4,4-Difluoro-1,3,5,7-tetramethyl-4-bora-3a,4a-diaza-*s*-indacene-2-yl)propionic Acid XVI**. *N*,*N*′-Disuccinimidyl carbonate (124 mg; 0.484 mmol) was added to a solution of **XV** (62 mg; 0.194 mmol) in acetonitrile (5.8 mL) and pyridine (65 μL). The mixture was stirred at room temperature for 12 h, and the solvents were evaporated at 35−40 °C. The residue was coevaporated with toluene (2 × 3 mL) to remove the traces of pyridine. Title compound **XVI** was obtained as a semisolid substance. UV−vis (CH_3CN) λ_{max} 518 nm (ϵ = 73000 M^{-1} cm^{-1}). Fluorescence (CH_3CN): λ_{max} 521 nm; Mp > 250 °C. MALDI TOF MS: calcd $C_{20}H_{22}BF_2N_3O_4$ (M^+) 417.21, found (M^+) 416.0.

Elongation Reactions with Alkyl Triphosphates Ia−g Catalyzed by TdT. The reaction mixture (10 μL) contained 200 mM cacodylate buffer (pH 7.2), 20 nM [5′-^{32}P]-18-mer primer, 0.1 mM DTT, 2 mM $CoCl_2$, 0.2 U of TdT, and compounds **Ia−g** at the concentrations indicated in the legend to Figure 1. After incubation for 10 min at 37 °C, the reactions were quenched by the addition of 5 μL of sequencing loading buffer containing 98% (v/v) deionized formamide/10 mM EDTA/1 mg/mL of bromophenol blue and xylene cyanol each. The reaction mixtures were loaded onto 20% denaturing PAAG and subjected to electrophoresis for approximately 3 h at 2000 V. The gels were exposed to X-ray film (Kodak RX).

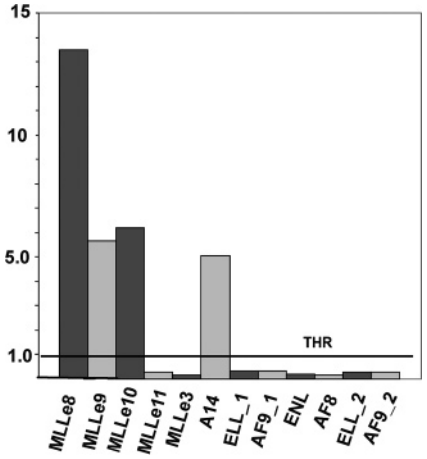


Figure 1. Histogram of a sample bearing t(4;11) translocation. The solid line indicates the cutoff value (THR = $<J> + 4\sigma$). Signals over the cutoff were recognized as true signals (MLLe8, MLLe9, MLLe10, AF4).

Microarray Analysis. The gel-based microarray developed for the analysis of MLL-translocations in leukemias was used as described earlier (*16*, *17*). Oligonucleotides for immobilization were synthesized on a 394 DNA/RNA automated synthesizer (Applied Biosystems) by the standard phosphoroamidite method. A spacer contained a free amino group at the 3′-end, which was introduced during synthesis with a C7 CPG 500 3′-amino modifier (Glen Research). Microarrays were obtained by photoinducible copolymerization of oligonucleotides and PAAG components as described previously (*16*). To prepare fluorescent labeled DNA, the target RNA was isolated from bone marrow of a leukemic patient and reverse transcribed, and cDNA was used as a matrix in multiplex PCR with specific primers. The two-round nested multiplex PCR was performed as described earlier (*18*). The 1/50 of reverse transcriptase reaction mixture (an equivalent of 20 000 cells) was added to 25-μL multiplex mixture containing 11 mM Tris-HCl (pH 8.3), 55 mM KCl, 1.5 mM $MgCl_2$, 0.2 mM each of deoxynucleotide triphosphates, a mixture of primers (0.2 μM each), and 1.5 units of Taq-polymerase (Sileks, Russia). Twenty-five cycles per each round were performed: 94 °C for 30 s, 58 °C for 30 s, and 72 °C for 1 min; the second round was followed by an extension at 72 °C for 4 min. In the case of translocation the estimated range of PCR products were from 150 to 300 bp in dependence on the breakpoint region in MLL-gene and gene-partner involved in translocation. To determine the sensitivity of the tests, cDNA from leukemic cells was serially diluted (10^{-4} up to 10^{-1} times) with cDNA from HL-60 cells carrying no translocations, and then the mixture was used in multiplex RT-PCR, followed by hybridization.

The PCR product was labeled with the synthesized monoesters of triphosphoric acid **Id−f** in the reactions catalyzed by TdT. The reaction mixture (50 μL) contained 200 mM cacodylate buffer, pH 7.2, 25 mM Tris, 0.01% Triton X-100, 2 mM $CoCl_2$, 30 units of TdT, and 500 pmol of synthesized compounds. DNA fragments labeled with Bio-dUTP or Cy5-dUTP were used as controls. The reactions were carried out at 37 °C for 1 h. The labeled DNA fragments were hybridized with an oligonucleotide microchip at 37 °C for 12 h. The microchip was washed briefly with distilled water and dried. For biotin-labeled probes, the microchip was washed and

$$[5'\text{-}^{32}P](pdN)_n + ppp\text{-}O\text{-}X\text{-}R \rightarrow [5'\text{-}^{32}P](pdN)_np\text{-}O\text{-}X\text{-}R + pp_i$$

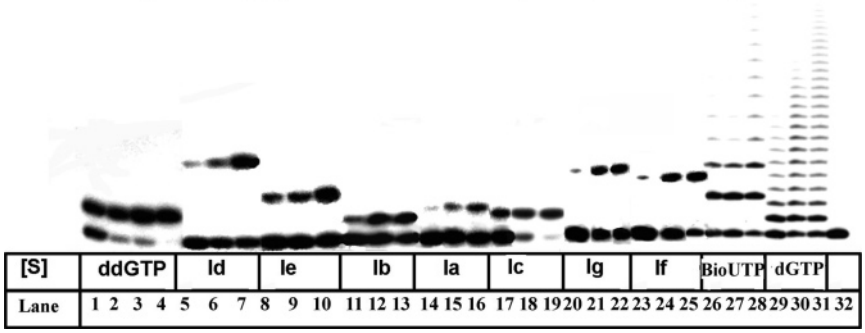


Figure 2. Dose-dependent TDT-catalyzed incorporation of compounds **Ia**−**g** into 18-mer primer 3′-ends: (lanes 8−10), DNP (**Ib**) 2, 10, 20 μM (lanes 11−13), DNS (**Ia**) 2, 10, 20 μM (lanes 14−17), DNS (**Ic**) 1, 5, 10 μM (lanes 17−19), Flu (**Ig**) 0.5, 2, 10 μM (lanes 20−22), Bio (**If**) 2, 5, 10 μM (lanes 23−25), Bio-dUTP 1, 2, 5 μM (lanes 26−28), dGTP 1, 2, 5 μM (lanes 29−31). The reaction conditions are given in Experimental Procedures. Lane 32 represents the reaction mixture containing all components except the substrate. The scheme of the reaction is presented above the picture.

Table 2. Nucleotide Sequences of Immobilized Oligonucleotides

translocation	gene	name	sequence from 5′ to 3′
all *MLL*-translocatio ns	*MLL*	*MLL* 3981	TGGTGGTGGAGGCTGCTTTTTCTTG
		MLL 4013	CACTTTTTTCTGTTTGCTCTGCTCTGGAC
		MLL 4194	CTTAAAGTCCACTCTGATCCTGTGG
		MLL 4297	CCTGGGTGTTATAGGAACAGAAGTCAAGA
Dup11 *MLL/MLL*	*MLL*	*MLL* 454	GCACTCTGACTTCTTCATCTGAGCC
t(4;11) *MLL/AF4*	*AF4*	*AF4* 1532	CTGTACTAGGCGTATGTATTGCTGTCA
t(9;11) *MLL/AF9*	*AF9*	*AF9* 1685	TTCATCTAGGTATGCCTTGTCACATTCAC
	AF9	*AF9* 1323	GCTGGCAGGACTGGGTTGTTCA
t(11;19) *MLL/ ENL*	*ENL*	*ENL* 83	ACAAACACCATCCAGTCGTGAGTGA
t(11;19) *MLL/ ELL*	*ELL*	*ELL* 149	CGGATAGATGGCCTAGTGAAACAGAAT
	ELL	*ELL* 241	CCGATGTTGGAGAGGTAGAAGGAGAA
t(6;11) *MLL/AF6*	*AF6*	*AF6* 197	AGCGTTTCGATTACATCTTGAGTGGTGG

incubated with streptavidin conjugated with Cy5 in 0.9% NaCl for 1 h at 37 °C, washed again, and dried. The fluorescent signal was registered using a portable biochip analyzer equipped with CCD camera. The input data for the analysis were obtained from measurements of fluorescent intensity $J_m = (C_m - B_m)/B_m$, where C_m is the intensity per unit area in the internal region of a pad, B_m is the background intensity, and m is the enumerated pads on the chip ($m = 1, ...48$). Signal intensities of the translocation-specific probes that were spotted in quadruplicate were averaged, and the obtained values (group signals) were used in the posterior calculations. The five most outlying group signals equal to the maximal number of perfect duplexes formed in the presence of translocation in the sample were excluded. The remaining values J_m for oligonucleotide groups were defined as background signals. The mean $<J>$ and standard deviation σ of background signals were calculated, and THR = $<J> + 4 \times \sigma$ was established as the cutoff level (Figure 1). We regarded any signal over the cutoff level to be a significant signal.

RESULTS AND DISCUSSION

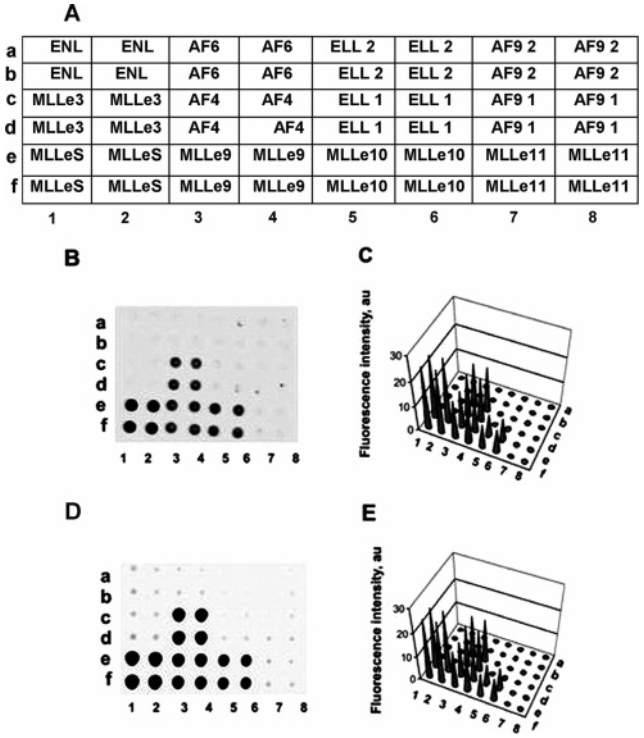
Synthesis of Triphosphoric Acid Monoesters. Two approaches were used for the synthesis of triphosphoric acid monoesters bearing fluorescent groups or biotin (Scheme 1). According to method A, the activated substance containing the marker group was coupled with the linker followed by phosphorylation. Compounds **IIa**,**b** were obtained by the reaction of DNS-Cl or DNP-F with ϵ-aminocaproic acid. Activation of **IIa**,**b** with CDI followed by the treatment with 2-aminoethylphosphate resulted in **IIIa**,**b**. For **IIIc** synthesis, 4-amino-1-butanol was treated with DNS-Cl followed by phosphorylation of alcohol **IV** with $POCl_3$. Compounds **IIIa**−**c** were diphosphorylated to give **Ia**−**c** by the imidazole method (*19*).

Compounds **Id**−**g** were synthesized by method B. The procedure included the synthesis of triphosphates bearing linkers followed by the addition of fluorescent labels or biotin. The key Fmoc-aminoalkyl esters of triphosphoric acid **Va**,**b** were prepared by the earlier developed procedure (*10*). The Fmoc-groups of **Va**,**b** were removed with aqueous ammonia, and the resulting **VIa**,**b** were coupled with either RdB *N*-methylimidazole or Flu isothiocyanates to give **Id** and **Ig**, respectively, or with *N*-hydroxysuccinimide esters of BDI or Bio to give **Ie** and **If**, respectively (*19*). Compounds of type **I** were purified by successive ion-exchange chromatography on DEAE-cellulose and reversed-phase silica gel chromatography. The structures of the compounds were confirmed by UV and ^1H and ^{31}P NMR spectra.

The diaza-bora-indacene dye (DBI) was synthesized (Scheme 2) using modified methods (*20*−*23*). The key 3-(4,4-difluoro-1,3,5,7-tetramethyl-4-bora-3a,4a-diaza-*s*-indacene-2-yl)propionic acid **XV** was obtained by condensation of boron trifluoride diethyl etherate and 4-(2″-carboxyethyl)-3,3′,5,5′-tetramethylpyrromethene hydrobromide **XIV** (*20*, *21*). The latter was prepared by the condensation of pyrroledicarbonic acid **XI** and formylpyrrole **XIII** according to the method described by Fischer and Orth (*22*). *N*-Hydroxysuccinimide ester **XVI** was obtained by the reaction of **XV** with *N*,*N*′-disuccinimidyl carbonate (*23*) and used without purification.

Substrate Properties. Substrate properties of alkyl triphosphates **I** toward TdT were evaluated by the ability of TdT to elongate the [5′-^{32}P]-primer in the presence of the synthesized **Ia**−**g** under the conditions described earlier (*8*, *9*). As reference compounds, ddGTP, dGTP, and Bio-dUTP were used.

Reaction products were analyzed by electrophoresis in 20% denaturing PAAG. Figure 2 presents the dose-dependent incorporation of **Ia**−**g** into the 18-mer primer 3′-ends. Bio-dUTP, ddGTP, and dGTP were used as control samples. As one can see, the compounds **Ia**−**g** could elongate the oligonucleotide, albeit with different potencies. The comparison of the intensities of the bands above the primer position shows that the substrate efficacies of **Ia**−**g** were 5−50-fold lower than that of ddGTP (lanes 1−4). In contrast to chain terminators **1a**−



	1	2	3	4	5	6	7	8
a	ENL	ENL	AF6	AF6	ELL 2	ELL 2	AF9 2	AF9 2
b	ENL	ENL	AF6	AF6	ELL 2	ELL 2	AF9 2	AF9 2
c	MLLe3	MLLe3	AF4	AF4	ELL 1	ELL 1	AF9 1	AF9 1
d	MLLe3	MLLe3	AF4	AF4	ELL 1	ELL 1	AF9 1	AF9 1
e	MLLeS	MLLeS	MLLe9	MLLe9	MLLe10	MLLe10	MLLe11	MLLe11
f	MLLeS	MLLeS	MLLe9	MLLe9	MLLe10	MLLe10	MLLe11	MLLe11

Figure 3. Scheme of microarray (A). Examples of hybridization of the PCR-product obtained from the clinical sample carrying the translocation t(4;11) and labeled with **Id** (B, C) and Cy5-dUTP (D, E). The fluorescent signals on diagrams C and E above the threshold line indicate the presence of translocation.

g, Bio-dUTP (lanes 26−28) can be incorporated by TdT several times similarly to dGTP (lanes 29−31). Triphosphates bearing RdB residue **Id** (lanes 5−7) and DBI residue **Ie** (lanes 8−10) were the most effective substrates. Their efficacies differed from that of ddGTP by approximately fivefold. Compound **Ia** bearing a DNS residue and a long linker (lanes 14−16) was incorporated less effectively if compared with **Ic** (lanes 17−19) containing a DNS residue but a short linker. These results correlate with the previously reported data showing the dependence of substrate properties on length and structure of linker (*8*−*11*).

Microarray Analysis Using Fluorescent Labeled DNA Targets. The synthesized alkyl triphosphates **Id**−**f** were used for fluorescent labeling of DNA fragments during post-PCR target preparation for microarray analysis. Cy5-dUTP and Bio-dUTP were used as reference samples. The microarray was developed for the analysis of six translocations in leukemias, involving the *MLL*-gene: t(4;11) *MLL/AF4*, t(6;11) *MLL/AF6*, t(9,11) *MLL/AF9*, t(11;19) *MLL/ ELL*, t(11;19) *MLL/ENL*, and dup(11) *MLL/MLL* (*17*). The oligonucleotide sequences are given in Table 2. As a result of translocation, a fusion gene is formed, where the 5′-part is presented by the *MLL*-gene and the 3′-part is originated from one of the gene-partners. Chimeric RNA expressed in leukemic cells was the molecular target for the analysis. After RNA isolation and reverse transcription, the multiplex PCR with specific primers is used for the amplification of DNA fragment for further hybridization with microarray. The forward primer is located in the *MLL*-gene and the reverse one in gene-partner, so that PCR-product is formed only in the case of translocation. Figure 3 shows the microarray plot (A) and hybridization patterns of the clinical sample bearing translocation t(4;11) after labeling of PCR products with **Id** (B and C) and Cy5 dUTP (D and E). The rows (**a**−**d**) of the microarray (A) show the immobilized probes specific to different gene partners, and the rows (**e**, **f**) present oligonucleotide probes specific to different exons of MLL-gene. According to the hybridization pattern, the molecular structure of chimeric transcript was

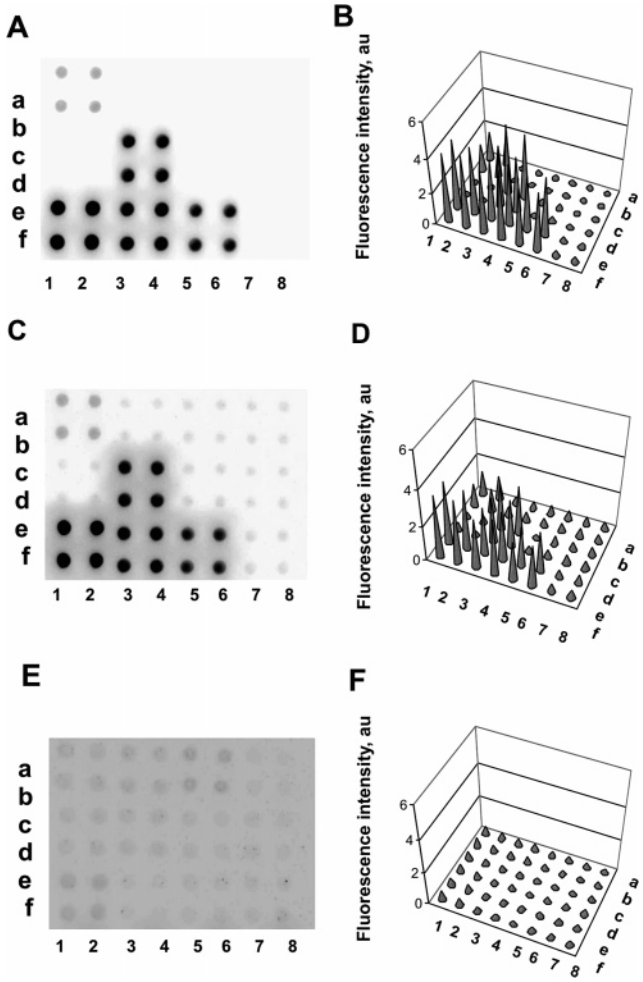


Figure 4. Examples of hybridization of the PCR-product obtained from the clinical sample carrying the translocation t(4;11) and labeled with **If** (A, B) and Bio-dUTP (C, D). Absence of fluorescent signals from the control sample carrying no translocation (E and F).

determined as *MLLex9/AF4*. The results of hybridization with microarray after labeling with **1f** (A and B) and Bio-dUTP (C and D) are presented in Figure 4. The fluorescent signals on diagrams (B and D) above the threshold line indicate the presence of t(4;11) translocation. In the case of negative sample carrying no translocation, no fluorescent signals were observed (E and F). Comparing the results of hybridization of PCR DNA fragments labeled with **1d** or commercially available Cy5-dUTP, we could notice that both compounds gave more sharp signals with lower background than that labeling with biotin-containing compounds. The efficacy of hybridization using compound **Id** is the same as that with Cy5-dUTP. The efficacy of hybridization of DNA labeled with **If** is even higher than that in the case of Bio-dUTP. The limit of detection was defined as dilution of cDNA carrying translocation with cDNA sample noncarrying translocation, which still allowed revealing the chimeric transcript using multiplex PCR and hybridization with biochips. For all translocations, the detection limit was found to be the dilution up to 10^{-3}, which corresponded to the detection of one blast cell per 10^3 normal cells. The sensitivity assay performed for **Id** or Cy5-dUTP compounds revealed the similar results for both labels.

To conclude, we developed a simple method of DNA labeling using monoesters of triphosphoric acid bearing fluorescent or ligand groups attached to the triphosphate moiety through different linkers. Two methods were used for the preparation of fluorescent triphosphates. According to the first method, the activated compounds bearing fluorescent labels were coupled

with a linker followed by phosphorylation. The second one included the initial synthesis of triphosphates coupled with linker followed by incorporation of fluorescent labels. This procedure allowed using different types of activating groups, namely sulfonyl chlorides, isothiocyanates, or *N*-hydroxysuccinimide esters for triphosphate labeling depending on ligand structure. All the synthesized compounds bearing fluorescent groups or biotin were successfully applied for effective labeling of DNA targets in microarray analysis during post-PCR target preparation.

ACKNOWLEDGMENT

The work was supported by the Russian Foundation for Basic Research, project no. 04-04-49500, and grant of Presidium of Russian Academy of Sciences on Molecular and Cellular Biology.

LITERATURE CITED

(1) Hermanson, G. T. (1996) *Bioconjugate Techniques*, pp 640−671, Academic Press, New York.
(2) Kricka, L. J. (1992) *Nonisotopic DNA probe techniques*, Academic Press, San Diego.
(3) Ranasinghe, R. T., and Brown, T. (2005) Fluorescent based strategies for genetic analysis. *Chem. Commun.* 5487−5502.
(4) Duthie, R. S., Kalve, I. M., Samols, S. B., Hamilton, S., Livshin, I., Khot, M., Nampalli, S., Kumar, S., and Fuller, C. W. (2002) Novel Cyanine Dye-labeled Dideoxynucleoside Triphosphates for DNA Sequencing. *Bioconjugate Chem. 13*, 699−706.
(5) Godovikova, T. S., Kolpashchikov, D. M., Orlova, T. N., Richter, V. A., Ivanova, T. M., Grochovsky, S. L., Nasedkina, T. V., Victorova, L. S., and Poletaev, A. I. (1999) 5-[3-(*E*)-4-Azido-2,3,5,6-tetrafluorobenzamido)propenyl-1]-2′-deoxyuridine-5′-triphosphate substitutes for thymidine-5′-triphosphate in the polymerase chain reaction. *Bioconjugate Chem. 10*, 529−537.
(6) Giller, G., Tasara, T., Angerer, B., Mulleger, K., Amacker, M., and Winter, H. (2003) Incorporation of reporter molecule-labeled nucleotides by DNA polymerases. I. Chemical synthesis of various reporter group-labeled 2′-deoxyribonucleoside-5′-triphosphates. *Nucleic Acids Res. 31, 2630−2635.*
(7) Tasara, T., Angerer, B., Damond, M., Winter, H., Dorhofer, S., Hubscher, U., and Amacker, M. (2003) Incorporation of reporter molecule-labeled nucleotides by DNA polymerases. II. High-density labeling of natural DNA. *Nucleic Acids Res. 31,* 2636−2646.
(8) Arzumanov, A. A., Victorova, L. S., and Jasko, M. V. (2000) Synthesis of non-nucleoside triphosphate analogues, a new type of substrates for terminal deoxynucleotidyl transferase. *Nucleosides, Nucleotides Nucleic Acids 19*, 1787−1793.
(9) Arzumanov, A. A., Victorova, L. S., Jasko, M. V., Yesipov, D. S., and Krayevsky, A. A. (2000) Terminal Deoxynucleotidyl Transferase Catalyzes the Reaction of DNA Phosphorylation. *Nucleic Acids Res. 28,* 1276−1281.
(10) Khandazhinskaya, A. L., Kukhanova, M. K., and Jasko, M. V. (2005) New nonnucleoside substrates for terminal deoxynucleotidyl transferase: synthesis and the dependence of substrate properties on structure. *Bioorg. Chem. (Russian) 31*, 394−398.
(11) Crespan, E., Zanoli, S., Khandazhinskaya, A., Shevelev, I., Jasko, M., Alexandrova, L., Kukhanova, M., Blanca, G, Villani, G., Hubscher, U., Spadari, S., and Maga, G. (2005) Incorporation of non-nucleoside triphosphate analogues opposite to an abasic site by human DNA polymerases beta and lambda. *Nucleic Acids Res. 33*, 4117−4127.
(12) Langer, P. R., Waldrop, A. A., and Ward, D. C. (1981) Enzymatic synthesis of biotin-labeled polynucleotides: Novel nucleic acid affinity probes. *Proc. Natl. Acad. Sci. U.S.A. 78*, 6633−6637.
(13) Alexandrova, L. A., Atrazhev, A. M., Kukhanova, M. K., and Krayevsky, A. A. (1987) Incorporation into DNA chain of fluorescent derivative 2′-deoxyuridilic acid at the catalysis by *E. coli* DNA polymerase. *Bioorg. Chem.* (Russian) *13*, 643−647.
(14) Becker, M., and Makela, O. (1975) Modification of bacteriophage with hapten-epsilon-aminocaproyl-N-hydroxysuccinimide esters. *Immunochemistry 12*, 329−331.
(15) Sambrook, G., Fritch, E. F., and Manniatis, T. (1989) *Molecular Cloning*: *A Laboratory Manual*, Cold Spring Harbor Laboratory Press, Cold Spring Harbor, NY.
(16) Mityaeva, O. N., Nasedkina, T. V., Zharinov, V. S., Turygin, A. Yu., Chupeeva, V. V., Kreindlin, E. Yu., and Mirzabekov, A. D. (2004) Analysis of chromosome translocations involving MML by hybridization with an oligonucleotide microarray. *Mol. Biol. (Mosk.) 38*, 449−456.
(17) Nasedkina, T. V., Zharinov, V. S., Isaeva, E. A., Mityaeva, O. N., Yurasov, R. N., Surzhikov, S. A., Turygin, A. Yu., Rubina, A. Yu., Karachunskii, A. I., Gartenhaus, R. B., and Mirzabekov, A. D. (2003) Clinical screening of gene rearrangements in childhood leukemia using a multiplex PCR-microarray approach. *Clin. Cancer Res. 9*, 5620−5629.
(18) Rubina, A. Yu., Pan'kov, S. V., Dementieva, E. I., Pen'kov, D. N., Butygin, A. V., Vasiliskov, V. A., Chudinov, A. V., Mikcheikin, A. L., Mikhailovich, V. M., and Mirzabekov, A. D. (2004) Hydrogel drop microchip with immobilized DNA: properties and methods for large-scale production. *Anal. Biochem. 325*, 92−106.
(19) Alexandrova, L. A., Skoblov, A. Yu., Jasko, M. V., Victorova, L. S., and Krayevsky, A. A. (1998) 2′-Deoxynucleoside 5′-triphosphates modified at α-, β- and γ-phosphates as substrates for DNA polymerases. *Nucleic Acids Res. 26*, 778−786.
(20) Treibs, A., und Kreuzer, F. H. (1968) Difluorboryl-komlexe von Di- und Tripyrrylmethenen. *Liebigs Ann. Chem. 718*, 208−223.
(21) Shah, M., Thangaraj, K., Soong, M. L., Wolford, L. T., Boyer, J. H., Politzer, I. R., and Pavlopoulos, T. G. (1990) Pyrromethene-BF_2 complexes as laser dyes: 1. *Heteroatom Chem. 1*, 389−399.
(22) Fischer, H., and Orth, H. (1937) A. Zweikernige Pyrrolsysteme. In *Die Chimie des Pyrrols, II Brand*, pp 1−59, Leipzig Akademische Verlaggeselschaft, Pyrrolfarbstoffe, Leipzig.
(23) Ogura, H., Kobayashi, T., Shimizu, K., Kawabe, K., and Takeda, K. (1979) A novel active ester synthesis reagent (N,N′-disuccinimidyl carbonate). *Tetrahedron Lett. 49*, 4745−4746.

BC060213Z

The Same Drug but a Different Mechanism of Action: Comparison of Free Doxorubicin with Two Different *N*-(2-Hydroxypropyl)methacrylamide Copolymer-Bound Doxorubicin Conjugates in EL-4 Cancer Cell Line

Lubomír Kovář,*,† Jiří Strohalm,‡ Petr Chytil,‡ Tomáš Mrkvan,† Marek Kovář,† Ondřej Hovorka,† Karel Ulbrich,‡ and Blanka Říhová†

Department of Immunology and Gnotobiology, Institute of Microbiology ASCR, v.v.i., Vídeňská 1083, 142 20 Prague 4, Czech Republic, and Department of Biomedical Polymers, Institute of Macromolecular Chemistry ASCR, v.v.i., Heyrovský Square 2, 162 06 Prague 6, Czech Republic. Received August 8, 2006; Revised Manuscript Received February 8, 2007

Doxorubicin is one of the most potent anti-tumor drugs with a broad spectrum of use. To reduce its toxic effect and improve its pharmacokinetics, we conjugated it to an HPMA copolymer carrier that enhances its passive accumulation within solid tumors via the EPR effect and decreases its cytotoxicity to normal, noncancer cells. In this study, we compared the antiproliferative, pro-survival, and death signals triggered in EL-4 cancer cells exposed to free doxorubicin and doxorubicin conjugated to a HPMA copolymer carrier via either enzymatically (PK1) or hydrolytically (HYD) degradable bonds. We have previously shown that the intracellular distribution of free doxorubicin, HYD, and PK1 is markedly different. Here, we demonstrated that these three agents greatly differ also in the antiproliferative effect and cell death signals they trigger. JNK phosphorylation sharply increased in cells treated with HYD, while treatment with free doxorubicin moderately decreased and treatment with PK1 even strongly decreased it. On the other hand, treatment with free doxorubicin greatly increased p38 phosphorylation, while PK1 and HYD increased it slightly. PK1 also significantly increased ERK phosphorylation, while both the free doxorubicin and HYD conjugate slightly decreased it. Long-term inhibition of JNK significantly increased both proliferation and viability of EL-4 cells treated with free doxorubicin, showing that the JNK signaling pathway could be critical for mediating cell death in EL-4 cells exposed to free doxorubicin. Both activation of caspase 3 and decreased binding activity of the p50 subunit of NFκB were observed in cells treated with free doxorubicin and HYD, while no such effects were seen in cells incubated with PK1. Analysis of the expression of genes involved in apoptosis and regulation of the cell cycle demonstrated that free doxorubicin and HYD have very similar mechanisms of action, while PK1 has very different characteristics.

INTRODUCTION

Doxorubicin is one of the most effective anthracycline antibiotics with a broad anti-tumor spectrum. Unfortunately, numerous side effects such as severe cardiotoxicity, bone marrow suppression, and alopecia limit its use. Development of tumor-targeted formulations is one of the main lines of research for improving the safety and efficacy of anthracyclines. For this purpose, we have used a water-soluble, nontoxic copolymer based on *N*-(2-hydroxypropyl)methacrylamide (HPMA) as a carrier for anti-cancer drugs. Covalent conjugation of doxorubicin to HPMA copolymer eliminates its adverse cytotoxicity, as this conjugate is biologically inactive when circulating in the bloodstream (*1*). Enhanced and tumor-selective accumulation of HPMA conjugate within the solid tumor is achieved either passively due to the enhanced permeability and retention (EPR) effect (*2*) or actively by addition of a targeting moiety (e.g., antibodies, lectins, carbohydrates) (*3*).

Anthracyclines cause apoptosis of cancer cells by a complex network of events which include intercalation into the DNA, generation of reactive oxygen species, topoisomerase II inhibition, and DNA damage (*4*). HPMA conjugate that contains doxorubicin bound via a pH-sensitive bond (HYD) possesses similar biological properties as free doxorubicin (*5*), because doxorubicin is released inside the cell and then acts analogously to free doxorubicin. Controlled release of doxorubicin within cancer cells is achieved by hydrolysis of hydrazone conjugates having doxorubicin bound via pH-sensitive bonds (*6*). Those bonds are stable at physiological pH 7.4, but are effectively degraded at pH 5. Inside the cell, doxorubicin is released quickly in endosomes or lysosomes. Conjugates with doxorubicin bound to the HPMA carrier through a hydrazone bond are highly cytotoxic and cytostatic in vitro and in vivo (*7*).

On the other hand, intracellular events triggered by HPMA copolymer-conjugated doxorubicin via an enzymatically degradable bond (PK1) remain unclear. These conjugates were originally designed to release the drug from the oligopeptide side chain by the activity of lysosomal proteases (*8*). Some authors initially demonstrated that HPMA copolymer conjugates with enzymatically degradable bonds can be stronger pro-apoptotic inducers than free doxorubicin (*9*). However, later it was shown that both apoptosis and necrosis are induced in cells exposed to proteolytically cleavable HPMA copolymer conjugates (*10*−*12*). Our recent data do not support the idea that the enzymatic degradation and doxorubicin release from PK1 are the most important mechanisms responsible for target cell death. They rather suggest that immediately after penetrating the plasma membrane the whole conjugate intercalates into the membrane system of the cell, causing its collapse and death (*10*, *11*).

PK1 with enzymatically degradable bond between the oligopeptide spacer GFLG and doxorubicin was tested in phase I

* Corresponding author. Tel.: +420241062158. Fax: +420241721143. E-mail address: lkovar@biomed.cas.cz.

† Institute of Microbiology ASCR.

‡ Institute of Macromolecular Chemistry ASCR.

10.1021/bc060246e CCC: $37.00 © 2007 American Chemical Society
Published on Web 04/03/2007

and was recommended for phase II of clinical study (*13*). A conjugate similar to PK1 but containing human nonspecific antibody was used for the treatment of patients with advanced cancer (*14*).

In this study, we used the EL-4 T-cell lymphoma to determine the differences in intracellular action of free doxorubicin, PK1, and HYD. We determined their impact on intracellular signaling pathways (mitogen-activated protein kinases, NFκB, and apoptosis) and expression of genes involved in the regulation of cell cycle, and showed differences in their intracellular distribution.

EXPERIMENTAL PROCEDURES

Materials. Hydrazine monohydrate, methacryloyl chloride, 1-aminopropan-2-ol, 4-nitrophenol, 6-aminohexanoic acid, glycyl-L-phenylalanine, L-leucylglycine, 2,2′-azobis(isobutyronitrile) (AIBN), 2-(dimethylamino)ethyl methacrylate, dimethylformamide (DMF), *N*,*N*′-dicyclohexylcarbodiimide (DCC), 1-hydroxybenzotriazole (HOBT), dimethyl sulfoxide (DMSO), *tert*-butylcarbazate, and doxorubicin hydrochloride (Dox.HCl) were purchased from Fluka Chemie AG. 2,4,6-Trinitrobenzene-1-sulfonic acid was purchased from SERVA Feinbiochemica Heidelberg. All other reagents and solvents were of analytical grade.

Synthesis and Characterization of Monomers. *N*-(2-Hydroxypropyl)methacrylamide (HPMA) was synthesized as described in (*15*) using Na_2CO_3 as a base in the methacryloylation reaction (mp 70 °C; elemental analysis (calcd/found): 58.80/58.98% C; 9.16/9.18% H; 9.79/9.82% N). *N*-(*tert*-Butoxycarbonyl)-*N*′-(6-methacrylamidohexanoyl)hydrazine (Ma-AH-NHNH-Boc) was prepared by a two-step synthesis consisting of methacryloylation of 6-aminohexanoic acid followed by reaction of the resulting *N*-methacryloyl-6-aminohexanoic acid with *tert*-butylcarbazate as described in (*7*). Yield: 6.06 g (46%). Mp 110−114 °C. Elemental analysis: calcd C 57.70%, H 8.33%, N 13.46%; found C 58.66%, H 8.84%, N 13.16%.

N-Methacryloylglycyl-DL-phenylalanyl-L-leucylglycine and *N*-methacryloylglycyl-DL-phenylalanyl-L-leucylglycine 4-nitrophenyl ester (Ma-GFLG-ONp) were synthesized as described earlier (*1*). Mp 134−136 °C. Amino acid analysis: Gly/L-Phe/D-Phe/L-Leu = 2.05/0.54/0.47/1.00. Elemental analysis (calcd/found): C 59.89/59.21%; H 6.07/6.25%; N 12.04/12.32%. HPLC showed two peaks of equal areas at 14.41 min (L-Phe peptide) and 14.71 min (D-Phe peptide).

Purity of all monomers was examined by HPLC (LDC Analytical, U.S.A.) using a reversed-phase column Tessek SGX C_{18} (15 × 33 mm) with UV detection at 230 nm, eluent water−methanol with gradient 50−100 vol % methanol, flow rate 0.5 mL/min.

Synthesis of Polymer Precursors. *Copolymer poly(HPMA-co-MA-AH-NHNH$_2$)*. Copolymer poly(HPMA-*co*-MA-AH-NHNH-Boc) was prepared by radical solution polymerization (AIBN, 1 wt %; monomer concentration, 14 wt % in methanol solution; molar ratio HPMA/MA-AH-NHNH-Boc 93/7; 60 °C; 23 h) in a sealed ampule under nitrogen. The copolymer was isolated by precipitation into a mixture of acetone/diethyl ether (2:1). The protecting Boc group was removed by dissolution of the polymer in concd trifluoroacetic acid (TFE), and a final polymer was isolated after dilution with methanol by precipitation into ethyl acetate and purified by gel filtration using a column filled with Sephadex LH-20 and methanol as a solvent. The poly(HPMA-*co*-MA-AH-NHNH$_2$) was isolated by precipitation into ethyl acetate, separated by filtration, and dried in vacuum to constant weight.

Poly(HPMA-*co*- Ma-GFLG-ONp) was prepared by radical precipitation polymerization as described in (*15*).

HPMA homopolymer poly(HPMA) was prepared by radical solution polymerization using AIBN as initiator (0.8 wt %) and monomer concentration 16 wt % in methanol. Polymerization was carried out at 60 °C for 22 h in a sealed ampule under nitrogen; the polymer was isolated by precipitation into acetone and reprecipitated from methanol into acetone.

Synthesis and Characterization of Polymer−Dox Conjugates. The conjugate bearing Dox attached via a pH-sensitive hydrazone bond poly(HPMA-*co*-MA-AH-NHN = Dox) (HYD) and the conjugate bearing Dox attached via the enzymatically degradable oligopeptide sequence poly(HPMA-*co*- Ma-GFLG-Dox) (PK1) were prepared as described earlier, HYD in (*6*) and PK1 in (*15*).

The polymer−drug conjugates were freed of low-molecular-weight impurities (such as Dox, 4-nitrophenol) by gel filtration using a Sephadex LH-20 column with methanol elution and tested for the content of the free drug using a Pharmacia FPLC equipped with a Superose 6 column and by HPLC after extraction of free Dox from an aqueous polymer solution into chloroform. HPLC analysis of monomers was conducted on an HPLC analyzer (LDC Analytical, U.S.A.) using a reversed-phase column Tessek SGXC18 (125 × 4 mm) with UV detection at 230 nm, solvent methanol−water, gradient 50−100% methanol, and flow rate 0.5 mL/min. Content of Dox in the conjugates was measured spectrophotometrically in water using ϵ = 11 500 L mol^{-1} cm^{-1} at λ = 488 nm).

Amino acid analysis was performed using an amino acid analyzer (LDC Analytical, U.S.A.) (precolumn OPA derivatization, reversed-phase column Tessek SGX C_{18}, 250 × 4 mm, gradient sodium acetate buffer−methanol, fluorescence detector Fluoromonitor 4100).

Determination of the molecular weight of all polymers was carried out with a FPLC Pharmacia system equipped with RI, UV, and multiangle light scattering DAWN DSP-F (Wyatt Co., U.S.A.) detectors using 0.3 M acetate buffer pH 6.5 and a Superose 6 column.

The content of hydrazide groups in a precursor and HYD conjugate was determined by a modified TNBSA assay as described (*16*).

The following polymers were prepared: HPMA copolymer bearing Dox attached via enzymatically degradable spacer (PK1), M_w = 24.8 kDa, M_w/M_n = 1.5, total Dox content 5.2 wt %, free Dox content <0.1%. HPMA copolymer bearing Dox attached via pH-sensitive hydrazone bond (HYD), M_w = 25 kDa, M_w/M_n = 1.8, total Dox content 5.2 wt %, free Dox content <0.3%.

Detection of MAPK Phosporylation by Immunoblotting. 1−5 × 10^7 EL-4 cells were incubated with tested samples at a concentration corresponding to 3, 10, or 50 × IC_{50} of doxorubicin equivalent. After incubation periods of 5, 15, 30, 60, or 120 min, the media from the cell culture were aspirated, and cells were washed twice with an ice-cold Tris-buffered saline (TBS) with 1 μM Na_3VO_4 (phosphatase inhibitor) and centrifuged (4000 *g*, 4 °C). Then, EL-4 cells were resuspended in Extract buffer composed of 1% Nonidet P-40 (Pierce), 1 mM Na_3VO_4, 1 mM EDTA, 2 mM EGTA, 10 mM NaF, 1 mM DTT, 5% Protease mix (Sigma), 1 mM PMSF phenylmethylsulfonyl fluoride (PMSF), and TBS of pH 7.4, and passed ten times through a syringe needle (25-30G). After 60 min of incubation at 4 °C, cell lysates were centrifuged at 14 000 *g* (4 °C), and protein concentration in aspirated supernatants was determined by the Bradford method. 20 μg protein (final protein load per lane) aliquots were mixed 2:1 with 3× sample buffer composed of 62.5 mM Tris, 30% glycerol, 20.8 μM SDS, 50 mM DTT, and 0.03% w/v bromophenol blue and stored at −20 °C until needed. Then, standard electrophoresis using 10% polyacrylamide gel followed by standard blotting semidry procedure with

nitrocellulose membrane was performed. 5 μL of a biotinylated protein ladder (Cell Signaling, MA) was used to estimate the molecular weight of protein bands. The membrane was washed in 25 mL of TBS and blocked for 60 min in 5% low-fat milk or 2% BSA in TBS at room temperature before overnight incubation with 1:1000 primary rabbit-anti-mouse phospho-p38, phospho-SAPK/JNK, or anti-mouse phospho-ERK antibodies (Cell Signaling, MA) at 4 °C in TBS with 0.1% Tween 20 and 5% BSA. Proper washing with TBS containing 0.1% Tween 20 (TBS/T) preceded 60−120 min of incubation with anti-rabbit or anti-biotin, HRP-linked IgG (1:1000) (Cell Signaling, MA) in 5% low-fat milk or 2% BSA in TBS at room temperature. Finally, the membranes were washed in TBS/T, developed by chemiluminescence reaction and exposed to LAS-1000 CCD camera (Fujifilm). Then, the *Aida Image Analyzer* v 3.2.8. (Raytest, Germany) was used for data quantification.

The molecular weights of the respective kinases were used as internal standards of assay specificity. The molecular weights of detected phospho-proteins were determined by using protein markers, compared with the data provided by the manufacturer and found to be identical with respective MAPKs. Untreated cells were used as another internal control. The level of respective phosphorylated MAPK in the untreated cell was regarded as a reference value to which all other values were referred.

In Vitro Proliferation Assay. An EL-4 murine T-cell lymphoma cell line was grown in cultivation flasks at 37 °C with 5% CO_2 in RPMI 1640 medium supplemented with heat-inactivated 10% fetal calf serum (FCS), 2 mM L-glutamine, 50 mM 2-mercaptoethanol, 4.5 g/L glucose, 1 mM sodium pyruvate, 100 U/mL penicillin, and 100 μg/mL streptomycin. 2×10^5 cells/mL were cultured in Nunc 96-well flat-bottom plates with or without Dox.HCl, HYD, or PK1, and/or MAPK inhibitors. In order to exclude any effect of tested agents on noninhibited kinase pathways, EL-4 cells were pretreated with SP600125 (JNK inhibitor), SB203580 (p38 inhibitor), or with U0126 (ERK inhibitor) (Sigma) MAPK inhibitors for 30 min prior to addition of Dox, PK1, or HYD in 48 h proliferation assays. In short-term assays, which were performed in order to avoid indirect effects such as changes in gene expression that could happen during the 48 h inhibition, inhibitors were added 30 min prior to [^{3}H]thymidine addition in 5 h MAPK inhibition assays. All samples were tested in pentaplets. The plates were then cultured in 5% CO_2 for 48 h at 37 °C. 18.5 kBq of [^{3}H]-thymidine in 50 μL was added per well for the last 5 h of incubation. The cells were then harvested (Tomtec, Orange, CT) onto glass filter mats. After drying, the fiber filter was placed into a sample bag, a solid scintillator MeltiLex A (Wallac, Turcu, Finland) was applied, and the bags were sealed (Microsealer, Wallac). Counting was performed in a 1450 MicroBeta TriLux scintillation counter (Wallac).

Flow Cytometry. Control, Dox, HYD, or PK1 treated cells were incubated for 24 or 48 h with or without MAPK inhibitors, as described in the In Vitro Proliferation Assay section. To exclude any unspecific effect of tested agents on noninhibited kinase pathways, kinase inhibitors were added 30 min prior to Dox, HYD, or PK1 treatment. All agents were used at a concentration of $1 \times IC_{50}$. After incubation, cells were washed and collected at 4 °C in PBS. Then, 0.01 μg/mL of Hoechst 33258 (Molecular Probes, Oregon) in 10 μL was added. After 20 min of incubation at 4 °C in the dark, 50 μL of ice-cold PBS was added, and at least 50 000 cells were analyzed by FACS (LSRII, BD, San Jose, CA) with the use of *FowJo* software (Tree Star, San Carlos, CA).

Detection of Caspase 3 Activity. 5×10^6 EL-4 cells were incubated with tested samples at a concentration corresponding to $3 \times IC_{50}$ for different time intervals. After the incubation periods, the cells were washed twice with PBS, and the pellets were resuspended in 50 μL of Lysis buffer (Caspase 3 Assay Kit, Sigma). Cells were lysed on ice for 20 min, and 50 μL of supernatant was collected after centrifugation (12 000 rpm, 5 min, 4 °C). The Bradford method was used to determine protein concentration in cell lysates. The activity in cell lysates was measured spectrophotometrically at 405 nm using the Caspase 3 Assay Kit (Sigma). Caspase 3 activity was finally expressed as the amount of *p*-nitroaniline (nmol) released from synthetic Caspase 3 substrate/μg of total protein in cell lysate.

Binding Activity of NFκB. 5×10^6 EL-4 cells were incubated with tested samples at a concentration corresponding to $10 \times IC_{50}$ for different time intervals. After the incubation period, the cells were washed twice with PBS, and the pellets were resuspended in Lysis buffer (Nuclear Extraction Kit, Chemicon). Cells were lysed on ice and passed five times through syringe with small (25−30) gauge needle. After centrifugation at 8 000 *g* for 20 min at 4 °C, the pellets were resuspended in nuclear extraction buffer, and nuclei were disrupted by lysis with the use of a 27G needle. After centrifugation (16 000 *g*, 5 min, 4 °C), protein concentration was determined with the use of the Bradford method, and aliquots were frozen at −80 °C until needed. Then, the binding assay was performed with the use of the NFκB p50/p65 Assay Kit (Chemicon). Briefly, in the streptavidin-coated 96-well plate, the biotinylated DNA binding sequence for NFκB was mixed with nuclear extract. After addition of specific antibodies, the amount of p50 or p65 subunits was detected spectrophotometrically at 450/650 nm. The NFκB binding activity was finally expressed as percent of controls.

Intracellular Localization of Doxorubicin. 1×10^6 cells were incubated for 24 h with 5 μg/mL of free doxorubicin or an adequate equivalent contained in HYD conjugate. For PK1 conjugate, a concentration corresponding to 20 μg of doxorubicin per mL was used. The excitation of doxorubicin at 488 nm and emission at 560 nm was used to visualize the intracellular localization of doxorubicin under Leica TCS-SP2 Multiphoton Confocal Laser Scanning Microscope (TCS−MP). Intensity profiles were performed by using *AnalySIS* Software (SIS software, Germany).

RNase Protection Assay. Total RNA was extracted from EL-4 cells exposed to $3 \times IC_{50}$ for different time intervals using the RNA blue reagent (Top-Bio, Czech Republic). Total RNA was quantified specrophotometrically and dried by vacuum centrifugation for 1 h. To determine the levels of cytokine mRNA transcripts, a RiboQuant Multi-probe RNase Protection Assay System (Pharmingen) was used following the manufacturer's instruction. α[^{32}P] UTP (Izotop, Budapest, Hungary) was used for the synthesis of antisense RNA probe sets. ^{32}P-labeled protected fragments were resolved by electrophoresis on 5% long ranger gel (BMA, Rockland, Maine). Gels were dried and radioactivity visualized by phosphorimaging. The level of mRNA was evaluated for the genes involved in cell cycle regulation (cyclin A1, A2, B1, B2, C, D1, D2, D3, sin3, c-, n-, l-, b-myc, max, mad, mxi, mad3, mad4, mnt) and genes involved in apoptosis signaling (caspase 8, fasL, fas, fadd, fap, faf, trail, TNFRp55, tradd, rip, bcl-W, bfl-1, bcl-x, bak, bax, bcl-2, bad). For each individual sample including the control, mRNA levels for the genes listed above were expressed in % of mRNA level for the L32 housekeeping gene. Final results are presented as a ratio of mRNA levels for the particular gene in treated cells and nontreated controls.

Statistical Analysis. The significance of any differences obtained between experimental groups was evaluated by the Student's *t*-test. In all statistical analyses, significance was assessed at the $P \leq 0.05$ level.

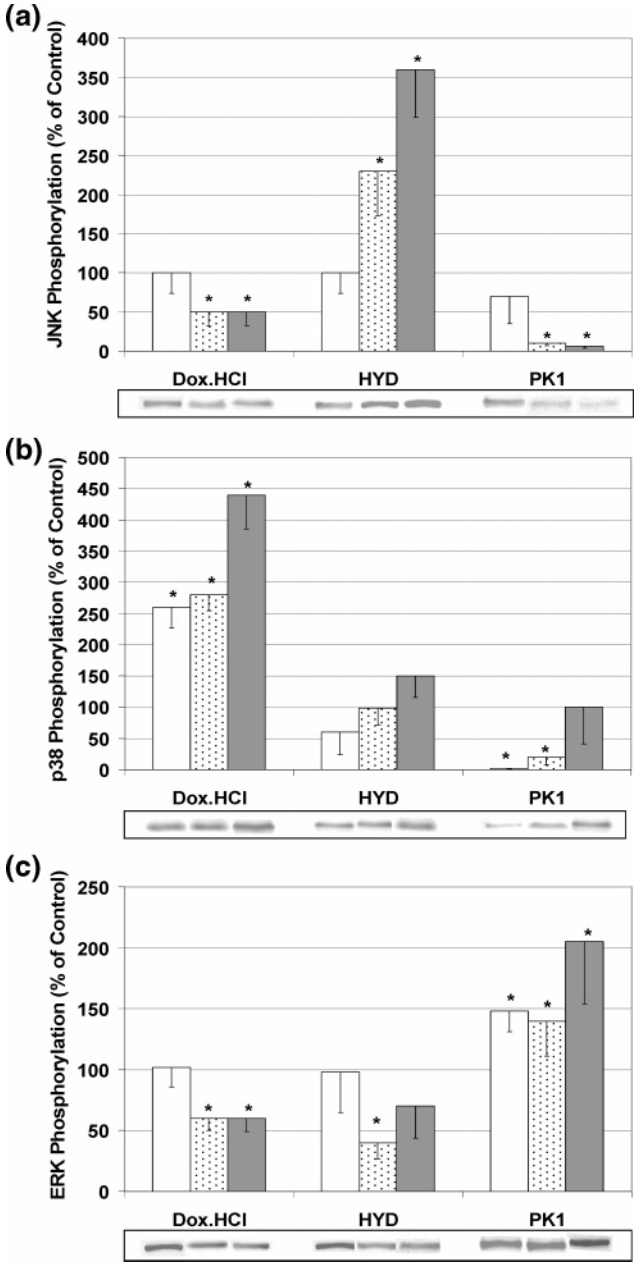


Figure 1. Phosphorylation of MAPKs in EL-4 cells treated with different forms of doxorubicin. Phosphorylation of JNK (a), p38 (b), and ERK (c) MAP kinases in lysates of EL-4 cells after 5 min (empty bars), 30 min (dotted bars), or 120 min (full bars) treatment with different forms of doxorubicin (50 × IC_{50}) relative to control cells (100%). Representative western blot bands are shown for each sample below the corresponding column. Dox.HCl, free doxorubicin; HYD, doxorubicin bound to HPMA copolymer via hydrolytically degradable bond; PK1, doxorubicin bound to HPMA copolymer via enzymatically cleavable bond. *The difference against control was significant at $P < 0.05$ (Student's *t*-test).

RESULTS

MAPKs Phosphorylation. In preliminary studies, we used the concentrations of 3×, 10×, and 50× IC_{50} of Dox, HYD, and PK1 on MAPK phosphorylation (not shown). The highest phosphorylation rates were achieved with the highest concentration of 50 × IC_{50}, and it was used in assays with phosphorylated JNK (Figure 1a), p38 (Figure 1b), and ERK (Figure 1c). Incubation of EL-4 cells with free doxorubicin stimulated phosphorylation of p38 kinase up to 450% of control, whereas it inhibited phosphorylation of JNK and ERK almost by 50% in comparison with control cells. The maximum stimulation of p38 phosphorylation was achieved during the longest incubation lasting 120 min, and inhibition of JNK and ERK was acheived during both the 30 and 120 min incubation periods. Hydrazone conjugate (HYD) stimulated the phosphorylation of the stress-activated protein kinase JNK up to 360% of controls in the 2 h incubation period. ERK phosphorylation was inhibited after both the 30 and 120 min incubation periods with HYD, whereas a slight inhibition of p38 phosphorylation turned into minute enhancement during the long-term incubation. Phosphorylation of ERK was enhanced up to 205% of controls after incubation with PK1 conjugate. PK1 achieved an almost total (95%) inhibition of JNK phosphorylation. During incubation of EL-4 cells with PK1 conjugate, previous almost absolute inhibition of p38 phosphorylation turned into the same level of phoshorylation as that of the control after longer incubation.

Table 1. Cytostatic Effects of Free Doxorubicin, HPMA-Bound Doxorubicin, and MAPK Inhibitors[a]

sample	IC_{50} concentration (μM) ± S.D.
Dox.HCl	0.014 ± 0.001
HYD	0.066 ± 0.013
PK1	45.970 ± 3.844
SP600125	6.36 ± 0.921
SB203580	8.12 ± 0.725
U0126	38.00 ± 3.453

[a] IC_{50} values determined in EL-4 cell line for free doxorubicin, HYD, PK1 conjugate, and JNK inhibitor SP600125, p38 inhibitor SB203580, and inhibitor of MEK/ERK U0126.

EL-4 Cell Proliferation Assay and IC_{50} Values. IC_{50} values summarized in Table 1 represent the concentration of doxorubicin or MAPK inhibitors required for 50% inhibition of EL-4 cell proliferation after 48 h. Free doxorubicin exhibited the highest cytostatic effect at 0.014 μM, IC_{50} value of hydrazone conjugate was 0.066 μM (doxorubicin equivalent), while PK1 conjugate showed the lowest cytostatic effect of 45.97 μM. IC_{50} of SP600125, SB203580, and U0126 were 6.36 μM, 8.12 μM, and 38 μM, respectively.

After 48 h of incubation with 1 × IC_{50} value of SP600125 (JNK pathway inhibitor), EL-4 cells proliferated about 50% less when coincubated with or without hydrazone or PK1. On the other hand, when coincubated with free doxorubicin, EL-4 cells proliferated twice more in comparison with control cells incubated only with free doxorubicin without SP600125. EL-4 cells incubated for 48 h with free doxorubicin or HYD conjugate followed by 5 h of JNK inhibition with SP600125 proliferated about 50% less than cells without SP600125 inhibitor with free doxorubicin or HYD conjugate. This short-term, 5 h JNK pathway inhibition did not have any effect on proliferation of control or PK1-treated cells (Figure 2a).

Neither 5 (not shown) nor 48 h inhibition of both the p38 pathway by SB203580 (Figure 2b) and ERK pathway by U0126 (Figure 2c) caused any significant differences in the proliferation of controls or cells treated with doxorubicin, HYD, or PK1. In those incubation assays, proliferation of all cells was inhibited approximately by 50% relative to corresponding untreated control cells.

FACS Analysis of Cell Viability. Inhibition of the JNK pathway by SP600125 (Figure 3a) for 48 h had no significant effect on cellular viability in controls, HYD-, or PK1-treated cells. Coincubation of EL-4 cells with doxorubicin and SP600125 reduced cellular viability up to 86% relative to the cells with uninhibited JNK pathway, whereas cells exposed only to Dox.HCl reduced their viability by approximately up to 60%. On the other hand, inhibition of the JNK pathway had no significant effect on viability of cells exposed to HYD or PK1 conjugates. A 24 h inhibition of the JNK pathway did not significantly affect the number of dead cells in controls or any tested samples.

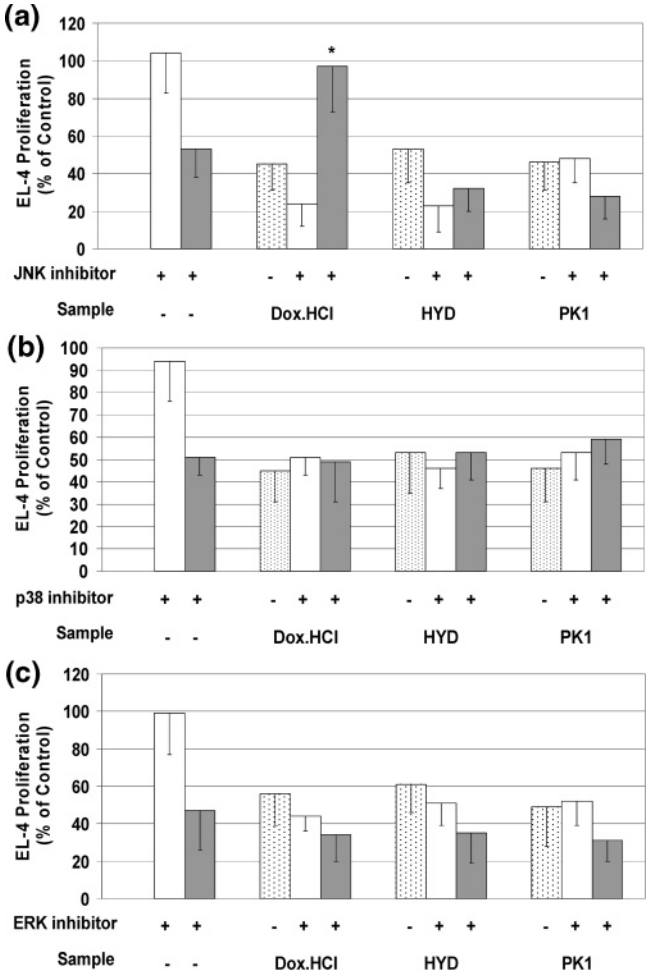


Figure 2. Proliferative activity of EL-4 cells incubated with different forms of doxorubicin and with/without MAPK inhibitors. Proliferation of EL-4 cells after a 48 h treatment with different forms of doxorubicin ($1 \times IC_{50}$) relative to control cells (100%). Dox.HCl, free doxorubicin; HYD, doxorubicin bound to HPMA copolymer via hydrolytically degradable bond; PK1, doxorubicin bound to HPMA copolymer via proteolytically cleavable bond. Cells were coincubated either for 5 h (empty bars) or for 48 h (full bars) with MAPKs inhibitors ($1 \times IC_{50}$) or without MAPK inhibitors (dotted bars). Inhibition of JNK (a), p38 (b), or inhibition of ERK (c). *The difference against the group without inhibitor but exposed to the same form of doxorubicin was significant at $P < 0.05$ (Student's *t*-test).

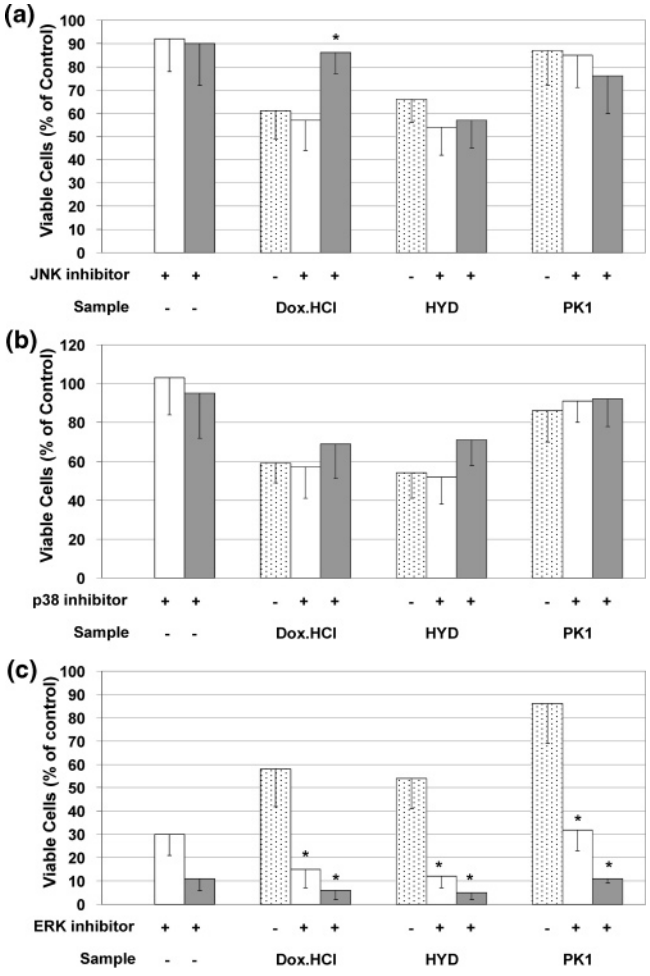


Figure 3. Viability of EL-4 cells incubated with different forms of doxorubicin and with/without MAPK inhibitors. Viability of EL-4 cells after a 48 h treatment with different forms of doxorubicin ($1 \times IC_{50}$) relative to control cells (100%). Dox.HCl, free doxorubicin; HYD, doxorubicin bound to HPMA copolymer via hydrolytically degradable bond; PK1, doxorubicin bound to HPMA copolymer via enzymatically cleavable bond. Cells were coincubated either for 24 h (empty bars) or for 48 h (full bars) with MAPKs inhibitors ($1 \times IC_{50}$) (a) inhibiting JNK, (b) p38, or (c) inhibiting ERK. Dotted bars show cells without inhibited MAPK pathway incubated with different forms of doxorubicin. *The difference against the group without inhibitor, but exposed to the same form of doxorubicin was significant at $P < 0.05$ (Student's *t*-test).

Inhibition of the p38 kinase pathway (Figure 3b) for 24 or 48 h did not significantly affect the viability of control cells nor of those treated with Dox.HCl, HYD, and PK1 conjugate when compared to cells exposed to free doxorubicin or HPMA conjugates without inhibitor.

U0126 inibitor had been shown to have toxic effects even on control EL-4 cells incubated in cultivation media only. Coincubation with free doxorubicin or HPMA conjugate enhanced U0126 toxicity. Cells exposed to Dox.HCl, HYD, or PK1 conjugate showed reduced viability by 94%, 95%, and 89%, respectively, in 48 h incubation. 24 h incubation showed 85%, 88%, and 68% viability reduction in Dox.HCl, HYD, and PK1 treated cells, respectively (Figure 3c).

Caspase 3 Activity. Caspase 3 was rapidly activated in EL-4 cells after treatment with free doxorubicin or hydrazone conjugate, and its activity increased more than 7- and 5-fold relative to controls, respectively. PK1 conjugate did not enhance the activity of this effector caspase even over an incubation period as long as 30 h (Figure 4a).

NFκB Binding Activity. The NFκB p50 binding activity was significantly reduced in cell lysates after treatment with free doxorubicin and hydrazone conjugate at all tested time intervals. The lowest binding was detected in the longest 16 h treatment and was as low as 43% with Dox.HCl and 42% with hydrazone conjugate, as compared with controls. On the other hand, in PK1-treated cells, the p50 binding was significantly reduced only after 4 and 8 h incubation (Figure 4b). The binding activity of the p65 subunit was not significantly changed either with Dox.HCl and with hydrazone, or in PK1-treated cells (data not shown).

Intracellular Localization. The confocal laser scanning microscopy visualizing the intracellular localization of free or HPMA-conjugated doxorubicin in native cells showed differences in the intracellular fate of these agents. The fluorescence of free doxorubicin was localized mainly inside the nucleus and endosomes, whereas the fluorescence of doxorubicin in the PK1 conjugate was clearly localized in cell membranes (cytoplasmic, nuclear, endosomal, Golgi apparatus, etc.). The doxorubicin contained in the hydrazone conjugate was shown to be localized in endosomes and lysosomes, and released doxorubicin was detected inside the nucleus (Figure 4c).

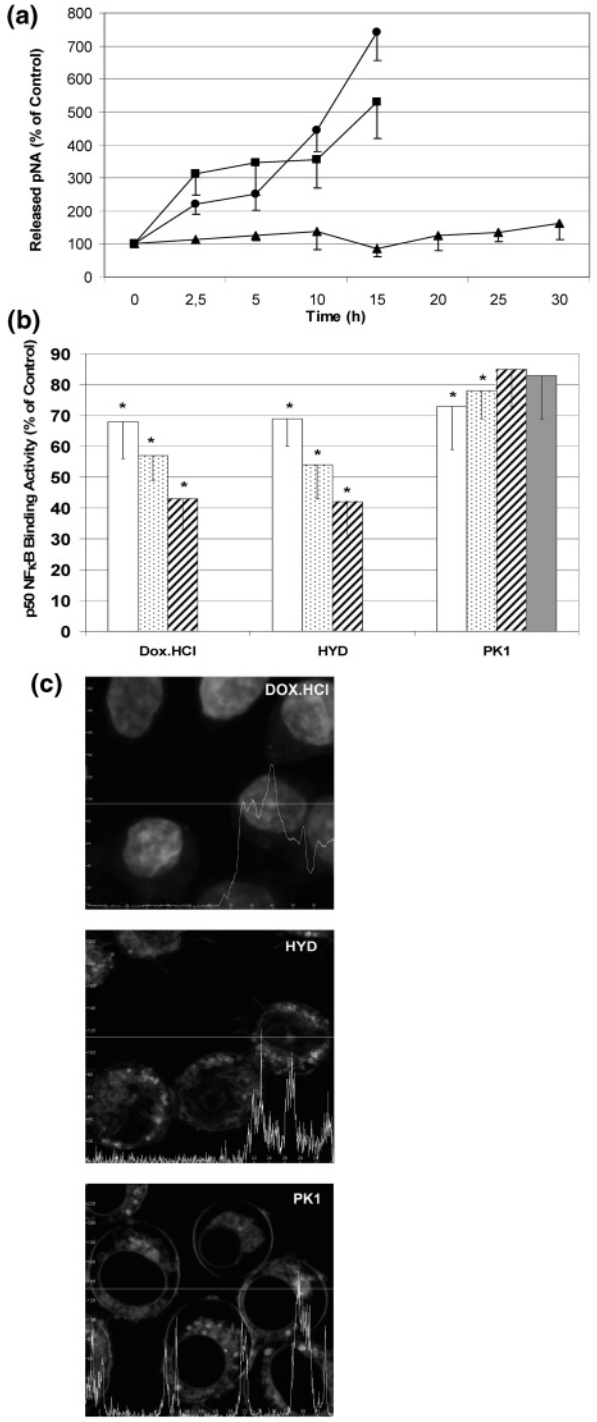


Figure 4. Caspase 3 activity, binding activity of p50 subunit of NFκB and intracellular distribution in EL-4 cells after treatment with different forms of doxorubicin. (a) The activity of caspase 3 in cells incubated with different forms of doxorubicin ($3 \times IC_{50}$). Caspase 3 activity is expressed as the amount of *p*-nitroaniline (nmol) released from synthetic caspase 3 substrate/μg of total protein in cell lysate and are related to control (control cells = 100%). (b) Binding activity of p50 subunit of NFκB in cells treated with $10 \times IC_{50}$ of different forms of doxorubicin for 4 (empty bars), 8 (dotted bars), 16 (hatched bars), or 24 (full bars) hours relative to control cells (100%). *The difference against control was significant at $P < 0.05$ (Student's *t*-test). (c) Intracellular localization of free doxorubicin, hydrazone conjugate, both with 5 μg of doxorubicin per mL and with PK1 conjugate with 20 μg of doxorubicin per mL in EL-4 cells after 24 h of treatment. Cross-section lines represent the intensity profiles demonstrating the fluorescence of doxorubicin. Free doxorubicin (-●-, Dox.HCl), doxorubicin bound to HPMA copolymer via hydrolytically degradable bond (-■-, HYD), doxorubicin bound to HPMA copolymer via proteolytically cleavable bond (-▲-, PK1).

Expression of Genes Involved in the Regulation of Cell Cycle and Apoptosis. Expression of selected mRNA for genes involved in the regulation of cell cycle and apoptosis was determined in EL-4 cells treated with $3 \times IC_{50}$ values of tested conjugates. The results for the most important genes with significantly altered expression are shown in Figure 5. Expression of an important proapoptotic gene bad was elevated up to 112% and 127% after incubation with free doxorubicin and the hydrazone conjugate, respectively, whereas the PK1 conjugate significantly reduced the level of mRNA for this gene to 48%, as compared with controls. Expression of another gene involved in apoptosis signaling − fas, were elevated after incubation with all tested forms of doxorubicin. The enhancement caused with the PK1 conjugate is significantly lower and more time-dependent in comparison with free doxorubicin or hydrazone conjugate. We did not observe any changes in the expression of bcl-2 family members tested, nor in the expression of bax and bak.

PK1-treated cells exhibited significantly increased levels of c-myc and max that are important for cell cycle progression. This nearly 150% and 120% increase of c-myc and max, respectively, turned into inhibition later on. Free doxorubicin and HYD conjugate quickly and strongly reduced the amount of those two genes.

The expression of all tested cyclines was quickly reduced after incubation with Dox.HCl and HYD conjugated, but this inhibition was slighter and slower after incubation of EL-4 cells with PK1 conjugates. Cyclines A2 and D2 are shown as typical indicators of action of tested forms of doxorubicin on expression of cycline genes.

DISCUSSION

The MAPK transfers signals from the cell membrane to the nucleus by phosphorylation of transcription factors like Elk-1. JNK, p38, and ERK are serine/threonine kinases that are activated by dual phosphorylation of the threonine/tyrosine motif by upstream kinases (*17*). Using specific antibodies, we found that Dox.HCl, HYD, and PK1 conjugates activate different MAPKs. Free doxorubicin and HYD activated the p38 and JNK, respectively. These kinases are typically activated in response to cell stress, DNA damage, and precede apoptotic cell death (*18*). Moreover, both the free drug and HYD conjugate enhanced the expression of proapoptotic gene bad and increased the activity of caspase 3, an effector apoptotic caspase whose activation is an irreversible step in apoptotic cell death. Both the Dox.HCl and HYD conjugate also increased the expression of Fas and thus made the cells more sensitive to FasL-mediated apoptotic cell death. These two agents also inhibited the activation of the p50 subunit of NFκB transcription factor that provides antiapoptotic signals.

On the other hand, the PK1 conjugate activated the ERK that is usually associated with cell growth and differentiation (*17*). In contrast to free doxorubicin and HYD conjugate, the PK1 conjugate reduced the expression of bad, did not enhance the activity of caspase 3 (up to 30 h of incubation), and was not inhibitory for p50 activation in longer time intervals. Surprisingly, neither free drug nor HPMA conjugates changed the expression of antiapoptotic genes as well as the expression of cyclin-dependent kinases (data not shown).

The mode of action of the HYD conjugate resembles that of free doxorubicin, as doxorubicin is released from the HYD conjugate by hydrolysis, a relatively fast process, and it acts as free doxorubicin by triggering apoptosis. This explains the similar mode of action of these agents in our study that has been demonstrated previously with another cell line (*5*). In contrast, the mechanism of action of the PK1 conjugate is less clear. Recently, we have shown new data which do not support the enzymatic degradation of PK1 conjugate in vivo and thus

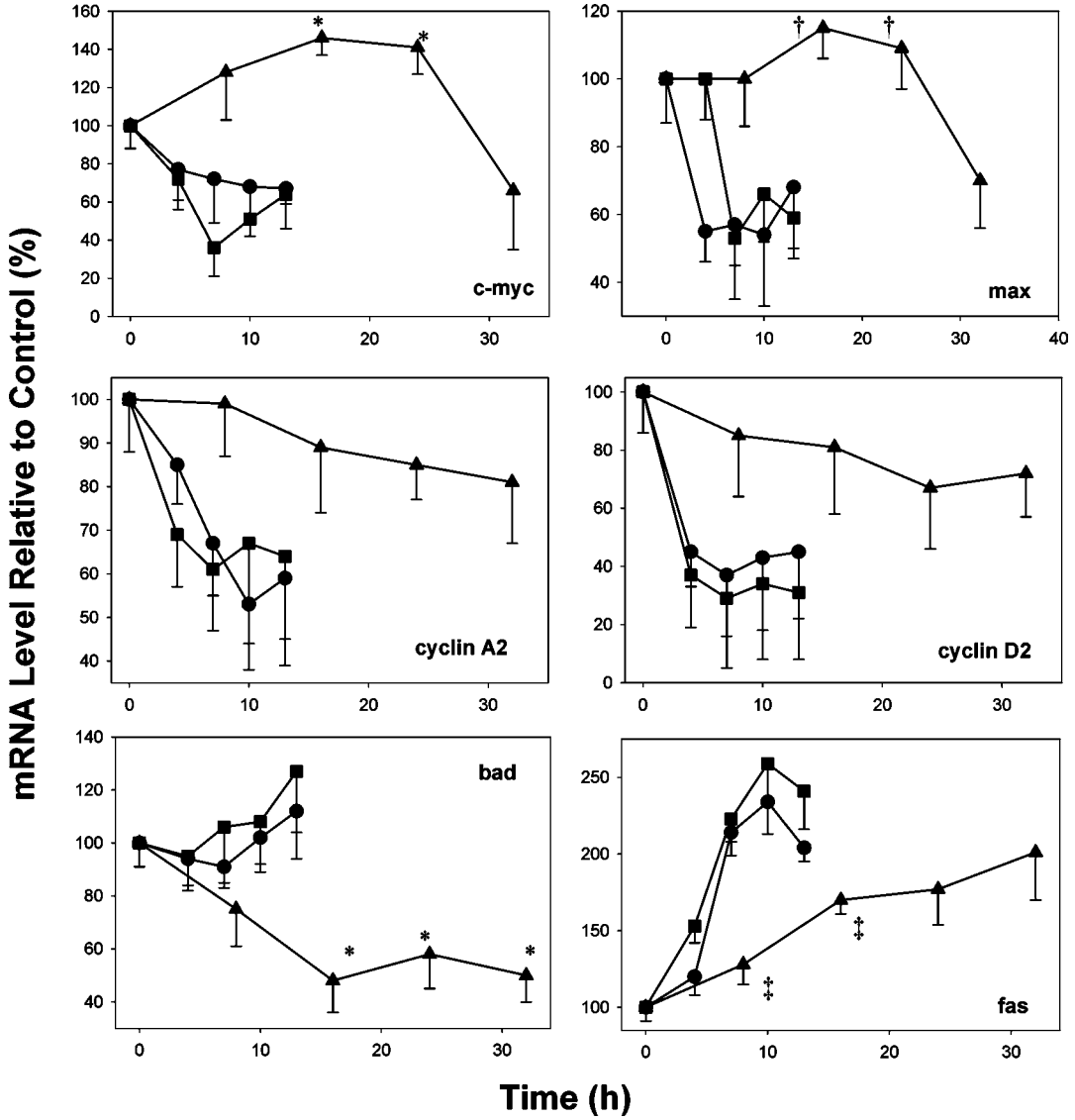


Figure 5. Expression of selected genes on mRNA level in EL-4 cells treated with different forms of doxorubicin. The level of mRNA for selected genes determined by RNAse protection assay in the EL-4 cells after treatment with different forms of doxorubicin ($3 \times IC_{50}$). For each individual sample including control, mRNA levels were expressed in % of mRNA level for L32 housekeeping gene. Final results are presented as a ratio of mRNA levels for the particular gene in treated cells and non-treated controls. Free doxorubicin (-●-), doxorubicin bound to HPMA copolymer via hydrolytically degradable bond (-■-), doxorubicin bound to HPMA copolymer via proteolytically cleavable bond (-▲-). *The difference against the free doxorubicin and hydrazone-treated groups was significant at $P < 0.05$. †The difference against the free doxorubicin and hydrazone (except for the 4 h incubation period with hydrazone) treated groups was significant at $P < 0.05$. ‡The difference against the free doxorubicin and hydrazone (except for the 4 h incubation period with both free doxorubicin and hydrazone) treated groups was significant at $P < 0.05$ (Student's *t*-test).

show that the release of free doxorubicin is not a dominant mechanism (*15*). Instead, we suggest that the whole PK1 conjugate interacts with cell membranes, causing their damage (changed permeability, blockade of intracellular trafficking, etc.) and subsequently resulting in cell death (*10, 11*). These data are supported by our recent finding that both the Dox.HCl and HYD conjugate trigger stress-activated signaling pathways JNK and p38 and strongly induce apoptosis. On the other hand, the PK1 conjugate activates ERK and suppresses the activation of JNK. Thus, PK1 shows an opposite pattern in activation of different MAPKs in comparison to Dox.HCl and HYD.

The data showing the effect of free or HPMA-conjugated doxorubicin on expression of genes involved in cell cycle (c-myc, max, and cyclines) demonstrate that Dox.HCl and HYD conjugate inhibit cell proliferation quickly, whereas the PK1 conjugate does not inhibit the cell cycle efficiently within the first 24 h.

Further, we used inhibitors specific for JNK, p38, and ERK to evaluate their impact on proliferation and cell death. These inhibitors alone showed some inhibition of proliferation which is shown in Table 1. Doxorubicin-treated cells with inhibited JNK proliferated more than twice as much as the cells without JNK inhibitor. Moreover, the viability of the cells with inhibited JNK was higher than that of cells treated only with free doxorubicin, which clearly shows that JNK plays a key role in mediating the cytostatic and cytotoxic effect of Dox.HCl. On the other hand, the death of control cells and HPMA conjugate treated cells was not significantly changed after treatment with the JNK inhibitor. It seems that, in doxorubicin treated cells, the JNK pathway triggers a lethal, probably proapoptotic signal, and blocking of this signal protects cells against doxorubicin-induced cell death (*19*). In contrast, this important role of the JNK pathway was not seen in cells treated with PK1 and even with HYD conjugate. This is surprising, because the HYD conjugate has been reported to possess properties very similar to the free drug (*5*). As shown previously with different cell lines (*10, 11*), the intracellular distribution of the PK1 conjugate greatly differs from that of free doxorubicin and the hydrazone

conjugate. These data discussed previously support our present results and show one of the possible mechanisms of action.

Furthermore, we used a confocal laser scanning microscopy to visualize the intracellular localization of doxorubicin in living cells exposed to different forms of doxorubicin. We demonstrated significant differences in the intracellular fate of these agents. The cells treated with free doxorubicin showed localization of the drug mainly inside the nucleus and acidic organelles (*10*). The fluorescence pattern within cells incubated with hydrazone conjugate was similar to that of the free drug, and the strong signal within the nucleus verified the effective release of doxorubicin from its carrier. By contrast, the fluorescence signal in cells treated with the PK1 conjugate was clearly localized almost solely within cell membranes (cytoplasmic, nuclear, endosomal, Golgi apparatus, etc.), and we were not able to detect any nuclear fluorescence. The latter finding indicates that PK1 conjugate was not intracellularly degraded and doxorubicin was not released in sufficient amount to be detected within cell nucleus. This seems to be in contradiction to the data published by Duncan's team (*20*), as well as two other groups who demonstrated nuclear localization of doxorubicin presumably released from the PK1 conjugate (*21, 22*). To put these conflicting data into accord, we propose that the differences might be due to the use of different cancer cell lines for the studies, as different cells have different trafficking pathways and the level of enzymes capable of cleaving doxorubicin from its carrier. Another explanation might be that doxorubicin detected within the nucleus was due to a contamination of the PK1 conjugate by free doxorubicin rather than to its intracellular release from the conjugate. This assumption is based on the fact that Duncan's group (*20*) reported that the PK1 conjugate used in their study contained 0.39% of free doxorubicin, while the content of free doxorubicin in our PK1 conjugate is up to the limit of 0.1% of total doxorubicin. In fact, the content of free doxorubicin in the PK1 conjugate synthesized by us is probably much lower, but the 0.1% content of free doxorubicin corresponds to doxorubicin concentration which is near the detection limit of the analytical assay. Unfortunately, the two remaining papers (*21, 22*) demonstrating the doxorubicin release from the PK1 conjugate do not even indicate free doxorubicin content in their PK1 conjugates and therefore neither disprove nor corroborate our hypothesis.

To sum up, we demonstrated that the conjugation of doxorubicin to HPMA copolymer carrier modulates the mechanism of its intracellular action. As mentioned before (*5*), the intracellular action of hydrazone conjugate resembles that of free doxorubicin, but in this study we have found different roles for MAP kinases. The PK1 conjugate has different and in some parameters opposite mechanisms of action from both free doxorubicin and the hydrazone conjugate. Since PK1 triggers different intracellular pathways involved in regulation of cell death and/or proliferation than free doxorubicin, one can hypothesize that there can also be a different spectrum of tumors sensitive to PK1. As an example, Dox.HCl is not used for the treatment of colorectal cancer at all, but PK1 showed some therapeutic effect in patients with this type of cancer (*13*). If such a hypothesis is shown to be true, the finding that the cancerostatic activity of a particular cytostatic drug toward different types of tumor can be modified by binding to a polymeric carrier is both scientifically interesting and important for the development of new polymer-bound drugs for treatment of tumors resistant to this drug in the free form.

ACKNOWLEDGMENT

This research was supported by the Grant Agency of the Czech Republic (grants 305/05/2268 and 310/03/H147), the grant of MEYS CR 1M0505, and by the Institutional Research Concept AV0Z50200510.

LITERATURE CITED

(1) Rihova, B., Bilej, M., Vetvicka, V., Ulbrich, K., Strohalm, J., Kopecek, J., and Duncan, R. (1989) Biocompatibility of N-(2-hydroxypropyl) methacrylamide copolymers containing adriamycin. Immunogenicity, and effect on haematopoietic stem cells in bone marrow in vivo and mouse splenocytes and human peripheral blood lymphocytes in vitro. *Biomaterials 10*, 335−42.

(2) Maeda, H. (2001) The enhanced permeability and retention (EPR) effect in tumor vasculature: the key role of tumor-selective macromolecular drug targeting. *Adv. Enzyme Regul. 41*, 189−207.

(3) Rihova, B. (1995) Antibody-targeted polymer-bound drugs. *Folia Microbiol. (Prague, Czech Repub.) 40*, 367−84.

(4) Minotti, G., Menna, P., Salvatorelli, E., Cairo, G., and Gianni, L. (2004) Anthracyclines: molecular advances and pharmacologic developments in antitumor activity and cardiotoxicity. *Pharmacol. Rev. 56*, 185−229.

(5) Kovar, M., Kovar, L., Subr, V., Etrych, T., Ulbrich, K., Mrkvan, T., Loucka, J., and Rihova, B. (2004) HPMA copolymers containing doxorubicin bound by a proteolytically or hydrolytically cleavable bond: comparison of biological properties in vitro. *J. Controlled Release 99*, 301−14.

(6) Etrych, T., Chytil, P., Jelinkova, M., Rihova, B., and Ulbrich, K. (2002) Synthesis of HPMA copolymers containing doxorubicin bound via a hydrazone linkage. Effect of spacer on drug release and in vitro cytotoxicity. *Macromol. Biosci. 2*, 43−52.

(7) Mrkvan, T., Sirova, M., Etrych, T., Chytil, P., Strohalm, J., Plocova, D., Ulbrich, K., and Rihova, B. (2005) Chemotherapy based on HPMA copolymer conjugates with pH-controlled release of doxorubicin triggers anti-tumor immunity. *J. Controlled Release 110*, 119−129.

(8) Kopecek, J., Rejmanova, P., Strohalm, J., Ulbrich, K., Rihova, B., Chytrý, V., Duncan, R., and Lloyd, J. B. (1991) Synthetic polymeric drugs. U.S. Patent 5,037,883.

(9) Minko, T., Kopeckova, P., and Kopecek, J. (2001) Preliminary evaluation of caspases-dependent apoptosis signaling pathways of free and HPMA copolymer-bound doxorubicin in human ovarian carcinoma cells. *J. Controlled Release 71*, 227−37.

(10) Hovorka, O., St'astny, M., Etrych, T., Subr, V., Strohalm, J., Ulbrich, K., and Rihova, B. (2002) Differences in the intracellular fate of free and polymer-bound doxorubicin. *J. Controlled Release 80*, 101−17.

(11) Hovorka, O., Etrych, T., Šubr, V., Strohalm, J., Ulbrych, K., and Říhová, B. (2005) HPMA based macromolecular therapeutics: internalization, intracellular pathway and cell death depend on the character of covalent bond between the drug and the peptidic spacer and also on spacer composition. *J. Drug Targeting 14*, 391−403.

(12) Demoy, M., Minko, T., Kopeckova, P., and Kopecek, J. (2000) Time- and concentration-dependent apoptosis and necrosis induced by free and HPMA copolymer-bound doxorubicin in human ovarian carcinoma cells. *J. Controlled Release 69*, 185−196.

(13) Vasey, P. A., Kaye, S. B., Morrison, R., Twelves, C., Wilson, P., Duncan, R., Thomson, A. H., Murray, L. S., Hilditch, T. E., Murray, T., Burtles, S., Fraier, D., Frigerio, E., and Cassidy, J. (1999) Phase I clinical and pharmacokinetic study of PK1 [N-(2-hydroxypropyl)-methacrylamide copolymer doxorubicin]: first member of a new class of chemotherapeutic agents−drug-polymer conjugates. *Clin. Cancer Res. 5*, 83−94.

(14) Rihova, B. (2003) Antibody-targeted HPMA copolymer-bound anthracycline antibiotics. *Drugs Future 28*, 1189−1210.

(15) Ulbrich, K., Subr, V., Strohalm, J., Plocova, D., Jelinkova, M., and Rihova, B. (2000) Polymeric drugs based on conjugates of synthetic and natural macromolecules. I. Synthesis and physicochemical characterisation. *J. Controlled Release 64*, 63−79.

(16) Etrych, T., Jelinkova, M., Rihova, B., and Ulbrich, K. (2001) New HPMA copolymers containing doxorubicin bound via pH-sensitive linkage: synthesis and preliminary in vitro and in vivo biological properties. *J. Controlled Release 73*, 89−102.

(17) Kyosseva, S. (2004) Mitogen-activated protein kinase signaling. *Int. Rev. Neurobiol. 59*, 201−20.

(18) Wada, T., and Penninger, J. (2004) Mitogen-activated protein kinases in apoptosis regulation. *Oncogene 23*, 2838−49.

(19) Brantley-Finley, C., Lyle, C., Du, L., Goodwin, M., Hall, T., Szwedo, D., Kaushal, G., and Chambers, T. (2003) The JNK, ERK and p53 pathways play distinct roles in apoptosis mediated by the antitumor agents vinblastine, doxorubicin, and etoposide. *Biochem. Pharmacol. 66*, 459−69.

(20) Seib, F. P., Jones, A. T., and Duncan, R. (2006) Establishment of subcellular fractionation techniques to monitor the intracellular fate of polymer therapeutics I. Differential centrifugation fractionation B16F10 cells and use to study the intracellular fate of HPMA copolymer - doxorubicin. *J. Drug Targeting 14*, 375−90.

(21) Nan, A., Ghandehari, H., Hebert, C., Siavash, H., Nikitakis, N., Reynolds, M., and Sauk, J. J. (2005) Water-soluble polymers for targeted drug delivery to human squamous carcinoma of head and neck. *J. Drug Targeting 13*, 189−97.

(22) Omelyanenko, V., Kopeckova, P., Gentry, C., and Kopecek, J. (1998) Targetable HPMA copolymer-adriamycin conjugates. Recognition, internalization, and subcellular fate. *J. Controlled Release 53*, 25−37.

BC060246E

Peptidyl Molecular Imaging Contrast Agents Using a New Solid-Phase Peptide Synthesis Approach

Byunghee Yoo and Mark D. Pagel*

Case Center of Imaging Research and Department of Biomedical Engineering, Case Western Reserve University, 10900 Euclid Avenue, Cleveland, Ohio 44106. Received August 11, 2006; Revised Manuscript Received November 1, 2006

A versatile method is disclosed for solid-phase peptide synthesis (SPPS) of molecular imaging contrast agents. A DO3A moiety was derivatized to introduce a CBZ-protected amino group and then coupled to a polymeric support. CBZ cleavage with Et_2AlCl/thioanisole was optimized for SPPS. Amino acids were then coupled to the aminoDOTA-loaded resin using conventional stepwise Fmoc SPPS to create a product with DOTA coupled to the C-terminus of the peptide. In a second study, the DO3A moiety was coupled to a glycine-loaded polymeric support, and amino acids were then coupled to the amino-DOTA-peptide-loaded resin using SPPS to incorporate DOTA within the peptide sequence. The peptide-(Tm^{3+}-DOTA) amide showed a paramagnetic chemical exchange saturation transfer (PARACEST) effect, which demonstrated the utility of this contrast agent for molecular imaging. These results demonstrate the advantages of exploiting SPPS methodologies through development of unique DOTA derivatives to create peptide-based molecular imaging contrast agents.

INTRODUCTION

Macrocyclic metal chelates using DOTA[1] (1,4,7,10-tetraazacyclododecane-*N*,*N*′,*N*″,*N*‴-tetraacetic acid) are often administered to patients and animal models to create or enhance contrast in biomedical molecular imaging studies (*1*, *2*). More recently, metal−DOTA chelates have been conjugated to peptides to affect the in vivo pharmacokinetics of the metal−DOTA imaging agent over a wide range of spatial scales. For example, subcellular scales can be assessed by coupling DOTA to membrane-penetrating peptides (*3*, *4*), cellular scales are assessed with cell receptor-targeting peptides attached to DOTA (*5*), and tissue scales are investigated with DOTA-bound peptides that interact with extracellular matrices (*6*) and have dramatically altered renal clearance rates (*7*). Numerous other applications have been reported, including peptide-DOTA probes for multimodality imaging studies (*8*−*10*).

To synthesize these peptidyl molecular imaging contrast agents, the carboxylates of DOTA have been conjugated to the amines of peptides, including the N-terminus of the backbone and the side chain of lysine (*5*, *11*−*19*). Other DOTA derivatives have been devised for conjugation to peptide amino groups, such as succinimide DOTA derivatives (*20*) and isothiocyanato DOTA derivatives (*21*). Unnatural amino acid derivatives have also been developed to couple DOTA to peptidyl amines, such as *p*-NH_2-phenylalanine (*13*) and diaminopropionic acid residues (*15*).

Standard solid-phase peptide synthesis (SPPS) methods have been used to couple DOTA to the backbone N-terminus of peptides bound to a PEGA Rink amide resin (*5*, *14*−*19*). Similar SPPS methodologies can be used to couple DOTA to other side chain amines of resin-bound peptides (*13*, *15*). However, coupling DOTA only to N-terminus or side chain amines of peptides can limit synthesis methodologies and may compromise the utility of the peptidyl contrast agent for molecular imaging applications (*22*). To alleviate this limitation, we developed an amine-derivatized DOTA (aminoDOTA) that can couple to the carboxylates of peptides (Scheme 1). We linked the aminoDOTA to a resin **8a** for use in standard SPPS methodologies in order to synthesize peptide-DOTA imaging agents with DOTA coupled to the C-terminus of the peptide (Scheme 2). We also linked aminoDOTA to an amino acid residue on the resin **8b** to demonstrate that this methodology can incorporate DOTA at any location within the peptide backbone (Schemes 1 and 2). Lanthanide chelates of the peptide-DOTA amide products were shown to affect magnetic resonance signals, thereby demonstrating that the peptide-bound DOTA moiety has practical utility for molecular imaging. This new approach greatly expands the opportunities to create peptide-based molecular imaging probes and is completely compatible with standard SPPS methods for facile production of products with good yield and high purity.

EXPERIMENTAL PROCEDURES

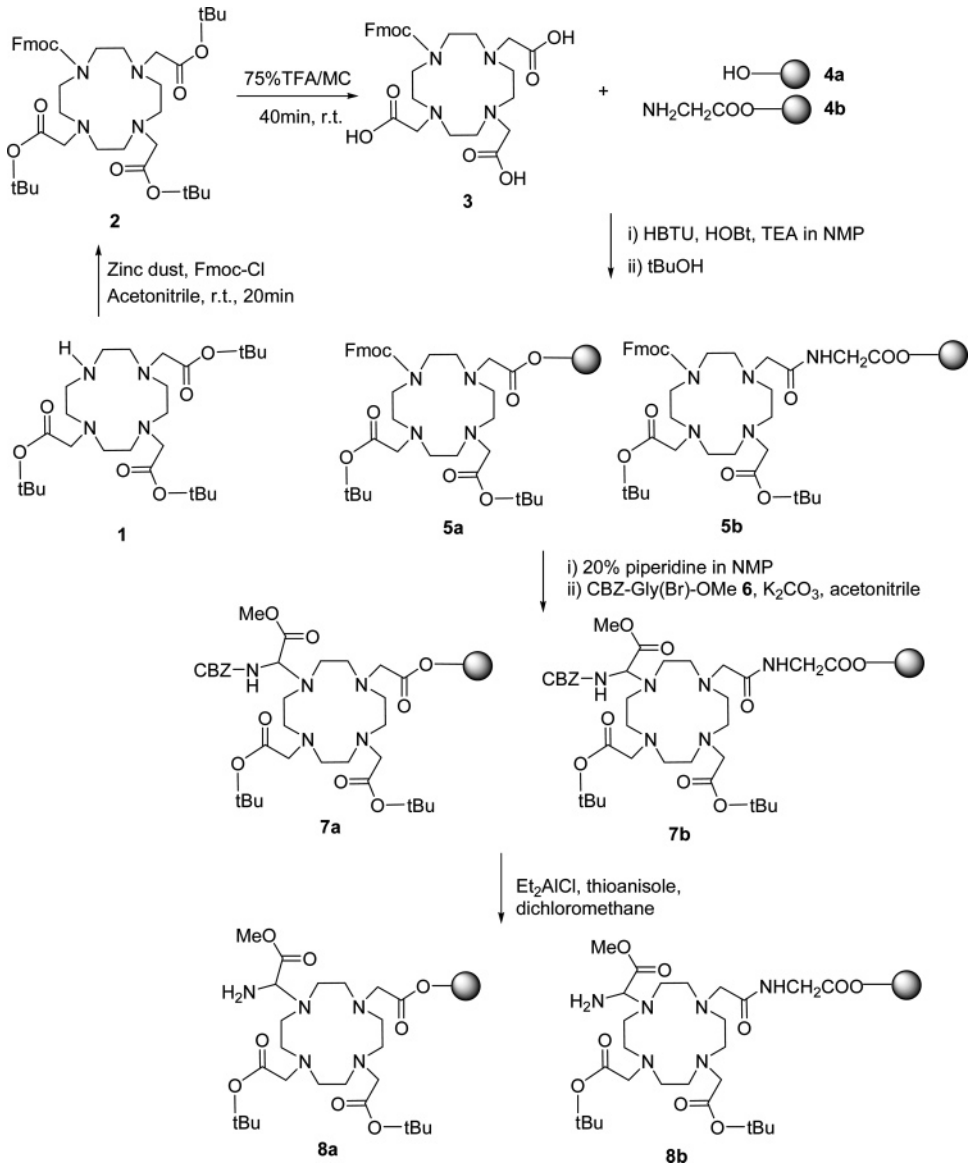
General Methods. All reactions were carried out under argon atmosphere. Dichloromethane (DCM) and carbon tetrachloride (CCl_4) were freshly distilled over phosphorus pentoxide (P_2O_5). Acetonitrile (ACN) was distilled over barium oxide (BaO). The peptide synthesis reagents fluorenylmethyloxycarbonyl (Fmoc) protected amino acids, *N*-hydroxybenzotriazole (HOBt), 2-(1*H*-benzotriazole-1-yl)-1,1,3,3-tetramethyluronium hexafluorophosphate (HBTU), acetic anhydride (Ac_2O), piperidine, triethylamine (TEA), *N*,*N*-diisopropylethylamine (DIEA), *N*,*N*-dimethylformamide (DMF), and *N*-methylpyrrolidone (NMP) were purchased from Applied Biosystems Co. (Foster City, CA). The 1,4,7,10-tetraazacyclododecane-*N*,*N*′,*N*″-tri(*tert*-butylacetate) (DO3A-tBu) was purchased from Macrocyclics Co. (Dallas, TX), and other reagents were purchased from Sigma-Aldrich Corp. (St. Louis, MO) and Fisher Scientific International, Inc. (Hampton, NH). Peptides were synthesized using a Wang resin

* To whom correspondence should be addressed. Tel.: +216 368 8519. Fax: 216 368 4969. E-mail: mpagel@case.edu.

[1] Abbreviations: Ac_2O, acetic anhydride; BaO, barium oxide; CCl_4, carbon tetrachloride; DCM, methylene chloride; DIEA, *N*,*N*-diisopropylethylamine; DMF, *N*,*N*-dimethylformamide; DO3A-tBu, 1,4,7,10-tetraazacyclododecane-*N*,*N*′,*N*″-tri(*tert*-butylacetate); DOTA, 1,4,7,10-tetraazacyclododecane-*N*,*N*′,*N*″,*N*‴-tetraacetic acid; Et_2AlCl, diethylaluminum chloride; Fmoc, fluorenylmethyloxycarbonyl; HBTU, 2-(1*H*-benzotriazole-1-yl)-1,1,3,3-tetramethyluronium hexafluorophosphate; HOBt, *N*-hydroxybenzotriazole; MeCN, acetonitrile; NMP, *N*-methylpyrrolidone; P_2O_5, phosphorous pentoxide; TEA, triethylamine.

10.1021/bc060250q CCC: $37.00 © 2007 American Chemical Society
Published on Web 03/02/2007

Scheme 1. Preparation of Amino-DOTA Preloaded Polymeric Support[a]

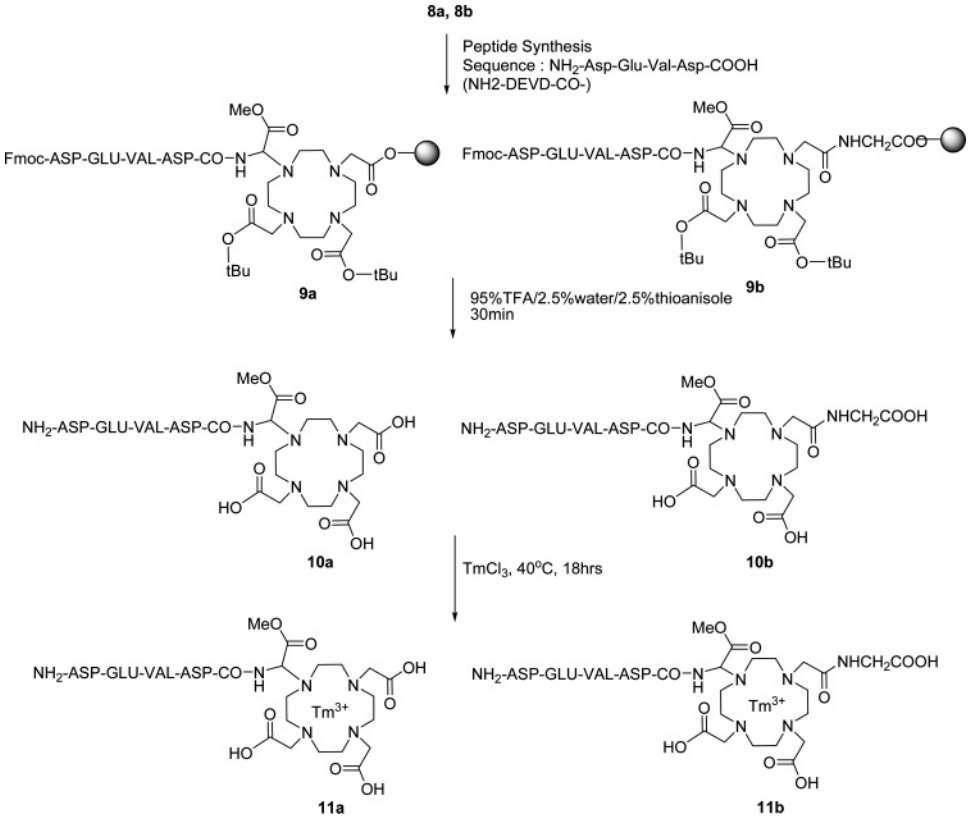


[a] For clarity, **5a**−**8a** and **5b**−**8b** only show ligands coupled to the cyclen ring in a 1,4 configuration. However, a 1,7 configuration is also possible.

(Fluka, Buchs Switzerland) and followed Fmoc chemistry methods with HOBt and HBTU as coupling agents (*23, 24*). The efficiencies of coupling DO3A-Fmoc **3** to resin **4b** and coupling **6** to resin Fmoc-deprotected **5a** and **5b** were checked with the Kaiser ninhydrin test (*25*−*27*). The starting resin had 1.0 mmol/g of hydroxyl groups or amino groups, and the scale of the peptide synthesis was calculated based on the substitution ratio of the resin. The loading efficiencies of the Fmoc compounds and the amine content of the resin were quantitatively analyzed with UV−vis/fluorescence spectroscopy using a Molecular Devices SpectraMax M2 spectrophotometer. IR spectroscopy was used to analyze the functional groups on the resin using an ABB BOMEM MB-104 spectrophotometer operating from 600 to 4000 cm^{-1}. To analyze the peptides and the peptide-DOTA amide final product, HPLC was used with a Grace Vydac OD-300 C-18 reverse-phase analytical column and a Perkin-Elmer Series 200 HPLC pump and UV detector operating at 222 nm. The lanthanide complexation reaction between peptide-DOTA amide and $TmCl_3$ was evaluated with an Arsenazo III solution color test (*28, 29*). ^1H and ^{13}C spectra were measured with a Varian Gemini 300 MHz NMR spectrometer and Varian Inova 600 MHz NMR spectrometer using $CDCl_3$ and DMSO-d_6 as solvents depending on solubility. Paramagnetic chemical exchange saturation transfer (PARACEST) spectra were measured in a solution of 5% D_2O in water (*30, 31*) using a Varian Inova 600 MHz NMR spectrometer. A series of 1D NMR spectra of the water signal were acquired with a selective saturation in 1 ppm increments between 100 and −100 ppm, and selective saturation was performed with a continuous wave pulse applied for 4 s at 31 μT. Analytical thin layer chromatography was performed on Merck silica gel 60 F254 plates. Compounds were visualized using a UV lamp operating at 254 nm, an iodine chamber, and ninhydrin solution. High-resolution mass spectral analyses were performed with a Bruker Daltonics Esquire HCT mass spectrometer and a Bruker BIFLEX III MALDI-TOF mass spectrometer using 3,5-dimethoxy-4-hydroxycinnamic acid as a matrix compound. Molecular modeling was accomplished using InsightII with the Discover-3 (Molecular Simulations Inc.).

Synthesis and Analysis. *Synthesis of 4,7,10-Tri(tert-butylacetate)-1-fluorenylmethoxycarbonyl-1,4,7,10-tetraazacyclododecane (Fmoc-DO3A-tBu)* ***2*** (*32*). To a solution of **1** (2.57 g, 5 mmol) in 10 mL of acetonitrile, activated zinc dust was added in small portions until the reaction mixture attained neutral pH.

Scheme 2. Synthesis of Peptidyl Contrast Agents[a]



[a] For clarity, **8a**−**9a** and **8b**−**11b** only show ligands coupled to the cyclen ring in a 1,4 configuration. However, a 1,7 configuration is also possible.

A solution of Fmoc-Cl (1.35 g, 5 mmol, 1 equiv) in 5 mL of ACN and zinc dust (325 mg, 5 mmol, 1 equiv) was added to the reaction mixture in one portion, and the reaction mixture was stirred at room temperature for 20 min. The progress of the reaction was monitored by TLC ($CHCl_3$/MeOH = 1/1, R_f = 0.75). The reaction mixture was filtered and dried in vacuo, yielding 3.32 g of white solid (yield 90%): ^{1}H NMR (600 MHz, DMSO-d_6) δ 1.47 (s, 27H), 2.50 (s, 8H), 2.71 (t, 4H), 2.79 (t, 4H), 3.39 (s, 6H), 5.15 (t, 1H), 6.29 (d, 2H), 7.42 (t, 2H), 7.47 (t, 2H), 7.63 (d,2H), 7.84 (d, 2H); ^{13}C (125 MHz, DMSO-d_6) δ 170.61, 153.83, 135.59, 135.36, 129.47, 127.23, 123.88, 121.36, 119.99, 81.22, 65.88, 55.14, 53.53, 50.48, 48.44, 47.10, 27.75; MALDI-mass *m*/*z* (calcd 736.94), 737.96 $[M + H]^+$.

Synthesis of 4,7,10-Tri(carboxymethyl)-1-fluorenylmethoxycarbonyl-1,4,7,10-tetraazacyclododecane (Fmoc-DO3A) ***3***. A 2.94 g (4 mmol) amount of **2** was dissolved in 5 mL of 75% TFA in DCM and treated for 40 min. The reaction was traced by TLC (chloroform/methanol = 1.1, R_f = 0.22). The solution was dried under reduced pressure. The remaining solid was redissolved in DCM and precipitated with diethyl ether. The precipitated solid was filtered and dried in vacuo, yielding 1.70 g (3.0 mmol, yield 75%): ^{1}H NMR (600 MHz, DMSO-d_6) δ 3.05 (s, 4H), 3.20 (s, 4H), 3.45 (t, 4H), 3.62 (t, 4H), 3.60 (s, 6H), 4.25 (t, 1H), 4.55 (d, 2H), 7.35 (t, 2H), 7.42 (t, 2H), 7.65 (d,2H), 7.94 (d, 2H); ^{13}C (125 MHz, DMSO-d_6) δ 174.21, 155.44, 143.85, 140.63, 127.08, 125.07, 120.01, 67.24, 54.30, 51.88, 50.65, 48.68, 45.79; MALDI-mass *m*/*z* (calcd 568.62), 569.64 $[M + H]^+$.

Coupling of Fmoc-DO3A on the Resin ***5a, 5b.*** To prepare **5a**, 1.0 g of Wang resin **4a** (substitution level = 1 mmol/g) was used after complete drying. Compound **3** (1.14 g, 2 mmol), HBTU (2.5 g, 6.6 mmol, 3.3 equiv), and HOBt (1.0 g, 6.6 mmol, 3.3 equiv) were dissolved in 30 mL of NMP for 40 min to activate carboxylates, and the solution was added to the peptide reaction vessel containing the resin. TEA (1.82 mL, 13 equiv) was added, and the reaction was continued for 12 h. After filtration, the resin was dispersed in a solution of *tert*-butyl alcohol (*t*-BuOH, 1.48 g, 20 mmol, 20 equiv) in 20 mL of NMP and the reaction was continued for 1 h. The resin was washed and dried in vacuo. To prepare **5b**, 1.3 g of **4b** (substitution level = 0.78 mmol/g) was treated with **3** following the same synthetic method as **4a**. During the reaction, a small amount of resin was sampled for uncoupled amines using the Kaiser test.

Loading Efficiency (Fmoc Titration). The Fmoc concentration on the resin was measured according to a previously reported method (*33*). Fmoc amino acyl resins (4−8 mg) were shaken or stirred in piperidine−DMF (3:7) (0.5 mL) for 30 min, after which MeOH (6.5 mL) was added and the resin was allowed to settle. The resultant fulvene−piperidine adduct had UV absorption maxima at 267 (ϵ = 17 500 M^{-1} cm^{-1}), 290 (ϵ = 5800 M^{-1} cm^{-1}), and 301 nm (ϵ = 7800 M^{-1} cm^{-1}). For reference, a piperidine−DMF−MeOH solution (0.3:0.7:39) was prepared. Spectrophotometric analysis was carried out at 301 nm with comparison to a free Fmoc amino acid (Fmoc-Ala) of known concentration treated under identical conditions. The measured Fmoc concentrations were determined to be 0.45 (±0.05) mmol per gram of resin (calcd 0.64 mmol/g) for **5a** and 0.47 (±0.05) mmol per gram of resin (calcd 0.54 mmol/g) for **5b**, based on 3 repetitions to synthesize each product.

Methyl N-(Benzyloxycarbonyl)-α-bromoglycinate ***6***. Phosphorus tribromide (8.2 g, 30 mmol, 3 equiv) was added to a suspension of methyl *N*-(benzyloycarbonyl)-α-methoxyglycinate (2.51 g, 10 mmol) in carbon tetrachloride (100 mL) under an argon atmosphere. The reaction mixture was stirred at room temperature for 7 days. The reaction solution was then concentrated in vacuo and triturated with dry *n*-hexane (100 mL) for 24 h. The reaction mixture was then filtered, yielding a white solid (75% to quantitative yield measured by weight): ^{1}H NMR (300 MHz, $CDCl_3$) δ 3.80 (s, 3H), 5.22 (s, 2H), 6.20 and 6.45 (split, 1H), 7.55 (s,5H); ^{13}C (125 MHz, DMSO-d_6) δ

170.71, 156.07, 137.37, 129.03, 128.57, 128.53, 73.78, 66.25; MS-ESI *m/z* (calcd 302.99), 304.07 $[M + H]^+$

*Coupling of **6** on the Resin **7a, 7b***. Both **5a** (2.22 g, substitution level = 0.45 mmol/g) and **5b** (2.13 g, substitution level =0.47 mmol/g) were treated with 20% piperidine for 30 min and sequentially washed with NMP, DCM, acetone, and acetonitrile. The Kaiser test was used to measure the content of free secondary amines after Fmoc deprotection. The resin was transferred to a flask with **6** (0.6 g, 2 mmol, 4.3 equiv) and K_2CO_3 (1.66 g, 12 mmol, 25.5 equiv) in dry acetonitrile (100 mL). The solution was stirred and heated to 70 °C for 6 h in anhydrous conditions. After the solution was filtered, the resin was sequentially washed with 50% MeOH in water, MeOH, and DCM and then dried in vacuo. The Kaiser test was used to monitor the coupling of **6** to **7b** by measuring the concentration of remaining free amines.

*Cleavage of the CBZ Group from the Resin **8a, 8b***. In each of three flasks, 0.20 g (0.1mmol) of **7a** was dispersed and swelled in DCM (5 mL) for 1 h and cooled to −78 °C. Et_2AlCl (*34*) was transferred into each flask with an airtight syringe in 1, 2, and 5 equiv amounts, and the mixture was stirred for 15 min. Aliquots of 2, 4, and 10 equiv of thioanisole (the molar ratio of Et_2AlCl:thioanisole was fixed at 1:2) were added to each flask, and portions of the resin were extracted after 5, 15, 30, and 60 min of cleavage reaction time. The sampled resin was immediately washed with DCM and titrated with picric acid according to a previously reported method (*35*). To account for tertiary amines on the cyclen ring, a CBZ-protected resin was treated and compared as a reference. CBZ cleavage was performed with conditions of 1 equiv of 33% Et_2AlCl in thioanisole for 20 min at −78 °C. The average amine content was 0.31 (±0.05) mmol/g for **8a** and 0.33 (±0.05) mmol/g for **8b**, based on 3 repetitions to synthesize each product.

*Peptide Synthesis **9a, 9b***. A 1.63 g (0.5 mmol) amount of **8a** was used to synthesize **9a** using standard SPPS methods. Fmoc-Asp(O^tBu)-OH (0.2 g, 0.5 mmol), Fmoc-Val-OH (0.17 g, 0.5 mmol), and Fmoc-Glu(O^tBu)-OH (0.23 g, 0.5 mmol) were used as building amino acids, and HBTU (0.19 g, 0.5 mmol) and HOBt (73 mg, 0.5 mmol) were used as coupling agents. Freshly distilled TEA (140 μL, 1 mmol) was used as a base in 70 mL of NMP. A solution of 20% piperidine in NMP was used to cleave the Fmoc groups on the resin, after which 1 equiv of an amino acid was reacted with the resin-bound peptide-DOTA amine. This coupling was repeated with a second reaction that was not preceded with Fmoc deprotection in order to follow a double-coupling SPPS strategy, which yielded 1.94 g of **9a** (calcd 1.97 g, yield 93%). Using the same procedure, 0.42 g (0.14 mmol) of **8b** was treated to synthesize 0.50 g of **9b** (calcd 0.52 g, yield 90%).

*Peptide Cleavage from the Resin and Characterization of **10a** and **10b***. After peptide synthesis, the Fmoc group of **9a** (0.55 g, 0.2 mmol) was removed from the resin and **10a** was cleaved from the resin with a 95% TFA/2.5% water/2.5% thioanisole cocktail for 40 min (*36*−*38*). After removing solvents, the product was washed with diethyl ether and dried in vacuo. The final product was purified with an Amberlite column, yielding 150 mg (0.17 mmol, yield 85%). Following the same procedure, 0.29 g of **9b** (0.1 mmol) was used to obtain 87 mg of **10b** (92 μmol, yield 92%). In both cases, the Amberlite column was used to remove impurities and residue from the cleavage cocktail and not intended to purify isomeric forms of **10a** or **10b**. The obtained products **10a** and **10b** were characterized by MALDI-mass (**10a** *m/z* (calcd 891.88): 892.89 $[M + H]^+$, 914.89 $[M + Na]^+$; **10b** *m/z* (calcd 948.93): 949.94 $[M + H]^+$, 971.95 $[M + Na]^+$) and HPLC (column: Symmetry C-18 3.5 μm, 4.6 × 75 mm, detector: 222 nm, flow rate: 0.5 mL/min, eluent: 0.1% TFA in water/acetonitrile, gradient from 100%/0% to 90%/10% for 5 min, 90%/10% for 25 min; retention time = 6.1 min for **10a** and **10b**).

*Complexation of Tm^{3+} with **11a** and **11b***. The obtained **10a** (100 mg, 0.11 mmol) was dissolved in water (3 mL) at pH 6.5 and 40 °C, and $TmCl_3$ (27 mg, 0.1 mmol) in water (0.5 mL) was added dropwise for 1 h and adjusted to pH 7.5 with 0.5 N NaOH. The solution was stirred for 18 h at 40 °C and adjusted to pH 7.5 when the pH dropped below 5. Complete complexation was evaluated with an Arsenazo III color test (*29*). When the test showed negative results for free lanthanide ions, the reaction mixture was cooled to room temperature. The pH was adjusted to 9, and the residual lanthanide−hydroxide white precipitate was removed by filtration. The solution was freeze-dried, yielding product **11a (**MALDI-mass *m/z* (calcd 1060.81): 1061.83 $[M + H]^+$, 1083.85 $[M + Na]^+$). **10b** was treated with a similar procedure to obtain the final product **11b (**MALDI-mass *m/z* (calcd 1117.86): 1118.87 $[M + H]^+$, 1140.92 $[M + Na]^+$).

RESULTS AND DISCUSSION

Scheme 1 demonstrates the synthesis strategies that were employed to create a DOTA-loaded resin for SPPS. Compound **2** was prepared by coupling **1** and Fmoc-Cl with activated Zn dust (*32*). Consequently, **2** was treated with 75% TFA in DCM for 40 min to remove ^{t}Bu esters. The deprotected product was a complex of **3** and TFA salt, as indicated by the NMR chemical shifts of the cyclen ring that were shifted to 3.05−3.62 ppm, relative to the NMR chemical shifts of 2.50−2.79 ppm of the cyclen ring of TFA-free **2**.

Compound **3** was coupled to a Wang resin **4a** (sub. lev. = 1.0 mmol/g) and a glycine-preloaded Wang resin **4b** (sub. lev. = 0.78 mmol/g) to create **5a** and **5b**, respectively. Compound **4b** was prepared to demonstrate the feasibility of incorporating DOTA within a peptide sequence. Compounds **5a** and **5b** showed 70% and 83% loading, respectively, as measured by quantitatively titrating the Fmoc group with a UV spectrometer operating at 301 nm. The lower loading of **5a** relative to **5b** is presumably caused by the closer proximity required by the hydrophilic **3** and relatively hydrophobic surface of **5a** in order to couple **3** to the short linker of **5a**. Adding an amino acid to the Wang resin lengthened the linker in **5b** and led to an improved loading efficiency, and comparable or improved results are anticipated if the Wang resin is preloaded with a longer peptide that would have even less potential for potentially adverse DOTA−resin interactions.

At the end of the coupling reaction to create **5a** and **5b**, an excess amount of *t*-BuOH was added to convert the remaining active carboxylates to *t*-Bu esters, and finally acetic anhydride was used to cap remaining functional active sites on the Wang resin (*39*, *40*). No active sites remained after this esterification and capping because analysis of **10a** and **10b** showed no evidence of synthesized peptide without DOTA or DOTA coupled to more than one peptide, which would be expected from any active sites that remain at this stage.

For clarity, Scheme 1 only shows coupling to the Wang resin at position 1 and Fmoc protection at position 4 (or 10) of the cyclen ring, and yet the Fmoc protection may also occur at position 7. This difference is inconsequential for **5a** because the resin is eventually cleaved from the DOTA to create **10a**. This difference may be significant for **5b** as the two peptidyl ligands of **10b** may have a 1,4 or 1,7 configuration. For comparison, studies of 1,4-DO2A vs 1,7-DO2A have demonstrated that the 1,4 isomer makes a more stable complex with manganese (*41*). Studies of RRSS and RSRS tetra(carboxyethyl) DOTA derivatives indicated different ratios of the 'major' square antiprismatic geometric isomer (M) vs the 'minor' twisted square-antiprismatic geometric isomer (m), although no sig-

nificant differences in hydration states were observed from these particular isomers (*42*). Yet the stabilities, hydration states, and water exchange rates of DOTA derivatives are known to be affected by different m/M geometric ratios (*43*, *44*). Therefore, more detailed investigations of the effects of 1,4 and 1,7 isomers on stabilities and water exchange rates of DOTA derivatives are warranted, and the SPPS methodology described herein may provide the versatility for synthesizing isomers for these investigations.

The α-bromo glycine template **6** was produced as racemates at approximately a 1 to 1 ratio, which was indicated by the NMR doublet on 5.20 and 5.46 ppm. The diastereomers of consequent steps were also determined to be the same ratio as **6**. The presence of diastereomers within a peptide may raise concerns because peptide conformations critically depend on the stereochemistry of each amino acid. However, this strategy to conjugate DOTA to peptide carboxylates is intended to label a peptide with an imaging contrast agent and not designed so that the DOTA directly participates in the conformation or biological function of the peptide. Therefore, racemization of **6** is acceptable for molecular imaging applications that simply require DOTA labeling of peptides. Use of brominated amino acid templates provides additional flexibility for creating peptide-DOTA imaging contrast agents, although other brominated amino acids besides bromoglycine were not investigated in this particular study.

After removal of the Fmoc group of **5a** and **5b** with 20% piperidine in NMP, **5a** and **5b** were coupled with α-brominated CBZ-Gly-OMe (*45*) **6** to obtain **7a** and **7b**, respectively. A comparison of results from the Fmoc titration and a Kaiser test of Fmoc-deprotected **5a** and **5b** indicated complete removal of the Fmoc groups. Similarly, a Kaiser test of **7a** and **7b** indicated that loading **6** onto the resin was performed with quantitative yield.

The CBZ group is commonly used to orthogonally protect amine groups in organic syntheses. Cleavage of CBZ groups is typically performed with H_2/Pd−C or 1,4-cyclohexadiene/Pd−C in EtOH (*46*). However, these cleavage conditions are not compatible with SPPS using polymeric supports, which lead to difficult problems with separation and purification. In this study, selective CBZ cleavage conditions were tested for SPPS. BF_3·Et_2O/dimethylthioether (*47*−*49*), trimethylsilyl iodide (*50*, *51*), and Et_2AlCl/thioanisole (*34*) conditions were investigated during initial trials. From the results of tracing the reactions for **7a** and **7b** with the Kaiser test, the strong Lewis acids BF_3·Et_2O/dimethylthioether and trimethylsilyl iodide were found to rapidly cleave the Wang linker on the resin and therefore failed to selectively cleave the CBZ group. Fortunately, the CBZ group was found to be selectively cleaved with Et_2AlCl/thioanisole by reducing the temperature to −78 °C and carefully controlling the reaction time and molar ratio of Et_2AlCl/thioanisole to optimize reaction conditions (Figure 1). The reaction rates were assessed by measuring the amine contents of ∼25 mg of resin after the start of the reaction using a picric acid titration and UV−vis spectrometer operating at 358 nm (*35*). These results were compared to the measured Fmoc concentrations of **5a** and **5b**. To eliminate the effect of tertiary amines in the cyclen ring, the results of picric acid titration of **7a** and **7b** that were not subjected to Et_2AlCl/thioanisole were subtracted from the measurements of the cleavage reaction. Optimized conditions were determined to consist of a reaction time of 15 min at −78 °C, 1 equiv of Et_2AlCl, and 2 equiv of thioanisole relative to the CBZ concentration on the resin. Under these conditions, cleavage of the benzyl ether group of the Wang linker or incomplete CBZ cleavage limited the overall yield of **8a** and **8b** to 70%. For the purposes of this particular study, a 70% yield was acceptable for subsequent steps. Although cross-

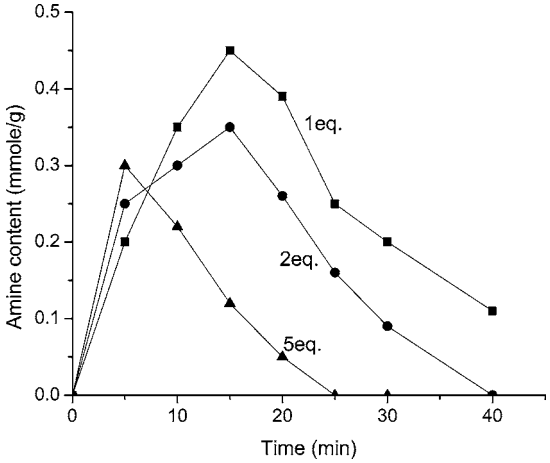


Figure 1. Amine content following CBZ cleavage versus reaction time. For 5 equiv of Et_2AlCl/thioanisole, the reaction was too fast to control cleavage of the CBZ group and benzyl ether linker group. A 1 equiv amount of Et_2AlCl/thioanisole showed the best CBZ cleavage conditions, and a similar reaction rate was obtained with 2 equiv of Et_2AlCl. The optimized CBZ cleavage reaction was carried out for 15 min with 1 equiv of Et_2AlCl at −78 °C.

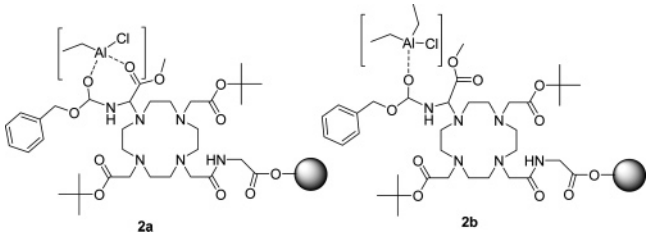


Figure 2. Two possible transition states of Et_2AlCl and CBZ-aminoDOTA Wang resin. The transition state in Figure 2a shows the bridging of Et_2AlCl between two carbonyl groups. This arrangement requires formation of an unstable 7-membered ring that also suffers from planar constraints of the amide and ester groups. Figure 2b represents a more stable interaction that forms a single bond between Et_2AlCl and one carbonyl group. This single-bond transition state is supported by mass spectral results of **10a** and **10b**.

linking between DOTA carboxylates and amines may also account for reduced yield after CBZ cleavage, MALDI-MS analyses of **10a** and **10b** showed no evidence for cross-linking, which is presumably due to the sparse population of DOTA within the Wang resin.

Additional temperature- and time-dependent studies to improve this deprotection step were under investigation in our laboratory as CBZ deprotection during SPPS has great potential for orthogonal synthetic strategies. The expected transition state is shown in Figure 2. Previous reports have shown that Et_2AlCl can bridge two carbonyl groups in a 1,3 position to form a stable 6-membered ring, which leads to bond cleavage adjacent to either carbonyl group (*52*−*53*). However, Et_2AlCl would form an unstable 7-membered ring by bridging the two carbonyl groups of CBZ-Gly-OMe, and this bridge would be further destabilized by the additional planar constraints of the amide and ester groups, so that Et_2AlCl is more likely to form a strong interaction with just one carbonyl group. This hypothesis is confirmed by the absence of cleavage of the methyl ester group as shown in the mass spectrum of **10a** and **10b**, which also shows that interaction of Et_2AlCl only occurs with the ester of the CBZ group.

As shown in Scheme 2, conventional Fmoc SPPS methods were then employed to perform stepwise coupling of amino acids to the aminoDOTA Wang resin (*33*). An Asp-Glu-Val-Asp (DEVD) peptide sequence was chosen for this demonstration because this peptide sequence is preferentially cleaved by the caspase-3 enzyme that is a focus of our molecular imaging

research (*55*). To enhance the coupling efficiency, two sequential applications (i.e., double coupling) of 4 equiv of each amino acid were applied to the SPPS after initial Fmoc deprotection. The total yield of stepwise SPPS of the four amino acids to aminoDOTA was 90% and 93% for the synthesis of **10a** and **10b**, respectively, as determined by weighing. Therefore, the coupling efficiency for coupling the first amino acid to aminoDOTA is no lower than 93%. This high coupling efficiency indicates that the CBZ-protected amine is sufficiently exposed after deprotection, even in the presence of the bulky DOTA moiety.

The SPPS products **10a** and **10b** were cleaved from the resin **9a** and **9b**. HPLC analyses of **10a** and **10b** showed a single peak, indicating that the peptide was successfully synthesized without additions or deletions of amino acids. HPLC analyses showed no evidence for separating stereoisomers of **10a** or **10b** or different relative ligand positions around the cyclen ring of **10b**.

These SPPS products **10a** and **10b** were used to chelate thulium using standard conjugation methods and an Arsenazo III color test (*29*) to create **11a** and **11b**. The weight of the reactants (including salt) and product indicated that chelation was quantitative. Although the final product was not desalted to approximate isotonic conditions during subsequent analyses, the presence of salts did not affect determination of the yield. In addition, mass spectrometry did not detect the presence of **10a** or **10b**, further indicating that complexation was quantitative. However, low amounts of unchelated **10a** and **10b** may still exist within the final product. Chelation of the lanthanide ion required lower temperatures and shorter reaction times relative to lanthanide chelations of DOTA-amide derivatives prepared in our laboratory. This facile chelation is attributed to the presence of three carboxylates and one carbonyl in **10a** and two carboxylates and two carbonyls in **10b** that participate in metal chelation relative to metal chelation with amide carbonyl groups in DOTA-amide derivatives. These results are similar to detailed chelation studies of other DOTA derivatives that indicate the advantage of employing carboxylates for metal binding, (*56*, *57*) and may indicate an improved stability and reduced toxicity of **11a** and **11b** relative to DOTA-amide formulations. Deprotection of the methyl ester of **11a** or **11b** would improve chelation. This deprotection was not performed in this study because the methyl ester group provides unique functionality for further derivatization of the peptide's C-terminus.

To demonstrate the application of the final product for molecular imaging, **11a** and **11b** were detected through the effect of paramagnetic chemical exchange saturation transfer (PARACEST) (*30*, *31*). The PARACEST effect is created by saturating a unique NMR chemical shift corresponding to an amide hydrogen (or more generally, a hydrogen of a functional group that that exchanges with water at a rate of approximately 100−5000 s^{-1}), and the effect is detected by observing a decrease in the water signal caused by transferring the saturation through chemical exchange. This novel mechanism for detecting imaging contrast agents has many advantages for biomedical applications that use magnetic resonance imaging. PARACEST exploits the close proximity between the amide group and the lanthanide ion to create a very unique NMR chemical shift for the amide group of the imaging agent, which facilitates selective saturation of this chemical shift. The synthesis strategy presented in this report is specifically designed to place amide groups in close proximity to the lanthanide ion.

Selective radio frequency irradiation at −51 ppm created a 7.8% PARACEST effect from 25 mM of **11a** (Figure 3). This PARACEST effect of **11a** occurs at the same chemical shift frequency and at a similar signal strength reported for a similar

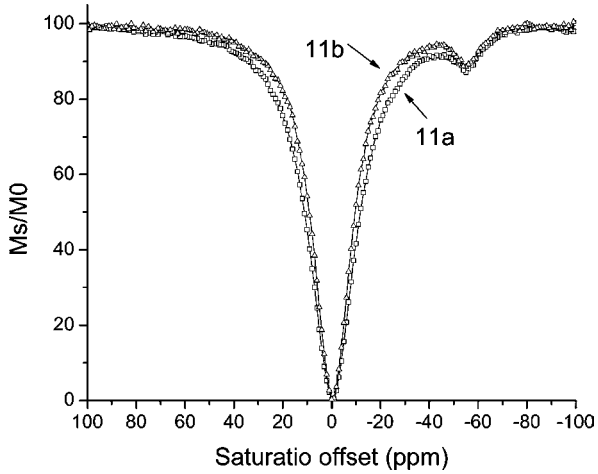


Figure 3. PARACEST spectrum of **11a** (25 mM in 5% D_2O in H_2O) and **11b** (12 mM in 5% D_2O in H_2O). PARACEST spectra were acquired using a Varian Inova 600 MHz NMR spectrometer with a modified presaturation pulse sequence that included a continuous wave saturation pulse, saturation pulse power of 31 μT, and saturation delay of 4 s. The 1D NMR spectra of water used to construct the PARACEST spectra were acquired with saturation in 1 ppm increments from 100 ppm to −100 ppm.

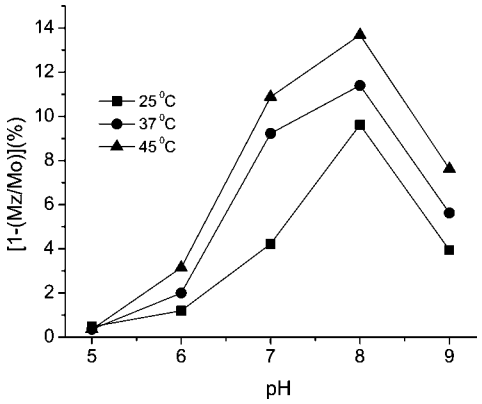


Figure 4. Effect of pH and temperature on the PARACEST effect of 25 mM of **11a**. PARACEST spectra were acquired using a Varian Inova 600 MHz NMR spectrometer with a modified presaturation pulse sequence that included a continuous wave saturation pulse, saturation pulse power of 31 μT, and saturation delay of 4 s at −51 and +51 ppm.

compound, DOTAMGly-Tm^{3+} (*58*). In addition, the PARACEST effect of **11a** shows good sensitivity at physiological pH and temperature, indicating that this contrast agent can be used for in vivo molecular imaging (Figure 4).

A similar PARACEST effect of 7.3% was observed from 12 mM **11b**. The PARACEST effects from the two amide hydrogens (Hb and Hc in Figure 5) both occurred at −51 ppm and were not distinguishable. To investigate the basis for this similarity, molecular modeling of the DOTA core of **11b** was performed with carboxylates constrained to conjugate the Tm^{3+} ion. These results revealed that Hb is positioned 4.1−4.3 Å from Tm^{3+} and Hc is positioned 4.9−5.1 Å from Tm^{3+}. Although a more detailed analysis of Tm^{3+} molecular orbitals is required for an accurate analysis of NMR chemical shifts, the very similar proximities of Hb and Hc to the lanthanide ion are sufficient to justify indistinguishable PARACEST effects that are measured in relatively coarse 1 ppm increments. The PARACEST effect is proportional to the number of water-exchangeable hydrogens that have the same NMR chemical shift. **11b** showed a PARACEST effect that was twice as strong as **11a** (on a per molar basis), demonstrating that multiple peptidyl ligands can

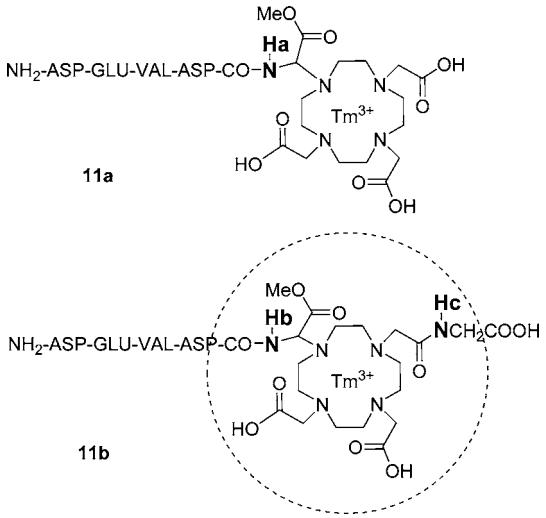


Figure 5. Proximity of amide hydrogens to Tm^{3+} in **11a** and **11b**. Molecular modeling results indicated that Hb is positioned 4.1−4.3 Å from Tm^{3+} and Hc is positioned 4.9−5.1 Å from Tm^{3+}. The dotted line of the 2D schematic is 5.4 Å from the lanthanide ion is provided as a visual aid. The PARACEST effects from two different amide hydrogens Hb and Hc were not distinguishable as only one PARACEST effect was detected at −51 ppm, which is consistent with the similar proximities of these hydrogens to the Tm^{3+}.

improve the detection sensitivity of PARACEST imaging contrast agents.

This synthesis methodology may also be applied to couple peptides to other metal chelators that are used for molecular imaging. For example, diethylenetriaminetetraacetic acid (DTTA) may be used in place of **1** to couple a peptide to diethylenetriaminepentaacetic acid (DTPA) (*1*, *59*). To couple more than two peptides to a molecular imaging contrast agent, 1,4,7,10-tetraazacyclododecaneacetic acid (DO1A) may be used in place of **1** to couple three peptides to DOTA following the scheme to synthesize **10a** or to couple four peptides to DOTA following the scheme to synthesize **10b**. Similarly, diethylenetriamineacetic acid (DT1A) may be used in place of **1** to couple four or five peptides to DTPA.

Larger derivatives of DOTA and DTPA, such as hexaazacyclohexadecane-*N*,*N*′,*N*″,*N*‴,*N*⁗,*N*⁗′-hexaacetic acid (HEHA) (*60*) and triethylenetetraaminehexaacetic acid (TTHA) (*61*), provide opportunities to couple additional peptides to a single molecular imaging agent. If the chemical shifts of all amides within multiple peptide−chelator linkages have the same MR chemical shift, then exploiting this SPPS method to link multiple peptides to a single chelator may increase the strength of the PARACEST effect and improve detection of these molecular imaging contrast agents.

This synthesis methodology may address other important applications in molecular imaging. Employment of standard SPPS techniques provides a convenient and robust method for synthesizing libraries of molecular imaging contrast agents, which may be useful for high-throughput screening to identify molecular imaging contrast agents with optimal properties. Because DOTA macrocyclic rings can strongly chelate a variety of ions, the peptide-DOTA product can be used to develop molecular imaging contrast agents for relaxivity-based MRI using Gd^{3+} or Dy^{3+} (*1*, *62*) or nuclear imaging using ^{64}Cu (*63*) or ^{111}In (*64*) in addition to PARACEST MRI as demonstrated in this report. Therefore, this synthesis strategy represents a platform technology for molecular imaging.

CONCLUSION

To summarize, a new SPPS approach has been developed to couple DOTA to the C-terminus of a peptide and incorporate DOTA within the peptide sequence in order to synthesize peptidyl contrast agents for molecular imaging. Selective cleavage of CBZ protecting groups in SPPS was investigated and optimized for the DOTA-loaded resin. The CBZ deprotection step and the step to load DOTA onto the resin were accomplished with acceptable yields for SPPS. Although *R*,*S* stereoisomers and 1,4 and 1,7 ligand isomers did not affect subsequent analyses in this report, the effect of isomeric forms on chelation stability, hydration, and water exchange rates is warranted, and development of isomeric forms for studies of isomers may be facilitated by this new SPPS strategy. Peptide-DOTA products were used to chelate thulium to create PARACEST imaging contrast agents that demonstrated good detection sensitivities at physiological conditions. This synthesis strategy provides great flexibility for coupling one or more peptides to DOTA to create peptide-DOTA imaging contrast agents for many molecular imaging applications.

ACKNOWLEDGMENT

This work was supported by the U.S. Army Medical Research and Materiel Command under W81XWH-04-1-0731. This work was also supported by the Northeastern Ohio Animal Imaging Resource Center, an NIH-funded program, R24CA110943, as part of the Case Center for Imaging Research.

LITERATURE CITED

(1) Caravan, P., Ellison, J. J., McMurray, T. J., and Lauffer, R. B. (1999) Gadolinium(III) Chelates as MRI Contrast Agents: Structure, Dynamics, and Applications. *Chem. Rev. 99*, 2293−2352.

(2) Anderson, C. J., and Welch, M. J. (1999) Radiometal-labeled agents (non-technetium) for diagnostic imaging. *Chem. Rev. 99*, 2219−2234.

(3) Allen, M. J., and Meade, T. J. (2003) Synthesis and visualization of a membrane-permeable MRI contrast agent. *J. Biol. Inorg. Chem. 8*, 746−750.

(4) Prantner, A. M., Sharma, V., Garbow, J. R., and Piwnica-Worms, D. (2003) Synthesis and characterization of a Gd-DOTA-D-permeation peptide for magnetic resonance relaxation enhancement of intracellular targets. *Mol. Imaging 2*, 333−341.

(5) De Leon-Rodriquez, L. M., Ortiz, A., Weiner, A. L., Zhang, S., Kovacs, Z., Kodadek, T., and Sherry, A. D. (2002) Magnetic resonance imaging detects a specific peptide-protein binding event. *J. Am. Chem. Soc. 124*, 3514−3515.

(6) Saab-Ismail, N. H., Simor, T., Gaszner, B., Lorand, T., Szollosy, M., and Eglavish, G. A. (1999) Synthesis and in vivo evaluation of new contrast agents for cardiac MRI. *J. Med. Chem. 42*, 2852−2861.

(7) Lu, Z.-R., Wang, X., Parker, D. L., Goodrich, K. C., and Buswell, H. R. (2003) Poly(l-glutamic acid) Gd(III)-DOTA conjugate with a degradable spacer for magnetic resonance imaging. *Bioconjugate Chem. 14*, 715−719.

(8) Achilefu, S., Bloch, S., Markiewicz, M. A., Zhong, T., Ye, Y., Dorshow, R. B., Chance, B., and Liang, K. (2005) Synergistic effects of light-emitting probes and peptides for targeting and monitoring integrin expression. *PNAS 102*, 7976−7981.

(9) Miao, Y., Whitener, D., Feng, W., Owen, N. K., Chen, J., and Quinn, T. P. (2003) Evaluation of the human melanoma targeting properties of radiolabeled α-melanocyte stimulating hormone peptide analogues. *Bioconjugate Chem. 14*, 1177−1184.

(10) Zhang, Z., Liang, K., Bloch, S., Berezin, M., and Achilefu, S. (2005) Monomolecular multimodal fluorescence-radioisotope imaging agents. *Bioconjugate Chem. 16*, 1232−1239.

(11) Lewis, M. R., Jia, F., Gallazzi, F., Wang, Y., Zhang, J., Shenoy, N., Lever, S. Z., and Hannink, M. (2002) Radiometal-labeled peptide-PNA conjugates for targeting *bcl-2* expression: preparation, characterization, and in vitro mRNA binding. *Bioconjugate Chem. 13*, 1176−1180.

(12) Schottelius, M., Schwaiger, M., and Wester, H.-J. (2003) Rapid and high-yield solution-phase synthesis of DOTA-Tyr^3-octoreotide and DOTA-Tyr^{3+}-octoreotate using unprotected DOTA. *Tetrahedron Lett. 44*, 2393−3496.

(13) De Leon-Rodriguez, L. M., Kovacs, Z., Dieckmann, G. R., and Sherry, A. D. (2004) Solid-phase synthesis of DOTA-peptides. *Chem. Eur. J. 10*, 1149−1155.

(14) Peterson, J. J., Pak, R. H., and Meares, C. F. (1999) Total solid-phase synthesis of 1,4,7,10-tetraazacyclododecane-*N*,*N*′,*N*″,*N*‴-tetraacetic acid-functionalized peptides for radioimmunotherapy. *Bioconjugate Chem. 10*, 316−320.

(15) Becker, C. F., Clayton, D., Shapovalov, G., Lester, H. A., and Kochendoerfer, G. G. (2004) On-resin assembly of a linkerless lanthanide(III)-based luminescence label and its application to the total synthesis of site-specifically labeled mechanosensitive channels. *Bioconjugate Chem. 15*, 1118−1124.

(16) Albert, R., Smith-Jones, P., Stolz, B., Simeon, C., Knecht, H., Bruns, C., and Pless, J. (1998) Direct synthesis of [DOTA-DPhe^1]-octoreotide and [DOTA-DPhe^1,Tyr^3]-octoreotide (SMT487): two conjugates for systemic delivery of radiotherapeutical nuclides to somatostatin receptor positive tumors in man. *Bioorg. Med. Chem. Lett. 8*, 1207−1210.

(17) Hsei, H.-P., Wu, Y.-T., Chen, S.-T., and Wang, K.-T. (1999) Direct solid-phase synthesis of octoreotide conjugates: precursors for use as tumor-targeted radiopharmaceuticals. *Bioorg. Med. Chem. 7*, 1797−1803.

(18) Gali, H., Sieckman, G. L., Hoffman, T. J., Owen, N. K., Mazuru, D. G., Forte, L. R., and Volkert, W. A. (2002) Chemical synthesis of *Escherichia Coli* ST_h analogues by regioselective disulfide bond formation: biological evaluation of an ^{111}In-DOTA-Phe^{19}-ST_h analogue for specific targeting of human colon cancers. *Bioconjugate Chem. 13*, 224−231.

(19) Graham, K. A., Wang, Q., Eisenhut, M., Haberkorn, U., and Mier, W. (2002) A general method for functionalizing both the C- and N-terminals of Tyr^3-octoreotate. *Tetrahedron Lett. 43*, 5021−5024.

(20) Lewis, M. R., Kao, J. Y., Anderson, A. L., Shively, J. E., and Raubitschek, A. (2001) An improved method for conjugating monoclonal antibodies with N-hydroxysulfosuccinimidyl DOTA. *Bioconjugate Chem. 12*, 320−324.

(21) Chappell, L. L., Rogers, B. E., Khazaeli, M. B., Mayo, M. S., Buchsbaum, D. J., and Brechbiel, M. W. (1999) Improved synthesis of the bifunctional chelating agent 1,4,7,10-tetraaza-N-(1-carboxy-3-(4-nitrophenyl)propyl)-N′,N″,N‴-tris(acetic acid)cyclododecane (PA-DOTA). *Bioorg. Med. Chem. 7, 2313−2320.*

(22) Kruper, W. J., Rudolf, P. R., Jr., and Langhoff, C. A. (1993) Unexpected selectivity in the alkylation of polyazamacrocycles. *J. Org. Chem. 58*, 3869−3876.

(23) Fields, C. G., Lloyd, D. H., Macdonald, R. L., Otteson, K. M., and Noble, R. L. (1991) HBTU activation for automated Fmoc solid-phase peptide synthesis. *Peptide Res. 4*, 95−101.

(24) Beck-Sickinger, A. G., Durr, H., and Jung, G. (1991) Semiautomated T-bag peptide synthesis using 9-fluorenyl-methoxycarbonyl strategy and benzotriazol-1-yl-tetramethyl-uronium tetrafluoroborate activation. *Peptide Res. 4*, 88−94.

(25) Kaiser, E., Colescott, R. L., Bossinger, C. D., and Cook, P. I. (1970) Color test for detection of free terminal amino groups in the solid-phase synthesis of peptides. *Anal. Biochem. 34*, 595−598.

(26) Sarin, V. K., Kent, S. B., Tam, J. P., and Merrifield, R. B. (1981) Quantitative monitoring of solid-phase peptide synthesis by the ninhydrin reaction. *Anal. Biochem. 117*, 147−157.

(27) Madder, A., Farcy, N., Hosten, N. G. C., Muynck, H. D., De Clercq, P. J., Barry, J., and Davis, A. P. (1999) A novel sensitive colorimetric assay for visual detection of solid-phase bound amines. *Eur. J. Org. Chem. 11*, 2787−2791.

(28) Pippin, C. G., Parker, T. A., McMurry, T. J., and Brechbiel, M. W. (1992) Spectrophotometric method for the determination of a bifunctional DTPA ligand in DTPA-monoclonal antibody conjugates. *Bioconjugate Chem. 3*, 342−345.

(29) Rohwer, H., Collier, N., and Hosten, E. (1995) Spectrophotometric study of arsenazo III and its interactions with lanthanides. *Anal. Chim. Acta 314*, 219−223.

(30) Ward, K. M., Aletras, A. H., Balaban, R. S. (2000) A new class of contrast agents for MRI based on proton chemical exchange dependent saturation transfer (CEST). *J. Magn. Reson. 143*, 79−87.

(31) Zhang, S., Merritt, M., Woessner, D. E., Lenkinski, R. E., and Sherry, A. D. (2003) PARACEST agents: modulating MRI contrast via water proton exchange. *Acc. Chem. Res. 36*, 783−790.

(32) Gopi, H. N., and Suresh Babu, V. V. (2000) Zinc-promoted simple synthesis of oligomer-free N(α)-Fmoc-amino acids using Fmoc-Cl as an acylating agent under neutral conditions. *J. Peptide Res. 55*, 295−299.

(33) Fields, G. B., Tian, Z., and Barany, G. (1992) In *Synthetic Peptides- A User's Guide* (Grant, G. A., Ed.) W. H. Freeman, New York, 77−183.

(34) Tsujimoto, T., and Murai, A. (2002) Efficient Detachment of N-Benzyl Carbamate Group. *Synlett 8*, 1283−1284.

(35) Gisin, B. F. (1972) The monitoring of reactions in solid-phase peptide synthesis with picric acid. *Anal. Chim. Acta 58*, 248−249.

(36) King, D. S., Fields, C. G., and Fields, G. B. (1990) A cleavage method which minimizes side reactions following Fmoc solid phase peptide synthesis. *Int. J. Peptide Protein Res. 36*, 255−266.

(37) Albericio, F., Kneib-Cordonier, N., Biancalana, S., Gera, L., Masada, R. I., Hudson, D., and Barany, G. (1990) Comparison of methods for the Fmoc solid-phase synthesis and cleavage of a peptide containing both tryptophan and arginine. *J. Org. Chem. 55*, 3730−3743.

(38) Riniker, B., and Hartmann, A. (1990) In *Peptides: Chemistry, Structure, and Biology* (Rivier, J. E., Marshall, G. R., Ed.), pp 950−952, Escom press, Leiden.

(39) Fujisawa, F., Mori, T., Fukumoto, K., and Sato, T. (1982) *N*,*N*,*N*′,*N*′-Tetramethylchloroformamidinium chloride as an efficient condensation reagent for a novel esterification applicable to the macrolide synthesis. *Chem. Lett. 11*, 1891−1894.

(40) Dhaon, M. K., Olsen, R. K., and Ramasamy, K. (1982) Esterification of N-protected α-amino acids with alcohol/carbodiimide/4-(dimethylamino)pyridine. Racemization of aspartic and glutamic acid derivatives. *J. Org. Chem. 47*, 1962−1965.

(41) Bianchi, A., Calabi, L., Giorgi, C., Losi, P., Mariani, P., Palano, D., Paoli, P., Rossi, P., Valtancoli, B. (2001) Thermodynamic and structural aspects of manganese(II) complexes with polyaminopolycarboxylic ligands based upon 1,4,7,10-tetraazocyclododecane (cyclen). Crystal structure of dimeric $[MnL]_2 2CH_3OH$ containing the new lignad 1,4,7,10-tetraaza-cyclododecane-1,4-diacetate. *Dalton Trans.* 917−922.

(42) Woods, M., Aime, S., Botta, M., Howard, J. A. K., Moloney, J. M., Navet, M., Parker, D., Port, M., Rousseaux, O. (2000) Correlation of water exchange rate with isomeric composition in diastereomeric gadolinium complexes of tetra(carboxyethyl)dota and related macrocyclic ligands. *J. Am. Chem. Soc. 122*, 9871−9792.

(43) Dunand, F. A., Dickins, R. S., Parker, D., and Merbach, A. E. (2001) Towards rational design of fast water-exchanging Gd(dota-like) contrast agents? Importance of the M/m ratio. *Chem.*−*Eur. J. 7* (23), 5160−5167.

(44) Zhang, S., Kovacs, Z., Burgess, S., Aime, S., Terreno, E., and Sherry, A. D. (2001) [DOTA-bis(amide)]lanthanide complexes: NMR evidence for differences in water-molecule exchange rates for coordination isomers. *Chem.*—Eur. J. *7* (1), 288−296.

(45) Williams, R. M., Aldous, D. J., and Aldous, S. C. (1990) General synthesis of *β*,*γ*-alkynylglycine derivatives. *J. Org. Chem. 55*, 4657−4663.

(46) Bodanszky, M., and Bodanszky A. (1984) *The practice of peptide synthesis*, pp 153−158, Springer-Verlag, Berlin.

(47) Sanchez, I. H., Lopez, F. J., Soria, J. J., Larraza, M. I., and Flores, H. J. (1983) Total synthesis of (±)-elwesine, (±)-epielwesine, and (±)-oxocrinine. *J. Am. Chem. Soc. 105*, 7640−7643.

(48) Winkler, J. D., Scott, R. D., and Williard, P. G. (1990) Asymmetric induction in the vinylogous amide photocyclo addition reaction. A formal synthesis of vindorosine. *J. Am. Chem. Soc. 112*, 8971−8975.

(49) Subhas, B. D., and Thurston, D. E. (1990) Boron trifluoride promoted cleavage of benzyl carbamates. *Tetrahedron Lett.* 31, 6903−6906.

(50) Bolos, J., Perez-Beroy, A., Gubert, S., Anglada, L., Sacristan, A., and Orbitz, J. A. (1992) Asymmetric synthesis of pyrrolo[2,1-b]-[1,3,4]thiadiazepine derivatives. *Tetrahedron 48*, 9567−9576.

(51) Ihara, M., Taniguchi, N., Noguchi, K., Fukumoto, K., and Kametani, T. (1988) Total synthesis of hydrocinchonidine and hydrocinchonine via photooxygenation of an indole derivative. *J. Chem. Soc. Perkin trans. 1*, 1277−1281.

(52) Ferreira, V. F., Pinheiro, S., Perrone, C. C., and Costa, P. R. R. (2000) Synthesis of new chiral auxiliares from carbohydrates for Et_2AlCl-promoted Diels-Alder reactions. *J. Braz. Chem. Soc. 11*, 266−273.

(53) Yang, D., Gao, Q., Zheng, B. F., and Zhu, N. Y. (2004) Et_2AlCl-promoted asymmetric phenylseleno group transfer radical cyclization reactions of unsaturated β-hydroxy esters. *J. Org. Chem. 69*, 8821−8828.

(54) Li, G., Wei, H. X., Whiteney, B. R., and Batrice, N. N. (1999) Novel asymmetric C-C bond formation process promoted by Et_2-AlCl and its application to the stereoselective synthesis of unusual β-branched Baylis−Hillman adducts. *J. Org. Chem. 64*, 1061−1064.

(55) Garcia-Calvo, M., Peterson, E. P., Leiting, B., Ruel, R., Nicholson, D. W., and Thornberry, N. A. (1998) Inhibition of human caspases by peptide-based and macromolecular inhibitors. *J. Biol. Chem. 273*, 32608−32613.

(56) Paul-Roth, C., and Raymond, K. N. (1995) Amide Functional Group Contribution to the Stability of Gadolinium(III) Complexes: DTPA Derivatives. *Inorg. Chem. 34*, 1408−1412.

(57) Sarka, L., Burai, L., Kiraly, R., Zekany, L., and Brucher, E. (2002) Studies on the kinetic stabilities of the Gd (3+) complexes formed with the N-mono(methylamide), N′-mono(methylamide) and N,N″-bis(methylamide) derivatives of diethylenetriamine-N,N,N′,N″,N″-pentaacetic acid. *J. Inorg. Biochem. 91*, 320−326.

(58) Aime, S., Barge, A., Castelli, D. D., Fedeli, F., Mortillaro, A., Nielson, F. U., Terreno, E. (2002) Paramagnetic lanthanide(III) complexes as pH-sensitive chemical exchange saturation transfer (CEST) contrast agents for MRI applications. *Magn. Reson. Med. 47*, 639−648.

(59) Peters, J. A., Zitha-Bovens, E., Corsi, D. M., and Geraldes, C. F. G. C. (2001) In *The chemistry of contrast agents in medicinal magnetic resonance imaging* (Merbach, A. E., Toth, E., Eds.) Chapt 8, Wiley, New York.

(60) Kodama, M., Koike, T., Mahatma, A. B., and Kimura, E. (1991) Thermodynamic and kinetic studies of lanthanide complexes of 1,4,7,10,13-pentaazacyclopentadecane-N,N′,N″,N‴,N⁗-pentaacetic acid and 1,4,7,10,13,16-hexaazacyclooctadecane-N,N′,N″,N‴,N⁗, N⁗′-hexaacetic acid. *Inorg. Chem. 30*, 1270−3.

(61) Chu, S. C., Pike, M. M., Fossel, E. T., Smith, T. W., Balschi, J. A., and Springer, S. S. (1984) Aqueous shift reagents for high resolution cationic nuclear magnetic resonance III $Dy(TTHA)^{3-}$, $Tm(TTHA)^{3-}$ and $Tm(PPP)_2^{7-}$. *J. Magn. Reson. 56*, 33−47.

(62) Elst, L. V., Roch, A., Gillis, P., Laurent, S., Botteman, F., Bulte, J. W. M., and Muller, R. (2000) Dy-DTPA derivatives as relaxation agents for very high field MRI: The beneficial effect of slow water exchange on the transverse relaxivities. *Magon Resn. Med. 47*, 1121−1130.

(63) Chen, X., Liu, S., Hou, Y., Tohme, M., Park, R., Bading, J. R., and Conti, P. S. (2004) MicroPET imaging of breast cancer αv-Integrin expression with 64Cu-labeled dimeric RGD peptides. *Mol. Imaging Biol. 6*, 350−359.

(64) Rodrigues, M., Traub-Weidinger, T., Li, S., Ibi, B., and Virgolini, I. (2006) Comparison of 111In-DOTA-Dphe1-Tyr3-octreotide and 111In-DOTA-lanreotide scintigraphy and dosimetry in patients with neuroendocrine tumours. *Eur. J. Nucl. Med. Mol. Imaging 33*, 532−540.

BC060250Q

Synthesis and Radiolabeling of Selective High-Affinity Ligands Designed to Target Non-Hodgkin's Lymphoma and Leukemia

Saphon Hok,[†] Arutselvan Natarajan,[‡] Rod Balhorn,[†] Sally J. DeNardo,[‡] Gerald L. DeNardo,[‡] and Julie Perkins*,[†]

Chemistry, Materials and Life Sciences Directorate, Lawrence Livermore National Laboratory, Livermore, California 94551, and Radiodiagnosis and Therapy Laboratory, University of California, Davis, Sacramento, California 95816. Received October 2, 2006; Revised Manuscript Received January 25, 2007

Selective high-affinity ligands (SHALs) were synthesized as molecular targeting agents for HLA-DR10, a cell surface receptor upregulated on malignant B-cell lymphocytes in non-Hodgkin's lymphoma and leukemia. SHALs are designed to mimic the affinity and selectivity of Lym-1, an antibody that binds to the β-subunit of HLA-DR10. To bind selectively to HLA-DR10, SHALs were constructed to bind to two adjacent pockets on the surface of the β-subunit of HLA-DR10 located within an epitope recognized by the Lym-1 antibody. A series of multivalent SHALs with molecular masses of 1500−3000 Da were synthesized using solid/polymer-supported synthesis on chlorotrityl chloride resin in 50−80% yield. To enable their use as radionuclide carriers in mouse studies, SHALs were conjugated to DOTA in a solution-phase reaction with 70−100% yield. $^{57}Co/CoCl_2$ titrations revealed that 50−60% of the DOTA in the DOTA-conjugated SHALs was available for radiometal chelation. These DOTA−SHALs were labeled with ^{111}In and used to carry out pharmacokinetic studies in mice. Radiolabeling reactions of DOTA−SHALs, with exactly one DOTA entity per targeting SHAL molecule, yielded products with greater than 90% radiochemical purity and specific activities ranging from 97 to 150 μCi/μg.

INTRODUCTION

Antibodies have evolved to be one of nature's most selective molecular targeting agents. These large proteins bind their target (small and large biological molecules) through two Fab arms, effectively a bivalent system. They typically have affinity constants ranging from 10^{-5} to 10^{-12} M for their target and are often used as therapeutic agents (*1*, *2*) among many other uses. The IgG_{2a} antibody, Lym-1, binds to the β-subunit of HLA−DR10, a surface-bound/trans-membrane protein found on lymphocytes (*3*−*5*). HLA−DR10 is more abundant on malignant lymphocytes than their normal precursor cells, and therefore, Lym-1 has been employed as a radionuclide carrier for the treatment of non-Hodgkin's lymphoma (*6*−*10*). While minimizing exposure to healthy cells (*11*, *12*), however, there are some disadvantages to using antibodies for treatment and imaging. As macromolecules, they have long residence time in the circulation, which limits the target contrast that can be achieved in tumor imaging (thus decreasing tumor detection). The long residence time also decreases the therapeutic index (ratio of damage to cancer cells relative to damage to normal cells) that can be obtained. Therefore, the design and realization of an alternative ligand that mimics the binding affinity and specificity of an antibody but with improved pharmacokinetic properties is an important contribution to future imaging and radiotherapeutic applications (*13*).

Although small molecules typically have low to moderate affinity for protein targets, linking two or more small molecules generates ligands that can exhibit a polyvalent effect (*14*−*19*). Affinity is a qualitative term commonly used to describe a binding constant. However, avidity refers to the association constant of a polyvalent interaction (*19*). Establishing the magnitude and individual contribution of the thermodynamic parameters of polyvalent interactions is complicated, however; it is generally accepted that multiple interactions or contacts on the surface of protein targets generally increases the avidity of the polyvalent ligand for the target (*19*). In many cases, the avidity of the polyvalent ligand is greater than the sum of the individual affinities of the component small molecules.

Small (molecular weight <300 Da) molecules, previously established to bind to the HLA−DR10 protein (*20*, *21*), have been linked together using a lysine/poly(ethylene glycol)-based linker to generate selective high-affinity ligands (SHALs), polyvalent ligands that exhibit multiple sites of contact with the target protein surface. These SHALs were shown to bind to lymphoma cells expressing HLA−DR10 with high specificity and nanomolar to picomolar binding avidity (*21*). The multiple sites of attachment generated SHALs with avidity and selectivity similar to Lym-1.

Here, the synthesis of six SHALs, the conversion of these SHALs to the DOTA−SHALs and the experimental determination of the radiochemical purity and specific activities of ^{111}In-DOTA−SHALs are described. Whole cell binding experiments to demonstrate specificity of the SHALs exhibiting the most promising binding properties for subsequent pharmacokinetic studies in mice are also briefly described.

EXPERIMENTAL PROCEDURES

Materials and Abbreviations. Unless otherwise stated, all reagents and solvents were obtained from commercial suppliers, were ACS grade or higher, and used as received. 2-Chlorotrityl chloride resin (100−200 mesh, 1% DVB, 1.2 mmol/g loading) and all Fmoc-protected amino acids were obtained from Novabiochem, Inc. Fmoc-8-amino-3,6-dioxaoctanoic acid was purchased from Peptides Int. The hexafluorophosphate (PF_6) salt of 1,4,7,10-tetraazacyclododecane-1,4,7,10-tetraacetic acid mono-*N*-hydroxysuccinimide (DOTA−NHS) ester was purchased from Macrocyclics. *N*-Benzoyl-L-arginyl-4-amino-benzoic acid (Ba) was obtained from Bachem, Inc. *N*-(Biotinyloxy)-

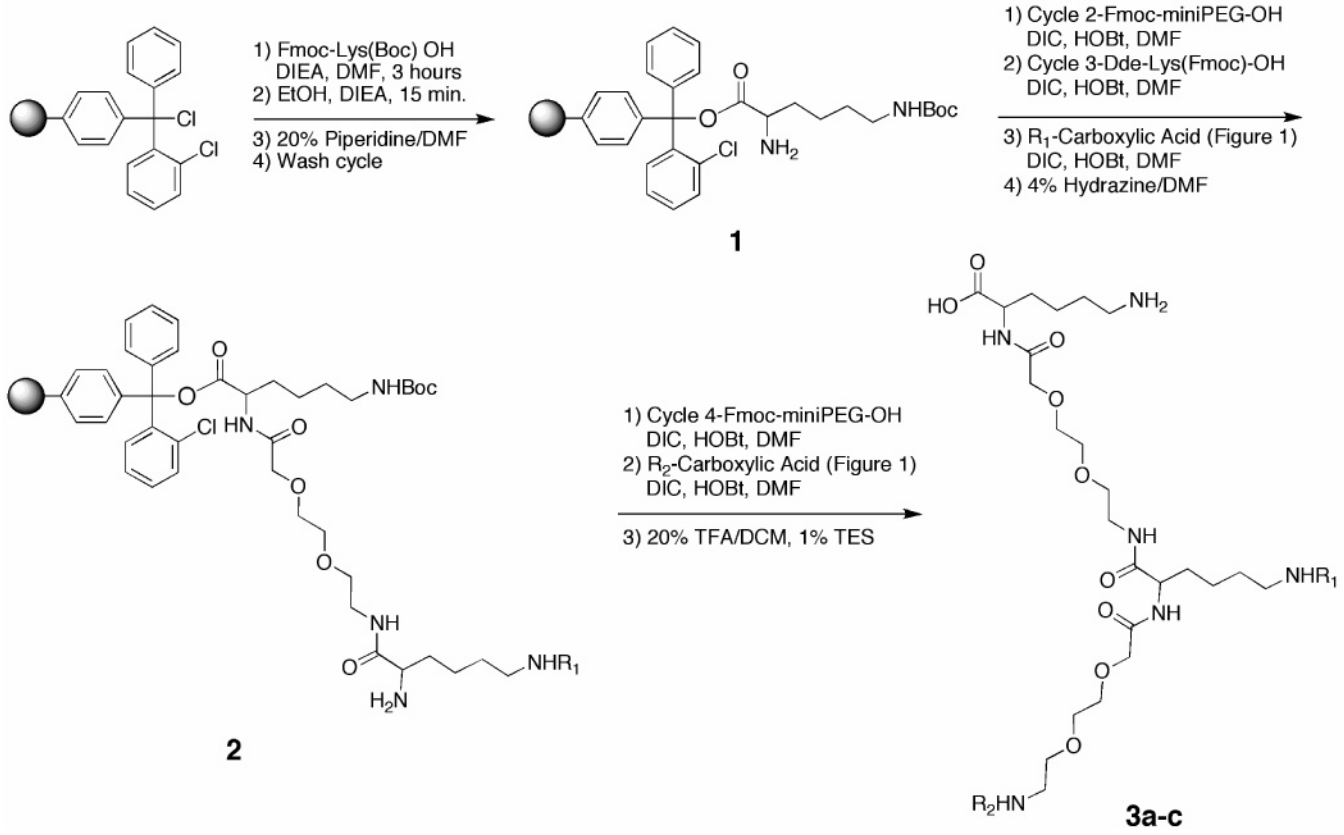
* Julie Perkins, Lawrence Livermore National Laboratory, 7000 East Avenue, California 94551. Tel: (925) 422-7319. FAX: (925) 422-3570. E-mail: perkins14@llnl.gov.

[†] Lawrence Livermore National Laboratory.

[‡] University of California, Davis.

10.1021/bc060305o CCC: $37.00 © 2007 American Chemical Society
Published on Web 03/21/2007

Scheme 1. Solid-Phase Synthesis of Bidentate SHALs 3a−c



succinimide (biotinyl-OSu) was purchased from BACHEM. Dabsyl-L-valine (Dv) was purchased from TCI, Inc., and Boc-L-thyronine (T) was obtained from AnaSpec, Inc. Deoxycholic acid (D), 3,3′,5-triido-L-thyronine, diisopropylethylamine (DIEA), di-*tert*-butyldicarbonate (Boc-anhydride), hydrazine, trifluoroacetic acid (TFA), 1,3-diisoproylcarbodiimide (DIC), 1-hydroxybenzotriazole (HOBt), 20% piperidine/dimethylformamide (DMF), and triethylsilane (TES) were purchased from Sigma-Aldrich. Boc-L-triiodothyronine (It) was synthesized from 3,3′,5-triiodo-L-thyronine using standard coupling protocols with Boc-anhydride (*22*). Carrier-free $^{111}InCl_3$ was purchased from MDS Nordion (Vancouver, Canada) as the chloride in 0.05 M hydrochloric acid solution. $^{57}CoCl_2$ was obtained from ICN Radiochemicals (Irvine, CA). Streptavidin−horseradish peroxidase (HRP) was obtained from Invitrogen, goat anti-mouse IgG-HRP from Kirkegaard and Perry Laboratories (Gaithersburg, MD), and 2,2′-azino-bis(3-ethylbenzthiazoline-6-sulfonic acid) (ABTS) substrate and bovine serum albumin (BSA) were obtained from Sigma-Aldrich.

Instrumentation. Solid-supported syntheses were carried out in Pierce Biotechnology polyethylene columns (5 mL). All SHALs were purified by semipreparative HPLC at 10 mL/min on a Waters preparative machine with photodiode array detection (Waters Symmetryprep C18, 7 μm, 19 × 300 mm column) and lyophilized using a Kinetics Flexi-Dry freeze-dryer. The purity was confirmed by analytical HPLC carried out at 1 mL/min on an Agilent 1100 machine (Waters Symmetry C18, 5 μm, 4.2 × 150 mm column, diode array detector) with a linear gradient from 95% H_2O (1% TFA) to 80% MeCN (1% TFA) over 12 min. Nuclear magnetic resonance (NMR) spectra were obtained on a Bruker 500 MHz or a Varian 600 MHz machine in d_6-DMSO. Mass spectra were acquired on a Micromass Quattro Micro API mass spectrometer operating in positive ion mode. The samples were dissolved in MeCN/H_2O (1:1), 0.1% formic acid, for mass spectrometry analysis. Radiolabeled SHALs were purified and analyzed using a Beckman Coulter System Gold 128 HPLC system with a radioactive detector (Raytest USA, Wilmington, NC). Radioactivity of cellulose acetate electrophoresis (CAE) (Gelman Sciences, Inc., Ann Arbor, MI) was performed using 0.05 M sodium barbital buffer, pH 8.6, and a current of 5 mA per strip was applied. Radioactivity was counted by scanning on Fuji film BAS-1800 imager. Quality assurance (QA) of the radiochemical and purification was carried out using HPLC (Beckman Coulter System Gold, 128 with Ray test radioactive detector) and a linear gradient from 95% H_2O (1% TFA) to 90% CH_3CN (1% TFA) over 12 min. DOTA−SHALs were dissolved in 5−10% DMSO in PBS for radiolabeling experiments.

Preparation of Resin 1. (Scheme 1) 2-Chlorotrityl chloride resin (*23*, *24*) (150 mg, 0.18 mmol or 50 mg, 0.06 mmol) was suspended in dichloromethane (DCM) for 30 min and washed 3× with anhydrous DMF. The resin was treated with Fmoc-Lys(Boc)-OH (468.5 g/mol; 40 mg (85 μmol) for a larger or 20 mg (43 μmol) for a smaller-scale reaction) and DIEA (50 μL, 287 μmol) in 1.0 mL anhydrous DMF (Scheme 1). The reaction mixture was agitated on a nutator for 3 h. Ethanol (1.0 mL) and DIEA (100 μL) was added and agitated for 15 min to quench the excess chlorotrityl chloride groups. The reaction solution was removed by filtration, and the resin was washed 3× with DMF and treated with 20% piperidine in DMF (1 mL) for 20 min for fluorenylmethoxycarbonyl (Fmoc) deprotection (*25*, *26*). The Fmoc-deprotected resin-bound Boc-lysine was washed with DMF and subsequently coupled to the next Fmoc-protected residue using amide coupling chemistry employing 3 mol equiv of DIC and 3 mol equiv of HOBt (*25*, *27*). The washing and filtration cycle with DMF (2 mL, 3×, 1 min) was performed between every deprotection and coupling step.

Preparation of Resin 2. (Scheme 1) Resin **1** was treated with a solution of Fmoc-8-amino-3,6-dioxaoctanoic acid, DIC, and HOBt (3 equiv) in 1.0 mL anhydrous DMF for 3−5 h (coupling cycle 2). The resin was then treated with Dde-Lys-(Fmoc)-OH, HOBt, and DIC (3 equiv) in 1.0 mL anhydrous

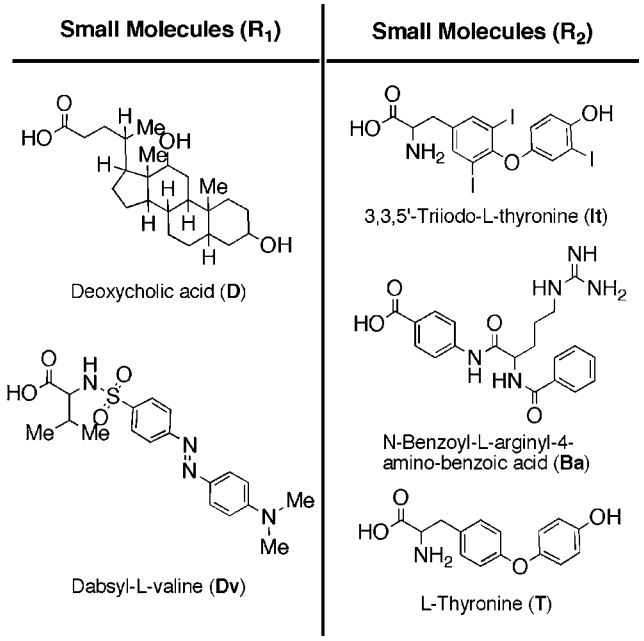


Figure 1. Chemical structure of molecules predicted to bind to two unique sites on the surface of target protein HLA−DR10.

DMF for 5 h (coupling cycle 3). Following Fmoc deprotection, the resultant free amine was subsequently coupled to one of the molecules R_1 in Figure 1 (2−3 equiv), HOBt, and DIC (3 equiv) in 1.0 mL anhydrous DMF for 5−12 h depending on molecule R_1. The reaction solution was filtered, and the resin was washed and treated twice with 4% hydrazine in DMF (40 μL hydrazine in 900 μL DMF for 10 min) to remove the 1-(4,4-dimethyl-2,6-dioxacyclohex-ylidene)ethyl (Dde) protecting group (*25*, *28*). After washing, resin **2** with a free α-amino on the second lysine residue was obtained.

Synthesis of SHALs (3a−c). (Scheme 1) Resin **2** was treated with a solution of Fmoc-8-amino-3,6-dioxaoctanoic acid, HOBt, and DIC (3 equiv) in 1.0 mL anhydrous DMF for 3−5 h (coupling cycle 4). Following Fmoc deprotection, the resultant free amine was subsequently coupled to one of the molecules R_2 in Figure 1 (2−3 equiv), HOBt, and DIC (3 equiv) in 1.0 mL anhydrous DMF for 5 h. The solvent was exchanged to DCM (2 mL). The washed resin was then treated with 2 mL of 20% TFA/1% TES in DCM for 30 min to cleave the product from the resin and the Boc-protecting group on the ϵ-amine of the first lysine. The cleaved solution was filtered and collected, the resin washed with DCM, and the combined filtrate was reduced to dryness. The crude sample was analyzed by analytical HPLC to determine the ratio of product to impurities in the cleaved material using UV absorbance peak areas at 254 nm. Purification was performed using semipreparative HPLC, and the product fractions were lyophilized to dryness. Analytical HPLC chromatograms, electron spray ionization mass spectroscopy (ESI-MS), ^{1}H NMR spectra for **3a**−**c**, and ^{13}C NMR spectrum for **3a** are provided in the Supporting Information.

*SHAL **3a** (DLPItPLA).* Crude **3a** was treated with 100 mM NH_4HCO_3 to cleave TFA esters formed on deoxycholate alcohols during deprotection. HPLC of the crude material gave approximately 50% product (Rt = 8.44 min). This NH_4HCO_3/crude was lyophilized and purified by HPLC (85% H_2O (0.1% TFA) to 70% MeCN (0.1% TFA), 25 min gradient). The combined product fractions were lyophilized to yield 40 mg of isolated **3a**. ESI-MS: *m*/*z* calcd for $C_{79}H_{122}I_3N_{11}O_{22}$ $(M + H)^+$ 1573.21, found 1572.41; calcd for $(M + 2H)^{2+}$ 787.11, found 786.78.

*SHAL **3b** (DvLPBaPLA).* HPLC of the crude material gave approximately 73% product (Rt = 7.29 min), and 20 mg of red solid **3b** was isolated. ESI-MS: *m*/*z* calcd for $C_{63}H_{91}N_{15}O_{15}S$ $(M + H)^+$ 1331.58, found 1331.47; calcd for $(M + 2H)^{2+}$ 666.29, found 665.96; calcd for $(M + 3H)^{3+}$ 444.53, found 444.06.

*SHAL **3c** (DvLPTPLA).* HPLC of the crude material gave approximately 80% product (Rt = 7.31 min), and 20 mg of red solid **3c** was isolated. ESI-MS: *m*/*z* calcd for $C_{58}H_{83}N_{11}O_{15}S$ $(M + H)^+$ 1207.44, found 1206.49; calcd for $(M + 2H)^{2+}$ 604.22, found 603.89; calcd for $(M + 3H)^{3+}$ 403.15, found 402.95

Preparation of Resin 5. (Scheme 2) Resin **1** was treated with Dde-Lys(Fmoc)-OH, HOBt and DIC (3 equiv) in 1.0 mL anhydrous DMF for 5 h (coupling cycle 2). The reaction solution was filtered, and the washed resin was treated twice with 4% hydrazine/DMF (40 μL hydrazine in 900 μL DMF for 10 min) to remove the Dde protecting group (Scheme 2). In coupling cycle 3, Fmoc-8-amino-3,6-dioxaoctanoic acid (6 equiv) was coupled to the resin with DIC and HOBT (6 equiv) in 1.0 mL anhydrous DMF for 3 h. The washed resin was then treated with Dde-Lys(Fmoc)-OH, HOBt, and DIC (6 equiv) in 1.0 mL anhydrous DMF for 5 h (coupling cycle 4). Following Fmoc deprotection, the resultant free amine was subsequently coupled to one of the molecules R_1 in Figure 1 (2−3 equiv), HOBt, and DIC (6 equiv) in 1.0 mL anhydrous DMF for 5−12 h, depending on the R_1 molecule. The mixture was filtered, and the washed resin was treated twice with 4% hydrazine/DMF to remove the two Dde protecting groups. After washing, resin **5** with two primary amines (one on each lysine) was obtained.

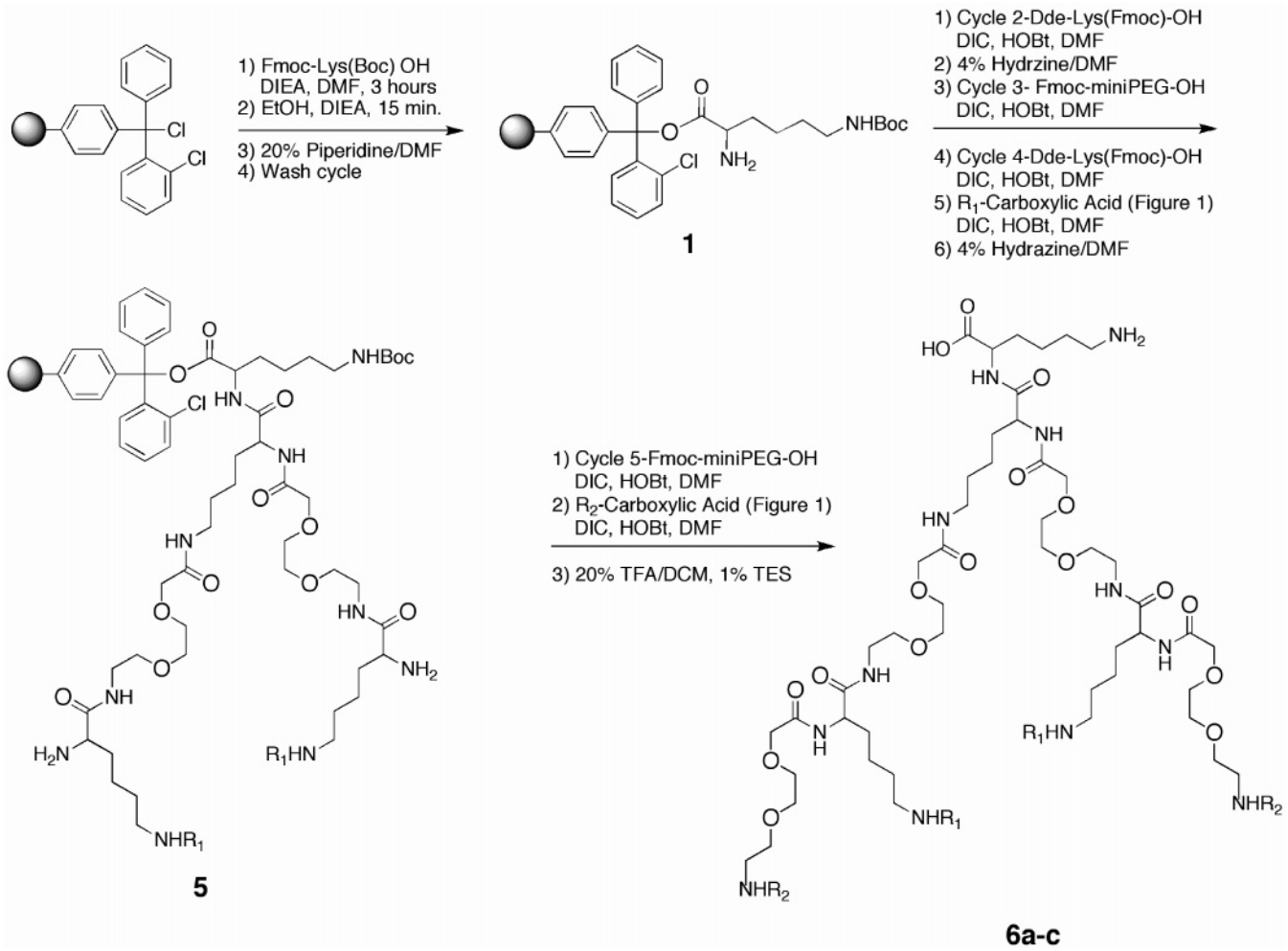
Synthesis of SHALs (6a−c). (Scheme 2) Resin **5** was treated with a solution of Fmoc-8-amino-3,6-dioxaoctanoic acid, HOBt, and DIC (6 equiv) in 1.0 mL anhydrous DMF for 5 h (coupling cycle 5). Following Fmoc deprotection, the resultant free amine was subsequently coupled to one of the molecules R_2 in Figure 1 (2−3 equiv), HOBt, and DIC (6 equiv) in 1.0 mL anhydrous DMF for 5 h. The solvent was exchanged to dichloromethane (DCM, 2 mL). The washed resin was treated with 2 mL of 20% TFA/1% TES in DCM for 30 min to cleave the product from the resin and the Boc-protecting group on the ϵ-amine of the first lysine. The cleaved solution was filtered and collected, the resin washed with DCM, and the combined filtrate was concentrated. A sample was analyzed by analytical HPLC to determine the ratio of product to impurities in the cleaved material using UV absorbance peak areas at 254 nm. Purification was performed using semipreparative HPLC, and the product fractions were lyophilized to dryness. Analytical HPLC, ESI-MS, ^{1}H NMR for all compounds, and ^{13}C NMR spectra for **3a** and **6a** are provided in Supporting Information.

*SHAL **6a** ((DLPItP)$_2$LLA).* HPLC of the crude material gave approximately 65% product (Rt = 9.73 min), and 96 mg of white solid **6a** was isolated. ESI-MS: *m*/*z* calcd for $C_{126}H_{190}I_6N_{14}O_{29}$ $(M + 2H)^{2+}$ 1564.21, found 1564.10; calcd for $(M + 3H)^{3+}$ 1043.14, found 1043.15.

*SHAL **6b** ((DvLPBaP)$_2$LLA):* HPLC of the crude material gave approximately 62% product (Rt = 7.86 min), and 60 mg of red solid **6b** was isolated. ESI-MS: *m*/*z* calcd for $C_{126}H_{180}N_{30}O_{29}S_2$ $(M + 2H)^{2+}$ 1322.57, found 1322.43; calcd for $(M + 3H)^{3+}$ 882.05, found 881.92; calcd for $(M + 4H)^{4+}$ 661.05, found 661.51; calcd for $(M + 5H)^{5+}$ 529.63, found 529.42.

*SHAL **6c** ((DvLPTP)$_2$LLA):* HPLC of the crude material gave approximately 63% product (Rt = 8.09 min), and 40 mg of red solid **6c** was isolated. ESI-MS: *m*/*z* calcd for $C_{116}H_{164}N_{22}O_{29}S_2$ $(M + 2H)^{2+}$ 1198.43, found 1198.18; calcd for $(M + 3H)^{3+}$ 799.29, found 799.16; calcd for $(M + 4H)^{4+}$ 599.72, found 599.54; calcd for $(M + 5H)^{5+}$ 479.98, found 479.73.

Scheme 2. Solid-Phase Synthesis of Bisbidentate SHALs 6a−c



Synthesis of DOTA SHALs. 3a−c and **6a−c** were converted to DOTA derivatives **4a−c** and **7a−c**, respectively (Scheme 3). Generally, a SHAL was dissolved in 500 μL anhydrous DMF and 100 μL DIEA. The PF_6 salt of DOTA NHS ester (933.36 g/mol, 0.95−1.1 equiv) was added to the mixture as a solid. The reaction was nutated for 15 min, and the reaction was monitored by analytical HPLC. Upon completion, the reaction solution was diluted with 300 μL H_2O and 300 μL MeCN, both containing 1% TFA, and directly HPLC purified into two 600 μL aliquots. The resulting purified lyophilized DOTA SHALs were analyzed by HPLC and ESI-MS (spectra provided in Supporting Information).

*DOTA SHAL **4a** (DLPItPLDo).* Reaction of **3a** (5.3 mg, 3.37 μmol) with DOTA NHS ester (3.5 mg, 3.75 μmol) gave 100% (Rt = 8.29 min) conversion by analytical HPLC and yielded **4a** (8.0 mg, white solid) after purification. ESI-MS: *m/z* calcd for $C_{79}H_{122}I_3N_{11}O_{22}$ $(M + H)^+$ 1959.62, found 1959.26; $(M + 2H)^{2+}$ 980.31, found 980.07.

*DOTA SHAL **4b** (DvLPBaPLDo).* Reaction of **3b** (6.2 mg, 4.66 μmol) with DOTA NHS ester (4.8 mg, 5.14 μmol) gave 93% (Rt = 7.07 min) conversion by crude analytical HPLC and yielded **4b** (6.5 mg, red solid) after purification. ESI-MS: *m/z* calcd for $C_{79}H_{117}N_{19}O_{22}S$ $(M + H)^+$ 1717.99, found 1718.20; calcd for $(M + 2H)^{2+}$ 859.49, found 859.46; calcd for $(M + 3H)^{3+}$ 573.33, found 573.29.

*DOTA SHAL **4c** (DvLPTPLDo).* Reaction of **3c** (5.8 mg, 4.81 μmol) with DOTA NHS ester (4.3 mg, 4.61 μmol) gave 75% (Rt = 7.17 min) conversion by crude analytical HPLC and yielded **4c** (7.0 mg, red solid) after purification. ESI-MS: *m/z* calcd for $C_{74}H_{109}N_{15}O_{22}S$ $(M + H)^+$ 1593.84, found 1594.01; calcd for $(M + 2H)^{2+}$ 797.42, found 797.36; calcd for $(M + 3H)^{3+}$ 531.42, found 531.88.

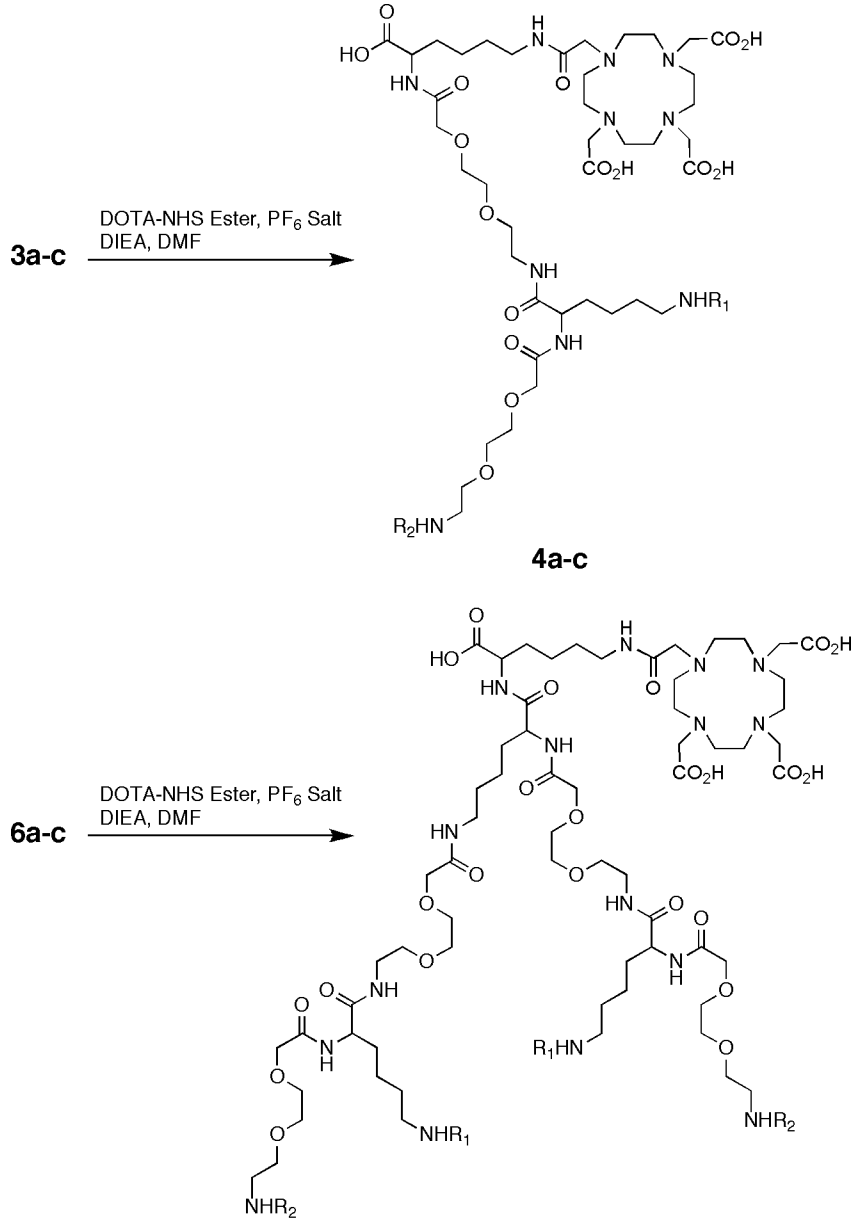
*DOTA SHAL **7a** ((DLPItP)$_2$LLDo).* Reaction of **6a** (11.0 mg, 3.52 μmol) with DOTA NHS ester (3.6 mg, 3.86 μmol) gave 70% (Rt = 9.53 min) conversion by crude analytical HPLC and yielded **7a** (12.0 mg, white solid) after purification. ESI-MS: *m/z* calcd for $C_{142}H_{216}I_6N_{18}O_{36}$ $(M + 2H)^{2+}$ 1757.41, found 1757.37; calcd for $(M + 3H)^{3+}$ 1171.94, found 1171.85; calcd for $(M + 4H)^{4+}$ 879.21, found 879.16.

*DOTA SHAL **7b** ((DvLPBaP)$_2$LLDo).* Reaction of **6b** (18.0 mg, 6.81 μmol) with DOTA NHS ester (8.0 mg, 8.57 μmol) gave 80% (Rt = 7.76 min) conversion by crude analytical HPLC and yielded **7b** (7.0 mg, red solid) after purification. ESI-MS: *m/z* calcd for $C_{142}H_{206}N_{34}O_{36}S_2$ $(M + 3H)^{3+}$ 1010.85, found 1010.82; calcd for $(M + 4H)^{4+}$ 758.39, found 758.30; calcd for $(M + 5H)^{5+}$ 606.91, found 606.78.

*DOTA SHAL **7c** ((DvLPIP)$_2$LLDo).* Reaction of **6c** (5.0 mg, 2.09 μmol) with DOTA NHS ester (2.5 mg, 2.68 μmol) gave 80% (Rt = 7.72 min) conversion by crude analytical HPLC and yielded **7c** (4.0 mg, red solid) after purification. ESI-MS: *m/z* calcd for $C_{132}H_{190}N_{26}O_{36}S_2$ $(M + 2H)^{2+}$ 1391.63, found 1391.41; calcd for $(M + 3H)^{3+}$ 928.09, found 928.11; calcd for $(M + 4H)^{4+}$ 696.31, found 696.33; calcd for $(M + 5H)^{5+}$ 557.26, found 557.21.

Synthesis of Biotinylated SHALs. 3b and **6b** were converted to the biotin derivatives **8b** and **9b**, respectively (Scheme 4). Generally, a SHAL was dissolved in 500 μL anhydrous DMF and 100 μL DIEA and biotinyl-OSu (341.39 g/mol, 1.1 equiv) was added to the mixture as a solid. The reaction was nutated for 15 min, and the reaction was monitored by analytical HPLC.

Scheme 3. Synthesis of DOTA-SHALs 4a−c and 7a−c. Free Amine of SHALs 3a−c and 6a−c were Reacted with the PF_6 Salt of DOTA−NHS Ester to Generate 4a−c and 7a−c, Respectively



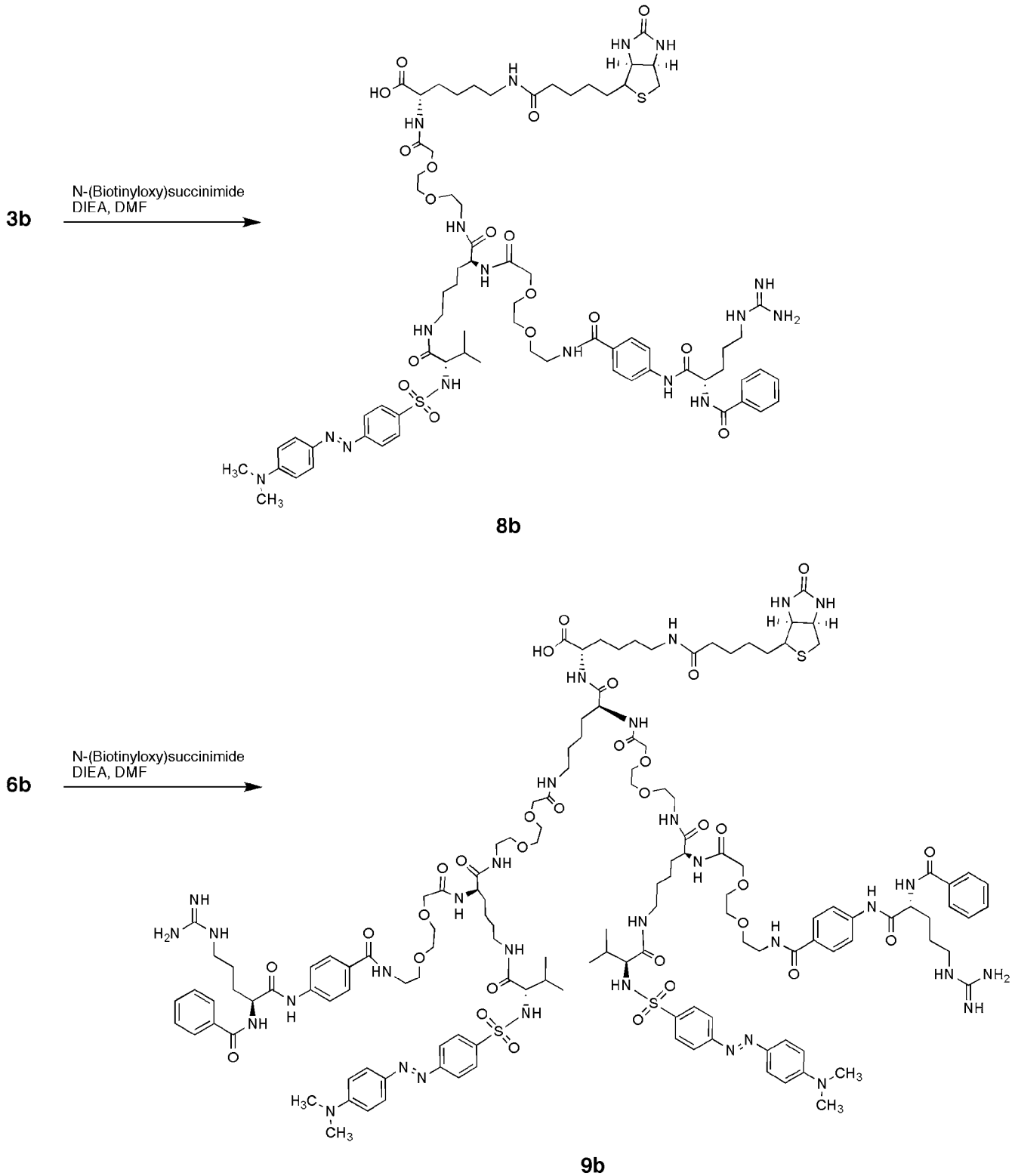
Upon completion, the reaction solution was diluted with 300 μL H_2O and 300 μL MeCN, both containing 1% TFA, and directly HPLC purified into two 600 μL aliquots. The resulting purified/lyophilized biotinylated SHALs were analyzed by HPLC and ESI-MS (spectra provided in Supporting Information).

Biotin SHAL ***8b*** *(DvLPBaPLB).* Reaction of **3b** (10.0 mg, 7.52 μmol) with biotinyl-OSu (3.5 mg, 8.20 μmol) gave 100% (Rt = 7.70 min) conversion by analytical HPLC and yielded **8b (**7.0 mg, red solid) after purification. ESI-MS: *m*/*z* calcd for $C_{73}H_{105}N_{17}O_{17}S_2$ $(M + H)^+$ 1557.88, found 1557.99; $(M + 2H)^{2+}$ 779.44, found 779.41; $(M + 3H)^{3+}$ 519.96, found 519.80.

Biotin SHAL ***9b*** *((DvLPBaP)$_2$LLB).* Reaction of **6b** (10.0 mg, 3.78 μmol) with biotinyl-OSu (1.5 mg, 4.39 μmol) gave 100% (Rt = 8.23 min) conversion by crude analytical HPLC and yielded **9b** (8.7 mg, red solid) after purification. ESI-MS: *m*/*z* calcd for $C_{136}H_{194}N_{32}O_{31}S_3$ $(M + 2H)^{2+}$ 1435.72, found 1435.78; calcd for $(M + 3H)^{3+}$ 957.49, found 957.52; calcd for $(M + 4H)^{4+}$ 718.37, found 718.35; calcd for $(M + 5H)^{5+}$ 574.86, found 574.85.

Determination of metal-free DOTA. DOTA−SHALs **4a−c** and **7a−c** were assayed in triplicate using a cobalt metal binding assay to determine the ratio of DOTAs available, following synthetic and purification procedures, for metal chelation. The binding assay was modified from previously described procedures (*29*−*31*). Generally, an aliquot of DOTA−SHAL in 10% DMSO in PBS was diluted into 0.1 M $(NH_4)_3PO_4$, pH 5.3, and excess standardized aqueous solution of $^{57}CoCl_2$ was added (manufacturer provided batch-specific specific activity information). The final solution was adjusted to pH 7.0 using NH_4-OAc, and this mixture was held for 30 min at room temperature. The initial concentration of the metal-free DOTA−SHAL was estimated from HPLC peak area with UV absorbance at 254 nm. Subsequently, aqueous EDTA (Fisher Scientific) was added to a final concentration of 10 mM and incubated for 15 min to sequester nonspecifically bound and excess cobalt ions. Radiolabeled ^{57}Co-DOTA−SHAL was estimated by TLC (precoated silica gel plates (EM Science, Gibbstown, NJ) with 10% NH_4-OAc−MeOH 1:1 v/v as the eluent). The concentration of the cobalt chelated by the DOTA−SHALs was determined by

Scheme 4. Synthesis of Biotinylated SHALs 8b and 9b



radiation counting using 1282 Compu Gamma Counter (Pharmacia, Piscataway, NJ, or a Fuji film BAS-1800 imager) against a known quantity of standardized $^{57}CoCl_2$ solution. The metal-chelatable DOTA was calculated as the ratio of the molar concentration of the ^{57}Co-DOTA−SHAL chelate and metal-free DOTA−SHAL ligand (Table 3).

Radiolabeling with ^{111}In. DOTA−SHALs **4a-c** and **7a−c** were labeled with $^{111}InCl_3$ (*31*). Generally, an aliquot of $^{111}InCl_3$ (4−5 mCi, 150−185 MBq, 15−20 μL) was added to a solution of DOTA−SHAL (25−50 μg) in 0.1 M $NH_4CO_2CH_3$ (50 μL). The final pH of the reaction mixture was adjusted to 6.5 by adding 4 M NH_4OAc and incubated for 1 h at 37 °C. After 1 h, 0.1 M EDTA (10−20 μL) was added to sequester excess, free $^{111}In^{3+}$. The radiolabeled product was purified by HPLC with a 1000 Da cutoff dialysis membrane using PBS as dialyzer. The ^{111}In-conjugated DOTA−SHAL was eluted between 8 and 10 min. The radiopharmaceutical purity of the radiolabeled SHALs was determined by TLC (10% NH_4OAc−MeOH 1:1), HPLC, and Cellulose-acetate electrophoresis (CAE) (Table 3). HPLC-purified pharmaceuticals were concentrated using Speed-

Table 1. Crude Percent Yield and Milligrams of Isolated Yield of SHALs[a]

SHAL	R_1	R_2	crude yield (%)	isolated yield (mg)
3a	D	It	50	40
3b	Dv	Ba	73	20
3c	Dv	T	80	20
6a	D	It	65	96
6b	Dv	Ba	62	60
6c	Dv	T	63	40

[a]Crude percent yield was estimated from SHAL absorbance of analytical HPLC trace at 254 nm.

Table 2. Crude Reaction Yield and Milligrams of Isolated Yield of DOTA−SHALs 4a−c and 7a−c

SHAL	R_1	R_2	crude yield (%)	isolated yield (mg)
4a	D	It	100	8.0
4b	Dv	Ba	93	6.5
4c	Dv	T	75	7.0
7a	D	It	70	12.0
7b	Dv	Ba	80	7.0
7c	Dv	T	70	4.0

Table 3. Quantitative Characterization of the Radiochemical and Purified Products

SHAL	metal chelatable DOTA to SHAL ratio	isolated product yield (%)	purity of In^{3+} labeled SHAL				specific activity μCi/μg
			TLC (%)	HPLC (%)	CAE 11′ (%)	CAE 45′ (%)	
4a	0.54	70	92	90	85	86	110
4b	0.60	95	95	94	95	95	150
4c	0.50	95	95	95	95	95	97
7a	0.52	75	96	95	95	97	102
7b	0.54	90	97	95	95	94	100
7c	0.55	90	95	96	95	96	101

vac SC110 (Savant Instruments, Holbrook, NJ) and the product redissolved in 10% DMSO in PBS for further use.

Live Cell ELISA. Washed cells (1×10^6/100 μL) were added to wells of a 96-well plate containing either 10 μM biotinylated SHALs **8b** or **9b** that has been preincubated with 10 μg/mL of streptavidin−HRP or 10 nM Lym-1 that has been preincubated with 0.5 μg/mL of goat anti-mouse IgG-HRP (1 h preincubation at rt) and incubated at room temperature for 1 h with nutation. For control wells, cells were incubated with 10 μg/mL of streptavidin−HRP in assay buffer (PBS, 1% BSA pH 7.2).

After 1 h, the plate was centrifuged for 5 min at 300 *g*, the supernatant was carefully removed, and the wells washed three times. For each wash, the cells were resuspended in 200 μL assay buffer, centrifuged, and the supernatant removed. After the third wash, the cells were resuspended in 200 μL assay buffer, transferred to a new plate, and washed twice more with PBS. The supernatant was removed, and cells were resuspended in 200 μL ABTS substrate and incubated at rt for 20 min. The plate was centrifuged, 100 μL of the supernatant was transferred to a flat-bottom ELISA plate, and the OD 405 was determined using a Dynatech MRX ELISA plate reader.

RESULTS AND DISCUSSION

Small molecules that bind to two unique, but structurally distinct, cavities located on the surface of the β-subunit of HLA−DR10, an abundant cell surface HLA−DR protein found on non-Hodgkin's lymphoma and leukemia cells, have been identified using computational docking techniques (*32*, *33*). Pairs of these small molecules have been covalently linked and radiolabeled to generate multivalent ligands, termed SHALs, that exhibit high avidity for HLA-DR10 and potentially create a new generation of radiopharmaceuticals. Computational docking methods predicted two molecules shown in Figure 1, deoxycholic acid (D) and dabsyl-L-valine (Dv), to bind to one cavity on the surface of the β-subunit of HLA−DR10 (*34*). Three additional molecules, also shown in Figure 1, 3,3′,5-triido-L-thyronine (It), L-thyronine (T), and *N*-benzoyl-L-arginyl-4-aminobenzoic acid (Ba), were predicted to bind to an adjacent cavity. Subsequently, all five of these molecules have experimentally been shown to bind to native HLA−DR10 isolated from Raji cells and a recombinant form of the β-subunit (*20*, *21*). One attractive feature of all five molecules is that they each contain a carboxylic acid, which provides a convenient site for covalent attachment of a pair of these molecules onto a multivalent scaffold using amide coupling chemistry. Furthermore, the structure of the molecules predicted to bind to each site are sufficiently different to suggest that SHALs produced using each combination of molecules will exhibit differing properties in vivo.

SHALs **3a−c** were conveniently synthesized using a combination of orthogonally protected lysines and the incremental use of a commercially available Fmoc-protected poly(ethylene glycol) spacer unit to generate an amine-functionalized scaffold. Subsequently, the carboxylic acid-functionalized molecules shown in Figure 1 were coupled to the amine groups before the completed SHAL was cleaved from the resin. Scheme 1 shows the initial coupling of Fmoc-Lys(Boc)-OH to chlorotrityl chloride resin using standard procedures (*25*, *27*). The Boc-protected lysine was included to generate a free amine after cleavage of the SHAL from the resin to allow labeling of the SHAL with DOTA or biotin for example for subsequent binding assays. The Fmoc-protected poly(ethylene glycol) spacer was introduced to separate the target binding portion of the SHALs and the radiolabel. Finally, Dde-Lys(Fmoc)-OH was used to sequentially generate free amines to sequentially couple the small molecules (R_1 and R_2, Figure 1) predicted to bind to the two different sites on the target protein. The SHALs were cleaved from the resin and the Boc group removed by TFA treatment and the SHALs were purified using semipreparative HPLC. The SHALs cleaved from the resin were generally of high purity (Table 1), indicating that each coupling step went to near completion. SHALs were synthesized on various scales, yielding 20−100 mg of purified product (Table 1). However, the SHALs could be synthesized on a much larger scale using these solid-phase synthetic methods. During initial synthetic development, it was important to determine that the small molecules R_1 (Figure 1) could withstand the Dde-deprotection conditions (4% hydrazine in DMF). This was determined by small-scale reactions and mass spectrometry confirmation of product integrity. In addition, both R_1 and R_2 were determined to withstand TFA treatment for resin cleavage and Boc deprotection. SHALs containing deoxycholate (D) as R_1 required a treatment with 100 mM NH_4HCO_3 before purification to displace the TFA esters formed on the deoxycholate alcohols during resin cleavage.

SHALs **6a−c**, bis-versions of SHALs **3a−c**, were generated in an effort to increase avidity of the SHALs for the target protein even further. The increased multivalency of SHALs **6a−c** potentially increases avidity of the SHALs for tumor cells in two ways. First, it is possible that increasing the multivalency of the SHAL increases the local concentration of the binding molecules R_1 and R_2 at the protein surface, thereby increasing the likelihood that the two molecules are bound to the protein at the same time. Second, it is also possible that SHALs **6a−c** can bind to neighboring HLA−DR10 molecules, increasing avidity for the tumor cell. The distance between the covalently linked molecules R_1 and R_2 is sufficient to allow the SHALs **6a−c** to bind neighboring HLA−DR10 molecules. SHALs **6a−c** were synthesized using an incremental approach as outlined in Scheme 2. The use of these solid-phase scaffolds to

generate multivalent ligands allows the rapid generation of SHALs with a variety of small molecule pairs for subsequent radiolabeling and binding assays.

SHALs **3a**−**c** and **6a**−**c** were constructed for convenient conjugation to metal-chelating molecules DOTA (Scheme 3) or affinity tags, such as biotin (Scheme 4). The reaction between the commercially available NHS ester of the DOTA hexafluorophosphate (PF_6) salt with SHALs **3a**−**c** and **6a**−**c** in DMF and DIEA gave 70−100% conversion to DOTA−SHALs after 5−15 min as monitored by analytical HPLC (Table 2). Biotin-derivatized SHALs **8b** and **9b** were synthesized starting from **3a** and **6b**, respectively, using similar conditions (Scheme 4) to generate SHALs suitable for subsequent use in cell binding assays. Subsequently, the DOTA−SHALs were labeled with ^{57}Co to determine the ratio of DOTAs available for radiolabel chelation following synthetic and purification procedures. Generally, 50−60% of the DOTAs were available for radiolabel chelation (Table 3). While the percentage DOTAs available for chelation are in an acceptable range for the synthesis of a radiotherapy agent, this can be further improved through the implementation of stringent metal-free conditions during synthesis, and especially purification, to produce better radiolabeling yields and consequently higher specific activities.

Reaction parameters were optimized to achieve maximum efficiency in radiolabeling the DOTA−SHALs with ^{111}In. The concentration of DOTA−SHAL was varied from 0.5 to 12.5 nmol; it was observed that, while 40% complexation was achieved at 0.5 nmol, 90% complexation was achieved at 5 nmol DOTA−SHAL, determined by titration with an excess amount of ^{111}In. Therefore, 5 nmol DOTA−SHAL was the minimum concentration used in labeling reactions. The chelation yield was determined over pH range 5−7, with a maximum observed at pH 5.5, consistent with previous reports of the radiolabeling of immunoconjugates (*31*). The chelation reaction was incubated at 37 °C, and the yield was estimated over 90 min. Incubation for 60 min was sufficient to achieve the maximum chelation.

The ^{111}In-DOTA−SHAL conjugates were characterized by TLC and HPLC. The radiochemical yield and purity were further confirmed by CAE to estimate the degree of aggregation of the DOTA−SHAL, if any, during the radiolabeling process. In general, the CAE assay showed very distinct resolution between the ^{111}In-DOTA−SHALs and ^{111}In-EDTA complexes, and the radioactive peaks were observed at 2.3−2.7 cm and >6.5 cm, respectively (Table 3). No radioactivity peak was observed at the origin of the CAE, indicating that no aggregation had occurred. The same trend was observed in the TLC assay; the ^{111}In-DOTA−SHALs showed very little migration from the point of spotting (R_F = 0.25−0.3), whereas the ^{111}In-EDTA complex moved further toward the solvent front (R_F = 0.6). Conversely, HPLC analysis showed the ^{111}In-EDTA at 2.5−3.0 min and the ^{111}In-DOTA−SHALs at 9.5−10 min. This distinct resolution facilitated the HPLC purification of the radiolabeled products. CAE, TLC, and HPLC were also used to determine the stability of the radiolabeled conjugate, and the ^{111}In-DOTA−SHALs were stable up to 72 h at room temperature with radiochemical purity of >85%. Radiolabeled product yields are shown in Table 3 and are similar to those obtained when generating antibody agents, and those needed for practicality, but can be further optimized for large-scale use where 80−90% yield is desirable. If radiochemical yield is greater than 90%, then the elimination of a final purification step can be considered with additional improvements in product yield.

In comparison to antibody agents, SHALs have a 1:1 ratio of protein binding sites to DOTA. Generally, radiolabeled monoclonal antibodies are modified to optimally contain an average of two DOTAs in order to preserve immunoreactivity, but can have up to a maximum of four DOTAs per macromolecule. One DOTA per SHAL with a molecular weight of ∼3000 Da compared to 2 DOTAs per monoclonal antibody with a molecular weight of ∼150 000 Da translates to a potentially higher specific activity (μCi/μg) for SHALs, although μCi/μmol may be less. Considering their relative mass differences of a factor of 50−100, and DOTA per molecule of about 2 in the opposite direction, then SHALs with specific activities 25−50 times greater than those for antibodies is theoretically feasible.

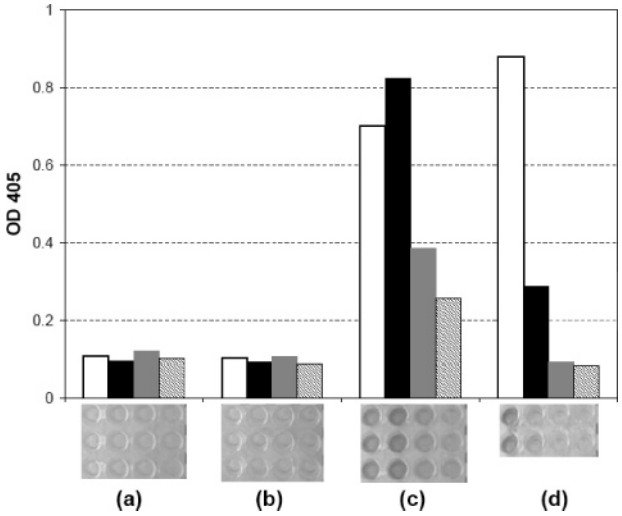


Figure 2. Live cell ELISA. (a) Buffer blank. (b) 10 μM biotinylated SHAL **8b**. (c) 10 μM biotinylated SHAL **9b**. (d) 0.5 μg/mL Lym 1. Cells: white, Raji; black, Nu-DHL-1; gray, MCF7; hashed, HBT-3477. Raji and Nu-DHL-1 are malignant lymphoma HLA−DR10 expressing cell lines, MCF7 and HBT-3477 are HLA−DR10-negative human breast epithelial cancer cell lines.

Whole-cell binding experiments conducted in vitro with ^{111}In-labeled SHALs **4b** and **7b** showed that both SHALs bind Raji HLA−DR10 positive non-Hodgkin's lymphoma cells. Linking the two molecules dabsyl-L-valine and *N*-benzoyl-L-arginyl-4-aminobenzoic acid together using a single lysine and poly(ethylene glycol) spacer resulted in the generation of a SHAL (**4b**) that binds to HLA−DR10-containing Raji cells with a K_d of ∼80 nM. Moreover, the bis-version of **4b**, SHAL **7b**, exhibited an avidity of 93 pM for Raji lymphoma cells (*21*). Biotinylated derivatives **8b** and **9b** of the two DOTA−SHALs **4b** and **7b** (in which biotin was conjugated to each SHAL in place of DOTA) were assessed using a live-cell ELISA, and the results are shown in Figure 2. The biotinylated SHALs were assayed against four cell types, two malignant lymphoma cell lines expressing HLA−DR10 (Raji and Nu-DHL-1) and two human breast epithelial cancer cell lines, known to not express HLA−DR10 (MCF7 and HBT-3477). Clearly, SHAL **9b** exhibits a much higher avidity than **8b**, again indicating that increased multivalency increases binding interactions. Morover, the SHAL **9b** exhibits a similar pattern of specificity to Lym-1, more specifically binding HLA−DR10-expressing cell lines.

The results presented here demonstrate that it is possible to create small-molecule-based targeting agents with an overall relatively small molecular weight (<5000 Da) that exhibit high avidity and specificity for their target protein, can be labeled with the appropriate radiolabel in high yield, and may prove useful as alternatives to traditional antibody-based targeting systems.

In conclusion, a convenient and rapid procedure for the generation of SHALs, relatively small molecular weight ligands, designed to bind HLA−DR10 has been established. In addition, the conditions for the reproducible radiolabeling of these SHALs have been determined. Significantly, it appears that increasing multivalent interactions significantly increases the avidity of a SHAL for the target protein. SHALs are a potential alternative

to antibodies as molecular targeting agents for the targeted radiotherapy of non-Hodgkin's lymphoma. By judicious selection of the small-molecule pairs used to generate SHALs, it should be possible to produce SHALs using the methods and procedures presented here that will not be significantly taken up by organs (liver, kidney) and are rapidly excreted, significantly decreasing the targeting agent's clearance time from the bloodstream. Synthetic molecules offer the additional advantage that they can be reproducibly synthesized in large amounts (g to kg), under QA procedures, while antibody production can be variable from batch to batch. Moreover, synthetic molecules can be produced in forms that are usually stable and do not degrade over prolonged periods of time. Small synthetic molecules are also less likely to elicit an immune response, and the small size of the reagent would allow it to penetrate tumors more effectively than an antibody counterpart, thereby increasing ionizing radiation to tumor cells, resulting in more homogeneous irradiation and hypothetically a better response.

ACKNOWLEDGMENT

Financial support for this work was provided by the National Cancer Institute (PO1-CA47829). This work was performed under the auspices of the U. S. Department of Energy by University of California, Lawrence Livermore National Laboratory, under contract W-7405-Eng-48.

Supporting Information Available: HPLC, ESI-MS, ^{1}H spectra, and selected ^{13}C NMR spectra. This material is available free of charge via the Internet at http://pubs.acs.org.

LITERATURE CITED

(1) Carter, P. J. (2006) Potent antibody therapeutics by design. *Nat. Rev. Immunol. 6*, 343−357.

(2) Presta, L. G. (2005) Selection, design and engineering of therapeutic antibodies. *J. Allergy Clin. Immunol. 116*, 731−736.

(3) Rose, L. M., Gunasekera, A. H., DeNardo, S. J., DeNardo, G. L., and Meares, C. F. (1996) Lymphoma selective antibody Lym-1 recognizes a discontinuous epitope on the light chain of HLA-DR10. *Cancer Immunol. Immunother. 43*, 26−30.

(4) Epstein, A. L., Marder, R. J., Winter, J. N., Stathopoulos, E., Chen, F. M., Parker, J. W., and Taylor, C. R. (1987) 2 new monoclonal-antibodies, Lym-1 and Lym-2, reactive with human B-lymphocytes and derived tumors, with immunodiagnostic and immunotherapeutic potential. *Cancer Res. 47*, 830−840.

(5) Rose, L. M., Deng, C. T., Scott, S. L., Xiong, C. Y., Lamborn, K. R., Gumerlock, P. H., DeNardo, G. L., and Meares, C. F. (1999) Critical Lym-1 binding residues on polymorphic HLA-DR10 molecules. *Mol. Immunol. 36*, 789−787.

(6) Cheson, B. D. (2003) Radioimmunotherapy of non-Hodgkin lymphomas. *Blood 101*, 391−398.

(7) DeNardo, G. L., O'Donnell, R. T., Oldham, R. K., and DeNardo, S. J. (1998) A revolution in the treatment of non-Hodgkin's lymphoma. *Cancer Biother. Radiopharm. 13*, 213−223.

(8) DeNardo, G. L. (2005) Treatment of non-Hodgkin's lymphoma (NHL) with radiolabeled antibodies (mAbs). *Semin. Nucl. Med. 35*, 202−211.

(9) Juweid, M. E. (2002) Radioimmunotherapy of B-cell non-Hodgkin's lymphoma: From clinical trials to clinical practice. *J. Nucl. Med. 43*, 1507−1529.

(10) DeNardo, G. L., DeNardo, S. J., Goldstein, D. S., Kroger, L. A., Lamborn, K. R., Levy, N. B., McGahan, J. P., Salako, Q., Shen, S., and Lewis, J. P. (1998) Maximum-tolerated dose, toxicity, and efficacy of (131)I-Lym-1 antibody for fractionated radioimmunotherapy of non-Hodgkin's lymphoma. *J. Clin. Oncol. 16*, 3246−3256.

(11) Goldenberg, D. M. (2001) The role of radiolabeled antibodies in the treatment of non-Hodgkin's lymphoma: the coming of age of radioimmunotherapy. *Crit. Rev. Oncol. Hemat. 39*, 195−201.

(12) Cutler, C. S., Smith, C. J., Ehrhardt, G. J., Tyler, T. T., Jurisson, S. S., and Deutsch, E. (2000) Current and potential therapeutic uses of lanthanide radioisotopes. *Cancer Biother. Radiopharm. 15*, 531−545.

(13) Imai, K., and Takoaka, A. (2006) Comparing antibody and small-molecule therapies for cancer. *Nat. Rev. Cancer 6*, 714−727.

(14) Shuker, S. B., Hajduk, P. J., Meadows, R. P., and Fesik, S. W. (1996) Discovering high-affinity ligands for proteins: SAR by NMR. *Science 274*, 1531−1534.

(15) Kramer, R. H., and Karpen, J. W. (1998) Spanning binding sites on allosteric proteins with polymer-linked ligand dimers. *Nature (London) 395*, 710−713.

(16) Maly, D. J., Choong, I. C., and Ellman, J. A. (2000) Combinatorial target-guided ligand assembly: Identification of potent subtype-selective c-Src inhibitors. *Proc. Natl. Acad. Sci. U.S.A. 97*, 2419−2424.

(17) Kitov, P. I., Sadowska, J. M., Mulvey, G., Armstrong, G. D., Ling, H., Pannu, N. S., Read, R. J., and Bundle, D. R. (2000) Shiga-like toxins are neutralized by tailored multivalent carbohydrate ligands. *Nature (London) 403*, 669−672.

(18) Fan, E. K., Zhang, Z. S., Minke, W. E., Hou, Z., Verlinde, C., and Hol, W. G. J. (2000) High-affinity pentavalent ligands of *Escherichia coli* heat-labile enterotoxin by modular structure-based design. *J. Am. Chem. Soc. 122*, 2663−2664.

(19) Mammen, M., Choi, S. K., and Whitesides, G. M. (1998) Polyvalent interactions in biological systems: Implications for design and use of multivalent ligands and inhibitors. *Angew. Chem., Int. Ed. Engl. 37*, 2755−2794.

(20) Albrecht, H., Cosman, M., Ngu-Schwemlein, M., Corzett, M., Curran, K. W., Hok, S., Dolan, C., Fang, X., DeNardo, S. J., DeNardo, G. L., and Balhorn, R. Recombinant HLA-DR10 beta-subunit for developing novel targeting agents for non-Hodgkin's lymphoma. Submitted.

(21) Balhorn, R., Hok, S., Burke, P. A., Lightston, F. C., Cosman, M., Zemla, A., Mirick, G., Perkins, J., Natarajan, A., Corzett, M., DeNardo, S. J., Lehner, T. A., Albrecht, H., Gregg, J. P., and DeNardo, G. L. (2007) Selective high affinity ligand antibody mimics for cancer diagnosis and therapy: Initial application to lymphoma/leukemia. *Clin. Cancer Res.*, in press.

(22) Charton, J., Gassiot, A. C., Girault-Mizzi, S., Debreu-Fontaine, M. A., Melnyk, P., and Sergheraert, C. (2005) Synthesis and pharmacological evaluation of Tic-hydantoin derivatives as selective sigma(1) ligands. Part 1. *Bioorg. Med. Chem. Lett. 15*, 4833−4837.

(23) Barlos, K., Gatos, D., Kallitsis, J., Papaphotiu, G., Sotiriu, P., Yao, W. Q., and Schafer, W. (1989) Synthesis of protected peptide-fragments using substituted triphenylmethyl resins. *Tetrahedron Lett. 30*, 3943−3946.

(24) Barlos, K., Gatos, D., Kapolos, S., Papaphotiu, G., Schafer, W., and Yao, W. Q. (1989) Esterification of partially protected peptide-fragments with resins - Utilization of 2-chlorotritylchloride for synthesis of leu-15-gastrin-I. *Tetrahedron Lett. 30*, 3947−3950.

(25) Chan, W. C., and White, P. D. (2000) *Fmoc solid phase peptide synthesis. A practical approach*. Oxford University Press, Oxford.

(26) Kates, S. A., Sole, N. A., Beyermann, M., Barany, G., and Albericio, F. (1996) Optimized preparation of deca(L-alanyl)-L-valinamide by 9-fluorenylmethyloxycarbonyl (Fmoc) solid-phase synthesis on polyethylene glycol-polystyrene (PEG-PS) graft supports, with 1,8-diazobicyclo[5.4.0]-undec-7-ene (DBU) deprotection. *Pept. Res. 9*, 106−113.

(27) Carpino, L. A. (1993) 1-Hydroxy-7-azabenzotriazole - an efficient peptide coupling additive. *J. Am. Chem. Soc. 115*, 4397−4398.

(28) Diaz-Mochon, J. J., Bialy, L., and Bradley, M. (2004) Full orthogonality between Dde and Fmoc: The direct synthesis of PNA-peptide conjugates. *Org. Lett. 6*, 1127−1129.

(29) Meares, C. F., McCall, M. J., Reardan, D. T., Goodwin, D. A., Diamanti, C. I., and McTigue, M. (1984) Conjugation of antibodies with bifunctional chelating-agents - Isothiocyanate and bromoacetamide reagents, methods of analysis, and subsequent addition of metal-Ions. *Anal. Biochem. 142*, 68−78.

(30) Goodwin, D. A., Meares, C. F., Watanabe, N., McTigue, M., Chaovapong, W., Ransone, C. M., Renn, O., Greiner, D. P., Kukis, D. L., and Kronenberger, S. I. (1994) Pharmacokinetics of pretargeted monoclonal-antibody 2d12.5 and Y-88 Janus-2-(P-Nitrobenzyl)-1,4,7,10-tetraazacyclododecanetetraacetic acid (Dota) in balb/C Mice

with Khjj mouse adenocarcinoma - a model for Y-90 radioimmunotherapy. *Cancer Res. 54*, 5937−5946.
(31) Kukis, D. L., Denardo, G. L., Denardo, S. J., Mirick, G. R., Miers, L. A., Greiner, D. P., and Meares, C. F. (1995) Effect of the extent of chelate substitution on the immunoreactivity and biodistribution of 2it-bat-Lym-1 immunoconjugates. *Cancer Res. 55*, 878−884.
(32) Ewing, T. J. A., and Kuntz, I. D. (1997) Critical evaluation of search algorithms for automated molecular docking and database screening. *J. Comput. Chem. 18*, 1175−1189.
(33) Cosman, M., Lightstone, F. C., Krishnan, V. V., Zeller, L., Prieto, M. C., Roe, D. C., and Balhorn, R. (2002) Identification of novel small molecules that bind to two different sites on the surface of tetanus toxin C fragment. *Chem. Res. Toxicol. 15*, 1218−1228.
(34) DeNardo, G. L., O'Donnell, R. T., Rose, L. M., Mirick, G. R., Kroger, L. A., and DeNardo, S. J. (1999) Milestones in the development of Lym-1 therapy. *Hybridoma 18*, 1−11.

BC060305O

Quaternized Poly(4-vinylpyridine)s as Model Gene Delivery Polycations: Structure−Function Study by Modification of Side Chain Hydrophobicity and Degree of Alkylation

Aurélie San Juan,[†] Didier Letourneur,[†] and Vladimir A. Izumrudov*[,‡]

Inserm, U698, Department of Bioengineering, X. Bichat Hospital, University Paris 7, Paris, F-75018, France, Institut Galilee, University Paris 13, Villetaneuse, F-93430, France, and M. V. Lomonosov Moscow State University, Department of Chemistry, 119992 Moscow, Russia. Received October 10, 2006; Revised Manuscript Received February 6, 2007

To optimize polycation-based gene delivery agents, the influence of molecular characteristics of the polycations on physicochemical properties of polycation/DNA complexes and their relationships to cellular gene transfer need to be understood. With this aim, we have synthesized a series of model polymers based on quaternized poly(4-vinylpyridine)s (C_nPVP-β) with the same DP of 1600 but differing by the number n of methylene groups in N-alkyl ester substituents from 1 to 6 and/or by degree of alkylation β from 25% to 95%. For polycations C_nPVP-95, the efficiency of transfection of a plasmid vector expressing a secreted form of alkaline phosphatase started to be detectable at $n = 4$, noticeable at $n = 5$, and again undetectable at $n = 6$. A decrease in β of active C_5PVP-95 from 95% to 65% resulted in a further noticeable increase of activity with a 9-fold increase for C_5PVP-65. This finding was attributed to the proton sponge mechanism due to protonation of non-alkylated pyridine moieties of C_nPVP-β/DNA complexes in slightly acidic media that was supported by the fluorescence quenching assay. The data demonstrate the advantages of partial alkylation of tertiary polyamines with medium-length alkyl agents for preparation of efficient nonviral gene delivery vectors.

INTRODUCTION

Gene therapy refers to the transfer of DNA encoding a therapeutic gene of interest into the target cells or organs with consequent expression of the transgene. In the past decade, gene therapy has received significant attention due to its potential application for treatment of acquired diseases (*1*, *2*). The most effective vectors for gene transfection are those based on viruses and viral peptide sequences (*3*, *4*). However, concerns with immunogenic and long-term oncogenic effects have prompted the concurrent development of synthetic gene delivery systems, such as liposomes, lipids, or polycations (*5*, *6*). Although naked DNA has been found to transfect some cells like the skeletal muscle cells of the cardiac and diaphragm regions, the pronounced negative charge of the double helix tends to inhibit DNA from entering cell membranes. Moreover, the unprotected DNA is rapidly degraded by nucleases. Linear cationic polymers, such as poly(lysine) and its conjugates (*7*−*9*), poly(*N*-ethyl-4-vinylpyridinium) bromide and its derivatives (*10*, *11*), branched polymers such as poly(ethylene imine) (*12*), and poly(amidoimine) dendrimers (*13*, *14*) effectively bind to the negatively charged DNA to form a polyelectrolyte complex that can be taken up by cells. The electrostatic binding of the polycation to the phosphate groups leads to DNA compaction. By being packed in the polyelectrolyte complex, DNA is shielded from contact with nucleases. It has been observed that in vitro transfection becomes efficient when complexes have a net positive charge to interact with negatively charged cell membranes.

Numerous works on liposomes or polymers for gene therapy indicated that the modification of positively charged chains with hydrophobic residues enhances their binding to cell membranes and penetration into cells. For gene transfer with cationic oligomers, long alkyl sequences were commonly used. For instance, the transformation of various mammalian cells was performed by DNA complexes with lipospermines that were synthesized by chemical modification of natural oligocation spermine with two long C_{18} alkyl tails (*15*, *16*). N-Terminal stearylation of oligoarginines consisting of 4−16 repeat units increased the transfection efficiency by 100 times with the maximal efficiency displayed by stearyl-Arg_8 (*17*), but the decrease in the number of methylene groups from 16 in the stearyl-Arg_8 to 10 in N-terminal lauryl-Arg_8 significantly reduced the efficiency. Few detailed reports are available for higher molecular weight structures. Thus, the introduction of 3−4% of C_{16} N-alkyl moieties in poly(*N*-ethyl-4-vinylpyridinium) bromide noticeably enhanced its affinity with DNA to negatively charged phosphatidylcholine/cardiolipin liposomes used as models of biological membranes (*18*). However, the hydrophobized polycation exhibited less transfection efficacy than unmodified poly(*N*-ethyl-4-vinylpyridinium) bromide (*19*, *20*). In another study, an increase of a number of methylene moieties in the side chain charge groups of cationic polyphosphoesters from 2 to 6 was accompanied by a 3-fold increase of the transfection efficacy (*21*). Similarly, an increase of the length of hydrophobic groups incorporated into the backbone of cationic polyvinyl ethers from 1 to 4 carbons was shown to significantly improve the transfection efficacy (*22*).

In the present study, combinations of length of the hydrophobic side chains and their content were evaluated using a series of model cationic copolymers of 4-vinylpyridine and *N*-alkyl-4-vinylpyridinium obtained by quaternization with ω-bromoesters. The hydrophobicity of the copolymers was controlled by a number of methylene groups in the ω-bromoesters and the degree of the quaternization. The main advantages of such model copolymers are their controllable hydrophilic−lipophilic balance and the presence of pH-induced ionizing 4-vinylpyridine units in their chains.

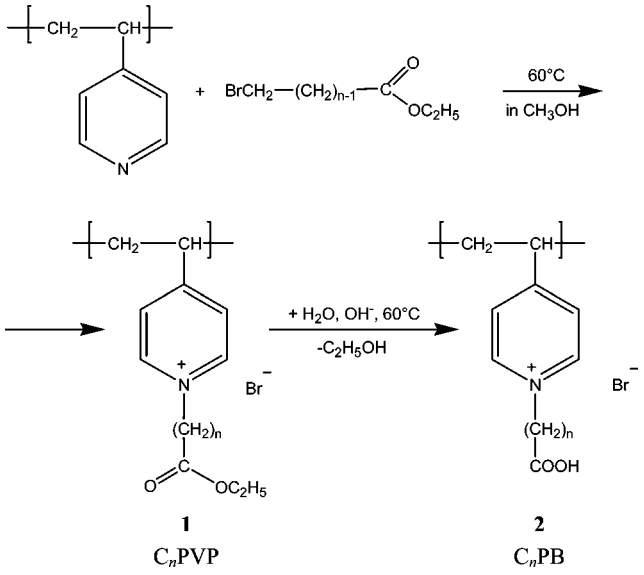
* Corresponding author. Moscow State University, Department of Chemistry, Leninskiye Gori V-234, 119992 Moscow, Russia. Telephone 7-4959393117, fax 7-4959390174, E-mail: izumrud@genebee.msu.su.

[†] University Paris.

[‡] M. V. Lomonosov Moscow State University.

10.1021/bc060317+ CCC: $37.00 © 2007 American Chemical Society
Published on Web 04/03/2007

Scheme 1. Synthesis Route for Quaternization of Poly(4-vinylpyridine) Yielding (1) Exhaustively Alkylated Polycations C_nPVP (n = 1 to 6) and (2) Polycarboxybetaines C_nPB



1 C_nPVP **2** C_nPB

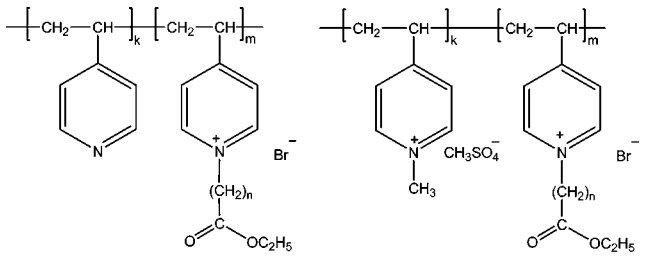
EXPERIMENTAL SECTION

Materials. NaOH, HCl, 3-(4,5-dimethylthiazol-2-yl)-2,5-diphenyltetrazolium bromide (MTT), Tris, MES, and HEPES buffers were purchased from Sigma (St. Louis, MO). In all experiments, twice-distilled water was used and purified by Milli-Q (Millipore, U.S.A.). Dulbecco's modified Eagle's media (DMEM) and fetal calf serum were obtained from BioMedia, France. Ethidium bromide was purchased from Sigma (St. Louis, MO). Concentration of ethidium bromide in solution was determined spectrophotometrically assuming molar extinction coefficient 5600 $L \cdot mol^{-1}\ cm^{-1}$ at 480 nm (*23*). Poly(ethylene imine) (PEI) was purchased from Aldrich (MW = 25 000 g/mol) or from Euromedex (ExGen 500, MW = 22 000 g/mol). Na salt of highly polymerized calf thymus DNA (~10 000 base pairs) was purchased from Sigma (St. Louis, MO) and used without further treatment. Concentration of DNA phosphate groups in the solutions was determined by UV absorbance measurements at 260 nm assuming molar extinction coefficient 6500 $L \cdot mol^{-1}\ cm^{-1}$ (*24*). pcDNA3-SEAP2 expression plasmid (pSEAP; 7443 base pairs) driven by the cytomegalovirus promoter was obtained by inserting the EcoRI-SalI fragment of the pSEAP2-control plasmid (Clontech), which contains the cDNA encoding for a secreted form of alkaline phosphatase (SEAP) preceded by the Kozak consensus translation initiation site and followed by the late polyadenylation signal of simian virus SV40, at the EcoR-SalI cloning sites of the pcDNA3 expression plasmid (Invitrogen).

Characterization Techniques. ^1H NMR spectra were recorded with a VARIAN Unity Inova 500 MHz spectrometer at 500.6 MHz using D_2O as solvent. IR spectroscopy was performed using a ThermoNicolet AVATAR 370 FTIR spectrometer (Thermo Electron Corparation, Waltham, MA).

Synthesis of Quaternized Poly(4-vinylpyridine)s (C_nPVP) (1). Quaternized poly(4-vinylpyridine)s that possessed the same average degree of polymerization, DP 1600, but differed by the number n of methylene groups in N-alkyl ester substituents (n = 1 to 6) were synthesized by alkylation of poly(4-vinylpyridine) sample (MW = 168 000 g/mol; Aldrich, U.S.A.) with esters of corresponding ω-bromocarboxylic acid (Scheme 1) as described elsewhere (*25*). The values of degree of alkylation of C_nPVP samples that were determined by FTIR measurements as described elsewhere (*26*) were 95 ± 3%.

Scheme 2. Structural Formulas of Copolymers (3) of 4-Vinylpyridine and *N*-Alkyl-4-vinylpyridinium (C_nPVP-β) with Different Content of N-Alkylpyridinium Moieties (β from 25% to 95%) and Copolymers (4) of *N*-Methyl-4-vinylpyridinium and *N*-Alkyl-4-vinylpyridinium (DMS−C_nPVP-β) Obtained by Exhaustive Alkylation of 4-Vinylpyridine Units of C_nPVP-β Samples with Dimethylsulfate



3 C_nPVP-β **4** DMS-C_nPVP-β

Synthesis of Polycarboxybetaines (C_nPB) (2). Polycarboxybetaines were obtained from the corresponding C_nPVP (n = 4 and 5) (Scheme 1) by alkaline hydrolysis that was performed by dropwise addition of concentrated NaOH solution to the solution of C_nPVP at 60 °C for several hours (*25*) according to the procedure described in ref 27. The hydrolysis was estimated from the potentiometric titration curves of aqueous solutions of the products that were conducted in the presence of sodium poly(styrene sulfonate) as described (*25*). The assay of aqueous solution of parent C_nPVP, as well as C_nPVP-β by the same approach, evidenced the absence of spontaneous hydrolysis in neutral media at room temperature even after storage of solutions for 2 weeks.

Synthesis of Copolymers of 4-Vinylpyridine and *N*-Alkyl-4-vinylpyridinium (C_nPVP-β) (3). Copolymers of 4-vinylpyridine and *N*-alkyl-4-vinylpyridinium (C_nPVP-β) with different content of N-alkylpyridinium moieties (β from 25% to 95%) were obtained by partial quaternization of poly(4-vinylpyridine) with the esters (Scheme 2). Samples were successively withdrawn from the reaction mixture during the course of the alkylation, and the values of β were estimated by FTIR spectroscopy (*26*). The presence of N-alkylpyridinium moieties in the copolymers was evidenced by ^1H NMR (e.g., the spectrum of C_5PVP-65 in D_2O with δ = 8.60, 7.43, 4.16, 2.41, 1.96, 1.67, and 1.26 ppm is depicted in Figure 1).

Synthesis of Copolymers of *N*-Methyl-4-vinylpyridinium and *N*-Alkyl-4-vinylpyridinium (DMS−C_nPVP-β) (4). Copolymers of *N*-methyl-4-vinylpyridinium and *N*-alkyl-4-vinylpyridinium (DMS−C_nPVP-β) were obtained by exhaustive

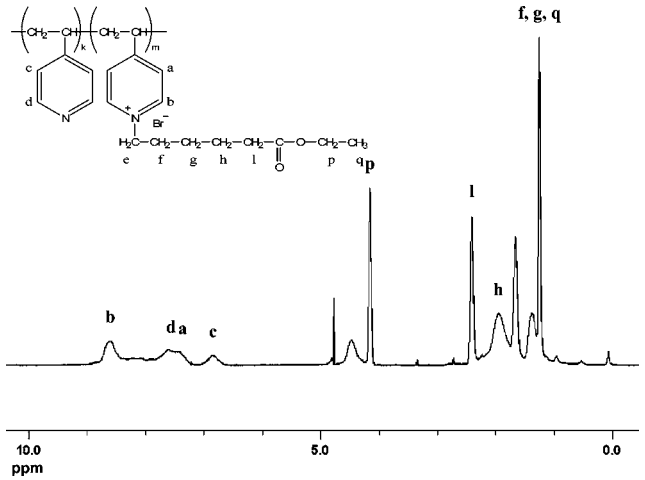


Figure 1. ^1H NMR spectrum of C_5PVP-65 copolymer. 500 MHz spectra were recorded using D_2O as solvent.

alkylation of 4-vinylpyridine units of C_nPVP-β samples with dimethylsulfate in methanol at room temperature.

Spectrophotometric Measurements were performed using Hitachi 150−20 Spectrometer (Japan) in water-thermostatic cell at 25 °C.

Fluorescence Measurements. Fluorescence intensity of the solutions was measured using a Jobin Yvon-3CS spectrofluorimeter (France) with water-thermostatic stirred cell holder. The measurements were made in a capped quartz fluorescence cell upon permanent stirring at 25 °C. The excitation and emission wavelengths in experiments with ethidium bromide were set at 535 and 595 nm, respectively.

Stability of C_nPVP/DNA Complexes in Water−Salt Solutions. The DNA solution was directly mixed in the fluorescence cell with ethidium bromide at a molar ratio [ethidium bromide]/[P] = 0.25 where [P] is molar concentration of DNA phosphate groups. At this ratio corresponding to 1 molecule of ethidium bromide per 2 base pairs (4 nucleotides), the maximum of ethidium bromide fluorescence intensity was observed (*28*). The concentration of DNA phosphate groups was 4×10^{-5} mol·L^{-1}. The solution of DNA/ethidium bromide complex was titrated with C_nPVP solution that was accompanied by quenching of ethidium bromide fluorescence due to displacement of the intercalated dye from DNA to the solution. The fluorimetric titration was conducted until the quenching was completed at a charge ratio [+]/[−] of 1.5. The mixtures were titrated with 4 M NaCl solution with a time interval between the titrant additions of 5 min. Destruction of the ion pairs in the C_nPVP/DNA polyelectrolyte complex by the added salt was monitored by the increase in fluorescence intensity I of the solution caused by re-intercalating of the dye into free sites of DNA. In parallel, a solution of DNA/ethidium bromide complex at the same concentration was titrated with 4 M NaCl solution, and the fluorescence intensity I_0 was measured. The stability of C_nPVP/DNA complexes was estimated by values of the salt concentration, [NaCl]*, corresponding to $I/I_0 = 1$, i.e., when a complete dissociation of the complex C_nPVP/DNA occurred (*29*). Note that the presence of the intercalated dye in the double helix weakens DNA binding to the polycations (*28*), but the contribution of this factor to the complex stability is relatively low and identical for all samples (*29*).

pH Profiles of Polycations with DNA. The fluorimetric titrations of DNA/ethidium bromide complex with solutions of C_5PVP-25, C_5PVP-65, or PEI were conducted at different pH values in 0.01 M MES or HEPES buffer solutions. This approach particularly applies for polycations with a large content of the ionizable amino groups that provides high accuracy in the calculations of a degree of conversion Θ in the polyelectrolyte coupling reaction (where Θ is the ratio of a current number of the protonated amino groups to the ultimate one). In neutral and slightly acidic media, the fluorescence intensity decreased linearly with the increase in charge ratio from 0 to 1 (*30*). The degree of conversion was determined in an equimolar mixture ([+]/[−] = 1) of polycations and DNA. The pH-independent contribution of (100 − β)% of N-alkylated units of C_5PVP-β polymers to the interaction with DNA that was accompanied by a displacement of ethidium bromide was determined but not taken into account upon calculation of the pH profile.

In Vitro Cell Transfection. Transfection experiments were carried out on rabbit vascular smooth muscle cells (SMCs; Rb-1 cell line (*31*)) cultured in DMEM supplemented with 1% penicillin, streptomycin, and amphotericin, 2% HEPES buffer, 1% glutamine, and 10% fetal calf serum. C_nPVP-β polycation and pSEAP solutions were filtered onto 0.22 μm Millipore filters before use. Twenty-four well plates were seeded with 5×10^4 cells per well 24 h before transfection. Ten microliters of pSEAP solution at 1 μg/μL was mixed with 10 μL of C_nPVP-β polycation solution at a concentration ranging from 0.06 μg/μL to 0.98 μg/μL, depending on the polycation, and corresponding to a charge ratio [+]/[−] of 1 or 5, assuming all amines were cationic. The resulting complex solution was diluted to a final volume of 50 μL with either serum-free or serum-containing culture medium, vortexed for 10 s, and allowed to stand at room temperature for 30 min. Cells were washed, and 450 μL of serum-free or serum-containing culture medium per well was added. The complex solution (C_nPVP-β/pSEAP) was then added to the wells, and cells were incubated at 37 °C in 95% air/5% CO_2 for 24 h. Cells were cultured for 72 h in serum-containing medium, and then the conditioned culture medium was removed and analyzed for SEAP activity. Phospha-Light kit (Tropix, Bedford, MA) was used for the measurement of SEAP activity, according to the manufacturer's protocol. Light output was measured using a luminometer (LUMAT LB9501, Berthold, Wildbach, Germany), as described elsewhere (*32*). SEAP activity was expressed as relative light units (RLU) per 10^5 cells. Cells incubated with culture medium alone or with pSEAP alone were used as controls. Cytotoxicity was assessed by the 3-(4,5-dimethylthiazol-2-yl)-2,5-diphenyltetrazolium bromide (MTT) assay (see below). For each condition, at least 3 experiments were performed.

Cell Viability. Evaluation of cell viability was performed with the MTT assay. At the end of the transfection experiments, the culture medium was replaced with 500 μL of fresh Hanks' Balanced Salt Solution and 50 μL of 5 mg/mL MTT. After 1 h incubation at 37 °C, MTT-containing medium was removed and 300 μL of DMSO was added to dissolve the formazan crystal formed by viable cells. Absorbance was measured at 540 nm. Cell viability was calculated according to the following equation: Cell viability (%) = $(OD_{540(sample)}/OD_{540(control)}) \times 100$, where the $OD_{540(control)}$ is measured with cells incubated in control medium.

Size and ζ-Potential Measurements. For each measurement, 750 μL of pSEAP at 0.03 μg/μL was mixed with 750 μL of polycation at concentrations ranging from 0.15 μg/μL to 0.29 μg/μL corresponding to a charge ratio [+]/[−] of 5. All the solutions were prepared in Tris buffer (pH = 7.4). The resulting mixtures were vortexed for 10 s and incubated for 30 min at room temperature before analysis. The size of polycation/DNA complexes was determined by quasi-elastic light scattering with a ZetaSizer 3000 instrument (λ = 633 nm, Malvern Instruments, U.K.) at 25 °C, using a sample refractive index of 1.59 and a viscosity of 0.89 cP. Data were collected at a scattering angle of 90° and sizes calculated from the correlation function using an automated method. Three series of five measurements were performed. ζ potentials were measured on the same instrument. Complexes used for the size determination were recovered and injected into the cell. The system was calibrated with a -50 ± 5 mV ζ-potential polystyrene standard from Malvern. The analysis parameters were as follows: viscosity = 0.89 cP, dielectric constant = 79, temperature = 25 °C, Smoluchowsky constant F (ka) = 1.50, dispersant refractive index = 1.33.

Statistical Analysis. All results are expressed as mean ± SD. Statistical comparisons were performed with the use of ANOVA and post-hoc PLSD test. A value of $p < 0.05$ was considered significant.

RESULTS AND DISCUSSION

A series of cationic copolymers based on quaternized poly(4-vinylpyridine) was synthesized. Schemes 1 and 2 indicate the synthesis conditions and the general formula of compounds from **1** to **4**. The advantages of utilizing quaternized poly(4-vinylpyridines) as model polycations were as follows: (i) All polycations possessed the same average degree of polymeriza-

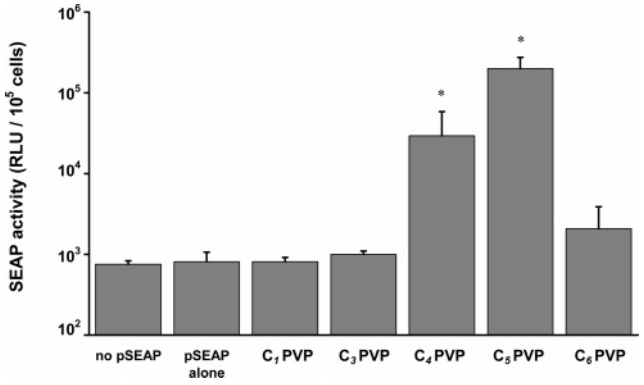


Figure 2. Effect of the number *n* of methylene groups in N-alkyl side chains of C_nPVP polycations on cell transfection efficacy. Plasmid pSEAP (1 μg) was used alone or with C_nPVP polycation solutions at charge ratio [+]/[−] of 5 in serum-free culture medium. The degree of alkylation was 95% for all polymers. Gene expression was measured 3 days after transfection. Transfection efficacy is expressed as relative light units (RLU) per 10^5 cells. Results represent the mean and standard deviation of 3 experiments. *, $p < 0.0001$ vs pSEAP alone.

tion, DP = 1600, that provided high stability of DNA/polycations and allowed circumvention of the possible influence of DP on the transfection efficiency (*33*). (ii) The opportunity to terminate the N-alkyl side chains with carboxylic groups by hydrolysis of the ester moieties (Scheme 1) allowed comparison of the transfection efficiency of polycarboxybetaines (**2**) to their parent polycations (**1**). (iii) The polycations remained soluble in aqueous media upon variation of the number of methylene groups in N-alkyl side chains (**3**) from 1 to 6 and/or the degree of alkylation $\beta \geq 25\%$. And, finally, (iv) non-alkylated pyridine units of all studied copolymers were accessible according to Scheme 2 to the alkylating agent dimethylsulfate, that allowed their quantitative quaternization (**4**) to establish the role of the pyridine groups in the transfection.

Alkylated C_nPVP Polycations (1). To elucidate the effect of hydrophobicity of the side chain on cell transfection, quaternized poly(4-vinylpyridine) polymers with the degree of quaternization of 95 ± 3% and an increasing number *n* of methylene groups from 1 to 6 in the N-alkyl substituents (Scheme 1) have been synthesized. The transfection efficiency was first estimated in the conditioned culture medium 3 days after incubation of cells for 24 h with mixtures of C_nPVP and a plasmid DNA encoding for the secreted form of alkaline phosphatase (pSEAP) in DMEM. No toxicity was noticed after incubation of cells with pSEAP and C_nPVP polycations (cell viability was 88.2 ± 9.9%). At a charge ratio [+]/[−] of 1, C_1PVP and C_5PVP were both inactive ($1.2 \pm 0.1 \times 10^3$ RLU/10^5 cells), whereas significant SEAP activity ($1.2 \pm 0.2 \times 10^5$ RLU/10^5 cells) was found with C_5PVP at a charge ratio [+]/[−] of 5. When all exhaustively alkylated poly(4-vinylpyridine) polymers were evaluated at a charge ratio [+]/[−] of 5, SEAP activity remained rather low for C_nPVP polycations with short N-alkyl substituents containing 1 to 3 methylene groups (Figure 2). At $n = 4$, there was noticeable SEAP activity that became pronounced at $n = 5$. However, at $n = 6$, the activity was rather low (Figure 2).

The *n*-dependent increase of transfection capacity correlated with previously reported data on transfection performed by cationic polyvinyl ethers with C_1−C_4 side chains in the backbone (*22*) whose efficacy was low with methyl- and ethyl-containing side chains, noticeably higher in the case of propyl residues, and significant with butyl moieties. Interestingly, C_6PVP was inactive as a gene transfer agent with cells (Figure 2). The reason is most likely the hydrophobic interactions between side chains that are strengthened upon lengthening of the side chains. In the case of C_6 N-alkyl substituents, the contribution of these intramolecular hydrophobic interactions could be large enough to hinder significantly the interaction of the C_6PVP polycation with DNA in a physiological buffer (DMEM; pH = 7, NaCl 0.15 M). This assumption is based on the *n*-dependent stability of C_nPVP/DNA complexes against the added salt that we studied by ethidium bromide displacement assay as described in the Experimental Section. The values of critical salt concentration determined by this approach for all C_nPVP polycations are listed in Table 1. It can be seen that the increase in *n* from 1 to 4 was accompanied by a progressive decrease in critical salt concentration [NaCl]* corresponding to complete dissociation of the C_nPVP/DNA complex. In the case of C_5PVP and most notably C_6PVP, the critical salt concentration was reduced markedly, suggesting that the side chains induced a pronounced steric hindrance that encumbered the electrostatic interactions between the charged pyridinium moieties and DNA phosphate groups.

Table 1. Critical Salt Concentration, [NaCl]*, Corresponding to Complete Dissociation of Different C_nPVP/DNA Complexes Measured by Ethidium Bromide Displacement Assay

C_nPVP	$n = 1$	$n = 2$	$n = 3$	$n = 4$	$n = 5$	$n = 6$
[NaCl]*, M	0.40	0.35	0.34	0.31	0.24	0.15

Thus, the maximum transfection capacity displayed by C_nPVP at $n = 5$ could be the result of optimal structure and composition of the C_5PVP chain that provided the balance between hydrophobic and electrostatic interactions needed for the transfection.

Polycarboxybetaines C_nPB (2). C_4PVP and C_5PVP polycations that exhibited significant transfection activity were transformed to the corresponding polycarboxybetaines, C_4PB and C_5PB (Scheme 1). The synthesis was performed by an exhaustive hydrolysis of ester moieties that terminated the N-alkyl substituents of polycations. Figure 3 shows the transfection efficacy determined upon incubation of cells with the polycarboxybetaine/DNA complexes. From the cell viability tests, it can be concluded that C_4PB and C_5PB polycarboxybetaines were nontoxic. Substitution in side chains of the ester moiety with a carboxylic group resulted in the complete loss of transfection activity for both polycarboxybetaines (Figure 3). For comparison, transfection activity for the parent polycations is also plotted in Figure 3. From a physicochemical point of view, the substitution is accompanied by a noticeable change of the hydrophilic−lipophilic balance of the side chain. Polycarboxybetaines that possess carboxylic groups are much more hydrophilic as compared to their precursors and, hence, less

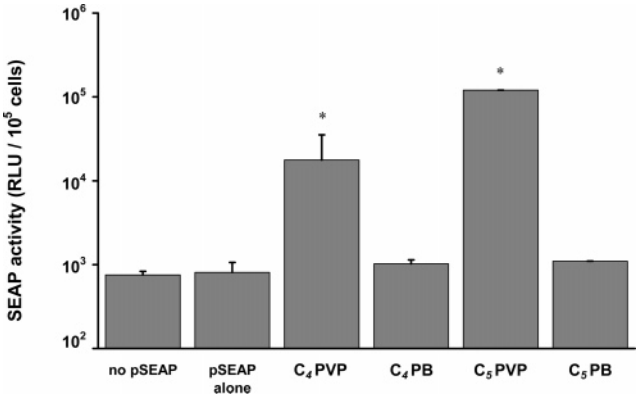


Figure 3. Cell transfection with polycarboxybetaines C_4PB and C_5PB. Plasmid pSEAP (1 μg) was used alone or with C_nPB polycation solutions at charge ratio [+]/[−] of 5 in serum-free culture medium. C_4PVP and C_5PVP (with similar methylene groups) are plotted for comparison. The degree of alkylation was 95% for all polymers. Gene expression was measured 3 days after transfection. Transfection efficacy is expressed as relative light units (RLU) per 10^5 cells. Results represent the mean and standard deviation of 3 experiments. *, $p < 0.0001$ vs pSEAP alone.

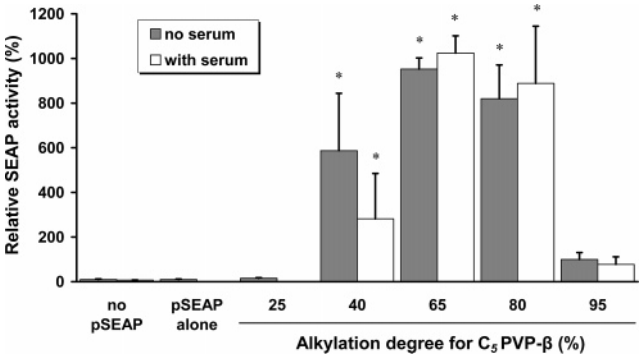


Figure 4. Effect of the alkylation degree (β) for C_5PVP-β polycations on cell transfection. Complex formation and incubation of cells were performed with either serum-free or serum-containing culture medium. Plasmid pSEAP (1 μg) was used alone or with C_5PVP-β solutions at charge ratio [+]/[−] of 5. Gene expression was measured 3 days after transfection. The data are presented as the relative SEAP activity taking as 100% the activity displayed by the corresponding exhaustively alkylated C_5PVP-95 in serum-free medium. Results represent the mean and standard deviation of 3 experiments. *, $p < 0.0001$ vs control (β = 95% in serum-free medium).

active in transfection. Besides, the carboxylic group being ionized in neutral media forms an ion pair with the pyridinium group in the betaine moiety. This weakens the electrostatic binding with DNA. Thus, the C_5PB/DNA complex was destroyed at physiological ionic strength (*25*).

Partially Alkylated C_nPVP-β Polycations (3) and Exhaustively Alkylated DMS−C_nPVP-β Polycations (4). To ascertain combinations of the length of the hydrophobic side chains and their content in the macromolecule, we have synthesized several series of cationic copolymers C_nPVP-β that possessed the same n but differed by degree of alkylation β. Note that the non-alkylated 4-vinylpyridine units are uncharged at physiological pH and their protonation occurred in acidic media according to the relatively low value of the apparent pK_a = 3.25 of poly(4-vinylpyridine). So, the composition of mixtures of partially alkylated polycations with pSEAP defined as a charge ratio [+]/[−] of 5 corresponds to the ratio of molar concentration of the quaternized N-alkylpyridinium moieties to molar concentration of phosphate groups. Figure 4 shows the transfection results obtained with the use of different C_5PVP-β copolymers. The data are presented as the relative SEAP activity taking the activity obtained with C_5PVP-95 in DMEM to be 100%. It can be seen that a decrease in β enhances the transfection of C_5PVP-95, with a maximal 9-fold increase for C_5PVP-65. For comparison, the relative SEAP activity obtained under the same conditions with ExGen 500, a commercial poly(ethylenimine) that is considered an excellent transfecting agent, was 6000%. It is remarkable that a further decrease in β for C_5PVP-β copolymers reduced the transfection efficiency that became negligible at β = 25%. Interestingly, cell transfection from inactive and highly hydrophobic C_6PVP-95 increased by reducing the alkylation degree with an optimum of significant transfection activity (85-fold increase from background level) at β = 40%.

To characterize the complex particles formed by C_5PVP-β with pSEAP, size and ζ-potential measurements were carried out at charge ratio [+]/[−] of 5 (Figure 5). It can be seen that all studied complexes including the complexes with exhaustively alkylated polycations did not differ both in size and in ζ potential being 150 ± 15 nm and 12 ± 2 mV, respectively. This suggests that the trends in transfection ability of C_5PVP-β copolymers cannot be attributed to the change of these parameters.

Contribution of N-alkyl substituents to intramolecular hydrophobic interactions may reduce flexibility of polycations and, hence, hinder their matching with DNA. To modulate polymer

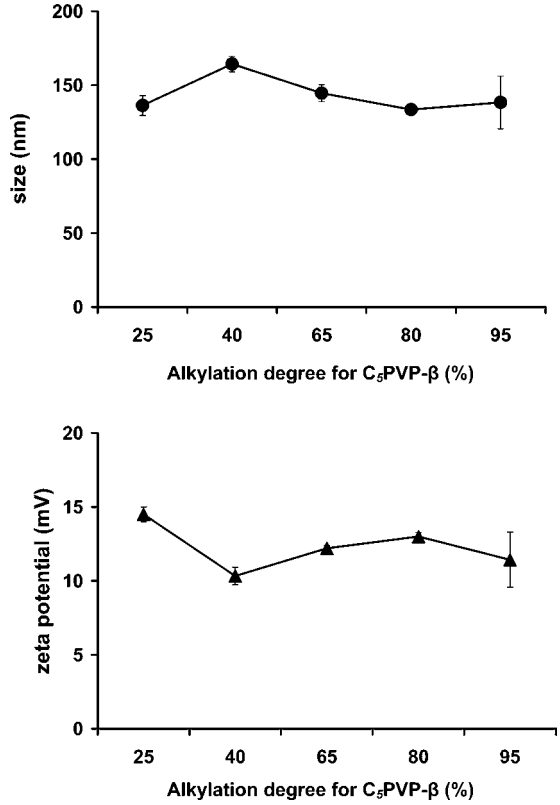


Figure 5. Size and ζ potential of complexes obtained with C_5PVP-β polycations and plasmid pSEAP. Sizes (circles) and ζ potentials (triangles) were measured in Tris buffer (pH 7.4) at a charge ratio [+]/[−] of 5 for all polycations.

flexibility, we performed quantitative alkylation of non-alkylated pyridine units of C_nPVP-β with dimethylsulfate treatment (**4**). The alkylation did not change the content and distribution of hydrophobic side chains along the macromolecule but transformed hydrophobic 4-vinylpyridine units that are not charged at physiological pH (non-alkylated poly(4-vinylpyridine) is insoluble in water at pH > 3.5) to hydrophilic quaternized 4-vinylpyridinium moieties containing relatively small N-methyl substituents (Scheme 2). Despite the higher net mean positive charge of the hydrophilized DMS−C_nPVP-β, the gene transfer activity of all these polycations was negligible (Figure 6).

pH Profiles of DNA Interaction with Polycations. The plausible explanation of the transfection activity of partially alkylated C_nPVP-β polycations is based on the ability of non-alkylated pyridine groups to be protonated in acidic media, according to a mechanism generally referred to as the "proton sponge hypothesis". When applied to a cell, the polycation/DNA complexes are thought to mediate transfection via a multistage process that includes hydrophobic and/or cationic binding to the cell membrane, internalization by endocytosis, and subsequent entry into the cytoplasm (*12*). The hypothesis asserts that polymers with high cationic charge potential, such as poly(ethylene imine) (PEI), act as a proton sponge upon acidification within endosomes or lysosomes. Under the acidic environment within lysosomes, every third nitrogen atom is protonated. The highly branched network of PEI absorbs a large amount of proton ions, like a sponge, upon lowering of the pH. The increased osmolarity resulted in endosomal or lysosomal swelling and subsequent escape of DNA into the cytosol. The proton sponge hypothesis has been built essentially around the transfecting activities of some cationic polymers such as PEI, PAMAM dendrimers, or polyhistidine (*34*) with apparent pK_a values close to pH 5.5, in relation to the acidic environment of endosomes and lysosomes. Yet, partially alkylated C_nPVP-β should be protonated in more acidic media, since aromatic

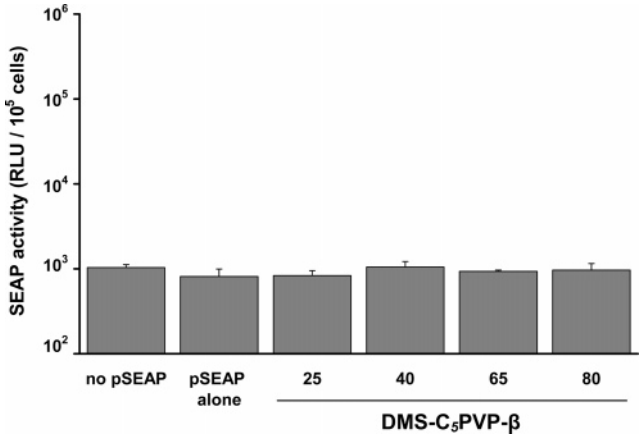


Figure 6. Effect of the exhaustive quaternization of C_5PVP-β polycations with DMS on cell transfection efficacy. Plasmid pSEAP (1 μg) was used alone or with the exhaustively quaternized DMS−C_5PVP-β polycation solutions at charge ratio [+]/[−] of 5 for the indicated alkylation degree (β). Gene expression was measured 3 days after transfection. Transfection efficacy is expressed as relative light units (RLU) per 10^5 cells. Results represent the mean and standard deviation of 3 experiments.

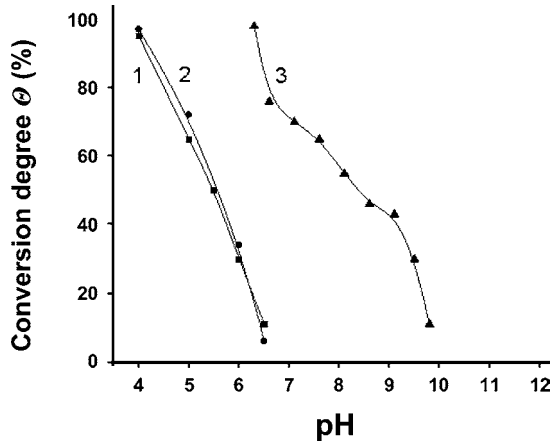


Figure 7. Protonation profiles of C_5PVP-25 (1), C_5PVP-65 (2), and PEI (3) determined by the ethidium bromide displacement assay. The degree of conversion (Θ) is plotted at the indicated pH for equimolar mixtures of polyamines and DNA (charge ratio [+]/[−] of 1).

tertiary amino groups of pyridine rings define relatively low apparent pK_a of 3.25 determined for poly(4-vinylpyridine) (*35*). As documented in Figure 7 by fluorimetric titration of polycations in the mixtures with DNA, the DNA promotes the protonation of polyamines that could occur with a ΔpH shift up to 2−3 units in the alkaline media as compared to ionization of free polyamine (*36*). The experimental procedure of estimating the protonation degree Θ of amino groups of polyamine bound in the complex with DNA is based on the ethidium bromide displacement assay performed at different pH (*29*). Figure 7 (curve 3) shows the protonation profile of PEI determined in an equimolar ([+]/[−] = 1) mixture of PEI and DNA. The inflection on curve 3 is in accordance with the basicity of the tertiary amino groups that noticeably differs from basicity of the primary and secondary amino groups of PEI. It is seen that the whole profile of PEI/DNA protonation is arranged in neutral, but not in slightly acidic, media, and hence, the transfection efficacy of PEI could not be attributed to protonation of the complex. Note that transfection with PEI or other polycations is commonly performed with a large excess of the polyamine. Consequently, apart from the ionizable amino group of PEI bound with DNA, a large number of amino groups that are not influenced by DNA are presented in endosomes and lysosomes and protonated in the acidic environment according to their intrinsic basicity. The protonation of these unbound amino groups appears to be the main reason for the well-documented high transfection efficacy of branched PEI. We used the same titration procedure for C_5PVP-65 (the most effective C_nPVP-β transfection agent) and for C_5PVP-25 that possessed the greatest amount of ionizable non-alkylated pyridine moieties in the series of C_5PVP-β copolymers but still remained soluble in aqueous media. The protonation profiles determined in equimolar mixtures of DNA with C_5PVP-25 (curve 1) or C_5PVP-65 (curve 2) are depicted in Figure 7. The left position of the protonation profile of C_5PVP-25 is in agreement with low pK_a of the pyridine rings. Nevertheless, the profile is markedly shifted to the right as compared to the ionization of free poly(4-vinylpyridine) (*35*). The protonation profile of the C_5PVP-65 copolymer (curve 2) practically coincided with the profile of C_5PVP-25 (curve 1) and also arranged in slightly acidic media. These findings support the hypothesis that the transfection activity of partially alkylated C_5PVP-β polycations could be related to the proton sponge mechanism that is accomplished due to protonation of non-alkylated pyridine moieties of C_nPVP-β/DNA complexes in slightly acidic media.

Complexation in Physiological Conditions. According to the literature, the transfection activity of polycations in the presence of serum could be noticeably reduced due to the interaction of the unbound polycation chains with serum proteins. In the present study, all studied C_nPVP polycations were shown to form stable complexes with DNA in salt concentration above the physiological conditions (Table 1). Moreover, complexation and incubation of cells with C_5PVP-β copolymers in serum-containing media resulted in transfection activity (Figure 4). No significant loss in SEAP activities was observed as compared to serum-free medium. The transfection capacity of C_5PVP-65 and C_5PVP-80 copolymers was even slightly higher in serum-containing medium. This finding also supports the explanation of their high activity by protonation of C_nPVP-β/DNA complexes and evidenced a suitable chemical structure of these polycations to bind to DNA in physiological conditions (Table 1, Figure 4) and then transfer pSEAP inside the cell, providing successful gene expression.

CONCLUSION

The data demonstrate the advantages of partial alkylation of tertiary polyamines with medium-length alkyl agents for the preparation of future efficient nonviral gene delivery vectors. With the DNA binding effect on protonation of polyamines in endosomes and lysosomes, this extends the range of polycations capable of improving the transfection, even in physiological conditions, by involvement of polyamines with tertiary amino groups that possess relatively low pK_a.

ACKNOWLEDGMENT

The authors are grateful to Laurent Véron and Thierry Delair (CNRS-bioMérieux, UMR 2714, ENS Lyon, France) for size and ζ-potential measurements and to Erwann Guénin (CNRS, UMR 7033 University Paris 13, France) for NMR measurements. This work was supported by INSERM, University Paris 7, and University Paris 13. Vladimir A. Izumrudov thanks University Paris 13 for invitations as visiting professor that supported this work.

LITERATURE CITED

(1) Huang, L., and Viroonchatapan, E. (1999) In *Non-viral vector for gene therapy* (L. Huang, M.-Ch. Hung, and E. Wagner, Eds.) pp 3−22, Academic Press, New York.

(2) Marxhall, J., Yew, N., Eastman, S., Jiang, C., Scheule, R., and Cheng, S. (1999) In *Non-viral vector for gene therapy* (L. Huang, M.-Ch. Hung, and E. Wagner, Eds.) pp 39−68, Academic Press, New York.

(3) Kabanov, A. (1998) *Self-assembling complexes for gene delivery: from laboratory to clinical trial*. J. Wiley & Sons, New York.
(4) Cho, Y. W., Kim, J. D., and Park, K. (2003) Polycation gene delivery systems: escape from endosomes to cytosol. *J. Pharm. Pharmacol. 55*, 721−734.
(5) Behr, J.-P. (1993) Synthetic gene-transfer vectors. *Acc. Chem. Res. 26*, 274−278.
(6) Wagner, E., and Cotten, M. (1993) Non-viral approaches to gene therapy. *Curr. Opin. Biotechnol. 4*, 705−710.
(7) Curiel, D. (1994) High efficiency gene transfer mediated by adenovirus-polylysine-DNA complexes. *Ann. N. Y. Acad. Sci. 716*, 36−56.
(8) Wagner, E., Cotten, M., Foisner, R., and Birnstiel, M. (1991) Transferrin-polycation DNA complexes: the effect of polycation on the structure of the complex and DNA delivery to cells. *Proc. Natl. Acad. Sci. U.S.A. 88*, 4255−4259.
(9) Stankovitcs, J., Crane, A., Andrews, E., Wu, C. H., Wu, G., and Ledley, F. (1994) Overexpression of human methylmalonyl CoA mutase in mice after in vivo gene transfer with asialoglycoprotein/polylysine/DNA complexes. *Hum. Gene Ther. 5*, 1095−1104.
(10) Kabanov, A., Kiselyov, V., Chikindas, M., Astafieva, I., Glukhov, A., Gordeev, S., Izumrudov, V., Zezin, A., Levashov, A., Severin, E., and Kabanov, V. (1989) Transformation activity of plasmid DNA is enhanced by complexation with a hydrocarbon polycation. *Dokl. Acad. Nauk. 306*, 226−229.
(11) Kabanov, A., and Kabanov, V. (1995) DNA complexes with polycations for the delivery of genetic materials into cells. *Bioconjugate Chem. 4*, 372−379.
(12) Boussif, O., Lezoualc'h, F., Zanta, M. A., Mergny, M. D., Scherman, D., Demeneix, B., and Behr, J. P. (1995) A versatile vector for gene and oligonucleotide transfer into cells in culture and in vivo: polyethylenimine. *Proc. Natl. Acad. Sci. U.S.A. 92*, 7297−7301.
(13) Haensler, J., and Szoka, F. (1993) Functionalization of polyamidoamine cascade polymers and their use for efficient transfection of cells in culture. *Bioconjugate Chem. 4*, 372−379.
(14) Tang, M., Redemann, C., and Szoka, F. (1996) In vitro gene delivery by degradated polyamidoamine dendrimers. *Bioconjugate Chem. 7*, 703−714.
(15) Remy, J.-S., Sirlin, C., Vierling, P., and Behr, J.-P. (1994) Gene transfer with a series of lipophilic DNA-binding molecules. *Bioconjugate Chem. 5*, 647−654.
(16) Behr, J.-P. (1994) Gene transfer with synthetic cationic amphiphiles: prospects for gene therapy. *Bioconjugate Chem. 5*, 382−389.
(17) Futaki, S., Ohashi, W., Suzuki, T., Niwa, M., Tanaka, S., Ueda, K., Harashima, H., and Sugiura, Y. (2001) Stearylated arginine-rich peptides: a new class of transfection systems. *Bioconjugate Chem. 12*, 1005−1011.
(18) Yaroslavov, A., Sukhishvili, S., Obolsky, O., Yaroslavova, E., Kabanov, A., and Kabanov, V. (1996) DNA affinity to biological membranes is enhanced due to complexation with hydrophobized polycation. *FEBS Lett. 384*, 177−180.
(19) Kabanov, A., Astafieva, I., Chikindas, M., Rosenblat, G., Kiselev, V., Severin, E., and Kabanov, V. (1991) DNA interpolyelectrolyte complexes as a tool for efficient cell transformation. *Biopolymers 31*, 1437−1443.
(20) Kabanov, A., Astafieva, I., Maksimova, I., Lukandin, E., Georgiev, G., and Kabanov, V. (1993) Efficient transformation of mammalian cells using DNA interpolyelectrolyte complexes with carbon chain polycations. *Bioconjugate Chem. 4*, 448−454.
(21) Wang, J., Huang, S.-W., Zhang, P.-C., Mao, H.-Q., and Leong, K. (2003) Effect of side-chain structures on gene transfer efficiency of biodegradable cationic polyphosphoesters. *Int. J. Pharm. 265*, 75−84.
(22) Wakefield, D., Klein, J., Wolff, J., and Rozema, D. (2005) Membrane activity and transfection ability of amphipathic polycations as a function of alkyl group size. *Bioconjugate Chem. 16*, 1204−1208.
(23) Waring, M. (1965) Complex formation between ethidium bromide and nucleic acids. *J. Mol. Biol. 13*, 269−282.
(24) Olins, D., Olins, A., and von Hippel, P. (1967) Model nuclear protein complexes: studies on the interaction of cationic homopolypeptides with DNA. *J. Mol. Biol. 24*, 157−176.
(25) Izumrudov, V., Domashenko, N., Zhiryakova, M., and Davydova, O. (2005) Interpolyelectrolyte reactions in solutions of polycarboxybetaines, 2. Influence of alkyl spacer in the betaine moieties on complexing with polyanions. *J. Phys. Chem. B 109*, 17391−17399.
(26) Starodubtsev, S., Kirsh, Y. E., and Kabanov, V. (1977) Solvation effects and reactivity of free pyridine residues in macromolecules of poly-4-vinylpiridine. *Eur. Polym. J. 10*, 739−742.
(27) Bohrisch, J., Schimmel, T., Engelhardt, H., and Jaeger, W. (2002) Charge interaction of synthetic polycarboxybetaines in bulk and solution. *Macromolecules 35*, 4143−4149.
(28) Le-Pecq, J.-B., and Paoletti, C. (1967) A fluorescent complex between ethidium bromide and nucleic acids. Physical-chemical characterization. *J. Mol. Biol. 27*, 87−106.
(29) Izumrudov, V., Zhiryakova, M., and Kudaibergenov, S. (2000) Controllable stability of DNA-containing polyelectrolyte complexes in water-salt solutions. *Biopolymers 52*, 94−108.
(30) Izumrudov, V., Zhiryakova, M., and Akritskaya, N. (2003) Fluorescence quenching technique for study of DNA-containing polyelectrolyte complexes. In *Advanced Macromolecular and Supramolecular Materials and Processes* (Geckeler, K., Ed.) pp 277−289, Kluwer Academic/Plenum Publishers, Dordrecht.
(31) Nachtigal, M., Nagpal, M. L., Greenspan, P., Nachtigal, S. A., and Legrand, A. (1989) Characterization of a continuous smooth muscle cell line derived from rabbit aorta. *In Vitro Cell Dev. Biol. 25*, 892−898.
(32) Elmadbouh, I., Rossignol, P., Meilhac, O., Vranckx, R., Pichon, C., Pouzet, B., Midoux, P., and Michel, J. B. (2004) Optimization of in vitro vascular cell transfection with non-viral vectors for in vivo applications. *J. Gene Med. 6*, 1112−1124.
(33) Zelikin, A., Putnam, D., Shastri, P., Langer, R., and Izumrudov, V. (2002) Aliphatic ionenes as gene delivery agents: elucidation of structure-function relationship through modification of charge density and polymer length. *Bioconjugate Chem. 13*, 548−553.
(34) Pack, D., Putnam, D., and Langer, R. (2000) Design of imidazole−containing endosomolytic biopolymers for gene delivery. *Biotechnol. Bioeng. 67*, 217−223.
(35) Kirsh, Y., Komarova, O., and Lukovkin, G. (1973) Physicochemical study of ionic equilibria for poly-2 and poly-4-vinylpyridines in alcohol-water solutions. *Eur. Polym. J. 9*, 1405−1408.
(36) Kabanov, V. (1994) in *Macromolecular complexes in chemistry and biology* (Dubin, P., Bock, J., Davies, R. M., Schulz, D. N., Thies, C., Eds.) pp 151−174, Springer-Verlag B-H, Berlin.

BC060317+

Impact of Bidentate Chelators on Lipophilicity, Stability, and Biodistribution Characteristics of Cationic ^{99m}Tc-Nitrido Complexes

Young-Seung Kim, Zhengjie He, Wen-Yuan Hsieh, and Shuang Liu*

Civil Engineering Building, School of Health Sciences, Purdue University, 550 Stadium Mall Drive, West Lafayette, Indiana 47907. Received October 11, 2006; Revised Manuscript Received January 2, 2007

This report describes synthesis and evaluation of novel cationic ^{99m}Tc-nitrido complexes, $[^{99m}TcN(L)(PNP)]^+$ (L = ma, ema, tma, etma and mpo; PNP = PNP5, PNP6, and L6), as potential radiotracers for heart imaging. Cationic complexes $[^{99m}TcN(L)(PNP)]^+$ were prepared in two steps. For example, reaction of succinic dihydrazide with $^{99m}TcO_4^-$ in the presence of excess stannous chloride and PDTA resulted in the $[^{99m}TcN(PDTA)_n]$ intermediate, which then reacted Hmpo and PNP6 at 100 °C for 10−15 min to give $[^{99m}TcN(mpo)(PNP6)]^+$ in >90% yield. It was found that bidentate chelators have a significant impact on lipophilicity, solution stability, biodistribution, and metabolic stability of cationic ^{99m}Tc-nitrido complexes. The fact that $[^{99m}TcN(ema)(PNP6)]^+$ decomposes rapidly in the presence of cysteine (1 mg/mL) while $[^{99m}TcN(etma)(PNP6)]^+$ and $[^{99m}TcN(mpo)(PNP6)]^+$ remain stable for >6 h under the same conditions strongly suggests that thione-S donors in bidentate chelators increase the solution stability of their cationic ^{99m}Tc-nitrido complexes. Biodistribution studies were performed on four cationic ^{99m}Tc-nitrido complexes in Sprague−Dawley rats. $[^{99m}TcN(etma)(PNP5)]^+$ is of particular interest due to its high initial heart uptake (1.81 ± 0.35 %ID/g at 5 min postinjection), and long myocardial retention (1.99 ± 0.47 %ID/g at 120 min postinjection). The heart/liver ratio of $[^{99m}TcN(etma)(PNP5)]^+$ (6.06 ± 1.48) at 30 min postinjection is almost identical that of ^{99m}TcN-DBODC5 (6.01 ± 1.45), and is >2 times better than that of ^{99m}Tc-sestamibi (2.90 ± 0.22). Results from metabolism studies show that $[^{99m}TcN(etma)(PNP5)]^+$ has no significant metabolism in the urine, but it does show significant metabolism in feces samples at 120 min postinjection. Planar imaging studies suggest that $[^{99m}TcN(etma)(PNP5)]^+$ might be able to give clinically useful images of the heart as early as 30 min postinjection. $[^{99m}TcN(etma)(PNP5)]^+$ is a very promising candidate for more preclinical evaluations in various animal models.

INTRODUCTION

Recently, we reported a series of crown ether-containing cationic complexes $[^{99m}TcN(DTC)(PNP)]^+$ (Figure 1: DTC = L1−L5; PNP = PNP5 and L6)[1] as potential radiotracers for heart imaging (*1*). Results from biodistribution studies have clearly demonstrated that crown ether groups are very useful for improvement of the liver clearance of cationic ^{99m}Tc-nitrido complexes, some of which have the heart uptake comparable to that of ^{99m}Tc-sestamibi, the most successful radiotracer for myocardial perfusion imaging, with the heart/liver ratios being 4−5 times better than that of ^{99m}Tc-sestamibi at 120 min postinjection (p.i.). Results from imaging studies suggested that they might be able to give clinically useful images of heart as early as 30 min p.i. These promising results led us to explore other bidentate chelators for preparation of cationic ^{99m}Tc-nitrido complexes that have the heart/liver ratio substantially better than that of ^{99m}Tc-sestamibi while maintaining their high heart uptake.

As an extension of our previous studies, we now report the use of maltol (Hma), thiomaltol (Htma), ethylmaltol (Hema), ethylthiomaltol (Hetma), and 2-mercaptopyridine oxide (Hmpo) as the bidentate chelators for preparation of cationic complexes $[^{99m}TcN(L)(PNP)]^+$ (Figure 1: L = ma, ema, tma, etma, and mpo; PNP = PNP5, PNP6, and L6). These cationic ^{99m}Tc-nitrido complexes are designed in such a way that the lipophilicity and biodistribution characteristics can be modified by the choice of bidentate chelators and bisphosphines. Compared to the crown ether-containing DTCs (Figure 1: L1−L5), these bidentate chelators offer a greater structural diversity, which is very important for modification of biodistribution properties of cationic ^{99m}Tc radiotracers. To demonstrate their potential as radiotracers for heart imaging, we carried out biodistribution studies on four cationic ^{99m}Tc-nitrido complexes in Sprague−Dawley rats. Results from these studies will be compared to those of ^{99m}Tc-sestamibi and ^{99m}TcN-DBODC5 (DBODC = *N*,*N*-bis(ethyoxythyl)dithiocarbamate) reportedly having the best heart/liver ratio among the known cationic ^{99m}Tc radiotracers (*2*−*4*).

It is well-documented that maltol and ethylmaltol form neutral complexes with many biologically important metal ions (*5*−*10*). Their vanadyl(IV) complexes have been reported to possess insulin enhancing activity (*11*−*15*). The Co(II), Cu(II), and Cr(III) complexes of maltol have also been studied for their antihypoglycemic activity (*16*). Recently, thiolmaltol and ethylthiomaltol and their N-substituted derivatives have been used for preparation of their Cu(II), Ni(II), Zn(II), V(IV), group 13 and lanthanide metal complexes (*17*−*21*). The study described herein represents the first one to use these bidentate chelators to prepared cationic complexes $[^{99m}TcN(L)(PNP)]^+$ (Figure 1: L = ma, ema, tma, etma, and mpo; PNP = PNP5, PNP6, and L6).

* To whom correspondence should be addressed. Phone: 765-494-0236; fax 765-496-1377; e-mail: lius@pharmacy.purdue.edu.

[1] Abbreviations: 1,2-diaminopropane-*N*,*N*,*N*′,*N*′-tetraacetic acid (PDTA), maltol (Hma), thiomaltol (Htma), ethylmaltol (Hema), ethylthiomaltol (Hetma), and 2-mercaptopyridine oxide (Hmpo), *N*-ethoxyethyl-*N*,*N*-bis[2-(bis(3-methoxypropyl)phosphino)ethyl]amine (PNP5), *N*-ethoxyethyl-*N*,*N*-bis[2-(bis(3-ethoxypropyl)phosphino)ethyl]amine (PNP6), *N*-methoxy-ethyl-*N*,*N*-bis[2-(bis(3-ethoxypropyl)phosphino)-ethyl]amine (L6).

10.1021/bc0603182 CCC: $37.00 © 2007 American Chemical Society
Published on Web 03/13/2007

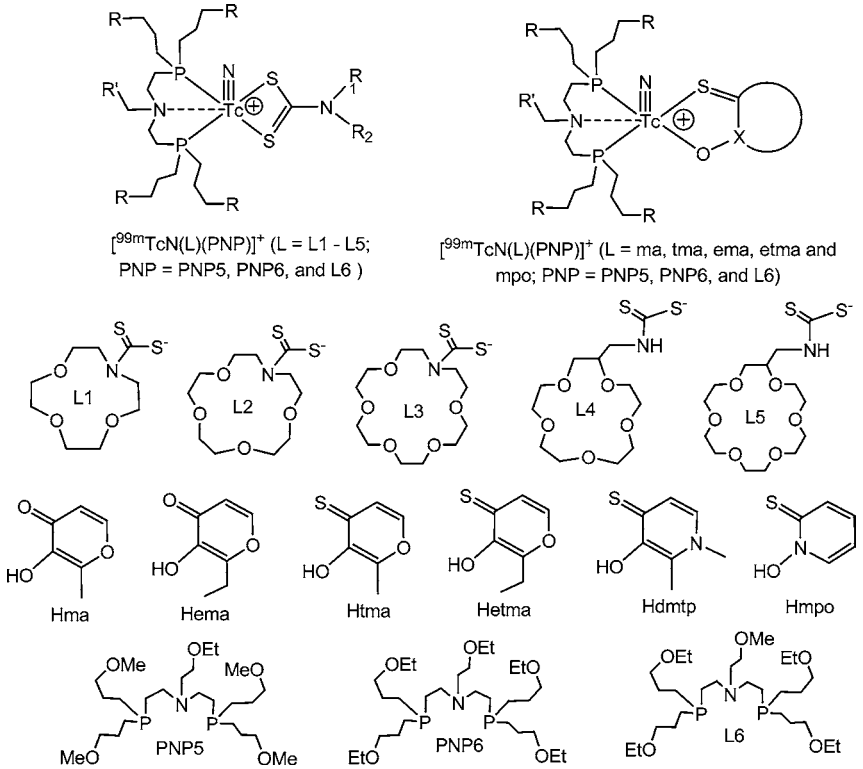
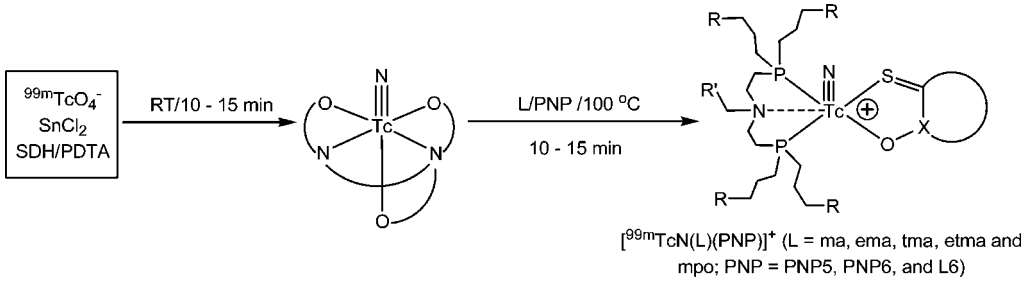


Figure 1. Bidentate chelators (Hma, Hema, Htma, Hetma, and Hmpo), bisphosphines (PNP5, PNP6, and L6), and their cationic ^{99m}Tc-nitrido complexes $[^{99m}TcN(L)(PNP)]^+$ (L = ma, ema, tma, etma, and mpo; PNP = PNP5, PNP6, and L6).

Scheme 1 . Synthesis of Cationic Complexes $[^{99m}TcN(L)(PNP)]^+$ (L = Ma, Ema, Tma, Etma, and Mpo; PNP = PNP5, PNP6 and L6).



EXPERIMENTAL SECTION

Materials. Chemicals, such as 1,2-diaminopropane-*N*,*N*,*N*′,*N*′-tetraacetic acid (PDTA), maltol (Hma), ethylmaltol (Hema), and mercaptopyridine oxide (Hmpo), were purchased from *Sigma*/*Aldrich* (St. Louis) and were used as received. Thiomaltol (Htma) and ethylthiomaltol (Hetma) were prepared according to the literature methods (*17*−*21*). Synthesis of *N*-ethoxyethyl-*N*,*N*-bis[2-(bis(3-methoxypropyl)phosphino)ethyl]amine (PNP5), *N*-ethoxyethyl-*N*,*N*-bis[2-(bis(3-ethoxypropyl)phosphino)ethyl]-amine (PNP6), and *N*-methoxyethyl-*N*,*N*-bis[2-(bis(3-ethoxypropyl)phosphino)ethyl]amine (L6) has been described in our previous report (*1*). ^{99m}TcN-DBODC5 was prepared according to the literature method (*2*−*4*). *Cardiolite* vials were obtained as a gift from Bristol Myers Squibb Medical Imaging (North Billerica, MA) and were reconstituted according to the manufacturer's insert.

Methods. The radio-HPLC method used a LabAlliance semi-prep HPLC system with a β-Ram IN-US detector, and a Zorbax Rx C_8 column (4.6 mm x 150 mm, 100 Å pore size). The flow rate was 1 mL/min. The mobile phase was isocratic with 30% solvent A (25 mM NH_4OAc buffer, pH = 6.8) and 70% solvent B (methanol) at 0−5 min, followed by a gradient from 70% solvent B at 5 min to and 90% solvent B at 15 min.

General Procedure for Preparation of Cationic ^{99m}Tc-Nitrido Complexes. The solution containing SDH and PDTA was prepared according to the procedure described in our previous communication (*1*). To a 5 cc vial were added 1.0 mL of the solution containing SDH (5 mg/mL) and PDTA (5 mg/mL), 1.0 mL of $^{99m}TcO_4^-$ solution (2−10 mCi), and 20 μL of $SnCl_2$ solution (1 mg/mL in 1.0 N HCl). The reaction mixture was kept at room temperature for 15−30 min to form the ^{99m}Tc-nitrido intermediate. After addition of 0.5 mL of the solution containing the bidentate chelator (5−10 mg/mL) and the bisphosphine (5−10 mg/mL), the reaction mixture was heated at 95 °C for 10−15 min. After completion of radiolabeling, the vial was placed back into lead pig and allowed to stand at room temperature for 5−10 min. A sample of the resulting solution was analyzed by the radio-HPLC. The radiochemical purity (RCP) was >95% with minimal amount (<0.5%) of [^{99m}Tc]colloid formation.

Composition Studies. The mixed-ligand experiments were performed to determine the number of bidentate chelators or bisphosphines in cationic ^{99m}Tc-nitrido complexes according to the method described in our previous communication (*1*). The radiolabeling procedure was identical to that above except that two bidentate chelators or PNP-type bisphosphines were used as competing ligands in a the same vial. For example, a mixture of Hma (2 mg) and Hema (2 mg) was used to determine the number of bidentate chelators in cationic complexes [^{99m}TcN-

(L)(PNP6)]$^+$. The number of bisphosphines was determined in a similar fashion using a mixture L6 (2 mg) and PNP6 (2 mg).

Doses for Animal Studies. For biodistribution studies on [^{99m}TcN(L)(L6)]$^+$ (L = ema, tma and etma) and [^{99m}TcN(etma)-(PNP5)]$^+$, the radiotracer was purified by HPLC to remove all radioimpurities. Volatiles in the mobile phase were evaporated under reduced pressure. Doses were made by dissolving the residue to ~10 μCi/mL in saline with 15% (w/w) propylene glycol. The resulting solution was filtered with a 0.20 μm filter unit to eliminate particles before being injected into animals. The injection volume was 0.1 mL for each animal in biodistribution studies. For imaging studies with [^{99m}TcN(etma)-(PNP5)]$^+$ was first purified by HPLC. Volatiles in the mobile phase were completely removed under the reduced pressure. Doses were made by dissolving the residue to ~2.5 mCi/mL in saline containing ~15% (w/w) propylene glycol. The injection volume was ~0.25 mL for each animal in the imaging studies.

Determination of Log *P* Values. Log *P* values of cationic ^{99m}Tc-nitrido complexes were determined using the following procedure: the ^{99m}Tc radiotracer was prepared and purified by HPLC. The collected mobile phases were evaporated, and the residue was dissolved in a mixture of equal volume (3 mL:3 mL) of n-octanol and 25 mM phosphate buffer (pH = 7.4). After being vortexed for >20 min, the mixture was centrifuged at 8000 rpm for 5 min. Samples (in triplets) from aqueous and n-octanol were obtained and counted separately in a gamma counter (Beckman Gama 8000). The partition coefficients were calculated using the equation: P = (activity concentration in n-octanol)/(activity concentration in aqueous layer). The log *P* value was measured three different times and reported as an average of three different measurements.

Solution Stability. For solution stability in kit matrix, the radiotracer was prepared and analyzed by radio-HPLC at 0, 1, 2, 3, and 6 h postlabeling. For cysteine challenging experiment, the resulting reaction solution was mixed with an equal volume of a cysteine (1 mg/mL) solution. Samples of the mixture were analyzed by radio-HPLC at 0, 1, 2, 3, and 6 h.

Biodistribution Studies. Biodistribution studies were performed using Sprague−Dawley rats in compliance with NIH animal experiment guidelines (*Principles of Laboratory Animal Care*, NIH Publication No. 86−23, revised 1985). This animal model has been used as the screening tool for cationic ^{99m}Tc radiotracers (*51*−*56*). The protocols for these studies have been approved by the Purdue University Animal Care and Use Committee (PACUC). In short, 16 Sprague−Dawley rats (200−250 g) were anesthetized with intramuscular injection of a mixture of ketamine (80 mg/kg) and xylazine (19 mg/kg). A jugular vein was surgically exposed, and each animal was administered 1−3 μCi of the purified radiotracer in 100 μL of 10−20% propylene glycol. Four animals were sacrificed by sodium pentobarbital overdose at each time point (5, 30, 60, and 120 min p.i.). Blood was withdrawn from the heart through a syringe. Organs of interest (heart, brain, lung, liver, spleen, kidneys, muscle, and intestine) were excised, rinsed with saline, dried with tissues, weighed, and counted on a gamma counter (Beckman RD8000). Four extra standard doses were also weighed and counted before and after tissue samples. The organ uptake was calculated as a percentage of the injected dose per gram of wet tissue mass (%ID/g) and a percentage of the injected dose per wet organ (%ID/organ). The biodistribution data and T/B ratios are reported as an average plus the standard variation.

Imaging Studies. Two Sprague−Dawley rats (200−250 g) were anesthetized with intramuscular injection of a mixture of ketamine (80 mg/kg) and xylazine (19 mg/kg). The radiotracer (300−500 μCi) was administered via surgically exposed jugular vein. Animals will be monitored on the gamma camera (PhoGama large field-of-view Anger camera and NucLearMac computer system). Sequential anterior images were collected for 5 min at the specified time (5, 15, 30, 60, and 120 min) using 256 × 256 image matrix while animal are still under anesthesia. Images of rats administered with ^{99m}Tc-sestamibi and ^{99m}TcN-DBODC5 were obtained using the same protocol. After imaging, the animals were sacrificed by sodium pentobarbital overdose. The urine and feces samples were collected for metabolism studies.

Table 1. RCP Data and Radio-HPLC Retention Times of Cationic ^{99m}Tc-nitrido Complexes

compound	radiochemical purity (%)	HPLC retention time (min)	log *P* value
^{99m}Tc-sestamibi	>98	16.5	1.29 ± 0.15
^{99m}TcN-DBODC5	>90	16.2	1.10 ± 0.07
[^{99m}TcN(ma)(PNP5)]$^+$	90.5	9.3	-0.01 ± 0.01
[^{99m}TcN(ema)(PNP5)]$^+$	90.3	10.7	0.53 ± 0.08
[^{99m}TcN(tma)(PNP5)]$^+$	91.0	9.9	0.38 ± 0.10
[^{99m}TcN(etma)(PNP5)]$^+$	90.0	15.5	0.67 ± 0.15
[^{99m}TcN(mpo)(PNP5)]$^+$	91.2	15.8	0.51 ± 0.05
[^{99m}TcN(ma)(PNP6)]$^+$	91.2	15.8	1.19 ± 0.13
[^{99m}TcN(ema)(PNP6)]$^+$	90.8	16.7	1.48 ± 0.02
[^{99m}TcN(tma)(PNP6)]$^+$	85.7	15.3	1.29 ± 0.02
[^{99m}TcN(etma)(PNP6)]$^+$	92.5	16.4	1.51 ± 0.01
[^{99m}TcN(mpo)(PNP6)]$^+$	90.3	16.7	1.49 ± 0.05
[^{99m}TcN(ma)(L6)]$^+$	90.1	14.2	0.92 ± 0.16
[^{99m}TcN(ema)(L6)]$^+$	90.2	15.2	1.22 ± 0.13
[^{99m}TcN(tma)(L6)]$^+$	85.8	15.7	1.09 ± 0.17
[^{99m}TcN(etma)(L6)]$^+$	85.6	16.6	1.43 ± 0.05
[^{99m}TcN(mpo)(L6)]$^+$	90.3	13.4	1.32 ± 0.13

Metabolism. The urine samples were collected from rats at 30 and 120 min p.i. by manual void and were mixed with an equal volume of acetonitrile. The mixture was centrifuged at a speed of 8000 rpm. The supernatant was collected and filtered through a 0.20 μm Millex-LG syringe driven filter unit. The filtrate was analyzed by radio-HPLC. The feces samples were collected once they were sacrificed after the imaging study (at ~120 min p.i.). The sample was suspended in a mixture of 50% acetonitrile aqueous solution, and the resulting mixture was vortexed for 5−10 min. After centrifugation, the supernatant was collected and passed through a 0.20 μ filter. The filtrate was analyzed by radio-HPLC.

Data and Statistical Analysis. The biodistribution data and T/B ratios are reported as an average plus the standard variation based on the results from four animals for each time point. Comparison between two different radiotracers was made using the one-way ANOVA test. The level of significance was set at $p = 0.05$.

RESULTS

Radiochemistry. Cationic complexes [^{99m}TcN(L)(PNP)]$^+$ (L = ma, ema, tma, etma and mpo; PNP = PNP5, PNP6, and L6) were prepared according to Scheme 1. First, ^{99m}TcO$_4^-$ was allowed to react with SDH in the presence of excess PDTA and stannous chloride. The reaction mixture was allowed to stand at room temperature for 15−30 min to form the [^{99m}TcN-(PDTA)$_n$] intermediate, which was then reacted with the bidentate chelator and bisphosphine at 100 °C for 10−15 min to give the cationic complex [^{99m}TcN(L)(PNP)]$^+$ (L = ma, ema, tma, etma, and mpo; PNP = PNP5, PNP6, and L6). Using this procedure, all new radiotracers had >85% RCP with minimal amount (<0.5%) of [^{99m}Tc]colloid formation.

A reversed phase radio-HPLC method was used to analyze cationic complexes [^{99m}TcN(L)(PNP)]$^+$ (L = ma, ema, tma, etma, and mpo; PNP = PNP5, PNP6, and L6). Their HPLC retention times are listed in Table 1. Figure 2 illustrates representitive radio-HPLC chromatograms of [^{99m}TcN(ma)-(PNP6)]$^+$ and [^{99m}TcN(ema)(PNP6)]$^+$. There is always an impurity peak (5−10%) in their radio-HPLC chromatograms.

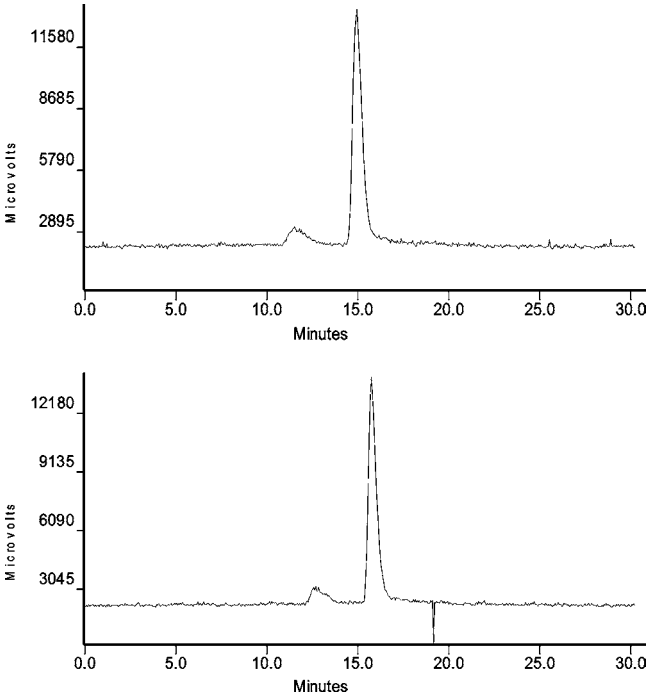


Figure 2. Typical radio-HPLC chromatograms of $[^{99m}TcN(ma)(PNP6)]^+$ (top) and $[^{99m}TcN(ema)(PNP6)]^+$ (bottom).

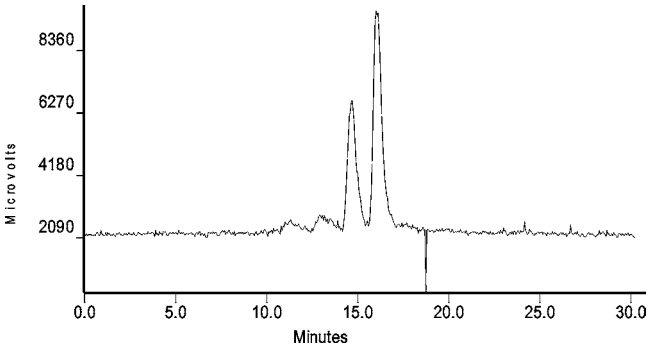


Figure 3. Radio-HPLC chromatogram of the reaction mixture containing $[^{99m}TcN(ma)(PNP6)]^+$ (left) and $[^{99m}TcN(ema)(PNP6)]^+$ (right).

These radioimpurities are most likely due to partial oxidation of the bisphosphine ligand during preparation or radiolabeling. This explanation is supported by the fact that the radioimpurities could be totally eliminated when the extra pure bisphosphine was used for radiolabeling.

The mixed-ligand experiment was performed to determine the composition (the number of bidentate chelators and bisphosphine ligands) of cationic ^{99m}Tc-nitrido complexes. In the first experiment, we used PNP6 as the bisphosphine ligand, and Hma and Hema as the competing chelators. After radiolabeling, the reaction mixture was analyzed by radio-HPLC. Figure 3 shows the typical radio-HPLC chromatogram of the reaction mixture containing $[^{99m}TcN(ma)(PNP6)]^+$ and $[^{99m}TcN(ema)(PNP6)]^+$. If only one bidentate chelator is bonded to the Tc, the HPLC chromatogram should show two peaks: one from $[^{99m}TcN(ma)(PNP6)]^+$ and the other from $[^{99m}TcN(ema)(PNP6)]^+$. If two bidentate chelators were bonded to the Tc, there would have been a third peak from the mixed-ligand complex, $[^{99m}TcN(ma)(ema)(PNP6)]$. The presence of two distinctive peaks at ~14.5 min and ~16.5 min for $[^{99m}TcN(ma)(PNP6)]^+$ and $[^{99m}TcN(ema)(PNP6)]^+$, respectively, clearly demonstrates that there is only one bidentate chelator in cationic complex $[^{99m}TcN(L)(PNP)]^+$. The number of bisphosphines in cationic complex $[^{99m}TcN(L)(PNP)]^+$ was determined in a similar fashion using Hema as the bidentate chelator, and L6 and PNP6 as the competing ligands. Figure 4 shows the radio-HPLC chromatogram of the resulting reaction mixture containing $[^{99m}TcN(ema)(L6)]^+$ and $[^{99m}TcN(ema)(PNP6)]^+$. The peak at 14.0 min is due to $[^{99m}TcN(ema)(L6)]^+$ and the peak at 15.5 min is from $[^{99m}TcN(ema)(PNP6)]^+$. This clearly demonstrates that there is only one bisphosphine in $[^{99m}TcN(L)(PNP)]^+$. Once again, the radioimpurities (~20%) at 10−12 min are caused by the partial oxidation of PNP6 during preparation.

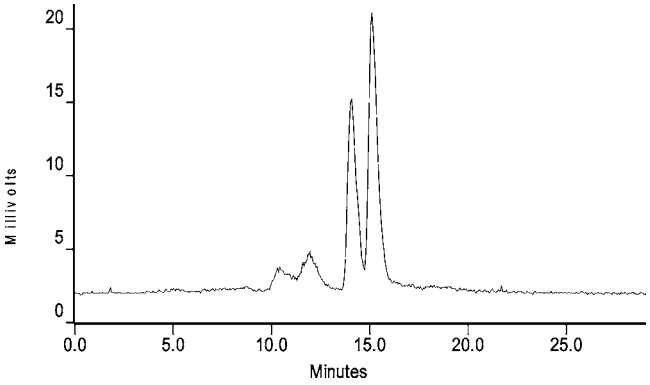


Figure 4. Radio-HPLC chromatogram of the reaction mixture containing $[^{99m}TcN(ma)(L6)]^+$ (left) and $[^{99m}TcN(ma)(PNP6)]^+$ (right). The radioimpurities (~20%) at 10−12 min are caused by the partial oxidation of PNP6.

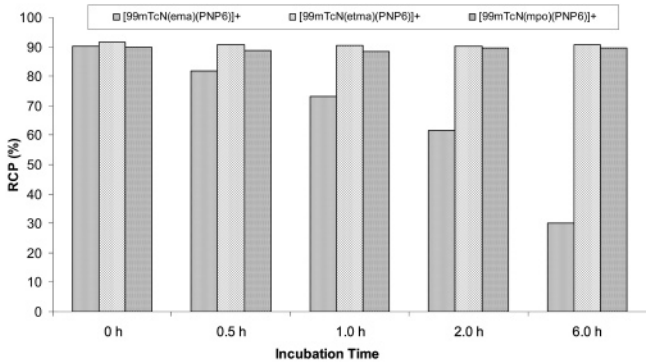


Figure 5. Solution Stability data for $[^{99m}TcN(ema)(PNP6)]^+$, $[^{99m}TcN(etma)(PNP6)]^+$ and $[^{99m}TcN(mpo)(PNP6)]^+$.

We studied the solution stability of $[^{99m}TcN(L)(PNP)]^+$ (L = ma, ema, tma, etma, and mpo; PNP = PNP5, PNP6 and L6) in the kit matrix and after purification. It was found that they all remain stable for more than 6 h. The cysteine challenge experiment was also performed for $[^{99m}TcN(L)(PNP6)]^+$ (L = ema, etma, and mpo). It was found that $[^{99m}TcN(ema)(PNP6)]^+$ decomposes rapidly in the presence of cysteine (~1.0 mg/mL). The RCP was >90% in the kit matrix and decreased to 61.6% at 2 h and 30.1% at 6 h (Figure 5). In contrast, $[^{99m}TcN(etma)(PNP6)]^+$ and $[^{99m}TcN(mpo)(PNP6)]^+$ remain stable (>6 h) in presence of excess cysteine (1.0 mg/mL) at ambient temperature (Figure 5). The use of thione-S donors in bidentate chelators increases solution stability of their cationic ^{99m}Tc-nitrido complexes.

Lipophilicity plays a significant role in the heart uptake and excretion kinetics of cationic ^{99m}Tc radiotracers (*1, 22−25*). Thus, it is important to explore the impact of bidentate chelators and bisphosphines on lipophilicity of their cationic ^{99m}Tc-nitrido complexes. Partition coefficient constants of $[^{99m}TcN(L)(PNP)]^+$ (L = ma, ema, tma, etma, and mpo; PNP = PNP5, PNP6, and L6) were determined by measuring their distribution in a mixture of equal volume n-octanol and 25 mM phosphate buffer (pH = 7.4). HPLC purification was needed to minimize the interference from other radioimpurities. The log *P* values are summarized in Table 1. In general, cationic complexes $[^{99m}TcN(L)(PNP)]^+$ (L = ma and tma) have lower lipophilicity than $[^{99m}TcN(L)$-

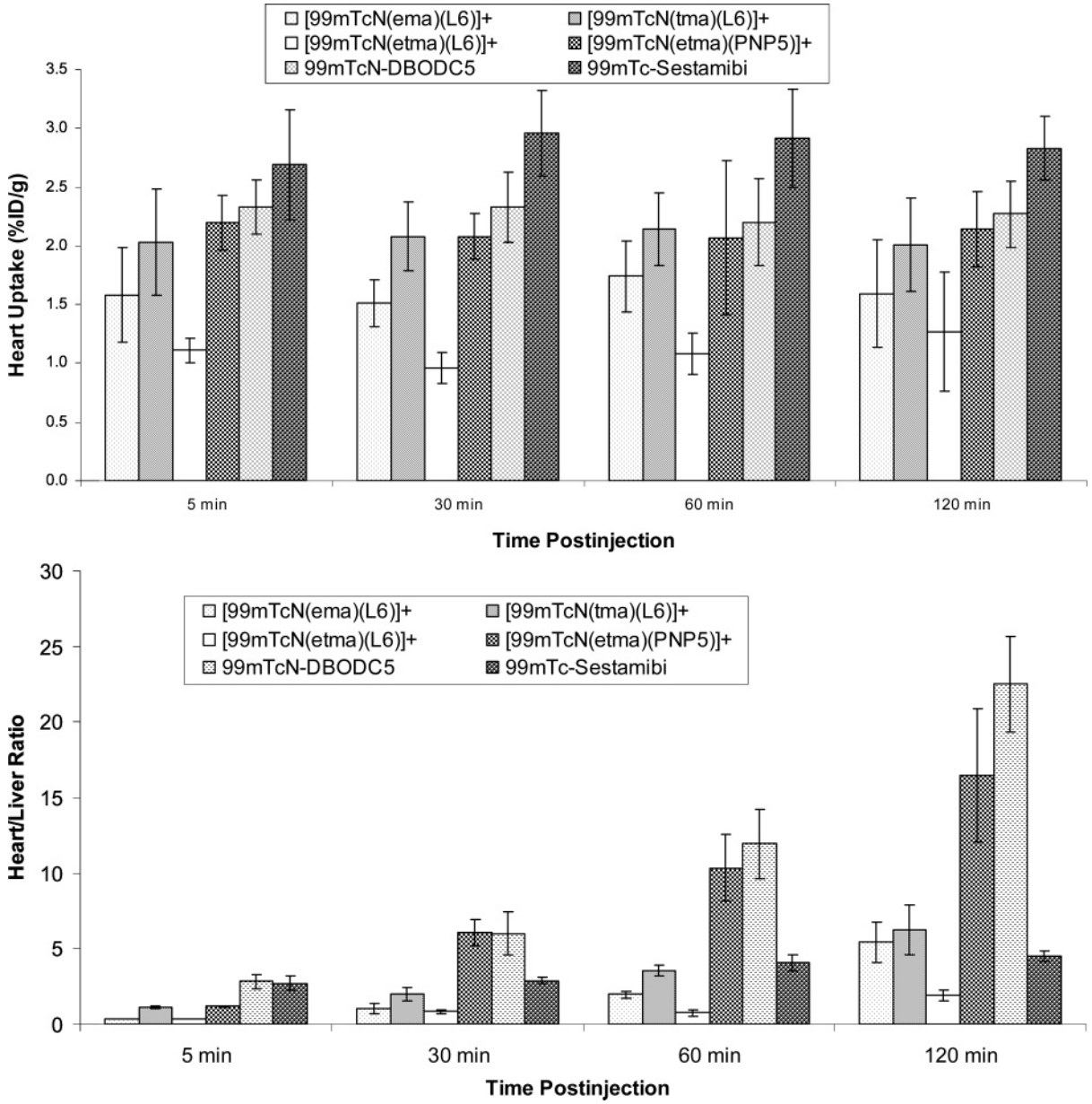


Figure 6. Comparison of heart uptake (top) and heart/liver (bottom) ratios between $[^{99m}TcN(ema)(L6)]^+$, $[^{99m}TcN(tma)(L6)]^+$, $[^{99m}TcN(etma)(L6)]^+$, $[^{99m}TcN(etma)(PNP5)]^+$, ^{99m}TcN-DBODC5, and ^{99m}Tc-Sestamibi.

$(PNP)]^+$ (L = ema and etma) due to the extra methylene group. $[^{99m}TcN(L)(PNP)]^+$ (L = tma and etma) are more lipophilic than $[^{99m}TcN(L)(PNP)]^+$ (L = ma and ema) due to the presence of thione-S donor. $[^{99m}TcN(L)(PNP6)]^+$ is more lipophilic than $[^{99m}TcN(L)(PNP5)]^+$ due to the presence of four ethoxypropyl groups in PNP6 instead of four methoxypropyl groups in PNP5. The lipophilicity of $[^{99m}TcN(mpo)(PNP)]^+$ is between that of $[^{99m}TcN(tma)(PNP)]^+$ and $[^{99m}TcN(etma)(PNP)]^+$.

Biodistribution Characteristics. Biodistribution studies in rats were performed on $[^{99m}TcN(etma)(PNP5)]^+$, $[^{99m}TcN(ema)(L6)]^+$, $[^{99m}TcN(tma)(L6)]^+$, and $[^{99m}TcN(etma)(L6)]^+$. We choose these four radiotracers to demonstrate the impact of solution stability and lipophilicity on their biodistribution characteristics. The biodistribution data and T/B ratios are listed in Tables SI−SIV. Figure 6 shows a direct comparison of their heart uptake and heart/liver ratios with those of ^{99m}Tc-sestamibi and ^{99m}TcN-DBODC5. Biodistribution data for ^{99m}Tc-sestamibi and ^{99m}TcN-DBODC5 in the same animal model were obtained from our previous report (*1*).

$[^{99m}TcN(ema)(L6)]^+$ has a lop *P* value of 1.22 ± 0.13, which is almost identical to that of ^{99m}Tc-sestamibi (1.29 ± 0.13). It had a moderate heart uptake (1.58 ± 0.41 %ID/g at 5 min p.i. and 1.60 ± 0.48 %ID/g at 120 min p.i.) with the heart/liver ratios being 0.35 ± 0.04, 1.06 ± 0.34, 2.56 ± 0.23, and 5.43 ± 1.37 at 5, 30, 60, and 120 min p.i., respectively. $[^{99m}TcN(etma)(L6)]^+$ has the log *P* of 1.43 ± 0.05. It has a low heart uptake (1.10 ± 0.10 %ID/g at 5 min p.i. and 1.27 ± 0.51 %ID/g at 120 min p.i.) and poor heart/liver ratios (0.37 ± 0.01, 1.21 ± 0.16, 1.17 ± 0.19, and 1.91 ± 0.31 at 5, 30, 60, and 120 min p.i., respectively). $[^{99m}TcN(tma)(L6)]^+$ has the log *P* value (1.09 ± 0.17) that is almost identical to that of ^{99m}TcN-DBODC5 (1.10 ± 0.07). It shows a high initial heart uptake (2.03 ± 0.75 %ID/g at 5 min p.i.) with a long myocardial retention (2.01 ± 0.40 %ID/g at 120 min p.i.). Its heart/liver ratios are 1.10 ± 0.09, 2.01 ± 0.41, 3.55 ± 0.34, and 6.25 ± 0.68 at 5, 30, 60, and 120 min p.i., respectively. The log *P* value of $[^{99m}TcN(etma)(PNP5)]^+$ is 0.67 ± 0.15. It has a relatively high heart uptake (1.81 ± 0.35 %ID/g at 5 min p.i.), a long myocardial retention (1.99 ± 0.47 %ID/g at 120 min p.i.), and high heart/liver ratios (6.06 ± 0.90, 10.36 ± 2.25, and 16.46 ± 4.24 at 30, 60, and 120 min p.i., respectively).

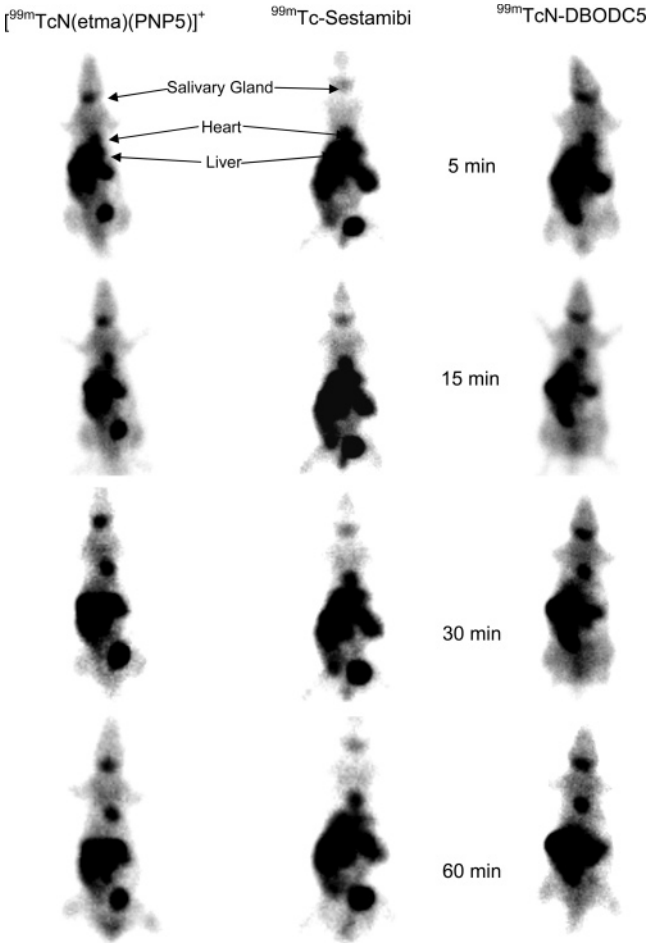


Figure 7. Planar images of rats administered with ~500 μCi of $[^{99m}TcN(etma)(PNP5)]^+$, ^{99m}Tc-sestamibi, and ^{99m}TcN-DBODC5. Arrows indicate the location of the heart, liver, and salivary gland (as determined by ex vivo gamma counting).

Imaging Studies. $[^{99m}TcN(etma)(PNP5)]^+$ was chosen for the imaging study in rats due to its much better heart/liver ratios than those of ^{99m}Tc-sestamibi. For comparison purposes, we also obtained images of rats administered with ^{99m}Tc-sestamibi and ^{99m}TcN-DBODC5. Figure 7 illustrates planar images of rats administered with $[^{99m}TcN(etma)(PNP5)]^+$, ^{99m}Tc-sestamibi, and ^{99m}TcN-DBODC5. In general, all the images acquired at 5 min p.i. show a very high liver uptake adjacent to the heart, but the lung activity was low for all three radiotracers. At 30 min p.i., the liver activity for $[^{99m}TcN(etma)(PNP5)]^+$ and ^{99m}TcN-DBODC5 is reduced significantly. By 60 min p.i., the liver activity almost disappeared for $[^{99m}TcN(etma)(PNP5)]^+$ and ^{99m}TcN-DBODC5 while the liver activity level for ^{99m}Tc-sestamibi remained high.

Metabolism. We examined metabolism of $[^{99m}TcN(etma)(PNP5)]^+$ by analyzing the urine and feces samples from the rats used in imaging studies. Figure 8 shows its radio-HPLC chromatograms in the kit matrix (A), in urine at 30 min p.i. (B), in urine at 120 min p.i. (C), and in feces at 120 min p.i. (D). Obviously, a very small amount of metabolite was detected in the urine samples (Figure 8: B and C), but a significant metabolism was observed in feces samples of rats administered with $[^{99m}TcN(etma)(PNP5)]^+$ (Figure 8D).

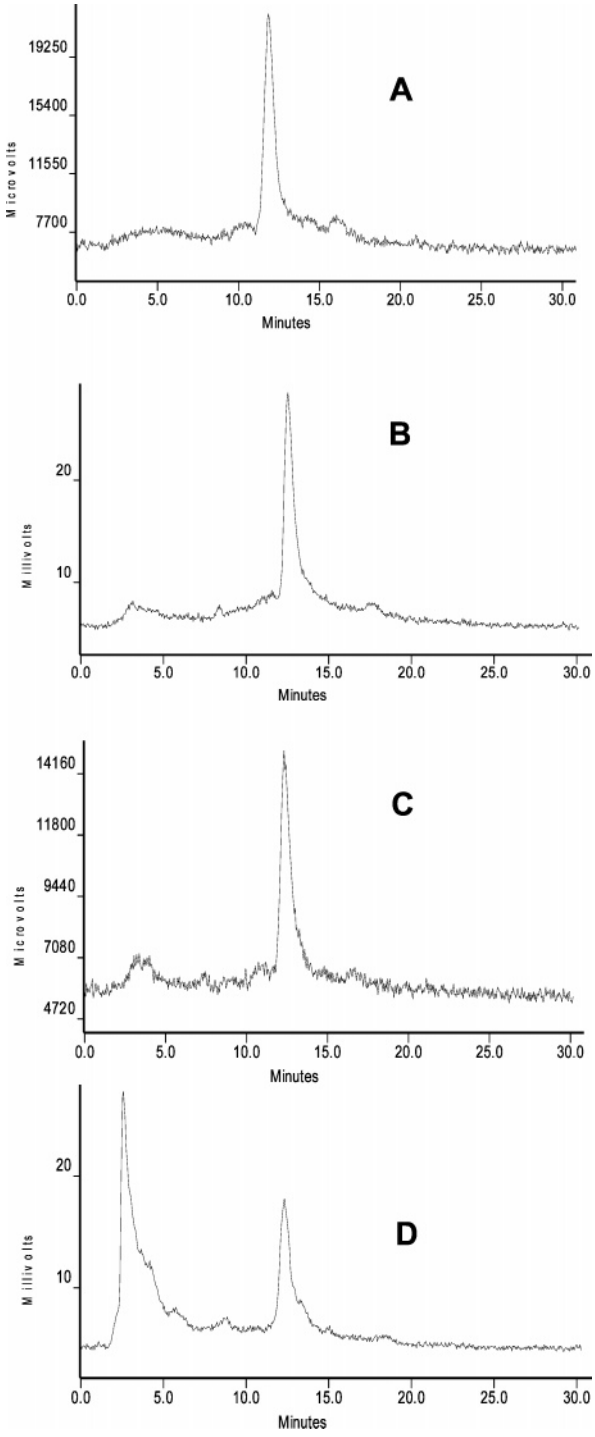


Figure 8. Radio-HPLC chromatograms of $[^{99m}TcN(etma)(PNP5)]^+$ in the kit matrix before injection (A), in the urine at 30 min p.i. (B), in the urine at 120 min p.i. (C), and in feces at 120 min p.i. (D). Each rat was administered with ~500 μCi of $[^{99m}TcN(etma)(PNP5)]^+$.

DISCUSSION

Myocardial perfusion imaging with radiotracers is an integral component of the clinical evaluation of patients with known or suspected coronary artery disease (*26*−*29*). Since the early 1980s, intensive research efforts have been directed toward development of cationic ^{99m}Tc complex radiotracers for heart imaging (*26, 27*). As a result these efforts, ^{99m}Tc-sestamibi and ^{99m}Tc-tetrofosmin have been approved as commercial products for myocardial perfusion imaging. Despite their widespread applications, both ^{99m}Tc-sestamibi and ^{99m}Tc-tetrofosmin do not meet the requirements of an ideal perfusion imaging agent, at least in part, due to their high liver uptake (*30*). Therefore, it would be a great advantage to develop a new radiotracer with substantially better heart/liver ratio than that of ^{99m}Tc-sestamibi.

The factors affecting biodistribution patterns of radiotracers include the charge, solution stability, lipophilicity, and protein-binding capability. For example, $[^{99m}TcN(ema)(L6)]^+$ and

^{99m}Tc-sestamibi share the same cationic charge and have very high lipophilicity (1.22 ± 0.13 and 1.29 ± 0.13, respectively). However, the heart uptake and heart/liver ratios of [^{99m}TcN-(tma)(L6)]$^+$ are significantly lower ($P < 0.01$) than that of ^{99m}Tc-sestamibi at 5−60 min postinjection. This difference is probably related to its solution instability of [^{99m}TcN(ema)(L6)]$^+$ in the presence of cysteine (Figure 5). The solution instability of [^{99m}TcN(ema)(L6)]$^+$ may also contribute to its high protein binding as indicated by its relatively high blood activity and low heart/blood ratios (Table SIII).

Compared to [^{99m}TcN(ema)(L6)]$^+$, [^{99m}TcN(etma)(L6)]$^+$ has better solution stability due to the thione-S donor atom in etma. However, it has a low heart uptake with low heart/lung and heart/liver ratios, suggesting that it is probably too lipophilic (log $P = 1.43 \pm 0.05$) to achieve the high heart uptake and fast liver clearance. [^{99m}TcN(tma)(L6)]$^+$ has a high solution stability. Its log P value is almost identical to that of ^{99m}TcN-DBODC5 (Table 1). The heart uptake of [^{99m}TcN(tma)(L6)]$^+$ is comparable to that of ^{99m}TcN-DBODC5 (Figure 6), but its heart/liver and heart/liver ratios are significantly lower ($p < 0.01$) than that of ^{99m}TcN-DBODC5 over the 2 h study period. In contrast, [^{99m}TcN(etma)(PNP5)]$^+$ is less lipophilic (log $P = 0.67 \pm 0.15$). Its heart uptake is comparable to that of ^{99m}TcN-DBODC5 within the experimental error (Figure 6). The heart/liver ratio of [^{99m}TcM(etma)(PNP5)]$^+$ is very similar to that of ^{99m}TcN-DBODC5 at 5−60 min p.i.

Another important factor influencing the *in vivo* biological properties of cationic ^{99m}Tc radiotracers is their metabolic properties. Cationic ^{99m}Tc radiotracers are generally excreted via hepatobiliary and renal routes. Metabolic products can be readily detected by analyzing the urine (renal excretion) and feces (hepatobiliary excretion) samples. In this study, we used a reversed phase radio-HPLC method to analyze the urine and feces samples from the rats administered with ~500 μCi of [^{99m}TcN(etma)(PNP5)]$^+$. The results indicated that [^{99m}TcN-(etma)(PNP5)]$^+$ remained intact in the urine over 2 h study period (Figure 8C), but it shows a significant metabolism (>70%) in feces samples at 120 min p.i. (Figure 8D). In contrast, ^{99m}TcN-DBODC5, which shares the same PNP5 bisphosphine ligand with [^{99m}TcN(etma)(PNP5)]$^+$, has very little metabolism in both urine and feces of rats under anesthesia (*1*). Changing the bidentate chelator from DBODC to ethylthiomaltolate (etma) has a significant impact on the metabolic fate of the cationic ^{99m}Tc-nitrido complex. The metabolic instability of [^{99m}TcN-(etma)(PNP5)]$^+$ may contribute to its lower heart/liver ratio than that of ^{99m}TcN-DBODC5 at 120 min p.i. (Figure 6).

It is well-documented that cationic ^{99m}Tc radiotracers, such as ^{99m}Tc-sestamibi and ^{99m}Tc-tetrofosmin, are able to penetrate plasma and mitochondrial membranes and accumulated in mitochondria because of the negative mitochondrial potential (*31*−*35*). Due to their similarity in molecular charge with ^{99m}Tc-sestamibi and ^{99m}Tc-tetrofosmin, it is reasonable to believe that cationic ^{99m}Tc-nitrido complexes might share the same localization mechanism. The difference in the heart uptake of cationic ^{99m}Tc radiotracers is most likely caused by their lipophilicity and capability to across the plasma and mitochondrial membranes. Cationic ^{99m}Tc radiotracers with the log $P >$ 1.5 often have a low heart uptake and a slow liver clearance while more hydrophilic cationic radiotracers with log $P < 0$ tend to show fast washout from the myocardium (*1*−*3*, *22*−*25*). In both cases, the heart/liver ratio is low because of either high liver uptake or fast myocardial washout. While there is no clear-cut "optimal" log P values, we believe that cationic ^{99m}Tc radiotracers should have a log P value of 0.6−1.2 in order to achieve a high heart uptake with the fast liver clearance at the same time.

CONCLUSIONS

This report describes synthesis and evaluation of cationic complexes [^{99m}TcN(L)(PNP)]$^+$ (Figure 1: L = ma, ema, tma, etma, and mpo; PNP = PNP5, PNP6, and L6) as potential radiotracers for heart imaging. The key finding of this study is that bidentate chelators have a significant impact on lipophilicity, solution stability, biodistribution patterns, and metabolism of their cationic ^{99m}Tc-nitrido complexes. The results from solution stability studies indicate that the thione-S donors in bidentate chelators increase solution stability of cationic ^{99m}Tc-nitrido complexes. Among four radiotracers evaluated in Sprague−Dawley rats for their biodistribution characteristics, [^{99m}TcN-(etma)(PNP5)]$^+$ has a high heart uptake, long myocardial retention, and fast liver clearance with the heart/liver ratio being >2 times better than that of ^{99m}Tc-sestamibi at 30 min p.i. Results from planar imaging studies are completely consistent with those from biodistribution studies. The fast liver clearance suggests that [^{99m}TcN(etma)(PNP5)]$^+$ might give clinically useful images of heart as early as 30 min p.i. [^{99m}TcN(etma)-(PNP5)]$^+$ is a promising candidate for evaluation of its blood flow characteristics in larger animal models, such as dogs and pigs. It is interesting to note that the heart/liver ratio of [^{99m}TcN(etma)(PNP5)]$^+$ is not as good as that of ^{99m}TcN-DBODC5 at 120 min p.i. probably due to its metabolic instability in the hepatobiliary system. Therefore, our future research will focus more on cationic ^{99m}Tc-nitrido complexes with better metabolic stability.

ACKNOWLEDGMENT

Authors would like to thank Lee Ann Grote, Carol Dowell, and Cheryl Anderson from the Department of Veterinary Clinical Sciences, Purdue University, for their assistance with biodistribution and imaging studies. This work is supported, in part, by Purdue University and research grants AHA0555659Z (S.L.) from the Greater Midwest Affiliate of American Heart Association, 5 R21 EB003419-02 (S.L.) from National Institute of Biomedical Imaging and Bioengineering (NIBIB), and 1 R21 HL083961-01 (S.L.) from National Heart, Lung, and Blood Institute (NHLBI).

Supporting Information Available: Experimental details. This material is available free of charge via the Internet at http://pubs.acs.org.

LITERATURE CITED

(1) Liu, S., He, Z. J., and Hsieh, W. Y. (2006) Evaluation of novel crown ether-containing cationic ^{99m}Tc-nitrido complexes as new radiopharmaceuticals for heart imaging. *Nucl. Med. Biol. 33*, 419−432.

(2) Boschi, A., Bolzati, C., Uccelli, L., Duatti, A., Benini, E., Refosco, F., Tisato, F., and Piffanelli, A. (2002) A class of asymmetrical nitrido ^{99m}Tc heterocomplexes as heart imaging agents with improved biological properties. *Nucl. Med. Commun. 23*, 689−693.

(3) Boschi, A., Uccelli, L., Bolzati, C., Duatti, A., Sabba, N., Moretti, E., Di, Domenico, G., Zavattini, G., Refosco, F., and Giganti, M. (2003) Synthesis and biologic evaluation of monocationic asymmetrical ^{99m}Tc-nitride heterocomplexes showing high heart uptake and improved imaging properties. *J. Nucl. Med. 44*, 806−814.

(4) Hatada, K., Riou, L. M., Ruiz, M., Yamamichi, Y., Duatti, A., Lima, R. L., Goode, A. R., Watson, D. D., Beller, G. A., and Glover, D. K. (2004) ^{99m}Tc-N-DBODC5, a new myocardial perfusion imaging agent with rapid liver clearance: comparison with ^{99m}Tc-sestamibi and ^{99m}Tc-tetrofosmin in rats. *J. Nucl. Med. 45*, 2095−2101.

(5) Nelson, W. O., Rettig, S. J., and Orvig, C. (1987) The exoclathrate $Al(C_7H_8NO_2)_3 \cdot 12H_2O$. A facial geometry imposed by extensive hydrogen bonding with the ice I structure. *J. Am. Chem. Soc. 109*, 4121−4123.

(6) Bernstein, L. R., Tanner, T., Godfrey, C., and Noll, B. (2000) Chemistry and pharmacokinetics of gallium maltolate, a compound with high oral gallium bioavailability. *Metal Based Drugs 7*, 33−47.

(7) Matsuba, C. A., Nelson, W. O., Rettig, S. J., and Orvig, C. (1988) Neutral water-soluble indium complexes of 3-hydroxy-4-pyrones and 3-hydroxy-4-pyridinones. *Inorg. Chem. 27*, 3935−3939.

(8) Hsieh, W. Y., Zaleski, C. M., Pecoraro, V. L., and Liu, S. (2006) Mn(II) Complexes of Monoanionic Bidentate Chelators: the X-Ray Crystal Structures of $Mn(DHA)_2(CH_3OH)_2$ (DHA = Dehydroacetic Acid) and $[Mn(ema)_2(H_2O)]_2 \cdot 2H_2O$ (Hema = 2-Ethyl-3-Hydroxy-4-Pyrone. *Inorg. Chim. Acta 359*, 228−236.

(9) Hsieh, W. Y., and Liu, S. (2005) Synthesis, characterization and structures of Mn(III) complexes $Mn(DMHP)_3 \cdot 12H_2O$ and $Mn(DMHP)_2Cl \cdot 0.5H_2O$ (DMHP = 1,2-dimethyl-3-hydroxy-4-pyridinone). *Inorg. Chem. 44*, 2031−2038.

(10) Hsieh, W. Y., and Liu, S. (2005) Synthesis, characterization and structures of Cr(III) complexes with 3-hydroxy-4-pyrones and 1,2-dimethyl-3-hydroxy-4-pyridinone. *Synth. React. Inorg., Met.-Org. Chem. 35*, 61−70.

(11) McNeill, J. H., Yuen, V. G., Hoveyda, H. R., and Orvig, C. (1992) Bis(maltolato)-oxovanadium(IV) is a potent insulin mimic. *J. Med. Chem. 35*, 1489−1491.

(12) Caravan, P., Gelmini, L., Glover, N., Herring, F. G., Li, H. L., McNeill, J. H., Rettig, S. J., Setyawati, I. A., Shuter, E., Sun, Y., Tracey, A. S., Yuen, V. G., and Orvig, C. (1995) Reaction chemistry of BMOV, bis(maltolato)oxovanadium(IV), a potent insulin mimetic agent. *J. Am. Chem. Soc. 117*, 12759−12770.

(13) Thompson, K. H., and Orvig, C. (2001) Coordination chemistry of vanadium in metallopharmaceutical candidate compounds. *Coord. Chem. Rev. 219*, 1033−1053., references therein.

(14) Thompson, K. H., and Orvig, C. (2000) Design of vanadium compounds as insulin enhancing agents. *J. Chem. Soc., Dalton Trans.* 2885−2892; references therein.

(15) Saatchi, K., Thompson, K. H., Patrick, B. O., Pink, M., Yuen, V. G., McNeill, J. H., and Orvig, C. (2005) Coordination chemistry and insulin-enhancing behavior of vanadium complexes with maltol $C_6H_6O_3$ Structural isomers. *Inorg. Chem. 44*, 2689−2697.

(16) Thompson, K. H., Chiles, J., Yuen, V. G., Tse, J., McNeill, J. H., and Orvig, C. (2004) Comparison of anti-hyperglycemic effect amongst vanadium, molybdenum and other metal maltol complexes. *J. Inorg. Biochem. 98*, 683−690.

(17) Lewis, J. A., Puerta, D. T., and Cohen, S. M. (2003) Metal complexes of the trans-Influencing ligand thiomaltol. *Inorg. Chem. 42*, 7455−7459.

(18) Lewis, J. A., and Cohen, S. M. (2004) Addressing lead toxicity: complexation of lead(II) with thiopyrone and hydroxypyridinthione O, S mixed chelators. *Inorg. Chem. 43*, 6534−6536.

(19) Monga, V., Patrick, B. O., and Orvig, C. (2005) Group 13 and lanthanide complexes with mixed O, S anionic ligands derived from maltol. *Inorg. Chem. 44*, 2666−2677.

(20) Monga, V., Thompson, K. H., Yuen, V. G., Sharma, V., Patrick, B. O., McNeil, J. H., and Orvig, C. (2005) Vanadium complexes with mixed O,S anionic ligands derived from maltol: synthesis, characterization, and biological studies. *Inorg. Chem. 44*, 2678−2688.

(21) Lewis, J. A., Tran, B. L., Puerta, D. T., Rumberger, E. M., Hendrickson, D. N., and Cohen, S. M. (2005) Synthesis, structure and spectroscopy of new thiopyrone and hydroxypyridinethione transition metal complexes. *Dalton Trans.* 2588−2596.

(22) Jones, A. G., Abrams, M. J., Davison, A., Brodack, J. W., Toothaker, A. K., Adelstein, S. J., and Kassis, A. I. (1984) Biological studies of a new class of technetium complexes: the hexakis-(alkylisonitrile)technetium(I) cations. *Int. J. Nucl. Biol. 11*, 225−234.

(23) Marmion, M. E., Woulfe, S. R., Neumann, W. L., Nosco, D. L., and Deutsch, E. (1999) Preparation and characterization of technetium complexes with Schiff-base and phosphine coordination. 1. Complexes of technetium-99g and -99m with substituted $acac_2$en and trialkyl phosphines (where $acac_2$en = N,N′-ethylenebis[acetylacetone iminatol]). *Nucl. Med. Biol. 26*, 755−770; references therein.

(24) Tisato, F., Maina, T., Shao, L. R., Heeg, M. J., and Deutsch, E. (1996) Cationic $[^{99m}Tc^{III}(DIARS)_2(SR)_2]^+$ complexes as potential myocardial perfusion imaging agents (DIARS = o-phenylenebis-(dimethylarsine); SR^- = thiolate). *J. Med. Chem. 39*, 1253−1261.

(25) Lisic, E. C., Heeg, M. J., and Deutsch, E. (1999) $^{99m}Tc(L\text{-}L)_3^+$ complexes containing ether analogs of DMPE. *Nucl. Med. Biol. 26*, 563−571.

(26) Jain, D. (1999) Technetium-99m labeled myocardial perfusion imaging agents. *Semin. Nucl. Med. 29*, 221−236.

(27) Acampa, W., Di Benedetto, C., and Cuocolo, A. (2000) An overview of radiotracers in nuclear cardiology. *J. Nucl. Cardiol. 7*, 701−707.

(28) Beller, G. A., and Zaret, B. L. (2000) Contributions of nuclear cardiology to diagnosis and prognosis of patients with coronary artery disease. *Circulation 101*, 1465−1478.

(29) Banerjee, S., Pillai, M. R. A., and Ramamoorthy, N. (2001) Evolution of Tc-99m in diagnostic radiopharmaceuticals. *Semin. Nucl. Med. 31*, 260−277.

(30) Llaurado, J. G. (2001) The quest for the perfect myocardial perfusion indicator... still a long way to go. *J. Nucl. Med. 42*, 282−284.

(31) Mousa, S. A., Cooney, J. M., and Williams, S. J. (1987) Flow-distribution characteristics of Tc-99m-Hexakis-2-methoxy-2-methylpropyl isonitrile in animal-models of myocardial-ischemia and perfusion (abstract). *J. Am. Coll. Cardiol. 9*, A137.

(32) Piwnica-Worms, D., Kronauge, J. F., and Chiu, M. L. (1990) Uptake and retention of hexakis(2-methoxyisobutylisonitrile) technetium(I) in cultured chick myocardial cells: mitochondrial and plasma membrane potential dependence. *Circulation 82*, 1826−1838.

(33) Carvalho, P. A., Chiu, M. L., Kronauge, J. F., Kawamura, M., Jones, A. G., Holman, B. L., and Piwnica-Worms, D. (1992) Subcellular distribution and analysis of technetium-99m-MIBI in isolated perfused rat hearts. *J. Nucl. Med. 33*, 1516−1521.

(34) Crane, P., Laliberte, R., Heminway, S., Thoolen, M., and Orlandi, C. (1993) Effect of mitochondrial viability and metabolism on technetium-99m-sestamibi myocardial retention. *Eur. J. Nucl. Med. 20*, 20−25.

(35) Herman, L. W., Sharma, V., Kronauge, J. F., Barbarics, E., Herman, L. A., and Piwnica-Worms, D. (1995) Novel hexakis-(arenisonitriles)technetium(I) complexes as radioligands targeted to the multidrug resistance P-glycoprotein. *J. Med. Chem. 38*, 2955−2936.

BC0603182

Synthesis and Assessment of First-Generation Polyamidoamine Dendrimer Prodrugs to Enhance the Cellular Permeability of P-gp Substrates

Mohammad Najlah,[†] Sally Freeman, David Attwood, and Antony D'Emanuele*,[†]

School of Pharmacy and Pharmaceutical Sciences, University of Manchester, Manchester M13 9PL, UK.
Received October 19, 2006; Revised Manuscript Received January 13, 2007

The aim of this study is to evaluate the potential use of first-generation (G1) polyamidoamine (PAMAM) dendrimers as drug carriers to enhance the permeability, hence oral absorption, of drugs that are substrates for P-glycoprotein (P-gp) efflux transporters. G1 PAMAM dendrimer-based prodrugs of the water-insoluble P-gp substrate terfenadine (Ter) were synthesized using succinic acid (suc) or succinyl−diethylene glycol (suc−deg) as a linker/spacer (to yield G1−suc−Ter and G1−suc−deg−Ter, respectively). In addition, the permeability of G1−suc−deg−Ter was enhanced by attaching two lauroyl chains (L) to the dendrimer surface (L2−G1−suc−deg−Ter). All of the G1 dendrimer−terfenadine prodrugs were more hydrophilic than the parent drug, as evaluated by drug partitioning between 1-octanol and phosphate buffer at pH 7.4 (log K_{app}). The influence of the dendrimer prodrugs on the integrity and viability of human Caucasian colon adenocarcinoma cells (Caco-2) was determined by measuring the transepithelial electrical resistance (TEER) and leakage of lactate dehydrogenase (LDH) enzyme, respectively. The LDH assay indicated that the dendrimer prodrugs had no impact on the viability of Caco-2 cells up to a concentration of 1 mM. However, the IC_{50} of the prodrugs was lower than that of G1 PAMAM dendrimer because of the high toxicity of terfenadine. Measurements of the transport of dendrimer prodrugs across monolayers of Caco-2 cells showed an increase of the apparent permeability coefficient (P_{app}) of terfenadine in both apical-to-basolateral (A → B) and basolateral-to-apical (B → A) directions after its conjugation to G1 PAMAM dendrimer. The A → B P_{app} of the dendrimer prodrugs was significantly greater than B → A P_{app}. The surface-modified dendrimer prodrug L2−G1−suc−deg−Ter showed the highest A → B permeability among the conjugates.

INTRODUCTION

There has been growing interest in polyamidoamine (PAMAM) dendrimers as hyperbranched polymers possessing a well-defined structure that allow precise control of size, shape, and terminal group functionality (*1*). Dendrimers show potential as carriers for the development of drug delivery systems (*2*) that can be used in several pharmaceutical fields (*2*, *3*).

Dendrimers have the ability to cross cell barriers (*4*−*6*) by both paracellular and transcellular pathways (*7*, *8*). The cytotoxicity and permeability of PAMAM dendrimers were found to be concentration, generation, and charge dependent (*7*). Low-generation PAMAM dendrimers (G0 and G1) exhibit significantly less cytotoxicity and higher permeability than higher generations (G2, G3, and G4) (*9*). However, a significant reduction in cytotoxicity and enhancement in permeability can be achieved by surface-engineered cationic PAMAM dendrimers (*7*, *10*).

Recent observations on intestinal absorption of drugs suggest that an intestinal secretion process mediated by P-glycoprotein (P-gp) limits the bioavailability of drugs that are P-gp substrates, such as terfenadine, after peroral administration (*11*, *12*). Several attempts have been reported to enhance the oral absorption of P-gp substrates by (1) inhibiting the P-gp secretion activity using P-gp inhibitors such verapamil and nifedipine (*13*), (2) co-administrating with excipients such as Tween 80 and acacia which are known to inhibit the P-gp efflux activity (*14*), (3) improving the paracellular transport by co-administrating modulators of tight junctions such as sodium caprate (C10) (*15*), and (4) changing the physicochemical properties of the drug by synthesis of a prodrug that is able to bypass the P-gp efflux pump, for example, attaching paclitaxel to PEG 5000 resulted in a prodrug with a higher bioavailability than the parent drug (*16*).

Previous work by our group reported potential drug carrier systems based on third-generation (G3) PAMAM dendrimer that may be used to enhance the transport of propranolol across Caco-2 cells. Propranolol has poor water solubility and is a substrate for the P-glycoprotein (P-gp) efflux transporter. When conjugated to surface-modified G3 PAMAM dendrimer, propranolol was shown to bypass the efflux system. Thus, dendrimer prodrugs may be used to enhance the bioavailability of drugs that are substrates of efflux transporters and therefore overcome cellular barriers such as the gastrointestinal epithelium and the blood brain barrier (*6*, *17*). A natural extension of this work is the inclusion of a linker between the drug and the dendrimer to control drug release, use of a lower generation (less toxic) carrier than G3 PAMAM dendrimer, and use of a stronger and more unambiguous P-gp substrate than propranolol to confirm that PAMAM dendrimers have the ability to bypass P-gp efflux transporters. More recently, we explored the nature of the linker between the drug and the dendrimer. It is important to design a linker that is robust enough for the drug−dendrimer prodrug to be absorbed intact yet labile once absorbed. It has been found that a diethylene glycol linker between the drug and dendrimer gave esters with a high chemical stability in buffers, which readily released the drug in plasma. PAMAM dendrimer conjugates incorporating this linker have potential as carriers for low-bioavailability drugs (*18*).

In the present study, the design, characterization, and in vitro evaluation of a novel drug carrier system based on first-

* To whom correspondence should be addressed. Phone: +44(0) 1772 895801. Fax: +44(0)7092 030763. E-mail: Antony@DEmanuele.net, www: http://www.dendrimerweb.com.

[†] Present address: School of Pharmacy and Pharmaceutical Sciences, University of Central Lancashire, Preston PR1 2HE, U.K.

10.1021/bc060325q CCC: $37.00 © 2007 American Chemical Society
Published on Web 03/14/2007

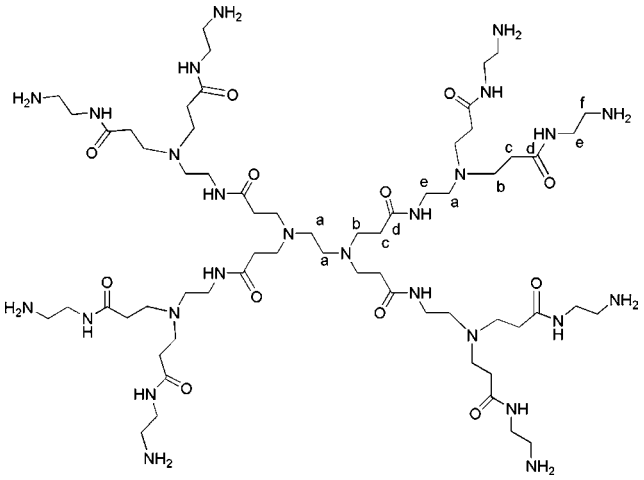


Figure 1. G1 PAMAM dendrimer (letters on G1 PAMAM dendrimer are included to aid NMR assignments).

generation PAMAM dendrimers (G1) (Figure 1) and utilizing a diethylene glycol linker are described. Terfenadine was selected as an unambiguous P-gp substrate and water-insoluble drug. It was attached to the dendrimer surface using succinyl linker (single ester linker) to give G1−suc−Ter or succinic−diethylene glycol linker (double ester linker) to give G1−suc−deg−Ter. The biological evaluation of both conjugates and the surface-modified conjugate (L2−G1−suc−deg−Ter) involved cytotoxicity studies (LDH assay) and measurement of transport across Caco-2 monolayers.

EXPERIMENTAL PROCEDURES

Materials. First-generation PAMAM dendrimers (G1) with ethylenediamine cores were purchased from Dendritech Inc. (Michigan). Trifluoroacetic acid (TFA), triethylamine (TEA), terfenadine, 4-nitrophenyl chloroformate, succinic anhydride, 1-dodecanol (lauroyl alcohol), trypan blue, 4-dimethylaminopyridine (DMAP), ethylenediamine tetraacetic acid (EDTA), lactate dehydrogenase assay kits, Sephadex 15, and Sephadex LH-20 were purchased from Sigma-Aldrich Co. Ltd. *N*-Hydroxysuccinimide (NHS), *N*,*N*′-dicyclohexylcarbodiimide (DCC), and diethylene glycol were purchased from Fluka (Poole, Dorset, U.K.). Cell culture materials were from Gibco BRL Life Technologies (Paisley, Scotland). Polycarbonate cell culture inserts (Transwell 12 mm diameter) and cluster plates (96 well) were purchased from Corning Costar UK (High Wycombe, Bucks, U.K.).

Dendrimer−terfenadine conjugates were characterized by ^{13}C and ^{1}H NMR spectroscopy (Bruker Avance 300, Bruker, Coventry, U.K.). ^{13}C NMR spectra were assigned with the aid of DEPT-135. HPLC analyses were carried out using a Hewlett-Packard Series II 1090 (Germany) instrument equipped with a Luna 5 μm, C18 column (250 × 4.6 mm, Phenomenex, Cheshire, U.K.). For the transport and partition studies the solvent systems were methanol:acetonitrile (ACN):H_3PO_4 (0.05% w/v) (48:32:20) with phenanthrene as internal standard for G1 conjugates, and ACN:Walpole's acetate buffer (pH = 4.5): methanol (40:48:12) with naproxen as internal standard for terfenadine, Ter−suc, and Ter−suc−deg. The flow rate was 1.2 mL/min, and UV detection was at λ = 230 nm. For characterization of dendrimer−terfenadine conjugates, the solvent system was 10:32:58 methanol:acetonitrile (ACN):H_3PO_4 (0.05% w/v) for 2 min then 48:32:20 methanol:acetonitrile-(ACN):H_3PO_4 for the remaining elution time. The flow rate was 1.2 mL/min, and UV detection was at λ = 230 nm.

Synthesis of Terfenadine−Succinyl (Ter−suc). Terfenadine (471.7 mg, 1 mmol) was added to a solution of succinic anhydride (200 mg, 2 mmol) and 4-dimethylaminopyridine (DMAP) (12.2 mg, 0.1 mmol) (previously dried under vacuum for 2 h) in DMF (4 mL). Dry pyridine (0.8 mL) was added, and the solution was stirred overnight at room temperature. DMF was evaporated under vacuum, and the residue was washed with petroleum ether and purified by silica gel column chromatography, eluting with chloroform:methanol (90:10) to give Ter−suc with a yield of 91% (R_f = 0.3) (mp = 198−199 °C). ^{1}H NMR ($CDCl_3$): 1.29 (9H, s, $-Bu^t$) 1.51 (2H, br d, $NCH_2CH_2CH_2CH$, J = 13.4), 1.95−1.69 (4H, m, 2 × $CHCH_2CH_2N$), 2.21−2.01 (2H, m, $NCH_2CH_2CH_2CH$), 2.90−2.38 (9H, m, 2 × $CHCH_2CH_2N$, $CHCH_2CH_2N$, $CO-CH_2-CH_2-CO$), 3.39 (H, br d, J_1 = 13.8, $NCH_2CH_2CH_2$), 3.44 (H, br d, J_2 = 13.8, $NCH_2CH_2CH_2$), 5.81 (1H, br d, J = 7.9, CH−O), 7.55−7.10 (14H, m, Ar). ^{13}C NMR ($CDCl_3$): 20.0 ($NCH_2CH_2CH_2$), 23.4 (2 × $CHCH_2CH_2N$), 31.0 (CH_2COO), 31.1 (3 × CH_3), 31.3 (CH_2COOH), 33.7 ($NCH_2CH_2CH_2CH$), 42.6 ($-C(CH_3)_3$), 52.7 ($CHCH_2CH_2N$), 53.0 ($CHCH_2CH_2N$), 56.1 ($CHCH_2CH_2N$), 60.4 ($NCH_2CH_2CH_2$), 73.8 (CH−O), 78.7 (C−OH), 125.4 (2 × CH, Ar), 125.6 (4 × CH, Ar), 125.9 (2 × CH, Ar), 126.5 (2 × CH, Ar), 128.2 (4 × CH, Ar), 137.2 (C, Ar), 145.9 (2 × C, Ar), 150.8 (C, Ar), 173.1 (COO), 177.2 (COOH). (+)-ESI-MS: 572 [M^+ + H]. Accurate MS ($C_{36}H_{46}O_5N_1$): 572.3372 (theoretical: 572.3370).

Synthesis of Terfenadine−Succinyl−Diethylene Glycol (Ter−suc−deg). CDI (65 mg, 0.4 mmol) was added portion wise to a solution of Ter−suc (200 mg, 0.35 mmol) in DCM (10 mL). The mixture was stirred for 4 h at room temperature. An excess of diethylene glycol (deg) (149 mg, 1.43 mmol) was added and stirred overnight. The reaction mixture was washed with water (2 × 10 mL), aqueous 0.1 M HCl (2 × 10 mL), aqueous 0.1 M NaOH (2 × 10 mL), and water (2 × 10 mL), dried (anhydrous Na_2SO_4), filtered, and evaporated to dryness in vacuo. The product was purified by size exclusion chromatography using Sephadex LH 20 and eluting with methanol: water (5:1) to give Ter−suc−deg as an oil with a yield of 69%. TLC: R_f = 0.16 (chloroform:methanol, 90:10). ^{1}H NMR ($CDCl_3$): 1.29 (9H, s, $-Bu^t$), 1.60−1.38 (6H, m, $NCH_2CH_2CH_2$ and 2 × $CHCH_2CH_2N$), 1.99−1.83 (2H, m, $NCH_2CH_2CH_2CH$), 2.75−2.35 (9H, m, 2 × $CHCH_2CH_2N$, $CHCH_2CH_2N$, $CO-CH_2-CH_2-CO$), 2.98−2.87 (2H, m, $NCH_2CH_2CH_2$), 3.69−3.52 (6H, m, $COOCH_2CH_2OCH_2CH_2OH$), 4.28−4.15 (2H, m, $COOCH_2CH_2OCH_2CH_2OH$), 5.76−5.69 (1H, dd, J = 6.5 and 13.7, CH−O), 7.55−7.12 (14H, m, Ar). ^{13}C NMR ($CDCl_3$): 22.9 ($NCH_2CH_2CH_2$), 26.1 (2 × $CHCH_2CH_2N$), 29.0 (CH_2COO), 29.1 (CH_2COO), 31.3 (3 × CH_3), 34.2 ($NCH_2CH_2CH_2CH$), 44.1 ($-C(CH_3)_3$), 53.9 ($CHCH_2CH_2N$), 54.0 ($CHCH_2CH_2N$), 58.2 ($CHCH_2CH_2N$), 61.6 ($NCH_2CH_2CH_2$), 61.7 (OCH_2CH_2OH), 63.7 ($COOCH_2CH_2O$), 67.0 ($COOCH_2CH_2O$), 68.8 (OCH_2CH_2OH), 72.5 (CH−O), 79.4 (C−OH), 125.0 (2 × CH, Ar), 125.6 (4 × CH, Ar), 125.9 (2 × CH, Ar), 126.4 (2 × CH, Ar), 128.1 (4 × CH, Ar), 137.2 (C, Ar), 146.0 (C, Ar), 150.8 (C, Ar), 155.0 (C, Ar), 171.6 (COO), 172.2 (COOH). (+)-ESI-MS: 660 [M^+ + H]. Accurate MS ($C_{40}H_{54}O_7N_1$): 660.3893 (theoretical: 660.3895).

Synthesis of G1 Dendrimer−Succinyl−Terfenadine (G1−suc−Ter). DCC (93 mg, 0.45 mmol) was added to a solution of Ter−suc (200 mg, 0.35 mmol) in 3 mL of DMF. The mixture was stirred for 1 h, after which time NHS (52 mg, 0.45 mmol) was added and the mixture was stirred for 24 h. The reaction mixture was filtered, and the filtrate was concentrated. The residue was dissolved in DCM, washed with water (2 × 10 mL), aqueous 0.1 M HCl (2 × 10 mL), aqueous 0.1 M NaOH (2 × 10 mL), and water (2 × 10 mL), dried (anhydrous Na_2SO_4), filtered, evaporated to dryness in vacuo, and dissolved in DMF (3 mL). The solution was added dropwise (during 6 h) to 2 mL of DMF containing G1 dendrimer (429 mg, 0.3 mmol),

stirred for 5 days, and evaporated under vacuum. The residue was dissolved in 3 mL of water and filtered. The filtrate was purified by size exclusion chromatography, using Sephadex 15 and eluting with methanol:water (1:5). The product was further purified using Sephadex LH 20 and eluting with methanol:water (5:1). The yield of G1−suc−Ter was 39%. ^{1}H NMR (d_4-MeOD): 1.28 (9H, s, −Bu^t), 1.95−1.42 (8H, m, $NCH_2CH_2CH_2$, 2 × $CHCH_2CH_2N$, and $NCH_2CH_2CH_2CH$, Ter), 2.45−2.18 (61H, m, c-G1), 3.05−2.50 (61H, 3 m, a-G1, (2 × $CHCH_2CH_2N$, Ter), ($CHCH_2CH_2N$, Ter), (CO−CH_2−CH_2−CO, Suc), b-G1, f-G1), 3.73−3.10 (26H, e-G1 and ($NCH_2CH_2CH_2$, Ter)), 5.80−5.60 (1H, m, CH−O), 7.65−7.05 (14H, m, Ar). ^{13}C NMR (d_4-MeOD): 22.0 ($NCH_2CH_2CH_2$), 25.9 and 26.0 (2 × $CHCH_2CH_2N$), 30.8 (CH_2COO), 31.8 (3 × CH_3), 34.7 (12 × c-G1), 35.4 (CH_2CONH, Suc), 37.0 ($NCH_2CH_2CH_2CH$), 38.6 (8 × f-G1), 41.4 (12 × e-G1) 43.6 (−$C(CH_3)_3$), 51.1 (12 × b-G1), 52.2 ($CHCH_2CH_2N$), 53.0 ($CHCH_2CH_2N$), 53.4 (6 × a-G1), 54.3 ($CHCH_2CH_2N$), 57.8 ($NCH_2CH_2CH_2$), 75.8 (C−OH), 80.0 (CH−O), 126.4 (2 × CH, Ar), 127.0 (4 × CH, Ar), 127.1 (2 × CH, Ar), 127.5 (2 × CH, Ar), 129.1 (4 × CH, Ar), 138.9 (C, Ar), 147.5 (2 × C, Ar), 152.0 (C, Ar), 174.6 (COO), 175.2 (CONH, 12 × d-G1), 175.7 (CONH, Suc).

Synthesis of G1 Dendrimer−Succinyl−Diethylene Glycol−Terfenadine (G1−suc−deg−Ter). Ter−suc−deg (139 mg, 0.21 mmol) was dissolved in THF (5 mL), and TEA (43 mg, 0.42 mmol) was added. The mixture was stirred for 10 min, after which 4-nitrophenyl chloroformate (85 mg, 0.42 mmol) was added portion wise and stirred for 24 h at room temperature. THF was evaporated under vacuum, and the residue was dissolved in DCM, filtered, and concentrated. The residue was dissolved in DMF (1 mL) and added dropwise (during 6 h) to a stirred solution of G1 dendrimer (200 mg, 0.14 mmol) in DMF (2 mL). The reaction mixture was stirred for 5 days. DMF was evaporated under vacuum, and the residue was purified by size exclusion chromatography using Sephadex LH 20 and eluting with methanol:water (5:1). The yield of G1−suc−deg−Ter was 72%. ^{1}H NMR (d_4-MeOD): 1.29 (9H, s, −Bu^t), 2.10−1.38 (8H, m, $NCH_2CH_2CH_2$, 2 × $CHCH_2CH_2N$, and $NCH_2CH_2CH_2CH$, Ter), 2.44−2.24 (24H, m, c-G1), 3.11−2.47 (61H, 3 m, a-G1, (2 × $CHCH_2CH_2N$, Ter), ($CHCH_2CH_2N$, Ter), (CO−CH_2−CH_2−CO, Suc), b-G1, f-G1), 3.79−3.11 (30H, m, e-G1, ($NCH_2CH_2CH_2$, Ter), $COOCH_2CH_2OCH_2CH_2O$−, deg), 4.32−4.10 (4H, m, $COOCH_2CH_2OCH_2CH_2O$−), 5.84−5.73 (1H, t, J = 6.7, CH−O), 7.55−7.05 (14H, m, Ar). ^{13}C NMR (d_4-MeOD): 23.5 ($NCH_2CH_2CH_2$), 27.1 (2 × $CHCH_2CH_2N$), 29.9 (CH_2COO), 30.3 (CH_2COO), 31.8 (3 × CH_3), 34.4 (12 × c-G1), 35.4 ($NCH_2CH_2CH_2CH$), 38.6 (8 × f-G1), 41.4 (12 × e-G1) 45.2 (−$C(CH_3)_3$), 51.2 (12 × b-G1), 52.3 (2 × $CHCH_2CH_2N$), 53.5 (6 × a-G1), 55.1 ($CHCH_2CH_2N$), 59.3 ($NCH_2CH_2CH_2$), 62.2 ($COOCH_2CH_2OCH_2CH_2O$−), 65.1 ($COOCH_2CH_2OCH_2CH_2O$−), 68.1 ($COOCH_2CH_2OCH_2CH_2O$−), 70.5 ($COOCH_2CH_2OCH_2CH_2O$−), 77.3 (CH−O), 80.3 (C−OH), 127.0 (2 × CH, Ar), 127.2 (4 × CH, Ar), 127.3 (2 × CH, Ar), 128.3 (2 × CH, Ar), 128.9 (4 × CH, Ar), 137.0 (C, Ar), 138.9 (C, Ar), 148.0 (C, Ar), 152.0 (C, Ar), 156.6 (OCONH−), 173.4 (COO), 174.0 (COO), 175.2 (CONH, 12 × d-G1).

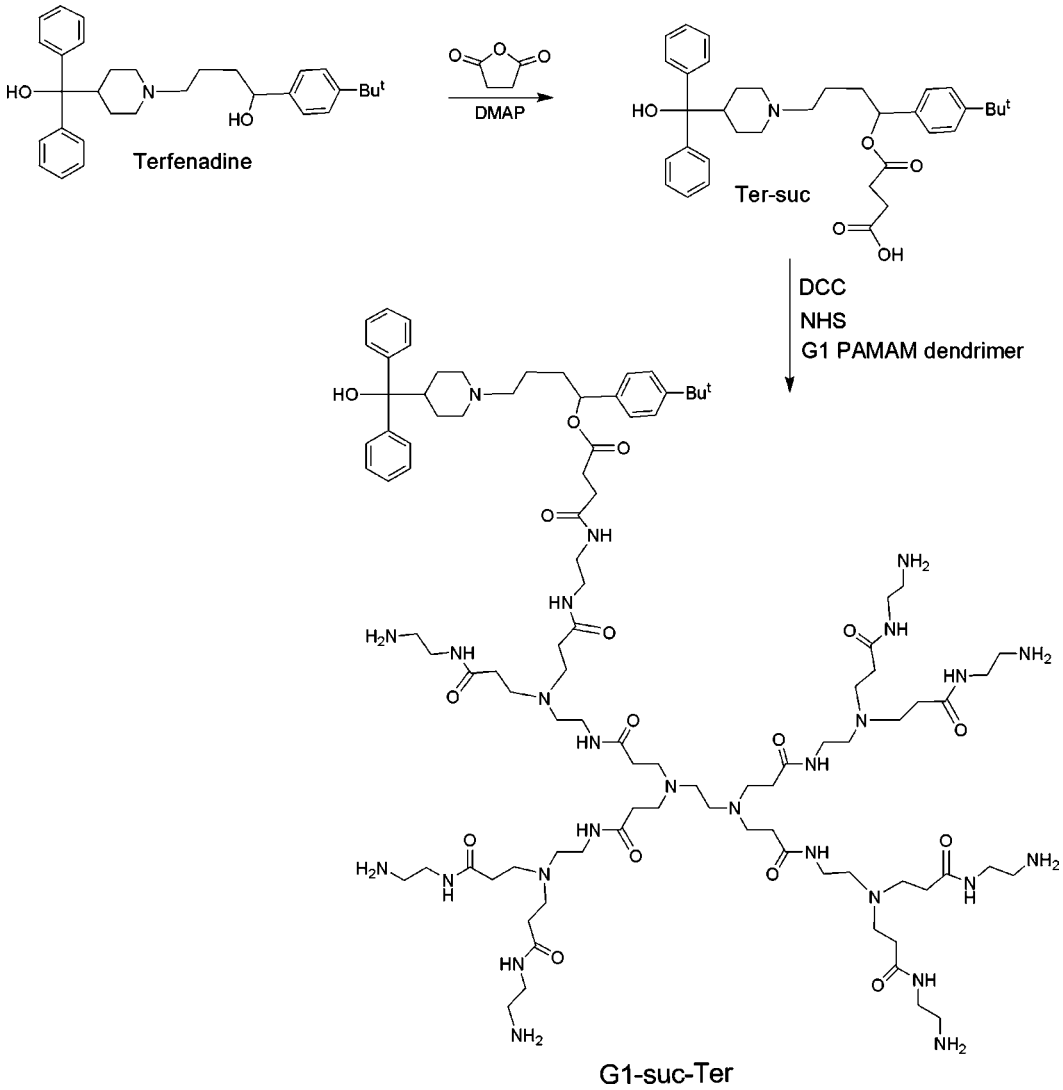
Synthesis of Lauroyl 4-Nitrophenyl Carbonate. Lauroyl alcohol (0.93 g, 5 mmol) was dissolved in THF (10 mL), and TEA (1.02 g, 10 mmol) was added. The mixture was stirred for 10 min, after which 4-nitrophenyl chloroformate (2.01 g, 10 mmol) was added portion wise and stirred for 24 h at room temperature. THF was evaporated under vacuum, and the residue was dissolved in hexane:EtOAc (85:15), filtered, and purified by silica gel column chromatography, eluting with the same solvent system to give lauroyl 4-nitrophenyl carbonate (R_f = 0.4) with a yield of 84%.^{1}H NMR ($CDCl_3$): 0.80 (3H, t, J = 6.9, CH_3), 1.35−1.15 (18H, m, 9 × $-CH_2-$), 1.68 (2H, pentet, J = 6.8, $-CH_2-$), 4.20 (2H, t, J = 6.8, $-CH_2-O-CO-$), 7.35−7.25 (2H, m, Ar), 8.2−8.15 (2H, m, Ar). ^{13}C NMR ($CDCl_3$): 14.5 ($-CH_3$), 23.1 ($-CH_2-$), 26.0 ($-CH_2-$), 30.0−28.9 (7 × $-CH_2-$), 32.3 ($-CH_2-$), 70.0 ($-CH_2-O-CO-$), 122.1 (2 × CH, Ar), 125.6 (2 × CH, Ar), 145.7 (CH, Ar), 152.9 (CH, Ar), 156.0 ($-CO-$).

Synthesis of (Lauroyl)$_2$−G1−suc−deg−Ter (L2−G1−suc−deg−Ter). Lauroyl 4-nitrophenyl carbonate (25 mg, 0.07 mmol) in DMF (1 mL) was added dropwise to a stirred solution of G1−suc−deg−Ter (51 mg, 0.023 mmol) in DMF (2 mL). The reaction mixture was stirred for 5 days. DMF was evaporated under vacuum, and the residue was purified by size exclusion chromatography using Sephadex LH 20 and eluting with methanol:water (5:1). The resulting product was dissolved in water and filtered; the filtrate was concentrated under vacuum and purified again by size exclusion chromatography (same conditions). The yield of L2−G1−suc−deg−Ter was 57%. ^{1}H NMR (d_4-MeOD): 0.89 (6H, t, J = 6.8, 2 × CH_3, L), 2.11−1.20 (60H, m, (−Bu^t, Ter), 2 × (10 × $-CH_2-$, L)), ($NCH_2CH_2CH_2$, 2 × $CHCH_2CH_2N$, and $NCH_2CH_2CH_2CH$, Ter)), 2.46−2.22 (24H, 24, c-G1), 3.78−2.48 (91H, 4 m, a-G1, (2 × $CHCH_2CH_2N$, Ter), ($CHCH_2CH_2N$, Ter), (CO−CH_2−CH_2−CO, suc), b-G1, f-G1, e-G1, ($NCH_2CH_2CH_2$, Ter), ($COOCH_2CH_2OCH_2CH_2O$−, deg)), 4.32−3.92 (8H, (2 × CH_2−O, L), ($COOCH_2CH_2OCH_2CH_2O$−, deg)), 5.76−5.66 (1H, t, J = 6.7, CH−O), 7.55−7.05 (14H, m, Ar). ^{13}C NMR (d_4-MeOD): 14.1 (2 × $-CH_3$, L), 22.8 ($NCH_2CH_2CH_2$), 23.4 (2 × $-CH_2-$, L), 26.6 (2 × $CHCH_2CH_2N$), 29.9 (CH_2COO), 30.1 (CH_2COO), 30.4 (14 × $-CH_2-$, L), 31.4 (3 × CH_3), 32.7 (2 × $-CH_2-$, L), 34.3 (12 × c-G1), 35.4 ($NCH_2CH_2CH_2CH$), 38.2 (8 × f-G1), 41.4 (12 × e-G1), 44.8 (−$C(CH_3)_3$), 50.7 (12 × b-G1), 51.8 (2 × $CHCH_2CH_2N$), 53.0 (6 × a-G1), 54.7 ($CHCH_2CH_2N$), 58.0 ($NCH_2CH_2CH_2$), 61.8 (2 × $-CH_2-$, L), 64.7 ($COOCH_2CH_2OCH_2CH_2O$−), 65.6 ($COOCH_2CH_2OCH_2CH_2O$−), 69.6 ($COOCH_2CH_2OCH_2CH_2O$−), 70.1 $COOCH_2-CH_2OCH_2CH_2O$−), 76.8 (CH−O), 79.9 (C−OH), 126.0 (2 × CH, Ar), 126.8 (4 × CH, Ar), 126.9 (2 × CH, Ar), 128.5 (2 × CH, Ar), 128.8 (4 × CH, Ar), 135.0 (C, Ar), 138.1 (C, Ar), 147.5 (2 × C, Ar), 156.6 (3 × OCONH−), 174.4 (2 × COO), 174.8 (CONH, 12 × d-G1).

Determination of Partition Coefficients. The apparent partition coefficients (P_{app}) of terfenadine and conjugates between 1-octanol and phosphate buffer (pH 7.4) were determined at 37 °C. Before use, the 1-octanol was saturated with phosphate buffer for 24 h by vigorous stirring. A known concentration of compound in phosphate buffer (pH 7.4, 5 mL) was shaken for 72 h with 1-octanol (5 mL) to achieve equilibrium, and the phases were separated by centrifugation at 9000*g* for 5 min. All experiments were performed in triplicate. The concentrations of the compounds in the buffer phase before and after partitioning were determined by HPLC.

Lactate Dehydrogenase (LDH) Leakage Assay (Cytotoxicity Studies). Human Caucasian colon adenocarcinoma cells (Caco-2) (passage 101−105) were seeded at 10 000 cells/well in 96-well plates and maintained at 37 °C in an atmosphere of 5% CO_2 and 95% relative humidity in Dulbecco's Modified Eagle's Medium (DMEM) supplemented with 1% foetal bovine serum, 1% nonessential amino acids, 50 IU/mL penicillin, and 50 mg/mL streptomycin. After 24 h the medium was removed and the cells were washed in phosphate-buffered saline. Hanks Balanced Salt Solution (HBSS, 200 μL) containing G1 PAMAM dendrimer, conjugates, or third-generation (G3) PAMAM dendrimer at concentrations of up to 1 mM was added to Caco-2 cells. Caco-2 cells were also treated with blank HBSS and 1% Triton X-100 as negative and positive controls, respectively. After 3 h of incubation at 37 °C, 100 μL/well supernatant was removed carefully and transferred into corresponding wells of an optically clear 96-well flat bottom microplate.

Scheme 1. Synthesis of G1−suc−Ter



LDH leakage in the compartment was quantified using an LDH assay kit following the manufacturer's specifications.

Transport Studies of Ter, Ter−suc, Ter−suc−deg, and G1 PAMAM Dendrimer Conjugates. Caco-2 cells (passage 104−112) were seeded onto polycarbonate filters (pore size 3.0 μm) at a density of 1.2×10^5 cells/cm^2. Cells were grown at 37 °C in an atmosphere of 5% CO_2 and 95% relative humidity in DMEM supplemented with 10% foetal bovine serum, 1% nonessential amino acids, 50 IU/mL penicillin, and 50 mg/mL streptomycin. The medium was changed every other day for 21−22 days. The integrity of each batch of cells was tested by measuring the TEER using a voltohmmeter (EVOM, World Precision Instruments, Sarasota, FL) before and after the experiments. Before the experiments, cells were equilibrated with HBSS for 20 min at 37 °C and the TEER was determined. The TEER value, corrected for the blank filter resistance, was in the range 800−1000 Ω cm^2. Only confluent monolayers were used for the transepithelial transport studies. Transport was determined in both A → B and B → A directions. The transport medium (TM) was HBSS with *N*-2-hydroxyethylpiperazine-*N*′-2-ethanesulfonic acid (HEPES, 25 mM) and placed in the donor and receiver compartments. Terfenadine, terfenadine prodrugs (each equivalent to 50 μM of terfenadine), or a mixture of G1 and terfenadine (50 μM each) was placed in the donor compartment, and cells were incubated in a humidified atmosphere at 37 °C. TEER was measured every 30 min during the experiment; samples (50 μL) were removed from the receiver compartment at time zero and after 60, 120, and 180 min and from the donor compartment after 180 min. The samples were analyzed by HPLC. The apparent permeability coefficient (P_{app}) was calculated from

$$P_{app} = dQ/dt \times (V/AC_o)\ (\text{cm s}^{-1})$$

where dQ/dt is the change in the donor concentration over time (mol L^{-1} s^{-1}), V is the volume in the reservoir in the receiver side (cm^3), C_o is the initial concentration in the donor compartment (mol L^{-1}), and A is the surface area of the membrane (cm^2).

RESULTS AND DISCUSSION

Synthesis and Characterization of Dendrimer−Ter Conjugates. A prodrug consisting of four components, the dendrimer, the drug, the spacer, and the permeability enhancer group, was synthesized. G1 dendrimer-based prodrugs of terfenadine with a succinyl linker (single ester linker, G1−suc−Ter) and succinic−diethylene glycol linker (double ester linker, G1−suc−deg−Ter) were evaluated in vitro as drug carriers.

G1−suc−Ter. Terfenadine was linked by its secondary hydroxyl (butan-1-ol) group with succinic anhydride (Scheme 1). The resulting product Ter−suc was characterized by ^{1}H NMR, ^{13}C NMR, and mass spectroscopy. Successful formation

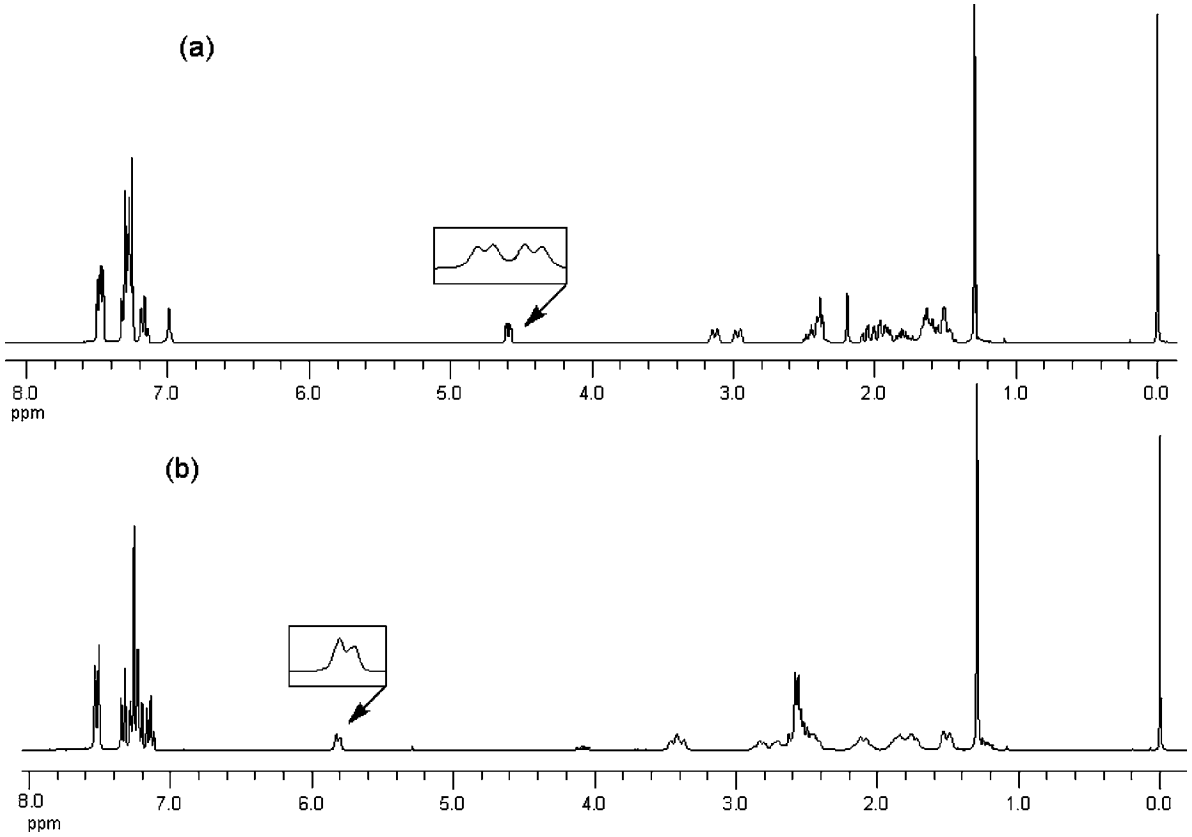


Figure 2. ^{1}H NMR spectra (300 MHz) of (a) terfenadine ($CDCl_3$) and (b) Ter−suc ($CDCl_3$).

of the ester bond between the secondary hydroxyl group of terfenadine and the carboxyl group of succinyl linker was demonstrated by a downfield shift in the ^{1}H NMR chemical shift of the methine group (CH−O) from 4.60 ppm in terfenadine to 5.81 ppm in Ter−suc (Figure 2). Accurate mass spectrometry confirmed that only one succinyl group was attached to terfenadine via the secondary hydroxyl group and that the tertiary hydroxyl diphenyl group ($Ph_2C(OH)$−) remained free. The carboxyl group of the succinyl linker was utilized to conjugate Ter−suc to a surface amine group of the G1 dendrimer using the active ester method involving NHS (Scheme 1) as this method of dendrimer conjugation was found to be more efficient than direct condensation using coupling agents such as CDI (*18*). In order to obtain an approximately 1:1 ratio of dendrimer and terfenadine, Ter−suc or Ter−suc−deg was added to the reaction in quantities slightly higher than the equimolar ratio to dendrimer.

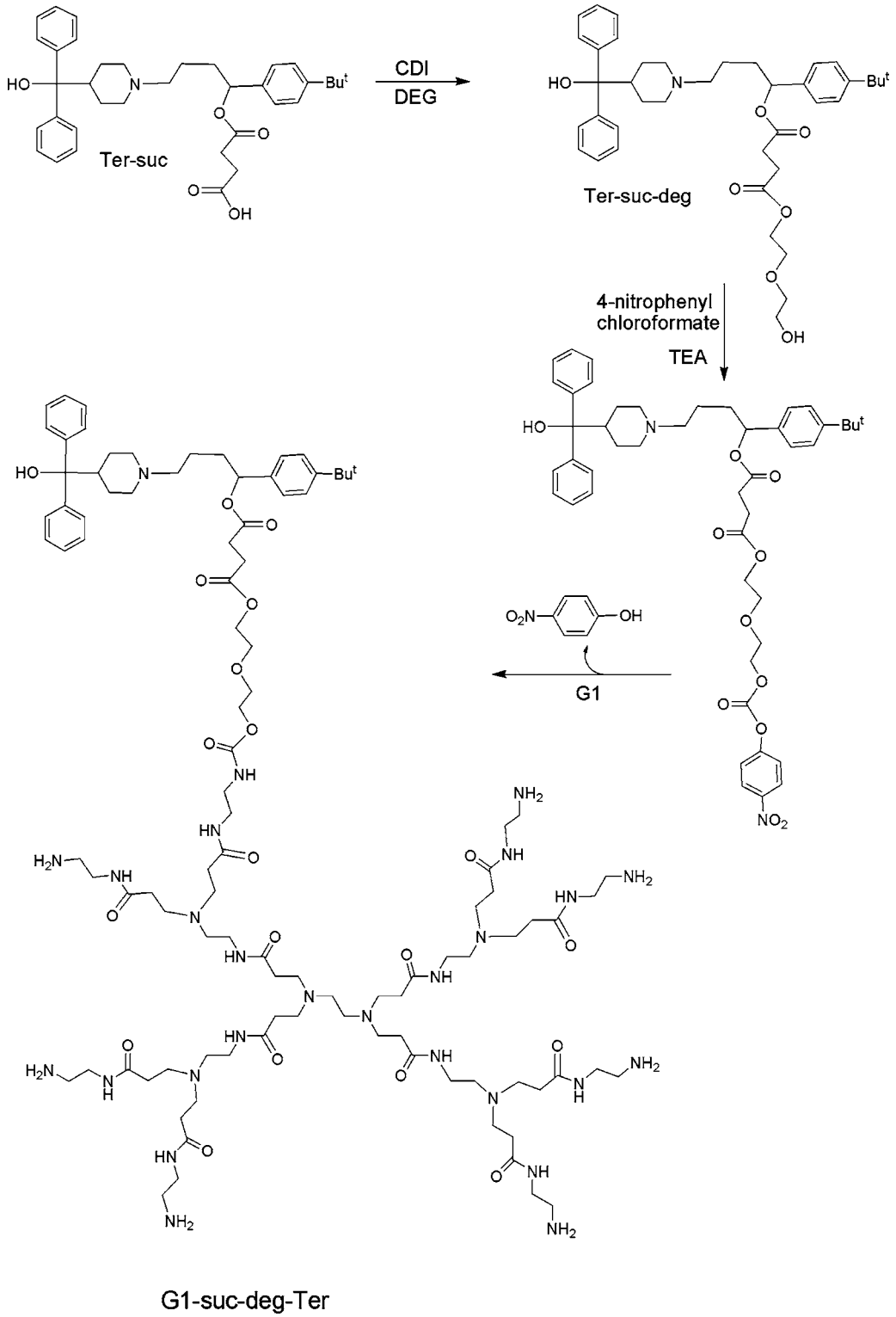
G1−suc−deg−Ter. Synthesis of Ter−suc−deg was performed by condensing diethylene glycol to the carboxyl of the succinic linker using CDI as coupling agent (Scheme 2). Adding diethylene glycol to Ter−suc changed its physical state from a solid to an oil without any noticeable enhancement in the water solubility. Ter−suc−deg (Scheme 2) and lauroyl alcohol (Scheme 3) were attached to the primary amines of G1 dendrimer using the 4-nitrophenyl chloroformate activation method.

Dendrimer conjugates were purified by size exclusion chromatography, solubilization in water (as terfenadine and lauroyl alcohol are insoluble in water), and dialysis (M_W cutoff = 1000 Da) for 48 h. The resulting conjugates were characterized by ^{1}H and ^{13}C NMR spectroscopy and RP-HPLC. As shown in Figure 3, the RP-HPLC chromatograms of the conjugates confirm that the drug is covalently bound to G1 PAMAM dendrimers; no traces of the free drug or drug linker were detected. The drug payloads in the conjugates were estimated using the relative intensities of the peaks in the ^{1}H NMR spectrum originating from attached compound compared to those of dendrimer (Table 1). In the ^{13}C NMR spectrum, the covalent bond between the succinyl linker and dendrimer was confirmed by the appearance of a new amide carbonyl peak at 175.7 ppm (CONH, Suc) for G1−suc−Ter. Similarly, the carbamate bond between diethylene glycol linker and/or lauroyl chain and G1 were represented by carbamate carbonyl peaks at 156.6 ppm for G1−suc−deg−Ter and L2−G1−suc−deg−Ter.

Partition Coefficients of Dendrimer Conjugates. Terfenadine, as an insoluble drug (*19*, *20*), is attached to the surface of a highly water-soluble dendrimer. Determination of solubility would require the synthesis of large amounts of the conjugates; therefore, the apparent partition coefficients (K_{app}) of terfenadine and conjugates between 1-octanol and phosphate buffer (pH 7.4) were determined as a parameter reflecting the change in the lipophilicity of terfenadine after attaching to G1 PAMAM dendrimer. Table 2 shows a significant decrease in the lipophilicity of terfenadine following its conjugation to the highly water-soluble G1 PAMAM dendrimer. L2−G1−suc−deg−Ter shows the highest lipophilicity among the G1−terfenadine conjugates (but lipophilicity is still significantly lower than that of terfenadine) as a result of the presence of two lipophilic lauroyl chains on the surface of the G1 PAMAM dendrimer.

Effect of PAMAM Dendrimer Prodrugs on Caco-2 Cell Viability (LDH Assay). The influence of PAMAM dendrimer prodrugs on the viability of Caco-2 cells was determined using the LDH assay. LDH, a cytosolic enzyme, has been found to leak into the culture medium upon damage to cell membranes (*21*). As shown in Figure 4, G1 PAMAM dendrimer was relatively nontoxic to Caco-2 cells, with less than 10% cytotoxicity at concentrations of 1 mM after 180 min incubation. A comparison between the IC_{50} of G1 and that of G3 PAMAM dendrimer shows that G1 is significantly less toxic than G3 (Table 3). This result is in agreement with previous observations which showed that the cytotoxicity of PAMAM dendrimers was concentration, generation, and charge dependent (*7*, *9*). Attach-

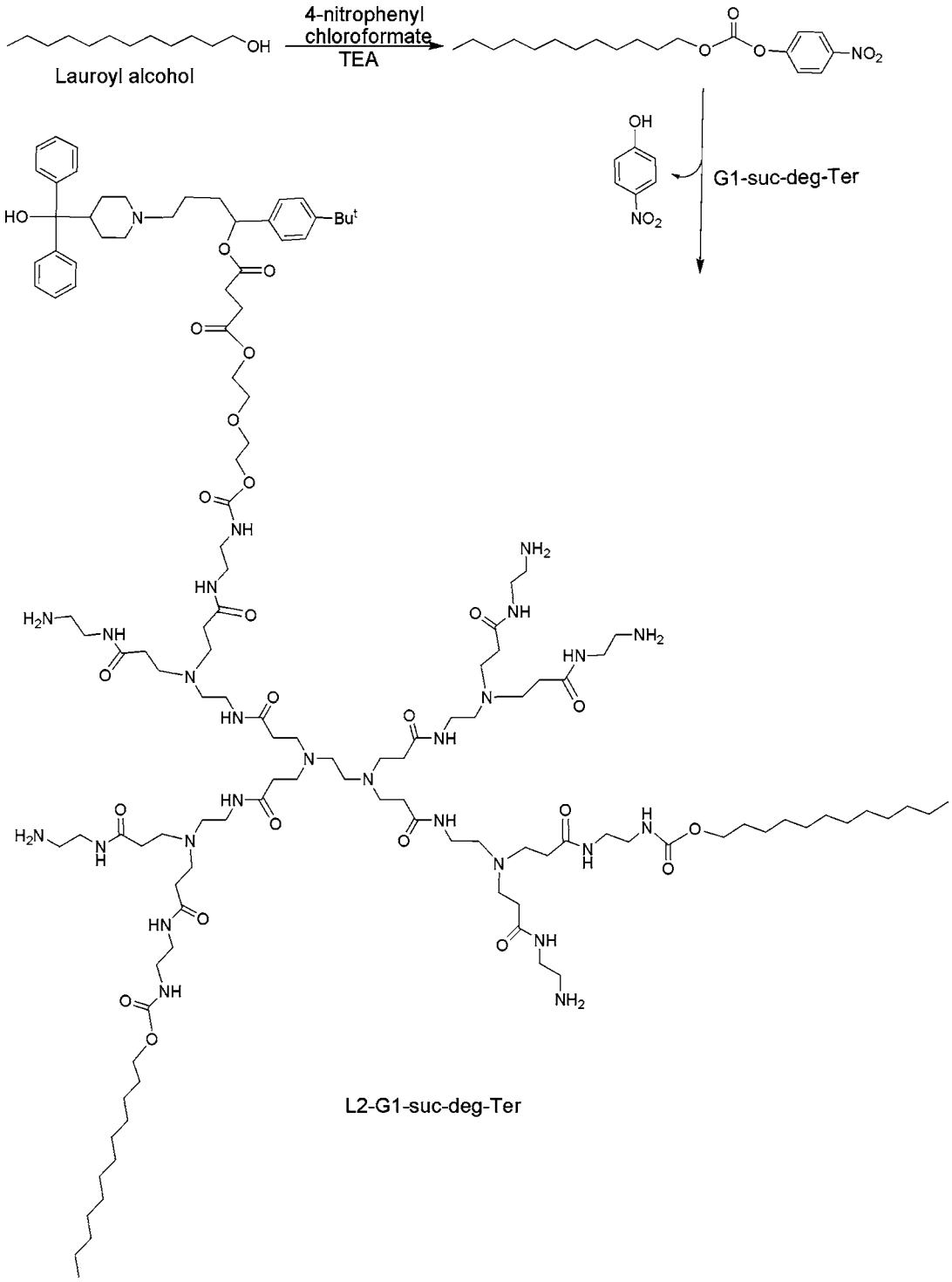
Scheme 2. Synthesis of G1−suc−deg−Ter



ing terfenadine via a linker to the G1 PAMAM dendrimer decreased the viability of Caco-2 cells as indicated by IC_{50} results (Table 3). G1 dendrimer−terfenadine conjugates showed concentration-dependent toxicity with a leakage of approximately 100% LDH for concentrations of 1 mM (Figure 4). These results are explained by the high toxicity of terfenadine, which has been reported to be both time and dose dependent as indicated by leakage of LDH from rat myocardial cells *(in vitro)* (*22*). However, G1 dendrimer−terfenadine conjugates were nontoxic toward Caco-2 cells at the concentration used in the transport study (50 μM).

Transport Studies of Ter, Ter−suc, Ter−suc−deg, and G1 PAMAM Dendrimer Conjugates Across Caco-2 Monolayers. The transport of terfenadine and prodrugs across Caco-2 monolayers was investigated in the A → B and B → A directions at nontoxic concentrations (as determined by the LDH assay). The stability of Ter−dendrimer conjugates was evaluated at pH 1.2, 7.4, and 8.5. After 24 h of incubation, the conjugates remained intact and no traces of drug were detected using HPLC (data not shown). Following transport studies, no free drug was detected in the receiver compartment.

Scheme 3. Synthesis of L2−G1−suc−deg−Ter



The apparent permeability coefficient (P_{app}) of terfenadine and prodrugs in both directions at 3 h is shown in Figure 5. Terfenadine, known as a strong substrate for the intestinal P-gp efflux transporter, showed B → A P_{app} significantly greater than A → B P_{app}, confirming previous reports showing the transport profile of terfenadine across Caco-2 monolayers (*23*). No significant difference can be observed on the permeability of terfenadine after attaching succinyl or succinic−diethylene glycol chains as shown in Figure 5 for Ter−suc or Ter−suc−deg. This suggests that attaching a linker to terfenadine had no impact on the permeability of the resulting prodrug.

In the presence of G1 there was no change in the transport profile of terfenadine in both directions (Figure 5). However, the permeability of G1−suc−Ter and G1−suc−deg−Ter across Caco-2 monolayers, especially in the A → B direction, was significantly higher than that of terfenadine, suggesting the ability of G1 dendrimer conjugates to bypass the P-gp efflux transporter. These results are in agreement with a previous report showing that propranolol (P-gp substrate) conjugated to G3 PAMAM dendrimer was also able to bypass the P-gp efflux system in Caco-2 monolayers (*17*). In the present study, terfenadine, an unambiguous, stronger P-gp substrate (*12*), was attached to G1 PAMAM dendrimer, a less toxic dendrimer than G3 PAMAM (*9*), via a linker/spacer. In addition, the A → B permeability of G1 PAMAM dendrimers was found to be several-fold higher than the A → B permeability of higher generations (G3 and G4) (*9*).

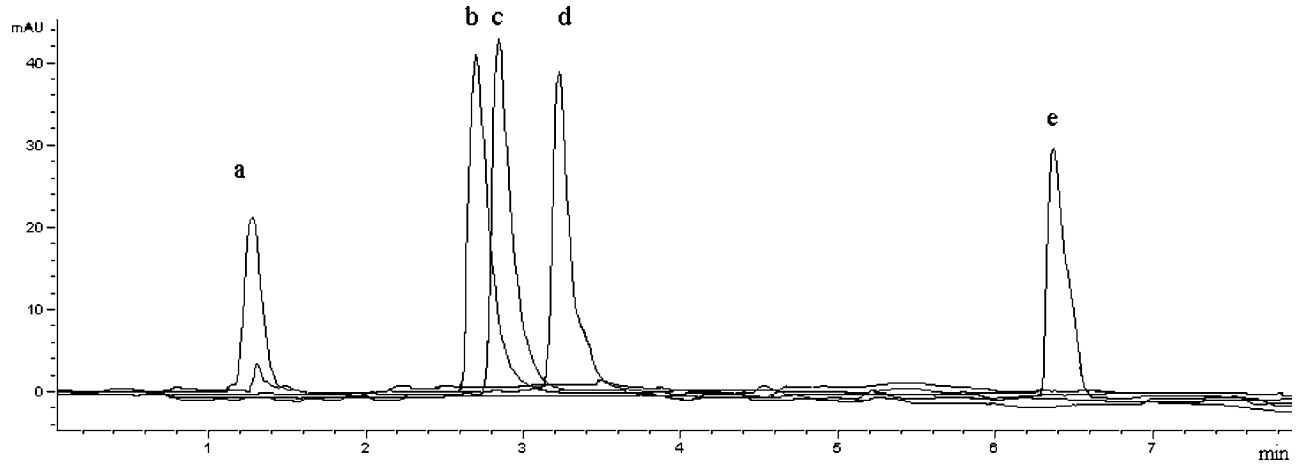


Figure 3. RP-HPLC chromatograms of (a) G1 PAMAM dendrimer, (b) G1−suc−deg−Ter, (c) G1−suc−Ter, (d) L2−G1−suc−deg−Ter, and (e) terfenadine.

Table 1. Properties and Concentrations of G1−Terfenadine Conjugates Used in Transport Studies

	conjugation ratio G1:terfenadine[a]	conjugation ratio G1:lauroyl chain[a]	average mol wt (g/mol)	conjugate concentration (μM)	equivalent concentration of terfenadine (μM)
G1	N/A	N/A	1429.9	N/A	N/A
G1−suc−Ter	1:1.14	N/A	1983.6	43.9	50
G1−suc−deg−Ter	1:1.11	N/A	2115.7	45.0	50
L2−G1−suc−deg−Ter	1:0.95	1:2.16	2540.4	52.6	50

[a] Determined by ^{1}H NMR spectroscopy.

Table 2. Log $K_{o/w}$ (pH 7.4) Values of Terfenadine and its Conjugates at 37 °C

compound	log $K_{o/w}$ (pH 7.4)
Ter	1.25 ± 0.17
Ter−suc	1.38 ± 0.22
Ter−suc−deg	1.15 ± 0.22
G1−suc−Ter	−0.11 ± 0.08
G1−suc−deg−Ter	−0.16 ± 0.07
L2−G1−suc−deg−Ter	0.15 ± 0.06

Table 3. Effect of G1 PAMAM Dendrimer, G1−Terfenadine Conjugates, and G3 PAMAM Dendrimer on the Viability of Caco-2 Cells As Determined by IC_{50} (mean ± SD, $n = 4$)

compound	IC_{50} (mM)
G1	6.23 ± 1.20
G1−suc−Ter	0.52 ± 0.08
G1−suc−deg−Ter	0.55 ± 0.10
L2−G1−suc−deg−Ter	0.48 ± 0.04
G3	0.25 ± 0.09

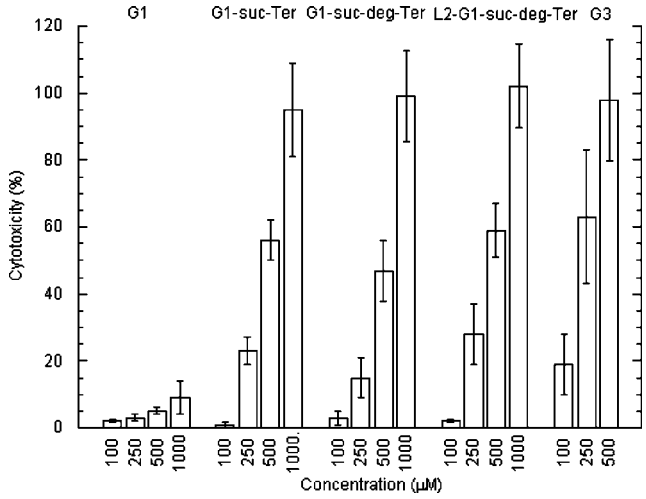


Figure 4. Effect of G1 PAMAM dendrimer, G1−terfenadine conjugates, and G3 PAMAM dendrimer on the viability of Caco-2 cells (LDH assay) (mean ± SD, $n = 4$).

The high permeability of G1 PAMAM−terfenadine conjugates may be attributed to the positively charged amine groups of the G1 PAMAM dendrimers. It has been reported that positively charged molecules permeate at a higher rate across Caco-2 monolayers compared to neutral or anionic molecules because of the favorable electrostatic interaction with the negatively charged epithelial surfaces (*24*). In addition, Jevprasesphant and co-workers found that the permeability of positively charged PAMAM dendrimers was higher than that of anionic PAMAM dendrimers (*7*). The apparent lack of impact of the G1 dendrimer on the transport profile of terfenadine may be a consequence of the transcellular rather than paracellular transport of terfenadine; G3 dendrimer was reported to enhance paracellular transport by opening up the tight junctions (*7*). Moreover, the significant increase in the permeability of terfenadine was only shown when terfenadine was covalently bound to G1 PAMAM dendrimers. It is proposed that G1 PAMAM dendrimer enhances the permeability of the conjugated drug by acting as an efficient carrier across the cellular membrane rather than influencing the transport mechanism of the drug. This suggestion is confirmed by reports showing that PAMAM dendrimers are neither P-gp inhibitors nor P-gp substrates (*8, 17*).

Lauroyl alcohol, known to function as a permeability enhancer (*25*), was used as a surface modifier of G1 PAMAM dendrimers to enhance the permeability of the resulting conjugates. Surface-modified dendrimers with medium chain fatty acids were also found to be significantly less cytotoxic and exhibited enhanced permeation through Caco-2 monolayers (*7*). Two lauroyl chains were attached to the surface amine group of G1−suc−deg−Ter to give the conjugate L2−G1−suc−deg−Ter. This conjugate showed the highest permeability in both directions across Caco-2 cell monolayers of all the G1 conjugates of this study with an A → B permeability over 25-fold higher than that of terfenadine alone.

Transepithelial electrical resistance (TEER) measurements were used to assess the influence of G1−terfenadine conjugates on the integrity of Caco-2 monolayers. TEER values were measured following apical incubation with Ter, Ter−suc, Ter−

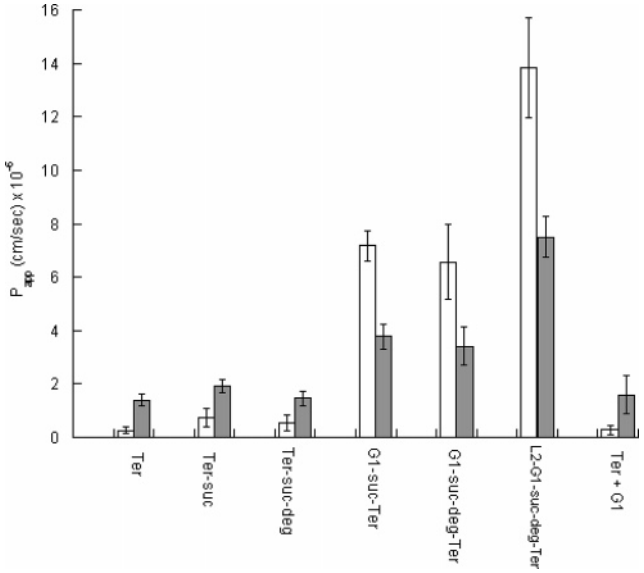


Figure 5. A → B (□) and B → A (■) permeability after 3 h across Caco-2 cell monolayers at 37 °C of free terfenadine, conjugates, and terfenadine in the presence of G1 PAMAM dendrimer (mean ± SD, $n = 4$).

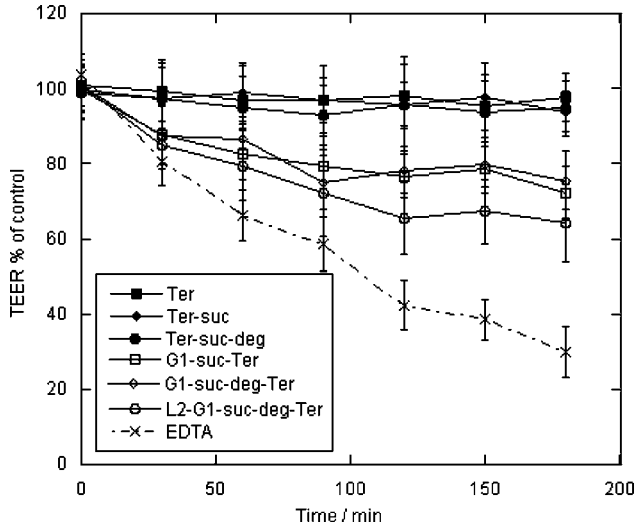


Figure 6. Effect of terfenadine and terfenadine prodrugs (each equivalent to 50 μM terfenadine) and EDTA (1 mM) on the TEER of Caco-2 cell monolayers after apical incubation (mean ± SD, $n = 4$).

suc−deg, and G1 PAMAM dendrimer conjugates (each equivalent to 50 μM of Ter) and EDTA (1 mM). EDTA (anionic permeation enhancer) was used as a positive control, modulating the tight junction by chelating the extracellular Ca^{2+} and Mg^{2+} ions required to maintain the integrity of tight junctions (*26*). Figure 6 shows that EDTA decreased the TEER values by approximately 65% compared to the control (HBSS with 25 mM HEPES) after 3 h of incubation. Ter, Ter−suc, and Ter−suc−deg had no significant impact on TEER values, which may suggest transcellular transport for these compounds. However, TEER values decreased by approximately 25% when exposed to G1−suc−Ter and G1−suc−deg−Ter and by approximately 35% for L2−G1−suc−deg−Ter. This suggests that the enhancement of permeability may be partly due to modulation of the tight junction. A previous report showed that transport of propranolol was increased when conjugated to lauroyl-modified G3 PAMAM and that this increase might involve endocytosis-mediated transport (*17*). However, as no significant differences were observed between the TEER values for L2−G1−suc−deg−Ter and other G1 conjugates, it is unlikely that the observed increase in the permeability of L2−G1−suc−deg−Ter (Figure 6) results from dilation of tight junctions, which suggests that transport of L2−G1−suc−deg−Ter may also involve a transcellular pathway. Previous work has demonstrated that transepithelial transport of dendrimer conjugates involves both paracellular and transcellular pathways (*6*).

CONCLUSIONS

The design, synthesis, characterization, and transport studies of terfenadine conjugates of G1 PAMAM dendrimer using biodegradable spacer/linkers are reported. Partition coefficient results indicate that the G1−terfenadine conjugates were significantly more hydrophilic than the parent drug. Cytotoxicity studies showed that G1 PAMAM dendrimer was only slightly toxic to Caco-2 monolayers with a significantly lower toxicity than that of G3 PAMAM dendrimer. The presence of G1 PAMAM dendrimer in the transport medium had no impact on the transport profile of terfenadine, but attaching terfenadine to the surface of G1 PAMAM dendrimers via a covalent bond significantly increased its A → B permeability across Caco-2 cell monolayers. A more pronounced increase of A → B terfenadine permeability was reported when lauroyl-modified dendrimer prodrug was used as a carrier. The transport mechanism of G1−terfenadine conjugates is thought to involve both transcellular and paracellular pathways. Our results suggest that G1 PAMAM dendrimers demonstrate potential as nanocarriers for enhancement of oral bioavailability of terfenadine as a model for low-solubility drugs that are P-glycoprotein substrates.

ACKNOWLEDGMENT

We thank Dr. Jeff Penny for use of Caco-2 cell facilities and Al-Baath University for financial support.

LITERATURE CITED

(1) Tomalia, D. A., Baker, H., Dewald, J., Hall, M., Kallos, G., Martin, S., Roeck, J., Ryder, J., and Smith, P. (1985) A new class of polymers: Starburst-dendritic macromolecules. *Polym. J. (Tokyo, Jpn.) 17*, 117−32.

(2) D'Emanuele, A., and Attwood, D. (2005) Dendrimer-drug interactions. *Adv. Drug Delivery Rev. 15*, 2147−2162.

(3) D'Emanuele, A., Attwood, D., and Abu-Rmaileh, R. (2003) Dendrimers. In *Encyclopedia of Pharmaceutical Technology* (Swarbrick, B. J. C., Ed.) pp 1−21, Marcel Dekker, New York.

(4) Florence, A. T., Sakthivel, T., and Toth, I. (2000) Oral uptake and translocation of a polylysine dendrimer with a lipid surface. *J. Controlled Release 65*, 253−259.

(5) Wiwattanapatapee, R., Carreno-Gomez, B., Malik, N., and Duncan, R. (2000) Anionic PAMAM dendrimers rapidly cross adult rat intestine in vitro: a potential oral delivery system? *Pharm. Res. 17*, 991−998.

(6) Najlah, M., and D'Emanuele, A. (2006) Crossing cellular barriers using dendrimer nanotechnologies. *Curr. Opin. Pharmacol. 6*, 522−527.

(7) Jevprasesphant, R., Penny, J., Attwood, D., McKeown, N. B., and D'Emanuele, A. (2003) Engineering of dendrimer surfaces to enhance transepithelial transport and reduce cytotoxicity. *Pharm. Res. 20*, 1543−1550.

(8) El-Sayed, M., Rhodes, C. A., Ginski, M., and Ghandehari, H. (2003) Transport mechanism(s) of poly (amidoamine) dendrimers across Caco-2 cell monolayers. *Int. J. Pharm. 265*, 151−7.

(9) El-Sayed, M., Ginski, M., Rhodes, C., and Ghandehari, H. (2002) Transepithelial transport of poly(amidoamine) dendrimers across Caco-2 cell monolayers. *J. Controlled Release 81*, 355−365.

(10) Jevprasesphant, R., Penny, J., Jalal, R., Attwood, D., McKeown, N. B., and D'Emanuele, A. (2003) The influence of surface modification on the cytotoxicity of PAMAM dendrimers. *Int. J. Pharm. 252*, 263−266.

(11) Saitoh, H., and Aungst, B. J. (1995) Possible involvement of multiple P-glycoprotein-mediated efflux systems in the transport of

verapamil and other organic cations across rat intestine. *Pharm. Res. 12*, 1304−10.
(12) Polli, J. W., Wring, S. A., Humphreys, J. E., Huang, L., Morgan, J. B., Webster, L. O., and Serabjit-Singh, C. S. (2001) Rational use of in vitro P-glycoprotein assays in drug discovery. *J. Pharmacol. Exp. Ther. 299*, 620−628.
(13) Trambas, C. M., Muller, H. K., and Woods, G. M. (1997) P-glycoprotein mediated multidrug resistance and its implications for pathology. *Pathology 29*, 122−130.
(14) Lo, Y. L., Hsu, C. Y., and Huang, J. D. (2005) Comparison of effects of surfactants with other MDR reversing agents on intracellular uptake of epirubicin in Caco-2 cell line. *Anticancer Res. 18*, 3005−9.
(15) Tomita, M., and Hayashi, M. (2005) Improvement of intestinal drug absorption based on structural changes of tight junction and functional changes of P-glycoprotein. *Drug Delivery Syst. 20*, 416−423.
(16) Choi, J. S., Jo, B. W., and Kim, Y. C. (2004) Enhanced paclitaxel bioavailability after oral administration of paclitaxel or prodrug to rats pretreated with quercetin. *Eur. J. Pharm. Biopharm. 57*, 313−8.
(17) D'Emanuele, A., Jevprasesphant, R., Penny, J., and Attwood, D. (2004) The use of a dendrimer-propranolol prodrug to bypass efflux transporters and enhance oral bioavailability. *J. Controlled Release 95*, 447−453.
(18) Najlah, M., Freeman, S., Attwood, D., and D'Emanuele, A. (2006) Synthesis, characterization and stability of dendrimer prodrugs. *Int. J. Pharm. 308*, 175−182.
(19) Loftsson, T., Hreinsdottir, D., and Masson, M. (2005) Evaluation of cyclodextrin solubilization of drugs. *Int. J. Pharm. 302*, 18−28.
(20) Choi, H.-G., Lee, B.-J., Han, J.-H., Lee, M.-K., Park, K.-M., Yong, C. S., Rhee, J.-D., Kim, Y.-B., and Kim, C.-K. (2001) Terfenadine-β-cyclodextrin inclusion complex with antihistaminic activity enhancement. *Drug. Dev. Ind. Pharm. 27*, 857−862.
(21) Decker, T., and Lohmann-Matthes, M. L. (1998) A quick and simple method for the quantitation of lactate dehydrogenase release in measurements of cellular cytotoxicity and tumor necrosis factor (tnf) activity. *J. Immunol. Methods 115*, 61−69.
(22) Melchert, R. B., Levin, P. S., and Acosta, D., Jr. (1996) Cardiotoxicity of nonsedating antihistamines in vitro. *In Vitro Toxicol. 9*, 431−440.
(23) Raeissi, S. D., Hidalgo, I. J., Segura-Aguilar, J., and Artursson, P. (1999) Interplay between CYP3A-mediated metabolism and polarized efflux of terfenadine and its metabolites in intestinal epithelial Caco-2 (TC7) cell monolayers. *Pharm. Res. 16*, 625−632.
(24) Knipp, G. T., Ho, N. F. H., Barsuhn, C. L., and Borchardt, R. R. (1997) Paracellular diffusion in Caco-2 cell monolayers: effect of perturbation on the transport of hydrophilic compounds that vary in charge and size. *J. Pharm. Sci. 86*, 1105−1110.
(25) Aungst, B. J. (2000) Intestinal Permeation Enhancers. *J. Pharm. Sci. 89*, 429−442.
(26) Noach, A. B. J., Kurosaki, Y., Blom-Roosemalen, M. C. M., de Boer, A. G., and Breimer, D. D. (1993) Cell-polarity dependent effect of chelation on the paracellular permeability of confluent Caco-2 cell monolayers. *Int. J. Pharm. 90*, 229−237.

BC060325Q

Improvement of a Recombinant Anti-Monkey Anti-CD3 Diphtheria Toxin Based Immunotoxin by Yeast Display Affinity Maturation of the scFv

Zhirui Wang, Geun-Bae Kim,† Jung-Hee Woo,‡ Yuan Yi Liu, Askale Mathias, Scott Stavrou, and David M. Neville, Jr.*

Section on Biophysical Chemistry, Laboratory of Molecular Biology, National Institute of Mental Health, Building 10 Rm 3D46, 10 Center Drive, Bethesda, Maryland 20892-1216. Received November 2, 2006; Revised Manuscript Received December 28, 2006

Recently, a bivalent recombinant anti-human CD3 diphtheria toxin (DT) based immunotoxin derived from the scFv of UCHT1 antibody has been made that shows enhanced bioactivity and is free from the side effects of Fc receptor interaction. In this case, the diminution of CD3 binding due to the placement of the scFv domain at the C-terminus of the truncated DT in single scFv immunotoxins was compensated by adding an additional scFv domain. However, this strategy was less successful for constructing an anti-rhesus recombinant immunotoxin derived from the scFv of FN18 antibody due to poor binding of the anti-rhesus bivalent immunotoxin. We report here that, by increasing the FN18 scFv affinity through random mutagenesis and selection with a dye-labeled monkey CD3$\epsilon\gamma$ recombinant heterodimer, we greatly improved the bioactivity of FN18 derived immunotoxin. The best mutant, C207, contained nine mutations, two of which were located in CDRs that changed the charge from negative to positive. Binding affinity of the C207 scFv to the monkey T cell line HSC-F increased 9.8-fold. The potency of the C207 bivalent immunotoxin assayed by inhibition of protein synthesis increased by 238-fold.

INTRODUCTION

Anti-CD3 immunotoxins induce profound but transient T cell depletion in vivo by inhibiting eukaryotic protein synthesis, and they have utility in nonhuman primate models of transplantation tolerance and autoimmune disease therapy. The chemically conjugated anti-human immunotoxin, UCHT1−CRM9, depleted 3 logs of xenografted human T leukemic cells in nude mice resulting in long-term regressions of 86% of the tumors in an animal model of T cell leukemia/lymphoma (*1*). The chemically conjugated anti-monkey immunotoxin, FN18−CRM9, depleted 1.5−2.0 logs of T cells from the lymph node compartment and markedly prolonged the survival of kidney allografts (*2*, *3*). In combination with a short-term course of deoxyspergualin, FN18−CRM9 produced long-term tolerance to pancreatic islet allografts in 3 out of 7 recipients (functioning graft survival over 5 years) (*4*). An anti-porcine anti-T cell conjugate was effective in maintaining long-term hematopoietic stem cell transplants in the absence of graft versus host disease (*5*). These conjugated immunotoxins were formed by chemically cross-linking the antibody or antibody fragment to a diphtheria toxin binding site mutant, CRM9. In this way, the binding site of the immunotoxin was dictated by the antibody moiety (*6*). Analysis of these 1:1 conjugates by SDS[1] reducing gels revealed that all of the possible linkages between the toxin A and B chains and the antibody heavy and light chains were formed, even though the average link per molecule was maintained at one. Although immunoglobulin receptor interactions could be eliminated by conjugation with $F(ab')_2$[2] antibody fragments, purified yields were low (2% of toxin input) and linkage heterogeneity remained.

In order to overcome the disadvantages of chemically conjugated immunotoxins, recombinant anti-human anti-T cell immunotoxins were developed. These immunotoxins, utilizing diphtheria toxin truncated at amino acid residue 390, were restricted to having the antibody moiety placed C-terminal to the truncated toxin, because antibody domains fused to the N-terminal of the toxin interfered with translocation of biologically active A chain (*7*, *8*). However, it was found that when the scFv of UCHT1 was fused to the C-terminus of DT390 its binding activity toward T cells was reduced by a factor of 0.033 compared to the free scFv. Since the monovalent scFv was reduced in binding by a factor of 0.3 compared to the parental divalent antibody, the overall binding reduction of this fusion immunotoxin was 0.01 compared to the parental antibody. By adding a second scFv moiety separated through a $(G_4S)_3$ linker, a 10-fold increase in binding activity was achieved compared

* Corresponding author. National Institute of Mental Health, Bldg 10, Rm 3D46, 10 Center Drive, Bethesda, Maryland 20892-1216, Tel: (301) 496 6807, Fax: (301) 480 0446, E-mail: davidn@mail.nih.gov.

† Current address: Department of Animal Science and Technology, Chung-Ang University, Gyeonggi-Do 456-756 Korea.

‡ Current address: Cancer Research Institute of Scott and White Memorial Hospital, 5701 South Airport Road, Temple, Texas 76502.

[1] Abbreviations: SDS, sodium dodecyl sulfate; dH_2O, deionized H_2O; FACS, fluorescent activated cell sorting; TE buffer, a buffer containing tris[hydroxymethyl]aminomethane and EDTA; TEG buffer, a similar buffer with the addition of 5% glycerol; 7-AAD, amino-actinomycin D; FITC, fluorescein; MCF, mean channel fluorescence; MCF′, background corrected mean channel fluorescence; PE, phycoerythrin.

[2] Abbreviations of antibody fragments and recombinant antibodies and immunotoxins: $F(ab')_2$, pepsin generated NH_2 terminal antibody fragment containing the both variable light chains, VL, and both the variable heavy chains, VH, the constant light and heavy chains and the interchain disulfide hinge; FR, framework region of variable light or heavy chains; CDR, complimentary determining region of variable light or heavy chains; scFv, recombinant single chain variable region VL-L-VH where in this work L represents a glycine serine (G4S)3 linker; biscFv, a recombinant tandem repeat of scFv, VL1-L-VH1-L-VL2-L-VH2, numerals indicate the order of the chains; DT390-biscFv, a recombinant immunotoxin consisting of the catalytic and translocation domain of diphtheria toxin truncated at residue 390 and preceded by an alanine residue and containing a double mutation, dm, removing glycosylation sites fused to a biscFv following residue 390. Writing in parenthesis following Fv indicates the lineage of the Fv.

10.1021/bc0603438 Not subject to U.S. Copyright. Published 2007 by American Chemical Society
Published on Web 03/13/2007

to monovalent fusion immunotoxin. This fusion immunotoxin, A-dmDT390biscFv(UCHT1), displayed an increase in potency of 10- to 30-fold compared to the chemically conjugated immunotoxin and depleted 2.4 logs of T cells in the lymph node compartment of transgenic mice expressing human CD3ϵ (*9*). The increase in potency of the fusion immunotoxins over the chemical conjugate normalized for equal cell binding was ascribed to an increase in the efficiency of postbinding processes within the intoxication pathway (*10*). The in vivo potency of the divalent fusion immunotoxin, A-dmDT390biscFv(UCHT1), was considered acceptable for clinical development. The expression and purification of this immunotoxin from *P. pastoris* under GMP compliant conditions has been described (*11*, *12*). Currently, gram quantities have been produced and are undergoing testing for an IND (investigational new drug) submission for the treatment of refractory human T cell leukemia (*36*).

This paper describes the steps used to develop a monkey analogue of the recombinant anti-T cell immunotoxin being readied for clinical trials. A monkey analogue is needed to explore preclinical immune tolerance protocols using a fusion immunotoxin that has similar potency, similar serum half-lives, and biodistribution as the clinical reagent. Preliminary evidence indicated that the scFv of the anti-monkey T cell antibody FN18 was even more sensitive than UCHT1 to positional affects of a neighboring DT390 domain, resulting in a much greater loss in affinity (*13*). We reasoned that increasing the affinity of FN18-scFv would compensate for the loss in affinity of recombinant immunotoxins and consequently increase their bioactivity. Therefore, we endeavored to affinity mature the scFv of FN18 through random mutagenesis and selection by sorting flow cytometry using dye-labeled CD3$\epsilon\gamma$ ectodomain heterodimers, and techniques developed by Boder and Wittrup (*14*). Here, we report the selection of scFv(FN18) mutants with increased binding affinity and the bioactivities of recombinant immunotoxins made with the highest affinity mutants. In additionally, we compare binding data of scFv(UCHT1) and biscFv(UCHT1) to those of the mutant scFv(FN18) and mutant biscFv(FN18) to illustrate differences in the divalent character of biscFvs made from FN18 versus UCHT1.

EXPERIMENTAL PROCEDURES

Plasmids, Bacterial and Yeast Strains, Antibodies, Cell Lines. *Pichia pastoris* strain GS115, plasmids pPICZα and pPIC9K, *Saccharomyces cerevisiae* strain EBY100, and anti-V5 monoclonal antibody were purchased from Invitrogen. Plasmids pET17b and pET27b and *E. coli* BL21 (DE3) pLysS were purchased from Novagen. Goat anti-mouse IgG2a antibody conjugated with PE /FITC was purchased from Caltag. Streptavidin Alexa Fluor-488 conjugate and streptavidin-FITC was from Molecular Probes. Goat anti-mouse IgG-HRP was purchased from Santa Cruz Biotechnology and used to detect the expression of FN18 scFv in *E. coli* BL21 (DE3) pLysS. The hybridoma secreting FN18 was kindly provided by Dr. Margreet Jonker, Biomedical Primate Research Center Rijswijk, and was produced and purified by the National Cell Culture Center, Minneapolis, MN. Chemically conjugated anti-monkey anti-CD3 immunotoxin, FN18−CRM9, was prepared as previously described (*15*). Biocytin-labeled monkey cyno/rhesus CD3$\epsilon\gamma$ ectodomain heterodimer ligand with alanine or valine at amino acid residue 35 of CD3ϵ was prepared as described by Wang and Neville (*16*). The Herpes Saimiri virus transformed cynomolgous cell T cell line HSC−F (*17*) was supplied by the Centralized Facility for AIDS Reagents supported by EU Programme EVA and the U.K. Medical Research Council. This cell line exhibits the moderate binding FN18 phenotype (*37*). The Herpes Saimiri transformed rhesus cell T cell line Mm357−2 was supplied by the NIH Nonhuman Primate Reagent Resource, Beth Israel Deaconess Medical Center, Boston MA. This cell line exhibits the high binding FN18 phenotype (*37*).

Codon Optimization of scFv(FN18) and Construction of biscFv(FN18). Footnote 2 details the protein domain structure of the recombinant monovalent and bivalent single chain antibody fragments scFv, and biscFv and the diphtheria toxin based immunotoxins derived from these single chain antibodies.

Our lab reported that codon optimization is necessary to express DT390-based immunotoxins in *Pichia pastoris* (*18*). We used the optimized DT390 nucleotide sequence described by Woo et al. (*18*) for the DT390 domain of the new anti-monkey immunotoxins. The initial anti-monkey immunotoxin A-dmDT390biscFv(FN18) was constructed from the scFv of FN18 following the strategy used to construct A-dmDT390biscFv-(UCHT1) in *P. pastoris* (*18*). A-dmDT390biscFv(FN18) was cloned into pnPICZα (*Xho*I-*Eco*RI), subcloned into pPIC9K (*Sac*I-*Eco*RI), which was used to transform *P. pastoris* strain GS115. Low yields (see results) prompted us to rebuild the new scFv(FN18) DNA using the *P. pastoris* preferred codons (*19*). Eight primers for VL and 10 primers for VH of scFv(FN18) were designed to cover the full length of scFv(FN18). The primer length was kept under 70 bases. There was about a 21 base overlap between any of the neighboring primers. Ten picomoles of the first and the last primers and 2 pmol of the rest of the primers were used. The PCR program was, after heating at 95 °C for 4 min, 25 cycles of 95 °C for 30 s, 55 °C for 30 s, 72 °C for 1 min, and then extension for another 10 min. The PCR products were checked with 1% agarose gel electrophoresis. The band with the correct size was cut out and extracted with the QIAquick Gel Extraction Kit. The VL PCR product was digested with *Bam*HI and the VH PCR product with *Bgl*II. Then, the VL part and VH part were ligated together with T4 ligase for 6 h. PCR amplification was done with the first primer (VL1a) of the VL carrying *Nco*I site at the 5′ end and the last primer of the VH (VH10b) carrying the *Eco*RI site at the 3′ end to get the full length of scFv(FN18). The PCR product was checked again with 1% agarose gel electrophoresis. The band with the correct size (VL + VH) was cut out and extracted with the QIAquick Gel Extraction Kit. The PCR product was digested with both *Nco*I and *Eco*RI and cloned into pET17b-DT390 at *Nco*I-*Eco*RI for sequencing analysis and *E. coli* BL21 expression analysis. To construct the rebuilt biscFv(FN18), we amplified the first scFv(FN18) with primers VL1a carrying *Nco*I site and VH10a carrying *Bam*HI site. We amplified the second scFv(FN18) with VL1b carrying *Bgl*II site and VH10b carrying stop codon and *Eco*RI site. Then, we cloned the first scFv(FN18) into pET27b and the second scFv(FN18) into pET17b for sequencing analysis. Then, the first and second scFv(FN18) were subcloned together into pET17b-DT390 (*Nco*I-*Bam*HI/*Bgl*II-stop codon-*Eco*RI) and confirmed by *E. coli* BL21 expression analysis. The DT390-biscFv(FN18) was then subcloned into pnPICZα (*Xho*I-*Eco*RI) (*18*) and then subcloned into pPIC9K (*Sac*I-*Eco*RI). The rebuilt DT390-biscFv(FN18) in pPIC9K was transformed into *Pichia pastoris* GS115.

Random Mutagenesis. The optimized scFv(FN18) sequence insert described in the previous section was randomly mutated with error-prone PCR using nucleotide analogues (*20*) as described by Colby et al. (*21*). Briefly, 6 of 50 μL-PCR reactions were set up with different concentration (200, 20, and 2 μM; two reactions for each of the concentrations) of the two nucleotide analogues: 8-oxo-dGTP and dPTP (8-oxo-2′-deoxyguanosine-5′-triphosphate and 2′-deoxy-p-nucleoside-5′-triphosphate, respectively, both from TriLink Biotech). Other components of the PCR mix were as follows: 10× PCR buffer without $MgCl_2$, 2 mM of $MgCl_2$, 0.5 μM of forward primer PYD5 For (5′ CAG TTA CTT CGC TGT TTT TCA ATA TTT TCT GTT ATT GCT AGC 3′, *Nhe*I site underlined), 0.5 μM

of reverse primer PYD5 Rev (5′ ATC GAG ACC GAG GAG AGG GTT AGG GAT AGG CTT ACC GAA TTC 3′, *Eco*RI site underlined), 200 μM of dNTP, 0.1−1 ng of pYD5 DNA containing the codon optimized FN18-scFv DNA, 2.5 units of Taq polymerase, adding dH_2O to the final volume of 50 μL. The PCR program used was 94 °C for 3 min; then cycles of 94 °C for 45 s, 55 °C for 30 s, 72 °C for 1 min, and finally an extension for another 10 min. PCR cycles were different for varying concentration of the nucleotide analogues (200 μM for 5 cycles, 200 μM for 10 cycles, 20 μM for 10 cycles, 20 μM for 20 cycles, 2 μM for 10 cycles, 2 μM for 20 cycles). The mutagenic PCR products were purified from SYBR Gold (Molecular Probes) stained agarose gel (1%) with QIAquick Gel Extraction Kit. In order to clear the DNA of incorporated nucleotide analogues and to generate sufficient mutated DNA for the transformations, a second round of PCR reactions was performed in the absence of the nucleotide analogues. Six 50 μL reactions were set up for each PCR product from the previous mutagenic reactions. This time, the PCR mix contained 2 μL of the gel-purified mutagenized DNA, 10× PCR−$MgCl_2$ buffer, 1.5 mM of $MgCl_2$, 0.2 μM of forward primer (same as above), 0.2 μM of reverse primer (same as above), 200 μM of dNTP, and 5 units of platinum Taq polymerase, with dH_2O added to the final volume. The PCR program was 95 °C for 5 min, 30 cycles of 95 °C for 30 s, 55 °C for 30 s, 72 °C for 1 min, and extension for another 10 min at 72 °C. The PCR products were again gel-purified. This protocol produces 40−100 μg of PCR products.

Preparation of the FN18-scFv Yeast Display Library. pYD5 (*13*) was digested with both *Nhe*I and *Eco*RI and purified with the QIAquick Gel Extraction Kit as the linear vector. The inserts produced by PCR and the linear vector were cotransformed into yeast *Saccharomyces cerevisiae* EBY100 using the standard transformation procedure in the Gietz Lab Transformation kit (Genomics One International, Inc., Buffalo, NY) as described by the instructions. The inserts were flanked by ∼42 nucleotides homologous to the 5′ and 3′ ends of the open vector, thus permitting homologous combination between the open vector and the insert within the yeast (upstream from *Nhe*I in the aga2 signal peptide region and downstream from *Eco*RI in the V5 epitope region). Transformations utilizing homologous recombination are highly efficient in *S. cerevisiae* (*22*).

Library size (number of transformants) was determined by plating 0.1 μL, 1 μL, and 10 μL of the 1 mL of the resuspended transformed *Saccharomyces cerevisiae* EBY100 cells onto a 100 mm screening plate. Using 1 μg of the linear pYD5 vector DNA (*Nhe*I-*Eco*RI) and 10 μg of the mutagenized library insert DNA (PCR product) cotransformed into 1×10^8 yeast *Saccharomyces cerevisiae* EBY100 cells, we obtained about 1×10^6 transformants. Normally, ten reactions were done and pooled, yielding about 1×10^7 transformants.

Growth and Induction. The growth and induction phases were modified as described by Wang et al. (*13*). The yeast display medium contained 0.67% YNB (Q.Biogene, with ammonium sulfate, without amino acids), 2% glucose (or galactose), 0.5% casamino acids (DIFCO), adjusting pH to 6.0 with pH 6.0 sodium phosphate buffer, 20 μg/mL of ampicillin, 20 μg/mL of kanamycin, 100 units/mL penicillin, and 100 μg/mL streptomycin. For plates, 1.5% agar and 1 M sorbitol were added to the medium. In the growth phase, glucose was used as the carbon source at 30 °C for 24 h, and in the induction phase, galactose was used as the carbon source at 20 °C for 24 h.

FACS Analysis, Sorting, and Sequencing. FACS analysis of yeast displayed scFv and K_D determination were conducted using biocytin-labeled monkey cyno/rhesus CD3$\epsilon\gamma$ ectodomain heterodimer ligand as described by Wang et al. (*13*). The sorting for higher-affinity FN18 sFv displaying yeast cells was performed on an Epics Elite ESP cell sorter (Beckman Coulter). The number of yeast cells screened was set as a factor of 10 greater than the library size to ensure that no unique clones were overlooked. Yeast cells were stained with anti-V5 antibody (Invitrogen) and CD3$\epsilon\gamma$ biocytin labeled ligand at 4 °C for 1.5 to 2 h. The amount of V5 antibody used was 1 μL/10^6 cells, while the molar amount of CD3$\epsilon\gamma$ biocytin to be used was predetermined by analytical FACS analysis and average K_D measurement on the mixed clone population (usually 0.1−0.05 × K_D). Yeast samples were then washed twice at 5000 *g* for 5 min at 4 °C. Staining with secondary reagents was done for 1 h at 4 °C with goat anti-mouse IgG2a-PE (Caltag) 5 μL and streptavidin Alexa Fluor 488 (Molecular Probes) 2 μL/10^6 cells, respectively. Samples were then washed twice at 5000 *g* for 5 min at 4 °C. Screening was done with an equilibrium screen (*21*) utilizing bivariate plots of the stained V5 and CD3$\epsilon\gamma$ ligand. Cells were initially gated on the characteristic of their forward and side light scatter to avoid cellular clumps and debris. If in the sort sample a double-positive diagonal was observed, the sample was sorted with a diagonal edge to normalize for expression of the scFv. In cases where no double-positive diagonal was present, almost the entire dual positive quadrant was collected. The first rounds of sorting were given a generous sort gate anywhere from 1% to 4% utilizing the gated logic mode. The purity mode was used for the third and fourth rounds as gate stringency was increased, reaching 0.1%. Sorted events were collected in yeast growth medium (see Growth and Induction section). After each round of mutagenesis, we did four rounds of sorting. Then, random clones picked up from selection plates were propagated, induced, and analyzed by FACS for their binding affinities as previously described (*13*). The yeast mutant plasmid DNA was extracted with a Zymoprep Yeast Plasmid Minipreparation kit (Zymo Research, Orange, CA) from those clones with the highest affinity and then transformed into *E. coli*. After the amplification in *E. coli*, the plasmid DNA was sequenced to determine the mutation(s) in the scFv sequence or used as template DNA for the next round of mutagenesis. We repeated the process until we failed to generate any new higher-affinity mutants. In this study, we did three rounds of the mutagenesis. Site-directed mutagenesis was applied to combine some the higher-affinity mutations into a single plasmid clone using a QuickChange Site-Directed Mutagenesis Kit (Stratagene, La Jolla, CA).

Expression and Purification of Mutant Immunotoxins in *P. pastoris*. To make DT390-biscFv(FN18−M20) bivalent immunotoxin, the first scFv(FN18−M20) and second scFv-(FN18−M20) genes were amplified by PCR (template DNA, M20 yeast plasmid; primers for the first scFv, WP-051 and WP-053; primers for the second scFv, WP-054 and WP-052. All of the WP and GP primers are listed in Table 1). The first scFv PCR product was digested with *Nco*I and *Bam*HI, and the second scFv PCR product was digested with *Bam*HI and *Eco*RI. Then, the two fragments were inserted into *Nco*I and *Eco*RI sites of pET17b-DT390 (pJW1019). The DT390-biscFv(FN18−M20) gene was subcloned into *Xho*I and *Eco*RI sites of pnPICZα. The resulting plasmid (pJW1020) was transformed into *Pichia pastoris* JW107, and the transformants were selected on YPD plates containing zeocin (100 μg/mL). Six colonies were randomly selected and cultivated in test tubes containing 5 mL YPD at 28 °C at 250 rpm for 2 days. The cultures were induced with methanol for 1 day, and then the culture supernatants were analyzed on SDS-PAGE under nonreducing condition. One clone (JW132) was selected and cultivated in shake-flasks to purify DT390-biscFv(FN18−M20) by phenyl hydrophobic interaction chromatography and then Super Q anion exchange chromatography. Solid sodium sulfate was added to 595 mL of culture supernatant to a final concentration of 500 mM. The

Table 1. Primer Sequence for the Construction of scFvs and Immunotoxins[a]

primers	sequence (5′→3′)
WP−051	TTCTT GCCAT GG**GAC GTTGT TATGT CTCAA TCT**
WP−052	CGTGA ATTC**T TAAGA GGAGA CGGTG ACAGA GGT**
WP−053	ATGGA ATTCA TGGGA TCCAC CGCCT CCGCT GCCTC CGCCT CCAG**A GGAGA CGGTG ACAGA GGT**
WP−054	GGTGG ATCCG GAGGG GGAGG CTCG**G ACGTT GTTAT GTCTC AATCT**
WP−061	TTCTT GCTCG AGAAA AGA**GA CGTTG TTATG TCTCA ATCT**
WP−073	TACAT ATTTT TGTTT TTGCT GTCAT TCGTT CAAGG C**GACG TTGTT ATGTC TCAAT CT**
WP−075	ATGTT CGAAA CGATG AATAT ATTT**T ACATA TTTTT GTTTT TGCTG TCA**
GP−080	TACAT ATTTT TGTTT TTGCT GTCAT TCGTT CAAGG CGACA TTGTT ATGTC TCAAT CT
GP−089	TTCTT GCCAT GGGAC TTTGT TATGT CTCAA TCT
GP−090	GGTGG ATCCG GAGGG GGAGG CTCGG ACTTT GTTAT GTCTC AATCT
GP−102	**TACAT ATTTT TGTTT TTGCT GTCA**T TCGTT CAAGG CGACT TTGTT ATGTC TCAAT CT

[a] Restriction sites are underlined. Boldface indicates the DNA sequences used to anneal two primers.

sample was loaded onto 50 mL phenyl 650M (Tosoh) in a 5 cm × 30 cm × K50 column (Amersham Biosciences). The bound DT390-biscFv(FN18−M20) was eluted with TEG buffer containing 5% glycerol, 20 mM Tris−HCl, and 1 mM EDTA (pH 8.0). Pooled fractions containing DT390-biscFv(FN18−M20) were dialyzed 3 times against TE buffer. The dialyzed sample was loaded to 3.5 mL of Super Q 650M (Tosoh) in a 1.5 cm × 10 cm Flex column (Kontes Glass Company). The bound DT390-biscFv(FN18−M20) was eluted with 50 mM NaCl in TEG buffer.

To make DT390-biscFv(FN18−C207) bivalent immunotoxin, the first scFv(FN18−C207) and second scFv(FN18−C207) genes were amplified by PCR (template DNA, C207 yeast display plasmid; primers for the first scFv, GP-089 and WP-053; primers for the second scFv, GP-090 and WP-052). The first scFv PCR product was digested with *Nco*I and *Bam*HI, and the second scFv PCR product was digested with *Bam*HI and *Eco*RI. Then, the two scFv parts in the vector pJW1020 (DT390-biscFv(FN18−M20) in pnPICZα) were sequentially replaced with C207 counterparts using *Nco*I and *Bam*HI for the first scFv and *Bam*HI and *Eco*RI for the second scFv. Purification of DT390-biscFv(FN18−C207) was performed as described for DT390-biscFv(FN18−M20) except that the loading of the anion exchange column was performed at pH 9.0 instead of pH 8.0 and the protein was eluted with 50 mM sodium borate at pH 8.5. In addition, the DT390-biscFv(FN18−C207) immunotoxin was fractionated on Superdex-200 10/300 GL to remove lower molecular weight breakdown products. Purity of both immunotoxins was judged by SDS gel electrophoresis and HPLC size exclusion chromatography on Superdex-200 10/300 GL (Amersham Biosciences).

Expression and Purification of Wild-Type, Mutant scFvs and biscFvs. For the production of the following scFvs and biscFvs, the original α-factor signal sequence in the vector system was replaced with killer toxin (kt) signal peptide due to the incomplete cleavage in the Kex2 cleavage site between the α-factor signal sequence and the inserted protein sequences of interest. This cleavage can be variable, since it is influenced by the first two amino acid residues of the post-Kex2 insert (*13*). To obtain scFv(FN18-WT), the scFv(FN18-WT) gene was PCR-amplified from the scFv(FN18-WT) yeast display plasmid using the primers (GP-080 and WP-052). After the PCR product was purified by gel elution, it was used for the second PCR using the primers WP-075 and WP-052. Primer WP-075 contained the 5′-sequence of the signal sequence of killer toxin from *Kluyveromyces lactis*. After the second PCR, the product was digested with *Sfu*I and *Eco*RI and purified by gel elution, and the treated PCR fragment was cloned into pwPICZα, which now contained the killer toxin signal peptide. The scFv(FN18−M20) and scFv(FN18−C207) genes were obtained by the same procedure using different primer sets for the first PCR (WP-073 and WP-052 for M20; GP-102 and WP-052 for C207). To make biscFv(FN18−C207), the first scFv(FN18−C207) and second scFv(FN18−C207) genes were PCR-amplified from the C207 yeast display plasmid. The first scFv was obtained by the two-step PCR as described in the previous section (primers GP-102 and WP-053 for the first PCR; primers WP-075 and WP-053 for the second PCR) and the second scFv was PCR-amplified using the primers (GP-090 and WP-052). The first scFv PCR product was digested with *Sfu*I and *Eco*RI, purified by gel elution, and cloned into pwPICZα. This constructed vector was digested with *Bam*HI and *Eco*RI and ligated with the scFv PCR product treated with the same enzymes. Transformation, growth, and induction conditions were similar to those used for the immunotoxins with the exception of biscFv(FN18−C207) where a modified version of strain mutEF2JC307 was used (*23*, *36*). Protein L affinity chromatography was used to purify the scFv and biscFv constructs; 1.8 mL of 5 M NaCl was added to 58 mL of culture supernatant and then loaded to 4 mL of Protein L agarose (Pierce) in a 1.5 cm × 10 cm Flex column (Kontes Glass Company) that was equilibrated with 100 mM potassium phosphate buffer, 150 mM NaCl (pH 7.0). The bound scFv(FN18−M20) was eluted with 100 mM glycine buffer (pH 2.5). 100 μL of 1 M Tris−HCl buffer (pH 8.0) was added to the eluted fractions. The eluted fractions were pooled and concentrated using an Amicon Ultra-4 (10 000 MWCO, Millipore). Purity was judged by SDS gel electrophoresis and HPLC Superdex 200 10/300 GL gel filtration (Amersham Biosciences). Purity was above 95% in all cases. Concentration was determined from the calculated absorption coefficients based on the amino acid sequences located at http://researchlink.labvelocity.com/tools/conversionTools/proteinExtinction.jhtml.

Protein Synthesis Inhibition Assay. This was performed by measuring the incorporation of ^{3}H-labeled leucine into HSC−F cells after a 20 h exposure to immunotoxins at different concentrations. Means and standard deviations of six replicates were calculated and divided by the means of non-immunotoxin treated controls × 100 to give % control protein synthesis as previously described (*9*).

T Cell Binding Assay of Recombinant scFv Antibodies And Immunotoxins. FN18−FITC conjugate was purchased from Biosource and added to 250 000 HSC−F cells at 5×10^{-9} M in the presence of varying concentrations of scFv and immunotoxin binding competitors at 4 °C for 30 min. The displacement of FN18−FITC was measured by FACS on a Beckman-Coulter Cytomics FC 500 instrument after washing the cells two times at 400 *g* at 4 °C and resuspending in 0.5 mL of 1 × PBS containing 2.5 μg of propidium iodide to exclude dead cells from further analysis. Mean channel fluorescent values, MCI, were corrected (MCF′) by subtracting an appropriate FITC-labeled isotope control from both the FN18−FITC tracer and the FN18−FITC tracer plus competitor MCF values. The % inhibition was determined as $[(MCF'_{FN18-FITC} - MCF'_{FN18-FITC+competitor})/MCF'_{FN18-FITC}] \times 100$. The relative binding affinity between any two competitors was determined

by dividing their respective concentrations at equal % inhibition obtained from plots of % inhibition versus concentration as previously described (*9*).

Immunotoxin-Induced Loss of $CD3^+CD4^+$ Resting Monkey T Cells. T cells from normal monkeys were isolated from blood by two centrifugations through Lymphocyte Separation Medium from BioWhittaker following the manufacturer's directions. The cells were washed and incubated in RPMI 1640 medium containing 25 mM HEPES with 10% fetal calf serum + 2 g/L $NaHCO_3$, adjusted to pH 7.4, plus 0.1 mM nonessential amino acids, 1.0 mM sodium pyruvate, and 50 μg/L of gentamicin sulfate with and without varying concentrations of immunotoxins for 72 h at 5% CO_2, 37 °C. Cells were washed and then stained for 30 min at 4 °C with anti-CD3 (SP34−2-PE BD Pharmingen), anti-CD4-FITC (BD Pharmingen), CD20-PE Cy7 (BD Biosciences), and the vital dye 7-ADD (BD Pharmingen) and analyzed on a Beckman-Coulter Cytomics FC 500 instrument counting 10^4 events. Cells were analyzed for uptake of the vital dye, the percent of cells within the lymphocyte forward scatter/side scatter gate, and the percent of cells within the lymphocyte gate within the quadrant displaying the $CD3^+$ and $CD4^+$ epitopes by two-color FACS. The % of cells within the lymphocyte gate at each immunotoxin concentration was divided by % of cells within the lymphocyte gate for the 72 h no-treatment control (G1). The % of cells within the $CD3^+CD4^+$ quadrant at each immunotoxin concentration was divided by % of cells within the $CD3^+CD4^+$ quadrant for the 72 h no-treatment control (Q1). The % loss of $CD3^+CD4^+$ cells was calculated as G1 × Q1 × 100.

RESULTS

Higher Immunotoxin Expression with Codon-Optimized scFv(FN18). Before codon optimization of the biscFv(FN18) domain of DT390biscFv(FN18), expression in *P. pastoris* strain GS115 yielded shake-flask culture supernatants with a barely visible band at 96.3 kDa corresponding to the DT390biscFv-(FN18) by Coomassie staining of SDS gels. Five clones screened from 91 clones by dot blots for higher expression gave supernatant concentrations of 1.3 to 2.7 ng/μL by comparison with a known concentration standard of DT390biscFv(UCHT1) in SDS gels. After rebuilding, 5 out of 12 transformants in GS115 had supernatant concentrations equal to 11 ng/μL after 24 h of induction judged by SDS gels (gel data not shown). A four-step purification procedure utilized absorption to Thiophilic Resin (Clonetech) followed by elution according to manufacturer's directions, dialysis versus 20 M Tris−HCl, pH 7.0, application to DEAE Sepharose (Amersham) followed by a step elution with 0.5 M NaCl and finally application to a Zorbax GF-250 column (DuPont). The major peak ran as a single band when analyzed on HPLC with a Zorbax GF-250 column. Purity was estimated as 95% by HPLC size exclusion and SDS gels.

Higher-Binding Mutants Selected with CD3$\epsilon\gamma$ Ectodomain Heterodimer. When this work was begun (*16*), we were using the monkey CD3ϵ sequence reported by Uda et al. (*24*) for the selecting ligand in the CD3$\epsilon\gamma$ ectodomain heterodimer used in flow cytometry. We encountered very low binding for the wild-type (WT) displayed scFvs and the initial mutant scFvs (*13*). Subsequently, through consulting the rhesus genome data base and by sequencing the CD3ϵ ectodomain of 24 rhesus and cynomolgous monkeys, we determined that high FN18-binding monkeys have a valine at amino acid residue 35 of CD3ϵ. The presence of alanine at this position is a frequently occurring polymorphism that reduces FN18 binding even when present in the heterozygote state (*37*). In our recent work, mutant selections utilized valine at position 35 of CD3ϵ of CD3$\epsilon\gamma$ ectodomain heterodimer. However, the change from A35 to V35 failed to select any new mutations.

Table 2. Representative scFv(FN18) Mutants Obtained from Yeast Display Selection[a]

scFv clones			Wt	L1	M20	C207
K_D[b] (nM)			13.9 ± 1.0	5.5 ± 0.3	4.4 ± 1.1	2.9 ± 0.3
mutations and locations	I 2 F	VL-FR1				+
	I 2 V	VL-FR1			+	
	K 18 R	VL-FR1		+	+	+
	S 32 F	VL-CDR1		+	+	+
	Q 35 R	VL-CDR1				+
	K 166 R	VH-FR2		+	+	+
	R 168 K	VH-FR2		+	+	+
	E 184 G	VH-CDR2				+
	A 207 V	VH-FR3				+
	S 225 A	VH-FR3			+	+

[a] Clone name indicates the mutation and residue within the scFv. Residue numbering proceeds from the NH_2 terminus of VL, the (G4S)3 linker and VH. [b] Mean equilibrium dissociation constants, K_D, determined as in Figure 1 from two titrations and curve fittings with CD3$\epsilon\gamma$ ectodomain heterodimer-35V batch L5−5. Errors are ±1 SD.

Random mutagenesis of yeast displayed FN18 scFv libraries selected by dye-labeled ectodomain CD3$\epsilon\gamma$ heterodimers for increased affinity yielded 43 mutations. Seven occurred in the first round in 3 clones, 31 in the second round in 20 clones, and 27 in the third round in 14 clones. Of these 43 mutations, only 9 showed significant increases in affinity when combined in single clones. These 10 mutations and their locations are summarized in Table 2. Three of these mutations occur in the complementary determining regions (CDR), two in the VL and one in the VH chains. The highest-affinity mutant, C207, contains a net increase of two positive charges over the wild-type. C207 was first made by combining several mutations by site-directed mutagenesis after the second round of mutagenesis and selection. However, C207 appeared spontaneously after three rounds of mutagenesis and selection. After the second round of mutagenesis and selection, no new affinity-enhancing mutants were found, although new favorable combinations were found in the third round of mutagenesis and selection.

The affinity of the yeast displayed scFv(FN18−C207) was increased 4.8-fold over the wild-type (WT) scFv. The titration curve and curve fitting for C207 and the WT scFv are shown in Figure 1. The binding curves appear saturable by inspection, and this is supported by the fact that the R values are >0.99 using a fitting equation that contains only a saturable term (see inserts in Figure 1 for the binding fitting equation and fit parameters). Nonspecific binding is by definition nonsaturable (*25*). If it were present here, it would appear as a linear increase in MFI as a function of ligand concentration superimposed on the saturable curve, and it would lower the R values (unless a nonsaturable term was added to the fitting equation). These considerations demonstrate that the measured increase in affinity caused by the C207 mutations is due to an increase in specific binding rather than nonspecific binding. The maximum mean fluorescent intensity at saturation increases by 2.4-fold in the C207 mutant compared to the WT, suggesting that the mutant has an increased protein folding stability within the yeast secretory pathway (*26*).

Purity of *P. pastoris* Mutant Immunotoxins. Following the three-step purification procedure, DT390-biscFv(FN18−M20) and DT390-biscFv(FN18−C207) displayed a major band on Coomassie-stained SDS nonreducing gels (Figure 2) migrating near the 97.3 kDa marker. DT390-biscFv(FN18−C207) showed several faint bands migrating near the 66.3 and 55.4 kDa markers. Western blots identified these as breakdown products. On Superdex-200 chromatography, these appeared as a small trailing shoulder accounting for 5.4% of the major band peak height. These bands were removed by subsequent fractionation on Superdex-200 as shown in the Figure 3 SDS nonreducing gel.

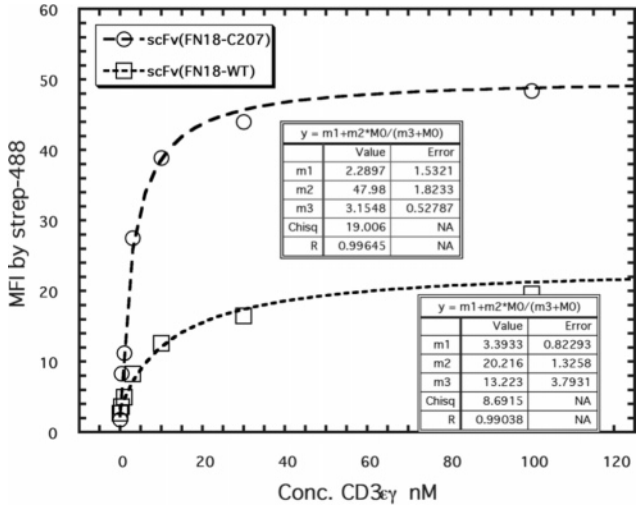


Figure 1. A comparison of titrations of CD3$\epsilon\gamma$ ectodomains labeled with streptavidin-488 on yeast displaying the wild-type scFv(FN18-WT), (□); and the highest-affinity selected mutant, scFv(FN18−C207), (○), is shown. The mean fluorescence intensity, MFI, is plotted vs the CD3$\epsilon\gamma$ concentration on the *x*-axis. The data points are fitted using nonlinear least-squares by *KaleidaGraph* software (Synergy Software, Reading, PA) using the hyperbolic equation $y = m_1 + m_2 \times M_0/(m_3 + M_0)$, where y = MFI at the given ligand concentration M_0, m_1 = MFI at 0 ligand concentration, m_2 = MFI at saturation minus m_2, and $m_3 = K_D$, the equilibrium dissociation constant in nM units. The top inserted box contains the C207 mutant fit data with a K_D of 3 nM. The CD3ϵ preparation contains V at residue 35.

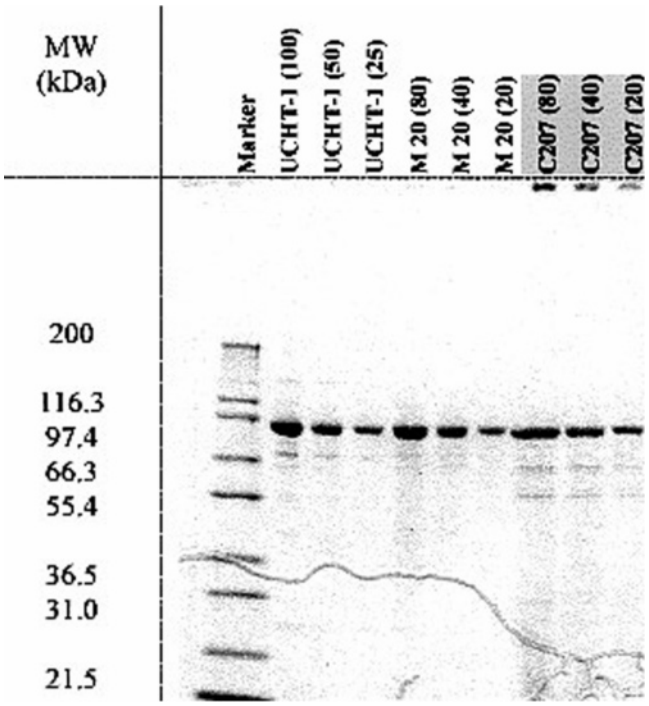


Figure 2. SDS 12% acrylamide bis-tris nonreducing gel of immunotoxins DT390biscFv(FN18−M20) and DT390biscFv(FN18−C207) are shown after the three-step purification procedure. From left to right, the lanes are (1) molecular weight markers, (2−4) immunotoxin standard DT390biscFv(UCHT1), (5−7) DT390biscFv(FN18−M20), and (8−10) DT390biscFv(FN18−C207). Numbers at the top indicate the load in μg applied. Marker MWs are given at the left.

Binding of Mutant scFvs and Their Derived Immunotoxins to T Cells. The binding activity of the *P. pastoris* expressed mutants and their derivative immunotoxins to the monkey TCR was explored in a binding competition assay using the continuous cultured monkey T cell line HSC−F. A tracer amount of FITC-labeled FN18 antibody was added to HSC−F cells along with varying concentrations of competitors, and the % inhibition of the FN18−FITC binding was determined by FACS (Figure 4). The binding activity of the scFv(FN18-WT) is reduced over the parental divalent FN18 by a factor of 0.29. Likewise, the binding activity of the immunotoxin derived from the scFv-(FN18-WT) is reduced by a factor of 0.01 compared to the parental antibody and by 0.04 compared to scFv(FN18-WT) as judged by the ratio of competitor concentrations at equal % inhibition values shown in Figure 4. The loss of binding activity of scFvs placed C-terminal to DT390 and other large proteins has been previously reported (*9*). However, the extent of the binding loss is 10-fold greater in the FN18 constructs compared to the anti-human CD3 UCHT1 constructs. This observation prompted us to undertake the affinity maturation of FN18 scFv in order to regain binding affinity within the immunotoxin

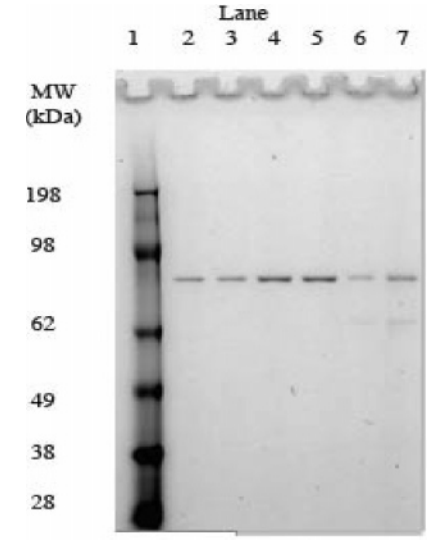


Figure 3. SDS 4−12% gradient tris-glycine nonreducing gel of DT390biscFv(FN18−C207) after an additional purification step of fractionation on Superdex-G200 to remove lower molecular weight contaminants. From left to right, the lanes are (1) molecular weight markers, (2,3) 22 μg of DT390biscFv(FN18−C207), (4,5) 44 μg of DT390biscFv(FN18−C207), and (6,7) standard DT390biscFv(UCHT1).

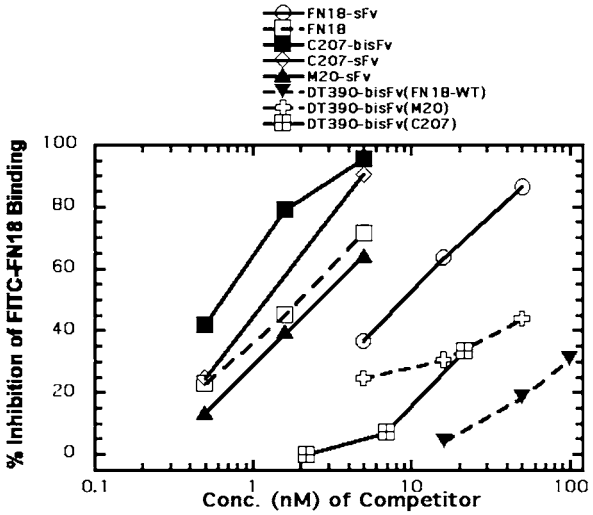


Figure 4. The % inhibition of tracer FITC-labeled FN18 binding to HSC−F monkey T cells is plotted vs the concentration of binding competitors consisting of mutant and wild-type scFvs, biscFvs, and immunotoxins derived from these scFvs. The relative binding affinity for any two competitors can be estimated from the ratio of their concentrations at equal % inhibition values. Estimates are considered to be reliable when comparing parallel curves or parallel curve regions. Means from replicate experiments comparing binding affinities relative to scFv(FN18-WT) are shown in Table 3.

Table 3. Relative Affinity Changes of Mutant scFvs(FN18)[a]

	mutant scFv affinity increase by yeast display relative to scFv-WT	*P. pastoris* expressed mutant scFv affinity increase by T cell binding relative to scFv-WT[b]
	scFv	
WT	1.0 ± 0.07	1.0 ± 0.014
M20	2.5 ± 0.14	3.0 ± 0.14
C207	4.8 ± 0.4	9.8 ± 0.2.4
	biscFv	
C207		16.7 ± 0.3

[a] Results are means + 1 SD for 2 or 3 determinations. [b] T cell binding affinity was measured displacement of FN18-FITC tracer from HSF cells by scFv competitors and ratioing equal displacement concentrations.

format. The scFv(FN18−M20) and scFv(FN18−C207) do exhibit increased binding in this assay, and the binding of biscFv(FN18−C207) is further enhanced. These results are summarized in Table 3, right-hand column, where the mean increases in binding affinity of the mutant scFvs relative to scFv-(FN18-WT) are listed from Figure 4 data and replicate experiments. The relative affinity changes determined from the yeast display K_D values are also listed for comparison. In Figure 4, the increase in the scFv(FN18−M20) is seen to be effective in increasing the affinity of the M20 derived immunotoxin, DT390-biscFv(FN18−M20). However, the increase is only about 4-fold over the WT immunotoxin, DT390-biscFv(FN18-WT). The DT390biscFv(FN18−C207) immunotoxin binding was not significantly different from the DT390-biscFv(FN18−M20) immunotoxin over the concentration range covered, although the steeper curve suggests that a difference might be observed at higher concentrations.

Increased Cytotoxicity of FN18−scFv Mutant-Derived Immunotoxin. In spite of the relatively small increase in binding affinity provided by the mutant M20 and C207 immunotoxins, the bioactivity of these immunotoxins exhibited large increases over the WT immunotoxins. Dose−response curves of a protein synthesis inhibition assay in HSC−F cells are shown in Figure 5 after a 20 h exposure to immunotoxins. In comparison to the DT390-biscFv(FN18-WT) immunotoxin, the M20 mutant immunotoxin is increased 68-fold, while the C207 mutant immunotoxin is increased 228-fold. Relative to the chemically conjugated immunotoxin, FN18−CRM9, these two mutant immunotoxins are increased 17- and 57-fold respectively. The receptor specificity of the assay is shown by the ability of a 10-fold excess of the FN18 antibody to compete with the cytotoxicity of each mutant immunotoxin at its highest concentration (filled symbols), and the lack of toxicity of the non-cross-reacting anti-human immunotoxin DT390biscFv(UCHT1). In another continuously cultured rhesus cell line, Mm357−2, M20 and C207 immunotoxins were increased 7-fold and 35-fold, respectively, over the chemically conjugated immunotoxin (data not shown).

In order to more closely replicate the in vivo status of T cells, we assayed the effects of these immunotoxins on freshly isolated T cells from peripheral monkey blood. Because the majority of these T cells are resting, the level of protein synthesis is too low to measure by the incorporation of labeled amino acids. However, resting T cells exposed to immunotoxins do incorporate the vital dye 7-AAD that is normally excluded from viable cells. We have found that these T cells also disappear from the normal lymphocyte gate. Those T cells that remain in the gate lose surface CD3 and CD4 epitopes in an immunotoxin dose- and time-dependent fashion. In Figure 6a, the DT390biscFv-(FN18−C207) mutant is seen to be 7.7-fold more potent than the chemical conjugate, 5.4-fold ± 3.3 for two replicate assays, while in Figure 6b, the DT390biscFv(FN18−M20) mutant is

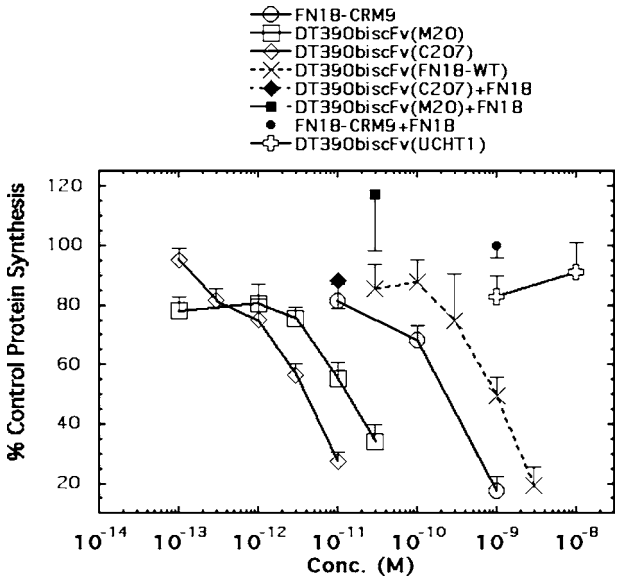


Figure 5. The % control inhibition of protein synthesis for four immunotoxins on HSC−F monkey T cells is plotted vs the immunotoxin concentrations on the *x*-axis after a 24 h exposure. Each point is the mean of six replicates and the positive sides of 1 SD single-sided error bars are shown. The mutant recombinant immunotoxin DT390-biscFv(FN18−C207) is the most potent immunotoxin, exceeding the wild-type recombinant immunotoxin by 238-fold. The receptor specificity of the assay is shown by the ability of a 10-fold excess of the FN18 antibody to compete the cytotoxicity of each immunotoxin at its highest concentration (filled symbols) and the lack of toxicity of the non-cross-reacting anti-human immunotoxin DT390biscFv(UCHT1).

seen to be 0.4-fold less potent than the chemical conjugate. Therefor, enhanced potency for the C207 mutant relative to the M20 mutant is 13.5-fold in resting T cells. Similar results were found when the assay measures the loss of the $CD3^+CD4^-$ cell population (data not shown). The possible causes for differences in relative potency between resting T cells and continuously cultured T cell lines are considered in the next section.

DISCUSSION

We increased the affinity of the anti-CD3 antibody FN18 by random mutagenesis combined with sorting flow cytometry selection using dye-labeled monkey CD3$\epsilon\gamma$ heterodimeric ectodomains. Although the affinity increase was modest in the best mutant, C207 (4.8-fold by yeast display), the increase was greater when judged by binding assays to T cells (9.8-fold) and further increased in the biscFv format used in diphtheria toxin based immunotoxins (16.7-fold). This resulted in an increase in bioactivity of 228-fold when measured on a continuously cultured monkey T cell line referenced to immunotoxin made with the wild-type scFv. Bioactivity toward monkey resting T cells isolated from peripheral blood increased 5.4-fold over the chemically conjugated immunotoxin, FN18−CRM9, that depletes resting T cells in monkey lymph nodes by 1.5−2 logs (*2*). Although the wild-type and the two mutant immunotoxins show the same rank order with regard to bioactivity between resting and transformed T cells, the large numerical differences imply differing rate-limiting steps within the intoxication pathway in resting versus transformed T cells. The rate-limiting step in diphtheria toxin intoxication of cells actively synthesizing protein has been ascribed to the translocation step of the toxin A chain into the cytosol compartment (*27*). However, resting T cells have very low rates of protein synthesis unless activated (*28*). In this situation, the toxin substrate, elongation factor-2, is continuously bound to the ribosome (as opposed to cycling on and off) and is protected against enzymatic inactivation by the toxin A chain (*29*). The rate of protein synthesis would then

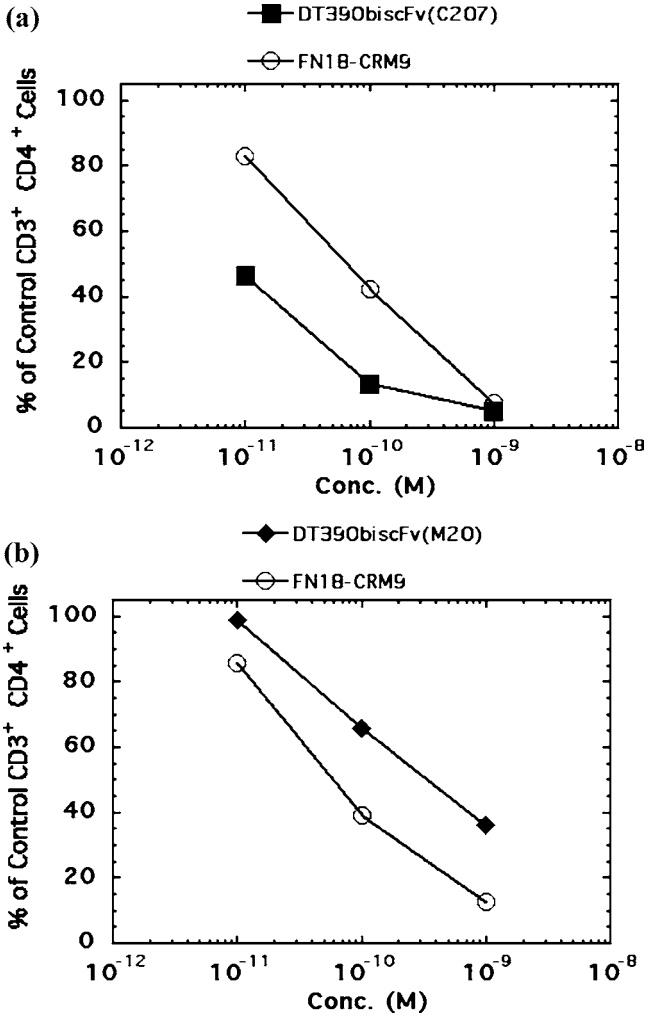


Figure 6. The loss of monkey peripheral blood $CD3^+CD4^+$ T cells from the FACS lymphocyte gate is shown after a 72 h exposure to immunotoxins as a function of immunotoxin concentration. In part a, the DT390biscFv(FN18−C207) mutant is seen to be 7.7-fold more potent than the chemical conjugate, 5.4-fold + 3.3 for two replicate assays; while in part b, the DT390biscFv(FN18−M20) mutant is seen to be 0.4-fold less potent than the chemical conjugate. The enhanced potency for the C207 mutant relative to the M20 mutant is 13.5-fold in resting T cells.

become rate-limiting for the intoxication process. It has been shown that the antibody moiety of an immunotoxin interacting with CD3ϵ provides an activating signal (*30*). The strength of this interaction may be determined by subtle features of the interaction and thus could enhance the intoxication rate. These considerations may explain why recombinant immunotoxins made with mutant C207 are active in depleting blood and lymph node T cells in monkeys in vivo, providing a homogeneous reagent for preclinical testing of tolerance induction in organ transplantation protocols (*38*).

The current study exploited the advantages of using *Pichia pastoris* for recombinant protein expression. All of the FN18 derivatives, mutant scFv, biscFv, and recombinant immunotoxins were expressed in *P. pastoris* using the secretory pathway ensuring optimal folding of each. This gave us confidence that the comparative numbers in binding and bioactivity assays reflected the advantages of the mutations rather than differences in protein folding that are often encountered when refolding proteins from insoluble granules in *E. coli*. Varying the signal peptide was found to be a valuable tool in optimizing the expression of these different constructs.

Analysis of the mutations in mutant C207 revealed that there was a net gain of two positive charges over the WT scFv within two CDR regions. Two recent crystallographic structures of anti-human CD3 antibodies OKT3 and UCHT1 bound to the human CD3$\epsilon\gamma$ (*31*) and human CD3$\epsilon\delta$ ectodomains (*32*) showed that the antibodies bind to an electronegative area on the exposed surface of CD3ϵ. It is possible that these new positive charges in the mutant are aiding the antibody CD3ϵ interaction.

The new mutations present in the C207 immunotoxin might cause some increase in immunogenicity and possibly compromise this methodology for human use. However, the major immunogen in this case is the toxin moiety. Preclinical animal studies have shown that T cell depletion sufficient for tolerating transplant protocols can be achieved with only 4 days of consecutive dosing, prior to the initiation of either a primary or secondary antibody response (*9*).

Our binding studies show that the scFv of FN18 loses affinity by a factor of 0.29 compared to the parental divalent antibody. This is nearly identical to the case of UCHT1 (0.3-fold) (*9*). Both scFvs lose affinity when placed C-terminal to DT390 (*33*). The strategy of using the biscFv format in DT-based immunotoxins was to compensate for this positional loss of affinity by introducing a bivalent interaction. However, the binding data presented here show that the biscFv format works less well for DT390-biscFv(FN18) than for DT390-biscFv(UCHT1), and the difference is 10-fold. The increase in affinity on going from scFv(UCHT1) to biscFv(UCHT1) is 5-fold (*9*). The increase in affinity on going from C207-scFv to C207-biscFv is only 16.7/9.8- or 1.7-fold (Table 3). This suggests that the biscFv of FN18 mutants has less divalent character than the UCHT1 biscFv. This could be the result of pairing preferences. In the biscFv structure, VL1-L-VH1-L-VL2-L-VH2, optimal divalent character will be achieved by binding of VL1 with VH1 and VL2 with VH2. However, other options for pairing are possible that will limit the divalent character of the biscFv. In the future, it will be necessary to explore other antibody formats for the biscFv domain of the anti-monkey immunotoxins derived from FN18. Diabody constructs with shortened linkers may be an option to force optimal pairing to achieve better divalent character (*34*, *35*).

ACKNOWLEDGMENT

This research was supported by the Intramural Research Program of NIMH, NIH. We thank Jim Nagle of the NINDS/NIH DNA Sequencing Facility for their generous support.

Supporting Information Available: The eight primers for VL and ten primers for VH to rebuild the scFv(FN18) for *P. pastoris* optimized codons. This material is available free of charge via the Internet as http://pubs.acs.org/BC.

LITERATURE CITED

(1) Neville, D. M., Jr., Scharff, J., and Srinivasachar, K. (1992) In vivo T cell ablation by a holo-immunotoxin directed at human CD3. *Proc. Natl. Acad. Sci. U.S.A. 89*, 2585−2589.

(2) Hu, H., Stavrou, S., Baker, B. C., Tornatore, C., Scharff, J., Okunieff, P., and Neville, D. M., Jr. (1997) Depletion of T lymphocytes with immunotoxin retards the progress of experimental allergic encephalomyelitis in rhesus monkeys. *Cell. Immunol. 177*, 26−34.

(3) Fechner, J. H., Jr., Vargo, D. J., Geissler, E. K., Graeb. C., Wang, J., Hanaway, M. J., Watkins, D. J., Piekarczyk, M., Neville, D. M., Jr., and Knechtle, S. J. (1997) Split tolerance induced by immunotoxin in a rhesus kidney allograft model. *Transplantation 63*, 1339−1345.

(4) Contreras, J. L., Jenkins, S., Eckhoff, D. E., Hubbard, W. J., Lobashevsky, A., Bilbao, G., Thomas, F. T., Neville, D. M., Jr., and Thomas, J. M. (2003) Stable α- and β-islet cell function after tolerance induction to pancreatic islet allografts in diabetic primates. *Am. J. Transplant. 3*, 128−138.

(5) Cina, R. A., Wikiel, K. J., Lee, P. W., Cameron, A. M., Hettiarachy, S., Rowland, H., Goodrich, J., Colby, C., Spitzer, T. R., Neville, D. M., Jr., and Huang, C. A. (2006) Stable multilineage chimerism without graft versus host disease following nonmyeloablative haploidentical hematopoietic cell transplantation. *Transplantation 81*, 1677−1685.
(6) Neville, D. M., Jr., Scharff, J., Rigaut, K., Hu, H., Shiloach, J., Slingerland, W., and Jonker, M. (1996) A new reagent for the induction of T cell depletion, anti-CD3-CRM9. *J. Immunother. Emphasis Tumor Immunol. 19*, 85−92.
(7) Madshus, I. H., Olsnes, S., and Stenmark, H. (1992) Membrane translocation of diphtheria toxin carrying passenger protein domains. *Infect. Immun. 60*, 3296−3302.
(8) Hexham, J. M., Dudas, D., Hugo, R., Thompson, J., King, V., Dowling, C., Neville, D. M., Jr., Digan, M. E., and Lake, P. (2001) Influence of relative binding affinity on efficacy in a panel of anti-CD3 scFv immunotoxins. *Mol. Immunol. 38*, 397−408.
(9) Thompson, J., Stavrou, S., Weetall, M., Weetall, M., Hexam, M., Digan, M. E., Wang, Z., Woo, J. H., Yu, Y., Mathias, A., Liu, Y. Y., Ma, S., Gordienko, I., Lake, P., and Neville, D. M., Jr. (2001) Improved binding of a bivalent single-chain immunotoxin results in increased efficacy for *in vivo* T-cell depletion. *Protein Eng. 14*, 1035−1041.
(10) Liu, Y. Y., Gordienko, I., Mathias, A., Ma, S., Thompson, J., Woo, J. H., and Neville, D. M., Jr. (2000) Expression of an anti-CD3 single-chain immunotoxin with a truncated diphtheria toxin in a mutant CHO cell line. *Protein Expr. Purif. 19*, 304−311.
(11) Woo, J. H., and Neville, D. M., Jr. (2003) Separation of bivalent anti-T cell immunotoxin from *P. pastoris* glycoproteins by borate anion exchange. *Biotechniques 35*, 392−398.
(12) Woo, J. H., Liu, Y. Y., and Neville, D. M., Jr. (2006) Minimization of aggregation of secreted bivalent anti-human T cell immunotoxin in *Pichia pastoris* bioreactor culture by optimizing culture for protein secretion. *J. Biotechnol. 121*, 75−85.
(13) Wang, Z., Mathias, A., Stavrou, S., and Neville, D. M., Jr. (2005) A new yeast display vector permitting free scFv amino termini can augment ligand binding affinities. *Protein Eng. Des. Sel. 18*, 337−343.
(14) Boder, E. T., and Wittrup, K. D. (1997) Yeast surface display for screening combinatorial polypeptide libraries. *Nat. Biotechnol. 15*, 553−557.
(15) Neville, D. M., Jr., Srinivasachar, K., Stone, R., and Scharff, J. (1989) Enhancement of immunotoxin efficacy by acid cleavable crosslinking agents utilizing diphtheria toxin and toxin mutants. *J. Biol. Chem. 264*, 14653−14661.
(16) Wang, Z., and Neville, D. M., Jr. (2004) Expression and characterization of recombinant soluble monkey CD3 molecules: mapping the FN18 polymorphic epitope. *Mol. Immunol. 40*, 1179−1188.
(17) Akari, H., Mori, K., Terao, K., Otani, I., Fukasawa, M., Mukai, R., and Yoshikawa, Y. (1996) In vitro immortalization of Old World monkey T lymphocytes with *Herpes* virus saimiri: its susceptibility to infection with simian immunodeficiency viruses. *Virology 218*, 382−388.
(18) Woo, J. H., Liu, Y. Y., Mathias, A., Stavrou, S., Wang, Z., and Neville, D. M., Jr. (2002) Gene optimization is necessary to express a divalent anti-T cell immunotoxin in *Pichia pastoris. Protein Expr. Purif. 25*, 270−282.
(19) Sreekrishna, K. (1993) Strategies for optimizing protein expression and secretion in the methylotrophic yeast *Pichia pastoris*. In *Industrial Microorganism: Basic and Applied Molecular Genetics* (Baltz, R. H., Hegeman, G. D., Skatrud, P. L., Eds.) pp 119−126, American Society of Microbiology, Washington, DC.
(20) Zaccolo, M., and Gherardi, E. (1999) The effect of high-frequency random mutagenesis on in vitro protein evolution: a study on TEM-1 beta-lactamase. *J. Mol. Biol. 285*, 775−783.
(21) Colby, D. W., Kellogg, B. A., Graff, C. P., Yeung, Y. A., Swers, J. S., and Wittrup, K. D. (2004) Engineering antibody affinity by yeast surface display. *Methods Enzymol. 388*, 348−358.
(22) Swers, J. S., Kellogg, B. A., and Wittrup, K. D. (2004) Shuffled antibody libraries created by in vivo homologous recombination and yeast surface display. *Nucleic Acid Res. 32*, e36.
(23) Liu, Y. Y., Woo, J. H., and Neville, D. M., Jr. (2003) Targeted introduction of a diphtheria toxin resistant mutation into the chromosomal EF-2 locus of *Pichia pastoris* and expression of immunotoxin in the EF-2 mutants. *Protein Expr. Purif. 30*, 262−274.
(24) Uda, A., Tanabayashi, K., Mukai, R., Yachi, M., Nam, K. H., and Yamada, A. (2001) CD3 polymorphism in cynomolgus monkeys (*Macaca fascicularis*). *J. Med. Primatol. 30*, 141−147.
(25) Kahn, C. R., Freychet, P., Roth, J., and Neville, D. M., Jr. (1974) Quantitative aspects of the insulin-receptor interaction in liver plasma membranes. *J. Biol. Chem. 249*, 2249−2257.
(26) Shusta, E. V., Kiete, M. C., Parke, E., Kranz, D. M., and Wittrup, K. D. (1999) Yeast polypeptide fusion surface display levels predict thermal stability and soluble secretion efficiency. *J. Mol. Biol. 292*, 949−956.
(27) Neville, D. M., Jr., and Hudson, T. H. (1986) Transmembrane transport of diphtheria toxin, related toxins, and colicins. *Annu. Rev. Biochem. 55*, 195−224.
(28) Preijers, F. W., Tax, W. J., Wessels, J. M., Capel, P. J., De Witte, T., and Haanen, C. (1988) Different susceptibilities of normal T cells and T cell lines to immunotoxins. *Scand. J. Immunol. 27*, 533−540.
(29) Gill, D. M. (1978) Seven toxic peptides that cross cell membranes. In *Bacterial toxins and cell membranes* (Jeljaszewicz, J., and Wadstrom, T., Eds.) pp 291−332, Academic Press, New York.
(30) Hamawy, M. M., Tsuchida, M., Cho, C. S., Manthei, E. R., Fechner, J. H., and Knechtle, S. J. (2001) Immunotoxin FN18-CRM9 induces stronger T cell signaling than unconjugated monoclonal antibody FN18. *Transplantation 72*, 496−503.
(31) Kjer-Nielsen, L., Dunstone, M. A., Kostenko, L., Ely, L. K., Beddoe, T., Mifsud, N. A., Purcell, A. W., Brooks, A. G., McCluskey, J., and Rossjohn, J. (2004) Crystal structure of the human T cell receptor CD3 epsilon gamma heterodimer complexed to the therapeutic mAb OKT3. *Proc. Natl. Acad. Sci. U.S.A. 101*, 7675−7680.
(32) Arnett, K. L., Harrison, S. C., and Wiley, D. C. (2004) Crystal structure of a human CD3-epsilon/delta dimer in complex with a UCHT1 single-chain antibody fragment. *Proc. Natl. Acad. Sci. U.S.A. 101*, 16268−16273.
(33) Ma, S., Hu, H., Thompson, J., Stavrou, S., Scharff, J., and Neville, D. M. Jr. (1997) Genetic construction and characterization of an anti-monkey CD3 single-chain immunotoxin with a truncated diphtheria toxin. *Bioconjugate Chem. 8*, 695−701.
(34) Holliger, P., Prospero, T., and Winter, G. (1993) "Diabodies": small bivalent and bispecific antibody fragments. *Proc. Natl. Acad. Sci. U.S.A. 90*, 6444−6448.
(35) Krauss, J., Arndt, M. A. E., Vu, B. K., Newton, D. L., Seeber, S., and Rybak, S. M. (2005) Efficient killing of CD22+ tumor cells by a humanized diabody-RNase fusion protein. *Biochem. Biophys. Res. Commun. 331*, 595−602.
(36) Frankel, A., and Woo, J.-H., January 2007, personal communication.
(37) Liu, Y. Y., Wang, Z., Thomas, J., Goodwin, K. J., Stavrou, S., Neville, D. M. Jr. (2007) Polymorphisms of CD3ϵ in cynomolgus and rhesus monkeys and their relevance to anti-CD3 antibodies and immunotoxins. *Immunol. Cell Biol.*, in press.
(38) Kim, G. B., Wang, Z., Liu, Y. Y., Stavrou, S., Mathias, A., Goodwin, K. J., Thomas, J. M., and Neville, D. M. Jr. A fold-back single-chain diabody format enhances the bioactivity of an anti-monkey anti-CD3 recombinant diphtheria toxin based immunotoxin. January 2007, unpublished data.

BC0603438

Construction of Intramolecular Luciferase Complementation Probe for Detecting Specific RNA

Tamaki Endoh,[†] Masayasu Mie,[†] Hisakage Funabashi,[†] Tatsuya Sawasaki,[‡] Yaeta Endo,[‡] and Eiry Kobatake[†,*]

Department of Biological Information, Graduate School of Bioscience and Biotechnology, 4259, Nagatsuta, Midori-ku, Yokohama, 226-8501, Japan, and Department of Applied Chemistry, Faculty of Engineering, Ehime University, Matsuyama 790-8577, Japan. Received November 9, 2006; Revised Manuscript Received January 12, 2007

Intermolecular enzyme complementation assay is a useful method for detecting protein−protein interactions. Specifically, bioluminescent signals produced from reconstructed split luciferase fragments are powerful tools for *in vivo* analysis because the bioluminescent signals have been visualized both in cultured cells and living animals. However, they are limited for detection and evaluation of biological events relevant to intermolecular protein−protein interactions. In this study, we constructed an intramolecular luciferase complementation probe for detecting target biomolecules other than protein−protein interactions. It consists of peptide-inserted firefly luciferase (PI-FLuc) containing a short peptide between internally divided firefly luciferase. The inserted short peptide triggers FLuc complementation or discomplementation and subsequent reactivation or inactivation of FLuc activity through its induced fit conformational changes. We chose RNA binding arginine rich motif (ARM) peptides, Rev and/or Tat, for model peptide insertion, and expressed constructed PI-FLuc probe variants using a wheat germ cell-free protein synthesis system. They showed FLuc activity changes, reactivation, or inactivation after binding to their specific RNA targets. Furthermore, to expand the versatility of the PI-FLuc RNA detection system, we designed split-RNA probes built to reform the ARM peptide binding site in the presence of arbitrarily selected target-RNA. As a result, the target RNA was homogeneously detected by FLuc luminescent signals mediated by a cooperative function of the PI-FLuc and split-RNA probe sets.

INTRODUCTION

Enzyme complementation and fluorescent resonance energy transfer (FRET) are typical assay systems for the detection of protein−protein interactions. The FRET assay is useful as a high-resolution assay since fluorescent signals provide both temporal and spatial resolution (*1*, *2*). In contrast, enzyme complementation is more precise than FRET, because enzymatic signals provide quantitative readout and signal amplification, resulting in more sensitive assays (*3*, *4*). Several proteins, such as dihydrofolate reductase (DHFR), β-galactosidase, and β-lactamase, have been used as reporter proteins, indicating intermolecular complementation and activity reconstruction (*4*−*8*). Recently, it was discovered that firefly luciferase (FLuc) and renilla luciferase (RLuc) could correspondingly function as reporter proteins for intermolecular complementation (*9*, *10*). Luciferase produces low background and highly sensitive bioluminescent signals simply by the administration of an appropriate substrate in the presence of cofactors. In addition, the bioluminescent signals produced from luciferase may be noninvasively visualized both in cultured cells and in living animals using cooled charge-coupled device (CCD) cameras (*11*, *12*). As a result, they are now becoming one of the most useful reporter proteins for analyzing protein−protein interactions especially for *in vivo* analysis. Using intermolecular luciferase complementation, previous studies have also reported direct protein−protein interactions or conditional protein−protein interactions mediated by chemical molecules in the living mouse (*9*, *13*, *14*).

In the meantime, there have also been efforts to construct recombinant protein probes, that can detect target biomolecules and antibodies intramolecularly, using an enzyme complementation assay (*15*−*18*). These recombinant proteins have been constructed by inserting domains or epitopes into internally divided reporter proteins. The inserted domains function as a response unit, undergoing conformational changes in response to the target biomolecules such as specific ligand bindings and signal transductions. In turn, conformational changes of the response units induce activity changes in reporter enzymes through a structural reorientation of the internally divided reporter enzyme. Such constructs would provide an advanced tool for analyzing target biomolecules other than protein−protein interactions and could be applied to *in vivo* analysis, especially in mammalian cells and living animals. However, until now it has seemed difficult to construct the intramolecular enzyme complementation probes via domain insertion as compared to similarly assembled intramolecular FRET probes (*19*−*22*). Only some enzymes are known to be available as reporter proteins, and only some domains have been successfully used for domain insertion (*18*). In the case of luciferase, just one group reported a successfully constructed intramolecular luciferase complementation probe (*23*, *24*). We posit that this failure is due to the detection principle of enzyme complementation. An intramolecular enzyme complementation probe requires the rational structural reconfiguration of divided reporter enzymes following the conformational changes of the response units, while FRET protein probes can detect such alterations directly by distant changes in fluorescent proteins (*25*). Therefore, the construction of an intramolecular luciferase complementation probe would be quite difficult if the inserted response unit is a relatively large domain.

In a previous report, we constructed an intramolecular FRET protein probe by using short peptides as response units for detecting specific RNAs (*26*). In that study, HIV-1 Rev-peptide (17 a.a.), which specifically binds to RRE-RNA and Rev-

* To whom correspondence should be addressed. Tel: +81-45-924-5760, FAX: +81-45-924-5779, E-mail: ekobatak@bio.titech.ac.jp.
[†] Tokyo Institute of Technology.
[‡] Ehime University.

10.1021/bc060351o CCC: $37.00 © 2007 American Chemical Society
Published on Web 03/17/2007

aptamer, was inserted between EYFP and ECFP. The resulting FRET protein probe indicated FRET increase and decrease as mediated by the peptide's conformational change after binding to RRE-RNA and Rev-aptamer, respectively. Moreover, we were able to detect arbitrarily selected target-RNA by designing split-RNA probes containing variable sequence regions. On the basis of these results, we expected that the construction of an intramolecular luciferase complementation probe should be possible by inserting short peptides as response units. In this study, we constructed a novel peptide-inserted firefly luciferase (PI-FLuc) probe by using short RNA-binding peptides for insertion. We expected that the constructed PI-FLuc probe would retain FLuc activity since the inserted peptide was sufficiently small so as not to disturb the steric configurations of native FLuc. We also expected that the conformational change of the inserted peptide following specific RNA binding would induce FLuc activity changes through a structural reorientation of the internally divided FLuc domains, either by FLuc complementation or discomplementation.

EXPERIMENTAL SECTION

Plasmid Construction. All PI-FLuc probe variants were constructed on cloning vector pBluescript II SK (+) (Stratagene). Gene fragments coding NFLuc (N437, N445), CFLuc (C438, C446) and Full-FLuc were respectively amplified by PCR from PicaGene Basic Vector 2 (Toyo Ink) using primers combinations. Forward primers were split-FLuc-s (5′-GCGACTAGTATGGAATTCGAAGACGCCAAAAACATAAAG-3′), split-CFLuc-s438 (5′-GCGAGATCTCTGAAGTCTCTGATTAAGTAC-3′) and split-CFLuc-s446 (5′-CTTAGATCTGGCTATCAGGTGGCTCCCGCT-3′). Reverse primers were split-FLuc-as (5′-CTTGGGCCCGCGGCCGCTTAAGGCCTCGCGACCACGGCGATCTTTCC GCCCTT-3′), split-NFLuc-as437 (5′-GCGGGATCCGCGGTCAACGATGAAGAAGTG-3′) and split-NFLuc-as445(5′-GCGGGATCCTTTGTACTTAATCAGAGACTT-3′). Underlined bases are the restriction enzyme sites for gene recombination. Rev-peptide-inserted PI-FLuc probe variants were constructed replacing the EYFP and ECFP regions of FRET protein probe (YRG0C-11ad) (*26*) by NFLuc and CFLuc, respectively. Tat-peptide gene fragment was obtained from annealed oligonucleotide pair (5′-CAGACCTAGAGGCACCAGAGGCAAGGGCAGAAGAATCAGAAGAGGCGGCA-3′ and 5′-GATCTGCCGCCTCTTCTGATTCTTCTGCCCTTGCCTCTGGTGCCTCTAGGTCTGGTAC-3′), and Tat-peptide-inserted PI-FLuc probe variants were constructed replacing the Rev-peptide region by Tat-peptide coding annealed oligonucleotide. FLAG-tag gene fragment was obtained from annealed oligonecleotide pair (5′-CTAGTATGAGGCCTGATTACAAGGATGACGACGATAAGGAATTCTAAG CGGCCGCGGGCC-3′ and 5′-CGCGGCCGCTTAGAATTCCTTATCGTCGTCATCCTTGTAATCAGGCCTCATA-3′), and *Stu* I cut C-terminus FLAG-tag sequence was inserted between *Stu* I and *Apa* I site of PI-FLuc variants or Full-FLuc. Then, the constructed probe variants were transferred to expression plasmid for wheat germ cell free protein synthesis system (pEU-E01-MCS) using *Spe* I and *Not* I.

Protein Expression and RNA Synthesis. Constructed PI-FLuc probe variants and Full-FLuc were expressed using a cell-free protein synthesis system with wheat germ extract (*27*). Transcriptional templates were amplified by PCR from the constructed plasmids to make DNA fragments containing SP6 promoter sequence. Then, mRNAs were transcribed using SP6 RNA polymerase and translated according to a previously reported bilayer cell-free protein synthesis system (*28*). Translated protein variants were confirmed by SDS-PAGE and Western blotting using anti-FLAG M2 antibody (Eastman Kodak).

All short RNA oligonucleotides, RNA-targets, and split-RNA probes were synthesized and purified according to a previously reported method (*26*).

Native-PAGE Western Blotting. Five microliters of translated products in wheat germ extract and 30 pmol of synthesized RNA oligonucleotides were mixed in 15 μL of interaction buffer (10 mM HEPES−KOH, 100 mM KCl, 1 mM $MgCl_2$, 0.5 mM EDTA, 1 mM DTT, 10% glycerol, pH = 7.4). After 30 min of incubation on ice, samples were resolved on a 10% nondenaturing polyacrylamide gel with Tris/glycine running buffer at 4 °C. Then resolved proteins were transferred to PVDF membrane with Tris/glycine transfer buffer for 80 min at 350 mA. The PI-FLuc probe variants in transferred membrane were labeled using anti-FLAG M2 antibody and Alexa-546 conjugated anti-mouse IgG antibody and visualized using FluorImager595 (Molecular Dynamics).

FLuc Activity Assay. FLuc activities were evaluated using luminometer (Luminous CT-9000D: Dia-Iatron). One microliter of translated products were mixed with an aliquot amount of RNA-targets or constructed hybridized complexes in 50 μL of interaction buffer using 96-well black plates (Sumilon). After 30 min of incubation at room temperature, luminescent signals were measured by addition of 50 μL of substrate (Picagene Luciferase Assay Kit: Toyo Ink) and counting for 10 s. The luminescent signals were normalized by subtracting the signal obtained from nontranslated wheat germ extract.

Target-RNA Homogeneous Assay. Two microliters of translated products and a pair of split-RNA probes (final concentration at 500 nM) were previously mixed in interaction buffer. Varied concentrations of specific or nonspecific target-RNA were immediately added to the premixed probes in total 100 μL of interaction buffer using nonadsorption 96-well black plates (Sumilon). Luminescent signals were measured by addition of 100 μL of substrate and counting for 10 s after 90 min of incubation at 37 °C followed by 30 min of incubation at room temperature. The luminescent signals were normalized by subtracting the signal obtained from nontranslated wheat germ extract.

RESULTS

Design and Expression of PI-FLuc Probes. To construct an intramolecular luciferase complementation probe, two ARM peptides, HIV-1 Rev-peptide (17 a.a.) and BIV Tat-peptide (13 a.a.) peptide, were selected for insertion. These two peptides are both well-characterized RNA-binding peptides, showing induced fit conformational changes following specific RNA binding. NMR and circular dichroism experiments indicate that the BIV Tat-peptide undergoes a change to a β-sheet structure upon binding to TAR-RNA (*29*−*31*), while HIV-1 Rev-peptide takes on α-hilical and elongated conformation upon binding to RRE-RNA and Rev-aptamer, respectively (*32*−*35*). FLuc was selected as a reporter luciferase, and two dividing points after 437th arginine and 445th lysine were chosen for peptide insertion, referring the previously reported intermolecular FLuc complementation probes (*9*, *12*, *14*).

Then, eight variants of PI-FLuc probes were constructed by combining NFLuc domains (N437 and N445), CFLuc domains (C438 and C446), and ARM peptides (Rev and Tat) (Figure 1a). A FLAG-tag sequence was connected to the C terminus of each for subsequent Western blotting. These variants were expected to alter FLuc activity after binding specific RNA-targets via conformational changes of the ARM peptides. If RNA binding broke the steric configuration of the connected FLuc domains, we should expect FLuc activity and luminescent signal to decrease. On the other hand, if RNA binding corrected the steric configuration of connected FLuc domains, we would expect FLuc activity and luminescent signal to increase (Figure

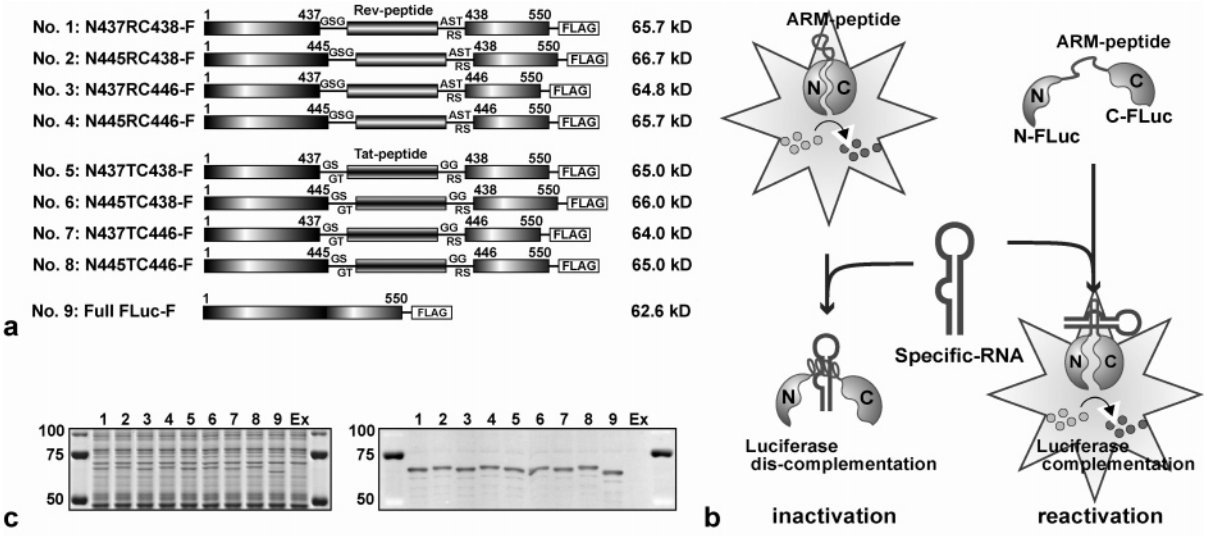


Figure 1. Principle of intramolecular luciferase complementation assay and PI-FLuc probe construction. (a) Rev-peptide (-TRQARRNRRRRWR-ERQR-) or Tat-peptide (-RPRGTRGKGRRIRR-) was inserted between NFLuc (N437, N445) and CFLuc (C438, C446). Control FLuc (No. 9) was constructed as wild type FLuc. A FLAG-tag sequence (-DYKDDDDK-) was connected to the C terminus of constructed variants. (b) PI-FLuc probes specifically bind to RNA-targets reflecting the inserted ARM peptide characteristics. If RNA binding induce discomplementation of the divided FLuc domains, luminescent signal would decrease (left). If RNA binding induce complementation of the divided FLuc domains, luminescent signal would increase (right). (c) Constructed split-FLuc probe variants were translated using a wheat germ cell-free protein synthesis system. An aliquot amount of translated products was resolved on an 8% SDS-PAGE and analyzed by CBB staining (3 μL: left) or Western blotting (1 μL: right). Lane numbers correspond to the numbers in part a). Nontranslated wheat germ extract was resolved as negative control (Ex).

1b). All constructed variants (Nos. 1−8) and the wild type FLuc (Full-FLuc No. 9) were expressed using a wheat germ cell-free protein synthesis system and confirmed by both SDS-PAGE and Western blotting (Figure 1c).

Characterization of Constructed PI-FLuc Probes. We next investigated whether the PI-FLuc probes have an ability to bind to specific RNA-targets (RRE-RNA, Rev-aptamer, TAR-RNA; see Figure 2a). The translated PI-FLuc probe variants and synthetic RNA were mixed in an interaction buffer and resolved on native-PAGE. After a transfer reaction to PVDF membrane, we analyzed gel-mobility shifted bands using anti-FLAG antibody (Figure 2b). In all constructed PI-FLuc probe variants, we found specific signal bands at the lanes mixed with their RNA targets, while there were no discriminative signal bands at control lanes (RNA −). In the case of Rev-peptide-inserted variants (Nos. 1−4), signal bands were observed at the lanes mixed with RRE-RNA and Rev-aptamer, which were the targets of the Rev-peptide. There were trends that the signal bands had clearly converged with RRE-RNA and widely spread with Rev-aptamer, except for variant No. 4. In constrast, in the case of Tat-peptide-inserted variants (Nos. 5−8), clearly converged signal bands were observed at the lanes mixed with TAR-RNA, the target of the Tat-peptide. Further, in all variants there were no distinctive signal bands at the lanes mixed with nonspecific RNAs corresponding to the control lanes. These results indicate that each inserted peptide has the ability to specifically bind to their corresponding RNA-targets.

Next, to evaluate whether PI-FLuc probe variants showed appropriate FLuc activity changes following specific RNA binding, we measured the luminescent signal produced after the addition of the respective RNA (Figure 2c). The results confirmed that the PI-FLuc probe variants, containing the N437 domain (Nos. 1, 3, 5, 7), have almost lost FLuc activity. These probes had luminescent signals as weak as the background signals obtained from nontranslated wheat germ extract (Ex) and did not show any luminescent signal change with addition of the relevant RNAs. In contrast, other variants, containing the N445 domain (Nos. 2, 4, 6, 8), retained FLuc activity. In addition, three of these four variants showed FLuc activity changes after addition of specific RNA-targets. Interestingly,

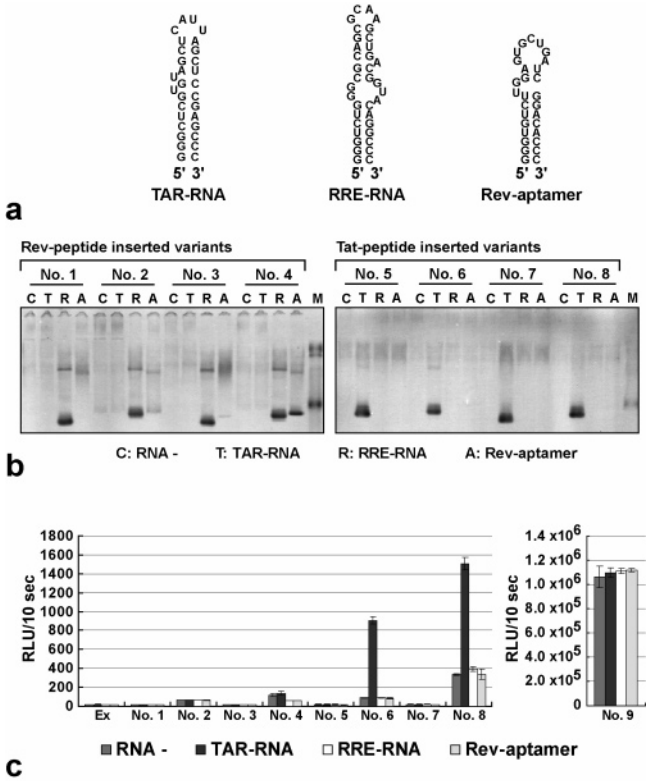


Figure 2. Detection of specific RNA-target with PI-FLuc probe. (a) Secondary structure of respective RNA-targets (TAR-RNA, RRE-RNA, Rev-aptamer). (b) Specific RNA binding was confirmed by native-PAGE gel mobility shift assay. Five microliters of translated products was mixed with 30 pmol of RNAs (C: RNA −, T: TAR-RNA, R: RRE-RNA, A: Rev-aptamer) and resolved on a 10% nondenaturing polyacrylamide gel. Transferred PI-FLuc probes were detected using Western blotting. (c) Luminescent signals were evaluated after the binding reaction of 1 μL of translated products and 25 pmol of respective RNAs. Values were average with standard deviation (n = 3).

in the case of the Rev-peptide-inserted variant No. 4, FLuc was inactivated after the addition of both RRE-RNA and Rev-

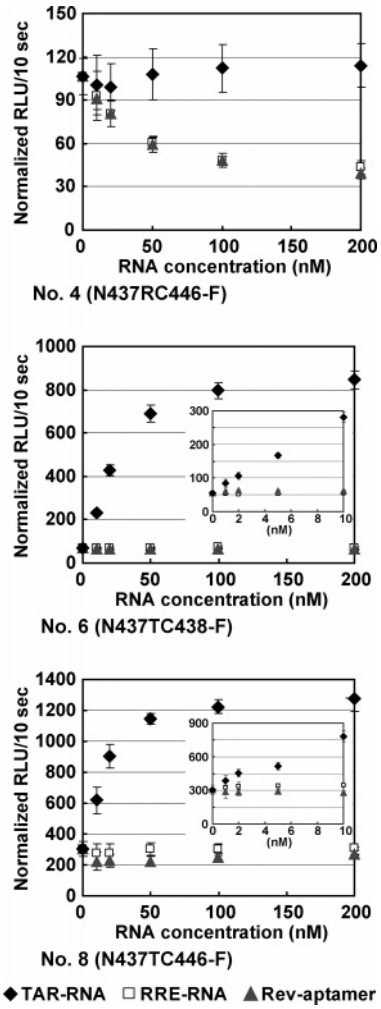


Figure 3. RNA concentration dependency in intramolecular luciferase complementation assay. Luminescent signals were evaluated after binding reaction of 1 μL of translated products and varied concentrations of respective RNAs. Values were average with standard deviation (n = 3).

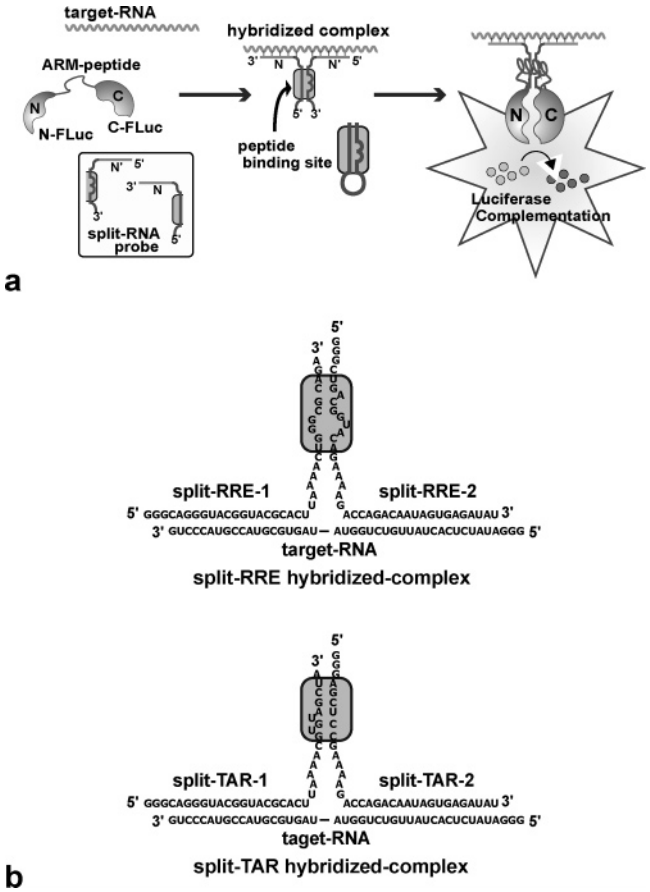


Figure 4. Principle of intramolecular luciferase complementation assay for arbitrarily selected target-RNA. (a) A pair of split-RNA probe hybridizes to an arbitrarily selected target-RNA and reforms the ARM peptide binding site. PI-FLuc probe binds to the ARM peptide binding site constructed on the hybridized complex. They indicate luminescent signal changes thorough the ARM peptide conformational change. (b) Secondary structure and sequence of designed hybridized complex. Surrounded region indicates minimal element necessary for the ARM peptide binding.

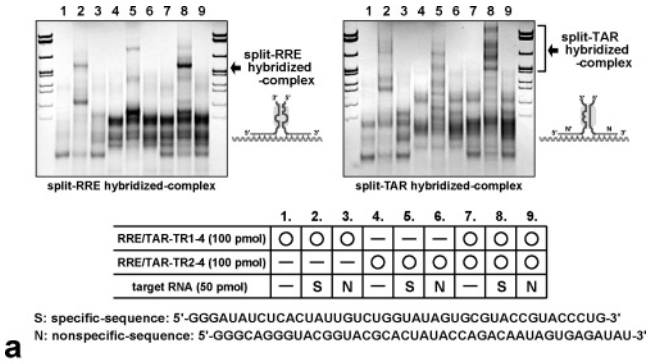
aptamer. On the other hand, in the case of the Tat-peptide-inserted variants No. 6 and No. 8, FLuc was reactivated after addition of the TAR-RNA. Moreover, no variants showed any change in their FLuc activity after the addition of nonspecific RNA.

RNA Detection by Intramolecular FLuc Complementation. We also investigated the RNA concentration dependency of FLuc activity changes in three variants (Nos. 4, 6, 8) (Figure 3). Varied concentrations of the RNA-targets were mixed with translated PI-FLuc variants, and FLuc activity was evaluated after the binding reaction. Variants No. 6 and No. 8 showed dose-dependent FLuc reactivation with TAR-RNA, while there were no signal changes with other RNAs. The signal change ratios corresponded to Figure 2c. In contrast, variant No. 4 showed dose-dependent FLuc inactivation with RRE-RNA and/or Rev-aptamer, while there were no signal changes with TAR-RNA. These results indicate that the RNA-targets were homogeneously detected by luminescent signal changes with sufficient specificity.

Intramolecular Complementation Assay for Arbitrarily-Selected Target-RNA. For detection of arbitrarily selected target-RNA other than specific RNA-targets, we designed split-RNA probes built to reform the ARM peptide binding site in the presence of the target-RNA. The split-RNA probes containing variable sequence regions respond to any target-RNAs. First, a split-RRE-RNA probe was constructed as previously described (*26*). Second, we designed a split-TAR-RNA probe according to our previous methodology. The TAR-RNA was split at its loop region, and RNA oligonucleotides containing complementary sequences of arbitrarily selected target-RNA were connected at the 5′ or 3′ end of the split-TAR-RNA. A minimal sequence for Tat-peptide recognition was retained for the split-TAR-RNA. Additionally, spacer-like sequences were inserted between the complementary sequence region and the split-TAR-RNA region.

By this design, the constructed split-RNA probes hybridize to adjacent regions of the arbitrarily selected target-RNA, and the ARM peptide binding site is subsequently reformed on the hybridized complex. Next, the PI-FLuc probe binds to the hybridized complex with the conformational change of the ARM peptide. Therefore, following this last step, the arbitrarily selected target-RNA should be detectable by FLuc luminescent signals through the cooperative functions of such self-assembled probe sets as the PI-FLuc probe and the split-RNA probe (Figure 4a). The secondary structure and sequence of the hybridized complexes (split-RRE hybridized complex and split-TAR hybridized complex) are displayed in Figure 4b.

Detection of Hybridized Complexes. To detect hybridized complexes, we first mixed split-RNA probes with arbitrarily selected target-RNA (specific-sequence) and confirmed hybridized formation by a polyacrylamide gel mobility shift assay (Figure 5a). Complementary sequence of the specific sequence was prepared as negative control (nonspecific-sequence). We found that there were new mobility shifted bands, indicative of



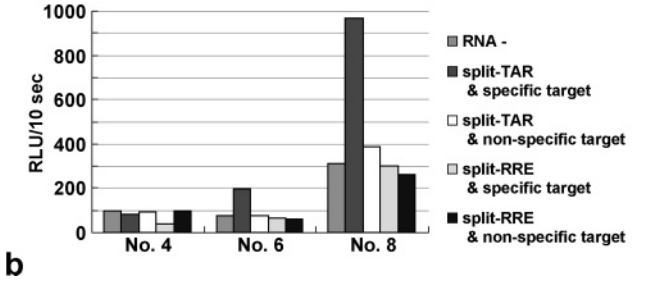


Figure 5. Detection of hybridized complex by luminescent signal change. (a) Construction of the hybridized complexes was confirmed by gel mobility shift assay. One-hundred picomoles of respective split-RNA probes was mixed with 50 pmol of specific-sequence or nonspecific-sequence. After 60 min of incubation at 37 °C, they were resolved on a 15% polyacrylamide gel and stained by EtBr. (b) An aliquot amount of hybridized complexes constructed in part a (50 pmol of split-RNA probes and 25 pmol of target-RNA) was mixed with 1 μL of translated products. Luminescent signals were evaluated after the binding reaction.

the hybridized complex, in the sample lanes including all components, split-RNA probe pair and specific-sequence (lane No. 8). To check for valid reporter activity, we next investigated whether the PI-FLuc probe reflected FLuc activity changes after the addition of the hybridized complexes. Aliquot amounts of the constructed hybridized complexes were mixed with translated products of the PI-FLuc probe variants, and luminescent signals were analyzed after a 30-min incubation at room temperature (Figure 5b). Three PI-FLuc probe variants (Nos. 4, 6, 8) showed FLuc activity changes corresponding to the addition of just the appropriate RNA-target. The Rev-peptide-inserted PI-FLuc probe variant showed FLuc inactivation with the addition of the hybridized complex constructed from the split-RRE-RNA probe (split-RRE hybridized complex). The Tat-peptide-inserted PI-FLuc probe variants showed FLuc reactivation with the addition of the hybridized complex constructed from the split-TAR-RNA probe (split-TAR hybridized complex). Further, neither showed FLuc activity changes with hybridized complexes constructed from nonspecific-sequence or nonspecific split-RNA probes. These results confirm that the observed FLuc activity changes were mediated by the binding of the correct hybridized complex, recognized by the inserted ARM peptide.

Homogeneous Detection of Arbitrarily-Selected Target-RNA. Arbitrarily selected target-RNA can also be homogeneously detected by FLuc activity changes. Figure 6 shows the target-RNA concentration dependency in a homogeneous assay. All PI-FLuc probe variants (Nos. 4, 6, 8) decreased or increased their luminescent signals through the intramolecular FLuc discomplementation or complementation. These probes also showed good concentration dependency with the specific-sequence, as well as no signal changes in the presence of nonspecific-sequence. Especially in the case of Tat-peptide-inserted PI-FLuc probe variants, relatively small error bars were

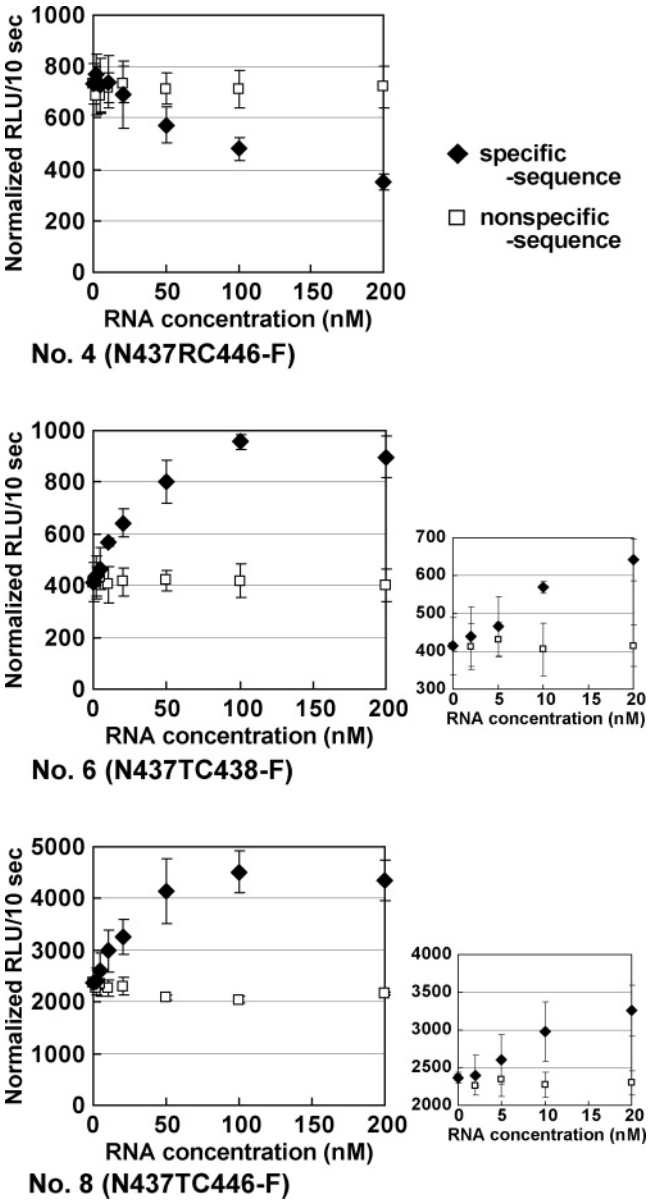


Figure 6. Homogeneous detection of arbitrarily selected target-RNA by intramolecular luciferase complementation assay. Varied concentrations of the target-RNA were mixed with a pair of split-RNA probes (final concentration at 500 nM) and 2 μL of translated products. Luminescent signals were evaluated after binding reaction. Values were average with standard deviation ($n = 3$).

observed at low target-RNA concentrations, and we obtained a significant increase of luminescent signal at 10 nM concentration. These results suggest that arbitrarily selected target-RNA was homogeneously and specifically detected by the cooperative function of PI-FLuc and split-RNA probes.

DISCUSSION

This study attempted to construct peptide-inserted FLuc (PI-FLuc) probes producing a high sensitivity luminescent signal mediated by intramolecular luciferase complementation in response to target biomolecules. Two essential factors were presumed to be required to achieve this objective. First, the PI-FLuc probe must be able to recognize target molecules reflecting inserted peptide characteristics. Second, the PI-FLuc probe must partly retain luciferase activity after peptide insertion. Consequently, we decided to construct several PI-FLuc probe variant patterns. Previously reported crystal structure analysis had demonstrated that FLuc could be separated to two distinct

domains (NFLuc and CFLuc) connected by a flexible linker-like amino acid sequence (*12*, *36*) Additionally, previously constructed intermolecular FLuc complementation probes had been divided into two parts around a linker-like amino acid sequence (*9*, *12*, *14*). This indicates that the linker-like region is not essential for enzymatic activity and can accept some degree of structural configuration variation. Making use of these results, we selected both ends of the linker-like amino acid sequence as the basis for FLuc dividing points, and eight variants of a PI-FLuc probe were constructed (Figure 1a).

The binding ability of PI-FLuc probes was confirmed by native-PAGE Western blotting (Figure 2b). We proposed that the converged signal bands, especially in the lanes with RRE-RNA (Nos. 1−4) and TAR-RNA (Nos. 5−8), indicated structural stabilization of PI-FLuc probes after the binding of respective RNA-targets, and that the spread signal bands in the lanes with Rev-aptamer (Nos. 1−3) indicated structural ambiguity after the binding of Rev-aptamer. We suspect that the complexes efficiently migrated in native-PAGE and transferred to PVDF membrane due to the negative charge of bound RNA, while the monomeric PI-FLuc probes in control and nonspecific RNA lanes did not migrate and transfer due to the positive charge of the inserted ARM peptide. In contrast, the monomeric wild type FLuc migrated in native-PAGE and an obvious signal band was observed by Western blotting, although band patterns were not changed by the addition of RNA (data not shown).

Retained FLuc activities and its alteration were evaluated via luminescent signal changes after RNA binding (Figure 2c and Figure 3). Since we could assess the expression levels of PI-FLuc probes equal via Western blotting (Figure 1c), we estimated that the variants Nos. 2, 4, 6, 8 retained FLuc activities approximately 0.01−0.03% of wild type FLuc. Although it was relatively low compared to our expectations, variants Nos. 4, 6, 8 showed dose-dependent FLuc inactivation or reactivation after RNA addition. We hypothesize that FLuc inactivation in the Rev-peptide-inserted variant is due to the intramolecular discomplementaion of divided FLuc domains mediated by intruding RNA (Figure 1a, left). We also suggest that FLuc reactivation in the Tat-peptide-inserted variants is due to the intramolecular complementation of divided FLuc domains mediated by domain contiguity outside TAR-RNA, because Tat-peptide takes on a β-sheet-like turned conformation in conjunction with TAR-RNA (Figure 1a, right). In addition, in the case of Tat-peptide-inserted variants, it seems that variant No. 6 shows a more effective structural reconfiguration after TAR-RNA binding, because No. 6 had higher relative FLuc activity without TAR-RNA versus with TAR-RNA addition (∼10.8) as compared to variant No. 8 (∼4.4). Moreover, both Tat-peptide-inserted variants displayed significant luminescent signal increases at 1.0 nM TAR-RNA concentration. Given these PI-FLuc probe characteristics, we conclude that the Tat-peptide-inserted PI-FLuc probes are potentially sensitive and useful RNA indicators, because their relative activity levels were higher and their RNA detection limits were lower than our previous FRET protein probe (*26*).

To expand the versatility of the intramolecular FLuc complementation assay system, we attempted to detect an arbitrarily selected target-RNA through the formation of hybridized complexes. From Figure 5a, it was suggested that some expanded bands, observed in the case of the split-TAR-RNA probe, represented structural variations of the split-TAR hybridized complex. Then, the arbitrarily selected target-RNA was dose-dependently detected under homogeneous and biocompatible conditions, namely, simultaneous incubation of all probe components at 37 °C (Figure 6). Particularly in the case of Tat-peptide-inserted variants No. 6 and No. 8, the resulting luminescent signal saturated when it reached 100 nM target-RNA levels. This corresponds to the detection of TAR-RNA alone, because the mixed PI-FLuc probes were at twice the volume of Figure 3, whose signal saturations were observed to be at 50 nM TAR-RNA levels. Furthermore, the relative FLuc activities after saturation of the signal increase (2.0−2.5) were at lower levels compared to the detection of TAR-RNA alone. We believe that the reason for lower relative FLuc activity in this case is due to the tertiary structure of the hybridized complex, specifically the more bulky and rigid structure of the target-RNA hybridized complex. Even so, the 10 nM detection limit of the arbitrarily selected target-RNA is relatively lower than other intramoleculer FRET detection or intramolecular enzyme complementation probes (*15*, *16*, *20*, *21*). In addition, we expect that this response could be improved by optimizing the design of hybridized complexes, as demonstrated in our previous report (*26*).

In this RNA detection system, the increase or decrease of luminescent signals is due to the intramolecular complementation or discomplementation of internally divided FLuc domains mediated by the inserted peptide's conformations changes. To extend this idea, recently peptides have drawn attention in the form of molecular recognition materials, such as peptide arrays and peptide aptamers (*37*, *38*). Some of these peptides may also have the necessary characteristics to show induced fit conformational changes after binding to their target molecules (*39*−*41*). If so, it is expected that the construction of PI-FLuc probes that target biomolecules other than RNA molecules would be possible by the same methodology. However, we suppose some more improvements are required in aspects of absolute activity and relative activity, because 10-s counting was needed to obtain sufficient luminescent signals and S/N values. It would require certain trial and error tests to optimize PI-FLuc variants. Even though these potential problems exist, we envisage that PI-FLuc probes could be an alternative strategy to the intramolecular FRET detection system for target biomolecules especially for in vivo detection, because PI-FLuc probes can be produced in living cells.

ACKNOWLEDGMENT

We thank Takashi Masaoka for assistance with translation of PI-FLuc probe variants using wheat germ extract. This study was in part supported by Grants-in-Aid from the Ministry of Education, Culture, Sports, Science and Technology (MEXT), Japan.

LITERATURE CITED

(1) Llopis, J., Westin, S., Ricote, M., Wang, Z., Cho, C. Y., Kurokawa, R., Mullen, T. M., Rose, D. W., Rosenfeld, M. G., Tsien, R. Y., and Glass, C. K. (2000) Ligand-dependent interactions of coactivators steroid receptor coactivator-1 and peroxisome proliferator-activated receptor binding protein with nuclear hormone receptors can be imaged in live cells and are required for transcription. *Proc. Natl. Acad. Sci. U.S.A. 97*, 4363−4368.

(2) Truong, K., and Ikura, M. (2001) The use of FRET imaging microscopy to detect protein-protein interactions and protein conformational changes *in vivo*. *Curr. Opin. Struct. Biol. 11*, 573−578.

(3) Michnick, S. W. (2001) Exploring protein interactions by interaction-induced folding of proteins from complementary peptide fragments. *Curr. Opin. Struct. Biol. 11*, 472−477.

(4) Rossi, F. M., Blakely, B. T., and Blau, H. M. (2000) Interaction blues: protein interactions monitored in live mammalian cells by β-galactosidase complementation. *Trends Cell Biol. 10*, 119−122.

(5) Rossi, F., Charlton, C. A., and Blau, H. M. (1997) Monitoring protein-protein interactions in intact eukaryotic cells by β-galactosidase complementation. *Proc. Natl. Acad. Sci. U.S.A. 94*, 8405−8410.

(6) Pelletier, J. N., Campbell-Valois, F. X., and Michnick, S. W. (1998) Oligomerization domain-directed reassembly of active dihydrofolate reductase from rationally designed fragments. *Proc. Natl. Acad. Sci. U.S.A. 95*, 12141−12146.

(7) Wehrman, T., Kleaveland, B., Her, J. H., Balint, R. F., and Blau, H. M. (2002) Protein-protein interactions monitored in mammalian cells via complementation of β-lactamase enzyme fragments. *Proc. Natl. Acad. Sci. U.S.A. 99*, 3469−3474.

(8) Galarneau, A., Primeau, M., Trudeau, L. E., and Michnick, S. W. (2002) β-lactamase protein fragment complementation assays as *in vivo* and *in vitro* sensors of protein protein interactions. *Nat. Biotechnol. 20*, 619−622.

(9) Paulmurugan, R., Umezawa, Y., and Gambhir, S. S. (2002) Noninvasive imaging of protein-protein interactions in living subjects by using reporter protein complementation and reconstitution strategies. *Proc. Natl. Acad. Sci. U.S.A. 99*, 15608−15613.

(10) Paulmurugan, R., and Gambhir, S. S. (2003) Monitoring protein−protein interactions using split synthetic renilla luciferase protein-fragment-assisted complementation. *Anal. Chem. 75*, 1584−1589.

(11) Honigman, A., Zeira, E., Ohana, P., Abramovitz, R., Tavor, E., Bar, I., Zilberman, Y., Rabinovsky, R., Gazit, D., Joseph, A., Panet, A., Shai, E., Palmon, A., Laster, M., and Galun, E. (2001) Imaging transgene expression in live animals. *Mol. Ther. 4*, 239−249.

(12) Paulmurugan, R., and Gambhir, S. S. (2005) Firefly luciferase enzyme fragment complementation for imaging in cells and living animals. *Anal. Chem. 77*, 1295−1302.

(13) Kaihara, A., Kawai, Y., Sato, M., Ozawa, T., and Umezawa, Y. (2003) Locating a protein-protein interaction in living cells via split Renilla luciferase complementation. *Anal. Chem. 75*, 4176−4181.

(14) Luker, K. E., Smith, M. C., Luker, G. D., Gammon, S. T., Piwnica-Worms, H., and Piwnica-Worms, D. (2004) Kinetics of regulated protein-protein interactions revealed with firefly luciferase complementation imaging in cells and living animals. *Proc. Natl. Acad. Sci. U.S.A. 101*, 12288−12293.

(15) Feliu, J. X., Ramirez, E., and Villaverde, A. (1998) Distinct mechanisms of antibody-mediated enzymatic reactivation in β-galactosidase molecular sensors. *FEBS Lett. 438*, 267−271.

(16) Tucker, C. L., and Fields, S. (2001) A yeast sensor of ligand binding. *Nat. Biotechnol. 19*, 1042−1046.

(17) Guntas, G., Mansell, T. J., Kim, J. R., and Ostermeier, M. (2005) Directed evolution of protein switches and their application to the creation of ligand-binding proteins. *Proc. Natl. Acad. Sci. U.S.A. 102*, 11224−11229.

(18) Ostermeier, M. (2005) Engineering allosteric protein switches by domain insertion. *Protein Eng. Des. Sel. 18*, 359−364.

(19) Truong, K., and Ikura, M. (2001) The use of FRET imaging microscopy to detect protein-protein interactions and protein conformational changes in vivo. *Curr. Opin. Struct. Biol. 11*, 573−578.

(20) Miyawaki, A., Llopis, J., Heim, R., McCaffery, J. M., Adams, J. A., Ikura, M., and Tsien, R. Y. (1997) Fluorescent indicators for Ca2+ based on green fluorescent proteins and calmodulin. *Nature 388*, 882−887.

(21) Honda, A., Adams, S. R., Sawyer, C. L., Lev-Ram, V., Tsien, R. Y., and Dostmann, W. R. (2001) Spatiotemporal dynamics of guanosine 3′,5′-cyclic monophosphate revealed by a genetically encoded fluorescent indicator. *Proc. Natl. Acad. Sci. U.S.A. 98*, 2437−2442.

(22) Sasaki, K., Sato, M., and Umezawa, Y. (2003) Fluorescent indicators for Akt/protein kinase B and dynamics of Akt activity visualized in living cells. *J. Biol. Chem. 278*, 30945−30951.

(23) Paulmurugan, R., Gambhir, S. S. (2005) Novel fusion protein approach for efficient high-throughput screening of small molecule-mediating protein-protein interactions in cells and living animals. *Cancer Res. 65*, 7413−7420.

(24) Paulmurugan, R., Gambhir, S. S. (2006) An intramolecular folding sensor for imaging estrogen receptor-ligand interactions. *Proc. Natl. Acad. Sci. U.S.A. 103*, 15883−15888.

(25) van Kuppeveld, F. J., Melchers, W. J., Willems, P. H., and Gadella, T. W., Jr. (2002) Homomultimerization of the coxsackievirus 2B protein in living cells visualized by fluorescence resonance energy transfer microscopy. *J. Virol. 76*, 9446−9456.

(26) Endoh, T., Funabashi, H., Mie, M., and Kobatake, E. (2005) Method for detection of specific nucleic acids by recombinant protein with fluorescent resonance energy transfer. *Anal. Chem. 77*, 4308−4314.

(27) Madin, K., Sawasaki, T., Ogasawara, T., and Endo, Y. (2000) A highly efficient and robust cell-free protein synthesis system prepared from wheat embryos: plants apparently contain a suicide system directed at ribosomes. *Proc. Natl. Acad. Sci. U.S.A. 97*, 559−564.

(28) Sawasaki, T., Hasegawa, Y., Tsuchimochi, M., Kamura, N., Ogasawara, T., Kuroita, T., and Endo, Y. (2002) A bilayer cell-free protein synthesis system for high-throughput screening of gene products. *FEBS Lett. 514*, 102−105.

(29) Puglisi, J. D., Chen, L., Blanchard, S., and Frankel, A. D. (1995) Solution structure of a bovine immunodeficiency virus Tat-TAR peptide-RNA complex. *Science 270*, 1200−1203.

(30) Calabro, V., Daugherty, M. D., and Frankel, A. D. (2005) A single intermolecular contact mediates intramolecular stabilization of both RNA and protein. *Proc. Natl. Acad. Sci. U.S.A. 102*, 6849−6854.

(31) Chen, L., and Frankel, A. D. (1995) A peptide interaction in the major groove of RNA resembles protein interactions in the minor groove of DNA. *Proc. Natl. Acad. Sci. U.S.A. 92*, 5077−5081.

(32) Battiste, J. L., Mao, H., Rao, N. S., Tan, R., Muhandiram, D. R., Kay, L. E., Frankel, A. D., and Williamson, J. R. (1996) α helix-RNA major groove recognition in an HIV-1 rev peptide-RRE RNA complex. *Science 273*, 1547−1551.

(33) Tan, R., and Frankel, A. D. (1994) Costabilization of peptide and RNA structure in an HIV Rev peptide-RRE complex. *Biochemistry 33*, 14579−14585.

(34) Xu, W., and Ellington, A. D. (1996) Anti-peptide aptamers recognize amino acid sequence and bind a protein epitope. *Proc. Natl. Acad. Sci. U.S.A. 93*, 7475−7480.

(35) Ye, X., Gorin, A., Ellington, A. D., and Patel, D. J. (1996) Deep penetration of an α-helix into a widened RNA major groove in the HIV-1 rev peptide-RNA aptamer complex. *Nat. Struct. Biol. 3*, 1026−1033.

(36) Conti, E, Franks, N. P., and Brick, P. (1996) Crystal structure of firefly luciferase throws light on a superfamily of adenylate-forming enzymes. *Structure 4*, 287−298.

(37) Hoppe-Seyler, F., Crnkovic-Mertens, I., Tomai, E., and Butz, K. (2004) Peptide aptamers: specific inhibitors of protein function. *Curr. Mol. Med. 4*, 529−538.

(38) Troitskaya, L. A., and Kodadek, T. (2004) Peptides as modulators of enzymes and regulatory proteins. *Methods 32*, 406−415.

(39) Wright, P. E., and Dyson, H. J. (1999) Intrinsically unstructured proteins: re-assessing the protein structure-function paradigm. *J. Mol. Biol. 293*, 321−331.

(40) Williamson, J. R. (2000) Induced fit in RNA-protein recognition. *Nat. Struct. Biol. 7*, 834−837.

(41) Tan, R., and Frankel, A. D. (1995) Structural variety of arginine-rich RNA-binding peptides. *Proc. Natl. Acad. Sci. U.S.A. 92*, 5282−5286.

BC060351O

Mannose Glycoconjugates Functionalized at Positions 1 and 6. Binding Analysis to DC-SIGN Using Biosensors

José J. Reina,[†] Olivia S. Maldonado,[†] Georges Tabarani,[‡] Franck Fieschi,[‡,*] and Javier Rojo[†,*]

Grupo de Carbohidratos, Instituto de Investigaciones Químicas, CSIC, Américo Vespucio 49, E-41092 Sevilla, Spain, IBS, Institut de Biologie Structurale Jean-Pierre Ebel, CEA, CNRS, Université Joseph Fourier, 41 rue Jules Horowitz, F-38027 Grenoble, France. Received November 28, 2006; Revised Manuscript Received January 11, 2007

The design of glycoconjugates to allow the generation of multivalent ligands capable of interacting with the receptor DC-SIGN is a topic of high interest due to the role played by this lectin in pathogen infections. Mannose, a ligand of this lectin, could be conjugated at two different positions, 1 and 6, not implicated in the binding process. We have prepared mannose conjugates at these two positions with a long spacer to allow their attachment to a biosensor chip surface. Analysis of the interaction between these surfaces and the tetravalent extracellular domain (ECD) of DC-SIGN by SPR biosensor has demonstrated that both positions are available for this conjugation without affecting the protein binding process. These results emphasize the possibility to conjugate mannose at position 6, allowing the incorporation of hydrophobic groups at the anomeric position to interact with hydrophobic residues in the carbohydrate recognition domain of DC-SIGN, increasing binding affinities. This fact is relevant for the future design of new ligands and the corresponding multivalent systems for DC-SIGN.

INTRODUCTION

Carbohydrate−protein interactions are involved in several cell adhesion and cell communication processes that govern basically the social behavior of cells. Inflammation (*1*), tumor progression and metastasis (*2*), cell development and embryogenesis (*3*), and infection (*4*) are some of the important biological events where carbohydrates play a key role through the interaction with their corresponding protein receptors (*5*, *6*). These carbohydrate interactions are highly selective, calcium dependent, and very weak (*7*). Nature has overcome this problem with a multivalent presentation of carbohydrate epitopes such as glycosphingolipid clustering into lipid rafts and presentation of multiple copies of carbohydrates on glycoproteins. Therefore, the design and development of chemical tools to understand and intervene into these processes involving carbohydrates require the appropriate multivalent scaffolds that can be functionalized with selected carbohydrates (*8*−*10*).

Our research interest has been focused during the last years on a lectin named DC-SIGN[1] (dendritic cell-specific ICAM-3 grabbing nonintegrin) or CD209. This C-type lectin is expressed at the surface of immature dendritic cells and presents at its C-terminus a carbohydrate recognition domain (CRD) (*11*, *12*). Recognition of pathogens by dendritic cells takes place through an interaction involving glycosylated proteins at the surface of pathogens and the receptor DC-SIGN (*13*−*16*). This recognition process is one of the first steps in a complex pathway of events controlled by the immune system. Previous work of our laboratory has demonstrated that multivalent systems based on mannose as carbohydrate and hyperbranched dendritic polymer Boltorn as a multivalent scaffold are capable to interact with DC-SIGN and inhibit the infection process of a pseudotyped viral particle that expresses the GP1 glycoprotein of Ebola virus (*17*−*19*).

Functionalization of mannose to create these glycodendritic polymers was performed at the anomeric position. This election was based on two main reasons. First of all, the hydroxyl groups of mannose implicated on binding with C type lectins are those presented at positions 2, 3, and 4 (*20*). Second, the easiest position to functionalize carbohydrates to generate glycoconjugates is the anomeric position. Position 6 could be considered as another possibility to be functionalized, taking into account that this hydroxyl group is well differentiated from the others (it is the only primary hydroxy group on the sugars), and also it does not seem to participate in the recognition process by the C-type lectin (*21*). Moreover, introducing hydrophobic residues, such as aromatic rings, at the anomeric position can improve the binding affinities of mannoses due to noncovalent van der Waals contacts with amino acid residues of a hydrophobic pocket present at the carbohydrate recognition domain of the lectin (*22*, *23*). As proved previously in several examples, aryl mannopyranosides show higher binding affinities than the corresponding mannose with a free anomeric position (*24*−*27*). This fact could also be applied for DC-SIGN presenting this hydrophobic pocket, and it would mean a considerable increase of mannose binding affinity. Depending on the residues introduced at the anomeric position, in some cases it could be necessary to conjugate these mannose derivatives at a position different from the anomeric one, mainly at position 6 of the mannose.

To prove that functionalization of mannose position 6 with a linker will not interfere in the binding process with DC-SIGN, we have prepared two mannose conjugates with a linker at position 6 and position 1 (anomeric), respectively. We have studied the binding process of these mannoses with the tetrameric extracellular domain (ECD) of DC-SIGN using a biosensor with surface plasmon resonance (SPR) detection. The

* Corresponding authors. Franck.fieschi@ibs.fr (FF), Fax: +33 (0)4 38 78 54 94; Tel: +33 (0)4 38 78 91 77. javier.rojo@iiq.csic.es (JR). Fax: +34 954 46 05 65; Tel: +34 954 48 95 68.

[‡] Institut de Biologie Structurale.

[†] Grupo de Carbohidratos.

[1] Abbreviations: CRD, carbohydrate recognition domain; DC-SIGN, dendritic cell-specific; ICAM-3, grabbing nonintegrin; DIC, diisopropylcarbodiimide; ECD, extra cellular domain; EDC, *N*-(3-dimethylaminopropyl)-*N*-ethylcarbodiimide; EDTA, ethylenediaminetetraacetic acid; HOBt, 1-hydroxybenzotriazole; ICAM, intercellular adhesion molecule; NHS, *N*-hydroxysuccinimide; RU, response units; SPR, surface plamon resonance

10.1021/bc060369z CCC: $37.00 © 2007 American Chemical Society
Published on Web 03/10/2007

glycoconjugates were prepared using a selected linker long enough to allow the attachment of these molecules to the biosensor chip surface without interfering in the binding process with the lectin. This biosensor is a very useful tool that provides quantitative analysis of binding processes in flow conditions using a tiny amount of ligands and receptors without any label (*28*). Biosensors have been succesfully used to measure binding affinities of carbohydrate ligands with lectins (*29*−*34*). In fact, a comparison of these binding affinities provides a rapid method to evaluate the best ligands for a specific receptor.

The mannose conjugates and the corresponding control surfaces have been used with a biosensor with SPR detection, and the analyses of the sensorgrams have demonstrated that both positions (1 and 6) of mannose were adequate to create glycoconjugates that can be used as monomers to prepare the corresponding multivalent systems.

MATERIALS AND METHODS

Materials. All purchased chemicals were used without further purification. Synthetic compounds were purified by flash chromatography using medium or fine silica gel. Reaction completion was observed by TLC using as development reagents phosphomolibdic acid, 10% sulfuric acid in methanol, or anisaldehyde. ^{1}H and ^{13}C NMR were recorded on Bruker Avance DPX 300 and DRX 500 MHz spectrometers. Chemical shift are in ppm with respect to TMS (tetramethylsylane) using the manufacturer indirect referencing method. IR spectra were recorded on a Bruker Vector 22. Optical rotations were measured with a Perkin-Elmer 341 polarimeter. Mass spectra were carried out with an Esquire 6000 ESI-Ion Trap from Bruker Daltonics. Methyl α-D-mannopyranoside (**7**) and 4,7,10-trioxa-1,13-tridecanediamine (**5**) were purchased from Aldrich.

Fmoc-Protected Mannose Derivative with a Linker at Position 1 (5). To a solution of **4** (18 mg, 0.088 mmol) and **7** (50 mg, 0.092 mmol) in DMF (3 mL) were added diisopropylcarbodiimine (DIC) (27 μL, 0.18 mmol) and hydroxybenzotriazole (HOBt) (24 mg, 0.18 mmol). The reaction mixture was stirring at 60 °C during 24 h and then evaporated. The final product was purified first by sephadex LH-20 (eluent: CH_2Cl_2−MeOH, 1:1) to eliminate the HOBt and later by silica gel column chromathography (eluent: CH_2Cl_2−MeOH, 9:1) to give **5** as a syrup (37 mg, 66%). $[\alpha]_D$ (MeOH, *c* 0.46) = +21.78; ^{1}H NMR (CD_3OD, 500 MHz) δ (ppm) 7.77 (d, 2H, J = 7.5 Hz, CH_{ArFmoc}), 7.62 (d, 2H, J = 7.5 Hz, CH_{ArFmoc}), 7.36 (t, 2H, J = 7.5 Hz, CH_{ArFmoc}), 7.28 (d, 2H, J = 7.5 Hz, CH_{ArFmoc}), 4.72 (d, 1H, J = 2.0 Hz, H_1), 4.34 (d, 2H, J = 6.5 Hz, CH_{2Fmoc}), 4.17 (t, 1H, J = 6.5 Hz, CH_{Fmoc}), 3.81 (dd, 1H, J = 2.0 and 11.7 Hz, H_6), 3.78 (dd, 1H, J = 1.5 and 3.0 Hz, H_2), 3.75−3.63 (m, 4H, $H_3 + H_4 + H_{6'} + H_7$), 3.63−3.45 (m, 14H, 6 × CH_2O, $H_{7'}$, H_5), 3.42−3.35 (m, 1H, H_8), 3.34−3.29 (m, 1H, H_8), 3.20 (t. 2H, J = 6.5 Hz, CH_2NH), 3.17 (t. 2H, J = 6.5 Hz, CH_2NH), 2.55−2.39 (m, 4H, $HNOCCH_2CH_2CONH$), 1.74−1.66 (m, 4H, 2 × $HNCH_2CH_2CH_2O$); ^{13}C NMR (CD_3OD, 125 MHz) δ (ppm) 173.4 (C═O), 173.1 (C═O), 144.0 (CAr_{Fmoc}), 141.2 (CAr_{Fmoc}), 127.4 (CAr_{Fmoc}), 126.7 (CAr_{Fmoc}), 124.7 (CAr_{Fmoc}), 119.5 (CAr_{Fmoc}), 100.3 (C_1), 73.4 (C_5), 71.1 (C_3), 70.7 (C_2), 70.1, 69.8, 68.5, 68.3, 67.3 (CH_2O− + C_4) 66.1 (CH_{2Fmoc}), 65.8 (C_7), 61.6 (C_6), 38.9 (C_8), 37.7 (CH_2NH), 36.5 (CH_2NH), 30.9 (N(O)CCH_2), 30.8 (N(O)CCH_2), 29.4 ($NHCH_2CH_2$-CH_2O), 29.0 ($NHCH_2CH_2CH_2O$); ESI-MS for $C_{37}H_{53}N_3O_{13}$: calcd, 747,4; found, 770.4 $(M + Na)^+$,786.3 $(M + K)^+$

Mannose Derivative with a Linker at Position 1 (1). 5 (7 mg, 9.36 × 10^{-3} mmol) was dissolved in DMF (1 mL), piperidine 20% in DMF (200 μL) was added, and the reaction was stirred during 2 h. Then the solvent was removed under low pressure. The residue was dissolved in water (10 mL) and washed with CH_2Cl_2 (10 mL). The water was eliminated under reduced pressure to give the desired product **1** as an oil (4 mg, 80%). $[\alpha]_D$ (MeOH, *c* 0.3) = + 23.20; ^{1}H NMR (CD_3OD, 500 MHz) δ (ppm) 4.73 (d, 1H, J = 1.7 Hz, H_1), 3.81 (dd, 1H, J = 2.0 Hz and 11.5 Hz, $H_{6'}$), 3.78 (dd, 1H, J = 1.7 Hz and 3.5 Hz, H_2), 3.74−3.71 (m, 1H, $H_{7'}$), 3.71−3.46 (m, 17 H, H_7, H_6, H_4, H_5, H_3 and 6x CH_2O), 3.46−3.37 (m, 1H, H_8), 3.35−3.29 (m, 1H, $H_{8'}$), 3.22 (t, 1H, J = 7.0 Hz, CH_2NH), 3.08 (t, 1H, J = 6.5 Hz, CHNH), 2.49−2.43 (m, 4H, $HNOCCH_2CH_2CONH$), 1.79−1.64 (m, 4H, 2 × $HNCH_2CH_2CH_2O$); ^{13}C NMR (CD_3OD, 125 MHz) δ (ppm) 173.4 (C═O), 173.1 (C═O), 100.3 (C_1), 73.4 (C_5), 71.9, 70.8, 70.1, 70.0, 69.7, 69.6, 69.0, 68.3, 67.3 (6 × CH_2O, C_2, C_3, C_4), 65.8 (C_7), 61.5 (C_6), 38.9 (C_8), 38.8 (CH_2NH), 38.3 (CH_2NH), 30.7 (N(O)CCH_2), 30.6 (N(O)-CCH_2), 29.3 ($NHCH_2CH_2CH_2O$), 29.3 ($NHCH_2CH_2CH_2O$); ESI-MS for $C_{22}H_{43}N_3O_{11}$: calcd, 525,3; found, 526.3 $(M + H)^+$

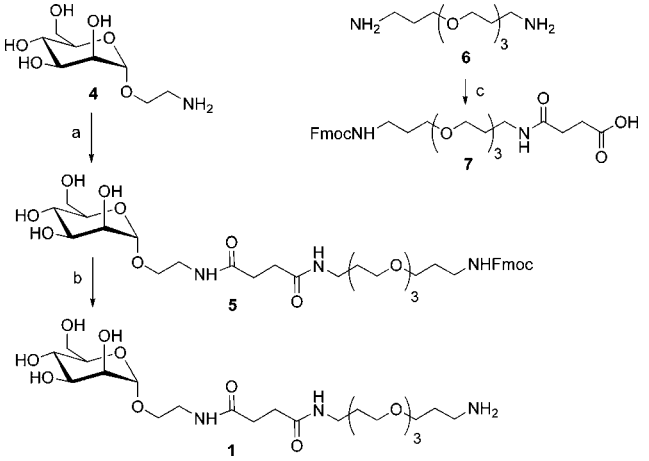
α-Methyl 6-tosylmannopyranoside (9) (*35*). α-Methyl mannopyranoside (**8**) (2.0 g, 10.30 mmol) was dissolved in dry pyridine (30 mL) and cooled to 0 °C. Then tosyl chloride (2.77, 14.53 mmol) was slowly added. The reaction was kept stirring at 0 °C overnight. The solvent was removed under reduced pressure, and the residue was purified by flash chromatography with silica gel (eluent: Hex−AcOEt, 7:1) to afford the desired product (5.1 g, 70% yield) as a white solid. $[\alpha]_D$ ($CHCl_3$, *c* 1.00) = +47.3; ^{1}H NMR ($CDCl_3$, 300 MHz) δ (ppm) 7.80 (d, 2H, J = 8.3 Hz, 2H Ts), 7.33 (d, 2H, J = 2H, J = 8.0 Hz, 2H Ts), 4.67 (d, 1H, J = 1.2 Hz, H_1), 4.35(dd, 1H, J = 10.7 and 4.1 Hz, H_6), 4.26 (dd, 1H, J = 4 Hz and 10.7 Hz, H_6), 3.95−3.87 (m, 1H, H_2), 3.78−3.62 (m, 3H, $H_3 + H_4 + H_5$), 3.30 (s, 3H, OCH_3), 2.42 (s, 3H, CH_3−Ar); ^{13}C NMR ($CDCl_3$, 125 MHz) δ (ppm) 145.0 (C_{Ts}), 132.7 (C_{Ts}), 129.9 (CH_{Ts}), 128.0 (CH_{Ts}), 100.9 (C_1), 71.6 (C_3), 70.5 (C_2), 69.8 (C_4), 69.1 (C_6), 67.3 (C_5), 55.2(OCH_3), 21.7 (CH_{3Ts}); ESI-MS for $C_{14}H_{20}O_8S$: calcd, 348.1; found, 386.9 $(M + K)^+$

α-Methyl 6-Azido-6-deoxymannopyranoside (10). A mixture of α-methyl 6-tosylmannopyranoside (**9**) (2.8 g, 8.04 mmol) and sodium azide (4.18 g, 64.35 mmol) in dry DMF (40 mL) was stirred at 60 °C overnight. After the reaction was complete, the solvent was removed *in vacuo* and the residue was dissolved in ethyl acetate. The excess of sodium azide and sodium tosylate was removed by filtration, and the filtrate was evaporated and purified by flash chromatography (eluent: DCM−MeOH, 9.5:0.5) to afford **9** as an oil (1.52 g, 98% yield). $[\alpha]_D$ (MeOH, *c* 1.00) = +54.80; ^{1}H NMR (CD_3OD, 500 MHz) δ (ppm) 4.62 (d, 1H, J = 1.4 Hz, H_1), 3.77 (dd, 1H, J = 1.6 Hz and 3.2 Hz, H_2), 3.60 (dt, 1H, J = 3.3 Hz and 9.3 Hz, H_3), 3.61−3.56 (m, 1H, H_5) 3.54 (c, 1H, J = 9.3 Hz, H_4), 3.45 (dd, 1H, J = 2.2 Hz and 12.9 Hz, H_6), 3.43 (dd, 1H, J = 6.0 Hz and 12.9 Hz, H_6) 3.38 (s, 3H, OCH_3); ^{13}C NMR (CD_3OD, 125 MHz) δ (ppm) 101.5 (C_1), 72.3 (C_5), 71.0 (C_3), 70.6 (C_2), 68.1 (C_4), 53.9 (C_6), 51.5 (OCH_3); ESI-MS for $C_7H_{13}N_3O_5$: calcd, 219.1; found, 242.0 $(M + Na)^+$

α-Methyl 6-Amino-6-deoxy- mannopyranoside (11). α-Methyl 6-azido-6-deoxy mannopyranoside (**10**) (130 mg, 0.59 mmol) was dissolved in MeOH (30 mL). Pd−C 10% (cat) was added, and the reaction mixture was saturated with hydrogen (1 bar) until reduction was complete to give **11** (120 mg, quant.) as a white solid. $[\alpha]_D$ (MeOH, *c* 1.00) = +49.3; ^{1}H NMR (CD_3OD, 300 MHz) δ (ppm) 4.67 (d, 1H, J = 1.1 Hz, H_1), 3.84−3.74 (m, 1H, H_2), 3.71−3.63 (m, 1H, H_3) 3.60−3.45 (m, 2H, H_4 and H_5), 3.40 (s, 3H, OCH_3), 3.13 (d, 1H, J = 12 Hz, H_6), 2.95 (dd, 1H, J = 6 Hz and 13.2 Hz, H_6); ^{13}C NMR (CD_3OD, 75 MHz) δ (ppm) 102.9 (C_1), 72.7 (C_4), 72.3 (C_3), 72.0 (C_2), 69.7 (C_5), 55.5 (OCH_3), 43.0 (C_6); ESI-MS for $C_7H_{15}NO_5$: calcd, 193.1; found, 194.0 $(M + H)^+$ and 220.0 $(M + Na)^+$

Fmoc-Protected Mannose Derivative with a Linker at Position 6 (12). To a solution of **11** (33 mg, 0.175 mmol) and **7** (100 mg, 0.092 mmol) in DMF (7 mL) were added DIC (60

Scheme 1. Synthesis of Mannose Derivative 1 Functionalized at the Anomeric Position and Synthesis of Linker 7[a]



[a] a) **7**, DIC, HOBt, DMF, 66%; b) Piperidine, DMF, 80%; c) Succinic anhydride; Fmoc-OSuc, 66%.

μL, 0.35 mmol) and HOBt (47 mg, 0.35 mmol). The reaction mixture was stirring at 60 °C during 24 h, and then the solvent was removed under low pressure. The final product was purified first by sephadex LH-20 (eluent: CH_2Cl_2−MeOH, 1:1) to eliminate the HOBt and later by silica gel column chromatography (eluent: CH_2Cl_2−MeOH, 95:5) to give **12** (75 mg, 60%) as a syrup. $[\alpha]_D$ (MeOH, *c* 1.00) = +19.02; ^{1}H NMR (CD_3-OD, 300 MHz) δ (ppm) 7.81 (d, 2H, J = 7.5 Hz, $CHAr_{Fmoc}$), 7.66 (d, 2H, J = 7.2 Hz, $CHAr_{Fmoc}$), 7.43 (t, 2H, J = 7.5 Hz, $CHAr_{Fmoc}$), 7.32 (t, 2H, J = 7.5 Hz, $CHAr_{Fmoc}$), 4.62 (d, 1H, J = 1.5 Hz, H_1), 4.38 (d, 2 H, J = 6.6 Hz, CH_{2Fmoc}), 4.21 (t, 1 H, J = 6.3 Hz, CH_{Fmoc}), 3.80 (dd, 1H, J = 1.8 and 3.3 Hz, H_2), 3.72−3.45 (m, 17H, 6 × CH_2O + H_3 + H_4 + H_5 + 2H_6), 3.35 (s, 3H, OCH_3), 3.29−3.17 (m, 4H, 2 × CH_2NH), 2.56−2.44 (m, 4H, 2 × N(O)CCH_2), 1.80−1.69 (m, 4H, 2 × $NHCH_2CH_2$-CH_2O); ^{13}C NMR (CD_3OD, 75 MHz) δ (ppm) 175.1 (C═O), 174.5 (C═O), 145.3 (CAr_{Fmoc}), 142.6 (CAr_{Fmoc}), 128.7 ($CHAr_{Fmoc}$), 128.1 ($CHAr_{Fmoc}$), 126.1 ($CHAr_{Fmoc}$), 121.9 ($CHAr_{Fmoc}$), 102.8 (C_1), 72.4, 72.2, 72.1, 71.5, 71.2, 69.8, 69.7, 69.4 ((CH_2O + C_2 + C_3 + C_4 + C_5), 67.5 (CH_{2Fmoc}), 55.3 (C_6), 48.5 (CH_{Fmoc}), 41.3 (CH_2NH), 39.1 (CH_2NH), 37.9 (CH_2NH), 32.3 (N(O)CCH_2), 32.2 (N(O)CCH_2), 30.8 ($NHCH_2CH_2CH_2O$), 30.3 ($NHCH_2CH_2CH_2O$); ESI-MS for $C_{36}H_{51}N_3O_{12}$: calcd, 717.3; found, 740.3 (M + Na)$^+$ and 756.3 (M + K)$^+$.

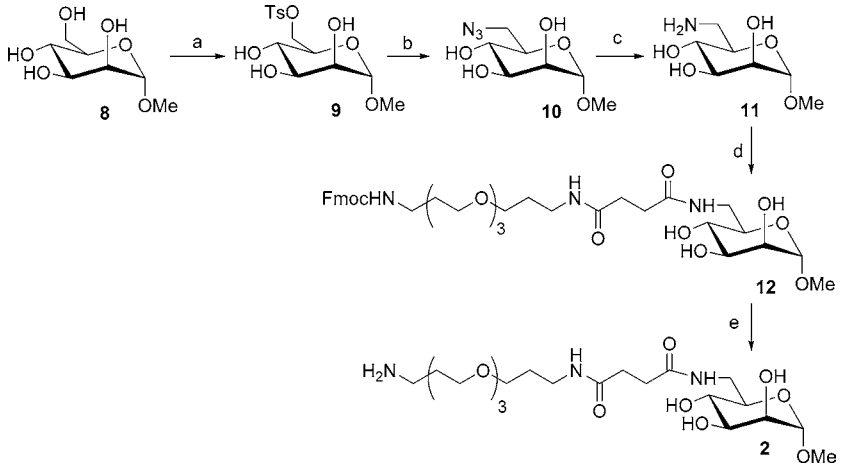
Mannose Derivative with a Linker at Position 6 (2). 12 (25 mg, 0.035 mmol) was dissolved in DMF (2 mL). Piperidine 20% in DMF (400 μL) was added, and the reaction was stirred during 2 h. Then the solvent was evaporated. The residue was dissolved in water (20 mL) and washed with CH_2Cl_2 (20 mL). The water was eliminated under reduce pressure to give the desired product **2** as an oil (17 mg, quant). $[\alpha]_D$ (MeOH, *c* 1.00) = +20.9; ^{1}H NMR (CD_3OD, 300 MHz) δ (ppm) 4.63 (d, 1H, J = 1.8 Hz, H_1), 3.80 (dd, 1H, J = 1.8 Hz and 3.6 Hz, H_2), 3.70−3.56 (m, 13H, H_3, H_5, H_4, 5 × CH_2O) 3.56−3.48 (m, 6H, 2H_6, CH_2O), 3.37 (s, 3H, OCH_3), 3.27 (t, 2 H, J = 6.9 Hz, CH_2NH), 2.85 (t, 2H, J = 6.9 Hz, CH_2NH), 2.57−2.44 (m, 4H, 2 × N(O)CCH_2), 1.86−1.71 (m, 4H, 2 × $NHCH_2CH_2$-CH_2O); ^{13}C NMR (CD_3OD, 75 MHz) δ (ppm) 175.1 (C═O), 174.6 (C═O), 102.8 (C_1), 72.4, 72.2, 72.1, 71.5, 71.4, 71.2, 71.1, 70.4, 69.8, 69.4 (C_2, C_3, C_4, C_5, 6 × CH_2O), 55.3 (OCH_3), 41.3 (C_6), 40.1 (CH_2NH), 37.8 (CH_2NH), 32.3 (N(O)CCH_2), 32.1 (N(O)CCH_2), 31.9 (C $CH_2CH_2CH_2O$), 30.4 (C CH_2CH_2-CH_2O); ESI-MS for $C_{21}H_{41}N_3O_{10}$: calcd, 495; found, 496.3 (M + H)$^+$.

Fmoc-Protected 4,7,10-Trioxa-1,13-tridecanediamine Succinimic Acid (7) (*36*). 4,7,10-Trioxa-1,13-tridecanediamine (**6**) (1.11 g, 5.045 mmol) was dissolved in acetonitrile (25 mL), and succinic anhydride (0.5 g, 5.045 mmol) in acetonitrile (12.5 mL) was added slowly over 1 h. The reaction was stirred at room temperature for an additional 3 h. Then the organic layer was decanted, the waxy oil was redissolved in 50% aqueous acetonitrile (50 mL) and cooled at 0 °C for 1 h, and then 1.3 equiv of Fmoc-OSu (2.2 g, 6.52 mmol) in acetonitrile (12.5 mL) was added slowly together with diisopropylethylamine to maintain pH 8−9. After stirring overnight at room temperature, solvents were removed under low pressure and the residue was dissolved in 5% $NaHCO_3$ (50 mL) and washed with AcOEt. The organic layer was discarded, and the aqueous phase was acidified to pH 2 with 5% HCl. Then the aqueous phase was extracted with AcOEt (3 × 25 mL). The combined organic layers were dried (Na_2SO_4), and the solvent was evaporated to give **7** (1.8 g, 66%). ^{1}H NMR (CD_3OD, 500 MHz) δ (ppm) 7.77 (d, 1H, J = 7.5 Hz, CH_{ArFmoc}), 7.62 (d, 1H, J = 7.5 Hz, CH_{ArFmoc}), 7.36 (d, 1H, J = 7.5 Hz, CH_{ArFmoc}), 7.28 (d, 1H, J = 7.5 Hz, CH_{ArFmoc}), 4.34 (d, 2H, J = 7.0 Hz, CH_{2Fmoc}), 4.17 (t, 1H, J = 6.5 Hz, CH_{Fmoc}), 3.62−3.42 (m, 12H, 6 × CH_2O), 3.21 (t, 2H, J = 6.5 Hz,), 3.16 (t, 2H, J = 6.5 Hz,) 2.53 (t, 2H, J = 6.7 Hz, N(O)CCH_2), 2.41 (t, 2H, J = 6.7 Hz, N(O)CCH_2), 1.75−1.66 (m, 2 × $NHCH_2$-CH_2CH_2O,); ^{13}C NMR (CD_3OD, 125 MHz) δ (ppm) 175.9 (C═O), 159.7 (C═O), 146.2 (C_{ArFmoc}), 143.5 (C_{ArFmoc}), 129.6 (C_{ArFmoc}), 129.0 (C_{ArFmoc}), 127.0 (C_{ArFmoc}), 121.8 (C_{ArFmoc}), 72.4 (CH_2O), 72.0 (CH_2O), 70.7 (CH_2O), 70.6 (CH_2O), 68.3 (CH_2O), 39.9 (CH_2NH), 38.6 (CH_2NH), 33.5 (N(O)CCH_2), 32.9 (N(O)CCH_2), 31.6 ($NHCH_2$-CH_2CH_2O), 31.2 ($NHCH_2$-CH_2CH_2O); ESI-MS for $C_{29}H_{38}N_2O_8$: calcd, 542.3; found, 543.3 (M + H)$^+$, 565.3 (M + Na)$^+$, and 581.2 (M + K)$^+$.

Fmoc-Protected Linker Ethanolamine (13). To a solution of 2-aminoethanol (5.5 μL, 0.092 mmol) and **7** (50 mg, 0.092 mmol) in DMF (4 mL) were added DIC (29 μL, 0.184 mmol) and HOBt (25 mg, 0.184 mmol). The reaction mixture was stirring at 60 °C during 24 h, and then the solvent was evaporated. The final product was first purified by sephadex LH-20 (eluent: CH_2Cl_2−MeOH, 1:1) to eliminate the HOBt and later by silica gel column chromatography (eluent: CH_2-Cl_2−MeOH, 95:5) to give **13** (34 mg, 64%) as a syrup. ^{1}H NMR (CD_3OD, 500 MHz) δ (ppm) 7.77 (d, 2H, J = 7.5 Hz, $CHAr_{Fmoc}$), 7.62 (d, 2H, J = 7.5 Hz, $CHAr_{Fmoc}$), 7.38 (t, 2H, J = 7.5 Hz, $CHAr_{Fmoc}$), 7.28 (t, 2H, J = 7.5 Hz, $CHAr_{Fmoc}$), 4.34 (d, 2 H, J = 6.5 Hz, CH_{2Fmoc}), 4.17 (t, 1 H, J = 6.5 Hz, CH_{Fmoc}), 3.65−3.50 (m, 12 H, CH_2O), 3.46 (m, 4 H, $NHCH_2CH_2CH_2O$), 3.26 (t, 2H, J = 5.5 Hz, CH_2NH), 3.20 (t, 2H, J = 6.5 Hz, CH_2NH), 3.16 (t, 2H, J = 5.5 Hz, CH_2NH), 2.47−2.41 (m, 4 H, N(O)CCH_2) 1.73−1.71 (m, 4 H, $NHCH_2CH_2CH_2O$). ^{13}C NMR (CD_3OD, 125 MHz) δ (ppm) 173.5 (C═O), 173.1 (C═O), 144.0 (CAr_{Fmoc}), 141.2 (CAr_{Fmoc}), 127.4 ($CHAr_{Fmoc}$), 126.7 ($CHAr_{Fmoc}$), 124.7 ($CHAr_{Fmoc}$), 119.5 ($CHAr_{Fmoc}$), 70.1 (CH_2O), 69.8 (CH_2O), 68.5 (CH_2O), 68.3 (CH_2O), 66.1 (CH_{2Fmoc}), 60.2 (CH_2OH), 47.2 (CH_{Fmoc}), 41.6 (CH_2NH), 37.7 (CH_2NH), 36.4 (CH_2NH), 30.9 (2 × N(O)CCH_2), 29.4 ($NHCH_2CH_2CH_2O$), 29.0 ($NHCH_2CH_2CH_2O$). ESI-MS for $C_{31}H_{43}N_3O_8$: calcd, 585.3; found, 608.3 (M + Na)$^+$ and 624.2 (M + K)$^+$.

Linker Ethanolamine (3). 13 (10 mg, 0.017 mmol) was dissolved in DMF (2 mL), and 20% of piperidine in DMF (400 μL) was added. The reaction was stirred during 2 h. Then the solvent was evaporated. The residue was dissolved in water (10 mL) and washed with CH_2Cl_2 (10 mL). The water was eliminated under reduce pressure to give the desired product **3** as an oil (6 mg, quant). ^{1}H NMR (CD_3OD, 500 MHz) δ (ppm) 3.65−3.50 (m, 12H, 5 × CH_2O− + CH_2OH), 3.49 (t, 2H, J = 6.0 Hz, CH_2O), 3.26 (t, 2H, J = 6.5 Hz, CH_2NH), 3.22 (t, 2H, J = 6.5 Hz, CH_2NH), 2.86 (t, 2H, J = 6.5 Hz, CH_2NH), 2.46−2.43 (m, 4H, 2 × N(O)CCH_2), 1.79 (q, 2H, J = 6.0 Hz, 2 ×

Scheme 2. Synthesis of Mannose Conjugate 2[a]



[a] a) TsCl, Pyr, rt; 60%; b) NaN_3, DMF, 60 °C, 98%; c) H_2, Pd/C, MeOH, 100%; d) **7**, DIC, HOBt, DMF, 60%; e) Piperidine, DMF, 100%.

$NHCH_2CH_2CH_2O$), 1.72 (q, 2H, $J = 6.0$ Hz, 2 × $NHCH_2CH_2$-CH_2O); ^{13}C NMR (CD_3OD, 125 MHz) δ (ppm) 173.5 (C═O), 173.2 (C═O), 70.1, 70.0, 69.8, 69.7, 69.0, 68.4, 60.2 (6 × CH_2O + CH_2OH), 41.6 (CH_2NH), 38.7 (CH_2NH), 36.4 (CH_2NH), 30.8 ($N(O)CCH_2$), 30.8 ($N(O)CCH_2$), 29.8 ($CH_2CH_2CH_2O$), 29.0 ($CH_2CH_2CH_2O$); ESI-MS for $C_{16}H_{33}N_3O_6$: calcd, 363.2; found, 386.2 $(M + Na)^+$

DC-SIGN ECD Expression and Purification. Plasmids pET30b (Novagen) containing a cDNA encoding the extracellular-domain of DC-SIGN (DC-SIGN ECD corresponding to amino acids 66−404) were used for protein overproduction as previously described (*29*). Proteins produced in inclusion bodies have been refolded as already described (*12*). Purification of functional DC-SIGN proteins were achieved by an affinity chromatography on Mannan-agarose column (Sigma) equilibrated with 25 mM Tris-HCl pH 7.8, 150 mM NaCl, 4 mM $CaCl_2$ (Buffer A) and eluted in same buffer lacking $CaCl_2$ but supplement with 10 mM EDTA. This step was followed by a Superose 6 size exclusion chromatography (Amersham) equilibrated in buffer A. Proteins were concentrated, frozen in liquid nitrogen, and stored at minus 80 °C.

Biosensor Experiments. Experiments have been conducted on a BIAcore 3000 instrument. Lyophilized compounds **1**, **2**, and **3** have been solubilized in HBS-N buffer reagent from BIAcore. These derivatives have then been used for functionalization of a CM5 chips (BIAcore). Flow cells were activated with a 50 μL injection of an EDC-NHS mixture as described by manufacturer and blocked, after functionalization, with 50 μL of 1 M ethanolamine. Flow cell one (control flow cell), two, and three were functionalized with 70 μL of control compound **3**, mannose conjugate compound **2**, and mannose conjugate compound **1** diluted at 50 μM in 10 mM acetate buffer pH 4, respectively. The corresponding immobilization levels were of 793, 961, and 848 RU for the flow cell one, two, and three, respectively.

For binding studies, 50 μL of DC-SIGN ECD, in running buffer A supplemented in 0.005% P20 surfactant, was injected, at a flow rate of 20μL.min^{-1}, onto the functionalized surfaces at increasing concentrations.

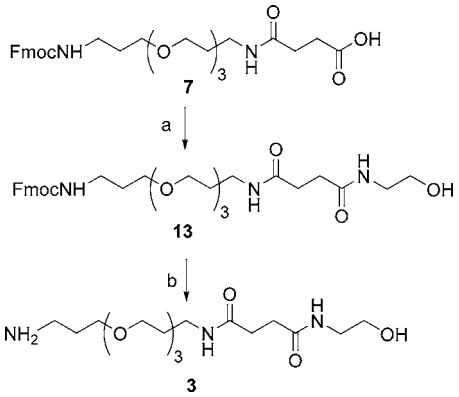
RESULTS AND DISCUSSION

Synthesis of Glycoconjugates. The 2-aminoethyl α-D-mannopyranoside (**4**) has been previously prepared in our laboratory and was used as starting material to prepare the mannose conjugate functionalized at position 1. We have considered that a longer linker should be more adequate to allow its attachment to the biosensor chip surface. For this reason, mannose derivative **4** was conjugated with linker **7** via an amide bond formation to obtain the glycoconjugate **1** with a longer spacer, after Fmoc removal. Linker **7** was prepared in two steps as described in the literature (*36*) from commercially available 4,7,10-trioxa-1,13-tridecanediamine (**6**) by reaction with succinic anhydride and subsequent amine protection as a carbamate with *N*-(9-fluorenylmethoxycarbonyloxy)succinimide (Fmoc-Osu) (Scheme 1). Reaction of 2-aminoethyl α-D-mannopyranoside (**4**) with linker **7** in the presence of DIC and HOBt at 60 °C gave selectively the mannose derivative **5** with an amide linkage in 66% yield. Using these conditions was not necessary to protect the mannose hydroxyl groups. After this coupling, the Fmoc protecting group was easily removed by treatment with 20% of piperidine in DMF at room temperature to give compound **1** in 80% yield, the mannosyl glycoconjugate functionalized at position 1 (Scheme 1).

To prepare a mannose derivative functionalized at position 6 we used as starting material the commercially available methyl α-D-mannopyranoside (**8**). To use the same type of linkage as that used with mannose derivative **4** we decided to introduce a primary amine at position 6 of the mannose. The 6-deoxy-6-aminomannose derivative **11** was prepared in three steps using the methodology described (*35*), introducing some modifications. We converted the 6-hydroxyl group into a good leaving group by reaction with tosyl chloride at 0 °C in pyridine using the procedure described in the literature (*35*) to give the mannose derivative **9** in 70% of yield. Then the tosyl group was substituted by an azide group by reaction with an excess of sodium azide in DMF. We tried the conditions previously described (*35*) to substitute the tosyl group by azide in a mixture acetone−water (*3*−*2*) under reflux, but the attempts using these conditions were fruitless, recovering the starting material in all the cases. Using DMF as solvent at 60 °C, the reaction was complete overnight to yield the methyl 6-deoxy-6-azidomannopyranoside (**10**) in 98% of yield. The last step to get the amine group at position 6 was the catalytic hydrogenation of the azide group using Pd/C at 1 atm of H_2 to obtain the methyl 6-deoxy-6-aminomannopyranoside (**11**) in quantitative yield (*35*) (Scheme 2).

Once the mannose derivative **11** was obtained, the coupling with the linker **7** was performed using the same conditions as those used with mannose derivative **4**, i.e., DIC and HOBt in DMF at room temperature, to give the glycoconjugate **12** in 60% of yield with the linker at the anomeric position. Again, the last step was the removal of Fmoc protecting group with 20% piperidine in DMF at room temperature to obtain mannose conjugate **2** in quantitative yield (Scheme 2).

Scheme 3. Synthesis of Control Compound 3[a]



[a] a) DIC, HOBt, ethanolamine, DMF, 64%; b) piperidine, DMF, 100%.

Finally, a control for the binding studies was prepared. We used the same spacer **7** coupled with ethanolamine using DIC and HOBt in DMF at 60 °C to give compound **13** in 64% of yield. Again, deprotection of amine group with 20% piperidine in DMF at room temperature gave compound **3** in quantitative yield which will be used as control (Scheme 3).

Surface Functionalization. In our mannose derivatives, the spacer added on position 6 or 1 has been designed with an amine terminal group. This function will allow further functionalization in order to produce future multivalent dendrimeric compounds. But this extremity can also be considered here as a mimics of a lysine side chain and may be used to functionalize the SPR surfaces using *N*-hydroxysuccinamide and EDC chemistry as usually done to covalently link proteins. Such protein functionalization methods lead to covalent attachment of the lysine residue to the carboxylic groups harbored by the dextran polymer present at the sensorchip surface. Similarly, compounds **1**−**3** were used to functionalize a CM5 sensorchip surface after activation with a mixed solution of EDC-NHS. After injections of the different compounds, an increase of the immobilization level (in resonance units) has been observed in the sensorgrams as a clear signal of covalent attachment of these compounds to the activated carboxylic acid surface via amide linkages (data not shown). An immobilization level of 793, 961.5, and 848 RU has been obtained for compounds **1**, **2**, and **3,** respectively. This validates this chemical strategy of "building block" production with this type of spacer, allowing a functional test of the carbohydrate unit in SPR analysis before getting to the expensive and time-consuming chemical step assembly of multivalent dendrimeric compounds. These functionalized surfaces were used to study the binding process with the ECD of DC-SIGN in a flow mode.

Surface Plasmon Resonance Binding Assays. Binding assays were performed using increasing concentrations of DC-SIGN ECD ranging from 0.1 μM to 100 μM. These solutions of lectin were injected over the functionalized surfaces. The interaction profile of DC-SIGN ECD (Figure 1) with the functionalized surfaces is indicative of a rapid association and dissociation process (high k_{on} and k_{off}) and of a weak affinity of DC-SIGN ECD for the monosaccharide derivatives used here, compounds **1** and **2**. This is in accord with the previously reported affinity for mannose of the DC-SIGN CRD in the millimolar range (*12*). By contrast, the surface functionalized with the control compound **3** only showed a small nonspecific response presenting the same RU level as observed on a surface without any functionalization (data not shown). This background interaction obtained with the control surface was subtracted from the signals obtained with surfaces functionalized with compounds **1** and **2** (Figure 1).

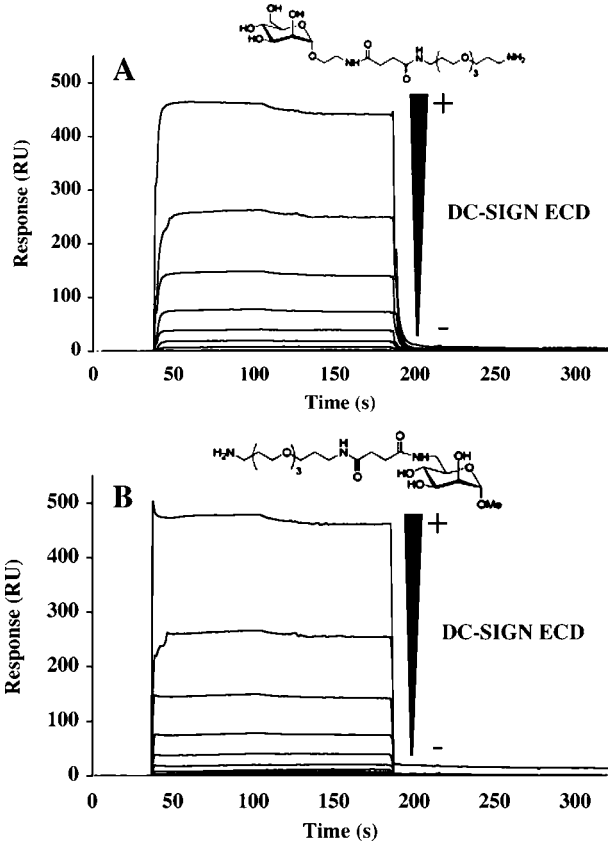


Figure 1. Sensorgrams corresponding to the injection of different concentrations of DC-SIGN ECD with surfaces functionalized with compound **1** (A) and compound **2** (B). The concentrations used were 0.1, 0.2, 0.4, 0.8, 1.55, 3.1, 6.2, 12.5, 25, 50, and 100 μM.

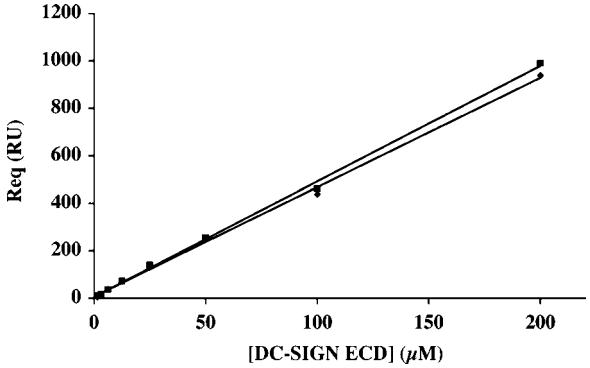


Figure 2. Representation of steady states response level (R_{eq}) for surfaces functionalized with glycoconjugates **1 (**filled diamond**)** and **2** (filled square) as a function of DC-SIGN ECD concentration.

An analysis of these curves by representation of DC-SIGN ECD concentration against the steady-state response level (R_{eq}) observed for each functionalized surface showed a similar behavior for both types of surfaces (functionalized, at an equivalent density, with the mannose conjugate linked at position 6 or at the anomeric position) (Figure 2). Because of the weak affinity observed for these carbohydrate−protein interactions, the saturation curve did not present a maximum because it was not possible to reach the saturation situation in the concentration range used for the DC-SIGN ECD. To get access to a K_d would require a high amount of DC-SIGN ECD and at a concentration in the millimolar range that may not be accessible for solubility reasons. Here we have access to the ascending part of the saturation curve. In the case of a marked difference in affinity of DC-SIGN ECD for both types of modified mannose, the change in K_d will be reflected not in the value of the maximum

plateau reached but rather in the position and evolution of the ascending part of the saturation curve. Here Figure 2 shows that there is no significant difference between the glycoconjugates **1** and **2**.

Our basic interest was centered on the qualitative comparison of both surfaces to determine if both positions in the mannose ring (anomeric position and position 6) were feasible as focal points for linkage of this carbohydrate in order to prepare glycoconjugates and finally multivalent systems. This SPR analysis demonstrated that both positions were appropriate to be used as points of functionalization to generate glycoconjugates, and it is also reasonable to say that position 6, as can be observed in Figure 2, is a good or even better than the anomeric position which is usually used to prepare carbohydrates conjugates.

CONCLUSIONS

In this work we have prepared two mannosyl conjugates at different positions, position 6, and position 1 or the anomeric position of the carbohydrate. With these conjugates, a CM5 chip surface of a biosensor was functionalized to create a carbohydrate surface to study the interaction with the tetrameric ECD of DC-SIGN. The analysis of the obtained sensorgrams showed that this binding process was fast and weak. In fact, for the concentration of protein used, it was not possible to reach saturation and therefore a quantitative calculation of K_d was not possible. However, an important feature of this binding process with the lectin DC-SIGN was demonstrated for the first time; functionalization of mannose at position 6 is a very good alternative, as good as glycoconjugates functionalized at the anomeric position, to prepare glycoconjugates.

This fact opens new possibilities in the design of ligands for this receptor. The introduction of selected hydrophobic groups at the anomeric position of the reducing end of the corresponding carbohydrate can be envisaged. These hydrophobic groups could establish contact with hydrophobic residues present in the carbohydrate recognition domain and increase the affinity of these ligands for the receptor. Introduction of linkers at position 6 will allow the preparation of glycoconjugates with these ligands without loss of activity and also will allow the preparation of the corresponding multivalent systems to interact with DC-SIGN.

ACKNOWLEDGMENT

One of us (J.R.) thanks FIS (PI030093) and the Spanish Ministry of Education and Science (Acción Integrada HF2005-0212) for funding support. O.S.M. thanks the CSIC and the European Social Funds (I3P program) for a fellowship. G.T. thanks the CEA for a Ph.D. Fellowship, and F.F. thanks Ensemble contre le SIDA-Sidaction for funding support.

Supporting Information Available: ^{1}H and ^{13}C NMR spectra of compounds **1**−**3**. This material is available free of charge via the Internet at http://pubs.acs.org.

LITERATURE CITED

(1) Lasky, L. A. (1995) Selectin-carbohydrate interactions and the initiation of the inflammatory response. *Annu. Rev. Biochem. 64*, 113−139.

(2) Fenderson, B. A., Eddy, E. M., and Hakomori, S. (1990) Glycoconjugate expression during embryogenesis and its biological significance. *Bioessays 12*, 173−179.

(3) Hakomori, S. (1984) Tumor-associated carbohydrate antigens. *Annu. Rev. Immunol. 2*, 103−126.

(4) Karlsson, K. A. (1995) Microbial recognition of target-cell glycoconjugates. *Curr. Opin. Struct. Biol. 5*, 622−635.

(5) Varki, A. (1993) Biological roles of oligosaccharides: all of the theories are correct. *Glycobiology 3*, 97−130.

(6) Lee, Y. C., and Lee, R. T. (1995) Carbohydrate-protein interactions: basis of glycobiology. *Acc. Chem. Res. 28*, 321−327.

(7) Burkhalter, N. F., Dimick, S. M., and Toone, E. J. (2000) Protein-carbohydrate interactions: Fundamental consideractions. In *Carbohydrates in Chemistry and Biology* (Ernst, B., Hart, G. W., Sinaÿ, P., Eds.) pp 863−911, Chapter 31, Part I, Vol. 2, Wiley-VCH, Weinheim.

(8) Mammen, M., Choi, S.-k., and Whitesides, G. M. (1998) Polyvalent interactions in biological systems: implications for design and use of multivalent ligands and inhibitors. *Angew. Chem., Int. Ed. 37*, 2754−2794.

(9) Kiessling, L. L., Gestwicki, J. E., and Strong, L. E. (2000) Synthetic multivalent ligands in the exploration of cell-surface interactions. *Curr. Opin. Chem. Biol. 4*, 696−703.

(10) Choi, S.-k. (2004) *Synthetic multivalent molecules: concepts and biomedical applications*, John Wiley & Sons, Inc., Hoboken, NJ.

(11) Geijtenbeek, T. B. H., Torensma, R., van Vliet, S. J., van Duijnhoven, G. C. F., Adema, G. J., van Kooyk, Y., and Figdor, C. G. (2000) Identification of DC-SIGN, a novel dendritic cell-specific ICAM-3 receptor that supports primary immune responses. *Cell 100*, 575−585.

(12) Mitchell, D. A., Fadden, A. J., and Drickamer, K. (2001) A novel mechanism of carbohydrate recognition by the C-type lectins DC-SIGN and DC-SIGNR. *J. Biol. Chem. 276*, 28939−28945.

(13) Geijtenbeek, T. B. H., Kwon, D. S., Torensma, R., van Vliet, S. J., van Duijnhoven, G. C. F., Middel, J., Cornelissen, I. L. M. H. A., Nottet, H. S. L. M., KewalRamani, V. M., Littman, D. R., Figdor, C. G., and van Kooyk, Y. (2000) DC-SIGN, a dendritic cell-specific HIV-1 binding protein that enhances trans-infection of T cells. *Cell 100*, 587−597.

(14) Appelmelk, B. J., van Die, I., van Vliet, S. J., Vandenbroucke-Grauls, C. M. J. E., Geijtenbeek, T. B. H., and van Kooyk, Y. (2003) Cutting edge: Carbohydrate profiling identifies new pathogens that interact with dendritic cell-specific ICAM-3-grabbing nonintegrin on dendritic cells. *J. Immunol. 170*, 1635−1639.

(15) van Kooyk, Y., C. M. J. E., and Geijtenbeek, T. B. H. (2003) DC-SIGN: escape mechanism for pathogens. *Nat. Rev. Immunol. 3*, 697−709.

(16) Cambi, A., de Lange, F., van Maarseveen, N. M., Nijhuis, M., Joosten, B., van Dijk, E. M. H. P., de Bakker, B. I., Fransen, J. A. M., Bovee-Geurts, P. H. M., van Leeuwen, F. N., van Hulst, N. F., and Figdor, C. G. (2004) Microdomains of the C-type lectin DC-SIGN are portals for virus entry into dendritic cells. *J. Cell Biol. 164*, 145−155.

(17) Arce, E., Nieto, P. M., Díaz, V., Castro, R. G., Bernad, A., and Rojo, J. (2003) Glycodendritic structures based on Boltorn hyperbranched polymers and their interactions with *Lens culinaris* lectin. *Bioconjugate Chem. 14*, 817−823.

(18) Lasala, F., Arce, E., Otero, J. R., Rojo, J., and Delgado, R. (2003) Mannosyl glycodendritic structure inhibits DC-SIGN-mediated Ebola virus infection *in cis* and *in trans*. *Antimicrob. Agents Chemother. 47*, 3070−3972.

(19) Rojo, J., and Delgado, R. (2004) Glycodendritic structures: promising new antiviral drugs. *J. Antimicrob. Chemother. 54*, 579−581.

(20) Weis, W. I., and Drickamer, K. (1996) Structural basis of lectin-carbohydrate recognition. *Annu. Rev. Biochem. 65*, 441−473.

(21) Kötter, S., Krallmann-Wenzel, U., Ehlers, S., and Lindhorst, T. K. (1998) Multivalent ligands for the mannose-specific lectin on type 1 fimbriae of *Escherichia coli*: syntheses and testing of trivalent α-D-mannoside clusters. *J. Chem. Soc., Perkin Trans. 1* 2193−2200.

(22) Feinberg, H., Mitchell, D. A., Drickamer, K., and Weis, W. I. (2001) Structural basis for selective recognition of oligosaccharides by DC-SIGN and DC-SIGNR. *Science 294*, 2163−2166.

(23) Guo, Y., Feinberg, H., Conroy, E., Mitchell, D. A., Alvarez, R., Blixt, O., Taylor, M. E., Weis, W. I., and Drickamer, K. (2004) Structural basis for distinct ligand-binding and targeting properties of the receptors DC-SIGN and DC-SIGNR. *Nat. Struct. Mol. Biol. 11*, 591−598.

(24) Firon, N., Ashkenazi, S., Mirelman, D., Ofek, I., and Sharon, N. (1987) Aromatic alpha-glycosides of mannose are powerful inhibitors of the adherence of type 1 fimbriated *Escherichia coli* to yeast and intestinal epithelial cells. *Infect. Immunol. 55*, 472−476.

(25) Hamodrakas, S. J., Alexandraki, E., Troganis, A., and Stassinopoulou, C. I. (1989) Models of binding of 4′-nitrophenyl α-D-mannopyranoside to the lectin concanavalin A. *Int. J. Biol. Macromol. 11*, 17−22.

(26) Lee, R. T., Ichikawa, Y., Fay, M., Drickamer, K., Shao, M.-C., and Lee, Y. C. (1991) Ligand-binding characteristics of rat serum-type mannose-binding protein (MBP-A). *J. Biol. Chem. 266*, 4810−4815.

(27) Pagé, D., Zanini, D., and Roy, R. (1996) Macromolecular recognition: effect of multivalency in the inhibition of binding of yeast mannan to concanavalin A and pea lectin by mannosylated dendrimers. *Bioorg. Med. Chem. 4*, 1949−1961.

(28) McDonnell, J. M. (2001) Surface plasmon resonance: towards an understanding of the mechanisms of biological molecular recognition. *Curr. Opin. Chem. Biol. 5*, 572−577.

(29) Halary, F., Amara, A., Lortat-Jacob, H., Messerle, M., Delaunay, T., Houlès, C., Fieschi, F., Arenzana-seisdedos, F., Moreau, J.-F. and Déchanet-Merville, J. (2002) Human citomegalovirus binding to DC-SIGN is required for dendritic cell infection and target cell *trans*-infection. *Immunity 17*, 653−664.

(30) Lozach, P.-Y., Lortat-Jacob, H., de Lacroix de Lavalette, A., Staropoli, I., Foung, S., Amara, A., Houlès, C., Fieschi, F., Schwartz, O., Virelizier, J.-L., Arenzana-Seisdedos, F., and Altmeyer, R. (2003) DC-SIGN and L-SIGN are high affinity binding receptors for hepatitis C virus glycoprotein E2. *J. Biol. Chem. 278*, 20358−20366.

(31) Navarro-Sanchez, E., Altmeyer, R., Schwartz, O., Fieschi, F., Virelizier, J.-L., Arenzana-Seisdedos, F., and Desprès, P. (2003) Dendritic-cell specific ICAM-3-grabbing non-integrin is essential for the productive infection of human dendritic cells by mosquito-cell-derived dengue viruses. *EMBO Rep. 4*, 1−6.

(32) Smith, E. A., Thomas, W. D., Kiessling, L. L., and Corn, R. M. (2003) Surface plasmon resonance imaging studies of protein-carbohydrate interactions. *J. Am. Chem. Soc. 125*, 6140−6148.

(33) Duverger, E., Frison, N., Roche, A.-C., and Monsigny, M. (2003) Carbohydrate-lectin interactions assesed by surface plasmon resonance. *Biochemie 85*, 167−179.

(34) Tabarani, G., Reina, J. J., Ebel, C., Vivès, C., Lortat-Jacob, H., Rojo, J., and Fieschi, F. (2006) Mannose hyperbranched dendritic polymers interact with clustered organization of DC-SIGN and inhibit gp120 binding. *FEBS Lett. 580*, 2402−2408.

(35) Wang, P., Shen, G.-J., Wang, Y.-F., Ichikawa, Y., and Wong, C.-H. (1993) Enzymes in oligosaccharide synthesis: active-domain overproduction, specific study, and synthetic use of an α-1,2-mannosyltransferase with regeneration of GDP-Man. *J. Org. Chem. 58*, 3895−3990.

(36) Zhao, Z. G., Im, J. S., Lam, K. S., and Lake, D. F. (1999) Site-specific modification of a single-chain antibody using a novel glyoxylyl-based labeling reagent. *Bioconjugate Chem. 10*, 424−430.

BC060369Z

Overcoming Limiting Side Reactions Associated with an NHS-Activated Precursor of Polymethacrylamide-Based Polymers

Sharon Y. Wong[†] and David Putnam*[,†,‡]

Department of Biomedical Engineering and the School of Chemical and Biomolecular Engineering, Cornell University, Ithaca, New York 14853. Received December 7, 2006; Revised Manuscript Received February 12, 2007

Combinatorial polymer libraries have recently gained popularity for the development of novel materials for a variety of biomedical applications including non-viral gene delivery systems and biodegradable polymers for tissue engineering. To streamline the nontrivial task of library synthesis, activated ester homopolymers have been used to serve as a backbone to which primary amine-containing functional groups (NH_2-FGs) can be covalently bound at varying ratios. Polymethacryloxysuccinimide (poly(MAOS)) is one such homopolymer that was previously reported to be an attractive precursor for polymeric drug and gene delivery systems. The reported functionalization protocols entailed conjugating the precursor with 2 equiv of the NH_2-FG at a reaction concentration of 25 mg poly(MAOS)/150 μL DMSO for either 5 h at 50 °C or 16 h at 25 °C. More recently, both protocols were revealed to be associated with ring-opening and glutarimide-forming side reactions that compromise the utility of the homopolymer. Using 1-dimensional and 2-dimensional NMR spectroscopy techniques, we have characterized the side product distributions that result from conjugations performed at 50 °C/5 h and 25 °C/16 h. Moreover, by systematically altering the equivalents of the NH_2-FGs, polymer concentration, reaction time, and reaction temperature, we have established a protocol that overcomes these side reactions. Using a final reaction protocol of 5 equiv of the NH_2-FG at a reaction concentration of 25 mg poly(MAOS)/600 μL DMSO for 24 h at 75 °C, we have obtained functionalized polymers with minimal side products. This protocol is applicable for polymers ranging from 5000 to 50 000 g/mol, compatible with a variety of functional groups, and amenable to conjugating combinations of functional groups.

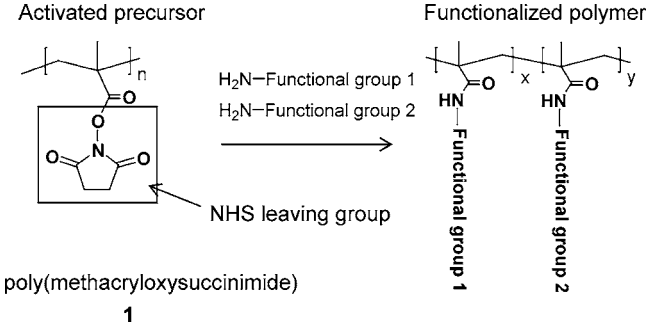
INTRODUCTION

With the ever-increasing demand for more sophisticated, multifaceted polymeric materials in various applications, many researchers have begun looking to combinatorial approaches to facilitate the materials discovery process. One of the first successful demonstrations of employing combinatorial strategies to develop degradable polymers for medical applications was reported almost a decade ago by Kohn and co-workers (*1*, *2*). Their work exemplified how combinatorial strategies can (1) offer a systematic approach to designing libraries of compounds that encompass a broad range of physicochemical properties and (2) assist in identifying structure−function relationships that correlate a polymeric structural feature to a biological response.

Building on this work, Brocchini and co-workers, Haddleton and co-workers, and others have applied the combinatorial approach toward developing water-soluble polymers for drug and gene delivery systems (*3*−*9*). To expedite the library synthesis process, the former two groups employed the use of the activated homopolymeric precursor, polymethacryloxysuccinimide (poly(MAOS) (**1**), to which primary amine-containing functional groups (NH_2-FGs) can be covalently bound via amidation chemistry (*10*) (Scheme 1).

Recently, greater resolution of the potential side reactions that can occur with the poly(MAOS) precursor was reported (*11*). In our hands, we also observed similar problems upon functionalizing poly(MAOS) that resulted in at least two unexpected side reactions: (1) ring opening of the succinimide moiety and (2) glutarimide formation between presumably neighboring active esters. These side products were confirmed by ^{1}H NMR, diffusion ordered spectroscopy (DOSY), heteronuclear multibond correlation spectroscopy (HMBC), and homonuclear correlated spectroscopy (COSY) analyses (Scheme 2).

Scheme 1. Theoretical Synthetic Scheme for Functionalizing the *N*-Hydroxysuccinimide (NHS)-Activated Precursor, Polymethacryloxysuccinimide (poly(MAOS) (1) to Form Polymethacrylamide-Based Polymers



However, these limitations do not ultimately preclude the use of this polymeric precursor as was previously suggested (*11*). In this report, we describe the protocol that we have established to overcome these side reactions allowing poly(MAOS) to serve as a viable precursor for polymethacrylamide-based materials. Additionally, we show that this protocol is applicable for polymers ranging from 5000 to 50 000 g/mol, compatible with a variety of functional groups, and amenable to conjugating combinations of functional groups.

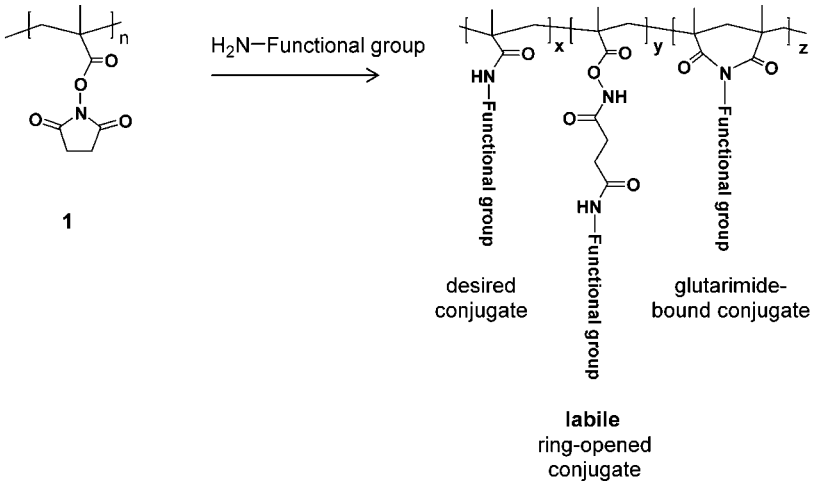
* To whom correspondence should be addressed: 270 Olin Hall Ithaca, New York 14853. Tel: (607) 255-4352. Fax: (607) 255-1136. E-mail: dap43@cornell.edu.

[†] Department of Biomedical Engineering.

[‡] School of Chemical and Biomolecular Engineering.

10.1021/bc0603790 CCC: $37.00 © 2007 American Chemical Society
Published on Web 04/20/2007

Scheme 2. Side Reactions Can Occur during Conjugation of NH_2-FGs to 1 Resulting in a Functionalized Polymer with Three Pendant Groups: the Desired Amide-Bound Conjugate; a Hydrolytically Unstable Ring-Opened Conjugate; and a Glutarimide-Bound Conjugate



Scheme 3. Resultant Functionalized Polymer Produced from Previously Reported Protocols[a]



[a] Two unexpected side reaction products accompany the desired conjugation: (1) a labile ring-opened conjugate and (2) a glutarimide-bound conjugate. (protocol 1—ref 3; protocol 2—ref 4)

EXPERIMENTAL PROCEDURES

N-Methacryloxysuccinimide monomer was synthesized as previously reported (*12*). Cu(I)Br (99.999%), Cu(II)Br_2 (99.999%), 2,2′-dipyridyl (≥99%), ethyl 2-bromoisobutyrate (98%), benzylamine (≥99.5%), *n*-butylamine (≥99.5%), hexylamine (≥99.5%), 1-amino-2-propanol (≥98%), N-Boc-*N*-methylethylenediamine (≥98.0%), N-Boc-ethylenediamine (≥98%), *N*,*N*-dimethylethylenediamine (≥98%), 2-(aminoethyl)trimethylammonium chloride—HCl (99%), histamine (≥97%), anhydrous DMSO, DMSO-d_6, abd DMF-d_7 were all purchased from Aldrich.

General Procedure for Synthesis of Poly(methacryloxysuccinimide) (poly(MAOS)). The polymer precursor was synthesized with a slight modification to a previously reported method (*5*). A 5 mL pear-shaped flask with a flea magnetic stir bar was fitted with a rubber septum and flame-dried while purging with N_2(g) until cooled to ambient temperature. *N*-Methacryloxysuccinimide (0.5 g, 2.73 mmol), Cu(I)Br (0.0078 g, 0.055 mmol), Cu(II)Br_2 (0.0122 g, 0.055 mmol), and 2,2′-dipyridyl (0.0171 g, 0.11 mmol) were placed in the flask and placed under a nitrogen atmosphere for 10 min. Cu(II)Br_2 was added to the reaction as an inhibitor of chain terminations to control polydispersities (*13*). Deoxygenated anhydrous DMSO (0.2 mL) was injected into the flask, and the contents were stirred until dissolved. Ethyl-2-bromoisobutyrate (81 μL, 0.55 mmol) was weighed directly into a separate dram vial and dissolved in deoxygenated anhydrous DMSO (0.5 mL). Upon complete dissolution of the contents, a 1/10 aliquot (50 μL) of the ethyl 2-bromoisobutyrate solution was injected into the flask and immersed into a 100 °C thermostated oil bath. To stop the polymerization, the flask was quenched in an ice bath and the product was diluted with anhydrous DMSO (1.5 mL). The final polymer was isolated as a white powder by precipitating into stirring acetone. ^{1}H NMR (DMSO-d_6) δ: 1.44 (b, 3H, CH_3), 2.41 (b, 2H, CH_2), 2.78 (b, 4H, CH_2CH_2).

Molecular weight and polydispersity were determined by hydrolyzing poly(MAOS) to its Na salt. Upon dissolving poly(MAOS) (0.010 g, 0.055 mmol) in DMSO (0.080 mL), 22 μL of 5 M NaOH was added dropwise to the reaction and allowed to stir for 7 h at room temperature. The cloudy solution was redissolved with 0.8 mL of filtered deionized water and allowed to stir overnight at room temperature. The reaction was then dialyzed against deionized water using Spectra/Por regenerated cellulose tubing (MWCO 3500 Da) for 3 days. The dialysate was subsequently lyophilized to give a white feathery powder.

General Procedure for Functionalized Poly(MAOS). Prior to each reaction, a 5 mL pear-shaped flask with a flea magnetic stir bar was fitted with a rubber septum and flame-dried while purging with N_2(g) until cooled to ambient temperature. Poly(MAOS) (0.025 g, 0.14 mmol) was added to the flask and dissolved with deoxygenated anhydrous DMSO (0.6 mL). Upon dissolution of the contents, 5 equiv of the NH_2-FG was dropwise added via a Hamilton syringe and immersed in a 75 °C thermostated oil bath. For the binary conjugations, the first amine was dropwise added via a Hamilton syringe, followed immediately by dropwise addition of the second amine via a separate Hamilton syringe. The flask was removed from the oil bath after 24 h and the septum removed. To remove excess solvent, the flask mouth was covered with Parafilm, punctured approximately seven times with a 21 gauge needle, and placed in vacuo for 4 h. The final product was isolated via dropwise addition into stirring acetone and filtered through a fine-fritted

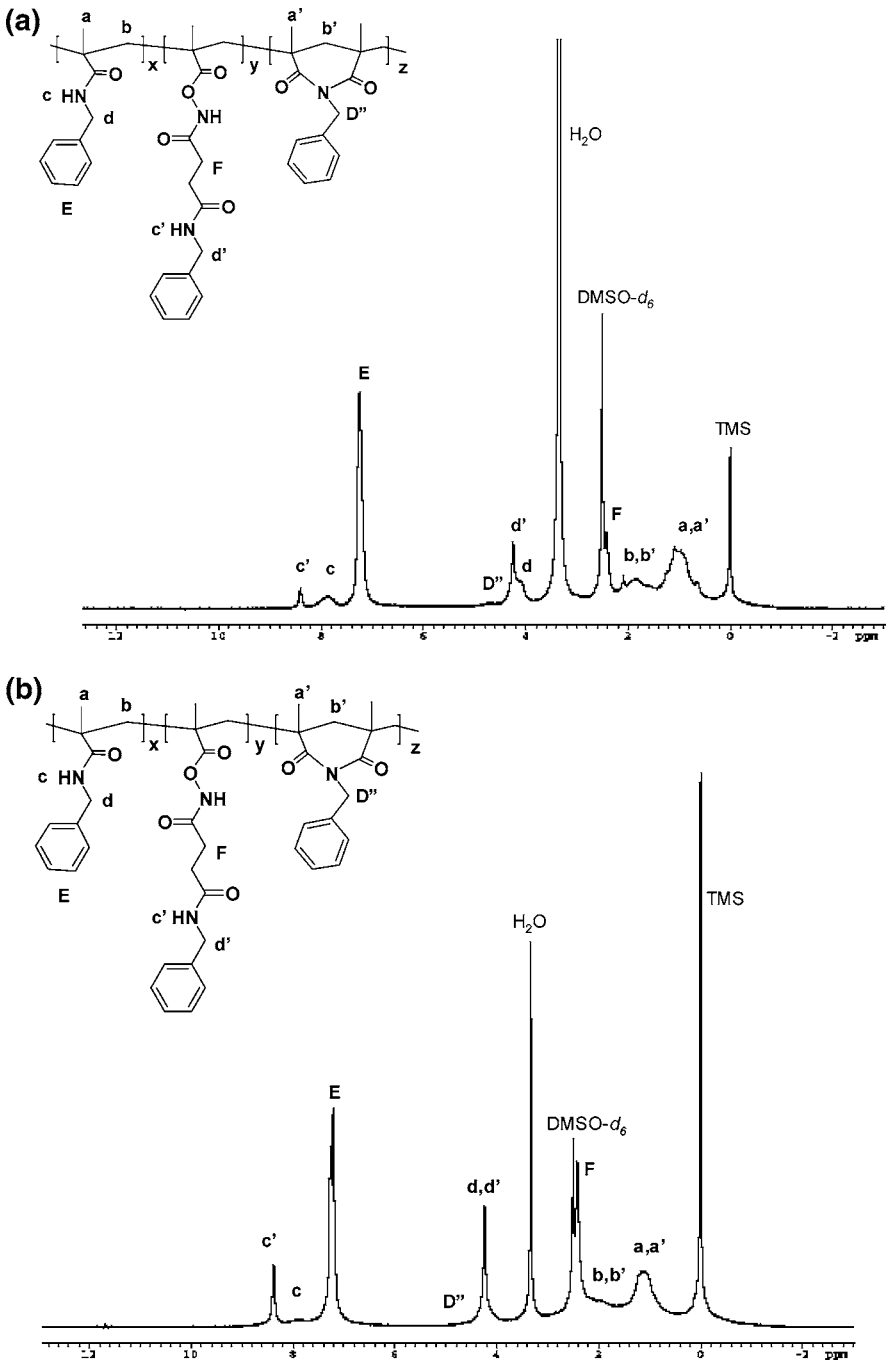


Figure 1. Representative ^{1}H NMR spectra of resultant functionalized polymer produced from (a) protocol 1 (2 equiv benzylamine, 50 °C, 5 h, 25 mg poly(MAOS)/150 μL DMSO) and (b) protocol 2 (2 equiv benzylamine, 25 °C, 16 h, 25 mg poly(MAOS)/150 μL DMSO). Both spectra provide evidence of a ring-opened side product (indicated by peaks F, d′, and c′) and glutarimide-bound side product (indicated by peak D′′). Peaks labeled in capital letters were used for quantification via signal integration of the respective pendant groups. Note: These spectra were obtained during our analysis but are consistent with the results of Devenish et al. and are shown here to clarify the method of quantification.

Buchner funnel and washed twice with acetone, twice with diethyl ether, and dried overnight in vacuo. N-Boc-protected functionalized polymers were isolated via dropwise addition into diethyl ether. The gummy precipitate was redissolved in methylene chloride and reprecipitated into diethyl ether as a white flaky powder. The powder was filtered through a fine-fritted Buchner funnel and immediately deprotected with 20 equiv of neat trifluoroacetic acid for 8 min. The final product was isolated via dropwise addition into stirring diethyl ether and filtered through a fine-fritted Buchner funnel. Polymers functionalized with water-solubilizing FGs, including all binary conjugations, were redissolved in, and dialyzed against, 0.1 N HCl in Spectra/Por regenerated cellulose tubing (MWCO 3500 Da) for 4 days. The dialysate was subsequently lyophilized to give a flaky solid.

Characterization. Benzylamine-functionalized poly (MAOS): ^{1}H NMR (DMSO-d_6) δ 0.89 (b, 3H, CH_3), 1.89 (b, 2H, CH_2), 7.86 (b, 1H, NH), 4.11 (b, 2H, CH_2), 7.26 (b, 5H, C_6H_5), 4.68 (b, 2H, glutarimide-CH_2). Butylamine-functionalized poly-(MAOS): ^{1}H NMR (DMSO-d_6) δ 0.89 (b, 3H, CH_3), 1.89 (b, 2H, CH_2), 7.29 (b, 1H, NH), 2.93 (b, 2H, CH_2), 1.25 (b, 4H, CH_2CH_2), 0.86 (b, 3H, CH_3). Hexylamine-functionalized poly-(MAOS): ^{1}H NMR (DMSO-d_6) δ 0.89 (b, 3H, CH_3), 1.89 (b, 2H, CH_2), 7.29 (b, 1H, NH), 2.93 (b, 2H, CH_2), 1.24 (b, 8H, $(CH_2)_4$), 0.86 (b, 3H, CH_3). Ethylenediamine-functionalized poly(MAOS): ^{1}H NMR (D_2O) δ 1.14 (b, 3H, CH_3), 1.84 (b,

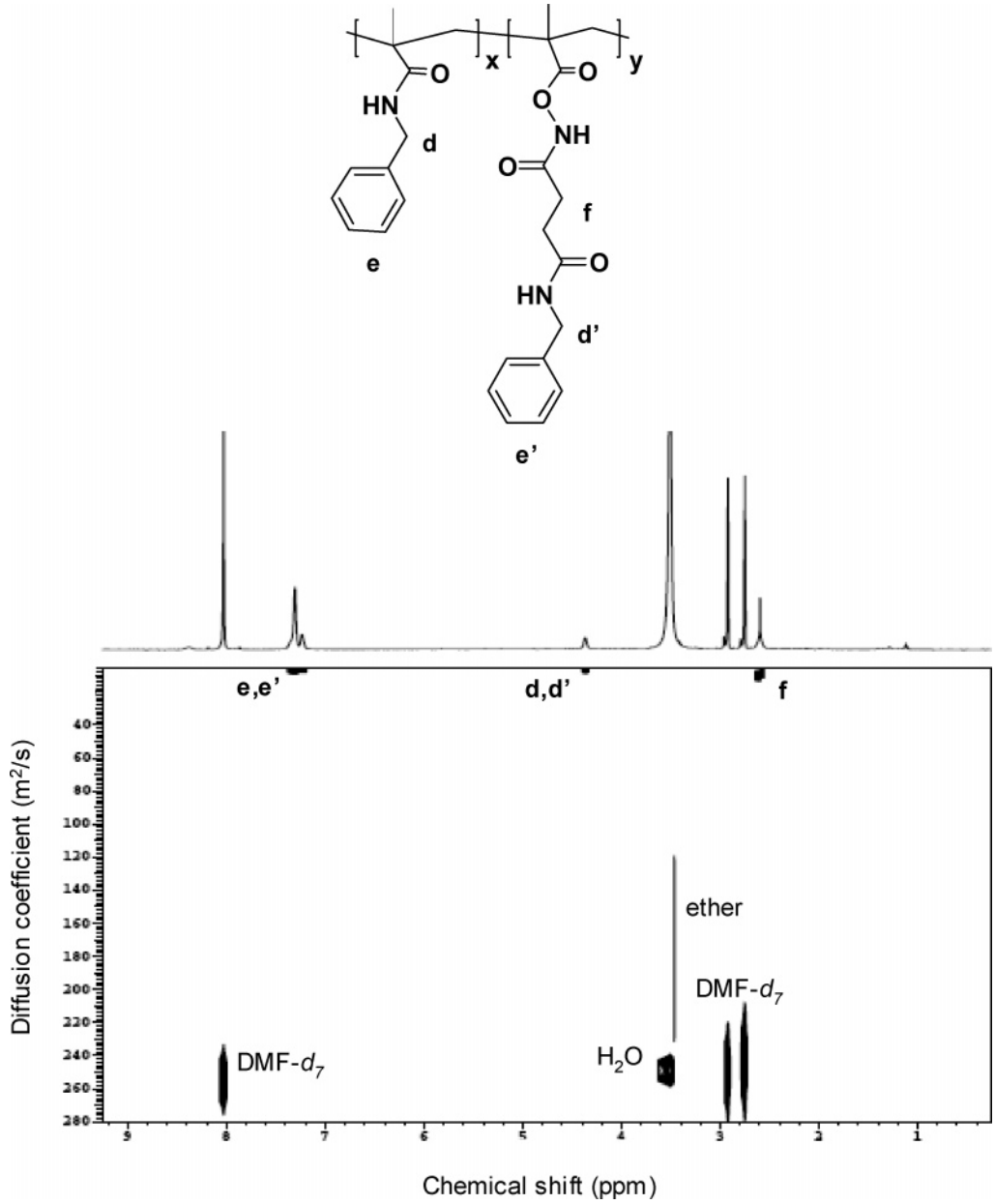


Figure 2. [1]H-detected DOSY spectrum of poly(MAOS) functionalized with benzylamine following protocol 2 (2 equiv benzylamine, 25 °C, 16 h, 25 mg poly(MAOS)/150 μL DMSO). Peak f, corresponding to the methylene protons of the ring-opened side product, has a similar diffusion coefficient as the rest of the polymer, providing evidence that the side reaction product is covalently bound to the polymer. Peaks corresponding to low molecular weight solvents are shown to diffuse faster as expected.

2H, CH_2), 3.43 (b, 2H, CH_2), 3.13 (b, 2H, CH_2). *N*-Methylethylenediamine-functionalized poly(MAOS): [1]H NMR (D_2O) δ 1.14 (b, 3H, CH_3), 1.84 (b, 2H, CH_2), 3.44 (b, 2H, CH_2), 3.17 (b, 2H, CH_2), 2.76 (b, 3H, CH_3). *N*,*N*-Dimethylethylenediamine-functionalized poly(MAOS): [1]H NMR (D_2O) δ 1.14 (b, 3H, CH_3), 1.84 (b, 2H, CH_2), 3.52 (b, 2H, CH_2), 3.28 (b, 2H, CH_2), 2.94 (b, 6H, CH_3CH_3), 4.05 (b, 2H, glutarimide-CH_2). 2-(Aminoethyl)trimethylammonium-functionalized poly(MAOS): [1]H NMR (D_2O) δ 1.14 (b, 3H, CH_3), 1.84 (b, 2H, CH_2), 3.61 (b, 2H, CH_2), 3.44 (b, 2H, CH_2), 3.20 (b, 6H, $(CH_3)_3$), 4.15 (b, 2H, glutarimide-CH_2). 1-Amino-2-propanol-functionalized poly(MAOS): [1]H NMR (D_2O) δ 1.14 (b, 3H, CH_3), 1.84 (b, 2H, CH_2), 3.14 (b, 2H, CH_2), 3.91 (b, 1H, CH), 1.17 (b, 3H, CH_3). Histamine-functionalized poly(MAOS): [1]H NMR (D_2O) δ 1.14 (b, 3H, CH_3), 1.84 (b, 2H, CH_2), 3.43 (b, 2H, CH_2), 2.93 (b, 2H, CH_2), 7.29 (b, 1H, CH), 8.61 (b, 1H, CH), 3.97 (b, 2H, glutarimide-CH_2).

Determination of Relative Percent Conjugation. For monofunctionalized conjugations, a sample calculation of the relative percent conjugation of each pendant group is demonstrated with benzylamine-conjugated poly(MAOS) as determined from the [1]H NMR spectra using the following equations:

$$\% Z = \frac{I_{4.68}}{2} \times 100$$

$$\% Y = \frac{I_{2.4}}{4} \times 100$$

$$\% X = 100 - \% Y - \% Z$$

where Z = glutarimide-bound conjugate, Y = ring-opened conjugate, X = desired amide-bound conjugate, $I_{4.68}$ = signal intensity of the two glutarimide methylene protons, and $I_{2.4}$ =

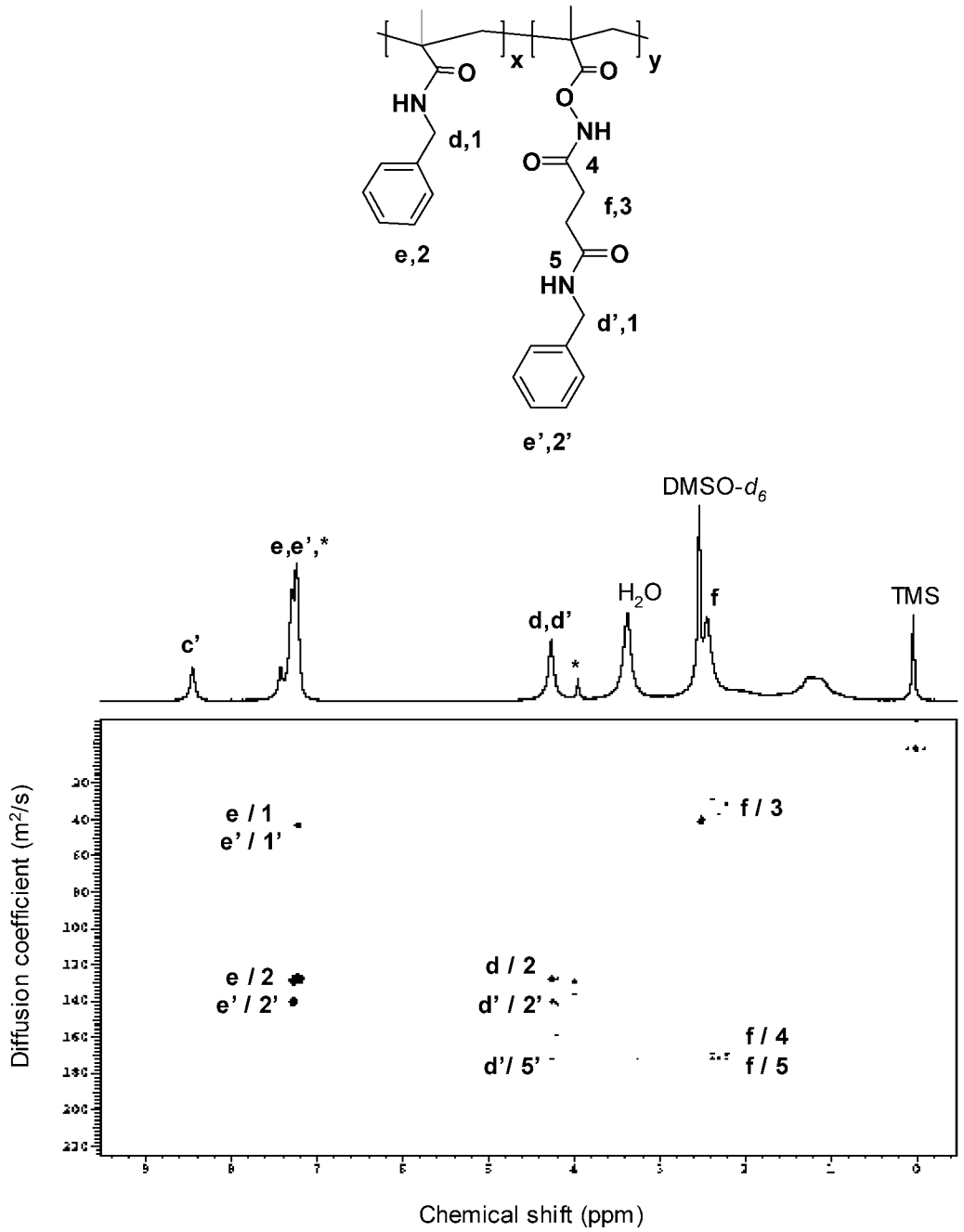


Figure 3. $^1H-^{13}C$ HMBC spectrum of poly(MAOS) functionalized with benzylamine following protocol 2 (2 equiv benzylamine, 25 °C, 16 h, 25 mg poly(MAOS)/150 μL DMSO). Peak f, corresponding to the ring-opened side product, is shown to correlate with carbonyl carbons, thus providing further evidence of the presence and identity of the ring-opened side product (correlations f/4 and f/5). Peaks labeled with letters correspond to protons, and numbers correspond to carbons. (* = excess benzylamine.)

signal intensity of the four ring-opened methylene protons. I_δ = signal intensity at δ ppm when $I_{7.26} = 5.0$.

For binary conjugations, the relative percent conjugation of each functional group is demonstrated with the *N*,*N*-dimethylethylenediamine(3N)/benzylamine conjugation as determined from the ^1H NMR spectra using the following equations:

$$\%\ \text{Benzylamine} = \frac{\frac{I_{7.26}}{5}}{1 + \frac{I_{7.26}}{5}} \times 100$$

$$\%\ 3N = 100 - \%\ \text{Benzylamine}$$

where $I_{7.26}$ = peak intensity of the five benzyl protons at 7.26 ppm when $I_{2.94} = 6.0$. $I_{2.94}$ = peak intensity of the six methyl protons of 3N.

Molecular Weight Characterization. Gel permeation chromatography was carried out using Waters Ultrahydrogel 250 and 500 columns in series coupled to UV (Waters 2487) and RI (Waters 2414) detectors. The mobile phase was phosphate buffered saline (pH = 7.4) at a flow rate of 0.8 mL/min at 30 °C. Calibration was performed using PMAA-Na standards (Polysciences, Inc., and Polymer Standards Service-USA, Inc.) in the range of 1.6 kg mol^{-1} to 110 kg mol^{-1}.

NMR Spectroscopy. All NMR analyses were performed with 7 mg of sample dissolved in 1 mL of deuterated solvent, and all spectra were processed using standard Varian software. One-

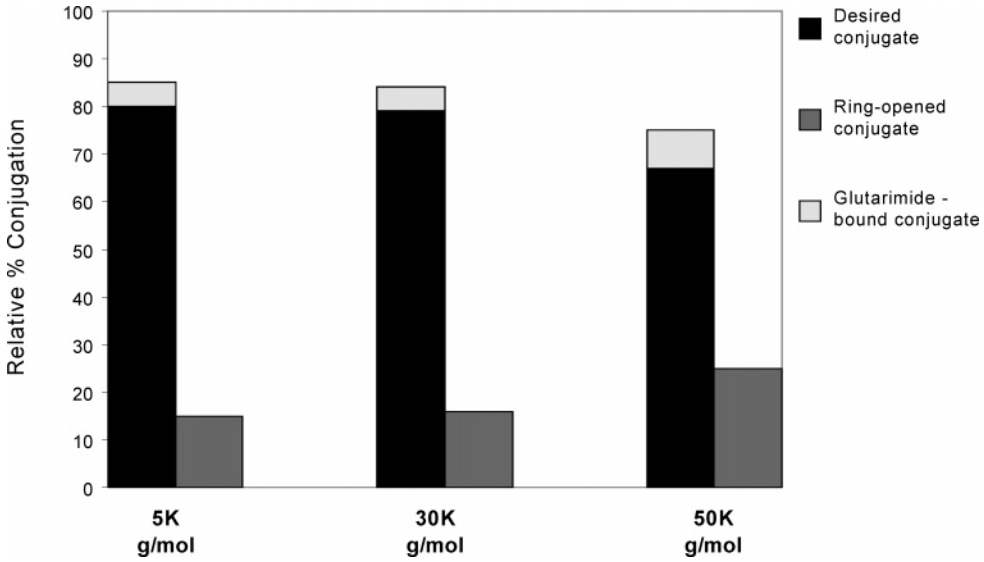


Figure 4. The effect of molecular weight on conjugation profile following protocol 1 (2 equiv benzylamine, 50 °C, 5 h, 25 mg poly(MAOS)/150 μL). Pendant distribution remained similar for all three molecular weights evaluated.

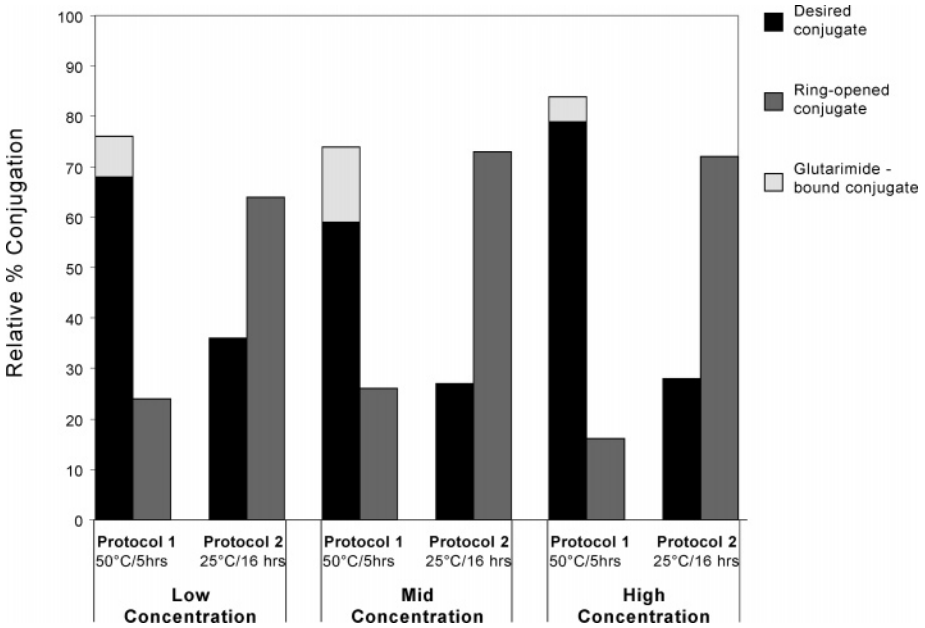
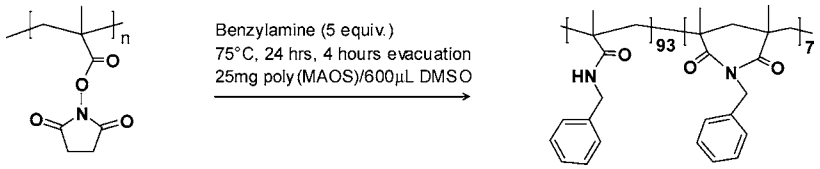


Figure 5. The effect of poly(MAOS) concentration on conjugation profile following two reported protocols. Each protocol results in similar pendant distributions regardless of precursor concentration. Low concn = 25 mg poly(MAOS)/1 mL DMSO; middle concn = 25 mg poly(MAOS)/600 μL DMSO; high concn = 25 mg poly(MAOS)/150 μL DMSO. 30 000 g/mol poly(MAOS) was used for all reactions. Reactions performed at low and mid concentrations included an additional 4 h in vacuo concentration of the reaction mixture prior to precipitation.

Scheme 4. Preparation of Functionalized Poly(MAOS) Free of Ring-Opened Side Product



dimensional ^{1}H NMR analyses were performed at room temperature on an Inova 600 MHz spectrometer with a proton observation frequency of 599.8 MHz. Chemical shifts were referenced relative to tetramethylsilane (0.0 ppm) when possible or the residual solvent signal: D_2O (4.8 ppm), DMSO-d_6 (2.5 ppm), or DMF-d_7 (2.75 ppm). Spectra were acquired with a 5.6 μs pulse width corresponding to a 45° flip angle, 3 s acquisition time, 4.8 kHz spectral width, 16 transients, and a 1 s recycle delay. An exponential multiplication of approximately 0.3 Hz was applied prior to Fourier transformation.

Proton homonuclear correlated spectroscopy (^{1}H−^{1}H COSY) was performed at 120 °C on an Inova 500 MHz spectrometer with a proton observation frequency of 499.9 MHz. Spectra were obtained using the gCOSY pulse program in the *VnmrJ* software with 1024 (t_2) × 512 (t_1) data points collected at two scans per t_1 increment. Spectral widths of 6.4 kHz in F2 and F1 were used along with a 0.1608 s acquisition time and a 1 s recycle delay time. Fourier transformation was done on a 2000 × 2000 data matrix with sine bell window function applied to F1 and F2.

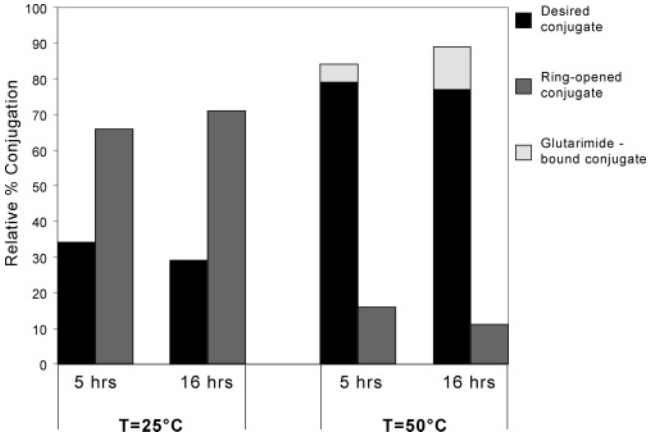
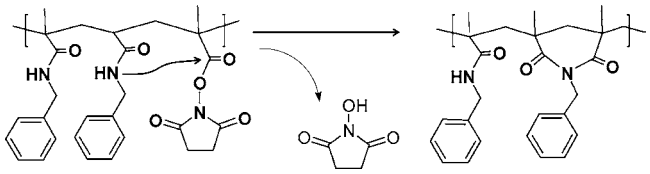


Figure 6. The effect of reaction time and temperature on conjugation profile. Increasing temperature leads to a greater proportion of the desired and glutarimide-bound conjugates and less of the ring-opened conjugate. 2 equiv benzylamine, 25 mg poly(MAOS)/150 μL DMSO, 30 000 g/mol poly(MAOS) was used for all reactions.

The long-range $^{1}H-^{13}C$ correlation spectroscopy (HMBC) was performed at room temperature on an Inova 600 MHz spectrometer with a proton frequency of 599.8 MHz. Spectra were obtained using the gHMBC pulse program in the *VnmrJ* software with 1024 (t_2) $\times$ 400 (t_1) data points collected at 28 scans per t_1 increment. Spectral widths of 7 kHz in F2 and 36.2 kHz in F1 were used along with a 0.1608 s acquisition time and a 1 s recycle delay. Fourier transformation was done on a 1000 (F2) $\times$ 4000 (F1) data matrix with Gaussian processing applied to F2 only.

Diffusion-Ordered NMR Spectroscopy (DOSY). ^{1}H detected DOSY experiments were performed at 22 °C on an Inova 600 MHz spectrometer equipped with a triple-resonance probe head capable of producing gradients in the *z* direction with strength of up to 70 G cm^{-1}. DOSY experiments were performed using a bipolar pulse pair double stimulated echo experiment. The gradient strength was logarithmically incremented in 16 steps from 2.3 up to 60 G cm^{-1}. Diffusion times and gradient pulse durations were optimized for each experiment in order to achieve a 90% decrease in the resonance intensity at the largest gradient amplitude. Diffusion times varied between 600 and 900 ms, and bipolar rectangular gradient pulses of 2 ms were employed. Data were analyzed using the *VnmrJ* software package.

Scheme 5. Proposed Route for N-Substituted Glutarimide Formation Presumably between Amide-Bound Conjugates and Neighboring Active Esters



RESULTS AND DISCUSSION

Our initial attempts to conjugate benzylamine to poly(MAOS) following two independent protocols resulted in two unexpected side reactions that accompanied the desired conjugation: (1) ring opening of the succinimide moiety and (2) glutarimide formation between presumably neighboring active esters. These side reactions were thoughtfully characterized and recently reported by Devenish et al. and shown again in Scheme 3 and Figure 1 for ease of reference (*11*).

To further verify that the ^{1}H NMR peak corresponding to the methylene protons of the ring-opened pendant group (peak F in Figure 1) was not just residual low molecular weight byproduct, we performed DOSY experiments to provide evidence of covalent linkage to the backbone (*14*). This pulsed field gradient NMR experiment yields a 2D spectrum with NMR chemical shifts on the horizontal axis and relative diffusion coefficients on the vertical axis. DOSY has been used for the analysis of polymer mixtures to determine the molecular weight (MW) of individual components (*15*). In this paper, DOSY was utilized to confirm that the ring-opened side reaction product was diffusing at a similar rate as the polymer and thus covalently bound to the polymer as evidenced in Figure 2. Additionally, HMBC experiments were performed to identify long-range (2−3 bonds) correlations between protons and neighboring carbons. Figure 3 reveals that the ring-opened methylene protons (peak f) are correlated to carbonyl carbons (carbons 4 and 5). Taken together, these data provide strong evidence that the ring-opened pendant group is indeed covalently bound to the polymer.

Using signal integration of the ^{1}H NMR spectra (Figure 1) to quantify the relative degree of conjugation of each pendant

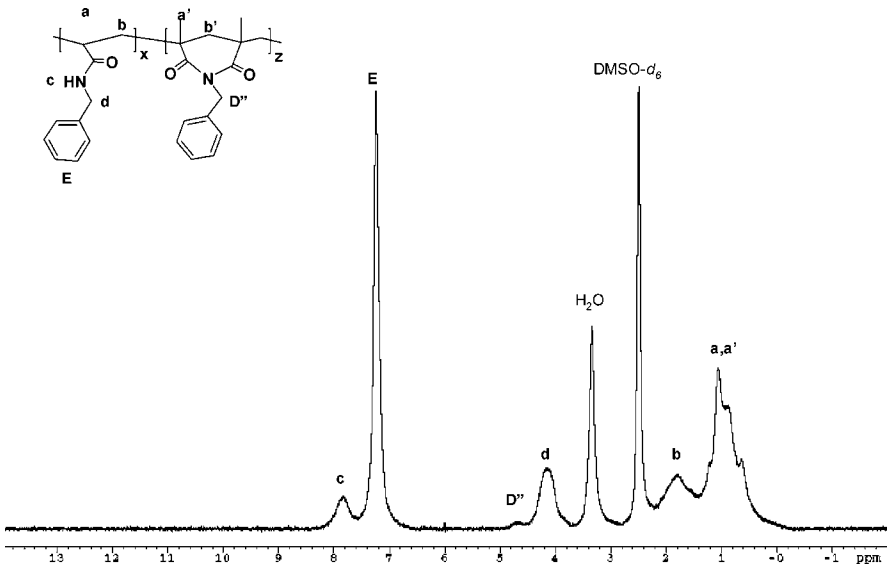
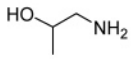
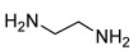
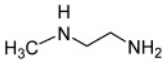
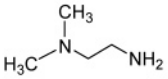
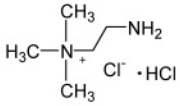
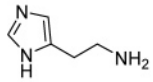


Figure 7. Representative ^{1}H NMR spectra of resultant functionalized polymer produced from the revised protocol (5 equiv benzylamine, 75 °C, 24 h, 4 h evacuation, 25 mg poly(MAOS)/600 μL DMSO) showing the absence of the ring-opened side product. Peaks labeled in capital letters were used for quantification via signal integration of respective pendant groups.

Table 1. Diverse Functional Groups Conjugated to Poly(MAOS)

Alkyl Functional Groups		
Name		Structure
butylamine		
hexylamine		
Water Solubilizing Functional Groups		
Name	Abbreviation	Structure
1-amino-2-propanol	1A2P	
ethylenediamine [a]	1N	
N-methylethylenediamine [a]	2N	
N,N-dimethylethylenediamine	3N	
2-(aminoethyl)-trimethylammonium chloride-HCl	4N	
histamine		

[a] derived from its N-Boc-protected precursor

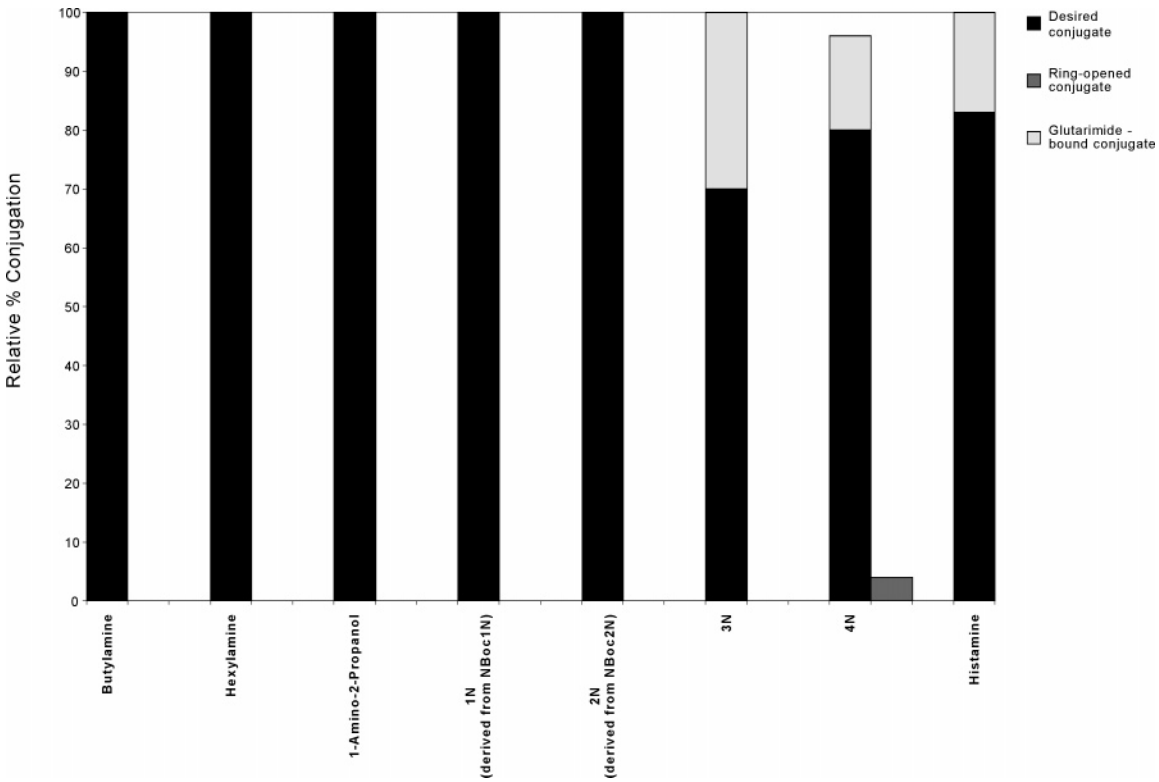


Figure 8. Conjugation profile of various NH_2-FGs to poly(MAOS). The revised protocol (5 equiv NH_2-FG, 75 °C, 24 h, 4 h evacuation, 25 mg poly(MAOS)/600 μL DMSO) results in the absence of any labile ring-opened conjugates for a diverse set of functional groups with only a minimal amount (~4%) remaining for the 4N conjugation. 50 000 g/mol poly(MAOS) was used for all reactions.

group, we observed a marked disparity in pendant distribution between the two protocols which essentially differ only by time and temperature. Protocol 1 produces approximately 75% of the desired conjugation (x), 20% ring-opened side product (y),

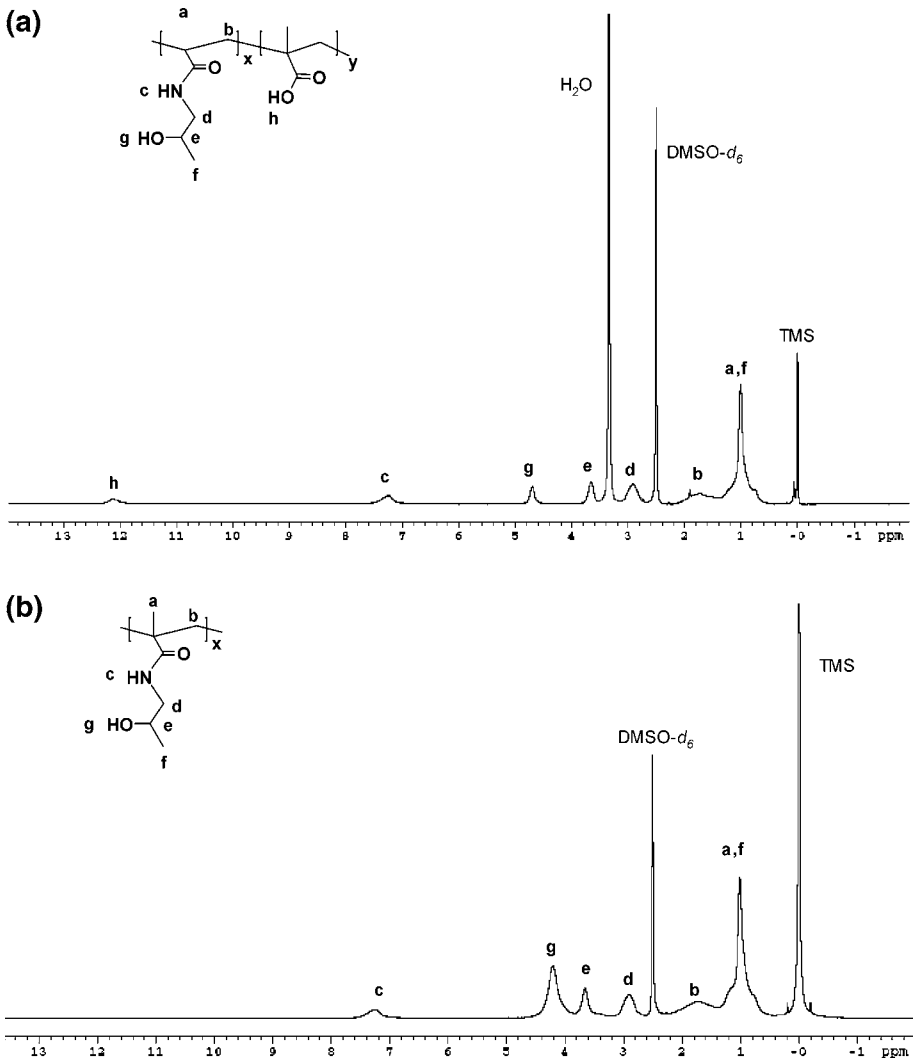


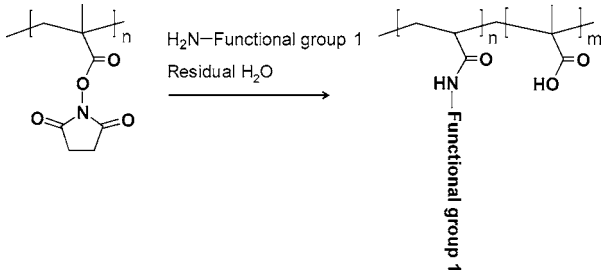
Figure 9. [1]H NMR spectra of poly(MAOS) functionalized with (a) 1A2P as received and (b) 1A2P dried over 3 Å molecular sieves. Note the absence of the hydroxyl peak in (b), thus indicating that premature hydrolysis of the activated ester to its carboxylic acid did not occur. Both conjugations followed the revised protocol (5 equiv 1-amino-2-propanol, 75 °C, 24 h, 4 h evacuation, 25 mg poly(MAOS)/600 μL DMSO). 50 000 g/mol poly(MAOS) was used for all reactions.

and 5% glutarimide-bound conjugate (z). Protocol 2 generates conjugations estimated to be about 30%, 70%, and 0%, respectively.

Monge and Haddleton's look at the feasibility of conjugating benzylamine to poly(MAOS) following protocol 1 resulted in a product whose published [1]H NMR spectrum appeared to be free of the ring-opened side product with only a small amount of the glutarimide-bound side product (*3*). By repeating their procedure following two alternative workup protocols—(1) direct purification of the reaction mixture through chromatography columns and (2) in vacuo concentration of the reaction mixture for 7 days at room temperature, followed by purification through chromatography columns—Devenish et al. reported a significant reduction of the ring-opened side product afforded by the latter workup protocol (*11*). This finding proposes the absence of any ring-opened side product in Monge and Haddleton's spectrum to be the result of longer than reported exposure to the benzylamine nucleophile upon in vacuo concentration of the reaction mixture prior to precipitation (*11*).

Incidentally, the benzylamine-conjugated polymer synthesized by Monge and Haddleton employed a low MW polymer precursor (~3000 g/mol). To examine whether MW might play a role in the resultant conjugation profile, we evaluated protocol 1 at three different MWs: 5000, 30 000, and 50 000 g/mol. We also explored the effects of several other reaction parameters,

Scheme 6. Potential Hydrolysis of NHS-Activated Ester to Methacrylic Acid from Residual Water May Occur during the Conjugation or Isolation Process[a]



[a] Due to proton exchange between the hydroxyl proton of the carboxylic acid and deuterium in D_2O, NMR analysis was performed in DMSO-d_6 to ensure the absence of a hydroxyl peak.

namely, poly(MAOS) concentration, reaction time, and reaction temperature, on the resultant conjugation profile. The data shown in Figures 4−6 suggest that the pendant distribution is independent of MW, precursor concentration, and reaction time, yet greatly dependent upon reaction temperature where an increase in temperature leads to a greater proportion of the desired and glutarimide-bound conjugates and less of the ring-opened conjugate. In contrast to the time dependency of the resultant conjugation profile reported by Devenish et al., our examination

did not reveal any appreciable reduction in the ring-opened side product at either temperature evaluated (25 °C and 50 °C). However, the reaction time range of 5 to 16 h evaluated in our study contrasts sharply with that of Devenish et al.'s 5 h to 7 days. As such, our time range may have been too narrow to produce any noticeable effects on conjugation profile and does not necessarily contradict the findings by Devenish et al.

Guided by the apparent time and temperature dependency of poly(MAOS) conjugation, we modified the previously reported protocols by increasing time, temperature, and equivalents of NH_2-FG while decreasing the precursor concentration. This revised protocol minimizes both labile ring-opened side products (as indicated by the disappearance of the 2.4, 4.3, and 8.4 ppm peaks) with a minimal amount of the glutarimide-bound conjugate (~7%) remaining. (Scheme 4, Figure 7) Because the glutarimide linkage is stable, its minimal presence is acceptable for polymer library synthesis. The revised protocol was further verified to be independent of MWs ranging from 5000 to 50 000 g/mol and reaction concentrations ranging from 25 mg poly(MAOS)/600 μL DMSO to 25 mg poly(MAOS)/mL DMSO (data not shown).

To address our initial goal of utilizing poly(MAOS) to synthesize molecularly diverse libraries, we extended the conjugation protocol to both single and binary conjugations of other alkyl (e.g., butylamine, hexylamine) and water-solubilizing functional groups (e.g., histamine, 1-amino-2-propanol) (Table 1).

No apparent side reaction conjugations resulted from butylamine and hexylamine functionalization presumably due to less steric hindrance relative to benzylamine functionalization. In the case of the water-solubilizing moieties, solvent solubility appears to be the predominant factor affecting conjugation dynamics. 3N and histamine, both soluble in DMSO in their free base state, render poly(MAOS) notably less soluble in DMSO upon functionalization, which we believe results in an increased presence of glutarimide-bound conjugation relative to the alkyl functional group conjugations. We hypothesize that, as conjugation proceeds, the decreasing solubility causes the semifunctionalized polymer precursor to assume a more tightly coiled and closed conformation. Consequently, accessibility of the primary amine to the activated esters becomes limited, leaving any remaining esters to form N-substituted glutarimides with neighboring amides (Scheme 5) (*11*).

To further support this hypothesis, we look to the 1A2P, 1N, and 2N conjugations. 1A2P, also miscible in DMSO in its primary amine reactant state, renders poly(MAOS) readily soluble in both water and DMSO upon conjugation. The proposed effect of the polymer coiling up upon conjugation would not be expected to occur to any appreciable degree which is supported by the absence of the glutarimide-indicating ^{1}H NMR peak. In the case of the 1N and 2N pendant groups, it is important to clarify that their pendant distributions shown in Figure 8 were quantified from polymers that were synthesized by functionalizing poly(MAOS) with their respective Boc-protected precursor and subsequently deprotected. Because 1N and 2N would render poly(MAOS) relatively insoluble in DMSO, one might expect their conjugation profiles to be like that of 3N conjugation. However, their conjugation dynamics were dictated by their Boc-protected precursor which results in a readily DMSO-soluble functionalized polymer. Thus, it is not surprising that their conjugation profiles are similar to those of other DMSO-soluble polymers, namely, the alkyl-functionalized polymers. Furthermore, direct conjugation of 2N (i.e., no Boc-protected precursor was used) resulted in a polymer whose NMR spectra yielded the expected desired and glutarimide-bound conjugates, presumably influenced by the hypothesized coiling-up effect, in addition to other side reaction products, presumably between the 2° amine and activated esters.

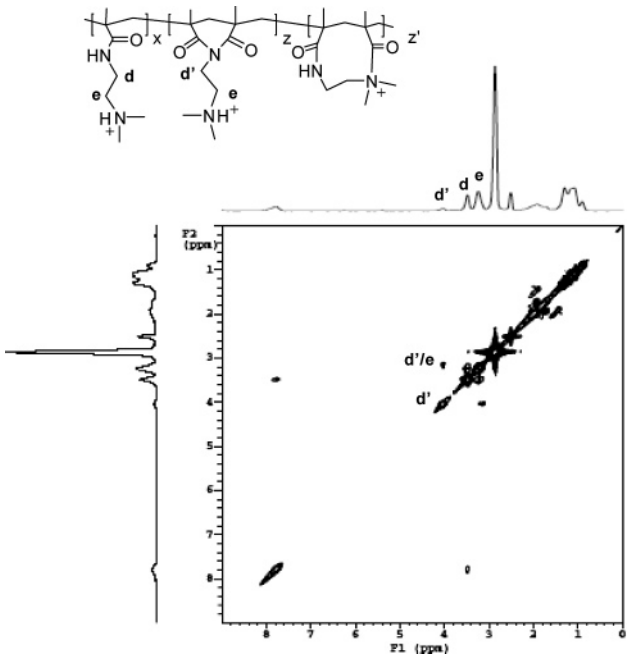


Figure 10. ^{1}H−^{1}H COSY of poly(MAOS) functionalized with *N*,*N*-dimethylethylenediamine (3N) following the revised protocol (5 equiv amine, 75 °C, 24 h, 4 h evacuation, 25 mg poly(MAOS)/600 μL DMSO. The correlation between the d′ and e protons provide evidence that side product z is formed as opposed to z′.

In addition to the solubility effects of the functionalized polymer, the solubility of the nucleophilic reactant also appears to influence conjugation behavior. 4N, insoluble in DMSO both in its salt reactant state and upon conjugating to poly(MAOS) resulted in a small, but persistent amount of the ring-opened pendant group remaining on the functionalized polymer. Efforts to eliminate all ring-opened conjugates by varying temperature and time conditions were ineffective and resulted in a similar pendant distribution at all conditions (See Supporting Information). Nevertheless, the conjugation behavior of 4N provides evidence that the solubility of both the nucleophilic reactant and the functionalized polymer plays a role in conjugation behavior.

Due to proton exchange between hydroxyl protons and deuterium in D_2O, ^{1}H NMR analysis was also performed for all water-soluble samples in DMSO-d_6 (*16*). This additional analysis was performed to ensure that premature hydrolysis of the activated ester to its carboxylic acid did not occur during either the conjugation reaction or isolation process (Scheme 6). The ^{1}H NMR spectra of the functionalized polymers in DMSO-d_6 were evaluated for the presence of a hydroxyl peak.

Polymers functionalized with 4N and 1N (i.e., NBoc-1N deprotected to the 1N form) were insoluble in DMSO and prevented this additional evaluation. To illustrate the analysis, Figure 9a shows the ^{1}H NMR spectrum of a polymer functionalized with 1A2P that was used as-received from the manufacturer. Residual water in the 1A2P may have contributed to premature hydrolysis of the activated esters during conjugation, resulting in the presence of a hydroxyl peak in the ^{1}H NMR spectrum (peak h in Figure 9a). Drying the 1A2P over 3 Å molecular sieves resulted in a functionalized polymer with no apparent hydrolysis as shown in Figure 9b. This analysis demonstrates the importance of using dried reagents with poly(MAOS) to ensure the desired products.

For functional groups with other nucleophilic atoms (e.g., 3° NH_2 on *N*,*N*-dimethylethylenediamine, imidazole on histamine), ^{1}H−^{1}H COSY was used to determine the presence of any

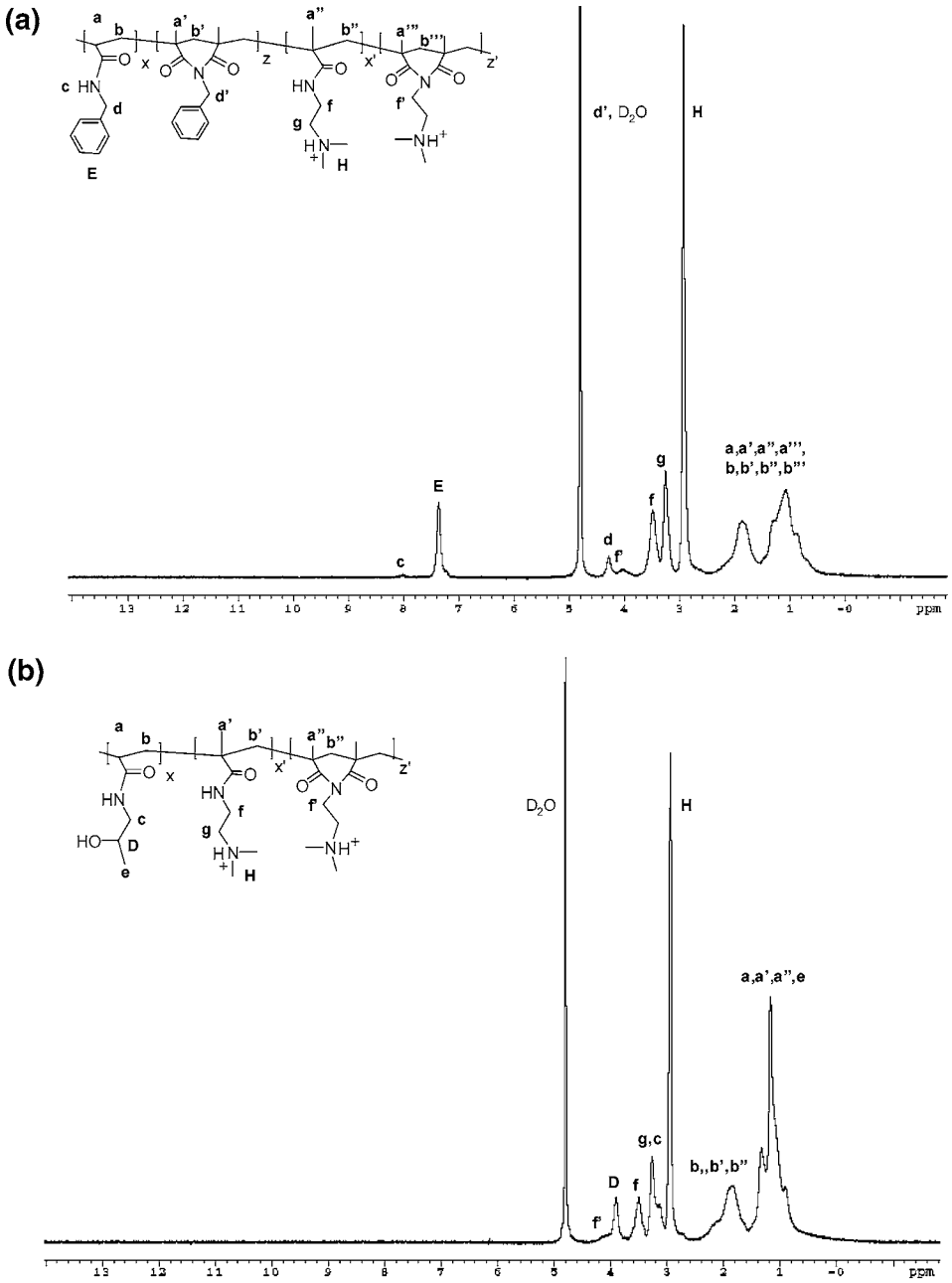


Figure 11. Representative ^{1}H NMR spectrum of poly(MAOS) functionalized with a binary mixture of (a) 2.5 equiv of *N*,*N*-dimethylethylenediamine (3N) and 2.5 equiv of benzylamine and (b) 2.5 equiv of *N*,*N*-dimethylethylenediamine (3N) and 2.5 equiv of 1-amino-2-propanol (1A2P). Both conjugations followed the revised protocol (5 total equiv of amine, 75 °C, 24 h, 4 h evacuation, 25 mg poly(MAOS)/600 μL DMSO). 50 000 g/mol poly(MAOS) was used for all reactions. Peaks labeled in capital letters were used for quantification via signal integration of respective pendant groups.

additional side reactions. Figure 10 exemplifies how we used this technique to determine the side reaction products for the 3N-conjugated polymer. The peak at 4.0 ppm (peak d′ in Figure 10) is shown to correlate with the 3.8 ppm peak (peak e in Figure 10), thus indicating the formation of side reaction z as opposed to side reaction z′.

Finally, we extended our protocol to binary conjugations using (1) benzylamine and 3N and (2) 1A2P and 3N as two independent model functional groups. Figure 11 shows the representative ^{1}H NMR spectra for both binary conjugations that were used to quantify the relative percent conjugations.

Figure 12 summarizes the conjugation profiles at various 3N equivalents for both binary conjugation experiments. The conjugation profile for the 3N/benzylamine system appears to follow a logarithmic trend compared to the linearly trending 3N/1A2P system. The difference in profiles is likely due to a dissimilarity in the degree of nucleophilicity between the conjugating pairs (i.e., 3N compared to benzylamine; 3N compared to 1A2P) (*17*). Further parametric studies, such as the effects of introducing each functional group at various times during the conjugation reaction, may be conducted to optimize the ligand distribution.

In conclusion, we have established a protocol that overcomes the side reactions that are associated with the NHS-activated polymer precursor, poly(MAOS). The revised protocol entails conjugating poly(MAOS) in the presence of a 5 mol excess of the primary amine-containing nucleophile for 24 h at 75 °C at a reaction concentration of 25 mg poly(MAOS)/600 μL DMSO. Using ^{1}H NMR and ^{1}H−^{1}H COSY analyses, we have quantified and characterized the resultant monofunctionalized polymer for a diverse range of functional groups. Moreover, we have also characterized the conjugation of two model binary systems: (1)

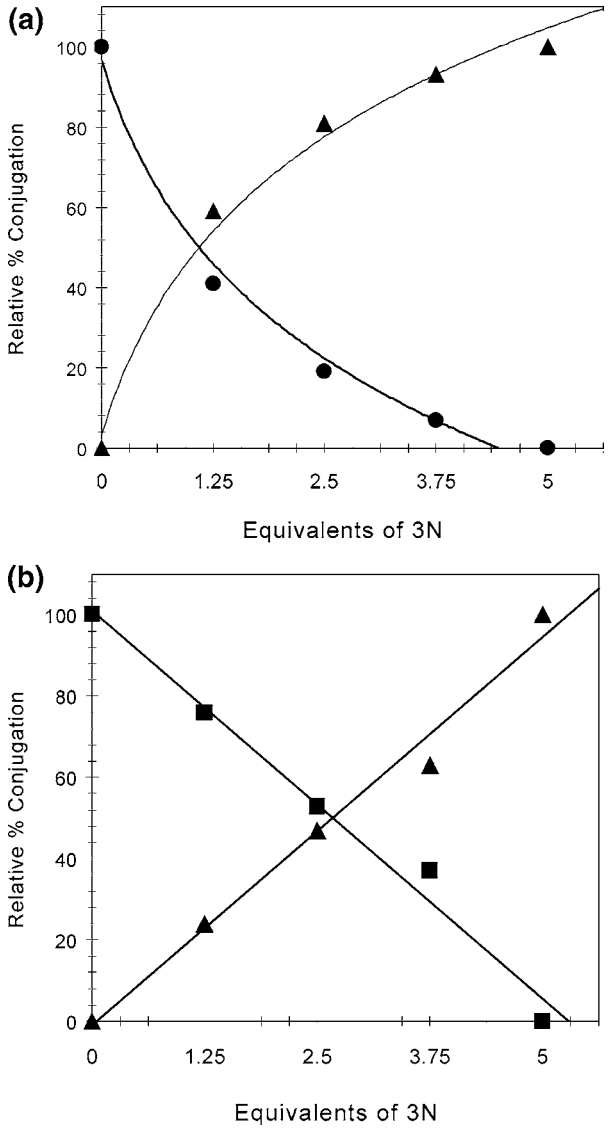


Figure 12. Conjugation profiles of (a) *N*,*N*-dimethylethylenediamine (3N) (▲)/benzylamine (●) binary mixtures (logarithmic fit; R^2 = 0.9893) and (b) 3N (▲) /1-amino-2-propanol (1A2P) (■) binary mixtures (linear fit; R^2 = 0.9844) at various feed equivalents of 3N. The conjugation profile of the 3N/1A2P mixtures resembles the theoretical conjugation and is likely due to a similar degree of nucleophilicity in contrast to the 3N/benzylamine conjugation profile.

N,*N*-dimethylethylenediamine (3N) and benzylamine and (2) *N*,*N*-dimethylethylenediamine (3N) and 1-amino-2-propanol (1A2P). Both systems were evaluated at various binary mixture compositions to demonstrate the compatibility of our protocol to conjugations comprising combinations of various functional groups.

An important and active area of research for which this work is applicable is the use of chemically and structurally diverse combinatorial libraries to develop polymeric biomaterials for drug and gene delivery systems. This area of research faces multiple challenges, including (1) a limited understanding of the biochemical and physical environment the materials must withstand, thereby making rational design an extremely difficult task, and (2) resource constraints associated with synthesizing and evaluating a large number of diverse compounds efficiently.

Combinatorial strategies offer a systematic approach to designing libraries of polymer candidates that encompass a broad range of properties. Subsequent screening of each polymer enables the identification of both "hits"—specific polymers that possess desirable properties—and trends that demonstrate how an incrementally varied feature affects the measured output (*1*). Hits are desired because they identify specific polymers that possess the desired biophysical and chemical properties (e.g., high drug/gene transfer efficiency, low cytotoxicity) as determined by screening assays. Equally important are the trends that are observed between polymers that share an incrementally varied feature. These trends may provide information about the functional effects of a particular structural feature and potentially shed light on the underlying biochemical and physical environment and mechanisms that govern the system. Ultimately, the information gained from these libraries can point to ways to improve the design of drug and gene delivery systems.

The protocol that we have established offers a facile method to use poly(MAOS) precursor as the molecular backbone for each compound in a combinatorial library where chemical and structural properties can be easily imparted and modified by conjugating different functional groups at various ratios to the precursor. Coupled with high throughput methods, these libraries can be feasibly synthesized and evaluated efficiently and reliably, posing the potential for these promising research tools to significantly change the way new materials are discovered.

ACKNOWLEDGMENT

The authors thank Dr. Ivan Keresztes for his expertise and assistance with the NMR work. This research was supported by a Biomedical Research Grant from the Whitaker Foundation.

Supporting Information Available: Additional conjugation profile. This material is available free of charge via the Internet at http://pubs.acs.org.

LITERATURE CITED

(1) Brocchini, S., James, K., Tangpasuthadol, V., and Kohn, J. (1997) A combinatorial approach for polymer design. *J. Am. Chem. Soc. 119*, 4553−4553.

(2) Brocchini, S., James, K., Tangpasuthadol, V., and Kohn, J. (1998) Structure−property correlations in a combinatorial library of degradable biomaterials. *J. Biomed. Mater. Res. 42*, 66−75.

(3) Monge, S., and Haddleton, D. (2004) Synthesis of precursors of poly(acryl amides) by copper mediated living radical polymerization in DMSO. *Eur. Polym. J. 40*, 37−45.

(4) Pedone, E., Li, X., Koseva, N., Alpar, O., and Brocchini, S. (2003) An information rich biomedical polymer library. *J. Mater. Chem. 13*, 2825−2837.

(5) Godwin, A., Hartenstein, M., Muller, A., and Brocchini, S. (2001) Narrow molecular weight distribution precursors for polymer-drug conjugates. *Angew. Chem. 113*, 614−617.

(6) Rickerby, J., Prabhakar, R., Patel, A., Knowles, J., and Brocchini, S. (2005) Water-soluble polyacetals derived from diphenols. *J. Controlled Release 101*, 21−34.

(7) Lynn, D., Anderson, D., Putnam, D., and Langer, R. (2001) Accelerated discovery of synthetic transfection vectors: parallel synthesis and screening of a degradable polymer library. *J. Am. Chem. Soc. 123*, 8155−8156.

(8) Anderson, D., Levenberg, S., and Langer, R. (2004) Nanoliter-scale synthesis of arrayed biomaterials and application to human embryonic stem cells. *Nat. Biotechnol. 22*, 863−866.

(9) Anderson, D., Peng, W., Akinc, A., Hossain, N., Kohn, A., Padera, R., Langer, R., and Sawicki, J. (2004) A polymer library approach to suicide gene therapy for cancer. *Proc. Natl. Acad. Sci. U.S.A. 101*, 16028−16033.

(10) Hermanson, G. (1996) *Bioconjugate Techniques*, Academic Press, New York.

(11) Devenish, S., Hill, J., Blunt, J., Morris, J., and Munro, M. (2006) Dual side-reactions limit the utility of a key polymer therapeutic precursor. *Tetrahedron Lett. 47*, 2875−2877.

(12) Ferruti, P., Bettelli, A., and Fere, A. (1972) High polymer of acrylic and methacrylic esters of N-hydroxysuccinimide as polyacrylamide and polymethacrylamide precursors. *Polymer 13*, 462−464.

(13) Perrier, S., Armes, S., Wang, X. S., Malet, F., and Haddleton, D. (2001) Copper(I)-mediated radical polymerization of methacrylates in aqueous solution. *J. Polym. Sci., Part A: Polym. Chem. 39,* 1696−1707.

(14) Morris, K., and Johnson, C. (1992) Diffusion-ordered two-dimensional nuclear magnetic resonance spectroscopy. *J. Am. Chem. Soc. 114,* 3139−3141.

(15) Viel, S., Capitani, D., Mannina, L., and Segre, A. (2003) Diffusion-ordered NMR spectroscopy: a versatile tool for the molecular weight determination of uncharged polysaccharides. *Biomacromolecules 4,* 1843−1847.

(16) Macomber, R. (1988) *NMR Spectroscopy: Basic Principles and Applications,* Harcourt Brace Jovanovich, Florida.

(17) Cline, G., and Hanna, S. (1987) The aminolysis of N-hydroxysuccinimide esters. A structure−reactivity study. *J. Am. Chem. Soc. 109,* 3087−3091.

BC0603790

TECHNICAL NOTES

An Improved Method for Covalently Conjugating Morpholino Oligomers to Antitumor Antibodies

Jiang He,[†] Guozheng Liu, Shuping Dou, Suresh Gupta, Mary Rusckowski, and Donald Hnatowich*

Division of Nuclear Medicine, Department of Radiology, University of Massachusetts Medical School, 55 Lake Avenue North, Worcester, Massachusetts 01655. Received July 10, 2006; Revised Manuscript Received December 13, 2006

Whether for conventional pretargeting, amplification pretargeting, or affinity enhancement pretargeting, it will be necessary to conjugate an antitumor antibody as the first injectate. This laboratory is investigating phosphorodiamidate morpholinos (MORFs) for pretargeting, and accordingly we are examining methods of attaching MORFs to antitumor antibodies that provide at least one group per molecule (gpm) without adversely influencing antibody properties. The aim of this investigation was to evaluate the commercial Hydralink for the conjugation of the anti-CEA MN14 antibody with an 18 mer amine-derivatized MORF. The conjugation was approached in both directions by first reacting MN14 with the NHS derivatives of 4-hydrozinonicotinate acetone hydrazone (SANH) or 4-formylbenzoate (SFB) and then combining with MORF that was previously reacted with SFB or SANH to yield MN14(SANH)−MORF and MN14(SFB)−MORF respectively. The storage stability, immunoreactive fraction, and the biodistribution in normal mice were compared for both conjugates. Thereafter, MN14(SANH)−MORF was used in a pretargeting study in tumored nude mice, and the results were compared to that obtained historically with MN14−MORF prepared by carbodiimide (EDC) coupling. Both new methods of conjugation provided between 1 and 2 gpm compared to 0.2 achieved previously by EDC. Furthermore, by repeat SE HPLC with and without CEA, both showed an unimpaired immunoreactive fraction. MN14(SANH)−MORF tolerated long-term storage best. More importantly, when labeled by hybridization with ^{99m}Tc-labeled complementary MORF (^{99m}Tc-cMORF), the biodistribution of MN14(SANH)−MORF was more favorable than that of MN14(SFB)−MORF in normal mice with lower liver (5.7 vs 9.4 %ID/g at 18 h) and spleen (3.5 vs 8.4 %ID/g) accumulations and higher blood levels (4.8 vs 3.4 %ID/g). Accordingly, only MN14(SANH)−MORF was used in a pretargeting study in tumored mice. When targeted with ^{99m}Tc-cMORF and at 2 days postinjection of antibody−MORF, the results obtained with 6 μg of antibody prepared in this way were essentially identical to that obtained previously with 30 μg of antibody prepared via EDC. Hydralink was used successfully to conjugate MORF to MN14 at higher gpm than that achieved earlier and without an obvious compromise of properties. Using MN14(SANH)−MORF, the influence of the higher gpm on pretargeting permitted lowering the dosages of MN14 administered and may permit administering higher levels of radioactivity in connection with therapy.

INTRODUCTION

Pretargeting has become an important approach to improve tumor targeting. In pretargeting, the long-circulating antitumor antibody conjugate is first administered and allowed time for specific localization in tumor and clearance from blood and other normal tissues before the injection of a short-circulating small radiolabeled effector. This technique has been shown to provide tumor targeting comparable to that of conventional direct targeting with directly labeled antibody but much earlier at 1−3 h post-administration of radiolabeled effector and, moreover, to dramatically improve the target/nontarget ratio. The three approaches to pretargeting that have been reported thus far use biotin−(strep)avidin, bispecific antibodies, or oligonucleotides. Regardless of the approach, the high affinity and binding specificity of a tumor-associated antibody is employed as the first injectate (*1*−*5*). The effector molecule is usually monovalent, but bivalent effectors can show greatly enhanced residence time in tumor (*6*) by what has been called affinity enhancement (*3*, *7*, *8*).

This laboratory has recently begun exploring DNA and other oligomers, in particular phosphorodiamidate morpholios (MORFs), for amplification pretargeting (*9*, *10*), conventional pretargeting (*4*, *5*) and, most recently, affinity enhancement pretargeting (*11*). Our preliminary in vitro studies of affinity enhancement using surface plasmon resonance has shown that the target density is an important determinant of affinity enhancement pretargeting (*12*). One method of achieving the required higher density in MORF pretargeting is to increase the number of MORFs attached to each antibody. It therefore has become important to develop methods of conjugating antitumor antibodies with several MORFs per molecule and without compromising antibody immunoreactivity or adversely influencing antibody pharmacokinetics. We report herein on the use of commercially available reagents (Hydralink) for the conjugation of the antitumor antibody MN14 with MORF (Scheme 1).

MATERIALS AND METHODS

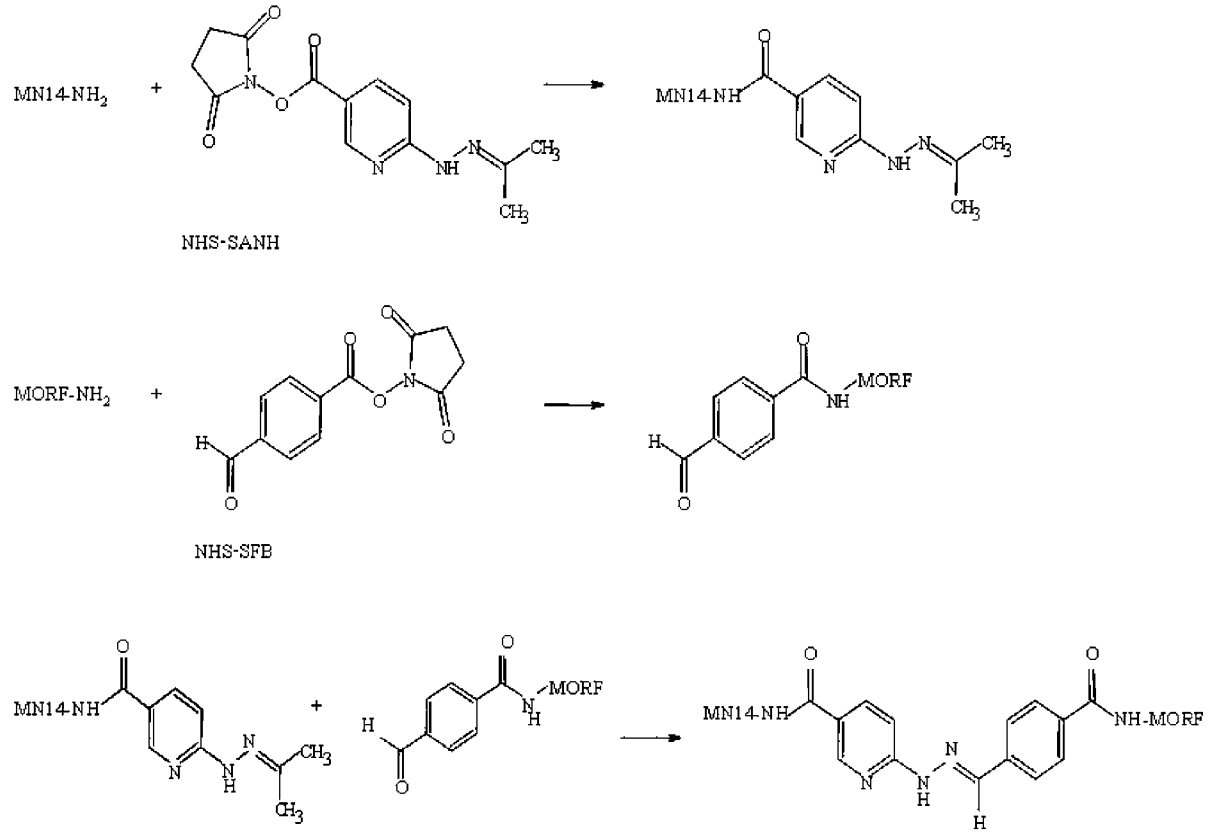
Reagents. All MORFs were purchased from Gene Tools (Philomath, OR) with an amine group on the 3′ equivalent

* Corresponding author. Tel: 1-508-856-4256; fax: 1-508-856-4572; e-mail: Donald.hnatowich@umassmed.edu.

[†] Present address: Department of Radiology, University of California San Francisco, San Francisco, CA 94143. Jiang.he@radiology.ucsf.edu.

10.1021/bc060208v CCC: $37.00 © 2007 American Chemical Society
Published on Web 03/27/2007

Scheme 1. Hydralink Approach to Conjugation of MN14 with MORF



terminus for conjugation with either SANH/SFB or *S*-acetyl mercaptoacetyltriglycine (MAG3). Each MORF was analyzed by the manufacturer using size-exclusion high-performance liquid chromatography (HPLC) and MALDI-TOF MS to ensure quality. The base sequences and molecular weights of the 18 mer MORF and its complement (cMORF) are shown below: MORF: 5′-TCTTCTACTTCACAACTA-linker-amine, 6164 Da cMORF: 5′-TAGTTGTGAAGTAGAAGA-linker-amine, 6422 Da

The linker is $C(O)CH_2CH_2NH_2$ for primary amine modification. A high-affinity murine anti-CEA antibody (MN14, IgG 1 subtype, MW 160 kDa) was a gift from Immunomedics (Morris Plains, NJ). The CEA antigen from human liver metastasis of a primary colon carcinoma (180 kDa) was purchased from Scripps Laboratories (San Diego, CA). NHS-MAG3 was synthesized in house (*13*) and the structure confirmed by elemental analysis, proton NMR, and mass spectroscopy. The PD-10 column was purchased from Amersham Pharmacia Biotech (Piscataway, NJ). The ^{99m}Tc-pertechnetate was eluted from a ^{99}Mo-^{99m}Tc generator (Bristol-Myers Squibb Medical Imaging Inc., North Billerica, MA). A commercially available conjugation kit (Hydralink) consisting of acetone 5-(succinimidyloxycarbonyl)-pyridine-2-ylhydrazone (NHS-SANH), succinimidyl 4-formylbenzoate (NHS-SFB), and other reagents were purchased from Solulink (San Diego, CA). All other chemicals were reagent grade and were used without purification.

High Performance Liquid Chromatography. Size-exclusion HPLC analysis was performed on a Superose-12 HR10/30 column with an optimal separation range between 1×10^3 and 3×10^5 Da (Amersham Pharmacia Biotech, Piscataway, NJ) using 0.10 M pH 7.2 phosphate buffer as eluant at a flow rate of 0.6 mL/min. The HPLC was equipped with both an in-line radioactivity detector and a Waters 2487 dual wavelength absorbance detector (Milford, MA).

MN14−MORF Conjugation, Evaluation, and Radiolabeling. For the preparation of MN14(SANH)−MORF, typically the MN14 antibody was incubated with a 5- to 10-fold molar excess of NHS-SANH in 100 mM PBS (pH = 8.0) for 1 h at room temperature. The reaction mixture was purified on a PD-10 column using conjugation buffer (pH 5, 100 mM MES, 150 mM NaCl) as eluant. At the same time, the MORF was incubated with a 50-fold molar excess of NHS-SFB in 100 mM PBS (pH = 8.0), and after 1 h at room temperature, this reaction mixture was also purified on a PD-10 column with the same conjugation buffer. The degree of modification of both the SANH (hydrazine)-modified MN14 (i.e., MN14(SANH)) and SFB (aldehyde)-modified MORF (i.e., MORF(SFB)) were determined as described below. Thereafter, conjugation was achieved simply by mixing solutions of modified antibody with a 5-fold molar excess of modified MORF in conjugation buffer (pH = 5.0) overnight. The product was purified by dialysis against 100 mM PBS buffer (pH = 7.2) at 4 °C for 72 h and the purity of MN14−MORF established by HPLC. A similar procedure was applied to the conjugation and evaluation of MN14(SFB)−MORF.

MN14−MORF Immunoreactivity. A measurement of immunoreactivity (i.e., immunoreactive fraction) of the antibody conjugated by both methods was obtained by an HPLC shift assay of the antibody, radiolabeled by addition of trace ^{99m}Tc-cMORF, before and after the addition of a 3-fold molar excess of CEA. In this assay, immunoreactive antibody will bind to the excess CEA and shift to shorter elution times

Quantitation of Hydrazine and Aldehyde Modification and MN14 Conjugation. Originally, the intermediate incorporation of hydrazine or aldehyde on MN14 and the incorporation of MORF on MN14 was quantitated according to the manufacture's recommendations. In the course of these measurements, a modified and simpler approach to quantitation was developed as described below.

Alternative Quantitation of Hydrazine and Aldehyde Modification of MN14. To the 10 μL MN14 and NHS-SANH

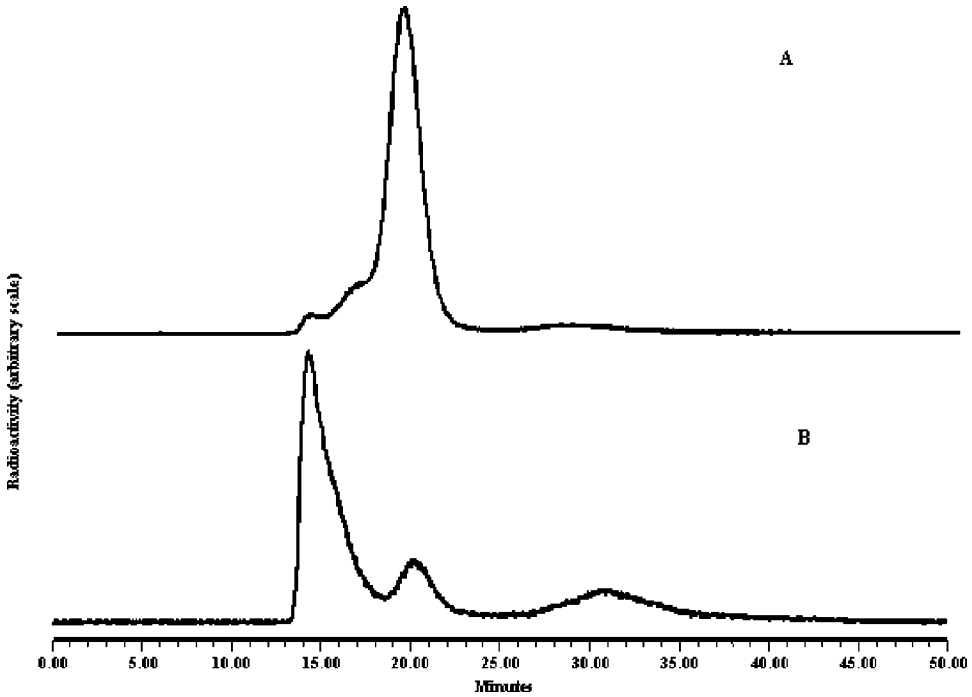


Figure 1. Size exclusion HPLC radiochromatograms of MN14(SANH)−MORF before (panel A) and after (panel B) the addition of CEA.

reaction mixture was added *p*-nitrobenzaldehyde in 200 μL of conjugation buffer at a 10-fold molar excess and the solution incubated at room temperature for 2 h. The free and antibody-bound hydrazone was then analyzed by size exclusion HPLC. The average number of SANH groups on MN14 (gpm) was then calculated from the initial molar ratio of SANH to MN14 corrected by the molar ratio of the MN14-bound SANH peak to that of free SANH quantitated by UV absorbance at 380 nm. The concentration of purified MN14(SANH) was taken as the initial MN14 concentration times the dilution factor of hydrazone concentration before and after purification and assuming the same loss of MN14 and MN14(SANH) during purification. The quantitation of the aldehyde modification of MN14 was achieved in a similar fashion but with corresponding solution of 0.50 mM 2-hydrazinopyridine (2-HP) in 100 mM MES, pH 4.7.

Quantitation of MORF Modification of MN14. Complete charcterization of the antibody−MORF conjugate requires measuring both the MORF gpm attached and the antibody concentration. In addition, for pretargeting, the "accessible" MORF gpm must also be measured since the number of MORF attached may not be equal to the number accessible. In this investigation, a method using UV absorbance at 265 and 280 nm was employed to measure the average number of attached groups (*16*).

Using a scanning UV spectrophotometer (U-2000, Hitachi Instruments, Inc, Danbury, CT), the maximum absorbance of MN14 was found to be at 280 nm and that of MORF at 265 nm (*16*). However since the SANH or SFB groups on MORF-conjugated MN14 contributes to UV absorbance, the UV absorbance of SANH and SFB was also measured by subtracting the absorbance of NHS from NHS-SANH or NHS-SFB at both wavelengths. Thus concentration curves were constructed by measuring the absorbance at different concentrations of native MN14, MORF, SANH, and SFB at both 280 and 265 nm. Under the assumption that the absorbance coefficients of MN14 and MORF do not change after conjugation, it was possible to plot the ratio of MN14−MORFs absorbance at 265 and 280 nm vs apparent gpm (i.e., molar ratio) of MORFs to MN14. This plot was also in agreement with the calculation based on derived equations from the relevant molar extinctions coefficients at 280 and 265 nm and then used to determine the MORF gpm "attached" in the conjugation solution by the absorbance ratio of 265 nm/280 nm of the MN14−MORF peak by size exclusion HPLC. The number of "accessible" groups was then determined by a size exclusion HPLC shift assay in which trace radiolabeled cMORF is added to the conjugation reaction mixture before purification.

Radiolabeling of cMORF. As previously described, cMORFs were conjugated with NHS-MAG_3 via the 3′ derivatized amine (*5*). Briefly, 1 mg of cMORF in 200 μL of 0.2 M pH 8.0 HEPES buffer was added to a vial containing 1.7−2.0 mg of *S*-acetyl NHS-MAG_3. The vial was vortexed immediately and incubated for 1 h at room temperature. The cMORF was then purified on a 0.7 × 20 cm P4 column with 0.25 M pH 5.2 NH_4OAc buffer as eluant. The peak fractions were pooled and were then adjusted from pH 5.2 to pH 7.6 with a pH 9.2 buffer (0.5 M Na_2HCO_3, 0.25 M NH_4OAc, 0.175 M NH_3). After heating for 20 min, the solution was again purified over P4 using the pH 5.2 NH_4OAc buffer as eluant. The peak fractions were again pooled as before and the concentration quantitated by UV absorbance at 265 nm (*5*). The ^{99m}Tc-cMORF-MAG_3 was prepared and analyzed as described previously (*5*). Radiolabeling was achieved by first adding ^{99m}Tc-pertechnetate generator eluant to a solution of 25 mL of cMORF-MAG_3 (concentrations 0.2−0.4 μg/μL), 25 μL of 0.25 mol/L ammonium acetate buffer, pH 5.2, 10 μL of pH 9.2 tartrate solution (50 μg sodium tartrate dehydrate per μL), and 4 μL of stannous chloride solution (1 μg stannous chloride dihydrate and 1 μg sodium ascorbate per μL in 10 mmol/L HCl), followed by heating in boiling water for 20 min. The product was purified on a P-4 column with 0.1mol/L phosphate buffer, pH 7.2, as eluant.

Animal Studies. All animal studies were performed with the approval of the UMMS Institutional Animal Care and Use Committee. The biodistribution of both MN14−MORFs radiolabled with trace ^{99m}Tc complementary MORF were evaluated in normal CD-1 mice (Charles River, Wilmington, MA). Each mouse was injected with 10 μg of MN14−MORF in 200 μL with 3.70 MBq (100 μCi). After sacrifice either at 1 h or 18 h postinjection, blood and selected organs were removed, weighed,

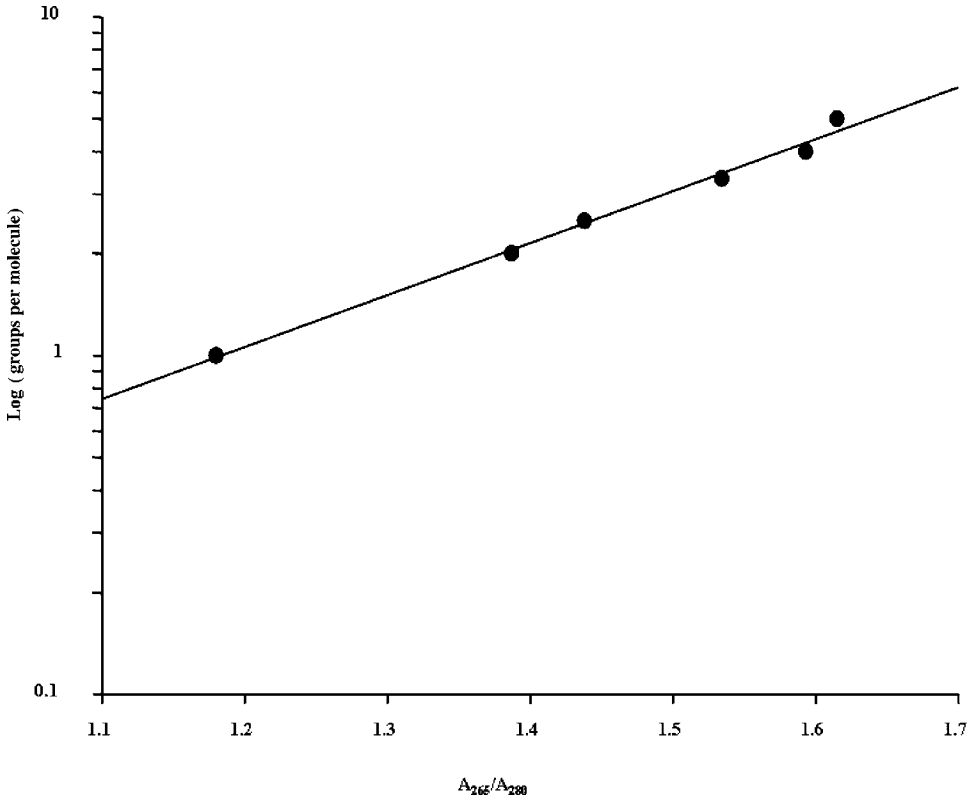


Figure 2. A standard curve for determination of MORF groups on MN14.

Table 1. Biodistribution of Both ^{99m}Tc-cMORF-MN14(SAHN)−MORF and ^{99m}Tc-cMORF-MN14(SFB)−MORF Conjugates in Normal Mice at 1 and 18 h Postinjection[a]

	MN14(SANH)−MORF				MN14(SFB)−MORF			
	1 h		18 h		1 h		18 h	
organs	mean	SD	mean	SD	mean	SD	mean	SD
				%ID/g				
liver	6.86	1.67	5.67	0.57	8.40	1.23	9.36	0.96
heart	2.65	0.29	1.39	0.45	3.13	0.53	1.71	0.19
kidney	4.65	0.46	2.02	0.64	4.97	0.59	2.50	0.19
lung	3.89	0.98	1.80	0.69	4.63	1.17	1.79	0.41
spleen	2.98	0.57	3.54	0.44	4.90	1.45	8.42	1.52
muscle	0.32	0.01	0.47	0.14	0.33	0.07	0.32	0.04
blood	10.8	0.59	4.76	1.46	15.2	1.93	3.39	0.96
				%ID/organ				
liver	14.5	3.74	13.5	2.41	18.1	3.62	23.4	2.40
heart	0.49	0.06	0.26	0.07	0.51	0.10	0.33	0.05
kidney	3.03	0.45	1.56	0.32	3.17	0.30	1.84	0.22
lung	0.96	0.22	0.42	0.17	1.04	0.19	0.41	0.08
spleen	0.38	0.04	0.43	0.11	0.64	0.08	1.25	0.30
stomach	0.56	0.07	0.30	0.04	0.49	0.07	0.52	0.14
sm. int.	1.95	0.12	1.30	0.17	2.03	0.36	2.33	0.50
lg. int.	0.49	0.04	0.50	0.11	0.37	0.14	0.82	0.17
muscle	4.79	0.39	7.43	2.33	5.01	1.01	5.37	0.88
blood	28.3	3.11	12.9	3.77	40.6	2.96	10.1	2.99
whole body	63.5	1.34	51.3	1.09	74.8	2.90	59.9	0.89

[a] Results presented as %ID/g and %ID/organ with one SD of the mean. $N = 4$.

and counted in a NaI(Tl) well counter (Cobra II, Packard Instrument Company, CT) along with a standard of the injectate. Blood and muscle were assumed to constitute 7% and 40% of the body weight, respectively. In the case of tumored mice, the tumored thigh was also excised for counting but after the skin, and as much as possible of the muscle and bone had been removed. Radioactivity remaining in the carcass was measured in a dose calibrator. Summation of radioactivity in all organs sampled and in the remaining carcass was taken as the whole-body radioactivity.

Pretargeting Comparison. Pretargeting studies were conducted in Swiss NIH nude mice (Taconic Farms, Germantown, NY) bearing LS174T tumors of 0.6−0.8 g. Each animal received either 6 or 30 μg of MN14(SANH)−MORF 2 days before the administration of 0.2 μg or 1.0 μg, respectively, of ^{99m}Tc-cMORF with 3.70 MBq (100 μCi). Thus, the ratio of pretargeting antibody to effector was kept constant. The animals were sacrificed at 3 h postinjection of the radioactivity. The results are compared with those obtained in this laboratory earlier in identical studies using MN14−MORF conjugate via the EDC approach (*5*).

RESULTS

Preparation and Characterization of MN14−MORF Conjugates. The average number of SANH and SFB groups per antibody was between 2−4 for both while the average number

Table 2. Biodistribution by Pretargeting at 3 h of Either 0.2 or 1.0 μg of ^{99m}Tc-cMORF Administered to Tumored Mice Having Received 2 d Earlier the MN14(SANH)−MORF Conjugate at 6 or 30 μg, Respectively

	30 μg MN14 (1.0 μg cMORF)		6 μg MN14 (0.2 μg cMORF)	
organs	mean	SD	mean	SD
	%ID/g			
Liver	1.93	0.24	1.94	0.17
Heart	0.80	0.11	0.61	0.02
Kidney	8.79	1.38	10.2	1.19
Lung	1.01	0.17	0.86	0.08
Spleen	1.13	0.18	1.01	0.08
Muscle	0.36	0.12	0.17	0.02
Tumor	3.96	0.70	3.00	0.72
Blood	1.98	0.24	1.37	0.23
	%ID/organ			
liver	3.23	0.11	2.92	0.17
heart	0.12	0.01	0.08	0.01
kidney	5.51	1.00	5.63	0.74
lung	0.17	0.04	0.16	0.01
spleen	0.12	0.00	0.13	0.01
stomach	0.85	0.13	0.73	0.08
sm. int.	1.22	0.21	1.27	0.06
lg. int.	1.20	0.12	1.03	0.15
muscle	4.60	1.24	2.05	0.25
tumor	3.09	0.56	1.85	0.60
blood	4.43	0.44	2.97	0.56
whole body	33.8	1.87	29.4	3.37

Results presented as %ID/g and %ID/organ with one SD of the mean. $N = 4$.

of MORFs incorporated was 1−2 per antibody. The yield in the modification of both the MORF and the antibody with SANH or SFB was 80−90%, and the antibody yield in the final conjugation step was 50−80%. The immunoreactivity measurements showed that greater than 86% of both MN14−MORFs were shifted by the addition of the antigen. In the only apparent difference, MN14(SFB)−MORF solution was cloudy and MN14(SANH)−MORF clear after storage at refrigerator temperatures for 6 months. Analysis by HPLC of the former conjugate also showed lower recoveries. Typical HPLC profiles of radiolabeled MN14(SANH)−MORF before (panel A) and after (panel B) the addition of CEA antigen are presented in Figure 1 and show an 86% shift of the radioactivity to higher molecular weight as the antibody binds to its antigen. The profiles for MN14(SFB)−MORF) were essentially identical.

Both MN14(SANH)−MORF and MN14(SFB)−MORF) were found to be virtually identical in properties. Averaged over two to six preparations, the attached MORFs per MN14 was identical within experimental error at 1.1−2.0 gpm while the average accessible MORF per MN14 was also identical at 1.0−2.0 gpm.

Figure 2 provides the standard curve (semilog scale) of gpm vs the 265 and 280 nm absorbance ratio for mixtures of MN14 to which MORF was added at designated molar ratios. The results obtained in this manner show a 90% agreement with the results obtained by the hydrazone bond method described by the Hydralink manufacturer (data not presented).

Animal Studies. Table 1 compares the biodistribution in normal mice at 1 and 18 h postinjection of both MN14(SFB)−MORF and MN14(SANH)−MORF radiolabeled by hybridization with ^{99m}Tc-cMORF. The results show no significant differences between the two conjugates except in the statistically higher liver and spleen values at 18 h postinjection in the case of MN14(SFB)−MORF ($p < 0.05$). Because of the lower liver and spleen accumulations and because of the higher storage stability mentioned above, the MN14(SANH)−MORF conjugate was used in all subsequent studies.

Table 2 presents the pretargeting results obtained in nude mice bearing LS174T tumors in one thigh and receiving either 0.2 or 1.0 μg of ^{99m}Tc-cMORF 3 h earlier to tumored mice having received 2 d earlier the MN14(SANH)−MORF conjugate at dosages of 6 μg or 30 μg, respectively. No significant differences in radiolabeled cMORF accumulation between the two dosages of antibody occurred in tissues ($p > 0.05$). Further, when compared with an earlier study using antibody conjugate with EDC (*5*), these results showed comparable tumor uptake (3.96 $\pm$ 0.70 vs 3.62 $\pm$ 0.45) %ID/g.

DISCUSSION

Some of the existing methods to couple DNA oligonucleotides and other oligomers to antibodies use biotin−streptavidin, use glutaraldehyde to cross-link amino groups (*17*−*22*), react sulfhydryl group-containing oligonucleotides with maleimide-modified antibodies (*23*−*25*), or cross-link a carboxyl group on an antibody with an amine-derivatized oligomer using EDC (*4*, *5*). The goal of this study was to evaluate Hydralink, a commercially available conjugation kit to conjugate the MN14 anti-CEA antibody with MORF for use in tumor pretargeting studies.

A novel and convenient method to determine the average gpm of attached MORF per MN14 conjugate was employed based on differential absorbance at 265 and 280 nm. By plotting the ratio of MN14−MORF absorbance at 265 and 280 nm vs gpm, the degree of conjugation during the conjugation reaction could be monitored by size-exclusion HPLC. The measurement of the degree of modification of an antibody or MORF in this manner by HPLC is possible because the UV absorbance of hydrazone is not affected by the presence of either the antibody or MORF.

The antibody conjugation was approached in both directions by first reacting MN14 with the NHS-SANH or NHS-SFB and then combined with MORF previously reacted with NHS-SFB or NHS-SANH respectively to yield MN14(SANH)−MORF and MN14(SFB)−MORF. We demonstrate that both approaches are effective and provide an average gpm of between 1 and 2 and therefore higher than the 0.2 value achieved earlier in this laboratory using a conventional EDC carbodiimide method (*5*). Because the pharmacokinetics in normal mice was slightly more favorable for the MN14(SANH)−MORF compared to the MN14(SFB)−MORF and because the former was more stable to storage, presumably due to side reaction from excess SFB on antibody which would require a blocking agent to eliminate, subsequent studies concentrated on MN14(SANH)−MORF. The MN14(SANH)−MORF was found to retain more than 86% immunorectivity (i.e., immunoreactive fraction), and when used in a pretargeting strategy, the biodistribution of MN14−MORF conjugates in tumored mice following a pretargeting strategy showed only minor differences in terms of tumor uptake between the two methods despite the order of magnitude difference in gpm.

In conclusion, the commercial Hydralink was shown to be an efficient and convenient method to conjugate MORF, and probably other oligomers, to antibodies or other biomolecules under mild conditions without compromising their properties.

ACKNOWLEDGMENT

Financial support for this investigation was provided, in part, by the National Institutes of Health (CA 94994).

LITERATURE CITED

(1) Goodwin, D. A., Meares, C. F., McTigue, M., McCall, M. J., and David, G. S. (1986) Rapid localization of haptens in sites containing previously administrated antibody for immunoscintigraphy with short half-life tracers [abstract]. *J Nucl Med. 27(suppl*), 959.

(2) Hnatowich, D. J., Virzi, F., and Rusckowski, M. (1987) Investigations of avidin and biotin for imaging applications. *J. Nucl. Med. 28*, 1294−1302.

(3) Chang, C. H., Sharkey, R. M., Rossi, E. A., Karacay, H., McBride, W., Hansen, H. J., Chatal, J.-F., Barbet, J., and Goldenberg, D. M. (2002) Molecular advances in pretargeting radioimmunotherapy with bispecific antibodies. *Mol. Cancer Ther. 1*, 553−563.

(4) Liu, G., Mang'era, K., Liu, N., Gupta, S., Rusckowski, M., and Hnatowich, D. J. (2002) Tumor pretargeting in mice using 99mTc labeled morpholinos, a DNA analog. *J. Nucl. Med. 43*, 384−391.

(5) Liu, G. Z., He, J., Dou, S. P., Gupta, S., Vanderheyden, J.-L., Rusckowski, M., and Hnatowich, D. J. (2004) Pretargeting in tumored mice with radiolabeled morpholino oligomer showing low kidney uptake. *Eur. J. Nucl. Med. Mol. Imaging 31*, 417−424.

(6) Le Doussal, J. M., Martin, M., Gautherot, E., Delaage, M., and Barbet, J. (1989) In vitro and in vivo targeting of radiolabeled monovalent and divalent haptens with dual specificity monoclonal antibody conjugates. *J. Nucl. Med. 30*, 1358−1366.

(7) Goodwin, D. A., Meares, C. F., McTigue, M., Chaovapong, W., Diamanti, C. I., Ransone, C. H., and McCall, M. J. (1992) Pretargeted immunoscintigraphy: effect of hapten valency on murine tumor uptake. *J. Nucl. Med. 33*, 2006−2013.

(8) Boerman, O. C., Kranenborg, M. H. G. C., Oosterwijk, E., Griffiths, G. L., McBride, W. J., Oyen, W. J., de Weijert, M., Oosterwijk, J., Hansen, H. J., and Corstens, F. H. M. (1999) Pretargeting of renal cell carcinoma: Improved tumor targeting with a bivalent chelate. *Cancer Res. 59*, 4400−4405.

(9) Wang, Y., Chang, F., Zhang, Y., Liu, N., Liu, G., Gupta, S., Rusckowski, M., and Hnatowich, D. J. (2001) Pretargeting with amplification using polymeric peptide nucleic acid. *Bioconjugate Chem. 12*, 807−816.

(10) He, J., Liu, G. Z., Gupta, S., Zhang, Y. M., Rusckowski, M., and Hnatowich, D. J. (2004) Amplification Targeting: A Modified Pretargeting Approach with Potential for Signal Amplification−Proof of a Concept. *J. Nucl. Med. 45*, 1087−1095.

(11) He, J., Liu, G. Z., Vanderheyden, J.-L., Dou, S. P., Rusckoswki, M., and Hnatowich, D. J. (2005) Affinity enhancement bivalent morpholino for pretargeting: Initial evidence by surface plasmon resonance. *Bioconjugate Chem. 16*, 338−45.

(12) He, J., Liu, X. R., Zhang, S. R., Liu, G. Z. and Hnatowich, D. J. Bivalent morpholinos for affinity enhancement pretargeting: Surface plasmon resonance studies of molecular dimensions. *Bioconjugate Chem. 16*, 1098−1104.

(13) Winnard, P., Jr., Chang, F., Rusckowski, M., Mardirossian, G., and Hnatowich, D. J. (1997) Preparation and use of NHS-MAG3 for technetium-99m labeling of DNA. *Nucl. Med. Biol. 24*, 425−432.

(14) He, J., Liu, G., Zhang, S., Rusckowski, M., and Hnatowich, D. J. (2003) Pharmacokinetics in mice of four oligomer-conjugated polymers for amplification targeting. *Cancer Biother. Radiopharm. 18*, 941−947.

(15) Liu, G., Liu, C., Zhang, S., He, J., Liu, N., Gupta, S., Rusckowski, M., and Hnatowich, D. J. (2003) Investigations of technetium-99m morpholino pretargeting in mice. *Nucl. Med. Commun. 24*, 697−705.

(16) Liu, G., Zhang, S., He, J., Liu, N., Gupta, S., Rusckowski, M., and Hnatowich, D. J. (2002) The influence of chain length and base sequence on the pharmacokinetic behavior of 99mTc-morpholinos in mice. *Quart. J. Nucl. Med. 46*, 233−243.

(17) Niemeyer, C. M., Adler, M., Pignataro, B., Lenhert, S., Gao, S., Chi, L., Fuchs, H., and Blohm, D. (1999) Self-assembly of DNA-streptavidin nanostructures and their use as reagents in immuno-PCR. *Nucleic Acids Res. 27*, 4553−4561.

(18) Sano, T., Smith, C. L., and Cantor, C. R. (1992) Immuno-PCR: very sensitive antigen detection by means of specific antibody-DNA conjugates. *Science 258*, 120−122.

(19) Sugawara, K., Kobayashi, D., Saito, K., Furuya, D., Araake, H., Yagihashi, A., Yajima, T., Hosoda, K., Kamimura, T., and Watanabe, N. (2000) A highly sensitive immuno-polymerase chain reaction assay for human angiotensinogen using the identical first and second polyclonal antibodies. *Clin. Chim. Acta. 299*, 45−54.

(20) Brem, R. B., Yvert, G., Clinton, R., and Kruglyak, L. (2002) Genetic dissection of transcriptional regulation in budding yeast. *Science 296*, 752−755.

(21) Niemeyer, C. M., Sano, T., Smith, C. L., and Cantor, C. R. (1994) Oligonucleotide-directed self-assembly of proteins: semisynthetic DNA−streptavidin hybrid molecules as connectors for the generation of macroscopic arrays and the construction of supramolecular bioconjugates. *Nucleic Acids Res. 22*, 5530−5539.

(22) Zhang, H. T., Kacharmina, J. E., Miyashiro, K., Greene, M. I., and Eberwine, J. (2001) Protein quantification from complex protein mixtures using a proteomics methodology with single-cell resolution. *Proc. Natl. Acad. Sci. U.S.A. 98*, 5497−5502.

(23) Hendrickson, E. R., Truby, T. M., Joerger, R. D., Majarian, W. R., and Ebersole, R. C. (1995) High sensitivity multianalyte immunoassay using covalent DNA-labeled antibodies and polymerase chain reaction. *Nucleic Acids Res. 23*, 522−529.

(24) Schweitzer, B., Wiltshire, S., Lambert, J., O'Malley, S., Kukanskis, K., Zhu, Z., Kingsmore, S. F., Lizardi, P. M., and Ward, D. C. (2000) Inaugural article: immunoassays with rolling circle DNA amplification: a versatile platform for ultrasensitive antigen detection. *Proc. Natl. Acad. Sci. U.S.A. 97*, 10113−10119.

(25) Bos, E. S., Kuijpers, W. H. A, Meesters-Winters, M., Pham, D. T., Haan, A. S., Doornmalen, A. M., Kaspersen, F. M., Boeckel, C. A. A., and Gougeon-Bertrand, F. (1994) In vitro Evaluation of DNA-DNA hydridization as a two-step approach in radioimmunotherapy of cancer. *Cancer Res. 54*, 3479−3486.

BC060208V

"Click Labeling" with 2-[^{18}F]Fluoroethylazide for Positron Emission Tomography

Matthias Glaser and Erik Årstad*

Hammersmith Imanet Ltd, Cyclotron Building, Du Cane Road, London W12 ONN, U.K. Received September 29, 2006; Revised Manuscript Received March 1, 2007

As an effort in the development of more flexible ^{18}F-labeling chemistry, we report herein on the use of the Cu(I)-catalyzed Huisgen cycloaddition, also known as the "click reaction", to form ^{18}F-labeled 1,2,3-triazoles. Nucleophilic fluorination of 2-azidoethyl-4-toluenesulfonate followed by distillation provided 2-[^{18}F]fluoroethylazide in 55% radiochemical yield (decay-corrected). 2-[^{18}F]fluoroethylazide was reacted with a small library of terminal alkynes in the presence of excess Cu^{2+}/ascorbate or copper powder. The most reactive alkyne, *N*-benzylpropynamide provided nearly quantitative incorporation of 2-[^{18}F]fluoroethylazide after 15 min at ambient temperature, whereas the majority of the alkyne substrates provided excellent yields of the corresponding ^{18}F-labeled 1,2,3-triazoles following heating to 80 °C. Using the method described, a model peptide was obtained in 92.3 ± 0.3% (n = 3) radiochemical yield (decay-corrected) after purification by semipreparative HPLC.

INTRODUCTION

Positron emission tomography (PET) allows high-resolution quantitative imaging of biochemical processes in vivo by detecting the distribution pattern of labeled biomarkers over time. PET is increasingly used for diagnostic imaging, medical research, and drug development (*1*−*3*). ^{18}F is particularly attractive for PET, as it can be produced in high yields and has favorable decay characteristics ($t_{1/2}$ = 110 min) (*4*−*6*). As formation of electrophilic ^{18}F-labeling agents invariably leads to isotopic dilution (*2*), the use of nucleophilic [^{18}F]fluoride, which can be produced with excellent specific activity, is usually preferred for labeling. However, due to the low reactivity and high proton affinity of [^{18}F]fluoride, ^{18}F-labeled prosthetic groups are necessary for labeling complex biomolecules such as peptides and small molecules with H-acidic functions (*7*).

Currently, peptide labeling is mostly confined to conjugation of free amino groups, either by direct acylation using ^{18}F-fluorinated activated esters (*7*) or indirectly by functionalization, e.g., to an aminooxy group, which subsequently can undergo condensation with ^{18}F-fluorinated aldehydes (*8*). The lack of alternative labeling positions and the high lipophilicity of the coupling groups that are formed make optimization of peptide-based biomarkers difficult. An additional limitation is that ^{18}F-labeling agents often are complicated to produce, which restricts their use to specialized centers.

The recent discovery that Cu(I) catalyzes the Huisgen 1,3-dipolar cycloaddition of terminal alkynes and organic azides to form 1,2,3-triazoles (*9*, *10*) often referred to as "click chemistry" (*11*) has proven particularly valuable in combinatorial chemistry (*12*−*16*). The reaction provides a versatile tool for coupling druglike fragments in high yields and under mild conditions, and the 1,2,3-triazole formed is biologically stable, with a polarity and size similar to amide bonds (*17*). The reaction can be carried out in aqueous media, and as both alkynes and organic azides are relatively inert, there is no need for protection groups. In addition, there is a wide selection of commercially available alkynes, providing building blocks for library synthesis.

* Erik Årstad, E-mail: erik.arstad@ge.com, Tel. +44 208 383 3714, Fax +44 208 383 8573.

As an effort in the development of more flexible ^{18}F-labeling chemistry, we report herein on the use of Cu(I)-catalyzed Huisgen cycloaddition to form ^{18}F-labeled 1,2,3-triazoles (*18*).

EXPERIMENTAL PROCEDURES

General. Reagents and solvents were purchased from Sigma-Aldrich Co. Ltd. (Gillingham, United Kingdom) and used without further purification. Ethyl-2-acetylamino-4-pentynoate was purchased from Bachem (Merseyside, U.K.). The model peptide **11** was provided by the Proteomics and Peptide Synthesis Facility, MRC Clinical Science Center/Imperial College, Hammersmith Hospital London. Mass spectra were recorded on a Finnigan LCQ system using electrospray ionization (ESI). MALDI-TOF mass spectra were measured on a Finnigan Lasermat 2000 instrument. Accurate mass spectra (HRMS) were measured on a Micromass Q-Tof Ultima machine coupled with a nanoLC system using *Mass Lynx 3.5* software. NMR spectra were obtained from a JEOL Eclipse instrument (500 MHz), and the chemical shifts are reported in parts per million (ppm) relative to residual solvent peaks. The melting points were measured using an SMP-1 apparatus (Fisher Scientific UK). GC-MS data were acquired under electron ionization using an Agilent 6890N system. FT-IR spectra were recorded with a SpectrumBX2 (Perkin-Elmer). Analytical HPLC was carried out using a Beckman Gold instrument with *Karat32* software. The radio HPLC system was a Beckman System Gold instrument equipped with a γ detector (Bioscan Flow-count). A Phenomenex Luna C18(2) column (50 × 4.6 mm, 3 μm; flow rate 1 mL/min) was used for analytical HPLC. A semipreparative column (Phenomenex Onyx Monolithic C18, 100 × 10 mm, with a flow rate of 4 mL/min) was used for the final purification of the peptide [^{18}F]**12**. The following mobile phase systems were used both for analytical and preparative HPLC: solvent A, water/TFA (0.1%); solvent B, acetonitrile/TFA (0.1%); linear gradient of 5−80% solvent B over 15 min (gradient I), 5−60% solvent B over 15 min (gradient II), or 30−80% solvent B over 15 min (gradient III). Non-radioactive compounds were purified using an automated flash machine (Companion Presearch Ltd., 4 g RediSep silica cartridges, flow rate 18 mL/min), with the exception of peptide **12**, which was purified using a preparative HPLC (Agilent1200, column Phenomenex Luna C18(2), 75 ×

10.1021/bc060301j CCC: $37.00 © 2007 American Chemical Society
Published on Web 04/13/2007

30 mm, 5 μm, gradient I, flow rate 15 mL/min). [^{18}F]Fluoride was produced by a cyclotron (Scanditronix MC40) using the ^{18}O(p,n)^{18}F nuclear reaction with 19 MeV proton irradiation of an enriched [^{18}O]H_2O target.

2-Fluoroethylazide (2). To a solution of 2-fluoroethyl-4-toluenesulfonate (**1**) (*19*) (128 mg, 0.586 mmol) in DMF (anhydr., 10 mL) was added sodium azide (114 mg, 1.76 mmol), and the resulting mixture was stirred at ambient temperature for 48 h. The reaction mixture was filtered, and the filtrate containing the title compound was used without isolation for subsequent reactions.

WARNING: Attempts to isolate neat 2-fluoroethylazide may result in an explosion.

1-(2-Fluoroethyl)-4-phenyl-1*H*-[1,2,3]triazole (3). To a stirred solution of copper(II) sulfate pentahydrate (12 mg, 0.0489 mmol) and L-ascorbic acid (16 mg, 0.0977 mmol) in water (0.3 mL) under nitrogen was added a solution of phenylacetylene (105 μL, 0.977 mmol) in DMF (1 mL). After addition of 2-fluoroethylazide (1.172 mmol) in DMF (5 mL), stirring was continued at room temperature for 21 h. The reaction mixture was diluted with water (5 mL), and the crude product was extracted with dichloromethane (3 × 5 mL) and washed with sodium bicarbonate solution (10%, 3 × 10 mL) and brine (1 × 5 mL). After drying over sodium sulfate, the solvent was removed under reduced pressure, and the crude material purified by means of flash chromatography (25% to 100% ethyl acetate in hexane for 10 min, t_R = 3.0 min) to provide the title compound (32 mg, 17% yield) as a white crystalline material. mp 83−85 °C. ^{1}H NMR ($CDCl_3$): δ 4.70 (m, 1H, CH_2), 4.76 (m, 1H, CH_2), 4.80 (m, 1H, CH_2), 4.89 (m, 1H, CH_2), 7.35 (tt, $J_{4,2}$ = 1.0 Hz, $J_{4,3}$ = 7.5 Hz, 1H, HAr), 7.44 (m, 2 H, HAr), 7.84 (m, 2H, HAr), 7.89 (d, J = 1.0 Hz, 1H, CH-triazole). GC-MS: m/z = 191 [M]$^+$. TOF-ES-MS: found m/z = 192.0935 [MH]$^+$, calcd for $C_{10}H_{10}N_3F$ m/z = 192.0932 [MH]$^+$.

1-(2-Fluoroethyl)-1*H*-[1,2,3]triazol-4-yl]carboxylic Acid (4). To a stirred solution of copper(II) sulfate pentahydrate (12 mg, 0.0489 mmol) and L-ascorbic acid (34 mg, 0.135 mmol) in water (0.4 mL) under nitrogen was added a solution of propargylic acid (60 μL, 0.977 mmol) in DMF (0.5 mL). After addition of 2-fluoroethylazide (1.172 mmol) in DMF (2.5 mL), stirring was continued at ambient temperature for 4 h. The reaction mixture was quenched with HCl (20 mL, 1 M), and the crude product was extracted with ethyl acetate (3 × 20 mL). After washing with brine (5 mL) and drying over sodium sulfate, the solvent was removed under reduced pressure. The residue was purified by recrystallization from ethyl acetate/hexane to give the title compound (16 mg, 10% yield) as a white crystalline material. mp 160−165 °C. ^{1}H NMR (DMSO-d_6): δ 4.74 (m, 1H, CH_2), 4.80 (m, 2H, CH_2), 4.90 (m, 1H, CH_2), 8.71 (s, 1H, CH-triazole). TOF-ES-MS: found m/z = 160.0518 [MH]$^+$, calcd for $C_5H_6N_3O_2F$ m/z = 160.0517 [MH]$^+$.

4-[1-(2-Fluoroethyl)-1*H*-[1,2,3]triazol-4-yl]benzoic Acid (5). To a stirred solution of copper(II) sulfate pentahydrate (3.7 mg, 0.0149 mmol) and L-ascorbic acid (10.5 mg, 0.0595 mmol) in water (0.2 mL) under nitrogen was added a solution of sodium 4-ethynylbenzoate (50 mg, 0.297 mmol) in DMF (1.5 mL). After addition of 2-fluoroethylazide (0.356 mmol) in DMF (0.76 mL), stirring was continued at ambient temperature for 12 h. The reaction mixture was diluted with HCl (20 mL, 1 M), the crude product was extracted with ethyl acetate (3 × 10 mL), and the organic phase washed with brine (10 mL). After drying over sodium sulfate, the solvent was removed under reduced pressure, and the crude material recrystallized from ethyl acetate/hexane to give the title compound (37 mg, 52% yield) as a white crystalline material. mp 236−240 °C (decomp.). ^{1}H NMR (DMSO-d_6): δ 4.74 (m, 1H, CH_2), 4.80 (m, 2H, CH_2), 4.90 (m, 1H, CH_2), 7.99 (m, 4H, HAr), 8.70 (s, 1H, CH-triazole). TOF-ES-MS: found m/z = 236.0838 [MH]$^+$, calcd for $C_{11}H_{10}N_3O_2F$ m/z = 236.0830 [MH]$^+$.

4-[1-(2-Fluoroethyl)-1*H*-[1,2,3]triazol-4-yl]aniline (6). To a stirred solution of copper(II) sulfate pentahydrate (129 mg, 0.516 mmol) and L-ascorbic acid (182 mg, 1.032 mmol) in water (1.2 mL) under nitrogen was added a solution of 4-ethynylaniline (40 mg, 0.344 mmol) in DMF (0.7 mL). After addition of 2-fluoroethylazide (0.287 mmol) in DMF (2.45 mL), stirring was continued at ambient temperature for 4 h. The reaction mixture was quenched with sodium hydroxide solution (1 M, 5 mL). The product was extracted with ethyl acetate (3 × 5 mL), and the organic phase was washed with water (5 mL) and brine (2 mL). After drying over sodium sulfate, the solvent was removed under reduced pressure and the crude material purified by means of flash chromatography (40% to 90% ethyl acetate in hexane for 10 min, t_R = 8.0 min) to give the title compound (15 mg, 25% yield) as a tan crystalline material. mp 79−82 °C. ^{1}H NMR ($CDCl_3$): δ 4.70 (m, 1H, CH_2), 4.72 (m, 1H, CH_2), 4.77 (m, 1H, CH_2), 4.88 (m, 1H, CH_2), 6.74 (d, J = 8.7 Hz, 2H, HAr), 7.64 (d, J = 8.7 Hz, 2H, HAr), 7.74 (d, J = 0.1 Hz, 1H, CH-triazole). TOF-ES-MS: found m/z = 207.1030 [MH]$^+$, calcd for $C_{10}H_{11}N_4F$ m/z = 207.1040 [MH]$^+$.

***N*-Benzyl-[1-(2-Fluoroethyl)-1*H*-[1,2,3]triazol-4-yl]formamide (7).** A solution of *N*-benzylpropynamide (*20*) (50 mg, 0.314 mmol) in DMF (1 mL) was added to a stirred solution of copper(II) sulfate pentahydrate (3.9 mg, 0.0157 mmol) and L-ascorbic acid (11 mg, 0.0628 mmol) in water (0.4 mL) under nitrogen. After addition of 2-fluoroethylazide (0.377 mmol) in DMF (3.2 mL), stirring was continued at room temperature for 48 h. The reaction mixture was diluted with sodium bicarbonate (10%, 5 mL), the crude product extracted with dichloromethane (3 × 5 mL), and the organic phase washed with brine (5 mL). After drying over sodium sulfate, the solvent was removed under reduced pressure and the crude material purified by recrystallization from ethyl acetate/diethyl ether to give the title compound (8 mg, 10% yield) as a white crystalline material. mp 165−167 °C. ^{1}H NMR ($CDCl_3$): δ 4.70 (m, 6H, CH_2), 7.34 (m, 5H, HAr), 7.46 (m, 1H, NH), 8.20 (s, 1H, CH-triazole). TOF-ES-MS: found m/z = 249.1143 [MH]$^+$, calcd for $C_{12}H_{13}N_4OF$ m/z = 249.1146 [MH]$^+$.

***N*-Benzyl-3-[1-(2-fluoroethyl)-1*H*-[1,2,3]triazol-4-yl]propionamide (8).** *N*-Benzyl-4-pentynamide was prepared from 4-pentynoic acid according to the method of Coppola and Damon (*20*). The spectroscopic data were consistent with reported values (*21*). To a stirred suspension of copper(I) iodide (255 mg, 1.335 mmol) in methanol (0.8 mL) under nitrogen was added a solution of *N*-benzyl-4-pentynamide (50 mg, 0.267 mmol) in methanol (0.5 mL), 2-fluoroethylazide (0.320 mmol) in DMF (2.62 mL), and diisopropylamine (0.233 mL, 1.335 mmol). Stirring was continued at ambient temperature for 2 h. The reaction mixture was diluted with a solution of sodium hydrogen phosphate (1 g) in water (10 mL) and filtered through Celite. The crude product was extracted with ethyl acetate (3 × 20 mL), and the organic phase was washed with brine (20 mL). After drying over sodium sulfate, the solvent was removed under reduced pressure and the crude material purified by column chromatography (silica, conditioned with ethyl acetate/hexane 1:1, elution with ethyl acetate/hexane 4:1) to afford the title compound (19 mg, 26% yield) as a white crystalline material. mp 127−133 °C. ^{1}H NMR ($CDCl_3$): δ 2.66 (t, J = 7.0 Hz, 2H, CH_2), 3.09 (t, J = 7.0 Hz, 2H, CH_2), 4.40 (d, J = 5.7 Hz, 2H, CH_2-benzyl), 4.56 (m, 1H, CH_2), 4.61 (m, 1H, CH_2), 4.70 (m, 1H, CH_2), 4.80 (m, 1H, CH_2), 6.0 (s, 1H, NH), 7.25 (m, 5H, HAr), 7.44 (s, 1H, CH-triazole). TOF-ES-MS: found m/z = 277.1474 [MH]$^+$, calcd for $C_{14}H_{17}N_4OF$ m/z = 277.1459 [MH]$^+$.

Ethyl-(2-acetylamino-3-[1-(2-fluoroethyl)-1*H*-[1,2,3]triazol-4-yl])propionate (9). A solution of ethyl-2-acetylamino-4-pentynoate (146 mg, 0.799 mmol) in DMF (1 mL) was added to copper powder (200 mg, 40 mesh) under nitrogen, followed by a solution of 2-fluoroethylazide (0.799 mmol) in DMF (2.16 mL). The mixture was stirred and heated at 80 °C for 3 h. Purification by means of reversed-phase flash chromatography (4.3 g RediSep C18-RP cartridge, 5% to 95% acetonitrile in water for 10 min, $t_R = 3.5$ min) provided the title compound as a white solid (196 mg, 90% yield). mp 55−60 °C. ^{1}H NMR (DMSO-d_6): δ 1.13 (t, $J = 7.1$ Hz, 3H, CH_2CH_3), 1.82 (s, 3H, CH_3), 3.02 (m, 2H, CH_2-propionate), 4.05 (m, 2H, OCH_2CH_3), 4.47 (m, 1H, CH), 4.46 (m, 1H, CH_2), 4.64 (m, 1H, CH_2), 4.70 (m, 1H, CH_2), 4.81 (m, 1H, CH_2), 7.89 (s, 1H, CH-triazole), 8.31 (d, 1H, NH). TOF-ES-MS: found $m/z = 273.1372$ $[MH]^+$, calcd for $C_{11}H_{17}N_4O_3F$ $m/z = 273.1357$ $[MH]^+$.

***N*-[1-(2-Fluoroethyl)-1*H*-[1,2,3]triazol-4-ylmethylene]benzamide (10).** A solution of *N*-propargylbenzamide (*22*) (100 mg, 0.628 mmol) in DMF (1 mL) was added to copper powder (200 mg, 200 mesh) under nitrogen followed by a solution of 2-fluoroethylazide (0.628 mmol) in DMF (1.75 mL). The mixture was stirred for 30 min at ambient temperature and subsequently heated to 80 °C for 1 h. After evaporation of the solvent under high vacuum, water (5 mL) and saturated sodium bicarbonate (1 mL) were added. The crude product was extracted with ethyl acetate (3 × 10 mL), and the organic phase was washed with brine (5 mL), filtered, and dried over sodium sulfate. The triazole **10** was obtained by recrystallization from ethyl acetate/hexane as a white solid (68 mg, 44% yield). mp 100−105 °C. ^{1}H NMR ($CDCl_3$): δ 4.63 (t, $J = 17.0$ Hz, 1H, CH_2), 4.68 (t, $J = 17.0$ Hz, 1H, CH_2), 4.75 (t, $J = 17.0$ Hz, 1H, CH_2), 4.84 (t, $J = 17.0$ Hz, 1H, CH_2), (d, $J = 23$ Hz, 2H, CH_2-amide), 6.87 (s, 1H, NH), 7.43 (m, 3H, HAr), 7.73 (s, 1H, CH-triazole), 7.85 (m, 2H, HAr). TOF-ES-MS: found $m/z = 249.1133$ $[MH]^+$, calcd for $C_{12}H_{13}N_4OF$ $m/z = 249.1146$ $[MH]^+$.

(*S*)-6-Amino-2-(2-{(*S*)-2-[2-((*S*)-6-amino-2-{[4-(2-fluoroethyl)-1*H*[1,2,3]triazol-4-yl-1-carbonyl]amino}hexanoylamino)-acetyl-amino]-3-phenylpropionylamino}acetylamino)-hexanoic Acid (12). To a stirred mixture of **11** (20.7 mg, 35.2 μmol), copper powder (200 mg, 40 mesh), and sodium phosphate buffer (0.2 mL, pH 6.0, 0.25 M) under nitrogen was added a solution of **2** (36.8 μmol) in DMF (97 μL). The mixture was heated to 80 °C for 2 h, the heating bath was removed, and stirring was continued for 48 h. The filtered solution was concentrated under vacuum and purified by means of preparative HPLC to provide the title compound **12** as a colorless oil (12 mg, 50% yield). MALDI-MS: found $m/z = 676.18$ $[M]^+$, calcd for $C_{30}H_{45}N_{10}O_7F$ $m/z = 676.75$ $[M]^+$.

Radiochemistry. 2-[^{18}F]Fluoroethylazide ([^{18}F]2). A mixture of Kryptofix 222 (5 mg, 13.3 μmol), potassium carbonate (1 mg, 7.2 μmol, dissolved in 50 μL water), and acetonitrile (1 mL) was added to [^{18}F]fluoride (74−370 MBq) in water (1 mL). The solvent was removed by heating at 80 °C under a stream of nitrogen (100 mL/min). Afterward, acetonitrile (0.5 mL) was added, and the distillation was continued. This procedure was repeated twice. After cooling to room temperature, a solution of 2-azidoethyl-4-toluenesulfonate (**1**) (1.5 μL, 7.5 μmol) in anhydrous acetonitrile (0.2 mL) was added. The reaction mixture was stirred for 15 min at 80 °C. After addition of acetonitrile (0.3 mL), [^{18}F]**2** was distilled at 130 °C under a flow of nitrogen (15 mL/min) into a trapping vial containing acetonitrile (0.1 mL). Compound [^{18}F]**2** was collected with a radiochemical yield of 54% (decay-corrected) and 63% distillation efficiency.

Preparation of [^{18}F]3-10 (See Table 1 for reaction times, temperatures, and yields). *Method A.* To a solution of copper-(II) sulfate (50 μL, 0.45 M), sodium L-ascorbate (50 μL, 1.5 M), and sodium phosphate buffer (100 μL, pH 6.0, 50 mM) under nitrogen was added a solution of the alkyne (0.015 mmol) in DMF (0.1 mL) followed by [^{18}F]**2** in acetonitrile (0.2 mL, 18.5−37 MBq).

Method B: To a mixture of sodium phosphate buffer (200 μL, pH 6.0, 50 mM) and copper powder (200 mg, 70 μm) was added a solution of the alkyne (0.015 mmol) in DMF (0.1 mL) followed by [^{18}F]**2** in acetonitrile (0.2 mL, 18.5−37 MBq).

[^{18}F](*S*)-6-Amino-2-(2-{(*S*)-2-[2-((*S*)-6-amino-2-{[4-(2-fluoroethyl)-1*H*[1,2,3]triazol-4-yl-1-carbonyl]amino}-hexanoylamino)acetylamino]-3-phenylpropionylamino}-acetylamino)hexanoic Acid ([^{18}F]12). To a solution of copper(II) sulfate pentahydrate (4.3 mg, 17 μmol) in water (50 μL) was added sodium ascorbate (3.4 mg, 17 μmol) in water (50 μL) under nitrogen. After 1 min at room temperature, a solution of alkyne peptide precursor **11** was added (2 mg, 3.4 μmol, in sodium phosphate buffer, pH 6.0, 0.5 M, 50 μL), followed by a solution of [^{18}F]**2** (24−32 MBq) in acetonitrile (50 μL). The mixture was left at room temperature for 15 min and diluted with HPLC mobile phase **A** (0.3 mL). The labeled peptide [^{18}F]**12** was isolated using semipreparative HPLC (gradient II, UV at 216 nm, $t_R = 6.4$ min).

RESULTS AND DISCUSSION

2-[^{18}F]-Fluoroethylazide ([^{18}F]**2**) was designed as the labeling agent, since alkynes in general are more readily available and less hazardous than organic azides. Nucleophilic fluorination of 2-azidoethyl-4-toluenesulfonate (**1**) (*23*) with anhydrous no-carrier-added Kryptofix 222 $K^+[^{18}F]F^-$ (acetonitrile, 80 °C, 15 min) provided the azide [^{18}F]**2** in 95% analytical yield, of which 55% yield (decay-corrected) was isolated by distillation (Scheme 1). While the "click reaction" has been extensively studied, the conditions reported so far either involve too long reaction times for ^{18}F-labeling or the use of microwave heating, which is difficult to implement in automated radiotracer production. Our main concern was therefore to investigate the scope and efficiency of the reaction with conventional heating within a time frame suitable for PET. Reportedly, the two most robust catalytic systems, Cu^{2+}/ascorbate (*10*) (method A) and copper metal (*24*) (method B), were used to evaluate the reaction of 2-[^{18}F]fluoroethylazide ([^{18}F]**2**) with a small library of terminal alkynes (Scheme 1, Table 1). The reactions were carried out in a buffered solution (pH 6.0, water/acetonitrile/DMF) under an inert atmosphere, using excess copper relative to the alkynes.

In order to evaluate the effect of the catalytic systems and the functional groups on the kinetics, radiochemical yields were measured after 15 min reaction time at ambient temperature and following subsequent heating to 80 °C for an additional 15 min. At ambient temperature, the degree of incorporation of [^{18}F]**2** varied considerably depending on the alkyne substrate and the catalytic system. *N*-Benzylpropynamide (entry 5, method A) performed particularly well, providing 98% yield as measured by radio-HPLC. Following heating to 80 °C for 15 min, excellent conversions of 2-[^{18}F]fluoroethylazide ([^{18}F]**2**) to the corresponding 1,2,3-triazoles were observed for the majority of the substrates, with the exception of propargylic acid, which provided 61% radiochemical yield (entry 2, method A). Thus, the click reaction is indeed compatible with the half-life of ^{18}F and has a high tolerance for functionalities α to terminal alkynes, including N- and C-terminal amides, which are attractive for labeling of peptides. With a suitable match of catalytic system and alkyne substrate, excellent yields can be obtained within a short time under very mild conditions, i.e., ambient temperature and neutral pH, which opens up the possibility of labeling fragile biomolecules that otherwise cannot be labeled with ^{18}F.

To further investigate the scope of the method, propargylic acid was coupled to a model peptide to provide the *N*-

Scheme 1. Radiosynthesis of 2-[^{18}F]fluoroethylazide ([^{18}F]2) and 1,3-Dipolar Cycloaddition with Terminal Alkynes

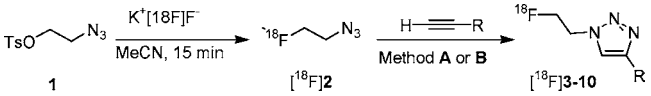
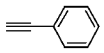
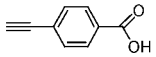
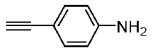
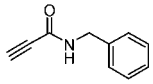
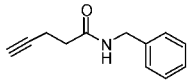
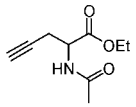
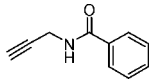


Table 1. Alkyne Substrates and Radiolabeling Yields with 2-[^{18}F]fluoroethylazide ([^{18}F]2)[a]

		Radiochemical yield[a] in %	
Entry	Substrate	Method **A**	Method **B**
1		84 (7)	56 (10)
2		61 (15)	29 (0)
3		93 (40)	15 (6)
4		>98 (12)	96 (33)
5		>98 (>98)	>98 (70)
6		98 (9)	76 (26)
7		>98 (31)	97 (90)
8		>98 (34)	92 (51)

[a] Yields measured by analytical radio-HPLC after 15 min reaction time at ambient temperature (in brackets) and after subsequent heating to 80 °C for 15 min. Method A: To a solution of copper(II) sulfate (50 μL, 0.45 M), sodium L-ascorbate (50 μL, 1.5 M), and sodium phosphate buffer (100 μL, pH 6.0, 50 mM) under nitrogen was added a solution of the alkyne (0.015 mmol) in DMF (0.1 mL) followed by [^{18}F]**2** in acetonitrile (0.2 mL). Method B: To a mixture of sodium phosphate buffer (200 μL, pH 6.0, 50 mM) and copper powder (200 mg, 70 μm) was added a solution of the alkyne (0.015 mmol) in DMF (0.1 mL) followed by [^{18}F]**2** in acetonitrile (0.2 mL).

propargylamide precursor **11**. In accordance with previous reports (*17*), "click labeling" (method A, 15 min room temperature, Scheme 2) was unaffected by the functional groups present and provided nearly quantitative incorporation of 2-[^{18}F]-fluoroethylazide ([^{18}F]**2**) to form the corresponding triazole [^{18}F]-**12**. Purification by means of semipreparative HPLC provided [^{18}F]**12** in 92.3 $\pm$ 0.6% (n = 3) radiochemical yield (decay-corrected) with a radiochemical purity of 99% (Figure 1).

While the click reaction proceeds well in a wide range of pH values (*10*), it should be noted that 2-[^{18}F]fluoroethylazide ([^{18}F]**2**) rapidly decomposes in the presence of copper and trifluoroacetic acid (*25*). Interestingly, the labeling agent [^{18}F]**2** appears otherwise to be stable in acidic media and also in the presence of copper at neutral or basic pH values. As peptides often contain residual trifluoroacetic acid, the addition of a buffer to the reaction mixture is therefore recommended to achieve optimal results for click labeling with [^{18}F]2-fluoroethylazide ([^{18}F]**2**).

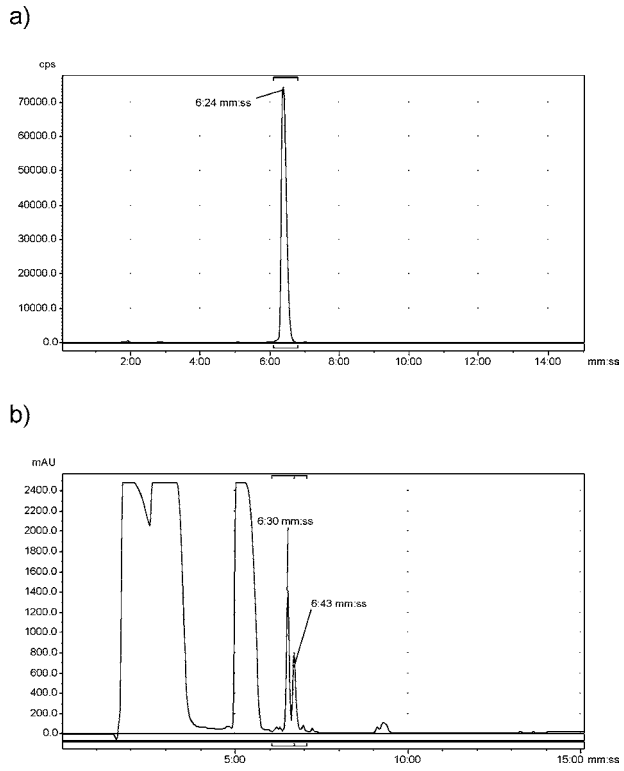
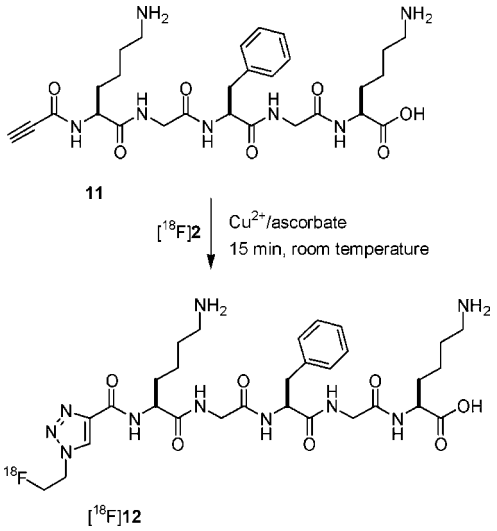


Figure 1. Preparative HPLC trace of a reaction mixture containing [^{18}F]**12**. (a) Radioactivity channel, [^{18}F]**12** at 6:24 min. (b) UV channel at 216 nm.

Scheme 2. Labeling of Model Peptide 11 with 2-[^{18}F]fluoroethylazide ([^{18}F]2) Using Cu^{2+}/Ascorbate Catalysis (method A)



CONCLUSION

The Cu-catalyzed Huisgen 1,3-dipolar cycloaddition provides a simple, flexible and highly efficient method for ^{18}F-labeling of small molecules and peptides. The labeling agent 2-[^{18}F]-fluoroethylazide ([^{18}F]**2**) can be produced in high yield in a one-step procedure, and subsequent Cu-catalyzed coupling with terminal alkynes to form the corresponding 2-[^{18}F]-fluoroethyl-1,2,3-triazoles proceeds in excellent yields within a short time under mild conditions.

ACKNOWLEDGMENT

We thank Geeta Patel (Proteomics and Peptide Synthesis Facility, MRC Clinical Science Center/Imperial College, Ham-

mersmith Hospital London) for the preparation of the model peptide and Emmanuel Samuel, School of Pharmacy London, for carrying out the mass spectrometry analysis. Finally, we thank Colin Steel and the cyclotron operators of Hammersmith Imanet Ltd. for providing us with ^{18}F.

Supporting Information Available: HPLC chromatograms of reference compounds and ^{18}F-labeled derivatives. This material is available free of charge via the Internet at http://pubs.acs.org.

LITERATURE CITED

(1) Stahl, A., Wieder, H., Piert, M., Wester, H.-J., Senekowitsch-Schmidtke, R., and Schwaiger, M. (2004) Positron emission tomography as a tool for translational research in oncology. *Mol. Imaging Biol. 6*, 214−224.

(2) Welch, M. J., and Redvanly, C. S. (2003) *Handbook of Radiopharmaceuticals, Radiochemistry and Applications*, John Wiley & Sons Ltd, Chichester.

(3) Heiss, W.-D., and Herholz, K. (2006) Brain receptor imaging. *J. Nucl. Med. 47*, 302−312.

(4) Stoecklin, G. (1998) Is there a future for clinical fluorine-18 radiopharmaceuticals (excluding FDG)? *Eur. J. Nucl. Med. 25*, 1612−1616.

(5) Qaim, S. M. (1986) Recent developments in the production of ^{18}F, ^{75,76,77}Br and ^{123}I. *Appl. Radiat. Isot. 37*, 803−810.

(6) Adam, M. J., and Wilbur, D. S. (2005) Radiohalogens for imaging and therapy. *Chem. Soc. Rev. 34*, 153−163.

(7) Wester, H.-J., Hamacher, K., and Stoecklin, G. (1996) A comparative study of NC. A. Fluorine-18 labeling of proteins via acylation and photochemical conjugation. *Nucl. Med. Biol. 23*, 365−372.

(8) Poethko, T., Schottelius, M., Thumshirn, G., Hersel, U., Herz, M., Henriksen, G., Kessler, H., Schwaiger, M., and Wester, H.-J. (2004) Two-step methodology for high-yield routine radiohalogenation of peptides: ^{18}F-labeled RGD and Octreotide analogs. *J. Nucl. Med. 45*, 892−902.

(9) Tornøe, C. W., Christensen, C., and Meldal, M. (2002) Peptidotriazoles on solid phase: [1,2,3]-triazoles by regiospecific copper-(I)-catalyzed 1,3-dipolar cycloadditions of terminal alkynes to azides. *J. Org. Chem. 67*, 3057−3064.

(10) Rostovtsev, V. V., Green, L. G., Fokin, V. V., and Sharpless, K. B. (2002) A stepwise Huisgen cycloaddition process: copper(I)-catalyzed regioselective "ligation" of azides and terminal alkynes. *Angew. Chem., Int. Ed. 41*, 2596−2599.

(11) Kolb, H. C., Finn, M. G., and Sharpless, K. B. (2001) Click chemistry: diverse chemical function from a few good reactions. *Angew. Chem., Int. Ed. 40*, 2004−2021.

(12) Pagliai, F., Pirali, T., Grosso, E. D., Brisco, R. D., Tron, G. C., Sorba, G., and Genazzani, A. A. (2006) Rapid synthesis of triazole-modified Resveratrol analogues via click chemistry. *J. Med. Chem. 49*, 467−470.

(13) Burley, G. A., Gierlich, J., Mofid, M. R., Nir, H., Tal, S., Eichen, Y., and Carell, T. (2006) Directed DNA metallization. *J. Am. Chem. Soc. 128*, 1398−1399.

(14) Whiting, M., Muldoo, J., Lin, Y.-C., Silverman, S. M., Lindstrom, W., Olson, A. J., Kolb, H. C., Finn, M. G., Sharpless, K. B., Elder, J. H., and Fokin, V. V. (2006) Inhibitors of HIV-1 protease by using in situ click chemistry. *Angew. Chem., Int. Ed. 45*, 1435−1439.

(15) Krasinski, A., Radic, Z., Manetsch, R., Raushel, J., Taylor, P., Sharpless, K. B., and Kolb, H. C. (2005) In situ selection of lead compounds by click chemistry: target-guided optimization of acetylcholinesterase inhibitors. *J. Am. Chem. Soc. 127*, 6686−6692.

(16) Agard, N. J., Prescher, J. A., and Bertozzi, C. R. (2004) A strain-promoted [3+2] azide-alkyne cycloaddition for covalent modification of biomolecules in living systems. *J. Am. Chem. Soc. 126*, 15046−15047.

(17) Bock, V. D., Hiemstra, H., and van Maarseveen, J. H. (2006) Cu^{I}-Catalyzed alkyne-azide "Click" cycloadditions form a mechanistic and synthetic perspective. *Eur. J. Org. Chem.* 51−68.

(18) While this manuscript was in preparation, a similar account on the use of click chemistry for ^{18}F-labeling of peptides was published (Marik, J., and Sutcliffe, J. L. (2006) Click for PET: Rapid preparation of [^{18}F]fluoropeptides using Cu^{I} catalyzed 1,3-dipolar cycloaddition. *Tetrahedron Lett. 47*, 6681−6684).

(19) van Velzen, E. U. T., Engbersen, J. F. J., and Reinhoudt, D. T. (1995) Synthesis of self-assembling resorcin[4]arene tetrasulfide adsorbates. *Synthesis* 989−997.

(20) Coppola, G. M., and Damon, R. E. (1993) Acetylenic amides. i: synthesis of N-substituted-2-propynamide. *Synth. Commun. 23*, 2003−2010.

(21) Jacobi, P. A., Brielmann, H. L., and Hauck, S. I. (1996) Toward the synthesis of biologically important chlorines, isobacteriochlorins, and corrins. Cyclic enamides from acetylenic amides. *J. Org. Chem. 61*, 5013−5023.

(22) Hashmi, A. S. K., Weyrauch, J. P., Frey, W., and Bats, J. W. (2004) Gold catalysis: mild conditions for the synthesis of oxazoles from N-propargylcarboxamides and mechanistic aspects. *Org. Lett. 6*, 4391−4394.

(23) Demko, Z. P., and Sharpless, K. B. (2001) An intramolecular [2+3] cycloaddition route to fused 5-heterosubstituted tetrazoles. *Org. Lett. 3*, 4091−4094.

(24) Himo, F., Lovell, T., Hilgraf, R., Rostovtsev, V. V., Noodleman, L., Sharpless, K. B., and Fokin, V. V. (2004) Copper(I)-catalyzed synthesis of azoles. DFT study predicts unprecedented reactivity and intermediates. *J. Am. Chem. Soc. 127*, 210−216.

(25) A solution of [^{18}F]**2** (13 MBq) in acetonitrile (50 μL) was added to a mixture of trifluoroacetic acid in water (5%, 50 μL) and copper powder (200 mg, 200 mesh). The resulting mixture was left for 15 min at room temperature. Subsequent HPLC analysis revealed a new peak (45%) that was assigned to [^{18}F]fluoride. No decomposition was detected after incubation of [^{18}F]**2** in 5% TFA solution only.

BC060301J

Chiral *O*-(Z-α-Aminoacyl) Sugars: Convenient Building Blocks for Glycopeptide Libraries

Alan R. Katritzky,* Parul Angrish, and Tamari Narindoshvili

Center for Heterocyclic Compounds, Department of Chemistry, University of Florida, Gainesville, Florida 32611-7200.
Received November 27, 2006; Revised Manuscript Received January 25, 2007

1,2:3,4-Di-*O*-isopropylidene-α-D-galactopyranose (**2**), 1,2:5,6-di-*O*-isopropylidene-D-glucose (**5**), and 2,3:5,6-di-*O*-isopropylidene-α-D-mannofuranose (**7**) are efficiently O-acylated in 78−96% yields with readily available *N*-(Z-α-aminoacyl)benzotriazoles **1a**−**e**, **1d**+**1d′** under microwave irradiation to give chiral **3a**−**d**, **4**, **6a**−**d**, **8a**,**b** and diastereomeric mixtures **(3d**+**3d′)**, **(6a**+**6a′)**, and **(6d**+**6d′)**. The original chirality was retained as evidenced by HPLC. The diisopropylidene protecting groups were removed from compounds **3a**,**d**, **6d** to give the free *O*-(Z-α-aminoacyl) sugars **9a**,**b**, **10**.

INTRODUCTION

Various potential biologically active molecules cannot be used in the clinic due to undesirable physical properties such as low water solubility, low permeability in biological membranes, and rapid loss by metabolic degradation (*1*−*3*). For example, the intrinsic flexibility of short peptides can lead to multiple conformations which can consequently reduce the binding efficiency to a critical receptor and/or induce undesirable effects due to binding with other receptors present (*4*). Many of these drawbacks can be significantly mitigated by derivatization of the biomolecules. Thus, the incorporation of saccharide units into the peptide moiety can improve the physiochemical properties of various bioactive peptides and inter alia increase their immunizing performance (*5*), intestinal permeability (*6*), resistance to enzymatic degradation (*7*), molecular recognition, (*8*, *9*), and rigidity of the peptide backbone (*10*−*12*). Advantageously, sugar−amino acid conjugates can offer both improved properties and access to significant diversification. Such efficacy arises from the fact that these hybrids are made up of two biocompatible components with almost unlimited potential structural variations (*13*, *14*). Such findings have established a pivotal role for a carbohydrate moiety in numerous biological processes ranging from cell−cell communication, cell adhesion, protein folding, and their implication in various diseases such as chronic inflammation, microbial infections, and cancers (*10*, *15*−*35*).

In the past several years, considerable efforts have been devoted to the synthesis of sugar-amino acid conjugates utilizing solution and solid-phase methodologies and enzymatic synthesis. In solution-phase methodology, the desired conjugates are obtained using coupling reagents like DCC/DMAP, (*36*−*40*) succinic anhydride/DMAP (*40*), or $COCl_2$−pyridine in dichloromethane (*41*). Examples prepared using these reagents utilize hexose moieties with all hydroxyl groups protected except for 6-OH, which enters into the coupling reaction.

Coupling of an unprotected sugar with an N-protected amino acid can also be achieved via an active ester such as a pentachlorophenyl ester, in the presence of imidazole as catalyst (*3*, *12*, *42*−*46*) which requires reaction times of 20−24 h and provides a yield of 30−50% (*3*, *45*, *46*). Recently, solid-phase methodology has also been utilized for the preparation of such conjugates, (*47*) utilizing coupling reagents like DCC and DIC in the presence of a catalytic amount of DMAP in DMF as solvent on a solid support bound to the protected sugar template with a free 6-OH. Finally, sugar-amino acid conjugates are also prepared by enzymatic synthesis in pyridine using commercial protease, Optimase M-440 (*48*).

We have already used *N*-acylbenzotriazoles extensively for [N-acylation] (*49*−*53*), [C-acylation] (*54*−*58*), and [O-acylation] (*58*). Previously, 1-(α-Boc-, -Z-, and -Fmoc-aminoacyl)benzotriazoles enabled the preparation of chiral di-, tri-, and tetrapeptides in average yields of 88% from natural unprotected amino acids, both without (L-Ala, L-Phe, L-Val, L-Leu) and with unprotected side chain functionality (L-Trp, L-Tyr, L-Gln, L-Ser, L-Cys, L-Asn), in aqueous acetonitrile (*59*−*63*), as well as amino-amides from chiral amines (*50*). The original chirality was preserved in all cases (>95% as evidenced by NMR and >99% by HPLC) (*59*−*63*). Herein, we present a convenient and efficient formation of α-amino acid−sugar conjugates derived from *N*-(Z-α-aminoacyl)benzotriazoles (*59*−*61*) and sugar −OH groups under microwave irradiation.

EXPERIMENTAL PROCEDURES

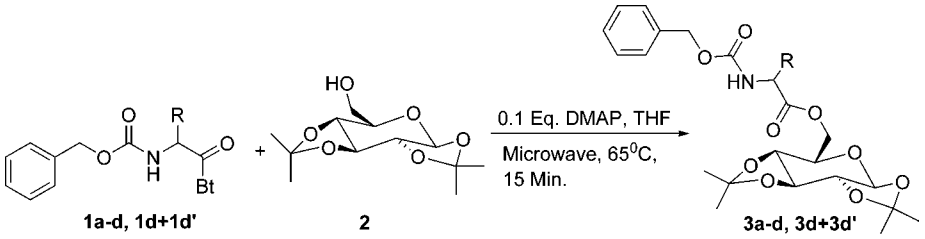
General Methods. Melting points were determined on a capillary point apparatus equipped with a digital thermometer. NMR spectra were recorded in $CDCl_3$ or DMSO-d_6 with TMS for ^{1}H (300 MHz) and ^{13}C (75 MHz) as an internal reference. *N*-Z-Amino acids and amino acids were purchased from Fluka and Acros and were used without further purification. All the reactions were carried out under microwave irradiation with a single mode cavity Discover Microwave Synthesizer (CEM Corporation, NC) producing a continuous irradiation at 2450 MHz. Elemental analyses was performed on a Carlo Erba-1106 instrument. Optical rotation values were measured with the use of sodium D line. Column chromatography was performed on silica gel (200−425 mesh). HPLC analyses were performed on Beckman system gold programmable solvent module 126 using Chirobiotic T column (4.6 × 250 mm), detection at 254 nm, flow rate 1.0 mL/min, and methanol as solvent.

General Procedure for the Preparation of *O*-(Z-α-Aminoacyl)diisopropylidene Sugars 3, 4, 6, 8 under Microwave Irradiation. A dried heavy walled Pyrex tube containing a small stir bar was charged with *N*-(Z-α-aminoacyl)benzotriazole **1** (1.0 mmol), sugars **2**, **5**, **7** (1.5 mmol), DMAP (0.2 mmol), and THF (0.5 mL). For the preparation of **4**, 1.0 equiv of

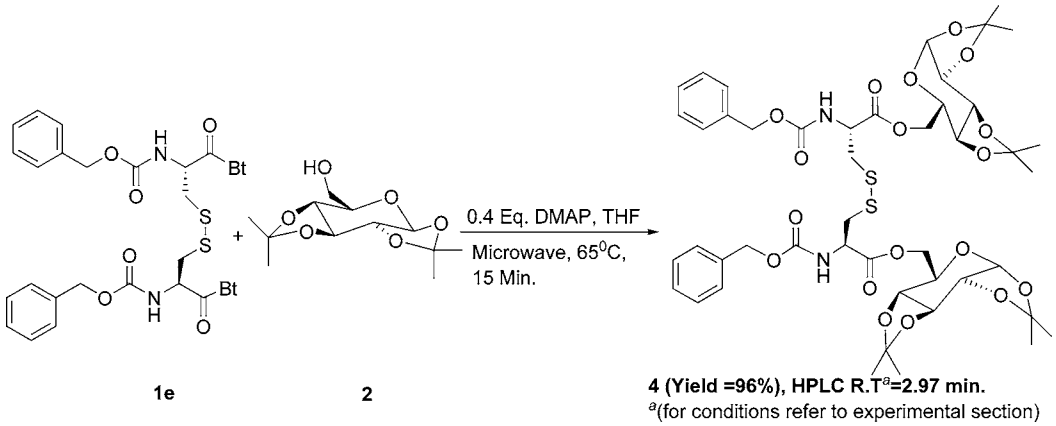
* Corresponding author. E-mail: katritzky@chem.ufl.edu.

10.1021/bc0603687 CCC: $37.00 © 2007 American Chemical Society
Published on Web 04/19/2007

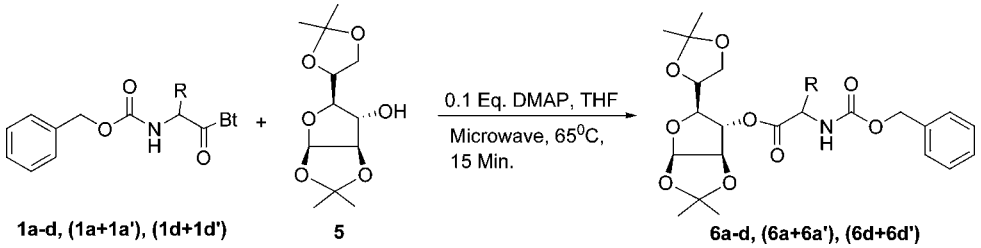
Scheme 1



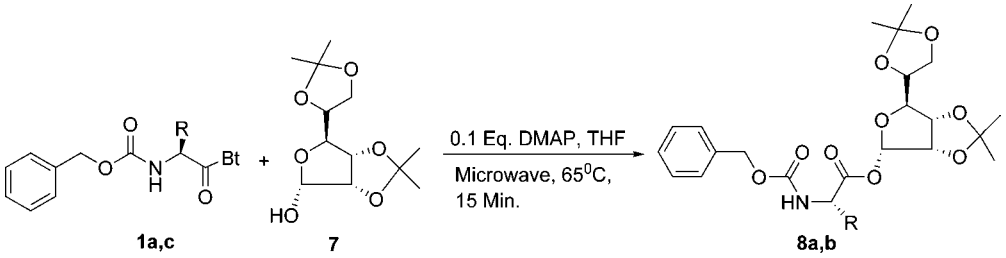
Scheme 2



Scheme 3



Scheme 4



1e, 2.5 equiv of **2**, and 0.4 equiv of DMAP in 0.5 mL of dry THF were utilized. The reaction mixture was exposed to microwave irradiation (100 W) for 15 min (to obtain **3**, **4**, **6**, **8**) and 1 h [to obtain the diastereomeric mixtures[1] **(3d**+**3d′)**, **(6a**+**6a′)** and **(6d**+**6d′)**] at a temperature of 65 °C. After the irradiation, the reaction mixture was allowed to cool through an inbuilt system in the instrument until the temperature had fallen below 30 °C (ca. 10 min). The reaction mixture was subjected to silica-gel column chromatography using ethyl acetate/hexanes (2:1) as eluent to afford the desired glycosyl amino acids **3**, **4**, **6**, **8**. Compounds **3b**−**d**, **4**, **6a**,**d**, **(6a**+**6d′)**, **8a** were recrystallized from CH_2Cl_2/hexane unless specified, otherwise Compounds **3a**, **6b**,**c**, **8b** were obtained as colorless oils.

[1] Compound numbers in brackets represent the diastereomeric mixtures of two components.

[(5*R*,5a*S*,8a*S*,8b*R*)-2,2,7,7-Tetramethyltetrahydro-3a*H*-di-(1,3)dioxolo[4,5-*b*:4′,5′-*d*]pyran-5-yl]methyl (2*S*)-2-[(benzyloxy)carbonyl]amino-3-phenylpropanoate, Z-L-Phe-*O*-galactopyranose, 3a: Colorless oil (93%), $[\alpha]^{23}_D = -20.4$ (*c* 2.25, CH_2Cl_2); ^{1}H NMR ($CDCl_3$) δ 1.33 (s, 6H), 1.45 (s, 3H), 1.52 (s, 3H), 3.13 (quintet, J = 6.0 Hz, 2H), 3.97−4.01 (m, 1H), 4.07 (d, J = 8.0 Hz, 1H), 4.26 (dd, J = 11.5, 4.9 Hz, 2H), 4.31−4.37 (m, 1H), 4.60 (dd, J = 7.6, 2.2 Hz, 1H), 4.67−4.73 (m, 1H), 5.06 (d, J = 12.3 Hz, 1H, B part of AB system), 5.11 (d, J = 12.4 Hz, 1H, A part of AB system), 5.22 (d, J = 7.9 Hz, 1H), 5.53 (d, J = 5.0 Hz, 1H), 7.12−7.14 (m, 2H), 7.22−7.27 (m, 3H), 7.30−7.38 (m, 5H). ^{13}C NMR ($CDCl_3$) δ 24.4, 24.9, 25.9, 26.0, 38.2, 54.8, 64.1, 65.8, 66.9, 70.4, 70.6, 70.8, 96.2, 108.8, 109.6, 127.0, 128.0, 128.1, 128.5, 128.6, 129.4, 135.7, 136.2, 155.6, 171.4. Anal. Calcd for $C_{25}H_{35}NO_9$: C, 64.31; H, 6.51; N, 2.59. Found: C, 64.04; H, 6.62; N, 2.55.

Table 1. Preparation of *O*-(Z-α-Aminoacyl)diisopropylidene Sugars 3a−d and the Diastereomeric Mixture (3d+3d′) from 2

R	product	yield[a] (%)	t_R (min)[b]
$CH_2C_6H_5$ **1a**	Z-L-Phe-*O*-galactopyranose **3a**	93	3.01
CH_2(3-indolyl) **1b**	Z-L-Trp-*O*-galactopyranose **3b**	88	3.08
CH_2CH_2SMe **1c**	Z-L-Met-*O*-galactopyranose **3c**	90	2.99
CH_3 **1d**	Z-L-Ala-*O*-galactopyranose **3d**	87	3.00
CH_3 **1d+d**	Z-DL-Ala-*O*-galactopyranose (**3d+3d**)	91	3.01, 3.35

[a] Isolated yield. [b] For conditions, refer to Experimental Section.

Table 2. Preparation of *O*-(Z-α-Aminoacyl)diisopropylidene Sugars 6a−d and Diastereomeric Mixtures (6a+6a′), (6d+6d′) from 5

R	product	yield[a] (%)	t_R (min)[b]
$CH_2C_6H_5$ **1a**	Z-L-Phe-*O*-diacetone glucose **6a**	83	2.99
$CH_2C_6H_5$ **1a+1a**	Z-DL-Phe-*O*-diacetone glucose **(6a+6a)**	82	2.99, 3.23
CH_2(3-indolyl) **1b**	Z-L-Trp-*O*-diacetone glucose **6b**	94	3.01
CH_2CH_2SMe **1c**	Z-L-Met-*O*-diacetone glucose **6c**	93	2.99
CH_3 **1d**	Z-L-Ala-*O*-diacetone glucose **6d**	83	2.99
CH3 **1d+1d**	Z-DL-Ala-*O*-diacetone glucose (**6d+6d**)	91	2.99, 3.36

[a] Isolated yield. [b] For conditions, refer to Experimental Section.

General Procedure for the Cleavage of Diisopropylidene Group Present in *O*-(Z-α-Aminoacyl)diisopropylidene Sugars 3a,b, 6d. TFA−H_2O mixture was added to **3a,b, 6d** (0.200 g) at room temperature and were then stirred until **3a**,**b**, **6d** were completely consumed as monitored by TLC. The resulting mixture was concentrated under vaccum followed by washings with diethyl ether (5−6 times) and drying under reduced pressure to afford the desired compound **9a**,**b**, **10** with free OH groups.

(3,4,5,6-Tetrahydroxytetrahydro-2*H*-pyran-2-yl)methyl (2*S*)-2-[(benzyloxy)carbonyl]amino-3-phenylpropanoate, Z-L-Phe-*O*-D-glucose, 9a: White solid (92%), mp 110 °C, decomposed and turned black brown: $[\alpha]^{23}_D = +3.4$ (*c* 2.50, DMF); ^{1}H NMR (DMSO-d_6) δ α/β: 2.81−2.92 (m, 1H), 3.00−3.14 (m, 1H), 3.44−3.62 (m, 2H), 3.68−3.95 (m, 2H), 4.05−4.18 (m, 2H), 4.23−4.38 (m, 2H), 4.40−4.80 (m, 3H), 4.92−4.94 (m, 1H), 4.98 (s, 2H), 7.19−7.37 (m, 10H), 7.78−7.85 (m, 1H). ^{13}C NMR (DMSO-d_6) δ α/β: 36.5, 55.5, 64.1, 65.4, 67.4, 67.5, 71.7, 71.8, 73.0, 75.9, 81.2, 82.6, 92.7, 97.4, 101.8, 126.5, 127.6, 127.6, 127.8, 128.3, 128.3, 129.1, 136.9, 137.4, 137.6, 155.9, 171.8. Anal. Calcd for $C_{23}H_{27}NO_9$: C, 59.86; H, 5.90; N, 3.04. Found: C, 59.58; H, 5.92; N, 2.94.

RESULTS AND DISCUSSION

Preparation of *O*-(Z-α-aminoacyl)diisopropylidene sugars 3a-d, the diastereomeric mixture (3d+3d′) and Bis-*O*-(Z-α-aminoacyl)diisopropylidene Sugar 4 from 1,2:3,4-Di-*O*-isopropylidene-α-D-galactopyranose 2. *O*-(Z-α-Aminoacyl)-diisopropylidene sugars **3a−d**, **(3d+3d′)**, and **4** were prepared by coupling *N*-(Z-α- aminoacyl)benzotriazoles **1a−d, 1d+1d′**, and **1e**, respectively, with 6-OH present in **2**. In the presence of a catalytic amount of DMAP (0.2 equiv), under 100 W microwave irradiation at 65 °C for 15 min; the acylating reagent **1a−d** was completely consumed (Scheme 1). However, for the preparation of **(3d+3d′)** under similar conditions, the reaction takes 1 h to complete. This could be attributed to the slow reactivity of the D-component present in the DL-amino acid moiety. For the preparation of **4**, 0.4 equiv of DMAP were utilized (Scheme 2). The crude products **3a−d**, **(3d+3d′)**, **4** were subjected to silica-gel column chromatography using ethyl acetate/hexane (2:1) as an eluent. The desired products **3a−d**, **4**, and the diastereomeric mixture **(3d+3d′)** were obtained in yields of 88−96%.

NMR and HPLC analysis of **3a−d** and **4** revealed no detectable racemization. ^{1}H NMR of **3a−d**, **4** showed a prominent doublet for the α-NH proton of the amino acid fragment in the range of 5.30−5.45 ppm in $CDCl_3$. All the methyl protons from the diisopropylidene group in sugar appeared as singlets in the NMR analysis, supporting the absence of any undesired isomers of **3a−d**, **4**. In the ^{1}H NMR of **3d**, the doublet arising from the methyl protons present in the Ala fragment overlapped with one of the methyl protons of the sugar moiety. In addition, a clear doublet arising from the α-NH proton was observed. No splitting of the peaks was observed in the ^{13}C NMR of **3d**, in contrast to its corresponding diastereomeric mixture **(3d+3d′)**, supporting the enantiopurity of **3d**. HPLC analysis of **3a−d**, **4** gave single retention times whereas **(3d+3d′)** gave two retention times, confirming the enantiopurity of **3a−d**, **4** (Table 1 and Scheme 2).

Table 3. Preparation of *O*-(Z-α-Aminoacyl)diisopropylidene Sugars 8a,b from 7

R	product	yield[a] (%)	t_R (min)[b]
$CH_2C_6H_5$ **1a**	Z-L-Phe-*O*-mannofuranose **8a**	78	2.99
CH_2CH_2SMe **1c**	Z-L-Met-*O*-mannofuranose **8b**	93	3.00

[a] Isolated yield. [b] For conditions, refer to Experimental Section.

Table 4. Cleavage of Diisopropylidene Groups Present in 3a,d Using TFA−H_2O (9:1; 5 mL)

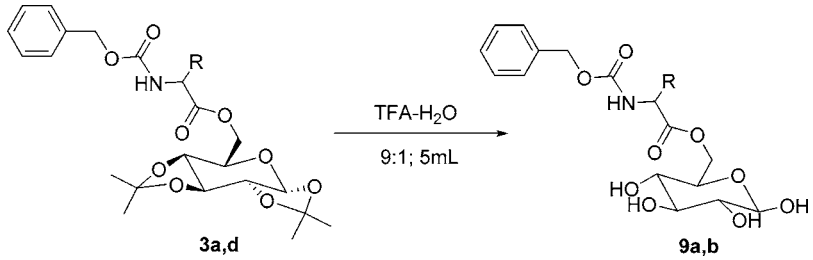
entry	*O*-(Z-α-aminoacyl) diisopropylidene sugars	*O*-(Z-α-aminoacyl) sugars	yield[a]
1	**3a**	**9a**	92
2	**3d**	**9b**	94

[a] Isolated yield.

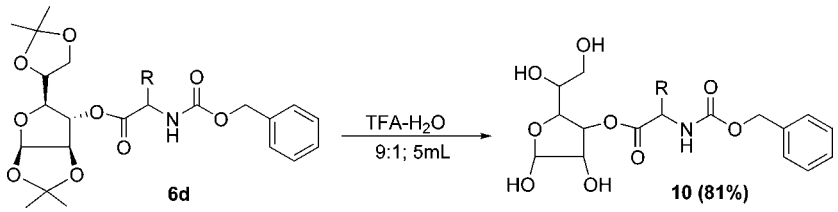
Preparation of *O*-(Z-α-Aminoacyl)diisopropylidene Sugars 6a−d, 8a,b and Diastereomeric Mixtures (6a+6a′), (6d+6d′) Using 1,2:5,6-Di-*O*-isopropylidene-D-glucose 5 and 2,3:5,6-Di-*O*-isopropylidene-α-D-mannofuraanose 7. *O*-(Z-α-Aminoacyl)diisopropylidene sugars **6a−d** were prepared by coupling *N*-(Z-α-aminoacyl)benzotriazoles **1a−d** with 3-OH of **5**, and the products **8a**,**b** were prepared by coupling **1a** and **1c** with 1-OH present in **7**, using similar reactions conditions as used for **3** (Scheme 3 and 4). However, for the preparation of **(6a+6a′)** and **(6d+6d′)** under similar microwave conditions, the reaction takes 1 h to complete (Scheme 3). The products **6a−d**, **8a**,**b** and the diastereomeric mixtures **(6a+6a′)** and **(6d+6d′)** were obtained in yields 78−94%.

NMR analysis of **6a−d**, **8a**,**b** revealed no detectable racemization. ^{1}H NMR demonstrated a prominent doublet for the α-NH proton of the amino acid fragment in the range of 5.44−5.66 ppm in $CDCl_3$. All the methyl protons from the diisopropylidene groups in the sugar appeared as singlets in the NMR spectra indicating the absence of any undesired isomers of **6a−d**, **8a**,**b**. For example, in **6d**, the methyl groups gave the desired singlet at 1.39 ppm and a doublet at 1.43 ppm as compared to the corresponding mixture **(6d+6d′)** which gave a multiplet at

Scheme 5



Scheme 6



1.37−1.42 ppm and two doublets at 1.43 and 1.45 ppm. HPLC analysis of **6a**−**d**, **8a**,**b** each gave single retention times whereas **(6a**+**6a′)** and **(6d**+**6d′)** gave two retention times, confirming the enantiopurity of **6a**−**d**, **8a**,**b** (Tables 2 and 3).

Cleavage of the Diisopropylidene Groups Present in *O*-(Z-α-aminoacyl)diisopropylidene Sugars 3a,d, 6d. The diisopropylidene protecting groups were cleaved using TFA−H_2O (9:1; 5 mL) (Scheme 5 and 6). The TFA−H_2O mixture was added to *O*-(Z-α-aminoacyl)diisopropylidene sugars **3a**,**d**, **6d** (0.200 g) at room temperature and was stirred until **3a**,**d**, **6d** were completely consumed as monitored by TLC. Each resulting mixture was concentrated under reduced pressure followed by subsequent washings with diethyl ether (5−6 times). The free amino acid−sugar conjugates **9a**,**b**, **10** were obtained in yields of 92−94% (Table 4 and Scheme 6) and characterized by ^{1}H and ^{13}C NMR spectroscopy, elemental analysis, melting point, and ORP. The other diastereomer was also observed in the NMR analysis, to the extent of 40−50%.

CONCLUSIONS

In conclusion, we have demonstrated a convenient and efficient preparation of chiral *O*-(Z-α-aminoacyl)diisopropylidene sugars **3a**−**d**, **4**, **6a**−**d**, **8a**,**b** and diastereomeric mixtures **(3d**+**3d′)**, **(6a**+**6a′)**, **(6d**+**6d′)** in yields of 78−96%. The original chirality of the resulting products was preserved in >97% ee as evidenced by NMR and HPLC. These advantages also suggest N-protected-(α-aminoacyl)benzotriazoles as a preferred choice for esterification among conventional coupling agents.

Supporting Information Available: Compound characterization data for all the compounds. This material is available free of charge via the Internet at http://pubs.acs.org

LITERATURE CITED

(1) Eisele, F., Owen, D. J., and Waldmann, H. (1999) Peptide conjugates as tools for the study of biological signal transduction. *Bioorg. Med. Chem. 7*, 193−224.

(2) Wang, W., Jiang, J., Ballard, C. E., and Wang, B. (1999) Prodrug approaches to the improved delivery of peptide drugs. *Curr. Pharm. Des. 5*, 265−287.

(3) Jeric, I., and Horvat, S. (2001) Novel ester-linked carbohydrate-peptide adducts: Effect of the peptide substituent on the pathways of intramolecular reactions. *Eur. J. Org. Chem.*, 1533−1539.

(4) Chakraborty, T. K., Ghosh, S., and Jayaprakash, S. (2002) Sugar amino acids and their uses in designing bioactive molecules. *Curr. Med. Chem. 9*, 421−435.

(5) Glunz, P. W., Hintermann, S., Williams, L. J., Schwarz, J. B., Kuduk, S. D., Kudryashov, V., Lloyd, K. O., and Danishefsky, S. J. (2000) Design and synthesis of Le(y)-bearing glycopeptides that mimic cell surface Le(y) mucin glycoprotein architecture. *J. Am. Chem. Soc. 122*, 7273−7279.

(6) Han, H. K., de Vrueh, R. L. A., Rhie, J. K., Covitz, K. M. Y., Smith, P. L., Lee, C. P., Oh, D. M., Sadee, W., and Amidon, G. L. (1998) 5′-Amino acid esters of antiviral nucleosides, acyclovir, and AZT are absorbed by the intestinal PEPT1 peptide transporter. *Pharm. Res. 15*, 1154−1159.

(7) Kihlberg, J., Ahman, J., Walse, B., Drakenberg, T., Nilsson, A., Soderbergahlm, C., Bengtsson, B., and Olsson, H. (1995) Glycosylated Peptide-Hormones - Pharmacological Properties and Conformational Studies of Analogs of [1-Desamino,8-D-Arginine] Vasopressin. *J. Med. Chem. 38*, 161−169.

(8) Monsigny, M., Roche, A. C., and Midoux, P. (1988) Endogenous Lectins and Drug Targeting. *Ann. N.Y. Acad. Sci. 551*, 399−414.

(9) Stahl, P. D., Rodman, J. S., Miller, M. J., and Schlesinger, P. H. (1978) Evidence for Receptor-Mediated Binding of Glycoproteins, Glycoconjugates, and Lysosomal Glycosidases by Alveolar Macrophages. *Proc. Natl. Acad. Sci. U.S.A. 75*, 1399−1403.

(10) Paulsen, H., Busch, R., Sinnwell, V., and Pollexkruger, A. (1991) Conformation Analysis .29. Conformation Analysis of O-Glycopeptide Sequences with D-Xylose Group. *Carbohyd. Res. 214*, 227−234.

(11) vonRoedern, E. G., Lohof, E., Hessler, G., Hoffmann, M., and Kessler, H. (1996) Synthesis and conformational analysis of linear and cyclic peptides containing sugar amino acids. *J. Am. Chem. Soc. 118*, 10156−10167.

(12) Horvat, S., Roscic, M., Varga-Defterdarovic, L., and Horvat, J. (1998) Intramolecular rearrangement of the monosaccharide esters of an opioid pentapeptide: formation and identification of novel Amadori compounds related to fructose and tagatose. *J. Chem. Soc., Perkin Trans. 1*, 909−913.

(13) Schweizer, F. (2001) Glycosamino acids: Building blocks for combinatorial synthesis - Implications for drug discovery. *Angew. Chem. Int. Ed. 41*, 230−253.

(14) Gruner, S. A. W., Locardi, E., Lohof, E., and Kessler, H. (2002) Carbohydrate-based mimetics in drug design: Sugar amino acids and carbohydrate scaffolds. *Chem. Rev. 102*, 491−514.

(15) Osborn, H. M. I., and Khan, T. H. (1999) Recent developments in polymer supported syntheses of oligosaccharides and glycopeptides. *Tetrahedron 55*, 1807−1850.

(16) Boons, G. J. (1996) Synthetic oligosaccharides: Recent advances. *Drug Discovery Today 1*, 331−342.

(17) Karlsson, K. A. (1991) Glycobiology - a Growing Field for Drug Design. *Trends Pharm. Sci. 12*, 265−272.

(18) Sharon, N., and Lis, H. (1993) Carbohydrates in Cell Recognition. *Sci. Am. 268*, 84.

(19) Dwek, R. A. (1996) Glycobiology: Toward understanding the function of sugars. *Chem. Rev. 96*, 683−720.

(20) Varki, A. (1993) Biological Roles of Oligosaccharides - All of the Theories Are Correct. *Glycobiology 3*, 97−130.
(21) Barkley, A., and Arya, P. (2001) Combinatorial chemistry toward understanding the function(s) of carbohydrates and carbohydrate conjugates. *Chem. Eur. J. 7*, 555−563.
(22) Fukuda, M. (2002) Roles of mucin-type O-glycans in cell adhesion. *Biochim. Biophys. Acta 1573*, 394−405.
(23) Ohyama, C., Tsuboi, S., and Fukuda, M. (1999) Dual roles of sialyl Lewis X oligosaccharides in tumor metastasis and rejection by natural killer cells. *EMBO J. 18*, 1516−1525.
(24) Macmillan, D., and Daines, A. M. (2003) Recent developments in the synthesis and discovery of oligosaccharides and glycoconjugates for the treatment of disease. *Curr. Med. Chem. 10*, 2733−2773.
(25) Varki, A., Cumnings, R., Esko, J., Freeze, H., and Hart, G. (2002) *Essentials of Glycobiology*, 2 ed., Cold Spring Harbor Laboratory Press, Woodbury, NY.
(26) Hart, G. W. (1992) Glycosylation. *Curr. Opin. Cell Biol. 4*, 1017−1023.
(27) Feizi, T., and Childs, R. A. (1985) Carbohydrate Structures of Glycoproteins and Glycolipids as Differentiation Antigens, Tumor-Associated Antigens and Components of Receptor Systems. *Trends Biochem. Sci. 10*, 24−29.
(28) Rademacher, T. W., Parekh, R. B., and Dwek, R. A. (1988) Glycobiology. *Ann. Rev. Biochem. 57*, 785−838.
(29) Paulson, J. C. (1989) Glycoproteins - What Are the Sugar Chains For. *Trends Biochem. Sci. 14*, 272−276.
(30) Gagneux, P., and Varki, A. (1999) Evolutionary considerations in relating oligosaccharide diversity to biological function. *Glycobiology 9*, 747−755.
(31) Varki, A. (1994) Selectin Ligands. *Proc. Natl. Acad. Sci. U.S.A. 91*, 7390−7397.
(32) Reuter, G., and Gabius, H. J. (1999) Eukaryotic glycosylation: whim of nature or multipurpose tool? *Cell. Mol. Life Sci. 55*, 368−422.
(33) Giannis, A. (1994) The Sialyl Lewis(X) Group and Its Analogs as Ligands for Selectins - Chemoenzymatic Syntheses and Biological Functions. *Angew. Chem., Int. Ed. 33*, 178−180.
(34) Jung, K. H., Muller, M., and Schmidt, R. R. (2000) Intramolecular O-glycoside bond formation. *Chem. Rev. 100*, 4423.
(35) Boyer, V., Stanchev, M., Fairbanks, A. J., and Davis, B. G. (2001) Ready protease-catalyzed synthesis of carbohydrate-amino acid conjugates. *Chem. Commun.*, 1908−1909.
(36) Tennant-Eyles, R. J., Davis, B. G., and Fairbanks, A. J. (1999) Peptide templated glycosidic bond formation: a new strategy for oligosaccharide synthesis. *Chem. Commun.*, 1037−1038.
(37) Tennant-Eyles, R. J., Davis, B. G., and Fairbanks, A. J. (2003) Solid phase peptide templated glycosidic bond formation. *Tetrahedron-Asymmetry 14*, 1201−1210.
(38) Tennant-Eyles, R. J., Davis, B. G., and Fairbanks, A. J. (2000) Peptide templated glycosylation reactions. *Tetrahedron-Asymmetry 11*, 231−243.
(39) Tennant-Eyles, R. J., and Fairbanks, A. J. (1999) Novel ester linked glycosyl amino acids: convenient building blocks for the synthesis of glycopeptide libraries. *Tetrahedron-Asymmetry 10*, 391−401.
(40) Geurtsen, R., and Boons, G. J. (2002) Regioselective glycosylations in solution and on soluble and insoluble polymeric supports. *Eur. J. Org. Chem.*, 1473−1477.
(41) Burt, J., Dean, T., and Warriner, S. (2004) The parallel synthesis of a disaccharide library using a solid phase, peptide-templated strategy. *Chem. Commun.*, 454−455.
(42) Horvat, S., Horvat, J., Kantoci, D., and Varga, L. (1989) Glycoconjugates of Opioid Peptides-Iii+ - a Novel Regioselective Synthesis of 6-O-Peptidyl-D-Glycopyranoses Using Unprotected Sugars. *Tetrahedron 45*, 4579−4584.
(43) Horvat, Š., Varga-Defterdarović L., Horvat, J., Modrić-Žganjar, S., Chung, N. N., and Schiller, P. W. (1996) Alterations in biological activities induced by glycation of leucine-enkephalin with different monosaccharide moieties *Lett. Pept. Sci. 2*, 363−368.
(44) Horvat, S., Varga-Defterdarovic, L., Roscic, M., and Horvat, J. (1998) Synthesis of novel imidazolidinones from hexose-peptide adducts: model studies of the Maillard reaction with possible significance in protein glycation. *Chem. Commun.* 1663−1664.
(45) Jeric, I., Simicic, L., Stipetic, M., and Horvat, S. (2000) Synthesis and reactivity of the monosaccharide esters of amino acids as models of teichoic acid fragment. *Glycoconjugate J. 17*, 273−282.
(46) Varga-Defterdarovic, L., and Hrlec, G. (2004) Synthesis and intramolecular reactions of Tyr-Gly and Tyr-Gly-Gly related 6-O-glucopyranose esters. *Carbohyd. Res. 339*, 67−75.
(47) Opatz, T., Kallus, C., Wunberg, T., and Kunz, H. (2004) Combinatorial synthesis of amino acid- and peptide-carbohydrate conjugates on solid phase. *Tetrahedron 60*, 8613−8626.
(48) Park, O. J., Jeon, G. J., and Yang, J. W. (1999) Protease-catalyzed synthesis of disaccharide amino acid esters in organic media. *Enzyme Microb. Technol. 25*, 455−462.
(49) Katritzky, A. R., He, H. Y., and Suzuki, K. (2000) N-acylbenzotriazoles: Neutral acylating reagents for the preparation of primary, secondary, and tertiary amides. *J. Org. Chem. 65*, 8210−8213.
(50) Katritzky, A. R., Wang, M. Y., Yang, H. F., Zhang, S. M., and Akhmedov, N. G. (2002) 1-(alpha-Boc-aminoacyl)benzotriazoles: Stable chiral alpha-aminoacylation reagents. *Arkivoc*, 134−142.
(51) Katritzky, A. R., Yang, H. F., Zhang, S. M., and Wang, M. Y. (2002) An efficient conversion of carboxylic acids into Weinreb amides. *Arkivoc*, 39−44.
(52) Katritzky, A. R., Yang, B. Z., and Semenzin, D. (1997) (Trifluoroacetyl)benzotriazole: A convenient trifluoroacetylating reagent. *J. Org. Chem. 62*, 726−728.
(53) Katritzky, A. R., Wang, M. Y., and Zhang, S. M. (2001) One-pot synthesis of cinnamoyl hydrazides. *Arkivoc 2*, 19−23.
(54) Katritzky, A. R., and Pastor, A. (2000) Synthesis of beta-dicarbonyl compounds using 1-acylbenzotriazoles as regioselective C-acylating reagents. *J. Org. Chem. 65*, 3679−3682.
(55) Katritzky, A. R., Abdel-Fattah, A. A. A., and Wang, M. Y. (2003) Expedient acylations of primary and secondary alkyl cyanides to (alpha-substituted beta-ketonitriles. *J. Org. Chem. 68*, 4932−4934.
(56) Katritzky, A. R., Suzuki, K., Singh, S. K., and He, H. Y. (2003) Regiospecific C-acylation of pyrroles and indoles using N-acylbenzotriazoles. *J. Org. Chem. 68*, 5720−5723.
(57) Katritzky, A. R., Suzuki, K., and Singh, S. K. (2004) C-acylation of 2-methylfuran and thiophene using N-acylbenzotriazoles. *Croat. Chem. Acta 77*, 175−178.
(58) Katritzky, A. R., Pastor, A., and Voronkov, M. V. (1999) Efficient general synthesis of 1-(benzotriazol-1-yl)alkyl esters. *J. Heterocycl. Chem. 36*, 777−781.
(59) Katritzky, A. R., Suzuki, K., and Singh, S. K. (2004) Highly diastereoselective peptide chain extensions of unprotected amino acids with N-(Z-alpha-aminoacyl)benzotriazoles. *Synthesis*, 2645−2652.
(60) Katritzky, A. R., Angrish, P., Hur, D., and Suzuki, K. (2005) N-(Cbz- and Fmoc-alpha-aminoacyl)benzotriazoles: Stable derivatives enabling peptide coupling of Tyr, Trp, Cys, Met, and Gln with free amino acids in aqueous media with complete retention of chirality. *Synthesis*, 397−402.
(61) Katritzky, A. R., Angrish, P., and Suzuki, K. (2006) The efficient preparation of di- and tripeptides by coupling N-(Cbz- or Fmoc-alpha-aminoacyl)benzotriazoles with unprotected amino acids. *Synthesis*, 411−424.
(62) Katritzky, A. R., Todadze, E., Cusido, J., Angrish, P., and Shestopalov, A. A. (2006) Selective peptide chain extension at the n-terminus of aspartic and glutamic acids utilizing 1-(N-protected-alpha-aminoacyl)benzotriazoles. *Chem. Biol. Drug Des. 68*, 37−41.
(63) Katritzky, A. R., Todadze, E., Shestopalov, A. A., Cusido, J., and Angrish, P. (2006) Selective peptide chain extension at the C-terminus of aspartic and glutamic acids utilizing N-protected (alpha-aminoacyl)benzotriazoles. *Chem. Biol. Drug Des. 68*, 42−47.

BC0603687

Binding of Streptavidin with Biotinylated Thermosensitive Nanospheres Based on Poly(*N*,*N*-diethylacrylamide-*co*-2-hydroxyethyl methacrylate)

M. Colonne, Y. Chen, K. Wu, S. Freiberg, S. Giasson, and X. X. Zhu*

Département de Chimie, Université de Montréal, C.P. 6128, Succursale Centre-ville, Montréal, QC, H3C 3J7, Canada.
Received September 29, 2006; Revised Manuscript Received February 19, 2007

Thermosensitive polymer nanospheres based on *N*,*N*-diethylacrylamide and 2-hydroxyethyl methacrylate (HEMA) have been prepared, characterized, and conjugated with biotin. The thermosensitivity of poly(*N*,*N*-diethylacrylamide) was enhanced by the incorporation of HEMA up to about 40 mol %. Atomic force microscopic images show that these particles can be closely packed even without the surface charges as in the latex particles. Biotinylation reduces the thermosensitivity of the copolymer nanospheres. The biotinylated hydrogel nanospheres showed a reduction in size upon binding with streptavidin, indicating the formation of a less hydrophilic conjugate. No aggregation of the biotinylated particles due to the cross-linking effect of streptavidin was observed. This size change could be reversed by the addition of free biotin to the system. The interaction is specific, and no such changes were observed when streptavidin was replaced by bovine serum albumin.

INTRODUCTION

Biologically reactive polymer hydrogels represent an extension of the temperature- or pH-activated systems (*1*). Miyata et al. reported on the preparation of hydrogels conjugated with an antibody that exhibited a reduction in volume in response to a specific antigen by forming cross-links in the gel network that can be reversed upon the addition of free antigen (*2*). Thermosensitive hydrogels are known to swell in water below the lower critical swelling temperature (LCST) due to hydrogen bonding with water (*3*, *4*). Above the LCST, hydrogen bonds with water are disrupted, resulting in a shrinkage of the gels. Such hydrogels can be made into nanospheres by emulsion polymerization, and the size of spheres can be modulated by temperature (*5*, *6*). Bead size modulation by biochemical interactions may lead to biosensor applications. Using charged polystyrene particles which can form colloidal crystal arrays (CCA) induced by electrostatic repulsion, Asher and co-workers built biological sensing systems by embedding them in thermosensitive gels and monitoring the changes of interparticle distances (*7*−*10*). Polymerized CCA of charged particles based on thermosensitive poly(*N*-isopropylacrylamide) (PNIPAM) were also embedded in polyacrylamide matrix to induce a fast response to changes in temperature (within nanoseconds) (*9*).

The high and specific affinity between streptavidin and biotin (association constant, $K_a \approx 10^{15}$) is well-known, and their coupling has been used for the rapid isolation of biomolecules such as proteins (*11*, *12*) or for the preparation of biosensors (*13*−*17*). Streptavidin (60 kDa) is a tetrameric protein that can bind four biotin molecules. Hoffman, Stayton, and co-workers used linear thermosensitive polymers such as PNIPAM or poly(*N*,*N*-diethyl acrylamide) (PDEA) to conjugate genetically engineered streptavidin and then immobilized them on magnetic microbeads (*18*−*22*). Depending on the pH and temperature, the polymers could block biotin binding (*22*). Steric restriction could change the nature of streptavidin binding and cause streptavidin to bind only two biotin molecules instead of four (*18*). The preparation of fiberoptic biosensors (*14*) was also realized by attaching a biotinylated polymeric thin film to the end-face of an optic fiber. It was shown that the system linked to avidin can support biotinylated antigens or antibodies that can be used to detect an anti-cholera toxin antibody with satisfactory performance (*14*).

The change in hydrophilicity of the thermosensitive polymers can be caused not only by a temperature change but also by the interactions between conjugated biological molecules such as streptavidin and biotin. We have prepared a model system with noncharged thermosensitive polymeric nanospheres that can be biotinylated so that they can respond to the presence of streptavidin. PDEA was selected as the polymer matrix with varying amounts of 2-hydroxyethyl methacrylate (HEMA) as functional comonomers. The copolymer nanoparticles were conjugated with biotin, and the binding with streptavidin and the specificity of the binding have been investigated.

EXPERIMENTAL PROCEDURES

Materials and Chemicals. All chemicals were purchased from Aldrich-Sigma. Tetrahydrofuran (THF) was purified and dried prior to use. Biotin, streptavidin, bovine serum albumin (BSA), scandium triflate, potasium persulfate (KPS), sodium dodecyl sulfate (SDS), and 2-(4′-hydroxyazobenzene)benzoic acid (HABA) were used without further purification. *N*,*N*′-Methylene bis(acrylamide) (BA) was recrystallized from methanol. *N*,*N*-Diethylacrylamide (DEA) was prepared from diethylamine and acryloyl chloride (*4*, *23*) and vacuum-distilled before use. HEMA was also vacuum-distilled before use.

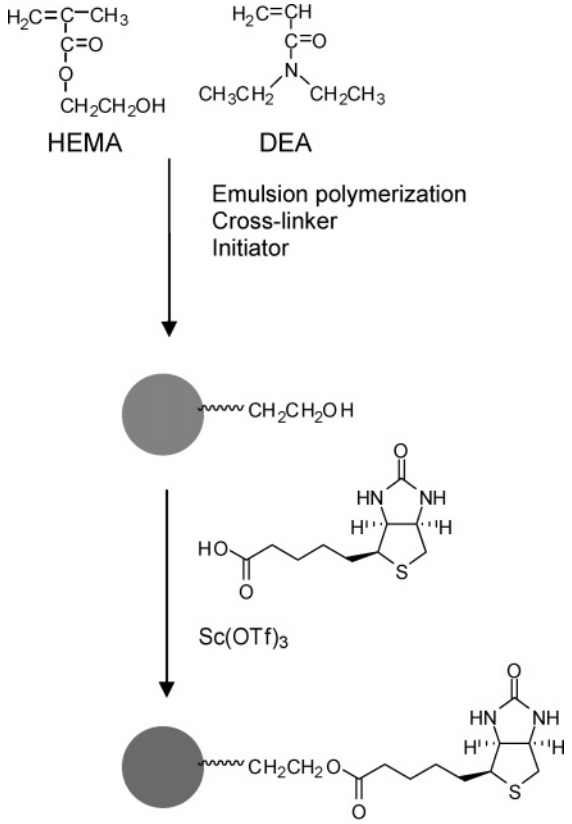
Cellulose sacks for dialysis (MW > 12 000) and Millipore Isopore membrane filters (2.0 μm) were purchased from Sigma. Water was purified by a water purification system from Millipore.

Preparation of Nanospheres and Biotinylation. The preparation of the biotinylated polymer nanospheres is shown in Scheme 1. Emulsion polymerization was done in a 500 mL three-necked flask with mechanical agitation at a constant rate of about 240 rpm. The monomers (DEA and HEMA), BA, and SDS were added to 200 mL of stirred Milli-Q water followed by nitrogen purging for 30 min at 70 °C. KPS, dissolved in 15 mL of Milli-Q water, was added to the solution. The mixture contained 1.5 mol % BA, 0.040 g SDS, and 0.120 g of KPS. A total amount of 26.5 mmol of monomers was used with HEMA

* Corresponding author. Fax: 514-340-5290; E-mail: julian.zhu@umontreal.ca.

10.1021/bc060302b CCC: $37.00 © 2007 American Chemical Society
Published on Web 04/13/2007

Scheme 1. Preparation of the Biotinylated Polymer Nanospheres



content varying from 0 to 100 mol %. The reaction was continued for 4 h and allowed to cool to room temperature before filtering the milky suspensions through 2.0 μm Millipore Isopore membrane filters. The filtrate was centrifuged for 40 min at about 15 000 rpm (relative centrifuge force (RCF) = 32 583 × *g*). The polymer spheres were collected and purified by dialysis for 1 week in Milli-Q water.

To conjugate biotin to the nanospheres containing HEMA, biotin (50 mg, 0.205 mmol) and scandium triflate (20 mg, 0.04 mmol) were stirred in an 8% solution of the spheres containing 0.205 mmol HEMA at 70 °C for 4 days. The resulting solution was centrifuged (15 000 rpm, RCF = 32 583 × *g*) at 20 °C for 20 min, rinsed with Milli-Q water, and dialyzed for 1 week.

For the binding studies, typically, 1 mg of streptavidin (17 nmol) was added directly to the biotinylated spheres in water (10 mL) in a cuvette and mixed for 30 min without filtration.

Sample Characterization and Binding Studies. To determine the amount of biotin attached on the nanospheres, the avidin−HABA assay (*24*−*26*) was used by monitoring the absorbance values at 500 nm for the avidin−HABA reagent and for the solution after addition of biotinylated nanospheres. UV−visible spectra were collected on a Cary 300 Bio UV−visible spectrophotometer. A calibration curve was generated by measuring the change in UV absorbance upon the gradual addition of free biotin of known concentration sequentially into the avidin−HABA reagent. The equivalent amount of free biotin available on the biotinylated nanospheres was calculated by comparing the absorbance change to that of the calibration curve.

Dynamic light scattering (DLS) was performed using a Brookhaven BI-200SM light scattering instrument setup with a Science/Electronics temperature controller and a 532 nm green JDS laser. Samples were prepared by suspending 1−2 drops of polymer spheres in about 20 mL of Milli-Q water followed by filtration through a 2 μm filter. To ensure data reproducibility, measurements were taken 25 min after the temperature was stabilized. At each temperature, 8 measurements were taken to determine the average diameter of the particles, and each temperature cycle was repeated at least 3 times per sample. The size variation due to measurement error is considered to be within 5% as confirmed by multiple measurements carried out by using the same sample on various heating and cooling cycles. The LCST of the aqueous system of the particles is defined as the midpoint of the inflection of the size change during heating.

Diffraction measurements were taken on a home-assembled spectrophotometer (Gamble Technologies USB2000) of wavelengths ranging from 350 to 1000 nm with a tungsten halogen source and an R200−7 VIS/NIR reflection probe. Measurements were taken after sample centrifugation at 15 000 rpm (RCF = 32 583 × *g*) for 30 min at 20 °C and ensuring that the reflectance probe was held 90° to the bead-containing cuvette.

Atomic force microscopy **(**AFM) was performed on a Digital Instruments Nanoscope III (Dimension 3100) in tapping mode with image set point at 75% of the pop-off value.

Table 1. Composition and Thermosensitive Properties of Poly(DEA-*co*-HEMA) Nanospheres

	HEMA/DEA molar ratio			
sample	feed	final[a]	LCST (°C)	size change[b] (%)
100% DEA	0/100	0/00	28	66.7
2% HEMA	2.5/97.5	2/98	28	68.9
9% HEMA	5/95	9/91	28	70.2
15% HEMA	10/90	15/85	25	75.9
27% HEMA	20/80	27/73	23	70.1
37% HEMA	30/70	37/63	23	77.8
48% HEMA	40/60	48/52	20	71.0
54% HEMA	50/50	54/46	25	66.7
100% HEMA	100/0	100/0		7.7

[a] Measured by elemental analyses of the samples. [b] Particle size variation between 10 and 50 °C vs size at 10 °C.

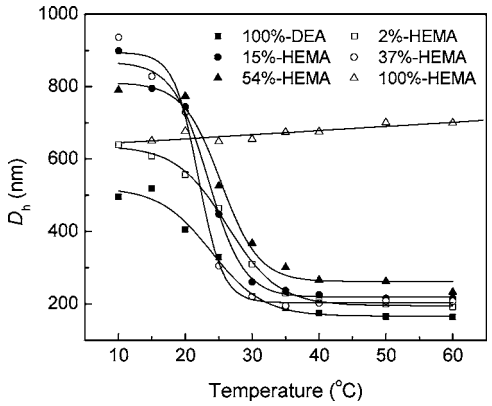


Figure 1. Thermosensitivity of the poly(DEA-*co*-HEMA) nanospheres as studied by DLS. HEMA enhances the thermosensitivity of the beads containing DEA, even if the homopolymer of HEMA itself does not exhibit thermosensitivity.

RESULTS AND DISCUSSION

Preparation and Thermosensitivity of the Nanospheres. Table 1 shows the list of the nanospheres prepared and the resulting compositions as obtained by elemental analysis. Colloidal stability is evident below a HEMA content of 48 mol %, but precipitation occurred over a period of several days with a higher HEMA content. At high HEMA contents (88 and 100 mol %), the samples precipitated readily, although dilute suspensions can be maintained.

DLS results at different temperatures are shown in Figure 1. It is interesting to note that the nanospheres made of PDEA alone, known to be thermosensitive, exhibited lower thermosensitivity than some of the copolymers with HEMA, although the HEMA homopolymer beads do not show any size change with

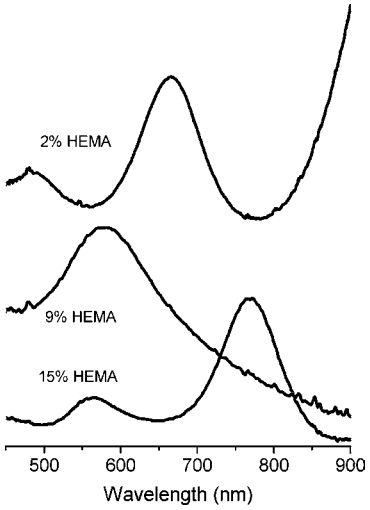


Figure 2. Poly(DEA-*co*-HEMA) nanospheres with different HEMA contents can diffract visible light at specific wavelengths as a result of the well-packed nanospheres of uniform size. Size of particles (measured by DLS at 20 °C): 15% HEMA, 744 nm; 9% HEMA, 571 nm; 2% HEMA, 556 nm.

temperature (Figure 1). The size differences (between 50 and 10 °C) of the thermosensitive nanospheres also increased with the HEMA content up to 37 mol % HEMA (Table 1). It is clear that HEMA enhances significantly the thermosensitivity of the PDEA beads at lower HEMA contents (even at just 2 mol % HEMA). At higher HEMA contents (above 50%), however, the opposite effect on thermosensitivity of the copolymers was observed. The results indicate an enhanced hydrogen bonding in the presence of small quantities of HEMA in the copolymer, with corresponding enhancement in the thermosensitivity of the gel. An increase in the HEMA content may result in a more rigid structure that is harder to contract upon the disruption of hydrogen bonds, which means that the enhancement of the thermosensivity was not accompanied by an enhanced hydrophilicity of the copolymers. The LCST of the spheres (Table 1) shows a general decreasing trend with increasing HEMA content to 48 mol %.

Self-Assembly of the Nanospheres. The centrifugation of the nanospheres (white color for a stable suspension) yielded samples that were iridescent when the HEMA content was less than 40 mol %. The color of the sample is dependent on the viewing angle. This indicates that the beads are packed in a regular fashion meeting conditions of the Bragg's law in the visible light wavelength range. Diffraction spectra obtained for various polymers are shown in Figure 2, and constructive interference is observed at specific wavelengths.

Self-assembly of the nanoparticles is also clearly seen by AFM (Figure 3). Upon spin-casting of the mixture, the beads assembled into hexagonally ordered arrays. AFM images of 37% HEMA beads showed that these soft beads are compressed from their expected spherical diameters. In solution, the particles are spherical with a diameter of approximately 450 nm at room temperature (obtained by DLS, Figure 1), but the dried samples form disclike particles with an average diameter of approximately 425 nm and a height of about 85 nm (data not shown). In an attempt to increase the spherical character of the particles after spin-casting and drying, beads with a higher degree of cross-linking (10% cross-linking agent) and 2.5% HEMA in the feed were synthesized. It was hoped that increased cross-linking density might reduce the amount of particle deformation upon drying. Figure 3 shows both the height and phase images of the particles. However, the AFM images still show they were in the form of discs (ca. 420 nm in diameter and ca. 110 nm in height). The phase image in Figure 3B shows

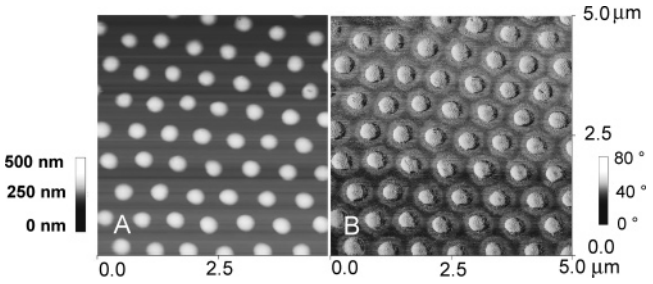


Figure 3. AFM images of hexagonally ordered poly(DEA-*co*-HEMA) nanospheres with 2% HEMA (size 394 nm measured by DLS at 20 °C) beads after spin-casting. (A) Height image. (B) Phase image showing a thin layer of polymer mass forming a ring around the core of the particles.

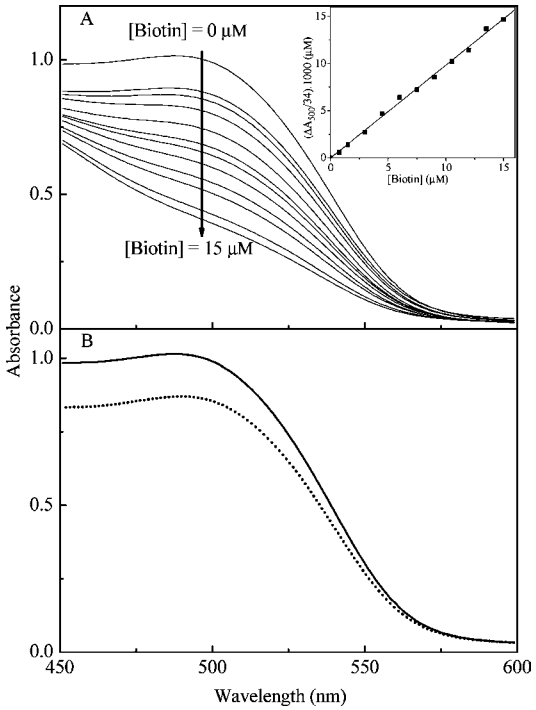


Figure 4. (A) The UV−visible spectra of the avidin−HABA complex, showing a decrease in the absorbance of the complex as free biotin concentration changed from 0 to 15 μM. The inset shows the calibration curve of the changes in absorbance as a function of biotin concentration (*26*). (B) UV−visible spectra of the avidin−HABA complex without (solid line) and with (dotted line) added biotinylated poly(DEA-*co*-HEMA) nanospheres containing 37% HEMA.

that each particle has a core size of ca. 420 nm surrounded by additional ring of ca. 120−130 nm in thickness increasing the diameter to ca. 670 nm. Therefore, this moderate increase in the degree of cross-linking did not help the particles to retain their spherical form upon centrifugation and dehydration.

The Biotinylated Spheres and Their Interaction with Streptavidin. The chemical conjugation of biotin to the polymer nanospheres (formation of an ester bond) can be evidenced by the reduced thermosensitivity of particles as shown in the example of the spheres containing 37% HEMA (Figure 5). Before biotinylation, the particles exhibited a sharp reduction in size from ca. 900 to 200 nm in water when the temperature was raised from 10 to 50 °C. After biotinylation, the change in size becomes much smaller (from ca. 800 to 450 nm). The results suggest a reduction in hydrophilicity upon biotinylation. Biotin coupling to the bead surface may render the outer layer of particle more hydrophobic, causing reduced thermosensitivity.

The amount of biotin attached on the polymer particles was quantified by the avidin−HABA assay (*24*−*26*). Figure 4 shows the UV−visible spectra of the avidin−HABA complex and the

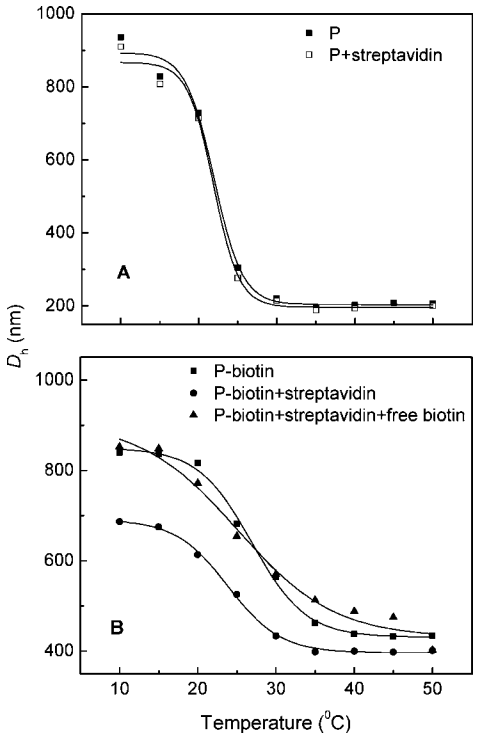


Figure 5. Thermosensitivity of the poly(DEA-*co*-HEMA) nanospheres (A) before and (B) after biotinylation, and in the presence or absence of streptavidin. "P" indicates the polymer particles containing 37 mol % HEMA.

spectroscopic changes of the complex upon the addition of biotinylated particles. The absorbance of the avidin−HABA complex at 500 nm decreased when biotinylated particles were added, since HABA (dissociation constant $K_d \approx 10^{-6}$ M) was replaced by biotin, which has a much higher binding affinity to avidin ($K_d \approx 10^{-15}$ M for avidin complex with free biotin) (*26*). On the basis of the calibration curve in Figure 4A, the amount of available biotin on the biotinylated particles was calculated (ca. 9.8 nmol/mL of the particle solution). The value can be further converted to ca. 2.0 μmol/g of particles. The amount of biotin detected may only correspond to those accessible for the avidin−HABA test, which may underestimate the total amount of biotin attached. The amount of biotin estimated in this test is still meaningful, since only the accessible biotin molecules can participate in the subsequent interaction studies. This amount corresponds only to 0.1% of the HEMA groups on the polymer spheres.

Figure 5A shows a blank experiment with unbiotinylated particles containing 37% HEMA. The addition of free streptavidin to these particles did not cause any appreciable change of their thermosensitivity, indicating the absence of any interactions. When streptavidin was added to a solution of biotinylated beads (Figure 5B), however, the change in the thermosensitivity curves is clearly shown. The size of these particles was reduced upon the interaction between steptavidin and biotin throughout the entire temperature range, with the largest reduction in size at temperatures below the LCST. The overall complex became less thermosensitive with a smaller size change than the original particles before the binding. Figure 6 shows that the change in particle size became more pronounced with subsequent additions of streptavidin due to increased biotin−streptavidin interactions. At the relatively low concentrations of the spheres used in this study, we did not observe any aggregation of the particles that may be caused by the cross-linking effect of streptavidin for the nanospheres. The reduction in size is due to reduced hydrophilicity of the particles upon binding with streptavidin,

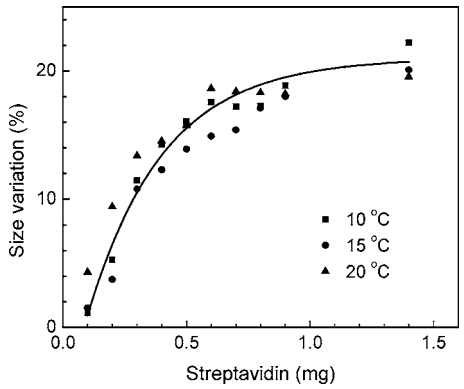


Figure 6. Size variation of biotinylated poly(DEA-*co*-HEMA) nanospheres containing 37% HEMA with different amounts of added streptavidin to 10 mL of a sample containing the nanospheres at three different temperatures.

similar to the process experienced by the thermosensitive particles upon heating.

Even at such low biotinylation levels, the presence of streptavidin was still clearly sensed by the biotinylated spheres. A high level of immobilized biotin may be desirable for a more efficient binding; care should be taken here since increased biotinylation may also reduce the thermosensitivity of the spheres (*19*) and hence its sensitivity toward the protein.

It is interesting to note that the binding between the protein (streptavidin) and the biotinylated particles was reversible. Figure 5B shows that the addition of free biotin to the streptavidin-containing system actually restored the particle size and their thermosensitivity to a state similar to that before their binding with streptavidin. Clearly, streptavidin has a higher affinity to free biotin than to the biotinylated particles. This reversibility indicates that such a system can even be reused if necessary. Results in Figure 5 also suggest that the streptavidin binding to the biotinylated particles may be disrupted above the LCST (as shown by the size change of the particles), which was suggested previously (*22*).

An experiment was performed to study the size variation of the beads at three different temperatures when increasing amounts of streptavidin were added to a sample containing 37% HEMA (Figure 6). The profiles are rather similar below the LCST of the gels. It is shown that the size change becomes more pronounced when the amount of streptavidin reaches about 0.6 mg (9 nmol) in 10 mL of the aqueous mixture which contains 2 mg of solid polymer particles (the amount of available biotin is 4 nmol). It is known that 1 molecule of streptavidin can bind up to 4 molecules of biotin. Therefore, this much lower stoichiometric ratio indicates that steric hindrance may have inhibited the binding of the immobilized biotin on the particles to streptavidin and that not all the binding sites were occupied.

To verify the specificity of the interaction between the biotinylated nanospheres and streptavidin, BSA, with a similar molecular weight (66 000 Da) to that of streptavidin, was also added to a solution of the beads. No size change of the nanospheres occurred, which indicates that the complexation is specific to the coupling between biotin and streptavidin.

CONCLUSION

It is clear that the hydrophilicity of the biotinylated hydrogel nanospheres changes upon binding with streptavidin. The biotin loading on the polymer spheres was relatively low, but already effective in triggering a response of the polymer spheres upon interaction with the protein. This is rather similar to the dehydration of the thermosensitive polymers in water when the temperature is raised, caused by the disruption of hydrogen bonds. The size change of the particles is more pronounced at

lower temperatures when the particles are most hydrated. The binding is reversible upon the addition of free biotin to the mixture, indicating its higher binding affinity in the solution in comparison to the biotinylated beads.

It may be interesting to selectively introduce extra HEMA surface groups to the particles by a delayed addition of HEMA during the polymerization. This may help in the optimization of this model sensor system. This work sets an example to attach other bioactive molecules in a similar fashion to noncharged soft hydrogel spheres for the development of useful biosensing systems with specificity.

ACKNOWLEDGMENT

Financial support FQRNT of Quebec, NSERC of Canada, and the Canada Research Chair program is gratefully acknowledged.

LITERATURE CITED

(1) Bae, Y. H., Okano, T., and Kim, S. W. (1991) "On−off" thermocontrol of solute transport. I. Temperature dependence of swelling of *N*-isopropylacrylamide networks modified with hydrophobic components in water. *Pharm. Res. 8*, 531−537.

(2) Miyata, T., Asami, N., and Uragami, T. (1999) A reversibly antigen-responsive hydrogel. *Nature (London) 399*, 766−769.

(3) Liu, H. Y., and Zhu, X. X. (1999) Lower critical solution temperatures of *N*-substituted acrylamide copolymers in aqueous solutions. *Polymer 40*, 6985−6990.

(4) Nichifor, M., and Zhu, X. X. (2003) Copolymers of *N*-alkylacrylamides and styrene as new thermosensitive materials. *Polymer 44*, 3053−3060.

(5) McPhee, W., Tam, K. C., and Pelton, R. (1993) Poly(*N*-isopropylacrylamide) lattices prepared with sodium dodecyl sulfate. *J. Colloid Interface Sci. 156*, 24−30.

(6) Pelton, R. H., Pelton, H. M., Morphesis, A., and Rowell, R. L. (1989) Particle sizes and electrophoretic mobilities of poly(*N*-isopropylacrylamide) latex. *Langmuir 5*, 816−818.

(7) Asher, S. A., Holtz, J., Liu, L., and Wu, Z. (1994) Self-assembly motif for creating submicron periodic materials. Polymerized crystalline colloidal arrays. *J. Am. Chem. Soc. 116*, 4997−4998.

(8) Reese, C. E., Baltusavich, M. E., Keim, J. P., and Asher, S. A. (2001) Development of an intelligent polymerized crystalline colloidal array colorimetric reagent. *Anal. Chem. 73*, 5038−5042.

(9) Holtz, J. H., and Asher, S. A. (1997) Polymerized colloidal crystal hydrogel films as intelligent chemical sensing materials. *Nature (London) 389*, 829−832.

(10) Asher, S. A., Alexeev, V. L., Goponenko, A. V., Sharma, A. C., Lednev, I. K., Wilcox, C. S., and Finegold, D. N. (2003) Photonic crystal carbohydrate sensors: Low ionic strength sugar sensing. *J. Am. Chem. Soc. 125*, 3322−3329.

(11) Furukawa, H., Shimojyo, R., Ohnishi, N., Fukuda, H., and Kondo, A. (2003) Affinity selection of target cells from cell surface displayed libraries: a novel procedure using thermo-responsive magnetic nanoparticles. *Appl. Microbiol. Biotechnol. 62*, 478−483.

(12) Garret-Flaudy, F., and Freitag, R. (2001) Use of the avidin (imino)-biotin system as a general approach to affinity precipitation. *Biotechnol. Bioeng. 71*, 223−234.

(13) Kumpumbu-Kalemba, L., and Leclerc, M. (2000) Electrochemical characterization of monolayers of a biotinylated polythiophene: Towards the development of polymeric biosensors. *Chem. Commun.* 1847−1848.

(14) Marks, R. S., Novoa, A., Thomassey, D., and Cosnier, S. (2002) An innovative strategy for immobilization of receptor proteins on to an optical fiber by use of poly(pyrrole-biotin). *Anal. Bioanal. Chem. 374*, 1056−1063.

(15) Glidle, A., Yasukawa, T., Hadyoon, S, C., Anicet, N., Matsu, T., Nomura, M., and Cooper, J. M. (2003) Analysis of protein adsorption and binding at biosensor polymer interfaces using X-ray photon spectroscopy and scanning electrochemical microscopy. *Anal. Chem. 75*, 2559−2570.

(16) Shim, M., Kam, N. W. S., Chen, R. J., Li, Y., and Dai, H. (2002) Functionalization of carbon nanotubes for biocompatibility and biomolecular recognition. *Nano Lett. 2*, 285−288.

(17) Lee, K-B., Yoon, K. R., Woo, S. I., and Choi, I. S. (2003) Surface modification of poly(glycolic acid) for biomedical applications. *J. Pharm. Sci. 92*, 933−937.

(18) Ding, Z., Fong, R. B., Long, C. J., Stayton, P. S., and Hoffman, A. S. (2001) Size-dependent control of the binding of biotinylated proteins to streptavidin using a polymer shield. *Nature (London) 411*, 59−62.

(19) Bulmus, V., Ding, Z., Long, C. J., Stayton, P. S., and Hoffman, A. S. (2000) Site-specific polymer-streptavidin bioconjugate for pH-controlled binding and triggered release of biotin. *Bioconjugate Chem. 11*, 78−83.

(20) Malmstadt, N., Hyre, D. E., Ding, Z., Hoffman, A. S., and Stayton, P. S. (2003) Affinity thermoprecipitation and recovery of biotinylated biomolecules via a mutant streptavidin-smart polymer conjugate. *Bioconjugate Chem. 14*, 575−580.

(21) Kulkarni, S., Schilli, C., Müller, A. H. E., Hoffman, A. S., and Stayton, P. S. (2004) Reversible meso-scale smart polymer-protein particles of controlled sizes. *Bioconjugate Chem. 15*, 747−753.

(22) Ding, Z., Long, C. J., Hayashi, Y., Bulmus, E. V., Hoffman, A. S., and Stayton, P. S. (1999) Temperature control of biotin binding and release with a streptavidin-poly(*N*-isopropylacrylamide) site-specific conjugate. *Bioconjugate Chem. 10*, 395−400.

(23) Shea, K. J., Stoddard, G. J., Shavelle, D. M., Wakui, F., and Choate, R. M. (1990) Synthesis and characterization of highly crosslinked poly(acrylamides) and poly(methacrylamides). A new class of macroporous polyamides. *Macromolecules 23*, 4497−4507.

(24) Green, N. M. (1975) Avidin. In *Advances in in Protein Chemistry*, Vol 29, pp 85−133, Academic Press, New York.

(25) Green, N. M. (1970) Spectrophotometric determination of avidin and biotin. *Methods Enzymol. 18*, 418−424.

(26) Qi, K., Ma, Q. G., Remsen, E. E., Clark, C. G., and Wooley, K. L. (2004) Determination of the bioavailability of biotin conjugated onto shell cross-linked (SCK) nanoparticles. *J. Am. Chem. Soc. 126*, 6599−6607.

BC060302B

Testing Oligothiophene Fluorophores under Physiological Conditions. Preparation and Optical Characterization of the Conjugates of Bovine Serum Albumin with Oligothiophene *N*-Hydroxysuccinimidyl Esters

Massimo Zambianchi,[†,*] Andrea Barbieri,[†] Alfredo Ventola,[‡] Laura Favaretto,[†] Cristian Bettini,[‡] Matteo Galeotti,[‡] and Giovanna Barbarella[†,*]

Istituto per la Sintesi Organica e la Fotoreattività (ISOF), Consiglio Nazionale delle Ricerche (CNR) and Mediteknology srl, Via Piero Gobetti 101, 40129 Bologna, Italy. Received October 24, 2006; Revised Manuscript Received January 22, 2007

Bovine serum albumin (BSA) was reacted with linear and newly synthesized branched oligothiophene *N*-hydroxysuccinimidyl ester fluorophores (TSEs) in moderately basic carbonate buffer solution. Optically stable BSA−TSE conjugates were obtained with a degree of labeling depending on experimental conditions. Conjugates with high fluorophore to BSA ratios (F/BSA = 8) displayed fluorescence quantum yields in the range of 10−30% in water at pH = 7.2, comparable to the quantum yield (25%) of the BSA−FITC conjugate prepared under the same conditions and with the same degree of labeling.

INTRODUCTION

Currently, there is a wide interest in polythiophenes as optical reporters of events of biological interest (*1*−*4*). Indeed, besides being important semiconductor materials, thiophene oligomers and polymers may also be strongly fluorescent compounds (*5*), and their optical properties are very sensitive to conformational changes induced by the environment (*6*). Charged polythiophenes have been used for polynucleotide detection, DNA hybridization, and sequence characterization, showing high selectivity and sensitivity useful for applications in medical diagnostics (*1*−*4*). The fluorescence properties of charged polythiophenes have been used for the specific detection of nucleic acids in sub-micromolar concentrations (*7*). Furthermore, it has been demonstrated that the optical phenomena observed in solution upon interaction of polynucleotides with charged polythiophenes can also be induced on surfaces, indicating that there is room for the development of inexpensive polythiophene-based gene chips for DNA detection (*3*).

Our interest in the field of biodiagnostics has brought us to develop new classes of thiophene-based fluorophores emitting light in the visible range and characterized by remarkable optical stability and fluorescence intensity (*8*, *9*). In particular, we have developed a rapid and high yield synthetic pattern for the preparation of oligothiophene *N*-hydroxysuccinimidyl esters and demonstrated that these fluorophores can be covalently linked to biological molecules and can be used to image specific antibody−antigen interactions in tumor cells by fluorescence microscopy or monitor polynucleotides hybridization by fluorescence spectroscopy methods (*9*).

Development of innovative fluorescent probes is highly required by the increasing number of applications of fluorescence techniques in biotechnologies (*10*, *11*). Fluorescence is a widely used readout modality employed in medical diagnostics, cellular imaging, microarrays, etc. and there is a recognized shortage of efficient fluorophores for biological applications. Developing new markers as probes for protein binding, DNA hybridization, immunoistochemistry, or other applications requires detailed knowledge on the spectroscopic and chemical properties of fluorophore-biopolymer conjugates to provide a basis for such applications. Newly developed markers should be easy to handle and to couple to biopolymers, be highly fluorescent under aqueous conditions, be resistant to photobleaching, and have large Stokes shifts between emission and absorption to facilitate fluorescence detection. The fluorophores should also be available in a great number of shades for multilabeling experiments and should be easy to couple to biopolymers with the same standard chemical methodology in all colors. Moreover, it is greatly desirable that all colors be excitable by means of the same light source. However, developing new fluorophores with all these characteristics at the same time is challenging, mainly because the optical response to excitation of a given molecular structure is not easy to predict. In this respect, thiophene oligomers are intriguing compounds, since the balance between radiative and nonradiative deexcitation pathways is greatly affected by the nature and the position of substituents, oligomers size, environment, etc. (*6*, *12*, *13*).

We report here a study on the optical properties of a set of newly synthesized oligothiophene *N*-hydroxysuccinimidyl esters (TSEs), together with the preparation and the optical characterization of the conjugates of linear and branched TSEs with bovine serum albumin (BSA). BSA, a major component in plasma protein, is one of the cheapest commercially available proteins and has been used as a model in a variety of studies (*14*−*16*). In the context of the present investigation, BSA is used to test the amino-reactive TSEs in the formation of bioconjugates in aqueous solvents and assess their fluorescence properties in physiological conditions.

MATERIALS AND METHODS

General Details. Bovine serum albumin (BSA), 2-bromothiophene (**3a**), succinic anhydride, aluminum chloride ($AlCl_3$), *N*-hydroxysuccinimide (HOSu), *N*,*N*′-dicyclohexylcarbodiimide (DCC), *N*-bromosuccinimide (NBS), tris(dibenzylideneacetone)dipalladium(0)−chloroform adduct, Tween-20, and triphenylarsine are commercially available compounds.

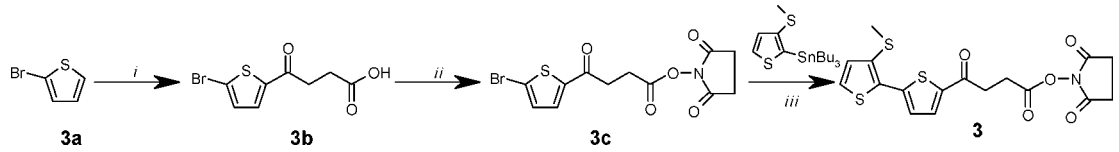
* Authors to whom the correspondence should be adressed. E-mail: barbarella@isof.cnr.it.

[†] Istituto per la Sintesi Organica e la Fotoreattività (ISOF).

[‡] Mediteknology srl, Consiglio Nazionale Ricerche, Via Piero Gobetti 101, 40129 Bologna, Italy.

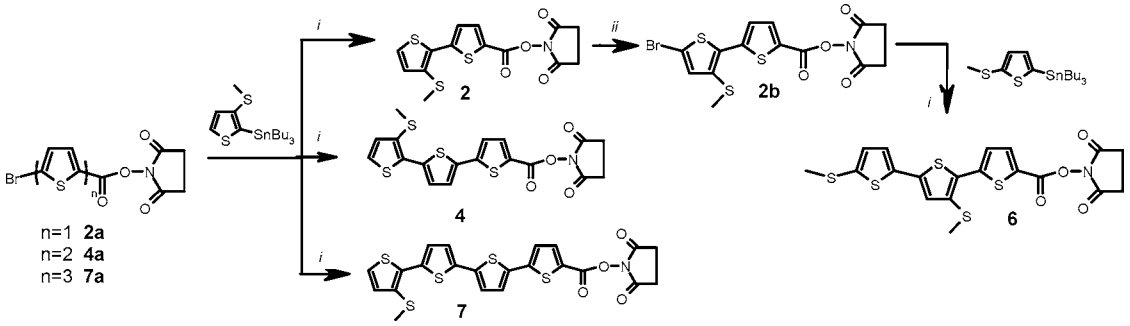
10.1021/bc060332e CCC: $37.00 © 2007 American Chemical Society
Published on Web 03/23/2007

Scheme 1 [a]



[a] Reagents and conditions: (*i*) (I) Succinic anhydride, $AlCl_3$, (II) aq. HCl 4N; (*ii*) HOSu, DCC; (*iii*) $Pd(AsPh_3)_4$.

Scheme 2 [a]



[a] Reagents and conditions: (*i*) $Pd(AsPh_3)_4$; (*ii*) NBS.

Synthesis of Fluorophores. The synthesis of compounds **1** and **5** has already been reported (*9*). The synthesis of compound **3** was performed as shown in Scheme 1. The synthesis of compounds **2**, **4**, **6**, **7** was performed as shown in Scheme 2.

4-(3′-Methylsulfanyl-[2,2′]bithiophenyl-5-yl)-4-oxo-butyric Acid 2,5-Dioxo-pyrrolidin-1-yl Ester (**3**). Yield: 55%. Pale yellow solid, mp 153−155 °C. EI-MS *m*/*z* 409 (M^+). ^{1}H NMR ($CDCl_3$, TMS/ppm) δ 7.69 (d, ^3J = 4.0 Hz, 1H), 7.35 (d, ^3J = 4.0 Hz, 1H), 7.31 (d, ^3J = 4.8 Hz, 1H), 7.07 (d, ^3J = 4.8 Hz, 1H), 3.36 (t, ^3J = 6.8 Hz, 2H), 3.10 (t, ^3J = 6.8 Hz, 2H), 2.84 (s, 4H), 2.51 (s, 3H); ^{13}C NMR ($CDCl_3$, TMS/ppm) δ 189.1, 168.9, 168.2, 144.2, 141.4, 132.8, 132.3, 131.8, 130.4, 126.2, 125.5, 33.3, 25.6, 25.4, 18.6. Anal. Calcd for $C_{17}H_{15}NO_5S_3$ (409.50): C, 49.86; H, 3.69. Found: C, 49.95; H, 3.81.

3′-Methylsulfanyl-[2,2′]bithiophenyl-5-carboxylic Acid 2,5-dioxo-pyrrolidin-1-yl Ester (**2**). Yield: 71%. Microcrystalline bright yellow solid, mp 131 °C; EI-MS *m*/*z* 353 (M^+); ^{1}H NMR ($CDCl_3$, TMS/ppm) δ 7.94 (d, ^3J = 4.4 Hz, 1H), 7.38 (d, ^3J = 4.4 Hz, 1H), 7.34 (d, ^3J = 5.2 Hz, 1H), 7.09 (d, ^3J = 5.2 Hz, 1H), 2.90 (s, 4H), 2.51 (s, 3H); ^{13}C NMR ($CDCl_3$, TMS/ppm) δ 169.1, 157.4, 145.9, 136.5, 133.2, 131.7, 130.7, 126.1, 125.8, 125.1, 25.6, 18.7. Anal. Calcd for $C_{14}H_{11}NO_4S_3$ (352.99): C, 47.58; H, 3.14. Found: C, 47.66; H, 3.23.

3′′-Methylsulfanyl-[2,2′;5′,2′′]terthiophene-5-carboxylic Acid 2,5-Dioxo-pyrrolidin-1-yl Ester (**4**). Yield: 80%. Microcrystalline bright orange solid, mp 156 °C; EI-MS *m*/*z* 435 (M^+); ^{1}H NMR ($CDCl_3$, TMS/ppm) δ 7.92 (d, ^3J = 4.0 Hz, 1H), 7.29 (d, ^3J = 4.0 Hz, 1H), 7.28 (d, ^3J = 4.0 Hz, 1H), 7.25 (d, ^3J = 5.2 Hz, 1H), 7.24 (d, ^3J = 4.0 Hz, 1H), 7.06 (d, ^3J = 5.2 Hz, 1H), 2.90 (s, 4H), 2.50 (s, 3H); ^{13}C NMR ($CDCl_3$, TMS/ppm) δ 169.1, 157.1, 147.6, 137.6, 137.4, 135.2, 132.9, 130.7, 130.6, 126.8, 126.1, 124.3, 124.1, 124.0, 25.6, 18.8. Anal. Calcd for $C_{18}H_{13}NO_4S_4$ (434.97): C, 49.64; H, 3.01. Found: C, 49.73; H, 3.07.

5′-Bromo-3′-methylsulfanyl-[2,2′]bithiophenyl-5-carboxylic Acid 2,5-Dioxo-pyrrolidin-1-yl Ester (**2b**). Under exclusion of light *N*-bromosuccinimide (0.33 g, 1.87 mmol) was added stepwise to a solution of **2** (0.60 g, 1.70 mmol) in acetic acid/methylene chloride 1:1 (30 mL). The mixture was left to stir overnight and then quenched with ice. After separation of layers, the aqueous phase was extracted with dichloromethane. The resulting organic layers were washed with potassium hydroxide (2 × 50 mL, 10% aqueous) and then dried over anhydrous sodium sulfate. Evaporation of the solvent under reduced pressure gave the crude product, which was isolated by flash chromatography on silica with increasing amounts of ethyl acetate in petroleum ether as eluent. Yield: 0.47 g (64%). Polycrystalline yellow solid; EI-MS *m*/*z* 432 (M^+); ^{1}H NMR ($CDCl_3$, TMS/ppm) δ 7.13 (d, ^3J = 4.0 Hz, 1H), 7.27 (d, ^3J = 4.0 Hz, 1H), 7.04 (s, 1H), 2.90 (s, 4H), 2.50 (s, 3H).

5′′-Methylsulfanyl-3′-methylsulfanyl-[2,2′;5′,2′′]terthiophene-5-carboxylic Acid 2,5-Dioxo-pyrrolidin-1-yl Ester (*6*). To a 5 mL dry toluene solution containing 0.0025 mmol of tetrakis-(triphenylarsine)palladium(0) prepared in situ was added compound **2b** (22 mg, 0.05 mmol) in toluene (2 mL). The mixture was heated to 80 °C, and 2-tributylstannyl-5-(methylthio)-thiophene (21 mg, 0.05 mmol) dissolved in 2 mL of toluene was added dropwise. The reaction mixture was stirred for 4 h at this temperature, and then the solvent was removed under reduced pressure. The crude mixture was purified by flash chromatography (silica gel, petroleum ether/ ethyl acetate 1:1) to provide 16 mg (66% yield) of the title product as microcrystalline yellow ocher solid, mp 106−108 °C; EI-MS *m*/*z* 481 (M^+); ^{1}H NMR ($CDCl_3$, TMS/ppm) δ 7.93 (d, ^3J = 4.0 Hz, 1H), 7.34 (d, ^3J = 4.0 Hz, 1H), 7.06 (d, ^3J = 4.0 Hz, 1H), 7.05 (s, 1H), 6.98 (d, ^3J = 4.0 Hz, 1H), 2.90 (s, 4H), 2.54 (s, 3H), 2.53 (s, 3H); ^{13}C NMR ($CDCl_3$, TMS/ppm) δ 169.2, 157.4, 145.5, 138.5, 137.2, 136.9, 136.5, 134.2, 131.3, 130.1, 126.3, 125.8, 125.0, 124.9, 25.8, 21.8, 18.7. Anal. Calcd for $C_{19}H_{15}NO_4S_5$ (481.65): C, 47.38; H, 3.14. Found: C, 47.61; H, 3.22.

3′′′-Methylsulfanyl-[2,2′;5′,2′′;5′′,2′′′]quaterthiophene-5-carboxylic Acid 2,5-Dioxo-pyrrolidin-1-yl Ester (**7**). Yield: 72%. Microcrystalline red-orange solid, mp 195 °C; EI-MS *m*/*z* 517 (M^+); ^{1}H NMR ($CDCl_3$, TMS/ppm) δ 7.92 (d, ^3J = 4.0 Hz, 1H), 7.27 (d, ^3J = 4.0 Hz, 1H), 7.26 (d, ^3J = 4.0 Hz, 1H), 7.21 (d, ^3J = 5.2 Hz, 1H), 7.20 (d, ^3J = 4.0 Hz, 1H), 7.16 (d, ^3J = 4.0 Hz, 1H), 7.15 (d, ^3J = 4.0 Hz, 1H), 7.04 (d, ^3J = 5.2 Hz, 1H), 2.89 (s, 4H), 2.50 (s, 3H); ^{13}C NMR ($CDCl_3/CS_2$, TMS/ppm) δ 168.6, 156.8, 147.2, 139.1, 137.3, 136.2, 135.6, 134.0, 133.4, 130.6, 130.0, 127.0, 126.6, 124.5, 124.3, 124.1, 124.0, 123.8, 25.6, 18.8. Anal. Calcd for $C_{22}H_{15}NO_4S_5$ (516.96): C, 51.04; H, 2.92. Found: C, 51.27; H, 3.05.

General Procedure for the Preparation of BSA−TSE Conjugates. In a 2 mL microtube with screw cap was dissolved the appropriate amount of BSA (calculated on the basis of a 1:15 BSA/fluorophore molar ratio) in a 0.05 M buffer carbonate/bicarbonate solution (1 mL, pH 9.3) at room temperature. Tween-20 (0.5%, w/v) was added to the buffered solution to

promote the solubility of the fluorophore in the aqueous medium. Then 100 μL of a dry DMF solution containing the fluorophore dissolved in concentration 2.5 mg/mL was added slowly to the BSA solution with gentle swirling, care being taken to avoid foaming. The microtube was then put on a rotating plate mixer (25 rpm), and conjugation was allowed to proceed at room temperature (21−24 °C) with continuous mixing for 30 min. The unreacted fluorophore was removed by passing the conjugate mixture through a Sephadex column (G-25, medium grade), previously equilibrated using phosphate-buffered saline (PBS, 80 mL, pH 7.4). Using this buffer as eluent, 500 μL fractions were collected at room temperature. All fractions were analyzed using a Perkin-Elmer spectrophotometer Lamda 20 for reading the absorbances. The conjugate was found in fractions 6−8 that were pooled in a 2 mL micro tube. Since the absorbance of these fractions was sometimes above 2, a 500 μL aliquot of the pooled solution was diluited 1:10 with PBS to give measurable readings. Before storing the solutions of the conjugates at 4 °C, sodium azide (0.1%, w/v) was added to inhibit bacterial growth. The protein content and the degree of labeling were determined by spectroscopic measurements as described (*17*).

Absorption and Photoluminescence Measurements. The absorption spectra of dilute solutions of TSEs alone and of their conjugates with BSA were obtained with a Perkin-Elmer Lambda 45 UV/vis spectrophotometer. The luminescence spectra were measured at room temperature using a Spex Fluorolog II spectrofluorimeter, equipped with a Hamamatsu R928 phototube. Air-equilibrated sample solutions were excited at the indicated wavelength, and the concentration was adjusted to obtain absorption values ≤0.15 at the excitation wavelengths. While uncorrected luminescence band maxima were used throughout the text, corrected spectra were employed for the determination of the luminescence quantum yields (ϕ). The correction procedure was based on the use of a software taking care of the wavelength dependent response of the phototube. Luminescence quantum efficiencies (ϕ_{em}) were evaluated by comparing wavelength integrated intensities (I) with reference to quinine sulfate as the standard ($\phi_r = 0.546$ in air-equilibrated 1 N H_2SO_4) and by using the following equation:

$$\phi_{em} = \frac{In^2}{OD} \cdot \frac{OD_r}{I_r n_r^2} \cdot \phi_r$$

where OD and n are absorbance values at the employed excitation wavelength, and refractive index of the solvent, respectively. Band maxima and relative luminescence quantum yields were obtained with uncertainty of 2 nm and 20%, respectively. The luminescence lifetimes (τ) were obtained with an IBH single photon counting equipment by using pulsed diode NanoLED sources with excitation at 278 and 331 nm. Analysis of the luminescence decay profiles against time was accomplished by using software provided by the manufacturers, with an estimated error on the lifetime results of 10%.

RESULTS

The molecular structures of all oligothiophene *N*-hydroxysuccinimidyl esters employed in this study are reported in Table 2 (see below). The tuning of the emission color from blue to orange was obtained by changing the oligomer size from dimer to tetramer and the number and the position of methylsulfanyl (SCH_3) substituents.

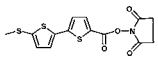
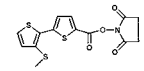
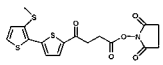
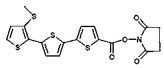
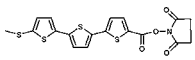
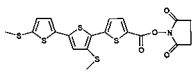
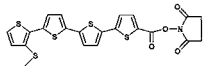
All fluorophores were soluble in DMF, while solubility in water was achieved by addition of a small amount (<1% v/v) of the Tween-20 surfactant. Owing to molecular distortion which prevents aggregation, fluorophores with substituents in β positions are the most soluble in all solvents.

Table 1. Effect of BSA to Fluorophore Molar Ratio, Reaction Time, pH, and Fluorophore Concentration on the Yields of Formation of the BSA−1 Conjugate in Phosphate-Buffered Solution

BSA−fluorophore molar ratio (60 min, pH 9.3, fluorophore 10 mg/mL)	F/BSA ratio[a]	reaction time (1:15 molar ratio, pH 9.3, fluorophore 10 mg/ mL)	F/BSA ratio[a]
1:20	4.9	120 min	5.4
1:15	4.4	60 min	4.4
1:10	4.8	45 min	4.0
1:5	2.6	30 min	3.7
		15 min	3.5
pH (30 min, 1:15, molar ratio fluorophore 10 mg/mL)	**F/BSA ratio[a]**	**fluorophore concentration (30 min, pH 9.3, 1:15 molar ratio)**	**F/BSA ratio[a]**
8.1	1.1	20 mg/mL	3.2
8.5	1.8	10 mg/mL	3.3
9.0	2.9	5 mg/mL	5.9
9.3	4.0	2.5 mg/mL	8.1
		1.25 mg/mL	7.2

[a] Expressed in moles of fluorophore per mole BSA.

Table 2. Molecular Structure, Maximum Absorption (λ_{max}, nm) and Emission (λ_{PL}, nm) Wavelengths, and Molar Absorption Coefficients (ϵ, cm^{-1} M^{-1}) of Oligothiophene Fluorophores 1−7[a] and λ_{max}, λ_{PL} Values of the Corresponding Conjugates with BSA[b]

		λ_{max}	λ_{PL}	ϵ	F/BSA[c]
	**1**	370	476	27300	
	BSA-1	353	461		8.1
	**2**	370	454	15200	
	BSA-2	350	445		8.4
	**3**	372	457	13000	
	BSA-3	376	481		8.2
	**4**	403	518	23400	
	BSA-4	391	509		7.2
	**5**	407	554	29900	
	BSA-5	373	464		8.0
	**6**	418	538	33000	
	BSA-6	412	546		7.0
	**7**	427	562	38100	
	BSA-7	405	498		8.6

[a] 10^{-4} M in CH_2Cl_2. [b] 10^{-6} M in phosphate buffer solution pH 7.2. [c] Moles of fluorophore per mole BSA.

1. Optimization of the Preparation Conditions of BSA−TSE Conjugates. The conjugation conditions were investigated by varying the BSA to fluorophore molar ratio, reaction time, pH, and fluorophore concentration on conjugation yields. Representative results are summarized in Table 1 for the BSA−**1** conjugate.

At pH = 9.3, reaction time 60 min, fluorophore **1** concentration 10 mg/mL, and a BSA−fluorophore **1** molar ratio of 1:5, a value F/BSA = 2.6 was obtained. For molar ratios of 1:10, 1:15, and 1:20 the F/BSA values were 4.8, 4.4, and 4.9, respectively. These values indicate that at the molar ratio 1:10 the fluorophore has already bound all the available (for conjugation) amino sites of the BSA.

In the subsequent step the BSA−fluorophore **1** molar ratio was kept at a value of 1:15, the pH at 9.3 and the fluorophore concentration at 10 mg/mL, while the reaction time was progressively incremented up to 120 min (Table 1). The F/BSA

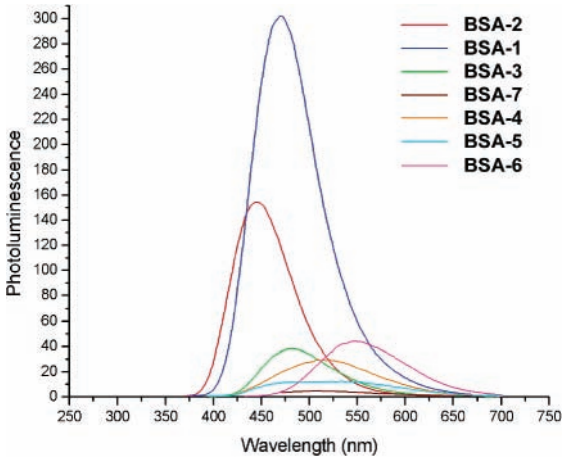


Figure 1. Photoluminescence spectra of the conjugates of BSA with fluorophores **1**−**7** (dilution 1:10) in PBS/Tween.

ratio increased upon an increase in the incubation time, from 3.5 (15 min) to 5.4 (120 min).

The effect of the pH value on the final BSA−**1** ratio was investigated using an incubation time of 30 min, a molar ratio BSA−fluorophore **1** of 1:15, and a fluorophore concentration at 10 mg/mL. The pH was varied from 8.1 to 8.5, 9.0 and 9.3. The F/BSA ratios were 1.1, 1.8, 2.9, and 4.0, respectively, indicating that only at pH value ≥9 conjugates with a good BSA to fluorophore ratios are obtained.

Finally, with an incubation time of 30 min, the pH at 9.3, and the BSA−fluorophore **1** molar ratio at 1:15, the fluorophore concentration was changed from 1.25 mg/mL to 2.5, 5.0, 10, and 20 mg/mL. The measured F/BSA ratios were 7.2, 8.1, 5.9, 3.3, and 3.2, respectively, indicating that the molar ratio needed to obtain the highest F/BSA ratio is 2.5 mg/mL.

On the basis of these results, the following conditions were employed for the conjugation of all fluorophores with BSA: pH 9.3, 1:15 BSA−fluorophore molar ratio, 2.5 mg/mL fluorophore concentration, and 30 min reaction time. Using these parameters about half of the employed fluorophore moles were bound to the protein, affording F/BSA ratios of 7−8 (Table 2).

For comparison, the BSA conjugate with FITC (fluorescein isothiocyanate), one of the most commonly employed fluorophores (*10*, *18*), was prepared using the same experimental conditions. A FITC/BSA ratio of 8.0 was measured under these conditions, the same value obtained for the conjugate of fluorophore **1** with BSA, as shown in Table 1.

2. Optical Properties. The absorption and emission data of free TSEs and of the corresponding conjugates with BSA obtained as described above are summarized in Table 2.

Figure 1 shows the photoluminescence spectra of the conjugates of the fluorophores with BSA. It is seen that the relative photoluminescence intensities at the maximum emission wavelength are: 1.00(BSA−**1**), 0.51 (BSA−**2**), 0.13 (BSA−**3**), 0.10 (BSA−**4**), 0.04 (BSA−**5**), 0.15 (BSA−**6**), 0.02 (BSA−**7**).

The width at half-maximum emission wavelength is 80−85 nm for the conjugates of **1**−**3**, 120 nm for that of **4**, 150 nm for **5** and 100 nm for the conjugates of **6**−**7**.

Fluorophores **1** and **5** have already been used for the labeling of monoclonal antibodies and toxins and demonstrated to be useful in cell imaging (*9*). We have now measured the fluorescence quantum yields and fluorescence lifetimes of these compounds and of their conjugates with BSA and compared to those of FITC and its conjugate with BSA under the same conditions. The fluorescence radiative constants, k_r, have been calculated from the relation $k_r = \phi/\tau$. The results are given in Table 3.

Table 3. Optical Properties of Fluorophores 1, 5 and FITC[a] in Different Solvents and in Conjugates with BSA

fluorophore	solvent	λ_{max} (nm)	ϕ	τ (ns)	k_r (s^{-1})
1	DCM	476	1.00 ± 0.05	2.87	3.76×10^8
	PBS	465	0.54 ± 0.01	3.44	1.57×10^8
	BSA-1	461	0.31 ± 0.01	3.13	0.99×10^8
5	DCM	554	0.76 ± 0.05	2.47	3.08×10^8
	PBS	559	0.17 ± 0.01	3.21	0.53×10^8
	BSA-5	464	0.10 ± 0.01	2.56	0.39×10^8
FITC	PBS	516	0.10 ± 0.01	3.99	0.25×10^8
	BSA−FITC	519	0.25 ± 0.01	3.71	0.67×10^8

[a] Fluorescein isothiocyanate.

Table 3 shows that fluorophore **1**, a bithiophene derivative, in dichloromethane reaches a remarkable 100% fluorescence quantum yield (ϕ), almost 2 orders of magnitude higher than that of unsubstituted bithiophene (1.4−2.6%) in the same solvent (*6*).

Fluorophore **5**, a derivative of terthiophene, in dichloromethane achieves a fluorescence quantum yield of 76%, more than 1 order of magnitude greater than that (5.7−7.0%) of unsubstituted terthiophene (*6*). The ϕ values are drastically reduced in PBS (54 and 17% for **1** and **5**, respectively) and even more lowered in the corresponding conjugates with BSA (31 and 10%, respectively). Table 3 also shows that the conjugate of BSA with fluorescein displays a fluorescence quantum yield of 25%. The fluorescence lifetimes of free **1** and **5** in DCM are of the same order as those of unsubstituted oligothiophenes (*6*). Change of solvent from DCM to PBS increases slightly the fluorescence lifetimes, which are near those in the conjugates and similar to that of fluorescein. The bioconjugates can undergo several cycles of irradiation without significantly altering their structure and their optical properties and mantain their characteristics after storage for months.

DISCUSSION

It is well-known that *N*-hydroxysuccinimidyl esters react selectively with the aliphatic amino groups of proteins, generally the ϵ-amino group of lysine residues, to form a relatively stable amide bond (*10*):

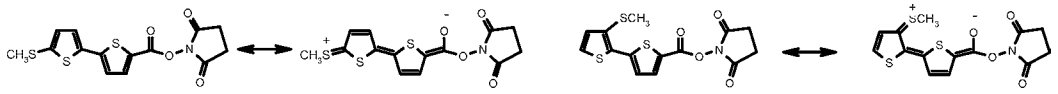
$$\text{Protein-NH}_2 + \text{R-C(O)-O-Nsucc} \rightarrow \text{Protein-NH-C(O)-R}$$

Our data confirm that amino-reactive oligothiophene *N*-hydroxysuccinimidyl esters can easily be conjugated to proteins in aqueous conditions, achieving high fluorophore to protein ratios. The degree of labeling varies with the pH, the reaction time, the BSA to fluorophore molar ratio, and the fluorophore concentration. As shown in Table 1, conditions may be selected to obtain the desired degree of labeling in short conjugation times.

The fluorescence quantum yields measured for fluorophores **1** and **5** in methylene chloride (100% and 70%, respectively) are 2 orders of magnitude greater than those measured for unsubstituted bi- and terthiophene (*6*). Moreover, the molar absorption coefficients of these and the other fluorophores of Table 2 are much higher than those of unsubstituted oligothiophenes of the same size (compare, for example, the ϵ value of bithiophene, 12440 mol^{-1} cm^{-1} (*6*), with that of compound **1**, 27300 mol^{-1} cm^{-1}, or even **2**, 15200 mol^{-1} cm^{-1}). Also the absorption and emission wavelengths of the fluorophores are much larger (compare, for example, the λ_{max} and λ_{PL} values of **1**, 370 and 479 nm, with those of α-bithiophene, 303 an 362 nm (*6*)).

All these characteristics are likely to be related to the peculiar electronic structure of the fluorophores. Indeed, all compounds bear one or two methylsulfanyl (SCH_3) substituents. The electron donor nature of the SCH_3 substituent and the electron

Scheme 3. Mesomeric Effect in Fluorophores 1 and 2



1 **2**

acceptor properties of the carbonyl group at the opposite end of the molecule confer to the fluorophores of Table 2 the nature of 'push−pull' compounds (*19*), with extended delocalization of the $\pi-\pi$ system. Scheme 3 illustrates the mesomeric effect of α and β SCH_3 substituents (*20*) in fluorophores **1** and **2**.

Table 3 shows that in PBS the fluorescence efficiencies of **1** and **5** drop to 54% and 17%, respectively. The fact that the decrease in fluorescence quantum yields is much more accentuated in **5** than in **1** suggests that this might be related to the higher number of conformations of the terthiophene derivative, allowing for more vibrational deactivation pathways. On the basis of literature data (*21*), also an effect due to the presence of the surfactant could be operative.

Table 3 also shows that binding to the protein leads to a further fluorescence quantum yield decrease of **1** and **5**, as generally observed for most commercially available fluorophores (*21*). In the conjugates with BSA, **1** and **5** show fluorescence quantum yields of 31% and 10%, respectively. This decrease is probably due to the proximity of the dyes because of the high degree (8:1) of labeling and fluorophore−fluorophore interactions which lead to partial quenching (*22*). It is known that FITC can be quenched up to the 70% for a dye to protein ratio of 5 (*17*). In agreement with this, we observed for FITC in the conjugate with BSA and a dye−protein ratio of 8:1 a quantum yield of 25%, much lower than the >90/% efficiency of FITC in alkaline aqueous solutions (*22*). However, the flexibility of conjugation conditions of TSEs illustrated in Table 1 should allow the optimization, case by case, of the labeling degree of proteins with oligothiophene fluorophores to minimize self-quenching phenomena. Work is currently under way in this direction to establish the dependence of the fluorescence quantum yield of TSEs on the degree of labeling.

It is worth noting that what is important in the present context is that the molar absorption coefficients of TSEs fluorophores and their fluorescence quantum yields are sufficiently high to allow the easy detections of protein−fluorophore conjugates in micromolar and even lower concentrations. It is also to note that the fluorophores are characterized by linewidths on the order of 100 nm and by very large Stokes shifts between absorption and emission signals. These large Stokes shifts are even increased in the conjugates with proteins with respect to the free fluorophores. Moreover, as already observed in the case of oligothiophene isothiocyanates (*8*), the fluorophores show high resistence to photobleaching.

CONCLUSION

We have shown that oligothiophene *N*-succinimidyl esters, built using a few repeating and simple structural elements, i.e., thienyl and α or β SCH_3 substituents and characterized by efficient emission in the blue-orange interval, can easily be bound to BSA achieving high fuorophore to protein ratios. The fluorophore to protein ratio can be controlled by an accurate choice of the experimental conditions. BSA−TSE conjugates in water in physiological conditions display fluorescence quantum yields that are comparable to that of BSA−FITC conjugates in similar conditions. Considering the synthetic versatility of thiophene (*5*), it is easy to predict that thiophene-based fluorophores even more efficient than those described here will rapidly be developed.

ACKNOWLEDGMENT

This work was partially supported by the project "Synthesis of novel organic materials and supramolecular architectures for high efficiency optoelectronic and photonic systems" (SYNERGY, FIRB RBNE03S7XZ_005) and by CNR Projects PM.P04.010 and "Functional organic materials for Hi-Tech applications" (MAFO-HT). Thanks are also due to Mediteknology srl for providing some of the compounds used in this study.

LITERATURE CITED

(1) Béra-Abérem, M., Ho, H. A., and Leclerc, M. (2004) Functional polythiophenes as optical chemo- and biosensors. *Tetrahedron 60*, 11169−11173.

(2) Ho, A., Boissinot, M., Bergeron, M. G., Corbeil, G., Doré, K., Boudreau, D., and Leclerc, M. (2002) Colorimetric and Fluorometric Detection of Nucleic Acids Using Cationic Polythiophene Derivatives. *Angew. Chem., Int. Ed. 41*, 1548−1551.

(3) Nilsson, K. P. R., and Inganäs, O. (2003) Chip and solution detection of DNA hybridization using a luminescent zwitterionic polythiophene derivative. *Nat. Mater. 2*, 419−424.

(4) Ho, A., Doré, K., Boissinot, M., Bergeron, M. G., Tanguay, R. M., Boudreau, D., and Leclerc, M. (2005) Direct Molecular Detection of Nucleic Acids by Fluorescence Signal Amplification. *J. Am. Chem. Soc. 127*, 12673−12676.

(5) Barbarella, G., Melucci, M., and Sotgiu, G. (2005) The versatile thiophene: an verview of recent research on thiophene based materials. *Adv. Mater. 17*, 1581−1593.

(6) Becker, R. S., Seixas de Melo, J., Maçanita, A. L., and Elisei, F. (1996) Comprehensive evaluation of the absorption, photophysical, energy transfer, structural and theoretical properties of α-oligothiophenes with one to seven rings. *J. Phys. Chem. 100*, 18683−18695.

(7) Doré, K., Dubus, S., Ho, H. A., Lévesque, I., Brunette, M., Corbeil, G., Boissinot, M., Boivin, G., Bergeron, M. G., Boudreau, D., and Leclerc, M. (2004) Fluorescent polymeric transducer for the rapid, simple, and specific detection of nucleic acids at the zeptomole level. *J. Am. Chem. Soc. 126*, 4240−4244.

(8) Barbarella, G., Zambianchi, M., Pudova, O., Paladini, V., Ventola, A., Cipriani, F., Gigli, G., Cingolani, R., and Citro, G. (2001) Oligothiophene Isothiocyanates as a New Class of Fluorescent Markers for Biopolymers. *J. Am. Chem. Soc. 123*, 11600−11607.

(9) Barbarella, G., Zambianchi, M., Ventola, A., Fabiano, E., Della Sala, F., Gigli, G., Anni, M., Bolognesi, A., Polito, L., Naldi, M., and Capobianco, M. (2006) Bright oligothiophene *N*-succinimidyl esters for efficient fluorescent labeling of proteins and oligonucleotides. *Bioconjugate Chem. 17*, 58−67.

(10) Haugland, R. P. (2005) *A Guide to Fluorescent Probes and Labeling Technologies*; Molecular Probes Inc.: Eugene, OR.

(11) Powe, A. M., Fletcher, K. A., St. Luce, N. N., Lowry, M., Neal, S., McCarroll, M. E., Oldham, P. B., McGown, L. B., and Warner, I. M. (2004) Molecular Fluorescence, Phosphorescence, and Chemiluminescence Spectrometry. *Anal. Chem. 76*, 4614−4634.

(12) Brédas, J. L., Cornil, J., Beljonne, D., Dos Santos, D. A., and Shuai, Z. (1999) Excited- State Electronic Structure of Conjugated Oligomers and Polymers: A Quantum-Chemical Approach to Optical Phenomena. *Acc. Chem. Res. 32*, 267−276.

(13) Fabiano, E., Della Sala, F., Barbarella, G., Lattante, S., Anni, M., Sotgiu, G., Hattig, C., Cingolani, R., and Gigli, G. (2006) Optical properties of *N*-succinimidyl bithiophene and the effects of the binding to biomolecules: Comparison between coupled-cluster and time-dependent density functional theory calculations and experiments. *J. Phys. Chem. B 110*, 18651−18660.

(14) Carter, D. C., and Ho, J. X. (1994) Structure of serum-albumin. Structure of serum albumin. *Adv. Protein Chem. 45*, 153−203.

(15) Wang, Q., Kuo, Y., Wang, Y., Shin, G., Ruengruglikit, C., and Huang, Q. (2006) Luminescent Properties of Water-Soluble Denatured Bovine Serum Albumin-Coated CdTe Quantum Dots. *J. Phys. Chem. B 110*, 16860−16866.

(16) Jiang, X. J., Huang, J. D., Zhu, Y. J., Tang, F. X., Ng, D. K. P., and Sunc, J. C. (2006) Preparation and in vitro photodynamic activities of novel axially substituted silicon (IV) phthalocyanines and their bovine serum albumin conjugates. *Bioorg. Med. Chem. Lett. 16*, 2450−2453.

(17) Brinkley, M. (1992) A Brief Survey of Methods for Preparing Protein Conjugates with Dyes, Haptens, and Cross-Linking Reagents. *Bioconjugate Chem. 3*, 2−13.

(18) Sjöback, R., Nigren, J., and Kubista, M. (1998) Characterization of fluorescein-oligonucleotide conjugates and measurement of local electrostatic potential. *Biopolymers 46*, 445−453.

(19) Meier, H. (2005) Conjugated Oligomers with Terminal Donor−Acceptor Substitution. *Angew. Chem. Int. Ed. 44*, 2482−2506.

(20) Barbarella, G., Zambianchi, M., Antolini, L., Folli, U., Goldoni, F., Iarossi, D., Schenetti, L., and Bongini, A. (1995) Conformational properties of 3,3′-, 3,4′-, and 4,4′-dimethyl and bis-(methylsulphanyl)-2,2′-bithiophenes. *J. Chem. Soc., Perkin Trans. 2*, 1869−1873.

(21) Lavigne, J. J., Broughton, D. L., Wilson, J. N., Erdogan, B., and Bunz, U. H. F. (2003) "Surfactochromic" Conjugated Polymers: Surfactant Effects on Sugar-Substituted PPEs. *Macromolecules 36*, 7409−7412.

(22) Berlier, J. E., Rothe, A., Buller, G., Bradford, J., Gray, D. R., Filanoski, B. J., Telford, W. G., Yue, Liu, J., Cheung, C. Y., Chang, W., Hirsch, J. D., Beechem, J. M., Haugland, R. H., and Haugland, R. P. (2003) Quantitative Comparison of Longwavelength Alexa Fluor Dyes to Cy Dyes: Fluorescence of the Dyes and Their Bioconjugates. *J. Histochem. Cytochem. 51*, 1699−1712.

BC060332E

Proton-Actuated Membrane-Destabilizing Polyion Complex Micelles

Marie-Andrée Yessine,[†] Marie-Hélène Dufresne,[†] Christian Meier,[‡] Hans-Ulrich Petereit,[‡] and Jean-Christophe Leroux*,[†]

Canada Research Chair in Drug Delivery, Faculty of Pharmacy, Université de Montréal, C.P. 6128 Succ. Centre-Ville, Montreal, Quebec, H3C 3J7, Canada, and Degussa, Pharma Polymers, Röhm GmbH and Co. KG, Kirschenallee, D-64293 Darmstadt, Germany. Received June 8, 2006; Revised Manuscript Received February 5, 2007

The efficiency of nucleic acid-based drugs is usually hampered by the fact that, following their uptake by the cell, these drugs end up in acidic organelles (i.e., endosomes/lysosomes) from which they barely escape. This work relates to the preparation and characterization of polyion complex micelles (PICM) formed by the self-assembly of three polyelectrolytes: a diblock cationic copolymer; a membranolytic, methacrylic acid copolymer; and an oligonucleotide. It is demonstrated that a synthetic membrane-active polyanion can be successfully integrated within the structure of PICM to yield well-defined, narrowly distributed micelles (30 nm) with a core/shell architecture. Besides their ability to protect the oligonucleotide against nuclease degradation, PICM partly dissociate under mildly acidic conditions, releasing chain clusters that destabilize bilayer membranes. This association/dissociation behavior illustrates the potential of these pH-sensitive PICM for the transport and efficient delivery of polyionic drugs.

INTRODUCTION

Recent advances in the field of nanotechnology have led to the design of highly sophisticated nanoscale constructs and supramolecular assemblies prepared from well-defined synthetic macromolecules (*1*). Of such assemblies, micelles formed by the self-association of block copolymers in aqueous medium have received much attention due to their potential applications in the biomedical and pharmaceutical fields (*2*, *3*). In particular, colloidal carrier systems prepared from the complexation of a polynucleotide and a diblock copolymer composed of polycation and poly(ethylene oxide) (PEO) segments are being developed for the delivery of nucleic acids (*4*−*7*). Neutralization of the charged segments through electrostatic interactions yields hydrophobic complexes that self-assemble into polyion complex micelles (PICM) presenting a core/shell architecture. These micelles present numerous advantages including their straightforward preparation, high colloidal stability, solubility in aqueous media, small size, and narrow size distribution. Furthermore, they represent a promising approach to improve the in vivo efficiency of nucleic acid-based drugs, since protection against nuclease degradation and prolonged circulation times in the blood compartment would allow for enhanced drug deposition at the target site (*8*).

However, despite these attractive properties, the intracellular bioavailability of polynucleotides remains limited due to their sequestration in the endosomal/lysosomal compartment following the uptake of PICM by the cell. The escape of biomolecules from endosomes generally requires a membrane-destabilizing agent, which will provoke the release of the internalized compounds into the cytoplasm before they reach the lysosomes. Synthetic titratable polyanions can achieve such a goal by destabilizing membrane bilayers at pH values typically found in endosomes. Indeed, polymers such as poly(ethylacrylic acid) (PEAA) and poly(propylacrylic acid) (PPAA) undergo a pH-triggered conformational change at slightly acidic pH values (*9*, *10*). Upon protonation and charge neutralization in the acidic environment of endosomes, PPAA was shown to disrupt selectively the endosomal membrane (*11*), thereby enhancing the cytoplasmic delivery of macromolecules such as plasmid DNA and polymer−antibody complex (*12*, *13*).

Recently, our group demonstrated that pH-sensitive methacrylic acid (MAA) copolymers can also be used to improve the cellular delivery of nucleic acid-based drugs (*14*). In that study, nanoparticles in suspension were obtained following the electrostatic complexation of an MAA copolymer, a model oligodeoxynucleotide (ODN), and a cationic lipid. The particles bore a positive surface charge which facilitated their internalization into cultured cells. However, given their cationic nature, the complexes were unstable in physiological conditions (Yessine et al., unpublished observations), thus compromising their applicability for systemic administration. The present work describes the incorporation of an MAA copolymer into a system that could be more suitable for in vivo applications. We demonstrate that the copolymer can be intimately integrated within the structure of neutral, water-soluble, and well-defined PICM. More importantly, we show that, upon a decrease in pH, the resulting PICM partially dissociate to release membrane-active fragments that efficiently destabilize lipid bilayers.

EXPERIMENTAL PROCEDURES

Materials. Poly(ethylene oxide)-*b*-poly(aminoethyl methacrylate) (PEO-*b*-PAEMA, 75/25 mol %, M_n 4700) was synthesized by atom transfer radical polymerization as described previously (*15*). Poly(methacrylic acid-*co*-ethyl acrylate-*co*-butyl methacrylate) (P(MAA-*co*-EA-*co*-BMA), 50/40/10 mol %, M_n 19 800) was provided by Röhm GmbH (Darmstadt, Germany). It was prepared by free radical polymerization involving dodecyl mercaptane as chain transfer agent. The polymer was dissolved in ethanol and dialyzed against water for at least 5 days prior to use. P(MAA-*co*-EA-*co*-BMA) was labeled with Lissamine rhodamine B ethylenediamine (Molecular Probes, Eugene, OR) as described previously (*14*). Twenty-mer phosphorothioate ODN (5′-GTTCTCGCTGGTGAGTTTCA-3′) and its fluores-

* Corresponding author. Tel: (514) 343-6455; Fax: (514) 343-6871; E-mail: Jean-Christophe.Leroux@umontreal.ca.

[†] Université de Montréal.

[‡] Röhm GmbH and Co..

10.1021/bc060159m CCC: $37.00 © 2007 American Chemical Society
Published on Web 04/03/2007

cein- labeled derivative were provided by Medicorp, Inc. (Montreal, QC, Canada).

Preparation of the Ternary Polyion Complex Micelles (PICM). PEO-*b*-PAEMA (500 μg) was incubated with P(MAA-*co*-EA-*co*-BMA) (216 μg) in tris(hydroxymethyl)aminoethane (Tris) buffer (10 mM, pH 7.4) for 5 min at room temperature under mild agitation. The ODN (20 μg) was then added, and the formulation was incubated further for 5 min. The charge ratio was calculated from the degree of ionization of the polymers, as determined from titration experiments (Supporting Information). Micelles containing PMAA were prepared using a similar procedure using the same amounts of each component. Salt-containing samples were prepared by adding 0.5 mL of micelles to 0.5 mL of Tris 0.1 M, pH 7.4, containing 300 mM sodium chloride (NaCl) to yield a final salt concentration of 150 mM (isotonic conditions).

Determination of the Critical Association Concentration. The critical association concentration (CAC) was measured by the steady-state pyrene fluorescence method (*16*) based on the I_{336}/I_{333} intensity ratio of the excitation spectra of pyrene following its translocation from water to the PICM hydrophobic core. Serial dilutions of a stock solution of ternary PICM in Tris buffer, pH 7.4, were prepared to contain 2×10^{-7} M of pyrene (Sigma, St-Louis, MO) and were stirred overnight in the dark. Fluorescence intensity was measured ($\lambda_{ex1} = 333$ nm, $\lambda_{ex2} = 336$, $\lambda_{em} = 390$ nm) at room temperature or at 37 °C using a Series 2 Aminco Bowman fluorimeter (Spectronic Instruments, Inc., Rochester, NY). Experiments were performed in triplicate.

Dynamic Light Scattering, Multiangle Static Light Scattering, and ζ-Potential Measurements. Size, M_w, and ζ potential of the ternary PICM were all determined in triplicate in Tris buffer of the appropriate pH following filtration of the micelles through a 0.45 μm GHP filter. The mean hydrodynamic diameter, PI, and scattering intensity of PICM were determined using a Malvern Autosizer 4800 or a Malvern ZetaSizer Nanoseries ZS (Malvern Instruments, Worcestershire, U.K.). Measurements were performed at a scattering angle of 90° and temperatures of 25 and 37 °C. The *CONTIN* program was used to extract size distributions from the autocorrelation functions. Alternatively, MASLS measurements were conducted using a Malvern Autosizer 4800 at 25 °C at seven angles ranging from 70° to 130° for four micelle concentrations. The M_w values of the complexes were derived from eq 1, which describes the intensity of light scattered from a dilute solution of macromolecules. In this equation, *c* stands for the solution concentration

$$\frac{\mathrm{K}c}{R_0} = \frac{1}{M_w P(\theta)} + 2A_2 c + 3A_3 c^2 \qquad (1)$$

in PICM, R_0 is the Rayleigh ratio, and A_2 and A_3 are the second and third virial coefficients. K is in turn defined by

$$\mathrm{K} = \frac{4\pi^2 n_0{}^2 \left(\frac{\mathrm{d}n}{\mathrm{d}c}\right)^2}{\lambda^4 N} \qquad (2)$$

where n_0 is the refractive index of the solvent, λ the laser wavelength in vacuo, and *N* Avogadro's number. The specific refractive index increment ($\mathrm{d}n/\mathrm{d}c = 0.174$) was determined using a differential Rudolph J157 automatic refractometer (Rudolph Research Analytical, Flanders, NJ), at a wavelength of 589.3 nm. ζ potential was evaluated with a Malvern ZetaSizer Nanoseries ZS.

Transmission Electron Microscopy Imaging. Copper grids (200 mesh) were coated with pioloforme resin. Prior to sample deposition, a drop of an aqueous solution of poly(lysine) (17% w/v, Sigma) was placed onto the grid for 5 min. The excess solution was wicked off, the grid was allowed to dry, and a drop of ternary PICM (5 μL) in Tris buffer (pH 7.4 or 5.0) was placed onto the grid for 2 min. After removal of the excess solution, the sample was stained using uranyl acetate (3.5% w/v in water) for 5 min. The grid was then gently washed with water and allowed to dry. Prepared samples were imaged using a Philips CM100 transmission electron microscope (FEI Company, Japan) operating at 60 kV. Micrographs were taken at a 46 000 magnification.

Nuclear Magnetic Resonance Analysis. Polymer and micelle samples were prepared in deuterated Tris buffer (10 mM) adjusted to pH 7.4 using DCl and NaOD solutions (CDN Isotopes, Pointe-Claire, QC, Canada). Prior to analysis, the PICM were eluted on a Sephacryl 200 HR column (Sigma) to completely remove any free polymer in solution and concentrated at room temperature using a vacuum concentrator (Savant SpeedVac SC210A, Thermo Electron Corp., Waltham, MA). The NMR spectrum of the micelles was first acquired at pH 7.4 using a Bruker spectrometer operating at 400 MHz (Bruker, Milton, ON, Canada). The pH of the sample was then adjusted to 5.0 using DCl and the NMR acquisition repeated.

Enzymatic Degradation of ODN Incorporated into the Ternary PICM. Naked fluorescent ODN or fluorescent ternary PICM were incubated with DNAse I (50 U/μg ODN) (Sigma) in the presence of $MgCl_2$ (5 mM) at 37 °C. At predetermined time points, aliquots were withdrawn and degradation was stopped by adding EDTA (10 mM). Before being loaded onto a 20% polyacrylamide gel, heparin (280 μM) was added to the samples to induce ODN release from the PICM. Following migration, ODN was visualized directly on the gel after exposition to UV light using a ChemiImager 5500 imaging system (Alpha Innotech Corp., San Leandro, CA). The amount of intact ODN was quantified relatively to the fluorescent signal obtained with a sample containing 100% intact ODN (nonexposed to DNAse).

Assessment of Membrane-Destabilizing Properties of Micelles Using Liposomes as an Endosomal Membrane Model. Unilamellar liposomes (40 mM total lipid) mimicking the composition of the endosomal membrane (egg phosphatidylcholine/cholesterol/dioleoylphosphatidylethanolamine/dimiristoylphosphatidylglycerol, 61:17:16:6 molar ratio) (*17*) were prepared by hydration of a dried lipid film, followed by repeated extrusion through a 0.2 μm pore size membrane at room temperature. The highly water-soluble fluorophore trisodium 8-hydroxypyrene trisulfonate (HPTS) and the collisional quencher *p*-xylene-bis-pyrimidium (DPX) were included in the lipid hydration buffer (Tris 10 mM, NaCl 48 mM, HPTS 35 mM, DPX 50 mM, pH 7.4). Untrapped dye was removed by gel filtration on Sepharose 2B (Sigma). The membrane-destabilizing properties of the micelles were evaluated at 37 °C at different pH values by adding liposomes (10 μL) to the ternary PICM (previously purified on Sephacryl 200HR to remove free P(MAA-*co*-EA-*co*-BMA) or PMAA) in isotonic buffer of the appropriate pH. In all cases, the final MAA copolymer concentration was adjusted to 85 μg/mL. The release of liposome content was monitored for 20 min at 37 °C by a fluorescence dequenching assay (*18*). The extent of release was calculated from HPTS fluorescence ($\lambda_{ex} = 412$ nm, $\lambda_{em} = 513$ nm) relative to the fluorescence intensity measured following liposome lysis in 0.5% (v/v) Triton X-100, which accounted for the complete release of encapsulated HPTS and DPX.

Intracellular Distribution of the ODN. U937 cells were plated in 6-well tissue culture plates (1 mL medium containing 1×10^6 viable cells) containing coverslips and differentiated into macrophages using 80 nM phorbol myristate (Sigma). After 72 h, the phorbol was rinsed, and ternary micelles (2 mg PEO-

Table 1. Characteristics of the Ternary PICM

pH	diameter (nm) [PI]	scattering intensity (Kcps)	M_w[a] (Da)	ζ potential ± SD (mV)
7.4	29.5 [0.13]	41.2	829 400	0.0 ± 2.6
6.2	31.5 [0.19]	30.8	752 900	1.4 ± 0.9
5.5	28.1 [0.24]	19.7	658 700	2.1 ± 1.2
5.0	29.1 [0.21]	17.0	362 200	1.8 ± 3.6

[a] Determined by static light scattering. Below pH 7.4, the M_w is an average for whole micelles, chain clusters, and free polymeric chains.

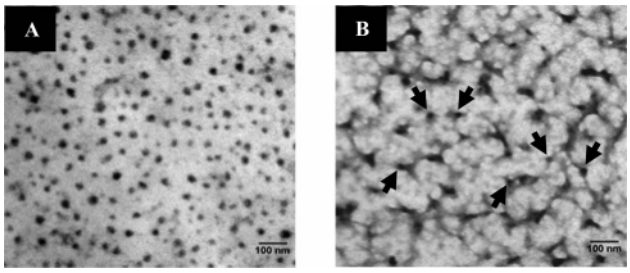


Figure 1. TEM analysis of ternary PICM at pH 7.4 (A) and 5.0 (B).

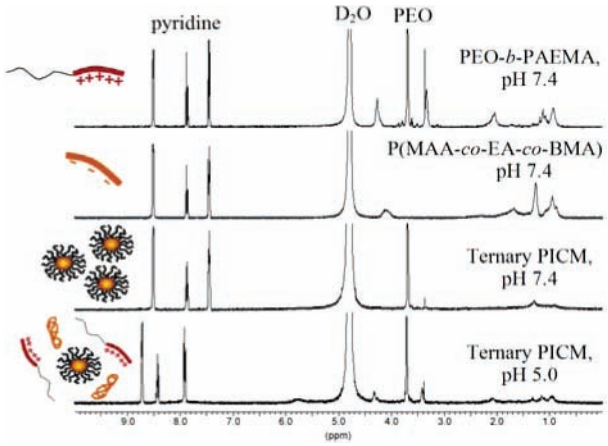


Figure 2. ^{1}H NMR spectra of the polymers alone and ternary PICM in deuterated Tris buffer. Pyridine was used as an internal standard.

b-PAEMA, 0.862 mg P(MAA-*co*-EA-*co*-BMA) or PMAA, 80 μg ODN) containing fluorescein-labeled ODN (50% of total ODN) were prepared as described above and incubated with cells for 4 h at 37 °C in a humid atmosphere containing 5% CO_2. Two hours before the end of the incubation period, LysoTracker red (Invitrogen, Burlington, ON, Canada) was added to each well at a final concentration of 80 nM. After 4 h, the cells were washed three times with cold PBS and mounted on slides which were kept on ice. Live cells were then examined by laser scanning confocal microscopy (LSCM) under a Leica DMIRBE inverted microscope coupled with a Leica TCS SP confocal system (Leica Microsystems, Heidelberg, Germany). The cells were excited at 488 or 568 nm, and fluorescence was collected by emission windows set at 505−555 and 585−635 nm, respectively. Images collected by *LCS Lite* software (Leica Microsystems) were exported as TIFF files and prepared for publication by *Adobe Photoshop* v 7.0 software (Adobe Systems, San Jose, CA).

RESULTS AND DISCUSSION

At pH 7.4 and room temperature, small-sized (30 nm), narrowly distributed (PI ≈ 0.1) and neutral PICM were obtained at the nearly stoichiometric ± ratio of 0.7/1 (PEO-*b*-PAEMA/P(MAA-*co*-EA-*co*-BMA)/ODN 68%/29%/3% w/w) (Table 1 and Figure 1A). The size and PI of the micelles barely changed at 37 °C (data not shown). Micelles were formed when the PEO-*b*-PAEMA concentration reached the critical values of 11.7 and

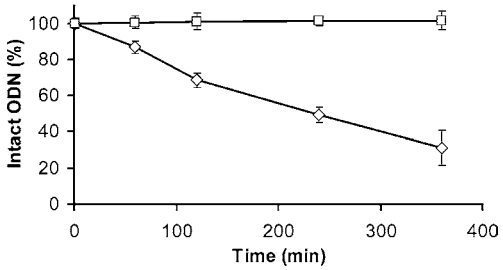


Figure 3. Stability toward nuclease degradation of naked ODN (◇) and ODN incorporated into ternary PICM (□) over a 6 h period.

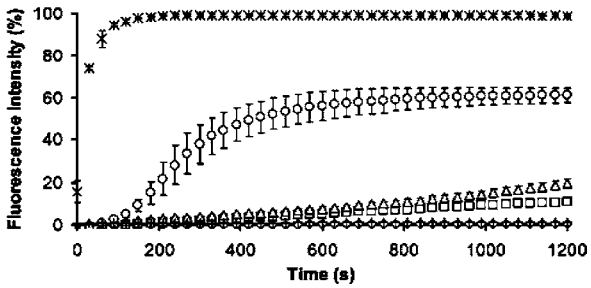


Figure 4. HPTS release induced by the ternary micelles at 37 °C and pH 7.4 (◇), 6.2 (□), 5.5 (△), and 5.0 (○). Star symbols represent the release induced by free P(MAA-*co*-EA-*co*-BMA) at pH 5.0 at equivalent concentration. Release induced by ternary micelles prepared with PMAA, pH 5.0, is represented by (+). Mean ± S.D. (n = 3).

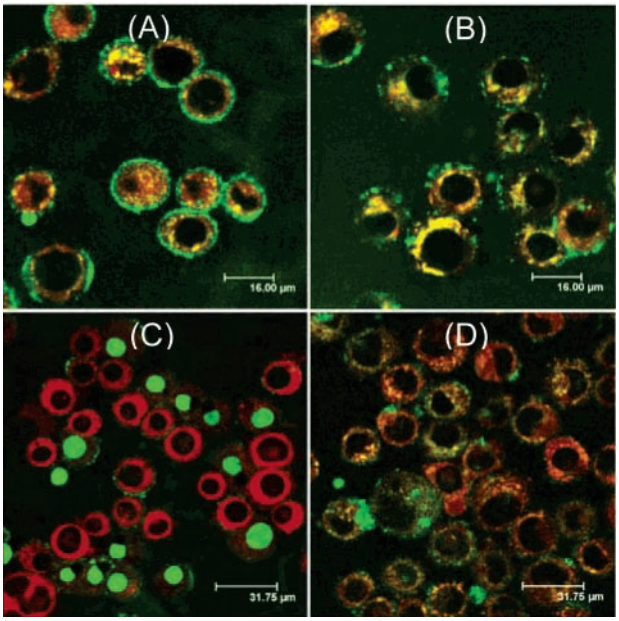


Figure 5. U937 macrophages on coverslips were incubated with ternary micelles prepared with P(MAA-*co*-EA-*co*-BMA) (A,C) or the non-endosomolytic polymer PMAA (B,D) for 4 h at 37 °C. Micelles were prepared using a fluorescein-labeled ODN, and acidic organelles were stained with LysoTracker red. After a 4 h incubation period at 37 °C, the cells were rinsed with cold PBS, mounted on slides, and kept on ice. Live cells were examined by LSCM 45 min (A,B) and 2 h (C,D) following the incubation period.

19.1 μg/mL at 25 and 37 °C, respectively, and remained stable in the presence of 150 mM NaCl (isotonic conditions). Incorporation levels of ODN and P(MAA-*co*-EA-*co*-BMA) reached 100% and 90%, respectively, as determined by gel electrophoresis and ultrafiltration of micelles containing a fluorescein-labeled ODN or a rhodamine-labeled copolymer (see Supporting Information). Table 1 reports the characteristics of the PICM at different pH values in Tris buffer. It is noteworthy that the individual copolymers did not self-associate in solution.

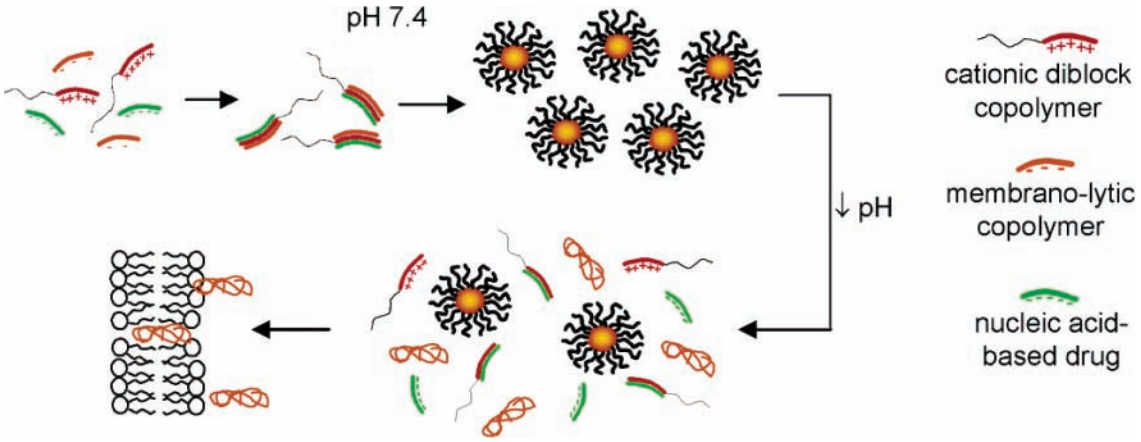


Figure 6. Schematic representation of the association/dissociation behavior of the ternary PICM as a function of pH.

At acidic pH, the micelle PI increased substantially. Moreover, upon lowering the pH from 7.4 to 5.0, a 2.3-fold decrease in the PICM M_w was observed, along with a decreased scattering intensity. This indicates partial dissociation and release of chain clusters and/or free polymeric chains in the external medium at acidic pH. The fact that 30 nm aggregates were still detected at pH 5.0 implies that micelle disruption was not complete. This was confirmed by TEM analysis (Figure 1B), which revealed the presence of small particles of appearance and size similar to those observed at neutral pH (see arrows), along with an excess of noncondensed material.

The association of the copolymers into a core/shell architecture was corroborated by ^{1}H NMR spectroscopy. Prior to analysis, the PICM were eluted on a Sephacryl column to completely remove any free polymer in solution. Figure 2 shows that PICM formation at neutral pH resulted in an important decrease in the intensity of the peaks corresponding to P(MAA-*co*-EA-*co*-BMA), while the signal of the PAEMA block completely disappeared. Interestingly, the peak attributed to the PEO block remained visible, confirming the micellization of the copolymers into core/shell assemblies (*19*). Indeed, the PEO chains forming the outer corona remain hydrated, while the (meth)acrylate monomers are segregated into a more viscous, less solvated internal core, causing a partial suppression of their signals. When the pH was reduced to 5.0, peaks corresponding to the cationic copolymer reappeared to some extent, which points toward enhanced solvation of the micellar core and/or polymer release due to partial micellar dissociation. No signal increase corresponding to P(MAA-*co*-EA-*co*-BMA) was observed at acidic pH because the relatively high concentrations required for the NMR analysis exceeded the copolymer solubility.

ODN stability toward nucleases was assessed by incubating free fluorescent ODN or ternary micelles containing the fluorescent ODN with DNAse I (50 U/μg ODN, 37 °C). Gel electrophoresis of aliquots withdrawn at predetermined time points showed that only 30% of the naked ODN remained intact after a 6 h incubation period. In contrast, no degraded ODN could be detected in the micellar samples at the end of the study (Figure 3). Thus, it is possible to protect the ODN upon incorporation in the ternary PICM structure.

The membrane-destabilizing properties of the micelles were evaluated at different pH values following removal of uncomplexed polymer. To do so, artificial phospholipid vesicles were used to mimic the endosomal membrane. The vesicles were loaded with the water-soluble fluorophore HPTS. They were then added to an isotonic micellar solution prepared at the appropriate pH value. Figure 4 illustrates the release profiles of the encapsulated probe. At pH 7.4, the ternary PICM did not destabilize the phospholipid bilayer as shown by the absence of released dye. As the pH was reduced, the extent of leakage progressively increased, reaching up to 60% at pH 5.0. When comparing the release kinetics obtained in the presence of free P(MAA-*co*-EA-*co*-BMA) to that associated with PICM at pH 5.0, one can note that the latter caused a lowered and delayed HPTS release. This suggests that the protonation of P(MAA-*co*-EA-*co*-BMA) led to its progressive removal from the micelles and to the subsequent destabilization of the vesicle membranes. Chung et al. (*20*) have reported that PEAA induces the formation of cation-selective channels through artificial membranes in a pH-dependent manner. Since P(MAA-*co*-EA-*co*-BMA) is structurally related to PEAA, a similar mechanism of vesicle destabilization may be hypothesized, although the exact nature of the membrane defects remains to be determined. Interestingly, control ternary PICM (35 nm) prepared using a well-known non-membranolytic polymer (PMAA) (*21*) instead of P(MAA-*co*-EA-*co*-BMA) were unable to trigger HPTS release at pH 5.0 (Figure 4), confirming that PEO-*b*-PAEMA does not destabilize the vesicles.

To verify whether the ternary micelles could facilitate the transfer of the ODN from the endosome to the cytoplasm, the intracellular distribution of the ODN in macrophages was examined by LSCM. In these in vitro experiments, macrophages were used, since the uptake of the PICM in non-phagocytic cells is inefficient due to the steric barrier created by the PEG corona (unpublished observations). Live cells were analyzed since it was previously demonstrated that cell fixation could affect membrane permeability and cause artifacts (*22*). Forty-five minutes after the incubation period, macrophages treated with ternary endosomolytic micelles showed multiple fluorescent intracellular vesicles, probably corresponding to phagocytic/endocytic compartments (Figure 5A). Colocalization of ODN and LysoTracker red was detected in most cells (yellow color), indicating that some micelles were localized in acidic organelles. Similar subcellular distribution was observed with the control micelles prepared with PMAA (Figure 5B). Two hours after the incubation period, bright green nuclear fluorescence could be seen in several cells incubated with endosomolytic micelles, indicating that the ODN was released from the endodomal/lysosomal compartments (Figure 5C) (*23*, *24*). These cells also exhibited a decreased red fluorescence indicating disruption of most of the acidic organelles. At that stage, the control, non-endosomolytic micelles were still mainly localized in intracellular globular compartments (Figure 5D), and staining of the nucleus of the cells was weak and, most of the time, undetectable. Collectively, these preliminary findings clearly demonstrate that cytoplasmic delivery of the ODN was facilitated by the incorporation of an endosomolytic polymer into PICM.

In conclusion, ternary PICM with a core/shell architecture, small size, and narrow size distribution were successfully

obtained at physiological pH following the sequential addition of a cationic diblock copolymer, an MAA copolymer, and an ODN. Besides their ability to protect the ODN against nuclease degradation, the ternary micelles were shown to release chain clusters capable of inducing membrane destabilization at slightly acidic pH and improving substantially the ODN subcellular distribution. This association/dissociation behavior is represented in Figure 6 and highlights the potential of these pH-sensitive PICM for the efficient transport and delivery of polyionic drugs. Future work will aim at evaluating the ability of the system to increase the efficacy of ODNs into human tumoral cells. To promote cellular internalization, the micelles will have to be decorated with a targeting ligand.

ACKNOWLEDGMENT

This work was financially supported by the NSERC and the Canada Research Chair Program. M.-A. Yessine acknowledges a scholarship from the FRSQ.

Supporting Information Available: Molecular weight determination, potentiometric titration, and ^{1}H NMR spectra of the copolymers in deuterated Tris. Experimental details on the determination of the critical association concentration of the ternary PICM and the quantification of complexed ODN and P(MAA-*co*-EA-*co*-BMA). This material is available free of charge via the Internet at http://pubs.acs.org.

LITERATURE CITED

(1) Hawker, C. J., and Wooley, K. L. (2005) The convergence of synthetic organic and polymer chemistries. *Science 309*, 1200−5.

(2) Kataoka, K., Harada, A., and Nagasaki, Y. (2001) Block copolymer micelles for drug delivery: design, characterization and biological significance. *Adv. Drug Delivery Rev. 47*, 113−31.

(3) Gillies, E. R., and Frechet, J. M. J. (2005) pH-responsive copolymer assemblies for controlled release of doxorubicin. *Bioconjugate Chem. 16*, 361−8.

(4) Rungsardthong, U., Ehtezazi, T., Bailey, L., Armes, S. P., Garnett, M. C., and Stolnik, S. (2003) Effect of polymer ionization on the interaction with DNA in nonviral gene delivery systems. *Biomacromolecules 4*, 683−90.

(5) Kataoka, K., Togawa, H., Harada, A., Yasugi, K., Matsumoto, T., and Katayose, S. (1996) Spontaneous formation of polyion complex micelles with narrow distribution from antisense oligonucleotide and cationic block copolymer in physiological saline. *Macromolecules 29*, 8556−7.

(6) Kabanov, A. V., Vinogradov, S. V., Suzdaltseva, Y. G., and Alakhov, V. Y. (1995) Water-soluble block polycations as carriers for oligonucleotide delivery. *Bioconjugate Chem. 6*, 639−43.

(7) Rungsardthong, U., Deshpande, M., Bailey, L., Vamvakaki, M., Armes, S. P., Garnett, M. C., and Stolnik, S. (2001) Copolymers of amine methacrylate with poly(ethylene glycol) as vectors for gene therapy. *J. Controlled Release 73*, 359−80.

(8) Kakizawa, Y., and Kataoka, K. (2002) Block copolymer micelles for delivery of gene and related compounds. *Adv. Drug Delivery Rev. 54*, 203−22.

(9) Murthy, N., Robichaud, J. R., Tirell, D. A., Stayton, P. S., and Hoffman, A. S. (1999) The design and synthesis of polymers for eukaryotic membrane disruption. *J. Controlled Release 61*, 137−43.

(10) Lackey, C. A., Murthy, N., Press, O. W., Tirell, D. A., Hoffman, A. S., and Stayton, P. S. (1999) Hemolytic activity of pH-responsive polymer−streptavidin bioconjugates. *Bioconjugate Chem. 10*, 401−5.

(11) Jones, R. A., Cheung, C. Y., Black, F. E., Zia, J. K., Stayton, P. S., Hoffman, A. S., and Wilson, M. R. (2003) Poly(2-alkylacrylic acid) polymers deliver molecules to the cytosol by pH-sensitive disruption of endosomal vesicles. *Biochem. J. 372*, 65−75.

(12) Cheung, C. Y., Murthy, N., Stayton, P. S., and Hoffman, A. S. (2001) A pH-sensitive polymer that enhances cationic lipid-mediated gene transfer. *Bioconjugate Chem. 12*, 906−10.

(13) Lackey, C. A., Press, O. W., Hoffman, A. S., and Stayton, P. S. (2002) A biomimetic pH-responsive polymer directs endosomal release and intracellular delivery of an endocytosed antibody complex. *Bioconjugate Chem. 13*, 996−1001.

(14) Yessine, M. A., Meier, C., Petereit, H.-U., and Leroux, J. C. (2006) On the role of methacrylic acid copolymers in the intracellular delivery of antisense oligonucleotides. *Eur. J. Pharm. Biopharm. 63*, 1−10.

(15) Dufresne, M. H., and Leroux, J. C. (2004) Study of the micellization behavior of different order amino block copolymers with heparin. *Pharm. Res. 21*, 160−9.

(16) Astafieva, I., Zhong, X. F., and Eisenberg, A. (1993) Critical micellization phenomena in block polyelectrolyte solutions. *Macromolecules 26*, 7339−52.

(17) Darnell, J., Lodish, H., and Baltimore, D. (1990) *Molecular Cell Biology*, 2nd ed., p 493, Scientific American Books, New York.

(18) Daleke, D. L., Hong, K., and Papahadjopoulos, D. (1990) Endocytosis of liposomes by macrophages: binding, acidification and leakage of liposomes monitored by a new fluorescence assay. *Biochim. Biophys. Acta 1024*, 352−66.

(19) Weaver, J. V. M., Armes, S. P., and Liu, S. Y. (2003) A "holy trinity" of micellar aggregates in aqueous solution at ambient temperature: unprecedented self-assembly behavior from a binary mixture of a neutral-cationic diblock copolymer and an anionic polyelectrolyte. *Macromolecules 36*, 9994−8.

(20) Chung, J. C., Gross, D. J., Thomas, J. L., Tirrell, D. A., and Opsahl-Ong, L. R. (1996) pH-sensitive, cation-selective channels formed by a simple synthetic polyelectrolyte in artificial bilayer membranes. *Macromolecules 29*, 4636−41.

(21) Thomas, J. L., You, H., and Tirrell, D. A. (1995) Tuning the response of a pH-sensitive membrane switch. *J. Am. Chem. Soc. 117*, 2949−50.

(22) Richard, J. P., Melikov, K., Vives, E., Ramos, C., Verbeure, B., Gait, M. J., Chernomordik, L. V., and Lebleu, B. (2003) Cell-penetrating peptides. A reevaluation of the mechanism of cellular uptake. *J. Biol. Chem. 278*, 585−90.

(23) Loke, S. L., Stein, C. A., Zhang, X. H., Mori, K., Nakanishi, M., Subasinghe, C., Cohen, J. S., and Neckers, L. M. (1989) Characterization of oligonucleotide transport into living cells. *Proc. Natl. Acad. Sci. U.S.A. 86*, 3474−8.

(24) Chin, D. J., Green, G. A., Zon, G., Szoka, F. C., Jr., and Straubinger, R. M. (1990) Rapid nuclear accumulation of injected oligodeoxyribonucleotides. *New Biol. 2*, 1091−100.

BC060159M

CORRECTIONS

Volume 17, Number 3, May/June 2006.

Timothy L. Kelly, Michael C. W. Lam, and Michael O. Wolf*

CARBOHYDRATE-LABELED FLUORESCENT MICROPARTICLES AND THEIR BINDING TO LECTINS

The stereochemistry of compound **1a** was incorrectly assigned as the β-anomer. It is the α-anomer, as determined by the $^1J_{C1-H1} = 176$ Hz coupling constant.

BC060127Z

10.1021/bc060127z
Published on Web 05/02/2007

Volume 17, Number 1, January/February 2006.

Giovanna Barbarella,* Massimo Zambianchi, Alfredo Ventola, Eduardo Fabiano, Fabio Della Sala, Giuseppe Gigli, Marco Anni, Andrea Bolognesi, Letizia Polito, Marina Naldi, and Massimo Capobianco

BRIGHT OLIGOTHIOPHENE *N*-SUCCINIMIDYL ESTERS FOR EFFICIENT FLUORESCENT LABELING OF PROTEINS AND OLIGONUCLEOTIDES

In our work (*1*), we have discovered an inconsistency in the definition of the molecular geometry of compound **5** used in the theoretical calculations. We used a molecular structure with a C═C double bond on the *succinimidyl* group, while the succinimidyl group instead has single C—C bonds. The structure employed in calculations is known as *maleimide* instead.

We repeated the theoretical calculations using the correct molecular structure. We found small changes in the electronic structure and optical properties. Molecular orbitals localized on the succinimidyl group are shifted in energy, so that now the LUMO is no longer localized on the succinimidyl group but rather on the bithiophene. New HOMO and LUMO orbitals are reported in Figure 1. The optically active state (computed at the CC2 level) is found at 4.01 eV, almost the same energy as in previous calculations, since the side group has a negligible effect on it, but now it is the lowest excited state and it is characterized by a HOMO → LUMO transition.

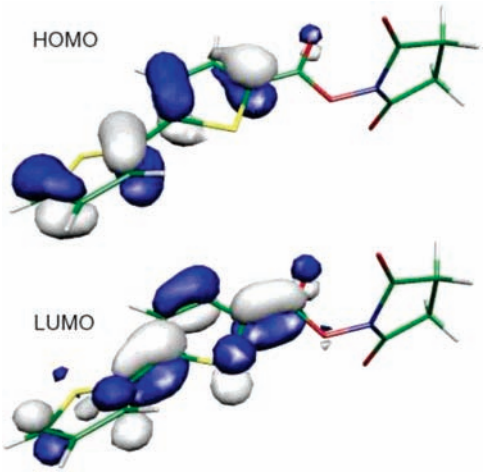


Figure 1. HOMO and LUMO wave functions for *N*-succinimidyl ester **5**.

Finally, we emphasize that the main conclusions drawn from theoretical calculations, based on considerations of optically active states and analysis of model compound **AT2**, still hold unaffected.

LITERATURE CITED

(1) Barbarella, G., Zambianchi, M., Ventola, A., Fabiano, E., Della Sala, F., Gigli, G., Anni, M., Bolognesi, A., Polito, L., Naldi, M., and Capobianco, M. (2006) Bright oligothiophene *N*-succinimidyl esters for efficient fluorescent labeling of proteins and oligonucleotides. *Bioconjugate Chem. 17*, 58−67.

BC060331M

10.1021/bc060331m
Published on Web 04/11/2007

JULY/AUGUST 2007
Volume 18, Number 4

© *Copyright 2007 by the American Chemical Society*

Bioconjugate Chemistry

COMMUNICATIONS

Studies on Aminoisonucleoside Modified siRNAs: Stability and Silencing Activity

Zong-Sheng Li,[†,#] Ren-Ping Qiao,[†,#] Quan Du,[‡] Zhen-Jun Yang,*[,†] Liang-Ren Zhang,[†] Pei-Zhuo Zhang,[§] Zi-Cai Liang,[‡] and Li-He Zhang*[,†]

State Key Laboratory of Natural and Biomimetic Drugs, School of Pharmaceutical Sciences, Peking University, Beijing, 100083, Institute of Molecular Medicine, Peking University, Beijing, 100871, and Shanghai GenePharma Co. Ltd., Z-J High Tech Park, Shanghai, 201203, China. Received December 26, 2006; Revised Manuscript Received May 11, 2007

A novel class of aminoisonucleoside was synthesized and incorporated into a luciferase gene-targeting siRNA. Structural and functional analyses of such a kind of siRNAs indicated that sense strand modifications with aminoisonucleoside at the 3′ or 5′ terminal, such as **ssIso-1** and **ssIso-2**, have less effect on RNA duplex thermal and serum stabilities, and their functional activities are also comparable to their native siRNAs. In contrast, antisense strand modifications with aminoisonucleoside at the corresponding positions, such as **asIso-2** or **asIso-1**, bring a striking negative effect on RNA duplex stability but still maintain around 40−50% of gene knockdown.

INTRODUCTION

RNAi[1] was first reported by A. Fire and co-workers in *Caenorhabditis elegans* (*1*) and represents a ubiquitous pathway of post-transcriptional gene silencing in nearly every eukaryote studied thus far. The real trigger of RNAi is a small double-stranded RNA (siRNA) that is ∼19 bases in length which assembles with RISC in the cytoplasm and initiates a complicated cascade for the ultimate degradation of sequence-homologous RNAs, The sequence-selective gene knockdown by siRNA and its rapid adoption as a powerful tool for gene regulation in mammalian cells has generated the expectation for its use to improve target therapeutics for cancer, metabolic, inflammatory, infectious, neurological, and other types of diseases (*2*).

Although a variety of methods have been developed to generate siRNA, such as plasmid vectors for transient transfection and viral vectors for stable transduction (*2*), chemical synthesis of siRNAs represents a more attractive resource for clinical purpose and has great advantages in accommodating chemical modifications and dosing changes (*3*−*6*). However, like the hindrances in development of antisense technology, which is the previous generation of RNA-targeting small RNA molecules, siRNA-based therapeutics is also obstructed by its intrinsic qualities, such as poor intracellular uptake, limited blood stability, and nonspecific immune stimulation, and so forth.

* To whom correspondence should be addressed. E-mail: zdszlh@bjmu.edu.cn, yangzj@bjmu.edu.cn; Tel: +86- 10-82802503, Fax: +86-10-82802503.

[†] School of Pharmaceutical Sciences, Peking University.

[‡] Institute of Molecular Medicine, Peking University.

[§] Shanghai GenePharma Co. Ltd.

[#] The authors contributed equally to this paper.

[1] Abbreviations: RNAi, RNA interference; siRNA, small interfering RNA; dsRNA, double-stranded RNA; RISC, RNA-induced silencing complex; LNA, locked nucleic acid; DMF, *N*,*N*-dimethyl foramide; THF, tetrahydrofuran; DIPEA, diisopropylethylamine; TMSCl, chlorotrimethylsilane; DMT, 4,4-dimethoxytrityl chloride; T, thymidine; A, adenosine; U, uridine; EDTA, ethylenediaminetetraacetic acid, disodium salt; SVPDE, snake venom phosphodiesterase; FBS, fetal bovine serum; ATP, adenosine triphosphate.

10.1021/bc060398+ CCC: $37.00 © 2007 American Chemical Society
Published on Web 06/01/2007

Table 1. Sequences of Native siRNA (ssNC/asNC) and Aminoisonucleoside-Modified Sense Strand siRNA (ssIso-1−ssIso-5) or Aminoisonucleoside-Modified Antisense Strand siRNA (asIso-1−asIso-5)[a]

NC	**ssNC/asNC:**	5′-CUG GUA AAG CAU UCA GUA Utt-3′ (Sense) 3′-ttGAC CAU UUC GUA AGU CAU A-5′ (Antisense)

Sense strand modification			Antisense strand modification		
	Name	**Sequence**		**Name**	**Sequence**
a	**ssIso-1**	5′-CUGGUAAAGCAUUCAGUA***T***tt-3′	**f**	**ssNC**	5′-CUGGUAAAGCAUUCAGUAUtt-3′
	asNC	3′-ttGACCAUUUCGUAAGUCAUA-5′		**asIso-1**	3′-ttGACCAUUUCGUAAGUCAU***A***-5′
b	**ssIso-2**	5′-C***T***GGUAAAGCAUUCAGUAUtt-3′	**g**	**ssNC**	5′-CUGGUAAAGCAUUCAGUAUtt-3′
	asNC	3′-ttGACCAUUUCGUAAGUCAUA-5′		**asIso-2**	3′-ttG***A***CCAUUUCGUAAGUCAUA-5′
c	**ssIso-3**	5′-CUGGUAA***A***GCAUUCAGUAUtt-3′	**h**	**ssNC**	5′-CUGGUAAAGCAUUCAGUAUtt-3′
	asNC	3′-ttGACCAUUUCGUAAGUCAUA-5		**asIso-3**	3′-ttGACCAUUUCGU***A***AGUCAUA-5′
d	**ssIso-4**	5′-C***T***GGUAAAGCAUUCAGUAU***T***t-3′	**i**	**ssNC**	5′-CUGGUAAAGCAUUCAGUAUtt-3′
	asNC	3′-ttGACCAUUUCGUAAGUCAUA-5′		**asIso-4**	3′-t***T***GACCAUUUCGUAAGUCAU***A***-5′
e	**ssIso-5**	5′-C***T***GGU***A***AAGCAUUC***A***GUA***T***t-3′	**j**	**ssNC**	5′-CUGGUAAAGCAUUCAGUAUtt-3′
	asNC	3′-ttGACCAUUUCGUAAGUCAUA-5′		**asIso-5**	3′-t***T***GACC***A***UUUCGU***A***AGUCAU***A***-5′

[a] Top strand depicts the sense strand in the 5′−3′ direction (same as the target sequence). Bottom strand depicts the antisense strand in the 3′−5′ direction (complementary to the target sequence). ***A*** and ***T*** letters indicate the aminoisonucleotide.

Chemical modification has been extensively explored to improve antisense serum stability and pharmacokinetics so as to extend circulation in blood for a sufficiently long time (*7*−*12*). Many modified antisense oligos are being tested in clinical trials with fomivirsen (Vitravene; Isis) as the first oligo drug approved by the U.S. FDA for the treatment of eye cytomegalovirus infection. Currently, such chemical modifications are also being applied to synthetic siRNAs, and some modified siRNAs have been reported to be more potent and stable than their native siRNAs (*6*, *13*−*15*). For example, phosphorothioate modification throughout the siRNA duplexes significantly enhanced gene-silencing activities (*16*, *17*). Alternative modification, 2′-position methylation within the pentose sugar, was generally well tolerated with siRNA silencing activity being comparable with the native form. Modification on base moieties is relatively less attempted with N^3-methyluridine, 5-bromouracil, 5-iodouracil, 2,6-diaminopurine, and inosine being reported so far (*3*, *16*). However, all three modifications resulted in a slight decrease of siRNA activity. Recently reported backbone modification, boranophosphate linkage, seems to be more attractive, since it makes siRNA 300-fold more active than the native form and 2-fold more stable than the classic phosphorothioate (*18*). Several of the siRNA reagents have already made their way into clinical trials, one with initially positive indications reported (*19*).

Isonucleosides represent a novel class of carbohydrate-modified nucleoside in which the nucleobase is linked to various positions of ribose other than C-1′, and some of these nucleosides have shown interesting biological activities. In our previous reports for synthesis and incorporation of isonucleosides into antisense oligos, we found that modified antisense oligos not only possess strong nuclease resistance but more interestingly become good substrates of RNase H (*20*). CD spectra and molecular modeling demonstrated that isonucleoside-modified DNA duplexes still adopt a B-like conformation, but the formation of Watson−Crick hydrogen bonding was perturbed by the torsion of the backbone (*21*, *22*), while isonucleoside-modified oligonucleotide/RNA duplex formed an A-like conformation in solution (*23*). An introduction of an amino group into the isonucleoside may increase the thermal stability of the isonucleoside-modified oligonucleotide with its complementary sequence. Here, we report the chemical synthesis and incorporation of aminoisonucleosides into the siRNA duplex and analyze the effect of such a modification at different positions on siRNA structural stability and functional activity.

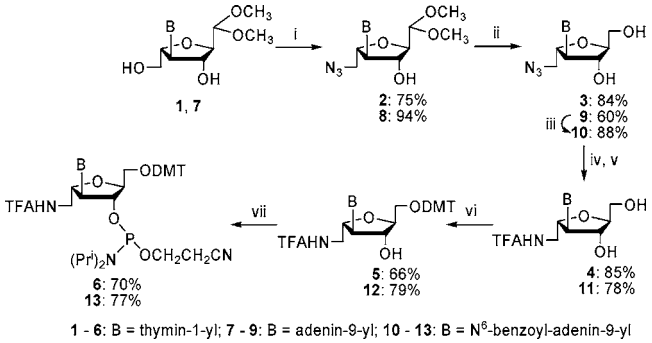
Members of the wee1 kinase family control the timing of cell cycle events by acting as a negative regulator of entry into mitosis (G2 to M transition) by protecting the nucleus from cytoplasmically activated cyclin B1-complexed CDC2 before the onset of mitosis. These kinases have been evaluated as promising anticancer target genes. siRNA is used in the current experiment as designed against the 3′ end of the coding sequence of the wee1 mRNA (Table 1) (*24*).

MATERIALS AND METHODS

General. All solvents were dried and distilled prior to use. Chemical reagents were purchased from Acros and Sigma Co. Thin layer chromatography was performed on silica gel GF-254 (Qing-Dao Chemical Co., China) plates with detection by UV or by heating. Silica gel (200−300 mesh; Qing-Dao Chemical Co.) was used for short column chromatography. NMR spectra were recorded on a Varian VXR-300, Varian Inova-500 instrument. ^{1}H NMR spectra were referenced using internal standard TMS and ^{31}P NMR spectra using external standard 85% H_3PO_4. Mass spectra (ESI-TOF$^+$ MS) and high-resolution mass spectra (ESI-TOF$^+$ HRMS) were obtained at MDS SCIEX QSTAR and Bruker DALTONICS APEX IV 70e instruments. MALDI-TOF mass spectra for oligonucleotides were obtained at SIMADZU AXIMA CFR plus, and the data are reported in *m*/*e* (intensity to 100%). Optical rotations were recorded on Perkin-Elmer 243B Polarimeter. 4-Deoxy-4-(thymin-1-yl)-2,5-anhydro-L-mannofuranose dimethylacetal (**1**) and 4-deoxy-4-(adenine-9-yl)-2,5-anhydro-L-mannofuranose dimethylacetal (**7**) were synthesized according to Yang et al. (*22*) (Scheme 1).

Synthesis. 4,6-Dideoxy-4-(thymin-1-yl)-6-azido-2,5-anhydro-L-mannofuranose dimethyl acetal (**2**). To a mixture of compound **1** (4.41 g, 13.95 mmol), triphenylphosphine (4.02 g, 15.35 mmol), and sodium azide (5.00 g, 76.92 mmol) in dry DMF (100 mL) was added carbon tetrabromide (4.90 g, 14.80 mmol) at room temperature. The mixture was stirred at room temperature for 48 h, and then methanol was added until the mixture turned into clear solution. Stirring was continued for another hour. The solvent was removed under vacuum, and the residue was purified by a short-column chromatography using a gradient of MeOH in CH_2Cl_2 (2−2.5%) to yield **2** (3.57 g, 75%) as white foam. UV (CH_3OH): λ_{max} = 270.5 (ϵ = 8804). $[\alpha]_D^{20}$ = −34.50 (C 0.004 g/mL, CH_3OH). ^{1}H NMR (DMSO-d_6, 500 MHz): δ 1.79 (s, 3H, 5-CH_3), 3.29−3.54 (m, 2H, H-6′), 3.34 (s, 3H, 1′-OCH_3), 3.35 (s, 3H, 1′-OCH_3), 3.81 (t, $J_{2',1'} = J_{2',3'}$

Scheme 1 . Synthesis of 6 and 13[a]



[a] Reagents and conditions: (i) $Ph_3P/CBr_4/NaN_3$/DMF/rt; (ii) a. 1% HCl, reflux; b. 2N NaOH/$NaBH_4$, rt; (iii) TMSCl/Py/BzCl/Py, rt; (iv) 10% Pd/C/H_2 /EtOH, rt; (v) $CF_3COOC_2H_5/Et_3N/CH_3OH$, rt; (vi) DMTrCl/Py, rt; (vii) 2-cyanoethyl-*N*,*N*-diisopropyl-chlorophosphoramidite/ $Et(Pr^i)_2N$/THF, rt.

= 5.5 Hz, 1H, H-2′), 4.16 (m, 1H, H-5′), 4.40 (m, 1H, H-3′), 4.49 (d, $J_{1',2'}$ = 5.5 Hz, 1H, H-1′), 4.65 (dd, J = 8 Hz, J = 9 Hz, 1H, H-4′), 5.58 (d, J = 5.5 Hz, 1H, 3′-OH), 7.54 (d, J = 1 Hz, 1H, H-6), 11.30 (s, 1H, N-3). ^{13}C NMR(DMSO-d_6, 125.7 MHz): δ (5-CH_3), 51.2 (C-6′), 53.8 (1′-OCH_3), 54.3 (1′-OCH_3), 64.0 (C-4′), 73.5 (C-3′), 77.0 (C-5′), 81.6 (C-2′), 103.9 (C-1′), 109.5 (C-5), 138.1 (C-6), 151.1 (C-4), 163.6 (C-2). HRMS (ESI-TOF$^+$) calcd for $C_{13}H_{20}N_5O_6$ (M^+ + H): 342.1408. Found: 342.1424.

4,6-Dideoxy-4-(thymin-1-yl)-6-azido-2,5-anhydro-L-mannitol (**3**). Compound **2** (0.15 g, 0.44 mmol) was dissolved in 1% hydrochloric acid in 50% water/50% THF (10 mL) and refluxed overnight. After cooling to 0 °C and neutralization with 2 M NaOH, sodium borohydride (0.032 g, 0.86 mmol) was added. The solution was stirred at room temperature for 4 h, then neutralized with 1% HCl at 0 °C. The solvent was removed under vacuum, and the residue was dissolved in C_2H_5OH. After filtration, the mixture was purified by a short-column chromatography using a gradient of MeOH in CH_2Cl_2 (5%) to yield **3** (0.11 g, 84%) as white foam. UV (CH_3OH): λ_{max} = 271 (ϵ = 8802). $[\alpha]_D^{20}$ = −48.25 (C 0.004 g/mL, CH_3OH). ^{1}H NMR (DMSO-d_6, 500 MHz) δ 1.77 (s, 3H, 5-CH_3), 3.32−3.63 (m, 2H, H-6′), 3.74−3.77 (m, 1H, H-2′), 4.09−4.12 (m, 1H, H-5′), 4.09−4.27 (m, 1H, H-3′), 4.71 (t, J = 8.5 Hz, 1H, H-4′), 4.81 (t, J = 5 Hz, 1′-OH), 5.57 (d, J = 5.5 Hz, 1H, 3′-OH), 7.56 (s, 1H, H-6), 11.27 (s, 1H, N-3). ^{13}C NMR (DMSO-d_6, 125.7 MHz): δ 12.0 (5-CH_3), 51.8 (C-6′), 61.4 (C-1′), 63.1 (C-4′), 72.4 (C-3′), 77.0 (C-5′), 83.0 (C-2′), 109.5 (C-5), 137.8 (C-6), 151.2 (C-2), 163.7 (C-4). HRMS (ESI-TOF$^+$) calcd for $C_{11}H_{16}N_5O_5$ (M^+ + H): 298.1145; Found: 298.1150.

4,6-Dideoxy-4-(thymin-1-yl)-6-trifluoroacetylamino-2,5-anhydro-L-mannitol (**4**). To a solution of compound **3** (0.37 g, 1.25 mmol) in 10 mL anhydrous methanol was added 10% Pd/C (0.18 g), then the mixture was reduced by hydrogen (4 kg/cm^2) for 16 h. After filtration, the solvent was removed under vacuum and the residue was dissolved in 25 mL methanol; triethylamine (0.96 mL, 6.90 mmol) and ethyl trifluoroacetate (0.5 mL, 4.14 mmol) were added, and the mixture was reacted overnight at room temperature. The solvent was removed under vacuum and the residue was purified by a short-column chromatography using a gradient of MeOH in CH_2Cl_2 (7%) to yield **4** (0.39 g, 85%) as white foam. UV (CH_3OH): λ_{max} = 271 (ϵ = 7965). $[\alpha]_D^{20}$ = −3.00 (C 0.004 g/mL, CH_3OH). ^{1}H NMR(DMSO-d_6, 500 MHz) δ 1.78 (s, 3H, 5-CH_3), 3.32−3.64 (m, 4H, H-1′ and H-6′), 3.75−3.78 (m, 1H, H-2′), 4.13−4.17 (m, 1H, H-5′), 4.26−4.30 (m, 1H, H-3′), 4.53 (t, J = 7.5 Hz, 1H, H-4′), 4.81 (t, J = 5.0 Hz, 1′-OH), 5.59 (d, J = 5.5 Hz, 1H, 3′-OH), 7.54 (d, J = 1.0 Hz, 1H, H-6), 9.51 (t, J = 5.0 Hz, 1H, 6′-NH-), 11.32 (s, 1H, N-3). ^{13}C NMR (DMSO-d_6, 125.7 MHz): δ 12.0 (5-CH_3), 41.9 (C-6′), 61.1 (C-1′), 65.3 (C-4′), 72.9 (C-3′), 76.1 (C-5′), 83.1 (C-2′), 109.5 (C-5), 138.2 (C-6), 151.0 (C-2), 156.3 and 156.5 (CF_3CO), 163.6 (C-4). Anal. Calcd. for $C_{13}H_{16}F_3N_3O_6$ (367.1) C 42.51, H 4.39, N 11.44. Found: C 42.28, H 4.60, N 11.20.

1-*O*-Dimethoxytrityl-4,6-dideoxy-4-(thymin-1-yl)-6-trifluoroacetylamino-2,5-anhydro-L-mannitol (**5**). Compound **4** (0.41 g, 1.1 mmol) was dissolved in dry pyridine (10 mL), and dimethoxytrityl (DMT) chloride (0.38 g, 1.1 mmol) was added at 0 °C. The solution was stirred at room temperature for 23 h. After evaporation, the mixture was purified by a short-column chromatography using a gradient of MeOH in CH_2Cl_2 (1.5%, 1% Et_3N added) to yield **5** (0.49 g, 66%) as white foam. ^{1}H NMR (DMSO-d_6, 500 MHz) δ 1.70 (s, 3H, 5-CH_3), 3.08−3.47 (m, 4H, H-1′ and H-6′), 3.73 (s, 6-H, Ph−OCH_3), 3.97−4.00 (m, 1H, H-2′), 4.24−4.29 (m, 2H, H-3′ and H-5′), 4.53 (t, J = 8.0 Hz, 1H, H-4′), 5.60 (d, J = 5.5 Hz, 3′-OH), 6.87−7.43 (m, 13H, Ph), 7.51 (s, 1H, H-6), 9.66 (t, J = 5.5 Hz, 1H, 6′-NH-), 11.34 (s, 1H, N-3). ^{13}C NMR (DMSO-d_6, 125.7 MHz): δ 11.9 (5-CH_3), 41.9 (C-6′), 54.9 (Ph−OCH_3), 64.3 (C-1′), 65.3 (C-4′), 72.8 (C-3′), 75.4 (C-5′), 81.1 (C-2′), 109.4 (C-5), 113.3, 126.6, 127.7, 129.7, 135.6 (Ph), 138.3 (C-6), 151.0 (C-2), 158.0 (CF_3CO), 163.6 (C-4). Anal. Calcd. for $C_{34}H_{34}F_3N_3O_8$ (669.2) C 60.98, H 5.12, N 6.27. Found: C 60.96, H 5.17, N 6.24.

1-*O*-Dimethoxytrityl-3-*O*-(2-cyanoethyl-*N*,*N*-diisopropyl)-phosphoramidite-4,6-dideoxy-4-(thymin-1-yl)-6-trifluoroacetylamino-2,5-anhydro-L-mannitol (**6**). Compound **5** (0.47 g, 0.7 mmol) was dissolved in anhydrous THF (5 mL) under argon. To this solution was added diisopropylethylamine (DIPEA, 0.5 mL, 2.8 mmol) and 2-cyanoethyl-*N*,*N*-diisopropylchlorophosphoramidite (0.3 mL, 1.4 mmol). The mixture was stirred at 0 °C for 10 min, then at room temperature for 2 h. The reaction mixture was quenched by addition of MeOH (0.6 mL). After stirring for 15 min, EtOAc (40 mL) was added, and the organic layer was washed with 5% aqueous $NaHCO_3$ (10 mL × 2), followed by H_2O (10 mL × 2) and saturated NaCl solution (10 mL × 2). The solution was dried (Na_2SO_4), then evaporated under vacuum to oil, and the oil was purified by a short-column chromatography eluting with petroleum ether/EtOAc (6:1−3:2, 0.5% Et_3N) to afford compound **6** as a white foam solid (0.43 g, 70%). ^{1}H NMR ($CDCl_3$, 500 MHz): δ 0.58 (d, J = 7.0 Hz, 3H, CH_3), 0.74 (d, J = 6.5 Hz, 3H, CH_3), 0.92 (d, J = 7.0 Hz, 6H, CH_3), 1.18 (t, J = 7.0 Hz, 2H, CH_2CN), 1.70 (s, 3H, 5-CH_3), 2.41 (m, 2H, CH), 3.08−3.47 (m, 6H, H-1′, H-6′ and -$POCH_2$), 3.72 (s, 6-H, Ph−OCH_3), 3.98−4.01 (m, 1H, H-2′), 4.22−4.28 (m, 2H, H-3′ and H-5′), 4.53 (t, J = 8.0 Hz, 1H, H-4′), 6.86−7.42 (m, 13H, Ph), 7.50 (s, 1H, H-6), 9.67 (t, J = 5.5 Hz, 1H, 6′-NH-), 11.30 (s, 1H, N-3). ^{31}P NMR ($CDCl_3$, 121.5 MHz): δ 154.18 and 154.84.

4,6-Dideoxy-4-(adenin-9-yl)-6-azido-2,5-anhydro-L-mannofuranose dimethyl acetal (**8**). Compound **8** (white foam, 2.15 g, 94%) was prepared from compound **7** (2.12 g, 6.52 mmol) in the same way as compound **2** from compound **1**. UV (CH_3OH): λ_{max} = 262 (ϵ = 13452). $[\alpha]_D^{20}$ = −27.50 (C 0.004 g/mL, CH_3OH). ^{1}H NMR (DMSO-d_6, 500 MHz): δ 3.36 (s, 3H, 1-OCH_3), 3.37 (s, 3H, 1-OCH_3), 3.29−3.56−3.47 (m, H-6′), 3.91 (t, J = 5.5 Hz, 1H, H-2′), 4.56−4.59 (m, 2H, H-1′ and H-5′), 4.72−4.80 (m, 2H, H-3′ and H-4′), 5.73 (d, J = 6.0 Hz, 1H, 3′-OH), 7.26 (br. s, 2H, 6-NH_2), 8.15 (s, 1H, H-2), 8.23 (s, 1H, H-8). ^{13}C NMR (DMSO-d_6, 125.7 MHz): δ 51.1 (C-6′), 53.8 (1′-OCH_3), 54.4 (1′-OCH_3), 63.4 (C-4′), 74.7 (C-3′), 77.6 (C-5′), 82.0 (C-2′), 103.7 (C-1′), 119.1 (C-5), 139.9 (C-8), 149.6 (C-4), 152.4 (C-2), 156.0 (C-6). HRMS (ESI-TOF$^+$) calcd for $C_{13}H_{19}N_8O_4$ (M^+ + H): 351.1523. Found: 351.1519.

4,6-Dideoxy-4-(adenin-9-yl)-6-azido-2,5-anhydro-L-mannitol (**9**). Compound **9** (white foam, 0.40 g, 60%) was prepared from compound **8** (0.74 g, 2.1 mmol) in the same way as

compound **3** from compound **2**. UV (CH_3OH): $\lambda_{max} = 260.5$ ($\epsilon = 12802$). $[\alpha]_D^{20} = -13.8$ (C 0.004 g/mL, CH_3OH). ^1H NMR (DMSO-d_6, 500 MHz): δ 3.31−3.69 (m, 4H, H-1′ and H-6′), 3.84−3.87 (m, 1H, H-2′), 4.54−4.57 (m, 1H, H-5′), 4.64−4.68 (m, 1H, H-3′), 4.77 (t, $J = 8.5$ Hz, 1H, H-4′), 4.88 (t, $J = 5.5$ Hz, 1H, 1′-OH), 5.68 (d, $J = 5.5$ Hz, 1H, 3′-OH), 7.24 (br. s, 2H, 6-NH_2), 8.13 (s, 1H, H-2), 8.24 (s, 1H, H-8). ^{13}C NMR (DMSO-d_6, 125.7 MHz): δ 51.7 (C-6′), 61.3 (C-1′), 62.8 (C-4′), 73.3 (C-3′), 77.4 (C-5′), 83.4 (C-2′), 119.1 (C-5), 139.9 (C-8), 149.6 (C-4), 152.4 (C-2), 156.0 (C-6). HRMS (ESI-TOF$^+$) calcd for $C_{11}H_{15}N_8O_3$ ($M^+ + H$): 307.1261. Found: 307.1263.

4,6-Dideoxy-4-(N^6-benzoyladenin-9-yl)-6-azido-2,5-anhydro-L-mannitol (**10**). Compound **9** (0.33 g, 1.1 mmol) was dissolved in dry pyridine (10 mL) and TMSCl (1.4 mL, 11 mmol) was added at 0 °C. The solution was stirred at room temperature for 2 h. Then, benzyl chloride (0.7 mL, 6 mmol) was added at 0 °C and the solution was stirred at room temperature for 4 h. Then, the pH of the solution was adjusted to 8−9 by NH_4OH at 0 °C. After evaporation, the mixture was dissolved in CH_2Cl_2. After filtration, the solvent was evaporated under vacuum, and the residue was purified by short-column chromatography using a gradient of MeOH in CH_2Cl_2 (3.5%) to yield **10** (0.39 g, 88%) as white foam. UV (CH_3OH): $\lambda_{max} = 280.5$ ($\epsilon = 13051$). $[\alpha]_D^{20} = -14.5$ (C 0.004 g/mL, CH_3OH). ^1H NMR (DMSO-d_6, 500 MHz): δ 3.32−3.71 (m, 4H, H-1′ and H-6′), 3.88−3.91 (m, 1H, H-2′), 4.59−4.63 (m, 1H, H-5′), 4.69−4.73 (m, 1H, H-3′), 4.90−4.95 (m, 2H, H-4′ and 1′-OH), 5.77 (d, $J = 6.0$ Hz, 1H, 3′-OH), 7.52−8.04 (5H, Ph), 8.62 (s, 1H, H-2), 8.74 (s, 1H, H-8), 11.16 (s, 1H, 6-NH-). ^{13}C NMR (DMSO-d_6, 125.7 MHz): δ 51.7 (C-6′), 61.2 (C-1′), 62.9 (C-4′), 73.4 (C-3′), 77.4 (C-5′), 83.3 (C-2′), 125.8 (C-5), 128.4, 132.4 and 133.3 (Ph), 143.5 (C-8), 150.2 (C-4), 151.4 (C-2), 152.6 (C-6), 165.5 (Ph−CO-). HRMS (ESI-TOF$^+$) calcd for $C_{18}H_{19}N_8O_4$ ($M^+ + H$): 411.1523. Found: 411.1514.

4,6-Dideoxy-4-(N^6-benzoyl-adenin-9-yl)-6-trifluoroacetylamino-2,5-anhydro-L-mannitol (**11**). Compound **11** (white foam, 0.40 g, 89%) was prepared from compound **10** (0.39 g, 0.94 mmol) in the same method as compound **4** from compound **3**. UV (CH_3OH): $\lambda_{max} = 279$ ($\epsilon = 13764$). $[\alpha]_D^{20} = -17.00$ (C 0.004 g/mL, CH_3OH). ^1H NMR (DMSO-d_6, 500 MHz): δ 3.39−3.71 (m, 4H, H-1′ and H-6′), 3.87−3.90 (m, 1H, H-2′), 4.61−4.64 (m, 1H, H-5′), 4.69−4.73 (m, 1H, H-3′), 4.79 (t, $J = 8.0$ Hz, 1H, H-4′), 4.91 (t, $J = 5.5$ Hz, 1H, 1′-OH), 5.77 (d, $J = 6.0$ Hz, 1H, 3′-OH), 7.54−8.05 (5H, Ph), 8.53 (s, 1H, H-2), 8.73 (s, 1H, H-8), 9.56 (t, $J = 5.5$ Hz, 1H, 6′-NH-), 11.16 (s, 1H, 6-NH-). ^{13}C NMR (DMSO-d_6, 125.7 MHz): δ 41.7 (C-6′), 61.0 (C-1′), 64.5 (C-4′), 73.5 (C-3′), 76.3 (C-5′), 83.3 (C-2′), 125.8 (C-5), 128.4, 132.4 and 133.3 (Ph), 143.7 (C-8), 150.3 (C-4), 151.3 (C-2), 152.3 (C-6), 156.4 and 156.6 (CF_3CO), 165.5 (Ph−CO-). HRMS (ESI-TOF$^+$) calcd for $C_{20}H_{20}N_6O_5F_3$ ($M^+ + H$): 481.1441. Found: 481.1463.

1-*O*-Dimethoxytrityl-4,6-dideoxy-4-(N^6-benzoyladenin-9-yl)-6-trifluoroacetylamino-2,5-anhydro-L-mannitol (**12**). Compound **12** (white foam, 0.35 g, 79%) was prepared from compound **11** (0.27 g, 0.56 mmol) in the same method as that of compound **5** from compound **4**. ^1H NMR (DMSO-d_6, 500 MHz): δ 3.21−3.56 (m, 4H, H-1′ and H-6′), 3.74 (s, 6H, Ph−OCH_3), 4.07−4.10 (m, 1H, H-2′), 4.78−4.90 (m, 3H, H-3′, H-4′ and H-5′), 5.78 (d, $J = 6.0$ Hz, 1H, 3′-OH), 6.89−8.06 (18H, Ph), 8.51 (s, 1H, H-2), 8.74 (s, 1H, H-8), 9.66 (t, 1H, 6′-NH-), 11.16 (s, 1H, 6-NH-). ^{13}C NMR (DMSO-d_6, 125.7 MHz): δ 41.7 (C-6′), 54.9 (Ph−OCH_3), 63.7 (C-1′), 64.5 (C-4′), 73.0 (C-3′), 75.6 (C-5′), 81.1 (Ph_3C), 85.2 (C-2′), 111.3, 126.0, 126.6, 127.7, 128.4, 129.8, 132.4, 133.3, 135.6 (Ph), 144.0 (C-8), 150.3 (C-4), 151.2 (C-2), 152.3 (C-6), 156.4 and 156.7 (CF_3CO), 165.5 (Ph−CO-). Anal. Calcd. for $C_{41}H_{37}F_3N_6O_7$ (782.2) C 62.91, H 4.76, N 10.74. Found C 62.77, H 4.83, N 10.51.

1-*O*-Dimethoxytrityl-3-*O*-(2-cyanoethyl-*N*,*N*-diisopropyl) phosphoramidite-4-dideoxy-4-(N^6- benzoyladenin-9-yl)-6-trifluoroacetylamino-2,5-anhydro-L-mannitol (**13**). Compound **13** (white foam, 0.31 g, 77%) was prepared from compound **12** (0.32 g, 0.41 mmol) in the same method as compound **6** from compound **5**. ^1H NMR ($CDCl_3$, 500 MHz): δ 0.58 (d, $J = 7.0$ Hz, 3H, CH_3), 0.74 (d, $J = 6.5$ Hz, 3H, CH_3), 0.92 (d, $J = 7.0$ Hz, 6H, CH_3), 1.18 (t, $J = 7.0$ Hz, 2H, CH_2CN), 2.41 (m, 2H, CH), 3.21−3.56 (m, 6H, H-1′, H-6′ and -$POCH_2$), 3.74 (s, 6H, Ph−OCH_3), 4.08 (m, 1H, H-2′), 4.78−4.90 (m, 3H, H-3′, H-4′ and H-5′), 5.78 (d, $J = 6.0$ Hz, 1H, 3′-OH), 6.89−8.06 (18H, Ph), 8.51 (s, 1H, H-2), 8.73 (s, 1H, H-8), 9.65 (t, 1H, 6′-NH-), 11.14 (s, 1H, 6-NH). ^{31}P NMR ($CDCl_3$, 121.5 MHz): δ 153.98 and 154.56.

Oligonucleotides. siRNAs (21 nt, Table 1) were chemically synthesized by automatic DNA synthesizer (model NW3900) using commercial phosphoramidities as building blocks (Shanghai Gene Biotech Co.). Aminoisonucleoside-modified siRNAs were synthesized by the same method but replacing the regular **T** and **A** unit with building blocks **6** and **13** at the defined positions (Table 1) (synthesis scale, 0.2 μmol; coupling time, 10 min). Cleavage and deprotection of RNA oligos were carried out according to the standard protocol (treated with 29% $NH_3 \cdot H_2O$ in sealed vessel at 55 °C for 16 h; the trifluoroacetyl group was removed at this stage (*25*); then, treated with Bu_4NF; TBDMS group was removed). The synthetic oligoribonucleotides were then purified by reverse-phase HPLC (Shimadzu LC-6AD, C-18 column, 10 × 250 mm) eluting with 0.1 M TEAA/MeCN, and the pure oligonucleotides were lyophilized and stored at −20 °C. siRNA duplexes were prepared by mixing complementary sense- and antisense-strand RNAs at equal 50 μm in MQ water, and then incubated in boiling water for 1 min, followed by gradual temperature decrease to room temperature and then 4 °C, allowing the efficient formation of siRNA duplex. The quality of the RNA duplexes was assessed on a 15% PAGE gel.

T_m Measurement. UV melting experiments were recorded with a Pharmacia LKB Biochrom 4060 spectrophotomer. Samples were dissolved in a buffer solution containing 0.14 M NaCl, 0.01 M Na_2PO_4, and 0.1 mM EDTA, pH 7.2. The solution containing the sense-strand siRNA and complementary antisense-strand siRNA were heated to 95 °C for 3 min, then cooled gradually to 4 °C and used for the thermal denaturation studies. Thermally induced transitions of each mixture were monitored at 260 nm. Sample temperature was increased at 0.5 °C/min between 15 and 85 °C. In all experiments, the concentration of each oligonucleotide strand was 2 μM.

Serum Stability. Duplexes of single-stranded RNA or siRNA (330 ng/μl) were incubated at 37 °C in 500 μL of 50% fetal bovine serum containing 7.5 μL TBST. Aliquots of 5 μL were withdrawn at different time points and immediately frozen in 15 μL × TBE-loading buffer. Samples were subjected to electrophoresis in 15% polyacrylamide−TBE under nondenaturing conditions and visualized by staining with SYBR Gold nucleic acid staining reagents and quantified by Storm 840 hardware and *Imagequant* software (Amersham Biosciences, Uppsala, Sweden).

Transfection and Dual-Luciferase Assay. Human embryonic kidney cells (HEK293) were grown in DMEM (Life Technologies, Gibco) and seeded in 24-well plates. After the cells reached about 50% confluence, the culture medium was changed to OPTIMEM (Gibco) and then transfected with plasmids and siRNA duplex in the presence of 0.17% Lipofectamine 2000 (Invitrogen). For each well, 0.17 g of recombination plasmid and 0.017 g pRL-TK were used. The final

Table 2. MALDI-TOF Mass Spectrum DATA for Modified Oligonucleotides

	ssNC	ssIso-1	ssIso-2	ssIso-3	ssIso-4	ssIso-5
calcd.	6652	6679	6679	6665	6708	6734
found	6650	6678	6679	6662	6713	6732
	asNC	**asIso-1**	**asIso-2**	**asIso-3**	**asIso-4**	**asIso-5**
calcd.	6628	6641	6641	6641	6670	6670
found	6627	6642	6643	6643	6671	6670

concentration of siRNA is 13 nM. The transfection medium was changed to culture medium (1 mL) after 4 h. All experiments were performed in triplicate and repeated at least twice. Cells were harvested 24 h after transfection and lyzed by passive cell lysis. Dual-luciferase assay was conducted. Luciferase activities were determined with 10 μL cell lysate using the Dual-Luciferase Assay System (Promega) by NOVOStar (BMG Labtechnologies Gmbh, Germany). The ratio between *firefly* and *Renilla* luciferase readings was generated for each well, and the inhibition efficiency of each siRNA was calculated by normalizing to respective buffer control.

RESULTS

Chemical Synthesis. Building blocks **6** and **13** for solid-phase oligonucleotide synthesis were synthesized from starting materials **1** and **7** (*22*), respectively (Scheme 1). The general method for synthesis of azido isonucleoside intermediates is to introduce a leaving group first and then substituted by azido group. Here, we developed a one-step method (step I) in which, at room temperature, compound **1** or **7** was directly reacted with sodium azide in the presence of triphenyl phosphine and carbon tetrabromide, giving the key intermediate **2** or **8** in good yield (*26*). Treatment of compound **2** or **8** with 1% HCl followed by sodium hydroxide and sodium borohydride in a second one-pot reaction at 0 °C (step II) gave unprotected azido isonucleoside **3** or **9** in 84% or 76% yield, respectively. Conversion of azidoisonucleosides into aminoisonucleosides was carried out by catalytic hydrogenation (step III). Prior to this reaction, compound **9** was first preprotected by a benzoyl group at the 6-amino group of the adenine moiety. After hydrogenation, the amino groups within the aminoisonucleosides were protected by trifluoroacetyl (step IV), yielding compounds **4** and **11**, which were then protected by a DMT group and a 2-cyanoethyl-*N*,*N*-diisopropylphosphoramidite group (steps V and VI) at the 1-hydroxyl and 3-hydroxyl positions for solid-phase chemistry.

Oligonucleotides. The obtained building blocks **6** and **13** were finally incorporated into the sequences of sense or antisense strand of designed siRNAs according to the solid-phase protocols. The coupling efficiency was determined by the release of DMT, and the efficiency was over 90% for coupling **6** and **13**. After the usual workup and purification by C-18 reverse HPLC, ten kinds of aminoisonucleoside-incorporated oligonucleotides were synthesized (Table 1). On the basis of the MALDI-TOF MS, the molecular weights of the aminoisonucleoside-modified sense strand and antisense strand of siRNA are concordant with the calculated value of the designed sequence (Table 2). The assessment results on a 20% PAGE gel showed the high quality of the RNA duplexes (Figure 1).

Thermal and Serum Stability of siRNA Duplexes. It has been reported that isonucleoside modification confers high nuclease resistance to oligonucleotides, but decreases the oligonucleotide binding ability to the complementary strand (*22*). In order to overcome the poor binding issue, we incorporated aminoisonucleosides instead of isonucleosides into siRNA duplexes. We found that incorporation of one aminoisonucleoside at the 3′ or 5′ terminal of sense strand of siRNA exhibited no effect on the duplex thermal stability with T_m = 66 °C for both **ssIso-1**/**asNC** and **ssIso-2**/**asNC**, which were equal to native siRNA form, **ssNC**/**asNC**. However, internal incorporation of one aminoisonucleoside into siRNA duplexes decreased the thermal stability with T_m = 62 °C for **ssIso-3**/**asNC**. Furthermore, when two or more aminoisonucleosides were incorporated into siRNAs, T_m values decreased strikingly with T_m = 56 °C for **ssIso-4**/**asNC** and 36 °C for **ssIso-5**/**asNC** (Table 3). Incorporation of aminoisnucleoside at a different position of the antisense strand of siRNA showed the same effect as the case of **ssIso1**−**5**/**asNC** (data were not shown).

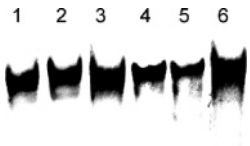


Figure 1. PAGE analysis of siRNAs: **ssNC/asNC** and **ssIsoX/asNC**. 20% polyacrylamide denaturing (7 M urea) gel electrophoresis and visualized by staining with SYBR gold and quantified by Model & Storm 860 hardware and *Imagequant* software (Amersham Biosciences, PKU, China). Lanes 1 to 6 represent: (1) **ssNC/asNC**; (2) **ssIso-1/asNC**; (3) **ssIso-2/asNC**; (4) **ssIso-3/asNC**; (5) **ssIso-4/asNC**; (6) **ssIso-5/asNC**.

Table 3. T_m and Serum Stability ($T_{1/2}$) of siRNAs: NC (ssNC/asNC) and ssIso-X/asNC (X = 1−5)

name	NCss NC/asNC	a ssIso-1/ asNC	b ssIso-2/ asNC	c ssIso-3/ asNC	d ssIso-4/ asNC	e ssIso-5/ asNC
T_m (°C)	66	66	66	62	56	36
$T_{1/2}$ (h)	16.53	14.96	13.79	13.51	4.06	5.86

After incubation of siRNAs with 50% FBS at 37 °C, the results indicated that siRNAs with a single aminoisonucleoside modification at the sense strand, such as **ssIso-1**/**asNC**, **ssIsio-2**/**asNC**, and **ssIso-3**/**asNC**, exhibited a slight decrease of serum stability compared with their native siRNA with all degraded in 24 h (Figure 2, **I**, **II**, and **III**) (Table 3). Modified siRNAs with two or more aminoisonucleosides at the sense strand, such as **ssIso-4**/**asNC** and **ssIso-5**/**asNC**, showed further weaker serum stability compared with the native siRNA and rapidly degraded within 1.5 h (Figure 2, **IV** and **V**) (Table 3).

Gene-Silencing Activities of Aminoisonucleoside-Modified siRNA. The firefly luciferse-targeting modified siRNAs with aminoisonucleosides in either the sense strand or antisense strand were evaluated on the basis of a dual-luciferase assay in which renillar luciferase acts as an internal control. We found that sense strand-modified siRNAs with a single aminoisonucleoside at the 3′- or 5′-end, such as **ssIso-1**/**asNC** and **ssIso-2**/**asNC**, exhibited comparative and even better activity than the native siRNA (**NC**) (Figure 3, Table 4). However, such an advantage was not observed when 3′- and 5′-terminal modifications combined together, such as **ssIso-4**/**asNC**; instead, the silencing activity somehow decreases. Alternative modifications with aminoisonucleoside at the siRNA internal region, such as **ssIso-3**/**asNC**, bring some negative effect on siRNA activity compared with the terminal modification, and such a negative effect further becomes apparent when internal and terminal modification in the sense strand were combined together, such as **ssIso-5**/**asNC**, which only maintains about 40% of gene-silencing activity (13 nM) (Figure 3, Table 4).

In contrast to the tolerance toward sense strand modifications, antisense strand modification brings a strikingly negative effect on the siRNA activity. We found that replacement of a single nucleotide with an aminoisonucleoside at the 5′-end of the antisense strand, such as **ssNC**/**asIso-2**, reduced siRNA activity by almost 60%. A similar modification at the 3′-end of the antisense strand, such as **ssNC**/**asIso-1**, reduced siRNA activity by around 50%, somehow better than the 5′-end modification.

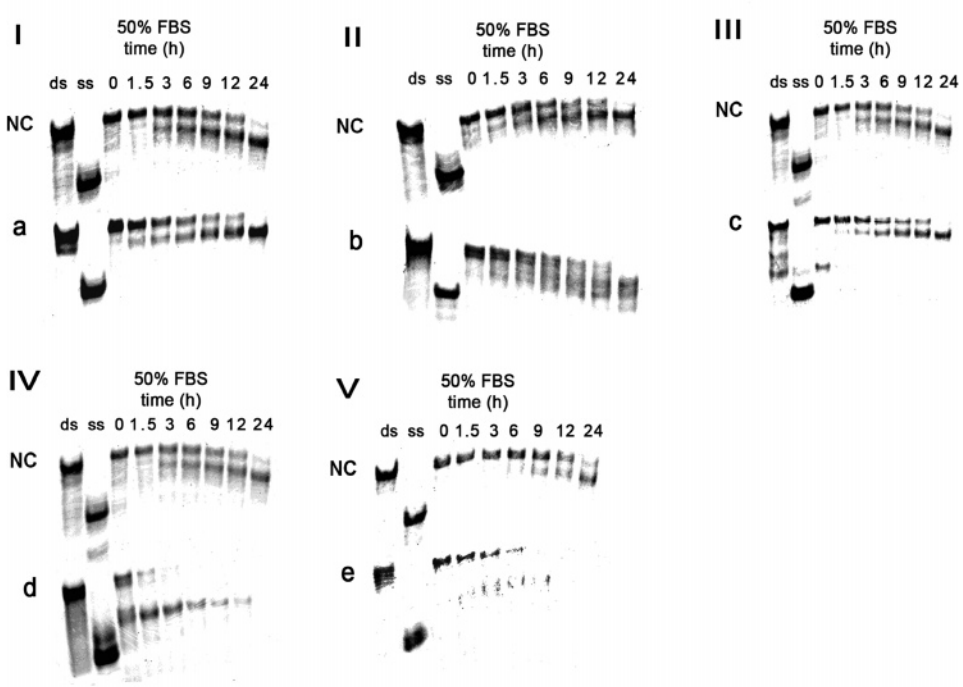


Figure 2. Serum stability of siRNAs: **NC** (**ssNC/asNC**) and **ssIso-X/asNC** (X = 1−5). The different **ssIso-X/asNC** were incubated in 50% FBS at 37 °C and withdrawn at indicated time points. The oligos were separated by PAGE and visualized with SYBR gold. ds depicts double-stranded siRNA marker and ss single-stranded. (a) **ssIso-1/asNC (I)**; (b) **ssIso-2/asNC(II)**; (c) **ssIso-3/asNC (III)**; (d) **ssIso-4/asNC(IV)**; (e) **ssIso-v/asNC(V)**.

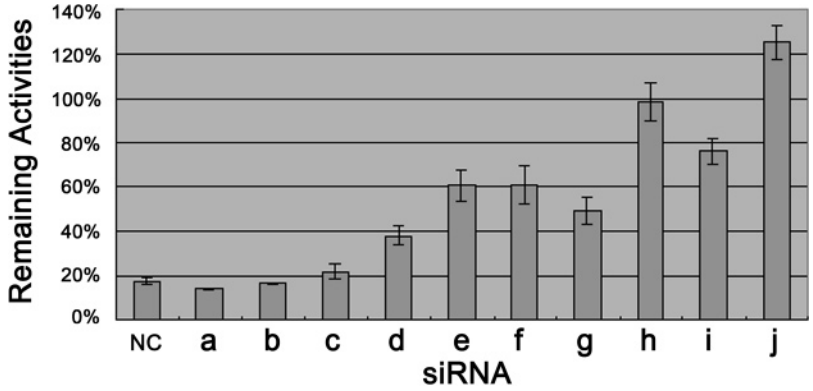


Figure 3. *Firefly renilla* luciferase activities of siRNAs: **NC (ssNC/asNC)**, **ssIso-X/asNC**, and **ssNC/asIso-X** (X = 1−5). All experiments were performed in triplicate and repeated at least twice.

Table 4. *Firefly renilla* Luciferase Activities of siRNAs: NC (ssNC/asNC), ssIso-X/asNC, and ssNC/asIso-X (X = 1−5)

NC ssNC/ asNC	a ssIso-1/ asNC	b ssIso-2/ asNC	c ssIso-3/ asNC	d ssIso-4/ asNC	e ssIso-5/ asNC
	15%	17%	22%	38%	61%
	f	**g**	**h**	**i**	**j**
18%	ssNC/ asIso-1	ssNC/ asIso-2	ssNC/ asIso-3	ssNC/ asIso-4	ssNC/ asIso-5
	61%	50%	98%	77%	126%

Simultaneous modifications of the 3′- and 5′-ends of the antisense strands by aminoisonucleosides lead to a further negative effect with just 20% activity remaining for **ssNC/asIso-4**. We also found that internal modification on siRNA antisense strand by replacing a single nucleoside with an aminoisonucleoside, such as **ssNC/asIso-3**, or combination of the terminal modification with internal modification on the antisense strand almost abolished the silencing activity, such as **ssNC/asIso-5** (Figure 3, Table 4).

DISCUSSION

RNA interference (RNAi) is the process of using a double-stranded RNA (dsRNA) with specific sequence to regulate the expression of a sequence-homologous gene. According to the RNAi pathway, the siRNA duplex is first incorporated into a large multiprotein known as RNAi-induced silencing complex (RISC), by which the sense strand is excluded via an undefined mechanism, and then the antisense strand together with RISC recognizes and cleaves the target mRNA (*27*−*30*). Therefore, the sense strand is more like a courier that delivers the antisense strand, the main effective component of RNAi, into the RISC complex. As a result, many different chemical modifications can be accommodated in the sense strand but not in the antisense strand. Schwarz et al. reported that siRNA duplexes function asymmetrically with two strands not equally eligible for assembly into RISC (*31*). By statistical analyses of the internal stability of siRNA, Khvorova et al. found that the functional siRNAs display lower stability at 5′ end of the antisense strand than nonfunctional dsRNAs, suggesting that altering the nature of the dsRNA, chemically or structurally, might be a means for optimization of siRNA activity (*32*).

Among the chemical modifications, aminoisonucleoside may represent a novel direction in which the nucleobase is linked to the 4-position rather than C1 of the sugar ring. It has been shown that incorporation of isonucleotides into a oligonucleotide causes a change in the conformation of 2,5-anhydro-L-mannitol, bringing torsion angles in the sugar−phosphate backbones. This alternation might make the modified oligonucleotide less recognized by nucleases and thus increase its stability toward various enzymes (*20*−*22*). However, the conformational change within isonucleotise-modified oligonucleotides decreases RNA duplex thermal stability with a lower T_m value. For aminoisonucleotide-modified oligonucleotides, the introduction of amino groups may increase their thermal stability via the strong binding of cationic amino groups with negatively charged phosphate backbones of the complementary sequences, as shown from the identical T_m values by comparisons of **ssIso-1**/**asNC** and **ssIso-2**/**asNC** with their native siRNA, **ssNC**/**asNC** (Table 1).

On the other hand, the alternations in torsion angles of the backbone of the oligonucleotide might promote the strand separation of the siRNA duplex that could potentially increase silencing activity. It might provide an explanation for the data above in which the siRNA duplex **ssIso-1**/**asNC** and **ssIso-2**/**asNC** with aminoisonucleoside substitution at the 3′-end or 5′-end of the sense strand exhibited better activity than the native siRNA (**NC**).

The comparable gene-silencing activities of **ssIso-1**/**asNC**, **ssIso-2**/**asNC**, and **ssIso-3**/**asNC** with their wild-type siRNA (Figure 3) indicate that introduction of a single aminoisonucleoside in the sense strand, at either the 3′-end or 5′-end or internally, is quite tolerant for maintaining siRNA activity. However, introduction of multiple aminoisonucleosides into the siRNA sense strand, such as **ssIso-4**/**asNC** and **ssIso-5**/**asNC**, seriously reduced its activity (Figure 3), potentially due to the lower serum and thermal stability (Table 1 and Figure 3). Even so, the combination of internal and terminal modifications at the sense strand, such as **ssIso-5**/**asNC** (T_m = 36 °C), still retains 40% (at 13 nM) gene-silencing activity. On the contrary, introduction of a single aminoisonucleoside at the antisense strand, either 3′- or 5′-end, such as **ssNC**/**asIso-2** or **ssNC**/**asIso-1**, strikingly affects siRNA function with 40% to 50% of gene-silencing activity left. Modification of the antisense strand at both ends, such as **ssNC**/**asIso-4**, further reduces siRNA silencing activity with just ∼20% left.

Hohjoh et al. have investigated the relationship of siRNA activity versus sense−antisense strand terminal mismatches, and found that the strand whose 3′-end is relatively easily unwound would be employed as the guider strand to incorporate into RISC for gene knockdown (*33*). Here, we conclude that siRNA sense-strand modification has less effect on siRNA activity, while antisense-strand modification significantly reduces siRNA activity. Our data also suggests the following: (i) the bases in modified siRNAs, despite their lower activity, retain their hybridization properties with complementary sequences; (ii) the torsion angles in the sugar−phosphate backbones would not perturb the entry of the modified siRNA into RISC; and (iii) the two strands of the siRNA duplex are not equally eligible for assembly into RISC.

The siRNA stability depends on the thermal stability of the siRNA duplex and the serum stability of each individual strand. We have found that single-stranded RNA oligos containing aminoisonucleoside were degraded rapidly when incubated with serum (data was not shown), but the siRNA duplex with aminoisonucleoside at either the 3′- or 5′-end of the sense strand exhibited a slight serum stability decrease compared with the unmodified siRNA. However, incorporation of two or four aminoisonucleosides into the sense strand reduces the duplex thermal and serum stability, which were potentially due to the combined torsion on siRNA backbone and the loose structure on the siRNA duplex.

Many efforts have been made to increase siRNA stability at the cost of a slight reduction of siRNA efficacy. Here, the aminoisonucleoside modification is superior to other chemical modifications, since such modified RNAs are good substrates of RNase H (*20*), and isonucleoside triphosphates can be recognized by many different DNA polymerases (*34*). Furthermore, siRNA sense-strand modification with aminoisonucleoside at the 3′- or 5′-end showed comparable gene-silencing activity and serum stability as their native siRNA. Taken together, aminoisonucleoside-modified oligonucleotide represents a novel direction and is a good mimic of natural oligonucleotide with the required biological and chemical properties.

SUMMARY

Ten modified siRNAs with aminoisonucleoside at various positions were synthesized and their thermal and serum stabilities and gene-silencing activities were studied. The sense-strand modification with aminonucleoside at the 3′- and 5′-end siRNAs showed similar duplex thermal and serum stability as the natural one. The identical gene activities indicated that such a modified siRNA is compatible with the intracellular siRNA machinery. It was also found that antisense strand modification with aminoisonucleoside, despite the reduction of gene-silencing activity, is still somehow tolerated. These findings are worthy of the further study.

ACKNOWLEDGMENT

This work was supported by the National Natural Science Foundation of China (20332010 and SFCBIC 20320130046), the Ministry of Science and Technology of China (2005BA-711A04), and a Foundation for the Author of National Excellent Doctoral Dissertation of PR China (FANEDD200265).

LITERATURE CITED

(1) Fire, A., Xu, S., Montgomery, M. K., Kostas, S. A., Driver, S. E., and Mello, C. C. (1998) Potent and specific genetic interference by double-stranded RNA in *Caenorhabditis elegans*. *Nature (London) 391*, 806−811.

(2) Zhou, D., He, Q. S., Wang, C., Zhang, J., and Wong-Staal, F. (2006) RNA Interference and potential applications. *Curr. Top. Med. Chem. 6*, 901−911.

(3) Chiu, Y. L., and Rana, T. M. (2003) siRNA function in RNAi: A chemical modification analysis. *RNA 9*, 1034−1048.

(4) Czauderna, F., Fechtner, M., Dames, S., Aygün, H., Klippel, A., Pronk, G. J., Giese, K., and Kaufmann, J. (2003) Structural variations and stabilising modification of synthetic siRNAs in mammalian cells. *Nucleic Acids Res. 31*, 2705−2716.

(5) Amarzguioui, M., Holen, T., Babaie, E., and Prydz, H. (2003) Tolerance for mutations and chemical modifications in a siRNA. *Nucleic Acids Res. 31*, 589−595.

(6) Elmén, J., Thonberg, H., Ljungberg, K., Frieden, M., Westergaard, M., Xu, Y., Wahren, B., Liang, Z., Ørum, H., Koch, T., and Wahlestedt, C. (2005) Locked nucleic acid (LNA) mediated improvements in siRNA stability and functionality. *Nucleic Acids Res. 33*, 439−447.

(7) Crooke, S. T. (1999) Molecular mechanisms of action of antisense drugs. *Biochim. Biophys. Acta 1489*, 31−44.

(8) Geary, R. S., Watanabe, T. A., Truong, L., Freier, S. M., Lesnik, E. A., Sioufi, N. B., Sasmor, H., Manoharan, M., and Levin, A. A. (2001) Pharmacokinetic properties of 2′-*O*-(2-methoxyethyl) modified oligonucleotide analogs in rats. *J. Pharmacol. Exp. Ther. 296*, 890−897.

(9) Geary, R. S., Yu, R. Z., and Levin, A. A. (2001) Pharmacokinetics of phosphorothioate antisense oligonucleotides. *Curr. Opin. Invest. Drugs 2*, 562−573.

(10) Kurreck, J. (2003) Antisense technologies: improvement through novel chemical modifications. *Eur. J. Biochem. 270*, 1628−1644.

(11) Cummins, L. L., Owens, S. R., Risen, L. M., Lesnik, E. A., Freier, S. M., McGee, D., Guinosso, C. J., and Cook, P. D. (1995) Characterization of fully 2′-modified oligoribonucleotide heteroduplex and homoduplex hybridization and nuclease sensitivity. *Nucleic Acids Res. 23*, 2019−2024.

(12) Kawasaki, A. M., Casper, M. D., Freier, S. M., Lesnik, E. A., Zounes, M. C., Cummins, L. L., Gonzalez, C., and Cook, P. D. (1993) Uniformly modified 2′-deoxy-2′-fluoro-phosphorothioate oligonucleotides as nuclease-resistant antisense compounds with high affinity and specificity for RNA targets. *J. Med. Chem. 36*, 831−841.

(13) Dande, P., Prakash, T. P., Sioufi, N., Gaus, H., Jarres, R., Berdeja, A., Swayze, E. E., Griffey, R. H., and Bhat, B. (2006) Improving RNA interference in mammalian cells by 4′-thio-modified small interfering RNA (siRNA): effect on siRNA activity and nuclease stability when used in combination with 2′-*O*-alkyl modifications. *J. Med. Chem. 49*, 1624−1634.

(14) Hall, A. H. S., Wan, J., Shaughnessy, E. E., Shaw, B. R., and Alexander, K. A. (2004) RNA interference using boranophosphate siRNAs: structure-activity relationships. *Nucleic Acids Res. 32*, 5991−6000.

(15) Allerson, C. R., Sioufi, N., Jarres, R., Prakash, T. P., Naik, N., Berdeja, A., Wanders, L., Griffey, R. H., Swayze, E. E., and Bhat, B. (2005) Fully 2′-modified oligonucleotide duplexes with improved in vitro potency and stability compared to unmodified small interfering RNA. *J. Med. Chem. 48*, 901−904.

(16) Parrish, S., Fleenor, J., Xu, S., Mello, C., and Fire, A. (2000) Functional anatomy of a dsRNA trigger: differential requirement for the two trigger strands in RNA interference. *Mol. Cell 6*, 1077−1087.

(17) Harborth, J., Elbashir, S. M., Vandenburgh, K., Manninga, H., Scaringe, S. A., Weber, K., and Tuschl, T. (2003) Sequence, chemical, and structural variation of small interfering RNAs and short hairpin RNAs and the effect on mammalian gene silencing. *Antisense Nucleic Acid Drug Dev. 13*, 83−105.

(18) Hall, A. H. S., Wan, J., Shaughnessy, E. E., Ramsay, Shaw, B., and Alexander, K. A. (2004) RNA interference using boranophosphate siRNAs: structure-activity relationships. *Nucleic Acids Res. 32*, 5991−6000.

(19) Whelan, J. (2005) First clinical data on RNAi. *Drug Discovery Today 10*, 1014−1015.

(20) Wang, Z., Shi, J., Jin, H., Zhang, L., Lu, J., and Zhang, L. (2005) Properties of isonucleotides-incorporated oligodeoxynucleotides and inhibition of the expression of spike protein of SARS-CoV. *Bioconjugate Chem. 16*, 1081−1087.

(21) Lei, Z., Zhang, L., Zhang, L., Chen, J., Min, J., and Zhang, L. (2001) Hybrid characteristics of oligonucleotides consisting of isonucleoside 2′,5′-anhydro-3′-deoxy-3′-(thymin-1-yl)-D-mannitol with different linkage modes. *Nucleic Acids Res. 29*, 1470−1475.

(22) Yang, Z., Zhang, H., Min, J., Ma, L., and Zhang, L. (1999) Synthesis and duplex stabilization of oligonucleotides consisting of isonucleosides. *Helv. Chim. Acta 82*, 2037−2043.

(23) Guan, Z., Tian, X. B., Zhang, L. R., Min, J. M., and Zhang, L. H. (2002) Synthesis and hybridization properties of an oligonucleotide consisting of 1′,4′-anhydro-2′,5′-dideoxy-2′-(thymin-1-yl)-D-Altritol. *Helv. Chim. Acta 85*, 1479−1484.

(24) Harvey, S. L., Charlet, A., Haas, W., Gygi, S. P., and Kellogg, D. R. (2005) Cdk1-dependent regulation of the mitotic inhibitor Wee1. *Cell 122*, 407−420.

(25) (a) Cuenoud, B., Casset, F., Hüsken, D., Natt, F., Wolf, R. M., Altmann, K.-H., Martin, P., and Moser, H. E. (1998) Dual recognition of double-stranded DNA by 2′-aminoethoxy-modified oligonucleotides. *Angew. Chem., Int. Ed. 37* (9), 1288−1291. (b) Ueno, Y., Nagasawa, Y., Sugimoto, I., Kojima, N., Kanazaki, M., Shuto, S., and Matsuda, A. (1998) Nucleosides and nucleotides 174. Synthesis of oligodeoxynucleotides containing 4-C-[2-[[N-(2-aminoethyl) carbamoyl] oxy]ethyl] thymidine and their thermal stability and nuclease-resistance properties. *J. Org. Chem. 63*, 1660−1667.

(26) Li, Z. S., Qiao, R. P., Yang, Z. J., Zhang, L. R., and Zhang, L. H. (2006) One-step synthesis of novel tricyclic isomeric azidonucleosides. *Tetrahedron: Asymmetry 17* (7), 1056−1061.

(27) Liu, J., Carmell, M. A., Rivas, F. V., Marsden, C. G., Thomson, J. M., Song, J. J., Hammond, S. M., Joshua-Tor, L., and Hannon, G. J. (2004) Argonaute2 is the catalytic engine of mammalian RNAi. *Science 305*, 1437−1441.

(28) Schwarz, D. S., Tomari, Y., and Zamore, P. D. (2004) The RNA-induced silencing complex is a Mg^{2+}-dependent endonuclease. *Curr. Biol. 14*, 787−791.

(29) Song, J. J., Smith, S. K., Hannon, G. J., and Joshua-Tor, L. (2004) Crystal structure of Argonaute and its implications for RISC slicer activity. *Science 305*, 1434−1437.

(30) Xia, H., Mao, Q., Paulson, H. L., and Davidson, B. L. (2002) siRNA-mediated gene silencing in vitro and in vivo. *Nat. Biotechnol. 20*, 1006−1010.

(31) Schwarz, D. S., Hutvagner, G., Du, T., Xu, Z., Aronin, N., and Zamore, P. D. (2003) Asymmetry in the assembly of the RNAi enzyme complex. *Cell 115*, 199−208.

(32) Khvorova, A., Reynolds, A., and Jayasena, S. D. (2003) Functional siRNAs and miRNAs exhibit strand bias. *Cell 115*, 209−216.

(33) Hohjoh, H. (2004) Enhancement of RNAi activity by improved siRNA duplexes. *FEBS Lett. 557*, 193−198.

(34) Jiang, C.W., Li, B. C., Guan, Z, Yang, Z. J., Zhanga, L. R., Zhang, L. H. (2007) Synthesis and recognition of novel isonucleoside triphosphates by DNA polymerases. *Bioorg. Med. Chem. 15*, 3019−3025.

BC060398+

Nanoparticles That Display Short Collagen-Related Peptides. Potent Stimulation of Human Platelet Aggregation by Triple Helical Motifs

Mabel A. Cejas, Cailin Chen, William A. Kinney,* and Bruce E. Maryanoff

Vascular Research Team, Johnson & Johnson Pharmaceutical Research and Development, Spring House, Pennsylvania 19477-0776. Received March 23, 2007; Revised Manuscript Received May 23, 2007

Collagen plays a key role in the activation and adhesion of blood platelets via their cell-surface receptors. Normally, collagen-related peptides (CRPs), even one as long as a 30-mer (10 Gly-Pro-Hyp (GPO) repeats), are unable to effectively express collagen's platelet-activating behavior. We attached two short CRPs, AcHN-(Gly-Pro-Hyp)$_n$Gly-OH with $n = 5$ (**1**) and $n = 10$ (**2**), via the C-terminus to amino-functionalized latex nanoparticles to create a multimeric display of triple helical motifs. These nanomaterials were characterized by dynamic light scattering and environmental scanning electron microscopy. The nanoparticles bearing the 31-mer CRP sequence, **2**, but not the 16-mer sequence, **1**, effectively induced the aggregation of human platelets, with a potency level approaching that of native type I collagen. Our results highlight the importance of presenting triple helical CRP motifs of sufficient length on a suitable scaffold in order to stimulate platelets.

Blood platelets are crucial for maintaining normal hemostasis. Through their activation and aggregation, platelets arrest bleeding caused by vascular injury and then encourage wound healing. However, excessive platelet-rich thrombus formation, especially in high-sheer arterial environments, can promote chronic cardiovascular diseases, such as unstable angina, acute myocardial infarction, and stroke (*1*). Collagen plays a pivotal role in initiating platelet activation and adhesion via two main collagen receptors: glycoprotein VI (GPVI) and the integrin $\alpha_2\beta_1$ (*2*−*5*). There are several types of collagen present in the blood vessel wall, with fibrillar type I and type III predominating in the subendothelial matrix. When a vessel's endothelial layer is damaged, such as in atherosclerosis, the underlying collagen fibers are exposed, thereby inducing platelet aggregation and triggering adverse cardiovascular events.

Synthetic triple helical peptides containing the main collagen repeat Gly-Pro-Hyp (GPO) have been used as models to study the structural basis of platelet activation by collagen (*6*−*13*). Rao et al. (*6*) were the first to report the promotion of platelet adhesion and aggregation by synthetic collagen-related peptides (CRPs). By using a branched assembly of three peptide chains containing a $(GPO)_8$ CRP and an α_1(IV)1263−1278 cell adhesion sequence, they demonstrated that a triple helix is required for platelet activation and suggested a role for the extra sequence. However, the potency observed in their study was much less than that of native collagen (by ∼1000-fold). A different approach involving the polymerization of short CRPs by cross-linking to obtain quaternary structures resulted in materials that were highly platelet-aggregatory (*7*), through direct action on GPVI (*8*). Interestingly, monomeric CRPs absorbed onto a glass surface can be as potent as cross-linked CRPs in aggregating platelets (*9*). Relative to structure−function requirements, Asselin et al. (*10*) found that short GPO containing monomeric CRPs are just partial agonists of GPVI, and in a review Nieswandt and Watson (*11*) present evidence that lengthy CRPs in a multimeric format are important for the clustering of GPVI and for robust signaling. The structural hypothesis for the collagen−GPVI interaction is supported by an X-ray investigation on the GPVI dimer (*12*).

Further understanding of the structural requirements for platelet signal transduction through GPVI could emerge from a system in which the CRPs are covalently attached to an inert support in a well-defined (nonrandom) manner. Such a construct would supply information about the importance of multivalency, spatial orientation, and chain length on collagen function. Thus, we sought to immobilize short CRPs of varying lengths onto a stable surface to present multiple peptide helices to platelets in a defined orientation. We now report a study in which we have covalently attached two different short CRPs by the C-terminus to the surface of latex nanoparticles. Some of these nanoparticle constructs, with a multimeric display of triple helical motifs, were able to induce the aggregation of human platelets with a potency level approaching that of native type I collagen.

Latex nanoparticles were chosen as a support because they are available in diameters similar to the diameters of the exposed collagen fibers in a damaged blood vessel (∼50 nm, Figure 1A) (*14*). In addition, they contain various chemical functionalities for attachment of the probe peptide ligands of interest. Nanoparticle scaffolds have been used effectively in drug delivery and diagnostics (*15*), as chemical sensors (*16*), and in presenting biomacromolecules for molecular recognition (*17, 18*). Recently, the preparation of gold CRP-coated nanoparticles and their interaction with collagen fibers has been described (*19*).

Peptides AcHN-(Gly-Pro-Hyp)$_n$Gly-OH, with $n = 5$ (**1**) and $n = 10$ (**2**), were synthesized on solid phase using standard FastMoc chemistry with an ABI 433A synthesizer (*20*). The N-terminus of the peptides was acetylated to avoid polymerization during the reaction with the nanoparticles. These CRPs were purified by HPLC and characterized by MALDI-TOF MS and CD spectroscopy. Their CD spectra showed a positive band at 225 nm, which is characteristic of a collagen triple helix (*21, 22*). The 225 nm band was more intense for 31-mer **2** vs 16-mer **1**, indicating that **2** has a more robust triple helical structure.

Each peptide was conjugated through its carboxyl terminus (via carbodiimide coupling) to 200 nm latex nanoparticles bearing primary amine-terminated, six-carbon spacer units. The degree of functionalization was determined by measuring the

* To whom correspondence should be addressed. Phone: (215) 628-5908. Fax: (215) 628-4985. E-mail: wkinney1@prdus.jnj.com.

10.1021/bc070105s CCC: $37.00 © 2007 American Chemical Society
Published on Web 06/21/2007

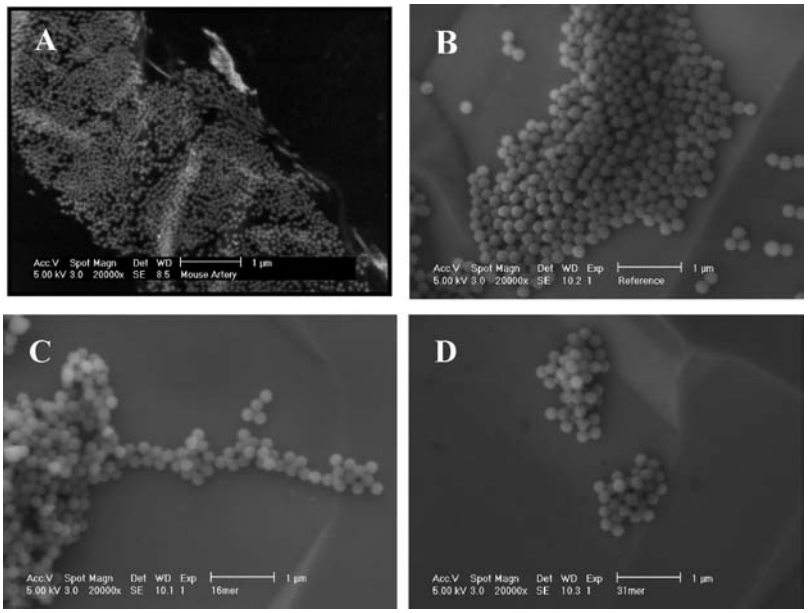


Figure 1. ESEM images of (A) collagen fibrils from a murine vessel, (B) reference nanoparticles, (C) 16-mer (**1**) modified nanoparticles, and (D) 31-mer (**2**) modified nanoparticles.

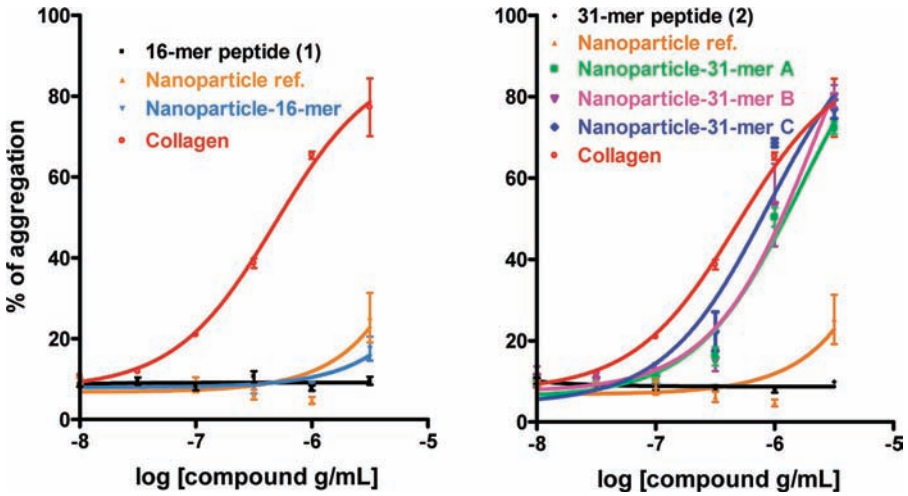


Figure 2. Percentage of platelet response to collagen, peptides, and nanoparticles before and after functionalization with CRPs.

amount of peptide that was cleaved off the nanoparticles following acid hydrolysis.[1] The amino acid analysis indicated that ~10% of the amino groups (molar basis) on the surface of the particles were conjugated to the peptides. The particle size of the resulting material was estimated by dynamic light scattering (DLS).[2] The average diameter of the reference particles suspended in water was determined to be approximately 200 nm, as expected. The values for the functionalized nanoparticles in solution were about 1000 nm, due to conglomeration.

The morphology of the various nanoparticles was visualized by environmental scanning electron microscopy (ESEM, Figure 1). The images illustrate that both functionalized nanoparticles tended to adhere to one another (Figure 1C,D) probably because of peptide−peptide interaction, while the reference nanoparticles remained loose (Figure 1B). The sizes of conglomerates here are larger than those determined by DLS, perhaps because of different experimental conditions. For DLS the nanoparticle clusters were moving freely in solution, whereas for ESEM the material was deposited on a solid support by drying a suspension. The display presented by multiple triple helices attached to the clustered nanoparticles is strikingly similar to the surface created by a severed murine blood vessel (compare part A of Figure 1 with parts C and D of Figure 1).

The effect of collagen nanoparticles on platelet function was evaluated in an in vitro platelet aggregation assay. Washed platelets were prepared from human platelet-rich plasma (from healthy volunteers), and platelet aggregation measurements were performed (*21*).[2] As depicted in Figure 2, free peptides **1** and **2**, unmodified nanoparticles, and nanoparticles functionalized with 16-mer **1** failed to aggregate platelets at concentrations below 1 μg/mL.[3] In sharp contrast, nanoparticles functionalized with 31-mer **2** markedly induced platelet aggregation in a dose-dependent manner (EC_{50} = 0.60 μg/mL). The potency of this material was comparable to that of equine type I collagen (EC_{50} = 0.40 μg/mL).

Experiments with three 31-mer nanoparticle preparations proved to be highly reproducible (experiments A−C). In the

[1] In preliminary experiments, smaller nanoparticles (20 nm) were found to be impractical because they did not centrifuge well and tended to associate.

[2] See Supporting Information.

[3] This concentration is based on peptide content in peptide-containing materials. Unmodified nanoparticles were processed in the same way, and used in the same volume, as the modified nanoparticles.

case of experiment B, the peptide was dissolved in MES buffer and kept at 4 °C for 1 h. The triple helix conformation was verified by CD before conjugation to the particles. For experiments A and C, the peptide was coupled without previous equilibration. The fact that all preparations yielded similar results in the platelet assays indicates the formation of a triple helix structure on the particle surface. Interestingly, while both conjugates form conglomerates of similar size, only the conjugate bearing the 31-mer peptide (**2**) is effective in the platelet aggregation assay, suggesting that functional activity depends on the nature of the peptide triple helix and not just on the multiple display.

Our study demonstrates that a CRP with a 31-mer sequence can mimic the function of collagen when this peptide is displayed in a multivalent fashion by linking its C-terminus to a nanoparticle scaffold. These results support the importance of multiple triple helical motifs for robust stimulation of platelets by CRPs via the GPVI receptor (*7*−*9*). Looking ahead, the covalent attachment of short CRPs to nanoparticles should provide a useful means to acquire new information about the structural requirements of such peptides for collagen-like function in cell biology.

ACKNOWLEDGMENT

We thank Pratik P. Joshi (Center for Advance Microscopy, University of Miami) for ESEM measurements. We also acknowledge the valuable guidance provided by Marian Kruszynski, Tami Raguse, and Albert Schmidt.

Supporting Information Available: Details on materials and methods, peptide synthesis, CD spectroscopy, nanoparticle functionalization, DLS, and platelet aggregation. This material is available free of charge via the Internet at http://pubs.acs.org.

LITERATURE CITED

(1) Jackson, S. P., and Schoenwaelder, S. M. (2003) Antiplatelet therapy: in search of the "magic bullet". *Nat. Rev. Drug Discovery 2*, 1−15.

(2) Clemetson, J. M., Polgar, J., Magnenat, E., Wells, T. N. C., and Clemetson, K. J. (1999) The platelet collagen receptor glycoprotein VI is a member of the immunoglobulin superfamily closely related to FcαR and the natural killer receptors. *J. Biol. Chem. 274*, 29019−29024.

(3) Siljander, P. R.-M., Munnix, I. C. A., Smethurst, P. A., Deckmyn, H., Lindhout, T., Ouwehand, W. H., Farndale, R. W., and Heemskerk, J. W. M. (2004) Platelet receptor interplay regulates collagen-induced thrombus formation in flowing human blood. *Blood 103*, 1333−1341.

(4) Penz, S., Reininger, A. J., Brandl, R., Goyal, P., Rabie, T., Bernlochner, I., Rother, E., Goetz, C., Engelman, B., Smethurst, P. A., Ouwehand, W. H., Farndale, R., Nieswandt, B., and Siess, W. (2005) Human atheromatous plaques stimulate thrombus formation by activating platelet glycoprotein VI. *FASEB J. 19*, 898−909.

(5) Heemskerk, J. W. M., Kuijpers, M. J. E., Munnix, I. C. A., and Siljander, P. R. M. (2005) Platelet collagen receptors and coagulation. A characteristic platelet response as possible target for antithrombotic treatment. *Trends Cardiovasc. Med. 15*, 86−92.

(6) Rao, G. H. R., Fields, C. G., White, J. G., and Fields, G. B. (1994) Promotion of human platelet adhesion and aggregation by a synthetic, triple-helical "mini-collagen". *J. Biol. Chem. 269*, 13899−13903.

(7) Morton, L. F., Hargreaves, P. G., Farndale, R. W., Young, R. D., and Barnes, M. J. (1995) Integrin $\alpha 2\beta 1$-independent activation of platelets by simple collagen-like peptides: collagen tertiary (triple-helical) and quaternary (polymeric) structures are sufficient alone for $\alpha 2\beta 1$-independent platelet reactivity. *Biochem. J. 306*, 337−344.

(8) Knight, C. G., Morton, L. F., Onley, D. J., Peachy, A. R., Ichinohe, T., Okuma, M., Farndale, R. W., and Barnes, M. J. (1999) Collagen-platelet interaction: Gly-Pro-Hyp is uniquely specific for platelet Gp VI and mediates platelet activation by collagen. *Cardiovasc. Res. 41*, 450−457.

(9) Heemskerk, J. W. M., Siljander, P., Vuist, W. M. J., Breikers, G., Reutelingsperger, C. P. M., Barnes, M. J., Knight, C. G., Lassila, R., and Farndale, R. W. (1999) Function of glycoprotein VI and integrin $\alpha 2\beta 1$ in the procoagulant response of single, collagen-adherent platelets. *Thromb. Haemostasis 81*, 782−792.

(10) Asselin, J., Knight, C. G., Farndale, R. W., Barnes, M. J., and Watson, S. P. (1999) Monomeric (glycine-proline-hydroxyproline)$_{10}$ repeat sequence is a partial agonist of the platelet collagen receptor glycoprotein VI. *Biochem. J. 339*, 413−418.

(11) Nieswandt, B., and Watson, S. P. (2003) Platelet-collagen interaction: Is GPVI the central receptor? *Blood 102*, 449−461.

(12) Horii, K., Kahn, M. L., and Herr, A. B. (2006) Structural basis for platelet collagen responses by the immune-type receptor glycoprotein VI. *Blood 108*, 936−942.

(13) Farndale, R. W. (2006) Collagen-induced platelet activation. *Blood Cells, Mol. Dis. 36*, 162−165.

(14) Finlay, H. M., Whittaker, P., and Canham, P. B. (1998) Collagen organization in the branching region of human brain arteries. *Stroke 29*, 1595−1601.

(15) Emerich, D. F., and Thanos, C. G. (2006) The pinpoint promise of nanoparticle-based drug delivery and molecular diagnosis. *Biomol. Eng. 23*, 171−184.

(16) Clark, H. A., Kopelman, R., Tjalkens, R., and Philbert, M. A. (1999) Optical nanosensors for chemical analysis inside single living cells. 2. Sensors for pH and calcium and the intracellular application of PEBBLE sensors. *Anal. Chem. 71*, 4837−4843.

(17) Verma, A., and Rotello, V. M. (2005) Surface recognition of biomacromolecules using nanoparticle receptors. *Chem. Commun.* 303−312.

(18) Kelly, T. L., Lam, M. C. W., and Wolf, M. O. (2006) Carbohydrate-labeled fluorescent microparticles and their binding to lectins. *Bioconjugate Chem. 17*, 575−578.

(19) Mo, X., An, Y., Yun, C.-S., and Yu, S. M. (2006) Nanoparticle-assisted visualization of binding interactions between collagen mimetic peptide and collagen fibers. *Angew. Chem., Int. Ed. 45*, 2267−2270.

(20) *Fmoc Solid-Phase Peptide Synthesis. A Practical Approach* (Chan, W. C., and White, P. D., Eds.) Oxford University, New York, 2003.

(21) Cejas, M. A., Kinney, W. A., Chen, C., Leo, G. C., Tounge, B. A., Vinter, J. G., Joshi, P. P., and Maryanoff, B. E. (2007) Collagen-related peptides: self-assembly of short, single strands into a functional biomaterial of micrometer scale. *J. Am. Chem. Soc. 129*, 2202−2203.

(22) Feng, Y., Melacini, G., Taulane, J. P., and Goodman, M. (1996) Acetyl-terminated and template-assembled collagen-based polypeptides composed of Gly-Pro-Hyp sequences. 2. Synthesis and conformational analysis by circular dichroism, ultraviolet absorbance, and optical rotation. *J. Am. Chem. Soc. 118*, 10351−10358.

BC070105S

ARTICLES

Role of Sulfhydryl Groups in Transfection? A Case Study with Chitosan−NAC Nanoparticles

Brigitta Loretz, Marlene Thaler,† and Andreas Bernkop-Schnürch*

Department of Pharmaceutical Technology, Institute of Pharmacy, and Institute of Zoology, Leopold-Franzens-University Innsbruck, 6020 Innsbruck, Austria. Received October 4, 2006; Revised Manuscript Received February 20, 2007

This study investigated the use of chitosan−*N*-acetylcysteine (NAC) as a non-viral gene carrier. In particular, we aimed to elucidate whether the advantage of thiolation was more pronounced in the stabilization of particles or in the effect of nonspecific sulfhydryl reduction of the target cells. Low-viscosity chitosan was modified by covalent binding of NAC. The resulting conjugate displayed 1.35 mM SH/g polymer. Particles produced via self-assembly of chitosan conjugate and pDNA had a mean particle size of 113.7 nm and a positive ζ-potential. Sulfhydryl group content on the particle surface was investigated by Ellman's test and papain reactivation assay, with the result of about 100 nM SH groups/mL nanoparticle suspension. An oxidation step was performed to stabilize polyplexes via disulfide bonds. The enhanced stability of oxidized particles against both polyanion heparin and alkaline pH was proven by a gel retardation assay. The stabilization was demonstrated to be reversible by treatment with glutathione. Further, the effect of immobilized SH groups and of supplementation with free NAC on transfection efficacy on Caco-2 cells was investigated. The expression of the transgene was raised 2.5-fold and 10-fold with nonoxidized thiomer polyplexes in comparison to polyplexes of unmodified chitosan and oxidized chitosan−NAC, respectively. The impact of sulfhydryl reduction on transfection was assessed via thiol group inactivation with 5,5′-dithiobis-(2-nitrobenzoic acid) (DNTB). This inactivation resulted in a decrease of transfection efficacy. In conclusion, chitosan−NAC conjugate was demonstrated to be beneficial for transfection, either for stabilization via disulfide bonds or for raising the expression of transgene via shifting the redox potential of the target cells.

INTRODUCTION

Results in recent clinical trials have renewed interest in nucleic acid-based therapeutics. The transition of these promising molecules into drugs needs to address the still most urgent problem of efficient delivery (*1*). Development of novel delivery platforms that prevent their degradation and facilitate specific uptake into target tissues is therefore a key issue. Here, in particular, the field of nanotechnology is raising expectations and is a main focus of many recent approaches (*2*−*5*). Currently, there is an enormous interest in non-viral vectors in general and in cationic polymer-based gene delivery systems, so-called polyplexes, in particular (*2*, *6*−*9*). These systems have several advantages, such as ease of production and modification, lack of mutagenesis, and reduced potential of immunogenicity, in comparison to viral vectors.

Recently, thiolated polymers have been reported as a promising tool in gene delivery. Reversible cross-linking via disulfide bonds was proposed as a strategy to keep the polyplex structure stable in the extracytoplasmic environment, while inducing the efficient release of entrapped pDNA from the polyplexes after their arrival in the cytoplasmic compartment (*10*−*14*). This tuneable release should be triggered by the large concentration differential of intracellular glutathione compared to extracellular levels. In the intracellular reductive environment, the disulfide bonds should be cleaved. Few references so far have proposed that the reduced sulfhydryl group itself may enhance the transfection (*15*−*17*).

The present study aims to examine the role and potential of sulfhydryl groups for enhancement of transfection efficiency. The new thiomer chitosan−NAC was chosen because of the comparatively high degree of modification and the low toxicity of the ligand *N*-acetylcysteine. Particular attention was paid to the quantification of thiol groups displayed by the gene carrier system. Effects of cross-linked and non-cross-linked thiolated particles on stability and transfection efficacy were assessed *in vitro*. As a control and to get the first clues about the functional mechanism of thiolation-related improvement of transfection, experiments with thiol-inactivating agent 5,5′-dithiobis-(2-nitrobenzoic acid) (DNTB) were performed.

EXPERIMENTAL PROCEDURES

Polymer Synthesis and Characterization. For the synthesis of chitosan−*N*-acetylcysteine, 0.5 g of low-viscosity chitosan (Fluka, Vienna, Austria, lot number 455080/1) was dissolved in 50 mL 0.1% (v/v) acetic acid. *N*-Acetylcysteine (Fluka, Vienna, Austria) was dissolved in distilled water to obtain a 1 M solution. The pH of both solutions was adjusted to 5.0. The coupling reaction between the amino group of chitosan and the carboxyl group of *N*-acetylcysteine was mediated by 1′-ethyl-3(3-dimethylaminopropyl)carbodiimide-HCl (EDAC). Initially,

* Corresponding author. Phone: +43-512-507-5371. Fax: +43-512-507-2933. E-mail: andreas.bernkop@uibk.ac.at. Address: Dep. of Pharmaceutical Technology, Univ. Innsbruck, Innrain 52c, Josef-Möller-Haus, 6020 Innsbruck, Austria.

† Institute of Zoology.

10.1021/bc0603079 CCC: $37.00 © 2007 American Chemical Society
Published on Web 06/07/2007

250 mg of EDAC was added to 50 mL of the chitosan solution and stirred shortly before 25 mL of the NAC solution was added. This reaction mix was stirred at room temperature for 2 h. Subsequently, the polymer solution was extensively dialyzed in five steps for 12 h each. The first dialysis was performed against 5 L distilled water containing 0.2 mM HCl, the second against 5 L distilled water, 0.2 mM HCl, and 2 μM EDTA; and finally, three more times against 5 L distilled water containing 0.2 mM HCl. The purified polymer solution was frozen and lyophilized. Freeze-dried polymers were stored at 4 °C.

Determination of the Thiol Group Content. The amount of reduced sulfhydryl groups on modified chitosan was determined using the photometrical Ellman's test as described previously (*18*).

To determinate the total amount of sulfhydryl groups on the polymer, all disulfide bonds were reduced with an excess of sodium borohydride, following Leitner et al. (*19*). The amount of disulfide bonds was calculated by substracting the quantity of free thiol groups from the totality of thiol moieties present on the polymer and dividing the result by two.

Preperation of Nanoparticles. Unmodified chitosan and chitosan−NAC were dissolved in distilled water in final concentrations of 0.02% and 0.1% (w/v), respectively. The pH of both polymer solutions was adjusted to 4.5 with acetic acid, and the solutions were filtered through sterile filters with 0.2 μm pore size. As model plasmid pEGFP-C2 (Clontech, Mountain View, CA) coding for enhanced green fluorescence protein was used. DNA solution was prepared in distilled water with a pDNA content of 100 μg/mL. Polymer solutions and DNA solution were separately heated to 50 °C for 10 min. For formation of chitosan control particles (Cs NP), 400 μL of the 0.02% chitosan solution was added to 250 μL of pDNA solution, followed by immediate vortexing for 30 s. Chitosan−NAC nanoparticles (NAC NP) were produced in the same way with the modification that 250 μL of pDNA solution was diluted with 306 μL of distilled water before 94 μL of 0.1% chitosan−NAC solution was added.

In the case of oxidized nanoparticles (oxid. NP), immediately after preparation 3 and 6 μL of a 3% hydrogen peroxide solution, respectively, were added to the nanoparticle suspensions and mixed briefly.

A higher amount of chitosan−NAC polymer than unmodified chitosan was used in order to obtain particles of comparable size distribution and ζ potential. The calculated ratio of amino groups to phosphate groups was 5:1 for chitosan control particles and 4.7:1 for chitosan−NAC particles.

Characterization of Nanoparticles. *Photon Correlation Spectroscopy.* To determinate the hydrodynamic diameters of the polyplexes, dynamic light scattering measurements were carried out using PSS Nicomp 380 ZLS instrument (Nicomp Particle Sizing Systems, Santa Barbara, CA). At least 6 samples of each nanoparticle suspension were measured for 3 cycles of 5 min. The data obtained at a detection angle of 90° at 23 °C were analyzed by the Gauss volume-weighted method to calculate the mean diameter.

ζ-Potential Measurement. Determination of ζ potential was performed with a 1:5 dilution of nanoparticle suspensions in distilled water to reduce the shielding effect of ions in the suspension. A scattering angle of 14.7° and an electronical field of 5 V/cm were used for analysis.

Transmission Electron Microscopy. Nanoparticle suspensions were analyzed after 2 h of incubation at room temperature. Drops of 10 μL particle solution were placed on pioloform-coated grids and air-dried for 10 min. The redundant fluid was removed while the dried nanoparticles remained on the grids. These grids were dried and examined by a transmission electron microscope (ZEISS LIBRA120) with an in-column energy filter (EFTEM). Digital micrographs were obtained from a ProScan Slow Scan CCD camera system using *iTEM 5.0* Software from Soft Imaging System GmbH.

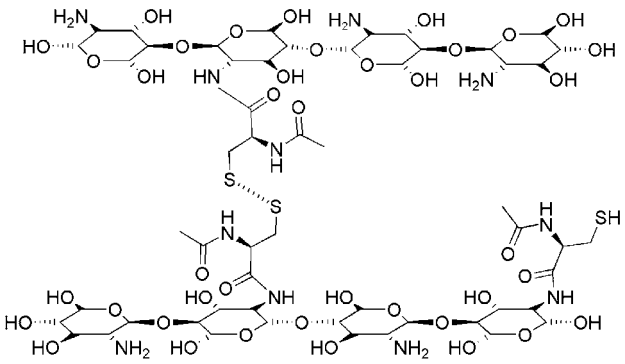


Figure 1. Chemical structure of chitosan−NAC as synthesized within this study. In addition, the possibility of cross-linking via disulfide bonds between two acetyl residues is displayed.

Table 1. Particle Characterization[a]

sample	mean size [nm]	ζ-potential [mV]
Cs NP	107.1 ± 29.2	+9.48 ± 1.2
NAC NP	113.7 ± 32.3	+6.54 ± 0.6
ox. NAC NP	73.0 ± 6.0	+17.01 ± 3.2

[a] Particle size and ζ potential of particles in suspension determined by photon correlation spectroscopy. Unmodified chitosan nanoparticles (Cs NP), chitosan−NAC nanoparticles (NAC NP), and disulfide-cross-linked chitosan−NAC particles (ox. NAC NP) all generated at 4.7:1 N/P ratio. Indicated values are means ± SD of at least six experiments.

Papain Reactivation Assay. Papain (Sigma-Aldrich, Vienna, Austria) was inactivated to papain−S−SCH_3 following the method of Singh (*20*). The papain reactivation assay was performed basically in the same way as described by Singh et al. (*20*) and Wright and Viola (*21*). Degassing of the solutions was not performed. For standards, a dilution series ranging from 0.9375 to 120 nM NAC was used. To aliquotes of 120 μL nanoparticle suspension, 14 μL of 100 mM sodium acetate buffer pH 4.5 were added. All samples were brought to the same volume of 280 μL by the addition of distilled water. An excess of papain (700 μL, 0.6 mg/mL) was added to each sample. The reaction mixtures were kept at room temperature for 1 h. Subsequently, 1 mL of 3.4 mM *N*-benzoyl-L-arginine-*p*-nitroanilide solution was added to all sample tubes. After 1 h further incubation at room temperature, the samples were briefly centrifuged. Finally, the absorbance was measured at 410 nm. The concentration of thiol groups in the test solutions was calculated with the linear function obtained from the calibration curve.

Ellman's Test. Aliquots of 120 μL of nanoparticle suspensions were diluted with 160 μL of 0.5 M PO_4 buffer, pH 8, before adding 280 μL of Ellman's reagent (0.3 mg/mL 5,5′-dithiobis-(2-nitrobenzoic acid) (DNTB)) dissolved in phosphate buffer. Following 2 h incubation at room temperature in the dark, the samples were briefly centrifuged, and the absorbance was measured at 450 nm.

Stability Test. Stability of various nanoparticle suspensions was investigated under challenging conditions such as 80-fold concentration of polyanion heparin (Sigma-Aldrich, Vienna, Austria) or minimum essential medium (MEM), pH 10, including 20% serum. For these assays, 50 μL aliquots of nanoparticle suspensions were mixed with 50 μL of aqueous heparin solution (16 mg/mL) and MEM medium, respectively. After an incubation period of 2 h at 37 °C and 400 rpm in an Eppendorf shaker, electrophoretic mobility assay on 0.7% agarose gel was performed.

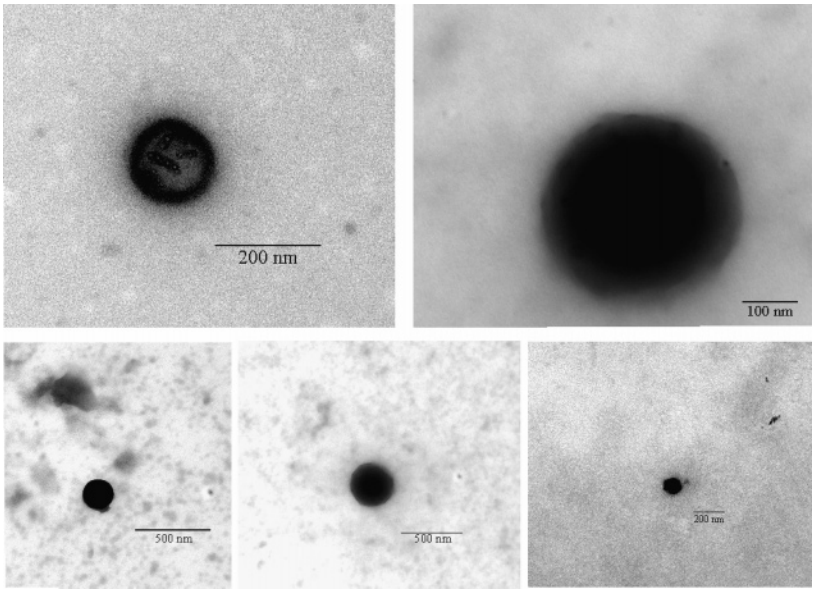


Figure 2. TEM micrograph of nonoxidized chitosan−NAC/pDNA nanoparticles at N/P ratio 4.7:1.

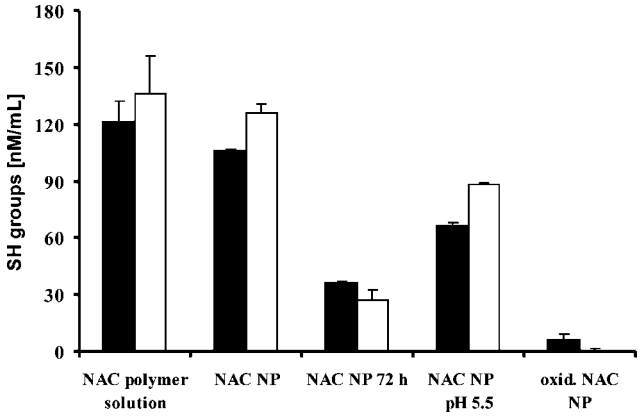


Figure 3. Quantization of thiol groups by two independent spectrophotometric assays. Black bars indicating the results of Ellman's test and open bars of papain reactivation assay. Investigated samples were 0.1% chitosan−NAC polymer solution, suspension of chitosan−NAC/pDNA nanoparticles, nanoparticle suspension after 72 h incubation at room temperature, suspension of chitosan−NAC/pDNA particles produced at pH 5.5, and nanoparticle suspension after oxidation step with 3 μL H_2O_2.

The degree of enzymatic degradation was analyzed by digestion of 50 μL nanoparticle suspension in 1×DNaseI buffer pH 8 (Promega, Madison, WI) with 0.2 units DNaseI (Promega, Madison, WI) at 37 °C for 30 min and subsequent gel electophoresis.

Release of pDNA charge from oxidized particles in a reducing environment like in cytoplasm was assessed in MEM medium containing 0 to 10 mM glutathione.

Cytotoxicity Tests. *LDH.* The Caco-2 human colon carcinoma cells (ATCC Nr. HTB-37) were grown in 12-well plates at an initial seeding density of 1×10^5 cells in 1 mL Eagle minimum essential medium (MEM) supplemented with 2.2 g/L sodium bicarbonate, 2 mM L-glutamine, penicillin/streptomycin, and 20% FCS (Gibco, Nr. 26140−079, Invitrogen, Lofer, Austria). After 24 h incubation, cells were washed once with phosphate buffered saline (PBS) before transfection with 260 μL of nanoparticle suspension per milliliter MEM was performed. MEM medium without serum and without phenol red was used during the cytotoxicity test. As a low control, cells were incubated with medium only. The high control was prepared with medium plus 2% Trition-X100. Samples of 100 μL supernatants were taken after 14 h of incubation and analyzed according to the manufactures protocol from Cytotoxicity Detection Kit (LDH) from Roche (Vienna, Austria). Cytotoxicity was calculated with the equation

$$\text{cytotoxicity [\%]} = (\text{experimental value} - \text{low control})/(\text{high control} - \text{low control}) \times 100$$

MTT. Caco-2 cells were plated into 12-well plates at a density of 5×10^4 cells/mL. After 24 h preincubation, culture medium was replaced by culture medium plus 260 μL nanoparticle suspension/well. Cells were incubated for 14 h before the medium with test solution was aspirated. Cells were washed once with PBS to remove traces of the particle solution. Subsequently, 1 mL MEM without phenol red, containing 0.5 mg/mL (3-(4,5-dimethylthiazol-2-yl)-2,5-diphenyl tetrazolium bromide) (MTT), was added to each well. After 3 h of further incubation, the medium with unreacted dye was aspirated. The converted dye was solubilized with 1 mL acidic isopropanol (0.04 M HCl in absolute isopropanol) by pipetting several times. The dye solution was transferred into tubes and centrifuged 2 min at 15.000 *g* prior to measurement of OD 570 nm with background subtraction of OD 650 nm. The relative cell viability [%] related to control wells was calculated according to the equation

$$\text{viability [\%]} = (\text{test Abs 570 nm} - \text{Abs 650 nm})/(\text{control Abs 570 nm} - \text{Abs 650 nm}) \times 100$$

Transfection. 1×10^5 Caco-2 cells in 1 mL MEM medium were seeded into 12-well plates and incubated for 24 h. Medium was aspirated, and cells were washed once with PBS. First, 260 μL nanoparticle suspension, containing 10 μg of pDNA, was added to the cells and overlaid with 740 μL medium including 20% serum. Cells were incubated with the nanoparticles for 14 h. After this transfection step, cells were washed once with PBS, fed with 1 mL fresh medium, and incubated for another 48 h. Fluorescent cells were monitored with a fluorescent microscope using UV light and the appropriate filter for green fluorescence. Cells were washed once with PBS. Thereafter, 100 μL lysis buffer (0.25 M Tris, pH 7.4, 0.25% (v/v) Trition X-100 and 2.5 mM EDTA) were added and the plate shaken at room temperature for 5 min. To enhance cell lysis, a freeze−thaw

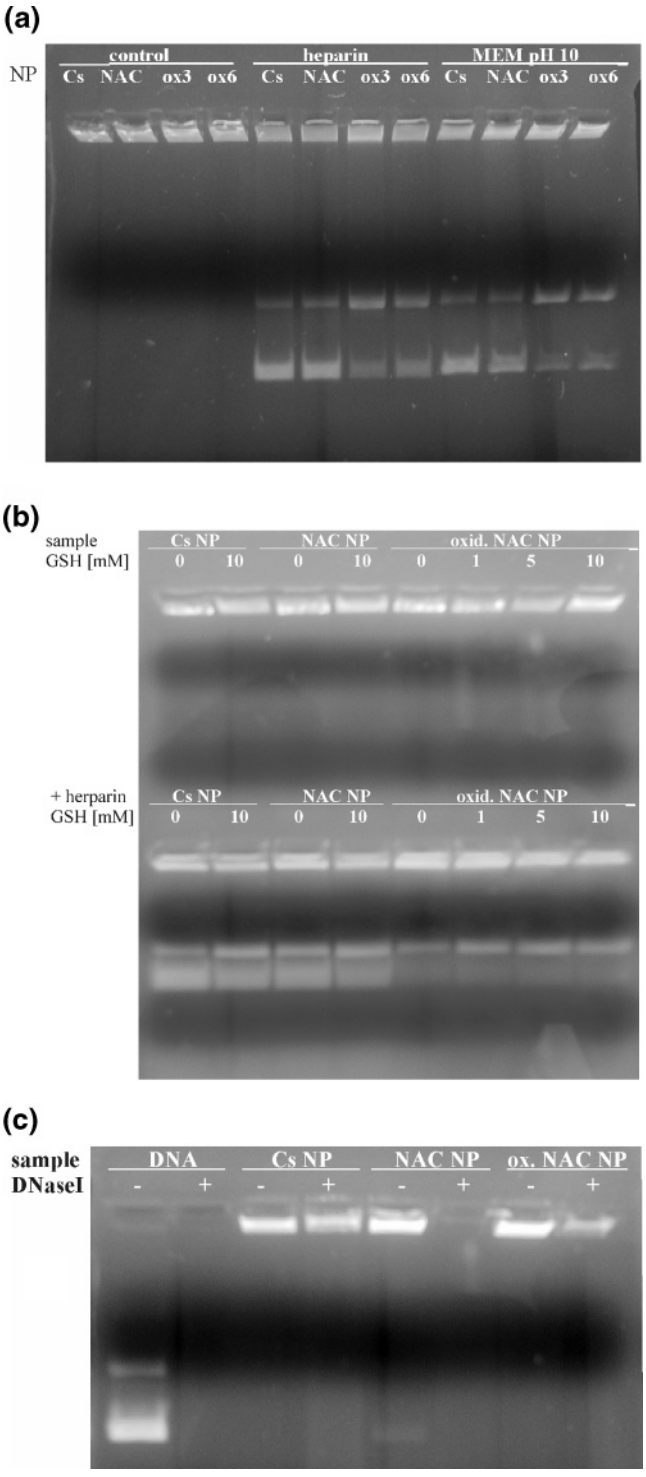


Figure 4. (a) Gel retardation assay for particles of unmodified chitosan (Cs), chitosan−NAC nanoparticles, (NAC) and oxidized Cs-NAC nanoparticles treated with 3 and 6 μL H_2O_2, respectively (ox3 and ox6) (lanes 1−4), and release of pDNA after challenge with 80-fold excess of heparin (lanes 5−8) and at pH 10 (lanes 9−12). (b) Release of pDNA from non-thiolated chitosan particles (Cs NP), thiolated nonoxidized particles (NAC NP), and oxidized chitosan−NAC particles (oxid. NP) achieved by treatment with 10 mM glutathione. (c) Agarose-gel electrophoresis after 30 min DNaseI (0.2 unit) digestion of chitosan control particles (Cs NP), nonoxidized (NAC NP) and oxidized Cs-NAC particles (oxid.NP).

cycle was performed. Cell lysate was transferred into tubes and cell debris was separated by centrifugation. For fluorescence measurement, 50 μL of cellular extract were transferred into a microtiter plate, and the fluorescence was measured at 485/520 nm excitation/emission. Fluorescence of untransfected cells was substracted as background.

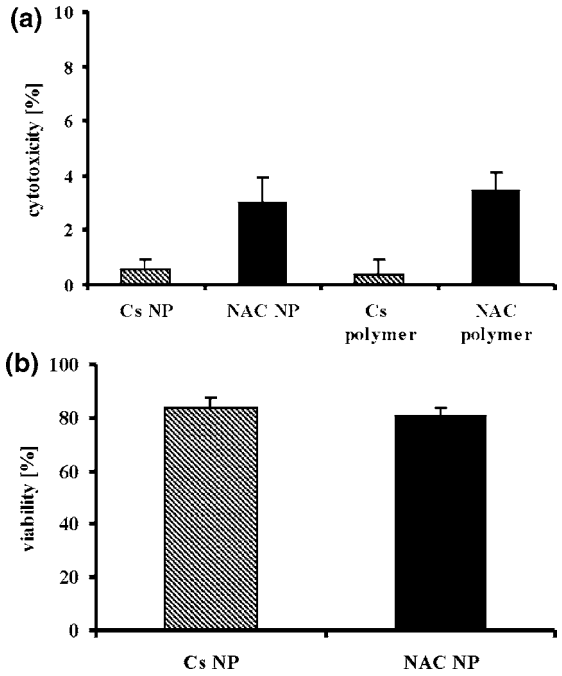


Figure 5. Toxicity of nanoparticle suspensions and viability of Caco-2 cells after challenge, respectively, were determined by (a) lactate dehydrogenase assay and (b) MTT assay. For both cytotoxicity tests, 14 h incubation was performed. Samples: 260 μL chitosan/pDNA nanoparticle suspension (Cs NP), 260 μL chitosan−NAC/pDNA nanoparticle suspension (NAC NP) 38 μL chitosan solution 0.1% 38 μL chitosan−NAC solution 0.1%.

Effect of Thiol Group Modification by DNTB. The dithiol-oxidizing agent 5,5′-dithiobis-(2-nitrobenzoic acid) (DNTB) was used to inactivate sulfhydryl groups on both cell surface and nanoparticles, to study the impact of active sulfhydryl group on the expression of transgene. A solution of 10 mM DNTB in 0.5 M phosphate buffer pH 8 was freshly prepared before every experiment. Caco-2 cells were treated with 200 μM DNTB in cell culture medium for 5 min followed by washing with PBS immediately before transfection. In a second experiment, DNTB solution was added to the nanoparticle suspension to reach a final concentration of 100 μM DNTB and preincubated for 30 min. The transfection was performed as described in the previous section.

Statistical Data Analysis. Results were depicted as mean value ± SD from at least three experiments. Significance among the mean values was calculated using Student's *t* test (software package *SPSS 11.0*). Probability value $p < 0.05$ was considered significant.

RESULTS

***N*-Acetylcysteine-Modified Chitosan.** Chitosan−NAC conjugates, as shown in Figure 1, were synthesized by covalent attachment of *N*-acetylcysteine to the amino group of the chitosan backbone. The colorimetric quantification of free sulfhydryl groups on the conjugate by Ellman's test displayed a thiol content of 1.356 mM/g polymer. Investigation of the amount of disulfide bonds present in the conjugate without any oxidation process performed revealed 0.484 mM disulfide bonds per gram polymer.

The lyophilized chitosan−NAC conjugate had the appearance of a white, odorless, fibrously structured substance. The conjugate was easily dissolved in 0.1% acetic acid. In aqueous solution of pH 4.5 and stored at 4 °C, it was stable for up to 1 month without detectable loss in transfection efficiency.

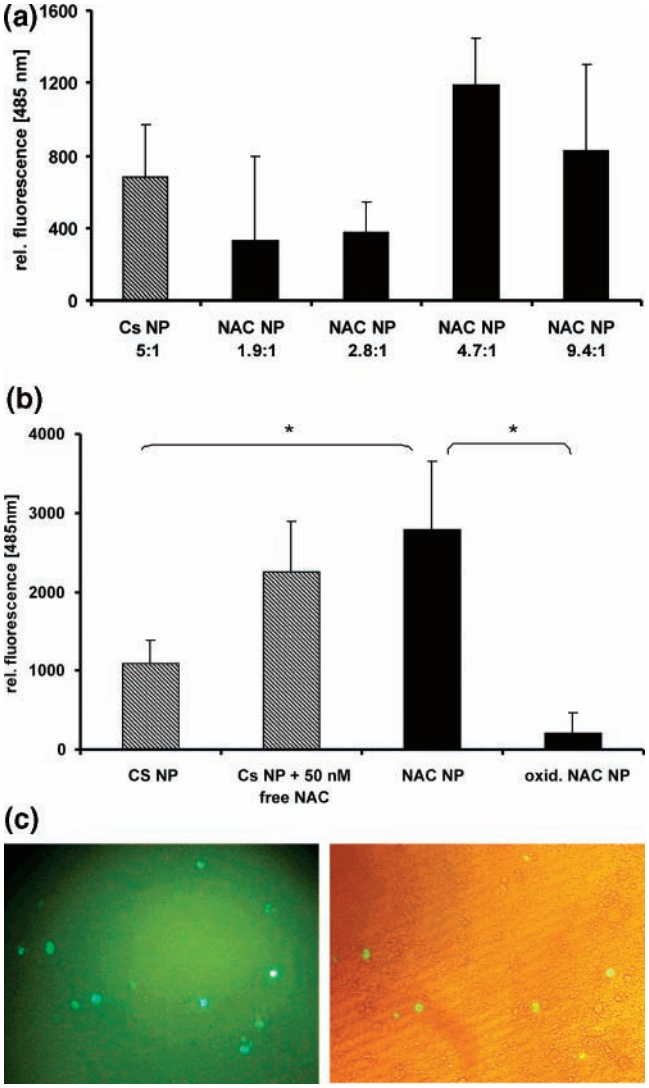


Figure 6. (a) Impact of N/P ratio on the transfection efficancy. Transfection of sub-confluent Caco-2 cells was performed for 14 h with nanoparticle suspension containing 10 μg pDNA each. (b) Gene expression of pEGFP after transfection of Caco-2 cells with suspension of chitosan nanoparticles (Cs NP), chitosan nanoparticle suspension supplemented with 50 mM NAC solution, nonoxidized (NAC NP) and oxidized chitosan−NAC nanoparticle (oxid. NAC NP) suspension. Dose of pDNA was 10 μg/well in all cases. *Significance level of $p < 0.05$. (c) Qualitative analysis of green fluorescence protein expression. Fluorescence microscopy image of chitosan−NAC transfected Caco-2 cells without and with overlaid light microscopy image.

Chitosan−*N*-Acetylcysteine Nanoparticles. Particles produced at N/P ratio 5:1 for chitosan and 4.7:1 for chitosan−NAC, respectively, were characterized. The measured mean size of 113.7 nm (±32.3 nm) for chitosan−NAC nanoparticles was in a comparable range to that of the control particles of unmodified chitosan at 107.1 nm (±29.2 nm). Disulfide bond stabilization caused a decrease in size down to 73.0 nm (±6.0 nm). Chitosan−NAC particles as well as chitosan control particles displayed positive ζ potentials of +6.54 mV and +9.48 mV, respectively (Table 1). The moderate decline in ζ potential was based in the slightly lower N/P ratio.

Transmission electron microscopy images, shown in Figure 2, supported the nanoscale size of the particles. Sedimentation and subsequent removal of the solution favored the small fraction of bigger particles in the suspension. This effect might also explain the bigger size of particles in TEM micrographs compared to the measured mean size with photon correlation spectroscopy. Particles displayed spherical shape and high density, indicating tight packing of polymer and nucleic acid chains.

Evaluation of the thiol group content was done with two methods, papain reactivation assay and Ellman's test, respectively. The results, as presented in Figure 3, obtained with both tests are in good accordance. The advantage of papain activation assay and possibly the reason for higher values determined with this assay was the incubation at pH 7.5 instead of pH 8 in Ellman's buffer. Moreover, the papain assay should measure just the thiol groups displayed on the particle surface, as the size of the enzyme does not allow its penetration into inner parts of the particles. Freshly prepared non-oxidized chitosan−NAC nanoparticle suspension displayed about 100−120 nM/mL SH groups. During 3 days storage at room temperature, the suspension lost about two-thirds of its functional SH groups. Preparation with polymer solution above pH 5 resulted in a loss of SH groups in the nanoparticle suspension. The comparatively milder oxidation processes was sufficient to oxidize almost all sulfhydryl groups present on the polymer.

Reversible Stabilization via Disulfide Bonds. To investigate the enhanced stability of oxidized chitosan−NAC/DNA particles, an excess of the polyanion heparin and pH 10 was used. In these extreme environments, the stabilizing effect of disulfide bonds was clearly demonstrated (Figure 4a). Further, the triggered release of payload in the reducing milieu of 10 mM glutathione was shown in the gel retardation assay illustrated in Figure 4b. The agarose gel shown in Figure 4c demonstrated the stabilization against nuclease challenge. Oxidized chitosan−NAC particles were more stable in comparison to nonoxidized chitosan−NAC particles, but not more stable than control particles of unmodified chitosan.

Moderate Toxicity of Chitosan−NAC Nanoparticles. Since chitosan−NAC is a new polymer, we were also interested in the possible toxic effects of this polymer and the resulting chitosan−NAC/pDNA nanoparticles.

The level of plasma membrane damage was investigated with lactate dehydrogenase assay (Figure 5a). In addition, the viability of Caco-2 cells after overnight exposure at the same concentrations and conditions as in transfection was assessed with MTT assay (Figure 5b).

Both toxicity tests revealed moderate toxicity. The membrane damage was higher with chitosan−NAC compared to unmodified chitosan, although overall in the moderate range of less than 4% cytotoxicity. The increase in acetylation by attaching *N*-acetylcysteine should not have caused the higher damage, since other research groups reported a higher toxicity of chitosan with a high degree of deacetylation (*22*, *23*). The difference in cell viability between exposure to chitosan nanoparticles and to chitosan−NAC nanoparticles assessed with MTT assay was less pronounced.

Transfection Enhancement with Chitosan−NAC Nanoparticles. To maximize transfection efficiency, the optimum ratio of polymer/pDNA was determined. At N/P ratio of 4.7:1, chitosan−NAC particles resulted in the highest expression of transgene as demonstrated in Figure 6a. Particles suitable for transfection were prepared at ratios from 1.9:1 to 9.4:1, indicating the broad range of loading capacity.

Figure 6b illustrates the effect of chitosan−NAC for transfection. These thiomer particles enhanced transfection 2.5-fold in comparison to unmodified chitosan. The dilution of nanoparticle suspension in cell culture medium reached a final concentration of 31 nmol SH /mL. The addition of 50 nmol/mL free *N*-acetylcysteine to control chitosan nanoparticles also led to an increase in transgene expression, but not to the same extent as immobilized NAC. Oxidized chitosan−NAC nano-

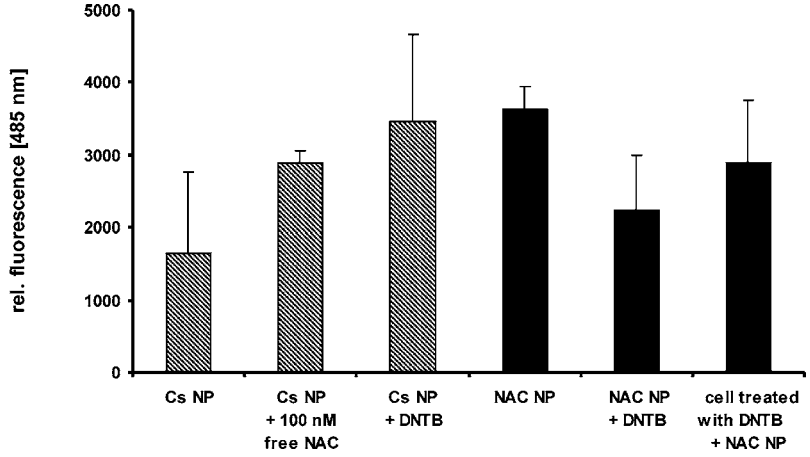


Figure 7. Partial reversibility of transfection enhancement by inhibition of thiol groups with DNTB. Nanoparticle suspension was supplemented with DNTB solution to achieve a final concentration of 100 μM and preincubated 30 min prior to transfection. Cells were pretreated with 200 μM DNTB for 5 min prior to transfection. Hatched bars indicate suspension of unmodified chitosan nanoparticles and black bars chitosan−NAC nanoparticles.

particles were apparently overstabilized for *in vitro* transfection. Their efficiency was decreased below the efficiency of control particles.

As a qualitative control of transfection, UV microscopy images overlaid with light microscopy images are displayed in Figure 6c.

Reversal of the Transfection Enhancement by DNTB Treatment. If SH groups acted as functional groups to enhance transgene expression, the inactivation of these SH via the quantitative formation of S−S bonds performed with DNTB should inhibit the enhancement. Results of sulfhydryl group inactivation are shown in Figure 7. Because DNTB is a cell-impermeable agent, treatment of Caco-2 cells inactivated just the accessible SH groups of proteins on the outside of the plasma membranes. This inhibition caused a decrease in transfection efficiency. The decrease was more pronounced when the SH groups on the nanoparticles were inactivated. Addition of DNTB to control chitosan nanoparticles caused an increase in transfection. Since unmodified chitosan did not carry any sulfhydryl groups to which DNTB could bind, the reagent remained in an active form in solution and resulted in a comparable effect to free NAC.

DISCUSSION

Chitosan−*N*-acetylcysteine represents an interesting new thiomer, as it exhibits a comparatively high amount of immobilized thiol groups and low toxicity. The relative reactivities of thiols with oxidants were demonstrated to be inversely related to the pK of the thiol group (*24*). The thiol group of *N*-acetylcysteine has a pK_a of 9.5 and is therefore a compromise between highly reactive thiols like glutathione (pK_a = 8.8) and cysteine (9.2) and more stable thiols like thioglycolic acid (pK_a = 10.4). This should facilitate the production by preventing excessive loss of SH at alkaline conditions and further grant a moderate but effective action in physiologic pH range.

The formulation process of nanoparticles demonstrated in this study is simple and feasible for a broad range of polymer/DNA ratios. The obtained nanoparticles were of a size which facilitates endocytosis (*25*). Polyplexes have been demonstrated to be taken up by two mechanisms, clathrin-coated pits and caveolae-mediated endocytosis, depending on particle size (*26*). Particles <200 nm in diameter were rapidly internalized via clathrin-coated pits, while particles between 200 and 500 nm in diameter were more slowly internalized via caveolae-mediated uptake (*26*). According to these results, the vast majority of chitosan−NAC/DNA nanoparticles should have been taken up by the clathrin-mediated process. The size of all used nanoparticles was in the same range and seems therefore not to be responsible for differences in the obtained transfection efficacy.

The particles employed in this study had no specific targeting ligand. A positive ζ potential of particles was therefore desired. Particle immobilization on the cell surface resulted in nonspecific ionic interaction between the positive charge of the particles and the negative charge of the cell surface, such as, for example, heparin sulfate proteoglycans that may act as nonspecific receptors for cationic charged molecules.

Results of papain and Ellman's test indicated that almost all thiol groups present on the polymer were displayed on the particle surface. A likely explanation for this result was the excess of polymer in solution. Unfortunately, particles and polymer could not be separated by centrifugation to avoid this distorting effect. However, it made sense to determine the amount of sulfhydryl groups in particle suspension, like it was applied in transfection.

In recent years, it has been well-established that chitosan/DNA particles provide good stability (*27*−*29*). Nevertheless, *in vivo* results are still rare and rather moderate (*30*, *31*), In particular, for challenging routes of application like the oral route, the stability still may be not adequate. Beyond this, to be useful, *in vivo* extracellular stability needs to be changed to lability once the nanoparticles have entered the cytoplasm. The intracellular reducing environment was reported to be in the range 1−10 mM glutathione, depending on the cell type (*11*). An amount of 10 mM glutathione was shown to be sufficient to reduce disulfide cross-linking to thiol groups within this study. However, troubles encountered with these oxidized nanoparticles in Caco-2 cell transfection demonstrated that Caco-2 cells did not exhibit enough intracellular reducing properties for a rapid onset of transcription. The combination of two stabilizing mechanisms, strong electrostatic interaction between negatively charged DNA and positively charged polymer, and, additionally, disulfide bond cross-linking caused overstabilization. The effect of overstabilization was also reported by Miyata et al. for block catiomer polyplexes stabilized via disulfide bonds (*11*). This research group suggested the use of a modification where a disulfide bond replaces amino groups. Although coupling of NAC to chitosan effected such a replacement, the degree of modification was probably not sufficient to prevent overstabilization in a cell culture experiment. Nevertheless, in some cell types of high intracellular glutathione levels, stabilized particles

may be favorable. Moreover, *in vivo* results of stabilized particles may be different from the controlled environment of cell culture model.

Transfection efficacy was also raised by addition of unbound *N*-acetylcysteine. The difference was not highly significant in the cell culture. *In vivo*, the immobilization via covalent attachment of the thiol groups on the particles will prevent dilution. Thus, the advantage of covalently attached thiol groups against supplementation of free SH groups should be more pronounced *in vivo*.

What are the mechanisms by which thiol groups act on transfection efficacy? A first attempt to answer this question was made by the inhibition with DNTB. Sulfhydryl groups may act as an anchor to tightly bind particles to the cell surface via S−S bonds to SH groups of plasma membrane proteins. However, the effect of blocking SH on the cell membrane was not the same effect as the blocking on the particles. Moreover, the addition of free, not attached to the particle, *N*-acetylcysteine also had a positive effect. Therefore, disulfide bonds to cell surface proteins may be one, but presumably not the only, mode of action of thiol groups.

There is evidence that reduced thiol groups may also have an important role in transport processes and/or translational processes. For example, the human cytomegalovirus infectivity could be blocked by DNTB (*32*). Treatment of normal primary keratinocytes with NAC was shown to result in a 10-fold greater rapid differentiation (*33*). The nonspecific sulfhydryl reduction by supplementation of 0.1−10 mM NAC led to terminal differentiation of normal and cancer cells (*34*). Transgene protein expression could possibly take advantage of the differentiation process. Further, the antioxidant *N*-acetylcysteine, a membrane-permeable aminothiol, is able to reduce oxidized glutathione and to act as a precursor for cellular cysteine and glutathione. A great deal of further experiments will be needed to resolve the mechanism and to check whether the results obtained here are conferrable to other cell lines and tissues.

CONCLUSION

Our data indicate a different potential role of thiol groups in the efforts to raise transfection efficacy of non-viral vectors. For cell culture applications, the reduced sulfhydryl groups enhanced transfection efficacy and were of more benefit than stabilization. In contrary, for challenging *in vivo* applications, like oral gene delivery, the stabilization may be of higher impact.

Moreover, we conclude that the chitosan−NAC conjugate may be an interesting vector for gene delivery, offering opportunities to perform both sulfhydryl reduction and stabilization via disulfide bonds.

LITERATURE CITED

(1) Patil, S. D., Rhodes, D. G., and Burgess, D. J. (2005) DNA-based therapeutics and DNA delivery systems: a comprehensive review. *AAPS J. 7* (1), E61−77.

(2) Ravi Kumar, M., Hellermann, G., Lockey, R. F., and Mohapatra, S. S. (2004) Nanoparticle-mediated gene delivery: state of the art. *Expert Opin. Biol. Ther. 4* (8), 1213−24.

(3) Kommareddy, S., Tiwari, S. B., and Amiji, M. M. (2005) Long-circulating polymeric nanovectors for tumor-selective gene delivery. *Technol. Cancer Res. Treat. 4* (6), 615−25.

(4) Mao, H. Q., and Leong, K. W. (2005) Design of polyphosphoester-DNA nanoparticles for non-viral gene delivery. *Adv. Genet. 53*, 275−306.

(5) Dobson, J. (2006) Gene therapy progress and prospects: magnetic nanoparticle-based gene delivery. *Gene Ther. 13* (4), 283−7.

(6) Tiera, M. J., Winnik, F. O., and Fernandes, J. C. (2006) Synthetic and natural polycations for gene therapy: state of the art and new perspectives. *Curr. Gene Ther. 6* (1), 59−71.

(7) Wagner, E., Culmsee, C., and Boeckle, S. (2005) Targeting of polyplexes: toward synthetic virus vector systems. *Adv. Genet. 53PA*, 333−354.

(8) Neu, M., Fischer, D., and Kissel, T. (2005) Recent advances in rational gene transfer vector design based on poly(ethylene imine) and its derivatives. *J. Gene Med. 7* (8), 992−1009.

(9) Medberry, P., Dennis, S., Van Hecke, T., and DeLong, R. K. (2004) pDNA bioparticles: comparative heterogeneity, surface, binding, and activity analyses. *Biochem. Biophys. Res. Commun. 319* (2), 426−32.

(10) Carlisle, R. C., Etrych, T., Briggs, S. S., Preece, J. A., Ulbrich, K., and Seymour, L. W. (2004) Polymer-coated polyethylenimine/DNA complexes designed for triggered activation by intracellular reduction. *J. Gene Med. 6* (3), 337−44.

(11) Miyata, K., Kakizawa, Y., Nishiyama, N., Harada, A., Yamasaki, Y., Koyama, H., and Kataoka, K. (2004) Block catiomer polyplexes with regulated densities of charge and disulfide cross-linking directed to enhance gene expression. *J. Am. Chem. Soc. 126* (8), 2355−61.

(12) Kommareddy, S., and Amiji, M. (2005) Preparation and evaluation of thiol-modified gelatin nanoparticles for intracellular DNA delivery in response to glutathione. *Bioconjugate Chem. 16* (6), 1423−32.

(13) Schmitz, T., Bravo-Osuna, I., Vauthier, C., Ponchel, G., Loretz, B., and Bernkop-Schnürch, A. (2007) Development and in vitro evaluation of a thiomer-based nanoparticulate gene delivery system. *Biomaterials 28* (3), 524−31.

(14) Cavallaro, G., Campisi, M., Licciardi, M., Ogris, M., and Giammona, G. (2006) Reversibly stable thiopolyplexes for intracellular delivery of genes. *J. Controlled Release 115* (3), 322−34.

(15) Kichler, A., Remy, J. S., Boussif, O., Frisch, B., Boeckler, C., Behr, J. P., and Schuber, F. (1995) Efficient gene delivery with neutral complexes of lipospermine and thiol-reactive phospholipids. *Biochem. Biophys. Res. Commun. 209* (2), 444−50.

(16) Martien, R., Loretz, B., Thaler, M., Majzoob, S., and Bernkop-Schnürch, A. (2007) Chitosan-thioglycolic acid conjugate: An alternative carrier for oral nonviral gene delivery? *J. Biomed. Mater. Res. 82A* (1), 1−9.

(17) Lee, D., Zhang, W., Shirley, S. A., Kong, X., Hellermann, G. R., Lockey, R. F., and Mohapatra, S. S. (2007) Thiolated chitosan/DNA nanocomplexes exhibit enhanced and sustained gene delivery. *Pharm. Res. 24* (1), 157−67.

(18) Hornof, M. D., Kast, C. E., and Bernkop-Schnürch, A. (2003) In vitro evaluation of the viscoelastic properties of chitosan-thioglycolic acid conjugates. *Eur. J. Pharm. Biopharm. 55* (2), 185−90.

(19) Leitner, V. M., Walker, G. F., and Bernkop-Schnürch, A. (2003) Thiolated polymers: evidence for the formation of disulphide bonds with mucus glycoproteins. *Eur. J. Pharm. Biopharm. 56* (2), 207−14.

(20) Singh, R., Blattler, W. A., and Collinson, A. R. (1995) Assay for thiols based on reactivation of papain. *Methods Enzymol. 251*, 229−37.

(21) Wright, S. K., and Viola, R. E. (1998) Evaluation of methods for the quantitation of cysteines in proteins. *Anal. Biochem. 265* (1), 8−14.

(22) Schipper, N. G., Varum, K. M., Stenberg, P., Ocklind, G., Lennernas, H., and Artursson, P. (1999) Chitosans as absorption enhancers of poorly absorbable drugs. 3: Influence of mucus on absorption enhancement. *Eur. J. Pharm. Sci. 8* (4), 335−43.

(23) Huang, M., Khor, E., and Lim, L. Y. (2004) Uptake and cytotoxicity of chitosan molecules and nanoparticles: effects of molecular weight and degree of deacetylation. *Pharm. Res. 21* (2), 344−53.

(24) Winterbourn, C. C., and Metodiewa, D. (1999) Reactivity of biologically important thiol compounds with superoxide and hydrogen peroxide. *Free Radical Biol. Med. 27* (3−4), 322−8.

(25) Rejman, J., Oberle, V., Zuhorn, I. S., and Hoekstra, D. (2004) Size-dependent internalization of particles via the pathways of clathrin- and caveolae-mediated endocytosis. *Biochem. J. 377* (Pt 1), 159−69.

(26) Rejman, J., Bragonzi, A., and Conese, M. (2005) Role of clathrin- and caveolae-mediated endocytosis in gene transfer mediated by lipo- and polyplexes. *Mol. Ther. 12* (3), 468−74.

(27) Strand, S. P., Danielsen, S., Christensen, B. E., and Varum, K. M. (2005) Influence of chitosan structure on the formation and stability of DNA-chitosan polyelectrolyte complexes. *Biomacromolecules 6* (6), 3357−66.

(28) Romoren, K., Aaberge, A., Smistad, G., Thu, B. J., and Evensen, O. (2004) Long-term stability of chitosan-based polyplexes. *Pharm. Res. 21* (12), 2340−6.
(29) Borchard, G. (2001) Chitosans for gene delivery. *Adv. Drug. Delivery Rev. 52* (2), 145−50.
(30) Chen, J., Yang, W. L., Li, G., Qian, J., Xue, J. L., Fu, S. K., and Lu, D. R. (2004) Transfection of mEpo gene to intestinal epithelium in vivo mediated by oral delivery of chitosan-DNA nanoparticles. *World J. Gastroenterol. 10* (1), 112−6.
(31) Roy, K., Mao, H. Q., Huang, S. K., and Leong, K. W. (1999) Oral gene delivery with chitosan−DNA nanoparticles generates immunologic protection in a murine model of peanut allergy. *Nat. Med. 5* (4), 387−91.
(32) Mirazimi, A., Mousavi-Jazi, M., Sundqvist, V. A., and Svensson, L. (1999) Free thiol groups are essential for infectivity of human cytomegalovirus. *J. Gen. Virol. 80* (Pt 11), 2861−5.
(33) Edlundh-Rose, E., Kupershmidt, I., Gustafsson, A. C., Parasassi, T., Serafino, A., Bracci-Laudiero, L., Greco, G., Krasnowska, E. K., Romano, M. C., Lundeberg, T., Nilsson, P., and Lundeberg, J. (2005) Gene expression analysis of human epidermal keratinocytes after N-acetyl L-cysteine treatment demonstrates cell cycle arrest and increased differentiation. *Pathobiology 72* (4), 203−12.
(34) Parasassi, T., Brunelli, R., Bracci-Laudiero, L., Greco, G., Gustafsson, A. C., Krasnowska, E. K., Lundeberg, J., Lundeberg, T., Pittaluga, E., Romano, M. C., and Serafino, A. (2005) Differentiation of normal and cancer cells induced by sulfhydryl reduction: biochemical and molecular mechanisms. *Cell Death Differ. 12* (10), 1285−96.

BC0603079

Design and Synthesis of Efficient Fluorescent Dyes for Incorporation into DNA Backbone and Biomolecule Detection

Wei Wang[†] and Alexander D. Q. Li*

Department of Chemistry and Center for Materials Research, Washington State University, Pullman, Washington 99164. Received June 1, 2006; Revised Manuscript Received January 11, 2007

We report here the design and synthesis of a series of π-conjugated fluorescent dyes with D-A-D (D, donor; A, acceptor), D-π-D, A-π-A, and D-π-A for applications as the signaling motif in biological−synthetic hybrid foldamers for DNA detection. The Horner−Wadsworth−Emmons (HWE) reaction and Knoevenagel condensation were demonstrated as the optimum ways for construction of long π-conjugated systems. Such rodlike chromophores have distinct advantages, as their fluorescence properties are not quenched by the presence of DNA. To be incorporated into the backbone of DNA, the chromophores need to be reasonably soluble in organic solvent for solid-phase synthesis, and therefore a strategy of using flexible tetraethylene glycol (TEG) linkers at either end of these rodlike dyes was developed. The presence of TEG facilitates the protection of the chain-growing hydroxyl group with DMTrCl (dimethoxytrityl chloride) as well as the activation of the coupling step with phosphoramidite chemistry on an automated DNA synthesizer. To form fluorescence resonance energy transfer (FRET) pairs, six synthetic chromophores with blue to red fluorescence have been developed, and those with orthogonal fluorescent emission were chosen for incorporation into DNA−chromophore hybrid foldamers.

INTRODUCTION

Syntheses of deoxyribonucleic acid (DNA) and dye conjugates (*1*−*3*) have enabled many optical probes; these conjugate probes provide a means to study biomolecules within living cells in detail via fluorescence imaging (*4*, *5*) and single-molecule fluorescence spectroscopy (*6*−*8*). However, introducing multiple fluorescent dyes ($N > 2$) into the backbone of a single DNA chain remains largely an unsolved challenge for organic chemistry. To study complex biochemical assemblies and reactions, it is necessary in some systems to have multiple fluorescence probes on a single DNA chain. One such interesting architectural motif in supramolecular chemistry is to use the self-assembling amphiphilic properties of the dyes to induce folded nanostructures with alternating single-strand DNA looping around the folded cores (*9*). Using this principle, hybrid biological and synthetic foldamers have been readily developed for DNA detection (*10*). The strategy is that organic fluorescence chromophores function as an optical reporter while the biological domain, in this case, a specific DNA sequence, functions as a high-fidelity molecular recognition element. The rationale here is that, when the built-in DNA sequences in the hybrid foldamer complement the target DNA in a completely or partially matched situation, the folded nanostructure of the foldamer will be converted to an extended one, a process in which the fluorescence color of the foldamer will change dramatically because of FRET between two adjacent chromophores (*11*). Different mismatched DNA sequences lead to various degrees of emission color changes due to different levels of FRET between the organic chromophores at a given time. From the structural skeleton point of view, molecular beacons usually have organic dyes at both ends of a single DNA sequence, and therefore their termini are a dead-end for incorporation into long DNA sequences (*12*−*16*); the hybrid foldamers have the organic dyes inserted between multiple DNA sequences, which allow further biological manipulation such that the DNA ends can be cut by endonucleases and incorporated into genes with a DNA polymerase or ligase. These special structural features make the hybrid foldamers unique and suitable candidates for studying biological mechanisms.

Since the foldamer probe with alternating hydrophobic and hydrophilic structures is constructed via solid-phase synthesis using an automated DNA synthesizer (Applied Biosystem 8909) (*9*), it is imperative to develop fluorescent building blocks with an activated linker which can be attached to the growing end of the DNA chain and a temporary blocking group to prevent undesired coupling reactions and permit further chain extension after deprotection. The resulting hybrid foldamers have multiple fluorescent chromophores, and the emission color is controlled by the distance between the chromophores separated by the DNA sequences (Figure 1). For completely mismatched sequences, no hybridization occurs between the foldamer and the mismatched target; therefore, the flexible single-stranded DNA chains allow individual chromophores to come in close proximity due to the hydrophobic and π-stacking effect, and the net result is that fluorescence emission is in the long-wavelength region because of the high degree of FRET between individual organic dyes. For perfect matched sequences, however, hybridization turns flexible single-stranded DNA into rigid double helixes, which in turn separates chromophores and reduces the level of FRET between the organic dyes. In this case, the emission color from the foldamer will depend on the short-wavelength chromophore. Therefore, we have designed and synthesized a series of fluorescent chromophores with emission wavelength ranging from blue to red; all fluorescent compounds bear tetraethylene glycol side chains with −OH termini, which are amenable to DMTr protection and phosphoramidite chemistry.

As a class of bis(styryl)benzene derivatives, the donor-π-donor (D-π-D), acceptor-π-acceptor (A-π-A), donor-acceptor-donor (D-A-D), and acceptor-donor-acceptor (A-D-A) structural motifs have received a great deal of attention, because they exhibit exceptionally large two-photon absorption cross sections,

* Corresponding author E-mail: dequan@wsu.edu.

[†] Current address: Department of Chemistry, University of California, One Shields Avenue, Davis, California 95616.

10.1021/bc060151c CCC: $37.00 © 2007 American Chemical Society
Published on Web 05/18/2007

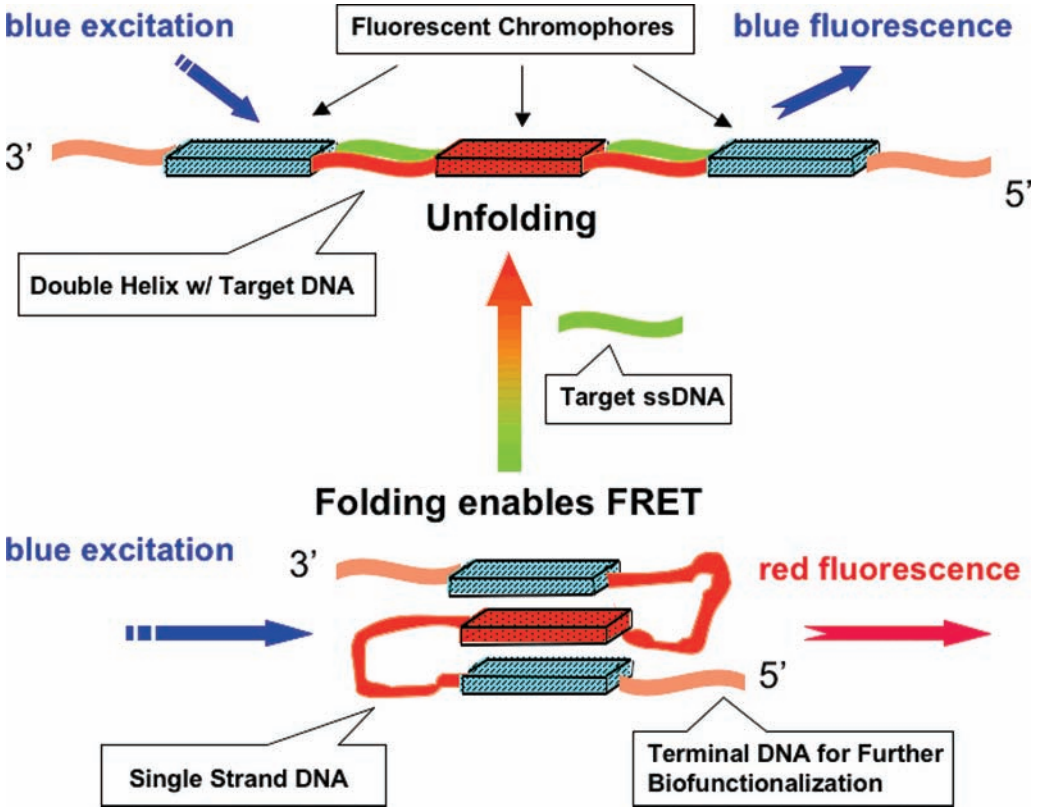


Figure 1. Incorporation of highly fluorescent chromophores into DNA main chains enables many biotechnologies, including DNA monitoring and detection.

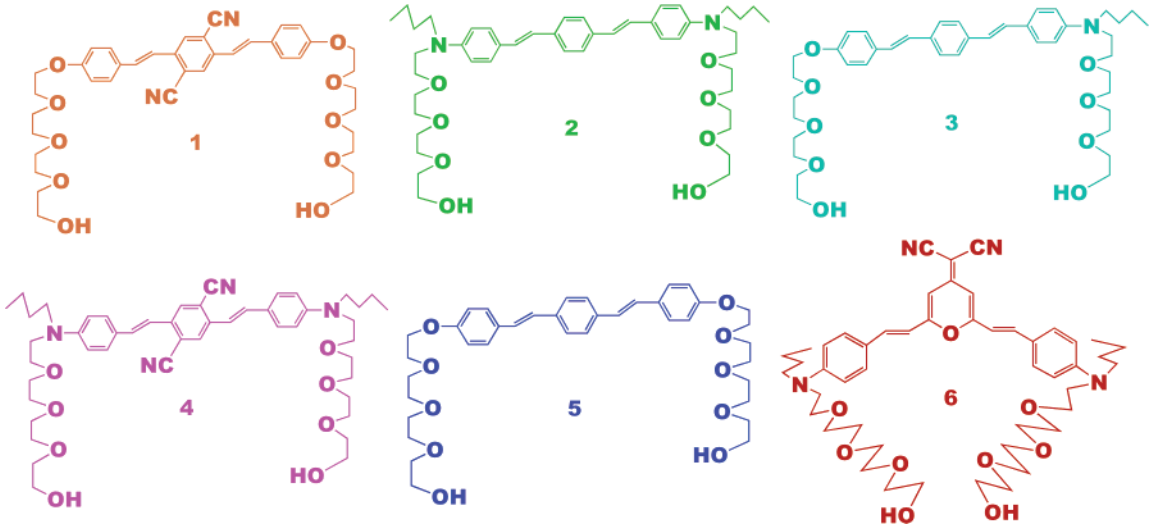


Figure 2. Chemical structures of highly fluorescent dye molecules that are amenable to the general strategy developed here: one hydroxyl group is protected with a dimethoxy trityl (DMTr) group and the other hydroxy group is activated with phosphoramidite.

up to ~400 times that of trans-stilbene (*17*). Compared to our prior perylene tetracarboxylic diimide unit, these new chromophores have desired features such as higher fluorescence quantum yield when incorporated into DNA, and adjustable excitation and emission wavelength via structural variations on similar molecular architectures. Meanwhile, a red fluorescence dye based on the symmetric structure of (2,6-dimethyl-4*H*-pyran-4-ylidene)malononitrile (DCM laser dye) has been developed according to a recent report (*18*); the large dipole moment and high decomposition temperature of this Y-shaped structure make it an attractive candidate for red fluorescence signaling reporter. Consequently, we have developed a series of organic chromophores with different fluorescent colors as molecular building blocks (Figure 2), which are suitable for construction of new hybrid foldamers as molecular probes (*10*).

EXPERIMENTAL SECTION

General Methods. Solvents and reagents were purified where necessary using literature methods (*31*). In particular, *N*,*N*-dimethylformamide (DMF) was distilled from 4 Å MS (molecular sieve) under reduced pressure and stored under argon. Acetonitrile (MeCN) was heated under reflux over calcium hydride and distilled under argon. MALDI mass spectra was obtained with an ABVS-2025 spectrometer. ^{1}H NMR spectra were recorded with a Mercury 300 (300 MHz) spectrometer for solutions in $CDCl_3$ (CD_3OD) at ambient temperature. ^{13}C NMR spectra were recorded at 75.48 MHz with a Mercury 300

spectrometer for solutions in $CDCl_3$ (CD_3OD) adopting 77.23 ppm for the central line of $CDCl_3$. ^{31}P NMR chemical shifts were reported in ppm using 85% H_3PO_4 as an external reference. Reactions were monitored by thin-layer chromatography (TLC) on a precoated plate of silica gel 60 F_{254} (EM Science). Column chromatography was performed on silica gel 60 (230−400 mesh, EM Science).

Compounds in Tetraethylene Chain Optimization and Modification. *4-(2-(2-(2-Hydroxyethoxy)ethoxy)ethoxy)benzaldehyde (**7**).* A mixture of 2-(2-(2-Chloroethoxy)ethoxy)-ethanol (commercial) (1.0 g, 5.9 mmol), 4-hydroxybenzaldehyde (0.8 g, 6.5 mmol, 1.1 equiv), and K_2CO_3 (1.8 g, 2.2 equiv) in dry *N,N*-dimethylformamide (DMF) (10 mL) was heated to 120 °C (oil bath 110 °C) under argon. After the stirring was continued at this temperature for 16 h, the reaction mixture was cooled to room temperature. The solvent (DMF) was evaporated in vacuum, and the residue was diluted with $CHCl_3$. The obtained suspension was suction-filtered and the filtrate was collected. After drying over Na_2SO_4, the organic phase was concentrated, and the residue was purified by chromatography on a silica gel column eluted with EtOAc/MeOH (20:1) to give the title product (950 mg, yield, 63%) as a yellow oil. R_f = 0.33 (EtOAc/MeOH 20/1). ^1H NMR ($CDCl_3$) δ (ppm): 9.89 (s, 1H, -C*H*O), 7.82 (dt, 2H, J_1 = 9.0 Hz, J_2 = 2.7 Hz, benzaldehyde), 7.02 (dt, 2H, J_1 = 9.0 Hz, J_2 = 2.7 Hz, benzaldehyde), 4.21 (t, 2H, J = 4.8 Hz, triethylene glycol chain), 3.89 (t, 2H, J = 4.8 Hz, triethylene glycol chain), 3.75−3.67 (m, 6H, triethylene glycol chain), 3.61 (bt, 2H, J = 4.8 Hz, triethylene glycol chain), 2.40 (bt, 1H, J = 6.0 Hz, -O*H*).

*4-(2-(2-(2-Trityloxyethoxy)ethoxy)ethoxy)benzaldehyde (**8**).* A mixture of **7** (0.5 g, 2.0 mmol), trityl chloride (1.2 g, 4.3 mmol, 2.2 equiv), and a catalytic amount of 4-(dimethylamino)pyridine (DMAP) in dry pyridine (5 mL) was heated to 40−50 °C under argon. After the stirring was continued at this temperature for 24 h, the reaction mixture was cooled to room temperature. The solvent was removed in vacuum, and the residue was diluted with EtOAc. The obtained suspension was suction-filtered and the filtrate was collected. After drying over Na_2SO_4, the organic phase was concentrated, and the residue was purified by chromatography on a silica gel column eluted with cyclohexane/EtOAc/pyridine (300/100/4, v/v) to give the title product (770 mg, yield 99%). R_f = 0.31 (300/100/4, v/v). ^1H NMR ($CDCl_3$) δ (ppm): 9.87 (s, 1H, -C*H*O), 7.80 (dt, 2H, J_1 = 8.7 Hz, J_2 = 2.1 Hz, benzaldehyde), 7.48−7.43 (m, 6H, benzene ring of trityl group), 7.46−7.18 (m, 9H, benzene ring of trityl group), 6.98 (dt, 2H, J_1 = 8.7 Hz, J_2 = 2.1 Hz, benzaldehyde), 4.20 (bt, 2H, J = 4.8 Hz, triethylene glycol chain), 3.92 (bt, 2H, J = 4.8 Hz, triethylene glycol chain), 3.78−3.67 (m, 6H, triethylene glycol chain), 3.24 (t, 2H, J = 4.8 Hz, triethylene glycol chain).

*4-[2-[2-[2-(2-hydroxyethoxy)ethoxy]ethoxy]ethoxy]-benzaldehyde (**10**).* A mixture of 2-(2-(2-(2-chloroethoxy)-ethoxy)ethoxy)ethanol (**9**) (*19*) (2.0 g, 9.4 mmol), 4-hydroxy-benzaldehyde (1.4 g, 1.2 equiv), and K_2CO_3 (2.5 g, 2 equiv) in dry *N,N*-dimethylformamide (DMF) (10 mL) was heated to 100 °C (oil bath 110 °C) under argon. The stirring was continued at this temperature for 72 h. After the reaction mixture was cooled to room temperature, the solvent (DMF) was evaporated in vacuum and the residue was diluted with $CHCl_3$. The obtained suspension was suction-filtered and the filtrate was collected. After drying over Na_2SO_4, the organic phase was concentrated, and the residue was purified by chromatography on a silica gel column eluted with EtOAc/MeOH (20:1) to give the title product (2.25 g, yield 80%) as a yellow oil. R_f = 0.3 (EtOAc/MeOH 20/1). ^1H NMR ($CDCl_3$) δ (ppm): 9.87 (s, 1H, -CHO), 7.82 (dt, 2H, J_1 = 9.0 Hz, J_2 = 2.7 Hz, benzaldehyde), 7.01 (dt, 2H, J_1 = 9.0 Hz, J_2 = 2.7 Hz, benzaldehyde), 4.22 (bt, 2H, J = 4.8 Hz, tetraethylene glycol chain), 3.89 (bt, 2H, J = 4.8 Hz, tetraethylene glycol chain), 3.77−3.59 (m, 12H, tetraethylene glycol chain), 2.53 (t, 1H, J = 6.0 Hz, -O*H*). ^{13}C NMR ($CDC1_3$) δ (ppm): 190.9, 163.9, 132.1, 130.1, 115.0, 72.65, 71.07, 70.86, 70.78, 70.53, 69.68, 67.92, 61.95. MS (MALDI-TOF): 299.01 $[M + H]^+$, 320.99 $[M + Na]^+$.

*4-(2-(2-(2-(2-(Bis(4-methoxyphenyl)phenylmethoxy)ethoxy)-ethoxy)ethoxy)ethoxy)benzaldehyde (**11**).* A mixture of **10** (0.5 g, 1.7 mmol), DMTrCl (1.2 g, 3.5 mmol, 2 equiv), and a catalytic amount of 4-(dimethylamino)pyridine (DMAP) in dry pyridine (10 mL) was stirred at room temperature under argon. After 6 h, the reaction solvent was removed in vacuum, and the residue was directly subjected to a silica gel column eluted with cyclohexane/EtOAc (gradient elution with 1% pyridine: 500/150 → 300/150 → 150/150, v/v) to give the title product (1.056 g, yield 96%). R_f = 0.42 (cyclohexane/EtOAc 1/1, v/v). ^1H NMR ($CDCl_3$) δ (ppm): 9.87 (s, 1H, -C*H*O), 7.79 (dt, 2H, J_1 = 8.7 Hz, J_2 = 2.1 Hz, benzaldehyde), 7.45 (m, 2H, benzene ring of DMTr group), 7.36−7.15 (m, 3H, benzene ring of DMTr group), 7.34 (dt, 4H, J_1 = 9.0 Hz, J_2 = 2.7 Hz, methoxybenzene ring of DMTr group), 6.97 (dt, 2H, J_1 = 8.7 Hz, J_2 = 2.1 Hz, benzaldehyde), 6.81 (dt, 4H, J_1 = 9.0 Hz, J_2 = 2.7 Hz, methoxybenzene ring of DMTr group), 4.15 (bt, 2H, J = 4.8 Hz, tetraethylene glycol chain), 3.87 (bt, 2H, J = 4.8 Hz, tetraethylene glycol chain), 3.77 (s, 6H, -OC*H*$_3$), 3.77−3.64 (m, 10H, tetraethylene glycol chain), 3.22 (t, 2H, J = 4.8 Hz, tetraethylene glycol chain). ^{13}C NMR ($CDC1_3$) δ (ppm): 191.0, 164.0, 158.5, 145.3, 136.5, 132.1, 130.3, 130.2, 128.4, 127.9, 126.8, 123.9, 115.1, 113.2, 86.2, 71.2, 71.1, 71.0, 69.7, 68.0, 63.4, 55.5, 27.3.

*2-(2-(2-(2-N-n-Butylaminoethoxy)ethoxy)ethoxy)ethanol (**12**).* To a solution of 2-(2-(2-(2-chloroethoxy)ethoxy)ethoxy)ethanol (2 g, 9.4 mmol) in *n*-butylamine 10 mL at room temperature was added K_2CO_3 (1 g, 0.77 equiv). The reaction mixture was heated to reflux for 24 h. Then, another 10 mL of *n*-butylamine was added into the mixture, and the reaction was continued to reflux another 12 h. The reaction mixture was cooled to room temperature, and the *n*-butylamine was removed in vacuum. The residue was diluted with $CHCl_3$ and the suspension was suction-filtered. The filtrate was collected and concentrated to give the title product as a yellow syrup in quantitative yield, which could be used directly in the next step without further purification. ^1H NMR ($CDCl_3$) δ (ppm): 3.55−3.51 (m, 14H, tetraethylene glycol chain), 2.66 (bt, 2H, J = 5.1 Hz, tetraethylene glycol chain), 2.47 (t, 2H, J = 7.2 Hz, *n*-butyl chain), 1.43−1.31 (m, 2H, *n*-butyl chain), 1.30−1.16 (m, 2H, *n*-butyl chain), 0.80 (t, 3H, J = 7.2 Hz, *n*-butyl chain). ^{13}C NMR ($CDC1_3$) δ (ppm): 72.9, 70.6, 70.4, 70.3, 70.2, 61.3, 49.5, 49.2, 32.1, 20.6, 14.1. MS (MALDI-TOF): 249.92 $[M + H]^+$, 271.92 $[M + Na]^+$, 287.86 $[M + K]^+$.

*4-N-n-Butyl-N-[2-[2-[2-(2-hydroxyethoxy)ethoxy]ethoxy]ethyl]-amino benzaldehyde (**13**).* A mixture of 2-[2-[2-(2-*N*-*n*-butylaminoethoxy)ethoxy]ethoxy]ethanol (**12**) (2.3 g, 9.4 mmol), 4-fluorobenzaldehyde (1.0 mL, 9.4 mmol), and K_2CO_3 (1.5 g, 1.1 equiv) in dry *N,N*-dimethylformamide (DMF) (10 mL) was heated with stirring to 120 °C (oil bath 128 °C) under argon. The stirring was continued at this temperature for 72 h, and the reaction mixture was cooled to room temperature. After the solvent (DMF) was evaporated in vacuum, the residue was diluted with $CHCl_3$. The obtained suspension was washed with brine (2 × 200 mL) and dried over Na_2SO_4. The organic layer was concentrated, and the residue was purified by chromatography on a silica gel column eluted with EtOAc/MeOH (20:1) to give the title product (1.2 g, 36% in two steps based on **9** as a yellow oil. R_f = 0.4 (EtOAc/MeOH 20/1). ^1H NMR ($CDCl_3$) δ (ppm): 9.56 (s, 1H, -CHO), 7.57 (bd, 2H, J = 9.3 Hz, aromatic ring), 6.58 (bd, 2H, J = 8.7 Hz, aromatic ring), 3.65−3.40 (m, 16H, tetraethylene glycol chain), 3.29 (t, 2H, J = 7.8

Hz, *n*-butyl chain), 1.59−1.40 (m, 2H, *n*-butyl chain), 1.30−1.18 (m, 2H, *n*-butyl chain), 0.85 (t, 3H, $J = 7.5$ Hz, *n*-butyl chain). ^{13}C NMR ($CDC1_3$) δ (ppm): 189.7, 152.4, 131.9, 124.5, 110.6, 72.4, 70.5, 70.4, 70.3, 70.1, 68.1, 61.4, 51.1, 50.3, 28.9, 20.0, 13.9. MS (MALDI-TOF): 353.23 $[M]^+$.

*4-((2-(2-(2-(2-(Bis(4-methoxyphenyl)phenylmethoxy)ethoxy)-ethoxy)ethoxy)ethyl)butylamino)benzaldehyde (**14**).* A mixture of **13** (475 mg, 1.35 mmol), DMTrCl (912 mg, 2.7 mmol, 2 equiv), and a catalytic amount of 4-(dimethylamino)pyridine (DMAP) in dry pyridine (10 mL) was stirred at room temperature under argon. After the stirring was continued overnight, the reaction solvent was removed in vacuum and the residue was directly subject to a silica gel column eluted with cyclohexane/EtOAc (gradient elution with 1% pyridine: 500/150 → 300/150 → 150/150, v/v) to give the title product (800 mg, yield 90%). $R_f = 0.19$ (cyclohexane/EtOAc 1/1, v/v). ^{1}H NMR ($CDCl_3$) δ (ppm): 9.69 (s, 1H, -C*H*O), 7.68 (bd, 2H, $J = 9.0$ Hz, benzaldehyde), 7.46 (m, 2H, benzene ring of DMTr group), 7.32−7.15 (m, 3H, benzene ring of DMTr group), 7.34 (dt, 4H, $J_1 = 9.0$ Hz, $J_2 = 3.0$ Hz, methoxybenzene ring of DMTr group), 6.81 (dt, 4H, $J_1 = 9.0$ Hz, $J_2 = 3.0$ Hz, methoxybenzene ring of DMTr group), 6.66 (bd, 2H, $J = 9.0$ Hz, benzaldehyde), 3.77 (s, 6H, -OCH_3), 3.68−3.53 (m, 14H, tetraethylene glycol chain), 3.37 (bt, 2H, $J = 7.9$ Hz, -NCH_2CH$_2$CH$_2$CH$_3$), 3.22 (t, 2H, $J = 5.2$ Hz, tetraethylene glycol chain), 1.62−1.52 (m, 2H, -NCH$_2$CH_2CH$_2$CH$_3$), 1.40−1.28 (m, 2H, -NCH$_2$CH$_2$CH_2CH$_3$), 0.95 (t, 3H, $J = 7.2$ Hz, -NCH$_2$CH$_2$CH$_2$CH_3).

Compounds in Preparation of Asymmetric Pyridinium Bistyryl Benzene. *4-(2-(2-(2-(2-(tert-Butyldimethylsilanyloxy)-ethoxy)ethoxy)ethoxy)ethoxy)benzaldehyde (**20**).* A mixture of **10** (1.4 g, 4.7 mmol), *tert*-butyldimethylsilyl chloride (TBDMSCl) (0.85 g, 5.6 mmol, 1.2 equiv), and *N*,*N*-diisopropylethylamine (DIPEA) (1.2 mL, 1.5 equiv) in dry CH_2Cl_2 (15 mL) was stirred at room temperature under argon. After 5 h, half of the starting material had gone. Another batch of DIPEA and TBDMSCl as well as a catalytic amount of DMAP was added. The reaction mixture was stirred overnight. The solvent (CH_2Cl_2) was evaporated in vacuum, and the residue was purified by chromatography on a silica gel column eluted with cyclohexane/EtOAc (1/1) to give the title product (1.5 g, yield 77%). $R_f = 0.44$ (cyclohexane/EtOAc, 1/1). ^{1}H NMR ($CDCl_3$) δ (ppm): 9.88 (s, 1H, -C*H*O), 7.83 (dt, 2H, $J_1 = 9.0$ Hz, $J_2 = 2.1$ Hz, benzaldehyde), 7.02 (dt, 2H, $J_1 = 9.0$ Hz, $J_2 = 2.1$ Hz, benzaldehyde), 4.22 (t, 2H, $J = 5.1$ Hz, tetraethylene glycol chain), 3.89 (t, 2H, $J = 5.1$ Hz, tetraethylene glycol chain), 3.75 (bt, 2H, $J = 5.1$ Hz, tetraethylene glycol chain), 3.71−3.59 (m, 8H, tetraethylene glycol chain), 3.49 (bt, 2H, $J = 5.1$ Hz, tetraethylene glycol chain), 0.83 (s, 9H, -Si(CH$_3$)$_2$C(CH_3)$_3$), 0.06 (s, 6H, -Si(CH_3)$_2$C(CH$_3$)$_3$). ^{13}C NMR ($CDC1_3$) δ (ppm): 190.9, 164.0, 132.1, 130.2, 115.1, 72.9, 71.2, 71.0, 70.99, 70.94, 69.7, 68.0, 63.0, 26.3, 18.7, −4.9.

*4-(2-(4-(2-(2-(2-(2-(tert-Butyldimethylsilanyloxy)ethoxy)ethoxy)-ethoxy)ethoxy)phenyl)vinyl)benzonitrile (**22**).* A solution of diisopropylamine (3.2 mL, 22.8 mmol, 4.3 equiv) in THF (40 mL) at room temperature under argon was cooled to −78 °C, and *n*-BuLi (12.5 mL, 1.6 M in hexanes, 3.8 equiv) was added via syringe. The mixture was warmed to 0 °C for 30 min and recooled to −78 °C. A solution of 4-cyanobenzylphosphonic acid diethyl ester **21** (2.3 g, 9 mmol) in THF (15 mL) was precooled and transferred via cannula into the LDA solution at −78 °C, and then the reaction mixture was warmed up to 0 °C. Another solution of **20** (2.2 g, 5.3 mmol) in THF (15 mL) was added into the reaction via cannula at 0 °C, and the reaction was warmed up to room temperature. After 24 h of stirring at room temperature, the reaction mixture was diluted with CH_2Cl_2 and the organic phase was washed with aqueous $NaHCO_3$ twice, then brine. The solvent (CH_2Cl_2) was evaporated in vacuum, and the residue was purified by chromatography on a silica gel column eluted with CH_2Cl_2/EtOAc (5/1, v/v) to give the title product (2.1 g, yield 84%). $R_f = 0.66$ (DCM/EtOAc, 5/1). ^{1}H NMR ($CDCl_3$) δ (ppm): 7.61 (dt, 2H, $J_1 = 8.7$ Hz, $J_2 = 1.8$ Hz, styryl benzene), 7.55 (dt, 2H, $J_1 = 8.7$ Hz, $J_2 = 1.8$ Hz, styryl benzene), 7.45 (dt, 2H, $J_1 = 8.7$ Hz, $J_2 = 2.1$ Hz, ethoxybenzene), 7.14 (d, 2H, $J = 16.2$ Hz, double bond trans linkage), 6.94 (d, 2H, $J = 16.2$ Hz, double bond trans linkage), 6.93 (dt, 2H, $J_1 = 8.7$ Hz, $J_2 = 2.1$ Hz, ethoxybenzene), 4.16 (t, 2H, $J = 4.8$ Hz, tetraethylene glycol chain), 3.88 (t, 2H, $J = 4.8$ Hz, tetraethylene glycol chain), 3.76 (bt, 2H, $J = 4.8$ Hz, tetraethylene glycol chain), 3.76−3.64 (m, 8H, tetraethylene glycol chain), 3.56 (bt, 2H, $J = 4.8$ Hz, tetraethylene glycol chain), 0.89 (s, 9H, -Si(CH$_3$)$_2$C(CH_3)$_3$), 0.06 (s, 6H, -Si(CH_3)$_2$C-(CH$_3$)$_3$). ^{13}C NMR ($CDC1_3$) δ (ppm): 159.5, 142.4, 132.7, 132.1, 129.4, 128.4, 126.8, 124.8, 119.4, 115.2, 110.3, 72.9, 71.2, 71.0, 70.99, 70.95, 70.0, 67.8, 63.0, 26.3, 18.7, −4.7.

*4-(2-(4-(2-(2-(2-(2-(tert-Butyldimethylsilanyloxy)ethoxy)ethoxy)-ethoxy)ethoxy)phenyl)vinyl)benzaldehyde (**23**).* A solution of **22** (710 mg, 1.47 mmol) in Et_2O (40 mL) was cooled to −78 °C. DIBALH (2.9 mL, in hexane 1 M, 2 equiv) was added to the reaction solution dropwise via syringe in two equal portions. The reaction was stirred for 7 h at −78 °C, then for 30 min at 0 °C. The reaction mixture was transferred via cannula into 10% AcOH aqueous solution (150 mL) with stirring. The obtained solution was stirred vigorously until the organic layer was separated from the aqueous layer. The organic layer was washed twice with aqueous $NaHCO_3$ (sat). Then, the solvents were evaporated in vacuum, and the residue was purified by chromatography on a silica gel column eluted with CH_2Cl_2/EtOAc (5/1, v/v) to give the title product (428 mg, yield 57%). $R_f = 0.50$ (CH_2Cl_2/EtOAc, 5/1). ^{1}H NMR ($CDCl_3$) δ (ppm): 9.98 (s, 1H, -C*H*O), 7.85 (bd, 2H, $J = 8.4$ Hz, benzaldehyde), 7.62 (bd, 2H, $J = 8.4$ Hz, benzaldehyde), 7.47 (dt, 2H, $J_1 = 8.7$ Hz, $J_2 = 1.8$ Hz, ethoxybenzene), 7.19 (d, 2H, $J = 16.2$ Hz, double bond trans linkage), 7.02 (d, 2H, $J = 16.2$ Hz, double bond trans linkage), 6.93 (dt, 2H, $J_1 = 8.7$ Hz, $J_2 = 1.8$ Hz, ethoxybenzene), 4.16 (t, 2H, $J = 4.8$ Hz, tetraethylene glycol chain), 3.88 (t, 2H, $J = 4.8$ Hz, tetraethylene glycol chain), 3.76 (bt, 2H, $J = 5.1$ Hz, tetraethylene glycol chain), 3.76−3.66 (m, 8H, tetraethylene glycol chain), 3.56 (bt, 2H, $J = 5.1$ Hz, tetraethylene glycol chain), 0.89 (s, 9H, -Si(CH$_3$)$_2$C(CH_3)$_3$), 0.06 (s, 6H, -Si(CH_3)$_2$C(CH$_3$)$_3$). ^{13}C NMR ($CDC1_3$) δ (ppm): 191.7, 159.3, 144.0, 135.1, 131.9, 130.4, 129.6, 128.3, 126.7, 125.3, 115.1, 72.9, 71.1, 71.0, 70.93, 70.88, 69.9, 67.7, 62.9, 26.2, 18.7, −4.9.

*4-(2-(4-(2-(2-(2-(2-Hydroxyethoxy)ethoxy)ethoxy)ethoxy)-phenyl)vinyl)benzaldehyde (**24**).* To a solution of **23** (100 mg, 0.19 mmol) in THF (10 mL) was added tetrabutylammonium fluoride (TBAF) (0.2 mL, 1.1 equiv, 1.0 M in THF) slowly at room temperature. After 5 min, another 0.1 mL TBAF was added. Then, several drops of 10% AcOH/THF was added to quench the reaction. The solvent was evaporated in vacuum, and the crude product was purified by flash chromatography on a silica gel column eluted with CH_2Cl_2/MeOH (20/1) to give the title product (78 mg, yield 100%). From ^{1}H NMR, the isomers (trans/cis double bond linkages) were observed. The isomerization was conducted: the isomers were dissolved in DMF (12 mL), and a catalytic amount of I_2 was added. The system was heated to 140 °C for 36 h to give the trans product (ee ≥ 95%). $R_f = 0.26$ (CH_2Cl_2/MeOH, 20/1). ^{1}H NMR ($CDCl_3$) δ (ppm): 9.93 (s, 1H, -C*H*O), 7.80 (bd, 2H, $J = 8.4$ Hz, benzaldehyde), 7.57 (bd, 2H, $J = 8.4$ Hz, benzaldehyde), 7.43 (bd, 2H, $J = 9.0$ Hz, ethoxybenzene), 7.15 (d, 2H, $J = 16.5$ Hz, double bond trans linkage), 6.96 (d, 2H, $J = 16.5$ Hz, double bond trans linkage), 6.90 (bd, 2H, $J = 9.0$ Hz, ethoxybenzene), 4.12 (t, 2H, $J = 4.8$ Hz, tetraethylene glycol chain), 3.84

(t, 2H, $J = 4.8$ Hz, tetraethylene glycol chain), 3.74−3.62 (m, 10H, tetraethylene glycol chain), 3.60−3.55 (m, 2H, tetraethylene glycol chain).

*4-(2-(4-(2-(2-(2-(2-(Bis(4-methoxyphenyl)phenylmethoxy)ethoxy)ethoxy)ethoxy)ethoxy)phenyl)vinyl)benzaldehyde (**25**).* A mixture of **24** (180 mg, 0.45 mmol), DMTrCl (0.5 g, 1.5 mmol, 3 equiv), and a catalytic amount of 4-(dimethylamino)pyridine (DMAP) in dry pyridine (5 mL) was stirred at room temperature under argon. After the stirring was continued overnight, the reaction solvent was removed in vacuum and the residue was directly subject to a silica gel column eluted with CH_2Cl_2/EtOAc/pyridine (100/10/1, v/v) to give the title product (210 mg, yield 66%). $R_f = 0.36$ (CH_2Cl_2/EtOAc 10/1, v/v). ^{1}H NMR ($CDCl_3$) δ (ppm): 9.98 (s, 1H, -C*H*O), 7.85 (bd, 2H, $J = 8.4$ Hz, benzaldehyde), 7.62 (bd, 2H, $J = 8.4$ Hz, benzaldehyde), 7.46 (m, 2H, benzene ring of DMTr group), 7.45 (bd, 2H, $J = 8.7$ Hz, ethoxybenzene), 7.34 (dt, 4H, $J_1 = 9.0$ Hz, $J_2 = 2.4$ Hz, methoxybenzene ring of DMTr group), 7.32−7.15 (m, 4H, benzene ring of DMTr group and double bond trans linkage), 7.00 (d, 1H, $J = 16.2$ Hz, double bond trans linkage), 6.91 (dt, 2H, $J_1 = 8.7$ Hz, $J_2 = 2.1$ Hz, ethoxybenzene), 6.81 (dt, 4H, $J_1 = 9.0$ Hz, $J_2 = 2.4$ Hz, methoxybenzene ring of DMTr group), 4.12 (bt, 2H, $J = 4.8$ Hz, tetraethylene glycol chain), 3.86 (bt, 2H, $J = 4.8$ Hz, tetraethylene glycol chain), 3.77 (s, 6H, -OC*H*$_3$), 3.74−3.65 (m, 10H, tetraethylene glycol chain), 3.22 (t, 2H, $J = 5.1$ Hz, tetraethylene glycol chain).

*4-(2-(4-(2-(2-(2-(2-(Bis(4-methoxyphenyl)phenylmethoxy)ethoxy)ethoxy)ethoxy)phenyl)vinyl)phenyl)vinyl)-1-(2-(2-(2-hydroxyethoxy)ethoxy)ethoxy)ethyl)pyridinium Chloride (**26**).* A mixture of **25** (200 mg, 0.28 mmol), 1-(2-(2-(2-(2-hydroxyethoxy)ethoxy)ethoxy)ethyl)-4-methylpyridinium chloride (90 mg, 0.29 mmol, 1 equiv), and a catalytic amount of piperidine in absolute EtOH (30 mL) was heated to 80 °C for 12 h. After the system was cooled to room temperature, the reaction solvent was removed in vacuum and the residue was directly subject to a silica gel column eluted with CH_2Cl_2/MeOH/pyridine/H_2O (400/60/5/5, v/v) to give the title product (85 mg, yield 30%). $R_f = 0.32$ (CH_2Cl_2/MeOH/pyridine/H_2O, 400/60/5/5, v/v). ^{1}H NMR ($CDCl_3$) δ (ppm): 9.27 (d, 2H, $J = 6.6$ Hz, pyridinium), 7.91 (d, 2H, $J = 6.6$ Hz, pyridinium), 7.64 (d, 1H, $J = 16.8$ Hz, double bond trans linkage), 7.60 (d, 2H, $J = 8.4$ Hz, styryl benzene), 7.53 (d, 2H, $J = 8.4$ Hz, styryl benzene), 7.47−7.42 (m, 2H, benzene ring of DMTr group), 7.45 (bd, 2H, $J = 8.7$ Hz, ethoxybenzene), 7.34 (dt, 4H, $J_1 = 9.0$ Hz, $J_2 = 2.1$ Hz, methoxybenzene ring of DMTr group), 7.28−7.15 (m, 3H, benzene ring of DMTr group), 7.16 (d, 1H, $J = 16.5$ Hz, double bond trans linkage), 7.12 (d, 1H, $J = 16.8$ Hz, double bond trans linkage), 6.97 (d, 1H, $J = 16.5$ Hz, double bond trans linkage), 6.89 (bd, 2H, $J = 8.7$ Hz, ethoxybenzene), 6.81 (dt, 4H, $J_1 = 9.0$ Hz, $J_2 = 2.1$ Hz, methoxybenzene ring of DMTr group), 5.07 (bt, 2H, tetraethylene glycol chain), 4.12 (bt, 4H, $J = 4.8$ Hz, tetraethylene glycol chain), 3.85 (bt, 2H, $J = 4.8$ Hz, tetraethylene glycol chain), 3.77 (s, 6H, -OC*H*$_3$), 3.74−3.55 (m, 22H, tetraethylene glycol chain), 3.22 (t, 2H, $J = 5.1$ Hz, tetraethylene glycol chain).

*Detritylation of **26** (**34**).* To a solution of **26** (20 mg, 0.02 mmol) in $CHCL_3$ (5 mL) was added Cl_2HCOOH (1 drop with a 9 in Pasteur pipet). After the completion of the reaction, the solvent was removed in vacuum and the residue was directly subjected to a silica gel column eluted with CH_2Cl_2/MeOH/pyridine/H_2O (400/60/5/5, v/v) to give the detritylated product **34** in quantitative yield. $R_f = 0.23$ (CH_2Cl_2/MeOH/pyridine/H_2O, 400/60/5/5, v/v). ^{1}H NMR ($CDCl_3$) δ (ppm): 9.11 (bs, 2H, pyridinium), 7.92 (bs, 2H, pyridinium), 7.60 (d, 1H, $J = 16.5$ Hz, double bond trans linkage), 7.55 (d, 2H, $J = 8.4$ Hz, styryl benzene), 7.47 (d, 2H, $J = 8.4$ Hz, styryl benzene), 7.42 (d, 2H, $J = 8.7$ Hz, ethoxybenzene), 7.10 (d, 1H, $J = 16.2$ Hz, double bond trans linkage), 7.06 (d, 1H, $J = 16.5$ Hz, double bond trans linkage), 6.91 (d, 1H, $J = 16.2$ Hz, double bond trans linkage), 6.89 (d, 2H, $J = 8.7$ Hz, ethoxybenzene), 4.91 (bs, 2H, tetraethylene glycol chain), 4.15 (bt, 2H, $J = 4.8$ Hz, tetraethylene glycol chain), 4.02 (bs, 2H, tetraethylene glycol chain), 3.86 (bt, 2H, $J = 4.8$ Hz, tetraethylene glycol chain), 3.78−3.55 (m, 24H, tetraethylene glycol chain).

*1-(2-(2-(2-(2-Hydroxyethoxy)ethoxy)ethoxy)ethyl)-4-methylpyridinium Tetraphenylborate (**27**).* A mixture of picoline (1 g, 11 mmol) and 2-(2-(2-(2-chloroethoxy)ethoxy)ethoxy)ethanol (1.5 g, 7.1 mmol) was heated to 140 °C for 4−6 h under argon. After the system was cooled to room temperature, the excess picoline was removed in vacuum. The obtained brown oil was dissolved in acetonitrile, and tetraphenylboron sodium (2.5 g, 7.3 mmol) was added into the solution. The mixture was refluxed for 20 min and concentrated to a residue, which was directly subjected to a silica gel column eluted with CH_2Cl_2/MeOH (10/1, v/v) to give the title product (4.2 g) in a quantitative yield. $R_f = 0.42$ (CH_2Cl_2/MeOH, 10/1, v/v). ^{1}H NMR ($CDCl_3$) δ (ppm): 7.52−7.44 (m, 8H, benzene ring of BPh_4), 6.96 (t, 8H, $J = 7.2$ Hz, benzene ring of BPh_4), 6.80 (bt, 4H, $J = 7.2$ Hz, benzene ring of BPh_4), 6.63 (d, 2H, $J = 7.5$ Hz, pyridinium), 6.60 (d, 2H, $J = 7.5$ Hz, pyridinium), 3.67−3.34 (m, 12H, tetraethylene glycol chain), 3.22−3.16 (m, 4H, tetraethylene glycol chain), 2.49 (t, 1H, $J = 6.0$ Hz, -O*H*), 2.21 (s, 3H, -C*H*$_3$). ^{13}C NMR ($CDC1_3$) δ (ppm): 165.2, 164.5, 163.9, 163.2, 158.2, 143.2, 136.2, 128.0, 126.2, 126.1, 122.3, 72.6, 70.7, 70.5, 70.3, 70.27, 68.8, 61.8, 59.9, 22.2.

*1-(2-(2-(2-(2-(Bis(4-methoxyphenyl)phenylmethoxy)ethoxy)ethoxy)ethoxy)ethyl)-4-methylpyridinium Tetraphenylborate (**28**).* A mixture of **27** (510 mg, 0.87 mmol), DMTrCl (600 mg, 1.77 mmol, 2 equiv), and a catalytic amount of 4-(dimethylamino)-pyridine (DMAP) in dry pyridine (10 mL) was stirred at room temperature under argon. After 12 h, the reaction solvent was removed in vacuum, and the residue was directly subjected to a silica gel column eluted with CH_2Cl_2/MeOH/pyridine (750/25/7, v/v) to give the title product (450 mg, yield 58%). $R_f = 0.33$ (CH_2Cl_2/MeOH/pyridine 750/25/7, v/v). ^{1}H NMR ($CDCl_3$) δ (ppm): 7.52−7.44 (m, 10H, benzene ring of BPh_4 and DMTr groups), 7.32 (bd, 4H, $J = 9$ Hz, methoxybenzene ring), 7.34−7.15 (m, 3H, benzene ring of DMTr group), 6.96 (t, 8H, $J = 7.2$ Hz, benzene ring of BPh_4), 6.80 (bt, 4H, $J = 7.2$ Hz, benzene ring of BPh_4), 6.79 (bd, 4H, $J = 9$ Hz, methoxybenzene ring), 6.67 (bd, 2H, $J = 6.9$ Hz, pyridinium), 6.63 (bd, 2H, $J = 6.9$ Hz, pyridinium), 3.75 (s, 3H, -OC*H*$_3$), 3.67−3.60 (m, 4H, tetraethylene glycol chain), 3.58−3.52 (m, 2H, tetraethylene glycol chain), 3.52−3.44 (m, 2H, tetraethylene glycol chain), 3.44−3.36 (m, 2H, tetraethylene glycol chain), 3.24−3.14 (m, 6H, tetraethylene glycol chain), 2.17 (s, 3H, -C*H*$_3$). ^{13}C NMR ($CDC1_3$) δ (ppm): 165.2, 164.6, 163.9, 163.3, 158.6, 158.1, 145.2, 143.2, 136.3, 136.2, 130.3, 128.4, 128.00, 127.97, 127.3, 127.0, 126.2, 126.1, 122.3, 113.3, 86.2, 71.0, 70.9, 70.88, 70.7, 70.5, 68.8, 63.4, 59.9, 55.6, 22.1.

*1-(2-(2-(2-(2-(Bis(4-methoxyphenyl)phenylmethoxy)ethoxy)ethoxy)ethoxy)ethyl)-4-(2-(4-(2-4-(2-(2-(2-(2-hydroxyethoxy)ethoxy)ethoxy)phenyl)vinyl)phenyl)vinyl)pyridinium Tetraphenylborate (**29**).* A mixture of **28** (230 mg, 0.26 mmol), **24** (105 mg, 0.26 mmol, 1 equiv), and a catalytic amount (6 drops, 9 in Pasteur pipet) of piperidine in absolute EtOH (30 mL) was heated to 100 °C for 12 h. After the reaction was cooled to room temperature, the reaction solvent was removed in vacuum and the residue was directly subject to a silica gel column eluted with CH_2Cl_2/MeOH/pyridine/H_2O (800/60/4/3, v/v) to give the title product (73 mg, yield 22%). $R_f = 0.37$ (CH_2Cl_2/MeOH/pyridine/H_2O, 400/60/5/5, v/v). ^{1}H NMR ($CDCl_3$) δ (ppm): 7.56−7.43 (m, 16H, benzene ring of BPh_4 (8H), benzene ring of DMTr group (2H), styryl benzene (6H)), 7.36−

7.18 (m, 4H, benzene ring of DMTr group (3H) and double bond trans linkage (1H)), 7.32 (bd, 4H, J = 9 Hz, methoxybenzene ring), 7.17 (d, 1H, J = 15.9 Hz, double bond trans linkage), 7.06 (d, 2H, J = 8.7 Hz, pyridinium), 7.02 (t, 8H, J = 7.5 Hz, benzene ring of BPh_4), 6.98 (d, 1H, J = 15.9 Hz, double bond trans linkage), 6.94 (d, 2H, J = 8.7 Hz, pyridinium), 6.85 (bt, 4H, J = 7.5 Hz, benzene ring of BPh_4), 6.78 (bd, 4H, J = 9 Hz, methoxybenzene ring), 6.74 (d, 1H, J = 16.2 Hz, double bond trans linkage), 4.18 (bt, 2H, J = 4.8 Hz, tetraethylene glycol chain), 3.88 (t, 2H, J = 4.8 Hz, tetraethylene glycol chain), 3.73 (s, 6H, -OCH_3), 3.78−3.58 (m, 18H, tetraethylene glycol chain), 3.58−3.52 (m, 2H, tetraethylene glycol chain), 3.52−3.47 (m, 2H, tetraethylene glycol chain), 3.46−3.36 (m, 4H, tetraethylene glycol chain), 3.23 (bt, 2H, J = 4.8 Hz, tetraethylene glycol chain). ^{13}C NMR ($CDC1_3$) δ (ppm): 158.2, 152.5, 149.5, 144.8, 143.7, 141.1, 135.9, 134.5, 132.8, 130.3, 129.9, 129.5, 128.6, 128.0, 127.9, 127.6, 126.9, 126.7, 125.8, 125.7, 125.2, 123.6, 122.8, 121.9, 114.8, 112.9, 85.8, 72.4, 70.7, 70.6, 70.5, 70.3, 70.2, 69.6, 68.8, 67.4, 63.0, 61.7, 55.1.

*2-(2-(2-(2-(4-(E-2-(4-(E-2-Pyridin-4-yl-vinyl)phenyl)vinyl)-phenoxy)ethoxy)ethoxy)ethoxy)ethanol (**30**).* A mixture of **24** (180 mg, 0.45 mmol), 4-picoline (1 mL, 10.3 mmol, 23 equiv), acetic anhydride (1.3 mL), and acetic acid (0.6 mL) was heated to 100 °C for 12 h. A complex was then obtained after chromatography. The improved procedure is as follows: A mixture of **24** (60 mg, 0.15 mmol), 4-picoline (1.8 mL, 18 mmol), and 37% HCl (0.72 mL, 8.8 mmol) gave a yellow solution. The reaction mixture was heated to 100 °C for 48 h and cooled to room temperature. The reaction was diluted with $CHCl_3$, washed with aqueous $NaHCO_3$, and extracted with $CHCl_3$. The organic layer was collected, dried over Na_2SO_4, and concentrated, and the residue was subjected to a silica gel column eluted with CH_2Cl_2/MeOH (20/1, v/v) to give the title product (18 mg, yield 25%). R_f = 0.28 (CH_2Cl_2/MeOH, 20/1, v/v). ^{1}H NMR ($CDCl_3$) δ (ppm): 8.57 (d, 2H, J = 6.0 Hz, pyridinium), 7.51 (bs, 4H, styryl benzene), 7.44 (dt, 2H, J_1 = 8.7 Hz, J_2 = 1.8 Hz, ethoxybenzene), 7.37 (bd, 2H, J = 6.0 Hz, pyridinium), 7.28 (d, 1H, J = 16.2 Hz, double bond trans linkage), 7.10 (d, 1H, J = 16.5 Hz, double bond trans linkage), 7.02 (d, 1H, J = 16.5 Hz, double bond trans linkage), 6.98 (d, 1H, J = 16.2 Hz, double bond trans linkage), 6.92 (dt, 2H, J_1 = 8.7 Hz, J_2 = 1.8 Hz, ethoxybenzene), 4.16 (bt, 2H, J = 4.8 Hz, tetraethylene glycol chain), 3.87 (t, 2H, J = 4.8 Hz, tetraethylene glycol chain), 3.77−3.64 (m, 10H, tetraethylene glycol chain), 3.61 (bt, 2H, J = 5.1 Hz, tetraethylene glycol chain). ^{13}C NMR ($CDC1_3$) δ (ppm): 158.8, 150.2, 145.0, 138.4, 135.1, 133.1, 130.3, 129.1, 128.0, 127.6, 126.9, 126.1, 125.6, 121.0, 115.1, 72.8, 71.1, 71.0, 70.9, 70.6, 70.0, 67.7, 62.1.

*2-(2-(2-(2-(Bis(4-methoxyphenyl)phenylmethoxy)ethoxy)ethoxy)-ethoxy)ethylene Chloride (**32**).* A mixture of 2-(2-(2-(2-chloroethoxy)ethoxy)ethoxy)ethanol (1.5 g, 4.7 mmol), DMTrCl (3.18 g, 9.4 mmol, 2 equiv), and a catalytic amount of 4-(dimethylamino)pyridine (DMAP) in dry Pyridine (40 mL) was stirred at room temperature under argon. After 12 h, the reaction solvent was removed in vacuum. The reaction mixture was diluted with CH_2Cl_2 and washed with aqueous $NaHCO_3$ and brine. The organic layer was collected, dried over Na_2SO_4, and concentrated, and the residue was subject to a silica gel column eluted with cyclohexane/EtOAC (3/1 w/ 1% pyridine, v/v) to give the title product in a quantitative yield. R_f = 0.35 (cyclohexane/EtOAc 3/1, v/v). ^{1}H NMR ($CDCl_3$) δ (ppm): 7.44 (bd, 2H, J = 7.2 Hz, benzene ring of DMTr group), 7.36 (dt, 4H, J_1 = 9.0 Hz, J_2 = 2.1 Hz, methoxybenzene ring of DMTr group), 7.28 (bt, 2H, J = 7.2 Hz, benzene ring of DMTr group), 7.20 (tt, 1H, J_1 = 7.2 Hz, J_2 = 2.1 Hz, benzene ring of DMTr group), 6.83 (dt, 4H, J_1 = 9.0 Hz, J_2 = 2.4 Hz, methoxybenzene ring of DMTr group), 3.78 (s, 6H, -OCH_3), 3.74 (bt, 2H, J = 5.1 Hz, tetraethylene glycol chain), 3.71−3.66 (m, 10H, tetraethylene glycol chain), 3.60 (bt, 2H, J = 5.7 Hz, tetraethylene glycol chain), 3.24 (t, 2H, J = 5.1 Hz, tetraethylene glycol chain). ^{13}C NMR ($CDC1_3$) δ (ppm): 158.5, 145.3, 136.5, 130.3, 128.4, 128.0, 126.9, 113.3, 86.2, 71.6, 71.1, 71.0, 70.99, 63.4, 55.5, 43.1, 27.3.

*2-(2-(2-(2-(Bis(4-methoxyphenyl)phenylmethoxy)ethoxy)ethoxy)-ethoxy)ethylene Iodide (**33**).* A mixture of **32** (506 mg, 0.98 mmol), KI (1.4 g, 8.4 mmol, 8.6 equiv), and NaI (1.2 g, 8 mmol, 8 equiv) in dry acetone (25 mL) was stirred at room temperature. During the reaction, another two batches of NaI (3 g) were added. After 72 h, the reaction solvent was removed in vacuum. The reaction mixture was diluted with CH_2Cl_2 and washed with aqueous $NaHCO_3$ and brine. The organic layer was collected, dried over Na_2SO_4, and concentrated, and the residue was subjected to a silica gel column eluted with cyclohexane/EtOAc (3/1 w/ 1% Pyridine, v/v) to give the title product in a 90% yield. R_f 0.38 (Cyclohexane/EtOAc, 3/1, v/v). ^{1}H NMR ($CDCl_3$) δ (ppm): 7.46 (bd, 2H, J = 7.2 Hz, benzene ring of DMTr group), 7.35 (dt, 4H, J_1 = 9.0 Hz, J_2 = 2.4 Hz, methoxybenzene ring of DMTr group), 7.28 (bt, 2H, J = 7.2 Hz, benzene ring of DMTr group), 7.20 (tt, 1H, J_1 = 7.2 Hz, J_2 = 2.4 Hz, benzene ring of DMTr group), 6.82 (dt, 4H, J_1 = 9.0 Hz, J_2 = 2.4 Hz, methoxybenzene ring of DMTr group), 3.78 (s, 6H, -OCH_3), 3.74 (bt, 2H, J = 6.9 Hz, tetraethylene glycol chain), 3.71−3.66 (m, 10H, tetraethylene glycol chain), 3.23 (bt, 2H, J = 6.9 Hz, tetraethylene glycol chain). ^{13}C NMR ($CDC1_3$) δ (ppm): 158.5, 145.3, 136.5, 130.3, 128.4, 128.0, 126.9, 113.3, 86.2, 71.6, 71.1, 71.0, 70.99, 63.4, 55.5, 43.1, 27.3.

*1-(2-(2-(2-(2-(Bis(4-methoxyphenyl)phenylmethoxy)ethoxy)-ethoxy)ethoxy)ethyl)-4-(2-(4-(2-(4-(2-(2-(2-hydroxyethoxy)-ethoxy)ethoxy)ethoxy)phenyl)vinyl)phenyl)vinyl)pyridinium Iodide (**31**).* A mixture of **30** (18 mg, 0.038 mmol) and **33** (60 mg, 0.1 mmol, 2.6 equiv) in anhydrous CH_2Cl_2 (10 mL) was heated to 60 °C for 24 h. After the system was cooled to room temperature, the reaction solvent was removed in vacuum and the residue was directly subject to a silica gel column eluted with CH_2Cl_2/MeOH/pyridine/H_2O (400/60/5/5, v/v) to give the title product (20 mg, yield 49%). R_f = 0.5 (CH_2Cl_2/MeOH/pyridine/H_2O, 400/60/5/5, v/v). ^{1}H NMR ($CDCl_3$) δ (ppm): 9.07 (bs, 2H, pyridinium), 7.89 (bs, 2H, pyridinium), 7.52 (s, 4H, styryl benzene), 7.51 (d, 1H, J = 16.2 Hz, double bond trans linkage), 7.46 (d, 2H, J = 9.0 Hz, ethoxybenzene), 7.48−7.42 (m, 2H, benzene ring of DMTr group), 7.33 (dt, 4H, J_1 = 9.0 Hz, J_2 = 2.1 Hz, methoxybenzene ring of DMTr group), 7.28−7.15 (m, 3H, benzene ring of DMTr group), 7.16 (d, 1H, J = 15.3 Hz, double bond trans linkage), 6.98 (d, 1H, J = 16.2 Hz, double bond trans linkage), 6.97 (d, 1H, J = 15.3 Hz, double bond trans linkage), 6.93 (bd, 2H, J = 9.0 Hz, ethoxybenzene), 6.78 (dt, 4H, J_1 = 9.0 Hz, J_2 = 2.1 Hz, methoxybenzene ring of DMTr group), 4.17 (bt, 2H, J = 4.8H, tetraethylene glycol chain), 4.05 (bs, 2H, tetraethylene glycol chain), 3.88 (bt, 4H, J = 4.8 Hz, tetraethylene glycol chain), 3.75 (s, 6H, -OCH_3), 3.76−3.55 (m, 22H, tetraethylene glycol chain), 3.24 (bt, 2H, J = 4.8 Hz, tetraethylene glycol chain).

Compounds in Preparation of *E,E*-1,4-Bis-4,4′-(2-(2-(2-(2-hydroxyethoxy)ethoxy)ethoxy)ethoxy)styryl Benzene Derivatives. *E,E-1,4-Bis-4,4′-(2-(2-(2-tritylethoxy)ethoxy)ethoxy)-styryl Benzene (**15** trans).* To a solution of 1,4-phenylenebis-(methylene)bis(chlorotriphenyl) phosphorane (500 mg, 0.715 mmol) in THF (5 mL) was added *n*-BuLi (0.89 mL, 1.4 mmol, 1.6 M in hexanes) at 0 °C under argon. The mixture was stirred at room temperature for 0.5 h and cooled to −78 °C. A solution of **8** (770 mg, 1.55 mmol) in THF (4 mL) was precooled and added dropwise to the cooled mixture via syringe. After 0.5 h, the reaction mixture was warmed up to room temperature and

stirred for another 1 h. The reaction solvents were removed in vacuum, and the reaction mixture was diluted with $CHCl_3$. The organic phase was washed with brine, dried over Na_2SO_4, and concentrated. Then, the title product was precipitated with ethanol or methanol as a yellow solid. Isomerization: the solid was dissolved in DMF with a catalytic amount of I_2 and the mixture was refluxed overnight. After evaporation of the solvent, the residue was purified by chromatography on a silica gel column eluted with cyclohexane/EtOAc (2/1, v/v) to give the double bond trans linked product in a yield of 17%. $R_f = 0.38$ (cyclohexane/EtOAc, 2/1). ^{1}H NMR ($CDCl_3$) δ (ppm): 7.51−7.46 (m, 16H, benzene ring of styryl benzene and trityl group), 7.44 (d, 4H, $J = 8.7$ Hz, ethoxybenzene), 7.30 (bt, 12H, $J = 6.9$ Hz, benzene ring of trityl group), 7.23 (bt, 6H, $J = 7.2$ Hz, benzene ring of trityl group), 7.07 (d, 2H, $J = 16.2$ Hz, double bond trans linkage), 6.97 (d, 2H, $J = 16.2$ Hz, double bond trans linkage), 6.91 (d, 4H, $J = 8.7$ Hz, ethoxybenzene), 4.16 (bt, 4H, $J = 4.8$ Hz, tetraethylene glycol chain), 3.91 (t, 4H, $J = 4.8$ Hz, tetraethylene glycol chain), 3.80−3.68 (m, 20H, tetraethylene glycol chain), 3.26 (bt, 2H, $J = 5.1$ Hz, tetraethylene glycol chain).

*For the Double Bond Cis Linked Product: Z, Z-1,4-Bis-4,4′-(2-(2-(2-tritylethoxy)ethoxy)ethoxy)styryl Benzene (**15** cis).* ^{1}H NMR ($CDCl_3$) δ (ppm): 7.48−7.44 (m, 12H, benzene ring of trityl group), 7.26 (bt, 12H, $J = 6.9$ Hz, benzene ring of trityl group), 7.19 (bt, 3H, $J = 6.9$ Hz, benzene ring of trityl group), 7.15 (bd, 4H, $J = 9.0$ Hz, ethoxybenzene), 7.12 (bs, 4H, styryl benzene), 6.74 (bd, 4H, $J = 9.0$ Hz, ethoxybenzene), 6.48 (d, 2H, $J = 12.3$ Hz, double bond cis linkage), 6.42 (d, 2H, $J = 12.3$ Hz, double bond cis linkage), 4.07 (bt, 4H, $J = 4.8$ Hz, tetraethylene glycol chain), 3.85 (bt, 4H, $J = 4.8$ Hz, tetraethylene glycol chain), 3.76−3.64 (m, 20H, tetraethylene glycol chain), 3.23 (bt, 2H, $J = 5.1$ Hz, tetraethylene glycol chain).

*E,E-1,4-Bis-4,4′-(2-(2-(2-(2-(Bis(4-methoxyphenyl)phenylethoxy)ethoxy)ethoxy) ethoxy)ethoxy)styryl Benzene (**17**).* To a solution of bis-ylide precursor, 1,4-phenylenebis(methylene)bis(chlorotriphenyl) phosphorane (550 mg, 0.79 mmol) in THF (5 mL) was added *n*-BuLi (1 mL, 1.6 mmol, 1.6 M in hexanes) dropwise at 0 °C under argon. The mixture was stirred at room temperature for 0.5 h and cooled to −78 °C. A solution of **11** (1 g, 1.6 mmol) in THF (5 mL) was precooled and added dropwise to the cooled mixture via syringe. After 0.5 h, the reaction mixture was warmed up to room temperature and stirred for another 4 h. The reaction solvents were removed in vacuum and the reaction mixture was diluted with $CHCl_3$. The organic phase was washed with brine, dried over Na_2SO_4, and concentrated. Then, the residue was dissolved with $CHCl_3$ and precipitated with ethanol. A yellow solid was collected as the title product with pure double bond trans linkages (150 mg, yield 15%). $R_f = 0.5$ (cyclohexane/EtOAc 1/2). Isomerization: the impure part (trans−cis double bond linkages) was deprotected (DMTr-group off) via Cl_2HCOOH in CH_2Cl_2. The obtained solid was dissolved in DMF with a catalytic amount of I_2, and the mixture was refluxed for 4 days. After evaporation of the solvent, the residue was purified by chromatography on a silica gel column eluted with CH_2Cl_2/MeOH (400/30, v/v) to give the double bond trans linked product (190 mg) in a yield of 35%. $R_f = 0.31$ (CH_2Cl_2/MeOH, 20/1.5). For **17**: ^{1}H NMR ($CDCl_3$) δ (ppm): 7.49−7.43 (m, 8H, benzene ring of DMTr group and styryl benzene), 7.42 (d, 4H, $J = 8.7$ Hz, ethoxybenzene), 7.34 (bd, 8H, $J = 9.0$ Hz, methoxybenzene ring of DMTr group), 7.31−7.23 (m, 4H, benzene ring of DMTr group), 7.19 (bt, 2H, $J = 7.2$ Hz, benzene ring of DMTr group), 7.05 (d, 2H, $J = 16.2$ Hz, double bond trans linkage), 6.96 (d, 2H, $J = 16.2$ Hz, double bond trans linkage), 6.89 (d, 4H, $J = 8.7$ Hz, ethoxybenzene), 6.81 (bd, 4H, $J = 9.0$ Hz, methoxybenzene ring of DMTr group), 4.12 (bt, 4H, $J = 4.8$ Hz, tetraethylene glycol chain), 3.85 (bt, 4H, $J = 4.8$ Hz, tetraethylene glycol chain), 3.77 (s, 12H, -OCH_3), 3.75−3.64 (m, 20H, tetraethylene glycol chain), 3.22 (t, 4H, $J = 5.1$ Hz, tetraethylene glycol chain). ^{13}C NMR ($CDC1_3$) δ (ppm): 158.7, 158.6, 145.3, 136.8, 136.5, 130.5, 130.3, 128.4, 128.1, 128.0, 127.9, 126.9, 126.8, 126.5, 115.1, 113.3, 86.2, 71.2, 71.1, 71.06, 70.0, 67.7, 63.5, 55.5.

*E,E-1,4-Bis-4,4′-((2-(2-(2-(2-(Bis(4-methoxyphenyl)phenylmethoxy)ethoxy)ethoxy)ethoxy)ethyl)butylamino)styryl Benzene (**18**).* To a solution of bis-ylide precursor, 1,4-phenylenebis(methylene)bis(chlorotriphenyl) phosphorane (430 mg, 0.62 mmol), in THF (5 mL) was added *n*-BuLi (0.76 mL, 1.2 mmol, 1.6 M in hexanes) dropwise at 0 °C under argon. The mixture was stirred at room temperature for 0.5 h and cooled to −78 °C. A solution of **14** (800 mg, 1.2 mmol) in THF (7 mL) was precooled and added dropwise to the cooled mixture via syringe. After 0.5 h, the reaction mixture was warmed up to room temperature and stirred for another 12 h. The reaction solvents were removed in vacuum and the reaction mixture was diluted with $CHCl_3$. The organic phase was washed with brine, dried over Na_2SO_4, and concentrated, and the residue was purified by chromatography on a silica gel column eluted with cyclohexane/EtOAc/pyridine (300/200/5, v/v) to give the double bond trans linked product (220 mg, yield 26%). $R_f = 0.32$ (cyclohexane/EtOAc, 3/2). Isomerization: the impure part (trans−cis double bond linkages) was detritylated (DMTr-group off) via Cl_2HCOOH in CH_2Cl_2 within 3 h. The deprotection reaction then was diluted with $CHCl_3$, washed with $NaHCO_3$ aqueous solution/brine, and concentrated. The obtained solid was dissolved in DMF with a catalytic amount of I_2 and the mixture was refluxed for 12 h. After evaporation of the solvent, the residue was purified by chromatography on a silica gel column eluted with CH_2Cl_2/MeOH (400/20, v/v) to give the double bond trans linked product **2** (27 mg) in a yield of 5.6%. $R_f = 0.31$ (CH_2Cl_2/MeOH, 20/1). For **18**: ^{1}H NMR ($CDCl_3$) δ (ppm): 7.56−7.50 (m, 4H, benzene ring of DMTr group), 7.48−7.38 (m, 8H, styryl benzene and ethoxybenzene), 7.42 (bd, 8H, $J = 9.0$ Hz, methoxybenzene ring of DMTr group), 7.36−7.20 (m, 6H, benzene ring of DMTr group), 7.06 (d, 2H, $J = 16.2$ Hz, double bond trans linkage), 6.92 (d, 2H, $J = 16.2$ Hz, double bond trans linkage), 6.86 (bd, 4H, $J = 9.0$ Hz, methoxybenzene ring of DMTr group), 6.70 (d, 4H, $J = 8.7$ Hz, methoxybenzene), 3.78 (s, 12H, -OCH_3), 3.76−3.64 (m, 24H, tetraethylene glycol chain), 3.61−3.54 (bt, 4H, $J = 5.4$ Hz, tetraethylene glycol chain), 3.40−3.31 (m, 4H, -NCH_2CH_2CH_2CH_3), 3.29 (bt, 4H, $J = 5.1$ Hz, tetraethylene glycol chain), 1.68−1.56 (m, 4H, -NCH$_2$CH_2CH$_2$CH$_3$), 1.46−1.31 (m, 4H, -NCH$_2$CH$_2$CH_2CH$_3$), 0.997 (t, 6H, $J = 7.2$ Hz, -NCH$_2$CH$_2$CH$_2$CH_3). ^{13}C NMR ($CDC1_3$) δ (ppm): 158.6, 147.7, 145.4, 136.9, 136.6, 130.3, 128.5, 128.4, 128.0, 126.9, 126.5, 125.3, 124.0, 113.3, 112.0, 86.2, 71.1, 71.09, 68.9, 63.5, 55.5, 51.6, 50.9, 29.7, 21.0, 14.5.

HWE reagent tetraethyl 1,4-xylylenediphosphonate was obtained according to literature (*32, 33*).

*E,E-1,4-Bis-4,4′-(2-(2-(2-(2-hydroxyethoxy)ethoxy)ethoxy)-ethoxy)styryl Benzene (**5**).* A mixture of tetraethyl 1,4-xylylenediphosphonate (1.05 g, 2.78 mmol) and 3 equiv of 4-[2-[2-[2-(2-hydroxyethoxy)ethoxy]ethoxy]ethoxy]benzaldehyde (**10**) (2.45 g, 8.22 mmol) was dried in vacuum overnight and dissolved in anhydrous DMF (25 mL) under argon. To the stirred solution of bisphosphonate and aldehyde at 0 °C was added dropwise a solution of potassium *tert*-butoxide (KOtBu) (922 mg, 3 equal) in anhydrous DMF (15 mL) over 15 min by syringe. After stirring for 0.5 h at 0 °C, the reaction mixture was slowly warmed up to room temperature and stirred for another 12 h, then the reaction was quenched with water. The crude product was collected by suction filtration and the filtrate was evaporated to dryness. The residue was resolved with $CHCl_3$ and washed

with water (2 × 100 mL). The organic layer was dried over Na_2SO_4 and concentrated to dryness. The crude product was then purified by being washed with tetrahydrofuran (THF) twice to give 1.69 g (91%) of the title compound (**5**). ^{1}H NMR ($CDCl_3$) δ (ppm): 7.47 (s, 4H, aromatic ring), 7.45 (d, 4H, J = 8.7 Hz, aromatic ring), 7.06 (d, 2H, J = 16.2 Hz, double bond trans linkage), 6.97 (d, 2H, J = 16.2 Hz, double bond trans linkage), 6.92 (d, 4H, J = 8.7 Hz, aromatic ring), 4.16 (bt, 4H, J = 4.8 Hz, tetraethylene glycol chain), 3.87 (bt, 4H, J = 4.8 Hz, tetraethylene glycol chain), 3.78−3.58 (m, 24H, tetraethylene glycol chain). ^{13}C NMR ($CDC1_3$/CD_3OD, 0.3 mL/0.2 mL) δ (ppm): 158.2, 136.5, 130.3, 127.6, 127.5, 126.4, 126.2, 114.6, 72.5, 70.55, 70.50, 70.38, 70.02, 69.63, 67.3, 61.2. MS (MALDI-TOF): m/z 666.8 $[M]^+$, 667.8 $[M + 1]^+$, 689.7 $[M + Na]^+$.

*Monotritylation of E,E-1,4-Bis-4,4′-(2-(2-(2-(2-hydroxyethoxy)-ethoxy)ethoxy)ethoxy)styryl Benzene (**40**).* *E,E*-1,4-Bis-4,4′-(2-(2-(2-(2-hydroxyethoxy)ethoxy)ethoxy)styryl benzene (**5**) (375 mg, 0.56 mmol) was dissolved in dry pyridine (50 mL), followed by addition of DMTrCl (415 mg, 1.23 mmol) and DMAP (∼10 mg). The mixture was stirred at room temperature under argon overnight, and TLC monitoring (10/0.75, CH_2Cl_2/MeOH) showed the formation of monosubstituted (R_f 0.32) and disubstituted (R_f 0.74) products, as well as the starting material (R_f 0.14). The reaction mixture was concentrated in vacuum, and the residue was subject to a silica gel column with CH_2Cl_2/MeOH/pyridine (100/5/0.5) as eluents affording the title product (160 mg, yield 30%) as a yellow powder. Meanwhile, the disubstituted fraction was also collected, and further monodetritylation was carried out as follows: A detritylation solution was made by mixing $ZnCl_2$ (1.5 g) into 110 mL of CH_2Cl_2/MeOH (10/1, v/v). Then, the disubstituted compound (150 mg, 0.12 mmol) was dissolved by 50 mL of the detritylation solution, and the reaction mixture was monitored by TLC (20/1, CH_2Cl_2/MeOH). As soon as the spot corresponding to starting material (*E,E*-1,4-bis-4,4′-(2-(2-(2-(2-hydroxyethoxy)-ethoxy)ethoxy)ethoxy)styryl benzene) appeared on the TLC plate, the reaction was quenched by pouring into a saturated aq $NaHCO_3$ solution. The mixture was extracted by $CHCl_3$, and the organic layer was washed with brine, collected, dried over Na_2SO_4, concentrated, and subjected to a silica gel column (100/5/0.5, CH_2Cl_2/MeOH/pyridine) to give the title product **40** (48 mg, yield 42%). On the basis of the starting material, the total yield of the monosubstituted product is 38%. The product is stored with a stabilizer (diisopropylethylamine) under argon at −80 °C. ^{1}H NMR ($CDCl_3$) δ (ppm): 7.46 (s, 4H, aromatic ring of styryl benzene), 7.49−7.38 (m, 6H, aromatic rings of styryl benzene and DMTr), 7.34 (dt, 4H, J_1 = 8.7 Hz, J_2 = 2.3 Hz, methoxylbenzene ring), 7.31−7.15 (m, 3H, benzene ring of DMTr), 7.06 (d, 1H, J = 16.2 Hz, double bond trans linkage), 7.05 (d, 1H, J = 16.2 Hz, double bond trans linkage), 6.96 (d, 1H, J = 16.2 Hz, double bond trans linkage), 6.95 (d, 1H, J = 16.2 Hz, double bond trans linkage), 6.94−6.84 (m, 4 H, aromatic ring of styryl benzene), 6.81 (dt, 4H, J_1 = 8.7 Hz, J_2 = 2.3 Hz, methoxylbenzene ring), 4.19−4.08 (m, 4H, tetraethylene glycol chain), 3.89−3.82 (m, 4H, tetraethylene glycol chain), 3.80−3.58 (m, 28H, C*H*$_3$O and tetraethylene glycol chain), 3.22 (t, 2H, J = 5.1 Hz, DMTrOC*H2*). ^{13}C NMR ($CDC1_3$) δ (ppm): 158.57, 158.55, 158.43, 145.2, 136.74, 136.70, 136.4, 130.47, 130.40, 130.2, 128.3, 128.00, 127.96, 127.87, 127.79, 126.77, 126.67, 126.44, 126.38, 115.0, 113.2, 86.1, 72.7, 71.09, 71.04, 70.98, 70.95, 70.88, 70.81, 70.56, 69.95, 67.64, 63.4, 62.0, 55.4.

*The Phosphoramidite of Monotritylated E,E-1,4-Bis-4,4′-(2-(2-(2-(2-hydroxyethoxy)ethoxy)ethoxy)ethoxy)styryl Benzene (**43**).* To a solution of monotritylated *E,E*-1,4-bis-4,4′-(2-(2-(2-(2-hydroxyethoxy)ethoxy)ethoxy)ethoxy)styryl benzene (**40**) (86 mg, 0.089 mmol) in 15 mL CH_2Cl_2 (dry) was added 5 equiv of diisopropylethylamine (0.08 mL). Then, chloro-*N,N*-diisopropylaminocyanoethoxyphosphane (0.04 mL, 0.18 mmol, ∼2 equal) was added dropwise at room temperature under argon. After 20 min of stirring under argon at room temperature, the reaction mixture was diluted with 100 mL of CH_2Cl_2/Et_3N (300/15, v/v), and the organic phase was washed with a saturated aq $NaHCO_3$ solution and brine. The organic layer was dried over Na_2SO_4, filtered, and evaporated to dryness. The residue was subject to a silica gel column (CH_2Cl_2/EtOAc/Et_3N, 3/6/1) to give the title product (88 mg, yield 85%) as a yellow powder, which should be used freshly for the next phosphotriester step in order to achieve a higher coupling yield.

*E,E-1,4-Bis-4,4′-((2-(2-(2-(2-hydroxyethoxy)ethoxy)ethoxy)-ethyl)butylamino)styryl Benzene (**2**).* To a solution of tetraethyl 1,4-xylylenediphosphonate (1.5 g, 3.9 mmol) and 4-*N*-*n*-butyl-*N*-[2-[2-[2-(2-hydroxyethoxy)ethoxy]ethoxy]ethyl]amino benzaldehyde (**13**) (4 g, 11 mmol, 3 equiv) in anhydrous DMF (20 mL) was added KOBut (1.2 g, 11 mmol, 3 equiv) predissolved in DMF (10 mL) dropwise via syringe at 0 °C under argon. After stirring for 0.5 h at 0 °C, the reaction mixture was slowly warmed up to room temperature and stirred for another 12 h, and then the reaction was quenched with water. The crude product was collected by suction filtration and the filtrate was evaporated to dryness. The residue was redissolved with $CHCl_3$ and washed with brine (2 × 100 mL). The organic layer was dried over Na_2SO_4 and concentrated to dryness. The crude product was then purified by chromatography on a silica gel column eluted with EtOAc/MeOH (20/1, v/v) to give the double bond trans linked product (1.54 g, yield 51%). R_f = 0.33 (EtOAc/MeOH, 20/1). ^{1}H NMR ($CDCl_3$) δ (ppm): 7.42 (s, 4H, styryl benzene), 7.36 (bd, 4H, J = 8.7 Hz, ethoxybenzene), 7.02 (d, 2H, J = 16.2 Hz, double bond trans linkage), 6.88 (d, 2H, J = 16.2 Hz, double bond trans linkage), 6.66 (d, 4H, J = 8.7 Hz, ethoxybenzene), 3.76−3.51 (m, 28H, tetraethylene glycol chain), 3.34 (bt, 4H, J = 7.5 Hz, -NC*H*$_2$CH$_2$CH$_2$CH$_3$), 1.65−1.52 (m, 4H, -NCH$_2$C*H*$_2$CH$_2$CH$_3$), 1.44−1.28 (m, 4H, -NCH$_2$-CH$_2$C*H*$_2$CH$_3$), 0.96 (t, 6H, J = 7.5 Hz, -NCH$_2$CH$_2$CH$_2$C*H*$_3$). ^{13}C NMR ($CDC1_3$) δ (ppm): 147.7, 136.8, 128.3, 127.9, 126.4, 125.3, 124.0, 111.9, 72.8, 71.0, 70.9, 70.88, 70.6, 68.8, 62.1, 51.5, 50.7, 29.6, 20.6, 14.4. MS (MALDI-TOF): 776.6 $[M]^+$.

*E,1-(4-((2-(2-(2-(2-(Bis-(4-methoxyphenyl)phenylmethoxy)-ethoxy)ethoxy)ethoxy)ethyl)butylamino)styryl)-E,4-(4-((2-(2-(2-(2-(bis-(4-methoxyphenyl)phenylmethoxy)ethoxy)ethoxy)ethoxy)-ethyl)butylamino)styryl) Benzene (**39**).* *E,E*-1,4-Bis-4,4′-((2-(2-(2-hydroxyethoxy)ethoxy)ethoxy)ethyl)butylamino)styryl benzene (**2**) (1.116 g, 1.44 mmol) was dissolved in dry pyridine (50 mL), followed by addition of DMTrCl (1.55 g, 4.3 mmol, 3 equiv) and DMAP (∼10 mg). The mixture was stirred at room temperature under argon overnight, and TLC monitoring (CH_2Cl_2/MeOH, 400/15, v/v) showed the formation of monosubstituted (R_f = 0.64) and disubstituted (R_f = 0.88) products, as well as the starting material (R_f = 0.31). The reaction mixture was concentrated in vacuum, and the residue was subject to a silica gel column with CH_2Cl_2/MeOH/pyridine (400/15/2) as eluents to give the title product (390 mg, yield 25%) as a yellow powder. Meanwhile, the disubstituted fraction was also collected, and further monodetritylation was carried out as follows: A detritylation solution was made by mixing $ZnCl_2$ (1.5 g) with 110 mL of CH_2Cl_2/MeOH (10/1, v/v). Then, the disubstituted compound (1150 mg, 0.83 mmol) was dissolved by 50 mL of the detritylation solution and the reaction mixture was monitored by TLC (CH_2Cl_2/MeOH, 400/15). As soon as the spot corresponding to starting matrerial **2** appeared on the TLC plate, the reaction was quenched by pouring into a saturated aq $NaHCO_3$ solution. The mixture was extracted by chloroform, and the organic layer was washed with brine, collected, dried over Na_2-

SO_4, concentrated, and subjected to a silica gel column (CH_2Cl_2/MeOH/pyridine, 400/15/2) to give the title product (470 mg, yield 53%).

On the basis of the starting material, the total yield of the monosubstituted product is 55%. The product is stored with a stabilizer (diisopropylethylamine) under argon at −80 °C. ^{1}H NMR ($CDCl_3$) δ (ppm): 7.48−7.44 (m, 2H, benzene ring of DMTr group), 7.42 (bs, 4H, styryl benzene), 7.40−7.32 (m, 4H, butylaminobenzene), 7.34 (bd, 4H, J = 9.0 Hz, methoxybenzene ring of DMTr group), 7.31−7.24 (m, 2H, benzene ring of DMTr group), 7.19 (bt, 1H, J = 7.2 Hz, benzene ring of DMTr group), 7.02 (d, 1H, J = 16.2 Hz, double bond trans linkage), 7.01 (d, 1H, J = 15.9 Hz, double bond trans linkage), 6.88 (d, 2H, J = 16.2 Hz, double bond trans linkage), 6.87 (d, 1H, J = 15.9 Hz, double bond trans linkage), 6.81 (bd, 4H, J = 9.0 Hz, methoxybenzene ring of DMTr group), 6.67 (d, 2H, J = 8.7 Hz, butylaminobenzene), 6.64 (d, 2H, J = 8.7 Hz, butylaminobenzene), 3.77 (s, 6H, -OCH_3), 3.76−3.50 (m, 30H, tetraethylene glycol chain), 3.38−3.26 (m, 4H, -NCH_2CH$_2$CH$_2$-CH$_3$), 3.22 (bt, 2H, J = 5.1 Hz, tetraethylene glycol chain), 1.64−1.52 (m, 4H, -NCH$_2$CH_2CH$_2$CH$_3$), 1.42−1.28 (m, 4H, -NCH$_2$CH$_2$CH_2CH$_3$), 0.96 (t, 3H, J = 7.2 Hz, -NCH$_2$CH$_2$-CH$_2$CH_3), 0.94 (t, 3H, J = 7.2 Hz, -NCH$_2$CH$_2$CH$_2$CH_3). ^{13}C NMR ($CDC1_3$) δ (ppm): 158.5, 147.7, 145.3, 136.9, 136.9, 136.5, 130.3, 128.4, 128.2, 128.2, 127.94, 127.91, 126.9, 126.4, 125.3, 125.3, 123.9, 123.9, 113.2, 111.92, 111.89, 86.2, 72.8, 71.1, 71.0, 70.98, 70.95, 70.88, 70.6, 68.8, 63.4, 62.1, 55.5, 51.5, 50.8, 29.6, 20.6, 14.4.

*The Phosphoramidite of E,1-(4-((2-(2-(2-(2-(Bis(4-methoxyphenyl)phenylmethoxy)ethoxy)ethoxy)ethoxy)ethyl)butylamino)-styryl)-E,4-(4-((2-(2-(2-(2-(Bis(4-methoxyphenyl)phenylmethoxy)-ethoxy)ethoxy)ethoxy)ethyl)butylamino)styryl) Benzene (**41**).* To a solution of *E*,1-(4-((2-(2-(2-(2-(bis(4-methoxyphenyl)phenyl-methoxy)ethoxy)ethoxy)ethoxy)ethyl)butylamino)styryl)-*E*,4-(4-((2-(2-(2-(2-(bis(4-methoxyphenyl)phenylmethoxy)ethoxy)ethoxy)-ethoxy)ethyl)butylamino)styryl) benzene (**39**) (770 mg, 0.71 mmol) in 80 mL CH_2Cl_2 (dry) was added 7 equiv of diisopropylethylamine (0.8 mL). Then, chloro-*N*,*N*-diisopropylaminocyanoethoxyphosphane (0.47 mL, 2.1 mmol, ∼3 equiv) was added dropwise at room temperature under argon. After 20 min of stirring under argon at room temperature, the reaction mixture was diluted with 100 mL of CH_2Cl_2/Et_3N (300/15, v/v), and the organic phase was washed with a saturated aq $NaHCO_3$ solution and brine. The organic layer was dried over Na_2SO_4, filtered, and evaporated to dryness. The residue was subject to a silica gel column (CH_2Cl_2/EtOAc/Et_3N, 3/6/1) to give the title product (870 mg, yield 96%) as a yellow powder, which should be used freshly for the next phosphotriester step in order to achieve a higher coupling yield. ^{1}H NMR ($CDCl_3$) δ (ppm): 7.48−7.44 (m, 2H, benzene ring of DMTr group), 7.42 (bs, 4H, styryl benzene), 7.40−7.32 (m, 4H, butylaminobenzene), 7.34 (bd, 4H, J = 9.0 Hz, methoxybenzene ring of DMTr group), 7.31−7.15 (m, 3H, benzene ring of DMTr group), 7.01 (d, 1H, J = 16.2 Hz, double bond trans linkage), 7.00 (d, 1H, J = 16.2 Hz, double bond trans linkage), 6.88 (d, 2H, J = 16.2 Hz, double bond trans linkage), 6.87 (d, 1H, J = 16.2 Hz, double bond trans linkage), 6.81 (bd, 4H, J = 9.0 Hz, methoxybenzene ring of DMTr group), 6.67 (d, 2H, J = 8.7 Hz, butylaminobenzene), 6.64 (d, 2H, J = 8.7 Hz, butylaminobenzene), 3.77 (s, 6H, -OCH_3), 3.90−3.75 (m, 2H, -OCH_2CH$_2$CN), 3.70−3.48 (m, 32H, -N(CH(CH$_3$)$_2$)$_2$ and tetraethylene glycol chain), 3.38−3.26 (m, 4H, -NCH_2CH$_2$CH$_2$CH$_3$), 3.22 (bt, 2H, J = 5.1 Hz, tetraethylene glycol chain), 2.63 (bt, 2H, J = 6.5 Hz, -OCH$_2$CH_2-CN), 1.64−1.52 (m, 4H, -NCH$_2$CH_2CH$_2$CH$_3$), 1.42−1.28 (m, 4H, -NCH$_2$CH$_2$CH_2CH$_3$), 1.19 (d, 6H, J = 6.8 Hz, -CH(CH_3)$_2$), 1.17 (d, 2H, J = 6.8 Hz, -CH(CH_3)$_2$), 0.96 (t, 3H, J = 7.2 Hz, -NCH$_2$CH$_2$CH$_2$CH_3), 0.94 (t, 3H, J = 7.2 Hz, -NCH$_2$CH$_2$-CH$_2$CH_3). ^{13}C NMR ($CDC1_3$) δ (ppm): 158.6, 147.7, 145.3, 136.9, 136.6, 130.3, 128.4, 128.3, 128.3, 127.98, 127.95, 126.9, 126.4, 125.37, 125.32, 124.0, 123.95, 113.3, 111.9, 86.1, 71.5, 71.4, 71.0, 70.98, 70.94, 70.90, 70.8, 68.8, 63.4, 62.9, 62.7, 58.9, 58.6, 55.4, 51.4, 50.7, 43.4, 43.2, 29.6, 24.93, 24.86, 24.83, 24.77, 20.6, 20.5, 14.4, 14.3. ^{31}P NMR ($CDC1_3$) δ (ppm): 149.6.

*(4-(2-(4-(Butyl-(2-(2-(2-(2-hydroxyethoxy)ethoxy)ethoxy)ethyl)-amino)phenyl)vinyl)benzyl)phosphonic Acid Diethyl Ester (**19**).* To a solution of tetraethyl 1,4-xylylenediphosphonate (466 mg, 1.2 mmol, 1.2 equiv) and 4-*N*-*n*-butyl-*N*-[2-[2-[2-(2-hydroxy-ethoxy)ethoxy]ethoxy]ethyl]amino benzaldehyde (**13**) (360 mg, 1.1 mmol) in anhydrous DMF (15 mL) was added KOBut (123 mg, 1.1 mmol, 1 equiv) predissolved in DMF (4 mL) dropwise via syringe at 0 °C under argon. After stirring for 0.5 h at 0 °C, the reaction mixture was slowly warmed up to room temperature and stirred for another 12 h. The crude product was then purified by chromatography on a silica gel column eluted with EtOAc/MeOH (20/1, v/v) to give the double bond trans linked product **2** (130 mg, yield 31%) and the title product (trans/cis 3/1) in a yield of 45% (281 mg). R_f = 0.25 (EtOAc/MeOH, 20/1). ^{1}H NMR ($CDCl_3$) δ (ppm): double bond trans/cis linkage (3/1): 7.40 (d, 2H (3/4), J = 8.1 Hz, aromatic ring), 7.35 (d, 2H (3/4), J = 8.7 Hz, aromatic ring), 7.28 (d, 2H (1/4), J = 8.4 Hz, aromatic ring), 7.24 (dd, 2H (3/4), J_1 = 8.1 Hz, J_2 = 2.4 Hz, aromatic ring), 7.16 (dd, 2H (1/4), J = 8.4 Hz, aromatic ring), 7.10 (d, 2H (1/4), J = 8.7 Hz, aromatic ring), 7.00 (d, 1H (3/4), J = 16.5 Hz, double bond trans linkage), 6.84 (d, 1H (3/4), J = 16.5 Hz, double bond trans linkage), 6.65 (d, 2H (3/4), J = 8.7 Hz, aromatic ring), 6.48 (d, 2H (1/4), J = 8.7 Hz, aromatic ring), 6.42 (d, 1H (1/4), J = 12.3 Hz, double bond cis linkage), 6.33 (bd, 1H (1/4), J = 12.3 Hz, double bond cis linkage), 4.06−3.95 (m, 4H, -OCH_2CH$_3$), 3.74−3.46 (m, 16H, tetraethylene glycol chain), 3.35 (bt, 2H (3/4), J = 7.5 Hz, -NCH_2-CH$_2$CH$_2$CH$_3$), 3.27 (bt, 2H (1/4), J = 7.5 Hz, -NCH_2CH$_2$CH$_2$-CH$_3$), 3.17 (bs, 1H (3/4), benzyl), 3.16 (bs, 1H (1/4), benzyl), 3.10 (bs, 1H (3/4), benzyl), 3.08 (bs, 1H (1/4), benzyl), 1.63−1.50 (m, 2H, -NCH$_2$CH_2CH$_2$CH$_3$), 1.40−1.28 (m, 2H, -NCH$_2$-CH$_2$CH_2CH$_3$), 1.24 (t, 6H, J = 7.1 Hz, -OCH$_2$CH_3), 0.95 (t, 3H (3/4), J = 7.2 Hz, -NCH$_2$CH$_2$CH$_2$CH_3), 0.92 (t, 3H (1/4), J = 7.2 Hz, -NCH$_2$CH$_2$CH$_2$CH_3). MS (MALDI-TOF): 576.6 [M]$^+$.

*E,1-(4-((2-(2-(2-(2-Hydroxyethoxy)ethoxy)ethoxy)ethyl)-butylamino)styryl)-E,4-(4-(2-(2-(2-(2-hydroxyethoxy)ethoxy)-ethoxy)ethoxy)styryl Benzene (**3**).* To a solution of **19** (87 mg, 0.15 mmol) and **10** (90 mg, 0.3 mmol, 2 equiv) in anhydrous DMF (8 mL) was added KOBut (35 mg, 0.31 mmol, 2 equiv) predissolved in DMF (4 mL) dropwise via syringe at 0 °C under argon. After stirring for 0.5 h at 0 °C, the reaction mixture was slowly warmed up to room temperature and stirred for another 12 h. Water was added to quench the reaction. After evaporation of the solvent, the crude product was purified by chromatography on a silica gel column eluted with EtOAc/MeOH (10/1, v/v) to give the title product (60 mg) in a yield of 55%. R_f = 0.39 (EtOAc/MeOH, 10/1). ^{1}H NMR ($CDCl_3$) δ (ppm): 7.45 (bs, 4H, styryl benzene), 7.44 (bd, 2H, J = 9.0 Hz, ethoxybenzene), 7.38 (d, 2H, J = 8.7 Hz, butylaminobenzene), 7.04 (d, 1H, J = 16.2 Hz, double bond trans linkage), 7.03 (d, 1H, J = 16.2 Hz, double bond trans linkage), 6.97 (d, 1H, J = 16.2 Hz, double bond trans linkage), 6.92 (bd, 2H, J = 9.0 Hz, ethoxybenzene), 6.88 (d, 1H, J = 16.2 Hz, double bond trans linkage), 6.66 (d, 2H, J = 8.7 Hz, butylaminobenzene), 4.16 (bt, 2H, J = 4.8 Hz, tetraethylene glycol chain), 3.87 (bt, 2H, J = 4.8 Hz, tetraethylene glycol chain), 3.76−3.51 (m, 28H, tetraethylene glycol chain), 3.34 (bt, 2H, J = 7.5 Hz, -NCH_2-CH$_2$CH$_2$CH$_3$), 2.53 (bt, 1H, J = 6.9 Hz, -OH), 2.47 (bt, 1H, J = 6.9 Hz, -OH), 1.65−1.52 (m, 2H, -NCH$_2$CH_2CH$_2$CH$_3$), 1.44−

1.28 (m, 2H, -$NCH_2CH_2CH_2CH_3$), 0.96 (t, 3H, J = 7.5 Hz, -$NCH_2CH_2CH_2CH_3$). ^{13}C NMR ($CDC1_3$) δ (ppm): 158.5, 147.7, 137.5, 136.1, 130.7, 128.7, 127.97, 127.8, 127.6, 126.7, 126.4, 125.2, 123.8, 115.0, 111.9, 72.4, 72.4, 70.7, 70.6, 70.56, 70.50, 70.2, 69.6, 68.4, 67.3, 61.7, 51.1, 50.3, 29.2, 20.2, 14.0. MS (MALDI-TOF): 721.3 $[M]^+$.

HWE reagent tetraethyl-2,5-dicyano-1,4-xylylenediphosphonate was obtained according to literature (*27*, *28*).

*2,5-Dicyano-E,E-1,4-Bis-4,4′-((2-(2-(2-(2-hydroxyethoxy)-ethoxy)ethoxy)ethyl)butylamino)styryl Benzene (**4**).* To a solution of tetraethyl-2,5-dicyano-1,4-xylylenediphosphonate (186 mg, 0.43 mmol) and 4-*N*-*n*-butyl-*N*-[2-[2-[2-(2-hydroxyethoxy)-ethoxy]ethoxy]ethyl]amino benzaldehyde (**13**) (460 mg, 1.3 mmol, 3 equiv) in anhydrous DMF (10 mL) was added KOBut (155 mg, 1.3 mmol, 3 equiv) predissolved in DMF (10 mL) dropwise via syringe at 0 °C under argon. After stirring for 0.5 h at 0 °C, the reaction mixture was slowly warmed up to room temperature and stirred for another12 h, then the reaction was quenched with water. The crude product was collected by suction filtration and the filtrate was evaporated to dryness. The residue was redissolved with $CHCl_3$ and washed with brine (2 × 100 mL). The organic layer was dried over Na_2SO_4 and concentrated to dryness. The crude product was then purified by chromatography on a silica gel column eluted with EtOAc/MeOH (20/1, v/v) to give the double bond trans linked product (233 mg, yield 65%). R_f = 0.23 (EtOAc/MeOH, 20/1). ^{1}H NMR ($CDCl_3$) δ (ppm): 7.94 (bs, 2H, styryl benzene), 7.44 (d, 4H, J = 8.7 Hz, butylaminobenzene), 7.19 (d, 2H, J = 16.2 Hz, double bond trans linkage), 7.10 (d, 2H, J = 16.2 Hz, double bond trans linkage), 6.68 (d, 4H, J = 8.7 Hz, butylaminobenzene), 3.74 (bt, 4H, J = 4.5 Hz, tetraethylene glycol chain), 3.71−3.55 (m, 28H, tetraethylene glycol chain), 3.37 (bt, 2H, J = 7.5 Hz, -$NCH_2CH_2CH_2CH_3$), 2.62 (bs, 2H, -O*H*), 1.65−1.52 (m, 2H, -$NCH_2CH_2CH_2CH_3$), 1.37 (sext, 2H, J = 7.5 Hz, -$NCH_2CH_2CH_2CH_3$), 0.97 (t, 3H, J = 7.5 Hz, -$NCH_2CH_2CH_2CH_3$). ^{13}C NMR ($CDC1_3$) δ (ppm): 149.1, 138.8, 134.6, 129.2, 129.1, 123.4, 117.4, 116.9, 114.2, 111.9, 72.7, 71.0, 70.89, 70.81, 70.6, 68.7, 62.0, 51.4, 50.6, 29.4, 20.5, 14.2. MS (MALDI-TOF): 827.0 $[M]^+$.

*2,5-Dicyano-E,E-1,4-bis-4,4′-(2-(2-(2-(2-hydroxy-ethoxy)-ethoxy)ethoxy)ethoxy) styryl Benzene (**1**).* To a solution of tetraethyl-2,5-dicyano-1,4-xylylenediphosphonate (200 mg, 0.47 mmol) and **10** (418 mg, 1.4 mmol, 3 equiv) in anhydrous DMF (15 mL) was added KOBut (160 mg, 1.4 mmol, 3 equiv) predissolved in DMF (10 mL) dropwise via syringe at 0 °C under argon. After stirring for 0.5 h at 0 °C, the reaction mixture was slowly warmed up to room temperature and stirred for another 12 h, then the reaction was quenched with water. The crude product was collected by suction filtration and the filtrate was evaporated to dryness. The residue was redissolved with $CHCl_3$ and washed with brine (2 × 100 mL). The organic layer was dried over Na_2SO_4 and concentrated to dryness. The crude product was then purified by chromatography on a silica gel column eluted with EtOAc/MeOH (10/1, v/v) to give the double bond trans linked product (201 mg, yield 60%). R_f = 0.20 (EtOAc/MeOH, 20/1). ^{1}H NMR ($CDCl_3$) δ (ppm): 7.97 (s, 2H, styryl benzene), 7.50 (bd, 4H, J = 8.7 Hz, ethoxybenzene), 7.23 (d, 2H, J = 16.2 Hz, double bond trans linkage), 7.18 (d, 2H, J = 16.2 Hz, double bond trans linkage), 6.95 (d, 4H, J = 8.7 Hz, ethoxybenzene), 4.16 (bt, 4H, J = 4.8 Hz, tetraethylene glycol chain), 3.87 (bt, 4H, J = 4.8 Hz, tetraethylene glycol chain), 3.78−3.64 (m, 20H, tetraethylene glycol chain), 3.60 (bt, 4H, J = 4.8 Hz, tetraethylene glycol chain), 2.95 (bs, 2H, -O*H*). ^{13}C NMR ($CDC1_3$) δ (ppm): 160.1, 138.9, 134.6, 129.6, 129.0, 128.7, 119.7, 117.0, 115.3, 114.8, 72.8, 71.0, 70.85, 70.77, 70.5, 69.8, 67.7, 61.9. MS (MALDI-TOF): 739.9 $[M + Na]^+$.

Compounds in Preparation of *E,E*-4-Dicyanomethylene-2,6-bis-*p*-*N,N′*-*n*-butyl-*N,N′*-(2-(2-(2-(2-hydroxyethoxy)ethoxy)-ethoxy)ethyl)aminostyryl Pyran Derivatives. *E,E-4-Dicyanomethylene-2,6-bis-p-N,N′-n-butyl-N,N′-(2-(2-(2-(2-hydroxyethoxy)ethoxy)ethoxy)ethyl)aminostyryl Pyran (**6**).* A mixture of 2,6-dimethyl-4-(dicyanomethylene) pyran (220 mg, 1.28 mmol), 4-*N*-*n*-butyl-*N*-[2-[2-[2-(2-hydroxyethoxy)ethoxy]-ethoxy]ethyl]aminobenzaldehyde (1.0 g, 2.8 mmol), and piperidine (1 mL, 10 mmol) in toluene (25 mL) was heated to reflux with a Dean−Stark trap under argon overnight. Then, the reaction was cooled and the solvent was evaporated to dryness in vacuum. $CHCl_3$ was added to dilute the residue, and the organic layer was washed with water (100 mL) and brine (100 mL). After drying over Na_2SO_4, the organic phase was concentrated, and the residue was purified by chromatography on a silica gel column eluted with EtOAc/MeOH (20/1) to give the title product (538 mg, yield 50%) as a red powder. R_f = 0.14 (EtOAc/MeOH 20/1). ^{1}H NMR ($CDCl_3$) δ (ppm): 7.42 (d, 4H, J = 9.0 Hz, aromatic ring), 7.41 (d, 2H, J = 16.2 Hz, double bond trans linkage), 6.69 (d, 4H, J = 9.0 Hz, aromatic ring), 6.51 (s, 2H, pyran ring), 6.47 (d, 2H, J = 16.2 Hz, double bond trans linkage), 3.55−3.51 (m, 32H, tetraethylene glycol chain), 3.39 (t, 4H, J = 7.5 Hz, *n*-butyl chain), 1.70−1.52 (m, 4H, *n*-butyl chain), 1.46−1.30 (m, 4H, *n*-butyl chain), 0.98 (t, 6H, J = 7.5 Hz, *n*-butyl chain). ^{13}C NMR ($CDC1_3$) δ (ppm): 159.4, 156.2, 149.8, 138.2, 129.9, 122.1, 116.5, 112.8, 111.7, 105.3, 72.6, 70.9, 70.8, 70.7, 70.4, 68.5, 61.8, 51.4, 50.5, 29.4, 20.4, 14.2. MS (MALDI-TOF): *m*/*z* 844.2 $[M + 1]^+$.

*E,E-4-Dicyanomethylene-2,6-bis-4.4′-(2-(2-(2-(2-hydroxy-ethoxy)ethoxy)ethoxy)ethyl)styryl Pyran (**37**).* A mixture of 2,6-dimethyl-4-(dicyanomethylene) pyran (206 mg, 1.2 mmol), **10** (800 mg, 2.68 mmol), acetic acid (0.5 mL, 8.5 mmol), and piperidine (1 mL, 10 mmol) in toluene (25 mL) was heated to reflux with a Dean−Stark trap under argon for 36 h. Then, the reaction was cooled and the solvent was evaporated to dryness in vacuum. $CHCl_3$ was added to dilute the residue, and the organic layer was washed with brine (2 × 100 mL). After drying over Na_2SO_4, the organic phase was concentrated, and the residue was purified by chromatography on a silica gel column eluted with EtOAc/MeOH (10:1) to give the title product (130 mg, yield 15%). R_f = 0.23 (EtOAc/MeOH 20/1). ^{1}H NMR ($CDCl_3$) δ (ppm): 7.52 (bd, 4H, J = 9.0 Hz, ethoxybenzene), 7.46 (d, 2H, J = 16.2 Hz, double bond trans linkage), 6.98 (d, 4H, J = 9.0 Hz, ethoxybenzene), 6.64 (s, 2H, pyran), 6.63 (d, 2H, J = 16.2 Hz, double bond trans linkage), 4.20 (bt, 4H, J = 4.8 Hz, tetraethylene glycol chain), 3.89 (bt, 4H, J = 4.8 Hz, tetraethylene glycol chain), 3.78−3.64 (m, 20H, tetraethylene glycol chain), 3.62 (bt, 4H, J = 4.8 Hz, tetraethylene glycol chain). ^{13}C NMR ($CDC1_3$) δ (ppm): 161.0, 158.8, 137.8, 129.7, 127.7, 116.5, 115.7, 115.5, 106.7, 72.7, 71.1, 70.88, 70.81, 70.5, 69.8, 67.8, 62.0. MS (MALDI-TOF): 731.7 $[M]^+$, 787.8 $[M + K + H_2O]^+$.

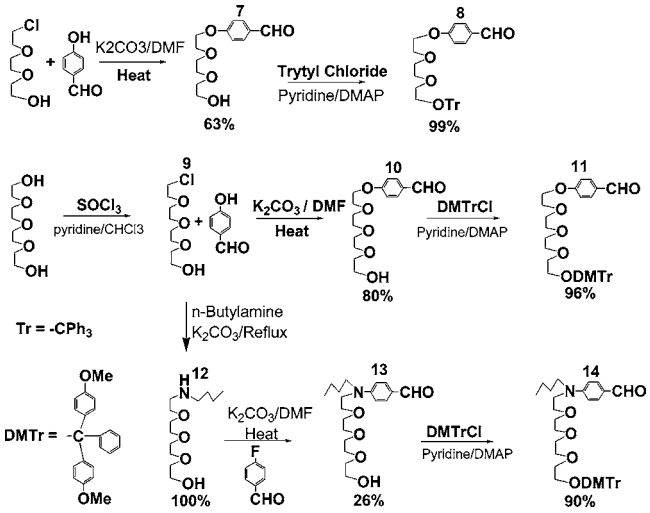
*Monotritylation of E,E-4-Dicyanomethylene-2,6-bis-p-N,N′-n-butyl-N,N′-(2-(2-(2-(2-hydroxyethoxy)ethoxy)ethoxy)ethyl)-aminostyryl Pyran (**38**).* *E,E*-4-Dicyanomethylene-2,6-bis-*p*-*N,N′*-*n*-butyl-*N,N′*-(2-(2-(2-(2-hydroxyethoxy)ethoxy)ethoxy)-ethyl)aminostyryl pyran (**6**) (538 mg, 0.64 mmol) was dissolved in dry pyridine (50 mL), followed by addition of 3 equiv of DMTrCl (684 mg) and DMAP (∼10 mg). The mixture was stirred at room temperature under argon for 5 days, and TLC monitoring (20/1, CH_2Cl_2/MeOH) showed the formation of monosubstituted (R_f = 0.25) and disubstituted (R_f = 0.98) products, as well as the starting material (R_f = 0.09). The reaction mixture was concentrated in vacuum, and the residue was directly subjected to a silica gel column using the gradient elution technique with CH_2Cl_2/MeOH/pyridine (500/10/3 to 500/20/3) as eluents affording the monosubstituted product (250 mg,

yield 35%), disubstituted product, and recovered starting material (123 mg). Meanwhile, the disubstituted fraction was collected, and further monodetritylation was carried out according to the following procedure: A detritylation solution was made by mixing $ZnCl_2$ (1.5 g) with 110 mL of CH_2Cl_2/MeOH (10/1, v/v). Then, the crude disubstituted compound (~900 mg) was dissolved by 50 mL of the detritylation solution, and the reaction mixture was monitored by TLC (20/1, CH_2Cl_2/MeOH). As soon as the spot corresponding to the starting material (*E,E*-4-dicyanomethylene-2,6-bis-*p*-*N,N′*-*n*-butyl-*N,N′*-(2-(2-(2-(2-hydroxyethoxy)ethoxy)ethoxy)ethyl)aminostyryl pyran) appeared on the TLC plate, the reaction was quenched by addition of a saturated aq $NaHCO_3$ solution (100 mL). The mixture was extracted by chloroform, and the organic layer was washed with brine, collected, dried over Na_2SO_4, concentrated, and subjected to a silica gel column (500/10/3, CH_2Cl_2/MeOH/pyridine) to give the title product **38** (128 mg, yield 17.5%). If the recovered starting material was counted, the total yield of the monotritylation would be 67% based on the consumed starting material. ^{1}H NMR ($CDCl_3$) δ (ppm): 7.49−7.38 (m, 8H, aromatic rings and double bond trans linkage), 7.34 (dt, 4H, $J_1 = 2.7$ Hz, $J_2 =$ 9 Hz, methoxylbenzene ring), 7.31−7.15 (m, 3H, benzene ring), 6.81 (dt, 4H, $J_1 = 2.7$ Hz, $J_2 = 9$ Hz, methoxylbenzene ring), 6.69 (d, 2H, $J = 8.7$ Hz, benzene ring), 6.66 (d, 2H, $J = 9.0$ Hz, benzene ring), 6.54 (d, 1H, $J = 2.1$ Hz, pyran ring), 6.52 (d, 1H, $J = 2.1$ Hz, pyran ring), 6.48 (d, 1H, $J = 15.9$ Hz, double bond trans linkage), 6.46 (d, 1H, $J = 15.9$ Hz, double bond trans linkage), 3.77 (s, 6H, C*H*$_3$O), 3.56−3.50 (m, 30H, tetraethylene glycol chain), 3.44−3.31 (m, 4H, *n*-butyl chain), 3.22 (t, 2H, $J = 5.1$ Hz, tetraethylene glycol chain), 1.69−1.49 (m, 4H, *n*-butyl chain), 1.48−1.42 (m, 4H, *n*-butyl chain), 0.97 (t, 3H, $J = 7.5$ Hz, *n*-butyl chain), 0.96 (t, 3H, $J = 7.5$ Hz, *n*-butyl chain). ^{13}C NMR ($CDC1_3$) δ (ppm): 159.5, 158.4, 156.2, 149.8, 145.1, 138.2, 136.4, 130.2, 129.9, 128.3, 127.8, 126.7, 122.2, 122.1, 116.5, 113.1, 112.94, 112.88, 111.8, 111.7, 105.4, 86.1, 72.7, 71.0, 70.92, 70.84, 70.76, 70.5, 68.6, 63.3, 61.9, 56.1, 55.4, 51.4, 50.6, 29.4, 20.5, 14.3. MS (ESI): *m*/*z* 1145.6 $[M]^+$.

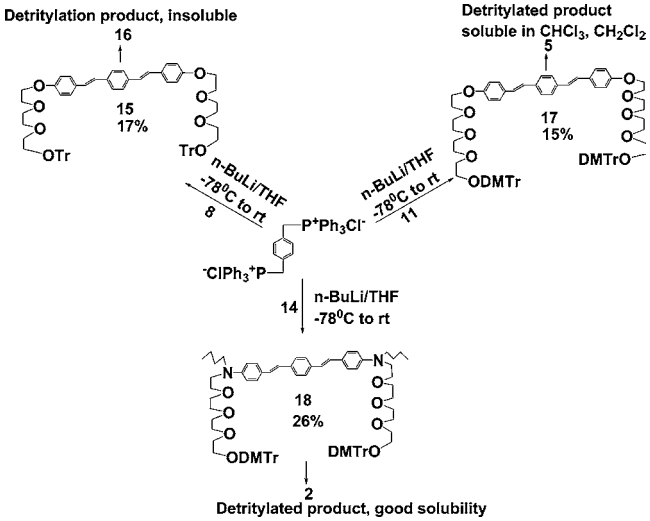
*The Phosphoramidite of Monotritylated E,E-4-Dicyanomethylene-2,6-bis-p-N,N′-n-butyl-N,N′-(2-(2-(2-(2-hydroxyethoxy)-ethoxy)ethoxy)ethyl)aminostyryl Pyran (**42**).* To a solution of monotritylated *E,E*-4-dicyanomethylene-2,6-bis-*p*-N,N′-*n*-butyl-N,N′-(2-(2-(2-(2-hydroxyethoxy)ethoxy)ethoxy)ethyl)-aminostyryl pyran (**38**) (200 mg, 0.17 mmol) in dry CH_2Cl_2 (20 mL) was added 2.7 equiv of diisopropylethylamine (0.08 mL). Then, chloro-*N,N*-diisopropylaminocyanoethoxyphosphane (0.05 mL, ~1.2 equiv) was added dropwise at room temperature under argon. After 20 min of stirring under argon at room temperature, the reaction mixture was diluted with CH_2Cl_2/Et_3N (300/15, v/v) 100 mL, and the organic phase was washed with a saturated aq $NaHCO_3$ solution and brine. The organic layer was dried over Na_2SO_4, filtered, and evaporated to dryness. The residue was immediately subjected to a silica gel column (CH_2Cl_2/EtOAc/Et_3N, 3/6/1) to give the title product (200 mg, yield 88%) as a red powder, which should be used freshly for the next phosphotriester step in order to achieve a higher coupling yield. ^{1}H NMR ($CDCl_3$) δ (ppm): 7.48−7.38 (m, 8H, aromatic rings and double bond trans linkage), 7.34 (dt, 4H, $J_1 = 2.4$ Hz, $J_2 = 9$ Hz, methoxylbenzene ring), 7.31−7.15 (m, 3H, benzene ring of DMTr group), 6.81 (dt, 4H, $J_1 = 2.4$ Hz, $J_2 =$ 9 Hz, methoxylbenzene ring), 6.69 (d, 2H, $J = 8.7$ Hz, benzene ring), 6.67 (d, 2H, $J = 9.0$ Hz, benzene ring), 6.56 (d, 1H, $J =$ 2.1 Hz, pyran ring), 6.54 (d, 1H, $J = 2.1$ Hz, pyran ring), 6.50 (d, 1H, $J = 15.9$ Hz, double bond trans linkage), 6.48 (d, 1H, $J = 15.6$ Hz, double bond trans linkage), 3.91−3.70 (m, 4H, -C*H*$_2$CH$_2$CN, -C*H*(CH$_3$)$_2$), 3.77 (s, 6H, C*H*$_3$O), 3.70−3.50 (m, 30H, tetraethylene glycol chain), 3.44−3.31 (m, 4H, -NC*H*$_2$-CH$_2$CH$_2$CH$_3$), 3.22 (t, 2H, $J = 5.4$ Hz, tetraethylene glycol chain), 2.64 (t, 2H, $J = 6.5$ Hz, -CH$_2$C*H*$_2$CN), 1.70−1.52 (m, 4H, -NCH$_2$C*H*$_2$CH$_2$CH$_3$), 1.48−1.30 (m, 4H, -NCH$_2$CH$_2$C*H*$_2$-CH$_3$), 1.18 (d, 6H, $J = 6.9$ Hz, -CH(C*H*$_3$)$_2$), 1.17 (d, 6H, $J =$ 6.6 Hz, -CH(C*H*$_3$)$_2$), 0.97 (t, 3H, $J = 7.5$ Hz, -NCH$_2$CH$_2$-CH$_2$C*H*$_3$), 0.96 (t, 3H, $J = 7.5$ Hz, -NCH$_2$CH$_2$CH$_2$C*H*$_3$). ^{13}C NMR ($CDC1_3$) δ (ppm): 159.2, 158.1, 155.9, 149.5, 144.9, 137.9, 136.1, 129.9, 129.6, 128.0, 127.5, 126.5, 121.9, 121.8, 117.6, 116.2, 112.8, 112.7, 111.5, 105.1, 85.8, 71.2, 71.1, 70.7, 70.6, 70.53, 70.49, 68.3, 63.0, 62.6, 62.4, 58.5, 58.3, 55.9, 55.1, 51.1, 50.3, 46.1, 43.1, 42.9, 29.1, 24.65, 24.58, 24.55, 24.49, 20.3, 20.24, 20.18, 14.0. ^{31}P NMR ($CDC1_3$) δ (ppm): 149.5.

Solid-Phase Synthesis of DNA−Chromophore Conjugates. The solid-phase syntheses were carried out on an Expedite Nucleic Acid Syntheses System. The DNA bases were synthesized on either glass beads or polystyrene spheres using software protocol supplied by PerSeptive Biosystems (Framingham, MA), and the phosphoramidite reagents of DNA bases were obtained from Applied Biosystems. The phosphoramidite reagents of organic chromophores were synthesized according to procedures described in this report, and their solid-phase syntheses were carried out using custom protocol in order to improve the reaction yields. Typically, the phosphoramidite concentrations of the organic dyes used for the solid-phase syntheses were greater than 40 mg/mL. Standard DNA base coupling delivers the phosphoramidite reagent with activator to the

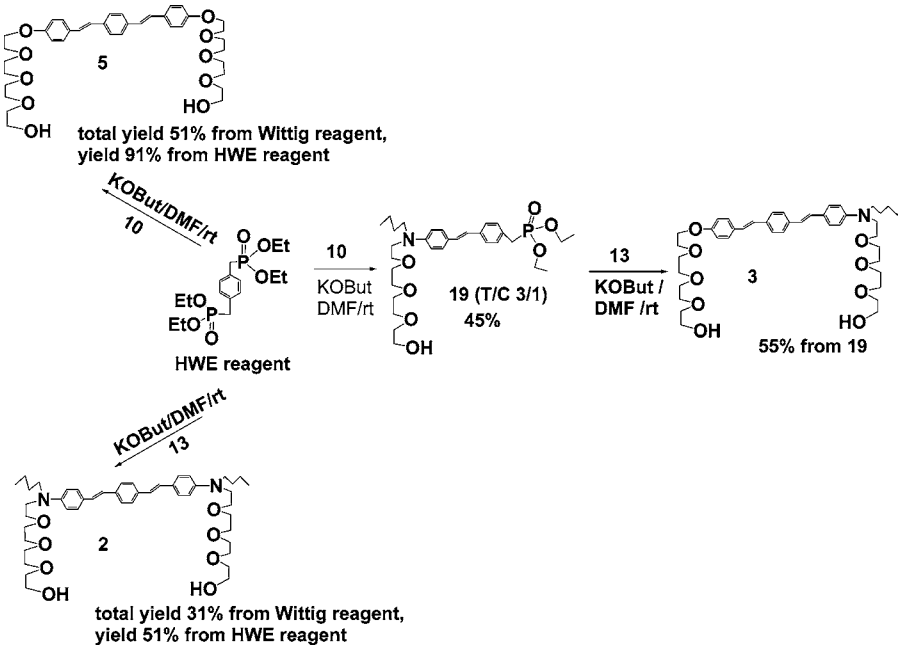
Scheme 1



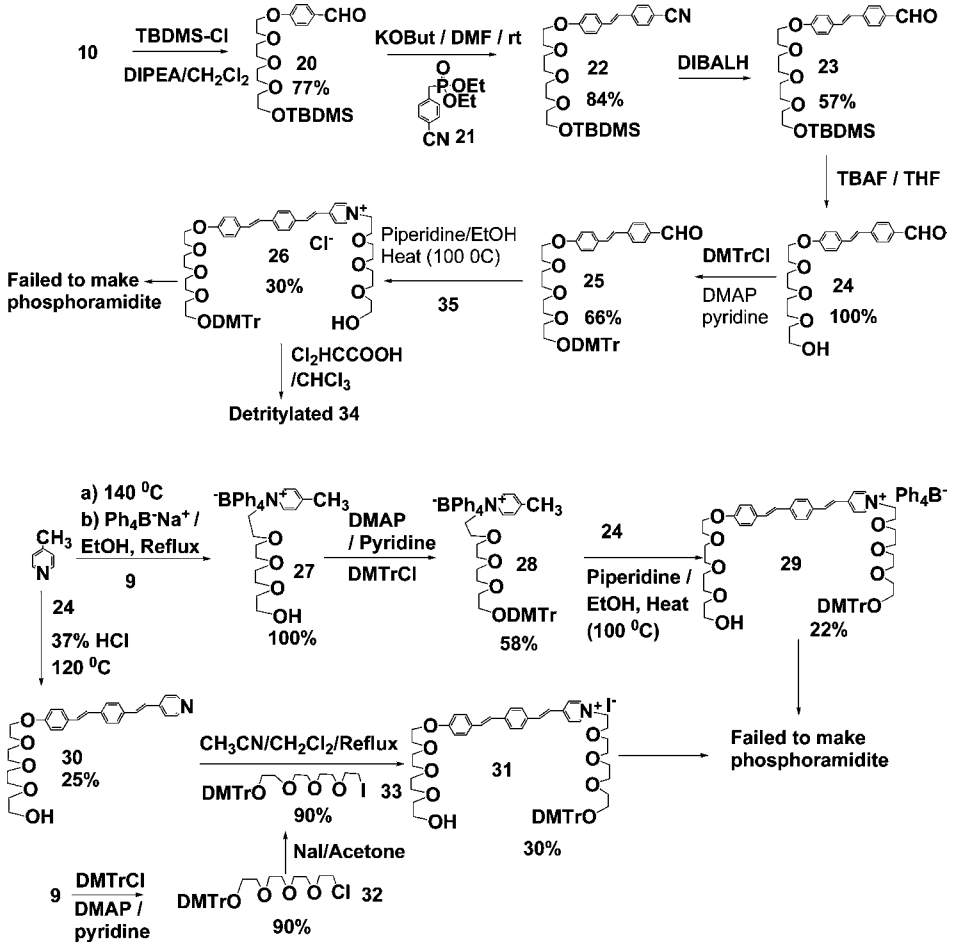
Scheme 2



Scheme 3

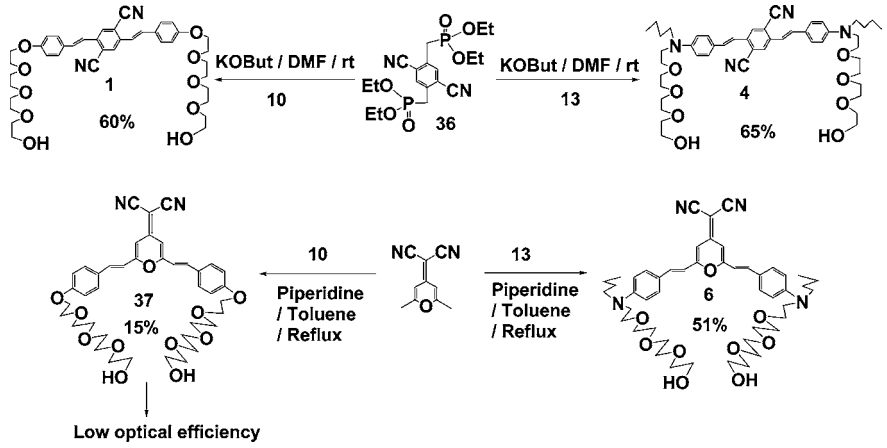


Scheme 4

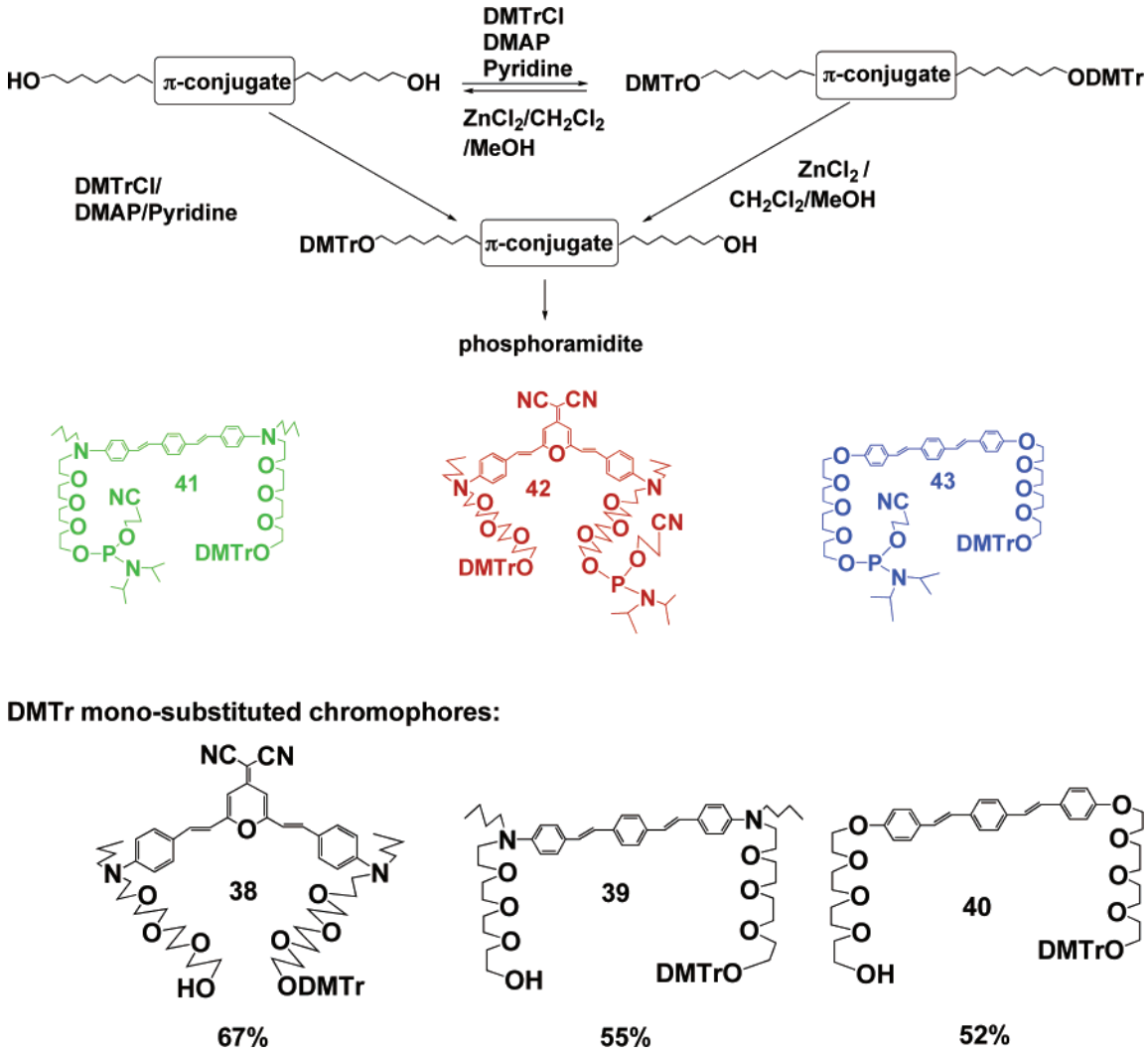


solid-phase column immediately and allows 47 s for coupling reaction. This reaction time is not adequate for coupling chromophoric phosphoramidite to DNA bases, and hence, the chromophoric coupling protocol was modified by delivering the phosphoramidite reagents to the column over a 4 s period (instead of immediately) and the reaction time was extended to 140 s (instead of 47 s). For a high yield of coupling, phosphoramidite reagents must be prepared and purified with silica gel columns immediately before carrying out the solid-phase syntheses. Using the modified protocol described here, the yield of the coupling reaction is typically greater than 80% as indicated by the trityl data.

Scheme 5



Scheme 6

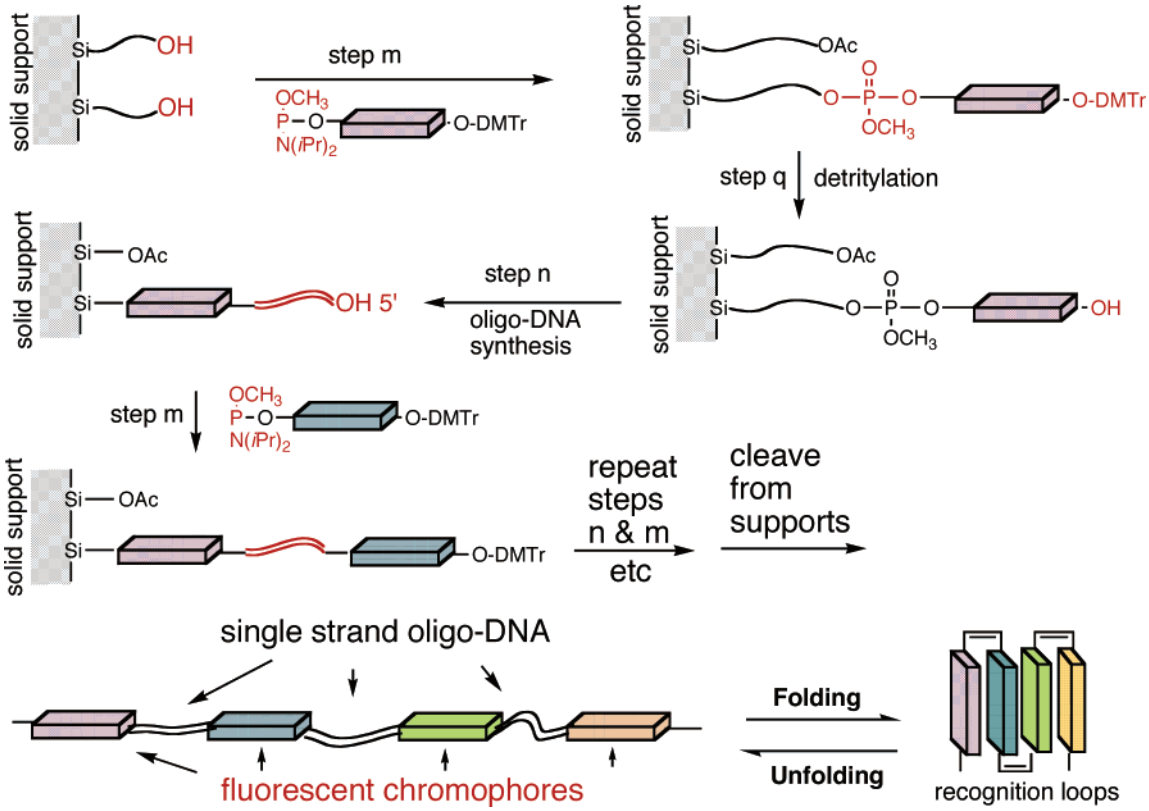


RESULTS AND DISCUSSION

The strategy for incorporating rigid dyes, which typically have poor solubility, into biomolecules is to functionalize them with very soluble ethylene glycol chains. In Scheme 1, all precursor compounds with flexible ethylene glycol chains were synthesized (*19*, *20*) as the appropriate benzaldehyde **7**−**14**, which can be further condensed with ylids to make large π-conjugated systems. The experimental procedures for the synthesis are described in the Experimental Section.

Our initial attempt was to use commercially available monochlorotriethylene glycol as the precursor for introducing soluble groups. Accordingly, in Scheme 2, compound **15** was synthesized using the conventional Wittig reaction with poor yield, and its detritylated derivative **16** is insoluble in organic solvents. The poor solubility of the final product **16** hinders further chemical manipulation and promotes us to make a longer tetraethylene glycol chain for more soluble amphiphilic chromophores. Again, the Wittig reaction was used in the initial

Scheme 7



coupling reaction between the desired aldehyde **11** and the bis-ylid precursor. The reaction yielded only 15% of all-trans **17**, mainly due to the formation of cis−trans isomers of **17** at low temperature (−78 °C). Detritylation of **17** yielded the final product **5**, which could be dissolved in chloroform or dichloromethane. Following the above procedure, soluble compound **2** was also synthesized. Comparing the solubility difference between **16** and **2** or **5**, we have concluded that tetraethylene glycol was an excellent flexible spacer for enhancing solubility of rigid chromophores. Furthermore, tetraethylene glycol proved to be an excellent hinge when inserted into the DNA sequence, and the influence of the spacers on the folding or unfolding behaviors of resulting hybrid foldamers was minimal.

However, the above method for synthesizing all-trans double bond π-conjugates still needs improvement. Thus, the Horner−Wadsworth−Emmons (HWE) reaction was used instead of the conventional Wittig reaction, and all three bis(styryl)benzene derivatives were synthesized again by condensing the phosphonate ylid with corresponding benzaldehyde derivatives as shown in Scheme 3. The HWE reagent (phosphonate ylid) was readily prepared from α,α′-dibromo-*p*-xylene according to the reported procedure (*21*). In dried DMF, 3 equiv of desired aldehyde **10** or **13** was reacted with phosphonate ylid using KOBut as the promoter at room temperature to give the final product **2** or **5** in a high yield. Even with the bulky tetraethylene glycol chain, the HWE condition still favored the formation of all-trans double bond configuration. To prepare polar chromophore **3**, intermediate **19** was prepared following the same procedure for **2** and **5** except that 1 equiv of benzaldehyde **10** was used. Then, final stepwise coupling reaction of **19** and **13** afforded the asymmetric π-conjugate **3**.

It was reported (*22*) that different donor or acceptor substituents on the ends of bis(styryl)benezene π-conjugate could significantly change their emission colors because of the electron donating or withdrawing effects. The oxygen substituents on both ends of the π-conjugate in **5** can be regarded as weak electron donors, involving in the symmetric electron transfer from both ends to the middle of the conjugated system; compound **5** has bright blue fluorescence. In **2**, *n*-butyl amino groups were used to terminate the π-conjugate instead of an oxygen atom as the electron donor to make a stronger donor-π-donor system, which gives green fluorescence. The trend appears that stronger electron donating groups will red-shift fluorescence emission. Following this trend, the featured asymmetric compound **3** has a fluorescence emission wavelength between those of **2** and **5**. The fact that asymmetric compound **3** does not have a fluorescence emission longer than that of symmetric compound **2** may suggest that an acceptor is required in the asymmetric compound in order to have yellow to red fluorescence. With efficient blue fluorophores in hand, our efforts have shifted to prepare similar bis(styryl)benzene structures with red fluorescent emission; the strategy is to vary the structure of the middle π-conjugated bridge and tune the electronic properties of the end substituents. In Scheme 4, three asymmetric bis(styryl)benzene structures were synthesized with the pyridinium ion as an extremely strong electron acceptor in the π-conjugated structure (**20**−**33**); the resulting D-π-A structures have yellow-orange emissions (*23*−*26*). However, the phosphoramidite products of all three precursors, **26**, **29**, and **31**, were not isolated because of low mobility on the silica column despite the fact that three different counterions with various polarity and DMTr protection were attempted (Experimental Section).

Scheme 5 shows the syntheses of the chromophore blocks with red-orange fluorescence based on a donor-acceptor-donor (D-A-D) structure with electron rich-poor-rich distribution. Phosphonate ylid **36** was synthesized as reported previously (*27*, *28*). The same HWE procedures as described for preparation of **2** and **5** were carried out except that tetraethyl 1,4-xylylenediphosphonate was replaced by **36**; consequently, **1** and **4** were synthesized in good yields. Because of the electron withdrawing properties of the dicyano groups, the hydrogen atoms on the methyl group of (2,6-dimethyl-4*H*-pyran-4-ylidene)malononitrile are acidic, and in the presence of base,

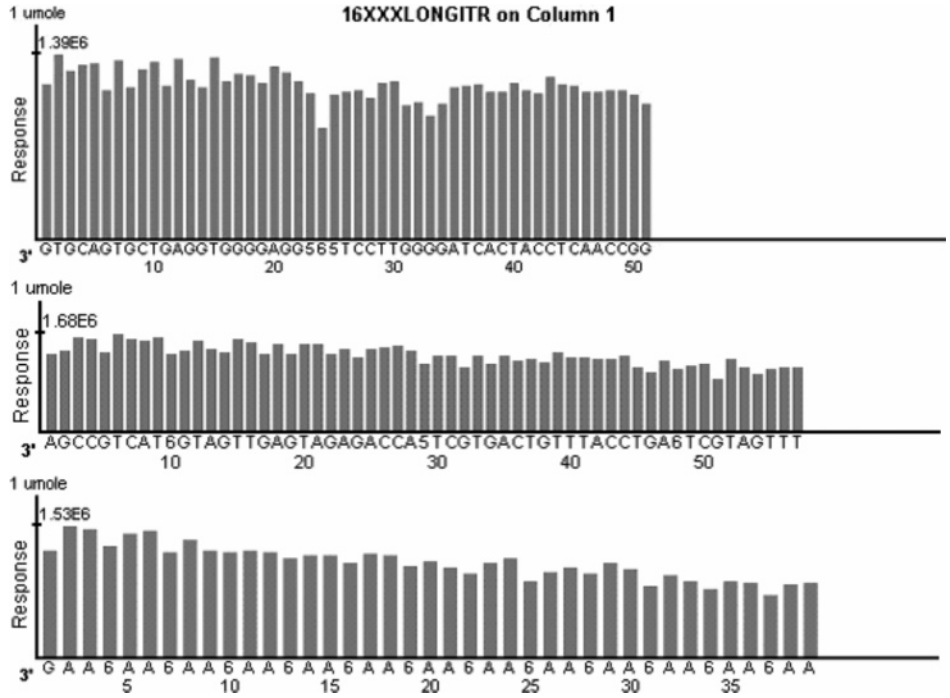


Figure 3. A, T, C, and G stand for single DNA bases linked by phosphotriester and number "5" or "6" stands for synthetic chromophores. Specifically, number "6" here is the red-emitting chromophore with TEG chains linked by phosphotriester (compound **42**) with either DNA bases or chromophores, and number "5" represents the blue-emitting chromophore with TEG chains linked by phosphotriester (compound **41**) with other DNA bases or chromophores. Note that the coupling yields for the two chromophores to DNA bases are almost as high as those of the coupling efficiency of DNA bases. Conversely, coupling of DNA bases to the chromophores is equally high.

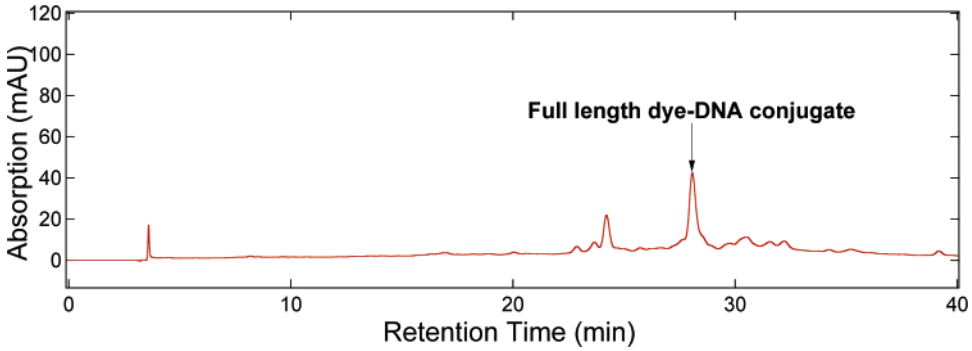


Figure 4. HPLC purification of a DNA 40mer containing one orange-fluorescence dye (compound **42**) and two blue-fluorescence dyes (compound **43**) in the sequence. Full-length DNA sequence containing three organic dyes has an elution time of approximate 28 min while using a linear gradient of H_2O and acetonitrile containing 0.1 M TEAA (triethylamine acetate).

the methyl groups can directly react with a desired aldehyde in a Knoevenagel condensation. The simplicity of the Knoevenagel condition leads to compounds **6** and **37** in one step (*18*). While compound **37** has low optical density and weak fluorescence properties, compound **6** emits impressive red fluorescence with peak maximum at 612 nm in organic solvents.

One important requirement for these fluorescent chromophores is to have asymmetric substitutions at either end of the rodlike or Y-shaped structure. This way, they can be protected with a DMTr group on one end and activated with a phosphoramidite group on the other. Such DMTr-protected and phosphoramidite-activated chromophores are suitable for incorporation into automated DNA synthesis.

Therefore, one of the key steps is the phosphoramidite activation and its efficiency will depend on the yield and purity of its precursor—monotritylated derivative of the chromophoric building blocks. To improve the yield of the monotritylated product, we have developed an efficient route as shown in Scheme 6. In a typical monotritylation process, two products were formed: monotritylated product and bistritylated product. The monotritylated product was purified as the desired product, while the bistritylated product can be further converted to the monotritylated product using a weak Lewis acid zinc chloride as the detritylation reagent (*29*).

A typical detritylation solution consists of $ZnCl_2$ (1.5 g) with 110 mL of CH_2Cl_2/MeOH (10/1, v/v). The detritylation procedure involves treating the bistritylated product in the detritylation solution. The reaction can be monitored with TLC, and typically detritylation finishes within an hour. Once the spot corresponding to the original, nonsubstituted chromophore appeared on the TLC plate, the reaction was quenched by pouring its contents into an aqueous solution saturated with $NaHCO_3$. After chromatography, the yield of the monotritylated product exceeded 40% based on the bistritylated compound. While combining with the direct monotritylation product, the total yield of the monotritylated product had been significantly improved (from ~30% to 56−77%). This method can

Table 1. UV and Fluorescence Data[a]

chromophore	absorbance (λ_{max}) wavelength (nm)	excitation wavelength (nm)	emission (λ_{max}^{EM}) wavelength (nm)
1	379	379	469
2	398	399	473
3	369	384	454
4	477	477	559
5	359	360	409, 430
6	488	490	612
29	433	418	581

[a] The solvent used is chloroform; the concentrations of various chromophores are ~10 μM.

be applied to large-scale preparation of monotritylated derivatives of chromophoric building blocks, and the resulting monosubstituted products can be kept in an −80 °C freezer under basic atmosphere for several months without noticeable decomposition.

Finally, a few fluorescent chromophores, which have orthogonal fluorescence emission, were chosen for phosphoramidite activation. They are compound **38**, the precursor **6** of which emits red fluorescence with an intensity maximum at 612 nm, compound **40**, the precursor **5** of which emits blue fluorescence with an emission maximum at 430 nm, and compound **39**, the precursor **2** of which emits (at 473 nm) in the blue-green region (Table 1). The fluorescence spectra of the red-blue or red-blue/green FRET pairs have little overlap, hence are orthogonal in fluorescent emissions. For efficient FRET pairs, the absorption maximum of the red-fluorescence chromophore (488 nm) should overlap perfectly with the fluorescent emission of the blue-fluorescence donor.

The phosphoramidite derivatives were made according to our prior report (*30*). It is worth mentioning that methylene chloride or methylene chloride/acetonitrile (1/1) was employed as the reaction solvent to ensure the maximum solubility of the chromophore precursor, as is the key point to reach the highest yield of the phosphoramidite derivatives. Also, 5−10% triethylamine in the system was necessary to stabilize the phosphoramidite compounds. The procedure describing the synthesis of phosphoramidites is presented in the Experimental Section. The yields of crude phosphoramidites from the monotritylated derivatives usually exceeded 90%, suitable for solid-state synthesis of phosphoramidite chemistry. The stability of these phosphoramidite chromophores was not optimum in solutions such that the phosphoramidite reagents must be prepared immediately before solid-phase synthesis. Because of the presence of tetraethylene glycol units, the phosphoramidite reagents usually cannot be purified with crystallization, but flash chromatography was effective for their final purification before usage. Additionally, the dumbbell-shaped spots on TLC plates, which correspond to the two steric isomers due to the chiral phosphorus atom in the phosphoramidite of normal DNA bases, were hardly observed in these phosphoramidite chromophores.

Solid-phase synthesis was employed to incorporate the final chromophoric candidates into single-strand DNA backbones as shown in Scheme 7. Our ability to synthesize asymmetrically substituted chromophoric building blocks has established a firm foundation for preparation of foldamers with a controlled molecular orientation, well-defined biological and synthetic sequences. All fluorescent chromophores have been functionalized with hydroxyl groups at their termini. Furthermore, one hydroxyl group will be protected with DMTr and the other will be activated with the β-cyanoethyl phosphoramidite group.

Foldamer synthesis employs the same strategy as DNA synthesis, i.e., one end of the chromophore is activated with phosphoramidite group for attacking the hydroxyl group at the growing chain terminal, and the other end can be regenerated for chain growth by removing the DMTr protected hydroxyl group. The essential steps are coupling between a chain-terminal hydroxyl group and a phosphoramidite group, followed by detritylation to regenerate the chain-terminal hydroxyl group for chain growth.

Unlike DNA synthesis that uses phosphoramidite on the *secondary* hydroxyl group of deoxyribose, the chromophoric blocks use phosphoramidite groups on *primary* hydroxyl groups, which have *completely different* inherent activities. Therefore, their stability and activity toward hydroxyl groups at chain termini are critical to the success of solid-phase synthesis. Nonetheless, we have achieved coupling yields as high as 95% by increasing the phosphoramidite concentration and reaction time and by repeating the coupling step. The *solid-phase synthesis* of foldamer is compatible with DNA synthesis; fluorescent chromophores can be incorporated *anywhere* in the sequence, for example, a juxtaposition of blue and red chromophores (**41-42-41**) embedded in the DNA main chains as shown in Figure 3 (51-mer). Using the trityl monitor reading of the five bases before the three chromophore sequence and five bases after the chromophore sequence, we obtained a *total yield* for coupling three chromophores consecutively of 92%, which corresponds to 97% yield per chromophore coupling. When the chromophore is coupled to a DNA base, followed by another DNA base (57-mer), the yield is also very high. For example, at the 48th position, chromophore **42** is introduced, and the yield of 95% is obtained using the three bases immediately before and after this position. Although trityl absorption does not provide extremely accurate yields for coupling reactions, it should be a good indicator to gauge these high yield coupling reactions

Another example of our state-of-the-art coupling synthesis is shown in Figure 3 with alternating sequences of **42** and double A bases (39-mer); again, the yields of each individual step are high. For example, using the ratio of the two bases before and after position 13 (**42**), we obtained a yield of 92%. Because of such high coupling efficiency, the overall yield is 40% at 39-mer. In the finished sequence, altogether 12 fluorescent dyes are introduced into the DNA backbone; this demonstrates the power of synthetic organic chemistry in biological applications.

As long as the dye number density in the DNA sequence is not too high, the resulting hybrid sequence behaves frequently like oligo-DNA. For example, the dye−DNA conjugates can be cleaved from the solid support using concentrated ammonium hydroxide, and the crude product can be further purified with HPLC as shown in Figure 4. Monitoring at the absorption ($\lambda^{max} \approx 485$ nm) of the red-fluorescence dye (**42**), the major isolated product is, typically, the desired full-length dye−DNA conjugates. The HPLC-purified dye−DNA conjugates have good purity and are suitable for most biological assays.

51-mer: 5'-GGC CAA CTC CAT CAC TAG GGG TTC CT-**41**-**42**-**41**-GGA GGG GTG GAG TCG TGA CGT G-3'

57-mer: 5'-TTT GAT GCT-**42**-AGT CCA TTT GTC AGT GCT-**41**-ACC AGA GAT GAG TTG ATG-**42**-TAC TGC CGA-3'

39-mer: 5'-AA-**42**-AA-**42**-AA-**42**-AA-**42**-AA-**42**-AA-**42**-AA-**42**-AA-**42**-AA-**42**-AA-**42**-AA-**42**-AA-**42**-AA-**42**-AA-**42**-**AAG**-3'

CONCLUSION

In conclusion, we have developed a new method for converting normal organic fluorescent dyes into asymmetrically functionalized phosphoramidite reagents, which has enabled bioconjugation of many fluorescent chromophores at multiple desired positions of DNA backbones. By using the Horner−Wadsworth−Emmons (HWE) reaction and Knoevenagel condensation, a series of highly fluorescent amphiphilic compounds was constructed; these compounds are suitable for labeling DNA since they can be conveniently protected with DMTr and activated with phosphoramidite and their fluorescence is not quenched by the presence of DNA bases.

ACKNOWLEDGMENT

The authors acknowledge the support of National Institute of General Medical Sciences (grant GM065306) and the Arnold and Mabel Beckman Foundation. ADQL is a Beckman Young Investigator (BYI). We thank LBB2 for the Mass measurement and Maggie Tam for the valuable suggestion.

LITERATURE CITED

(1) Letsinger, R. L., and Wu, T. F. (1995) Use of a stilbenedicarboxamide bridge in stabilizing, monitoring, and photochemically altering folded conformations of oligonucleotides. *J. Am. Chem. Soc*. *117*, 7323−7328.

(2) Lewis, F. D., Wu, T. F., Burch, E. L., Bassani, D. M., Yang, J. S., Schneider, S., Jager, W., and Letsinger, R. L. (1995) Hybrid oligonucleotides containing stilbene units−excimer fluorescence and photodimerization. *J. Am. Chem. Soc*. *117*, 8785−8792.

(3) Bevers, S., O'Dea, T. P., and McLaughlin, L. W. (1998) Perylene- and naphthalene-based linkers for duplex and triplex stabilization. *J. Am. Chem. Soc*. *120*, 11004−11005.

(4) (a) Xu, X. H. N., Brownlow, W., Huang, S., and Chen, J. (2003) Single-molecule detection of efflux pump machinery in *Pseudomonas aeruginosa*. *Biochem. Biophys. Res. Commun*. *305*, 79−86.

(5) Martin, R. M., Leonhardt, H., and Cardoso, M. C. (2005) DNA labeling in living cells. *Cytometry, Part A 67A*, 45−52.

(6) Hards, A., Zhou, C. Q., Seitz, M., Brauchle, C., and Zumbusch, A. (2005) Simultaneous AFM manipulation and fluorescence imaging of single DNA strands. *ChemPhysChem 6*, 534−540.

(7) Ishikawa, M., Maruyama, Y., Ye, J. Y., and Futamata, M. (2002) Single-molecule imaging and spectroscopy using fluorescence and surface-enhanced Raman scattering. *J. Biol. Phys*. *28*, 573−585.

(8) Garcia-Parajo, M. F., Veerman, J. A., van Noort, S. J. T., de Grooth, B. G., Greve, J., and van Hulst, N. F. (1998) Near-field optical microscopy for DNA studies at the single molecular level. *Bioimaging 6*, 43−53.

(9) Wang, W., Wan, W., Zhou, H.-H., Niu, S., and Li, A. D. Q. (2003) Alternating DNA and π-conjugated sequences. Thermophilic foldable polymers. *J. Am. Chem. Soc. 125*, 5248−5249.

(10) Wang, W., Wan, W., Stachiw, A., and Li, A. D. Q. (2005) Foldamers with hybrid biological and synthetic sequences as selective DNA fluorescent probes. *Biochemistry 44*, 10751−10756.

(11) Schleifenbaum, A., Stier, G., Gasch, A., Sattler, M., and Schultz, C. (2004) Genetically encoded FRET probe for PKC activity based on pleckstrin. *J. Am. Chem. Soc. 126*, 11786−11787.

(12) Fujimoto, K., Shimizu, H., and Inouye, M. (2004) Unambiguous detection of target DNAs by excimer-monomer switching molecular beacons. *J. Org. Chem. 69*, 3271−3275.

(13) Du, H., Disney, M. D., Miller, B. L., and Krauss, T. D. (2003) Hybridization-based unquenching of DNA hairpins on Au surfaces: Prototypical "molecular beacon" biosensors. *J. Am. Chem. Soc. 125*, 4012−4013.

(14) Fang, X. H., Li, J. J., and Tan, W. H. (2000) Using molecular beacons to probe molecular interactions between lactate dehydrogenase and single-stranded DNA. *Anal. Chem. 72*, 3280−3285.

(15) Tsourkas, A., Behlke, M. A., Xu, Y., and Bao, G. (2003) Spectroscopic features of dual fluorescence/luminescence resonance energy-transfer molecular beacons. *Anal. Chem. 75*, 3697−3703.

(16) Antony, T., Thomas, T., Sigal, L. H., Shirahata, A., and Thomas, T. J. (2001) A molecular beacon strategy for the thermodynamic characterization of triplex DNA: Triplex formation at the promoter region of cyclin D1. *Biochemistry 40*, 9387−9395.

(17) Albota, M., Beljonne, D., Brédas, J.-L., Ehrlich, J. E., Fu, J.-Y., Heikal, A. A., Hess, S. E., Kogej, T., Levin, M. D., Marder, S. R., McCord-Maughon, D., Perry, J. W., Röckel, H, Rumi, M., Subramaniam, G., Webb, W. W., Wu, X., and Xu, C. (1998) Design of organic molecules with large two-photon absorption cross sections. *Science 281*, 1653−1656.

(18) Moylan, C. R., Ermer, S., Lovejoy, S. M., McComb, I.-H., Leung, D. S., Wortmann, R., Krdmer, P., and Twieg, R. J. (1996) (Dicyanomethylene)pyran derivatives with C-2v symmetry: An unusual class of nonlinear optical chromophores. *J. Am. Chem. Soc. 118*, 12950−12955.

(19) Amabilino, D. B., Ashton, P. R., Brown, C. L., Cordova, E., Godinez, L. A., Goodnow, T. T., Kaifer, A. E., Newton, S. P., Pietraszkiewicz, M., Philp, D., Raymo, F. M., Reder, A. S., Rutland, M. T., Slawin, A. M. Z., Spencer, N., Stoddart, J. F., and Williams, D. J. (1995) Molecular meccano 2. Self-assembly of [eta]catenanes. *J. Am. Chem. Soc. 117*, 1271−1293.

(20) Maeda, H., Furuyoshi, S., Nakatsuji, Y., and Okahara, M. (1982) Intramolecular cyclization of N,N-bis(oligooxyethylene)amines: a new synthesis of monoaza crown ethers. *Tetrahedron 38*, 3359−3362.

(21) Pond, S. J. K., Tsutsumi, O., Rumi, M., Kwon, O., Zojer, E., Brédas, J.-L., Marder, S. R., and Perry, J. W. (2004) Metal-ion sensing fluorophores with large two-photon absorption cross sections: Aza-crown ether substituted donor-acceptor-donor distyryl benzenes. *J. Am. Chem. Soc. 126*, 9291−9306.

(22) Bartholomew, G. P., and Bazan, G. C. (2002) Synthesis, characterization, and spectroscopy of 4,7,12,15-[2.2]paracyclophane containing donor and acceptor groups: Impact of substitution patterns on through-space charge transfer. *J. Am. Chem. Soc. 124*, 5183−5196.

(23) For TBDMS manipulation: Lombardo, L. (1984) Diisopropylethylamine: an effective catalyst for the introduction of the tert-butyldimethylsilyl group. *Tetrahedron Lett. 25*, 227−228.

(24) Corey, E. J., and Venkateswarlu, A. (1972) Protection of hydroxyl groups as tert-butyldimethylsilyl derivatives. *J. Am. Chem. Soc. 94*, 6190−6191.

(25) For ion replacement: Brimacombe, J. S., and Kabir, A. K. M. S. (1988) Higher-carbon sugars. Part 10. The synthesis and osmylation of 7,8-dideoxy-1,2:3,4-di-O-isopropylidene-b-L-glycero-D-galacto-oct-7-enopyranose and related studies. *Carbohydr. Res. 174*, 37−45.

(26) For condensation: Maekawa, Y., Kato, S., Saigo, K., Hasegawa, M., and Ohashi, Y. (1991) Crystallographic interpretation of the topochemical behavior of alkyl alpha-cyano-4-[2-(4-pyridyl)ethenyl]-cinnamates in the crystalline state-enhancement of photopolymerizability by complex-formation. *Macromolecules 24*, 2314−2322.

(27) Wenseleers, W., Stellacci, F., Meyer-Friedrichsen, T., Mangel, T., Bauer, C. A., Pond, S. J. K., Marder, S. R., and Perry, J. W. (2002) Five orders-of-magnitude enhancement of two-photon absorption for dyes on silver nanoparticle fractal clusters. *J. Phys. Chem. B106*, 6853−6863.

(28) Ngola, S. M., Kearney, P. C., Mecozzi, S., Russell, K., and Dougherty, D. A. (1999) A selective receptor for arginine derivatives in aqueous media. Energetic consequences of salt bridges that are highly exposed to water. *J. Am. Chem. Soc. 121*, 1192−1201.

(29) Ding, X. L., Wang, W., and Kong, F. Z. (1998) Detritylation of mono- and di-saccharide derivatives using ferric chloride hydrate. *Carbohydr. Res*. *303*, 445−448.

(30) Wang, W., Li, L-S., Helms, G., Zhou, H-H., and Li, A. D. Q. (2003) To fold or to assemble? *J. Am. Chem. Soc. 125*, 1120−1121.

(31) Perrin, D. D., and Armarego, W. L. F. (1988) *Purification of Laboratory Chemicals*, 3rd ed., Pergamon Press, New York.

(32) Stuhr-Hansen, N., Christensen, J. B., Harrit, N., and Bjrnholm, T. (2003) Novel synthesis of protected thiol end-capped stilbenes and oligo(phenylenevinylene)s (OPVs). *J. Org. Chem. 68*, 1275−1282.

(33) Schwöppe, D., and Meier, H. (2000) Crown ether substituted 1,4-distyrylbenzene and their complexation with alkali picrates. *J. Prakt. Chem. 342* (5), 459−464.

BC060151C

Use of Lanthanide-Grafted Inorganic Nanoparticles as Effective Contrast Agents for Cellular Uptake Imaging

Pierre Voisin,[‡] Emeline Julie Ribot,[‡] Sylvain Miraux,[‡] Anne-Karine Bouzier-Sore,[‡] Jean-François Lahitte,[†,‡] Véronique Bouchaud,[‡] Stéphane Mornet,[§] Eric Thiaudière,[‡] Jean-Michel Franconi,[‡] Lydia Raison,[†] Christine Labrugère,[||] and Marie-Hélène Delville*[,†]

Institut de Chimie de la Matière Condensée de Bordeaux, UPR CNRS 9048, Université Bordeaux 1, 87 Avenue du Docteur A. Schweitzer, F-33608 Pessac cedex, France, Résonance Magnétique des Systèmes Biologiques, UMR CNRS 5536, 146 rue Léo Saignat, F-33076 Bordeaux cedex France, Imagerie Moléculaire et Nano-Bio-Technologie, IECB, UMR-CNRS 5471 Avenue des Facultés, Université Bordeaux 1, F-33405 Talence, France, and Cecama, 87 Avenue du Docteur A. Schweitzer, F-33608 Pessac cedex, France. Received September 1, 2006; Revised Manuscript Received March 24, 2007

The improvement of commonly used Gd^{3+}-based MRI agents requires the design of new systems with optimized *in vivo* efficacy, pharmacokinetic properties, and specificity. To design these contrast agents, two parameters are usually considered: increasing the number of coordinated water molecules or increasing the rotational correlation time by increasing molecular weight and size. This has been achieved by noncovalent or covalent binding of low-molecular weight Gd^{3+} chelates to macromolecules or polymers. The grafting of these high-spin paramagnetic gadolinium chelates on metal oxide nanoparticles (SiO_2, Al_2O_3) is proposed. This new synthetic strategy presents at least two main advantages: (1) a high T_1-relaxivity for MRI with a 275% increase of the MRI signal and (2) the ability of nanoparticles to be internalized in cells. Results indicate that these new contrast agents lead to a huge reconcentration of Gd^{3+} paramagnetic species inside microglial cells. This reconcentration phenomenon gives rise to high signal-to-noise ratios on MR images of cells after particle internalization, from 1.4 to 3.75, using Al_2O_3 or SiO_2 particles, respectively. The properties of these new particles will be further used to get new insight into gene therapy against glioma, using microglial cells as vehicles to simultaneously transport a suicide gene and contrast agents. Since microglia are chemoattracted to brain tumors, the presence of these new contrast agents inside the cells will lead to a better MRI determination of the *in vivo* location, shape, and borders of the tumors. These Gd^{3+}-loaded microglia can therefore provide effective localization of tumors by MRI before applying any therapeutic treatment. The rate of carcinoma remission following a suicide gene strategy is also possible.

INTRODUCTION

Numerous strategies have been developed for cellular imaging (*1*, *2*). Noninvasive imaging techniques such as magnetic resonance imaging (MRI) appear suitable since they can operate on soft tissues and cells in real time. When highly paramagnetic contrast agents are used, this technique allows for high contrast as well as spatial resolution (*3*, *4*). Such an approach strongly improves the analysis of images and facilitates their interpretation (*5*−*11*). Further developments for specific cellular imaging require the synthesis of new contrast agents, which should be able on one hand to increase contrast and on the other hand, to target cells.

Previous studies have demonstrated the utility of using circulating cells of the immunological system like lymphocytes, monocytes, and microglial cells after the uptake of contrast agents with a superparamagnetic core (*12*, *13*). These contrast agents with various and controlled sizes are easily taken up. With their high susceptibility effect, iron oxide nanoparticles can be detected at very low concentration at high magnetic fields. With T_2* weighted images, they allow the detection of single cells *in vitro* (*4*). Nevertheless, in this situation, the signal due to the iron oxide nanoparticles can only be a hyposignal, and this appears as a limit in image analysis (*12*). Moreover, the precise anatomic localization of this iron contrast agent is limited by the breakdown of spatial resolution due to a high local susceptibility effect. Consequently, the detection of a defined cellular population in a localized area *in vivo* becomes a major difficulty.

Therefore, there is a real need to design MRI contrast agents, which can produce detectable changes in the MR signal intensity of the target tissue or organ by changing their MR relaxation properties (*14*, *15*). Among them, the Gd^{3+} DTPA chelate was the first FDA approved contrast agent in clinical use (*16*). These contrast agents require (i) a large number of paramagnetic centers (seven unpaired electrons for Gd^{3+}) selectively bound to the target tissue and (ii) an adapted molecular weight of the MRI agents in order to extend their vascular retention (*17*, *18*) and to slow their tissue clearance (*19*).

Over the past decade, various approaches have been used to address both of these issues such as the conjugation of paramagnetic chelates to macromolecules (*20*) and linear polymers (*21*). Recent reports are on polymeric paramagnetic liposomes (*22*, *23*), micelles (*24*), and dendrimer-based metal chelates (*25*). These studies have shown that Gd-DTPA (DTPA: diethylenetriaminepentaacetic acid)-based contrast agents of high molecular weight have extended circulation times and can accumulate at specific sites. The liposomes are made by incorporating DTPA-conjugated lipids into liposomes. The conjugated lipids form chelating sites for gadolinium ions. Because of its excellent metal-chelating properties, DTPA is one of the most widely used organic ligands in MRI and positron emission tomography (PET) (*26*−*28*). This approach can be

* Corresponding author. E-mail: delville@icmcb-bordeaux.cnrs.fr.
[†] Institut de Chimie de la Matière Condensée de Bordeaux.
[‡] Résonance Magnétique des Systèmes Biologiques.
[§] Imagerie Moléculaire et Nano-Bio-Technologie.
[||] Cecama.

10.1021/bc060269t CCC: $37.00 © 2007 American Chemical Society
Published on Web 05/19/2007

extended to the MR imaging of any receptors once the targeting ligands are conjugated to the lipids.

A new class of polymeric metal-loaded nanoparticles with core−shell morphology has been developed and shows a great potential as a contrast agent for medical imaging (*29*). The Gd^{3+}-loaded nanoparticles could reduce relaxation times *in vitro*, and provide excellent contrast when used to image the heart and the gastrointestinal tract in rat animal models.

However, the utility of these contrast agents might be limited. First, the relaxivity of the entrapped paramagnetic species is lowered because of the limited exchange of bulk water with the contrast agents (*30*, *31*). Indeed, this exchange is dependent on the permeability of the liposome or polymeric membrane to water (*29*, *32*).

For this reason, the development of biocompatible nanoparticles with an external shell of high-spin paramagnetic lanthanide contrast agents like gadolinium chelate appears to be advantageous for targeted imaging (*33*). The gadolinium nucleus generates a hypersignal with a T_1-weighted sequence, even at high magnetic field and, consequently, a much easier interpretation of the MR images. However, these low molecular weight gadolinium chelates accumulate in the extra cellular space only where the "blood−brain barrier" breakdown took place. They undergo rapid diffusion through the interstitial as well as renal elimination and therefore have the limitation of providing a time-dependent image of tumor margins (*34*).

The chemical grafting of such contrast agents on metal oxide nanoparticles will be an alternative route to change their biodistribution and increase their half-lives, since they are internalized by macrophages. Moreover, they will also exhibit a more pronounced hypersignal with a T_1-weighted sequence. Indeed, silica, for example, would be an excellent carrier for the lanthanide chelates, as it is porous enough for water to freely move in and out of the frame. The size of the particles will slow the rotational movement of the chelates and improve the relaxation of water. Additionally, the biocompatible silica particles (*35*, *36*) can be easily derivatized, and targeted contrast agents can be synthesized (*37*). These nanoparticles could be radio-opaque and thus show X-ray contrast due to the presence of these electron-dense metal ions. Nanosized particles of about 20 nm, are small enough to pass through the body, and above all are able to enter cells since they can be easily internalized (pynocytosis, phagocytosis, or both). In the following experiments, we have modified SiO_2 nanoparticles and alumina nanoparticles with an aminosilane to bind Gd^{3+}-DTPA on their surface. Then, *in vitro* microglial cells were used to validate the increased MRI contrast, owing to internalized gadolinium particles and not free particles located in the intercellular space. These experiments were performed with the particles linked to tetramethyl rhodamine isothiocyanate (TRITC) as a fluorochrome and analyzed by microscopy and flow cytometry before the MRI characterizations and observations.

EXPERIMENTAL PROCEDURES

Characterizations. TEM was performed at room temperature on a JEOL JEM-2000 FX transmission electron microscope using an accelerating voltage of 200 kV. DRIFT characterizations were performed using a Bruker IFS Equinox 55FTIR spectrometer (signal averaging 64 scans at a resolution of 4 cm^{-1} in KBr pellets containing ca. 2 mass % of material). The zeta potential of the nanoparticles was assessed by using a Zetasizer 3000HSA setup (Malvern Instruments) equipped with a He−Ne laser (50 mW, 532 nm). The zeta potential measurement based on laser Doppler interferometry was used to assess the electrophoretic mobility of nanoparticles. Measurements were performed for 20 s using a standard capillary electrophoresis cell. The dielectric constant was set to 80.4 and the Smoluchowsky constant f(ka) was 1.5. Thermogravimetric analyses (TGA) were performed using a SETARAM apparatus (5 °C min^{-1} from 30 to 600 °C, air with a 2-h plateau at 170 °C). X-ray photoelectron spectra were recorded with a VG 220i-XL ESCALAB spectrometer. Irradiation was a non-monochromatized Al source operating at 110W ($h\nu = 1486.6$ eV). Acquisition was done at constant pass energy (i.e., 40 eV for high resolution) with a flood gun, and analyzed area was about 150 μm diameter. Spectra were fitted with the AVANTAGE software by THERMO Election. Fluorescence analysis by flow cytometry was performed on a FACScan cytometer (BD BioSciences, Le pont de Claix, France) using Cell Quest Pro software.

X-ray photoelectron spectra were obtained using a VG 220i-XL Escalab spectrometer, employing non-monochromatized Mg Kα source ($h\nu = 1253.6$ eV). The X-ray gun was operated at 10 kV and 20 mA (pressure: 10^{-8} bar). Powdered samples were pressed onto small indium foils and survey spectra obtained in the constant pass energy mode of 150 eV. The C1s contamination line (BE = 284.6 eV) was used to calibrate all binding energy values.

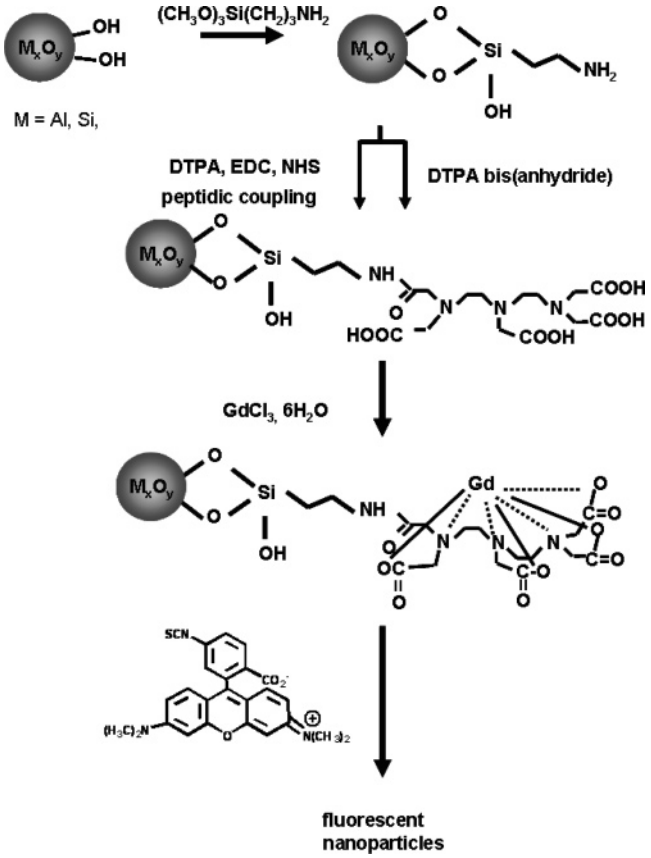
MR images were acquired on a 4.7 T Biospec system (Bruker, Ettlingen, Germany). The system was equipped with a 6-cm BG6 gradient system capable of 950 mT/m maximum strength. Measurements were performed with a birdcage resonator (35-mm diameter and 80-mm length) tuned at 200.3 MHz. Longitudinal relaxation time constants were measured with the inversion recovery technique (48 points, inversion delay from 20 to 5000 ms) and transverse relaxation time using the CPMG pulse sequence (32 echoes) on different nanoparticle concentrations (20.4, 17, 14.57, 12.75, 11.33, 10.2, 6.8, 5.1 μM). 2D images were acquired with a T_1-weighted sequence (FLASH sequence, TE/TR = 2/75 ms, flip angle: 75°, 8 slices, FOV = 27 × 27 mm, matrix = 128 × 128, average of 16, total acquisition time = 2 min 35 s) on microglial cell phantoms before and after internalization of the MRI contrast agent particles. For Al_2O_3 particles, TE/TR was 1.7/100 ms and the flip angle was 90°. T_1-relaxation time was also evaluated on these two samples.

The lanthanide content has been measured by inductively coupled plasma mass spectrometer ICP-MS (HP 4500, Agilent Technologies) equipped with a crossflow nebulizer. The instrumental conditions have been optimized with a 10 μg/L solution of lithium, yttrium, and bismuth. Plasma gas flow rate: 15 L/min; auxiliary gas flow rate: 0.8 L/min; nebulizer gas flow rate: 1.1 L/min; power: 1350 W; oxide (CeO/Ce): <0.5%; doubly charged (Ba^{2+}/Ba): <3%. The analyses have been performed using an external calibration. A 1 g/L gadolinium solution has been used to prepare the standard solutions (Techlab, Metz, France). Rhodium (Techlab, Metz, France) has been used as internal standard to evaluate the instrumental drift.

Materials. $LnCl_3{:}6H_2O$, tetramethyl rhodamine isothiocyanate (TRITC), 3-aminopropyltrimethoxy-silane (APS), diethylenetriamine pentaacetic acid (DTPA), diethylenetriamine pentaacetic anhydride (DTPAA) (Aldrich), SiO_2 (negatively charged silica sol Ludox HS-40 (DuPont) (composition: 40% SiO_2, 60% H_2O, <1% Na_2O, average diameter of 20 nm, surface area ~220 m^2/g), ammonia, ethanol, and DMF from Aldrich were used without further purification. Alumina C (with an average diameter of 13 nm according to the manufacturer, surface area ~ 100 m^2/g) was generously provided by Degussa.

(1) Synthesis of APS-Grafted Nanoparticles. A 2 g amount of the metal oxide nanoparticles was dispersed by sonication in 100 mL of distilled water purged with argon or anhydrous toluene. A 2 mL amount of freshly distilled APS was added under argon and maintained under rapid stirring for 36 h. The suspension was then put under reflux for 2 h to achieve the

Scheme 1. Chemical Modification of the Metal Oxide Nanoparticles



reaction. The nanoparticles were then washed and purified by centrifugation four times with ethanol and then water to remove unreacted APS. The samples were redispersed and stored in water in which they are stable for months or dried at 70 °C under low pressure for 24 h for analysis.

(2) Synthesis of DTPA-Grafted Nanoparticles. Two ways of synthesis have been used and gave similar results. In the first method, the amine nanoparticles prepared above were diluted with 50 mL of water or 50 mL of DMF. Diethylene triaminepentaacetic anhydride (DTPAA) was slowly added to the solution (10/1 DTPAA/-NH_2 for the synthesis in water and 2/1 DTPAA/-NH_2 for the synthesis in DMF). After 24 h in both cases, the particles were filtered and purified five times by centrifugation−redispersion in water. The final products were stored in water as colloidal suspensions (at a concentration of 100 g/L) or dried at 70 °C under low pressure for 24 h for analysis.

In the second method, DTPA is linked to amino group using peptide synthesis with a carbodiimide coupling agent in the presence of NHS (*N*-hydroxysuccinimide) (*38*). A suspension of 2 g of the amino nanoparticles in 50 mL of water was prepared. A pH 5 solution of 1.67 g of DTPA in water was activated with 1.1 g of EDC (1-ethyl-3-(3-dimethylaminopropyl)carbodiimide) and 1.1 g of NHS (*39*, *40*). The resulting solution was added into the colloidal suspension while maintaining pH 5 (HEPES buffer) and reacted for 24 h. The nanoparticles were washed and cleaned five times by centrifugation−redispersion in water. The final product was stored in water as a colloidal suspension or dried at 70 °C under low pressure for 24 h for analysis. This second procedure was finally chosen because H_2O is the only solvent used for the entire synthesis.

(3) Synthesis of Lanthanide Chelate-Grafted Nanoparticles. A colloidal suspension of 1 g of DTPA-grafted nanoparticles in 20 mL of water was added to 0.5 g of hydrated

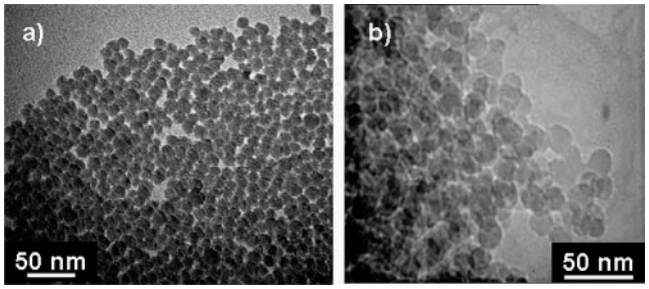


Figure 1. TEM images of (a) bare and (b) APS-grafted silica nanoparticles.

Table 1. Grafted-APS Surface Density for Al_2O_3 and SiO_2 Nanoparticles

	H_2O	toluene
Al_2O_3−APS	5.1 ± 0.3 μmol/m^2	12.8 ± 0.3 μmol/m^2
SiO_2−APS	5.3 ± 0.3 μmol/m^2	9.0 ± 0.3 μmol/m^2

$GdCl_3$:$6H_2O$ at room temperature. After 24 h, the excess of unreacted Gd(III) was removed by centrifugation−redispersion five times in water, and the absence of free Ln(III) was checked with arsenazo III indicator. The final product was stored in water as a colloidal suspension or dried at 70 °C under low pressure for 24 h for analysis.

(4) Synthesis of Rhodamine-Loaded Nanoparticles. A colloidal suspension of 0.25 g of amino-grafted nanoparticles in 50 mL of water was added to 0.5 g of tetramethyl rhodamine isothiocyanate (TRITC) and reacted for 5 h in a 0.1 M carbonate/bicarbonate buffer at pH 9. The excess of unreacted TRITC was removed by five cycles of centrifugation−redispersion until no more signals was detected in the supernatant by UV−visible spectroscopy. The final product was stored in water as a colloidal suspension.

(5) Cell Culture. Human microglial cell line was grown as a monolayer. C6 glioma rat membrane extracts and serum starvation were used in this study to activate microglial cells 24 h before the experiments (this allows the cells to acquire phagocytosis ability). After a 4-h incubation with the lanthanide-grafted nanoparticles (170 nmol/L), the cellular monolayers were washed three times with phosphate-buffered saline (PBS), collected, fixed, and trapped in agarose gels (1% in H_2O) for the MRI analysis. The biological internalization characterization of the contrast agent by the microglia was controlled using nanoparticles modified with TRITC fluorochrome (0.5 mM) and both qualitative microscopy and quantitative flow cytometric measurements.

RESULTS AND DISCUSSION

The choice of approach of silica and alumina nanoparticles grafted with lanthanide contrast agents was motivated because they present a large range of particle sizes (10 to 1000 nm) which can be tailored to the requirements of biological applications (intravenous (IV) injections for example). They also exhibit a good selectivity, low cytotoxicity (SiO_2 (*41*), Al_2O_3 (*42*), and high tissue clearance properties. These particles are modified with Gd^{3+} to provide contrast in MR, and a fluorescent probe for cytometry analysis. The grafting of the metal oxide nanoparticles (Al_2O_3, SiO_2) was performed according to Scheme 1.

The surface of the nanoparticles were chemically modified by reacting the surface hydroxyl groups with the 3-aminopropyltrimethoxysilane (APS) leading to an aminated surface. This reaction was stirred overnight at room temperature and for 2 h under a gentle reflux to promote covalent bonding of the organosilane to the surface of the nanoparticle (*43*). The

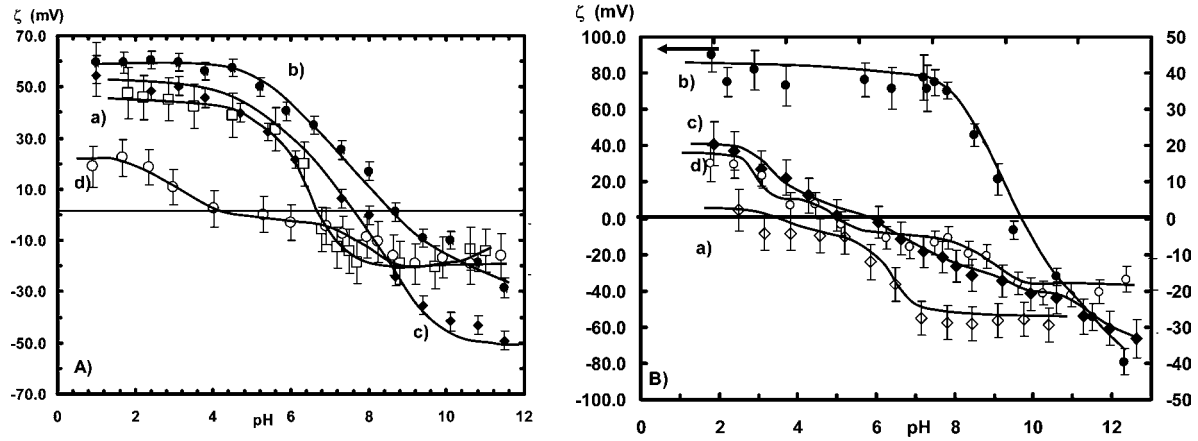


Figure 2. Zeta potential titration as a function of pH of the (A) (a) Al_2O_3, (b) Al_2O_3-APS, (c) $Al_2O_3-APS-DTPA$, (d) $Al_2O_3-APS-DTPA$-Gd dispersions; (B) (a) SiO_2, (b) SiO_2-APS, (c) $SiO_2-APS-DTPA$, (d) $SiO_2-APS-DTPA$-Gd dispersions. Lines are guides for the eyes. In B, consider right scale for a, c, and d.

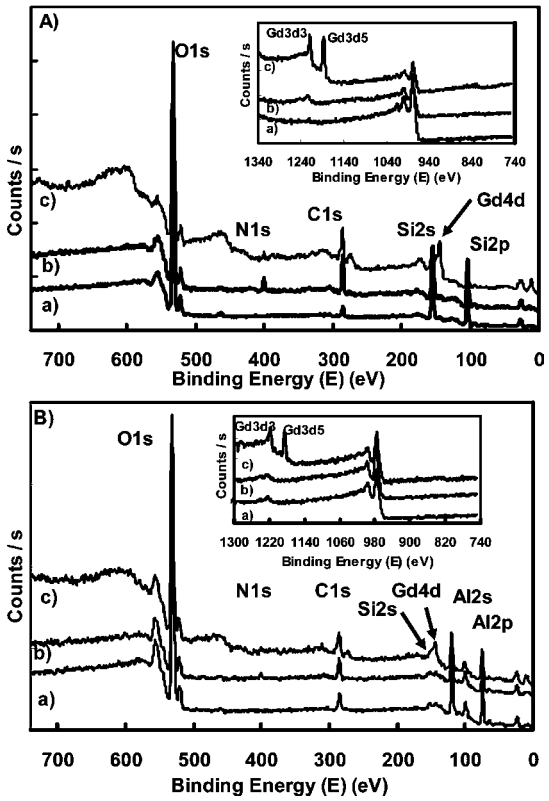


Figure 3. (A) XPS data of the (a) SiO_2, (b) SiO_2-APS, and (c) $SiO_2-APS-DTPA$ Gd nanoparticles (0−740 eV survey); insert: 740−1340 eV survey. (B) XPS data of the (a) Al_2O_3, (b) Al_2O_3-APS, and (c) $Al_2O_3-APS-DTPA$ Gd nanoparticles (0−740 eV survey); insert: 740−1340 eV survey.

chemical attachment of DTPA to these aminated nanoparticles was carried out by the formation of an amide linkage between the primary amine group and one of the five carbonyl groups of DTPA, using either a reaction directly with the dianhydride or a peptidic coupling by esterification with EDC catalyzed by NHS (*38*) to facilitate the amide linkage (*39*). The coordination of DTPA with Gd^{3+} was subsequently followed by reaction with an aqueous solution of $GdCl_3{:}6H_2O$.

The particles were characterized at each step to ensure the efficiency of the chemical modification. Quantification of the grafting agent was calculated from the thermogravimetric mass loss. The APS surface density is expressed in mol/m^2 as $d_{APS} = \Delta m/M_{cx}Spm$, on the assumption that the thermal degradation proceeds (*44*) at the Si−C bond breaking level between 200 and 650 °C (Table 1). $\Delta m/m$ is the measured mass loss between the two concerned temperatures (200 and 650 °C), M_{cx} is the molecular weight of the concerned fragment, and Sp the specific surface area of metal oxide (220 m^2/g for Ludox and 100 m^2/g for alumina C).

The APS surface density is higher when the reaction is performed in refluxing toluene for both nanoparticles. This is characteristic of the formation of more than one monolayer of silane at the surface of the particles (*45*). Ishida estimated that the surface area occupied by an APS molecule is $S_{APS} = 40$ Å^2 (*46*). The number of APS layers (NL_{APS}) can be estimated according to the following equation: $NL_{APS} = N_A \times d_{APS} \times S_{APS}$ where N_A is the Avogadro's constant $= 6.02 \times 10^{23}$ molecules mol^{-1} and d_{APS} is the silane surface density, given in Table 1. The number of layers (between 2 and 3) depends on the reaction solvent (*47, 48*) and does not modify the particle size, as shown by TEM images (Figure 1).

Diffuse reflectance infrared Fourier transform (DRIFT) spectroscopy is another very useful technique for probing the effectiveness of the chemical grafting (*48*). The bare silica nanoparticles present simple infrared spectra, with two kinds of hydroxyl groups: (i) the bound Si−OH, characterized by a very broad IR absorption band in the 2800−3700 cm^{-1} region; (ii) the so-called free Si−OH groups, which provide a narrow IR absorption band at 3750 cm^{-1}. The stretching at 1622 cm^{-1} still shows the presence of residual physisorbed water molecules. The large bands centered on 1866, 1093, 794 are assigned to the Si−O and Si−O−Si stretching modes. Alumina nanoparticles exhibit a large band (3200−3800 cm^{-1}) centered at 3450 cm^{-1} coupled with a thinner one at 1634 cm^{-1} attributed to the deformation mode of the hydroxyl groups. The subsequent effective APS-silanization of the mineral oxides is evidenced by the modification of the DRIFT spectrum of the resulting powders. Grafting of the organic APS on the silica particles is illustrated by (i) the disappearance of the single Si−OH (with respect to the Al−OH) vibration; (ii) the shape modification of the band around 3500 cm^{-1}, due to the NH vibrations, and the 2937 and 2873 cm^{-1} bands of the grafted alkyl chain which are assigned to the asymmetric and symmetric stretching vibrations of CH_2 groups, confirming that the amino propyl groups get anchored; and (iii) the presence of the 1624 and 1544 (respectively, the free and hydrogen-bonded NH_2), 787 (NH bending mode), and 1406 ($SiCH_2$) cm^{-1}. The chemical grafting of the DTPA units is pointed out by the new stretching bands due to the amide and carboxylic functions (1660, 1635, 1542 cm^{-1}) while the complexation with Gd^{3+} induces a slight

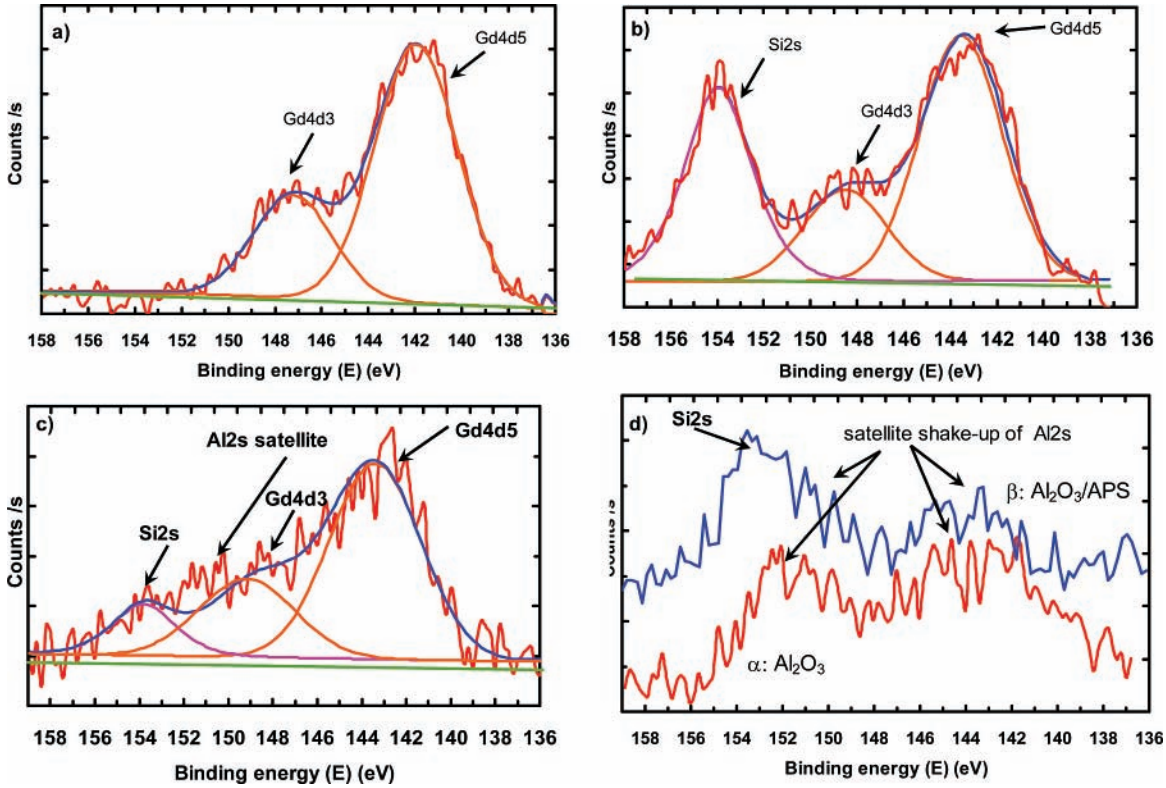


Figure 4. High resolution spectra of the 136−158 eV zone for (a) commercial Gd DTPA complex, (b) SiO_2−APS−DTPA Gd nanoparticles, (c) Al_2O_3−APS−DTPA Gd nanoparticles, (d) (α) satellite "shake-up" of Al2s in the 136−158 eV zone for pristine Al_2O_3 and (*β*) satellite "shake-up" of Al2s in the 136−158 eV zone for Al_2O_3/APS particles showing both the satellite "shake-up" of Al2s and the Si2s peak.

Table 2. Surface Elemental Composition of Al_2O_3, SiO_2 Particles before and after Chemical Modification

	Al_2O_3						SiO_2				
atomic %	C	O	Al	Si	N	Gd	C	O	Si	N	Gd
unmodified	10.2	58.4	31.4	-	-	-	8.1	64.7	27.2	-	-
APS	13.1	52.8	29.9	2.6	1.6	-	20.7	50.8	23.9	4.6	-
DTPA	10.5	54.1	31.9	1.6	1.9	-	22.5	49.4	22.8	5.0	-
Gd	15.0	54.9	24.0	2.9	1.0	2.2	27.7	46.6	18.2	3.5	3.9

bathochromic shift of these bands to 1632, 1592, 1561 cm^{-1} respectively. As far as the grafted alumina particles are concerned, identical trends were observed, with an additional vibration attributed to the Al−O−Si vibration located at 1152 cm^{-1} (*44*).

Zeta potential titrations as a function of pH (obtained by adding 0.01 M HNO_3 or KOH solutions) were realized to verify the isoelectric points (IEP) of Al_2O_3 and SiO_2 as well as their pH range of stability (Figure 2). The IEP values were 7.8 and 2.3, respectively. The evolution of the IEPs with the different modification steps also provided an additional confirmation of the silane immobilization as well as the lanthanide complexation. Indeed, after the APS coating, the two suspensions exhibited isoelectric points of 8.4 (Figure 2a) and 10.2 (Figure 2b), respectively. This IEP displacement toward higher values is characteristic of the presence of free amines on the surface of the particles. Once the peptidic coupling was achieved, there was another shift of the IEP toward lower pH values due to the introduction of the pentaacid ligand. The final IEPs were, respectively, 4.5 and 4.2 pH units for Al_2O_3 and SiO_2 nanoparticles, which confers upon them a high stability in a medium with a pH down to 4.5.

XPS studies were carried out for the different samples. Figure 3 shows the XPS general survey scans of the SiO_2 and Al_2O_3 nanoparticles at each step of the chemical modification (traces a, b, and c) until the final coating with DTPA-Gd complex (*49*).

No nitrogen was detected on the unmodified particles, but an unavoidable contaminant carbon peak due to impurities from processing (*50*) was observed. However, the increase of the C1s peak as well as the presence of the N1s peak in trace b) for the SiO_2−APS and Al_2O_3−APS nanoparticles confirms that the reaction with the aminopropylsilane occurred (Table 2).

In the case of the alumina particles, a detectable Si2s contribution is due to the silicon atom of the aminosilane. SiO_2−APS−DTPA and Al_2O_3−APS−DTPA samples presented the same trends (data not shown). The introduction of the gadolinium ion is illustrated by the appearance of the Gd photoelectron peaks at a binding energy of 143 eV for Gd4d and at 1186 and 1219 eV for $Gd3d_{5/2}$ and $Gd3d_{3/2}$, respectively (Figure 3A and 3B inserts). Study of the high-resolution $Gd4d_{5/2}$ and $Gd4d_{3/2}$ spectra lead to a quantitative estimation of Gd grafted onto silica or alumina materials. As the literature gives poor information on the sensitivity factor of Gd (*51*), we carried out a calibration using a commercial reference of Gd-DTPA complex, adjusting the $Gd4d_{5/2}$ and $Gd4d_{3/2}$ sensitivity factors from a Scofield table to obtain the ratios expected between chemical elements (i.e., 6.5 for $Gd4d_{5/2}$ after Gd4d fitting, Figure 4a).

In the case of silica nanoparticles, fitting in the 136−158 eV binding energy range gave the well-defined Si2s and $Gd4d_{3/2}$−$Gd4d_{5/2}$ components (Figure 4b) leading to a surface quantification of 4 atomic % of Gd (Table 2). Concerning alumina, fitting

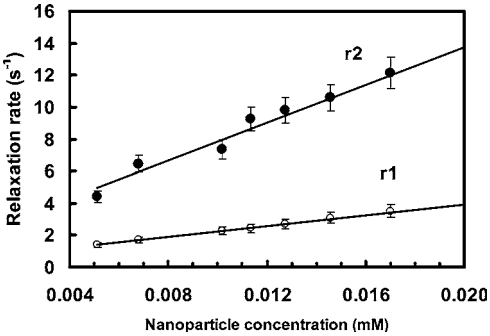


Figure 5. Plots of the relaxation rates R1 and R2 with respect to the concentrations of SiO_2−APS−DTPA Gd nanoparticles (20.4; 17; 14.57; 12.75; 11.33; 10.20; 6.8; 5.1 μM of beads). Proton relaxivities (r_1 and r_2) were determined based on these linear relationships.

of the same energy range (Figure 4c) was more complex due to the presence of satellite "shakeup" of Al2s (Figure 4dα) and Si2s photoelectron peaks from APS (Figure 4dβ) observed, in addition to the chemical modification of alumina with the aminosilane. The percentage of Gd on Al_2O_3 was found to be around 2 atomic % (Figure 4c, Table 2)).

These nanoparticles were also studied by NMR. They generated contrast on both longitudinal and transverse proton relaxation time-weighted sequences. The proton relaxivities were calculated by measuring the change in R1 and R2 for increasing concentrations of nanoparticles in distilled water (Figure 5). The r_1 and r_2 relaxivities of these Gd-doped silica nanoparticles were, respectively, 168 ± 4 mM^{-1} s^{-1} and 589 ± 38 mM^{-1} s^{-1} at 4.7 T, respectively.

The relaxivity of the SiO_2−APS−DTPA Gd nanoparticles is much higher than the one determined for commercial Gd-DOTA (DOTAREM, Guerbet, Aulnay-sous-Bois, France, r_1 = 4.5 mM^{-1} s^{-1} at 4.7 T). An amount of four Gd complexes per silica bead has been estimated by ICP MS titration of Gd^{3+}. This means that the relaxivity of this kind of Gd-DTPA is very high (42 mM^{-1} s^{-1}). This value is of the same order as those obtained for similar sized Gd-loaded dendrimers: 36 mM^{-1} s^{-1} (*52*) or 40 mM^{-1} s^{-1} despite a very low number of Gd per particle. This enhancement could be explained by a slow down of the rotational motion of the particle (*17*, *53*). This increase in relaxivity is thus consistent with the increase in rotational correlation time, which results both from the increase in molecular weight and maximum compactness of the SiO_2 structure as compared to organic molecules. Indeed, the rigid nature of the inorganic nanoparticle tends to avoid the Gd^{3+} chelate from freely rotating or even folding back (*54*).

The other advantage of Gd inorganic nanoparticles is that they exhibit a high ability for internalization in cells, inducing a relatively close vicinity of the contrast agents which could also be responsible for this strong increase in the r_1 value. Furthermore, these particles, once internalized in specific cells, favor the visualization and the characterization of tissue territories where these cells can accumulate during long periods. In fact, their biological half-life inside the cell is increased as compared to that in the extracellular circulating stream (*12*).

The cellular uptake of the Gd-TRITC fluorochrome-modified nanoparticles were tested for internalization in microglial cells. Microglial cells were grown as monolayer cultures. After activation, they were first incubated with the TRITC fluorescent particles (0.5 mM) and studied by fluorescence microscopy. An illustration of modified silica nanoparticle internalization is given in Figure 6. The results concerning Al_2O_3 nanoparticle uptake are given in Supporting Information.

Microglia monolayer cultures displayed a typical morphology with either elongated (Figure 6b, top thin arrow) or ovoid cell bodies (Figure 6b, bottom thin arrow). When activated, these

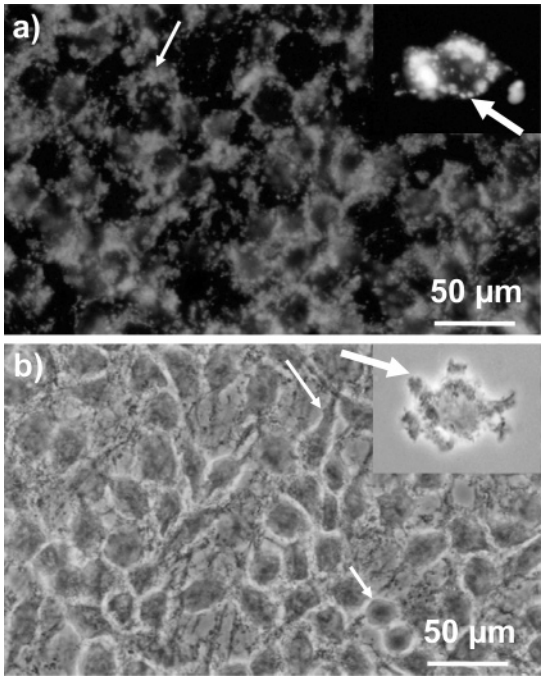


Figure 6. (a) Fluorescence microscopy (λ_{ex} = 546 nm and λ_{en} = 590 nm) imaging of monolayer cultures of microglial cells after incubation with TRITC fluorescent nanoparticles. (b) Phase contrast image of the field shown in part a. Thin arrows point both elongated and ovoid microglia. In the inserts, bold arrow shows (a) vesicles of internalized nanoparticles; (b) a typical membrane bud of activated microglia.

cells changed their shape and became ovoid with buds at the external border of the cytoplasm membrane (Figure 6b, insert). These outgrowths were characteristic of the macrophagic behavior induced by the activation with C6 extracts.

The fluorescent particles appeared both inside the cells with a perinuclear location and adsorbed at their surface (Figure 6a, thin arrow). The large dots at the periphery of the cell bodies were strongly fluorescent with a size suggesting that the beads concentrated as aggregates whatever the internalization processes (Figure 6a, insert). Independently of the chemical nature of the particles, they appear highly taken up by the activated microglial cells.

Flow cytometry is a system for sensing cells or particles as they move in a liquid stream through a laser or light beam past a sensing area. The flow cytometric analyses were performed on three sets of samples: (i) fluorescent nanoparticles alone and (ii) on microglial cells before and (iii) after fluorescent nanoparticles uptake (Figure 7). A procedure makes it possible to trace areas delimiting the interesting statistical events (cell population or free nanoparticles), called gates G1 and G2, on the "dots plots", from which the one-dimensional histograms are generated. This technique was used to estimate the contribution of the fluorescent signal of each sample and to check the contribution of the free nanoparticles, which remain in the cellular samples despite all the washing procedures.

Microglia cells (Figure 7A, gate 2) can be easily distinguished from free nanoparticles (Figure 7C, gate 1) because of their higher size. Indeed, gate 1 area gathered most of the free nanoparticles, whereas the cells spread in the area defined by gate 2. The cells, whatever the situation (after particle uptake (Figure 7F) or not (Figure 7A)), displayed similar distributions, and the overlapping distribution of free nanoparticles is very low. The analysis of fluorescence in the different gates in all the cases (control cells, free nanoparticles, cells with internalized nanoparticles) allowed us to estimate the contribution of free nanoparticles to the microglia signal. Indeed, from the histograms, it is possible to obtain, for either the whole statistical

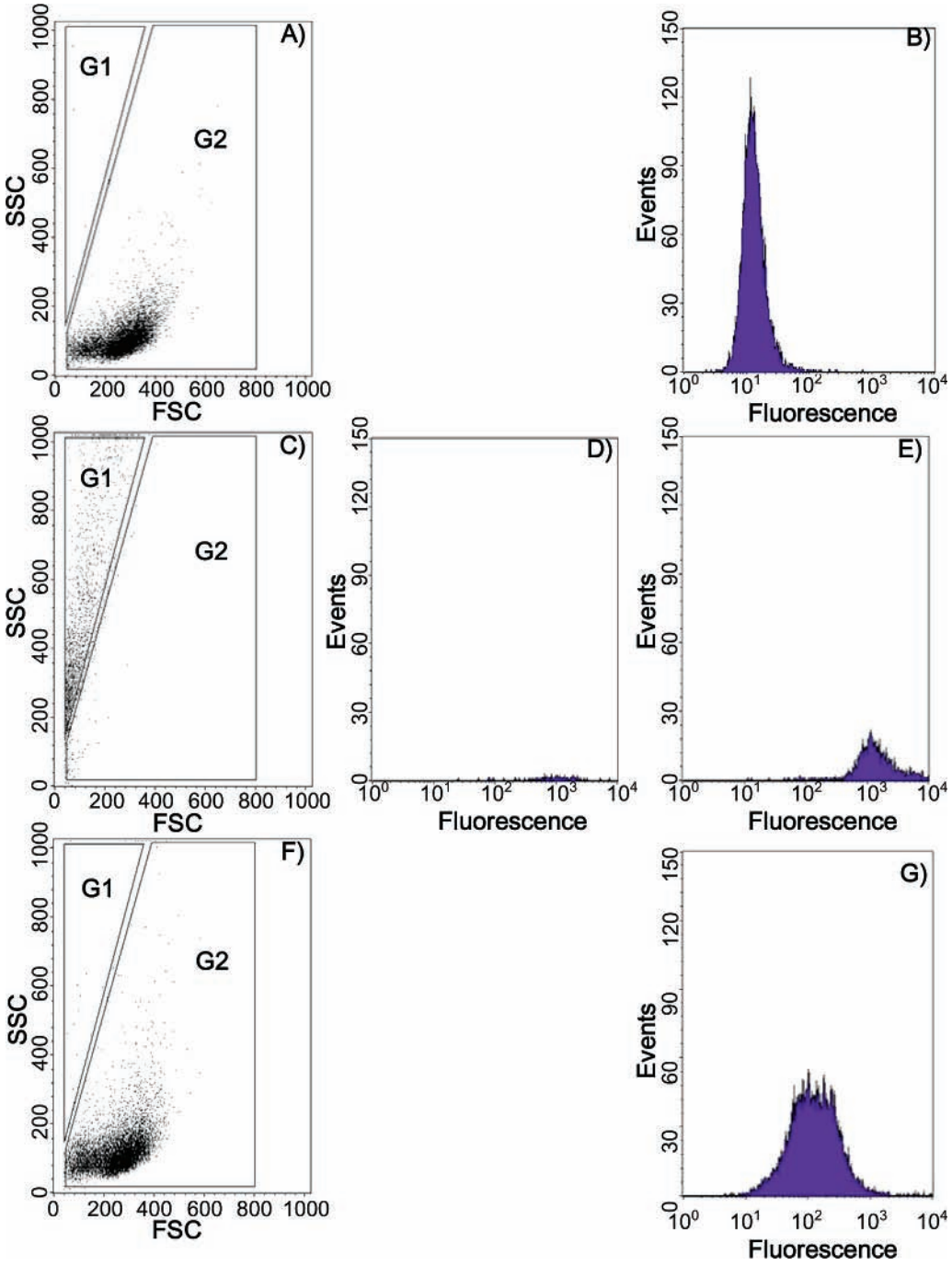


Figure 7. Flow cytometric data. The flow cytometric analyses were performed with control microglial cell cultures (A and B), free fluorescent nanoparticles (C, D, and E), and microglial cells after incubation with these particles (F and G). A, C, and F represent dot-plot of the scatters FSC (Forward SCatter, representative of the cell size, transmitted light) and SSC (Side SCatter, representative of the cell granularity, which depends on the density and the volume of intracellular organelles, diffracted light). B, D, E, and G are histograms of fluorescence: B, D, and G represent fluorescence observed in gate 2, and E, fluorescence observed in gate 1. Each dot represents one event. The scales in A, C, F (0−1000) are arbitrary scales representing increasing intensity of signal.

event or those inside each gate area, their contribution to the signal (% of events), their fluorescence average value, and the percentage of the total response (*P*) (Table 3).

The *P* assessment for the microglial cells before the uptake defines the level of contribution of the autogenerated fluorescence due to the cells themselves which also contributes to the total signal after the uptake (Figure 7B, 14 arbitrary units (a.u.); see Table 3). The contribution to the final signal *P* of the free particles, which are still present despite the various rinses at the end of the particle incubation with the cells, has been estimated in both G1 and G2 gated areas. In the G1 area, it is around 1.5 au (Table 3). The 5% contamination rate of free particles (Figure 7C, Table 3) in gate 2 has been used to estimate the contribution of the free remaining nanoparticles in the cellular sample (Figure 7F, Table 3). This contribution was less than 0.1% ($1.5 \times 5\% = 0.075$, to be compared to 166). Therefore, the relative contributions to the final fluorescence signal *P* (166 a.u.) of microglia cells after particle uptake are 91.5% from internalized particles, 8.4% from cellular autofluorescence ($14 \times 99.3\% = 13.9$ to be compared to 166), and 0.1% from free nanoparticles.

MR images were achieved on activated microglia (trapped in agarose gel) before and after incubation with of the two sets of metal oxide nanoparticles: Al_2O_3−APS−DTPA Gd (Figure

Table 3. Fluorescence Characterization of the Microglial Cells and the Fluorescent Nanoparticles

	% of events[a]		avg fluoresc, f_{av}[b]		$P = \% \times f_{av}$ (a.u.)[c]	
	G1	G2	G1	G2	G1	G2
unlabeled cells	0.7	99.3	14	14	0.1	14
free particles	94	5	1500	1100	1410	55
microglia cells after particle uptake	0.2	99.3	774	167	1.5	166

[a] The percentage of events (% of events) characterizes the statistical repartition of the populations (cells or particles) as defined in gates 1 (G1) and 2 (G2) (Figure 7). [b] The mean fluorescence is representative of the statistical average value after analysis of the fluorescence as described in these areas (Figure 7). [c] $P = \% \times f_{av}$ is the product of (% of events) by the average fluorescence and evaluates the relative contribution of the particles inside the microglial gate (G2) in the global signal of fluorescence. The reported values are the average of three independent experiments with a relative error that did not exceed 6%.

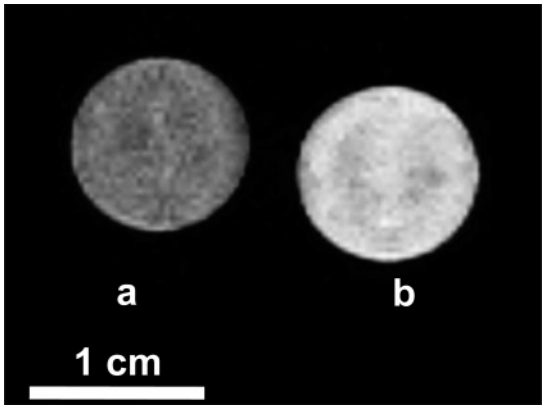


Figure 8. T_1-weighted images of microglia before and after incubation with 170 nM Al_2O_3−APS−DTPA-Gd. Images were performed with a typical T_1-weighted FLASH sequence as described in Experimental Procedures: (a) image of the control microglia before exposition to nanoparticles, (b) image of the microglia after incubations with the MRI contrast agents.

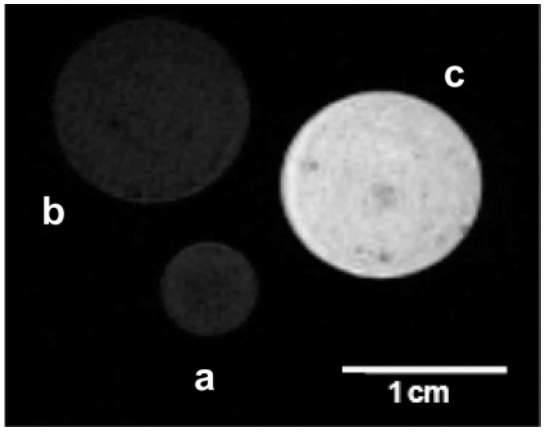


Figure 9. T_1-weighted image of microglial cells before and after incubation with 170 nM SiO_2−APS−DTPA-Gd. (a) 170 nM nanoparticles in solution, (b) microglial cells control, and (c) microglial cells after nanoparticle incubation. The signal-to-noise ratio of samples was homogeneous on all the slices.

8) and SiO_2−APS−DTPA Gd (Figure 9). Figure 8 shows a 2D slice of these cells obtained at 4.7 T with a T_1-weighted image (TE/TR = 1.7/100 ms, flip angle: 90°). The microglia cells exhibited T_1-relaxation times of 2357 and 1470 ms, respectively, before and after the internalization of Al_2O_3−APS−DTPA Gd.

The signal-to-noise ratios for cells before (Figure 8a) and after (Figure 8b) the uptake of Al_2O_3−APS−DTPA-Gd nanoparticles were 14.8 ± 1 and 20.7 ± 1, respectively. This 1.4 factor observed between the two images has been evaluated on the entire samples. This phenomenon was due to a decrease in water T_1-relaxation time once microglia cells were exposed to nanoparticles.

In the case of SiO_2−APS−DTPA-Gd nanoparticles, (Figure 9), the signal-to-noise ratio values on T_1-weighted images increased from 12 to 45, before and after nanoparticle incubation, respectively (3.75 ratio). This higher contrast of the SiO_2-based particles is directly correlated to a higher concentration of Gd^{3+} ions on the particles and therefore to the higher specific surface area (220 m^2/g) as compared to Al_2O_3 particles which only exhibit a 100 m^2/g specific surface area.

The determination of the relaxivity of the different samples (nanoparticles at 170 nM, microglia before and after nanoparticle internalization) shows that T_1 decreases from 2482 ± 10 ms (microglia control) to 753 ± 10 ms once nanoparticles were internalized; T_1 for the 170 nM nanoparticles solution was 1700 ± 10 ms.

These data allowed the estimation of the nanoparticle amount accumulated in microglia cells. Indeed, a 4.6 μM concentration of the cell-internalized nanoparticles can be deduced from the relaxivity curve of the SiO_2−APS−DTPA Gd nanoparticles (Figure 5). This value is 27-fold higher than that of incubated solution (170 nM). However, this high concentration value may nevertheless be strongly minimized because of two phenomena. On one hand, the relaxation time measured by MRI has two components: one obtained from the cellular content and the other from the agarose gel in which the microglia cells were diluted (as described in Experimental Procedures). Indeed, the cellular volume (20×10^6 microglia cells used in this experiment) was about 100 μL, representing one tenth of the volume of the entire sample. Thus, the nanoparticle concentration in the cells could be, in fact, ten-times higher than 4.6 μM. Moreover, assuming that the particles present in the cells are in vesicles, the contrast agent concentration may even be higher. On the other hand, Terreno et al. have already demonstrated that a T_1-saturation effect occurred when the nanoparticles are concentrated in the cell vesicles (*55*, *56*). Indeed, high concentrations of macromolecules, stored in these compartments, significantly reduce the mobility of water and of the gadolinium chelates, resulting in a "quench" of the relaxation enhancement. Thus, it again induces an underestimation of the amount of internalized gadolinium-grafted nanoparticles in the microglia cells.

With regards to these *in vitro* results, we may assume that this reconcentration of nanoparticles in microglial cells will allow *in vivo* experiments to be performed. Indeed, when chemoattracted to brain tumors these microglial cells increase the concentration of MRI agents in the desired area. Additionally, even if the nanoparticle amount in the cells decreases with time because of, for example, the release of the contrast agents or mitosis, their vesicle concentration will still be high enough to generate a positive contrast on MR images, since the "quench-effect" is lower.

Moreover, the imaging sequences used to detect the lanthanide contrast agents display a low sensitivity to susceptibility effects and minimize the imaging artifacts at high fields. These sequences are currently used for clinical MRI detection of

tumors as well as angiography. In fact, T_1-weighted MRI showed a strong *in vitro* contrast between control microglial cells and those after Gd nanoparticle uptake (a 3.75 ratio). Indeed, Vuu et al. have already demonstrated that Gd−Rh−NP which exhibited a 146% increase when internalized *in vitro*, were also visualized *in vivo* (*57*). The comparison with these results suggests that more reliable information than with iron oxide particles are expected in the next future for *in vivo* studies (*12*). In addition, the development of other specific sequences and the ease in their application such as magnetization transfer or inversion recovery will also lead to the achievement of higher contrasts and the adaptation of the contrast level to the studied tissue versus its environment.

CONCLUSION

The grafting of high-spin paramagnetic gadolinium chelates on nanoparticle surfaces such as alumina and silica nanoparticles offers a new strategy for the synthesis of contrast agents for MRI detection of cell populations capable of phagocytosis. In this situation, the advantage of gadolinium as a contrast agent is to generate a hypersignal for the observed populations, and the role of the nanoparticles is to facilitate the internalization through the membrane as well as to induce high local concentration of Gd^{3+} ion around the particle. This internalization property is a characteristic function of activated macrophages known to be chemoattracted and strongly accumulate particularly in brain pathological situations, including tumors. This type of detection will be straightforward for *in vivo* analysis in association with a high spatial resolution and open the route for more efficient contrast agents for MR cell tracking than the superparamagnetic contrast agents.

ACKNOWLEDGMENT

This work was performed in the frame of the European network of excellence "FAME" (http://www.famenoe.org/). The authors thank Dr. S. Augagneur (LPTC, Bordeaux) for ICP-MS assistance, Ph. Dagault (ICMCB) for TGA technical assistance, and the CNRS, the CNRS-CEA Small Animal Imaging program, and the Région Aquitaine for their financial support.

Supporting Information Available: Fluorescence microscopy imaging of a monolayer culture of microglial cells after incubation with Gd TRITC fluorescent Al_2O_3 nanoparticles. (b) Phase contrast image of the field shown in part a. Inserts are the fluorescent and phase contrast images of two single cells. This material is available free of charge via the Internet at http://pubs.acs.org.

LITERATURE CITED

(1) Wunderbaldinger, P., Bogdanov, A., and Weissleder, R. (2000) New approaches for imaging in gene therapy. *Eur. J. Radiol. 34*, 156−165.

(2) Nichol, C., and Kim, E. E. (2001) Molecular imaging and gene therapy. *J. Nucl. Med. 42*, 1368−1374.

(3) Benveniste, H., Einstein, G., Kim, K. R., Hulette, C., and Johnson, G. A. (1999) Detection of neuritic plaques in Alzheimer's disease by magnetic resonance microscopy. *Proc. Natl. Acad. Sci. U.S.A. 96*, 14079−14084.

(4) Dodd, S. J., Williams, M., Suhan, J. P., Williams, D. S., Koretsky, A. P., and Ho, C. (1999) Detection of single mammalian cells by high-resolution magnetic resonance imaging. *Biophys. J. 76*, 103−109.

(5) Caravan, P., Ellison, J. J., McMurry, T. J., and Lauffer, R. B. (1999) Gadolinium(III) chelates as MRI contrast agents: Structure, dynamics, and applications. *Chem. Rev. 99*, 2293−2352.

(6) Goldstein, H., Lumma, W., and Rudzik, A. (1989) Contrast media for magnetic resonance imaging. *Annu. Rep. Med. Chem. 24*, 265−276.

(7) Lauffer, R. B. (1987) Paramagnetic metal complexes as water proton relaxation agents for NMR imaging: theory and design. *Chem. Rev. 87*, 901−927.

(8) Toth, E., Helm, L., and Merbach, A. E. (2002) Relaxivity of MRI contrast agents. *Top. Curr. Chem. 221*, 61−101.

(9) Meade, T. J., Taylor, A. K., and Bull, S. R. (2003) New magnetic resonance contrast agents as biochemical reporters. *Curr. Opin. Neurobiol. 13*, 597−602.

(10) Zhang, S. R., Merritt, M., Woessner, D. E., Lenkinski, R. E., Sherry, A. D., Zhang, S. R., Merritt, M., Woessner, D. E., Lenkinski, R. E., and Sherry, A. D. (2003) PARACEST agents: Modulating MRI contrast via water proton exchange. *Acc. Chem. Res. 36*, 783−790.

(11) Raymond, K. N., and Pierre, V. C. (2005) Next Generation, High Relaxivity Gadolinium MRI Agents. *Bioconjugate Chem. 16*, 3−8.

(12) Fleige, G., Nolte, C., Synowitz, M., Seeberger, F., Kettenmann, H., and Zimmer, C. (2001) Magnetic labeling of activated microglia in experimental gliomas. *Neoplasia 3*, 489−499.

(13) Weissleder, R., Cheng, H. C., Bogdanova, A., and Bogdanov, A., Jr. (1997) Magnetically labeled cells can be detected by MR imaging. *J. Magn. Reson. Imaging 7*, 258−263.

(14) Mornet, S., Vasseur, S., Grasset, F., and Duguet, E. (2004) Magnetic nanoparticle design for medical diagnosis and therapy. *J. Mater. Chem. 14*, 2161−2175.

(15) Kobayashi, H., Kawamoto, S., Jo, S. K., Jr., Bryant, H. L., Brechbiel, M. W., and Star, R. A. (2003) Macromolecular MRI contrast agents with small dendrimers: pharmacokinetic differences between sizes and cores. *Bioconjugate Chem. 14*, 388−394.

(16) Runge, V. M. (2000) Safety of approved MR contrast media for intravenous injection. *J. Magn. Reson. Imaging 12*, 205−213.

(17) Langereis, S., de Lussanet, Quido, G., van Genderen, Marcel, H. P., Meijer, E. W., Beets-Tan, Regina, G. H., Griffioen, Arjan, W., van Engelshoven, Jos, M. A., Backes, and Walter, H. (2006) Evaluation of Gd(III)DTPA-terminated poly(propylene imine) dendrimers as contrast agents for MR imaging. *NMR Biomed. 19* (1), 133−141.

(18) (a) Cong, L., Ying-Xia, L., Ga-Lai, L., Kwan, M., Wing-Tak, W., and Hao, L. (2006) Fast Water-Exchange Gd3+-(DO3A-like) Complex Functionalized with Aza-15-Crown-5 Showing Prolonged Residence Lifetime in Vivo. *Bioconjugate Chem. 17*, 571−574. (b) Ito, M., Ogino, H., Oshima, H., Shiraki, N., Shibamoto, Y., Kasai, H., Mase, M., Kawamura, Y., and Miyati, T. (2006) Evaluation of CH3-DTPA-Gd (NMS60) as a new MR contrast agent: early phase II study in brain tumors and dual dynamic contrast-enhanced imaging. *Magn. Reson. Med. 24* (5), 625−630.

(19) Nunn, A. D., Linder, K. E., and Weedle, M. F. (1997) Can receptors be imaged with MRI agents? *Q. J. Nucl. Med. 41*, 155−162.

(20) Brasch, R. C. (1991) Rationale and applications for macromolecular Gd-based contrast agents. *Magn. Reson. Med. 22*, 282−287.

(21) (a) Shreve, P., and Aisen, A. M. (1986) Monoclonal antibodies labeled with polymeric paramagnetic ion chelates. *Magn. Reson. Med. 3*, 336−340. (b) Perkins, A. C. (1998) Polymer diagnostics. The next generation of image contrast agents. *J. Drug Targeting 6*, 79−84.

(22) (a) Mulder, W. J. M., Strijkers, G. J., van Tilborg, G. A. F., Griffioen, A. W., and Nicolay, K. (2006) Lipid-based nanoparticles for contrast-enhanced MRI and molecular imaging. *NMR Biomed. 19* (1), 142−164. (b) Parac-Vogt, T. N., Kimpe, K., Laurent, S., Pierart, C., Vander Elst, L., and Muller, R. N. (2006) Paramagnetic liposomes containing amphiphilic bisamide derivatives of Gd-DTPA with aromatic side chain groups as possible contrast agents for magnetic resonance imaging. *Eur. Biophys. J. 35*, 136−144.

(23) (a) Storrs, R. W., Tropper, F. D., Li, H. Y., Song, C. K., Kuniyoshi, Jeremy, K., Sipkins, D. A., Li, King, C. P., and Bednarski, M. D. (1995) Paramagnetic Polymerized Liposomes: Synthesis, Characterization, and Applications for Magnetic Resonance Imaging. *J. Am. Chem. Soc. 117*, 7301−7306. (b) Li, K. C., Bednarski, M. D., Storrs, R. W., Li, H. Y., Trooper, F. D., Song, C. K. H., Sipkins, D. A., and Kuniyoshi, J. K. (1996) Targeted polymerized liposome contrast agents. U.S. Patent 5,512,294 A. (c) Tilcock, C. (1994) Liposomal blood pool agents for nuclear medicine and magnetic resonance

imaging. *J. Liposome Res. 4*, 909−936. (d) Torchilin, V. P., and Trubetskoy, V. S. (1995) In vivo visualizing of organs and tissues with liposomes. *J. Liposome Res. 5*, 795−812.

(24) Parac-Vogt, T. N., Kimpe, K., Laurent, S., Pierart, C., Vander, Elst, L., Muller, Robert, N., and Binnemans, K. (2004) Gadolinium DTPA-monoamide complexes incorporated into mixed micelles as possible MRI contrast agents. *Eur. J. Inorg. Chem. 17*, 3538−3543.

(25) (a) Kim, Y., and Zimmerman, S. C. (1998) Applications of dendrimers in bio-organic chemistry. *Curr. Opin. Chem. Biol. 2*, 733−742. (b) Schmitt-Willich, H., Platzek, J., Muehler, A., and Frinzel, T. (1995) Metal complex of dendritic polymer as NMR and X-ray diagnostic agent. Ger. Patent 4344460. (c) Wiener, E. C., Brechbiel, M. W., Brothers, H., Magin, R. L., Gansow, O. A., Tomalia, D. A., and Lauterbur, P. C. (1994) Dendrimer-based metal chelates: a new class of magnetic resonance imaging contrast agents. *Magn. Reson. Med. 31*, 1−8. (d) Wiener, E. C., Konda, S., Shadron, A., Brechbiel, M. W., and Gansow, O. (1997) Targeting dendrimer-chelates to tumors and tumor cells expressing the high-affinity folate receptor. *Invest. Radiol. 32*, 748−754.

(26) (a) Aime, S., Crich, Geninatti, S., Gianolio, E., Giovenzana, G. B., Tei, L., and Terreno, E. (2006) High sensitivity lanthanide(III) based probes for MR-medical imaging. *Coord. Chem. Rev. 250*, 1562−1579. (b) Aime, S., Botta, M., Fasano, M., and Terreno, E. (1998) Lanthanide(III) chelates for NMR biomedical applications. *Chem. Soc. Rev. 27*, 19−29.

(27) Caravan, P., Ellison, J. J., McMurry, T. J., and Lauffer, R. B. (1999) Gadolinium(III) Chelates as MRI Contrast Agents: Structure, Dynamics, and Applications. *Chem. Rev. 99*, 2293−2352.

(28) Woods, M., Kovacs, Z., and Sherry, A. D. (2002) Targeted Complexes of Lanthanide(III) Ions as Therapeutic and Diagnostic Pharmaceuticals. *J. Supramol. Chem. 2*, 1−15.

(29) Reynolds, C. H., Annan, N., Beshah, K., Huber, J. H., Shaber, S. H., Lenkinski, R. E., and Wortman, J. A. (2000) Gadolinium-Loaded Nanoparticles: New Contrast Agents for Magnetic Resonance Imaging. *J. Am. Chem. Soc. 122*, 8940−8945.

(30) Tilcock, C., Unger, E., Cullis, P., and MacDougall, P. (1989) Liposomal Gd-DTPA: preparation and characterization of relaxivity. *Radiology 171*, 77−80.

(31) Unger, E., Shen, D. K., Wu, G. L., and Fritz, T. (1991) Liposomes as MR contrast agents: pros and cons. *Magn. Reson. Med. 22*, 304−308.

(32) Koenig, S. H., Ahkong, Q. F., Brown, R. D., III, Lafleur, M., Spiller. M., Unger, E., and Tilcock, C. (1992) Permeability of liposomal membranes to water: results from the magnetic field dependence of T1 of solvent protons in suspensions of vesicles with entrapped paramagnetic ions. *Magn. Reson. Med. 23*, 275−286.

(33) Zhu, D., White, R. D., Hardy, P. A., Weerapreeyakul, N., Sutthanut, K., and Jay, M. J. (2006) Biocompatible nanotemplate-engineered nanoparticles containing gadolinium: stability and relaxivity of a potential MRI contrast agent. *Nanosci. Nanotechnol. 6*, 996−1003.

(34) Ruehm S. G., Christina H, Violas X, Corot C., and Debatin J. F. (2002) MR angiography with a new rapid-clearance blood pool agent: Initial experience in rabbits. *Magn. Reson. Med. 48* (5), 844−851.

(35) Radu, D. R., Lai, C. Y., Jeftinija, K., Rowe, E. W., Jeftinija, S., and Lin, V. S. Y. (2004) A Polyamidoamine Dendrimer-Capped Mesoporous Silica Nanosphere-Based Gene Transfection Reagent. *J. Am. Chem. Soc. 126*, 13216−13217.

(36) Ribot E., Bouzier-Sore A. K., Bouchaud V., Miraux S., Delville M. H., Franconi J. M., and Voisin, P. (2007) Microglia used as vehicles for both inducible thymidine kinase gene therapy and MRI contrast agents for glioma therapy. *Cancer Gene Ther.*, in press.

(37) Santra, S., Bagwe, R. P., Dutta, D., Stanley, J. T., Walter, G. A., Tan, W., Moudgil, B. M., and Mericle, R. A. (2005) Synthesis and characterization of fluorescent, radio-opaque, and paramagnetic silica nanoparticles for multimodal bioimaging applications. *Adv. Mater. 17*, 2165−2169.

(38) Tedder, J. M., Nechvatal, A., Murray, A. W., and Carnduff, J. (1972) Amino-acids and proteins. In *Basic organic chemistry*, Chapter 6, pp 305−342, John Wiley & Sons, London,

(39) Sehgal, D., and Vijay, I. K. (1994) A Method for the High Efficiency of Water-Soluble Carbodiimide-Mediated Amidation. *Anal. Biochem. 218*, 87−89.

(40) Staros, J. V., Wright, R. W., and Swingle, D. M. (1986) Enhancement by N-hydroxysulfo-succinimide of water-soluble carbodiimide-mediated coupling reactions. *Anal. Biochem. 156*, 220−222.

(41) Kneuer, C., Sameti, M., Bakowsky, U., Schiestel, T., Schirran, H., Schmidt, H., and Lehr, C. M. (2000) A Nonviral DNA Delivery System Based on Surface Modified Silica-Nanoparticles Can Efficiently Transfect Cells in Vitro. *Bioconjugate Chem. 11*, 926−932.

(42) (a) Catelas, I., Petit, A., Zukor, D. J., Marchand, R., Yahia, L. H., and Huk, O. L. (1999) Induction of macrophage apoptosis by ceramic and polyethylene particles in vitro. *Biomaterials 20*, 625−630. (b) Hanawa, T., Kaga, M., Itoh, Y., Echizenya, T., Oguchi, H., and Ota, M. (1992) Cytotoxicities of oxides, phosphates and sulphides of metals. *Biomaterials 13*, 20−24. (c) Germain, M. A., Hatton, A., Williams, S., Matthews, J. B., Stone, M. H., Fisher, J., and Ingham, E. (2003) Comparison of the cytotoxicity of clinically relevant cobalt-chromium and alumina ceramic wear particles in vitro. *Biomaterials 24*, 469−479.

(43) (a) Van Blaaderen, A., and Vrij, A. (1993) Synthesis and characterization of monodisperse colloidal organo-silica spheres. *J. Colloid Interf. Sci. 156*, 1−18. (b) Waddell, T. G., Leyden, Donald E., DeBello, and Mary T. (1981) The nature of organosilane to silica-surface bonding. *J. Am. Chem. Soc. 103*, 5303−5307.

(44) Abboud, M., Turner, M., and Duguet, E., and Fontanille, M. (1997) PMMA-based composite materials with reactive ceramic fillers. Part 1.-Chemical modification and characterization of ceramic particles. *J. Mater. Chem. 7*, 1527−1532.

(45) Vandenberg, E. T., Bertilsson, L., Liedberg, B., Uvdal, K., Erlandsson, R., Elwing, H., and Lundstroem, I. (1991) Structure of 3-aminopropyl triethoxy silane on silicon oxide. *J. Colloid Interface Sci. 147*, 103−118.

(46) Naviroj, S., Culler, S. R., Koenig, J. L., and Ishida, H. (1984) Structure and adsorption characteristics of silane coupling agents on silica and E-glass fiber; dependence on pH. *J. Colloid Interface Sci. 97*, 308−317.

(47) Etienne, M., and Walcarius, A. (2003) Analytical investigation of the chemical reactivity and stability of aminopropyl-grafted silica in aqueous medium. *Talanta 59*, 1173−1188.

(48) (a) De Haan, J. W., Van Den Bogaert, H. M., Ponjee, J. J., and Van De Ven, L. J. M. (1986) Characterization of modified silica powders by Fourier transform infrared spectroscopy and cross-polarization magic angle spinning NMR. *J. Colloid Interface Sci. 110*, 591−600. (b) Vrancken, K. C., Van Der Voort, P., Possemiers, K., and Vansant, E. F. (1995) Surface and structural properties of silica gel in the modification with γ-aminopropyltriethoxysilane. *J. Colloid Interface Sci. 174*, 86−91.

(49) Jiang, X., Yu, H., Frayne, R., Unal, O., and Strother, C. M. (2002) Surface Functionalization of Polyethylene for Magnetic Resonance Signal-Enhancing Coating Materials. *Chem. Mater. 14*, 1914−1920.

(50) Popat, K. C., Swan, E. E. L., and Desai, T. A. (2005) Modeling of RGDC Film Parameters Using X-ray Photoelectron Spectroscopy. *Langmuir 21*, 7061−7065.

(51) Raiser, D., and Deville, J. P. (1991) Study of XPS photoemission of some gadolinium compounds. *J. Electron Spectrosc. Relat. Phenom. 57*, 91−97.

(52) (a) Bryant, L. H., Jr., and Bulte, J. W. M. (2001) Dendrimers: Chemical principles and biotechnology applications. In *Focus on Biotechnology* (*Physics and Chemistry*: *Basis of Biotechnology*), pp 47−69, Kluwer Academic Publishers, Dordrecht. (b) Bryant, L. H., Jr., Jordan E. K., Bulte J. W. M., Herynek, V., and Frank J. A. (2002) Pharmacokinetics of a high-generation dendrimer-Gd-DOTA. *Acad. Radiol. 9 Suppl 1* S29−S33. (c) Laus, S., Sour, A., Ruloff, R., Toth, E., and Merbach, A. E. (2005) Rotational dynamics account for pH-dependent relaxivities of PAMAM dendrimeric, Gd-based potential MRI contrast agents. *Chem. A. Eur. J. 11*, 3064−3076.

(53) Pierre, V. C., Botta, M., and Raymond, K. N. (2005) Dendrimeric Gadolinium Chelate with Fast Water Exchange and High Relaxivity at High Magnetic Field Strength. *J. Am. Chem. Soc. 127* (2), 504−505.

(54) Nicolle, G. M., Toth, E., Schmitt-Willich, H., Raduchel, B., and Merbach, A. E. (2002) The impact of rigidity and water exchange on the relaxivity of a dendritic MRI contrast agent. *Chem. Eur. J. 8*, 1040−1048.

(55) Terreno, E., Crich, S. G., Belfiore, S., Biancone, L., Cabella, C., Esposito, G., Manazza, A. D., and Aime, S. (2006) Effect of the intracellular localization of a Gd-based imaging probe on the relaxation enhancement of water protons. *Magn. Reson. Med. 55* (3), 491−497.

(56) Stanisz, G. J., and Henkelman, R. M. (2000) Gd-DTPA relaxivity depends on macromolecular content. *Magn. Reson. Med. 44*, 665−667.

(57) Vuu, K., Xie, J., McDonald, M. A., Bernardo, M., Hunter, F., Zhang, Y., Li, K., Bednarski, M., and Guccione, S. (2005) Gadolinium-Rhodamine Nanoparticles for Cell Labeling and Tracking via Magnetic Resonance and Optical Imaging. *Bioconjugate Chem. 16* (4), 995−999.

BC060269T

General Method for Site-Specific Protein Immobilization by Staudinger Ligation

Jeet Kalia,[†] Nicholas L. Abbott,*[,‡] and Ronald T. Raines*[,†,§]

Departments of Biochemistry, Chemical and Biological Engineering, and Chemistry, University of Wisconsin−Madison, Madison, Wisconsin 53706. Received September 30, 2006; Revised Manuscript Received February 20, 2007

Protein microarrays are playing an increasingly important role in the discovery and characterization of protein−ligand interactions. The uniform orientation conferred by site-specific immobilization is a demonstrable advantage in using such microarrays. Here, we report on a general strategy for fabricating gold surfaces displaying a protein in a uniform orientation. An azido group was installed at the C-terminus of a model protein, bovine pancreatic ribonuclease, by using the method of expressed protein ligation and a synthetic bifunctional reagent. This azido protein was immobilized by Staudinger ligation to a phosphinothioester-displaying self-assembled monolayer on a gold surface. Immobilization proceeded rapidly and selectively via the azido group. The immobilized enzyme retained its catalytic activity and was able to bind to its natural ligand, the ribonuclease inhibitor protein. This strategy provides a general means to fabricate microarrays displaying proteins in a uniform orientation.

INTRODUCTION

Protein−protein, protein−DNA, and protein−small-molecule interactions underlie biological chemistry. High-throughput approaches for the discovery and characterization of these various protein−ligand interactions can elucidate complicated biological pathways. In addition, the screening of small-molecule libraries for agonists and antagonists can provide leads for drug development. Recyclable devices that detect biomarkers in body fluids can be used to diagnose human diseases. All of these challenges could be met with the use of protein microarrays (*1*−*7*).

Microarrays that present proteins in a uniform orientation exhibit both a markedly greater capacity to bind ligands (*8*−*11*) and more reproducible biological function (*12*) than do protein arrays generated by random immobilization. Microarrays of uniformly oriented DNA have long been produced on a large scale and used with notable success in studies of gene function (*13*−*16*). The production of DNA microarrays is made facile by the ease with which oligonucleotides can be prepared by chemical synthesis (*17*) and incorporated into large fragments by DNA polymerase (*18*). By comparison, the fabrication of protein microarrays is much more arduous. Notable advances are being made in the chemical synthesis of proteins (*19*), but this technology is still nascent. The immobilization of natural proteins is complicated by their chemical complexity, as each of the 20 proteinogenic amino acids bears a side chain with distinct physicochemical properties, and the reactivity of the same amino acid can vary according to its position in the three-dimensional structure. Post-translational modifications confer additional diversity (*20*). Other difficulties result from the intrinsic fragility of proteins, which have modest conformational stability and can be damaged upon chemical modification. Accordingly, new strategies are needed to immobilize proteins while maintaining their integrity.

Proteins have been immobilized on surfaces, both noncovalently and covalently (*21*). Noncovalent immobilization has been achieved by physical adsorption (*22*, *23*) and affinity tag-mediated complex formation (*24*, *25*). Covalent immobilization, however, results in more robust arrays. A common strategy, immobilization by attack of the nucleophilic side chain of lysine or cysteine residues, typically proceeds at multiple sites and thus yields an array in which the proteins have a random orientation (*26*, *27*). In contrast, site-specific covalent immobilization, via a unique natural (*8*, *11*, *28*) or nonnatural residue, affords a uniformly oriented protein array.

The azido group is chemically inert to the functional groups found in nature. Accordingly, the azido group is being exploited widely by chemical biologists (*29*), including in the site-specific immobilization of proteins and peptides by the Huisgen 1,3-dipolar azide−alkyne cycloaddition (*30*−*32*) and Staudinger ligation (*32*−*34*). A limitation, however, has been the difficulty of installing an azido group in a particular position in a protein. Recently, we developed a general method for appending the C-terminus of proteins with an azido group (*35*). Specifically, we used a bifunctional reagent bearing an α-hydrazino acetamido and azido group to cleave the transient thioester generated on the C-terminus of the target protein fused to an intein, thereby labeling the protein with an azido group on the C-terminus (Scheme 1). This azido group was available for site-specific installation of a fluorophore by the Huisgen 1,3-dipolar azide−alkyne cycloaddition.

Here, we report a general method for the site-specific immobilization of a protein. As a model protein, we choose one of the most thoroughly studied enzymes, bovine pancreatic ribonuclease (RNase A (*36*); EC 3.1.27.5). The immobilized protein was detected with a standard immunoassay, which does not report on the integrity of the protein. The choice of RNase A provides two rigorous means to assess its structure and function. First, RNase A is an efficient catalyst of RNA cleavage, and its catalytic activity provides a measure of its conformational integrity. Second, the affinity of the ribonuclease inhibitor protein (RI) for RNase A is extremely high (*37*), and this interaction provides an independent report on the structure

* Corresponding authors to whom correspondence should be addressed. R.T.R., Department of Biochemistry, University of Wisconsin−Madison, 433 Babcock Drive, Madison, WI 53706-1544. Tel: 608-262-8588. Fax: 608-262-3453. E-mail: raines@biochem.wisc.edu. N.L.A., Department of Chemical and Biological Engineering, University of Wisconsin−Madison, 1415 Engineering Drive, Madison, WI 53706-1691. Tel: 608-265-5278. Fax: 608-262-5434. E-mail: abbott@engr.wisc.edu.

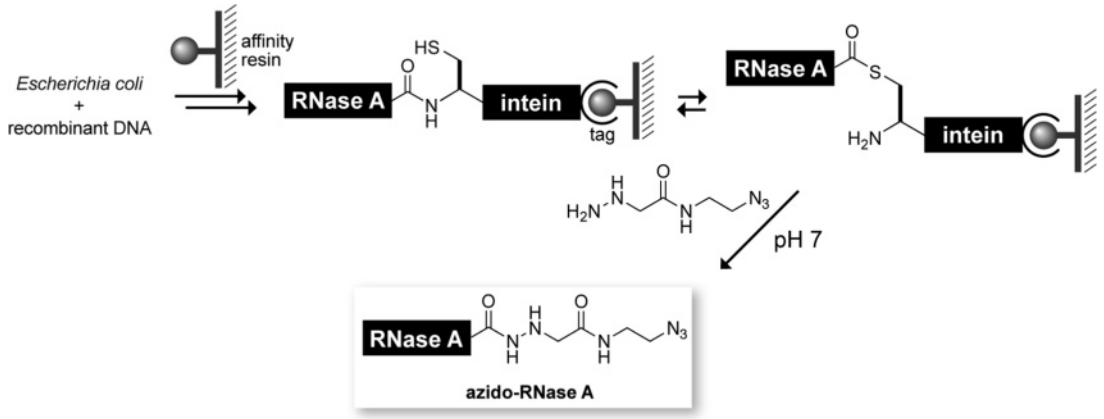
[†] Department of Biochemistry.

[‡] Department of Chemical and Biological Engineering.

[§] Department of Chemistry.

10.1021/bc0603034 CCC: $37.00 © 2007 American Chemical Society
Published on Web 05/09/2007

Scheme 1. Semisynthesis of Azido-RNase A (*35*)



and function of the immobilized protein. Our strategy was to react an azido-RNase A (Scheme 1) (*35*) with a phosphinothioester group displayed on self-assembled monolayers (SAMs) of alkane thiols on a gold surface (Scheme 2). The resulting Staudinger ligation (*19, 38*−*40*) immobilized the protein in a form that retained its biological function.

MATERIALS AND METHODS

Materials. Silicon chips coated with gold prepared by physical vapor deposition as described previously (*41*) and were a generous gift from C.-H. Jang. Alkane thiols $HS(CH_2)_{11}(OCH_2CH_2)_6OCH_2CO_2H$ and $HS(CH_2)_{11}(OCH_2CH_2)_3OH$ were from Prochimia (Gdansk, Poland). A fluorogenic ribonuclease substrate, 6-carboxyfluorescein−dArU$(dA)_2$−6-carboxytetramethylrhodamine (6-FAM−dArU$(dA)_2$−6-TAMRA), was from Integrated DNA Technologies (Coralville, IA). Two-hand AtmosBags were from Sigma−Aldrich (St. Louis, MO).

Azido-RNase A was produced as described previously (Scheme 1) (*35*). Wild-type RNase A was from Sigma−Aldrich. Human RI was prepared as described previously and was a generous gift from R. J. Johnson and G. A. Ellis. Anti-RNase A rabbit primary antibody was from Biodesign International (Kennebunk, ME). AlexaFluor 488-conjugated anti-rabbit secondary antibody was from Molecular Probes (Eugene, OR). Anti-RI chicken primary antibody was from Genetel (Madison, WI). Fluorescein-conjugated anti-chicken secondary antibody was from Abcam (Cambridge, MA).

Instrumentation. Fluorescence measurements for assaying ribonucleolytic activity were made with a QuantaMaster 1 photon-counting spectrofluorimeter equipped with sample stirring (Photon Technology International, South Brunswick, NJ). Immunoassays of immobilized RNase A and RI bound to the immobilized RNase A were visualized with a GeneTac UC4 × 4 fluorescence scanner (Genomic Solutions, Ann Arbor, MI). The optical thickness of SAMs and proteins on the gold chips was determined with a AutoEL ellipsometer (Rudolf Research, Flanders, NJ).

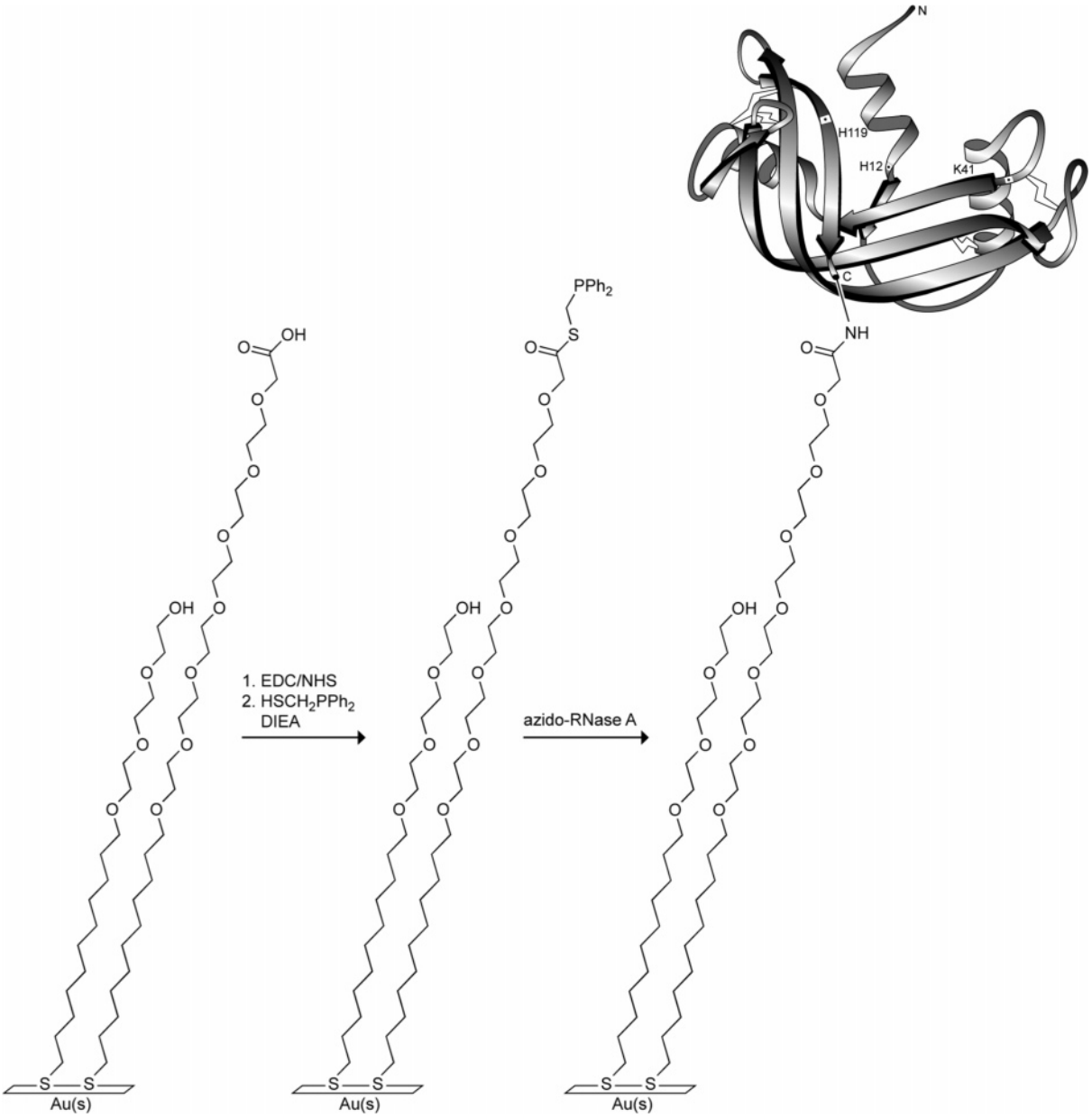
Preparation of Phosphinothioester-Displaying SAMs of Alkane Thiols on Gold Chips. Alkane thiol solutions were prepared by dissolving $HS(CH_2)_{11}(OCH_2CH_2)_6OCH_2CO_2H$ and $HS(CH_2)_{11}(OCH_2CH_2)_3OH$ in ethanol to a final concentration of 0.25 mM each. The oligo(ethylene oxide) $HS(CH_2)_{11}(OCH_2CH_2)_3OH$ is included to discourage the nonspecific adsorption of protein (*42*), which can be problematic (*43*). Gold chips were cleaned under a stream of Ar(g) and immersed in the alkane thiol solution for at least 18 h. After rinsing thoroughly with ethanol and drying under a stream of Ar(g), the chips were overlaid with an aqueous solution containing *N*-hydroxysuccinimide (NHS, 50 mM) and 1-ethyl-3-(3-dimethylaminopropyl)carbodiimide (EDC, 200 mM) for 7 min to generate succinimidyl esters in situ. Diphenylphosphinomethanethiol (PPh_2CH_2SH) was synthesized as described earlier previously (*44*), and was dissolved in anhydrous DMF to a concentration of 0.10 M. *N,N*-Diisopropylethylamine (DIEA) was added to a concentration of 0.12 M. The resulting solution (in a 25 mL flask), succinimidyl ester displaying chips (in a Petri dish containing a water-soaked absorbent paper to serve as a humid chamber), and azido-RNase A (10 μM in 5% v/v DMF(aq)) were placed in a two-hand AtmosBag along with vials containing anhydrous DMF (20 mL/vial), water (20 mL/vial), and 25 mM sodium phosphate buffer at pH 7.5 (20 mL/vial). The AtmosBag was sealed and connected to the house vacuum on one end and an Ar(g) supply on the other end. The air inside the bag was removed by using the house vacuum and flushing twice with Ar(g) before finally filling up the bag with Ar(g). The diphenylphosphinomethanethiol−DIEA solution was transferred into a small empty vial, and succinimidyl ester displaying chips were incubated in that vial for 2 h. The phosphinothioester-displaying chips thus produced were rinsed with DMF (2 × 20 mL) and then with water (2 × 20 mL).

Immobilization of Azido-RNase A by Staudinger Ligation. Azido-RNase A (1 μL, 10 μM in 5% v/v DMF(aq)) was incubated on phosphinothioester-displaying chips for 1, 5, 10, and 15 min inside the AtmosBag (Figure 1). The chips were subsequently rinsed with 25 mM sodium phosphate buffer at pH 7.5 (20 mL) and removed from the AtmosBag. They were then incubated in 25 mM sodium phosphate buffer at pH 7.5 (1.0 mL) for 30 min to remove protein bound nonspecifically.

Detection of Immobilized RNase A. A chip displaying immobilized RNase A was overlaid with anti-RNase A rabbit primary antibody (100 μg/mL in 25 mM sodium phosphate buffer at pH 7.5) for 30 min. The chip was then rinsed with 25 mM sodium phosphate buffer at pH 7.5 (2 × 20 mL), and incubated in the same buffer for 15 min. The chip was subsequently overlaid with AlexaFluor 488-conjugated anti-rabbit secondary antibody (2.0 μg/mL in 25 mM sodium phosphate buffer at pH 7.5) for 30 min. Finally, the chip was rinsed with 25 mM sodium phosphate buffer at pH 7.5 (2 × 20 mL), incubated in the same buffer for 15 min, and scanned with a Genomic Solutions GeneTac UC4 × 4 Fluorescence Scanner using a gain of 50.

Ribonucleolytic Activity Assay on Immobilized RNase A. A phosphinothioester-displaying chip was overlaid with azido-RNase A (10 μM in 5% v/v DMF(aq)) in an Ar(g) atmosphere to immobilize RNase A. The chip was rinsed with 25 mM sodium phosphate buffer at pH 7.5 (2 × 20 mL) and then introduced into a vial containing a solution (22 mL) of 0.10 M 2-(*N*-morpholino)ethanesulfonic acid (MES)−NaOH buffer at pH 6.0 containing 0.10 M NaCl. A fluorogenic substrate of RNase A, 6-FAM−dArU$(dA)_2$−6-TAMRA (10 μL of a 40 μM

Scheme 2. Site-Specific Protein Immobilization on a SAM by Staudinger Ligation[a]



[a] The three active-site residues and N- and C-termini are indicated explicitly.

solution) was introduced into the vial, and the vial was placed on a shaker. Aliquots (2.0 mL) were withdrawn at known time intervals, and their fluorescence was measured ($\lambda_{ex} = 493$ nm, $\lambda_{em} = 515$ nm). After 1 h, excess wild-type RNase A (20 μL of a 2.8 mg/mL solution) was added to obtain a value of fluorescence after complete cleavage of the substrate. A phosphinothioester-displaying chip was overlaid with wild-type RNase A (10 μM in 5% v/v DMF(aq)), and the assay was performed again. As a negative control, a similar assay was performed on a phosphinothioester-displaying chip which was not overlaid with RNase A. The percentage of the fluorescent substrate cleaved at various time intervals in the negative control was subtracted from the corresponding values for azido- and wild-type RNase A, and plotted against time to generate the graph in Figure 2.

Detection of RI Bound to Immobilized RNase A. Azido-RNase A (1 μL, 10 μM in 5% v/v DMF(aq)) was spotted on phosphinothioester-displaying SAMs on a gold chip for 15 min in an AtmosBag filled with Ar(g). The chip was removed from the bag, rinsed with 25 mM sodium phosphate buffer at pH 7.5 (2 × 20 mL), and incubated in the same buffer for 30 min to remove nonspecifically bound RNase A. RI (10 μM in 25 mM sodium phosphate buffer at pH 7.5 containing 10 mM DTT) was overlaid on the chip for 10 min at 4 °C. The chip was then rinsed with 25 mM sodium phosphate buffer at pH 7.5 containing 10 mM DTT (2 × 20 mL) and incubated in the same buffer for 15 min.

Immunoassay. After RI binding, the chip was overlaid with bovine serum albumin (2.0 mg/mL in 25 mM sodium phosphate buffer at pH 7.5) for 15 min. The chip was rinsed with 25 mM sodium phosphate buffer at pH 7.5 (2 × 20 mL), and subsequently incubated with anti-RI chicken primary antibody (12.5 μg/mL in 25 mM sodium phosphate buffer at pH 7.5) for 15 min. The chip was rinsed with 25 mM sodium phosphate buffer at pH 7.5 (2 × 20 mL), incubated in the same buffer for 15 min, and subsequently overlaid with fluorescein-conjugated anti-chicken secondary antibody (1.5 μg/mL in 25 mM sodium phosphate buffer at pH 7.5) for 15 min. The chip was rinsed with 25 mM sodium phosphate buffer at pH 7.5 (2 × 20 mL), incubated in the same buffer for 15 min, and then scanned with

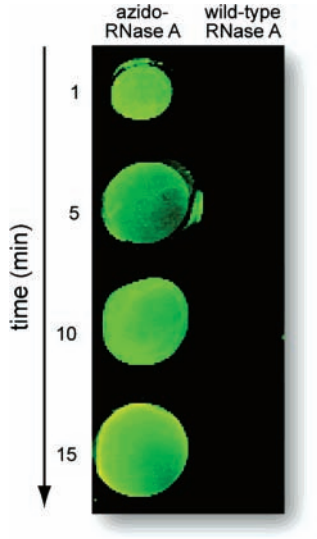


Figure 1. Time course and specificity of immobilization of azido-RNase A. Azido-RNase A and wild-type RNase A (each 10 μM) were spotted on a phosphinothioester-displaying chip for various times. The chip was overlaid with an anti-RNase A primary antibody (10 μg/mL) and a secondary antibody conjugated to AlexaFluor 488 (2 μg/mL).

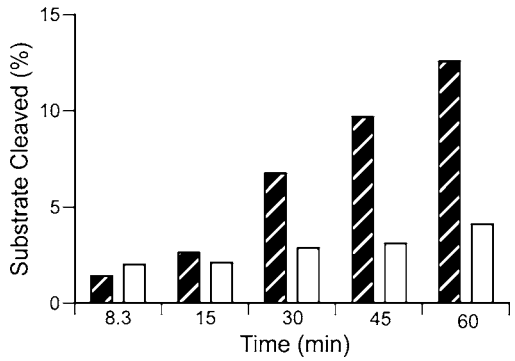


Figure 2. Catalytic activity of immobilized RNase A. Phosphinothioester-displaying chips were incubated with azido-RNase A (hatched bars) or wild-type RNase A (open bars), and assayed for ribonucleolytic activity by using a fluorogenic substrate.

a Genomic Solutions GeneTac UC4 × 4 fluorescence scanner using a gain of 50.

Ellipsometry. Ellipsometric measurements were performed to determine the optical thicknesses of the SAMs, RNase A, and RI on the gold surface. The measurements were performed with a wavelength of 632 nm and an angle of incidence of 70°. The optical thickness reported is the average from seven different surface locations. A slab model was used to interpret these constants in which the slab (SAM and protein) was assumed to have an index of refraction of 1.46.

RESULTS AND DISCUSSION

Generation of Phosphinothioester-Displaying SAMs on Gold. SAMs of alkane thiols on gold were prepared by incubating gold-coated silicon chips in an ethanolic solution containing equimolar quantities of $HS(CH_2)_{11}(OCH_2CH_2)_6OCH_2CO_2H$ and $HS(CH_2)_{11}(OCH_2CH_2)_3OH$. Subsequently, the chips were overlaid with an aqueous solution of EDC/NHS to produce succinimidyl ester-displaying chips. Diphenylphosphinomethanethiol was synthesized in multigram quantities by a procedure described previously (*44*), and was reacted with succinimidyl ester-displaying chips to generate phosphinothioester-displaying chips. The resultant phosphinothioester-displaying SAMs of alkane thiols on gold surfaces provide a highly homogeneous surface for performing the Staudinger ligation. These surfaces are significantly better defined than that of a glass slide, which had been used previously for Staudinger ligation (*33*, *34*, *45*), thereby enabling the use of high-precision techniques such as ellipsometry, surface plasmon resonance (*46*), and liquid crystal methods (*11*, *47*) for the detection of ligand binding.

Azido-RNase A Immobilization by Staudinger Ligation. Azido-RNase A (in 5% v/v DMF(aq)) was incubated on phosphinothioester-displaying chips for immobilization by Staudinger ligation (Scheme 2). A time course of immobilization of azido-RNase A is depicted in Figure 1. The immobilized RNase A was detected by an immunoassay utilizing a primary anti-RNase A antibody and a fluorescent secondary antibody. Protein immobilization proceeded rapidly, with a significant fluorescence signal being clearly observable after only 1 min. The rapidity of this reaction is reminiscent of that for the immobilization of azido-peptides to glass slides with a phosphinothioester-mediated Staudinger ligation (*33*).

Exposure of a protein to a phosphinothioester-displaying chip could lead to undesirable protein immobilization via a side chain of the protein. For example, RNase A has 10 lysine residues, any one of which could attack the phosphinothioester via its nucleophilic ϵ-amino group, thereby resulting in random immobilization. Additionally, the protein could be immobilized noncovalently onto the surface by hydrophobic interactions with the phenyl groups of the phosphinothioester. To probe for these possible immobilization routes, wild-type RNase A was incubated adjacent to azido-RNase A on phosphinothioester-displaying SAMs on gold. No significant immobilization of wild-type RNase A was observed during the time scale required for substantial azido-RNase A immobilization (Figure 1), thereby establishing that the immobilization of azido-RNase A proceeded exclusively via the azido group. Longer incubation times (>1 h) did result in detectable immobilization of wild-type RNase A (data not shown), highlighting the benefit of the rapidity of the Staudinger ligation.

Attempts to immobilize azido-RNase A in purely aqueous solutions of various pH were unsuccessful (data not shown). The presence of a small quantity of polar organic solvent (here, 5% v/v DMF) is required, perhaps for adequate solubilization of the immobilized phosphinothioester. A version of the Staudinger ligation has been used to immobilize proteins in purely aqueous solutions (*34*), though this method requires a long incubation period (4 h) and installs a racemic nonnatural moiety—a phosphine oxide—into the immobilized protein.

Activity of Immobilized RNase A. Enzymatic activity assays were performed with phosphinothioester-displaying chips incubated with azido-RNase A for 10 min. These chips were incubated in solutions containing 6-FAM−$dArU(dA)_2$−6-TAMRA, which is a fluorogenic substrate for RNase A (*48*). After 1 h, the fluorescence intensity from a chip incubated with azido-RNase A had increased substantially relative to one incubated with wild-type RNase A (Figure 2). Thus, the azido-RNase A was immobilized preferentially, and immobilization did not destroy its enzymatic activity.

Binding to Immobilized RNase A. A phosphinothioester-displaying chip was overlaid with azido-RNase A, and subsequently overlaid with RI. Another phosphinothioester-displaying chip was incubated with wild-type RNase A, and then overlaid with RI. Both chips were assayed for the presence of RI by an immunoassay that involved a primary antibody to RI and a fluorescent secondary antibody. The chip that was overlaid with azido-RNase A had a high fluorescence signal, whereas the chip incubated with wild-type RNase A produced negligible fluorescence (Figure 3A). This result demonstrated that the RI detected on the surface was bound to

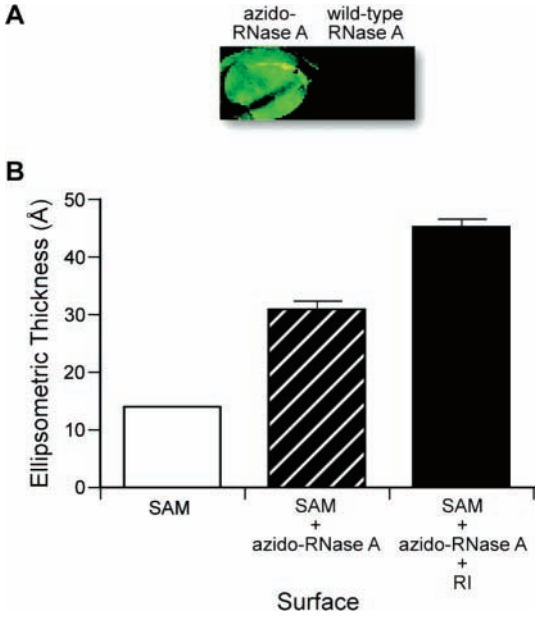


Figure 3. Binding of RI to immobilized RNase A. (A) Immunoassay with a primary anti-RI antibody and a secondary antibody conjugated to fluorescein. (B) Ellipsometric thickness before and after incubation with azido-RNase A, and after the addition of RI.

the immobilized RNase A, and was not binding to the surface nonspecifically.

Ellipsometric measurements corroborated these findings (Figure 3B). Upon incubation of azido-RNase A on phosphinothioester chips for 10 min, the ellipsometric thickness of the surface increased by 16.9 Å. Exposure to RI resulted in a further increase of 14.3 Å. That the increase in thickness upon RI binding was less than the increase in thickness upon azido-RNase A immobilization is surprising, as RI (molecular mass ~51 kDa) is a larger protein than RNase A (molecular mass ~14 kDa). One explanation is that the immobilization of RNase A via its C-terminus forces RI to bind obliquely to the surface, causing a smaller increase in the thickness than expected from lineal binding. Another explanation is that the binding of RI molecules to a few immobilized RNase A molecules creates steric hindrance to other incoming RI molecules. Consequently, not all of the immobilized RNase A molecules would form a complex with RI, producing a smaller than expected increase in ellipsometric thickness. To obtain additional information, we measured the ribonucleolytic activity of the immobilized RNase A after incubation with excess RI. Only half of the activity was lost, consistent with steric hindrence preventing half of the RNase A molecules from forming a complex with RI.

SUMMARY

We have developed a general strategy for the site-specific immobilization of a protein on SAMs on a gold surface. Immunoassays, assays of enzymatic activity, and ellipsometric measurements revealed that the immobilized protein retained its structure and function. We envisage numerous applications of our strategy, which could be applicable to any protein. For example, we expect that our strategy could be useful for the high-throughput screening of ligands, in diagnostic applications that detect disease markers in clinical samples, and in industrial processes that utilize immobilized enzymes as recyclable catalysts (*49*).

ACKNOWLEDGMENT

We are grateful to C.-H. Jang, R. J. Johnson, and G. A. Ellis for supplying reagents, and T. J. Rutkoski for contributive discussions. This work was supported by Grants GM44783 and CA108467 (NIH), and the Materials Research Science and Engineering Center at the University of Wisconsin−Madison (NSF DMR-0520527).

LITERATURE CITED

(1) Wilson, D. S., and Nock, S. (2003) Recent developments in protein microarray technology. *Angew. Chem., Int. Ed. 42*, 494−500.
(2) Schena, M., Ed. (2004) *Protein Microarrays*, Jones and Bartlett, Boston, MA.
(3) Kambhampati, D., Ed. (2004) *Protein Microarray Technology*, Wiley−VCH, Weinheim, Germany.
(4) Merkel, J. S., Michaud, G. A., Salcius, M., Schweitzer, B., and Predki, P. F. (2005) Functional protein microarrays: Just how functional are they? *Curr. Opin. Biotechnol. 16*, 447−452.
(5) Hultschig, C., Kreutzberger, J., Seitz, H., Konthus, Z., Bussow, K., and Lehrach, H. (2006) Recent advances in protein microarrays. *Curr. Opin. Chem. Biol. 10*, 4−10.
(6) Hu, Y., Uttamchandani, M., and Yao, S. Q. (2006) Microarray: A versatile platform for high-throughput functional proteomics. *Comb. Chem. High Throughput Screening 9*, 203−212.
(7) Kingsmore, S. F. (2006) Multiplexed protein measurement: Technologies and applications of protein and antibody arrays. *Nat. Rev. Drug Discovery 5*, 310−320.
(8) Sweeney, R. Y., Kelemen, B. R., Woycechowsky, K. J., and Raines, R. T. (2000) A highly active immobilized ribonuclease. *Anal. Biochem. 286*, 312−314.
(9) Peluso, P., Wilson, D. S., Do, D., Tran, H., Venkatasubbaiah, M., Quincy, D., Heidecker, B., Poindexter, K., Tolani, H., Phelan, M., Witte, K., Jung, L. S., Wagner, P., and Nock, S. (2003) Optimizing antibody immobilization strategies for the construction of protein microarrays. *Anal. Biochem. 312*, 113−124.
(10) Du, Y.-Z., and Saavedra, S. S. (2003) Molecular orientation distributions in protein films. V. Cytochrome *c* adsorbed to a sulfonate-terminated self-assembled monolayer. *Langmuir 19*, 6443−6448.
(11) Luk, Y.-Y., Tingey, M. L., Dickson, K. A., Raines, R. T., and Abbott, N. L. (2004) Comparison of the binding activity of randomly oriented and uniformly oriented proteins immobilized by chemoselective coupling to a self-assembled monolayer. *J. Am. Chem. Soc. 126*, 9024−9032.
(12) Cha, T., Guo, A., and Zhu, X. Y. (2005) Enzymatic activity on a chip: The critical role of protein orientation. *Proteomics 5*, 416−419.
(13) Lipshutz, R. J., Fodor, S. P. A., Gingeras, T. R., and Lockhart, D. J. (1999) High density synthetic oligonucleotide arrays. *Nat. Genet. 21*, 20−24.
(14) Brown, P. O., and Botstein, D. (1999) Exploring the new world of the genome with DNA microarrays. *Nat. Genet. 21*, 33−37.
(15) Singh-Gasson, S., Green, R. D., Yue, Y., Nelson, C., Blattner, F., Sussman, M. R., and Cerrina, F. (1999) Maskless fabrication of light-directed oligonucleotide microarrays using a digital micromirror array. *Nat. Biotechnol. 17*, 974−978.
(16) Hoheisel, J. D. (2006) Microarray technology: Beyond transcript profiling and genotype analysis. *Nat. Rev. Genet.* 200−210.
(17) Caruthers, M. H. (1991) Chemical synthesis of DNA and DNA analogues. *Acc. Chem. Res. 24*, 278−284.
(18) Mullis, K. B. (1994) The polymerase chain reaction (Nobel lecture). *Angew. Chem., Int. Ed. Engl. 33*, 1209−1213.
(19) Nilsson, B. L., Soellner, M. B., and Raines, R. T. (2005) Chemical synthesis of proteins. *Annu. Rev. Biophys. Biomol. Struct. 34*, 91−118.
(20) Walsh, C. T. (2005) *Posttranslational Modification of Proteins: Expanding Nature's Inventory*, Roberts, Englewood, CO.
(21) Yeo, D. S., Panicker, C., Tan, L. P., and Yao, S. Q. (2004) Strategies for immobilization of biomolecules in a microarray. *Comb. Chem. High Throughput Screening 7*, 213−221.
(22) Butler, J. E., Ni, L., Nessler, R., Joshi, K. S., Suter, M., Rosenberg, B., Chang, J., Brown, W. R., and Cantarero, L. A. (1992) The physical and functional behavior of capture antibodies adsorbed on polystyrene. *J. Immunol. Methods 150*, 77−90.
(23) Duburcq, X., Olivier, C., Malingue, F., Desmet, R., Bouzidi, A., Zhou, F., Auriault, C., Gras-Masse, H., and Melnyk, O. (2004)

Peptide−protein microarrays for the simultaneous detection of pathogen infections. *Bioconjugate Chem. 15*, 307−316.
(24) Paborsky, L. R., Dunn, K. E., Gibbs, C. S., and Dougherty, J. P. (1996) A nickel chelate microtiter plate assay for six histidine-containing proteins. *Anal. Biochem. 234*, 60−65.
(25) Zhu, H., Bilgin, M., Bangham, R., Hall, D., Casamayor, A., Bertone, P., Lau, N., Jansen, R., Bidlingmaier, S., Houfek, T., Mitchell, T., Miller, P., Dean, R. A., Gerstein, M., and Snyder, M. (2001) Global analysis of protein activities using proteome chips. *Science 293*, 2101−2105.
(26) Lahiri, J. I. L., Tien, J., and Whitesides, G. M. (1999) A strategy for the generation of surfaces presenting ligands for studies of binding based on an active ester as a common reactive intermediate: a surface plasmon resonance study. *Anal. Chem. 71*, 777−790.
(27) MacBeath, G., and Schreiber, S. L. (2000) Printing proteins as microarrays for high-throughput function determination. *Science 289*, 1760−1763.
(28) Liu, X., Jang, C.-H., Zheng, F., Jürgensen, A., Denslinger, J. D., Dickson, K. A., Raines, R. T., Abbott, N. L., and Himpsel, F. J. (2006) Characterization of protein immobilization at silver surfaces by near edge X-ray absorption fine structure spectroscopy. *Langmuir 22*, 7719−7725.
(29) Bräse, S., Gil, C., Knepper, K., and Zimmermann, V. (2005) Organic azides: An exploding diversity of a unique class of compounds. *Angew. Chem., Int. Ed. 44*, 5188−5240.
(30) Sun, X. L., Stabler, C. L., Cazalis, C. S., and Chaikof, E. L. (2006) Carbohydrate and protein immobilization onto solid surfaces by sequential Diels−Alder and azide−alkyne cycloadditions. *Bioconjugate Chem. 17*, 52−57.
(31) Duckworth, B. P., Xu, J., Taton, T. A., Guo, A., and Distefano, M. D. (2006) Site-specific, covalent attachment of proteins to a solid surface. *Bioconjugate Chem.* 967−974.
(32) Gauchet, C., Labadie, G. R., and Poulter, C. D. (2006) Regio- and chemoselective covalent immobilization of proteins through unnatural amino acids. *J. Am. Chem. Soc. 128*, 9274−9275.
(33) Soellner, M. B., Dickson, K. A., Nilsson, B. L., and Raines, R. T. (2003) Site-specific protein immobilization by Staudinger ligation. *J. Am. Chem. Soc. 125*, 11790−11791.
(34) Watzke, A., Kohn, M., Gutierrez-Rodriguez, M., Wacker, R., Schroder, H., Breinbauer, R., Kuhlmann, J., Alexandrov, K., Niemeyer, C. M., Goody, R. S., and Waldmann, H. (2006) Site-selective protein immobilization by Staudinger ligation. *Angew. Chem., Int. Ed. 45*, 1408−1412.
(35) Kalia, J., and Raines, R. T. (2006) Reactivity of intein thioesters: Appending a functional group to a protein. *ChemBioChem 7*, 1375−1383.
(36) Raines, R. T. (1998) Ribonuclease A. *Chem. Rev. 98*, 1045−1066.
(37) Dickson, K. A., Haigis, M. C., and Raines, R. T. (2005) Ribonuclease inhibitor: Structure and function. *Prog. Nucleic Acid Res. Mol. Biol. 80*, 349−374.
(38) Nilsson, B. L., Kiessling, L. L., and Raines, R. T. (2001) High-yielding Staudinger ligation of a phosphinothioester and azide to form a peptide. *Org. Lett. 3*, 9−12.
(39) Kohn, M., and Breinbauer, R. (2004) The Staudinger ligation−A gift to chemical biology. *Angew. Chem., Int. Ed. 43*, 2−12.
(40) Soellner, M. B., Nilsson, B. L., and Raines, R. T. (2006) Reaction mechanism and kinetics of the traceless Staudinger ligation. *J. Am. Chem. Soc. 128*, 8820−8828.
(41) Jang, C.-H., Cheng, L.-L., Olsen, C. W., and Abbott, N. L. (2006) Anchoring of nematic liquid crystals on viruses with different envelope structures. *Nano Lett. 6*, 1053−1058.
(42) Prime, K. L., and Whitesides, G. M. (1993) Adsorption of proteins onto surfaces containing end-attached oligo(ethylene oxide): A model system using self-assembled monolayers. *J. Am. Chem. Soc. 115*, 10714−10721.
(43) Wood, L. L., Cheng, S.-S., Edmiston, P. L., and Saavedra, S. S. (1997) Molecular orientation in protein films. 2. Site-directed imobilization of yeast cytochrome c on thiol-capped, self-assembled monolayers. *J. Am. Chem. Soc. 119*, 571−576.
(44) Soellner, M. B., Nilsson, B. L., and Raines, R. T. (2002) Staudinger ligation of α-azido acids retains stereochemistry. *J. Org. Chem. 67*, 4993−4996.
(45) Kohn, M., Wacker, R., Peters, C., Schroder, H., Soulere, L., Breinbauer, R., Niemeyer, C. M., and Waldmann, H. (2003) Staudinger ligation: A new immobilization strategy for the preparation of small-molecule arrays. *Angew. Chem., Int. Ed. 42*, 5830−5834.
(46) Green, R. J., Frazier, R. A., Shakesheff, K. M., Davies, M. C., Roberts, C. J., and Tendler, S. J. (2000) Surface plasmon resonance analysis of dynamic biological interactions with biomaterials. *Biomaterials 21*, 1823−1835.
(47) Gupta, V. K., Skaife, J. J., Dubrovsky, T. B., and Abbott, N. L. (1998) Optical amplification of ligand-receptor binding using liquid crystals. *Science 279*, 2077−2080.
(48) Abel, R. L., Haigis, M. C., Park, C., and Raines, R. T. (2002) Fluorescence assay for the binding of ribonuclease A to the ribonuclease inhibitor protein. *Anal. Biochem. 306*, 100−107.
(49) Chibata, I., Tosa, T., Sato, T., and Mori, T. (1979) In *Immobilized Enzymes: Research and Development* (Chibata, I., Ed.) pp 148−264, John Wiley & Sons, New York.

BC0603034

Tailoring Protease-Sensitive Photodynamic Agents to Specific Disease-Associated Enzymes

Doris Gabriel,† Marino A. Campo,† Robert Gurny, and Norbert Lange*

Laboratory of Pharmaceutics and Biopharmaceutics, Section of Pharmaceutical Sciences, University Lausanne, University Genève, 30 Quai Ernest-Ansermet, CH-1211, Geneva, Switzerland. Received October 13, 2006; Revised Manuscript Received March 27, 2007

We have developed novel polymeric photosensitizer prodrugs (PPPs) for improved photodynamic therapy. In PPPs, multiple photosensitizer units are covalently coupled to a polymeric backbone via protease-cleavable peptide linkers. These initially non-photoactive compounds become fluorescent and phototoxic after specific enzymatic cleavage of the peptide linkers and subsequent release of the photosensitizer moieties. Tethering the photosensitizer via a short and easily modified amino acid sequence to the polymeric backbone allows for the targeting of a wide variety of proteases. Model compounds, sensitive to trypsin-mediated cleavage, with different pheophorbide a-peptide loading ratios and backbone net charges were evaluated with respect to their solubility, "self-quenching" capacity of fluorescence emission, and reactive oxygen species (ROS) generation. In addition, linker sequence impaired selectivity toward enzymatic cleavage was demonstrated either by incubating PPPs with different enzymes having trypsin-like activity or by introducing a single D-arginine mutant in the peptide sequence. In vitro cell culture tests confirmed dose-dependent higher phototoxicity of enzymatically activated PPPs compared to the nonactivated conjugate after irradiation with white light. These data suggest that similar compounds adapted to disease-associated proteases can be used for selective photodynamic therapy.

INTRODUCTION

Photodynamic therapy (PDT[1]) has emerged as a promising therapeutic option for the treatment of cancer and other nonmalignant diseases. It combines the simultaneous use of a photosensitizer (PS), oxygen, and light to locally generate cytotoxic reactive oxygen species (ROS) causing the destruction of unwanted tissues (*1*, *2*). This treatment has several advantages over surgery and radiotherapy: it is comparatively noninvasive, it can be targeted accurately, repeated doses can be given without the total-dose limitations associated with radiotherapy, and the healing progress results in little or no scarring. PDT can usually be done on an outpatient or day-case basis; it is convenient for the patient and has few or no side effects. However, one of the main drawbacks of PDT is unfavorable biodistribution and lack of selective accumulation of conventional PSs in the target tissue. Although passive and active targeting strategies have been shown to enhance the specific delivery of PS to the site of disease, none of the exploited active targeting strategies has led to the development of a clinically relevant compound until today (*3*).

Photodynamically induced collateral damage to vital tissue structures within the irradiated area demand that PSs or PS precursors become photoactive specifically at the target site, in response to the disease environment. Exploiting enhanced proteolytic activities, a hallmark in several pathologic conditions involving tissue remodeling and invasion (*4*−*8*), is a novel concept for enzyme-mediated activation of polymeric photosensitizer prodrugs (PPPs). In so-called first-generation conjugates, multiple PSs are directly coupled to a poly(L-lysine) backbone (PLL). In this configuration, the PPP is non-phototoxic due to energy transfer between PS moieties. Proteolytic cleavage of the polymeric backbone by enzymes leads to PS activation and to an increase in phototoxicity. We and others have already demonstrated the advantages of such strategy in vitro (*9*) and in vivo (*10*). Nonetheless, these photodynamic agents are limited to targeting selected proteases capable of degrading the polymeric backbone. In order to broaden the spectrum of this targeting strategy to a wide variety of disease-related proteases, we propose the use of a peptidic linker between the PS and a stable polymeric backbone, whose sequence will determine the proteolytic enzyme being targeted. This approach will allow for a more specific targeting of proteases and prevent nonspecific activation by backbone degradation.

In the present study, we describe the synthesis and evaluation of novel PPPs that follow this strategy. Activation of the PPP occurs by abrogation of the intramolecular interaction between photosensitzers, induced by enzymatic cleavage of the polymer−photosensitizer linker and release of truncated photosensitizer−peptide fragments. In contrast to first-generation conjugates, where enzymatic cleavage occurs on the polymeric backbone, the loading ratio and restoration of phototoxicity are limited by neither available cleavage sites on the polymeric backbone nor the release of potentially quenched fragments.

* Norbert.Lange@pharm.unige.ch.

† Both authors contributed equally to the present work.

[1] Abbreviations: aq, aqueous; equiv, equivalents; DCM, dichloromethane; DMAP, 4-*N*,*N*-dimethylaminopyridine; DMF, *N*,*N*-dimethylformamide; DMSO, dimethysulfoxide; EDC, *N*-(3-dimethylaminopropyl)-*N*′-ethyl-carbodiimide hydrochloride; EDTA, ethylenediaminetetraacetic acid; EPR, enhanced permeability and retention effect; ES, electrospray; FL, fluorescence intensity; F_o, fluorescence intensity of conjugate carrying one photosensitizer unit per polymer chain; FCS, fetal calf serum; FL_E, fluorescence intensity of a control enzyme solution without PPP; FL_{max}, maximum fluorescence intensity after enzymatic activation; FL_o, fluorescence intensity of undigested conjugate; Fmoc, 9-fluorenylmethyloxycarbonyl; GFP, green fluorescent protein; HBSS, Hank's balanced salt solution; MS, mass spectrometry; MW, molecular weight; NHS, *N*-hydroxysuccinimide; PBS, phosphate saline buffer; PDT, photodynamic therapy; PLL, Poly(L-lysine); PPP, polymeric photosensitizer prodrug; PS, photosensitizer; ROS, reactive oxygen species; RP-HPLC, reversed-phase high pressure liquid chromatography; SEC, size exclusion chromatography; UV, ultraviolet; vis, visible.

10.1021/bc060321l CCC: $37.00 © 2007 American Chemical Society
Published on Web 05/04/2007

These newly designed second-generation pheophorbide a-peptide−poly(L-lysine) conjugates are designed to have molecular weights (≥50kDa) above the renal excretion limit and are, thus, expected to have prolonged plasma half-lives and EPR targeting capability (*11*). Small water-solubilizing backbone protecting units will maintain the resulting conjugate at an estimated size of 70 kDa, therefore helping the PPP to elude the immune system and prevent a reaction from the organism after repeated treatments.

In our studies, pheophorbide a was chosen as the photosensitizer because of its photochemical properties, including high absorption in the range 660−680 nm, allowing for deeper tissue penetration (*12*, *13*). Furthermore, pheophorbide a is a natural compound with a known toxicological profile. However, the developed synthetic strategy can be easily adapted to other photosensitizer moieties.

EXPERIMENTAL PROCEDURES

Chemicals. All commercial reagents were used as obtained. Anhydrous forms of acetonitrile, *N*,*N*-dimethylformamide (DMF), dimethylsulfoxide (DMSO), dichloromethane (DCM), diethyl ether, methanol, and ethyl acetate, as well as *N*-(3-dimethylaminopropyl)-*N*′-ethylcarbodiimide hydrochloride (EDC), *N*-hydroxysuccinimide (NHS), *N*,*N*-diisopropylethylamine (DIPEA), trypsin (bovine pancreas), poly(L-lysine) HBr (25 KDa), HGly-2-chlorotrityl resin (1.1 mmol/g), FmocAlaOH, Fmoc-D-Arg(Pbf)OH, Fmoc-L-Arg(Pbf)OH, FmocGlyOH, FmocPheOH, FmocSer(*t*-Bu)OH, FmocThr(*t*-Bu)OH, O-(7-azabenzotriazol-1-yl)-*N*,*N*,*N*,*N*-tetramethyluronium hexafluorophosphte (HATU), and 1 M picrylsulfonic acid aqueous solution were purchased from Fluka (Buchs, Switzerland). Pheophorbide a was purchased from Frontier Scientific (Logan, UT). D-MEM+GlutaMAX I medium, as well as HBSS and D-PBS solutions were purchased from GIBCO (Invitrogen, Basel, Switzerland). 4-Aminobenzamidine dihydrochloride, thrombin (bovine plasma), and elastase (type l, porcine pancreas) were obtained from Sigma-Aldrich (Buchs, Switzerland).

General Procedures. Mass spectra were recorded using a Finnigan MAT SSQ 7000 (Thermo Electron Co. Waltham, MA). Fluorescence measurements were done with a SPEX Fluoromax (Perkin-Elmer, Wellesley, MA excitation at 400 nm and emission at 670 nm). UV/vis data were obtained using a Cintra 40 UV/vis spectrometer (GBC, Dandenong, Australia).

Preparation of Pheophorbide a-NHS Ester and *N*-Succinimidyl (1-methyl-3-pyridinio)formate Iodide. Synthesis of Pheophorbide a-NHS ester using EDC/NHS chemistry, as well as preparation of *N*-succinimidyl (1-methyl-3-pyridinio)formate iodide, was done as described previously (*9*, *14*).

Peptide Synthesis. The synthesis of the trypsin-cleavable peptide Gly-Thr-Phe-(L)Arg-Ser-Ala-Gly and the control Gly-Thr-Phe-(D)Arg-Ser-Ala-Gly were performed manually on HGly-2-chlorotrityl resin 200−400 mesh (1.1 mmol/g, 0.355 g, 0.39 mmol) using the standard FMOC strategy (*15*). Peptides were purified by RP-HPLC and obtained in >95% purity. ES-MS: 695.6 ($[M + H]^+ = 695.4$ calculated for $C_{29}H_{47}N_{10}O_{10}^+$) and 348.3 ($[M + 2H]^{2+} = 348.2$ calculated for $C_{29}H_{48}N_{10}O_{10}^{2+}$).

Pheophorbide−Peptide Conjugates. To a solution of the corresponding peptide (15 mg, 1.62×10^{-5} mol) in DMSO (1.0 mL) was added pheophorbide a-NHS ester (0.5 equiv, 5.6 mg) in DMSO (1.5 mL). The reaction was allowed to proceed for 4 h after the dropwise addition of DIPEA (2.0 equiv). The reaction was quenched by adding water (2.5 mL) and TFA to pH 3. Pheophorbide−peptide conjugates were purified by preparative RP-HPLC (Waters Delta 600 HPLC) on a C8, Nucleosil 300−10 column (Macherey-Nagel) using a 0.1% TFA water/acetonitrile gradient (flow rate = 20 mL/min). Eluting products were monitored by dual UV/vis absorbance at 230 nm and 400 nm and were obtained as green solids after lyophilization. ESI-MS: 1269.9 ($[M + H]^+ = 1269.6$ calculated for $C_{64}H_{81}N_{14}O_{14}^+$) obtained for both L and D configured pheophorbide−peptide conjugates.

Final Assembly of PPP. To a solution of the corresponding pheophorbide−peptide (1.8 mg, 1.3×10^{-6} mol), PLL (25 kDa) (1.07 mg, 4.34×10^{-8} mol, 5.1×10^{-6} mol of ϵ-NH_2 functions), and HATU (1.3 equiv based on pheophorbide−peptide to be activated) in DMSO (0.5 mL) was added DIPEA (3 equiv based on the number of ϵ-NH_2 functions of PLL) and the mixture was stirred under argon overnight (14 h). Loading of 30 PS units per PLL was confirmed by analytical RP-HPLC monitoring of the reference pheophorbide−peptide peak ($\lambda_{abs} = 400$ nm), which completely disappeared during the reaction, giving rise to a single, new, and broader peak corresponding to the polymeric conjugate.

In order to cap the remaining free ϵ-NH_2 functions of PLL, *N*-succinimidyl (1-methyl-3-pyridinio)formate iodide (1.5 mg, 1.1 equiv based on the number of free ϵ-NH_2 functions remaining on PLL) in DMSO (0.1 mL) was added to the reaction mixture and the reaction allowed to proceed for 1 h. The reaction mixture was then quenched by adding a water/acetonitrile (70/30) mixture (3.0 mL) and TFA to pH 3. The resulting solution was filtered and purified by SEC using a Sephacryl S-100 (Amersham Biosciences, Otelfingen, Switzerland) column and 30:70:0.00025 acetonitrile/water/TFA as eluent. The fraction containing the product was lyophilized to yield the desired product as a green solid. UV/vis (H_2O): 287.6 (29 707 M^{-1} cm^{-1}), 390.0 (122 128 M^{-1} cm^{-1}), 504.4 (13 803 M^{-1} cm^{-1}), 623.6 (8402 M^{-1} cm^{-1}), 667.6 (43 510 M^{-1} cm^{-1}).

Note: Conjugates carrying 6 and 18 PS moieties per PLL chain were prepared by a similar procedure as the one described above but used the corresponding amounts of pheophorbide−peptide (0.3 mg and 1.08 mg, respectively) and *N*-succinimidyl (1-methyl-3-pyridinio)formate iodide (1.9 mg and 1.7 mg, respectively).

Enzymatic Cleavage of Pheophorbide−L-Peptide and Control Pheophorbide−D-Peptide. Enzymatic cleavage of the pheophorbide−peptide by trypsin (0.5 mg/mL) was confirmed by monitoring the released fragment pheophorbide a-Gly-Thr-Phe-Arg by analytical HPLC. Either pheophorbide−L-peptide or control pheophorbide−D-peptide at equimolar concentration with respect to pheophorbide a in PBS was incubated with the enzyme at 37 °C. After 30 min, aliquots of the digestion mixture were quenched with TFA and subjected to analytical HPLC analysis, using a Nucleodur C18 gravity 3 μ CC 125/4 column from Macherey-Nagel and a linear acetonitrile/0.1% TFA−water gradient. Fluorescence was detected on a Merck Hitachi FL detector L7480 at an emission wavelength of 670 nm and excitation wavelength at 405 nm. The same conditions were used to monitor the release of cleaved fragments from the PPP.

Fluorescence Measurements of Undigested PPP. The optical density for each of the aqueous solutions containing the PPP carrying either 6, 18, or 30 PS units per PLL chain was adjusted to 0.125 at 667 nm, setting the PS concentration to 3.5 μM. The fluorescence intensity of each of these equimolar solutions was measured at 37 °C using a SPEX Fluoromax (Perkin-Elmer, Wellesley, MA) setting the excitation at 400 nm and emission at 670 nm.

ROS Measurements in Aqueous Media Using Iodide. ROS were measured by a modified procedure previously described by Mosinger (*16*), in which the I_3^- (286 nm absorbance band) generated by ROS oxidation of I^- in aqueous media was monitored (*9*). Briefly, to 0.6 mL of D-PBS buffered solutions containing PPPs at equimolar concentrations with respect to pheophorbide a, NaI was added in aqueous solution to obtain a final concentration of 0.625 M, and the

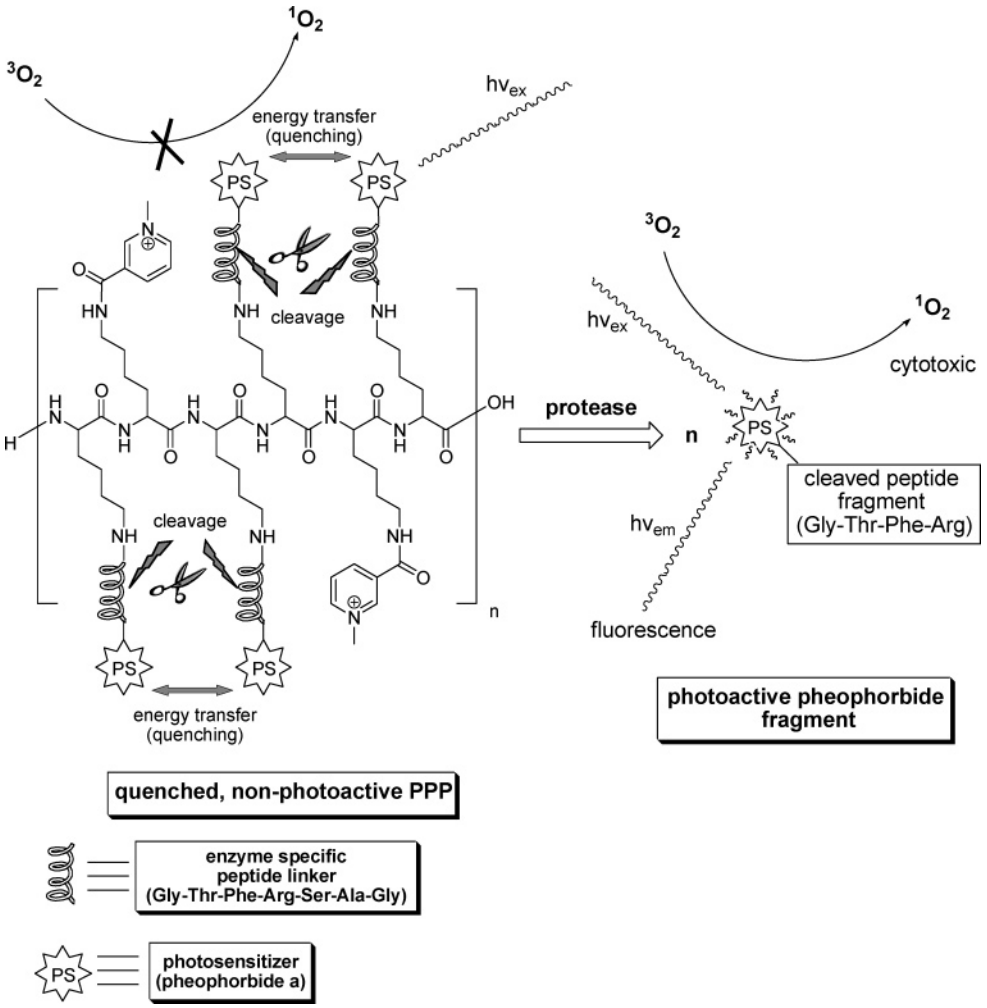


Figure 1. Principle of probe activation and schematic structure. Intramolecular energy transfer between closely positioned photosensitizers is assumed to efficiently depopulate irradiation-excited first and triplet states, resulting in reduced fluorescence and energy transfer to molecular triplet oxygen. Enzymatic cleavage leads to the release of photosensitizer−peptidyl fragments, which in turn are free to diffuse and fully photoactive again.

UV−vis spectra were recorded as background. Then, the mixtures were irradiated with white light (3.72 J/cm^2), and the UV−vis spectra were again recorded to yield the actual increase in optical density.

In Vitro Enzymatic Activation of PPPs. For in vitro protease-mediated activation, PBS buffered solutions of the PPP (corresponding to 10 μM pheophorbide a) containing 2.5% DMSO were treated with trypsin, thrombin, and elastase (180 μL, 7 nmol/mL). Samples were incubated at 37 °C in the dark, and aliquots were sampled in DMSO (75%) to measure the fluorescence spectra in a quartz microcuvette at 37 °C using $\lambda_{ex} = 400$ nm and $\lambda_{em} = 675$ nm. Activation experiments with the control PPP were performed under identical conditions. The relative increase in fluorescence was calculated as follows: $(FL_{max} - FL_E)/(FL_0)$, where FL_{max} is the fluorescence of the activated probe after 15 min, FL_E the fluorescence of the enzyme in buffer, and FL_0 corresponds to the fluorescence of the nondigested PPP.

Cell Culture. GFP transfected human urothelial bladder cancer cell line T24 was grown as monolayers and was a kind gift from S. Cloutier (CHUV Hospital, Lausanne, Switzerland). The cells were routinely maintained by serial passage in D-MEM+GlutaMAX I medium supplemented with 10% FCS, 100 μL/mL streptomycin, and 100 IE/mL penicillin in 5% CO_2/95% air at 37 °C.

Cell Culture Toxicity Studies. 3-(4,5-Dimethylthiazol-2-yl)-2,5-diphenyl-2*H*-tetrazolium bromide assay (MTT assay) was used to assess dark and phototoxicity of activated and nonactivated PPP. For this, 100 μL of a cell suspension (seeding density: 85 000 cells/mL) were plated into 96-well plates and allowed to grow overnight.

Cells were exposed for 30 min to increasing concentrations of either intact or predigested PPP in complete medium containing 10% FCS, 2.5% DMSO, and the trypsin inhibitor *p*-aminobenzamidine (2 mg/mL) for the enzyme (0.3 mg/mL) predigested PPP. After incubation, cells were washed three times with HBSS, complete medium was added, and cells were irradiated with white light (13.5 J/cm^2). Dark toxicity was determined in an identical manner but without irradiation. Cell survival was assessed 18 h later by adding 50 μL MTT (1 mg/mL) in complete medium. Following incubation for 3 h at 37 °C, formazan crystals were dissolved with 200 μL DMSO per well. Absorbance at 525 nm was read after overnight incubation with a Bio Rad (model 550) plate reader. The signal was normalized to 100% viable cells (incubated with 2.5% DMSO for PPP or 2.5% DMSO, trypsin [0.3 mg/mL] and *p*-aminobenzamidine (2 mg/mL) in complete medium for preactivated PPP) and 0% viable cells (incubated with 0.25% Triton X in D-PBS). Thus, percentage survival was calculated as follows:

$$(A_{(\text{conc.X})} - A_{(0\%\text{survival})})/(A_{(100\%\text{survival})} - A_{(0\%\text{survival})}) \times 100$$

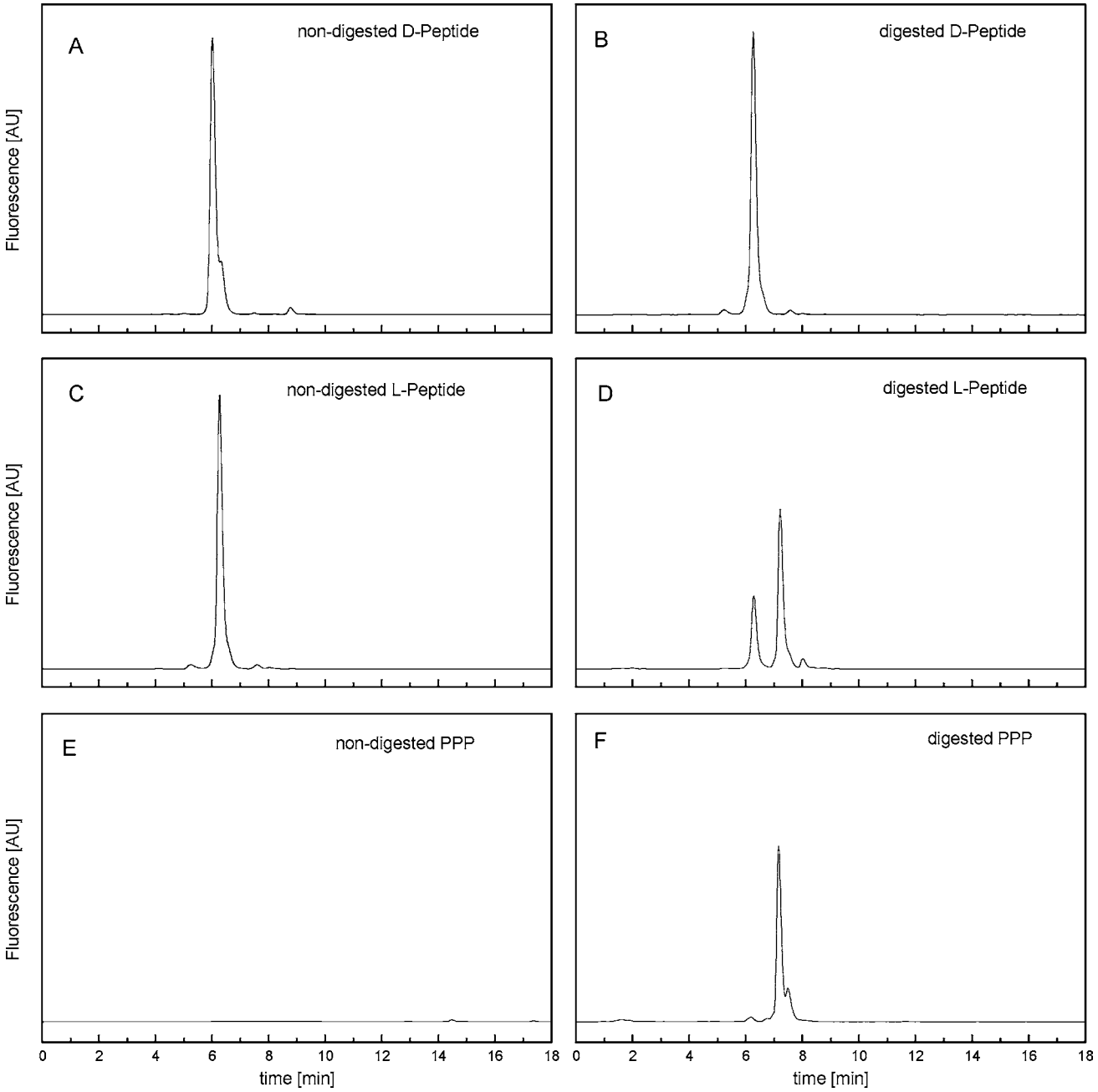


Figure 2. Analytical HPLC trace of the undigested (A,C,E) and digested (B,D,F) pheophorbide−peptide and PPP, respectively. (A) The negative control peptide pheophorbide-Gly-Thr-Phe-(D)Arg-Ser-Ala-Gly before enzymatic degradation. (B) The control peptide pheophorbide-Gly-Thr-Phe-(D)Arg-Ser-Ala-Gly following incubation with trypsin; the D-arginine-containing control peptide was not cleaved. (C) The pheophorbide-Gly-Thr-Phe-(L)Arg-Ser-Ala-Gly and (D) after incubation with trypsin gives rise to a new peak corresponding to the more lipophilic pheophorbide-Gly-Thr-Phe-(L)Arg fragment. (E) The corresponding HPLC trace of the nondigested PPP. (F) After incubation of the PPP, a peak corresponding to the cleaved fragment observed in (D) appears.

where $A_{(\text{conc.X})}$ corresponds to the absorbance of wells incubated with various concentrations of PPP or activated PPP; $A_{(100\%\text{survival})}$ represents the positive and $A_{(0\%\text{survival})}$ the negative control values.

All results were obtained from six replicate measurements per condition.

Confocal Fluorescence Microscopy. T24+ cells were seeded into falcon cell culture inserts (Becton Dickinson Labware, Franklin Lakes, NJ) and allowed to attach overnight. Cells were then incubated for 30 min with either the activated or nonactivated PPP at a final concentration of 5 μM pheophorbide a equivalents, in a mixture of D-PBS, medium, and FCS (6:3:1). To avoid cell detachment, *p*-aminobenzamidine (2 mg/mL) was added to the medium containing the trypsin (0.3 mg/mL) activated conjugate prior to incubation. Cells were washed three times with 2 mL HBSS before visualization of fluorescence and cellular localization pattern of the photosensitizer by confocal fluorescence microscopy using a Zeiss Axiovert 510 microscope (Carl Zeiss, Jena, Germany). Fluorescence emission was monitored at $\lambda > 650$ nm for the photosensitizer and from 520 to 550 nm for GFP, using a diode laser excitation at 405 nm.

Statistical Analysis. Statistical significance between the different values was assessed with a Student's *t*-test, and results were expressed as means ± S.D. p values ≤ 0.05 were considered significant.

RESULTS

Synthetic Strategy. PPPs were prepared using a convergent strategy in the following fashion. First, a peptide substrate with

Table 1. Direct Comparison between Second- and First-Generation PPP (data given in brackets from ref 1)[a]

PS units/PLL chain	Water solubility (in terms of PS concentration (mM))	Quenching efficiency[b] (1-FL/FL_o)	Quenching factor[b] (FL_o/FL)	Relative photodynamic response[c] (optical density at 286 nm)
1	[10]	[0]	[1]	[40.0] ± 2.4
6	> 10[10]	0.930[0.972]	14.2[35.4]	6.67[9.29] ± 0.4
18	7.8[1.3]	0.988[0.992]	84.6[131.7]	3.01[1.05] ± 0.18
30	0.06[0.01]	0.999[0.998]	705.2[626.8]	1.28[0.0] ± 0.08

[a] FL_o = fluorescence intensity of the nonquenched conjugate carrying one PS unit per chain, and FL = fluorescence intensity of conjugate carrying a given number of PS units per chain. [b] Measurements were carried out under identical concentrations of the PS by adjusting the optical density at 667 nm. [c] Relative photodynamic response of PPP was noted after irradiating with white light (3.7 J/cm^2) the solutions containing the PPP + NaI under equimolar concentration of the PS. Photodynamic response was measured by monitoring the increase in optical density at 286 nm (I_3^-). The following formula was used to calculate the normalized *x*-fold increase in optical density at 286 nm [value = (increase in optical density for PPP*x* − increase in optical density for reference PPP (loaded with 30 PS units per chain)) increase in optical density for reference PPP)].

an amino acid sequence that is recognized and cleaved by trypsin was assembled manually on the solid phase using the Fmoc strategy. Chemoselective conjugation of pheophorbide a to the N-terminus of the peptide via a stable amide bond produced pheophorbide a−peptide conjugates, which were then covalently coupled via the C-terminus to the ϵNH_2 functions of PLL (25 kDa) at different loading ratios. Finally, in order to increase water solubility and to protect the polymer backbone from nonspecific enzymatic degradation, the free remaining lysine chains of PLL were capped with 1-methylnicotinic acid units. A schematic representation of PPPs and activation mechanism is given in Figure 1.

Synthesis of the Pheophorbide−Peptide Conjugates and Evaluation of the Trypsin Substrate Specifity. The peptide sequence Gly-Ala-Leu-Ala-Thr-Phe-Arg-Ser-Ala−Ala-Val-Ser-Thr has been reported as a good substrate for trypsin and chymotrypsin (*17*). The core parent sequence Thr-Phe-Arg-Ser-Ala was slightly modified by introducing a glycine spacer at the N and C-termini, respectively, for covalent attachment to either the photosensitizer pheophorbide a or to the ϵ-NH_2 of the PLL backbone. Substituting the L-arginine by a D-arginine residue gave a noncleavable control sequence. The identity of the two peptides was confirmed by ES-MS analysis (695.6 ([M + H]$^+$ = 695.4 calculated for $C_{29}H_{47}N_{10}O_{10}^+$ and 348.3 ([M + 2H]$^{2+}$ = 348.2 calculated for $C_{29}H_{48}N_{10}O_{10}^{2+}$) after purification of the resulting crudes by preparative RP-HPLC. The subsequent chemoselective coupling of *N*-hydroxysuccinimide pheophorbide a activated ester to the N-terminus of either of the two peptides yielded pheophorbide a-Gly-Thr-Phe-(L)Arg-Ser-Ala-Gly (pheophorbide−L-peptide) and pheophorbide a-Gly-Thr-Phe-(D)Arg-Ser-Ala-Gly (pheophorbide−D-peptide). ESI-MS analysis after preparative RP-HPLC purification confirmed the identity of the obtained products (1269.9 ([M + H]$^+$ = 1269.6 calculated for $C_{64}H_{81}N_{14}O_{14}^+$).

Analytical RP-HPLC analysis was used to monitor the cleavage of the two pheophorbide−peptides by trypsin, revealing that only the substrate pheophorbide−L-peptide was recognized and cleaved by the enzyme, whereas the control was stable to enzymatic cleavage (Figure 2). Furthermore, the site of cleavage for the L-arginine-containing sequence was confirmed to be at the C-terminus of the arginine residue in accordance with reported preferential trypsin cleavage sites (*18*). This was determined by ESI-MS analysis of the isolated pheophorbide a-Gly-Thr-Phe-(L)ArgOH fragment obtained after enzymatic digestion [M + H]$^+$ = 1054.51 calculated for $C_{56}H_{68}N_{11}O_{10}^+$.

Synthesis and Physicochemical Properties of Trypsin-Selective PPPs. Finally, trypsin-sensitive PPPs were assembled by chemoselective conjugation of the C-terminal carboxylic function of the pheophorbide−peptide conjugates to the PLL backbone. The remaining free side chains of the PLL backbone were capped by reaction with *N*-succinimidyl(1-methyl-3-pyridinio)formate iodide salt to yield the final conjugates. This

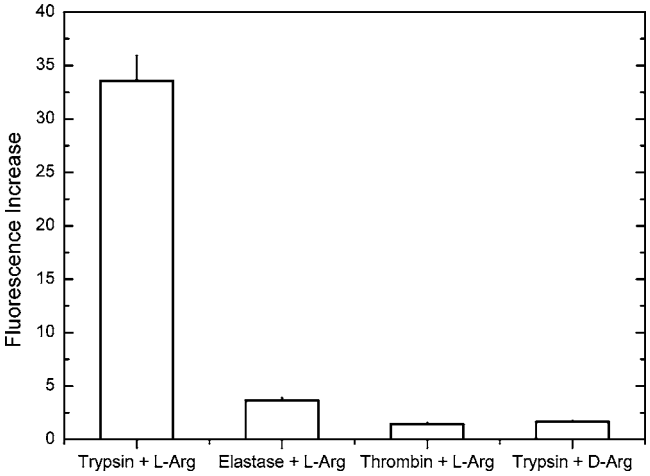


Figure 3. Increase in fluorescence emission of PPP following incubation with trypsin, thrombin, and elastase 15 min after enzyme addition and expressed as times increase compared to a PBS-treated PPP. As control, a PPP with a D-Arg mutation was incubated under the same conditions.

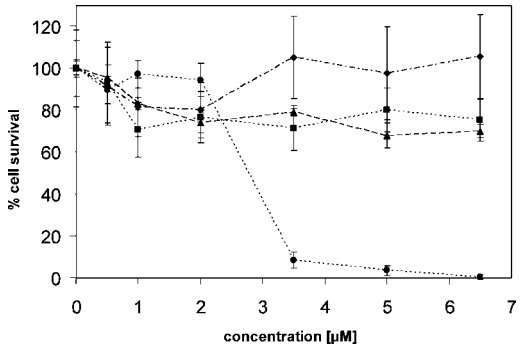


Figure 4. Normalized percentage cell survival of nonirradiated and irradiated T24+ cells after 30 min of incubation with increasing concentrations of activated or nonactivated PPP. Dark toxicity of intact PPP, - -♦- -♦- -; and enzyme-activated PPP, - -■- - -■- -. Phototoxicity of intact PPP, - -▲- -▲- -; and enzyme-activated PPP, - -●- -●- -; after irradiation with white light 13.5 J/cm^2. Concentration is expressed as pheophorbide a equivalents and percentage cell survival are mean ± S.D. values of six replicate measurements.

moiety was used to enhance PPP water solubility and to protect the polymeric backbone from nonspecific enzymatic degradation.

Covalent coupling of different amounts of pheophorbide−peptide moieties to ϵ-NH_2 functions of the polymer resulted in PPPs carrying 6, 18, and 30 PS units per polymer chain. RP-HPLC monitoring of coupling reactions confirmed them to be quantitative for all investigated loading ratios.

A direct correlation between fluorescence quenching and ROS generation of the PS pheophorbide a is well-documented in the literature using dendrimer constructs (*19*). Data for the quench-

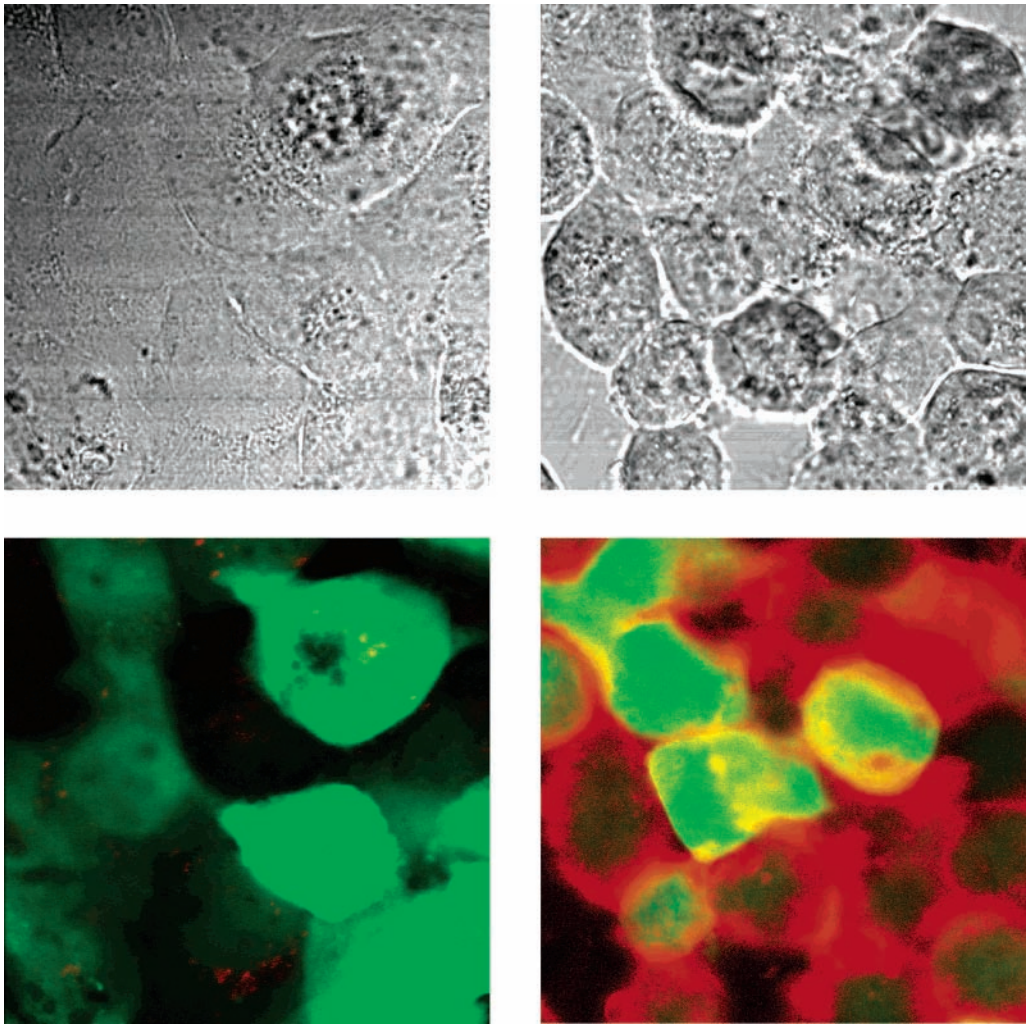


Figure 5. Confocal fluorescence micrographs (bottom panel) and corresponding trans-illumination images (top panel) (magnification 120×) of T24+ cells incubated with nondigested PPP (left panel) and with digested PPP (right panel).

ing of fluorescence emission and ROS generation of fully assembled second generation PPP with different photosensitizer loadings are summarized in Table 1. Photodynamic response and fluorescence emission decrease with increasing loading to a similar extent as for first-generation conjugates. Water solubility of both generations PPPs decreased with photosensitizer loading, although the second-generation PPPs were more soluble, probably due to the use of the alleged solubilizing moieties.

Enzymatic Activation of PPP in Vitro. Peptide linker imparted selectivity of photosensitizer activation was demonstrated by assaying PPP cleavage with different trypsin-like proteases. Figure 3 shows the relative increase in fluorescence emission after in vitro digestion with trypsin, elastase, and thrombin, respectively. Incubation with the control PPP gave essentially no change in fluorescence. Furthermore, protease-mediated fluorescence activation was prevented by inhibiting trypsin activity with *p*-aminobenzamidine (data not shown). These results indicate that N-terminal introduction of the relative bulky, hydrophobic photosensitizer pheophorbide a and C-terminal coupling to the polymeric backbone did not interfere with enzymatic cleavage of the peptide substrate. Furthermore, there are similarities in the sequence of our peptide linker and a previously reported substrate for plasmin and human kallikrein 2, two cancer-related enzymes (*20*).

Phototoxicity Evaluation in Vitro. Dark and phototoxicity of the PPP carrying 30 PS units per chain were evaluated on a human T-24 bladder epithelium cancer cell line. In vitro predigestion of our model compounds was a necessary step for PPP activation, as levels of secreted proteases within the cell culture medium are generally low. In addition, the trypsin-like enzymes meant to be targeted with the chosen peptide linker are rapidly neutralized in the presence of serum, and the locally enhanced proteolytic activity within cancerous or inflamed tissue is difficult to mimic in cell cultures. Normalized percentages of cell survival of irradiated and nonirradiated cells after incubation with increasing concentrations of the corresponding activated or nonactivated PPP are shown in Figure 4. Within the studied concentration range, neither the activated PPP nor the nonactivated PPP showed significant dark toxicity. However, upon white light irradiation (13.5 J/cm^2), the activated PPP showed a significantly higher phototoxicity than the nonactivated one ($p < 0.05$), in the 3.5−6.5 μM concentration range.

Intracellular Localization. The subcellular localization of the PPP in its active and inactive forms within T24+ cells was visualized by confocal fluorescence microscopy. Pictures were taken after 30 min of incubation and thorough washing under identical microscope settings. Figure 5 shows a granular distribution pattern for the nonactivated PPP versus a more homogeneous distribution for the activated PPP within the GFP expressing cells. Cells treated with the activated PPP appeared brightly fluorescent when compared to those treated with the nonactivated PPP. Although GFP is not equally expressed at the same level in all T24+ cells, phase contrast images (top panel) show that porphyrin-mediated fluorescence is associated with the presence of cells. In the case of the

nonactivated PPP in the left panel of Figure 5, small fluorescent spots presumably due to nonspecific lysosomal degradation can be seen.

DISCUSSION

Protease-mediated release of prodrugs and toxins for cancer chemotherapy has been proposed already some years ago (*21*−*25*). Recent research aims to further enhance prodrug delivery using long-circulating polymeric conjugates (*26*−*28*) or additional targeting moieties (*29*).

By using first-generation PPPs, it has been shown recently that this approach can successfully be implemented into PDT in vitro and in vivo. Although these conjugates have a substantially higher molecular weight than our novel second-generation PPPs, tumor eradication was demonstrated in a mouse xenograph model (*10*). The latter emphasizes that despite this high molecular weight sufficient tumor penetration can be achieved with these compounds. However, as mentioned above, the application of first-generation PPPs is limited to the targeting of proteases able to digest the polymeric backbone such as the lysosomal cystein−protease Cathepsin B. Therefore, nonspecific activation in normal cells might occur with such compounds. Our "low" molecular weight second-generation PPPs might circumvent this drawback and allow for the targeting of other disease-specific proteolytic activities. Furthermore, nonspecific degradation of the polymeric backbone could be totally prevented by our protecting moieties, avoiding nonspecific activation by lysosomal proteases to a large extent.

We suggest that our newly developed polymeric protease-mediated photodynamic agents are of particular value for cancer phototherapy for the following reasons: First, the use of polymeric conjugates allows for passive targeting by the EPR effect. Second, specific proteolytic activation of the PPP at the tumor site will minimize collateral damage to healthy tissue structures within the irradiated area. The use of a peptide linker makes this strategy amenable to targeting a wide variety of disease-related extracellular proteases. Third, tumor penetration and uptake of photosensitizer−peptidyl fragments into cells might be facilitated by passive diffusion. Furthermore, released photosensitizer−peptide fragments are lipophilic and only poorly water-soluble, which is expected to result in slower systemic clearance. Finally, light is applied specifically at the tumor site, and thus cytotoxic ROS are efficiently produced only within the irradiated area in the presence of activated photosensitizer and oxygen.

In the current research, we have prepared second-generation PPPs for the targeting of enzymes with trypsin-like activity. These PPPs are water-soluble and have a polymeric backbone that is stable to nonspecific enzymatic degradation. The developed synthetic strategies can be easily adapted to other peptide linkers whose sequences will determine the enzyme being targeted. Protease-mediated activation of these PPP gave rise to a pronounced increase in fluorescence and phototoxicity in vitro.

Together, the gathered in vitro data suggest that the developed PPPs are promising for the systemic delivery of photodynamic agents, and further in vivo studies are currently underway.

ACKNOWLEDGMENT

The authors would like to thank the Swiss National Foundation (grant no. 205321-102009 and (grant no. 205320-112234)), Oncosuisse (grant no. F16476), and the Novartis-Consumer Health Foundation for their financial support.

LITERATURE CITED

(1) Hopper, C. (2000) Photodynamic therapy: a clinical reality in the treatment of cancer. *Lancet Oncol. 1*, 212−219.

(2) Dolmans, D. E., Fukumura, D., and Jain, R. K. (2003) Photodynamic therapy for cancer. *Nat. Rev. Cancer 3*, 380−387.

(3) Lange, N. (2003) Controlled drug delivery in photodynamic therapy and fluorescence-based diagnosis of cancer. *Handbook of Biomedical Fluorescence* (Mycek, M.-A., and Pogue, W. B., Eds.) pp 563−635, Chapter 16, Marcel Dekker Inc., New York, Basel.

(4) Egeblad, M., and Werb, Z. (2002) New functions for the matrix metalloproteinases in cancer progression. *Nat. Rev. Cancer 2*, 161−174.

(5) Berdowska, I. (2004) Cysteine proteases as disease markers. *Clin. Chim. Acta 342*, 41−69.

(6) Dano, K., Romer, J., Nielsen, B. S., Bjorn, S., Pyke, C., Rygaard, J., and Lund, L. R. (1999) Cancer invasion and tissue remodeling−cooperation of protease systems and cell types. *APMIS 107*, 120−127.

(7) Van Kempen, L. C., de Visser, K. E., and Coussens, L. M. (2006) Inflammation, proteases and cancer. *Eur. J. Cancer 42*, 728−734.

(8) Myöhänen, H., and Vaheri, A. (2004) Regulation and interactions in the activation of cell-associated plasminogen. *Cell. Mol. Life Sci. (CMLS) 61*, 2840−2858.

(9) Campo, M. A., Gabriel, D., Kucera, P., Gurny, R., and Lange, N. (2007) Polymeric photosensitizer prodrugs for photodynamic therapy. *Photochem. Photobiol.* (in press).

(10) Choi, Y., Weissleder, R., and Tung, C. H. (2006) Selective antitumor effect of novel protease-mediated photodynamic agent. *Cancer Res. 66*, 7225−7229.

(11) Maeda, H., Wu, J., Sawa, T., Matsumura, Y., and Hori, K. (2000) Tumor vascular permeability and the EPR effect in macromolecular therapeutics: a review. *J. Controlled Release 65*, 271−284.

(12) Krasnovsky, A. A., Jr., Neverov, K. V., Egorov, S. Y., Roeder, B., and Levald, T. (1990) Photophysical studies of pheophorbide a and pheophytin a. Phosphorescence and photosensitized singlet oxygen luminescence. *J. Photochem. Photobiol., B 5*, 245−254.

(13) Stiel, H., Marlow, I., and Roeder, B. (1993) Photophysical properties of the photosensitizer pheophorbide a studied at high photon flux densities. *J. Photochem. Photobiol., B 17*, 181−186.

(14) Tedjamulia, M. L., Srivastava, P. C., and Knapp, F. F., Jr. (1985) Evaluation of the brain-specific delivery of radioiodinated (iodophenyl)alkyl-substituted amines coupled to a dihydropyridine carrier. *J. Med. Chem. 28*, 1574−1580.

(15) Chan, W. C., and White, P. D. (2000) *Fmoc Solid Phase Peptide Synthesis: A Practical Approach* (Chan, W. C., and White, P. D., Eds.) pp 9−76, Chapter 2−3, The Practical Approach Series, Oxford University Press, Oxford.

(16) Mosinger, J., and Micka, Z. (1997) Quantum yields of singlet oxygen of metal complexes of meso-tetrakis(sulphonatophenyl) porphine. *J. Photochem. Photobiol., A 107*, 77−82.

(17) Felber, L. M., Cloutier, S. M., Kundig, C., Kishi, T., Brossard, V., Jichlinski, P., Leisinger, H. J., and Deperthes, D. (2004) Evaluation of the CFP-substrate-YFP system for protease studies: advantages and limitations. *Biotechniques 36*, 878−885.

(18) Craik, C. S., Largman, C., Fletcher, T., Roczniak, S., Barr, P. J., Fletterick, R., and Rutter, W. J. (1985) Redesigning trypsin: alteration of substrate specificity. *Science 228*, 291−297.

(19) Hackbarth, S., Ermilov, E. A., and Roder, B. (2005) Interaction of Pheophorbide a molecules covalently linked to DAB dendrimers. *Opt. Commun. 248*, 295−306.

(20) Janssen, S., Jakobsen, C. M., Rosen, D. M., Ricklis, R. M., Reineke, U., Christensen, S. B., Lilja, H., and Denmeade, S. R. (2004) Screening a combinatorial peptide library to develop a human glandular kallikrein 2-activated prodrug as targeted therapy for prostate cancer. *Mol. Cancer Ther. 3*, 1439−1450.

(21) Carl, P. L., Chakravarty, P. K., Katzenellenbogen, J. A., and Weber, M. J. (1980) Protease-activated "prodrugs" for cancer chemotherapy. *Proc. Natl. Acad. Sci. U.S.A. 77*, 2224−2228.

(22) Devy, L., de Groot, F. M., Blacher, S., Hajitou, A., Beusker, P. H., Scheeren, H. W., Foidart, J. M., and Noel, A. (2004) Plasmin-activated doxorubicin prodrugs containing a spacer reduce tumor growth and angiogenesis without systemic toxicity. *FASEB J. 18*, 565−567.

(23) Albright, C. F., Graciani, N., Han, W., Yue, E., Stein, R., Lai, Z., Diamond, M., Dowling, R., Grimminger, L., Zhang, S. Y., Behrens, D., Musselman, A., Bruckner, R., Zhang, M., Jiang, X., Hu, D., Higley, A., Dimeo, S., Rafalski, M., Mandlekar, S., Car, B., Yeleswaram, S., Stern, A., Copeland, R. A., Combs, A., Seitz,

S. P., Trainor, G. L., Taub, R., Huang, P., and Oliff, A. (2005) Matrix metalloproteinase-activated doxorubicin prodrugs inhibit HT1080 xenograft growth better than doxorubicin with less toxicity. *Mol. Cancer Ther. 4*, 751−760.

(24) Liu, S., Aaronson, H., Mitola, D. J., Leppla, S. H., and Bugge, T. H. (2003) Potent antitumor activity of a urokinase-activated engineered anthrax toxin. *Proc. Natl. Acad. Sci. U.S.A. 100*, 657−662.

(25) Abi-Habib, R. J., Liu, S., Bugge, T. H., Leppla, S. H., and Frankel, A. E. (2004) A urokinase-activated recombinant diphtheria toxin targeting the granulocyte-macrophage colony-stimulating factor receptor is selectively cytotoxic to human acute myeloid leukemia blasts. *Blood 104*, 2143−2148.

(26) Chau, Y., Tan, F. E., and Langer, R. (2004) Synthesis and characterization of dextran-peptide-methotrexate conjugates for tumor targeting via mediation by matrix metalloproteinase II and matrix metalloproteinase IX. *Bioconjugate Chem. 15*, 931−941.

(27) Chau, Y., Padera, R. F., Dang, N. M., and Langer, R. (2006) Antitumor efficacy of a novel polymer-peptide-drug conjugate in human tumor xenograft models. *Int. J. Cancer 118*, 1519−1526.

(28) Satchi, R., Connors, T. A., and Duncan, R. (2001) PDEPT: polymer-directed enzyme prodrug therapy. I. HPMA copolymer-cathepsin B and PK1 as a model combination. *Br. J. Cancer 85*, 1070−1076.

(29) De Groot, F. M., Broxterman, H. J., Adams, H. P., van Vliet, A., Tesser, G. I., Elderkamp, Y. W., Schraa, A. J., Kok, R. J., Molema, G., Pinedo, H. M., and Scheeren, H. W. (2002) Design, synthesis, and biological evaluation of a dual tumor-specific motive containing integrin-targeted plasmin-cleavable doxorubicin prodrug. *Mol. Cancer Ther. 1*, 901−911.

BC060321L

Synthesis and in Vitro Testing of a Pyropheophorbide-*a*-Fullerene Hexakis Adduct Immunoconjugate for Photodynamic Therapy

Fiorenza Rancan,*[,†] Matthias Helmreich,[‡] Andreas Mölich,[§] Eugeny A. Ermilov,[||] Norbert Jux,*[,‡] Beate Röder,[||] Andreas Hirsch,[‡] and Fritz Böhm[†]

Universitätsklinikum Charité, Hautklinik, Photobiologisches Labor, Berlin, Germany, Institut für Organische Chemie, Universität Erlangen-Nürnberg, Erlangen, Germany, Institut für Biologie, Tierphysiologie, Humboldt Universität, Berlin, Germany, and Institut für Physik, Photobiophysik, Humboldt-Universität zu Berlin, Berlin, Germany. Received October 24, 2006; Revised Manuscript Received February 13, 2007

The employment of carriers to enhance drug selectivity is one of the strategies to increase the efficacy and reduce the side effects of antitumor therapy. The concept of a modular carrier system (MCS) was developed to construct a complex drug having a high efficacy and selectivity. An MCS employs diverse units or modules: beside the therapeutic unit, an addressing unit (e.g., an antibody) serves to direct the drug to its target, and a multiplying unit has the role of increasing the number of biological active moieties the system can carry. In this paper, we report on the synthesis of a modular carrier system in which the role of multiplying unit is given to a [5:1]-fullerene hexakis adduct. This fullerene hexaadduct has five malonate spacers which can bind two therapeutic units (the photosensitizer pyropheophorbide-*a*) each, for a total of ten, and a longer malonate spacer which serves for the conjugation to the addressing unit, the monoclonal antibody rituximab. Confocal microscopy studies using Epstein−Barr virus-transformed B-lymphocytes and Jurkat cells showed that the antibody conjugate conserves the affinity for its receptor (CD20) and its selectivity toward CD20 positive B-lymphocytes. On the contrary, the antibody-free complex did not show any bounding or intracellular uptake.

INTRODUCTION

The enhancement of drug selectivity is the most important task of modern investigations directed to improve the efficacy and reduce the side effects of anticancer therapy. The idea of binding a drug to an addressing unit with specificity for tumor tissue was formulated a long time ago (*1*). Several carrier systems have been used for this purpose, like liposomes (*2*), lipoproteins (*3*), dendrimers (*4*), or polymers (*5*), but antibodies or antibody fragments were the most selective molecules (*6*, *7*). One inconvenience of using tumor-specific antibodies is the loss of their biological activity when many drug units are covalently bound to their peptide backbone (*8*). The concept of the modular carrier system (MCS) was developed as a solution to this problem (*9*). In an MCS, diverse units or modules are combined to construct a complex drug with diverse specific functions. Besides the therapeutic unit, an addressing unit (e.g., an antibody) serves to direct the drug to the target, and a multiplying unit has the role of increasing the number of drug moieties the system can carry. In this way, a number of drug units can be loaded on a tumor-specific antibody. Dendrimers and polymers were proposed as multiplying units (*10*, *11*). In particular, dendrimers became of rising interest in different fields of biophysical research due to their highly branched and well-defined architecture having a high number of functional end groups (*12*). C_{60}-fullerene adducts are good candidates to be used as the core of multiplying units. Fullerene hexakis adducts have an octahedral addition pattern, which allows the six substituents occupying spread positions with minimal steric interactions (*13*). So-called [5:1]hexaadducts are well-known in fullerene chemistry. In such adducts, one position can be occupied by the addressing unit, while the other five positions are suitable for spacers bearing drug moieties. The fullerene's ability to scavenge free radicals (*14*) and its spherical shape, which could adapt to active sites of enzymes (*15*), make the use of C_{60} in medical research particularly interesting. Recently, a communication appeared reporting the conjugation of fullerene derivatives with the antibody ZME-18 (*16*). The authors used water-soluble fullerenes and reached C_{60}/antibody molar ratios of 42:1 and 15:1 without the loss of antigen binding ability. Although one of the two water-soluble derivatives had no activated group for covalent binding to the monoclonal antibody (mAb), it still showed similar results to the derivative with a binding site. The authors therefore concluded that in such immunoconjugates the fullerene moieties are not necessarily connected to the antibody through a covalent bond.

In this paper, we report the synthesis of a modular carrier system in which the role of multiplying unit is given to a [5:1]-fullerene hexakis adduct. This fullerene hexaadduct has five malonate addends, which can bind two pyropheophorbide-*a* **2** units each, and a longer malonate spacer with an activated ester moiety, which serves for the conjugation to one addressing unit, the mAb rituximab. Rituximab is a genetically engineered chimeric murine/human mAb directed against the CD20 antigen found on the surface of normal and malignant B lymphocytes (*17*). The antibody is an IgG_1 κ immunoglobulin containing murine light- and heavy-chain variable region sequences and human constant region sequences. Rituximab is composed of two heavy chains of 451 amino acids and two light chains of 213 amino acids (based on cDNA analysis) and has an

* Corresponding authors: Fiorenza Rancan, Universitätsklinikum Charité, Photobiologisches Labor, Ziegelstr. 5-9, 10117 Berlin, Germany. Tel. +49 30 450518085, Fax. +49 30 450513941, E-mail: fiorenza.rancan@charite.de. Dr. Norbert Jux, Institut für Organische Chemie, Universität Erlangen-Nürnberg, Henkestr. 42, D-91054 Erlangen, Germany. Tel. +49 9131 8522976, Fax. +49 9131 8526864, E-mail: norbert.jux@chemie.uni-erlangen.de.

[†] Universitätsklinikum Charité.

[‡] Universität Erlangen-Nürnberg.

[§] Institut für Biologie, Tierphysiologie, Humboldt Universität.

[||] Institut für Physik, Photobiophysik, Humboldt-Universität zu Berlin.

10.1021/bc0603337 CCC: $37.00 © 2007 American Chemical Society
Published on Web 06/06/2007

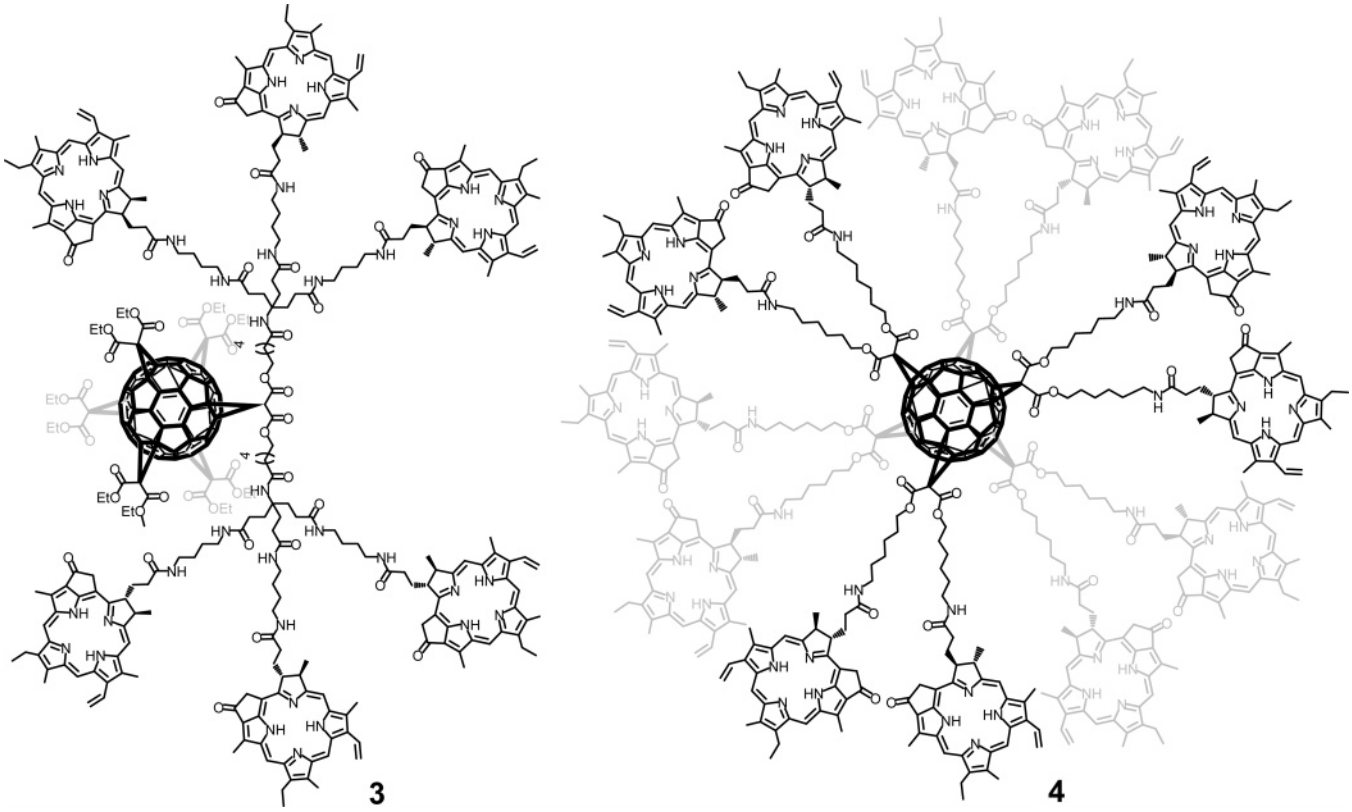


Figure 1. [5:1]Fullerene hexaadduct **3** and fullerene hexaadduct **4** carrying 6 and 12 pyropheophorbide-*a* moieties, respectively.

approximate molecular weight of 145 kDa. Rituximab has a binding affinity for the CD20 antigen of approximately 8.0 nM (*17*). This monoclonal antibody is an already approved drug and is indicated for the treatment of patients with relapsed or refractory, low-grade or follicular, CD20-positive, B-cell non-Hodgkin's lymphoma (NHL).

The therapeutic unit, pyropheophorbide-*a* (**2**) (*18*) is a photosensitizer (PS) which might be used in photodynamic therapy (PDT). This is a treatment of cancerous and noncancerous diseases (*19*), which involves the administration of a PS and light. By irradiation of the region to be treated, the PS is activated and can induce the generation of singlet molecular oxygen followed by a sequence of reactions generating other reactive oxygen species (*20*). **2** has optimal photophysical properties for its use as PS: it has an absorption maximum at 668 nm with high extinction coefficient ($\epsilon_{668\ nm} = 4 \times 10^4\ M^{-1}\ cm^{-1}$) and an emission maximum at 672, and the singlet oxygen quantum yield in ethanol using pheophorbide-*a* as reference was estimated to be 0.52 (*21*). Moreover, it has a free carboxylic group which can be used for attaching it to the multiplying unit.

In previous works, in which we employed antibodies as carriers for photosensitizers, we found that the dye's ability to produce singlet oxygen and the antibody's ability to recognize its antigen strongly decrease when a high number of dye molecules are covalently bound to the antibody (*8*). We concluded that the use of a multiplying unit may be necessary to increase the local concentration of drugs without a decrease of the antibody's biological activity. The choice of a [5:1]-fullerene hexakis adduct as the multiplying unit came after several studies with different fullerene adducts carrying a different number of photosensitizers. First, we prepared fullerene mono- and hexaadducts carrying two pyropheophorbide-*a* (**2**) moieties. The investigation of the photophysical properties of these derivatives showed that in the fullerene monoadduct an efficient photoinduced electron transfer occurs between the exited pyropheophorbide-*a* (**2**) moieties and the fullerene core. This event results in a dramatic reduction of PSs singlet oxygen quantum yield. On the contrary, in the fullerene hexaadduct, the π-system is broken up and C_{60} cannot act as a strong electron-acceptor anymore (*22*−*24*). As a direct consequence, the in vitro phototoxicity of the fullerene monoadduct was significantly inferior to that of the fullerene hexaadduct carrying the same number of PSs (*25*). Successively, we synthesized fullerene hexaadducts carrying six (**3**) (*26*, *27*) and twelve (**4**) (*27*, *28*) pyropheophorbide-*a* moieties (Figure 1). It was found that dye molecules covalently linked to one fullerene moiety could interact with each other, forming energy traps. A very fast and efficient delivery of the excitation energy to a trap can therefore occur. As a result, the fluorescence as well as the singlet oxygen quantum yields of the different complexes were reduced with increasing number of dye molecules per complex (*26*−*28*). This was confirmed by in vitro cell experiments (*36*): While the fullerene adduct loaded with six PS moieties (**3**) still has a significant phototoxic activity against lymphoid T-cells, the [6:0] adduct loaded with twelve PSs (**4**) is not phototoxic.

A [5:1]fullerene adduct analogous to **4** and carrying ten pyropheophorbide-*a* moieties (**5**) has been prepared for the coupling with the mAb. **5** has an activated carboxylic ester group at the end of a long alkyl chain, which serves for the covalent binding to an amino group of the antibody. The reason we chose **5** for the coupling with rituximab is that the analogous compound **4** turned out to be photostable even under high-energy irradiation while other carriers (diaminobutane dendrimers) were completely fragmented under the same conditions (*28*). In this way, we avoid a possible overlap of the conjugate biological activity and light-caused effects like disconnection of the antibody from the fullerene adduct.

EXPERIMENTAL PROCEDURES

Chemicals and Characterization of the Samples. C_{60} was obtained from Hoechst AG/Aventis and separated from higher

fullerenes by a plug filtration process (*29*, *30*). The monoclonal antibody rituximab was bought as pharmaceutical preparation Mabthera, (Roche, Germany). The antibody concentration in the preparation is 10 mg/mL. Chemicals and solvents were used as received unless otherwise noted. Solvents were dried using standard procedures (*31*). Pyropheophorbide-*a*-NHS ester and malonate **6** and malonate **7** were prepared according to literature procedures (*26*). Column chromatography was performed on silica gel 32-63, 60 Å, MP Biomedicals. ^{1}H and ^{13}C NMR spectra were recorded on JEOL JMM EX 400 and JEOL GX 400 instruments; an asterisk indicates a resonance of a pyropheophorbide-*a* proton or carbon atom; the atom indices are given according to the literature (*32*). FAB mass spectrometry was performed with Micromass Zabspec and Varian MAT 311A instruments; MALDI-TOF mass spectrometry was done on an AUTOFLEX instrument from Bruker Daltonics GmbH. Standard UV/vis spectra were recorded on a Shimadzu UV-3102 PC UV/vis NIR scanning spectrophotometer. IR spectra were either taken with a Bruker Vector 22 spectrometer or an ASI React IR-1000 spectrometer. HPLC was performed with a Shimadzu Liquid Chromatograph LC-10AT equipped with an SCL-10AVP system controller, LC-8A preparative liquid chromatographs, a diode array detector, and a UV/vis detector, on a Nucleosil 100−5 column. All compounds decomposed prior to melting. All reactions were performed in nitrogen atmosphere.

Synthesis. *20-Hydroxyeicosyl Methylmalonate **9***. A solution of 1,20-dihydroxyeicosane **8** (4.13 g, 13 mmol) and pyridine (4 mL, 52 mmol) in dry THF (500 mL) was cooled in an ice bath under nitrogen. Malonyl dichloride (1.4 mL, 13 mmol) was diluted in dry THF (20 mL) and added dropwise over a period of 1 h via a dropping funnel. The reaction mixture was stirred for 6 h at room temperature. CH_2Cl_2 (200 mL) was added, and the mixture was washed with water (150 mL, three times). After drying over $MgSO_4$, the solvent was removed in vacuo. Flash chromatography on silica (1. $CHCl_3$ 2. $CHCl_3$/ethyl acetate 95:5) yielded **9** as a white solid (yield: 1.96 g, 37%). ^{1}H NMR (400 MHz, $CDCl_3$, 25 °C, TMS): δ = 4.11 (t, ^3J = 6.7 Hz, 2H, $COOCH_2$), 3.72 (s, 3H, CH_3), 3.61 (t, ^3J = 6.6 Hz, 2H, CH_2O), 3.36 (s, 2H, $OOCCH_2COO$), 2.61 (tt, ^3J = 6.8 Hz, ^3J = 6.8 Hz, 2H, CH_2CH_2O), 1.63 (tt, ^3J = 6.8 Hz, ^3J = 6.7 Hz, 2H, $COOCH_2CH_2$), 1.39 (bs, 32H, CH_2). ^{13}C NMR (100 MHz, $CDCl_3$, 25 °C, TMS): δ = 176.1 (CO), 166.6 (CO), 65.7, 63.1, 52.5, 41.4, 32.8, 29.7, 29.6, 29.5, 29.4, 29.2, 28.4, 26.2, 25.7, 25.7, 23.5. IR (ATR): ν = 3331 cm^{-1}, 2918, 2849, 1737 (CO), 1463, 1339, 1200, 1154, 1061, 1031, 729. MS (FAB, NBA): *m*/*z* = 416 [M$^+$]. Anal. calcd (%) for $C_{24}H_{46}O_5$ (414.34): C 69.52, H 11.18. Found: C 69.74, H 10.98.

*[1-(Methoxycarbonyl)-1-(20-hydroxyeicosyl)oxycarbonyl]-1,2-methano [60]-fullerene **10***. C_{60} (2.5 g, 3.47 mmol) was dissolved in dry toluene (1200 mL), resulting in a dark purple solution. The solution was stirred until the C_{60} was completely dissolved. Afterward, CBr_4 (1.7 g, 5.1 mmol) and the malonate **9** (1.4 g, 3.37 mmol) were added. DBU (800 μL, 5.2 mmol) was diluted in toluene (50 mL) and added dropwise over a period of 1 h to the stirred solution at room temperature. After the solution was stirred for another 12 h, the reaction mixture was controlled by thin layer chromatography to reveal unreacted C_{60}, the monoadduct **10**, as well as traces of bis- and trisadducts. The toluene was almost completely removed in vacuo and the remaining solution transferred to a flash chromatography column. Flash chromatography on silica gel with toluene yielded unreacted C_{60} as first fraction (0.98 g, 39%). **10** was obtained as a brown powder which was dried in vacuo (yield: 1.65 g, 42%). ^{1}H NMR (400 MHz, $CDCl_3$, 25 °C, TMS): δ = 4.48 (t, ^3J = 6.5 Hz, 2H, $COOCH_2$), 4.07 (s, 3H, CH_3), 3.61 (t, ^3J = 6.7 Hz, 2H, CH_2O), 1.81 (tt, ^3J = 6.6 Hz, ^3J = 6.7 Hz, 2H, $COOCH_2CH_2$), 1.54 (m, 2H, CH_2CH_2O), 1.44 (m, 2H, $CH_2CH_2CH_2O$), 1.22 (bs, 30H, CH_2). ^{13}C NMR (100 MHz, $CDCl_3$, 25 °C, TMS): δ = 164.5 (CO), 163.9 (CO), 145.4, 145.4, 145.4, 145.1, 144.9, 144.9, 144.1, 143.3, 143.3, 142.4, 142.2, 142.1, 141.2, 139.4, 139.1 (58C, C_{60} sp^2), 71.5 (2C, C_{60} sp^3), 67.5, 63.2, 53.9, 52.4, 32.6, 29.5, 29.4, 29.3, 29.0, 28.4, 25.8, 25.58. IR (KBr): ν = 2921 cm^{-1}, 2851, 1741 (CO), 1462, 1430, 1267, 1233, 1187, 1060, 749. MS (FAB, NBA): *m*/*z* = 1132 [M$^+$]$^+$, 720 [C_{60}^+]. UV/vis (CH_2Cl_2): λ_{max} (ϵ) = 257 nm (113 000 mol^{-1} dm^3 cm^{-1}), 325 (35 000), 425 (2100). Anal. calcd (%) for $C_{84}H_{44}O_5 \times 0.5CHCl_3$ (1191.3): C 85.08, H 3.76. Found: C 85.58, H 3.63.

*[5:1]Hexakis Adduct **11***. Monoadduct **10** (1.37 mg, 1.2 mmol) was dissolved in degassed, dry toluene (250 mL). 9,10-Dimethylanthracene (2.50 mg, 12 mmol) was added and the mixture stirred for 12 h at room temperature under protection from light. Malonate **7** (6.10 g, 12.1 mmol) and CBr_4 (4.03 g, 12.1 mmol) were added subsequently to the reaction flask. DBU (3.18 mL, 21.0 mmol) was diluted in dry toluene (20 mL) and added dropwise over a period of 1 h. Precleaning on silica gel (CH_2Cl_2/ethyl acetate 60:40) and subsequent purification by preparative HPLC (Nucleosil 5 μm, CH_2Cl_2/ethyl acetate 74:26) gave **11** as a yellow solid (yield: 1.07 g, 24.1%). ^{1}H NMR (400 MHz, $CDCl_3$, 25 °C, TMS): δ = 4.76 (bs, 10H, NH), 4.22 (t, ^3J = 6.3 Hz, 20H, $COOCH_2$), 4.22 (t, ^3J = 6.3 Hz, 2H, $COOCH_2$), 3.83 (s, 3H, OCH_3), 3.60 (t, ^3J = 6.6 Hz, 2H, CH_2O), 3.06 (m, 20H, NCH_2), 1.66 (m, 22H, $COOCH_2CH_2$), 1.54 (m, 2H, CH_2CH_2O), 1.40 (s, 90H, CH_3), 1.50−1.20 (m, 94H, CH_2). ^{13}C NMR (100 MHz, $CDCl_3$, 25 °C, TMS): δ = 164.3 (CO), 163.8 (CO), 156.0 (NHCO), 145.7 (C_{60} sp^2), 141.1 (C_{60} sp^2), 78.9 (10C, $OC(CH_3)_3$), 69.1 (C_{60} sp^3), 66.9, 63.0, 53.6, 45.5, 40.5, 32.8, 29.9, 29.7, 29.6, 29.4, 28.4, 28.3, 26.4, 25.7, 25.6. IR (ATR): ν = 2975 cm^{-1}, 2930, 2856, 1743, 1689, 1516, 1365, 1244, 1212, 1165, 714. MS (FAB, NBA): *m*/*z* = 3635 [M$^+$], 3579 [M − *t*Bu$^+$], 3536 [M$^+$ − Boc], 3479 [M$^+$ − Boc-*t*Bu], 3435 [M$^+$ − 2×Boc], 3336 [M$^+$ − 3×Boc], 3235 [M$^+$ − 4×Boc], 3135 [M$^+$ − 5×Boc]. UV/vis (CH_2Cl_2): λ_{max} (ϵ) = 244 nm (93 600 mol^{-1} dm^3 cm^{-1}), 280 (73 100), 496 (500). Anal. calcd for $C_{209}H_{264}N_{10}O_{45} \times 2CH_2Cl_2$ (3801.8): C 66.58, H 7.10, N 3.68. Found: C 66.65, H 7.08, N 3.67.

*[5:1]Hexaadduct Tosylate **12***. The hexaadduct **11** (460 mg, 0.126 mmol), trimethylamine hydrochloride (102 mg, 1.07 mmol), and triethyamine (2 mL, 14 mmol) were dissolved in dry CH_2Cl_2 (150 mL). The reaction mixture was cooled to 0 °C. Tosyl chloride (182 mg, 1 mmol) was dissolved in CH_2Cl_2 (30 mL) and added dropwise over a period of 1 h, keeping the temperature below 5 °C. After the mixture was stirred for 12 h at room temperature, the solvent was evaporated. Flash chromatography on silica (1. CH_2Cl_2, 2. CH_2Cl_2/ethyl acetate 70:30) yielded **12** as an orange solid (yield: 380 mg, 79%). ^{1}H NMR (400 MHz, $CDCl_3$, 25 °C, TMS): δ = 7.75 (d, ^3J = 8.2 Hz, 2H, aryl-H), 7.31(d, ^3J = 8.3 Hz, 2H, aryl-H), 4.75 (bs, 10H, NH), 4.22 (t, ^3J = 6.3 Hz, 20H, $COOCH_2$), 3.98 (t, ^3J = 6.5 Hz, 2H, CH_2OSO_2), 3.82 (s, 3H, OCH_3), 3.06 (m, 20H, NCH_2), 2.42 (s, 3H, aryl-CH_3), 1.65 (m, 22H, $COOCH_2CH_2$), 1.61 (m, 2H, $CH_2CH_2OSO_2$), 1.40 (s, 90H, CH_3), 1.50−1.20 (m, 94H, CH_2). ^{13}C NMR (100 MHz, $CDCl_3$, 25 °C, TMS): δ = 164.3 (CO), 163.8 (CO), 156.0 (NHCO), 145.7 (C_{60} sp^2), 144.6, 141.1 (C_{60} sp^2), 133.2, 129.7, 127.8, 78.9 ($OC(CH_3)_3$), 70.7, 69.1, 69.0 (C_{60} sp^3), 67.1, 66.8, 53.5, 45.5, 40.5, 29.9, 29.7, 29.6, 29.5, 29.4, 29.2, 28.9, 28.8, 28.4, 28.3, 28.1, 27.9, 26.4, 25.7, 25.6, 25.3, 21.6 (1C, 27). IR (ATR): ν = 2976 cm^{-1}, 2930, 2857, 1742, 1692, 1515, 1365, 1242, 1214, 1167, 1043, 753, 714. MS (FAB, NBA): *m*/*z* = 3789 [M$^+$], 3733 [M$^+$ − *t*Bu], 3690 [M$^+$ − Boc], 3633 [M$^+$ − Boc-*t*Bu], 3490 [M$^+$ − 3×Boc], 3390 [M$^+$ − 4×Boc], 3289 [M$^+$ − 5×Boc], 3188 [M$^+$ − 6×Boc]. UV/vis (CH_2Cl_2): λ_{max} (ϵ) = 244 nm (90 100 mol^{-1} dm^3 cm^{-1}), 280 (69 000), 496 (420). Anal. calcd

for $C_{216}H_{270}N_{10}O_{47}S \times 2CH_2Cl_2$ (3955.8): C 66.11, H 6.97, N 3.54, S 0.81. Found: C 65.83, H 7.14, N 3.56, S 0.47.

*[5:1]Hexaadduct Azide **13***. The hexaadduct **12** (202 mg, 0.053 mmol) and sodium azide (60 mg, 0.9 mmol) were dissolved in 4 mL of dry DMF and stirred for 16 h at room temperature. The solvent was removed in vacuo. Flash chromatography on silica (CH_2Cl_2/ethyl acetate 70:30) yielded **13** as an orange solid (yield: 160 mg, 82%). ^{1}H NMR (400 MHz, $CDCl_3$, 25 °C, TMS): $\delta = 4.76$ (bs, 10H, NH), 4.22 (t, $^3J = 6.5$ Hz, 20H, $COOCH_2$), 4.14 (t, 2H, $COOCH_2$), 3.83 (s, 3H, OCH_3), 3.22 (t, $^3J = 6.9$ Hz, 2H, CH_2N_3), 3.06 (m, 20H, $NHCH_2$), 1.66 (m, 20H + 2H, $COOCH_2CH_2$), 1.56 (tt, 2H, CH_2-CH_2N_3), 1.40 (s, 90H, CH_3), 1.45−1.20 (m, 94H, CH_2). ^{13}C NMR (100 MHz, $CDCl_3$, 25 °C, TMS): $\delta = 164.3$ (CO), 163.8 (CO), 156.0 (NHCO), 145.7 (C_{60} sp^2), 141.1 (C_{60} sp^2), 78.9 ($OC(CH_3)_3$), 69.1 (C_{60} sp^3), 66.9, 53.6, 51.5, 45.4, 40.5, 29.9, 29.7, 29.7, 29.6, 29.6, 29.5, 29.4, 29.2, 28.8, 28.3, 28.3, 26.7, 26.4, 25.7, 25.6. IR (ATR): $\nu = 2976$ cm^{-1}, 2930, 2856, 2097, 1743, 1691, 1514, 1365, 1244, 1213, 1166, 753, 715. MS (FAB, NBA): $m/z = 3682$ [M + Na$^+$], 3659 [M$^+$], 3603 [M$^+$ − *t*Bu], 3561 [M$^+$ − Boc], 3504 [M$^+$ − Boc-*t*Bu], 3359 [M$^+$ − 2×Boc], 3259 [M$^+$ − 3×Boc], 3160 [M$^+$ − 4×Boc]. UV/vis (CH_2Cl_2): λ_{max} (ϵ) = 243 nm (95 400 mol^{-1} dm^3 cm^{-1}), 270 (70 900), 280 (72 500). Anal. Calcd for $C_{209}H_{263}N_{13}O_{44} \times CH_2Cl_2$ (3742.82): C 67.33, H 7.13, N 4.86. Found: C 67.36, H 7.30, N 5.00.

*Decakis Pyropheophorbide-a[5:1]fullerene Hexaadduct Azide **14***. The hexakis adduct **13** (160 mg, 0.04 mmol) was dissolved in methanol (30 mL) and hydrochloric acid (5 mL, 4 N in 1,4-dioxane) was added. After stirring for 3 h at room temperature, the solvent was removed in vacuo. The orange decakis ammonium salt was used without any further purification for the next transformation. The deprotected hexakis adduct (55 mg, 0.018 mmol) was dissolved in brine (50 mL). $CHCl_3$ (50 mL) and triethylamine (200 μL) were added, and the organic layer was washed twice with brine. After this solution was dried over Na_2SO_4, pyropheophorbide-*a*-NHS ester **6** (170 mg, 0.27 mmol) was added and the solution stirred for 72 h at room temperature. Evaporation of the solvent and subsequent size exclusion chromatography (1. Bio-Beads SX3 2. Bio-Beads SX1, $CHCl_3$) yielded a black−green solid. Additional flash chromatography with silica ($CHCl_3$/methanol, 93.5:7.5) yielded **14** as a dark green solid (yield: 85 mg, 74%). ^{1}H NMR (400 MHz, $CDCl_3$, 25 °C, TMS): $\delta = 8.83$* (m, 10H, β), 8.54* (m, 10H, α), 8.20* (m, 10H, δ), 7.48* (m, 10H, 2a), 6.21* (bs, 2H + 1H, CONH, $NHCO-C_4H_8$), 6.11* (bs, 8H, CONH), 5.86* (m, 20H, 2b), 4.91* (m, 10H, 10), 4.64* (m, 10H, 10), 4.22* (m, 10H, 7), 3.96* (m, 10H, 8), 3.96 (m, 20H + 2H, $COOCH_2$), 3.64 (s, 3H, OCH_3), 3.25−2.60* (m, 30H + 30H + 20H + 30H + 20H + 2H, 1a, 3a, 4a, 5a, $NHCH_2$, CH_2N_3), 2.40* (m, 10H, 7a/b), 2.10* (m, 20H, 7a/b), 1.88* (m, 10H, 7a/b), 1.54* (m, 30H, 8a), 1.35* (m, 30H + 20H + 2H, 4b, $COOCH_2CH_2$), 1.24−1.03 (m, 94H, CH_2), −0.15* (bs, 10H, NH), −2.16* (s, 10H, NH). ^{13}C NMR (100 MHz, $CDCl_3$, 25 °C, TMS): $\delta = 195.9$, 172.4, 171.5, 164.1, 163.6, 160.3, 154.7, 150.2, 148.4, 146.0, 144.5, 141.0, 140.8, 137.1, 135.7, 135.5, 131.1, 129.5, 129.5, 128.7, 127.2, 121.9, 107.9, 105.5, 105.5, 103.2, 96.5, 92.6, 69.0, 67.6, 66.7, 51.6, 51.4, 49.6, 49.4, 47.8, 45.4, 39.1, 32.8, 31.9, 30.2, 29.6, 29.5, 29.4, 29.1, 28.7, 28.1, 26.6, 26.2, 25.3, 23.9, 22.7, 18.9, 17.2, 11.8, 11.2, 11.1, 10.9. IR (ATR): $\nu = 2961$ cm^{-1}, 2923, 2855, 2095, 1743, 1688, 1617, 1498, 1367, 1260, 1218, 1057, 978, 793. MS (Maldi-TOF, 2,5-dihydroxybenzoic acid): $m/z = 7833$ [M$^+$] (calcd 7826.55). MS (FAB, NBA): $m/z = 7821$ [M$^+$]. UV/vis (CH_2Cl_2): λ_{max} (ϵ) = 281 nm (184 600 mol^{-1} dm^3 cm^{-1}), 324 (220 900), 400 (623 200), 413 (621 300), 509 (708 000), 540 (60 600), 613 (55 900), 669 (287 600). Anal. Calcd for $C_{489}H_{503}N_{53}O_{44} \times 1.5CHCl_3$ (7997.75): C 73.59, H 6.35, N 9.27. Found: C 73.42, H 6.44, N 9.90.

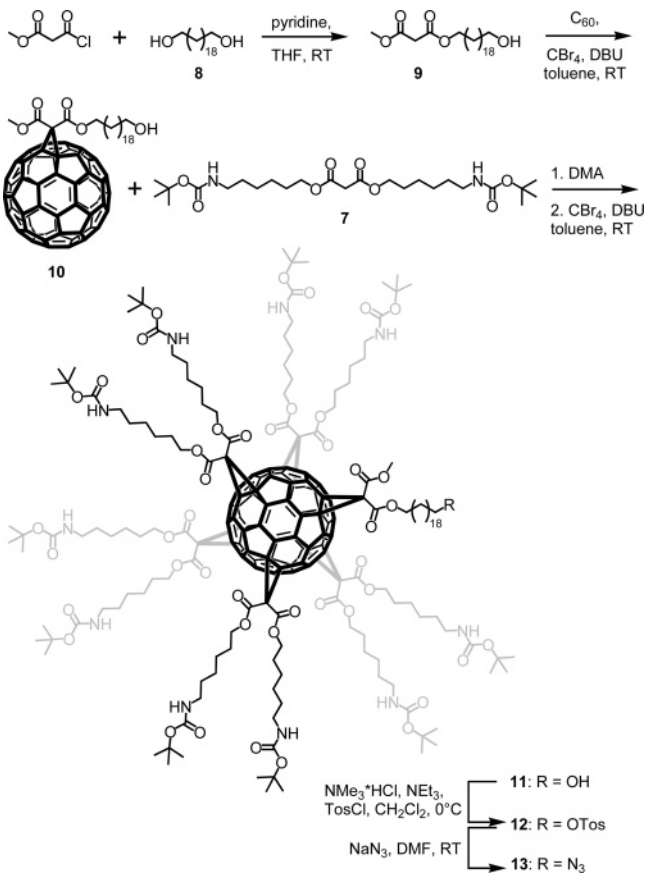
*Decakis Pyropheophorbide-a[5:1]fullerene Hexaadduct Adipinic Acid Active Ester **5**.* To a solution of hexakis adduct **14** (25 mg, 0.003 mmol) in THF (2 mL) and water (0.2 mL), trimethyl phosphine (1 mL, 1 mol solution in toluene, 1 mmol) was added. After stirring for 16 h at room temperature, the solvent was removed in vacuo. The dark green residue **15** was used without any further purification in the next transformation. The amino hexakis adduct **15** (25 mg, 0.003 mmol) was dissolved in dry CH_2Cl_2 (5 mL) and adipinic acid bis-(hydroxysuccinimide) ester **16** (50 mg, 0.14 mmol) was added. After stirring for 16 h at room temperature and subsequent size exclusion chromatography (Bio-Beads SX3 CH_2Cl_2), **5** was obtained as a black−green solid (yield: 22 mg, 91%). ^{1}H NMR (400 MHz, $CDCl_3$, 25 °C, TMS): $\delta = 8.83$* (m, 10H, β), 8.53* (m, 10H, α), 8.19* (m, 10H, δ), 7.48* (m, 10H, 2a), 6.18* (bs, 2H, CONH), 6.10* (bs, 8H, CONH), 5.81* (m, 10H, 2b), 4.91* (m, 10H, 10), 4.63* (m, 10H, 10), 4.21* (m, 10H, 7), 3.96* (m, 10H, 8), 3.96 (m, 20H + 2H, $COOCH_2$), 3.64 (m, 3H, OCH_3), 3.30−2.60* (m, 30H + 30H + 20H +30H + 20H + 2H + 4H + 4H, 1a, 3a, 4a, 5a, $NHCH_2$, adipinic $OOCCH_2$, succinyl-CH_2), 2.40* (m, 10H, 7a/b), 2.10* (m, 20H, 7a/b), 1.88* (m, 4H + 10H, adipinic $OOCCH_2CH_2$, 7a/b), 1.54* (bs, 30H, 8a), 1.35* (bs, 52H, 4b, $COOCH_2CH_2$), 1.24−1.03 (m, 98H, CH_2), −0.14* (bs, 10H, NH), −2.18* (s, 10H, NH). ^{13}C NMR (100 MHz, $CDCl_3$, 25 °C, TMS): $\delta = 195.9$, 172.3, 171.4, 163.6, 160.3, 154.7, 150.2, 148.4, 145.6, 144.5, 141.0, 137.1, 135.7, 135.5, 135.1, 131.1, 129.6, 129.5, 128.7, 127.2, 121.9, 105.6, 103.2, 96.6, 92.7, 69.1, 66.7, 51.6, 49.7, 47.8, 45.5, 39.1, 32.9, 30.2, 29.5, 29.4, 29.1, 28.1, 26.2, 25.4, 22.8, 19.0, 17.2, 11.8, 11.3, 10.9. IR (ATR): $\nu = 2963$ cm^{-1}, 2921, 2865, 1741, 1685, 1617, 1497, 1410, 1259, 1218, 1082, 1014, 866, 792. MS (Maldi-TOF, 2,5-dihydroxybenzoic acid): $m/z = 8028.57$ [M$^+$] (calcd 8025.76), 7803, 7394. UV/vis (CH_2Cl_2): λ_{max} (ϵ) = 279 (175 900 mol^{-1} dm^3 cm^{-1}), 322 (211 900), 399 (592 980), 413 (588 100), 510 (67 200), 540 (57 500), 613 (53 100), 669 (273 300).

Rit*−*5. The conjugation of **5** with the antibody Rituximab **Rit** was performed by dissolving **5** (5.5 mg, ∼0.7 μmol) in a little DMF (∼3 mL), which was then added to a stirred solution of **Rit** (10 mg/mL in 100 mg solution, ∼0.7 μmol) at pH 9. The concentration of DMF in the final reaction mixture did not exceed 35%. After 12 h at 4 °C, the crude mixture was purified by size exclusion chromatography (Bio-Gel P-60 eluent: PBS/DMF 80:20) to give a light green fraction of **Rit**−**5**. Unreacted **5** was recovered in the second fraction. The yield of the antibody conjugate **Rit**−**5** was calculated to be about 90% by adjusting the antibody's protein absorption to that before the reaction. Thus, the sample contained approximately 10% of nonreacted antibody.

Cell Culture. Epstein−Barr virus (EBV) transformed human B-lymphocytes, B-lymphoma cells (Ramos), and human T-lymphocytes (Jurkat cells: clone E 6−1) were used. Jurkat and Ramos cells were purchased from ACACC. EBV transformed B-lymphocytes were kindly provided by Dr. S. Lobitz (Otto-Heubner-Centrum für Kinder- and Jugendmedizin, Charité, Berlin). Cell lines were cultivated in 50 mL flasks in 5 mL RPMI 1640 medium containing Glutamax-I, supplemented with 10% fetal calf serum (FCS), 100 μg/mL streptomycin, and 100 IE/mL penicillin. Cells were cultivated at 37 °C in 100% humidity and 5% CO_2 and were seeded in new medium every 2−3 days.

Laser Scan Microscopy. The ability of the conjugate to bind the antigen CD20 was proven using a confocal laser scanning microscope (CLSM 510, Zeiss) equipped with a Helium-Neon

Scheme 1. Synthesis of the [5:1]Fullerene Hexaadduct Azide 13



laser. Pictures of the fluorescence of pyropheophorbide-*a* (**2**) were taken by exciting the PS at $\lambda_{exc} = 633$ nm and capturing the fluorescence at an emission wavelength $\lambda_{em} > 650$ nm using a long-pass filter (LP 650). Cells were incubated 24 h with the conjugate **Rit**−**5** (0.5 μmol as determined from the intensity of the last Q-band of the absorption spectrum of **Rit**−**5**), with the fullerene adduct **5** (0.5 μmol) and with compound **3** (0.8 μmol), which served as the positive control (*30*). The final concentration of the pyropheophorbide-*a* moieties was approximately 5 μmol (equivalent concentration). Cells incubated with the solvent were used as the negative control. After incubation, the cells were washed twice with phosphate buffered solution (PBS) and observed at the CLSM. Pictures were taken of transmitted light as well as fluorescence light. Transmitted and fluorescent light were then merged using the *Paint Shop Pro 7* software.

Cell Vitality and Proliferation. Cell vitality and proliferation were measured by the XTT test (Roche). The assay is based on the conversion of the yellow tetrazolium salt XTT into an orange formazane dye by the activity of mitochondria dehydrogenase in metabolically active cells. The amount of formazane product was analyzed spectrophotometrically at the absorbance of 492 nm. The reference wavelength was at 650 nm. The blank optical density (OD) was subtracted from the samples OD, and the percentage of cell vitality and proliferation was determined as follows: $(OD_{sample}/OD_{reference}) \times 100$. Bars represent the standard deviations for three experiments.

RESULTS AND DISCUSSION

Synthesis. After establishing a protocol for the synthesis of multi-pyropheophorbide-*a* conjugates (*26*, *27*), we applied it to the preparation of the synthetically much more demanding system **5** (Scheme 2). **5**, which is a fullerene [5:1]hexakis adduct, has a lower symmetry than the previously synthesized C_{60} hexakis adduct **4** (*26*); even more challenging is the attachment of an activated ester for coupling of the whole carrier system to an antibody. Due to the various reaction conditions during the synthesis of **5** and the inherent sensitivity of the pyropheophorbide-*a* moieties, very mild methods had to be used for generating the active ester unit. It also should be introduced at a very late point in the synthesis.

We decided to make an azide derivative which can be reduced easily to an amine and then coupled to a diester derivative, preferably the bis-active ester of an aliphatic dicarboxylic acid. The size of monoclonal antibodies, typically around 130−150 kDa, as well as the dimensions of the fullerene−pyropheophorbide-*a* conjugate **5**, requires the introduction of a long spacer unit between fullerene and active ester to allow for an efficient coupling reaction.

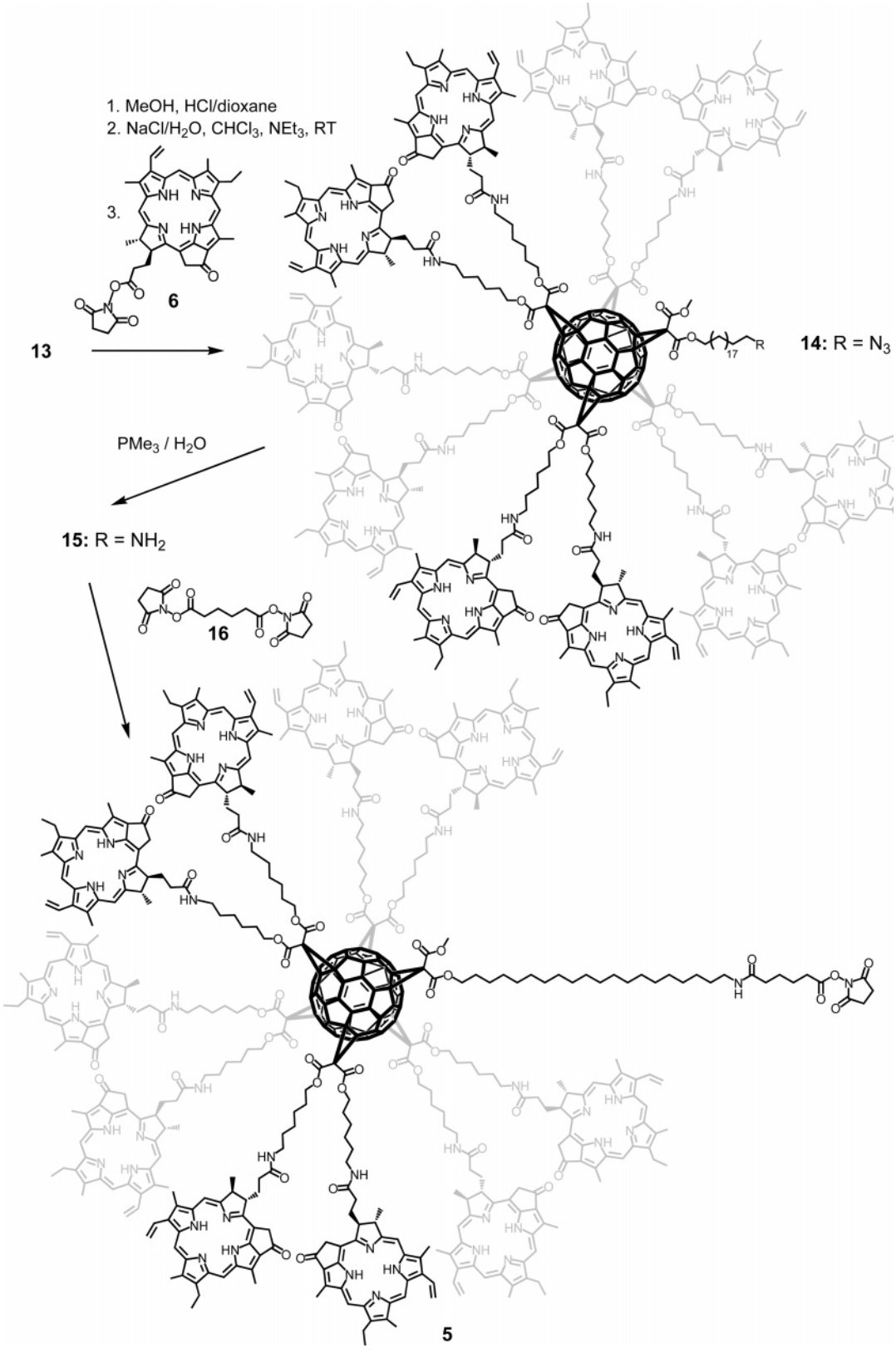
Starting from 1,20-dihydroxyeicosane **8**, the coupling with methyl malonylchloride yielded the corresponding malonate **9** in 37%; given the fact that **8** is poorly soluble, this yield is quite acceptable. The malonate **9** was attached to C_{60} by the well-established Bingel reaction (*33*) giving the monoadduct **10** in good yields. Subsequent coupling of five BOC-protected malonates **7** (*26*) to the monoadduct **10** by using the template activation method with 9,10-dimethyl anthracene (*34*) yielded the [5:1]hexakis adduct **11**. Here, purification with preparative HPLC was necessary to remove the pentakis adduct impurities. The overall yield after the purification steps was 24%.

The spectroscopic properties of **11** clearly show its constitution. Of particular importance are the resonances of the sp^3-carbon atoms of the fullerene core at 69.1 ppm. The typical C_{60} hexakis adduct bands at 271 and 281 nm in the UV/vis spectrum adds further support to the [5:1] structure. Tosylation of the free alcohol functionality of **11** gave the fullerene tosylate **12** which, after substitution of the tosyl group with sodium azide in DMF, gave the azido compound **13** in high yields (Scheme 1). The azide stretching vibration at 2095 cm^{-1} together with the NMR data unambiguously prove the formation of **13**. It should be pointed out that **13** not only is a very useful precursor for the project presented here, but may also be employed as a carrier/docking unit for other drugs.

After removal of the BOC protecting groups with HCl in dioxane, which liberates a decaamino compound (not isolated), and subsequent coupling with the NHS-active ester of pyropheophorbide-*a* **6** (*26*), the decapyropheophorbide-*a* [5:1]-fullerene hexaadduct **14** with an intact azide group was obtained. The reduction of the azido group of **14** to an amino group was performed by a modified Staudinger reaction (*35*) using trimethylphosphine in THF/water (Scheme 2). The resulting amine **15** could not be isolated or characterized. Nevertheless, the MALDI-TOF mass spectrum of the crude mixture shows clearly the molecular ion peak of the amino compound **15** at 7807.20 (calculated 7800.56) as the main signal. The molecular ion peak of the adduct **14** appears as a small signal at 7836.22 (calculated 7826.55) (see Supporting Information). Compounds **6**−**14** were fully characterized by standard spectroscopic and analytical methods.

The reaction of **15** with a large excess of adipinic acid−bis-NHS ester **16** gave compound **5** with one remaining activated carboxylic acid group. This active ester group is the aforementioned coupling unit which provides the covalent bond between the fullerene−pyropheophorbide-*a* residue and the monoclonal antibody Rituximab—or, in the future, other proteins. The ^1H NMR spectrum of **5** (see Supporting Information) shows quite well resolved signals, which is in contrast to the spectrum of the symmetrical dodecakis pyropheophorbide-*a* fullerene conjugate **4** (*26*) where all signals were rather broad. The signals of the chlorin moiety can be clearly assigned as well as those of the malonate spacer groups. Unfortunately, the resonances

Scheme 2. Synthesis of the Decakis Pyropheophorbide-*a* [5:1]Fullerene Hexaadduct 5 with Active Ester Docking Unit



of the active ester unit cannot be resolved, because they are hidden under the much more intense signals of the other groups. Fortunately, the successful generation of the active ester **5** can be proven with the MALDI-TOF mass spectrum (see Supporting Information). The main signal at 8028.82 can be assigned to the molecular ion peak (calculated 8025.76), whereas the smaller signal at 7802.34 can be assigned to either the unreacted amino compound **15** (calculated 7800.56) or a fragmentation product. This proves clearly the formation of compound **5** as the main component.

Synthesis of the Antibody Conjugate. We used the monoclonal antibody Rituximab (**Rit**) which was obtained from Hoffmann La Roche and is distributed under the commercial name MabThera. MabThera is a sterile, clear, colorless,

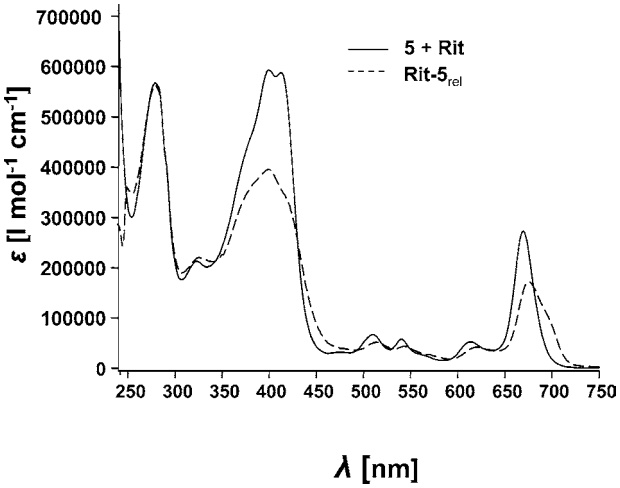


Figure 2. UV−vis spectrum of a mixture of compound **5** with the pure antibody and of the antibody conjugate (**Rit**-**5**).

preservative-free liquid concentrate for intravenous administration, supplied at a concentration of 10 mg/mL in 100 mg (10 mL) single-use vials. The product is formulated for intravenous administration in 9.0 mg/mL sodium chloride, 7.35 mg/mL sodium citrate dihydrate, 0.7 mg/mL polysorbate 80, and sterile water for injection. The pH is adjusted to 6.5.

The conjugation of **5** with the antibody **Rit** was performed by dissolving **5** in as little DMF as possible to allow solubility but to prevent denaturation of **Rit**. This solution was then added to the aforementioned solution of the antibody adjusted to pH 9, keeping the total amount of DMF below 35%. The separation from unreacted **5** and other small-molecule impurities was achieved by size exclusion chromatography (Bio-Gel P-60 eluent: PBS/DMF 80/20) to give a light green fraction of **Rit**−**5**. Figure 2 reports the UV−vis absorption spectra of the immunoconjugate **Rit**−**5** and a solution of **5** and Rituximab (1:1). In order to estimate the antibody/C_{60} ratio, we adjusted the conjugate's protein absorption band at 270 nm to that of the unreacted antibody. By integration over the last Q-band of **5** which stems from the pyropheophorbide *a* units, and comparison of this value with that one of **Rit**−**5**, we determined that the antibody/C_{60} ratio is approximately 1:0.9. It has to be noted that the Q-band of the antibody−fullerene complex is much broader compared to that of **5**. This means that the antibody strongly affects the pyropheophorbide-*a* moiety even in the ground state.

We are convinced that we have achieved a covalent attachment—and not an electrostatic interaction—of the fullerene derivative **5** to the antibody **Rit**, because (i) we observed clear bands on the chromatography column in contrast to broad or tailing bands in case of a breakup of electrostatically coupled components, and (ii) **5** does not contain charged groups or highly polarizable substituents, which could form coulomb complexes. In our opinion, it is more convenient that the drug complex is covalently bonded to the addressing unit. If a drug is merely absorbed on the mAb, once the carrier system is administered, it could be released or sequestered from other plasma proteins (i.e., albumin) before it has reached the target tissue.

Antigen Binding Ability. The monoclonal antibody rituximab **Rit** binds to the membrane receptor (CD20), which is exclusively expressed by normal B-lymphocytes or cancer B-cells, i.e., non-Hodgkin's lymphoma. The binding of the antibody conjugate **Rit**−**5** to the complement protein CD20 was tested on transformed B-lymphocytes by detecting the fluorescence of pyropheophorbide-*a* moieties with a confocal fluorescence microscope. The selectivity of the immunoconjugate **Rit**−**5** for the targeted B-cells was tested by comparison with its binding efficiency to cells which do not express the CD20 receptor (Jurkat cells). The uptake of C_{60} derivatives **5** and **3** was also tested on both cell lines. The comparison of the uptake of **5** with that of the conjugate **Rit**−**5** should give an idea of the efficiency of the antibody as addressing unit. **3**, a [5:1]-fullerene hexaadduct loaded with six pyropheophorbide-*a* moieties, which was shown to be taken up by Jurkat cells, served as positive control for cellular internalization. All dyes were applied in concentrations as such that the equivalent concentration of pyropheophorbide-*a* in each sample was approximately 5 μmol. Finally, cells incubated without any photosensitizer or antibody conjugate were used as reference to distinguish the autofluorescence of the cells. Fluorescence pictures were taken 24 h after incubation. Four different fields were observed with a confocal laser scan microscope. Pictures of both transmitted and fluorescence light were taken for each sample. Superimposed images were then created to clearly show the localization of the fluorescence on cell membranes or in the cell. Figure 3 reports a summary of the analyzed cells.

The T-lymphocytes used as reference did not show any autofluorescence, while a weak autofluorescence was detected in B-lymphocytes. The fluorescence of bound or taken-up photosensitizer (i.e., cells incubated with **3**, Figure 3C) had higher intensity than the autofluorescence of the cells and was clearly discernible from it. The hexakis pyropheophorbide-*a* [5:1]fullerene hexaadduct **3** was taken up by both cell types, and its fluorescence was detected mainly in the cytoplasm and in the perinuclear region. Compound **5** was not taken up by Jurkat and B-cells, which has obviously nothing to do with the size of the fullerene adduct; otherwise, **3** would not have been taken up either. The long lipophilic chain of **5** may have a detrimental influence on its intracellular uptake. The fact that **5** is not taken up makes the enhancement of delivery efficiency that can be reached by the use of an addressing unit even more remarkable. In fact, B-cells incubated with the antibody conjugate **Rit**−**5** had a bright fluorescence on a restricted region of the plasma membrane. The pictures clearly show that the immunoconjugate binds to surface receptors and that it is not internalized by the cells. These results demonstrate that the conjugation with the fullerene adduct **5** does not negatively influence the affinity of the antibody for its antigen. No fluorescence was detected when the same immunoconjugate was incubated with Jurkat cells. This means that **Rit**−**5** selectively recognizes B-lymphocytes without binding to T-cells which do not express the CD20 membrane receptor. In cytotoxicity experiments, the **Rit**−**5** preparation exhibited dark toxicity toward Ramos cells (CD20+ B-lymphoma cells) but not toward Jurkat cells (Figure 4). The immunoconjugate preparation gave the same cytotoxicity as the pure antibody. This means that the immunocojugate **Rit**−**5** has the same affinity for the CD20 receptor as the pure antibody and, furthermore, the same biological activity. However, it has to be considered that the immunoconjugate preparation may contain unreacted rituximab together with **Rit**−**5**, which may be the cause for the dark cytotoxicity. Further experiments considering dark and phototoxicity dependent on the incubation concentration of the **Rit**−**5** preparation will better demonstrate the biological activity of the immunoconjugate.

Our results show that fullerene hexakis adducts are useful multiplying units for modular carrier systems to be used in photodynamic therapy and can be potentially useful in any therapy in which a higher selectivity for the target is required. The special structure and chemistry of C_{60} and the use of long spacers allow the coupling of many drug moieties to a monoclonal antibody avoiding the inactivation of the antibody antigen-specific site. Confocal microscopy studies showed that the antibody conjugate **Rit**−**5** conserves its affinity for the CD20

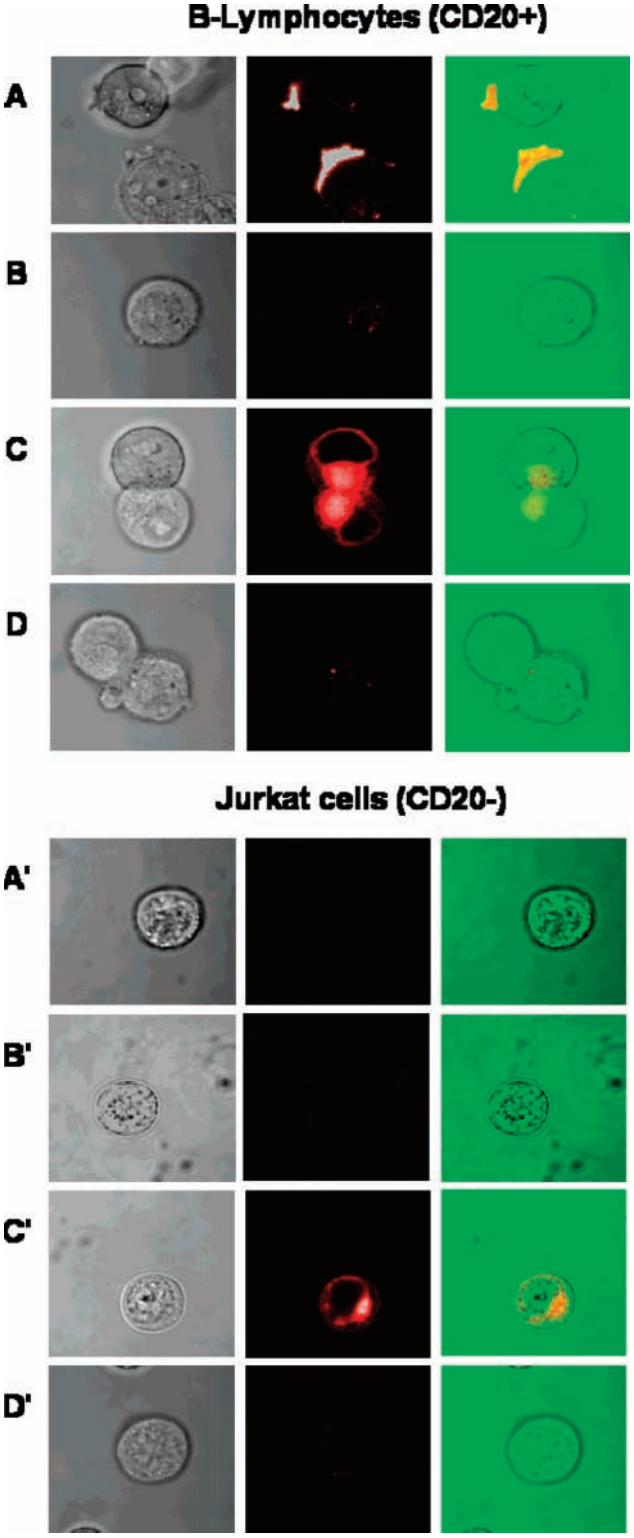


Figure 3. Binding of the conjugated antibody **Rit-5** to CD20 positive (CD20+) B-lymphocytes, and CD20 negative (CD20−) Jurkat cells. Both cells lines were incubated with the conjugated antibody (A, A′) and with the fullerene complexes **5** (B, B′) and **3** (C, C′) at a final pyropheophorbide-*a* equivalent concentration of ∼5 μmol. Cells incubated without any PS were used as reference (D, D′). After incubation, cells were washed twice and observed at the confocal laser scanning microscope (CLSM 510, Zeiss) using λ_{exc} = 633 nm and λ_{em} > 650 nm.

receptor and its selectivity toward CD20 positive B-lymphocytes. On the contrary, the antibody-free complex **5** did not show any bounding or intracellular uptake.

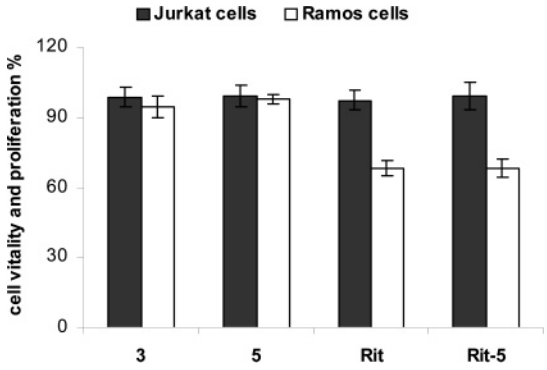


Figure 4. Cytotoxicity of immunoconjugate **Rit-5** toward Ramos cells (CD20+) and Jurkat cells (CD20−). Cells were incubated 24 h with 0.1 μmol **Rit-5**, fullerene adducts **5** and **3**, and the pure antibody rituximab (**Rit**). Cells incubated without any compound were used as reference. Cell vitality and proliferation were detected with the XTT test 24 h after incubation. Percentages were calculated with respect to reference cells.

In our future work, the introduction of a photounstable bond at the PS side will be pursued. In this way, once the modular carrier system has reached the target cells, the drug moieties can be released through irradiation and successively reach those intracellular compartments where the phototoxic effect is mostly efficient.

ACKNOWLEDGMENT

The authors thank the Deutsche Forschungsgemeinschaft (DFG) for financial support (F.R., F.B.: grant no. BO 1353/2-1,2; E.A.E., B.R.: grant no. RO 1042/9-3,4; E.A.E., B.R.: grant no. RO 1042/11-1,2; A. H., M. H., N. J.: grant no. HI 468/11-1). We also thank Mrs. Gisela Wöhlecke (Berlin) for technical assistance and Priv.-Doz. Dr. Andreas Humeny (Erlangen) for performing the MALDI-TOF experiments.

Supporting Information Available: ^{1}H NMR spectrum of **5** and MALDI-TOF spectra of **5** and of crude **15**. This material is available free of charge via the Internet at http://pubs.acs.org/BC.

LITERATURE CITED

(1) Ehrlich, P. (1906) *Studies in Immunity* (Wiley, J. & Sons, Eds.) Plenum Press, New York.

(2) Harashima, H., Shinohara, Y., and Hiroshi, K. (2001) Intracellular control of gene trafficking using liposomes as drug carriers. *Eur. J. Pharm. Sci. 13*, 85−89.

(3) Matsumura, Y., and Maeda, H. (1986) A new concept for macromolecular therapeutics in cancer chemotherapy: mechanism of tumoritropic accumulation of proteins and the antitumor agent smancs. *Cancer Res. 46*, 6387−6392.

(4) Svenson, S., and Tomalia, D. A. (2005) Dendrimers in biomedical applications-reflections on the field. *Adv. Drug Delivery Rev. 57*, 2106−2129.

(5) Putnam, D., and Kopeček, J. (1995) Polymer conjugates with anticancer activity. *Adv. Polym. Sci. 122*, 55−123.

(6) Guillemard, V., and Saragovi, H. U. (2001) Taxane-antibody conjugates afford potent cytotoxicity, enhanced solubility, and tumor target selectivity. *Cancer Res. 61*, 694−699.

(7) Patri, A. K., Myc, A., Beals, J., Thomas, T. P., Bander, N. H., and Baker, J. R., Jr. (2004) Synthesis and in vitro testing of J591 antibody-dendrimer conjugates for targeted prostate cancer therapy. *Bioconjugate Chem. 15*, 1174−1181.

(8) Dressler, C., Möller, U., Lewald, T., Berlien, H. P., Röder, B., and Risse, H. J. (1992) Introduction of a simple model for testing immunoconjugates with photosensitizers. *Laser Med. Sci. 7*, 164−168.

(9) Röder, B. (2000) Photodynamic therapy. In *Encyclopedia of Analytical Chemistry* (Meyers, A. Ed.) pp 302−320, John Wiley & Sons, Chichester, UK.
(10) Patri, A. K., Majoros, I. J., and Baker, J. R., Jr. (2002) Dendritic polymer macromolecular carriers for drug delivery. *Curr. Opin. Chem. Biol. 6*, 466−471.
(11) van Vlerken, L. E., and Amiji, M. M. (2006) Multi-functional polymeric nanoparticles for tumor-targeted drug delivery. *Expert Opin. Drug Delivery 3*, 205−216.
(12) Gillies, E. R., and Fréchet, J. M. J (2005) Dendrimers and dendritic polymers in drug delivery. *Drug Discovery Today 10*, 35−43.
(13) Herzog, A., Hirsch, A., and Vostrowsky, O. (2000) Dendritic mixed hexakis adducts of C_{60} with a T_h symmetrical addition pattern. *Eur. J. Org. Chem.* 171−180.
(14) Dugan, L. L., Turetsky, D. M., Du, C., Lobner, D., Wheeler, M., Almli, C. R., Shen, C. K.-F., Luh, T.-Y., Choi, D. W., and Lin, T.-S. (1997) Carboxyfullerenes as neuroprotective agents. *Proc. Natl. Acad., Sci. U.S.A. 94*, 9434−9439.
(15) Nakamura, E., and Isobe, H. (2003) Functionalized fullerenes in water, the first 10 years of their chemistry, biology, and nanoscience. *Acc. Chem. Res. 36*, 807−815.
(16) Ashcroft, J. M., Tsyboulsky, D. A., Hartman, K. B., Zakharian, T. Y., Marks, J. W., Weisman, R. B., Rosenblum, M. G., and Wilson, L. J. (2006). *Chem. Commun.* 3004−3006.
(17) (a) Reff, M. E., Carner, C., Chambers, K. S., Chinn, P. C., Leonard, J. E., Raab, R., Hanna, N., and Anderson, D. R. (1994) Depletion of B cells in vivo by a chimeric mouse human monoclonal antibody to CD20. *Blood 83*, 435−445. (b) Demidem, A., Lam, T., Alas, S., Hariharan, K., Hanna, N., and Bonavida, B. (1997) Chimeric anti-CD20 (IDEC-C2B8) monoclonal antibody sensitizes a B cell lymphoma cell line to cell killing by cytotoxic drugs. *Cancer Biother. Radiopharm. 12*, 177−186. (c) Berinstein, N. L., Grillo-López, A. J., White, C. A., Bence-Bruckler, I., Maloney, D., Czuczman, M., Green, D., Rosenberg, J., McLaughlin, P., and Shen, D. (1998) Association of serum Rituximab (IDEC-C2B8) concentration and anti-tumor response in the treatment of recurrent low-grade or follicular non-Hodgkin's lymphoma. *Ann. Oncol. 9*, 995−1001. See also: http://www.gene.com/gene/products/information/oncology/rituxan/insert.jsp.
(18) Shimokawa, K., Hashizume, A., and Shioi, Y. (1990) Pyropheophorbide-*a*, a catabotite of ethylene-induced chlorophyll a degradation. *Phytochemistry 29*, 2105−2106.
(19) Levy, J. G., and Obochi, M. (1996) New applications in photodynamic therapy introduction. *Photochem. Photobiol. 64*, 737−739.
(20) Dougherty, T. J., Gomer, C. J., Henderson, B. W., Jori, G., Kessel, D., Korbelik, M., Moan, J., and Peng, Q. (1998) Photodynamic therapy. *J. Natl. Cancer Inst. 90*, 889−905.
(21) Spiller, W., Kliesch, H., Wöhrle, D., Hackbarth, S., Röder, B., and Schnurpfeil, G. (1998) Singlet oxygen quantum yields of different photosensitizers in polar solvents and micellar solutions. *J. Porphyrins Phthalocyanines 2*, 145−158.
(22) Ermilov, E. A., Al-Omari, S., Helmreich, M., Jux, N., Hirsch, A., and Röder, B. (2004) Photophysical properties of fullerene-dendron-pyropheophorbide supramolecules. *Chem. Phys. 301*, 27−31.
(23) Ermilov, E. A., Al-Omari, S., Helmreich, M., Jux, N., Hirsch, A., and Röder, B. (2004) Steady-state and time-resolved studies on the photophysical properties of fullerene-pyropheophorbide a complexes in polar and nonpolar solvents. *Opt. Commun. 234*, 245−252.
(24) Al, Omari, S., Ermilov, E. A., Helmreich, M., Jux, N., Hirsch, A., and Röder, B. (2004) Transient absorption spectroscopy of a monofullerene C60-bis-(pyropheophorbide a) molecular system in polar and nonpolar environments. *Appl. Phys. B 79*, 617−622.
(25) Rancan, F., Helmreich, M., Mölich, A., Jux, N., Hirsch, A., Röder, B., Witt, C., and Böhm, F. (2005) Fullerene−pyropheophorbide *a* complexes as sensitizer for photodynamic therapy: uptake and photo-induced cytotoxicity on Jurkat cells. *J. Photochem. Photobiol., B 80*, 1−8.
(26) Helmreich, M., Ermilov, E. A., Meyer, M., Jux, N., Hirsch, A., and Röder, B. (2005) Dissipation of electronic excitation energy within a C60 [6:0]-hexaadduct carrying twelve pyropheophorbide a moieties. *J. Am. Chem. Soc. 127*, 8376−8385.
(27) Ermilov, E. A., Hackbarth, St., Al-Omari, S., Helmreich, M., Jux, N., Hirsch, A., and Röder, B. (2005) Trap formation and energy transfer in the hexapyropheophorbide a-fullerene C60 hexaadduct molecular system. *Opt. Commun. 250*, 95−104.
(28) Röder, B., Ermilov, E. A., Hackbarth, St., Helmreich, M., and Jux, N. (2006) Trap formation and energy transfer in pheophorbide a-DAB-dendrimers and pyropheophorbide a-fullerene C60 hexaadduct molecular systems. *SPIE 6192*, 495−507.
(29) Reuther, U. (2001) Evaluation of synthetic pathways for the heterofullerene $C_{58}N_2$ and introduction of the first concept for a completely regioselective control of multiple adduct formation of C_{60}. Ph.D. Dissertation, University of Erlangen-Nürnberg, Germany.
(30) Isaacs, L., Wehrsig, A., and Diederich, F. (1993) Improved purification of C60 and formation of σ- and π-homoaromatic methano-bridged fullerenes by reaction with alkyl diazoacetates. *Helv. Chim. Acta 76*, 1231−1250.
(31) Perrin, D. D., and Amarego, W. L. F. (1988) Purification of laboratory chemicals, Pergamon Press, Oxford, UK.
(32) (a) Closs, G. L., Katz, J. J., Pennington, F. C., Thomas, M. R., and Strain, H. H. (1963) Nuclear magnetic resonance spectra and molecular association of chlorophylls a and b, methyl chlorophyllides, pheophytins, and methyl pheophorbides. *J. Am. Chem. Soc. 85*, 3809−3821. (b) Smith, K. M., and Unsworth, J. F. (1975) Carbon-13 NMR spectra of some chlorins and other chlorophyll degradation products. *Tetrahedron 31*, 367−375.
(33) Bingel, C. (1993) Cyclopropanation of fullerenes. *Chem. Ber. 126*, 1957−1959.
(34) Lamparth I., Maichle-Mössmer C., and Hirsch, A. (1995) Reversible template-directed activation of equatorial double bonds of the fullerene framework: regioselective direct synthesis, crystal structure, and aromatic properties of T_h-$C_{66}(COOEt)_{12}$. *Angew. Chem., Int. Ed. Engl. 34*, 1607−1609.
(35) (a) Staudinger, H., and Meyer, J. (1919) New organic compounds of phosphorus. III. Phosphinemethylene derivatives and phosphinimines. *Helv. Chim. Acta 2*, 635−646. (b) Garcia, J., Urpí, F., and Vilarrasa, J. (1984) New synthetic tricks. Triphenylphosphine-mediated amide formation from carboxylic acids and azides. *Tetrahedron Lett. 25*, 4841−4844.
(36) Rancan, F., Helmreich, M., Mölich, A., Jux, N., Hirsch, A., Röder, B., Böhm, F. Unpublished results.

BC0603337

Coupling of Biotin−(poly(ethylene glycol))amine to Poly(D,L-lactide-*co*-glycolide) Nanoparticles for Versatile Surface Modification

Barbara Weiss,[‡] Marc Schneider,[‡] Leon Muys,[‡] Sebastian Taetz,[‡] Dirk Neumann,[§] Ulrich F. Schaefer,[‡] and Claus-Michael Lehr*[,‡]

Biopharmaceutics and Pharmaceutical Technology, and Junior Research Group Drug Transport, Center for Bioinformatics, Saarland University, Saarbruecken, Germany. Received November 2, 2006; Revised Manuscript Received April 1, 2007

Generally, polymeric nanoparticles (NP) for drug targeting are designed to entrap the drug moiety in the core and to present the targeting moiety on the surface. However, in most cases, common preparation techniques of polymeric NP need to be specifically arranged for each compound to be entrapped or attached. In the present work, we introduce a method for versatile conjugation of targeting moieties to the surface of preformed, polymeric NP. Moreover, due to taking advantage of biotin−avidin interactions, our regime opens the additional possibility of a rapid fluorescence labeling of NP. Poly(D,L-lactide-*co*-glycolide) (PLGA) NP in the size of 210 nm were prepared by the classic oil-in-water method. Such NP were functionalized with biotin−(poly(ethylene glycol))amine (BPEG) by means of cyanuric chloride chemistry. The amount of surface-associated biotin was 850 pmol per milligram of polymer, corresponding to roughly 2650 molecules of biotin per NP. When drawn to scale, such surface coating appeared to be well-suited for subsequent binding of avidin or avidin-linked ligands. By resonant mirror measurements, we could prove specific binding of biotinylated NP to a NeutrAvidin (NAv)-coated surface. Furthermore, after coupling of NAv-linked fluorescence dyes to BPEG-functionalized NP, differences in binding and uptake could be demonstrated using two epithelial cell lines (Caco-2, A549).

1. INTRODUCTION

Polymeric nanoparticles (NP) have turned out to be a promising carrier system for a number of active pharmacological ingredients (API), because they allow controlled release, drug targeting, and overcoming certain biological barriers such as the blood−brain barrier (*1*−*4*), the skin (*5*−*9*), or the intestinal mucosa (*10*−*13*).

In this context, biocompatible and biodegradable polymers are highly preferred, as they are eliminated from the body as small, nontoxic fragments after having served their intended purpose (*14*). Well-known examples of such polymers are the aliphatic poly(esters) poly(lactic acid) (PLA), poly(glycolic acid) (PGA), and their copolymers poly(lactic acid-*co*-glycolic acid) (PLGA); they have been extensively used since the 1970s for biomedical applications like sutures, fibers, fracture repairs, implants, and vascular grafts (*15*). Later, mainly PLA and PLGA have also been applied for the preparation of NP (*4*, *6*, *16*−*21*), which resulted in a variety of well-established methods for preparation and drug entrapment (*14*, *15*). Nowadays, a major interest of research is the synthesis of novel biodegradable polymers for the preparation of NP with different drug-loading properties, controlled release, and predictable degradation (*22*−*28*). Most of them are block copolymers (*22*, *23*, *26*) or polymer blends (*27*), often also containing PLGA or PLA subunits (*26*−*28*).

Generally, nanoparticulate drug targeting systems may bear different functionalities. The inner functionality is reflected by the NP core encapsulating the active moiety, small drug molecules (*6*, *8*, *29*−*32*), or therapeutic proteins (*16*, *33*−*35*). The active compound is stabilized toward the physiological environment, and its release can be controlled by the composition and structure of the polymer matrix. Complementarily, the outer functionality of a NP is represented by the NP surface which may establish specific and nonspecific interactions with the target, e.g., some particular cells, tissues, or organs. With regard to drug targeting, specific interactions between NP and the target cells or tissues are favored, requiring a sufficient number of targeting ligands on the NP surface to be available for such interaction (*36*−*38*).

In literature, diverse approaches describe the preparation of biodegradable biotinylated homopolymers (*39*) and block copolymers (*40*−*42*), which may be subjected to nanoparticle preparation. The aim of this study was to develop a procedure for surface functionalization of preformed NP for a subsequent versatile conjugation of targeting ligands and/or fluorescence dyes under mild conditions. Such a method may be applicable to various formulations of PLGA NP, which may eventually already contain an API, without any alteration of the NP preparation procedure. For this purpose, we chose the avidin−biotin system, as avidin (Av) and its homologues streptavidin (SAv) and NeutrAvidin (NAv) exhibit very high affinities ($K_d = 10^{-13}-10^{-16}$ M) and rapid and stable binding to biotin (*43*, *44*). Taking into consideration the presence of free carboxylic acid groups on the surface of NP made of poly(esters) like PLA, PLGA, PGA, and diverse lactide and/or glycolide containing blends and block copolymers (*23*, *26*, *27*), we have opted for an approach where surface-biotinylated NP bind to conjugates of avidin (or homologues). Consequently, both targeting moieties (antibodies, Fab fragments, etc.) as well as fluorescence labels can be easily linked to the surface of thus-functionalized NP as long as they are available as conjugates of avidin (or homologues) (Figure 1A).

In the present study, an effective surface biotinylation of preformed PLGA NP cores could be demonstrated. PLGA NP were characterized for their size, ζ potential, and surface

* Corresponding author. Prof. Dr. Claus-Michael Lehr, Biopharmaceutics and Pharmaceutical Technology, Saarland University, 66123 Saarbruecken, Germany. Tel: +49-681-302-3039. Fax: +49-681-302-4677. E-mail: lehr@mx.uni-saarland.de.

[‡] Biopharmaceutics and Pharmaceutical Technology.

[§] Junior Research Group Drug Transport, Center for Bioinformatics.

10.1021/bc060342f CCC: $37.00 © 2007 American Chemical Society
Published on Web 06/23/2007

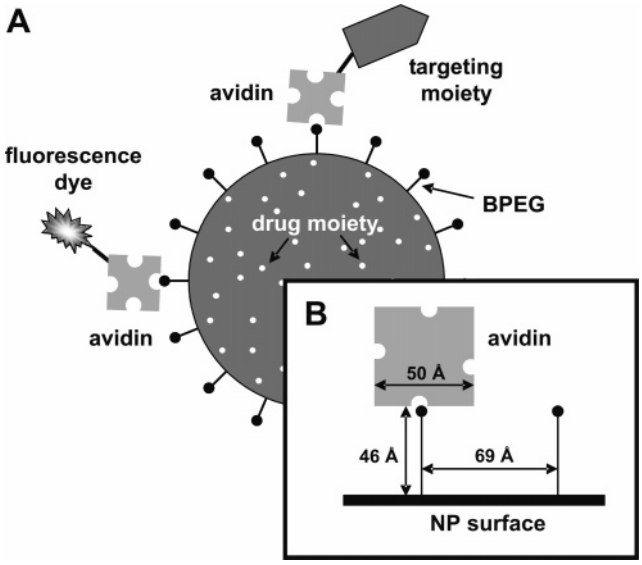


Figure 1. Schematic illustration of a surface-modified PLGA NP by means of BPEG. Part A gives an overview of the aims of the study. Versatile binding of targeting moieties is realized by employing avidin (and homologues) conjugates. Binding of fluorescence dye conjugated avidin (and homologues) introduces the possibility of additional fluorescence labeling of the NP. Part B represents a virtual zoom into the NP surface. Assuming homogeneous distribution of the BPEG molecules on the NP surface, the mean distance is calculated to 69 Å. The length of the BPEG molecule is determined to be roughly 46 Å. The size of avidin is reported to 50 Å × 50 Å × 40 Å with the biotin binding sites at a distance of 29.5 and 20 Å.

characteristics before and after biotin functionalization. The particle-associated biotin amount was determined to scale. Resonant mirror measurements gave evidence for specific binding of biotinylated NP to a NAv surface. For the first evaluation of the ease of application in a biological system, differences in binding and uptake of NP were studied in two epithelial cell lines after labeling the NP with different Av-linked fluorescence dyes.

2. METHODS AND MATERIALS

2.1. Materials. Poly(D,L-lactide-*co*-glycolide) (PLGA) (Resomer RG 50:50 H; inherent viscosity 0.31 dL/g) was kindly provided by Boehringer Ingelheim (Boehringer Ingelheim GmbH & Co. KG, Ingelheim, GE). Biotin−(poly(ethylene glycol))amine (BPEG) was obtained from Sigma (Sigma Chemical Co., St. Louis, MO). Poly(vinyl alcohol) (PVA) (Mowiol 4−88) was bought from Kuraray (Kuraray Specialities GmbH, Frankfurt am Main, GE). NeutrAvidin biotin-binding protein (NAv), avidin−FITC conjugate (FITC-Av), streptavidin−FITC conjugate (FITC-SAv), and NeutrAvidin−FITC conjugate (FITC-NAv) were purchased from Pierce (Perbio Science Deutschland GmbH, Bonn, GE). NeutrAvidin−Rhodamin Red−X conjugate (Rho-NAv) was obtained from Invitrogen (Molecular Probes, Inc., Eugene, OR). Rhodamine ricinus communis agglutinin I (Rho-RCA) and fluorescein wheat germ agglutinin (FITC-WGA) were obtained from Vector (Vector Laboratories, Inc., Burlingame, CA). Dulbecco's modified Eagle's medium (DMEM), RPMI-1640, nonessential amino acids (NeAA), and fetal bovine serum (FBS) were bought from GIBCO (Invitrogen Corp., Carlsbad, CA). All other chemicals were of analytical grade. Phosphate buffered solution pH 7.4 (PBS) was composed of KCl 0.20 g/L, NaCl 8.00 g/L, KH_2PO_4 0.20 g/L, and $Na_2HPO_4 \cdot 2H_2O$ 1.44 g/L.

2.2. Preparation of Biotin−(Poly(ethylene glycol)amine-Coated PLGA Nanoparticles. PLGA NP were prepared by a single emulsion method (*45*). Briefly, 100 mg of PLGA was dissolved in 5 mL of ethyl acetate and emulsified into a 1% PVA solution. The system was stirred at room temperature for 2 h at 800 rpm on a magnetic stirrer and then homogenized for 10 min using an Ultra-Turrax T 25 Mixer (Janke and Kunkel GmbH & Co., Staufen, GE) at 13 500 rpm. The volume was filled up to 50 mL with demineralized water, and the organic solvent was evaporated using a rotary evaporator.

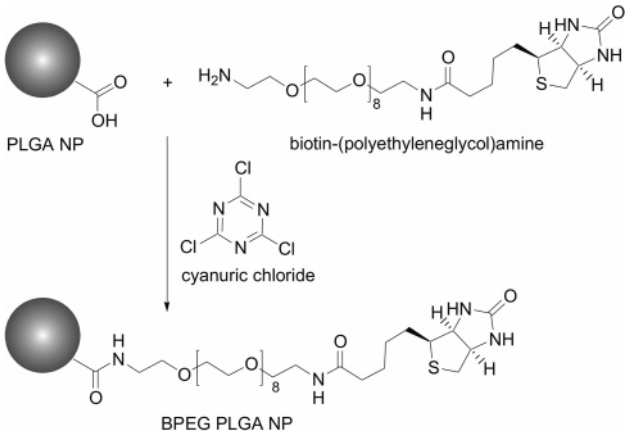


Figure 2. Reaction of chemical surface modification of PLGA NP resulting in BPEG PLGA NP.

BPEG-coated PLGA NP (BPEG PLGA NP) were generated from PLGA NP via a triazine-promoted amidation of the carboxylic acid groups present on the PLGA NP surface. The technique has been frequently described in the literature (*46*−*48*); here, it was adapted to surface modification of PLGA NP. The carboxylic acid groups formed activated intermediates with cyanuric chloride and, subsequently, the desired carboxyl amides in a single one-step reaction (Figure 2). The amino groups for the amidation reaction were derived from BPEG. 1 mL of PLGA NP suspension was supplemented with 1 mL of saturated cyanuric chloride solution and 50 μL of 10 mg/mL BPEG solution and incubated at room temperature for 24 h under gentle shaking on a horizontal shaker. BPEG PLGA NP were rinsed from excessive reagents by dialysis against 2 L of demineralized water for 24 h using a dialysis membrane with a cutoff of 100 000 Da (Spectra Por CE, Carl Roth GmbH, Karlsruhe, GE). The dialysis water was renewed after 8 h of dialysis time. In case blank PLGA NP were used for comparison, they were also dialyzed as described above. The NP concentration was determined via the residue of a defined volume of NP suspension after lyophilization. NP were prepared with a total of $n = 3$ to 5 batches.

2.3. Physicochemical Characterization of the Nanoparticles. *2.3.1. Particle Size and Surface Charge (ζ potential).* For determination of particle size and ζ potential, the NP suspensions were 100-fold diluted in demineralized water and analyzed using a Zetasizer Nano ZS (Malvern Instruments, Malvern, UK). The measurement of the NP size was based upon photon correlation spectroscopy (PCS). This technique yields the particle mean diameter and the polydispersity index (PI), which is a dimensionless measure for the broadness of the particle size distribution. The ζ potential was analyzed by laser Doppler anemometry using the same instrument in appropriate settings. Results are expressed as mean ± SD.

2.3.2. Morphology Study. NP shape and surface properties were imaged by means of scanning probe microscopy (SPM). NP samples were prepared as dense layers by mounting a drop of a freshly prepared NP suspension on a silicon wafer and air-drying. Imaging was performed using a Bioscope SPM and a Nanoscope IV controller (Veeco Instruments, Santa Barbara, CA) in a vibration-free environment. For all measurements, tapping mode was employed using a commercially available

pyramidal tip (silicon, Ultrasharp, MikroMasch, Tallinn, EST) on a cantilever with a length of 230 μm. The resonance frequency was approximately 170 kHz, the nominal force constant 40 N/m, and the scan frequency between 0.1 and 1 Hz.

2.4. Particle-Associated Biotin Amount. The amount of biotin on BPEG PLGA NP was determined by means of FluoReporter Biotin Quantitation Assay (Molecular Probes, Invitrogen GmbH, Karlsruhe, GE). This assay uses Biotective Green reagent which consists of Av labeled with a fluorescence dye and with quencher dye ligands occupying the biotin binding sites. The ligand quenches the fluorescence through fluorescence resonance energy transfer. By addition of any biotin, the ligand is displaced from Biotective Green reagent, yielding fluorescence proportional to the amount of added biotin. The assay was performed according to the protocol of the manufacturer. NP suspensions were used in concentrations between 0.49 and 0.88 mg/mL, and experiments were performed with three batches and with a total of $n = 2$ to 3 samples each. The background was subtracted. Results are expressed as mean $\pm$ SD.

2.5. Modeling of Biotin−(Poly(ethylene glycol))amine. To determine the dimensions of BPEG, we built a single stretched molecule using the program *HyperChem Professional 7.1* (Hypercube, Inc., Gainesville, FL). The geometry optimization was performed on a personal computer employing the MM+ force field. For the energy minimization, we used a conjugate gradient method with a termination value of the root-mean-square gradient of 0.1 kcal/mol/Å according to the HyperChem manual.

2.6. Binding of FITC Conjugated Proteins (FITC-Av, FITC-SAv, FITC-NAv) to Nanoparticles. 100 μL samples of BPEG PLGA NP and PLGA NP suspensions ($\sim$1 mg/mL) were incubated with 25 μL of FITC-Av (1 mg/mL), FITC-SAv (1 mg/mL), and FITC-NAv (1 mg/mL), respectively, for 10 min under gentle shaking and protection from light. The suspensions were centrifuged for 5 min at 23 147 $\pm$ 66 g, and the supernatant was removed. NP were washed by resuspension in 1 mL of PBS, centrifuged again, and finally resuspended in 50 μL of PBS. In all resuspension steps, NP pellets were treated with ultrasound for 2 min ($n = 3-5$). In pre-experiments, a separation of NP on the size order of 210 nm by centrifugation at 23 147 $\pm$ 66 g (no NP detectable in the supernatant by PCS) and a complete removal of free proteins in solution by the described washing procedure were confirmed.

The binding of FITC conjugated proteins to BPEG PLGA NP and PLGA NP was investigated and visualized by confocal laser scanning microscopy (CLSM) which was performed using a Bio-Rad MRC-1024 CLSM (Bio-Rad Laboratories, Hercules, CA) equipped with an argon/krypton laser. The objective used was an oil immersion objective 40$\times$ (NA = 1.3). The excitation wavelength was $\lambda = 488$ nm, and the fluorescence signal was collected with a band-pass filter (Zeiss 520/35) in the green wavelength range. For each set of samples, the same detector settings were chosen.

2.7. Resonant Mirror System (RMS) Adhesion Studies. The interaction of BPEG PLGA NP and PLGA NP with two differently modified surfaces was examined by means of a RMS (IAsys, Cambridge, UK). First, the interaction of the NP with a NAv-coated surface was investigated.

In a second run, the binding sites of NAv were blocked using a 0.02 mg/mL BPEG solution (incubation time $\sim$4.5 min) to study possible nonspecific binding of NP with this surface.

Briefly, NP suspensions were added to the coated sensor chip and allowed to bind to the surface. The adhesion process was monitored, and the measurements were stopped after 5 to 10 min. The vertical displacement of the vibrostirrer was set to 0.425 mm, and the temperature of the instrument was set to 25 °C.

Table 1. Size, Polydispersity Index (PI), and ζ Potential of PLGA NP and BPEG PLGA NP

	size [nm]	PI	ζ potential [mV]
PLGA NP	207 $\pm$ 4	0.042 $\pm$ 0.017	−32.0 $\pm$ 3.6
BPEG PLGA NP	207 $\pm$ 2	0.051 $\pm$ 0.004	−23.0 $\pm$ 4.1

The concentrations of BPEG PLGA NP and PLGA NP were 0.5 and 1.2 mg/mL, respectively. The NAv-functionalized surface was generated by incubating a biotin-coated cuvette (Thermo Electron LED GmbH, Langenselbold, GE) with NAv as described in the IAsys standard immobilization protocol. All reactions were performed in PBS.

2.8. Cell Culture. *2.8.1. Caco-2 Cells.* Caco-2 cells, clone C2BBe1, were purchased at passage 60 from American Tissue Culture Collection (ATCC; Manassas, VA) and used at passages 70 to 91. Cells were grown to a confluency of approximately 90% in 75 cm^2 T-flasks with DMEM supplemented with 10% FBS and 1% NeAA. Thereby, the culture medium was changed every second day, and the temperature was 37 °C in an atmosphere of around 85% relative humidity and 5% CO_2.

2.8.2. A549 Cells. A549 cells (ATCC no. CCL-185) were purchased at passage 82 from ATCC (American Type Culture Collection, Manassas, VA) and used at passages 88 to 110. Cells were grown to a confluency of approximately 90% in 75 cm^2 T-flasks with RPMI-1640 supplemented with 10% FBS. Thereby, the culture medium was changed every second day, and the temperature was 37 °C in an atmosphere of around 85% relative humidity and 5% CO_2.

2.8.3. Uptake Studies. After trypsinization, Caco-2 and A549 cells were seeded on LAB-TEK chamber slides (Nalge Nunc International, Rochester, NY) at densities of roughly 20 000 and 12 500 cells/mL, respectively, and grown for 3 days. Uptake of test substances was evaluated after 6 and 24 h of incubation with a test substance at 37 °C under protection from light. In the case of the 24 h incubation time, the supernatant was replaced by cell culture medium after 6 h. For localization of fluorescent NP, cell membranes were stained using Rho-RCA and FITC-WGA, respectively, by incubation with a 5 μg/mL solution in PBS for 10 min at 37 °C under protection from light. Cells were washed twice with PBS and fixed by 10 min of incubation with 4% formaldehyde solution at room temperature under protection from light. Again, cells were washed twice and then subjected to CLSM, which was performed as described in section 2.6. In the red wavelength range, the excitation wavelength was $\lambda = 568$ nm, and the fluorescence signal was collected with a long-pass filter (Zeiss LP585). Test substances were 0.5 mg/mL BPEG PLGA NP, which were preincubated with FITC-NAv or Rho-NAv in excess for 30 min, dialyzed in order to remove unbound proteins, and 1:1 diluted with the respective growth medium. References were as follows: (i) blank growth medium, (ii) a 25 μg/mL FITC-NAv or Rho-NAv solution in the respective growth medium, and (iii) a 25 μg/mL FITC-NAv or Rho-NAv solution in the respective growth medium additionally containing 0.5 mg/mL of blank PLGA NP. The concentrations of the FITC-NAv and Rho-NAv solutions were well above the maximum of NP-associated fluorescent proteins in a 0.25 mg/mL BPEG PLGA NP solution when all biotin molecules bound to one FITC-NAv or Rho-NAv molecule.

3. RESULTS

3.1. Physicochemical Properties of Biotinylated Nanoparticles. PCS measurements showed that size and PI of BPEG PLGA NP and PLGA NP were practically the same, i.e., there was no measurable increase in size of the original PLGA NP after functionalization with BPEG. Particle size distributions were monodisperse. However, the ζ potential changed from −32 mV to −23 mV (Table 1).

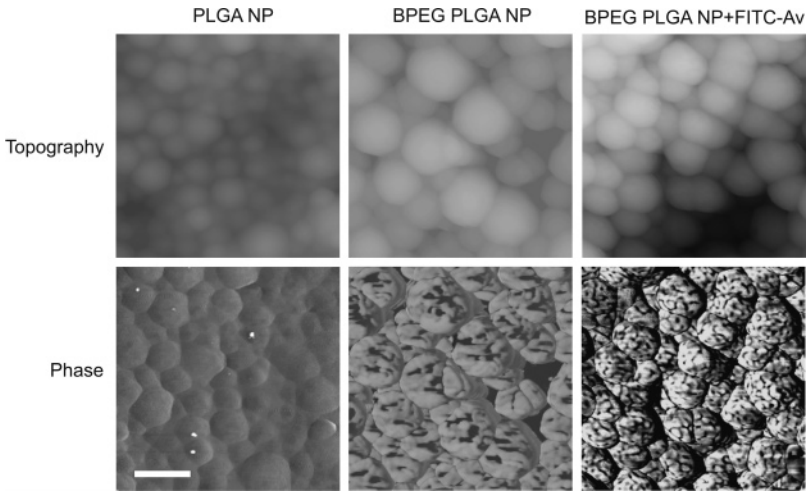


Figure 3. SPM topography and phase images of PLGA NP, BPEG PLGA NP, and BPEG PLGA NP with associated FITC-Av (bar = 250 nm).

Figure 3 presents SPM images of PLGA NP, BPEG PLGA NP, and BPEG PLGA NP with associated FITC-Av. Before subjection to SPM measurements, successful binding of FITC-Av to BPEG PLGA NP was confirmed via CLSM. The SPM topography images show the particle shape and surface structure. Blank PLGA NP exhibited a spherical particle shape and a smooth surface. Obviously, these properties were not affected by surface modification, as can be seen from the height images of BPEG PLGA NP and BPEG PLGA NP with associated FITC-Av. However, the phase images of those samples showed clear structural differences, in contrast to the original PLGA NP. These alterations reflect changes of the local elastic and/or adhesive properties as a consequence of surface biotinylation of PLGA NP and also due to the binding of FITC-Av to thus-modified surface.

FluoReporter Biotin Quantitation Assay was used to quantitatively analyze the extent of surface modification of PLGA NP resulting in BPEG PLGA NP. By that method, an amount of 845 ± 145 pmol of biotin attached to the surface of 1 mg of BPEG PLGA NP was determined. Assuming a particle density of 1.25 g/mL (which corresponds to the real density of PLGA according to the information of the manufacturer), an approximate number of 2600 biotin molecules on the surface of one single average-sized (210 nm) BPEG PLGA NP could be calculated. Assuming that BPEG chains are evenly distributed on the NP surface, the mean distance of two chains would be 69 Å. The length of the BPEG chains was calculated to maximally 46 Å. In solution, we would expect the BPEG molecule to adopt a more or less coiled conformation; here, however, to roughly estimate surface conditions we deliberately assumed the molecule to exist in a stretched conformation. The size of Av is reported to be 50 Å × 50 Å × 40 Å with the biotin binding sites being distances of 29.5 and 20 Å from each other (*49*). The dimensions of such a BPEG-functionalized NP surface are drawn to scale in Figure 1B, indicating that each single BPEG graft on the NP surface should be well accessible to Av.

3.2. Selection of Suitable Avidin Homologues for Further Functionalization. Each of the three proteins FITC-Av, FITC-SAv, and FITC-NAv bound to BPEG PLGA NP, whereas only FITC-Av and FITC-SAv exhibited binding to blank PLGA NP, obviously due to nonspecific interactions. In these cases, we could visualize green fluorescent single NP or particle aggregates by means of CLSM. Figure 4A shows an image of BPEG PLGA NP with surface-bound FITC-NAv. In contrast, we did not find binding of FITC-NAv to blank PLGA NP (Figure 4B). Consequently, due to apparently weak nonspecific particle binding, we chose NAv for further RMS measurements and ligand coupling.

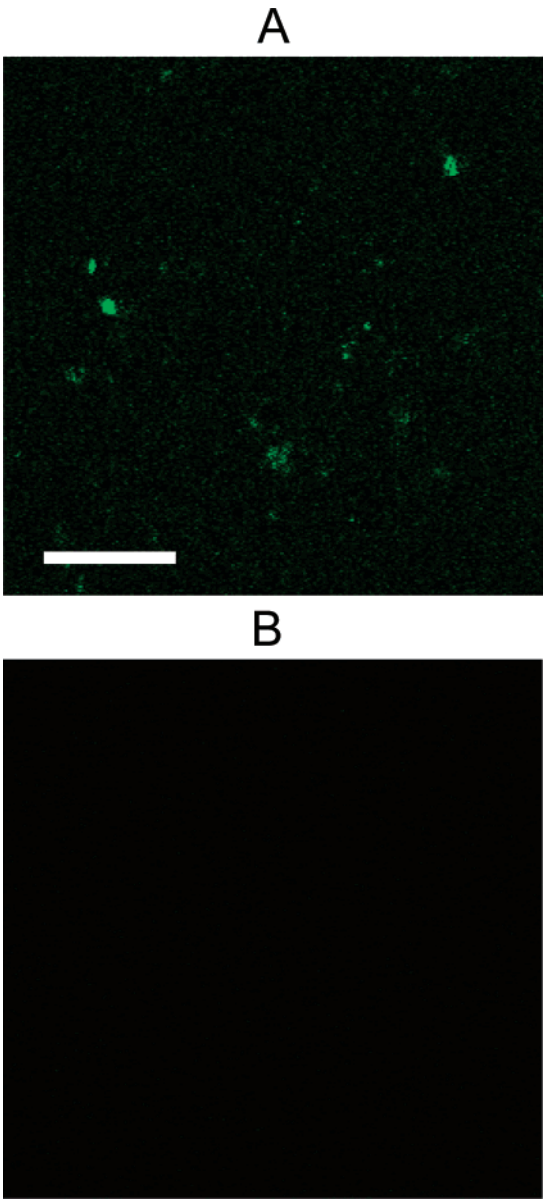


Figure 4. CLSM visualization of FITC-NAv-treated BPEG PLGA NP (A) and PLGA NP (B) (bar = 20 μm).

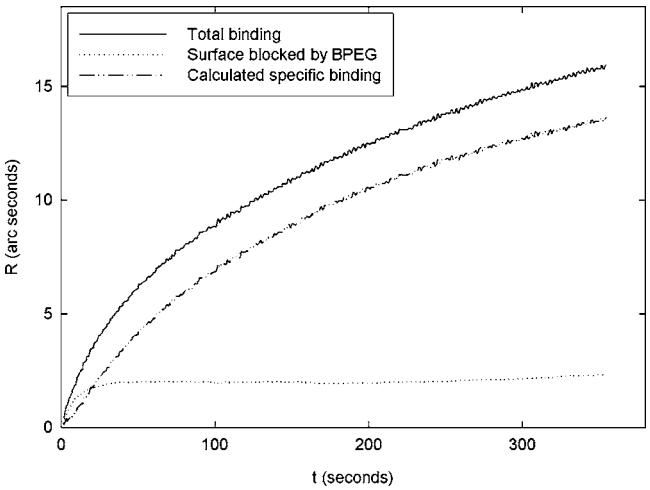


Figure 5. Results of resonant mirror system (RMS) adhesion studies: interactions of BPEG PLGA NP with a NeutrAvidin (NAv) surface and a NAv surface with BPEG-blocked biotin binding sites. An additional curve calculated as the difference of both binding curves represents the extent of specific binding.

BPEG PLGA NP and PLGA NP without protein treatment and BPEG PLGA NP and PLGA NP which were incubated with FITC-NAv with blocked biotin binding sites were imaged as a control. Those samples did not exhibit any fluorescence under the same conditions, indicating that there was no binding of FITC-NAv to the NP under such conditions.

3.3. RMS Measurements. Using RMS, we first studied the binding of BPEG PLGA NP with a NAv-functionalized surface (total binding) (Figure 5). We obtained a clear response; however, the binding curve did not reach equilibrium during the measurement, possibly due to particle rearrangement on the NAv-coated surface. There was no observable NP dissociation, and particles could not be washed easily from the surface, indicating a strong binding. In a second experiment, nonspecific binding was studied by blocking the biotin binding sites of a NAv-coated functionalized cuvette using free BPEG. Here, we received only a small response. The extent of specific binding of BPEG PLGA NP to the NAv surface is described by a calculated curve, which was obtained by subtracting the curve representing the nonspecific binding from the curve representing the total binding. Again, the curve did not reach equilibrium for reasons described above.

For comparison, we also investigated the binding behavior of nonfunctionalized PLGA NP to a NAv surface. Here, the equilibrium response was very small and readily established after approximately 100 s.

3.4. Uptake Studies. Figure 6 shows *xz* cross sections from a stack of confocal laser scans of Rho-RCA-stained A549 cells, Rho-RCA-stained Caco-2 cells, and FITC-WGA-stained Caco-2 cells after 6 and 24 h incubation with fluorescent NP formulations. In order to investigate and visualize binding and uptake, we applied FITC-NAv-labeled NP if the cell membranes were stained with Rho-RCA and Rho-NAv-labeled NP if the membranes were stained with FITC-WGA.

In the case of A549 cells, NP appeared in close association with the cell membranes after 6 h of incubation, whereas we found a clear NP uptake after 24 h. In the case of Caco-2 cells, there was no particle uptake even after 24 h of incubation. However, particles were attached to the cell membranes.

These results in Caco-2 cells were found with both FITC-NAv and Rho-NAv labeled BPEG PLGA NP, thus evidencing the suitability of this approach for rapid versatile fluorescence labeling.

In the case of all references, no fluorescence within the cells or at the cell membranes was found that had derived from the protein solutions (images not shown).

4. DISCUSSION

The overall goal of this study was the evaluation of a procedure for surface functionalization of preformed NP made from biodegradable polymers such as PLGA. Surface-modified NP are intended to be used for subsequent versatile conjugation of targeting moieties and for rapid fluorescence labeling under mild conditions.

Preformed PLGA NP were modified by easy covalent binding of a biotin derivative via a short PEG spacer (Figure 2). The biotinylated particle surface forms a platform for further specific binding of Av (and homologues) conjugated compounds, which may be either targeting moieties or fluorescence dyes, by brief incubation in aqueous medium (Figure 1A). By this NP modification method, harsh preparation conditions like shearing or heating or the presence of organic solvents are avoided. Another benefit of this technique concerns the detachment of compounds from the NP surface for potential targeting purposes. If NP are made from functionalized polymers (*39*, *42*, *50*), ongoing polymer erosion may uncover further active groups, thus leading to a subsequent rebinding of detached proteins. Using this preparation, it cannot be entirely excluded that BPEG and the activating agent cyanuric chloride might also interpenetrate the NP cores during biotinylation reaction. However, due to selected process parameters (i.e., aqueous dispersion, hydrophobic polymer), the reaction is supposed to preferably take place at the NP−water interface. Therefore, in contrast to NP from modified polymers, the core of the BPEG PLGA NP is not expected to provide further biotin groups as soon as they are cleaved from the surface, i.e., specific rebinding is most unlikely.

Regarding the biocompatibility of BPEG PLGA NP, biotin is a natural vitamin, and both substances, PEG and PLGA, may be considered nontoxic (as they are part of FDA-approved drug products for parenteral administration).

Surface functionalization of PLGA NP to yield BPEG PLGA NP did not involve an increase in size as determined by PCS, i.e., any change in the hydrodynamic diameter was beneath the detection limit (Table 1). As evidenced in SPM studies, surface modification of PLGA NP and binding of Av to BPEG PLGA

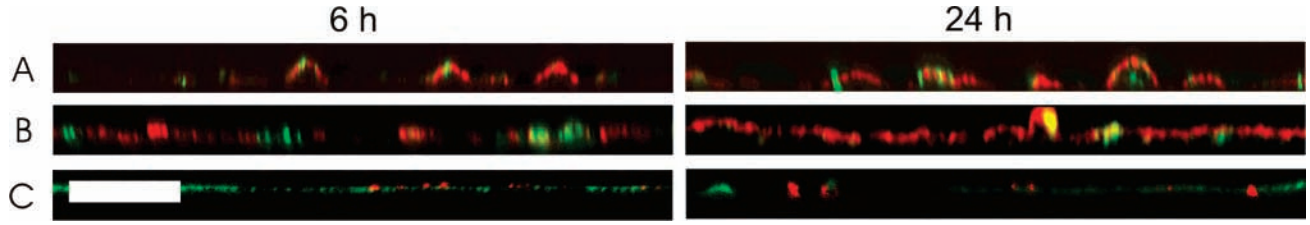


Figure 6. *xz* cross sections from a stack of confocal laser scans (apical up) of Rho-RCA-stained A549 cells (A), Rho-RCA-stained Caco-2 cells (B), and FITC-WGA-stained Caco-2 cells (C). Cells were imaged after 6 and 24 h incubation with FITC-NAv-labeled BPEG PLGA NP (in the case of Rho-RCA-stained A549 and Caco-2 cells) and Rho-NAv-labeled BPEG PLGA NP (in the case of FITC-WGA-stained Caco-2 cells) (rows A and B: bar = 50 μm × 5 μm. row C: bar = 20 μm × 9 μm).

NP did not lead to changes in particle shape and surface structure (Figure 3). Obviously, however, as indicated in the phase images, those modifications resulted in changes of elasticity or adhesion of the cantilever tip.

We found a decrease in the ζ potential for the BPEG PLGA NP in comparison to nonmodified PLGA NP (Table 1). The negative surface charge of both particle species is attributed to the presence of carboxyl end groups derived from PLGA chain ends. However, in the case of the BPEG PLGA NP, the particle surface was partially shielded, owing to covalent modification of the carboxyl groups by means of BPEG molecules. The PEG chain linking the biotin compound with the NP core consisted of ten ethylene oxide subunits and was conceived to facilitate the surface-modification reaction by provision of amino groups and, at the same time, to increase biotin flexibility while protein binding.

Studying the binding specificity of Av and its homologues to BPEG PLGA NP and PLGA NP, we found specific binding to BPEG PLGA NP only in the case of NAv. This finding has to be attributed to the character of the proteins: Av and its bacterially produced counterpart SAv represent positively charged glycoproteins with a well-known tendency of nonspecific interactions with negatively charged compounds, e.g., PLGA NP. NAv is manufactured from Av by deglycosylation, consequently, reducing charge and nonspecific binding (*51*).

The binding specificity was confirmed in RMS measurements where BPEG PLGA NP showed specific binding to a NAv-coated surface (Figure 5). Attachment of BPEG PLGA NP to the NAv surface did not reach equilibrium during the measurement, which probably is to be attributed to particle rearrangement; in contrast, minor nonspecific binding of PLGA NP was completed rapidly.

For drug delivery applications, investigation and imaging of NP in biological systems, their penetration pathways, and their final localization at cellular or tissue level is of major interest (*9*, *18*, *52*). Common strategies represent the entrapment of fluorescence markers or visualizable drugs and the imaging of NP by fluorescence, confocal, or multiphoton microscopy (*6*, *9*, *52*, *53*). The present work illustrates the application of fluorescence-labeled BPEG PLGA NP to demonstrate differences in binding and uptake behavior between flat squameous epithelial cells from the alveolar epithelium (A549) in comparison to the relatively thick columnar epithelial cells from the intestinal mucosa (Caco-2) (Figure 6). Moreover, dependent on the staining of the cell membranes, we applied NP decorated with different fluorescent NAv conjugates, thus demonstrating the ease of versatile fluorescence labeling of BPEG PLGA NP.

From calculations to scale of the surface of BPEG PLGA NP, we hypothesized that particles are optimally covered by BPEG molecules. Presumably, those molecules are able to reach each site on the particle surface due to the flexibility of their PEG spacer in order to mediate specific binding of Av (and homologues). Considering Av and homologues that are tetrameric, with four biotin binding sites, it is evident that this fact may lead to binding of biotin molecules derived from several NP, and subsequently to cross-linking. Nowadays, in order to overcome this cross-linking problem, one can find different approaches in the literature. Active monomeric Av and SAv mutants have been produced by means of biotechnological methods (*54*, *55*). Since monomerization of those proteins generally involves loss of biotin binding affinity, a NAv-coated tetramer with only one functional biotin binding subunit was recently developed (*56*).

Those protein mutants would help to avoid particle cross-linking, whereas the choice of NAv as biotin binding protein can further minimize nonspecific binding. Such a refinement of our approach by using monovalent NAv appears very possible; however, this is still a subject of ongoing research.

5. CONCLUSION

Successful surface biotinylation of preformed PLGA NP, representing a model for NP from any other polymer exhibiting free carboxylic acid groups, can be demonstrated. Without interfering with or being dependent on the methods of NP preparation and drug loading, our approach allows versatile surface decoration with targeting moieties and fluorescence labels under mild conditions, provided they are available as conjugates of NAv. Binding studies and calculations to scale of the surface conditions of biotinylated NP revealed optimal conditions for subsequent specific binding of Av conjugated ligands. In a first biological evaluation with A549 and Caco-2 cells, BPEG PLGA NP enabled us to demonstrate differences in binding and uptake.

ACKNOWLEDGMENT

Boehringer Ingelheim is kindly acknowledged for providing the polymer. We would like to thank Jens Schaefer (Department of Pharmaceutics and Biopharmacy, Philipps-University Marburg) for his help with the Zetasizer measurements. D. Neumann is financially supported by the Deutsche Forschungsgemeinschaft (DFG grant BIZ 4/1).

LITERATURE CITED

(1) Koziara, J. M., Lockman, P. R., Allen, D. D., and Mumper, R. J. (2004) Paclitaxel nanoparticles for the potential treatment of brain tumors. *J. Controlled Release 99*, 259−269.

(2) Ambruosi, A., Gelperina, S., Khalansky, A., Tanski, S., Theisen, A., and Kreuter, J. (2006) Influence of surfactants, polymer and doxorubicin loading on the anti-tumour effect of poly(butyl cyanoacrylate) nanoparticles in a rat glioma model. *J. Microencapsulation 23*, 582−592.

(3) Aktas, Y., Yemisci, M., Andrieux, K., Gursoy, R. N., Alonso, M. J., Fernandez-Megia, E., Novoa-Carballal, R., Quinoa, E., Riguera, R., Sargon, M. F., Celik, H. H., Demir, A. S., Hincal, A. A., Dalkara, T., Capan, Y., and Couvreur, P. (2005) Development and brain delivery of chitosan-PEG nanoparticles functionalized with the monoclonal antibody OX26. *Bioconjugate Chem. 16*, 1503−1511.

(4) Costantino, L., Gandolfi, F., Tosi, G., Rivasi, F., Vandelli, M. A., and Forni, F. (2005) Peptide-derivatized biodegradable nanoparticles able to cross the blood-brain barrier. *J. Controlled Release 108*, 84−96.

(5) Alvarez-Roman, R., Naik, A., Kalia, Y. N., Guy, R. H., and Fessi, H. (2004) Enhancement of topical delivery from biodegradable nanoparticles. *Pharm. Res. 21*, 1818−1825.

(6) Luengo, J., Weiss, B., Schneider, M., Ehlers, A., Stracke, F., Konig, K., Kostka, K. H., Lehr, C. M., and Schaefer, U. F. (2006) Influence of nanoencapsulation on human skin transport of flufenamic acid. *Skin Pharmacol. Physiol. 19*, 190−197.

(7) Shim, J., Seok, Kang, H., Park, W. S., Han, S. H., Kim, J., and Chang, I. S. (2004) Transdermal delivery of mixnoxidil with block copolymer nanoparticles. *J. Controlled Release 97*, 477−484.

(8) Simeonova, M., Velichkova, R., Ivanova, G., Enchev, V., and Abrahams, I. (2003) Poly(butylcyanoacrylate) nanoparticles for topical delivery of 5-fluorouracil. *Int. J. Pharm. 263*, 133−140.

(9) Stracke, F., Weiss, B., Lehr, C. M., Konig, K., Schaefer, U. F., and Schneider, M. (2006) Multiphoton microscopy for the investigation of dermal penetration of nanoparticle-borne drugs. *J. Invest. Dermatol. 126*, 2244−2233.

(10) Lamprecht, A., Schaefer, U. F., and Lehr, C. M. (2001) Size-dependent bioadhesion of micro- and nanoparticulate carriers to the inflamed colonic mucosa. *Pharm. Res. 18*, 788−793.

(11) Borges, O., Borchard, G., Verhoef, J. C., de Sousa, A., and Junginger, H. E. (2005) Preparation of coated nanoparticles for a new mucosal vaccine delivery system. *Int. J. Pharm. 299*, 155−166.

(12) Shakweh, M., Besnard, M., Nicolas, V., and Fattal, E. (2005) Poly (lactide-co-glycolide) particles of different physicochemical properties and their uptake by peyer's patches in mice. *Eur. J. Pharm. Biopharm. 61*, 1−13.

(13) Weiss, B., Schaefer, U. F., Zapp, J., Lamprecht, A., Stallmach, A., and Lehr, C.-M. (2006) Nanoparticles made of fluorescence-labelled PLGA: preparation, stability and biocompatibility. *J. Nanosci. Nanotechnol. 6*, 3048−3056.
(14) Bala, I., Hariharan, S., and Kumar, M. N. (2004) PLGA nanoparticles in drug delivery: the state of the art. *Crit. Rev. Ther. Drug Carrier Syst. 21*, 387−422.
(15) Jain, R. A. (2000) The manufacturing techniques of various drug loaded biodegradable poly(lactide-co-glycolide) (PLGA) devices. *Biomaterials 21*, 2475−2490.
(16) Bilati, U., Allemann, E., and Doelker, E. (2005) Poly(D,L-lactide-co-glycolide) protein-loaded nanoparticles prepared by the double emulsion method−processing and formulation issues for enhanced entrapment efficiency. *J. Microencapsulation 22*, 205−214.
(17) Higaki, M., Ishihara, T., Izumo, N., Takatsu, M., and Mizushima, Y. (2005) Treatment of experimental arthritis with poly(D,L-lactic/glycolic acid) nanoparticles encapsulating betamethasone sodium phosphate. *Ann. Rheum. Dis. 64*, 1132−1136.
(18) Horisawa, E., Kubota, K., Tuboi, I., Sato, K., Yamamoto, H., Takeuchi, H., and Kawashima, Y. (2002) Size-dependency of D,L-lactide/glycolide copolymer particulates for intra-articular delivery system on phagocytosis in rat synovium. *Pharm. Res. 19*, 132−139.
(19) Kristl, A., Allemann, E., and Gurny, R. (1996) Formulation and evaluation of zinc phthalocyanine-loaded poly(D,L-lactic acid) nanoparticles. *Acta Pharm. 46*, 1−12.
(20) McClean (1998) Binding and uptake of biodegradable poly-D,L-lactide micro- and nanoparticles in intestinal epithelia. *Eur. J. Pharm. Sci. 6*, 153−163.
(21) Nobs, L., Buchegger, F., Gurny, R., and Allemann, E. (2004) Poly(lactic acid) nanoparticles labeled with biologically active Neutravidin for active targeting. *Eur. J. Pharm. Biopharm. 58*, 483−490.
(22) Shenoy, D., Little, S., Langer, R., and Amiji, M. (2005) Poly(ethylene oxide)-modified poly(beta-amino ester) nanoparticles as a pH-sensitive system for tumor-targeted delivery of hydrophobic drugs: part 2. In vivo distribution and tumor localization studies. *Pharm. Res. 22*, 2107−2114.
(23) Duan, Y., Sun, X., Gong, T., Wang, Q., and Zhang, Z. (2006) Preparation of DHAQ-loaded mPEG-PLGA-mPEG nanoparticles and evaluation of drug release behaviors in vitro/in vivo. *J. Mater. Sci.: Mater. Med. 17*, 509−516.
(24) Lescure, F., Seguin, C., Breton, P., Bourrinet, P., Roy, D., and Couvreur, P. (1994) Preparation and characterization of novel poly(methylidene malonate 2.1.2.)-made nanoparticles. *Pharm. Res. 11*, 1270−1277.
(25) Akagi, T., Higashi, M., Kaneko, T., Kida, T., and Akashi, M. (2006) Hydrolytic and enzymatic degradation of nanoparticles based on amphiphilic poly(gamma-glutamic acid)-graft-L-phenylalanine copolymers. *Biomacromolecules 7*, 297−303.
(26) Farokhzad, O. C., Cheng, J., Teply, B. A., Sherifi, I., Jon, S., Kantoff, P. W., Richie, J. P., and Langer, R. (2006) Targeted nanoparticle-aptamer bioconjugates for cancer chemotherapy in vivo. *Proc. Natl. Acad. Sci. U.S.A. 103*, 6315−6320.
(27) Dong, Y., and Feng, S. S. (2006) Nanoparticles of poly(D,L-lactide)/methoxy poly(ethylene glycol)-poly(D,L-lactide) blends for controlled release of paclitaxel. *J. Biomed. Mater. Res., Part A 78*, 12−19.
(28) Lee, C. T., Huang, C. P., and Lee, Y. D. (2007) Synthesis and characterizations of amphiphilic poly(l-lactide)-grafted chondroitin sulfate copolymer and its application as drug carrier. *Biomol. Eng. 24*, 131−139.
(29) Ahlin, P., Kristl, J., Kristl, A., and Vrecer, F. (2002) Investigation of polymeric nanoparticles as carriers of enalaprilat for oral administration. *Int. J. Pharm. 239*, 113−120.
(30) Ubrich, N., Bouillot, P., Pellerin, C., Hoffman, M., and Maincent, P. (2004) Preparation and characterization of propranolol hydrochloride nanoparticles: a comparative study. *J. Controlled Release 97*, 291−300.
(31) Yoo, H. S., Oh, J. E., Lee, K. H., and Park, T. G. (1999) Biodegradable nanoparticles containing doxorubicin-PLGA conjugate for sustained release. *Pharm. Res. 16*, 1114−1118.
(32) Polakovic, M., Gorner, T., Gref, R., and Dellacherie, E. (1999) Lidocaine loaded biodegradable nanospheres. II. Modelling of drug release. *J. Controlled Release 60*, 169−177.
(33) Raghuvanshi, R. S., Katare, Y. K., Lalwani, K., Ali, M. M., Singh, O., and Panda, A. K. (2002) Improved immune response from biodegradable polymer particles entrapping tetanus toxoid by use of different immunization protocol and adjuvants. *Int. J. Pharm. 245*, 109−121.
(34) Zambaux, M. F., Bonneaux, F., Gref, R., Dellacherie, E., and Vigneron, C. (1999) Preparation and characterization of protein C-loaded PLA nanoparticles. *J. Controlled Release 60*, 179−188.
(35) Sanchez, A., Tobio, M., Gonzalez, L., Fabra, A., and Alonso, M. J. (2003) Biodegradable micro- and nanoparticles as long-term delivery vehicles for interferon-alpha. *Eur. J. Pharm. Sci. 18*, 221−229.
(36) Dinauer, N., Balthasar, S., Weber, C., Kreuter, J., Langer, K., and von Briesen, H. (2005) Selective targeting of antibody-conjugated nanoparticles to leukemic cells and primary T-lymphocytes. *Biomaterials 26*, 5898−5906.
(37) Gupta, P. N., Mahor, S., Rawat, A., Khatri, K., Goyal, A., and Vyas, S. P. (2006) Lectin anchored stabilized biodegradable nanoparticles for oral immunization 1. Development and in vitro evaluation. *Int. J. Pharm. 318*, 163−173.
(38) Weissenbock, A., Wirth, M., and Gabor, F. (2004) WGA-grafted PLGA-nanospheres: preparation and association with Caco-2 single cells. *J. Controlled Release 99*, 383−392.
(39) Tosi, G., Rivasi, F., Gandolfi, F., Costantino, L., Vandelli, M. A., and Forni, F. (2005) Conjugated poly(D,L-lactide-co-glycolide) for the preparation of in vivo detectable nanoparticles. *Biomaterials 26*, 4189−4195.
(40) Ben-Shabat, S., Kumar, N., and Domb, A. J. (2006) PEG-PLA block copolymer as potential drug carrier: preparation and characterization. *Macromol. Biosci. 6*, 1019−1025.
(41) Salem, A. K., Cannizzaro, S. M., Davies, M. C., Tendler, S. J., Roberts, C. J., Williams, P. M., and Shakesheff, K. M. (2001) Synthesis and characterisation of a degradable poly(lactic acid)-poly(ethylene glycol) copolymer with biotinylated end groups. *Biomacromolecules 2*, 575−580.
(42) Gref, R., Couvreur, P., Barratt, G., and Mysiakine, E. (2003) Surface-engineered nanoparticles for multiple ligand coupling. *Biomaterials 24*, 4529−4537.
(43) Green, N. M. (1975) Avidin. *Adv. Protein Chem. 29*, 85−133.
(44) Green, N. M. (1990) Avidin and streptavidin. *Methods Enzymol. 184*, 51−67.
(45) Quintanar-Guerrero, D., Fessi, H., Allemann, E., and Doelker, E. (1996) Influence of stabilizing agents and preparative variables on the formation of poly(D,L-lactic acid)nanoparticles by an emulsification-diffusion technique. *Int. J. Pharm. 143*, 133−141.
(46) Bradley, A. J., and Scott, M. D. (2004) Separation and purification of methoxypoly(ethylene glycol) grafted red blood cells via two-phase partitioning. *J. Chromatogr., B: Anal. Technol. Biomed. Life Sci. 807*, 163−168.
(47) Rayle, H., and Fellmeth, L. (1999) Development of a process for triazine-promoted amidation of carboxylic acids. *Org. Process Res. Dev. 3*, 172−176.
(48) Moghimi, S. M. (2002) Chemical camouflage of nanospheres with a poorly reactive surface: towards development of stealth and target-specific nanocarriers. *Biochim. Biophys. Acta 1590*, 131−139.
(49) Pugliese, L., Coda, A., Malcovati, M., and Bolognesi, M. (1993) Three-dimensional structure of the tetragonal crystal form of egg-white avidin in its functional complex with biotin at 2.7 Å resolution. *J. Mol. Biol. 231*, 698−710.
(50) Cannizzaro, S. M., Padera, R. F., Langer, R., Rogers, R. A., Black, F. E., Davies, M. C., Tendler, S. J., and Shakesheff, K. M. (1998) A novel biotinylated degradable polymer for cell-interactive applications. *Biotechnol. Bioeng. 58*, 529−535.
(51) *Avidin and NeutrAvidin biotin-binding proteins and conjugates* (2002) Molecular Probes, Eugene, OR; http://probes.invitrogen.com/media/pis/mp000887.pdf.
(52) Weissenboeck, A., Bogner, E., Wirth, M., and Gabor, F. (2004) Binding and uptake of wheat germ agglutinin-grafted PLGA-nanospheres by caco-2 monolayers. *Pharm. Res. 21*, 1917−1923.
(53) Saxena, V., Sadoqi, M., and Shao, J. (2004) Indocyanine green-loaded biodegradable nanoparticles: preparation, physicochemical characterization and in vitro release. *Int. J. Pharm. 278*, 293−301.
(54) Laitinen, O. H., Nordlund, H. R., Hytonen, V. P., Uotila, S. T., Marttila, A. T., Savolainen, J., Airenne, K. J., Livnah, O., Bayer, E.

A., Wilchek, M., and Kulomaa, M. S. (2003) Rational design of an active avidin monomer. *J. Biol. Chem. 278*, 4010−4014.
(55) Qureshi, M. H., Yeung, J. C., Wu, S. C., and Wong, S. L. (2001) Development and characterization of a series of soluble tetrameric and monomeric streptavidin muteins with differential biotin binding affinities. *J. Biol. Chem. 276*, 46422−46428.
(56) Howarth, M., Chinnapen, D. J., Gerrow, K., Dorrestein, P. C., Grandy, M. R., Kelleher, N. L., El-Husseini, A., and Ting, A. Y. (2006) A monovalent streptavidin with a single femtomolar biotin binding site. *Nat. Methods 3*, 267−273.

BC060342F

Biodelivery of a Fullerene Derivative

Bogdan Belgorodsky, Ludmila Fadeev, Jenny Kolsenik, and Michael Gozin*

School of Chemistry, Raymond and Beverly Sackler Faculty of Exact Sciences, Tel Aviv University, Tel Aviv 69978, Israel.
Received November 21, 2006; Revised Manuscript Received March 29, 2007

Most current nanotoxicology research is focused on examining the influence of nanomaterials at the tissue and cellular levels. To explore these interactions on the molecular level, new carboxyfullerenes interact with transport proteins at the molecular level. The carboxyfullerenes exhibited an unusual mode of binding outside the calyx of β-lactoglobulin (a typical representative of lipocalin family of barrier liquid proteins). The complexes were studied by various techniques, including mass spectrometry, UV/vis and circular dichroism spectroscopy, chromatographic methods, gel electrophoresis, and dynamic light scattering. The fullerene ligands were transferred from β-lactoglobulin to human serum albumin (a representative of a blood transport protein), thus providing a model of how fullerene-based nanomaterials interact with biomolecules and are transported in biological systems.

INTRODUCTION

During the past decade, research related to carbonaceous nanomaterials has increased, because these materials have potential in applications ranging from biosensor components (*1*, *2*) to therapeutics (*3*) to diagnostic agents (*4*). In this context, fullerenes and their derivatives have great potential because of their unique structural (*5*, *6*), physical (*7*, *8*), and chemical properties (*9*−*12*). Bioactivity of fullerenes has been demonstrated in antibacterial (*13*), neuroprotection (*14*), DNA cleavage (*15*, *16*), and apoptosis (*17*) assays.

Taking into account that fullerene industrial production approaches the scale of tens of tons per year (and may reach hundreds of tons in the future), human and environmental exposure to carbonaceous nanomaterials will undoubtedly increase. In a light of this prospect, studies have begun to appear in the literature addressing the toxicity of nanomaterials. Specifically, acute toxicity studies of nanocolloidal suspensions of C_{60} fullerene clusters (nanoC_{60}) in water have been performed on several environmentally relevant species, such as freshwater crustaceans and fish (*14*). Hughes and co-workers found that growth of prokaryotic cells is inhibited upon exposure to low concentrations of nanoC_{60} (*18*). Cytotoxicity of fullerene has been shown for both normal (*19*−*22*) and carcinogenic cells (*20*−*22*). West and co-workers reported that nanoC_{60} suspensions disrupt normal cellular function through lipid peroxidation (*21*). All these studies indicate the potential risk of uncontrolled exposure to our environment to fullerene-based nanomaterials.

Current knowledge of the toxicology of carbonaceous nanomaterials suggests that these materials may have adverse effects at their portals of entry into living organisms, particularly the respiratory and digestive systems and the skin (*23*). Most nanotoxicology research is focused on examining the influence of nanomaterials at the tissue and cellular levels, while interactions of carbon nanomaterials with native proteins, especially transport proteins, remain mostly unexplored. Only a few complexes of fullerene derivatives with proteins have been reported. This includes enzyme inhibition by fullerene-based compounds (*24*, *25*) and interactions with some other proteins such as a fullerene-specific antibody (*26*, *27*), lysozyme (*28*), cytochrome C (*29*), bovine and human serum albumins (*30*−*32*), and apomyoglobin (*33*, *34*). However, in most cases, the reported information provides only partial data on the structure and properties of these fullerene−protein complexes.

Our recent studies have been aimed at preparing novel complexes of fullerenes with transport proteins in an attempt to elucidate the structure and properties of these materials. These studies should lead to better understanding of the biodelivery of carbon nanomaterials. In the present study, we focused on lipocalins, a family of transport proteins present in serum, lymph, and barrier liquids, such as saliva and mucus. The lipocalins are a family of small secreted proteins, characterized by similarity in their tertiary structures and molecular recognition properties. These proteins bind to hydrophobic molecules (such as retinol) and to specific cell-surface receptors (to promote endocytosis) (*35*, *36*).

Bovine β-lactoglobulin (β-LG) is a typical representative of the lipocalin family of proteins and was selected as a model compound for the preparation of lipocalin−fullerene complexes. Here, we report preparation of complexes formed by interaction of β-LG with carboxyfullerene (CF) and structural characterization of these compounds. We then showed how a fullerene ligand could be transported to the human serum albumin (HSA) to model carbonaceous nanomaterial delivery from an epithelial liquid barrier protein to a major blood transport protein.

EXPERIMENTAL SECTION

Preparation and Separation of β-LG/CF Complexes. Carboxyfullerene was synthesized according to previously reported methods (*37*−*39*). Bovine β-lactoglobulin, fine chemicals, and solvents were purchased from Sigma-Aldrich. A solution of 4.0 mg of β-LG (1 equiv) in 2 mL of sodium phosphate buffer (20 mM, pH 7.2) and 4, 10, 20, or 40 μL of 100 mM CF in DMSO (2, 5, or 10 equiv, respectively) was incubated for 2 h at 37 °C and then overnight at 10 °C. Additional incubations were prepared in phosphate buffer (20 mM) at pH 6.2 and pH 8.2 at the same concentrations. The complexes were separated from noncomplexed CF on a Sephadex G-25 gel permeation column (Pharmacia Biotech) with sodium phosphate buffer (20 mM, pH 7.2). No differences in the extent of complexation were found among incubations with β-LG A, β-LG B, or a mixture of these proteins; therefore, the latter was used in our further studies.

The buffer concentration was reduced by reloading the complex-containing fraction on a second Sephadex G-25 column

* Corresponding author: Telephone: +972-3-6405878. Fax: +972-3-6405879. E-mail: cogozin@mgchem.tau.ac.il.

10.1021/bc060363+ CCC: $37.00 © 2007 American Chemical Society
Published on Web 06/09/2007

and eluting the complex with sodium phosphate buffer (1 mM, pH 7.2). The resulting solution was lyophilized for storage and further experiments. After reconstitution in water, the concentration of complex in solution was determined by UV−vis spectroscopy and a BioRad protein assay (BioRad).

Liquid Chromatography. All HPLC analyses were performed on an Agilent 1100 chromatograph equipped with diode-array detector (Agilent). Size-exclusion liquid chromatography of β-LG, CF, and β-LG/CF complexes was performed on a 4.6 mm × 3.0 cm TSK-gel Super SW2000 column (Tosoh Bioscience) using a sodium phosphate/sodium chloride buffer (100 mM sodium phosphate, pH 7.2, and 100 mM sodium chloride) as the isocratic eluent at a flow rate of 0.2 mL/min.

Ion exchange chromatography analyses of starting materials and incubated mixtures were performed on an SP Sepharose column (HiTrap SP FF, Amersham Biosciences) using sodium phosphate/citric acid (20 mM, pH 4.2) as the starting buffer and sodium phosphate/citric acid/sodium chloride (100 mM sodium phosphate, pH 7.2, and 400 mM sodium chloride) as the elution buffer. A total of 72 fractions (200 μL each) were collected on a Costar UV 96-well plate (Corning), and absorption of each fraction was analyzed by a microplate reader (SpectraMax M2, Molecular Devices) at 280 and 485 nm.

Mass Spectrometry. Mass spectrometric analyses were performed on a Finnigan LCQ Classic ion-trap mass spectrometer (Finnigan) equipped with a standard ESI source. The ESI source was operated at 3.5 kV, and the capillary was set to 150 °C and 50 V. Raw data were processed using *ZNova ProMass* version 1.4 software (Novatia).

Dynamic Light Scattering. Particle sizing was performed at 25 °C using a high-performance particle size analyzer ALV-NIBS/HPPS (ALV-Laser Vertriebsgesellschaft). Freshly prepared solutions of β-LG, CF, and β-LG/CF complex in sodium phosphate buffer (20 mM, pH 7.2) were filtered through a 0.2 μm filter. In all experiments, a final concentration of 100 μM protein was used. The particle size was calculated by the autocorrelation function of the ALV sizer software.

Circular Dichroism. Circular dichroism measurements were performed on a spectrophotometer equipped with a temperature-controlled cell holder (202 Model, Aviv Biomedical). Spectra of protein samples (2 μM) dissolved in a sodium phosphate buffer (20 mM, pH 7.2) were recorded at room temperature in the 190−400 nm spectral range (in 1 nm steps); each spectrum (averaged over 10 scans) was corrected according to the appropriate blank.

Docking Studies. The three-dimensional structure of the β-LG protein was obtained from Protein Data Bank (1BEB). A three-dimensional structure of CF was obtained from Hartee-Fock energy-minimization calculations (*Gaussian 03*, Gaussian.com). Molecular docking calculations were performed using the PatchDock algorithm (*40*, *41*). In order to estimate the CF binding site on β-LG, the PatchDock algorithm was applied without any a priori data to indicate putative CF binding sites.

RESULTS AND DISCUSSION

***β*-LG/CF Complexes Preparation.** A series of incubations of native β-LG A, β-LGB, or a mixture of these proteins was performed with different amounts of CF ligand (under various pH conditions and salt concentrations). Using the analytical methods described below, all these experiments produced very similar results and showed the formation of stable β-LG/CF complexes.

Size Exclusion Chromatography. Analyses of the β-LG/CF complexes were performed by high-performance, size exclusion liquid chromatography (SEC-HPLC) coupled to a diode array UV−vis detector. Figure 1 presents chromatograms of the CF ligand, the β-LG protein, and the β-LG/CF complex.

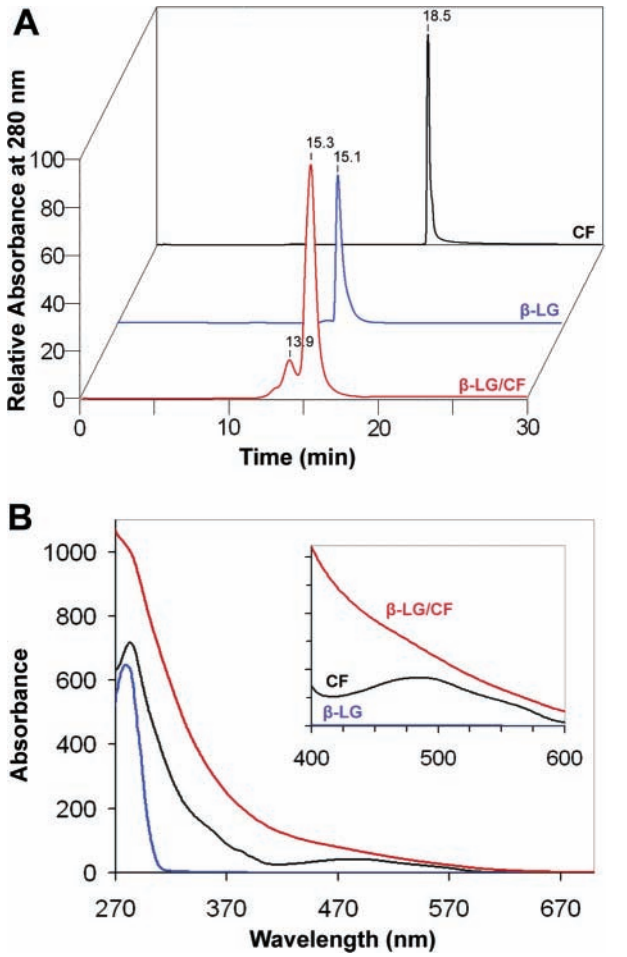


Figure 1. (A) Size exclusion chromatograms (monitored at 280 nm): blue, β-LG protein; red, β-LG/CF complex; black, unbound CF ligand. (B) Corresponding UV−vis spectra obtained using a diode array detector: blue, β-LG protein; red, β-LG/CF complex; black, unbound CF ligand.

Table 1. CF Content (equivalents) in β-LG/CF Complexes

incubation ratio [β-LG]:[CF]	ratio of [CF]:[β-LG] in β-LG/CF complex		
	pH 7.2	pH 6.2	pH 8.2
1:2	1:1.0	1:1.7	1:1.0
1:5	1:1.9	1:2.9	1:2.0
1:10	1:2.6	1:3.2	1:2.8

These size exclusion chromatograms clearly show that under our elution conditions the retention time of the proposed β-LG/CF complex (RT = 15.3 min) closely matched that of the free β-LG host (RT = 15.1 min), unambiguously showing very similar sizes of both molecules.

Determination of CF Ligand Binding Stoichiometry. Different host-to-ligand ratios were present in the β-LG/CF complexes. Protein-to-ligand ratios were obtained from analyses of purified complexes prepared under various experimental conditions by comparing the amount of the CF ligand in a certain complex (determined at $\lambda_{max} = 485$ nm, $\epsilon = 4800$ M^{-1} cm^{-1}) to the amount of β-LG protein in the same complex (determined by the BioRad protein assay). Our quantitative analyses of complexes showed that these complexes contained up to three bound CF ligands per a single β-LG host, depending on the amount of the CF ligand used in complexes preparation (Table 1). These unusually high binding ratios between the β-LG host and the CF ligand are in contrast to the typical binding mode of this protein, in which a calix hydrophobic cavity functions

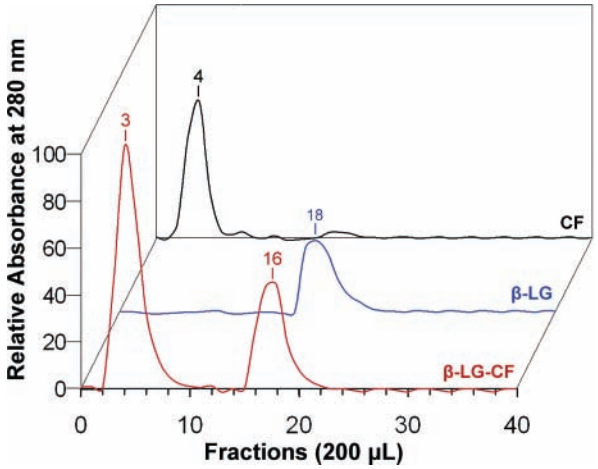


Figure 2. Ion-exchange chromatograms (monitored at 280 nm): blue, β-LG protein; red, β-LG/CF complex; black, unbound CF ligand.

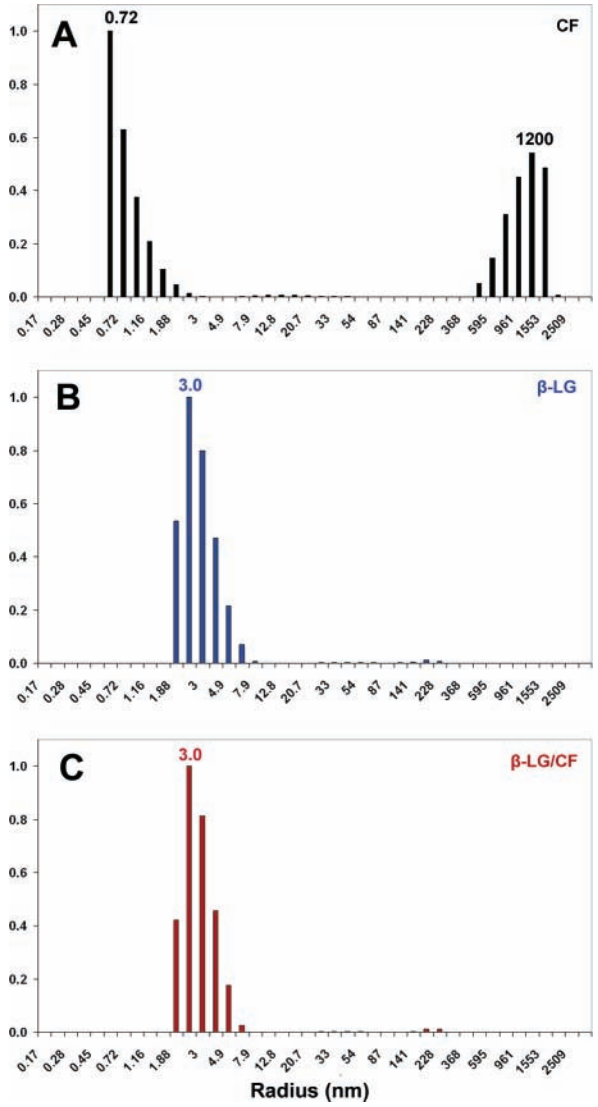


Figure 3. DLS analyses. (A) Unbound CF ligand. (B) Dimer of β-LG protein. (C) β-LG/CF complex.

as a single binding site for ligand (*35*). This observation suggests that there are alternative sites for ligand binding or aggregates formation.

Ion Exchange Chromatography. We first explored the possibility that binding between CF and β-LG is stabilized through ionic interactions by analyzing the complexes by ion exchange chromatography (IEC); IEC should disrupt most ionic interactions. On IEC, the free β-LG protein and β-LG/CF complex were observed, unambiguously showing that the interactions between the CF ligand and the β-LG host are mostly hydrophobic. There was only a small difference in retention time between complex and free protein. This could be explained by small differences in the overall charge of the free host versus the complex, as the latter contains more carboxylic groups (Figure 2).

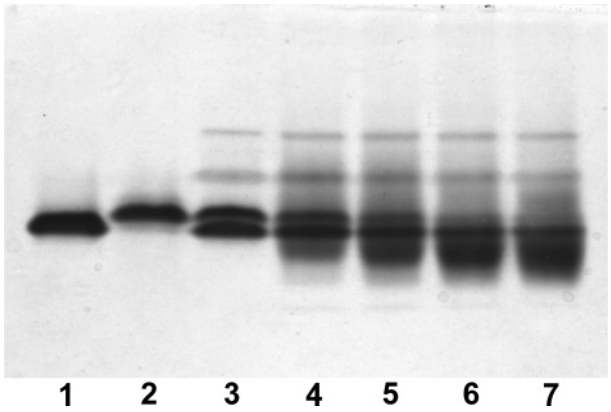


Figure 4. Native polyacrylamide gel electrophoresis of β-LG/CF complexes. Lanes contain (1) β-LG A; (2) β-LG B; (3) β-LG A/β-LG B mixture; β-LG/CF at ratios of (4) 1:2, (5) 1:5, (6) 1:10, and (7) 1:20.

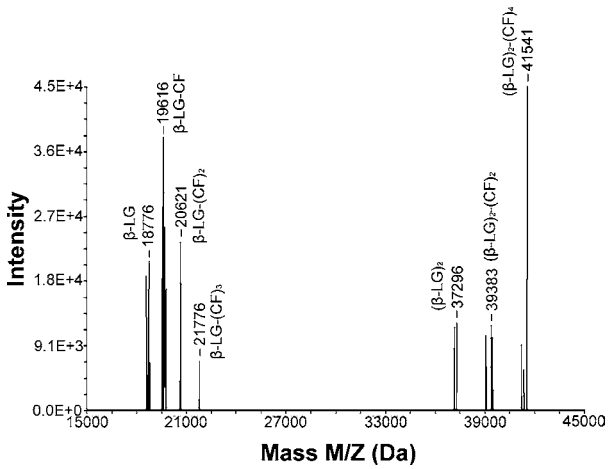


Figure 5. Deconvoluted ESI-mass spectra of β-LG/CF complex.

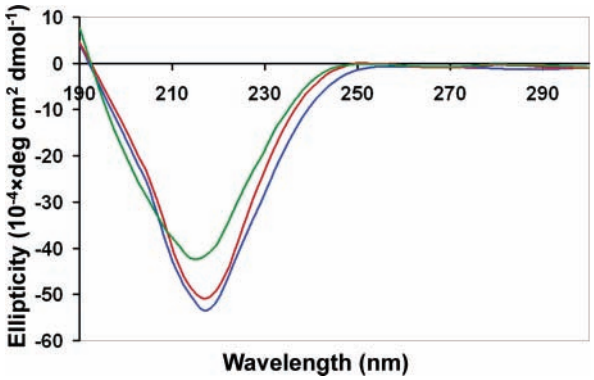


Figure 6. Circular dichroism spectra of β-LG protein (blue) and β-LG/CF mixtures in ratios of 1:5 (red) and 1:20 (green).

Dynamic Light Scattering. Our next step was to exclude the possibility of nonspecific binding of β-LG protein to clusters formed by CF molecules (*42*). We performed dynamic light scattering (DLS) experiments, examining aqueous solutions of the CF ligand, the free β-LG protein, and the purified β-LG/CF complex. In aqueous solution, we observed two populations

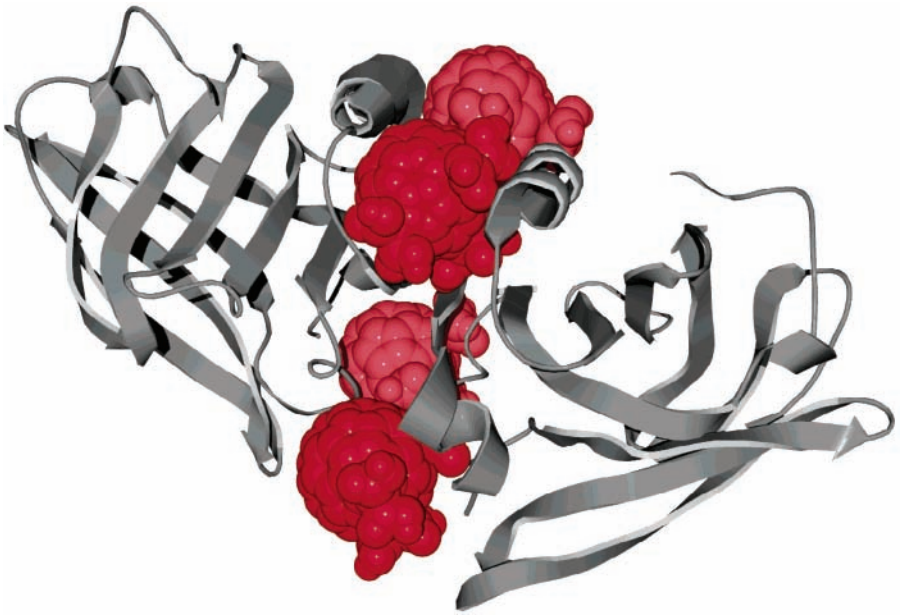


Figure 7. Representative, high-score docking model of the β-LG/CF complex; the β-LG dimer is shown as a ribbon model (gray) and the four CF ligands as space-filling models (red).

of CF particles with average sizes of 1 and 1200 nm (broadly distributed), corresponding to single CF molecules and large CF clusters, respectively (Figure 3A). In solutions of the free β-LG protein and the purified β-LG/CF complex, only one type of CF species was observed with an average size of 3 nm (Figure 3B,C). The latter results are in excellent agreement with the approximately 3.5 nm size structure reported for β-LG dimer (PDB: 1BEB) (*43*). The DLS experiment results suggest that a process of β-LG−CF complex formation proceeds through CF clusters dissolution by β-LG protein and may represent a mechanism by which fullerene nanoclusters undergo an uptake into biological systems.

Gel Electrophoresis. Native polyacrylamide gel electrophoresis (PAGE) was used as an additional technique to examine the size, the overall charge, and the stability of the β-LG/CF complexes. The PAGE results showed progressive disappearance of bands of the free protein and appearance of diffuse bands with that migrated more rapidly through the gel than free protein, corresponding to complexes, as the concentration of CF increased (Figure 4). The faster mobility of β-LG/CF complexes probably results from a larger number of the incorporated CF ligands, producing compounds with higher overall negative charge, but similar size to native proteins, as shown in the DLS experiments.

Mass Spectrometry. Electrospray mass spectrometry (ESI-MS) analysis of a representative purified β-LG/CF complex was performed. The deconvoluted ESI-MS spectrum of this material (Figure 5) revealed the presence of a β-LG dimer bound to up to four CF ligands and additional peaks corresponding to β-LG/CF complexes with 1:3 binding stoichiometry. These β-LG/CF complexes had remarkable stability, as most noncovalent protein complexes do not remain intact under these mass spectrometry conditions. Notably, these results are in agreement with the data obtained by UV−vis spectroscopy and the stoichiometry determination previously described (Table 1), which showed 1:2.8 protein-to-ligand ratio for the same complex.

Circular Dichroism. To assess the structural features of these complexes, we explored whether the β-LG protein remains folded close to its native conformation in the β-LG/CF complex. For these purposes, circular dichroism (CD) spectroscopy studies of β-LG/CF complexes were performed. All the measured CD spectra of these complexes exhibited a typical negative peak with a minimum around 215 nm, as previously reported for β-LG (*44*). A series of complexes in which the ratio between β-LG and CF was progressively increased were evaluated. The ellipticity of the complex noticeably decreased upon addition of 20 excess equivalents of the CF ligand (Figure 6). These results strongly suggest that the native structure of the β-LG protein is only slightly affected (mostly in α-helix regions) by binding of CF, even when multiple CF ligands are bound.

Docking Studies. To explore possible CF-binding sites on the β-LG dimer interface, docking calculations were performed using the dimer (PDB: 1BEB) structure of β-LG (*40*, *41*). In our models, the first CF unit was located in the interface formed between β-LG monomers, near the α-helix (Figure 7). The resulting structure was used as a basis for further docking experiments as more CF units were added in each round of calculations, producing a model in which four ligands bound near the dimerization site (Figure 7). These docking results are strongly supported by experimental observations; we found that CF binding by β-LG was unaffected by changes in pH conditions and therefore nonrelated to the Tanford transition (*45*), as the Tanford transition involves pH-dependent movement of EF loop, controlling the entry to β-LG's calyx binding site. Moreover, in good correlation with CD results, docking studies showed interactions between CF units and the main α-helices of β-LG dimer, located near the dimerization site.

Delivery of CF from the β-LG/CF Complex to HSA. Nanomaterials can enter the human body through different ports, including lungs and intestines, and then undergo rapid translocation through the bloodstream to other vital organs (*23*). The pharmacokinetic behavior of different types of nanoparticles requires detailed investigation, starting at the molecular biochemical level. For the first time, we were able to monitor the transport of nanomaterial between two biochemical systems: CF dissociated from the β-LG/CF complex, where β-LG represented a barrier liquid protein, and bound to a blood plasma protein (represented by HSA). Specifically, 25 μM β-LG/CF complex (at a 1:3 ratio) was incubated with 25 μM HSA protein in phosphate buffer (20 mM, pH 7.2). Transport of CF ligand from the β-LG/CF complex to HSA was monitored by SEC-HPLC (Figure 8), using the previously described HSA-CF complex as a reference standard (*31*). At 485 nm, the noncomplexed proteins exhibited almost no absorbance (dark blue

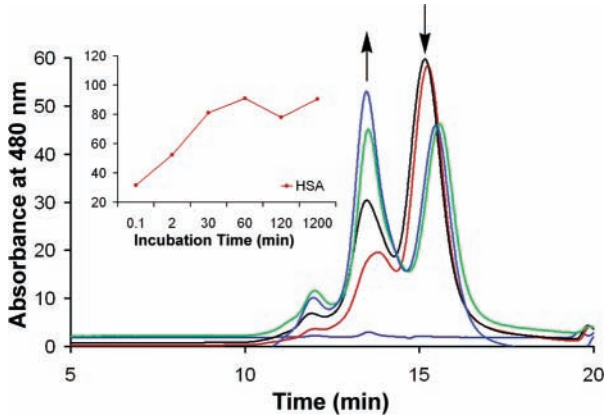


Figure 8. Delivery of CF ligand from β-LG/CF complex to HSA, monitored by size exclusion chromatography (at 485 nm). Dark blue, HSA and β-LG proteins without CF; red, after incubation of 0.1 min; black, 2 min; green, 120 min; light blue, 1200 min. Inset: time-dependent changes in relative fullerene content in HSA-CF complexes during CF delivery process.

chromatogram; Figure 8), thus allowing us to detect only CF-containing compounds. As expected, the larger-size HSA-CF complex eluted with a shorter retention time than β-LG/CF (13.6 and 15.3 min, respectively). CF uptake by HSA was clearly observed even at the beginning of the process (after only 0.1 min incubation, red chromatogram; Figure 8). Over the time course, the intensity of the peak at 13.6 min gradually increased, while the peak at 15.3 min decreased (insert, Figure 8). The HSA-CF complex in these experiments was spectroscopically and chromatographically identical to the previously reported HSA-CF (1:1 protein-to-ligand) complex (*31*). The observed process of CF transfer from β-LG/CF to HSA is very rapid, which could be explained by significant differences in CF affinity toward these proteins. The HSA-CF complex has a relatively high binding constant of 1.2×10^7 M^{-1} as determined by fluorescence titration (*31*). A binding constant for CF to β-LG could not be precisely determined due to the presence of multiple competing binding sites (see Supporting Information). After 60 min of incubation, CF uptake by HSA reached a maximum. However, it is expected that, in the real world, the amount of serum albumin protein will be far greater than the amount of lipocalin, thus leading to more complete ligand depletion in β-LG/CF complex.

CONCLUSIONS

The characterization of the complex formed by CF and β-LG reported here provides insight into how fullerene-based nanomaterials interact with native liquid barrier proteins. Capable of multiple carbonaceous ligand binding, a representative lipocalin protein, β-lactoglobulin, bound efficiently to carboxyfullerene. Moreover, we provide the first example of transfer of CF from one protein, β-lactoglobulin, to another, albumin, in a model of the delivery process of nanomaterials in biological systems.

ACKNOWLEDGMENT

The authors thank the Israeli Science Foundation for their generous financial support.

Supporting Information Available: Addtional experimental details. This material is available free of charge via the Internet at http://pubs.acs.org.

LITERATURE CITED

(1) Katz, E., and Willner, I. (2004) Nanobiotechnology: integrated nanoparticle-biomolecule hybrid systems: Synthesis, properties, and applications. *Angew. Chem., Int. Ed. 43*, 6042−6108.
(2) Bakker, E., and Qin, Y. (2006) Electrochemical sensors. *Anal. Chem. 78*, 3965−3984.
(3) Da Ros, T., and Prato, M. (1999) Medicinal chemistry with fullerenes and fullerene derivatives. *Chem. Commun. 8*, 663−669.
(4) Bosi, S., Da Ros, T., Spalluto, G., and Prato, M. (2003) Fullerene derivatives: an attractive tool for biological applications. *Eur. J. Med. Chem. 38*, 913−923.
(5) Kroto, H. W., Heath, J. R., O'Brien, S. C., Curl, R. F., and Smalley, R. E. (1985) C60: buckminsterfullerene. *Nature (London) 318*, 162−163.
(6) Kraetschmer, W., Lamb, L. D., Fostiropoulos, K., and Huffman, D., R. (1990) Solid C60: a new form of carbon. *Nature (London) 347*, 354−358.
(7) Guldi, D. M., and Martin, N. (2002) *Fullerenes: From Synthesis to Optoelectronic Properties*. Kluwer Academic Publishers, Dordrecht.
(8) Guldi, D. M., and Prato, M. (2000) Excited-state properties of C_{60} fullerene derivatives. *Acc. Chem. Res. 33*, 695−703.
(9) Birkett, P. R. (2006) Fullerenes. *Annu. Rep. Prog. Chem., Sect. A: Inorg. Chem. 102*, 420−448.
(10) Hirsch, A. (1994) *Chemistry of the fullerenes*. Thieme, Stuttgart.
(11) Diederich, F., and Kessinger, R. (2000) Regio- and stereoselective multiple functionalization of fullerenes. *Templated Org. Synth.* 189−218.
(12) Nakamura, E., and Isobe, H. (2003) Functionalized fullerenes in water. The first 10 years of their chemistry, biology, and nanoscience. *Acc. Chem. Res. 36*, 807−815.
(13) Mashino, T., Nishikawa, D., Takahashi, K., Usui, N., Yamori, T., Seki, M., Endo, T., and Mochizuki, M. (2003) Antibacterial and antiproliferative activity of cationic fullerene derivatives. *Bioorg. Med. Chem. Lett. 13*, 4395−4397.
(14) Ali, S. S., Hardt, J. I., Quick, K. L., Sook K.-Han, J., Erlanger, B. F., Huang, T.-T., Epstein, C. J., and Dugan, L. L. (2004) A biologically effective fullerene (C60) derivative with superoxide dismutase mimetic properties. *Free Radical Biol. Med. 37*, 1191−1202.
(15) Da Ros, T., Spalluto, G., Boutorine, A., and Prato, M. (2001) Fullerene derivatives as potential DNA photoprobes. *Aus. J. Chem. 54*, 223−224.
(16) Ikeda, A., Ejima, A., Nishiguchi, K., Kikuchi, J.-I., Matsumoto, T., Hatano, T., Shinkai, S., and Goto, M. (2005) DNA-photo-cleaving activities of water-soluble carbohydrate-containing non-ionic homooxacalix[3]arene [60]fullerene complex. *Chem. Lett. 34*, 308−309.
(17) Fumelli, C., Marconi, A., Salvioli, S., Straface, E., Malorni, W., Offidani, A. M., Pellicciari, R., Schettini, G., Giannetti, A., Monti, D., Franceschi, C., and Pincelli, C. J. (2000) Carboxyfullerenes protect human keratinocytes from ultraviolet-B-induced apoptosis. *Invest. Dermatol. 115*, 835−841.
(18) Fortner, J. D., Lyon, D. Y., Sayers, C. M., Boyd, A. M., Falkner, J. C., Hotze, E. M., Alemany, L. B., Tao, Y. J., Guo, W., Ausman, K. D., Colvin, V. L., and Hughes, J. B. (2005) C60 in water: nanocrystal formation and microbial response. *Environ. Sci. Technol. 39*, 4307−4316.
(19) Jia, G., Wang, H., Yan, L., Wang, X., Pei, R., Yan, T., Zhao, Y., and Guo, X. (2005) Cytotoxicity of carbon nanomaterials: single-wall nanotube, multi-wall nanotube, and fullerene. *Environ. Sci. Technol. 39*, 1378−1383.
(20) Bosi, S., Feruglio, L., Da Ros, T., Spalluto, G., Gremoretti, B., Terdoslavich, M., Decorti, G., Passamonti, S., Moro, S., and Prato, M. (2004) Hemolytic effects of water-soluble fullerene derivatives. *J. Med. Chem. 47*, 6711−6715.
(21) Sayers, C. M., Gobin, A. M., Ausman, K. D., Mendez, J., West, J. L., and Colvin, V. L. (2005) Nano-C60 cytotoxicity is due to lipid peroxidation. *Biomaterials 26*, 7587−7595.
(22) Sayers, C. M., Fortner, J. D., Guo, W., Lyon, D., Boyd, A. M., Ausman, K. D., Tao, Y. J., Sitharaman, B., Wilson, L. J., Hughes, J. B., West, J. L., and Colvin, V. L. (2004) The differential cytotoxicity of water-soluble fullerenes. *Nano Lett. 4*, 1881−1887.
(23) Oberdorster, G., Oberdorster, E., and Oberdorster, J. (2005) Nanotoxicology: an emerging discipline evolving from studies of ultrafine particles. *Environ. Health Perspect. 113*, 823−839.
(24) Wolff, D. J., Barbieri, C. M., Richardson, C. F., Schuster, D. I., and Wilson, S. R. (2002) Trisamine C60-fullerene adducts inhibit neuronal nitric oxide synthase by acting as highly potent calmodulin antagonists. *Arch. Biochem. Biophys. 399*, 130−141.

(25) Mashino, T., Okuda, K., Hirota, T., Hirobe, M., Nagano, T., and Mochizuki, M. (2001) Inhibitory effect of fullerene derivatives on glutathione reductase. *Fullerene Sci. Technol. 9*, 191−196.
(26) Utz, N., and Koslowski, T. (2006) Charge transfer through a protein-nano junction. *J. Phys. Chem. B 110*, 9333−9338.
(27) Braden, B. C., Goldbaum, F. A., Chen, B.-X., Kirschner, A. N., Wilson, S. R., and Erlanger, B. F. (2000) X-ray crystal structure of an anti-Buckminsterfullerene antibody Fab fragment: biomolecular recognition of C60. *Proc. Nat. Acad. Sci. U.S.A. 97*, 12193−12197.
(28) Prabha, C. R., Patel, R., and Murthy, C. N. (2004) Studies on protein-[60]fullerene interactions: the lysozyme-c[60]fullerene model system. *Fullerenes, Nanotubes, Carbon Nanostruct. 12*, 405−412.
(29) Zilbermann, I., Lin, A., Hatzimarinaki, M., Hirsch, A., and Guldi, D. M. (2004) Electrostatically arranged cytochrome c-fullerene photoelectrodes. *Chem. Commun. 1*, 96−97.
(30) Laus, S., Sitharaman, B., Toth, E., Bolskar, R. D., Helm, L., Asokan, S., Wong, M. S., Wilson, L. J., and Merbach, A. E. (2005) Destroying gadofullerene aggregates by salt addition in aqueous solution of $Gd@C_{60}(OH)x$ and $Gd@C_{60}[C(COOH)_2]_{10}$. *J. Am. Chem. Soc. 127*, 9368−9369.
(31) Belgorodsky, B., Fadeev, L., Ittah, V., Benyamini, H., Zelner, S., Huppert, D., Kotlyar, A. B., and Gozin, M. (2005) Formation and characterization of stable human serum albumin-tris-malonic acid[C60]fullerene complex. *Bioconjugate Chem. 16*, 1058−1062.
(32) Belgorodsky, B., Fadeev, L., Kolsenik, J., and Gozin, M. (2006) Formation of a soluble stable complex between pristine C60-fullerene and a native blood protein. *ChemBioChem 11*, 1783−1789.
(33) Kolsenik, J., Belgorodsky, B., Fadeev, L., and Gozin, M. (2007) Can apomyoglobin form a complex with a spherical ligand? *J. Nanosci. Nanotechnol. 3*, 1−5.
(34) Kotelnikova, R. A., Bogdanov, G. N., Frog, E. C., Kotelnikov, A. I., Shtolko, V. N., Romanova, V. S., Andreev, S. M., Kushch, A. A., Fedorova, N. E., Medzhidova, A. A., and Miller, G. G. (2003) Nanobionics of pharmacologically active derivatives of fullerene C60. *J. Nanopart. Res. 5*, 561−566.
(35) Flower, D. R. (1996) The lipocalin protein family: structure and function. *Biochem. J. 318*, 1−14.
(36) Flower, D. R. (2000) Beyond the superfamily: the lipocalin receptors. *Biochim. Biophys. Acta 1482*, 327−336.
(37) Dugan, L. L., Turetsky, D. M., Du, C., Lobner, D., Wheeler, M., Almli, C. R., Shen, C. K. F., Luh, T.-Y., Choi, D. W., and Lin, T.-S. (1997) Carboxyfullerenes as neuroprotective agents. *Proc. Nat. Acad. Sci. U.S.A. 94*, 9434−9439.
(38) Foley, S., Curtis, A. D. M., Hirsch, A., Brettreich, M., Pelegrin, A., Seta, P., and Larroque, C. (2002) Interaction of a water soluble fullerene derivative with reactive oxygen species and model enzymatic systems. *Fullerenes, Nanotubes, Carbon Nanostruct. 10*, 49−67.
(39) Tsao, N., Luh, T.-Y., Chou, C.-K., Chang, T.-Y., Wu, J.-J., Liu, C.-C., and Lei, H.-Y. (2002) In vitro action of carboxyfullerene. *J. Antimicrob. Chemother. 49*, 641−649.
(40) Schneidman-Duhovny, D., Inbar, Y., Polak, V., Shatsky, M., Halperin, I., Benyamini, H., Barzilai, A., Dror, O., Haspel, N., Nussinov, R., and Wolfson, H. J. (2003) Taking geometry to its edge: fast unbound rigid (and hinge-bent) docking. *Proteins 52*, 107−112.
(41) Benyamini, H., Shulman-Peleg, A., Wolfson, H. J., Belgorodsky, B., Fadeev, L., and Gozin, M. (2006) Interaction of C60-fullerene and carboxyfullerene with proteins: docking and binding site alignment. *Bioconjugate Chem. 17*, 378−386.
(42) Sitharaman, B., Asokan, S., Rusakova, I., Wong, M. S., and Wilson, L. J. (2004) Nanoscale aggregation properties of neuroprotective carboxyfullerene (C3) in aqueous solutions. *Nano Lett. 4*, 1759−1762.
(43) Brownlow, S., Morais Cabral, J. H., Cooper, R., Flower, D. R., Yewdall, S. J., Polikarpov, I., North, A. C., and Sawyer, L. (1997) Bovine beta-lactoglobulin at 1.8 A resolution−still an enigmatic lipocalin. *Structure 5* (4), 481−495.
(44) Townend, R., Kumosinski, T. F., and Timasheff, S. N. (1967) The circular dichroism of variants of lactoglobulin. *J. Biol. Chem. 242*, 4538−4545.
(45) Ragona, L., Fogolari, F., Catalano, M., Ugolini, R., Zetta, L., and Molinaris, H. (2003) EF loop conformational change triggers ligand binding in β-lactoglobulins. *J. Biol. Chem. 287*, 38840−38846.

BC060363+

Synthesis and Evaluation of Bivalent NDP-α-MSH(7) Peptide Ligands for Binding to the Human Melanocortin Receptor 4 (hMC4R)

Heather L. Handl,[‡,§] Rajesh Sankaranarayanan,[†,§] Jatinder S. Josan,[†] Josef Vagner,[†] Eugene A. Mash,[†] Robert J. Gillies,[‡] and Victor J. Hruby*[,†]

Department of Chemistry, University of Arizona, Tucson, Arizona 85721, and Departments of Radiology, Biochemistry, and Molecular Biophysics, Arizona Cancer Center, Tucson, Arizona 85724. Received November 22, 2006; Revised Manuscript Received April 19, 2007

We demonstrate the potential utility of multivalent ligands as targeting agents for cancer imaging or therapy by determining the binding of homobivalent ligands to their corresponding receptors. This manuscript details the synthesis and evaluation of a series of bivalent ligands containing two copies of the truncated heptapeptide version of [Nle^4-D-Phe^7]-α-melanocyte stimulating hormone (NDP-α-MSH), referred to as MSH(7). These were connected with various semirigid linkers containing Pro-Gly repeats, with or without flexible poly(ethylene glycol) (PEGO) moieties at their termini. Modeling data suggest a distance of 20−50 Å between the ligand binding sites of two adjacent G-protein coupled receptors, GPCRs. These bivalent ligands were observed to bind with higher affinity compared to their monovalent counterparts. Data suggest these ligands may be capable of cross-linking adjacent receptors. An optimal linker length of 25 ± 10 Å, inferred from these ligands, correlated well with the inter-receptor distance estimated through modeling. Although there was no difference in maximal binding affinities between the ligands constructed with the Pro-Gly repeats versus those constructed with the PEGO inserts, the PEGO-containing ligands bound with high affinities over a greater range of linker lengths.

INTRODUCTION

Current cancer treatments suffer from a lack of specificity for cancer cells. Using peptide ligands for specific delivery of a drug or a contrast agent to the site of action has been demonstrated for a number of cancers using many different ligand−receptor pairs (*1*). However, a limitation of this approach is that targeting an individual receptor requires that it be overexpressed or mutated in the cancer and nowhere else in the body. While such target receptors may be available for some cancers, they are not widely prevalent. Hence, alternative targeting strategies are required. We hypothesize that specific targeting of cancer cells could be achieved through the development of multivalent ligands directed toward unique combinations of cell surface proteins that are expressed on the target cancer cells compared to normal cells. By targeting combinations, these ligands can be more specific for the cells of interest while circumventing nonspecific interaction with healthy tissues. As a proof of the concept that such cell surface proteins can indeed be targeted specifically, we chose to mimic the cancer cells through overexpression of MC4 receptors because of our considerable experience with MC4 receptors (*2, 3*). Thus, in order to demonstrate that multivalent peptide ligands bind to their target receptors with increased affinity and cooperativity, we have constructed ligands containing two copies of MSH(7),[1] a truncated version of [Nle^4-D-Phe^7]-α-melanocyte stimulating hormone (NDP-α-MSH) (*2*), a peptide hormone analogue that binds specifically to the melanocortin receptors. These two MSH(7) ligands are separated by a linker, which is constructed with different amino acids and/or organic derivatives in order to provide differences in flexibility and length.

Previously, we described the synthesis and evaluation of a series of short homobivalent MSH(4) His-D-Phe-Arg-Trp-NH_2 and MSH(6) Nle-Glu-His-D-Phe-Arg-Trp-NH_2 ligands which bind to cells expressing the human melanocortin 4 receptor (hMC4R) with increased affinity and apparent cooperativity compared to their monovalent counterparts (*3*). However, the linkers used in these studies were likely too short to allow for cross-linking of multiple receptors. Thus, the increased binding affinity and positive cooperativity observed in these studies were most likely due to "statistical" binding, wherein affinity is apparently increased through increased local concentrations, and not receptor "clustering", wherein multiple receptors are bound by the same multivalent ligand (*4*) (Figure 1). In order to improve the likelihood that multivalent ligands simultaneously cross-link receptors, we have constructed homobivalent MSH(7) ligands with linkers that are longer and more flexible than those previously investigated.

It has been documented that the hMC4 receptors can form homodimers (*5*) and that other melanocortin receptors can form

* Address correspondence to Prof. Victor J. Hruby, Regents Professor of Chemistry, Department of Chemistry, 1306, E. University, P.O. Box 210041, Department of Chemistry, University of Arizona, Tucson, Arizona 85721 USA; Phone (520) 621-6332; FAX (520) 621-8407. Email: hruby@u.arizona.edu.

† University of Arizona.

‡ Arizona Cancer Center.

§ H.L.H. and R.S. contributed equally to this work.

[1] Abbreviations: α-MSH, α-melanocyte stimulating hormone; NDP-α-MSH, Nle^4-D-Phe^7-α-melanocyte stimulating hormone; hMC4R, human melanocortin 4 receptor; Boc, *tert*-butyloxycarbonyl; BSA, bovine serum albumin; DMEM, Dulbecco's Modified Eagle Medium; ESI-MS, electrospray ionization-mass spectrometry; FBS, fetal bovine serum; Fmoc, 9-fluorenylmethyloxycarbonyl; FT-ICR, Fourier transform-Ion Cyclotron Resonance; GPCR, G-protein coupled receptor; HCTU, *O*-[1*H*-6-chlorobenzotriazol-1-yl)(dimethylamino)methylene]uranium hexafluorophosphate *N*-oxide; HOBt, 1-hydroxybenzotriazole; HOCt, 6-chloro-1-hydroxybenzotriazole; MALDI-TOF, matrix-assisted laser desorption ionization time-of-flight; MMFF, Merck molecular force field; MSH(7), des-{Ser^1-Tyr^2-Gly^{10}-Lys^{11}-Pro^{12}-Val^{13}}-Nle^4-D-Phe^7-α-melanocyte stimulating hormone; PEGO, 19-amino-5-oxo-3,10,13,-16-tetraoxa-6-azanonadecan-1-oic acid; Pbf, 2,2,4,6,7-pentamethyldihydrobenzofuran-5-yl sulfonyl; TFA, trifluoroacetyl; TRF, time-resolved fluorescence; Trt, triphenylmethyl (trityl).

10.1021/bc0603642 CCC: $37.00 © 2007 American Chemical Society
Published on Web 06/26/2007

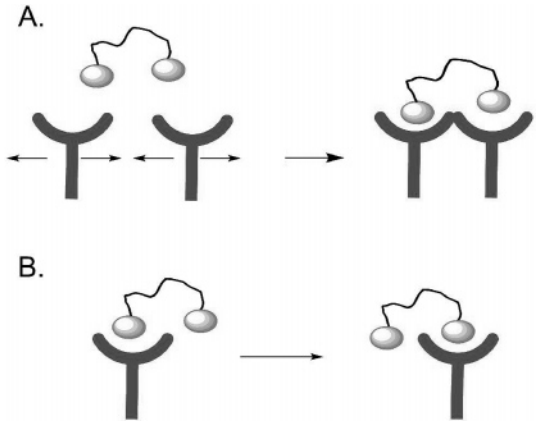


Figure 1. Two of the four potential modes of multivalent ligand binding. A. The *cluster effect* results in recruitment of receptors on the cell surface to allow for multiple receptor−ligand interactions. B. The *statistical effect* allows ligands to bind to single binding sites on a receptor based on increased local effective concentration of the ligand.

homo- or heterodimers (*6*). The lack of high-resolution data for G-protein coupled receptors (GPCRs) has made it difficult to elucidate the 3D structure of these receptors, thus further complicating the task of rationally designing multivalent ligands that could span the distance between adjacent GPCRs. Early estimates suggest that this distance is at least 40 Å (*7*−*9*). The crystal structure of rhodopsin (*10*) has made it possible to model the structures of additional members of the GPCR family of proteins based on computer-aided modeling by homology. For example, the human melanocortin 4 receptor (hMC4R) has been modeled on the basis of sequence homology and the known rhodopsin structure (*11*). This model was used to assist in the determination of the linker lengths needed to span the distance between adjacent GPCR binding sites.

In addition to difficulties in estimating the size and location of the receptor binding pockets, it is also relatively difficult to estimate the actual length of the linkers in question. This difficulty arises due to the fact that the peptide type linkages used to construct these linkers will be flexible, thus permitting folding and secondary structure. We used the estimation that one amino acid residue is roughly equivalent to 1.2 Å, an estimation based on the average linear distance between atoms in a peptide bond and the assumption that at least one conformer of these linkers can exist in a stretched conformation with little or no secondary structure (*12*). Upon binding, the linker may lose its folding to be stretched in extended conformations.

This manuscript details the construction and evaluation of a family of homobivalent MSH(7) ligands with linkers ranging in length from 18 to 148 atoms that could span distances over 100 Å (Table 1). A series of control ligands also were constructed in which MSH(7) was attached to only one end of the various linkers (ligands **1**−**5**, Table 1) to allow for a direct determination of the influence of the linker on the binding affinity of the ligand to the receptor. Pro-Gly repeats were chosen as the building blocks for the linker unit, as this semirigid construct provided the best results in our initial studies (*3*). The Pro residues add rigidity to the overall linker structure, while the Gly residues provide for some flexibility. Five bivalent ligands were synthesized with these Pro-Gly repeat regions (ligands **6**−**10**, Table 1) directly corresponding to the monovalent ligands. As an added feature, PEGO units were either themselves used as linkers or were incorporated into the termini of Pro-Gly repeats (ligands **11**−**16**, Table 1). As it has been proposed that the first binding event serves to tether the multivalent ligand to the cell surface (*13*), we hypothesized that the addition of these flexible PEGO moieties to the ends of the linkers would provide a greater opportunity for the ligand to explore more volume and thus have greater opportunity to find and bind multiple receptors at once.

EXPERIMENTAL PROCEDURES

Chemical Materials. *N*-α-Fmoc-protected amino acids were purchased from SynPep (Dublin, CA) or from Novabiochem (San Diego, CA). Rink amide Tentagel S resin was acquired from Rapp Polymere (Tubingen, Germany). HCTU, HOBt, and HOCt were purchased from IRIS Biotech (Marktredwitz,

Table 1. The Ligands Synthesized[a]

Compound	No of atoms present in the linker	Estimated linker length (Å)	EC_{50} (nM)	n
(1)	18	5-10	99±13	244
(2)	36	10-20	82±12	306
(3)	54	15-30	236±24	295
(4)	72	20-40	188±25	303
(5)	90	25-50	428±55	276
(6)	18	5-10	39±8	230
(7)	36	10-20	11±2	236
(8)	54	15-30	15±3	238
(9)	72	20-40	22±3	225
(10)	90	25-50	22±4	257
(11)	20	4-18	16±2	261
(12)	40	8-36	13±1	279
(13)	58	13-46	16±2	277
(14)	76	18-56	11±2	256
(15)	112	28-76	19±13	259
(16)	148	38-96	34±8	272

◇ = MSH (7); ▬ = $(Pro\text{-}Gly)_3$; ∿ = Pego linker

[a] Ligands **1**−**5** represent the control monovalent ligands which are similar in structure to the bivalent ligands **6**−**10**. Ligands **11**−**16** have the PEGO units incorporated into the linker structure for added flexibility. *n* indicates the total number of data points used to generate the binding curve and the resulting EC_{50} value.

Germany). For the *N*-α-Fmoc-protected amino acids, the following side chain protecting groups were used: Arg(N^g-Pbf); Glu(*O*-*t*Bu); His(N^{im}-Trt); Ser(*O*-*t*Bu); Trp(N^i-Boc). Peptide synthesis solvents, reagents, and acetonitrile for HPLC were reagent grade, were acquired from VWR (West Chester, PA) or Aldrich-Sigma (Milwaukee, WI), and were used without further purification unless otherwise noted. The solid-phase synthesis was performed in fritted syringes using Domino manual synthesizer obtained from Torviq (Niles, MI).

The purity of the final products was checked by analytical RP-HPLC using a Waters Alliance 2695 separation model with a Waters 2487 dual wavelength detector (220 and 280 nm) on a reverse-phase column (Waters Symmetry 4.6 × 75 mm, 3.5 μm). Peptides were eluted with a linear gradient of aqueous CH_3CN/0.1% CF_3CO_2H at a flow rate of 1.0 mL/min. Purification of ligands was achieved on a Waters 600 HPLC using a reverse-phase column (Vydac C-18, 15−20 μm, 22 × 250 mm). Peptides were eluted with a linear gradient of CH_3CN/0.1% CF_3CO_2H at a flow rate of 5.0 mL/min. Separation was monitored at 230 and 280 nm.

Size exclusion chromatography was performed on a borosilicate glass column (2.6 × 250 mm, Sigma, St. Louis, MO) filled with medium-sized Sephadex G-25 or G-10. The compounds were eluted with an isocratic flow of 1.0 M aqueous AcOH. Structures were characterized by ESI (Finnigan, Thermoquest LCQ ion trap instrument) or MALDI-TOF (Bruker Reflex-III, α-cyanocinnamic acid as a matrix). For internal calibration, an appropriate mixture of standard peptides was used with an average resolution of 8000−9000. High-resolution mass measurements were carried out on a FT-ICR IonSpec 4.7T instrument.

Solid-Phase Synthesis. The Rink resin was washed with DMF, and the N^α-Fmoc protecting group was removed with 1:1 or 1:4 piperidine in DMF, as the case may be (1 × 2 min and 1 × 20 min). The resin was washed successively with DMF, DCM, DMF, and then a solution of 1.0 M HOBt in DMF, and DMF, and the next N^α-Fmoc amino acid was coupled using preactivated 0.3 M HOCt or HOBt esters in THF (3 equiv of N^α-Fmoc amino acid, 3 equiv of HOCt/HOBt, and 3 equiv of DIC). The resin slurry was stirred for 2 h or until the bromophenol test became negative. If the test failed, the resin was washed with DMF, and the amino acid was coupled again by the HCTU/2,4,6-lutidine procedure (0.3 M solution of 3 equiv of N^α-Fmoc amino acid, 3 equiv of HCTU, and 6 equiv of 2,4,6-lutidine in DMF) for 3 h or by a preformed symmetric anhydride (3 equiv of N^α-Fmoc amino acid and 1.5 equiv of DIC in a 1:1 DMF−DCM mixture) until the Kaiser test was negative. If the second coupling did not result in a negative Kaiser test, the resin was washed with DMF, and the free amino groups were capped with 50% Ac_2O in pyridine for 10 min.

After coupling Trp(N^i-Boc), Arg(N^g-Pbf), D-Phe, His(N^{im}-Trt), Glu(*O*-*t*Bu), Nle, and Ser(*O*-*t*Bu) sequentially to the Rink amide resin, Gly and Pro were attached alternatively as many times as needed to synthesize the control ligands **1**−**5** (Scheme 1). Assembly of the second ligand, MSH(7), was carried out by the procedure described above to give ligands **6**−**10**. Similarly for the synthesis of ligands **11**−**16**, after the assembly of MSH(7) sequence on the resin, the flexible linker PEGO was attached, by first adding diglycolic anhydride and then activating the free carboxylate as an imidazolide for the attachment of 4,7,10-trioxa-1,13-tridecanediamine (*3*). This was followed by stepwise assembly of repetitive Pro-Gly linker units. Another PEGO attachment followed by the second MSH(7) sequence and N-terminal acetylation yielded resin bound protected precursors of compounds **11**−**16** (Scheme 1). A cleavage cocktail (10 mL per 1 g of the resin) consisting of CF_3CO_2H (91%), H_2O (3%), $HSCH_2CH_2SH$ (3%), and PhSMe (3%) was injected into the resin, and the mixture was agitated at room temperature for 3 h. The solution was filtered off, the resin was washed with CF_3CO_2H (2 × 3 min), the liquid phases were concentrated under a stream of nitrogen, and the product was precipitated using cold Et_2O. The products **1**−**16** were washed three times with cold Et_2O, lyophilized, purified, and characterized as described above. Mass spectral and HPLC characterization data are given in Table 2.

Molecular Modeling. Conformational searches and molecular dynamics were performed with *MacroModel* v 9.1 implemented under the Maestro 7.5 interface on a Linux workstation. The *MacroModel* implementations of Merck Molecular Force Field (MMFF), AMBER*, and OPLS all-atom force fields were used (*14*). AMBER* is a reparametrized AMBER force field containing a new set of torsional parameters that more closely reproduces *ab initio* calculations on the conformational preferences of simple peptides (*15*). For solution-phase calculations, the GB/SA continuum model for water was used. Amide bonds were required to be trans except in the case of proline whose imide bonds were intentionally sampled and accepted with either cis or trans geometry in the conformational searches.

Conformation Search. Conformational searches were performed with the systematic Monte Carlo method of Goodman and Still (*16*). For each search, 5000 starting structures were generated and minimized until the gradient was less than (0.05 kJ/mol)/Å, using the truncated Newton−Raphson method implemented in *MacroModel*. Duplicate conformations and those with energy greater than 50 kJ/mol above the global minimum were discarded.

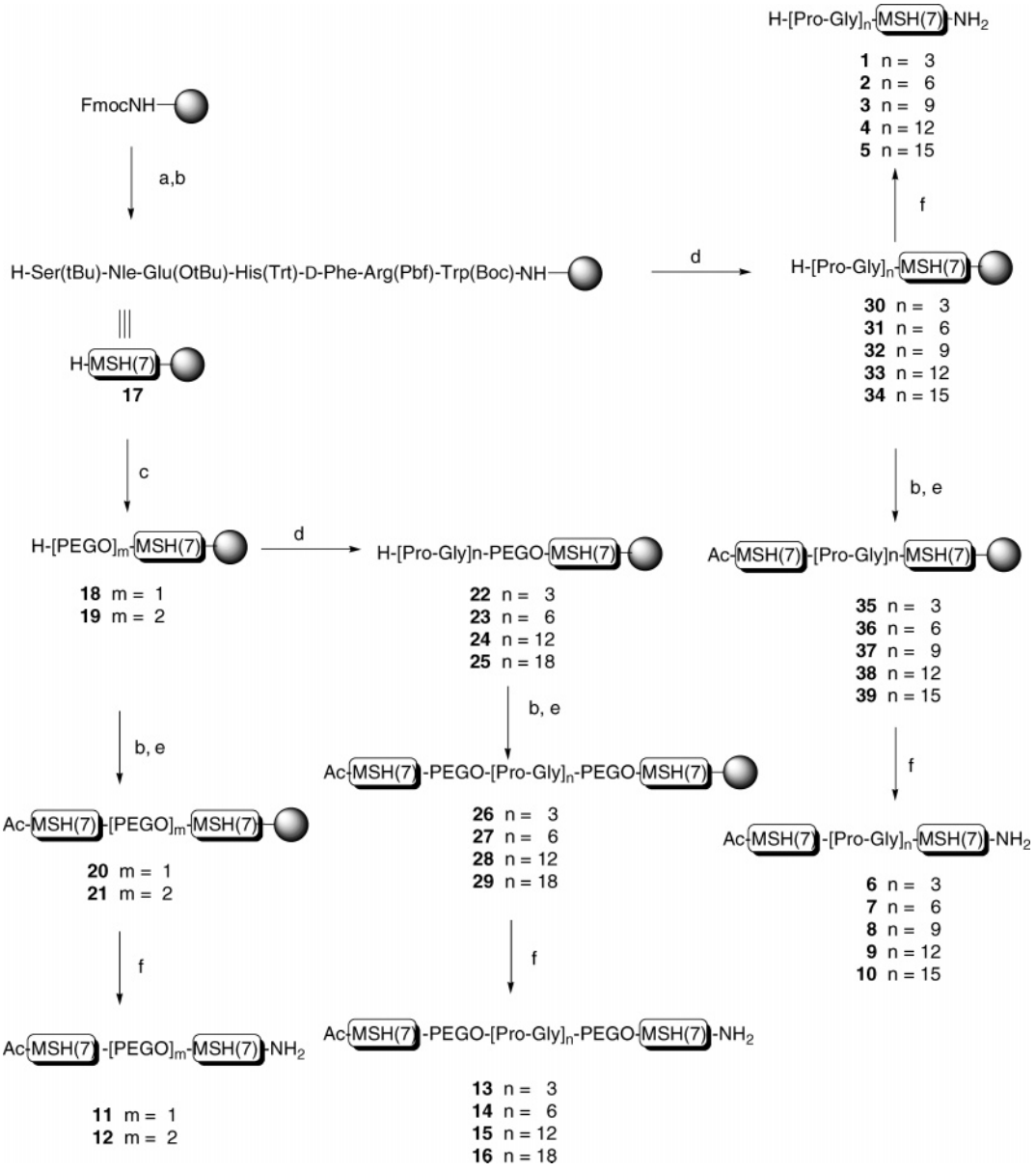
Monte Carlo/Stochastic Dynamics. All simulations were performed at 310 K with Monte Carlo/stochastic dynamics (MC/SD) hybrid simulation algorithm (*17*) with either the AMBER* all-atom force field or the new OPLS-2005 force field in *MacroModel 9.1*. A time step of 1.5 fs was used for the stochastic dynamics (SD) part of the algorithm. The MC part of the algorithm used random torsional rotations between ±60° and ±180° that were applied to all rotatable bonds except the proline amide C−N bond where the random rotations between ±0° and ±180° were applied. No torsion rotations were applied to bonds in the pyrrolidine ring of proline, as the barriers are low enough to permit adequate sampling from the SD part of the simulation. The total simulation time was 1000 ps, and samples were taken at 1 ps interval, yielding 1000 conformations for analysis.

G-Protein Coupled Receptor Size Estimations. The PDB file of a recently described bovine rhodopsin protein in a trigonal crystal form (1GZM) (*18*) was loaded into the *DeepView* program (Swiss-Pdb Viewer Program, http://www.expasy.org/spdbv/). This program allows distances between different residues on the GPCR structure to be measured. Several residues on the outer edges of the transmembrane domain were chosen, and distances across the GPCR were measured. The "width" of the GPCR was taken as the average of eight of these measured distances.

Cell Culture. HEK293 cells overexpressing the human melanocortin 4 receptor (hMC4R) were used to assess the binding at the hMC4R. The hMC4R vector was originally received from Dr. Ira Gantz, University of Michigan (*19*). The coding region of the hMC4R gene was expressed in pcDNA3.1 (Invitrogen, V790−20). Hek293/hMC4R cells were grown in Dulbecco's Modified Eagle Medium (DMEM) supplemented with 10% FBS.

Lanthanide-Based Binding Assays. Lanthanide-based competitive binding assays were conducted according to the method which has been previously described (*20*). In brief, HEK293/hMC4R cells were plated in black and white 96-well isoplates

Scheme 1. Solid-Phase Synthesis of MSH(7) Peptides 1−16[a]



[a] Reagents and conditions**:** (a) 1:1 or 1:4 piperidine in DMF. (b) Fmoc/*t*Bu solid-phase synthesis. (c) PEGO attachment (ref 3). (d) Fmoc/*t*Bu solid-phase synthesis of Pro-Gly repeats. (e) pyridine/Ac_2O (50/50). (f) $CF_3CO_2H/HSCH_2CH_2SH/PhSMe/H_2O$ (91/3/3/3).

(Wallac, 1450−584) at a density of 12 000 cells/well and were allowed to grow for 3 days. On the day of the experiment, media was aspirated from all wells. 50 μL of nonlabeled ligand and 50 μL of Eu-labeled ligand (final concentration of 10 nM for Eu-NDP-α-MSH) were added to each well. Ligands were diluted in binding media (DMEM, 1 mM 1,10-phenanthroline, 200 mg/L bacitracin, 0.5 mg/L leupeptin, 0.3% BSA), and samples were tested in quadruplicate, unless otherwise noted. Cells were incubated in the presence of ligand for 1 h at 37 °C. Following the incubation, cells were washed 3× with 250 μL wash buffer (50 mM Tris−HCl, 0.2% BSA, 30 mM NaCl). Enhancement solution (Perkin-Elmer; 1244−105) was added (100 μL/well), and the plate was incubated for at least 30 min at 37 °C prior to reading. The plates were read on a Wallac VICTOR^3 instrument using the standard Eu TRF measurement (340 nm excitation, 400 μs delay, and emission collection for 400 μs at 615 nm).

Data Analysis. Data from at least five independent binding experiments were compiled into a single competition curve and were analyzed with *GraphPad Prism* software using the sigmoidal dose−response (variable slope) classical equation for nonlinear regression analysis. The total number of data points used to generate each binding curve is indicated by *n* in Table 1.

RESULTS

Synthesis. The synthesis of ligand dimers **6**−**16** consisting of two MSH(7) ligands connected in a head-to-tail fashion by PEGO and/or Pro-Gly linkers and monovalent controls **1**−**5** is depicted in Scheme 1. The heptapeptide MSH(7) was constructed on Rink amide Tentagel S resin (initial loading 0.2 mmol/g). Resin **17** retained all side chain protecting groups, except for the *N*-terminal Fmoc protecting group. PEGO linkers were attached to the *N*-terminal of **17**, giving $[PEGO]_m$ resins **18** and **19.** The resin **18** was proportionally split for synthesis of compounds **11** and **12** or for synthesis of longer ligands **13**−**16**. For the ligands **11** and **12**, the free amine groups of resins **18** and **19** were coupled with Fmoc-Trp(N^i-Boc)-OH, and solid-phase peptide synthesis continued to complete the second MSH-

Table 2. Analytical Data for Synthetic Peptide Conjugates

compound	mass calculated[a]	mass found	t_R(purity %)	K'
1 ($C_{67}H_{94}N_{20}O_{16}$)	718.3657 $(M+2)^{2+}$	718.3658$(M+2)^{2+}$	12.6[b] (98.8)	18.5
2 ($C_{88}H_{124}N_{26}O_{22}$)	633.3206 $(M+3)^{3+}$	633.3193$(M+3)^{3+}$	13.2[b] (100)	11.35
3 ($C_{109}H_{154}N_{32}O_{28}$)	787.3948$(M+3)^{3+}$	787.3972$(M+3)^{3+}$	13.4[b] (98.4)	9.62
4 ($C_{130}H_{184}N_{38}O_{34}$)	706.3538 $(M+4)^{4+}$	706.354$(M+4)^{4+}$	13.6[b] (98.5)	11.42
5 ($C_{151}H_{214}N_{44}O_{40}$)	821.9094 $(M+4)^{4+}$	821.9074$(M+4)^{4+}$	13.7[b] (82.3)	11.58
6 ($C_{131}H_{180}N_{38}O_{32}$)	700.3485$(M+4)^{4+}$	700.3455$(M+4)^{4+}$	22.6[c] (100)	15.44
7 ($C_{138}H_{190}N_{40}O_{34}$)	984.8201$(M+3)^{3+}$	984.8166$(M+3)^{3+}$	22.4[c] (100)	17.62
8 ($C_{159}H_{220}N_{46}O_{40}$)	683.7397$(M+5)^{5+}$	683.7428$(M+5)^{5+}$	22.3[c] (100)	15.4
9 ($C_{180}H_{250}N_{52}O_{46}$)	646.9882$(M+6)^{6+}$	646.9911$(M+6)^{6+}$	22.2[c] (97.5)	19.94
10 ($C_{201}H_{280}N_{58}O_{52}$)	724.0253$(M+1)^{6+}$	724.0284$(M+1)^{6+}$	22.2[c] (100)	19.92
11 ($C_{108}H_{153}N_{29}O_{27}$)	573.0451 $(M+4)^{4+}$	573.0441 $(M+4)^{4+}$	20.0[b] (92.9)	9.43
12 ($C_{122}H_{179}N_{31}O_{33}$)	869.7839$(M+3)^{3+}$	869.7818$(M+3)^{3+}$	20.4[b] (83.7)	8.26
13 ($C_{143}H_{209}N_{37}O_{39}$)	768.1455$(M+4)^{4+}$	768.1487$(M+4)^{4+}$	20.0[b](83.1)	8.27
14 ($C_{166}H_{242}N_{44}O_{46}$)	897.9566$(M+4)^{4+}$	897.9605$(M+4)^{4+}$	22.6[c] (100)	15.72
15 ($C_{208}H_{302}N_{56}O_{58}$)	645.6136$(M+7)^{7+}$	645.6156$(M+7)^{7+}$	22.3[c] (100)	17.44
16 ($C_{250}H_{362}N_{68}O_{70}$)	680.5935$(M+8)^{8+}$	680.5965$(M+8)^{8+}$	22.2[c] (100)	15.33

[a] The exact molecular mass of the structure, calculated using the atomic masses of the most common isotope for the element. [b] Linear gradient of 10−40% B in 30 min. [c] Linear gradient of 5−45% B in 30 min. 0.1% aqueous TFA (A) and CH_3CN (B).

(7) sequence, then acetylated, giving resins **20** and **21**. To the second portion of resin **18** already split into four reactors, Pro-Gly linkers were alternatively coupled to the *N*-terminus of **18**, giving resins **22**−**25**. PEGO linker was attached, and the second ligand was built up similar to **20** and **21**, giving acetylated resins **26**−**29**. Analogously, resin **17** was split into five portions for the attachment of Pro-Gly linkers, giving resins **30**−**34**. For the synthesis of monomers **1**−**5** and dimers **6**−**10**, each of the above resins **30**−**34** was split. The synthesis of second ligand was carried out, giving resins **35**−**39**. All resin precursors **20** and **21** and **26**−**39** were simultaneously deprotected and cleaved from the Rink resin using a mixture of trifluoroacetic acid, 1,2-ethanedithiol, thioanisole, and water (91/3/3/3) that produced the desired compounds **1**−**16**. Peptides **1**−**16** were purified by size exclusion chromatography and reverse-phase C_{18} preparative HPLC and were characterized by ESI-MS and/or MALDI-TOF mass spectrometry, and/or FT-ICR (Table 2).

Linker Length Estimate. The 3D structure of the hMC4R has been modeled on the basis of the sequence homology and crystal structure of rhodopsin (*11*). We used the crystal structure of a recently published bovine rhodopsin protein, with two protein molecules per asymmetric unit (*18*) to determine the width of the hMC4R and to estimate the distance between two adjacent ligand binding sites. Using the *DeepView/Swiss-Pdb Viewer* program to visualize the 3D structure of rhodopsin, we measured the "width" of the GPCR dimer and found that the average distance from edge to edge was ∼70 Å at the widest point (Figure 2A).

For the hMC4R, four transmembrane domains (TM), viz., TM3, TM4, TM5 and TM6, are integral in forming the ligand-binding pocket of this GPCR. On the basis of this arrangement of the TM domains, the center of the binding pocket is estimated to be located ∼12 Å from the nearest edge of the receptor (Figure 2A). If two adjacent receptors have their binding pockets facing each other in a head-to-head arrangement (Figure 2B), the distance between the centers of these binding pockets would be ∼25 Å. If the binding pockets are arranged in a head-to-tail fashion or a tail-to-tail fashion, the distance between the binding sites would be expected to increase (Figure 2C,D, respectively). Additionally, it must be noted that annular lipids may be associated with receptors and thus would be expected to add an additional 8 Å to the distance based on an estimated cross-sectional area of ∼45 $Å^2$ (*21*−*23*). Furthermore, these estimations assumed that, upon dimerization, each receptor maintained its overall dimensions and that the two receptors did not participate in domain swapping. With these assumptions, the length needed to span the distance between these binding sites was estimated to be between 20 and 50 Å. This estimation implies that linkers shorter than 20 Å (e.g., (*3*)) cannot cross-link multiple GPCRs.

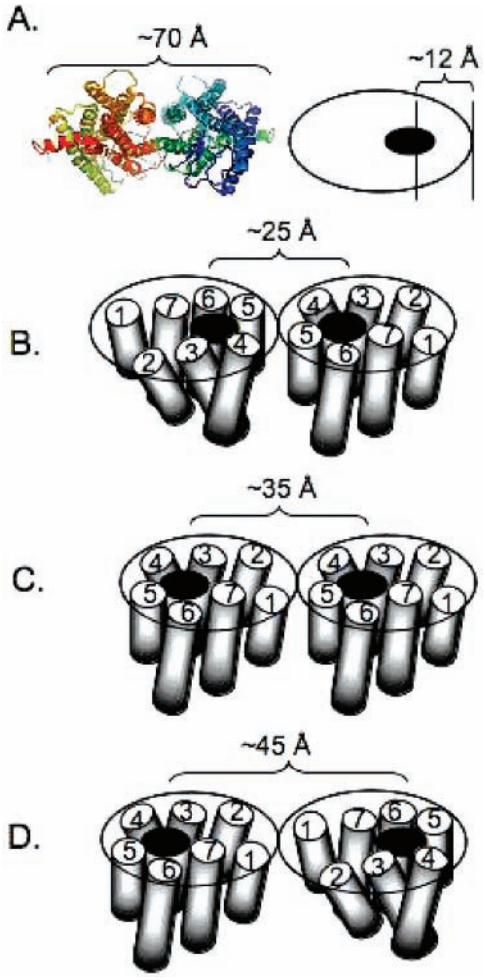


Figure 2. The distance estimations between the binding sites of two adjacent GPCRs (modeled from pdb 1GZM). A. The binding site is estimated to be ∼12 Å from the nearest edge of the receptor. When the receptors are arranged in a head-to-head (B), tail-to-head (C), or tail-to-tail fashion (D), the estimated distances between the binding pockets are 25, 35, and 45 Å, respectively. These distances do not account for the presence of additional lipids or domain swapping as was discussed in the text.

Modeling of Linkers and Homobivalent Ligands. The compounds **7**, **8**, and **14** (Table 1) displayed the highest affinity in our lanthanide-based binding assays. As is evident, the linker

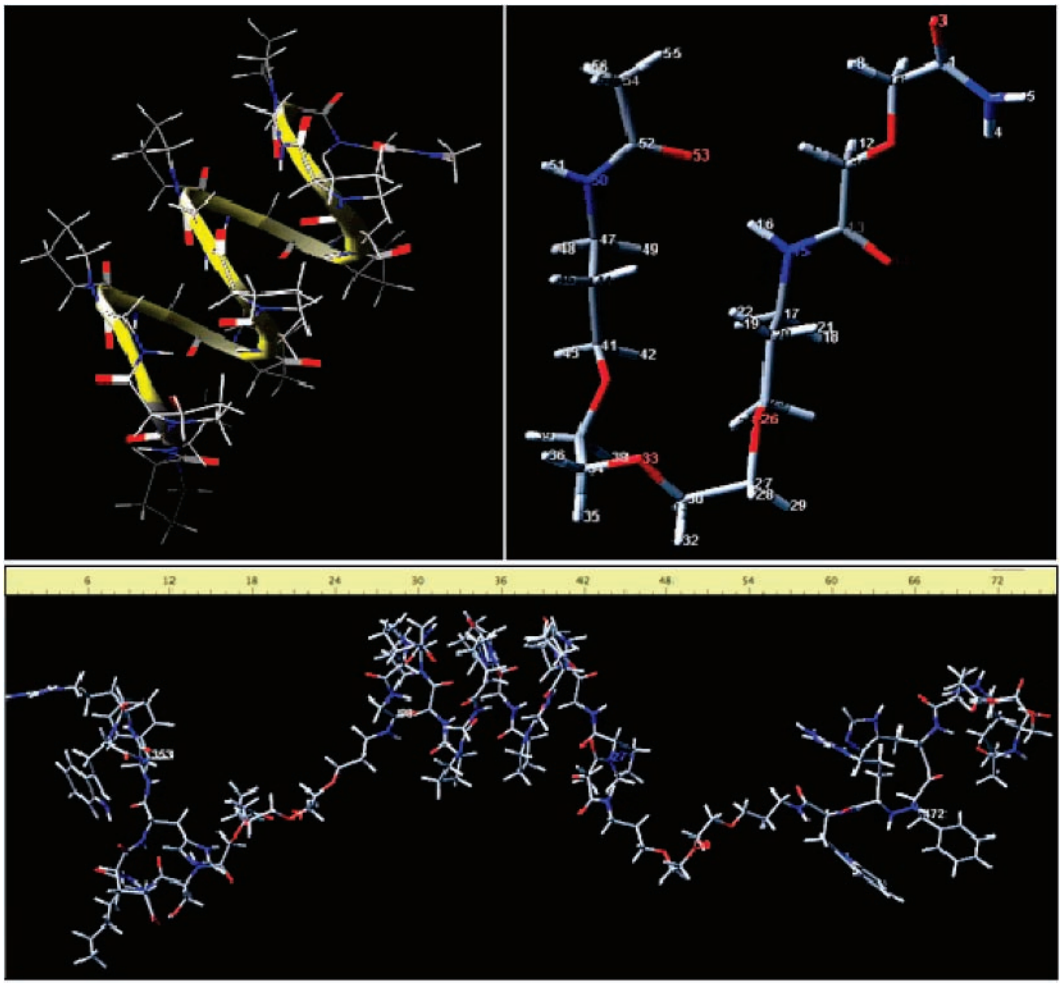


Figure 3. Computational study of -[Pro-Gly]- and -[PEGO]- linkers and a model homobivalent ligand to investigate the conformation, distance span of the linkers, and overall linker moiety. Part A (top left) shows a $[PG]_9$ repeat taking a 6_{17}-helical conformation. MD simulation of this conformation at 310 K shows a significant helical pattern in the entire sample set of 1000 conformations with length ranging from 15 to 29 Å. Part B (top right) shows the PEGO linker in a bent conformation at global minimum. As expected, the linker shows a high degree of flexibility in MD simulations, with distance span between two ends ranging from 4 to 18 Å. Part C (bottom) shows a hypothetical homobivalent ligand, with ruler above, to indicate the approximate distance span of different subunits. The distances calculated from the GPCR dimer study and the modeling of linkers correlate quite well with the binding data.

lengths in terms of atoms do not bear any correlation with activity, as a whole range of compounds having linker lengths from 36 to 76 atoms displayed similar affinities, irrespective of the nature of the linkers. This indicates either a secondary structure formation or a large degree of inherent flexibility of the linkers such that the bivalent mode of binding of MSH epitopes is preserved but the overall conformation of the linker region is reasonably different among compounds. Modeling of the Pro-Gly repeats and PEGO linkers bears out both of these possibilities. These maximum entropy methods indicated that a semirigid helical structure for Pro-Gly-based linkers and a very flexible conformation for PEGO spacers were allowable conformations.

Initially, Monte Carlo conformational searches were performed separately on model rigid linker peptides $[PG]_n$ ($n = 3$, 6, 9) and the flexible linker PEGO. As can be seen from Figure 3a, an 18-mer Pro-Gly (PG) sequence folded into a helical structure in the lowest-energy conformer with a triangular shape (viewed perpendicular to axis) similar to a polyproline helix type II (*24*). However, the Pro-Gly helix was broader with a pitch of 5 Å per seven residues. This lowest-energy conformer was further investigated using Monte Carlo/stochastic dynamics simulations at 310 K for 1000 ps of simulation time. This revealed that this 18-mer could span a distance of 5−10 Å per seven-residue turn with an average of 7 Å from the population sample set, while still retaining a significant helical shape. Therefore, the PG repeat is predicted to be stabilized in a semirigid conformation as was anticipated in the initial design of our rigid linkers. Additionally, the per-residue span of 0.8−1.6 Å indicated here roughly correlates with the span of 1.2 Å unit from linear sequence estimations that were used initially. However, it must be noted here that the distance ranges from dynamic simulations are not linear distances measured along the C_α backbone but instead are spatial distances based upon the pitch of modeled helix. Further experimental verification of these results is presently being investigated in our group.

A similar study set of conformational searches and MD simulations on the flexible PEGO linker revealed that it could assume a bent conformation at the global minimum, as one would expect (Figure 3b) and that the population contained many low-energy conformers with linear (open) shapes. This indicates that a 20-atom PEGO spacer can take any number of conformations with a distance range 4−18 Å long. The fact is evident, as the solvent medium can easily replace most of the hydrogen bonds in the open conformation that it forms with itself in the bent conformation.

We also investigated a model ligand, Ac-MSH(7)-PEGO-$[PG]_9$-PEGO-MSH(7)-NH_2 to investigate the conformation and dynamics of this compound with respect to linker mobility and space interrogation by the attached ligands. Figure 3c shows

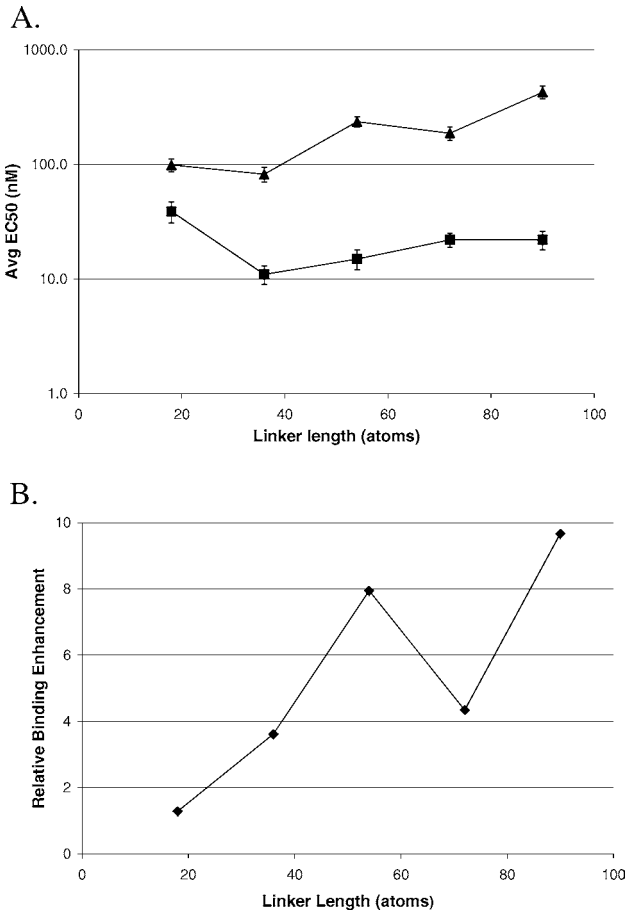


Figure 4. Binding results of monovalent ligands versus bivalent ligands. Binding of the ligands was tested via competition with Eu-NDP-α-MSH. A. Bivalent ligands (■) bind with a higher affinity than their corresponding monovalent ligands (▲). B. The affinity enhancement was calculated by the equation: EC_{50}monovalent/2(EC_{50}bivalent). Results represent the average of at least five independent experiments, each done in quadruplicate, and error bars indicate the standard deviation.

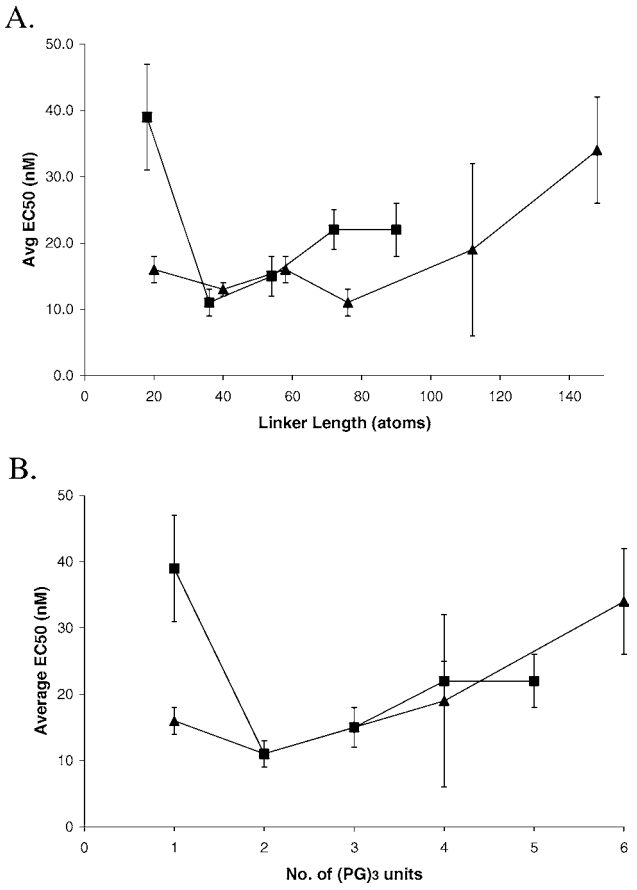


Figure 5. A. Binding results of the two classes of bivalent MSH(7) ligands. Binding of the ligands was tested via competition with Eu-NDP-α-MSH. The bivalent ligands constructed with the PEGO inserts (▲) do not bind with higher affinity compared to the bivalent ligands constructed primarily from Pro-Gly repeats (■). Results represent the average of at least five independent experiments, each done in quadruplicate, and error bars indicate the standard deviation. B. Comparison of compounds with the same number of PG repeats. Only one set of compounds showed increased binding affinity upon incorporation of PEGO inserts.

the ligand along with a ruler in angstrom units. The MD simulation results included populations of both open and closed conformations (MSH epitopes either further apart or closer together). Although the difference in energy between these two conformations was quite large, we believe the binding of MSH epitopes to the receptors could relieve this energy difference. Therefore, the open conformation may more closely resemble the binding mode. Upon the basis of these models, the lengths spanned by the linkers in the ligand library were estimated, as shown in Table 1. It is worth noting that these linker lengths correlated quite well with the inter-receptor distances of 25 ± 10 Å estimated from the modeled GPCR dimers reported above and in the literature (*25*).

Homobivalent Ligands with Longer Linkers Bind with an Increased Affinity. Ligand binding was evaluated via the lanthanide-based binding assay that has been described previously (*20*). In all cases, the bivalent constructs of MSH(7) bound with more than 10-fold higher affinities compared to the ligands composed of monovalent MSH(7) plus the linker (Figure 4A). In order to assess the enhancement in binding affinity of the bivalent ligand relative to the monovalent ligand, the EC_{50} of the monovalent ligand was divided by twice the EC_{50} for the bivalent ligand, accounting for the presence of two binding subunits in the bivalent ligand compared to only one in the monovalent ligand. Even following this correction, Figure 4B indicates that a significant enhancement is still detected when observing bivalent versus monovalent ligand binding. The trend relating linker length to average EC_{50} followed a similar pattern for the control monomers and the dimers.

Ligands **7** and **8**, with linker lengths of 36 and 54 atoms (10−20 Å and 15−30 Å, respectively), showed the highest binding affinity of all compounds in the Pro-Gly series. The estimated linker lengths for these compounds (25 ± 10 Å), were identical to the estimated inter-receptor distance obtained through modeling.

Addition of Flexible Ends to Overall Rigid Linkers Provides no Further Increase in Affinity. Although compounds **11**−**14** have similar and appreciable activity, the flexibility of the PEGO linkers precluded using these compounds for distance estimation (*vide infra*; see also Figure 3B). Nonetheless, it was notable that, while the maximum affinities of the PEGO series were not higher than those of the Pro-Gly series, they retained high-affinity binding over a wider range of ligand sizes (Table 1, Figure 5A). Notably, 20-atom compound **11** and 76-atom compound **14** bound with significantly higher affinity ($p < 0.001$) compared to the similarly sized, 18-atom compound **6** and 72-atom compound **9**, respectively. To directly compare compounds with and without PEGO units, binding data were plotted as a function of Pro-Gly units. In this analysis (Figure 5B), only the shortest PEGO compound showed significant improvement in binding over PG alone. It is also noteworthy that, for both series, the affinity decreases

with increasing linker length, after the minimum, optimal length criterion of 2 PG repeats is met.

DISCUSSION

We have synthesized 16 MSH(7)-containing ligands and confirmed their binding to the hMC4R in whole cell assays. All 11 of the homobivalent ligands bound with at least a 10-fold greater affinity than the corresponding monovalent controls. The conjugation of linkers to monovalent MSH(7) did not significantly decrease the binding affinity of the ligand when linkers were shorter than 40 atoms. As the linker lengths increased beyond 40 atoms, significant decreases in the binding affinities were observed. This can be attributed to the increased translational and rotational entropies associated with longer linkers (*26*). Thus, the linker is interfering with the ligand receptor interactions leading to a decreased affinity.

Bivalent ligands bound with an enhanced affinity compared to monovalent ligands. On the basis of our modeling studies, linkers longer than ~25 Å allowed both ligands to reach and simultaneously bind adjacent receptors. Although we hypothesize that the enhanced affinity observed with the bivalent ligands is a result of the receptor clustering mechanism, we cannot conclusively demonstrate this in this experimental system. Such a demonstration will require a heterobivalent system, which is currently under investigation.

We originally hypothesized that the addition of flexible PEGO moieties to the ends of the otherwise relatively rigid linker would enhance ligand binding by allowing the dimer to investigate more space, thus increasing the likelihood of finding and binding to a second receptor. While this may be the case, the results are not dramatic. The 76-atom PEGO-decorated dimer **14** bound with an EC_{50} of 11 ± 2 nM, while the corresponding 72-atom [PG] dimer **9** bound with a significantly higher 22 ± 3 nM. However, the 112-atom compound **15** (19 nM) and the 90-atom compound **10** (22 nM) were not significantly different. This would suggest that either the structures or the distance spans of these linkers are similar enough that they do not demonstrate any effects on ligand binding. The effect of PEGO was most evident in the short linkers. The 20-atom PEGO-linked dimer **11** bound with significantly higher affinity (EC_{50} = 16 ± 2 nM) compared to the corresponding 18-atom PG-linked dimer **6** (39 ± 8 nM). Both Pro-Gly and PEGO-$[PG]_n$-PEGO-based linkers were expected to possess a certain degree of inherent flexibility, especially the PEGO-based linker. Computational modeling revealed that linkers could assume multiple conformations with a range of distance due to this inherent flexibility. Whereas Pro-Gly may maintain a more or less rigid structure (as evident from the helical structure in MD simulations, the PEGO-$[PG]_n$-PEGO was more free to take a linear or bent shape overall and could assume a wider range of distances. For example, compound **14** had a predicted linker length of 18−56 Å, which was a larger range compared to compound **7,** which had a range of only 10−20 Å. Thus, it is predicted that these two linker types can assume different overall geometries. Because of lower flexibility, the Pro-Gly series provided a clearer picture of the distance between two receptors. Notably, the PEGO series maintained high-affinity binding, even out to lengths of 100 atoms, beyond which there appeared to be a decrease in binding affinity.

In summary, the optimal linker length to span two GPCRs in our model was 25 ± 10 Å, and this generally fits with the binding data for the Pro-Gly series. However, the significant bioactivity of compound **6** suggests that a distance may be less than 25 Å. This may indicate either a statistical effect of two epitopes or domain swapping among receptors. The present study cannot make a conclusive statement with respect to this mode, and additional work will need to be completed to further assess the actual optimal linker length and differentiation in binding modes. Moreover, this distance will most likely vary depending on the exact receptor evaluated and may change when evaluating heterovalent binding which involves different types of receptors. Finally, the only way to demonstrate actual cross-linking of multiple receptors using our experimental system requires the evaluation of heterovalent ligands. Such work is currently underway, and the results from the experiments reported here will be used to design linkers for our future work involving heterovalent ligands for direct targeting of cancer cells.

ACKNOWLEDGMENT

We thank Ms. Lucinda Begay for technical assistance. The work was supported by grants R33 CA 95944 and RO1 CA 97360 from the National Cancer Institute.

LITERATURE CITED

(1) Reubi, J. C. (2003) Peptide receptors as molecular targets for cancer diagnosis and therapy. *Endocr. Rev. 24*, 389−427.

(2) Sawyer, T. K., Sanfilippo, P. J., Hruby, V. J., Engel, M. H., Heward, C. B., Burnett, J. B., and Hadley, M. E. (1980) 4-Norleucine, 7-D-phenylalanine-α-melanocyte-stimulating hormone: A highly potent α-melantropin with ultra-long biological activity. *Proc. Natl. Acad. Sci. U.S.A. 77*, 5754−5758.

(3) Vagner, J., Handl, H. L., Gillies, R. J., and Hruby, V. J. (2004) Novel targeting strategy based on multimeric ligands for drug delivery and molecular imaging: homooligomers of α-MSH. *Bioorg. Med. Chem. Lett. 14*, 211−215.

(4) Kiessling, L. L., Gestwicki, J. E., Strong, L. E. (2000) Strong, synthetic multivalent ligands in the exploration of cell-surface interactions. *Curr. Opin. Chem. Biol. 4*, 696−703.

(5) Biebermann, H., Krude, H., Elsner, A., Chubanov, V., Gudermann, T., and Gruters, A. (2003) Autosomal-dominant mode of inheritance of a melanocortin-4 receptor mutation in a patient with severe early-onset obesity is due to a dominant-negative effect caused by receptor dimerization. *Diabetes 52*, 2984−2988.

(6) Mandrika, I., Petrovska, R., and Wikberg, J. (2005) Melanocortin receptors form constitutive homo- and heterodimers. *Biochem. Biophys. Res. Commun. 326*, 349−354.

(7) Schertler, G. F. X., Villa, C., and Henderson, R. (1993) Projection structure of rhodopsin. *Nature (London) 362*, 770−772.

(8) Schertler, G. F. (2005) Structure of rhodopsin and the metarhodopsin I photointermediate. *Curr. Opin. Struct. Biol. 15*, 408−415.

(9) Guo, W., Shi, L., and Javitch, J. A. (2003) The fourth transmembrane segment forms the interface of the dopamine D2 receptor homodimer. *J. Biol. Chem. 278*, 4385−4388.

(10) Palczewski, K., Kumasaka, T., Hori, T., Behnke, C. A., Motoshima, H., Fox, B. A., Trong, I. L., Teller, D. C., Okada, T., Stenkamp, R. E., Yamamoto, M., and Miyano, M. (2000) Crystal structure of rhodopsin: A G protein-coupled receptor. *Science 289*, 739−745.

(11) Xiaonan, Y. (2003) Modeling and docking of the three-dimensional structure of the human melanocortin 4 receptor. *J. Protein Chem. 22*, 335−344.

(12) Pauling, L., Corey, R. B., and Branson, H. R. (1951) The structure of proteins: two hydrogen-bonded helical configurations of the polypeptide chain. *Proc. Natl. Acad. Sci. U.S.A. 37*, 205−211.

(13) Handl, H. L., Vagner, J., Han, H. Y., Mash, E., Hruby, V. J., and Gillies, R. J. (2004) Hitting multiple targets with multimeric ligands. *Exp. Opin. Ther. Targets 8*, 565−586.

(14) Mohmadi, F., Richards, N. G. J., Guida, W. C., Lizkamp, R., Lipton, M., Caulfield, C., Chang, G., Hendickson, T., and Still, W. C. (1990) Macromodel − an integrated software system for modeling organic and bioorganic molecules using molecular mechanics. *J. Comput. Chem. 11*, 440−467.

(15) McDonald, D. Q., and Still, W. C. (1992) AMBER* torsional parameters for the peptide backbone. *Tetrahedron Lett. 33*, 7743−7746.

(16) Goodman, J. M., and Still, W. C. (1991) An unbounded systematic search of conformational space. *J. Comput. Chem. 12*, 1110−1117.
(17) Guarnieri, F., and Still, W. C. (1994) A rapidly convergent simulation method: mixed Monte Carlo/stochastic dynamics. *J. Comput. Chem. 15*, 1302−1310.
(18) Li, J., Edwards, P. C., Burghammer, M., Villa, C., and Schertler, G. F. X. (2004) Strucuture of bovine rhodopsin in a trigonal crystal form. *J. Mol. Biol. 343*, 1409−1438.
(19) Gantz, I., Miwa, H., Konda, Y., Shimoto, Y., Tashiro, T., Watson, S. J., Delvalle, J., and Yamada, T. (1993) Molecular cloning, expression, and gene localization of a 4th melanocortin receptor. *J. Biol. Chem. 268*, 15174−15179.
(20) Handl, H. L., Vagner, J., Yamamura, H. I., Hruby, V. J., and Gillies, R. J. (2004) Lanthanide-based time-resolved fluorescence of in cyto ligand-receptor interactions. *Anal. Biochem. 330*, 242−250.
(21) Israelachvili, J. N., and Mitchell, D. J. (1975) A model for the packing of lipids in bilayer membranes. *Biochim. Biophys. Acta 389*, 13−19.
(22) Israelachvili, J. N., Mitchell, D. J., and Ninham, B. W. (1977) Theory of self-assembly of lipid bilayers and vesicles. *Biochim. Biophys. Acta 470*, 185−201.
(23) Carnie, S., Israelachvili, J. N., and Pailthorpe, B. A. (1979) Lipid packing and transbilayer asymmetries of mixed lipid vesicles. *Biochim. Biophys. Acta 554*, 340−357.
(24) Cubellis, M. V., Caillez, F., Blundell, T. L., and Lovell, S. C. (2005) Properties of polyproline II, a secondary structure element implicated in protein-protein interactions. *Proteins 58*, 880−892.
(25) Portoghese, P. S. (2001) From models to molecules: opioid receptor dimers, bivalent ligands, and selective opioid receptor probes. *J. Med. Chem. 44*, 2259−2269.
(26) Mammen, M., Choi, S. -K., and Whitesides, G. M. (1998) Polyvalent interactions in biological systems: implications for design and use of multivalent ligands and inhibitors. *Angew. Chem., Int. Ed. 37*, 2754−2796.

BC0603642

In Vitro and in Vivo Evaluation of ^{64}Cu-Labeled DOTA−Linker−Bombesin(7−14) Analogues Containing Different Amino Acid Linker Moieties

Jesse J. Parry,[†] Thomas S. Kelly,[†] Rebecca Andrews,[†] and Buck E. Rogers[†,‡,*]

Department of Radiation Oncology and the Alvin J. Siteman Cancer Center, Washington University School of Medicine, St. Louis, Missouri 63110. Received December 7, 2006; Revised Manuscript Received March 13, 2007

The gastrin-releasing peptide receptor (GRPR) is overexpressed on a variety of tumor types and has been targeted with radiolabeled peptides for detection and therapy of these cancers. Analogues of the 14 amino acid bombesin (BN) peptide have been radiolabeled with both gamma- and positron-emitting radionuclides for detection of GRPR-expressing tumors. We have previously evaluated BN analogues radiolabeled with the positron-emitter, copper-64 (^{64}Cu), that contained various aliphatic linkers placed between the BN peptide and the 1,4,7,10-tetraazacyclododecane-1,4,7,10-tetraacetic acid (DOTA) chelator. These studies showed that the analogues could be used for positron-emission tomographic (PET) imaging of GRPR-positive tumors in mice but clinical translation would be hindered by significant uptake in background tissues. Therefore, the purpose of this study was to determine if the use of amino acid linkers placed between the DOTA chelate and the BN peptide would reduce nontarget tissue uptake, while maintaining good prostate tumor uptake. The linkers studied utilized three amino acid combinations of glycine (G), serine (S), or glutamic acid (E). *In vitro* assays in PC-3 cells showed that the glutamic acid-containing linkers had poor binding and internalization, while the other analogues had IC_{50} values <100 nM and good internalization. *In vivo*, these same analogues demonstrated tumor-specific uptake and good imaging characteristics that were comparable to, or better than the previously reported ^{64}Cu-labeled DOTA−BN analogues. Overall, this study shows that BN analogues containing amino acid linkers can be used for the PET imaging of GRPR-expressing prostate cancer and that these linkers lead to lower background tissue uptake.

INTRODUCTION

Bombesin (BN) is a 14 amino acid peptide that was originally purified from amphibian skin (*1*). This peptide is also active in mammals exerting various physiological effects such as regulating smooth muscle contraction, stimulating action of gastric contraction, and increasing insulin secretion (*2*). BN and BN-like peptides exert their effect through binding to members of the BN receptor family that consists of four receptor subtypes including the neuromedin B receptor (BB1), the gastrin-releasing peptide receptor (GRPR, BB2), the orphan receptor subtype (BB3), and the amphibian receptor (BB4) (*3*−*6*). The bombesin receptor subtype 2 (GRPR) has been shown to be overexpressed on various human tumors and tumor cell lines and thus has been a successful target for the detection and treatment of these cancers. Therapeutic targeting of GRPR has been accomplished through a number of approaches including the development of BN antagonists, conjugation of cytotoxic agents to BN analogues, and attachment of therapeutic radionuclides to BN analogues (*7*−*12*). Similarly, diagnostic radionuclides have been attached to BN analogues for the noninvasive detection of GRPR-expressing neoplasms via imaging.

Noninvasive imaging of GRPR-expressing tumors has been proposed using BN analogues radiolabeled with ^{99m}Tc or ^{111}In for gamma ray scintigraphy or with positron-emitting radionuclides for imaging by positron-emission tomography (PET) (*13*−*20*). In general, BN agonists consisting of either the full length BN peptide (*15*, *20*) or just the C-terminal amino acids of BN have been evaluated (*17*, *18*), although there are some examples of BN antagonists being used (*21*). Our previous studies have used the C-terminal amino acids of BN (BN(7−14)) conjugated to the macrocyclic chelate 1,4,7,10-tetraazacyclododecane-1,4,7,10-tetraacetic acid (DOTA) for radiolabeling with ^{64}Cu for PET imaging of GRPR-expressing tumors (*17*, *22*). These studies used aliphatic linkers between the DOTA and BN(7−14) which likely led to their excretion via the hepatobiliary pathway and is one possible reason for the high retention of radioactivity in the liver. The goal of this study was to evaluate ^{64}Cu-labeled DOTA−BN(7−14) analogues that contain amino acid linkers between DOTA and BN(7−14) in order to reduce the accumulation of radioactivity in the liver that is observed with the aliphatic linkers. Another source of accumulation of radioactivity in the liver that will not be addressed in these studies is from the known dissociation of ^{64}Cu from the DOTA complex.

The amino acid linkers in this study contain glycine (G), serine (S), and glutamic acid (E), and we specifically evaluated GGG, GSG, GSS, GEG, and GEE as linkers. The DOTA−linker−BN(7−14) conjugates evaluated in this manuscript are shown in Figure 1. We hypothesized that the insertion of the serines into the linker would reduce the lipophilicity of the conjugate and thus reduce liver accumulation of radioactivity, while the insertion of glutamic acids would decrease the lipophilicity, but also increase the overall negative charge of the conjugate and therefore reduce kidney accumulation. The conjugates were evaluated for binding to PC-3 human prostate cancer cells, and the ^{64}Cu-labeled conjugates were evaluated for internalization into these cells. The tumor localization and normal tissue accumulation of the ^{64}Cu-labeled analogues were then analyzed in acute *in vivo* biodistribution studies and in

* Corresponding author. Buck E. Rogers, Ph.D., Washington University School of Medicine, Department of Radiation Oncology, 4511 Forest Park Blvd., Suite 411, St. Louis, MO 63108. Phone: 314-362-9787. Fax: 314-362-9790. E-mail: rogers@radonc.wustl.edu.

[†] Department of Radiation Oncology.

[‡] Alvin J. Siteman Cancer Center.

10.1021/bc0603788 CCC: $37.00 © 2007 American Chemical Society
Published on Web 05/16/2007

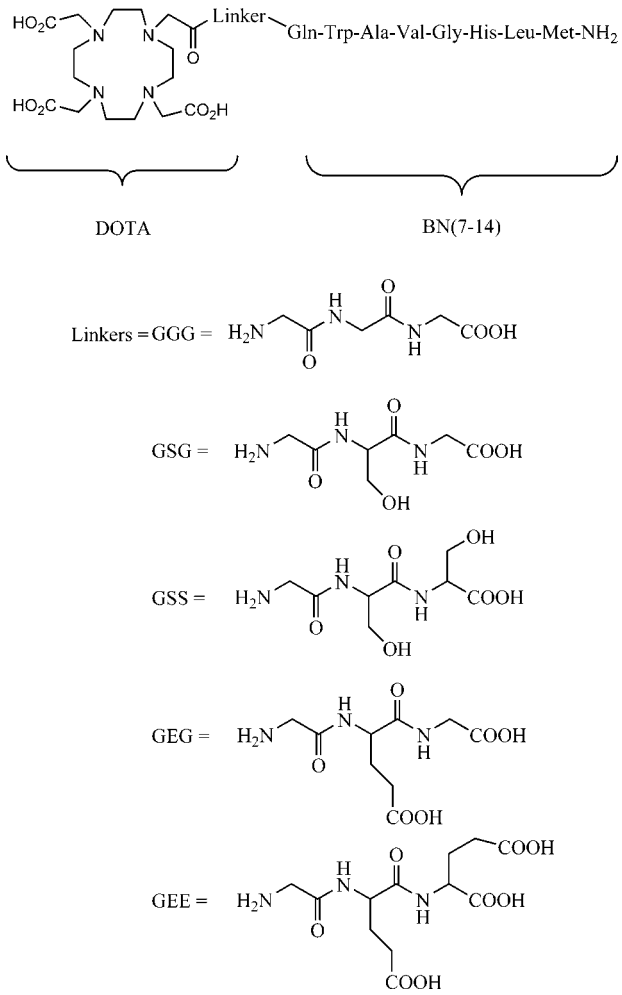


Figure 1. Structures and amino acid sequences of the DOTA−linker−BN(7−14) peptides.

noninvasive small animal PET imaging studies using mice bearing PC-3 xenografts.

EXPERIMENTAL PROCEDURES

Cell Line and Bombesin Analogues. The human prostate adenocarcinoma cell line PC-3 was obtained from the American Type Tissue Culture Center (Manassas, VA), and the cells were maintained in 45% RPMI 1640, 45% Ham's F-12, and 10% heat inactivated fetal bovine serum (FBS). The media components were obtained from Invitrogen (Carlsbad, CA), with FBS from Sigma Chemical Company (St. Louis, MO). Five DOTA−linker−BN(7−14) analogues (DOTA−GGG−BN(7−14), DOTA−GSG−BN(7−14), DOTA−GSS−BN(7−14), DOTA−GEG−BN(7−14), and DOTA−GEE−BN(7−14)) were synthesized by CS Bio Co. (Menlo Park, CA) using standard Fmoc chemistry. The DOTA as the tris(*tert*-butyl)-protected, mono-(*N*-hydroxysuccinimide ester) was purchased from Macrocyclics Inc. (Dallas, TX) for use in solid-phase synthesis. The crude synthetic yield of all peptide analogues was >90% of theoretical yield. The crude peptides were then purified by semipreparative HPLC to give a 10% yield of pure peptide. Final purity was determined by reversed-phase HPLC with a gradient of 80% Solvent A (0.1% CF_3COOH/H_2O) to 50% Solvent B (CF_3COOH/CH_3CN) over 20 min. The purities were: DOTA−GGG−BN(7−14) 97.88%; DOTA−GSG−BN(7−14) 95.67%; DOTA−GSS−BN(7−14) 98.34%; DOTA−GEG−BN(7−14) 94.34%; DOTA−GEE−BN(7−14) 96.85%. Peptide identities were confirmed by ES-MS: DOTA−GGG−BN(7−14) ($C_{65}H_{101}N_{20}O_{19}S_1$), calcd $(M + H)^+$ *m/z* 1497.25, found 1497.60; DOTA−GSG−BN(7−14) ($C_{66}H_{103}N_{20}O_{20}S_1$), calcd $(M + H)^+$ *m/z* 1527.28, found 1527.40; DOTA−GSS−BN(7−14) ($C_{67}H_{105}N_{20}O_{21}S_1$), calcd $(M + H)^+$ *m/z* 1557.30, found 1557.40; DOTA−GEG−BN(7−14) ($C_{68}H_{105}N_{20}O_{21}S_1$), calcd $(M + H)^+$ *m/z* 1569.30, found 1569.40; DOTA−GEE−BN(7−14) ($C_{71}H_{109}N_{20}O_{23}S_1$), calcd $(M + H)^+$ *m/z* 1641.32, found 1641.67.

Competitive Binding Assay. The IC_{50} values of the five individual DOTA−linker−BN(7−14) analogues were determined using a competitive binding assay with ^{125}I-Tyr^4−BN (Amersham Biosciences, Piscataway, NJ) as previously described (*23*). Briefly, PC-3 cells were grown to confluence and collected in cold 4 mM EDTA + 0.05% potassium chloride. Increasing amounts of the DOTA−linker−BN(7−14) analogues ranging from 0.1 ng to 10 μg in 10 μL PBS + 0.1% BSA were added to 1×10^6 cells (100 μL) in triplicate. To this was added 100 μL of ^{125}I-Tyr^4−BN (0.05 nM) to each tube such that the final concentration of the analogues ranged from 1 nM to 100 μM. The tubes were then incubated at 4 °C with shaking for 1 h. After incubation, 3 mL of cold PBS + 0.1% BSA were added to each tube, and all of the tubes were centrifuged at 1500 rpm for 10 min at 4 °C. The supernatants were then aspirated, and the amount of cell-associated radioactivity was determined by gamma counting on a Packard II gamma counter (Perkin-Elmer, Boston, MA). The data were then plotted in GraphPad Prism 3 Software (San Diego, CA) using the sigmoidal dose response equation, with % radioactivity bound versus log of the DOTA−linker−BN(7−14) concentration for the determination of the IC_{50} values.

Radiolabeling of Bombesin Analogues. Positron-emitting copper-64 (^{64}Cu, $t_{1/2} = 12.7$ h, β^+, 0.656 MeV, 17.4%; β^-, 0.573 MeV, 39%) was produced on a CS-15 cyclotron at Washington University School of Medicine (St. Louis, MO) as described (*24*). All five bombesin analogues were radiolabeled with ^{64}Cu as previously described (*17*). Briefly, $^{64}CuCl_2$ (~300 μCi) was diluted with at least a 10-fold excess of 0.1 M NH_4OAc (pH = 5.5) and added to 3 μg of the BN analogues such that the final volume was ~100 μL. The mixture was incubated at room temperature for 30 min in the presence of 2,5-dihydroxybenzoic acid (100 μg) to prevent radiolysis. The radiochemical purity of the radiolabeled peptides was determined using radioTLC on Whatman $MKC_{18}F$ reversed-phase TLC plates (Whatman Inc., Florham Park, NJ) with 10% ammonium acetate:methanol (30:70) as the mobile phase. The TLC plates were scanned on a BioScan Imaging Scanner (Washington, D.C.), and the radiolabeled peptides were used immediately without purification for in vitro and in vivo assays.

Internalization of Radiolabeled Bombesin Analogues. Confluent PC-3 cells were collected and plated in six-well plates at a concentration of 5×10^5 cells per well. On the following day, the cells were washed with Hank's Balanced Salts Solution (HBSS) and 1 mL of internalization media (DMEM plus 30 mM HEPES, 2 mM L-glutamine, 1 mM sodium pyruvate, and 1% BSA) was added. To three of the six wells per plate was added 10 μg of Tyr^4−BN (Sigma Chemical Company, St. Louis, MO) to act as a block. Following the addition of block, ^{64}Cu-labeled BN peptides were added to each well (0.5 μCi), such that the final concentration of the radiolabeled peptide was approximately 1 nM. The plates were then incubated at 37 °C for 15, 30, 60, 120, 240, or 1200 min, upon which the media was aspirated, and the cells were washed twice with cold HBSS. The cells were then washed twice with HBSS plus 20 mM sodium acetate, pH 4.0, and these washes were collected for the determination of surface-bound radioactivity. Then to each well was added 1 mL of 10 mM sodium borate + 1% SDS to facilitate cell lysis. The lysates were then collected to determine

Table 1. IC_{50} Values of DOTA−linker−BN(7−14) Peptides versus ^{125}I-Tyr^4−BN[a]

compound	IC_{50} (nM)
DOTA−GGG−BN(7-14)	50.0 ± 16.2
DOTA−GSG−BN(7-14)	81.8 ± 34.3
DOTA−GSS−BN(7-14)	31.7 ± 6.0
DOTA−GEG−BN(7-14)	2160 ± 718
DOTA−GEE−BN(7-14)	19300 ± 4050

[a] The data are shown as nM ± SEM for 4−6 experiments, each performed in triplicate.

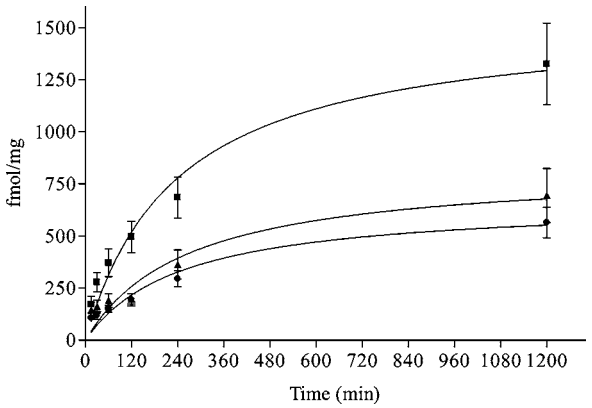


Figure 2. Internalization of ^{64}Cu-DOTA−GGG−BN(7−14) (circles), ^{64}Cu-DOTA−GSG−BN(7−14) (triangles), and ^{64}Cu-DOTA−GSS−BN(7−14) (squares) into PC-3 cells. Cells were incubated with the ^{64}Cu-labeled analogues for various times with or without Tyr^4−BN as an inhibitor. After acid washing of the cells to remove cell surface radioactivity, the cells were lysed and collected, and the amount of internalized radioactivity was counted. The data are shown as the mean of 3−4 experiments ± SEM, with each experiment being performed in triplicate.

the internalized fraction of the radiolabeled BN analogues. Both surface-bound radioactivity and internalized radioactivity were determined by counting the samples in a Packard II gamma counter. The data were normalized to protein amounts in which the protein content of the wells was determined using the Pierce BCA Protein Assay Kit (Rockford, IL) in a separate set of plates in which no radioactivity was added. The data are represented as fmol/mg internalized radioactivity versus time.

Biodistribution Studies. All animal studies were performed under the Guidelines for the Care and Use of Research Animals through the Washington University Animal Studies Committee. Female 3−4 week-old SCID mice (Taconic, Hudson, NY) were implanted subcutaneously (s.c.) on the rear flank with 1×10^7 PC-3 cells, which had been mixed 1:1 with Matrigel Basement Membrane Matrix (Becton Dickinson, Palo Alto, CA), to a volume of 200 μL. The tumors were allowed to grow for 21 days (tumor weight ∼230 mg) upon which the mice ($n = 3-5$ per group) were intravenously (i.v.) injected with ∼7 μCi (∼60 ng) of ^{64}Cu-DOTA−linker−BN(7−14). The animals were then sacrificed either 1, 4, or 24 h postinjection, and blood, liver, kidney, muscle, pancreas, and tumor were extracted, weighed, and processed for gamma counting. For each biodistribution, one additional group of mice were coinjected i.v. with 100 μg of Tyr^4−BN to act as a block and the mice were sacrificed at 1 h postinjection. The percent injected dose per gram of tissue (% ID/g) was determined by decay correction of the ^{64}Cu-DOTA−linker−BN(7−14) for each sample normalized to a standard of known weight, which was representative of the injected dose.

Imaging of PC-3 Xenografts. PC-3 cells were implanted as described above, but on the axillary thorax instead of the hind limb. The mice ($n = 3-4$ per group) were injected i.v. with ∼100 μCi (∼300 ng) of ^{64}Cu-DOTA−linker−BN(7−14) with or without 100 μg of Tyr^4−BN, anesthetized with 1−2% isoflurane, positioned supine, and imaged on a microPET FOCUS 220 (Concorde Microsystems, Knoxville, TN) (*25*) at 1, 4, and 24 h after injection of the radiolabeled analogues. CT images were obtained using a MicroCAT II System (ImTek Inc., Knoxville, TN) at 1 and 24 h after administration and coregistered with the microPET images at those time points. The microPET acquisition times were 10 min for the 1 and 4 h images and 20 min for the 24 h images. The images were reconstructed with an Ordered-Subset Estimation Maximization (OSEM) algorithm and employing the corrections for scatter and attenuation. The scanner was cross-calibrated using an ^{18}F-filled mouse-size cylindrical uniform phantom with a known activity. The relative beta decay branching ratios of ^{64}Cu to ^{18}F were taken into account for absolute quantitation measurements. Regions of interest were drawn to encompass the entire tumor to determine an average activity concentration (nCi/cc) in the tumor. To calculate the % ID/g of tumor, the nCi/cc was divided by the nCi injected (decay corrected to the scan start time) and multiplied by 100.

Statistical Analysis. All data are presented as the mean ± SEM. The Student's *t*-test was used to determine statistical significance at the 95% confidence level, with $p < 0.05$ being considered significantly different.

Table 2. Biodistribution of ^{64}Cu-DOTA−Linker−BN(7−14) in Mice Bearing PC-3 Tumors (% ID/g ± SEM; $n = 3-5$) at 1, 4, and 24 h

tissue	1 h	4 h	24 h
	^{64}Cu-DOTA−GGG−BN(7−14)		
blood	0.808 ± 0.092	0.566 ± 0.104	0.477 ± 0.080
lung	2.527 ± 0.424	1.978 ± 0.455	1.689 ± 0.256
liver	7.737 ± 0.943	4.689 ± 0.954	3.976 ± 0.565
spleen	2.413 ± 0.593	1.198 ± 0.239	1.243 ± 0.177
kidney	5.353 ± 0.603	2.999 ± 0.475	2.643 ± 0.347
muscle	0.540 ± 0.067	0.207 ± 0.038	0.155 ± 0.023
bone	1.149 ± 0.205	0.389 ± 0.087	0.232 ± 0.085
pancreas	10.053 ± 0.710	8.051 ± 0.832	5.242 ± 0.849
tumor	4.577 ± 0.441	4.013 ± 0.609	2.752 ± 0.281
	^{64}Cu-DOTA−GSG−BN(7−14)		
blood	0.399 ± 0.047	0.381 ± 0.059	0.393 ± 0.094
lung	0.788 ± 0.068	1.041 ± 0.196	1.200 ± 0.250
liver	2.078 ± 0.370	4.953 ± 1.043	2.688 ± 0.618
spleen	0.614 ± 0.100	1.055 ± 0.093	1.028 ± 0.325
kidney	2.872 ± 0.234	2.733 ± 0.416	1.605 ± 0.302
muscle	0.291 ± 0.026	0.147 ± 0.044	0.374 ± 0.105
bone	0.248 ± 0.157	0.553 ± 0.140	0.675 ± 0.205
pancreas	10.891 ± 0.403	5.795 ± 0.973	3.237 ± 0.509
tumor	2.810 ± 0.183	2.060 ± 0.257	1.735 ± 0.202
	^{64}Cu-DOTA−GSS−BN(7-14)		
blood	0.775 ± 0.086	0.580 ± 0.081	0.270 ± 0.049
lung	1.583 ± 0.177	1.351 ± 0.145	0.853 ± 0.178
liver	4.918 ± 0.527	2.925 ± 0.586	2.148 ± 0.467
spleen	1.287 ± 0.254	0.830 ± 0.181	0.777 ± 0.148
kidney	5.481 ± 0.435	4.442 ± 0.410	1.571 ± 0.250
muscle	0.327 ± 0.017	0.353 ± 0.100	0.108 ± 0.023
bone	0.626 ± 0.111	0.451 ± 0.053	0.189 ± 0.059
pancreas	12.282 ± 0.792	1.409 ± 0.493	2.606 ± 0.274
tumor	3.751 ± 0.209	1.677 ± 0.121	2.149 ± 0.245

RESULTS

Competitive Binding Assay. The relative affinity of the five BN analogues was determined in a competitive binding assay, where various concentrations of the analogues were used to inhibit the binding of ^{125}I-Tyr^4−BN to PC-3 cells. The IC_{50} values for the analogues are shown in Table 1. The IC_{50} values for the analogues containing the GGG, GSG, and GSS linkers were not significantly different from each other but were significantly less than the GEG and GEE linkers. The IC_{50} of DOTA−GEG−BN(7−14) was significantly less than for DO-

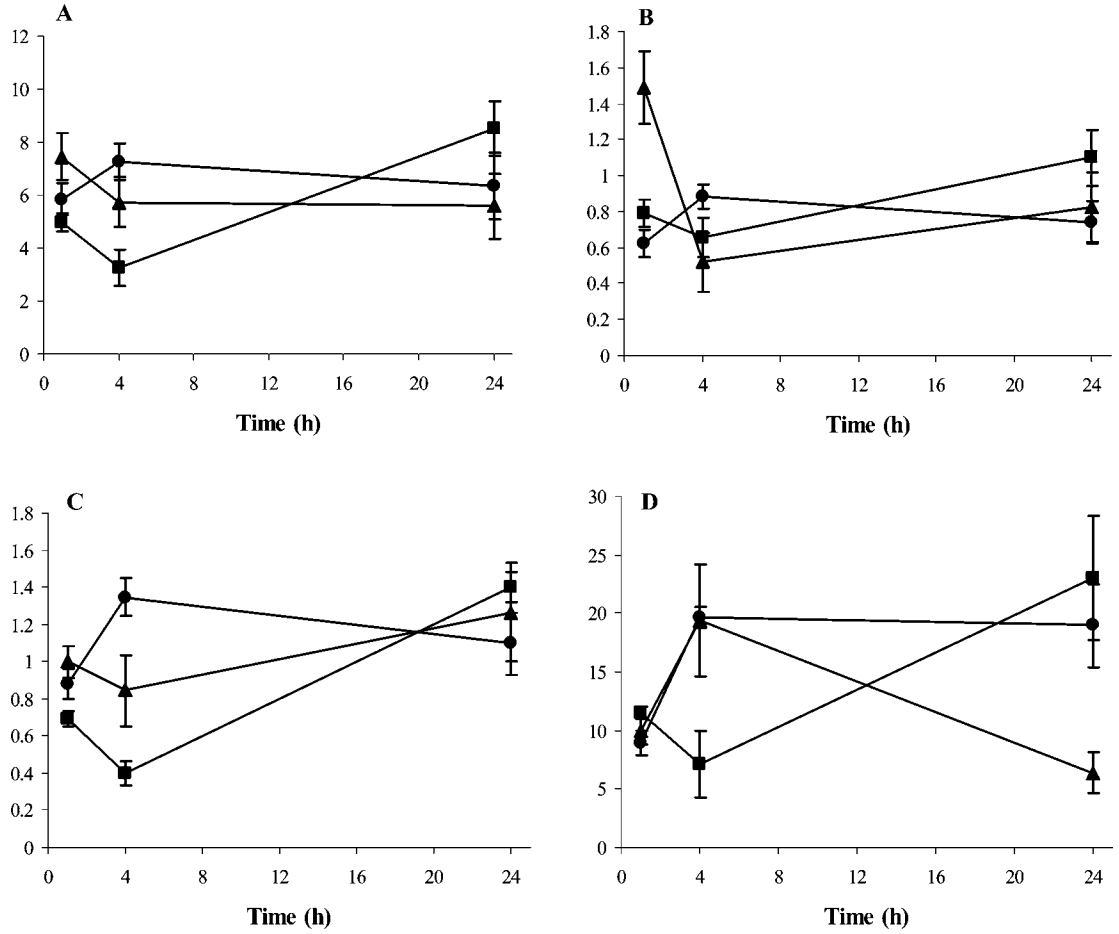


Figure 3. Tumor/blood (A), tumor/liver (B), tumor/kidney (C), and tumor/muscle (D) ratios for ^{64}Cu-DOTA−GGG−BN(7−14) (circles), ^{64}Cu-DOTA−GSG−BN(7−14) (triangles), and ^{64}Cu-DOTA−GSS−BN(7−14) (squares) in mice bearing PC-3 xenografts. The data are expressed as the mean ± SEM of the tumor-to-tissue ratio for each mouse for 3−5 mice per time point.

TA−GEE−BN(7−14) (2.2 ± 0.7 μM vs 19.3 ± 4.0 μM respectively, $p < 0.001$).

Radiolabeling and Internalization. The five BN analogues were all radiolabeled with ^{64}Cu in >95% radiochemical purity and at a specific activity of ∼100 μCi/μg (∼157 Ci/mmol) for the internalization and biodistribution studies. A specific activity of ∼300 μCi/μg (∼470 Ci/mmol) was used for the small animal PET imaging studies. Figure 2 shows that the internalization of ^{64}Cu-DOTA−GGG−BN(7−14) was similar to the internalization of ^{64}Cu-DOTA−GSG−BN(7−14), with no significant differences in the amount internalized at any of the time points. The amount of ^{64}Cu-DOTA−GSS−BN(7−14) internalized was significantly greater than the amount of ^{64}Cu-DOTA−GGG−BN(7−14) and ^{64}Cu-DOTA−GSG−BN(7−14) internalized at all time points except for 15 min. Curve fitting showed that the maximum internalizations were 670, 830, and 1550 fmol/mg for ^{64}Cu-DOTA−GGG−BN(7−14), ^{64}Cu-DOTA−GSG−BN-(7−14), and ^{64}Cu-DOTA−GSS−BN(7−14), respectively. The initial velocities of internalization were 0.83, 0.93, and 2.12 fmol/mg/min for ^{64}Cu-DOTA−GGG−BN(7−14), ^{64}Cu-DOTA−GSG−BN(7−14), and ^{64}Cu-DOTA−GSS−BN(7−14), respectively, as determined by linear regression of the data from 0 to 240 min. There was a small amount of internalization of ^{64}Cu-DOTA−GEG−BN(7−14) over the first 4 h (<30 fmol/mg) that increased to ∼160 fmol/mg at 20 h. No significant internalization was observed for ^{64}Cu-DOTA−GEE−BN(7−14) over the time course of the study. The amount of surface-bound radioactivity for all of the BN analogues was never greater than 140 fmol/mg at any of the time points measured. Since the internalization of ^{64}Cu-DOTA−GEG−BN(7−14) and ^{64}Cu-DOTA−GEE−BN(7−14) was negligible and their affinity for GRPR was low, we did not evaluate these compounds further in the *in vivo* biodistribution and imaging studies.

Biodistribution Studies. Both ^{64}Cu-DOTA−GGG−BN(7−14) and ^{64}Cu-DOTA−GSS−BN(7−14) demonstrated good blood clearance from 1 to 24 h, while ^{64}Cu-DOTA−GSG−BN-(7−14) showed relatively constant blood values (Table 2). However, the blood levels of ^{64}Cu-DOTA−GSG−BN(7−14) were significantly lower than ^{64}Cu-DOTA−GGG−BN(7−14) at 1 h ($p < 0.005$) and ^{64}Cu-DOTA−GSS−BN(7−14) at 1 h ($p < 0.005$) and 4 h ($p < 0.05$). Similar to the blood, the liver activity of ^{64}Cu-DOTA−GSG−BN(7−14) did not significantly decrease over time and was significantly lower than ^{64}Cu-DOTA−GGG−BN(7−14) and ^{64}Cu-DOTA−GSS−BN(7−14) at 1 h ($p < 0.003$ for both). The liver activity of ^{64}Cu-DOTA−GSS−BN(7−14) was also significantly lower than for ^{64}Cu-DOTA−GGG−BN(7−14) at 1 h ($p = 0.03$) and 24 h ($p = 0.04$). The amount of radioactivity in the kidneys was significantly lower for ^{64}Cu-DOTA−GSG−BN(7−14) at 1 h ($p = 0.005$) and 24 h ($p = 0.05$) compared to ^{64}Cu-DOTA−GGG−BN(7−14) and at 1 h ($p < 0.001$) and 4 h ($p < 0.02$) compared to ^{64}Cu-DOTA−GSS−BN(7−14). Thus, at early time points, ^{64}Cu-DOTA−GSG−BN(7−14) generally had lower normal tissue accumulation compared to the other analogues.

The ^{64}Cu-DOTA−GSG−BN(7−14) had significantly less tumor uptake than ^{64}Cu-DOTA−GGG−BN(7−14) at all time points ($p < 0.02$) and ^{64}Cu-DOTA−GSS−BN(7−14) at 1 h ($p < 0.01$). The tumor uptake of all compounds was significantly inhibited by administration of an excess of Tyr^4−BN ($p < 0.001$; Figure 5A) at 1 h. The GRPR-positive pancreas also

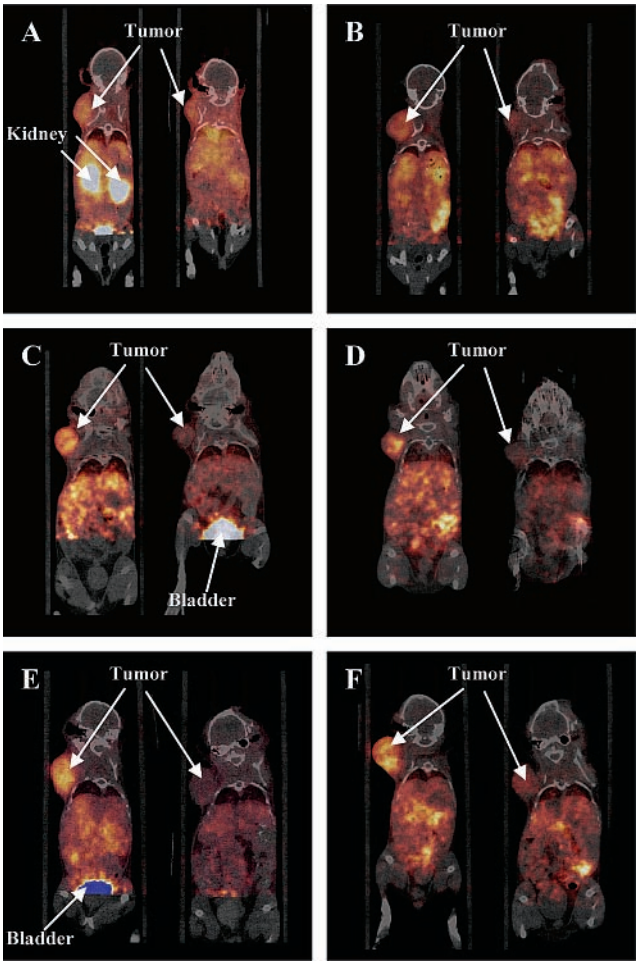


Figure 4. Coronal microPET images with coregistered CT of mice bearing PC-3 xenografts in the axillary thorax at 1 h (A, C, E) and 24 h (B, D, F). The mice were injected i.v. with ^{64}Cu-DOTA−GGG−BN(7−14) (A, B), ^{64}Cu-DOTA−GSG−BN(7−14) (C, D), or ^{64}Cu-DOTA−GSS−BN(7−14) (E, F). The mice on the left of each frame were not injected with blocking agent, while the mice on the right received 100 μg of Tyr^4−BN as an inhibitor.

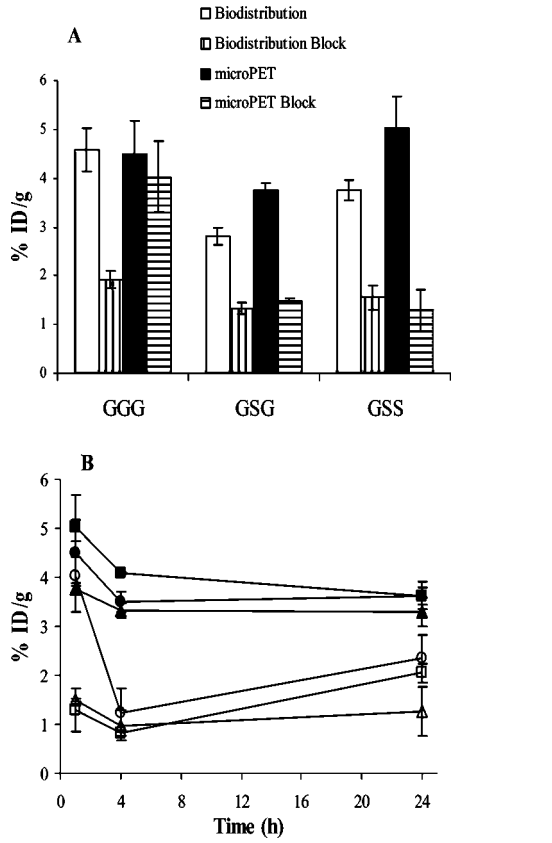


Figure 5. Comparison of tumor uptake at 1 h between biodistribution data (white bars) and microPET imaging data (black bars) for the ^{64}Cu-labeled analogues containing the GGG, GSG, and GSS linkers (A). GRPR-mediated uptake is demonstrated by the hatched bars for both the biodistribution (vertical) and imaging (horizontal) studies. The tumor uptake of ^{64}Cu-DOTA−GGG−BN(7−14) (circles), ^{64}Cu-DOTA−GSG−BN(7−14) (triangles), and ^{64}Cu-DOTA−GSS−BN(7−14) (squares) over time as determined by microPET imaging is shown in part B. The open symbols represent the ^{64}Cu-labeled analogue that was coinjected with blocking agent. The biodistribution data represent the mean ± SEM of 3−5 mice per group, while the imaging data represent the mean ± SEM of 2−3 mice per group.

showed good uptake of all of the ^{64}Cu-labeled analogues (>10% ID/g at 1 h) and all were significantly inhibited ($p < 0.0002$) by administration of the blocking agent. Approximately 70−80% of the radioactivity cleared from the pancreas from 1 to 24 h for ^{64}Cu-DOTA−GSG−BN(7−14) and ^{64}Cu-DOTA−GSS−BN(7−14), while only ∼50% cleared for ^{64}Cu-DOTA−GGG−BN(7−14). This is in contrast to the tumors, where ∼40% of the radioactivity cleared for all of the analogues.

The tumor/blood, tumor/liver, tumor/kidney, and tumor/muscle ratios for the analogues over time are shown in Figure 3. Although ^{64}Cu-DOTA−GSG−BN(7−14) generally had lower normal tissue uptake than the other analogues, the tumor uptake was also lower and thus greater tumor/normal tissue ratios were not achieved. An exception to this is the tumor/liver ratios at 1 h (Figure 3B). ^{64}Cu-DOTA−GSG−BN(7−14) had a significantly higher ($p < 0.02$) tumor/liver ratio (1.49 ± 0.20) at 1 h than either ^{64}Cu-DOTA−GGG−BN(7−14) (0.62 ± 0.08) or ^{64}Cu-DOTA−GSS−BN(7−14) (0.79 ± 0.08). In fact, there were no other significant differences in tumor/liver ratios between the analogues at any of the other time points. ^{64}Cu-DOTA−GSG−BN(7−14) had significantly higher tumor/blood and tumor/kidney ratios than ^{64}Cu-DOTA−GSS−BN-(7−14) at 1 and 4 h ($p < 0.05$ for all). There were no differences observed between the analogues at 24 h except for the tumor/muscle, where ^{64}Cu-DOTA−GSG−BN(7−14) was significantly less than the other analogues ($p < 0.02$). In general, the tumor/tissue ratios are similar for the various analogues except that the ^{64}Cu-DOTA−GSS−BN(7−14) is inferior to the other analogues in terms of the blood and kidney ratios at early time points.

Imaging of PC-3 Xenografts. Small animal PET/CT images of ^{64}Cu-DOTA−GGG−BN(7−14), ^{64}Cu-DOTA−GSG−BN-(7−14), ^{64}Cu-DOTA−GSS−BN(7−14) at 1 and 24 h are shown in Figure 4. This figure shows a representative single slice of the coronal PET/CT images for mice bearing PC-3 xenografts. The mice on the left did not receive blocking agent, while the mice on the right received 100 μg of Tyr^4−BN. These images show good tumor uptake of the three analogues at both 1 and 24 h that was inhibited when an excess of Tyr^4−BN was administered. The 1 and 24 h blocking of ^{64}Cu-DOTA−GGG−BN(7−14) was not as efficient as with the other two analogues and this was confirmed in the quantitative data (Figure 5A). Background activity is observed due to the hepatobiliary clearance of the analogues. Figure 5A shows a comparison of the PC-3 tumor uptake of the analogues as determined from the biodistribution studies and the microPET imaging studies. This shows that the tumor uptake of the analogues were similar between the biodistribution studies and the imaging studies, although the tumor uptake was significantly higher as determined by microPET for ^{64}Cu-DOTA−GSG−BN(7−14) ($p <$ 0.02). The tumor uptake of all of the analogues was significantly inhibited by administration of the blocking agent in the

biodistribution studies, while significance was not reached for ^{64}Cu-DOTA−GGG−BN(7−14) in the imaging studies. Figure 5B shows that all of the analogues had similar tumor uptake over time with the GSS linker having significantly better uptake than the other two at 4 h ($p < 0.05$).

DISCUSSION

Numerous BN analogues have been radiolabeled with a variety of radioactive metals for detection and therapy of GRPR-expressing neoplasms and discussed in a recent review (*19*). In general, most of these studies have utilized γ-emitting radiometals for their potential as single photon emission computed tomographic (SPECT) imaging agents. Recently, there has been an interest in developing radioactively labeled BN analogues for PET imaging utilizing ^{64}Cu, ^{68}Ga, and ^{18}F (*14*, *17*, *18*, *20*, *22*, *26*). Our laboratory has focused on BN analogues labeled with ^{64}Cu for PET imaging of both breast and prostate cancer (*17*, *22*). These analogues have utilized aliphatic linkers between the DOTA chelator and the BN peptide and have shown good tumor localization and imaging. However, they have also resulted in high accumulation of radioactivity in the liver and kidneys. In this study, we report the evaluation of analogues that contain amino acid linkers between DOTA and BN(7−14) that alter the overall lipophilicity and charge with the intention of lowering background activity. The analogues were evaluated for their binding to GRPR, internalization into PC-3 human prostate cancer cells, and *in vivo* tumor localization by biodistribution and imaging studies.

The purpose of this study was to evaluate three amino acid linkers between the chelator and BN(7−14). We hypothesized that the introduction of amino acids that were hydrophilic or contained a negative charge would help reduce radioactive accumulation in the liver and kidneys. Thus, serines (S) were used to add hydrophilicity to the linker because of the presence of the hydroxyl group side chain, and glutamic acids (E) were used to add negative charges to the linker. The pK_a of the acid side chain of glutamic acid is 4.07 and thus should be highly deprotonated at physiologic pH, leading to the negative charge. Since positively charged compounds are known to accumulate in the kidneys, these negative charges should reduce the kidney accumulation. A recent study by Alves et al. compared a GGG linker between BN(7−14) and a ^{99m}Tc-chelate complex to a SSS linker (*27*). This study showed that the analogue with the GGG linker had liver and kidney uptakes of 5.8% and 7.9% ID/g, respectively, at 1 h postinjection that dropped to 2.1% and 2.7% when the SSS linker was used. Thus, it has been demonstrated that changes in the amino acid linker sequence can have a profound effect on normal tissue uptake.

As seen in Table 1, the peptides that had linkers containing glutamic acids (E) had significantly higher IC_{50} values than the other peptides. The IC_{50} values (∼30 nM to 80 nM) of the other analogues were similar to that previously reported by our group for an analogue with an aliphatic linker (DOTA−Aoc−BN(7−14) = 90 nM). Johnson et al. shows the three-dimensional structure of ^{177}Lu-DOTA−Aoc−BN(7−14) as determined from two-dimensional NMR (*9*). This shows the helical structure of BN(7−14) that is responsible for binding to GRPR, with the linker and metal-chelator extending away from the peptide. The low affinity binding of the glutamic acid-containing linkers in this study may be due to a disruption of this helical structure by the negative charges of the linker.

The internalization of the analogues containing the GGG, GSG, and GSS linkers are shown in Figure 2 and demonstrate agonist-like behavior that is consistent with similar constructs (*27*). The internalization curves are similar for ^{64}Cu-DOTA−GGG−BN(7−14) and ^{64}Cu-DOTA−GSG−BN(7−14), while ^{64}Cu-DOTA−GSS−BN(7−14) shows a more rapid internalization as well as a higher degree of internalization. Other reports have shown a more rapid internalization of radiolabeled BN analogues in PC-3 cells where saturation was reached in 1 to 2 h (*14*, *16*, *27*, *28*), while this study shows that analogues only reached ∼44% saturation by 4 h. It is not clear why ^{64}Cu-DOTA−GSS−BN(7−14) internalizes more rapidly than the other analogues or why internalization appears to be slower than reported by others in this cell line. It has generally been thought that internalization of these analogues is important for their use as diagnostic imaging agents, although a recent publication suggests that noninternalizing somatostatin antagonists are preferred for imaging rather than internalizing agonists (*29*).

The biodistribution study (Table 2) shows that ^{64}Cu-DOTA−GSG−BN(7−14) has lower liver uptake at 1 h compared to the other analogues, while ^{64}Cu-DOTA−GSS−BN(7−14) has lower uptake at 4 and 24 h. This would agree with the hypothesis that the addition of serines to the linker will lead to lower liver accumulation of radioactivity, although, one might predict that the liver radioactivity of ^{64}Cu-DOTA−GSS−BN(7−14) should also be lower than ^{64}Cu-DOTA−GSG−BN(7−14) at 1 h. The liver uptake of ^{64}Cu-DOTA−GSS−BN(7−14) at 1, 4, and 24 h was lower than we had previously reported for similar analogues containing 6-, 8-, or 12-carbon linkers between DOTA and BN(7−14) where the values ranged from ∼7.0 to 8.8% ID/g at 1 h and ∼4.1 to 9.6% ID/g at 24 h. Yang et al. has shown a similarly high liver uptake of ^{64}Cu of ∼9 to 12% ID/g from 1.5 to 12 h using an ϵ-aminocaproic acid linker between DOTA and BN(7−14) (*20*). They also demonstrated that the liver uptake was reduced to ∼4% ID/g from 1 to 4 h when the full length BN peptide was used and DOTA was conjugated to a lysine substituted in the third position (*20*). It has also been shown that ^{64}Cu dissociates from DOTA *in vivo* and transchelates to other proteins that can lead to high blood and liver accumulation of radioactivity (*30*). Thus, the use of other chelators that have improved *in vivo* stability for their copper complexes may reduce the liver uptake even further. Two recent examples of chelators with improved stability for their copper complexes include the cross-bridged cyclam chelator, CBTE2A, and the hexa-aza cage chelator, SarAr (*31*−*33*).

As previously mentioned, the analogues containing the glutamic acid linkers were not evaluated *in vivo* due to their low binding and internalization into PC-3 cells. Therefore, we did not determine if these analogues had lower uptake of radioactivity in the kidney compared to the other analogues. ^{64}Cu-DOTA−GSG−BN(7−14) generally had lower kidney uptake than the other analogues, and all three analogues demonstrated GRPR-specific tumor uptake as determined by the blocking studies. The amount of tumor uptake ranged from ∼2.8 to 4.6% ID/g for the three analogues. This tumor uptake was similar to that reported for other ^{64}Cu-labeled analogues in the same animal model that ranged from ∼3.0 to 5.5% ID/g at 1 h or 2 h postinjection (*14*, *17*, *20*). We previously reported that ^{64}Cu-DOTA−Aoc−BN(7−14) had tumor/blood and tumor/liver ratios of ∼4 and ∼0.4, respectively, in this tumor model (*17*). Here we show (Figure 3) that the tumor/blood and tumor/liver ratios generally range from ∼4 to 8 and ∼0.6 to 1.2, respectively. These ratios are also improved compared to a recent study where aliphatic linkers were evaluated in a breast tumor model (*22*). Thus, these studies show that the ^{64}Cu-labeled analogues with the amino acid linkers had comparable tumor uptake to other ^{64}Cu-labeled analogues previously reported, but with improved tumor/tissue ratios due to lower radioactive accumulation in normal tissues.

The PET/CT images (Figure 4) show good tumor uptake of ^{64}Cu-DOTA−GGG−BN(7−14), ^{64}Cu-DOTA−GSG−BN(7−14), and ^{64}Cu-DOTA−GSS−BN(7−14) (mice on the left) which confirms the uptake observed in the biodistribution studies. The

tumor uptake was specific, as the signal decreased upon administration of the blocking agent (mice on the right), although the 1 h image for ^{64}Cu-DOTA−GGG−BN(7−14) did not show efficient receptor blockade. The images also show the background hepatobiliary clearance of the peptides, and the 1 h PET/CT slice for ^{64}Cu-DOTA−GGG−BN(7−14) (Figure 4A) shows the kidney and bladder radioactivity. Analysis of the imaging data shows that there is good agreement with the biodistribution data (Figure 5A) and that the tumor uptake of the analogues was inhibited at all time points except for ^{64}Cu-DOTA−GGG−BN(7−14) at 1 h (Figure 5B). These images show that the tumor can be clearly delineated with these analogues but that the background activity in the intestinal tract and rapid clearance of the activity through the bladder may preclude imaging of lesions in these areas.

In conclusion, we evaluated five ^{64}Cu-DOTA−linker−BN(7−14) analogues that consisted of different amino acid linkers and found that the use of negatively charged glutamic acid residues significantly reduced the affinity of these analogues for GRPR as well as internalization into GRPR-expressing cells. The other analogues showed specific tumor uptake and good imaging characteristics that were comparable to or better than previously reported ^{64}Cu-labeled DOTA−BN analogues. However, these results may be further improved by additional modification of the linkers and/or use of chelators that are more kinetically inert when forming complexes with copper than the DOTA chelator evaluated here.

ACKNOWLEDGMENT

The authors gratefully acknowledge Nicole Fettig, Margaret Morris, Amanda Roth, Lori Strong, and Dawn Werner for performing the biodistribution and imaging studies. Jerrel Rutlin and Dr. Richard LaForest are thanked for analysis and helpful discussions of the imaging data. Dr. Jason Lewis and Ronald Chen are thanked for critical reading of the manuscript. This work was supported, in part, by a grant from the American Cancer Society (RSG-00-067-04-CCE). The production of ^{64}Cu at Washington University School of Medicine is supported by NCI Grant R24 CA86307, and small animal imaging is supported by an NIH/NCI SAIRP Grant R24 CA83060.

LITERATURE CITED

(1) Anastasi, A., Erspamer, V., and Bucci, M. (1971) Isolation and structure of bombesin and alytesin, 2 analogous active peptides from the skin of the European amphibians Bombina and Alytes. *Experientia 27*, 166−167.

(2) Ohki-Hamazaki, H., Iwabuchi, M., and Maekawa, F. (2005) Development and function of bombesin-like peptides and their receptors. *Int. J. Dev. Biol. 49*, 293−300.

(3) Battey, J. F., Way, J. M., Corjay, M. H., Shapira, H., Kusano, K., Harkins, R., Wu, J. M., Slattery, T., Mann, E., and Feldman, R. I. (1991) Molecular cloning of the bombesin/gastrin-releasing peptide receptor from Swiss 3T3 cells. *Proc. Natl. Acad. Sci. U.S.A. 88*, 395−399.

(4) Fathi, Z., Corjay, M. H., Shapira, H., Wada, E., Benya, R., Jensen, R., Viallet, J., Sausville, E. A., and Battey, J. F. (1993) BRS-3: a novel bombesin receptor subtype selectively expressed in testis and lung carcinoma cells. *J. Biol. Chem. 268*, 5979−5984.

(5) Nagalla, S. R., Barry, B. J., Creswick, K. C., Eden, P., Taylor, J. T., and Spindel, E. R. (1995) Cloning of a receptor for amphibian [Phe^{13}]bombesin distinct from the receptor for gastrin-releasing peptide: Identification of a fourth bombesin receptor subtype (BB4). *Proc. Natl. Acad. Sci. U.S.A. 92*, 6205−6209.

(6) Wada, E., Way, J., Shapira, H., Kusano, K., Lebacq-Verheyden, A. M., Coy, D., Jensen, R., and Battey, J. (1991) cDNA cloning, characterization, and brain region-specific expression of a neuromedin-B-preferring bombesin receptor. *Neuron 6*, 421−430.

(7) Bajo, A. M., Schally, A. V., Krupa, M., Hebert, F., Groot, K., and Szepeshazi, K. (2002) Bombesin antagonists inhibit growth of MDA-MB-435 estrogen-independent breast cancers and decrease the expression of the ErbB-2/HER-2 oncoprotein and c-jun and c-fos oncogenes. *Proc. Natl. Acad. Sci. U.S.A. 99*, 3836−3841.

(8) Buchholz, S., Keller, G., Schally, A. V., Halmos, G., Hohla, F., Heinrich, E., Koester, F., Baker, B., and Engel, J. B. (2006) Therapy of ovarian cancers with targeted cytotoxic analogs of bombesin, somatostatin, and luteinizing hormone-releasing hormone and their combinations. *Proc. Natl. Acad. Sci. U.S.A. 103*, 10403−10407.

(9) Johnson, C. V., Shelton, T., Smith, C. J., Ma, L., Perry, M. C., Volkert, W. A., and Hoffman, T. J. (2006) Evaluation of combined ^{177}Lu-DOTA-8-AOC-BBN(7−14)NH_2 GRP receptor-targeted radiotherapy and chemotherapy in PC-3 human prostate tumor cell xenografted SCID mice. *Cancer Biother. Radiopharm. 21*, 155−166.

(10) Lantry, L. E., Cappelletti, E., Maddalena, M. E., Fox, J. S., Feng, W., Chen, J., Thomas, R., Eaton, S. M., Bogdan, N. J., Arunachalam, T., Reubi, J. C., Raju, N., Metcalfe, E. C., Lattuada, L., Linder, K. E., Swenson, R. E., Tweedle, M. F., and Nunn, A. D. (2006) ^{177}-Lu-AMBA: Synthesis and characterization of a selective ^{177}Lu-labeled GRP-R agonist for systemic radiotherapy of prostate cancer. *J. Nucl. Med. 47*, 1144−1152.

(11) Safavy, A., Raisch, K. P., Matusiak, D., Bhatnagar, S., and Helson, L. (2006) Single-drug multiligand conjugates: synthesis and preliminary cytotoxicity evaluation of a paclitaxel−dipeptide "scorpion" molecule. *Bioconjugate Chem. 17*, 565−570.

(12) Schwartsmann, G., DiLeone, L. P., Horowitz, M., Schunemann, D., Cancella, A., Pereira, A. S., Richter, M., Souza, F., da Rocha, A. B., Souza, F. H., Pohlmann, P., and De Nucci, G. (2006) A phase I trial of the bombesin/gastrin-releasing peptide (BN/GRP) antagonist RC3095 in patients with advanced solid malignancies. *Invest. New Drugs 24*, 403−412.

(13) Breeman, W. A. P., de Jong, M., Erion, J. L., Bugaj, J. E., Srinivasan, A., Bernard, B. F., Kwekkeboom, D. J., Visser, T. J., and Krenning, E. P. (2002) Preclinical comparison of ^{111}In-labeled DTPA- or DOTA-bombesin analogs for receptor-targeted scintigraphy and radionuclide therapy. *J. Nucl. Med. 43*, 1650−1656.

(14) Chen, X., Park, R., Hou, Y., Tohme, M., Shahinian, A. H., Bading, J. R., and Conti, P. S. (2004) MicroPET and autoradiographic imaging of GRP receptor expression with ^{64}Cu-DOTA-[Lys^3]-bombesin in human prostate adenocarcinoma xenografts. *J. Nucl. Med. 45*, 1390−1397.

(15) Lin, K. S., Luu, A., Baidoo, K. E., Hashemzadeh-Gargari, H., Chen, M. K., Brenneman, K., Pili, R., Pomper, M., Carducci, M. A., and Wagner, H. N. J. (2005) A new high affinity technetium-99m-bombesin analogue with low abdominal accumulation. *Bioconjugate Chem. 16*, 43−50.

(16) Nock, B. A., Nikolopoulou, A., Galanis, A., Cordopatis, P., Waser, B., Reubi, J. C., and Maina, T. (2005) Potent bombesin-like peptides for GRP-receptor targeting of tumors with ^{99m}Tc: A preclinical study. *J. Med. Chem. 48*, 100−110.

(17) Rogers, B. E., Bigott, H. M., McCarthy, D. W., Della Manna, D., Kim, J., Sharp, T. L., and Welch, M. J. (2003) MicroPET imaging of a gastrin-releasing peptide receptor-positive tumor in a mouse model of human prostate cancer using a ^{64}Cu-labeled bombesin analogue. *Bioconjugate Chem. 14*, 756−763.

(18) Schuhmacher, J., Zhang, H., Doll, J., Macke, H. R., Matys, R., Hauser, H., Henze, M., Haberkorn, U., and Eisenhut, M. (2005) GRP receptor-targeted PET of a rat pancreas carcinoma xenograft in nude mice with a 68Ga-labeled bombesin(6−14) analog. *J. Nucl. Med. 46*, 691−699.

(19) Smith, C. J., Volkert, W. A., and Hoffman, T. J. (2005) Radiolabeled peptide conjugates for targeting of the bombesin receptor superfamily subtypes. *Nucl. Med. Biol. 32*, 733−740.

(20) Yang, Y. S., Zhang, X., Xiong, Z., and Chen, X. (2006) Comparative in vitro and in vivo evaluation of two ^{64}Cu-labeled bombesin analogs in a mouse model of human prostate adenocarcinoma. *Nucl. Med. Biol. 33*, 371−380.

(21) Nock, B., Nikolopoulou, A., Chiotellis, E., Loudos, G., Maintas, D., Reubi, J. C., and Maina, T. (2003) [^{99m}Tc]Demobesin 1, a novel potent bombesin analogue for GRP receptor-targeted tumour imaging. *Eur. J. Nucl. Med. Mol. Imaging 30*, 247−258.

(22) Parry, J. J., Andrews, R., and Rogers, B. E. (2006) MicroPET imaging of breast cancer using radiolabeled bombesin analogs targeting the gastrin-releasing peptide receptor. *Breast Cancer Res. Treat, 101*, 175−183.

(23) Rogers, B. E., Della Manna, D., and Safavy, A. (2004) In vitro and in vivo evaluation of a ^{64}Cu-labeled polyethylene glycol bombesin conjugate. *Cancer Biother. Radiopharm. 19*, 25−34.

(24) McCarthy, D. W., Shefer, R. E., Klinkowstein, R. E., Bass, L. A., Margeneau, W. H., Cutler, C. S., Anderson, C. J., and Welch, M. J. (1997) Efficient production of high specific activity ^{64}Cu using a biomedical cyclotron. *Nucl. Med. Biol. 24*, 35−43.

(25) Tai, Y. C., Ruangma, A., Rowland, D., Siegal, S., Newport, D. F., Chow, P. L., and Laforest, R. (2005) Performance evaluation of the microPET Focus: A third-generation microPET scanner dedicated to animal imaging. *J. Nucl. Med. 46*, 455−463.

(26) Zhang, X., Cai, W., Cao, F., Schreibmann, E., Wu, Y., Wu, J. C., Xing, L., and Chen, X. (2006) ^{18}F-labeled bombesin analogs for targeting GRP receptor-expressing prostate cancer. *J. Nucl. Med. 47*, 492−501.

(27) Alves, S., Correia, J. D. G., Santos, I., Veerendra, B., Sieckman, G. L., Hoffman, T. J., Rold, T. L., Figueroa, S. D., Retzloff, L., McCrate, J., Prasanphanich, A., and Smith, C. J. (2006) Pyrazolyl conjugates of bombesin: a new tridentate ligand framework for the stabilization of fac-$[M(CO)_3]^+$ moiety. *Nucl. Med. Biol. 33*, 625−634.

(28) La Bella, R., Garcia-Garayoa, E., Langer, M., Blauenstein, P., Beck-Sickinger, A. G., and Schubiger, P. A. (2002) In vitro and in vivo evaluation of a ^{99m}Tc(I)-labeled bombesin analogue for imaging of gastrin releasing peptide receptor-positive tumors. *Nucl. Med. Biol. 29*, 553−560.

(29) Ginj, M., Zhang, H., Waser, B., Cescato, R., Wild, D., Wang, X., Erchegy, J., Rivier, J., Macke, H. R., and Reubi, J. C. (2006) Radiolabeled somatostatin receptor antagonists are preferable to agonists for in vivo peptide receptor targeting of tumors. *Proc. Natl. Acad. Sci. U.S.A. 103*, 16436−16441.

(30) Boswell, C. A., Sun, X., Niu, W., Weisman, G. R., Wong, E. H., Rheingold, A. L., and Anderson, C. J. (2004) Comparative in vivo stability of copper-64-labeled cross-bridged and conventional tetraazamacrocyclic complexes. *J. Med. Chem. 47*, 1465−1474.

(31) DiBartolo, N., Sargeson, A. M., and Smith, S. V. (2006) New ^{64}Cu PET imaging agents for personalised medicine and drug development using the hexa-aza cage, SarAr. *Org. Biomol. Chem. 4*, 3350−3357.

(32) Sprague, J. E., Peng, Y., Sun, X., Weisman, G. R., Wong, E. H., Achilefu, S., and Anderson, C. J. (2004) Preparation and biological evaluation of copper-64-labeled Tyr^3-octreotate using a cross-bridged macrocyclic chelator. *Clin. Cancer Res. 10*, 8674−8682.

(33) Sun, X., Wuest, M., Weisman, G. R., Wong, E. H., Reed, D. P., Boswell, C. A., Motekaitis, R., Martell, A. E., Welch, M. J., and Anderson, C. J. (2002) Radiolabeling and in vivo behavior of copper-64-labeled cross-bridged cyclam ligands. *J. Med. Chem. 45*, 469−477.

BC0603788

A Novel Conjugable Translocator Protein Ligand Labeled with a Fluorescence Dye for in Vitro Imaging

Mingfeng Bai,[†] Shelby K. Wyatt,[†] Zeqiu Han,[‡] Vassilios Papadopoulos,[‡] and Darryl J. Bornhop*[,†]

Department of Chemistry, Vanderbilt University, VU Station B 351822 Nashville, Tennessee 37235-1822, and Department of Biochemistry & Molecular and Cellular Biology, Georgetown University Medical Center, BSB Room 315, 3900 Reservoir Road NW, Washington, DC 20057. Received December 11, 2006; Revised Manuscript Received April 2, 2007

A conjugable analogue of the benzodiazepine 4′′-chlorodiazepam (Ro5-4864), C_6Ro5-4864 was synthesized to probe the binding sites of translocator protein (18 kDa; TSPO), previously known as the peripheral benzodiazepine receptor for molecular imaging. The amino group in this analogue allows universal conjugation to signaling molecules. Lissamine−C_6Ro5-4864, synthesized from C_6Ro5-4864 and a lissamine fluorescence dye, was investigated in this study. This imaging agent exhibited micromolar binding affinity ($K_i = 2.6\ \mu$M) to TSPO and was successfully imaged in TSPO rich glioma and breast cancer cell lines. These findings suggest that C_6Ro5-4864 may provide opportunities in imaging disease states where TSPO levels are affected, such as cancer and neurologic diseases.

INTRODUCTION

Molecular imaging (MI) has emerged as an important multidisciplinary area which involves radiology, chemistry, biology, biochemistry, physics, engineering, and medicine. MI combines molecular agents with imaging tools to follow specific molecular pathways in the body and can be widely applied in locating, diagnosing, and treating disease. Synthetic chemistry is essential to MI by providing potent imaging agents.

The translocator protein (18 kDa), TSPO, previously known as the peripheral-type benzodiazepine receptor has become an interesting target in MI (*1*). TSPO is a mitochondrial protein which is associated with a variety of biological activities such as cell proliferation, apoptosis, immunomudulation, steroidogenesis, and transport of porphyrin and heme (*1*−*3*). TSPO is ubiquitously expressed in human body, with high level of expression in non-neoplastic diseases such as ischemia, brain damage induced by toxins, viral encephalitis, hepatic encephalopathy, epilepsy, nerve degeneration, and trauma (*4*). TSPO overexpression has also been observed in various cancers including breast, glioma, prostate, colorectal, esophageal, ovarian, and small cell lung cancer (*4*).

Several selective and potent TSPO ligands have been developed, such as benzodiazepines (Ro5-4864), isoquinoline carboxamides (PK11195), indolacetamide derivatives (FGIN-1−27), pyrisanoindole derivatives (SSR180575), and phenoxylphenyl acetamide derivatives (DAA1106 or DAA1097). The study of TSPO, an important mitochondrial membrane protein is currently limited because only two ligands that exist are conjugable to signaling moieties for tracking and quantitation. An FGIN analogue was labeled with a fluorophore (NBD) which is not ideal for in vitro imaging due to the low molar extinction coefficient ($\sim$ 8000 L mol^{-1} cm^{-1}) (*5*, *6*). Our lab developed a PK11195 analogue which has a six-carbon linker and a terminal primary amino group (*7*). Development of conjugable forms of the numerous PBR ligands would facilitate the study of TSPO and possibly allow for it to be used as a target for in vivo imaging.

A conjugable form of PK11195 has been reported, and the molecule has been coupled to a lanthanide chelate (*7*) and a fluorescence dye (*8*). These TSPO-targeted agents showed good TSPO binding activity, allowing in vitro molecular imaging studies. Ro5-4864 and PK11195 are reversible competitive inhibitors of each other, and they show distinct biological properties in inflammation (*9*), depression (*10*), nociception (*11*), and apoptosis enhancement (*4*). Given these facts, to further study TSPO function in relation to its expression levels, a conjugable form of Ro5-4864 was deemed as a necessity.

We report herein the synthesis of a conjugable form of Ro5-4864 having a six-carbon spacer (C_6Ro5-4864). Through the primary amino group, this molecule can be conjugated to a variety of signaling moieties, thus allowing the use of different imaging modalities. Lissamine−rhodamine B sulfonyl chloride, a fluorescence dye with a high molar extinction coefficient (88 000 L/mol cm in methanol), was selected for conjugation to C_6Ro5-4864. The resulting TSPO-targeted fluorophore, lissamine−C_6Ro5-4864, labels TSPO-expressing cells selectively and shows promise for MI studies in imaging disease states where TSPO levels are affected, either as the cause or the outcome of the disease.

EXPERIMENTAL PROCEDURES

7-Chloro-5-(4-chlorophenyl)-1-methyl-1*H*-benzo[1,2,4]-triazepin-2-one (2). (5-Chloro-2-(methylamino)phenyl)(4-chlorophenyl)methanone **1** (2 g, 7 mmol) and ethyl carbazate (1.5 g, 17 mmol) were stirred at 210 °C for 3.5 h. After the reaction was cooled to room temperature, the product was purified by column chromatography on silica gel by eluting with 1:3 ethyl acetate/hexanes to yield **2** as a yellow solid (774 mg, 34%). ^{1}H NMR (300 MHz, $CDCl_3$) δ 7.38−7.53 (6H, m), 7.15 (1H, d, J = 8.7 Hz), 7.05 (1H, d, J = 2.7 Hz), 3.29 (3H, s); MS (MALDI)$^+$ m/z 320.3 ([M + H]$^+$, 100%).

(6-Bromohexyloxy)(*tert*-butyl)dimethylsilane (4). To a solution of 6-bromo-1-hexanol (906 mg, 5 mmol) in dichloromethane (25 mL) at 0 °C was added imidazole (1.02 g, 15 mmol). After 5 min, 4-(dimethylamino)pyridine (DMAP) (60 mg, 0.5 mmol) was added, followed by *tert*-butyldimethylsilyl chloride (1.5 g, 10 mmol). The resulting solution was stirred at 0 °C for 2 h, quenched with 30 mL water, and extracted with

* Corresponding author. Tel: 615.322.4226. Fax: 615.343.1234. E-mail: darryl.bornhop@vanderbilt.edu.

[†] Vanderbilt University.

[‡] Georgetown University Medical Center.

10.1021/bc060381r CCC: $37.00 © 2007 American Chemical Society
Published on Web 06/07/2007

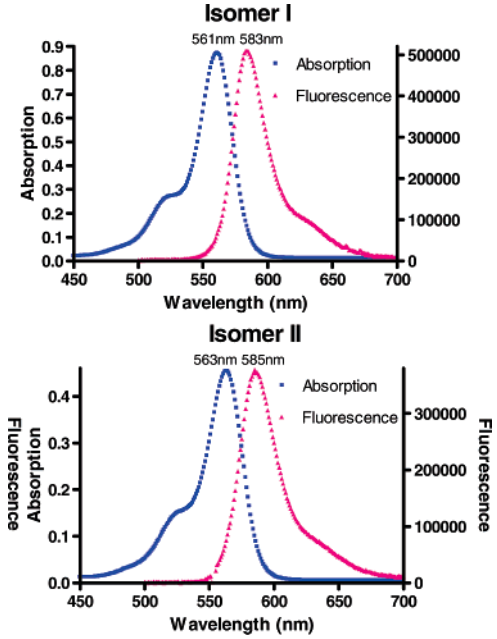


Figure 1. Lissamine−C_6Ro5-4864 isomer I (left) and isomer II (right) absorption and fluorescence curves.

dichloromethane (3 × 30 mL). The organic layers were combined, dried over sodium sulfate, and concentrated by vacuum rotary evaporation. The product was purified by silica gel chromatography using 1:20 ethyl acetate/hexanes as the eluent. Compound **4** was isolated as a colorless liquid (1.3 g, 88%). ^{1}H NMR 300 MHz ($CDCl_3$) δ 3.60 (t, J = 6.3 Hz, 2H), 3.40 (t, J = 6.9 Hz, 2H), 1.86 (q, J = 5.1 Hz, 2H), 1.54−1.35 (m, 6H), 0.89 (s, 9H), 0.04 (s, 6H). MS (GC): 295, 293 [M•].

(*Z*)-3-(6-(*tert*-Butyldimethylsilyloxy)hexyl)-7-chloro-5-(4-chlorophenyl)-1-methyl-1*H*-benzo[*e*][1,2,4]triazepin-2(3*H*)-one (5). Sodium hydride (60% in mineral oil) (20 mg, 0.5 mmol) was added to a stirring solution of compound **2** (256 mg, 0.8 mmol) in dry DMF (4 mL). The mixture was stirred under argon for 30 min. Compound **4** was then added to the mixture, and the resulting mixture was stirred for another 30 min. The reaction solution was poured into 50 mL of a stirring 1 M ammonium chloride solution at 0 °C. The mixture was transferred to a separation funnel and extracted with ethyl ether (3 × 40 mL). The organic layers were combined, dried over sodium sulfate, and concentrated by vacuum rotary evaporation. The crude product was purified by silica gel chromatography using gradient 1:20 to 1:4 ethyl acetate/hexanes as the eluent to give a yellow oil (349 mg, 89%). ^{1}H NMR 400 MHz ($CDCl_3$) δ 7.55−7.53 (m, 2H), 7.46 (dd, J = 8.8, 2.4 Hz, 1H), 7.41−7.39 (m, 2H), 7.12 (d, J = 8.8 Hz, 1H), 7.06 (d, J = 2.4 Hz, 1H), 3.73 (bs, 1H), 3.55 (t, J = 2.4 Hz, 2H), 3.23 (s, 3H), 1.65 (bs, 2H), 1.49−1.43 (m, 2H), 1.33−1.24 (m, 5H), 0.88 (s, 9H), 0.02 (s, 6H). MS (ESI)$^+$: 556.2 Da [M + Na]$^+$.

(*Z*)-7-Chloro-5-(4-chlorophenyl)-3-(6-hydroxyhexyl)-1-methyl-1*H*-benzo[*e*][1,2,4]triazepin-2(3*H*)-one (6). Tetrabutylammonium fluoride (TBAF) (3.5 mL 1 M solution in THF) was added to a stirring solution of compound **5** (377 mg, 0.7 mmol) in THF (2.5 mL) at 0 °C. The reaction solution was stirred at 0 °C for 3 h, quenched with 30 mL of water, and extracted with ethyl ether three times. The organic layers were combined, dried over sodium sulfate, and concentrated by vacuum rotary evaporation. The crude product was purified by column chromatography (silica gel) using 1:2 ethyl acetate/hexanes as eluent. Compound **6** was collected as a pale yellow oil (281 mg, 95%). ^{1}H NMR 300 MHz ($CDCl_3$) δ 7.55−7.53 (m, 2H), 7.46 (dd, J = 9.0, 2.4 Hz, 1H), 7.41−7.38 (m, 2H), 7.12 (d, J = 8.7 Hz, 1H), 7.06 (d, J = 2.4 Hz, 1H), 3.72 (bs, 1H), 3.61−3.56 (m, 3H), 3.23 (s, 3H), 1.69−1.62 (m, 2H), 1.57−1.48 (m, 2H), 1.37−1.24 (m, 5H). ^{13}C NMR 75 MHz ($CDCl_3$) δ 163.6, 161.1, 145.5, 136.5, 134.5, 131.7, 130.3, 129.2, 129.0, 128.8, 128.5, 120.9, 62.8, 51.5, 35.5, 32.6, 27.7, 26.6, 25.4. MS (ESI)$^+$: 442.2 Da [M + Na]$^+$.

(*Z*)-6-(7-Chloro-5-(4-chlorophenyl)-1-methyl-2-oxo-1*H*-benzo[*e*][1,2,4]triazepin-3(2*H*)-yl)hexyl 4-Methylbenzenesulfonate (7). A solution of compound **6** (182 mg, 0.43 mmol) and triethylamine (188 μL, 1.3 mmol) in dry dichloromethane (6 mL) was stirred at 0 °C for 5 min. *p*-Toluenesulfonyl chloride (298 mg, 1.56 mmol) was added slowly to the above solution. The resulting mixture was warmed to room temperature and stirred overnight. The reaction was then quenched with 20 mL of water and extracted with dichloromethane (3 × 20 mL). The combined organic layers were dried over sodium sulfate and concentrated by vacuum rotary evaporation. The crude product was purified by silica gel chromatography using a 1:19 to 2:3 ethyl acetate/hexanes gradient as eluent. Compound **7** was isolated as a yellow oil (238 mg, 96%). ^{1}H NMR 300 MHz ($CDCl_3$) δ 7.77 (dm, J = 8.1 Hz, 2H), 7.54−7.51 (m, 2H), 7.46 (dd, J = 8.7, 2.4 Hz, 1H), 7.52−7.39 (m, 2H), 7.33 (d, J = 7.8 Hz, 2H), 7.12 (d, J = 8.7 Hz, 1H), 7.06 (d, J = 2.4 Hz, 1H), 3.97 (t, J = 6.3 Hz, 2H), 3.70−3.40 (m, 2H), 3.23 (s, 3H), 2.44 (s, 3H), 1.62−1.55 (m, 4H), 1.31−1.21 (m, 4H). MS (ESI)$^+$: 596.3 Da [M + Na]$^+$.

C_6Ro5-4864 (8). A sealed tube with a solution of compound **7** (25 mg, 44 μmol) in methanol (1 mL) was cooled to −78 °C and flushed with ammonia gas. After about 2.5 mL liquid ammonia was condensed, the tube was sealed and warmed to room temperature. The reaction was stirred under room temperature overnight. The mixture was concentrated by nitrogen flow, redissolved by dichloromethane, and treated with a saturated sodium bicarbonate solution. The mixture was extracted with dichloromethane three times. The organic layers were combined, dried over sodium sulfate, and concentrated by vacuum rotary evaporation. The crude product was purified by column chromatography (silica gel) using a gradient with dichloromethane and dichloromethane/methanol/ammonia (6:1:0.1) as the eluent. C_6Ro5-4864 was collected as a pale yellow oil (14 mg, 77%). ^{1}H NMR 300 MHz ($CDCl_3$) δ 7.55−7.51 (m, 2H), 7.45 (dd, J = 8.7, 2.4 Hz, 1H), 7.41−7.37 (m, 2H), 7.12 (d, J = 8.7 Hz, 1H), 7.06 (d, J = 2.4 Hz, 1H), 3.80−3.45 (m, 2H), 3.23 (s, 3H), 2.62 (bs, 2H), 1.65 (bs, 2H), 1.49−1.38−1.24 (m, 8H). ^{13}C NMR 75 MHz ($CDCl_3$) δ 163.6, 161.1, 145.5, 136.4, 134.5, 131.7, 130.2, 129.2, 129.0, 128.8, 128.5, 120.9, 51.5, 42.1, 35.5, 33.7, 27.7, 26.6, 26.5. MS (ESI)$^+$: 419.3 Da [M + H]$^+$.

Lissamine−C_6Ro5-4864. A mixture of lissamine rhodamine B sulfonyl chloride (mixed isomers) (10 mg, 17 μmol), C_6-Ro5-4864 (8 mg, 19 μmol), and triethylamine (15 μL) in dry dichloromethane (1.6 mL) was stirred at room temperature under argon flow for 2 h. The product was purified through column chromatography (silica gel) using a mixture of 24:1 dichloromethane:methanol as the eluent. Lissamine−C_6Ro5-4864 was isolated as a pink solid (Isomer I, 3.2 mg, 19%; Isomer II, 2.2 mg, 13%). ^{1}H NMR 500 MHz ($CDCl_3$) **Isomer I**: δ 8.81 (d, J = 2.0 Hz, 1H), 7.96 (dd, J = 8.0, 1.5 Hz, 1H), 7.55−7.53 (m, 2H), 7.47 (dd, J = 8.5, 2.5 Hz, 1H), 7.41−7.39 (m, 2H), 7.29 (d, J = 9.5 Hz, 2H), 7.20 (d, J = 8.0 Hz, 1H), 7.15 (d, J = 9.0 Hz, 1H), 7.07 (d, J = 2.0 Hz, 1H), 6.81 (dd, J = 9.5, 2.5 Hz, 2H), 6.66 (d, J = 2.5 Hz, 2H), 4.99 (t, J = 6.5 Hz, 1H), 3.50−3.59 (m, 8H), 3.23 (s, 3H), 3.01 (q, J = 7.0 Hz, 2H), 1.69−1.58 (m, 6H), 1.55−1.50 (m, 2H), 1.29 (t, J = 7.5 Hz, 14H). **Isomer II**: δ 8.66 (s, 1H), 8.38 (dd, J = 8.0, 1.0 Hz, 1H), 7.52−7.50 (m, 2H), 7.46 (dd, J = 8.5, 2.5 Hz, 1H), 7.38−7.36 (m, 2H), 7.23 (d, J = 7.5 Hz, 1H), 7.17 (d, J = 9.5 Hz, 1H), 7.14 (d, J = 9.0 Hz, 1H), 7.04 (d, J = 2.5 Hz, 1H), 6.85 (dd,

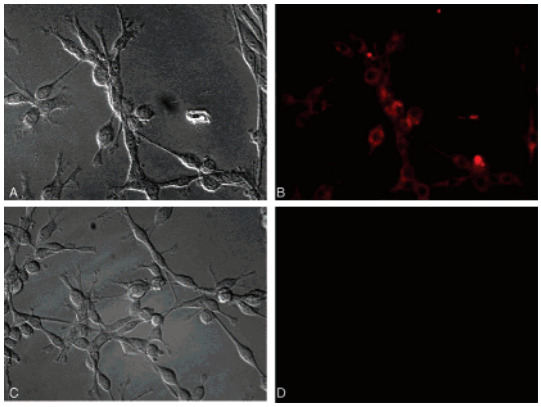


Figure 2. Fluorescence imaging of C6 rat glioma cells: (A) phase contrast microscopy of cells dosed with lissamine−C_6Ro5-4864; (B) fluorescence imaging of cells dosed with 100 nM lissamine−C_6Ro5-4864; (C) phase contrast microscopy of cells dosed with lissamine dye; (D) fluorescence imaging of cells dosed with 100 nM lissamine dye (control).

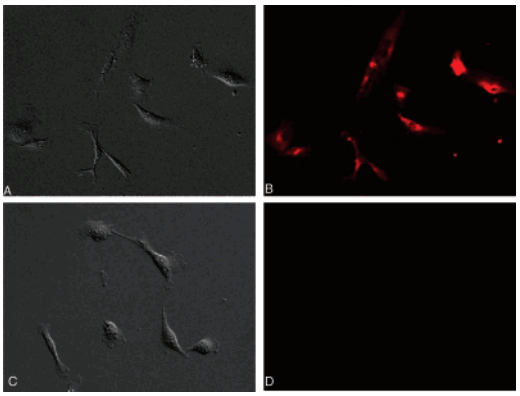


Figure 3. Fluorescence imaging of MDA-MB-231 human breast cancer cells: (A) Phase contrast microscopy of cells dosed with lissamine−C_6Ro5-4864; (B) fluorescence imaging of cells dosed with 100 nM lissamine−C_6Ro5-4864; (C) Phase contrast microscopy of cells dosed with lissamine dye; (D) fluorescence imaging of cells dosed with 100 nM lissamine dye (control).

J = 9.5, 1.5 Hz, 2H), 6.70 (d, J = 2.5 Hz, 2H), 5.24 (bs, 1H), 3.63−3.55 (m, 8H), 3.21 (s, 3H), 2.89 (q, J = 6.5 Hz, 2H), 1.72−1.61 (m, 9H), 1.33 (t, J = 7.5 Hz, 14H). MS $(ESI)^+$: 981.4 Da $[M + Na]^+$. Rf 0.23 (Isomer I), 0.14 (Isomer II) (4% methanol in dichloromethane).

Spectroscopic Characterization. The lissamine−C_6Ro5-4864 absorption and emission spectra (Figure 1) were obtained using a Shimadzu 1700 UV−vis spectrophotometer and ISS PCI spectrofluorometer at room temperature on a 5 μM sample.

Binding Studies. C6 glioma cells were cultured in Dulbecco's modified Eagle medium (DMEM)-F12 medium (Gibco/Invitrogen) supplemented with 0.5% FBS and 2.5% horse serum (HS) at 3.7% CO_2. Cells were scraped from 150 mm culture dishes into 5 mL of phosphate-buffered saline (PBS), dispersed by trituration, and centrifuged at 500*g* for 15 min. Cell pellets were resuspended in PBS and assayed for protein concentration. [^{3}H]PK11195 binding studies on 30 μg of protein from cell suspensions were performed as previously described (*12*). Displacement studies using increasing concentrations of lissamine−C_6Ro5-4864 were performed in the presence of 15 nM [^{3}H]PK11195. Data were analyzed using PRISM software (vs 4.0, GraphPad, Inc., San Diego, CA).

Cell Imaging. C6 rat glioma and MDA-MB-231 human breast carcinoma cells were plated in MaTek dishes. The growth media was removed and replaced with media containing the contrast agent. C6 and MDA-MB-231 cells were dosed with 100 nM lissamine−C_6Ro5-4864 for 30 min at 37 °C under 5% CO_2. Cells dosed with 100 nM free lissamine dye were imaged as control. At the end of the incubation time, cells were rinsed with PBS three times and imaged under a Nikon Eclipse TE2000-U microscope (Lewisville, TX).

In Vitro Competition. MDA-MB-231 human breast carcinoma cells were plated in MaTek dishes. The growth media was removed and replaced with media containing the contrast agent. Unchallenged MDA-MB-231 cells were dosed with 5 μM lissamine−C_6Ro5-4864. Unchallenged cells were dosed with 5 μM lissamine−C_6Ro5-4864 and PK1195 (500 nM, 5 μM or 50 μM). All cells were incubated for 30 min at 37 °C under 5% CO_2. At the end of the incubation time, cells were rinsed with PBS three times and imaged under a Nikon Eclipse TE2000-U microscope (Lewisville, TX).

RESULTS AND DISCUSSION

Synthesis. The overall goal of this synthetic effort was to construct a conjugable TSPO ligand with a biologically active portion of Ro5-4864. (5-Chloro-2-(methylamino)phenyl)(4-chlorophenyl)methanone **1** was synthesized from commercially available 4-chloro-phenylacetonitrile and 4-chloronitrobenzene as reported (*13*). After several unsuccessful attempts using semicarbazide and high-boiling solvents to induce a ring-closure reaction with **1**, we synthesized the triazepinone **2** by heating a mixture of ethyl semicarbazide and **1** at 210 °C without any solvent (Scheme 1). The *tert*-butyldimethylsilyl (TBS)-protected six-carbon linker **4** was added to **2** by an N-alkylation reaction. It is noteworthy that two other linkers, 1,3-dihydro-1,3-dioxo-2*H*-isoindole-2-hexanoic acid and 6-nitrohexanoic acid were also employed, but we were unsuccessful in achieving the final product. After the TBS group in **5** was removed via TBAF, the hydroxyl group in **6** was converted to a tosyl group and subsequently reacted with ammonia to yield the final product **8**.

Since the commercially available lissamine−rhodamine B sulfonyl chloride is a mixture of two isomers (Scheme 2), the N-sulfonylation reaction between C_6Ro5-4864 and the fluorescence dye produced two isomer products. It was possible to isolate these two products through silica gel column chromatograph (R_f is 0.23 for isomer I and 0.14 for isomer II in 4% methanol in dichloromethane). Isomers I and II have a similar maximum absorption (isomer I: 561 nm; isomer II: 563 nM) and emission (isomer I: 583 nm; isomer II: 585 nm) wavelength to that of the free lissamine dye (Abs = 568 nm and Fluo = 583 nm) and Liss-ConPK11195 (Abs = 571 nm and Fluo = 585 nm) (Figure 1) (*8*). However, the molar extinction coefficients of the produced isomers are significantly different (isomer I: 175 000 L/mol cm; isomer II: 91 000 L/mol cm). Isomer I has much higher ϵ than lissamine−rhodamine B sulfonyl chloride (ϵ = 88 000 L/mol cm), which indicates that C_6Ro5-4864 produces a positive effect on lissamine's absorptive property. The molar extinction coefficient of Liss-ConPK11195 was reported as 350 000 L/mol cm, which is lower than isomer I but higher than isomer II. Isomer I was selected for imaging due to the relative high absorption and fluorescence (Figure 1).

Cell Imaging and Binding Study. The cellular uptake of lissamine−C_6Ro5-4864 was examined in C6 rat glioma and MDA-MB-231 human mammary adenocarcinoma cells by fluorescence microscopy. Both cell types were previously shown to contain relatively high levels of TSPO (*14*, *15*). The resulting images were compared with those obtained using the same concentrations of the free lissamine dye as control. Cell uptake of lissamine−C_6Ro5-4864 was observed in fluorescence images of both cell lines (Figures 2and 3, panel B) while the control exhibited no significant fluorescence. Images using Liss-ConPK11195 showed similar quality (*8*).

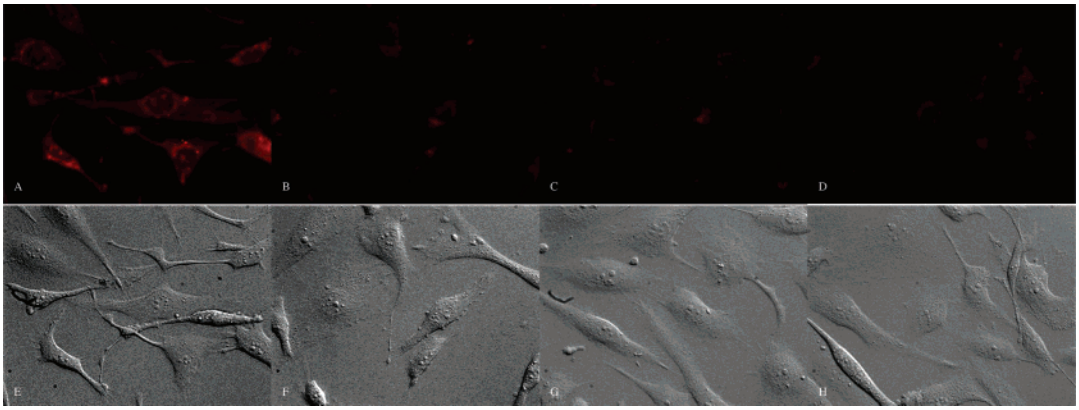
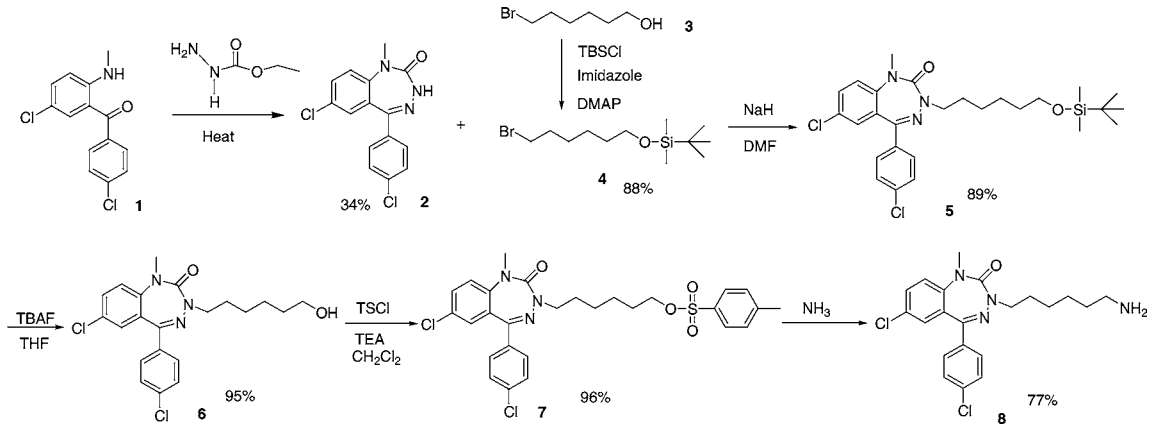
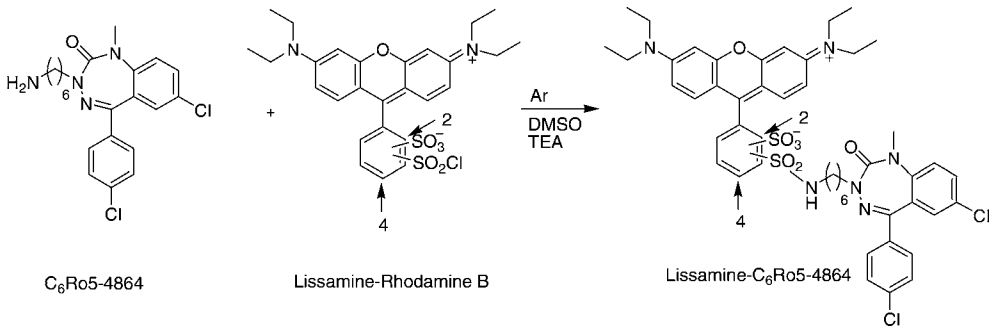


Figure 4. Fluorescence imaging of MDA-MB-231 human breast cancer cells: (A) fluorescence imaging of cells dosed with 5 μM lissamine−C_6Ro5-4864; (B) fluorescence imaging of cells dosed with 5 μM lissamine−C_6Ro5-4864 and 500 nM PK11195; (C) fluorescence imaging of cells dosed with 5 μM lissamine−C_6Ro5-4864 and 5 μM PK11195; (D) fluorescence imaging of cells dosed with 5 μM lissamine−C_6Ro5-4864 and 50 μM PK11195; (E−H) corresponding phase contrast microscopy.

Scheme 1 . Synthesis of C_6-Ro5-4864



Scheme 2 . Synthesis of Lissamine−C_6Ro5-4864



Radioligand binding studies further demonstrated specific binding of lissamine−C_6Ro5-4864 to the TSPO protein. In these studies, [^{3}H]PK11195, the well characterized diagnostic TSPO drug ligand, was used as the competitive radioligand. The concentration of lissamine−C_6Ro5-4864 tested varied from 10^{-11} M to 10^{-4} M in the competitive binding assays performed. The K_i value derived from IC_{50} was calculated to be 2.6 ± 1.4 μM, which is similar to Liss-ConPK11195 (1 μM) (*8*). Even though the binding affinity is significantly lower than that of [^{3}H]Ro5-4864 (K_i = 5 nM) (*16*), the selective binding of lissamine−C_6Ro5-4864 to TSPO is clearly shown and visualized. The specificity of lissamine−C_6Ro5-4864 to TSPO is further verified by in vitro competition study. In this experiment, MDA-MB-231 cells were treated with 5 μM lissamine−C_6Ro5-4864 and PK11195 with different concentrations as competitor. Challenged cells showed reduced fluorescence signal compared to unchallenged cells (Figure 4). Taken together these data suggest that lissamine−C_6Ro5-4864 is a promising TSPO targeted MI agent.

CONCLUSIONS

We synthesized and characterized a conjugable form of the benzodiazepine Ro5-4864, C_6Ro5-4864, which can be conjugated to a variety of signaling moieties for TSPO-targeted imaging. This TSPO ligand has been coupled to a fluorescent dye, and the resulting imaging agent, lissamine−C_6Ro5-4864, displays attractive optical properties for fluorescence microscopy imaging. The specific binding of this agent to TSPO was demonstrated by radioligand binding studies and live cell imaging on MDA-MB-231 breast cancer and C6 glioma cells.

ACKNOWLEDGMENT

This work was supported by grants from the National Science Foundation (Bes-0323281) and Department of Defense (W81XWH-

04-1-0432). We thank Coe Foutch and Kathryn Stinson for assistance with cell preparation.

LITERATURE CITED

(1) Papadopoulos, V., Baraldi, M., Guilarte, T. R., Knudsen, T. B., Lacapere, J. J., and et al. (2006) Translocator protein (18 kDa): new nomenclature for the peripheral-type benzodiazepine receptor based on its structure and molecular function. *Trends Pharmacol. Sci. 27*, 402−409.

(2) Casellas, P., Galiegue, S., and Basile, A. S. (2002) Peripheral benzodiazepine receptors and mitochondrial function. *Neurochem. Int. 40*, 475−486.

(3) Taketani, S., Kohno, H., Furukawa, T., and Tokunaga, R. (1995) Involvement of Peripheral-Type Benzodiazepine Receptors in the Intracellular-Transport of Heme and Porphyrins. *J. Biochem. 117*, 875−880.

(4) Decaudin, D., Castedo, M., Nemati, F., Beurdeley-Thomas, A., De, Pinieux, G., and et al. (2002) Peripheral benzodiazepine receptor ligands reverse apoptosis resistance of cancer cells in vitro and in vivo. *Cancer Res. 62*, 1388−1393.

(5) Kozikowski, A. P., Kotoula, M., Ma, D. W., Boujrad, N., Tuckmantel, W., and et al. (1997) Synthesis and biology of a 7-nitro-2,1,3-benzoxadiazol-4-yl derivative of 2-phenylindole-3-acetamide: A fluorescent probe for the peripheral-type benzodiazepine receptor. *J. Med. Chem. 40*, 2435−2439.

(6) Shilova, N. V., and Bovin, N. V. (2003) Fluorescent labels for the analysis of mono- and oligosaccharides. *Russ. J. Bioorg. Chem. 29*, 309−324.

(7) Manning, H. C., Goebel, T., Marx, J. N., and Bornhop, D. J. (2002) Facile, efficient conjugation of a trifunctional lanthanide chelate to a peripheral benzodiazepine receptor ligand. *Org. Lett. 4*, 1075−1078.

(8) Manning, H. C., Smith, S. M., Sexton, M., Haviland, S., Bai, M. F., and et al. (2006) A peripheral benzodiazepine receptor targeted agent for in vitro imaging and screening. *Bioconjugate Chem. 17*, 735−740.

(9) Farges, R. C., Torres, S. R., Ferrara, P., and Ribeiro-Do-Valle, R. M. (2004) Involvement of steroids in anti-inflammatory effects of peripheral benzodiazepine receptor ligands. *Life Sci. 74*, 1387−1395.

(10) Gavioli, E. C., Duarte, F. S., Bressan, E., Ferrara, P., Farges, R. C., and et al. (2003) Antidepressant-like effect of Ro5-4864, a peripheral-type benzodiazepine receptor ligand, in forced swimming test. *Eur. J. Pharmacol. 471*, 21−26.

(11) DalBo, S., Nardi, G. M., Ferrara, P., Ribeiro-do-Valle, R., and Farges, R. C. (2004) Antinociceptive effects of peripheral benzodiazepine receptors. *Pharmacology 70*, 188−194.

(12) Garnier, M., Dimchev, A. B., Boujrad, N., Price, J. M., and Musto, N. A., and et al. (1994) In-Vitro Reconstitution of a Functional Peripheral-Type Benzodiazepine Receptor from Mouse Leydig Tumor-Cells. *Mol. Pharmacol. 45*, 201−211.

(13) Vejdelek, Z., Polivka, Z., and Protiva, M. (1985) Synthesis of 7-Chloro-5-(4-Chlorophenyl)-1-Methyl-1,3-Dihydro-1,4-Benzodiazepin-2-one. *Collect. Czech. Chem. Commun. 50*, 1064−1069.

(14) Papadopoulos, V., Guarneri, P., Krueger, K. E., Guidotti, A., and Costa, E. (1992) Pregnenolone Biosynthesis in C6−2b Glioma Cell Mitochondria - Regulation by a Mitochondrial Diazepam Binding Inhibitor Receptor. *Proc. Natl. Acad. Sci. U.S.A. 89*, 5113−5117.

(15) Hardwick, M., Fertikh, D., Culty, M., Li, H., Vidic, B., and et al. (1999) Peripheral-type benzodiazepine receptor (PBR) in human breast cancer: Correlation of breast cancer cell aggressive phenotype with PBR expression, nuclear localization, and PBR-mediated cell proliferation and nuclear transport of cholesterol. *Cancer Res. 59*, 831−842.

(16) Boujrad, N., Gaillard, J. L., Garnier, M., and Papadopoulos, V. (1994) Acute Action of Choriogonadotropin on Leydig Tumor-Cells - Induction of a Higher Affinity Benzodiazepine-Binding Site Related to Steroid-Biosynthesis. *Endocrinology 135*, 1576−1583.

BC060381R

Synthesis and Testing of a Binary Catalytic System for Imaging of Signal Amplification *in Vivo*

Alexei Bogdanov, Jr.,* Hye-Won Kang, Manuel Querol, P. Hendrik Pretorius, and Anna Yudina†

Department of Radiology, University of Massachusetts Medical School, 55 Lake Avenue North, Worcester, Massachusetts 01655. Received December 18, 2006; Revised Manuscript Received February 21, 2007

We report a binary targeted enzymatic system that is composed of two covalent monoclonal antibody conjugates for specific labeling of cellular targets *in vivo*. The system utilizes low-molecular weight peroxidase-reducing substrates synthesized by linking 5-hydroxytryptamine (serotonin) with DTPA (5HT−DTPA) for magnetic resonance and radionuclide imaging or with Cy5.5 for near-infrared optical imaging. Initially, the conjugation reaction conditions were optimized to achieve a low level of antiepidermal growth factor receptor (EGFR) antibody (EMD 72000) modification with the *N*-hydroxysuccinimide ester of 4-hydrazinonicotinate acetone hydrazone (SANH), yielding mAb−HNH conjugate. The resultant modified antibodies were incubated with the periodate-oxidized peroxidase (HRP) or 4-formylbenzoyl-conjugated glucose oxidase (GO), followed by the purification of the resultant mAb−enzyme conjugates by size-exclusion HPLC. The conjugates were further characterized by electrophoresis and were tested by cross-titration on A431 EGFR+ squamous carcinoma or SW620 adenocarcinoma cells (negative control). The conjugates at the optimized concentration ratios were further tested using near-infrared fluorescence microscopy in the presence of Cy5.5 monocarboxy-5-hydroxytryptamide. Further *in vitro* experiments demonstrated that (1) antibody binding was specific and could be inhibited by free antibody; (2) both antibody conjugates exhibited high enzymatic activity after the binding to the cells; (3) ^{111}In-labeled 5-HT−DTPA was avidly binding to EGFR-positive cells only if both HRP- and GO-conjugates were bound to the cells. The conjugates were tested *in vivo* using a SPECT imaging experiment, which demonstrated the accumulation of ^{111}In-labeled 5-HT−DTPA substrate at the site containing both conjugates.

INTRODUCTION

In vivo targeting of disease-specific molecules has been a subject of investigation as a diagnostic tool for decades, primarily with a goal of detecting and treating cancer (*1*). Recent advances in the use of therapeutic monoclonal antibodies suggested that the old paradigm has been finally transformed into a highly important clinical tool (*2*). The two major reasons for this success are (1) identification of relevant target molecules and signaling cascades; (2) elimination of immunogenicity through new technologies, i.e., antibody engineering (including humanization of monoclonal antibodies) (*3*). In addition, a variety of semisynthetic and engineered alternatives to mouse hybridoma-secreted monoclonal antibodies have emerged since the 1990s, including single chain antibodies (*4*) and minibodies (*5*), phage display library-derived peptides (*6*, *7*), and aptamers (*8*, *9*). In general, the use of protein engineering and combinatorial techniques are expected to significantly shorten the development of new targeted agents and to utilize mainly *in vitro*-based selection procedures. The engineered molecules with a single target-binding domain or sequence can be further di- or multimerized to increase the avidity and target tissue accumulation (*10*). In diagnostic imaging this is frequently achieved by using the imaging component (i.e., nanoparticle) as a multimeric reactive center (*11, 12*). Regardless of whether single-, bi-, or multimeric targeted molecules are used for delivery of diagnostic compounds, the results of *in vivo* imaging depend largely on the distribution of the image signal-generating component of the targeted imaging drug or a construct (reviewed in (*13*)). This component can be linked to targeting molecules either directly (i.e., radionuclide (*14*) or a fluorochrome (*15*)) or indirectly (e.g., linked via polymeric carrier (*16*, *17*) and incorporated into liposomes or micelles (*18*)).

Alternatively, a pretargeting approach can be used for *in vivo* imaging and therapy (*19*−*21*). This concept includes *in vivo* administrations of targeting and imaging compounds that are separated in time. This approach is based on high affinity/complementarity of imaging compounds or conjugates to targeting molecules, which are administered first. By carefully choosing pharmacokinetics of the first (targeted) molecule and the second (imaging ligand) molecule, it is feasible to improve sensitivity of imaging because of the higher target-to-background ratios. Since most of the high-affinity receptor-specific molecules (e.g., antibodies, their fragments, and dimerized scFv (*14*, *22*)) have relatively long blood half-lives, the availability of a "waiting time window" allows clearance of free targeting molecules. This eliminates the unnecessary and lengthy exposure to imaging ligand that could lead to increased immunogenicity and/or undesirable dosimetry profiles. Consequently, the pretargeting approach was adapted to labeled biotin (*23*), small molecular weight imaging ligands (*24*, *25*), oligonucleotides (*26*), oligonucleotide analogues (*27*), polymers (*28*), and conjugates of avidin with imaging ligands (*29*).

We hypothesized that pretargeting strategy could be combined with enzyme-mediated signal amplification for *in vivo* imaging (*30*) and applied this concept for imaging cell-surface receptors in human carcinomas using MRI (*31*). We report here a binary EGF[1]-receptor (EGFR) targeted catalytic system based on enzymatically coupled conversion of fluorochrome- and radionuclide-labeled imaging substrates into the tissue-bound species

* To whom correspondence should be addressed. E-mail: Alexei.Bogdanov@umassmed.edu, tel.: 508-856-5571, fax: 508-856-1860.

† Current address: University Hospital Utrecht, Heart Lung Institute, Heidelberglaan 100, 3584 CX Utrecht, The Netherlands.

10.1021/bc060392k CCC: $37.00 © 2007 American Chemical Society
Published on Web 05/18/2007

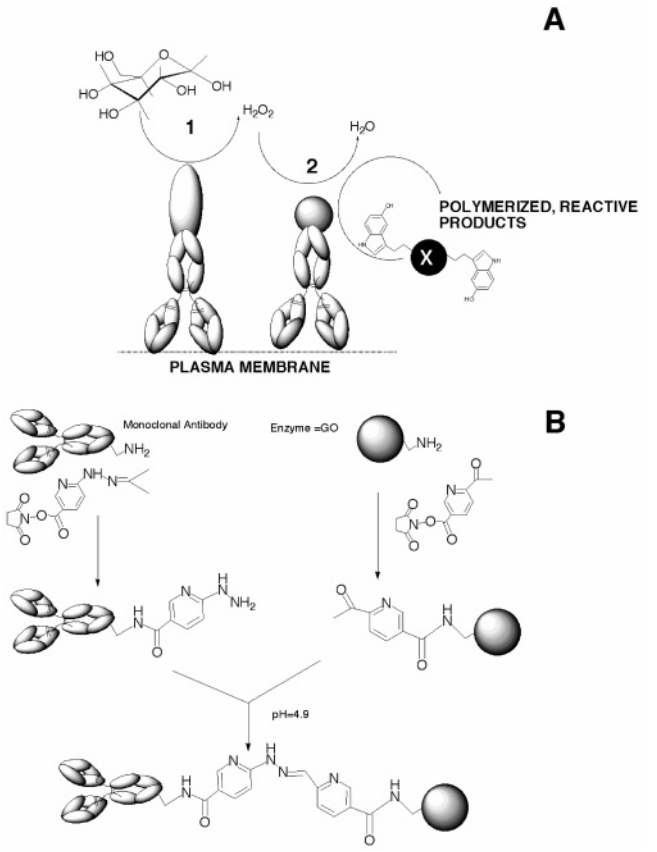


Figure 1. A. A scheme of the proposed two-enzyme (binary) targeted signal amplification system. The first conjugate (mAb−GO) provides the source of peroxide by oxidizing glucose, which is present in the extracellular milieu. The second conjugate (mAb−HRP) reduces peroxide and oxidizes imaging substrates bearing hydroxyindole or hydroxybenzene groups. X = paramagnetic element, radionuclide, fluorochrome. B. Antibody−enzyme conjugation via the formation of a stable hydrazone.

(schematically shown in Figure 1A). We anticipate that such binary systems could be useful for single- or multimodality imaging of EGFR and other cancer-specific cell-surface targets.

MATERIALS AND METHODS

Peroxidase-Reducing Substrate Synthesis and Characterization. Synthesis of di-5-hydroxytryptamide−DTPA (5HT−DTPA) was performed as described by us previously (*32*, *33*). Briefly, to a suspension of DTPA-bis(anhydride) (0.357 g, 1 mmol) in 30 mL of dry DMF was added a solution of 2.2 mmol of dry triethylamine and 2.2 mmol of 5-hydroxytryptamide (serotonin) in 10 mL under argon, and the mixture was stirred at room temperature for 48 h. The completion of the reaction was determined by using C18 RP-TLC. The solvent was removed under vacuum, and the crude mixture was solubilized in 50 mL of 0.5 M triethylammonium acetate in water (50 mL, pH 7.0). The solution was washed twice with 25 mL of methylene chloride and evaporated again to give a white powder. The powder was solubilized in MeOH and precipitated by slow acetone diffusion. This procedure was repeated three times to afford di-5-hydroxytryptamide−DTPA with a yield of 58%. ^{1}H NMR (DMSO-d_6), δ (ppm): 2.70 (4H, t, J = 7.6 Hz), 2.89 (4H, t, J = 7.6 Hz), 3.10 (4H, m), 3.21 (4H, s), 3.24 (4H, s), 3.29−3.31 (4H, m), 3.46 (2H, s), 6.56 (2H, dd, J_1 = 6.4 Hz, J_2 = 2.2 Hz), 6.93 (2H, d, J = 2.1 Hz), 7.02 (2H, d, J = 2.1 Hz), 7.09 (2H, d, J = 8.6 Hz), 8.42−8.45 (2H, m), 10.05 (2H, s). FAB-MS: 710, $^+$. The obtained chelate was purified by using preparative HPLC (HAISIL 100 C-8, Higgins Analytical, 10−90% acetonitrile/water gradient (yield, 40%).

Fluorescent substrate (Cy5.5 monocarboxy-5-hydroxytryptamide, Figure 1S) was synthesized by reacting 1.1 molar excess of 5-hydroxytryptamine with Cy5.5-NHS (GE Healthcare Bio-Sciences Corp., Piscataway NJ) in DMF in the presence of triethylamine. The reaction product was precipitated using 10 volumes of acetone:diethyl ether (1:2 by vol), dried under argon, and purified by using C18 HPLC (Discovery C18 column, Supelco, St. Louis, MO) and a gradient of acetonitrile in 0.1 M triethylammonium acetate, pH 7.0 (see Supporting Information).

The peroxidase-reducing properties of synthesized substrates were tested by spectrofluorometry (5HT−Cy5.5) using a Cary Eclipse instrument (Varian Inc., Palo Alto, CA) as well as test labeling with ^{111}In and analytical separation on a C18 HPLC column (Discovery, Supelco, Sigma-Aldrich, St. Louis, MO). Approximately 1 μg of peroxidase and glucose oxidase conjugates was combined with various concentrations of substrates in the presence of 5 mM glucose in PBS, pH 7.5, and incubated for 10 min. Additionally, human serum albumin was added at 40 mg/mL (final concentration) in some experiments. Fluorescence was assayed by measuring changes of fluorescence spectra in the range of 690−800 nm using excitation at 675 nm (Cary Eclipse, Varian) in the presence or absence of serum albumin (see Figure 2S).

Synthesis of Antibody Conjugates. Monocolonal antibodies (humanized EMD72000 mAb (*34*) and mouse mAb 425 (*35*, *36*) were provided by Merck KGaA, Darmstadt, Germany. Antibodies were dialyzed against 10 mM PBS, pH 7.5, before use. The concentration of NHS esters in commercially available preparations of *N*-hydroxysuccinimidyl 4-hydrazinonicotinate acetone hydrazone (SANH) and *N*-hydroxysuccinimidyl-C6−4-formylbenzoate (C6-SFB, both were obtained from Pierce Chemical Co., Rockford, IL) was determined by measuring *N*-hydroxysuccinimide release upon hydrolysis at pH 8.5 using spectrophotometry at 260 nm (ϵ_{260} = 8500 M^{-1} cm). Twelve nanomoles of mAb in 0.2 mL of 0.1 M sodium bicarbonate, pH 8, was covalently modified using 1.5 μL of SANH in DMF (60 nmol of active ester, i.e., 5-fold molar excess over the protein) and incubated for 30 min at room temperature. The modified antibodies were purified on Tween-20 blocked BioSpin P-30 minicolumns (Bio-Rad, Hercules, CA) equilibrated with 0.1 M sodium acetate, pH 4.9.

Stock solution of recombinant glucose oxidase (GO) from *Aspergillus niger* (EMD Merck-Calbiochem) was dialyzed with 0.1 M sodium acetate, pH 4.9. To 0.2 mL of 120 μM glucose oxidase (24 nmol) in 0.1 M sodium bicarbonate, pH 8, was added 2 μL of 44 mM C6-SFB (88 nmol) in DMF on a Vortex mixer. After 30 min incubation, GO-formyl benzoate was purified on BioSpin P-30 minicolumns as described above. Horseradish peroxidase (100 nmol, Type IX, Sigma) in 0.25 mL of 0.1 M sodium acetate, pH 7, was oxidized using a 5-fold molar excess of sodium periodate for 30 min in the dark, and the reaction was stopped by adding 0.1 M glycerol (final concentration) and purified as above. The amount of covalently conjugated 4-hydraziniumnicotinate was determined by using 4-nitrobenzaldehyde and measuring absorbance at 380 nm (ϵ = 22000 M^{-1} cm); conjugated 4-formylbenzoyl groups were determined by spectrophotometry at 350 nm (ϵ = 18000 M^{-1} cm). Protein concentrations were determined by using Micro BCA assay (Pierce).

4-Hydraziniumnicotinate-modified antibodies (final concentration, 2 mg/mL) were combined with the enzymes bearing aldehyde groups at molar ratios ranging from 1:3 to 1:1.5

[1] Abbreviations: DPBS, Dulbecco's phosphate-buffered saline; EGF, epidermal growth factor; GO, glucose oxidase; HRP, horseradish peroxidase; mAb, monoclonal antibody; DTPA, diethylenetriamine pentaacetic acid; SPECT, single photon emission computed tomography.

(antibody:enzyme) at pH 4.9. The incubation was completed in 12 h, and 2-hydrazinopyridine was added (final concentration 0.1 mM) to block the remaining aldehyde groups. The reaction mixture was loaded onto a Superdex 200 column (GE-Healthcare) and eluted with 0.1 M ammonium acetate, pH 7.0, at 0.5 mL/min. The peaks that were eluted earlier than 150 kD IgG marker protein and containing peroxidase or glucose oxidase activity were pooled separately, concentrated, and washed with PBS using Amicon Ultra-4 centrifugal filter units with an Ultracel-50 membrane (Millipore, Billerica MA) at 2800*g*. Concentrated conjugates were analyzed using 4−15% gradient SDS-PAGE minigels run at 60 V, followed by gel fixation and staining with Flamingo fluorescent reagent (Bio-Rad).

Radioiodination and Fluorescent- and ^{111}In-Labeling. A 100 μL amount of monoclonal antibodies (A425 mAb and EMD72000 mAb at 1 mg/mL) was radioiodinated by using Na^{125}I (Perkin-Elmer, Boston, MA) using Iodogen-coated tubes (Pierce) as described by the manufacturer and purified by using PD10 columns (GE-Healthcare). Radiochemical purity by ITLC-G was higher than 98% and exceeded 90% by SDS electrophoresis. Fluorescent labeling of A425 mAb was achieved by using a 5-fold molar excess of Alexa Fluor 488 NHS ester (Invitrogen) in 0.1 M sodium carbonate, pH 8.5, followed by purification on Bio-Spin P30 minicolumns (Bio-Rad).

Labeling of 5-HT−DTPA was performed by adding 800 μCi of ^{111}In chloride to a solution of 50 μg 5-HT−DTPA (65 nmol) in 0.1 mL of 10 mM sodium citrate, pH 5.0. After 15 min incubation, HPLC runs on a Discovery C18 analytical column eluted with a 10−75% acetonitrile gradient in water routinely showed a 95% binding of ^{111}In radioactivity to 5-HT−DTPA.

Cell Culture Experiments. A431 human squamous carcinoma, SW620 human adenocarcinoma, and MDCK epithelial cells were obtained and grown as recommended by ATCC. Cells were seeded on the surface of coverslip-bottomed chambers (Lab-Tek Chambered glass coverslips, Electron Microscopy Sciences, Hatfield, PA) for fluorescence microscopy or in 96-well plates for antibody-binding experiments. Alternatively, cells were detached using nonenzymatic methods, fixed with 4% formaldehyde, and used at $2-4 \times 10^5$/well for binding experiments. Binding experiments were performed in triplicate, curve fitting, and statistical analysis performed by using Prism 4 (Graph Pad Software Inc.).

EGFR expression on A431 cells was monitored by using Alexa Fluor 488-labeled A425 mouse monoclonal antibodies followed by flow cytometry (FACSCalibur, Beckton-Dickinson). In all binding experiments 0.2 μm-filtered 5% horse serum in DPBS, pH 7.2, was used for serial dilutions of the antibodies and conjugates. Peroxidase activity was determined by using ABTS substrate (Sigma-Aldrich). Glucose oxidase activity was determined by using a 1 μg/mL solution of horseradish peroxidase in 2 mM ABTS, 5 mM glucose, 10 mM sodium citrate, pH 6.0. In both cases, endpoint changes of optical density were measured at 405 nm after a 30 min incubation at room temperature (M5 plate reader, Molecular Devices Inc.).

Fluorescence microscopy was performed using inverted Nikon TE2000 Eclipse microscope equipped with Cy5.5 excitation/emission epifluorescence filters and CoolSNAP-HQ CCD (MVI Inc., Avon, MA). Cells were incubated with mAb−enzyme conjugates (1 μg/mL each conjugate in 0.2% BSA/DPBS) followed by washing in DPBS and incubating with 2 μM 5HT−Cy5.5, 5 mM glucose in DPBS. Control experiments were performed in the presence of Cy5.5-labeled A425 anti-EGFR antibody or 2 μM 5HT−Cy5.5, 5 mM glucose in DPBS in the absence of conjugates.

Experiments with 5-HT−[^{111}In]DTPA were performed in A431 cells or SW620 cells seeded in 96-well plates. Cells were incubated with various amounts of mAb−GO/mAb−HRP conjugate mixtures (concentration range 0−10 μg/mL of each mAb conjugate) or mAb conjugates incubated with the cells individually at the same concentrations. Cells were washed with 0.2% horse serum in DPBS followed by adding 1 nmol of 5-HT−[^{111}In]DTPA/well in 0.2 mL of 5 mM glucose in DPBS. In 30 min at room temperature, the cells were lysed and radioactivity was determined by gamma-counting (Packard Cobra 5003 gamma counter).

***In Vivo* Single Photon Computed Tomography Imaging (SPECT).** *In vivo* experiments were approved by UMass Medical School Institutional Animal Care and Use Committee. Initially, 0.25 mL of Matrigel (BD Biosciences, San Jose, CA) was mixed on ice with 5 μL aliquots of 0.2 mg/mL mAb−HRP and mAb−GO conjugate, respectively. Athymic (*nu/nu*) female mice (NCI) were injected with the above solution in a femoral muscle. The contralateral femoral muscle was injected with 0.25 mL of Matrigel alone. After Matrigel solidification, 0.2 mL of saline containing 500 μCi of 5HT−DTPA[^{111}In] was injected into a tail vein. HiSPECT imaging was performed at 4 h postadministration of the labeled substrate using Prism 3000 3-head SPECT (Picker, Cleveland, OH) using pyramid collimators equipped with six-pinhole whole body aperture plates allowing 40 × 90 mm field-of-view (Bioscan, Washington, D.C./Scivis Gmbh). The images were collected under anesthesia for a total of 20 min and reconstructed using Bioscan software. Biodistributions were performed after the experiment, and radioactivity was determined as above.

RESULTS

Characterization of Model Cell Lines. Using fluorescent anti-EGFR antibody and SW620 cells as negative control, we initially verified that A431 cells were more than 95% positive for EGFR expression by flow cytometry. In experiments with radiolabeled anti-EGFR monoclonal antibodies (mouse A425 anti-EGFR and EMD72000 mAbs), we determined that nonfixed A431 cells had approximately 1.06×10^6 total binding/uptake sites per cell. As shown by using fixed cells, at least 60% of these sites represented the true receptor binding sites. On the average, 425−450 ng of antibody saturated all binding sites on the surface of one million live A431 cells. EGFR-negative cells showed negligible amounts of cell surface association: the experiments with both MDCK and SW620 cells showed no concentration-dependent binding in both cell-based ELISAs and radioimmunoassays.

Conjugate Synthesis. Initially, we tested hydrazone bond formation between the SANH-modified antibody and SFB-modified glucose oxidase (Figure 1B) using hydraziniumnicotinate:mAb ratios in the range of 15:1 to 10:1 and various SFB:GO ratios. As a result, coincubation of the modified proteins resulted in a very rapid formation of conjugates. Within 2 h, light scattering at 600 nm increased two times. The conjugates formed at 80% antibody consumption yield showed little precipitation after centrifuging at 13000*g* for 10 min and eluted in the void volume of Superdex 200 columns (1.3×10^6 D exclusion limit). However, cell ELISA and cross-titration on A431 cells with HRP and GO mAb conjugates (Figure 2A) showed that GO conjugates were outcompeted by peroxidase conjugates in cell-based ELISA assays, indicating a substantial loss of antibody affinity in large conjugates formed with GO. According to the results of the 4-nitrobenzaldehyde reaction, after lowering SANH:mAb molar ratio to 5:1, four hydraziniumnicotinate groups were covalently linked per protein molecule, on the average. At this mAb modification ratio, the formation of large conjugates was avoided if both GO and HRP were reacted with mAbs at the ratio of 1.5 mol of enzyme per 1 mol of antibody. Higher enzyme:mAb ratios usually resulted in undesirable large macromolecular conjugates. Conjugates

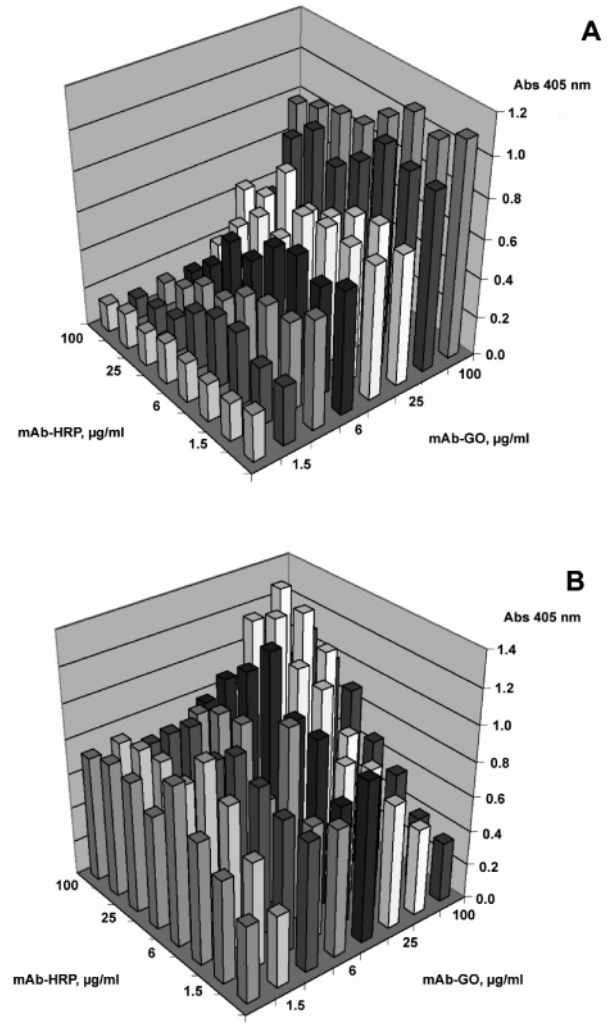


Figure 2. Cross-titration of A431 cells in 96-well plates using EMD72000 antibody conjugates. A. An example of titration results showing mAb−GO conjugates outcompeted by mAb−HRP. B. an example of titration using optimized mAb−GO conjugates that preserve binding affinity.

obtained by using lower active ester/mAb ratios showed more favorable cross-titration profiles (Figure 2B) with less competition between the conjugates for cell binding sites. The preparative size-exclusion chromatography results (Figure 3A) suggest that two major peaks corresponding to 670 and 410 kD products in the case of GO and one peak having an average mass of 400 kD in the case of HRP were formed as a result of covalent conjugation. The corresponding SDS gel electrophoresis (Figure 3B) revealed heterogeneity of conjugation products showing the 400 kD HRP-linked product alongside higher order conjugates. The analysis of glucose oxidase−mAb conjugation products showed some dissociation into a free GO subunit and remaining conjugated product (320 kD, free 90 kD subunit and 410 kD conjugate). The first peak of eluted GO conjugates showed the presence of conjugates with a higher molecular mass. After blocking free aldehyde groups, the conjugates preserved their immunoreactivity and stability for 10−14 days with no detectable changes in enzymatic activity.

Cell Culture Experiments. Testing of conjugates using cross-titration showed that there is an optimal range of 5−1.2 μg conjugate/96 wells of GO and HRP (i.e., per 5×10^4 cells, on the average) which resulted in similar optical density values (greater than 1 AU under conditions used) and showed only a minor apparent concentration-dependent competition for cell binding sites. In these experiments the rate-limiting hydrogen peroxide was supplied by glucose oxidase-mediated oxidation

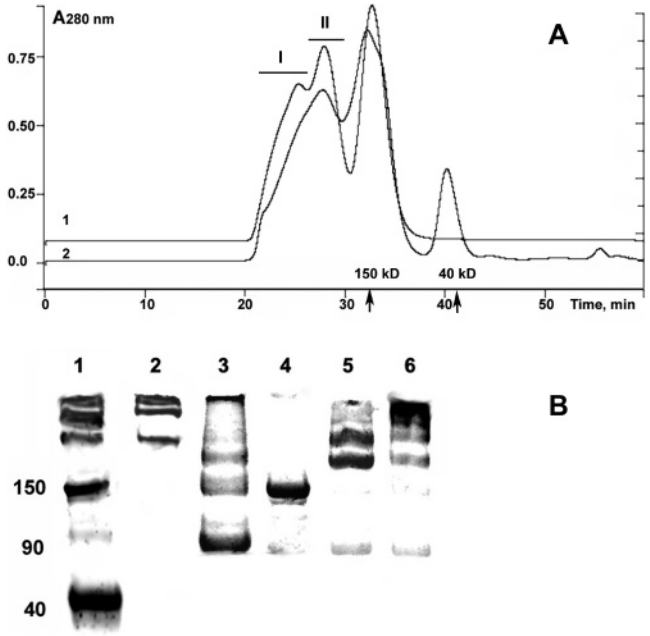


Figure 3. A. Size-exclusion HPLC separation of mAb conjugates with GO from the free antibody/GO peak (indicated by an arrow below "150 kD") (profile 1) and mAb−HRP conjugate separation from free HRP ("40 kD" arrow, profile 2). B. Gradient is 5−15% acrylamide/SDS gel electrophoresis: lane 1, mAb−HRP reaction mixture; lane 2, mAb−HRP conjugates; lane 3, mAb−GO reaction mixture; lane 4, mAb standard; lane 5, lower molecular weight conjugate peak of purified mAb−GO conjugates (peak II, Figure 3A); lane 6, higher molecular weight mAb−GO conjugates (peak I, Figure 3A).

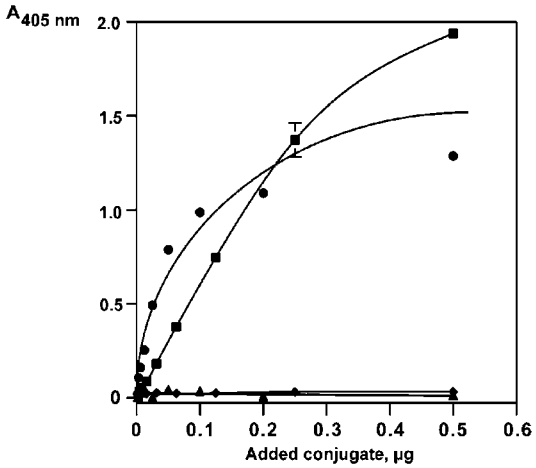


Figure 4. Cell ELISA: the dependence of peroxidase ABTS reaction signal from the conjugate concentration. HRP activity was determined directly (circles); GO activity was determined indirectly by using a 1 μg/mL solution of horseradish peroxidase in 2 mM ABTS, 5 mM glucose, 10 mM sodium citrate, pH 6.0 (squares). Nonspecific cell-associated activities of peroxidase (triangles) and glucose oxidase (diamonds) were measured in the presence of the excess of nonconjugated mAb (10 μg/mL). Data presented as mean ± SD ($n = 3$).

of D-glucose, which was present at 5 mM non-rate-limiting concentration. The enzymatic activity in the wells was then monitored after the conjugates were separately incubated with the cells (Figure 4). The ABTS reaction was performed either directly, i.e., in the presence of noninhibiting concentrations of hydrogen peroxide for determining mAb−HRP concentration-dependent binding, or indirectly, in the presence of an excess amount of HRP (0.1 μg of peroxidase/well) and 5 mM glucose to track the concentration dependence of mAb−GO binding. These experiments revealed the concentration-dependent binding of HRP conjugate and GO concentration-dependent hydrogen

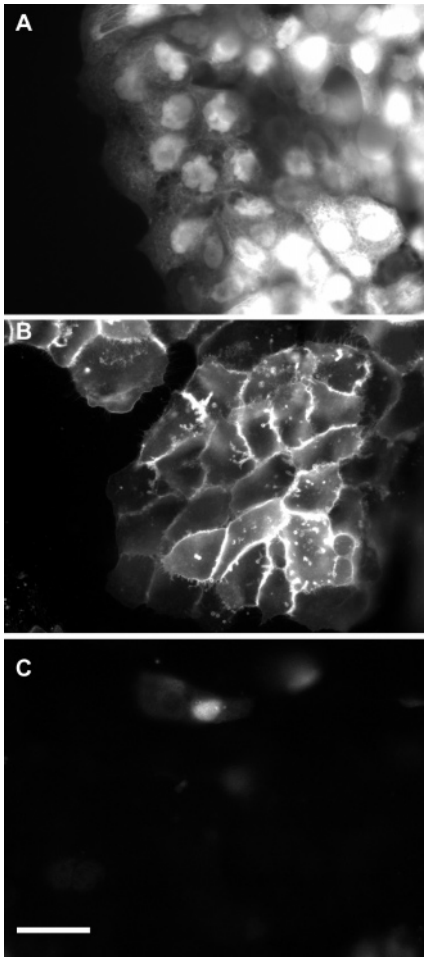


Figure 5. A. Fluorescence microscopy of A431 cells incubated with a mAb−HRP and mAb−GO conjugates (1 μg/mL) followed by 2 μM 5HT−Cy5.5 substrate, 5 mM glucose in DPBS. B. Fluorescence microscopy of A431 cells stained with Cy5.5-labeled A425 anti-EGFR monoclonal antibody (10 μg/mL). C. A431 cells incubated with a free 2 μM 5HT−Cy5.5 substrate in the absence of antibody conjugates.

peroxide release that was detected by enzymatically coupled HRP/ABTS reaction. In the presence of 10 μg of free mAb, enzymatic activity was completely absent due to binding inhibition (Figure 4).

Cells were then incubated in the presence of a mixture of 1 μg of mAb−HRP and mAb−GO each, washed, and treated with a near-infrared fluorescent substrate 5HT−Cy5.5 (see Figure 1S). This substrate was efficiently oxidized in the presence of glucose, GO, and HRP with a resultant loss of fluorescence (Figure 2S). However, if albumin was present in the solution, about 50% of the fluorescence was rescued (Figure 2S). After adding the substrate to cells, we observed a bright labeling of cell membranes, cytoskeleton, and nucleus (Figure 5A). The observed distribution of oxidized 5HT−Cy5.5 in the cells was markedly different from the distribution of Cy5.5−mAb (either 425 or EMD72000) on the surface of the cells (Figure 5B). If cells were incubated with the free dye in the absence of conjugates, only very few cells were permeated by the substrate (Figure 5C).

The formation of cell-bound products of 5-hydroxytryptamide oxidation was proven by using radioactively labeled di-5HT−[^{111}In]DTPA (90% radiochemical purity, see Figure 3S). In the presence of both HRP− and GO−mAb conjugates we observed binding of radioactivity to cells (Figure 5). The obtained cell protein-normalized binding curves suggested that the simultaneous presence of both conjugates in the well was essential for ^{111}In radioactivity association with cells since none of the

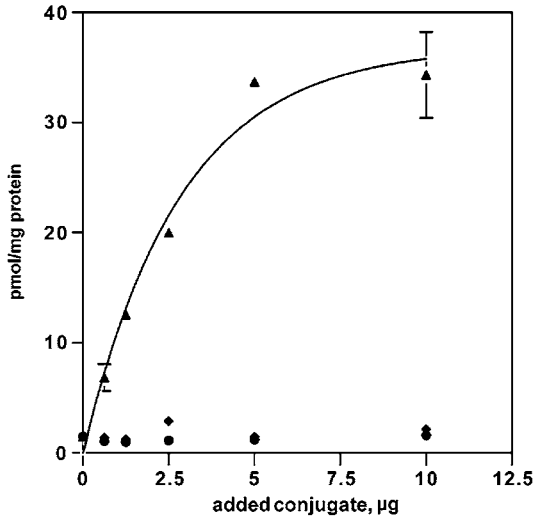


Figure 6. A431 cells incubated with a mixture of mAb−GO and mAb−HRP antibody conjugates at the concentrations indicated (triangles) or each conjugate separately (mAb−GO, diamonds; mAb−HRP, circles) in the presence of 5-HT−[^{111}In]DTPA (1 nmol/well in 5 mM glucose/DPBS). Data presented as mean ± SD (n = 3).

conjugates that individually bound to A431 cells showed the ability to oxidize the substrate with the formation of the cell-binding species.

***In Vivo* Experiments.** Finally, to establish whether the presence of conjugates can be detected *in vivo*, we performed a feasibility experiment by using a model *in vivo* system. We used a Matrigel semipermeable matrix pellet that served as a colocalization site of both conjugates used at the optimized concentrations. On the basis of *in vitro* data, the estimated 1 μg of each of the conjugates in 0.25 mL of Matrigel was the lowest saturating concentration required for the HRP−GO-coupled system to oxidize and convert the substrate with high efficacy. We mixed the conjugates with Matrigel at 4 °C and injected the solution into femoral muscles of mice. Contralateral enzyme-free Matrigel muscle injection served as a control. After the injection of a dose of [^{111}In]-labeled di-5HT−DTPA and 4 h of waiting to ensure the clearance of free molecule, we assessed binding of the substrate to Matrigel using SPECT imaging with subsequent biodistribution. The imaging allowed reconstruction of the remaining radioactivity (11% of injected dose, 60 μCi/mouse) distribution in the animals. We observed the overall higher signal in the conjugate-containing Matrigel implant if compared to the control. SPECT imaging allowed us to establish that the reacted substrate was retained primarily in the outer layer of Matrigel (Figure 6A). The model colocalization implant had bound [111In] radioactivity (5.2% injected dose/g) that was 7 times higher than the control (0.7% injected dose/g). The biodistribution showed that other major sites of activity accumulation were colon (1.1% injected dose/g) and bladder, suggesting some hepatobiliary excretion in addition to kidney filtration.

DISCUSSION

We previously reported that gadolinium (Gd) relaxivity increases as a result of oligomerization of phenolic chelates of Gd (*32*, *37*). The applications of this water relaxation effect ("MR signal amplification") were reported for imaging myeloperoxidase activity in model systems (*33*, *38*). The extension of this imaging approach beyond MRI suggested that similar substrates labeled with radionuclides could also be useful for imaging endogenous peroxidase activity (*39*). The accumulated data suggests that targeted delivery of enzymes capable of converting "imaging prodrugs" into reactive species could be

potentially used for imaging of a variety of target molecules *in vivo*. Recent reports describing metabolic cell surface biotinylation for cell targeting (*40*), as well the use Gd-amplification step for MRI of human carcinoma-targeted delivery (*31*), demonstrated the feasibility of the developed approach for *in vivo* imaging. Importantly, the use of "in situ catalysis" allows signal amplification in one step, without the need for additional adaptor proteins or multivalent particles. The approach is based on the delivery of targeted enzymes *in vivo* through biodistribution and clearance, followed by a chase with the imaging substrate ("prodrug"), biodistribution phase, and rapid clearance of free substrate. The latter scenario was modeled *in vivo* in this study. In addition, we summarized the results of the experiments aimed at synthesis, characterization, and testing of a binary catalytic targeted system that could be used for amplification-pretargeting of cell receptors *in vivo*.

We chose humanized anti-EGF receptor antibody (matuzumab) as a model because of the emerging use of these antibodies in treating advanced pancreatic cancer (*41*) and non-small cell lung cancer (*42*) as well as squamous cell carcinomas of head and neck (*43*). Our preliminary experiments demonstrated that hydrazone bond formation offers a simple and reliable approach allowing conjugation of these antibodies with glucose oxidase and peroxidase, respectively. However, the preservation of affinity of the resultant conjugates was critically dependent on the degree of antibody modification and molar ratios of reacting macromolecules. Only by selecting low modification ratios could we obtain conjugates with average masses lower than 700 kD that retained high affinity to cell EGF receptors. The optimized ratios of obtained purified conjugates were used to test two potential imaging substrates.

First, a covalent conjugate of 5-hydroxytryptamide and Cy5.5 dye was tested as a potential candidate for optical imaging of amplification-pretargeting. Near-infrared fluorochrome conjugation was chosen because of the known favorable tissue scattering and absorption characteristics of near-infrared fluorescence *in vivo* (*44*). Fluorescence microscopy of A431 cells incubated with GO− and HRP−mAb conjugates followed with a near-infrared substrate showed that unlike Cy5.5-labeled antibodies or nonoxidized substrate, the oxidized substrate was interacting with intracellular components (cytoskeleton and nuclei) which suggests chemical reactivity of the oxidized 5HT−Cy5.5. Apparently, the behavior of oxidized substrate was similar to that of myeloperoxidase-treated 5HT−DTPA(Gd) (*33*). The latter was binding tightly to albumin only after the enzyme-mediated oxidation. Overall, HRP-mediated oxidation of the near-infrared substrate resulted in a loss of fluorescence which was dramatically lowered by the presence of proteins or cells in the incubation medium.

Fluorescence microscopy results were supported by a demonstration of a highly specific cell binding of the second substrate tested in this study (5HT−[^{111}In]DTPA). The binding of radioactivity to cells was detected only if both GO and HRP conjugates were bound to the cells. The high specificity of radioactive substrate conversion into cell-binding species suggested that a colocalization of both conjugates at the same site or organ could potentially lead to very high target/background ratios provided the nonbound substrate does not have secondary nonspecific sites of accumulation *in vivo*. To test the potential use of the targeted catalytic system for imaging in live animals, we chose a model system previously used by us for myeloperoxidase activity imaging *in vivo* (*38*, *39*). This model system allows creation of a semipermeable reservoir that provides an artificial binding site for the enzyme-specific substrate.

On the basis of SPECT image reconstruction results (Figure 7), we concluded that imaging allows differentiation between artificial extracellular matrix implants which contained both conjugates and control implants lacking HRP and GO activity. This study suggested the need for further optimization of the time window between the administration of the radioactive substrate and imaging. It also suggested potential feasibility of targeted imaging in realistic models of human cancers. The advantage of such systems is in the potential high specificity of the imaging signal, which depends on efficiency of colocalization of both conjugates at the target site. However, there are still unsolved problems associated with the use of multicomponent targeting systems: (1) the need to account for potential differences in biodistribution between two conjugate components; (2) to need to attenuate the potential immune response to enzymes; (3) the need to control the size of conjugates to avoid nonspecific trapping of aggregated glucose oxidase-conjugated antibodies in the lung capillaries (*45*). It has been shown in the past that conjugated and unconjugated glucose oxidase has low systemic toxicity (*46*). The problem of conjugate aggregation was, in general terms, solved by developing an optimized conjugation protocol. However, the toxicity to tumor cells as a result of targeted delivery (*47*, *48*) should be treated as a factor that could potentially influence the imaging results.

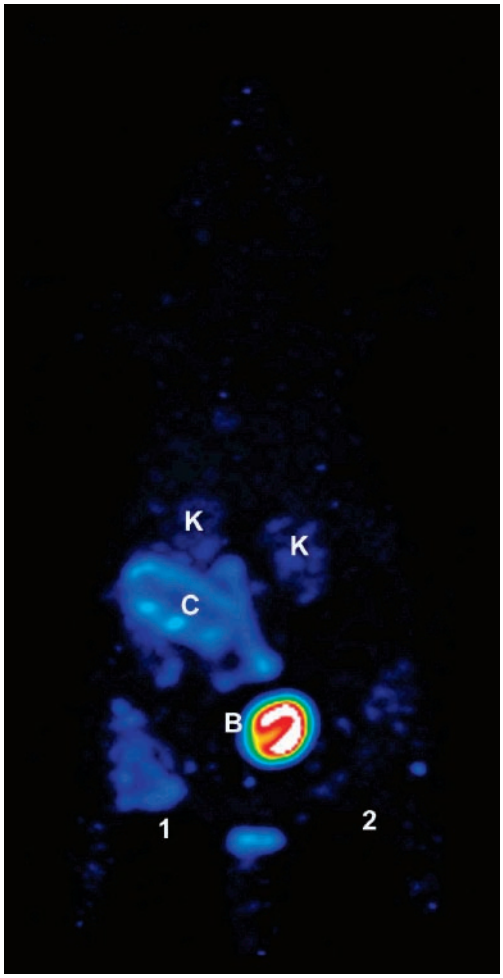


Figure 7. Single photon imaging of a mouse injected with a 0.25 mL Matrigel implant containing 1 μg each of mAb−HRP and mAb−GO (indicated as 1) and control implant 2. The animal was injected with 500 μCi of 5-HT−[^{111}In]DTPA followed by a 4 h waiting time window. SPECT imaging (20 min acquisition) was performed using Bioscan pinhole collimators using a three-head SPECT instrument.

In conclusion, we demonstrated that (1) the optimization of conjugation conditions results in stable covalent conjugates of antibodies with high yields of minimally cross-linked products; (2) the use of binary catalytic system could be potentially applied to several molecular imaging techniques (MRI, optical, and

radionuclide imaging); (3) binary targeted catalytic system enables imaging based on site-specificity, reducing substrate conversion into the cell-reactive species.

ACKNOWLEDGMENT

The authors acknowledge the input by Dr. Iris Verel (Philips Research) made during the initial phase of this work; Oncology Research, Global Preclinical R&D Merck KGaA for providing EMD72000 (Matuzumab). We are grateful to Dr. Mary Rucskowski (UMMS) for her help with radiochemical facility support. This work was supported in part by NIH RO1 EB000858.

Supporting Information Available: HPLC profiles of Cy5.5−monocarboxy-5-hydroxytryptamide and di-5-hydroxytryptamide−[^{111}In]DTPA. This material is available free of charge via the Internet at http://pubs.acs.org/BC.

LITERATURE CITED

(1) Torchilin, V. (1995) *Targeted delivery of imaging agents* p 732, CRC Press, Boca Raton, FL.
(2) Sharkey, R. M., and Goldenberg, D. M. (2006) Targeted therapy of cancer: New prospects for antibodies and immunoconjugates. *CA Cancer J. Clin. 56* , 226−43.
(3) Carter, P., and Merchant, A. M. (1997) Engineering antibodies for imaging and therapy. *Curr. Opin. Biotechnol. 8*, 449−54.
(4) Adams, G. P., and Schier, R. (1999) Generating improved single-chain fv molecules for tumor targeting. *J. Immunol. Methods 231*, 249−60.
(5) Hu, S., Shively, L., Raubitschek, A., Sherman, M., Williams, L. E., Wong, J. Y., Shively, J. E., and Wu, A. M. (1996) Minibody: A novel engineered anti-carcinoembryonic antigen antibody fragment (single-chain fv-ch3) which exhibits rapid, high-level targeting of xenografts. *Cancer Res. 56*, 3055−61.
(6) Ladner, R. C. (1999) Polypeptides from phage display. A superior source of in vivo imaging agents. *Q. J. Nucl. Med. 43*, 119−24.
(7) Nahrendorf, M., Jaffer, F. A., Kelly, K. A., Sosnovik, D. E., Aikawa, E., Libby, P., and Weissleder, R. (2006) Noninvasive vascular cell adhesion molecule-1 imaging identifies inflammatory activation of cells in atherosclerosis. *Circulation 114*, 1504−11.
(8) Lupold, S. E., Hicke, B. J., Lin, Y., and Coffey, D. S. (2002) Identification and characterization of nuclease-stabilized rna molecules that bind human prostate cancer cells via the prostate-specific membrane antigen. *Cancer Res. 62*, 4029−33.
(9) Mi, J., Zhang, X., Giangrande, P. H., McNamara, J. O., 2nd, Nimjee, S. M., Sarraf-Yazdi, S., Sullenger, B. A., and Clary, B. M. (2005) Targeted inhibition of alphavbeta3 integrin with an rna aptamer impairs endothelial cell growth and survival. *Biochem. Biophys. Res. Commun. 338*, 956−63.
(10) Williams, L. E., Wu, A. M., Yazaki, P. J., Liu, A., Raubitschek, A. A., Shively, J. E., and Wong, J. Y. (2001) Numerical selection of optimal tumor imaging agents with application to engineered antibodies.[see comment]. *Cancer Biother. Radiopharm. 16*, 25−35.
(11) Kang, H. W., Josephson, L., Petrovsky, A., Weissleder, R., and Bogdanov, A., Jr. (2002) Magnetic resonance imaging of inducible e-selectin expression in human endothelial cell culture. *Bioconjugate Chem. 13*, 122−7.
(12) Tsourkas, A., Shinde-Patil, V. R., Kelly, K. A., Patel, P., Wolley, A., Allport, J. R., and Weissleder, R. (2005) In vivo imaging of activated endothelium using an anti-vcam-1 magnetooptical probe. *Bioconjugate Chem. 16*, 576−81.
(13) Britz-Cunningham, S. H., and Adelstein, S. J. (2003) Molecular targeting with radionuclides: State of the science. *J. Nucl. Med. 44*, 1945−61.
(14) Olafsen, T., Kenanova, V. E., Sundaresan, G., Anderson, A. L., Crow, D., Yazaki, P. J., Li, L., Press, M. F., Gambhir, S. S., Williams, L. E., Wong, J. Y., Raubitschek, A. A., Shively, J. E., and Wu, A. M. (2005) Optimizing radiolabeled engineered anti-p185her2 antibody fragments for in vivo imaging. *Cancer Res. 65*, 5907−16.
(15) Ballou, B., Fisher, G. W., Waggoner, A. S., Farkas, D. L., Reiland, J. M., Jaffe, R., Mujumdar, R. B., Mujumdar, S. R., and Hakala, T. R. (1995) Tumor labeling in vivo using cyanine-conjugated monoclonal antibodies. *Cancer Immunol. Immunother. 41*, 257−63.
(16) Torchilin, V., Klibanov, A. L., Nossiff, N., Slinkin, M. A., Strauss, H., Haber, E., Smirnov, V. N., and Khaw, B. (1987) Monoclonal antibody modification with chelate-linked high-molecular-weight polymers: Major increases in polyvalent cation binding without loss of antigen binding. *Hybridoma 6*, 229−240.
(17) Kang, H., Weissleder, R., and Bogdanov, A. J. (2002) Targeting of mpeg-protected polyamino acid carrier to human e-selectin in vitro. *Amino Acids 23*, 301−308.
(18) Erdogan, S., Roby, A., Sawant, R., Hurley, J., and Torchilin, V. P. (2006) Gadolinium-loaded polychelating polymer-containing cancer cell-specific immunoliposomes. *J. Liposome Res. 16*, 45−55.
(19) Sharkey, R. M., Karacay, H., Cardillo, T. M., Chang, C. H., McBride, W. J., Rossi, E. A., Horak, I. D., and Goldenberg, D. M. (2005) Improving the delivery of radionuclides for imaging and therapy of cancer using pretargeting methods. *Clin. Cancer Res. 11*, 7109s-7121s.
(20) Wilkins, D. K., and Mayer, A. (2006) Development of antibodies for cancer therapy. *Expert Opin. Biol. Ther. 6*, 787−96.
(21) Meredith, R. F., and Buchsbaum, D. J. (2006) Pretargeted radioimmunotherapy. *Int. J. Radiat. Oncol. Biol. Phys. 66*, S57−9.
(22) Xiong, C. Y., Natarajan, A., Shi, X. B., Denardo, G. L., and Denardo, S. J. (2006) Development of tumor targeting anti-muc-1 multimer: Effects of di-scfv unpaired cysteine location on pegylation and tumor binding. *Protein Eng., Des. Select. 19*, 359−67.
(23) Rusckowski, M., Fritz, B., and Hnatowich, D. J. (1992) Localization of infection using streptavidin and biotin: An alternative to nonspecific polyclonal immunoglobulin. *J. Nucl. Med. 33*, 1810−5.
(24) van Schaijk, F. G., Oosterwijk, E., Soede, A. C., Broekema, M., Frielink, C., McBride, W. J., Goldenberg, D. M., Corstens, F. H., and Boerman, O. C. (2005) Pretargeting of carcinoembryonic antigen-expressing tumors with a biologically produced bispecific anticarcinoembryonic antigen x anti-indium-labeled diethylenetriaminepentaacetic acid antibody. *Clin. Cancer Res. 11*, 7130s−7136s.
(25) Corneillie, T. M., Whetstone, P. A., and Meares, C. F. (2006) Irreversibly binding anti-metal chelate antibodies: Artificial receptors for pretargeting. *J. Inorg. Biochem. 100*, 882−90.
(26) Kuijpers, W. H., Bos, E. S., Kaspersen, F. M., Veeneman, G. H., and van Boeckel, C. A. (1993) Specific recognition of antibody−oligonucleotide conjugates by radiolabeled antisense nucleotides: A novel approach for two-step radioimmunotherapy of cancer. *Bioconjugate Chem. 4*, 94−102.
(27) He, J., Liu, G., Gupta, S., Zhang, Y., Rusckowski, M., and Hnatowich, D. J. (2004) Amplification targeting: A modified pretargeting approach with potential for signal amplification-proof of a concept. *J. Nuclear Med. 45*, 1087−95.
(28) del Rosario, R. B., and Wahl, R. L. (1993) Biotinylated iodopolylysine for pretargeted radiation delivery. *J. Nuclear Med. 34*, 1147−51.
(29) Artemov, D., Mori, N., Ravi, R., and Bhujwalla, Z. M. (2003) Magnetic resonance molecular imaging of the her-2/neu receptor. *Cancer Res. 63*, 2723−7.
(30) Bogdanov, A. J., Matuszewski, L., Bremer, C., Petrovsky, A., and Weissleder, R. (2002) Oligomerization of paramagnetic substrates results in signal amplification and can be used for mr imaging of molecular targets. *Mol. Imaging 1*, 16−23.
(31) Bogdanov, A. J., Kang, H., Bennett, D., Querol, M., Yudina, A., Verel, I., and Sotak, C. (2006) *Proc. Intl. Soc. Mag. Reson. Med. 14*, p 685, ISMRM, Berkeley, CA.
(32) Querol, M., Chen, J. W., Weissleder, R., and Bogdanov, A., Jr. (2005) Dtpa-bisamide-based mr sensor agents for peroxidase imaging. *Org. Lett. 7*, 1719−22.
(33) Querol, M., Chen, J. W., and Bogdanov, A. A., Jr. (2006) A paramagnetic contrast agent with myeloperoxidase-sensing properties. *Org. Biomol. Chem. 4*, 1887−95.
(34) Bier, H., Hoffmann, T., Haas, I., and van Lierop, A. (1998) Anti-(epidermal growth factor) receptor monoclonal antibodies for the induction of antibody-dependent cell-mediated cytotoxicity against squamous cell carcinoma lines of the head and neck. *Cancer Immunol., Immunother. 46*, 167−73.

(35) Murthy, U., Basu, A., Rodeck, U., Herlyn, M., Ross, A. H., and Das, M. (1987) Binding of an antagonistic monoclonal antibody to an intact and fragmented EGF-receptor polypeptide. *Arch. Biochem. Biophys. 252*, 549−60.

(36) Rodeck, U., Herlyn, M., Herlyn, D., Molthoff, C., Atkinson, B., Varello, M., Steplewski, Z., and Koprowski, H. (1987) Tumor growth modulation by a monoclonal antibody to the epidermal growth factor receptor: Immunologically mediated and effector cell-independent effects. *Cancer Res. 47*, 3692−6.

(37) Bogdanov, A., Jr., Matuszewski, L., Bremer, C., Petrovsky, A., and Weissleder, R. (2002) Oligomerization of paramagnetic substrates result in signal amplification and can be used for mr imaging of molecular targets. *Mol Imaging 1*, 16−23.

(38) Chen, J. W., Querol Sans, M., Bogdanov, A., Jr., and Weissleder, R. (2006) Imaging of myeloperoxidase in mice by using novel amplifiable paramagnetic substrates. *Radiology 240*, 473−81.

(39) Querol Sans, M., Chen, J. W., Weissleder, R., and Bogdanov, A. A., Jr. (2005) Myeloperoxidase activity imaging using Ga-67 labeled substrate. *Mol. Imaging Biol. 7*, 403−10.

(40) Tannous, B., Grimm, J., Perry, K., Chen, J., Weissleder, R., and Breakefield, X. (2006) Metabolic biotinylation of cell surface receptors for in vivo imaging. *Nat. Methods 3*, 291−396.

(41) Graeven, U., Kremer, B., Sudhoff, T., Killing, B., Rojo, F., Weber, D., Tillner, J., Unal, C., and Schmiegel, W. (2006) Phase 1 study of the humanised anti-EGFR monoclonal antibody matuzumab (EMD 72000) combined with gemcitabine in advanced pancreatic cancer. *Br. J. Cancer 94*, 1293−9.

(42) Tiseo, M., Loprevite, M., and Ardizzoni, A. (2004) Epidermal growth factor receptor inhibitors: A new prospective in the treatment of lung cancer. *Curr. Med. Chem. Anti-Cancer Agents 4*, 139−48.

(43) Bier, H., Hoffmann, T., Hauser, U., Wink, M., Ochler, M., Kovar, A., Muser, M., and Knecht, R. (2001) Clinical trial with escalating doses of the antiepidermal growth factor receptor humanized monoclonal antibody EMD 72000 in patients with advanced squamous cell carcinoma of the larynx and hypopharynx. *Cancer Chemother. Pharmacol. 47*, 519−24.

(44) Frangioni, J. V. (2003) In vivo near-infrared fluorescence imaging. *Curr. Opin. Chem. Biol. 7*, 626−34.

(45) Christofidou-Solomidou, M., Pietra, G. G., Solomides, C. C., Arguiris, E., Harshaw, D., Fitzgerald, G. A., Albelda, S. M., and Muzykantov, V. R. (2000) Immunotargeting of glucose oxidase to endothelium in vivo causes oxidative vascular injury in the lungs. *Amer. J. Physiol., Lung Cell Mol. Physiol. 278*, L794−805.

(46) Samoszuk, M., Ehrlich, D., and Ramzi, E. (1993) Preclinical safety studies of glucose oxidase. *J. Pharm. Exp. Ther. 266*, 1643−8.

(47) Muzykantov, V. R., Sakharov, D. V., Sinitsyn, V. V., Domogatsky, S. P., Goncharov, N. V., and Danilov, S. M. (1988) Specific killing of human endothelial cells by antibody-conjugated glucose oxidase. *Anal. Biochem. 169*, 383−9.

(48) Samoszuk, M. K., Wimley, W. C., and Nguyen, V. (1996) Eradication of interleukin 5-transfected J558i plasmacytomas in mice by hydrogen peroxide-generating stealth liposomes. *Cancer Res. 56*, 87−90.

BC060392K

In Vivo Antitumor Activity of the Folate-Conjugated pH-Sensitive Polymeric Micelle Selectively Releasing Adriamycin in the Intracellular Acidic Compartments

Younsoo Bae,[†,‡] Nobuhiro Nishiyama,[†,‡] and Kazunori Kataoka*[,†,‡,§]

Center for Disease Biology and Integrative Medicine, Graduate School of Medicine, The University of Tokyo, 7-3-1 Hongo, Bunkyo-ku, Tokyo 113-0033, Japan, and Center for NanoBio Integration and Department of Materials Engineering, The University of Tokyo, 7-3-1 Hongo, Bunkyo-ku, Tokyo 113-8656, Japan. Received December 26, 2006; Revised Manuscript Received March 2, 2007

Cancer treatment efficacy and safety of the environmentally sensitive polymeric micelle drug carriers were significantly increased by optimizing the number of ligands on their surface. These micelles were designed to target the cancerous tumors through the interaction between folate and its receptors that overexpress on the cancer cell membrane while achieving pH-controlled drug release in the intracellular acidic compartments such as endosomes and lysosomes. In order to elucidate the effects of folate on cytotoxicity, biodistribution, anticancer activity, and pharmacological properties, folate concentration on the surface of the micelles was controlled by precise synthesis of two different amphiphilic block copolymers that self-assemble into spherical micelles, folate−poly(ethylene glycol)−poly(aspartate-hydrazone-adriamycin) with γ-carboxylic acid activated folate and methoxy-poly(ethylene glycol)−poly(aspartate-hydrazone-adriamycin) without folate. It is of significance that, although folate conjugation induced an extremely small change in tumor accumulation of the micelles, folate-conjugated micelles showed lower in vivo toxicity and higher antitumor activity over a broad range of the dosage from 7.50 to 26.21 mg/kg, which was 5-fold broader than free drugs.

INTRODUCTION

Precise control of the amount and uniform distribution of ligands on nanoparticles is one of the most challenging assignments in the design of polymeric drug carriers for successful active drug targeting (*1*−*3*). Indeed, a large number of studies have shown that active drug targeting is promising for effective cancer treatment (*4*−*7*). However, the questions about how many ligands are necessary for achieving efficient active drug targeting of the polymeric drug carriers are still controversial and remain to be elucidated further. In particular, when such drug carriers are tailored to deliver anticancer drugs to cancer cells systemically, it is of significant importance to confirm whether the ligand conjugation maintains their pharmacokinetic properties without decreasing antitumor activity. It is because anticancer drugs are normally highly toxic, inducing serious side effects, and although ligands can increase the interaction between the drug carriers and targeted cells in the body, they might also induce an increase in the cellular interaction with nontargeted cells, that we are not willing to deliver drugs. In order to answer these questions, we have to prepare first a drug carrier with optimal amounts of ligands, whose chemical and biological properties are fairly well established and then ascertain whether ligand installation induces any change in its biological properties.

The rationales for tumor-specific drug delivery with polymers have been reported during the past decades and are based on the characteristics of tumor tissues such as disordered and leaky vasculatures, a thick extracellular matrix, and other microenvironmental peculiarities including the hypoxic environment, expression of cancer-specific receptors, and excessive secretion of cytokines (*8*−*9*). One of the widely accepted methodologies for polymeric drug delivery is to target leaky tumor vessels and the poorly developed lymphatic drainage in the tumor tissues so that polymers and their drug conjugates can pass the tumor blood vessel wall and then accumulate in tumor tissue for a prolonged time. This methodology is explained as the enhanced permeability and retention (EPR) effect, providing the most probable theory for passive drug targeting (*10*). Nevertheless, recent studies have revealed that tumor-targeting drug delivery cannot be completely achieved only by the EPR effect because polymeric drug carriers often encounter difficulties in accessing cancer cells in the deeper place of the tumor tissues or in interacting with the targeted cells after accumulation (*11, 12*). Polymeric drug carriers are normally required to have biocompatibility and high molecular weight to prevent protein adsorption that induces recognition by the body defense system and to increase the tumor accumulation via the EPR effect, respectively. However, these efforts frequently result in low cellular uptake of polymeric drug carriers after extravasation, reducing the actual drug concentration within the tumor due to the stagnation around the tumor tissue. As a result, we should inject polymeric drug carriers with a higher amount compared to free drugs to deliver a sufficient amount of drugs to the tumor. This is also the reason the current polymeric drug delivery systems urgently need to improve their targeting efficiency. From these aspects, active targeting has been believed to clear the problems by facilitating polymeric drug delivery systems (*13*). Active targeting can be achieved by installing ligands to the polymers or polymer assemblies so that they can interact with receptors that express on the targeted sites such as cancer cell membranes. Nevertheless, it is obvious that active targeting

* To whom correspondence should be addressed: Kazunori Kataoka, Ph.D. Professor, Department of Materials Engineering, Graduate School of Engineering, The University of Tokyo, 7-3-1 Hongo, Bunkyo-ku, Tokyo 113-8656, Japan. Phone +81-3-5841-7138, Fax +81-3-5841-7139, E-mail: kataoka@bmw.t.u-tokyo.ac.jp.

[†] Graduate School of Medicine.

[‡] Center for NanoBio Integration.

[§] Department of Materials Engineering.

10.1021/bc060401p CCC: $37.00 © 2007 American Chemical Society
Published on Web 05/09/2007

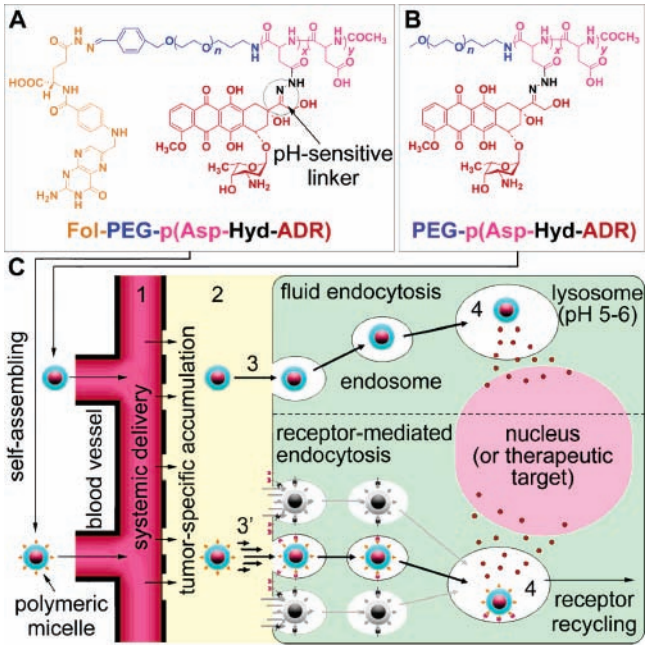


Figure 1. Design of polymeric micelles and the rationale for active drug delivery. Chemical structures of folate−poly(ethylene glycol)−poly(aspartate-hydrazone-adriamycin) and methoxy-poly(ethylene glycol)−poly(aspartate-hydrazone-adriamycin) block copolymers (A and B). As shown in panel C, these polymers can self-assemble into the polymeric micelles that can effectively achieve systemic drug delivery and tumor-specific accumulation (1 and 2). The micelles are then uptaken by the cancer cells via fluid endocytosis (3) or receptor-mediated endocytosis (3′) depending on surface design for accelerating endocytosis (e.g., folate conjugation). Anticancer drugs, adriamycin (ADR), that are conjugated through a pH-sensitive hydrazone bond can be released from the micelles in the acidic intracellular compartments such as endosomes or lysosomes where pH ranges from 5 to 6 (4).

cannot be achieved until passive targeting of drug carriers is successfully accomplished.

Amphiphilic block copolymers are useful tools for the preparation of supramolecular assemblies. By precisely controlling their molecular weight and the hydrophilic/hydrophobic balance, we can prepare spherical supramolecular nanoassemblies, also known as "the polymeric micelles", with a hydrophilic shell that envelopes a hydrophobic core (*14*). The polymeric micelle is considered to be one of the most successful polymeric drug carrier formulations, because it is characterized by high drug loading contents, prolonged blood circulation, and selective tumor accumulation (*15*). Most notably, their chemical, biological, and pharmacological properties have been widely studied, and thus we can easily investigate the effect of active targeting (*16, 17*). In this study, poly(ethylene glycol)−poly(β-benzyl-L-aspartate) block copolymers (PEG−PBLA) were synthesized for the basic platform for the preparation of the polymeric micelles, and these micelles were further functionalized to conjugate anticancer drugs and ligands. Figure 1 shows the chemical structures of the block copolymers used in this study. Anticancer drugs, adriamycin (ADR), were conjugated to the side chains of the core-forming poly(aspartic acid) block through a hydrazone linkage, which can be selectively cleaved under the acidic conditions with pH ranging from 5 to 6, corresponding to the intracellular vesicles such as the endosomes and lysosomes (*18*). In our previous studies, we have reported that this intracellular pH-sensitive polymeric micelle showed remarkably low toxicity and high in vivo efficacy (*19*). It was also confirmed that the pH-sensitive micelles can release drugs selectively by responding to a decrease in intracellular pH of the cell, and therefore, drug leakage from the micelles decreases during the blood circulation and tumor-specific drug delivery efficiency increases. In the meantime, folate was conjugated at the end of the shell-forming poly(ethylene glycol) (PEG) block for active targeting. Folate, an anionic form of folic acid, is a vitamin B9 that helps the production and maintenance of new cells. Originally, folate was necessary for the restoration of the DNA damage that may induce cancer. However, interestingly, cancer cells overexpress folate-binding proteins (FBPs) on their cell membranes (*20, 21*). This is probably due to the DNA replication that is supported by folate, which is also a prerequisite for the cancer growth. More interestingly, cancer cells are believed to reduce chemotherapeutical response by regulating intracellular folate concentration (*22*). Therefore, we can actively guide polymeric drug carriers to cancer cells in the body by folate conjugation (*23*). It must be noticed that FBP binding activity of folate drastically changes depending on its activated state, which is distinguished by an inactive α- and active γ-carboxyl activated form (*24*). Herein, we conjugated folate to PEG at its γ-carboxyl position to maintain its activity by precision synthesis as reported elsewhere (*25*−*27*).

The objectives of this research are to ascertain whether folate conjugation can enhance antitumor efficacy of the pH-sensitive micelles without deteriorating the characteristics of the micelles as a long-circulating drug carrier with high tumor accumulation, and to determine how much folate concentration is optimum for achieving effective passive and active drug targeting simultaneously. Such information would be beneficial to the future design and preparation of ligand-installed multifunctional polymeric drug carriers for cancer treatment.

EXPERIMENTAL PROCEDURES

Materials and Devices. Acetic anhydride (AA), chloroform ($CHCl_3$), *N*,*N*-dimethyl formamide (DMF), dimethyl sulfoxide (DMSO), hexane, methanol (MeOH), methanesulfonyl chloride (CH_3SO_2Cl), triethylamine (TEA), trifluoroacetic acid (TFA), trifluoroacetic anhydride (TFAA), and tetrahydrofuran (THF) were purchased from Wako Pure Chemical Industries, Japan. DMF, hexane, and THF were distilled twice following standard procedures. Carbazic acid *tert*-butyl ester (CAt-BE) and potassium carbonate (K_2CO_3) were purchased from Tokyo Kasei Organic Chemicals, Japan. These chemicals were used without further purification. Daunorubicin (DAU), folic acid (Fol), 4-(diethoxymethyl)benzaldehyde, and sodium borohydride ($NaBH_4$) were purchased from Sigma Chemical, U.S.A. Ethylene oxide (EO) was from Sumitomo Seika Chemicals, Japan, and dried over calcium hydride followed by distillation. β-Benzyl-L-aspartate (BLA) was from Sigma, and α-methoxy-ω-amino-poly(ethylene glycol) (MeO-PEG-NH_2) was from Nippon Oil and Fats, Japan. PEG was purified using an ion-exchange gel column (CM-Sephadex C-50, Amersham Pharmacia Biotech, U.S.A.) prior to the synthesis of the block copolymers. Adriamycin hydrochloride (ADR) was kindly provided by Nippon Kayaku, Japan, and its purity was checked by reversed-phase liquid chromatograpy (RPLC). Sephadex LH-20 gel was from Amersham Pharmacia Biotech, Sweden. Gel permeation chromatography (GPC) analysis was carried out using a TOSOH HLC-8220 equipped with TSK-GEL columns (G4000PWXL and G3000PWXL). Internal refractive index (RI) and ultraviolet−visible absorption (UV) detectors were used. DMF containing 10 mM of LiCl was used as an eluant at a flow rate of 0.8 mL/min at 40 °C. ^1H NMR spectra were measured with a JEOL EX300 spectrometer (JEOL, Japan). Flow cytometric analysis was performed with EPICS XL Flow Cytometry Systems (Beckman Coulter, U.S.A.). The multimode reader Mithras LB 940 (Berthold Technologies, U.S.A.) was used for in vitro cytotoxicity evaluation using a CellTiter-Glo luminescent cell viability assay kit (Promega, U.S.A.).

Cell Lines and Animals. A human pharyngeal cancer cell line KB was purchased from Health Science Research Resources Bank, Japan. Cells were cultured in Dulbecco's Modified Eagle cell culture Medium (DMEM, Sigma, U.S.A.) containing 10% FBS under a humidified atmosphere with 5% CO_2 at 37 °C. CD-1 nude mice (female, 6-week-old) were purchased from Charles River, Japan. The animals were cared for and all experiments were performed in compliance with the Guide for the Care and Use of Laboratory Animals as adopted and promulgated by the National Institutes of Health. The number of independent experiments is stated as *n*, and the experimental data are expressed as mean and mean ± SEM for relative and absolute values, respectively.

Synthesis of Self-Assembling Amphiphilic Block Copolymers. In this study, we synthesized two different types of self-assembling amphiphilic block copolymers for the preparation of the micelles, folate−poly(ethylene glycol)−poly(aspartate-hydrazone-adriamycin) [Fol−PEG−p(Asp-Hyd-ADR)] and methoxy-poly(ethylene glycol)−poly(aspartate-hydrazone-adriamycin) [PEG−p(Asp-Hyd-ADR)]. Synthesis methods for these block copolymers were previously reported elsewhere (*25*). Briefly, Fol−PEG−p(Asp-Hyd-ADR) was synthesized via seven steps as follows.

a. Synthesis of Heterobifunctional α*-4-(Diethoxymethyl)-benzylacetal-*ω*-amine-poly(ethylene glycol) (aceBz-PEG-NH_2).* 4-(Diethoxymethyl)benzaldehyde (5 g) was reduced with $NaBH_4$ (1 g) in dry ethanol (100 mL). Obtained 4-(diethoxymethyl)-benzylalcohol (0.19 g) was then mixed with potassium naphthalene (115 mg) in dry THF (30 mL) to prepare potassium 4-(diethoxymethyl)benzylalkoxide, followed by the addition of distilled EO (11.9 g) for anionic polymerization to obtain aceBz-PEG-OH. After 2 days of reaction at 25 °C, CH_3SO_2Cl (0.62 g) and TEA (0.82 g) were added to aceBz-PEG-OH in 25 mL of THF to prepare an intermediate product aceBz-PEG-OSO_2CH_3, which was then mixed with ammonia solution (25%) to produce aceBz-PEG-NH_2.

b. Selective Functionalization of Folic Acid at its γ*-Position of the Glutamate Residue with Hydrazide (Fol-hyd).* An excess amount of TFAA (3 mL) was added dropwisely to folic acid (2 g) in THF (20 mL) to prepare N_{10}-(trifluoroacetyl)pyrofolic acid. This pyrofolic acid (500 mg) was reacted with CAt-BE (1.6 g) in 20 mL of dry DMF at 40 °C overnight. Prepared folate-hydrazide-BOC was treated with TFA to obtain Fol−Hyd.

c. Preparation of β*-benzyl-*L*-aspartate N-Carboxy Anhydride (BLA−NCA).* 5.77 g of triphosgene was added to 10 g of β-benzyl-L-aspartate in 150 mL of dry THF at 40 °C, and the reaction was allowed to proceed until the solution became clear. Prepared β-benzyl-L-aspartate *N*-carboxy anhydride (BLA−NCA) was purified by recrystallization from hexane.

*d. Ring-Opening Polymerization of BLA−NCA by Using aceBz-PEG-NH_2 as a Macroinitiator to Obtain 4-(Diethoxymethyl)benzyl Acetal−poly(ethylene glycol)−poly(*β*-benzyl-*L*-aspartate) (aceBz−PEG−PBLA).* 6 g of aceBz−PEG−NH_2 with molecular weight of 12 000 and 5 g of BLA−NCA were dissolved in 30 mL and 10 mL of DMSO, respectively. NCA solution was added to PEG solution at 40 °C, and the reaction was allowed to proceed for 2 days.

e. ω*-Amino Group Protection for aceBz−PEG−PBLA Block Copolymers, Followed by* α*-Acetal Group Deprotection and Subsequent Conjugation of Fol−hyd at the End of the PEG Chain (Fol−PEG−PBLA).* The ω-amino group of aceBz−PEG−PBLA was protected by AA to prevent dimerization between aldehyde−benzyl−poly(ethylene glycol)−poly(β-benzyl-L-aspartate) (CHO−Bz−PEG−PBLA) block copolymers, which can be prepared by deprotecting acetal groups of aceBz−PEG−PBLA with 0.1 N HCl aqueous solution. End-group protected CHO−Bz−PEG−PBLA (250 mg) was then mixed with Fol−Hyd (50 mg) in dry DMF to prepare Fol−PEG−PBLA.

Table 1. Polymer Compositions

compound	composition[a]	polydispersity index[d] (Mw/Mn)	drug loading content (wt %)
PEG-PBLA	12−42[b]	1.12	
Fol-PEG-PBLA	12−40[b]	1.14	
PEG-p(Asp-Hyd-ADR)	12−42−33−15[c]		33.84
Fol-PEG-p(Asp-Hyd-ADR)	12−40−34−14[c]		34.32

[a] The compositions of the block copolymers are abbreviated *X*−*Y* and *X*−*Y*−*Z*−*A*. The letter *X* stands for molecular weight × 10^{-3} of poly(ethylene glycol), while *Y*, *Z*, and *A* denote the numbers of aspartic acid, hydrazide, and adriamycin (ADR), respectively. [b] The values were calculated from the peak area ratio determined by ^{1}H NMR between poly(ethylene glycol) and benzyl groups of the PBLA block. [c] The numbers of hydrazide groups and ADR were determined by ^{1}H NMR and reversed-phase liquid chromatography (RPLC), respectively. [d] Polydispersity was measured for PEG−PBLA and Fol−PEG−PBLA to ensure the purity of starting materials.

f. Substitution Benzyl Esters at the Side Chain of Fol−PEG−PBLA with Drug-Binding Hydrazide Groups to Prepare Fol−PEG−p(Asp-Hyd). 500 mg of Fol−PEG−PBLA was dissolved in 10 mL of dry DMF, and anhydrous hydrazine (0.62 mg) was added to the solution. The reaction was allowed to proceed at 40 °C for 2 h, followed by deprotection of remained benzyl groups with 0.1 N NaOH aqueous solution at 25 °C. Polymers were dialyzed against 0.25% ammonia solution and collected by freeze-drying.

g. Conjugation of ADR at Its 13-C Carbonyl with the Hydrazide Groups of Fol−PEG−p(Asp-Hyd) through a pH-Sensitive Schiff Base Linkage. Fol−PEG−p(Asp-Hyd) (100 mg) in 50 mL of DMSO was mixed with an excess amount of ADR-HCl (100 mg) with respect to drug-binding hydrazide residues. The mixed solution was stirred at room temperature for 3 days. After precipitation from ether, Fol−PEG−p(Asp-Hyd-ADR) was redissolved in 10 mL of DMF and purified by gel filtration using a Sephadex LH-20 column. In the case of PEG−p(Asp-Hyd-ADR), MeO-PEG-NH_2 was used as a macroinitiator for BLA−NCA polymerization at step (d) instead of aceBz−PEG-NH_2, following the procedures from steps (e) to (g).

Preparation of the Folate-Conjugated pH-Sensitive Polymeric Micelles. The folate-conjugated pH-sensitive polymeric micelles were prepared from Fol−PEG−p(Asp-Hyd-ADR) alone or in combination with PEG−p(Asp-Hyd-ADR) block copolymers in various molar ratios to change folate contents (0%, 1%, 2%, 5%, 10%, 25%, 50%, and 100%). We distinguish the micelles from Fol−PEG-p(Asp-Hyd-ADR) and PEG−p(Asp-Hyd-ADR) by the notations of FMA and MA, which denote folate-conjugated micellar adriamycin and micellar adriamycin, respectively. For the preparation of FMA and MA, 250 mg of each Fol−PEG−p(Asp-Hyd-ADR) and PEG−p(Asp-Hyd-ADR) were dissolved in 5 mL of DMSO. Polymer solutions were then added dropwise into 95 mL of Tris−HCl buffer solution (10 mM, pH 7.4), sonicated at 25 °C for 10 min, and diluted further with 900 mL of Tris−HCl buffer. The polymer solutions were concentrated by Amicon Ultra-15 Centrifugal Filter Units (Millipore, U.S.A.) with molecular weight cutoff (MWCO) 30 000 kDa. 12 mL of the solutions in each swinging bucket rotor were spun at 1500 *g* at 25 °C for 15 min. During repetitive centrifugation, additional Tris−HCl buffer was added to the solutions until DMSO was completely removed. Concentrated micelle solutions were filter-sterilized and stored in aliquots at 4 °C for future use. Drug concentration was determined by UV at 490 nm, based on the calibration curve of free ADR.

Table 2. Particle Size and ζ Potential of the Micelles with Varying Folate Contents

	folate conjugation[a] (%)							
	0 (MA)	1 (FMA1)	2 (FMA2)	5 (FMA5)	10 (FMA10)	25 (FMA25)	50 (FMA50)	100 (FMA100)
particle size[b] (nm)	64.21	65.34	63.79	68.35	69.22	72.51	77.47	91.29
polydispersity index (μ/Γ^2)	0.1018	0.0951	0.1096	0.1232	0.1318	0.1437	0.1661	0.1973
ζ potential (mV)	−0.39	0.11	−0.67	−1.07	−1.98	−2.33	−6.95	−9.25

[a] It was determined by the mixing ratio of folate-conjugated block copolymers to the block copolymers without folate conjugation. [b] The micelles were filter-sterilized using 0.45 μm filter units (Millex-HV, Millipore, Co., Ltd., U.S.A.) prior to the measurements.

In Vitro Cytotoxicity Assay. In order to determine in vitro cytotoxicity of the micelles, a human pharyngeal cancer cell line KB was incubated with FMA, MA, and free ADR in various concentrations, changing exposure time. Exponentially growing KB cells were seeded on a 96-well culture plate (2000 cells/well) and preincubated for 24 h, followed by coincubation with the samples. After 3 and 24 h, cell culture media were replaced with fresh media, and the cells were incubated further for additional 24 h. The number of viable cells was determined by CellTiter-Glo luminescent cell viability assay ($n = 8$) that provides a convenient, rapid, and sensitive procedure based on quantitation of ATP, which signals the presence of metabolically active cells (*28*).

Flow Cytometric (FCM) Analysis. Cellular uptake of the micelles was analyzed by an EPICS XL Flow Cytometry Systems (Beckman Coulter, U.S.A.) monitoring autofluorescence of ADR accumulated in the cell. KB cells were seeded on a 12-well culture plate (30 000 cells/well) and preincubated for 24 h, followed by coincubation with FMA, MA, and ADR (10 mg/mL) for 3 and 24 h. The cells were then washed three times with PBS, detached by trypsinization, spun down by centrifugation, and dispersed again in PBS for FCM analysis. Data were acquired and processed with the accompanying software (*EXPO 32*).

Surface Plasmon Resonance (SPR) Analysis. Interaction between FBP and the micelles was analyzed by surface plasmon resonance (SPR) measurements using BIAcore 3000 (Biacore, Sweden). FBP was immobilized on the surface of a sensor chip (3 ng/mm^2 of FBP per channel), following the procedures provided by the manufacturer. FBP binding effects of both FMA and MA were evaluated at a flow rate of 10 μL/min with a concentration of 200 μg/mL. The micelles were allowed to flow for 30 min, and all samples were tested by replacing sensor chips on which FBPs were newly immobilized.

Pharmacological Study. Tumor-bearing mice were prepared by transplanting KB cells on the abdominal region of CD-1 nude mice (female, 6-week-old, $n = 6$, Charles River, Japan). When the tumor volume reached 100 mm^3, the micelles and free ADR as control were intravenously injected in a volume of 0.1 mL/10 g body weight. The drug dose was 10 mg/kg for both free ADR and the micelles (ADR equivalent). After drug injection, the blood, tumor, and major organs (heart, kidney, liver, and spleen) were collected at 0.5, 1, 3, 6, 9, and 24 h, followed by HPLC analysis as previously reported (*19*). Briefly, plasma was separated from the blood, and the tissues were homogenized prior to the measurements. Daunorubicin (DAU) was added to the specimens as an internal standard in 2 μg/mL, depending on sample amount. 200 μL of 10 mM HCl solution was then added to the specimens to cleave drug conjugation, and 1 mL of 100 mM ammonia buffer (pH 9.0) was applied after 24 h incubation. 5 mL of $CHCl_3$/MeOH (2:1) mixed solution was also added to the solution, and ADR and DAU were extracted by vigorous vortexing at 25 °C for 15 min. The organic layer was collected using Pasteur pipets and evaporated at 40 °C after centrifugation (1900 *g*, 15 min, 4 °C). Dry drugs were redissolved in 100 μL of DMF and injected to RPLC equipped with a μ Bondasphere 5μ C4 300 column and a fluorescence detector (Ex 485 nm, Em 560 nm). The area under the curve of concentration (AUC) vs time was calculated by the trapezoidal rule with the time points of 0.5, 1, 3, 6, 9, and 24 h. The unit for AUC is defined as % dose/mL plasma × h or % dose/g organ × h for the blood or other tissues (tumor, kidney, liver, spleen, and heart), respectively.

Table 3. Time-Dependent Increase in Cytotoxicity and Cellular Uptake of the Micelles ($n = 8$)[a]

sample	exposure time (h)	IC_{50}[b] (μg/mL ± SD)	relative index[c]	cellular uptake[d] (%)
ADR	3	0.069 ± 0.014	1.97	100.00
	24	0.035 ± 0.011	1	100.00
FMA100	3	0.172 ± 0.017	4.91	92.51
	24	0.041 ± 0.012	1.17	94.95
MA	3	N.D.[e]	N.D.[e]	40.20
	24	0.263 ± 0.013	7.51	82.05

[a] Data were obtained from the eight independent experiments using a human pharyngeal cancer cell KB. [b] IC_{50} means the inhibitory concentration of the drugs required for reducing 50% of cell proliferation. The drug concentration of the micelles was calculated with respect to free ADR equivalents. [c] Relative index means the ratio between the IC_{50} of free ADR after 24 h incubation and the samples. [d] Cellular uptake of the micelles was analyzed by flow cytometric analysis monitoring autofluorescence of ADR accumulated in the cell. [e] N.D. means not determined.

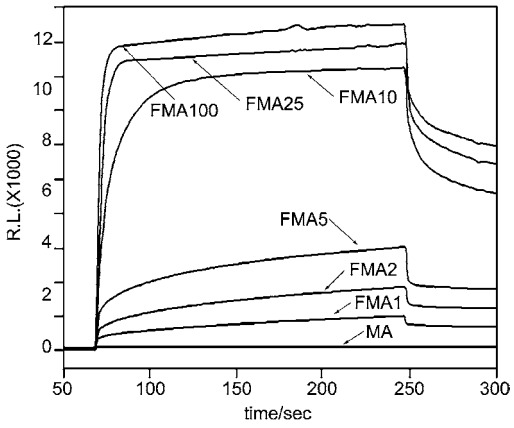


Figure 2. Surface plasmon resonance (SPR) analysis. FBP-binding selectivity of folate-conjugated micelles was evaluated by SPR measurements (eluent, 100 mM phosphate buffer; pH 7.4; flow rate, 10 mL/min; density of folate-binding protein, 3 ng/mm per channel; sample concentration, 200 μg/mL). Folate concentration on the surface of the micelles was varied to determine the optimum substitution rate.

In Vivo Antitumor Activity Evaluation. Tumor-bearing mice were prepared as described above. The micelles were injected from the tail vein three times with a four day interval in various doses (5, 10, 20, and 40 mg/kg). This administration schedule was based on the optimum regimen for free ADR as a control. However, free ADR was applied to the mice in limited doses (5, 10, and 15 mg/kg) due to the serious toxicity. Tumor growth and body weight of mice were checked at every second day. Tumor volume was calculated as volume $V = {}^1/_2 \times LW^2$, where the letters L and W denote the long and short diameters of the tumor tissue. Cancer treatment efficacy was analyzed by a treatment to control (T/C) ratio $= (V_c - V_t) \times 100/V_c$, where

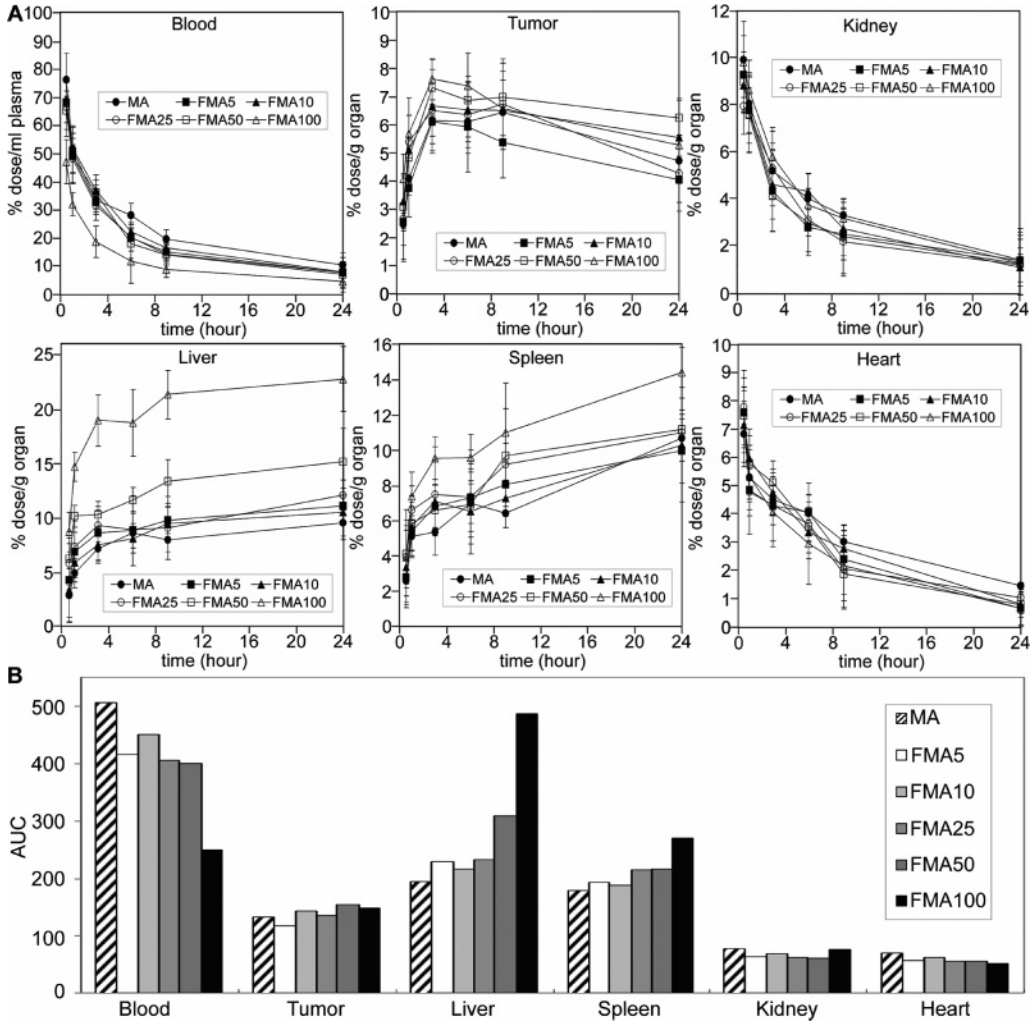


Figure 3. Pharmacokinetic profiles. Distribution of the micelles with varying folate amounts was measured in the blood compartment, tumor tissue, and major organs such as the liver, spleen, kidney, and heart (A). Experiments were carried out using tumor-bearing CD-1 nude mice (female, 6-week-old, $n = 6$) when the tumor volume reached 100 mm^3. Data are expressed as mean and mean ± SEM for relative and absolute values, respectively. Accumulation amounts for each micelle are compared in terms of the areas under the curve of concentration (AUC) vs time up to 24 h time period (B).

V_c and V_t are the mean tumor volumes of the control and the treated mice, respectively. The effective dose (ED) of each micelle was determined as the T/C ratio = 50, which means the average tumor volume of the mice decreased 50% of control values by drug treatments. The toxic dose (TD) was defined as the dose that causes 20% decrease in body weight of the mice after drug injection.

RESULTS AND DISCUSSION

Preparation of the Folate-Conjugated pH-Sensiive Polymeric Micelles (FMA). The molecular weight and composition distributions of self-assembling amphiphilic block copolymers, folate−poly(ethylene glycol)−poly(aspartate-hydrazone-adriamycin) [Fol−PEG−p(Asp-Hyd-ADR)] and α-methoxy-poly(ethylene glycol)−poly(aspartate-hydrazone-adriamycin) [PEG−p(Asp-Hyd-ADR)], were determined by GPC and ^{1}H NMR. Table 1 shows that these block copolymers were successfully prepared with a controlled number of hydrazide groups and ADR. It is noticeable that Fol−PEG−p(Asp-Hyd-ADR) block copolymers did not form any dimers or aggregates after folate conjugation. In addition, most notably, folate was functionalized only at γ-carboxylate position of its glutamate residue in this study by precision synthesis, as we previously reported elsewhere (*25*). This enables every folate molecule that is conjugated to the block copolymers to remain active, distinguishing our system from other folate conjugates. In many studies, folate molecules have been conjugated by using carbodiimide coupling reagents. The folate conjugated in this way is prone to making a mixture of α- and γ-carboxylate-functionalized forms. Because the α-carboxylate-functionalized form of folate loses its activity, the carbodiimide coupling method is substantially accompanied by the problems of undesirable introduction of inactive folate, which induces insufficient conjugation or incorrect quantification of active folate (*23*, *24*). To the contrary, herein we can exclude the possibility that folate becomes inactive after conjugation, and therefore, it is able to clearly investigate the effects of folate conjugation on the biological properties of the micelles.

The particle size and ζ potential of the micelles were analyzed by Zetasizer Nano (Malvern, U.K.), and data are summarized in Table 2. Each micelle from Fol−PEG−p(Asp-Hyd-ADR) and PEG−p(Asp-Hyd-ADR) was abbreviated as FMA and MA, which denote folate micellar adriamycin and micellar adriamycin (without folate), respectively. The successive number after the abbreviated term of FMA in some descriptions indicates the mol % of Fol−PEG−p(Asp-Hyd-ADR) block copolymers in the micelles. For instance, FMA10 means that the micelles were prepared from 10% of Fol−PEG−p(Asp-Hyd-ADR) and 90% of PEG−p(Asp-Hyd-ADR) block copolymers. In all cases, the micelles exhibited particle sizes between 60 and 90 nm, while the distribution was narrow and monodisperse. Surface charge

of the micelles became negative, which is probably due to the carboxylic group remaining at the α-position of glutamate of the folate molecule. Although the micelle size slightly increased as folate concentration increased, these data demonstrate that the size and surface charge of the prepared micelles were still suitable for tumor-specific accumulation via the EPR effect after folate conjugation. When the micelle solutions were concentrated, however, aggregation between particles was observed in the case of FMA100. Such aggregation was able to be suppressed by decreasing the folate substitution ratio. Considering that MA (or FMA0) showed no aggregation during concentration, it is most probable that folate substitution increases the local concentration of folate molecules on the micelle surface, and thus, FMA aggregated due to the intermicellar hydrophobic interaction (*29*). Nevertheless, it must be noted that the micelles stably dispersed with 60−90 nm diameter up to 5 mg/mL concentration irrespective of folate substitution ratio. Because a high drug loading content (∼30 wt %) is one of the characteristic advantages of the micelles, injecting the micelles above this concentration would not be realistic in terms of determining the injection dosage of ADR whose lethal dose ranges from 12.7 to 13.2 mg/kg. Therefore, it is concluded that the micelles with varying folate contents were stable at a size suitable for systemic drug delivery with sufficient drug concentration.

Folate Conjugation Significantly Increased in Vitro Cytotoxicity and Cellular Uptake of the Micelles. Table 3 shows a change in proliferation of KB cells treated by FMA100, MA, and free ADR and cellular uptake. It is of interest that the 50% inhibitory concentrations (IC_{50}) of cell growth decreased significantly in the case of the micelles by folate conjugation. Notably, cytotoxicity of FMA100 was as high as that of free ADR after 24 h incubation despite their different internalization mechanisms. In our previous studies, it is confirmed that this pH-sensitive micelle, which was designed to selectively release drugs in the intracellular region, requires relatively long exposure time sufficient for inhibiting cell growth (>10 h). It is because the micelles are required to enter the cell first and to release drug by sensing pH so that the released drugs accumulate in cell nuclei to intercalate with DNA, inducing cell death. In comparison with MA, FMA100 showed efficient cytotoxicity with a short exposure time of 3 h. These results suggest that folate conjugation promotes the interaction between the micelles and the cell. It is generally known that KB cells overexpress folate-binding proteins (FBPs) on the cell membrane, and therefore the FBPs can take up FMA100 to the cell interior efficiently via receptor-mediated endocytosis. Such enhanced cellular uptake probably induced higher cytotoxicity of FMA100 even with short exposure time. This hypothesis was also confirmed by flow cytometric analysis. As also summarized in Table 3, cellular uptake of FMA100 increased by folate conjugation, and such an increment corresponds well with enhanced cytotoxicity. Consequently, it is confirmed that folate conjugation enhanced cytotoxicity of the micelles by increasing cellular uptake and intracellular drug concentration.

FMA Recognized Folate-Binding Proteins (FBPs) Selectively and Strongly. Although in vitro cytotoxicity assay and flow cytometric analysis have proven that high efficacy of FMA was due to the increased intracellular drug concentration, the scientific evidence that elucidates the role of folate in accelerating cellular uptake was still required. In order to confirm the interaction between FMA and folate binding proteins (FBPs), we carried out surface plasmon resonance (SPR) analysis by using a sensor chip on which FBP molecules were immobilized. It is also of great importance to verify how folate concentrations affect FBP binding properties of the micelles, so we prepared FMA with varying folate substitution rates from 100% to 0%.

Table 4. Tumor-Specific Accumulation of the Micelles

sample	blood	tumor	liver	spleen	kidney	heart
AUC[a]						
MA	506.42	132.67	194.45	179.37	76.96	69.48
FMA5	415.53	117.13	229.35	193.65	63.15	57.01
FMA10	450.38	143.60	215.97	187.98	68.45	61.79
FMA25	405.17	135.48	233.33	215.24	61.58	55.59
FMA50	400.76	155.13	308.99	216.80	60.91	54.99
FMA100	250.16	147.86	487.30	270.14	76.10	51.87
			K_b value[b]			
MA	1	0.26	0.38	0.35	0.15	0.14
FMA5	1	0.28	0.55	0.47	0.16	0.15
FMA10	1	0.32	0.48	0.42	0.16	0.15
FMA25	1	0.33	0.58	0.53	0.17	0.16
FMA50	1	0.39	0.77	0.54	0.16	0.15
FMA100	1	0.59	1.95	1.08	0.30	0.25
			tumor to organ ratio[c] (AUC_{tumor}/AUC_{organ})			
MA	−	1	0.68	0.74	1.72	1.91
FMA5	−	1	0.51	0.60	1.81	1.92
FMA10	−	1	0.66	0.76	2.04	2.12
FMA25	−	1	0.58	0.63	1.94	2.16
FMA50	−	1	0.50	0.72	2.48	2.59
FMA100	−	1	0.30	0.55	1.94	2.41

[a] AUC denotes the area under a concentration curve that is obtained from the pharmacokinetic study with time points at 0.5, 1, 3, 6, 9, and 24 h. Values were calculated on the basis of the trapezoidal rule up to 24 h after intravenous injection. The unit for AUC is defined as % dose/mL plasma × h or % dose/g organ × h for the blood or other tissues (tumor, kidney, liver, spleen, and heart), respectively. [b] K_b value is defined as [$K_b = C_{tissue}/C_{blood}$] where C_{tissue} and C_{blood} are the drug concentrations in the tissue and the blood, respectively. Each K_b value indicates distribution of the drugs in the vascular space ($K_b < 0.1$), extracellular space ($0.1 < K_b < 0.5$), and intracellular space ($0.5 < K_b$). [c] Tumor selectivity of the micelles was determined by calculating the relative accumulated concentrations between the tumor tissues and each organ (AUC_{tumor}/AUC_{organ}).

Figure 2 shows SPR signal intensity versus time for individual micelle samples. The micelles were flowed into the sensor channel for 3 min and rinsed with fresh buffer solution. The signal change indicates that FMA binds promptly and strongly to FBP in various folate contents while MA showed no interaction with FBP. Interestingly, FMA was able to recognize FBP even with 10% folate substitution ratio. However a significant decrease was found in the FBP binding effect between FMA10 and FMA5. In the meantime, the folate substitution rates can be converted from a percent to mol wt % on the basis of the molecular weight of block copolymers and the mixing ratio. It shows that 100% folate substitution ratio corresponds to 16.9 mmol wt % for a single micelle, and FMA10 and FMA5 were calculated to contain 1.7 and 0.8 mmol % of folate molecules, respectively. Therefore, these data revealed that the micelles require only a small quantity of folate to recognize FBPs. Folate is known to have a high affinity for FBP ($K_d < 1$ nM), and such high affinity seems to provide a strong binding property of FMA (*23, 24*).

Optimum Amounts of Folate-Facilitated Tumor Targeting Properties of the Micelles with Long Blood Circulation. The information regarding the relation between the amount of folate and biodistribution of the micelles is of primary importance to determining the compositions of FMA. Such compositions should be considered to maintain the balance between passive and active tumor targeting to realize an ultimate goal of drug delivery systems. For these reasons, we have investigated the biodistribution of FMA by changing folate contents. Figure 3 shows the distribution of the micelles in the blood compartment, tumor tissues, and major organs such as the liver, spleen, kidney, and heart after the intravenous injection. The area under a concentration curve (AUC) shows that the micelles circulated

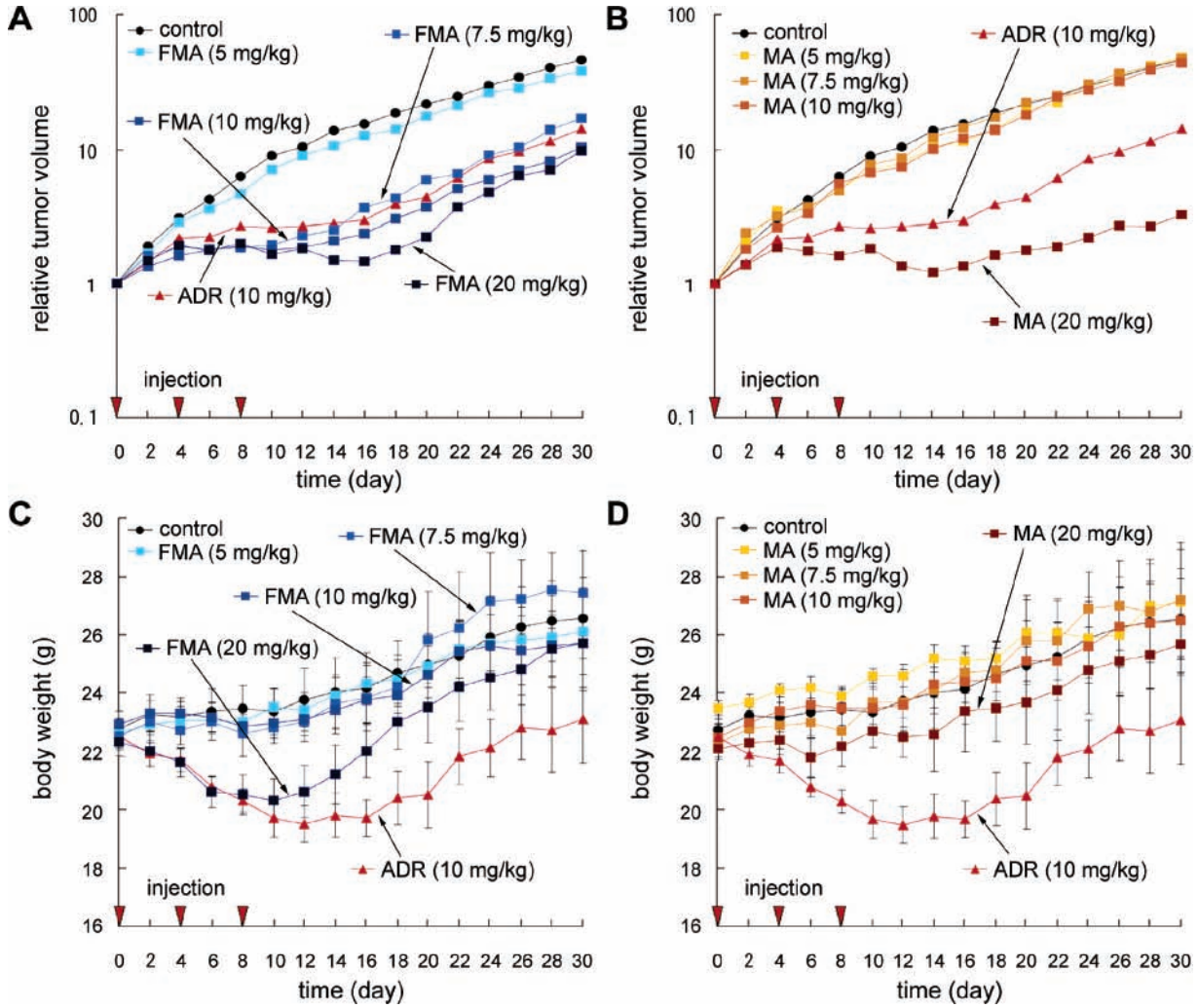


Figure 4. Tumor size and body weight change. The figure shows effective tumor-suppressing activity and low change in body weights over a broad range of injection doses of the folate-conjugated micelles (A and C). It clearly shows that the dose for effective tumor treatments decreased by folate conjugation compared to the micelles without folate, while toxicity remained lower than free drugs (B and D). Administrations were carried out 3 times with a 4 day interval into tumor-bearing CD-1 nude mice (female, 6-week-old, $n = 6$). The micelle doses are shown as ADR equivalents. Data are expressed as mean and mean ± SEM for relative and absolute values, respectively.

in the blood for a long time and their accumulation in tumor tissue increased significantly during the period of 24 h compared to normal organ. In the case of MA, the results correspond well with our previous data that revealed that the intracellular pH-sensitive micelles are characterized by prolonged circulation time in blood and tumor-specific accumulation (*19*). Such characteristic pharmacokinetic properties are considered to result from controlled drug release that can enhance the drug delivery efficiency of the micelles to the solid tumors. Regarding FMA, it is of interest that folate conjugation does not significantly affect the long-term circulation property of the micelles. FMA circulated in the blood for a prolonged time irrespective of folate content. However, the micelle accumulation in the liver as well as in the tumor changes obviously depending on the folate amount. As summarized in Table 4, a clear difference in tumor-specific accumulation was found between FMA and MA. The AUC values for each organ exhibit that FMA with a higher folate content showed a lower tumor-targeting property compared to MA. These results might be due to an increase in accumulation in the liver. Micelle accumulation in the liver was most probably due to the high FBP affinity of the micelles with increased folate concentration. In the meantime, the K_b values, which indicate the drug distribution within inter- and intracellular compartments, show that cellular uptake of FMA increased in tumor cells while remaining low in normal tissues. Nevertheless, the pharmacokinetic data also indicate that the possibility cannot be completely excluded that the micelles underwent nonspecific accumulation in normal organs after folate conjugation. It is not only because the K_b values increased, but also because the tumor to organ ratio (TOR) decreased as folate amounts increased. Accumulation in the liver increased, predominantly decreasing tumor-specific delivery efficiency. One of the previous studies showed that folate conjugation can induce higher hepatic clearance of the conjugates (*30*). Although expression of FBP in the liver would be suggested as a likely reason for the hepatic clearance, we considered that excessive conjugation of folate could increase accumulation of the micelles in normal organs. Therefore, it is concluded that the amount of folate should be carefully determined to facilitate tumor-targeting properties while maintaining long-term blood circulation. This would help us to minimize nonspecific distribution of the micelles in the body. Most noticeably, accumulation of the micelles in the tumor tissues did not significantly differ before and after folate conjugation in terms of pharmacokinetic profile. These findings indicate that the EPR effect seems to still be a major factor in determining the tumor accumulation of drug carriers for active targeting within a 24 h time range. In other words, folate conjugation would mainly affect the distribution of the micelles after extravasation rather than regulate migration of the micelles from the blood compartments to the tumor tissue.

FMA Showed Lower Toxicity and Higher Efficacy than Free Drug. The SPR analysis and biodistribution studies revealed that the optimum amount of folate conjugation is of significant importance to achieve passive and active drug targeting simultaneously. From the obtained data above, we selected FMA10 as the optimum micelle composition for further studies, which was believed to be the most suitable for the best performance in terms of tumor-specific drug delivery. In order to elucidate how folate affects in vivo antitumor activity of the micelles in detail, we have injected FMA, MA, and free ADR into the CD-1 nude mice implanted with human pharyngeal cancer KB cells by changing the dosage. Figure 4 show the changes in tumor size and body weight after drug administration. Free ADR was injected as a control, and it suppressed tumor growth at a dose of 10 mg/kg. The mice were also treated with different doses of free ADR, but there was no effect at 5 mg/kg. At a dose of 15 mg/kg, free ADR showed severe toxicity. These results indicated that free ADR was safe to exhibit the efficacy only within an extremely narrow dose range from 10 to 15 mg/kg. Indeed, body weight reduction was observed even at a dose of 10 mg/kg in the case of free ADR. In contrast to free ADR, MA was able to suppress tumor growth over a broad range of doses ranging from 20 to 40 mg/kg, while its toxicity was significantly low. Such effective and safe antitumor activity of the micelles was consistent with our previous results, which demonstrated the usefulness of intracellular pH-sensitive drug delivery (*18, 19*). Nevertheless, the effective dose (ED) of MA was relatively high compared to free ADR. In case of FMA, however, tumor growth was effectively suppressed with the same dose range of MA, but surprisingly, its ED decreased from 20 to 7.5 mg/kg while toxicity remained low. This value is even lower than the ED of free ADR (10 mg/kg), indicating that the micelles became more effective than free drug by folate conjugation. Therefore, these experimental data clearly elucidate that the drug carrier can show higher efficacy than free drug by optimally balancing passive and active tumor targeting properties as well as controlling drug release profile. It should be emphasized that, although the pharmacokinetic study showed that folate conjugation did not significantly improve the tumor-specific accumulation of the micelles, in vivo antitumor activity experiments clearly show that FMA is more effective to the cancer treatment than free ADR in terms of efficacy and safety. These results also support our hypothesis described above that active targeting seems to mainly affect the distribution profile of the drug carriers within the tumor tissues after extravasation rather than in the blood compartment. It is certain that more studies on this topic should be investigated further in the future. Nevertheless, it is of great importance that the ED of FMA decreased compared to free ADR as well as MA. A lowered dose is obviously beneficial for preventing possible long-term toxicity to the patients. From these aspects, it is concluded that our in vivo studies clearly demonstrate the effects of folate conjugation on active targeting drug delivery.

Folate Conjugation Decreased Effective Dose while Maintaining the Broad Therapeutic Window of the Micelles. The range of drug concentrations that provide the efficacy safely is known as the therapeutic window. If the injection dose is lower than this range, the drug cannot show its efficacy. To the contrary, if the injection dose is higher than the therapeutic window, the drug will induce either acute or chronic toxicity. In this study, animal studies have shown that FMA is more effective and safer than free drugs. In order to provide more objective criteria for evaluating efficacy of FMA, we analyzed antitumor activity of the micelles by calculating a treatment to control (T/C) ratio. Figure 5 exhibits the relation between the T/C ratio and a dosage. Each curve provides information about the tumor-suppressing efficacy of FMA, MA, and free ADR with respect to the control. Effective dose (ED) and toxic dose (TD) were defined as the doses that induce 50% of tumor growth (ED_{50}) and reduce 20% of body weight during the treatment, respectively. As drug concentrations increased, tumor growth suppression efficiency increased by all drug formulations. However, when we compare the effective doses, ED_{50} of free ADR is obviously close to its TD while ED_{50} of the micelles remained low compared to their TD. Namely, the safe dose of free ADR was only 3.96 mg/kg, but in contrast, FMA and MA were safely injectable between 20.03 and 23.75 mg/kg, respectively. These values correspond to 5.05- and 5.99-fold broader dose ranges than free drug. In particular, ED_{50} of FMA became lower than that of free ADR, and these results exemplify how active drug targeting is promising for cancer treatment. Most notably, such low toxicity and high efficacy were achieved by determining the optimum amount of folate on the micelle surface.

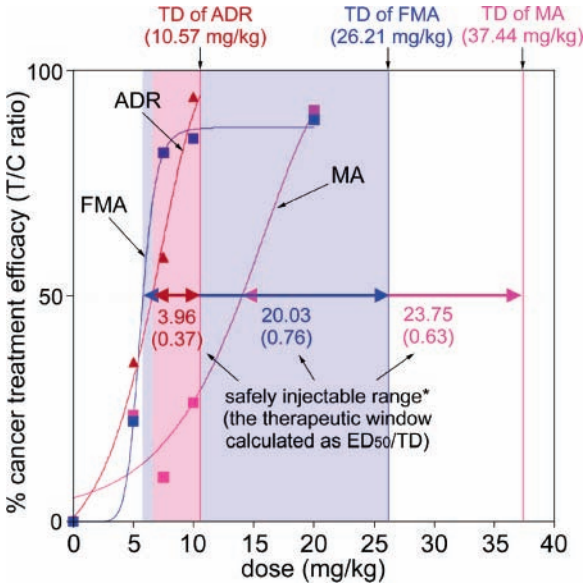


Figure 5. Treatment-to-control (T/C) ratio. Cancer treatment efficacy of the micelles was evaluated by comparing the therapeutic windows of FMA10, MA, and ADR, which were calculated from the ratio of ED_{50} to TD. ED_{50} and TD were defined as the effective dose that induces 50% decrease in tumor volume and the toxic dose that reduces 20% of body weight of mice, respectively. The data show the dose range in which each sample can be safely injected while achieving effective cancer treatments.

CONCLUSIONS

Integration of multiple functions into a single nanoparticle can broaden the possibilities of the macromolecular drug delivery systems for their future applications in the clinic. In this study, we have prepared a multifunctional polymeric micelle that is implemented with intracellular pH-dependent drug-releasing functionality and folate-mediated cancer cell targeting property simultaneously. By precision synthesis and preparation of the pH-sensitive micelles with varying folate contents, we were able to elucidate that the ligand-installed micelles for active drug targeting can be more effective than free drug in terms of antitumor activity, safety, pharmacokinetics, and bioavailability. It is of great interest that folate conjugation did not significantly improve the tumor accumulation of the micelles in the body because it induced a prominent increase in accumulation in the liver. However, when folate concentration was adjusted to achieve minimum ligand−receptor interaction, folate-conjugated micelles showed an effective cancer treatment efficiency that was even higher than free drugs as well as the micelles without folate conjugation. These findings clearly demonstrated that the

balance between passive and active drug targeting should be carefully considered to maximize the drug delivery efficiency as well as cytotoxic activity of the polymeric drug carriers.

ACKNOWLEDGMENT

The authors wish to express their thanks for the Project on the Materials Development for Innovative Nano-Drug Delivery Systems from the Ministry of Education, Culture, Sports, Science and Technology (MEXT), Japan.

LITERATURE CITED

(1) Duncan, R. (2006) Polymer conjugates as anticancer nanomedicines. *Nat. Rev. Cancer 6*, 688−701.

(2) Low, P. S., and Antony, A. C. (2004) Folate receptor-targeted drugs for cancer and inflammatory diseases. *Adv. Drug Delivery Rev. 56*, 1055−1058.

(3) Allen, T. M. (2002) Ligand-targeted therapeutics in anticancer therapy. *Nat. Rev. Drug Discovery 2*, 750−763.

(4) Lee, E. S., Na, K., and Bae, Y. H. (2005) Doxorubicin loaded pH-sensitive polymeric micelles for reversal of resistant MCF-7 tumor. *J. Controlled Release 103*, 405−418.

(5) Xu, Z., Gu, W., Huang, J., Sui, H., Zhou, Z., Yang, Y., Yan, Z., and Li, Y. (2005) In vitro and in vivo evaluation of actively targetable nanoparticle for paclitaxel delivery. *Int. J. Pharm. 288*, 361−368.

(6) Oyewumia, M. O., Yokela, R. A., Jaya, M., Coakleyb, T., and Mumper, R. J. (2004) Comparison of cell uptake, biodistribution, and tumor retention of folate-coated and PEG-coated gadolinium nanoparticles in tumor-bearing mice. *J. Controlled Release 95*, 613−626.

(7) Gabizon, A., Horowitz, A. T., Goren, D., Tzemach, D., Shmeeda, H., and Zalipsky, S. (2003) In vivo fate of folate-targeted polyethyleneglycol liposomes in tumor-bearing mice. *Clin. Cancer Res. 9*, 6551−6559.

(8) Jain, R. K. (1998) Delivery of molecular and cellular medicine to solid tumors. *J. Controlled Release 53*, 49−67.

(9) Matsumura, Y., and Maeda, H. (1986) A new concept for macromolecular therapeutics in cancer chemotherapy: mechanism of tumoritropic accumulation of proteins and the antitumor agent Smancs. *Cancer Res. 46*, 6387−6392.

(10) Maeda, H. (2001) SMANCS and polymer-conjugated macromolecular drugs advantages in cancer chemotherapy. *Adv. Drug Delivery Rev. 46*, 169−185.

(11) Minchinton, A. I., and Tannock, I. F. (2006) Drug penetration in solid tumours. *Nat. Rev. Cancer 6*, 583−592.

(12) Kamb, A. (2005) What's wrong with our cancer models? *Nat. Rev. Drug Discovery 4*, 161−165.

(13) Atkins, J. H., and Gershell, L. J. (2002) Selective anticancer drugs. *Nat. Rev. Cancer 1*, 645−646.

(14) Kataoka, K., Harada, A., and Nagasaki, Y. (2001) Block copolymer micelles for drug delivery: design, characterization and biological significance. *Adv. Drug Delivery Rev. 47*, 113−131.

(15) Nishiyama, N., and Kataoka, K. (2006) Nanostructured devices based on block copolymer assemblies for drug delivery: designing structures for enhanced drug function. *Adv. Polym. Sci. 193*, 67−101.

(16) Nishiyama, N., Bae, Y., Miyata, K., Fukushima, S., and Kataoka, K. (2005) Smart polymeric micelles for gene and drug delivery. *Drug Discovery Today*: *Technol. 2*, 21−26.

(17) Lavasanifar, A., Samuel, J., and Kwon, G. S. (2002) Poly(ethylene oxide)-block poly(L-amino acid) micelles for drug delivery. *Adv. Drug Delivery Rev. 54*, 169−190.

(18) Bae, Y., Fukushima, S., Harada, A., and Kataoka, K. (2003) Design of environment-sensitive supramolecular assemblies for intracellular drug delivery: polymeric micelles that are responsive to intracellular pH change. *Angew. Chem., Int. Ed. 42*, 4640−4643.

(19) Bae, Y., Nishiyama, N., Fukushima, S., Koyama, H., Matsumura, Y., and Kataoka, K. (2005) Preparation and biological characterization of polymeric micelle drug carriers with intracellular pH-triggered drug release property: tumor permeability, controlled subcellular drug distribution, and enhanced in vivo antitumor efficacy. *Bioconjugate Chem. 16*, 122−130.

(20) Mantovani, L. T., Miotti, S., Menard, S., Canevari, S., Raspagliesi, F., Bottini, C., Bottero, F., and Colnaghi, M. I. (1994) Folate binding protein distribution in normal tissues and biological fluids from ovarian carcinoma patients as detected by the monoclonal antibodies MOv18 and MOv19. *Eur. J. Cancer 30A*, 363−369.

(21) Weitman, S. D., Lark, R. H., Coney, L. R., Fort, D. W., Frasca, V., Zurawski, V. R., Jr., and Kamen, B. A. (1992) Distribution of the folate receptor GP38 in normal and malignant cell lines and tissues. *Cancer Res. 52*, 3396−3401.

(22) Hooijberg, J. H., de Vries, N. A., Kaspers, G. J. L., Pieters, R., Jansen, G., and Peters, G. J. (2005) Multidrug resistance proteins and folate supplementation: therapeutic implications for antifolates and other classes of drugs in cancer treatment. *Cancer Chemother. Pharmacol. 58*, 1−12.

(23) Leamon, C. P., and Reddy, J. A. (2004) Folate-targeted chemotherapy. *Adv. Drug Delivery Rev. 56*, 1127−1141.

(24) Lee, R. J., and Low, P. S. (1994) Delivery of liposomes into cultured KB cells via folate receptor-mediated endocytosis. *J. Biol. Chem. 269*, 3198−3204.

(25) Bae, Y., Jang, W.-D., Nishiyama, N., Fukushima, S., and Kataoka, K. (2005) Multifunctional polymeric micelles with folate-mediated cancer cell targeting and pH-triggered drug releasing properties for active intracellular drug delivery. *Mol. BioSyst. 1*, 242−250.

(26) Akiyama, Y., Nagasaki, Y., and Kataoka, K. (2004) Synthesis of heterotelechelic poly(ethylene glycol) derivatives having α-benzaldehyde and ω-pyridyl disulfide groups by ring opening polymerization of ethylene oxide using 4-(diethoxymethyl)benzyl alkoxide as a novel initiator. *Bioconjugate Chem. 15*, 424−427.

(27) Luo, J., Smith, M. D., Lantrip, D. A., Wang, S., and Fuchs, P. L. (1997) Efficient synthesis of pyrofolic acid and pteroyl A azide, reagents for the production of carboxyl differentiated derivatives of folic acid. *J. Am. Chem. Soc. 119*, 10004−10013.

(28) Crouch, S. P., Kozlowski, R., Slater, K. J., and Fletcher, J. (1993) The use of ATP bioluminescence as a measure of cell proliferation and cytotoxicity. *J. Immunol. Methods 160*, 81−88.

(29) Kanie, K., Nishii, M., Yasuda, T., Taki, T., Ujiieb, S., and Kato, T. (2001) Self-assembly of thermotropic liquid-crystalline folic acid derivatives: hydrogen-bonded complexes forming layers and columns. *J. Mater. Chem. 11*, 2875−2886.

(30) Shinoda, T., Takagi, A., Maeda, A., Kagatani, S., Konno, Y., and Hashida, M. (1998) In vivo fate of folate-BSA in non-tumor- and tumor-bearing mice. *J. Pharm. Sci. 87*, 1521−1526.

BC060401P

Dual-Surface-Modified Bacteriophage MS2 as an Ideal Scaffold for a Viral Capsid-Based Drug Delivery System

Ernest W. Kovacs, Jacob M. Hooker, Dante W. Romanini, Patrick G. Holder, Katherine E. Berry, and Matthew B. Francis*

Department of Chemistry, University of California, Berkeley, California 94720-1460, and Materials Sciences Division, Lawrence Berkeley National Labs, Berkeley, California 94720. Received January 8, 2007; Revised Manuscript Received February 16, 2007

With the development of covalent modification strategies for viral capsids comes the ability to convert them into modular carrier systems for drug molecules and imaging agents. With this overall goal in mind, we have used two orthogonal modification strategies to decorate the exterior surface of genome-free MS2 capsids with PEG chains, while installing 50−70 copies of a fluorescent dye inside as a drug cargo mimic. Despite the very high levels of modification, the capsids remained in the assembled state, as determined by TEM, size-exclusion chromatography, and dynamic light scattering analysis. The ability of the polymer coating to block the access of polyclonal antibodies to the capsid surface was probed using a sandwich ELISA, which indicated a 90% reduction in binding. Further experiments indicated that biotin groups placed at the distal ends of the polymer chains were still capable of binding to streptavidin, despite their proximity to the PEG layer. Finally, a modular strategy was developed for the attachment of small-molecule targeting groups to the polymer chains through an efficient oxime formation reaction. As a result of these studies, a robust and versatile new platform has emerged for the potential delivery of therapeutic cargo.

INTRODUCTION

The robust, monodisperse architectures of viral capsids have emerged as attractive scaffolds for the construction of new materials (*1*). With the goal of adding new function to these structures, numerous studies have demonstrated that their exterior surfaces can be functionalized with peptides (*2*), fluorescent dyes (*3, 4*), polymers (*5*−*8*), carbohydrates (*9*, *10*), oligonucleotides (*11*), and other organic molecules (*2*, *3*, *8*) through the use of carefully planned bioconjugation reactions. In terms of inorganic materials, the capsids have also served as templates for the positioning of gold nanoparticles (*12*), the deposition of metal oxides (*13*), and the coordination of gadolinium ions (*3*, *14*) for magnetic resonance imaging (MRI). Similarly, the interior surfaces of some viral capsids have been exploited as "cages" that can template the growth of inorganic nanocrystals (*1*, *15*−*17*) and display organic functionality (*8*, *18*). Beyond these synthetic methods, much attention has also been devoted to the genetic manipulation of capsid proteins to present peptide sequences with desired function. Specifically, capsid protein fusions have been expressed to display antigenic peptides on their surfaces (*19*−*22*), and the evolution of peptide sequences via phage display (*23*−*25*) has achieved promising and widely applicable success for a number of applications.

In terms of biomedical applications, the construction of spherical nanomaterials with differentiated surfaces could offer particularly attractive systems for the delivery of therapeutic agents. As suggested in Figure 1, an ideal construct for these purposes would consist of an externally modified surface presenting multiple copies of a ligand that targets specific cell receptors, while also providing resistance to antibody binding that would neutralize the carriers before reaching their destinations. Interior modification strategies could then be used to install a high payload of imaging agents, drug cargo, or other molecules of biomedical interest in a modular fashion, with the advantage that internal functionality would be expected to exert minimal effects on biodistribution. Even in the absence of specific targeting ligands, passive accumulation of these materials could occur in solid tumors through the enhanced permeability and retention (EPR) effect (*26*−*28*). Though we have previously demonstrated the dual surface covalent modification of the tobacco mosaic virus (TMV) with small molecules and polymers (*8*), there remain no examples of spherical capsids that have been simultaneously modified on both their exterior and interior surfaces to access these materials. This is largely due to structural instabilities that are introduced upon high levels of modification and the relatively limited number of bioconjugation strategies that are available to differentiate the two surfaces.

As part of our efforts to build such materials, we have constructed the first genome-free icosahedral capsids selectively modified on both their exterior and interior surfaces. Utilizing orthogonal coupling strategies, we have successfully appended over 180 PEG chains, average molecular weight 2000 or 5000 (PEG-2000 or PEG-5000), to the exterior surface of bacteriophage MS2, while decorating its interior surface with 50−70 fluorescein molecules as our initial drug cargo mimic. This dual-surface modification has been achieved in only two protein modification steps with high overall recovery. In vitro ELISA assays, furthermore, have shown that the extensive PEGylation achieved in our system effectively masks the epitopes of the native capsid surface. We have also developed a modular strategy to attach targeting groups to the distal ends of the polymer chains through chemoselective oxime formation reactions. These constructs represent the complete synthetic exploitation of the three-dimensional space afforded by the capsids and provide a promising platform for future biomedical applications.

EXPERIMENTAL PROCEDURES

General Procedures and Materials. Unless otherwise noted, all chemicals were analytical grade, obtained from commercial sources, and used without further purification. All nonaqueous

* francis@cchem.berkeley.edu.

10.1021/bc070006e CCC: $37.00 © 2007 American Chemical Society
Published on Web 06/30/2007

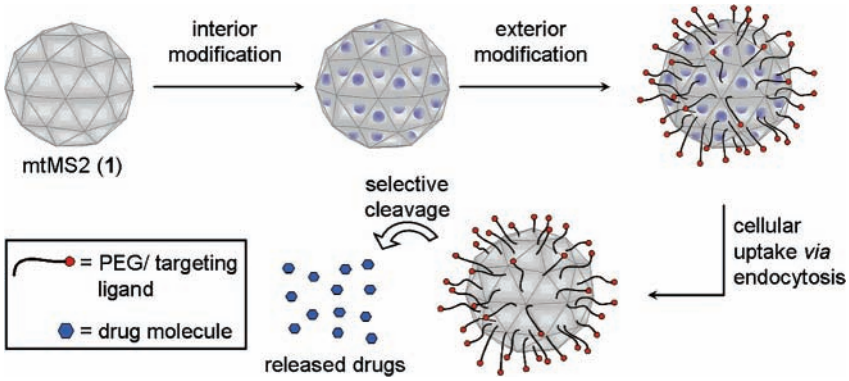


Figure 1. General strategy for the construction of multifunctional drug delivery vessels derived from genome-free (mtMS2) viral capsids.

reactions were carried out under a nitrogen atmosphere using distilled solvents. Water (ddH_2O) used in biological procedures or as a reaction solvent was deionized using a NANOpure purification system (Barnstead, USA). All organic solvents were removed under reduced pressure using a rotary evaporator. PEG polymers were purchased from Nektar Therapeutics. Fluorescein derivative FAM-SE was purchased from Molecular Probes.

Instrumentation. UV−vis spectroscopic measurements were conducted on a Tidas-II benchtop spectrophotometer (J&M, Germany). General desalting and removal of other small molecules of protein samples were achieved using BioSpin G-25 centrifuge columns (Amersham Biosciences, USA) or NAP-5 gel filtration columns (Amersham Biosciences, USA). Protein samples were concentrated by way of centrifugal ultrafiltration using Amicon Ultra-4 or Ultra-15 100 kDa molecular weight cutoff spin columns (Millipore, USA).

^{1}H NMR and ^{13}C NMR spectra were measured with a Bruker AVQ-400 (400 MHz) spectrometer. Chemical shifts are reported as δ in units of parts per million (ppm) relative to dimethyl sulfoxide-d_6 (δ 2.50, pentet) or chloroform-d_3 (δ 7.26, singlet). Multiplicities are reported as follows: s (singlet), d (doublet), t (triplet), q (quartet), dd (doublet of doublets), m (multiplet), br (broadened), or app (apparent). Coupling constants are reported as a J value in hertz (Hz). The number of protons (n) for a given resonance is indicated nH and is based on spectral integration values. ^{13}C NMR spectra are reported as δ in units of parts per million (ppm) relative to dimethyl sulfoxide-d_6 (δ 39.50, septet) or chloroform-d_3 (δ 77.2, singlet).

Transmission electron microscopy (TEM) images were obtained at the UC-Berkeley Electron Microscope Lab using a FEI Tecnai 12 transmission electron microscope with 100 kV accelerating voltage. Protein samples were prepared for TEM analysis by applying 5 μL of an analyte solution at approximately 0.1 mg/mL to carbon-coated copper grids for 3 min followed by rinsing with ddH_2O. The grids were then exposed to 5 μL of a 1% solution of uranyl acetate (UA) for 1.5 min as a negative stain. After excess stain was removed by blotting, the grid was allowed to dry until analysis.

Matrix assisted laser desorption−ionization time-of-flight (MALDI-TOF) mass spectra were obtained on a Voyager-DE system (Appled Biosystems, USA). Application of 0.5 μL of a matrix solution containing 2,4,6-trihydroxyacetophenone (THAP) (38 mg/mL in 2:1 MeCN/ddH_2O with 7 mg/mL ammonium chloride) was followed immediately by simultaneous application of 1 μL of analyte solution in ddH_2O and 0.5 μL of glacial acetic acid. A repeat addition of another 0.5 μL aliquot of the THAP matrix solution was followed by air-drying for 0.5 h or until analysis.

For protein analysis, sodium dodecyl sulfate−polyacrylamide gel electrophoresis (SDS-PAGE) was accomplished on a Mini-Protean apparatus from Bio-Rad (Hercules, CA). Samples were combined 1:1 (v/v) with gel loading buffer containing SDS, DTT, and bromophenol blue and heated at 95 °C for approximately 15 min. After removal of the completed gels from their cassettes, the bottom portions containing unbound dye were excised promptly, after which the gels were submerged in the appropriate solution for rinsing or imaging. Commercially available markers (Bio-Rad) were applied to at least one lane of each gel for calculation of apparent molecular masses. Fluorescence visualization of gels was obtained by UV transillumination at 302 nm. Visualization of protein bands was accomplished by staining with Coomassie Brilliant Blue R-250. Gel imaging was performed on an EpiChem3 Darkroom system (UVP, USA). Protein recovery and/or degree of modification was estimated from standard optical density measurements of the observed gel bands with *LabWorks* software (version 4.0.0.8, UVP).

All size, ζ potential, and protein melting curve data were obtained using a Zetasizer Nano Series (Malvern Instruments Limited, UK). For size and melting curve measurements, analyte solution at approximately 0.5 mg/mL in aqueous buffer was sterile-filtered into glass cuvettes equipped with a Teflon cap. For ζ potential measurements, analyte solution at approximately 0.5 mg/mL in 10 mM Na_2HPO_4, pH 7.3, was sterile-filtered directly into disposable ζ cells equipped with electrodes and a folded capillary (Malvern Instruments Limited, UK).

MS2 (natMS2 and mtMS2). Routine propagation, purification, and characterization of the native bacteriophage MS2 (natMS2) followed by subsequent production of genome-free "empty" MS2 capsids (mtMS2) was accomplished using previously reported methods (*18*, *44*, *45*). A typical 1 L culture of natMS2 yields approximately 30 mg of phage. Genome removal is accomplished with over 90% protein recovery.

5-Amino-*N*-(2-amino-ethyl)-2-nitrobenzamide (4). A 200 mL flame-dried round-bottom flask equipped with a magnetic stir bar was charged with a solution of 5-amino-2-nitrobenzoic acid (750 mg, 4.12 mmol, 1 equiv) in distilled pyridine (25 mL) under an argon atmosphere. To the stirred solution was added 1,1′-carbonyldiimidizole (CDI, 1.00 g, 6.18 mmol, 1.5 equiv) at rt. After 45 min, all of the 5-amino-2-nitrobenzoic acid had been converted to the active imidizole amide, at which point the reaction solution was cooled to 0 °C and treated with a solution of ethylene diamine (1.48 g, 24.7 mmol, 6 equiv) in pyridine (25 mL). Reaction progress was monitored by TLC (1:1 MeOH/CH_2Cl_2). The reaction solution was heated to 80 °C. After 12 h, the solution was cooled to rt and concentrated under reduced pressure. Purification was accomplished by flash chromatography (1:9 $CHCl_3$/MeOH) affording **4** as a pure yellow solid (767 mg, 83% yield): ^{1}H NMR (400 MHz, DMSO-d_6): δ, 2.60 (t, 2H, J = 6.0 Hz), 3.14 (app q, 2H, J = 6.0 Hz), 6.43 (d, 1H, J = 2.4 Hz), 6.56 (dd, 1H, J = 2.4, 9.2 Hz), 6.72 (br s, 2H), 7.89 (d, 1H, J = 9.2 Hz), 8.27 (t, 1H, 5.6 Hz). ^{13}C NMR (100 MHz, DMSO-d_6): δ, 41.6, 43.3, 112.3, 112.7, 127.9,

133.3, 137.7, 155.1, 167.5. HRMS (EI+) calculated for $C_9H_{12}N_4O_3$ ($[M + H]^+$) 225.0982, found 225.0984.

5-Amino-*N*-(2-[FAM-amido]-ethyl)-2-nitrobenzamide (5). To a microcentrifuge tube was added **4** (10 mg, 45 μmol), FAM-SE (23 mg, 49 μmol), anhydrous triethylamine (12.4 μL, 89 μmol), and anhydrous DMF (77 μL). After thorough vortexing, the resulting dark orange mixture was protected from light and heated at 65 °C for 1.5 h. (Reaction progress was monitored by way of C8 reversed-phase HPLC followed by MALDI-TOF MS.) After cooling to room temperature, the resulting product mixture was used without further purification. Unused portions were protected from light and stored in aliquots at 4 °C.

FAM-Azo-labeled mtMS2 Conjugate (2). *(a) Formation of Diazonium Salt **6**.* To a 50 μL solution of **5** in DMF (100 mM) chilled to 4 °C was added 25 μL of a 4 °C aqueous solution of *p*-toluene sulfonic acid monohydrate (800 mM), followed immediately by 25 μL of a 4 °C aqueous solution of sodium nitrite (200 mM). The resulting bright yellow mixture was thoroughly vortexed and allowed to incubate at 4 °C for 15 min.

(b) Diazonium Coupling Reaction. To a 12.2 mL aqueous buffered solution of mtMS2 (1.0 mg/mL, 0.89 μmol of Y85, pH 8.5, 100 mM NaHPO4) at 4 °C was added 89 μL of a solution of **6** (4.45 μmol). After briefly vortexing, the resulting orange solution was held at 4 °C for 15 min. The reaction mixture was then diluted to 14 mL, after which 1.4 g of poly(ethylene glycol), average molecular weight 6000 (PEG-6000), and 409 mg of NaCl were added. The resulting heterogeneous mixture was then centrifuged at 13 000 rcf for 0.5 h to precipitate assembled MS2 capsids selectively. Further purification via FPLC removed residual polymer and free dye, while final centrifugal ultrafiltration yielded intact, pure, stable FAM-MS2 conjugate **2** with an overall protein recovery of approximately 90% with conversion levels of 50−80 FAM/capsid.

General Procedure for PEGylation of MS2 Capsids. To 100 μL of an MS2 sample (1 mg/mL, 70 μM in 150 mM $NaHCO_3$ buffer, pH 8.4) was added 1.82 mmol of PEG-NHS (MW = 2000 or 5000). The reaction mixture was vortexed gently for 18 h at room temperature and then subjected to FPLC purification and final centrifugal ultrafiltration as described above.

Production of Polyclonal Anti-MS2 Antibodies. The production of polyclonal anti-MS2 antibody (Ab) sera was performed as a 90 d accelerated protocol by Covance Research Products (Denver, PA).

Sandwich ELISA Assay. Affinity-purified polyclonal anti-MS2 Abs were diluted 1000-fold into 50 mM $NaHCO_3$ buffer, pH 8.2, added (50 μL/well) to Reacti-Bind 96-Well EIA Plates (Pierce Endogen, USA), and incubated overnight at 4 °C. The plates were then washed once with phosphate buffered saline containing 0.1% Tween-20 and 0.05% NaN_3 (PBSTween/azide), followed by a single wash with PBS/azide, before being blocked with 2% bovine serum albumin (BSA) in PBS/Tween/azide. After 2 h of incubation at rt, the plates were washed three times with PBS/Tween/azide, once with PBS/azide, and dried briefly. To each well was next added 50 μL of the appropriate MS2 or control protein sample at a concentration of 10−100 000 ng/mL, diluted in 2% BSA in PBS/Tween/azide. After 2 h of incubation at rt, the plates were washed as before. A previously prepared polyclonal anti-MS2 Ab-horseradish peroxidase (Ab-HRP) conjugate was diluted 100-fold in PBS/Tween (no azide) and added (50 μL/well) to the plates, which were then incubated at room temperature for 2 h. The plates were washed three times with PBS/Tween and once with PBS before addition (100 μL/well) of 1-Step ABTS substrate solution (Pierce Endogen). Following a 15−30 min incubation at room temperature, each well was quenched with 100 μL of a 1% aqueous solution of SDS. Absorbance readings were measured at 405 and 410 nm on a 96-well plate reader.

Biotin-Conjugated MS2 Pull-Down Assay. A 50 μL slurry of Immunopure Immobilized Avidin (Pierce) was washed several times with 50 mM NaH_2PO_4 buffer (pH 7.4) before a final centrifugation (1 min, 5000 rcf). After removal of the resulting supernatant, 50 μL of biotin-conjugated MS2 (0.5 mg/mL in NaH_2PO_4 buffer, pH 7.4) or an appropriate control was added. The resulting heterogeneous mixture was vortexed moderately for 15 h at rt, with one aliquot (20 μL) being removed after 1 h following centrifugation of the mixture. Removed aliquots were subjected to SDS-PAGE gel analysis as described above.

Bis-*N*-alkoxyphthalimido−poly(ethylene glycol), M_n 2291. A flame-dried, nitrogen-purged 250 mL round-bottom flask equipped with a magnetic stir bar was charged with *N*-hydroxyphthalimide (3.58 g, 22 mmol), triphenylphosphine (5.5 g, 21 mmol), and poly(ethylene glycol) (M_n 2000, 20 g, 10 mmol). The flask was evacuated and purged with nitrogen. Freshly distilled methylene chloride (100 mL) was added, and the mixture was stirred at rt to dissolve the solids. After 15 min, some heterogeneity persisted. While stirring, the mixture was treated in small portions with diisopropyl azodicarboxylate (DIAD, 4.3 mL, 22 mmol). The rate of addition was determined by the persistence of an orange color. The color was allowed to fade between each addition of DIAD (~0.25 mL). Once the DIAD addition was complete, the solution became homogeneous. After 12 h of stirring, the solution was diluted into 3 L of diethyl ether and stirred vigorously at 4 °C for 30 min. The white precipitate was collected via suction filtration and dried in vacuo for 3 h. ^{1}H NMR of the dried precipitate indicated unreacted poly(ethylene glycol) in addition to the desired product. The collected material was subjected to identical reaction conditions and purification above, ultimately yielding bis-*N*-alkoxyphthalimido−poly(ethylene glycol) as a pure white solid (15.4 g, 6.72 mmol, 67%). ^{1}H NMR (400 MHz, $CDCl_3$): δ 3.4−3.8 (poly(ethylene glycol) signals), 3.85, (t, 4H), 4.36, (t, 4H), 7.75 (m, 4H), 7.82 (m, 4H).

Bis(aminooxy)poly(ethylene glycol), M_n 2030 (12). A 100 mL round-bottom flask was charged with a solution of bis-*N*-alkoxyphthalimido−poly(ethylene glycol) (7.5 g, 3.3 mmol) in methylene chloride (35 mL). The solution was treated in one portion with hydrazine hydrate (0.9 mL, 7.2 mmol, ~22% in H_2O) and stirred vigorously at rt for 1 h. The resulting, pasty off-white solid was removed by filtration. The clear eluent was diluted into 2.5 L of diethyl ether and stirred vigorously for 1 h at 4 °C, yielding a fine white precipitate. The solid was isolated by filtration and dried in vacuo for 3 h, affording **12** as a white powder (6.1 g, 3.0 mmols, 91%), which was used without further purification. ^{1}H NMR (400 MHz, $CDCl_3$): δ 3.4−3.8 (poly(ethylene glycol) signals), 5.5 (s, amine signals).

Coumarin−PEG Conjugate (14). To a stirred solution of coumarin-334 (**13**, 8.5 mg, 0.03 mmol) in methylene chloride (5 mL) was added **12** as a solid (38 mg, 0.02 mmol). Once the solid had dissolved completely, trifluoroacetic (20 μL) acid was added. After 2 h at rt, the reaction solution was poured slowly into 250 mL of diethyl ether. Precipitation occurred slowly over the course of 1 h, at which time the mother liquor was carefully decanted. The yellow solid was dissolved in ~2 mL of CH_2Cl_2 and again precipitated from diethyl ether. The yellow solid was used without further purification. Reversed-phase HPLC analysis of the solid indicated a ratio of 1:2 single/double coupled coumarin−PEG with no free coumarin-334 remaining. Stoichiometry for protein reactions was estimated on the basis of this ratio.

4-Formylbenzoic Acid 2,5-Dioxopyrrolidin-1-yl Ester (15). A stirred solution of *p*-formylbenzoic acid (200 mg, 1.33 mmol), *N*-hydroxysuccinimide (230 mg, 2.0 mmol), and *N*,*N*-diisopropylethylamine (520 μL, 3.0 mmol) in dry THF (25 mL) was cooled to 0 °C and treated in one portion with *N*,*N*-dicyclohexylcarbodiimide (310 mg, 1.5 mmol). The solution was stirred at 0 °C for 30 min and then allowed to warm to rt. Reaction progress was monitored by TLC (EtOAc). After 2 h at rt, the solution was concentrated under reduced pressure and then diluted with methylene chloride (25 mL). Insoluble material was removed by filtration, and the solution was again concentrated under reduced pressure. The remaining mixture was again filtered, and the eluent was applied to a silica-gel column. Flash chromatography (EtOAc/hexanes) afforded **15** as a pure white solid (310 mg, 94% yield). ^{1}H NMR (500 MHz, $CDCl_3$): δ 2.92 (s, 4H), 8.01 (d, 2H, $J = 8.0$ Hz), 8.28 (d, 2H, $J = 8.0$ Hz), 10.12 (s, 1H). ^{13}C NMR (125 MHz, $CDCl_3$): δ 25.7, 129.7, 130.0, 131.2, 140.3, 161.1, 168.9, 191.2.

Aldehyde-Functionalized mtMS2 Capsids (16). A 1.0 mL buffered solution of mtMS2 (100 μM in "monomer", 100 mM NaH_2PO_4, pH 9.0) was treated with 50 μL of a solution of **15** (20 mM in DMF). The resulting solution was incubated at rt on a rotating shaker for 2 h. The mtMS2 conjugate was purified from unreacted small-molecule impurities using size-exclusion chromatography (NAP-10). Labeling efficiency was determined by ESI-MS to be ~1:3:2 (unlabeled/single conjugate/double conjugate) distribution of adducts with a small amount of triple modification noted.

RESULTS AND DISCUSSION

Our target scaffold, bacteriophage MS2, possesses many desirable features with regard to both processing and synthesis. It is a $T = 3$ icosahedral virus, with a 27 nm protein capsid composed of 180 identical copies of a 13.7 kDa subunit (*29*, *30*). Native MS2 (natMS2) is safe, easily handled, readily propagated in multi-milligram quantities in broth cultures, and remains indefinitely stable upon storage in aqueous buffer at 4 °C (*31*, *32*). In addition, we have previously shown that natMS2 possesses impressive stability to a broad range of temperature, pH, ionic strength, and organic cosolvent conditions, and is capable of forming genome-free "empty" capsid shells (mtMS2, **1**) that exhibit nearly identical resistance to disassembly and denaturation under extreme conditions to that of natMS2 (*18*). Crucial to our internal modifications is the fact that MS2 possess 32 pores per capsid, each approximately 1.8 nm in diameter. These structural features provide ready access to its interior space for moderately sized particles and reagents, including functionalized drug molecules, for covalent attachment.

The abundance of reactive amines (the coat protein N-terminus, Lys 106, and Lys 113) presented on the nat- or mtMS2 exterior allows for facile and high-yielding modification via *N*-hydroxysuccinimide esters (Figure 2b). However, the key to selectivity for our dual surface modification strategy is the targeting of an interior amino acid side chain with orthogonal reactivity to lysine and cysteine residues. We have previously shown that this can be accomplished by functionalizing Tyr 85, which is displayed on the interior face of each monomer after capsid assembly. Following the removal of the RNA genome, this residue can undergo a rapid and efficient coupling to the diazonium salt of p-nitroaniline to install an azo linkage *ortho* to the phenolic moiety of the tyrosine (Figure 2a) (*18*).

As an elaboration of this strategy, the current study began with the synthesis of aniline **4**, which bears the nitro group that is required to achieve high coupling efficiency and an aliphatic amino group that can be functionalized selectively with virtually any commercially available NHS-ester. This is demonstrated for fluorescein derivative FAM-SE in Figure 3. The resulting aniline derivative (**5**) was then converted to diazonium salt **6** before being exposed to mtMS2 in a 5-fold excess (relative to capsid monomers) for 15 min. After gel filtration to remove small molecules and any dissociated monomers, the resulting conjugate (**2**) was recovered at 90% with each intact particle encapsidating 50−70 fluorescein dyes (as determined by MALDI-TOF MS and UV−vis analysis). We were particularly interested in these fluorescent anilines, as they can serve as useful visualization probes for subsequent cell-based assays. In addition, the large size of the aniline−dye conjugate (MW $\approx$ 600) demonstrates that access to the capsid interior is permitted for relatively large molecules, potentially including many drugs.

With the internally labeled capsids in hand, the exterior surface was passivated through the attachment of poly(ethylene glycol) (PEG) chains (*33*, *34*). As previously demonstrated for a vast array of biomacromolecules and small molecules (*35*, *36*), PEG conjugation reduces the humoral immune response in vivo, improves serum half-life, enhances bioavailability, and minimizes proteolytic cleavage. In the case of viral capsids, PEG conjugation has been shown to reduce the immunogenicity of adenovirus-based gene delivery vectors (*37*), as well as improve its prospects for oral delivery (*38*). In addition, PEG conjugation to cowpea mosaic virus (CPMV) has been observed to alter the levels of serum antibodies following inoculation (*7*). Through the clever use of blue fluorescent antibodies, PEG chains have also been shown to prevent the binding of small molecule antigens displayed on the surface of CPMV.

In the context of MS2, the attachment of PEG chains was first accomplished through the reaction of **2** with commercially available PEG-NHS esters (MW = 2000 or 5000), affording conjugates **3a** and **3b** with essentially complete conversion (Figure 2c). Gel filtration using S-300 resin followed by centrifugal concentration removed the excess PEG after bioconjugation was complete. For both polymers, single, doubly, and triply modified capsid monomers were observed by SDS-PAGE. In comparison to other viral capsid-based scaffolds, this level of PEG coverage is unprecedented, adding over 1800 kD of polymer (in the case of the PEG-5000) to the surface of each capsid. This coverage was obtained without any observable protein precipitation or denaturation, in contrast to what has been observed previously for other viral particles. Fluorescence imaging of the gel for conjugates **3a** and **3b** confirmed that the PEG-modified capsid monomers retained the dye molecules attached to the inner surface. The selectively differentiated conjugates were obtained with an overall protein recovery (two steps) of over 80%.

The assembly state of the doubly modified capsids was determined using several analytical techniques. Analytical size exclusion chromatography and TEM analysis (Figure 2d,e) indicated the presence of intact capsids with no indication of protein monomers. In addition, the spherical nature of the capsid conjugates made them particularly amenable to characterization by dynamic light scattering (DLS) (Table 1). Virtually identical particle diameters were observed for natMS2, mtMS2, and **2**, each measuring 27−29 nm. Upon conjugation of the PEG-2000 chains (**3a**), an effective diameter of 34 nm was observed, with a further increase to 41 nm upon conjugation of the PEG-5000 chains (**3b**). Further determination of each particle's ζ potential indicated that the inherent excess negative surface charge of MS2 (−19.40 mV) is reduced significantly upon PEGylation, a property that is highly desirable to avoid bioaccumulation in drug delivery formulations (*39*, *40*). Interestingly, thermal denaturation studies (also monitored using DLS) indicated that the dual surface-functionalized particles remained fully assembled up to 58 °C, with no apparent effects from the polymer coating. This value is identical to that measured for natMS2 itself.

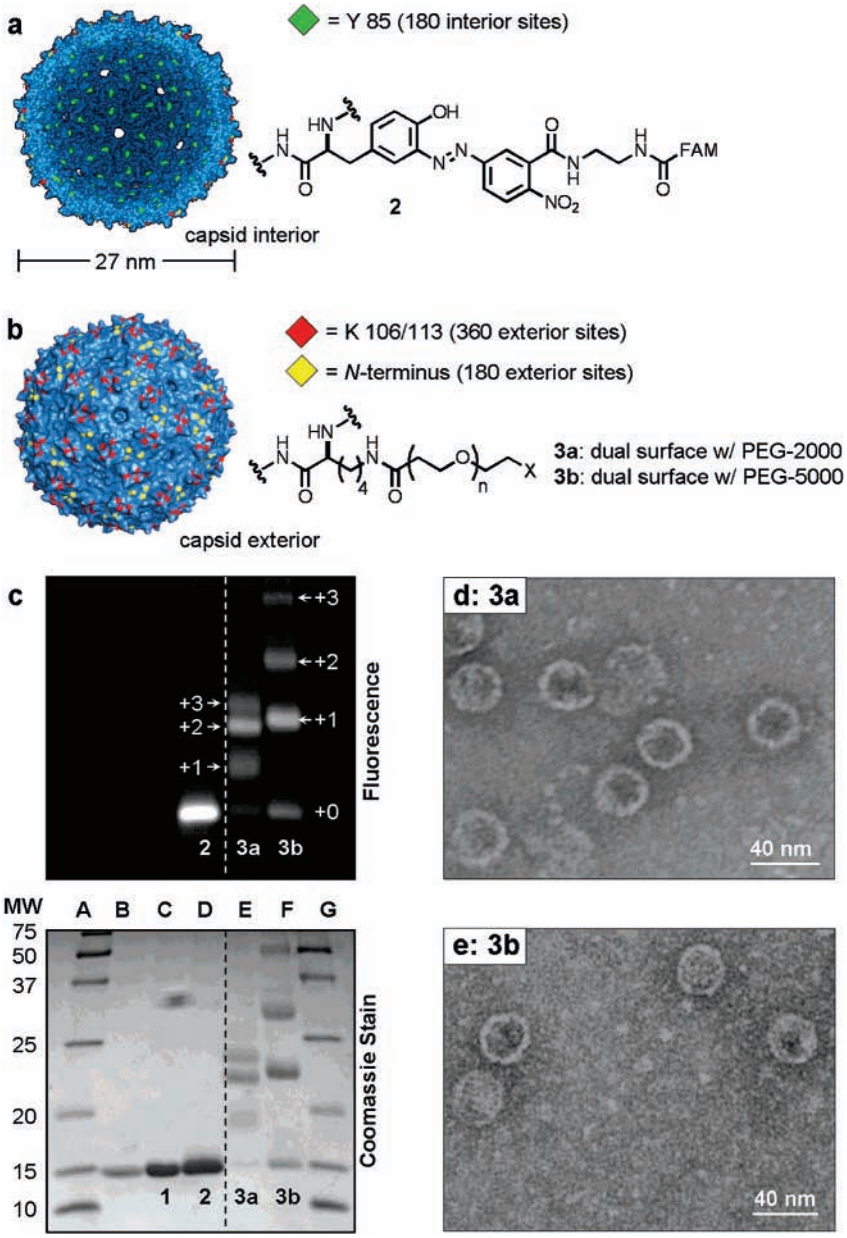


Figure 2. Dual surface modification of MS2 capsids. (a) Tyrosine 85 of the interior capsid surface undergoes rapid diazonium coupling with *p*-nitroaniline derivatives, including large dye conjugates. (b) Up to 360 accessible amino groups (lysines 106, 113, and the *N*-terminus) on the capsid exterior are readily modified with PEG-NHS esters. (c) SDS-PAGE analysis confirming both PEGylation (via MW shift) and dye attachment (fluorescent bands) for capsid monomers after disassembly. The arrows indicate coat proteins modified with 1, 2, or 3 PEG chains. Lanes A and G: MW markers, listed in kDa. Lane B: natMS2. Lane C: mtMS2 (**1**) + aniline **5**. Lane D: **2**. Lane E: **3a**. Lane F: **3b**. (d,e) In addition to other methods, the assembly state of the modified capsids was confirmed by TEM analysis after staining with $UO_2(OAc)_2$.

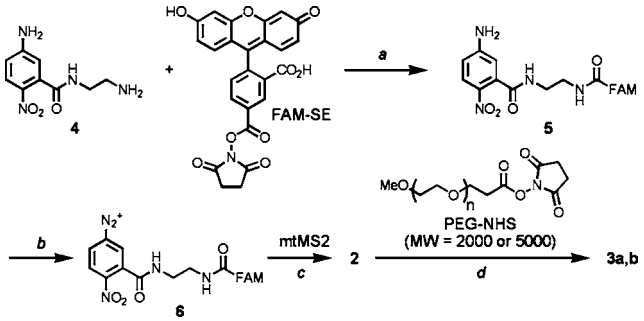


Figure 3. Dual surface modification sequence. Reagents and conditions: (a) DMF, Et_3N, 65 °C, 1.5 h, >95%; (b) $NaNO_2$, *p*-TsOH, 0 °C, 0.75 h; (c) **6** (5 equiv), pH 8.5, 0 °C, 5 min, 90% protein recovery; (d) pH 8.4, rt, 15 h, 90% protein recovery.

To determine the ability of the PEG chains to mask the capsid surface from antibody recognition, we subjected our samples to a sandwich ELISA assay. Using rabbit-derived anti-native MS2 polyclonal antibodies for detection and capture, identical maximum antibody binding was achieved with natMS2, mtMS2, or conjugate **2** under the full range of protein concentrations tested. This indicates that the native epitopes of the MS2 capsid remain intact after genome removal and subsequent internal modification with **6** (Figure 4). In contrast, PEG-2000 conjugate

Table 1. Properties of MS2 Conjugates Obtained from DLS Measurements[a]

sample	avg particle size[a]	ζ potential[b]	disassembly temp[c]
mtMS2	28.9 ± 1.1 nm	−19.4 ± 2.3 mV	58−61 °C
2	27.5 ± 0.9 nm	−21.5 ± 1.4 mV	58−61 °C
3a	34.5 ± 0.7 nm	−11.4 ± 0.6 mV	58−61 °C
3b	40.9 ± 1.0 nm	−5.0 ± 2.1 mV	58−61 °C

[a] Average of ten separate measurements. [b] Average of three separate measurements. [c] Reported as the point at which additional peaks (±50% of established particle size) emerge as >4% of the volume distribution for a single particle size measurement.

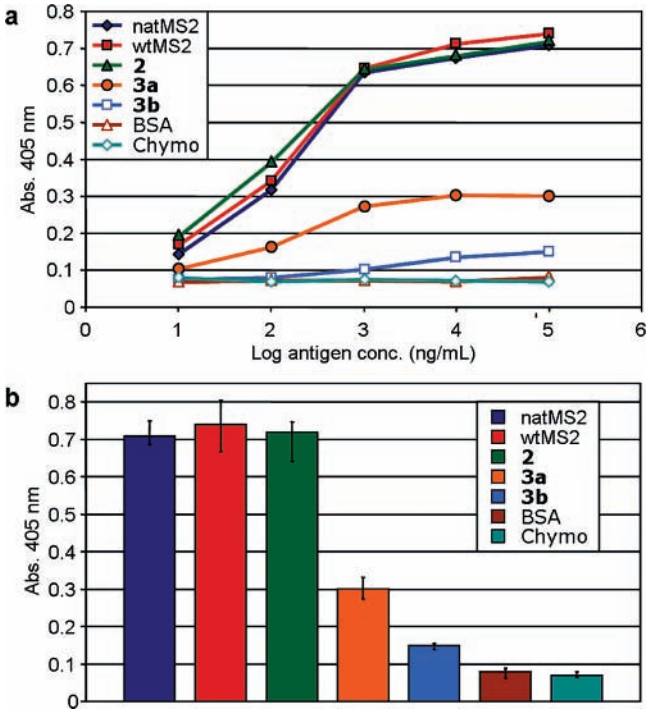


Figure 4. Polyclonal anti-natMS2 antibody response to MS2 capsids, as determined by ELISA. (a) ELISA response for the sample antigen concentration from 10 ng/mL to 0.1 mg/mL. (b) Comparative antibody binding for antigen concentration at 0.1 mg/mL. BSA = bovine serum albumin and chymo = α-chymotrypsinogen (negative controls).

3a exhibited greater than 65% reduction in antibody binding, while PEG-5000 conjugate **3b** showed nearly 90% reduction at the highest concentration of antigen sample tested (Figure 4b).

A number of functional groups have been shown to direct attached cargo to specific tissue types in vivo. In terms of small molecules, folate (*41*), transferrin (*42*), and vitamin B_{12} (*43*, *44*), have been particularly successful for the targeting of solid tumors, and a growing collection of peptides that target organs of interest have been identified through the use of phage display techniques (*45*). In addition to shielding the capsid surface from antibody recognition, it was envisioned that the polymer chains could be used to display these molecules to gain similar control of cellular uptake for MS2-derived drug carriers. However, a key consideration of this technique is the ability of the small molecules to reach their targets in the presence of the PEG layer. To test this, samples of mtMS2 capsids were biotinylated using commercially available NHS esters bearing (in the case of **8a** and **8b**) or lacking (in the case of **7**) PEG chains, Figure 5a. For biotin-3k-PEG conjugate **8a**, SDS-PAGE analysis indicated that 30% of the monomers had been functionalized, while for biotin-PEG-5000 conjugate **8a**, the level of modification was 70%. These differences in reactivity were attributed to degradation of the NHS esters during storage prior to use. Nonetheless, this method produced samples displaying 50−100 biotin groups at the end of the polymer chains.

The resulting samples were exposed to avidin beads for 1 and 15 h, after which the samples were centrifuged to remove the captured MS2 from solution. SDS-PAGE analysis of the remaining supernatants revealed 82% recovery for mtMS2 capsids as a negative control, Figure 5b,c. Surprisingly, similar levels (87%) of mtMS2 capsids functionalized with biotin (**7**) were also recovered, suggesting that the capsid surface hinders the ability of the avidin groups to reach the displayed ligands. In contrast, both of the PEG−biotin conjugates were removed from solution using this method, indicating that the small-molecule ligands had access to the solution surrounding the PEG layer. After 15 h of exposure to the resin, 90% of the capsids

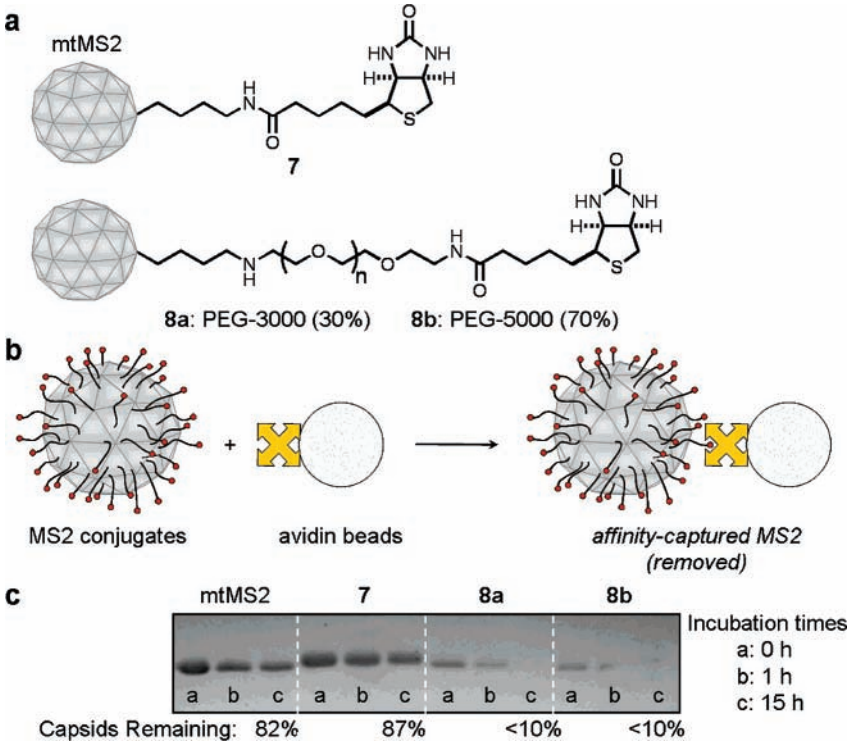


Figure 5. Accessibility of small molecules displayed on the distal ends of MS2-PEG conjugates. (a) Biotinylated samples of MS2 were prepared through reaction of the corresponding NHS esters with genome-free capsids. Densitometry measurements after SDS-PAGE analysis and Coomassie staining indicated that ∼30% of the monomers were labeled in the case of **8a** and 70% of the monomers were labeled in the case of **8b**. (b) Conjugates **7**, **8a**, and **8b** were incubated with avidin beads for 0, 1, and 15 h. (c) Following centrifugation, the MS2 remaining in the supernatant was analyzed by SDS-PAGE. The percentages reported were determined by densitometry analysis after Coomassie staining. For the polymer-conjugated samples, only the band corresponding to unlabeled monomers is shown.

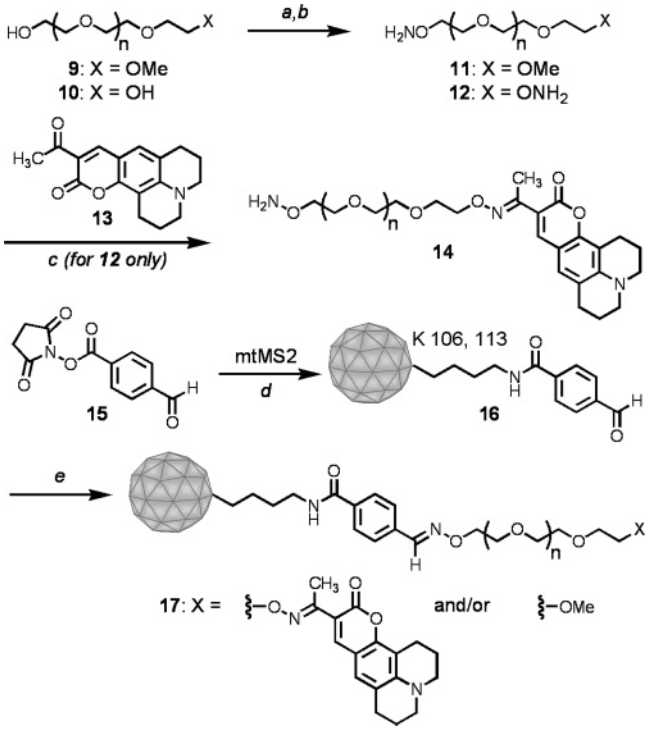


Figure 6. Chemical strategy for the installation of PEG chains bearing small-molecule targeting groups. Reagents and conditions: (a) DIAD, *N*-hydroxyphthalimide, CH_2Cl_2, rt, 12 h (see Experimental Procedures); (b) $NH_2NH_2 \cdot xH_2O$ (2.2 equiv), CH_2Cl_2, rt, 1 h; (c) CH_2Cl_2, 0.1% TFA; (d) 100 mM NaH_2PO_4 aqueous buffer, pH 9.0, rt, 2 h; (e) 25 mM NaH_2PO_4 aqueous buffer, pH 6.5, 1.5 h, rt.

were removed from solution for both **8a** and **8b**. It should be noted that these effects will vary dramatically for each ligand−receptor combination; however, this experiment serves to validate the placement of targeting groups at the ends of the polymer chains.

Following the success of this experiment, the final synthetic component of these studies was the development of a modular strategy for the coupling of a wide variety of small molecules to the ends of the PEG chains. Oxime formation was chosen for this purpose, as it proceeds rapidly and chemoselectively under mild reaction conditions in aqueous media (*46*). In a previous report, we have explored the use of singly functionalized PEG−alkoxyamines, such as methoxy-terminated **11**, for the modification of ketones introduced on the surface of the tobacco mosaic virus (*8*). For this study, precursors to doubly functionalized PEG-bis-alkoxyamines were prepared through the displacement of the alcohol groups of PEG-diol **10** using hydroxyphthalamides under Mitsunobu conditions (Figure 6). Hydrazinolysis subsequently afforded bis-alkoxyamine **12**, which could be condensed with ketones and aldehydes in CH_2Cl_2 using catalytic TFA. Fluorescent coumarin−ketone **13** was used in these model studies, as it can be visualized readily after SDS-PAGE analysis of the bioconjugates.

To bind to the remaining alkoxyamine group of **14**, aldehydes were installed on the surface of mtMS2 capsids using NHS ester **15**. Following removal of the small molecules using gel filtration, MALDI-MS analysis indicated ~90% conversion of the capsid monomers to single, double, and triple conjugates. These groups were attached to the alkoxyamine groups in aqueous phosphate buffer, pH 6.5, in 1.5 h at rt. The unreacted PEG chains were removed using gel filtration, and the samples were analyzed using SDS-PAGE with fluorescence visualization of the attached coumarin, followed by Coomassie staining. Using this method, high levels of conversion could be obtained to the singly, doubly, and triply conjugated species (Figure 7). Using

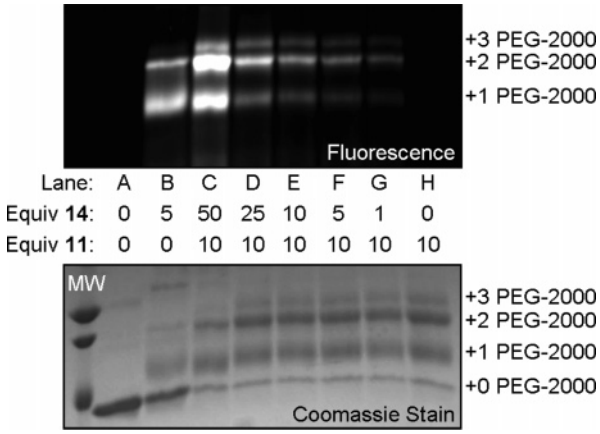


Figure 7. Attachment of functionalized PEG chains to the aldehyde groups of MS2 conjugate **16** through oxime formation. All reactions were carried out in 25 mM phosphate buffer, pH 6.5, for 1.5 h, using the indicated ratios of **14** and **11**. The remaining polymer was removed via gel filtration before SDS-PAGE analysis. From bottom to top, the MW markers correspond to 15, 20, and 25 kD.

this method, the number of ligands that are displayed can be modulated by varying the ratio of labeled PEG (**17**) to methoxy-PEG (**11**), as observed by changes in fluorescence intensity for samples with the same overall PEG coverage.

Through these studies, we have demonstrated the ability of MS2 viral capsids to undergo a facile, site-selective dual surface modification to afford unique hybrid drug delivery vehicles. These conjugations were achieved in high overall yield, were accomplished without the need for site-directed mutagenesis, and produced particles that are as resistant to disassembly and denaturation as the native capsid. Our exterior PEGylation levels match or exceed previous reports for other viral particles, resulting in a nearly 90% reduction in antibody binding of the capsid surface. The interior modification strategy demonstrates that access to the interior is readily permitted for large "druglike" dye molecules, while further expanding the utility of tyrosine-selective reactions to achieve bioconjugations that are orthogonal to lysine and cysteine modification strategies. Further studies are underway to monitor the biodistribution and serum half-life of these particles in vivo using animal models. In addition, we are investigating the optimal degradable linkage for the interior surface attachment of drug cargo. The ability of targeting ligands to enhance capsid uptake in specific cell lines is also being explored.

ACKNOWLEDGMENT

These studies were generously supported by the Chemical Biology Graduate Program in the Department of Chemistry at UC Berkeley (NRSA Training Grant 1 T32 GMO66698), the Biomolecular Materials Program at Lawrence Berkeley National Labs (DE-AC02-05CH11231), and the NIH (GM072700-01). J.M.H. was supported by a graduate fellowship from the NSF.

LITERATURE CITED

(1) Douglas, T., and Young, M. (1998) Host-guest encapsulation of materials by assembled virus protein cages. *Nature (London) 393*, 152−155.

(2) Sen Gupta, S., Kuzelka, J., Singh, P., Lewis, W. G., Manchester, M., and Finn, M. G. (2005) Accelerated bioorthogonal conjugation: A practical method for the ligation of diverse functional molecules to a polyvalent virus scaffold. *Bioconjugate Chem. 16*, 1572−1579.

(3) Anderson, E. A., Isaacman, S., Peabody, D. S., Wang, E. Y., Canary, J. W., and Kirshenbaum, K. (2006) Viral nanoparticles donning a paramagnetic coat: Conjugation of MRI contrast agents to the MS2 capsid. *Nano Lett. 6*, 1160−1164.

(4) Gillitzer, E., Willits, D., Young, M., and Douglas, T. (2002). Chemical modification of a viral cage for multivalent presentation. *Chem. Commun.* 2390−2391.

(5) O'Riordan, C. R., Lachapelle, A., Delgrado, C., Parkes, V., Wadsworth, S. C., Smith, A. E., and Francis, G. E. (1999) PEGylation of adenovirus with retention of infectivity and protection from neutralizing antibody in vitro and in vivo. *Hum. Gene Ther. 10*, 1349−1358.

(6) Croyle, M. A., Yu, Q. C., and Wilson, J. M. (2000) Development of a rapid method for the PEGylation of adenoviruses with enhanced transduction and improved stability under harsh storage conditions. *Hum. Gene Ther. 11*, 1713−1722.

(7) Raja, K. S., Wang, Q., Gonzalez, M. J., Manchester, M., Johnson, J. E., and Finn, M. G. (2003) Hybrid virus-polymer materials. 1. Synthesis and properties of PEG-decorated cowpea mosaic virus. *Biomacromolecules 4*, 472−476.

(8) Schlick, T. L., Ding, Z. B., Kovacs, E. W., and Francis, M. B. (2005). Dual-surface modification of the tobacco mosaic virus. *J. Am. Chem. Soc. 127*, 3718−3723.

(9) Raja, K. S., Wang, Q., and Finn, M. G. (2003) Icosahedral virus particles as polyvalent carbohydrate display platforms. *Chembiochem 4*, 1348−1351.

(10) Sen Gupta, S., Raja, K. S., Kaltgrad, E., Strable, E., and Finn, M. G. (2005). Virus-glycopolymer conjugates by copper(I) catalysis of atom transfer radical polymerization and azide-alkyne cycloaddition. *Chem. Commun.* 4315−4317.

(11) Strable, E., Johnson, J. E., and Finn, M. G. (2004) Natural nanochemical building blocks: Icosahedral virus particles organized by attached oligonucleotides. *Nano Lett. 4*, 1385−1389.

(12) Klem, M. T., Willits, D., Young, M., and Douglas, T. (2003) 2D array formation of genetically engineered viral cages on Au surfaces and imaging by atomic force microscopy. *J. Am. Chem. Soc. 125*, 10806−10807.

(13) Shenton, W., Douglas, T., Young, M., Stubbs, G., and Mann, S. (1999) Inorganic-organic nanotube composites from template mineralization of tobacco mosaic virus. *Adv. Mater. 11*, 253−256.

(14) Allen, M., Bulte, J. W. M., Liepold, L., Basu, G., Zywicke, H. A., Frank, J. A., Young, M., and Douglas, T. (2005) Paramagnetic viral nanoparticles as potential high-relaxivity magnetic resonance contrast agents. *Magn. Reson. Med. 54*, 807−812.

(15) Douglas, T., and Young, M. (1999) Virus particles as templates for materials synthesis. *Adv. Mater. 11*, 679−681.

(16) Douglas, T., Strable, E., Willits, D., Aitouchen, A., Libera, M., and Young, M. (2002). Protein engineering of a viral cage for constrained nanomaterials synthesis. *Adv. Mater*. 415−418.

(17) Loo, L., Guenther, R. H., Basnayake, V. R., Lommel, S. A., and Franzen, S. (2006) Controlled encapsidation of gold nanoparticles by a viral protein shell. *J. Am. Chem. Soc. 128*, 4502−4503.

(18) Hooker, J. M., Kovacs, E. W., and Francis, M. B. (2004) Interior surface modification of bacteriophage MS2. *J. Am. Chem. Soc. 126*, 3718−3719.

(19) Mastico, R. A., Talbot, S. J., and Stockley, P. G. (1993) Multiple presentation of foreign peptides on the surface of an RNA-free spherical bacteriophage capsid. *J. Gen. Virol. 74*, 541−548.

(20) Burke, K. L., Dunn, G., Ferguson, M., Minor, P. D., and Almond, J. W. (1988) Antigen chimeras of poliovirus as potential new vaccines. *Nature (London) 332*, 81−82.

(21) van Meerten, D., Olsthoorn, R. C. L., van Duin, J., and Verhaert, R. M. D. (2001) Peptide display on live MS2 phage: restrictions at the RNA genome level. *J. Gen. Virol. 82*, 1797−1805.

(22) Ochoa, W. F., Chatterji, A., Lin, T. W., and Johnson, J. E. (2006) Generation and structural analysis of reactive empty particles derived from an icosahedral virus. *Chem. Biol. 13*, 771−778.

(23) Zwick, M. B., Shen, J. Q., and Scott, J. (1998) Phage-displayed peptide libraries. *Curr. Opin. Biotechnol. 9*, 427−436.

(24) Whaley, S. R., English, D. S., Hu, E. L., Barbara, P. F., and Belcher, A. M. (2000) Selection of peptides with semiconductor binding specificity for directed nanocrystal assembly. *Nature (London) 405*, 665−668.

(25) Lee, S.-W., Mao, C., Flynn, C. E., and Belcher, A. M. (2002) Ordering of quantum dots using genetically engineered viruses. *Science 296*, 892−895.

(26) Matsumura, Y., and Maeda, H. (1986) A new concept for macromolecular therapeutics in cancer-chemotherapy - Mechanism of tumoritropic accumulation of proteins and the antitumor agent SMANCS. *Cancer Res. 46*, 6387−6392.

(27) Seymour, L. W., Ulbrich, K., Steyger, P. S., Brereton, M., Subr, V., Strohalm, J., and Duncan, R. (1994) Tumor tropism and anticancer efficacy of polymer-based doxorubicin prodrugs in the treatment of subcutaneous murine B16F10 melanoma. *Br. J. Cancer 70*, 636−641.

(28) Gianasi, E., Wasil, M., Evagorou, E. G., Keddle, A., Wilson, G., and Duncan, R. (1999) HPMA copolymer platinates as novel antitumour agents: In vitro properties, pharmacokinetics and antitumour activity in vivo. *Eur. J. Cancer 35*, 994−1002.

(29) Valegard, K., Liljas, L., Fridborg, K., and Unge, T. (1990) The 3-dimensional structure of the bacterial-virus MS2. *Nature (London) 345*, 36−41.

(30) Golmohammadi, R., Valegard, K., Fridborg, K., and Liljas, L. (1993) The refined structure of bacteriophage-MS2 at 2.8 Angstrom resolution. *J. Mol. Biol. 234*, 620−639.

(31) Strauss, J. H., and Sinsheimer, R. L. (1963) Purification and properties of bacteriophage MS2 and of its ribonucleic acid. *J. Mol. Biol. 7*, 43.

(32) Cargile, B. J., McLuckey, S. A., and Stephenson, J. L., Jr. (2001) Identification of bacteriophage MS2 coat protein from *E. coli* lysates via ion trap collisional activation of intact protein ions. *Anal. Chem. 73*, 1277−1285.

(33) Bailon, P., and Berthold, W. (1998) Polyethylene glycol-conjugated pharmaceutical proteins. *Pharm. Sci. Technol. Today 1*, 352−356.

(34) Zalipsky, S., and Harris, J. M. (1997) Introduction to chemistry and biological applications of poly(ethylene glycol). *Poly(Ethylene Glycol*) *680*, 1−13.

(35) Harris, J. M., and Chess, R. B. (2003) Effect of pegylation on pharmaceuticals. *Nat. Rev. Drug Discovery 2*, 214−221.

(36) Duncan, R. (2003) The dawning era of polymer therapeutics. *Nat. Rev. Drug Discovery 2*, 347−360.

(37) Croyle, M. A., Chirmule, N., Zhang, Y., and Wilson, J. M. (2001) "Stealth" adenoviruses blunt cell-mediated and humoral immune responses against the virus and allow for significant gene expression upon readministration in the lung. *J. Virol. 75*, 4792−4801.

(38) Cheng, X., Ming, X., and Croyle, M. A. (2003) PEGylated adenoviruses for gene delivery to the intestinal epithelium by the oral route. *Pharm. Res. 20*, 1444−1451.

(39) Moghimi, S. M., Hunter, A. C., and Murray, J. C. (2001) Long-circulating and target-specific nanoparticles: Theory to practice. *Pharmacol. Rev. 53*, 283−318.

(40) Chellat, F., Merhi, Y., Moreau, A., and Yahia, L. (2005) Therapeutic potential of nanoparticulate systems for macrophage targeting. *Biomaterials 26*, 7260−7275.

(41) Leamon, C. P., and Reddy, J. A. (2004) Folate-targeted chemotherapy. *Adv. Drug Delivery Rev. 56*, 1127−1141.

(42) Gomme, P. T., and McCann, K. B., and Bertolini, J. (2005) Transferrin: structure, function and potential therapeutic actions. *Drug Discovery Today 10*, 267−273.

(43) Hogenkamp, H. P. C., Collins, D. A., Grissom, C. B., and West, F. G. (1999) *Chemistry and Biochemistry of B12*, Banerjee, R., Ed., Wiley, New York, p 921.

(44) Bagnato, J. D., Eilers, A. L., Horton, R. A., and Grissom, C. B. (2004) Synthesis and characterization of a cobalamin-colchicine conjugate as a novel tumor-targeted cytotoxin. *J. Org. Chem. 69*, 8987−8996.

(45) Krumpe, L. R. H., and Mori, T. (2006) The use of phage-displayed peptide libraries to develop tumor-targeting drugs. *International Journal of Peptide Research and Therapeutics 12*, 79−91.

(46) Jencks, W. P. (1959). Studies on the mechanism of oxime and semicarbazone formation. *J. Am. Chem. Soc.* 475−481.

BC070006E

Synthesis and Characterization of PAMAM Dendrimer-Based Multifunctional Nanodevices for Targeting $\alpha_v\beta_3$ Integrins

Wojciech G. Lesniak,[†,§] Muhammed S. T. Kariapper,[†,§] Bindu M. Nair,[†] Wei Tan,[‡] Alan Hutson,[‡] Lajos P. Balogh,*[,†] and Mohamed K. Khan[†]

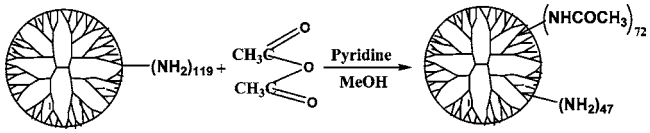
NanoBiotechnology Center at RPCI, Department of Radiation Medicine, and Department of Biostatistics, Roswell Park Cancer Institute, Elm and Carlton Streets, Buffalo, New York 14263. Received January 10, 2007; Revised Manuscript Received April 2, 2007

We have synthesized a stable and clinically relevant nanodevice (cRGD-BT-ND; ND for short) that exhibits superior binding to the biologic target $\alpha_v\beta_3$ integrins, when either compared to the same free cRGD peptide or to the biotinylated nanodevice without covalently attached peptides (BT-ND). Selective targeting of $\alpha_v\beta_3$ integrins was achieved by coupling cyclic cRGD peptides to the nanodevice (ND) surface, while biotin groups (BT) were used for amplified detection of bound cRGD-BT-ND by anti-biotin antibody or avidin linked to horseradish peroxidase after binding. The synthesis involved the following steps: the amino-terminated ethylenediamine core generation 5 poly(amidoamine) (PAMAM_E5.NH_2) dendrimer was first partially acetylated and then biotinylated, and residual primary amine termini were converted to succinamic acid groups (SAH), some of which finally were conjugated with cRGD peptide residues through the amino group of the lysine side chain. The starting material and all derivatives were extensively characterized by polyacrylamide gel electrophoresis (PAGE), size exclusion chromatography (SEC), potentiometric acid−base titration, MALDI-TOF, and NMR. Cytotoxicity of all dendrimer derivatives was examined in B16F10 melanoma cell cultures using the XTT colorimetric assay for cellular viability. Binding of nanodevices to the biological target was determined using plates coated with human $\alpha_v\beta_3$ integrin and $\alpha_v\beta_3$ receptor expressing human dermal microvascular endothelial cells (HDMECs). The PAMAM_E5.$(NHAc)_{72}(NHBT)_8(NHSAH)_{35}(NHSA\text{-}cR\ GD)_4$ nanodevice is nontoxic within physiologic concentration ranges and specifically binds to the $\alpha_v\beta_3$ integrins, apparently much stronger than the cyclic cRGD peptide itself.

INTRODUCTION

We are developing a novel Systemic Targeted Radiation Therapy (START) approach utilizing a dendrimer-based platform to detect and treat primary and metastatic cancers. As a first step using poly(amidoamine) (PAMAM) dendrimer we have synthesized the multifunctional nanodevice that selectively binds to $\alpha_v\beta_3$ integrins. PAMAM dendrimers are water soluble, well-defined polymers, built from symmetric dendrons, containing β-alanine subunits, emanating from a core (*1*, *2*). These polymers are nearly ideal delivery vehicles, as they are not broken down by enzymes and are generally removed from the bloodstream by the filter organs (*3*−*6*). PAMAMs can be prepared to be nonimmunogenic, nonmutagenic, and nontoxic (see, e.g., *7*). Modifiable terminal functionalities of dendrimers offer a multipurpose mode to covalently attach drugs, diagnostic/imaging modules, and targeting moieties (*8*). PAMAMs have been already used as delivery vehicles for oligonucleotides, antisense oligonucleotides, oligonucleotide arrays, and chemotherapeutic cancer drugs (*9*−*11*). They have also been utilized as templates for composite nanoparticles, which allows them to host inorganic nanoclusters (*12*), thus providing a way to integrate desirable properties of inorganic materials and biofriendly polymers, and yielding several new imaging and therapy applications (*13*−*15*).

Scheme 1



During the design of this ND[1], we considered the following. The $\alpha_v\beta_3$ integrins are highly overexpressed on the angiogenic endothelial cells present in tumors, and are not available for binding in normal blood vessels (*16*). This feature can be exploited to target nanodevices (NDs) to endothelial cells of tumor microvasculature by covalently attaching $\alpha_v\beta_3$ targeting peptides to the surface of each nanodevice. For this purpose four copies of a specific cyclic RGD peptide (Phe(f)-Lys-Arg-Gly-Asp, abbreviated to cRGD) were conjugated with dendrimer. We used a peptide that strongly binds to the $\alpha_v\beta_3$ integrins and is already in clinical trials (*17*), making the nanodevice potentially more clinically useful than other permutations of RGD peptides (*10*). Additionally, it is a more stable cyclic RGD peptide compared to cyclization achieved via disulfide bond.

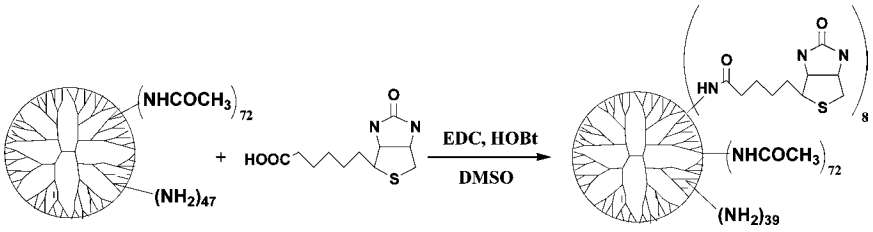
During the design, we have considered that toxicity of nanodevices, including dendrimers, often results from the presence of excessive positive charges (*7*, *11*, *15*). For this reason, we converted the unused primary amine surface groups that would have been positively charged (thus potentially toxic) at biologic pH values (pH = 5.5−7.5), to carboxylate groups by reacting them with succinamic anhydride.

* Author to whom correspondence should be addressed. Phone: 716-845-3886, fax: 716-845-8254; e-mail: lajos.balogh@roswellpark.org.
[†] Department of Radiation Medicine.
[‡] Department of Biostatistics.
[§] Equally contributed to this research.

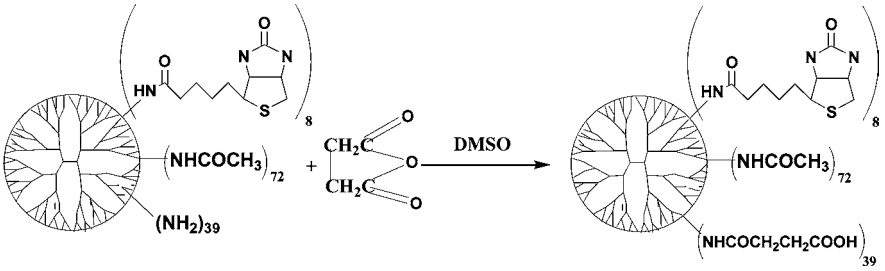
[1] Abbreviations: PAMAM_E5.NH_2, amine-terminated, ethylenediamine core generation 5 poly(amidoamine) dendrimer; ND, nanodevice; BT, biotin.

10.1021/bc070008z CCC: $37.00 © 2007 American Chemical Society
Published on Web 06/13/2007

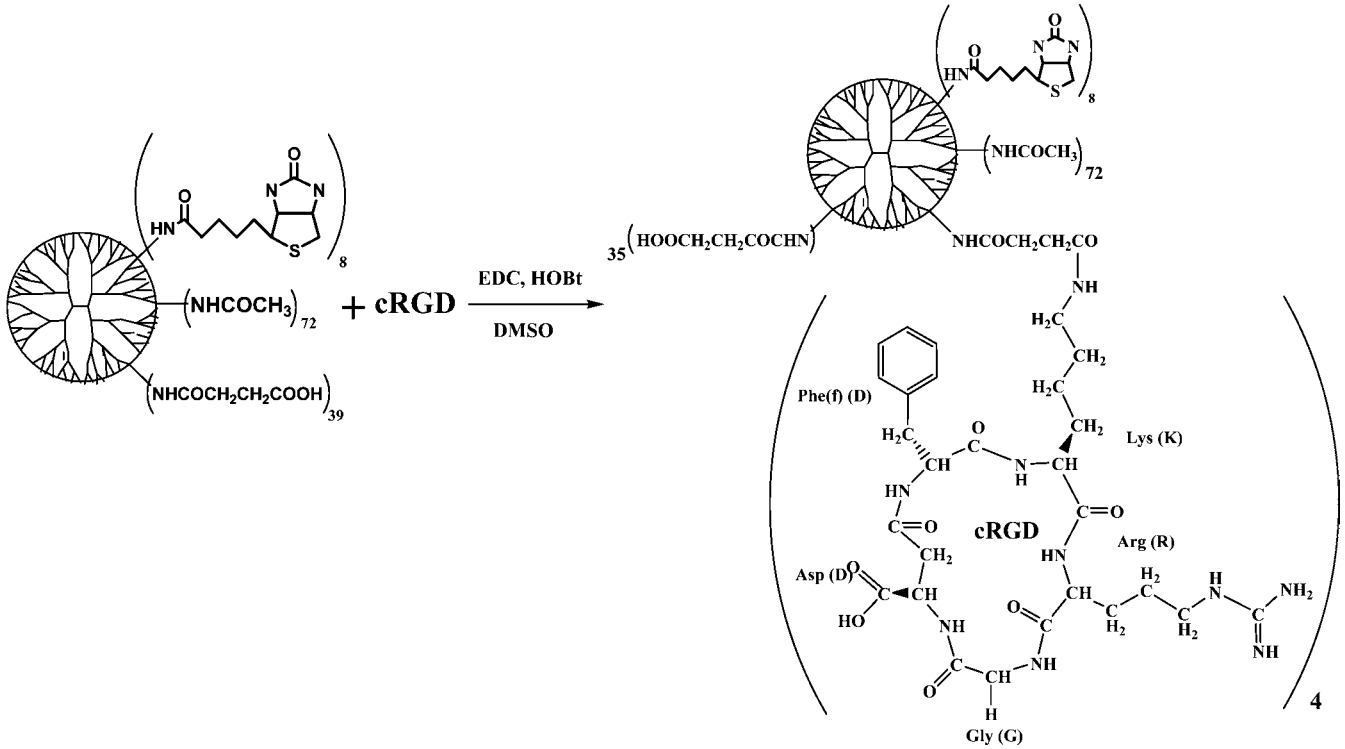
Scheme 2



Scheme 3



Scheme 4



Exact measurement of biodistribution is a prerequisite for the construction of efficient medical nanodevices that carry therapeutic or imaging agents to cancer cells. In the present literature, dendrimer-based nanodevices are often tracked by covalently attaching fluorescent dye molecules to the macromolecules. The apparent disadvantage of that method is that attaching large aromatic molecules to a dendrimer surface has to change the biodistribution of the dendrimer nanodevices. In our ND we used biotin as a label on the ND that can selectively be detected by labeled antibodies. We have conjugated eight biotin moieties per dendrimer to detect the presence of dendrimers sensitively and selectively after localization, as it is described in Experimental Procedures below. Using nanodevices labeled with multiple biotin units results in considerable signal amplification, while it does not disturb the biodistribution of the nanodevice.

EXPERIMENTAL PROCEDURES

General. Ethylenediamino-core poly(amidoamine) PAMAM dendrimer of generation 5 (PAMAM_E5.NH_2) was purchased from Dendritech Midland, MI, in methanol solution (14.17 wt %). Succinic anhydride, pyridine, acetic anhydride, biotin, bovine serum albumin, absolute methanol, dimethyl sulfoxide (DMSO), 1-(3-dimethylaminopropyl)-3-ethylcarbodiimide, and 1-hydroxybenzotriazole were obtained from Aldrich and used as received. Cyclic RGD peptide (Phe(f)-Lys-Arg-Gly-Asp) was acquired from Peptides International (Louisville, KY) and characterized by HPLC, electrospray ionization-TOF MS, and amino acid analysis before use. $\alpha_v\beta_3$ Integrin was purchased from Chemicon International (Temecula, CA). Immuno-Pure Avidin HRP and *o*-phenylenediamine were obtained from Pierce (Rockford, IL). Regenerated cellulose dialysis membranes

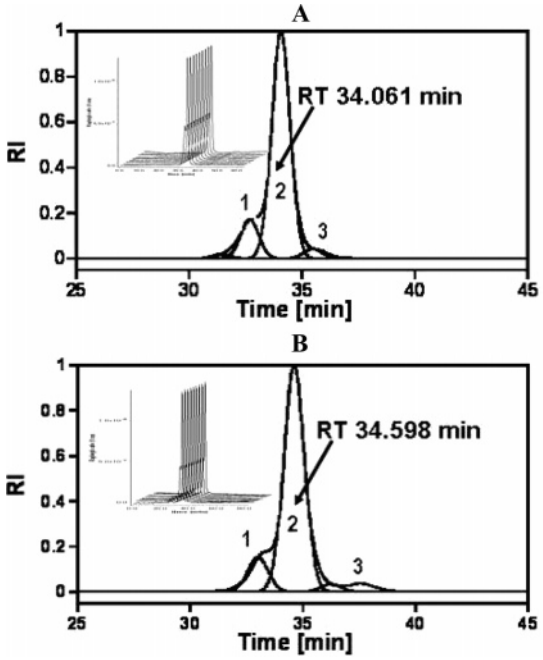


Figure 1. (A) Molecular mass distributions of the starting material E5.NH_2 dendrimer, and (B) the E5.$(NHAc)_{72}(NHB)_8(NHSAH)_{35}$-$(NHSAcRGD)_4$ nanodevice shown by their RI signals (insert, MALLS data). Fit of RI signals was performed using Gaussian deconvolution of SEC chromatograms using PeakFit software. The starting material contains (A1) $(E5.NH_2)_2$ dimers (16.42%), (A2) E5.NH_2 generation five dendrimers (80.42%), and (A3) a small amount of trailing generation E4.NH_2 (3.15%). Average molecular mass of M_n = 27 280, M_w = 30 280 with a polydispersity of M_w/M_n = 1.110 were obtained for this material. The final product (B) contains modified dimers (B1 = 16.32%); modified E5 derivatives (B2 = 80.22%) and a small amount of modified trailing generation (B3 = 3.46%). (Respective molecular masses calculated from PeakFit are M_n = 34080, M_w = 38 067, and M_w/M_n = 1.117).

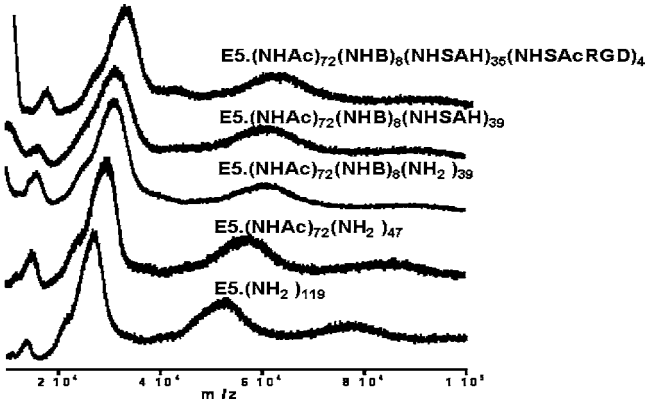


Figure 2. MALDI-TOF spectra of starting dendrimer, of the intermediates, and of the final nanodevice using 2,5-dihydroxybenzoic acid (DHB) as a matrix.

(MWCO = 2000 and 10 000) were acquired from Fisher. Water used in the experiments was purified by a Milli-Q Plus 185 water purification system (Millipore, Bedford, MA) with resistivity higher than 18 MΩ cm^{-1}. Starting material and all derivatives were characterized by polyacrylamide gel electrophoresis (PAGE), and size exclusion chromatography equipped with three detectors: multiangle laser light scattering, UV−vis diode-array, and refractive index (SEC-MALLS-DAD-RI), potentiometric acid−base titration, matrix assisted laser desorption ionization-time-of-flight (MALDI-TOF) mass spectrometry, and nuclear magnetic resonance (NMR).

Synthesis of PAMAM_E5.$(NHAc)_{72}(NHBT)_8(NHSAH)_{35}$-$(NHSAcRGD)_4$. *(1) Synthesis of PAMAM_E5.$(NAc)_{72}(NH_2)_{47}$ Dendrimer (Scheme 1).* A 100 mL amount of methanol solution containing 3.08 g ($n = 1.13 \times 10^{-4}$ mol) of PAMAM_E5.NH_2 dendrimer was placed in a 250-mL round-bottom flask. Then 100 mL of methanol solution with 1.53 g ($n = 1213 \times 10^{-2}$ mol) of pyridine and 0.98 g ($n = 9.60 \times 10^{-3}$ mol) of acetic anhydride was added. After 24 h, methanol was evaporated on a rotary evaporator. The residue was dissolved in water and dialyzed (using cellulose membrane with 2000 MWCO) against water for 3 days to remove byproducts and excess reactants. The obtained solution was filtered and lyophilized.

(2) Synthesis of PAMAM_E5.$(NHAc)_{72}(NHBT)_8(NH_2)_{39}$. Nanodevice (Scheme 2). A 0.08 g biotin ($n = 3.28 \times 10^{-4}$ mol) was dissolved in 50 mL of dimethyl sulfoxide (DMSO) in a 250-mL round-bottom flask then 0.13 g ($n = 6.78 \times 10^{-4}$ mol) of 1-(3-dimethylaminopropyl)-3-ethylcarbodiimide (EDC) and 0.09 g ($n = 6.66 \times 10^{-4}$ mol) 1-hydroxybenzotriazole (HOBt) was added and mixed for 0.5 h at room temperature to obtain active ester. Then 50 mL of DMSO solution containing 1.04 g ($n = 3.55 \times 10^{-5}$ mol) of PAMAM_E5.$(NAc)_{72}(NH_2)_{47}$ dendrimer (product obtained in the first step of the synthesis) was added to the mixture and stirred for an additional 24 h under nitrogen atmosphere. The reaction mixture was diluted with water and dialyzed for 3 days using cellulose membrane with 10 000 MWCO, filtered, and lyophilized.

(3) Synthesis of PAMAM_E5.$(NHAc)_{72}(NHBT)_8(NHSAH)_{39}$ Nanodevice (Scheme 3). A 0.83341 g ($n = 2.73 \times 10^{-5}$ mol) of PAMAM_E5.$(NAc)_{72}(NH-BT)_8(NH_2)_{39}$ (product obtained in the second step of the synthesis) was dissolved in 50 mL of DMSO solution and placed in a 250-mL round-bottom flask. Then 0.68 g ($n = 6.73 \times 10^{-3}$ mol; 4 mol equivalents compared to the remaining terminal NH_2 groups; number of amino termini was calculated based potentiometric titrations) of succinic anhydride was added with vigorous stirring. The reaction was stopped after 24 h by diluting the reaction mixture with water. Byproducts and excess reactants were removed by dialysis using cellulose membrane with 10 000 Da MWCO. The retentate was filtered, and the resulting solution was lyophilized.

(4) Synthesis of PAMAM_E5.$(NHAc)_{72}(NHBT)_8(NHSAH)_{35}$ $(NHSAcRGD)_4$ Nanodevice (Scheme 4). A 50 mL amount of DMSO stock solution containing 0.19 g ($n = 6.00 \times 10^{-6}$ mol) of PAMAM_E5.$(NHAc)_{72}(NHBT)_8(NHSAH)_{39}$ (product obtained in the previous step of synthesis) was placed in a 250-mL round-bottom flask. Then 0.19 g of EDC and 0.08 g HOBt (4 mol equiv compared to terminal COOH groups) were added and stirred for 0.5 h to form active ester. Then 50 mL of DMSO solution containing 0.03 g ($n = 4.97 \times 10^{-5}$ mol) of c-RGD peptide was added. Reaction was stopped after 24 h by diluting the reaction mixture with water. Byproducts and excess reactants were removed by dialysis using cellulose membrane with 10 000 Da MWCO. The retentate was filtered, and the resulting solution was lyophilized.

Analytical Methods. *Size Exclusion Chromatography (SEC).* Analysis was performed using an Alliance Waters 2690 separation module equipped with a Waters UV−vis detector, a Wyatt Dawn laser photometer, Optilab interferometric refractometer, and Waters Ultrahydrogel columns. Phosphate buffer (0.05 M, pH 2.5) with 0.025% sodium azide was used as mobile phase. The flow rate was maintained at 0.6 mL/min. Sample concentration was kept at 2 mg/mL, and 100 μL was injected. Data was elaborated using Astra and PeakFit software.

Potentiometry. Dendrimers were dissolved in NaCl (0.1 M) solution at a concentration of 0.5 mg/mL, and the pH was set to around 3. In the case of each sample, the same number of moles (adjusted by the volume) was titrated. Titrations were performed at room temperature, under nitrogen atmosphere,

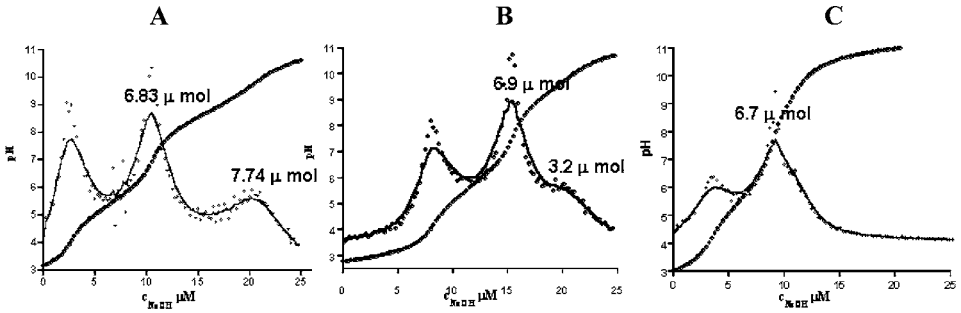


Figure 3. Potentiometric titration curves of (A) the PAMAM_E5.NH_2 amino-terminated dendrimer (starting material), (B) its acetylated derivative obtained after the first step of synthetic path, clearly showing shift of the end point of titration of primary aminogroups upon acetylation, and (C) E5.$(NHAc)_{72}(NHBT)_8(NHSAH)_{39}$ showing disappearance of NH_2 groups.

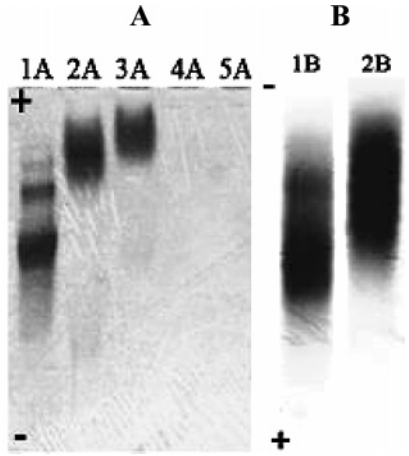


Figure 4. PAGE of starting dendrimer, nanodevice intermediates, and the final product: (1A) E5.$(NH_2)_{119}$, (2A) E5.$(NHAc)_{72}(NH_2)_{47}$, (3A) E5.$(NHAc)_{72}(NHBT)_8(NH_2)_{39}$, (4A) E5.$(NHAc)_{72}(NHBT)_8(NHSAH)_{39}$, (5A) E5.$(NHAc)_{72}(NHBT)_8(NHSAH)_{35}$-$(NHSAcRGD)_4$, (1B) E5.-$(NHAc)_{72}(NHBT)_8(NHSAH)_{39}$, (2B) E5.$(NHAc)_{72}(NHBT)_8(NHSAH)_{35}$-$(NHSAcRGD)_4$.

using Molspin automated titration system, a Mettler-Toledo combination InLab electrode, and NaOH (0.1 M) as a titrant.

Polyacrylamide Gel Electrophoresis. PAGE of PAMAM dendrimers was performed using a vertical electrophoresis system (Model FB-VE10-1 FisherBiotech) with a commercial power supply (Model EC135−90; Thermo Electron Corporation), precast 4−20% gradient express gels for PAGE (BioExpress), and Tris-glycine (TG) native (pH = 8.3). Separations typically required 1.5 h min at 200 V. Into each sample well, 2 μL of a sample solution composed of 2 or 3 μL of 1 mg/mL PAMAM dendrimer and 2 or 3 μL of sucrose dye solutions (50% sucrose, 1% methylene blue) was injected. Developed gel was stained with 0.025% Comassie Blue R-250 in 40% methanol and 7% acetic acid aqueous solution overnight. The gels were destained with 7% (v/v) acetic acid and 5% (v/v) methanol in water.

Matrix-Assisted Laser Desorption Ionization-Time-of-Flight Mass Spectrometry. Spectra of dendrimer nanodevices were recorded on a Bruker Biflex IV spectrophotometer, using 2,5-dihydroxybenzoic acid (DHB) as a matrix. First 0.5 μL of matrix was placed on the target, plated, and evaporated. Then 0.5 μL of the dendrimer (~1.5 mg/mL) was spotted over the matrix. Matrix and dendrimer were dissolved in 75% ACN and 0.1% TFA aqueous solution. For each spectrum, 100 shots and 50% of laser power was applied. For each spectrum, 100 shots and 50% of laser power was applied.

Nuclear Magnetic Resonance. Spectra were recorded using Bruker AMX 400 MHz, D_2O as solvent, and at sample concentrations 20 mg/mL.

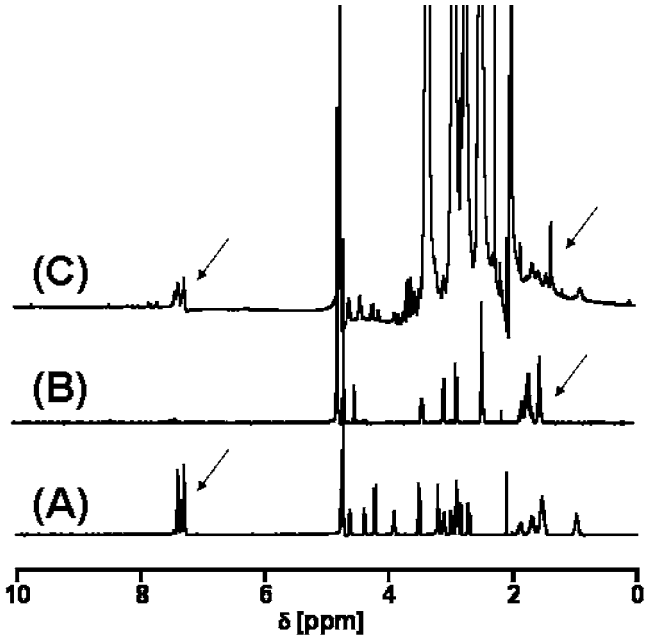


Figure 5. ^{1}HNMR spectra of (A) c-RGD, (B) biotin, and (C) cRGD-BT-ND revealing the presence of c-RGD peptide and biotin in the sample of cRGB-BT-ND well seen in the aromatic range of the spectrum pointed by arrows.

Biological Studies. *Toxicology Studies of the cRGD-BT-ND and the Four Intermediate Materials Leading Up to Its Synthesis.* Toxicity studies were conducted *in vitro*, using MatLyLu prostate cancer cells and B16F10 melanoma cells in tissue culture and 10, 100, 250, 500, 1000, and 2000 nM of ND. All samples were replicated in quintuplets. Tissue culture-treated 96-well microtiter plates were coated with cells and incubated at 37 °C, 5% CO_2, for 24 h. The following day, nanodevices in defined amounts were added to the plates, which were further incubated for 24 h and 48 h. To measure cell viability at different time points, plates were then treated with XTT (sodium 3′-[1-(phenylaminocarbonyl)-3,4-tetrazolium]-bis-(4-methoxy-6-nitro)benzenesulfonic acid hydrate) according to manufacturer's instructions (Roche Diagnostics Corporation, Indianapolis, IN). Briefly, at 0, 24, and 48 h time points, cell culture medium was removed, and an aliquot of 100 μL of fresh medium was added to each well. Then an aliquot of 50 μL of XTT working solution prepared according to manufacturer instructions was added to each well using multichannel pipet. After 3 h incubation in the dark at 37 °C, the absorbance at 490 nm was recorded using a plate reader.

Statistical Analysis of the Toxicity Experiment. To assess differences among six dose levels at each time reading and differences among three time readings at each dose level, the

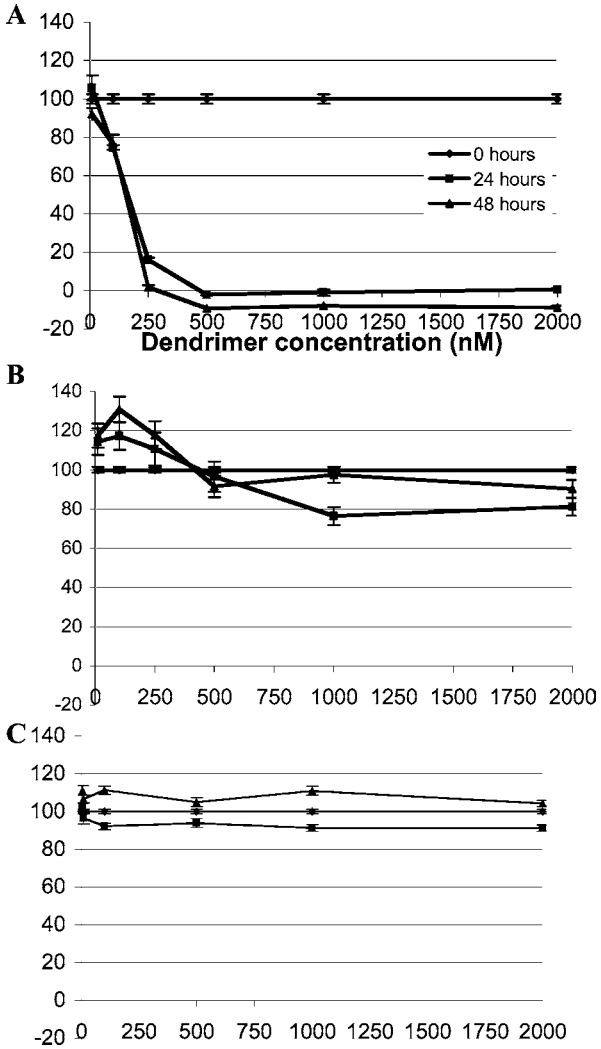


Figure 6. B16 cell viability in the presence of (A) PAMAM_E5.NH_2 and (B) cRGD-BT-ND and (C) HDMEC viability in the presence of cRGD-BT-ND at 0, 10, 100, 250, 500, 1000, and 2000 nM concentrations and 0, 1, and 2 days.

Wilcoxon test was used. Tests for overall group differences were done at a 0.05 level of significance. If there was a significant difference for overall comparison, the Bonferroni adjusted test was used to perform pairwise comparisons. All statistical analyses were carried out using SAS (version 9.1) statistical software (Cary, NC).

Nanodevice Binding to $\alpha_v\beta_3$ Integrin in Vitro. An aliquot of 100 μL (0.5 μg/mL) of purified $\alpha_v\beta_3$ integrin receptor (Chemicon Int., Temecula, CA) in coating buffer (50 mM Tris, pH 7.4; 100 mM NaCl and 1 mM each of $CaCl_2$, $MnCl_2$, and $MgCl_2$,) was immobilized in a 96-well microtiter plate overnight at 4 °C. The wells were washed once with binding buffer (50 mM Tris HCl, pH 7.4, 100 mM NaCl, 1 mM $CaCl_2$, 1 mM $MnCl_2$, 1 mM $MgCl_2$, and 35 mg/mL bovine serum albumin) and incubated with the same for 2 h at room temperature. The plate was then washed three times with binding buffer and an aliquot of 100 μL of BT-ND or cRGD-BT-ND (13.8 μM) added and incubated for 3 h at 4 °C. Competition assay was conducted adding 4-, 40-, and 400-fold excess of cRGD-peptide (Peptide International, Louisville, KY) simultaneously with the nanodevice. At the end of this incubation period, the plate was washed five times with binding buffer. The bound biotinylated NDs were detected by Immuno-Pure Avidin conjugated with horseradish peroxidase (product no. 21123; Pierce, Rockford, IL), which was subsequently developed using *o*-phenylenediamine and the absorbance at 450 nm recorded according to the manufacturer's directions (*18*).

Nanodevice Binding to Human Dermal Microvasculature Cells (HDMECs). HDMECs were seeded (50 000 cells per well) and grown on chamber slides (Lab Tek) in conditioned endothelial culture medium EBM Bullet kit 2 (Cambrex, Walkersville, MD). After 2 days at 50% confluence, cells were treated with 1 μM nanodevices for 5 h at 37 °C and washed five times with PBS buffer, fixed with cold acetone, and dried. Cells were then freeze-thawed (−80 °C) and blocked for 1 h with 4 mg/mL BSA in PBS followed by 1 h incubation with FITC labeled anti-biotin antibody (Vector Labs, Burlingame, CA) according to the manufacturer's instruction at room temperature. Cells were washed four times with PBS buffer, and DAPI counterstain was added.

RESULTS AND DISCUSSION

We have synthesized the targeted dendrimer nanodevice (cRGD-BT-ND) as follows. The starting material, PAMAM_E5.NH_2 amino-terminated dendrimer (abbreviated as E5.NH_2), was partially acetylated (1, NHAc) and then biotinylated (2, NHBT), followed by converting the rest of primary amine termini to succinamic acid groups (3, NHSAH), and finally conjugated with four cRGD peptides (4, NHSAcRGD) as described by the following reaction sequence (in which subscripts correspond to number of measured functional groups):

$$\text{E5.}(NH_2)_{119} \Rightarrow \text{E5.}(NHAc)_{72}(NH_2)_{47} \quad (1)$$

$$\text{E5.}(NHAc)_{72}(NH_2)_{47} \Rightarrow \text{E5.}(NHAc)_{72}(NHBT)_8(NH_2)_{39} \quad (2)$$

$$\text{E5.}(NHAc)_{72}(NHBT)_8(NH_2)_{39} \Rightarrow \text{E5.}(NHAc)_{72}(NHBT)_8(NHSAH)_{39} \quad (3)$$

$$\text{E5.}(NHAc)_{72}(NHBT)_8(NHSAH)_{39} \Rightarrow \text{E5.}(NHAc)_{72}(NHBT)_8(NHSAH)_{35}(NHSAcRGD)_4 \quad (4)$$

The acetylation was performed first to obtained a more uniform distribution of the functional groups within nanodevice (ND) molecules and decrease their toxicity since positively charged (amino-terminated) PAMAM dendrimers are know to be toxic (*7*). Biotin (BT) was selected as the reporter moiety for ND detection using labeled antibodies. In addition it is much smaller compared to commonly used fluorescent dyes that can potentially affect biological activity of NDs. Last, carboxyl groups of succinamic acid were used for cRGD peptides conjugation via amide bound with lysine side chain amino group, which is not involved in the binding of the peptide to $\alpha_v\beta_3$ integrins. Derivatives in each synthetic step were purified and characterized by polyacrylamide gel electrophoresis (PAGE) and size exclusion chromatography equipped with three detectors: multiangle laser light scattering, UV−vis diode-array and refractive index (SEC-MALLS-DAD-RI), potentiometric acid−base titration, matrix assisted laser desorption ionization - time-of-flight (MALDI-TOF) mass spectrometry, and nuclear magnetic resonance (NMR), providing complementary results for thorough analysis.

SEC was used to determine the composition, average molecular mass, and polydispersity of the nanodevices. Figure 1 compares the SEC data of the (A) starting material and of the (B) final product (cRGD-BT-ND). The value of polydispersity index (M_w/M_n) changed only by 0.007, indicating that all components of the starting material were equally modified. Light scattering data confirmed the corresponding increase of the molecular mass throughout the synthesis, even though the hydrodynamic volume slightly decreased as indicated by longer

Table 1. Characterization of Dendrimer Nanodevices

no.[a]	functional groups	no. of groups measured by potentiometry	no. of groups measured by SEC	no. of groups measured by MALDI	mass measured by SEC	mass measured by MALDI[b]
1	NH_2	119	–	–	27180	26572
2	NHAc	72	51	55	29300	28887
3	NHBT	8	5	6	30530	30369
4	NHSAH	39	11	10	31650	31416
5	NHSAcRGD	–	4	2	34110	32691

[a] 1, PAMAM_E5.$(NH_2)_{119}$ (starting material); 2, PAMAM_E5.$(NHAc)_{72}(NH_2)_{47}$ (partially acetylated derivative); 3, PAMAM_E5.$(NHAc)_{72}(NHB)_8(NH2)_{39}$ (biotinylated and partially acetylated derivative); 4, PAMAM_E5.$(NHAc)_{72}(NHB)_8(NHSAH)_{39}$ (partially acetylated, biotinylated, and succinaminated compound); 5, PAMAM_E5.$(NHAc)_{72}(NHB)_8(NHSAH)_{35}(NHSAcRGD)_4$ (cRGD peptides conjugated to compound, for short RGD targeted and biotinylated nanodevice. [b] Molecular mass of the highest frequency fragment in the major peak in Figure 2.

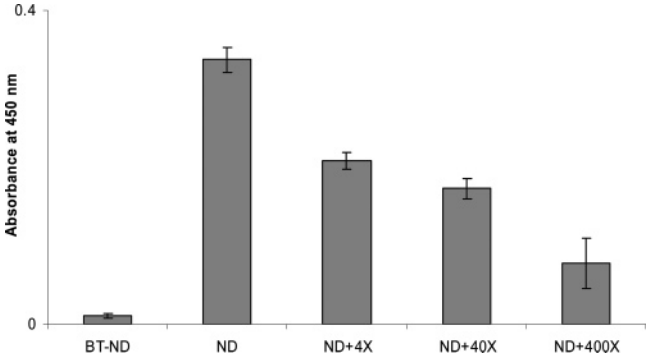


Figure 7. Nanodevice binding to integrin receptors in an *in vitro* plate binding assay: Plates coated with $\alpha_v\beta_3$ integrins were treated with the respective nanodevices (eq 4, i.e., with and without covalently bound cRGD targeting moieties) and the cRGD competitor peptide. The bound NDs were detected by their biotin functions using avidin linked to horseradish peroxidase, and the color was developed with *o*-phenylenediamine. The labels 4X, 40X, and 400X denote 4, 40, and 400 times of molar excess of cRGD mixed with the cRGD-BT-ND nanodevice, respectively, competing for the binding sites.

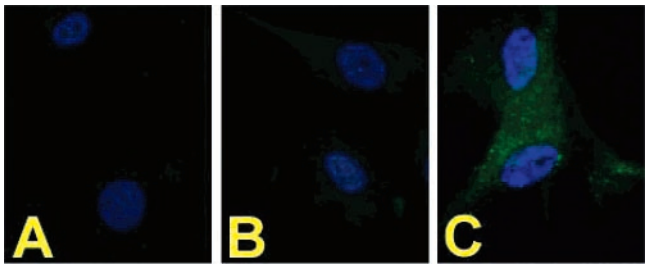


Figure 8. Fluorescence microscopy of $\alpha_v\beta_3$ receptor-overexpressing HDMEC cells exposed to cRGD-BT-ND: FITC labeled anti-biotin antibody (green) labels the RGD-BT-ND, and DAPI (blue) stains the nuclei. A: No treatment, B: BT-ND treated, C: cRGD-BT-ND treated.

retention times (as pointed out in the graph). Unmodified and fully protonated PAMAM_E5.NH_2 dendrimer is in an extended conformation at acidic pH (pH = 2.5 for SEC-MALLS). This extended structure reduces in size after its terminal amino groups are substituted, accompanied by the decrease of charge of the nanodevice. Figure 2 presents successive mass spectra of all analyzed compounds. The shift in the spectra toward higher molecular masses after each synthesis step indicates successful modifications of intermediates with the selected terminal functional groups during the construction of the required ND structure. Figure 3 shows examples of titration curves and their derivatives for the (A) PAMAM_E5.$(NH_2)_{119}$ dendrimer, (B) its partially acetylated derivative (PAMAM_E5.$(NHAc)_{72}$-$(NH_2)_{47}$), and (C) the E5.$(NHAc)_{72}(NHBT)_8(NHSAH)_{39}$ intermediate. Degree of acetylation can be precisely measured by acid–base titration, because the acetamide termini cannot be protonated within the investigated pH range. The inflection point related to deprotonation of primary amino groups shifts from 7.74 (Figure 3A) to 3.2 mol equiv (Figure 3B) of the titrant, indicating that 60% of initial amino groups were acetylated. However, position of end points of titration of tertiary amines does not change (Figure 3A 6.83 μmol and Figure 3B 6.9 μmol; the observed 0.07 μmol difference is within the experimental error). Similarly, the number of conjugated BT molecules and succinamic acid termini can be determined since amide groups formed upon modification of terminal NH_2 groups with these functionalities cannot be protonated, eventually leading to the disappearance of the deprotonation peak as shown in the titration curve of the intermediate obtained after succinamination (Figure 4C). In polyacrylamide gel electrophoresis (PAGE) (Figure 4) all synthetic products exhibited different electrophoretic mobilities as expected, indicating the decrease of positive charge due to increasing substitution of free terminal amine groups of NDs. After conversion of the primary amines to succinamic acid termini, the resulting intermediates become negatively charged and migrate toward the positive electrode (image B in Figure 4). Change of polarity indicates that substitution of remaining amino groups of E5.$(NHAc)_{72}(NHB)_8(NH_2)_{39}$ biotinylated dendrimer with succinamic acid was successful. ^{1}H NMR confirmed the presence of all functional groups in the cRGD-BT-ND (Figure 5). Average numbers of functional groups in the consecutive products were determined by analyzing all characterization data collected in Table 1. It must be pointed out that increase of the molecular mass of the nanodevice after succinamination, as measured by MALDI and MALLS, indicates conversion of only 10–11 primary amino groups, which is most likely due to structural changes occurring upon modification (decrease of hydrodynamic radius changing dn/dc values). However, potentiometric titration indicated the conversion of all terminal NH_2 groups into succinamic acid (Figure 3C), which was further confirmed by PAGE analysis (Figure 4B). In this scenario, the number of succinamic acid moieties must equal to 39, the number of available amine groups.

We next carried out biologic characterization of the NDs, namely *in vitro* toxicity and binding to integrins. Cytotoxicity of all dendrimer derivatives, concentrations varying from 10 to 2000 nM, was examined in B16F10 melanoma cell cultures using the XTT colorimetric assay for cellular viability. Only the positively charged surfaced starting material PAMAM_E5.NH_2 was toxic to B16F10 cells at or above 250 nM (Figure 6A), killing the cells after 24 h incubation. cRGD-BT-ND did not show any significant reduction in cell viability up to a device concentration of 500 nM. At very high concentrations, at or above 1000 nM, we observed ~20% decrease in the cell viability after 24 h posttreatment compare to untreated cells (statistical analysis by Wilcoxon test indicated $p = 0.0003$ compare to untreated). The cell viability was recovered to the levels of the untreated cell after 2 days posttreatment at 2000 nM concentration ($p = 0.2991$). The cRGD-BT-ND was also nontoxic to MatLyLu prostate cancer cells at all concentrations tested, with proliferation rates close to that of control cells (data not shown). We also tested the effect of cRGD-BT-ND on

human dermal microvasculature cells (HDMEC). The cRGD-BT-ND did not show any significant toxicity toward HDMECs (Figure 6C). At 24 h the statistical test gave a significant ($p = 0.0283$) but biologically irrelevant (<10%) difference, and by 48 h posttreatments, there was no significant different in the overall value for all six dose levels tested ($p = 0.0977$).

The cRGD-BT-NDs were then shown to specifically bind *in vitro* to plates coated with human $\alpha_v\beta_3$ integrin. The cRGD targeted ND displayed superior specific binding compared to the control (biotinylated ND without cRGD, i.e., E5.$(NHAc)_{72}$-$(NHBT)_8(NHSAH)_{39}$). Even a 400-fold excess of free cyclic cRGD peptide was unable to displace over 25% bound RGD-BT-ND (Figure 7) in a competitive binding experiment. The binding of NDs to cultured cells was performed using $\alpha_v\beta_3$ receptor-expressing human dermal microvascular endothelial cells (HDMECs). Our results show that only the cRGD-coupled biotinylated NDs notably bind to HDMECs (Figure 8C). This is the first *in vitro* data showing specific ligand (cRGD)$-\alpha_v\beta_3$ receptor binding by these NDs.

In summary, we have synthesized biotinylated and cRGD peptide-conjugated carboxylate-terminated dendrimer NDs from commercially available amino-terminated PAMAM_E5.NH_2 dendrimer. Importantly, we attached a form of cRGD that is already in clinical trial as an anti-angiogenic agent and therefore may have more applicability in humans than other forms. Analytical data indicate successful modifications of dendrimers according to designed terminal functionalities. We have determined the composition of the ND (cRGD-BT-ND) by comparing results of different analytical methods to provide insight into the complex structure of these dendrimer-based NDs. Detailed characterization is a crucial factor in understanding their biological response. The final ND is nontoxic within physiologic concentration ranges and shows superior binding to the biologic target $\alpha_v\beta_3$. Strong binding is a prerequisite for constructing targeted NDs that can carry therapeutic or imaging agents to cancer cells (*19*).

ACKNOWLEDGMENT

This research was funded with Federal Funds from the National Institutes of Health, National Cancer Institute (NCI) (no. R01-CA-104479-01) and from the Department of Defense (grant no. DAMD17-03-1-0018).

LITERATURE CITED

(1) Tomalia, D., and Dvornic P. (1996) Starburst polyamidoamine dendrimers. *Polymeric Materials Encyclopedia 3*, pp 1814−1830, CRC Press, Boca Raton, FL.

(2) Mansfield, M., and Klushin, L. (1993) Monte Carlo studies of dendrimer macromolecules. *Macromolecules 26*, 4262−4268.

(3) Malik, N., Evagorou, E., and Duncan, R. (1999) Dendrimer-platinate: a novel approach to cancer chemotherapy. *Anticancer Drugs 10*, 767−776.

(4) Malik, N., Wiwattanapatapee, R., Klopsch, R., Lorenz, K., Frey, H., Weener, J. W., Meijer, E. W., Paulus, W., and Duncan, R. (2000) Dendrimers: Relationship between structure and biocompatibility in vitro and preliminary studies on the biodistribution of ^{125}I-labelled PAMAM dendrimers in vivo. *J. Controlled Release 65*, 133−148.

(5) El-Sayed, M., Kiani, M., Naimark, M., Hikal, A. H., and Ghandehari, H. (2001) Extravasation of poly(amidoamine) (PAMAM) dendrimers across microvascular network endothelium. *Pharm. Res. 18*, 23−28.

(6) Nigavekar, S. S., Sung, L. Y., Llanes, M., El-Jawahri, A., Lawrence, T. S., Becker, C. W., Balogh, L., and Khan, M. K. (2004) 3H dendrimer nanoparticle organ/tumor distribution *Pharm. Res. Pharm. Res. 21*, 476−483.

(7) Roberts, J. C., Bhalgat, M. K., and Zera, R. T. (1996) Preliminary biological evaluation of polyamidoamine (PAMAM) Starburst™ dendrimers. *J. Biomed. Mater. Res. 30*, 53.

(8) Bielinska, A., Kukowska-Latallo, J. F., Johnson, J., Tomalia, D. A., and Baker, J. R., Jr. (1996) Regulation of in vitro gene expression using antisense oligonucleotides or antisense expression plasmids transfected using starburst PAMAM dendrimers. *Nucleic Acids Res. 24*, 2176−2182.

(9) Majoros, I. J., Thommey, P. T., Chandan, B. M., and Baker, J. R., Jr. (2005) Dendrimer-Based Multifunctional Engineered Nanodevice for Cancer Therapy. *J. Med. Chem. 48*, 5892−5899.

(10) Shukla, R., Thomas, T. P., Peters, J., Kotlyar, A., Myc, A., Baker, J. R., Jr. (2005) Tumor angiogenic vasculature targeting with PAMAM dendrimer-RGD conjugates. *Chem. Commun.* 5739−5749.

(11) Eichman, J., Bielinska, A., Kukowska-Latallo, J., and Baker, J. R., Jr. (2000) The Use of PAMAM Dendrimers in the Efficient Transfer of Genetic. *Pharm. Sci. Technol. Today 3*, 232−245.

(12) Balogh, L., Laverdure, K. S., Gido. S. P., Mott, A. G., Miller, M. J., Ketchel, B. P., and Tomalia, D. A. (1999) Organic/Inorganic Hybrid Materials. *Mater. Res. Soc. Symp. Proc. 576*, 69−75.

(13) Balogh, L., Bielinska, A., Eichman, J. D., Valluzzi, R., Lee, I., Baker, J. R., Lawrence, T. E., and Khan, M. K. (2002) Dendrimer nanocomposites in medicine. *Chim. Oggi 20*, 35−40.

(14) Balogh, L., Nigavekar, S., Cook, A., Minc, L., and Khan, M. K. (2003) Dendrimer-Gold Radioactive Nanocomposites to Treat Cancer Microvasculature. *PharmaChem. 2*, 94−99.

(15) Khan, M. K., Nigavekar, S. S., Minc, L. D., Kariapper, M. S. T., Nair, B. M., Lesniak, W. G., and Balogh, L. P. (2005) Host-Guest Nanodevices: In Vivo Biodistribution of Dendrimers and Dendrimer Nanocomposites - Implications for Cancer Imaging and Therapy. *Technol. Cancer Res. Treat. 4*, 603−613.

(16) Stromblad, S., and Cheresh, D. A. (1996) Integrins, angiogenesis and vascular cell survival. *Chem. Biol. 3*, 881−885.

(17) Ragusea, J., Gatha, H., Biera, J., Riess, H., and Oettle, H. (2004) Predictive factors and distribution of lymph node metastasis in lip cancer patients and their implications on the treatment of the neck. *Oral Oncol. 40*, 228−30.

(18) Smith, J., Vestal, D., Irwin, S., Burke, T., and Cheresh, D. (1990) Purification and functional characterization of integrin $\alpha_v\beta_5$: an adhesion receptor for vitronectin. *J. Biol. Chem. 265*, 11008−11013.

(19) Kukowska-Latallo, J. F., Kimberly, A., Zhengyi, C., Nigavekar, S. S., Majoros, I. J., Thomas, T. P., Balogh, L. P., Khan, M. K., and Baker, J. R. Jr. (2005) Nanoparticle targeting of anticancer drug improves therapeutic response in animal model of human epithelial cancer. *Cancer Res. 65*, 5317−5324.

BC070008Z

Multiplex Targeting, Tracking, and Imaging of Apoptosis by Fluorescent Surface Enhanced Raman Spectroscopic Dots

Kyeong Nam Yu,[†,#] Sang-Myung Lee,[‡,#] Ji Yun Han,[§,#] Hyunmi Park,[§] Min-Ah Woo,[†] Mi Suk Noh,[†] Soon-Kyung Hwang,[†] Jung-Taek Kwon,[†] Hua Jin,[†] Yong-Kweon Kim,[||] Paul J. Hergenrother,[⊥] Dae Hong Jeong,*[,§] Yoon-Sik Lee,*[,‡] and Myung-Haing Cho*[,†]

Laboratory of Toxicology, College of Veterinary Medicine, School of Chemical and Biological Engineering, Department of Chemistry Education, and School of Electrical Engineering and Computer Science, Seoul National University, Seoul 151-742, Korea, and Department of Chemistry, University of Illinois, Urbana, Illinois 61801. Received January 11, 2007; Revised Manuscript Received April 26, 2007

We have developed multifunctional fluorescent surface enhanced Raman spectroscopic tagging material (F-SERS dots) composed of silver nanoparticle-embedded silica spheres with fluorescent organic dye and specific Raman labels for multiplex targeting, tracking, and imaging of cellular/molecular events in the living organism. In this study, F-SERS dots fabricated with specific target antibodies (BAX and BAD) were employed for the detection of apoptosis. The F-SERS dots did not show any particular toxicity in several cell lines. The F-SERS dots could monitor the apoptosis effectively and simultaneously through fluorescent images as well as Raman signals in both cells and tissues with high selectivity. Our results clearly demonstrate that F-SERS dots can be easily applicable to multiplex analysis of diverse cellular/molecular events important for maintaining cellular homeostasis.

INTRODUCTION

The current development of nanotechnology has led to a strong motivation for the connection between nanoscience and biology. In fact, scientific interests between nanotechnology and biology are based on the perceptions that nanotechnology offers biology new tools and that biology offers nanotechnology access to new types of functional nanosystems (*1*). In this regard, recent efforts in such nanobio fusion technology have been partly focused on the development of nonradioactive tagging technology for the investigation of complex interplay of biomolecules, because it may provide safe, specific, and stable alternatives. Up to now, several types of tagging materials have been developed for the application into biology. For example, fluorescence-based materials and semiconductor quantum dots have been used widely. However, some intrinsic problems such as broad emission profiles leading to peak overlapping in fluorescence/emission tagging, difficulties in surface modification, and potential safety issues in quantum dots have impeded the practical application into biology (*2*).

Apoptosis, a form of programmed cell death, plays a critical role in the maintenance of cells by providing a controlled cell deletion to a balanced cell proliferation. Apoptosis is characterized by specific morphological changes such as nuclear fragmentation, membrane blebbing, and cell shrinkage. At the molecular level, apoptosis represents a collection of intricate pathways with many proteins actively participating in activities from cell signals. Failure of tumor cells to undergo apoptosis translates into malignant potential (*3*). Therefore, multiplex detection of several key targets important for apoptosis should provide critical clues for cells/tissues to cope with diverse abnormal cellular stimulation.

Up to the present, diverse bioapplications have emerged from several nanoparticles. The addition of fluorescence properties to nanoparticles may offer new potential for *in vitro* and *in vivo* imaging (*4*). There have been several reports on tagging strategy using Raman spectroscopy featuring the narrow band structure for multiplex biological targeting (*5*−*10*). However, such previous reports have still not reached a stage for multiplex detection at once. Recently, our multidisciplinary research group reported a simple and highly reproducible procedure to generate a new type of Raman tag called surface-enhanced Raman spectroscopic dots (SERS dots) in which Raman scatterings of the molecules adsorbed thereon are dramatically enhanced (*2*). Current study, therefore, has been motivated by the exploratory use of unique advantages of fluorescence-based tracking and imaging of the site of interest as a first step and then subsequent characterization by SERS-based multiplex reading of signals important for cellular/molecular changes. For this purpose, we have developed specific fluorescent SERS dots (F-SERS dots) composed of silver nanoparticle-embedded silica spheres with fluorescent dye and specific Raman labels. Here, we report that F-SERS dots can be employed for multiplex targeting, tracking, and imaging of apoptosis at once in cells/tissues. This concept of multifunctional F-SERS dots may serve as a platform technology for the diagnostic as well as therapeutic application in the future.

EXPERIMENTAL PROCEDURES

Preparation of F-SERS Dot. Silica nanoparticles of *ca.* 120 nm size were prepared by the Stöber method (*11*). A 1 mL portion of ammonium hydroxide (27%) was added into 78 mL

* Corresponding authors. Dae Hong Jeong, Ph.D., Department of Chemistry Education, Seoul National University, Seoul 151-742, Korea, E-mail: jeongdh@snu.ac.kr. Yoon-Sik Lee, Ph.D., School of Chemical and Biological Engineering, Seoul National University, Seoul 151-742, Korea, E-mail: yslee@snu.ac.kr. Myung-Haing Cho, D.V.M., Ph.D., Laboratory of Toxicology, College of Veterinary Medicine, Seoul National University, Seoul 151-742, Korea, E-mail: mchotox@snu.ac.kr.

[†] College of Veterinary Medicine, Seoul National University.

[‡] School of Chemical and Biological Engineering, Seoul National University.

[§] Department of Chemistry Education, Seoul National University.

[||] School of Electrical Engineering and Computer Science, Seoul National University.

[⊥] University of Illinois.

[#] These authors contributed equally to this work.

10.1021/bc070011i CCC: $37.00 © 2007 American Chemical Society
Published on Web 06/29/2007

ethanol (95%) and 10 mL H_2O, and then 5 mL (22.4 mmol) of tetraethylorthosilicate (TEOS) was added into the solution. The solution was stirred with a magnetic bar vigorously for 12 h at 25 °C. The resulting silica colloids were centrifuged and washed with ethanol several times. To obtain mercapto-functionalized silica nanoparticles (MSNP), 300 mg portion of silica nanoparticles was dispersed in ethanol, and then 150 μL of 3-mercaptopropyltrimethoxysilane (MPTS) and 300 μL of ammonium hydroxide were added to the colloidal solution. The mixture was stirred with a magnetic bar vigorously for 12 h at 25 °C again. The resulting MSNPs were centrifuged and washed with ethanol several times to remove excess reagents. Silver nanoparticles were embedded on the surfaces of silica nanoparticles by the Sn^{2+}-reduction method (*12*). At first, 160 mg of silica nanoparticles were dispersed in water/ethanol solution (15 mL/15 mL), and then 100 μL of trifluoroacetic acid (TFA) and 100 mg of $SnCl_2$ were added. The mixture was stirred vigorously for 1 h at 25 °C. The resulting silica nanoparticles were centrifuged and washed with ethanol (20 mL × 3). The Sn^{2+}-coated silica nanoparticles were redispersed in 250 mL of water, and 50 mL of 6 mM $AgNO_3$ was added dropwise under vigorous magnetic stirring at 25 °C. The dispersion was centrifuged and washed with water (30 mL × 2 times) and ethanol (30 mL × 2 times) to remove excess reagents.

In order to introduce the dual signals of Raman spectroscopy and fluorescence to the silica nanoparticles, 4-aminothiophenol (ATP) and 4-mercaptotoluene (MT) were used as Raman spectroscopic coding chemicals, and fluoresceinisothiocyanate (FITC) and Alexafluoro 647 (AF647) as fluorescent tagging chemicals. First of all, Raman chemicals were introduced together with MPTS allowing a self-assembled monolayer on the silver surface of silica nanoparticles. Raman chemicals (10 mL of 5 mM in ethanol) and MPTS (10 mL of 50 mM in ethanol) were mixed and added into a 50 mg portion of silver-embedded silica nanoparticles. The dispersion was stirred vigorously for 1 h at 25 °C. The colloids were centrifuged and washed with ethanol (20 mL × 3 times) and water (20 mL). These silica nanoparticles were dispersed in 20 mL of water, and 30 μL of aqueous sodium silicate (27%) was added into the dispersion and stirred vigorously for 12 h at 25 °C (*13*). The resulting colloids were centrifuged and washed with water (20 mL × 3) and ethanol (20 mL) to remove excess reagents. In the next step, a fluorescent layer was introduced onto silica nanoparticles labeled with Raman signals. For this process, the conjugates of 3-aminopropyltriethoxysilane (APS) and fluorescence dyes were synthesized. In the case of FITC, FITC (10 μL of 8 mM in DMSO) was added into the APS (100 μL of 19.2 mM in ethanol), and the resulting solution was stirred for 6 h at 25 °C. Then, the FITC−APS conjugate, 20 μL of TEOS, and 40 μL of aqueous ammonium hydroxide (25%) were added into the 20 mg portion of silica nanoparticles with Raman labels. The mixture was stirred vigorously for 12 h at 25 °C. The resulting nanoparticles (F-SERS dots) were centrifuged and washed with ethanol thoroughly. Thereafter, the surface of F-SERS dots was modified with a hydrophilic spacer, *N*-fluorenylmethylcarbonyl-NH-triethylene glycol-NH-$COCH_2$-CH_2COOH (Fmoc-TEG-COOH). This spacer was synthesized from 4,7,10-trioxa-1,13-tridecanediamine by the literature procedure (*14*). F-SERS dots (20 mg) were dispersed in *N*,*N*-dimethylformamide (DMF) and aliquots (0.1 mmol) of Fmoc-TEG-COOH, *N*,*N*-diisopropylcarbodiimide (DIC), *N*-hydroxybenzotriazole (HOBT), and diisopropylethylamine (DIEA) were added into the dispersion, consecutively. The mixture was shaken vigorously for 6 h at 30 °C. After the coupling reaction, Fmoc protecting groups were removed from the spacer on F-SERS dots by 20 vol % piperidine/DMF solution for 30 min at 25 °C. The resulting triethylene glycol (TEG) grafted F-SERS dots (F-SERS dots/TEG-NH_2) were centrifuged and washed with ethanol thoroughly.

Antibody Conjugation onto F-SERS Dots. F-SERS dots/TEG-NH_2 were treated with 0.1 mmol of 3-maleimidopropionic acid *N*-hydroxysuccinimide ester in DMF for 2 h at 25 °C. The resulting nanoparticles were centrifuged and washed with DMF, water, and PBS (100 mM, pH 7.4). Before antibody conjugation, full-bodied antibody was reduced and fragmented into two parts (*15*). This procedure was applied to bcl2-associated death promoter (BAD) and bcl2-associated X protein (BAX) antibodies. Antibody (20 μL, 100 μg/mL) was pretreated with 5 μL of ethylenediaminetetraaceticacid (EDTA, 0.5 M, pH 8.0), and then followed by adding 2 μL of 2-mercaptoethylamine (MEA, 0.312 mmol) and 5 μL of 0.5 M EDTA in 200 μL of PBS (pH 7.4). The mixture was incubated at 37 °C for 90 min. The resulting half-fragmented antibody was purified by gel filtration using Sephadex G-25 and then used for conjugation without additional handling. The 200 μL of reduced antibody solution was added into 10 mg portion of maleimide-modified F-SERS dots dispersed in PBS (100 mM, pH 7.4). The dispersion was incubated at 25 °C for 2 h. The F-SERS dots/TEG−antibody conjugates were centrifuged and washed with PBS containing 0.1 wt % Tween 20 (1 mL × 3 times), and PBS (1 mL × 2 times), consecutively.

Annexin V Conjugation onto the F-SERS Dots. The amine termini of F-SERS dots/TEG-NH_2 were modified to carboxyl termini for immobilizing Annexin V. F-SERS dots/TEG-NH_2 (10 mg) was dispersed in 10 mM succinic anhydride and 10 mM DIEA in DMF, and shaken for 2 h at 30 °C. They were centrifuged and washed with DMF (1 mL × 3 times), H_2O (1 mL × 3 times). They were redispersed in 2-(*N*-morpholino)-ethanesulfonic acid buffer (MES, 25 mM, pH 6.0), followed by adding 50 μL of 5 mg/mL 1-ethyl-3-[3-(dimethylamino)-propyl]carbodiimide hydrochloride (EDC) and 50 μL of 5 mg/mL *N*-hydroxysuccinimide (NHS) in MES buffer. The dispersion was incubated for 1 h at 25 °C. The activated nanoparticles were washed with MES (1 mL × 3 times) and redispered in MES buffer. Immediately, 20 μL of 100 μg/mL Annexin V was added into the activated nanoparticles mixture and incubated for 2 h at 25 °C. The resulting F-SERS dots−Annexin V conjugates were treated with 10 mM ethanolamine in PBS for 30 min for quenching the unreacted activating sites, and washed with PBS containing 0.1 wt % Tween 20 (1 mL × 3 times), and PBS (1 mL × 2 times), consecutively.

Cell Culture and Viability Assay. Normal lung epithelial cells (WI-38), and breast mammary gland epithelial cancer cell (SK-BR3) were obtained from Korea Cell Line Bank (Seoul, Korea), and lung squamous carcinoma cells (H226) were obtained from ATCC (American Type Culture Collection). H226 and SK-BR3 cells were cultured in RPMI-1640 with 10% fetal bovine serum (FBS, Hyclone, Logan, UT), and WI-38 cells were cultured in MEM with 10% FBS. Cultures were maintained at 37 °C in 5% CO_2 atmosphere. Effects of F-SERS dots on viability of several cell lines were determined using a CCK-8 assay kit according to manufacturer's protocol (Dojindo, Kumamoto, Japan). Briefly, cells were seeded at 5×10^4 cells on each well and treated with F-SERS dots for 24 h. Samples were analyzed in triplicate. Results were expressed as a percentage of viable cells of untreated control.

Detection of Apoptosis in Cells. Cells were treated with 0.1 μM staurosporine (STS, Sigma-Aldrich, St. Louis, MO) for 24 h in order to induce apoptosis. Our preliminary works indicate that STS at this concentration is sufficient to induce significant apoptosis in diverse cell lines used in this study. Annexin V is a calcium-dependent phospholipid-binding protein with high affinity for phosphatidylserine (*16*). Therefore, Annexin V-

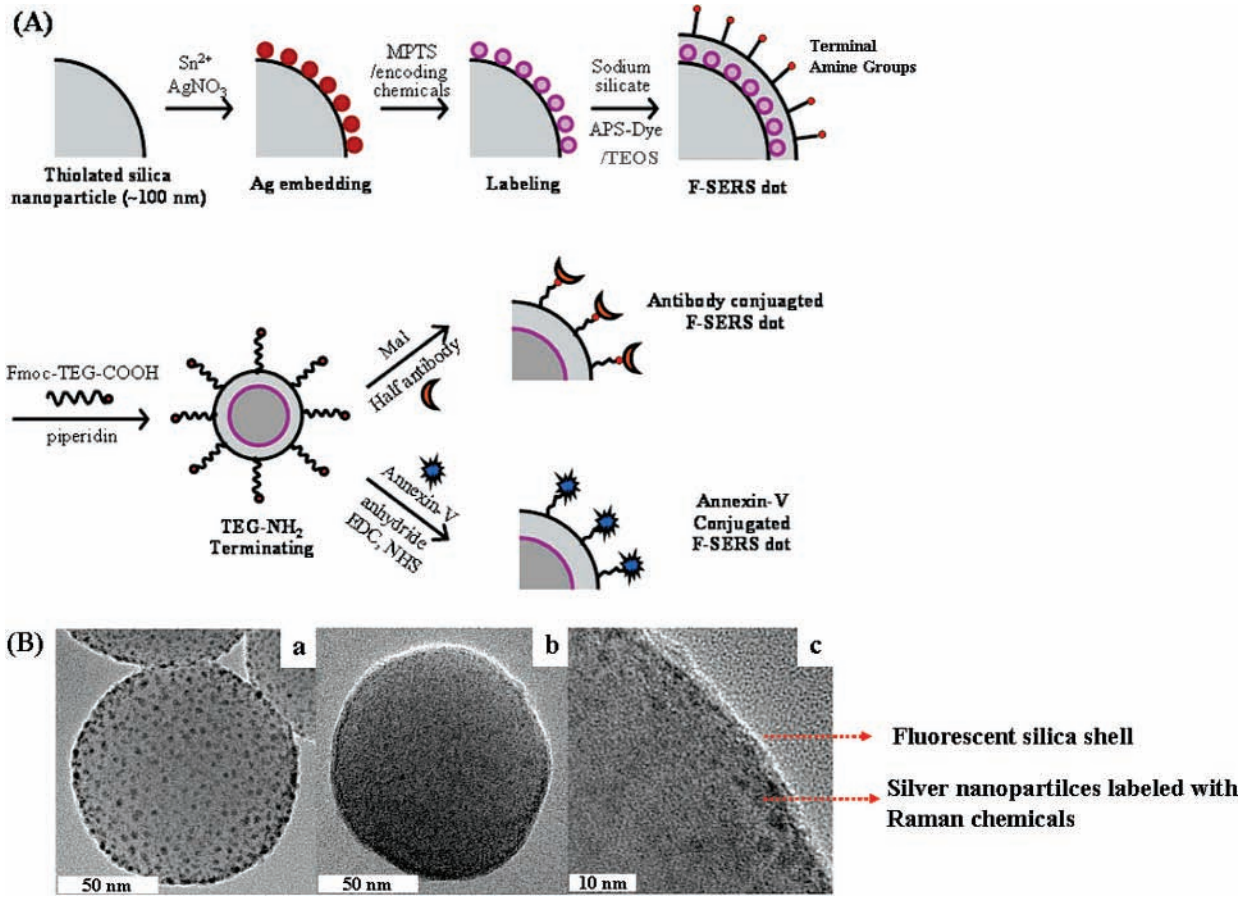


Figure 1. Synthetic scheme of F-SERS dots. Preparation of fluorescent Raman active silica nanoparticle and surface modification of the F-SERS dots with antibody or Annexin V (A). HR-TEM images of silica nanoparticles embedded with silver nanoparticles by Sn^{2+}-reduction method (B-a), after silica shell encapsulation, and then amino-functionalized F-SERS dots labeled with ATP and FITC (B-b) and high-magnification image (B-c).

conjugated F-SERS dots were employed to detect the translocation of phosphatidylserine residues from the inner layer to the outer layer of the plasma membrane. Briefly, cells were grown on chamber slides (Nalge Nunc, Naperville, IL) and treated with STS for 24 h. Then, Annexin V-conjugated F-SERS dots were added and then incubated for 6 h. Slides were then washed with PBS and fixed in 4% paraformaldehyde for 10 min. The slides were examined using a confocal laser scanning microscope (CLSM, Nikon, Tokyo, Japan).

Detection of Apoptosis in Murine Lung Cancer Tissues. Apoptosis study on tissue with the F-SERS dots was carried out onto PAC-1 treated murine lung cancer tissues. Our previous works demonstrated that PAC-1 induced apoptosis significantly through activation of procaspase-3 to caspase-3 in the lungs from mice carrying lung cancer (*17*). Therefore, we adopted the lung samples for current study. The immunohistochemistry on lung tissue was performed with BAX and BAD antibodies with a slightly modified method from Jin et al. (*18*). For the immunoassay with antibody-conjugated F-SERS dots, sample slides were processed according to the same procedures of immunohistochemistry until the blocking process. At the blocking step, F-SERS dots diluted in PBS were added into tissue slides. The slides were incubated for 24 h under dark condition. After incubation, the site of apoptosis was initially identified by fluorescence signals, and then, multiplex targeting was characterized by Raman analysis using a confocal Raman system (LabRam 300, JY-Horiba, Edison, NJ) equipped with an optical microscope (Olympus, Tokyo, Japan). In this system, the Raman scattering signals were collected in a 180° scattering geometry and detected by a spectrometer equipped with a thermoelectrically cooled CCD detector. A 514.5 nm laser line from Ar ion laser (35-MAP-321, Melles Griot, Carlsbad, CA) was used as an excitation source. The strong Rayleigh line was eliminated by a holographic notch filter placed in the collection path. Raman scattered light was collected with a 100× objective microscope (0.95 NA, Olympus). Approximately less than 1 mW of laser irradiation was used to excite samples for Raman measurements. The signal collection time was 30 s.

RESULTS

Synthesis of Annexin V-Conjugated F-SERS Dots. The silica nanoparticles (*ca.*120 nm) as a supporting material were successfully synthesized (Figure 1A). As shown, silver nanoparticles were produced by the Sn^{2+}-reduction method and embedded onto the silica nanoparticles, which were fabricated with Raman chemicals such as ATP or MT and MPTS. The Ag nanoparticle-embedded silica nanoparticles, which contained Raman chemicals, were overcoated with silica shell. The nanoparticles were then treated with APS−organic dye (FITC or AF647)/TEOS under basic conditions to form F-SERS dots. In order to conjugate F-SERS dots with half-fragmented antibody (BAD and BAX), the surface of F-SERS dots was modified with hydrophilic spacer (Fmoc-TEG-COOH). The half-antibodies were prepared by reducing disulfide bonds of the antibody heavy chain using MEA. Also, in the case of Annexin V conjugation for specific targeting to phosphatidylserine, the F-SERS dots were further treated with APS for amine termination and then coupled with the carboxylic group of Annexin V

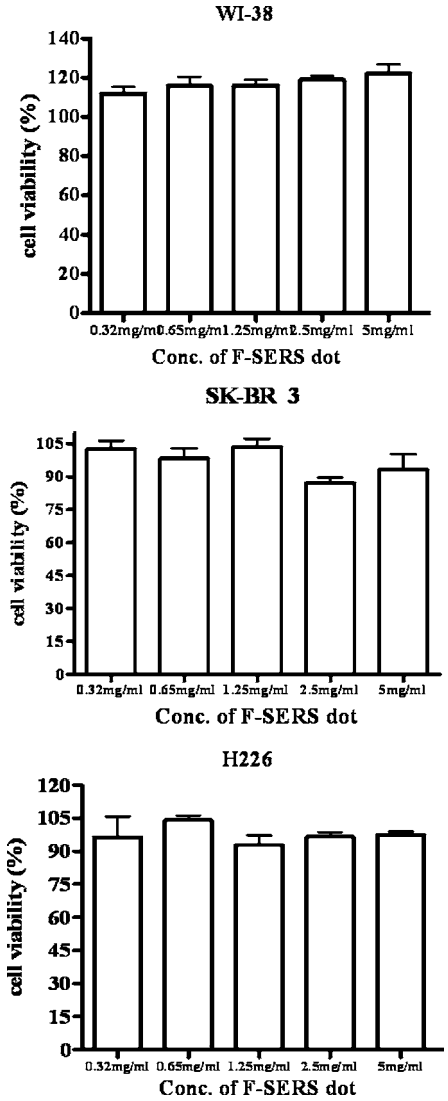


Figure 2. Cell viability assay for potential cytotoxicity of F-SERS dots in various cell lines (WI-38, SK-BR3, and H226). Each cell seeded at 5×10^4 cells/cm^2 was treated with F-SERS dots at different concentrations and incubated for 24 h. All cell viability was expressed as a percentage of viable cells with untreated control cells set at 100%.

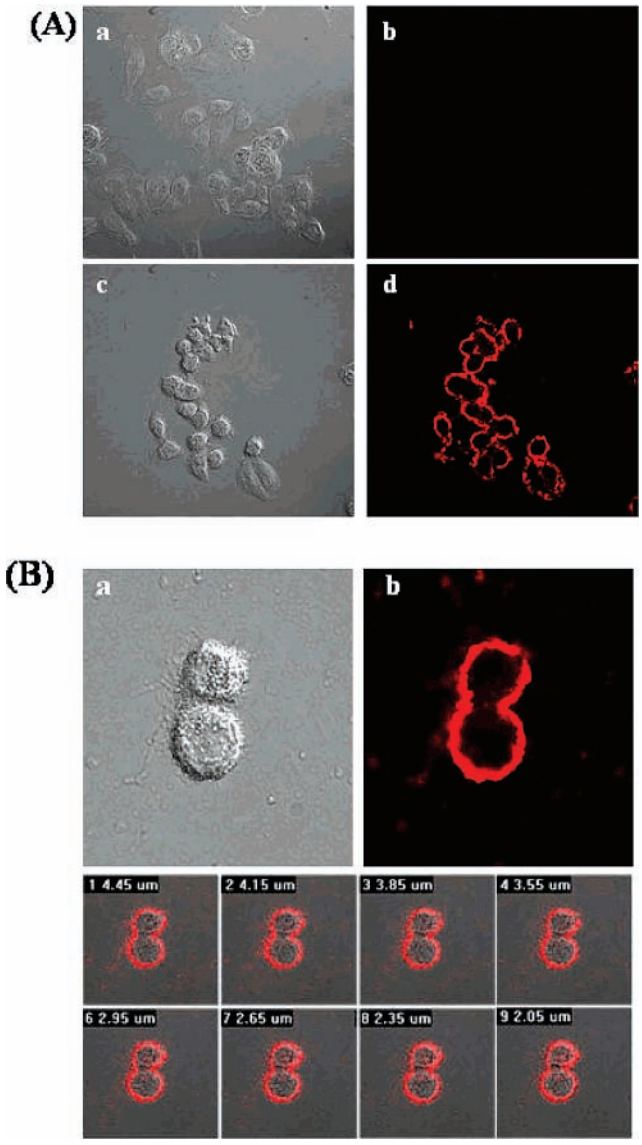


Figure 3. CLSM analysis of specific phosphatidylserine targeting with Annexin-V conjugated F-SERS dots in SK-BR3 cells. (A-a,b) Normal untreated cell. (A-c,d) STS treated cell. (B-a,b) High-magnification images (600×) from apoptotic cell. (B, bottom) *z*-Section images of apoptosis cells (scanned interval of 0.3 μm). A-a, A-c, and B-a are bright field images; A-b, A-d, and B-b are fluorescence images.

leading to amide bond formation. Figure 1B exhibited that the silver nanoparticles were successfully embedded and overcoated with silica shell. The thickness of overcoated silica shell was about 3 nm by high-resolution transmission electron microscope (HR-TEM).

Cytotoxicity Study of F-SERS Dots. The cytotoxicity of the F-SERS dots in various cell lines such as WI-38, SK-BR3, and H226 cells was evaluated (Figure 2). All cell lines were incubated for 24 h at 37 °C, 5% CO_2, and the F-SERS dots containing media were discarded for CCK-8 assay. Our data strongly suggest that F-SERS dots fabricated in this study are not toxic, because cell viabilities remained over 90%.

Specific Targeting with Annexin V-Conjugated F-SERS Dots in the Apoptotic Cells. To demonstrate the specific targeting of phosphatidylserine with Annexin V-conjugated F-SERS dots which were tagged with ATP as Raman chemical and anchored with AF647 (red color), we performed an assay with the cells pretreated with STS. At first, in order to confirm the specific targeting ability, FITC (green color) labeled Annexin V was monitored within STS-treated SK-BR3 cells by CLSM and FACS (see the Supporting Information, SI-Figure 1). We confirmed that FITC-labeled Annexin V could target the apoptosis successfully, because green color was only found in the outer cell membrane (SI-Figure 1A-c), while such staining was not observed in control cells (SI-Figure 1A-a). Such apoptosis was also confirmed by flow cytometry analysis (SI-Figure 1B), thus suggesting that used STS was sufficient to induce apoptosis. Figure 3A showed that the Annexin V-conjugated F-SERS dots could recognize the apoptosis in outer plasma membrane where Annexin V bound to phosphatidylserine selectively. In comparison to STS-treated cells (Figure 3A-d), such red signals were not observed in control cells (Figure 3A-b). Please note that the red fluorescence from F-SERS dots was detected at most of the apoptotic cells. In Figure 3B, high-magnification *z*-section images of cells exhibited clear evidence of reddish nanoparticle location at the outer cell membrane. In contrast, F-SERS dots without Annexin V were internalized into the cells, and such uptake of nonmodified F-SERS dots into the cells was clearly observed in the study

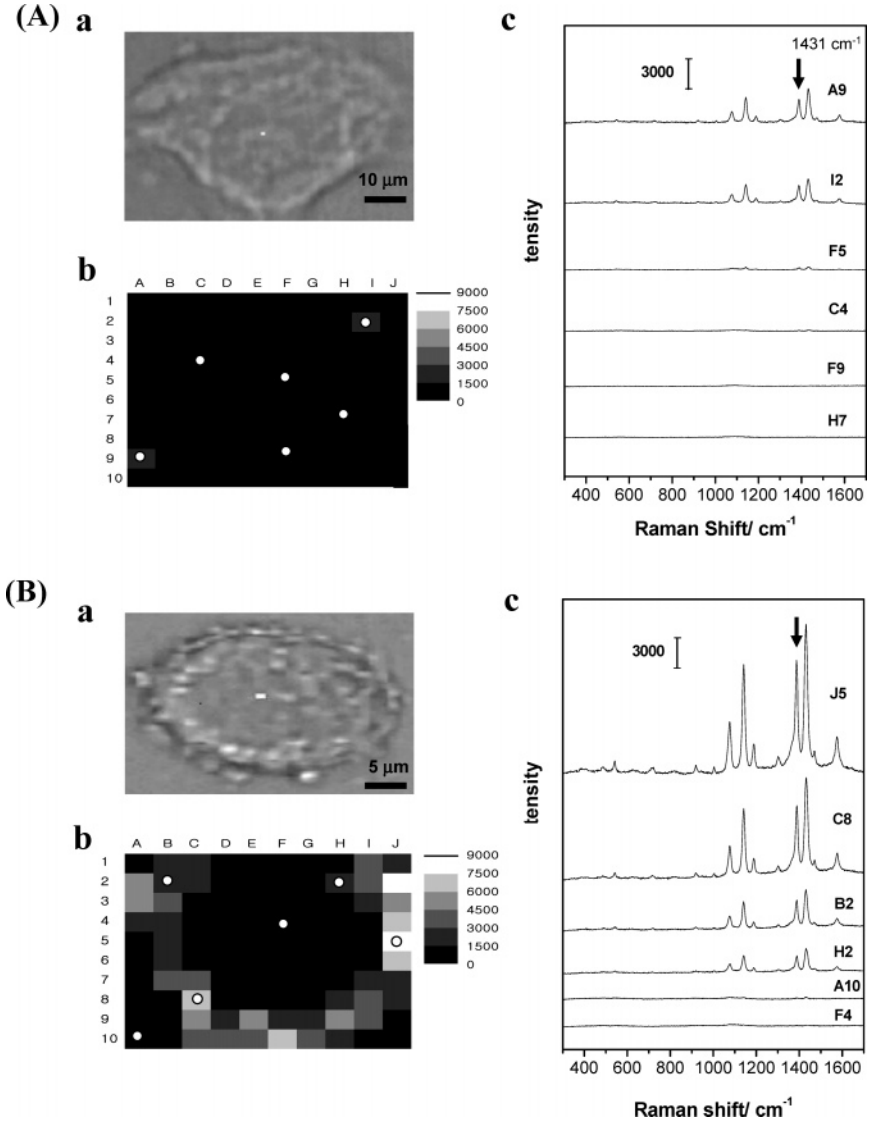


Figure 4. SERS analysis of specific phosphatidylserine targeting with Annexin V conjugated F-SERS dots. A and B represent a control normal cell and a STS-treated cell, respectively. A-a and B-a are bright field optical images of normal and treated cells, respectively. A-b and B-b are SERS intensity maps for 1431 cm^{-1} Raman band, and A-c and B-c depict SERS spectra at several positions indicated as white dots in parts A-b and B-b, respectively. The whole area was scanned by 10 × 10 steps, and Raman signals were collected for 30 s each step.

by CLSM and Raman analysis (SI-Figure 2). According to *z*-section scanning of CLSM, we knew that the internalized F-SERS dots were primarily located at the cytoplasm of the cells. The F-SERS dots were not present in the nucleus, which was confirmed by nucleus staining with DAPI (SI-Figure 2A). Raman spectra were detected in all areas of fluorescence (SI-Figure 2B). Together, F-SERS dots with Annexin V could detect the apoptosis effectively through specific binding to phosphatidylserine in outer plasma membrane.

Since the fluorescence and SERS spectra of F-SERS dots were spectrally well-separated, we could obtain the SERS spectra from cells emitting fluorescence lights (Figure 4). When the cells were not treated with STS, the SERS signals from the F-SERS dots were not detected in most of cell region (Figure 4A). On the other hand, the SERS signals were clearly observed in the cells treated with STS (Figure 4B). Figure 4A-b,B-b demonstrated the SERS intensity maps for the 1431 cm^{-1} Raman band of ATP corresponding to the regions shown in Figure 4A-a,B-a images, respectively. The same scales of the brightness for both SERS intensity maps were used to visualize their different intensities. White blocks represent stronger SERS signals compared to black blocks. Selected SERS spectra for cells with and without STS treatment are shown in Figure 4A-c and B-c, respectively. Most regions of the cell without STS exhibited no SERS signals, but some parts depicted SERS signals with very weak intensity, such as at A9 and I2 positions in Figure 4A-b reflecting a noncorrelated distribution with cell morphology presumably due to nonspecifically bound F-SERS dots. However, the cell treated with STS exhibited a highly correlated distribution of strong intensity with cell morphology as well as strong SERS spectra as shown in Figure 4B-c.

Detection of Multiple Targets of Apoptosis in the Murine Lung Tissues with F-SERS Dots at once. In order to locate the expressed sites of BAX and BAD proteins on the tumor tissue, an immunoassay with F-SERS dots was performed in the murine lung cancer tissues adopted from previous study (*17*). Please note that brown color indicates the apoptotic proteins such as BAX (Figure 5A upper left (×200), lower left (×400)) and BAD (Figure 5A upper right (×200), lower right (×400)). The white arrows are position markers in sequential slices. On the basis of the effective searching the sites of apoptosis by fluorescence signals (representative white square in Figure 5), we tried to characterize the apoptosis through Raman scattering. The green blocks in Figure 6a indicate the SERS intensity of

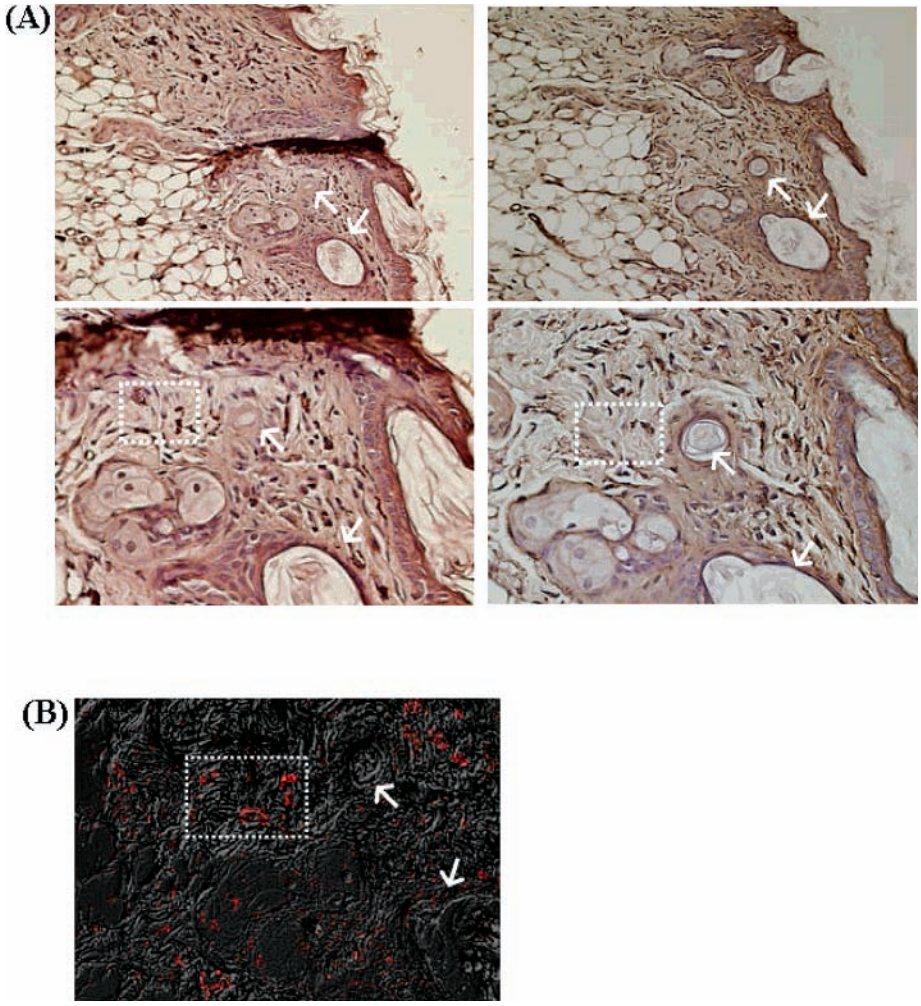


Figure 5. Immunohistochemistry and CLSM image of BAX/BAD protein on PAC-1 induced apoptosis in murine lung tissue. (A) Immunohistochemistry images of BAX (left)/BAD (right) and low magnification (up, 200×)/high magnification (down, 400×). (B) Fluorescent images of F-SERS dots (400×). White square indicates the same areas scanned by Raman analysis. White arrows are the position markers.

the 384 cm^{-1} Raman band of MT (signal of BAX), and the red blocks in Figure 6b indicate the SERS intensity of the 1431 cm^{-1} Raman band of ATP (signal of BAD). Figure 6c is a merged image of both images to illustrate the distributions of BAX and BAD proteins in the tissue. In most parts, occurrences of BAX and BAD were similarly distributed with some exceptions such as positions C and D marked in Figure 6c. The representative SERS spectra from the tissue are depicted in Figure 6d. As illustrated, F-SERS dots were able to detect the multiple targets of apoptosis in the murine lung cancer tissue at once.

DISCUSSION

Nanotechnology has been applied to various biological areas such as specific targeting, cell sorting, and fluorescent or magnetic imaging. The increased application of nanotechnology can, however, be either positive or negative or a mix of both (*19*). Therefore, the biocompatibility of nanomaterials is a very important factor. In this regard, we performed a cytotoxicity study of F-SERS dots on several cell lines (Figure 2). On the basis of our results, F-SERS dots seemed to be nontoxic, thus suggesting that F-SERS dots may be used as a biocompatible tool.

Analysis of current literature suggests that combining several biomarkers improves sensitivity and specificity of many diseases dramatically (*20*). Therefore, a multimarker approach for detection and monitoring of disease status should have a great potential in the future (*21*). In this regard, several research groups have successfully linked fluorescent nanoparticles to peptides, proteins, and oligonucleotides (*22*). Quantum dots are fluorescent nanoparticles and emit narrow symmetrical emission peaks with minimum overlap between spectra, thus allowing unique resolution of their spectra. These key advantages make it possible to label molecular targets by quantum dots both *in vitro* and *in vivo* (*23*). However, the use of quantum dots may be limited by the difficulty in surface modification and the potential toxic effects of the heavy metal core (*24*). The use of organic fluorescent molecules as tags for the probe of interest also has some limitations such as influence on fluorescence intensity from environmental molecules, broad emission profiles, and photobleaching problems (*25*).

SERS has gaining attention because it is another sensitive method for spectroscopic detection of multiple targets in aqueous and solid samples (*26*). The benefit of SERS and nanoparticles in terms of sensitivity, specificity, and selectivity has been previously proven by our previous works (*2*). In this study, F-SERS dots were successfully synthesized by the well-established procedure, and the size and the shape were well-characterized by TEM (Figure 1). Moreover, the modified F-SERS dots could provide a rapid and specific way to monitor the apoptosis in both cells and tissues by simultaneous use of

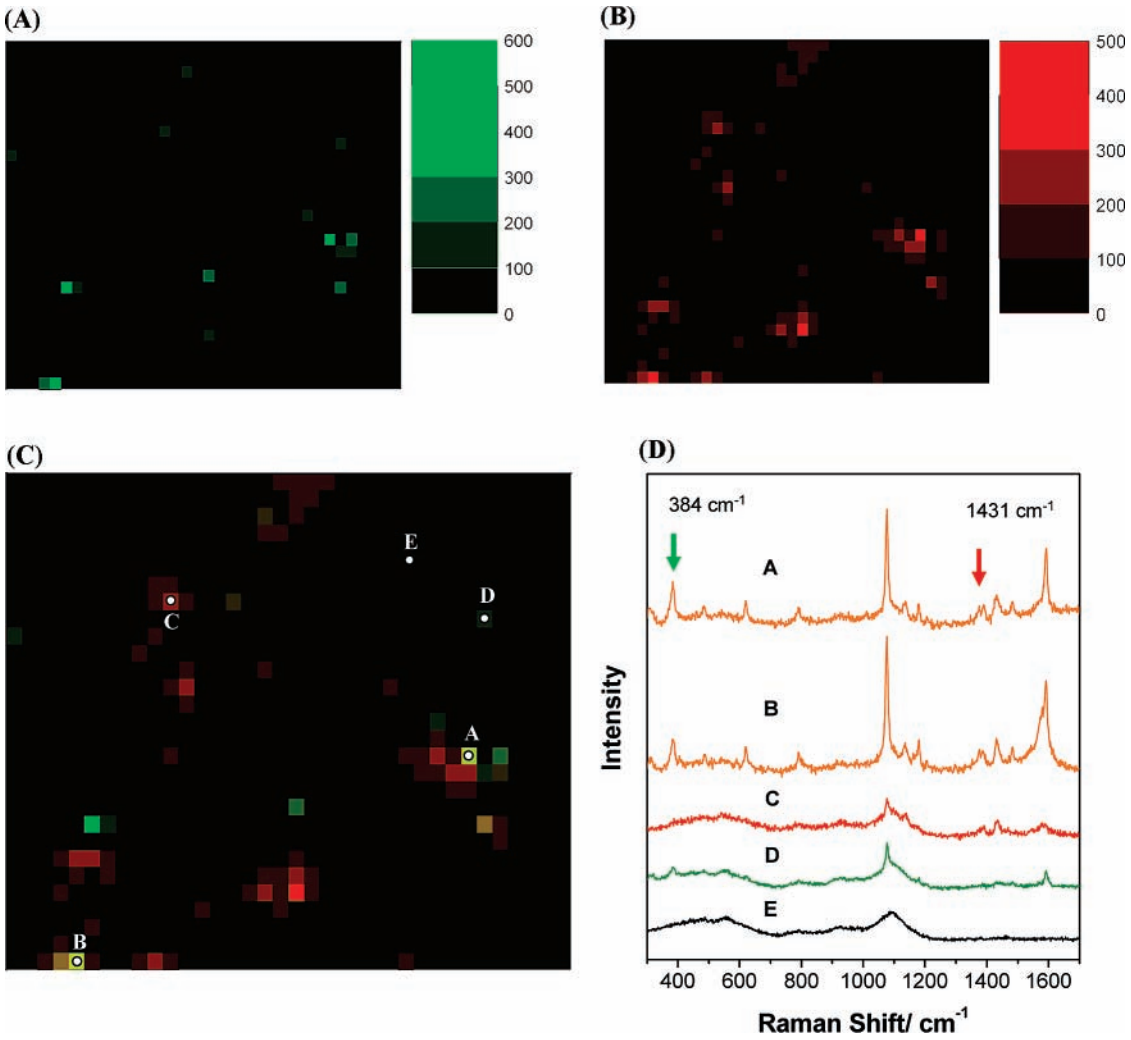


Figure 6. SERS intensity maps indicating distribution of BAX and BAD proteins on the tumor tissue. The maps were produced using the baseline-corrected intensities of the 384 cm^{-1} Raman band of MT corresponding to BAX proteins (a) and the 1431 cm^{-1} Raman band of ATP corresponding to BAD proteins (b), respectively. Part c represents the merged figure of parts a and b to illustrate the distribution of both apoptotic proteins.

fluorescence and Raman signals (Figures 3−6). Interestingly, Annexin V-conjugated F-SERS dots remained in the outer plasma membrane due to the selective binding to phosphatidylserine (*27*), while F-SERS dots without Annexin V were translocated into the cells; thus, we could confirm the specificity and selectivity of F-SERS dots (Figure 3, and Supporting Information). Furthermore, multiplex targeting under the guide of tracking and imaging of F-SERS dots were clearly demonstrated in the study done with murine lung cancer tissue samples. In a classical study of immunohistochemistry, it is difficult to detect multiple targets in one time process. Moreover, immunohistochemistry takes a relatively long time (more than 72 h). In contrast to such time-consuming immunohistochemistry, however, multiplex targeting of BAX/BAD protein expression by F-SERS dots with different encoding chemicals was simple, accurate, effective, and reproducible (Figures 5 and 6). Immunoassay with F-SERS dots just requires one sample due to the multifunction of fluorescence and Raman signals. Taken together, the simplicity and specificity of F-SERS dots for the simultaneous multidetection of apoptosis at cells or tissues were proven clearly. In conclusion, our results strongly demonstrate that F-SERS dots may be applicable to multiplex analysis of diverse cellular/molecular events important for maintaining cell/tissue homeostasis in the future.

ACKNOWLEDGMENT

This work is partly supported by NCI-NCRC program of KOSEF.

Supporting Information Available: Additional imaging as described in the text. This material is available free of charge via the Internet at http://pubs.acs.org.

LITERATURE CITED

(1) Whitesides, G. M. (2003) The 'right' size in nanobiotechnology. *Nat. Biotechnol. 21* (10), 1161−1165.
(2) Kim, J. H., Kim, J. S., Choi, H., Lee, S. M., Jun, B. H., Yu, K. N., Kuk, E., Kim, Y.−K., Jeong, D. H., Cho, M.−H., and Lee, Y.−S. (2006) Nanoparticle probes with surface enhanced Raman spectroscopic tags for cellular cancer targeting. *Anal. Chem. 78*, 6967−6973.
(3) Khan, N., Afag, F., and Mukhtar, H. (2007) Apoptosis by dietary factors: the suicide solution for delaying cancer growth. *Carcinogenesis 28* (2), 233−239.
(4) Bertorelle, F., Wilhelm, C., Roger, J., Gazeau, F., Menager, C., and Cabuil, V. (2006) Fluorescence-modified superparamagnetic nanoparticles: intracellular uptake and use in cellular imaging. *Langmuir 22*, 5385−5391.
(5) Cao, Y. C., Jin, R., and Mirkin, C. A. (2002) Nanoparticles with Raman spectroscopic fingerprints for DNA and RNA detection. *Science 297*, 1536.

(6) Doering, W. E., and Nie, S. (2003) Spectroscopic tags using dye-embedded nanoparticles and surface-enhanced Raman scattering. *Anal. Chem. 75* (22), 6171−6176.
(7) Fenniri, H., Chun, S., Ding, L., Zyrianov, Y., and Hallenga, K. (2003) Preparation, physical properties, on-bead binding assay and spectroscopic reliability of 25 barcoded polystyrene-poly(ethylene glycol) graft copolymers, *J. Am. Chem. Soc*. *125* (35), 10546−10560.
(8) Grubisha, D. S., Lipert, R. J., Park, H. Y., Driskell, J., and Porter, M. D. (2003) Femtomolar detection of prostate-specific antigen: an immunoassay based on surface-enhanced Raman scattering and immunogold labels. *Anal. Chem*. *75* (21), 5936−5943.
(9) Halas, N. (2005) Playing with plasmons: tuning the optical resonant properties of metallic nanoshells. *MRS Bull. 30*, 362−367.
(10) Jackson, J. B., and Halas, N. J. (2004) Surface-enhanced Raman scattering on tunable plasmonic nanoparticle substrates. *Proc. Natl. Acad. Sci. U.S.A. 101* (52), 17930−17935.
(11) Stöber, W., Fink, A., and Bohn, E. (1968) Controlled growth of monodisperse silica spheres in micron size range. *J. Colloid Interface Sci*. *26*, 62−69.
(12) Kobayashi, Y., Salgueirño-Maceira, V., and Liz-Marzán, L. M. (2001) Deposition of silver nanoparticles on silica spheres by pre-treatment steps in electroless plating. *Chem. Mater*. *13*, 1630−1633.
(13) Liz-Marzan, L. M., Giersig, M., and Mulvaney, P. (1996) Synthesis of nanosized gold-silica core-shell particles. *Langmuir*. *12* (18), 4329−4335.
(14) Song, A., Wang, X., Zhang, J., Marik, J., Lebrilla, C. B., and Lam, K. S. (2004) Synthesis of hydrophilic and flexible linkers for peptide derivatization in solid phase. *Bioorg. Med. Chem. Lett*. *14*, 161−165.
(15) Yoon, T. J., Yu, K. N., Kim, E., Kim, J. S., Kim, B. G., Yun, S. H., Sohn, B. H., Cho, M. H., Lee, J. K., and Park, S. B. (2006) Specific targeting, cell sorting, and bioimaging with smart magnetic silica core−shell nanomaterials. *Small 2*, 209−215.
(16) Martin, S. J., Reutelingsperger, C. P. M., McGahon, A. J., Rader, J. A., van Schie, R. C. A. A., LaFace, D. M., and Green, D. R. (1995) Early redistribution of plasma membrane phosphatidylserine is a general feature of apoptosis regardless of the initiating stimulus: inhibition of overexpression of Bcl-2 and Abl. *J. Exp. Med*. *182*, 1545−1556.
(17) Putt, K. S., Chen, G. W., Pearson, J. M., Sandhorst, J. S., Hoagland, M. S., Kwon, J. T., Hwang, S. K., Jin, H., Churchwell, M. I., Cho, M. H., Doerge, D. R., Helferich, W. G., and Hergenrother, P. J. (2006) Small-molecule activation of procaspase-3 to caspase-3 as a personalized anticancer strategy. *Nat. Chem. Biol*. *2* (10), 543−550.
(18) Jin, H., Kim, T. H., Hwang, S. K., Chang, S. H., Kim, H. W., Anderson, H. K., Lee, H. W., Lee, K. H., Colburn, N. H., Yang, H. S., Cho, M. H., and Cho, C. S. (2006) Aerosol delivery of urocanic acid-modified chitosan/programmed cell death 4 complex regulated apoptosis, cell cycle, and angiogenesis in lung of K-ras null mice. *Mol. Cancer Ther*. *5* (4), 1041−1049.
(19) Oberdorster, G., Oberdorster, E., and Oberdorster, J. (2005) Nanotoxicology: an emerging discipline evolving from studies of ultrafine particles. *Environ. Health Perspect. 113*, 823−839.
(20) Su, X., Zhang, J., Sun, L., Koo, T., Chan, S., Sundararajan, N., Yamakawa, M., and Berlin, A. A. (2005) Composite organic-inorganic nanoparticle (COINs) with chemically encoded optical signatures. *Nano Lett. 5*, 49−54.
(21) Yurkovetsky, Z. R., Linkov, F. Y., Malenhorn, D. E., and Lokshin, A. E. (2006) Multiple biomarker panels for early detection of ovarian cancer. *Future Oncol*. *2* (6), 733−741.
(22) Fortina, P., Kricka, L. J., Surrey, S., and Grodzinski, P. (2005) Nanobiotechnology: the promise and reality of new approaches to molecular recognition. *Trends Biotechnol. 23*, 168−173.
(23) Medintz, I. L., Uyeda, H. T., Goldman, E. R., and Mattoussi, H. (2005) Quantum dot bioconjugates for imaging, labeling and sensing. *Nat. Mater*. *4*, 435−446.
(24) Hardman, R. (2006) A toxicologic review of quantum dots: toxicity depends on physicochemical and environmental factors. *Environ. Health Perspect. 114*, 165−172.
(25) Xiao, Y., and Barker, P. E. (2004) Semiconductor nanocrystal probes for human metaphase chromosomes. *Nucleic Acids Res. 32* (3), e28.
(26) Bell, S. E., and Sirimuthu, N. M. (2006) Surface-enhanced Raman spectroscopy (SERS) for sub-micromolar detection of DNA/RNA mononucleotides. *J. Am. Chem. Soc*. *128* (49), 15580−15581.
(27) Van Blerkom, J., and Davis, P. W. (1998) DNA strand breaks and phosphatidylserine redistribution in newly ovulated and cultured mouse and human oocyte: occurrence and relationship to apoptosis. *Hum. Reprod*. *13*, 1317−1324.

BC070011I

Synthesis of Poly(amidoamine) Dendron-Bearing Lipids with Poly(ethylene glycol) Grafts and Their Use for Stabilization of Nonviral Gene Vectors

Toshinari Takahashi, Jun Hirose, Chie Kojima, Atsushi Harada, and Kenji Kono*

Department of Applied Chemistry, Graduate School of Engineering, Osaka Prefecture University, 1-1 Gakuen-cho, Naka-ku, Sakai, Osaka 599-8531, Japan. Received January 16, 2007; Revised Manuscript Received April 10, 2007

Recently, we developed a new type of cationic lipid that consists of an amine-terminated poly(amidoamine) dendron and two long alkyl groups. These dendron-bearing lipids achieved efficient gene transfection of cells through synergetic action of the proton sponge effect and membrane fusion in combination with fusogenic lipid dioleoylphosphatidylethanolamine. Using those dendron-bearing lipids as a base material, we developed in this study a functional component of gene vectors that stabilizes lipoplexes by multiple PEG chains and promotes gene transfection through the proton sponge effect. We combined a poly(ethylene glycol) (PEG, 550 Da) graft to each of four chain ends of the G2 dendron-bearing lipid (P4-DL). An analogous molecule having single PEG graft was also synthesized using the G0 dendron-bearing lipid (P1-DL). Inclusion of P4-DL decreased the size of the G3 dendron-bearing lipid-based lipoplexes more efficiently than P1-DL. In addition, P4-DL-containing lipoplexes exhibited two-orders-higher transfection efficiency than P1-DL-containing lipoplexes with the same PEG graft density. These results indicate the superiority of multiple attachments of PEG graft chains to a lipid for heightened ability to increase colloidal stability of lipoplexes while retaining their transfection activity. The lipoplexes stabilized by P4-DL were small, around 250 nm, and achieved efficient transfection in the presence of serum. Therefore, P4-DL and its analogues will form the basis for production of efficient nonviral vectors for *in vivo* use.

INTRODUCTION

Development of nonviral vector systems that deliver therapeutic genes to targets cells is an important step for gene therapy. Cationic lipids are the most extensively studied among nonviral vectors. These lipids can associate with DNA and form complexes, which are termed lipoplexes (*1*, *2*). Lipoplexes are widely used because of their low immunogenic nature, ability to deliver large pieces of DNA, and ease of handling and preparation. However, lipoplexes also pose inherent problems. They are generally heterogeneous, often aggregating and exhibiting transfection activities that vary from sample to sample. Furthermore, despite demonstrating reasonable transfection activity *in vitro*, their large size and overall positive charge engenders rapid clearance by the cells of the reticuloendothelial system (RES) and to nonspecific association with the extracellular matrix *in vivo*; therefore, the highest levels of transfection activity are apparent in the first-pass organs such as the lung, liver, and spleen (*3*−*7*). The instability of lipoplexes limits their use for systemic injection *in vivo*.

To overcome such drawbacks, lipoplexes can be coated with highly hydrophilic and flexible polymers such as poly(ethylene glycol) (PEG), which forms a steric barrier on the surface (*8*−*10*). In fact, various lipoplexes modified with PEG-modified lipids exhibit prolonged circulation in blood (*10*, *11*). Moreover, PEG lipids can inhibit intensive aggregation and fusion during complexation with DNA, engendering formation of small lipoplexes with high stability (*8*, *11*). However, incorporation of PEG chains onto the lipoplex surface often induces a marked reduction of its transfection activity because PEG chains cover its surface and suppress direct contact with cell membranes. For that reason, it is desired to develop a PEGylation methodology that provides high colloidal stability and high transfection activity.

In general, PEG-modified lipids used for stabilization of lipoplexes have a structure in which a single PEG chain is conjugated to the head group of phospholipids. However, considering that conformation of PEG chains grafted onto the lipoplex membranes and distribution of the PEG chains in the lipoplex membrane might affect the ability of PEG to stabilize lipoplex particles and interaction between the lipoplex and a cell, the use of PEG-modified lipids that have multiple PEG chains might be of interest.

In a previous study, we developed a novel type of cationic lipid that consists of two dodecyl or octadecyl groups and a poly(amidoamine) (PAMAM) dendron as a head group (*12*, *13*). The PAMAM dendron possesses many tertiary amines, which become protonated under weakly acidic conditions (*14*−*16*). Those amines suppress the lowering of pH in endosomes and lysosomes by adsorbing protons and prohibiting degradation of DNA in the lysosome. In addition, the endosome buffering ability of PAMAM dendron is believed to induce osmotic swelling of the endosome interior, thereby engendering rupture of the endosome and the subsequent release of DNA into the cytoplasm (*17*). Such a function of these tertiary amine groups of PAMAM dendron, the so-called proton sponge effect, is considered to contribute to their high transfection activity (*18*).

As a new type of PEG-bearing lipid, we prepared in this study a PAMAM dendron-bearing lipid having four PEG chains at the dendron chain ends, which is termed P4-DL. Such a PEG-modified dendron lipid can efficiently increase the colloidal stability of lipoplexes by multiple PEG chains and enhance gene transfection of cells through the proton sponge effect (Figure 1). As a control, DL-G0-2C_{18} having a single PEG chain at its chain terminal, so-called P1-DL, was also synthesized (Figure 1). We examined advantages using a lipid having multiple PEG

* Corresponding author. E-mail: kono@chem.osakafu-u.ac.jp. Tel: +81-722549330. Fax: +81-722549330.

10.1021/bc070014v CCC: $37.00 © 2007 American Chemical Society
Published on Web 06/15/2007

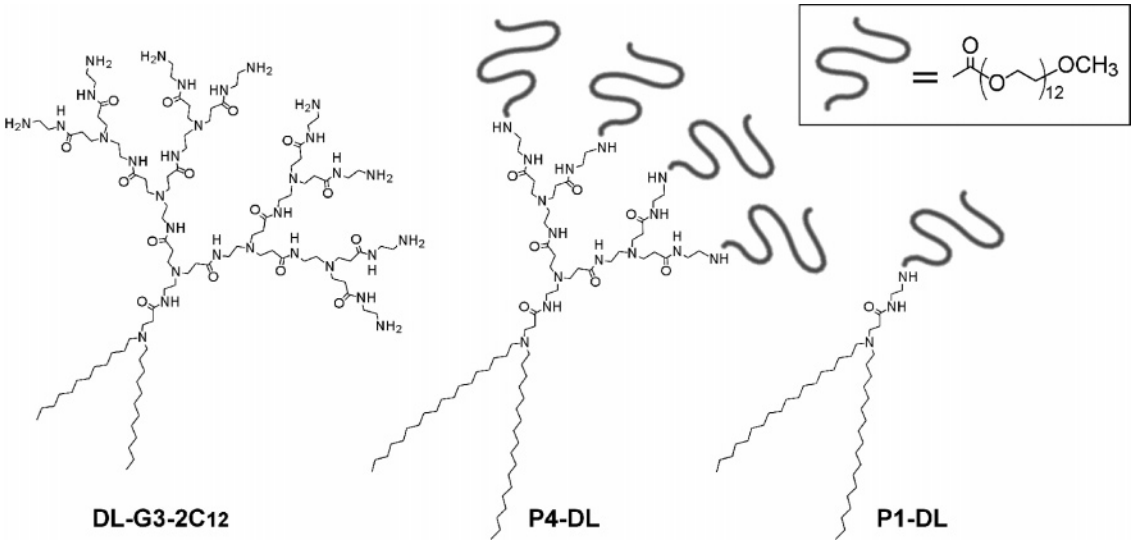
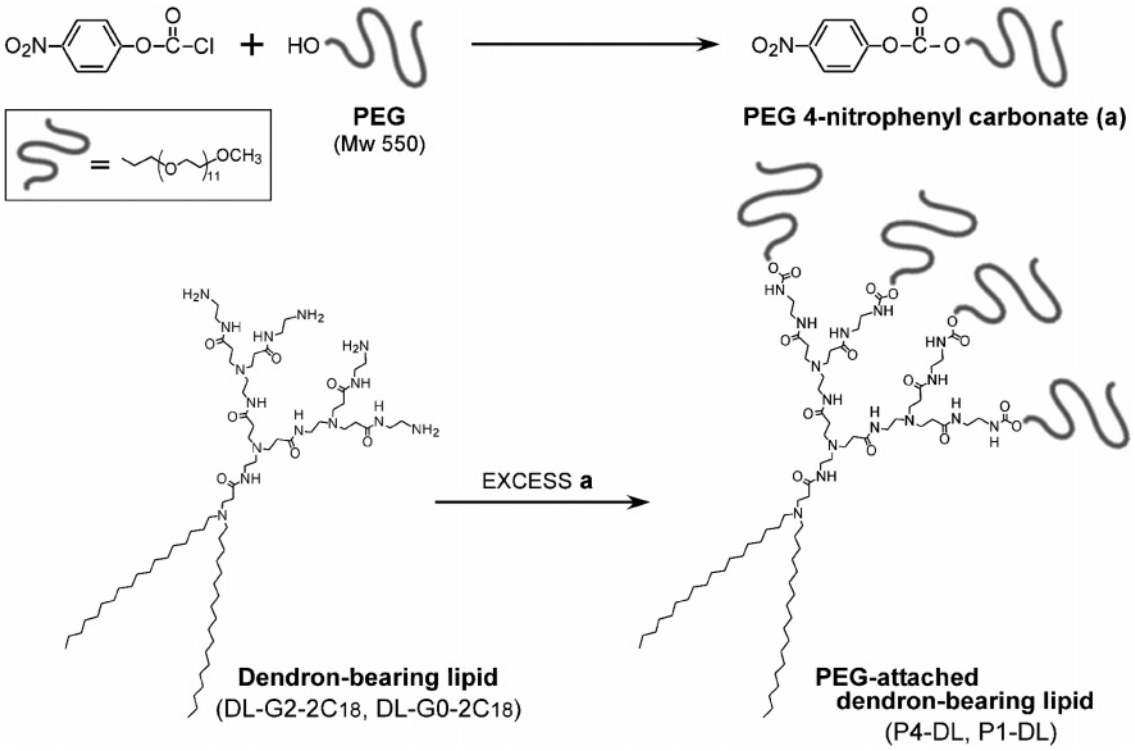


Figure 1. Structures of DL-G3-2C_{12}, P4-DL, and P1-DL.

Scheme 1. Synthetic Route for PEG-Attached Dendron-Bearing Lipids



chains to obtain lipoplexes with increased colloidal stability and enhanced transfection activity.

EXPERIMENTAL PROCEDURES

General Methods. PEG with the number average molecular weights of 550 [PEG-(550)] was purchased from Aldrich Chemical (Milwaukee, WI). 4-Nitrophenyl chloroformate was obtained from Tokyo Kasei Kogyo (Tokyo, Japan). Tris-(hydroxymethyl)aminomethane (Tris), triethylamine (TEA), tetrahydrofuran (THF), and dimethyl sulfoxide (DMSO) were supplied from Kishida Chemical (Osaka, Japan). Ethidium bromide was supplied from Wako Pure Chemical Industries (Osaka, Japan). Fetal calf serum (FCS) was obtained from PAA Laboratories GmbH (Pasching, Austria). Dulbecco's modified Eagle's medium (DMEM) was from Nissui Pharmaceutical (Tokyo, Japan). Agarose was purchased from Nacalai Tesque (Kyoto, Japan). DOPE was kindly donated by Nippon Oil and Fats Co. (Tokyo, Japan).

DL-G0-2C_{18}, DL-G2-2C_{18}, and DL-G3-2C_{12} were synthesized by the method previously reported (*12*, *13*). Plasmid DNA pCMV-Luc, which contains the cDNA of firefly luciferase driven by a human cytomegalovirus immediate-early promoter, was a gift from Dr. Kazuo Maruyama, Teikyo University, and amplified in the *E. coli*, isolated, and purified using a QIAGEN plasmid Maxi Kit.

Synthesis of PEG-Attached Dendron-Bearing Lipids. The PEG-attached DL-G2-2C_{18} (P4-DL) and PEG-attached DL-G0-2C_{18} (P1-DL) were synthesized via the procedure shown in Scheme 1 as reported by Kojima et al. (*19*).

PEG 4-Nitrophenyl Carbonate. PEG-(550) (1.1 mmol) was dissolved in THF (12 mL). To the solution were added 4-nitrophenyl chloroformate (4.3 mmol) and TEA (4.3 mmol),

followed by stirring for 24 h at room temperature. PEG 4-nitrophenyl carbonate was recovered by evaporation of the reaction mixture and purified using a Sephadex LH-20 column with methanol as the eluent. Yeild. 82%; ^{1}H NMR ($CDCl_3$): δ 3.38 (s, OCH_3), δ 3.54−3.83 (m, CH_2CH_2O), δ 4.44 (m, $OCOOCH_2$), δ 7.40 (d, aromatic), δ 8.28 (d, aromatic).

PEG-Attached Dendron-Bearing Lipids. The PEG-attached DL-G2-2C_{18} (P4-DL) was synthesized via the procedure shown in Scheme 1. To a solution of the DL-G2-2C_{18} (38 μmol) in DMSO (12 mL) was added PEG 4-nitrophenyl carbonate (0.76 mmol), and the solution was stirred for 5 days at room temperature. The solution was diluted with distilled water and dialyzed using a dialysis bag (molecular weight 1000 cut off) against distilled water for 24 h. The crude compound was lyophilized and then purified by a Sephadex LH-20 column using methanol as the eluent. In the case of PEG-attached DL-G0-2C_{18} (P1-DL), to a solution of the DL-G0-2C_{18} (63 μmol) in chloroform (6 mL) was added PEG 4-nitrophenyl carbonate (0.32 mmol), and the solution was stirred for 5 days at room temperature. The obtained material was chromatographed on silica gel using chloroform−methanol (95/5, v/v) and then chloroform−methanol (90/10, v/v) as eluent. The solution was diluted with distilled water and dialyzed using a dialysis bag (molecular weight 1000 cut off) against distilled water for 24 h. The P1-DL was recovered by lyophilization. Yields of P4-DL and P1-DL were 49 and 89%, respectively. ^{1}H NMR for P4-DL ($CDCl_3$): δ_{Alkyl} 0.88 (m, $CH_3(CH_2)_{15}$), δ_{Alkyl} 1.25 (s, $CH_3(CH_2)_{15}$), δ_{Alkyl} 1.53 (br, CH_2CH_2N), $\delta_{Alkyl/PAMAM}$ 2.37 (br, CH_2N, CH_2CONH), δ_{PAMAM} 2.53 (br, $CONHCH_2CH_2$), δ_{PAMAM} 2.72 (br, CH_2CH_2CONH), δ_{PAMAM} 3.28−3.33 (br, $CONHCH_2$, CH_2NHCOO), δ_{PEG} 3.38 (s, OCH_3), δ_{PEG} 3.54−3.82 (m, CH_2CH_2O), δ_{PEG} 4.18 (br, $NHCOOCH_2$). ^{1}H NMR for P1-DL ($CDCl_3$): δ_{Alkyl} 0.88 (m, $CH_3(CH_2)_{15}$), δ_{Alkyl} 1.26 (s, $CH_3(CH_2)_{15}$), δ_{Alkyl} 1.43 (br, CH_2CH_2N), δ_{PAMAM} 2.35 (m, CH_2CONH), δ_{Alkyl} 2.44 (m, CH_2N), δ_{PAMAM} 2.67 (br, CH_2CH_2CONH), δ_{PAMAM} 3.28−3.34 (m, $CONHCH_2$, CH_2NHCOO), δ_{PEG} 3.38 (s, OCH_3), δ_{PEG} 3.54−3.82 (m, CH_2CH_2O), δ_{PEG} 4.20 (br, $NHCOOCH_2$).

Preparation of Lipoplexes. The composition of basic components for the lipoplex, namely, DL-G3-2C_{12} and DOPE, was fixed at the ratio of 1/10 (mol/mol) throughout the experiment. To a dry thin membrane of a mixture of the DL-G3-2C_{12}, DOPE and a given amount of PEG-attached dendron-bearing lipids (P4-DL or P1-DL), phosphate-buffered saline (PBS) was added and sonicated for 2 min using a bath-type sonicator to afford a lipid suspension. Plasmid DNA (1 μg) was dissolved in 20 mM Tris-HCl buffer (pH7.4, 50 μL), mixed with the lipid suspension (50 μL), and incubated for 30 min at room temperature to afford a lipoplex with a ratio of primary amine of DL-G3-2C_{12} to DNA phosphate (N/P ratio) of 4.

Agarose Gel Electrophoresis. The lipoplexes with a given amount of PEG-attached dendron-bearing lipids were prepared by mixing plasmid DNA (1 μg) dissolved in 20 mM Tris-HCl buffer (5 μL) and lipid suspension (5 μL). After 30 min incubation at room temperature, the samples (10 μL) were electrophoresed on 0.6 wt % agarose gel in 40 mM Tris, 20 mM sodium acetate, and 2 mM EDTA buffer (pH 8.0) containing 1 μg/mL ethidium bromide at 100 V for 30 min. The ethidium bromide-stained bands were visualized using a LAS-1000UVmini (Fujifilm, Japan) and analyzed with Science Lab 2003 Multi Gauge software (Fujifilm, Japan).

Zeta Potential Measurement. The zeta potential values were determined by a Nicomp PSS ZW380 instrument (Santa Barbara, CA). Lipoplexes with a given amount of PEG-attached dendron-bearing lipids were prepared by mixing plasmid DNA (20 μg) and the lipid suspension and incubated for 30 min as described above. The measurement was performed in triplicate.

Dynamic Light Scattering (DLS) Measurement. To estimate the hydrodynamic diameters of lipoplexes, dynamic light scattering (DLS) was analyzed using an electrophoretic light scattering spectrometer ELS-8000F (Otsuka Electronics Co, Ltd., Japan). Lipoplexes with a given amount of PEG-attached dendron-bearing lipids were prepared by mixing plasmid DNA (20 μg) and the lipid suspension and incubated for 30 min as described above. The data obtained at a detection angle of 90° at 25 °C were analyzed by the cumulant method to obtain the hydrodynamic diameters of the lipoplexes.

Atomic Force Microscopy (AFM). AFM measurements were performed by SPI3800 probe station and SPA400 unit system of the scanning probe microscopy system (Seiko Instruments Inc, Japan). The cantilever was made of silicon (SI-DF40; Seiko Instruments Inc, Japan), and its spring constant was 38 N/m. Lipoplexes were formed at a total of 100 μg/mL of plasmid DNA concentration. Lipoplexes containing 0.5 μg of plasmid DNA were applied to freshly cleaved mica and incubated on the mica for 5 min. After incubation, excess fluid was dried under air flow. The measurements were performed in a dynamic force mode (noncontact mode). Raw AFM images have been processed only for background removal (flattening) using the microscope manufacturer's image-processing software.

Transfection. Transfection of HepG2 cells was done according to the following procedures unless otherwise noted in the text. The cells were seeded in 0.5 mL of DMEM supplemented with 10% FCS in 24-well culture plates at 5.0×10^4 cells per well the 2 days before transfection. The cells were washed with PBS containing 0.36 mM $CaCl_2$ and 0.42 mM $MgCl_2$ [PBS(+)] and then covered with DMEM supplemented with a given amount of FCS (1 mL). The lipoplexes containing plasmid DNA were added gently to the cells and incubated for 24 h at 37 °C. Then, the cells were rinsed with PBS(+), covered with DMEM containing 10% FCS, and incubated at 37 °C. After 24 h, the cells were lysed by adding 50 μL of Luc-PGC-50 detergent (Toyo Ink, Japan). A 20 μL aliquot from each dish was used for one luciferase assay using a kit (Toyo Ink) and a Lumat LB9507 luminometer (Berthold, Bad Wildbad, Germany). The protein content of the lysate was measured by Coomassie Protein Assay Reagent (Pierce, IL) using bovine serum albumin as the standard.

RESULTS AND DISCUSSION

Design and Synthesis of PEG-Attached Dendron-Bearing Lipids. In a previous study, we developed a new type of cationic lipid consisting of two dodecyl or octadecyl groups and PAMAM dendron of varying generations (*12*, *13*, *20*).

We examined conjugation of PEG chains to amino groups at chain ends of the PAMAM G2 and G0 dendron-bearing lipids (DL-G2-2C_{18} and DL-G0-2C_{18}) through urethane bonds (Scheme 1). We showed that PEG chains are attachable to terminal amino groups of the PAMAM dendrimers using 4-nitrophenyl chloroformate (*19*). In this study, we combined PEG chains with the PAMAM dendron chain ends using the same method. We synthesized DL-G2-2C_{18}, which has four PEG grafts at chain terminals; it is called P4-DL. As a control lipid, DL-G0-2C_{18} was also synthesized; it has a single PEG graft at its chain terminal, and is termed P1-DL. Characterization using ^{1}H NMR showed good correspondence between the theoretically expected and experimentally obtained values for the synthesized products, as described in the Experimental section.

Evaluation of Complex Formation with Plasmid DNA. In a previous study, we established the composition of a lipoplex comprising DL-G3-2C_{12}, DOPE, and plasmid DNA with high transfection activity in the presence and in the absence of serum. Specifically, we showed that a lipoplex with an N/P ratio of 4 and DL-G3-2C_{12}/DOPE ratio of 1/10 exhibited the highest

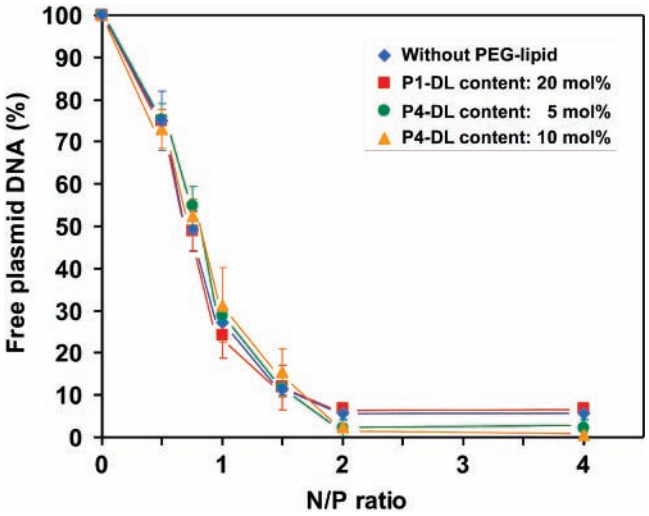


Figure 2. Complexation between DL-G3-2C_{12}−DOPE mixtures containing varying amounts of P1-DL or P4-DL and plasmid DNA. Percent of free plasmid DNA after the complexation was estimated using gel electrophoresis and plotted against N/P ratio of DL-G3-2C_{12} to plasmid DNA. Each point represents the mean ± SD (n = 3).

activity (*20*). Suspensions of a mixture of DL-G3-2C_{12} and DOPE with that composition can form complexes efficiently with plasmid DNA through electrostatic interaction between protonated primary amines of the DL-G3-2C_{12} and negatively charged phosphate groups of DNA (*20*). Nevertheless, addition of the dendron-bearing lipid with hydrophilic PEG chains to the mixture of DL-G3-2C_{12} and DOPE might affect their complex formation with plasmid DNA. For that reason, we examined complexation among DL-G3-2C_{12}–DOPE mixtures containing varying amounts of PEG-bearing lipids with plasmid DNA.

The plasmid DNA (1 μg) was incubated with suspensions of DL-G3-2C_{12}−DOPE mixtures containing varying amounts of P4-DL or P1-DL at varying N/P ratios for 30 min and electrophoresed on an agarose gel. Figure 2 shows the formation of lipoplexes of the DL-G3-2C_{12}−DOPE mixtures containing varying amounts of the PEG-lipids with plasmid DNA. Irrespective of the type of PEG-lipids and their contents, there is essentially no difference among them. Free DNA was not detected at the N/P ratio of 2 for complexation with these mixtures. All plasmid DNA molecules were associated with mixtures at this N/P ratio. Therefore, influence of these PEG-grafted lipids could be only slight for the complex formation of the DL-G3-2C_{12}-DOPE mixture with DNA.

Effects of PEG-Modified Dendron-Bearing Lipids on Lipoplex Characteristics. Figure 3A presents zeta potentials of the lipoplexes containing varying amounts of PEG-attached dendron-bearing lipids. The DL-G3-2C_{12}−DOPE lipoplex without the PEG-modified lipid exhibited zeta potentials of about 10 mV. However, their zeta potentials decreased with increasing amounts of P4-DL or P1-DL and reached a constant value of about 3−4 mV at P4-DL contents above 2 mol % or P1-DL contents above 20 mol %. The lipoplex containing 2 mol % of P4-DL and that containing 8 mol % of P1-DL have the same PEG density on the surface, which suggests that the P4-DL has greater ability to cover the lipoplex surface and shield its positive charge.

Effects of inclusion of the PEG-modified dendron-bearing lipids on the lipoplex size were examined using DLS. As shown in Figure 3B, the lipoplex without the PEG-modified lipids exhibited an 800-nm diameter. However, the lipoplexes containing the PEG-modified dendron-bearing lipids showed much smaller diameters. Their size decreased markedly with increasing PEG-attached dendron-bearing lipid contents and reached

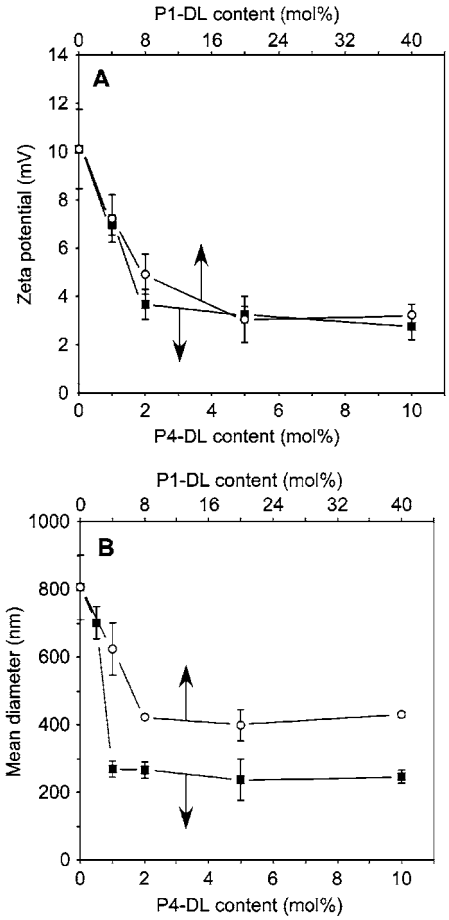


Figure 3. Zeta potentials (A) and mean diameters (B) of lipoplexes with varying P4-DL (■) and P1-DL (○) contents. Each lipoplex was prepared at N/P ratio of 4 and DOPE/DL-G3-2C_{12} ratio of 10. Each point represents the mean ± SD (n = 3).

constant values of 250 nm for lipoplexes containing P4-DL greater than 1 mol % and 400 nm for lipoplexes containing P1-DL greater than 8 mol %. This result is indicative that the lipid with multiple PEG chains has greater ability to decrease the lipoplexes' particle size.

The lipoplexes were further characterized using AFM. For lipoplexes that did not contain the PEG-modified dendron-bearing lipid, particles with irregular shapes and wide size distribution were observed, implying that these particles were formed by aggregation and fusion of smaller lipoplexes (Figure 4A). In contrast, lipoplexes containing 5 mol % of the P4-DL showed spherical particles with much smaller diameter and more uniform particle size of about 200 nm (Figure 4B) compared to the plain lipoplex. For lipoplexes containing P1-DL content of 20 mol %, spherical particles with a wider size distribution between 250 and 500 nm were observed. These particles were smaller than those of the plain lipoplex, but more heterogeneous than those of the lipoplex containing P4-DL (Figure 4C). These results indicate that lipids having multiple PEG chains to the lipid are more effective to stabilize lipoplex than those having a single PEG chain. We confirmed that the lipoplexes with P4-DL contents greater than 1 mol % were highly stable and that their size did not change over a period of more than 10 days in saline (see Supporting Information).

Transfection Activity of Lipoplexes Containing PEG-Modified Dendron-Bearing Lipids. Lipoplexes are known to lose their transfection activity readily in the presence of serum because negatively charged serum proteins bind to the lipoplexes and induce their destabilization and/or aggregation (*21, 22*). Modification of lipoplexes with PEG-lipids might increase the

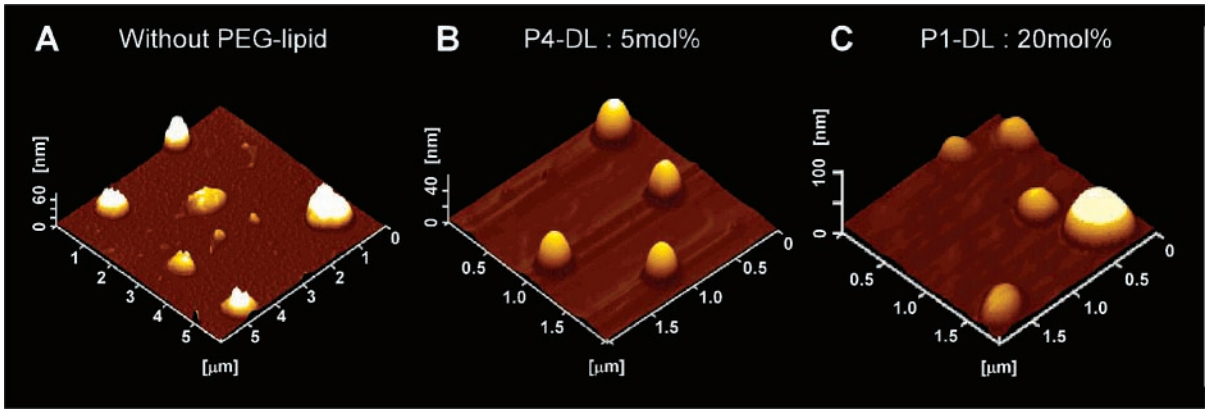


Figure 4. AFM images of plain (A), P4-DL-containing (B), and P1-DL-containing (C) DL-G3-2C_{12}–DOPE lipoplexes. Contents of P4-DL (B) and P1-DL (C) were 5 and 20 mol %, respectively. N/P and DOPE/DL-G3-2C_{12} ratios of lipoplexes were 4 and 10, respectively.

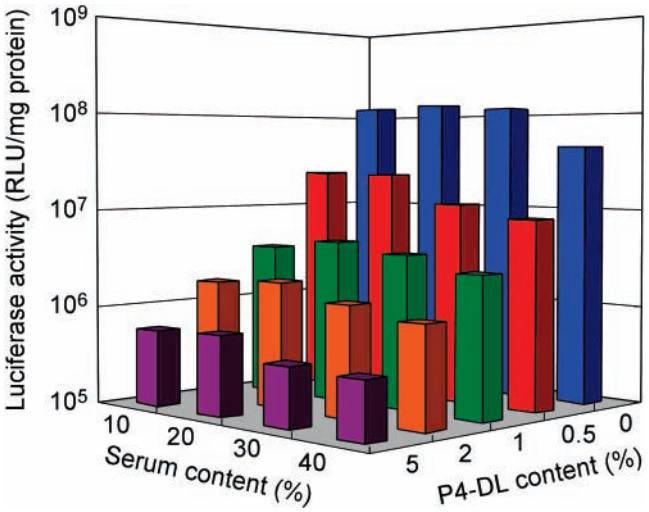


Figure 5. Luciferase activities of HepG2 cells treated with lipoplexes containing varying amounts of P4-DL. N/P and DOPE/DL-G3-2C_{12} ratios of lipoplexes were 4 and 10, respectively. The cells (5×10^4) were treated with the lipoplexes containing 1μg plasmid DNA in the medium with varying contents of FCS. Each bar represents the mean ($n = 5$).

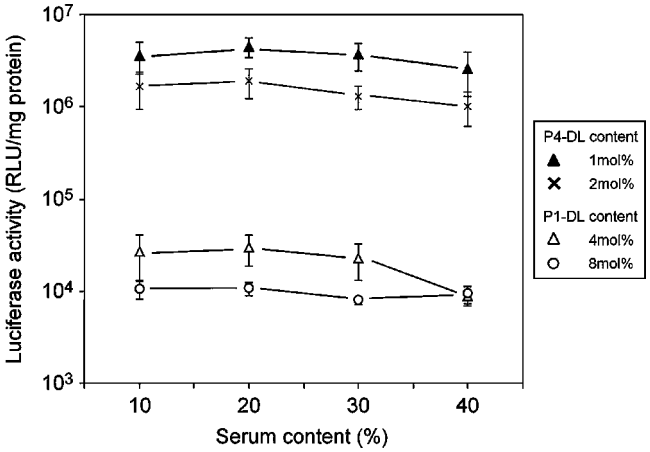


Figure 6. Comparison of transfection activity of lipoplexes containing varying amounts of P4-DL or P1-DL. N/P and DOPE/DL-G3-2C_{12} ratios of lipoplexes were 4 and 10, respectively. The cells (5×10^4) were treated with the lipoplexes containing 1 μg plasmid DNA in the medium with varying contents of FCS. Each point represents the mean $\pm$ SD ($n = 5$).

colloidal stability of lipoplexes because highly hydrated PEG chains shield the positively charged surface of lipoplexes. However, incorporation of PEG chains onto lipoplex surfaces often substantially reduces their transfection activity because PEG chains suppress interaction with cell membranes simultaneously (*23*−*25*). Therefore, PEGylation that increases colloidal stability of the lipoplexes without a concomitant decrease in transfection activity is desired to obtain nonviral vectors for use in biological fluids.

As described above, P4-DL increased colloidal stability of the dendron-bearing lipid-based lipoplexes more efficiently than P1-DL. Consequently, the influence of inclusion of P4-DL on transfection activity of the lipoplexes was examined in a medium with varying serum contents. The HepG2 cells were treated with the P4-DL-modified lipoplexes containing luciferase gene. As shown in Figure 5, transfection activity of the lipoplexes decreased gradually with increasing P4-DL content in the lipoplexes, probably because hydrophilic PEG chains suppress their interaction with the cell membrane. However, these lipoplexes exhibited excellent serum resistance: their transfection activity decreased only slightly with increasing serum content.

Next, we examined the influence of multiple attachments of PEG chains to the dendron-bearing lipid by comparing transfection of lipoplexes containing either P4-DL or P1-DL. Figure 6 shows the dramatic difference observed in their transfection efficiencies. Despite the same PEG chain density in the lipoplex surfaces, the lipoplexes with the P1-DL content of 4 mol % induced production of luciferase that was 2 orders of magnitude less than the lipoplex containing 1 mol % of P4-DL. A similar situation was observed when the transfection efficiency of the lipoplexes containing 2 mol % of P4-DL and that of the lipoplex containing 8 mol % of P1-DL were compared.

In this study, we compared stability and transfection activity of the PEG-modified dendron-bearing lipid based lipoplexes and showed the superiority of multiple attachments of PEG chains to the lipid head group for production of lipoplexes with high colloidal stability and high transfection activity. The distance between neighboring polymer chains is known to affect their conformation (*26*). Thus, PEG chains grafted to lipid membrane surface change their configuration from a hydrated mushroom structure to a more stretched brush structure, depending on their density in the lipid membrane. For example, Bartucci et al. reported that PEG (350 Da) chain grafted to a dipalmitoylphosphatidylcholine (DPPC) membrane converts its configuration from a mushroom-like structure to a more stretched brush-like structure at mole fractions greater than 0.07 in the DPPC membrane (*27*). Therefore, it is possible that multiple attachments of PEG (550 Da) chains to a lipid head group induced a more extended conformation than the case of single attachment of PEG chain. The extended PEG chains tethered to the lipoplex

surface can form a thicker hydration layer and increase the colloidal stability of the lipoplexes.

Hydrophobic chains of the PEG-grafted lipid might be another means to modify the lipoplexes' properties. In general, lipids with unsaturated alkyl chains, such as DOPE, are used as a helper lipid for preparation of potent lipoplexes because these lipids increase the fusion ability of the lipoplexes (*28*, *29*). However, inclusion of a large amount of PEG-modified lipid with saturated alkyl chains might induce alteration of physical properties of the lipoplex and decrease its transfection activity. In fact, efficient stabilization of the lipoplexes was obtained at P1-DL contents above 8 mol %, whereas the same PEG chain density is attainable at 2 mol % of PEG-grafted lipid using P4-DL (Figure 3B). Furthermore, tertiary amines of the dendron contained in P4-DL might help retain the ability of the dendron-bearing lipid based lipoplexes to induce the proton sponge effect, although the contribution might not be important, considering the content of P4-DL in the lipoplexes.

In this study, we prepared a new type of a functional PEG-grafted lipid, P4-DL, by PEGylation of a PAMAM dendron-bearing lipid DL-G2. When included in the DL-G3-based lipoplexes, this PEG-grafted lipid increased the colloidal stability of the dendron-based lipoplexes more efficiently than P1-DL, which has a single PEG chain, as do PEG-lipids of the conventional type generally used for lipoplex stabilization. The lipoplexes stabilized with P4-DL displayed a small particle size with narrow size distribution and much higher transfection activity than the lipoplexes stabilized with P1-DL. The results demonstrate the superiority of multiple attachments of PEG chains to a lipid molecule for production of PEG-stabilized lipoplexes with high transfection activity in the presence of serum. Indeed, optimizations of the number and length of PEG chains are necessary. However, information obtained through this study will be useful for production of highly potent gene vectors.

ACKNOWLEDGMENT

This work was partly supported by a Grant-in-aid for Scientific Research from the Ministry of Education, Science, Sports, and Culture in Japan. T. Takahashi thanks the Research Fellowships of the Japan Society for the Promotion of Science for Young Scientists.

Supporting Information Available: Change of mean diameters of lipoplexes with varying amounts of P4-DL as a function of time. This material is available free of charge via Internet at http://pubs.acs.org.

LITERATURE CITED

(1) Felgner, P. L., Gadek, T. R., Holm, M., Roman, R., Chan, H. W., Wenz, M., Northrop, J. P., Ringold, G. M., and Danielsen, M. (1987) Lipofection: a highly efficient, lipid-mediated DNA-transfection procedure. *Proc. Natl. Acad. Sci. U.S.A. 84*, 7413−7417.

(2) de Lima, M. C. P., Simoes, S., Pires, P., Faneca, H., and Duzgunes, N. (2001) Cationic lipid-DNA complexes in gene delivery: from biophysics to biological applications. *Adv. Drug Delivery Rev. 47*, 277−294.

(3) Hofland, H. E. J., Nagy, D., Liu, J. J., Spratt, K., Lee, Y. L., Danos, O., and Sullivan, S. M. (1997) In vivo gene transfer by intravenous administration of stable cationic lipid DNA complex. *Pharm. Res. 14*, 742−749.

(4) Huang, L., and Li, S. (1997) Liposomal gene delivery: a complex package. *Nat. Biotechnol. 15*, 620−621.

(5) Mori, A., Chonn, A., Choi, L. S., Israels, A., Monck, M. A., and Cullis, P. R. (1998) Stabilization and regulated fusion of liposomes containing a cationic lipid using amphipathic polyethyleneglycol derivatives. *J. Liposome Res. 8*, 195−211.

(6) Templeton, N. S., Lasic, D. D., Frederik, P. M., Strey, H. H., Roberts, D. D., and Pavlakis, G. N. (1997) Improved DNA: liposome complexes for increased systemic delivery and gene expression. *Nat. Biotechnol. 15*, 647−652.

(7) Thierry, A. R., Lunardiiskandar, Y., Bryant, J. L., Rabinovich, P., Gallo, R. C., and Mahan, L. C. (1995) Systemic gene-therapy-biodistribution and long-term expression of a transgene in mice. *Proc. Natl. Acad. Sci. U.S.A. 92*, 9742−9746.

(8) Hong, K., Zheng, W., Baker, A., and Papahadjopoulos, D. (1997) Stabilization of cationic liposome-plasmid DNA complexes by polyamines and poly(ethylene glycol)-phospholipid conjugates for efficient in vivo gene delivery. *FEBS Lett. 400*, 233−237.

(9) Tam, P., Monck, M., Lee, D., Ludkovski, O., Leng, E. C., Clow, K., Stark, H., Scherrer, P., Graham, R. W., and Cullis, P. R. (2000) Stabilized plasmid-lipid particles for systemic gene therapy. *Gene Ther. 7*, 1867−1874.

(10) Kim, K. J., Choi, S. H., Kim, C. O., Park, J. S., Ahn, W. S., and Kim, C. K. (2003) Enhancement of polyethylene glycol (PEG)-modified cationic liposome-mediated gene deliveries: effects on serum stability and transfection efficiency. *J. Pharm. Pharmacol. 55*, 453−460.

(11) Nicolazzi, C., Mignet, N., de la Figuera, N., Cadet, M., Ibad, R. T., Seguin, J., Scherman, D., and Bessodes, M. (2003) Anionic polyethyleneglycol lipids added to cationic lipoplexes increase their plasmatic circulation time. *J. Controlled Release 88*, 429−443.

(12) Takahashi, T., Kono, K., Itoh, T., Emi, N., and Takagishi, T. (2003) Synthesis of novel cationic lipids having polyamidoamine dendrons and their transfection activity. *Bioconjugate Chem. 14*, 764−773.

(13) Takahashi, T., Kojima, C., Harada, A., and Kono, K. (2007) Alkyl chain moieties of polyamidoamine dendron-bearing lipids influence their function as a nonviral gene vector. *Bioconjugate Chem.*, in press.

(14) Haensler, J., and Szoka, F. C., Jr. (1993) Polyamidoamine cascade polymers mediate efficient transfection of cells in culture. *Bioconjugate Chem. 4*, 372−379.

(15) Tang, M., Redemann, C. T., and Szoka, F. C., Jr. (1996) In vitro gene delivery by degraded polyamidoamine dendrimers. *Bioconjugate Chem. 7*, 703−714.

(16) Kukowska-Latallo, J. F., Bielinska, A. U., Johnson, J., Spindler, R., Tomalia, D. A., and Baker, J. R., Jr. (1996) Efficient transfer of genetic material into mamalian cells using Starburst polyamidoamine dendrimers. *Proc. Natl. Acad. Sci. U.S.A. 93*, 4897−4902.

(17) Sonawane, N. D., Szoka, F. C., Jr., and Verkman, A. S. (2003) Chloride accumulation and swelling in endosomes enhances DNA transfer by polyamine-DNA polyplexes. *J. Biol. Chem. 278*, 44826−44831.

(18) Boussif, O., Lezoualc'h, F., Zanta, M. A., Mergny, M. D., Scherman, D., Demeneix, B., and Behr, J. P. (1995) A versatile vector for gene and oligonucleotide transfer into cells in culture and in vivo: polyethylenimine. *Proc. Natl. Acad. Sci. U.S.A. 92*, 7297−7301.

(19) Kojima, C., Kono, K., Maruyama, K., and Takagishi, T. (2000) Synthesis of polyamidoamine dendrimers having poly(ethylene glycol) grafts and their ability to encapsulate anticancer drugs. *Bioconjugate Chem. 11*, 910−917.

(20) Takahashi, T., Harada, A., Emi, N., and Kono, K. (2005) Preparation of efficient gene carriers using a polyamidoamine dendron-bearing lipid: improvement of serum resistance. *Bioconjugate Chem. 16*, 1160−1165.

(21) Yang, J. P., and Huang, L. (1997) Overcoming the inhibitory effect of serum on lipofection by increasing the charge ratio of cationic liposome to DNA. *Gene Ther. 4*, 950−960.

(22) Li, S., Tseng, W. C., Stolz, D. B., Wu, S. P., Watkins, S. C., and Huang, L. (1999) Dynamic changes in the characteristics of cationic lipidic vectors after exposure to mouse serum: implications for intravenous lipofection. *Gene Ther. 6*, 585−594.

(23) Harvie, P., Wong, F. M. P., and Bally, M. B. (2000) Use of poly-(ethylene glycol)-lipid conjugates to regulate the surface attributes and transfection activity of lipid−DNA particles. *J. Pharm. Sci. 89*, 652−663.

(24) Song, L. Y., Ahkong, Q. F., Rong, Q., Wang, Z., Ansell, S., Hope, M. J., and Mui, B. (2002) Characterization of the inhibitory effect of PEG-lipid conjugates on the intracellular delivery of plasmid and

antisense DNA mediated by cationic lipid liposomes. *Biochim. Biophys. Acta 1558*, 1−13.
(25) Shi, F. X., Wasungu, L., Nomden, A., Stuart, M. C. A., Polushkin, E., Engberts, J. B. F. N., and Hoekstra, D. (2002) Interference of poly(ethylene glycol)-lipid analogues with cationic-lipid-mediated delivery of oligonucleotides; role of lipid exchangeability and non-lamellar transitions. *Biochem. J. 366*, 333−341.
(26) Kent, M. S. (2000) A quantitative study of tethered chains in various solution conditions using Langmuir diblock copolymer monolayers. *Macromol. Rapid Commun. 21*, 243−270.
(27) Bartucci, R., Pantusa, M., Marsh, D., and Sportelli, L. (2002) Interaction of human serum albumin with membranes containing polymer-grafted lipids: spin-label ESR studies in the mushroom and brush regimes. *Biochim. Biophys. Acta 1564*, 237−242.
(28) Monkkonen, J., and Urtti, A. (1998) Lipid fusion in oligonucleotide and gene delivery with cationic lipids. *Adv. Drug Delivery Rev. 34*, 37−49.
(29) Farhood, H., Serbina, N., and Huang, L. (1995) The role of dioleoyl phosphatidylethanolamine in cationic liposome mediated gene transfer. *Biochim. Biophys. Acta 1235*, 289−295.

BC070014V

Comparison of Several Linear Fluorophore- and Quencher-Conjugated Oligomer Duplexes for Stability, Fluorescence Quenching, and Kinetics in Vitro and in Vivo in Mice

Surong Zhang, Guozheng Liu, Xinrong Liu, Dongguang Yin, Shuping Dou, Jiang He,† Mary Rusckowski, and Donald J. Hnatowich*

Department of Radiology, University of Massachusetts Medical School, Worcester, Massachusetts 01655. Received January 21, 2007; Revised Manuscript Received April 11, 2007

A useful property of optical imaging is the potential to modulate the detectable signal to improve target/nontarget ratios. When administered as a dimer of a fluorophore- and a quencher-conjugated duplex arranged to inhibit fluorescence but designed to dissociate only in the presence of its target, the fluorescence signal should in principle appear only in the target. This laboratory has demonstrated the feasibility of this approach by using a duplex consisting of a linear oligomer conjugated with Cy5.5 (emitter) hybridized to another linear oligomer conjugated with Iowa Black (quencher) in a pretargeting optical study. Now eight duplexes consisting of combinations of 18 mer linear phosphodiester (PO) and phosphorothioate (PS) DNAs and phosphorodiamidate morpholinos (MORFs) conjugated with Cy5.5 (emitter) and Iowa Black (quencher) were variously screened for in vitro duplex stability. The MORF/PO duplex was selected for further study based on evidence of stability in 37 °C serum. Simultaneously, the kinetics of quenching were investigated in vitro and in vivo in mice. Thereafter, mice were implanted in one thigh with MORF/PO Cy 5.5 microspheres and the complementary PS Iowa Black administered iv to measure the extent and kinetics of duplex formation in the target. While all duplexes were stable in buffer, only the MORF/PO duplexes and possibly all PS containing duplexes were stable in 37 °C serum for at least 4 h. The kinetics of quenching were found to be rapid in vitro, with a 80−90% decrease in Cy5.5 fluorescence immediately following formation of a PS/PS homoduplex, and in vivo, with a 27 to 38% decrease in target thigh/nontarget ratio within 1 h following administration of the complementary PS Iowa Black complementary DNA but not the random control DNA to mice implanted with MORF/PO Cy5.5 microspheres. This investigation has provided additional evidence that Cy5.5 may be efficiently and rapidly quenched by Iowa Black when both are conjugated to complementary oligomers and that the resulting inhibition of fluorescence is sufficiently persistent for imaging.

INTRODUCTION

While nuclear imaging offers many advantages including high sensitivity of detection, quantitation accuracy, and the availability of numerous contrast agents, the physics involved does not permit varying the nuclear emissions. By contrast, a property of optical imaging unique among most molecular imaging modalities is the potential to modulate the detectable signal in the target. By bringing into close proximity a fluorophore and its quencher, it is possible to inhibit fluorescence by contact fluorescence inhibition (*1*). This laboratory is investigating antisense and pretargeting of tumor and other applications of radiolabeled oligomers (*2*−*4*). In the course of these investigations, it became apparent that the hybridization properties of oligomers may have applications in optical imaging as well. When properly designed, it should be possible with fluorophore-conjugated linear duplexes to limit fluorescence in a living subject except at the target site presenting a complementary oligomer capable of dissociating the duplex. Molecular beacons consisting of DNAs in the form of hairpins with two fluorophores or a fluorophore and a quencher on opposite ends are already in use in a similar manner for in vitro assays and for in vivo studies as well (*5*−*11*). Possible applications include antisense targeting in which the target mRNA serves as the complementary oligomer and pretargeting in which the complementary oligomer is localized in the target by a preliminary administration. This laboratory has recently reported on a poof of concept study of optical pretargeting showing that a linear fluorophore/quencher-conjugated oligomer duplex may be designed to dissociate in its target with the release of fluorescence inhibition (*12*). The further development of optical imaging using linear duplexes will require additional investigations of imaging sensitivity, duplex stability, and the kinetics of fluorescent inhibition.

We report herein on the screening of duplexes consisting of phosphodiester (PO) and phosphorothioate (PS) DNAs and/or phosphodiamidate morpholinos (MORFs) conjugated with Cy5.5 as emitter and Iowa Black as quencher to evaluate duplex stability in vitro and in vivo and to measure the pharmacokinetic and optical imaging properties of a stable duplex in a mouse microsphere model. The results of these measurements will be required to select duplexes for future investigations.

EXPERIMENTAL PROCEDURES

All oligomers were either uniform PO, PS, or MORF throughout their length. All DNAs, fluorophore/quencher conjugated or native, were purchased HPLC purified (Integrated DNA Technologies, Inc., Coralville, IA) as were the MORFs, biotin conjugated, or native (GeneTools, Philomath, OR). The DNAs were purchased with the fluorophore/quenchers attached directly while the biotin was attached to the MORF via a six-

* For correspondence, contact Donald J. Hnatowich, Ph.D., Dept. of Radiology, H2-579, Univ. of Massachusetts Medical School, 55 Lake Ave. North, Worcester, MA 01655. Tel: (508) 856-4256; Fax: (508) 856-4572. E-mail: donald.hnatowich@umassmed.edu.

† Current address: Department of Radiology, University of California San Francisco, San Francisco, CA 94143.

10.1021/bc070021j CCC: $37.00 © 2007 American Chemical Society
Published on Web 05/19/2007

Table 1. Base Sequences of the PO and PS DNAs and MORF of this Investigation[a]

oligomer type	base sequence	modifications
MORF1, 18 mer	5′-TCT-TCT-ACT-TCA-CAA-CTA	native or 3′ biotin conjugated
PO DNA1, 18 mer	5′-TCT-TCT-ACT-TCA-CAA-CTA	native only
PO cc′DNA 36 mer	5′-TAG-TTG-TGA-AGT-AGA-AGA-GGT-GTA-GGA-GTC-GGT-GTT	native and 3′ Cy5.5 conjugated
PS DNA1 18 mer	5′-TCT-TCT-ACT-TCA-CAA-CTA	native and 3′ Iowa Black conjugated
PS cDNA1 18 mer	5′-TAG-TTG-TGA-AGT-AGA-AGA	5′ Cy5.5 conjugated
PS random rDNA1 18 mer	5′-AGA-ATG-ATG-GTT-ATA-AGG	5′ Cy5.5 conjugated
PS random rDNA2 18 mer	5′-ATA-CCA-ACC-GCC-TCC-ACA	5′ Iowa Black conjugated
PS DNA2 18 mer	5′-AAC-ACC-GAC-TCC-TAC-ACC	5′ Iowa Black conjugated
PS cc′DNA 36 mer	5′-TAG-TTG-TGA-AGT-AGA-AGA-GGT-GTA-GGA-GTC-GGT-GTT	native

[a] Complementary DNAs identified as cDNAs, random DNAs identified as rDNAs, DNAs with two complementary regions identified as cc′DNAs.

carbon linker. The oligomer base sequences of this investigation are shown in Table 1. For convenience, the 18 mer sequence was selected as the standard sequence of ongoing pretargeting studies in this laboratory (*13*). The calculated melting temperatures of PO homoduplexes with the 18 mer standard sequence and with the new sequence of this investigation are above 43 °C. The melting temperatures of the PS and MORF duplexes of this investigation are also expected to exceed 37 °C whether native or with fluorophore/quencher attached (*14, 15*). Complementary sequences are designated herein as cDNA or c′DNA and random sequences are designated as rDNAs. The base sequence of both the 36 mer PO and PS DNAs consisted of two complementary regions, an 18 mer sequence complementary to the above standard sequence (i.e., cDNA1) and an additional 18 mer new sequence (i.e., c′DNA2) complementary to that of a new 18 mer PS DNA2 sequence. Therefore, in this article, both the 36 mer PO and PS DNAs are represented as cc′DNAs to illustrate this structure. The new sequence was selected to avoid hairpin formation and to bring the fluorophore/quencher into the proper configuration for quenching after hybridization (Scitools OligoAnalyzer 3.0, Integrated DNA Technologies). The control PS rDNA1 and PS rDNA2 were also 18 mer but with randomized sequences. The 1.0 μm streptavidin-coated polystyrene microspheres had a 3.5 μg/mL biotin binding capacity (Polysciences, Inc., Warrington, PA).

All centrifuge tubes, pipet tips, and PBS buffers were autoclaved before use. The Cy5.5 fluorophore was selected because its emission maximum is at 694 nm and therefore in the near-infrared where light absorbance in tissue reaches a minimum. The Cy5.5 fluorescence can therefore be detected in vivo at subnanomolar concentrations and at depths sufficient for experimental studies in small animals and possibly in patients (*16*−*19*). The Iowa Black RQ dye was selected because it has a broad absorbance spectrum ranging from 500 to 700 nm with peak absorbance at 656 nm and therefore that overlaps the emission spectrum of Cy5.5 such that the emissions of Cy5.5−DNA may be efficiently inhibited (quenched). The Cy5.5 fluorescence was detected using a 615−665 nm excitation filter combined with a 695−770 nm emission bandpass filter on a IVIS 100 optical camera (Xenogen, Alameda, CA). Regions of interest were set and data were analyzed with Living Image software (Xenogen). To reduce autofluorescence, the animals were hairless male SKH-1 (Charles River Breeding Labs, Wilmington, MA) and were fed on a chlorophyll-free diet (AIN-93G Purified Diet, Harlan Teklad, Madison, WI).

Duplex Stability Studies by PAGE. All oligomers for the duplex stability studies were native rather than fluorophore/quencher conjugated and all were prepared at 10 μM concentration. The PAGE Ready Gel 15% TBE gel was purchased (Bio-Rad, Richmond, CA) and run in 1 ×TBE (Tris-borate buffer) at 87 v for 1 h then stained with ethidium bromide (0.5 mg/mL in 1× Tris-borate buffer). The following four duplexes were prepared: PO DNA1/PO cc′DNA; MORF1/PO cc′DNA; MORF1/PS cc′DNA; and PO DNA1/PS cc′DNA. All duplexes were first formed by heating at 90 °C for 10 min before cooling to room temperature. Samples were then incubated in PBS at 37 °C for 2, 4, or 9 h before analysis. For analysis, 1 μL was added to each well. Samples were also incubated in fresh mouse serum by adding 10 μL of each sample to 30 μL of serum followed by incubation at 37 °C for 2 or 4 h before analysis. For analysis, 4 μL was added to each well except for serum alone in which 3 μL was added.

Confirmation of Fluorescence Hybridization Quenching in Vitro. The 18 mer PS Cy5.5 cDNA1 was first added in triplicate to Costar 96 well black polystyrene flat bottom assay plates (Corning Incorporated, Corning, NY) at concentrations of 1, 2, or 5 μM in room-temperature 50 μL PBS (pH 7.4) or 75% fresh mouse serum followed immediately by the addition of the 18 mer PS Iowa Black DNA1 to the wells at different cDNA1:DNA1 molar ratios. Fluorescence intensity was measured over 1.5 h thereafter on the IVIS camera. As control, the identical study was repeated with the random control PS Cy5.5 rDNA1 in place of the study PS Cy5.5 cDNA1. The kinetics of quenching was also measured in 75% fresh mouse serum in wells containing 5 μM PS Cy5.5 cDNA1 to which the PS Iowa Black DNA1 was added at a 1:1 molar ratio.

Before performing imaging studies on animals implanted with microspheres, the ability of PS Iowa Black DNA2 to quench the fluorescence of PO Cy5.5 cc′DNA immobilized on microspheres was established. Streptavidin-coated microspheres (100 μL) were added to a solution of 0.8 nmol of the duplex formed previously between biotin-MORF1 and PO cc′DNA and incubated at room temperature for 30 min. Thereafter the microspheres were separated by centrifugation and washed in PBS/BSA binding buffer three times.

Approximately 20 μL of these microspheres (Cy5.5 concentration 2 μM) were added to each well of the flat bottom assay plate and suspended in 50 μL of PBS/BSA binding buffer. Thereafter, the PS Iowa Black DNA2 was added at different cc′DNA:DNA2 molar ratios followed by agitation to suspend the microspheres. The fluorescence intensity was measured at room-temperature 20 and 60 min later on the IVIS camera, and the results were analyzed by Living Image software as before.

Animal Studies. All animal studies were performed with the approval of the UMMS Institutional Animal Care and Use Committee. For in vivo studies, the identical illumination settings (lamp voltage, filters) were used for all images, and fluorescence emission was normalized to photons per second per centimeter squared per steradian (p/s/cm^2/sr). All data were processed by Living Image 2.50 software (Xenogen). Prior to performing the imaging studies on microsphere implanted animals, the stoichiometry and kinetics of fluorescence hybridization quenching was studied in vivo. In groups of 3 to 4, male SKH-1 mice were injected via a tail vein with either 0.3 nmol (2 μg) or 0.8 nmol (5 μg) of the PS Cy5.5 cDNA1 in 0.1 mL, and thereafter each received via a tail vein either 0.3 nmol, 0.8 nmol or 2.4 nmol of PS Iowa Black DNA1. The molar ratios of Iowa Black DNA1 to Cy5.5 cDNA1 were either 1:1 or 3:1. The animals were then anesthetized using ketamine (90 mg/kg) and xylazine (10 mg/kg) and imaged on the IVIS camera

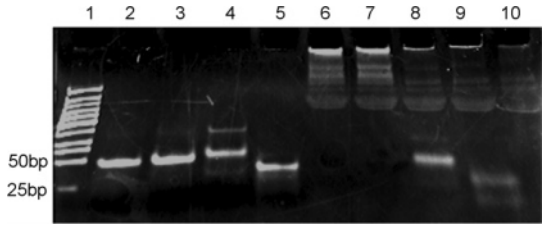


Figure 1. PAGE gel photograph presenting results of stability measurements after 2 h of incubation at 37 °C. Lane 1, low molecular weight DNA ladder; lane 2, PBS incubation of PO DNA1/PS cc′DNA; lane 3, PBS incubation of MORF1/PS cc′DNA; lane 4, PBS incubation of MORF1/PO cc′DNA; lane 5, PBS incubation of PO DNA1/PO cc′DNA; lane 6, serum incubation of PO DNA1/PS cc′DNA; lane 7, serum incubation of MORF1/PS cc′DNA; lane 8, serum incubation of MORF1/PO cc′DNA; lane 9, serum incubation of PO DNA1/PO cc′DNA; lane 10, serum alone.

both in the ventral and dorsal views at various times postinjection while under continuous sedation. All images were acquired with 1 s exposure (f/stop = 2). A large region of interest was set about the whole animal for quantitation.

Approximately 30 μL of the microspheres prepared as described and carrying 0.06 nmol of Cy5.5 were implanted intramuscularly in one thigh of each SKH-1 mice. After 15 min, each animal received either 0.06 nmol ($N = 2$), 0.6 nmol ($N = 2$) or 6.0 nmol ($N = 4$) of the PS Iowa Black DNA2 by iv administration and was imaged in both the dorsal and ventral view immediately thereafter. The fluorescence intensity in a region of interest about both thighs was recorded, and target to nontarget ratios were compared before and after the administration of PS Iowa Black DNA2 with any decrease defined as the quenching efficiency. As a control, one implanted animal received 6.0 nmol of the random Iowa Black rDNA2.

Although the amount of microspheres implanted was identical, the depth of intramuscular implantation varied from animal to animal and resulted in differences in the fluorescence intensity. To correct for absorption and scatter, the fluorescence intensity of all mice but one with implanted PO Cy5.5 cc′DNA microspheres were measured before the PS Iowa Black DNA2 was administrated. The remaining mouse left as a further control did not receive PS Iowa Black DNA2.

RESULTS

Duplex Stability Studies by PAGE. Figure 1 presents a photograph of the 2 h gel showing a molecular weight ladder in lane 1, the results of incubating at 37 °C in PBS in lanes 2 to 5, the results of incubating in serum in lanes 6 to 9 and serum alone in lane 10. The gels obtained in the 4 h incubations in PBS and serum and the 9 h incubation in PBS show the identical trends (data not presented).

As shown, all four duplexes with either the PS or PO cc′DNAs are stable in 37 °C PBS (lanes 2 to 5). In each case, one intense band at about 50 base pairs appears for both homoduplexes and the MORF1/PS cc′DNA heteroduplex. The two weaker bands in the case of the MORF1/PO cc′DNA heteroduplex (lane 4) appeared consistently in all gels.

However, also as shown in the figure, duplex stability in serum compared to PBS is obviously very different. Of the four duplexes, only the MORF1/PO cc′DNA duplex showed evidence of stability at the earliest time point at 2 h (lane 8). This band was weaker although still readily apparent at 4 h. The 9 h gels were equivocal as regards duplex stability (data not presented). The weak bands at low molecular weight in the case of the PO DNA1/PO cc′DNA (lane 9) are probably the result of the nuclease instability of this DNA. Finally, a band is apparent at the loading point in all serum samples, including that of serum alone. However, this band is much more intense in the case of the PS cc′DNA duplexes (lanes 6 and 7) presumably because of the protein binding affinity of this DNA. This analysis therefore cannot exclude the possibility that the duplexes with PS cc′DNA were also stable in serum but remained at the loading point.

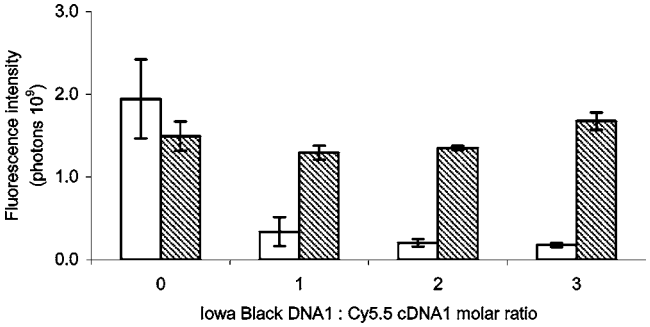


Figure 2. Fluorescence intensity of wells containing 5 μM of the study PS Cy5.5 cDNA1 (open bars) and control PS Cy5.5 rDNA (closed bars) 30 min after the addition of PS Iowa Black DNA1 at different DNA1:cDNA1 molar ratios from 0:1 to 3:1 in PBS buffer. Error bars represent one SD ($N = 3$).

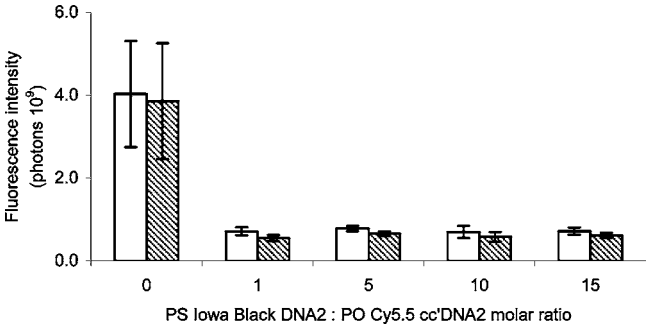


Figure 3. Fluorescence intensity of wells with MORF1/PO Cy5.5 cc′DNA microspheres at 20 min (open bars) and 60 min (hatched bars) following addition of PS Iowa Black DNA2 at 0 to 15 fold molar excess to PO Cy5.5 cc′DNA in PBS/BSA binding buffer. Error bars represent one SD ($N = 3$).

An additional four 18 mer duplexes were also investigated in buffer and in serum: MORF1/PO cDNA1; MORF1/PS cDNA1; PO DNA1/PO cDNA1; PO DNA1/PS cDNA1 (data not presented). The results show once again that at 2 and 4 h of incubation, the MORF1/PO cDNA is stable in serum.

It is possible to conclude from these duplex stability studies that the PO DNA homoduplex with overhang is unstable as expected due to the recognized instability to nucleases of a single chain PO DNAs (*20*, *21*). However nuclease attack on PO DNA, including the single chain overhang, appears to be less effective when hybridized to MORF.

The bead studies described below require streptavidin microspheres to which Cy5.5-conjugated oligomer are bound. Since neither a PO or PS DNA derivitized with both Cy5.5 and a biotin group on opposite ends were commercially available, the results of the above PAGE study provided confidence that microspheres prepared by the addition of biotinylated MORF1 first to the beads followed by addition of PO cc′DNA-conjugated Cy5.5 would be stable.

Confirmation of Fluorescence Hybridization Quenching in Vitro. The histograms of Figure 2 show that the fluorescence in PBS buffer of the PS Cy5.5 cDNA1 was reduced by more than 80% following addition of the PS Iowa Black DNA1 even at the lowest 1:1 cDNA1:DNA1 molar ratio and more than 90% at cDNA1:DNA1 molar ratios 1:2 or higher. This quenching of Cy5.5 fluorescence was not apparent when the Iowa Black was added to the control nonspecific PS Cy5.5 rDNA. The figure

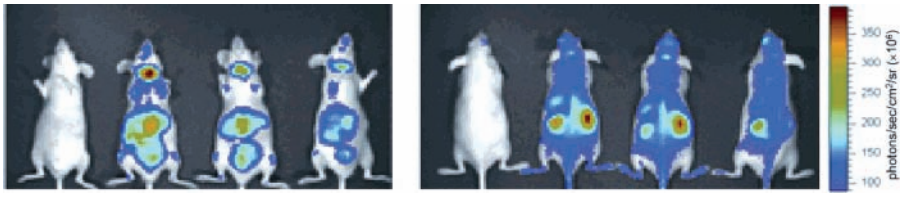


Figure 4. Whole body ventral (left panel) and dorsal (right panel) fluorescent images of SKH-1 mice. From left to right in both panels: blank control, Cy5.5 cDNA1 alone, 1:1 and 3:1 molar ratios of Iowa Black DNA1 to Cy5.5 cDNA1 with 10 min between administrations. Images at 30 min.

presents results ($N = 3$) obtained at 30 min and at the 5 μM concentration of PS Cy5.5 cDNA1.

The kinetics of quenching in wells ($N = 3$) with 5 μM PS Cy5.5 cDNA1 following addition of PS Iowa Black DNA1 at three cDNA1:DNA1 molar ratios from 1:1 to 1:3 showed that under the conditions of this in vitro study, quenching occurred extremely rapidly, reaching more than 80% within 5 min even at cDNA1:DNA1 molar ratio of 1:1 and greater than 90% at higher molar ratios. The quenching was persistent thereafter at least until the end of observation at 90 min. The quenching was found to be equally rapid in serum as well as in buffer (data not presented). Specifically compared to the fluorescence of wells without the Iowa Black, the fluorescence intensity in wells containing 5 μM PS Cy5.5 cDNA1 in 75% serum fell by 73% immediately upon addition of the PS Iowa Black DNA1 at 1:1 molar ratio at room temperature and rose only slightly to 77% and 83% at 8 and 57 min, respectively. However, the quenching efficiency was somewhat reduced in serum over the 80% achieved in buffer under essentially identical experimental conditions.

Figure 3 presents histograms showing that Cy5.5 on the 3′ end of the 36 mer PO cc′ DNA even when tethered via MORF1 to streptavidin-coated microspheres loses 82% of its fluorescence by the addition of Iowa Black DNA2 in PBS/BSA buffer within 20 min at room-temperature even at a 1:1 molar ratio with little change at higher molar ratios or at 60 min ($N = 3$).

Animal Studies. Camera sensitivity was sufficient to provide an acceptable fluorescence image within 10 min following the administration of 0.3 nmol of PS Cy5.5 cDNA1 alone. However following administration of PS Iowa Black DNA1, image quality was markedly superior when 0.8 nmol of PS Cy5.5 cDNA1 was initially administered. Accordingly, the 0.8 nmol dosage of Cy5.5 was selected for subsequent studies.

Figure 4 presents the images obtained in the study of the stoichiometry and kinetics of fluorescence hybridization quenching in vivo and shows both the ventral (left panel) and dorsal (right panel) whole body fluorescence images in animals receiving from left to right: nothing, PS Cy5.5 cDNA1 alone (0.8 nmol), and PS Cy5.5 cDNA1 followed by PS Iowa Black DNA1 at a 1 and 3 fold molar excess 10 min later and imaged 30 min thereafter. The figure shows obvious quenching in both the ventral and dorsal views of PS Cy5.5 cDNA1 fluorescence following administration of PS Iowa Black DNA1. As expected, the quenching is more pronounced following administration of PS Iowa Black DNA1 at a 3-fold molar excess. Fluorescence intensity in these hairless animals fed on a chlorophyll-free diet appears to be concentrated in the kidneys as evident in the dorsal view and in the GI tract and possibly the thyroid as evident in the ventral view. The fluorescence from these and other tissues tended to change over time (data not presented).

The quenching efficiency was determined by subtracting from unity the ratio obtained by dividing the whole body fluorescence intensity of the mice receiving both PS Cy5.5 cDNA1 and PS Iowa Black DNA1 by the fluorescence intensity of the mice receive PS Cy5.5 cDNA1 alone. As shown in Figure 5, when measured in this manner, the quenching efficiency at 20 min postadministration ($N = 3$ in all cases) at a 3 fold molar excess

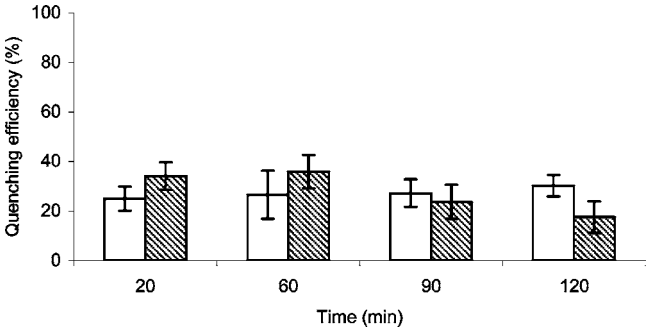


Figure 5. Histograms showing the quenching efficiency in SKH-1 mice receiving iv 0.8 nmol of PS Cy5.5 cDNA1 followed by a 3-fold molar excess of PS Iowa Black DNA1 10 min later. Results presented for both the dorsal view (open bars) and ventral view (hatched bars) obtained between 20 and 120 min thereafter. Error bars represent one SD ($N = 3$).

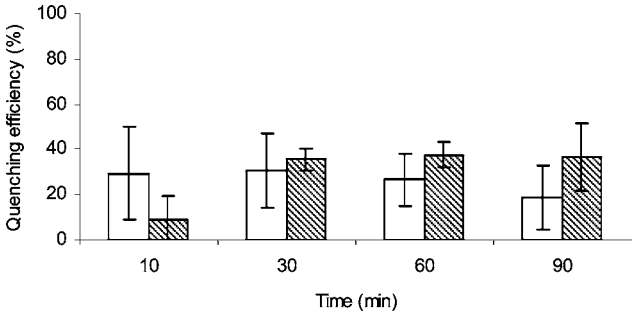


Figure 6. The quenching efficiency 10 to 90 min after iv administration of 6.0 nmol of PS Iowa Black DNA2 in SKH-1 mice implanted with 0.06 nmol PO Cy5.5 cc′DNA microspheres. Results presented for both dorsal view (open bars) and ventral view (hatched bars). Error bars represent one SD ($N = 4$).

of PS Iowa Black DNA1 was 25.0 ± 4.8% (dorsal view) and 34.1 ± 5.6% (ventral view) with little change at 60 min (26.6 ± 9.6% and 35.9 ± 6.7%, respectively).

Thereafter, the streptavidin microspheres carrying 0.06 nmol of biotinylated MORF1/PO Cy5.5 cc′DNA were implanted intramuscularly in one thigh of SKH-1 mice and, after 15 min, each animal received either 0.06 nmol ($N = 2$), 0.6 nmol ($N = 2$), or 6.0 nmol ($N = 4$) of the PS Iowa Black DNA2 by iv administration. One mouse received 6.0 nmol of the random PS Iowa Black rDNA2 as control. The animals were imaged in both the dorsal and ventral view immediately thereafter. The fluorescence intensity of the implanted thigh compared to that of the contralateral thigh was measured, and the decrease in this ratio after administration of the Iowa Black was defined as the percent quenching efficiency as before. Figure 6 presents the results obtained over 90 min in mice receiving 6.0 nmol of the PS Iowa Black DNA2 at a 100-fold molar excess over the PO Cy5.5 ($N = 4$). Lower dosage of Iowa Black DNA2 (10 and 1 fold molar excess) gave an unremarkable quenching effect.

Specifically mice implanted with streptavidin beads binding the 36 mer PO Cy5.5 cc′DNA showed a decrease in target/

nontarget ratio of 27% ± 12% (dorsal view) and 38% ± 6% (ventral view) within 1 h of administration of the 18 mer PS Iowa Black DNA2 but not the Iowa Black rDNA2 random control. When administered at a 100-fold molar excess, the target/nontarget ratio was *increased* 20% (dorsal view) and 14% (ventral view) at 40 min postadministration of the random Iowa Black rDNA2 control. Therefore, despite the barriers to in vivo hybridization including rapid clearance and poor access, the quenching of the tethered Cy5.5 fluorescence was remarkably effective following intravenous administration of the Iowa Black DNA2.

DISCUSSION

To the best of our knowledge, pretargeting and similar applications of optical imaging have not been previously considered especially with linear oligomers. This laboratory recently completed a optical pretargeting study in which microspheres with a 25 mer cMORF were implanted in mice that subsequently received a duplex consisting of a 25 mer Cy5.5-MORF hybridized with a 18 mer BHQ3-PS DNA (*12*). The results of that study confirm that fluorescent conjugated duplexes may be designed to dissociate rapidly in the presence of its target. We report herein on an investigation of the vivo stability of novel duplexes, the sensitivity of detection, the kinetics of hybridization and the pharmacokinetics of in vivo quenching. While these measurements are not directly related to pretargeting and similar applications of optical imaging, the results described herein will be required in the further development of optical imaging with linear duplexes.

Of the eight duplexes between PO DNA, PS DNA, and MORF, gel electrophoresis showed stability only for the MORF/PO DNA and possibly the MORF/PS DNA duplexes following incubations in 37 °C serum for 2 h (Figure 1) and 4 h (data not presented). To measure the kinetics of quenching, the fluorescence intensity of a Cy5.5 conjugated PS DNA was measured in vitro following addition of various molar ratios of Iowa Black conjugated complementary PS cDNA. The quenching was initially found to be essentially completed within 30 min (Figure 2) while a more focused study of kinetics indicated that quenching was completed within several minutes. By contrast no queching was observed if the study Cy5.5 cDNA was replaced with the control Cy5.5 rDNA. Quenching in vivo in mice was also found to be rapid and essentially completed within 20 min (Figure 5).

The most plausible mechanism to explain the fluorescence inhibition of a Cy5.5 conjugated PS DNA following addition of the Iowa Black complementary but not random control DNA is contact fluorescence inhibition following duplex formation. That the quenching and therefore hybidization is rapid is encouraging since rapid kinetics will be required for the in vivo applications contemplated. Rapid hybridization was previously observed in this laboratory by surface plasmon resonance in which a 25 mer Cy5.5 MORF duplexed with an 18 mer BHQ3 DNA was allowed to flow over an immobilized 18 mer PS DNA complementary to the MORF (*12*). Dissociation of the duplex with capture of the MORF was completed in less than 1 min.

Figure 4 presents whole body optical images of mice showing fluorescence inhibition at 30 min after the iv administration of Cy5.5-cDNA1 to mice administered iv Iowa Black-DNA1 10 min earlier. The results presented in Figure 5 show that at 20 min postadministration of Iowa Black DNA1, the quenching efficiency was 25 to 34% depending upon the view, with little change thereafter.

Fluorescence was apparent at all dosages in hairless SKH-1 mice administered iv Cy5.5 cDNA1 alone; however, the administration of 0.8 nmol (5 μg) of the Cy5.5 cDNA1 provided the most intense image. We conclude from these studies that the 0.8 nmol of Cy5.5 cDNA1 fluorescence may be detected with sufficient sensitivity and that the iv administration of 2.4 nmol of Iowa Black DNA1 (i.e., a 3 fold molar excess) provided obvious inhibition, superior to an equamolar administration and superior to the initial administration of 0.3 nmol of Cy5.5 cDNA1. The results confirm that a 0.8 nmol dosage of Cy5.5 cDNA1 provides sufficient fluorescence intensity for subsequent in vivo measurements with the camera used in this investigation, that fluorescence intensity is stable over at least 1 h, and that in vivo quenching of fluorescence occurs rapidly, consistent with the earliest practical times between administrations and imaging.

Having thus established that rapid fluorescence quenching follows hybridization in solution both in vitro and in vivo, we found it necessary to ensure that immobilization does not adversely influence these properties. Since MORF/PO DNA duplexes are stable in serum, an 18 mer PO immobilized microsphere was constructed, consisting of a biotinylated MORF1 added first to the streptavidin-coated bead followed by addition of the 36 mer PO Cy5.5 DNA with two 18 mer complementary regions, one against the standard sequence (i.e., cDNA1) and one against a new sequence (i.e., c′DNA2). Thereafter, the PS conjugated Iowa Black DNA2 quencher complementary to the 18 mer PO overhang of the bead duplex was administered, and the fluorescence intensity was measured. As shown in Figure 3, quenching inhibition in buffer was completed in 20 min or less and with about 82% inhibition at the lowest 1:1 molar ratio despite the immobilization.

Finally, as shown in Figure 6, in mice implanted with the 36 mer PO Cy5.5 cc′DNA microspheres showed a decrease in target/nontarget ratio of 27% (dorsal view) and 38% (ventral view) within 1 h of administration of the 18 mer PS Iowa Black DNA2 but not the Iowa Black rDNA2 random control. The quenching efficiency was therefore remarkable despite the rapid clearance from circulation of the PS Iowa Black DNA2 and the poor accessibility of the subcutaneous microspheres from the circulation.

In conclusion, the results of this proof of concept study show that duplexes of a fluorophore- and a quencher-conjugated linear oligomer can be designed to be sufficiently stable for use in vivo, that fluorescence quenching follows duplex hybridization of Cy 5.5 and Iowa Black conjugated oligomers and that this can be detected in mice at reasonable concentrations, that the hybridization and therefore quenching is rapid whether free or immobilized, and that the quenching is persistent. Future studies will apply the results of this investigation of fluorescent quenching to applications such as optical antisense and pretargeting imaging.

ACKNOWLEDGMENT

Financial support for this investigation was provided in part by the Office of Science, U.S. Department of Energy (DE-FG02-03ER63602) and the National Institutes of Health (CA94994).

LITERATURE CITED

(1) Marras, S. A., Kramer, F. R., and Tyagi, S. (2002) Efficiencies of fluorescence resonance energy transfer and contact-mediated quenching in oligonucleotide probes. *Nucleic Acids Res. 30,* e122.

(2) Liu, G., He, J., Dou, S., Gupta, S., Rusckowski, M., and Hnatowich, D. J. (2005) Further investigations of morpholino pretargeting in mice— establishing quantitative relations in tumor. *Eur. J. Nucl. Med. 32,* 1115−1123.

(3) He, J., Liu, X., Zhang, S., Liu, G., and Hnatowich, D. J. (2005) Affinity enhancement bivalent morpholino for pretargeting: surface plasmon resonance studies of molecular dimensions. *Bioconjugate Chem. 16,* 1098−1104.

(4) Liu, X., Nakamura, K., Wang, Y., Wang, Y., Liu, G., He, J., Ding, H., Lu, P., Rusckowski, M., Kubo, A., and Hnatowich, D. J. (2006)

Initial mechanistic studies of antisense targeting in cells. *J. Nucl. Med. 47*, 360−368.
(5) Tyagi, S., and Kramer, F. R. (1996) Molecular beacons: probes that fluoresce upon hybridization. *Nat. Biotechnol. 14*, 303−308.
(6) Silverman, A. P., and Kool, E. T. (2005) Quenched probes for highly specific detection of cellular RNAs. *Trends in Biotechnol. 23*, 225−230.
(7) Nitin, N., Santangelo, P. J., Kim, G., Nie, S., and Bao, G. (2004) Peptide-linked molecular beacons for efficient delivery and rapid mRNA detection in living cells. *Nucleic Acids Res. 32*, e58.
(8) McIntyre, J. O., Fingleton, B., Wells, K. S., Piston, D. W., Lynch, C. C., Gautam, S., and Matrisian, L. M. (2004) Development of a novel fluorogenic proteolytic beacon for in vivo detection and imaging of tumour-associated matrix metalloproteinase-7 activity. *Biochem. J. 377*, 617−628.
(9) Hoeflich, K. P., Gray, D. C., Eby, M. T., Tien, J. Y., Wong, L., Bower, J., Gogineni, A., Zha, J., Cole, M. J., Stern, H. M., Murray, L. J., Davis, D. P., and Seshagiri, S. (2006) Oncogenic BRAF is required for tumor growth and maintenance in melanoma models. *Cancer Res. 66*, 999−1006.
(10) Molenaar, C., Marras, S. A., Slats, J. C., Truffert, J. C., Lemaitre, M., Raap, A. K., Dirks, R. W., and Tanke, H. J. (2001) Linear 2′ O-Methyl RNA probes for the visualization of RNA in living cells. *Nucleic Acids Res. 29*, E89−9.
(11) Tyagi, S., and Alsmadi, O. (2004) Imaging Native beta-Actin mRNA in motile fibroblasts. *Biophys. J. 87*, 4153−4162.
(12) He, J., Rusckowski, M., Wang, Y., Dou, S., Liu, X., Zhang, S., Liu, G., and Hnatowich, D. J. (2007) Optical pretargeting of tumor with fluorescent MORF oligomers. *Mol. Imaging Biol. 9*, 17−23.
(13) Liu, G., He, J., Dou, S., Gupta, S., Vanderheyden, J. L., Rusckowski, M., and Hnatowich, D. J. (2004) Pretargeting in tumored mice with radiolabeled morpholino oligomer showing low kidney uptake. *Eur. J. Nucl. Med. Mol. Imaging 31*, 417−424.
(14) Zhang, Y., He, J., Liu, G., Vanderheyden, J. L., Gupta, S., Rusckowski, M., and Hnatowich, D. J. (2004) Initial Observations of 99mTc-labeled Locked Nucleic Acids for Antisense Targeting. *Nucl. Med. Commun. 25*, 1113−1116.
(15) Moreira, B. G., You, Y., Behlke, M. A., and Owczarzy, R. (2005) Effects of fluorescent dyes, quenchers, and dangling ends on DNA duplex stability. *Biochem. Biophys. Res. Commun. 327*, 473−484.
(16) Weissleder, R., Tung, C. H., Mahmood, U., and Bogdanov, A. Jr. (1999) In vivo imaging of tumors with protease-activated near-infrared fluorescent probes. *Nat. Biotechnol. 17*, 375−378.
(17) Petrovsky, A., Schellenberger, E., Josephson, L., Weissleder, R., and Bogdanov, A. Jr. (2003) Nearinfrared fluorescent imaging of tumor apoptosis. *Cancer Res. 63*, 1936−1942.
(18) Ke, S., Wen, X., Gurfinkel, M., Charnsangavej, C., Wallace, S., Sevick-Muraca, E. M., and Li, C. (2003) Near-infrared optical imaging of epidermal growth factor receptor in breast cancer xenografts. *Cancer Res. 63*, 7870−7875.
(19) Chen, X., Conti, P. S., and Moats, R. A. (2004) In vivo near-infrared fluorescence imaging of integrin alphavbeta3 in brain tumor xenografts. *Cancer Res. 64*, 8009−8014.
(20) Tidd, D. M., and Warenius, H. M. (1989) Partial protection of oncogene, anti-sense oligodeoxynucleotides against serum nuclease degradation using terminal methylphosphonate groups. *Br. J. Cancer 60*, 343−350.
(21) Shaw, J. P., Kent, K., Bird, J., Fishback, J., and Froehler, B. (1991) Modified deoxyoligonucleotides stable to exonuclease degradation in serum. *Nucleic Acids Res. 19*, 747−750.

BC070021J

A New, Simple Method for Linking of Antibodies to Atomic Force Microscopy Tips

Andreas Ebner,[†] Linda Wildling,[†] A. S. M. Kamruzzahan,[†] Christian Rankl,[†] Jürgen Wruss,[‡] Christoph D. Hahn,[†] Martin Hölzl,[†] Rong Zhu,[†] Ferry Kienberger,[†] Dieter Blaas,[‡] Peter Hinterdorfer,[†] and Hermann J. Gruber*[,†]

Institute of Biophysics, J. Kepler University, Altenberger Strasse 69, A-4040 Linz, Austria, and Max F. Perutz Laboratories, Institute of Medical Biochemistry, Dr. Bohr Gasse 9/3, Medical University of Vienna, Vienna A-1030, Austria. Received January 25, 2007; Revised Manuscript Received March 5, 2007

Functionalization of atomic force microscope (AFM) tips with bioligands converts them into monomolecular biosensors which can detect complementary receptor molecules on the sample surface. Flexible PEG tethers are preferred because the bioligand can freely reorient and locally palpate the sample surface while the AFM tip is moved along. In a well-established coupling scheme [Hinterdorfer et al. (1996) *Proc. Natl. Acad. Sci. U.S.A. 93*, 3477−3481], a heterobifunctional PEG linker is used to tether thiol-containing bioligands to amino-functionalized AFM tips. Since antibodies contain no free thiol residues, prederivatization with *N*-succinimidyl 3-(acetylthio)-propionate (SATP) is needed which causes a relatively high demand for antibody. The present study offers a convenient alternative with minimal protein consumption (e.g., 5 μg of protein in 50 μL of buffer) and no prederivatization, using a new heterobifunctional cross-linker that has two different amino-reactive functions. One end is an activated carboxyl (*N*-hydroxysuccinimide ester) which is much faster to react with the amino groups of the tips than the benzaldehyde function on its other end. The reactivity of the latter is sufficient, however, to covalently bind lysine residues of proteins via Schiff base formation. The method has been critically examined, using biotinylated IgG as bioligand on the tip and mica-bound avidin as complementary receptor. These experiments were well reproduced on amino-functionalized silicon nitride chips where the number of specifically bound IgG molecules ($\sim$2000 per μm^2) was estimated from the amount of specifically bound ExtrAvidin-peroxidase conjugate. For a bioscientific application, human rhinovirus particles were tethered to the tip, very-low-density lipoprotein receptor fragments were tethered to mica, and the specific interaction was studied by force microscopy.

INTRODUCTION

Atomic force microscopy (AFM[1]) can operate in aqueous solution under physiological conditions (*1*) and reveal fine details not resolved by electron microscopy (*2*). AFM is thus well suited for structural analysis of biomolecules and their assemblies (*1, 3*). In addition, the AFM tip can be upgraded into a monomolecular biosensor by coupling of a "ligand" molecule which is moved over the sample surface and recognized by complementary "receptor" molecules on the sample surface, yielding a map of recognition sites (*3, 4*). Binding is detected as a rupture event which is sensed by a vertically oscillated cantilever (*5*), preferably under simultaneous monitoring of sample topography (*6*−*8*). Moreover, fine biophysical and structural details of biomolecular interactions are obtained when measuring the unbinding forces at different force loading rates (*9*), interaction time before dissociation (*10*), biochemical modifications, and coassociation of third components (*11*), or with different mutants or truncated forms of the participating proteins (*12*).

Linear PEG chains have frequently been used to attach one or few sensor molecules to an AFM tip because the PEG itself is chemically and physically inert and it allows for rapid and free reorientation of the sensor molecule when the AFM tip approaches the surface (*6*−*8, 10*−*31*). Thus, even a single sensor molecule on the tip can recognize its cognate molecule on the target surface with up to 25% probability in one force−distance cycle with 100−800 nm vertical range and 1 s cycle time (*26*). Moreover, the nonlinear stretching behavior of the PEG tether helps to discriminate biospecific interactions from nonspecific tip−sample adhesion (*19, 21, 26*).

Small ligand molecules (exemplified by biotin or fluorescein) are usually first attached to the PEG linker before the ligand−PEG conjugate is attached to an amino-functionalized AFM tip (*8, 15, 26, 28, 32*). Flexible tethering of proteins to AFM tips, however, has always been performed by a three-step procedure, in which (i) reactive amino groups (*15, 25, 26, 33*) or thiol functions (*12, 18, 27*) are generated on the tip surface, (ii)

* To whom correspondence should be addressed. Tel.: +43 (732) 2468-9271. Fax: +43 (732) 2468-9270. E-mail: hermann.gruber@jku.at.

[†] J. Kepler University.

[‡] Medical University of Vienna.

[1] Abbreviations: AFM, atomic force microscope (or microscopy); aldehyde-PEG-COOH, see Figure 2; aldehyde-PEG-NHS, see Figure 2; biotin-cap-NHS, *N*-succinimidyl 6-(*N*-biotinoyl)-aminohexanoate; DMSO, dimethyl sulfoxide; EDTA, ethylenediamine *N,N,N′,N′*-tetraacetic acid; EGTA, ethylene glycol-bis(2-aminoethyl ether)-*N,N,N′,N′*-tetraacetic acid; ELISA, enzyme-linked immunosorbent assay; HBS, HEPES-buffered saline; HBS-Ca, HBS with 2 mM $CaCl_2$; HRV2, human rhinovirus serotype 2; MBP, maltose-binding protein; NH_2-PEG-NH_2, *O,O′*-bis(2-aminopropyl)-poly(ethylene glycol) 800; NH_2-PEG-COOH, *N*-glutaryl derivative of NH_2-PEG-NH_2, see Figure 2; NHS, *N*-hydroxysuccinimide; pdf, probability density function; PBS, phosphate-buffered saline; PDP, 3-(2-pyridyl)-dithiopropionyl group; PDP-PEG-NHS, see Figure4S in the Supporting Information; PEG, poly(ethylene glycol); SATP, *N*-succinimidyl 3-(acetylthio)-propionate; TBS, Tris-buffered saline; TBS-Ca, TBS with 2 mM $CaCl_2$; TSTU, *N,N,N′,N′*-tetramethyl(succinimidyl)uronium tetrafluoroborate; VLDL, very-low density lipoprotein; VLDLR, VLDL receptor; VLDLR1-8, the extracellular fragment of human VLDLR fused with MBP (N-terminus of VLDLR1-8) and His_6 peptide (C-terminus of VLDLR1-8).

10.1021/bc070030s CCC: $37.00 © 2007 American Chemical Society
Published on Web 05/22/2007

these are reacted with one end of the PEG linker, and (iii) the protein is coupled to the free PEG end (*6, 7, 10−14, 16−27, 30, 31*).

The heterobifunctional cross-linker most widely used for tip−PEG−protein linking is PDP-PEG-NHS (*6, 7, 10, 13, 16, 17, 19−24, 30, 31*). Its NHS ester function forms a stable amide bond with an amino group on the AFM tip and subsequently its pyridyldithiopropionyl (PDP) group reacts with a protein thiol, resulting in a disulfide linkage between PEG and protein (see Figure 6S in the Supporting Information). Use of this method is appropriate if the protein of interest contains a free thiol group (e.g., in case of $F_{ab'}$ or half antibodies, see ref 24). Most extracellular proteins (e.g., antibodies), however, possess no free thiol group, requiring artificial thiol functions to be introduced, e.g., with SATP (see Figure 6S in the Supporting Information). The procedure for SATP derivatization is quick and simple, however, unreacted SATP must rigorously be removed to ensure coupling of SATP-derivatized antibody, rather than of free SATP, to the AFM tip (*19*). Consequently, gel filtration must be used for removal of free SATP which cannot be done at a small scale such that 0.2−0.5 mg of antibody are required per batch. Moreover, refreezing of the modified protein is undesirable because of its low concentration after gel filtration.

The need for prederivatization of nonthiol proteins is eliminated if the tip is grafted with PEG chains carrying amino-reactive functions at their free ends. This allows for reaction with lysine residues which are abundant in most proteins. As an example, human antibodies have been shown to contain 80−90 lysines (*34*). Two different methods have been reported in which the tip-bound PEG still carries an NHS-ester function that can couple lysine residues. In the first method, the tip is prefunctionalized with a critically adjusted low density of amino groups which ensures that NHS-PEG-NHS (i.e., the bis-NHS ester of a PEG dicarboxylic acid) cannot form loops with two adjacent amino groups, thereby sparing one of the two NHS ester functions for protein coupling (*25, 35*). In the second method, a tip with a high area density of thiol functions is reacted with maleimide-PEG-NHS, expecting thioether formation between thiol and maleimide to predominate over thioester formation between thiol and NHS ester for kinetic reasons (*12, 18*). In this respect it is fortunate that maleimide−thiol coupling is exceptionally fast ($k \leq 10^5$ M^{-1} min^{-1}, see ref 36) because thiol groups are prone to react not only with maleimides but with the NHS ester functions as well, being much better nucleophiles than amino groups which are the typical targets of NHS esters. Probably the high lateral density of thiol groups on the tip ensured that a sufficient number of PEG linkers was unilaterally bound with the maleimide function only, even if a sizable fraction of PEGs may have been bound via both end groups.

The two above-described methods (with NHS-PEG-NHS or maleimide-PEG-NHS) have in common that both ends of the cross-linker have a considerable reactivity for the reactive groups on the tip surface (amine or thiol, respectively) and that the relative extent of desired univalent coupling as compared to undesired bivalent coupling of PEG on the tip is dependent on the lateral density of reactive groups on the tip, as well as on the length of the chosen PEG linker. Such interdependence of the experimental parameters is avoided if only one end of the PEG linker can react with the reactive groups on the tip surface. This requirement seems particularly difficult to fulfill if the PEG tether should react with amino groups on the tip surface and with amino functions on the protein. Nevertheless this situation is quite typical because most tip functionalization methods utilize amino groups (*8, 15, 26, 28, 32*) and because lysines are the most general coupling functions on proteins.

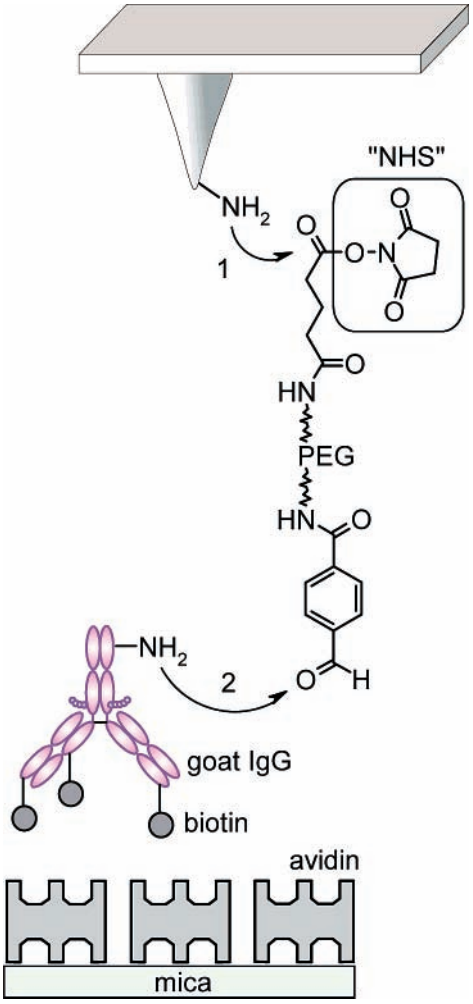


Figure 1. Schematic representation of the testing system for tip−antibody linking via lysine−aldehyde coupling. In the first step (in organic solvent), the NHS-ester of aldehyde-PEG-NHS reacts with the amino groups on the tip, while in the second step (in aqueous buffer), one of the antibody's lysines forms a Schiff base with the aldehyde function on the free end of the cross-linker. The Schiff base is reduced by $NaCNBH_3$ to form an irreversible bond (not shown). When brought into contact with avidin-covered mica, the biotin residues on the model antibody show reversible binding to, and unbinding from, immobilized avidin.

The present study ventured to solve this nontrivial problem by a newly synthesized heterobifunctional PEG linker (aldehyde-PEG-NHS, see Figure 1). Its NHS ester function has a much higher reactivity for amino groups than its benzaldehyde terminus, as previously observed with the short homologue (the NHS ester of formylbenzoic acid, see ref 37). Consequently, the reaction of aldehyde-PEG-NHS with an amino-functionalized tip yields a high number of tip-bound PEGs with intact benzaldehyde functions. The latter provide for easy and robust coupling of unmodified nonthiol proteins, as demonstrated below by quantitative analysis of AFM test experiments, as well as of surface functionalization performed on silicon nitride chips.

EXPERIMENTAL PROCEDURES

Materials. Analytical grade materials were used as long as they were commercially available. The starting materials were of highest available purity. NH_2-PEG-COOH was synthesized as described (*27*). *N*-Succinimidyl 4-formylbenzoate was synthesized similarly as described (*37*) (see Supporting Information). As shown in Figure 2, aldehyde-PEG-NHS was synthesized by reaction of *N*-succinimidyl 4-formylbenzoate with NH_2-PEG-COOH, followed by conversion of the terminal carboxyl

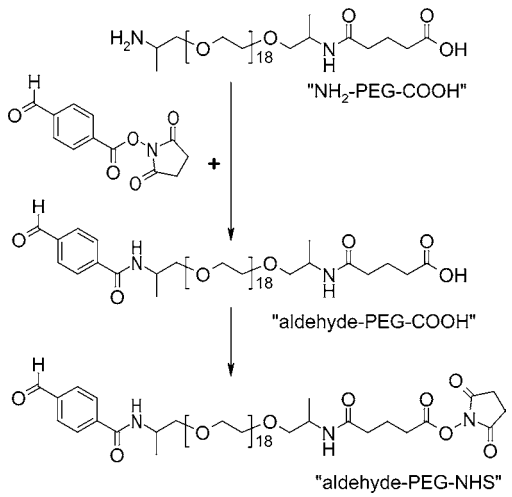


Figure 2. Synthesis of aldehyde-PEG-NHS. In the first step, NH_2-PEG-COOH (*27*) was reacted with *N*-succinimidyl 4-formylbenzoate in chloroform/triethylamine. In the second step, the terminal carboxyl was activated with TSTU in DMF/pyridine (*26*). The PEG chain length was not uniform but the chain length distribution was relatively narrow ($n = 18 \pm 2$), as determined by mass spectrometry (*26*).

function into an NHS ester (see Supporting Information). Muscovite mica sheets were supplied by Christiane Gröpl (Austria). Si_3N_4 measuring tips were bought from Veeco (Santa Barbara, CA) and Si_3N_4 chips from Wacker-Chemitronic GmbH (Germany). Biotin−IgG and biotin−IgG−SATP were prepared by derivatization of goat IgG with biotin−cap-NHS (and SATP), as described before (*19*). HRV2 viral particles (in HBS, 150 mM NaCl, 25 mM HEPES−NaOH, pH 7.4) were prepared by a published procedure (*38*). VLDLR1-8, an extracellular fragment of the human VLDL receptor, fused to MBP on the N-terminus and to His_6 peptide on the C-terminus, was produced as reported before (*39*). The latter was dialyzed to exchange TBS-Ca (150 mM NaCl, 2 mM $CaCl_2$, 25 mM Tris-HCl, pH 7.4) for HBS-Ca (150 mM NaCl, 2 mM $CaCl_2$, 25 mM HEPES−NaOH, pH 7.4) and thus to avoid the undesired reaction of Tris base with surface-bound aldehyde linkers.

Functionalization of AFM Tips with PEG Linkers and Antibodies or Virus Particles. AFM tips (Si_3N_4) were amino-functionalized as described before (*26*), using the room-temperature method for reaction with ethanolamine hydrochloride (see also Supporting Information). Attachment of aldehyde-PEG-NHS was performed by incubating the tip for 2 h in 0.5 mL of chloroform containing 6.6 mg/ mL of aldehyde-PEG-NHS and 0.5% (v/v) of triethylamine. After rinsing with chloroform, the tip was stored in an argon-filled desiccator for less than 5 days. For coupling of antibody, 40 μL of biotin−IgG (2.2 mg/mL) was mixed with 380 μL of buffer A (100 mM NaCl, 50 mM NaH_2PO_4, 1 mM EDTA, pH 7.5, adjusted with NaOH) and 8 μL of 1 M $NaCNBH_3$ (freshly prepared by dissolving 32 mg of $NaCNBH_3$ in 500 μL of 10 mM NaOH). Tips with aldehyde-PEG linkers were immersed in this solution for 1 h, washed in buffer A (2 ×) and PBS (2 ×), and stored in PBS at 4 °C until used (up to 3 days). The procedure for covalent binding of virus particles to the aldehyde termini of tip-linked PEG chains was similar (see Supporting Information for details).

Monitoring of Single Unbinding Events between Tip-Bound Biotin−IgG and Mica-Bound Avidin by AFM. Avidin (1 mg/mL in PBS, 150 mM NaCl, 5 mM NaH_2PO_4, pH 7.4, adjusted with NaOH) was diluted with 9 volumes of water and adsorbed to freshly cleaved mica. After 15 min, the substrate was extensively rinsed (25 ×) with a 1/9 mixture of PBS and water and imaged in PBS. Force measurements with biotin−IgG-functionalized AFM tips were performed in the fluid cell of a commercial AFM (Pico-SPM, Molecular Imaging, Phoenix, AZ) using a Nanoscope IIIA controller (Digital Instruments, Santa Barbara, CA). Force−distance cycles were recorded at a 1 Hz vertical scan rate and 300 nm *z*-amplitude. The measurements were done in PBS at a constant trace and retrace velocity of 600 nm/s. The spring constants of the levers were determined by the thermal noise method (*40, 41*).

Functionalization of Silicon Nitride Chips with Amines, PEG Linkers, and Biotin−IgG−SATP, and Quantitative Assay for Chip-Bound Biotin−IgG−SATP. Silicon nitride chips were precut, weighed for calculation of the effective surface area, precleaned, and amino-functionalized in a DMSO solution of ethanolamine hydrochloride (16 h), using the room-temperature method (*26*). After washing in DMSO (3×) and ethanol (3×), the chips were dried with nitrogen gas and derivatized with aldehyde-PEG-NHS exactly as described above for AFM tips. After binding of the PEG linkers, the chips were washed in chloroform (3 ×), dried with nitrogen, and placed in a polystyrene petri dish. Biotin−IgG (3.2 mg/mL) was mixed with buffer A and with 1 M $NaCNBH_3$ reagent (see above) to adjust to final concentrations of 0.5 mg/mL for biotin−IgG and of 20 mM for $NaCNBH_3$. A 50 μL aliquot of this solution was pipetted onto the surface of each chip. The petri dishes were covered with lids and incubated at room temperature for 60 min. The chips were removed and washed in buffer A (3 × 10 min) and PBS (3 × 10 min). The surface density of biotin−IgG bound to the silicon nitride chips was determined by specific binding of ExtrAvidin-peroxidase, as described before (*19, 26*).

Monitoring of Single Unbinding Events between Tip-Bound Virus Particles and Mica-Bound VLDL Receptor Fragments. Mica was treated with ethanolamine hydrochloride in DMSO to introduce amino functions (*42*). All further steps (reaction with aldehyde-PEG-NHS and coupling of VLDLR1-8) were analogous to the functionalization of AFM tips with aldehyde-PEG-NHS and biotin−IgG (see above) or virus particles (see Supporting Information for details). Unbinding events were measured in HBS-Ca. The specific interaction between virus and receptor protein was blocked by perfusion of the AFM measuring cell with HBS containing 1 mM EGTA instead of 2 mM $CaCl_2$.

RESULTS AND DISCUSSION

Synthesis of Aldehyde-PEG-NHS. The synthesis of aldehyde-PEG-NHS was analogous to that of other AFM-related cross-linkers (*26, 27*). The general precursor NH_2-PEG-COOH was first acylated with *N*-succinimidyl 4-formylbenzoate, yielding "aldehyde-PEG-COOH" (see Figure 2). Fortunately, the main product was indeed the amide conjugate shown in Figure 2 and not a Schiff base adduct of the formyl group with the amino group of NH_2-PEG-COOH. From this we conclude that under the reaction conditions (i.e., in chloroform/triethylamine) the kinetics of amide bond formation was much faster than that of Schiff base formation. Admittedly, the latter may also have occurred to a minor extent, since small amounts of side products were formed which could not be removed by gel filtration, neither in water (on Sephadex G-25) nor in organic solvent (on Sephadex LH-20). These were removed by a multistep extraction procedure (see Supporting Information). Subsequently, the carboxyl of aldehyde-PEG-COOH was activated as NHS ester to give the heterobifunctional cross-linker aldehyde-PEG-NHS (see Figure 2).

Recognition Force Spectroscopy with AFM Tip-Bound Biotin−IgG and Mica-Bound Avidin. In a preceding study, tip−PEG−protein linking via PDP-PEG-NHS was studied in detail, using biotinylated IgG in place of a specific antibody and avidin in place of an antigen (*19*). As a consequence, we could take advantage of the well-known rupture force of the

Table 1. Critical Test for the Specific Role of the Biotin Residues on TIP-Bound IgG[a]

tip number	tip functionalization	recognition, %
1	biotin−IgG	4
2	biotin−IgG	13
3	biotin−IgG	15
4	IgG	0
5	IgG	1
6	IgG	2

[a] Three measuring tips were functionalized with ethanolamine hydrochloride, aldehyde-PEG-NHS, and biotin−IgG as depicted in Figure 1. For control purposes, another three tips were functionalized in the same way, except for using unlabeled goat IgG in the third step. All tips were subsequently tested in the AFM for specific recognition of avidin on mica. Each tip was tested in five different locations, performing 999 force−distance cycles on each site. The fraction of force−distance cycles containing specific unbinding events was calculated for each tip. AFM experiments and data evaluation were done by a person not knowing which tip carried biotin−IgG or unlabeled IgG.

avidin−biotin bond (*15, 19, 26, 43−45*), of specific block with minute concentrations of D-biotin, and of the ease of avidin immobilization on bare mica (*8, 19, 26*). Biotin−IgG was prepared by statistic labeling with ∼5 biotin residues per IgG, and in addition ∼5 protected thiol groups were attached per IgG to provide for disulfide coupling to tip-bound PEG (see Figure 6S in the Supporting Information). In the present study, the same model system as before (*19*) was used to establish tip−PEG−protein coupling via aldehyde-PEG-NHS (see Figure 1); the essential difference was the omission of SATP for prederivatization of biotin−IgG.

Biotin−IgG was covalently tethered to AFM tips via aldehyde-PEG-NHS, as shown in Figure 1. The procedure consisted of three steps. First, amino groups were introduced as usual, i.e., by reaction of surface silanol groups with ethanolamine hydrochloride (*26*). Second, these amino groups were reacted with aldehyde-PEG-NHS, expecting to form amide bonds between an amino group on the tip and the "carboxy termini" of the PEG linkers while avoiding the undesired reaction of the aldehyde functions with the amino groups on the AFM tip. This reaction was analogous to the reaction of *N*-succinimidyl 4-formylbenzoate with NH_2-PEG-COOH (also in chloroform/triethylamine, first step in Figure 2) which had mainly resulted in the amide conjugate. Such analogy alone, however, was regarded insufficient to ensure complete suppression of Schiff base formation with amino groups on AFM tips. We were afraid that the free aldehyde end of the initially formed product ("aldehyde-PEG-CO-NH-tip") might still react with an adjacent amino group on the tip, forming a bivalently bound PEG linker that would have been refractive to further conjugation of protein. In order to minimize the extent of such PEG loop formation on the surface, we applied a much higher PEG linker concentration (6.6 mg/mL) than with PDP-PEG-NHS (1 mg/mL) in order to speed up surface grafting by amide bond formation as compared to loop formation. This notion was supported by the finding that tip functionalization with 1 mg/mL of aldehyde-PEG-NHS gave unsatisfactory results (data not shown) while, after reaction at 6.6 mg/mL, amino-functionalized AFM tips and silicon nitride chips were regularly seen to couple protein (*14*), as exemplified in Tables 1 and 2 (see below).

Tips with such PEG-linked biotin−IgG were tested for function by repeated approach to, and retraction from, a dense monolayer of avidin on mica (see Figure 1) while measuring the repulsive and attractive forces, as described in detail in our preceding studies (*19, 26, 27*). Typical results are shown in Figure 3. Panel A shows a force−distance cycle with a small adhesion event (at ∼1 nm tip−mica distance) and a specific unbinding event (at ∼20 nm tip−mica distance), exhibiting unbinding forces of ∼33 pN and ∼52 pN. The gradual downward deflection of the cantilever within $2 < x < 20$ nm and the sudden cantilever relaxation at $x > 20$ nm obviously reflect specific binding of tip-tethered biotin−IgG to mica-bound avidin, for the following reasons: (i) The nonlinear force−distance profile is very characteristic for the nonlinear elasticity of the PEG tether between tip and biotin−IgG (*21*). (ii) The tip−mica distance of ∼20 nm at the moment of rupture is explained by the length of the PEG tether (6−8 nm, see ref 26), the length of IgG (∼15 nm), and the height of avidin (∼4 nm), taking into account that the position of PEG attachment on IgG and on the tip is not defined and not known. (iii) The unbinding force of ∼52 pN is in good agreement with the values previously measured at similar force loading rates (*15, 19, 26, 43−45*). (iv) When the avidin molecules on the mica surface were blocked with D-biotin (0.1 mg/mL), the chance of observing traces like that in panel A was dramatically reduced (see below). Instead, almost all traces were as shown in panel B. Panel C shows the unbinding force distributions measured in absence (solid line) or presence of D-biotin (dotted line). In the absence of D-biotin, 131 out of 990 force−distance cycles showed typical avidin−biotin unbinding events (analogous to the virus−receptor unbinding event in Figure 5B, see below) corresponding to a binding probability of 13.2%. The force distribution of these avidin−biotin bond ruptures shows force maxima at ∼50, ∼100, and ∼150 pN. The same phenomenon had previously been observed when biotin−IgG−SATP had been tethered to AFM tips via PDP-PEG-NHS (*19*), and it obviously reflects the simultaneous binding/unbinding of one, two, or three biotin residues which are covalently linked to a single IgG molecule (see ref *19*).

Table 1 shows a comprehensive data set acquired with six different cantilevers functionalized as depicted in Figure 1. Three of the cantilevers were functionalized with biotin−IgG and assigned the numbers 1−3, the other three with unlabeled IgG and assigned the numbers 4−6 (see first two columns of Table 1). Each tip was tested for specific recognition by performing 999 force−distance cycles each on five different locations of avidin-covered mica, and the number of force−distance cycles containing a typical unbinding event was evaluated as described (*46*). As can be seen from Table 1, the tips with biotin−IgG showed much higher binding probabilities than the control tips which had been functionalized with unlabeled goat IgG. This finding agrees with the conclusion from Figure 2 that the large majority of unbinding curves derived from specific avidin−biotin interactions, as previously seen after tip functionalization with biotin−PEG-NHS (*26*) or PDP-PEG-NHS plus biotin−IgG−SATP (*19*).

Imitation of AFM Tip Functionalization by Functionalization of Silicon Nitride Chips for Semiquantitative Analysis of Efficiency. In our preceding model study on the sequential functionalization of AFM tips with ethanolamine, PDP-PEG-NHS, and biotin−IgG−SATP (see Figure 6S in the Supporting Information for illustration), the AFM data were complemented with parallel macroscopic experiments in which silicon nitride chips (same material as the tips) were functionalized by the same three-step protocol (*19*). The chip-bound biotin−IgG molecules were then quantified with the help of a conjugate between avidin and a marker enzyme (ExtrAvidin-peroxidase), similar as in other solid-phase assays such as ELISA. By analogy, we have now reacted amino-functionalized silicon nitride chips with aldehyde-PEG-NHS and subsequently coupled biotin−IgG via Schiff base formation, thereby simulating AFM tip functionalization (see Figure 1) on a macroscopic scale (see Figure 7S in the Supporting Information for a schematic illustration of these steps, as well as of the quantitation of bound IgG).

The number of covalently bound probe molecules (biotin−IgG) per μm^2 was estimated from the number of subsequently

Table 2. Tethering of Antibodies to Silicon Nitride Chips via PEG Linkers[a]

linker type	[linker] (mg/mL)	antibody	total sites (μm^{-2})	nonspecific sites (μm^{-2})	specific sites (μm^{-2})
PDP-PEG-NHS	1	biotin−IgG−SATP	2100 ± 300	130	2000 ± 400
PDP-PEG-NHS	1	biotin−IgG	130 ± 40	120	0 ± 100
aldehyde-PEG-NH S	1	biotin−IgG	2000 ± 200	190	1800 ± 300

[a] The chip surface was amino-functionalized with ethanolamine hydrochloride (room-temperature method, see ref 26) and reacted with the NHS-ester function of PDP-PEG-NHS (see Figure 6S in the Supporting Information) or of aldehyde-PEG-NHS (see Figure 1). For coupling of protein, the chips were incubated in aqueous solutions of biotin−IgG−SATP (pretreated with 50 mM hydroxylamine to unmask the protected thiol functions) or biotin−IgG (in presence of 20 mM $NaCNBH_3$) and washed. the number of biotinylated IgG molecules per μm^2 surface was estimated from the amount of bound ExtrAvidin-peroxidase, measured in the absence (total sites) or presence (nonspecific sites) of free D-biotin.

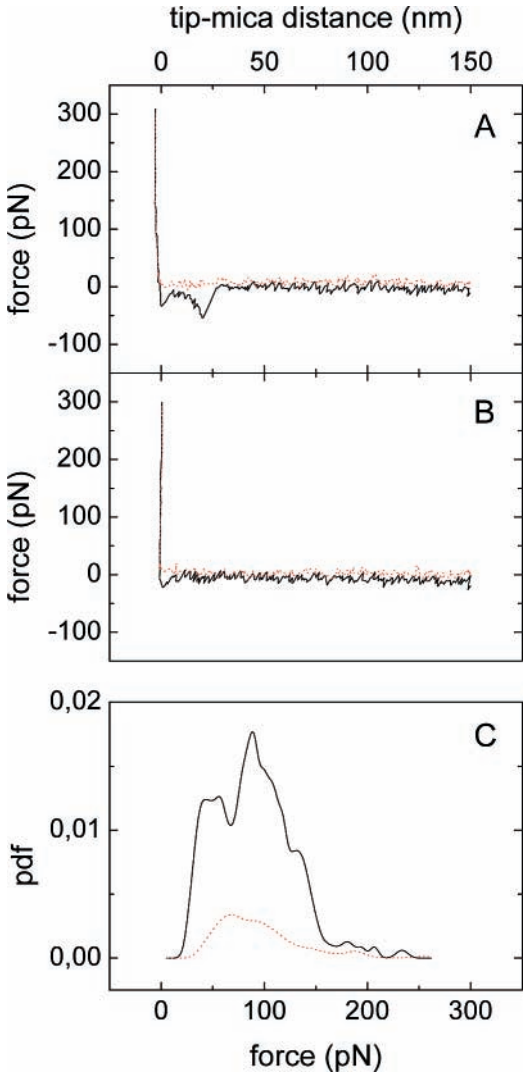


Figure 3. Force measurements of single avidin−biotin interactions. The amino-functionalized tip was derivatized with aldehyde-PEG-NHS and biotin−IgG, and avidin was irreversibly adsorbed to mica, as shown in Figure 1. The piezo movement in the approach-and-retraction cycles was ± 300 nm in 1 s, the force constant of the cantilever was 45 pN/nm, and the loading rate at unbinding was calculated as 2.7 nN/s, taking into account PEG elasticity at 50−100 pN pulling force (*21*). (A) Example of a force−distance cycle showing specific avidin−biotin unbinding in the absence of d-biotin. Unbinding occurred at a rupture force of 52 pN and at a tip−mica distance of 20 nm. (B) Example of a force−distance cycle performed in the presence of free D-biotin (0.1 mg/mL). (C) Probability density function (pdf) of the unbinding forces observed in 174 out of 705 force−distance cycles (solid line, 24.6% binding probability). In the presence of free D-biotin, only 80 out of 1767 force−distance cycles appeared to reflect specific binding (dotted line, 4.5% binding probability).

bound ExtrAvidin-peroxidase molecules, determined and calculated as described in detail in the previous study (*19*). Parallel controls were performed in which ExtrAvidin-peroxidase was blocked with excess of D-biotin in order to determine nonspecific adsorption of ExtrAvidin-peroxidase to the chip surface. As can be seen in Table 2, the extent of nonspecific adsorption (column 5) was very low in comparison to total binding in absence of D-biotin (column 4); thus, the number of specific binding sites (last column) could be estimated with confidence.

The data set in Table 2 was obtained with one batch of chips that had been amino-functionalized together in the same beaker to ensure the same amino group surface density. In addition, further reaction of all chips in lines 1 and 2 of Table 2 with PDP-PEG-NHS was done in a single batch, and the same applies to reaction with aldehyde-PEG-NHS in line 3. In this way the differences between line 1 and line 2 (∼2000 versus ∼0 IgG molecules per μm^2) are clearly attributed to the presence or absence of *S*-acetyl thiopropionyl residues on IgG (see Figure 6S for illustration); in other words, PDP-terminated PEG can only couple proteins which carry free thiol residues. In contrast, chips functionalized with aldehyde-PEG-NHS (see Figure 1) were able to couple biotin−IgG that had not been prederivatized with SATP, i.e., proteins without free thiol residues.

Mechanism of Schiff Base Formation between Protein and Aldehydes on PEG Tethers. The aldehyde function on the free termini of surface-linked PEG chains showed the same coupling efficiency with biotin−IgG as did surface-linked PEG-PDP tentacles with biotin−IgG−SATP (see last column in Table 2). In our preceding study we have shown that the observed efficiency of biotin−IgG−SATP coupling can only be understood by invoking preadsorption of IgG molecules next to surface-bound PEG-PDP chains because in absence of such preadsorption the disulfide coupling step should have taken several months, rather than the actually observed 1−2 h when working at <1 μM biotin−IgG−SATP (*19*). Preadsorption of one protein next to the surface-bound PEG has been estimated to result in a formal protein concentration of 3 mM within the volume that can be reached by the outer end of the 6−8 nm long PEG chain (*19*). Since Schiff base formation is known to be rather slow (*47*), the same preadsorption phenomenon must have helped in this study to achieve efficient AFM tip functionalization at micromolar biotin−IgG concentration.

On the basis of the preadsorption hypothesis, care must be taken to avoid components (e.g., detergents or high concentrations of glycerol) that could weaken the nonspecific adsorption of proteins to the AFM tip. Other forbidden additives are primary amines (e.g., Tris base) which would react with the benzaldehyde function of the PEG linker and de-activate it before protein is coupled. Azide is also likely to inhibit coupling because it is chemically similar to cyanide which is known to react with aldehyde functions. Microdialysis should suffice to eliminate all these components because minute traces of these components left after dialysis are not expected to have a significant effect.

A hitherto unaddressed aspect concerns the simultaneous inclusion of ∼20 mM $NaCNBH_3$ for immediate reduction of the initially formed Schiff bases. It is based on the finding that this concentration of $NaCNBH_3$ reduces only Schiff bases but not the aldehydes themselves (*47*). Moreover, this fixation reagent not only ensures irreversibility of coupling but also

enhances the yield of immobilization when added together with protein, rather than after aldehyde−protein coupling (*48*).

Lateral Density of Antibody Molecules on the Chip and Tip Surface. Table 1 indicates that ∼2000 ExtrAvidin-peroxidase molecules were bound per μm^2 of chip surface. This number is a crude estimate of the number of surface-bound biotinylated IgG molecules per μm^2, as explained before (*26*). With this uncertainty in mind, one can translate the area density of biotin−IgG from the chip assay into a number of functional biotin−IgG molecules per AFM tip. A lateral density of 2000 μm^{-2} corresponds to an average area of 500 nm^2 per biotin−IgG. Based on the nominal tip radii (10−20 nm), the foremost hemispheres of AFM tips should have areas between 600 and 2500 nm^2 and thus carry 1−5 biotin−IgG molecules. In order to be functional, one of the IgG-bound biotin residues must be able to reach beyond the apex of the tip in order to be recognized by mica-bound avidin (see Figure 1). Consequently, the grafting site of the PEG tether must not be higher up on the tip than the total length of the PEG tether (6−8 nm) plus the IgG molecule. In practice, only grafting sites in the lowest 10 nm region of the tip will provide for good functionality because the benzaldehyde terminus of PEG may often bind in the F_{ab} region of the antibody, rather than in the F_c region (as shown for simplicity in Figure 1). In conclusion, the data from the chip assay predict that roughly one functional biotin−IgG molecule should be found on one AFM tip when using the protocol in Figure 1. Taking into account that the chip assay tends to somewhat underestimate the number of surface-tethered biotin−IgG (*26*), the prediction should be modified to "one or several". This prediction has regularly been confirmed in our AFM studies (*10, 14, 16, 17, 19−24, 27*), whether antibodies had been tethered via aldehyde-PEG-NHS (Figure 1) or PDP-PEG-NHS (Figure 6S).

Tethering of Whole Virus Particles to Amino-Functionalized AFM Cantilevers via Aldehyde-PEG-NHS. The tethering of virus particles (human rhinovirus serotype 2, HRV2) to the surface of silicon nitride cantilevers is visualized in Figure 4. The cantilever shown in panel A had been amino-functionalized, reacted with aldehyde-PEG-NHS, and incubated with virus particles (0.1 mg/mL, with 20 mM $NaCNBH_3$) by a similar protocol as described above (for details see Supporting Information), resulting in a high density of virus particles that remained on the cantilever surface after washing. In order to check whether the viral particles had indeed been bound via Schiff base bonds, another cantilever was treated with ethanolamine to block the benzaldehyde residues before exposure to virus. As shown in panel B, a much lower number of virus particles remained on this cantilever surface after washing. The pronounced difference between panel A and panel B provides clear evidence that most virus particles had indeed been immobilized via Schiff base-type bonds.

Measurement of Interaction Forces between Virus Particles on AFM Tips and Virus Receptors on Mica Surfaces. Figure 4A is an image of the top surface of a cantilever densely covered with virus particles, most of which had been covalently tethered to the surface via aldehyde-PEG-NHS. Because of the high density of viral particles it was very likely that the measuring tip of the cantilever also carried at least one virus particle (15 nm radius) on the apex of the tip (10−20 nm radius). The virus-functionalized tip could thus be used to study specific binding to, and unbinding from, a virus-specific receptor protein. VLDLR1-8, a soluble fragment of the very-low-density lipoprotein receptor encompassing the entire ligand binding domain was chosen as the receptor protein. It contains 8 repeats many of which contribute to specific binding of HRV2 (*49*). VLDLR1-8 was tethered to amino-functionalized mica (*42*) via aldehyde-PEG-NHS by the usual protocol used in the present

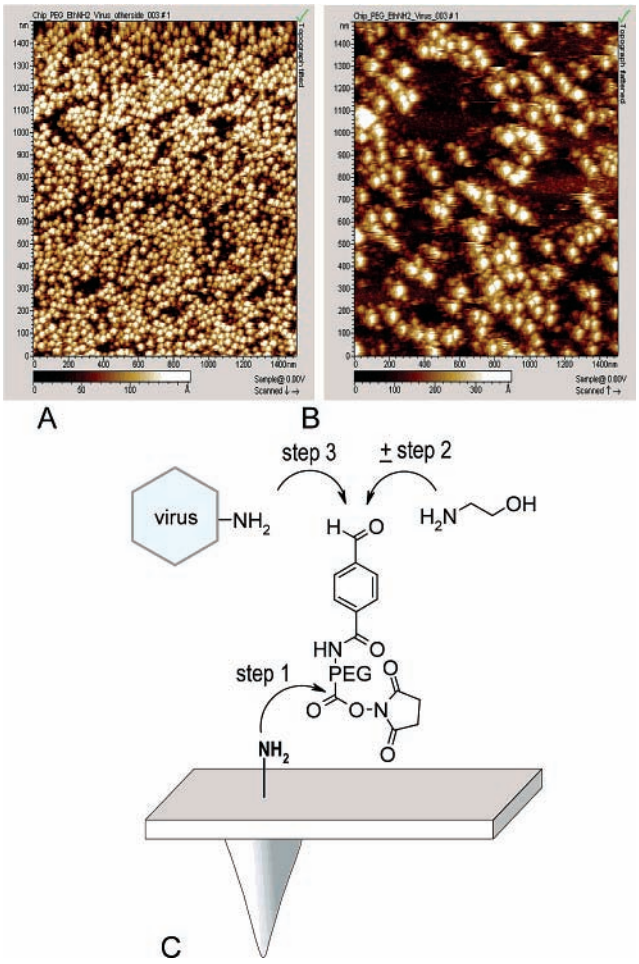


Figure 4. Quantitative study on the tethering of virus particles to the top side of two different silicon nitride cantilevers. This experiment served to characterize the preparation of virus-functionalized tips used for studying virus−receptor interactions as shown in Figure 5. Cantilevers A and B were functionalized with ethanolamine hydrochloride (not shown) and aldehyde-PEG-NHS (step 1 in panel C). On cantilever A, the virus particles were immediately added (step 3 in panel C), together with $NaCNBH_3$, incubated, and washed, and the top side of the cantilever was imaged with an unmodified cantilever (see panel A). On cantilever B, the free benzaldehyde groups on the outer end of the PEG linkers were blocked with ethanolamine and $NaCNBH_3$ (step 2 in panel C) before virus particles were added (step 3 in panel C), incubated, washed, and imaged with an unmodified cantilever (see panel B). In the latter panel, the virus particle look larger (i) because they were not as immobile as in panel A and (ii) because of the tip broadening effect. The latter effect was absent in panel A because the close proximity of the particles prevented the tip to reach the supporting surface in most places.

study, taking care to keep VLDLR1-8 native by inclusion of 2 mM Ca^{2+} (see Supporting Information).

The specific interaction of tip-tethered HRV2 and mica-bound VLDLR1-8 (see Figure 5A) was studied by performing force−distance cycles in which the cantilever base was repeatedly lowered and raised by 400 nm within 1 s while simultaneously recording cantilever bending. The latter was converted into force values (*y*-axis in Figure 5B and 5C) according to Hooke's law, based on the known force constant of the cantilever (23 pN/nm). In the presence of 2 mM Ca^{2+}, 118 out of 999 force distance cycles showed specific recognition events (as exemplified in Figure 5B). In the absence of free Ca^{2+} (1 mM EGTA), however, only 24 out of 999 measuring cycles exhibited some nonspecific recognition event (not shown), and all others were event-free, as shown in Figure 5C. The reduction in binding probability from 11.8% in 2 mM Ca^{2+} to 2.4% in Ca^{2+}-free

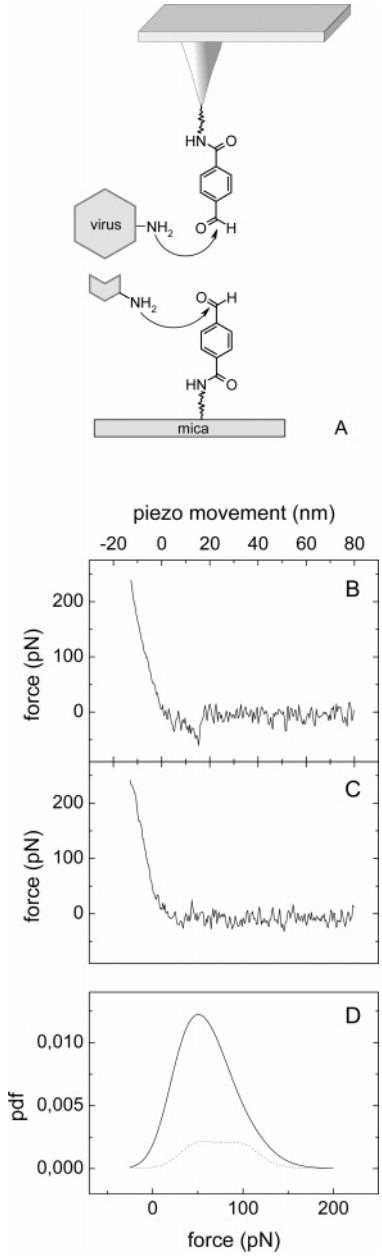


Figure 5. Force measurements between tip-linked virus particles (HRV2) and mica-bound virus receptor protein (VLDLR1-8, the extracellular fragment of human VLDL receptor). (A) Tip and mica were functionalized with ethanolamine hydrochloride and aldehyde-PEG-NHS (compare Figure 1) before virus and receptor were bound to the free aldehyde ends on tip and mica, respectively, and fixed by simultaneous application of $NaCNBH_3$. The piezo movement in the approach-and-retraction cycles was ±400 nm in 1 s, the force constant of the cantilever was 23 pN/nm, and the effective loading rate was 1.7 nN/s. (B) Example of a force−distance cycle showing specific virus−receptor unbinding. Unbinding occurred at a rupture force of 51 ± 18 pN. (C) Example of a force−distance cycle performed in the absence of Ca^{2+}, i.e. in Ca-free buffer containing 1 mM EGTA). (D) Probability density function (pdf) of the unbinding forces observed in 118 out of 999 force−distance cycles (11.8%, solid line). In the absence of Ca^{2+} (dotted line), only 24 out of 999 force−distance cycles (2.4%) appeared to reflect specific unbinding. The integrals of the two pdf curves were scaled to be proportional to the binding probabilities.

buffer indicates the specificity of virus−receptor interaction in the force distance cycles (*49*).

The rupture force distribution of the 118 specific unbinding events is shown in Figure 5D (solid line). The histogram peaks at a force of 50 pN, reflecting the well defined interaction of HRV2 particles with the VLDL receptor fragment. In contrast, the force distribution of the 24 unbinding events observed in EGTA buffer had no distinct maximum (Figure 5D, dotted line), providing further evidence that nonspecific adhesion caused very few apparent unbinding events only and most of the 118 events measured in presence of Ca^{2+} must have been specific in nature.

Meanwhile, promising experiments with other receptor constructs are under way which are expected to elucidate the contributions of the individual repeats to virus−receptor interaction (Rankl et al., manuscript in preparation). Moreover, tip functionalization with aldehyde-PEG-NHS has successfully been used for tethering of cytochrome C to the AFM tip in order to study its biospecific interaction of cytochrome C with azurin that had been immobilized on an ultraflat gold surface (*14*).

CONCLUSIONS

Force measurements of biospecific interactions between isolated purified molecules require linking of the interacting molecules to the AFM tip and to the sample surface. Long flexible linkers such as PEG chains are preferred because they allow for reorientation and local mobility of "receptor" and/or "ligand" molecule. The present study offers a straightforward method for the tethering of proteins via one of their many lysine residues, eliminating the need for endogenous or artificially introduced thiol groups. Minute amounts of protein (e.g., 5 μg in 50 μL of physiological buffer) are required to functionalize one AFM cantilever within 1−2 h incubation time.

ACKNOWLEDGMENT

We are indebted to Prof. Norbert Müller for use of NMR spectrometer facilities. This work was supported by the Austrian Science Funds (FWF projects P14549 and P-15295) and by EU project "Tips4Cells".

Supporting Information Available: Syntheses of *N*-succinimidyl 4-formylbenzoate, aldehyde-PEG-COOH, and aldehyde-PEG-NHS. Tethering of virus particles to AFM tips and of virus receptor to mica. Illustration of antibody coupling to AFM tips via disulfide bond formation. Illustration of silicon nitride chip functionalization and characterization with ExtrAvidin-peroxidase. This material is available free of charge via the Internet at http://pubs.acs.org.

LITERATURE CITED

(1) Hörber, J. K. H., and Miles, M. J. (2003) Scanning probe evolution in biology. *Science 302*, 1002−1005.
(2) Scheuring, S., Müller, D. J., Ringler, P., Heymann, J. B., and Engel, A. (1999) Imaging streptavidin 2D crystals on biotinylated lipid monolayers at high resolution with the atomic force microscope. *J. Microsc. 193*, 28−35.
(3) Kienberger, F., Ebner, A., Gruber, H. J., and Hinterdorfer, P. (2006) Molecular recognition imaging and force spectroscopy of single biomolecules. *Acc. Chem. Res. 39*, 29−36.
(4) Leckband, D., and Israelachvili, J. (2001) Intermolecular forces in biology. *Q. Rev. Biophys. 34*, 105−267.
(5) Radmacher, M., Cleveland, J. P., Fritz, M., Hansma, H. G., and Hansma, P. K. (1994) Mapping interaction forces with the atomic force microscope. *Biophys. J. 66*, 2159−2165.
(6) Stroh, C. M., Ebner, A., Geretschläger, M., Freudenthaler, G., Kienberger, F., Kamruzzahan, A. S. M., Smith-Gill, S. J., Gruber, H. J., and Hinterdorfer, P. (2004) Simultaneous topography and recognition imaging using force microscopy. *Biophys. J. 87*, 1981−1990.
(7) Stroh, C. M., Wang, H., Bash, R., Ashcroft, B., Nelson, J., Gruber, H. J., Lohr, D., Lindsay, S. M., and Hinterdorfer, P. (2004) Single-molecule recognition imaging microscopy. *Proc. Natl. Acad. Sci. U.S.A. 101*, 12503−12507.
(8) Ebner, A., Kienberger, F., Kada, G., Stroh, C. M., Geretschläger, M., Kamruzzahan, A. S. M., Wildling, L., Johnssohn, W. T.,

Ashcroft, B., Nelson, J., Lindsay, S. M., Gruber, H. J., and Hinterdorfer, P. (2005) Localization of single avidin-biotin interactions using simultaneous topography and molecular recognition imaging. *ChemPhysChem. 6*, 897−900.

(9) Evans, E., and Ritchie, K. (1997) Dynamic strength of molecular adhesion bonds. *Biophys. J. 72*, 1541−1555.

(10) Baumgartner, W., Hinterdorfer, P., Ness, W., Raab, A., Vestweber, D., Schindler, H., and Drenckhahn, D. (2000) Cadherin interaction probed by atomic force microscopy. *Proc. Natl. Acad. Sci. U.S.A. 97*, 4005−4010.

(11) Nevo, R., Stroh, C. M., Kienberger, F., Kaftan, D., Brumfeld, V., Elbaum, M., Reich, Z., and Hinterdorfer, P. (2003) A molecular switch between alternative conformational states in the complex of Ran and importin β1. *Nat. Struct. Biol. 10*, 553−557.

(12) Wieland, J. A., Gewirth, A. A., and Leckband, D. E. (2005) Single molecule adhesion measurements reveal two homophilic neural cell adhesion molecule bonds with mechanically distinct properties. *J. Biol. Chem. 280*, 41037−41046.

(13) Avci, R., Schweitzer, M., Boyd, R. D., Wittmeyer, J., Steele, A., Toporski, J., Beech, W., Arce, F. T., Spangler, B., Cole, K. M., and McKay, D. S. (2004) Comparison of antibody−antigen interactions on collagen measured by conventional immunological techniques and atomic force microscopy. *Langmuir 20*, 11053−11063.

(14) Bonanni, B., Kamruzzahan, A. S. M., Bizzarri, A. R., Rankl, C., Gruber, H. J., Hinterdorfer, P., and Cannistraro, S. (2005) Single molecule recognition between cytochrome C 551 and gold-immobilized azurin by force spectroscopy. *Biophys. J. 89*, 2783−2791.

(15) De Paris, R., Strunz, T., Oroszlan, K., Güntherodt, H.-J., and Hegner, M. (2000) Force spectroscopy and dynamics of the biotin-avidin bond studied by scanning force microscopy. *Single Mol. 1*, 285−290.

(16) Hinterdorfer, P., Baumgartner, W., Gruber, H. J., Schilcher, K., and Schindler, H. (1996) Detection and localization of individual antibody-antigen recognition events by atomic force microscopy. *Proc. Natl. Acad. Sci. U.S.A. 93*, 3477−3481.

(17) Hinterdorfer, P., Schilcher, K., Baumgartner, W., Gruber, H. J., and Schindler, H. (1998) A mechanistic study of the dissociation of individual antibody-antigen pairs by atomic force microscopy. *Nanobiology 4*, 177−188.

(18) Hukkanen, E., Wieland, J., Gewirth, A., Leckband, D., and Braatz, R. D. (2005) Multiple-bond kinetics from single-molecule pulling experiments: evidence for multiple NCAM bonds. *Biophys. J. 89*, 3434−3445.

(19) Kamruzzahan, A. S. M., Ebner, A., Wildling, L., Kienberger, F., Riener, C. K., Hahn, C. D., Pollheimer, P. D., Winklehner, P., Hölzl, M., Lackner, B., Schörkl, D. M., Hinterdorfer, P., and Gruber, H. J. (2006) Antibody linking to atomic force microscope tips via disulfide bond formation. *Bioconjugate Chem. 17*, 1473−1481.

(20) Kienberger, F., Kada, G., Gruber, H. J., Pastushenko, V. P., Riener, C. K., Trieb, M., Knaus, H.-G., Schindler, H., and Hinterdorfer, P. (2000) Recognition force spectroscopy studies of the NTA-His6 bond. *Single Mol. 1*, 59−65.

(21) Kienberger, F., Pastushenko, V. P., Kada, G., Gruber, H. J., Riener, C. K., Schindler, H., and Hinterdorfer, P. (2000) Static and dynamic properties of single poly(ethylene glycol) molecules investigated by force microscopy. *Single Mol. 1*, 123−128.

(22) Puntheeranurak, T., Wildling, L., Gruber, H. J., Kinne, R. K., and Hinterdorfer, P. (2006) Ligands on the string: single-molecule AFM studies on the interaction of antibodies and substrates with the Na^+-glucose co-transporter SGLT1 in living cells. *J. Cell. Sci. 114*, 2960−2967.

(23) Puntheeranurak, T., Wimmer, B., Castaneda, F., Gruber, H. J., Hinterdorfer, P., Kinne, R. K. H. (2007) Substrate specificity of sugar transport by rabbit SGLT1: single molecule AFM versus transport studies. *Biochemistry,* in press.

(24) Raab, A., Han, W., Badt, D., Smith-Gill, S. J., Lindsay, S. M., Schindler, H., and Hinterdorfer, P. (1999) Antibody recognition imaging by force microscopy. *Nature Biotechnol. 17*, 902−905.

(25) Ratto, T. V., Langry, K. C., Rudd, R. E., Balhorn, R. L., Allen, M. J., and McElfresh, M. W. (2004) Force spectroscopy of the double-tethered concanavalin-A mannose bond. *Biophys. J. 86*, 2430−2437.

(26) Riener, C. K., Stroh, C. M., Ebner, A., Klampfl, C., Gall, A. A., Romanin, C., Lyubchenko, Y. L., Hinterdorfer, P., and Gruber, H. J. (2003) Simple test system for single molecule recognition force microscopy. *Anal. Chim. Acta 479*, 59−75.

(27) Riener, C. K., Kienberger, F., Hahn, C. D., Buchinger, G. M., Egwim, I. O. C., Haselgrübler, T., Ebner, A., Romanin, C., Klampfl, C., Lackner, B., Prinz, H., Blaas, D., Hinterdorfer, P., and Gruber, H. J (2003) Heterobifunctional crosslinkers for tethering single ligand molecules to scanning probes. *Anal. Chim. Acta 497*, 101−114.

(28) Ros, R., Schwesinger, F., Anselmetti, D., Kubon, M., Schafer, R., Plückthun, A., and Tiefenauer, L. (1998) Antigen binding forces of individually addressed single-chain F_v antibody molecules. *Proc. Natl. Acad. Sci. U.S.A. 95*, 7402−7405.

(29) Strunz, T., Oroszlan, K., Schafer, R., and Güntherodt, H. J. (1999) Dynamic force spectroscopy of single DNA molecules. *Proc. Natl. Acad. Sci. U.S.A. 96*, 11277−11282.

(30) Wielert-Badt, S., Hinterdorfer, P., Gruber, H. J., Lin, J.-T., Badt, D., Wimmer, B., Schindler, H., and Kinne, R. K.-H. (2002) Single molecule recognition of protein binding epitopes in brush border membranes by force microscopy. *Biophys. J. 82*, 2767−2774.

(31) Willemsen, O. H., Snel, M. M. E., van der Werf, K. O., Gruber, H. J., Hinterdorfer, P., Schindler, H., van Kooyk, Y., de Grooth, B. G., Greve, J., and Figdor, C. G. (1999) Simultaneous height and adhesion imaging of antibody-antigen interactions by atomic force microscopy. *Biophys. J. 75*, 2220−2228.

(32) Schwesinger, F., Ros, R., Strunz, T., Anselmetti, D., Güntherodt, H. J., Honegger, A., Jermutus, L., Tiefenauer, L., and Plückthun, A. (2000) Unbinding forces of single antibody-antigen complexes correlate with their thermal dissociation rates. *Proc. Natl. Acad. Sci. U.S.A. 97*, 9972−9977.

(33) Ebner, A., Hinterdorfer, P., and Gruber, H. J. (2007) Comparison of different aminofunctionalization strategies for attachment of single antibodies to AFM cantilevers. *Ultramicroscopy,* in press.

(34) Dorner, M. M., Bassett, E W., Beiser, S. M., Kabat, E. A., and Tanenbaum, S. W. (1967) Studies on human antibodies: V. Amino acid composition of antidextrans of the same and of different specificities from several individuals. *J. Exp. Med. 125*, 823−831.

(35) Langry, K. C., Ratto, T. V., Rudd, R. E., and McElfresh, M. W. (2005) The AFM measured force required to rupture the dithiolate linkage of thioctic acid to gold is less than the rupture force of a simple gold−alkyl thiolate bond. *Langmuir 21*, 12064−12067.

(36) Gruber, H. J., Kada, G., Pragl, B., Riener, C., Hahn, C. D., Harms, G. S., Ahrer, W., Dax, T. G., Hohenthanner, K., and Knaus, H.-G. (2000) Preparation of thiol-reactive Cy5 derivatives from commercial Cy5 succinimidyl ester. *Bioconjugate Chem. 11*, 161−166.

(37) Kraehenbuhl, J: P., Galardy, R E., and Jamieson, J. D. (1974) Preparation and characterization of an immuno-electron microscope tracer consisting of a heme-octapeptide coupled to Fab. *J. Exp. Med. 139*, 208−223.

(38) Hewat, E. A., Neumann, E., Conway, J. F., Moser, R., Ronacher, B., Marlovits, T. C., and Blaas, D. (2000) The cellular receptor to human rhinovirus 2 binds around the 5-fold axis and not in the canyon: a structural view. *EMBO J. 19*, 6317−6325.

(39) Ronacher, B., Marlovits, T. C., Moser, R., and Blaas, D. (2000) Expression and folding of human very-low-density lipoprotein receptor fragments: neutralization capacity toward human rhinovirus HRV2. *Virology 278*, 541−550.

(40) Hutter, J., and Bechhoefer, J. (1993) Calibration of atomic-force microscope tips. *Rev. Sci. Inst. 64*, 1868−1873.

(41) Butt, H. J., and Jaschke, M. (1995) Calculation of the thermal noise in atomic force microscopy. *Nanotechnology 82*, 1−7.

(42) Klein, D. C. G., Stroh, C. M., Jensenius, H., van Es, M., Kamruzzahan, A. S. M., Stamouli, A., Gruber, H. J., Oosterkamp, T. H., and Hinterdorfer, P. (2003) Covalent immobilization of single proteins on mica for molecular recognition force microscopy. *ChemPhysChem. 4*, 1367−1371.

(43) Florin, E. L., Moy, V. T., and Gaub, H. E. (1994) Adhesion forces between individual ligand-receptor pairs. *Science 264*, 415−417.

(44) Ebner, A., Kienberger, F., Huber, C., Kamruzzahan, A. S., Pastushenko, V. P., Tang, J., Kada, G., Gruber, H. J., Sleytr, U. B., Sara, M., and Hinterdorfer, P. (2006) Atomic-force-microscopy imaging and molecular-recognition-force microscopy of recrystallized heterotetramers comprising an S-layer-streptavidin fusion protein. *ChemBioChem. 7*, 588−591.

(45) Ebner, A., Madl, J., Kienberger, F., Chtcheglova, L. A., Puntheeranurak, T., Zhu, R., Tang, J., Stroh, C., Gruber, H. J., Schütz, G. J.,

and Hinterdorfer, P. (2007) Single molecule force microscopy on cells and biological membranes. *Curr. Nanosci. 3,* in press.
(46) Baumgartner, W., Hinterdorfer, P., and Schindler, H. (2000) Data analysis of interaction forces measured with the atomic force microscope. *Ultramicroscopy 82,* 85−95.
(47) Peelen, D., and Smith, L. M. (2005) Immobilization of amine-modified oligonucleotides on aldehyde-terminated alkanethiol monolayers on gold. *Langmuir 21,* 266−271.
(48) Hahn, C. D., Leitner, C., Weinbrenner, T., Schlapak, R., Tinazli, A., Tampé, R., Lackner, B., Steindl, C., Hinterdorfer, P., Gruber, H. J., and Hölzl, M. (2007) Self-assembled monolayers with latent aldehydes for protein immobilization. *Bioconjugate Chem. 18,* 247−253.
(49) Verdaguer, N., Fita, I., Reithmayer, M., Moser, R., and Blaas, D. (2004) X-ray structure of a minor group human rhinovirus bound to a fragment of its cellular receptor protein. *Nat. Struct. Mol. Biol. 11,* 429−434.

BC070030S

Porphyrin−Retinamides: Synthesis and Cellular Studies

Martha Sibrian-Vazquez, Timothy J. Jensen, and M. Graça H. Vicente*

Department of Chemistry, Louisiana State University, Baton Rouge, Louisiana 70803. Received February 2, 2007; Revised Manuscript Received March 14, 2007

A series of four porphyrin−retinamides containing either all-trans- or 13-cis-retinoid acid residues, directly linked to the para-phenyl position of *meso*-tetraphenylporphyrin or via a low-molecular-weight PEG spacer, have been synthesized. The biological properties of these conjugates were evaluated in a model cell line, human HEp2, and in neuroblastoma SK-N-DZ cells, which exhibit moderate expression of retinoic acid receptors and retinoic acid-induced differentiation. The directly linked porphyrin−retinamides were taken up by a greater extent (20−50% more) in SK-N-DZ than in HEp2 cells. However, the PEG-containing conjugates accumulated maximally within both cell lines and approximately by the same amount, probably due to their increased amphiphilicity. Among all conjugates, the porphyrin-PEG-13-cis-retinamide accumulated the most in both cell lines (about 5 times more than the non-pegylated conjugates). None of the porphyrin−retinamide conjugates were toxic toward HEp2 cells at concentrations up to 100 μM, and only the hydrophobic non-pegylated conjugates were moderately toxic to SK-N-DZ cells [IC_{50} (dark) = 56−92 μM, and IC_{50} (at 1 J/cm^2) = 6−8 μM]. All conjugates preferentially localized within cellular vesicles that correlated well to the lysosomes and, in addition, the PEG-containing porphyrin−retinamides were also found in the ER.

INTRODUCTION

The receptor-mediated transport of drugs into targeted cells and sensitive intracellular sites is a valuable approach aimed at increasing the specificity of drugs for diseased tissue (*1*−*4*). Photodynamic therapy (PDT) is a binary modality for the treatment of cancer based on the activation of a tumor-accumulated photosensitizer with light of a wavelength, suitable for the excitation of the photosensitizer and for maximum tissue penetration (*5, 6*). The excited photosensitizer reacts with molecular oxygen and other surrounding molecules, generating radicals and reactive oxygen species (such as $^1O_2$) that cause irreversible photodamage to tumor tissues. Since $^1O_2$, the main cytotoxic agent generated in PDT, has a very short lifetime in biological systems and a very limited range in tissues (<0.05 μm), the site of photodamage is also the site of its generation. A particularly sensitive intracellular site is the cell nucleus, and DNA photodamage has been reported to occur in PDT (*7*−*10*), although porphyrin-based photosensitizers do not usually localize within cell nuclei (*11*). Therefore, the targeting of nuclear receptors by PDT photosensitizers might lead to increased therapeutic efficacy. Nuclear receptors consist of a vast family of proteins composed of steroid receptors, nonsteroidal receptors, thyroid hormone receptors, and retinoic acid receptors, all of which play a major role in intracellular signaling and carcinogenesis (*12, 13*). Among these, the retinoic acid receptor (RAR[1]) and the retinoic X receptor (RXR) belong to a large family of proteins that activate transcription in the presence of retinoic acids, the biologically active metabolites of vitamin A (retinol) and its active derivatives (*14, 15*). The use of retinoids to suppress tumor development has been evaluated in animal models of carcinogenesis including skin, breast, oral cavity, lung, hepatic, gastrointestinal, prostate, and bladder cancers (*16*−*18*). In these studies, all-trans retinoic acid derivatives have demonstrated chemopreventive activity both in vitro and in vivo (*19*−*25*). However, there are some disadvantages associated with the use of retinoids for cancer treatment, including retinoid-induced toxicity, resistance, and long-term side effects. As a result, the use of retinoids has been proposed only in an advanced disease state in order to enhance tumor sensitivity toward cytotoxic agents (*26*−*28*). It is possible that the combined use of retinoids and porphyrin-based photosensitizers might induce synergistic or additive effects that can lead to higher PDT therapeutic efficacy. We envisioned that the conjugation of a porphyrin photosensitizer to a retinoic acid might result in nucleus import of the resulting conjugate upon ligand recognition by the nuclear receptor, thus improving the biological efficacy of the photosensitizer while reducing the toxic effects of the retinoic acid moiety. Porphyrin-retinoid derivatives have been previously prepared, comprising either a *meso*-tetraphenylporphyrin (*29*) or a deuteroporphyrin-IX (*30*) macrocycle and aromatic derivatives of retinoic acid differing in the length of the conjugated side chains. However, only the energy transfer and primary charge separation characteristics of these conjugates were reported, and their biological properties were not investigated. Herein, we report the synthesis and in vitro biological evaluation of a series of new porphyrin−retinamides of the natural occurring all-trans- and 13-cis-retinoic acids, using both human carcinoma HEp2 and neuroblastoma SK-N-DZ cell lines. We studied the effects of (i) a low-molecular-weight PEG spacer between the porphyrin and retinoic acid moieties, (ii) the all-trans- vs 13-cis-retinoic acid moieties, and (iii) the use of a cell line (SK-N-DZ) known to respond to retinoic acid, on the cellular uptake, toxicity, and intracellular localization of the new porphyrin−retinamides.

EXPERIMENTAL PROCEDURES

Synthesis. Unless otherwise indicated, all commercially available starting materials were used directly without further

* Corresponding Author. E-mail: vicente@lsu.edu.

[1] Abbreviations: HOBt, 1-hydroxybenzotriazole; DMF, *N*,*N*-dimethylformamide; CCA, α-cyano-4-hydroxycinnamic acid; TFA, trifluoroactic acid; DIEA, *N*,*N*-diisopropylethylamine; TBTU, 2-(1*H*-benzotriazole-1-yl)-1,1,3,3-tetramethyluronium tetrafluoroborate; DMSO, dimethyl sulfoxide; Boc, *t*-butoxy carbonyl; HEPES, 4-(2-hydroxyethyl)-1-piperazine ethanesulfonic acid; PBS, phosphate buffer saline; FBS, fetal bovine serum; MEM, modified eagle medium; RAR, retinoic acid receptor; RXR, retinoic acid receptor; CRAPs, cellular retinoic acid binding proteins; SAR, structure−activity relationships; LBD, ligand binding domain.

10.1021/bc0700382 CCC: $37.00 © 2007 American Chemical Society
Published on Web 05/23/2007

purification. All reactions were monitored by TLC using Sorbent Technologies 0.25 mm silica gel plates with UV indicator (60F-254). Silica gel Sorbent Technologies 32−63 μm was used for flash column chromatography. NMR spectra were obtained on a ARX-300 Bruker or Bruker DPX 400 spectrometer. Chemical shifts (δ) are given in parts per million (ppm) relative to $CDCl_3$ (7.26 ppm, ^{1}H) unless otherwise indicated. Electronic absorption spectra were measured on a Perkin-Elmer Lambda 35 UV−vis spectrophotometer. Fluorescence spectra were measured on either a Perkin-Elmer LS55 spectrometer or a Florolog 3 Spectrofluorimeter. Mass spectra were obtained on a Bruker ProFLEX III MALDI-TOF mass spectrometer using CCA as the matrix.

Porphyrin−Retinamide 2. To a solution of all-trans-retinoic acid (0.0119 g, 0.0397 mmol) in DMF (500 μL) was added DIEA (0.0154 g, 0.119 mmol), followed by HOBt (0.006 g, 0.0397 mmol) and TBTU (0.0127 g, 0.0397 mmol). The reaction mixture was stirred 5 min, and then aminoporphyrin **1** (0.025 g, 0.0397 mmol) was added in one portion. The reaction mixture was stirred at room temperature for 24 h and then diluted with 50 mL of ethyl acetate. The organic phase was washed with saturated $NaHCO_3$ (100 mL) and water (100 mL), dried over Na_2SO_4, filtered, and the solvent evaporated under vacuum. The title compound was purified by flash chromatography on silica gel using CH_2Cl_2 for elution. Yield: 0.019 g, 51%. ^{1}H NMR ($CDCl_3$, 300 MHz): δ 8.89 (8H, s, β-H), 8.27 (6H, s, ArH), 8.19 (2H, d, J = 8.17 Hz, ArH), 7.92 (2H, d, J = 7.0 Hz, ArH), 7.81 (9H, s, ArH), 7.49 (1H, s, NHCO), 7.13 (1H, t, J = 14.68 Hz, =CH), 6.40 (1H, t, J = 15.56 Hz, =CH), 6.15−6.22 (3H, m, =CH), 5.98 (1H, s, =CH), 2.60 (3H, s, CH_3), 2.10 (5H, s, CH_3, CH_2), 1.8 (3H, s, CH_3), 1.69−1.75 (2H, m, CH_2), 1.59 (2H, s, CH_2), 1.11 (6H, s, CH_3), −2.71 (2H, s, NH). UV−vis ($CHCl_3$) λ_{max} (ϵ/M^{-1} cm^{-1}) 421 (618 000), 516 (19 000), 552 (10 600), 591 (6200), 647 (5100). LRMS (MALDI) *m*/*z* 911.75 (M^+).

Porphyrin−Retinamide 3. The title compound was synthesized as described above using 13-cis-retinoic acid. Yield: 0.0179 g, 49%. ^{1}H NMR ($CDCl_3$, 300 MHz): δ 8.87 (8H, s, β-H), 8.04−8.22 (8H, m, ArH), 7.87 (1H, d, J = 6.16 Hz, =CH), 7.77 (9H, s, ArH), 7.45 (1H, s, NHCO), 7.07 (1H, t, J = 13.73 Hz, =CH), 6.13−6.39 (3H, m, =CH), 5.79 (1H, s, =CH), 2.18 (3H, s, CH_3), 2.06 (5H, s, CH_3, CH_2), 1.74 (2H, s, CH_3), 1.63 (2H, s, CH_2), 1.49−1.54 (2H, m, CH_2), 1.06 (6H, s, CH_3), −2.73 (2H, s, NH). UV−vis ($CHCl_3$) λ_{max} (ϵ/M^{-1} cm^{-1}) 421 (605 000), 516 (18 000), 552 (10 000), 591 (5900), 647 (5900). LRMS (MALDI) *m*/*z* 911.76 (M^+).

Porphyrin−Retinamide 4. The monoaminoporphyrin (**1**) reacted with glycolic anhydride to give a carboxylic acid-terminated porphyrin, as previously described (*31*). To a solution of this porphyrin (0.100 g, 0.134 mmol) in DMF (2 mL) was added DIEA (0.1039 g, 0.8044 mmol), followed by HOBt (0.0205 g, 0.1348 mmol) and TBTU (0.043 g, 0.134 mmol). After 5 min, the monoprotected $NH_2CH_2CH_2(OCH_2CH_2)_6OCH_2CH_2NH^tBoc$ (0.0628 g, 0.134 mmol) was added and the mixture stirred at room temperature for 48 h. The reaction mixture was diluted with ethyl acetate (100 mL), the organic phase was treated as described above for the synthesis of compound **2**, and the ^{t}Boc-protected porphyrin−PEG was purified by flash chromatography using $CHCl_3/CH_3OH$ 9:1 for elution. Yield: 0.133 g, 83%. ^{1}H NMR ($CDCl_3$, 300 MHz): δ 8.87−8.90 (8H, m, β-H), 8.21−8.25 (8H, m, ArH), 8.22 (2H, d, J = 7.98 Hz, ArH), 7.57 (1H, s, NHCO), 7.78−7.85 (9H, m, ArH), 4.39 (2H, s, CH_2O), 4.32 (2H, s, CH_2O), 3.58−3.69 (26H, m, PEG-CH_2O), 3.49−3.55 (4H, m, CH_2NH, CH_2O), 3.30−3.31 (2H, m, CH_2-NH), 1.44 (9H, s, CH_3), −2.73 (2H, s, NH). UV−vis ($CHCl_3$) λ_{max} (ϵ/M^{-1} cm^{-1}) 420 (460 000), 516 (16 800), 552 (8300), 591 (5200), 646 (4500). LRMS (MALDI) *m*/*z* 1195.99 (M^+). The ^{t}Boc-protected porphyrin−PEG (0.133 g, 0.126 mmol) was dissolved in a 1:1 mixture of $CHCl_3$/TFA (2 mL) and stirred at room temperature for 4 h. After the solvent was evaporated under vacuum, the green residue was triturated with ethyl ether and then dried again under vacuum to give the free amino porphyrin−PEG in quantitative yield. ^{1}H NMR ($CDCl_3$, d-TFA, 300 MHz): δ 8.84−8.57 (18H, m, ArH), 7.97 (10H, s, ArH), 4.39 (2H, s, CH_2O), 4.33 (2H, s, CH_2O), 3.62−3.81 (30H, m, PEG-CH_2O), 3.30 (2H, s, CH_2NH), 0.38−0.48 (4H, br, NH^+). UV−vis ($CHCl_3$) λ_{max} (ϵ/M^{-1} cm^{-1}) 420 (670 000), 516 (16 100), 551(8100), 590 (5300), 646 (4100). LRMS (MALDI) *m*/*z* 1095.62 (M^+). Conjugation of this pegylated porphyrin intermediate (0.033 g, 0.03 mmol) to all-trans-retinoic acid amino (0.009 g, 0.03 mmol) was performed as described above for compound **2**. The title compound was purified by flash chromatography on silica gel using $CHCl_3/CH_3OH$ 9:1 for elution. Yield: 0.032 g, 78%. ^{1}H NMR ($CDCl_3$, 300 MHz): δ 8.85−8.89 (8H, m, β-H), 8.18−8.23 (8H, m, ArH), 8.11 (2H, d, J = 8.22 Hz, ArH), 7.86 (1H, s, NHCO), 7.75−7.77 (9H, m, ArH), 6.88 (1H, t, J = 11.34 Hz, =CH), 6.52−6.58 (1H, m, =CH), 6.03−6.05 (3H, m, =CH), 5.68 (1H, s, =CH), 4.37 (2H, s, CH_2O), 4.31 (2H, s, CH_2O), 3.44−3.66 (32H, m, PEG-CH_2O), 2.34 (3H, s, CH_3), 1.95 (3H, s, CH_3,CH_2), 1.65 (2H, s, CH_3), 1.43 (2H, s, CH_2), 1.26 (2H, s, CH_2), 0.98 (6H, s, CH_3), −2.65 (2H, s, NH). UV−vis ($CHCl_3$) λ_{max} (ϵ/M^{-1} cm^{-1}) 420 (670 000), 516 (17 900), 551 (9100), 590 (5900), 646 (4700). LRMS (MALDI) *m*/*z* 1377.57 (M^+).

Porphyrin−Retinamide 5. This compound was synthesized and isolated as described above for porphyrin−retinamide **4**, using 13-cis-retinoic acid amino (0.009 g, 0.03 mmol) and the same pegylated porphyrin intermediate (0.033 g, 0.03 mmol). Yield: 0.025 g, 60%. ^{1}H NMR ($CDCl_3$, 300 MHz): δ 8.87 (8H, s, β-H), 8.18−8.23 (8H, m, ArH), 8.10 (2H, d, J = 7.98 Hz, ArH), 7.85−7.90 (1H, m, =CH), 7.77 (9H, s, ArH), 6.80−6.95 (1H, m, =CH), 6.54 (1H, br, =CH), 6.07−6.28 (2H, m, =CH), 5.56 (1H, s, =CH), 4.37 (2H, s, CH_2O), 4.30 (2H, s, CH_2O), 3.45−3.36 (32H, m, PEG-CH_2O), 1.90−1.94 (8H, m, CH_3,CH_2), 1.68 (3H, s, CH_3), 1.59 (2H, s, CH_2), 1.45 (2H, s, CH_2), 1.00 (6H, s, CH_3), −2.77 (2H, s, NH). UV−vis ($CHCl_3$) λ_{max} (ϵ/M^{-1} cm^{-1}) 420 (528 000), 516 (17 300), 551 (8800), 590 (5800), 646 (4600). LRMS (MALDI) *m*/*z* 1377.50 (M^+).

Fluorescence Quantum Yields. All absorption spectra were acquired using 10 mm path length quartz cuvettes and the corresponding solvents as reference solutions. The optical density of the solutions used for the emission studies was below 0.05 at the excitation wavelength to eliminate inner filter effects. All the measurements were performed within 3 h of preparation of the solutions. Stock solutions (10 mM) of porphyrins **1**−**5** were prepared in DMSO. The quantum yields were calculated using a secondary standard method (*32*, *33*). Methylene blue, a dye with an established quantum yield, was used as a secondary standard. Using this method, the integrated fluorescence intensities of the analyte (I) and standard (I_R), the optical densities of the analyte (OD) and the standard (OD_R), and the refractive indexes of analyte solvent (n) and standard solvent (n_R) are related to the quantum yield of the analyte (Q) as follows:

$$Q = Q_R \frac{I}{I_R} \frac{OD_R}{OD} \frac{n^2}{n_R^2}$$

where Q_R is the quantum yield of the reference standard (0.03 for methylene blue). To account for incomplete spectra, the bands were extrapolated using appropriate fitting models whenever necessary.

Computer Simulations. The Gasteiger−Huckel computational model and the Tripos Force Field parameters incorporated into the software package *SYBYL 7.0* (Tripos St. Louis, USA)

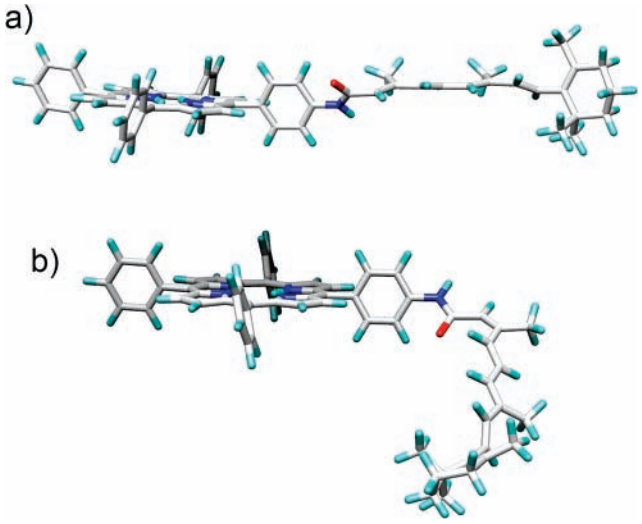


Figure 1. Energy-minimized conformations for conjugates (a) **2** and (b) **3** using the Gasteiger-Huckel model and the Tripos Force Field parameters incorporated into the software package *SYBYL 7.0*.

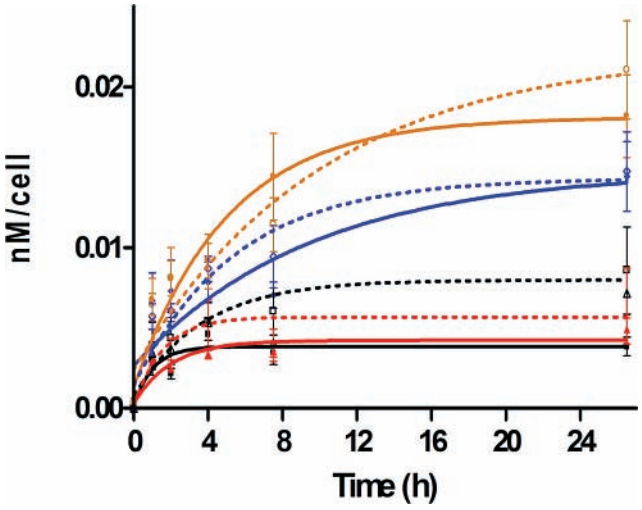


Figure 2. Time-dependent uptake of porphyrin−retinamides **2** (black), **3** (red), **4** (blue), and **5** (brown) at 10 μM by HEp2 cells (solid line) and SK-N-DZ cells (dashed line).

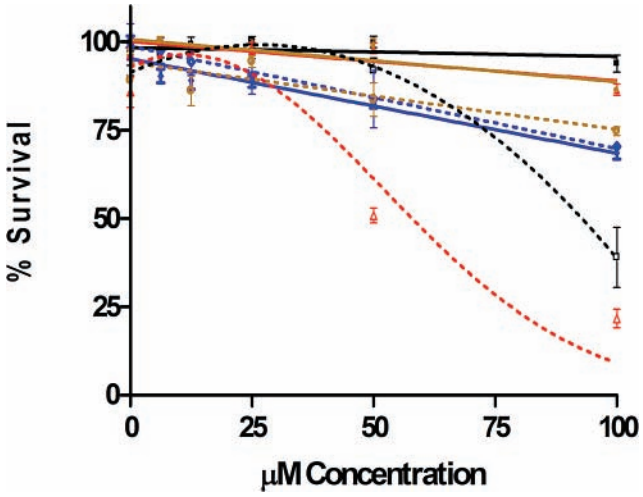


Figure 3. Dark toxicity of porphyrin−retinamides **2** (black), **3** (red), **4** (blue), and **5** (brown) toward HEp2 cells (solid line) and SK-N-DZ cells (dashed line) after 24 h, using the Cell Titer Blue assay.

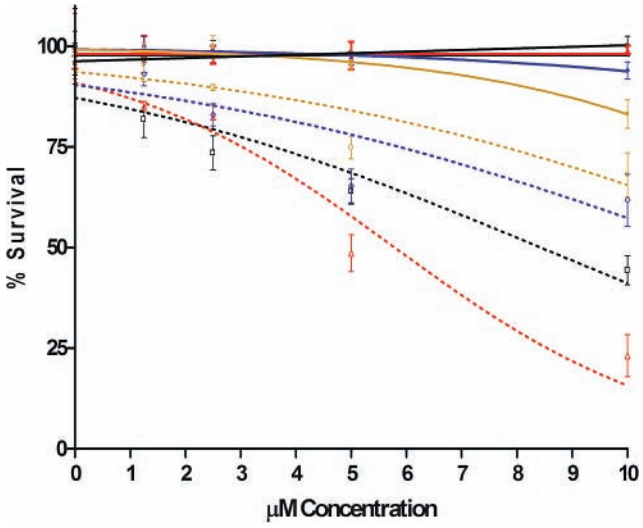


Figure 4. Phototoxicity of porphyrin−retinamides **2** (black), **3** (red), **4** (blue), and **5** (brown) toward HEp2 cells (solid line) and SK-N-DZ cells (dashed line) using 1 J/cm^2 light dose.

were used for the energy minimization calculations. After initial minimization for each molecule, a dynamics evaluation was performed by heating the molecules to 300 K and then cooling to 0 K over a period of 1000 fs.

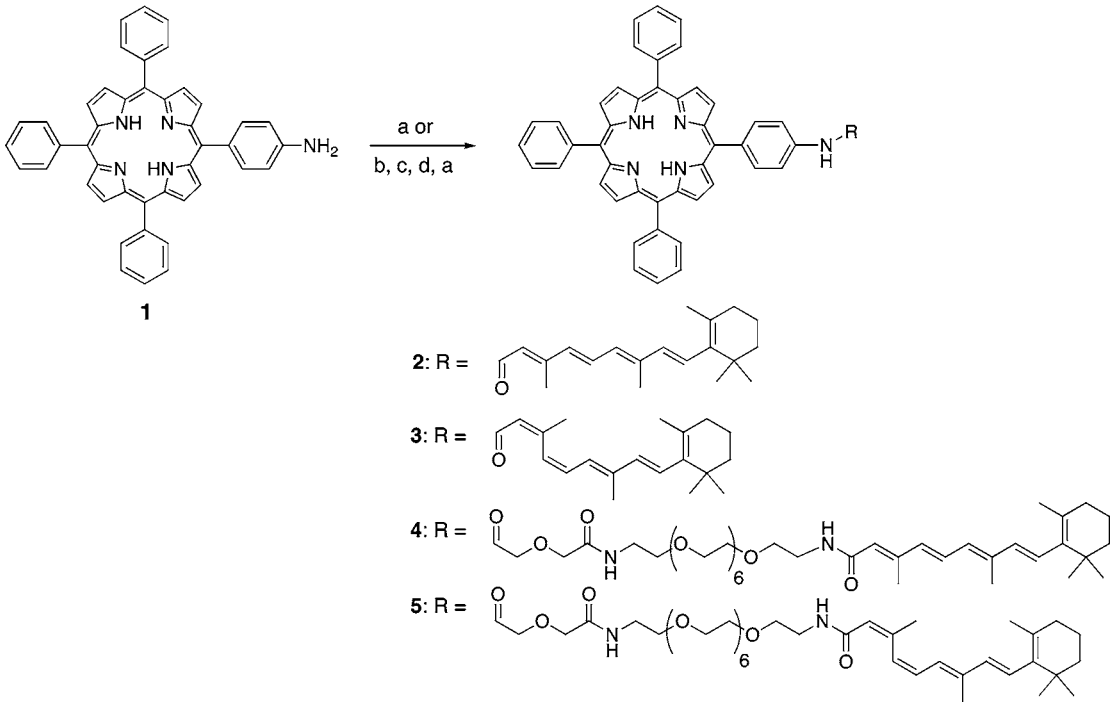
Cell Culture. All tissue culture media and reagents were obtained from Invitrogen. Human cervical carcinoma HEp2 and neuroblastoma SK-N-DZ cells were obtained from ATCC and maintained in a 50:50 mixture of DMEM/Advanced MEM containing 5% FBS. The cells were subcultured biweekly to maintain subconfluent stocks. The results shown in Figures 2−4 for the uptake and toxicity experiments are the average of three independent experiments, each performed in triplicate (i.e., nine wells per point).

Time-Dependent Cellular Uptake. HEp2 cells were plated at 10 000 per well and SK-N-DZ cells were plated at 50 000 per well in a Costar 96 well plate and allowed to grow 36−48 h. Porphyrin stocks were prepared in DMSO at a concentration of 10 mM and then diluted into medium to final working concentrations. The cells were exposed to 10 μM of each conjugate for 0, 1, 2, 4, 8, and 26.5 h. At the end of the incubation time, the loading medium was removed and the cells were washed with PBS. The cells were solubilized upon addition of 100 μL of 0.25% Triton X-100 (Calbiochem) in PBS. To determine the conjugate concentration, fluorescence emission was read at 410/650 nm (excitation/emission) using a BMG FLUOstar plate reader. The cell numbers were quantified using the CyQuant reagent (Molecular Probes).

Dark Cytotoxicity. The HEp2 cells and SK-N-DZ cells were plated as described above and allowed 36−48 h to attach. The cells were exposed to increasing concentrations of conjugate up to 100 μM and incubated for 24 h. The loading medium was then removed, and new medium containing Cell Titer Blue (Promega) was added as per manufacturer's instructions. Cell toxicity was then measured by reading the fluorescence at 520/584 nm using a BMG FLUOstar plate reader. The signal was normalized to 100% viable (untreated) cells and 0% viable (treated with 0.2% saponin) cells.

Phototoxicity. The HEp2 cells and SK-N-DZ cells were prepared as described above for the dark cytotoxicity assay and treated with conjugate concentrations of 0, 0.625, 1.25, 2.5, 5, and 10 μM. After compound loading, the medium was removed and replaced with medium containing 50 mM HEPES pH 7.4. The cells were then placed on ice and exposed to light from a 100 W halogen lamp filtered through a 610 nm long-pass filter (Chroma) for 20 min. An inverted plate lid filled with water to a depth of 5 mm acted as an IR filter. The total light dose was approximately 1 J/cm^2. The cells were returned to the incubator

Scheme 1[a]



[a]Conditions: (a) HOBt/TBTU/DIEA/DMF, 13-cis- or all-trans-retinoic acid, rt, 24 h (49−78%). (b) Glycolic anhydride/DMF, rt, 24 h, quantitative yield. (c) HOBt/TBTU/DIEA/DMF, $NH_2CH_2CH_2(OCH_2CH_2)_6OCH_2CH_2NH^tBoc$, rt, 48 h (83%). (d) $CHCl_3$/TFA 1/1, rt, 4 h, quantitative yield.

overnight and assayed for viability as described above for the dark cytotoxicity experiment.

Microscopy. The HEp2 cells were plated on LabTek 2 chamber coverslips and incubated overnight, before being exposed to 10 μM of conjugate for 24 h. For the colocalization experiments, the cells were incubated for 18 h concurrently with conjugate and one of the following organelle tracers, for 30 min: MitoTracker Green (Molecular Probes) 250 nM, LysoSensor Green (Molecular Probes) 50 nM, BODIPY FLC_5-Ceramide (Molecular Probes) 50 nM, and $DiOC_6$ (Molecular Probes) 5 μg/mL. The slides were washed three times with growth medium, and new medium containing 50 mM HEPES pH 7.4 was added. Fluorescent microscopy was performed using a Zeiss Axiovert 200M inverted fluorescent microscope fitted with standard FITC and Texas Red filter sets (Chroma). The images were aquired with a Zeiss Axiocam MRM CCD camera fitted to the microscope.

RESULTS

Synthesis. The new series of porphyrin conjugates to either all trans- or 13-cis-retinoic acids were prepared from monoaminoporphyrin **1** (*34*), as shown in Scheme 1, via amide bond formation. The retinoic acids were first activated as the hydroxybenzotriazole esters and then coupled to either aminoporphyrin **1** or to a pegylated monoaminoporphyrin using TBTU in the presence of DIEA, in 49−78% overall yields. The pegylated conjugates were also prepared from monoaminoporphyrin **1**, first by reaction with glycolic anhydride to afford a carboxyl-terminated porphyrin, followed by coupling to $NH_2CH_2CH_2(OCH_2CH_2)_6OCH_2CH_2NH^tBoc$ and deprotection using TFA in $CHCl_3$ (*31*). Conjugates **2** and **3** bearing a direct linkage between the retinoic acid moiety and the para-phenyl porphyrin position are highly hydrophobic, soluble only in organic solvents, such as hexane, dichloromethane, chloroform, and DMSO. In contrast, conjugates **4** and **5**, containing a low-molecular-weight PEG spacer between the porphyrin and the retinoid moiety, showed amphiphilic properties, being soluble in both organic and protic solvents, such as hexane, methanol, acetonitrile, and DMSO, and partially soluble in water. Furthermore, we anticipated that the PEG spacer would favor an extended conformation for conjugates **4** and **5**, which we believe is crucial for receptor binding (*31*). Indeed, we used computer calculations to determine the minimum-energy conformations for porphyrin−retinamides **2**−**5**. While the conformations of the PEG-containing conjugates were similarly extended (results not shown), those for the non-pegylated conjugates **2** and **3** were very different, as shown in Figure 1. The all-trans-retinoic acid conjugate **2** shows a planar conformation, while the 13-cis-retinoic acid conjugate **3** adopts a bend conformation. The structures of the new porphyrin−retinamide conjugates **2**−**5** were confirmed by MS, ^{1}H NMR, UV−vis, and fluorescence spectrophotometry. The UV−vis spectra of porphyrin−retinamides **2**−**5** show characteristic etio-type porphyrin spectra with a shoulder on the Soret band due to the presence of the retinoic acid moiety; retinoic acids typically have a broad absorption band at 390 nm (see Figure 1 of the Supporting Information). The emission spectra of aminoporphyrin **1** and of porphyrin−retinamides **2**−**5** in DMSO can be seen in Figure 2 of the Supporting Information. The fluorescence quantum yields determined for porphyrins **1**−**5** are shown in Table 1.

Cell Studies. The time-dependent cellular uptake of porphyrin−retinoid conjugates **2**−**5** was evaluated in both human carcinoma HEp2 and neuroblastoma SK-N-DZ cells at a concentration of 10 μM, and the results are shown in Figure 2. The HEp2 cell line is a convenient model for the evaluation of porphyrin-based in vitro biological properties (*31, 35*−*37*), while the SK-N-DZ cell line is known to respond to retinoic acid and

Table 1. Fluorescence Quantum Yields of Aminoporphyrin 1 and Porphyrin−Retinamides 2−5 in DMSO, Excitation at 605 nm

porphyrin	ϕ_f
1	0.0029
2	0.043
3	0.045
4	0.037
5	0.038

to retinoic acid-induced differentiation (*38*−*41*). Indeed, conjugates **2** and **3** bearing a direct linkage between the porphyrin and either all-trans- (**2**) or 13-cis-retinoic acid (**3**) were taken up to a greater extent (20−50%) by SK-N-DZ than HEp2 cells (Figure 2). However, conjugates **4** and **5**, containing a PEG spacer between the porphyrin and retinoic acid moieties, accumulated the most and approximately by the same extent within both cell lines. The PEG-containing 13-cis-retinoic acid conjugate **5** was the most taken up by both cell lines, at all time points studied, indicating that both the PEG and the nature of the retinoic acid moiety influence the cellular uptake of these conjugates. In contrast, the non-PEG-containing hydrophobic conjugates **2** and **3** were taken up similarly by HEp2 cells and the all-trans-retinamide **2** accumulated preferentially in SK-N-DZ cells. All conjugates exhibited similar uptake kinetics in both cell lines at short time points (within the first 1−2 h), but while the uptake of the hydrophobic conjugates **2** and **3** reached a plateau after 4 h, that of PEG-containing conjugates **4** and **5** continued to steadily increase over the 26.5 h period investigated.

The dark toxicity and phototoxicity of the porphyrin−retinamides **2**−**5** were investigated in both HEp2 and SK-N-DZ cells exposed to increasing concentrations of each conjugate, up to 100 μM for 24 h, and the results are shown in Figures 3 and 4, respectively. While none of the conjugates were found to be toxic toward HEp2 cells, both **2** and **3** showed low dark toxicity (IC_{50} = 92 and 56 μM, respectively) and moderate phototoxicity (IC_{50} = 8.4 and 5.8 μM, respectively, at 1 J/cm^2) toward SK-N-DZ cells.

The porphyrin-retinamides **2**−**5** showed similar fluorescence patterns in HEp2 and SK-N-DZ cells when investigated by fluorescence microscopy. Figures 5−8 show the fluorescence observed within HEp2 cells for retinoid conjugates **2**−**5**, respectively, and their overlay with the organelle specific fluorescent probes BODIPY Ceramide (Golgi network), $DiOC_6$ (ER), LysoSensor Green (lysosomes), and Mitotracker Green (mitochondria). The preferential sites of subcellular localization for conjugates **2** and **3** were found to be cellular vesicles that correlated well with the lysosomes, while conjugates **4** and **5** localized preferentially in both the lysosomes and the ER. Similar results (not shown) were observed in SK-N-DZ cells.

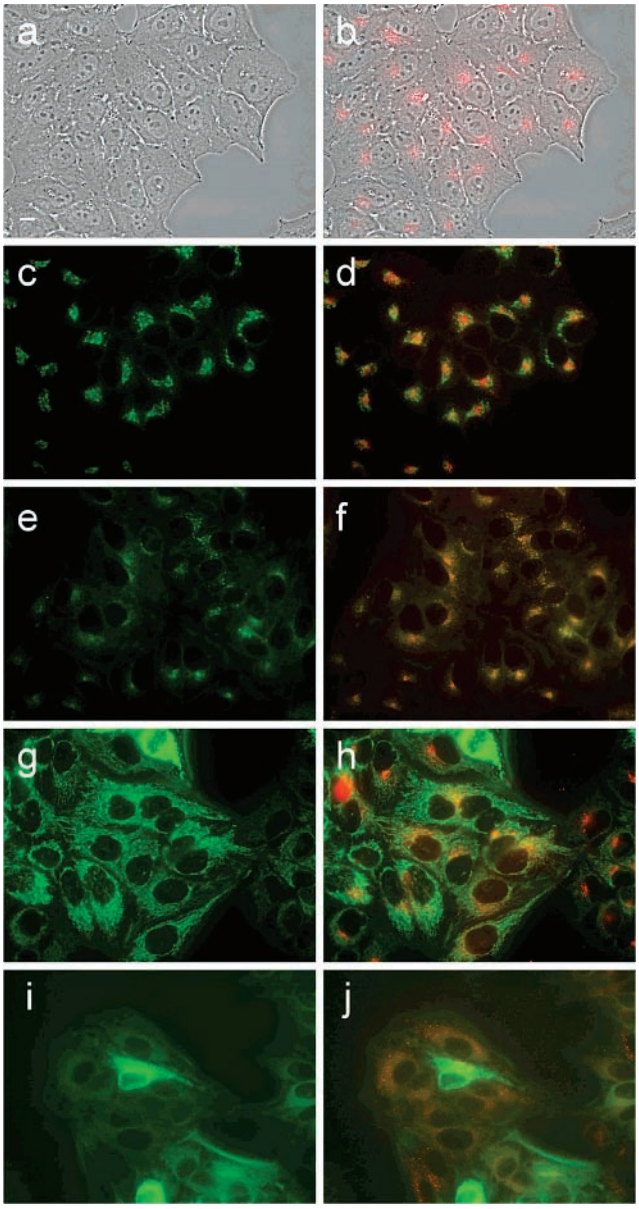


Figure 5. Subcellular localization of porphyrin−retinamide **2** in HEp2 cells at 10 μM for 24 h. (a) Phase contrast, (b) overlay of **2** fluorescence and phase contrast, (c) BODIPY ceramide fluorescence, (e) LysoSensor green fluorescence, (g) MitoTracker green fluorescence, (i) $DiOC_6$ fluorescence, (d,f,h,j) overlays of organelle tracers with **2** fluorescence. Scale bar: 10 μm.

DISCUSSION

The new porphyrin−retinoic acid conjugates were designed to contain either a all-trans retinoic acid moiety, due to its documented biological activity, or a 13-cis retinoic acid moiety, a naturally occurring metabolite also with reported biological activity (*19*−*25*). Ester and amide derivatives of retinoic acid have been previously prepared in low to moderate yields by the reaction of alcohols or amines with activated retinoic acids, for instance, as acid chlorides, retinoyl fluorides, or retinoyl imidazolides, and DCC as the coupling reagent (*29, 30, 42*−*44*). In our new synthesis of porphyrin−retinamides **2**−**5** (Scheme 1), the retinoic acids were activated as the hydroxybenzotriazole esters and subsequently coupled to monoaminoporphyrin **1** or to a pegylated porphyrin using TBTU as the coupling agent, in reproducibly high yields (49−78%). We have previously used this synthetic strategy for the conjugation of peptides and other molecules to porphyrin macrocycles (*31, 35, 36*). Conjugates **2** and **3**, with the retinoic acid moiety directly linked to the porphyrin para-phenyl position, are highly hydrophobic and not soluble in water. The all-trans-retinamide conjugate **2** has a planar conformation, while the 13-cis-retinamide conjugate **3** adopts a bent conformation (Figure 1), which might in part explain its preferential accumulation in SK-N-DZ cells in comparison with **3**. Furthermore, in comparison to all-trans-retinoic acid, 13-cis-retinoic acid exhibits lower binding affinity for nuclear retinoid receptors (*45, 46*). On the other hand, conjugates **4** and **5** containing a low-molecular-weight PEG linkage between the porphyrin and the retinoic acid moiety are amphiphilic, and thus soluble in polar and nonpolar organic solvents, as well as partially soluble in water. The PEG spacer was introduced not only to increase the water solubility and to decrease both inter- and intramolecular interactions, but also to favor an extended vs bent conformation of the conjugates, which is believed to be crucial for efficient binding to nuclear receptors. A low-molecular-weight PEG was chosen over a high-molecular-weight PEG in order to avoid the formation of mixtures due to the polydispersity of the high-molecular-weight PEGs (*47*−*49*).

The fluorescence quantum yields observed for porphyrin−retinamides **2**−**5** (Table 1) were significantly higher than that for the nonconjugated aminoporphyrin **1** and depended on the

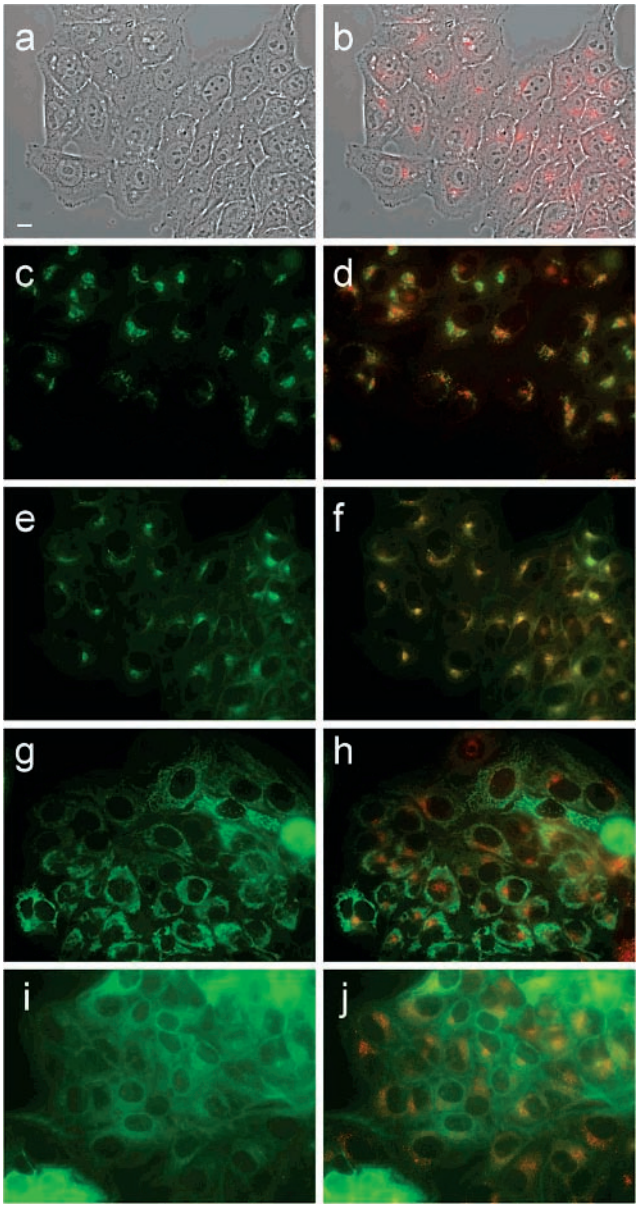


Figure 6. Subcellular localization of porphyrin−retinamide **3** in HEp2 cells at 10 μM for 24 h. (a) Phase contrast, (b) overlay of **3** fluorescence and phase contrast, (c) BODIPY ceramide fluorescence, (e) LysoSensor green fluorescence, (g) MitoTracker green fluorescence, (i) $DiOC_6$ fluorescence, (d,f,h,j) overlays of organelle tracers with **3** fluorescence. Scale bar: 10 μm.

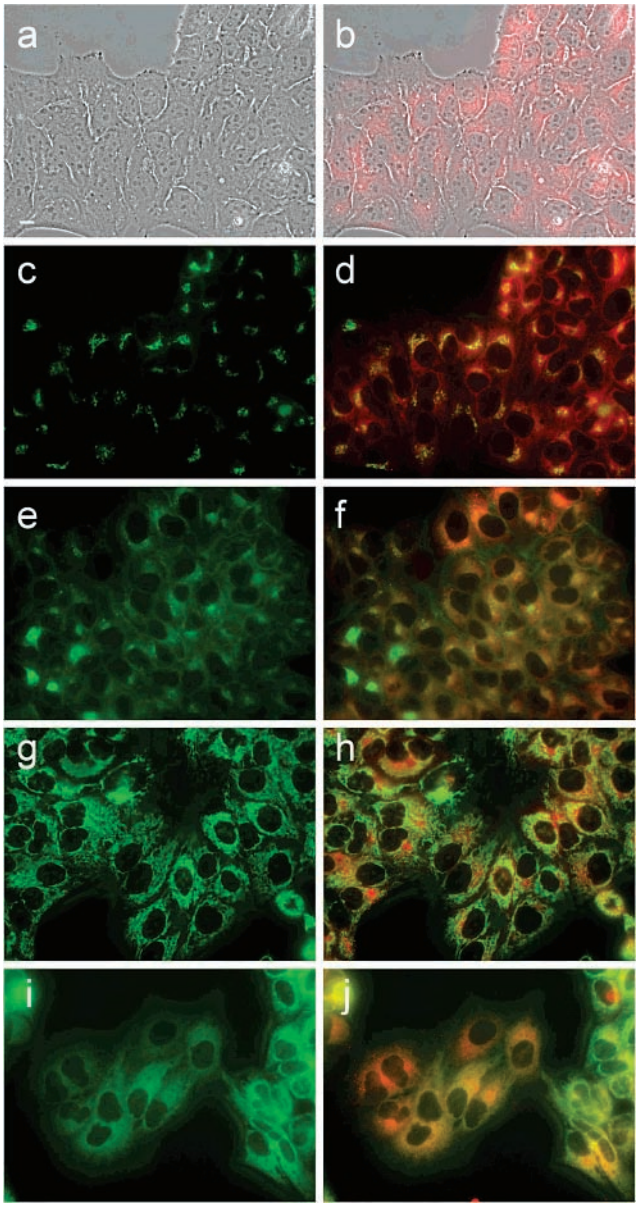


Figure 7. Subcellular localization of porphyrin−retinamide **4** in HEp2 cells at 10 μM for 24 h. (a) Phase contrast, (b) overlay of **4** fluorescence and phase contrast, (c) BODIPY ceramide fluorescence, (e) LysoSensor green fluorescence, (g) MitoTracker green fluorescence, (i) $DiOC_6$ fluorescence, (d,f,h,j) overlays of organelle tracers with **4** fluorescence. Scale bar: 10 μm.

presence of the PEG linker. Our results are in agreement with previous studies showing that the fluorescence of porphyrin macrocycles increases upon conjugation to carotenoids and other aromatic retinoid moieties (*29*). Porphyrin−retinamides **2** and **3** bearing the retinoid moiety directly linked to the porphyrin phenyl group showed the highest quantum yields of this series. In agreement with previous reports, the introduction of a PEG linker between the porphyrin and the retinoid moiety, as in conjugates **4** and **5**, decreases the fluorescence quantum yields (*50*).

The biological efficacy of the new porphyrin−retinamides was evaluated in a model cancer cell line, human carcinoma HEp2 cells, and in neuroblastoma SK-N-DZ cells, which are known to respond to retinoic acid (*38*−*41*). The cellular uptake of the porphyrin−retinamides was dependent on both the nature of the retinoid moiety (all-trans or 13-cis) and the presence of a PEG linker between the porphyrin and the retinoic acid. Among all conjugates, porphyrin−retinamide **5** bearing a PEG linker to a 13-cis-retinoid moiety accumulated the most within both cell lines, which indicates that the 13-cis-retinoid residue might be a better ligand for promoting conjugate translocation across the plasma membrane. Indeed, the PEG-containing conjugates **4** and **5** exhibited up to five times higher uptake than the non-PEG-containing retinamides **2** and **3** in both cell lines, probably because the PEG confers amphiphilic character to the otherwise highly hydrophobic conjugates, and it also favors an extended over a bent conformation of the conjugates, which might be required for receptor binding and efficient translocation across cellular membranes. While the PEG-containing conjugates **4** and **5** showed similar uptake in both cell lines, the hydrophobic conjugates **2** and **3** accumulated preferentially in SK-N-DZ rather than in HEp2 cells, probably due to the slightly higher expression of retinoic acid receptors in the SK-N-DZ cells. Furthermore, of the hydrophobic porphyrin−retinamides, the all-trans-retinoic acid conjugate **2**

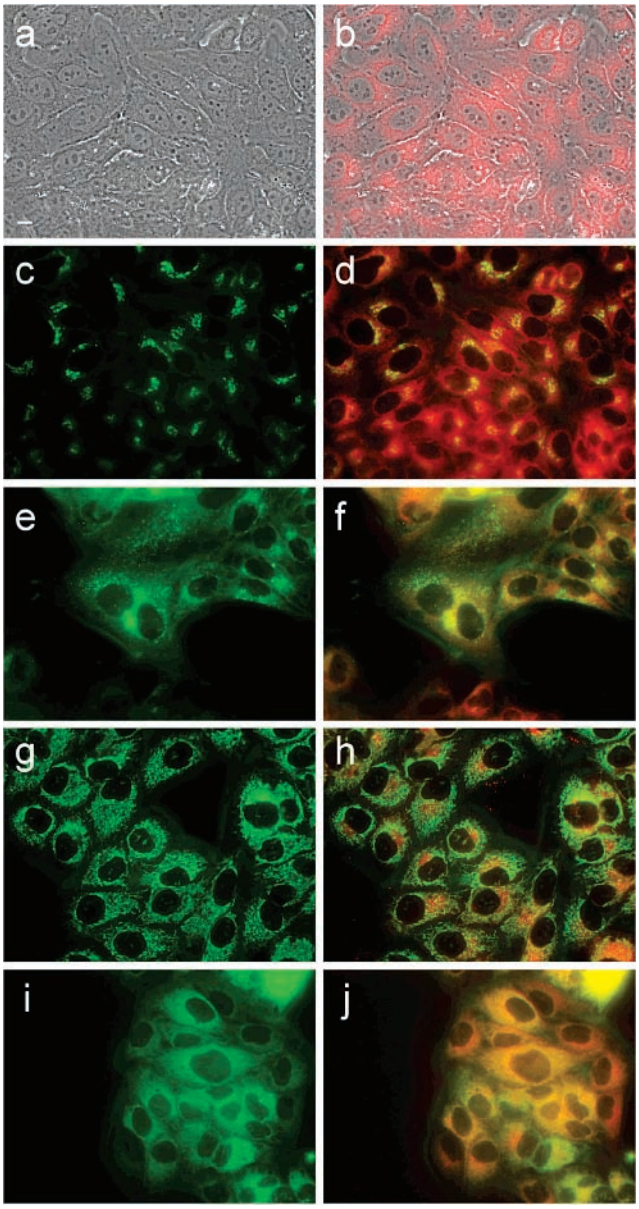


Figure 8. Subcellular localization of porphyrin−retinamide **5** in HEp2 cells at 10 μM for 24 h. (a) Phase contrast, (b) overlay of **5** fluorescence and phase contrast, (c) BODIPY ceramide fluorescence, (e) LysoSensor green fluorescence, (g) MitoTracker green fluorescence, (i) $DiOC_6$ fluorescence, (d,f,h,j) overlays of organelle tracers with **5** fluorescence. Scale bar: 10 μm.

accumulated to a slightly higher extent within SK-N-DZ cells than the 13-cis-retinoid analog **3**, probably because of its more favored planar conformation for receptor binding. Previously reported SAR studies in ligand−nuclear receptor binding suggest distinct levels of tolerance among receptors for alterations in ligand structure (*51*, *52*). Structural analysis of LBD−ligand complexes suggest a common ligand-binding mode for the nuclear-receptor family, the preferred ligands being small and hydrophobic, and falling within a narrow range of molecular volumes (250−350 Å^3) (*53*). For example, the all-trans-retinoic acid fits snugly into the hydrophobic pocket of the RAR ligand-binding domain, not leaving enough room for alternative geometries of the ligand. It has also been reported that 13-cis-retinoic acid exhibits lower binding affinity for cellular retinoic acid binding proteins (CRABPs) and retinoid receptors than all-trans-retinoic acid (*45*, *46*).

All porphyrin−retinamides **2**−**5** showed low phototoxicity (IC_{50} > 50 μM) toward HEp2 cells, and only the hydrophobic conjugates **2** and **3** showed moderate phototoxicity toward SK-N-DZ cells (IC_{50} = 8.4 and 5.8 μM, respectively, at 1 J/cm^2). Indeed, the 13-cis-retinoic acid-containing conjugate **3** was the most phototoxic of all conjugates studied. In agreement with our results, it was previously reported that 13-cis-retinoid acid is toxic to neuroblastoma SK-N-DZ cells in the concentration range 0.001−10 μM for 6 to 14 days (*38*). The higher phototoxicity observed for porphyrin−retinamides **2** and **3** which accumulated to a significantly smaller extent within cells than conjugates **4** and **5**, and in addition localized mainly within the cell lysosomes, while **4** and **5** were also found in the more sensitive ER, suggests that these porphyrin−retinamides induce cell death via different mechanisms. Previous studies have shown that retinoids are capable of mediating apoptosis, although the biological mechanisms leading to retinoid-induced cell death are poorly understood (*14*, *15*). It is possible that, upon light exposure, the lysosomal content is released into the cytoplasm where the hydrophobic porphyrin−retinamides **2** and **3** preferentially bind the CRABPs proteins in comparison with the more hydrophilic conjugates **4** and **5**. The CRABPs function as transport proteins to the nucleus and are also reported to facilitate the metabolic degradation of retinoic acids (*54*). Although we observed no nuclear localization of the porphyrin−retinamides, probably because of the large volume of these molecules (800−1200 Å^3) due to the porphyrin macrocycle, our studies show that there is a synergistic effect in the hydrophobic porphyrin−retinamides that leads to their increased phototoxicity in SK-N-DZ cells expressing retinoid receptors.

ACKNOWLEDGMENT

This work was supported by the National Science Foundation grant number CHE-304833.

Supporting Information Available: Additional spectra as discussed in the text. This material is available free of charge via the Internet at http://pubs.acs.org.

LITERATURE CITED

(1) Kim, C.-K., and Lim, S.-J. (2002) Recent progress in drug delivery systems for anticancer agents. *Arch. Pharm. Res. 25*, 229−239.

(2) Nori, A., and Kopecek, J. (2004) Intracellular targeting of polymer-bound drugs for cancer therapy. *Adv. Drug. Delivery Rev. 57*, 609−636.

(3) Rosenkranz, A. A., Jans, D. A., and Sobolev, A. S. (2002) Targeted intracellular delivery of photosensitizers to enhance photodynamic efficiency. *Immunol. Cell Biol. 78*, 452−464.

(4) Nyman, E. S., and Hynninen, P. H. (2004) Research advances in the use of tetrapyrrolic photosensitizers for photodynamic therapy. *J. Photochem. Photobiol., B 73*, 1−28.

(5) Dougherty, T. J., Gomer, C. J., Henderson, B. W., Jori, G., Kessel, D., Korbelik, M., Moan, J., and Peng, Q. (1998) Photodynamic therapy. *J. Natl. Cancer Inst. 90*, 889−905.

(6) Pandey, R. K., and Zheng, G. (2000). Porphyrins as photosensitizers in photodynamic therapy. In *The Porphyrin Handbook*. Volume 6: Applications: past, present and future (Kadish, K. M., Smith, K. M., Guilard, R., Eds.) pp 157−230, Chapter 43, Academic Press, New York.

(7) Moan, J., Waksvik, H., and Christensen, T. (1980) DNA Single-strand breaks and sister chromatid exchanges induced by treatment with hematoporphyrin and light or by X-rays in human NHIK 3025 cells. *Cancer Res. 40*, 2915−2918.

(8) Ramakrishnan, N., Oleinick, N. L., Clay, M. E., Horng, M. F., Antunez, A. R., and Evans, H. H. (1989) DNA lesions and DNA degradation in mouse lymphoma L5178Y cells after photodynamic treatment sensitized by chloroaluminum phthalocyanine. *Photochem. Photobiol. 50*, 373−378.

(9) Ruck, A., Kollner, T., Dietrich, A., Strauss, W., and Schneckenburger, H. (1992) Fluorescence formation during photodynamic

therapy in nucleus of cells incubated with cationic and anionic water-soluble photosensitizers. *J. Photochem. Photobiol., B 12*, 403−412.
(10) Penning, L. C., Lagerberg, J. W., Van Dierendonck, J. H., Cornelisse, C. J., Dubbelman, T. M., and Van Steveninck, J. (1996) The role of DNA damage and inhibition of poly(ADP-ribosyl) action in loss of clonogenicity of murine L929 fibroblasts, caused by photodynamically induced oxidative stress. *Cancer Res. 54*, 5561−5567.
(11) Kessel, D. (2004) Correlation between subcellular localization and photodynamic efficacy. *J. Porphyrins Phthalocyanines 8*, 1009−1014.
(12) Weatherman, R. V., Fletterick, R. J., and Scanlan, T. S. (1999) Nuclear-receptor ligands and ligand-binding domains. *Annu. Rev. Biochem. 68*, 559−581.
(13) Renaud, J. P., and Moras, D. (2000) Structural studies of nuclear receptors. *Cell. Mol. Life Sci. 57*, 1748−1769.
(14) Curley, R. W. and Robarge M. J. (1997) Retinoid structure, chemistry, and biological active derivatives. In *Retinoids: Their physiological function and therapeutic potential,* Advances in Organ Biology, Volume 3 (Bittar, E. E., Sherbet, G. V., Eds.) pp 1−34, Jai Press Inc., Greenwich, Connecticut.
(15) Marill, J., Idres, N., Capron, C. C., Nguyen, E., and Chabot, G. G. (2003) Retinoic acid metabolism and mechanism of action. *Curr. Drug Metabolism 4*, 1−10.
(16) Tallman, M. S., and Wiernik, P. H. (1992) Retinoids in cancer treatment. *J. Clin. Pharm. 32*, 868−888.
(17) Evans, T. R. J., and Kaye, S. B. (1999) Retinoids: present role and future potential. *Br. J. Cancer 80*, 1−8.
(18) Lei, M., and de The, H. (2003) Retinoids and retinoid acid receptor in cancer. *Eur. J. Cancer Suppl. 1*, 13−18.
(19) Panigot, M. J., Humphries, K. A., and Curley, R. W. (1994) Preparation of 4-retinamidophenyl- and 4-retinamidobenzyl-C-glycosyl and C-glucuronosyl analogs of the glucuronide of 4-hydroxyphenyl-retinamide as potential stable cancer chemopreventive agents. *J. Carbohydr. Chem. 13*, 303−321.
(20) Curley, R. W., and Robarge, M. J. (1996) Recent advances in the development of retinoids. *Curr. Med. Chem. 3*, 325−342.
(21) Redoules, D., and Perie, J. (1999) Stereospecific synthesis of retinoic acid glucoconjugates, as pseudo-substrates of epidermal beta-glucocerebrosidase. *Tetrahedron Lett. 40*, 4811−4814.
(22) Ruhl, R., Sass, J. O., Nau, H., and Klug, S. (2001) Effects of *all-trans*-retinoic acid and *all-trans*-retinoyl glucuronide in two in vitro systems of distinct biological complexity. *Arch. Tox. 75*, 497−504.
(23) Shealy, Y. F., Frye, J. L., and Schiff, L. J. (1988) N-(Retinoyl)-amino acids—synthesis and chemopreventive activity in vitro. *J. Med. Chem. 31*, 190−196.
(24) Manfredini, S., Simoni, D., Ferroni, R., Bazzanini, R., Vertuani, S., Hatse, S., Balzarini, J., and DeClercq, E. (1997) Retinoic acid conjugates as potential antitumor agents: synthesis and biological activity of conjugates with Ara-a, Ara-c, 3(2H)-furanone, and aniline mustard moieties. *J. Med. Chem. 40*, 3851−3857.
(25) Veal, G. J., Errington, J., Redfern, C. P. F., Pearson, A. D. J., and Boddy, A. V. (2002) Influence of isomerisation on the growth inhibitory effects and cellular activity of 13-*cis* and all-*trans* retinoic acid in neuroblastoma cells. *Biochem. Pharm. 63*, 207−215.
(26) Johnsen, J. I., Pettersen, I., Ponthan, F., Sveinbjornsson, B., Flaegstad, T., and Kogner, P. (2004) Synergistic induction of apoptosis in neuroblastoma cells using a combination of cytostatic drugs with interferon-gamma and TRAIL. *Int. J. Oncol. 25*, 1849−1857.
(27) Dalpiaz, A., Pavan, B., Scaglianti, M., Vitali, F., Bortolotti, F., Biondi, C., Scatturin, A., and Manfredini, S. (2005) Vitamin C and 6-amino-vitamin C conjugates of diclofenac: synthesis and evaluation. *Int. J. Pharm. 291*, 171−181.
(28) Hassan, H. T., and Rees, J. K. H. (1989) Triple combination of retinoic acid + aclcinomycin A + dimethylformamide induces differentiation of acute myeloid leukaemic blasts in primary culture. *Anticancer Res. 9*. 647−652.
(29) Filippovich, E. I., Evstigneeva, R. P., Luzgina, V. N., Egorova, T. G., Kurdyumova, N. R., Mikerin, I. E., and Makin, S. M. (1990) Energy transfer in the systems of covalently bound porphyrin and retinoic acid derivatives. *Zh. Obshch. Khim. 60*, 481−484.
(30) Gribkova, S. E., Evstigneeva, R. P., and Luzgina, V. N. (1993) Synthesis of molecular complexes based on porphyrins for the investigation of the energy transfer and primary charge separation in photosynthesis. *Russ. Chem. Rev. 62*, 963−979.
(31) Sibrian-Vazquez, M., Jensen, T. J., Hammer, R. P., and Vicente, M. G. H (2006) Peptide-mediated cell transport of water-soluble porphyrin conjugates. *J. Med. Chem. 49*, 1364−1372.
(32) Fery-Forgues, S., and Lavabre, D. (1999) Are fluorescence quantum yields so tricky to measure? A demonstration using familiar stationery products. *J. Chem. Ed. 76*, 1260−1264.
(33) Lakowicz, J. R. (1999) *Principles of Fluorescence Spectroscopy*, 2nd ed., pp 52−53, Chapter 2, Kluwer Academic/Plenum Publishers, New York.
(34) Luguya, R., Jaquinod, L., Fronczek, F. R., Vicente, M. G. H., and Smith, K. M. (2004) Synthesis and reactions of meso-(*p*-nitrophenyl)porphyrins. *Tetrahedron 60*, 2757−2763.
(35) Sibrian-Vazquez, M., Jensen, T. J., Fronczek, F. R., Hammer, R. P., and Vicente, M. G. H. (2005) Synthesis and characterization of positively charged porphyrin−peptide conjugates. *Bioconjugate Chem. 16*, 852−863.
(36) Sibrian-Vazquez, M., Hao, E., Jensen, T. J., and Vicente, M. G. H. (2006) Enhanced cellular uptake with a cobaltacarborane-porphyrin-HIV-1 Tat 48-60 conjugate. *Bioconjugate Chem. 17*, 928−934.
(37) Sibrian-Vazquez, M., Jensen, T. J., and Vicente, M. G. H. (2007) Synthesis and cellular studies of PEG-functionalized meso-tetraphenylporphyrins. *J. Photochem. Photobiol., B 86*, 9−21.
(38) Helson, L., and Helson, C. (1985) Human neuroblastoma cells and *13-cis*-retinoic acid. *J. Neuro-Oncol. 3*, 39−41.
(39) Lovat, P. E., Irving, H., Annicchiarico-Petruzzelli, M., Bernassola, F., Malcolm, A. J., Pearson, A. D. J., Melino, G., and Redfern, C. P. F. (1997) Retinoids in neuroblastoma therapy: Distinct biological properties of 9-cis- and all-trans-retinoic acid. *Eur. J. Cancer 33*, 2075−2080.
(40) Nagai, J., Yazawa, T., Okudela, K., Kigasawa, H., Kitamura, H., and Osaka, H. (2004) Retinoic acid induces neuroblastoma cell death by inhibiting proteasomal degradation of retinoic acid receptor alpha. *Cancer Res. 64*, 7910−7917.
(41) Armstrong, J. L., Ruiz, M., Boddy, A. V., Redfern, C. P. F., Pearson, A. D. J., and Veal, G. J. (2005) Increasing the intracellular availability of *all-trans* retinoic acid in neuroblastoma cells. *Br. J. Cancer 92*, 696−704.
(42) Shealy, Y. F., Frye, J. L., Odell, C. A., Thorpe, M. C., Kirk, M. C., Coburn, W. C., and Sporn, M. B. (1984) Synthesis and properties of some *13-cis*-retinamides and *all-trans*-retinamides. *J. Pharm. Sci. 73*, 745−751.
(43) Barua, A. B., Huselton, C. A., and Olson, J. A. (1996) Synthesis of novel glucuronide conjugates of retinoid carboxylic acids. *Synth. Commun. 26*, 1355−1361.
(44) Barua, A. B., and Olson, J. A. (1985) Preparation of retinamides by use of retinoyl fluoride. *J. Lipid Res. 26*, 258−262.
(45) Armstrong, J. L., Ruiz, M., Boddy, A. V., Redfern, C. P. F., Pearson, A. D. J., and Veal, G. J. (2005) Increasing the intracellular availability of all-*trans* retinoic acid in neuroblastoma cells. *Br. J. Cancer 92*, 696−704.
(46) Tsukada, M., Schroder, M., Roos, T. C., Chandraratna, R. A. S., Reichert, U., Merk, H. F., Orfanos, C. E., and Zouboulis, C. C. (2000) 13-*cis* Retinoic acid exerts its specific activity on human sebocytes through selectively intracellular isomerization to *all-trans* tetinoic acid and binding retinoid acid receptors. *J. Invest. Dermatol. 115*, 321−327.
(47) Greenwald, R. B., Choe, Y. H., McGuire, J., and Conover, C. D. (2003) Effective drug delivery by PEGylated drug conjugates. *Adv. Drug Delivery Rev. 55*, 217−250.
(48) Hamblin, M. R., Miller, J. L., Rizvi, I., Ortel, B., Maytin, E. V., and Hasan, T. (2001) Pegylation of a chlorin(e_6) polymer conjugate increases tumor targeting of photosensitizer. *Cancer Res. 61*, 7155−7162.
(49) Kim, Y. S., Song, R., Hyun, K. D., Jun, M. J., and Sohn, Y. S. (2003) Synthesis, biodistribution and antitumor activity of hematoporphyrin-platinum(II) conjugates. *Bioorg. Med. Chem. 11*, 1753−1760.
(50) Kanofsky, J. R. (1990) Quenching of singlet oxygen by human plasma. *Photochem. Photobiol. 51* 299−303.

(51) Dawson, M. I., Jong, L., Hobbs, P. D., Cameron, J. F., Chao, W., Pfahal, M., Lee, M., Shroot, B., and Pfhal, M. (1995) Conformational effects on retinoid receptor selectivity. 2. Effects of retinoid bridging group on retinoid X receptor activity and selectivity. *J. Med. Chem. 38*, 3368−3383.

(52) Silva, C. H. T. P., Almeida, P., and Taft, C. A. (2004) Density functional and docking studies of retinoids for cancer treatment. *J. Mol. Model. 10*, 38−43.

(53) Bogan, A. A., Cohen, F. E., and Scanlan, T. (1998) Natural ligands of nuclear receptors have conserved volumes. *Nat. Struct. Biol. 5*, 679−681.

(54) Yang, Q., Sakurai, T., and Kakudo, K. (2002) Retinoid, retinoic acid receptor β and breast cancer. *Breast Cancer Res. Treat. 76*, 167−173.

BC0700382

5′-Modified G-Quadruplex Forming Oligonucleotides Endowed with Anti-HIV Activity: Synthesis and Biophysical Properties

Jennifer D'Onofrio,[†] Luigi Petraccone,[‡] Eva Erra,[‡] Luigi Martino,[‡] Giovanni Di Fabio,[†] Lorenzo De Napoli,[†] Concetta Giancola,*[,‡] and Daniela Montesarchio*[,†]

Dipartimento di Chimica Organica e Biochimica, Università degli Studi di Napoli "Federico II", and Dipartimento di Chimica, Università degli Studi di Napoli "Federico II", Complesso Universitario di Monte S. Angelo, via Cintia, 4, I-80126 Napoli, Italy. Received February 23, 2007; Revised Manuscript Received April 19, 2007

Oligodeoxyribonucleotides of sequence d($^{5'}$TGGGAG$^{3'}$) carrying bulky aromatic groups at the 5′ end were found to exhibit potent anti-HIV activity [Hotoda, H., et al. (1998) *J. Med. Chem. 41,* 3655−3663 and references therein]. Structure−activity relationship investigations indicated that G-quadruplex formation, as well as the presence of large aromatic substituents at the 5′-end, were both essential for their antiviral activity. In this work, we synthesized some representative examples of the anti-HIV active Hotoda's 6-mers and analyzed the resulting G-quadruplexes by CD, DSC, and molecular modeling studies, in comparison with the unmodified oligonucleotide. In the case of the sequence carrying the 3,4-dibenzyloxybenzyl (DBB) group, identified as the best candidate for further drug optimization, we developed an alternative protocol to synthesize the 5′-DBB-thymidine phosphoramidite building block in higher yields. The thermodynamic and kinetic parameters for the association/dissociation processes of the 5′-conjugated quadruplexes, determined with respect to the unmodified one, were discussed in light of the molecular modeling studies. The aromatic groups at the 5′ position of d($^{5'}$TGGGAG$^{3'}$) dramatically enhance both the equilibrium and the rate of formation of the quadruplex complexes. The overall stability of the investigated quadruplexes was found to correlate with the reported IC_{50} values, thus furnishing quantitative evidence for the hypothesis that the G-quadruplex structures are the ultimate active species, effectively responsible for the biological activity.

INTRODUCTION

In the past decade, many synthetic oligonucleotides (ODNs) have been found to be potent antiviral agents, and a number of modified ODNs have been selected as promising drug candidates against HIV (*1*−*3*). The mechanisms of action of synthetic ODNs as antivirals are based on the inhibition and/or interference with the viral cycle at different levels, including HIV binding to target cells. Recently, Hotoda and co-workers demonstrated that various G-rich oligonucleotides, bearing aromatic moieties as the 4,4′-dimethoxytriphenylmethyl (DMT) group at their 5′-end, are non-antisense anti-HIV active compounds (*4*−*7*). Particularly, they identified the lead sequence $^{5'}$d(TGGGAG)$^{3'}$, active against HIV-1 only when conjugated at the 5′ position with large aromatic groups. The 6-mer bearing the 3,4-dibenzyloxybenzyl (3,4-DBB) group at the 5′-end and the 2-hydroxyethylphosphate group at the 3′-end (R-95288) showed the most potent activity and the least cytotoxicity among the synthesized analogues. This specific anti-HIV activity was correlated with the ability of G-rich sequences to form stable quadruplex structures (*8, 9*), postulated to be the ultimate active species, directly interacting with the *in vivo* targets. Evidence for quadruplex formation in 5′-substituted d($^{5'}$TGGGAG$^{3'}$) sequences was obtained by CD spectra, showing a large positive band at 263 nm, diagnostic of parallel, tetramolecular G-quadruplex structures (*4*). The hypothesized mechanism of action of these 5′-conjugated G-rich ODNs is based on the interference/inhibition of both cell-to-cell transmission and virus-to-cell transmission of HIV-1 by interaction with both the V3 loop and the CD4 binding site on viral gp120, in analogy with the behavior proposed for the phosphorothioate oligonucleotides d($^{5'}$TTGGGGTT$^{3'}$) (*10*) and d($^{5'}$GGGTTTTGGG$^{3'}$) (*11*), forming, respectively, tetramolecular and bimolecular G-quadruplex complexes.

Other examples of G-rich oligonucleotides folding into highly stable quadruplexes, found to be potent inhibitors of HIV replication in cell culture, are also known from the literature (*12, 13*). In particular, a recent study (*14*) has identified the 16-mer guanine-rich sequence d(GGGGTGGGAGGAGGGT), designated *93del*, which inhibits both the processing and strand transfer functions of HIV-1 integrase at nanomolar concentrations; and the NMR-based solution structure of this aptamer, adopting an unusually stable dimeric quadruplex architecture, has been described in detail (*15*).

Interestingly, Hotoda's unmodified d($^{5'}$TGGGAG$^{3'}$) showed no antiviral effects; no specific antiviral activity was also found when a relatively small aromatic residue, as the benzyl group, was inserted at the 5′ position of the same sequence. The antiviral activity of 5′-modified ODNs was therefore attributed to the presence of large aromatic groups at the 5′-end of the native ODN backbone, which could produce hydrophobic effects stabilizing quadruplex structures. CD spectra of the investigated ODNs were in agreement with the hypothesized relationship between G-quadruplex formation and antiviral activity, but no successive data appeared in the literature to analyze these G-quadruplex forming systems in a quantitative manner or to shed light on their conformational differences.

The final conclusion of the authors is that *both* the G-quadruplex forming ODN backbone *and* the cluster of 5′-end substituents contribute to the interaction of the 6-mers with viral gp120. These results can also be correlated to a previous study on the 20-mer phosphorothioate d($^{5'}$TGGGGCTTACCTTG-CGAACA$^{3'}$) carrying covalently attached cholesteryl tails (*16*).

* E-mail: montesar@unina.it.
[†] Dipartimento di Chimica Organica e Biochimica.
[‡] Dipartimento di Chimica.

10.1021/bc070062f CCC: $37.00 © 2007 American Chemical Society
Published on Web 06/15/2007

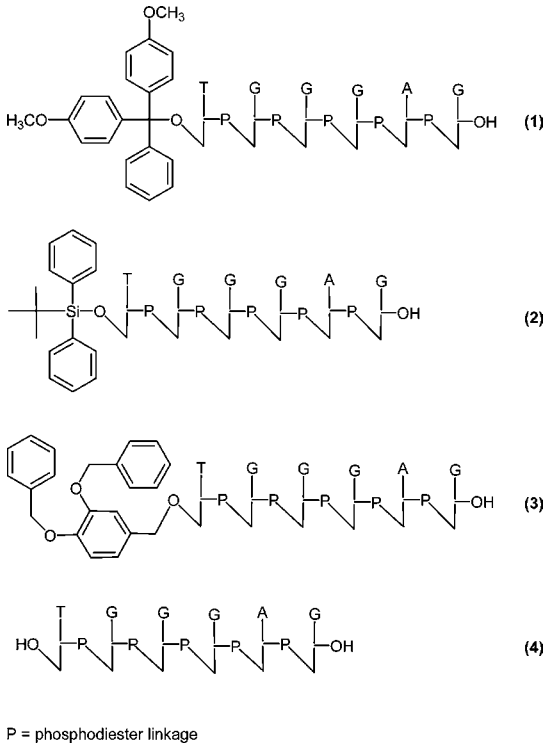


Figure 1. Oligonucleotides used.

In this work, the 3′-conjugated oligomer was showed to form a stable quadruplex aggregate; conversely, the corresponding 5′-conjugate was essentially present as a single strand, which was explained as a consequence of negative steric effects impeding efficient G-quartet formation.

Aiming at the design of novel, more efficient oligonucleotide-based antivirals, we focused our attention on Hotoda's 5′-conjugated d($^{5'}$TGGGAG$^{3'}$) sequences, chosen as model compounds, to determine the main physicochemical parameters of the corresponding quadruplex structures, presumably present also in physiological conditions. In this paper, we intend to explore possible direct relationships between the specific effects induced by the terminal groups and the thermodynamic and kinetic aspects of quadruplex formation. To this purpose, we have selected a set of 5′-substituted Hotoda's ODNs, among the ones showing the highest antiviral activity (*4*), *i.e.*, 5′-DMT, 5′-*tert*-butyldiphenylsilyl (TBDPS), and 5′-DBB-ether modified 6-mers (**1**, **2**, and **3**, Figure 1 and Table 1), and compared them to the natural sequence (**4**, Figure 1). In the case of ODN **3**, an alternative and more efficient procedure has been developed (*17*) for the synthesis of 5′-DBB-thymidine-phosphoramidite building block **13** (Scheme 2), used in the last coupling step of the automated ODN chain assembly.

In all the studied cases, a detailed CD investigation for the analysis of the conformational behavior, as well as a DSC analysis, have been carried out for the complete description of the thermodynamic and kinetic parameters governing the tetraplex formation processes in solution. The obtained experimental data have been examined in light of the molecular models, generated to directly investigate the main conformational differences of the quadruplex structures formed by 5′-conjugated ODNs **1**−**3** (here described, respectively, as Q-DMT, Q-TBDPS, and Q-DBB), in comparison to the quadruplex obtained by unmodified ODN **4** (Q-TGGGAG).

EXPERIMENTAL PROCEDURES

Synthesis and Characterization of Oligonucleotides 1−**4.** Phosphoramidite building blocks **6** and **13** were synthesized following the reactions described respectively in Schemes 1 and 2. In the case of 5′-*O*-*tert*-butyldiphenylsilylthymidine-3′-*O*-(2-cyanoethyl)-*N*,*N*-diisopropylphosphoramidite **6**, known procedures were essentially followed (*18*). An alternative, more efficient procedure was developed for the synthesis of 5′-DBB oligomer **3**, based on the usage of novel building block **13** (*17*). A full description of the synthetic procedures adopted for the preparation of 5′-modified thymidine phosphoramidites **6** and **13**, of the NMR and ESI-MS characterization for all the nucleoside intermediates and final compounds, and of the general experimental procedures are reported in the Supporting Information.

Oligonucleotides **1**−**4** were synthesized using standard solid-phase β-cyanoethyl phosphoramidite chemistry on a 15 μmol scale. In the case of oligomers **1** and **4**, starting from 100 mg of functionalized CPG[1]-dG support with 0.10 mequiv/g initial loading, the sequence $^{5'}$d(TG$_3$AG)$^{3'}$ was assembled by exploiting standard commercially available 3′-phosphoramidite 2′-deoxynucleoside monomers, respectively adopting the DMT-on, for oligomer **1**, and the DMT-off protocol, for oligomer **4**. Analogously, the solid-phase assembly of oligomers **2** and **3** was carried out starting from 100 mg of functionalized CPG-dG support with 0.10 mequiv/g initial loading, using, respectively, 5′-TBDPS- and 5′-DBB-thymidine phosphoramidite (**6**, Scheme 1; and **13**, Scheme 2) in the last coupling step of the chain assembly. Oligomers **1**, **2**, and **4** were detached from the solid support and deprotected by standard treatment with conc aq ammonia at 55 °C for 12 h. In the case of oligomer **3**, detachment from the solid support and full oligonucleotide deprotection, including complete thymidine unmasking, was successfully achieved by an overnight treatment at 50 °C with a 0.1 M NaOH solution.

The combined filtrates and washings were concentrated under reduced pressure, redissolved in H_2O, and analyzed and purified by HPLC on a Nucleosil RP18 column (Supelco, 100−5, C18, 4.6 × 250 mm, 7 μm), using a linear gradient from 20% to 100% of CH_3CN in 0.1 M TEAB in 20 min, flow rate 0.8 mL/min, and detection at λ = 260 nm. The isolated oligomers had the following retention times: **1** = 17.5 min; **2** = 14.0 min; **3** = 11.5 min. After HPLC purification, the oligonucleotide samples were desalted on a Sephadex G25 column eluted with H_2O/EtOH (4:1, v/v). The isolated oligomers proved to be more than 98% pure by ^{1}H NMR and RP-HPLC analysis and were characterized by ESI-MS and/or MALDI-TOF mass spectrometry.

Purification of the crude natural oligomer **4** was carried out on an analytical anion exchange Nucleogel SAX column (Macherey−Nagel, 1000−8/46, 4.6 × 50 mm, 5 μm), adopting the following eluents: buffer A, 20 mM KH_2PO_4/K_2HPO_4 aq solution (pH 7.0), containing 20% (v/v) CH_3CN; buffer B, 1 M KCl, 20 mM KH_2PO_4/K_2HPO_4 aq solution (pH 7.0), containing 20% (v/v) CH_3CN. Using a linear gradient from 0% to 100% B in 40 min, flow rate 0.8 mL/min, and detection at λ = 260 nm, two main peaks were observed, with retention times 15.5 min and 26.7 min. As also reported by Hotoda (*4*), in all the purification attempts on an anionic exchange HPLC column, the fastest eluting peak, attributed to the single-strand 6-mer, was always accompanied by a major peak, having a higher retention time. This additional peak was attributed to a G-quadruplex structure generated under HPLC elution conditions. In fact, by reinjecting on HPLC the isolated and desalted fastest

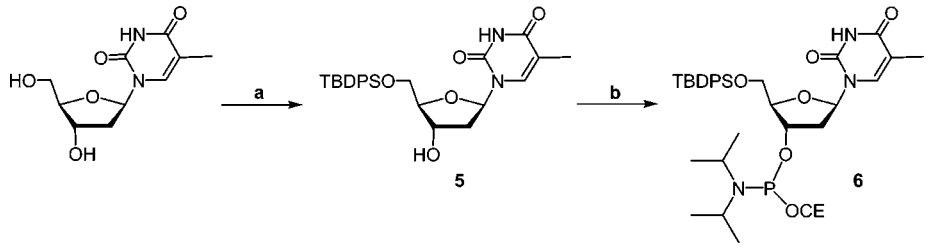
[1] Abbreviations: ADDP = 1,1′-(azodicarbonyl)dipiperidine; mCPBA = 3-chloroperbenzoic acid; CPG = controlled pore glass; DMAP = 4-dimethylaminopyridine; DMF = *N*,*N*-dimethylformamide; TBAF = tetrabutylammonium fluoride; TEA = triethylamine; TEAB = triethylammonium bicarbonate; TFA = trifluoroacetic acid; THF = tetrahydrofuran.

Table 1. Physical Data of ODNs 1−4

entry	sequence	HPLC,[a] t_R (min)	MS data[b] calcd	MS data[b] found	IC_{50} values[c] (μM)
1	DMT-$^{5'}$TGGGAG$^{3'}$	17.5	2173.49	2174.57	1.0 ± 0.21
2	TBDPS-$^{5'}$TGGGAG$^{3'}$	14.0	2109.48	2110.96	0.88 ± 0.070
3	DBB-$^{5'}$TGGGAG$^{3'}$	11.5	2173.49	2172.76	0.37 ± 0.060
4	$^{5'}$TGGGAG$^{3'}$	15.5 and 26.7	1871.36	1872.01	not active up to 40 μM

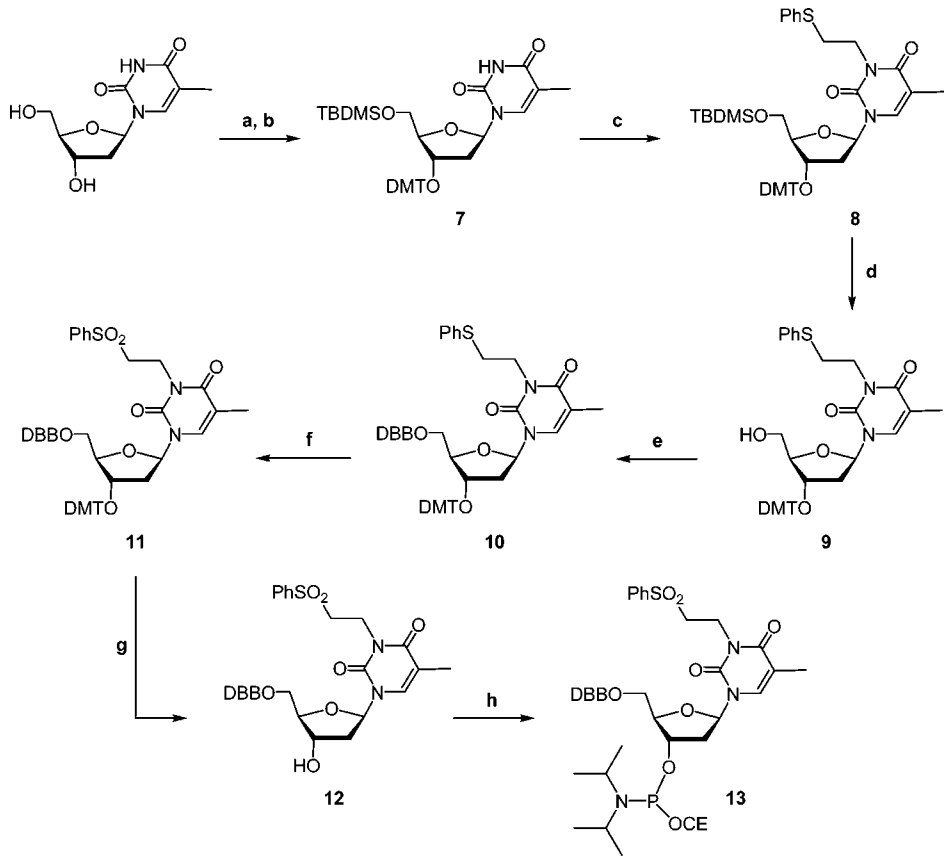
[a] HPLC conditions are described in Experimental Procedures. [b] See Supporting Information. [c] See ref 4.

Scheme 1 [a]



[a] Reagents and conditions: **a**, TBDPSCl, imidazole, DMF, 5 h, rt (95%); **b**, 2-cyanoethyl-*N*,*N*-diisopropylchlorophosphoramidite, TEA, CH_2Cl_2, 30 min, rt (92%).

Scheme 2 [a]



[a] Reagents and conditions: **a**, TBDMSCl, imidazole, DMF, 5 h, rt (quant.); **b**, DMTCl, DMAP, pyridine, 12 h, rt (95%); **c**, $PhSCH_2CH_2OH$, PBu_3-ADDP in benzene, 18 h, 0 °C to rt (90%); **d**, 1 M TBAF in THF, 30 min, rt (98%); **e**, NaH, DBBCl, NaI, DMF, 18 h, rt (70%); **f**, *m*CPBA, CH_2Cl_2, 1 h, rt (98%); **g**, 3% TFA in CH_2Cl_2, 30 min, rt (94%); **h**, 2-cyanoethyl-*N*,*N*-diisopropylchlorophosphoramidite, TEA, CH_2Cl_2, 30 min, rt (85%).

eluting peak, one could always observe the slowest eluting one also; in addition, the two isolated peaks, analyzed in the same conditions by ^{1}H NMR and ESI-MS spectra, always showed superimposable spectra.

In a typical experiment, starting from 100 mg of functionalized CPG-dG support, 110−150 OD units of purified **1**−**4** could be obtained.

Oligomer 1: Calcd mass for $C_{81}H_{92}N_{27}O_{36}P_5$: 2173.489; ESI-MS, found *m*/*z* 2174.57.

Oligomer 2: Calcd mass for $C_{76}H_{92}N_{27}O_{34}P_5Si$: 2109.476; ESI-MS, found *m*/*z* 2110.96.

Oligomer 3: Calcd mass for $C_{81}H_{92}N_{27}O_{36}P_5$: 2173.489; MALDI-TOF, found $[M - H]^-$: *m*/*z* 2172.76.

Oligomer 4: Calcd mass for $C_{60}H_{74}N_{27}O_{34}P_5$: 1871.358; ESI-MS, found *m*/*z* 1872.01.

Quadruplex Preparation. The quadruplex complexes were formed by dissolving the lyophilized compound in the appropriate buffer and annealed by heating at 95 °C for 5 min and slowly

cooling to room temperature. The buffer used was 10 mM potassium phosphate, 200 mM KCl, 0.1 mM EDTA at pH = 7.0. The concentrations of the dissolved oligonucleotides **1**−**3** were determined by UV measurements at 260 nm and at 95 °C, using, as the molar extinction coefficients, the values calculated by the nearest-neighbor model (*19*) for the sequence $^{5'}$GGGAG$^{3'}$, to which the ϵ coefficient determined for the corresponding 5′-conjugated thymidylic acid residue (9100, 8900, and 9000 cm^{-1} M^{-1}, respectively, for 5′-DMT, 5′-TBDPS, and 5′-DBB-thymidine-3′-monophosphate derivatives; for the synthesis of these nucleotides, see Supporting Information) was added.

Thermal Dissociation and Reassociation. Thermal dissociation and reassociation of the different quadruplexes were monitored by recording the CD spectra as a function of the temperature. The molar ellipticity was calculated from the equation $[\vartheta] = 100\vartheta/cl$, where ϑ is the ellipticity value, c is the concentration of the single strand (2.0×10^{-4} M), and l is the path length of the cell in centimeters. The temperature was increased or decreased at a rate of 1.0 °C/min. The melting and annealing profiles were not superimposable, indicating that the dissociation/reassociation reactions were not in thermodynamic equilibrium. Since the heating curves are not equilibrium curves, the melting temperatures obtained from these experiments were indicated as $T_{1/2}$ to distinguish them from the thermodynamic melting temperatures (indicated as T_m).

Dissociation Kinetics. The quadruplex dissociation kinetics were measured by rapidly increasing the temperature and following the change with time of the CD signal at 263 nm. All the experiments were performed at 2.0×10^{-4} M single-strand concentration and in 60−80 °C temperature range, conditions under which the reassociation reaction can be neglected. The kinetic constants were obtained by fitting the recorded time-dependent decrease in CD signal with a single-exponential function.

Isothermal Kinetic Analysis for Association. The association of single strands into a well-defined quadruplex structure was monitored for each sequence in the buffer 10 mM potassium phosphate, 200 mM KCl, 0.1 mM EDTA at pH = 7.0. The experiments were carried out at various strand concentrations (between 5×10^{-6} and 2×10^{-4} M single-strand concentration), depending on the kinetics. The samples were incubated at 90 °C for 5 min to allow for dissociation. The structural transition from the single strands to the tetramolecular quadruplex was monitored in the temperature range 10−30 °C by recording the CD spectra as a function of time. Assuming that the dissociation is negligible, the single-strand concentration at any time is given by

$$[S]_t^{1-n} - [S]_0^{1-n} = 4(n-1)k_{on}t \qquad (1)$$

where $[S]_t$ is the single-strand concentration at time t, $[S]_0$ is the initial single-strand concentration, n is the order of the reaction with respect to the single-strand concentration, and k_{on} is the rate constant for the single-strand disappearance. As previously described (*20*), the changes in CD spectra at a given time t can be related with the single-strand concentration according to the equation

$$\Theta_t = \Theta_\infty - [(\Theta_\infty - \Theta_0)^{1-n} + (n-1)k't]^{1/1-n} \qquad (2)$$

where Θ_∞ and Θ_0 correspond to the ellipticity of the final and initial state, respectively. Θ_t is the ellipticity at time t, and $k' = 4(\Theta_\infty - \Theta_0/[S]_0)^{1-n}k_{on}$.

The association rate constants and the reaction orders were obtained by fitting the ellipticity at 263 nm as a function of time by means of eq 2 using *Origin 7.5* software.

DSC Experiments. Differential scanning calorimetry measurements were carried out on a third-generation Setaram Micro-DSC. The excess heat capacity function $\langle \Delta C_P \rangle$ was obtained after baseline subtraction, assuming that the baseline is given by the linear temperature dependence of the native-state heat capacity (*21*). No baseline difference was observed before and after the transition, indicating a negligible heat capacity difference between the initial and final states. The transition enthalpies, ΔH°_{cal}, were obtained by integrating the area under the heat capacity vs temperature curves. The enthalpy change values are the averages of at least three different heating experiments. The reported errors are the standard deviations of the mean from the multiple determinations.

Molecular Modeling. The conformational features of the quadruplexes generated by modified ODNs **1**−**3** have been explored by means of molecular modeling studies. All the calculations were performed on a personal computer running the *HyperChem 7.5* suite of programs. To build the $[d(TG_3AG)]_4$ quadruplex, the T and dG nucleotide residues were generated by using the coordinates of the corresponding residues in a previously reported quadruplex structure (*22*), whereas the A-tetrad was generated by using the coordinates of the dA residues in the reported structure of the $[d(TTAG_3T)]_4$ (*23*).

The DMT, DBB, and TBDPS groups were generated using the *HyperChem 7.5* building tool. Partial charges for all the atoms in the DMT, DBB, and TBDPS moieties were assigned using the Gasteiger-Marsili algorithm (*24*) implemented in the QSAR module of the HyperChem suite. The Q-DMT, Q-DBB, and Q-TBDPS quadruplexes were then built by linking the appropriate groups to the 5′-ends of the unmodified quadruplex. The resulting coordinates of the modified quadruplexes were energy-minimized in vacuum for 500 steps of the steepest-descent method, keeping the DNA residues in fixed position, allowing only the DMT, DBB, and TBDPS atoms to relax. Potassium ions were positioned in the central channel between the G-tetrads to allow for coordination, for each potassium ion, with the eight carbonyl oxygen atoms of the two adjacent G-quartets completing the octahedral coordination sphere. The remaining potassium counterions were added to give electrical neutrality, and then the neutralized systems were solvated in a preequilibrated box of TIP3P water (*25*). The water molecules within a 2.6 Å radius from any solute atoms were removed. The Amber force field was used (*26*). A simulated annealing was performed on the modified T residues before the energy structure minimization. During the simulated annealing, the DNA coordinates were kept fixed, and only the modified T residues and the solvent (water molecules and ions) were allowed to move. The initial conformation was first heated to 500 K over 10 ps, simulated at 500 K for 70 ps, and finally cooled to 10 K for 20 ps. Then, the whole system was minimized using 1000 cycles of the steepest-descent method followed by the conjugate gradient method until convergence to an rms gradient of 0.1 kcal mol^{-1} $Å^{-1}$.

The contributions of the DBB, TBDPS, and DMT groups to the total solvent-accessible surface area (SASA) were calculated using the grid method (*27*) implemented in the QSAR module of the HyperChem suite. The SASA was obtained for each aromatic group both in the quadruplex ($SASA^{quadruplex}$) and in the dissociated single strand ($SASA^{single\ strand}$). The $SASA^{quadruplex}$ values were calculated using the minimized quadruplex structures, whereas the $SASA^{single\ strand}$ values were obtained under the assumption that the aromatic groups in the single strands are completely exposed to the solvent. The difference $\Delta(SASA) = SASA^{quadruplex} - (4 \times SASA^{single\ strand})$ represents the relative reduction of the solvent-accessible surface area of the 5′-aromatic substituents that occurs upon quadruplex formation.

RESULTS

For a detailed investigation of the structural and biophysical properties of 5′-modified d(5′TGGGAG3′) sequences, the preparation of the model oligonucleotides in the 3−5 mg scale was a prerequisite. The 5′-modified oligomer **1** could be easily achieved by standard ODN chain assembly procedures, simply involving a DMT-on synthetic routine to preserve the 4,4′-dimethoxytriphenylmethyl group at the 5′-end of the oligonucleotide. On the other hand, for the preparation of ODNs **2** and **3** special protocols were required. In their papers, Hotoda and co-workers synthesized the 5′-modified oligonucleotides by means of standard phosphoramidite chemistry (*28*) using tailored 5′-substituted thymidine derivatives as the 5′-terminal residues. 5′-*O*-TBDPS-thymidine derivative **6** was synthesized in two steps, starting from thymidine, with 46% overall yields. 5′-*O*-(3,4-dibenzyloxy)benzylthymidine-3′-*O*-(2-cyanoethyl)-*N*,*N*-diisopropylphosphoramidite was obtained in three steps and 20% overall yields starting from 3′-*O*-*tert*-butyldimethylsilylthymidine (3′-*O*-TBDMS-thymidine), which in turn can be typically prepared from thymidine in three straightforward, high-yielding reactions (*18*).

In our hands, the preparation of phosphoramidite **6** was successfully achieved with 88% overall yields. Conversely, we always failed in the synthesis of 6-mer **3** following Hotoda's procedure, particularly at the crucial stage of the insertion of the 3,4-DBB group at the 5′-OH of the thymidine monomer. In Hotoda's protocol, the 5′-DBB-ether was synthesized by reacting, in the presence of NaH, DBB bromide (*29*) with 3′-*O*-TBDMS-thymidine in THF. The 5′-alkylated compound, recovered by the authors in very modest yields (23%), after TBDMS removal, was then phosphitylated in 87% yields to give the corresponding 3′-phosphoramidite derivative, used as the last addition monomer in the oligonucleotide chain growth. Following the same alkylation procedure, with the sole difference of using the commercially available DBB chloride in lieu of the bromide, we could exclusively isolate from the reaction mixtures the undesired N3-alkylation product, even when varying several experimental conditions. When further forcing the reaction, two compounds, identified after column chromatography as the N3, O-bis-alkylated derivatives, were observed. In fact, as also reported by Kobe et al. (*30*), starting from 3′-*O*-TBDMS-thymidine the concomitant formation, in almost 1:1 ratio, of both the N3, O-5′- and the N3, O-3′-bis-alkylated derivative occurred, as a result of the hydride-mediated migration of the TBDMS group from the 3′- to the 5′-position. These results led us to develop an alternative protection strategy for the thymidine moieties to more efficiently obtain the 5′-alkylated nucleoside, based on (i) protection of the 3′-OH function with a group completely stable under basic conditions and reluctant to migrate to the 5′-OH and (ii) protection of the thymine base.

Having discarded the silyl ethers as the 3′-OH protecting groups, we moved to the DMT group, completely stable even to harsh basic media, and searched for a suitable heterocycle protection. A novel, two-stage protecting group, namely, the 2-(phenylthio)ethyl group, proved to be useful to our purposes, preventing otherwise predominant N-alkylation of thymine (*17*). The phenylthioethyl residue proved to be completely stable onto the heterocycle as such, but after oxidation of the tioether to sulfone, the resulting group could be easily removed *via* a β-elimination reaction. Treatment with a 0.1 M NaOH solution at 50 °C allowed complete thymine deblocking after 12 h, *i.e.*, under conditions usually adopted also for oligonucleotide deprotection and detachment from the solid support.

We therefore synthesized 5′-*O*-TBDMS-3′-*O*-DMT-thymidine **7** as the starting material and reacted it with 2-(phenylthio)-ethanol under standard Mitsunobu conditions (Scheme 2). Following this protocol, the N3-alkylated nucleoside **8** was obtained in 85% yields for the three steps. Subsequent standard triethylammonium fluoride treatment yielded the 5′-OH derivative **9** in almost quantitative yields, which was next reacted with DBBCl and NaH with cat. NaI, to give the desired 5′-DBB adduct **10** in 70% yields. After oxidation with mCPBA of the thioether function to sulfone **11**, addition of 3% TFA in CH_2Cl_2 led to **12**, which was finally phosphitylated to give desired **13**. Starting from 5′-*O*-TBDMS-3′-*O*-DMT-thymidine, 3′-phosphoramidite building block **13** was obtained in six straightforward steps and 48% overall yields (46% overall yields starting from thymidine).

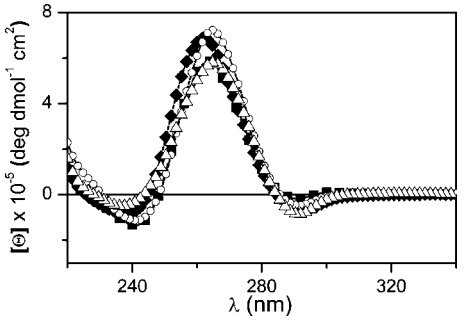


Figure 2. CD spectra of the Q-TGGGAG (squares), Q-DBB (open triangles), Q-TBDPS (open circles), and Q-DMT (diamonds). The spectra were recorded at 10 °C in a 10 mM potassium phosphate buffer (pH 7.0) supplemented with 200 mM KCl.

The assembly of oligomers **1**−**4** was then achieved on an automated DNA synthesizer by exploiting classical phosphoramidite chemistry, using a standard DMT-on protocol for 5′-conjugated **1**−**3**. In the case of the synthesis of **2** and **3**, the last coupling was carried out, respectively, using the building block 5′-TBDPS-thymidine phosphoramidite **6** or 5′-DBB-thymidine phosphoramidite **13**. Once the assembly of the desired sequence was completed, detachment from the solid support and full deprotection of the 5′-conjugated oligomer, including thymine protecting group removal for oligomer **3**, were achieved by an overnight treatment with 0.1 M NaOH.

Purification of the detached oligomers was carried out by HPLC on an analytical anionic exchange column in the case of **4** and on an analytical RP18 column for **1**−**3** (see Experimental Procedures). The isolated products, desalted on a Sephadex G25 column, were checked for purity by HPLC and characterized by mass analysis (Table 1).

The dissociation and reassociation of the tetramolecular quadruplexes were followed by circular dichroism. The CD spectra at 10 °C for all the studied sequences showed a positive band at 263 nm and a negative band at 243 nm (Figure 2), diagnostic of parallel-stranded tetramolecular quadruplex structures (*4*, *31*). In Figure 3, the melting and annealing CD profiles are shown for all the samples at the heating and cooling rate of 1.0 °C/min. All the quadruplexes show hysteresis between the melting and annealing profiles, which indicates that the association/dissociation reaction is not at thermodynamic equilibrium during the heating and cooling experiments (*32*, *33*). The melting temperatures obtained at 1.0 °C/min scan rate are very similar for the modified quadruplexes. Particularly, the $T_{1/2}$ values are 89 °C for the Q-TBDPS, 86 °C for the Q-DMT, and 83 °C for the Q-DBB, whereas the $T_{1/2}$ for the unmodified quadruplex is 60 °C. Q-DBB and Q-TBDPS show less pronounced hysteresis between melting and annealing curves than Q-DMT. In addition, almost no reassociation of the unmodified strands (Figure 3) was observed during the cooling curve. These findings suggest that Q-TBDPS and Q-DBB complexes are formed faster than Q-DMT and that all the modified strands associate faster than the unmodified strands. In the case of Q-DMT, the melting and annealing profiles were

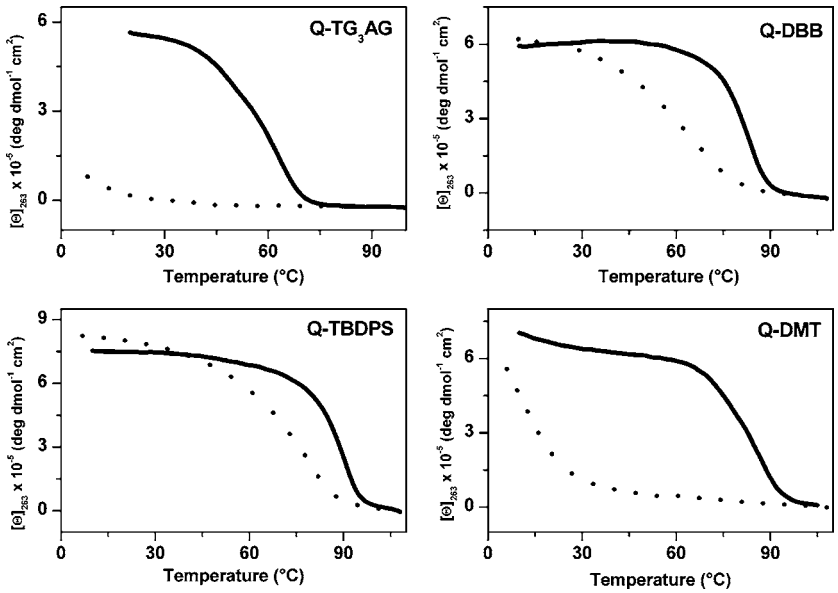


Figure 3. CD melting and annealing profiles for the studied quadruplexes. The solid lines are relative to melting profiles and the dot lines to annealing profiles. All the experiments were performed in a 10 mM potassium phosphate buffer (pH 7.0) supplemented with 200 mM KCl.

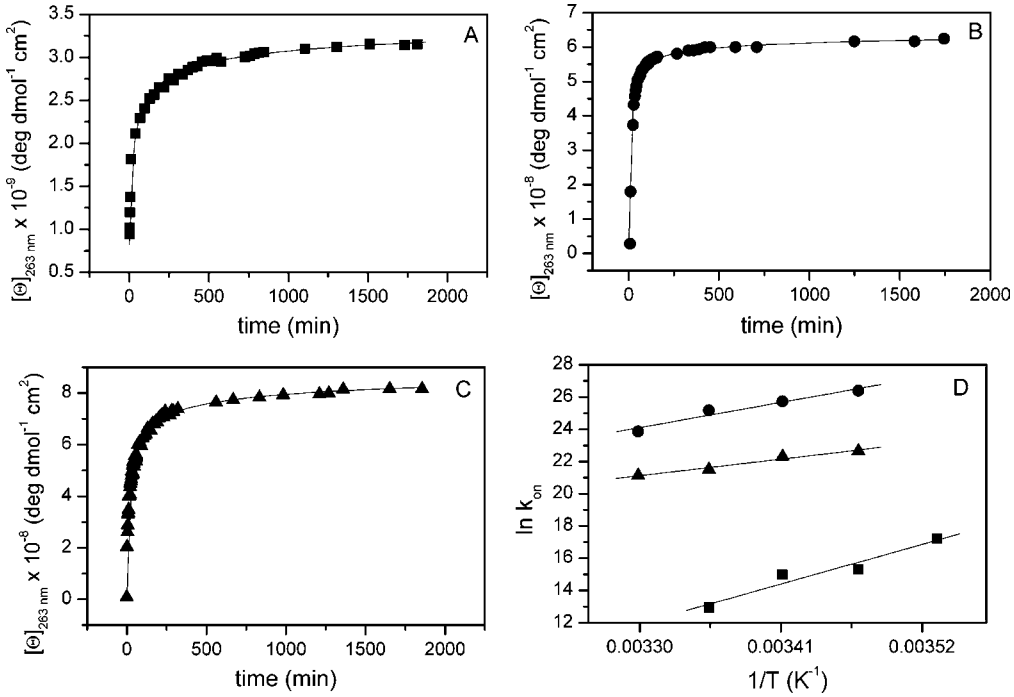


Figure 4. Kinetics of the quadruplex formation. Association profiles for **4** (A), **2** (B), and **3** (C) at 15 °C. Single-strand concentrations used: 2×10^{-5} M for **2**, 4.4×10^{-5} M for **3**, and 4.4×10^{-4} M for **4**. Quadruplex formation leads to an increase of molar ellipticity at 263 nm. Mathematical fits are shown in solid line. (D) Arrhenius plots for the association of **4** (squares), **2** (circles), and **3** (triangles). All the experiments were performed in a 10 mM potassium phosphate buffer (pH 7.0) supplemented with 200 mM KCl.

always found to be not fully reproducible (data not shown). This behavior was not completely unexpected, since the prolonged exposition to high temperatures is well-known to cause partial 5′-deprotection of 5′-DMT-oligonucleotides. To confirm this hypothesis, the Q-DMT samples were analyzed for integrity by RP HPLC after each heating experiment, resulting in a mixture of **1** and **4**. For this reason, the Q-DMT system could not be investigated in detail, and our efforts were then concentrated on more chemically stable ODNs **2**−**4**.

The kinetics of Q-DBB, Q-TBDPS, and Q-TGGGAG quadruplex association was directly measured. The rate of the association reaction was studied by monitoring the ellipticity at 263 nm as a function of time after heating the sample at 95 °C for 5 min and cooling rapidly. Representative molar ellipticity vs time profiles at 15 °C are shown in Figure 4. Similar profiles were obtained at the other investigated temperatures (see Figures S1−S3 in the Supporting Information).

The experimental curves were fitted by means of eq 2. All the data for the studied sequences were fitted well by reaction order of 4.0. The kinetic constants (k_{on}) for the studied sequences are compared in Table 2. The rate of quadruplex association follows the order Q-TBDPS > Q-DBB > Q-TGGGAG. The association rate constants at 25 °C were 8.6×10^{10} M^{-3} s^{-1} and 2.2×10^{9} M^{-3} s^{-1} for Q-TBDPS and Q-DBB, respectively. The corresponding value found for the unmodified sequence at the same temperature is 4.1×10^{5} M^{-3} s^{-1}.

The kinetic experiments were performed over the temperature range 10−30 °C. For all the sequences, the association rate

Table 2. Kinetic Parameters for the Quadruplex Formation[a]

quadruplex	temp (°C) ±1	n	k_{on} (M^{-3} s^{-1})[b]	E_{on} (kJ mol^{-1})
Q-TBDPS	15	4	$(2.9 \pm 0.5) \times 10^{11}$	
	20	4	$(1.5 \pm 0.6) \times 10^{11}$	
	25	4	$(8.6 \pm 0.5) \times 10^{10}$	-125 ± 19
	30	4	$(2.3 \pm 0.8) \times 10^{10}$	
Q-DBB	15	4	$(6.9 \pm 0.4) \times 10^{9}$	
	20	4	$(4.9 \pm 0.4) \times 10^{9}$	
	25	4	$(2.2 \pm 0.7) \times 10^{9}$	-90 ± 9
	30	4	$(1.5 \pm 0.3) \times 10^{9}$	
Q-TGGGAG	10	4	$(3.0 \pm 0.5) \times 10^{7}$	
	15	4	$(4.5 \pm 0.8) \times 10^{6}$	
	20	4	$(3.2 \pm 0.2) \times 10^{6}$	-190 ± 20
	25	4	$(4.1 \pm 0.3) \times 10^{5}$	

[a] All the values have been determined in a 200 mM KCl, 10 mM potassium phosphate, pH 7.0 buffer. [b] k_{on} is defined as $d[S]/dt = -4d[S_4]/dt = -k_{on}[S]^4$.

Table 3. Kinetic Parameters for the Quadruplex Dissociation[a]

quadruplex	temp (°C) ±1	$k_{off} \times 10^4$ [b] (s^{-1})	$t_{1/2}$ [c]	E_{off} (kJ mol^{-1})
Q-TBDPS	70	0.50 ± 0.03		
	73	0.83 ± 0.02		
	75	1.4 ± 0.4	591 days	
	77	2.3 ± 0.1		220 ± 20
	80	3.5 ± 0.3		
Q-DBB	65	1.8 ± 0.5		
	67	2.2 ± 0.5		
	70	5.0 ± 0.4	41 days	
	73	9.1 ± 0.3		210 ± 9
	75	15 ± 3		
Q-TGGGAG	63	40 ± 1		
	65	46 ± 1		
	67	67 ± 1	69 min	
	70	84 ± 5		105 ± 14
	73	120 ± 9		

[a] All the values have been determined in a 200 mM KCl, 10 mM potassium phosphate, pH 7.0 buffer. [b] k_{off} is defined as $d[S]/dt = -d[S_4]/dt = k_{off}[S_4]$. [c] Half-dissociation times of tetramolecular quadruplex at 37 °C.

Table 4. Thermodynamic Parameters for the Quadruplex Dissociation

quadruplex	T_m (°C) ±1	ΔH°_{cal} (kJ mol^{-1})	ΔH°_{kin} (kJ mol^{-1})	ΔS° (kJ mol^{-1} K^{-1})	ΔG°_{298} (kJ mol^{-1})
Q-TGGGAG	26	310 ± 12	295 ± 34	0.82 ± 0.03	66 ± 21
Q-DBB	72	320 ± 15	300 ± 17	0.71 ± 0.03	108 ± 15
Q-TBDPS	75	355 ± 15	345 ± 39	0.80 ± 0.03	117 ± 15
Q-DMT		330 ± 13			

decreases upon increasing the temperature, and this effect is more pronounced for the unmodified sequence. From the slope of the Arrhenius plots (Figure 4D), the activation energies (E_{on}) could be derived (Table 2). We found negative activation energies for all the sequences, as already reported in the literature for other quadruplexes and attributed to the existence of a rapid preequilibrium step involving intermediate species (*20*, *32*, *34*, *35*).

The kinetics of quadruplex dissociation was also investigated by performing temperature-jump experiments. In each experiment, the temperature of the sample was rapidly increased, and the rate of quadruplex dissociation was monitored by following the change of CD signal with time. Representative kinetic profiles obtained at 65 °C are shown in Figure 5. Similar profiles were obtained at the other investigated temperatures (see Figures S4−S6 in the Supporting Information). The dissociation rate constants were obtained by fitting these kinetic profiles with a single-exponential curve. The kinetic constants were then used to construct the Arrhenius plots (Figure 5D), so allowing the determination of the corresponding activation energies. The kinetic parameters for quadruplexes dissociation are summarized in Table 3. Both Q-TBDPS and Q-DBB have k_{off} values 10−100 times smaller than the corresponding value of Q-TGGGAG at the same temperature. Analogously, the modified quadruplexes have higher activation energies in comparison with the unmodified one. The values found for Q-TBDPS and Q-DBB are about 100 kJ mol^{-1} higher than the one found for Q-TGGGAG, proving that the presence of the aromatic groups significantly stabilizes the quadruplex structure. The kinetically most stable complex is Q-TBDPS, with a half-life of 591 days at 37 °C, whereas at the same temperature, the half-life for the unmodified quadruplex is 69 min.

Differential scanning calorimetry (DSC) experiments were performed on each quadruplex, and the corresponding calorimetric profiles at scan rate of 1.0 °C/min are shown in Figure 6. The calorimetric profiles and melting temperatures were influenced by the scan rate (Figure 7), indicating nonequilibrium conditions, analogous to the results already found in the CD-monitored melting experiments. Although the ΔS°, ΔG°, and T_m values cannot be derived from these measurements as they are not at equilibrium, the enthalpy changes measured can be correctly attributed to the quadruplex−single-strand transition, provided that the oligonucleotides are 100% structured in the quadruplex form at the starting temperature of the DSC scan. To ensure complete quadruplex formation, before DSC experiments, each sequence was annealed by heating at 95 °C for 5 min and slowly cooling to room temperature, and then incubated at low temperature for an appropriate time, depending on the known association kinetics. The enthalpy changes for all the quadruplexes are reported in Table 4. Note, however, that the value obtained here for Q-DMT is assumed to be less precise; in fact, it cannot be excluded that partial detritylation occurred when the sample was exposed to high temperatures. This event was indeed directly analyzed in the case of the samples prepared for the CD-monitored melting investigations.

The thermodynamic parameters for the dissociation of the quadruplexes were calculated from the rate constants and the activation energies (*35*, *36*). These kinetically derived thermodynamic parameters are reported in Table 4. There is a good agreement between the calorimetric $\Delta H^\circ_{cal}\Delta$ values and the kinetically derived values ($\Delta H^\circ = E_{on} - E_{off}$). It is noteworthy that all the modified quadruplexes show an equilibrium melting temperature (T_m) much higher than 37 °C, whereas the unmodified quadruplex show a lower equilibrium T_m (26 °C). The ΔS° and ΔG° values were calculated using the more accurate ΔH°_{cal} values.

The ΔH°_{cal} value for the unmodified quadruplex is 310 kJ mol^{-1}, which accounts for the formation of four G-tetrads (*31*, *37*, *38*) and suggests that both the dA and dG nucleotide at the 3′-ends of the ODN strand participate in the overall quadruplex stabilization. All the modified quadruplexes have higher enthalpic terms in comparison with the unmodified quadruplex. Particularly, the ΔH°_{cal} values of the modified quadruplexes follow the order Q-TBDPS > Q-DMT > Q-DBB. The same trend was observed for the ΔS° values of Q-TBDPS and Q-DBB, thus counterbalancing the contribution given by the ΔH°_{cal} and leading to comparable data for the T_m and free energy values for Q-TBDPS and Q-DBB.

We used molecular modeling to explore the main conformational differences induced by the presence of the DBB, DMT, and TBDPS groups at the 5′-end of the d(5′TGGGAG3′) quadruplex structures. In Figure 8, the minimized structures of the three modified quadruplexes are shown. In the top view, the central channel of the quadruplex structure is clearly visible for Q-TBDPS and Q-DMT, whereas in Q-DBB, it is hidden by the DBB groups, suggesting that only this moiety is able to span the distance between the 5′-ends of nonadjacent strands.

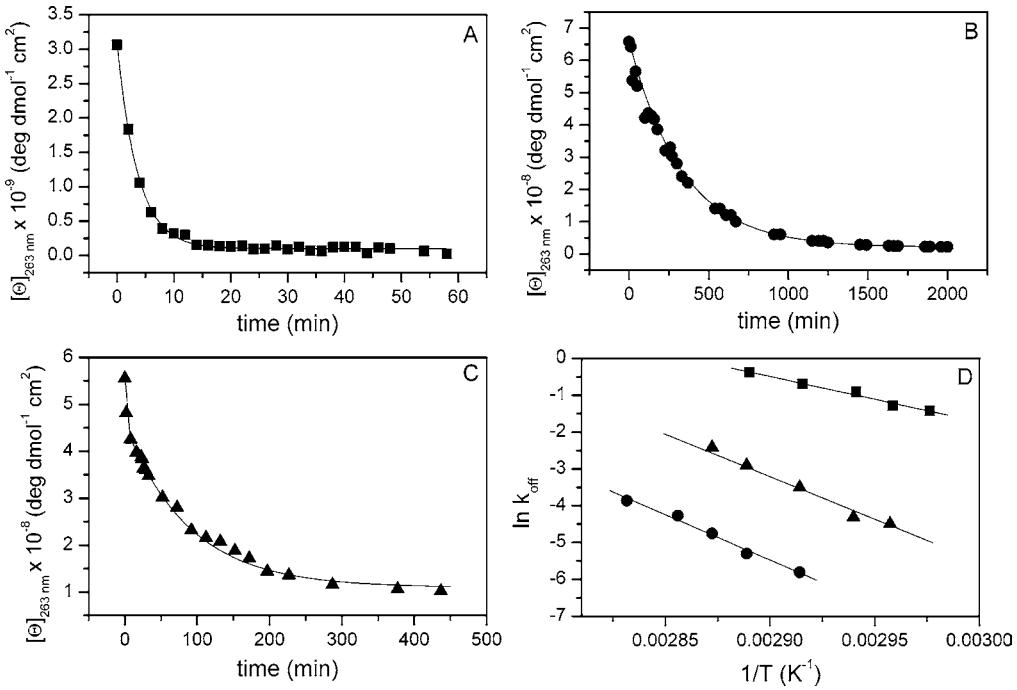


Figure 5. Kinetics of the quadruplex dissociation. Dissociation profiles for Q-TGGGAG (A) and Q-DBB (C), measured at 65 °C, and for Q-TBDPS (B) measured at 70 °C. Quadruplex dissociation leads to a decrease of the molar ellipticity at 263 nm. Mathematical fits are shown in solid line. (D) Arrhenius plots for the dissociation of the Q-TGGGAG (squares), Q-TBDPS (circles), and Q-DBB (triangles). All the experiments were performed in 10 mM potassium phosphate buffer (pH 7.0) supplemented with 200 mM KCl.

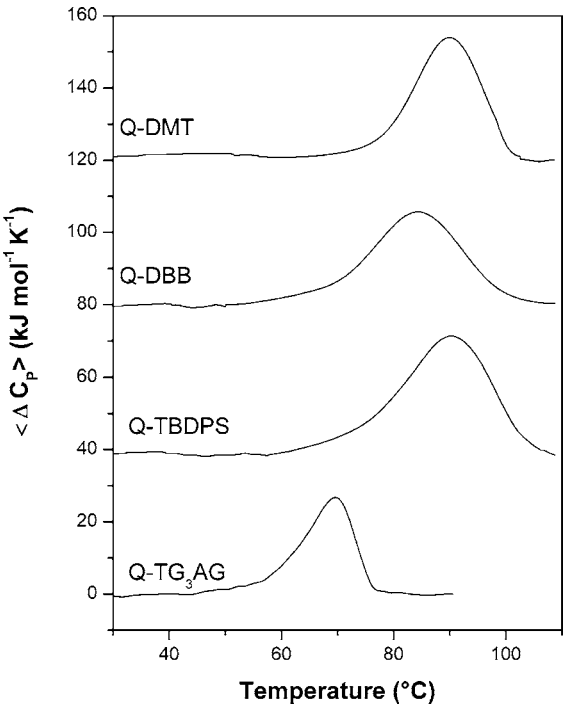


Figure 6. Calorimetric heat capacity vs temperature profiles at 1 °C/min for the studied quadruplexes. Excess capacity values have been shifted along the *y*-axis for ease of presentation. All the experiments were performed in a 10 mM potassium phosphate buffer (pH 7.0) supplemented with 200 mM KCl.

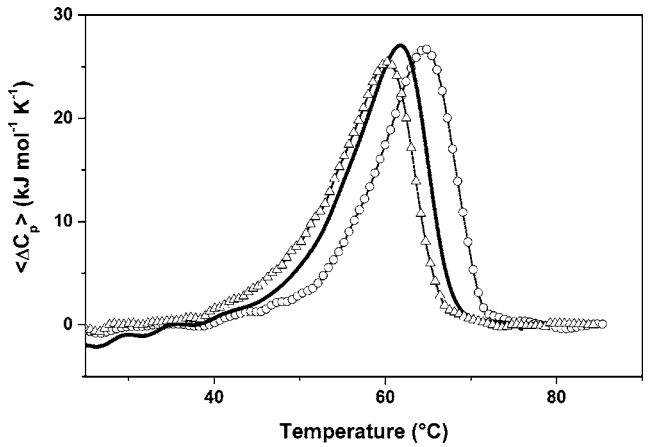


Figure 7. Calorimetric heat capacity vs temperature profiles at different scan rate 0.3 °C/min (open triangles), 0.5 °C/min (solid line), and 1 °C/min (open circles) for the Q-TGGGAG. All the experiments were performed in a 10 mM potassium phosphate buffer (pH 7.0) supplemented with 200 mM KCl.

Close inspection of the models reveals that the DBB aromatic rings form a network of noncovalent face-to-face and face-to-edge (T-shaped) aromatic interactions, so that the planar four thymines at the 5′-end of the strands are not exposed to the solvent.

Still being isomers, the DBB and the DMT groups confer different properties to the resulting quadruplex complexes. In the DBB group, the three phenyl rings are spaced by the flexible O−CH_2− linkers and can adopt different relative orientations, whereas in the DMT group, the three phenyl residues, being attached to the same carbon atom, show a significantly reduced flexibility and, to avoid steric crowding, are obliged to be approximately perpendicular to each other. In Q-DMT, the DMT group does not stack over the surface formed by the four thymine bases, with the three phenyl rings largely projected away from the helix axis, to minimize mutual steric hindrance interactions. However, in Q-DMT, a certain number of van der Waals contacts were observed between the aromatic groups of adjacent strands.

In Q-TBDPS, the TBDPS groups are not large enough to directly interact with each other over the quadruplex surface at the 5′-end and only show stacking interactions with the adjacent thymine base.

To compare the relative contributions of the modified groups to the hydrophobic interactions involved in the quadruplex

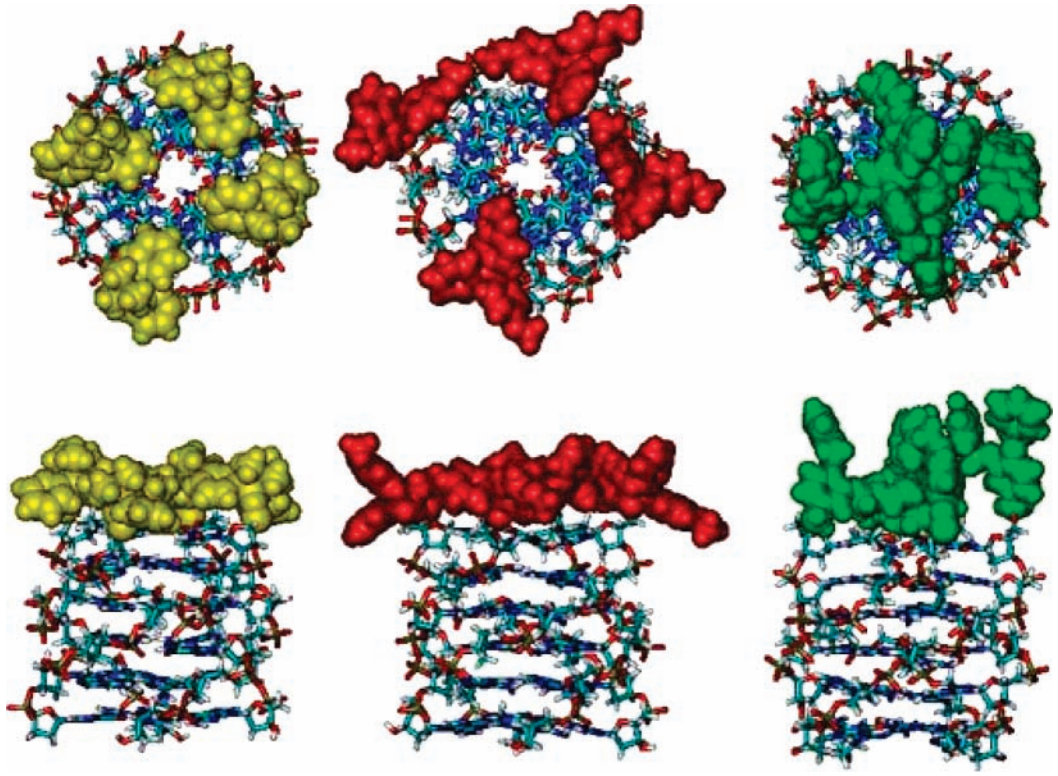


Figure 8. Top and lateral views of the molecular models of Q-TBDPS (left), Q-DMT (middle), and Q-DBB (right). The 5′-aromatic groups are shown with a space-filling representation.

Table 5. Contributions of the 5′-Aromatic Groups to the Total Solvent-Accessible Surface Area (SASA)

5′-aromatic groups	$SASA^{quadruplex}$ (Å^2)	$SASA^{single\ strand}$ (Å^2)	$\Delta(SASA)^a$ (Å^2)
DBB	1245	520	−835
TBDPS	1251	442	−517
DMT	1826	541	−338

^{a} $\Delta(SASA) = SASA^{quadruplex} - (4 \times SASA^{single\ strand})$.

formation, we calculated the relative decrease in the solvent-accessible surface area (SASA) for the DBB, TBDPS, and DMT groups in the quadruplex structure ($SASA^{quadruplex}$) with respect to the dissociated single strands ($SASA^{single\ strand}$). Inspection of the $\Delta(SASA)$ values (Table 5) reveals that the highest reduction in the solvent-accessible surface area upon quadruplex formation is observed in the case of the DBB group. This result suggests that the hydrophobic interactions play a major role in the Q-DBB quadruplex formation with respect to the other two modified quadruplexes.

DISCUSSION

In this work, we synthesized and characterized a set of 5′-substituted Hotoda's ODNs, among the ones showing the highest antiviral activity (*4*), *i.e.*, 5′-DMT, 5′-TBDPS, and 5′-DBB-ether modified 6-mers (**1**, **2**, and **3**, Figure 1 and Table 1). These ODNs were compared to the unmodified sequence, which showed no antiviral effects, in an attempt to put on a quantitative basis the hypothesized correlation between biological activity and physicochemical properties of these G-quadruplex-forming ODNs. Our results point out remarkable physicochemical differences between the Hotoda's 5′-substituted ODNs and the natural sequence. The insertion of large aromatic groups, as DMT, DBB, or TBDPS, at the 5′-end of the d($^{5'}$TGGGAG$^{3'}$) sequence has dramatic effects on the kinetics and thermodynamics of quadruplex formation. All the 5′-modified quadruplexes, showing comparable thermal stability, are far more stable than the natural quadruplex. Inspection of Table 4 reveals that the higher thermodynamic stability of Q-DBB and Q-TBDPS with respect to the natural quadruplex complex has different thermodynamic origins. Indeed, Q-DBB is entropically stabilized, whereas Q-TBDPS is mainly enthalpically stabilized in comparison with Q-TGGGAG. The low entropic term observed for the dissociation of the Q-DBB quadruplex can be due to a decrease of the solvation entropy of the DBB groups after the quadruplex dissociation. This hypothesis is supported by our molecular modeling results, revealing a significant increase of the solvent-accessible surface area (ΔSASA) of the DBB groups when they are not involved in the quadruplex structure. On the other hand, the formation of structured DBB groups in the Q-DBB quadruplex very weakly affects the overall enthalpic change involved in quadruplex formation, with this being the result of two opposite contributions: a positive contribution, due to hydrophobic factors, and a negative contribution, due to increased stacking and van der Waals interactions between the DBB groups. As a consequence, the enthalpic change for Q-DBB formation is very similar to the one measured for Q-TGGGAG.

Conversely, the higher thermodynamic stability of Q-TBDPS in comparison with the natural quadruplex is essentially due to the increased enthalpic term, suggesting that the hydrophobic effects play a minor role in this case, when compared to Q-DBB. This result is in agreement with the smaller $\Delta(SASA)$ value estimated from the molecular models (Table 5). Further, the stacking interactions between the TBDPS groups and the adjacent thymine bases, observed in the molecular models, can account for the higher enthalpic term measured in comparison with the natural quadruplex. In addition, in both Q-DBB and Q-TBDPS complexes, high activation energies were measured for the dissociation processes, consistent with the additional stacking and van der Waals interactions induced by the aromatic groups in these modified quadruplexes.

Another striking result of our study is that the introduction of the aromatic groups deeply affects the rate of quadruplex

formation. Under the same conditions, Q-TBDPS is assembled 10^5 times faster than Q-TGGGAG. The faster association kinetics of the modified single strand is probably due to hydrophobic interactions, which is consistent with the higher activation energies (hydrophobic interactions give a positive contribution to the total E_{on} value) measured for the modified strands with respect to the unmodified sequence.

Taken together, our data show that all the modified d(5′-TGGGAG3′) sequences are able to adopt stable G-quadruplex structures. On the contrary, the unmodified sequence forms a weak complex, with a T_m of 26 °C under the investigated conditions. Large aromatic groups at the 5′-end of the oligonucleotide chain dramatically stabilize the resulting G-quadruplex complexes on both a kinetic and a thermodynamic basis, with hydrophobic contributions on one side and additional stacking and van der Waals interactions on the other side playing major roles in the quadruplex formation processes. T_m values higher than 70 °C were found for Q-DBB and Q-TBDPS; similar indications were obtained also for Q-DMT from ΔH°_{cal} as obtained by DSC experiments, even if the latter case could not be further investigated in detail due to the intrinsic instability to high temperatures of the DMT ether linkage. High thermal stability, associated with a very fast association and slow dissociation, account for the 5′-modified ODNs fully structured in the form of quadruplex complexes; on the contrary, only a very small percentage of the unmodified oligomer is present in the aggregated form under physiological conditions. Since the physicochemical parameters for quadruplex stability reflect well the trend observed for the anti-HIV activity (see IC_{50} data reported in Table 1), our data can furnish indirect evidence that 5′-conjugated d(5′TGGGAG3′) oligomers interact with the HIV-1 gp120 target only if structured in the quadruplex form.

In conclusion, a systematic physicochemical characterization by DSC and CD analyses has been carried out on a representative set of 5′-modified d(5′TGGGAG3′) sequences, able to adopt stable G-quadruplex structures, to better understand the subtle features involved in the formation and stability of these complexes. The present results demonstrate that the large aromatic groups at the 5′-position of d(5′TGGGAG3′) play a decisive role in favoring the quadruplex formation processes. The unmodified sequence is indeed able to adopt a G-quadruplex structure, though it is not thermodynamically stable at physiological temperature and its formation is, in addition, very slow. Conversely, the 5′-modified quadruplexes are formed faster and, once formed, are very thermodynamically stable, with T_m values higher than 70 °C. These findings suggest a correlation between stability and rate of formation of the G-quadruplex structures on one side and anti-HIV activity of 5′-modified ODNs on the other side.

These results are useful not only to gain a critical insight into the biological behavior of Hotoda's 6-mers, but also to develop a general frame to better understand and, ultimately, roughly predict the effective potential as drugs of quadruplex-forming oligonucleotides. The very slow kinetics of quadruplex formation is one of the main drawbacks limiting efficient pharmacological applications of aptamers based on tetramolecular quadruplex structures. For this reason, it is highly desirable that, in a drug optimization process, most research efforts are concentrated on the rational search for well-tailored modifications to be inserted within the oligonucleotide backbone. Large aromatic groups may indeed be regarded as suitable appendages to enhance the biological activity of G-rich, quadruplex-forming ODNs, positively affecting both stability and rate of formation of quadruplex complexes.

This study, developed in the more general frame of the search for novel ODN analogues suitable for therapeutic applications, adds a further contribution to the research of biologically active quadruplex forming oligonucleotides, showing kinetic aspects as relevant as thermodynamic parameters in influencing the overall quadruplex formation process and therefore in affecting their biological role within the cell.

ACKNOWLEDGMENT

We acknowledge MIUR (PRIN) and Regione Campania (L5) for grants in support of this investigation. We also thank C.I.M.C.F., Università degli Studi di Napoli "Federico II", for the NMR, MS, and CD facilities.

Supporting Information Available: Synthetic procedures and characterization of phosphoramidite building blocks **6** and **13** and general experimental procedures and synthetic methods for the preparation of the 5′-DMT, 5′-TBDPS, and 5′-DBB nucleoside-3′-monophosphates for the ϵ calculation are reported. Kinetic profiles for the association process and for the dissociation process of Q-DBB, Q-TBDPS, and Q-TGGGAG at different temperatures are also available. This material is available free of charge via the Internet at htpp://pubs.acs.org/BC.

LITERATURE CITED

(1) Turner, J. J., Fabani, M., Arzumanov, A. A., Ivanova, G., and Gait, M. J. (2006) Targeting the HIV-1 RNA leader sequence with synthetic oligonucleotides and siRNA: chemistry and cell delivery. *Biochim. Biophys. Acta 1758*, 290−300.

(2) Markosian, M., and Hyde, R. M. (2005) Oligonucleotides and polyribonucleotides: a review of antiviral activity. *Antiviral Chem. Chemother. 16*, 91−102.

(3) Saravolac, E. G., Sun, L. Q., Cairns, M. J., and Wong, J. P. (2001) Nucleic acid-based drugs as antiviral agents. *Recent Dev. Antiviral Res. 1*, 117−141.

(4) Hotoda, H., Koizumi, M., Koga, R., Kaneko, M., Momota, K., Ohmine, T., Furukawa, H., Agatsuma, T., Nishigaki, T., Sone, J., Tsutsumi, S., Kosaka, T., Abe, K., Kimura, S., and Shimada, K. (1998) Biologically active oligodeoxyribonucleotides. 5. 5′-End-substituted d(TGGGAG) possesses anti-human immunodeficiency virus type 1 activity by forming a G-quadruplex structure. *J. Med. Chem. 41*, 3655−3663.

(5) Koizumi, M., Kaneko, M., Ohmine, T., Furukawa, H., and Nishigaki T. (1999) Patent no. JP98/04625, PCT/WO99/19474.

(6) Koizumi, M., Koga, R., Hotoda, H., Ohmine, T., Furukawa, H., Agatsuma, T., Nishigaki, T., Abe, K., Kosaka, T., Tsutsumi, S., et al. (1998) Biologically active oligodeoxyribonucleotides. Part 11: The least phosphate-modification of quadruplex-forming hexadeoxyribonucleotide TGGGAG, bearing 3′ -and 5′-end modification, with anti-HIV-1 activity. *Bioorg. Med. Chem. 6*, 2469−2475.

(7) Koizumi, M., Koga, R., Hotoda, H., Momota, K., Ohmine, T., Furukawa, H., Agatsuma, T., Nishigaki, T., Abe, K., Kosaka, T., et al. (1997) Biologically active oligodeoxyribonucleotides-IX. Synthesis and anti-HIV-1 activity of hexadeoxyribonucleotides, TGGGAG, bearing 3′- and 5′-end-modification. *Bioorg. Med. Chem. 5*, 2235−2243.

(8) Keniry, M. A. (2001) Quadruplex structures in nucleic acids. *Biopolymers 56*, 123−146.

(9) Petraccone, L., Barone, G., and Giancola, C. (2005) Quadruplex-forming oligonucleotides as tools in anticancer therapy and aptamers design: energetic aspects. *Curr. Med. Chem. Anticancer Agents 5*, 463−475.

(10) Wyatt, J. R., Vickers, T. A., Roberson, J. L., Buckheit, R. W., Klimkait, T., DeBaets, E., Davis, P. W., Rayner, B., Imbach, J. L., and Ecker, D. J. (1994) Combinatorially selected guanosine-quartet structure is a potent inhibitor of human immunodeficiency virus envelope-mediated cell fusion. *Proc. Natl. Acad. Sci. U.S.A. 91*, 1356−1360.

(11) Suzuki, J., Miyano-Kurosaki, N., Kuwasaki, T., Takeuchi, H., Kawai, G., and Takaku, H. (2002) Inhibition of human immunodeficiency virus type 1 activity in vitro by a new self-stabilized oligonucleotide with guanosine-thymidine quadruplex motifs. *J. Virol. 76*, 3015−3022.

(12) Cherepanov, P., Este, J. A., Rando, R. F., Ojwang, J. O., Reekmans, G., Steinfeld, R., David, G., De Clercq, E., and Debyser, Z. (1997) Mode of interaction of G-quartets with the integrase of human immunodeficiency virus type 1. *Mol. Pharmacol. 52*, 771−780.

(13) Rando, R. F., Ojwang, J., Elbaggari, A., Reyes, G. R., Tinder, R., McGrath, M. S., and Hogan, M. E. (1995) Suppression of human immunodeficiency virus type 1 activity in vitro by oligonucleotides which form intramolecular tetrads. *J. Biol. Chem. 270*, 1754−1760.

(14) de Soultrait, V. R., Lozach, P. Y., Altmeyer, R., Tarrago-Litvak, L., Litvak, S., and Andreola, M.-L. (2002) DNA aptamers derived from HIV-1 RNase H inhibitors are strong anti-integrase agents. *J. Mol. Biol. 324*, 195−203.

(15) Phan, A. T., Kuryavyi, V., Ma, J.-B., Faure, A., Andreola, M.-L., and Patel, D. J. (2005) An interlocked dimeric parallel-stranded DNA quadruplex: a potent inhibitor of HIV-1 integrase. *Proc. Natl. Acad. Sci. U.S.A. 102* (3), 634−639.

(16) Wolfe, J. L., and Goodchild, J. (1996) Modulation of tetraplex formation by chemical modifications of a G4-containing phosphorothioate oligonucleotide. *J. Am. Chem. Soc. 118*, 6301−6302.

(17) D'Onofrio, J., De Napoli, L., Di Fabio, G., and Montesarchio, D. (2006) 2-(Phenylthio)-ethyl as a novel two-stage base protecting group for thymidine analogues. *Synlett 6*, 845−848.

(18) Hotoda, H., Momota, K., Furukawa, H., Nakamura, T., and Kaneko, M. (1994) Biologically active oligodeoxyribonucleotides-II: structure activity relationships of anti-HIV-1 pentadecadeoxyribonucleotides bearing 5′-end-modifications. *Nucleosides Nucleotides 13*, 1375−1395.

(19) Cantor, C. R., Warshaw, M. M., and Shapiro, H. (1970) Oligonucleotide interactions. 3. Circular dichroism studies of the conformation of deoxyoligonucleotides. *Biopolymers 9*, 1059−1077.

(20) Petraccone, L., Pagano, B., Esposito, V., Randazzo, A., Piccialli, G., Barone, G., Mattia, C. A., and Giancola, C. (2005) Thermodynamics and kinetics of PNA-DNA quadruplex-forming chimeras. *J. Am. Chem. Soc. 127*, 16215−16223.

(21) Freire, E., and Biltonen, R. L. (1978) Thermodynamics of transfer ribonucleic acids: the effect of sodium on the thermal unfolding of yeast tRNAPhe. *Biopolymers 17*, 1257−1272.

(22) Laughlan, G., Murchie, A. I., Norman, D. G., Moore, M. H., Moody, P. C., Lilley, D. M., and Luisi, B. (1994) The high-resolution crystal structure of a parallel-stranded guanine tetraplex. *Science 265*, 520−524.

(23) Gavathiotis, E., and Searle, M. S. (2003) Structure of the parallel-stranded DNA quadruplex d(TTAGGGT)$_4$ containing the human telomeric repeat: evidence for A-tetrad formation from NMR and molecular dynamics simulations. *Org. Biomol. Chem. 1*, 1650−1656.

(24) Gasteiger, J., and Marsili, M. (1980) Iterative partial equalization of orbital electronegativity—a rapid access to atomic charges. *Tetrahedron 36*, 3219−3228.

(25) Jorgensen, W. L., Chandrasekhar, J., Madura, J. D., Impey, R. W., and Klein, M. L. (1983) Comparison of simple potential functions for simulating liquid water. *J. Chem. Phys. 79*, 926−935.

(26) Cornell, W. D., Cieplack, P., Bayly, C. I., Gould, I. R., Merz, K. M., Ferguson, D. M., Spellmeyer, D. C., Fox, T., Caldwell, J. W., and Kollmann, P. A. (1995) A second generation force field for the simulation of proteins, nucleic acids, and organic molecules. *J. Am. Chem. Soc. 117*, 5179−5197.

(27) Bodor, N., Gabanyi, C., and Wong, J. (1989) A new method for the estimation of partition coefficient. *J. Am. Chem. Soc. 111*, 3783−3786.

(28) Eckstein, F. (1991) *Oligonucleotides and analogues: a practical approach.* IRL Press, Oxford, UK.

(29) Reimann, E. (1969) Natürliche Stilbene. Synthese von Polyhydroxystillbenäthern durch Wittig-Reaktion. *Chem. Ber. 102*, 2881−2888.

(30) Jaksa, S., Kralj, B., Pannecouque, C., Balzarini, J., De Clercq, E., and Kobe, J. (2004) How a modification (8-aza-3-deaza-2′-deoxyguanosine) influences the quadruplex structure of Hotoda's 6-mer TGGGAG with 5′- and 3′-end modifications. *Nucleosides, Nucleotides Nucleic Acids 23*, 77−88.

(31) Petraccone, L., Erra, E., Esposito, V., Randazzo, A., Mayol, L., Nasti, L., Barone, G., and Giancola, C. (2004) Stability and structure of telomeric DNA sequences forming quadruplexes containing four G-tetrads with different topological arrangements. *Biochemistry 43*, 4877−4884.

(32) Mergny, J. L., De Cian, A., Ghelab, A., Saccà, B., and Lacroix, L. (2005) Kinetics of tetramolecular quadruplexes. *Nucleic Acids Res. 33*, 81−94.

(33) Petraccone, L., Erra, E., Esposito, V., Randazzo, A., Galeone, A., Barone, G., and Giancola, C. (2005) Biophysical properties of quadruple helices of modified human telomeric DNA. *Biopolymers 77*, 75−85.

(34) Petraccone, L., Erra, E., Randazzo, A., and Giancola, C. (2006) Energetic aspects of locked nucleic acids quadruplex association and dissociation. *Biopolymers 83*, 584−594.

(35) Wyatt, J. R., Davis, P. W., and Freier, S. M. (1996) Kinetics of G-quartet-mediated tetramer formation. *Biochemistry 35*, 8002−8008.

(36) Mergny, J. L., and Lacroix, L. (2003) Analysis of thermal melting curves. *Oligonucleotides 13*, 515−537.

(37) Shafer, R. H. (1998) Stability and structure of model DNA triplexes and quadruplexes and their interactions with small ligands. *Prog. Nucleic Acid Res. Mol. Biol. 59*, 55−94.

(38) Smirnov, I., and Shafer, R. H. (2000) Effect of loop sequence and size on DNA aptamer stability. *Biochemistry 39*, 1462−1468.

BC070062F

Design and Synthesis of Mono- and Multimeric Targeted Radiopharmaceuticals Based on Novel Cyclen Ligands Coupled to Anti-MUC1 Aptamers for the Diagnostic Imaging and Targeted Radiotherapy of Cancer

K. Eszter Borbas,[†,§] Catia S. M. Ferreira,[†,||] Alan Perkins,[‡] James I. Bruce,*[,†] and Sotiris Missailidis*[,†]

Chemistry Department, The Open University, Milton Keynes, U.K., and Department of Medical Physics, University of Nottingham, Nottingham, U.K.. Received March 6, 2007; Revised Manuscript Received May 1, 2007

Targeted radiopharmaceuticals offer the possibility of improved tumor imaging and radiotherapy, with reduced side effects. A variety of monoclonal antibodies and antibody fragments have previously been successfully radiolabeled and used in diagnostic imaging and targeted radiotherapy of cancer. Many such antibodies have been shown to recognize the well-characterized MUC1 tumor marker and have recently been in clinical trials. Furthermore, a number of chelators have been synthesized and are currently used as radiopharmaceuticals for imaging and therapy. We now report the synthesis of a novel, cyclen-based ligand with a sulfur-containing arm that offers increased stability of the ligand−metal complex. We have coupled this ligand with previously selected aptamers to the MUC1 tumor marker to generate a novel targeted radiopharmaceutical with improved properties. We have tested the complex against known, commercially available chelators such as MAG3 in model breast cancer systems. To improve the pharmacokinetic properties of the aptamer-based targeted radiopharmaceutical, we have generated multi-aptamer complexes around a central chelator. Such multi-aptamer complexes have increased retention of the complex in circulation, without affecting the lack of immunogenicity of the complex or altering its superior tumor penetration properties.

INTRODUCTION

MUC1 (*1*) is a large cell-surface mucin glycoprotein expressed in the extracellular matrix by most glandular and ductal epithelial cells and some hematopoietic cell lineages (*2, 3*). It is highly expressed by the majority of human adenocarcinomas and has been associated with poor clinical prognosis (*4*). MUC1 is found shed in the bloodstream of adenocarcinoma patients (*5*) and is the antigen in commercial serum tumor marker assays (CA15−3, Truquant-Br, CASA, CA549, MCA) (*6*−*11*).

The extracellular presentation of MUC1, its elongated structure, and characteristic under-glycosylation patterns allow the protein core to be exposed in neoplastic cells, thus making it a suitable target for immunotherapeutic and targeted radiotherapy approaches. These characteristics have been explored in immunotherapies, including radiolabeled antibodies (Abs) against breast (*12*−*14*) and bladder (*15*−*19*) cancers, with encouraging results that led to various clinical trials (*20, 21*). However, radiolabeled Abs are limited to modest amounts of activity (mCi), since with their long circulation time, bone marrow toxicity becomes a problem. Furthermore, a major problem is the antibodies' immunogenicity and poor tumor penetration. We have attempted to overcome such problems using aptamers as binding ligands to MUC1. Aptamers (*22*) are short (<100 bases) oligonucleotides selected from a pool of 10^{14}−10^{16} randomized sequences by binding to a target molecule. The strongest binders are amplified after the removal of the nonbinding sequences. Repetition of the selection-amplification procedure (typically 6−20 times) results in a small number of strongly binding oligonucleotides (*23*). Aptamers have been shown to present reduced immunogenecity and toxicity compared to other biological therapeutics, increased thermal stability and reproducibility compared to Abs, and the possibility of production using solid-phase synthesis (*24*−*26*). Furthermore, the radiolabeling of aptamers has been previously reported (*27*−*29*), raising the possibility of such targeting moieties being used in γ-camera imaging and targeted radiotherapy. In a recent example, aptamers selected against Tenascin-C were used in an *in vivo* preclinical targeting study, investigating the biodistribution of a radiolabeled anti-Tenascin-C aptamer in nude mice bearing either U251 glioblastoma or MDA-MB-435 breast tumor xenografts (*30*). The Tenascin-C targeting aptamer was radiolabeled with ^{99m}Tc using mercaptoacetyl glycine (MAG_2) and DTPA. Imaging studies of the complex demonstrated rapid blood clearance with a half-life of less than 10 min and rapid tumor penetration (6% injected dose per gram) at 10 min.

The chelators used in this study are shown in Chart 1. Macrocyclic chelates, such as DOTA and **MetCyc**, provide a more stable coordination environment compared to open-chain analogues by virtue of the "macrocyclic effect" (*31*). The addition of soft donor atoms, such as sulfur in MAG3 and **MetCyc**, also enhance the stability of the resulting complexes, since both technetium and rhenium prefer softer nitrogen and sulfur donors to harder oxygen in their coordination sphere. Thus, the ligand **MetCyc** combines the features of both commercially available DOTA and MAG3. The development and *in vitro* characterization of the aptamers have been described

* Corresponding author for aptamer studies: Dr. Sotiris Missailidis, Chemistry Department, The Open University, Walton Hall, Milton Keynes, MK7 6AA, UK. Phone: +44 1908 858382, Fax: +44 1908 858327, E-mail: s.missailidis@open.ac.uk. Corresponding author for cyclen ligand synthesis: Dr. James Bruce, Chemistry Department, The Open University, Walton Hall, Milton Keynes, MK7 6AA, UK. Phone: +44 1908. Phone: +44 1908 654171, Fax: +44 1908 858327, E-mail: J.I.Bruce@open.ac.uk.

† The Open University.

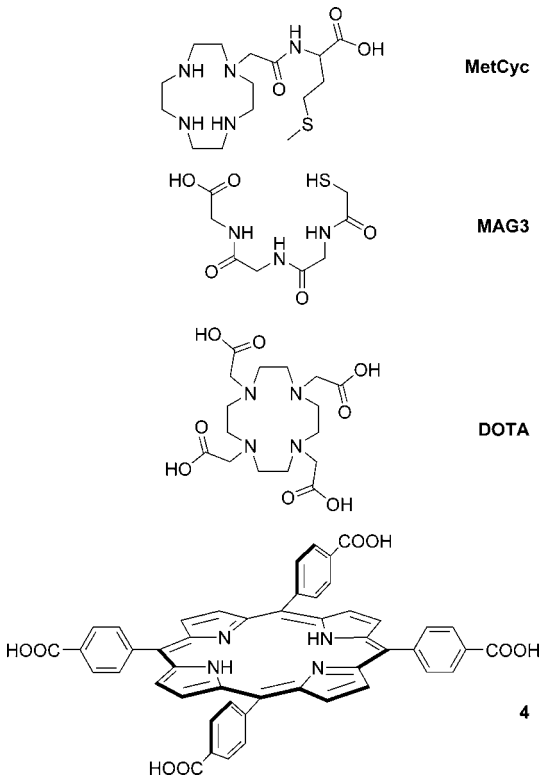
‡ University of Nottingham.

§ Current address: Department of Chemistry, North Carolina State University, Raleigh, NC 27695-8204, USA.

|| Current address: Ontario Cancer Institute, University of Toronto, 610 University Avenue, Toronto, Ontario, M5G 1J6, Canada.

10.1021/bc0700741 CCC: $37.00 © 2007 American Chemical Society
Published on Web 06/21/2007

Chart 1



previously (*32*). We now report the synthesis of the novel, cyclen-based bifunctional chelator **MetCyc**, the complexation of technetium-99m with **MetCyc** to generate the radioactive complex **Tc-MetCyc**, and the conjugation of **Tc-MetCyc** to an amino-modified aptamer to furnish conjugate **Tc-MetCyc-Apt**. Conjugate **Tc-MetCyc-Apt** has been compared with an analogous aptamer bioconjugate **Tc-MAG3-Apt**, prepared using the commercially available ligand MAG3 for metal binding.

As aptamers are known to have rapid clearance from the system due to their increased hydrophilicity and low molecular weight (*33*, *34*), we have generated multi-aptamer complexes around a central tetravalent chelator (DOTA and **4**), by reacting 1 equiv of the chelator with 4 equiv of aptamer in the presence of the water-soluble coupling reagent EDCI. The four aptamer molecules are attached via amide bonds formed between the carboxylic acids of the chelators and the 5′-amino group of the modified oligonucleotide. Apart from the stoichiometry, the conditions were identical to those used in the synthesis of the monomeric aptamers. The tetrameric conjugates are shown in Chart 2. These conjugates have approximately four times the molecular weight of a single aptamer and were expected to display increased retention in the circulation compared to the monomeric conjugates **Tc-MetCyc-Apt** and **Tc-MAG3-Apt**. They also have the ability to carry multiple ligands and radionuclides (Chart 3, M_1 and M_2), thus increasing the radioactive load delivered to the tumor site. Finally, the multi-aptamer complex offers potentially increased affinity for the MUC1 tumor marker, as the complex can bind to more than one target molecule on the surface of the tumor cell, as well as increased stability from nuclease degradation.

EXPERIMENTAL SECTION

General Procedures. $NaReO_4$, $NaBH_4$, DOTA, and MAG3 were purchased from Sigma Aldrich, UK. Porphyrin **4** was obtained from Strem Chemicals (UK). All other chemicals were purchased from Acros Organics and were used as received. Triethylamine (TEA) was distilled from CaH_2 under argon and

Chart 2

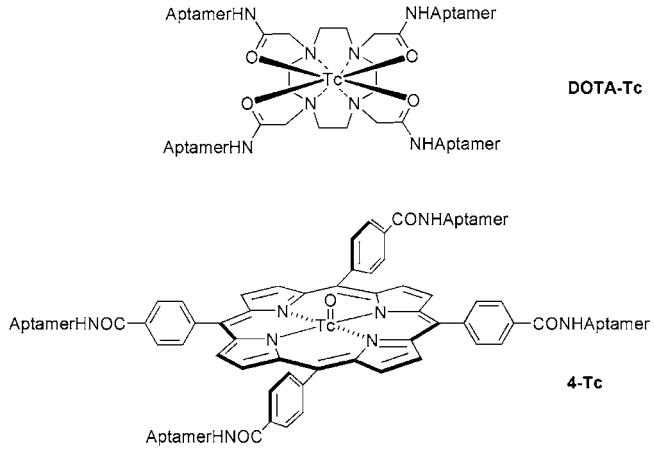
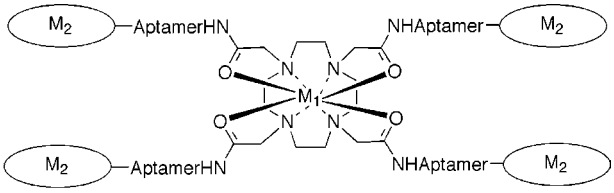


Chart 3



stored over molecular sieves. All other solvents were used as purchased from Fluka. Methionine ethyl ester was synthesized following standard literature procedures (*35*). Thin-layer chromatography was performed on Merck fluorescent silica or on Fluka fluorescent alumina plates with iodine, $KMnO_4$, or UV visualization. ^{1}H NMR (300 MHz) and ^{13}C NMR (75 MHz) spectra were recorded in $CDCl_3$ unless noted otherwise. ESI-MS (positive-ion mode) was performed on a VG Quattro 2 equipment. Samples were introduced by direct infusion of methanolic or aqueous solutions. UV−vis absorption spectra were recorded on a Uvikon XL (Bio-Tek Instruments) spectrometer.

Radioactive $NaTcO_4$ solution in saline was obtained from a Mo-99-Tc-99m generator (Shering, CIS bio international, Burgess Hill, Sussex, UK), with typical activity values being 2000−6000 MBq in 1−2 mL volume. Aptamers were selected as described previously (*32*), and modified aptamers were purchased from Sigma Gensys, UK. The radiolabeled aptamers were purified by size exclusion chromatography on NAP-10 SEC columns (Amersham Biosciences) by elution with sterile saline. Three-week-old nude female mice with MCF-7 xenografts in the left flank were supplied by the Cancer Studies Unit, Nottingham University, for imaging at the γ-camera facilities of the Department of Academic Medical Physics, University of Nottingham, Nottingham, UK. The animal experiments were conducted according to ethical committee approved protocols and regulations.

2. A mixture of DL-methionine ethyl ester (**1**, 0.18 g, 1.00 mmol) in CH_2Cl_2 (10 mL) and chloroacetic acid (0.18 g, 1.90 mmol) was treated with EDCI (0.38 g, 2.00 mmol). Stirring was continued at room temperature for 24 h. The sample was diluted with CH_2Cl_2 and water. The phases were separated, and the aqueous layer was extracted with CH_2Cl_2. The combined organic phases were washed with water, dilute acid (1 M HCl), and dilute base (1 M NaOH). The organic layer was dried ($MgSO_4$). Evaporation of the solvent afforded a colorless solid (0.24 g, 95%). ^{1}H NMR δ 1.16−1.26 (t, 3H, CH_3), 1.92−2.20 (m, 2H, CH_2), 2.02 (s, 3H, S−CH_3), 2.40−2.49 (t, 2H, CH_2), 2.78 (s, 1H, NH), 4.02 (s, 2H, $ClCH_2$), 4.60−4.67 (m, 1H, CH). ^{13}C NMR δ 14.09, 15.44, 29.81, 31.40, 42.41, 51.89, 61.87, 165.89, 171.18.

3. 1,4,7,10-Tetraazadodecane (cyclen, 4.71 g, 27.4 mmol) in 100% ethanol (25 mL) was treated with TEA (0.70 mL, 5.54 g, 54.9 mmol) for 10 min. A sample of **2** (4.64 g, 18.3 mmol) was added. The resulting solution was refluxed under an Ar atmosphere for 24 h. The sample was concentrated. The oily residue was dissolved in a mixture of CH_2Cl_2 and water. The phases were separated, and the aqueous phase was extracted with CH_2Cl_2. The organic layer was washed with water and dried ($MgSO_4$). Chromatography [basic alumina (pH 9.5), CH_2Cl_2/MeOH (0.2 → 4%)] afforded a colorless solid (0.96 g, 13.5%). ^{1}H NMR δ 1.21 (t, J = 7.2 Hz, 3H, CH_3), 1.87−2.15 (m, 2H, CH_2), 2.04 (s, 3H, SCH_3), 2.45−3.01 (m, 18H, CH_2), 3.15 (dd, J_1 = 17.4 Hz, J_2 = 12.5 Hz, 2H, CH_2), 4.11 (q, J = 7.2 Hz, 2H, CH_2), 4.57−5.65 (m, 1H, CH), 8.76 (d, J = 8.4 Hz, 1H, NH). ^{13}C NMR δ 14.07, 15.40, 30.37, 31.55, 45.84, 46.23, 47.19, 51.23, 53.43, 58.99, 61.32, 172.37.

MetCyc [4-Methylsulfanyl-2-(2−1,4,7,10-tetraaza-cyclododec-1-yl-acetylamino)-butyric acid]. A stirred sample of **3** (0.80 g, 2.06 mmol) in methanol (10 mL) was treated with aqueous NaOH (2 M, 10 mL). Stirring was continued at room temperature for 12 h. The pH of the solution was adjusted to 7.0 with dilute HCl (2 M). The sample was concentrated. The residue was suspended in a mixture of CH_2Cl_2 and MeOH (9:1). Filtration and concentration of the resulting solution afforded an off-white solid (0.56 g, 75%). ^{1}H NMR (CD_3OD) δ 1.77−2.23 (m, 5H, CH_2 + SCH_3), 2.08 (s, 3H, SCH_3), 2.45−3.76 (m, 21H, CH_2 + CH). ^{13}C NMR δ 14.02, 14.83, 24.85, 30.17, 52.65, 55.73, 128.94. ESI-MS obsd 361 $(M + H)^+$, 381 $(M + NH_4)^+$, calcd (361.2).

Digestion of MUC1 Aptamers by Blood Nuclease. Approximately 10 pmol of DNA MUC1 aptamers were suspended in 40 μL of fresh human serum (Sigma, UK). The serum was incubated at simulated body temperature for a series of times (5, 10, 20, 40, 80, and 160 min, and 6 and 12 h). Plasma was obtained by centrifugation (13 000× rpm for 30 min) and analyzed on a 2.5% agarose gel for 25 bp inserts.

Digestion of MUC1 Aptamers by Urine Nuclease. Approximately 10 pmol of MUC1 aptamers were suspended in 40 μL of fresh urine sample. The urine was incubated at simulated body temperature for a series of times (5, 10, 20, 40, 80, and 160 min, and 6 and 12 h). Constituents were separated by centrifugation (13 000× rpm for 30 min). Urine was analyzed on a 2.5% agarose gel for 25 bp inserts.

Tc-MetCyc and Re-MetCyc. Metastable sodium pertechnetate in saline (0.2 mL) or sodium perrhenate (25 mg, 0.10 mmol in 2 mL methanol) was treated with small portions of sodium borohydride (4 mg, 0.1 mmol). Stirring was continued for 10 min. A sample of **MetCyc** (36 mg, 0.1 mmol) in HPLC-grade methanol (2 mL) was added, and the reaction mixture was heated to reflux. The reaction was allowed to continue for 12 h. The mixture was allowed to cool back to room temperature, and the sample was filtered through a plug of cotton wool into ice-cold diethyl ether (5 mL). A white precipitate formed. The sample was centrifuged, and the solvents were decanted from the resulting pellet. The solid was dissolved in water, filtered, and freeze-dried to give an off-white solid [14% (**Tc-MetCyc**), 25% (**Re-MetCyc**)]: ESI-MS: 361 (**MetCyc** + H)$^+$.

Tc-MetCyc-Apt. Sodium pertechnetate in saline (1 mL, varying activity) was incubated with sodium borohydryde (4 mg, 0.11 mmol) at room temperature for 10 min. A sample of **MetCyc** (36 mg, 0.1 mmol) was added, and the solution was heated to approximately 60 °C for 30 min. The solution was allowed to cool back to room temperature and was used without further purification for the labeling of the amino-modified aptamers. Aptamer (25-mer, 5′-amino-3′-inverse thymine-modified, 11 mg) and EDCI (19 mg, 0.1 mmol) were added to the solution of the technetium complex, and the reaction was allowed to proceed for 45 min at room temperature. The reaction volume was adjusted to 3 mL with sterile distilled water, and the sample was applied onto a PD-10 SEC column. Elution with sterile deionized water yielded the labeled aptamer in the second, third, and fourth fractions, as indicated by UV−vis absorption spectroscopy (260 nm). The activity of the samples was measured, confirming the presence of the technetium in the bioconjugates. The complexed but unconjugated technetium eluted in fractions 5 to 8. Fraction 4, containing the highest concentration of labeled conjugate **Tc-MetCyc-Apt**, was used for the animal studies without further purification.

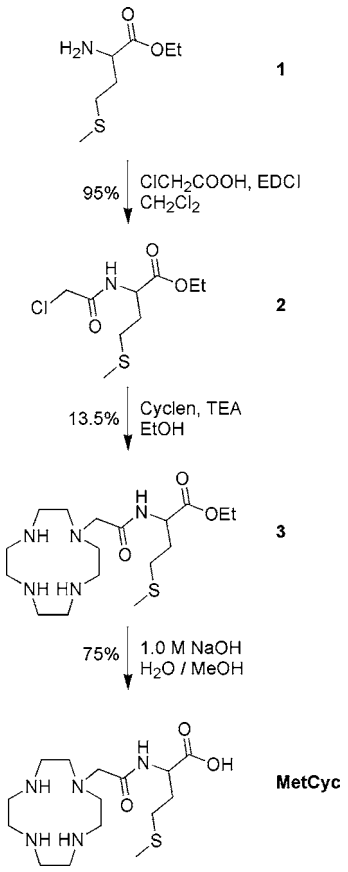
DOTA-Tc and 4-Tc. A mixture of aptamer (25-mer, 5′-amino-3′-inverse thymine-modified, 40 mg)/EDCI/chelator (DOTA or porphyrin **4**) in a 4:4:1 ratio in sodium bicarbonate buffer (1 M $NaHCO_3$, pH 8.3) was prepared, and the reaction was allowed to proceed overnight at room temperature. The crude product was analyzed on an acrylamide nondenaturing gel (15%). The band of interest (∼40 kDa) was excised and purified either by RP-HPLC using a C18 column or by precipitation with ethanol. The products were redissolved in a solution of reduced technetium (approximately 1 mL, prepared as before) and were allowed to react for 45 min at 60 °C. The labeled conjugates were purified by SEC on NAP-10 columns by elution with PBS. Fractions were analyzed as described for the monomeric conjugates **Tc-MetCyc-Apt** and **Tc-MAG3-Apt.**

RESULTS AND DISCUSSION

Aptamer Development and Modification. The development of the aptamers against MUC1 antigen has been previously reported (*32*). Briefly, libraries containing a variable region of 25 bases, flanked by primers on either side were designed and used for the selection of aptamers against synthetic MUC1 peptides of the variable tandem repeat sequence of this well-characterized tumor marker. MUC1 peptides were immobilized on an activated sepharose matrix in an affinity chromatography column. The aptamer library was added to the column and was allowed to interact with the peptides for 1 h at 37 °C. Unbound aptamers were washed away, and bound species were eluted using 3 M NaSCN or 1.5 M NaCl. Eluted aptamers were desalted, lyophilized, and PCR amplified using unidirectional PCR, to be returned to the chromatography column for subsequent rounds of selection and amplification. After 10 rounds of selection, aptamers were cloned and sequenced, resulting in a pool of selected aptamers with high affinity for the target peptides. Selected aptamers were synthesized bearing modifications in both the 5′ and 3′ ends of the aptamer. The NH_2 modification was selected at the 5′ end to facilitate coupling of the aptamer to the metal chelator, whereas an inverted thymine base has been selected for the 3′ end to confer additional nuclease resistance to the aptamer. Modified aptamers were characterized for nuclease degradation by both blood and urine nucleases and were found to be stable, with no indication of degradation for 12 h, as deemed by gel electrophoresis.

Ligand Synthesis and Aptamer Labeling. *Monomeric Conjugates.* A bifunctional chelator **MetCyc** was prepared in three steps from cyclen and methionine ethyl ester chloroacetamide as shown in Scheme 1. DL-Methionine was esterified in a standard procedure (*35*) with ethanol in the presence of 1.1 equiv of $TsOH\cdot H_2O$. The resulting **1** was acetylated with chloroacetic acid in CH_2Cl_2 in the presence of EDCI to furnish **2** in excellent yield as a colorless solid. An excess of cyclen in a refluxing mixture of absolute ethanol and TEA was treated with **2** under an inert atmosphere. The monoalkylated derivative **3** was isolated by conventional aqueous−organic workup, followed by column chromatography on basic alumina (pH 9.5). Hydrolysis of the ethyl ester with 1 M sodium hydroxide in

Scheme 1

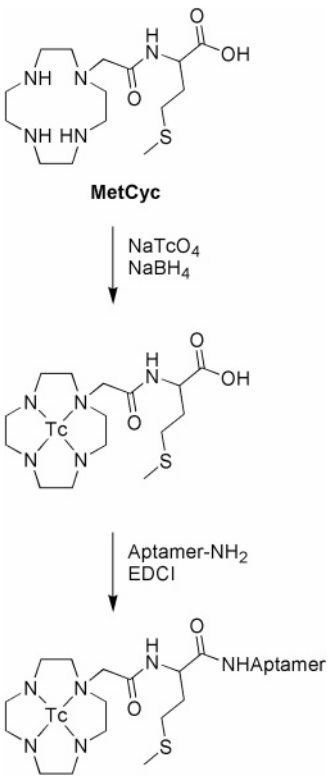


methanol/water (1:1), followed by recrystallization from methanol, afforded the bifunctional chelator **MetCyc**. The synthesis can be scaled up to provide up to 500 mg of **MetCyc** without significant decrease in yield. The methionine arm provides both the point of attachment of the targeting aptamer via the carboxylic acid group and an additional stabilizing sulfur donor which can coordinate to the central metal. In this respect, it is analogous to the lariat crown ethers (*36*) where the addition of a simple pendant arm or tail provided enhanced stability for the complex.

Ligand **MetCyc** was complexed with both rhenium and technetium. Both metals have isotopes relevant in radioimaging and/or -therapy (^{99m}Tc and ^{186}Re/^{188}Re) (*37*). To prepare **Re-MetCyc**, sodium perrhenate was reduced in a methanolic suspension with sodium borohydride, followed by treatment with a slight excess of **MetCyc** (*38*). The product was isolated by precipitation from cold diethyl ether, followed by freeze-drying from water. The non-radioactive technetium chelate **Tc-MetCyc** was prepared in a similar manner, with a slight modification (Scheme 2). Sodium pertechnetate was available as a solution in saline by allowing radioactive samples obtained from a Mo−Tc generator to decay over 1 week. Therefore, the reduction of pertechnetate with sodium borohydride was carried out in an aqueous medium. Complexation was carried out by the addition of a methanolic solution of **MetCyc** to the reduced sample. Yields were low to moderate (14% and 25% for **Tc-MetCyc** and **Re-MetCyc**, respectively). Upon ESI-MS analysis of the products, the protonated molecule ion peak corresponding to **MetCyc** (*m*/*z* 361) was observed. This is presumably due to the instability of the complexes under the analysis conditions, as TLC did not indicate the presence of free **MetCyc**.

The radioactive **Tc-MetCyc-Apt** conjugate was prepared by the reduction of an aqueous solution of sodium pertechnetate by sodium borohydride and heating the solution to 60 °C for 45 min (*39*). After cooling the sample back to room temperature,

Scheme 2



the complex was conjugated to the aptamer without isolation. After 1 h, the radiolabeled aptamer was isolated by size exclusion column chromatography on NAP-10 columns by elution with sterile deionized water. Characterization of the product (**Tc-MetCyc-Apt**) was possible by absorption spectroscopy (260 nm) and by measuring the activities of the isolated fraction with a scintillation counter. In an analogous reaction, technetium was complexed with the commercially available **MAG3** ligand, and this complex was attached to the aptamer. This enabled the comparison of the novel ligand to an already established label. Fractions 1−4 contained the labeled aptamer, while the uncomplexed salt eluted in fractions 5−8, as determined by absorption spectroscopy. The labeling efficiency, based on the number of aptamer molecules, was >90%. Using the conjugates, triplicate experiments with approximately 5 MBq activity in 0.1−0.2 mL volume were carried out *in vivo*.

Tetrameric Conjugates. It has been previously observed (*33*, *34*) that aptamers, due to their small size and high hydrophilicity, are rapidly cleared from the system through renal clearance and excreted in the urine, and appropriate modifications can improve their pharmacokinetic properties. To slow down renal clearance of the conjugates, two tetrameric conjugates were synthesized by the attachment of four aptamers to a central chelator. DOTA and the porphyrin ligand **4** were chosen for their commercial availability, known chelating properties and relative small size, as well as the presence of four arms bearing carboxyl groups available for coupling to the amino-modified aptamer. Syntheses of the tetrameric radiolabeled conjugates **DOTA-Tc** and **4-Tc** were carried out by allowing the stoichiometric mixtures of the aptamers, chelators (DOTA or **4**), and EDCI to react overnight, and separating the desired product from the excess starting material and the lower-substituted conjugates, followed by labeling with reduced technetium. The reversal of the complexation−conjugation sequence was necessary to minimize the decay of the technetium. As aptamers are known to retain their 3D structure even after prolonged heating, this was not expected to result in loss of binding affinity.

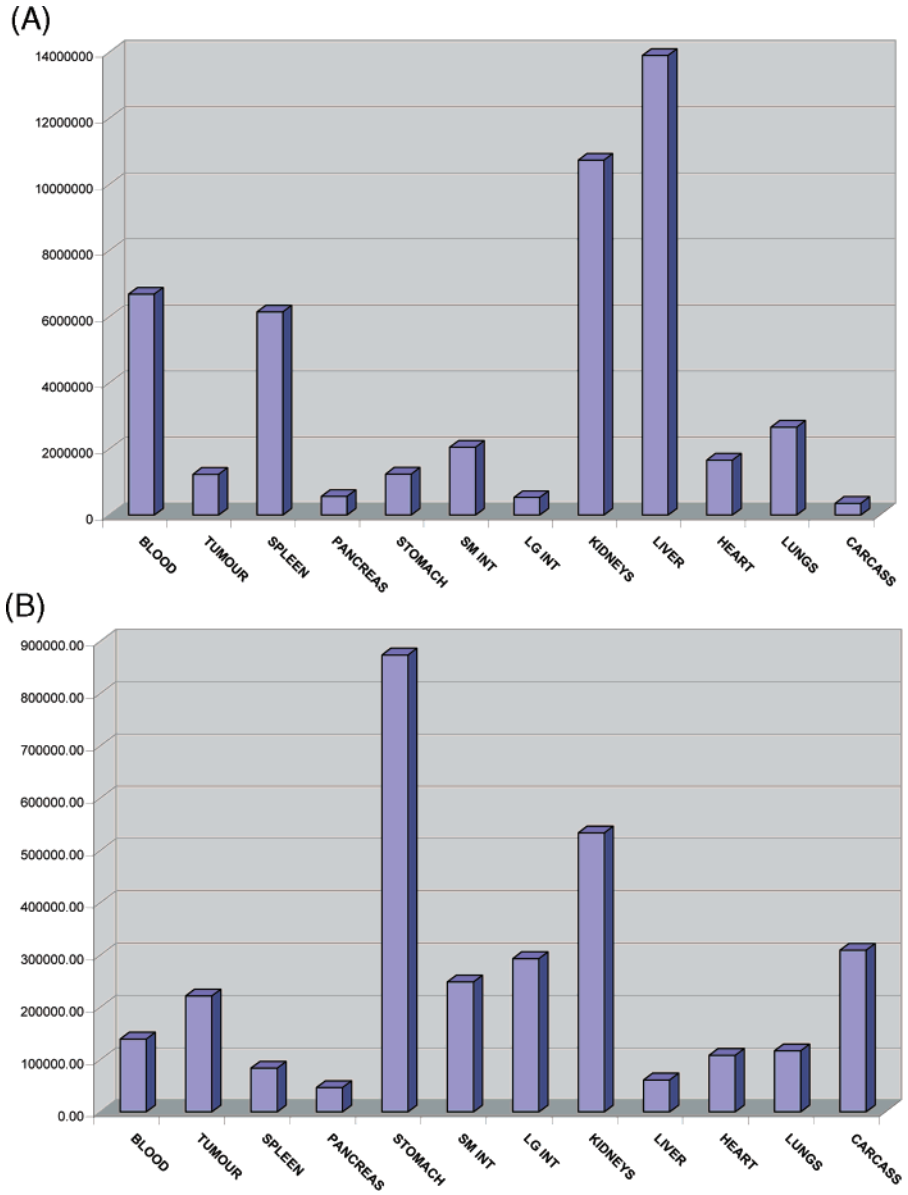


Figure 1. A. The biodistribution data using the monoaptamer labeled with ^{99m}Tc-**MAG3**. B. The biodistribution data using the monoaptamer labeled with the cyclen-ligand, ^{99m}Tc-**MetCyc**.

***In Vivo* Evaluation of the Radioactive Aptamer Complexes.** Radiolabeled aptamers were injected intravenously into nude mice bearing xenografted MCF7 breast cancer cell line tumors. Biodistribution data are shown in Figures 1 and 2. All biodistribution data are presented in counts/gram.

Both **MetCyc** and **MAG3** were labeled with more than 90% efficiency to generate conjugates **Tc-MetCyc-Apt** and **Tc-MAG3-Apt**, respectively, which were subsequently used in the biodistribution studies. The conjugate **Tc-MAG3-Apt** displayed high liver and kidney uptake. However, the kidney uptake was shown to be mainly excreted in the urine, rather than retained in the kidneys. Significant amounts of the conjugate were also observed in the liver. Although nearly 90% of the conjugate was rapidly eliminated through the kidneys in the first few minutes, the remaining conjugate was present in circulation for a long time, with high levels found after 6 h, at which point the animals were sacrificed and the activity was measured (Figure 1a).

Conjugate **Tc-MetCyc-Apt** gave very different biodistribution data from the **Tc-MAG3-Apt** complex. The overall labeling efficiency was somewhat lower than with the **Tc-MAG3-Apt**, presumably due to less efficient complexation of the technetium. This was also indicated by the high activity measured in the stomach, which is associated with the presence of free pertechnetate (*40*), rather than aptamer uptake. However, there was very little liver uptake, and the kidney uptake was smaller than with either of the other ligands (see below). This resulted in a perceptibly higher presence of the aptamer in the tumor at the 6 h study. The biodistribution data for **Tc-MetCyc-Apt** are shown in Figure 1b.

Both the DOTA and the porphyrin-based ligand **4** formed labile technetium complexes, resulting in the release of free technetium, as shown by TLC, and by the uncomplexed technetium found in the stomach and large intestine during the biodistribution studies. Furthermore, both conjugates, but in particular the porphyrin-based one **Tc-4**, gave high liver uptake, although it was hoped that the presence of the porphyrin would assist the conjugate in localizing preferentially in the tumor (*41*). The conjugate **Tc-DOTA** had smaller liver uptake than **Tc-4**, with higher excretion through the kidneys and into the urine. As before, up to 95% of the kidney radiation was actually shown to be in the urine and excreted from the system, which would

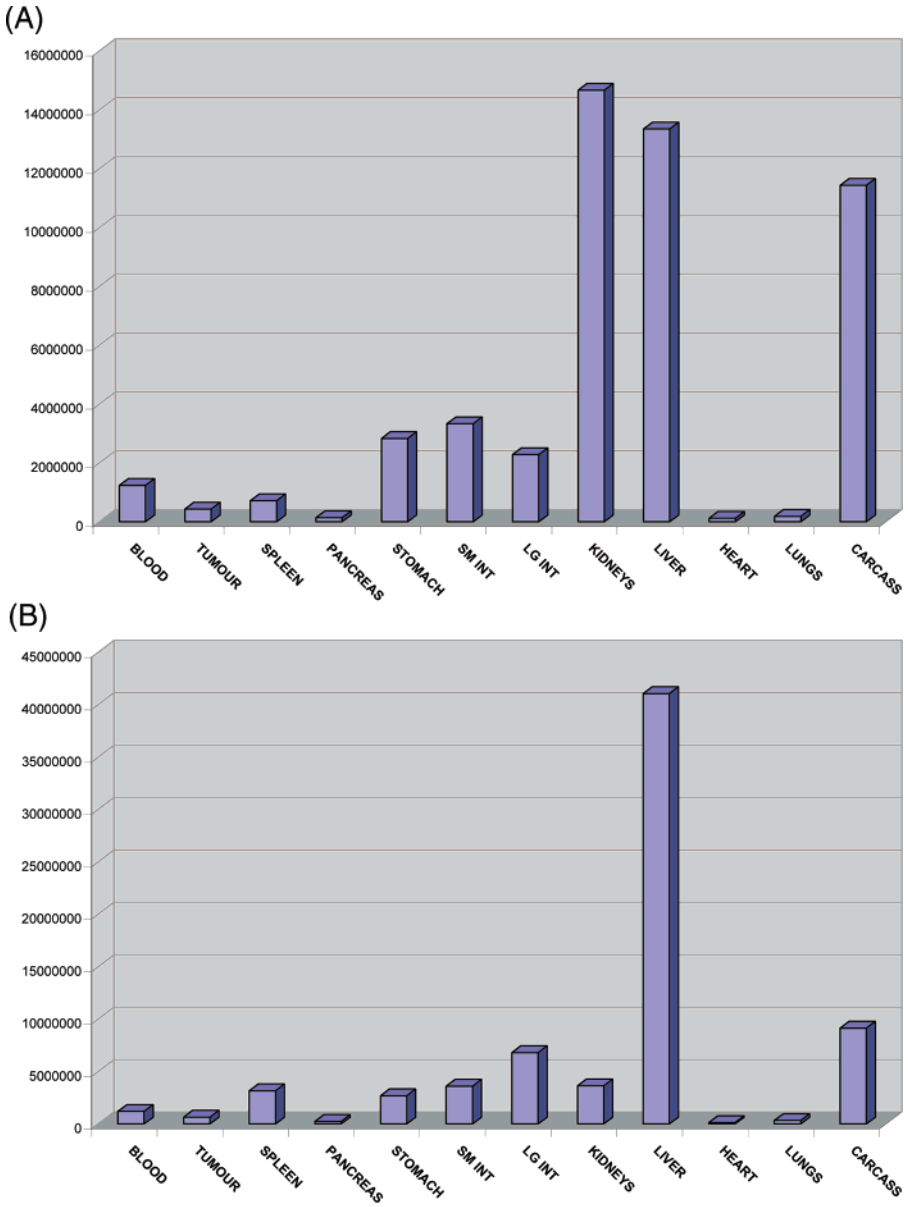


Figure 2. A. The biodistribution data using the tetra-aptamer labeled with ^{99m}Tc-DOTA. B. The biodistribution data using the tetra-aptamer labeled with the ^{99m}Tc-**4**.

indicate that no renal radioprotection would be necessary when the labeled aptamers are used as radiopharmaceuticals. Biodistribution data for **Tc-DOTA** and **Tc-4** are shown in Figure 2a,b, respectively.

Our studies, similarly to previous aptamer-related pharmacokinetic studies, indicate that aptamers alone are cleared rapidly through the kidneys and excreted through the urine, with the ability to localize in the tumor. The high radioactivity counts in the liver and stomach when the labeled aptamers were studied were most likely due to the label that increased the lipophilicity of the molecule, thus altering its pharmacokinetic properties and enabling liver uptake, or due to the presence of labeled unconjugated MAG3 that coeluted with the aptamer conjugate in the PD10 column. The stomach count is usually identified as free technetium in the system. The amount of aptamer in the kidneys was identified as excreted in the urine, again in accordance with other aptamer-related studies.

Electronic Direct β-Autoradiography. Electronic direct β-autoradiography or digital autoradiography combines high sensitivity with good spatial resolution ($<100\ \mu$m). The detector is based on proximity registration of β particles by radioisotope-free low-noise microchannel plates (MCPs) developed for photon counting of the X-ray emissions from active galactic nuclei (*42*). Recently, this technology has been applied in several applications for biological and medicinal research (*43*). The detectors can be used to monitor the uptake of radioactive-labeled material with emitted β radiation in tumors and other tissues (*44*) and has been used in this study to demonstrate the degree of tumor penetration. The tumors from mice numbers 1 and 2 were used to investigate the tumor penetration of the tetrameric carboxyporphyrin aptamer complexes. The tumor section was cut across the largest diameter, and 10 μm thin slices were cut using a cryosectioning manual machine, and two slices were wet-mounted onto a microscope slide. Exposure was measured over a period of 3 h in the electronic β autoradiography apparatus. After 3 h of exposure, and with more than half the life of the radionuclide having decayed (past 6 h), bright images of tumor perfusion and penetration across the tumor were observed (Figure 3). The images demonstrated the potential of these molecules in penetrating solid tumors, in a manner far superior to that observed with antibodies, thus indicating the

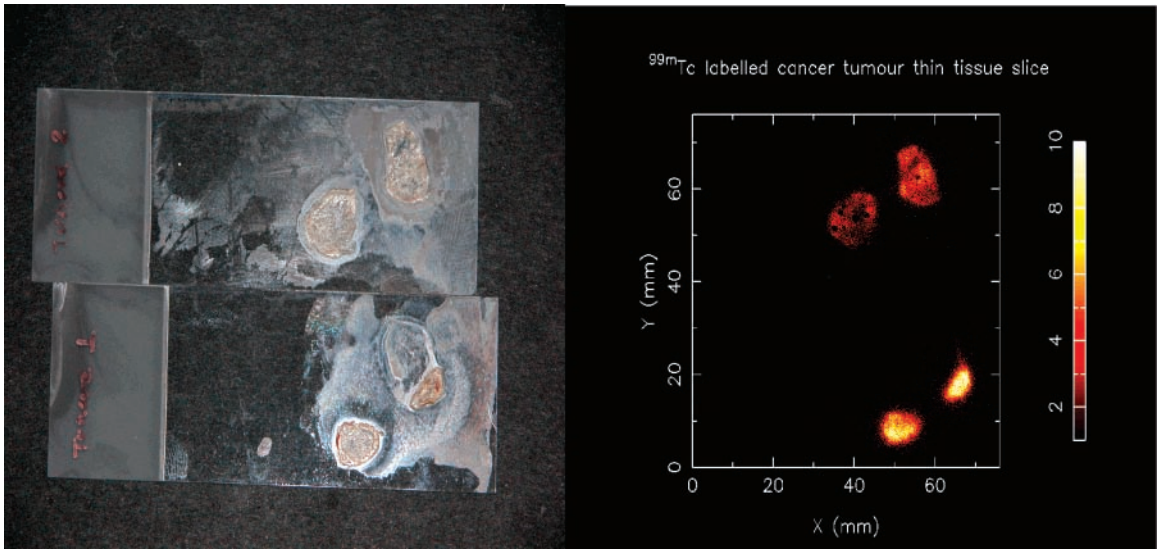


Figure 3. Microscope slides of wet-mounted MCF-7 tumor slices from nude mice numbers 1 and 2 used in biodistribution study (left). The same tumor slices presented on the left were imaged by electronic direct beta autoradiography courtesy of Dr. J. Lees, University of Leicester, UK, for radioactive load of ^{99m}Tc-labeled carboxyporphyrin aptamer.

great potential of aptamers in tumor radiotherapy (*44*). Furthermore, this study allowed us to observe that, once the aptamer molecules bind to the MUC1 on the surface of the tumor molecules, degradation by nucleases no longer occurs, allowing local irradiation to proceed for a longer time. We can thus demonstrate the ability of the aptamer to bind to the MUC1 tumor marker and its ability to penetrate the tumor mass for improved tumor imaging and molecular targeted radiotherapy.

CONCLUSIONS

A series of aptamers targeting MUC1 have been developed using the SELEX procedure. Chemical modifications, aimed at increasing the *in vivo* stability of the aptamers, have been introduced, including an inverted base at the 3′ end of the aptamer, as well as a 5′-amino group, to enable facile bioconjugation of radioactive and fluorescent labels. A novel, cyclen-based ligand for the complexation of Tc and Re has been designed. The synthesis of **MetCyc** can be accomplished using commercially available starting materials in three straightforward steps. The ligand **MetCyc** forms stable Tc and Re chelates owing to its cyclic tetraaza binding site, with its additional sulfur-containing arm. Furthermore, it contains a reactive carboxylic acid moiety, enabling bioconjugation to amino group-containing molecules, such as antibodies, peptides, or in this case the amino-modified aptamers.

Both monomeric and tetrameric aptamer conjugates (based on monovalent and tetravalent bifunctional chelators, respectively) were synthesized and tested *in vitro* and *in vivo*. The tetrameric aptamers displayed improved tumor-retention and pharmacokinetic properties compared to the monomers, due to their larger size, although the ligands were not ideal for metal binding, and additional ligands would need to be explored. The development of other multimeric aptamer bioconjugates with increased *in vivo* complex stability are currently underway in our laboratories, as well as the investigation of alternative ways to increase the molecular weight and further improve the pharmacokinetic properties of the radiolabeled aptamer as diagnostic imaging agents and targeted radiopharmaceuticals.

ACKNOWLEDGMENT

The authors would like to thank Dr. J. E. Lees of the Biomedical Imaging Unit at the Space Research Centre, University of Leicester, UK, for assistance with the autoradiographic studies. This work was supported by The Open University. KEB would like to thank Universities UK for an ORS Award.

Supporting Information Available: ^{1}H and ^{13}C NMR spectra for compounds **2**−**3**, and **MetCyc**. This material is available free of charge via the Internet at http://pubs.acs.org.

LITERATURE CITED

(1) von Mensdorff-Pouilly, S., Snijdewint, F. G. M., Verstraeten, A. A., Verheijen, R. H. M., and Kenemans, P. (2000) Human MUC1 mucin: a multifaceted glycoprotein. *Int. J. Biol. Markers 15*, 343−356.

(2) Zotter, S., Hageman, P. C., Lossnitzer, A., Mooi, and W. J., Hilgers (1988) J. Tissue and tumor distribution of human polymorphic epithelial mucin. *Cancer Rev. 11*−*12*, 55−101.

(3) Dent, G. A., Civalier, C. J., Brecher, M. E., and Bentley, S. A. (1999) MUC1 expression in hematopoietic tissues. *Am. J. Clin. Pathol. 111*, 741−747.

(4) Packer, L. M., Williams, S. J., Callaghan, S., Gotley, D. C., and McGuckin, M. A. (2004) Expression of the cell surface mucin gene family in adenocarcinomas. *Int. J. Oncol. 25*, 1119−1126.

(5) Burchell, J., Wang, D., and Taylor-Papadimitriou, J. (1984) Detection of the tumour-associated antigens recognized by the monoclonal antibodies HMFG-1 and 2 in serum from patients with breast cancer. *Int. J. Cancer 34*, 763−768.

(6) Tomlinson, I. P. M., Whyman, A., Barrett, J. A., and Kremer, J. K. (1995) Tumour marker CA15−3: Possible uses in the routine management of breast cancer. *Eur. J. Cancer 31A*, 899−902.

(7) Nicolini, A., Carpi, A., Michelassi, C., Spinelli, C., Conte, M., Miccoli, P., Fini, M., and Giardino, R. (2003) "Tumour marker guided" salvage treatment prolongs survival of breast cancer patients: final report of a 7-year study. *Biomed. Pharmacother. 57*, 452−459.

(8) Bon, G. G., van Kamp, G. J., Verstraeten, R. A., von Mensdorff-Pouilly, S., Hilgers, J., and Kenemans, P. (1999) Quantification of MUC1 in breast cancer patients. A method comparison study. *Eur. J. Obstet. Gynecol. Reprod. Biol. 83*, 67−75.

(9) Devine, P. L., McGuckin, M. A., Quin, R. J., and Ward, B. G. (1994) Serum markers CASA and CA 15−3 in ovarian cancer: all MUC1 assays are not the same. *Tumor Biol. 15*, 337−344.

(10) Cazin, J. L., Gosselin, P., Boniface, B., Demaille, M. C., and Demaille, A. (1992) An evaluation of CA549, a circulating marker of breast cancer using a procedure for comparision with CA15.3. *Anticancer Res. 12*, 719−724.

(11) Kuralay, F., Tokgöz, Z., and Cömlecki, A. (2000) Diagnostic usefulness of tumour marker levels in pleural effusions of malignant and benign origin. *Clin. Chim. Acta 300*, 43−55.

(12) Schuhmacher, J., Kaul, S., Klivényi, G., Junkermann, H., Magener, A., Henze, M., Doll, J., Haberkorn, U., Amelung, F., and Bastert, G. (2001) Immunoscintigraphy with positron emission tomography: Gallium-68 chelate imaging of breast cancer pretargeted with bispecific anti-MUC1/anti-Ga chelate antibodies. *Cancer Res. 61*, 3712−3717.

(13) Apostopoulos, V., Pietersz, G. A., Tsibanis, A., Tsikkinis, A., Drakaki, H., Loveland, B. E., Piddlesden, S. J., Plebanski, M., Pouniotis, D. S., Alexis, M. N., McKenzie, I. F., and Vassilaros, S. (2006) Pilot phase III immunotherapy study in early-stage breast cancer patients using oxidized mannan-MUC1 [ISRCTN71711835]. *Breast Cancer Res. 8*, R27.

(14) Richman, C. M., and DeNardo, S. J. (2001) Systemic radiotherapy in metastatic breast cancer using 90Y-linked monoclonal MUC-1 antibodies. *Crit. Rev. Oncol. Hematol. 38*, 25−35.

(15) Kunkler, R. B., Bishop, M. C., Green, D. J., Pimm, M. V., Price, M. R., and Frier, M. (1995) Targeting of bladder cancer with monoclonal antibody NCRC48 − a possible approach for intravesical therapy. *Br. J. Urol. 76*, 81−86.

(16) Hughes, O. D. M., Bishop, M. C., Perkins, A. C., Frier, M., Price, M. R., Denton, G., Smith, A., Rutherford, R., and Schubiger, P. A. (1997) Preclinical evaluation of copper-67 labeled anti-MUC1 mucin antibody C595 for therapeutic use in bladder cancer. *Eur. J. Nucl. Med. 24*, 439−443.

(17) Hughes, O. D. M., Bishop, M. C., Perkins, A. C., Wastie, M. L., Denton, G., Price, M. R., Frier, M., Denley, H., Rutherford, R., and Schubiger, P. A. (2000) Targeting superficial bladder cancer by the intravesical administration of copper-67-labeled anti-MUC1 mucin monoclonal antibody C595. *J. Clin. Oncol. 18*, 363−370.

(18) Simms, M. S., Murray, A., Denton, G., Scholfield, D. P., Price, M. R., Perkins, A. C., and Bishop, M. C. (2001) Production and characterisation of a C595 antibody-^{99m}Tc conjugate for immunoscintigraphy of bladder cancer. *Urol. Res. 29*, 13−19.

(19) Murray, A., Simms, M. S., Scholfield, D. P., Vincent, R. M., Denton, G., Bishop, M. C., Price, M. R., and Perkins, A. C. (2001) Production and characterization of ^{188}Re-C595 antibody for radioimmunotherapy of transitional cell bladder cancer. *J. Nucl. Med. 42*, 726−732.

(20) Gold, D. V., Schutsky, K., Modrak, D., and Cardillo, T. M. (2003) Low-dose radioimmunotherapy (Y-90-PAM4) combined with gemcitabine for the treatment of experimental pancreatic cancer. *Clin. Cancer Res. 9*, 3929S-3937S.

(21) Hughes, O. D. M., Perkins, A. C., Frier, M., Wastie, M. L., Denton, G., Price, M. R., Denley, H., and Bishop, M. C. (2001) Imaging for staging bladder cancer: a clinical study of ^{111}indium-labelled anti-MUC1 mucin monoclonal antibody C595. *Br. J. Urol. Int. 87*, 39−46.

(22) Pestourie, C., Tavitian, B., and Duconge, F. (2005) Aptamers against extracellular targets for in vivo applications. *Biochimie 87*, 921−930.

(23) Tuerk, C., and Gold, L. (1990) Systematic evolution of ligands by exponential enrichment: RNA ligands to bacteriophage T4 DNA polymerase. *Science 249*, 505−510.

(24) Eulberg, D., and Klussmann, S. (2003) Spiegelmers: biostable aptamers. *ChemBioChem 4*, 979−983.

(25) Kusser, W. (2000) Chemically modified nucleic acid aptamers for in vitro selections: evolving evolution. *Rev. Mol. Biotechnol. 74*, 27−38.

(26) Schmidt, K. S., Borkowski, S., Kurreck, J., Stephens, A. W., Bald, R., Hecht, M., Friebe, M., Dinkelborg, L., and Erdmann, V. A. (2004) Application of locked nucleic acids to improve aptamer *in vivo* stability and targeting function. *Nucleic Acids Res. 32*, 5757−5765.

(27) Hilger, C. S., Willis, M. C., Wolters, M., and Pieken, W. A. (1998) Synthesis of a Tc-99m-labeled, modified RNA. *Tetrahedron Lett. 39*, 9403−9406.

(28) Kuhnast, B., Klussmann, S., Hinnen, F., Boisgard, R., Rousseau, B., Fürste, J. P., Tavitian, B., and Dollé, F. (2003) Fluorine-18- and iodine-125-labelling of spiegelmers. *J. Labelled Compd. Radiopharm. 46*, 1205−1219.

(29) Tavitian, B. (2006) In vivo imaging with oligonucleotides for diagnosis and drug developement. *Gut 52* (Suppl IV), iv40−iv47.

(30) Hicke, B. J., Stephens, A. W., Gould, T., Chang, Y.-F., Lynott, C. K., Heil, J., Borkowski, S., Hilger, C.-S., Cook, G., Warren, S., and Schmidt, P. G. (2006) Tumor targeting by an aptamer. *J. Nucl. Med. 47*, 668−678.

(31) Lindoy, L. F. (1990) *The chemistry of macrocyclic ligand complexes*. Cambridge University Press, Cambridge, UK.

(32) Ferreira, C. S. M., Matthews, C. S., and Missailidis, S. (2006) DNA aptamers that bind to MUC1 tumour marker: Design and characterization of MUC1-binding single-stranded DNA aptamers. *Tumor Biol. 27*, 289−302.

(33) DeAnda, A., Jr., Coutre, S. E., Moon, M. R., Vial, C. M., Griffin, L. C., Law, V. S., Komeda, M., Leung, L. L., and Miller, D. C. (1994) Pilot-study of the efficacy of a thrombin inhibitor for use during cardiopulmonary bypass. *Ann. Thorac. Surg. 58*, 344−350.

(34) Lee, J. F., Stovall, G. M., and Ellington, A. D. (2006) Aptamer therapeutics advance. *Curr. Opin. Chem. Biol. 10*, 282−289.

(35) Bodanszky, M. (1984) *Principles of Peptide Synthesis*. Akad Verlag, Berlin.

(36) Gokel, G. W. (1992) Lariat ethers: from simple sidearms to supramolecular systems. *Chem. Soc. Rev. 21*, 39−47.

(37) Dilworth, J. R., and Parrott, S. J. (1998) The biomedical chemistry of technetium and rhenium. *Chem. Soc. Rev. 27*, 43−55.

(38) Kung, H. F., Yu, C. C., Billings, J., Molnan, M., and Blau, M. (1985) Synthesis of new bis(aminoethanethiol) (BAT) derivatives: possible ligands for ^{99m}Tc brain imaging agents. *J. Med. Chem. 28*, 1280−1284.

(39) Kasina, S., Sanderson, J. A., Fitzner, J. N., Srinivasan, A., Rao, T. N., Hobson, L. J., Reno, J. M., Axworthy, D. B., Beaumier, P. L., and Fritzberg, A. R. (1998) Simplified preformed chelate protein radiolabeling with technetium-99m mercaptoacetamidoadipoylglycylglycine (N_3S-adipate). *Bioconjugate Chem. 9*, 108−117.

(40) Schwartz, M. J., and Lewis, J. H. (1984) Meckel's diverticulum: pitfalls in scintigraphic detection in the adult. *Am. J. Gastroenterol. 79*, 611−618.

(41) Sternberg, E. D., Dolphin, D., and Bruckner, C. (1998) Porphyrin-based photosensitizers for use in photodynamic therapy. *Tetrahedron 54*, 4151−4202.

(42) Lees, J. E., Fraser, G. W., and Dinsdale, D. (1997) Direct beta autoradiography using microchannel plate (MCP) detectors. *Nucl. Instrum. Methods Phys. Res., Sect. A 392*, 349−353.

(43) Lees, J. E., and Richards, P. G. (1999) Rapid, high-sensitivity imaging of radiolabeled gels with microchannel plate detectors. *Electrophoresis 20*, 2139−2143.

(44) Lees, J. E., Murray, A., Perkins, A. C., and Fraser, G. W. (2002) Autoradiography of high-energy radionuclides using a microchannel plate detector. *IEEE Trans. Nucl. Sci. 49*, 153−155.

BC0700741

Pyrene Excimer Fluorescence as a Probe for Parallel G-Quadruplex Formation

Huihe Zhu and Frederick D. Lewis*

Department of Chemistry, Northwestern University, Evanston, Illinois 60208. Received September 8, 2006; Revised Manuscript Received February 16, 2007

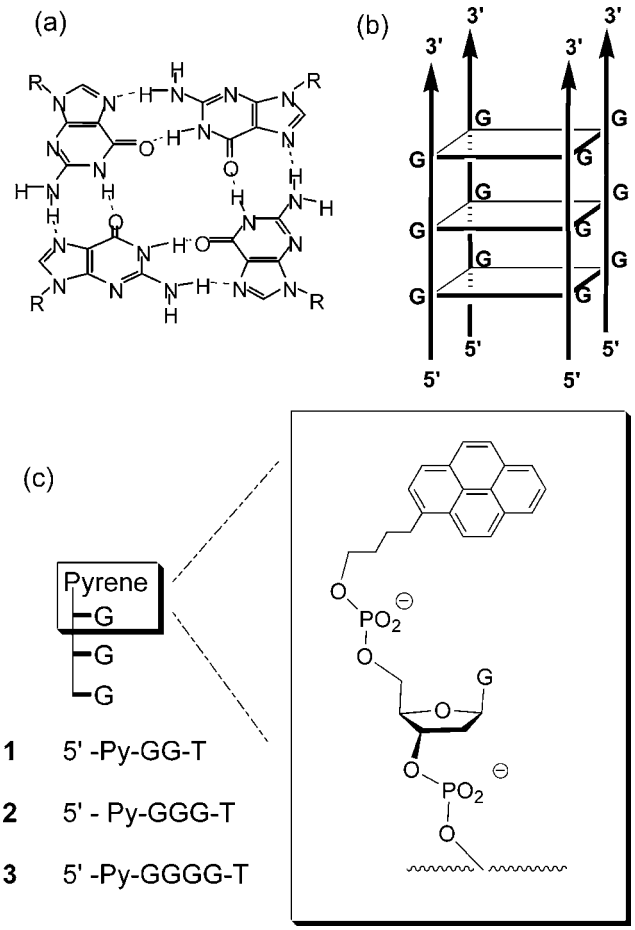
The formation and properties of G-quadruplex structures from short single-strand oligonucleotide conjugates possessing two to four guanines and a 5′-terminal pyrenebutanol are reported. The 4-G conjugate forms a stable G-quadruplex under low or high potassium ion concentrations, whereas the 3-G conjugate forms a stable G-quadruplex only in the presence of high potassium. The 2-G conjugate fails to form a stable G-quadruplex even at low temperature and high potassium concentration. Both pyrene monomer and excimer fluorescence are observed for the G-quadruplex structures, whereas only monomer fluorescence is observed for the single-strand conjugates. Thus, pyrene excimer fluorescence can be used as a probe for the formation of G-quadruplex structures. The excimer/monomer intensity ratios for the G-quadruplex structures are dependent upon both the temperature and potassium or lithium salt concentration. The salt effect is attributed to a change in the structure of the hydrophobic pyrene chromophores, which are assembled on the 5′-face of the G-quadruplex as a consequence of electrostriction.

INTRODUCTION

Pyrene excimer fluorescence has been widely employed as a probe for the structure of biopolymers possessing covalently attached pyrene chromophores in aqueous solution (*1*). Complementary oligodeoxynucleotides (ODNs) possessing pendant pyrene chromophores or pyrene-derived base surogates in both strands display either monomer or excimer fluorescence, depending upon the proximity of the pyrenes (*2*−*5*). ODNs possessing a single 5′- or 3′-terminal pyrene have been used to investigate the strand polarity (parallel vs antiparallel) of duplex and triplex structures (*6*, *7*). ODNs possessing bases modified with covalently attached pyrene groups have also been prepared and the fluorescence of their duplex structures studied (*2*, *8*−*12*). These studies have established that the proximity of two pyrenes is a necessary but not sufficient condition for the observation of excimer fluorescence. Ground-state conformations which disfavor the formation of a sandwich-type excimer structure for the electronically excited pyrene dimer give rise to monomer or broadened monomer fluorescence rather than excimer fluorescence (*1*). The pyrene excimer/monomer ratio in oligomeric pyrene-containing C-nucleosides increases with the length of the oligomer (*13*).

Guanine-rich ODNs can assemble to form G-quadruplex structures based on stacked arrays of G-quartets connected by Hoogsteen-type base pairing (Scheme 1a) (*14*, *15*). G-quadruplexes can be formed by the association of four ODNs possessing a single poly(dG) domain, dimerization of ODNs possessing two poly(dG) domains, or intramolecular folding of ODNs possessing four poly(dG) domains. Quadruplexes formed via intermolecular association in the presence of potassium generally have parallel structures (*16*, *17*), whereas hairpin dimers and intramolecular quadruplexes are highly polymorphic (*18*). Merkina and Fox (*19*) have recently reported the formation and kinetic stability of intermolecular G-quadruplex structures formed by the conjugate 5′-d(TGGGG)-FL (FL = fluorescein), which possess a covalently attached FL dye. Reduction in the FL fluorescence intensity of these ODNs upon quadruplex formation is attributed to self-quenching of the four dye molecules when assembled on the same face of the G-quadruplex structure (Scheme 1b); however, FL self-quenching

Scheme 1 [a]



[a] (a) Hoogsteen base pairing in a G-quartet; (b) parallel G-quadruplex structure formed by intermolecular association; (c) pyrene-modified poly(dG) sequences.

* Corresponding author. E-mail: fdl@northwestern.edu. Voice: +1-847-491-3441. Fax: +1-847-467-2184.

10.1021/bc060279u CCC: $37.00 © 2007 American Chemical Society
Published on Web 05/04/2007

does not result excimer fluorescence (*13*). It occurred to us that replacement of FL with pyrene might result in the formation of quadruplex structures with high excimer/monomer fluorescence ratios.

We report here the study of intermolecular G-quadruplex formation using short poly(dG) sequences possessing a 5′-pyrenebutanol fluorescent probe (Scheme 1c, **1**−**3**). Whereas the single-strand ODNs display structured monomer fluorescence, the quadruplex structures display a mixture of monomer and excimer fluorescence, both of which are assigned to parallel quadruplex structures. Thus, the appearance of excimer fluorescence can be used as a probe for parallel G-quadruplex formation. The ratio of excimer/monomer fluorescence intensity is dependent upon both the temperature and salt concentration. These observations are consistent with the presence of a mixture of pyrene geometries which either favor or disfavor excimer formation. Increased excimer fluorescence at high salt concentrations is attributed to a hydrophobic salt effect on the pyrene chromophore ground state-geometry.

EXPERIMENTAL PROCEDURES

Materials. 1-Pyrenebutanol was converted to its phosphoramidite by reaction with 2-cyanoethyl diisopropyl chlorophosphoramidite in tetrahydrofuran in the presence of diisopropylethylamine. The conjugates **1**−**3** were prepared by means of conventional phosphoramidite chemistry using a Millipore Expedite oligonucleotide synthesizer and reagents obtained from Glenn Research following the procedure of Letsinger and Wu (*20*) as implemented by Lewis et al. (*21*). Following synthesis, conjugates **1**−**3** were isolated by reverse phase (RP) HPLC and repurified as needed. HPLC analyses and purifications were performed using a Phenomenex HyperClone column (250 × 4.6 mm). Molecular weights were determined by means of MALDI-TOF mass spectrometry using a Perseptive Biosystems Voyager Pro DE spectrometer with a 2,4,6-trihydroxyacetophenone (THAP)/ammonium citrate matrix.

ODN **1**: calcd. 1236.96; found: 1239.21.
ODN **2**: calcd. 1566.17; found: 1568.73.
ODN **3**: calcd. 1895.37; found: 1897.37.

Electronic Spectra. UV spectra were performed with a Perkin-Elmer Lambda-2 UV spectrophotometer equipped with a Peltier temperature programmer to automatically increase the temperature at the rate of 0.5 °C/min. Fluorescent spectra were obtained using a Spex FluoroMax Fluorometer with temperature control provided by a Quantum Northwest TC 125 Peltier controller. Fluorescent spectra were collected after samples were deoxygenated by purging with dry nitrogen gas for 15 min. The spectra were excited at 336 nm and monitored from 360 to 600 nm. The integration time was 0.1 s, and slits for both excitation and emission were 5.0 nm. Temperature-dependent fluorescent spectra were collected with heating or cooling rate of 40 °C/h. All spectra were obtained on freshly prepared samples within 30 min of preparation. The concentration of single-strand sequences was determined from the extinction coefficient of 1-pyrenebutanol ($\epsilon_{340\ nm} = (5.0 \pm 0.04) \times 10^4\ M^{-1}\ cm^{-1}$ in THF solution).

CD Experiments. Circular dichroism (CD) spectra and thermal denaturation experiments were recorded using a Jasco J-715 circular dichroism spectrometer equipped with a Jasco Peltier temperature controller. Spectra were recorded at room temperature approximately 30 min after sample preparation in a 1 cm path length cuvette using either 1.0×10^{-6} or 5.0×10^{-6} M single-strand concentration. Spectra were obtained from the sum of five scans over the 200−400 nm wavelength range with a scan rate of 100 nm m^{-1}, a bandwidth of 2.0 nm, and a response time of 2 s. The spectra were normalized by subtraction of the background scan obtained with buffer solution. Temperature-dependent experiments were performed in the range 10−90 °C with a heating rate of 40 °C/h, monitoring the CD value (mdeg) at 265 nm.

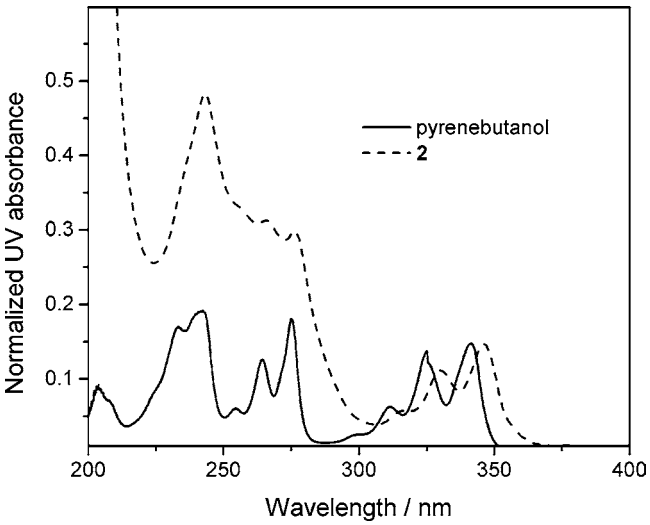


Figure 1. Absorption spectra of the pyrenebutanol in methanol solution and conjugate **2** in aqueous 0.1 M KCl, 10 mM potassium phosphate.

Electrophoresis. Samples for gel electrophoresis were equilibrated for 1 day at 4 °C prior to electrophoresis for 2 h at 150 V at 4 °C using a 15% nondenaturing polyacrylamide gel (PAGE) that contained 100 mM KCl in 1 × TBE, 10 mM potassium phosphate electrophoresis buffer. The fluorescence of the gel was observed over a UV transilluminator (312 nm), and then the gel was stained with Stains-All (Sigma).

RESULTS

The synthesis, purification, and characterization of conjugates **1**−**3** are described in the Experimental Procedures. The UV spectra of pyrenebutanol in methanol and conjugate **2** in aqueous buffer with 0.1 M KCl are shown in Figure 1. The spectrum of **2** in water is similar to that obtained in buffer. The long-wavelength π,π^* band of pyrenebutanol is red-shifted and broadened in the conjugate spectrum. The short-wavelength bands of the conjugate are assigned to overlapping absorption of the bases and pyrene. The spectra of **1** and **3** have band structures similar to that of **2**, but differ in the ratio of band intensities, as a consequence of the different number of dG bases.

The CD spectra of **1**−**3** in water and in 0.01 M phosphate with 0.1 M KCl at room temperature are shown in Figure 2. No CD peaks are observed for **1**, either with or without KCl at room temperature or at 5 °C. The CD spectrum of **2** in water is weaker than that with salt, whereas added salt has little effect on the CD spectrum of **3**. In addition to the short-wavelength bands characteristic of the parallel G-quadruplex structure at 265 and 240 nm, weaker long-wavelength CD bands having vibrational structure similar to that for pyrene UV absorption (Figure 1) are observed for **2** and **3** (Figure 2b). The intensity of the pyrene CD band for **2** increases as the salt concentration is increased from 0.1 to 0.5 M KCl (data not shown). The temperature dependence of the CD spectra of **2** (0.1 M KCl) and **3** (no added salt) are shown in Figure 3. The spectra of **3** are independent of temperature, whereas those of **2** display a marked decrease in CD intensity between 60 and 70 °C, which is largely reversible upon cooling (data not shown).

The fluorescence spectra of **1**−**3** in water and in 0.1 M KCl are shown in Figure 4. The spectra of **2** and **3** with salt and of **3** without salt display a mixture of structured pyrene monomer fluorescence and broad, red-shifted pyrene excimer fluorescence. Only monomer fluorescence is observed for conjugates **1** and

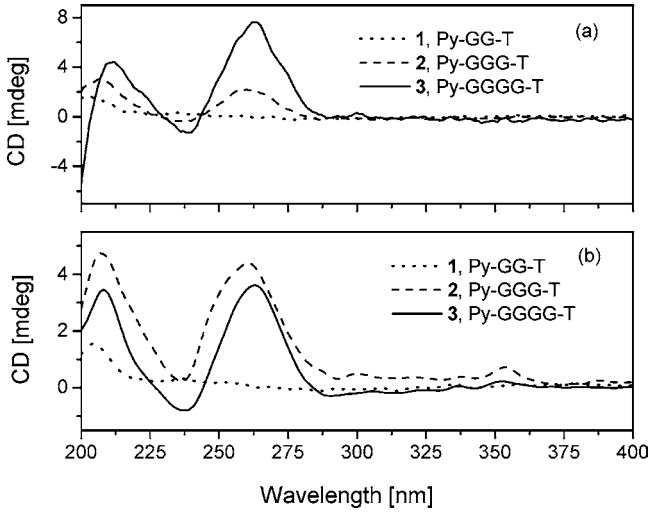


Figure 2. Circular dichroism spectra of 1×10^{-6} M conjugates **1**−**3** in (a) in water and (b) in 10 mM potassium phosphate with 0.1 M KCl.

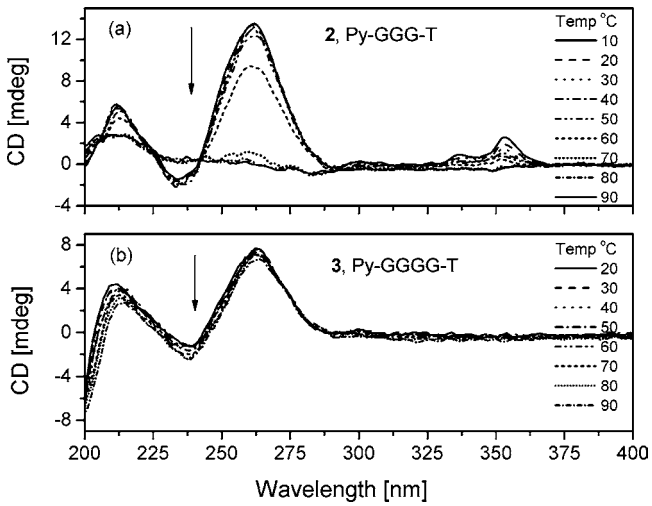


Figure 3. Temperature-dependent circular dichroism spectra of conjugates **2** and **3**. Heating rate: 1.5 min/°C. (a) 5×10^{-6} M conjugate **2** in 10 mM potassium phosphate with 0.1 M KCl and (b) 1×10^{-6} M conjugate **3** in water.

2 in water. The effect of added KCl and LiCl salts on the ratio of excimer to monomer fluorescence intensity for conjugate **2** is shown in Figure 5. The ratio I_{ex}/I_m increases with added KCl to a value of 1.4 at 0.2 M KCl but does not increase further at higher KCl concentrations. The I_{ex}/I_m ratio also increases upon addition of LiCl to a solution of **2** in 0.1 M KCl. Addition of LiCl results in values of I_{ex}/I_m somewhat smaller than that for 0.2 M KCl.

The effects of increasing temperature on the total fluorescence of **2** (with salt) and **3** (in buffer) are shown in Figure 6. The I_{ex}/I_m ratios obtained for both heating and cooling are shown in Figure 7. Heating of **2** results in a decrease in both monomer and excimer fluorescence intensity (Figure 6a). The ratio I_{ex}/I_m remains fairly constant up to ca. 50 °C but decreases at higher temperatures (Figure 7a). Cooling to 0 °C is necessary for recovery of the I_{ex}/I_m ratio. Heating of **3** results in a larger decrease in I_m than I_{ex} (Figure 6b), resulting in an increase in I_{ex}/I_m with increasing temperature (Figure 7b). Cooling results in lower values of I_{ex}/I_m than those observed at the same temperatures in the heating cycle.

Excimer fluorescence can also be used to visually detect G-aggregate formation using nondenaturing PAGE under a UV transilluminator, the eye being more sensitive to pyrene excimer vs monomer fluorescence. Electrophoresis of conjugates **2** and **3** (3.5×10^{-5} M or 0.3 mM in 0.1 M KCl) yields a single strongly fluorescence band, the band for **2** having a higher migration rate. In contrast, the faster-moving band from **1** cannot be detected visually without the addition of a staining agent (data not shown).

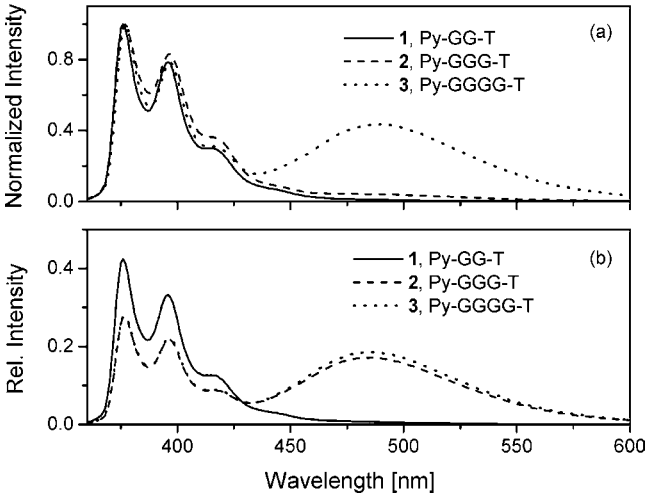


Figure 4. Room-temperature fluorescence spectra of 1×10^{-6} M conjugates **1**−**3** in different salt conditions: (a) in water and (b) in 0.1 M KCl, 10 mM potassium phosphate.

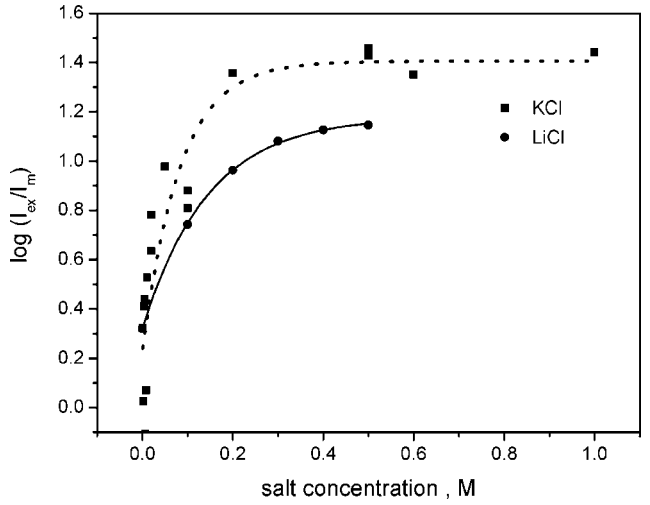


Figure 5. Salt concentration dependence of the pyrene excimer/monomer fluorescence intensity ratio for conjugate **2** (LiCl added to a solution containing 0.1 M KCl).

DISCUSSION

The ODNs d(TGGGT) and d(TGGGGT) are known to form stable parallel G-quadruplex structures in the presence of potassium ions (*17*, *22*). Parallel quadruplex formation has not been reported for d(TGGT); however, hairpin dimer and intramolecular G-quadruplex structures possessing only two G-quartets have been reported (*14*, *23*). The presence of the terminal thymines in the d(TG$_n$T) ODNs inhibits the formation of higher aggregates. The conjugates **1**−**3** are derived from these ODNs by replacement of the 5′-dT by pyrenebutanol (Scheme 1b,c). The 200−300 nm region of the CD spectra of **2** and **3** in the presence of KCl (Figure 2b) are identical, respectively, to those reported for d(TGGGT)$_4$ and for a G-quadruplex in which the 3′-thymines are connected by a branched linker which enforces a parallel structure (*24*, *25*).

The structure of **3** is similar to that of the conjugate d(TGGGG)-FL (FL = fluorescein) recently studied by Merkina

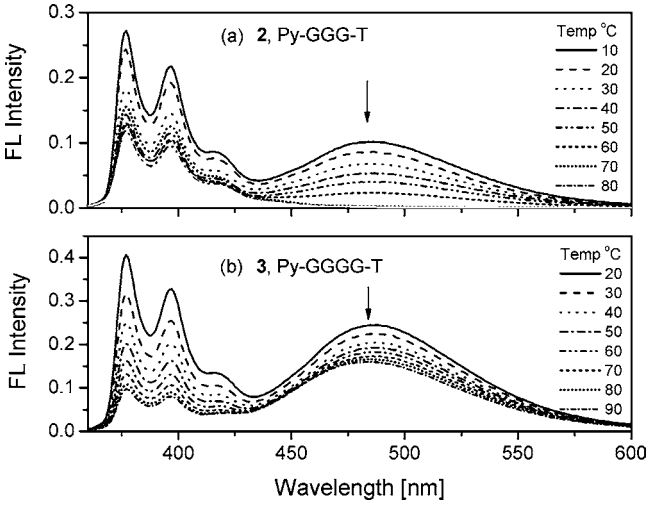


Figure 6. Temperature-dependent fluorescent spectra of conjugates **2** and **3**. Heating rate: 1.5 min/°C. (a) 5×10^{-6} M **2** in 10 mM potassium phosphate with 0.1 M KCl and (b) 1×10^{-6} M **3** in 10 mM potassium phosphate.

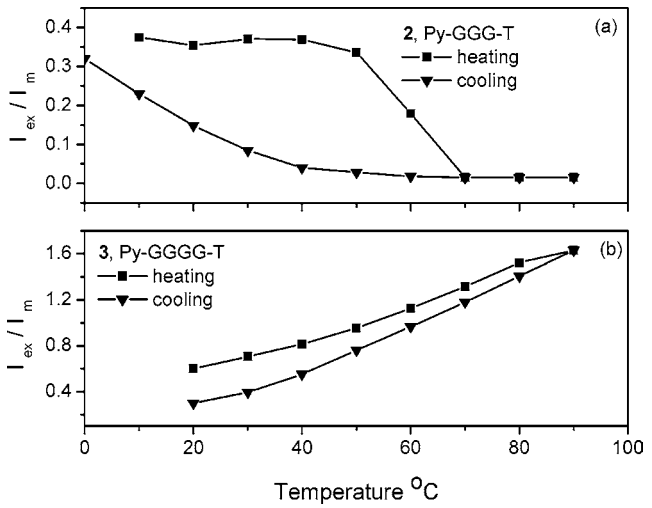


Figure 7. Excimer/monomer fluorescence intensity ratios for conjugates **2** and **3**. Heating and cooling rate: 1.5 min/°C. (a) 5×10^{-6} M **2** in 10 mM potassium phosphate with 0.1 M KCl and (b) 1×10^{-6} M **3** in 10 mM potassium phosphate.

and Fox (*19*). They report that the quadruplex formed by this conjugate is resistant to melting in the presence of 5 mM potassium. Stabilization of the FL-labeled quadruplex in sodium buffer when compared to an unlabeled quadruplex was attributed to stacking of the fluorophore on the exposed face of the terminal G-quartet, as observed for the complexes formed between G-quadruplexes and other planar hydrophobic organic molecules (*26*). We observe no change in the CD spectrum of **3** upon heating to 90 °C in the presence or absence of 10 mM potassium (Figure 3b), in accord with the high thermal stability observed for d(TGGGGT) or d(TGGGG)-FL (*13*, *17*). The failure of **2** to form a stable quadruplex structure under in water (Figure 2a) and the observation of "melting" of the high salt CD spectrum at ca. 60 °C (Figure 3a) is consistent with previous reports of the diminished stability of d(TGGGT) vs d(TGGGGT) (*17*). The failure of **1** to form a G-quadruplex structure even at high salt concentrations indicates that the hydrophobic association of four pyrenes is not sufficient to stabilize an intermolecular G-quadruplex structure possessing only two G-quartets.

The fluorescence spectra of **2** and **3** (Figure 4) consist of mixtures of monomer and excimer fluorescence, even though the CD spectra (Figure 2) are indicative of the formation of stable parallel G-quadruplex structures. It is possible that monomer and excimer fluorescence arise from different structures. However, PAGE gels for **2** and **3** display a single band, as visualized using pyrene excimer fluorescence. Low pyrene excimer/monomer fluorescence ratios have previously been observed upon duplex and triplex formation with pyrene end-labeled ODNs (*6*, *7*). A high excimer/monomer fluorescence ratio has been observed for oligomeric pyrene-containing C-nucleosides (*13*) and for an intramolecular G-quadruplex having pyrenes attached to the 3′- and 5′-ends of the sequence d(GGTTGGTGTGGTTGG) (*27*). However, only broadened monomer emission is observed for several duplexes bearing pyrenes as pendant groups on multiple adjacent dU bases (*9*, *10*). Studies of the fluorescence of conformationally constrained pyrene cyclophanes indicate that a full sandwich-like structure is required for the observation of long-wavelength excimer fluorescence, whereas structures with restricted overlap display small shifts or only broadened monomer emission (*1*, *28*).

We assume that the four pyrene chromophores occupy the 5′-face of the G-quartets formed by **2** and **3**, so as to minimize hydrophobic interactions of both the G-quartet and pyrenes with water. However, it is likely that some of the pyrene chromophores have ground-state geometries that disfavor formation of a sandwich excimer with a neighboring pyrene upon electronic excitation. Evidence for the clustering of pyrenes on a single face of the G-quadruplex is provided by the effect of added salts on the excimer/monomer fluorescence ratio (Figure 5). Both added KCl and LiCl cause an increase in the I_{ex}/I_m ratio, even though 0.01 M KCl is sufficient to effect G-quadruplex formation, as evidenced by the CD spectra. Since LiCl is unable to stabilize G-quadruplex structures (*29*, *30*), its influence on I_{ex}/I_m most likely is a consequence of a hydrophobic salt effect on the structure of the assembled pyrenes. LiCl and KCl have similar hydrophobic effects on the solubility of nonpolar molecules such as benzene in aqueous solution (*31*). Solvation of small ions by water results in collapse of the water molecules around the ions (*32*). This phenomenon, known as electrostriction, increases the energy required for creation of a space for a hydrophobic molecule such as pyrene and would force the four pyrenes attached to the quadruplex to occupy a smaller volume, plausibly favoring excimer formation.

In summary, evidence based on circular dichroism spectra indicates that both **2** and **3** form parallel quadruplex structures in which the appended pyrenes occupy the 5′-face of the quadruplex. Conjugate **1** fails to form a stable quadruplex structure even at low temperature in the presence of KCl. Conjugate **3**, which possesses a GGGG sequence, forms a stable quadruplex even in the absence of added salt and does not dissociate upon heating to 90 °C. In the presence of KCl, conjugate **2** forms a quadruplex structure that is stable at room temperature but undergoes thermal dissociation above 60 °C.

The fluorescence spectra of the quadruplexes formed by conjugates **2** and **3** display both monomer and excimer bands, whereas single-strand conjugates display only monomer fluorescence. Thus, excimer fluorescence can be used as a probe for intermolecular quadruplex formation, both in solution and in visualizing PAGE gels. Upon heating, the excimer/monomer band ratio for **2** deceases sharply above 50 °C, concomitant with thermal dissociation of the quadruplex. In contrast, the excimer/monomer ratio for **3** increases with temperature, indicative of a change in pyrene aggregate structure in a manner that favors the face-to-face geometry required for pyrene excimer fluorescence. The effect of added salts (KCl or LiCl) on the pyrene excimer/monomer ratio is attributed to electrostriction, which confines the hydrophobic pyrenes to a small volume.

ACKNOWLEDGMENT

Funding for this project was provided by a grant from the National Science Foundation (CHE-0400663).

LITERATURE CITED

(1) Winnik, F. M. (1993) Photophysics of preassociated pyrenes in aqueous polymer solutions and in other organized media. *Chem. Rev. 93*, 587−614.

(2) Hrdlicka, P. J., Babu, B. R., Sorensen, M. D., Harrit, N., and Wengel, J. (2005) Multilabeled pyrene-functionalized 2′-amino-LNA probes for nucleic acid detection in homogeneous fluorescence assays. *J. Am. Chem. Soc. 127*, 13293−13299.

(3) Kawai, K., Yoshida, H., Takada, T., Tojo, S., and Majima, T. (2004) Formation of pyrene dimer radical cation at the internal site of oligodeoxynucleotides. *J. Phys. Chem. B 108*, 13547−13550.

(4) Langenegger, S. M., and Haener, R. (2004) Excimer formation by interstrand stacked pyrenes. *Chem. Commun. 24*, 2792−2793.

(5) Paris, P. L., Langenhan, J. M., and Kool, E. T. (1998) Probing DNA sequences in solution with a monomer-excimer fluorescence color change. *Nucl. Acids Res. 26*, 3789−3793.

(6) Mohammadi, S., Slama-Schwok, A., Leger, G., El Manouni, D., Shchyolkina, A., Leroux, Y., and Taillandier, E. (1997) Triple helix formation and homologous strand exchange in pyrene-labeled oligonucleotides. *Biochemistry 36*, 14836−14844.

(7) Rippe, K., Fritsch, V., Westhof, E., and Jovin, T. M. (1992) Alternating d(G-A) sequences form a parallel-stranded DNA homoduplex. *EMBO J. 11*, 3777−86.

(8) Lewis, F. D., Zhang, Y., and Letsinger, R. L. (1997) Bispyrenyl excimer fluorescence: A sensitive oligonucleotide probe. *J. Am. Chem. Soc. 119*, 5451−5452.

(9) Barbaric, J., and Wagenknecht, H.-A. (2006) DNA as a supramolecular scaffold for the helical arrangement of a stack of 1-ethynylpyrene chromophores. *Org. Biomol. Chem. 4*, 2088−2090.

(10) Mayer-Enthart, E., and Wagenknecht, H.-A. (2006) Structure-sensitive and self-assembled helical pyrene array based on DNA architecture. *Angew. Chem., Int. Ed. 45*, 3372−*3375.*

(11) Nakamura, M., Ohtoshi, Y., and Yamana, K. (2005) Helical pyrene-array along the outside of duplex RNA. *Chem. Commun*, 5163−5165.

(12) Yamana, K., Takei, M., and Nakano, H. (1997) Synthesis of oligodeoxyribonucleotide derivatives containing pyrene labeled glycerol linkers: enhanced excimer fluorescence on binding to a complementary DNA sequence. *Tetrahedron Lett. 38*, 6051−6054.

(13) Cuppoletti, A., Cho, Y., Park, J.-S., Straessler, C., and Kool, E. T. (2005) Oligomeric fluorescent labels for DNA. *Bioconjugate Chem. 16*, 528−534.

(14) Keniery, M. A. (2001) Quadruplex structures in nucleic acids. *Biopolymers 56*, 123−146.

(15) Patel, D. J., Bouaziz, S., Kettani, A., and Wang, Y. (1998) Studies of guanine-rich and cytosine-rich quadruplexes formed *in vitro* by telomeric, centromeric, and triplet repeat disease DNA sequences. In *Oxford Handbook of Nucleic Acid Structure* (Neidle, S., Ed.), Oxford.

(16) Aboul-ela, F., Murchie, A. I. H., Norman, D. G., and Lilley, D. M. J. (1994) Solution structure of a parallel-stranded tetraplex formed by d(TG_4T) in the presence of sodium ions by NMR spectroscopy. *J. Mol. Biol. 243*, 458−471.

(17) Jin, R., Gaffney, B. L., Wang, C., Jones, R. A., and Breslauer, K. J. (1992) Thermodynamics and structure of a DNA tetraplex: a spectroscopic and calorimetric study of the tetramolecular complexes of d(TG_3T) and d($TG_3T_2G_3T$). *Proc. Natl. Acad. Sci. U.S.A. 89*, 8832−8836.

(18) Williamson, J. R. (1994) G-quartet structures in telomeric DNA. *Annu. Rev. Biophys. Biomol. Struct. 23*, 703−730.

(19) Merkina, E. E., and Fox, K. R. (2005) Kinetic stability of intermolecular DNA quadruplexes. *Biophys. J. 89*, 365−373.

(20) Letsinger, R. L., and Wu, T. (1995) Use of a stilbenedicarbxoamide bridge in stabilizing, monitoring, and photochemically altering folded conformations of oligonucleotides. *J. Am. Chem. Soc. 117*, 7323−7328.

(21) Lewis, F. D., Liu, X., Wu, Y., Miller, S. E., Wasielewski, M. R., Letsinger, R. L., Sanishvili, R., Joachimiak, A., Tereshko, V., and Egli, M. (1999) Structure and photoinduced electron transfer in exceptionally stable synthetic DNA hairpins with stilbenediether linkers. *J. Am. Chem. Soc. 121*, 9905−9906.

(22) Wyatt, J. R., Davis, P. W., and Freier, S. M. (1996) Kinetics of G-quartet mediated tetramer formation. *Biochemistry 35*, 8002−8008.

(23) Lewis, F. D., Wu, Y., and Zhang, L. (2004) Reversible formation of DNA G-quadruplex hairpin dimers from stilbenediether conjugates. *Chem. Commun*. 636−637.

(24) Oliviero, G., Borbone, N., Galeone, A., Varra, M., Piccialli, G., and Mayol, L. (2004) Synthesis and characterization of a bunchy oligonucleotide forming a monomolecular parallel quadruplex structure in solution. *Tetrahedron Lett.* 4869−4872.

(25) Oliviero, G., Amato, J., Borbone, N., Galeone, A., Petraccone, L., Varra, M., Piccialli, G., and Mayol, L. (2006) Synthesis and characterization of monomolecular DNA G-quadruplexes formed by tetra-end-linked oligonucleotides. *Bioconjugate Chem. 17*, 889−898.

(26) Clark, G. R., Pytel, P. D., Squire, C. J., and Neidle, S. (2003) Structure of the first parallel DNA quadruplex-drug complex. *J. Am. Chem. Soc. 125*, 4066−4067.

(27) Nagatoishi, S., Nojima, T., Juskowiak, B., and Takenaka, S. (2005) A pyrene-labeled G-quadruplex oligonucleotide as a fluorescent probe for potassium ion detection in biological applications. *Angew. Chem., Int. Ed. 44*, 5067−5070.

(28) Lewis, F. D., and Kurth, T. L. (2003) Intramolecular excimer fluorescence from folded ground state rotamers of N, N′-dimethyl-N, N′-dipyrenylurea protophanes. *Can. J. Chem. 81*, 770−776.

(29) Risitano, A., and Fox, K. R. (2004) Influence of loop size on the stability of intramoleclar DNA quadruplexes. *Nucl. Acids Res. 32*, 2598−2606.

(30) Sen, D., and Gilbert, W. (1992) Guanine quartet structures. *Methods Enzymol. 211*, 191−199.

(31) Long, F. A., and McDevit, W. F. (1952) Activity coefficeints of nonelectrolyte solutions in aqueous salt solutions. *Chem. Rev. 51*, 119−169.

(32) Breslow, R. (1991) Hydrophobic effects in simple organic reactions in water. *Acc. Chem. Res. 24*, 159−164.

BC060279U

An Acetal-Based PEGylation Reagent for pH-Sensitive Shielding of DNA Polyplexes

Veronika Knorr,[†] Lars Allmendinger,[‡] Greg F. Walker,[†] Franz F. Paintner,[‡] and Ernst Wagner*[,†]

Pharmaceutical Biology−Biotechnology and Pharmaceutical Chemistry, Department of Pharmacy Ludwig-Maximilians-Universität München, Butenandtstr. 5-13, D-81377 Munich, Germany. Received October 19, 2006; Revised Manuscript Received February 23, 2007

p-Piperazinobenzaldehyde methoxy poly(ethylene glycol) (mPEG, 5 kDa) acetal was synthesized by the Buchwald-Hartwig coupling reaction from piperazine and *p*-bromobenzaldehyde mPEG acetal. Introduction of a maleimide moiety yielded a novel acetal-based PEGylation reagent (PEG−acetal−MAL) for pH-sensitive conjugation of PEG to thiol-functionalized biomolecules. For reversible shielding of polyplexes, PEG−acetal−MAL was conjugated to polyethylenimine (PEI). At 37 °C, the PEG−acetal−PEI conjugate had a half-life of 3 min at endosomal pH 5.5 and 2 h at physiological pH 7.4, respectively. PEI polyplexes containing PEG−acetal−PEI had a ζ potential of +3 mV and were stable to salt-induced aggregation for 2 h at pH 7.4. In contrast, at endosomal pH, the particles were deshielded and aggregated within 0.5 h. Epidermal growth factor or transferrin receptor-targeted polyplexes shielded with the pH-sensitive PEG−acetal mediated enhanced luciferase gene expression in receptor-expressing target cells (Renca-EGFR or K562) as compared to stably shielded control polyplexes. Thus, the novel PEG−acetal−MAL reagent may present a versatile tool for drug and gene delivery formulations when pH-sensitive PEGylation is preferred.

INTRODUCTION

Nonviral vectors are receiving increasing attention due to their higher biosafety, compound stability, ease of chemical modification, and low cost compared to viral systems. In comparison with viruses, however, they suffer from lower gene transfer efficiency. Polyplexes belong to a subclass of nonviral vectors consisting of negatively charged DNA complexed with cationic polymers (*1*−*4*). Among the cationic polymers, polyethylenimine (PEI[1]) offers the advantage of efficient endosomal release due to its high pH-buffering capacity (*5*−*7*). An excess of PEI over DNA is usually required for high gene transfer activity (*8*), resulting in PEI polyplexes with a net positive surface charge. This charge, however, triggers nonspecific interactions with negatively charged physiological compounds. Systemic application of such polyplexes results in significant toxicity and/or poor efficiency due to binding to plasma proteins or blood cells and complement activation (*9*, *10*). The side effects can be reduced by surface neutralization by PEGylation, i.e., the modification with the hydrophilic polymer poly(ethylene glycol) (PEG). PEGylation covering the polyplex surface, however, reduces not only undesired interactions but also the desired binding to the negatively charged cell membrane (*11*). A reduced association and uptake into the cell can be overcome by the chemical attachment of a targeting ligand to the polyplex for receptor-mediated uptake. PEI polyplexes containing PEG and cell-targeting ligands have been successfully applied in vitro and in vivo (*11*−*17*).

Extensive PEGylation, though beneficial for systemic circulation, appears to negatively affect intracellular release of the delivered nucleic acid. Lipoplexes and polyplexes with a pH-sensitive PEG shield which can be removed upon endosomal acidification have been found to mediate enhanced gene transfer efficiency (*18*−*20*). In our previous work (*20*), reversible shielding of PEI polyplexes was achieved in an indirect manner by the conjugation of PEG to polylysine via a hydrazone bond. The chemistry was not applicable for direct conjugation of PEG to PEI because of insufficient stability of the resulting PEI conjugate. In their synthesis of bio-inspired polymeric carriers, Murthy et al. (*21*, *22*) synthesized hydrophobic, membrane-disruptive methacrylate polymers onto which hydrophilic PEG chains have been grafted through acid-degradable acetal linkages; a *p*-aminobenzaldehyde acetal linkage demonstrated a suitable hydrolysis profile at endosomal pH.

In our current work, a new PEGylation reagent was synthesized containing *p*-piperazinobenzaldehyde acetal linkage and a maleimide moiety which can be coupled to thiol-functionalized compounds. As a first application of this pH-sensitive PEGylation reagent, PEI conjugates were synthesized and used for shielding targeted PEI polyplexes. pH-triggered deshielding and higher gene transfer efficiency in comparison to analogous stable shielded polyplexes was demonstrated.

EXPERIMENTAL PROCEDURES

General Information. All chemical procedures were carried out in oven-dried glassware under a nitrogen atmosphere unless stated otherwise. Compound **6** was dried in a drying tube (KOH,

* Corresponding author. Pharmaceutical Biology - Biotechnology, Department of Pharmacy, Ludwig-Maximilians-Universität München, Butenandtstr. 5-13, Rm D 3.030. D-81377 Munich, Germany. E-mail: Ernst.Wagner@cup.uni-muenchen.de, Tel: +49 89 2180 77841, Fax: +49 89 2180 77791.

[†] Pharmaceutical Biology-Biotechnology.

[‡] Pharmaceutical Chemistry.

[1] Abbreviations: PEG, poly(ethylene glycol); mPEG, poly(ethylene glycol) monomethyl ether; PEG−acetal−MAL, *N*-(3-{4-[4-(1-{bis-[monomethoxy poly(ethylenoxy)]}methyl)phenyl]piperazinyl-]3-oxo-propyl)maleimide; PEI, polyethylenimine; PEG−A−PEI, poly(ethylene glycol) acetal conjugate with 25 kDa polyethylenimine; PEG−S−PEI, poly(ethylene glycol) stably conjugated with 25 kDa polyethylenimine; EGF, epidermal growth factor; Tf, transferrin; RLU, relative light units; SPDP, succinimidyl 3-(2-pyridyldithio)propionate; FCS, fetal calf serum; Hepes, *N*-2-hydroxyethylpiperazine-*N*′-2-ethane sulfonic acid; HBG, Hepes buffered glucose (5% (w/v) glucose, 20 mM Hepes, pH 7.4); 0.5× HBS, Hepes buffered salt (2.5% glucose (w/v), 75 mM NaCl, 20 mM Hepes, pH 7.4); rt, room temperature; sd, standard deviation.

10.1021/bc060327a CCC: $37.00 © 2007 American Chemical Society
Published on Web 05/04/2007

vacuum) for 3 days prior to use. Unless otherwise specified, all reagents were purchased from commercial suppliers and used without further purification. Toluene and tetrahydrofuran (THF) were distilled from sodium benzophenone ketyl radical; dimethyl sufoxide (DMSO) was distilled and stored over molecular sieves 4 Å under nitrogen. Ethyl acetate (EtOAc), chloroform, *n*-hexane, dichloromethane, diethyl ether, methanol, and *N*-ethyldimethylamine were distilled prior to use. Diethyl ether was stored over KOH. Methoxy poly(ethylene glycol)maleimide (PEG−MAL, average molecular weight of 5 kDa) was purchased from Nektar Therapeutics (Huntsville Alabama). Poly(ethylene glycol) 5 kDa monomethyl ether (mPEG) was purchased from Fluka Chemie GmbH (CH-9471 Buchs) and dried by heating to reflux (water separator) in toluene at an oil bath temperature of 170 °C for 20 h prior to use. Branched PEI with an average molecular weight of 25 kDa (PEI25) was purchased from Sigma-Aldrich (Steinheim, Germany). Linear PEI of 22 kDa (PEI22) was synthesized by acid-catalyzed deprotection of poly(2-ethyl-2-oxazoline) (50 kDa, Aldrich) in analogous form as described (*23*). It is also available from Polyplus Transfections (Strasbourg, France). Targeting conjugates (EGF−PEI and Tf−PEI) contain the ligands EGF or Tf linked with branched PEI 25 kDa by a heterobifunctional 3.4 kDa PEG linker and were synthesized as described previously (*13*−*24*). Succinimidyl 3-(2-pyridyldithio)propionate (SPDP) was purchased from Fluka (Steinheim, Germany). Tris-(dibenzylideneacetone)dipalladium ($Pd_2(dba)_3$) was a gift from Prof. Dr. Lorenz, LMU (Munich, Germany). Cell culture media, antibiotics, and fetal calf serum (FCS) were purchased from Life Technologies (Karlsruhe, Germany). Plasmid pCMVLuc (*Photinus pyralis* luciferase under control of the CMV enhancer/promoter) described in Plank et al. (*25*) was purified with the EndoFree Plasmid Kit from Qiagen (Hilden, Germany).

Column chromatography was performed on Merck silica gel 60 (40−63 μm). Gel filtration was performed on a Sephadex G-25 superfine, HR 10/30 column (Pharmacia, Sweden) in a 20 mM Hepes buffer pH 7.4 with 0.25 M NaCl, at a flow rate of 1 mL/min. Cation exchange was performed on a HR 10/10 column (BioRad, Munich, Germany) filled with Macro-prep High S. Infrared spectra were recorded on a Perkin-Elmer FT-IR Spectrometer Paragon 1000. ^{1}H NMR spectra were recorded on a Jeol JNMR-GX400 (400 MHz) or on a Jeol JNMR-GX500 (500 MHz) spectrometer. Chemical shifts are reported in parts per million (ppm) and refer to the solvent as internal standard (CH_2Cl_2 at 5.32 ppm). Data are reported as s = singulet, d = doublet, t = triplet, m = multiplet; coupling constants in hertz (Hz); integration. ^{13}C NMR spectra were recorded on a Jeol JNMR-GX500 (125 MHz) spectrometer. Chemical shifts are reported in ppm using solvent as an internal standard (CD_2Cl_2 at 53.8 ppm). Mass spectra were obtained on a Hewlett-Packard 5989A MS Engine with 59980B particle beam and on a Jeol MStation JMS-700. UV absorption and UV spectra were recorded on a GENESYS 10 Series Spectrometer.

Syntheses. *1-(4-Bromobenzene)-1-{bis[monomethoxypoly-(ethylenoxy)]}methane (**6**).* *p*-Bromobenzaldehyde (5.5506 g, 30 mmol) and *p*-TsOH·H_2O (19 mg, 0.1 mmol) were added to dried mPEG5kDa (10.0 g, 2 mmol) in toluene (50 mL), and the stirred reaction mixture was heated for 22 h at 170 °C (oil bath temperature). K_2CO_3 (276 mg, 2 mmol) was added, and after 45 min of stirring at room temperature (rt), the solidified reaction mixture was diluted with with CH_2Cl_2, filtered, and evaporated. For purification, the crude product was powdered, washed with Et_2O (7×), and finally dried under vacuum to afford **6** as a white powder (9.860 g, 97%).

^{1}H NMR (500 MHz, CD_2Cl_2): δ = 3.32 (s, CH_3 PEG5kDa), 3.37−3.79 (m, CH_2 PEG5kDa), 5.56 (s, 1 H), 7.34−7.40 (m, 2 H), 7.45−7.52 (m, 2 H).

*2-Trimethylsilylethyl 4-[4-(1{bis[monomethoxypoly(ethylenoxy)]}-methyl)phenyl]piperazine-1-carboxylate (**7**).* The following synthesis steps were carried out under an argon atmosphere. KO*t*Bu (19.1 mg, 0.17 mmol), $Pd_2(dba)_3$ (4.6 mg, 0.005 mmol), 2-(dicyclohexylphosphino)biphenyl, and dried **6** (1.0167 g, 0.1 mmol) were suspended in toluene (1 mL). A solution of 2-trimethylsilylethyl piperazine-1-carboxylate (**2**, Supporting Information) (34.5 mg, 0.15 mmol) in toluene (1 mL) was added, and the reaction mixture was stirred for 45 h at 90 °C. After cooling to rt, the mixture was treated with a saturated solution of $NaHCO_3$ (20 mL). The aqueous solution was extracted with CH_2Cl_2 (7 × 15 mL), and the combined organic layers were dried ($MgSO_4$), filtered, and evaporated under reduced pressure. To remove impurities, the resulting crude product was powdered and extracted with Et_2O (5×) to give **7** as a fawn powder (918 mg, 90%). The ^{1}H NMR shows this product contained about 82% of **7** and 18% of unreacted **6**, which could not be eliminated but also did not interfere in the following synthesis steps.

^{1}H NMR (500 MHz, CD_2Cl_2): δ = 0.04 (s, 9 H), 0.98−1.03 (m, 2 H), 3.13 (t, J = 5.0 Hz, 4 H), 3.32 (s, CH_3 PEG5kDa), 3.42−3.75 (m, CH_2 PEG5kDa, 4 H), 4.13−4.20 (m, 2 H), 5.50 (s, 1 H), 6.87−6.92 (m, 2 H), 7.31−7.36 (m, 2 H).

*1-[4-(1-{Bis[monomethoxypoly(ethylenoxy)]}methyl)phenyl]-piperazine (**8**).* To a suspension of **7** (310 mg, 0.03 mmol) in THF (1 mL), a solution of tetrabutylammonium fluoride trihydrate (TBAF·3H_2O) in THF (1 mL) was added dropwise. After slightly warming the reaction mixture, it was stirred at rt for 20 h. The mixture was then treated with a saturated solution of $NaHCO_3$ (5 mL). The aqueous solution was extracted with CH_2Cl_2 (5×), and the combined organic layers were dried ($MgSO_4$), filtered, and evaporated under reduced pressure. The resulting solid was powdered and washed with Et_2O (5 × 10 mL) to afford **8** as a beige powder (275.5 mg, 90%).

^{1}H NMR (500 MHz, CD_2Cl_2): δ = 2.94−2.99 (m, 4 H), 3.07−3.12 (m, 4 H), 3.33 (s, CH_3 PEG5kDa), 3.42−3.76 (m, CH_2 PEG5kDa), 5.49 (s, 1 H), 6.84−6.90 (m, 2 H), 7.28−7.33 (m, 2 H).

*N-(3-{4-[4-(1-{Bis[monomethoxypoly(ethylenoxy)]}methyl)-phenyl]piperazinyl-3-oxopropyl)maleimide (**9**).* *N*-Methylmorpholine (11 μL, 0.1 mmol) and *N*-succinimidyl-3-maleimidopropionate (13 mg, 0.05 mmol) were added subsequently to a suspension of **8** (101.9 mg, 0.01 mmol) in DMSO (0.5 mL) and stirred at rt for 30 min. The reaction mixture was then treated with phosphate buffer pH 7.4 [3 mL; KH_2PO_4 (250.0 mL, 0.2 M) + NaOH (393.4 mL, 0.1 M)] and extracted with CH_2Cl_2 (5 × 5 mL). The combined organic layers were dried ($MgSO_4$), filtered, and evaporated. The resulting beige solid was aliquoted into two portions of about 50 mg, dissolved in 20 mM Hepes buffer pH 7.4 with 0.25 M NaCl (2 mL) and purified by gel filtration chromatography. The fractions containing the desired product were extracted with CH_2Cl_2 (5 × 5 mL). The combined organic layers were dried ($MgSO_4$), filtered, and evaporated under reduced pressure to give **9** as a pale yellow solid (73.5 mg, 71%).

^{1}H NMR (500 MHz, CD_2Cl_2): δ = 2.63−2.70 (m, 2 H), 3.11−3.20 (m, 2 H), 3.32 (s, 6 H), 3.42−3.82 (m, CH_2 PEG5kDa, 4 H), 5.50 (s, 1 H), 6.69 (s, 2 H), 6.86−6.91 (m, 2 H), 7.32−7.36 (m, 2 H).

Thiolation of Branched Polyethylenimine. PEI25 (6 mg, 0.24 μmol) in 0.1 M Hepes buffer pH 7.4 (0.4 mL) was mixed with 0.6 μmol SPDP from a stock solution at 3 mg mL^{-1} in DMSO. The reaction was mixed overnight at rt, and the resulting product was purified by G-25 superfine gel filtration (*26*, *27*). The dithiopyridyl groups of the product were reduced with 50 mol equiv of DTT for 10 min, and the resulting thiol-modified PEI was purified by G-25 superfine gel filtration equilibrated in 20 mM Hepes pH 7.4 containing 0.25 M NaCl under argon.

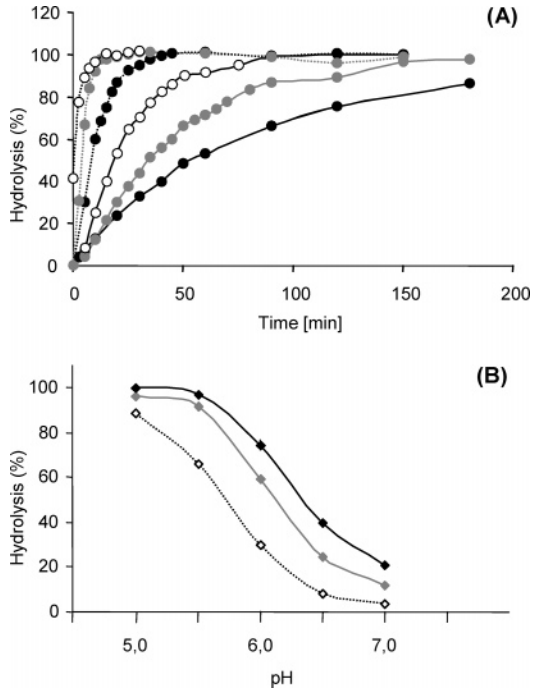


Figure 1. Time course of the cleavage of PEG−acetal−MAL **9** and formation of the corresponding aldehyde at 37 °C at different pH values (pH 7.4,−●−; pH 7.0, gray circles/solid lines; pH 6.5, −○−; pH 6.0, ···●···; pH 5.5, gray circles/dotted lines; pH 5.0, ···○···). (A). Hydrolysis rate of PEG−acetal−MAL **9** as a function of pH shown for different time points at 37 °C (5 min, ···◇···; 10 min, gray diamond/solid line; 15 min, −♦−) (B). Values are shown as duplicate.

The product was snap-frozen in liquid nitrogen and stored at −80 °C. PEI was quantified by the 2,4,6-trinitrobenzenesulfonic acid (TNBS) assay (*28*), and the amount of free mercapto groups was determined by the Ellman assay (*29*).

Poly(ethylene)glycol−polyethylenimine Conjugates. PEG−acetal−MAL **9** (0.2 mL, 0.12 μmol) or PEG−MAL (0.1 mL, 0.2 μmol) was dissolved in degassed 20 mM Hepes buffer pH 7.4 containing 0.25 M NaCl by brief sonication. PEG−acetal−MAL or PEG−MAL was mixed with PEI25-SH at 0.03 or 0.02 μmol (PEI), respectively (total volume 2 mL). After 10 min, the reaction was applied to the cation-exchange column, which was equilibrated in 20 mM Hepes buffer pH 7.4 containing 0.5 M NaCl. The salt concentration was increased with a linear gradient to 3 M NaCl (10 min) and maintained at 3 M NaCl for 15 min with a flow rate of 1 mL/min. The PEI product was eluted as a single peak at 3 M NaCl. PEI was quantified by the TNBS assay. PEG conjugation was monitored by measuring unbound PEG (*30*) and by ^{1}H NMR. The purified conjugates (PEG−A−PEI and PEG−S−PEI) were snap-frozen in liquid nitrogen and stored at −80 °C.

Hydrolysis Assay. The PEG−A−PEI conjugate (0.0092 μmol, 0.8 mL) was adjusted to pH 5 by the addition of sodium acetate (0.333 M) to a final concentration of 0.2 M total volume 2 mL and was incubated for 22 h at 37 °C. The reaction was applied to and separated on the cation-exchange column, the unbound PEG fractions were pooled, and the amount of PEG was quantified (*30*). For hydrolysis kinetic measurements in Figure 1, compound **9** was dissolved in the respective buffer (0.2 M Hepes buffer pH 7.4; 0.2 M Hepes buffer pH 7.0; 0.2 M phosphate buffer pH 6.5; 0.2 M phosphate buffer pH 6.0; 0.2 M phosphate buffer pH 5.5; 0.5 M NaOAc buffer pH 5.0) at a concentration of 1.5 mg/mL.

Formation of Polyplexes. DNA was mixed with PEI in HBG; complexes were formed at molar ratios of PEI nitrogen atoms to DNA phosphate (N/P) of 3 and 6. Various PEI derivatives were included in the formulation at the indicated ratios, as unmodified PEI (PEI22 or PEI25), targeting conjugate (EGF−PEI or Tf−PEI), or shielding conjugate (PEG−S−PEI or PEG−A−PEI). The DNA complexes were left at room temperature for 20 min prior to use.

Particle Size and ζ Potential. Particle size of DNA complexes was measured by laser-light scattering using a Malvern Zetasizer 3000HS (Malvern Instruments, Worcestershire, U.K.). For particle sizing, complexes were measured at a final DNA concentration of 10 μg/mL (total volume 1 mL). Measurements at pH 7.4 were performed in 0.5 × HBS pH 7.4, while for pH 5 measurements, a 20 mM NaOAc buffer pH 5.0, containing 75 mM NaCl, was used. For estimation of the surface charge, polyplexes were diluted 5-fold in 10 mM NaCl; ζ potential was measured as previously described (*24*).

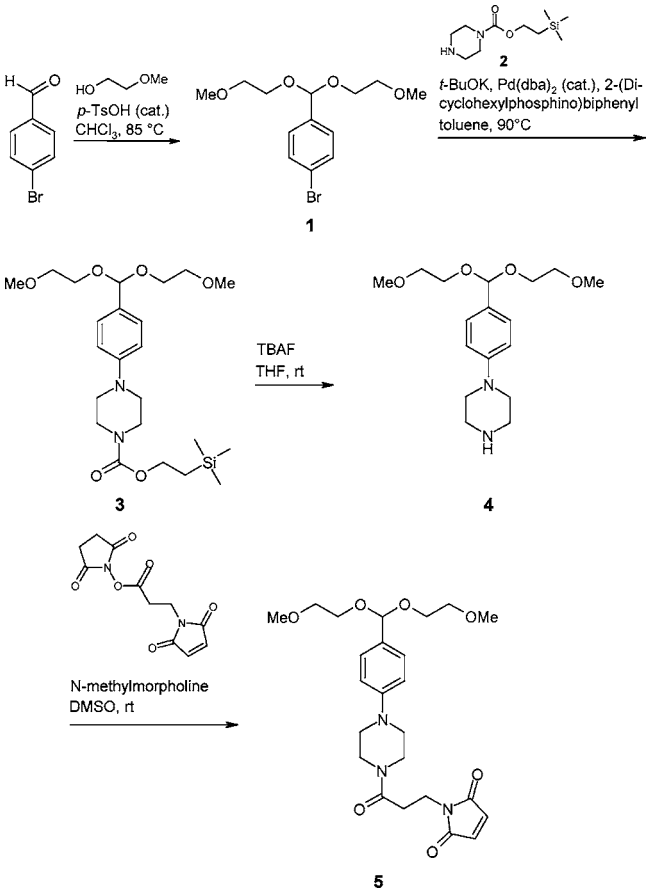
Cell Culture and Transfection. Renca-EGFR mouse renal carcinoma cells stably transfected with pLTR-EGFR and pSV2neo (kindly provided by Winfried Wels, Frankfurt am Main, Germany) and K562 suspension cells (ATCC CCL-243) were grown at 37 °C in a 5% CO_2 humidified atmosphere in RPMI-1640 with 4% Glutamax I medium supplemented with 10% FCS and 1% antibiotics (streptomycin, penicillin). Renca-EGFR cells were seeded in 96 well plates with 5×10^3 cells per well 24 h prior to transfection. K562 (2.5×10^5 cells in 0.75 mL) were plated in 24 well plates.

Transfection polyplexes at the indicated amounts of pCMVL plasmid DNA were added to each well. After 4 h incubation at 37 °C, the transfection medium was replaced by fresh culture medium. Luciferase gene expression was measured after 24 h as described (*24*). Values are given as relative light units (RLU) and represent the luciferase activity per 10^4 (Renca) or 2.5×10^5 (K562) cells. Two nanograms of recombinant luciferase (Promega, Mannheim, Germany) corresponds to 10^7 light units.

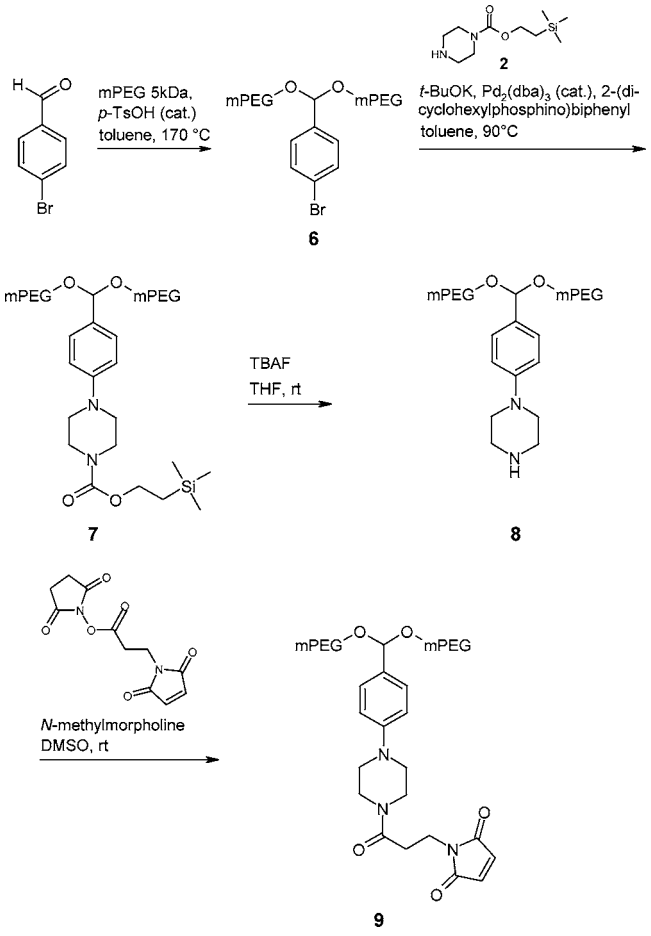
RESULTS

As shown in Scheme 1, the initial synthesis of the acetal linker was developed with 2-methoxyethanol instead of mPEG (see Supporting Information). This was necessary for optimization of the synthesis as well as for the characterization of the linker by NMR, as the PEG signal overlaps several signals of the synthesis intermediates. The synthesis of the methoxyethanol acetal (**5**) was achieved in four reaction steps, each of which was confirmed by NMR analysis. In a similar manner, the PEG acetal linker was synthesized as shown in Scheme 2. In the first step, *p*-bromobenzaldehyde was reacted with mPEG to generate the corresponding acetal (**6**) with a 97% yield. Formation of the acetal was confirmed by ^{1}H NMR, by appearance of a singlet at 5.56 ppm (acetal proton) and the disappearance of a singlet at 9.96 ppm (aldehyde proton). The bromo group of **6** was then substituted with trimethylsilylethyloxocarbonyl piperazine by the Buchwald-Hartwig reaction with 2-trimethylsilylethyl piperazine-1-carboxylate. ^{1}H NMR shows that the product obtained was a mixture of the piperazine-substituted acetal **7** (82%) and the starting material **6** (18%). The signals proving the existence of **7** appear as a singlet at 0.04 ppm belonging to the nine protons of the trimethylsilyl group, a multiplet of the methylene function next to the trimethylsilyl group at 0.98−1.03 ppm, and a triplet from four piperazine protons at 3.13 ppm; while the signal of the other four piperazine protons is overlapped by the PEG signal. For **6**, the acetal proton is represented at 5.56 ppm and the aromatic protons at 7.34−7.40 and 7.45−7.52 ppm. The respective signals for **7** are shifted to 5.50 ppm and to 6.87−6.92 and 7.31−7.36 ppm. The trimethylsilylethyloxocarbonyl protecting group of **7** was removed by reaction with TBAF·$3H_2O$, resulting in a 90% yield. Subsequent ^{1}H NMR analysis of the reaction product **8** showed the deprotection of the amine moiety by the appearance of a signal at 2.94−2.99 ppm which corresponds to the four protons at the carbons next to the

Scheme 1. Synthesis of the Methoxyethanol Acetal−MAL (5)



Scheme 2. Synthesis of PEG−acetal−MAL (9)

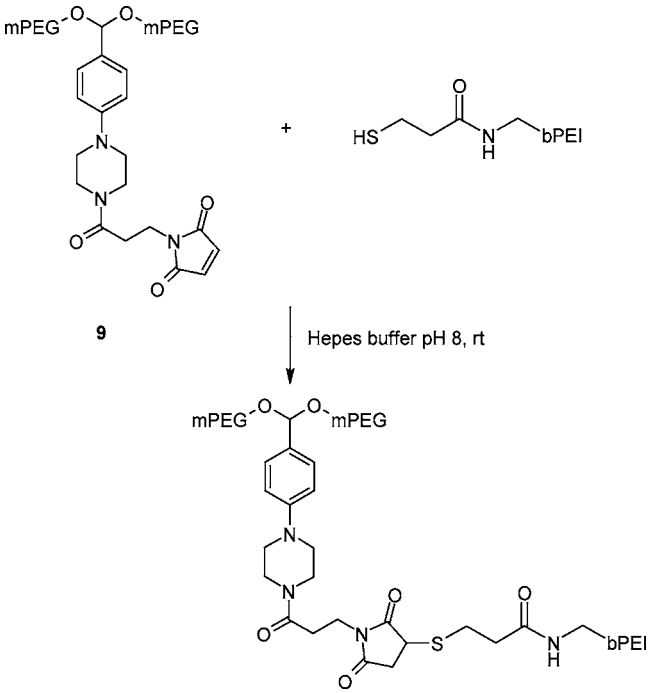


secondary amine. A 3-oxopropyl maleimido function was introduced at the deprotected amine by reacting **8** with *N*-succinimidyl-3-maleimidopropionate, resulting in a shift of the ^{1}H NMR signal from 2.94 to 2.99 ppm to lower field, which could not be observed due to the broad, overlapping PEG signal. Furthermore, a singlet appeared at 6.69 ppm, indicating the two methine protons of the maleimido group. In addition, a multiplet emerged at 2.63−2.70 ppm, corresponding to the two protons next to the carboxy group of the new substituent. Product **9**, the PEGylation reagent PEG−acetal−MAL used in the subsequent studies, was obtained with a 71% yield.

To ascertain the pH sensitivity of the linker, hydrolysis of **9** was carried out at pH 5.0, 5.5, 6.0, 6.5, 7.0, and 7.4 respectively. The assay was performed at 37 °C, and the hydrolysis was determined at different time points by measuring the absorbance at 340 nm, the main absorbance of the released aldehyde. Half-life continuously decreased with decreasing pH. At pH 7.4, the acetal hydrolyzed with a half-life of approximately 1 h, while at pH 5, the half-life was less than 3 min. At a pH of 6, which is relevant for PEI-containing endosomes (*6*, *31*), PEG−acetal−MAL degraded with a half-life of less than 10 min (Figure 1A). The curves in Figure 1B show the hydrolysis rates of PEG−acetal−MAL at defined time points as a function of the pH. For pH 5 at all three time points—5, 10, and 15 min—the reagent showed almost complete degradation, while for pH 7.0, between 96% and 80% remained intact during the indicated time periods.

Synthesis of the PEG−A−PEI conjugate was achieved by reacting the maleimide moiety of the PEG acetal linker **9** with mercapto-modified PEI25 (Scheme 3), resulting in a PEG/PEI molar ratio of approximately 3/1, corresponding to approximately 1.5 acetal moieties per PEI25 moiety. The hydrolytic profile of the PEG−A−PEI was measured at 340 nm in a similar manner to that of PEG−acetal−MAL. Figure 2 shows the time course of hydrolysis of the PEG−A−PEI conjugate at either

Scheme 3. Coupling of the PEG−acetal−MAL to Mercaptan-Modified Branched PEI25



pH 7.4 or pH 5.5 at 37 °C. The PEG−A−PEI had a half-life of approximately 3 min at pH 5.5, while the half-life was 2 h at pH 7.4.

To investigate the effect of PEG conjugates on the shielding of polyplexes, particle size and ζ potential were measured.

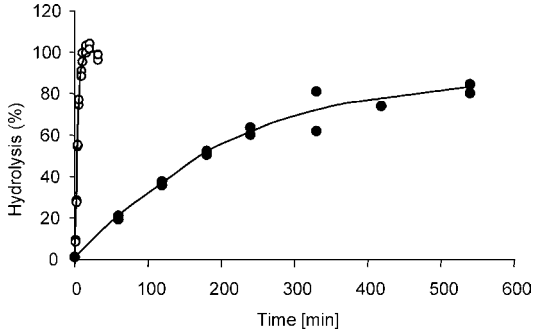


Figure 2. Time course of the cleavage of the acetal PEG−A−PEI25 and formation of the corresponding aldehyde at pH 7.4 (●) and at pH 5.5 (○) at 37 °C. Experiments were performed in duplicate.

Table 1. Particle Size and ζ Potential of Various Polyplex Formulations of N/P = 6[a]

	0 h		2 h	
formulation 70% PEI22 with:	size [nm]	ζ [mV]	size [nm]	ζ [mV]
20% PEI25, 10% EGF-PEG-PEI25	267	18.8	[b]	14.0
20% PEI25, 10% Tf-PEG-PEI25	[b]	18.2	[b]	13.7
20% PEG-S-PEI25, 10% PEI25	196	2.1	177	2.4
20% PEG-S-PEI25, 10% EGF-PEG-PEI25	232	3.0	251	2.7
20% PEG-S-PEI25, 10% Tf-PEG-PEI25	198	2.9	179	2.8
20% PEG-A-PEI25, 10% PEI25	204	3.2	169	3.2
20% PEG-A-PEI25, 10% EGF-PEG-PEI25	224	3.2	223	3.2
20% PEG-A-PEI25, 10% Tf-PEG-PEI25	211	3.0	203	3.1

[a] Data at the 0 and 2 h time points, pH 7.4. Each value represents the mean of at least three readings. [b] Aggregates with size over 1 μm formed.

Control PEI22 particles at N/P 6 without PEG and targeting ligands have a surface charge of about 30 mV and form aggregates (*24*). Table 1 shows particle sizes and ζ potentials of polyplexes containing targeting conjugate (EGF−PEI25 or Tf−PEI25) with and without PEG shield (PEG−S−PEI or PEG−A−PEI) at pH 7.4 and 37 °C. All PEGylated polyplexes remained shielded and stable for 2 h, whereas non-PEGylated polyplexes formed aggregates. Figure 3 shows the time-dependent changes of PEG−A−PEI shielded polyplexes incubated at either pH 5.0 or pH 7.4 and 37 °C. At pH 5.0, the PEG−A−PEI shielded polyplexes formed aggregates at the 0.5 h time point, indicating PEG removal under these conditions. In contrast, at pH 7.4 polyplexes were stable in size and retained low surface charge for the whole 2 h time period. Even after 4 h at pH 7.4—representing the incubation time of cells with polyplexes—particles remained shielded (data not shown). Different targeting conjugates (EGF in Figure 3A,B; Tf in Figure 3 C,D) did not significantly alter the biophysical properties. Polyplexes containing the nonreversible conjugate PEG−S−PEI did not change in size and remained shielded at both pH values (Table 1 and data not shown).

The transfection efficiency of the various polyplex formulations was tested using a luciferase gene expressing plasmid. EGF-containing polyplexes (*32*, *33*) were applied on Renca-EGFR cells and Tf-containing polyplexes (*24*, *26*) on K562 cells. To avoid extracellular deshielding, transfection medium was replaced after 4 h of incubation by fresh culture medium. All targeted, reversibly shielded polyplex formulations had greater gene transfer activity as compared to the analogous stably shielded formulations (see Figure 4 for Renca-EGFR and Figure 5 for K562). The effect of pH-sensitive PEGylation was most pronounced at a molar PEI nitrogen/DNA phosphate (N/P) ratio of 3 in Renca-EGFR, with a 14-fold enhanced gene expression compared to nonsensitive PEGylation (Figure 4). Analogously, for K562 cells the effect of pH-sensitive PEGylation was most pronounced at a molar N/P ratio of 6 resulting in 8-fold enhancement of gene expression (Figure 5). As polyplexes

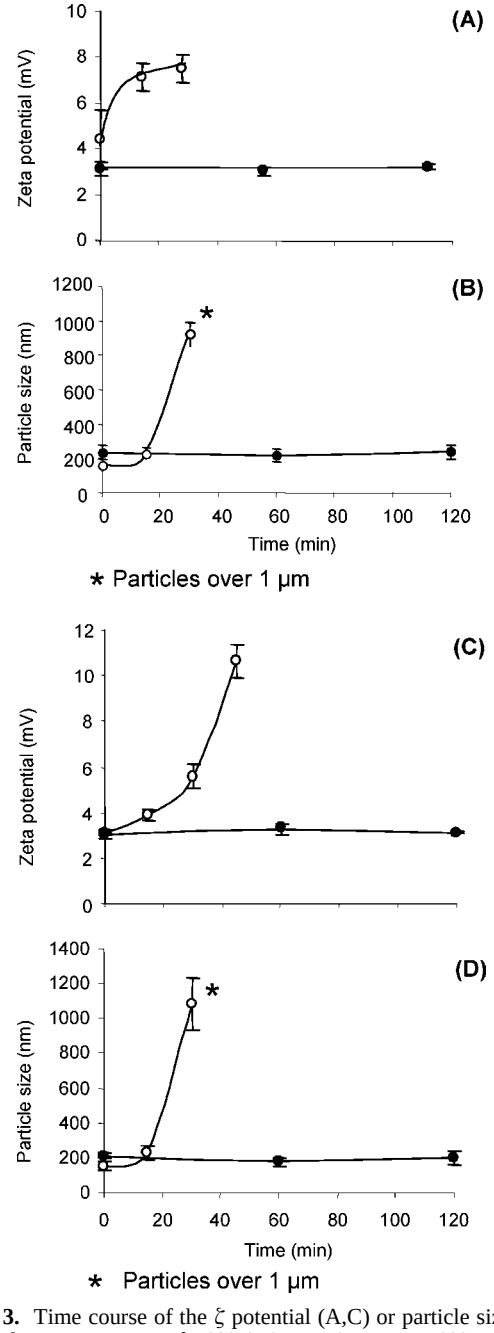


Figure 3. Time course of the ζ potential (A,C) or particle size (B,D) of polyplexes consisting of 70% (w/w; PEI) PEI22, 20% PEG−A−PEI, and 10% EGF−PEI (A,B) or 10% Tf−PEI (C,D) at pH 7.4 (●) and at pH 5.0 (○) at 37 °C. Each point represents the mean ± sd of three experiments.

remained shielded within the incubation time with cells, the higher transfection efficiency of reversibly shielded compared to stably shielded polyplexes is most probably due to intracellular deshielding.

DISCUSSION

Recent strategies for improving drug and gene delivery systems focus on the design of dynamic "stimuli-responsive" formulations (*34*). Similar to viruses in their infection process, these formulations may undergo programmed structural changes (*4*, *22*) which are induced by the particular microenvironment such as an intracellular reductive environment (*35*−*37*), enzymes (*38*), or altered pH (*19*, *22*, *39*), or are introduced externally by physical means (e.g., temperature, light, or magnetic field). The acidification of endosomes has been capitalized to trigger

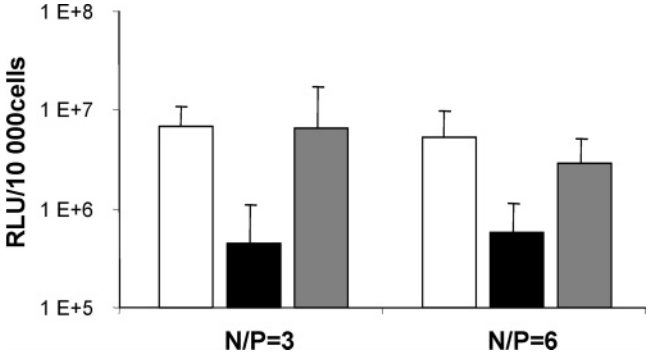


Figure 4. Luciferase gene expression by EGF-receptor-targeted polyplexes on Renca-EGFR cells. The experiments were performed using 200 ng pCMVLuc per well formulated at N/P ratios of 3 and 6. Polyplexes contain 70% PEI22, 10% EGF−PEI, and 20% of either PEI25 (nonshielded polyplexes, white bars), PEG−S−PEI (stably shielded polyplexes, black bars) or PEG−A−PEI (reversibly shielded polyplexes, gray bars). Each bar represents the mean ± sd of four independent experiments, each performed in triplicate.

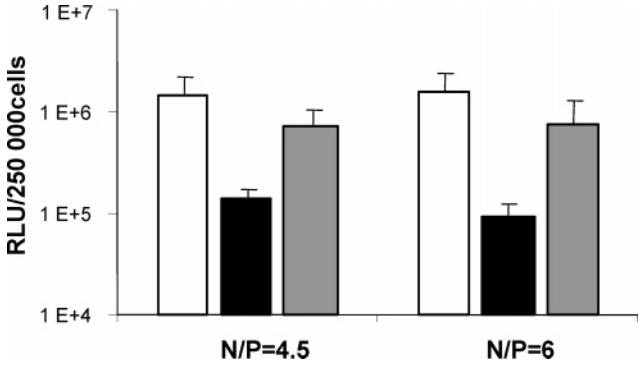


Figure 5. Luciferase gene expression by nonshielded (white bars), stably shielded (black bars), and reversibly shielded (gray bars) Tf-receptor-targeted polyplexes at N/P ratios of 4.5 and 6 on K562 cells. The experiments were performed using a pCMVLuc reporter gene at 2.5 μg per well. The values are mean ± sd of triplicates from a representative experiment out of three.

hydrolysis of acid-labile bonds in drug carriers and conjugates, such as ortho esters (*19*, *40*, *41*), acetals (*21*, *22*, *42*), or hydrazones (*20*, *39*, *43*). Among other applications, this strategy has been used for pH-responsive intracellular deshielding of nonviral gene vectors (*44*). Surface shielding of gene vectors by PEG (*24*) or other hydrophilic polymers (*45*) has been found to be very helpful for systemic circulation and reduced toxicity, but hampers intracellular delivery. Therefore, removal of the shield after delivery of the gene vector to the target cell would be desirable.

The current work describes the synthesis of a new acetal-linked PEGylation reagent that undergoes acidic triggered cleavage and is shown to be advantageous for reversible shielding of gene delivery particles. The novel PEGylation reagent **9** was synthesized following the steps shown in Scheme 2, after synthetic procedures were established using 2-methoxyethanol instead of mPEG. The Buchwald-Hartwig cross-coupling reaction is a powerful method for substitution of aromatic bromines with piperazine (*46*). In this report, the Buchwald-Hartwig amination reaction for substitution of the *p*-bromobenzaldehyde mPEG acetal with the monoprotected piperazine proved to be an efficient procedure affording the desired product with an 82% yield. To our knowledge, it is the first Buchwald-Hartwig cross-coupling reaction with a polymeric compound.

The pH within endosomes varies with the type of endosomal vesicle and the applied formulation (*6*, *31*, *31*). Therefore, hydrolysis studies with PEG−acetal−MAL were performed at several pHs to determine changes in the hydrolysis rate depending on the pH. As shown in Figure 1A, PEG−acetal−MAL hydrolysis revealed a strong pH specificity with a half-life of approximately 1 h at pH 7.4 and less than 3 min at pH 5. At pH 5.5 and 6, approximately the pHs existing in PEI-containing endosomes (*6*, *31*), PEG−acetal−MAL degraded with a half-life of less than 5 and 10 min, respectively (Figure 1A). Figure 1B shows the hydrolysis rates of PEG−acetal−MAL at defined time points as a function of the pH. For pH 5 at all three time points (5, 10, and 15 min), the reagent showed almost complete degradation, while for pH 7.0, between 96% and 80% remained intact during the indicated time periods. These data demonstrate a suitable pH dependence of the degradation rate of PEG−A−MAL.

Since these hydrolytic studies showed the PEG−acetal−MAL linker to be suitable for acid-specific hydrolysis, the reagent was used for PEGylation of the transfection reagent polyethylenimine (PEI) by reaction of the maleimide moiety with mercapto-modified PEI. Kinetic hydrolysis studies on the resulting conjugate PEG−A−PEI showed similar pH specificity (at 37 °C, half-life of about 2 h at pH 7.4 and 3 min at pH 5.5) as for PEG−acetal−MAL. Thus, this conjugate provides sufficient storage stability on one hand and allows polyplex deshielding even in PEI-buffered endosomes of pH 5.5 to 6 on the other hand. This observation was made both for branched PEI 25 kDa (this work) and for linear PEI 22 kDa conjugates (data not shown) and contrasts our previous work with acid-labile hydrazone linkers, where PEI triggers pronounced hydrolysis of the linker also at neutral pH (*20*).

From previous work (*20*, *24*), it is known that for the shielding of polyplexes only part of the polycation has to be replaced by its PEGylated version. The percentage of required PEG conjugate depends on the amount of PEG on the polycation as well as the PEG chain length and type of polycation; therefore, we determined in titration experiments with varying amounts of PEG−A−PEI the optimal amount of shielding conjugate in the formulation. Polyplexes with 20% of the PEG−A−PEI conjugate containing 1.5 acetals, i.e., three PEG chains per PEI were found to be most convenient. With this amount of PEG, polyplexes showed proper and persistent shielding at physiological pH but at the same time were deshielded quickly at the acidic pH of 5. This new acid-labile conjugate PEG−A−PEI was then incorporated into DNA polyplexes to evaluate the effect of pH-specific removal of the PEG shield. For receptor-mediated uptake, targeting conjugates EGF−PEI or Tf−PEI were incorporated into the polyplexes. EGF-containing polyplexes and Tf-containing polyplexes have been previously shown to be efficiently internalized into EGFR-overexpressing Renca cells (*33*, *47*) and transferrin receptor overexpressing K562 cells (*24*, *26*), respectively. To obtain sufficient surface neutralization, the pH-sensitive (PEG−A−PEI) or nonreversible (PEG−S−PEI) shielding conjugate was included in the polyplex at 20% (w/w; PEI), resulting in well-shielded particles with a ζ potential of +3 mV and particle sizes in the range of 200 nm. In order to follow the deshielding process, these particles were incubated at pH 7.4, representing the physiological pH of the blood, or at pH 5, representing endosomal pH. At pH 7.4, all polyplexes maintained their PEG shield for the 2 h time period, after which major receptor-mediated uptake should be completed (*48*). At pH 7.4, additional analysis of the polyplexes after 4 h was performed (data not shown) to ensure stability of the PEG shield during the incubation time in cell culture experiments. Polyplexes did not deshield within this time. Also, the polyplexes containing the nonreversible shielding conjugate PEG−S−PEI did not change their biophysical properties at pH 5 (data not shown). In contrast, the particles containing PEG−A−PEI at pH 5 within 30 min formed aggregates and increased in ζ

potential, indicating deshielding. The reversibly shielded (PEG−A−PEI) polyplexes were found to have approximately 10-fold enhanced gene transfer efficiency than stable shielded polyplexes when tested on the two different cell lines, Renca-EGFR cells and K562 cells. This is consistent also with our previous result using pH-labile hydrazone linkages (*20*).

The novel PEG−acetal−MAL reagent **9** described in this study, however, presents a more versatile tool for pH-sensitive PEGylation. Beyond the branched PEI as applied in this study, other mercapto-modified compounds may be modified for the development of more dynamic, pH-responsive drug and gene delivery systems.

ACKNOWLEDGMENT

We thank Olga Brück for skillful assistance in preparing the manuscript. This work was in part funded by the Deutsche Forschungsgemeinschaft, SFB 486 'Nanoman', excellence cluster NIM, and by the European Community FP6 network project 'GIANT'.

Supporting Information Available: Synthesis protocol for the model compound *N*-{3-[4-(4-{1-[bis-(2-methoxyethoxy)]methyl}-phenyl)piperazinyl]-3-oxopropyl}maleimide. This material is available free of charge via the Internet at http://pubs.acs.org/BC.

LITERATURE CITED

(1) Felgner, P. L., Barenholz, Y., Behr, J. P., Cheng, S. H., Cullis, P., Huang, L., Jessee, J. A., Seymour, L., Szoka, F., Thierry, A. R., Wagner, E., and Wu, G. (1997) Nomenclature for synthetic gene delivery systems. *Hum. Gene Ther. 8*, 511−512.

(2) Hughes, J. A., and Rao, G. A. (2005) Targeted polymers for gene delivery. *Expert Opin. Drug Delivery 2*, 145−157.

(3) Pack, D. W., Hoffman, A. S., Pun, S., and Stayton, P. S. (2005) Design and development of polymers for gene delivery. *Nat. Rev. Drug Discovery 4*, 581−593.

(4) Wagner, E. (2004) Strategies to improve DNA polyplexes for in vivo gene transfer: will "artificial viruses" be the answer? *Pharm. Res. 21*, 8−14.

(5) Boussif, O., Lezoualc'h, F., Zanta, M. A., Mergny, M. D., Scherman, D., Demeneix, B., and Behr, J. P. (1995) A versatile vector for gene and oligonucleotide transfer into cells in culture and in vivo: polyethylenimine. *Proc. Natl. Acad. Sci. U.S.A. 92*, 7297−7301.

(6) Sonawane, N. D., Szoka, F. C., Jr., and Verkman, A. S. (2003) Chloride accumulation and swelling in endosomes enhances DNA transfer by polyamine-DNA polyplexes. *J. Biol. Chem. 278*, 44826−44831.

(7) Akinc, A., Thomas, M., Klibanov, A. M., and Langer, R. (2005) Exploring polyethylenimine-mediated DNA transfection and the proton sponge hypothesis. *J. Gene Med. 7*, 657−663.

(8) Boeckle, S., von Gersdorff, K., van der Piepen, S., Culmsee, C., Wagner, E., and Ogris, M. (2004) Purification of polyethylenimine polyplexes highlights the role of free polycations in gene transfer. *J. Gene Med. 6*, 1102−1111.

(9) Plank, C., Mechtler, K., Szoka, F. C., Jr., and Wagner, E. (1996) Activation of the complement system by synthetic DNA complexes: a potential barrier for intravenous gene delivery. *Hum. Gene Ther. 7*, 1437−1446.

(10) Chollet, P., Favrot, M. C., Hurbin, A., and Coll, J. L. (2002) Side-effects of a systemic injection of linear polyethylenimine-DNA complexes. *J. Gene Med. 4*, 84−91.

(11) Erbacher, P., Bettinger, T., Belguise-Valladier, P., Zou, S., Coll, J. L., Behr, J. P., and Remy, J. S. (1999) Transfection and physical properties of various saccharide, poly(ethylene glycol), and antibody-derivatized polyethylenimines (PEI). *J. Gene Med. 1*, 210−222.

(12) Ogris, M., Brunner, S., Schuller, S., Kircheis, R., and Wagner, E. (1999) PEGylated DNA/transferrin-PEI complexes: reduced interaction with blood components, extended circulation in blood and potential for systemic gene delivery. *Gene Ther. 6*, 595−605.

(13) Wolschek, M. F., Thallinger, C., Kursa, M., Rossler, V., Allen, M., Lichtenberger, C., Kircheis, R., Lucas, T., Willheim, M., Reinisch, W., Gangl, A., Wagner, E., and Jansen, B. (2002) Specific systemic nonviral gene delivery to human hepatocellular carcinoma xenografts in SCID mice. *Hepatology 36*, 1106−1114.

(14) Ogris, M., Walker, G., Blessing, T., Kircheis, R., Wolschek, M., and Wagner, E. (2003) Tumor-targeted gene therapy: strategies for the preparation of ligand-polyethylene glycol-polyethylenimine/DNA complexes. *J. Controlled Release 91*, 173−181.

(15) Kim, W. J., Yockman, J. W., Lee, M., Jeong, J. H., Kim, Y. H., and Kim, S. W. (2005) Soluble Flt-1 gene delivery using PEI-g-PEG-RGD conjugate for anti-angiogenesis. *J. Controlled Release 106*, 224−234.

(16) Moffatt, S., Wiehle, S., and Cristiano, R. J. (2005) Tumor-specific gene delivery mediated by a novel peptide-polyethylenimine-DNA polyplex targeting aminopeptidase N/CD13. *Hum. Gene Ther. 16*, 57−67.

(17) Moffatt, S., Papasakelariou, C., Wiehle, S., and Cristiano, R. (2006) Successful in vivo tumor targeting of prostate-specific membrane antigen with a highly efficient J591/PEI/DNA molecular conjugate. *Gene Ther. 13*, 761−772.

(18) Choi, J. S., MacKay, J. A., and Szoka, F. C., Jr. (2003) Low-pH-sensitive PEG-stabilized plasmid-lipid nanoparticles: preparation and characterization. *Bioconjugate Chem. 14*, 420−429.

(19) Li, W., Huang, Z., MacKay, J. A., Grube, S., and Szoka, F. C., Jr. (2005) Low-pH-sensitive poly(ethylene glycol) (PEG)-stabilized plasmid nanolipoparticles: effects of PEG chain length, lipid composition and assembly conditions on gene delivery. *J. Gene Med. 7*, 67−79.

(20) Walker, G. F., Fella, C., Pelisek, J., Fahrmeir, J., Boeckle, S., Ogris, M., and Wagner, E. (2005) Toward synthetic viruses: endosomal pH-triggered deshielding of targeted polyplexes greatly enhances gene transfer in vitro and in vivo. *Mol. Ther. 11*, 418−425.

(21) Murthy, N., Campbell, J., Fausto, N., Hoffman, A. S., and Stayton, P. S. (2003) Design and synthesis of pH-responsive polymeric carriers that target uptake and enhance the intracellular delivery of oligonucleotides. *J. Controlled Release 89*, 365−374.

(22) Murthy, N., Campbell, J., Fausto, N., Hoffman, A. S., and Stayton, P. S. (2003) Bioinspired pH-responsive polymers for the intracellular delivery of biomolecular drugs. *Bioconjugate Chem. 14*, 412−419.

(23) Brissault, B., Kichler, A., Guis, C., Leborgne, C., Danos, O., and Cheradame, H. (2003) Synthesis of linear polyethylenimine derivatives for DNA transfection. *Bioconjugate Chem. 14*, 581−587.

(24) Kursa, M., Walker, G. F., Roessler, V., Ogris, M., Roedl, W., Kircheis, R., and Wagner, E. (2003) Novel shielded transferrin-polyethylene glycol-polyethylenimine/DNA complexes for systemic tumor-targeted gene transfer. *Bioconjugate Chem. 14*, 222−231.

(25) Plank, C., Zatloukal, K., Cotten, M., Mechtler, K., and Wagner, E. (1992) Gene transfer into hepatocytes using asialoglycoprotein receptor mediated endocytosis of DNA complexed with an artificial tetra-antennary galactose ligand. *Bioconjugate Chem. 3*, 533−539.

(26) Cotten, M., Langle-Rouault, F., Kirlappos, H., Wagner, E., Mechtler, K., Zenke, M., Beug, H., and Birnstiel, M. L. (1990) Transferrin-polycation-mediated introduction of DNA into human leukemic cells: stimulation by agents that affect the survival of transfected DNA or modulate transferrin receptor levels. *Proc. Natl. Acad. Sci. U.S.A. 87*, 4033−4037.

(27) Kircheis, R., Kichler, A., Wallner, G., Kursa, M., Ogris, M., Felzmann, T., Buchberger, M., and Wagner, E. (1997) Coupling of cell-binding ligands to polyethylenimine for targeted gene delivery. *Gene Ther. 4*, 409−418.

(28) Snyder, S. L., and Sobocinski, P. Z. (1975) An improved 2,4,6-trinitrobenzenesulfonic acid method for the determination of amines. *Anal. Biochem. 64*, 284−8.

(29) Riddles, P. W., Blakeley, R. L., and Zerner, B. (1979) Ellman's reagent: 5,5′-dithiobis(2-nitrobenzoic acid)−a reexamination. *Anal. Biochem. 94*, 75−81.

(30) Childs, C. E. (1975) The determination of polyethylene glycol in gamma globulin solutions. *Microchem. J. 20*, 190−192.

(31) Kulkarni, R. P., Mishra, S., Fraser, S. E., and Davis, M. E. (2005) Single cell kinetics of intracellular, nonviral, nucleic acid delivery vehicle acidification and trafficking. *Bioconjugate Chem. 16*, 986−994.

(32) Blessing, T., Kursa, M., Holzhauser, R., Kircheis, R., and Wagner, E. (2001) Different strategies for formation of pegylated EGF-conjugated PEI/DNA complexes for targeted gene delivery. *Bioconjugate Chem. 12*, 529−537.

(33) von Gersdorff, K., Ogris, M., and Wagner, E. (2005) Cryoconserved shielded and EGF receptor targeted DNA polyplexes: cellular mechanisms. *Eur. J. Pharm. Biopharm. 60*, 279−285.

(34) Oupicky, D., and Diwadkar, V. (2003) Stimuli-responsive gene delivery vectors. *Curr. Opin. Mol. Ther. 5*, 345−350.

(35) Saito, G., Swanson, J. A., and Lee, K. D. (2003) Drug delivery strategy utilizing conjugation via reversible disulfide linkages: role and site of cellular reducing activities. *Adv. Drug Delivery Rev. 55*, 199−215.

(36) Carlisle, R. C., Etrych, T., Briggs, S. S., Preece, J. A., Ulbrich, K., and Seymour, L. W. (2004) Polymer-coated polyethylenimine/DNA complexes designed for triggered activation by intracellular reduction. *J. Gene Med. 6*, 337−344.

(37) Chen, C. P., Kim, J. S., Steenblock, E., Liu, D., and Rice, K. G. (2006) Gene transfer with poly-melittin peptides. *Bioconjugate Chem. 17*, 1057−1062.

(38) Hatakeyama, H., Akita, H., Kogure, K., Oishi, M., Nagasaki, Y., Kihira, Y., Ueno, M., Kobayashi, H., Kikuchi, H., and Harashima, H. (2007) Development of a novel systemic gene delivery system for cancer therapy with a tumor-specific cleavable PEG-lipid. *Gene Ther. 14*, 68−77.

(39) Aissaoui, A., Martin, B., Kan, E., Oudrhiri, N., Hauchecorne, M., Vigneron, J. P., Lehn, J. M., and Lehn, P. (2004) Novel cationic lipids incorporating an acid-sensitive acylhydrazone linker: synthesis and transfection properties. *J. Med. Chem. 47*, 5210−5223.

(40) Guo, X., and Szoka, F. C., Jr. (2001) Steric stabilization of fusogenic liposomes by a low-pH sensitive PEG−diortho ester−lipid conjugate. *Bioconjugate Chem. 12*, 291−300.

(41) Masson, C., Garinot, M., Mignet, N., Wetzer, B., Mailhe, P., Scherman, D., and Bessodes, M. (2004) pH-sensitive PEG lipids containing orthoester linkers: new potential tools for nonviral gene delivery. *J. Controlled Release 99*, 423−434.

(42) Gillies, E. R., Goodwin, A. P., and Frechet, J. M. (2004) Acetals as pH-sensitive linkages for drug delivery. *Bioconjugate Chem. 15*, 1254−1263.

(43) Greenfield, R. S., Kaneko, T., Daues, A., Edson, M. A., Fitzgerald, K. A., Olech, L. J., Grattan, J. A., Spitalny, G. L., and Braslawsky, G. R. (1990) Evaluation in vitro of adriamycin immunoconjugates synthesized using an acid-sensitive hydrazone linker. *Cancer Res. 50*, 6600−6607.

(44) Meyer, M., and Wagner, E. (2006) pH-responsive shielding of non-viral gene vectors. *Expert Opin. Drug Delivery 3*, 563−571.

(45) Oupicky, D., Ogris, M., Howard, K. A., Dash, P. R., Ulbrich, K., and Seymour, L. W. (2002) Importance of lateral and steric stabilization of polyelectrolyte gene delivery vectors for extended systemic circulation. *Mol. Ther. 5*, 463−472.

(46) Clark, M. A., Duffy, K., Tibrewala, J., and Lippard, S. J. (2003) Synthesis and metal-binding properties of chelating fluorescein derivatives. *Org. Lett. 5*, 2051−2054.

(47) Blessing, T., Kursa, M., Holzhauser, R., Kircheis, R., and Wagner, E. (2001) Different strategies for formation of pegylated EGF-conjugated PEI/DNA complexes for targeted gene delivery. *Bioconjugate Chem. 12*, 529−537.

(48) Ogris, M., Steinlein, P., Carotta, S., Brunner, S., and Wagner, E. (2001) DNA/polyethylenimine transfection particles: Influence of ligands, polymer size, and PEGylation on internalization and gene expression. *AAPS Pharm. Sci. 3*, E21.

BC060327A

Reagents for Astatination of Biomolecules. 2. Conjugation of Anionic Boron Cage Pendant Groups to a Protein Provides a Method for Direct Labeling that is Stable to in Vivo Deastatination

D. Scott Wilbur,*,† Ming-Kuan Chyan,† Donald K. Hamlin,† Robert L. Vessella,‡ Timothy J. Wedge,§ and M. Frederick Hawthorne§

Departments of Radiation Oncology and Urology, University of Washington, Seattle, Washington 98195, and Department of Chemistry and Biochemistry, University of California, Los Angeles, California. Received November 3, 2006; Revised Manuscript Received April 25, 2007

Cancer-targeting biomolecules labeled with ^{211}At must be stable to in vivo deastatination, as control of the ^{211}At distribution is critical due to the highly toxic nature of α-particle emission. Unfortunately, no astatinated aryl conjugates have shown in vivo stability toward deastatination when (relatively) rapidly metabolized proteins, such as monoclonal antibody Fab′ fragments, are labeled. As a means of increasing the in vivo stability of ^{211}At-labeled proteins, we have been investigating antibody conjugates of boron cage moieties. In this investigation, protein-reactive derivatives containing a *nido*-carborane (**2**), a bis-*nido*-carborane derivative (Venus Flytrap Complex, **3**), and four 2-nonahydro-*closo*-decaborate(2-) derivatives (**4**−**7**) were prepared and conjugated with an antibody Fab′ fragment such that subsequent astatination and in vivo tissue distributions could be obtained. To aid in determination of stability toward in vivo deastatination, the Fab′−borane conjugates were also labeled with ^{125}I, and that material was coinjected with the ^{211}At-labeled Fab′. For comparison, direct labeling of the Fab′ with ^{125}I and ^{211}At was conducted. Direct labeling with Na[^{125}I]I and Chloramine-T gave an 89% radiochemical yield. However, direct labeling of the Fab′ with Na[^{211}At]At and Chloramine-T resulted in a yield of <1% after quenching with NaS_2O_5. As another comparison, the same Fab′ was conjugated with *p*-[^{211}At]astatobenzoate NHS ester, [^{211}At]**1c**-Fab′, and (separately) with *p*-[^{125}I]iodobenzoate NHS ester, [^{125}I]**1b**-Fab′. An evaluation in athymic mice demonstrated that [^{211}At]**1c**-Fab′ underwent deastatination. In contrast, the high in vivo stability of [^{125}I]-**1b**-Fab′ allowed it to be used as a tracer control for the natural distribution of Fab′. Although found to be much more stable in vivo than [^{211}At]**1c**-Fab′, the biodistributions of *nido*-carborane conjugated Fab′ ([^{125}I]**2**-Fab′/[^{211}At]**2**-Fab′) and the bis-*nido*-carborane (VFC) ([^{125}I]**3**-Fab′/[^{211}At]**3**-Fab′) had very different in vivo distributions than the control [^{125}I]**1b**-Fab′. Biodistributions of *closo*-decaborate(2-) conjugates ([^{125}I]**4**-Fab′/[^{211}At]**4**-Fab′, [^{125}I]-**6**-Fab′/[^{211}At]**6**-Fab′, and [^{125}I]**7**-Fab′/[^{211}At]**7**-Fab′) demonstrated that they were stable to in vivo deastatination and had distributions similar to that of the control [^{125}I]**1b**-Fab′. In contrast, a benzyl-modified *closo*-decaborate-(2-) derivative evaluated in vivo ([^{125}I]**5**-Fab′/[^{211}At]**5**-Fab′) had a very different tissue distribution from the control. This study has shown that astatinated protein conjugates of *closo*-decaborate(2-) are quite stable to in vivo deastatination and that some derivatives have little effect on the distribution of Fab′. Additionally, direct ^{211}At labeling of Fab′ conjugated with *closo*-decaborate(2-) derivatives provide very high (e.g., 58−75%) radiochemical yields. However, in vivo data also indicate that the *closo*-decaborate(2-) may cause some retention of radioactivity in the liver. Studies to optimize the *closo*-decaborate(2-) conjugates for protein labeling are underway.

INTRODUCTION

The α-particle emitting radionuclide ^{211}At is of interest in targeted radionuclide therapy of cancer (*3*−*7*). Due to its decay properties, it is particulary attractive for therapy of micrometastatic disease (*8*, *9*). To be effective against cancer and to circumvent its high cytotoxicity, it is important to couple ^{211}At to a cancer targeting agent such as a monoclonal antibody (mAb[1]). Indeed, the potential for its use in cancer therapy when coupled to a targeting antibody was suggested over a half-century ago (*10*). However, it became apparent in early studies with ^{211}At that, unlike radioiodine, direct electrophilic labeling of proteins (*11*, *12*) results in a product that is rapidly deastatinated in vivo (*13*, *14*). This problem was circumvented a few years later by the incorporation of ^{211}At into an aromatic diazonium salt-containing compound, which in a second step was conjugated with a protein (*15*−*17*). Many modifications of this labeling approach were subsequently made, including the use of organometallic intermediates for rapid and efficient incorporation of ^{211}At into vinyl and aromatic compounds prior to protein conjugation (*18*−*21*).

A number of studies have shown that stability toward deastatination is not a problem for mAbs labeled with astatobenzoate derivatives when slowly metabolized intact mAbs and

* Address correspondence to D. Scott Wilbur, Ph.D., Department of Radiation Oncology, University of Washington, Box 355016, 616 N.E. Northlake Place, Seattle, WA 98105. Phone: 206-616-9246, E-mail: dswilbur@u.washington.edu.

† Department of Radiation Oncology, University of Washington.

‡ Department of Urology, University of Washington.

§ University of California, Los Angeles.

[1] Abbreviations: CDI, 1,1′-carbonyldiimidazole; ChT, chloramine-T; cpm, counts per minute; EDC, 1-(3-dimethylaminopropyl)-3-ethylcarbodiimide; mAb, monoclonal antibody; NCS, *N*-chlorosuccinimide; NEM, *N*-ethylmaleimide; %ID/g, percent injected dose/gram; PBS, phosphate buffered saline; pi, postinjection; rt, room temperature; tBoc, *tert*-butoxycarbonyl; TCDI, 1,1′-thiocarbonyldiimidazole; TFA, trifluoroacetic acid; TFP, 2,3,5,6-tetrafluorophenyl; TFP-OH, 2,3,5,6-tetrafluorophenol; TFP-OTFA, 2,3,5,6-tetrafluorophenyl trifluoroacetate; VFC, "Venus Flytrap Complex".

10.1021/bc060345s CCC: $37.00 © 2007 American Chemical Society
Published on Web 06/21/2007

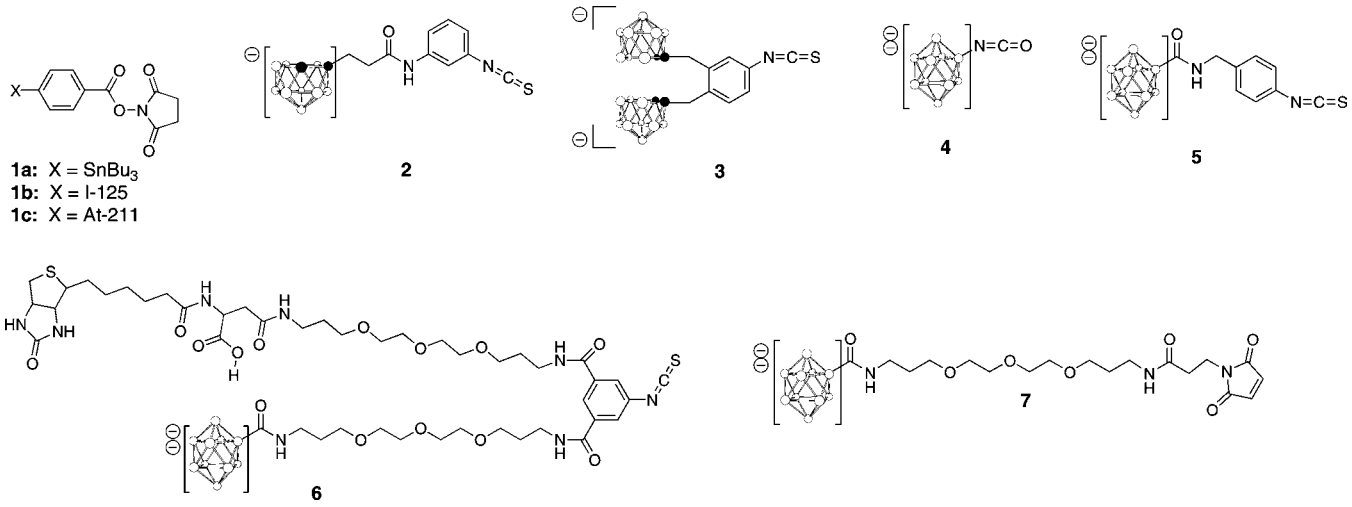


Figure 1. Structures of protein-reactive molecules used for conjugation with 107-1A4 Fab′. In the boron cage structures, white circles represent B or B−H atoms and black circles represent C or C−H atoms. In all conjugation reactions, except with **7**, the Fab′ sulfhydryl group was capped with NEM, and the conjugations were conducted by reaction with lysine amines at pH 8.5. Conjugation of compound **7** was conducted by reaction with the Fab′ sulfhydryl at pH 6.5 with the maleimide.

their $F(ab')_2$ fragments are used (*22*−*26*, *73*). However, when smaller, more rapidly metabolized mAb Fab′ fragments are used, deastatination occurs fairly rapidly. In our studies, the in vivo deastatination was surprising, as the ^{211}At-labeled Fab′ were quite stable to deastatination in vitro. The deastatination process observed for rapidly metabolized proteins is particularly problematic with ^{211}At, as its half-life is only 7.2 h. With such a short half-life, it is anticipated that smaller proteins and peptides will be required to adequately target the cancer before a significant fraction of the injected ^{211}At decays. Therefore, it is of critical importance to develop ^{211}At-labeling methods that circumvent the in vivo stability problem.

We have been investigating alternative methods for attaching ^{211}At to targeting molecules such that they are stable to in vivo deastatination (*27*, *28*). Although other investigators have evaluated a number of different aryl groups for ^{211}At labeling of mAbs (*29*, *30*), stability with the mAb Fab′ fragment has not been demonstrated. Thus, it seemed likely that a completely different approach might be required to obtain in vivo stability of more rapidly metabolized proteins, such as mAb Fab′ fragments, when labeled with ^{211}At. With this in mind, we are studying the use of boron cage moieties as pendant groups for radiolabeling of proteins and peptides with ^{211}At. The rationale behind this approach is that the boron−At bond should be stronger than a carbon−At bond based on the general trend for boron−halogen bond energies, and it may be more resistant to enzymatic reductive or oxidative cleavage. Prior studies involving small borane cage molecules have shown that some were deastatinated in vivo, but other boron cage molecules demonstrated in vivo stability, or the deastatination process was slower than for the aryl conjugates (*28*). An important aspect of using anionic boron cage moieties as pendant groups is that their astatination can be very rapid. This is important, as the alternative method, the two-step benzoate conjugation, is limited by hydrolysis to moderate overall radiochemical yields (40−60%). Therefore, we thought it might be possible to improve the in vivo stability and also improve the radiochemical yields if appropriate borane cage conjugates were used.

In the investigation described herein, the synthesis, conjugation, radiolabeling, and in vivo distribution of mAb Fab′ conjugated with a series of anionic boron cage-containing molecules was conducted. The boron cage molecules contained either a *nido*-carborane, a bis-*nido*-carborane, or *closo*-decaborate(2-) (*74*) cage moiety. The molecules conjugated with Fab′ in the studies are shown in Figure 1. The in vivo ^{211}At stability was assessed by coinjection of the same Fab′ conjugate radiolabeled with ^{125}I. Stability was noted by comparing the concentrations of ^{211}At and ^{125}I in the lung and spleen, tissues that localize ^{211}At but not radioiodine, and in the neck (containing thyroid) and stomach, tissues that localize both radionuclides when present as the halide. The rationale for using the mAb Fab′ in the study rather than another protein was based simply on the fact that prior studies had exhibited in vivo instability when labeled with *p*-[^{211}At]astatobenzoate. For comparison in this study, *p*-[^{211}At]astatobenzoyl- and *p*-[^{125}I]-iodobenzoyl-labeled Fab′ and directly labeled Fab′ were also prepared and evaluated in vivo.

EXPERIMENTAL PROCEDURES

General. Chemicals purchased from commercial sources were analytical grade or better and were used without further purification. 4-Pentynoic acid, **8**, was obtained from Lancaster (Windham, NC) or Farchan Laboratories (Gainesville, FL). Decaborane ($B_{10}H_{14}$) was obtained from Alfa Aesar (Ward Hill, MA). Chloramine-T (ChT) and phosphate buffered saline (PBS) were obtained from Sigma (St. Louis, MO). NHS-3-maleimidoproprionate, **24**, was obtained from Quanta BioDesign (Powell, OH; quantabiodesign.com). Iodobenzoic acid, 4-aminobenzylamine, **15**, 4,7,10-trioxatridecanediamine, **21**, and most other chemicals were obtained from Aldrich Chemical Co. (Milwaukee, WI). Solvents for HPLC analysis were obtained as HPLC grade and were filtered (0.2 μm) prior to use. Tetrafluorophenyl trifluoroacetate (TFP-OTFA) was prepared as previously described (*31*). Silica gel chromatography was conducted with 70−230 mesh 60 Å silica gel (Aldrich Chemical Co.). Sephadex G-25 desalting columns (PD-10 and NAP-10) were obtained from Amersham Biosciences (Piscataway, NJ). Centricon-30 centrifugation concentrators were obtained from Amicon (Beverly, MA). Melting points were obtained in open capillary tubes on a Mel-Temp II apparatus with a Fluke 51 K/J electronic thermometer and are uncorrected.

Radioactive Materials. All radioactive materials were handled according to approved protocols at the University of Washington. Standard methods for safely using radionuclides of iodine were employed (*32*). Na[^{125}I]I was purchased from Perkin-Elmer Life Sciences (Billerica, MA) as high concentration/high specific activity radioiodide in 0.1 N NaOH. Measurement of ^{125}I and ^{211}At were conducted on a Capintec CRC-15R Radioisotope Calibrator using calibration numbers 319 and 44, respectively

(designated by Capintec Technical Services). Tissue samples containing ^{211}At and ^{125}I were counted in a Wallac 1480 Wizard gamma counter (Perkin-Elmer Life and Analytical Services, Wellesley, MA). The tissue samples were initially counted to obtain both ^{211}At and ^{125}I counts, then were recounted after 3−5 days (0.1% or less ^{211}At remaining) to obtain ^{125}I counts. Radioactivity counts were imported into an *Excel* spreadsheet (Microsoft Corp., Redmond, WA) where calculations were made. The ^{211}At counts were obtained by subtracting ^{125}I counts from total counts. Individual tissue counts for ^{211}At were corrected for decay from the time of counting the first standard (at the beginning of the tissue counting process).

^{211}At was produced by irradiation of a thin layer (0.003 mm) bismuth metal (99.999%, Aldrich) with 28 MeV α-particles on a Scandatronix MP-50 cyclotron using the conditions previously described (*26*). All handling and processing of the irradiated target was done in a glove box (Innovative Technologies, Inc., radioisotope glove box) which was vented through a charcoal filter. During the study, varying distillation conditions were used. The following was found to provide the highest distillation yields.

Distillation of the ^{211}At from the irradiated target was conducted by first inserting the target into an oven heated to 650−700 °C under slightly negative pressure (vacuum pump on), followed by closure of the distillation apparatus to provide a slight vacuum with a flow of argon gas. The distilled ^{211}At was trapped in a coiled PEEK tube (1 mm i.d. × 35 cm length) which was cooled in a dry ice/$CHCl_3$ trap as previously described (*33*). The distillation process was monitored with a NaI detector by taking readings of the γ-rays emitted from the oven and PEEK tubing. When it was apparent that no additional ^{211}At was being distilled, the PEEK tubing was disconnected and rinsed into a vial with 0.6 mL of $CHCl_3$. Following this, an aliquot of 0.05 N aqueous NaOH (e.g., 0.5 mL) was added, and the mixture was shaken. Then, a portion of the activity in the aqueous layer was removed for use in the labeling experiments. The radioactive sample was tightly sealed, placed in a Ziploc plastic bag, then taken from the glove box and placed in the radiolabeling enclosure within a fume hood.

All radiohalogenation reactions were conducted in a charcoal-filtered Plexiglas enclosure (radioiodine fume hood, 20 × 24 × 36 in^3, Biodex Medical Systems Inc., Shirley, NY) housed within a radiochemical fume hood. The radiohalogenation reactions were conducted in vials capped with Teflon-coated septa and were vented through a 10 mL charcoal filled syringe. Additions of reagents to, or removal of materials from, the radiohalogenation vessel was conducted by passing a syringe needle through the septa.

Spectral Analyses. ^{1}H NMR and ^{11}B NMR spectra were obtained on either a Bruker AV 300 (300 MHz) or Bruker AV 500 (500 MHz) instrument. Proton chemical shifts are expressed as parts per million (ppm) using tetramethylsilane as an internal standard ($\delta = 0.0$ ppm). Boron chemical shifts used $BF_3{\cdot}OEt_2$ as an internal standard. High-resolution mass spectral (HRMS) data were obtained on a Bruker APEX III 47e Fourier transform mass spectrometer using electrospray ionization. For analysis, the samples were dissolved in 50/50 MeOH/H_2O and were introduced by an integral syringe infusion pump (Cole Parmer series 74900). Isothiocyanate derivatives (**5**, **6**) and the bis-TFP ester-containing compound **18** gave erroneous mass data under the conditions studied.

Analytical Chromatography. All synthetic reactions were monitored by HPLC. Samples were assessed on a system that contained a Hewlett-Packard quaternary 1050 gradient pump, a variable-wavelength UV detector (254 nm), and a Varex ELSD MKIII evaporative light-scattering detector. Analyses of HPLC data were conducted using Hewlett-Packard HPLC *ChemStation* software. Reversed-phase HPLC chromatography was carried out on an Alltech Altima C-18 column (5 μm, 250 × 4.5 mm) using a gradient solvent system at a flow rate of 1 mL/min. A gradient of MeOH and H_2O/0.1% HOAc was used. Starting with 40% MeOH, the initial solvent mixture was held for 2 min; then, the gradient was increased to 100% MeOH over the next 10 min and then held at 100% MeOH for 8 min. Retention times (t_R) under these conditions for biotin compounds are provided with the compound experimental.

Size exclusion HPLC (SE-HPLC) separations of the conjugates of Fab′ were obtained on Hewlett-Packard isocratic system consisting of a model 1050 pumping system and a model 1050 multiple wavelength detector (280 nm). Proteins were evaluated on a Protein Pak 300 SW glass size exclusion column (10 μm, 8 mm × 30 cm, Waters Corporation, Milford, MA) run at 1.0 mL/min eluting with 50 mM sodium phosphate buffer (pH 6.8) which contained 300 mM NaCl, 1 mM EDTA, and 1 mM sodium azide. Analyses of the HPLC data were conducted using Hewlett-Packard HPLC *ChemStation* software. Retention times (t_R) for F(ab′)$_2$ were 9.2 min and for Fab′ or its conjugates were ∼10.5 min.

Preparation of the following compounds was conducted as previously described: 4-(tri-*n*-butylstannyl)benzoic acid NHS ester **1a** (*34*); decahydro-*closo*-decaborate(2-) ion, [*closo*-$B_{10}H_{10}]^{2-}$ **13** (*35*); 1-(*N*-biotinyl)-L-aspartyl-4,7,10-trioxatridecane-1,13-diamine (TFA salt), **19** (*36*).

3-(*nido*-carboranyl)-*N*-3-isothiocyanatophenyl)propionamide, 2. This compound was prepared in five synthetic steps from 4-pentynoic acid, **8**, as previously described (*28*).

3,4-Bis-(*nido*-carboranylmethyl)phenylisothiocyanate, 3. The intermediate 3,4-bis(*nido*-carboranylmethyl)aniline **12** was prepared in six synthetic steps as previously described (*26*). A solution of **12** (12.6 mg; 25 μmol) and thiocarbonyldiimidazole (TCDI; 8.9 mg; 50 μmol) in anhydrous DMF (1 mL) was stirred at room temperature for 1 h. Then, the reaction mixture was dropped slowly into 20 mL of ether with stirring at room temperature. The precipitate was filtered and washed with ether to give 13 mg (95%) of **3** as a solid. Mp 114−116 °C. ^{1}H NMR (CD_3CN, 500 MHz): δ −0.37−2.30 (br m, 18H), 1.69 (br s, 4H), 2.73−2.78 (m, 3H), 2.79 (s, 4H), 2.92−2.97 (m, 2H), 5.75 (br s, 9H), 7.09−7.14 (m, 2H), 7.23 (dd, $J = 4.1$, 8.0 Hz, 1H), 7.34 (d, $J = 1.0$ Hz, 3H), 8.32 (s, 2H). ^{11}B NMR (CD_3CN, decoupled, 96.29 MHz): δ −9.5 (2B), −10.7 (2B), −13.2 (2B), −15.6 (2B), −18.7 (4B), −21.1 (2B), −32.7 (2B), −36.2 (2B). LRMS (ES^-) calcd for $C_{13}H_{28}B_{18}NS$ $(M-H)^-$: 428.4. Found: 428.4. HPLC: $t_R = 14.5-14.6$ min.

2-Isocyanatononahydro-*closo*-decaborate(2-) ion, [*closo*-2-$B_{10}H_9$-NCO]$^{2-}$ 4. This compound was prepared by reaction of $[Et_3NH]_2[B_{10}H_{10}]$, **13**, with oxalyl chloride and NaN_3 in acetonitrile as previously described (*37*).

2-Carbonylnonahydro-*closo*-decaborate(2-) ion, [*closo*-2-$B_{10}H_9$-CO]$^{1-}$ 14. This compound was prepared in 92% yield by the method previously described for preparation of the isocyanate **4**, but the NaN_3 addition was omitted (*37*).

2-(4′-Aminobenzyl)amidononahydro-*closo*-decaborate-(2), 16. Et_3N (0.12 mL, 0.86 mmol) was added to a solution containing 4-aminobenzylamine, **15** (0.35 g, 2.86 mmol), $[Et_3NH][B_{10}H_9$-CO], **14** (0.1 g, 0.40 mmol), and anhydrous CH_3CN (10 mL) at room temperature. The resultant solution was heated to reflux for 3 h. After the solution was cooled to room temperature, EtOAc (40 mL) was added to triturate the product. The residue was washed with EtOAc (3 × 20 mL) and dried under vacuum for 16 h to provide 124 mg (92%) of **16** as a tacky brown solid. ^{1}H NMR (500 MHz, DMSO-d_6): δ −0.05−3.49 (m, 9H), 3.66 (s, 2H), 5.04 (br s, 2H), 6.52 (d, $J = 8.4$ Hz, 2H), 7.03 (d, $J = 8.3$ Hz, 2H). ^{11}B NMR (*n*-Bu_4N salt, 160.43 MHz, CD_3CN): δ −0.90 (2B), −23.27 (2B),

−26.05 (2B), −26.85 (4B). LRMS (ES⁻) calcd for $C_8H_{17}B_{10}N_2O$ $(M-H)^-$: 267.2. Found: 267.1. HPLC: t_R = 2.4 min.

2-(4′-Isothiocyanatobenzyl)amidononahydro-*closo*-decaborate(2-), 5. TCDI (50 mg, 0.28 mmol) was added to a solution of compound $[Et_3NH]_2$**16** (100 mg, 0.21 mmol), Et_3N (60 mL, 0.43 mmol), and anhydrous DMF (8 mL) at room temperature, and the resultant solution was stirred for 1 h. EtOAc (30 mL) was added and stirred for another 20 min. The solvents were decanted, and the residue was washed with EtOAc (3 × 20 mL) and dried under vacuum to yield 98 mg (91%) of a tacky brown solid. A portion of the crude product was used directly for conjugation with the Fab′. ^{1}H NMR (500 MHz, DMSO-d_6): δ −0.53−3.47 (m, 9H), 7.94 (s, 4H), 9.16 (s, 2H), 10.71 (br s, 4H). ^{11}B NMR (*n*-Bu_4N salt, 160.43 MHz, CD_3CN): δ −0.84 (2B), −23.26 (2B), −26.03 (2B), −26.90 (4B). HPLC t_R = 2.5 min.

5-Aminoisophthalate Bis-tetrafluorophenyl Ester, 18. To a solution of of 5-aminoisophthalic acid, **17** (1.0 g, 5.52 mmol), and 2,3,5,6-tetrafluorophenol (2.02 g, 12.14 mmol) in 50 mL of anhydrous DMF was added EDC (2.33 g, 12.14 mmol). The reaction mixture was stirred at room temperature for 16 h, then the solution was evaporated to dryness. The crude product was purified by silica gel column (2.5 × 25 cm) eluting with 10% EtOAc/hexanes solution to afford 1.64 g (63%) of a colorless solid, mp 190.2−191.4 °C. ^{1}H NMR 500 MHz (CD_3CN): δ 4.53 (s, 2H), 7.12−7.19 (m, 2H), 7.76 (d, J = 1.4 Hz, 2H), 8.29 (t, J = 1.5 Hz, 1H). HPLC: t_R = 15.0 min.

5-Amino-(3-((15′-((*N*-biotinyl)-*β*-L-Aspartyl)-4,7,10-trioxapentadecanylamino)-isophtalamic Acid 2,3,5,6-tetrafluorophenyl Ester, 20. Biotin-Asp-OH-trioxadiamine TFA salt, **19** (71 mg, 0.11 mmol), and Et_3N (35 μL, 0.25 mmol) in anhydrous DMF (5 mL) was added slowly over 30 min to a solution containing 5-aminoisophthalate diTFP ester **18** (50 mg, 0.11 mmol) and anhydrous DMF (3 mL) at room temperature. The resultant mixture was then stirred at room temperature for an additional 10 min. The volatile materials were removed by rotoevaporation, and the residue was purified by silica gel column (1.5 × 25 cm, 40% MeOH/EtOAc) to yield 65 mg (71%) of **20** as a colorless tacky solid. ^{1}H NMR (CD_3OD, 500 MHz): δ 1.38−1.49 (m, 2H), 1.54−1.60 (m, 1H), 1.65 (t, J = 7.3 Hz, 2H), 1.69−1.74 (m, 3H), 1.87−1.92 (m, 2H), 2.19−2.29 (m, 2H), 2.58 (dd, J = 7.6, 14.8 Hz, 1H), 2.68 (d, J = 13.0 Hz, 1H), 2.75 (dd, J = 5.0, 14.8 Hz, 1H), 2.91 (dd, J = 5.0, 12.6 Hz, 1H), 3.16−3.20 (m, 1H), 3.30−3.31 (m, 2H), 3.23 (t, J = 7.1 Hz, 2H), 3.48 (q, J = 7.1 Hz, 3H), 3.52−3.54 (m, 2H), 3.59−3.66 (m, 7H), 4.30 (dd, J = 4.5, 8.0 Hz, 1H), 4.47 (dd, J = 4.6, 7.9 Hz, 1H), 4.56 (dd, J = 4.8, 7.3 Hz, 1H), 7.44−7.51 (m, 1H), 7.45 (s, 1H), 7.60 (s, 1H), 7.84 (s, 1H). HRMS (ES^+) calcd for $C_{38}H_{48}F_4N_6NaO_{11}S$ $(M+Na)^+$: 895.2936. Found: 895.2923. HPLC: t_R = 12.4 min.

[Et$_3$NH]B$_{10}$H$_9$-CO-trioxadiamine, 22. A reaction solution containing $[Et_3NH][B_{10}H_9-CO]^{1-}$, **14**, (0.50 g, 2.02 mmol) and 4,7,10-trioxa-1,13-tridecanediamine, **21**, (5 mL) was stirred at room temperature for 3 days. The solution was triturated with diethyl ether (15 mL). After solvents were removed, the residue was washed with diethyl ether (5 × 15 mL) and dried under vacuum to afford 0.55 g (68%) of **22** as a tacky light-brown solid, which was used directly for the next step reaction. ^{1}H NMR (CD_3CN, 500 MHz): δ 1.56 (t, J = 7.2 Hz, 18H), 2.24−2.26 (m, 2H), 2.68 (t, 7.1 Hz, 4H), 2.89 (s, 2H), 3.41−3.47 (m, 19H), 3.74 (t, J = 6.1 Hz, 4H), 3.78−3.89 (m, 12H), 3.98 (t, J = 7.2 Hz, 4H), 6.99 (br s, 1H), 7.06 (s, 2H), 7.07 (br s, 1H). ^{11}B NMR (*n*-Bu_4N salt, 160.43 MHz, CD_3CN): δ −0.92 (2B), −23.70 (2B), −27.85 (6B).

3-((15′-(*N*-Biotinyl)-*β*-L-aspartyl-4,7,10-trioxapentadecanylamino)-1-((13-nonahydro-*closo*-decaborate(2-))-4,7,10-trioxatridecanediamine)-aminoisophthalic Acid, 23. [Et_3NH]-$B_{10}H_9$-CO-trioxadiamine **22** (32 mg, 68.7 μmol) in anhydrous DMF (3 mL) was added dropwise to a solution containing **20** (60 mg, 68.7 μmol), Et_3N (20 μL, 0.143 mmol), and anhydrous DMF (5 mL) at room temperature. The resultant solution was stirred at room temperature for 10 min; then, EtOAc (40 mL) was added and stirred for another 10 min. After solvents was decanted, the residue was washed with 10% MeOH/EtOAc (3 × 30 mL) and dried under vacuum to afford 56 mg (76% yield) of **23** as a tacky light-brown solid. ^{1}H NMR (500 MHz, CD_3-OD): δ 1.38−1.47 (m, 2H), 1.52−1.75 (m, 8H), 1.85−1.94 (m, 8H), 2.19−2.30 (m, 2H), 2.63−2.78 (m, 4H), 2.88−2.93 (m, 1H), 3.07−3.11 (m, 2H), 3.15−3.19 (m, 1H), 3.21−3.25 (m, 2H), 3.29−3.31 (m, 2H), 3.45−3.48 (m, 8H), 3.51−3.54 (m, 2H), 3.58−3.67 (m, 24H), 4.29 (dd, J = 4.5, 8.0 Hz, 1H), 4.48 (dd, J = 4.6, 8.1 Hz, 1H), 4.71−4.74 (m, 1H), 7.21−7.23 (m, 2H), 7.43−7.45 (m, 1H). ^{11}B NMR (160.43 MHz, CD_3-OD): δ −0.98 (2B), −23.83 (2B), −28.06 (6B). LRMS (ES^-) calcd for $C_{43}H_{78}B_{10}N_8O_{14}S$ $(M)^-$: 1072.6. Found: 1072.5. HPLC: t_R = 11.4 min.

1-Isothiocyanato-3-((15′-(*N*-biotinyl)-*β*-L-aspartyl-4,7,10-trioxapentadecanylamino)-1-((13-nonahydro-decaborate(2-))-4,7,10-trioxatridecanediamine)-aminoisophthalic Acid, 6. A solution of compound **23** (50 mg, 42.6 mmol), TCDI (10 mg, 56.1 mmol), and anhydrous DMF (6 mL) was stirred at room temperature for 1 h. After the reaction solution was washed 5× with 20 mL 10% EtOAc/hexanes, the residue was dried under vacuum for 3 h to yield 51 mg (98%) of **6** as a tacky light-brown solid. ^{1}H NMR (500 MHz, CD_3OD): δ 1.40−1.47 (m, 2H), 1.54−1.73 (m, 6H), 1.86−1.92 (m, 6H), 2.20−2.30 (m, 2H), 2.62−2.77 (m, 3H), 2.89−2.93 (m, 1H), 3.17−3.24 (m, 4H), 3.29−3.31 (m, 3H), 3.46−3.51 (m, 8H), 3.54−3.65 (m, 18H), 4.31 (dd, J = 4.4, 8.0 Hz, 1H), 4.49 (dd, J = 4.5, 8.1 Hz, 1H), 4.64−4.68 (m, 1H), 7.87 (s, 1H), 8.21 (s, 1H), 8.27 (s, 1H). ^{11}B NMR (160.43 MHz, CD_3OD): δ −1.03 (2B), −23.85 (2B), −28.01 (6B). HPLC: t_R = 12.8 min.

***N*-(15-(Aminoacyldecaborate)-4,7,10-trioxatridecanyl)-3-maleimidopriopionamide, 7.** NHS-3-maleimidopropionate, **24** (70 mg, 0.26 mmol), was added to a solution of [Et_3NH]$B_{10}H_9$-CO-trioxadiamine, **22** (100 mg, 0.18 mmol), Et_3N (45 μL, 0.32 mmol), and anhydrous DMF (5 mL). The resultant solution was stirred at room temperature for 2 h. Then, 20 mL of hexanes/EtOAc (90/10) was added, and the solution was stirred for an additional 30 min at room temperature. The solvents were decanted, and the residue was washed with 20 mL of hexanes/EtOAc (90/10) three times. The residue dried under vacuum for 4 h to yield **7** as a light-yellow tacky solid. Yield 110 mg (87%). ^{1}H NMR (DMSO-d_6): δ 1.18 (t, J = 7.3 Hz, 9H), 1.52−1.66 (m, 6H), 1.72−1.81 (m, 3H), 2.31 (t, J = 7.3 Hz, 4H), 2.80−2.86 (m, 2H), 2.99−3.12 (m, 10H), 3.34−3.62 (m, 14H), 7.01 (s, 2H), 7.90−7.95 (m, 3H). LRMS (ES^-) calcd for $C_{18}H_{35}B_{10}N_3O_7$ $(M-2H)^-$: 515.4. Found: 515.4. HPLC: t_R = 7.0 min.

Preparation of Fab′-S-NEM. The monoclonal antibody 107-1A4, an IgG_1 mAb reactive with the PSMA antigen on prostate cells, was obtained and purified as previously described (*38*). Fragmentation of 107-1A4 was accomplished using pepsin (6.5 μg/mL in 10 mM NaOAc, pH 3.9) at 37 °C for 24 h. The resultant $F(ab')_2$ was purified on a Fractogel TMAE column (EM Science, Gibbstown, NJ). The isolated $F(ab')_2$ was concentrated to 8.4 mg/mL, and aliquots were stored.

To 500 μL of a 8.4 mg/mL solution of 107-1A4 $F(ab')_2$ was added 20 μL of a 100 mM DTT solution in H_2O. The solution was placed on a rotator for 1 h at room temperature. The progress of the reaction was evaluated by HPLC analysis of a small aliquot (e.g., 10 μL). After 1 h, the reaction was complete, so the reaction solution was placed on a Sephadex G-25 (PD-10) column that was equilibrated with 20 mM sodium phosphate, pH 6.5, containing 1 mM EDTA. The column was eluted with

the same buffer, collecting 1 mL fractions. The protein-containing fractions were combined, and protein recovery was evaluated by UV at 280 nm. A recovery of 99% was obtained in 2.2 mL at 1.9 mg/mL.

To 2 mL of a 1.9 mg/mL solution of Fab′ was added 76 μL (50 equiv, 10 mg/mL) of a solution containing *N*-ethylmaleimide (NEM) in DMSO. The reaction was allowed to proceed at room temperature for 30 min. Then, the reaction mixture was placed in a Centricon-30 ultracentifugation filter prewashed with 1 mL 20 mM phosphate buffer, pH 7.2, and centrifuged at 3200 rpm for 15 min to concentrate the solution to 100 μL. The centrifuge retentate was rinsed 4× using 500 μL of the phosphate buffer, reducing the volume to 100 μL each rinse. The final protein concentration was determined by UV as described above and gave 71% recovery (2.7 mg at 3.3 mg/mL).

Fab′-NEM Conjugations with 2, 3, 4, 5, or 6. To 500 μL of 107-1A4 Fab′-NEM (2 mg/mL in 50 mM $NaHCO_3$, pH 8.5) was added 5, 10, or 20 equiv of **2**, **3**, **4**, **5**, or **6** in 20 μL DMSO or 75 μL 10% DMSO in H_2O. The reaction solution was tumbled gently overnight at room temperature. The reaction solution was then placed on a Sephadex G-25 (PD-10) column that had been equilibrated in PBS, pH 7.2, and eluted with the same buffer. Fractions containing protein were combined and concentrated in a Centricon-30 ultracentrifugation unit to give 30−80% recovery.

Fab-SH Conjugation with 7. 107-1A4 Fab′-SH (without NEM capping) was prepared as described above. To 1 mL of a 1.9 mg/mL Fab′ solution was added 54 μL of a 10 mg/mL solution of **7** (20 equiv) in DMF. After 1 h at room temperature, the mixture was eluted on a Sephadex G-25 (PD-10) column that had been equilibrated in PBS, pH 7.2. The fractions containing protein were pooled and concentrated in a Centricon-30 to give a 1 mL volume of a 1.5 mg/mL solution (84% recovery).

Fab′ Conjugate Characterization. All Fab′ conjugates were evaluated by SE-HPLC as described above. All non-radioactive Fab′ conjugates were also evaluated on isoelectric focusing gels to determine changes in charge (pI) on the molecules as described below. Additional information on the number of conjugates per Fab′ was obtained for the conjugate of **6**, which contained the biotin moiety, by conducting a HABA analysis (*39*) as described below.

Isoelectric Focusing. IEF analyses were conducted on a Novex PowerEase 500 instrument with the XCell II chamber using Invitrogen (Novex) precast gels, pH 3−10 or pH 3−7 (1.0 mm × 12 well), running under the standard IEF program. The protein was stained with GelCode Blue Stain (Pierce). IEF standards were from Serva Electrophoresis GmbH: pH 10.7, cytochrome C; 9.5, ribonuclease A; 8.3, 8.0, 7.8, lectin; 7.4, 6.9, myoglobin; 6.0, carbonic anhydrase; 5.3, 5.2, β-lactoglobulin; 4.5, trypsin inhibitor; 4.2, glucose oxidase; 3.5, amyloglucosidase.

Biotin Quantification. Biotin quantification was accomplished using the HABA-avidin procedure as outlined by the manufacturer (Pierce Biotechnology, Inc., Rockford, IL). Briefly, a 900 μL aliquot of HABA-avidin solution is placed in a cuvette, and the UV absorbance was measured at 500 nm. Following that measurement, 100 μL of the conjugated antibody is added to the cuvette and mixed well. The UV absorbance is again measured at 500 nm, and the value is taken after it stabilizes for at least 15 s. This value is the A_{500} biotin from which the number of mmoles of biotin/mL mixture can be calculated. Once obtained, the calculated mmoles biotin/mL are divided by the mmol antibody/mL solution obtained from the BCA or UV analysis to give the number of conjugates per antibody.

Labeling with *p*-[^{211}At]astatobenzoate NHS Ester and *p*-[^{125}I]iodobenzoate NHS Ester. The *p*-stannylbenzoate NHS ester, **1a**, (100 μg) was dissolved in 100 μL MeOH/5% HOAc. To that solution was added a maximum of 20 μL (500 μCi to 1 mCi) Na[^{211}At]At or Na[^{125}I]I in 0.1 N NaOH, followed by 20 μL of a 1 mg/mL solution of *N*-chlorosuccinimide (NCS) in H_2O. After 5 min at room temperature, 20 μL of a 1 mg/mL solution of $Na_2S_2O_5$ was added. The reaction mixture was then reduced to dryness under a stream of Ar. To the residue was added 0.5−1 mg Fab'-NEM (5 mg/mL in 0.25 M Na Borate, pH 8.5). After 15 min at room temperature, the mixture was eluted with PBS, pH 7.2, over a preequilibrated Sephadex G-25 (PD-10) column. Protein fractions were combined, and the concentration was determined by UV_{280}.

General Method for Radiolabeling Fab′-S-NEM Conjugates of 2, 3, 4, 5, and 6 with Na[^{211}At]At and Na[^{125}I]I. To 500−800 μg of Fab′ conjugate in PBS was added 2−100 μL of Na[^{125}I]I or Na[^{211}At]At, then 20−40 μL of Chloramine-T (1 mg/mL) in H_2O. The reaction was allowed to proceed for 30 s to 2 min; then, 20−40 μL of a 1 mg/mL solution of $Na_2S_2O_5$ in H_2O was added to quench the reaction. The reaction mixture was placed on a NAP-10 column and was eluted with PBS. The amount of activity associated with the protein was measured in a dose calibrator.

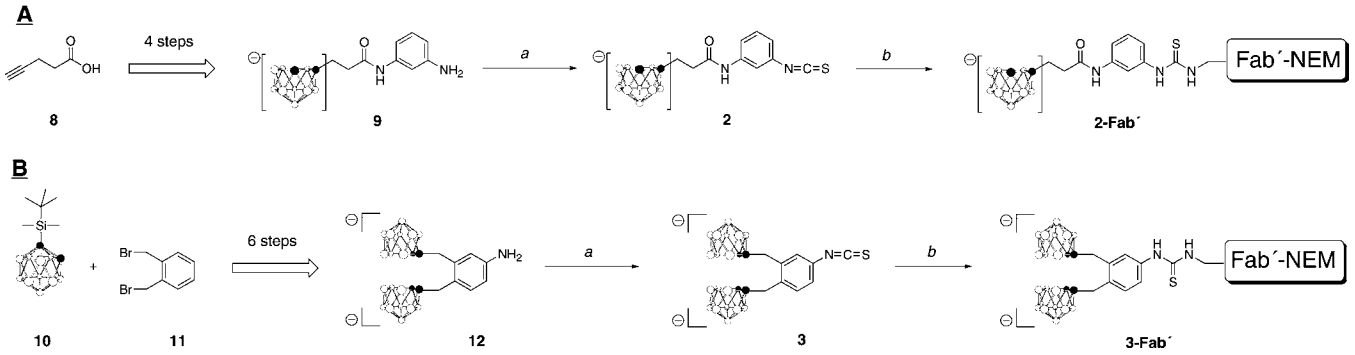
Biodistribution Studies. Animal use and procedures were approved by the University of Washington's Institutional Animal Care and Use Committee. All reagents were administered to BALB/c nu/nu mice in a total volume of approximately 100 μL (injectate weighed) via the lateral tail vein. Injections and euthanasia of the animals were done at predetermined times. Blood samples were obtained by cardiac puncture immediately before sacrifice. Urine samples were obtained by syringe bladder tap at the time the tissues were excised. The tissues excised included muscle, lung, kidney, spleen, liver, intestines, neck (with thyroid), and stomach. Excised tissues were blotted free of blood, weighed, and counted. Calculation of the percent injected dose (%ID) and percent injected dose per gram (%ID/g) of radioactivity in the tissues was based on standards containing 1 μL of the injected dose. The ^{211}At counts were corrected for decay. Total blood volume was estimated to be 8% of body weight. The data obtained are provided in Tables S1−S8 in the Supporting Information. The amount of ^{125}I and ^{211}At administered to mice and the average mouse weight in each biodistribution are provided in the table legends.

RESULTS

Synthesis of Protein-Reactive Boron Cage Molecules. The syntheses of the protein-reactive *nido*-carboranyl derivatives **2** and **3** are shown in Scheme 1 (sequences A and B). *N*-(3-Aminophenyl)-3-(*nido*-carboranyl)propionamide **9** was prepared in four synthetic steps as previously described (*28*). Conversion of the aniline amine in **9** to the amine-reactive isothiocyanate **2** was achieved in nearly quantitative yield using thiocarbonyldiimidazole (TCDI) in DMF at room temperature for 30 min. Likewise, 3,4-bis-(*nido*-carboranylmethyl)aniline, **12**, was prepared in six synthetic steps as previously described (*28*). Conversion of the aniline amine in **12** to the amine-reactive isothiocyanate **3** was achieved using the same condition as for **2** to give **3** in 95% yield.

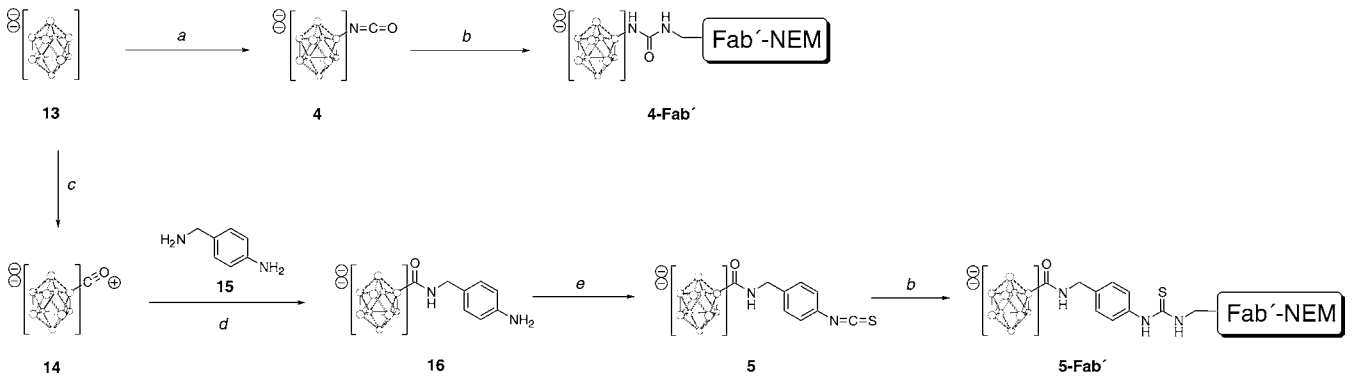
The syntheses of two amine-reactive decaborate(2-) derivatives, **4** and **5**, are shown in Scheme 2. Synthesis of 2-isothiocyanato-nonahydro-*closo*-decaborate(2-) ion [*closo*-2-$B_{10}H_9$-NCO]$^{2-}$, **4**, was accomplished in high yield by reaction of decahydro-*closo*-decaborate(2-) ion [*closo*-2-$B_{10}H_{10}$]$^{2-}$, **13**, with oxalyl chloride and NaN_3 as previously described (*37*). Synthesis of the 2-isocyanatobenzylamidononahydro-*closo*-decaborate(2-) derivative **5** began by reaction of decahydro-*closo*-decaborate(2-) ion [*closo*-2-$B_{10}H_{10}$]$^{2-}$, **13**, and oxalyl chloride to give 92% of 2-carbonylnonahydro-*closo*-decaborate(2-), **14**, as previously

Scheme 1 . Syntheses of Amine-Reactive *nido*-Carboranyl Derivatives 2 and 3 and Conjugation with Fab′-NEM[a]



[a] Reagents and conditions: (a) TCDI, DMF, RT, 30 min, 99%; (b) Fab′-NEM, H_2O, $NaHCO_3$, pH 8.5, **2** or **3** in DMSO/H_2O, RT, 16−20 h.

Scheme 2 . Synthesis of Amine-Reactive Decaborate(2-) Derivatives 4 and 5 and Conjugation with Fab′-NEM[a]



[a] Reagents and conditions: (a) ClCOCOCl, NaN_3, CH_3CN, RT, 16−20 h; (b) Fab′-NEM, H_2O, $NaHCO_3$, pH 8.5, **4** or **5** in DMSO/H_2O, RT, 16−20 h; (c) ClCOCOCl, CH_3CN, RT, 16−20 h; (d) **15**, Et_3N, CH_3CN, RT, 3h, 92%; (e) TCDI, DMF, RT, 30 min, 91%.

described (*37*). In the next step, refluxing **14** with 4-aminobenzylamine, **15**, and Et_3N in acetonitrile for 3 h provided the benzylamine adduct **16** in 92% yield. Reaction of **16** with TCDI in DMF at room temperature gave 91% yield of crude **5**.

Synthesis of the protein-reactive decaborate(2-) derivative that also contains a biotin moiety, **6**, is shown in Scheme 3. An initial attempt at synthesizing **6** began with N-Boc-protected aminoisophthalic acid (*40*), but deprotection in a later step was problematic. In the successful synthesis, the ditetrafluorophenyl ester, **18**, was prepared in 63% yield by reaction of aminoisophthalic acid, **17**, with tetrafluorophenol (TFP-OH) and EDC in DMF. Reaction of **18** with the biotin derivative **19** and Et_3N in DMF provided **20** in 71% yield. Biotin derivative **19** was prepared as previously described (*36*). The decaborate(2-) derivative **22** was prepared in 68% yield by reaction of 4,7,10-trioxatridecane-1,13-diamine, **21**, with the 2-carbonyl-nonahydro-*closo*-decaborate(2-) ion, **14**. After preparation of **22**, that compound was reacted with **20** and Et_3N in DMF to provide **23** in 76% yield. Reaction of **23** with TCDI in DMF for 1 h provided the protein-reactive **6** in 98% yield.

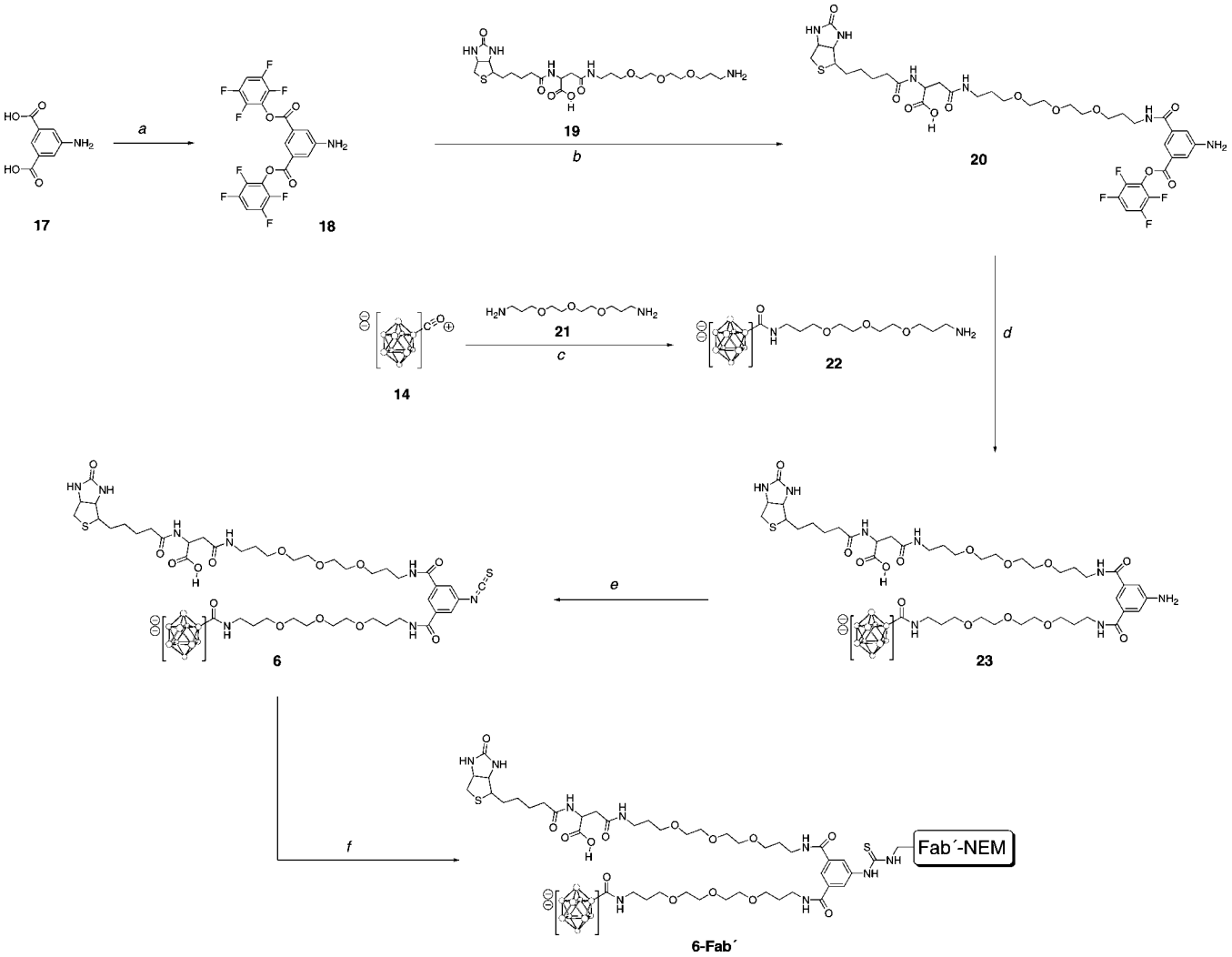
Synthesis of the protein reactive decaborate(2-) derivative containing a maleimide functionality, **7**, is shown in Scheme 4. The product was obtained in 87% yield by reaction of **22** with the commercially available reagent 3-maleimidopropionate *N*-hydroxysuccinimidyl ester, **24**, and Et_3N in DMF for 2 h.

Protein Conjugation. The protein used in the studies was a Fab′ fragment of the anti-PSMA antibody, 107-1A4 (*38*). To prepare the Fab′ fragment, the intact antibody was digested following standard procedures employing pepsin at 37 °C for 24 h to form the $F(ab')_2$ fragment, then reduced with 4 mM dithiotreitol (DTT) for 1 h at room temperature. For all conjugations, except for the maleimide-containing **7** conjugation, the sulfhydryl on Fab′ was reacted with *N*-ethylmaleimide (NEM) to ensure that it would not be involved in the reactions or reform the $F(ab')_2$. After the conjugation reactions were complete, size exclusion HPLC was run to evaluate the peak shape, rention time, and number of species present. Isoelectric focusing (IEF) gels were run on the isolated conjugates to help assess the extent of the conjugation.

Conjugations of the halobenzoate NHS esters, [^{125}I]**1b** or [^{211}At]**1c**, were conducted in borate buffer, pH 8.5, at room temperature for 15 min. Because the conjugations were conducted with a high specific activity material, very small amounts of the Fab′ were actually modified. Thus, radioHPLC traces look identical to that obtained for Fab′-NEM before conjugation with **1b** or **1c**.

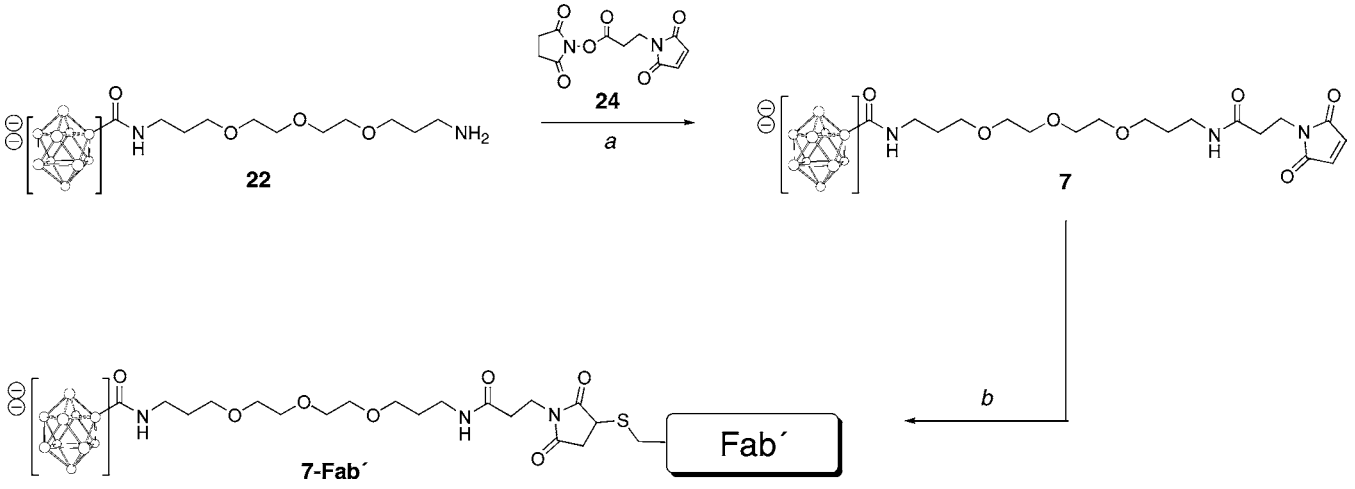
The amine-reactive borane cage compounds **2**, **3**, **4**, **5**, and **6** (Figure 1) were all conjugated with the Fab′-NEM under the same conditions. The conjugations were conducted by reaction of Fab′-NEM with 5, 10, or 20 equiv of the amine-reactive compound in 50 mM $NaHCO_3$ buffer, pH 8.5, for 16 h at room temperature. The conjugation reactions are depicted as the last steps in Schemes 1−3. Conjugation of Fab'-NEM with 20 equiv of **2** caused visible precipitation the Fab′. Conjugations involving lower number of equivalents (e.g., 5 or 10) of **2** with the protein did not cause visible precipitation, but the SE-HPLC chromatograms indicated that the protein properties had changed significantly (i.e., peaks were broadened) and that some higher molecular weight species (eluting before 10 min) were present. The SE-HPLC chromatogram for conjugation with 10 equiv of **2** (Figure 2, panel B) displayed only a small percentage (<5%) of high molecular weight contaminants (t_R = 6.3 min); however, when 20 equiv were reacted, that percentage went up (>30%), and when 50 equiv were reacted, almost all of the soluble protein was found to be high molecular weight species (Figure S1 in Supporting Information). Conjugation of 10 equiv of **3** caused extensive broadening of the chromatographic peak by SE-HPLC

Scheme 3 . Synthesis of Amine-Reactive Decaborate(2-) Derivative 6 and Conjugation with Fab′-NEM[a]



[a] Reagents and conditions: (a) TFP−OH, DMF, EDC, RT, 16 h, 63%; (b) **19**, Et_3N, DMF, RT, 30 min, 71%; (c) **21**, RT, 3 d, 68%; (d) **22**, DMF, RT, 10 min, 76%; (e) TCDI, DMF, RT, 1 h, 98%; (f) Fab′-NEM, H_2O, $NaHCO_3$, pH 8.5, **6** in DMSO/H_2O, RT, 16−20 h, 92% recovered.

Scheme 4. Synthesis of Sulfhydryl-Reactive Decaborate(2-) Derivative 7 and Conjugation with Fab′-SH[a]



[a] Reagents and conditions: (a) **24**, Et_3N, DMF, RT, 2 h, 87%; (b) Fab′-SH, PBS, **7** IN DMF, RT, 1 h, 84% (recovered).

(Figure 2, panel C), but there was no visible precipitation even at 20 equiv reacted.

In contast to the *nido*-carborane derivatives **2** and **3**, the Fab′ conjugates of decaborate(2-) derivatives **4**, **5**, **6**, and **7** did not cause visible precipitation or aggregation of Fab′-NEM, even when 20 equiv or more were offered. The conjugation product Fab′-**4** when analyzed by SE-HPLC (Figure 2, panel D) showed a single peak that was slightly broadened from the starting Fab'. Unfortunately, after the 16 h conjugation period, an IEF gel indicated there was Fab' remaining that was not conjugated with

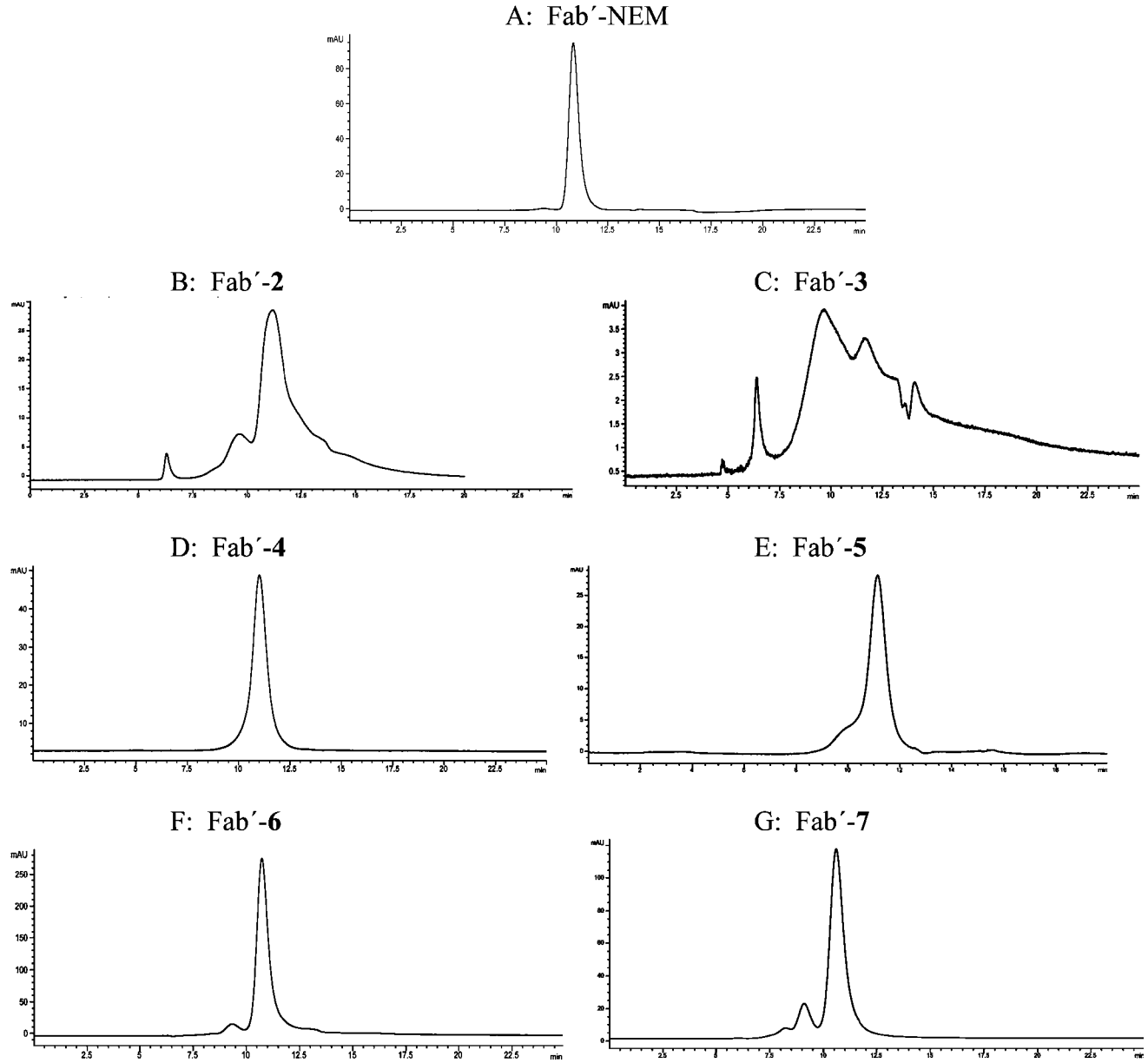


Figure 2. Size-exclusion HPLC chromatograms of 107-1A4 Fab′ conjugates prepared for the study. The conjugate in panel A has the sulfhydryl moiety capped with NEM but contains no borane cage. Chromatograms in panels B−F represent products obtained with 10 equiv of borane-containing reagent (**2**−**6**) offered for conjugation with Fab′-NEM. The chromatogram in panel G is from a conjugation reaction where 20 equiv of **7** were offered for reaction with Fab′-SH.

4. Reactions of **4** with compounds containing primary amines were found to be quite slow compared with other isocyanate derivatives (unreported results), presumably due to conjugation of the isocyanate functionality with the highly anionic borane cage. On the basis of this observation, we became interested in decaborate(2-) derivatives that have a higher reactivity with protein amines. Because we had observed that the carbonyl-substituted decaborate(2-) **14** (Scheme 2) was slightly more reactive than **4**, that compound was conjugated with Fab′-NEM. No aggregation was noted in this reaction, and an IEF gel indicated that a somewhat higher substitution may have been achieved. However, we felt that it was important to be able to have an even more reactive functional group in the conjugation reactions, as some proteins may be sensitive to the reaction conditions and time taken to complete the reactions. Therefore, an isothiocyanate-benzylamine adduct of decaborate(2-), **5**, was prepared and conjugated to the Fab′-NEM. Again, no visible aggregation was observed in the conjugation reactions, and little aggregation was noted by SE-HPLC (Figure 2, panel E). While an IEF gel indicated that conjugation had occurred (e.g., Figure S2, panel B; Supporting Information), it was not possible to quantify the number of conjugates added.

We felt that it was important to have a method for easily assessing the number of decaborate(2-) groups conjugated with the protein. To achieve this, the biotin-containing decaborate-(2-) derivative **6** was prepared and conjugated with Fab′-NEM. The inclusion of a biotin in the structure permits the use of the well-established HABA assay (*39*) to determine the number of biotin moieties present. After conjugation of **6** with Fab′-NEM, there was little change in the SE-HPLC (Figure 2, panel F), even at the highest offering of conjugate (20 equiv). Importantly, a dramatic change in the migration on the IEF gel was noted (Figure S1, panel B). Interestingly, the width of the Fab′ peak at half-height was not broadened from the standard (Figure 1, panels A and F), as was the case for conjugates of **4** and **5**. Assessment of the number of biotin derivatives by the HABA assay indicated that, with 10 equiv of **6** offered, 1.5 conjugates/

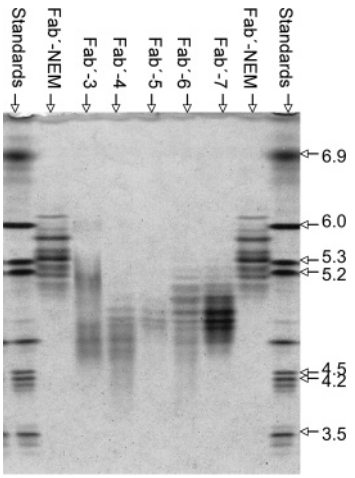


Figure 3. Digitized isoelectric focusing gel containing Fab′ conjugates prepared for the study. Standards are as follows: 6.9, myoglobin; 6.0, carbonic anhydrase; 5.3, 5.2, β-lactoglobulin; 4.5, trypsin inhibitor; 4.2, glucose oxidase; and 3.5, amyloglucosidase.

Fab′ were obtained. With 20 equiv of **6** offered, 2.1 conjugates/Fab′ were obtained.

In collaborative studies (*41*), a sulfhydryl-reactive decaborate-(2-) was desired, so conjugate **7** was prepared and included in this investigation. Conjugation of Fab′-SH using 20 equiv of **7** did not cause visible aggregation. A representative SE-HPLC (Figure 2, panel G) showed one major peak, but also had a minor peak at ~7.8 min which appears to be some reformation of the $F(ab')_2$. As with **6**, conjugation of **7** appears to have minimal affect on the HPLC profile of the Fab′.

For all except Fab′-**6**, the primary method for determining whether conjugations of the borane cage moieties with Fab′ had occurred was an IEF analysis. As the studies progressed, IEF were obtained on one or two boron-conjugated Fab′ species. In an attempt to obtain a better comparison of the anionic borane cage conjugates, a single IEF analysis was conducted with most of the Fab′ conjugates (all except Fab′-**2**). A digitized scan of that IEF is shown in Figure 3. In the samples examined, all conjugates except Fab′-**3** appear to have at least one conjugate on the protein, as none of the primary bands from the Fab′-NEM remain, indicating that at least one charge unit has been changed from the unmodified Fab′. This result is in constrast to an earlier IEF of Fab′-**4**, which indicated that some of the Fab′-NEM remained. The Fab′-**6** also displayed a different banding from those obtained with earlier samples. The difference is likely due to the fact that the Fab′-**6** sample examined in this IEF only had 1.1 biotins/Fab′. Unfortunately, samples shown in Figure 3 had been stored for varying lengths of time, which made comparisons with earlier IEF data difficult.

Radioiodination and Astatination. A key objective in the studies was to evaluate the use of boron conjugates to provide a method for stable attachment by directly labeling proteins with ^{211}At. Our hypothesis was that direct labeling can provide yields comparable to those obtained with direct radioiodination of a native (nonconjugated) protein. Therefore, examples of direct labeling of Fab'-NEM with Na[^{125}I]I/Na[^{131}I]I and Na[^{211}At]-At using the standard reagents (Chloramine-T) in PBS at pH 6.8 were conducted first. As is the general case with most proteins, very good radioiodine labeling yields were obtained (e.g., 75−89%). In contrast, essentially no (<1%) direct labeling was obtained with Na[^{211}At]At. A more effective method for labeling proteins with ^{211}At is to use ^{211}At-labeled benzoate NHS ester, **1c**, in a conjugation/labeling step. Therefore, for comparison, radiolabeling of the Fab′-NEM was conducted using the *p*-[^{125}I]iodobenzoate NHS ester, [^{125}I]**1b**, and the *p*-[^{211}At]-astatobenzoate NHS ester, [^{211}At]**1c**. The labeling of stannyl-benzoate **1a** was conducted in MeOH/5% HOAc using *N*-chlorosuccinimide as the oxidant and $Na_2S_2O_5$ as the quench. The crude residue, obtained after removal of solvent, was mixed with the Fab′-NEM in borate buffer, pH 8.5. The overall labeling yields 32% and 14% isolated yields of Fab′-[^{125}I]**1b** and Fab′-[^{211}At]**1c** (respectively). The yields are lower than obtained in many similar protein-labeling experiments previously conducted in our laboratory (e.g., usually 40−60% conjugation yields). Radiolabeling of the borane cage-conjugated Fab′ was conducted in H_2O using Chloramine-T as oxidant (pH ~7, rt, 30 s to 2 min) and NaS_2O_5 as quench. The yields obtained for radioiodination and astatination of Fab′ and its conjugates are shown in Table 1. The yields are for single labelings under similar conditions and are not optimized.

Table 1. Radiochemical Yields for Labeling 107-1A4 Fab′ Conjugates with Na[^{125}I]I and Na[^{211}At]At[a,b]

Fab′ conjugate reacted	^{125}I yield (%)	^{211}At yield (%)
Fab′ (direct label)	89[c]	<1
Fab′ + **1**b or **1**c	32	14
2-Fab′	75	28
3-Fab′	51	32
4-Fab′	33	36
5-Fab′	72	60
6-Fab′	70	58
7-Fab′	84	75

[a] Reaction conditions are described in the Experimental Section. Yields are for isolated Fab′ conjugates after radiolabeling reaction, quenching with NaS_2O_5, and PD-10 purification. Labeling yields are not optimized. [b] Fab′ sulfhydryl group is capped with NEM. [c] Na[^{131}I]I was used for labeling.

Biodistributions of Radiolabeled Fab′ Derivatives. Tissue distributions of coadministered ^{125}I- and ^{211}At-labeled conjugates of Fab′ were conducted in athymic mice to assess the stability of the ^{211}At label and to assess changes in the tissue concentrations brought about by the boron-containing conjugate. The data obtained for concentrations (%ID/g) of ^{125}I and ^{211}At in selected tissues at 1 and 4 h postinjection are shown as bar graphs (panels A−H) in Figure 4. The complete data obtained in each biodistribution study, including amounts injected, animal weights, and results of statistical significance (using Student's *t* test) are provided as Tables S1−S8 in the Supporting Information.

Panel A in Figure 4 shows the tissue distribution of Fab′-NEM directly labeled with ^{125}I. These data have been included for comparison with the radiolabeled conjugates. The data clearly show that directly labeled Fab′ releases radioiodine in vivo (as noted by neck and stomach concentrations). Direct labeling with ^{211}At gave a very low yield (<1%), so that material was not evaluated in vivo. Panel B in Figure 4 shows the tissue distribution of Fab′-NEM conjugated with [^{125}I]**1b** and [^{211}At]-**1c**. While catabolism of the directly labeled Fab′ releases iodide, catabolism of Fab′ conjugated with *p*-[^{125}I]iodobenzoate, [^{125}I]-**1b**, does not release radioiodine. For this reason, we use [^{125}I]-**1b** labeling as a control to provide the tissue distribution of the Fab′. The tissue distribution data for [^{125}I]**1b**-Fab′ can be used in comparisons with other radiolabeled Fab′ conjugates to determine whether a paricular conjugate has altered the Fab′ distribution. An important point to note in panel B is that the release of ^{211}At from [^{211}At]**1c**-Fab′ is evident due to higher concentrations of ^{211}At than ^{125}I found in lung, spleen, neck, and stomach tissues. Indeed, there was a significant difference in concentrations for the two radionuclides in all tissues except intestines and urine.

Biodistributions of the radiohalogenated *nido*-carborane-conjugated Fab′ derivatives, [^{125}I]**2**-Fab′/[^{211}At]**2**-Fab′ and [^{125}I]-**3**-Fab′/[^{211}At]**3**-Fab′, are shown graphically in Figure 4, panels C and D, respectively. The tissue distributions are very different from those of the Fab′-NEM when directly labeled (panel A) or labeled with the halobenzoates (panel B), suggesting that the

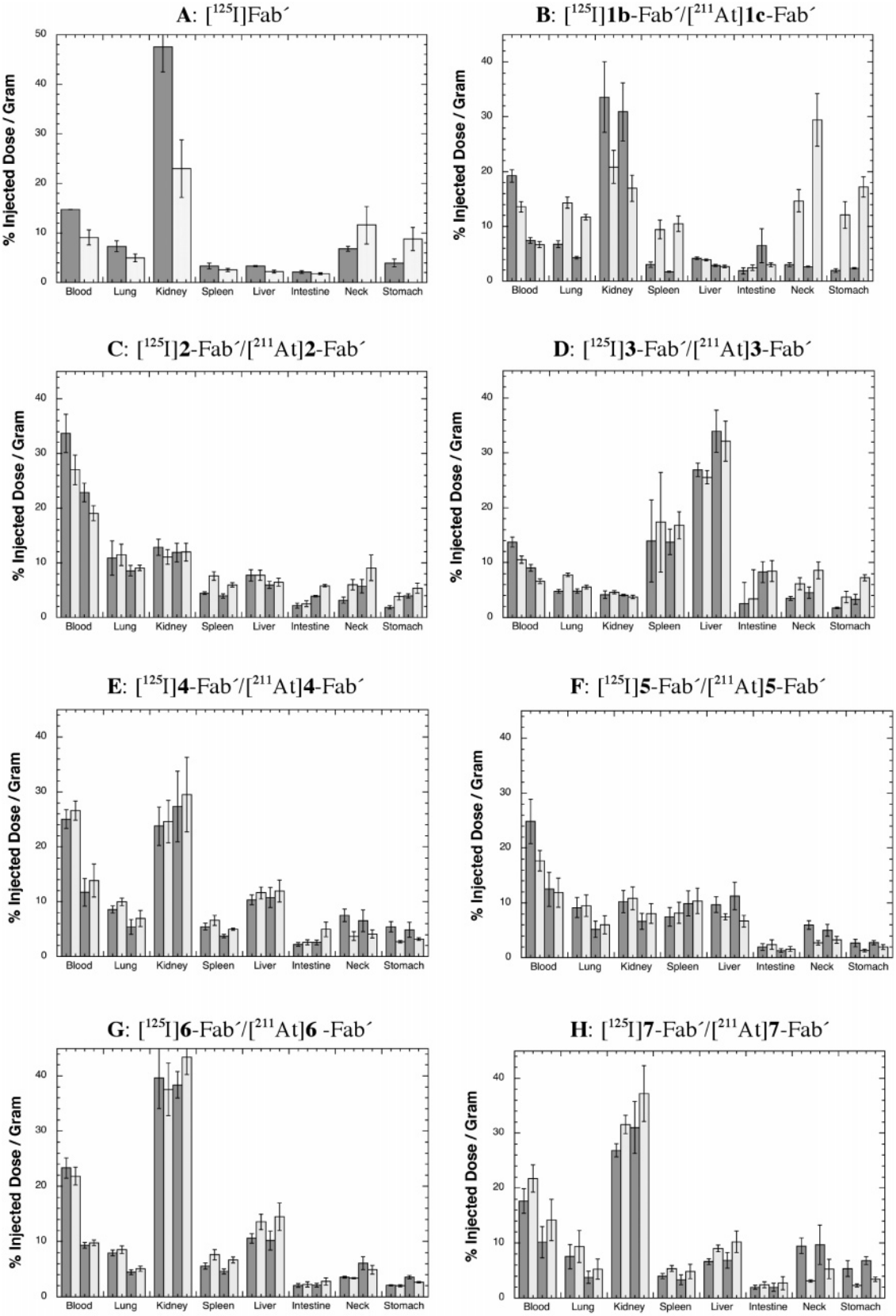


Figure 4. Graphs of tissue distributions of ^{125}I-labeled (dark gray bars) and ^{211}At-labeled (light gray bars) Fab′ and Fab′ conjugates in athymic mice. The heights of the bars (%ID/g) are based on the average %ID/g value obtained in five mice for each tissue, and the error bars are standard deviation of values in each tissue. The first two bars represent values obtained at 1 h postinjection, and the second two bars represent values obtained at 4 h postinjection. In panel A, only the 4 h timepoint is shown. The Fab′ conjugates studied are noted above each bar graph.

nido-carborane conjugates significantly alter the in vivo characteristics of the Fab′. Of particular note in both biodistributions are the low kidney concentrations, suggesting that the material injected aggregated or bound with blood components, resulting in an effective size larger than that of Fab′, causing them to be excluded from the kidney. Both of these conjugates displayed

a high propensity to aggregate during preparation, and additional aggregation may have occurred prior to injection or association with serum proteins occurred after injection. On the basis of the fact that the conjugates of the mono-*nido*-carborane derivative **2** have high concentrations in the blood (compared with the [^{125}I]**1b**-Fab′ standard) and low concentrations in the liver and spleen, it seems likely that this conjugate associates with the serum proteins. Statistical analysis (Student's *t* test) indicated that there were significant differences in the concentrations of radionuclides in blood, spleen, neck, and stomach. Since the concentration of ^{211}At was higher in spleen, neck and stomach, it is likely that some deastatination occurred.

In contrast to Fab′-**2**, blood concentrations are lower than the standard values for the bis-*nido*-carborane derivative **3**, and the concentrations in spleen and liver are higher, suggesting that larger aggregates may have been injected or were formed upon injection of that conjugate. It should be noted that there were small (but significant by Student's *t* test) differences in ^{211}At and ^{125}I concentrations seen in the lung, spleen, neck, and stomach suggesting that there is some instability of the label, but the stability is much higher than that of the astatobenzoate, [^{211}At]**1c**-Fab′ (panel B).

Biodistributions of two radiohalogenated decaborate(2-)-conjugated Fab′ derivatives [^{125}I]**4**-Fab′/[^{211}At]**4**-Fab′ and [^{125}I]-**5**-Fab′/[^{211}At]**5**-Fab′ are shown graphically in Figure 4, panels E and F, respectively. The isocyanato-decaborate(2-) conjugate **4**-Fab′ has a biodistribution that is very similar to the [^{125}I]**1b**-Fab′ standard (darker bars, panel B) indicating that it has minimal affect on the Fab′ distribution. Interestingly, the kidney concentration for the benzamidyldecaborate(2-) conjugate **5**-Fab′ is dramatically lower than expected. Since the liver and intestine concentrations are also relatively low, it seems *unlikely* that the protein is aggregating or the radioactive metabolites are being excreted through the hepatobiliary system rather than the renal system. It should be noted that for both conjugates the concentrations of radioactivity in the liver are higher than observed when the halobenzoates are used, suggesting that some deviation of the distribution or trapping of the radioactivity in the liver has occurred with the decaborate(2-) conjugates. Very small differences can be noted in the concentrations of ^{211}At and ^{125}I in lung and spleen (differences are significant in Fab′-**4**, but not in Fab′-**5**), indicating that the ^{211}At label is fairly stable to in vivo deastatination. It is interesting to note that the concentration of ^{125}I is higher than that of ^{211}At in the neck and stomach. This may be an indication that some of the radioiodine reacted with tyrosine residues on the Fab′ rather than with the decaborate(2-) cage.

Biodistributions of two additional radiohalogenated decaborate-conjugated Fab′ derivatives [^{125}I]**6**-Fab′/[^{211}At]**6**-Fab′ and [^{125}I]**7**-Fab′/[^{211}At]**7**-Fab′ are shown graphically in Figure 4, panels G and H, respectively. As with the isocyanatodecaborate-(2-) conjugate **4**, these more structurally complex decaborate-(2-)-containing conjugates, **6** and **7**, do not appear to significantly alter the in vivo distribution of the Fab′. However, similar to other decaborate(2-) conjugates, the liver concentrations are higher than expected on the basis of those obtained with the iodobenzoyl conjugate, [^{125}I]**1b**-Fab′ (panel B). The small differences in ^{211}At and ^{125}I concentrations in spleen and lung (not significant by Student's *t* test) indicate that the astatinated decaborate(2-) cage is quite stable to in vivo deastatination.

DISCUSSION

The utility of the α-particle-emitting radionuclide ^{211}At for targeted radionuclide therapy will be severely limited unless reagents that provide high in vivo stability toward deastatination are developed. The previously developed protein astatination reagents, such as *meta*-[^{211}At]astatobenzoate NHS ester (*22*) or *para*-[^{211}At]astatobenzoate NHS ester (*25*) are likely to be useful in applications where the protein is slowly metabolized or in applications where the radiolabeled protein is administered to a body compartment (e.g., intraperitoneal, intrathecal, etc.) and remains there during the ^{211}At decay period. One such use is being explored in a clinical study at Duke University. That study involves injection of the astatinated mAb into a resection cavity from brain surgery, similar to the studies being conducted with ^{131}I (*42*). Another potential use under investigation is application of ^{211}At-labeled mAbs for bone marrow conditioning (*43*). In this latter application, all of the astatinated targeting mAb should be bound with hematopoietic cells during the decay of the radionuclide (*44*).

The low in vivo stability toward deastatination of astatobenzene derivatives when used with rapidly metabolized proteins (and other biomolecules) is not their only limitation to their use. They can also be difficult to prepare and can display a low stability toward radiolysis. For example, when labeling with higher quantities of ^{211}At, the two-step preparation and conjugation has inherent problems associated with stability of the activated ester and the stannylbenzoate functionality. In spite of this, studies at Duke University have shown that reproducible clinical-level labelings can be prepared with *m*-[^{211}At]astatobenzoate NHS ester ([^{211}At]**1c**), and clinical studies (noted above) using that agent to label an anti-tenacin mAb (81C6) were initiated (*45*). In their early labeling studies, it was concluded that the labeling chemistry was not affected by radiolysis. More recently, problems with preparing clinical levels of the [^{211}At]astatobenzoate NHS ester were determined to be affected by radiolysis (*46*), particularly when chloroform was used as the solvent (*47*).

Due to the observed instability of ^{211}At-benzoate conjugate on mAb Fab′ fragments, we initiated the investigation using boron cage moieties as alternatives for use in labeling of biomolecules. It is our hypothesis that use of the appropriately functionalized boron cage moieties could provide in vivo stability of the ^{211}At and could also provide a more convenient and robust approach to labeling proteins with ^{211}At. Thus, the primary objective of this investigation was to prepare conjugates of a protein that contained boron cage moieties, such that they could be directly labeled with ^{211}At and evaluated in vivo to determine stability toward deastatination. To assist in determining whether the ^{211}At-labeled protein was stable to in vivo deastatination, it was necessary to also radiolabel the protein conjugates with radioiodine (^{125}I). The inclusion of ^{125}I in the studies made it important to employ boron cage moieties that are highly reactive with radioiodine, such that there is a high likelihood the radioiodine will react with the boron cage moiety in preference to the protein tyrosine residues. On the basis of their highly lipophilic nature and very low reactivity with iodine (*48*−*50*), neutral dicarbon carboranes were not considered appropriate for the studies. In our previous studies, it was noted that anionic *nido*-carboranes reacted much more rapidly with electrophilic iodine than tyrosine (*51*), so this moiety was of interest for the studies. Other boron cage moieties such as anionic monocarbon carboranes were considered nonoptimal due to their low reactivity with iodine (*52*). However, dianionic carborane cage moieties, *closo*-dodecaborate(2-) and *closo*-decaborate(2-), were also of high interest due to their reactivity with halogens (*53*).

In the studies described herein, an antibody Fab′ was chosen as a model system to evaluate the in vivo stability of (relatively) rapidly metabolized astatinated proteins. Prior studies had shown *p*-[^{211}At]astatobenzoyl-labeled A6H Fab′ (*26*) and NRML-05 Fab′ (*25*) underwent rapid deastatination in vivo, most likely after protein degradation. Similar results have been reported for *m*-[^{211}At]astatobenzoyl-labeled 3H11 Fab′ (*54*). As a control,

p-[^{211}At]astatobenzoyl-labeled 107-1A4 Fab′, [^{211}At]**1c**-Fab′, was prepared and evaluated in comparison with coinjected *p*-[^{125}I]iodobenzoyl-labeled 107-1A4 Fab′, [^{125}I]**1b**-Fab′. As in the prior studies, evidence for significant deastatination (Figure 4, panel B; lung, spleen, neck, stomach) was seen even at the 1 h time point.

The studies of boron cage conjugates began by preparation, radiolabeling, and in vivo evaluation of two *nido*-carborane conjugates of 107-1A4 Fab′. In prior studies directed at determining the stability of astatinated boron cage moieties in vivo, it was shown that a diaminobenzene adduct of *nido*-carboranylpropionate derivative, **2**, was more resistant to deastatination than *nido*-carboranylpropionate itself (*28*). Therefore, we chose this protein-reactive derivative **2** for study. In those same prior studies, bis-*nido*-carborane derivatives were shown to be stable to in vivo deastatination, so we chose the isothiocyanate derivative, **3**, for preparation and testing as well. While the studies were not extensive, nor optimized, the results obtained with the *nido*-carboranyl derivatives **2** and **3** indicated that they caused aggregation of the Fab′ when conjugated. Additionally, they also caused dramatic changes in the in vivo behavior of the Fab′. These negative characteristics appear unfavorable for use in astatination of proteins. However, it should be noted that in a series of studies involving a *nido*-carboranylphenyl diazonium salt (*55*) and its corresponding isothiocyanate (*56*, *57*) under optimized conjugation conditions allowed coupling of 12 or more *nido*-carborane moieties with good recovery of protein and retention of immunoreactivity of the antibody. More recently, this same *nido*-carborane derivative was successfully used for radiobromination of the anti-HER/neu/ErbB-2 monoclonal antibody (*58*). Similarly, prior studies demonstrated that the ^{211}At- and ^{125}I-labeled bis-*nido*-carborane derivatives (also referred to as Venus Flytrap Complex, VFC) used in this study localized to liver (*28*). Interestingly, studies with ^{57}Co complexed in a VFC showed no change in protein on conjugation (*59*). These examples tend to suggest that optimization studies might provide better protein conjugates of **2** and **3**, but our initial experience with these agents led us to explore other boron cage moieties for conjugation and astatination.

In prior studies, oxygen- (*60*, *61*), sulfur- (*62*, *63*), and nitrogen-bonded (*64*, *65*) *closo*-dodecaborate(2-) derivatives were prepared by other investigators, and some were conjugated with mAbs for direct labeling with radiobromine, radioiodine, and astatine (*66*−*68*). Our concern with the use of these reagents for direct radiohalogenation was that the dodecaborane(2-) cage moiety is deactivated in aqueous solution by protonation of the heteroatom adjacent to the highly anionic *closo*-dodecaborate-(2-) cage. In fact, some preliminary studies were conducted in this laboratory involving amine- and oxo-bonded *closo*-dodecaborates, and it was found that the iodinations were very much slower than with a *closo*-decaborate(2-) derivative (unreported results). Since it was desirable to directly radioiodinate the Fab' conjugates, we chose to prepare conjugates of the *closo*-decaborate(2-) cage system due to its high reactivity with halogens (*53*). An example of sulfur-bonded derivatives of *closo*-decaborate(2-) has also been previously reported (*69*). As with the *closo*-dodecaborate(2-) derivatives, it is likely that the sulfur is protonated under physiological conditions. Therefore, derivatives that have B-bonded functional groups that are unlikely to be protonated (e.g., amide bond, urea, etc.) were sought.

On the basis of the previously listed considerations, the protein-reactive 2-isocyanato-*closo*-decaborate(2-) derivative, **4**, was initially chosen due to its simple preparation (*37*). Unlike the Fab′ conjugates of *nido*-carborane derivatives **2** and **3**, in vivo evaluation of radiohalogenated Fab′ conjugated with **4** demonstrated that concentrations of ^{211}At and ^{125}I in kidney were similar to the control ([^{125}I]**1b**-Fab′; Figure 4, panel B). Importantly, very small differences in the concentrations of nuclides was seen in lung and spleen, providing evidence that the astatinated *closo*-decaborate(2-) cage was stable to in vivo deastatination. Interestingly, higher concentrations of ^{125}I were noted in the neck and stomach. The reason for this difference is uncertain. However, it might be speculated that some radioiodination occurred on protein tyrosine residues, and that radioactivity was released as free [^{125}I]iodide after catabolism of the protein. Importantly, the radiochemical yield was not as high (36%) as desired (i.e., 50+%) for a direct labeling procedure, so additional derivatives were sought.

The carbonylated decaborate(2-) derivative **14** was also used to prepare Fab′ conjugates. The Fab′ conjugate of 2-carbonyl-*closo*-decaborate(2-) derivative **14** was not astatinated or evaluated in vivo, as it seemed likely that would not be significantly different from Fab′ conjugates of **4**. Subsequently, another *closo*-decaborate(2-) derivative, **5**, which has the protein conjugation functionality a distance from the dianionic cage, was prepared and studied. A significantly improved radiolabeling yield was obtained (60%). Surprisingly, in vivo evaluation of the Fab′ conjugate of **5** provided biodistribution data (Figure 4, panel F) that was significantly different from the control ([^{125}I]**1b**-Fab′; Figure 4, panel B). While the ^{211}At and ^{125}I concentrations in blood, lung, spleen, and liver were not very different, the kidney concentrations were dramatically lower. Although the lower kidney values may be of importance in continued conjugate development, the high variation in tissue concentration from that obtained with [^{125}I]**1b** was not desired in this study, so an alternative *closo*-decaborate(2-) derivative was sought.

Difficulties with assessing the number of *closo*-decaborate-(2-) derivatives conjugated to the protein when **4**-Fab′ and **5**-Fab′ were studied led to the preparation of another *closo*-decaborate-(2-)-containing conjugate, **6**-Fab′. In previous studies, a series of mAb conjugates were prepared, which included a biotin moiety (*70*). The inclusion of a biotin in those conjugates was for its application to extracorporeal affinity absorption techniques (*71*), but it was noted that the presence of biotin also made quantification of the number of conjugates per mAb relatively easy when the "HABA" assay (*39*) was used. Conjugation of Fab′ with **6** provided an appropriate substitution (1.5−2 conjugates/Fab′). Interestingly, in the biodistribution (Figure 4, panel G), the two radionuclides on **6**-Fab′ had almost identical concentrations in most tissues examined, including neck and stomach. The fact that the concentrations of ^{211}At and ^{125}I were very similar in neck and stomach suggests that the radioiodine had reacted with the decaborate cage. However, it should be noted that tissue concentrations of radiolabeled **6**-Fab′ in liver and spleen are significantly higher than for the control ([^{125}I]**1b**-Fab′; Figure 4, panel B). This fact suggests that the protein modification with **6** has an effect, although fairly small, on the biodistribution.

The Fab′ conjugates described thus far were prepared by reaction with the protein lysine residues. A desire to couple the decaborate(2-) moiety to a protein sulfhydryl in a collaborative study (*41*) led to the preparation of a maleimide derivative, **7**. Conjugation of **7** with the sulfhydryl on Fab′ was accomplished at pH 6.5. At this pH, the conjugation would be expected to be highly selective for the thiol group. The yields for radioiodination and astatination were the highest obtained in the study (Table 1). This high yield may in part be due to having a thioether bond rather than a thiourea bond in the conjugate. Previous studies have provided data that suggest that radiohalogenations can be negatively affected in the presence of a thiourea functionality (*72*). The biodistribution data obtained from **7**-Fab′ is fairly consistent with data obtained with other decaborate(2-) conjugates.

CONCLUSION

The preparation, characterization, astatination, and in vivo characteristics of 107-1A4 Fab′ conjugated with a series of *nido*-carborane and *closo*-decaborate(2-) derivatives has been described. The primary goal of the studies was to obtain at least one astatinated protein conjugate that is both stable to in vivo deastatination and has a minimal affect on the in vivo characteristics of the protein. This goal was achieved, and studies involving conjugation and astatination of other proteins with the amine-reactive and sulfhydryl-reactive *closo*-decaborate(2-) derivatives **6** and **7** are planned. *We believe this report provides the first examples of direct labeling of proteins with ^{211}At which do not undergo deastatination in vivo.* A secondary goal of the studies was to simplify the protein astatination reactions and improve the radiochemical yields obtained. This goal was also achieved. *The radiochemical yields for Fab′ conjugates of **6** and **7** were similar to those obtained in direct radioiodination reactions,* and higher than previously attained with the two-step ^{211}At labeling procedures. Despite these very important steps forward, the results also indicate that *closo*-decaborate-(2-) conjugates are not optimal. It is apparent that concentrations of the radionuclides in some tissues (e.g., liver) are higher than obtained with unconjugated Fab′. The reason for the higher concentrations is not known, but it is likely that the dianionic nature of the *closo*-decaborate(2-) cage contributes to a longer residence time in those tissues. Therefore, studies are underway to chemically modify the *closo*-decaborate(2-) cage conjugates to improve their in vivo properties.

ACKNOWLEDGMENT

We thank Janna Quinn, Austin Odman, and Nicole Lavoie for their assistance in the animal biodistributions studies. We thank Quanta Biodesign (Powell, Ohio) for the gift of NHS-3-maleimidoproprionate. We thank the Department of Energy, Office of Isotope Programs (ANMI-DE-FG01-00NE22740), Department of Energy, Medical Applications and Biophysical Research Division, OHER, (DE-FG03-98-ER62572), and NIH (1 RO1 CA113431) for funding the studies described.

Supporting Information Available: SE-HPLC chromatograms for conjugation of varying quantities (10, 20, and 50 equiv) of **2** with Fab′-NEM are provided is Figure S1; digitized IEF gels run on some Fab′ conjugates is provided in Figure S2; and complete tissue distribution data for all in vivo studies are provided in Tables S1−S8. This material is available free of charge via the Internet at http://pubs.acs.org/BC.

LITERATURE CITED

(1) Yordanov, A. T., Garmestani, K., Zhang, M., Zhang, Z., Yao, Z., Phillips, K. E., Herring, B., Horak, E., Beitzel, M. P., Schwarz, U. P., Gansow, O. A., Plascjak, P. S., Eckelman, W. C., Waldmann, T. A., and Brechbiel, M. W. (2001) Preparation and in vivo evaluation of linkers for ^{211}At labeling of humanized anti-Tac. *Nucl. Med. Biol. 28,* 845−856.

(2) Talanov, V. S., Yordanov, A. T., Garmestani, K., Milenic, D. E., Arora, H. C., Plascjak, P. S., Eckelman, W. C., Waldmann, T. A., and Brechbiel, M. W. (2004) Preparation and in vivo evaluation of novel linkers for ^{211}At labeling of proteins. *Nucl. Med. Biol. 31,* 1061−1071.

(3) Couturier, O., Supiot, S., Degraef-Mougin, M., Faivre-Chauvet, A., Carlier, T., Chatal, J. F., Davodeau, F., and Cherel, M. (2005) Cancer radioimmunotherapy with alpha-emitting nuclides. *Eur. J. Nucl. Med. Mol. Imaging 32,* 601−14.

(4) Mulford, D. A., Scheinberg, D. A., and Jurcic, J. G. (2005) The promise of targeted {α}-particle therapy. *J. Nucl. Med. 46 Suppl 1,* 199S−204S.

(5) Imam, S. K. (2001) Advancements in cancer therapy with alpha-emitters: a review. *Int. J. Radiat. Oncol., Biol., Phys. 51,* 271−8.

(6) Zalutsky, M. R., and Vaidyanathan, G. (2000) Astatine-211-labeled radiotherapeutics: an emerging approach to targeted alpha-particle radiotherapy. *Curr. Pharm. Des. 6,* 1433−55.

(7) Wilbur, D. S. (1991) Potential use of alpha-emitting radionuclides in the treatment of cancer. *Antibody, Immunoconjugates, Radiopharm. 4,* 85−97.

(8) Humm, J. L. (1987) A microdosimetric model of astatine-211 labeled antibodies for radioimmunotherapy. *Int. J. Radiat. Oncol., Biol., Phys. 13,* 1767−1773.

(9) Kassis, A. I., Harris, C. R., Adelstein, S. J., Ruth, T. J., Lambrecht, R., and Wolf, A. P. (1986) The in vitro radiobiology of astatine-211 decay. *Radiat. Res. 105,* 27−36.

(10) Hughes, W. L., and Gitlin, D. (1955) Astatinated (At^{211}) organic compounds for production of highly localized radiobiological effects. *Am. Soc. Biol. Chem. 14,* 229.

(11) Smit, J. A., Myburgh, J. A., and Neirinckx, R. D. (1973) Specific inactivation of sensitized lymphocytes in vitro using antigens labelled with astatine-211. *Clin. Exp. Immunol. 14,* 107−116.

(12) Aaij, C., Tschroots, W. R. J. M., Lindner, L., and Feltkamp, T. E. W. (1975) The preparation of astatine labelled proteins. *Int. J. Appl. Radiat. Isot. 26,* 25−30.

(13) Vaughan, A. T. M., and Fremlin, J. H. (1978) The preparation of astatine labelled proteins using an electrophilic reaction. *Int. J. Nucl. Med. Biol. 5,* 229−230.

(14) Vaughan, A. T. M., Bateman, W. J., and Fisher, D. R. (1982) The in vivo fate of a ^{211}At labelled monoclonal antibody with known specificity in a murine system. *Int. J. Radiat. Oncol., Biol., Phy. 8,* 1943−1946.

(15) Friedman, A. M., Zalutsky, M. R., Wung, W., Buckingham, F., Harper, P. V., Scherr, G. H., Wainer, B., Hunter, R. L., Appelman, E. H., Rothberg, R. M., Fitch, F. W., Stuart, F. P., and Simonian, S. J. (1977) Preparation of a biologically stable and immunologically competent astatinated protein. *Int. J. Nucl. Med. Biol. 4,* 219−224.

(16) Vaughan, A. T. M. (1979) Labelling of proteins with ^{211}At using an acylation reaction. *Int. J. Appl. Radiat. Isot. 30,* 576−577.

(17) Harrison, A., and Royle, L. (1984) Preparation of a ^{211}At-IgG conjugate which is stable in vivo. *Int. J. Appl. Radiat. Isot. 35,* 1005−1008.

(18) Visser, G. W. M., Diemer, E. L., and Kaspersen, F. M. (1980) The preparation of aromatic astatine compounds through aromatic mercury-compounds. *J. Labelled Compd. Radiopharm. 17,* 657−665.

(19) Wilbur, D. S., Hylarides, M. D., and Fritzberg, A. R. (1989) Reactions of organometallic compounds with astatine-211. Application to protein labeling. *Radiochim. Acta 47,* 137−42.

(20) Zalutsky, M. R., and Narula, A. S. (1988) Radiohalogenation of a monoclonal antibody using an N-succinimidyl 3-(tri-*n*-butylstannyl)benzoate Intermediate. *Cancer Res. 48,* 1446−1450.

(21) Wilbur, D. S., Hylarides, M. D., Hadley, S., Schroeder, J., and Fritzberg, A. R. (1989) A general approach to radiohalogenation of proteins. Radiohalogenation of organometallic intermediates containing protein reactive substituents. *J. Labelled Compd. Radpharm. 26,* 316−318.

(22) Zalutsky, M. R., and Narula, A. S. (1988) Astatination of proteins using an *n*-succinimidyl tri-*n*-butylstannyl benzoate intermediate. *Appl. Radiat. Isot. 39,* 227−232.

(23) Zalutsky, M. R., Garg, P. K., Friedman, H. S., and Bigner, D. D. (1989) Labeling monoclonal antibodies and $F(ab')_2$ fragments with the α-particle-emitting nuclide astatine-211: Preservation of immunoreactivity and in vivo localizing capacity. *Proc. Natl. Acad. Sci. U.S.A. 86,* 7149−7153.

(24) Zalutsky, M. R., Stabin, M. G., Larsen, R. H., and Bigner, D. D. (1997) Tissue distribution and radiation dosimetry of astatine-211-labeled chimeric 81C6, an α-particle-emitting immunoconjugate. *Nucl. Med. Biol. 24,* 255−261.

(25) Hadley, S. W., Wilbur, D. S., Gray, M. A., and Atcher, R. W. (1991) Astatine-211 labeling of an antimelanoma antibody and its Fab fragment using *N*-succinimidyl *p*-[^{211}At]astatobenzoate: comparisons in vivo with the *p*-[^{125}I]iodobenzoyl conjugate. *Bioconjugate Chem. 2,* 171−9.

(26) Wilbur, D. S., Vessella, R. L., Stray, J. E., Goffe, D. K., Blouke, K. A., and Atcher, R. W. (1993) Preparation and evaluation of *para*-[^{211}At]astatobenzoyl labeled anti-renal cell carcinoma antibody A6H $F(ab')_2$. In vivo distribution comparison with *para*-[^{125}I]iodobenzoyl labeled A6H $F(ab')_2$. *Nucl. Med. Biol. 20,* 917−27.

(27) Wilbur, D. S., Chyan, M.-K., and Hamlin, D. K. (2005) Investigation of a decaborate(2-) containing conjugate for direct labeling of monoclonal antibodies with At-211. *J. Nucl. Med. 46*, 31P−32P (abstract).

(28) Wilbur, D. S., Chyan, M. K., Hamlin, D. K., Kegley, B. B., Risler, R., Pathare, P. M., Quinn, J., Vessella, R. L., Foulon, C., Zalutsky, M., Wedge, T. J., and Hawthorne, M. F. (2004) Reagents for astatination of biomolecules: comparison of the in vivo distribution and stability of some radioiodinated/astatinated benzamidyl and *nido*-carboranyl compounds. *Bioconjugate Chem. 15*, 203−23.

(29) Reist, C. J., Foulon, C. F., Alston, K., Bigner, D. D., and Zalutsky, M. R. (1999) Astatine-211 labeling of internalizing anti-EGFRvIII monoclonal antibody using N-succinimidyl 5-[^{211}At]astato-3-pyridinecarboxylate. *Nucl. Med. Biol. 26*, 405−411.

(30) Vaidyanathan, G., Affleck, D. J., and Zalutsky, M. R. (2003) N-Succinimidyl 3-[^{211}At]astato-4-guanidinomethylbenzoate: An acylation agent for labeling internalizing antibodies with alpha-particle-emitting ^{211}At. NUCL-101, *Abstracts of Papers*, 225th National Meeting of the American Chemical Society, New Orleans, LA, March 23−27, 2003.

(31) Gamper, H. B., Reed, M. W., Cox, T., Virosco, J. S., Adams, A. D., Gall, A. A., Scholler, J. K., and Meyer, R. B., Jr. (1993) Facile preparation of nuclease resistant 3′ modified oligodeoxynucleotides. *Nucleic Acids Res. 21*, 145−50.

(32) Wilbur, D. S., Hamlin, D. K., Vessella, R. L., Stray, J. E., Buhler, K. R., Stayton, P. S., Klumb, L. A., Pathare, P. M., and Weerawarna, S. A. (1996) Antibody fragments in tumor pretargeting. Evaluation of biotinylated Fab′ colocalization with recombinant streptavidin and avidin. *Bioconjugate Chem. 7*, 689−702.

(33) Lindegren, S., Back, T., and Jensen, H. J. (2001) Dry-distillation of astatine-211 from irradiated bismuth targets: a time-saving procedure with high recovery yields. *Appl. Radiat. Isot. 55*, 157−160.

(34) Wilbur, D. S., Hadley, S. W., Hylarides, M. D., Abrams, P. G., Beaumier, P. A., Morgan, A. C., Reno, J. M., and Fritzberg, A. R. (1989) Development of a stable radioiodinating reagent to label monoclonal antibodies for radiotherapy of cancer. *J. Nucl. Med. 30*, 216−26.

(35) Hawthorne, M. F., Pilling, R. L., and Knoth, W. H. (1967) 5. Bis(triethylammonium) decahydrodecaborate (2-). *Inorg. Synth. 9*, 16−19.

(36) Wilbur, D. S., Hamlin, D. K., Chyan, M. K., Kegley, B. B., and Pathare, P. M. (2001) Biotin reagents for antibody pretargeting. 5. Additional studies of biotin conjugate design to provide biotinidase stability. *Bioconjugate Chem. 12*, 616−23.

(37) Shelly, K., Knobler, C. B., and Hawthorne, M. F. (1992) Synthesis of monosubstituted derivatives of *closo*-decahydrodecaborate(2-). X-ray crystal structures of [*closo*-2-$B_{10}H_9Co]^-$ and [*closo*-2-$B_{10}H_9$-$NCO]^{2-}$. *Inorg. Chem. 31*, 2889−2892.

(38) Brown, L., Wegner, S., Wang, H., Buhler, K., Arfman, E., Lange, P., and Vessella, R. (1998) A novel monoclonal antibody 107−1A4 with high prostate specificity: generation characterization of antigen expression, and targeting of human prostate cancer xenografts. *Prostate Cancer and Prostatic Diseases 1*, 208−215.

(39) Green, N. M. (1965) A spectrophotometric assay for avidin and biotin based on binding of dyes by avidin. *Biochem. J. 94*, 23−24.

(40) Hamblett, K. J., Kegley, B. B., Hamlin, D. K., Chyan, M. K., Hyre, D. E., Press, O. W., Wilbur, D. S., and Stayton, P. S. (2002) A streptavidin-biotin binding system that minimizes blocking by endogenous biotin. *Bioconjugate Chem. 13*, 588−98.

(41) Steffen, A.-C., Almquist, Y., Chyan, M.-K., Lundquist, H., Tolmachev, V., Wilbur, D. S., and Carlsson, J. (2006) Biodistribution of ^{211}At-labeled HER-2 binding affibody molecules in mice. *Oncol. Rep. 17*, 1141−7.

(42) Reardon, D. A., Akabani, G., Coleman, R. E., Friedman, A. H., Friedman, H. S., Herndon, J. E., II, McLendon, R. E., Pegram, C. N., Provenzale, J. M., Quinn, J. A., Rich, J. N., Vredenburgh, J. J., Desjardins, A., Guruangan, S., Badruddoja, M., Dowell, J. M., Wong, T. Z., Zhao, X.-G., Zalutsky, M. R., and Bigner, D. D. (2006) Salvage radioimmunotherapy with murine iodine-131-labeled antitenascin monoclonal antibody 81C6 for patients with recurrent primary and metastatic malignant brain tumors: Phase II study results. *J. Clin. Oncol. 24*, 115−122.

(43) Bethge, W. A., and Sandmaier, B. M. (2004) Targeted cancer therapy and immunosuppression using radiolabeled monoclonal antibodies. *Semin. Oncol. 31*, 68−82.

(44) Sandmaier, B. M., Bethge, W. A., Wilbur, D. S., Hamlin, D. K., Santos, E. B., Brechbiel, M. W., Fisher, D. R., and Storb, R. (2002) Bismuth 213-labeled anti-CD45 radioimmunoconjugate to condition dogs for nonmyeloablative allogeneic marrow grafts. *Blood 100*, 318−26.

(45) Zalutsky, M. R., Zhao, X.-G., Alston, K. L., and Bigner, D. (2001) High-level production of α-particle-emitting 211At and preparation of ^{211}At-labeled antibodies for clinical use. *J. Nucl. Med. 42*, 1508−1515.

(46) Pozzi, O. R., and Zalutsky, M. R. (2005) Radiopharmaceutical chemistry of targeted radiotherapeutics, part 1: Effects of solvent on the degradation of radiohalogenation precursors by ^{211}At α-particles. *J. Nucl. Med. 46*, 700−706.

(47) Pozzi, O. R., and Zalutsky, M. R. (2005) Radiopharmaceutical chemistry of targeted radiotherapeutics, part 2: radiolytic effects of ^{211}At α-particles influence N-succinimidyl 3-^{211}At-astatobenzoate synthesis. *J. Nucl. Med. 46*, 1393−1400.

(48) Andrews, J. S., Zayas, J., and Jones, M., Jr. (1985) 9-Iodo-*o*-Carborane. *Inorg. Chem. 24*, 3715−3716.

(49) Li, J., Logan, C. F., and Jones, M., Jr. (1991) Simple syntheses and alkylation reactions of 3-iodo-*o*-carborane and 9,12-diiodo-*o*-carborane. *Inorg. Chem. 30*, 4866−4868.

(50) Srivastava, R. R., Hamlin, D. K., and Wilbur, D. S. (1996) Synthesis of highly iodinated icosahedral mono- and dicarbon carboranes. *J. Org. Chem. 61*, 9041−9044.

(51) Wilbur, D. S., Hamlin, D. K., Pathare, P. M., and Kegley, B. B. (1999) Synthesis of a *nido*-carborane derivative for use as a protein conjugate for direct radioiodination. *J. Labelled Compd. Radiopharm. 42*, S288−S290.

(52) Wilbur, D. S., Hamlin, D. K., Srivastava, R. R., and Chyan, M. K. (2004) Synthesis, radioiodination, and biodistribution of some *nido*- and *closo*-monocarbon carborane derivatives. *Nucl. Med. Biol. 31*, 523−30.

(53) Knoth, W. H., Miller, H. C., Sauer, J. C., Balthis, J. H., Chia, Y. T., and Muetterties, E. L. (1964) Chemistry of boranes. IX. Halogenation of $B_{10}H_{10}^{-2}$ and $B_{12}H_{12}^{-2}$. *Inorg. Chem. 3*, 159−167.

(54) Liu, N., Jin, J., Zhang, S., Mo, S., Yang, Y., Wang, J., and Zhou, M. (2001) ^{211}At labeling of a monoclonal antibody and its Fab fragment: cytotoxicity on human gastric cancer cells and biodistribution in nude mice with tumor xenografts. *J. Radioanal. Nucl. Chem. 247*, 129−133.

(55) Mizusawa, E., Dahlman, H. L., Bennett, S. J., Goldenberg, D. M., and Hawthorne, M. F. (1982) Neotron-capture therapy of human cancer: in vitro results on the preparation of boron-labeled antibodies to carcinoembryonic antigen. *Proc. Natl. Acad. Sci. U.S.A. 79*, 3011−3014.

(56) Mizusawa, E. A., Thompson, M. R., and Hawthorne, M. F. (1985) Synthesis and antibody-labeling studies with the *p*-isothiocyanatobenzene derivatives of 1,2-dicarba-*closo*-dodecaborane(12) and the dodecahydro-7,8-dicarba-*nido*-undecaborate(1-) ion for neutron-capture therapy of human cancer. Crystal and molecular stucture of Cs^+[*nido*-7-(*p*-C_6H_4NCS)-9-I-7,8-$C_2B_9H_{11}$]. *Inorg. Chem. 24*, 1911−1916.

(57) Varadarajan, A., Sharkey, R. M., Goldenberg, D. M., and Hawthorne, M. F. (1991) Conjugation of phenyl isothiocyanate derivatives of carborane to antitumor antibody and in vivo localization of conjugates in nude mice. *Bioconjugate Chem. 2*, 102−110.

(58) Winberg, K. J., Persson, M., Malmstrom, P.-U., Sjoeberg, S., and Tolmachev, V. (2004) Radiobromination of anti-HER2/neu/ErbB-2 monoclonal antibody using the *p*-isothiocyanatobenzene derivative of the [^{76}Br]undecahydro-bromo-7,8-dicarba-*nido*-undecaborate(1-) ion. *Nucl. Med. Biol. 31*, 425−433.

(59) Paxton, R. J., Beatty, B. G., Hawthorne, M. F., Varadarajan, A., Williams, L. E., Curtis, F. L., Knobler, C. B., and Shively, J. E. (1991) A Transition metal complex (Venus flytrap cluster) for radioimmunodetection and radioimmunotherapy. *Proc. Nat. Acad. Sci. U.S.A. 88*, 3387−3391.

(60) Sivaev, I. B., Sjuberg, S., Bregadze, V. I., and Gabel, D. (1999) Synthesis of alkoxy derivatives of dodecahdro-*closo*-dodecaborate anion $[B_{12}H_{12}]^{2-}$. *Tetrahedron Lett. 40*, 3451−4.

(61) Sivaev, I. B., Semioshkin, A. A., Brellochs, B., Sjoberg, S., and Bregadze, V. I. (2000) Synthesis of oxonium derivatives of the dodecahydro-*closo*-dodecaborate anion $[B_{12}H_{12}]^{2-}$. Tetramethylene oxonium derivative of $[B_{12}H_{12}]^{2-}$ as a convenient precursor for the synthesis of functional compounds for boron neutron capture therapy. *Polyhedron 19*, 627−632.

(62) Alam, F., Soloway, A. H., McGuire, J. E., Barth, R. F., Carey, W. E., and Adams, D. (1985) Dicesium *N*-succinimidyl 3-(undecahydro-*closo*-dodecaboranyldithio)propionate, a novel heterobifunctional boronating agent. *J. Med. Chem. 28*, 522−525.

(63) Tolmachev, V., Koziorowski, J., Sivaev, I., Lundqvist, H., Carlsson, J., Orlova, A., Gedda, L., Olsson, P., Sjoberg, S., and Sundin, A. (1999) *closo*-Dodecaborate(2-) as a linker for iodination of macromolecules aspects on conjugation chemistry and biodistribution. *Bioconjugate Chem. 10*, 338−45.

(64) Sivaev, I. B., Bruskin, A. B., Nesterov, V. V., Antipin, M. Y., Bregadze, V. I., and Sjoberg, S. (1999) Synthesis of Schiff bases derived from the ammoniaundecahydro-*closo*-dodecaborate(1-) anion, $[B_{12}H_{11}NH{=}CHR](-)$, and their reduction into monosubstituted amines $[B_{12}H_{11}NH_2CH_2R](-)$: a new route to water soluble agents for BNCT. *Inorg. Chem.* 5887−5893.

(65) Nestor, M., Persson, M., Cheng, J., Tolmachev, V., Van Dongen, G., Anniko, M., and Kairemo, K. (2003) Biodistribution of the chimeric monoclonal antibody U36 radioiodinated with a *closo*-dodecaborate-containing linker. Comparison with other radioiodination methods. *Bioconjugate Chem. 14*, 805−810.

(66) Bruskin, A., Sivaev, I., Persson, M., Lundqvist, H., Carlsson, J., Sjoberg, S., and Tolmachev, V. (2004) Radiobromination of monoclonal antibody using potassium [^{76}Br] (4-isothiocyanatobenzyl-ammonio)-bromo-decahydro-*closo*-dodecaborate (Bromo-DABI). *Nucl. Med. Biol. 31*, 205−211.

(67) Orlova, A., Lebeda, O., Tolmachev, V., Sjoberg, S., Carlsson, J., and Lundqvist, H. (1999) Astatination of *Closo*-dodecaborate(2-) anion. *J. Labelled Compd. Radiopharm. 42*, S735−S737.

(68) Orlova, A., Lebeda, O., Tolmachev, V., Sjoberg, S., Carlsson, J., and Lundqvist, H. (2000) *Closo*-dodecaborate (2-) anion as a potential prosthetic group for attachment of astatine to proteins. Aspects of the labelling chemistry with Chloramine-T. *J. Labelled Compd Radiopharm. 43*, 251−260.

(69) Sneath, R. L., Jr., Soloway, A. H., and Dey, A. S. (1974) Protein-binding polyhedral boranes. 1. *J. Med. Chem. 17*, 796−799.

(70) Wilbur, D. S., Chyan, M. K., Hamlin, D. K., Kegley, B. B., Nilsson, R., Sandberg, B. E., and Brechbiel, M. (2002) Trifunctional conjugation reagents. Reagents that contain a biotin and a radiometal chelation moiety for application to extracorporeal affinity adsorption of radiolabeled antibodies. *Bioconjugate Chem. 13*, 1079−92.

(71) Strand, S.-E., Sjogren, H.-O., Chen, J., Hindrof, C., Tennvall, J. G., Garkavij, M., Nilsson, R., and Sandberg, B. E. B. (2000) Extracorporeal techniques in radioimmunotherapy, in *Radioimmunotherapy of Cancer* (Abrams, P. G., and Fritzberg, A. R., Eds.) pp 223−243, Marcel Dekker, Inc., New York.

(72) Wilbur, D. S., Hamlin, D. K., Kegley, B. B., Chyan, M. K., Pathare, P. M., and Wan, F. (2001) Studies which indicate that thiourea bonds interfere with radioiodination reactions. *J. Labelled Compd. Radiopharm. 44*, S973−S975.

(73) Studies conducted at NIH by Brechbiel et al. have noted that Hu-anti-Tac antibody labeled with an astatobenzoate was subject to deastatination in vivo (*1*). Those investigators have developed another aryl reagent, *N*-succinimidyl N-4-[^{211}At]astatophenethyl)succinamate (SAPS), that has shown greater stability with some labeled mAbs. However, deastatination was noted when [^{211}At]SAPS was used with Herceptin (*2*).

(74) The terms decaborate(2-) and dodecaborate(2-) are used herein as simplified nomenclature for monosubstituted 2-nonahydro-*closo*-decaborate(2-) salt, $[closo\text{-}2\text{-}B_{10}H_9\text{-}R]^{2-}$, and monosubstituted undecahydro-*closo*-dodecaborate(2-) salt, $[closo\text{-}B_{12}H_{11}\text{-}R]^{2-}$. The counterion of the salt has been left off throughout the text for simplicity, but is generally $[Et_3NH]^+$ prior to protein conjugation.

BC060345S

Colloidal Au Replacement Assay for Highly Sensitive Quantification of Low Molecular Weight Analytes by Surface Plasmon Resonance

Seiji Takae,[†] Yoshitsugu Akiyama,[†] Yuichi Yamasaki,[†,‡] Yukio Nagasaki,[§] and Kazunori Kataoka*[,†,‡,||]

Department of Materials Engineering, Graduate School of Engineering, The University of Tokyo, 7-3-1 Hongo, Bunkyo-ku, Tokyo 113-8656, Japan, Center for NanoBio Integration, The University of Tokyo, 7-3-1 Hongo, Bunkyo-ku, Tokyo 113-0033, Japan, Tsukuba Research Center for Interdisciplinary Materials Science, Tsukuba University, Tennoudai 1-1-1, Tsukuba 305-8573, Japan, and Center for Disease Biology and Integrative Medicine, Graduate School of Medicine, The University of Tokyo, 7-3-1 Hongo, Bunkyo-ku, Tokyo 113-0033, Japan. Received November 9, 2006; Revised Manuscript Received April 16, 2007

A novel sensing method based on surface plasmon resonance (SPR) was developed for the highly sensitive quantification of low molecular weight (LMW) analytes (colloidal Au replacement assay). Gold nanoparticles (diameter = 20 nm) functionalized with lactosyl-poly(ethylene glycol) (PEG) were prepared and were specifically adsorbed onto a *Ricinus communis* agglutinin (RCA_{120})-immobilized SPR sensor chip surface. Subsequent injection of free D-galactose elicited the elution of the preadsorbed lactosyl-PEGylated gold nanoparticles in a manner proportional to the galactose concentration, achieving a substantial and quantitative analysis over a wide range of galactose concentrations (0.1−50 ppm). This method of D-galactose sensing through the substituted elution of preadsorbed nanoparticles from the sensor chip surface would be applicable for the highly sensitive SPR quantification of various LMW analytes, which are known to be difficult to detect by the conventional SPR sensing regime.

1. INTRODUCTION

The surface plasmon resonance (SPR) technique has been widely used in the real-time assay of biomolecular interactions (*1*−*4*). SPR is based on a change in the reflection of laser light from a metal−liquid surface, induced by a variation in the dielectric constant due to the adsorption of analyte molecules. Because this change is extremely sensitive and is correlated with the amount of adsorbed analytes, quantitative experiments with SPR are feasible for the monitoring of various biomacromolecules, including proteins, carbohydrates, and nucleic acid compounds. Nevertheless, the sensing of low molecular weight (LMW) compounds by SPR is generally difficult, mainly due to the inherently low response of analytes with a limited mass. An available method for the amplification of the SPR signal is the augmentation of the apparent mass of the analyte molecules. In this regard, gold nanoparticles modified with analytes were employed for the enhancement of the SPR signal (*5*−*7*). The amplification mechanisms of colloidal Au enhanced SPR are (i) the increased apparent mass of the analytes immobilized on gold nanoparticles and (ii) a coupling of the localized surface plasmon of gold nanoparticles with the propagating plasmon on the SPR gold surface. The colloidal Au enhanced SPR achieved the highly sensitive detection of the antigen−antibody interaction and DNA hybridization (*5*, *6*), but, as far as we know, this has not been applied to a direct quantitative assay of low molecular weight (LMW) analytes in sample solutions.

We now report a novel SPR method for the quantitative assay of LMW analytes (colloidal Au replacement assay) based on the elution of preadsorbed gold nanoparticles on the sensor chip surface induced by the injection of LMW analytes. In this method, it is crucial to minimize the nonspecific adsorption between the gold nanoparticles and the sensor chip surface. PEGylated gold nanoparticles possessing lactose moieties, as a ligand, at the distal end were then prepared by covering the nanoparticle with a densely tethered layer of a thiolated heterobifunctional PEG (*8*). Note that the hydrophilic PEG layer with a strong steric-repulsive property serves to minimize the nonspecific adsorption and agglomeration of gold nanoparticles in an aqueous medium (*9*). Eventually, the highly sensitive quantification of the label-free LMW compound, galactose, by SPR was achieved by monitoring the competitive elution of the lactosyl-PEGylated gold nanoparticles from a *Ricinus communis* agglutinin (RCA_{120}; a bivalent galactose-binding lectin)-immobilized sensor chip upon the injection of the sample solution containing a definite concentration of free galactose.

2. EXPERIMENTAL PROCEDURES

2.1. Materials. Gold nanoparticles (diameter = 20 nm) were purchased from British Biocell International (Cardiff, U.K.). Bovine serum albumin (BSA), lactosyl-albumin (lac-BSA), and NA3 glycan ($[Gal\text{-}GlcNAc]_3\text{-}Man_3\text{-}GlcNAc_2$, FW = 2006) were purchased from the Sigma-Aldrich Co. (St. Louis, MO). *Ricinus communis* agglutinin (RCA_{120}) was purchased from the Honen Co. (Tokyo, Japan). D-Galactose was purchased from Wako Pure Chemical Industries, Ltd. (Osaka, Japan). The CM3 sensor chip, acetate buffer (pH 5.5), and amine coupling kit were purchased from Biacore AB (Uppsala, Sweden). All reagents were used as received. The phosphate buffered saline (PBS, 150 mM, pH 7.4) was prepared using Dulbecco's PBS from the Dainippon-Sumitomo Pharma Co. (Osaka, Japan). Water was purified using a Milli-Q instrument (Millipore, Bedford, MA).

2.2 Preparation of PEGylated Gold Nanoparticles Possessing Varying Lactose Functionalities. PEGylated gold nanoparticles with varying lactose functionalities on the surface

* To whom correspondence should be addressed. Telephone: +81-3-5841-7138. Fax: +81-3-5841-7139. E-mail: kataoka@bmw.t.u-tokyo.ac.jp.

[†] Graduate School of Engineering, The University of Tokyo.

[‡] Center for NanoBio Integration, The University of Tokyo.

[§] Tsukuba University.

[||] Graduate School of Medicine, The University of Tokyo.

10.1021/bc0603541 CCC: $37.00 © 2007 American Chemical Society
Published on Web 06/19/2007

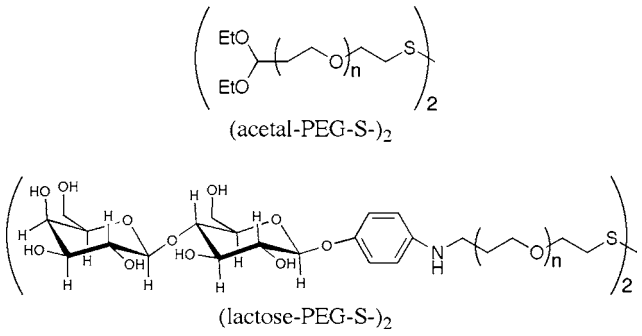


Figure 1. Chemical structures of (acetal-PEG-S-)$_2$ and (lactose-PEG-S-)$_2$.

were fabricated as previously reported (*10*). Briefly, a mixture of (acetal-PEG-S-)$_2$ (M_n = 12 100, Figure 1) and (lactose-PEG-S-)$_2$ (M_n = 12 200, Figure 1; the lactose functionality is 50%) of different molar ratios was added to the gold nanoparticle (diameter = 20 nm) solution (pH = 6.5) at room temperature. Lactose content on the gold nanoparticles was regulated by varying the feed molar ratio of (lactose-PEG-S-)$_2$ with (acetal-PEG-S-)$_2$ in the reaction mixtures. Since the reactivity of the disulfide group toward the surface of gold nanoparticles is likely to be equal between (lactose-PEG-S-)$_2$ and (acetal-PEG-S-)$_2$ because of their identical molecular weight with only a subtle change in the chain ends, the ratio of the lactose moieties on the gold surface is assumed to be equal to the feed ratio. Accordingly, the mol % of (lactose-PEG-S-)$_2$ in the feed was utilized to express the lactose functionalities (the fraction of tethered PEG having a lactosyl ligand at the distal end) on the PEGylated gold nanoparticles. Here, PEGylated gold nanoparticles with 0%, 25%, and 50% functionalities were prepared and abbreviated as lac0, lac25, and lac50, respectively. After 15 h of stirring, repetitive centrifugation and redispersion were carried out twice to remove any excess polymer from the solution. Finally, the nanoparticles were resuspended in PBS containing 0.01 wt % bovine serum albumin (BSA). The final concentration of the resuspended PEGylated gold nanoparticles was calculated from the absorbance at 523 nm using a UV−visible spectrophotometer (V-550 UV/vis spectrophotometer, JASCO, Japan). The calibration curve was prepared on the basis of the absorbance of the bare gold nanoparticles, because the UV−visible spectra revealed no substantial change even after the PEGylation of the gold nanoparticles (Supporting Information Figure S1).

2.3. Surface Plasmon Resonance Measurements. The SPR experiments were done using a Biacore 3000 instrument (Biacore AB, Uppsala, Sweden). RCA_{120} was immobilized on the surface of a CM3 carboxymethyl-dextran sensor chip using an amine coupling kit and 20 μg/mL RCA_{120} in 10 mM acetate buffer (pH 5.5) at the rate of 10 μL/min. Namely, carboxyl groups on the chip surface were activated by a mixture of succinimide (NHS) and carbodiimide (EDC) to form active esters, which then spontaneously react with the amino groups of RCA_{120}. Subsequently, excess ethanolamine was injected to deactivate the remaining active esters. The amount of the immobilized RCA_{120} was 1500 resonance units (RU) in all the experiments. A 0.1° SPR angle shift corresponds to 1000 RU, which is calibrated to be ca. 1 ng/mm^2, as provided by the manufacturer (Biacore) (*11*). Given that the molecular weight of RCA_{120} is ~120 000, it follows that 1500 RU = 1500 pg/mm^2 = 1.25×10^{-14} mol/mm^2 = 7.52×10^9 proteins/mm^2 = 7.52×10^{-3} proteins/nm^2. A similar procedure was carried out for a reference flow cell, for which the RCA_{120} injection is replaced with a blank injection of the buffer.

The lactosyl-PEGylated gold nanoparticles were then continuously injected over the flow cell modified with RCA_{120} and the unmodified flow cell at 25 °C. PBS containing 0.01 wt % BSA was used as the running buffer. All the data were obtained by signal subtraction of the blank flow cell injection from the RCA_{120}-immobilized flow cell, in order to remove any adverse contribution from the refractive index noise due to the bulk contribution of the sample injection. To assess the kinetic parameters, a global analysis of six concentrations of samples was performed using a 1:1 Langmuir model and bivalent model by *Biaevaluation 3.1* software.

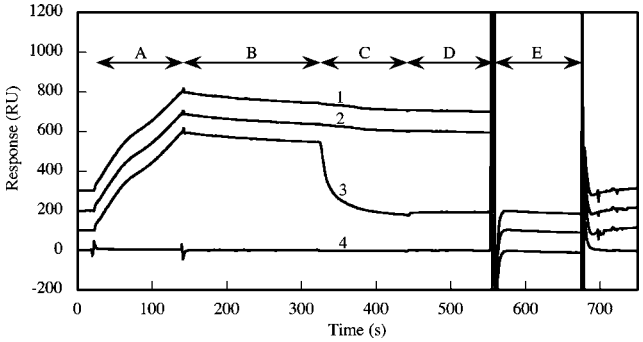


Figure 2. Sensorgrams for the interaction of PEGylated gold nanoparticles with RCA_{120} immobilized on the CM3 sensor chip. (region A): Injection of lac50 (lines 1−3) and lac0 (line 4). (region B): Flowing of running buffer (lines 1−4). (region C): Injection of running buffer (lines 1, 4), 100 μg/mL of glucose solution (line 2), and 100 μg/mL of galactose solution (line 3). (region D): Flowing of running buffer (lines 1−4). (region E): Injection of excess galactose (100 mg/mL, lines 1−4). All of these experiments were carried out at the flow rate of 5 μL/min.

2.4. Colloidal Au Replacement Assay. Lac25 and lac50 (15 nM and 5.2 nM particle concentrations, respectively) were injected over 1500 RU of an RCA_{120}-immobilized sensor chip at 10 μL/min for 5 and 3 min, respectively, producing a 900−1300 RU increase in the response. Subsequently, 0−100 ppm of galactose was injected for 5 min to elute the preadsorbed gold nanoparticles. In the elution sensorgram, the response level was normalized by the amount of the preadsorbed PEGylated gold nanoparticles (*12*, *13*). The dissociation rate constant (k_d) of the galactose-induced dissociation of lac25 and lac50 was calculated by a separate fitting against the first 15 s of the dissociation curves using a Langmuir model of the *Biaevaluation 3.1* software.

3. RESULTS AND DISCUSSION

3.1. Specificity of the Binding. Injection of lac50 (15 nM particle concentration) onto an RCA_{120}-immobilized CM3 sensor chip induced an obvious increase in the SPR signal (ca. 500 RU), in which lac0 was used as the control and conveyed low response (region A, Figure 2). The subsequent injection of 100 μg/mL galactose allowed a fast dissociation of the adsorbing lac50, whereas the same concentration of glucose did not trigger such a dissociation, and almost the same curve as the sensorgram recorded under the buffer injection was observed (region C, Figure 2), indicating the specific interaction of RCA_{120} with the lactose moieties on the PEGylated gold nanoparticles. The injection of a large excess of galactose (100 mg/mL) to the lac50-adsorbed sensor chip allowed the complete dissociation of the lac50, and eventually led to a regeneration of the sensor chip (region E, Figure 2).

3.2. SPR Response of PEGylated Gold Nanoparticles with Varying Lactose Surface Densities. Figure 3 shows the signal changes induced by the injection of the gold nanoparticles possessing various lactose densities (lac25, lac50) into a flow cell equipped with an RCA_{120}-immobilized sensor chip. Data for lac-BSA and NA3 glycan are also shown as controls. Obviously, the lactose-functionalized gold nanoparticles displayed a much higher response compared to the controls,

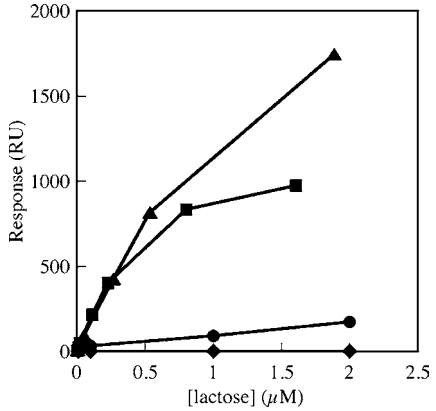


Figure 3. Binding response of various lactosylated substances onto an RCA_{120}-immobilized CM3 sensor chip (square, lac25; triangle, lac50; circle, lac-BSA; diamond, NA3 glycan). The samples were injected for 10 min at the flow rate of 5 μL/min.

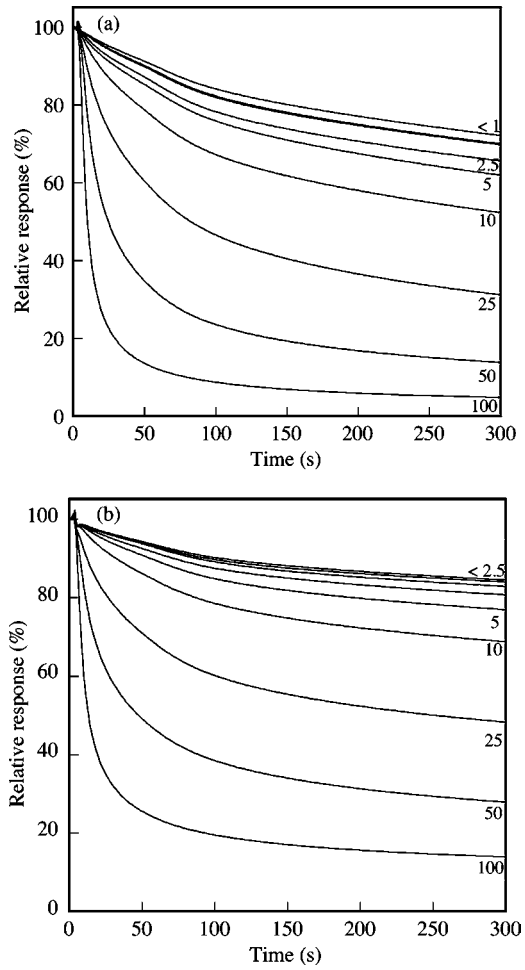


Figure 4. The elution profiles of preadsorbed lac25 (a) and lac50 (b) from an RCA_{120}-immobilized CM3 sensor chip induced by the injection of galactose. Lac25 and lac50 were injected over the sensor chip at the flow rate of 10 μL/min for 5 and 3 min, respectively. The elution of the preadsorbed nanoparticles was done by the injection of 0.1−100 ppm of galactose for 5 min. The magnitude of the net response increase from the baseline at the beginning of the elution phase was taken as 100% for each sensorgram for data normalization. The values indicated in each of the sensorgrams represent the injected galactose concentration (ppm).

indicating that the enhancement of the SPR signal based on the gold nanoparticles effectively worked. This is considered to be due to the large apparent mass and the coupling effect between the gold nanoparticles and gold surface on the sensor chip (*5*, *6*). Interestingly, the lac50 system revealed a more effective signal enhancement than the lac25 system at the same lactose concentration, even where the former has a particle concentration that is half of the latter, suggesting that the former has a higher binding affinity to the immobilized RCA_{120} than the latter.

Table 1. Kinetic Parameters for lac25-RCA_{120} and lac50-RCA_{120} Systems Determined from SPR Analysis

sample	k_a ($M^{-1}\,s^{-1}$)	k_d (s^{-1})	K_D (M)	χ^2
lac25	1.56×10^5	9.88×10^{-4}	6.34×10^{-9}	1.21
lac50	2.41×10^5	4.97×10^{-4}	2.06×10^{-9}	3.88

3.3. Kinetic Evaluations. To quantitatively assess the affinity of lac25 and lac50 to RCA_{120}, a kinetic analysis was carried out. A series of different concentrations of the samples was injected at the flow rate of 20 μL/min for 2 min, followed by the flowing of running buffer for 5 min to observe the dissociation phase of the samples (Figures S2 and S3). As shown in Table 1, the equilibrium dissociation constants (K_D) of the lac25-RCA_{120} and lac50-RCA_{120} systems were calculated to be 6.34×10^{-9} and 2.06×10^{-9} M, respectively, using global fitting of a Langmuir model. On the other hand, the K_D of a single lactose molecule with RCA_{120} was reported to be 3.7×10^{-3} M (*14*). It is notable that the lactosyl gold nanoparticles-RCA_{120} system has a K_D that is 6 orders smaller than the lactose-RCA_{120} system. In our previous report, lactose-installed polymeric micelles behave as a multivalent ligand for an RCA_{120}-immobilized sensor chip with a decrease in the K_D of the same order of magnitude as this system with respect to a monovalent interaction (*15*). Considering this previous report of multivalent interactions and several other references about multivalent glyconanoparticles (*16*, *17*), all of which showed that multivalency causes the nonlinear increase in the affinity, it is reasonable to also assume in this case the multivalent interactions: multiple lactose ligands on a single particle would bind with several lectin molecules on a sensor chip. In fact, in the global fitting of the sensorgrams of lac25 and lac50 using a bivalent model, a sufficiently low χ^2, a measure of the accuracy of the fitting, was obtained (1.26 and 4.03, respectively), making this fit acceptable by Biacore standards ($\chi^2 < 10$).

To gain insight into the multivalent interaction of lactose molecules on the gold nanoparticles with RCA_{120} on the sensor chip, the inter-lactose distance on the gold nanoparticles as well as the distance between two RCA_{120} molecules on the sensor chip were calculated on the basis of the following three assumptions; (i) uniform distribution of lactose molecules on the gold nanoparticles as well as of RCA_{120} molecules on the sensor chip, (ii) reduced apparent valency of an immobilized RCA_{120} molecule on the sensor chip from bivalent to monovalent against lactose molecules on the gold nanoparticles due to a steric restriction, and (iii) all of the lactose ligands accessible to the binding site of RCA_{120}, neglecting the possible decrease in the number of available lactose molecules due to the concealment of the chain end into the flexible PEG coils. As previously reported (*10*), the diameter including the PEG layer of the PEGylated gold nanoparticles was evaluated to be 33.3 nm from SEM, and the number of PEG chains on a single gold nanoparticle was estimated to be 520 chains/particle from a thermogravimetric analysis. Accordingly, the number of lactose molecules and the inter-lactose distance on lac25 and lac50 were calculated and summarized in Table 2 . Alternatively, on the basis of the RCA_{120} density described in the Experimental Section 2.3 (7.52×10^{-3} proteins/nm^2), the area occupied by a single RCA_{120} molecule on the sensor chip was calculated to be $(7.52 \times 10^{-3})^{-1} = 133$ nm^2/protein. Consequently, the average distance between RCA_{120} on the sensor chip surface is approximated to be $133^{0.5} = 11.5$ nm. It may be reasonable to then assume at least a bivalent interaction, because the inter-lactose distance on lac25 and lac50 is calculated to be less than

Table 2. Number of Lactose Molecules and Lactose Density on Gold Nanoparticles

	lac25	lac50
number of lactose molecules on a single particle[a]	130	260
area occupied by a single lactose molecule (nm^2)[b]	26.8	13.4
average distance between lactose moieties (nm)[c]	5.18	3.66

[a] Calculated from the number of PEG chains on a single gold nanoparticle (520 chains/particle) and the lactose functionality. [b] The surface area of PEGylated gold nanoparticles [$4\pi \times (33.3/2)^2 = 3.48 \times 10^3$ nm^2] was divided by the number of lactose molecules on a single gold nanoparticle. [c] Square root of the area occupied by one lactose molecule.

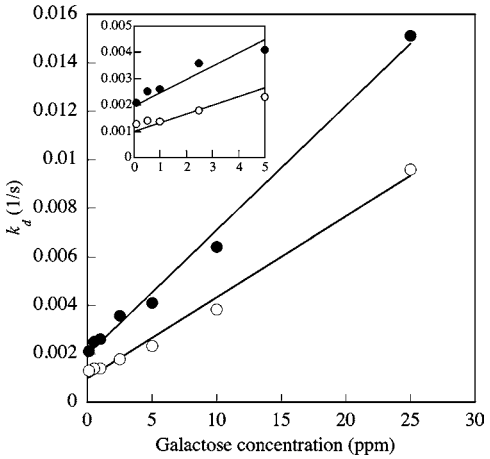


Figure 5. The relationship of the dissociation rate constant (k_d) to the injected galactose concentration. The k_d was obtained by curve fitting of the sensorgrams in Figure 4 as described in the Experimental Section. Closed circles indicate k_d of lac25 ($R^2 = 0.9924$, $\chi^2 = 3.83$), and open circles indicate k_d of lac50 ($R^2 = 0.9895$, $\chi^2 = 1.95$). The insert is the expanded figure in the range 0−5 ppm galactose.

half of the average distance between two RCA_{120} molecules on the sensor chip surface.

3.4. Colloidal Au Replacement Assay. The SPR signal enhancement by the lactosyl-PEGylated gold nanoparticles was then applied to the direct and quantitative detection of the LMW analyte, galactose. The novel method developed here (colloidal Au replacement assay) is based on the elution of the preadsorbed lactosyl-PEGylated gold nanoparticles from the sensor chip surface due to the substitution with galactose in the solution. A practical advantage of this method is that it does not require any labeling of the LMW analytes. The lactosyl-PEGylated gold nanoparticles (ca. 900−1300 RU) were initially adsorbed on the RCA_{120}-immobilized CM3 sensor chip. Free galactose, in varying concentrations (0.1−100 ppm), was then injected into the flow cell. During the elution phase of each sensorgram, the response level was normalized by the amount of the preadsorbed PEGylated gold nanoparticles as shown in Figure 4 (relative response) (*12*, *13*). Obviously, the elution of the gold nanoparticles correlated with the galactose concentration. To quantify the degree of galactose-induced dissociation, the dissociation rate constant (k_d) was calculated by curve fitting against the dissociation sensorgrams. Notably, the k_d has a linear relationship in the 0.1−25 ppm galactose concentration range for both lac25 and lac50 (Figure 5), thus permitting the quantitative analysis of galactose. Moreover, a decrease in the relative response fits nicely to a linear relationship with the galactose concentration for both lac25 (Figure 6A) and lac50 (Figure 6B) measured at several time points. As seen in the inserts of Figure 6A,B, a quantitative analysis is feasible from 0.1 to 50 ppm, indicating the significantly high sensitivity of this method. It is also noted that the linearity was valid for an appreciably wide

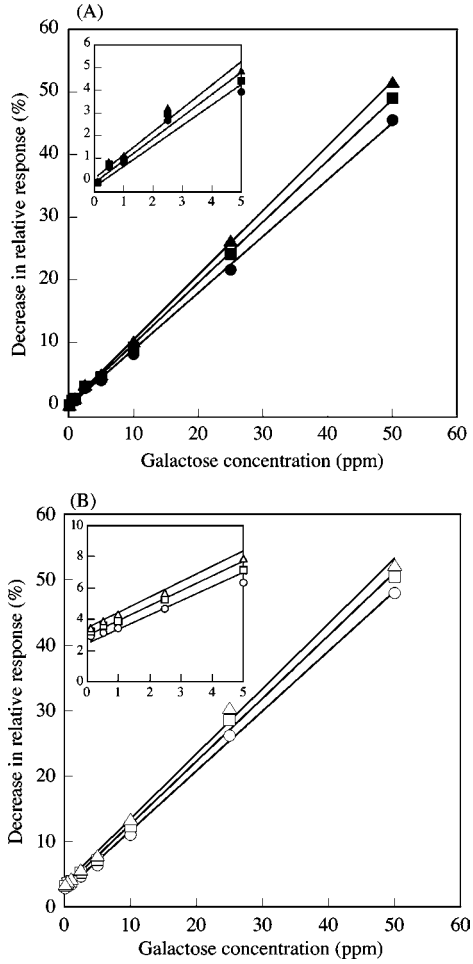


Figure 6. Relationship of the decrease in the relative response vs injected galactose concentration. All the plots in these figures were obtained by the subtraction of the relative response recorded under galactose-induced dissociation from the relative response recorded under only the running buffer. A linear response to the galactose concentration (0.1−50 ppm) was observed in all the plots ($R^2 > 0.997$). The inserts are the expanded figures in the range 0−5 ppm galactose. (A) Closed circles, squares, and triangles are the data corresponding to the time points at 25, 30, and 35 s in the sensorgrams of the lac25 elution (Figure 4a), respectively. (B) Open circles, squares, and triangles are the data points corresponding to the times of 50, 60, and 70 s in the sensorgrams of the lac50 elution (Figure 4b), respectively.

range of response times: 20−30 s for lac25 and 50−70 s for lac50. This linearity in the decrease of the relative response reveals a practical advantage of the colloidal Au replacement assay. Note that the colloidal Au replacement assay achieves a sensitivity comparable to that of ELISA in a much shorter operating time (∼5 min) without any cumbersome processes of multiple washing and separation steps, which are necessary for the ELISA assay.

This method may be applicable for the quantitative sensing of various LMW compounds of practical interest, including sugars (*18*, *19*), by utilizing an appropriate combination of analyte-installed PEGylated gold nanoparticles and immobilized ligands to construct a high-throughput screening system.

4. CONCLUSION

PEGylated gold nanoparticles with different lactose functionalities (0−50%) on the distal end of PEG were prepared in order to construct a novel method for the quantitative assay of LMW analytes by SPR (colloidal Au replacement assay). The lactosyl-PEGylated gold nanoparticles showed a specific adsorption on the sensor chip surface bearing the RCA_{120} lectin,

dependent on the lactose functionality on the surface of the gold nanoparticles due to the multivalent interaction of the nanoparticles with RCA_{120} immobilized on the sensor chip. Interestingly, preadsorbed lactosyl-PEGylated gold nanoparticles on the RCA_{120}-immobilized sensor chip were eluted from the sensor chip by the injection of galactose, in a manner proportional to the galactose concentration. Eventually, this method allowed for the quantitative assay over a wide range of galactose concentrations (0.1−50 ppm) within a short operating time (∼5 min). This concept of colloidal Au replacement assay would be applicable to the highly sensitive SPR quantification of various LMW analytes.

ACKNOWLEDGMENT

The authors acknowledge Dr. Eduardo Jule, the University of Tokyo, for his advice about the SPR experiments. This study was financially supported by Special Coordination Funds for Promoting Science and Technology from the Ministry of Education, Culture, Sports, Science and Technology of Japan (MEXT) as well as by the Core Research for Evolutional Science and Technology (CREST) from the Japan Science and Technology Agency (JST) and also by a Grant for the 21st Century COE Program "Human-Friendly Materials based on Chemistry" from MEXT. S.T. would like to express his special gratitude for the scholarship from the Asahi Glass Scholarship Foundation.

Supporting Information Available: Sensorgrams for the curve fitting of lac25 and lac50. This material is available free of charge via the Internet at http://pubs.acs.org/BC.

LITERATURE CITED

(1) Liedberg, B., Nylander, C., and Lundström, I. (1983) Surface plasmon resonance for gas detection and biosensing. *Biosensors and Actuators 4*, 299−304.

(2) Karlsson, R., Michaelsson, A., and Mattsson, L. (1991) Kinetic analysis of monoclonal antibody-antigen interactions with a new biosensor based analytical system. *J. Immunol. Methods 145*, 229−240.

(3) Homola, J., Yee, S. S., and Gauglitz, G. (1999) Surface plasmon resonance sensors: review. *Sens. and Actuators, B 54*, 3−15.

(4) Tawa, K., and Knoll, W. (2004) Mismatching base-pair dependence of the kinetics of DNA-DNA hybridization studied by surface plasmon fluorescence spectroscopy. *Nucleic Acids Res. 32*, 2372−2377.

(5) Lyon, L. A., Musick, M. D., and Natan, M. J. (1998) Colloidal Au-enhanced surface plasmon immunosensing. *Anal. Chem. 70*, 5177−5183.

(6) He, L., Musick, M. D., Nicewarner, S. R., Salinas, F. G., Benkovic, S. J., Natan, M. J., and Keating, C. D. (2000) Colloidal Au-enhanced surface plasmon resonance for ultrasensitive detection of DNA hybridization. *J. Am. Chem. Soc. 122*, 9071−9077.

(7) Hutter, E., Cha, S., Liu, J-F., Park, J., Yi, J., Fendler, J. H., and Roy, D. (2001) Role of substrate metal in gold nanoparticle enhanced surface plasmon resonance imaging. *J. Phys. Chem. B 105*, 8−12.

(8) Akiyama, Y., Otsuka, H., Nagasaki, Y., Kato, M., and Kataoka, K. (2000) Selective synthesis of heterobifunctional poly(ethylene glycol) derivatives containing both mercapto and acetal terminals. *Bioconjugate Chem. 11*, 947−950.

(9) Otsuka, H., Akiyama, Y., Nagasaki, Y., and Kataoka, K. (2001) Quantitative and reversible lectin-induced association of gold nanoparticles modified with α-lactosyl-ω-mercapto-poly(ethylene glycol). *J. Am. Chem. Soc. 123*, 8226−8230.

(10) Takae, S., Akiyama, Y., Otsuka, H., Nakamura, T., Nagasaki, Y., and Kataoka, K. (2005) Ligand density effect on biorecognition by PEGylated gold nanoparticles: regulated interaction of RCA_{120} lectin with lactose installed to the distal end of tethered PEG strands on gold surface. *Biomacromolecules 6*, 818−824.

(11) Stenberg, E., Persson, B., Roos, H., and Urbaniczky, C. (1991) Quantitative determination of surface concentration of protein with surface plasmon resonance using radiolabeled proteins. *J. Colloid Interface Sci. 143*, 513−526.

(12) Suzuki, F., Goto, M., Sawa, C., Ito, S., Watanabe, H., Sawada, J., and Handa, H. (1998) Functional interaction of transcription factor human GA-binding protein subunits. *J. Biol. Chem. 273*, 29302−29308.

(13) Murai, N., Taguchi, H., and Yoshida, M. (1995) Kinetic analysis of interactions between GroEL and reduced α-lactalbumin. *J. Biol. Chem. 270*, 19957−19963.

(14) Dooley, T. P., and Houston, L. L. (1982) Binding of two molecules of 4-methylumbelliferyl galactose or 4-methylumbelliferyl N-acetylgalactosamine to the B chains of ricin and ricinus communis agglutinin and to purified ricin B chain. *J. Biol. Chem. 257*, 4147−4151.

(15) Jule, E., Nagasaki, Y., and Kataoka, K. (2003) Lactose-installed poly(ethylene glycol)-poly(D,L-lactide) block copolymer micelles exhibit fast-rate binding and high affinity toward a protein bed simulating a cell surface. A surface plasmon resonance study. *Bioconjugate Chem. 14*, 177−186.

(16) Lin, C., Yeh, Y., Yang, C., Chen, G., Chen, Y., Wu, Y., and Chen, C. (2003) Quantitative analysis of multivalent interactions of carbohydrate-encapsulated gold nanoparticles with concanavalin A. *Chem. Commun.* 2920−2921.

(17) Hernaiz, M. J., de la Fuente, J. M., Barrientos, A. G., and Penades, S. (2002) A model system mimicking glycophingolipid clusters to quantify carbohydrate self-interaction by surface plasmon resonance. *Angew. Chem., Int. Ed. 41*, 1554−1557.

(18) Park, S., Boo, H., and Chung, T. D. (2006) Electrochemical non-enzymatic glucose sensors. *Anal. Chim. Acta 556*, 46−57.

(19) Perez-Olmos, R., Soto, J. C., Zarate, N., Araujo, A. N., Lima, J. L. F. C., and Saraiva, M. L. M. F. S. (2005) Application of sequential injection analysis (SIA) to food analysis. *Food Chem. 90*, 471−490.

BC0603541

Selective Fluorescence Probes for Dipeptidyl Peptidase Activity—Fibroblast Activation Protein and Dipeptidyl Peptidase IV

Koon Siew Lai,[†,§] Nan-Hui Ho,[†,§] Jonathan D. Cheng,[‡] and Ching-Hsuan Tung*[,†]

Center of Molecular Imaging Research, Massachusetts General Hospital, Harvard Medical School, Charlestown, Massachusetts 02129, and Department of Medical Oncology, Fox Chase Cancer Center, Philadelphia, Pennsylvania 19111. Received November 16, 2006; Revised Manuscript Received March 15, 2007

Development of suitable tools to assess enzyme activity directly from their complex cellular environment has a dramatic impact on understanding the functional roles of proteins as well as on the discovery of new drugs. In this study, a novel fluorescence-based chemosensor strategy for the direct readout of dipeptidase activities within intact living cells is described. Selective activity-based probes were designed to sense two important type II transmembrane serine proteases, fibroblast activation protein (FAP) and dipeptidyl peptidase IV (DPP-IV). These serine proteases have been implicated in diverse cellular activities, including blood coagulation, digestion, immune responses, wound healing, tumor growth, tumor invasion, and metastasis. Here, we validated that Ac-GPGP-2SBPO and GPGP-2SBPO probes are excellent reporters of both proteolytic activities. Furthermore, the novel probes can differentiate between FAP and DPP-IV proteolytic activities in cellular assay. Potentially, this assay platform is immediately useful for novel drug discovery.

INTRODUCTION

Fibroblast activation protein (FAP; EC: 3.4.21.B28) and dipeptidyl peptidase IV (DPP-IV; EC: 3.4.14.5) belong to a type II transmembrane serine protease family, and are capable of cleaving N-terminal dipeptides after a proline residue (*1*, *2*). Structurally, both proteases have a short cytoplasmic tail, a transmembrane domain, and a large C-terminal extracellular domain (ECD). The ECD domain consists of two characteristic subdomains, a β-propeller subdomain with several sites of N-linked glycosylation at the N-terminus and an α/β-hydrolase subdomain with the catalytic triad of serine, aspartate, and histidine residues at the C-terminus. The human FAP gene maps on chromosome 2 at 2q23, and the DPP-IV gene maps on the same chromosome at 2q24.3. Although FAP and DPP-IV share a high sequence identity and may have arisen by gene duplication, it was reported that each has a distinct enzyme activity profile. Apart from having prolyl exopeptidase activity like its DPP-IV homologue, FAP also functions as a prolyl endopeptidase (*3*, *4*) and has a collagenolytic activity capable of degrading gelatin and type I collagen (*5*, *6*).

In terms of expression, FAP is selectively expressed on reactive stromal fibroblasts in over 90% of common human epithelial cancers, such as colorectal, breast, and lung cancers (*7*). Expression of FAP is not detected in fibroblasts of benign epithelial tumors or normal adult tissues. High expression of FAP in tumors correlates with increased FAP activity relative to normal tissues (*4*, *8*, *9*). It has been suggested that FAP promotes tumor growth and proliferation (*10*). Currently, FAP inhibitor PT-100 (Val-boroPro) (*11*) is being tested in clinical trials to evaluate its efficacy to treat non-small-cell lung and other cancers (*12*). In contrast to FAP, DPP-IV is ubiquitously expressed in normal epithelial cells and melanocytes. It was originally identified as a protein expressed on the surface of T cells, and its expression is lost in various cancers (*13*−*15*). These suggest the involvement of DPP-IV in immunology, oncology, and other areas. DPP-IV has been recently validated as a therapeutic target for type 2 diabetics with the approval of the DPP-IV inhibitor sitagliptin phosphate (*16*). The proteolytic functions of these two proteins and their distinct expression distribution make them promising and attractive targets for new indications (*8*, *17*−*21*).

Protease-targeted fluorogenic substrates using 7-amino-4-methylcoumarin (AMC) or 7-amino-4-trifluoromethylcoumarin (AFC) as a reporter have commonly been used for detecting protease activity in vitro (*4*−*6*). The fluorescence property of the coumarin reporters is masked by the peptide amide linkage. Upon proteolytic conversion of the probes, the reporters are released as fluorescent free dyes. This type of probes has been widely used in cell-free assays; however, it cannot be directly applied to complex cellular environments. Limitations of these probes are attributed to two major factors. First, high autofluorescence background can be caused by the illumination of cells. Second, the poor aqueous solubility of the fluorophores often required DMSO as a cosolvent, which could lead to reduced enzymatic activity (*22*).

To develop methods that allow more direct and reliable assessment of enzyme activity in vivo, a water-soluble and far-red fluorescence-based probe having emission maxima between 650 and 900 nm is preferred. We recently validated the use of a new water-soluble far-red fluorogenic dye containing a disulfonated benzo[*a*]phenoxazine (2SBPO) scaffold for enzyme sensing (*23*). 2SBPO conjugated to a GPGP tetrapeptide is weakly fluorescent but displays strong fluorescence emission at 670 nm upon cleavage by DPP-IV. Here, we further demonstrate that the distinct proteolytic activities between FAP and DPP-IV could be assessed using preselected probes. The sensitivity and selectivity of these fluorescence-based chemosensors are sufficient to measure the prolyl-endopeptidase activities of FAP and the prolyl-exopeptidase activity of DPP-IV in living cells.

* Corresponding author: Ching H. Tung, PhD, Center for Molecular Imaging Research, Massachusetts General Hospital, 149 13th Street, Room 5406, Charlestown, MA 02129. Tel: 617-726-5779, Fax: 617-726-5708, E-mail: tung@helix.mgh.harvard.edu.

[†] Harvard Medical School.

[‡] Fox Chase Cancer Center.

[§] These authors contributed equally to this work.

10.1021/bc0603586 CCC: $37.00 © 2007 American Chemical Society
Published on Web 05/10/2007

MATERIALS AND METHODS

Synthesis of the Fluorescence-Based Chemosensors. The parent dye, 9-di-3-sulfonylpropylaminobenzo[*a*]phenoxazonium perchlorate (2SBPO), was synthesized as previously described (*24*). Amino acids were purchased from Novabiochem (San Diego, CA). All peptide substrates were prepared by solution-phase synthesis using N-Boc-protected amino acids and Ac-glycine for the acetyl-protected peptides using the same procedure as described for GPGP-2SBPO (*23*). The peptide substrates were purified on a C-18 Sep-Pak cartridge. Electrospray mass spectra were obtained on a Platform LCT mass spectrometer (Micromass, Beverly, MA), and MALDI mass spectra were measured on a Voyager linear mass spectrometer (Applied Biosystems; Framingham, MA). GPGP-2SBPO: HRMS (ES+/TOF) calcd for $C_{36}H_{44}N_7O_{11}S_2$ $(M)^+$ 814.2540, found 814.2538. Ac-GPGP-2SBPO: HRMS (ES+/TOF) calcd for $C_{38}H_{46}N_7O_{12}S_2$ $(M)^+$ 856.2640, found 856.2530. APAP-2SBPO: HRMS (ES+/TOF) calcd for $C_{38}H_{48}N_7O_{11}S_2$ $(M)^+$ 842.2848, found 842.2856. Ac-GP-2SBPO: MS (MALDI-TOF) calcd for $C_{31}H_{36}N_5O_{10}S_2$ $(M)^+$ 702.2, found 701.9. TSGP-2SBPO: MS (MALDI-TOF) calcd for $C_{36}H_{45}N_6O_{14}S_2$ $(M)^+$ 702.2, found 701.9.

Cell Lines. HT-29, human colon cancer cell line was obtained from American Type Culture Collection (Rockville, MD). To detect the FAP activity in culture assay, human embryonic kidney cell line, HEK293, stably transfected with full-length wild-type murine FAP (HEK-FAP) was used, and HEK293 cells stably transfected with empty vector alone (HEK-vector) were used as a control cell line (*9*). For recombinant murine FAP preparation, HEK293 stably transfected with murine FAP-ECD cDNA was used (HEK-FAP-ECD) (*9*, *10*). All cell lines were maintained in DMEM medium with 10% FBS.

In Vitro and Cell-Based Enzymatic Assay. Recombinant murine DPP-IV was purchased from R&D Systems (Minneapolis, MN), while murine FAP was purified from HEK-FAP-ECD cells as previously described (*9*, *10*). Purification of the FAP protein was confirmed by SDS-PAGE electrophoresis and staining with Gelcode blue stain reagent (Pierce, Rockford, IL). Concentration of the FAP protein was determined by using a BCA protein assay kit (Pierce, Rockford, IL).

All of the enzymatic assays were performed in triplicate on 96-well assay plates (Corning Inc., NY). Various substrates at 50 μM were tested in vitro with 10 nM of the respective recombinant murine DPP-IV and FAP enzymes under physiological conditions. A total of 200 μL of 10 mM PBS (pH 7.4) with substrate and enzyme, or with substrate alone as control, was incubated in the 96-well plate at 37 °C for 2 h. Fluorescence emission at 670 nm and excitation at 630 nm were measured by a fully modular monochromator-based plate reader (Safire2, Tecan, San Jose, CA). For cell-based enzymatic assays, the cells were first seeded at 50,000 cells/well in the 96-well assay plate. A day later, the serum-containing medium was removed and changed to 10 mM PBS (pH 7.4) with 20 μM of the substrate. Cells were then incubated with substrates at 37 °C for 3 to 5 h prior to fluorescence measurement.

Western Blot Analyses. HEK-vector, HEK-FAP, and HT-29 cells were lysed with M-PER mammalian protein extraction reagent (Pierce, Rockford, IL). Cell debris was removed by centrifugation, and clear cell lysates were transferred to new microfuge tubes. The protein concentrations were determined by using Bradford reagent (Sigma-Aldrich, St, Louis, MO). The cell lysates (50 μg) were loaded onto 10% SDS-PAGE gels and transferred to Immun-blot PVDF membranes (Bio-Rad, Hercules, CA). Anti-murine FAP monoclonal antibody (6E1) (*9*) was custom-made and used at a 1:100 dilution with 5% nonfat milk in PBS + 0.1% Tween. Anti-human DPP-IV polyclonal antibody was purchased from EM Biosciences (San Diego, CA) and used at a 1:1000 dilution. As a control for protein loading, actin antibody (C-11) from Santa Cruz Biotechnology, Inc. (Santa Cruz, CA), was used at a 1:1000 dilution. All immunoblots were analyzed by using the ECL detection system (Amersham Biosciences, U.K.).

Cell Proliferation Assay. MTS tetrazolium compound from Promega (Madison, WI) was used as a colorimetric indicator for determining the number of viable cells in proliferation or cytotoxicity assays. Assays were performed by adding 20 μL of MTS compound to each well containing the cells in 100 μL of assay medium. Absorbance at 490 nm was recorded after 1 h incubation at 37 °C in a humidified chamber with 5% CO_2.

RESULTS AND DISCUSSION

Fluorogenic Substrate Design. Recent study in substrate development has indicated that glycylprolyl dipeptide is an excellent substrate for DPP-IV; unfortunately, it can also be recognized by FAP (*3*). The result from a systematic screening of the proline-containing dipeptide library has suggested a broad substrate exopeptidase selectivity of these two proteases, especially DPP-IV (*5*). The best, maybe the only, approach to distinguish these two proteases is by measuring the exopeptidase and endopeptidase activity of DPP-IV and FAP, respectively (*6*).

A water-soluble DPP-IV sensitive probe, GPGP-2SBPO, was previously synthesized to measure dipeptidyl peptidase activity (*23*). The rationale of having a tetrapeptide to report the dipeptidase activity was the instability of the dipeptide and fluorogenic dye conjugate. GP-2SBPO underwent spontaneous nonenzymatic hydrolysis via intramolecular cyclization to give cyclo[Gly-Pro] and free 2SBPO in physiological conditions. To overcome the problem of this unexpected nonenzymatic hydrolysis, a second glycylprolyl dipeptide was added to the N-terminus of GP-2SBPO to generate the tetrapeptide substrate, GPGP-2SBPO, which was subsequently proven to be useful for DPP-IV sensing. On the basis of this finding, several tetrapeptide substrates were synthesized to detect exo and endo dipeptidyl protease activity (Figure 1).

Substrate Selectivity and in Vitro Enzymatic Activity. To evaluate the selectivity of these fluorogenic probes, recombinant murine FAP and DPP-IV enzymes were assayed for proteolytic activity in vitro. GPGP-2SBPO and APAP-2SBPO were used to compare the specific exopeptidase activity of FAP with DPP-IV. Fluorescence signals released from the substrates upon activation by their respective enzyme were monitored simultaneously in a 96-well assay plate. The fluorescence of the control referred to the background signal where no enzyme was added. Although both proteases exhibit exopeptidase activity, as shown in Figure 2A, FAP preferred the APAP-2SBPO substrate but showed no activity with the GPGP-2SBPO substrate. In contrast, DPP-IV readily cleaved both substrates (Figure 2B), and a greater than 6-fold increase in fluorescence signal was observed with GPGP-2SBPO. These results are consistent with the published data indicating that DPP-IV has broader substrate specificity for prolyl exopeptidase activity (*5*).

It has been reported that FAP, but not DPP-IV, possesses endopeptidase activity (*3*, *5*, *6*). To confirm the endopeptidase specificity of the protease, we assayed FAP and DPP-IV against TSGP-2SPO, Ac-GP-2SBPO, and Ac-GPGP-2SBPO (Figure 2). As expected, DPP-IV showed no activity against any of these substrates (Figure 2B). However, FAP showed a greater catalytic efficiency for Ac-GPGP-2SBPO than for Ac-GP-2SBPO and TSGP-2SBPO under the same assay reaction conditions.

Ac-GPGP-2SBPO was the most efficient substrate for FAP activation. Its cleavage yielded a 7-fold increase in fluorescence signal (Figure 2). Similar to our previous finding (*23*), following the specific FAP endopeptidase cleavage between the Pro and

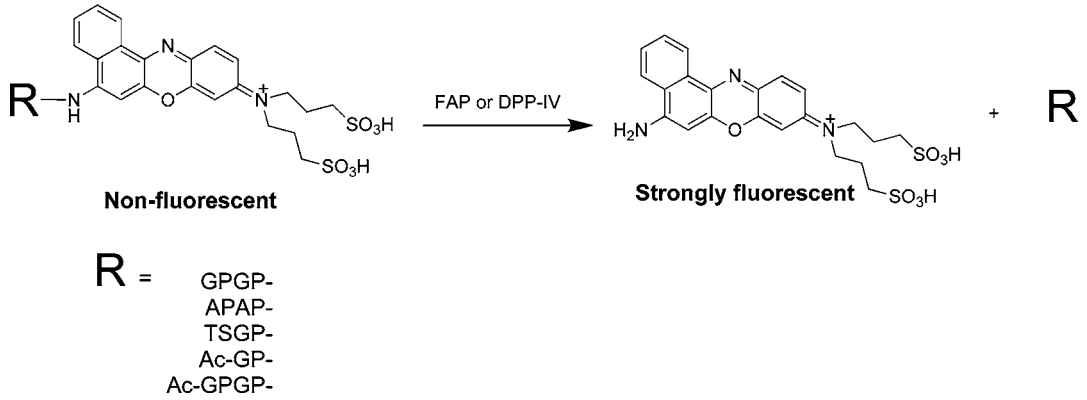


Figure 1. Structure and sequences of the synthesized fluorogenic probes.

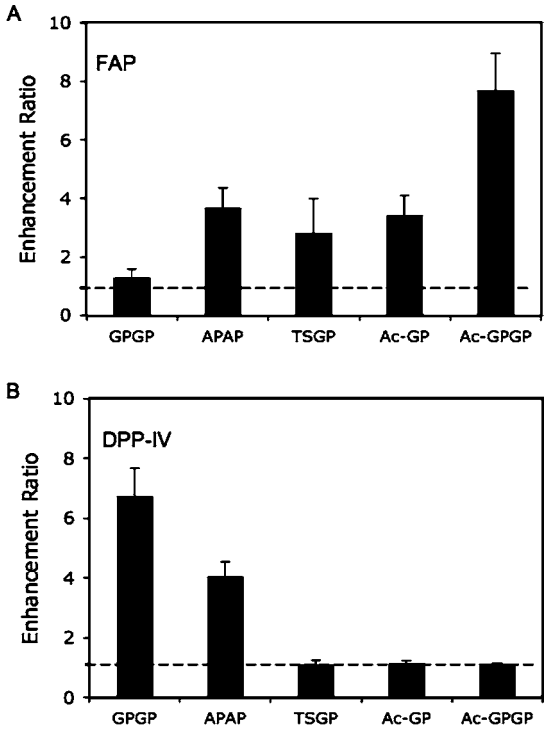


Figure 2. Substrate selectivity of FAP (A) and DPP-IV (B). The substrates (50 μM) were incubated with either protease (10 nM) in 10 mM PBS (pH 7.4) for 2 h. The measurement was collected with 630 nm excitation and 670 nm emission. The dotted lines indicate the background signal.

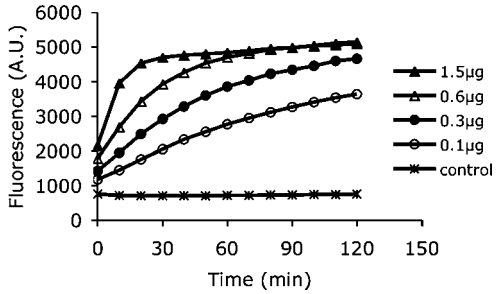


Figure 3. Dose response of fluorescence signal. The fluorescence signal was measured at various times with five different concentrations of FAP and a single Ac-GPGP-2SBPO substrate concentration at 10 uM in PBS. The increase in fluorescence emission was found to be enzyme concentration dependent. The fluorescence of the control referred to the background signal where no enzyme was added.

Gly residues, a spontaneous nonenzymatic hydrolysis of the resulting GP-2SBPO happened to free 2SBPO and emit fluorescence. In contrast, the smaller increases in fluorescence signal for Ac-GP-2SBPO and TSGP-2SBPO may be attributable to sequence preference.

To demonstrate the dose response of FAP enzymatic activity, 10 μM Ac-GPGP-2SBPO substrate was mixed with four different concentrations of FAP enzyme, and fluorescence signals were measured over a period of 2 h. The reaction progress curves, shown in Figure 3, approach a similar maximum plateau fluorescence value. This is an indication that FAP enzyme remains stable under the conditions tested. A nearly linear dose response ($R^2 = 0.98$) was observed in the first 10 min. These curves were also used to define the amount of FAP enzyme that was needed to maintain initial velocity conditions.

Cell-Based Enzymatic Studies. Having identified Ac-GPGP-2SBPO and GPGP-2SBPO probes as excellent reporter substrates of FAP and DPP-IV, respectively, we were interested to know whether these probes permit a direct and simple readout of the enzyme activity in intact mammalian cells. Three cell lines, i.e., (i) human colon cancer cells HT-29, (ii) human embryonic kidney HEK293 cells stably transfected with full length wild-type murine FAP (HEK-FAP), and (iii) HEK293 cells stably transfected with empty vector (HEK-vector), were used to monitor the selectivity of these two fluorogenic probes.

According to Western blot analyses, the HT-29 cell line expresses DPP-IV but not FAP (Figure 4A). On the other hand, HEK-FAP transfected cells show exogenous expression of FAP. For the HEK-vector control cell line, FAP expression is undetectable. It is also noteworthy that neither of these HEK cell lines express DPP-IV, as seen in the blot. Although FAP is not expressed in the HEK-vector control cell line, interestingly we observed an increase in fluorescence signal when Ac-GPGP-2SBPO substrates were directly incubated with HEK-vector cells in the growth medium which contains 10% fetal bovine serum (data not shown). Recent studies have reported the identification of soluble forms of FAP from human blood and bovine serum (*25*, *26*). In order to eliminate the interference and be able to monitor the transmembrane proteases in intact cells directly, a phosphate-buffered solution (10 mM) at pH 7.4 was used for subsequent cellular assays.

As shown in Figure 4B,C, the Ac-GPGP-2SBPO probe showed a 4-fold increase in fluorescence after direct incubation with HEK-FAP cells for 5 h at 37 °C. This result demonstrated that Ac-GPGP-2SBPO possesses significant selectivity for FAP in HEK-FAP cells as compared with HEK-vector control cells and HT-29 cells. In the case of GPGP-2SBPO, the substrate was selectively cleaved by the endogenous DPP-IV in HT-29 living cells and showed an approximately 3-fold increase in fluorescence in 5 h. The smaller increase in fluorescence may suggest that the level of activity corresponds to its lower expression level of DPP-IV within the cells, as supported by Western blot expression data.

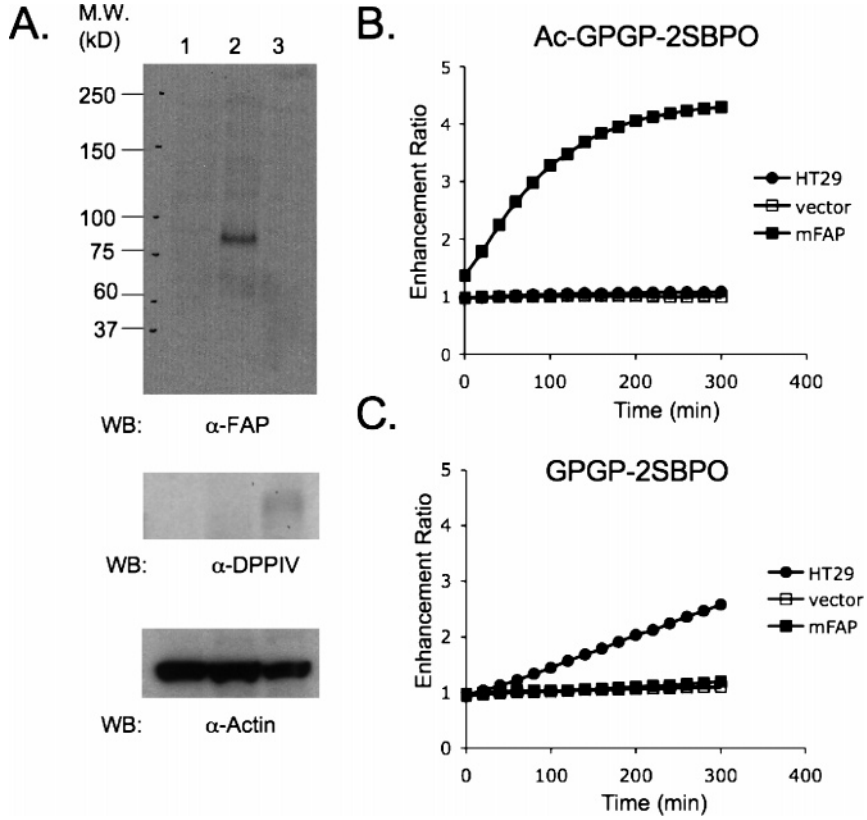


Figure 4. Western blot analysis and detection of dipeptidase activity by cell-based assays. (A) Western blots of cell lysates collected from HEK-vector (column 1), HEK-FAP (column 2), and HT-29 (column 3). (B) Activation of Ac-GPGP-2SBPO in 5 h. Only HEK-FAP was able to activate the probe. (C) Activation of GPGP-2SBPO in 5 h. Only HT-29 was able to activate the probe.

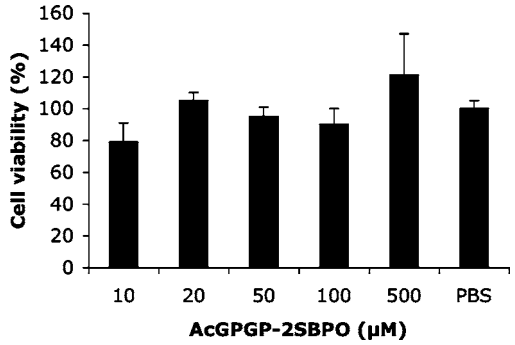


Figure 5. Effects of Ac-GPGP-2SBPO on cell toxicity. HEK-FAP cells were incubated with different concentrations of Ac-GPGP-2SBPO at 37 °C for 1 h. Experiments were performed in triplicate, mean ± SE.

Cell proliferation MTS assay was further performed to ensure that the probes are nontoxic to cells. HEK-FAP cells were treated with various concentrations of Ac-GPGP-2SBPO for 5 h. Then, MTS assay medium was added into each well and incubated for another 1 h. The absorbance readings at 490 nm showed no significant difference, suggesting that 2SBPO fluorogenic dye is nontoxic under the experimental condition (Figure 5).

CONCLUSIONS

In summary, a novel near-infrared optical probe has been developed to detect specific FAP endopeptidase activity by either in vitro or in cellular assays. Ac-GPGP-2SBPO is a water-soluble acetylated tetrapeptide fluorescent substrate with the excitation wavelength at 630 nm and emission wavelength at 670 nm. It contains the Gly-Pro dipeptide motif for the FAP-selective endopeptidase cleavage site. We also validated that Ac-GPGP-2SBPO and GPGP-2SBPO probes are excellent reporters for studying FAP and DPP-IV prolyl aminopeptidase activities in cell culture and can be readily adapted for a high-throughput drug screening format.

ACKNOWLEDGMENT

This research was supported in part by grants from NIH (CA86355, CA099385, and CA114149 to C.T.; CA090468, CA103991, and CA006927 to J.C.), and an appropriation from the Commonwealth of Pennsylvania (J.C.).

LITERATURE CITED

(1) Scanlan, M. J., Raj, B. K., Calvo, B., Garin-Chesa, P., Sanz-Moncasi, M. P., Healey, J. H., Old, L. J., and Rettig, W. J. (1994) Molecular cloning of fibroblast activation protein alpha, a member of the serine protease family selectively expressed in stromal fibroblasts of epithelial cancers. *Proc. Natl. Acad. Sci. U.S.A. 91*, 5657−5661.

(2) Cheng, J. D., and Weiner, L. M. (2003) Tumors and their microenvironments: tilling the soil. *Clin. Cancer Res. 9*, 1590−1595.

(3) Aertgeerts, K., Levin, I., Shi, L., Snell, G. P., Jennings, A., Prasad, G. S., Zhang, Y., Kraus, M. L., Salakian, S., Sridhar, V., Wijnands, R., and Tennant, M. G. (2005) Structural and kinetic analysis of the substrate specificity of human fibroblast activation protein alpha. *J. Biol. Chem. 280*, 19441−19444.

(4) Park, J. E., Lenter, M. C., Zimmermann, R. N., Garin-Chesa, P., Old, L. J., and Rettig, W. J. (1999) Fibroblast activation protein, a dual specificity serine protease expressed in reactive human tumor stromal fibroblasts. *J. Biol. Chem. 274*, 36505−36512.

(5) Edosada, C. Y., Quan, C., Wiesmann, C., Tran, T., Sutherlin, D., Reynolds, M., Elliott, J. M., Raab, H., Fairbrother, W., and Wolf, B. B. (2006) Selective inhibition of fibroblast activation protein protease based on dipeptide substrate specificity. *J. Biol. Chem. 281*, 7437−7444.

(6) Edosada, C. Y., Quan, C., Tran, T., Pham, V., Wiesmann, C., Fairbrother, W., and Wolf, B. B. (2006) Peptide substrate profiling defines fibroblast activation protein as an endopeptidase of strict Gly(2)-Pro(1)-cleaving specificity. *FEBS Lett. 580*, 1581−1586.

(7) Garin-Chesa, P., Old, L. J., and Rettig, W. J. (1990) Cell surface glycoprotein of reactive stromal fibroblasts as a potential antibody target in human epithelial cancers. *Proc. Natl. Acad. Sci. U.S.A. 87*, 7235−7239.

(8) Dolznig, H., Schweifer, N., Puri, C., Kraut, N., Rettig, W. J., Kerjaschki, D., and Garin-Chesa, P. (2005) Characterization of cancer stroma markers: in silico analysis of an mRNA expression database for fibroblast activation protein and endosialin. *Cancer Immun. 5*, 10.

(9) Cheng, J. D., Valianou, M., Canutescu, A. A., Jaffe, E. K., Lee, H. O., Wang, H., Lai, J. H., Bachovchin, W. W., and Weiner, L. M. (2005) Abrogation of fibroblast activation protein enzymatic activity attenuates tumor growth. *Mol. Cancer Ther. 4*, 351−360.

(10) Cheng, J. D., Dunbrack, R. L., Jr., Valianou, M., Rogatko, A., Alpaugh, R. K., and Weiner, L. M. (2002) Promotion of tumor growth by murine fibroblast activation protein, a serine protease, in an animal model. *Cancer Res. 62*, 4767−4772.

(11) Coutts, S. J., Kelly, T. A., Snow, R. J., Kennedy, C. A., Barton, R. W., Adams, J., Krolikowski, D. A., Freeman, D. M., Campbell, S. J., Ksiazek, J. F., and Bachovchin, W. W. (1996) Structure-activity relationships of boronic acid inhibitors of dipeptidyl peptidase IV. 1. Variation of the P2 position of Xaa-boroPro dipeptides. *J. Med. Chem. 39*, 2087−2094.

(12) Nemunaitis, J., Vukelja, S. J., Richards, D., Cunningham, C., Senzer, N., Nugent, J., Duncan, H., Jones, B., Haltom, E., and Uprichard, M. J. (2006) Phase I trial of PT-100, a cytokine-inducing small molecule, following chemotherapy for solid tumor malignancy. *Cancer Invest. 24*, 553−561.

(13) Wesley, U. V., Tiwari, S., and Houghton, A. N. (2004) Role for dipeptidyl peptidase IV in tumor suppression of human non small cell lung carcinoma cells. *Int. J. Cancer 109*, 855−866.

(14) Kelly, T. (2005) Fibroblast activation protein-alpha and dipeptidyl peptidase IV (CD26): cell-surface proteases that activate cell signaling and are potential targets for cancer therapy. *Drug Resist. Updates 8*, 51−58.

(15) Gorrell, M. D. (2005) Dipeptidyl peptidase IV and related enzymes in cell biology and liver disorders. *Clin. Sci. 108*, 277−292.

(16) Miller, S., and St. Onge, E. L. (2006) Sitagliptin: a dipeptidyl peptidase IV inhibitor for the treatment of type 2 diabetes. *Ann. Pharmacother. 40*, 1336−1343.

(17) Rosenblum, J. S., and Kozarich, J. W. (2003) Prolyl peptidases: a serine protease subfamily with high potential for drug discovery. *Curr. Opin. Chem. Biol. 7*, 496−504.

(18) Adams, S., Miller, G. T., Jesson, M. I., Watanabe, T., Jones, B., and Wallner, B. P. (2004) PT-100, a small molecule dipeptidyl peptidase inhibitor, has potent antitumor effects and augments antibody-mediated cytotoxicity via a novel immune mechanism. *Cancer Res. 64*, 5471−5480.

(19) Hu, Y., Ma, L., Wu, M., Wong, M. S., Li, B., Corral, S., Yu, Z., Nomanbhoy, T., Alemayehu, S., Fuller, S. R., Rosenblum, J. S., Rozenkrants, N., Minimo, L. C., Ripka, W. C., Szardenings, A. K., Kozarich, J. W., and Shreder, K. R. (2005) Synthesis and structure-activity relationship of N-alkyl Gly-boro-Pro inhibitors of DPP4, FAP, and DPP7. *Bioorg. Med. Chem. Lett. 15*, 4239−4242.

(20) Lee, J., Fassnacht, M., Nair, S., Boczkowski, D., and Gilboa, E. (2005) Tumor immunotherapy targeting fibroblast activation protein, a product expressed in tumor-associated fibroblasts. *Cancer Res. 65*, 11156−11163.

(21) Shreder, K. R., Wong, M. S., Corral, S., Yu, Z., Winn, D. T., Wu, M., Hu, Y., Nomanbhoy, T., Alemayehu, S., Fuller, S. R., Rosenblum, J. S., and Kozarich, J. W. (2005) Boro-norleucine as a P1 residue for the design of selective and potent DPP7 inhibitors. *Bioorg. Med. Chem. Lett. 15*, 4256−4260.

(22) Grant, S. K., Sklar, J. G., and Cummings, R. T. (2002) Development of novel assays for proteolytic enzymes using rhodamine-based fluorogenic substrates. *J. Biomol. Screen 7*, 531−540.

(23) Ho, N. H., Weissleder, R., and Tung, C. H. (2006) Development of a dual fluorogenic and chromogenic dipeptidyl peptidase IV substrate. *Bioorg. Med. Chem. Lett. 16*, 2599−2602.

(24) Ho, N. H., Weissleder, R., and Tung, C. H. (2006) Development of water-soluble far-red fluorogenic dyes for enzyme sensing. *Tetrahedron 62*, 578−585.

(25) Collins, P. J., McMahon, G., O'Brien, P., and O'Connor, B. (2004) Purification, identification and characterisation of seprase from bovine serum. *Int. J. Biochem. Cell Biol. 36*, 2320−2333.

(26) Lee, K. N., Jackson, K. W., Christiansen, V. J., Lee, C. S., Chun, J. G., and McKee, P. A. (2006) Antiplasmin-cleaving enzyme is a soluble form of fibroblast activation protein. *Blood 107*, 1397−1404.

BC0603586

From Phage Display to Magnetophage, a New Tool for Magnetic Resonance Molecular Imaging

Jérôme Segers,[§] Catherine Laumonier, Carmen Burtea, Sophie Laurent, Luce Vander Elst, and Robert N. Muller*

Department of General, Organic and Biomedical Chemistry, NMR and Molecular Imaging Laboratory, University of Mons-Hainaut, 24 Avenue du Champ de Mars, Mons B-7000, Belgium. Received December 7, 2006; Revised Manuscript Received March 23, 2007

Phage display, an extremely promising technology in the context of molecular imaging, allows for the selection of peptides interacting with virtually any target from a heterogeneous mixture of bacteriophages. In this work, we propose the concept of magnetophages, obtained by covalent coupling of ultrasmall particles of iron oxide (USPIO) to the proteins of the phage wall. To validate magnetophages as a magnetic resonance imaging contrast agent (MRI), we have used as a prototype the clone E3 because of its specific affinity for phosphatidylserine, a marker of apoptosis. Enzyme-linked immunosorbent assay showed that E3 magnetophages incubated with phosphatidylserine retained the properties of the nonmagnetically labeled phages. The usefulness of magnetophages as an MRI contrast agent was estimated by incubation with phosphatidylcholine and phosphatidylserine or with apoptotic and control cells. Under these conditions, E3 magnetophages allow the discrimination of phosphatidylserine from phosphatidylcholine and of apoptotic cells from control ones. Injected *in vivo*, magnetophages are rapidly cleared from the blood stream and internalized by the phagocytic cells of the liver. To abrogate this problem, USPIO were pegylated to obtain stealthy E3-PEG-magnetophages, invisible to phagocytic cells, which were successfully targeted to apoptotic liver. If this feature demonstrated for E3 magnetophages can be extrapolated to other phage display selected entities, magnetophages become an original system which allows validation of the candidate binding peptides before their synthesis is considered. The concept of the magnetophage could be extended to other imaging modalities by replacing USPIO with an adequate reporter (i.e., radiolabeled phages).

INTRODUCTION

Molecular imaging, a concept that has recently emerged, aims at visualizing molecules expressed in pathological conditions. It has therefore the potential of playing an important role in the early detection of pathologies and understanding their molecular mechanisms (*1*). Molecular imaging relies on the use of vectorized reporters acting as contrast agents. In magnetic resonance imaging (MRI), contrast agents are made of a magnetic center responsible for the modulation of the recorded signal, which is coupled to a targeting structure.

Phage-display technology is a powerful strategy for the selection and identification of peptidic sequences interacting with a target of interest (receptor, protein, etc.). It is based on the use of a phage library which is a heterogeneous mixture of phage clones, each carrying a different foreign DNA insert and therefore displaying a different peptide on its surface (*2*−*8*). The identification of binders specific to a target requires several rounds of selection and amplification during which the phage population is gradually enriched in high affinity binders, to finally obtain a population of phages specific for the target. Subsequent coupling of the selected peptide to a magnetic, optical, or radioactive reporter gives specific probes for molecular imaging.

We have previously applied this methodology to the design of a MRI contrast agent specific for apoptosis (*9*). In this study, we propose an alternative strategy: the direct use of the selected phages themselves as vectors of the contrast agent. The conjugation of ultrasmall particles of iron oxide (USPIO) to the phages generates a system that we have called "magnetophages". USPIO are indeed efficient magnetic reporters for MRI (*10, 11*), made of nanocrystals containing 2000 to 3000 Fe^{3+} atoms coated with dextran.

The aim of this work was to design, characterize, and evaluate the potential application of magnetophages as markers for magnetic resonance molecular imaging (MRMI). To evaluate this concept, phages displaying the peptide TLVSSL (corresponding to phage clone E3) identified in our previous work as a specific binder for phosphatidylserine (PS) (*9*), a biomarker of apoptosis (*12, 13*), were turned into magnetic labeled phages (magnetophages E3). Phages E3 and magnetophages E3 were used as prototypes.

EXPERIMENTAL PROCEDURES

The *in vivo* protocols of the experiments fulfill the prescriptions of the ethics committee of our institution.

Phage Display Library, Phage, and Bacterial Strains. A random linear hexapeptide library (fUSE5 vector) was used. The inserts are spliced into the gene corresponding to the minor coat protein pIII (*3*). In addition, the phages of this library contain a gene that confers resistance to tetracycline (Tc) to the infected bacteria. This library was kindly provided by Dr. Hans Ullrichts (KULAK, Kortrijk, Belgium). Nonselected phages, from the initial library, and a clone (E3), specific for phosphatidylserine (PS), were used to produce the corresponding magnetophages. The clone E3 was selected using the phage-display selection procedure carried out in a previous work (*9*). Bacteria used in this work belong to the enterobacterium *Escherichia coli* strain K91BluKAN provided by Dr. H. Ullrichts (KULAK, Kortrijk, Belgium). These bacteria contain the kanamycine (Kan) resistance gene.

Phage Amplification and Precipitation. Phages were amplified by infecting *E. coli* host strain K91BluKan. A culture flask

* Author to whom correspondence should be addressed. E-mail: Robert.Muller@umh.ac.be. Phone: +3265373520, Fax: +3265373520.

[§] Present address: INSERM U629, Institut Pasteur de Lille, 1 rue du Prof. Calmette, F-59019 Lille, France.

10.1021/bc060377f CCC: $37.00 © 2007 American Chemical Society
Published on Web 05/24/2007

containing LB (Luria−Bertani) medium supplemented with 100 μg/mL Kan was inoculated with a single bacteria colony. Bacteria were allowed to grow overnight at 37 °C with vigorous rotational shaking. The culture was then diluted 100 times in 100 mL LB medium supplemented with 100 μg/mL Kan and allowed to grow until bacteria reached the midlog phase ($OD_{600} \sim 0.8-0.9$). At that time, an amount of 2×10^{11} phages was added to the culture medium that was completed with 10 μg/mL Tc. The culture was allowed to grow overnight. During this phase, phages are secreted in the medium by infected bacteria.

Amplified phages were recovered by precipitation with poly(ethylene glycol) (PEG). Briefly, the culture was centrifuged at 10 000 rpm and 4 °C for 15 min. The supernatant was transferred to a new flask and 1/5 volume/volume PEG/NaCl was added (20% PEG 6000, 2.5 M NaCl). Phages were precipitated for 2 h at 4 °C and were then retrieved by centrifugation at 4 °C and 3200 rpm for 20 min. The phage pellet was suspended in 1 mL Tris-buffered saline (TBS, 50 mM Tris-HCl, 150 mM NaCl, pH 7.5), 200 μL PEG/NaCl was added, and a new precipitation was carried out for 1 h at 4 °C. A final centrifugation at 4 °C and 13 000 rpm for 5 min allowed the isolation of a pellet that was finally suspended in TBS at the suitable phage concentration.

Synthesis of Magnetophages. Magnetophages were obtained by reacting phages with activated USPIO obtained by pretreating USPIO with epichlorhydrin (Sigma, Bornem, Belgium).

A 1.5 mL amount of USPIO (30 mg of 22 nm Fe particles coated with dextran) was diluted in 5 mL of water and treated with 5 mL of 5 M NaOH and 2 mL of epichlorhydrin. The mixture was stirred for 24 h at 40 °C in the darkness and then dialyzed in a 5 mM citrate solution, pH = 8 (membrane cutoff: 12000−14000) to remove unreacted epichlorhydrin (*14*). A 400 μL amount of activated USPIO (150 mM Fe) was added to 600 μL of phage suspension in water at a concentration of 4×10^{12} phages per mL and incubated 24 h at 37 °C. Magnetophages were recovered by PEG-precipitation as described above. This process was repeated three times to ensure total elimination of free USPIO. The magnetophages were finally suspended in 500 μL of water.

Estimation of Apparent Affinity Constant $K_{a,app}$. The $K_{a,app}$ of E3 magnetophages for PS was determined by saturation experiments performed by enzyme-linked immunosorbent assay (ELISA). PS (1,2-dipalmitoyl-sn-glycero-3-phospho-L-serine, Genzyme Pharmaceuticals-Sygena Facility, Liestal, Switzerland) was dissolved in ethanol and immobilized on microplates (Greiner Gmbh, Frichenhausen, Germany) by overnight evaporation of the ethanol at room temperature. Plates were blocked with 200 μL of a blocking solution [4% milk powder in phosphate-buffered saline (PBS, 137 mM NaCl, 3.2 mM KCl, 6.4 mM Na_2HPO_4, 1.5 mM KH_2PO_4, pH 7.2−7.5)] for 2 h at room temperature. After rinsing three times with washing buffer (PBS completed with 0.1% Tween 20) using a microplate washer (Adil Instruments, Schiltigheim, France), serial magnetophage dilutions ranging from $\sim 10^{-8}$ to $\sim 10^{-16}$ M were prepared in a calcium buffer (2 mM $CaCl_2$, 150 mM NaCl, 10 mM HEPES, 3 mM NaN_3, pH 7.4). PS-coated plates were incubated with 200 μL of each dilution for 2 h at 37 °C. Plates were then rinsed six times with washing buffer. Bound phages were detected using the horseradish peroxidase (HRP)-conjugated anti-M13 antibody (HRP anti-M13, Amersham Pharmacia Biotech, Roosendaal, The Netherlands). The peroxidase staining reaction was performed with HRP substrate solution containing 100 mM citric acid pH 2, 200 mM Na_2HPO_4, 30% H_2O_2 (8 μL for 20 mL of substrate solution) and OPD (o-phenylenediamine dihydrochloride, ICN, Asse-Relegem, Belgium). After incubation with the substrate for 30 min, the reaction was stopped by addition of 50 μL/well of 4 M H_2SO_4. OD_{450} values were determined with Stat Fax-2100 ELISA plate reader (Awareness Technology, Palm City, FL). Titration curves were obtained by plotting OD_{450}, which reflects the number of phages bound to PS, against the logarithmic concentration of total magnetophages, expressed in mol/L. Curves were fitted according to a sigmoidal model. The phage concentration at half-saturation corresponds to $1/K_{a,app}$ (*7*).

Competition Experiments with Annexin V. Annexin V, a protein interacting specifically with PS (*15*), was used as competitor for E3 magnetophages. Serial dilutions from 6×10^{-4} to 10^{-10} M of annexin V (33 kDa from human placenta, Sigma-Aldrich, Bornem, Belgium) were prepared in calcium buffer. PS-coated plates were incubated with each dilution of annexin V during 30 min at 37 °C. E3 magnetophages were then added at the concentration yielding half-saturation and incubated for 90 min at 37 °C. The subsequent protocol was identical to that used in the previous section. The competition curve was obtained by plotting OD_{450} against the logarithmic concentration of total annexin V input, expressed in M.

Nuclear Magnetic Resonance Dispersion Profiles. Nuclear magnetic resonance dispersion (NMRD) profiles represent the relaxivity of the contrast agent as a function of the proton Larmor frequencies. Longitudinal relaxivities r_1 and transverse relaxivities r_2 were obtained respectively from longitudinal relaxation rate R_1 and the transverse relaxation rate R_2 at each field as described below. R_1 and R_2 are the reciprocals of the measured longitudinal relaxation time T_1 and the transverse relaxation time T_2 of water protons respectively, expressed in seconds. The relaxivity reflects the efficiency of a MRI contrast agent: the higher the relaxivity, the lower the amount of contrast agent needed to produce a given contrast enhancement in MRI. Relaxivity (r_1 or r_2, expressed in s^{-1} $mmol^{-1}$ L) is defined as the increase of relaxation rate (R_1 and R_2) produced by 1 mmol per liter of contrast agent. The r_1 and r_2 are the main physicochemical parameters that are considered in the development of an effective magnetic label. They depend essentially on the size and chemical structure of the magnetic center as well as on its accessibility to water molecules. The MRI contrast agents are indirect agents because they are not visible by themselves contrary to the situation encountered in other imaging modalities. Indeed, they enhance the difference between healthy and diseased tissues by modifying their intrinsic parameters, mainly the longitudinal, T_1, or transverse, T_2, relaxation times of the tissues water protons. Relaxivities and observed relaxation rates are linked by the following formula:

$$R_{i(obs)} = \frac{1}{T_{i(obs)}} = \frac{1}{T_{i(diam)}} + r_i C; \qquad i = 1 \text{ or } 2 \qquad (1)$$

where: $R_{i(obs)}$ and $1/T_{i(obs)}$ = global relaxation rate of the tissue (s^{-1}), $T_{i(diam)}$ = relaxation time of the tissue before the addition of the contrast agents, C = the concentration of the paramagnetic center (mmol L^{-1}), and r_i = the relaxivity (s^{-1} $mmol^{-1}$ L).

Iron concentration was determined as follows. Magnetophage samples were mineralized in nitric acid/hydrogen peroxide 3:1 volume/volume by microwave treatment (Milestone, Analis, Namur, Belgium). Fe content was then determined by inductively coupled plasma atomic emission spectrometry (ICP-AES, Jobin Yvon JY70+, Longjumeau, France). The iron concentration of mineralized samples was also estimated by relaxometry at 20 MHz from the known relaxivity of the Fe^{3+} ion in acidic solution.

R_1 and R_2 were recorded with different systems. For proton Larmor frequencies ranging between 0.01 and 15 MHz, R_1 was measured on a fast field cycling NMR relaxometer (Stelar spa, Mede, Italy). For 20 and 60 MHz, R_1 and R_2 were measured on

minispecs (PC-20 and mq-60, Bruker, Karlsruhe, Germany). At 200 MHz, R_1 and R_2 were estimated by image analysis on an Avance-200 vertical magnet spectrometer (Bruker, Karlsruhe, Germany). For R_1 determination, an inversion−recovery sequence was used [repetition time (TR)/echo time (TE) = 2004/8.1 ms, slice thickness = 1.5 mm, field of view (FOV) = 5 cm, matrix = 64]. R_1 was calculated by fitting the intensities observed for different inversion times (TI) with the equation

$$M_z(T_1) = M_z(0)[1 - (1 - \alpha) \times \exp^{TI/T_1}] \quad (2)$$

R_2 was obtained by a spin−echo T_2 sequence (TR/TE = 2062/6.6 ms, echo number (NE) = 24, slice thickness = 1 mm, FOV = 5 cm, matrix = 64). R_2 was calculated by fitting the curve representing the image intensities as a function of echo time according to the equation

$$M_{xy}(\mathrm{TE}) = A + C \times \exp^{TE/T_2} \quad (3)$$

MaLISA and C-MaLISA. MaLISA (magnetic-linked immunosorbent assay) is the MRI equivalent of ELISA (*16*). PS or phosphatidylcholine (PC, 1,2-dipalmitoyl-sn-glycero-3-phospho-L-choline, Genzyme Pharmaceuticals-Sygena Facility, Liestal, Switzerland) were adsorbed on a microtiter plate by overnight evaporation of a phospholipid solution (concentration: 25 mg/30 mL ethanol). Phospholipid-coated plates were then blocked by incubation with 200 μL of blocking solution (5 mg/mL BSA in PBS) for 90 min at 4 °C. After washing three times with 0.1% Tween 20 in PBS, serial magnetophage dilutions ranging from $\sim 10^{-8}$ to $\sim 10^{-16}$ M were prepared in calcium buffer. A 100 μL amount of each magnetophage dilution was added to the wells and incubated at 37 °C during 90 min. After washing six times with 0.1% Tween 20 in PBS, 100 μL of 0.2 M glycine-HCl (pH2.2) was added and a 10 min incubation was carried out in order to eluate bound magnetophages. This resuspension is necessary to obtain a homogeneous solution of magnetophage required for MRI measurements. As acidic solution can alter phages and digest iron particles, the pH was neutralized with 25 μL of 1 M Tris pH 8. Magnetophages were then detected by MRI using an Avance-200 imaging system equipped with a vertical magnet (Bruker, Karlsruhe, Germany). Images were acquired using the following parameters: TR/TE = 3000/20 ms, NE = 40, number of acquisitions (NA) = 2, slice thickness = 1.5 mm, FOV = 5 cm, matrix 256 × 256.

C-MaLISA, for cellular magnetic-linked immunosorbent assay, was performed with apoptotic and control Jurkat cells. Jurkat cells (contribution from Prof. Oberdan Leo, Free University of Brussels, IBMM, Belgium) were grown in RPMI-1640 medium (Sigma-Adrich, Bornem, Belgium) supplemented with 10% FCS (Fetal calf-serum, Gibco, Paisley, UK), and 1% antimycotic−antibiotic solution (Gibco, Paisley, UK). Apoptosis was induced with 1 mM campthotecin (ICN, Asse-Relegem, Belgium) (*17*). Cells were fixed in 0.5% formalin (37% formaldehyde solution, Sigma-Adrich, Bornem, Belgium) in PBS at a final concentration of 10^7 cells/mL. Wells were coated by evaporating 200 μL of the cell suspension at 37 °C (*18*). After blocking for 90 min at 4 °C with 200 μL/well of 5 mg/mL BSA in PBS, plates were washed three times with 0.1% Tween 20 in PBS. A 100 μL amount of each magnetophage dilution was incubated during 90 min at 37 °C. The subsequent steps of the protocol are the same as described above. Competition with annexin V was carried out at a final concentration of the competitor equal to 0.3 mM.

Stealthy Magnetophages. Stealthy magnetophages were obtained by covalent attachment of pegylated USPIO to the proteins of the phage wall using the protocol already described. USPIO were modified by monoamine polyethylene glycol 2000 (PEG, Shearwater Corporation, Huntsville, AL) as follows: 100 mg of PEG 2000 was incubated with 0.8 mL of activated USPIO (100 mM Fe) for 24 h at room temperature. Particles were dialyzed (membrane cut off: 12000−14000) and the resulting PEG-derivatized USPIO were again treated with epichlorydrin. These particles were finally incubated with phages to obtain stealthy magnetophages.

***In Vivo* Evaluation of Magnetophages.** Magnetophages (stealthy or not) were injected to Balb/c mice (5−6 weeks old, Universal Limited Hull, UK) in the caudal vein. The injected amount was 65 μL at an iron concentration of 2.4 mM. Animals were anesthetized by intraperitoneal injection of 60 mg/kg Nembutal (sodium pentobarbital, CEVA, Sanofi Santé Animale, Benelux). Apoptosis of hepatic cells was induced by intravenous injection of 10 μg anti-Fas antibody (Becton-Dickinson, Erembodeghem, Belgium) (*19*). TUNEL staining (terminal deoxynucleotidyl-transferase-mediated UTP end labeling) demonstrated that 70% of hepatocytes were apoptotic 2 h after treatment (results not shown).

Magnetic resonance images were acquired on a 4.7 T Avance-200 imaging system. Acquisition parameters were: TR = 2000 ms, TE = 20 ms, matrix = 128, slice thickness = 2.5 mm, FOV = 6 cm.

As explained above, the MRI contrast agent enhances the relaxations rates R_1 and R_2 of the water protons. The modification of the relaxation rates are reflected on the MR image by a local modification of the image intensity. The MRI signal was expressed as relative postcontrast enhancement (RE%), i.e., the signal modification related to the precontrast image. RE% is calculated by the following formula:

$$RE(\%) = \frac{\dfrac{I_i}{I_{ref,i}} - \dfrac{I_0}{I_{ref,0}}}{\dfrac{I_0}{I_{ref,0}}} \times 100 \quad (4)$$

where RE(%) is the relative enhancement expressed as a percentage, I_0 and $I_{ref,0}$ are respectively the image intensity measured in the liver and in the reference (tube containing an USPIO solution of 0.1 mM Fe) before administration of the contrast agent, and I_i and $I_{ref,i}$ are respectively the signal intensity in the liver and in the reference after the contrast agent administration. A decrease of the image intensity (negative enhancement, darkening of the image) or the increase of the image intensity (positive enhancement, brightening of the image) are respectively reflected by negative or positive RE(%). Intensities were measured in circular ROI (region of interest) drawn in the liver or in the external reference.

Statistics. Data are given as the mean ± SEM (standard error of the mean). Comparison between groups was performed with the Student *t* test and differences were considered to be significant for $p \leq 0.05$ and highly significant for $p \leq 0.01$.

RESULTS

Synthesis of Magnetophages. Magnetophages were obtained by linking of iron particles pretreated with epichlorhydrin directly to the amino functions of the phage proteins. We used previously similar experimental procedure to graft small peptides on USPIO, and we could estimate that less than five peptides were grafted on each particle (see ref 16, Burtea et al.). We can thus expect that each USPIO activated with epichlorydrin has only a few amine reactive sites and that the risk of cross-linking virions is low. Moreover, the water solubility of the synthesized magnetophages confirms the absence of considerable cross-linking of the virions.

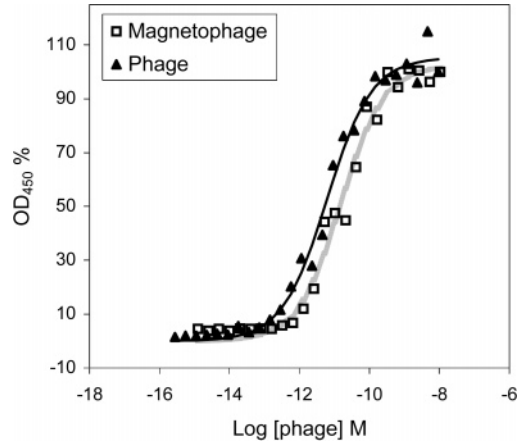


Figure 1. Estimation of $K_{a,app}$. OD_{450}% is the percentage ratio of OD_{450} related to OD_{450} measured for the maximal concentration. OD_{450} measured for magnetophages at maximal concentration was 1.3.

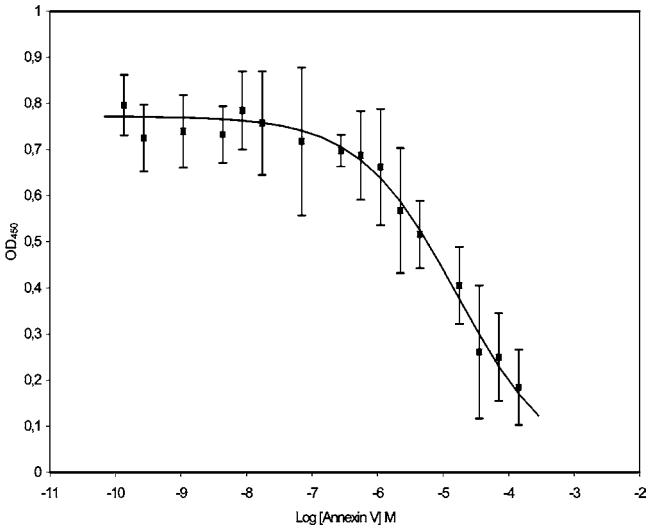


Figure 2. Competition between annexin V and E3 magnetophages for PS. Each value represents the mean of three measurements.

From the magnetophage concentration and the iron concentration (determined by ICP-AES), we evaluate the average number of USPIO per phage at 80 (160 000 to 240 000 iron atoms per virion) assuming that each USPIO contains 2000−3000 iron atoms.

Determination of $K_{a,app}$. The apparent association constant $K_{a,app}$ of E3 magnetophages for PS was compared to that of the nonmagnetically labeled E3 clone, previously determined (*9*), in order to evaluate the capacity of magnetophages to recognize their target. Figure 1 shows that the titration curve of magnetophages is shifted to the right, meaning that their $K_{a,app}$ is slightly decreased as compared to that of the nonmagnetically labeled phages. $K_{a,app}$ is equal to 1.6×10^{11} and 6.55×10^{10} M for phages E3 and magnetophages E3, respectively.

Specificity of the Interaction with Phosphatidylserine. To confirm the specific interaction between E3 magnetophages and PS, annexin V, known to bind PS with high affinity (*15*), was used in a competitive binding assay with E3 magnetophages. The amount of magnetophages bound to PS, as expressed by the OD_{450} value, decreased when the concentration of competitor was increased (Figure 2). These results confirmed that E3 magnetophages selectively interact with PS and not with other structures exposed during the ELISA experiments, such as polystyrene or blocking buffer.

Determination of Relaxivity. NMRD profiles reflect the relaxation rate as a function of field strength and allow for the determination of relaxivity at the magnetic field of interest. These profiles are largely used to characterize contrast agents because they reflect the efficacy of a MRI contrast agent and are very sensitive to the agents' structural modifications (*20*). They can be seen as a fingerprint of the MRI contrast agents. The NMRD profiles of the three magnetophage samples (Figure 3), synthesized under identical experimental conditions, were compared to those of the original USPIO (represented by black squares). Although small differences exist at lower magnetic fields, the three profiles corresponding to the three magnetophage samples mainly overlap above 5 MHz, confirming the reproducibility of our protocol. The low field r_1 and the high field r_2 are higher than those observed for the USPIO not conjugated to virion and are characteristic of some clustering of the magnetic centers as shown by Roch et al. (*21*). As compared to that of free USPIO, the high field r_2 of magnetophages (about 160 $s^{-1}mM^{-1}$ at 60 MHz) is indeed four times higher than that of unconjugated USPIO (about 40 $s^{-1}mM^{-1}$ at 60 MHz). As a result, a similar MRI contrast enhancement will be obtained with a four times lower amount of iron than with nonconjugated USPIO.

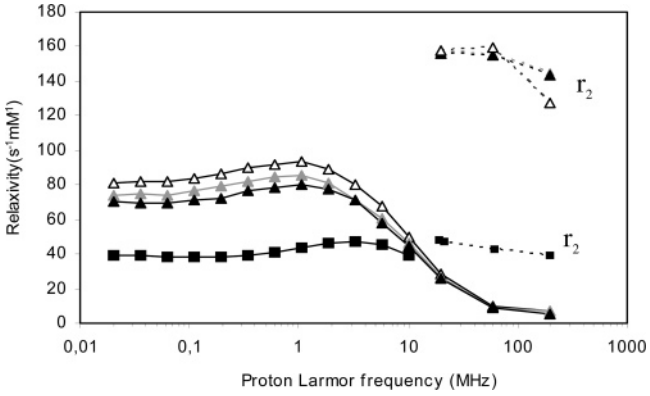


Figure 3. NMRD relaxivity profiles of magnetophages and USPIO. Black squares: USPIO. Black, gray, and white triangles: different samples of magnetophages. r_1 relaxivity: plain lines; r_2 relaxivity: dashed lines.

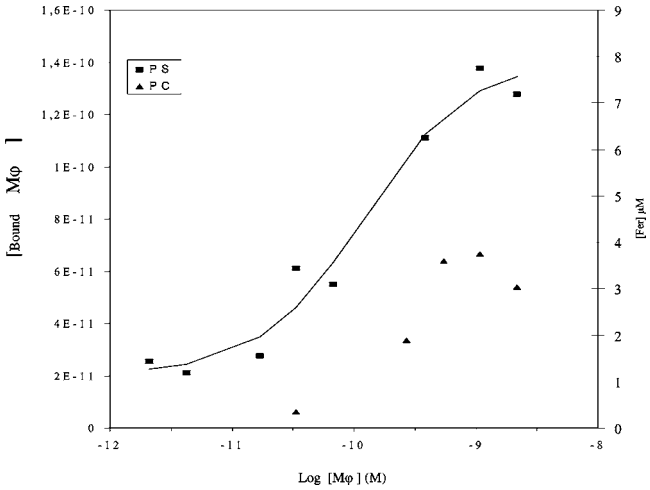


Figure 4. Titration curves obtained by MaLISA. They were obtained after incubation of E3 magnetophages (Mφ) with phosphatidylserine (PS) and phosphatidylcholine (PC).

MaLISA. Titration curves like those obtained by ELISA, which represent the amount of magnetophages bound to the target, can be obtained by MaLISA where the colorimetric evaluation is replaced by the measurement of signal intensity by MRI. The amount of bound magnetophages was determined from a calibration curve obtained from the MRI measurement of the transverse relaxation time T_2 as a function of iron

Table 1. T_2 (ms) Obtained in C-MaLISA after Incubation of E3 Magnetophages (Initial Concentration $\sim 10^{-8}$ M) with Apoptotic and Control Jurkat Cells in the Absence and in the Presence of the Competitor Annexin V[a]

[magnetophages], M	JURKAT apoptotic	JURKAT control	competition with annexin V
10^{-8} M	296	335	353
5×10^{-9} M	295	329	336
2.5×10^{-9} M	316	362	361
1.25×10^{-9} M	326	353	367

[a] E3 magnetophages (10^{-8} M corresponding to 6×10^{12} magnetophages/mL) were diluted, and each dilution was incubated with the cells.

concentration. The fixation curves for PS and PC obtained by MaLISA are represented in Figure 4. The fixation curve for PC is shifted to the right, suggesting that the affinity for PS of E3 magnetophages is much higher than for PC. The fitting of the fixation curve for PS gave a $K_{a,app}$ equal to 8.3×10^9 M.

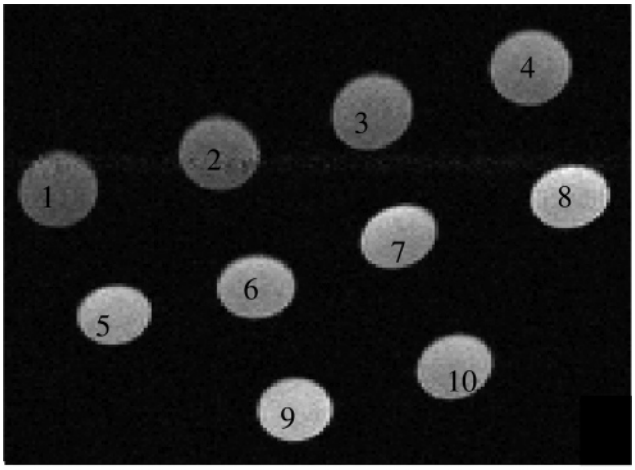
The same MaLISA protocol was used to validate the potential of magnetophages as an MRI contrast agent. The acquired image is represented in Figure 5. Signal intensities are lower and therefore T_2 values shorter in the wells coated with PS than in those coated with PC, confirming the selective binding of the E3 magnetophages. These results confirm that magnetophages are able to discriminate between PS and PC.

C-MaLISA. E3 magnetophages were incubated with apoptotic and control Jurkat cells by a C-MaLISA protocol. The T_2 values are given in Table 1. In the case of apoptotic Jurkat cells, E3 magnetophages induced a higher decrease of intensity than in the case of control Jurkat cells. Competition with annexin V weakened this interaction, confirming a specific interaction of E3 magnetophages with phosphatidylserine. These results corroborate the conclusion that magnetophages are able to discriminate apoptotic and normal structures at the cellular level.

***In Vivo* MRI Evaluation of Magnetophages: Stealthy Magnetophages.** Magnetophages, specific or not to PS, are rapidly sequestered by the liver (healthy or apoptotic) when they are injected in mice and induce a decrease of the relative enhancement (RE%) (Figure 6). As shown on Figure 7, stealthy nonspecific magnetophages, produced from the native phage display library, are not sequestrated by the liver, contrary to their nonstealthy analogs. Figure 7 shows that stealthy magnetophages specific to PS induce a decrease of RE% only in apoptotic livers, and not in healthy ones. These results are conceivably correlated with the specific accumulation of stealthy magnetophages specific to PS in apoptotic livers. The reasons for the increase of the signal intensity in the case of healthy mice treated with specific or nonspecific stealthy magnetophages remains to be explored. It could be attributed to a very low concentration of magnetic nanoparticles in the liver caused by an absence of immobilization and a rapid diffusion in the hepatic vascular tree (*22*).

DISCUSSION

The coupling of target-specific peptides identified by phage display technology with an appropriate reporter is a powerful strategy in the context of molecular imaging. This approach defines the new rationale in the design of novel MRI contrast agents pursued by our laboratory. However, the behavior of the peptide isolated from its phage carrier cannot be predicted after *in vivo* injection, since it could potentially interact less with its target and show unspecific binding with other structures. This is a consequence of a different spatial conformation of the target when immobilized on a solid support or from lower target concentration in an *in vivo* environment (*2*). To avoid these problems, and because phage production is more economical than peptide synthesis, we propose an alternative system, designated with the generic name "magnetophages", obtained by conjugation of USPIO to the phage clone presenting the highest affinity for the target.



Well	Intensity	T_2 (msec)
1	63	266
2	68	273
3	75	288
4	85	301
5	106	339
6	96	317
7	103	326
8	114	358
9	120	361
10	104	312

Figure 5. Image obtained after incubation of successive two-fold dilutions of E3 magnetophages with PS (1 to 4) and with PC (5 to 8). 9 and 10: PS and PC, respectively, without magnetophages.

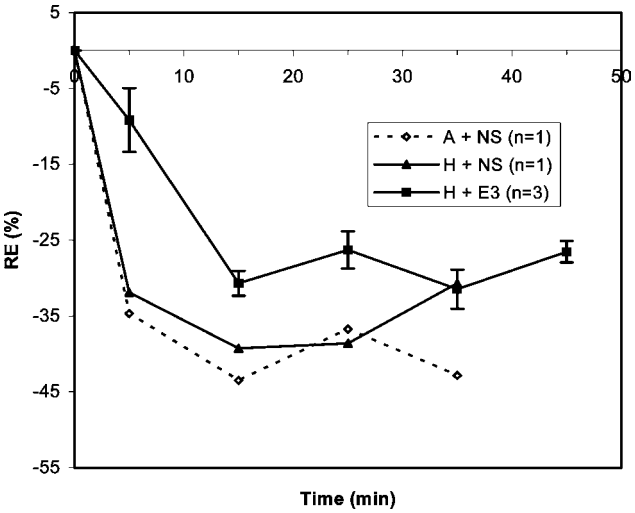


Figure 6. Relative enhancement of the NMR signal in apoptotic (A) or healthy (H) mouse liver after intravenous injection of nonspecific magnetophages (NS) or magnetophage E3 (E3). A + NS: injection of nonspecific magnetophage to apoptotic liver bearing mouse, H + NS: injection of nonspecific magnetophages to healthy liver bearing mouse, H + E3: injection of magnetophages carrying the peptide E3 specific for PS to mice with normal liver.

Magnetophages would be inoperative if the linkage of USPIO to the phage proteins would alter their capacity to interact with their target, an attribute conferred by the displayed peptide. To characterize magnetophages, and subsequently to evaluate them as a contrast agent, we synthesized magnetophages from the

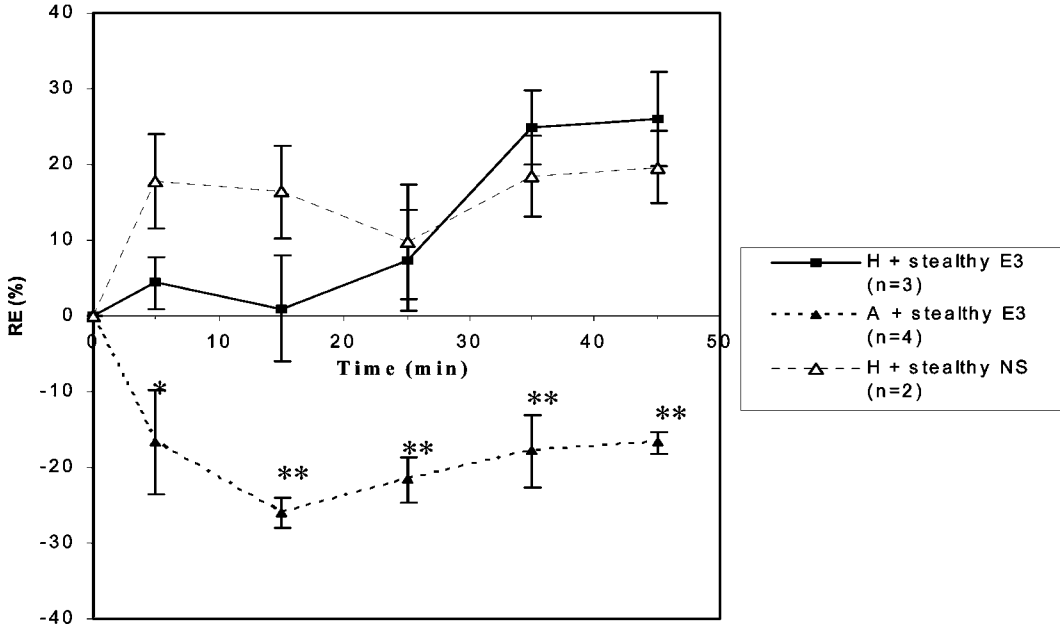


Figure 7. Relative enhancement of the NMR signal in healthy (H) or apoptotic (A) mouse liver (A) after intravenous injection of stealthy magnetophages carrying the peptide specific to PS (stealthy E3) or nonspecific stealthy magnetophages (NS). H + stealthy E3: injection of magnetophage E3 to mice with healthy liver, A + stealthy E3: injection of magnetophages E3 to mice with apoptotic liver, H + stealthy NS: injection of nonspecific magnetophages to mice with healthy liver. *: statistically significant ($p < 0.05$); **: highly statistically significant ($p < 0.01$).

phage clone E3 obtained in our laboratory to target PS. The titration curve of E3 magnetophages showed that the peptide ability to link to PS is maintained after the conjugation with USPIO to create magnetophages, although with a slightly decreased K_a. The specific interaction was further demonstrated by a competition experiment with annexin V, where the extent of PS binding decreased as a function of the competitor's concentration. These results suggest that USPIO do not significantly alter the potential of peptide displayed by magnetophages to interact with the target.

Relaxivity is a measure of the contrast agent efficiency and a way of characterization. NMRD profiles (Figure 3) showed that our protocol of synthesis gives magnetophages with reproducible magnetic properties. The relaxivity r_1 is similar for the three magnetophage batches and approaches 0 with increasing magnetic fields. As usual, this suggests that the T_1 effect of magnetophages at 200 MHz (4.7 T) would be very weak. However, at 20, 60, and 200 MHz, the r_2 relaxivity is constant and four times higher than that of USPIO. This suggests a strong T_2 effect at 200 MHz. Thus, magnetophages would act as a superparamagnetic contrast agent locally, disturbing the homogeneity of the magnetic field and inducing a subsequent suppression of the NMR signal. It has to be emphasized that these modifications of the NMRD profiles as compared to USPIO are characteristic of clustered systems and confirms the multiple USPIO attachment to each virion. This conclusion agrees with the determination of the number of USPIO particles per virion, based on the determination of the concentration of phages and of iron (calculation of 80 USPIO per virion, see above). Results obtained from the *in vitro* characterization of magnetophages encourage their use as a new kind of contrast agent for MRMI. In this context, two different *in vitro* protocols were used to evaluate magnetophages. These protocols basically rely on the ELISA technique and were adapted as an MRI application for biomedical research and clinical diagnosis. Under these conditions, immobilized targets (MaLISA) or intact cells (C-MaLISA) are detected with specifically targeted contrast agents. Hence, the ligand itself (e.g., phages) is labeled with a superparamagnetic moiety (USPIO), which directly reports on the interaction with the specific reporter. MaLISA and C-MaLISA revealed that E3 magnetophages interacted with apoptotic Jurkat cells at a higher level than with control cells and that this interaction was specific for phosphatidylserine, as confirmed by the competition experiment. In addition, it was possible to estimate the constant describing the interaction with the phospholipid by MaLISA. In these experiments, E3 magnetophages were able to discriminate PS from PC and apoptotic cells from nonapoptotic ones. They suggest that magnetophages can be used as contrast agents *in vitro*, playing the role of a reporter for the expression of cellular receptors in any type of biomedical screening. In our protocol of C-MaLISA, we have assumed that PS was not exposed (or was exposed at a lesser extent) in control samples as suggested by the lower level of magnetophage binding on control cells compared to apoptotic cells. Still, binding on controls could have been lower if cells would not have been fixed. However, our rationale was to propose a protocol for high-throughput MRI screening by using magnetophages instead of more complicated, expensive, and time-consuming ELISA protocols which use several antibodies to measure ligand−receptor interaction.

In the vascular system of a mammal, magnetophages are processed by the host's defense system, i.e., the immunologic response and the pathway of endocytosis by the phagocytic cells of the reticuloendothelial system (RES), such as Kupffer cells of the liver. It has been shown that circulating bacteriophages are rapidly sequestered by the RES (*23*). On the other hand, USPIO used to produce magnetophages are coated by dextran that adsorbs plasma proteins such as albumin, transferrin, and immunoglobulins. These proteins act as opsonins, facilitating endocytosis by Kupffer cells (*22*, *24*, *25*). Parameters like the size or the charge of USPIO favor the internalization by the cells of RES (*10*). The accumulation of magnetophages in the RES with a subsequent reduction of their bioavailability was confirmed by experiments summarized in Figure 6, where nonspecific magnetophages and E3 magnetophages (carrying a PS-specific peptide) were rapidly and nonspecifically taken up by healthy or apoptotic livers.

Stealthy nanoparticles have two characteristics: they are invisible to the RES, meaning a decrease of their capture by phagocytic cells, and they have a long vascular circulating time,

making them available to interact with the target (*26, 27*). As a consequence, these particles can act efficiently as biocarriers and are used in molecular targeting for both therapy and molecular imaging (*27, 28*). These properties are conferred by grafting PEG onto particles to prevent the absorption of the proteins and to reduce the phagocytosis. This is because of the fact that PEG is neutral and allows a relatively strong binding of water molecules around the polymer chain that induces high steric exclusion. In addition, pegylated surfaces are biocompatible and not immunogenic nor antigenic (*26, 29*−*32*). This approach has already been applied to liposomes and superparamagnetic nanoparticles, reducing their capture by Kupffer cells (*33, 34*). We employed the same procedure with magnetophages to fashion stealthy magnetophages. Stealthy E3 magnetophages (carrying a peptide specific for PS) were injected into healthy mice and into mice with apoptotic liver. The absence of signal depression in the liver on MR images of healthy mice and the negative signal enhancement of apoptotic livers (decrease of RE(%), Figure 7) confirm that these magnetophages were not internalized by the RES of healthy mice but are retained by apoptotic livers. These results are convincing arguments that stealthy E3 magnetophages can discriminate between apoptotic and normal livers.

CONCLUSIONS

E3 magnetophages selected for their affinity for apoptotic structures were able to discriminate apoptotic from normal cells and between PS and PC *in vitro*, while stealthy E3 magnetophages targeted *in vivo* apoptotic liver. If this feature demonstrated for E3 magnetophages can be extrapolated to other phage display selected entities, magnetophages become an original system which allows validation of the candidate binding peptide before their synthesis is considered. This means that the targeting peptide discovered by phage display can be investigated without having to incorporate those peptides into more conventional molecular imaging probes. Furthermore, magnetophages themselves can be used as an MRI contrast agent. Finally, the concept of magnetophage could be extended to other imaging modalities by replacing USPIO with an adequate reporter (i.e., radiolabeled phages).

ACKNOWLEDGMENT

The financial supports of the FNRS (Fonds National de la Recherche Scientifique), of the French Community of Belgium ARC (Concerted Research Action), of Region of Wallonia, of the NOMADE program, and of EU (EMIL Network of Excellency, FP6) are acknowledged. Mrs. Patricia De Francisco is thanked for her help in preparing the manuscript.

NOTE ADDED AFTER ASAP PUBLICATION

This manuscript was released ASAP on May 24, 2007 with a typographical error in Figure 5. The corrected version was posted on July 2, 2007.

LITERATURE CITED

(1) Weissleder, R. (1999) Molecular imaging: exploring the next frontier. *Radiology 212*, 609−614.

(2) Smith, G. P., and Petrenko, V. A. (1997) Phage display. *Chem. Rev. 97*, 391−410.

(3) Scott, J. K., and Smith, G. P. (1990) Searching for peptide ligands with an epitope library. *Science 249*, 386−390.

(4) Burritt, J. B., Bond, C. W., Doss, K. W., and Jesaitis, A. J. (1996) Filamentous phage display of oligopeptide libraries. *Anal. Biochem. 238*, 1−13.

(5) Zwick, M. B., Shen, J., and Scott, J. K. (1998) Phage-displayed peptide libraries. *Curr. Opin. Biotechnol. 9*, 427−436.

(6) Sidhu, S. S., Lowman, H. B., Cunningham, B. C., and Wells, J. A. (2000) Phage display for selection of novel binding peptides. *Methods Enzymol. 328*, 333−363.

(7) Cortese, R., Monaci, P., Luzzago, A., Santini, C., Bartoli, F., Cortese, I., Fortugno, P., Galfre, G., Nicosia, A., and Felici, F. (1996) Selection of biologically active peptides by phage display of random peptide libraries. *Curr. Opin. Biotechnol. 7*, 616−621.

(8) Rodi, D. J., and Makowski, L. (1999) Phage-display technology - finding a needle in a vast molecular haystack. *Curr. Opin. Biotechnol. 10*, 87−93.

(9) Laumonier, C., Segers, J., Laurent, S., Michel, A., Coppée, F., Belayew, A., Vander Elst, L., and Muller, R. N. (2006) A new peptidic vector for molecular imaging of apoptosis, identified by phage display technology. *J Biomol. Screen. 11*, 537−545.

(10) Weinmann, H-J., Ebert, W., Misselwitz, B., and Smitt-Willich, H. (2003) Tissue-specific MR contrast agents. *Eur. J. Radiol. 46*, 33−44.

(11) Pouliquen, D., Le Jeune, J. J., Perdrisot, R., Ermias, A., and Jallet, P. (1991) Iron oxide nanoparticles for use as MRI contrast agent : pharmacokinetics and metabolism. *Magn. Reson. Imaging 9*, 275−283.

(12) Van den Eijnde, S. M., Boshart, L., Reutelingsperger, C. P., De Zeeuw, C. I., and Vermeij-Keers, C. (1997) Phosphatidylserine plasma membrane asymetry in vivo : a pancellular phenomenon which alters during apoptosis. *Cell Death Differ. 4*, 311−316.

(13) Schlegel, R. A., and Williamson, P. (2001) Phosphatidylserine, a death knell. *Cell Death Differ. 8*, 551−563.

(14) . Josephson, L., Tung, CH., Moore, A., and Weissleder, R. (1999) High-efficiency intracellular magnetic labeling with novel superparamagnetic-Tat peptide conjugates. *Bioconjugate Chem. 10*, 186−91.

(15) Van Engeland, M., Nieland, L. J., Ramaekers, F. C., Schutte, B., and Reutelingsperger, C. P. (1998) Annexin V affinity assay : a review on a apoptosis detection system based on phosphatidylserine exposure. *Cytometry 31*, 1−9.

(16) Burtea, C., Laurent, S., Roch, A., Vander Elst, L., and Muller, R. N. (2005) C-MALISA (cellular magnetic-linked immunosorbent assay), a new application of cellular ELISA for MRI. *J. Inorg. Biochem. 99*, 1135−44.

(17) Johnson, N., Tony, T. C., and Parkin, J. M. (1997) Camptothecin causes cell cycle perturbations within T-lymphoblastoid cells followed by dose dependent induction of apoptosis. *Leuk. Res. 21*, 961−972.

(18) Walker, K. W., Llull, R., Balkian, G. K., Ko, H. S., Flores, K. M., Ramsamooj, R., Black, K. S., Hewitt, C. W., and Martin, D. C. (1992) A rapid and sensitive cellular enzyme-linked immunoabsorbent assay (CELISA) for the detection and quantitation of antibodies against cell surface determinants. A comparison of cell fixation and storage techniques. *J. Immunol. Methods 154*, 121−30.

(19) Ogasawara, J., Watanabe-Fukunaga, R., Adachl, M., Matsuzawa, A., and Kasugal, T. (1993) Lethal effect of the anti-Fas antibody in mice. *Nature 364*, 806−809.

(20) Muller, R. N., Vander Elst, L., Rinck, P. A., Vallet, P., Maton, F., Fischer, H., Roch, A., and Van Haverbeke, Y. (1988) The importance of nuclear magnetic relaxation dispersion (NMRD) profiles in MRI contrast media development. *Invest. Radiol. 23*, S229−31.

(21) Roch, A., Moiny, F., Gillis, P., and Muller, R. N. (2002) Water magnetic relaxation in superparamagnetic colloid suspensions : the effect of agglomeration. *NATO Sci. Ser. II 76*, 383−391.

(22) Oswald, P., Clement, O., Chambon, C., Schouman-Claeys, E., and Frija, G. (1997) Liver positive enhancement after injection of superparamagnetic nanoparticles: respective role of circulating and uptaken particles. *Magn. Reson. Imaging 15*, 1025−1031.

(23) Merril, C. R., Biswas, B., Carlton, R., Jensen, N. C., Creed, G. J., Zullo, S., and Adhya, S. (1996) Long-circulating bacteriophage as antibacterial agents. *Proc. Natl. Acad. Sci. U.S.A. 93*, 3188−3192.

(24) Van Beers, B., Sempoux, C., Materne, R., Delos, M., and Smith, A. M. (2001) Biodistribution of ultrasmall iron oxide particles in the rat liver. *J. Magn. Reson. Imaging 13*, 594−599.

(25) Moore, A. R., Weisleder, R., and Bogdanov, A. (1997) Uptake of dextran-coated monocrystalline iron oxides in tumour cells and macrophages. *J. Magn. Reson. Imaging 7*, 1140−1145.

(26) Monfardini, C., and Veronese, F. M. (1998) Stabilization of substances in circulation. *Bioconjugate Chem. 9*, 418−450.
(27) Moghimi, S., and Hunter, C. (2001) Capture of stealth nanoparticles by the body's defences. *Crit. Rev. Ther. Drug Carr. Syst. 8*, 527−550.
(28) Inada, Y., Furukawa, M., Sasaki, H., Kodera, Y., Hiroto, M., Nishimura, H., and Matsushima, A. (1995) Biomedical and biotechnological applications of PEG- and PM-modified proteins. *Trends Biotechnol. 13*, 86−91.
(29) Moghimi, S. M. (2002) Chemical camouflage of nanospheres with a poorly reactive surface: towards development of stealth and target-specific nanocarriers. *Biochim. Biophys. Acta 1590*, 131−139.
(30) Moghimi, S. M., Hunter, A. C., and Murray, J. C. (2001) Long-circulating and target-specific nanoparticles: theory to practice. *Pharmacol. Rev. 53*, 283−318.
(31) Bhadra, D., Bhadra, S., Jain, P., and Jain, N. K. (2002) Pegnology: a review of PEG-ylated systems. *Pharmazie 57*, 5−29.
(32) Li, Y., Pei, Y., Zhang, X., Gu, Z., Zhou, Z., Yuan, W., Zhou, J., Zhu, J., and Gao, X. (2001) PEGylated PLGA nanoparticles as protein carriers: synthesis, preparation and biodistribution in rats. *J. Controlled Release 71*, 203−211.
(33) Zalipsky, S., Brandeis, E., Newman, M. S., and Woodle, M. C. (1994) Long circulating, cationic liposomes containing amino-PEG-phosphatidylethanolamine. *FEBS Lett. 353*, 71−74.
(34) Zhang, Y., Kohler, N., and Zhang, M. (2002) Surface modification of superparamagnetic magnetite nanoparticles and their intracellular uptake. *Biomaterials 23*, 1553−1561.

BC060377F

Identification of an Orthogonal Peptide Binding Motif for Biarsenical Multiuse Affinity Probes

Baowei Chen, Haishi Cao, Ping Yan, M. Uljana Mayer, and Thomas C. Squier*

Cell Biology and Biochemistry Group, Biological Sciences Division, Pacific Northwest National Laboratory, P.O. Box 999, Richland, Washington 99352. Received December 18, 2006; Revised Manuscript Received April 5, 2007

Biarsenical multiuse affinity probes (MAPs) complexed with ethanedithiol (EDT) permit the selective cellular labeling of proteins engineered with tetracysteine motifs, but are limited by the availability of a single binding motif (i.e., CCPGCC or PG tag) that prevents the differential labeling of coexpressed proteins. To overcome this problem, we have used a high-throughput peptide screen to identify an alternate binding motif (i.e., CCKACC or KA tag), which has a similar brightness to the classical sequence upon MAP binding, but displays altered rates and affinities of association that permit the differential labeling of these peptide sequences by the red probe 4,5-bis(1,3,2-dithiarsolan-2-yl)-resorufin (ReAsH-EDT_2) or its green cognate 4′,5′-bis(1,3,2-dithoarsolan-2-yl)-fluorescein (FLAsH-EDT_2). The utility of this labeling strategy was demonstrated following the expression of PG- and KA-tagged subunits of RNA polymerase in *E. coli*. Specific labeling of two subunits of RNA polymerase in cellular lysates was achieved, whereby ReAsH-EDT_2 is shown to selectively label the PG-tag on RNA polymerase α-subunit prior to the labeling of the KA-tag sequence of the β-subunit of RNA polymerase with FlAsH-EDT_2. These results demonstrate the ability to selectively label multiple individual proteins with orthogonal sequence tags in complex cellular lystates with spectroscopically distinct MAPs, and indicate the absolute specificity of ReAsH to target expressed proteins with essentially no nonspecific binding interactions.

INTRODUCTION

Biarsenical multiuse affinity probes (MAPs[1]) based on a xanthene scaffold permit the selective labeling of expressed proteins that contain a tetracysteine motif and have been used for the affinity isolation of individual proteins and associated complexes, for the biophysical characterization of protein structure and binding interactions, and for cellular imaging and turnover measurements of protein expression (*1*−*10*). Specific labeling is accomplished through the chelation of each arsenic with a pair of vicinal cysteines within a tetracysteine tag sequence, which is uncommon within endogenously expressed proteins (*4*). Important to these applications has been (*1*) the ability to stabilize the arsenics through their reversible association with ethanedithiol (EDT) in order to enhance membrane permeability, decrease nonspecific binding, and protect the arsenic from oxidation and polymerization, and (*2*) the identification of an optimal 9−12 amino acid high-affinity binding motif involving a tetracoordinate linkage between the biarsenical and the vicinal thiols associated with a PG-tag sequence (i.e., a CCPGCC tag) (*11*, *12*). The commercially available red probe 4,5-bis(1,3,2-dithiarsolan-2-yl)-resorufin (ReAsH-EDT_2) and its green cognate 4′,5′-bis(1,3,2-dithoarsolan-2-yl)fluorescein (FlAsH-EDT_2) both bind with high affinity to the PG-tag sequence, permitting the use of competing dithiol reducing agents to minimize nonspecific binding (*12*).

To date, only a single high-affinity peptide motif has been identified, preventing the simultaneous use of ReAsH-EDT_2 and FlAsH-EDT_2 to label multiple tag sequences for structural measurements of protein dynamics or cellular colocalization. In fact, current approaches involve the pairing of a tetracysteine tag with a cyanofluorescent protein (CFP) derived from the jellyfish *Aequorea victoria* (*13*), whose relatively large size and slow folding kinetics have the potential to perturb both protein structure and cellular localization. ReAsH and FlAsH are synthesized as ethanedithiol adducts in order to protect the arsenic from oxidation and polymerization. In the initial study of the binding kinetics, the starting material was not this commercial form, but rather the arsenoxide (*11*). Since the reaction does not involve the thiol exchange necessary for the binding of the EDT chelates, the reported binding rates may overestimate the rates of reaction using the stable ReAsH-EDT_2 and FlAsH-EDT_2 compounds. Furthermore, it is commonly suggested that addition of 1,2-dithiol antidotes such as 1,2-ethanedithiol (EDT) or 2,3-dimercaptopropanol (BAL) into the reaction mixture can facilitate the reduction of nonspecific binding to endogenous cysteine-rich proteins (*12*, *14*), but the binding kinetics under conditions of competing dithiol ligand have not been reported.

To extend the applicability of MAPs, we have used a surface-bound peptide library to identify useful protein-encoded tags in addition to CCPGCC that would permit the specific labeling of distinct tag sequences with both ReAsH-EDT_2 and FlAsH-EDT_2. Through one round of selection, in which the two amino acids between the vicinal cysteines were substituted combinatorially, we identified an alternate binding sequence with the amino acids KA located between two pairs of vicinal cysteines (i.e., KA-tag), which has a similar brightness to the classical sequence upon MAP binding, but displays altered rates and affinities of association that permit the differential labeling of these peptide sequences engineered into the α- and β-subunits

* Correspondence should be addressed to: Thomas C. Squier, Pacific Northwest National Laboratory; P.O. Box 999; Mail Stop P7-53; Richland, WA 99352; e-mail: thomas.squier@pnl.gov; Tel: (509) 376-2218; FAX: (509) 372-1632.

[1] Abbreviations: β-ME, beta-mercaptoethanol; DTT, dithiotreitol; EDT, 1,2-ethanedithiol; FlAsH-EDT_2, 4,5-bis(1,3,2-dithioarsolan-2-yl)-fluorescein also known as fluorescein arsenical helix binder; HEPES, *N*-(2-hydroxyethyl)piperazine-*N*′-(2-ethanesulfonic acid); MAP, multiuse affinity probe; ReAsH-EDT_2, 4,5-bis(1,3,2-dithioarsolan-2-yl)-resorufin; SDS-PAGE, sodium dodecyl sulfate-polyacrylamide gel electrophoresis; TCEP, tris(carboxyethyl)phosphine.

10.1021/bc0603900 CCC: $37.00 © 2007 American Chemical Society
Published on Web 06/15/2007

of RNA polymerase by the red probe ReAsH-EDT_2 and its green cognate FlAsH-EDT_2.

EXPERIMENTAL PROCEDURES

Materials. 4,5-Bis(1,3,2-dithiarsolan-2-yl)-resorufin (ReAsH-EDT_2 or Lumio Red) and 4′,5′-bis(1,3,2-dithoarsolan-2-yl)-fluorescein (FLAsH-EDT_2 or Lumio Green) were synthesized as previously described (*3*, *11*) or, in the case of FlAsH-EDT_2, obtained commercially under the trade name Lumio Green (Invitrogen, Carlsbad, CA), *N*-(2-Hydroxyethyl)piperazine-*N*′-(2-ethanesulfonic acid) (HEPES) and tris(carboxyethyl)phosphine (TCEP) were obtained from Sigma (St. Louis, MO). 2-Mercaptoethanol (β-ME) and 1,2-ethanedithiol (EDT) were obtained from Aldrich (Milwaukee, WI). The peptides, AR-EACCPGCCK-$CONH_2$ (peptide PG) and AREACCKACCK-$CONH_2$ (peptide KA) were obtained from SynPep Corporation (Dublin, CA). The concentration of tetracysteine-containing peptide was measured as previously described (*15*). All other chemicals were the purest grade commercially available.

Peptide Arrays. The peptide library was from Sigma-Genosys (The Woodlands, Texas), which contained 208 different 15 amino acid acetylated peptides (5 nmol per spotted peptide) that were immobilized on a cellulose membrane through the C-terminus with the basic structure Ac-YYYYWDCCXXCC-KAA. The YYYY sequence at the N-terminus was constrained to be GGGG, AAAA, or the originally proposed AREA sequence (*11*), while XX was systematically varied. High-affinity binding sequences were identified following overnight incubation with FlAsH-EDT_2 (5 nmol). Sequences of each peptide and identified peptides that became very bright upon binding FlAsH-EDT_2 are provided in the Supporting Information.

Peptide-Tag Labeling. Peptide tags (1 μM) were placed in 50 mM HEPES (pH 7.5), 140 mM KCl, 1 mM β-ME, and 1 mM TCEP at room temperature for 1 h to reduce any disulfide bonds prior to incubation at 4 °C with either ReAsH-EDT_2 or FLAsH-EDT_2. Fluorescence emission spectra of ReAsH-peptide or FlAsH-peptide complexes were measured using a Fluoro Max-2 fluorometer (SPEX, Edison, NJ), with excitation and emission slits set at 5 nm. In all cases, the sample temperature was 25 °C. Apparent rate constants were calculated from the second-order reaction

$$\frac{F_t}{[\mathrm{L}]_{t=0} \times (F_{\max} - F_t)} = kt \quad (1)$$

where F_{max} is the fluorescence maximum, F_t is the fluorescence at time t, $[L]_{t=0}$ is the concentration of fluorescent probe at time zero, k is the second-order rate constant, and t is the time of reaction. For equilibrium binding measurements, the extent of labeling was assessed following 24 h, and the concentration of peptide that is in association with the fluorescent probe, i.e., $[FP]_{bound,}$ can be calculated such that

$$[\mathrm{FP}] = \frac{\Delta F}{\Delta F_{\max}} \times [\mathrm{F}]_{\mathrm{total}} = \left[\frac{|(F - F_0)|}{|(F_{\max} - F_0)|}\right] \times [\mathrm{F}]_{\mathrm{total}} \quad (2)$$

where F_0 is the initial fluorescence, F_{max} is the fluorescence observed in the presence of saturating concentrations of peptide, and F is the observed fluorescence at a particular peptide concentration. $[F]_{total}$ is the concentration of FlAsH-EDT_2 or ReAsH-EDT_2 in solution. Determination of the binding affinities assumes a ligand exchange mechanism whereby the binding of the vicinal cysteines within the target peptides to the two arsenics on the MAPs involves the displacement of the bound EDT, as described by the following equilibrium.

$$\mathrm{MAP} + \text{Peptide Tag} \rightarrow \text{MAP-Peptide complex} + 2\ \mathrm{EDT} \quad (3)$$

The dissociation constant, K_d, can be described as

$$K_{\mathrm{d}} = \frac{[\mathrm{F}][\mathrm{P}]}{[\mathrm{FP}][\mathrm{EDT}]^2} \quad (4)$$

where [F] and [P] represent the concentration of free dye and free peptide, respectively. [EDT] represents the concentration of ethanedithiol, which must be in large excess of the dye or peptide concentrations in order to calculate an apparent dissociation constant, K_{app}, as given by

$$K_{\mathrm{app}} = K_{\mathrm{d}}[\mathrm{EDT}]^2 = [\mathrm{F}][\mathrm{P}]/[\mathrm{FP}] \quad (5)$$

When the reaction is at equilibrium, then

$$[\mathrm{F}]_{\mathrm{total}} = [\mathrm{F}] + [\mathrm{FP}] \quad (6)$$

$$[\mathrm{P}]_{\mathrm{total}} = [\mathrm{P}] + [\mathrm{FP}] \quad (7)$$

where $[P]_{total}$ is the concentration of added peptide. After rearranging, the concentration of the dye−peptide complex [FP] can be solved, where

$$[\mathrm{FP}]^2 - ([\mathrm{F}]_{\mathrm{total}} + [\mathrm{P}]_{\mathrm{total}} + K_{\mathrm{app}})[\mathrm{FP}] + [\mathrm{F}]_{\mathrm{total}}[\mathrm{P}]_{\mathrm{total}} = 0 \quad (8)$$

$$[\mathrm{FP}] = \{([\mathrm{F}]_{\mathrm{total}} + [\mathrm{P}]_{\mathrm{total}} + K_{\mathrm{app}}) - [([\mathrm{F}]_{\mathrm{total}} + [\mathrm{P}]_{\mathrm{total}} + K_{\mathrm{app}})^2 - 4[\mathrm{F}]_{\mathrm{total}}[\mathrm{P}]_{\mathrm{total}}]^{1/2}\}/2 \quad (9)$$

Substitution of [FP] (see eq 2) yields

$$\Delta F = \Delta F_{\max}\{([\mathrm{F}]_{\mathrm{total}} + [\mathrm{P}]_{\mathrm{total}} + K_{\mathrm{app}}) - [([\mathrm{F}]_{\mathrm{total}} + [\mathrm{P}]_{\mathrm{total}} + K_{\mathrm{app}})^2 - 4[\mathrm{F}]_{\mathrm{total}}[\mathrm{P}]_{\mathrm{total}}]^{1/2}\}/2[\mathrm{F}]_{\mathrm{total}} \quad (10)$$

Cloning and Expression of RNA Polymerase Subunits. A C-terminus 52 amino acid sequence was appended onto the α- or β-subunit of RNA polymerase (SO0256 or SO0257) from *Shewanella oneidensis* cloned into the pBAD/DTOPO 202 vector (Invitrogen) containing in the following order a tetracysteine tag (either AREACCPGCCK or AREACCKACCK) adjacent to a V5 epitope (KGGRADPAFLYKVVINSKLEGK PIPNPLLGL) and His_6 sequence at the C-terminus, as previously described (*5*). The pBAD-TOPO expression system contains the promoter of the *araBAD* (arabinose) operon, which can be upregulated by arabinose and downregulated by glucose to permit optimal expression. Plasmids were maintained by addition of 20 μg/mL kanamycin.

Following transformation of *E. coli*, cells were grown in flasks in standard Luria-Bertani growth media. Cells were grown until the optical density was 0.4−0.6, and PG-tagged α- or KA-tagged β-subunits were expressed near native levels (about 0.5 pM). Following overnight growth at 30 °C, cells were collected by centrifugation and lysed. Cell lysates (5 mg/mL) in 50 mM HEPES (pH 7.5), 140 mM NaCl, 2 mM β-ME, and 5 mM TCEP were labeled in the dark (due to the photoinstability of ReAsH; see Figure S1 in Supporting Information) with either FlAsH-EDT_2 or ReAsH-EDT_2 (5 μM) for 20 min. Alternatively, equal amounts of lysate expressing either the PG-tagged α- or KA-tagged β-subunits were mixed prior to their sequential labeling, which involved first addition of ReAsH-EDT_2 (5 μM) for 20 min followed by the addition of FlAsH-EDT_2 (5 μM) for an additional 20 min. Proteins were then separated by sodium dodecyl sulfate−polyacrylamide gel electrophoresis (SDS-

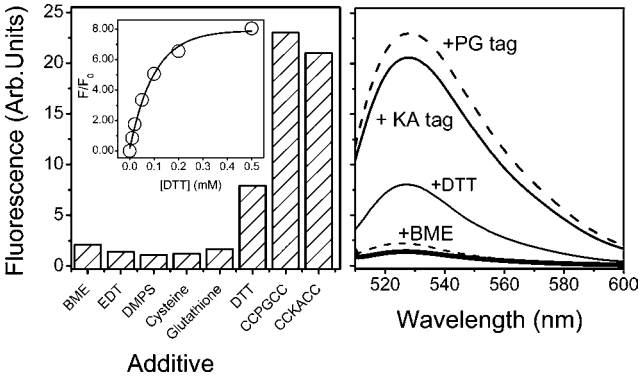


Figure 1. Maximal fluorescence intensities (left panel) and selected emission spectra (right panel) for FlAsH-EDT$_2$ (1 μM) in the presence of indicated thiol reagents (500 μM) or tetracysteine-containing peptide motifs (1 μM) in 50 mM HEPES (pH 7.5), 140 mM KCl, 1.0 mM EGTA, 1.0 mM β-ME, and 1.0 mM TCEP. Inset shows dependence of emission spectra on added DTT. Excitation was at 500 nm.

PAGE) and protein bands were visualized with GELCode Blue stain reagent (Pierce, Rockford, IL); the fluorescence was observed by Kodak IS2000MM illuminator with selected filters for excitation and emission.

RESULTS

Identification and Fluorescence Properties of Multiuse Affinity Probes Bound to Target Peptide. Currently, two commercially available biarsenical dyes, i.e., ReAsH-EDT$_2$ and FlAsH-EDT$_2$, permit the labeling of tagged proteins in cells, but cannot be used in multicolor experiments due to the current limitation of a single class of tetracysteine peptide motifs that bind these probes with similar affinities. To circumvent this problem, we have used a combinatorial peptide screen to identify new peptide motifs that differentially bind these commercially available MAPs. Briefly, this involved selection of a cellulose-derivatized peptide library containing 208 different peptide motifs for optimal candidate sequences that preferentially bind FlAsH-EDT$_2$ to form a highly fluorescent complex. Following overnight incubation with limiting amounts of FlAsH-EDT$_2$, 18 very bright peptides were identified that fall into 2 sequence classes corresponding to the previously identified CCPGCC motif (PG-peptide) (*11*, *12*) and a motif with a basic amino acid at the first position between the vicinal cysteines (i.e., KA-peptide) (see Supporting Information). Following identification of these candidate peptides, we have measured the binding kinetics and affinities of ReAsH-EDT$_2$ and FlAsH-EDT$_2$ to these two peptide motifs. Since all prior measurements of MAP binding to target peptides involved unchelated MAP (i.e., no bound EDT), we have also measured the apparent affinities and reaction rates for both FlAsH-EDT$_2$ and ReAsH-EDT$_2$ against both the classical PG-peptide and the newly introduced KA-peptide in the presence of both EDT (suggested to enhance labeling specificity) and other thiols that are either present within cells or have previously been suggested to reduce nonspecific binding (*9*).

As previously described (*4*, *11*), there is a large (i.e., >20-fold) increase in the fluorescence of FlAsH-EDT$_2$ or ReAsH-EDT$_2$ upon binding the PG-peptide (Figure 1) (see Supporting Information for photostability data). In the presence of a large excess of 1,2-ethanedithiol (EDT), 2,3-dimercapto-1-propanesulfonic acid (DMPS), cysteine, or glutathione, there is little change in the fluorescence. A similar large increase in fluorescence is observed upon binding to the KA-peptide or the dithiol DTT (albeit with a substantially reduced affinity; $K_d = 0.1$ mM; Figure 1), whose intensities are approximately 91% and 38% of that associated with binding to the PG-peptide. These latter results indicate that DTT cannot be used as a reducing agent in the application of biarsenical dyes due to substantially higher background fluorescence. A much smaller increase is observed in the presence of β-mercaptoethanol (β-ME), which has been suggested to reduce nonspecific binding in cell imaging measurements with reduced toxicity in comparison to the application of EDT (*9*).

The fluorescence enhancement upon binding to DTT further suggests the possible structural underpinning associated with the large fluorescence enhancements associated with binding to target peptides in comparison to other thiols. Our results suggest a relationship between the ring size between the arsenic atoms in FlAsH and the sulfur ligands. On the basis of the structure of thiol reagents, EDT and DMPS can form a complex with the arsenic in FlAsH to form a rigid five-membered ring that has a very low fluorescence. In contrast, following derivatization with DTT, a seven-membered ring is formed that has an intermediate fluorescence. Upon liganding to either PG-tag or KA-tag sequences, a nine-membered ring can form that is associated with the large fluorescence enhancement (Figure 1). Consistent with this model, there is a small increase in fluorescence for FlAsH in the presence of 0.5 mM β-ME that is significantly higher than observed in the presence of either EDT or DMPS. These results are consistent with the known hydrogen bonding character between proximal β-ME that can form upon the liganding of two β-ME with the arsenic atoms of FlAsH to form a transient nine-membered ring. Thus, our results demonstrate that binding of the small mono- and dithiols (i.e., β-ME and DTT) to FlAsH result in an enhanced fluorescence that, in the case of DTT, is comparable to that following peptide tag binding and correlates strongly with increases in ring size. We suggest that arsenic is capable of quenching fluorescein fluorescence, and that ability, in turn, is modulated by the ring strain induced by the arsenic liganding. This is in contrast to prior suggestions that attributed the low fluorescence of FlAsH-EDT$_2$ in comparison to the peptide bound dye to the greater mobility of the arsenic atoms bound to the small ligands that would act to "quench the fluorescence of fluorescein" (http://www.invitrogen.com/content/sfs/manuals/ lumiogreen-detection_man.pdf).

Rates of ReAsH− or FlAsH−Peptide Complex Formation. Under conditions in which there is a large molar excess of PG- or KA-peptide tag relative to ReAsH-EDT$_2$ or FlAsH-EDT$_2$, there is a linear relationship between the pseudo-first-order constant associated with fluorescent probe binding and the concentration of peptide, which is indicative of a reaction mechanism involving second-order kinetics (data not shown). Using equimolar stoichiometries of fluorescent probes and peptides, we find that ReAsH-EDT$_2$ preferentially binds to the PG-peptide with a nearly 50% rate enhancement in comparison to the KA-peptide (Figure 2; Table 1). In comparison, the rates of FlAsH-EDT$_2$ binding to these peptide tags are very similar. These results indicate that ReAsH-EDT$_2$ labeling is sensitive to the conformation of the peptide binding motif in a manner that is not possible for the bigger FlAsH-EDT$_2$ moiety.

Binding of Tetracysteine-Containing Peptides with ReAsH-EDT$_2$ and FlAsH-EDT$_2$. Peptide binding to ReAsH-EDT$_2$ or FlAsH-EDT$_2$ was measured using associated increases in the fluorescence intensity upon formation of the dye−peptide complex in the absence and presence of excess amounts of the competing dithiol EDT, whose presence diminishes the apparent affinity and permits an accurate determination of an apparent binding affinity (see eq 3 in Experimental Procedures). In all cases, it is apparent that FlAsH-EDT$_2$ binds to all peptide sequences with a higher affinity than ReAsH-EDT$_2$, and that the presence of EDT results in a reduction in the apparent affinity. In the absence of unliganded EDT, binding to both the

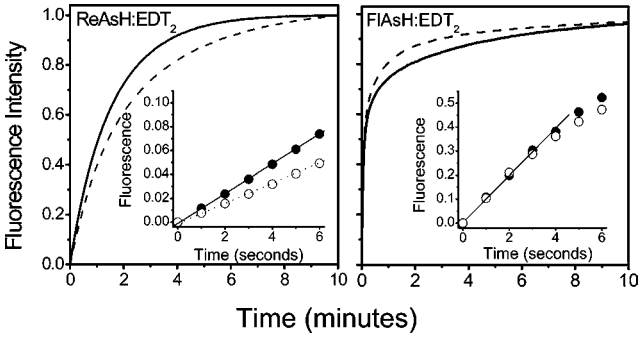


Figure 2. Binding kinetics of ReAsH-EDT_2 or FlAsH-EDT_2 (1 μM) to peptides (1 μM) AREACCPGCCK-$CONH_2$ (peptide PG) (solid line; closed circles) or AREACCKACCK-$CONH_2$ (peptide KA) (dashed line; open circles). In all cases, the reaction mixture contained 50 mM HEPES (pH 7.5), 140 mM KCl, 1.0 mM EGTA, 1.0 mM β-ME, and 1.0 mM TCEP. Lines represent fits to eq 1, where for ReAsH-binding to PG and KA peptides, $k = 12.5 \pm 0.1 \times 10^3\ M^{-1}\ s^{-1}$ and $8.47 \pm 0.07 \times 10^3\ M^{-1}\ s^{-1}$. For FlAsH-binding to PG and KA peptides, $k = 124 \pm 8 \times 10^3\ M^{-1}\ s^{-1}$ and $k = 143 \pm 8 \times 10^3\ M^{-1}\ s^{-1}$ (KA peptide). Fluorescence was measured at 530 and 608 nm with excitation at 500 and 593 nm for FlAsH and ReAsH, respectively.

Table 1. Binding Rates and Apparent Affinities of FlAsH-EDT_2 and ReAsH-EDT_2 to Peptide Tags

complex	k ($M^{-1}\ s^{-1}$)[a]	K_{app} (μM)[b]
ReAsH-Peptide PG	12 500 ± 1000	1.3 ± 0.2
ReAsH-Peptide KA	8470 ± 700	3.3 ± 1.2
FlAsH-Peptide PG	124 000 ± 8000	0.24 ± 0.09
FlAsH-Peptide KA	143 000 ± 8000	0.85 ± 0.23

[a] The second-order rate constant obtained from fitting the data in Figure 2 using eq 1 in Experimental Procedures. [b] Apparent dissociation constant in presence of 200 μM EDT obtained from fitting data in Figure 3 to eq 10 in Experimental Procedures, where $K_d = K_{app}/[EDT]^2$.

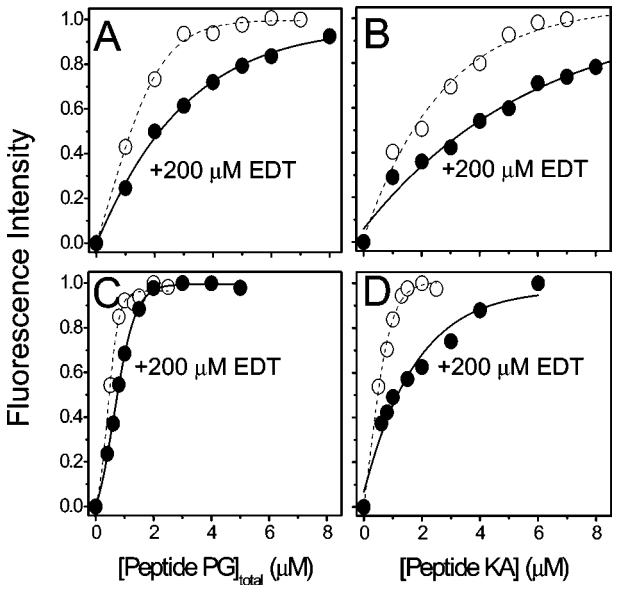


Figure 3. Equilibrium binding of ReAsH-EDT_2 (A, B) or FlAsH-EDT_2 (C, D) to peptides AREACCPGCCK-$CONH_2$ (peptide PG) or AREACCKACCK-$CONH_2$ (peptide KA) in the absence (○) or presence (●) of 200 μM EDT. Buffer contained 50 mM HEPES (pH 7.5), 140 mM KCl, 1.0 mM EGTA, 1.0 mM β-ME, and 1.0 mM TCEP at 25 °C. Dashed and solid lines represent fits to eq 10 in Experimental Procedures, assuming that respective concentrations of unliganded EDT in solution are negligible and 200 μM.

PG- and KA-peptide is essentially complete in the presence of equimolar amounts of FlAsH-EDT_2 and either peptide (Figure 3), consistent with prior estimates regarding the high-affinity binding of the unliganded bis-arsenoxide FlAsH probe to this peptide, whose K_d has been estimated to be approximately 10 pM (*11*).

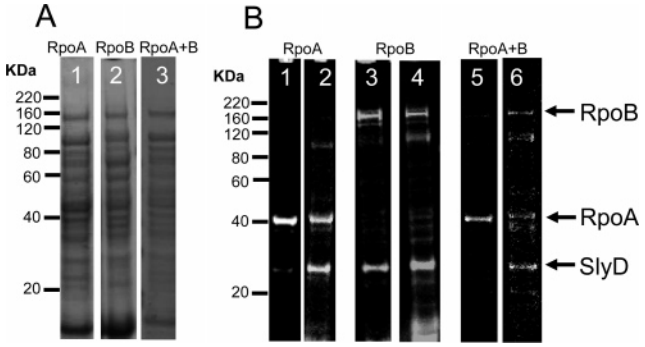


Figure 4. SDS-PAGE of cellular lysates corresponding to total protein gel-code blue protein stain (A) or fluorescence signals (B) associated with ReAsH (lanes 1, 3, and 5; $\lambda_{ex} = 555$ nm, $\lambda_{em} = 600$ nm) or FlAsH-labeling (lanes 2, 4, and 6; $\lambda_{ex} = 465$ nm, $\lambda_{em} = 535$ nm) of cellular lysates containing the α-subunit of RNA polymerase containing an engineered PG-tag (i.e., RpoA), the β-subunit of RNA polymerase containing an engineered KA-tag (i.e., RpoB), or equimolar amounts of both tagged proteins (i.e., RpoA+B). Labeling protocols are fully described in Experimental Procedures. Relative mobilities of molecular mass standards shown at left, and positions of RpoA, RpoB, and SlyD on SDS-PAGE obtained from authentic standards are indicated.

A quantitative determination of differences in binding affinities is possible in the presence of excess EDT, as the presence of EDT reduces the apparent dissociation constant (i.e., $K_{app} = K_d \times [EDT]^2$). The reduction in the apparent dissociation constant (K_{app}) in the presence of EDT permits the accurate measurement of differences in binding affinities for the different peptides, and in the presence of excess EDT, apparent dissociation constants can be obtained (Table 1). In the presence of 200 μM EDT, differences in FlAsH-EDT_2 binding to the PG- and KA-peptides are revealed, where complete binding of FlAsH-EDT_2 requires a 2- and 6-fold molar excess of the PG- and KA-peptide (Figure 3). Likewise, complete binding of ReAsH-EDT_2 is observed in the presence of an 8- and 20-fold molar excess of the PG- and KA-peptides (data not shown for the KA-peptide). These differences reflect 3−4-fold differences in binding affinities (Table 1), and suggest a strategy to selectively label these peptide motifs with these complementary dyes.

Selective Labeling of Tagged Subunits in RNA Polymerase. Tagged α- and β-subunits of RNA polymerase (RNAP) complex were respectively expressed in *E. coli* with the PG- and KA-tags located near their C-termini at nearly native levels of expression (about 0.5 pM), essentially as previously described (*5*, *16*). The specificity of ReAsH-EDT_2 and FlAsH-EDT_2 binding to individual proteins was determined following expression of either the PG-tagged α-subunit (RpoA) or KA-tagged β-subunit (RpoB) of RNA polymerase (Figure 4). Prior to labeling, cell lysates (5 mg protein/mL) were incubated with either ReAsH-EDT_2 or FlAsH-EDT_2 (5 μM) in buffer containing 50 mM HEPES (pH 7.5), 140 mM NaCl, 2 mM β-mercaptoethanol, and 5 mM TCEP for 20 min prior to separation and visualization of labeling specificity using SDS-PAGE.

ReAsH-EDT_2 and FlAsH-EDT_2 both label RpoA tagged with the PG-tag, which migrates as a 40 kDa band on SDS-PAGE (Figure 4). However, while ReAsH-EDT_2 specifically labels RpoA, we find that FlAsH-EDT_2 binds to a number of additional proteins, with apparent molecular masses 28 kDa, 39 kDa, and 100 kDa. These results indicate that both ReAsH-EDT_2 and FlAsH-EDT_2 permit the labeling of expressed proteins in cellular lysates, but that ReAsH-EDT_2 has the required affinity and selectivity for applications involving the fluorescent labeling of low abundance proteins. Complementary measurements

assessed the ability of both ReAsH-EDT_2 and FlAsH-EDT_2 to bind the KA-peptide tag engineered onto the β-subunit of RNA polymerase (RpoB). Consistent with measurements using the PG-tag on RpoA, we find that ReAsH-EDT_2 and FlAsH-EDT_2 both label RpoB, which migrates with an apparent mass of about 160 kDa (Figure 4). However, in this application, ReAsH-EDT_2 and FlAsH-EDT_2 bind several additional proteins, including the prominent band at about 28 kDa corresponding to the thiol-rich chaperone SlyD protein (*17*).

Multicolor Labeling of RNA Polymerase Subunits. Differences in the affinities and kinetics of ReAsH-EDT_2 binding to the PG- and KA-peptides suggest a strategy to differentially label subunits of RNA polymerase. As a proof of principle, lysate expressing PG-tagged α- and KA-tagged β-subunits of RNA polymerase (i.e., RpoA and RpoB) were mixed, and the α- and β-subunits were then sequentially labeled. First, ReAsH-EDT_2 (5 μM) is used to modify the PG-tag sequence on the α-subunit of RNA polymerase (RpoA), which is possible due to the 50% rate enhancement and 3-fold increase in binding affinity (i.e., $1/K_{app}$) of the PG-tag in comparison to the KA-tag (Table 1). Second, following the selective labeling of the PG-tag sequence, FlAsH-EDT_2 (5 μM) was used to selectively label the KA-tag sequence on the β-subunit of RNA polymerase (RpoB). Using this strategy, specific labeling of two subunits of RNA polymerase in cellular lysates from *E. coli* was achieved (Figure 4), whereby ReAsH-EDT_2 specifically labels the RNA polymerase α-subunit RpoA engineered with a PG-tag in the presence of an equimolar mixture of RpoA and RpoB (engineered with the KA-tag). Following labeling of RpoA, the KA-tag sequence of the RNA polymerase β-subunit RpoB can then be labeled with FlAsH-EDT_2. These results demonstrate the ability to differentially label multiple proteins engineered with orthogonal sequence tags in complex cellular lysates with spectroscopically distinct MAPs.

DISCUSSION

Summary of Results. Using a combinatorial approach involving a peptide array, we have identified an orthogonal peptide tag sequence (i.e., CCKACCK-$CONH_2$ or KA-tag) that in combination with the classical PG-tag sequence permits the use of the commercially available cell permeable MAPs ReAsH-EDT_2 (Lumio Red) and FlAsH-EDT_2 (Lumio Green) for multicolor measurements in which different proteins engineered with either tag can be differentially labeled. Upon binding to either peptide-tag, similar levels of brightness are observed (Figure 1). In addition, we have for the first time characterized the affinities and rates of binding of the commercially available and stable forms of these dyes. As expected, the chelation of ReASH or FlAsH with EDT reduces the rates of protein modification, where complete labeling requires approximately 10 min (Figure 2). Further, the commonly suggested inclusion of EDT to reduce nonspecific labeling (*12*) results in a substantial reduction in the apparent binding affinity (Figure 3). Indeed, in our hands, labeling of tagged proteins in cellular lysates is minimal in the presence of amounts of EDT suggested to be necessary to reduce nonspecific binding. Rather, we find that optimal amounts and specificities of labeling are observed in the presence of both 2 mM β-ME and 5 mM TCEP (but no competing EDT) (Figure 4). Under the latter conditions, we have demonstrated the ability to specifically modify a PG-tagged α-subunit of RNA polymerase (i.e., RpoA) with ReAsH-EDT_2 in the presence of an equimolar amount of the β-subunit of RNA polymerase engineered with the KA-tag (see lane 5 in Figure 4). This specificity of labeling permits the subsequent modification of the KA-tag on the β-subunit using FlAsH-EDT_2 for multicolor measurements.

Genetic Tagging and Cell Permeable Multiuse Affinity Probes. To understand the expression, localization, and fate of proteins in live cells, current approaches emphasize the engineering of GFP mutants with improved properties and altered colors that provide the basic tools to investigate more complex processes in live cells (*18*−*20*). However, because of the large size of GFP and its slow folding kinetics, it has the potential to alter the function, binding interactions, and localization of tagged proteins (*21*). Furthermore, in bacteria GFP labels are often incompatible with cellular export systems associated with the trafficking of proteins into the periplasm. The development of small molecular probes, i.e., the biarsenical dyes FlAsH and ReAsH, have largely overcome these prior limitations (*3*, *4*, *11*, *22*, *23*). The specific ligand for the labeling reaction is the small tetracysteine binding motif (i.e., CCXXCC), whose sequence is readily engineered within the gene encoding the protein of interest. Indeed, the small tag can be placed within the protein of interest to minimize the physical interference associated with N- or C-terminal tags, and to allow direct functional measurements of protein conformational change and binding interactions (*1*, *2*, *4*).

Recent improvements in the brightness and selectivity of FlAsH-EDT_2 analogs offer the potential to image low-abundance proteins in living cells (*24*, *25*). Nevertheless, the prior recognition of only a single binding motif has limited the application of multiuse affinity probes to imaging the cellular locations or turnover of individual proteins (*8*, *20*), while the identification of protein−protein interactions requires the use of Aequorea-derived fluorescent proteins such as YFP (*13*). In this respect, the identification of orthogonal tags using a combinatorial screen that permit the simultaneous use of both commercially available MAPS (i.e., ReAsH-EDT and FlAsH-EDT_2) to selectively modify the α- and β-subunits of RNA polymerase tagged, respectively, with PG- and KA-tags extends the range of possible applications of these cell-permeable reagents to selectively label multiple proteins to assess protein−protein interactions using, for example, fluorescence resonance energy transfer or colocalization single-molecule measurements in cell lysates. This strategy permits the validation of protein−protein interactions identified using high-throughput screens and mass spectrometry, when specific pairwise interactions are not certain. Thus, upon tagging multiple proteins, their association in a protein complex can be directly assessed using, for example, single-molecule methods that measure the association between tagged proteins to validate their interactions without the need to try to purify specific binding partners. In addition, these reagents permit fluorophore-assisted light inactivation (FALI) to selectively knock-out targeted protein activities to aid in the identification of their functions as well as the modulation of metabolic networks (*26*−*28*). However, additional specificity for cellular measurements will require the introduction of new biarsenical probes with different spacings between the arsenic ligands, providing greater labeling specificity.

Practical Considerations. Observed rates of binding for the commercially available and more stable reagents ReAsH-EDT_2 or FlAsH-EDT_2 to tag sequences are substantially slower than reported for the unliganded probes, which bind to peptide tags on the time scale of seconds, and require approximately 10 min for stoichiometric labeling due to the requirement for ligand exchange (Figure 2). Furthermore, the high-affinity association of the unliganded dyes with peptide tags (K_d = 10 pM) is substantially reduced in the presence of added EDT (Figure 3) (*11*). In the presence of 200 μM EDT, which has previously been suggested to minimize nonspecific binding (*12*), we find that apparent binding affinities are in the micromolar range (Table 1). Indeed, under the latter conditions, we observe low stoichiometries of peptide-tag modification in cellular lysates

(data not shown), limiting the ability of these reagents to image highly abundant proteins. In contrast, using other reducing reagents (e.g., β-mercaptoethanol and TCEP), we are able to selectively modify tagged proteins with nearly equimolar stoichiometries of either ReAsH-EDT_2 or FlAsH-EDT_2, permitting both enhanced detection of low-abundance proteins and multicolor experiments involving the differential labeling of PG- and KA-tags engineered onto different proteins. In this application, we take advantage of the substantially larger rates of labeling and binding affinity of ReAsH-EDT_2 binding against the PG-peptide tag in comparison to the KA-tag (Figure 4). Following the stoichiometric labeling of PG-tagged protein (RpoA) with ReAsH-EDT_2, it is then possible to label the KA-tagged protein (RpoB) with the higher-affinity FlAsH-EDT_2 probe with minimal cross-reactivity.

Conclusions and Future Directions. The identification of orthogonal peptide tags permits the simultaneous application of the commercially available and stable biarsenical dyes ReAsH-EDT_2 and FlAsH-EDT_2 to differentially label multiple proteins, providing a path forward for their use in multicolor measurements relating to protein associations and colocalization. Specificity of labeling is dependent on the reduction of peptide tags with the cell-permeant reducing agents β-mercaptoethanol and tris(carboxyethyl)phosphine (TCEP), which act to enhance binding to peptide tags without significantly affecting the binding affinity. These differences in binding specificities were demonstrated using a single peptide scaffold in which vicinal cysteines were separated by two amino acids whose sequence was altered, indicating that modest conformational differences in the binding sequence of the peptide tag can promote differences in binding specificity. These results suggest that further variation of the scaffold to vary the spatial separation between the biarsenical linkages within the probes will provide the required specificity to allow the generation of a family of cell-permeant affinity probes that permit simultaneous labeling and isolation of multiple tagged proteins, using peptide tags with variable spacing between the vicinal cysteine binding ligands.

ACKNOWLEDGMENT

This work was supported by the U.S. Department of Energy, Office of Science Genomics: GTL project. Pacific Northwest National Laboratory is operated for the U.S. Department of Energy by Battelle Memorial Institute under contract DE-AC05-76RLO 1830.

Supporting Information Available: Peptide sequences using an initial screen to identify orthogonal binding sequences for FlAsH-EDT_2 and ReAsH-EDT_2, as well as their photostability in the presence of room light levels (Figure S1). This material is available free of charge via the Internet at http://pubs.acs.org.

LITERATURE CITED

(1) Chen, B., Mayer, M. U., Markillie, L. M., Stenoien, D. L., and Squier, T. C. (2005) Dynamic motion of helix A in the amino-terminal domain of calmodulin is stabilized upon calcium activation. *Biochemistry 44*, 905−914.

(2) Chen, B., Mayer, M. U., and Squier, T. C. (2005) Structural uncoupling between opposing domains of oxidized calmodulin underlies the enhanced binding affinity and inhibition of the plasma membrane Ca-ATPase. *Biochemistry 44*, 4737−4747.

(3) Griffin, B. A., Adams, S. R., Jones, J., and Tsien, R. Y. (2000) Fluorescent labeling of recombinant proteins in living cells with FlAsH. *Methods Enzymol. 327*, 565−578.

(4) Griffin, B. A., Adams, S. R., and Tsien, R. Y. (1998) Specific covalent labeling of recombinant protein molecules inside live cells. *Science 281*, 269−272.

(5) Mayer, M. U., Shi, L., and Squier, T. C. (2005) One-step, non-denaturing isolation of an RNA polymerase enzyme complex using an improved multi-use affinity probe resin. *Mol. Biosys. 1*, 53−56.

(6) Thorn, K. S., Naber, N., Matuska, M., Vale, R. D., and Cooke, R. (2000) A novel method of affinity-purifying proteins using a bis-arsenical fluorescein. *Protein Sci. 9*, 213−217.

(7) Shi, L., Chen, B., Wang, Z., Elias, D. A., Mayer, M. U., Gorby, Y. A., Ni, S., Lower, B. H., Kennedy, D. W., Wunschel, D. S., Mottaz, H. M., Marshall, M. J., Hill, E. A., Beliaev, A. S., Zachara, J. M., Fredrickson, J. K., and Squier, T. C. (2006) Isolation of a high-affinity functional protein complex between OmcA and MtrC: Two outer membrane decaheme c-type cytochromes of Shewanella oneidensis MR-1. *J. Bacteriol. 188*, 4705−4714.

(8) Gaietta, G., Deerinck, T. J., Adams, S. R., Bouwer, J., Tour, O., Laird, D. W., Sosinsky, G. E., Tsien, R. Y., and Ellisman, M. H. (2002) Multicolor and electron microscopic imaging of connexin trafficking. *Science 296*, 503−507.

(9) Langhorst, M. F., Genisyuerek, S., and Stuermer, C. A. (2006) Accumulation of FlAsH/Lumio Green in active mitochondria can be reversed by beta-mercaptoethanol for specific staining of tetracysteine-tagged proteins. *Histochem. Cell Biol. 125*, 743−747.

(10) Panchal, R. G., Ruthel, G., Kenny, T. A., Kallstrom, G. H., Lane, D., Badie, S. S., Li, L., Bavari, S., and Aman, M. J. (2003) In vivo oligomerization and raft localization of Ebola virus protein VP40 during vesicular budding. *Proc. Natl. Acad. Sci. U.S.A. 100*, 15936−15941.

(11) Adams, S. R., Campbell, R. E., Gross, L. A., Martin, B. R., Walkup, G. K., Yao, Y., Llopis, J., and Tsien, R. Y. (2002) New biarsenical ligands and tetracysteine motifs for protein labeling in vitro and in vivo: synthesis and biological applications. *J. Am. Chem. Soc. 124*, 6063−6076.

(12) Martin, B. R., Giepmans, B. N., Adams, S. R., and Tsien, R. Y. (2005) Mammalian cell-based optimization of the biarsenical-binding tetracysteine motif for improved fluorescence and affinity. *Nat. Biotechnol. 23*, 1308−1314.

(13) Hoffmann, C., Gaietta, G., Bunemann, M., Adams, S. R., Oberdorff-Maass, S., Behr, B., Vilardaga, J. P., Tsien, R. Y., Ellisman, M. H., and Lohse, M. J. (2005) A FlAsH-based FRET approach to determine G protein-coupled receptor activation in living cells. *Nat. Methods 2*, 171−176.

(14) Stroffekova, K., Proenza, C., and Beam, K. G. (2001) The protein-labeling reagent FLASH-EDT2 binds not only to CCXXCC motifs but also non-specifically to endogenous cysteine- rich proteins. *Pflugers Archiv. 442*, 859−866.

(15) Gill, S. C., and von Hippel, P. H. (1989) Calculation of protein extinction coefficients from amino-acid sequence data. *Anal. Biochem. 182*, 319−326.

(16) Verma, S., Xiong, Y., Mayer, M. U., and Squier, T. C. (2007) Remodeling of bacterial RNA polymerase supramolecular complex in response to environmental conditions. *Biochemistry 46*, 3023−3035.

(17) Scholz, C., Eckert, B., Hagn, F., Schaarschmidt, P., Balbach, J., and Schmid, F. X. (2006) SlyD proteins from different species exhibit high prolyl isomerase and chaperone activities. *Biochemistry 45*, 20−33.

(18) Tsien, R. Y. (1998) The green fluorescent protein. *Annu. Rev. Biochem. 67*, 509−544.

(19) Zacharias, D. A., and Tsien, R. Y. (2006) Molecular biology and mutation of green fluorescent protein. *Methods Biochem. Anal. 47*, 83−120.

(20) Giepmans, B. N., Adams, S. R., Ellisman, M. H., and Tsien, R. Y. (2006) The fluorescent toolbox for assessing protein location and function. *Science 312*, 217−224.

(21) Andresen, M., Schmitz-Salue, R., and Jakobs, S. (2004) Short tetracysteine tags to beta-tubulin demonstrate the significance of small labels for live cell imaging. *Mol. Biol. Cell 15*, 5616−5622.

(22) Zhang, J., Campbell, R. E., Ting, A. Y., and Tsien, R. Y. (2002) Creating new fluorescent probes for cell biology. *Nat. Rev. Mol. Cell Biol. 3*, 906−918.

(23) Gaietta, G. M., Giepmans, B. N., Deerinck, T. J., Smith, W. B., Ngan, L., Llopis, J., Adams, S. R., Tsien, R. Y., and Ellisman, M. H. (2006) Golgi twins in late mitosis revealed by genetically encoded

tags for live cell imaging and correlated electron microscopy. *Proc. Natl. Acad. Sci. U.S.A. 103*, 17777−17782.

(24) Cao, H., Chen, B., Squier, T. C., and Mayer, M. U. (2006) CrAsH: a biarsenical multi-use affinity probe with low non-specific fluorescence. *Chem. Commun. (Cambridge, U.K.)* 2601−2603.

(25) Spagnuolo, C. C., Vermeij, R. J., and Jares-Erijman, E. A. (2006) Improved photostable FRET-competent biarsenical-tetracysteine probes based on fluorinated fluoresceins. *J. Am. Chem. Soc. 128*, 12040−12041.

(26) Yan, P., Xiong, Y., Chen, B., Negash, S., Squier, T. C., and Mayer, M. U. (2006) Fluorophore-assisted light inactivation of calmodulin involves singlet-oxygen mediated cross-linking and methionine oxidation. *Biochemistry 45*, 4736−4748.

(27) Surrey, T., Elowitz, M. B., Wolf, P. E., Yang, F., Nedelec, F., Shokat, K., and Leibler, S. (1998) Chromophore-assisted light inactivation and self-organization of microtubules and motors. *Proc. Natl. Acad. Sci. U.S.A. 95*, 4293−4298.

(28) Tour, O., Meijer, R. M., Zacharias, D. A., Adams, S. R., and Tsien, R. Y. (2003) Genetically targeted chromophore-assisted light inactivation. *Nat. Biotechnol. 21*, 1505−1508.

BC0603900

Radiolabeled Divalent Peptidomimetic Vitronectin Receptor Antagonists as Potential Tumor Radiotherapeutic and Imaging Agents

Thomas D. Harris,* Edward Cheesman, Anthony R. Harris, Richard Sachleben,[†] D. Scott Edwards, Shuang Liu,[‡] Judit Bartis,[§] Charles Ellars,[||] Dave Onthank, Padmaja Yalamanchili, Stuart Heminway,[⊥] Paula Silva, Simon Robinson, Joel Lazewatsky, Milind Rajopadhye,[▽] and John Barrett[#]

Discovery Research, Bristol−Myers Squibb Medical Imaging, 331 Treble Cove Road, North, Billerica, Massachusetts 01862.
Received January 2, 2007; Revised Manuscript Received May 1, 2007

The integrin receptor $\alpha_v\beta_3$ is overexpressed on the endothelial cells of growing tumors and on some tumor cells themselves. A radiolabeled $\alpha_v\beta_3$ antagonists belonging to the quinolin-4-one class of peptidomimetics (**TA138**) was previously shown to exhibit high affinity for integrin $\alpha_v\beta_3$ and high selectivity versus other integrin receptors. ^{111}In-**TA138** exhibited high tumor uptake in the c-neu Oncomouse mammary adenocarcinoma model and produced excellent scintigraphic images. This study describes the synthesis of eight divalent versions of **TA138** and their evaluation as potential tumor radiotherapeutic agents. The two main variables in this study were the length of the spacer bridging the biotargeting moieties and the total negative charge of the molecules imparted by the cysteic acid pharmacokinetic modifiers. Receptor affinity was evaluated in a panel of integrin receptor affinity assays, and biodistribution studies using the ^{111}In-labeled derivatives were carried out in the c-neu Oncomouse model. All divalent agents maintained the high receptor affinity and selectivity of **TA138**, and six of the eight ^{111}In derivatives exhibited blood clearance that was faster than ^{111}In-**TA138** at 24 h postinjection (PI). All divalent agents exhibited tumor uptake and retention at 24 h PI that was higher than ^{111}In-**TA138**. Tumor/organ ratios were improved for most of the divalent agents at 24 h PI in critical nontarget organs marrow, kidney, and liver, with the agents having intermediate-length spacers (29−43 Å) showing the largest improvement. As an example, ^{111}In-**15** showed tumor uptake of 14.3% ID/g at 24 h PI and tumor/organ ratios as follows: marrow, 3.24; kidney, 7.29; liver, 8.51. A comparison of therapeutic indices for ^{90}Y-**TA138** and ^{177}Lu-**15** indicate an improved therapeutic index for the divalent agent. The implications for radiotherapeutic applications and the mechanism of this multivalent effect are discussed.

INTRODUCTION

Integrins are a large family of transmembrane heterodimeric glycoprotein cell surface receptors formed by associations between α and β subunits. Integrins are important facilitators of cell−cell and cell−matrix interactions, and are also involved in cell signaling events (*1*). This has made integrins an important area of study in cancer metastasis and angiogenesis research (*2*−*5*). The integrin $\alpha_v\beta_3$ (vitronectin receptor or VnR) is generally expressed at low levels on normal tissues and quiescent blood vessels, but is significantly upregulated on the neovasculature found in tumors and in wound repair (*6*−*9*) and is also present on certain tumor cells, including melanoma, kidney, breast, and prostate, and squamous cell carcinoma (*10*−*13*). This differential expression has made the vitronectin receptor a promising target in anti-angiogenic research (*14*, *15*). For example, antagonists of integrin $\alpha_v\beta_3$ have been demonstrated to inhibit tumor angiogenesis and disrupt metastasis in a number of models (*16*−*19*).

We and others have utilized integrin $\alpha_v\beta_3$ antagonists for selective localization of diagnostic and therapeutic radionuclides in the vicinity of malignant tumors. Cyclic RGD peptides labeled with ^{18}F and ^{64}Cu for PET imaging (*20*−*22*) and with ^{99m}Tc and ^{111}In for SPECT imaging (*23*−*26*) have been shown to exhibit selective tumor uptake in a variety of murine tumor models, and a ^{18}F-labeled RGD peptide has recently been evaluated in 19 human patients with solid tumors (*27*). The use of radiolabeled peptides to image tumor angiogenesis has recently been reviewed (*28*−*30*). Our goal in this area was the development of an integrin $\alpha_v\beta_3$ antagonist platform that could be utilized to deliver both imaging and radiotherapeutic isotopes to tumors. While many radiolabeled RGD peptides have demonstrated potential as tumor imaging agents, none have been able to combine the high tumor uptake and retention and low uptake in critical nontarget tissues required of a radiotherapeutic agent (*29*). We reasoned that peptidomimetics having high affinity and selectivity for integrin $\alpha_v\beta_3$ offered the best opportunity to deliver diagnostically and therapeutically useful quantities of radionuclides to tumors while minimizing dose to nontarget organs. We recently described the synthesis and evaluation of a series of peptidomimetic antagonists to integrin $\alpha_v\beta_3$ based on a substituted quinolin-4-one ring system (*31*, *32*). The agent providing the best combination of tumor uptake and tumor/organ ratios was ^{111}In-**TA138** (Figure 1). This agent uses 2-aminoimidazole and a 2,3-diaminopropionate (DAP) arylsulfonamide as mimics of the guanidine and carboxylate groups of the RGD sequence, respectively. Macrocyclic chelator DOTA allows for chelation to both imaging (^{111}In) and therapeutic (^{90}Y, ^{177}Lu) radionuclides, and is conjugated to the aryl sulfonamide group through a short spacer that includes cysteic acid as a pharmacokinetic modifier (PKM). ^{111}In-**TA138** was evaluated in the c-neu Oncomouse model, providing tumor uptake of 9.39% ID/g at 2 h postinjection (PI) and selected tumor/organ ratios at 2 h PI as follows: blood, 17.5; muscle, 17.1; liver,

* To whom correspondence should be addressed. Phone: 603-893-0031. Fax: 603-898-4605. E-mail: tdharris911@comcast.net.
[†] Present address: Momenta Pharmaceuticals, Cambridge, MA.
[‡] Present address: Division of Nuclear Pharmacy, Purdue University, West Lafayette, IN.
[§] Present address: ArQule, Woburn, MA.
[||] Present address: AEA Technology QSA, Burlington, MA.
[⊥] Present address: Astra Zeneca Pharmaceutical, Wilmington, DE.
[▽] Present address: VisEn Medical Inc., Woburn, MA.
[#] Present address: Molecular Insight, Cambridge, MA.

10.1021/bc070002+ CCC: $37.00 © 2007 American Chemical Society
Published on Web 06/19/2007

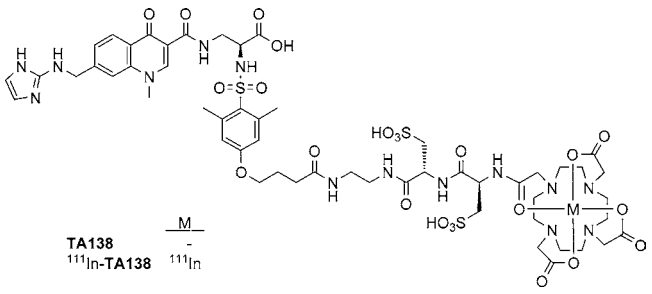


Figure 1. Structures of monovalent parent **TA138** and ^{111}In-**TA138**.

4.83; kidney, 4.04; bone 6.01. ^{111}In-**TA138** exhibited slow washout from the tumors, decreasing to 3.46% ID/g at 24 h PI.

These are excellent biodistribution properties from the viewpoint of an imaging agent, but they leave room for improvement for a radiotherapeutic agent. We were especially interested in a further slowing of tumor washout and in improving the tumor/organ ratios for critical nontarget organs such as kidneys and bone marrow. One technique that is commonly employed to improve receptor affinity and retention is polyvalency. Our early work with cyclic RGD peptides has shown that in the c-neu Oncomouse model (*33*), and in the OVCAR-3 xenograft model (*23*, *24*), divalent cyclic RGD peptide $\alpha_v\beta_3$ antagonists give superior tumor uptake and retention compared to the cyclic monovalent peptides. This polyvalency effect has also been noted by others for cyclic RGD peptides (*34*−*36*), for α-MSH receptor peptides (*37*), and for Tuftsin antagonist peptides (*38*). Herein, we report the complete details of the synthesis of eight divalent analogues of **TA138**, along with receptor affinity and biodistribution data of the ^{111}In-radiolabeled analogues. The general structures of these compounds are shown in Figure 2. The length of the spacer between the two biotargeting groups was varied over a wide range by the number and position of the cysteic acid PKMs and by the number of repeating PEG units, as shown in Table 1. Varying the total number of cysteic acid groups also provided control of the total charge on the molecule.

Table 1. Structural Features of Divalent Agents Shown in Scheme 1

compd	x	y	z	no. spacer atoms[a]	spacer length[b]	no. cysteic acids	Δ charge[c]
TA138	2	na	na	na	na	2	−
13	0	0	2	23	29	2	0
14	0	0	4	23	29	4	−2
15	1	0	0	29	36	2	0
16	1	0	1	29	36	3	−1
17	1	0	2	29	36	4	−2
18	2	0	0	35	43	4	−2
19	2	1	0	73	89	4	−2
20	2	2	0	111	134	4	−2

[a] Number of atoms between phenyl rings of arylsulfonamide groups. [b] Maximum spacer length calculated using an average interatomic distance of 1.2 Å, which takes into account the different bond angles and hybridization states of the atoms in the spacer. [c] Relative to **TA138**.

EXPERIMENTAL SECTION

General Experimental. All reactions were carried out under a dry nitrogen atmosphere at ambient temperatures, unless otherwise noted. All chemicals and solvents (reagent grade) were used as supplied from the vendors cited without further purification, unless otherwise noted. Solutions were concentrated under reduced pressure on a rotary evaporator, with final drying, if required, under high vacuum (<0.5 mmHg). Boc-Glu(OTfp)-OTfp was synthesized according to a previously published procedure (*39*). 3-((*tert*-Butoxy)carbonylamino)propyl bromide and 4,7,10-trioxa-1,13-tridecanediamine were purchased from Fluka. *tert*-Butyloxycarbonyl (Boc) amino acids and other starting amino acids were obtained from Bachem Inc., Bachem Biosciences Inc. (Philadelphia, PA), or Advanced ChemTech (Louisville, KY). 2-(1*H*-Benzotriazol-1-yl)-1,1,3,3-tetramethyluronium hexafluorophosphate (HBTU) and benzotriazol-1-yloxy-tris-pyrrolidinophosphonium hexafluorophosphate (PyBOP) were purchased from Advanced ChemTech. Ethyl acetate, chloroform ($CHCl_3$), methanol (MeOH), acetonitrile (ACN), dichloromethane (DCM), ethyl ether, acetone, and hydrochloric acid (HCl) were obtained from Baker. Anhydrous dimethylformamide (DMF), *N*-methylpyrrolidinone (NMP), acetonitrile (ACN), pyridine, triethylamine (TEA), and diisopropylethylamine (DIEA) were obtained from Aldrich in SureSeal bottles. Absolute ethanol was obtained from Quantum Chemical Corp. Merck silica gel, grade 9385, 230−400 mesh, 60 Å was used for flash chromatography. DOTA(O*t*-Bu)$_3$OH was obtained from Macrocyclics, Dallas, TX. Other reagents were obtained from Lancaster Synthesis, Inc., Aldrich Chemical Co, or Fluka Chemical Corp.

^{1}H NMR spectra were recorded on a Bruker Avance DRX (600 MHz) spectrometer. Chemical shifts are reported in parts per million (ppm) from tetramethylsilane with the residual

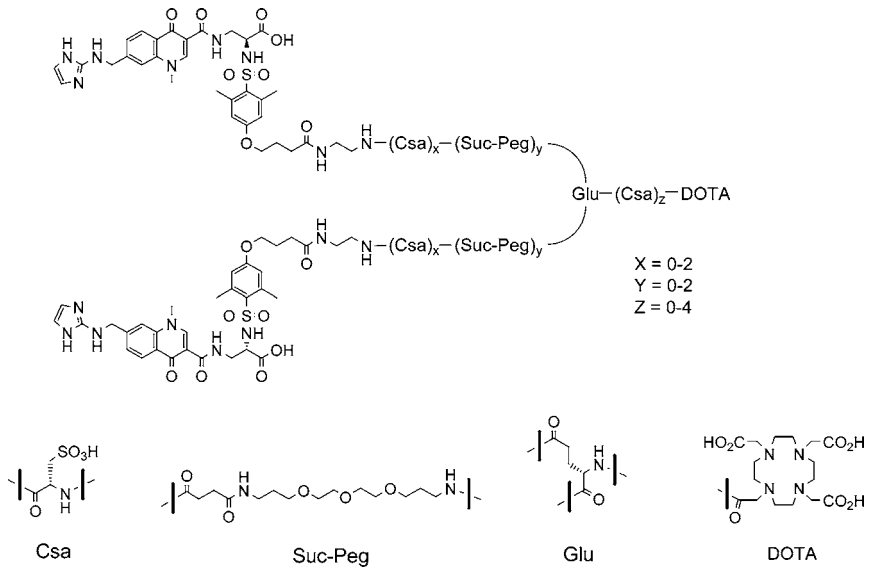


Figure 2. General structure of divalent integrin $\alpha_v\beta_3$ receptor antagonists of this study.

solvent resonance resulting from incomplete deuteration as the internal standard ($CDCl_3$, δ 7.25 ppm; ACN-d_3, δ 1.95 ppm; DMSO-d_6, δ 2.50 ppm). Data are reported as follows: chemical shift, multiplicity (s = singlet, d = doublet, t = triplet, q = quartet, quin = quintet, b = broad, m = multiplet), coupling constants, and integration. ^{13}C NMR spectra were recorded on a Bruker Avance DRX (150 MHz) with complete proton decoupling. Chemical shifts are reported in ppm from tetramethylsilane with the solvent as the internal reference ($CDCl_3$, δ 77.0 ppm; ACN-d_3, δ 118.1 ppm; DMSO-d_6, δ 39.5 ppm). Low-resolution mass spectra were recorded on an Agilent Technologies 1100 series LC/MS ESI-MS and are reported as *m/z*, fragment identification (C_4H_8 = isobutylene, Boc = isobutylene + CO_2, Trt = triphenylmethane), and percent relative abundance. High-resolution mass spectrometry was performed on an Ionspec Ultima FTMS; ESI-MS (positive mode). Chiral amino acid purity was determined according to a published GC-MS method (*40*). Melting points were determined using a Thomas-Hoover melting point apparatus and are uncorrected.

(VnR Antagonist)$_2$Glu-(Csa)2-DOTA (13). *Part A. Synthesis of (Trt-VnR Antagonist)$_2$Glu-H (**4**).* A solution of (*S*)-2-(4-(4-(2-aminoethylamino)-4-oxobutoxy)-2,6-dimethylphenylsulfonamido)-3-(1-methyl-4-oxo-7-((1-trityl-1*H*-imidazol-2-ylamino)methyl)-1,4-dihydroquinoline-3-carboxamido)-propanoic acid (1) (*41*) (1.41 g, 1.50 mmol) and DIEA (0.52 mL, 3.00 mmol) in DMF (14 mL) was treated with Boc-Glu-(OTfp)-OTfp (0.41 g, 0.75 mmol) and stirred for 18 h. The solution was concentrated, and the oily residue was triturated with EtOAc (2 × 25 mL) to give a dry, off-white solid. MS (ESI) *m/z* 1847.6 (M + H − Trt, 47), 1604.6 (M + H − 2Trt, 20), 1045.4 (M + 2H, 100), 924.0 (M + 2H − Trt, 42). The above solid was treated with 1:1 TFA/DCM (20 mL) and stirred for 1 h. The solution was concentrated, and the resulting red oil was triturated with diethyl ether (2 × 40 mL) to give a yellow solid. This crude product was divided into three portions, and these were individually purified by preparative HPLC on a Vydac C18 Pharmaceutical column (50 × 250 mm) using a 0.90%/min gradient of 22.5−72% ACN containing 1.65% TFA at a flow rate of 80 mL/min. The main product peak eluting at 15 min was collected and lyophilized to give the TFA salt of **4** as a colorless solid (1.36 g, 43%). MS (ESI) *m/z* 1989.6 (M + H, 40), 1747.6 (M + H − Trt, 45), 1626.5 (M + H − 2Trt, 10), 995.3 (M + 2H, 80).

*Part B. Synthesis of (Trt-VnR Antagonist)$_2$Glu-(Csa)$_2$-H (**9**).* A solution of Boc−L-cysteic acid (176 mg, 0.402 mmol), DIEA (640 μL, 3.68 mmol), and PyBOP (251 mg, 0.402 mmol) in DMF (15 mL) was stirred for 15 min and added to a previously prepared solution of **4** (800 mg, 0.380 mmol) and DIEA (365 μL, 2.09 mmol) in DMF (15 mL). The solution was stirred for 30 min and concentrated to an amber oil. The oil was triturated with EtOAc (2 × 25 mL) to give the Boc−cysteic acid conjugate as a dry, tan solid (884 mg). MS (ESI) *m/z* 2240.7 (M + H, 37), 1997.6 (M + H − Trt, 25), 1756.4 (M + H − 2Trt, 8), 1494.8 (2M + 3H, 8), 1120.8 (M + 2H, 75), 999.6 (M + 2H-Trt, 12). The above solid (884 mg) was dissolved in 1:1 TFA/DCM (20 mL), stirred for 45 min, and concentrated. The resulting oily residue was triturated with ether (2 × 50 mL) to give the amine TFA salt as a dry, off-white solid (865 mg). MS (ESI) *m/z* 1898.6 (M + H − Trt, 37), 1655.4 (M + H − 2Trt, 20), 1070.9 (M + 2H, 53), 949.4 (M + 2H − Trt, 25). A solution of Boc−L-cysteic acid (263 mg, 0.904 mmol), DIEA (315 μL, 1.81 mmol), and PyBOP (376 mg, 0.724 mmol) in DMF (15 mL) was stirred for 10 min and added to a previously prepared solution of the above amine salt (860 mg, 0.380 mmol). The solution was stirred for 30 min and concentrated to an oily yellow solid. Trituration of the solid with EtOAc (2 × 25 mL) gave a dry, pale yellow solid, which was divided into two portions, and these were individually purified by preparative HPLC on a Vydac C18 Pharmaceutical column (50 × 250 mm) using a 1.2%/min gradient of 31.5−67.5% ACN containing 0.1% TFA at a flow rate of 80 mL/min. The main product peak eluting at 18 min was collected and lyophilized to give the protected bis-cysteic acid conjugate as a colorless solid (670 mg, 74% from **4**). MS (ESI) *m/z* 1906.4 (M + H − 2Trt, 10), 1595.7 (2M + 3H, 12), 1196.2 (M + 2H, 45), 1074.9 (M + 2H − Trt, 30). A solution of this solid (670 mg, 0.280 mmol) in 1:1 TFA/DCM (20 mL) was stirred for 10 min and concentrated to give a yellow, oily solid. This solid was triturated with ether (2 × 50 mL) to give **9** as a pale yellow, dry solid (523 mg, 81%). MS (ESI) *m/z* 2050.4 (M + H − Trt, 19), 1806.4 (M + H − 2Trt, 10), 1146.3 (M + 2H, 42), 1024.8 (M + 2H − Trt, 28).

*Part C. Synthesis of **13**.* A solution of DOTA(O*t*-Bu)$_3$OH (210 mg, 0.366 mmol), DIEA (128 μL, 0.732 mmol), and HBTU (104 mg, 0.275 mmol) in DMF (15 mL) was stirred for 15 min and added to a previously prepared solution of the product from part B (520 mg, 0.227 mmol) and DIEA (192 μL, 1.10 mmol) in DMF (10 mL). The solution was stirred for 2.5 h and concentrated to a yellow solid, which was divided into two portions, and these were individually purified by preparative HPLC on a Vydac C18 Pharmaceutical column (50 × 250 mL) using a 1.20%/min gradient of 31.5−67.5% ACN containing 0.1% TFA at a flow rate of 80 mL/min. The main product peak eluting at 15 min was collected and lyophilized to give the TFA salt of the DOTA conjugate as a colorless solid (600 mg, 89%). MS (ESI) *m/z* 1898.1 (2M + 3H, 11), 1423.5 (M + 2H, 52), 1302.6 (M + 2H − Trt, 87), 1181.5 (M + 2H − 2Trt, 20). A solution of the DOTA conjugate (600 mg, 0.203 mmol) in 97:3 TFA/Et_3SiH (20 mL) was heated at 70 °C for 45 min and concentrated to an oily solid. The solid was partitioned between 10:90 ACN/H_2O (4.0 mL) and diethyl ether (2.0 mL). The aqueous phase was washed with additional diethyl ether (2 × 2 mL) and divided into two portions, and the portions were individually purified by preparative HPLC on a Vydac C18 Pharmaceutical column (50 × 250 mL) using a 0.75%/min gradient of 0.9−31.5% ACN containing 0.1% TFA at a flow rate of 80 mL/min. The main product peak eluting at 15 min was collected and lyophilized to give **13** (158 mg, 35%). MS (ESI) *m/z* 2193.4 (M + H, 6), 1463.0 (2M + 3H, 12), 1097.3 (M + 2H, 90), 731.8 (M + 3H, 100), 549.3 (M + 4H, 8). Amino acid analysis: L-Csa, 99.3%; L-Glu, 99.7%; L-DAP, 98.4%.

(VnR Antagonist)$_2$Glu-(Csa)$_4$-DOTA (14). *Part A. Synthesis of (Trt-VnR Antagonist)$_2$Glu-(Csa)$_4$-H (**10**).* A solution of Boc−L-cysteic acid (24 mg, 0.082 mmol), DIEA (64 μL, 0.368 mmol), and PyBOP (34 mg, 0.065 mmol) in DMF (5 mL) was stirred for 10 min and added to a previously prepared solution of **9** (130 mg, 0.054 mmol) and DIEA (98 μL, 0.57 mmol) in DMF (3.0 mL). The solution was stirred for 30 min and concentrated, and the resulting residue was triturated with EtOAc (2 × 25 mL) to give the Boc-protected conjugate as an off-white solid. MS (ESI) *m/z* 2301.3 (M + H − Trt, 13), 2057.4 (M + H − 2Trt, 9), 1695.5 (2M + 3H, 8), 1272.0 (M + 2H, 55), 1150.4 (M + 2H − Trt, 30). The solid was dissolved in 1:1 TFA/DCM (10 mL), stirred for 10 min, and concentrated to give **(Trt-VnR Antagonist)$_2$Glu-(Csa)$_3$-H**. MS (ESI) *m/z* 2200.4 (M + H − Trt, 9), 1958.2 (M + H − 2Trt, 10), 1548.3 (2M + 3H − Trt, 7), 1222.2 (M + 2H, 13), 1100.7 (M + 2H − Trt, 30). A solution of Boc−L-cysteic acid (36 mg, 0.123 mmol), DIEA (43 μL, 0.25 mmol), and PyBOP (51 mg, 0.098 mmol) in DMF (10 mL) was stirred for 10 min and added to a previously prepared solution of the tris-cysteic acid conjugate. The resulting solution was stirred for 30 min and concentrated, and the resulting residue was triturated with EtOAc (2 × 25 mL) to give a dry, off-white solid. The solid was purified by preparative

HPLC on a Vydac C18 Pharmaceutical column (21 × 250 mL) using a 0.9%/min gradient of 0−36% ACN containing 0.1% TFA at a flow rate of 20 mL/min. The main product peak eluting at 29 min was collected and lyophilized to give the Boc-protected tetra-cysteic acid conjugate as a colorless solid (80 mg, 55% over three reactions). MS (ESI) *m/z* 1347.3 (M + 2H, 24), 1226.2 (M + 2H − Trt, 17). A solution of the above solid (43 mg, 0.016 mmol) in 1:1 TFA/DCM (10 mL) was stirred for 10 min and concentrated to give **9** as a colorless solid. MS (ESI) *m/z* 2351.2 (M + H − Trt, 7), 2108.3 (M + H − 2Trt, 11), 1648.9 (2M + 3H − Trt, 10), 1297.3 (M + 2H, 12), 1176.3 (M + 2H − Trt, 36).

*Part B. Synthesis of **14**.* A solution of DOTA(O*t*-Bu)$_3$OH (18 mg, 0.032 mmol), DIEA (11 μL, 0.064 mmol), and HBTU (9.1 mg, 0.024 mmol) in DMF (10 mL) was stirred for 15 min and added to a previously prepared solution of the product from part A and DIEA (34 μL, 0.20 mmol) in DMF (5.0 mL). The resulting solution was stirred for 45 min and concentrated, and the resulting residue was triturated with EtOAc (2 × 10 mL) to give the protected DOTA conjugate as an off-white solid. MS (ESI) *m/z* 1574.7 (M + 2H, 12), 1454.4 (M + 2H − Trt, 32), 1332.9 (M + 2H − 2Trt, 13), 1050.2 (M + 3H, 10). A solution of the above solid in 97:3 TFA/Et_3SiH (10 mL) was heated at 70 °C for 1 h and concentrated to an oily solid. The solid was partitioned between 1:9 ACN/H_2O and diethyl ether, and the aqueous layer was purified by preparative HPLC on a Higgins Clipeus C18 column (20 × 250 mL) using a 0.22%/min gradient of 13.5−22.5% ACN containing 0.1% TFA at a flow rate of 15 mL/min. The main product peak eluting at 34 min was collected and lyophilized to give slightly impure product. The product was repurified on the same column using a 0.64%/min gradient of 9−31.5% ACN containing 0.1% formic acid at a flow rate of 15 mL/min. The main product peak eluting at 21 min was collected and lyophilized to give **14** (5.0 mg, 12% over three reactions). MS (ESI) *m/z* 2495.9 (M + H, 7), 1664.3 (2M + 3H, 10), 1248.8 M + 2H, 40), 832.7 (M + 3H, 100). Amino acid analysis: L-Csa, 99.6%; L-Glu, 99.7%; L-DAP, 98.9%.

(VnR Antagonist-Csa)$_2$Glu-DOTA (15). *Part A. Synthesis of (Trt-VnR Antagonist-Csa)$_2$Glu-H (**5**).* A solution of the TFA salt of (*S*)-2-(4-(4-(2-((*R*)-2-amino-3-sulfopropanamido)ethylamino)-4-oxobutoxy)-2,6-dimethylphenylsulfonamido)-3-(1-methyl-4-oxo-7-((1-trityl-1*H*-imidazol-2-ylamino)methyl)-1,4-dihydroquinoline-3-carboxamido)propanoic acid (**2**) (*41*) (317 mg, 0.264 mmol), HOAt (36 mg, 0.264 mmol), and DIEA (230 μL, 1.32 mmol) in DMF (5.0 mL) was treated with Boc-Glu-(OTfp)-OTfp (65 mg, 0.12 mmol) and stirred for 3.5 h. The reaction solution was concentrated, and the resulting amber oil was triturated with EtOAc (2 × 5 mL) to give a tan solid, which was purified by preparative HPLC on a Vydac C18 Pharmaceutical column (50 × 250 mm) using a 0.34%/min gradient of 32−49% ACN containing 0.1% TFA at a flow rate of 80 mL/min. The main product peak eluting at 36 min was collected and lyophilized to give the Boc-protected dimer as a colorless powder (212 mg, 74%). MS (ESI): *m/z* 2392.9 (M + H, 9), 2149.4 (M + H − Trt, 21), 1196.4 (M + 2H, 48). A solution of the above solid (212 mg, 0.0886 mmol) in 1:1 TFA/DCM (15 mL) was stirred for 10 min and concentrated under vacuum to give a pale yellow, glassy solid. The solid was dissolved in 1:1 ACN/H_2O and lyophilized to give amine **5** as an off-white solid (231 mg). MS (ESI): *m/z* 2049.5 (M + H − Trt, 19), 1806.4 (M + H − 2Trt, 12), 1146.1 (M + 2H, 17).

*Part B. Synthesis of **15**.* A solution of DOTA(O*t*-Bu)$_3$OH (26 mg, 0.045 mmol), DIEA (10 μL, 0.06 mmol), and HBTU (14 mg, 0.0375 mmol) in DMF (0.5 mL) was stirred for 20 min and added to a previously prepared solution of the product from part A (72 mg, 0.030 mmol) and DIEA (31 μL, 0.18 mmol) in DMF (2.0 mL). Additional DIEA (10 μL, 0.06 mmol) was added after 15 min to maintain a strongly basic solution. The solution was stirred for 3 h and concentrated to an amber oil. This oil was purified by preparative HPLC on a Vydac C-18 column (50 × 250 mm) using a 0.68%/min gradient of 31.5−58.5% ACN containing 0.1% TFA at a flow rate of 80 mL/min. The main product peak eluting at 20 min was collected and lyophilized to give the protected DOTA conjugate as a colorless solid (37 mg, 46%). MS (ESI): *m/z* 2604.9 (M + H − Trt), 1423.6 (M + 2H, 100), 1302.7 (M + 2H − Trt, 53), 1181.4 (M + 2H − 2Trt, 17). HRMS: Calcd for $C_{141}H_{174}N_{23}O_{33}S_4$ (M + H), 2846.1606; found, 2846.1580. A solution of the protected DOTA conjugate (35 mg, 0.0123 mmol) in 97:3 TFA/Et_3SiH (4.0 mL) was heated at 70 °C for 70 min. The solution was concentrated, and the resulting residue was purified by preparative HPLC on a Higgins C-18 Clipeus column (20 × 250 mm) using a 0.45%/min gradient of 9−27% ACN containing 0.1% TFA at a flow rate of 15 mL/min. The main product peak eluting at 29 min was collected and lyophilized to give **15** as a colorless solid (27 mg, 91%). MS (ESI): *m/z* 2193.9 (M + H, 8), 1462.4 (2M + 3H, 5), 1096.9 (M + 2H, 57), 731.8 (M + 3H, 100). HRMS: Calcd for $C_{91}H_{122}N_{23}O_{33}S_4$ (M + H), 2192.7458; found, 2192.7430. Amino acid analysis: L-Csa, 99.3%; L-Glu, 99.1%; L-DAP, 99.3%.

(VnR Antagonist-Csa)$_2$Glu-Csa-DOTA (16). *Part A. Synthesis of (Trt-VnR Antagonist-Csa)$_2$Glu-Csa-H (**11**).* A solution of Boc−L-cysteic acid (29 mg, 0.100 mmol), DIEA (23 μL, 0.134 mmol), and HBTU (32 mg, 0.0836 mmol) in DMF (1.0 mL) was stirred for 20 min and added to a previously prepared solution of 5 (161 mg, 0.0669 mmol) and DIEA (69 μL, 0.401 mmol) in DMF (2.5 mL). Additional DIEA (23 μL, 0.134 mmol) was added after 60 min to maintain a strongly basic solution. The solution was stirred a total of 3.5 h and concentrated under vacuum to a viscous amber oil. This oil was triturated with ether to give a dry solid (234 mg). MS (ESI): *m/z* 2300.6 (M + H − Trt, 14), 1271.8 (M + 2H, 50), 1150.5 (M + 2H − Trt, 23). The solid was dissolved in 1:1 TFA/DCM (6.0 mL) for 10 min and concentrated to give an amber oil. Trituration with ether gave **11** as an off-white solid (210 mg, 93%). MS (ESI): *m/z* 2201.1 (M + H − Trt, 8), 1958.3 (M + H − 2Trt, 9), 1221.7 (M + 2H, 17), 1100.9 (M + 2H − Trt, 19).

*Part B. Synthesis of **16**.* A solution of DOTA(O*t*-Bu)$_3$OH (37 mg, 0.065 mmol), DIEA (9.4 μL, 0.054 mmol), and HBTU (15 mg, 0.0405 mmol) in DMF (1.0 mL) was stirred for 20 min and added to a previously prepared solution of the product of part A (66 mg, 0.027 mmol) and DIEA (28 μL, 0.162 mmol) in DMF (1.3 mL). The solution was stirred for 2 h and concentrated to an amber oil. This oil was purified by preparative HPLC on a Vydac C-18 column (50 × 250 mm) using a 0.36%/min gradient of 36−54% ACN containing 0.1% TFA at a flow rate of 80 mL/min. The main product peak eluting at 23 min was collected and lyophilized to give the protected DOTA conjugate as a colorless solid (24 mg, 29%). MS (ESI): *m/z* 1499.4 (M + 2H, 30), 1377.9 (M + 2H − Trt, 38). The DOTA conjugate (22 mg, 0.00707 mmol) was dissolved in 97:3 TFA/Et_3SiH (6.0 mL) and heated at 70 °C for 1 h. The solution was concentrated, and the residue was purified by preparative HPLC on a Higgins Clipeus C-18 column (20 × 250 mm) using a 0.21%/min gradient of 10.8−22.5% ACN containing 0.1% TFA at a flow rate of 15 mL/min. The main product peak eluting at 48 min was collected and lyophilized to give **16** as a colorless solid (13 mg, 75%). MS (ESI) *m/z* 2345.3 (M + H, 7), 1173.3 (M + 2H, 45), 782.3 (M + 3H, 100). Amino acid analysis: L-Csa, 99.7%; L-Glu, 99.5%; L-DAP, 98.8%.

(VnR Antagonist-Csa)$_2$Glu-(Csa)$_2$-DOTA (17). *Part A. Synthesis of (Trt-VnR Antagonist-Csa)$_2$Glu-(Csa)$_2$-H (**12**).* A solution of Boc−L-cysteic acid (42 mg, 0.143 mmol), DIEA

(40 μL, 0.229 mmol), and HBTU (43 mg, 0.115 mmol) in DMF (1.5 mL) was stirred for 20 min and added to a previously prepared solution of **11** (140 mg, 0.0573 mmol) and DIEA (40 μL, 0.229 mmol) in DMF (2.5 mL). The solution was stirred for 4 h and concentrated to give a viscous amber oil. The oil was purified by preparative HPLC on a Vydac C-18 column (50 × 250 mm) using a 0.60%/min gradient of 18−54% ACN containing 0.1% TFA at a flow rate of 80 mL/min. The main product peak eluting at 54 min was collected and lyophilized to give the cysteic acid conjugate as a colorless solid (83 mg, 53%). MS (ESI) *m*/*z* 1347.1 (M + 2H), 1226.4 (M + 2H − Trt), 1176.8 (M + 2H − Boc − Trt), 1104.9 (M + 2H − 2Trt), 1055.5 (M + 2H − Boc − 2Trt). The solid (82 mg, 0.0305 mmol) was dissolved in 1:1 TFA/DCM (10 mL) for 15 min and concentrated to an amber oil. This oil was lyophilized from 1:1 ACN/H_2O to give **12** as colorless solid (79 mg, 100%). MS (ESI) *m*/*z* 2351.4 (M + H − Trt, 7), 2109.4 (M + H − 2Trt, 10), 1297.8 (M + 2H, 11), 1176.3 (M + 2H − Trt, 25).

*Part B. Synthesis of **17**.* A solution of DOTA(O*t*-Bu)$_3$OH (42 mg, 0.0734 mmol), DIEA (11 μL, 0.062 mmol), and HBTU (18 mg, 0.0462 mmol) in DMF (1.0 mL) was stirred for 20 min and added to a previously prepared solution of the product of part A (80 mg, 0.0308 mmol) and DIEA (44 μL, 0.208 mmol) in DMF (1.8 mL). The solution was stirred for 2 h and concentrated to give an amber oil, which was purified by preparative HPLC on a Vydac C-18 column (50 × 250 mm) using a 0.36%/min gradient of 36−54% ACN containing 0.1% TFA at a flow rate of 80 mL/min. The main product peak eluting at 40 min was collected and lyophilized to give the protected DOTA conjugate as a colorless solid (56 mg, 58%). MS (ESI) *m*/*z* 1572.2 (M + 2H, 16), 1453.9 (M + 2H − Trt, 32). A solution of this solid (54 mg, 0.0172 mg) in 97:3 TFA/Et_3SiH (5.0 mL) was heated at 70 °C for 1 h and concentrated to an oily, yellow solid. This solid was purified by preparative HPLC on a Higgins Clipeus C-18 column (20 × 250 mm) using a 0.24%/min gradient of 9−22.5% ACN containing 0.1% TFA at a flow rate of 15 mL/min. The main product peak eluting at 45 min was collected and lyophilized to give **17** (33 mg, 77%) as a colorless solid. MS (ESI) *m*/*z* 2496.1 (M + H, 14), 1664.7 (2M + 3H, 27), 1248.3 (M + 2H, 44), 832.5 (M + 3H, 100). Amino acid analysis: L-Csa, 99.2%; L-Glu, 98.9%; L-DAP, 98.8%.

(VnR Antagonist-(Csa)$_2$)$_2$Glu -DOTA (18). *Part A. Synthesis of (Trt-VnR Antagonist-(Csa)$_2$)$_2$Glu-H (**6**).* A solution of (*S*)-2-(4-(4-(2-((*R*)-2-((*R*)-2-amino-3-sulfopropanamido)-3-sulfopropanamido)ethylamino)-4-oxobutoxy)-2,6-dimethylphenylsulfonamido)-3-(1-methyl-4-oxo-7-((1-trityl-1*H*-imidazol-2-ylamino)methyl)-1,4-dihydroquinoline-3-carboxamido)propanoic acid (**3**) (*41*) (136 mg, 0.110 mmol) and DIEA (76 μL, 0.44 mmol) in DMF (3.0 mL) was treated with Boc-Glu(OTfp)-OTfp (27 mg, 0.050 mmol) and stirred for 7 h. The solution was concentrated, and the resulting amber oil was purified by preparative HPLC on a Vydac C-18 column (50 × 250 mm) using a 0.45%/min gradient of 45−63% ACN containing 0.1% TFA at a flow rate of 80 mL/min. The main product peak eluting at 16 min was collected and lyophilized to give the Boc-protected bis-conjugate as a colorless solid (129 mg, 96%). MS (ESI) *m*/*z* 1347.3 (M + 2H, 9), 1226.4 (M + 2H − Trt, 12), 1176.5 (M + 2H − Trt − Boc, 12). The above solid (95 mg, 0.0353 mmol) was dissolved in 1:1 TFA/DCM (20 mL), stirred for 20 min, and concentrated. The resulting solid was taken up in 1:1 ACN/H_2O and lyophilized to give **6** as a pale yellow solid (89 mg, 97%). MS (ESI) *m*/*z* 2351.9 (M + H − Trt, 6), 2110.2 (M + H − 2Trt, 7), 1298.0 (M + 2H, 16), 1176.4 (M + 2H − Trt, 18).

*Part B. Synthesis of **18**.* A solution of DOTA(O*t*-Bu)$_3$OH (63 mg, 0.110 mmol), DIEA (48 μL, 0.270 mmol), and HBTU (20 mg, 0.0514 mmol) in DMF (2.0 mL) was stirred for 20 min and added to a previously prepared solution of the product of part A (88 mg, 0.0340 mmol) and DIEA (48 μL, 0.270 mmol) in DMF (3.0 mL). The solution was stirred for 3 h. The solution was concentrated, and the resulting residue was purified by preparative HPLC on a Vydac C-18 column (50 × 250 mm) using a 0.36%/min gradient of 36−54% ACN containing 0.1% TFA at a flow rate of 80 mL/min. The main product peak eluting at 41 min was collected and lyophilized to give the protected DOTA conjugate as a colorless solid (42 mg, 39%). MS (ESI) *m*/*z* 1575.7 (M + 2H, 10), 1454.4 (M + 2H − Trt, 50). The above DOTA conjugate was dissolved in 97:3 TFA/Et_3SiH (5.0 mL) and heated at 70 °C for 45 min. The solution was concentrated, and the oily solid was purified by preparative HPLC on a Vydac C-18 column (50 × 250 mm) using a 0.68%/min gradient of 0−27% ACN containing 0.1% TFA at a flow rate of 80 mL/min. The main product peak eluting at 34 min was collected and lyophilized to give **18** as a colorless solid (23 mg, 73%). MS (ESI) *m*/*z* 2496.6 (M + H, 5), 1664.5 (2M + 3H, 10), 1248.2 (M + 2H, 25), 832.4 (M + 3H, 100). Amino acid analysis: L-Csa, 99.8%; L-Glu, 99.6%; L-DAP, 99.1%.

(VnR Antagonist-(Csa)$_2$-Suc-Peg)$_2$-Glu-DOTA (19). *Part A. Synthesis of (S)-tert-butyl 1,33-diamino-15,19-dioxo-4,7,10,-24,27,30-hexaoxa-14,20-diazatritriacontan-16-ylcarbamate ((H-Peg)$_2$Glu-Boc).* A solution of benzyl 3-(2-(2-(3-aminopropoxy)-ethoxy)ethoxy)propylcarbamate (*41*) (3.55 g, 10.0 mmol), Boc-Glu-OH (1.00 g, 4.05 mmol), DIEA (2.00 mL, 11.5 mmol), and PyBOP (8.00 g, 15.4 mmol) in NMP (45 mL) was stirred for 1 h and partitioned between EtOAc (175 mL) and 0.5 N HCl/NaCl (150 mL). The organic phase was washed consecutively with 0.5 N HCl/NaCl (3 × 50 mL), H_2O (50 mL), saturated $NaHCO_3$ (25 mL), and H_2O (25 mL). The aqueous phases were back-extracted with EtOAc (6 × 25 mL). The combined organic layers were dried (Na_2SO_4) and concentrated to give a pale yellow oil. This oil was purified by flash chromatography on SiO_2 (100 g) using a step gradient consisting of EtOAc (400 mL), 3:1 EtOAc/acetone (200 mL), 1:1 EtOAc/acetone (200 mL), 1:3 EtOAc/ acetone (200 mL), and acetone. Product fractions were combined and concentrated to give impure product as a colorless oil (4.30 g). This oil was repurified by flash chromatography using the above conditions to give pure bis-conjugate as a waxy solid (3.30 g, 88%). ^{1}H NMR ($CDCl_3$): δ 7.33−7.28 (m, 10H), 7.08 (bs, 1H), 6.69 (bs, 1H), 5.89 (bs, 1H), 5.59 (bs, 2H), 5.08 (s, 4H), 4.12−2.04 (m, 2H), 3.68−3.48 (m, 24H), 3.37−3.24 (m, 8H), 2.29−2.17 (m, 2H), 2.04−1.96 (m, 1H), 1.95−1.83 (m, 1H), 1.80−1.68 (m, 8H), 1.42 (s, 9H). ^{13}C NMR ($CDCl_3$): δ 172.69, 171.81, 156.52, 155.75, 136.66, 128.32, 127.92, 127.86, 79.57, 70.23, 70.20, 69.89, 69.86, 69.75, 69.46, 69.29, 69.17, 66.31, 38.80, 37.50, 37.21, 32.44, 29.31, 28.90, 28.74, 28.21. MS (ESI) *m*/*z* 920.5 (M + H, 100). The above solid (920 mg, 1.00 mmol) was dissolved in MeOH (25 mL) and hydrogenolyzed over 10% Pd/C (140 mg) at 60 psi for 6 h. The catalyst was removed by filtration through Celite, and the filtrate was concentrated to give a quantitative yield of (H-Peg)$_2$Glu-Boc. ^{1}H NMR ($CDCl_3$): δ 8.04 (bs, 1H), 7.67 (bs, 1H), 6.34 (bs, 1H), 4.08 (bs, 1H), 3.67−3.50 (m, 24H), 3.37−3.26 (m, 4H), 3.09 (t, J = 6.4 Hz, 4H), 2.28 (t, J = 7.0 Hz, 2H), 2.10−1.88 (m, 10H), 1.77 (quin, J = 6.2 Hz, 4H), 1.42 (s, 9H). ^{13}C NMR ($CDCl_3$): δ 173.17, 172.48, 155.02, 79.45, 70.28, 69.88, 69.86, 69.71, 69.68, 69.64, 69.45, 68.82, 68.63, 54.10, 38.70, 36.85, 36.67, 32.47, 29.18, 29.06, 29.02, 28.26, 27.12. MS (ESI) *m*/*z* 652.5 (M + H, 43), 326.8 (M + 2H, 100), 298.8 (M + 2H − C_4H_8, 20), 276.7 (M + 2H − Boc, 90).

*Part B. Synthesis of (H-Suc-Peg)$_2$-Glu-Boc (**22a**).* A solution of the product of part A (650 mg, 1.00 mmol) and succinic anhydride (226 mg, 2.26 mmol) in pyridine (10 mL) was

sonicated briefly to dissolve all solids and then stirred for 20 h. The solution was concentrated, and the residue was triturated with toluene (4 × 50 mL). The remaining residue was purified by preparative HPLC on a Vydac C-18 column (50 × 250 mm) using a 0.56%/min gradient of 13.5−36% ACN containing 0.1% TFA at a flow rate of 80 mL/min. The main product fractions were collected and lyophilized to give **22a** as a colorless solid (650 mg, 76%). ^{1}H NMR ($CDCl_3$): δ 7.70 (bs, 1H), 7.43 (bs, 1H), 7.05 (bs, 2H), 6.04 (bs, 1H), 4.11 (bs, 1H), 3.71−3.52 (m, 24H), 3.37−3.28 (m, 8H), 2.67 (t, J = 6.5 Hz, 4H), 2.51, (t, J = 6.6 Hz, 4H), 2.34−2.27 (m, 2H), 2.12−2.04 (m, 1H), 1.96−1.87 (m, 1H), 1.79−1.70 (m, 8H), 1.42 (s, 9H). MS (ESI) *m*/*z* 852.4 (M + H, 100), 376.8 (M + 2H − Boc, 50).

*Part C. Synthesis of (Trt-VnR Antagonist-(Csa)$_2$-Suc-Peg)$_2$-Glu-H (**7**).* A solution of the product of part B (20 mg, 0.024 mmol), DIEA (50 μL, 0.285 mmol), and HBTU (17 mg, 0.044 mmol) in DMF (0.5 mL) was stirred for 5 min and treated sequentially with 3 (*38*) (61 mg, 0.049 mmol), DIEA (42 μL, 0.240 mmol), and DMF (0.7 mL). The solution was stirred for 20 min and concentrated. The resulting residue was purified by preparative HPLC on a Vydac C-18 column (21 × 250 mm) using a 0.56%/min gradient of 22.5−45% ACN containing 0.1% TFA at a flow rate of 20 mL/min. The main product peak eluting at 35 min was collected and lyophilized to give the Boc-protected bis-conjugate as a colorless solid (35 mg, 50%). MS (ESI) *m*/*z* 1648.7 (M + 2H, 35), 1099.5 (M + 3H, 15). The above solid (35 mg, 0.011 mmol) was dissolved in 1:1 TFA/DCM (2.0 mL) and stirred for 15 min. The solution was concentrated, and the residue was taken up in 1:1 ACN/H_2O and lyophilized to give **7** as a colorless solid (34 mg, 100%). MS (ESI) *m*/*z* 1600.1 (M + 2H, 40), 1478.9 (M + 2H − Trt, 50).

*Part D. Synthesis of **19**.* A solution of DOTA(O*t*-Bu)$_3$OH (24 mg, 0.042 mmol), DIEA (43 μL, 0.247 mmol), and HBTU (12 mg, 0.032 mmol) in DMF (1.0 mL) was stirred for 15 min and treated sequentially with the product of part C (34 mg, 0.011 mmol), DIEA (20 μL, 0.115 mmol), and DMF (0.4 mL). The solution was stirred for 30 min and concentrated to an amber oil. This oil was purified by preparative HPLC on a Vydac C-18 column (50 × 250 mm) using a 0.68%/min gradient of 27−54% ACN containing 0.1% TFA at a flow rate of 80 mL/min. The main product peak eluting at 27 min was collected and lyophilized to give the protected DOTA conjugate as a colorless solid (16 mg, 40%). MS (ESI) *m*/*z* 1877.2 (M + 2H, 70), 1756.2 (M + 2H − Trt, 70), 1635.1 (M + 2H − 2Trt, 40), 1251.8 (M + 3H, 60), 1171.2 (M + 3H − Trt, 50). The above solid (12 mg, 0.0032 mmol) was dissolved in 97:3 TFA/Et_3SiH (1.3 mL), heated at 65 °C for 90 min, and concentrated to an oily solid. The solid was dissolved in 10:90 ACN/H_2O (3.0 mL) and washed with diethyl ether (2 × 4 mL) to remove triphenylmethane. The product in the aqueous layer was purified by preparative HPLC by direct injection of the solution on a Vydac C-18 column (21 × 250 mm) using a 0.36%/min gradient of 9−27% ACN containing 0.1% TFA at a flow rate of 20 mL/min. The main product peak eluting at 31 min was collected and lyophilized to give **19** as a colorless solid (7.4 mg, 75%). MS (ESI) *m*/*z* 1550.6 (M + 2H, 40), 1034.2 (M + 3H, 100), 775.8 (M + 4H, 90), 620.9 (M + 5H, 35). HRMS: Calcd for $C_{125}H_{186}N_{29}O_{51}S_6$ (M + 3H), 1034.0398; found 1034.0394. Amino acid analysis: L-Csa, 99.1%; L-Glu, 99.7%; L-DAP, 97.9%.

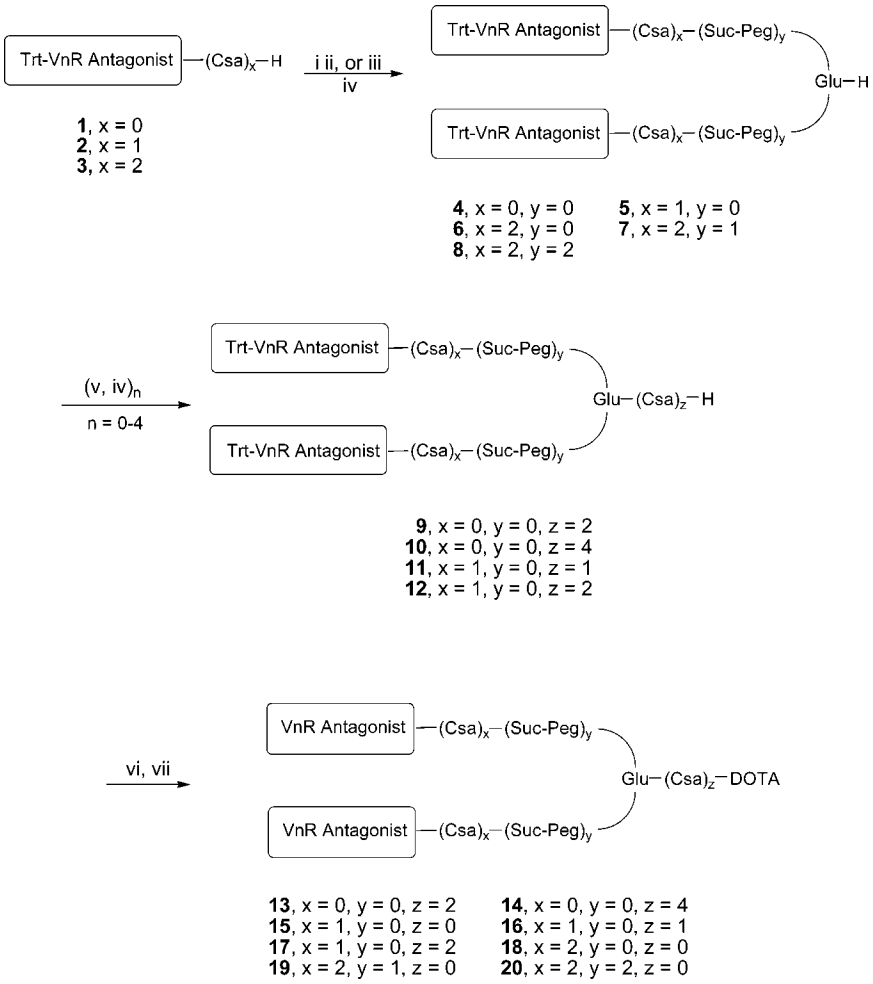
(VnR Antagonist-Csa-Csa-Suc-Peg-Suc-Peg)$_2$-Glu-DOTA (20). *Part A. Synthesis of (H-Peg-Suc-Peg)$_2$-Glu-Boc.* A solution of **22a** (850 mg, 1.00 mmol), DIEA (0.85 mL, 5.0 mmol), and HBTU (1.00 g, 2.60 mmol) in DMF (25 mL) was stirred for 5 min and treated with benzyl 3-(2-(2-(3-aminopropoxy)ethoxy)-ethoxy)propylcarbamate (1.00 g, 2.80 mmol). The solution was stirred for 1 h and concentrated to a red oil, which was triturated with H_2O (3 × 15 mL) and dissolved in DCM. The DCM solution was filtered, and the filtrate was concentrated to give a red−orange oil. This oil was purified by preparative HPLC on a Vydac C-18 column (50 × 250 mm) using a 0.90%/min gradient of 31.5−67.5% ACN containing 0.1% TFA at a flow rate of 80 mL/min. The main product fractions were collected and lyophilized to give the bis-conjugate as a colorless oil (1.282 g, 84%). MS (ESI) *m*/*z* 1524.7 (M + H, 32), 763.0 (M + 2H, 100). The above oil (1.20 g, 7.90 mmol) was hydrogenolyzed over 10% Pd/C (200 mg) in MeOH (25 mL) at 50 psi for 2 h. The catalyst was removed by filtration through Celite, and the filtrate was concentrated to give a quantitative yield of (H-Peg-Suc-Peg)$_2$-Glu-Boc. MS (ESI) *m*/*z* 1256.7 (M + H, 10), 629.0 (M + 2H, 100), 386.4 (M + 3H-Boc, 92).

*Part B. Synthesis of (H-(Suc-Peg)$_2$)$_2$-Glu-Boc (**22b**).* A solution of the product of part A (942 mg, 0.75 mmol) and succinic anhydride (250 mg, 2.50 mmol) in pyridine (10 mL) was sonicated briefly to dissolve solids and then stirred for 18 h. The solution was concentrated, and the resulting residue was purified by preparative HPLC on a Vydac C-18 column (50 × 250 mm) using a 0.90%/min gradient of 31.5−67.5% ACN containing 0.1% TFA at a flow rate of 80 mL/min. It was necessary to take fine heart cuts in order to remove closely eluting impurities. The pure product fractions were collected and lyophilized to give the **22b** (206 mg, 14%) as a colorless viscous oil. MS (ESI) *m*/*z* 1456.8 (M + H, 60), 729.0 (M + 2H, 100), 453.0 (M + 3H − Boc, 48).

*Part C. Synthesis of (Trt-VnR Antagonist-(Csa)$_2$-(Suc-Peg)$_2$)$_2$-Glu-H (**8**).* A solution of the product of part B (77 mg, 0.053 mmol), DIEA (52 μL, 0.30 mmol), and HBTU (38 mg, 0.100 mmol) in DMF (1.0 mL) was stirred for 10 min and treated sequentially with **3** (*38*) (142 mg, 0.112 mmol), DIEA (100 μL, 0.574 mmol), and DMF (0.5 mL). The solution was stirred for 2 h and concentrated. The resulting residue was purified by preparative HPLC on a Vydac C-18 column (50 × 250 mm) using a 0.60%/min gradient of 45−63% ACN containing 0.1% TFA at a flow rate of 80 mL/min. The main product peak eluting as a broad peak from 16−20 min was collected and lyophilized to give the bis-conjugate as a colorless solid (104 mg, 53%). MS (ESI) *m*/*z* 1952.3 (M + 2H, 32), 1831.3 (M + 2H − Trt, 55), 1709.3 (M + 2H − 2Trt, 34), 1302.2 (M + 3H, 72), 1221.2 (M + 3H − Trt, 58), 1140.8 (M + 3H − 2Trt, 22). A solution of the above solid (100 mg, 0.026 mmol) in 1:2 TFA/DCM (2.4 mL) was stirred for 25 min and concentrated. The resulting oil was taken up in 1:1 ACN/H_2O (40 mL) and lyophilized to give **8** as a colorless solid (99 mg, 100%). MS (ESI) *m*/*z* 1902.2 (M + 2H, 55), 1780.6 (M + 2H − Trt, 60), 1659.9 (M + 2H − 2Trt, 45), 1268.6 (M + 3H, 85), 1187.6 (M + 3H − Trt, 70).

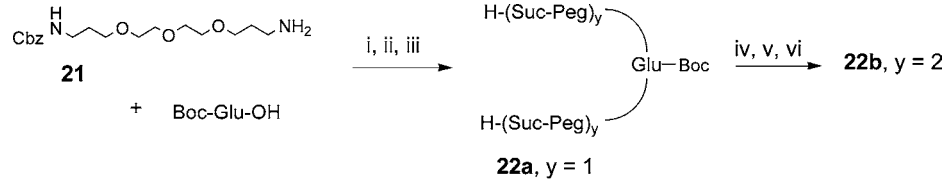
*Part D. Synthesis of **20**.* A solution of DOTA(O*t*-Bu)$_3$OH (24 mg, 0.042 mmol), DIEA (43 μL, 0.247 mmol), and HBTU (12 mg, 0.032 mmol) in DMF (1.0 mL) was stirred for 10 min and treated sequentially with the product of part C (97 mg, 0.0255 mmol) and DIEA (65 μL, 0.37 mmol). The resulting solution was stirred for 45 min and concentrated to an amber oil. This oil was purified by preparative HPLC on a Vydac C-18 column (50 × 250 mm) using a 0.54%/min gradient of 27−54% ACN containing 0.1% TFA at a flow rate of 80 mL/min. The main product peak eluting at 42 min was lyophilized to give the protected DOTA conjugate as a colorless solid (60 mg, 54%). MS (ESI) *m*/*z* 2179.6 (M + 2H, 30), 2058.1 (M + 2H − Trt, 30), 1936.8 (M + 2H − 2Trt, 25), 1453.4 (M + 3H, 70), 1372.8 (M + 3H − Trt, 100), 1241.6 (M + 3H − 2Trt, 60). A solution of the DOTA conjugate in 80:20 TFA/Et_3SiH (2.5 mL) was stirred at 60 °C for 95 min and concentrated to an oily solid. This solid was purified by preparative HPLC on a Vydac

Scheme 1. General Synthetic Route to Divalent Integrin $\alpha_v\beta_3$ Receptor Antagonists[a]



[a] Reagents: (i) Boc-Glu-(OTfp)-OTfp, HBTU, DIEA, DMF; (ii) **22a**, HBTU, DIEA, DMF; (iii) **22b**, HBTU, DIEA, DMF; (iv) TFA:DCM; (v) Boc-L-cysteic acid, HBTU, DIEA, DMF; (vi) DOTA(O*t*-BU)$_3$OH, HBTU, DIEA, DMF; (vii) TFA/Et$_3$SiH, 70 °C.

Scheme 2. Synthesis of (H-(Suc-PEG)$_y$)$_2$-Glu-Boc[a]



[a] Reagents: (i) PyBOP, DIEA, NMP, 88%; (ii) H_2, 10% Pd/C, 100%; (iii) succinic anhydride, pyridine, 76%; (iv) **21**, HBTU, DIEA, NMP, 84%; (v) H_2, 10% Pd/C, 100%; (vi) succinic anhydride, pyridine, 14%.

C-18 column (21 × 250 mm) using a 0.36%/min gradient of 9−27% ACN containing 0.1% TFA at a flow rate of 20 mL/min. The main product peak eluting at 34 min was lyophilized to give **20** as a colorless solid (31 mg, 75%). MS (ESI) *m*/*z* 1853.0 (M + 2H, 13), 1235.7 (M + 3H, 65), 927.0 (M + 4H, 100), 741.8 (M + 5H, 57), 618.3 (M + 6H, 27). HRMS: Calcd for $C_{153}H_{238}N_{33}O_{61}S_6$ (M + 3H), 1235.8304; found: 1235.830. Amino acid analysis: L-Csa, 99.5%; L-Glu, 99.7%; L-DAP, 98.6%.

Receptor Binding Assays. Affinity assays toward four integrin receptors were carried out according to previously published procedures (*31*, *43*) and are included in the Supporting Information.

Radiolabeling. ^{111}In-DOTA complexes used in this study were prepared in >95% radiochemical purity according to a previously published procedure (*41*). This procedure is included in the Supporting Information. ^{177}Lu-**15** was prepared in >95% radiochemical purity according to a previously published procedure (*42*). This procedure is included in the Supporting Information.

In Vivo Biodistribution Study. Biodistribution in the c-neu Oncomouse mammary adenocarcinoma model was carried out according to a previously published procedure (*41*) as described in the Supporting Information.

Scintigraphic Image Study. Scintigraphic images of ^{111}In-**TA138** and ^{111}In-**15** in the c-Neu Oncomouse model were acquired according to a previously published procedure (*31*). This procedure is reproduced in the Supporting Information.

RESULTS

Synthesis of Divalent $\alpha_v\beta_3$ Antagonists. The syntheses of vitronectin receptor antagonists **1**, **2**, and **3**, having zero, one, and two cysteic acid PKMs, respectively, were described previously (*41*). The general synthetic route from these three

starting materials to the divalent radiopharmaceuticals reported here is shown in Schemes 1 and 2. Conjugation of **1**, **2**, and **3**, with 0.5 molar equiv of Boc-Glu(OTfp)-OTfp in DMF gave the bis-conjugates in good to excellent yields. Treatment of these conjugates with 1:1 TFA/DCM removed the Boc protecting group from the glutamyl residue, while leaving intact the trityl protecting group on the imidazole rings, to give **4**, **5**, and **6** in purified yields of 43%, 74%, and 94%, respectively. Compound **4** was used to synthesize DOTA conjugates **13** and **14**, having two and four cysteic acid PKMs, respectively. These compounds are related in that the cysteic acids are conjugated to the glutamic acid α-amine, between the glutamic acid branch point and DOTA. Thus, the compounds have identical spacing between the two biotargeting groups but differ in their lipophilicity and charge. The cysteic acids were added in stepwise fashion using Boc−L-cysteic acid and PyBOP in DMF for the conjugation reactions and 1:1 TFA/DCM for Boc removal. Two coupling/deprotection cycles gave compound **9** in 60% yield over four reactions. Triturations were used to remove impurities in three of the four synthetic steps, with one HPLC purification used for final purification prior to DOTA conjugation. In a similar fashion, **9** was converted to tetra-cysteic acid derivative **10** in 55% overall yield. Conjugation of the bis- and tetra-cysteic acid derivatives to DOTA(O*t*-Bu)$_3$-OH was accomplished using HBTU in DMF. Global deprotection using 97:3 TFA/Et_3SiH at 70 °C gave final products **13** and **14** in 31% and 12% yield, respectively. The low yields for these final two steps were due in large part to very challenging HPLC purifications that necessitated taking small heart cuts from the product peaks.

Compound **5** was used to synthesize a trio of DOTA conjugates, **15**, **16**, and **17**, having a total of two, three, or four cysteic acid PKMs, respectively. All three of these compounds have a single cysteic acid PKM on each arm of the spacer, and either zero, one, or two cysteic acid PKMs conjugated to the glutamic acid α-amine. As a group, they have identical spacing between the biotargeting groups but differ in their lipophilicity and charge. Placing cysteic acids in the chain linking the biotargeting groups adds a total of six atoms to the spacer length. Conjugation of DOTA(O*t*-Bu)$_3$-OH directly to **5** followed by global deprotection gave **15** in 42% yield. Reaction of **5** with Boc−cysteic acid and HBTU, followed by removal of Boc using TFA/DCM, gave **11** in 93% yield. Addition of a second cysteic acid PKM to **11** using the same chemistry gave **12** in 53% yield. Compounds **11** and **12** were converted to DOTA conjugates **16** and **17** in 22% and 45% purified yields, respectively. Conjugation of DOTA(O*t*-Bu)$_3$-OH directly to **6** followed by global deprotection gave **18** in 28% yield.

The final two compounds of this study utilized Suc-PEG spacers to provide a large additional increase in the distance between the biotargeting groups. The spacer groups were added to Boc−glutamic acid in stepwise fashion as shown in Scheme 2. Conjugation of Boc−glutamic acid with 2 equiv of Cbz-protected PEG diamine **21**, followed by catalytic hydrogenolysis, and reaction of the resulting amine with succinic anhydride gave dicarboxylic acid **22a** in 67% overall yield. A second Suc-PEG spacer was added to each arm of **22a** using the same sequence of reactions to give **22b** in 12% overall yield. Conjugation of **22a** and **22b** with bis-cysteic acid $\alpha_v\beta_3$ receptor antagonist **3**, followed by removal of the Boc protecting groups, gave divalent antagonists **7** and **8** in 50% and 55% yields, respectively. HBTU-mediated conjugation of **7** and **8** to DOTA(O*t*-Bu)$_3$-OH followed by global deprotection gave **19** and **29** in 30% and 40% yields, respectively.

Receptor Binding Assays. Affinity assays toward four integrin receptors were used to measure the potency and selectivity of the divalent $\alpha_v\beta_3$ antagonist described here and to compare them to **TA138**. Our principle receptor $\alpha_v\beta_3$ assay was the 293β_3-fibrinogen ($\alpha_v\beta_3$-mediated) adhesion assay (*43*). Receptor selectivity was measured using the platelet aggregation $\alpha_{IIb}\beta_3$ assay (*43*), the human SKBR3 cell-vitronectin ($\alpha_v\beta_5$-mediated) adhesion assay (*31*), and the human lymphocyte (Jurkat)-fibronectin ($\alpha_5\beta_1$-mediated) adhesion assay (*31*). The affinity data in Table 2 show that all compounds have high affinity toward receptor $\alpha_v\beta_3$, with IC_{50} values of 6−58 nM in the 293β_3 assay. They also show good to excellent selectivity versus receptors $\alpha_{IIb}\beta_3$, $\alpha_v\beta_5$, and $\alpha_5\beta_1$.

Table 2. In Vitro Receptor Affinity of Quinolin-4-one DOTA Conjugates

	IC_{50}, nM (±SEM)[a]			
compd	$\alpha_v\beta_3$ (293β_3)[b]	$\alpha_{IIb}\beta_3$ (PRP[c])[b]	$\alpha_v\beta_5$ (SKB)[d]	$\alpha_5\beta_1$ (Jurkat)[d]
13	17 ± 5	>10 000	>10 000	4800
14	40 ± 24	>10 000	>10 000	ND[e]
15	9 ± 6	>10 000	>10 000	2000
16	57 ± 16	5000	>10 000	6100
17	42 ± 17	4400	>10 000	>10 000
18	58 ± 18	3600	>10 000	>10 000
19	6 ± 4	>10 000	>10 000	2900
20	15 ± 11	>10 000	>10 000	2100

[a] Performed in triplicate. [b] Assay performed according to procedures outlined in ref 42. [c] Platelet-rich plasma. [d] Assays performed according to procedures outlined in ref 31. [e] Not determined.

Radiolabeling. All DOTA conjugates of this study formed stable complexes with ^{111}In. The complexes were prepared according to a previously published procedure and isolated in >95% radiochemical purity (*41*).

In Vivo Biodistribution Study. The biodistribution properties of the compounds in this study were evaluated in the c-neu Oncomouse mammary adenocarcinoma model according to a previously published procedure (*41*). Compounds were evaluated as the ^{111}In complexes and administered at 2 mCi/Kg of body weight. Mice were euthanized and dissected at 2 and 24 h postinjection (PI), and activity in the organs and tumors was counted on a gamma counter. The biodistribution data are presented in Figures 3 and 4, expressed as % of injected dose/gram of tissue (%ID/g). All biodistribution data are decay-corrected. Tumor uptake was rapid for all divalent agents, ranging from 4.81% ID/g at 2 h PI for ^{111}In-**20** to 9.99% ID/g at 2 h PI for ^{111}In-**17**. The parent monovalent agent, ^{111}In-**TA138**, displayed slow washout from the tumor, decreasing from 9.39% ID/g at 2 h PI to 3.46% ID/g at 24 h PI. In contrast, tumor uptake for the divalent agents either remained constant or increased between 2 and 24 h, with ^{111}In-**15** showing the highest uptake at 14.3% ID/g at 24 h PI. This continuous uptake was also apparent in the colon and uterus, where the majority of divalent agents displayed increased uptake between 2 and 24 h. As shown in Figures 3 and 4, uptake in the kidneys, marrow, and liver decreased over 24 h for all agents. Uptake in organs not shown in the figures was low for all agents as follows at 24 h PI: eyes, muscle, heart, and bile, <1% ID/g; spleen, lung, and bone (excluding marrow), < 2% ID/g. Complete biodistribution data at 2 and 24 h PI for all of these organs, plus stomach, blood, and urine is available in the Supporting Information. All agents were excreted primarily through the kidneys. Blood clearance was fast for all agents, with seven of the eight divalent agents decreasing to lower levels than parent monovalent agent ^{111}In-**TA138** over a 2 h period, and six of the eight remaining below ^{111}In-**TA138** at 24 h PI (Figure 5).

DISCUSSION

Many interactions in biological systems are polyvalent in nature, including the DNA helix, carbohydrate interactions, and virus−cell wall interactions. However, the idea of using multiple, simultaneous interactions as a strategy in drug discovery and development is a relatively recent phenomenon.

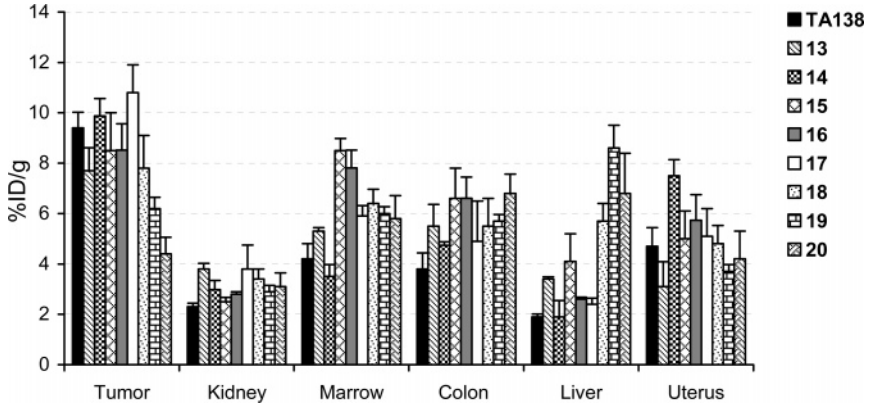


Figure 3. Biodistribution of the ^{111}In complexes of **TA138** and the eight divalent agents described in the text 2 h PI in the c-neu Oncomouse model at 2 mCi/Kg. Values are the average of three animals. The radiolabeling and biodistribution procedures were described in ref 41.

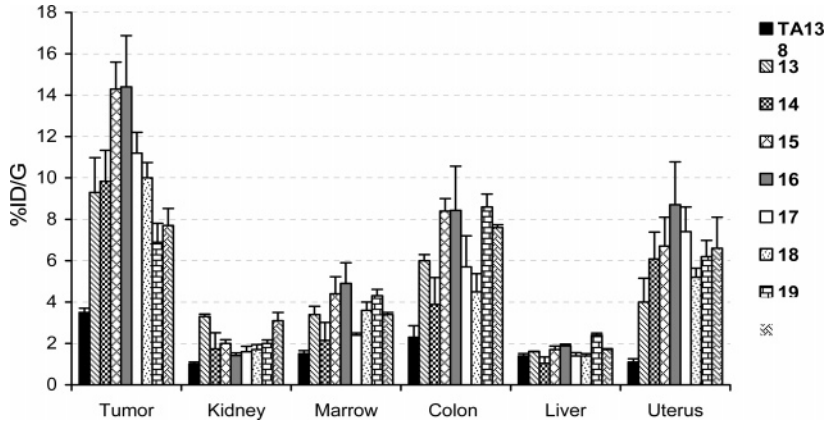


Figure 4. Biodistribution of the ^{111}In complexes of **TA138** and the eight divalent agents described in the text 24 h PI in the c-neu Oncomouse model at 2 mCi/Kg. Values are the average of three animals. The radiolabeling and biodistribution procedures are described in ref 41.

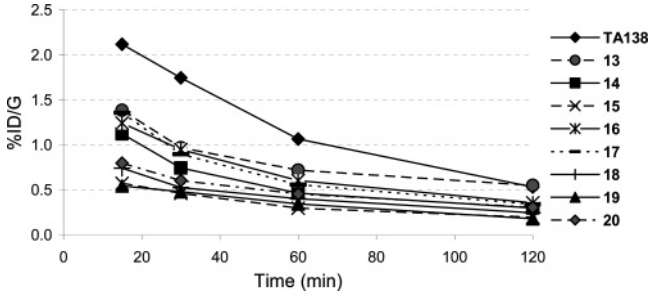


Figure 5. Blood clearance of the ^{111}In complexes of **TA138** and the eight divalent agents described in the text in the c-neu Oncomouse model at 2 mCi/Kg. Values are the average of three animals. The radiolabeling and biodistribution procedures are described in ref 41.

Polyvalency is a complex phenomenon, and the reader is referred to two recent reviews for an in-depth discussion (*44*, *45*). Past efforts by us and others to simultaneously achieve high tumor uptake and retention and favorable tumor/organ ratios for critical nontarget organs using polyvalent radiolabeled cyclic RGD peptide antagonists to receptor $\alpha_v\beta_3$ have led either to high tumor uptake or to improved tumor/organ ratios, but not both (*23*, *35*, *46*). Our main goal in this work was to determine whether polyvalency in peptidomimetic $\alpha_v\beta_3$ antagonists could be used as a means of improving tumor uptake and retention, and tumor/organ ratios for radiotherapeutic applications, where the radiation dose to nontarget organs, especially kidneys and bone marrow, becomes critically important.

We were also interested in understanding the nature of the polyvalent effect in $\alpha_v\beta_3$ antagonists, including the question of whether a polyvalent ligand can simultaneously bind to two or more $\alpha_v\beta_3$ receptors. The minimum spacer length required for homogeneous divalent association can be inferred from structural studies carried out on integrin receptors. Integrin $\alpha_v\beta_5$, which also recognizes the RGD binding motif, is an internalization receptor for adenovirus. Cryomicroscopy and difference map analyses of adenovirus complexed with an $\alpha_v\beta_5$ cluster were used to derive a 3D map of the extracellular domain of $\alpha_v\beta_5$ (*47*). Five integrin molecules form an integrin cluster and bind to the penton base of adenovirus. The penton base of adenovirus has five surface protrusions, which are believed to be the five RGD-containing surface loops that bind to the integrin cluster. The distance between any two adjacent loops was estimated to be 60 Å, suggesting a minimum length requirement of a spacer in order to achieve homogeneous divalent binding. The multivalent nature of the adenovirus−integrin cluster interaction was confirmed by kinetic analyses, which indicated 4.2 integrin molecules bound to each adenovirus penton base at close to saturation conditions. Additional structural information comes from the recently determined crystal structure of the extracellular segment of integrin $\alpha_v\beta_3$ in its activated state (*48*). The α and β subunits of $\alpha_v\beta_3$ assemble into an ovoid head having lateral dimensions of 60 Å by 90 Å. The putative $\alpha_v\beta_3$ binding site is centrally located on top of the head in the cleft between subunits. Below the integrin head, each subunit forms a thin cylindrical tail ~20 Å in diameter. Thus, the head dimensions determine the closest approach distance of two receptors and suggest that homogeneous bridging of adjacent receptors requires a minimum spacer length of 60−90 Å, depending on orientation of the two receptors.

All reported examples of the polyvalent effect in divalent cyclic RGD peptides have spacer lengths that fall far short of that required to simultaneously bridge the primary binding sites of adjacent integrin receptors (*23*, *24*, *33*−*36*). What, then, is

the source of the observed polyvalent effect? One explanation is the statistical effect, where increased affinity or retention is the result of increased effective local concentration of the binding moiety. Detachment of the ligand from the receptor is more likely to be followed by reattachment if there are multiple copies of the binding moiety near the receptor, effectively reducing the off-rate. Another possibility is the existence of secondary binding sites. A portion of the spacer or a portion of the second ligand may bind to what is commonly referred to as a subsite or exosite. These secondary binding sites are typically on the same receptor as the primary binding site and thus require a relatively short spacer for simultaneous attachment.

Given these previous studies, it was our expectation that we would observe a polyvalent effect with the quinolin-4-one vitronectin receptor antagonists using relatively short spacer lengths. The study design therefore consisted of a series of divalent structures having relatively short spacer lengths, which would not be predicted to bridge the primary binding sites of adjacent receptors but would be expected to produce a polyvalent effect by the statistical and/or exosite modes of binding. In addition, we synthesized and tested two divalent structures with spacer lengths greater than the estimated 60−90 Å required for simultaneous binding to the primary binding sites of adjacent receptors. To our knowledge, this is the first reported instance of divalent small molecule receptor $\alpha_v\beta_3$ antagonists having spacers that, in theory, are long enough to show true homogeneous divalent interactions. Such homogeneous divalent interactions would be evidenced by an increase in receptor affinity and target uptake when compared to those divalent agents binding by statistical and/or exosite divalent interactions. The structural features of all the divalent compounds in the study (structures **13**−**20**) are shown in Scheme 1 and in Table 1. The table also shows the length of the spacer groups as a function of the number of atoms in the spacers and as the maximum achievable length of the spacer in angstroms.

The structure of the spacer linking receptor-binding moieties plays an important role in the polyvalent process. The spacer must be of sufficient length to span the closest approach distance of the receptors, allow the pharmacophores to adopt the proper orientation to the receptors, and not interfere with binding. For short distances, we used spacers consisting of the ethylenediamine 4-oxobutyramide tether attached to the arylsulfonamide group of monomer **TA138**, plus cysteic acid PKMs (see structures **13**−**18**, Scheme 1 and Figure 2). For the longer distances (e.g., **19** and **20**), we added short diamino PEG units derivatized on one end with succinic acid (Suc-PEG in Figure 2). We reasoned that this PEG spacer should be neutral in its effect on the hydrophilic nature of the antagonist molecules. This spacer is also very flexible and will allow the molecules to acquire the necessary orientation for binding. Unfortunately, such extreme flexibility carries a thermodynamic penalty due to the increased entropy associated with divalent association. Entropy would be reduced with a rigid spacer of correct length and conformation. However, little is known about the optimum distance and conformation required for simultaneous binding to two $\alpha_v\beta_3$ receptors, and the flexible spacer approach was judged to be best in this instance.

The divalent compounds of this study can be grouped into two main series. The larger series consists of five compounds (**14** and **17**−**20**) having spacer lengths of 29−134 Å. These compounds have four cysteic acid PKMs and therefore have the same overall charge. The shortest spacers (compounds **14** and **17**) required a relocation of cysteic acid PKMs to a position between the glutamic acid branch point and DOTA. The lipophilicities of these five compounds are similar as judged by their elution properties on reverse-phase HPLC, where all compounds elute from a C18 column at 20−22% ACN under acidic mobile phase conditions. The principal variable in this series is therefore spacer length, and it was felt the biodistribution data would reveal information on the optimum spacer length and on the mechanism of the expected divalent effect in these molecules. The second series consists of three compounds (**15**, **16**, and **17**) having the same 36 Å spacer length, but having a total of either two, three, or four cysteic acid PKMs. This series was intended to reveal information on the role of charge and lipophilicity.

Receptor Affinity and Selectivity. Receptor affinity and selectivity of our divalent agents were measured in a panel of four integrin binding assays, as shown in Table 2. The affinity data for monovalent parent agent **TA138** are shown in line 1 of the table, with divalent agents following in order of increasing spacer length. Refer to Table 1 for spacer length data. The data show that all agents have high affinity toward the vitronectin receptor in the 293β_3-fibrinogen ($\alpha_v\beta_3$-mediated) adhesion assay, with IC_{50} values of 6−58 nM. There is no trend in the numbers that would suggest an optimum spacer length. For example, parent **TA138** has essentially the same affinity (IC_{50} = 12 nM) as **15** with a 36 Å spacer (IC_{50} = 9 nM) and **19** with a 89 Å spacer (IC_{50} = 6 nM). Receptor selectivities against receptors $\alpha_{IIb}\beta_3$, $\alpha_v\beta_5$, and $\alpha_5\beta_1$ are good for all agents. There are some minor differences, but no consistent pattern. For example, in the $\alpha_{IIb}\beta_3$ assay, the agents having intermediate-length spacers showed a slight reduction in selectivity, while in the $\alpha_5\beta_1$ assay, the shorter and longer spacers gave a slight reduction in selectivity. All compounds showed high selectivity in the $\alpha_v\beta_5$ assay. The two compounds with spacers long enough to simultaneously bind adjacent vitronectin receptors (**19** and **20**) have some of the best $\alpha_v\beta_3$ affinity numbers (IC_{50} = 6 and 15 nM, respectively), but the numbers are not orders of magnitude better than monomer **TA138**, as might be expected of a homogeneous divalent interaction. Thus, the receptor affinity data do not suggest simultaneous binding to two vitronectin receptors for compounds **19** and **20**. With regard to the effect of total charge of the molecules, there is no correlation between the negative charge imparted by the cysteic acid PKMs and affinity for $\alpha_v\beta_3$. These latter data support our earlier conclusion that the close proximity of the negatively charged cysteic acid PKM to the receptor does not negatively influence affinity for integrin $\alpha_v\beta_3$ (*41*). It is interesting that there is no correlation between affinity for $\alpha_v\beta_3$ and the tumor uptake of these agents (discussion to follow). It must be remembered that receptor affinity is only one of many variables that affect tissue uptake. Among these variables are protein binding, uptake and release by nontarget tissues, and blood clearance rates, and the role play by these variables will not be revealed by a simple in vitro affinity study.

In Vivo Biodistribution. We have previously shown that the ^{90}Y and ^{111}In complexes of **TA138** are biologically equivalent (*49*). We therefore assume that the ^{111}In complexes of these divalent antagonists can serve as reasonable surrogates for the corresponding therapeutic analogs. The ideal biodistribution and pharmacokinetic profile for a therapeutic radiopharmaceutical is one of rapid, high, and prolonged uptake in the target tissue, followed by rapid clearance from nontarget tissues and renal excretion. An agent with such a profile minimizes the radiation burden to the patient while maximizing the radiation dose to the target. Monovalent agent ^{111}In-**TA138** shows rapid tumor uptake in the c-neu Oncomouse model (9.39% ID/g at 2 h PI) with slow tumor washout (3.46% ID/g at 24 h PI), rapid blood clearance (Figure 5), and primarily renal excretion. Our principal goal in this study was to further reduce the already slow tumor washout shown by ^{111}In-**TA138**. This would allow us to take full advantage of the long half-life of therapeutic radionuclides such as ^{90}Y ($t_{1/2}$ = 64.1 h, 2.3 MeV β^- particle) and ^{177}Lu ($t_{1/2}$

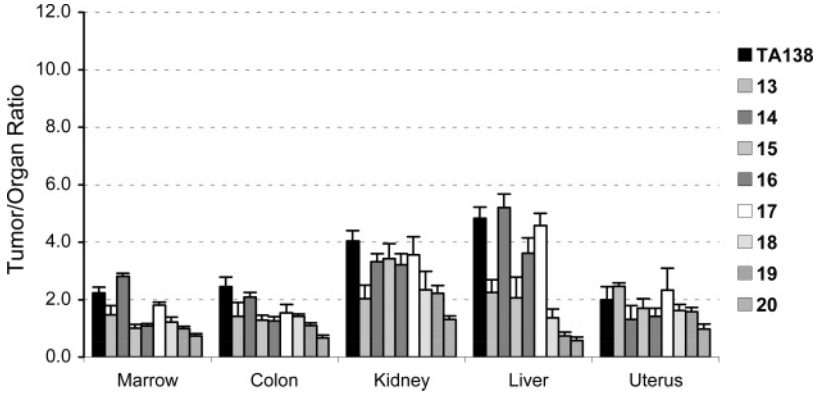


Figure 6. Tumor/organ ratios of the ^{111}In complexes of **TA138** and the eight divalent agents described in the text 2 h PI in the c-neu Oncomouse model at 2 mCi/Kg. Values are the average of three animals. The radiolabeling and biodistribution procedures are described in ref 41.

= 6.65 d, 0.48 MeV β^- particle). This goal has been achieved by all of the divalent agents of the study. The ^{111}In complexes of compounds **14**−**17** have tumor uptake at 2 h PI that is approximately equal to ^{111}In-**TA138**. But while ^{111}In-**TA138** washes out of tumors beyond 2 h PI, seven out of the eight divalent agents continue to accumulate in tumors, and by 24 h PI, all divalent agents display tumor uptake significantly higher than that of ^{111}In-**TA138** (Figure 4). It is interesting that the agents delivering the highest tumor uptake (^{111}In-**15**, ^{111}In-**16**, and ^{111}In-**17** with 14.3%, 11.1%, and 11.2% ID/g at 24 h PI, respectively) have the same intermediate-length spacers (36 Å). On the basis of the integrin structural studies discussed above, a 36 Å spacer is insufficient to provide simultaneous binding to two adjacent integrins. In contrast, the two agents having spacers sufficiently long to bridge the gap between adjacent integrins (^{111}In-**19** and ^{111}In-**20**) gave the lowest tumor uptake of the divalent agents at both 2 h PI (6.04% and 4.81% ID/g, respectively) and 24 h PI (6.87% and 7.69% ID/g, respectively). These data strongly suggest that ^{111}In-**19** and ^{111}In-**20** are also binding primarily by the statistical and/or exosite modes of polyvalent interaction, and the fact that they show the lowest tumor uptake of the divalent agents implies a thermodynamic penalty is being paid for having spacers longer than that required by the operative binding mechanism. Thus, while divalency has improved on the tumor uptake and retention of ^{111}In-**TA138** for all of the divalent agents, the data suggest that this is due in all cases to the statistical and/or exosite modes of polyvalent interaction rather than the simultaneous binding to two receptors.

Our calculations of organ doses from ^{111}In-**TA138** suggested that for a therapeutic version of **TA138** the kidneys and bone marrow would be the critical nontarget organs. The tumor/kidney ratios (Figures 6 and 7) for ^{111}In-**TA138** were 4.04 and 3.27 at 2 and 24 h PI, respectively, while the tumor/marrow ratios were constant at 2.30 from 2 to 24 h PI. The majority of divalent agents showed improved tumor/marrow and tumor/kidney ratios. The tumor/kidney ratios showed the largest improvement, with ^{111}In-**15**, ^{111}In-**16**, and ^{111}In-**17**, all with 36 Å spacers, having ratios of 3.42, 3.21, and 3.55 at 2 h PI, and increasing to 7.29, 8.51, and 6.82 at 24 h PI. The tumor/liver ratios showed a similar profile of improvement across the divalent agents, with the intermediate-length spacers providing the largest ratios. A much smaller improvement was observed for bone marrow, with ^{111}In-**14** and ^{111}In-**17** having nearly identical tumor/marrow ratios of 4.57 and 4.66 at 24 h PI. The colon and uterus displayed a pattern of uptake and retention noticeably different from other organs. Both showed uptake for all divalent agents at 24 h PI (Figure 4) that was significantly higher than ^{111}In-**TA138**, and the pattern of uptake was similar to that observed in the tumors. For example, from 2 to 24 h PI there was increased uterus uptake for seven of the eight divalent agents and increased colon uptake for four of the eight divalent

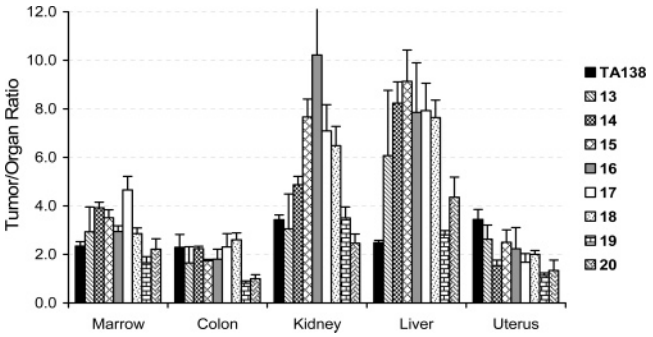


Figure 7. Tumor/organ ratios of the ^{111}In complexes of **TA138** and the eight divalent agents described in the text 24 h PI in the c-neu Oncomouse model at 2 mCi/Kg. Values are the average of three animals. The radiolabeling and biodistribution procedures are described in ref 41.

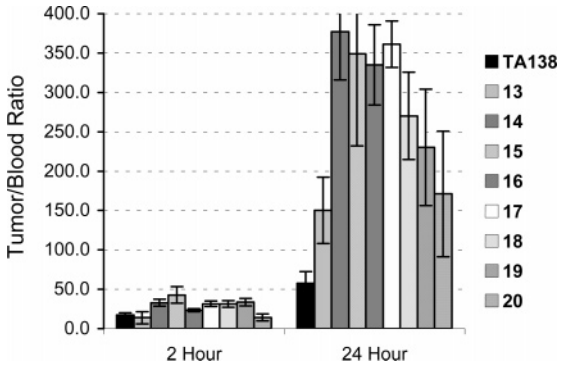


Figure 8. Tumor/blood ratios of the ^{111}In complexes of **TA138** and the eight divalent agents described in the text at 2 and 24 h PI in the c-neu Oncomouse model at 2 mCi/Kg. Values are the average of three animals. The radiolabeling and biodistribution procedures are described in ref 41.

agents. These findings are consistent with our previously reported competition studies with ^{111}In-**TA138**, which showed that uptake in colon and uterus was blocked to exactly the same degree as in tumors (*31*). It is our belief that uptake in these two organs is in large part receptor-mediated rather than the result of nonspecific binding. The rapid blood clearance and high tumor uptake provide very high tumor/blood ratios for all agents in the study (Figure 8).

The spacer that links the different binding moieties of a multivalent system is of paramount importance because it is responsible for the orientation that the binding ligands present to the biological target. The spacer must be of sufficient length to bridge the closest approach distance between receptors and

have a certain degree of flexibility to adjust to the changing conformation of the cellular surface. A spacer that is longer and more flexible than necessary will have increased conformational entropy and reduce the ability of all binding ligands to find their respective receptors. The current understanding of the optimum length and conformation required for simultaneous binding to two or more vitronectin receptors is very imprecise, and the divalent agents of this study were therefore joined by very flexible spacers. The increased thermodynamic penalty of the longest spacers presented here (i.e., ^{111}In-**19** and ^{111}In-**20**) is the most likely reason these agents did not display clear evidence of homogeneous divalent interaction with two vitronectin receptors. However, all of the divalent agents of this study displayed increased retention in tumors out to 24 h PI. Both the statistical and exosite binding modes are consistent with the observed results. While ^{111}In-**15**, ^{111}In-**16**, and ^{111}In-**17**, all with 36 Å spacers, gave the highest tumor uptake at 24 h PI, one must be careful about generalizing these results to other systems. The optimum spacer length will depend on a multitude of variables, including the receptor antagonist structure, spacer conformation, spacer rigidity, lipophilicity, protein binding, and so forth. The other variable in this study, the number of cysteic acid PKMs, appears to have little effect on the biodistribution properties of these divalent agents. Here again, one must be careful not to overanalyze these data, since the two series where cysteic acid is the only variable consist of only two and three compounds (**13** and **14**, and **15**−**17**). ^{111}In-**15** gave the best combination of tumor uptake and tumor/organ ratios for critical nontarget organs, and the ^{177}Lu analogue was used in the tissue residence time study below.

Tissue Residence Time Study. Of the readily available therapeutic radionuclides that form stable complexes with DOTA, ^{90}Y best fits the uptake and washout characteristics of ^{111}In-**TA138**. It has a relatively short $t_{1/2}$ of 64.1 h and decays to produce a very energetic 2.3 MeV β^- particle. One disadvantage of ^{90}Y is the relatively long 95% energy range (~5 mm in water), which means that a significant fraction of the decay energy escapes the tumor and is deposited in surrounding tissues. This fraction of lost energy increases as the size of the tumor decreases. The defining characteristic of the divalent agents in this study is the high and continuous tumor uptake in the c-neu Oncomouse model out to 24 h PI. This difference in tumor retention is more pronounced at later time points. For example, ^{111}In-**TA138** has a tumor uptake of 3.46% ID/g at 24 h PI, decreasing to 0.94% ID/g at 144 h PI, while divalent agent ^{111}In-**15** has a tumor uptake of 14.3% ID/g at 24 h PI, decreasing only slightly to 12.2% ID/g at 144 h PI. Complete biodistribution data for ^{111}In-**TA138** and ^{111}In-**15** from 2 to 144 h are provided in the Supporting Information. This prolonged tumor retention, coupled with the improved tumor/kidney and tumor/marrow ratios at later time points for the majority of divalent agents, suggested that they should exhibit an improved therapeutic index with radionuclides having relatively long half-lives, such as ^{177}Lu ($t_{1/2}$ = 6.65 d, 0.48 MeV β^- particle). The longer half-life of ^{177}Lu translates into a lower dose to nontarget organs at early time points while excess agent is clearing from the body, and the shorter 95% energy range (~0.8 mm in water) of the lower-energy β^- particle translates into less energy deposited outside the tumor. We therefore attempted to quantify this by comparing the therapeutic indices of monovalent agent ^{90}Y-**TA138** and divalent agent ^{177}Lu-**15** in our c-neu Oncomouse model. The biodistribution data of ^{90}Y-**TA138** used for these calculations has been reported previously (*49*). Biodistribution data for ^{177}Lu-**15** in critical nontarget organs are shown in Table 3 from 2 to 168 h PI. Complete biodistribution data are provided in the Supporting Information. The relative therapeutic indices of radiotherapeutic agents can be calculated by comparing the agent's tissue residence times. The tissue residence times of ^{90}Y-**TA138** and ^{177}Lu-**15** were compared after correcting for the difference in the energy released and retained between ^{90}Y and ^{177}Lu. Figure 9 shows the residence times (total disintegrations per unit injected dose per gram of tissue) for ^{90}Y-**TA138** and ^{177}Lu-**15** from 15 min PI to 168 h PI and extrapolated to infinity. The values are corrected using the ratio of the self-dose *S*-values for each organ. The *S*-value correction for the tumor was derived from thymus, which is similar in size to the tumors of this study. All *S*-values were taken from OLINDA/EXM (*50*). Relative to ^{90}Y-**TA138**, the residence time for ^{177}Lu-**15** decreases in the liver and kidney, is identical in the spleen, and increases in marrow, colon, and tumor. The tumor/organ residence time ratios (Figure 10) give a clearer picture of the relative radiation dose delivered to each organ. The tumor/organ residence time ratios for ^{177}Lu-**15** in the marrow and colon are identical to those for ^{90}Y-**TA138**, while the ratios in the liver, kidney, and spleen are considerably higher for ^{177}Lu-**15**, confirming the improved therapeutic index for this divalent $\alpha_v\beta_3$ antagonist.

Table 3. Biodistribution of ^{177}Lu-15 from 2−168 h PI, c-neu Oncomouse Mammary Adenocarcinoma Model

	organ uptake expressed as % ID/g (± SEM)[a]			
organ	2 h PI	24 h PI	48 h PI	168 h PI
liver	1.256 (0.108)	0.904 (0.071)	0.751 (0.047)	0.447 (0.022)
kidney	2.390 (0.223)	1.458 (0.169)	1.004 (0.073)	0.484 (0.027)
spleen	1.380 (0.148)	0.547 (0.037)	0.477 (0.042)	0.359 (0.028)
colon	2.677 (0.298)	3.160 (0.199)	3.179 (0.442)	0.746 (0.059)
marrow	2.527 (0.375)	1.356 (0.232)	0.913 (0.138)	1.119 (0.227)
tumor	6.867 (0.720)	7.285 (0.873)	7.165 (0.682)	8.048 (1.302)

[a] Values are the average of three animals. Test agents were administered at 2 mCi/Kg.

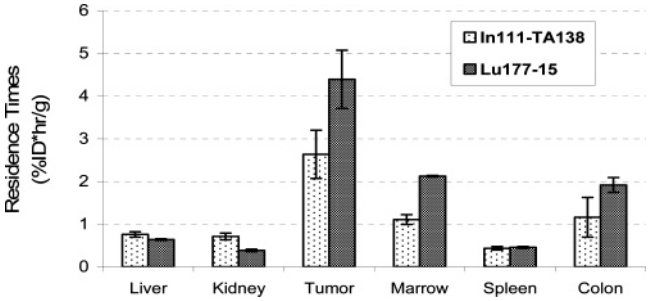


Figure 9. Residence times for ^{90}Y-**TA138** and ^{177}Lu-**15** corrected for isotope energy ratio and self-dose S-values for each organ.

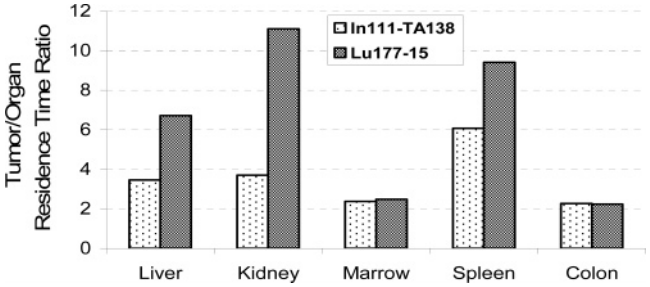


Figure 10. Tumor/organ residence time ratios for ^{90}Y-**TA138** and ^{177}Lu-**15** in the c-neu Oncomouse model at 2 mCi/Kg. Values are the average of three animals. The radiolabeling and biodistribution procedures are described in ref 41.

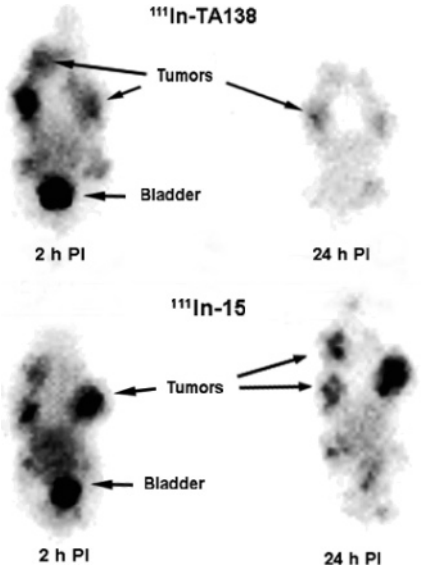


Figure 11. Representative scintigraphic images of ^{111}In-**TA138** and ^{111}In-**15** in the c-neu Oncomouse model at 2 mCi/Kg at 2 and 24 h PI.

Scintigraphic Image Study. As stated in the introduction, the primary goal of this study was the evaluation of these divalent agents as potential oncology radiotherapeutic agents. A secondary goal was their evaluation as potential imaging agents for detecting the overexpression of the vitronectin receptor. An examination of the tumor/organ ratios at 2 h PI (Figure 6) and 24 h PI (Figure 7) suggests that monovalent agent **TA138** should be the superior imaging agent at early time points due to rapid tumor uptake and relatively low nontarget uptake. At later time points, several of the divalent agents should be superior due to their continued tumor uptake and clearance from the majority of nontarget organs. This impression was confirmed in an imaging study comparing ^{111}In-**TA138** and ^{111}In-**15** in the c-neu Oncomouse model as shown in Figure 11. The excellent biodistribution properties of both agents are confirmed visually in the scintigraphic images. Both agents are able to clearly visualize tumors at 2 h PI, but ^{111}In-**TA138** gives a cleaner image with less background signal in the abdominal region. At 24 h PI, the ^{111}In-**TA138** image shows considerable washout from the tumors, making it difficult to clearly visualize the smaller tumors. In contrast, the image obtained with divalent agent ^{111}In-**15** very clearly shows even the smallest tumors. In addition, there is generally low background signal from the general musculature and abdomen. These data raise an interesting question: What is the optimum time postinjection required to obtain the ideal image with these divalent agents? The experiments required to answer that question were outside the scope of this study and will have to await further work.

CONCLUSIONS

In the present work, we have described synthetic methodology for the preparation of divalent versions of the quinolin-4-one class of receptor $\alpha_v\beta_3$ antagonists. A panel of integrin receptor affinity assays have shown that all of these agents have high affinity for receptor $\alpha_v\beta_3$ and good selectivity versus three other integrin receptors. Biodistribution studies in the c-neu Oncomouse revealed that compounds with intermediate-length spacers (29−43 Å) provide the highest tumor uptake and the best tumor/organ ratios. These data suggest that the primary mechanism for enhanced tumor uptake and retention is either the statistical effect or the subsite effect, rather than divalent homogeneous binding with two vitronectin receptors. The compound giving the best combination of tumor uptake and tumor/organ ratios for critical nontarget organs was ^{111}In-**15**, with a 36 Å spacer. A comparison of tissue residence times for ^{90}Y-**TA138** and ^{177}Lu-**15** show an improved therapeutic index for ^{177}Lu-**15** and suggest the potential application of these divalent vitronectin receptor antagonists as radiotherapeutic antitumor agents.

ACKNOWLEDGMENT

The authors with to thank Jeffrey Bogart, John Pietryka, and Neal Williams for analytical support.

Supporting Information Available: Additional experimental details. This material is available free of charge via the Internet at http://pubs.acs.org.

LITERATURE CITED

(1) van der Flier, A., and Sonnenberg, A. (2001) Function and interactions of integrins. *Cell Tissue Res. 305*, 285−298.
(2) Mizeiewski, G. J. (1999) Role of integrins in cancer: survey of expression patterns. *Proc. Soc. Exp. Biol. Med. 222*, 124−138.
(3) Hood, J. D., and Cheresh, D. A. (2002) Role of integrins in cell invasion and migration. *Nat. Rev. Cancer 2*, 91−100.
(4) Tucker, G. C. (2002) Inhibitors of integrins. *Curr. Opin. Pharm. 2*, 394−402.
(5) Jin, H., and Varner, J. (2004) Integrins: roles in cancer development and as treatment targets. *Br. J. Cancer 90*, 561−565.
(6) Max, R., Gerritsen, R. R. C. M., Nooijen, P. T. G. A., Goodman, S. L., Sutter, A., Keilholz, U., Ruiter, D. J., and De Waal, M. W. (1997) Immunohistochemical analysis of integrin $\alpha_v\beta_3$ expression on tumor-associated vessels of human carcinomas. *Int. J. Cancer 71*, 320−324.
(7) Christofidou-Solomidou, M., Bridges, M., Murphy, G. F., Albelda, S. M., and DeLisser, H. M. (1997) Expression and function of endothelial cell α_v integrin receptors in wound-induced human angiogenesis in human skin/SCID mice chimeras. *Amer. J. Pathol. 151*, 975−983.
(8) Cairns, R. A., Khokha, R., and Hill, R. P. (2003) Molecular mechanisms of tumor invasion and metastasis: an integrated view. *Curr. Mol. Med. 3*, 659−671.
(9) Felding-Habermann, B. (2003) Integrin adhesion receptors in tumor metastasis. *Clin. Exp. Metastasis 20*, 203−213.
(10) Mizejewski, G. J. (1999) Role of integrins in cancer: survey of expression patterns. *Proc. Soc. Exp. Biol. Med. 222*, 124−138.
(11) Liapis, H., Flath, A., and Kitazawa, S. (1996) Integrin $\alpha_v\beta_3$ expression by bone-residing breast cancer metastases. *Diagn. Mol. Pathol. 5*, 127−135.
(12) Wechsel, H. W., Petri, E., Feil, G., Nelde, H. J., Bichler, K. H., and Loesr, W. (1999) Renal cell carcinoma: immunohistological investigation of expression of the integrin $\alpha_v\beta_3$. *Anticancer Res. 19*, 1529−1532.
(13) Zheng, D., Woodard, A. S., Fornaro, M., Tallini, G., and Languino, L. R. (1999) Prostatic carcinoma cell migration via integrin $\alpha_v\beta_3$ is modulated by a focal adhesion kinase pathway. *Cancer Res. 59*, 1655−1664.
(14) Coleman, P. J., and Duong, L. T. (2002) Ligands to the integrin receptor $\alpha_v\beta_3$. *Expert Opin. Ther. Patents 12*, 1009−1021.
(15) Tucker, G. C. (2003) Alpha v integrin inhibitors and cancer therapy. *Curr. Opin. Invest. Drugs 4*, 722−731.
(16) Brooks, P. C., Montgomery, M. P., Rosenfeld, M., Reisfeld, R. A., Hu, T., Klier, G., and Cheresh, D. A. (1994) Integrin $\alpha_v\beta_3$ antagonists promote tumor regression by inducing apoptosis of angiogenic blood vessels. *Cell 79*, 1157−1164.
(17) Brooks, P. C., Stömblad, S., Klemke, R., Visscher, D., Sarkar, F. H., and Cheresh, D. A. (1995) Anti-integrin $\alpha_v\beta_3$ blocks human breast cancer growth and angiogenesis in human skin. *J. Clin. Invest. 96*, 1815−1822.
(18) Kumar, C. C., Malkowski, M., Yin, Z., Tanghetti, E., Yaremko, B., Nechuta, T., Varner, J., Liu, M., Smith, E. M., Neustadt, B., Presta, M., and Armstrong, L. (2001) Inhibition of angiogenesis and tumor growth by SCH221153, a dual $\alpha_v\beta_3$ and $\alpha_v\beta_5$ integrin receptor antagonist. *Cancer Res. 61*, 2232−2238.
(19) Kerr, J. S., Mousa, S. A., and Slee, A. M. (2001) $\alpha_v\beta_3$ Integrin in angiogenesis and restenosis. *Drug News Perspect. 14*, 143−150.

(20) Haubner, R., Kuhnast, B., Mang, C., Weber, W. A., Kessler, H., Wester, H.-J., and Schwaiger, M. (2004) [^{18}F]Galacto-RGD: synthesis, radiolabeling, metabolic stability, and radiation dose estimates. *Bioconjugate Chem. 15*, 61−69.

(21) Chen, X., Park, R., Shahinian, A. H., Tohme, M., Khankaldyyan, V., Bozorgzadeh, M. H., Bading, J. R., Moats, R., Laug, W. E., and Conti, P. S. (2004) ^{18}F-Labeled RGD peptide: initial evaluation for imaging brain tumor angiogenesis. *Nucl. Med. Biol. 31*, 179−189.

(22) Chen, X., Park, R., Tohme, M., Bading, J. R., and Conti, P. S. (2004) ^{18}F and ^{64}Cu-Labeled RGD peptide for imaging breast cancer in mice with microPET. *Bioconjugate Chem. 15*, 41−49.

(23) Janssen, M., Oyen, W. J. G., Massuger, L. F. A. G., Frielink, C., Dijkgraaf, I., Edwards, D. S., Radjopadhye, M., Corstens, F. H. M., and Boerman, O. C. (2002) Comparison of a monomeric and dimeric radiolabeled RGD-peptide for tumor targeting. *Cancer Biother. Radiopharm. 17*, 641−646.

(24) Janssen, M. L., Oyen, W. J., Dijkgraaf, I., Massuger, L. F., Frielink, C., Edwards, D. S., Rajopadhye, M., Boonstra, H., Corstens, F. H., and Boerman, O. C. (2002) Tumor targeting with radiolabeled $\alpha_v\beta_3$ integrin binding peptides in a nude mouse model. *Cancer Res. 62*, 6146−6151.

(25) Dijkgraaf, I., Kruijtzer, J. A. W., Frielink, C., Soede, A. C., Hilbers, H, W., Oyen, W. J. G., Corstens, F. H. M., Liskamp, R. M. J., and Boerman, O. C. (2006) Synthesis and biological evaluation of potent $\alpha_v\beta_3$ integrin receptor antagonists. *Nucl. Med. Biol. 33*, 953−961.

(26) Decristoforo, C., Faintuch-Linkowski, B., Rey, A., von Guggenberg, E., Rupprich, M., Hernandez-Gonzales, I., Rodrigo, T., and Haubner, R. (2006) [^{99m}Tc]HYNIC-RGD for imaging integrin $\alpha_v\beta_3$ expression. *Nucl. Med. Biol. 33*, 945−952.

(27) Beer, A. J., Haubner, R., Sarbia, M., Goebel, M., Luderschmidt, S., Grosu, A. L., Schnell, O., Niemeyer, M., Kessler, H., Wester, H. J., Weber, W. A., and Schwaiger, M. (2006) Positron emission tomography using [^{18}F]galacto-RGD identifies the level of integrin $\alpha_v\beta_3$ expression in man. *Clin. Cancer Res. 12*, 3942−3949.

(28) Haubner, R., and Wester, H.-J. (2004) Radiolabeled tracers for imaging of tumor angiogenesis and evaluation of anti-angiogenic therapies. *Curr. Pharm. Des. 10*, 1439−1455.

(29) Haubner, R. (2006) $\alpha_v\beta_3$-Integrin imaging: a new approach to characterise angiogenesis? *Eur. J. Nucl. Med. Mol. Imaging 33*, S54−S63.

(30) Liu, S. (2006) Radiolabeled multimeric cyclic RGD peptides as integrin $\alpha_v\beta_3$ targeted radiotracers for tumor imaging. *Mol. Pharm. 3*, 472−487.

(31) Harris, T. D., Kalogeropoulos, S., Nguyen, T., Liu, S., Bartis, J., Ellars, C., Edwards, D. S., Onthank, D., Silva, P., Yalamanchili, P., Robinson, R., Lazewatsky, J., Barrett, J., and Bozarth, J. (2003) Design, synthesis, and evaluation of radiolabeled integrin $\alpha_v\beta_3$ receptor antagonists for tumor imaging and radiotherapy. *Cancer Biother. Radiopharm. 18*, 627−641.

(32) Harris, T. D., Kalogeropoulos, S., Nguyen, T., Dwyer, G., Edwards, D. S., Liu, S., Bartis, J., Ellars, C., Onthank, D., Yalamanchili, P., Heminway, S., Robinson, S., Lazewatsky, J., and Barrett, J. (2006) Structure-activity relationships of ^{111}In- and ^{99m}Tc-labeled quinolin-4-one peptidomimetics as ligands for the vitronectin receptor: Potential tumor imaging agents. *Bioconjugate Chem. 17*, 1294−1313.

(33) Rajopadhye, M., Harris, A. R., Nguyen, H., Overoye, K. L., Bartis, J., Edwards, D. S., Liu, S., Onthank, D., and Barrett, J. A. (2000) The synthesis and evaluation of the ^{99m}Tc and ^{111}In complexes of cyclic RGD peptide antagonists of the integrin $\alpha_v\beta_3$. *J. Nucl. Med. 41*, 259P.

(34) Kok, R., Schraa, A. J., Bos, E. J., Moorlag, H. E., Asgeirsdottir, A., Everts, M., Meijer, D. K. F., and Molema, G. (2002) Preparation and functional evaluation of RGD-modified proteins as $\alpha_v\beta_3$ integrin directed therapeutics. *Bioconjugate Chem. 13*, 128−135.

(35) Cheng, Z., Wu, Y., Xiong, Z., Gambhir, S. S., and Chen. X. (2005) Near-infrared fluorescent RGD peptides for optical imaging of integrin $\alpha_v\beta_3$ expression in living mice. *Bioconjugate Chem. 16*, 1433−1441.

(36) Chen, X., Tohme, M., Park, R., Hou, Y., Bading, J. R., and Conti, P. S. (2004) Micro-PET imaging of $\alpha_v\beta_3$-integrin expression with ^{18}F-labeled dimeric RGD peptide. *Mol. Imaging 3*, 96−104.

(37) Vagner, J., Handl, H. L., Gillies, R. J., and Hruby, V. R. (2004) Novel targeting strategy based on multimeric ligands for drug delivery and molecular imaging: homooligomers of α-MSH. *Biorg. Med. Chem. Lett. 14*, 211−215.

(38) Tweedle, M. F. (2006) Adventures in multivalency: The Harry S. Fischer Memorial Lecture, CMR 2005; Evian, France. *Contrast Media Mol. Imaging 1*, 2−9.

(39) Harris, T. D., Barrett, J. A., Carpenter, A. P., and Rajopadhye, M. (2003) Vitronectin Receptor Antagonist Pharmaceuticals. U.S. Patent 6,511,649.

(40) Gerhardt, J. and Nicholson, G. J. (1994) Unambiguous determination of the optical purity of peptides via GC-MS. *Peptides: Chemistry, Structure, and Biology* (Hodges, R. S. and Smith, J. A., Eds) pp 241−243, Escom, Leiden.

(41) Harris, T. D., Kalogeropoulos, S., Nguyen, T., Dwyer, G., Edwards, D. S., Liu, S., Bartis, J., Ellars, C., Onthank, D., Yalamanchili, P., Heminway. S., Robinson, S., Lazewatsky, J., and Barrett, J. (2006) Structure-Activity Relationships of ^{111}In- and ^{99m}Tc-labeled quinolin-4-one peptidomimetics as ligands for the vitronectin receptor: potential tumor imaging agents. *Bioconjugate Chem. 17*, 1294−1313.

(42) Liu, S., Harris, T. D., Ellard, C. E., and Edwards, D. S. (2003) Anaerobic ^{90}Y- and ^{177}Lu-labeling of a DOTA-conjugated nonpeptide vitronectin receptor antagonist. *Bioconjugate Chem. 14*, 1030−1037.

(43) Pitts, W. J., Wityak, J., Smallheer, J. M., Tobin, A. E., Jetter, J. W., Buynitsky, J. S., Harlow, P. P., Solomon, K. A., Corjay, M. H., Mousa, S. A., Wexler, R. R., and Jadhav, P. K. (2000) Isoxazolines as potent antagonists of the integrin $\alpha_v\beta_3$. *J. Med. Chem. 43*, 27−40.

(44) Mammen, M., Choi, S. K., and Whitesides, G. M. (1998) Polyvalent interactions in biological systems: Implications for design and use of multivalent ligands and inhibitors. *Angew. Chem., Int. Ed. 37*, 2754−2794.

(45) Handl, H. L., Vagner, J., Han, H., Mash, E., Hruby, V. J., and Gillies, R. J. (2004) Hitting multiple targets with multimeric ligands. *Exp. Opin. Ther. Targets 8*, 565−586.

(46) Poethko, T., Schottelius, M., Thumshirn, G., Herz, M., Haubner, R., Henriksen, G., Kessler, H., Schwaiger, M., and Wester, H. J. (2004) Chemoselective pre-conjugate radiohalogenation of unprotected mono- and multimeric peptides via oxime formation. *Radiochim. Acta, 92*, 317−327.

(47) Chiu, C., Mathias, P., Nemerow, G. R., and Stewart, P. L. (1999) Structure of adenovirus complexed with its internalization receptor, $\alpha_v\beta_5$. *J. Virol. 73*, 6759−6768.

(48) Xiong, J.-P., Stehle, T., Diefenback, B., Zhang, R., Dunker, R., Scott, D. L., Joachimiak, A., Goodman, S. L., and Arnaout, M. A. (2001) Crystal structure of the extracellular segment of integrin $\alpha_v\beta_3$. *Science 294*, 339−345.

(49) Onthank, D. C., Liu, S., Silva, P. J., Barrett, J. A., Harris, T. D., Robinson, S. P., and Edwards, D. S. (2004) ^{90}Y and ^{111}In complexes of a DOTA-conjugated integrin $\alpha_v\beta_3$ receptor antagonist: different but biologically equivalent. *Bioconjugate Chem. 15*, 235−241.

(50) Stabin, M. G., Sparks, R. B., and Crowe, E. (2005) OLINDA/EXM: The second-generation personal computer software for internal dose assessment in nuclear medicine. *J. Nucl. Med. 46*, 1023−1027.

BC070002+

A Polysaccharide Carrier to Effectively Deliver Native Phosphodiester CpG DNA to Antigen-Presenting Cells

Naohiko Shimada,[†] Cevayir Coban,[§,▽] Yoichi Takeda,[†] Masami Mizu,[†] Jusaku Minari,[†] Takahisa Anada,[†] Yuichi Torii,[⊥] Seiji Shinkai,[‡,#] Shizuo Akira,[§,⊥,▽] Ken J. Ishii,[§,⊥] and Kazuo Sakurai[†,*]

Department of Chemical Processes & Environments, The University of Kitakyushu, 1-1, Hibikino, Wakamatu-ku, Kitakyushu, Fukuoka 808-0135, Japan, Department of Chemistry & Biochemistry, Graduate School of Engineering, and Center for Future Chemistry, Kyushu University, Motooka 744, Nishi-ku, Fukuoka 819-0395, Japan, Exploratory Research for Advanced Technology (ERATO), Japan Science and Technology Agency (JST), and Department of Host Defense, and The 21st Century COE, Combined Program on Microbiology and Immunology, Research Institute for Microbial Diseases, Osaka University, Osaka 565-0871, Japan Received January 18, 2007; Revised Manuscript Received March 22, 2007

Oligodeoxynucleotides containing unmethylated CpG sequences (CpG DNAs) activate the vertebrate innate immune system via toll-like receptor 9 (TLR-9). Although CpG DNA is a promising immunotherapeutic agent, its short circulation time in biological fluids due to nuclease is the major drawback. This paper proposes that a natural polysaccharide called schizophyllan (SPG) can be used as an effective CpG DNA carrier because SPG can complex with CpG DNA and the resultant complex shows the nuclease resistance of the bound DNA. In order to increase cellular uptake in vitro, we chemically attached spermine, cholesterol, arginine octamer, or RGD peptide to SPG. The complexes made of the chemically modified SPG and CpG DNA having a phosphorothioate (PS) or phosphodiester (PO) backbone led to increased secretion of cytokines of about 4- to 15-fold, compared with the uncomplexed dose. Furthermore, when PO CpG DNA was complexed with unmodified SPG, the IL-12 level increased by almost 3- to 11-fold compared with the naked dose. The PO CpG DNA/unmodified SPG complex data suggested that unmodified SPG might effectively deliver PO in vivo due to the electrically neutral nature of unmodified SPG. When the complexed CpG DNAs were injected intraperitoneally, a large amount of IL-12 production was observed compared with the uncomplexed material. Both in vivo and vitro assays indicated that the SPG complex may be of use for CpG DNA therapy.

INTRODUCTION

Oligodeoxynucleotides containing unmethylated CpG sequences (CpG DNAs) can activate the vertebrate immune system (*1*−*3*). The initial step of this event is cellular uptake of CpG DNAs by antigen-presenting cells (APCs), particularly dendritic cells, macrophages, and B-cells. Subsequently, CpG DNAs are transported through the endocytosis pathway, and during the transport they are recognized by a pattern recognition receptor called toll-like receptor 9 (TLR-9) in endosome vesicles (*4*). The recognition by TLR-9 triggers the secretion of cytokines, including IL-6, TNF-α, IFN-γ, and IL-12. These cytokines activate natural killer (NK) cells and dendric cells (DC) (*5*−*8*) and finally control adaptive immune responses toward Th1- and IgG2a-secreting B cell inductions. Therefore, the interaction between CpG DNAs and TLR-9 effectively bridges the innate and adaptive immune systems.

Recently, clinical trials have demonstrated that CpG DNAs can be useful as adjuvants for vaccines against infectious pathogens, cancer antigens, and allergens (*9*, *10*). However, there is a serious drawback in CpG DNA therapy. Generally, once naked DNAs are exposed to biological liquids, they are quickly eliminated by nuclease-mediated degradation and nonspecific binding with plasma proteins. To translate CpG DNAs to practical therapy, it is essentially important to deliver CpG DNAs to their target cells while avoiding these unfavorable interactions. Phosphorothioate (PS) DNA, an analogue of the natural type phosphodiester (PO) DNA, has relatively strong antinuclease capability, so that PS DNAs are used in clinical trials. Some recent studies pointed out the cytotoxicity of PS and unexpected biological responses, for example, inducing a nonspecific response from a complement system (*11*, *12*). These side effects can be ascribed to nonspecific binding to serum proteins and antigen nature of PS. It would be better if we can use PO by effectively protecting it from nuclease-mediated degradation and nonspecific binding.

Recent studies categorized CpG DNAs into at least two types of structurally and functionally different classes (*10*, *13*−*15*). One is denoted as K-type, which contains TCGT or TCGA motifs and activates plasmacytoid DCs to produce IL-6 and IL-12, but very little IFN-α or IFN-γ. K-type also stimulates B cells to proliferate and recreate IL-6 and IgM. The PS analogues of K-type show almost the same activity as native phosphodiesters. The other is called D-type. The structural distinction of D-type is an unmethylated CpG dinucleotide flanked by a palindromic sequence and G quartet attached to the 3′ end to increase the cellular uptake (*16*). D-type activates plasmacytoid DCs to secrete a large amount of IFN-α, causing stimulation of NK-cells to produce IFN-γ and differentiate monocytes into myeloid DCs (*14*). D-type does not stimulate B-cells and other subsets of DCs. Ballas et al. recently reported that D-type for immunotherapy of cancer was more effective than K-type in the therapy of murine melanoma (*17*). Verthelyi et al. also

* Corresponding author. Tel: +81-93-695-3294, Fax: +81-93-695-3368, e-mail: sakurai@env.kitakyu-u.ac.jp.
[†] The University of Kitakyushu.
[‡] Department of Chemistry & Biochemistry, Kyushu University.
[#] Center for Future Chemistry, Kyushu University.
[§] Japan Science and Technology Agency.
[⊥] Department of Host Defense, Osaka University.
[▽] The 21st Century COE, Combined Program on Microbiology and Immunology, Osaka University.

10.1021/bc0700178 CCC: $37.00 © 2007 American Chemical Society
Published on Web 05/27/2007

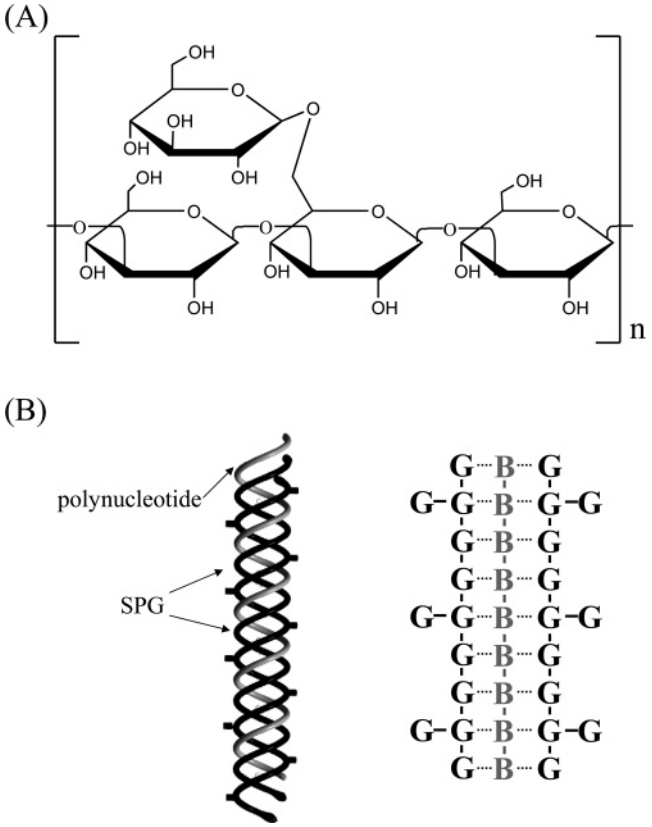


Figure 1. (A) Repeating unit of SPG, and (B) the structural model of the complex consisting of one polynucleotide and two SPG chains (*21*). The chemical modifications were carried out by the selective cleavage of the 1,2-diol group of the glycosyl side chain with periodate, leading to formyl group formation, and then subsequently introducing a chemical group (*27*). As presented in B, the complex forms a triple helix. The black lines and gray lines indicate SPG and polynucleotide, respectively (left). Two main-chain glucoses of SPG interact with one base of nucleotide. Capital letters of G and B indicate the glucoses of SPG and the base of polynucleotides (right).

reported that D-type as an adjuvant was superior to K-type in the magnitude of elicited antibody response by coadministered heat-killed *Leishmania* vaccine (*18*). Delivery system for D-type is required to protect against nuclease because the essential sequence of D-type cannot be replaced by PS (*13*).

There is a natural polysaccharide called schizophyllan (SPG) (Figure 1A), whose main chain consists of β-(1→3)-D-glucan and one β-(1→6)-D-glycosyl side chain links to the main chain at every three glucose residues (*19*). We found that SPG forms a novel complex with single-stranded homo polynucleotides (Figure 1B), and the fundamental properties of the complex have been examined by our group (*20*−*23*). Recently, we started to apply this complex to DNA delivery. Our communication preceding this paper showed a possibility to apply this complex to a CpG DNA carrier, showing that the complex can protect the bound DNA against unfavorable interactions with proteins and thus increase cytokine secretion (*24*, *25*). The previous paper used a classical K-type PS DNA and delivered it to macrophage-like cell lines (*24*). The promising results in the excellent antinuclease resistance of the complex compelled us to expand this research. This study utilized CpG DNA, having a PO backbone instead of a cytotoxic PS, spleen primary cells in vitro, and a preliminary in vivo assay.

MATERIALS AND METHODS

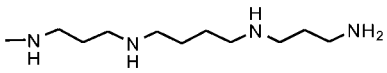
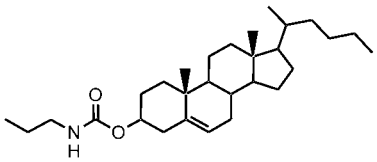
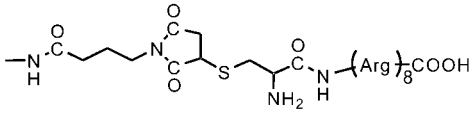
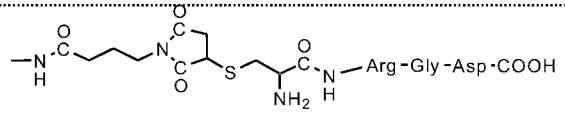
Materials. Mitsui Sugar Co., Ltd. (Japan) kindly supplied the SPG sample. The weight-average molecular weight (M_w) and the number of repeating units were found to be 1.5×10^5 and 231, respectively. We used this SPG sample unless mentioned. Additionally, two SPG samples with M_w of 2.5×10^6 and 2.5×10^4 were used to study the M_w dependence of the cytokine secretion. The molecular weight control of SPG and purification were described elsewhere (*26*). The cellular uptake efficiency of SPG itself was not significant *in vitro*; therefore, we modified SPG with a functional group that can induce passive cellular uptake. In this work, we introduced spermine (SP), arginine-glycine-aspartic acid tripeptide (RGD), octaarginine (R8), and cholesterol (Chol) (see Table 1). The experimental details and characterization for the modified SPG are described in our previous papers (*24*, *27*)

As a CpG DNA and its negative control, we adopted the two sequences of 5′-TCC ATG ACG TTC CTG ATG-3′ and 5′-TCC ATG AGC TTC CTG AGT-3′ (key sequence is underlined), respectively. To bind these sequences with SPG, we had to attach a poly(dA)$_{40}$ tail at the 3′ ends (*23*). In the present work, 5′-TCC ATG ACG TTC CTG ATG -(dA)$_{40}$-3′ and 5′-TCC ATG AGC TTC CTG ATG -(dA)$_{40}$-3′ were used and denoted by CpG DNA and non-CpG DNA, respectively. In addition to this classical sequence, we used typical K- and D-type DNAs, which were 5′-(dA)$_{40}$-ATC GAC TCT CGA GCG TTC TC-3′ ((dA)$_{40}$-K3) and 5′-(dA)$_{40}$-GGT GCA TCG ATG CAG GGG GG ((dA)$_{40}$-D35). PS analogues for the CpG DNA and non-CpG DNA were used to compare with PO. The sequences of the CpG DNA used in this work are summarized in Table 2. All DNAs were synthesized at Hokkaido System Science (Hokkaido, Japan) and purified with high-pressure liquid chromatography. The fetal bovine serum (FBS) and penicillin/streptomycin were purchased from Gibco/BRL. Dulbecco's modified Eagle's medium (DMEM) and RPMI1640 were obtained from Nissui Pharmaceutical Co., Ltd.

Complex Preparation. A 2 mg amount of PO CpG DNA or PS CpG DNA was dissolved in 10 mM Tris buffer solution (pH = 7.8) (1 mL). An appropriate concentration of unmodified or modified SPG/DMSO solution was added to the DNA solution so that the water volume fraction was always adjusted to be 0.9 after mixing. The molar ratio (M_{SPG}/M_{DNA}) was controlled to be 1.5, where M_{SPG} and M_{DNA} are the repeating molar concentration of SPG and DNA, respectively. After the DNA and SPG mixture was kept at 5 °C for 1 night to complete the complexation, DMSO was removed by ultrafiltration. After the filtration, the final concentration of DNA was determined by measuring the ultraviolet absorbance.

Mice and Cells. Seven- to eight-week-old female BALB/c or C57/B6 mice were purchased from Kyudo Co., Ltd., and CLEA, respectively. TLR-9 deficient mice were generated as previously described (*4*). Single spleen cell suspensions were prepared in RMPI1640 medium/10% FBS, 2 mM L-glutamine, 10 mM HEPES, and 0.11 mg/mL sodium pyruvate. Bone marrow dendric cells (BMDCs) were prepared as the established method (*28*). Flt3 ligand (Flt3L)-induced BMDCs (1×10^5 cells/well) were generated by culturing bone marrow cells with Flt3 ligand (100 ng/mL; PeproTech) for 8−9 days in DMEM medium containing 10% FBS. Murine macrophage-like cells (J774.A1) were cultured in DMEM containing 10% FBS and 1 wt % penicillin/streptomycin mixture. BALB/c spleen cells were maintained in RPMI1640 supplemented with 10% FBS. All medium contains a 1 wt % penicillin/streptomycin mixture. The cells were cultured at 37 °C in a 5% CO_2 incubator. Cells were stimulated in the presence of the indicated stimuli, and supernatants were collected for cytokine ELISA. For the in vivo assay, C57/B6 mice were injected intraperitoneally with 50 μg of CpG DNAs or the complex per mouse. Serum was collected in hours. The amount of IL-12p40 in serum was determined by ELISA.

Table 1. Sample Codes and the Introduced Chemical Groups

Sample code	Chemical group	Modification level [a]
SP-SPG		4.6 ±0.3 mol%
Chol-SPG		6.9 ±1.0 mol%
R8-SPG		0.5 ±0.1 mol%
RGD-SPG		1.3 ±0.3 mol%

[a] Determined by N elemental analysis. The experimental details and characterization for the modified SPG are described in our previous papers (*24*, *27*).

Table 2. Sequences of CpG DNAs

sample code	sequence[a]
PS CpG DNA	5′-TCC ATG ACG TTC CTG ATG -$(dA)_{40}$-3′
PS non-CpG DNA	5′-TCC ATG AGC TTC CTG ATG -$(dA)_{40}$-3′
PO CpG DNA	5′-TCC ATG ACG TTC CTG ATG -$(dA)_{40}$-3′
PO non-CpG DNA	5′-TCC ATG AGC TTC CTG ATG -$(dA)_{40}$-3′
$(dA)_{40}$-K3	5′-$(dA)_{40}$-ATC GAC TCT CGA GCG TTC TC-3′
$(dA)_{40}$-D35	5′-$(dA)_{40}$-GGT GCA TCG ATG CAG GGG GG-3′

[a] The key sequences are indicated as underlined text. All backbones of $(dA)_{40}$-K3 and $(dA)_{40}$-D35 are composed of phosphodiester.

ELISA. Spleen cells were plated in 48-well dishes using 2.5 $\times$ 10^6 cells/mL (1 well/1 mL) and were incubated 2 h at 37 °C. Naked CpG DNA or SPG/CpG DNA complexes were added to the cells. The cells were incubated at 37 °C for 24 h, and the supernatants were collected for ELISA assays (n = 4). The secretion of IL-6 and total IL-12 was determined using commercially available ELISA kits according to the instructions of the manufacturer (Endogen). For the experiments using BMDCs and in vivo experiments, IL-12 p40 and IFN-α (PBL Biomedical Laboratories) were measured either from the supernatants or the serum by ELISA according to the manufacturer's instructions (n = 4). R-848 and LPS were added to the cells at the concentration of 1 μM and 1 μg/mL, respectively. J774.A1 cells were plated in 48-well dishes using 1 $\times$ 10^6 cells/mL (1 well/200 μL) and were incubated 5 h at 37 °C, and then samples were added to the cells. The cells were incubated at 37 °C for 24 h, and the supernatants were collected for ELISA assays (n = 4). For all assays, each experiment was repeated at least twice.

RESULTS AND DISCUSSION

Comparison of the Cytokine Secretion between Phosphorothioate and Phosphodiester. Figure 2 shows the cytokine secretions from the spleen cells when PS CpG DNA (left panels) and PS non-CpG DNA (right panels) were administered. When naked CpG DNA was exposed at a concentration of 25 μg/mL, the secretion levels of IL-12 and IL-6 were 2.2 and 2.5 ng/mL, respectively. When the amount of dose was doubled, the secretion became almost 2-fold, 3.7 ± 0.5 ng/mL for IL-12 and 3.7 ± 0.4 ng/mL for IL-6. When CpG DNA was complexed with unmodified SPG, the secretions were increased to ~15% compared with the naked dose for IL-12 and IL-6. This increment can be ascribed to the fact that the complex can

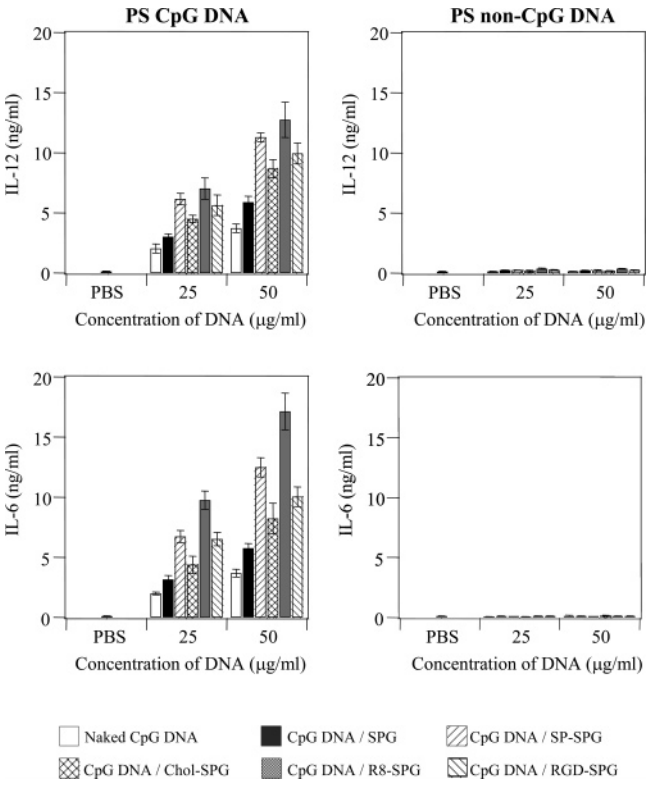


Figure 2. The cytokine secretions by various SPG/CpG DNA complexes when PS CpG was used. The spleen cells were stimulated with various concentrations of CpG DNA. The amount of secretions was determined with ELISA kits, after incubation of the cells in the presence of CpG DNA or its complex for 24 h. The molar ratio (M_{SPG}/M_{DNA}) is fixed at 1.5. Data represent the average ± SD (n = 4).

stabilize the bound DNA in the culturing medium, and thus it increases the population of CpG DNA that can reach the cell surface. The stabilization is effective even for PS, because BSA contained in the culturing medium tends to bind to PS to eliminate the activity (*29*). We carried out the control experiments using naked non-CpG DNA and complexed non-CpG DNA with SPG. Some results are presented in the right panels, showing essentially no secretions for all of the cytokines.

When we used the modified SPG samples, all of them increased the amount of secretions for IL-12 and IL-6 2- to

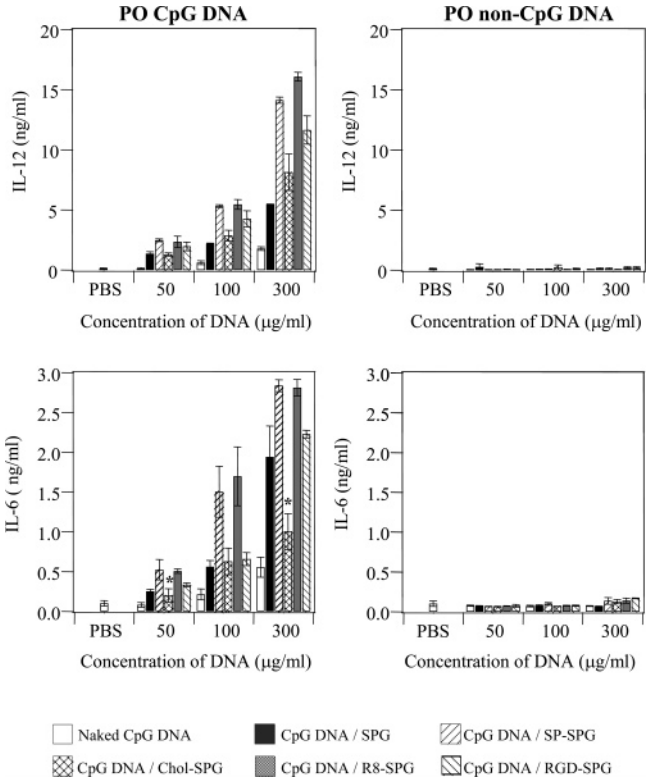


Figure 3. The cytokine secretions by various SPG/CpG DNA complexes when PO CpG was used. The spleen cells were stimulated with various concentrations of CpG DNA. The amount of secretions was determined with ELISA kits, after incubation of the cells in the presence of CpG DNA or its complex for 24 h. The molar ratio (M_{SPG}/M_{DNA}) is fixed at 1.5. Data represent the average ± SD ($n = 4$), *$p <$ 0.05 for naked PO CpG DNA dose.

4-fold, confirming the previous results obtained for the murine macrophage-like cells J774.A1 (*24*). The carriers themselves did not show any increment in the cytokines (data not shown). The increments in Figure 2 are ascribed to the increased cellular uptake mediated by the functional groups. Similar to the previous data, the R8−SPG complex was superior to the others. RGD−SPG, SP−SPG, and Chol−SPG ranked second, and RGD−SPG follows. According to previous work, the cellular uptake for the RGD, SP, and Chol complexes can be ascribed to normal endocytosis (*30*, *31*). On the other hand, the R8 complex is seemingly ingested by an endocytosis pathway different from the other functional groups, although there is still controversy over how R8 and its analogues are ingested by cells (*32*−*34*). R8 binds to heparan sulfate proteoglycan which is a sulfated polysaccharide anchored to the cell surface (*35*). The anchored heparan sulfate may release R8 and its cargo during the endocytosis transport (*36*). Since R8 has cationic charge, it can be ingested by normal electrostatic interactions similar to the other functional groups. The enhanced secretion for the R8−SPG complex may be caused by a combination of all of the endocytosis pathways.

Figure 3 shows the cytokine secretions when PO CpG DNAs were administered; here all the assays were carried out with the same conditions as those in Figure 2, except for using PO instead of PS. In contrast to the PS doses, naked PO CpG DNA did not show significant secretions unless the dose was increased over 100 μg/mL (PS showed appreciable secretion even at 25 μg/mL dose). This difference between PS and PO can be ascribed to two factors: PS is more stable against nuclease degradation than PO, and PS itself can be positively ingested by cells with an unidentified pathway (*37*). When PO CpG DNA was complexed with unmodified SPG, IL-12 level increased almost 11-fold at 50 μg/mL, 3.6-fold at 100 μg/mL, and 3.1-fold at 300 μg/mL, compared with the naked dose, respectively. In the case of PS, the complex with unmodified SPG increased the secretion level by 1.5-fold at most. The complexation increased the secretion level more efficiently in the PO system than in the PS system. This feature can be ascribed to the antinuclease protection effect of the complex (*25*) because naked PO DNAs should be more easily degraded than PS DNAs.

The modified SPG samples showed that the amount of secretions for IL-12 and IL-6 increased 4- to 15-fold, compared with the naked ones, similar to the PS results while the order of the superiority was different. R8−SPG and SP−SPG showed the highest increment, and RGD−SPG and Chol−SPG ranked second. Comparison between Figures 2 and 3 offers valuable insight. When we compared PO and PS at the same dose level, the complexed PO did not show the equivalent secretion with those of the complexed PS. For IL-12, we needed to increase the dose level to about 6 times to obtain the same secretion level (e.g., PS CpG DNA/SPG induced 5.5 ng/mL at 50 μg/mL dose, while PO CpG DNA/SPG induced 5.8 ng/mL at 300 μg/mL dose. Compare the black bars between Figures 2 and 3). This is because PS is positively introduced into cells but PO is not, and the complexation does not perfectly protect the bound PO from degradation. For IL-6, the secretion due to PO was much lower than that of PS (e.g., PS CpG DNA/R8 induced 17 ng/mL at 50 μg/mL dose, while PO CpG DNA/R8 induced 2.8 ng/mL at 300 μg/mL dose. Compare the gray bars between Figure 2 and 3). This difference in IL-6 secretion is due to the intrinsic difference between PS and PO reported by previous papers (*38*, *39*). A large amount of IL-6 secretion induces unfavorable side effects,(*40*) as in the case of TNF-α. Therefore, the lower induction of IL-6 from PO CpG DNA/SPG complexes can be an advantage as an adjuvant.

It is interesting that the complex of unmodified SPG showed a comparable effect with that of Chol−SPG and probably with that of RGD−SPG for IL-6. These results suggest that we can use unmodified SPG for CpG DNA carriers. A neutral or slightly anionic nature is favorable for the delivery in vivo, providing prolonged circulation time (*41*). This is because cations are generally easily absorbed by anionic proteins or the cellular surface and thus eliminated and/or inactivated in short period. Additionally, polycations can indeed induce side effects in the case of frequent doses, such as activation of complement, erythrocyte aggregation, and hemolysis. This is the main reason that the carriers with neutral and negative charge show good performance in vivo. On the basis of these facts, we decided to use unmodified SPG. An additional advantage to using unmodified SPG is that recent immunology (*42*, *43*) and our data (*44*) showed that SPG and other β-(1→3)-d-glucans can be recognized by dectin-I and thus ingested by APCs. This means that the unmodified SPG complex has the ability to deliver its cargo to APCs in vivo, where the target TLR-9 is present.

Many RGD-attached molecules have been studied as drug carriers to target to tumor cells in vivo (*45*−*47*), because the RGD motif can bind to integrin on the surface of the tumor cells (*48*) and also bind to newly formed endothelial cells (*49*). CpG DNA is required for uptake by APCs. This is why we did not use RGD−SPG.

SPG Molecular Weight Dependence of the Secretion. The M_w of SPG used in the above experiments was 1.5×10^5, which means 230 repeating units in one molecule. The stoichiometric number of the complex shows that two repeating units of SPG and three bases are interacting with each other; that is to say, two main-chain glucoses and one base are interacting (Figure 1B) (*21*). CpG DNA consists of 58 bases; therefore, one complex contains at least 11 CpG DNA molecules. [In this calculation, we assumed that the hetero sequence of CpG DNA

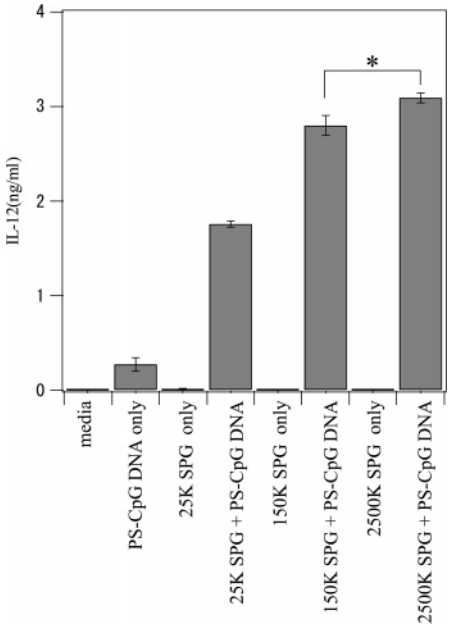


Figure 4. SPG molecular weight dependence of the secretion. J774.A1 (1×10^6 cells/mL, 200 μL) was stimulated with 25 μg/mL of PS CpG DNA and its SPG complex for 24 h. Data represent the average ± SD ($n = 4$), *$p < 0.001$.

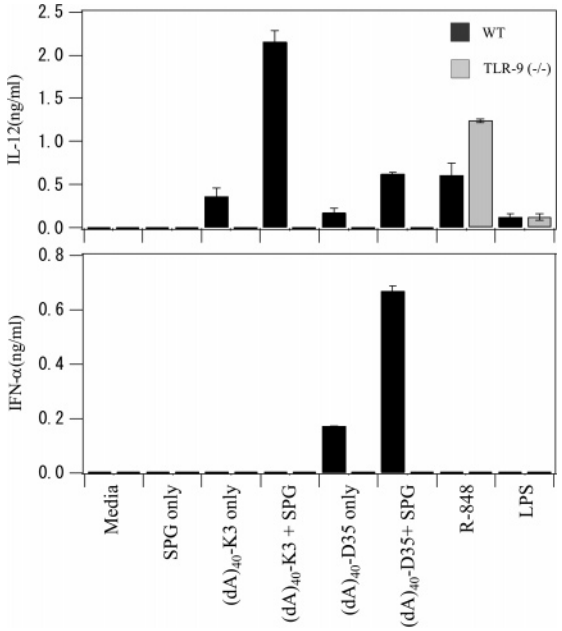


Figure 5. Difference of the cytokine secretions between K-type and D-type DNA with unmodified SPG. Flt3L-induced BMDCs were stimulated with CpG DNAs (30 μg/mL), R-848 (1 μM), or LPS (1 mg/mL) for 24 h. WT and TLR-9 (−/−) denote BMDCs obtained from wild type and TLR-9 knockout mice, respectively. Data represent the average ± SD ($n = 4$), *$p < 0.001$.

is complexed with SPG and one SPG chain is involved in one complex. In ref 23, we attached the $(dA)_{40}$ tail to a hetero sequence at the 3′ or 5′ end, where $(dA)_{40}$ can form a complex but the hetero sequence itself does not. After complexation with SPG, we compared the hydrolysis rate between the 3′- and 5′-$(dA)_{40}$ tailed hetero sequences using exonuclease I (hydrolyzes DNA from the 3′ end). We found that the hydrolysis rate was dramatically reduced for both 3′- and 5′-$(dA)_{40}$ tailed hetero sequences and there was no appreciable difference between them. This result implies that the hetero part is protected, suggesting that the complexation of the $(dA)_{40}$ part triggers additional complexation between the hetero part and SPG. If the hetero part is not involved in the complexation, 17 CpG DNA molecules are present in the complex.] We prepared two additional SPG samples with different M_w: 2.5×10^4 and 2.5×10^6. The same calculation shows that 2 and 200 CpG DNA molecules can be present in one complex, respectively. Figure 4 shows M_w dependence of the cytokine secretion for IL-12. The secretion was increased with increasing M_w. These results imply that the more CpG DNA molecules contained in the complex, the more cytokine secretion can be induced. A recent study reported the dramatic enhancement of cytokine secretion in the case of multiple CpG pairs in one DNA (*50*). Their results can be rationalized with the "cluster effect", which is normally termed for the case that branched oligosaccharides are bound much more tightly to receptors than monosaccharides or single chain oligosaccharides. We presume that the multiple CpG DNA pairs in one sequence can play the same role as the multiple oligosaccharides. A more recent study, by Wu et al., reported that the aggregation of CpG DNA due to the polymerization of G-quartet and palindrome enhanced the IL-12 secretion (*51*). This result can be explained with the cluster effect of CpG pairs. Our results in Figure 4 can be understood in the same framework as these two studies.

With increasing M_w, the size of the complex increases. Our dynamic light scattering determined the hydrodynamic diameter of the complexes using SPG with $M_w = 1.5 \times 10^4$ to be 100−300 nm and with $M_w = 2.5 \times 10^6$ to be 1000 nm, respectively (data not shown). Since SPG is internalized by dectin-I-mediated phagocytosis, such a large size of complex may not hinder the cellular uptake.

Distinct Cytokine Secretion with K-Type and D-Type CpG DNAs in Vitro. A distinctive difference between K- and D-type in the immunological response for the Flt3L-induced BMDCs can be determined by whether the secretion of IFN-α is induced. The resultant BMDCs contain $CD11c^+/B220^+$ and $CD11c^+/B220^-$ cells (*52*). K-type leads both cells to secrete IL-12; on the other hand, D-type leads to IFN-α secretion from $CD11c^+/B220^+$ and to IL-12 secretion from $CD11c^+/B220^-$. Therefore, when K-type is administered to the Flt3L-induced BMDCs, only IL-12 should be observed and the secretion level of IL-12 should be higher than that of D-type. On the other hand, both IL-12 and IFN-α should be secreted from the D-type administration.

The upper panel of Figure 5 shows the IL-12 secretion comparing $(dA)_{40}$-K3 and $(dA)_{40}$-D35, when the wild type and TLR-9-knockout (TLR-9 −/−) BMDCs were used. The IL-12 secretion was dramatically increased when $(dA)_{40}$-K3 was complexed. The increment due to the complexation was also observed for the case of $(dA)_{40}$-D35; however, the amount of the secretion was much smaller than those of $(dA)_{40}$-K3. These features are consistent with the difference between K- and D-types. The control experiment used with TLR-9 −/− BMDCs did not secret IL-12 at all for both $(dA)_{40}$-K3 and $(dA)_{40}$-D35 systems, while it showed a large amount of IL-12 for R848 and LPS doses, which are recognized by TLR-7 and TLR-4, respectively (*53*). This result indicates that the IL-12 productions by treatments of complex of both $(dA)_{40}$-K3 and $(dA)_{40}$-D35 are ascribed to the signal induced by TLR-9. The lower panel shows the IFN-α secretions. As in the case of IL-12, the advantage of the complexation is evidently demonstrated. The K-type did not show any secretion; on the other hand, the D-type clearly showed the secretion and the complex increased the secretion. The present IFN-α assay clarifies the advantage of using the SPG complex for the CpG DNA delivery.

IL-12 Secretion Induced by the Complex in Vivo. Figure 6 shows IL-12 p40 secretion of unmodified SPG/CpG DNA complex in vivo. IL-12 secretion was hardly observed by injection of unmodified SPG and naked CpG DNAs. On the other hand, injection of the complexes clearly exhibited 2−9 fold increase in IL-12 productions compared with those of naked

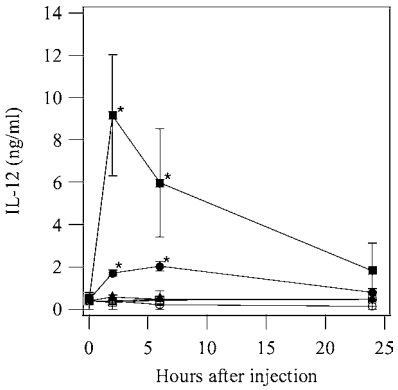


Figure 6. Time course of IL-12 p40 secretion in vivo, when CpG DNAs (50 μg) were intraperitoneally injected to C57/B6 mouse. Results represent the average ± SD of three mice per group. *$p < 0.05$ when compared with naked DNAs at each time. Naked $(dA)_{40}$-K3 and its SPG complex are indicated with unfilled and filled squares, respectively. Naked $(dA)_{40}$-D35 and its complex are indicated with unfilled and filled circles, respectively. PBS alone and SPG alone are indicated with open triangles and filled triangles, respectively.

doses. Maximum secretions appeared at 2−4 h. These enhancements can be ascribed to the stabilization due to the complex. Moreover, the complex with $(dA)_{40}$-K3 produced a large amount of IL-12 than that with $(dA)_{40}$-D35. This result agrees with in vitro study (Figure 5).

CONCLUSIONS

This paper showed that a natural polysaccharide called schizophyllan (SPG) can be used as a CpG DNA carrier. K- and D-type of phosphodiester CpG DNA were administered to Flt3L-induced BMDCs. K-type induced a large amount of IL-12 secretion; on the other hand, D-type led to the secretion of both IL-12 and IFN-α. The complexation increased the secretion in both cases, showing that the difference between K- and D-type was further enhanced. When CpG DNA was complexed with SPG and intraperitoneally injected to mouse, the maximum value of IL-12 for $(dA)_{40}$-K3 was 9-fold that of the naked dose. On the basis of these promising findings, the present paper proposes a new delivery method of CpG DNA and could lead to development of this therapy.

ACKNOWLEDGMENT

This work was finically supported by JST SORST and ERATO programs and Grant-in-Aid for Scientific Research (16350068 and 16655048).

LITERATURE CITED

(1) Wagner, H. (1999) Bacterial CpG DNA activates immune cells to signal infectious danger. *Adv. Immunol. 73*, 329−368.

(2) Krieg, A. M. (2002) CpG motifs in bacterial DNA and their immune effects. *Annu. Rev. Immunol. 20*, 709−760.

(3) Yamamoto, S., Yamamoto, T., and Tokunaga, T. (2000) The discovery of immunostimulatory DNA sequence. *Springer Semin. Immunopathol. 22*, 11−19.

(4) Hemmi, H., Takeuchi, O., Kawai, T., Kaisho, T., Sato, S., Sanjo, H., Matsumoto, M., Hoshino, K., Wagner, H., Takeda, K., and Akira, S. (2000) A Toll-like receptor recognizes bacterial DNA. *Nature 408*, 740−745.

(5) Klinman, D. M., Yi, A. K., Beaucage, S. L., Conover, J., and Krieg, A. M. (1996) CpG motifs present in bacteria DNA rapidly induce lymphocytes to secrete interleukin 6, interleukin 12, and interferon gamma. *Proc. Natl. Acad. Sci. U.S.A. 93*, 2879−2883.

(6) Yamamoto, S., Yamamoto, T., Kataoka, T., Kuramoto, E., Yano, O., and Tokunaga, T. (1992) Unique palindromic sequences in synthetic oligonucleotides are required to induce IFN [correction of INF] and augment IFN-mediated [correction of INF] natural killer activity. *J. Immunol. 148*, 4072−4076.

(7) Roman, M., Martin-Orozco, E., Goodman, J. S., Nguyen, M. D., Sato, Y., Ronaghy, A., Kornbluth, R. S., Richman, D. D., Carson, D. A., and Raz, E. (1997) Immunostimulatory DNA sequences function as T helper-1-promoting adjuvants. *Nat. Med. 3*, 849−854.

(8) Sparwasser, T., Miethke, T., Lipford, G., Erdmann, A., Hacker, H., Heeg, K., and Wagner, H. (1997) Macrophages sense pathogens via DNA motifs: induction of tumor necrosis factor-alpha-mediated shock. *Eur. J. Immunol. 27*, 1671−1679.

(9) Klinman, D. M. (2004) Immunotherapeutic uses of CpG oligodeoxynucleotides. *Nat. Rev. Immunol. 4*, 249−258.

(10) Ishii, K. J., Gursel, I., Gursel, M., and Klinman, D. M. (2004) Immunotherapeutic utility of stimulatory and suppressive oligodeoxynucleotides. *Curr. Opin. Mol. Ther. 6*, 166−174.

(11) Stein, C. A. (1997) Controversies in the cellular pharmacology of oligonucleotides. *Antisense Nucleic Acid Drug Dev. 7*, 207−209.

(12) Stein, C. A., and Cheng, Y. C. (1993) Antisense oligonucleotides as therapeutic agents−is the bullet really magical? *Science 261*, 1004−1012.

(13) Verthelyi, D., Ishii, K. J., Gursel, M., Takeshita, F., and Klinman, D. M. (2001) Human peripheral blood cells differentially recognize and respond to two distinct CPG motifs. *J. Immunol. 166*, 2372−2377.

(14) Gursel, M., Verthelyi, D., and Klinman, D. M. (2002) CpG oligodeoxynucleotides induce human monocytes to mature into functional dendritic cells. *Eur. J. Immunol. 32*, 2617−2622.

(15) Gursel, M., Verthelyi, D., Gursel, I., Ishii, K. J., and Klinman, D. M. (2002) Differential and competitive activation of human immune cells by distinct classes of CpG oligodeoxynucleotide. *J. Leukoc. Biol. 71*, 813−820.

(16) Prasad, V., Hashim, S., Mukhopadhyay, A., Basu, S. K., and Roy, R. P. (1999) Oligonucleotides tethered to a short polyguanylic acid stretch are targeted to macrophages: enhanced antiviral activity of a vesicular stomatitis virus-specific antisense oligonucleotide. *Antimicrob. Agents Chemother. 43*, 2689−2696.

(17) Ballas, Z. K., Krieg, A. M., Warren, T., Rasmussen, W., Davis, H. L., Waldschmidt, M., and Weiner, G. J. (2001) Divergent therapeutic and immunologic effects of oligodeoxynucleotides with distinct CpG motifs. *J. Immunol. 167*, 4878−4886.

(18) Verthelyi, D., Kenney, R. T., Seder, R. A., Gam, A. A., Friedag, B., and Klinman, D. M. (2002) CpG oligodeoxynucleotides as vaccine adjuvants in primates. *J. Immunol. 168*, 1659−1663.

(19) Tabata, K., Ito, W., Kojima, T., Kawabata, S., and Misaki, A. (1981) Ultrasonic degradation of schizophyllan, an antitumor polysaccharide produced by Schizophyllum commune Fries. *Carbohydr. Res. 89*, 121−135.

(20) Sakurai, K., and Shinkai, S. (2000) Molecular Recognition of Adenine, Cytosine, and Uracil in a Single-Stranded RNA by a Natural Polysaccharide: Schizophyllan. *J. Am. Chem. Soc. 122*, 4520−4521.

(21) Sakurai, K., Mizu, M., and Shinkai, S. (2001) Polysaccharide−polynucleotide complexes. 2. Complementary polynucleotide mimic behavior of the natural polysaccharide schizophyllan in the macromolecular complex with single-stranded RNA and DNA. *Biomacromolecules 2*, 641−650.

(22) Sakurai, K., Uezu, K., Numata, M., Hasegawa, T., Li, C., Kaneko, K., and Shinkai, S. (2005) beta-1,3-Glucan polysaccharides as novel one-dimensional hosts for DNA/RNA, conjugated polymers and nanoparticles. *Chem. Commun. (Camb*) 4383−4398.

(23) Mizu, M., Koumoto, K., Anada, T., Sakurai, K., and Shinkai, S. (2004) Antisense oligonucleotides bound in the polysaccharide complex and the enhanced antisense effect due to the low hydrolysis. *Biomaterials 25*, 3117−3123.

(24) Mizu, M., Koumoto, K., Anada, T., Matsumoto, T., Numata, M., Shinkai, S., Nagasaki, T., and Sakurai, K. (2004) A polysaccharide carrier for immunostimulatory CpG DNAs to enhance cytokine secretion. *J. Am. Chem. Soc. 126*, 8372−8373.

(25) Mizu, M., Koumoto, K., Kimura, T., Sakurai, K., and Shinkai, S. (2004) Protection of polynucleotides against nuclease-mediated hydrolysis by complexation with schizophyllan. *Biomaterials 25*, 3109−3116.

(26) Kimura, T., Koumoto, K., Sakurai, K., and Shinkai, S. (2000) Polysaccharide-Polynucleotide Complexes (III): A novel Interaction

between the b-1,3-Glucan Family and the Single-Stranded RNA Poly(C). *Chem. Lett.* 1242−1243.
(27) Matsumoto, T., Numata, M., Anada, T., Mizu, M., Koumoto, K., Sakurai, K., Nagasaki, T., and Shinkai, S. (2004) Chemically modified polysaccharide schizophyllan for antisense oligonucleotides delivery to enhance the cellular uptake efficiency. *Biochim. Biophys. Acta 1670*, 91−104.
(28) Coban, C., Ishii, K. J., Kawai, T., Hemmi, H., Sato, S., Uematsu, S., Yamamoto, M., Takeuchi, O., Itagaki, S., Kumar, N., Horii, T., and Akira, S. (2005) Toll-like receptor 9 mediates innate immune activation by the malaria pigment hemozoin. *J. Exp. Med. 201*, 19−25.
(29) Mizu, M., Koumoto, K., Anada, T., Karinaga, R., Kimura, T., Nagasaki, T., Shinkai, S., and Sakurai, K. (2004) Enhancement of the Antisense Effect of Polysaccharide?Polynucleotide Complexes by Preventing the Antisense Oligonucleotide from Binding to Proteins in the Culture Medium. *Bull. Chem. Soc. Jpn. 77*, 1101−1110.
(30) Heiniger, H. J., Kandutsch, A. A., and Chen, H. W. (1976) Depletion of L-cell sterol depresses endocytosis. *Nature 263*, 515−517.
(31) Colin, M., Harbottle, R. P., Knight, A., Kornprobst, M., Cooper, R. G., Miller, A. D., Trugnan, G., Capeau, J., Coutelle, C., and Brahimi-Horn, M. C. (1998) Liposomes enhance delivery and expression of an RGD-oligolysine gene transfer vector in human tracheal cells. *Gene Ther. 5*, 1488−1498.
(32) Nakase, I., Niwa, M., Takeuchi, T., Sonomura, K., Kawabata, N., Koike, Y., Takehashi, M., Tanaka, S., Ueda, K., Simpson, J. C., Jones, A. T., Sugiura, Y., and Futaki, S. (2004) Cellular uptake of arginine-rich peptides: roles for macropinocytosis and actin rearrangement. *Mol. Ther. 10*, 1011−1022.
(33) Ferrari, A., Pellegrini, V., Arcangeli, C., Fittipaldi, A., Giacca, M., and Beltram, F. (2003) Caveolae-mediated internalization of extracellular HIV-1 tat fusion proteins visualized in real time. *Mol. Ther. 8*, 284−294.
(34) Zaro, J. L., Rajapaksa, T. E., Okamoto, C. T., and Shen, W. C. (2006) Membrane transduction of oligoarginine in HeLa cells is not mediated by macropinocytosis. *Mol. Pharm. 3*, 181−186.
(35) Goncalves, E., Kitas, E., and Seelig, J. (2005) Binding of oligoarginine to membrane lipids and heparan sulfate: structural and thermodynamic characterization of a cell-penetrating peptide. *Biochemistry 44*, 2692−2702.
(36) Xu, Y., and Szoka, F. C., Jr. (1996) Mechanism of DNA release from cationic liposome/DNA complexes used in cell transfection. *Biochemistry 35*, 5616−5623.
(37) Krieg, A. M., and Stein, C. A. (1995) Phosphorothioate oligodeoxynucleotides: antisense or anti-protein? *Antisense Res. Dev. 5*, 241.
(38) Roberts, T. L., Sweet, M. J., Hume, D. A., and Stacey, K. J. (2005) Cutting edge: species-specific TLR9-mediated recognition of CpG and non-CpG phosphorothioate-modified oligonucleotides. *J. Immunol. 174*, 605−608.
(39) Baek, K. H., Ha, S. J., and Sung, Y. C. (2001) A novel function of phosphorothioate oligodeoxynucleotides as chemoattractants for primary macrophages. *J. Immunol. 167*, 2847−2854.
(40) Heikenwalder, M., Polymenidou, M., Junt, T., Sigurdson, C., Wagner, H., Akira, S., Zinkernagel, R., and Aguzzi, A. (2004) Lymphoid follicle destruction and immunosuppression after repeated CpG oligodeoxynucleotide administration. *Nat. Med. 10*, 187−192.
(41) Nicolazzi, C., Mignet, N., de la Figuera, N., Cadet, M., Ibad, R. T., Seguin, J., Scherman, D., and Bessodes, M. (2003) Anionic polyethyleneglycol lipids added to cationic lipoplexes increase their plasmatic circulation time. *J. Controlled Release 88*, 429−443.
(42) Adachi, Y., Ishii, T., Ikeda, Y., Hoshino, A., Tamura, H., Aketagawa, J., Tanaka, S., and Ohno, N. (2004) Characterization of beta-glucan recognition site on C-type lectin, dectin 1. *Infect. Immun. 72*, 4159−4171.
(43) Herre, J., Marshall, A. S., Caron, E., Edwards, A. D., Williams, D. L., Schweighoffer, E., Tybulewicz, V., Reis e Sousa, C., Gordon, S., and Brown, G. D. (2004) Dectin-1 uses novel mechanisms for yeast phagocytosis in macrophages. *Blood 104*, 4038−4045.
(44) Shimada, N., Ishii, K. J., Takeda, Y., Coban, C., Torii, Y., Shinkai, S., Akira, S., and Sakurai, K. (2006) Synthesis and in vitro characterization of antigen-conjugated polysaccharide as a CpG DNA carrier. *Bioconjugate Chem. 17*, 1136−1140.
(45) Schiffelers, R. M., Ansari, A., Xu, J., Zhou, Q., Tang, Q., Storm, G., Molema, G., Lu, P. Y., Scaria, P. V., and Woodle, M. C. (2004) Cancer siRNA therapy by tumor selective delivery with ligand-targeted sterically stabilized nanoparticle. *Nucleic Acids Res. 32*, e149.
(46) Arap, W., Pasqualini, R., and Ruoslahti, E. (1998) Cancer treatment by targeted drug delivery to tumor vasculature in a mouse model. *Science 279*, 377−3780.
(47) Janssen, M. L., Oyen, W. J., Dijkgraaf, I., Massuger, L. F., Frielink, C., Edwards, D. S., Rajopadhye, M., Boonstra, H., Corstens, F. H., and Boerman, O. C. (2002) Tumor targeting with radiolabeled alpha(v)beta(3) integrin binding peptides in a nude mouse model. *Cancer Res. 62*, 6146−6151.
(48) Tomiyama, Y., Brojer, E., Ruggeri, Z. M., Shattil, S. J., Smiltneck, J., Gorski, J., Kumar, A., Kieber-Emmons, T., and Kunicki, T. J. (1992) A molecular model of RGD ligands. Antibody D gene segments that direct specificity for the integrin alpha IIb beta 3. *J. Biol. Chem. 267*, 18085−18092.
(49) Janssen, M., Frielink, C., Dijkgraaf, I., Oyen, W., Edwards, D. S., Liu, S., Rajopadhye, M., Massuger, L., Corstens, F., and Boerman, O. (2004) Improved tumor targeting of radiolabeled RGD peptides using rapid dose fractionation. *Cancer Biother. Radiopharm. 19*, 399−404.
(50) Marshall, J. D., Hessel, E. M., Gregorio, J., Abbate, C., Yee, P., Chu, M., Van, Nest, G., Coffman, R. L., and Fearon, K. L. (2003) Novel chimeric immunomodulatory compounds containing short CpG oligodeoxyribonucleotides have differential activities in human cells. *Nucleic Acids Res. 31*, 5122−5133.
(51) Wu, C. C., Lee, J., Raz, E., Corr, M., and Carson, D. A. (2004) Necessity of oligonucleotide aggregation for toll-like receptor 9 activation. *J. Biol. Chem. 279*, 33071−33078.
(52) Hemmi, H., Kaisho, T., Takeda, K., and Akira, S. (2003) The roles of Toll-like receptor 9, MyD88, and DNA-dependent protein kinase catalytic subunit in the effects of two distinct CpG DNAs on dendritic cell subsets. *J. Immunol. 170*, 3059−64.
(53) Ito, T., Amakawa, R., Kaisho, T., Hemmi, H., Tajima, K., Uehira, K., Ozaki, Y., Tomizawa, H., Akira, S., and Fukuhara, S. (2002) Interferon-alpha and interleukin-12 are induced differentially by Toll-like receptor 7 ligands in human blood dendritic cell subsets. *J. Exp. Med. 195*, 1507−15012.

BC0700178

Synthesis, Liposomal Preparation, and *in Vitro* Toxicity of Two Novel Dodecaborate Cluster Lipids for Boron Neutron Capture Therapy

Eugen Justus,[†] Doaa Awad,[†] Michaela Hohnholt,[†] Tanja Schaffran,[†] Katarina Edwards,[‡] Göran Karlsson,[‡] Luminita Damian,[§] and Detlef Gabel*[,†]

Department of Chemistry, University of Bremen, PO Box 330440, D-28334 Bremen, Department of Physical Chemistry, Uppsala University, Box 579, S-75123 Uppsala, and School of Science and Engineering, Jacobs University Bremen, PO Box 750561, D-28725 Bremen. Received February 6, 2007; Revised Manuscript Received April 12, 2007

A new class of lipids, containing the *closo*-dodecaborate cluster, has been synthesized. Two lipids, *S*-(*N*, *N*-(2-dimyristoyloxyethyl)acetamido)thioundecahydro-*closo*-dodecaborate (2-) (**B-6−14**) and *S*-(*N*, *N*-(2-dipalmitoyloxyethyl)acetamido)thioundecahydro-*closo*-dodecaborate (2-) (**B-6−16**) are described. Both of them have a double-tailed lipophilic part and a headgroup carrying two negative charges. Differential scanning calorimetry shows that **B-6−14** and **B-6−16** bilayers have main phase transition temperatures of 18.8 and 37.9 °C, respectively. Above the transition temperature of 18.8 °C, **B-6−14** can form liposomal vesicles, representing the first boron-containing lipid with this capability. Upon cooling below the transition temperature, stiff bilayers are formed. When incorporated into liposomal formulations with equimolar amounts of distearoyl phosphatidylcholine (DSPC) and cholesterol, stable liposomes are obtained. The ζ-potential measurements indicate that both **B-6−14-** and **B-6−16**-containing vesicles are negatively charged, with the most negative potential described of any liposome so far. The liposomes are of high potential value as transporters of boron to tumor cells in treatments based on boron neutron capture therapy (BNCT). Liposomes prepared from **B-6−14** were slightly less toxic in V79 Chinese hamster cells (IC50 5.6 mM) than unformulated $Na_2B_{12}H_{11}SH$ (IC_{50} 3.9 mM), while liposomes prepared from **B-6−16** were not toxic even at 30 mM.

INTRODUCTION

In boron neutron capture therapy of tumors (BNCT[1]), successful treatment requires a selective delivery of boron-10 to tumor tissues to maximize damage to the tumor and to minimize damage to surrounding normal tissue (*1*). However, relatively large intracellular accumulations of boron (approximately 20−30 μg of boron-10 per gram of tumor) are necessary to produce cell death (*2*). Several means of selective targeting of boron-10 to tumors have been investigated. In 1964, Soloway suggested that antibodies might be used for delivering boron-10 to cancer cells (*3*). Assuming an antigen site density of 10^6 per tumor cell, this would require approximately 1000 boron-10 atoms per antibody molecule to attain 10^9 boron atoms per cell (approximately 20−50 μg boron-10/gram of tumor). The structures formed by linking 1000 boron atoms to an antibody molecule fail, however, to find their antigenic target (*4*). The increased rate of mitosis of malignant cells has inspired the synthesis of boron-containing nucleic acid precursors (*5*). Further, porphyrin derivatives that contain boron have been synthesized as capture agents for BNCT (*6*). However, significant normal tissue uptake of the boronated porphyrins (*7*, *8*) may limit their use in BNCT.

Liposomes show selective localization in tumors (*9*, *10*). The lipid carriers extravasate through the highly permeable microvessels of the tumors and remain locked in the interstitial fluid compartment due to a lack of functional lymphatic drainage (*11*). Liposomes might therefore be useful vehicles for transporting boron to the tumor site.

Two approaches are possible when using liposomes in boron delivery: encapsulation of boron compounds in the aqueous core of theliposome, and incorporation of boron-containing lipids in theliposome bilayer. Encapsulation of a boron compound in liposomes has been described by, e.g., Hawthorne, (*12*), Mehta (*13*), Johnsson (*14*), Maruyama (*15*), and Lee (*16*). Problems might arise by the encapsulation of these compounds into the liposomes through, e.g., low encapsulation efficiency and changes in the physical−chemical behavior through the presence of the boron compounds, and leakage upon storage and in contact with serum. The amount of boron which can be encapsulated in liposomes depends on the maximal concentration of the boron compound which is compatible with stability. For liposomes of 100 nm diameter, the encapsulated volume is about 2.5 L per mol lipid (*17*). With concentrations of the encapsulated agent of 0.1 M, about 0.25 mol can be encapsulated per mol of lipid. The alternative approach, incorporation of boron-containing amphiphilic molecules into liposomes, has been described by, e.g., Hawthorne (*18*), Nakamura (*19*), Tjarks (*20*), and Rossi (*21*, *22*). Many of the problems encountered in the encapsulation approach can be avoided by using the latter strategy. It is, in principle, not even necessary to prepare closed vesicles, as long as tumor accumulation is possible.

Boron-containing lipids constitute very interesting building blocks for the construction of boron-containing liposomes. A few approaches toward the synthesis of such lipids intended for incorporation into liposomes have been described in the literature.

Synthesis of a nido-carborane lipid with a one-tailed moiety (Figure 1, compound **1**) has been described, and the liposomal boron delivery using this compound and DSPC has been

* gabel@chemie.uni-bremen.de. Phone +49 421 2182200, fax +49 421 2182871.

[†] Department of Chemistry, University of Bremen.

[‡] Uppsala University.

[§] School of Science and Engineering, Jacobs University Bremen.

[1] Abbreviations: HEPES, 4-(2-hydroxyethyl)-1-piperazineethanesulfonic acid; CHOL, cholesterol; BNCT, boron neutron capture therapy; DSPC, distearoylphosphatidylcholine; BSH, $Na_2B_{12}H_{11}SH$; DSC, differential scanning calorimetry; DMPC, dimyristoylphosphatidylcholine; DPPC, dipalmitoylphosphatidylcholine; TEM, transmission electron microscopy.

10.1021/bc070040t CCC: $37.00 © 2007 American Chemical Society
Published on Web 06/15/2007

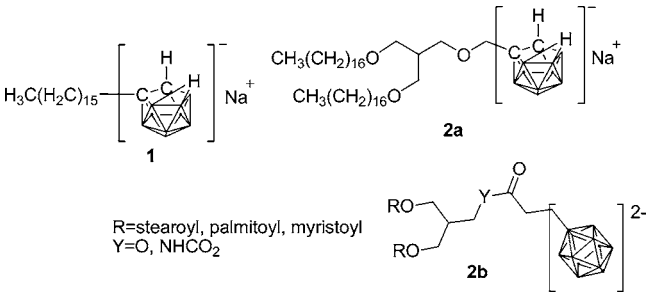


Figure 1. Structures of the boron cluster lipids **1** and **2**. Each unlabeled corner of the polyhedra corresponds to a BH unit.

examined in mice (*18*, *23*). Later, Nakamura designed a nido-carborane lipid with a double-tailed moiety for the purposes of high boron accumulation into liposomes (*19*) (Figure 1, compound **2a**). More recently, Hawthorne et al. described a very similar lipid (differing only in the number of methylene groups of the side chain) and investigated the in vivo toxicity of liposomes formed from the boron-containing lipid and helper lipids (distearoylphosphatidylcholine (DSPC), cholesterol (CHO)). They found that the liposomes were very toxic already at dosages of 6 mg boron per kg body weight (*24*). Nidocarborane lipids might therefore be problematic as agents for boron delivery in BNCT. A first dodecaborate-containing ether lipid (Figure **1**, compound **2b**) was recently described by Nakamura (*25*).

Our target was the preparation of $(B_{12}H_{11}S)^{2-}$-containing lipids, since mercaptoundecahydrododecaborate ($B_{12}H_{11}SH^{2-}$, BSH) is the only acceptable boron cluster compound that can be used at the present time in clinical trials in Japan, Europe, or the USA. Other suitable target species are under rapid development, but $B_{12}H_{11}SH^{2-}$ will probably remain as the baseline compound for clinical studies conducted in the immediate future (*26*). Soloway found that $B_{12}H_{11}SH^{2-}$ was sufficiently nontoxic ($LD_{50} = 73 \pm 4$ mg of boron per kg body weight in male CD1 Swiss mice by intraperitoneal injection) to be used clinically (*27*). Absence of toxicity in patients has later been proven in clinical trials (*28*). The boron compounds that are used as capture agents for BNCT should be nontoxic when administered in amounts required to obtain sufficient tumor concentrations and thus sustain a lethal $^{10}B(n,\alpha)^{7}Li$ reaction.

EXPERIMENTAL PROCEDURES

General. NMR spectra were recorded on a Bruker DPX 200 spectrometer. IR spectra of KBr pellet were collected on a BioRad FTS 155 spectrometer. Electrospray mass spectra were measured with a Bruker Esquire spectrometer. Charge was determined through isotope satellite peaks. For B-containing compounds, the peak with highest intensity is given. The peak multiplicity for B-containing compounds was compared to the theoretical pattern and found to agree for all B-containing compounds prepared. Melting points were measured on a Büchi 512 melting point apparatus.

Chemistry. *N,N-Bis-(2-dimyristoyloxyethyl)-2-chloracetamide (**4a**).* *N,N*-Bis-(2-myristoyloxyethyl)amine (**3a**) (5.23 g, 0.01 mol) and (1.11 g, 0.011 mol) triethylamine were dissolved in $CHCl_3$ (50 mL) and cooled to −10 °C. While stirring, chloroacetylchloride (1.24 g, 0.011mol) was added dropwise. After stirring the reaction mixture for 2−3 h, hexane was added until a precipitate (triethylamine hydrochloride) formed. The precipitate was removed by filtration, acetone (50 mL) was added, and the solution was kept at +4 °C overnight, whereupon the product precipitated. It was filtered off, dried, and recrystallized from $CHCl_3$. Yield 5.11 g (85%), mp 52−54 °C. IR (KBr): ν = 2956−2850 (C−H), 1732 (C═O), 1661 (-N−C═O), 1179 (C−O), 720 cm^{-1} (C−Cl). ^{1}H-NMR (200 MHz, $[D_1]$-$CDCl_3$, 25 °C, TMS): δ = 0.89 (t, *J*(H, H) = 3.0 Hz, 6H, C*H*$_3$−CH$_2$-), 1.27 (s, 40H, CH$_3$−(C*H*$_2$)$_{10}$−CH$_2$-), 1.51−1.69 (m, 4H, -CO−CH$_2$−C*H*$_2$-), 2.23−2.38 (m, 4H, -CO−C*H*$_2$-), 3.57−3.76 (m, 4H, -O−C*H*$_2$-), 4.19 (s, 2H, Cl−C*H*$_2$−CO-), 4.12−4.32 ppm (m, 4H, -N−C*H*$_2$-). MS (ESI, methanol, *m*/*z*): negative 636 $[M + Cl^-]^-$; positive 624 $[M + Na^+]^+$, 640 $[M + K^+]^+$.

*N,N-Bis-(2-dipalmitoyloxyethyl)-2-chloracetamide (**4b**).* Similar to **4a**. Yield 5.72 g (87%), mp 80−82 °C (hexane). IR (KBr): ν = 2917−2851 (C−H), 1732 (C═O), 1661 (−N−C═O), 1179 (C−O), 720 cm^{-1} (C−Cl). ^{1}H-NMR (200 MHz, $[D_1]CDCl_3$, 25 °C, TMS): δ = 0.89 (t, *J*(H, H) = 3.0 Hz, 6H, C*H*$_3$−CH$_2$-), 1.26 (s, 48H, CH$_3$−(C*H*$_2$)$_{12}$−CH$_2$-), 1.52−1.67 (m, 4H, -CO−CH$_2$−C*H*$_2$-), 2.26−2.37 (m, 4H, -CO−C*H*$_2$-), 3.60−3.73 (m, 4H, -O−C*H*$_2$-), 4.17 (s, 2H, Cl−C*H*$_2$−CO-), 4.23−4.33 ppm (m, 4H, -N−C*H*$_2$-). MS (ESI, methanol, *m*/*z*): negative 692 $[M + Cl^-]^-$; positive 680 $[M + Na^+]^+$, 696 $[M + K^+]^+$.

*S-(2-Cyanoethyl)-S-(N,N-(2-dimyristoyloxyethyl)acetamido)-sulfonioundecahydro-closo-dodecaborate (1-) Tetramethylammonium Salt (**5a**).* Bis-tetramethylammonium 2-cyanoethyl-thioundecahydro-*closo*-dodecaborate (2-) (**10**) (0.375 g, 1.0 mmol) and (1.2 g, 2.0 mmol) *N,N*-bis-(2-dimyristoyloxyethyl)-2-chloracetamide (**4a**) were suspended in acetonitrile (40 mL) for 24 h and then heated to 70 °C for 3 h. The mixture was cooled, and the solid was removed by filtration. The solvent was evaporated, and the product was dried at the oil pump. Yield 0.485 g (56%). IR (KBr): ν = 2923−2853 (C−H), 2487 (B−H), 1739 (C═O), 1651 (−N−C═O), 1175 cm^{-1} (C−O). ^{1}H-NMR (200 MHz, $[D_3]CD_3CN$, 25 °C, TMS): δ = 0.88 (t, *J*(H, H) = 3.2 Hz, 6H, C*H*$_3$−CH$_2$-), 1.27 (s, 40H, CH$_3$−(C*H*$_2$)$_{10}$−CH$_2$-), 1.48−1.63 (m, 4H, -CO−CH$_2$−C*H*$_2$-), 2.21−2.38 (m, 4H, -CO−C*H*$_2$-), 2.96−3.48 (m, 2H, -S−C*H*$_2$-), 3.12 (s, 12H, (C*H*$_3$)$_4$N), 3.24−3.37 (m, 2H, -C*H*$_2$−CN), 3.52−3.64 (m, 4H, -O−C*H*$_2$-), 4.12−4.20 (m, 4H, -N−C*H*$_2$-), 4.25 (s, 2H, S−C*H*$_2$−CO), 0.1−2.3 ppm (m, 11H, B-*H*). ^{11}B-NMR (200 MHz, $[D_6]$-DMSO, 25 °C): δ = −5.86 (1B), −14.56 ppm (11B). MS (ESI, acetonitrile, *m*/z): negative 794 $[A]^-$; positive 74 $[Kat]^+$, 942 $[A^- + 2Kat^+]^+$.

*S-(N,N-(2-Dimyristoyloxyethyl)acetamido)thioundecahydro-closo-dodecaborate (2-) Ditetramethylammonium Salt (**B-6**−**14**).* Method A. To a solution of **5a** (0.867 g, 1.0 mmol) in acetone, 1 equiv of a 25% solution of tetramethylammonium hydroxyde in methanol was added dropwise. The white precipitate of the product formed immediately. The precipitate was filtered off and dried. Yield 0.434 g (49%), mp 165 °C (decomp.). IR (KBr): ν = 2922−2853 (C−H), 2487 (B−H), 1739 (C═O), 1651 (−N−C═O), 1175 cm^{-1} (C−O). ^{1}H-NMR (200 MHz, $[D_3]CD_3CN$, 25 °C, TMS): δ = 0.85 (t, *J*(H, H) = 3.2 Hz, 6H, C*H*$_3$−CH$_2$-), 1.25 (s, 40H, CH$_3$−(C*H*$_2$)$_{10}$−CH$_2$-), 1.44−1.61 (m, 4H, -CO−CH$_2$−C*H*$_2$-), 2.21−2.37 (m, 4H, -CO−C*H*$_2$-), 3.11 (s, 24H, (C*H*$_3$)$_4$N), 3.16 (s, 2H, S−C*H*$_2$−CO), 3.38−3.62 (m, 4H, -O−C*H*$_2$-), 4.10−4.27 (m, 4H, -N−C*H*$_2$-), 0.2−2.3 ppm (m, 11H, B-*H*). ^{11}B-NMR (200 MHz, $[D_6]$DMSO, 25 °C): δ = −8.70 (1B), −13.23 (5B), −15.31 (5B), −18.80 ppm (1B). ^{13}C-NMR (400 MHz, $[D_3]CD_3CN$, 25 °C, TMS): δ = 174.16, 64.18, 62.39, 56.25, 56.19, 56.13, 48.80, 46.24, 36.25, 34.72, 34.66, 32.59, 30.31, 30.17, 30.03, 29.77, 27.59, 23.32, 14.33 ppm. MS (ESI, acetonitrile, *m*/*z*): negative 738 $[A^- - H^\bullet + H^+]^-$; positive 74 $[Kat]^+$, 963 $[A^{2-} + 3Kat^+]^+$.

Method B. To a solution of **9** (0.331 g 0.7 mmol) in dry CH_3-CN (30 mL), a 60% suspension of NaH in mineral oil (0.051 g, 1.8 mmol) was added. The mixture was stirred under N_2 for 30 min at RT, then for 30 min at 70 °C, and cooled to 25 °C. To the stirred mixture, myristoyl chloride (0.493 g, 2.0 mmol) was added dropwise at RT and stirred for 24 h. The solvent

was evaporated. The remaining oil was crystallized from 2−3 mL acetone. Yield 0.48 g (76%).

*S-(2-Cyanoethyl)-S-(N,N-(2-dipalmitoyloxyethyl)acetamido)-sulfonioundecahydro-closo-dodecaborate (1-) Tetramethylammonium Salt (**5b**).* Similar to **5a**. Yield 0.554 g (60%). IR (KBr): ν = 2935−2887 (C−H), 2491 (B−H), 1732 (C=O), 1651 (−N−C=O), 1175 cm^{-1} (C−O). ^{1}H-NMR (200 MHz, [D_3]CD_3CN, 25 °C, TMS): δ = 0.88 (t, J(H, H) = 3.1 Hz, 6H, CH_3−CH_2-), 1.27 (s, 48H, CH_3−(CH_2)$_{12}$−CH_2-), 1.45−1.62 (m, 4H, -CO−CH_2−CH_2-), 2.23−2.35 (m, 4H, -CO−CH_2-), 2.93−3.04 (m, 2H, -S−CH_2-), 3.07 (s, 12H, (CH_3)$_4$N), 3.22−3.36 (m, 2H, -CH_2−CN), 3.57−3.63 (m, 4H, -O−CH_2-), 4.12−4.20 (m, 4H, -N−CH_2-), 4.25 (s, 2H, S−CH_2−CO), 0.1−2.3 ppm (m, 11H, B-*H*). ^{11}B-NMR (200 MHz, [D_6]DMSO, 25 °C): δ = −5.86 (1B), −14.56 ppm (11B). MS (ESI, acetonitrile, *m*/*z*): negative 850 $[A]^-$; positive 74 $[Kat]^+$.

*S-(N,N-(2-Dipalmitoyloxyethyl)acetamido)thioundecahydro-closo-dodecaborate (2-) Ditetramethylammonium Salt (**B-6**−**16**).* Similar to **B-6**−**14**. Method A. Yield 0.518 g (55%), mp 179 °C (decomp). IR (KBr): ν = 2935−2867 (C−H), 2487 (B−H), 1732 (C=O), 1651 (−N−C=O), 1175 cm^{-1} (C−O). ^{1}H-NMR (200 MHz, [D_3]CD_3CN, 25 °C, TMS): δ = 0.88 (t, J(H, H) = 3.1 Hz, 6H, CH_3−CH_2-), 1.27 (s, 48H, CH_3−(CH_2)$_{12}$−CH_2-), 1.47−1.63 (m, 4H, -CO−CH_2−CH_2-), 2.23−2.33 (m, 4H, -CO−CH_2-), 3.10 (s, 24H, (CH_3)$_4$N), 3.16 (s, 2H, S−CH_2−CO), 3.47 (t, J(H, H) = 3.1 Hz, 2H, -N−CH_2-), 3.79 (t, J(H, H) = 2.8 Hz, 2H, -N−CH_2-), 4.08 (t, J(H, H) = 3.1, 2H, -O−CH_2-), 4.22 (t, J(H, H) = 2.8 Hz, 2H, -O−CH_2-), 0.2−2.3 ppm (m, 11H, B-*H*). ^{11}B-NMR (200 MHz, [D_6]DMSO, 25 °C): δ = −8.70 (1B), −13.23 (5B), −15.31 (5B), −18.80 ppm (1B). ^{13}C-NMR (400 MHz, [D_3]CD_3CN, 25 °C, TMS): δ = 174.60, 166.63, 64.63, 62.80, 56.57, 56.51, 49.20, 46.69, 36.68, 35.15, 35.06, 33.03, 30.78, 30.63, 30.48, 30.21, 26.02, 23.77, 14.78 ppm. MS (ESI, acetonitrile, *m*/*z*): negative 796 $[A^{2-} - H^{\bullet} + H^+]^-$; positive 74 $[Kat]^+$.

*N,N-Bis-(2-trimethylsilyloxyethyl)-2-chloracetamide (**8**).* A mixture of *N*,*N*-Bis-(2-trimethylsilyloxyethyl)amine **7** (23.23 g, 0.093 mol) (prepared by reacting diethanolamine with 1 equiv of bis(trimethylsilyl)disilazan without solvent) and triethylamine (13.0 mL, 0.093 mol) in THF (125 mL) was added dropwise to a solution of chloroacetylchloride (7.42 mL, 0.093 mol) in THF (60 mL) at −20 °C. The precipitated triethylammonium chloride was removed by filtration, and the solvent was evaporated. The remaining oil was distilled in vacuo at $1.4 \cdot 10^{-2}$ mbar (130−131 °C). Yield 28.5 g (94%). IR (KBr): ν = 2959−2875 (C−H), 1651 (C=O), 655 cm^{-1} (C−Cl). ^{1}H-NMR (200 MHz, [D_1]$CDCl_3$, 25 °C, TMS): δ = 0.087 (s, 18H, CH_3−Si-), 3.43 (t, J(H, H) = 2.9 Hz, 2H, N−CH_2), 3.52 (t, J(H, H) = 2.9 Hz, 2H, N−CH_2-), 3.57−3.73 (m, 4H, -O−CH_2-), 4.21 ppm (s, 2H, Cl−CH_2−CO-). MS (70 eV, EI, *m*/*z*): 325 [M].

*S-(N,N-(2-Dihydroxyethyl)acetamido)thioundecahydro-closo-dodecaborate (2-) Ditetramethylammonium Salt (**9**).* **10** (1.87 g 5.0 mmol) and **8** (2.44 g 7.5 mmol) were stirred in CH_3CN (40 mL) at RT and then heated to 70 °C for 2 h. The mixture was cooled, and tetramethylammonium chloride was removed by filtration. The solvent was evaporated. The residue was dissolved in acetone and treated with 1 equiv of a 25% solution of tetramethylammonium hydroxide in MeOH. The precipitate of **9** which formed immediately was removed by filtration and dried. Yield 1.5 g (65%). IR (KBr): ν = 3400 (O−H), 3036−2875 (C−H), 2484 (B−H), 1622 cm^{-1} (C=O). ^{1}H-NMR (200 MHz, [d_6]DMSO, 25 °C, TMS): δ = 2.99 ppm (s, 2H, S−CH_2-), 3.08 (s, 24H, (CH_3)$_4$N), 3.19−3.32 (m, 2H, -N−CH_2-), 3.33−3.44 (m, 2H, -N−CH_2-), 3.45−3.57 (m, 4H, -O−CH_2-), 4.50−4.90 (m, 2H, -CH_2−O*H*), 0.2−2.3 ppm (m, 11H, B-*H*). ^{11}B-NMR (200 MHz, [d_6]DMSO-d_6, 25 °C): δ = −8.70 (1B), −13.23 (5B), −15.31 (5B), −18.80 ppm (1B). MS (ESI, acetonitrile, *m*/*z*): negative 160 $[A]^{2-}$; positive 74 $[Kat]^+$, 542 $[A^{2-} + 3Kat^+]^+$.

Preparation of Liposomes. Each lipid mixture was dissolved in a mixture of acetonitrile and chloroform (2:1). The solution was dried to a thin film in a round-bottom flask. The dried lipid film was then hydrated and dispersed by vortexing in 10 mM HEPES buffer saline, pH 7.4 (150 mM NaCl, 10 mM HEPES buffer), to achieve a lipid concentration of 10 mg/mL. The resulting suspension was subjected to 10 cycles of freezing and thawing, then extruded through a polycarbonate membrane with a pore diameter of 100 nm (Avestin, Mannheim, Germany) at a temperature of 50 °C.

For preparation of liposomes in the absence of helper lipids, 20 mg of lipid was dissolved in acetonitrile and dried to a film. The film was then hydrated with 4 mL of 10 mM HEPES buffer saline, pH 7.4. The lipid suspension was subjected to 10 freeze−thaw cycles and then extruded as described previously.

Lipid contents was measured by the Stewart assay (*29*), using appropriate standard curves for the individual lipids.

Cryotransmission Electron Microscopy (cryo-TEM). The liposomal suspension was applied to a polymer-coated grid either at room temperature or (in the case of Figure 3a) at 30 °C. The sample was shock-frozen in liquid ethane. The vitrified sample was mounted and examined in a Zeiss EM 902 A electron microscope, operating at an accelerating voltage of 80 keV in filtered bright field image mode at ΔE = 0 eV. The stage temperature was kept below 108 K, and images were recorded at defocus settings between 1 and 3 μm. A large number of areas were examined in order to ensure the reproducibility of the results (*30*).

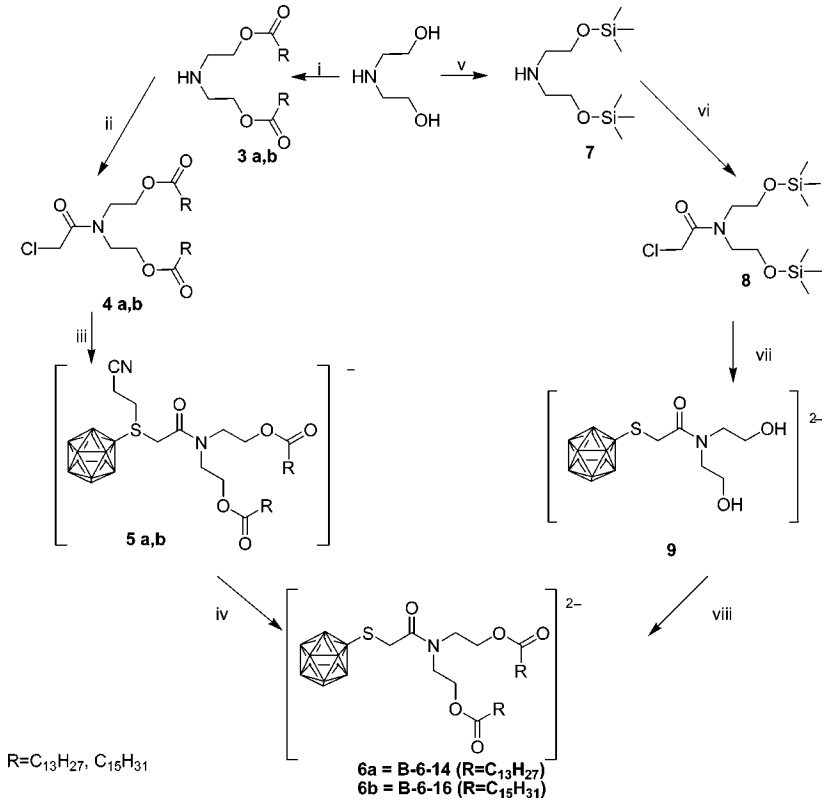
ζ-Potential and Size Measurements. ζ-potential and size were measured at 25 °C using a Malvern Zetasizer Nano ZS, Malvern Instruments Ltd., Malvern, U.K. The liposomes were diluted to a concentration of about 1 mg lipid per mL with 1 mM HEPES buffer (pH 7.4). For ζ-potential measurements, fifteen individual determinations were averaged. For size measurements, ten individual determinations were averaged.

Differential Scanning Calorimetry Measurements. Differential scanning calorimetry (DSC) measurements were carried out on a VP−DSC microcalorimeter from Microcal (Northampton, MA), using a lipid concentration of 5 mM. Samples were degassed under vacuum prior to the measurements. The upscans and downscans were recorded at a temperature range between 10 and 60 °C, a scan rate of 90 °C/h, and a filtering period of 2 s. A background scan collected with buffer in both cells was subtracted from each scan. For data analysis, the software package *ORIGIN* (Microcal) was used.

Cytotoxicity Determinations. The cytotoxicity of the boron-containing liposomes was assessed using the WST-1 assay (using the conversion of 4-[3-(4-iodophenyl)-2-(4-nitrophenyl)-2*H*-5-tetrazolio]-1,3-benzene disulfonate to a formazan) which is a colorimetric quantification of cell proliferation and cell viability. The WST-1 reagent was 4× diluted with 10 mM phosphate buffered saline pH 6.9 and then 1:10 diluted with the culture medium.

F10 medium supplemented with 10% newborn calf serum was used for V79 Chinese hamster cells (obtained from ATCC). The cells were harvested by trypsinization and plated at 11 000 cells/well in a 96 well plate and grown in a humidified atmosphere at 37 °C under 5% CO_2. Different concentrations of the liposomes were incubated with the cells for 24 h. At the end of the incubation time, the old medium was removed, and 100 μL of the diluted WST solution was added and allowed to react for 4 h in the incubator at 37 °C and 5% CO_2. The absorbance was measured at 450 and 620 nm using a Wallac 1420 Multilabel counter from Perkin-Elmer. A subtraction analysis of the dual wavelength measurement was performed

Scheme 1. Synthesis of Boron Lipids[a]



[a] (i) 1. HCl, $CHCl_3$, 2. RCOCl, $CHCl_3$, 3. KOH, $CHCl_3$; (ii) $ClCH_2COCl$, $(C_2H_5)_3N$, C_6H_6; (iii) $[(CH_3)_4N]_2^+[B_{12}H_{11}SCH_2CH_2CN]^{2-}$, acetonitrile; (iv) $(CH_3)_4NOH$, acetone; (v) $(CH_3)_3SiCl$, $(C_2H_5)_3N$, $CHCl_3$; (vi) $ClCH_2COCl$, $(C_2H_5)_3N$, THF; (vii) 1. $[(CH_3)_4N]^+[B_{12}H_{11}SCH_2CH_2CN]^-$, acetonitrile, 2. $(CH_3)_4NOH$, acetone; (viii) 1. NaH, acetonitrile, 2. RCOCl. Each unsubstituted corner of the clusters corresponds to a BH unit, a substituted corner to a B atom.

to increase the accuracy of the measurement. Controls were set to 100%. Experiments were run in three wells for each concentration and repeated once. As the data appeared essentially identical, they were pooled, and the pooled data (6 data points per concentration) were used to calculate the average survival and its standard deviation.

RESULTS

Chemistry. In this work, two different dodecaborate cluster-containing lipids, **B-6−14** and **B-6−16**, were synthesized according to Scheme 1. The structures are similar to those of **DC-6−14** (*O,O′*-ditetradecanoyl-*N*-(α-trimethylammonioacetyl)-diethanolamine chloride, described by Almofti et al. (*31*)) and are named accordingly. The synthesis followed either the work of Trowbridge and Falk (method A) (*32*) or through the *O*-protected diethanolamine (method B). The introduction of the boron cluster was achieved by alkylation with *S*-cyanoethylmercaptoundecahydrododecaborate **10** and subsequent alkaline removal of the cyanoethyl protecting group (*33*).

In method A, 2 equiv of the chloroanhydride of the fatty acids was allowed to react with diethanolamine. The resulting products *N,N*-(2-dimyristoyloxyethyl)- and *N,N*-(2-dipalmitoyloxyethyl)-amine **3a**,**b** were reacted with chloroacetylchloride in the presence of triethylamine to obtain **4a**,**b** in 87% yield. The reaction between the chloroacetamides **4a**,**b** and the tetramethylammonium salt of 2-cyanoethylmercaptoundecahydro-*closo*-dodecaborate (2-) produced sulfonium salts **5a**,**b** in 60% yield. The end products **B-6−14** and **B-6−16** were obtained from the reaction of sulfonium salts **5a**,**b** with tetramethylammonium hydroxide in acetone. The yield of lipids **B-6−14** and **B-6−16** is 48−55% (overall yield from diethanolamine 25−28%).

The lipids can also be obtained through method B. Here, the introduction of the fatty acid chain occurs later, and the intermediate **9** is therefore a suitable synthon when aiming at a variety of fatty acid derivatives. Two equivalents of chlorotrimethylsilane are reacted with diethanolamine in the presence of triethylamine. The trimethylsilyloxy derivative **7** is reacted with chloroacetylchloride in the presence of triethylamine to give **8** in 84% yield. **8** can react in analogy to path 1 with *S*-cyanoethylmercaptuundecahydrododecaborate. Starting from **9**, the yield of **B-6−14** was 76% (overall yield from diethanolamine 46%).

The synthesized compounds have two negative charges due to the presence of the undecahydro-*closo*-dodecaborate (2-) cluster in the head group. They are one of the examples of amphiphilic lipids which carry two negative charges in the part that would be in direct contact with water when incorporated into mixed lipid films, with phosphatidylglycerol lipids being another example.

Physical Characterization and Liposome Preparation. DSC results demonstrated that **B-6−14** and **B-6−16** alone exhibit a main phase transition at 18.8 and 37.9 °C, respectively (Figure 2). These temperatures are quite comparable to the transition temperatures of dimyristoyl- and dipalmitoylphosphatidylcholine (DMPC and DPPC, respectively), which are 24.3 and 41 °C, respectively (*34*). Phase transition data for the lead structure **DC-6−14** are not reported in the literature. Liposomes containing 33.3 mol % of either **B-6−14** or **B-6−16**, as well as the same mol % of DSPC and CHO, exhibit broad phase transitions, and the enthalpy of transition was low (data not shown), in accordance with literature observations (*35*, *36*).

Liposomes from pure **B-6−14** can be prepared by lipid film hydration and extrusion above the phase transition temperature

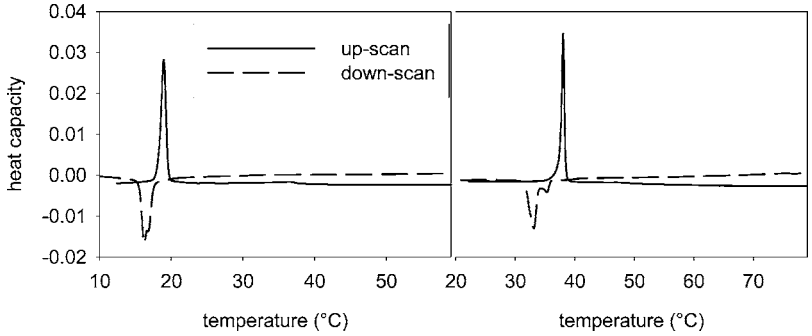


Figure 2. DSC of pure films of **B-6−14** (left) and **B-6−16** (right) (the first upscan and the first downscan are shown). Lipid concentration 5 mM.

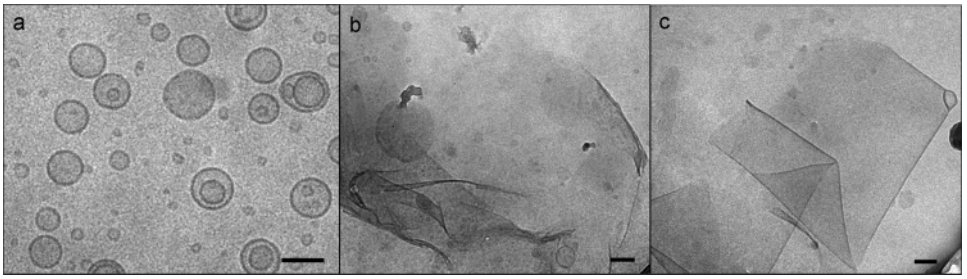


Figure 3. Cryo-TEM pictures of a preparation of **B-6−14** prepared by extrusion at 50 °C and vitrification from 30 °C (a), prepared by extrusion at 50 °C, storage at 4 °C for 1 week and vitrification from 25 °C (b) and **B-6−16** prepared as sample b (c). Scale bare 100 nm.

18.8 °C (Figure 3a). The liposomes are heterogeneous in size, and many have diameters well below the 100 nm size of the extrusion membrane. Important structural rearrangements take place upon cooling of the samples to temperatures below the phase transition temperature. As shown in Figure 3b, the liposomes transform into large open bilayer sheets when stored for some time at 4 °C. The equipment used for cryo-TEM in the present study did not allow vitrification from temperatures safely above the phase transition temperature for **B-6−16** (37.6 °C), and therefore, the possible formation of liposomes could not be verified for this lipid. As already observed for **B-6−14**, open bilayers are obtained when the sample is stored for some time at 4 °C (Figure 3c). Some of the large bilayer sheets of both lipids covered more than one of the holes in the supporting polymer net.

Nakamura et al. have previously shown that it is possible to prepare liposomes from the ether lipid **2a** (*19*). **B-6−14** represents, however, the first dodecaborate-containing lipid which has been proven to form liposomes without the addition of helper lipids.

From X-ray crystal analysis (see, e.g., (*37*)), the van der Waals radius of the dodecaborate cluster can be determined to be approximately 4 Å, giving an unsolvated cross section area of the head group of about 0.5 nm^2. This is close to the 0.6 nm^2 area occupied by lipids with saturated fatty acid chains in the gel phase (*34*).

Liposomes consisting of either a mixture of 33.3 mol % **B-6−14**, 33.3 mol % DSPC, and 33.3 mol % CHO or a mixture of 33.3 mol % **B-6−16**, 33.3 mol % DSPC, and 33.3 mol % CHO were successfully prepared (Figure 3) by thin film hydration and extrusion.

The mean diameters of the liposomes containing **B-6−14** and **B-6−16** in combination with DSPC and CHO were found to be 135 and 123 nm, respectively, when measured by dynamic light scattering. This value is corroborated by the results from cryo-TEM (see below). The liposomes containing 33.3 mol % of either **B-6−14** or **B-6−16** had ζ potentials of −67 and −63 mV, respectively, reflecting the double negative charge of the headgroup. Liposomes prepared by extrusion from neat **B-6−14** at 50 °C and analyzed at 30 °C had a ζ potential of −63 mV and showed a broad size distribution centered at 129 nm.

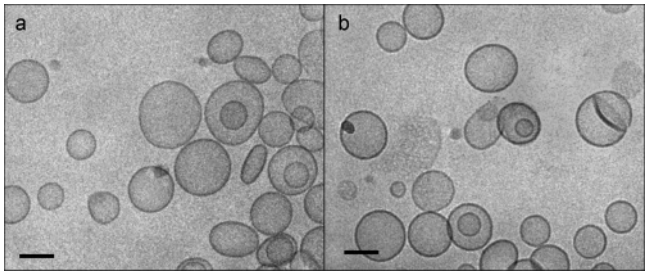


Figure 4. Cryo-TEM pictures of liposomes prepared from an equimolar mixture of DSPC, CHO and **B-6−14** (a), or **B-6−16** (b), respectively. Scale bar 100 nm.

The pictures obtained from cryo-TEM (Figure 4) showed formation of boron cluster-containing liposomes when an equimolar mixture of the boron lipid, DSPC, and CHO was used for liposome preparation. The micrographs confirm a size distribution centered around 100 nm as measured by dynamic light scattering. Cryo-TEM also revealed a certain degree of heterogeneity in the preparation. A few open structures were observed (see Figure 4b), but most of the material was present in the form of closed liposomes.

It has been shown before that liposomes composed of DSPC/CHO (60/40 molar ratio) and prepared by extrusion through 100 nm filters have a tendency to aggregate (*38*). As a consequence of the attractive interaction, the liposomes adapt a nonspherical, more elongated shape. The spherical shape of the liposomes displayed in Figure 4 is likely due to the presence of the boron-containing lipid and the repulsion caused by the negatively charged headgroups.

Cytotoxicity. We found that 5.6 mM of **B-6−14**-containing liposomes was required to inhibit cell growth by 50% (Figure 5. This value should be compared to the IC_{50} value of BSH in the same cell assay system, which is 3.9 mM. **B-6−16**-containing liposomes were added at different concentrations ranging from 0.5 to 30 mM. In this case, cell growth and activity was only weakly affected even at the highest concentration used, and accordingly, we could not determine an IC_{50} value.

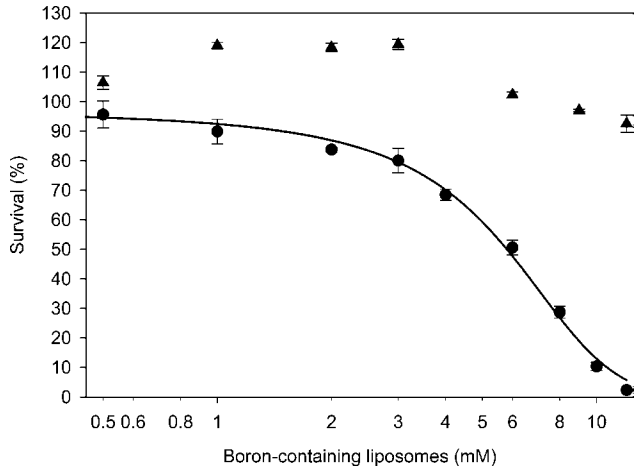


Figure 5. Survival of V79 Chinese hamster cells exposed to **B-6−14** (circles) and **B-6−16** (triangles), respectively. The solid line is the fitted curve from which the IC_{50} value was calculated.

DISCUSSION

Synthesis of two *closo*-dodecaborate cluster-containing lipids was achieved. Cryo-TEM results show that liposomesthat are stable above the transition temperature of the boron lipid can be prepared from pure **B-6−14**,. Although no evidence was collected in the present study, it is plausible that also **B-6−16** is capable of forming liposomes at temperatures above the phase transition temperature. Liposomes that are stable below the phase transition temperature can be prepared from mixtures containing equimolar amounts of the boron lipid, DSPC, and CHO. The liposomes containing the pure lipid are among the most boron-rich units prepared to date for BNCT. The structure of the liposomes provides two modes of delivery: encapsulation of boron and transport of boron-containing lipids. Previously, liposomes have been used to encapsulate concentrated aqueous solutions of water-soluble polyhedral borane anion salts (*12*, *13*, *15*) or to incorporate lipophilic boron-containing moieties embedded within the bilayer membrane (*18*, *19*, *21*, *23*, *24*).

The use of a boron-containing lipid circumvents problems with possible leakage of encapsulated material. The liposomes prepared here can most probably be tagged with tumor-seeking entities (*16*, *39*), and thereby, it should be possible to achieve selective tumor accumulation. Due to their high contents of boron, their relative lack of toxicity, and the known procedures by which liposomes can be targeted, they appear to be of great potential value for BNCT.

Successful BNCT is considered to require between 10 and 30 ppm boron in the target tissue, which corresponds to around $(1-3)\cdot10^9$ boron atoms for an average mammalian cell (*41*). Assuming an area per lipid molecule of 0.6 nm^2 (*34*), the bilayer of a unilamellar liposome with a diameter of 100 nm (and thus an area of $31\cdot10^3$ nm^2) contains about 10^5 lipid molecules. If composed purely of **B-6−14** or **B-6−16**, one such liposome will contain $1.2\cdot10^6$ boron atoms. Thus, the binding of 800−2500 liposomes would suffice to accumulate therapeutic amounts of boron. Naturally, the amount of boron carried by each liposome becomes lower if helper lipids, such as cholesterol and DSPC, are used in the preparation. The effective area per lipid molecule in bilayers containing DPPC and 33 mol % cholesterol is about 0.39 nm^2 (*41*), and a similar value may be assumed for bilayers based on DSPC and cholesterol. A 100 nm liposome will in this case contain approximately $1.6\cdot10^5$ lipid molecules. Assuming that the area per lipid remains close to 0.39 nm^2 when half the DSPC molecules are exchanged for boron lipids, a liposome composed of equimolar amounts of DSPC, cholesterol and boron lipid will contain about $6.5\cdot10^5$ boron atoms. This may be compared to the $3.8\cdot10^5$ boron atoms per liposome obtained when a water-soluble dodecaborate is encapsulated at a concentration of 0.1 M in 100 nm liposomes (assuming a volume per liposome of $5.2\cdot10^6$ nm^3) (see, e.g., (*15*)). In the latter case, leakage of the encapsulated compound might reduce the boron content even further, thus making the use of liposomes prepared from boron-containing lipids very attractive for BNCT.

ACKNOWLEDGMENT

E. J. acknowledges the support of Otto Benecke Stiftung. We are grateful for a gift of lipids from Lipoid GmbH, Ludwigshafen, Germany. D. G. acknowledges support from the German Research Foundation DFG and the German Academic Exchange Service DAAD. K. E. gratefully acknowledges financial support from the Swedish Research Council, the Swedish Cancer Society, and the Swedish Foundation for International Cooperation in Research and Higher Education STINT.

Supporting Information Available: ^{1}H-NMR spectra of compounds **4a**, **4b**, **5a**, **6a**, **6b**, **8**, **9**; ^{13}C-NMR spectra of compounds **6a** and **6b**; ESI mass spectra of compounds **5a**, **5b**, **6a**, **6b**. This material is available free of charge via the Internet at http://pubs.acs.org/BC.

LITERATURE CITED

(1) Barth, R. F., Soloway, A. H., and Fairchild, R. G. (1990) Boron neutron capture therapy of cancer. *Cancer Res. 50*, 1061−1070.

(2) Barth, R. F., Soloway, A. H., Fairchild, R. G., and Brugger, R. M. (1992) Boron neutron capture therapy for cancer. Realities and prospects. *Cancer 70*, 2995−3008.

(3) Soloway, A. H., Brownell, G. L., Ojemann, R. G., and Sweet, W. H. (1965) Boron-slow neutron capture therapy: present status. In *Proceedings of the International Symposium on the Preparation and Bio-Medical Application of Labeled Molecules*, pp 383−403, Venice, Italy.

(4) Alam, F., Barth, R. F., and Soloway, A. H. (1989) Boron containing immunoconjugates for neutron capture therapy of cancer and for immunocytochemistry. *Antibody, Immunoconjugates, Radiopharm. 2*, 145−163.

(5) Schinazi, R. F., and Prusoff, W. H. (1978) Synthesis and properties of boron and silicon substituted uracil of 2′-deoxyuridine. *Tetrahedron Lett. 50*, 4981−4984.

(6) Fairchild, R. G., Kahl, S. B., Laster, B. H., Kalef-Ezra, J., and Popenoe, E. A. (1990) In vitro determination of uptake, retention, distribution, biological efficacy, and toxicity of boronated compounds for neutron capture therapy: a comparison of porphyrins with sulfhydryl boron hydrides. *Cancer Res. 50*, 4860−4865.

(7) Miura, M., Gabel, D., Fairchild, R. G., Laster, B. H., and Warkentien, L. S. (1989) Synthesis and in vivo studies of a carboranyl porphyrin. *Strahlenther. Onkol. 165*, 131.

(8) Kahl, S. B., Laster, B. H., Kood, M.-S., Warkentien, L. S., and Fairchild, R. G. (1989) Distribution of a boronated porphyrin in murine tumors. In *Clinical Aspects of Neutron Capture Therapy* (Fairchild, R. G., Bond, V. P., Woodhead, A. D., Eds) pp 205−211, Plenum Press, New York.

(9) Pathak, A. P., Artemov, D., Ward, B. D., Jackson, D. G., Neeman, M., and Bhujwalla, Z. M. (2005) Characterizing extravascular fluid transport of macromolecules in the tumor interstitium by magnetic resonance imaging. *Cancer Res. 65*, 1425−32.

(10) Dreher, M. R., Liu, W., Michelich, C. R., Dewhirst, M. W., Yuan, F., and Chilkoti, A. (2006) Tumor vascular permeability, accumulation, and penetration of macromolecular drug carriers. *J. Natl. Cancer Inst. 98*, 335−44.

(11) Muggia, F. M. (1999) Doxorubicin-polymer conjugates: further demonstration of the concept of enhanced permeability and retention. *Clin. Cancer Res. 5*, 7−8.

(12) Feakes, D. A., Shelly, K., Knobler, C. B., and Hawthorne, M. F. (1994) $Na_3[B_{20}H_{17}NH_3]$- Synthesis and liposomal delivery to murine tumors. *Proc. Natl. Acad. Sci. U.S.A. 91*, 3029−3033.

(13) Mehta, S. C., Lai, J. C., and Lu, D. R. (1996) Liposomal formulations containing sodium mercaptoundecahydrododecaborate (BSH) for boron neutron capture therapy. *J. Microencapsul. 13*, 269−279.

(14) Johnsson, M., Bergstrand, N., and Edwards, K. (1999) Optimization of drug loading procedures and characterization of liposomal formulations of two novel agents intended for boron neutron capture therapy (BNCT). *J. Liposome Res. 9*, 53−79.

(15) Maruyama, K., Ishida, O., Kasaoka, S., Takizawa, T., Utoguchi, N., Shinohara, A., Chiba, M., Kobayashi, H., Eriguchi, M., and Yanagie, H. (2004) Intracellular targeting of sodium mercaptoundecahydrododecaborate (BSH) to solid tumors by transferrin-PEG liposomes, for boron neutron-capture therapy (BNCT). *J. Controlled Release 98*, 195−207.

(16) Pan, X., Wu, G., Yang, W., Barth, R. F., Tjarks, W., and Lee, R. J. (2007) Synthesis of cetuximab-immunoliposomes via a cholesterol-based membrane anchor for targeting of EGFR. *Bioconjugate Chem. 18*, 101−108.

(17) *Liposomes*, 2nd ed. (2003) (Torchilin, V. P. and Weissig, V., Eds.) Oxford University Press, Oxford, UK.

(18) Feakes, D. A., Shelly, K., and Hawthorne, M. F. (1995) Selective boron delivery to murine tumors by lipophilic species incorporated in the membranes of unilamellar liposomes. *Proc. Natl. Acad. Sci. U.S.A. 92*, 1367−1370.

(19) Nakamura, H., Miyajima, Y., Takei, T., Kasaoka, S., and Maruyama, K. (2004) Synthesis and vesicle formation of a nido-carborane cluster lipid for boron neutron capture therapy. *Chem. Commun. (Cambridge, U. K.)* 1910−1911.

(20) Thirumamagal, B. T., Zhao, X. B., Bandyopadhyaya, A. K., Naranyanasamy, S., Johnsamuel, J., Tiwari, R., Golightly, D. W., Patel, V., Jehning, B. T., Backer, M. V., Barth, R. F., Lee, R. J., Backer, J. M., and Tjarks, W. (2006) Receptor-targeted liposomal delivery of boron-containing cholesterol mimics for boron neutron capture therapy (BNCT). *Bioconjugate Chem. 17*, 1141−1150.

(21) Rossi, S., Karlsson, G., Martini, G., and Edwards, K. (2003) Combined cryogenic transmission electron microscopy and electron spin resonance studies of egg phophatidylcholine liposomes loaded with a carboranyl compound intended for boron neutron capture therapy. *Langmuir 19*, 5608−5617.

(22) Rossi, S., Schinazi, R. F., and Martini, G. (2005) ESR as a valuable tool for the investigation of the dynamics of EPC and EPC/cholesterol liposomes containing a carboranyl-nucleoside intended for BNCT. *Biochim. Biophys. Acta 1712*, 81−91.

(23) Watson-Clark, R. A., Banquerigo, M. L., Shelly, K., Hawthorne, M. F., and Brahn, E. (1998) Model studies directed toward the application of boron neutron capture therapy to rheumatoid arthritis: Boron delivery by liposomes in rat collagen-induced arthritis. *Proc. Natl. Acad. Sci. U.S.A. 95*, 2531−2534.

(24) Li, T., Hamdi, J., and Hawthorne, M. F. (2006) Unilamellar liposomes with enhanced boron content. *Bioconjugate Chem. 17*, 15−20.

(25) Lee, J.-D., Ueno, M., Miyajima, Y., and Nakamura, H. (2006) Synthesis of boron cluster lipids: *closo*-dodecaborate as an alternative hydrophilic function of boronated liposomes for neutron capture therapy. *Organic Lett. 9*, 323−326.

(26) Hawthorne, M. F. (1993) The role of chemistry in the development of boron neutron capture therapy of cancer. *Angew. Chem., Int. Ed. Engl. 32*, 950−984.

(27) Soloway, A. H., Hatanaka, H., and Davis, M. S. (1967) Penetration of brain and brain tumor. VII. Tumor-binding sulfhydryl boron compounds. *J. Med. Chem. 10*, 714−717.

(28) Gabel, D., Preusse, D., Haritz, D., Grochulla, F., Haselsberger, K., Fankhauser, H., Ceberg, C., Peters, H.-D., and Klotz, U. (1997) Pharmacokinetics of $Na_2B_{12}H_{11}SH$ (BSH) in patients with malignant brain tumours as prerequisite for a Phase I clinical trial of boron neutron capture. *Acta Neurochirurgica 139*, 606−612.

(29) Stewart, J. C. (1980) Colorimetric determination of phospholipids with ammonium ferrothiocyanate. *Anal. Biochem. 104*, 10−14.

(30) Almgren, M., Edwards, K., and Karlsson, G. (2000) Cryo transmission electron microscopy of liposomes and related structures. *Colloids Surf., A 174*, 3−21.

(31) Almofti, M. R., Harashima, H., Shinohara, Y., Almofti, A., Baba, Y., and Kiwada, H. (2003) Cationic liposome-mediated gene delivery: biophysical study and mechanism of internalization. *Arch. Biochem. Biophys. 410*, 246−253.

(32) Trowbridge, J. R., Falk, R. A., and Krems, I. J. (1955) Fatty acid derivatives of diethanolamine. *J. Org. Chem. 20*, 990−995.

(33) Gabel, D., Moller, D., Harfst, S., Rösler, J., and Ketz, H. (1993) Synthesis of S-alkyl and S-acyl derivatives of mercaptoundehydrododecaborate, a possible boron carrier for neutron capture therapy. *Inorg. Chem. 32*, 2276−2278.

(34) Nagle, J. F., and Tristram-Nagle, S. (2000) Structure of lipid bilayers. *Biochim. Biophys. Acta 1469*, 159−195.

(35) Lu, J. Z., Hao, Y. H., and Chen, J. W. (2001) Effect of cholesterol on the formation of an interdigitated gel phase in lysophosphatidylcholine and phosphatidylcholine binary mixtures. *J. Biochem. (Tokyo) 129*, 891−898.

(36) Lippert, J. L., and Peticolas, W. L. (1971) Laser Raman investigation of the effect of cholesterol on conformational changes in dipalmitoyl lecithin multilayers. *Proc. Natl. Acad. Sci. U.S.A. 68*, 1572−6.

(37) Azev, Y. A., Lork, E., Duelcks, T., and Gabel, D. (2004) New possibilities of 1,2,4-triazines functionalization: first examples of synthesis and structure of boron-containing 1,2,4-triazines. *Tetrahedron Lett. 45*, 3249−3252.

(38) Edwards, K., Johnsson, M., Karlsson, G., and Silvander, M. (1997) Effect of polyethyleneglycol-phospholipids on aggregate structure in preparations of small unilamellar liposomes. *Biophys. J. 73*, 258−266.

(39) Ishida, O., Maruyama, K., Tanahashi, H., Iwatsuru, M., Sasaki, K., Eriguchi, M., and Yanagie, H. (2001) Liposomes bearing polyethyleneglycol-coupled transferrin with intracellular targeting property to the solid tumors in vivo. *Pharm. Res. 18*, 1042−1048.

(40) Fairchild, R. G., and Bond, V. P. (1985) Current status of ^{10}B-neutron capture therapy: enhancement of tumor dose via beam filtration and dose rate, and the effects of these parameters on minimum boron content: a theoretical evaluation. *Int. J. Radiat. Oncol. Biol. Phys. 11*, 831−840.

(41) Ipsen, J. H., Mouritsen, O. G., and Bloom, M. (1990) Relationships between lipid membrane area, hydrophobic thickness, and acyl-chain orientational order. The effects of cholesterol. *Biophys. J. 57*, 405−412.

BC070040T

Reconstitution of Modular PDK1 Functions on Trans-Splicing of the Regulatory PH and Catalytic Kinase Domains

Hassan Al-Ali, Timothy J. Ragan, Xinxin Gao, and Thomas K. Harris*

Department of Biochemistry and Molecular Biology, Miller School of Medicine, University of Miami, P.O. Box 016129, Miami, Florida 33101-6129. Received February 16, 2007; Revised Manuscript Received March 29, 2007

The serine-threonine protein kinases PDK1 and PKB each contain a pleckstrin homology (PH) domain that binds the membrane-bound phosphatidylinositol 3,4,5-triphosphate [PI(3,4,5)P_3] second messenger and is required for PDK1-catalyzed phosphorylation and activation of PKB. While X-ray structures have been reported for the individual regulatory PH and catalytic kinase domain constructs of both PDK1 and PKB, diffraction quality crystals of full length constructs have yet to be obtained, likely due to conformational heterogeneity. In developing alternative approaches to understanding the potential role of conformational dynamics in regulating PKB phosphorylation by PDK1, an efficient in vitro method for protein trans-splicing was developed, which utilizes the N- and C-terminal split inteins of the gene *dnaE* from *Nostoc punctiforme* [(N)*Npu*DnaE] and *Synechocystis* sp. strain PCC6803 [(C)SspDnaE], respectively. For conjugating the regulatory PH domain to the catalytic kinase domain of PDK1, the recombinant trans-splicing fusion constructs KINASE(AEY)-(N)*Npu*DnaE-His_6 and GST-His_6-(C)*Ssp*DnaE-(CMN)PH were designed, PCR assembled, overexpressed, and affinity purified. The cross-reacting (N)*Npu*DnaE and (C)*Ssp*DnaE inteins generated full length spliced-PDK1 with $k_{obs} = (2.8 \pm 0.3) \times 10^{-5}$ s^{-1} and with ≤5% of any competing trans-cleavage reactions. Spliced-PDK1 was efficiently purified to ≥95% homogeneity from the reaction mixture by subsequent His_6 affinity and ion exchange chromatography steps. In vitro kinase assays and phosphopeptide mapping studies confirmed that spliced-PDK1 retained the ability to colocalize and selectively phosphorylate Thr-309 of PKBβ in a PI(3,4,5)P_3-dependent manner. The high-level production and reconstitution of functional spliced-PDK1 establishes the feasibility of incorporating domain-specific biophysical probes for spectroscopic studies of regulatory PH domain mediated catalytic specificity.

INTRODUCTION

Protein kinases comprise the largest enzyme family, with ~518 being encoded by the human genome (*1*). The large number of serine-threonine protein kinases (~80% of total protein kinases) reflects the large number of intracellular signal transduction pathways required in regulating proper cellular growth, survival, and proliferation. The complexity in elucidating intracellular signaling networks is compounded by analyses, indicating that individual protein kinases may target and phosphorylate numerous different protein substrates (*2*, *3*). Further complexities arise in the observation that individual protein kinases can be intricately regulated by multiple phosphorylation events catalyzed by numerous upstream kinases, as well as autocatalytically. On review of protein kinase sequence alignments, it becomes readily apparent that signaling complexity can be largely accounted for by a distinguishingly diverse arrangement of regulatory domains, which may exist contiguously N- or C-terminal to an otherwise structurally homologous catalytic kinase domain (*4*). Often such domains may serve in proper localization, but many have been shown to play direct roles in regulating kinase activity either intrinsically or through participation in docking-based substrate recognition.

While the functions of various regulatory domains of different protein kinases are steadily being recognized, progress toward molecular understanding of conformational interactions within full length multidomain kinases remains hampered. To date, no three-dimensional structure has been reported for any full length monomeric multidomain serine-threonine protein kinase. Rather for example, X-ray structures have been reported for the isolated catalytic kinase domains of multidomain AGC kinases including PDK1[1] (*5*), PKBβ (*6*, *7*), PKCθ (*8*), and PKCι (*9*); multidomain MAP kinases including B-RAF (*10*), MEK1,2 (*11*), MK2 (*12*), and MSK1 (*13*); and multidomain cell-cycle related kinases including CHK1 (*14*), Aurora A (*15*), and Aurora B (*16*). Likewise, X-ray or NMR structures have been reported for corresponding isolated regulatory domain constructs including the PH domains of PDK1 (*17*), PKBα (*18*), and PKBβ (*19*); the C1 domain of PKCγ (*20*); the *C*2 domains of PKCα (*21*, *22*), PKCβ (*23*), PKCδ (*24*, *25*), and PKCϵ (*26*); the CR1 domain of RAF1 (*27*); the FHA domain of CHK2 (*28*); and the PBD domain of PLK1 (*29*, *30*). The observation that suitable crystals for X-ray diffraction studies of full length multidomain monomeric protein kinases have not been obtained suggests an important role for intra-domain−domain conformational dynamics. Thus, alternative methodologies will be required for advanced understanding of such processes.

* Corresponding author. Tel: +1 305 243 3358; fax: +1 305 243 3955; e-mail: tkharris@miami.edu.

[1] Abbreviations: Aurora, Aurora kinase; C1, PKC first constant domain responsible for activation by diacylglycerol and phorbol esters; C2, PKC second constant domain responsible for activation by Ca^{2+}; CHK, checkpoint kinase; CR1, first conserved region (cysteine rich) domain of RAF1; 2,5-DHB, 2,5-dihydroxybenzoic acid; FHA, forkhead-associated domain; HM, hydrophobic motif; λPP, lambda protein phosphatase; MEK, MapK/ERK kinase; MK2, MAP KAP kinase-2; MSK, mitogen- and stress-activated kinase; PBD, polo-box domain; PC, 1,2-dioleoyl-*sn*-glycerol-3-phosphocholine; PDK1, phosphoinositide-dependent protein kinase-1; PH, pleckstrin homology; PIF, PDK1-interacting fragment; PI3K, phosphatidylinositol 3-kinase; PI(3,4,5)P_3, *sn*-1-stearoyl-2-arachidonyl D-phosphatidylinositol (3,4,5)-triphosphate; PLK, polo-like kinase; PKA, cAMP-dependent protein kinase; PKB, protein kinase B; PKC, Ca^{2+}-activated protein kinase; PS, 1,2-dioleoyl-*sn*-glycerol-3-phospho-L-serine; RAF, first identified downstream effector kinase of RAS; RAS, mitogen-activated G protein.

10.1021/bc070055r CCC: $37.00 © 2007 American Chemical Society
Published on Web 05/15/2007

One very promising approach toward better understanding conformational interactions within full length multidomain kinases involves the use of intein-based technologies to generate a native peptide bond between given pairs of contiguous regulatory and catalytic kinase domains (*31*−*34*). Successful peptide conjugation would facilitate domain-specific incorporation of biophysical probes (e.g., fluorophores and paramagnetic spin labels) and stable isotopes (e.g., ^{15}N and ^{13}C), enabling spectroscopic characterization of intra-domain−domain conformational dynamics in solution. While a large number of small C-terminal peptides have been successfully ligated to their cognate proteins, few cases have been reported in which two large functional domains have been conjugated to reconstitute regulatory function in a monomeric multidomain native enzyme (*34*). To begin addressing the possibility that intein-based technologies may be used to reconstitute a monomeric multidomain protein kinase for spectroscopic functional studies, we selected the human serine-threonine AGC protein kinase, PDK1, for which X-ray structures are known for both the N-terminal catalytic kinase (*5*) and the C-terminal PH domains (*17*). The C-terminal PH domain is required for PI(3,4,5)P_3-dependent colocalization and phosphoryaltion of PKB (*35*).

In this paper, we report efficient protein trans-splicing of the regulatory PH and catalytic kinase domains of human PDK1 by using naturally split DnaE inteins from two different organisms. In addition, spliced-PDK1 is shown to retain the ability to colocalize and selectively phosphorylate Thr-309 of PKBβ in a PI(3,4,5)P_3-dependent manner. The high-level production and reconstitution of functional spliced-PDK1 establishes the feasibility of generating full length PDK1 with either (i) segmental ^{15}N-isotopic labeling of the PH domain for NMR studies or (ii) simultaneous site-directed modifications of the PH and kinase domains with small molecule donor and acceptor fluorophores for FRET-based studies of conformational transitions related to docking-based catalytic specificity.

EXPERIMENTAL PROCEDURES

Materials. PDK1-Tide (acetyl-KTFCTGTPEYLAPEVRRE-PRILSEEEQEMFRDYIAD-WC) and Crosstide (acetyl-GR-PRTSSFAEG) were from 21st Century Biochemicals, Inc. (Marlboro, MA). [γ-^{32}P]ATP was from MP-Biomedical (Irvine, CA). 1,2-Dioleoyl-*sn*-glycerol-3-phosphocholine (PC), 1,2-dioleoyl-*sn*-glycerol-3-phospho-L-serine (PS), and *sn*-1-stearoyl-2-arachidonyl D-phosphatidylinositol-(3,4,5)-triphosphate [PI(3,4,5)P_3] were from Echelon Biosciences (Salt Lake City, UT). Full length His_6-PKBβ and His_6-PDK1 (residues 51−556) were expressed using the Bac-to-Bac Baculovirus Expression System (Invitrogen, Carlbad, CA) and His_6 affinity purified as described (*36*). Affinity-purified His_6-PKBβ was fully dephosphorylated by treatment with lambda protein phosphatase (λPP) as described (*36*).

PDK1 Trans-Splicing Strategy. Figure 1 shows the protein engineering strategy designed for trans-splicing of the regulatory PH and catalytic kinase domains of human PDK1. This strategy derives from recent reporting of the highly efficient in vivo cross trans-splicing reaction catalyzed between the N-terminal DnaE intein from *Nostoc punctiforme* [(N)*Npu*DnaE] and the C-terminal DnaE intein from *Synechocystis* sp. strain PCC6803 [(C)*Ssp*DnaE] (*37*). One additional advantage of utilizing (N)-*Npu*DnaE is that it has been demonstrated to be more tolerant of amino acid substitutions at the at the C-terminal side of the splice junction (*37*). Since three-dimensional structures have been reported for the N-terminal catalytic kinase domain (residues 51−359) (*5*) and the C-terminal regulatory PH domain (residues 409−556) (*17*), C385 was chosen as the optimal site of conjugation. In utilizing the (N)*Npu*DnaE and (C)*Ssp*DnaE cross trans-splicing intein pair, ^{382}QFG^{384} at the N-terminal side of the splice junction was replaced with ^{382}AEY^{384}. In addition, a conservative Q387N mutation gave ^{385}CMN^{387} residues at the C-terminal side of the splice junction, which has been shown to be equally effective as the native CFN sequence required for trans-splicing with the native (N/C)*Ssp*DnaE pair (*37*). In order to facilitate purification of spliced-PDK1 from cleaved and uncleaved DnaE intein containing fragments, His_6 affinity tags were joined to the corresponding DnaE inteins. Addition of GST significantly increased the overall protein yield and solubility over that obtained by expression of the His_6-(C)SspDnaE-(CMN)PH construct.

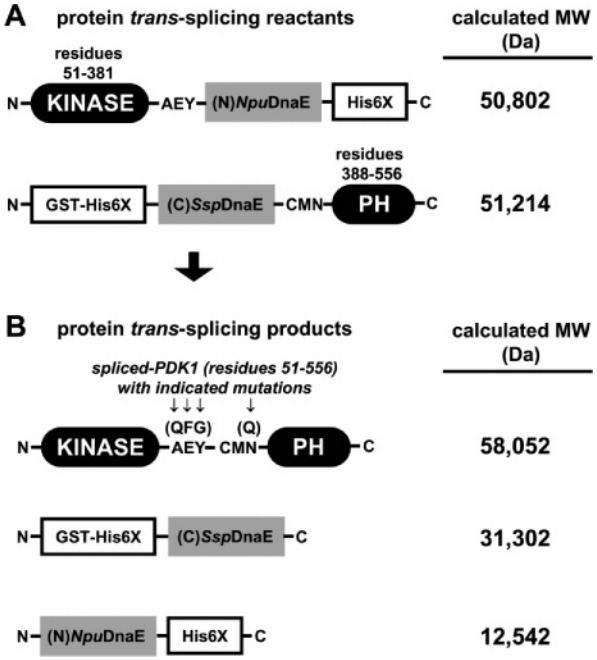


Figure 1. (A) Protein trans-splicing reactants. The N-terminal kinase domain of PDK1 (residues 51−381, black oval) is fused to the (N)-*Npu*DnaE trans-splicing intein (gray square) with a C-terminal His_6 affinity tag (open square). The N-terminal three residues flanking the splice junction (Q382, F383, and G384) were mutated to the preferred AEY sequence required in trans-splicing. The C-terminal PH domain of PDK1 (residues 388−556, black oval) is fused to the (C)*Ssp*DnaE trans-splicing intein (gray square) with an N-terminal GST-His_6 tag (open square). Whereas the His_6 tag was used for affinity purification, the GST tag significantly improved both expression yield and solution stability. For the native C-terminal three residues flanking the splice junction (C385, M386, and Q387), only Q387 was mutated to yield the preferred CMN sequence optimal for cross trans-splicing of the (C)*Ssp*DnaE intein with the (N)*Npu*DnaE intein. The (N)*Npu*DnaE and (C)*Ssp*DnaE split inteins associate with high affinity and catalyze trans-splicing of the regulatory PH and catalytic kinase domains by forming a native peptide bond between Tyr-384 and Cys-385. (B) Protein trans-splicing products. The primary domain arrangement of PDK1 is regenerated, which contains the Q382A, F383E, G384Y, and Q387N mutations that flank the spice junction. The affinity tagged trans-splicing inteins are indicated. Spliced-PDK1 is separated from the cleaved (N)-*Npu*DnaE-His_6 and GST-His_6-(C)*Ssp*DnaE split inteins, as well as any uncleaved intein fusion constructs by His_6 affinity purification. The calculated molecular weights (MW) of each trans-splicing reactant and product are indicated.

Baculovirus-Mediated Expression of KINASE(AEY)-(N)*Ssp*DnaE-His_6. Experimental procedures describing PCR engineering to generate an *EcoR*I-*Xba*I cDNA fragment containing the KINASE(AEY)-(N)*Npu*DnaE-His_6 fusion construct are given as described (Supporting Information). A sequence verified *EcoR*I-*Xba*I fragment containing the KINASE(AEY)-(N)*Npu*DnaE-His_6 construct (Figure 1) was removed from the pCR-Blunt II-TOPO cloning vector and ligated into pFastBac1 vector (Invitrogen) to generate recombinant baculovirus using the Bac-to-Bac Baculovirus Expression System (Invitrogen).

Recombinant P2 viral stocks were used to infect 200 mL spinner flask cultures of Sf9 cells in the midlogarithmic phase of growth (2×10^6 cells/mL) at a multiplicity of infection (MOI) of two viral particles/cell. The infected cells were incubated at 27 °C for 72 h and harvested by centrifugation for 10 min at 4 °C at 3000 rpm in a Beckman tabletop centrifuge. The cells were resuspended in 50 mL of buffer (50 mM Tris-HCl, pH 7.5, 300 mM NaCl, 50 mM imidazole, 1 mM 2-mercaptoethanol, 1 mM benzamidine, and 0.2 mM PMSF) and were immediately stored at −80 °C. The resuspended frozen cells were allowed to thaw on ice for 1 h, which resulted in efficient cell lysis. Cell debris was pelleted by centrifugation for 30 min at 4 °C at 12 000 rpm. The supernatants containing the soluble components of the cell lysate were collected, and the KINASE(AEY)-(N)-*Npu*DnaE-His_6 construct was His_6-affinity purified from the soluble lysate as described below.

Bacterial Expression of GST-His_6-(C)*Ssp*DnaE-(CMN)-PH. Experimental procedures describing PCR engineering to generate the *Sac*II-*Kpn*I fragment containing the (C)*Ssp*DnaE-(CMN)PH fusion construct are given as described (Supporting Information). A sequence-verified *Sac*II-*Kpn*I fragment containing the (C)*Ssp*DnaE-(CMN)PH construct was removed from the pCR-Blunt II-TOPO cloning vector and ligated into the pET-41b protein expression vector (Novagen), which provided N-terminal dual GST-His_6 affinity tags to yield the GST-His_6-(C)*Ssp*DnaE-(CMN)PH construct (Figure 1). The protein expression vector was transformed into the Rosetta (DE3) protein expression strain of *E. coli*. Cells were grown in 1 L of Luria Broth (LB) containing kanamycin (50 μg/mL) and chloramphenicol (37 μg/mL) at 37 °C until an OD of 0.4. Then the cell culture was transferred to 15 °C and grown until an OD of 0.8 before induction with 0.5 mM isopropyl β-D-thiogalactopyranoside (IPTG) for 16 h. The cells were harvested by centrifugation at 3500*g* for 20 min and then resuspended in 3 mL of PBS buffer per gram of cells (10 mM Na_2HPO_4 and 1.8 mM KH_2PO_4, pH 7.3, 140 mM NaCl, 2.7 mM KCl, 2 mM dithiothreitol, 1 mM benzamidine, and 0.2 mM PMSF). The cells were lysed using the EmulsiFlex-C3 high-pressure homogenizer (Avestin, Inc.), and particulates were removed from the lysate by centrifugation for 20 min at 14 000 rpm in the SS-34 Sorvall rotor. The GST-His_6-(C)*Ssp*DnaE-(CMN)PH construct was GST-affinity purified from the soluble lysate as described below.

His_6- and GST-Affinity Purification. The soluble Sf9 insect cell lysate containing the KINASE(AEY)-(N)*Npu*DnaE-His_6 recombinant fusion construct (Figure 1) was directly loaded by FPLC (1 mL/min) onto a 5 mL size Ni^{2+} Sepharose HiTrap HP affinity column (Amersham) equilibrated at 4 °C in 50 mM Tris-HCl, pH 7.5, 500 mM NaCl, 50 mM imidazole, 1 mM 2-mercaptoethanol. The soluble *E. coli* lysate containing the GST-His_6-(C)*Ssp*DnaE-(CMN)PH recombinant fusion construct (Figure 1) was directly loaded by FPLC (1 mL/min) onto a 5 mL size GST HiTrap HP affinity column (Amersham) equilibrated at 4 °C in PBS buffer (10 mM Na_2HPO_4 and 1.8 mM KH_2PO_4, pH 7.3, 140 mM NaCl, 2.7 mM KCl, and 2 mM dithiothreitol). The columns were subsequently washed until the absorbances at 260 and 280 nm returned to baseline. The KINASE(AEY)-(N)*Npu*DnaE-His_6 construct was eluted by linear increasing of the imidazole concentration from 50 to 500 mM at 1 mL/min for 30 min. The GST-His_6-(C)*Ssp*DnaE-(CMN)PH construct was eluted with buffer containing 50 mM Tris-HCl, pH 8.0, 2 mM dithiothreitol, and 20 mM glutathione. Chromatographic fractions (1 mL) containing the designated fusion protein were detected by absorbance at 280 nm and analyzed by SDS-PAGE. Fractions containing recombinant protein were pooled and subjected to gel exclusion chromatography for exchange to the protein trans-splicing buffer (50 mM Tris-HCl, pH 7.5, 500 mM NaCl, 0.5 mM TCEP, 0.5 mM EGTA, 1 mM EDTA, and 5% (v/v) glycerol). Protein was concentrated using a VivaSpin 20, 6, or 2 mL ultrafiltration concentrator (10 kDa molecular weight cutoff, VivaScience). Protein concentrations were determined by BioRad protein assay. Protease inhibitors (0.5 mM benzamidine and 0.1 mM PMSF) were added to each purified protein construct. A ~40 μM stock solution of the KINASE(AEY)-(N)*Npu*DnaE-His_6 construct was prepared using ~2 mg/mL total protein with ≥95% purity. A ~40 μM stock solution of the GST-His_6-(C)-*Ssp*Dna-(CMN)PH construct was prepared using ~2.8 mg/mL total protein with ≥60% purity. These solutions were stored at −80 °C.

PDK1 Trans-Splicing. Frozen aliquots containing ~40 μM of either the KINASE(AEY)-(N)*Npu*DnaE-His_6 or the GST-His_6-(C)*Ssp*Dna-(CMN)PH trans-splicing constructs were thawed at 21 °C. After 10 min microcentrifugation of each tube, the reaction was initiated by combining the clarified supernatants to yield ~20 μM of each construct. The reaction tube was incubated either at 4 °C or 21 °C, and at varying times (0, 1, 3, 6, 9, 12, and 18 h) 9 μL aliquots containing ~18−20 μg of total protein were removed and quenched by addition to 9 μL of 2× SDS sample buffer, heated at 95 °C for 2 min, and placed on ice for SDS-PAGE analysis of trans-splicing progress. At the end of the time course, the reaction mixture was buffer exchanged by gel exclusion chromatography to 50 mM Tris-HCl, pH 7.5, 500 mM NaCl, 50 mM imidazole, and 1 mM 2-mercaptoethanol, the equilibration buffer for His_6 affinity chromatography. The cleaved (N)*Npu*DnaE-His_6 and GST-His_6-(C)*Ssp*Dna products and any uncleaved KINASE(AEY)-(N)-*Npu*DnaE-His_6 and GST-His_6-(C)*Ssp*Dna-(CMN)PH reactants were removed by passage over a 5 mL size Ni^{2+} Sepharose HiTrap HP affinity column (Amersham). The column was subsequently washed until the absorbances at 260 and 280 nm returned to baseline. Flow-through fractions containing spliced-PDK1 were desalted and directly loaded by FPLC (0.5 mL/min) onto a Tricorn Mono Q 5/50 GL anion exchange column (Amersham) equilibrated at 4 °C in Tris-HCl buffer, pH 7.5, containing 2 mM 2-mercaptoethanol. Upon linear increasing of the NaCl concentration from 0 to 1 M at 1 mL/min for 1 h, ≥95% purified spliced-PDK1 eluted between 0.1 and 0.2 M NaCl. Fractions containing purified spliced-PDK1 (~35 μM or ~2 mg/mL) were combined, and protease inhibitors (0.5 mM benzamidine and 0.1 mM PMSF) were added before storage of either 50 μL or 1 mL aliquots at −80 °C.

SDS-PAGE and Western Analysis. Protein samples in SDS sample buffer were heated at 95 °C for 2 min and cooled on ice. Analytical SDS-PAGE was performed on 4−20% gradient polyacrylamide gels (GradiPore) developed at 150 V (constant) for 1 h or until the tracking dye reached the bottom of the slab. Coomassie staining was used to visualize total protein. Densitometric analysis was performed using the ImageQuant software (Molecular Dynamics). For Western analyses, protein was transferred from the gel to Nitrocellulose Membrane Filter Paper Sandwich (Invitrogen) in a semidry blotting apparatus using 0.7% (v/v) acetic acid as transferring solution. According to the manufacturer's instructions, purified KINASE(AEY)-(N)-*Npu*DnaE-His_6 was probed with phospho-PDK1 (Ser241) polyclonal rabbit antibody (Cell Signaling Technology), and His_6-PKBβ was probed with either phospho-PKB (Thr-308) or phospho-PKB (Ser473) polyclonal rabbit antibodies (Cell Signaling Technology). Detection of all immunoprotein complexes was carried out using secondary anti-rabbit antibody conjugated to horseradish peroxidase (HRP) and LumiGLO chemiluminescent reagent and peroxide.

Kinetic Assays and Phosphopeptide Mapping. V_{max} and K_m values at 30 °C and percent inactivation over time of purified 20 μM KINASE(AEY)-(N)*Npu*DnaE-His_6 in protein trans-

splicing buffer at 21 °C were measured by quantifying transfer of ^{32}P-radiolabel from [γ-^{32}P]ATP to the model PDK1-Tide substrate as described (*36*). PI(3,4,5)P_3-dependent phosphorylation of His$_6$-PKBβ by spliced-PDK1 and measurement of the resulting increase in His$_6$-PKBβ-catalyzed transfer of ^{32}P-radiolabel from [γ-^{32}P]ATP (100 μM) to the model Crosstide substrate (50 μM) was carried out as described (*36*). For both assays, one unit of activity was defined as the amount of enzyme required to catalyze phosphorylation of 1 nmol of peptide substrate in 1 min.

The ability of spliced-PDK1 to *selectively* phosphorylate Thr-309 in the activation loop of His$_6$-PKBβ was tested in a 1 mL reaction mixture containing 2 μM of each enzyme (60 μg or 1 nmol) in 50 mM Tris-HCl buffer, pH 7.5, 1 mM 2-mercaptoethanol, 10 mM $MgCl_2$, 0.2 mM sodium vanadate, and PC/PS/PI(3,4,5)P_3 vesicles. The reaction was initiated by addition of 100 μM [γ-^{32}P]ATP (~500 cpm/pmol) and allowed to proceed with continuous shaking at 30 °C for 40 min. The reaction was quenched by addition of urea to 6 M. Control assays were carried out in parallel in which either spliced-PDK1, PI(3,4,5)P_3 in the phospholipid vesicles, or both were omitted.

^{32}P-Radiolabeled His$_6$-PKBβ was affinity-purified from the quenched reaction mixture by addition of 200 μL of Ni-NTA agarose resin and shaking overnight at room temperature. After low-speed centrifugation, the supernatant was removed and the resin was washed twice with 1 mL of 50 mM Tris-HCl, pH 7.5, containing 6 M urea, 50 mM imidazole, 300 mM NaCl, and 1 mM 2-mercaptoethanol. ^{32}P-Radiolabeled His$_6$-PKBβ was eluted from the Ni-NTA agarose resin pellet with 100 μL of 50 mM Tris-HCl, pH 7.5, containing 6 M urea, 500 mM imidazole, 300 mM NaCl, and 1 mM 2-mercaptoethanol, and approximately 40−50% of enzyme (400−500 pmol) was recovered in the 100 μL elute. First, protein concentration was determined with the Bio-Rad protein assay kit, using 10 μL of the eluted enzyme. Second, the specific radioactivity of the ^{32}P-radiolabeled His$_6$-PKBβ construct ($SA^{PKB\beta}$, cpm/pmol) was determined from radioactivity detected by scintillation counting of the known amount of enzyme (~40−50 pmol) in 10 μL of the eluted enzyme. The mole fraction of total phosphorylated sites ($f_{mol}{}^{tot}$) was calculated according to $f_{mol}{}^{tot} = SA^{PKB\beta}/SA^{ATP}$.

To determine site-specific phosphorylation, the remaining amount (~80 μL with ~320−400 pmol) of affinity-purified His$_6$-PKBβ was used for trypsin digestion and HPLC resolution of ^{32}P-radiolabeled peptides. First, cysteine residues were reduced by addition of 0.5 mL of 50 mM Tris-HCl, pH 7.5, containing 20 mM 2-mercaptoethanol. Free cysteines were protected from reoxidation by subsequent addition of 50 μL of 500 mM iodoacetamide incubation in the dark at room temperature for 20 min. Excess unreacted iodoacetamide was depleted from the reaction mixture by further addition of 30 μL of 500 mM 2-mercaptoethanol and incubation at room temperature for 5 min. Proteolytic digestion was carried out by addition of 1 μg of trypsin and incubation at 37 °C for 5 h, followed by subsequent addition of 1 μg of trypsin and incubation at 37 °C overnight. The individual reaction mixtures (~200 μL) containing digested ^{32}P-radiolabeled His$_6$-PKBβ constructs were diluted to 1 mL with solvent A [0.1% (v/v) trifluoroacetic acid in water]. The 1 mL samples were directly loaded by HPLC (0.5 mL/min) onto a μRPC *C*2/C18 column (Amersham) equilibrated in 100% solvent A. The column was subsequently washed in this buffer for 5 min, and the peptides were eluted by linear increasing solvent B [80% acetonitrile and 0.07% (v/v) trifluoroacetic acid in water] from 0% to 50% in 1 h at a flow rate of 0.4 mL/min, while 300 μL was collected for each fraction. ^{32}P-Radiolabeled peptides were detected by scintillation counting of 30 μL of each chromatographic fraction.

The identity of the ^{32}P-radiolabeled peptide was confirmed by MALDI-TOF mass spectrometric analysis. The 300 μL fraction containing the ^{32}P-radiolabeled peptide was evaporated to dryness and resuspended in a small volume (10−30 μL) of 50% acetonitrile to yield a ^{32}P-peptide concentration of 10 pmol/μL, as indicated by the amount of radioactivity; 1 μL of saturated 2,5-dihydroxybenzoic acid (2,5-DHB) was added to 1 μL of the concentrated ^{32}P-peptide, and 1 μL of this mixture containing ~5 pmol of the ^{32}P-peptide was placed on a stainless steel MALDI-TOF target plate and allowed to dry. MALDI-TOF mass spectra were acquired on a Biflex IV MALDI-TOF mass spectrometer (Bruker Daltronics) in either linear (larger peptides) or reflectron (smaller peptides) mode. A N_2 laser was used to desorb/ionize the matrix/analyte material. Calibration was performed using angiotensin II (monoisotopic mass [MH^+] 1046.5423 Da), angiotensin I (monoisotopic mass [MH^+] 1296.6900 Da), bombesin (monoisotopic mass [MH^+] 1619.8229 Da), and adrenocorticotropic hormone clip 18−39 (monoisotopic mass [MH^+] 2465.2027 Da) (Sigma-Aldrich, St. Louis, MO).

RESULTS AND DISCUSSION

Development of PDK1 Cross Trans-Splicing Strategy. It has been underreported but overestablished that a majority of human protein kinases are poorly expressed and purified as inclusion bodies from both bacterial and yeast protein expression strains under a wide variety of growth and induction conditions. In addition, such kinase preparations have proven difficult to resolubilize into stable and active conformations. To date, baculovirus-mediated protein expression in either Sf9 or Sf21 insect cells has been the most effective method for generating high levels of soluble and active human protein kinases (*36*). Although the reason is not entirely clear, we observed that high production of the catalytic kinase domain constructs of PDK1, S6K1, and PKBβ, typically achieved by baculovirus-mediated expression in Sf9 insect cells, was severely attenuated when these constructs were fused with a C-terminal *active* intein (e.g., *Mxe* GyrA or VMA inteins available from New England Biolabs, Inc.) (unpublished results). In addition, the small amounts of expressed fusion protein (≤0.5 mg/200 mL Sf9 insect cell culture) were observed to be ≥80% hydrolyzed. Therefore, only very small quantities of N-kinase-intein fusion protein (≤0.1 mg/200 mL Sf9 insect cell culture) were available for thiolysis of the intein to generate the C-terminal thioester required for chemical ligation to the N-terminal cysteine residue of a C-terminal peptide fragment. Thus, we reasoned that high-level baculovirus-mediated expression in Sf9 insect cells of human catalytic kinase domains for engineered ligation could be better achieved if fused to an *inactive* intein fragment of a protein trans-splicing intein pair.

To date, the naturally occurring split *Ssp* DnaE intein (*38*−*40*) and the artificially split *Ssp* DnaB and *Sce* VMA inteins (*41*, *42*) have been best characterized with regard to achieving protein trans-splicing activity in the absence of protein refolding routines typically required of artificially split inteins. However, in all these cases, protein trans-splicing under native conditions has been compromised by competing cleavage of the protein trans-splicing reactants upon mixing, resulting in typical yields of only 40−50% spliced protein product. Encouragingly, highly efficient protein trans-splicing (≥98%) of two B1 domains of the IgG binding protein (GB1) was recently demonstrated when the His$_6$-GB1-(N)*Npu*DnaE and (C)*Ssp*DnaE-GB1 cross reacting trans-splicing constructs were coexpressed in *E. coli* (*37*). Since it is difficult to access contributions of endogenous chaperones and the reducing environment to the observed high splicing efficiency in *E. coli*, it became of immediate interest whether this highly efficient in vivo 'cross' trans-splicing strategy would translate to in vitro conditions.

Table 1. Purification of Recombinant KINASE(AEY)-(N)*Npu*DnaE-His$_6$ from Sf9 Insect Cells[a]

purification (step)	volume (mL)	concn (mg/mL)	yield (mg)	purification (fold)
crude lysate	50	2.2 ± 0.2	110 ± 10	N/A
Ni Sepharose	10	1.0 ± 0.2	10 ± 2	11

[a] All values are reported for purification from initial infection of 200 mL of insect Sf9 cells (2×10^6 cells/L) with recombinant baculovirus.

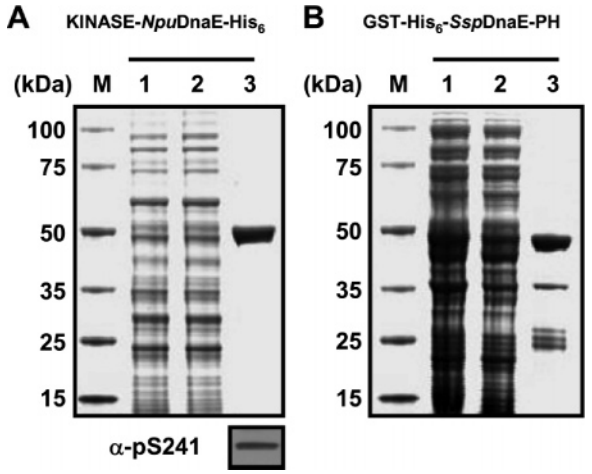


Figure 2. SDS-PAGE analysis of purification of protein trans-splicing reactants. (A) KINASE(AEY)-(N)*Npu*DnaE-His$_6$ was His$_6$ affinity purified from Sf9 insect cell lysate. (B) GST-His$_6$-(C)*Ssp*DnaE-(CMN)-PH was GST affinity purified from *E. coli* lysate. Lane 1 shows the total lysate; lane 2 shows protein species that were not retained by the affinity column, and lane 3 shows the affinity-purified recombinant protein trans-splicing construct. Molecular weight markers are indicated. Proteins were visualized by Coomassie staining.

Preparation of Cross Trans-Splicing Constructs. The KINASE(AEY)-(N)*Npu*DnaE-His$_6$ fusion construct of PDK1 (Figure 1) was generated by PCR and subcloned into the pFastBac1 vector for generation of recombinant baculovirus using the Bac-to-Bac Baculovirus Expression System (Invitrogen). Using MOI = 2 and a time of harvest 72 h after post infection, KINASE(AEY)-(N)*Npu*DnaE-His$_6$ was overexpressed and His$_6$ affinity purified, typically yielding 10 ± 2 mg from initial infection of 4×10^8 total Sf9 insect cells (Table 1). Figure 2A shows that the KINASE(AEY)-(N)*Npu*DnaE-His$_6$ was efficiently purified to ≥95% homogeneity (lane 3), as judged by Coomassie blue staining of 4−20% SDS-PAGE. Purified KINASE(AEY)-(N)*Npu*DnaE-His$_6$ migrates with an apparent molecular weight of 51 kDa, which agrees with its calculated molecular mass of 50 802 Da. Similar to the recombinant catalytic domain construct of PDK1 [His$_6$-PDK1(ΔPH), residues 51−359] (*5*), Western analysis showed that the KINASE(AEY)-(N)*Npu*DnaE-His$_6$ construct was purified in its Ser-241 phosphorylated and catalytically active form (Figure 2A, lower panel). The values of V_{max} = 200 ± 15 U/mg and $^{Tide}K_m$ = 70 ± 10 μM measured for KINASE(AEY)-(N)*Npu*DnaE-His$_6$-catalyzed phosphorylation of the model PDK1-Tide substrate were in the same range as those measured for native His$_6$-PDK1 (*36*).

The (C)*Ssp*DnaE-(CMN)PH fusion construct was cloned into pET-41b vector downstream of a GST-His$_6$ tag, yielding the coding sequence for the GST-His$_6$-(C)*Ssp*DnaE-(CMN)PH fusion protein (Figure 1). Recombinant protein expression of cell cultures (OD of 0.8) were induced with 0.5 mM IPTG for 16 h at 15 °C. Cell lysate from 1 L of culture was collected by homogenization, and GST affinity purification typically yielded 17 ± 3 mg total protein (Table 2). Figure 2B shows that the GST-His$_6$-(C)*Ssp*DnaE-(CMN)PH construct was purified to ∼60% homogeneity (lane 3), as judged by Coomassie blue staining of 4−20% SDS-PAGE. Affinity-purified GST-His$_6$-(C)*Ssp*DnaE-(CMN)PH showed anomalous slightly faster migration corresponding to an apparent molecular weight of 49 kDa compared with its calculated molecular mass of 51 214 Da. The ∼40% impurities retained after GST affinity purification of GST-His$_6$-(C)*Ssp*DnaE-(CMN)PH from the *E. coli* are primarily composed of a mixture of four protein species that migrate with apparent molecular weights of approximately 24, 25, 26, and 37 kDa, which were efficiently removed in subsequent chromatographic steps used to purify spliced-PDK1 from the trans-splicing reaction (see below).

Table 2. Purification of GST-His$_6$-(C)*Ssp*DnaE-(CMN)PH from *E. coli*[a]

purification (step)	volume (mL)	concn (mg/mL)	yield (mg)	purification (fold)
crude lysate	25	14 ± 2	350 ± 50	N/A
Ni Sepharose	10	1.7 ± 0.3	17 ± 3	21

[a] All values are reported for purification from expression in 1 L of *E. coli*.

PDK1 Cross Trans-Splicing Kinetics and Yield. Figure 3A shows the progress of protein trans-splicing that occurs over 12 h. The 10 mL protein trans-splicing reaction (21 °C) was initiated by combining 2 mmol of each of the protein trans-splicing reactants, KINASE(AEY)-(N)*Npu*DnaE-His$_6$ (species I) and GST-His$_6$-(C)*Ssp*Dna-(CMN)PH (species II) (∼20 μM each). SDS-PAGE with Coomassie staining shows decreasing band intensities corresponding to consumption of the trans-splicing reactants (species I and II) with a concomitant increasing band intensity corresponding to formation of full length spliced-PDK1 (species III). In addition, increasing band intensities were observed for formation of the cleaved affinity tagged intein constructs, GST-His$_6$-(C)*Ssp*Dna (species IV) and (N)-*Npu*DnaE-His$_6$ (species V). Densitometric analysis of multiple reaction gels indicated that PDK1 trans-splicing follows apparent first-order kinetics with $k_{obs} = (2.8 \pm 0.3) \times 10^{-5}$ s^{-1} (Figure 3B). This rate is approximately 10-fold slower than the $k_{obs} = (3.0 \pm 0.4) \times 10^{-5}$ s^{-1} reported for trans-splicing of the maltose binding protein and thioredoxin utilizing the native (N/C)-*Ssp*DnaE intein pair, which was also performed at room temperature (*40*). However, the fit of the kinetic data (Figure 3B) also indicated that the cross trans-splicing strategy facilitates a limiting reaction extent approaching 90 ± 10%. This is corroborated by observation of the faint band intensity indicated for KINASE(AEY) (species VI ≤ 5%), which results from trans-cleavage or hydrolysis of KINASE(AEY)-(N)*Npu*DnaE-His$_6$. The extent of the competing trans-cleavage reaction is significantly lower than those typically reported for the native (N/C)-*Ssp*Dna intein pair (*38*−*40*). Disappointingly, the trans-splicing reaction was much less efficient when performed at 4 °C.

Although the cross trans-splicing reaction at 21 °C should approach 90% yield, it was not reasonable to allow the reaction to proceed to such limits, as a $k_{obs} = (4.4 \pm 0.4) \times 10^{-6}$ s^{-1} was determined for KINASE(AEY)-(N)*Npu*DnaE-His$_6$ inactivation at 21 °C (Figure 3B). Thus, a reaction time of 18 h was selected as an optimal time for maximizing the yield of spliced-PDK1, while retaining significant enzyme stability and function (Figure 3C, lane 2). The reaction mixture was then buffer exchanged and subjected to His$_6$ affinity chromatography. Figure 3C (lane 3) shows that the cleaved affinity tagged intein constructs, GST-His$_6$-(C)*Ssp*Dna (species IV) and (N)*Npu*DnaE-His$_6$ (species V), as well as the remaining uncleaved KINASE-(AEY)-(N)*Npu*DnaE-His$_6$ and GST-His$_6$-(C)*Ssp*Dna-(CMN)PH reactants, were effectively retained by the column. In addition, three of the four contaminating protein impurities (24, 25, and 26 kDa) that copurified with GST-His$_6$-(C)*Ssp*Dna-(CMN)PH

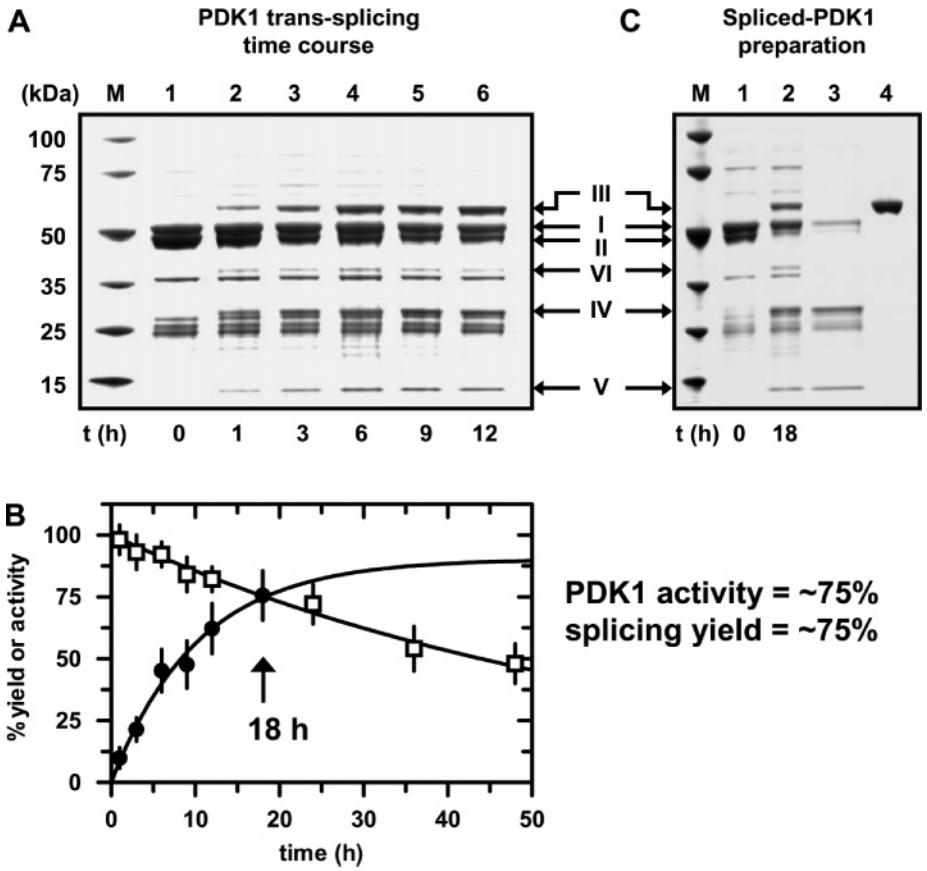


Figure 3. (A) Progress of PDK1 trans-splicing. Affinity-purified KINASE(AEY)-(N)*Npu*DnaE-His_6 and GST-His_6-(C)*Ssp*DnaE-(CMN)PH protein trans-splicing reactants were mixed and allowed to react at 21 °C. Aliquots of the reaction mixture were removed and analyzed by SDS-PAGE, which indicates the distribution of reactants and products at varying times of 0 h (lane 1), 1 h (lane 2), 3 h (lane 3), 6 h (lane 4), 9 h (lane 5), and 12 h (lane 6). (B) Time courses for KINASE(AEY)-(N)*Npu*DnaE-His_6 inactivation (□) and yield of spliced-PDK1 (●) at 21 °C. (C) Preparative amounts of trans-splicing reactants were mixed (lane 1) and allowed to react at 21 °C for 18 h (lane 2). Lane 3 shows the protein species in the reaction mixture that were retained by His_6 affinity chromatography. Lane 4 shows purified spliced-PDK1 (≥95%), which was resolved by MonoQ ion exchange chromatography from trace amounts of protein species that were not retained by His_6 affinity chromatography.

(Figure 3C, lane 3) were retained, suggesting that these may likely result from proteolytic degradation prior to cell lysis. Spliced-PDK1, the contaminating species (37 kDa), and the small amount of trans-cleaved KINASE(AEY), which were not retained by the His_6 affinity column were readily resolved by MonoQ ion exchange chromatography. Figure 3C (lane 4) shows that spliced-PDK1 is purified to ≥95% homogeneity. For this optimized preparative procedure, ∼1 mmol of purified spliced-PDK1 could be readily obtained from 2 mmol of each of the starting reactants.

PI(3,4,5)P_3-Dependent Phosphorylation of PKBβ by Spliced-PDK1. The best characterized function of the C-terminal PH domain of PDK1 is its ability to bind the PI(3,4,5)P_3 second messenger, causing its membrane colocalization with PKB, which also contains a PH domain that selectively binds PI(3,4,5)P_3 (*43*−*53*). At the membrane, PDK1 catalyzes phosphorylation of the critical residue in the activation loop of PKB, which is required for downstream PKB signaling activity. For the three known isoforms of PKB, the phosphorylation sites correspond to Thr-308, Thr-309, and Thr-305 in PKBα, PKBβ, and PKBγ, respectively. In vitro characterization of PDK1-catalyzed site-specific phosphorylation of PKB isoforms, which utilize phosphoinositide-containing vesicles, demonstrated an absolute requirement for PI(3,4,5)P_3-containing vesicles, as well as functional PH domains in both PDK1 and PKB (*45*, *46*, *50*). Since protein trans-splicing of the regulatory PH and catalytic kinase domains of PDK1 required mutation of ^{382}QFG^{384} to ^{382}AEY^{384} at the N-terminal side of the splice junction, as well as the Q387N mutation to give ^{385}CMN^{387} at the C-terminal side of the splice junction (Figure 1), it was very important to assess whether spliced-PDK1 retained the characteristic ability to specifically phosphorylate and activate PKB in a PI(3,4,5)P_3-dependent manner.

First, full length His_6-PKBβ was obtained by baculovirus-mediated expression and purification from Sf9 insect cells (*36*). As we have previously demonstrated, His_6-PKBβ purifies with minimal catalytic activity to the Crosstide substrate (∼0.3 U/mg) and displays very small but detectable amounts of both Thr-309 and Ser-474 phosphorylation, as detected by Western analysis (Figure 4A, lane 1). Previous isoelectric focusing studies, as well as ion exchange chromatography, could not resolve the phosphorylated isoforms, suggesting that the small detectable amount of phosphorylated His_6-PKBβ likely consists of a mixture of enzyme monophosphorylated either at Thr-309 or Ser-474 (*36*). Nevertheless, homogeneous unphosphorylated His_6-PKBβ with slightly lower Crosstide activity (∼0.2 U/mg) was readily generated by treatment with λPP (Figure 4A, lane 2). Western analysis further showed that λPP-treated unphosphorylated His_6-PKBβ did not catalyze autophosphorylation at either Thr-309 or Ser-474 when incubated in autophosphorylation reaction mixtures either in the absence (Figure 4A, lane 3) or presence of PI(3,4,5)P_3-containing vesicles (Figure 4A, lane 4). Most importantly, Western analysis detected significant Thr-309 phosphorylation of His_6-PKBβ only when incubated with spliced-PDK1 in the presence of PI(3,4,5)P_3-containing vesicles, and His_6-PKBβ catalytic activity to Crosstide increased ∼10-fold (Figure 4A, lanes 5 and 6). Affinity purification and phosphopeptide mapping of His_6-PKBβ from the phosphorylation reaction mixture containing both spliced-PDK1 and PI(3,4,5)P_3-containing vesicles (Figure 4A, lane 6) confirmed that

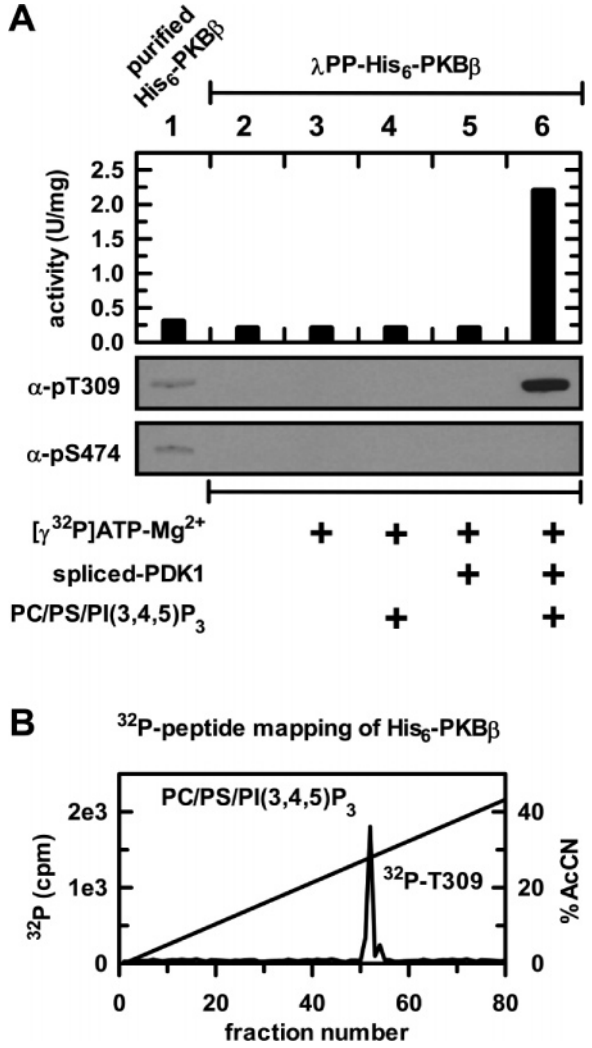


Figure 4. Site-specific Thr-309 phosphorylation by spliced-PDK1. (A) Preparation of His_6-PKBβ (lane 1), preparation of λPP-treated unphosphorylated His_6-PKBβ (lane 2), and affinity-purified λPP-treated His_6-PKBβ after 40 min incubation at 30 °C in phosphorylation reaction mixtures containing [γ-^{32}P]ATP-Mg^{2+} (lane 3), [γ-^{32}P]ATP-Mg^{2+} in the presence of PC/PS/PI(3,4,5)P_3 vesicles (lane 4), [γ-^{32}P]ATP-Mg^{2+} in the presence of spliced-PDK1 (lane 5), and [γ-^{32}P]ATP-Mg^{2+} in the presence of both spliced-PDK1 and PC/PS/PI(3,4,5)P_3 vesicles (lane 6). SDS-PAGE and Western analysis were used to visualize Thr-309 and Ser-474 phosphorylated His_6-PKBβ. Activities were determined for His_6-PKBβ-catalyzed phosphorylation of 100 μM of Crosstide (Ψ). (B) After 40 min incubation at 30 °C in the phosphorylation reaction mixture containing [γ-^{32}P]ATP-Mg^{2+}, affinity-purified λPP-treated His_6-PKBβ was digested with trypsin and subjected to reversed-phase HPLC. Scintillation counting of the individual fractions detected the ^{32}P-radiolabeled peptide that eluted near 28% acetonitrile, which was identified by MALDI-TOF (m/z = 2469.6) to be the monophosphorylated tryptic peptide containing Thr-309 (^{309}pTFCGTPEYLAPEVLEDNDYGR^{329}).

spliced-PDK1 catalyzed site-specific Thr-309 phosphorylation of His_6-PKBβ (Figure 4B), as no other ^{32}P-radiolabeled peptides were detected. The mole fraction of total phosphorylated sites (f_{mol}^{tot}) was calculated to be 0.65 ± 0.15, in agreement with previous reports (*50*).

PROSPECTIVE AND SUMMARY

Large efforts are being directed toward design of potent and selective inhibitors of well-established protein kinase drug targets (*54*, *55*). Since the overwhelming majority of protein kinase inhibitors bind in or near the ATP binding pocket shared by the structurally homologous catalytic domain shared by all kinases, very few serine-threonine protein kinase inhibitors have been clinically approved due to their broad specificity and overall high toxicity (*56*−*58*). Therefore, we are developing the hypothesis that serine-threonine protein kinase inhibitor selectivity may be better achieved by designing compounds that target interfacial clefts and crevices formed between contiguous regulatory and catalytic kinase domains, thereby 'allosterically' stabilizing inactive or autoinhibited conformations of multidomain protein kinases (*59*). In fact, validation of this hypothesis is exemplified by the recent discovery of the small molecule inhibitors, Akt-I-1 and Akt-I-1,2, which showed remarkable isozyme specificity toward PKB/Akt isozymes and did not significantly inhibit other closely related kinases (*60*). Most importantly, only the full length PKB/Akt isozymes containing the regulatory PH domain were sensitive to inhibition, suggesting an 'allosteric' mechanism in which high selectivity results from inhibitor binding at a site that stabilizes a PH domain-mediated autoinhibited form of the kinase.

The inability to obtain diffraction quality crystals for full length constructs of any of the large number of multidomain serine-threonine protein kinase drug targets suggests a large degree of conformational heterogeneity, which likely results from changes in relative orientations of contiguous regulatory and catalytic kinase domains. In order to better facilitate structure-based discovery or design of highly selective inhibitors (e.g., Akt-I-1 and Akt-I,2), development of alternative methodologies will be required to better understand autoinhibitory contiguous domain−domain interactions, and domain-specific incorporation of biophysical probes would greatly facilitate spectroscopic studies of these interactions in solution. Disappointingly, the use of intein-mediated chemical ligation for such purposes is largely precluded, as we found it difficult to purify from Sf9 insect cells adequate quantities of a number of protein kinases when fused with *active* inteins (e.g., *Mxe* GyrA and VMA). While the use of naturally [e.g., (N/C)*Ssp*DnaE] or artificially split intein pairs [e.g., (N/C)*Ssp*DnaB] circumvents decreased protein stability and intein self-cleavage issues during baculovirus-mediated expression in Sf9 insect cells, only 40−50% protein trans-splicing yields are typically achieved. On the basis of the recently reported highly efficient in vivo protein trans-splicing (≥98%) catalyzed between split DnaE inteins from two different organisms (*37*), we implemented and demonstrated that the 'cross' trans-splicing strategy was optimal for in vitro ligation of the regulatory PH and catalytic kinase domains of PDK1, and spliced-PDK1 was shown to retain the ability to specifically phosphorylate Thr-309 and activate PKBβ in a PI-(3,4,5)P_3-dependent manner. This bioconjugation strategy may prove useful for design of spectroscopic experiments to detect and characterize the elusive frontier of potential allosteric drug targeting sites, which may exist at interfacial clefts and crevices in flexible multidomain monomeric protein kinases.

ACKNOWLEDGMENT

This research was supported by a grant from the National Institute of General Medical Sciences (GM69868) to T.K.H.

Supporting Information Available: Experimental procedures describing PCR engineering to generate the *Eco*RI-*Xba*I cDNA fragment containing the KINASE(AEY)-(N)*Npu*DnaE-His_6 fusion construct and the *Sac*II-*Kpn*I fragment containing the (C)-*Ssp*DnaE-(CMN)PH fusion construct. This material is available free of charge via the Internet at http://pubs.acs.org/BC.

LITERATURE CITED

(1) Manning, G., Whyte, D. B., Martinez, R., Hunter, T., and Sudarsanam, S. (2002) The protein kinase complement of the human genome. *Science 298*, 1912−1934.

(2) Manning, B. D., and Cantley, L. C. (2002) Hitting the target: emerging technologies in the search for kinase substrates. *Sci. STKE 162*, PE49.

(3) Obenauer, J. C., and Yaffe, M. B. (2004) Computational prediction of protein-protein interactions. *Methods Mol. Biol. 261*, 445−468.

(4) Neidner, R. H., Buzko, O. V., Haste, N. M., Taylor, A., Gribskov, M., and Taylor, S. S. (2006) Protein kinase resource: an integrated environment for phosphorylation research. *Proteins 63*, 78−86.

(5) Biondi, R. M., Komander, D., Thomas, C. C., Lizcano, J. M., Deak, M., Alessi, D. R., and van Aalten, D. M. F. (2002) High resolution crystal structure of the human PDK1 catalytic domain defines the regulatory phosphopeptide docking site. *EMBO J. 21*, 4219−4228.

(6) Yang, J., Cron, P., Thompson, V., Good, V. M., Hess, D., Hemmings, B. A., and Barford, D. (2002) Molecular mechanism for the regulation of protein kinase B/Akt by hydrophobic motif phosphorylation. *Mol. Cell 9*, 1227−1240.

(7) Yang, J., Cron, P., Good, V. M., Thompson, V., Hemmings, B. A., and Barford, D. (2002) Crystal structure of an activated Akt/protein kinase B ternary complex with GSK3-peptide and AMP-PNP. *Nat. Struct. Biol. 9*, 940−944.

(8) Xu, Z.-B., Chaudhary, D., Olland, S., Wolfrom, S., Czerwinski, R., Malakian, K., Lin, L., Stahl, M. L., Joseph-McCarthy, D., Benander, C., Fitz, L., Greco, R., Somers, W. S., and Mosyak, L. (2004) Catalytic domain crystal structure of protein kinase C-θ (PKCθ). *J. Biol. Chem. 279*, 50401−50409.

(9) Messerschmidt, A., Maciera, S., Velarde, M., Bädeker, M., Benda, C., Jestel, A., Brandstetter, H., Neuefeind, T., and Blaesse, M. (2005) Crystal structure of the catalytic domain of human atypical protein kinase C-iota reveals interaction mode of phosphorylation site in turn motif. *J. Mol. Biol. 352*, 918−931.

(10) Wan, P. T. C., Garnett, M. J., Roe, S. M., Lee, S., Niculescu-Duvaz, D., Good, V. M., Jones, C. M., Marshall, C. J., Springer, C. J., Barford, D., and Marais, R. (2004) Cancer Genome Project Mechanism of activation of the RAF-ERK signaling pathway by oncogenic mutations of B-RAF. *Cell 116*, 855−867.

(11) Ohren, J. F., Chen, H., Pavlovsky, A., Whitehead, C., Zhang, E., Kuffa, P., Yan, C., McConnell, P., Spessard, C., Banotai, C., Mueller, W. T., Delaney, A., Omer, C., Sebolt-Leopold, J., Dudley, D. T., Leung, I. K., Flamme, C., Warmus, J., Kaufamn, M., Barrett, S., Tecle, H., and Hasemann, C. A. (2004) Structures of human MAP kinasekinase 1 (MEK1) and MEK2 describe novel noncompetitive kinase inhibition. *Nat. Struct. Mol. Biol. 11*, 1192−1197.

(12) Underwood, K. W., Parris, K. D., Federico, E., Mosyak, L., Czerwinski, R. M., Shane, T., Taylor, M., Svenson, K., Liu, Y., Hsiao, C.-L., Wolfrom, S., Maguire, M., Malakian, K., Telliez, J.-B., Lin, L.-L., Kriz, R. W., Seehra, J., Somers, W. S., and Stahl, M. L. (2003) Catalytically active MAP KAP kinase 2 structures in complex with staurosporine and ADP reveal differences with the autoinhibited enzyme. *Structure 11*, 627−636.

(13) Smith, K. J., Carter, P. S., Bridges, A., Horrocks, P., Lewis, C., Pettman, G., Clarke, A., Brown, M., Hughes, J., Wilkinson, M., Bax, B., and Reith, A. (2004) The structure of MSK1 reveals a novel autoinhibitory conformation for a dual kinase protein. *Structure 12*, 1067−1077.

(14) Zhang, B., Bower, M. J., McDevitt, P. J., Zhao, H., Davis, S. T., Johanson, K. O., Green, S. M., Concha, N. O., and Zhou, B.-B. S. (2002) Structural basis for Chk1 inhibition by UCN-01. *J. Biol. Chem. 277*, 46609−46615.

(15) Cheetham, G. M. T., Knegtel, R. M. A., Coll, J. T., Renwick, S. B., Swenson, L., Weber, P., Lippke, J. A., and Austen, D. A. (2002) Crystal structure of Aurora-2, an oncogenic serine/threonine kinase. *J. Biol. Chem. 277*, 42419−42422.

(16) Sessa, F., Mapelli, M., Ciferri, C., Tarricone, C., Areces, L. B., Schneider, T. R., Stukenberg, P. T., and Musacchio, A. (2005) Mechanism of Aurora B activation by INCENP and inhibition by hesperadin. *Mol. Cell 18*, 379−391.

(17) Komander, D., Fairservice, A., Deak, M., Kular, G. S., Prescott, A. R., Downes, C. P., Safrany, S. T., Alessi, D. R., and van Aalten, D. M. F. (2004) Structural insights into the regulation of PDK1 by phosphoinositides and inositol phosphates. *EMBO J. 23*, 3918−3928.

(18) Thomas, C. C., Deak, M., Alessi, D. R., and van Aalten, D. M. F. (2002) High-resolution structure of the pleckstrin homology domain of protein kinase B/Akt bound to phosphatidylinositol (3,4,5)-triphosphate. *Curr. Biol. 12*, 1256−1262.

(19) Auguin, D., Barthe, P., Augé-Sénégas, M.-T., Stern, M.-H., Noguchi, M., and Roumestand, C. (2004) Solution structure and backbone dynamics of the pleckstrin homology domain of the human protein kinase B (PKB/Akt). Interaction with inositol phosphates. *J. Biomol. NMR 28*, 137−155.

(20) Xu, R. X., Pawelczyk, T., Xia, T.-H., and Brown, S. C. (1997) NMR structure of a protein kinase C-γ phorbol-binding domain and study of protein−lipid micelle interactions. *Biochemistry 36*, 10709−10717.

(21) Ochoa, W. F., Corbalán-Garcia, S., Eritja, R., Rodríguez-Alfaro, J. A., Gómez-Fernández, J. C., Fita, I., and Verdaguer, N. (2002) Additional binding sites for anionic phospholipids and calcium ions in the crystal structures of complexes of the C2 domain of protein kinase Cα. *J. Mol. Biol. 320*, 277−291.

(22) Ochoa, W. F., Torrecillas, A., Fita, I., Verdaguer, N., Corbalán-Garcia, S., and Gómez-Fernández, J. C. (2003) Retinoic acid binds to the C2-domain of protein kinase Cα. *Biochemistry 42*, 8774−8779.

(23) Sutton, R. B., and Sprang, S. R. (1998) Structure of the protein kinase Cβ phospholipid-binding C2 domain complexed with Ca^{2+}. *Structure 6*, 1395−1405.

(24) Pappa, H., Murray-Rust, J., Dekker, L. V., Parker, P. J., and McDonald, N. Q. (1998) Crystal structure of the C2 domain from protein kinase C-δ. *Structure 6*, 885−894.

(25) Benes, C. H., Wu, N., Elia, A. E. H., Dharia, T., Cantley, L. C., and Soltoff, S. P. (2005) The C2 domain of PKCδ is a phosphotyrosine binding domain. *Cell 121*, 271−280.

(26) Ochoa, W. F., Garcia-Garcia, J., Fita, I., Corbalán-Garcia, S., Verdaguer, N., and Gómez-Fernández, J. C. (2001) Structure of the C2 domain from a novel protein kinase Cϵ. A membrane binding model for Ca^{2+}-independent C2 domains. *J. Mol. Biol. 311*, 837−849.

(27) Mott, H. R., Carpenter, J. W., Zhong, S., Ghosh, S., Bell, R. M., and Campbell, S. L. (1996) The solution structure of the Raf-1 cysteine-rich domain: a novel Ras and phospholipid binding site. *Proc. Natl. Acad. Sci. U.S.A. 93*, 8312−8317.

(28) Li, J., Williams, B. L., Haire, L. F., Goldberg, M., Wilker, E., Durocher, D., Yaffe, M. B., Jackson, S. P., and Smerdon, S. J. (2002) Structural and functional versatility of the FHA domain in DNA-damage signaling by the tumor suppressor kinase Chk2. *Mol. Cell 9*, 1045−1054.

(29) Cheng, K.-Y., Lowe, E. D., Sinclair, J., Nigg, E. A., and Johnson, L. N. (2003) The crystal structure of the human polo-likekinase-1 polo box domain and its phospho-peptide complex. *EMBO J. 22*, 5757−5768.

(30) Elia, A. E. H., Rellos, P., Haire, L. F., Chao, J. W., Ivins, F. J., Hoepker, K., Mohammad, D., Cantley, L. C., Smerdon, S. J., and Yaffe, M. B. (2003) The molecular basis for phosphodependent substrate targeting and regulation of Plks by the polo-box domain. *Cell 115*, 83−95.

(31) Muralidharan, V., and Muir, T. W. (2006) Protein ligation: an enabling technology for the biophysical analysis of proteins. *Nat. Methods 3*, 429−438.

(32) Xu, M.-Q., and Evans, T. C., Jr. (2005) Recent advances in protein splicing: manipulating proteins in vitro and in vivo. *Curr. Opin. Biotechnol. 16*, 440−446.

(33) Muir, T. W. (2003) Semisynthesis of proteins by expressed protein ligation. *Annu. Rev. Biochem. 72*, 249−289.

(34) Hofmann, R. M., and Muir, T. W. (2002) Recent advances in the application of expressed protein ligation to protein engineering. *Curr. Opin. Biotechnol. 13*, 297−303.

(35) Vanhaesebroeck, B., and Alessi, D. R. (2000) PI3K-PDK1 connection: more than just a road to PKB. *Biochem. J. 346*, 561−576.

(36) Gao, X., Yo, P., and Harris, T. K. (2005) Improved yields for baculovirus-mediated expression of human His_6-PDK1 and His_6-PKBβ/Akt2 and characterization of phospho-specific isoforms for design of inhibitors that stabilize inactive conformations. *Prot. Express. Purif. 43*, 44−56.

(37) Iwai, H., Züger, S., Jin, J., and Tam, P.-H. (2006) Highly efficient protein *trans*-splicing by a naturally split DnaE intein from *Nostoc punctiforme*. *FEBS Lett. 580*, 1853−1858.

(38) Evans, T. C., Jr., Martin, D., Kolly, R., Panne, D., Sun, L., Ghosh, I., Chen, L., Benner, J., Liu, X.-Q., and Xu, M.-Q. (2000) Protein

trans-splicing and cyclization by a naturally split intein from the dnaE gene of Synechocystis species PCC6803. *J. Biol. Chem. 275*, 9091−9094.
(39) Martin, D. D., Xu, M.-Q., and Evans, T. C., Jr. (2001) Characterization of a naturally occurring trans-splicing intein from Synechocystis sp. PCC6803. *Biochemistry 40*, 1393−1402.
(40) Nichols, N. M., and Evans, T. C., Jr. (2004) Mutational analysis of protein splicing, cleavage, and self association reactions mediated by the naturally split *Ssp* DnaE intein. *Biochemistry 43*, 10265−10276.
(41) Brenzel, S., Kurpiers, T., and Mootz, H. D. (2006) Engineering artificially split inteins for applications in protein chemistry: biochemical characterization of the split *Ssp* DnaB intein and comparison to the split *Sce* VMA intein. *Biochemistry 45*, 1571−1578.
(42) Ludwig, C., Pfeiff, M., Linne, U., and Mootz, H. D. (2006) Ligation of a synthetic peptide to the N terminus of a recombinant protein using semisynthetic protein trans-splicing. *Angew. Chem., Int. Ed. 45*, 5218−5221.
(43) Alessi, D. R., Andjelkovíc, M., Caudwell, B., Cron, P., Morrice, N., Cohen, P., and Hemmings, B. A. (1996) Mechanism of activation of protein kinase B by insulin and IGF-1. *EMBO J. 15*, 6541−6551.
(44) Alessi, D. R., James, S. R., Downes, C. P., Holmes, A. B., Gaffney, P. R. J., Reese, C. B., and Cohen, P. (1997) Characterization of a 3-phosphoinositide-dependent protein kinase which phosphorylates and activates protein kinase Bα. *Curr. Biol. 7*, 261−269.
(45) Alessi, D. R., Deak, M., Casamayor, A., Caudwell, F. B., Morrice, N., Norman, D. G., Gaffney, P., Reese, C. B., MacDougall, C. N., Harbison, D., Ashworth, A., and Bownes, M. (1997) 3-phosphoinositide-dependent protein kinase-1 (PDK1): structural and functional homology with the *Drosophila* DSTPK61 kinase. *Curr. Biol. 7*, 776−789.
(46) Stokoe, D., Stephens, L. R., Copeland, T., Gaffney, P. R. J., Reese, C. B., Painter, G. F., Holmes, A. B., McCormick, F., and Hawkins, P. T. (1997) Dual role of phosphatidylinositol-3,4,5-triphosphate in the activation of protein kinase B. *Science 277*, 567−570.
(47) Meier, R., Alessi, D. R., Cron, P., Andjelkovíc, M., and Hemmings, B. A. (1997) Mitogenic activation, phosphorylation, and nuclear translocation of protein kinase Bβ. *J. Biol. Chem. 272*, 30491−30497.
(48) Andjelkovíc, M., Alessi, D. R., Meier, R., Fernandez, A., Lamb, N. J. C., Frech, M., Cron, P., Cohen, P., Lucocq, J. M., and Hemmings, B. A. (1997) Role of translocation in the activation and function of protein kinase B. *J. Biol. Chem. 272*, 31515−31524.
(49) Stephens, L., Anderson, K., Stokoe, D., Erdjument-Bromage, H., Painter, G. F., Holmes, A. B., Gaffney, P. R. J., Reese, C. B., McCormick, F., Tempst, P., Coadwell, J., and Hawkins, P. T. (1998) Protein kinase B kinases that mediate phosphatidylinositol 3,4,5-triphosphate-dependent activation of protein kinase B. *Science 279*, 710−714.
(50) Walker, K. S., Deak, M., Paterson, A., Hudson, K., Cohen, P., and Alessi, D. R. (1998) Activation of protein kinase B β and γ isoforms by insulin *in vivo* and by 3-phosphoinositide-dependent protein kinase-1 *in vitro*: comparison with protein kinase B α. *Biochem. J. 331*, 299−308.
(51) Filippa, N., Sable, C. L., Hemmings, B. A., and van Obberghen, E. (2000) Effect of phosphoinositide-dependent kinase 1 on protein kinase B translocation and its subsequent activation. *Mol. Cell. Biol. 20*, 5712−5721.
(52) McManus, E. J., Collins, B. J., Ashby, P. R., Prescott, A. R., Murray-Tait, V., Armit, L. J., Arthur, J. S. C., and Alessi, D. R. (2004) The in vivo role of PtdIns(3,4,5)P_3 binding to PDK1 PH domain defined by knockin mutation. *EMBO J. 23*, 2071−2082.
(53) Hanada, M., Feng, J., and Hemmings, B. A. (2004) Structure, regulation and function of PKB/AKT-a major therapeutic target. *Biochim. Biophys. Acta 1697*, 3−16.
(54) Vieth, M., Sutherland, J. J., Robertson, D. H., and Campbell, R. M. (2005) Kinomics: characterizing the therapeutically validated kinase space. *Drug Discovery Today 10*, 839−846.
(55) Cohen, P. (2002) Protein kinases- the major drug targets of the twenty-first century? *Nat. Rev. Drug Discov. 1*, 309−315.
(56) Noble, M. E. M., Endicott, J. A., and Johnson, L. N. (2004) Protein kinase inhibitors: insights into drug design from structure. *Science 303*, 1800−1805.
(57) Davies, S. P., Reddy, H., Caivano, M., and Cohen, P. (2000) Specificity and mechanism of action of some commonly used protein kinase inhibitors. *Biochem. J. 351*, 95−105.
(58) Bain, J., Mclauchlan, H., Elliott, M., and Cohen, P. (2003) The specificities of protein kinase inhibitors: an update. *Biochem. J 371*, 199−204.
(59) Harris, T. K. (2003) PDK1 and PKB/Akt: ideal targets for development of new strategies to structure-based drug design. *IUBMB Life 55*, 117−126.
(60) Barnett, S. F., Defeo-Jones, D., Fu, S., Hancock, P. J., Haskell, K. M., Jones, R. E., Kahana, J. A., Kral, A. M., Leander, K., Lee, L. L., Malinowski, J., McAvoy, E. M., Nahas, D. D., Robinson, R. G., and Huber, H. E. (2005) Identification and characterization of pleckstrin-homology-domain-dependent and isozyme-specific Akt inhibitors. *Biochem. J. 385*, 399−408.

BC070055R

Novel Water-Soluble Near-Infrared Cyanine Dyes: Synthesis, Spectral Properties, and Use in the Preparation of Internally Quenched Fluorescent Probes

Cédric Bouteiller,[†,‡,§] Guillaume Clavé,[†,‡,§] Aude Bernardin,[†,‡] Bertrand Chipon,[†,‡] Marc Massonneau,[‡] Pierre-Yves Renard,*[,†] and Anthony Romieu*[,†]

IRCOF, Equipe de Chimie Bio-Organique, UMR 6014 CNRS, INSA de Rouen et Université de Rouen, 1, rue Lucien Tesnières, 76131 Mont-Saint-Aignan Cedex, France, and QUIDD, Technopôle du Madrillet, 50, rue Ettore Bugatti, 76800 Saint-Etienne du Rouvray, France. Received January 23, 2007; Revised Manuscript Received May 13, 2007

In this paper, we describe the synthesis and the photophysical properties of two novel near-infrared (NIR) cyanine dyes (**NIR5.5-2** and **NIR7.0-2**) which are water soluble potential substitutes of the commercially available Cy 5.5 and Cy 7.0 fluorescent labels respectively. For each one of these cyanine dyes, the synthetic strategy relies on the postsynthetic derivatization of a cyanine precursor in order to introduce the key functionalities required for bioconjugation of these NIR fluorophores. For **NIR5.5-2**, a reactive amino group was acylated with an original trisulfonated linker for water solubility. For **NIR7.0-2**, a vinylic chlorine atom was derivatized through a $S_{RN}1$ reaction for the introduction of a monoreactive carboxyl group for labeling purposes. Unexpectedly, when these two fluorophores were closely associated within a peptidic architecture, mutual fluorescence quenching between **NIR5.5-2** and **NIR7.0-2** was observed both at 705 (**NIR5.5-2**) and 798 nm (**NIR7.0-2**). On the basis of this property, a novel internally quenched caspase-3-sensitive NIR fluorescent probe was prepared.

INTRODUCTION

During the past decade, intensive research efforts have been devoted to the design and synthesis of novel water-soluble fluorescent organic dyes for life science applications (*1*). Indeed, despite the multitude of commercially available fluorophores, new fluorophoric systems, especially those with spectral properties in the near-infrared (NIR) region, are hotly sought for emerging and more challenging biotechnology and biomedical applications such as genetic analysis, DNA sequencing, *in vivo* imaging, and proteomics (*2*, *3*). Thus, numerous long-wavelength fluorophores belonging to the BODIPY (*4*), rhodamine (*5*, *6*), oxazine (*7*), or cyanine dyes (*8*−*10*) have been recently reported. Because of their large molar extinction coefficients, moderate-to-high fluorescence quantum yields, and a broad wavelength tunability, cyanine dyes have received considerable attention and can be considered as the main class of NIR fluorescent probes for biological applications at present (*11*, *12*). Cy 5.5 **1** and Cy 7.0 **2** (Figure 1) are two of these NIR fluorescent cyanine dyes, widely used for such bioanalytical purposes and commercially available from GE Healthcare (formerly Amersham-Biosciences). Despite its good optical properties in the NIR range, the sulfobenzoindocyanine **1** is prepared through a low-yield (15% as described) and poorly reproducible synthetic route using 6-amino-1,3-naphthalenedisulfonic acid as starting material (*13*). Major synthetic difficulties are related to the poor solubility of this latter amino-naphthalene derivative in organic media. This synthetic bottleneck and the drastic reaction conditions required explain why only two bioconjugatable derivatives (i.e., amine-reactive succinimidyl ester and thiol-reactive maleimide) of this fluorescent marker are available at present. As far as the heptamethine cyanine dye **2** (*14*) is concerned, its poor chemical stability restrains its use as fluorescent marker in numerous site-specific biolabeling strategies, especially those requiring additional purification steps by RP-HPLC. To overcome this limitation, numerous studies have shown that incorporating a rigid cyclohexenyl (or cyclopentenyl) ring in the polymethine chain increases the stability of the resulting Cy 7.0 analogue (*15*−*17*). Furthermore, the central cyclohexenyl (or cyclopentenyl) group offers a reactive site for labeling biomolecules *via* substitution of its *meso*-chlorine atom by nucleophiles (metal alcoholates, amines, and thiols) bearing an additional functional group (amine or carboxylic acid) through a $S_{RN}1$ mechanism. Thus, a variety of water-soluble heptamethine cyanine dyes containing aryl-ether, aryl-thioether and alkyl-ether linkages have been prepared using this route (*18*−*21*). However, the susceptibility of most of these dyes to form nonfluorescent aggregates (*18*) limits their use as probes in biological analysis.

With the goal in mind to develop new bright, monofunctional, water-soluble NIR fluorophores suitable for bioconjugation and easily accessible through high-yielding synthetic routes, we have explored an original approach to prepare Cy 5.5 and Cy 7.0 analogues based on the postsynthetic derivatization of cyanine precursors ("convertible cyanine dyes") readily available through standard cyanine synthesis protocols. This synthetic methodology has been already applied to the chemical derivatization of heptamethine cyanine dyes but never extended to cyanine dyes bearing a shorter polyene chain. We thought that the introduction of the key functionalities of a bioconjugatable NIR fluorophore (for instance hydrophilic moieties for water solubility or functional reactive groups for covalent attachment to biomolecules) in the last step of the synthetic process should improve its synthesis because the time-consuming handling and RP-HPLC purification of highly polar materials will be reduced only to the final dye product. Furthermore, both the level of byproducts resulting from interference of the functional reactive groups with the reagents currently used to achieve the condensa-

* Author to whom correspondence should be addressed. E-mail: pierre-yves.renard@univ-rouen.fr or anthony.romieu@univ-rouen.fr. Phone: +33-2-35-52-24-14 (or 24-15). Fax: +33-2-35-52-29-59.

[†] IRCOF, Equipe de Chimie Bio-Organique.

[‡] QUIDD.

[§] These authors contributed equally to this work.

10.1021/bc0700281 CCC: $37.00 © 2007 American Chemical Society
Published on Web 06/21/2007

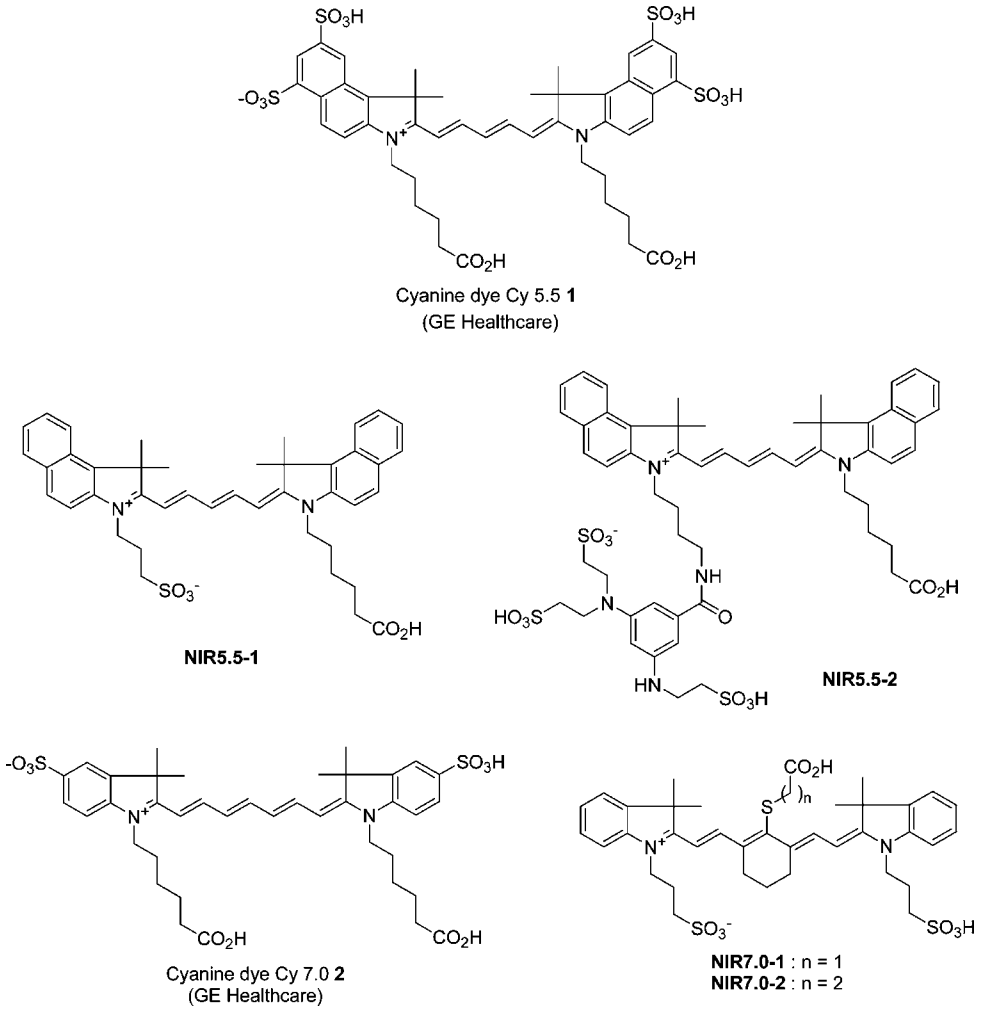


Figure 1. Structures of cyanine dyes Cy 5.5 and Cy 7.0 and their novel analogues studied in this work. An unsymmetrical derivative of cyanine dye Cy 5.5 **1** bearing the ethyl and carboxypentyl substituents is also commercially available, but its synthesis is not described in the literature.

tion reaction leading to the cyanine dye, and the limitation associated with drastic reaction conditions on those fragile polyconjugated scaffolds, should be minimized and consequently the overall yield of the synthesis significantly improved.

We describe here the synthesis and properties of two such novel NIR cyanine fluorophores **NIR5.5-2** and **NIR7.0-2** which are analogues of Cy 5.5 **1** and Cy 7.0 **2**, respectively. These two dyes display absorption and emission maxima in the NIR region, large extinction coefficients, excellent solubility, and no tendency to self-aggregate in aqueous solutions. Their conversion into thiol- and amine-reactive derivatives is also described. The utility of these latter fluorescent labeling reagents is illustrated by the preparation of an internally quenched fluorescent probe of caspase-3 protease.

EXPERIMENTAL PROCEDURES

Chemicals and Reagents. Column chromatography was performed on silica gel (40−63 μm) from SdS. Reversed-phase column flash-chromatography was performed on octadecyl-functionalized silica gel (mean pore size 60 Å) from Aldrich or Whatmann. TLC was carried out on Merck DC Kieselgel 60 F-254 aluminum sheets and visualized by employing a short wavelength UV lamp (i.e., λ = 254 nm). DMF was dried by distillation over BaO. DIEA, pyridine, and triethylamine were distilled from CaH_2 and stored over BaO. Chloro-substituted heptamethine sulfocyanine dye **12** was prepared from 2,3,3-trimethyl-3*H*-indole by using the multistep synthetic procedure developed by Strekowski et al. (*20*). Cyanine-based amino acid **6** was prepared in five steps from 1,1,2-trimethyl-1*H*-benz[*e*]-indole by using the convergent synthetic scheme recently reported by us (*22*, *23*). Malonaldehyde dianilido hydrochloride, sodium 2-bromoethanesulfonate, *N*-succinimidyl[4-iodoacetyl]-aminobenzoate (SIAB), sulfocyanine dye Cy 5.0, 1,1,2-trimethyl-1*H*-benz[*e*]indole and its derivatives *N*-(3-sulfonatopropyl)-1,1,2-trimethylbenzindolinium, inner salt **3**, and *N*-(γ-carboxypentyl)-1,1,2-trimethylbenzindolinium, bromine salt **4**, were prepared by using literature procedures (*14*, *24*−*29*). Hexapeptide Ac-Cys(StBu)-Asp-Glu-Val-Asp-Lys-NH_2 **16** was synthesized on an automated peptide synthesizer (ABI 433A, Applied Biosystems) using the stepwise solid-phase synthesis method and Fmoc amino acids, as previously described (*30*). Indocyanine green (ICG or IR-125, laser grade) was purchased from Acros. Recombinant human caspase-3 enzyme (5.52 U/mg) and Bovine Serum Albumin (BSA, ≥98%) were purchased from Sigma. The HPLC grade solvents (CH_3CN and MeOH) were obtained from Acros. Aqueous buffers for HPLC were prepared using water purified with a Milli-Q system. Triethylammonium acetate (1.0 M) (TEAA) and triethylammonium bicarbonate (1.0 M) (TEAB) buffers were prepared from distilled triethylamine and glacial acetic acid or CO_2 gas.

Instruments. ^1H and ^{13}C NMR spectra were recorded on a Bruker DPX 300 (Bruker, Wissembourg, France). Chemical shifts are expressed in parts per million (ppm) from D_2O (δ_H = 4.79) or DMSO-d_6 (δ_H = 2.54, δ_C = 40.45) (*31*). *J* values are expressed in Hz. Analytical HPLC was performed on a Thermo Electron Surveyor instrument equipped with a PDA

detector. Semipreparative HPLC was performed on a Finnigan SpectraSYSTEM liquid chromatography system equipped with a UV-Visible 2000 detector. UV−visible spectra were obtained on a Varian Cary 50 scan spectrophotometer. Fluorescence spectroscopic studies were performed either in a semi-micro fluorescence cell (Hellma, 104F-QS, 10 × 4 mm, 1400 μL) or in an ultra-micro fluorescence cell (Hellma, 105.51-QS, 3 × 3 mm, 45 μL) with a Varian Cary Eclipse spectrophotometer. Mass spectra were obtained with a Finnigan LCQ Advantage MAX (ion trap) apparatus equipped with an electrospray source. The purified peptides were characterized by MALDI-TOF mass spectrometry on a Voyager DE PRO in the reflector mode with CHCA as a matrix.

HPLC Separations. Several chromatographic systems were used for the analytical experiments and the purification steps. Each one of these systems was optimized in order to improve separation conditions.

System A: RP-HPLC (Thermo Hypersil GOLD C_{18} column, 5 μm, 4.6 × 150 mm) with CH_3CN and 0.1% aq trifluoroacetic acid (aq TFA, 0.1%, v/v, pH 2.0) as eluents, at a flow rate of 1 mL/min, with the following gradients:

A1: [80% TFA (5 min), linear gradient from 20 to 40% (5 min) and 40 to 100% (50 min) of CH_3CN]. Triple UV-visible detection was achieved at 260, 650, and 675 nm.

A2: [80% TFA (5 min), linear gradient from 20 to 30% (5 min) and 10 to 90% (50 min) of CH_3CN]. Triple UV-visible detection was achieved at 260, 650, and 675 nm.

A3: [80% TFA (5 min), linear gradient from 20 to 60% (30 min) of CH_3CN]. Dual UV-visible detection was achieved at 260 and 750 nm.

A4: [100% TFA (5 min), linear gradient from 0 to 60% (40 min) of CH_3CN]. Dual UV-visible detection was achieved at 260 and 750 nm.

System B: RP-HPLC (Thermo Hypersil GOLD C_{18} column, 5 μm, 4.6 × 150 mm) with CH_3CN and aq triethylammonium acetate buffer (TEAA, 0.1 M, pH 7.0) as eluents [100% TEAA (10 min), linear gradient from 0 to 60% (30 min) of CH_3CN] at a flow rate of 1 mL/min. Dual UV detection was achieved at 260 and 330 nm.

System C: RP-HPLC (Varian Kromasil C_{18} column, 10 μm, 21.2 × 250 mm) with CH_3CN and aq triethylammonium bicarbonate buffer (TEAB, 50 mM, pH 7.5) as eluents [100% TEAB (20 min), linear gradient from 0 to 30% (60 min) of CH_3CN] at a flow rate of 20 mL/min. Dual UV detection was achieved at 255 and 335 nm.

System D: RP-HPLC (Thermo Hypersil GOLD C_{18} column, 5 μm, 10 × 250 mm) with CH_3CN and 0.1% aq trifluoroacetic acid (aq TFA, 0.1%, v/v, pH 2.0) as eluents, at a flow rate of 5 mL/min, with the following gradients:

D1: [90% TFA (5 min), linear gradient from 10 to 30% (10 min) and 30 to 70% (55 min) of CH_3CN]. UV detection was achieved at 260 nm.

D2: [90% TFA (5 min), linear gradient from 10 to 40% (15 min) and 40 to 70% (40 min) of CH_3CN]. UV detection was achieved at 260 nm.

System E: RP-HPLC (Varian Kromasil C_{18} column, 10 μm, 21.2 × 250 mm) with CH_3CN and 0.1% aq TFA as eluents [95% TFA (5 min), linear gradient from 5 to 25% (5 min) and 5 to 75% (70 min) of CH_3CN] at a flow rate of 20 mL/min. UV-visible detection was achieved at 780 nm.

System F: RP-HPLC (Waters XTerra MS C_{18} column, 5 μm, 7.8 × 100 mm) with CH_3CN and 0.1% aq TFA as eluents, at a flow rate of 2.5 mL/min, with the following gradients:

F1: [100% TFA (5 min), linear gradient from 0 to 36% (18 min) and 36 to 60% (24 min) of CH_3CN]. UV detection was achieved at 260 nm.

F2: [100% TFA (5 min), linear gradient from 0 to 30% (15 min) and 30 to 60% (60 min) of CH_3CN]. Triple UV-visible detection was achieved at 260, 675 and 778 nm.

F3: [100% TFA (5 min), linear gradient from 0 to 30% (15 min), 30 to 35% (10 min) and 35 to 60% (125 min) of CH_3CN]. Dual UV-visible detection was achieved at 675 and 778 nm.

Preparation of NIR5.5-1. *(a) Hemicyanine Intermediate 5*. A solution of *N*-(3-sulfonatopropyl)-1,1,2-trimethylbenzindolinium, inner salt **3** (1 g, 3.0 mmol) and malonaldehyde dianilido hydrochloride (0.88 g, 3.42 mmol) in a mixture of acetic acid (5 mL) and acetic anhydride (5 mL) was heated under reflux. The reaction was checked for completion by UV-visible spectroscopy (the absorption maximum of **3** at $\lambda = 380$ nm has declined whereas the absorption maximum of hemicyanine intermediate **5** has appeared at $\lambda = 455$ nm). After 90 min, the reaction mixture was evaporated under reduced pressure without heating above 40 °C (to avoid the formation of some symmetrical dye). The resulting residue was dissolved in water and lyophilized. The crude hemicyanine intermediate was used without further purification in the next reaction.

(b) Preparation of Cyanine Dye. A solution of crude hemicyanine intermediate **5** (1.44 g, 2.77 mmol) and *N*-(γ-carboxypentyl)-1,1,2-trimethylbenzindolinium, bromine salt **4** (1.11 g, 2.77 mmol) in a mixture of acetic anhydride (5 mL) and dry pyridine (5 mL) was heated under reflux for 30 min. The reaction was checked for completion by UV-visible spectroscopy (the absorption maximum of **5** at $\lambda = 455$ nm has disappeared whereas the absorption maximum of cyanine dye **NIR5.5-1** has appeared at $\lambda = 679$ nm). The reaction mixture was evaporated under reduced pressure, dissolved in water, and lyophilized to give a blue solid (2.86 g). One gram of this crude product was purified by chromatography on a silica gel column (40 g) with a step gradient of MeOH (0−5%) in dichloromethane as the mobile phase. After drying under vacuum, **NIR5.5-1** was obtained as a blue solid (0.67 g, 0.97 mmol, yield 80%). $R_f = 0.35$ (CH_2Cl_2/MeOH 9/1, v/v). ^{1}H NMR (300 MHz, DMSO-d_6): δ 8.52 (t, 2H, $J = 13.2$ Hz), 8.29 (d, 2H, $J = 8.7$ Hz), 8.11 (m, 4H), 7.86 (d, 1H, $J = 9.0$ Hz), 7.77 (d, 1H, $J = 9.0$ Hz), 7.71 (t, 2H, $J = 7.5$ Hz), 7.54 (t, 2H, $J = 7.5$ Hz), 7.32 (s, 1H, NH), 7.15 (s, 1H, NH), 6.98 (s, 1H, NH), 6.65 (t, 1H, $J = 12.4$ Hz), 6.55 (d, 1H, $J = 13.9$ Hz), 6.41 (d, 1H, $J = 13.6$ Hz), 4.43 (m, 2H), 4.27 (m, 2H), 2.67 (t, 2H, $J = 6.4$ Hz), 2.25 (t, 2H, $J = 6.8$ Hz), 2.11−2.05 (m, 2H), 2.01 (s, 6H, Me), 1.99 (s, 6H, Me), 1.81−1.46 (m, 6H). HPLC (system A1): $t_R = 20.5$ min, purity >95%. UV-visible (DMSO, 25 °C): $\lambda_{max} = 688$ nm (147 000 M^{-1} cm^{-1}). UV-visible (EtOH, 25 °C): $\lambda_{max} = 681$ nm (156 000 M^{-1} cm^{-1}). Φ_F (DMSO, 25 °C): 0.27. Φ_F (EtOH, 25 °C): 0.17. MS (ESI, positive mode): *m/z* 691.40 $[M + H]^+$, 713.47 $[M + Na]^+$, 1381.40 $[2M + H]^+$, 1404.53 $[2M + Na]^+$, calcd exact mass for $C_{42}H_{46}N_2O_5S$ 690.91.

Trisulfonated Linker (9). A mixture of 3,5-diaminobenzoic acid (0.25 g, 1.6 mmol), sodium 2-bromoethanesulfonate (1.39 g, 6.6 mmol), KI (0.29 g, 1.8 mmol), and NaOH (64 mg, 1.6 mmol) in deionized water (3 mL) was heated under reflux for 4 days. After 24 and 48 h, further amounts of sodium bromoethanesulfonate (2 × 1.34 g, 2 × 6.4 mmol) and NaOH (2 × 0.64 mL of an aq 5 N solution, 2 × 3.2 mmol) were added. The reaction was checked for completion by RP-HPLC (system B) and purified by RP-HPLC (system C, 12 injections). The product-containing fractions were twice lyophilized (to remove excess of TEAB salts) to give **9** as a highly hygroscopic white powder (yield 36%). ^{1}H NMR (300 MHz, D_2O): δ 6.78 (s, 1H), 6.71 (s, 1H), 6.32 (s, 1H), 3.77 (m, 6H, N−CH_2−CH_2-SO_3^-), 3.11 (m, 30H, TEA & N$CH_2CH_2SO_3^-$), 1.21 (t, 36H, TEA, $J = 7.2$ Hz). ^{13}C NMR (75.5 MHz, D_2O): δ 175.1, 148.8, 147.7, 138.7, 104.9, 104.2, 100.8, 49.8 (2C), 48.3 (4C),

48.1 (4C), 46.9 (12C), 39.9 (2C), 8.5 (12C). HPLC (system B): $t_R = 7.0$ min. MS (ESI, negative mode): *m/z* 157.93 $[M - 3H]^{3-}$, 237.33 $[M - 2H]^{2-}$, 475.20 $[M - H]^-$, calcd for $C_{13}H_{20}N_2O_{11}S_3$ (acid form) 476.50.

Preparation of Trisulfonated Linker, Succinimidyl Ester (10). A mixture of trisulfonated linker **9** (50 mg, 56.7 μmol) and *N*-hydroxysuccinimide (7.2 mg, 62.0 μmol) was dissolved in dry DMF (100 μL). DCC (12.8 mg, 62.0 μmol) was added, and the resulting reaction mixture was stirred at room temperature for 20 h. After 3 h, further amounts of *N*-hydroxysuccinimide (5.8 mg, 50.8 μmol) and DCC (10.7 mg, 50.8 μmol) were added. The reaction was checked for completion by RP-HPLC (system B), and the resulting succinimidyl ester **10** was used without further purification. HPLC (system B): $t_R = 17.8$ and 18.6 min (broad peak, compared to $t_R = 7.0$ min for the free acid **9**). Two peaks are observed due to a counterion effect with the triethylammonium cations of HPLC eluent.

NIR5.5-2. A solution of cyanine-based amino acid **6** (39.5 mg, 45.5 μmol) in dry NMP (1 mL) was added to the solution of crude succinimidyl ester **10** (56.7 μmol) and DIEA (57.6 μL, 330 μmol). The resulting reaction mixture was protected from light and stirred at room temperature for 24 h. The reaction was checked for completion by RP-HPLC (system A1). Finally, the reaction mixture was quenched by dilution with aq TFA 0.1% and purified by RP-HPLC (system D1, 6 injections). Two products identified as the Cy 5.5 analogue **NIR5.5-2** (t_R = 27.0−28.8 min) and its corresponding succinimidyl ester **11** (29.4−31.2 min) were isolated. The product-containing fractions were lyophilized to give **NIR5.5-2** and **11** as blue amorphous powders (combined yield 70%). ^{1}H NMR (300 MHz, DMSO-d_6 + TFA): δ 8.56 (m, 2H), 8.47 (t, 1H, $J = 12.8$ Hz), 8.27 (m, 2H), 8.11 (m, 4H), 7.84−7.68 (m, 4H), 7.53 (m, 2H), 7.28 (bs, NH), 7.07 (bs, 1H, NH), 7.01 (bs, 1H, NH), 6.89 (bs, 1H, NH), 6.72 (t, 1H, $J = 12.5$ Hz), 6.44 (dd, 2H), 4.28 (m, 4H), 3.75 (m, 6H, $NCH_2CH_2SO_3^-$), 2.83 (m, 2H), 2.72 (m, 6H, $NCH_2CH_2SO_3^-$), 2.24 (t, 2H, $J = 7.2$ Hz), 1.99 (s, 12H), 1.83−1.01 (m, 10H). All spectroscopic characterizations are reported only for the free acid **NIR5.5-2** except for the HPLC and MS analyses. HPLC (system A1): $t_R = 17.8$ min (**NIR5.5-2**), 18.9 min (**11**). UV-visible (PBS, pH 7.4, 25 °C): $\lambda_{max} = 680$ nm (197 000 M^{-1} cm^{-1}). UV-visible (DMSO, 25 °C): $\lambda_{max} = 688$ nm (147 000 M^{-1} cm^{-1}). Φ_F (PBS, pH 7.4, 25 °C): 0.05. Φ_F (DMSO, 25 °C): 0.05. MS (MALDI-TOF, positive mode, CHCA matrix): *m/z* 1098.89 $[M + H]^+$. MS (ESI, negative mode): *m/z* 400.93 $[M - 3H+TEA]^{3-}$, 601.87 $[M - 2H+TEA]^{2-}$, calcd for $C_{56}H_{66}N_5O_{12}S_3$ (**NIR5.5-2**, acid form) 1097.37. MS (MALDI-TOF, positive mode, CHCA matrix): *m/z* 1195.93 $[M + H]^+$, calcd for $C_{60}H_{70}N_6O_{14}S_3$ (**11**, acid form) 1195.45.

Preparation of Thiol-Reactive NIR5.5-2 Derivative (15). *(a) Preparation of **NIR5.5-2** Carboxylic Acid, Succinimidyl Ester **11**.* Free carboxylic acid dye **NIR5.5-2** (10.5 mg, 9.6 μmol) was introduced into a Reacti-Vial and dissolved in 140 μL of dry NMP. A 20 μL amount of a solution of TSTU reagent in dry NMP (2.88 mg, 9.6 μmol) and 11.7 μL of DIEA (67.2 μmol) were added, and the resulting reaction mixture was protected from light and stirred at room temperature for 1 h. The reaction was checked for completion by RP-HPLC (system A1) and the resulting succinimidyl ester **11** was used without further purification. HPLC (system A1): t_R = 18.8 min (compared to $t_R = 17.8$ min for **NIR5.5-2** carboxylic acid, *vide supra*).

*(b) Synthesis of **NIR5.5-2** Amine **14**.* Ethylenediamine dihydrochloride (150 mg, 1.152 mmol) was dissolved in a mixture of deionized water (0.9 mL) and DMF (10 mL). The crude reaction mixture containing the succinimidyl ester **11** and a 10% solution of DIEA in DMF (0.9 mL, 537 μmol) were sequentially added, and the resulting reaction mixture was protected from light and stirred at room temperature for 1 h. The reaction was checked for completion by RP-HPLC (system A1), and the mixture was evaporated to dryness. The resulting residue was purified by RP-HPLC (system D2, 2 injections). The product-containing fractions were lyophilized to give the **NIR5.5-2** amine **14** as a blue amorphous powder (8.0 mg, yield 73%). HPLC (system A1): $t_R = 16.6$ min, purity >95%. MS (MALDI-TOF, positive mode, CHCA matrix): *m/z* 1140.98 $[M + H]^+$, calcd exact mass for $C_{58}H_{73}N_7O_{11}S_3$ 1140.46.

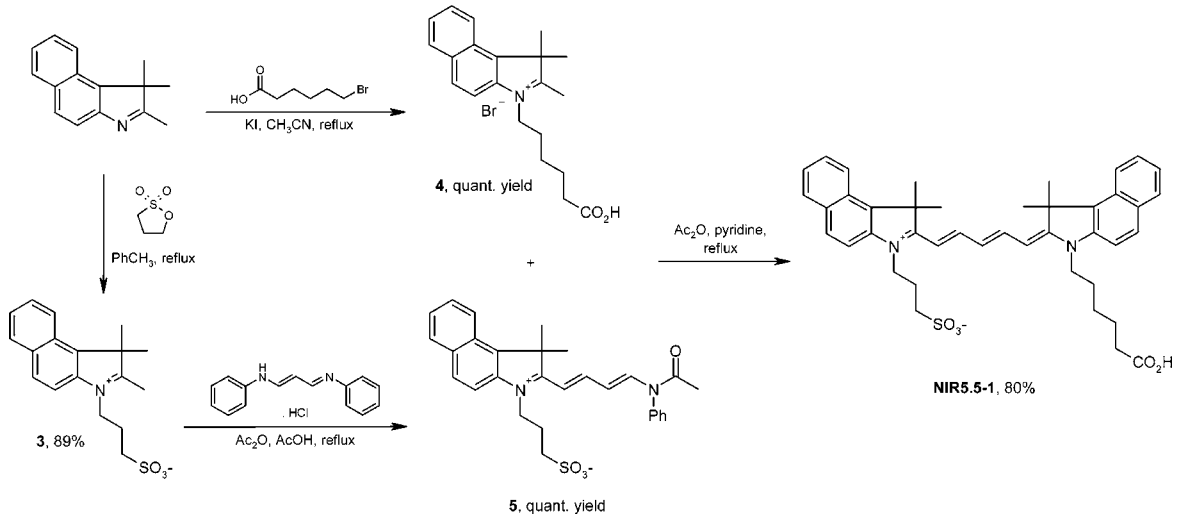
*(c) Preparation of **NIR5.5-2** SIAB Derivative **15**.* **NIR5.5-2** amine **14** (3.3 μmol) was dissolved in NMP (200 μL). $NaHCO_3$ (2.7 mg, 32.1 μmol) and a solution of SIAB reagent (2.5 mg, 6.3 μmol) in NMP (200 μL) were sequentially added. Thereafter, 0.1 M $NaHCO_3$ buffer (pH 8.5, 1 mL) was added, and the resulting reaction mixture was protected from light and stirred at room temperature for 2 h. The reaction was checked for completion by RP-HPLC (system A2). Finally, the reaction mixture was quenched by dilution with aq TFA 0.1% and purified by RP-HPLC (system D2, 2 injections). The product-containing fractions were lyophilized to give the thiol-reactive **NIR5.5-2** derivative **15** as a blue amorphous powder (3.8 mg, yield 80%). HPLC (system A2): $t_R = 23.2$ min (broad peak). Φ_F (PBS, pH 7.4, 25 °C): 0.056. Φ_F (DMSO, 25 °C): 0.145. MS (MALDI-TOF, positive mode, CHCA matrix): *m/z* 1299.96 $[(M - I)+H]^+$, 1427.85 $[M + H]^+$, calcd exact mass for $C_{67}H_{79}IN_8O_{13}S_3$ 1427.52.

NIR7.0-2. A mixture of crude chloro-substituted heptamethine sulfocyanine dye **12** (220 mg, 0.31 mmol) and 3-mercaptopropionic acid (107 μL, 1.22 mmol) in dry DMF (15 mL) was heated under reflux for 40 min. The reaction was checked for completion by RP-HPLC (system A3), and the mixture was evaporated to dryness. The resulting residue was purified by RP-HPLC (system E, three injections, t_R = 24.5−26.5 min). The product-containing fractions were lyophilized to give **NIR7.0-2** as a green amorphous powder (187 mg, 0.24 mmol, yield 80%). ^{1}H NMR (300 MHz, DMSO-d_6 + TFA-d_1): δ 8.70 (d, 2H, $J = 13.9$ Hz), 7.58 (d, 2H, $J = 7.5$ Hz), 7.49−7.37 (m, 4H), 7.24 (t, 2H, $J = 7.5$ Hz), 6.48 (d, 2H, $J = 13.9$ Hz), 4.34 (bt, 4H, $N^+CH_2CH_2CH_2SO_3^-$), 2.99 (t, 2H, $J = 6.8$ Hz), 2.66−2.49 (m, 10H), 2.05−1.80 (m, 6H), 1.68 (s, 12H). HPLC (system A3): $t_R = 20.6$ min, purity > 95%. HPLC (system A4): t_R = 34.6 min, purity >95%. UV-visible (PBS, pH 7.4, 25 °C): λ_{max} = 777 nm (120 000 M^{-1} cm^{-1}). UV-visible (DMSO, 25 °C): $\lambda_{max} = 802$ nm (146 000 M^{-1} cm^{-1}). UV-visible (EtOH, 25 °C): $\lambda_{max} = 790$ nm (171 000 M^{-1} cm^{-1}). Φ_F (PBS, pH 7.4, 25 °C): 0.025. Φ_F (DMSO, 25 °C): 0.092. MS (ESI, positive mode): *m/z* 769.60 $[M + H]^+$, MS (ESI, negative mode): *m/z* 767.80 $[M - H]^-$, calcd exact mass for $C_{39}H_{48}N_2O_8S_3$ 769.02.

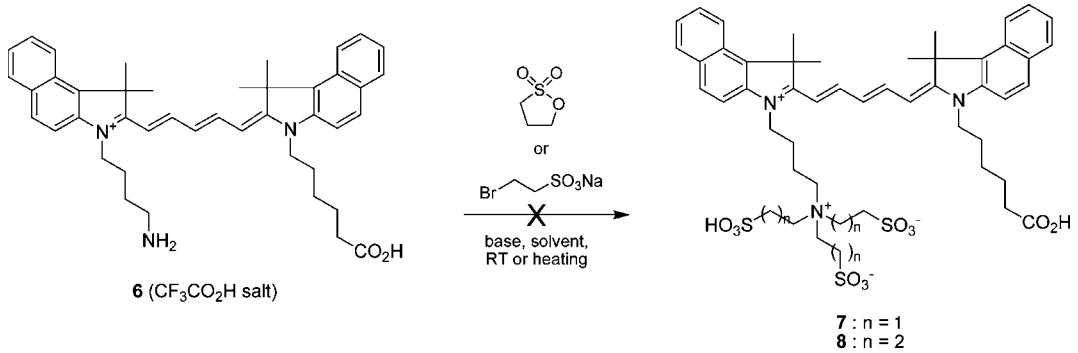
Preparation of NIR7.0-2 Carboxylic Acid, Succinimidyl Ester (13). NIR7.0-2 carboxylic acid (4.12 mg, 5.36 μmol) was introduced into a Reacti-Vial and dissolved in 50 μL of dry NMP. A 50 μL amount of a solution of TSTU reagent in dry NMP (1.94 mg, 6.45 μmol) and 1.86 μL of DIEA (10.72 μmol) were added, and the resulting reaction mixture was protected from light and stirred at room temperature for 35 min. The reaction was checked for completion by RP-HPLC (system A4), and the resulting succinimidyl ester **13** was used without further purification. HPLC (system A4): $t_R = 35.6$ min (compared to $t_R = 34.6$ min for **NIR7.0-2** carboxylic acid, *vide supra*).

Synthesis of Ac-Cys(StBu)-Asp-Glu-Val-Asp-Lys(NIR7.0-2)-NH_2(17). A 5.66 mg amount of crude peptide Ac-Cys(StBu)-Asp-Glu-Val-Asp-Lys-NH_2 **16** (5.95 μmol, weighed in a 1.0 mL Eppendorf tube) was dissolved in 100 μL of dry NMP, and 4.14 μL of DIEA (23.76 μmol) was added. After complete solubilization by vortexing, the resulting solution was added to the crude reaction mixture containing the succinimidyl ester of

Scheme 1



Scheme 2



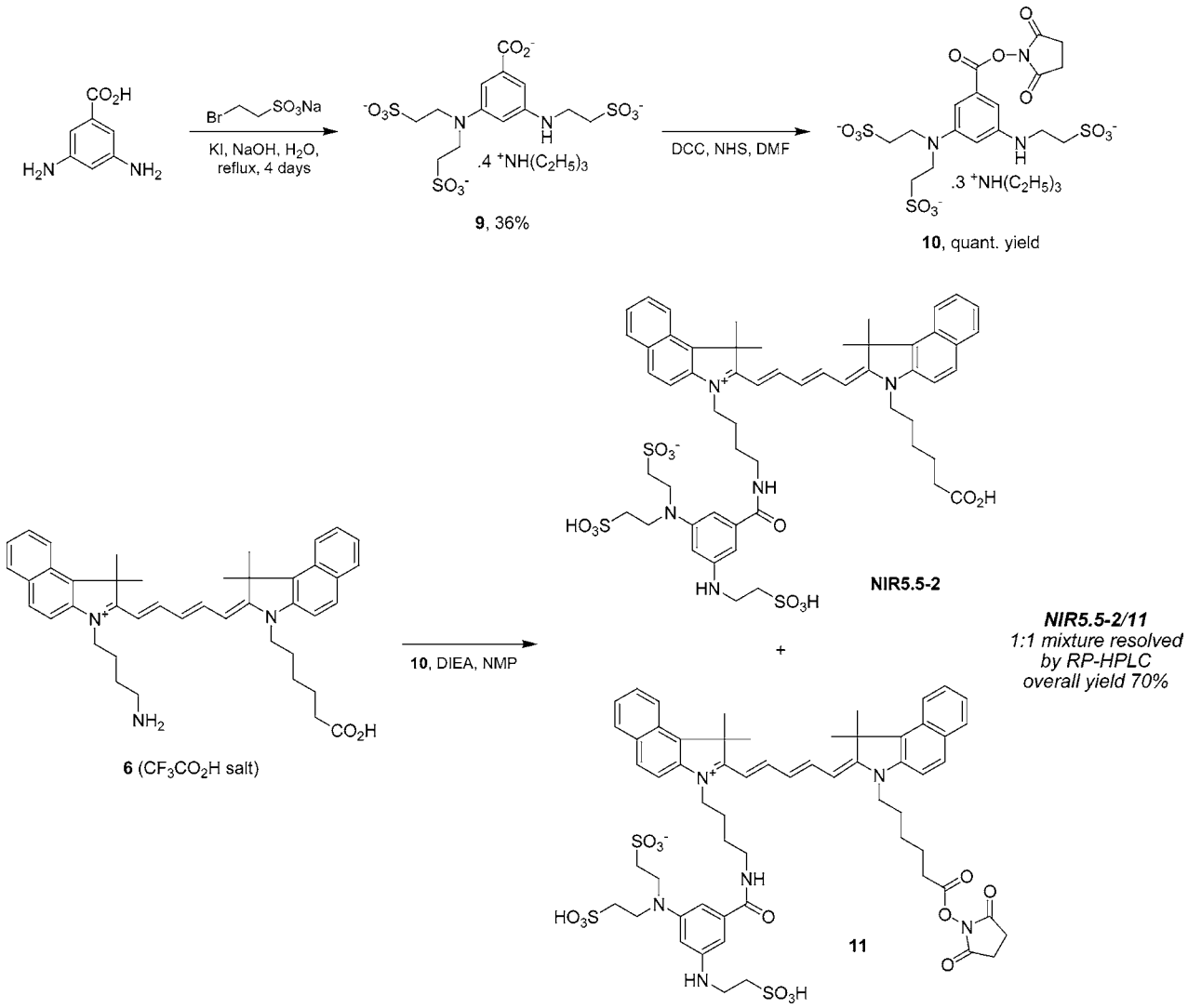
NIR7.0-2. The resulting reaction mixture was protected from light and stirred at room temperature for 1 h. The reaction was checked for completion by RP-HPLC (system A4). Finally, the reaction mixture was quenched by dilution with 1 mL of aq TFA 0.1% and purified by RP-HPLC (system F1, 2 injections, t_R = 27.0−28.5 min). The product-containing fractions were lyophilized to give the peptide-**NIR7.0-2** conjugate **17** as a green amorphous powder. Quantification was achieved by UV-visible measurements at λ_{max} = 777 nm of **NIR7.0-2** by using the ϵ value 120 000 M^{-1} cm^{-1} (yield estimated after RP-HPLC purification: 60%). HPLC (system A4): t_R = 35.0 min, purity 91%. MS (MALDI-TOF, positive mode, CHCA matrix): *m/z* 796.78 $[M + 2H]^{2+}$, 1590.03, $[M + H]^+$, 1625.99 $[M + K]^+$. MS (ESI, positive mode): *m/z* 825.00 $[M + Na + K]^{2+}$, 1609.60 $[M + Na]^+$, 1625.67 $[M + K]^+$, calcd exact mass for $C_{72}H_{102}N_{10}O_{20}S_5$ 1587.99.

Removal of *tert*-butylthio Group. Peptide Ac-Cys(StBu)-Asp-Glu-Val-Asp-Lys(**NIR7.0-2**)-NH_2 **17** (5.7 mg, 3.6 μmol) was introduced into a Reacti-Vial and dissolved in 0.1 M $NaHCO_3$ buffer (pH 8.5, 250 μL). A solution of DTT (8.03 mg in 500 μL, 52.1 μmol) in 0.1 M $NaHCO_3$ buffer (pH 8.5) was added. The reaction mixture was protected from light and stirred at room temperature for 2 h. The reaction was checked for completion by RP-HPLC (system A4). Finally, the reaction mixture was quenched by dilution with aq TFA 0.1% (1 mL) and purified by RP-HPLC (system F1, 2 injections, t_R = 26.5−27.5 min). The product-containing fractions were lyophilized to give the free sulfhydryl containing peptide-**NIR7.0-2** conjugate **18** as a green amorphous powder. Quantification was achieved by UV-visible measurements at λ_{max} = 777 nm of **NIR7.0-2** by using the ϵ value 120 000 M^{-1} cm^{-1} (estimated quantitative yield after RP-HPLC purification). HPLC (system A4): t_R = 33.8 min, purity >95%. MS (ESI, positive mode): *m/z* 752.13 $[M + 2H]^{2+}$, 1502.67 $[M + H]^+$; MS (ESI, negative mode): *m/z* 1500.60 $[M - H]^-$, calcd exact mass for $C_{68}H_{94}N_{10}O_{20}S_4$ 1499.82.

Synthesis of Ac-Cys(NIR5.5-2)-Asp-Glu-Val-Asp-Lys-(NIR7.0-2)-NH_2 (19). Peptide Ac-Cys-Asp-Glu-Val-Asp-Lys-(**NIR7.0-2**)-NH_2 **18** (2.3 mg, 1.56 μmol) was introduced into a Reacti-Vial and dissolved in 0.1 M $NaHCO_3$ buffer (pH 8.5, 200 μL). A 300 μL amount of a solution of iodoacetyl derivative **15** (0.75 mg, 0.52 μmol) in 0.1 M $NaHCO_3$ buffer (pH 8.5) was added. The reaction mixture was protected from light and stirred at room temperature for 2 h. The reaction was checked for completion by RP-HPLC (system F2). Finally, the reaction mixture was quenched by dilution with aq TFA 0.1% (1 mL) and purified by RP-HPLC (system F3, 2 injections, t_R = 45.0−46 min). Because of the small difference in polarity between the peptide **19** and iodoacetamido derivative **15**, it is essential to use a slow linear gradient of increasing acetonitrile (0.2%/min) in aq TFA to get peptide **19** in a pure form. The product-containing fractions were lyophilized to give the peptide Ac-Cys(**NIR5.5-2**)-Asp-Glu-Val-Asp-Lys(**NIR7.0-2**)-NH_2 **19** as a blue-green amorphous powder. Stock solution of this fluorogenic caspase-3 substrate was prepared in HPLC grade water and UV-visible quantification was achieved in DMSO at λ_{max} of **NIR7.0-2** by using the ϵ value 146 000 M^{-1} cm^{-1} (yield after RP-HPLC purification: 25%). HPLC (system F2): t_R = 39.9 min, purity >95%. UV-visible (water, 25 °C): λ_{max} = 649, 676 and 800 nm. UV-visible (DMSO, 25 °C): λ_{max} = 689 and 799 nm. MS (ESI, positive mode): *m/z* 1059.20 $[M + 2H]^{2+}$; calcd exact mass for $C_{99}H_{130}N_{16}O_{28}S_4$ 2120.49.

Optical Properties of Water-Soluble NIR Cyanine Dyes. The absorption spectra of NIR cyanine dyes **NIR5.5-1**, **NIR5.5-2**, and **NIR7.0-2** were recorded (220−900 nm) in deionized

Scheme 3



water, DMSO, and PBS (concentration: 1.0−5.0 μM) at 25 °C. Emission spectra were recorded under the same conditions after excitation at a wavelength 10 nm below the corresponding λ_{max} (excitation and emission slit = 5 nm). Relative quantum yields were measured in DMSO and/or PBS at 25 °C by a relative method using either sulfocyanine dye Cy 5.0 (for **NIR5.5-1** and **NIR5.5-2**, $\Phi_F = 0.20$ in PBS (*14*)) or ICG (for **NIR7.0-2**, $\Phi_F = 0.106$ in DMSO (*32*)) as a standard.

Steady-State Fluorescence Quenching Experiments of NIR5.5-2 SIAB Derivative 15 by NIR7.0-2. A Stern−Volmer plot for **NIR7.0-2** was obtained at 25 °C as follows. A solution of **NIR5.5-2** SIAB derivative **15** in PBS (0.72 μM) was treated with an increased amount of **NIR7.0-2** from 0 to 7.2 μM in PBS. The integrated fluorescence intensity F (area under the corrected emission curve in the range 670−900 nm after excitation at λ = 660 nm) was measured, and the relative fluorescence intensity F_0/F was plotted versus **NIR7.0-2** concentration. A straight line was obtained in the concentration range. The following equation was used to derive the Stern−Volmer quenching constant:

$$F_0/F = 1 + K_{sv}[\textbf{NIR7.0-2}]$$

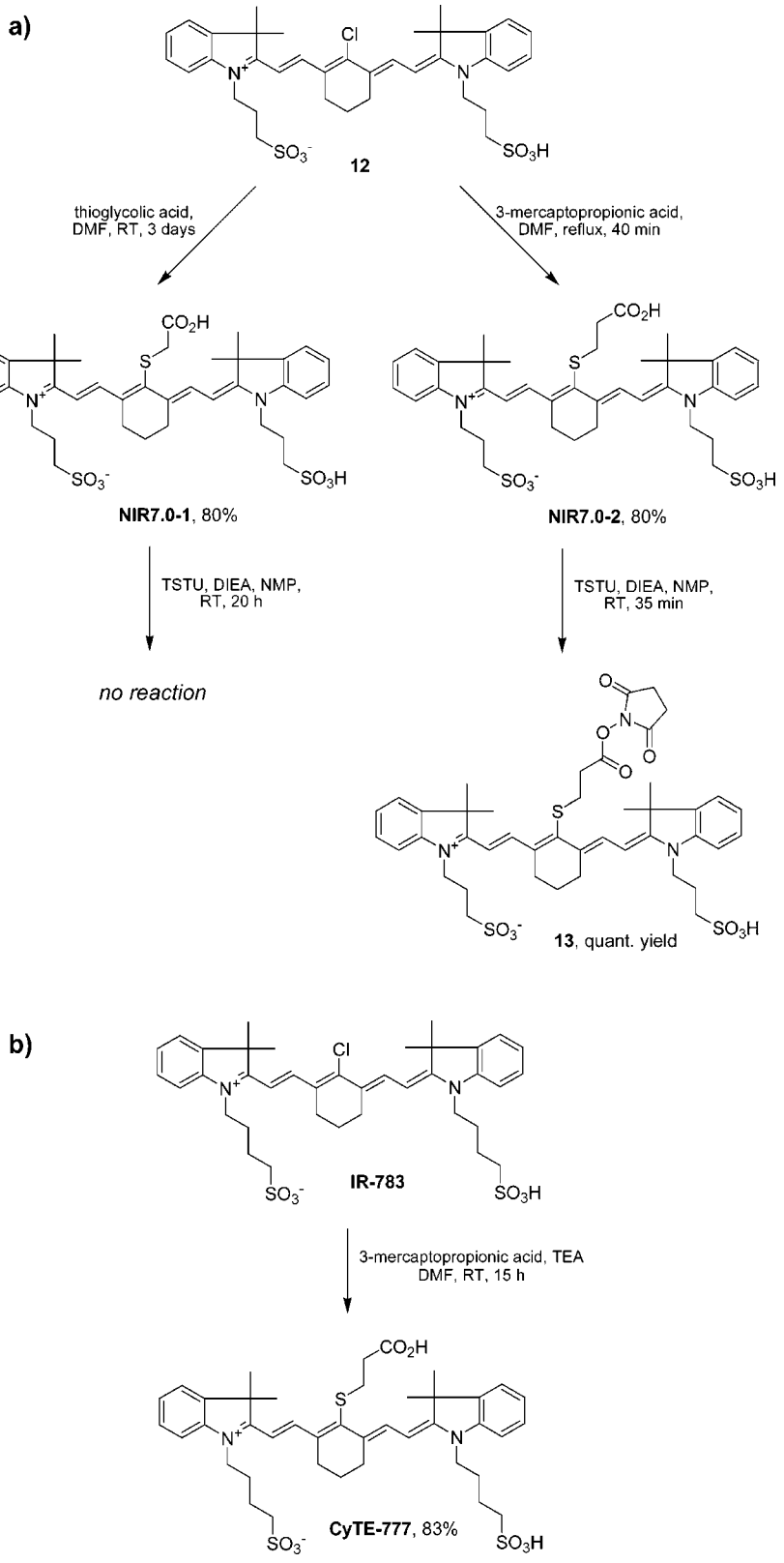
where F_0 is the integrated unquenched fluorescence intensity of **15** and K_{sv} is the static Stern−Volmer quenching constant (K_{sv} = 67500 M^{-1}, R^2 = 0.983).

***In Vitro* Peptide Cleavage by Recombinant Human Caspase-3.** A 1.0 μM solution of peptide **19** was prepared in 50 μL of caspase-3 buffer (100 mM NaCl, 40 mM HEPES, 10 mM DTT, 1 mM EDTA, 10% (w/v) sucrose and 0.1% (w/v) CHAPS, pH 7.4) and transferred into an ultra-micro fluorescence cell. A 2 μL amount of human recombinant caspase-3 (3.2×10^{-3} U) was added, and the resulting mixture was incubated at 37 °C. After excitation at 670 and 775 nm (excitation slit = 5 nm), fluorescence emission at 705 and 805 nm (emission slit = 5 nm) was monitored over time with measurements recorded every 5 s. Control experiment with BSA was performed under the same conditions by adding 2 μL of 1% (w/v) aq solution of this protein.

RESULTS AND DISCUSSION

Synthesis of the Cy 5.5 Analogues. Sulfobenzoindocyanine dye Cy 5.5 **1** is probably one of the most widely used NIR dyes as fluorescent reporter group in numerous molecular probes designed to facilitate the detection of molecular processes in solutions and living tissues (*33*−*36*). Indeed, this compound fulfils the most requirements expected for an ideal biomarker (i.e., narrow excitation and emission peaks in the NIR range, high quantum yield, high chemical and photostability, reasonable aqueous solubility, and a reactive carboxyl functional group for bioconjugation). However, as mentioned in Introduction, the multistep synthesis reported in 1996 by Mujumdar et al. (*13*) is not suitable for a convenient preparation of Cy 5.5 dye at a

Scheme 4



gram scale in good yields. We started the study related to the development of improved methods for the synthesis of cyanine dyes in our laboratory with the preparation of the Cy 5.5 analogue **NIR5.5-1**. Despite the presence of a single water-solubilizing sulfonated group on the cyanine core, we thought that the covalent association of **NIR5.5-1** with some biomolecules could lead to NIR fluorescent molecular probes suitable for various biomedical applications. Although this dye is commercially available (FEW Chemicals GmBH (www.few.de)), there is no detailed experimental procedure for its efficient synthesis. Thus, we have developed a practical high-yield synthesis of **NIR5.5-1** from relatively inexpensive precursors (Scheme 1). The nitrogen atom of 2,3,3-trimethyl-3*H*-indole was alkylated with propanesultone in dry toluene under reflux for 24 h to afford compound **3** in 89% yield, which was treated with malonaldehyde dianilido hydrochloride in a 1:1 mixture

Scheme 5

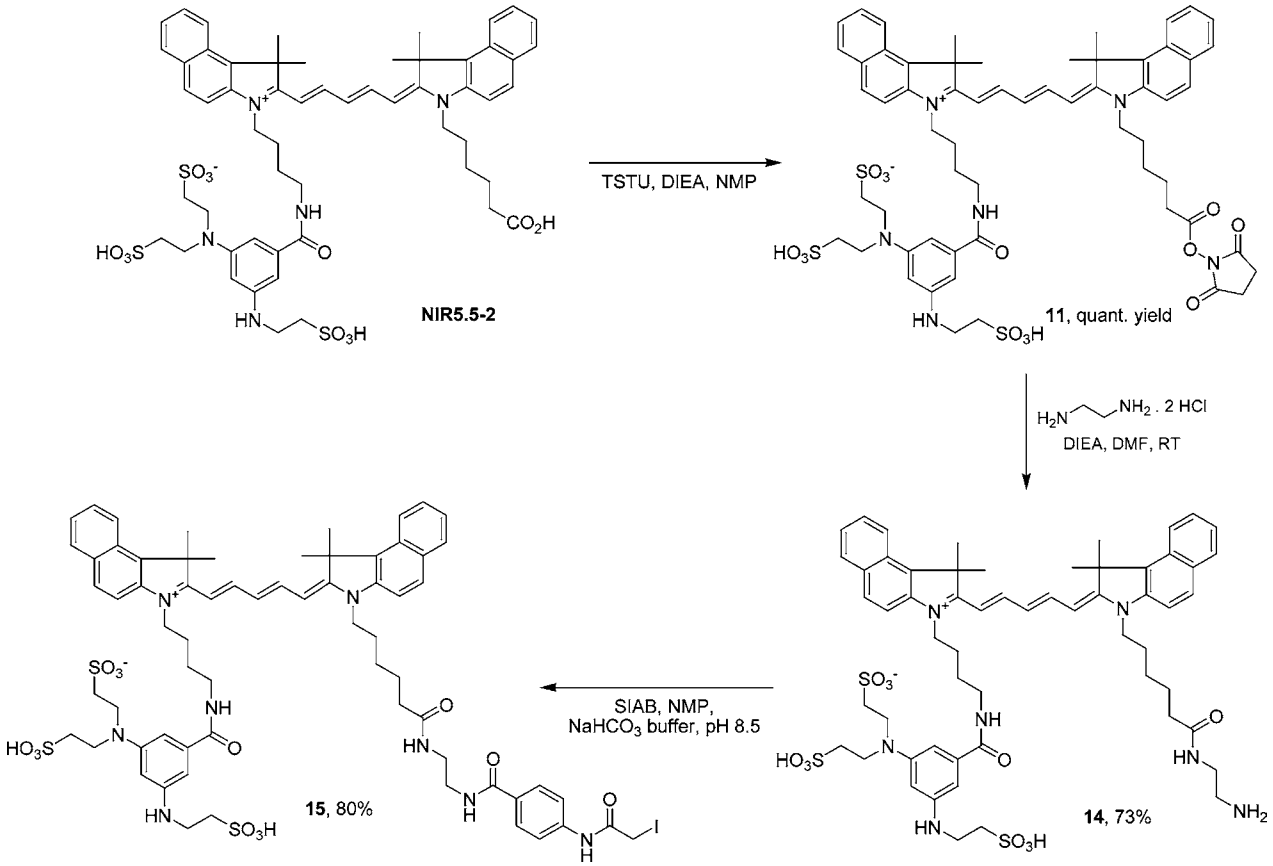


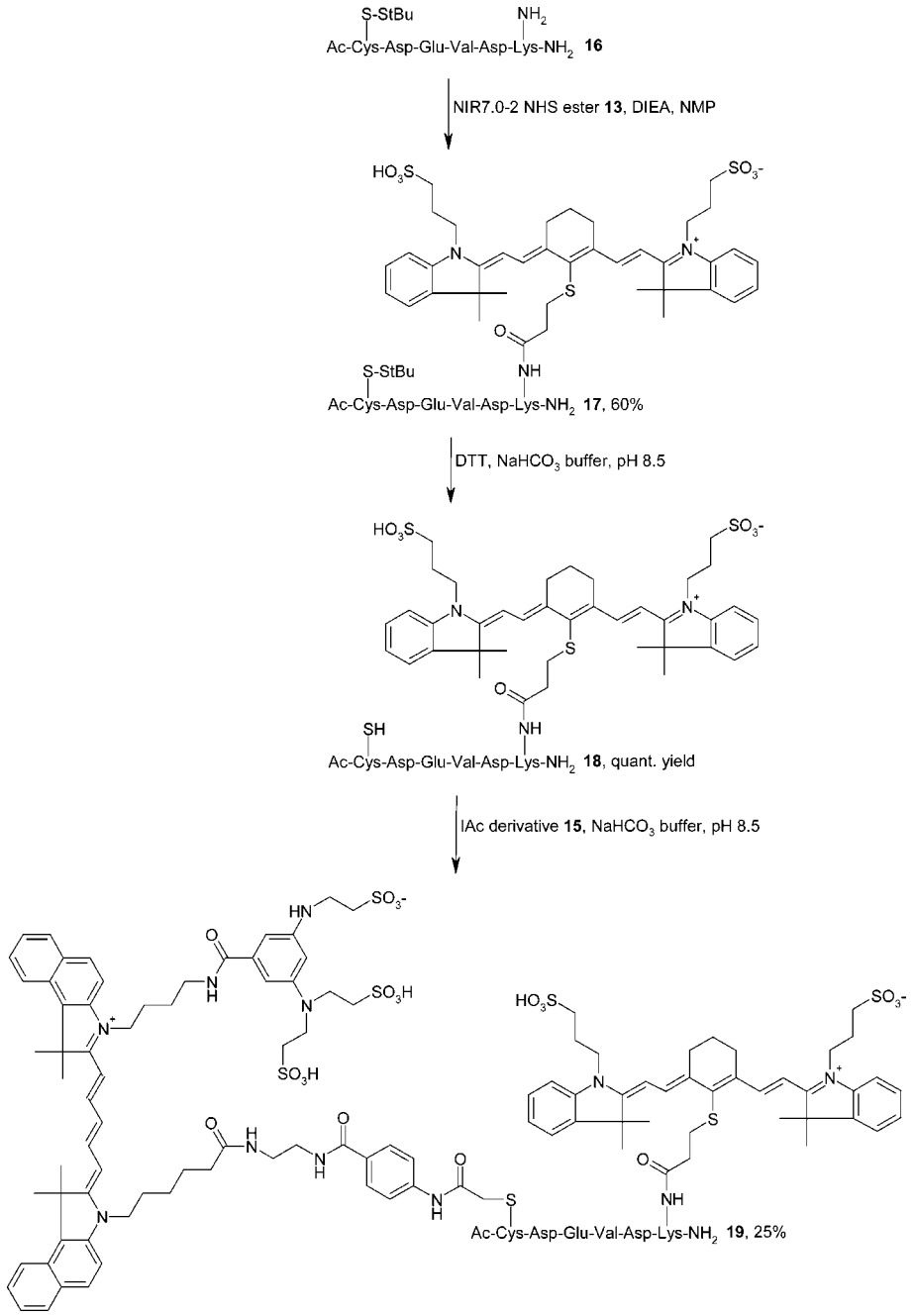
Table 1. Optical Properties of NIR Cyanine Dyes

compound	solvent	$\lambda_{max,abs}$ (nm)	$\lambda_{max,em}$ (nm)	Stokes shift (nm)	ϵ (M^{-1} cm^{-1})	Φ_F [b]
Cy 5.5[a]	PBS	674	694	20	195000	0.23
NIR5.5-1	DMSO	688	711	23	147000	0.27
NIR5.5-2	DMSO	688	714	26	147000	0.05
NIR5.5-2	PBS	680	710	30	197000	0.05
Cy 7.0[a]	PBS	750	777	27	200000	-
NIR7.0-2	DMSO	802	818	16	146000	0.09
NIR7.0-2	PBS	777	798	21	120 000	0.025

[a] Values reported by Mujumdar et al. (*13*, *14*). [b] Determined at 25 °C by using either sulfocyanine dye Cy 5.0 (for **NIR5.5-1** and **NIR5.5-2**, $\Phi_F = 0.20$ in PBS (*14*)) or ICG (for **NIR7.0-2**, $\Phi_F = 0.106$ in DMSO (*32*)) as a standard.

of acetic acid and acetic anhydride under reflux for 90 min to obtain hemicyanine intermediate **5** in a quantitative yield. Reaction of **5** with the carboxypentyl indole derivative **4** in a 1:1 mixture of acetic anhydride and pyridine under reflux for 30 min furnished **NIR5.5-1** which was isolated in good yield (80%) by silica gel chromatography. All spectroscopic data, especially NMR and mass spectrometry, were in agreement with the structure assigned. However, preliminary experiments on bioconjugation of **NIR5.5-1** to hydrophilic peptides have shown that the resulting fluorescent conjugates are poorly soluble in water and related aqueous buffers (see Supporting Information). We wished to improve the water solubility of this Cy 5.5 analogue by increasing the number of sulfonated groups on the backbone and to be able to modulate this solubility by varying the nature and the number of solubilizing moieties. Yet possibilities offered for such a further modification of **NIR5.5-1** dye were limited, and modulation of the solubility required starting again the synthesis from the beginning. In an effort to develop an improved and flexible synthetic methodology enabling an easy access to numerous analogues of this NIR fluorophore, we have explored the postsynthetic derivatization of the cyanine-based amino acid **6** (*22*, *23*). This amino acid offers two amenable groups; thus, the derivatization could be undertaken either on the amino group (for instance through selective acylation reactions) or on the carboxylic acid, and derivatizations or bioconjugations could be led successively on the two reactive functions. Moreover, the introduction of water-solubilizing groups after completion of the cyanine synthesis seems to be an interesting approach because it avoids the use of a highly polar naphthalene derivative (for instance, as described for the synthesis of Cy 5.5 itself, 6-amino-1,3-naphthalenedisulfonic acid) as starting material whose the restricted solubility in organic solvents made synthesis and purification of cyanine dye and its intermediates tricky. The backbone of this fluorescent amino acid **6** (two naphthalene rings and a pentamethine chain) has been chosen to get the same spectral properties as that of cyanine dye Cy 5.5. Furthermore, it is conveniently prepared using a five-step reaction (overall yield 42%) and could be purified by flash-chromatography on RP-C_{18} silica gel column at gram quantities. Therefore, we first tried to directly convert **6** into the sulfonated derivatives **7** and **8** by successive alkylations of the amino group with 1,3-propanesultone or sodium 2-bromoethanesulfonate. As described in a preliminary report (*22*, *23*), all our attempts to get **7** or **8** failed (Scheme 2). The amino acid **6** is either completely recovered or converted into decomposition products which were not characterized. Since the sulfonation of aniline derivatives is well described in the literature (*37*, *38*), we have explored the synthesis of an original polysulfonated linker derived from cheap, commercially available 3,5-diaminobenzoic acid and its subsequent covalent attachment to the aminobutyl arm of **6** (Scheme 3). Reaction of 3,5-diaminobenzoic acid with a large excess of sodium 2-bromoethanesulfonate and KI in aq NaOH under reflux for 4 days gave the trisulfonated derivative **9** as the major compound. This highly polar linker was purified by semipreparative RP-HPLC. For this latter chromatographic

Scheme 6



purification, it was essential to use a volatile aqueous buffer such as triethylammonium bicarbonate buffer (TEAB, 50 mM, pH 7.5) as eluent both (1) to get a good separation between **9** and the other residual sulfonated species and (2) to avoid after lyophilization its contamination with salts which may further react with the reagents used for the conversion into active ester in the next steps. Thereafter, benzoic acid **9** was quantitatively converted into the corresponding *N*-hydroxysuccinimidyl ester **10** by treatment with DCC and *N*-hydroxysuccinimide (NHS) in dry DMF. This reaction was found to be very slow (20 h) and required the use of an excess of reagents (2 equiv) to go to completion. Finally, acylation of amino acid **6** with this crude active ester **10** in near stoichiometric amounts in dry NMP in the presence of DIEA (7 equiv) gave a 1:1 mixture of dye **NIR5.5-2** and its NHS ester **11** which was readily purified by semipreparative RP-HPLC (overall yield 70%). Their structures were confirmed by detailed measurements, including MALDI-TOF mass spectrometry and NMR analyses. As expected, **NIR5.5-2** was found to be perfectly soluble in water and related aqueous buffers in the concentration range (1 μM to 5 mM) suitable for biomolecular labeling applications.

Synthesis of the Cy 7.0 Analogue. A variety of water-soluble Cy 7.0 analogues with a functional reactive group at cyclohexenyl bridge included in the heptamethine chain have been already reported in the literature (*15*−*20*). Most of them have been obtained from readily available chloro cyanine dye **12**. However, most of these dyes are not optimal for applications as biological markers. Although they are water-soluble, cyanine dyes containing an additional aryl group in the meso position through an ether or a thioether bridge show an increased tendency to aggregate in aqueous solution (*18*), and the aryl-(thio)ether linkage in some of these fluorophores is fragile and thus susceptible to cleavage (*39*). To circumvent these problems and further optimize the chemical and photochemical properties of these NIR fluorophores, Lee et al. have recently reported the preparation of heptamethine cyanine dyes with a robust C−C bond at the central position of the chromophore by an efficient Suzuki−Miyaura palladium-catalyzed cross-coupling reaction

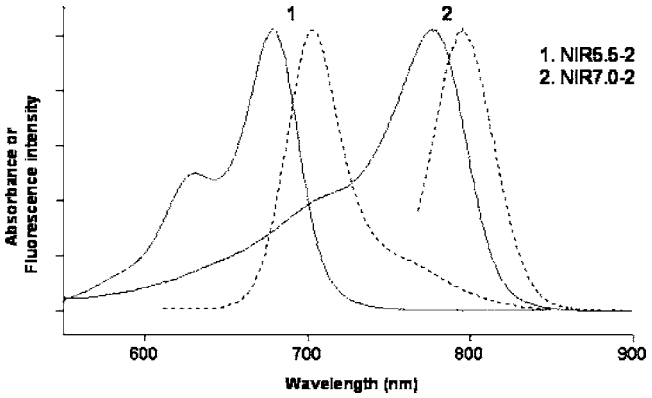


Figure 2. Normalized absorption (—) and emission (---) spectra of **NIR5.5-2** (Ex. $\lambda = 600$ nm) and **NIR7.0-2** (Ex. $\lambda = 760$ nm) in PBS at 25 °C.

(*40*). However, their spectral properties were investigated in MeOH or 20% aq DMSO, and no data about the fluorescence efficiency and aggregation tendency under physiological conditions are reported. Alternately, we have explored the postsynthetic derivatization of the precursor chloro cyanine dye **12** with a mercaptoalkyl carboxylic acid through an effective $S_{RN}1$ reaction of its *meso*-chlorine atom (Scheme 4a). Indeed, the introduction of a short alkyl linker between the reactive carboxyl group and the heptamethine chain should prevent the $\pi-\pi$ stacking interactions observed with the aryl linkers and so lead to fluorescent derivatives that are less likely to aggregate in aqueous solutions than their aryl-thioether congeners. As a starting point, we have developed a synthetic procedure that allows for the facile synthesis of dye **NIR7.0-1**. Reaction of the chloro-substituted heptamethine sulfocyanine dye **12** (*20*) with an excess of thioglycolic acid (3 equiv) in dry DMF gave the carboxylic acid functionalized **NIR7.0-1** in nearly quantitative yield. However, this dye proved to not be suitable for bioconjugation applications since its conversion into the *N*-hydroxysuccinimidyl ester or its direct activation with various peptide coupling reagents (i.e., phosphonium and uronium reagents) failed. Therefore, we have turned our attention to the carboxylic acid dye **NIR7.0-2** bearing a propanoic acid-based linker. [The Cy 7.0 analogue bearing an hexanoic acid based-based linker has also been also synthesized (by $S_{RN}1$ reaction between **12** and 6-mercaptohexanoic acid). These optical properties and its bioconjugation efficiency are similar to those reported for **NIR7.0-2**.] The synthesis of this new derivative was achieved by using the same synthetic procedure but required an additional heating of the reaction mixture (i.e., **12** and 3-mercaptopropionic acid in dry DMF) under reflux. Pure **NIR7.0-2** was obtained by RP-HPLC in 80% yield; its structure was confirmed by detailed measurements, including ESI mass spectrometry and NMR analyses. In addition to these characterizations, we have checked the reactivity of the free carboxylic acid functional group. Its activation was accomplished by treatment of **NIR7.0-2** with TSTU uronium salt in the presence of DIEA. Complete conversion to the *N*-hydroxysuccinimidyl ester **13** was observed by RP-HPLC. It is important to note that during the course of our work, a similar monofunctional NIR fluorophore namely **CyTE-777** was reported by Hilderbrand et al. (*10*). **CyTE-777** was obtained by postsynthetic derivatization of the commercially available dye IR-783 through the same $S_{RN}1$ reaction with 3-mercaptopropionic acid as described above (Scheme 4b). However, in this case, the use of a stoichiometric amount of triethylamine has enabled us to perform this reaction at room temperature.

Optical Properties. As expected, the two novel water-soluble cyanine fluorophores **NIR5.5-2** and **NIR7.0-2** display wavelength absorption and emission bands in the NIR range. The optical properties of these dyes are summarized in Table 1, and their absorption and emission spectra are displayed in Figure 2. **NIR5.5-2** has absorption and emission bands that match closely those of Cy 5.5 in PBS, which has an absorption maximum of 674 nm. There is no indication for dye−dye aggregation in PBS, which would manifest itself as a second absorption band at approximately 50 nm shorter wavelength (*13*). Indeed, the short wavelength shoulder visible in the absorption spectrum of **NIR5.5-2** is typical of cyanines and related polymethine dyes and attributed to transitions from different vibrational levels of the excited-state of fluorophore (i.e., vibronic shoulder) (*14*). The formation of dye−dye dimers and other aggregates is detrimental, because they frequently result in intermolecular quenching fluorescence emission. Thus, it appears that the three sulfonate groups introduced onto the 3,5-diaminobenzoic acid linker are sufficient to prevent dye−dye aggregation. The quantum yield of **NIR5.5-2** is significantly lower than that reported for Cy 5.5. This lower value may be explained by the presence of the trisulfonated aryl linker **9** because aromatic amines are known to quench the excited-state of some fluorophores through the photoinduced electron transfer (PET) process (*41*, *42*). This explanation was supported by the higher value of quantum yield determined for the Cy 5.5 analogue **NIR5.5-1**. Indeed, this dye contains a single sulfonatopropyl substituent which has no electron-donating ability for such PET to occur. However, the brightness or fluorescence intensity per dye molecule (i.e., the product of the fluorescence quantum yield and molar absorptivity) of **NIR5.5-2** is compatible with its use as a donor in NIR molecular probes relying on the fluorescence resonance energy transfer (FRET) process (*43*). Concerning the long wavelength dye **NIR7.0-2**, its absorption spectrum shows a characteristic band broadening, which is typical of heptamethine dyes with the absorption maxima in the range of 770−800 nm. As with **NIR5.5-2**, the Cy 7.0 analogue **NIR7.0-2** does not show any tendency to aggregate in aqueous solution. This indotricarbocyanine dye has a 20 nm Stokes shift of the fluorescence emission maximum and a quantum yield of 0.025 in PBS and 0.09 in DMSO. These latter values are comparable to those recently reported for other heptamethine cyanine dye derivatives (*17*, *40*, *44*). Furthermore, as illustrated in Figure 2, there is a good spectral overlap between the absorption of **NIR7.0-2** and emission of **NIR5.5-2**. Thus, **NIR7.0-2** might serve as an efficient acceptor for the fluorophores with emission around 700 nm in a FRET configuration.

Peptide Labeling. To demonstrate the general applicability of these novel water-soluble NIR cyanine dyes, **NIR5.5-2** and **NIR7.0-2** were converted into thiol- and amine-reactive derivatives for use in peptide labeling. As these two NIR fluorophores may act as an efficient FRET pair, their sequential and selective introduction within the same peptide architecture seems to be an interesting way to validate the labeling strategy leading to original NIR molecular probes relies on FRET process. We thus chose to couple our FRET pair to the caspase-3 cleavable peptide substrate Ac-Cys-Asp-Glu-Val-Asp-Lys-NH_2 **16** (cleavage site after the aspartic acid residue at the C-terminal side). Caspases are Cysteine-ASpartic-acid-ProteASES that play a critical role as mediators for apoptotic cell death (*45*). Caspase-3 has been specifically identified as being a key mediator of apoptosis in mammalian cells (*46*): activation of caspase-3 indicates that the apoptotic pathway has progressed to an irreversible stage. There is thus a growing interest in identifying caspase inhibitors to minimize cell death in pathological conditions (neurodegenerative diseases for instance) but also for inducing caspase activation in cancer cells (*47*, *48*). In addition, caspase-3 is widely used for monitoring apoptosis induction for general cytotoxicity screening. This interest for

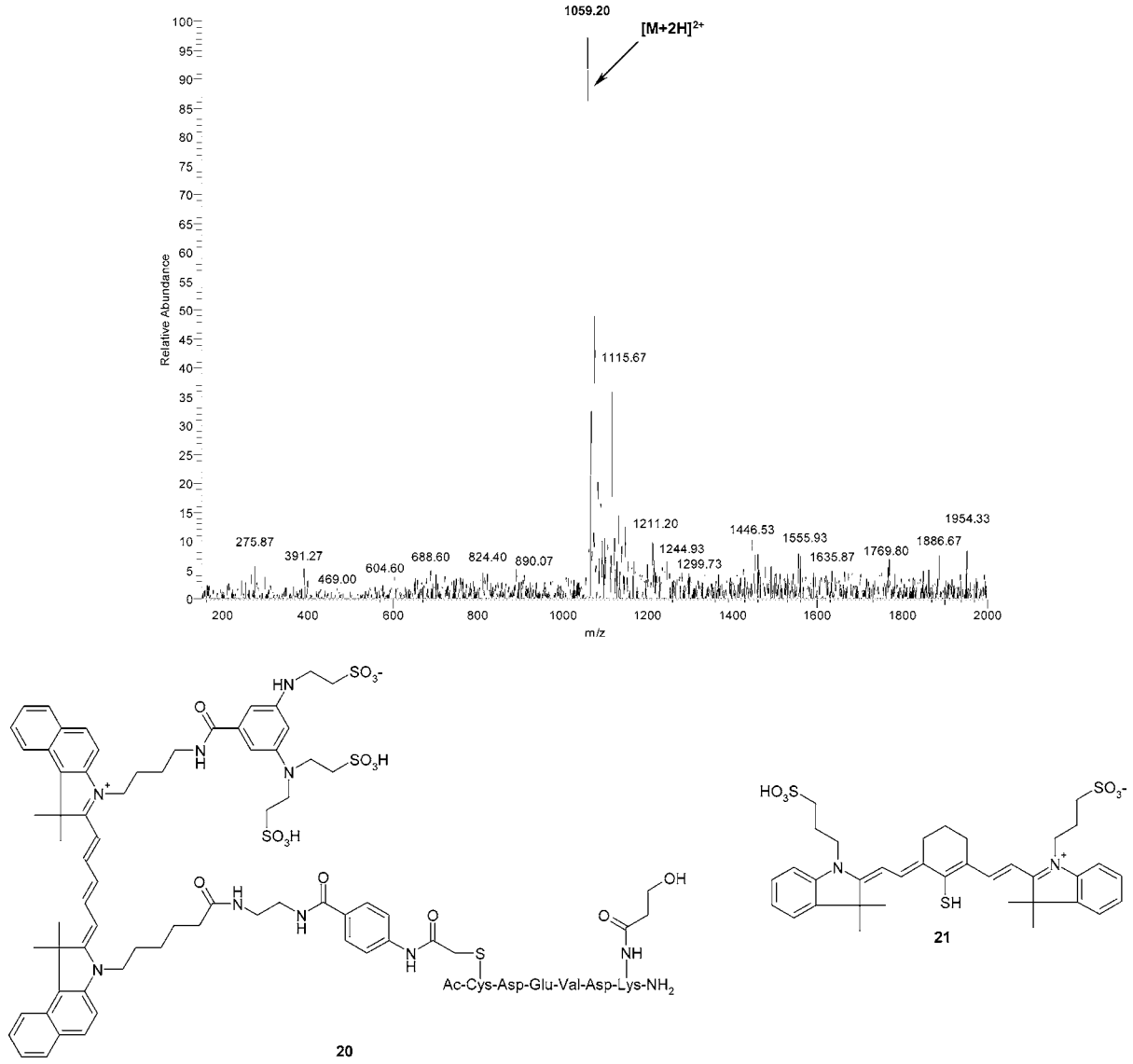


Figure 3. ESI mass spectrum of the fluorogenic substrate of caspase-3 protease **19**, in the positive mode, $[M + 2H]^{2+}$: m/z: calcd for $C_{99}H_{130}N_{16}O_{28}S_4$: 1061.24, found 1059.20. Loss of thiol NIR dye **21** occurred during the ionization process. Structures of peptide **20** and thiol NIR dye **21**.

caspase-3 resulted in the development of several assays using a variety of formats and amenable to high throughput screening (*49*−*54*). Hexapeptide **16** has thus been chosen as a suitable target in order to get a novel fluorogenic substrate useful for detecting apoptosis in whole cells and for cell-based high throughput screening assays for apoptosis inhibitors or inducers.(- For other examples of FRET-based probes used for caspase-3 detection, see refs 55−58.) To the core caspase-3 substrate sequence, cysteine and lysine residues were incorporated at N- and C-termini, respectively, as handles for the attachment of fluorophores. The use of a cysteine side-chain protecting group removable under mild reducing conditions (i.e., *tert*-butylthio group, StBu) has enabled the selective introduction of the two fluorescent labels within this peptide, thus obtaining the target FRET substrate through an efficient solution-phase labeling method.

First, **NIR5.5-2** was converted into the thiol-reactive iodoacetyl derivative **15** using a conventional three-step method (Scheme 5). **NIR5.5-2** *N*-hydroxysuccinimidyl ester **11**, generated by reaction with TSTU/ DIEA in dry NMP, was reacted with ethylenediamine under the conditions reported by Gruber et al. (*59*) to give **NIR5.5-2** amine **14** in 73% yield. Finally, acylation of the primary amino group of **14** with the heterobifunctional cross-linker reagent succinimidyl 4-[(iodoacetyl)-amino]benzoate (i.e., SIAB) in a mixture of NMP and aq sodium bicarbonate buffer (pH 8.5) provided, after RP-HPLC purification, the thiol-reactive Cy 5.5 analogue **15** (yield 80%). Its structure was confirmed by ESI mass spectrometry. Site-specific fluorescent labeling of caspase-3-cleavable peptide substrate started with the reaction between Ac-Cys(StBu)-Asp-Glu-Val-Asp-Lys-NH_2 **16** and the *N*-hydroxysuccinimidyl ester of **NIR7.0-2 13** in dry NMP in the presence of DIEA (Scheme 6). Purification by RP-HPLC provided the **NIR7.0-2**-labeled peptide Ac-Cys(StBu)-Asp-Glu-Val-Asp-Lys(**NIR7.0-2**)-NH_2 **17** in 60% yield. The removal of the StBu protecting group from the cysteine residue was achieved by treatment with an excess of dithiothreitol (DTT) in aq sodium bicarbonate buffer (pH 8.5). Purification of the free sulfhydryl-containing peptide−**NIR7.0-2** conjugate **18** was achieved by RP-HPLC. Finally, iodoacetamido-activated **NIR5.5-2 15** was attached on the free cysteine of peptide **18** by using a 3:1 molar excess (**18**/**15**) in aq sodium bicarbonate buffer (pH 8.5). The caspase-3 substrate **19** was obtained in a pure form after purification by RP-HPLC (yield 25%, purity >95%). When this fluorogenic substrate was analyzed by ESI mass spectrometry (Figure 3), the expected molecular ion $[M + H]^+$ around *m*/*z* 2800.00 Da was not observed. The mass spectrum shows a single peak at *m*/*z* 1059.20 Da corresponding to the positive ion $[M + 2H]^{2+}$ of

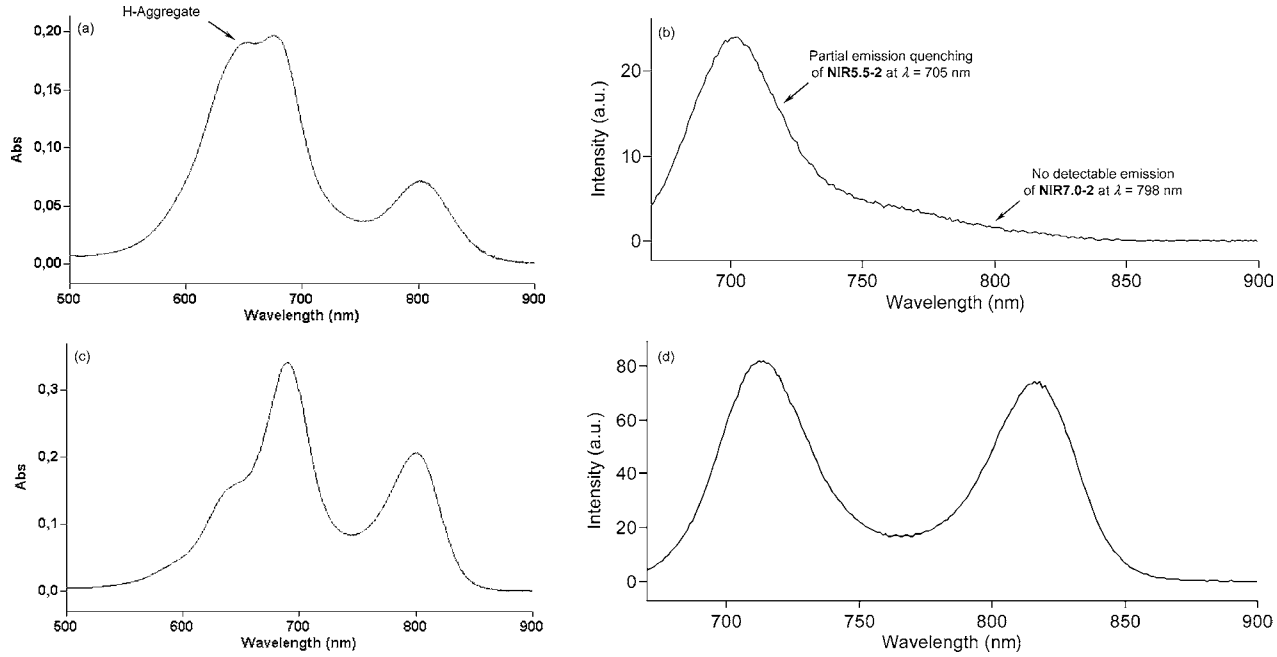


Figure 4. Absorption and emission (Ex. $\lambda = 660$ nm) spectra of probe **19** at 25 °C (concentration 2.6 μM). (a,b) In PBS. (c,d) In DMSO. The efficiency of this energy transfer (E) is typically measured using the relative fluorescence intensity of the donor (**NIR5.5-2**), in the absence (F_D) and presence (F_{DA}) of acceptor (**NIR7.0-2**): $E = 1 - (F_{DA}/F_D)$. For our fluorescent probe, this was accomplished by comparing the **NIR5.5-2** emission (i.e., area under the corrected emission curve in the range 670−760 nm after excitation at $\lambda = 660$ nm) for the iodoacetyl derivative **15** and peptide **19**. From these emission spectra, a value of F_{DA}/F_D close to 0.45 was found.

NIR5.5-2 derivative **20**. The formation of this single fluorescently labeled peptide was explained by the elimination of thiol **NIR7.0-2** derivative **21** (i.e., retro-Michael reaction) followed by the 1,4-addition of a water molecule onto the newly formed Michael olefin. This fragmentation pathway was also observed when the fluorogenic probe was subjected to a MALDI-TOF mass spectrometry analysis and observed with other FRET probes bearing the same NIR cyanine dye as energy acceptor (see Supporting Information). Furthermore, as the photophysical characterization (see below) has confirmed the presence and integrity of the two fluorophores **NIR5.5-2** and **NIR7.0-2** within the hexapeptide, the hydrolytic release of **21** obviously occurs during the ionization process.

Photophysical Characterization and *in Vitro* Cleavage by Caspase-3 of the Fluorogenic Peptide. The absorption and emission spectra of the probe **19** recorded in PBS and DMSO are shown in Figure 4. In DMSO, two major absorption peaks at 689 and 800 nm, indicating the presence of **NIR5.5-2** and **NIR7.0-2**, respectively, were observed. Surprisingly, a new peak at 649 nm, which is blue-shifted by about 30 nm from the absorption peak of the free **NIR5.5-2** dye, was observed for the probe dissolved in aqueous buffered solution. As the absorption peak of **NIR7.0-2** dye is also red-shifted by about 20 nm, it is clear that this probe displays significant dye−dye-aggregation leading to the formation of an intramolecular heterodimer (*60*). Further evidence for the formation of an H-aggregate within the dual-labeled peptide **19** was given by the fluorescence emission spectrum (recorded after excitation of the donor **NIR5.5-2** at 660 nm). Indeed, no significant emission at 798 nm corresponding to the **NIR7.0-2** fluorescence (see Supporting Information) or a minor emission at 705 nm (diminished by 3 times compared to the fluorescence of free **NIR5.5-2** dye at the same concentration) corresponding to the remaining untransferred **NIR5.5-2** fluorescence was observed. This quenching was not observed in the fluorescence emission spectrum recorded in DMSO, where an energy transfer efficiency close to 55% was found. Thus, **NIR7.0-2** acts as an efficient quencher for **NIR5.5-2**. As this quenching effect is also observed with the probe bearing the less polar Cy 5.5 analogue **NIR5.5-1** as donor (see Supporting Information) but not observed with the fluorogenic Cy 5.0/**NIR7.0-2** hexapeptide, dye−dye aggregation may result from strong $\pi-\pi$ stacking interactions between the benz[*e*]indole and indole units. To assess the quenching efficiency of the **NIR5.5-2**/**NIR7.0-2** pair, a Stern−Volmer plot was obtained from steady-state fluorescence intensity measurements of the donor **NIR5.5-2** with or without the acceptor **NIR7.0-2** (Figure 5). Since the structural features of the linker connecting the Cy 5.5 analogue to the peptide core may influence the quenching, this study was performed with iodoacetyl derivative **15** instead of the free carboxylic acid dye. The Stern−Volmer plot displays an upward curvature; this positive deviation from linearity with increasing **NIR7.0-2** concentrations indicates that static quenching is much higher than expected for a diffusion-controlled bimolecular reaction. This strongly supports the idea of the formation of a nonfluorescent ground-state complex between the two NIR cyanine dyes in aqueous solutions (*61*).

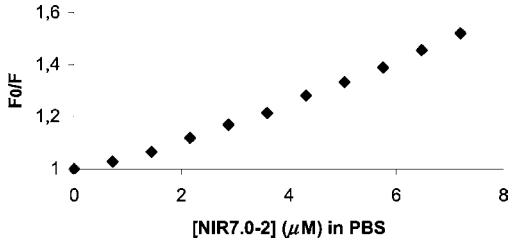


Figure 5. Static bimolecular Stern−Volmer plot for determining quenching efficiency of **NIR7.0-2** toward the idoacetyl derivative of **NIR5.5-2** in PBS. F_0 and F are fluorescence intensity of **15** (0.72 μM) in the absence and in the presence of **NIR7.0-2**, respectively.

Interestingly, a comprehensive study of the optical properties of the thiol-reactive Cy 5.5 analogue **15** has revealed that the chemical derivatization of **NIR5.5-2** with the SIAB cross-linker significantly increases the quantum yield of our Cy 5.5 analogue especially in DMSO ($\Phi_F = 0.145$ compared to $\Phi_F = 0.05$ for **NIR5.5-2**). We presume that this increase of fluorescence in **15** as compared with **NIR5.5-2** is due to the longer distance between the cyanine core and the aniline nitrogen atoms of the

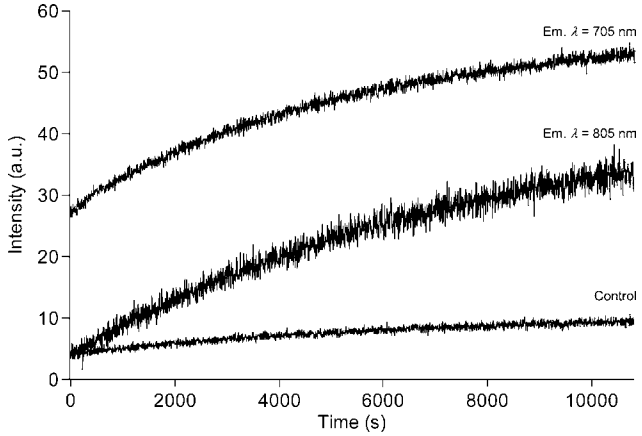


Figure 6. Fluorescence emission time course of probe **19** (concentration 1.0 μM) with recombinant human caspase-3 (3.2 10^{-3} U, incubation time 180 min) in caspase assay buffer (100 mM NaCl, 40 mM HEPES, 10 mM DTT, 1 mM EDTA, 10% (w/v) sucrose, and 0.1% (w/v) CHAPS, pH 7.2, 37 °C) at 705 nm (Ex. $\lambda = 670$ nm) and 805 nm (Ex. $\lambda = 770$ nm). To avoid overloading of this figure, only the emission at 805 nm (Ex. $\lambda = 770$ nm) is shown for the control reaction without caspase-3. The same straight line was obtained for the emission at 705 nm but at a fluorescence level around 25 a.u.

hydrophilic linker which acts as a quencher (see above). Indeed, strong $\pi-\pi$ stacking interactions between the benzene rings of trisulfonated linker **9** and SIAB cross-linker may favor a conformation in which the quencher−fluorophore distance is significantly increased. Thus, this conformational change would reduce the rate of the PET-based quenching process, thereby enhancing the fluorescence emission.

With this interesting tool in hand, the internally quenched fluorescent probe **19** was assayed against recombinant human caspase-3. Within 180 min, the fluorescence emission of **19** at 705 and 805 nm has increased about 2- and 8-fold, respectively, while no activation was observed when the peptide **19** was incubated only with the caspase-3 buffer (Figure 6). Furthermore, no fluorescence enhancement was obtained after prolonged incubation of **19** with BSA protein (see Supporting Information). This latter observation asserts that an hypothetical nonspecific binding between peptide **19** and protein (such as caspase-3) cannot induce the fluorescence revealing of both NIR dyes through conformational changes of the probe. Overall, these results confirm that the fluorogenic peptide-based probe **19** is a substrate for recombinant caspase-3 protease. However, fluorescence recovery was significantly lower than expected if complete proteolytic cleavage of **19** had occurred. One possible explanation for this result is the low accessibility of the enzyme cleavage site within the peptide backbone. As the enzyme activity and substrate recognition are usually extremely sensitive to peptide conformation, the formation of the intramolecular heterodimer has probably significantly modified the shape of the peptide recognition unit, and the activity rate was dramatically decreased.

CONCLUSION

In this paper, we have described the synthesis and photophysical properties of two novel water-soluble NIR cyanine dyes **NIR5.5-2** and **NIR 7.0-2** which are potential substitutes of the commercially available Cy 5.5 and Cy 7.0 labels. They are easily prepared in good yields by postsynthetic derivatization of an amino or a chloro cyanine precursor through an efficient acylation and a $S_{RN}1$ reaction respectively. These two derivatives display absorption and emission maxima in the NIR range and do not self-aggregate in aqueous solution, and their fluorescence efficiency is compatible with their use in a wide variety of optical imaging applications and NIR fluorescence studies. However, further efforts are required in order to improve the quantum yield of **NIR5.5-2** especially by introducing a polysulfonated aminoalkyl linker as water-solubilizing moiety onto the cyanine precursor. Efficient synthetic protocols were also found for conversion of **NIR5.5-2** and **NIR7.0-2** into thiol- and amine-reactive derivatives **13** and **15**. These novel fluorescent labeling reagents have been successfully used in solution-phase peptide labeling to provide an original peptide-based NIR probe of caspase-3 protease. Efficient quenching effect between **NIR5.5-2** and **NIR7.0-2** at 705 and 798 nm was demonstrated. In the caspase-3 model, the probe is able to release fluorescence signal by 8-fold at 805 nm after enzymatic degradation. However, enzyme activity is dramatically decreased compared with other fluorogenic FRET-based probes previously reported by us (*30*, *62*). Thus, further studies aimed at re-engineering the placement of the NIR dye labels and their covalent attachment, such that dimer formation will not alter the hexapeptide secondary structure, are necessary to get an internally quenched fluorescent probe suitable to assay caspase-3 activity both *in vitro* and *in vivo*. Yet, the observation of an efficient formation of an intramolecular heterodimer yielding a nonfluorescent ground-state complex between the two NIR cyanine dyes in aqueous solutions, even with a very short peptide which is unlikely to fold, opens the door to the use of this efficiently quenched fluorophore pair using coil-containing longer peptidic backbones.

ACKNOWLEDGMENT

The contribution of Dr. Jérôme Leprince (U 413 INSERM/IFRMP 23) to MALDI-TOF mass spectrometry measurements and solid-phase synthesis of hexapeptide **16** is greatly acknowledged. We thank Dr. Xavier Franck for helpful discussions concerning the sulfonation reactions of amines. The financial support of the "Région Haute Normandie" is gratefully acknowledged.

Supporting Information Available: Synthesis and characterization of thiol-reactive **NIR5.5-1** derivative **24**, detailed synthetic procedures and photophysical characterization of fluorogenic **NIR5.5-1**/**NIR7.0-2** hexapeptide. Photophysical characterization of fluorogenic **NIR5.5-2**/**NIR7.0-2** hexapeptide **19** and fluorescence emission time course of incubation with BSA. This material is available free of charge via the Internet at http://pubs.acs.org/ BC.

LITERATURE CITED

(1) Haugland, R. P. (2002) *Handbook of Fluorescence Probes and Research Products*, 9th ed., Molecular Probes, Inc., Eugene, OR.

(2) Buschmann, V., Weston, K. D., and Sauer, M. (2003) Spectroscopic study and evaluation of red-absorbing fluorescent dyes. *Bioconjugate Chem. 14*, 195−204 and references cited therein.

(3) Gómez-Hens, A., and Aguilar-Caballos, M. P. (2004) Long-wavelength fluorophores: new trends in their analytical use. *Trends Anal. Chem. 23*, 127−136.

(4) Zhao, W., and Carreira, E. M. (2006) Conformationally restricted aza-BODIPY: highly fluorescent, stable near-infrared absorbing dyes. *Chem. Eur. J. 12*, 7254−7263.

(5) Liu, J., Diwu, Z., Leung, W.-Y., Lu, Y., Patch, B., and Haugland, R. P. (2003) Rational design and synthesis of a novel class of highly fluorescent rhodamine dyes that have strong absorption at long wavelengths. *Tetrahedron Lett. 44*, 4355−4359.

(6) Bandichhor, R., Petrescu, A. D., Vespa, A., Kier, A. B., Schroeder, F., and Burgess, K. (2006) Synthesis of a new water-soluble rhodamine derivative and application to protein labeling and intracellular imaging. *Bioconjugate Chem. 17*, 1219−1225.

(7) Jose, J., and Burgess, K. (2006) Benzophenoxazine-based fluorescent dyes for labeling biomolecules. *Tetrahedron 62*, 11021−11037.

(8) Lin, Y., Weissleder, R., and Tung, C.-H. (2002) Novel near-infrared cyanine fluorochromes: synthesis, properties, and bioconjugation. *Bioconjugate Chem. 13*, 605−610.
(9) Mader, O., Reiner, K., Egelhaaf, H.-J., Fischer, R., and Brock, R. (2004) Structure property analysis of pentamethine indocyanine dyes: identification of a new dye for life science applications. *Bioconjugate Chem. 15*, 70−78.
(10) Hilderbrand, S. A., Kelly, K. A., Weissleder, R., and Tung, C.-H. (2005) Monofunctional near-infrared fluorochromes for imaging applications. *Bioconjugate Chem. 16*, 1275−1281.
(11) Patonay, G., Salon, J., Sowell, J., and Strekowski, L. (2004) Noncovalent labeling of biomolecules with red and near-infrared dyes. *Molecules 9*, 40−49.
(12) Tung, C.-H. (2004) Fluorescent peptide probes for in vivo diagnostic imaging. *Biopolymers 76*, 391−403 and references cited therein.
(13) Mujumdar, S. R., Mujumdar, R. B., Grant, C. M., and Waggoner, A. S. (1996) Cyanine-labeling reagents: sulfobenzindocyanine succinimidyl esters. *Bioconjugate Chem. 7*, 356−362.
(14) Mujumdar, R. B., Ernst, L. A., Mujumdar, S. R., Lewis, C. J., and Waggoner, A. S. (1993) Cyanine dye labeling reagents: sulfoindocyanine succinimidyl esters. *Bioconjugate Chem. 4*, 105−111.
(15) Narayanan, N., and Patonay, G. (1995) A new method for the synthesis of heptamethine cyanine dyes: synthesis of new near-infrared fluorescent labels. *J. Org. Chem. 60*, 2391−2395.
(16) Narayanan, N., Strekowski, L., Lipowska, M., and Patonay, G. (1997) Erratum to "A new method for the synthesis of heptamethine cyanine dyes: synthesis of new near infrared fluorescent labels". *J. Org. Chem. 62*, 9387.
(17) Song, F., Peng, X., Lu, E., Zhang, R., Chen, X., and Song, B. (2004) Syntheses, spectral properties and photostabilities of novel water-soluble near-infrared cyanine dyes. *J. Photochem. Photobiol. A. Chem. 168*, 53−57.
(18) Flanagan, J. H., Jr., Khan, S. H., Menchen, S., Soper, S. A., and Hammer, R. P. (1997) Functionalized tricarbocyanine dyes as near-infrared fluorescent probes for biomolecules. *Bioconjugate Chem. 8*, 751−756.
(19) Li, C., Greenwood, T. R., Bhujwalla, Z. M., and Glunde, K. (2006) Synthesis and characterization of glucosamine-bound near-infrared probes for optical imaging. *Org. Lett. 8*, 3623−3626.
(20) Strekowski, L., Mason, C. J., Lee, H., Gupta, R., Sowell, J., and Patonay, G. (2003) Synthesis of water-soluble near-infrared cyanine dyes functionalized with [(succinimido)oxy]carbonyl group. *J. Heterocycl. Chem. 40*, 913−916.
(21) Zhang, Z., and Achilefu, S. (2004) Synthesis and evaluation of polyhydroxylated near-infrared carbocyanine molecular probes. *Org. Lett. 6*, 2067−2070.
(22) Chipon, B., Clavé, G., Bouteiller, C., Massonneau, M., Renard, P.-Y., and Romieu, A. (2006) Synthesis and post-synthetic derivatization of a cyanine-based amino acid. Application to the preparation of a novel water-soluble NIR dye. *Tetrahedron Lett. 47*, 8279−8284.
(23) Chipon, B., Clavé, G., Bouteiller, C., Massonneau, M., Renard, P.-Y., and Romieu, A. (2007) Corrigendum to "Synthesis and post-synthetic derivatization of a cyanine-based amino acid. Application to the preparation of a novel water-soluble NIR dye". *Tetrahedron Lett. 48*, 501.
(24) Jung, M. E., and Kim, W.-J. (2006) Practical syntheses of dyes for difference gel electrophoresis. *Bioorg. Med. Chem. 14*, 92−97.
(25) Marvel, C. S., and Sparberg, M. S. (1930) Sodium 2-bromoethanesulfonate. *Organic Syntheses*, Coll. Vol. 10, pp 96−97, Wiley, New York.
(26) Leone-Bay, A., and Timony, P. E. (1988) A new synthesis of Sulfo-N-succinimidyl p-(iodoacetylamino)benzoate. *Synth. Commun. 18*, 1637−1640.
(27) Portoghese, P. S., Sultana, M., and Takemori, A. E. (1990) Design of peptidomimetic δ opioid receptor antagonists using the message-address concept. *J. Med. Chem. 33*, 1714−1720.
(28) Kappe, T., Fruhwirth, F., Roschger, P., Jocham, B., Kremsner, J., and Stadlbauer, W. (2002) Synthesis and reactions of 10,10-dimethyl-10H-pyrido[1,2-a]indol-6-ones. *J. Heterocycl. Chem. 39*, 391−397.
(29) Strekowski, L., Gorecki, T., Mason, J. C., Lee, H., and Patonay, G. (2001) New heptamethine cyanine reagents for labeling of biomolecules with a near-infrared chromophore. *Heterocycl. Commun. 7*, 117−122.
(30) Lapeyre, M., Leprince, J., Massonneau, M., Oulyadi, H., Renard, P.-Y., Romieu, A., Turcatti, G., and Vaudry, H. (2006) Aryldithioethyloxycarbonyl (Ardec): a new family of amine protecting groups removable under mild reducing conditions and their applications to peptide synthesis. *Chem. Eur. J. 12*, 3655−3671.
(31) Gottlieb, H. E., Kotlyar, V., and Nudelman, A. (1997) NMR chemical shifts of common laboratory solvents as trace impurities. *J. Org. Chem. 62*, 7512−7515.
(32) Reindl, S., Penzkofer, A., Gong, S. H., Landthaler, M., Szeimies, R. M., Abels, C., and Baeumler, W. (1997) Quantum yield of triplet formation for indocyanine green. *J. Photochem. Photobiol. A. Chem. 105*, 65−68.
(33) Cheng, Z., Wu, Y., Xiong, Z., Gambhir, S. S., and Chen, X. (2005) Near-infrared fluorescent RGD peptides for optical imaging of integrin αv. beta.3 expression in living mice. *Bioconjugate Chem. 16*, 1433−1441.
(34) Medarova, Z., Bonner-Weir, S., Lipes, M., and Moore, A. (2005) Imaging β-cell death with a near-infrared probe. *Diabetes 54*, 1780−1788.
(35) Vera, D. R., Hall, D. J., Hoh, C. K., Gallant, P., McIntosh, L. M., and Mattrey, R. F. (2005) Cy5.5-DTPA-galactosyl-dextran: a fluorescent probe for in vivo measurement of receptor biochemistry. *Nucl. Med. Biol. 32*, 687−693.
(36) Cheng, Z., Levi, J., Xiong, Z., Gheysens, O., Keren, S., Chen, X., and Gambhir, S. S. (2006) Near-infrared fluorescent deoxyglucose analogue for tumor optical imaging in cell culture and living mice. *Bioconjugate Chem. 17*, 662−669.
(37) Ho, N.-H., Weissleder, R., and Tung, C.-H. (2006) Development of water-soluble far-red fluorogenic dyes for enzyme sensing. *Tetrahedron 62*, 578−585.
(38) Jose, J., and Burgess, K. (2006) Syntheses and properties of water-soluble Nile Red derivatives. *J. Org. Chem. 71*, 7835−7839.
(39) Zaheer, A., Wheat, T. E., and Frangioni, J. V. (2002) IRDye78 conjugates for near-infrared fluorescence imaging. *Mol. Imaging 1*, 354−364.
(40) Lee, H., Mason, J. C., and Achilefu, S. (2006) Heptamethine cyanine dyes with a robust C−C bond at the central position of the chromophore. *J. Org. Chem. 71*, 7862−7865.
(41) Sasaki, E., Kojima, H., Nishimatsu, H., Urano, Y., Kikuchi, K., Hirata, Y., and Nagano, T. (2005) Highly sensitive near-infrared fluorescent probes for nitric oxide and their application to isolated organs. *J. Am. Chem. Soc. 127*, 3684−3685.
(42) Sparano, B. A., and Koide, K. (2005) A strategy for the development of small-molecule-based sensors that strongly fluoresce when bound to a specific RNA. *J. Am. Chem. Soc. 127*, 14954−14955.
(43) Sapsford, K. E., Berti, L., and Medintz, I. L. (2006) Materials for fluorescence resonance energy transfer analysis: beyond traditional donor-acceptor combinations. *Angew. Chem., Int. Ed. 45*, 4562−4588.
(44) Chen, X., Peng, X., Cui, A., Wang, B., Wang, L., and Zhang, R. (2006) Photostabilities of novel heptamethine 3H-indolenine cyanine dyes with different N-substituents. *J. Photochem. Photobiol. A. Chem. 181*, 79−85.
(45) Denault, J.-B., and Salvesen, G. S. (2002) Caspases: keys in the ignition of cell death. *Chem. Rev. 102*, 4489−4499.
(46) Kothakota, S., Azuma, T., Reinhard, C., Klippel, A., Tang, J., Chu, K., McGarry, T. J., Kirschner, M. W., Koths, K., Kwiatkowski, D. J., and Williams, L. T. (1997) Caspase-3-generated fragment of gelsolin: effector of morphological change in apoptosis. *Science 278*, 294−298.
(47) Talanian, R. V., Brady, K. D., and Cryns, V. L. (2000) Caspases as targets for anti-inflammatory and anti-apoptotic drug discovery. *J. Med. Chem. 43*, 3351−3371.
(48) Nuttall, M. E., Lee, D., McLaughlin, B., and Erhardt, J. A. (2001) Selective inhibitors of apoptotic caspases: implications for novel therapeutic strategies. *DDT 6*, 85−91.
(49) Tawa, P., Tam, J., Cassady, R., Nicholson, D. W., and Xanthoudakis, S. (2001) Quantitative analysis of fluorescent caspase substrate cleavage in intact cells and identification of novel inhibitors of apoptosis. *Cell Death Differ. 8*, 30−37.
(50) Waud, J. P., Bermudez Fajardo, A., Sudhaharan, T., Trimby, A. R., Jeffery, J., Jones, A., and Campbell, A. K. (2001) Measurement

of proteases using chemiluminescence-resonance-energy-transfer chimaeras between green fluorescent protein and aequorin. *Biochem. J. 357*, 687−697.

(51) Gopalakrishnan, S. M., Karvinen, J., Kofron, J. L., Burns, D. J., and Warrior, U. (2002) Application of micro arrayed compound screening (mARCS) to identify inhibitors of caspase-3. *J. Biomol. Screening 7*, 317−323.

(52) Karvinen, J., Hurskainen, P., Gopalakrishnan, S. M., Burns, D. J., Warrior, U., and Hemmila, I. (2002) Homogeneous time-resolved fluorescence quenching assay (LANCE) for caspase-3. *J. Biomol. Screening 7*, 223−231.

(53) Preaudat, M., Ouled-Diaf, J., Alpha-Bazin, B., Mathis, G., Mitsugi, T., Aono, Y., Takahashi, K., and Takemoto, H. (2002) A homogeneous caspase-3 activity assay using HTRF technology. *J. Biomol. Screening 7*, 267−274.

(54) O'Brien, M. A., Daily, W. J., Hesselberth, P. E., Moravec, R. A., Scurria, M. A., Klaubert, D. H., Bulleit, R. F., and Wood, K. V. (2005) Homogeneous, bioluminescent protease assays: caspase-3 as a model. *J. Biomol. Screening 10*, 137−148.

(55) Mizukami, S., Kikuchi, K., Higuchi, T., Urano, Y., Mashima, T., Tsuruo, T., and Nagano, T. (1999) Imaging of caspase-3 activation in HeLa cells stimulated with etoposide using a novel fluorescent probe. *FEBS Lett. 453*, 356−360.

(56) Komoriya, A., Packard, B. Z., Brown, M. J., Wu, M. L., and Henkart, P. A. (2000) Assessment of caspase activities in intact apoptotic thymocytes using cell-permeable fluorogenic caspase substrates. *J. Exp. Med. 191*, 1819−1828.

(57) Pham, W., Weissleder, R., and Tung, C.-H. (2002) An azulene dimer as a near-infrared quencher. *Angew. Chem., Int. Ed. 41*, 3659−3662.

(58) Bullok, K., and Piwnica-Worms, D. (2005) Synthesis and characterization of a small, membrane-permeant, caspase-activatable far-red fluorescent peptide for imaging apoptosis. *J. Med. Chem. 48*, 5404−5407.

(59) Gruber, H. J., Kada, G., Pragl, B., Riener, C., Hahn, C. D., Harms, G. S., Ahrer, W., Dax, T. G., Hohenthanner, K., and Knaus, H. G. (2000) Preparation of thiol-reactive Cy5 derivatives from commercial Cy5 succinimidyl ester. *Bioconjugate Chem. 11*, 161−166.

(60) Johansson, M. K., and Cook, R. M. (2003) Intramolecular dimers: a new design strategy for fluorescence-quenched probes. *Chem. Eur. J. 9*, 3466−3471.

(61) Marmé, N., Knemeyer, J.-P., Sauer, M., and Wolfrum, J. (2003) Inter- and intramolecular fluorescence quenching of organic dyes by tryptophan. *Bioconjugate Chem. 14*, 1133−1139.

(62) Poupart, S., Boudou, C., Peixoto, P., Massonneau, M., Renard, P.-Y., and Romieu, A. (2006) Aminopropargyl derivative of terpyridine-bis(methyl-enamine) tetraacetic acid chelate of europium (Eu (TMT)-AP3): a new reagent for fluorescent labelling of proteins and peptides. *Org. Biomol. Chem. 4*, 4165−4177.

BC0700281

Development of a Small Peptide Tag for Covalent Labeling of Proteins

Fujie Tanaka,* Roberta Fuller, Lily Asawapornmongkol, Axel Warsinke, Sarah Gobuty, and Carlos F. Barbas, III*

The Departments of Molecular Biology and Chemistry and The Skaggs Institute for Chemical Biology, The Scripps Research Institute, 10550 North Torrey Pines Road, La Jolla, California 92037. Received March 8, 2007; Revised Manuscript Received May 11, 2007

A 21-mer peptide that can be used to covalently introduce synthetic molecules into proteins has been developed. Phage-displayed peptide libraries were subjected to reaction-based selection with 1,3-diketones. The peptide was further evolved by addition of a randomized region and reselection for improved binding. The resulting 21-mer peptide had a reactive amino group that formed an enaminone with 1,3-diketone and was used as a tag for labeling of maltose binding protein. Using this peptide tag and 1,3-diketone derivatives, a variety of molecules such as reporter probes and functionalities may be covalently introduced into proteins of interest.

INTRODUCTION

Development of systems for labeling of proteins with synthetic molecules or small molecules is of considerable interest (*1*), because labeling systems can be used to address fundamental biological questions and can be used for the preparation of novel therapeutics. For example, labeling of proteins with fluorescent molecules allows tracking of the proteins within native environs (*2*−*4*). Whereas GFP variants have a given fluorescence, use of a tag-fusion protein allows for labeling with a variety of synthetic fluorescent molecules that differ in fluorescence. In addition, modifications to a tag-fusion protein are not limited to introduction of fluorescent molecules; other molecules can be introduced to the tag-fusion protein. Proteins conjugated with carbohydrates or lipids are tools for exploring interactions among these biomolecules on the cell surface and inside cells (*5*). Drug−protein conjugates, including antibody conjugates with cytotoxic molecules or radioisotopes, are often safer and more effective therapeutics than drug or protein alone (*6*−*9*). Proteins labeled with polymers are more stable than the corresponding unlabeled proteins in serum and are useful for therapeutic applications (*10*). Labeling reactions of proteins with synthetic molecules can also be used for covalently attaching proteins to the surfaces of microchips or microarrays (*11*−*13*).

In order to label a protein of interest selectively and specifically, several strategies and methods have been developed. For example, using a tag protein or peptide (either enzyme-derived or designed) that selectively reacts with designed synthetic molecules provides selective and specific labeling. Methods using a covalently modifiable tag fusion include labeling of O^6-alkylguanine-DNA alkyltransferase with O^6-benzylguanine derivatives (*3*, *14*), Sfp phosphopantetheinyl transferase-catalyzed labeling of a peptide excised from a nonribosomal peptide synthetase with an adenosine 3′-monophosphate derivative (*11*, *15*), phosphopantetheine transferase-catalyzed labeling of the acyl carrier protein with an adenosine 3′-monophosphate derivative (*4*), biotin ligase-catalyzed labeling of the acceptor peptide with a biotin-mimic derivative (*16*), labeling of a serine esterase cutinase with phosphate derivatives (*13*), and labeling of a tetracysteine α-helix motif with biarsenical ligands (*17*, *18*). Other useful covalent labeling methods include intein-mediated labeling (*19*−*21*), incorporation of an unnatural amino acid into a protein and labeling of the unnatural amino acid (*5*), and introduction of a N-terminal cysteine and its labeling with aldehyde derivatives (*22*). When serine or threonine is introduced at the N-terminus of a protein, oxidation of the N-terminal serine or threonine to form an aldehyde group followed by oxime or hydrazone formation reaction is another useful chemical modification method (*23*−*25*). Labeling of fusion proteins with noncovalent, but tight-binding compounds has also been reported. Examples include labeling of a dihydrofolate reductase (DHFR)-fusion with methotrexate conjugates (*26*, *27*), labeling of an FKBP12 mutant (F36V)-fusion with its ligand derivatives (*28*), labeling of a single chain antibody fusion with its hapten-conjugated molecules (*29*), and labeling of avidin fusion with biotin conjugates (*30*).

For labeling of fusion proteins, a smaller peptide tag is preferred as the fusion partner because a larger protein tag may affect the function of the protein of interest and because production of larger proteins is often more difficult. When multiple labeling of a protein of interest with different molecules is required, one convenient solution is the introduction of different tags into the protein at the same time followed by specific labeling of each tag of the fusion. For multiple labels, smaller fusion partners allow for the fusion protein to be of reasonable size. When small peptides are used, noncovalent binding is unlikely to provide sufficient hydrogen bonds and/or charge and hydrophobic interactions for tight binding. In contrast, a covalent bond is sufficient to retain the label and numerous noncovalent interactions are not necessary. Thus small peptides that form covalent bonds with designed compounds should be suitable for conjugation of the fusion proteins with synthetic molecules. In addition, it is preferred that labeling methods do not require additional catalysts or toxic metal reagents. Here we report the development of a small 21-mer peptide that forms an enaminone with 1,3-diketone derivatives. We have demonstrated that when fused to a protein of interest, the peptide can be used to introduce synthetic molecules into the fusion protein without the requirement of additional catalysts or reagents.

EXPERIMENTAL PROCEDURES

Selection of Peptides from Initial Libraries. Ph.D.-C7C, Ph.D.-7, and Ph.D.-12 phage display peptide libraries (New England Biolabs, NEB) were used for the selection. Wells of a microtiter plate (Costar 3690) were coated with **1**−bovine serum albumin conjugate (**1**−BSA) (2 μg/PBS 25 μL/well) at 4 °C

* To whom correspondence should be addressed. E-mail: ftanaka@scripps.edu, carlos@scripps.edu; fax: 858-784-2583; phone: 858-784-2559 (F.T.), 858-784-9098 (C.F.B).

10.1021/bc070080x CCC: $37.00 © 2007 American Chemical Society
Published on Web 06/30/2007

overnight, washed with H_2O two times, and blocked with 3% BSA/PBS (170 μL/well) at room temperature for 1.5 h (PBS is 10 mM Na_2HPO_4, 1.8 mM KH_2PO_4, 137 mM NaCl, 2.7 mM KCl, pH 7.4). Blocking solution was removed, and the library phage were added. After 2 h, the wells were washed 10 times with 0.5% Tween 20/PBS (PBST) to remove unbound phage. The bound phage were eluted by trypsin digestion (Difco Trypsin 1:250, 10 mg/mL in TBS, 50 μL/well) at 37 °C for 30 min, added to *E. coli* 2537 cells in LB medium, and grown using the procedures recommended by NEB. After four rounds of selection using each phage-displayed peptide library separately, panned libraries were combined and an additional three rounds of selection were performed. The DNA sequences of the clones from the seventh round were analyzed using procedures recommended by NEB. Individual clones were analyzed by ELISA for binding to **1**−BSA immobilized on wells of a microtiter plate using anti-M13 antibody−horseradish peroxidase conjugate (Amersham) and the peroxidase substrates 2,2′-azinobis(3-ethylbenzothiazoline-6-sulfonic acid) (ABTS) and hydrogen peroxide.

Construction of the Second and Third Libraries and Peptide Selections. The synthesized oligonucleotide library was amplified by PCR using 5′-primer SfiI-f (5′-GAGGAGGAG-GAGGCCCAGGCGGCC-3′) and 3′-primer SfiI-b (5′-GAG-GAGGAGGAGGCCGGCCTGGCC-3′). The PCR conditions as were follows: SfiI-f, 1 μg; SfiI-b, 1 μg; oligonucleotide library, 50 ng; 0.2 mM each dNTP; 10 μL of 10x PCR buffer; 2.5 units of Ampli Taq DNA polymerase (Roche) in a total volume of 100 μL. A program of 94 °C 1 min; 94 °C 15 s, 52 °C 15 s, 72 °C 30 s (25 times); 72 °C 10 min was used for amplification. The PCR products were purified, digested with *Sfi*I, and ligated to *Sfi*I-digested pComb3X using T4 DNA ligase (NEB). The following oligonucleotides were used (N = A, C, G, or T; K = G or T): PhD-C7C-NNK6 (5′-GGCCCAGGCGGCCTGTCAT-AATCATCAGAAGGCTACGTGCNNKNNKN NKNNKNN-KNNKGGCCAGGCCGGCC-3′), PhD7−2-NNK6-f (5′-GGCC-CAGGCGGCCGCTGCTGTGGCTAAGCCGCCGNNKNNKNN-KNNKNN KNNKGGCCAGGCCGGCC-3′), NNK6-PhD7-2-f (5′-GGCCCAGGCGGCCNNKNNKNNKNNKNNKNNKG-CTGCTGTGGCTAAGC CGCCGGGCCAGGCCGGCC-3′), PhD7-6-NNK6-f (5′-GGCCCAGGCGGCCGTGTCGGTGCA-GACTAAGTATNNKNNKNNKNNK NNKNNKGGCCAG-GCCGGCC-3′), NNK6-PhD7−6-f (5′-GGCCCAGGCGGCC-NNKNNKNNKNNKNNKNNKGTGTCGGTGCAGAC TAAG-TATGGCCAGGCCGGCC-3′), PhD7-14-NNK6-f (5′-GGCCCA-GGCGGCCAATCCGCTGGGTGCTAAGTTGNNKNNKNN-KNNK NNKNNKGGCCAGGCCGGCC-3′), NNK6-PhD7-14-f (5′-GGCCCAGGCGGCCNNKNNKNNKNNKNNKNNKAA-TCCGCTGGGTGCTAAGTTGGGCCAGGCCGGCC-3′), PhD12-3-NNK6-f (5′-GGCCCAGGCGGCCGCTGCTATGGATG-CTAAGAATTCTCCTGCTTCTGC TNNKNNKNNKNNKN-NKNNKGGCCAGGCCGGCC-3′), NNK6−PhD12−3-f (5′-GGCCCAGGCGGCCNNKNNKNNKNNKNNKNNKGCTGC-TATGGATGCT AAGAATTCTCCTGCTTCTGCTGGCCAG-GCCGGCC-3′), PhD12-9-NNK6-f (5′-GGCCCAGGCGGC-CGATTTGCCTATTCCTACTACGAAGCTTGGGCGGTCTNN-KNNKNNKNNKNNKNNKGGCCAGGCCGGCC-3′), and NNK6-PhD12-9-f (5′-GGCCCAGGCGGCCNNKNNKNNKNN-KNNKNNKGATTTGCCTATTCCTACTACGAAGCTTGGGCG-GTCTGGCCAGGCCGGCC-3′).

Construction of the third libraries was performed using the same procedures as used for construction of the second libraries. The following oligonucleotides were used: PhD-C7C-1319-NNK6 (5′-GGCCCAGGCGGCCTGTCATAATCATCAGAA-GGCTACGTGCACGGCGCAG GCGCAGAGTNNKNNKNN-KNNKNNKNNKGGCCAGGCCGGCC-3′), PhD-C7C-1320-NNK6 (5′-GGCCCAGGCGGCCTGTCATAATCATCA-GAAGGCTACGTGCCGGAGGATG CGGTCTAGGNNKNN-KNNKNNKNNKNNKGGCCAGGCCGGCC-3′), PhD-C7C-1322-NNK6(5′-GGCCCAGGCGGCCTGTCATAATCATCAGAA-GGCTACGTGCTCGTGGGTT CTTGTGCCGNNKNNKNN-KNNKNNKNNKGGCCAGGCCGGCC-3′), PhD-C7C-1326-NNK6 (5′-GGCCCAGGCGGCCTGTCATAATCATCAGA-AGGCTACGTGCCCGAGGGAT AGGCATGGGNNKNN-KNNKNNKNNKNNKGGCCAGGCCGGCC-3′), PhD7-14-2-NNK6 (5′-GGCCCAGGCGGCCAATCCGCTGGGTGCTA-AGTTGGCGGGTGTGTTTTGG TGGNNKNNKNNKNNK-NNKNNKGGCCAGGCCGGCC-3′), and PhD7-14-10-NNK6 (5′-GGCCCAGGCGGCCAATCCGCTGGGT-GCTAAGTTGGCTATGGCTATGTGG GGGNNKNNKNN-KNNKNNKNNKGGCCAGGCCGGCC-3′). The library size of the second and third libraries was between 2.3×10^7 and 3.1×10^8.

Ligation mixtures were ethanol precipitated and transformed into *E. coli* ER 2537 cells by electroporation. Immediately after transformation, 5 mL of SOC (2% trypton, 0.5% yeast extract, 0.05% NaCl, 2.5 mM KCl, 10 mM $MgCl_2$, 20 mM glucose) was added to each reaction, and the cells were grown at 37 °C. After 1 h, 10 mL of super broth (SB, 3% trypton, 2% yeast extract, 1% Mops) and carbenicillin (to 20 μg/mL) were added. After 1 h, additional carbenicillin was added to increase the final concentration to 50 μg/mL. After 1 h, helper phage VCS-M13 ($\sim 10^{13}$ pfu) were added, and the culture volume was increased to 100 mL by the addition of SB including carbenicillin (at 50 μg/mL). After 1.5 h, kanamycin (for a final concentration of 70 μg/mL) was added, and the culture was incubated at 37 °C over night. The cells were removed by centrifugation (4000 rpm, 30 min). Phage were purified by precipitation: Poly(ethylene glycol) 8000 (final concentration 4% w/v) and NaCl (final concentration 3% w/v) were added to the supernatant, and, after 30 min on ice, the mixture was centrifuged at 9000 rpm for 20 min. The phage precipitate was resuspended in 1% BSA/PBS (2 mL) and filtered (0.2 μm).

Selection was performed using **1**−BSA immobilized on wells in a microtiter plate as described above. The bound phage eluted by trypsin were added to *E. coli* ER2537 cells (20 mL in SB), and the culture was shaken at 37 °C. After 15 min, carbenicillin (for a final concentration of 20 μg/mL) was added. After 45 min, helper phage VCS-M13 ($\sim 10^{12}$ pfu) was added, and the culture was diluted to the total volume 100 mL with SB containing carbenicillin (50 μg/mL). After 1.5 h, kanamycin (final concentration of 70 μg/mL) was added, and the culture was incubated at the same temperature overnight. Phage were purified as described above and were used for further panning.

An enzyme-linked immunosorbent assay (ELISA) of individual clones against **1**−BSA immobilized on wells of a microtiter plate was performed using anti-decapeptide antibody−alkaline phosphatase conjugate (Pierce) and *p*-nitrophenyl phosphate.

Preparation rpf1368-MBP. The *Sfi*I-digested fragment of rpf1368 was ligated to *Sfi*I-digested pComb3-MBP vector (see below) with T4 DNA ligase. The ligation mixture was transformed into *E. coli* XL1-Blue cells (Stratagene) by electroporation. After transformation, SOC (2 mL) was immediately added, and the cells were grown at 37 °C. After 1 h, the culture (100, 10, and 1.0 μL) was plated on LB agar containing carbenicillin (100 μg/mL). Individual colonies were picked from the plates and grown in SB (5 mL) containing carbenicillin (50 μg/mL) at 37 °C for overnight. The culture was diluted 1:10 in SB containing 0.2% glucose and carbenicillin (50 μg/mL) and was grown for 2 h at 37 °C. Expression of the rpf1368-MBP genes was induced by addition of IPTG (1 mM), and the culture was incubated for additional 3 h. The culture was centrifuged

(3500 rpm) for 20 min, and the cells were resuspended in PBS (500 μL) and then freeze-thawed five times in a dry ice−ethanol bath and water bath. The lysate sample was spun in a microcentrifuge at maximum speed for 20 min, and the supernatant was used for the ELISA with **1**−BSA (see below). The sequence of rpf1368-MBP was confirmed by DNA sequencing of peptide rpf1368 region using primer Mal-B (5′-GAATTTCTCTTCCAGTTTATCCG-3′) as well as the positive signal in ELISA with **1**−BSA.

For large-scale production of rpf1368-MBP, the following procedures were used: The colony was picked from a plate and grown in SB (5 mL) containing carbenicillin (50 μg/mL) at 37 °C for overnight. A 1 mL aliquot of the culture was added into each of two flasks containing 100 mL of SB containing 0.2% glucose, 20 mM $MgCl_2$, and carbenicillin (50 μg/mL) and was grown for 7 h at 37 °C. Expression of the rpf1368-MBP genes was induced by addition of IPTG (1 mM), and the culture was incubated overnight. The culture was centrifuged (3500 rpm) for 20 min at 4 °C, and the cells were resuspended in amylose column buffer (5 mL) composed of 20 mM Tris-HCl, 200 mM NaCl, 1 mM EDTA, and 1 mM PMSF. The cells were sonicated on ice using Tekmer Sonic Disrupter. The lysate sample was centrifuged (3500 rpm) for 15 min at 4 °C, and the supernatant was filtered. The filtrate was applied to the amylose resin column (pre-equilibrated with the amylose column buffer). The column was washed with the column buffer and rpf1368-MBP was eluted with 10 mM maltose in column buffer. The combined eluted fractions were concentrated, and the buffer was changed to PBS using Centriprep-10 (Millipore). The protein purity was judged to be >95% by in gel electrophoresis.

Construction of pComb3-MBP. Cloning of the *Sfi*I-digested fragment from the pComb3X (*31*) into pComb3-MBP allowed the production of the MBP-fusion. Vector pComb3-MBP produces N-terminal MBP-fusion (protein/peptide of interest fused at the N-terminus of MBP), and the N-terminal sequence of protein/peptide of the MBP fusion is identical to that produced from the pComb3X system. Vector pComb3-MBP was prepared by replacing gene III of pComb3X with the MBP gene from pMAL-pIII (*32*).

PCR was performed using (i) primers Bseq (5′-GTGAGC-GAGGAAGCGGAAGAG-3′) and TT-SfiI-b (5′-CATCTGGC-CGGCCTGGCCACTAG-3′) and template pComb3X containing anti-tetanus toxoid Fab p313 gene (*33*) between the *Sfi*I sites, and (ii) primers SfiI-MBP-f (5′-GGCCAGGCCGGCCAGAT-GAAAATCGAAGAAGGTAAACTG-3′) and MBP-NotI-b (5′-GAGGAGGAGAAGCGGCCGCTTAAATTAATTAGCTA-GCTTAAGAGGAT CCAAATTCTGAAATCC-3′) which included a silent mutation to destroy an intrinsic *Eco*RI site in MBP (indicated by underlining) and template pMAL-pIII. The PCR fragments were fused using primers Bseq and MBP-NotI-b. The resulting PCR product was digested with *Eco*RI and *Not*I and purified. The fragment was ligated to *Eco*RI/*Not*I-digested pComb3X. The correct vector pComb3-MBP was identified by the production of anti-tetanus toxoid Fab fused to MBP and by ELISA against tetanus toxoid using detection of MBP. When the gene of a protein is cloned by the *Sfi*I sites into this vector and the protein is overproduced, the protein is delivered into the periplasm. Thus in this system disulfide bonds that are conformationally reasonable can form automatically in the periplasm when the protein is produced in *E. coli* cells.

ELISA of rpf1368-MBP. Wells of a microtiter plate (Costar 3690) were coated with **1**−BSA (1 μg/PBS 25 μL/well) at 37 °C for 1 h, washed with H_2O two times, and blocked with 3% BSA/PBS (170 μL/well) at 37 °C for 1 h. Blocking solution was removed, and ELISA sample (cell lysate or purified protein) was added (25 μL/well). After 2 h of incubation at room temperature, the wells were washed 10 times with water. The bound rpf1368-MBP was detected using mouse anti-MBP antibody clone MBP-17 (Sigma), goat anti-mouse antibody-alkaline phosphatase conjugate (Pierce), and the phosphatase substrate *p*-nitrophenyl phosphate. The resulting yellow color was measured at 405 nm. For the control MBP, MBP2* protein (NEB) was used.

For the ELISA using **1**−biotin (Figure 2b), wells of a microtiter plate (Costar 3690) were coated with NeutrAvidin (Pierce) (10 μg/PBS 25 μL/well) at 37 °C for 1 h and washed with H_2O two times, and **1**−biotin (80 μM/PBS, 25 μL) was added. After 2 h incubation at room temperature, the wells were washed with H_2O two times and were blocked with 3% BSA/PBS (170 μL/well) at room temperature for 1 h. Blocking solution was removed, and ELISA sample was added. The same procedure was then followed as described for the ELISA with **1**−BSA. For background ELISA, the same procedures were used except that **1**−biotin was added (i.e., wells coated with NeutrAvidin were used for background binding studies).

Whereas **1**−BSA possessed ∼30 diketone moieties per BSA molecule, each subunit of NeutrAvidin binds one molecule of biotin. Therefore, ELISA using **1**−BSA afforded greater signal (absorption at 405 nm) than that using **1**−biotin/NeutrAvidin. Because of the difference in the numbers of the diketone moieties presented on well surfaces, the ELISA signal difference between binding to **1**−BSA and to BSA (background) were also greater than that between binding to **1**−biotin/NeutrAvidin and to NeutrAvidin (background).

Reaction of rpf1368-MBP with 2,4-Pentanedione. Reactions were initiated by adding 2 μL of 2,4-pentanedione (20 mM in CH_3CN) to 78 μL of rpf1368-MBP solution in PBS at 25 °C. The final conditions were [rpf1368-MBP] 2 μM, [2,4-pentanedione] 500 μM in 2.5% CH_3CN/PBS (total volume 80 μL). Enaminone formation was measured by the increase in absorption at 318 nm using a spectrophotometer.

Peptide rpf1368. Peptide rpf1368 was synthesized on a peptide synthesizer using standard Fmoc solid-phase peptide synthesis chemistry, purified by HPLC to >95% purity, and characterized by mass spectrometry. An intramolecular S−S bond was formed when the peptide was stored in buffer under air at room temperature overnight or during the reaction with diketones. The cyclized form of the peptide was also characterized by mass analysis.

Mass Analysis for the Reaction of Peptide rpf1368 with Diketone 2. Reactions were initiated by adding 2.5 μL of diketone **2** (20 mM in CH_3CN) to a mixture of 47 μL of 50 mM Na phosphate, pH 7.0, and 0.5 μL of peptide rpf1368 (10 mM in H_2O). The final conditions were [rpf1368] 100 μM, [**2**] 1 mM in 5% CH_3CN−47 mM Na phosphate, pH 7.0 (total volume 50 μL). After 1 day, MALDI-TOF analysis was performed.

Synthesis of 1−Biotin. See Supporting Information. A mixture of EZ-Link Biotin PEO-LC-Amine (Pierce) (11.2 mg, 0.027 mmol) and diketone *N*-hydroxysuccinimide ester (*N*-hydroxysuccinimide ester rather than BSA amide in the structure of **1**−BSA shown in Figure 1; 9.3 mg, 0.022 mmol) in CH_3CN (0.2 mL)−MeOH (0.2 mL) was stirred at room temperature for 3 h. The mixture was purified by flash silica gel chromatography (EtOAc/MeOH = 4:1 to 2:1) to afford **1**−biotin (7.4 mg, 46%). ^{1}H NMR (500 MHz, CD_3OD) δ 7.50 (d, J = 8.5 Hz, 2H), 7.19 (d, J = 8.5 Hz, 2H), 4.52 (m, 1H), 4.33 (m, 1H), 3.70−3.62 (m, 8H), 3.59 (t, J = 5.5 Hz, 2H), 3.56 (t, J = 5.5 Hz, 2H), 3.41 (t, J = 5.5 Hz, 2H), 3.38 (t, J = 5.5 Hz, 2H), 3.24 (m, 1H), 2.99−2.86 (m, 2H), 2.92 (t, J = 7.4 Hz, 2H × 0.5), 2.74 (m, 1H), 2.63 (t, J = 7.4 Hz, 2H × 0.5), 2.44 (t, J = 7.4 Hz, 2H), 2.33 (t, J = 7.4 Hz, 2H), 2.25 (t, J = 7.4 Hz, 2H), 2.05 (s,

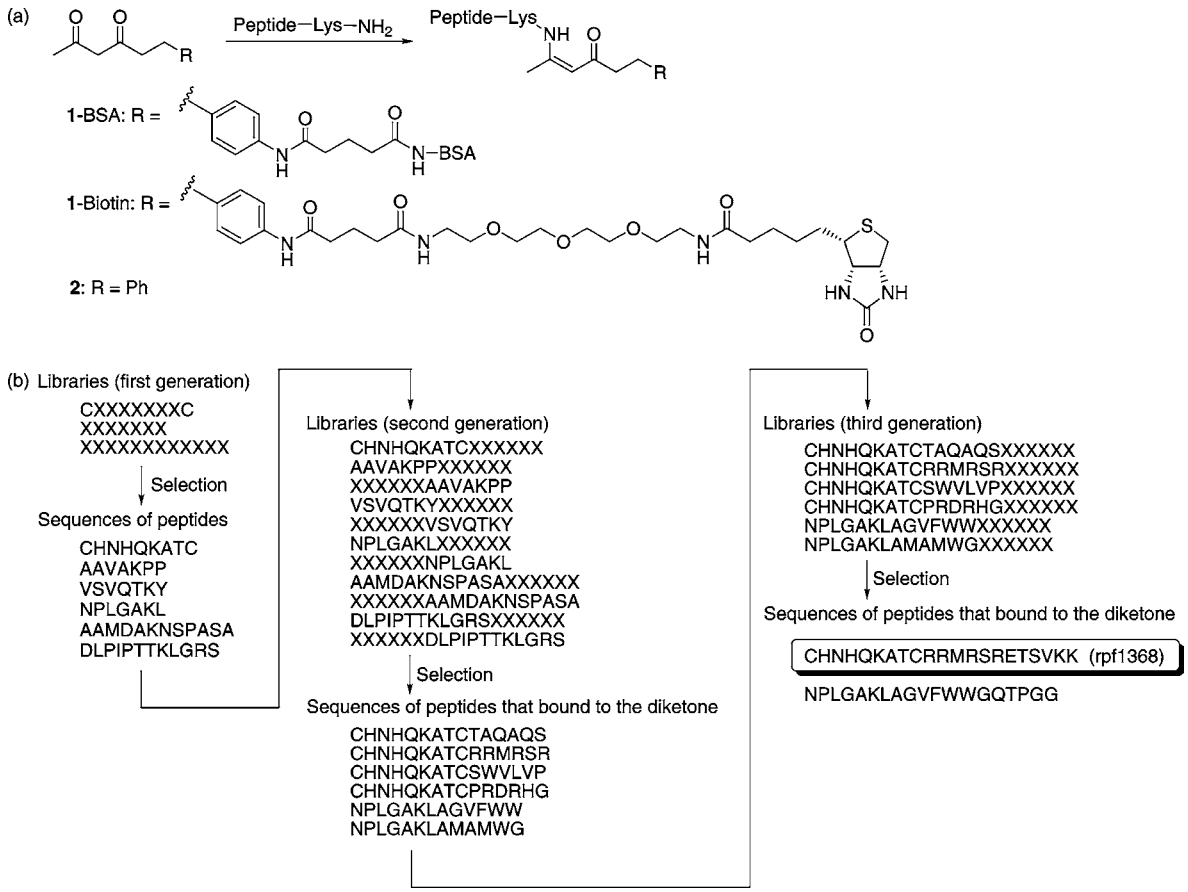


Figure 1. Selection of peptides that form enaminones with diketones. (a) 1,3-Diketones and enaminone formation. (b) Peptide libraries and selected peptide sequences. Selection implies selection using phage display with **1**−BSA immobilized on wells in a microtiter plate.

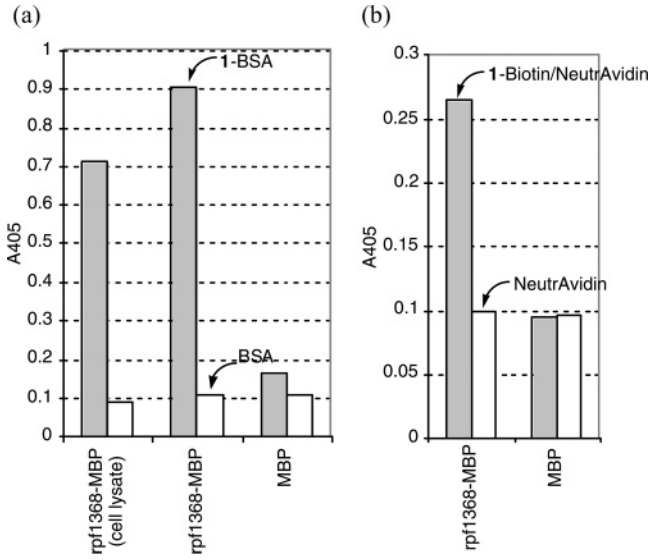


Figure 2. Binding assays of rpf1368-MBP to diketones. (a) ELISA with **1**−BSA. The cell lysate of *E. coli* cells expressing the fusion protein (labeled as cell lysate) was evaluated, as were purified proteins. Data of binding to **1**−BSA and to BSA (background) are shown: **1**−BSA (gray), BSA (white). Deviations were within ±10% of the indicated values. (b) ELISA with **1**−biotin. Data of binding to **1**−biotin supported on NeutrAvidin and to NeutrAvidin (background) are shown: **1**−biotin/NeutrAvidin (gray), NeutrAvidin (white). Deviations were within ±10% of the indicated values.

3H × 0.5), 2.02 (quintet, J = 7.4 Hz, 2H), 1.82−1.43 (m, 6H). MALDI-FTMS calcd for $C_{35}H_{54}N_5O_9S$ (MH^+) 720.3637, found 720.3590.

RESULTS AND DISCUSSION

Design of Labeling System Using Enaminone Formation and Selection of Peptides. Lysine ϵ-amino groups and N-terminal amino groups in proteins and peptides are not typically nucleophilic enough to form enaminones with 1,3-diketones at neutral pH, but certain enzymes have nucleophilic lysine ϵ-amino groups that are essential for catalysis (*34*, *35*). 1,3-Diketones act as inhibitors of such enzymes by formation of enaminones with the nucleophilic amino groups (*36*). Because of the π-conjugation, enaminones are very stable (*34*, *36*, *37*). In order for an amino group to be nucleophilic enough to allow for formation of an enaminone with diketones, the amino group must either have an electrostatic interaction with a positively charged residue or be present within a hydrophobic microenvironment (*35*, *38*, *39*). Only proteins and peptides that can provide such interactions/microenvironments can form enaminones with 1,3-diketones. Thus a small peptide that forms an enaminone with a 1,3-diketone derivative should provide selective and stable labeling of a protein of interest through the enaminone formation reaction with a diketone-labeling molecule conjugate.

Although peptides possessing lysine residues in α-helical structures whose lysine ϵ-amino groups are nucleophilic have also been developed by design (*40*, *41*−*43*), design of peptides that form an enaminone with 1,3-diketones is generally a difficult task. To efficiently develop proteins and peptides that have nucleophilic amino group(s), we have used selections from libraries based on formation of enaminones with 1,3-diketones. Using the enaminone formation reaction-based selections with 1,3-diketone derivatives from antibody libaries, we have previously developed catalytic antibodies that possess a nucleophilic lysine ϵ-amino group for catalysis (*33*, *34*, *44*). We have also demonstrated that peptides with improved activities for enamine

catalysis can be generated by the reaction-based selection with 1,3-diketones using phage displayed peptide libraries (*45*, *46*) and developed an RNase S-peptide-derived small peptide that forms an enaminone, upon interaction with RNase S-protein (*47*).

Here we have explored reaction-based selection with 1,3-diketone derivatives using peptide libraries that did not initially include helix or sheet structures. Peptide libraries composed of randomized amino acids that are not part of other folded proteins were previously used to identify peptides that noncovalently bind to small molecules (*48*). Although selections starting from a completely randomized 80-mer protein library have been performed to select ATP binding proteins (*49*), current methods allow for only a small portion of such libraries to be probed. Further, the results obtained from such libraries have not superseded results obtained with smaller peptide libraries. Thus, we started our selection using peptides containing seven to twelve randomized amino acids displayed on phage. Initially selected peptides were improved by extending their structure through the attachment of libraries composed of six randomized amino acids followed by the same reaction-based selections. Multiple rounds of peptide growth and selection were performed to access functional peptides without resorting to a longer peptide library where the theoretically diversity of the library would far exceed that examined in the actual experiment.

First, phage-displayed peptide libraries that contained seven randomized amino acids flanked by a pair of cysteine residues (CX_7C, X = any of the natural 20 amino acids), linear seven-mer peptides (X_7), and linear 12-mer peptides (X_{12}) fused via a short spacer to the N-terminus of a minor coat protein (pIII) of the filamentous bacteriophage M13 phage were screened in a covalent selection with a 1,3-diketone derivative (Figure 1). Four rounds of binding selection of each peptide-phage library were performed against diketone **1**−bovine serum albumin conjugate (**1**−BSA) (*34*) immobilized on wells in a microtiter plate. Phage from each of the selected libraries were combined, and three additional rounds of selection were performed. After the final round of selection from the first libraries, individual clones were examined for binding to the diketone in an enzyme-linked immunosorbent assay (ELISA) using **1**−BSA. The amino acid sequences of the 20 individual clones that showed positive signals, including those with borderline signals (the ELISA signal was above the background but less than 2-fold of the background) in the ELISA, were determined, and six different peptides (total 10 out of the 20) had at least one lysine residue. Since we were more interested in peptides that formed enaminones through lysine ϵ-amino groups than through the N-terminal amino group, these six peptide sequences were used as the starting points for further improvement. The peptides were elongated to evolve their activity by attachment of six randomized amino acid residues of each of the natural 20 amino acids. The resulting libraries (the second generation libraries) were selected against **1**−BSA for four rounds using the monovalent phage display system pComb3X (*31*). ELISA identified individual clones, from the final round of selection from the second-generation libraries, that bound to **1**−BSA, and the amino acid sequences of the bound clones were determined. These peptides were further elongated by attachment of six randomized amino acid residues, and the same phage selection procedure was used. After the selection from the third generation libraries, a peptide that showed a relatively strong ELISA signal (more than 5-fold of the background) against **1**−BSA, named rpf1368 (Figure 1b), was obtained, and this peptide was further characterized.

Preparation of the Fusion Protein and Evaluation of Diketone Labeling. In order to examine whether peptide rpf1368 could be used to label a protein, a fusion of this peptide with maltose binding protein (MBP) was prepared, and labeling

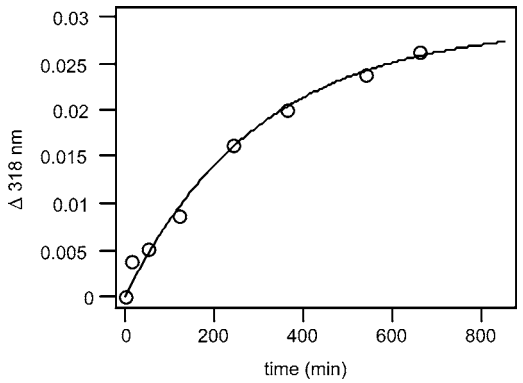


Figure 3. Time course of enaminone formation of rpf1368-MBP with 2,4-pentanedione. Increase in absorption at 318 nm, characteristic of the enaminone, was monitored. Conditions: [rpf1368-MBP] 2 μM and [2,4-pentanedione] 500 μM in 2.5% CH_3CN/PBS. The second-order rate constant k in this reaction {V (M/min) = k[2,4-pentanedione (M)][peptide rpf1368 (M)]} was 6.0 M^{-1} min^{-1}.

was analyzed by ELISA with **1**−BSA. The culture supernatant and lysates of *E. coli* cells that produced fusion protein rpf1368-MBP showed a positive signal in the ELISA, while the culture supernatant and lysate of *E. coli* cells that did not produce rpf1368-MBP or that produced only MBP were negative in the same ELISA. The ELISA results concerning these cell lysate experiments and those performed with the purified protein are shown in Figure 2a. Both the cell lysate containing rpf1368-MBP and the purified fusion protein rpf1368-MBP bound to the diketone conjugate **1**−BSA significantly better than to BSA. These results indicate that rpf1368 tagged protein can be labeled with diketone derivatives. Since MBP that was not fused to peptide rpf1368 did not bind to **1**−BSA, the peptide rpf1368 portion of rpf1368-MBP is essential for binding to the diketone. Note that MBP has 34 lysine residues per molecule. The ELISA results indicate that peptide rpf1368 has a different chemical reactivity with the 1,3-diketone and is selectively labeled.

Labeling of protein rpf1368-MBP was also analyzed using diketone−biotin conjugate **1**−biotin in ELISA experiments. Fusion protein rpf1368-MBP bound to **1**−biotin supported on a NeutrAvidin, but native MBP did not (Figure 2b). Biotin was introduced into rpf1368-MBP without requirements of the addition of any second catalysts or reagents. These results indicate that peptide rpf1368 functions as a fusion protein and that this peptide can be used as a tag for proteins to introduce compounds conjugated with the diketone.

Formation of enaminones can be monitored through the UV absorption characteristic of the enaminone at 318 nm (*34*), so enaminone formation of rpf1368-MBP was analyzed by monitoring this UV absorption band. When rpf1368-MBP was mixed with 2,4-pentanedione, the smallest compound containing the diketone structure, at pH 7.4, an increase in UV absorption at 318 nm was observed, indicating that rpf1368-MBP covalently bound to this diketone through formation of an enaminone linkage. When 500 μM of 2,4-pentanedione and 2 μM of rpf1368-MBP were mixed in buffer at pH 7.4, the enaminone formation reaction took approximately 10 h to reach >90% modification as shown in Figure 3. This reaction rate for enaminone formation between rpf1368 and 2,4-pentanedione should be acceptable for labeling. Fusion protein rpf1368-MBP was labeled at a low protein concentration (2 μM). When we studied our previously developed 24-mer peptide FT-YLK3 (*46*) that possesses nucleophilic lysine residues in a helical structure upon dimerization or oligomerization was fused to MBP, the labeling of FT-YLK3-MBP fusion with 1,3-diketones was not detected at 2 μM fusion protein concentration. At a high concentration, FT-YLK3-MBP formed oligomers, possibly based on oligomerization of the FT-YLK3 portion. Such

oligomerization typically is not suitable for many uses of labeled fusion proteins. Thus, as a labeling tag, peptide rpf1368 is superior to our previously developed small peptides containing helical structures where self-association is key for the conformation necessary to provide enaminone forming amino groups.

Characterization of the Labeling Reaction Using Synthetic Peptides. In order to characterize the peptide in more detail, the 21-mer peptide rpf1368 was chemically synthesized (with a C-terminal amide, in cyclic form due to the formation of a disulfide bond between cysteines) and evaluated. This synthesized peptide also showed an increase in UV absorption at 318 nm upon addition of 2,4-pentanedione, characteristic of enaminone formation. Enaminone formation was also confirmed by MALDI-TOF mass analysis. A mixture of peptide rpf1368 and diketone **2** gave isotopic mass *m*/*z* MH^+ of 2725 whereas peptide rpf1368 alone had isotopic mass *m*/*z* MH^+ of 2553 (see Supporting Information). One molecule of diketone **2** (MW 190) was incorporated per peptide rpf1368 and one molecule of H_2O (MW 18) was released, indicating the formation of the enaminone through an amino group of the peptide. Only one amino group of rpf1368 was nucleophilic. Another possible covalent modification, formation of the pyrimidine derivative with a guanidyl group of an arginine, was excluded by the mass analysis: If a guanidyl group reacted with diketone **2** and formed a derivative of pyrimidine (*50*), the mass MH^+ should be 2707 because two molecules of H_2O are released in the formation of pyrimidine. Unrelated peptides possessing lysine residue(s), ELLELDKWASLWNC, ELKDKWASLWNWFNIT, ELDKWASLWNWFDITGGC, and CDEKSKLQEIYQELTQLKAAVGEL, did not form an enaminone with 2,4-pentanedione; no changes in absorption at 318 nm were observed in the presence of 2,4-pentanedione for these peptides. The single reactive site within peptide rpf1368 is in contrast to our previously developed 24-mer and 35-mer peptides possessing a helical structure (*46*, *51*). Although multiple lysine groups are present in peptide rpf1368, only one amino group was nucleophilic enough to form the enaminone.

The conformation of peptide rpf1368 was critical for the reactivity. An intramolecular disulfide bond between the two cysteines of the peptide formed spontaneously in buffer under air at room temperature. The uncyclized peptide (prior to disulfide bond formation) did not react with 2,4-pentanedione. The cyclic constraint of rpf1368 by the disulfide bond provided for the formation of favorable electrostatic interactions or a microenvironment that tuned the reactivity of the amino group.

CONCLUSION

We have developed a small 21-mer peptide that possesses a single reactive amino group using a reaction-based selection with a 1,3-diketone derivative and phage-displayed peptide libraries. The libraries did not contain designed helix or sheet structures. We have demonstrated that the peptide can be used as a tag for a protein of interest to covalently label the protein with a synthetic molecule through enaminone formation. No enzyme and no additional reagents were necessary for the labeling of the peptide−protein fusion with the diketone derivatives. Although the reactivity of peptide rpf1368 is still moderate compared to existing covalent labeling tags that are derivatives of natural proteins, this peptide is the smallest peptide tag for covalent labeling with designed synthetic molecules without the requirement of additional catalysts or toxic metal reagents. We have demonstrated that small peptides that covalently react with designer synthetic molecules can be generated. Further improvement of this peptide should provide better small peptide tags for covalent labeling. Using these tags, a variety of molecules such as reporter probes and other functionalities may be conveniently and covalently introduced into proteins of interest.

ACKNOWLEDGMENT

This study was supported in part by The Skaggs Institute for Chemical Biology and by NIH R21GM078447.

Supporting Information Available: A scheme for synthesis of **1**−biotin and mass spectra for the reaction of peptide rpf1368 with diketone **2**. This material is available free of charge via the Internet at http://pubs.acs.org.

LITERATURE CITED

(1) Prescher, J. A., and Bertozzi, C. R. (2005) Chemistry in living systems. *Nat. Chem. Biol. 1*, 13−21.

(2) Giepmans, B. N. G., Adams, S. R., Ellisman, M. H., and Tsien, R. Y. (2006) The fluorescent toolbox for assessing protein location and function. *Science 312*, 217−224.

(3) Keppler, A., Pick, H., Arivoli, C., Vogel, H., and Johnsson, K. (2004) Labeling of fusion proteins with synthetic fluorophores in living cells. *Proc. Natl. Acad. Sci. U.S.A. 101*, 9955−9959.

(4) George, N., Pick, H., Vogel, H., Johnsson, N., and Johnsson, K. (2004) Specific labeling of cell surface proteins with chemically diverse compounds. *J. Am. Chem. Soc. 126*, 8896−8897.

(5) Zhang, Z., Gildersleeve, J., Yang, Y.-Y., Xu, R., Loo, J. A., Uryu, S., Wong, C.-H., and Schultz, P. G. (2004) A new strategy for the synthesis of glycoproteins. *Science 303*, 371−373.

(6) Hamann, P. R., Hinman, L. M., Hollander, I., Beyer, C. F., Lindh, D., Holcomb, R., Hallett, W., Tsou, H.-R., Upeslacis, J., Shochat, D., Mountain, A., Flowers, D. A., and Bernstein, I. (2002) Gemtuzumab ozogamicin, a potent and selective anti-CD33 antibody−calicheamicin conjugate for treatment of acute myeloid leukemia. *Bioconjugate Chem. 13*, 47−58.

(7) Lillo, A. M., Sun, C., Gao, C., Ditzel, H., Parrish, J., Gauss, G.-M., Moss, J., Felding-Habermann, B., Wirsching, P., Boger, D. L., and Janda, K. D. (2004) A human single-chain antibody specific for integrin $\alpha_3\beta_1$ capable of cell internalization and delivery of antitumor agents. *Chem. Biol. 11*, 897−906.

(8) Mohsin, H., Jia, F., Sivagura, G., Hudson, M. J., Shelton, T. D., Hoffmann, T. J., Cutler, C. S., Ketring, A. R., Athey, P. S., Simon, J., Frank, R. K., Jurisson, S. S., and Lewis, M. R. (2006) Radiolanthanide-labeled monoclonal antibody CC49 for radioimmunotherapy of cancer: Biological comparison of DOTA conjugates and ^{149}Pm, ^{166}Ho, and ^{177}Lu. *Bioconjugate Chem. 17*, 485−492.

(9) Antczak, C., Jaggi, J., LeFave, C. V., Curcio, M. J., McDevitt, M. R., and Scheinberg, D. A. (2006) Influence of the linker on the biodistribution and catabolism of actinium-225 self-immolative tumor-targeted isotope generators. *Bioconjugate Chem. 17*, 1551−1560.

(10) Cheng, T.-L., Chen, B.-M., Chan, L.-Y., Wu, P.-Y., Chern, J.-W., and Roffler, S. R. (1997) Poly(ethylene glycol)modification of β-glucuronidase-antibody conjugates for solid-tumor therapy by targeted activation of glucuronide prodrugs. *Cancer Immunol. Immunother. 44*, 305−315.

(11) Yin, J., Liu, F., Li, X., and Walsh, C. T. (2004) Labeling proteins with small molecules by site-specific posttranslational modification. *J. Am. Chem. Soc. 126*, 7754−7755.

(12) Phizicky, E., Bastiaens, P. I. H., Zhu, H., Snyder, M., and Fields, S. (2003) Protein analysis on a proteomic scale. *Nature 422*, 208−215.

(13) Hodneland, C. D., Lee, Y.-S., Min, D.-H., and Mrksich, M. (2002) Selective immobilization of proteins to self-assembled monolayers presenting active site-directed capture ligands. *Proc. Natl. Acad. Sci. U.S.A. 99*, 5048−5052.

(14) Keppler, A., Gendreizig, S., Gronemeyer, T., Pick, H., Vogel, H., and Johnsson, K. (2003) A general method for the covalent labeling of fusion proteins with small molecules in vivo. *Nat. Biotechnol. 21*, 86−89.

(15) Yin, J., Lin, A. J., Golan, D. E., and Walsh, C. T. (2006) Site-specific protein labeling by Sfp phosphopantetheinyl transferase. *Nat. Protocols 1*, 280−285.

(16) Chen, I., Howarth, M., Lin, W., and Ting, A. Y. (2005) Site-specific labeling of cell surface proteins with biophysical probes using biotin ligase. *Nat. Methods 2*, 99−104.
(17) Griffin, B. A., Adams, S. R., and Tsien, R. Y. (1998) Specific covalent labeling of recombinant protein molecules inside live cells. *Science 281*, 269−272.
(18) Martin, B. R., Giepmans, B. N. G., Adams, S. R., and Tsien, R. Y. (2005) Mammalian cell-based optimization of the biarsenical-binding tetracysteine motif for improved fluorescence and affinity. *Nat. Biotechnol. 23*, 1308−1314.
(19) Lesaicherre, M.-L., Lue, R. Y. P., Chen, G. Y. J., Zhu, Q., and Yao, S. Q. (2002) Intein-mediated biotinylation of proteins and its application in a protein microarray. *J. Am. Chem. Soc. 124*, 8768−8769.
(20) Wood, R. J., Pascoe, D. D., Brown, Z. K., Medlicott, E. M., Kriek, M., Neylon, C., and Roach, P. L. (2004) Optimized conjugation of a fluorescent label to proteins via intein-mediated activation and ligation. *Bioconjugate Chem. 15*, 366−372.
(21) Muralidharan, V., and Muir, T. W. (2006) Protein ligation: an enabling technology for the biophysical analysis of proteins. *Nat. Methods 3*, 429−438.
(22) Tolbert, T. J., and Wong, C.-H. (2002) New methods for proteomic research: Preparation of proteins with N-terminal cysteines for labeling and conjugation. *Angew. Chem., Int. Ed. 41*, 2171−2174.
(23) Chelius, D., and Shaler, T. A. (2003) Capture of peptides with N-terminal serine and threonine: A sequence-specific chemical method for peptide mixture simplification. *Bioconjugate Chem. 14*, 205−211.
(24) Dirksen, A., Hackeng, T. M., and Dawson, P. E. (2006) Nucleophilic catalysis of oxime ligation. *Angew. Chem., Int. Ed. 45*, 7581−7584.
(25) Dirksen, A., Dirlsen, S., Hackeng, T. M., and Dawson, P. E. (2006) Nucleophilic catalysis of hydrazone formation and implications for dynamic covalent chemistry. *J. Am. Chem. Soc. 128*, 15602−15603.
(26) Miller, L. W., Sable, J., Goelet, P., Sheetz, M. P., and Cornish, V. W. (2004) Methotrexate conjugates: A molecular in vitro protein tag. *Angew. Chem., Int. Ed. 43*, 1672−1675.
(27) Miller, L. W., Cai, Y., Sheetz, M. P., and Cornish, V. W. (2005) In vitro protein labeling with trimethoprim conjugates: a flexible chemical tag. *Nat. Methods 2*, 255−257.
(28) Marks, K. M., Braun, P. D., and Nolan, G. P. (2004) A general approach for chemical labeling and rapid, spatially controlled protein inactivation. *Proc. Natl. Acad. Sci. U.S.A. 101*, 9982−9987.
(29) Farinas, J., and Verkman, A. S. (1999) Receptor-mediated targeting of fluorescent probes in living cells. *J. Biol. Chem. 274*, 7603−7606.
(30) Wu, M. M., Llopis, J., Adams, S., McCaffery, J. M., Kulomaa, M. S., Machen, T. E., Moore, H.-P. H., and Tsien, R. Y. (2000) Organelle pH studies using targeted avidin and fluorescein-biotin. *Chem. Biol. 7*, 197−209.
(31) Rader, C., and Barbas, C. F., III (1997) Phage display of combinatorial antibody libraries. *Curr. Opin. Biotechnol. 8*, 503−508.
(32) Zwick, M. B., Bonnycastle, L. L. C., Noren, K. A., Venturini, S., Leong, E., Barbas, C. F., III, Noren, C. J., and Scott, J. K. (1998) The maltose-binding protein as a scaffold for movovalent display of peptides derived from phage libraries. *Anal. Biochem. 264*, 87−97.
(33) Tanaka, F., Fuller, R., Shim, H., Lerner, R. A., and Barbas, C. F., III. (2004) Evolution of aldolase antibodies in vitro: correlation of catalytic activity and reaction-based selection. *J. Mol. Biol. 335*, 1007−1018.
(34) Wagner, J., Lerner, R. A., and Barbas, C. F., III (1995) Efficient aldolase catalytic antibodies that use the enamine mechanism of natural enzymes. *Science 270*, 1797−1800.
(35) Westheimer, F. H. (1995) Coincidences, decarboxylation, and electrostatic effects. *Tetrahedron 51*, 3−20.
(36) Guidinger, P. F., and Nowak, T. (1991) An active-site lysine in avian liver phosphoenolpyruvate carboxykinase. *Biochemistry 30*, 8851−8861.
(37) Rader, C., Sinha, S. C., Popkov, M., Lerner, R. A., and Barbas, C. F., III (2003) Chemically programmed monoclonal antibodies for cancer therapy: Adaptor immunotherapy based on a covalent antibody catalyst. *Proc. Natl. Acad. Sci. U.S.A. 100*, 5396−5400.
(38) Zhu, X., Tanaka, F., Hu, Y., Heine, A., Fuller, R., Zhong, G., Olson, A. J., Lerner, R. A., Barbas, C. F., III, and Wilson, I. A. (2004) Theorigin of enantioselectivity in aldolase antibodies: Crystal structure, site-directed mutagenesis, and computational analysis. *J. Mol. Biol. 343*, 1269−1280.
(39) Tanaka, F., Thayumanavan, R., Mase, N., and Barbas, C. F., III (2004) Rapid analysis of solvent effects on enamine formation by fluorescence: how might enzymes facilitate enamine chemistry with primary amines? *Tetrahedron Lett. 45*, 325−328.
(40) Johnsson, K., Allemann, R. K., Widmer, H., and Benner, S. A. (1993) Synthesis, structure and activity of artificial, rationally designed catalytic polypeptides. *Nature 365*, 530−532.
(41) Perez-Paya, E., Houghten, R. A., and Blondell, S. E. (1996) Functionalized protein-like structures from conformationally defined synthetic combinatorial libraries. *J. Biol. Chem. 271*, 4120−4126.
(42) Allert, M., and Baltzer, L. (2002) A designed folded polypeptide model system that catalyzes the decarboxylation of oxaloacetate. *Chem. Eur. J. 8*, 2549−2560.
(43) Weston, C. J., Cureton, C. H., Calvert, M. J., Smart, O. S., and Allemann, R. K. (2004) A stable miniature protein with oxaloacetate decarboxylase activity. *ChemBioChem 5*, 1075−1080.
(44) Tanaka, F., Lerner, R. A., and Barbas, C. F., III (2000) Reconstructing aldolase antibodies to alter their substrate specificity and turnover. *J. Am. Chem. Soc. 122*, 4835−4836.
(45) Tanaka, F., Barbas, C. F., III. (2001) Phage display selection of peptides possessing aldolase activity. *Chem. Commun.* 769−770.
(46) Tanaka, F., Fuller, R., and Barbas, C. F., III (2005) Development of small designer aldolase enzymes: Catalytic activity, folding, and substrate specificity. *Biochemistry 44*, 7583−7592.
(47) Tanaka, F., and Fuller, F. (2006) Control of function of a small protein by a protein. *Bioorg. Med. Chem. Lett. 16*, 4059−4062.
(48) Rozinov, M. N., and Nolan, G. P. (1998) (2001) Evolution of peptides that modulate the spectral qualities ofbound, small-molecule fluorophores. *Chem. Biol. 5*, 713−728.
(49) Keefe, A. D., and Szostak, J. W. (2001) Functional proteins from a random-sequence library. *Nature 410*, 715−718.
(50) Gilbert, H., F., III, and O'Leary, M. H. (1975) Modification of arginine and lysine in proteins with 2,4-pentanedione. *Biochemistry, 14*, 5194−5199.
(51) Tanaka, F., and Barbas, C. F., III. (2002) A modular assembly strategy for improving the substrate specificity of small catalytic peptides. *J. Am. Chem. Soc. 124*, 3510−3511.

BC070080X

Pharmacokinetics, Biodistribution, Stability and Toxicity of a Cell-Penetrating Peptide−Morpholino Oligomer Conjugate

Adams Amantana,* Hong M. Moulton, Melissa L. Cate, Muralimohan T. Reddy, Tom Whitehead, Jed N. Hassinger, Derek S. Youngblood, and Patrick L. Iversen

AVI BioPharma, Inc., Corvallis, Oregon. Received February 22, 2007; Revised Manuscript Received April 27, 2007

Objective: Conjugation of arginine-rich cell-penetrating peptide (CPP) to phosphorodiamidate morpholino oligomers (PMO) has been shown to enhance cytosolic and nuclear delivery of PMO. However, the *in vivo* disposition of CPP−PMO is largely unknown. In this study, we investigated the pharmacokinetics, tissue distribution, stability, and safety profile of an anti-c-*myc* PMO conjugated to the CPP, $(RXR)_4$ (X = 6-aminohexanoic acid) in rats. Methods: The PMO and CPP−PMO were administrated intravenously into rats. The concentrations of the PMO and the CPP−PMO in plasma and tissues were monitored by HPLC. The stability of the CPP portion of the CPP−PMO conjugate in rat plasma and tissue lysates was determined by mass spectrometry. The safety profile of the CPP−PMO was assessed by body weight changes, serum chemistry, and animal behavior. Results: CPP conjugation improved the kinetic behavior of PMO with a 2-fold increase in the estimated elimination half-life, a 4-fold increase in volume of distribution, and increased area under the plasma concentration vs time curve. Consistent with the improved pharmacokinetic profile, conjugation to CPP increased the uptake of PMO in all tissues except brain, varied between organ type with greater uptake enhancement occurring in liver, spleen, and lungs. The CPP−PMO conjugate had greater tissue retention than the corresponding PMO. Mass spectrometry data indicated no observable degradation of the PMO portion, while there was identifiable degradation of the CPP portion. Time-dependent CPP degradation was observed in plasma and tissue lysates, with the degradation in plasma being more rapid. The pattern of degraded products differed between the plasma and lysates. Safety evaluation data showed that the CPP−PMO was well-tolerated at the dose of 15 mg/kg with no apparent signs of toxicity. In contrast, at the dose of 150 mg/kg, adverse events such as lethargy, weight loss, and elevated BUN ($p < 0.01$) and serum creatinine ($p < 0.001$) levels were recorded. Supplementation with free L-arginine *ad libitum* showed improved clearance of serum creatinine ($p < 0.05$) and BUN ($p < 0.01$) at the toxicological dose, suggesting that the CPP caused toxicity in kidney. Conclusion: This study demonstrates that conjugation of CPP to PMO enhances the PMO pharmacokinetic profile, tissue uptake, and subsequent retention. Therefore, when dosed at ≤15 mg/kg, CPP is a promising transporter for enhancing PMO delivery in therapeutic settings.

INTRODUCTION

Phosphorodiamidate morpholino oligomers (PMO[1]) are uncharged steric-blocking antisense compounds that can interfere with protein translation, pre-mRNA splicing, and RNA synthesis (*1*−*5*). The structure of PMO differs from DNA, with two major structural changes in the phosphorodiester internucleoside linkages and the five-membered ring of the deoxyribose sugar of DNA, as shown in Figure 1. Several animal models have demonstrated the antisense specificity and efficacy of PMOs against their targets (*6*−*15*). Like many macromolecules, the cellular uptake of PMOs is limited. Recently, several studies have reported success using arginine-rich cell-penetrating peptides (CPPs) to improve cytosolic and nuclear delivery of PMO in cell culture and *in vivo*. For instance, conjugation of CPPs to PMOs enhanced the ability of PMOs to inhibit replication of various viruses in cell culture (*3*, *16*−*22*) and *in vivo* (*19*, *23*), as well as to alter pre-mRNA splicing (*24*−*27*). The internalization of CPP−PMO conjugates may be through an endocytosis mechanism involving binding of cell surface proteoglycans through electrostatic interactions between cationic charges of the CPP and anionic charges of the proteoglycans (*28*).

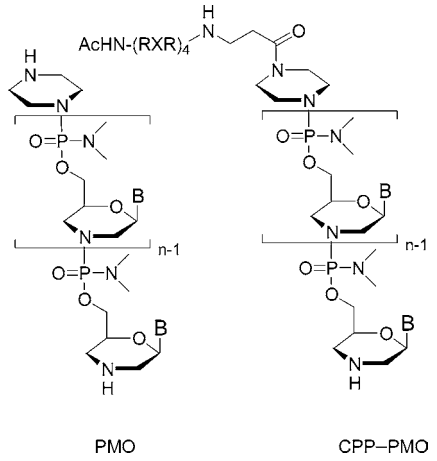


Figure 1. Structures of PMO and CPP−PMO.

These successes point to the potential of CPPs for the intracellular delivery of therapeutic PMO; however, there are no reports on the *in vivo* disposition of any CPP−PMO. Information regarding pharmacokinetics (PK), tissue distribution, dosing, and the safety profile of a CPP−PMO would be useful in designing animal experiments for various disease models.

* Corresponding author. Adams Amantana, Ph.D. Mailing Address: AVI BioPharma, Inc., 4575 SW Research Way, Corvallis, OR 97333. Phone (541) 753-3635; Fax (541) 754-3545. E-mail: (amantana@avibio.com).

[1] Abbreviations: CPP, cell-penetrating peptide; DMD, Duchene muscular dystrophy; MALDI-TOF, matrix-assisted laser desorption ionization time-of-flight mass spectrometry; *m*/*z*, mass-to-charge ratio; PBS, phosphate buffered saline; PMO: phosphorodiamidate morpholino oligomer; PNA, peptide nucleic acid.

10.1021/bc070060v CCC: $37.00 © 2007 American Chemical Society
Published on Web 06/21/2007

Therefore, the objective of this study was to evaluate the *in vivo* disposition of a PMO conjugated to a CPP having the $(RXR)_4XB$ sequence (X = 6-aminohexanoic acid, B = β-alanine, R = L-arginine). We chose this CPP for our study on the basis of the following. First, this CPP demonstrated greater serum stability compared to CPPs such as Tat and an oligoarginine (*29*). Second, PMO conjugated to this CPP had greater antisense activity than PMO conjugated to Tat and the oligoarginine CPP (*28*). Last, this CPP has been shown to successfully deliver PMO and caused specific antisense activities in several virus models (*3*, *17*, *18*, *23*) and in pre-mRNA splicing models (*24*, *25*, *28*). Here, we report the PK, tissue distribution, biological stability, and safety profile of the $(RXR)_4XB$−PMO conjugate (CPP−PMO) following intravenous injection in rats.

EXPERIMENTAL PROCEDURES

Synthesis of PMO, CPP, and CPP−PMO Conjugate. The PMO, CPP, and CPP−PMO conjugates were synthesized by AVI BioPharma (Corvallis, OR). The PMO with sequence 5′-ACGTTGAIIIGCATCGTCGC-3′ (I = inosine) was synthesized and purified to >90% by the previously described method (*1*, *30*). The peptide was synthesized and purified to >95% purity using the standard FMOC chemistry and HPLC method. The CPP−PMO conjugate was synthesized and purified according to a method described previously (*28*). The purity of the final conjugate was >90%.

PMO Quantitation. The concentration of PMO in tissue homogenates and plasma from the treated animals was evaluated by HPLC as described previously (*8*). An extra trypsin-digestion step was performed for the samples harvested from CPP−PMO treated rats. The trypsin-digestion step was used for removal of the CPP portion of the conjugate (*31*) and left the PMO portion for quantification. Briefly, a 100 μL aliquot of the plasma or tissue homogenate was mixed with 100 μL of trypsin solution (1.0 mg/mL in 1× PBS; Sigma Aldrich, St Louis, MO). The mixture was then incubated in a water bath at 37 °C overnight to facilitate the removal of the peptide from the CPP−PMO conjugate.

Animals and Husbandry. Experimentally naïve catheterized male Sprague−Dawley rats (Zivic Laboratories, Zelienople, PA) were used for this study. At the time of the experiment, the rats were 9−11 weeks old and weighed 200−250 g. On arrival, the animals were individually housed in stainless steel cages during the acclimatization and treatment periods in the laboratory animal resource center at Oregon State University (OSU), Corvallis, OR. The animals were exposed to a 12 h light/dark cycle in a temperature- and humidity-controlled environment and allowed access to commercially available rodent diet and city-supplied tap water. Temperature was maintained at 18−26 °C. The light/dark cycle was allowed to be interrupted for study-related activities. The animal studies were used in accordance with the guidelines established in the *Guide for the Care and the Use of Laboratory Animals of National Research Council* and was monitored by the institutional animal care and use committee, of OSU.

Treatments. Animals were randomly assigned to each treatment group. Each animal received intravenous (iv) bolus injection at 15, 30, and 150 mg/kg dosing levels of the CPP−PMO or PMO via an installed jugular vein catheter. In this study, the 150 mg/kg dose was chosen for toxicological evaluation. Blood samples were collected via the installed catheter at 0.2, 0.5, 1, 2, 4, 8, 12, and 24 h time points following a single dose for plasma PK evaluation. For the tissue uptake study, the animals were injected with a daily dose of 15 or 30 mg/kg for 5 days. The animals were euthanized 24 h or 5 days after the last injection by 100% carbon dioxide inhalation (in a plexiglass chamber). The liver, kidney, spleen, heart, brain, and lungs of the animals were harvested to assess the tissue distributions of the PMO and CPP−PMO.

Pharmacokinetic Evaluation. PK was characterized by compartmental analysis from the blood samples collected at different time points following the first administration. Plasma concentration versus time profiles were fitted into a two-compartmental open model with bolus intravenous input using the PK Solutions Software (Summit Research Services, Montrose, CO). The fitted PK parameters include the apparent elimination half-life ($T_{1/2}\beta$), plasma clearance (CL), volume of distribution (Vd), and the area under the concentration versus time curve (AUC). The AUC was estimated using the log-linear trapezoidal method. The plasma data were fitted to eq 1

$$C(t) = A\,e^{-\alpha t} + B\,e^{-\beta t} \quad (1)$$

where $C(t)$ is plasma concentration at time t; A and B are intercept terms; α is distribution rate constant; and β is elimination rate constant.

Biological Stability of CPP in Plasma and Tissues. Stability of the CPP−PMO was examined in the rat plasma and lysates of the liver, heart, and kidney. The tissue lysates were prepared as previously described (*32*). The CPP−PMO was incubated in the lysates or plasma at 37 °C for 1, 6, and 24 h periods. The PMO were extracted and subsequently analyzed by matrix-assisted laser desorption ionization time-of-flight mass spectrometry (MALDI-TOF MS) using a method described previously (*29*).

Safety Assessment. The safety of the CPP−PMO or PMO was evaluated on the basis of mortality as well as changes in physical appearance, behavior by cage-side observations, in-life body weight, and serum biochemistry profile. LD_{50} of the CPP−PMO was determined by iv administration of a single dose of the compound at the doses ranging from 1.2 to 400 mg/kg. The following serum components were monitored as part of the toxicological evaluation following administration of the CPP−PMO or PMO: serum alanine aminotransferase (ALT), lactate dehydrogenase (LDH), alkaline phosphatase, total bilirubin, albumin, total protein, glucose, cholesterol, blood urea nitrogen (BUN), and serum creatinine. All samples were evaluated by the analytical laboratory at OSU college of Veterinary Medicine.

Statistical Analysis. Data were analyzed using the statistical program *GraphPad Prism* v 4.01 (GraphPad Software, San Diego, CA). Statistical differences among compared groups were analyzed by one-way nonparametric ANOVA, and Tukey's multiple comparison post-test analysis with a p value less than 0.05 was considered statistically significant. Comparison of two dosage levels was conducted using the Student's t test. A two tailed p value less than 0.05 was considered statistically significant.

RESULTS

Plasma Pharmacokinetics. Conjugation of PMO to the CPP improved kinetic behavior of the PMO. Pharmacokinetic (PK) analysis was based on plasma data following a single intravenous injection. The plasma concentration data was described by a two-compartment PK model describing both the distribution and elimination phases. The plasma concentration vs time curves and the PK parameters of the CPP−PMO and PMO are presented in Figure 2 and Table 1 respectively. The plasma PK for the CPP−PMO was characterized by rapid distribution from the vascular space to tissues with an initial distribution half-life ($T_{1/2}\alpha$) ranging from 0.40 to 1.56 h. The CPP−PMO showed a prolonged elimination half-life ($T_{1/2}\beta$) ranging from 3.80 to 8.23 h, representing a 2-fold increase compared to the PMO at all three doses. Also, we observed a 4-fold increase in the

Table 1. Single-Dose Plasma Pharmacokinetics Following IV Bolus Administration of the CPP−PMO and PMO in Rats[a]

dose (mg/kg)	AUC (μg-hr/mL)	CL (L/hr)	Vd (L/kg)	$T_{1/2}\alpha$ (hr)	$T_{1/2}\beta$ (hr)
		PMO			
15	11.48 ± 1.44	0.32 ± 0.09	3.31 ± 0.17	0.44 ± 0.13	2.24 ± 0.91
30	44.58 ± 2.46	0.23 ± 0.02	4.81 ± 0.44	0.76 ± 0.04	2.83 ± 0.20
150	74.79 ± 6.77	0.47 ± 0.06	11.20 ± 2.26	0.80 ± 0.05	3.80 ± 0.54
		CPP−PMO			
15	13.50 ± 2.61	0.33 ± 0.01	12.10 ± 0.65[c]	0.40 ± 0.05	5.04 ± 0.06[d]
30	56.47 ± 1.61[c]	0.27 ± 0.02	11.23 ± 0.96[c]	0.63 ± 0.02	5.83 ± 0.86[d]
150	163.40 ± 5.52[b]	0.30 ± 0.04	15.22 ± 2.22	1.56 ± 0.10[b]	8.23 ± 0.07[c]

[a] Blood samples were collected at different time points over a 24 h period. Data were fit to the following equation $C(t) = A\ e^{-\alpha t} + B\ e^{-\beta t}$, where $C(t)$ is the plasma concentration at time t; A and B are intercept terms; α is distribution rate constant; and β is elimination rate constant. Each data point represents the mean ± SD of triplicate values. Student's t-test analysis: [b] $p < 0.001$, [c] $p < 0.01$, and [d] $p < 0.05$ CPP−PMO vs PMO treatment at equivalent dosing levels.

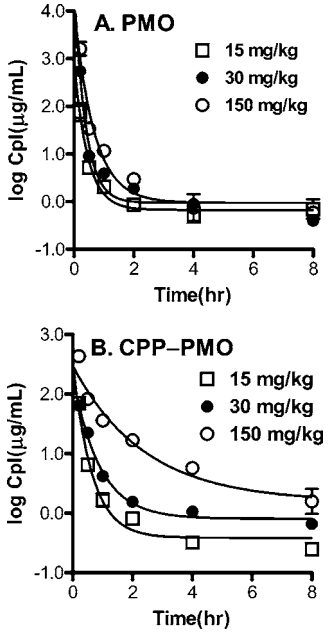


Figure 2. Plasma PMO concentration vs time profiles of (A) PMO and (B) CPP−PMO following a single iv bolus injection in rats at indicated dosing levels. Blood samples were collected at different time points over a 24 h period. The plasma PMO levels at the 12 and 24 h time points were below the lower limit of quantitation (LLOQ) of the detection method of 0.1 μg/mL. Each data point represents the mean ± SD of triplicate values.

Table 2. Safety Assessment of the PMO and CPP−PMO Conjugate[a]

dose (mg/kg)	Δwt (g)	BUN (mg/dL)	creatinine (mg/dL)
	PMO		
15	6.0 ± 6.93	24.50 ± 0.71	0.45 ± 0.07
30	8.7 ± 5.03	16.00 ± 1.41	0.20 ± 0.00
150	16.0 ± 8.72	21.50 ± 3.36	0.25 ± 0.07
	CPP−PMO		
15	16.0 ± 7.21	19.67 ± 3.79	0.37 ± 0.06
30	−19.0 ± 18.94	50.00 ± 36.77	0.55 ± 0.21
150	−39.3 ± 24.44[b]	106.00 ± 39.85[c]	2.03 ± 0.40[d]

[a] In-life body weight changes, serum BUN and creatinine data following iv bolus injection in rats. [b] Group received single daily injections for two consecutive days and animal body weight measured at the end of the 2 day period. The other groups received single daily injections for 5 days. [c] BUN ($p < 0.05$, one-way ANOVA, Tuckey's multiple comparison test). [d] Serum creatinine ($p < 0.001$, one-way ANOVA, Tukey's multiple comparison test). Reference range: BUN: 12−40 mg/dL, serum creatinine: 0.4−0.9 mg/dL.

volume of distribution (Vd) (12.10−15.22 L/kg body weight) at the 15 and 30 mg/kg doses following conjugation of the CPP to the PMO. There was a small but statistically significant increase in the area under the plasma concentration vs time curve (AUC) at the 30 mg/kg dose and a larger increase in AUC for the 150 mg/kg dose.

Tissue Distribution. Conjugation of PMO to the CPP increased the tissue uptake and retention of the PMO. The liver, kidney, spleen, heart, brain, and lungs of the animals were harvested 24 h following five single daily injections of 15 and 30 mg/kg PMO or CPP−PMO, to assess the tissue distribution of the PMO. The tissue recovery at the 15 mg/kg dose following a 5 day washout period was also evaluated. The data is presented in Figure 3A−C. The CPP−PMO showed a broad tissue distribution with the kidney and liver as the primary sites of accumulation. Relatively lower concentrations were detected in spleen, lungs, heart, and brain. At equivalent dose, the tissue recovery data showed that conjugation of the CPP improved tissue uptake of the PMO in all of these tissues except brain, with the liver, spleen, and lungs showing greater increases at compared to PMO both dosing levels. In addition, tissue concentrations of the CPP−PMO treated samples were greater than the PMO treated samples 5 days postdose (Figure 3C), indicating that CPP conjugation prolongs the duration of tissue retention.

Biological Stability of CPP−PMOs. The stability study found no evidence of PMO degradation, while the observed degradation of the CPP portion of CPP−PMO depended on time and tissue type. The degradation pattern varied among the tissue types and between tissue and plasma. The stability of the conjugate was examined in the plasma and the lysates of rat liver, heart, and kidney. The CPP−PMO was incubated with tissue lysates or plasma at 37 °C for 1, 6, and 24 h. The extracted materials were then analyzed by MALDI-TOF MS (*29*). The CPP portion of the conjugate degraded, more rapidly in plasma than in tissues (Figure 4). The intact CPP−PMO was observable in the plasma up to 6 h. A 24 h treatment resulted in complete degradation of the intact conjugate from $(RXR)_4XB$−PMO to RXRXB−PMO. However, degradation of CPP was slower in tissue homogenates, with no apparent degradation at 6 h but much degradation at 24 h. Unlike the heart and kidney, some intact CPP was detectable in the liver at the 24 h time point. Therefore, the biological stability of the CPP was ranked in the order of liver > heart = kidney > plasma. In the plasma, cleavage appeared to occur between adjacent L-arginine residues with the appearance of an m/z peak corresponding to RXR, which is consistent with the data observed in human serum (*29*). Comparatively, in the liver and kidney, degradation was observed to occur between adjacent L-arginine and 6-amino-hexanoic acid residues with m/z peaks corresponding to XR-(RXR) and $XR(RXR)_2$. CPP degradation in the heart homogenate reflected a combination of the degradation patterns observed for plasma, liver, and kidney.

Safety Assessment. Animals were observed for changes in behavior, appearance, or eating and drinking habits during the course of the study. Body weight measurements and serum chemistry were also used for the safety evaluation as shown in Table 2. The CPP−PMO conjugate did not cause detectable toxicity at the 15 mg/kg dose. It was well-tolerated, with no

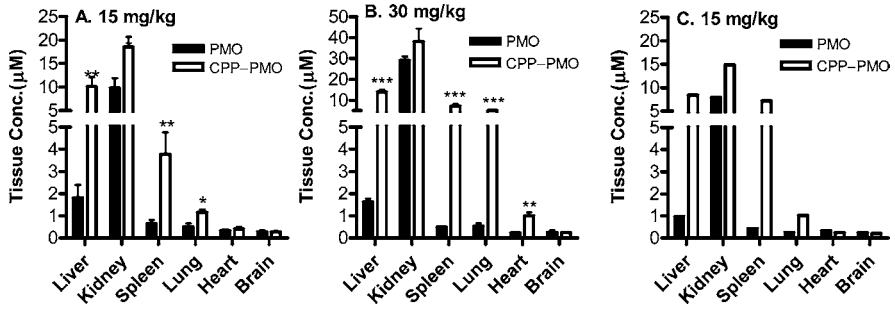


Figure 3. PMO concentration detected in tissue lysates. Rats were administrated with the PMO or the CPP−PMO at 15 mg/kg (A) and 30 mg/kg (B) with single daily iv injection for 5 days, and tissues were harvested 24 h after the last administration. Each data point represents mean ± SD of replicate values ($N = 5$). (C) Rats were administrated with the PMO or the CPP−PMO at 15 mg/kg with single daily iv injection for 5 days, and the tissue were harvested 5 days after the last administration. The lower limit of quantitation (LLOQ) of the HPLC method was 0.075 μM. *p < 0.05, **p < 0.01, ***p < 0.001 (Student's t test).

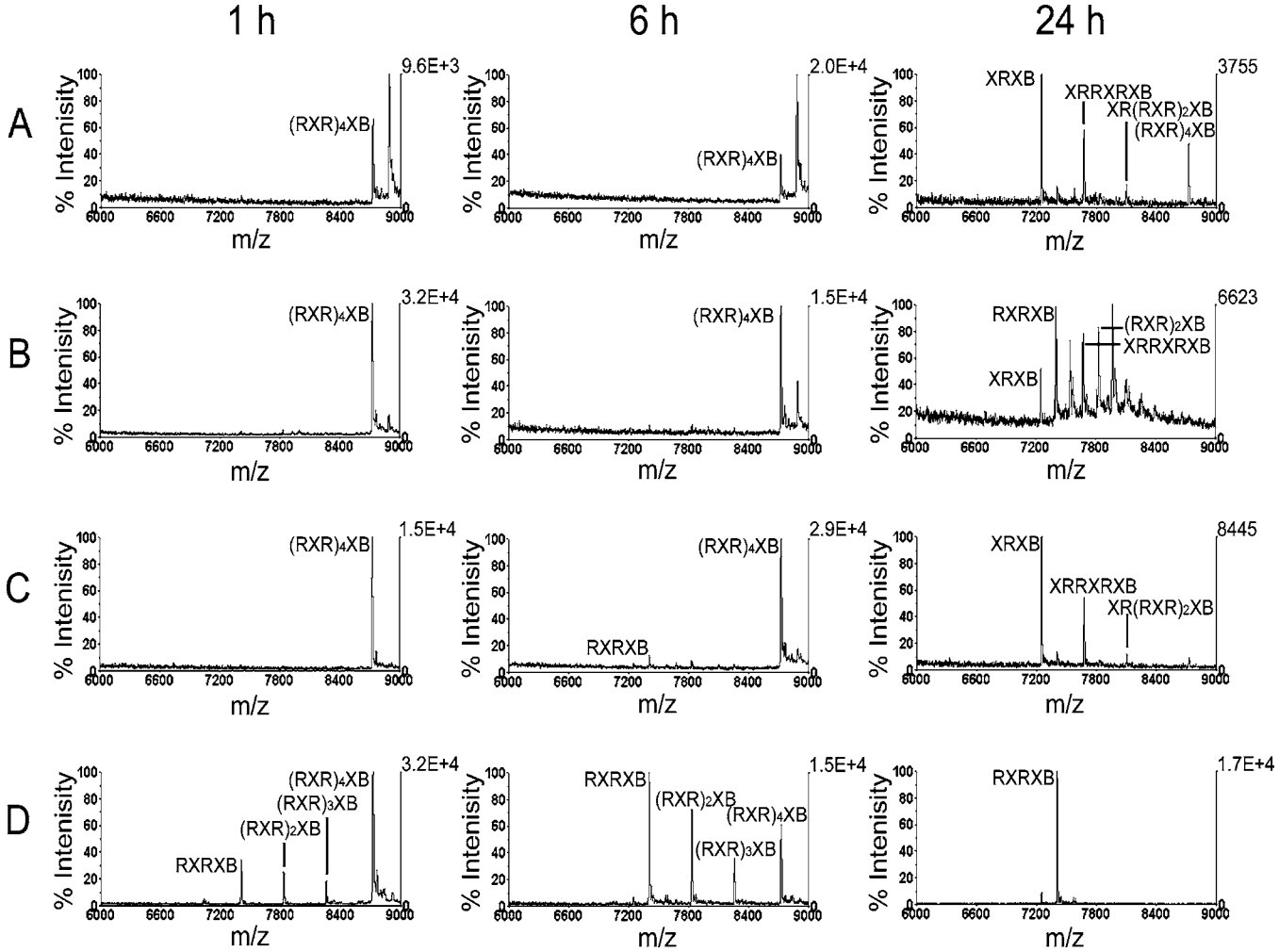


Figure 4. Biological stability of the peptide portion of the CPP−PMO conjugate in the rat tissue lysate or plasma. The mass spectrometry spectra of the samples are shown. Rat liver lysate (A), heart lysate (B), kidney lysate (C), and plasma (D) were treated with conjugate at 34 μM for 1, 6, and 24 h at 37 °C. The extracted materials were then analyzed by MALDI-TOF MS.

apparent adverse events. At 30 mg/kg, there was a decrease in body weight and a slight elevation in BUN levels but not creatinine. At 150 mg/kg, there was a greater decrease in body weight and a greater increase in BUN ($p < 0.05$) and serum creatinine ($p < 0.001$) levels. Animals appeared to be lethargic within minutes after the injection of 150 mg/kg of the conjugate. No changes were observed in albumin, total protein, glucose billirubin, cholesterol, electrolytes, as well as formed elements of blood (including red cells, neutrophils, and platelets) or serum enzymes such as LDH, or ALT (data not shown) at any dose level.

Free L-arginine was administered *ad libitum* in an attempt to restore BUN and serum creatinine to the normal plasma levels alongside treatment with CPP−PMO at a dose of 150 mg/kg. This was based on earlier reports demonstrating L-arginine to be effective against renal toxic or ischemic injury (*33*−*39*). L-Arginine supplementation significantly improved BUN ($p < 0.01$)) and serum creatinine ($p < 0.05$) clearance, as shown in Figure 5A and B, respectively.

The data in Figure 6 show that the LD_{50} of the conjugate administered iv in rats was between 210 and 250 mg/kg. Death was observed at 3 h postdose at 400 mg/kg and was preceded

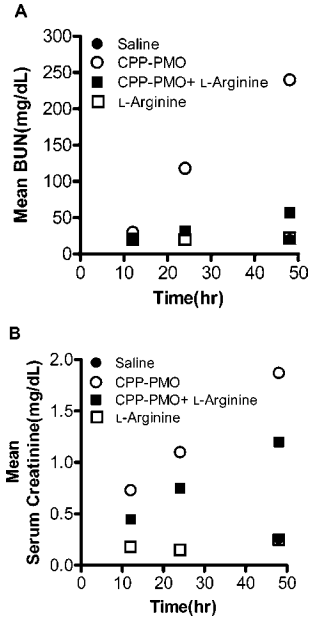


Figure 5. Coadministration of L-arginine reduced serum BUN and creatinine levels. Mean serum creatinine and BUN levels vs time following iv administration of the CPP−PMO at a single 150 mg/kg dose and 0.5 g/animal L-arginine administered *ad libitum*. Serum creatinine and BUN following CPP−PMO + L-arginine treatment were significantly lower than the CPP−PMO alone, $p < 0.05$ and $p < 0.01$, respectively (one-way ANOVA, Tukey's multiple comparison test).

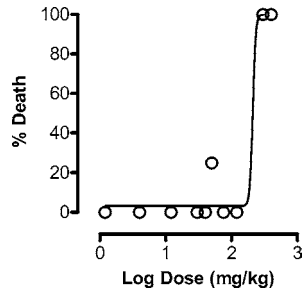


Figure 6. Percent animal death vs log dose of the CPP−PMO following a single iv injection in rats.

by mild to severe lethargy, decreased food and water consumption, and ruffled fur.

DISCUSSION

PMOs have been shown to have good biological stability (*29*), RNA binding affinity and specificity (*2, 31*), efficacy, and safety profiles (*7, 13, 40*). In spite of these qualities, delivery of PMOs into cells is limited. The arginine-rich cell-penentrating peptides, Tat, oligoarginine, and $(RXR)_4$, have been shown to enhance the cytosolic and nuclear delivery of PMO (*3, 23, 26*−*28*). The $(RXR)_4$ peptide has been found to be more efficacious (*28*) and more stable (*29*) than the Tat and oligoarginine peptides, and may have the potential to deliver therapeutic PMO. Therefore, evaluation of the PK, tissue distribution, biological stability, and safety of the $(RXR)_4$−PMO conjugate is an important step for its therapeutic development.

Conjugation of PMO to the $(RXR)_4$ CPP improved kinetic behavior of the PMO as reflected by prolonged elimination half-life, increased AUC, and volume of distribution (Vd). Since the AUC and Vd are directly related to bioavailability and tissue uptake, respectively, it is expected that increases in these pharmacokinetic parameters will lead to increased tissue uptake. Indeed, the CPP−PMO demonstrated broad tissue distribution with increased uptake compared to PMO alone in all tissues except brain. This is in agreement with an earlier study which demonstrated enhanced tissue uptake of a Tat-protein-conjugated PMO compared to the same PMO in a nonconjugated form (*41*). Kidney and liver were the sites of the highest accumulation of CPP−PMO in our study, with relatively lower concentrations observed in the lungs, spleen, heart, and brain. The broad distribution of the PMO is therapeutically valuable, because it is targeted to c-*myc* which is ubiquitously expressed in nearly all replicating cells. c-*myc* is expressed in the process of liver regeneration following partial hepatectomy, polycystic kidney disease, and other cell proliferation disorders. Therefore, the observed accumulation of the CPP−PMO in tissues such as the liver and kidney may be therapeutically valuable. Once delivered to the tissues, CPP−PMO showed extensive retention time as shown by the tissue concentration of the compound detected 5 days after the last injection as shown in Figure 3C. This observation further goes to demonstrate a slow efflux of the compound from tissues back to the vascular space, which is vital in determining the dosing schedule in future clinical studies.

Electrostatic interaction between the positively charged conjugate and cell surface proteoglycans is one of the factors that account for increased tissue uptake of CPP−PMO compared to PMO. The exact mechanism by which conjugated CPPs facilitate PMO delivery into the cytosolic and nuclear compartments of cells is not fully understood, although proteoglycan-involved endocytosis has been suggested (*28*).

The CPP had moderate biological stability with intact CPP detectable up to 6 h in plasma. This, along with the CPP−PMO having an estimated distribution half-life ($T_{1/2}\alpha$) range from 0.4 to 1.56 h, suggests that CPP−PMO will likely have sufficient time for distribution from plasma to peripheral tissues before the CPP component is completely degraded. Once the CPP−PMO reached the tissues, it had a high degree of stability, with the majority of the conjugate still intact up to 6 h in all three tissue types examined. It is interesting that the rate and pattern of CPP degradation differed among the tissues. No detectable intact conjugate was found in heart and kidney after 24 h incubation, but the intact conjugate was still detectable in liver.

Safety was assessed on the basis of changes in the animals' physical appearance and activity, food and water consumption, in-life body weight, and serum biochemistry. The CPP−PMO conjugate was well-tolerated at 15 and 30 mg/kg doses, with no evidence of clinical abnormalities. This observation further emphasizes the therapeutic utility of this CPP−PMO conjugate, since the effective dose has been shown in previous studies to be several fold less than the lowest dose used in this study (*13, 42*). However, the 150 mg/kg dose caused adverse events such as lethargy and elevated BUN and serum creatinine levels. It must be noted that the 150 mg/kg dose was chosen to exclusively examine the toxicological profile of the CPP−PMO conjugate and therefore has no therapeutic relevance. BUN and creatinine are cleared from the plasma mainly by the kidneys, and a decrease in renal output leads to a simultaneous elevation of BUN and creatinine in plasma. We note that L-arginine is a known precursor for urea and creatinine biosynthesis in the liver and kidneys (*43*−*46*). It is therefore possible that the elevated BUN and serum creatinine levels could be due in part to the CPP degradants. However, the degree of elevation of serum creatinine and BUN levels appear to be significant and may not have been generated from the CPP portion of the CPP−PMO. Therefore, we hypothesize that the observed simultaneous increase in serum creatinine and BUN concentrations is a result of reduced renal output.

To test this hypothesis, L-arginine was administered *ad libitum* in an attempt to rescue the animals from the apparent peptide-induced renal failure. Like other cationic amino acids, L-arginine is transported into cells and tissues via the Na^+-independent cationic amino acid transporter system y^+, which is encoded

by the *Cat* gene (*47*−*52*). We speculate that the delivery peptide which is arginine-rich utilizes the y^+ system for transport into the kidney but with lower affinity compared to L-arginine. Therefore, L-arginine may be expected to displace the CPP−PMO conjugate from the transporter, thereby reducing the delivery of the CPP−PMO to the kidney cells. Displacement of the CPP−PMO conjugate from the transporter by L-arginine may lead to reduced kidney exposure, and hence, the effect of the CPP−PMO on the kidney could be reduced. Also, L-arginine has been shown to increase renal glomerular filtration rate (GFR) either via nitric oxide (NO) production or stimulation of glucagon secretion (*33*−*39*). Indeed, our results showed improved renal clearance of creatinine and BUN following L-arginine supplementation.

In conclusion, pharmacokinetic, tissue distribution, biological stability, and safety profiles of a CPP−PMO have been established by this study. CPP conjugation improved the kinetic behavior and tissue uptake of PMO. The CPP component has moderate stability in plasma and tissues. At ≤15 mg/kg, CPP−PMO appeared to be nontoxic. Hence, the data from this study provide useful information when designing future CPP−PMO *in vivo* efficacy studies.

ACKNOWLEDGMENT

The authors thank the chemistry team at AVI BioPharma for the synthesis and purification and analysis of the PMO and CPP−PMO used in this study and the technical assistance provided by Oregon State University laboratory animal resource center (LARC) and Ariel Eberle. Also, we would like to thank Dave A. Stein for the critical reading of this manuscript.

LITERATURE CITED

(1) Summerton, J., and Weller, D. (1997) Morpholino antisense oligomers: design, preparation, and properties. *Antisense Nucleic Acid Drug Dev. 7*, 187−195.

(2) Summerton, J. (1999) Morpholino antisense oligomers: the case for an RNase H-independent structural type. *Biochim. Biophys. Acta 1489*, 141−158.

(3) Deas, T. S., Binduga-Gajewska, I., Tilgner, M., Ren, P., Stein, D. A., Moulton, H. M., Iversen, P. L., Kauffman, E. B., Kramer, L. D., and Shi, P. Y. (2005) Inhibition of flavivirus infections by antisense oligomers specifically suppressing viral translation and RNA replication. *J. Virol. 79*, 4599−4609.

(4) Sazani, P., Kang, S. H., Maier, M. A., Wei, C., Dillman, J., Summerton, J., Manoharan, M., and Kole, R. (2001) Nuclear antisense effects of neutral, anionic and cationic oligonucleotide analogs. *Nucleic Acids Res. 29*, 3965−3974.

(5) Sazani, P., and Kole, R. (2003) Therapeutic potential of antisense oligonucleotides as modulators of alternative splicing. *J. Clin. Invest. 112*, 481−486.

(6) Iversen, P. L. (2001) In *Antisense Drug Technology-Principles, Strategies, and Applications.* (Crooke, S. T., Ed.) pp 375−389, Marcel Dekker, Inc., New York.

(7) Arora, V., Cate, M. L., Ghosh, C., and Iversen, P. L. (2002) Phosphorodiamidate morpholino antisense oligomers inhibit expression of human cytochrome P450 3A4 and alter selected drug metabolism. *Drug Metab. Dispos. 30*, 757−762.

(8) Arora, V., Knapp, D. C., Reddy, M. T., Weller, D. D., and Iversen, P. L. (2002) Bioavailability and efficacy of antisense morpholino oligomers targeted to c-Myc and cytochrome P-450 3A2 following oral administration in rats. *J. Pharm. Sci. 91*, 1009−1018.

(9) Arora, V., Hannah, T. L., Iversen, P. L., and Brand, R. M. (2002) Transdermal use of phosphorodiamidate morpholino oligomer AVI-4472 inhibits cytochrome P450 activity in male rats. *Pharm. Res. 19*, 1465−1470.

(10) McCaffrey, A. P., Meuse, L., Karimi, M., Contag, C. H., and Kay, M. A. (2003) A potent and specific morpholino antisense inhibitor of hepatitis C translation in mice. *Hepatology 38*, 503−508.

(11) Kipshidze, N., Moses, J., Shankar, L. R., and Leon, M. (2001) Perspectives on antisense therapy for the prevention of restenosis. *Curr. Opin. Mol. Ther. 3*, 265−277.

(12) Kipshidze, N. N., Kim, H. S., Iversen, P., Yazdi, H. A., Bhargava, B., New, G., Mehran, R., Tio, F., Haudenschild, C., Dangas, G., Stone, G. W., Iyer, S., Roubin, G. S., Leon, M. B., and Moses, J. W. (2002) Intramural coronary delivery of advanced antisense oligonucleotides reduces neointimal formation in the porcine stent restenosis model. *J. Am. Coll. Cardiol. 39*, 1686−1691.

(13) Iversen, P. L., Arora, V., Acker, A. J., Mason, D. H., and Devi, G. R. (2003) Efficacy of antisense morpholino oligomer targeted to c-myc in prostate cancer xenograft murine model and a Phase I safety study in humans. *Clin. Cancer Res. 9*, *2510*−*2519.*

(14) Alter, J., Lou, F., Rabinowitz, A., Yin, H., Rosenfeld, J., Wilton, S. D., Partridge, T. A., and Lu, Q. L. (2006) Systemic delivery of morpholino oligonucleotide restores dystrophin expression bodywide and improves dystrophic pathology. *Nat. Med. 12*, 175−177.

(15) Fletcher, S., Honeyman, K., Fall, A. M., Harding, P. L., Johnsen, R. D., and Wilton, S. D. (2006) Dystrophin expression in the mdx mouse after localised and systemic administration of a morpholino antisense oligonucleotide. *J Gene Med. 8*, 207−216.

(16) Neuman, B. W., Stein, D. A., Kroeker, A. D., Paulino, A. D., Moulton, H. M., Iversen, P. L., and Buchmeier, M. J. (2005) Antisense morpholino-oligomers directed against the 5′ end of the genome inhibit coronavirus proliferation and growth. *J. Virol. 78*, 5891−5899.

(17) Kinney, R. M., Huang, C. Y., Rose, B. C., Kroeker, A. D., Dreher, T. W., Iversen, P. L., and Stein, D. A. (2005) Inhibition of dengue virus serotypes 1 to 4 in vero cell cultures with morpholino oligomers. *J. Virol. 79*, 5116−5128.

(18) Ge, Q., Pastey, M., Kobasa, D., Puthavathana, P., Lupfer, C., Bestwick, R. K., Iversen, P. L., Chen, J., and Stein, D. A. (2006) Inhibition of multiple subtypes of influenza A virus in cell cultures with morpholino oligomers. *Antimicrob. Agents Chemother. 50*, 3724−3733.

(19) Enterlein, S., Warfield, K. L., Swenson, D. L., Stein, D. A., Smith, J. L., Gamble, C. S., Kroeker, A. D., Iversen, P. L., Bavari, S., and Muhlberger, E. (2006) VP35 knockdown inhibits Ebola virus amplification and protects against lethal infection in mice. *Antimicrob. Agents Chemother. 50*, 984−993.

(20) Holden, K. L., Stein, D. A., Pierson, T. C., Ahmed, A. A., Clyde, K., Iversen, P. L., and Harris, E. (2006) Inhibition of dengue virus translation and RNA synthesis by a morpholino oligomer targeted to the top of the terminal 3′ stem-loop structure. *Virology 344*, 439−452.

(21) Alonso, M., Stein, D. A., Thomann, E., Moulton, H. M., Leong, J. C., Iversen, P., and Mourich, D. V. (2005) Inhibition of infectious haematopoietic necrosis virus in cell cultures with peptide-conjugated morpholino oligomers. *J Fish Dis. 28*, 399−410.

(22) Neuman, B. W., Stein, D. A., Kroeker, A. D., Churchill, M. J., Kim, A. M., Kuhn, P., Dawson, P., Moulton, H. M., Bestwick, R. K., Iversen, P. L., and Buchmeier, M. J. (2005) Inhibition, escape, and attenuated growth of severe acute respiratory syndrome coronavirus treated with antisense morpholino oligomers. *J. Virol. 79*, 9665−9676.

(23) Yuan, J., Stein, D. A., Lim, T., Qiu, D., Coughlin, S., Liu, Z., Wang, Y., Blouch, R., Moulton, H. M., Iversen, P. L., and Yang, D. (2006) Inhibition of coxsackievirus B3 in cell cultures and in mice by peptide-conjugated morpholino oligomers targeting the internal ribosome entry site. *J. Virol. 80*, 11510−11519.

(24) McClorey, G., Fall, A. M., Moulton, H. M., Iversen, P. L., Rasko, J. E., Ryan, M., Fletcher, S., and Wilton, S. D. (2006) Induced dystrophin exon skipping in human muscle explants. *Neuromuscul. Disord. 16*, 583−590.

(25) McClorey, G., Moulton, H. M., Iversen, P. L., Fletcher, S., and Wilton, S. D. (2006) Antisense oligonucleotide-induced exon skipping restores dystrophin expression in vitro in a canine model of DMD. *Gene Ther. 13*, 1373−1381.

(26) Moulton, H. M., Hase, M. C., Smith, K. M., and Iversen, P. L. (2003) HIV Tat peptide enhances cellular delivery of antisense morpholino oligomers. *Antisense Nucleic Acid Drug Dev. 13*, 31−43.

(27) Moulton, H. M., Nelson, M. H., Hatlevig, S. A., Reddy, M. T., and Iversen, P. L. (2004) Cellular uptake of antisense morpholino

oligomers conjugated to arginine-rich peptides. *Bioconjugate Chem. 15*, 290−299.
(28) Abes, S., Moulton, H. M., Clair, P., Prevot, P., Youngblood, D. S., Wu, R. P., Iversen, P. L., and Lebleu, B. (2006) Vectorization of morpholino oligomers by the (R-Ahx-R)4 peptide allows efficient splicing correction in the absence of endosomolytic agents. *J. Controlled Release 116*, 304−313.
(29) Youngblood, D. S., Hatlevig, S. A., Hassinger, J. N., Iversen, P. L., and Moulton, H. M. (2007) Stability of cell-penetrating Peptide-morpholino oligomer conjugates in human serum and in cells. *Bioconjugate Chem. 18*, 50−60.
(30) Summerton, J., and Weller, D. (1993) Uncharged morpholino-based polymers having phosphorus containing chiral intersubunit linkages. U.S. Patent 5,185,444.
(31) Nelson, M. H., Stein, D. A., Kroeker, A. D., Hatlevig, S. A., Iversen, P. L., and Moulton, H. M. (2005) Arginine-rich peptide conjugation to morpholino oligomers: effects on antisense activity and specificity. *Bioconjugate Chem. 16*, 959−966.
(32) Mangino, M. J., Ametani, M., Szabo, C., and Southard, J. H. (2004) Poly(ADP-ribose) polymerase and renal hypothermic preservation injury. *Am. J. Physiol. Renal Physiol. 286*, F838−F847.
(33) Schramm, L., Heidbreder, E., Lopau, K., Schaar, J., De Cicco, D., Gotz, R., and Heidland, A. (1994) Toxic acute renal failure in the rat: effects of L-arginine and N-methyl-L-arginine on renal function. *Nephrol., Dial., Transplant. 9*, 88−93.
(34) Lopau, K., Kleinert, D., Erler, J., Schramm, L., Heidbreder, E., and Wanner, C. (2000) Tacrolimus in acute renal failure: does L-arginine-infusion prevent changes in renal hemodynamics? *Transplant Int. 13*, 436−442.
(35) Valdivielso, J. M., Lopez-Novoa, J. M., Eleno, N., and Perez Barriocanal, F. (2000) Role of glomerular nitric oxide in glycerol-induced acute renal failure. *Can. J. Physiol. Pharmacol. 78*, 476−482.
(36) Schramm, L., La, M., Heidbreder, E., Hecker, M., Beckman, J. S., Lopau, K., Zimmermann, J., Rendl, J., Reiners, C., Winderl, S., Wanner, C., and Schmidt, H. H. (2002) L-Arginine deficiency and supplementation in experimental acute renal failure and in human kidney transplantation. *Kidney Int. 61*, 1423−1432.
(37) Sabbatini, M., Pisani, A., Uccello, F., Fuiano, G., Alfieri, R., Cesaro, A., Cianciaruso, B., and Andreucci, V. E. (2003) Arginase inhibition slows the progression of renal failure in rats with renal ablation. *Am. J. Physiol. Renal Physiol. 284*, 680−687.
(38) Zhang, X. Z., Ghio, L., Ardissino, G., Tirelli, A. S., Dacco, V., Testa, S., and Claris-Appiani, A. (1999) Renal and metabolic effects of L-arginine infusion in kidney transplant recipients. *Clin. Nephrol. 52*, 37−43.
(39) Solerte, S. B., Rondanelli, M., Giacchero, R., Stabile, M., Lovati, E., Cravello, L., Pontiggia, B., Vignati, G., Ferrari, E., and Fioravanti, M. (1999) Serum glucagon concentration and hyperinsulinaemia influence renal haemodynamics and urinary protein loss in normotensive patients with central obesity. *Int. J. Obes. Relat. Metab. Disord. 23*, 997 -1003.
(40) McCaffrey, A. P., Meuse, L., Karimi, M., Contag, C. H., and Kay, M. A. (2003) A potent and specific morpholino antisense inhibitor of hepatitis C translation in mice. *Hepatology 38*, 503−508.
(41) Pooga, M., Soomets, U., Hallbrink, M., Valkna, A., Saar, K., Rezaei, K., Kahl, U., Hao, J. X., Xu, X. J., Wiesenfeld-Hallin, Z., Hokfelt, T., Bartfai, T., and Langel, U. (1998) Cell penetrating PNA constructs regulate galanin receptor levels and modify pain transmission *in vivo*. *Nat. Biotechnol. 16*, 857−861.
(42) Arora, V., Knapp, D. C., Smith, B. L., Statdfield, M. L., Stein, D. A., Reddy, M. T., Weller, D. D., and Iversen, P. L. (2000) c-Myc antisense limits rat liver regeneration and indicates role for c-Myc in regulating cytochrome P-450 3A activity. *J. Pharmacol. Exp. Ther. 292*, 921−928.
(43) Cynober, L., Le Boucher, J., and Vasson, M-P. (1995) Arginine metabolism in mammals. *J. Nutr. Biochem. 6*, 402−403.
(44) Morel, F., Hus-Citharel, A., and Levillain, O. (1996) Biochemical heterogeneity of arginine metabolism along the kidney proximal tubules. *Kidney Int. 49*, 1608−1610.
(45) Visek, W. J. (1986) Arginine needs physiological state and usual diets. A reevaluation. *J. Nutr. 116*, 36−46.
(46) Perez, G. O., Epstein, M., Rietberg, B., and Loutzenhiser, R. (1978) Metabolism of arginine by the isolated perfused rat kidney. *Am. J. Physiol. 235*, F376−380.
(47) MacLeod, C. L. (1996) Regulation of cationic amino acid transporter (CAT) gene expression. *Biochem. Soc. Trans. 24*, 846−852.
(48) Kim, J. W., Closs, E. I., Albritton, L. M., and Cunningham, J. M. (1991) Transport of cationic amino acids by the mouse ecotropic retrovirus receptor. *Nature (London) 352*, 725−728.
(49) Wang, H., Kavanaugh, M. P., North, R. A., and Kabat, D. (1991) Cell-surface receptor for ecotropic murine retroviruses is a basic amino-acid transporter. *Nature (London) 352*, 729−731.
(50) MacLeod, C., Finley, K., Kakuda, D., Kozak, C., and Wilkinson, M. (1990) Activated T cells express a novel gene on chromosome 8 that is closely related to the murine ecotropic retroviral receptor. *Mol. Cell. Biol. 10*, 3663−3674.
(51) Ito, K., and Groudine, M. (1997) A new member of the cationic amino acid transporter family is preferentially expressed in adult mouse brain. *J. Biol. Chem. 272*, 26780−26786.
(52) White, M. F., Gazzola, G. C., and Christensen, H. N. (1982) Cationic amino acid transport into cultured animal cells. I. Influx into cultured human fibroblasts. *J. Biol. Chem. 257*, 4443−4449.

BC070060V

TECHNICAL NOTES

^{99m}Tc(CO)$_3$-15-[*N*-(Acetyloxy)-2-picolylamino]pentadecanoic Acid: A Potential Radiotracer for Evaluation of Fatty Acid Metabolism

Byung Chul Lee,[†,§] Dong Hyun Kim,[‡] Jae Hak Lee,[†] Hyun Ju Sung,[†] Yearn Seong Choe,*[,‡] Dae Yoon Chi,[†] Kyung-Han Lee,[‡] Yong Choi,[‡] and Byung-Tae Kim[‡]

Department of Chemistry, Inha University, 253 Yonghyundong, Namgu, Inchon 402-751, Korea, and Department of Nuclear Medicine, Samsung Medical Center, Sungkyunkwan University School of Medicine, 50 Ilwon-dong, Kangnam-ku, Seoul 135-710, Korea. Received September 23, 2006; Revised Manuscript Received January 20, 2007

^{99m}Tc(CO)$_3$-15-[*N*-(Acetyloxy)-2-picolylamino]pentadecanoic acid (**1a**) was prepared by incorporating [^{99m}Tc(CO)$_3$]$^+$ into 15-[*N*-(hydroxycarbonylmethyl)-2-picolylamino]pentadecanoic acid (**2a**). The overall radiochemical yield of **1a** after HPLC purification was 60−63%. Radiotracer **1a** was found to be chemically stable when incubated in human plasma for 4 h at 37 °C. Tissue distribution studies showed that high radioactivity accumulated in the heart with rapid clearance. The maximum heart-to-blood uptake ratio was 1.87 at 5 min after a tail-vein injection. Radioactive metabolites were analyzed in urine samples of mice and corresponded to a 9.3:1 ratio of ^{99m}Tc(CO)$_3$-5-[*N*-(acetyloxy)-2-picolylamino]pentanoic acid (**1b**) to ^{99m}Tc(CO)$_3$-3-[*N*-(acetyloxy)-2-picolylamino]-propionic acid (**1c**), indicating that **1a** is mainly metabolized to **1b** via β-oxidation in the body. These results suggest that **1a** is a promising radiotracer for evaluation of fatty acid metabolism in myocardium.

INTRODUCTION

Fatty acids are important substrates for adenosine triphosphate (ATP) production in myocardium. In the fasting state, fatty acid oxidation is enhanced and anaerobic glycolysis is suppressed, whereas in the nonfasting state, fatty acid oxidation decreases and glucose is utilized as an energy source (*1*). In myocardium, long-chain fatty acids are usually metabolized via β-oxidation, which degrades fatty acids by removing two-carbon units, and only a small fraction of the fatty acids is stored in the intracellular lipid pool as triglyceride (*2*−*4*). Disturbances in fatty acid metabolism often reflect myocardial damage, such as myocardial ischemia and cardiomyopathy; for example, fatty acid metabolism is impaired due to a reduced oxygen supply during myocardial ischemia (*1*, *5*).

Therefore, radiolabeled fatty acid analogs have been investigated for evaluating fatty acid metabolism in myocardium using single-photon emission computed tomography (SPECT) and positron emission tomography (PET). 1-[^{11}C]Palmitate, which reflects the metabolism of its natural counterpart, showed biexponential clearance, indicating rapid washout resulting from β-oxidation and slow washout due to slow turnover of the intracellular lipid pool (*5*, *6*). ω-[^{11}C]Palmitate showed greater heart uptake than 1-[^{11}C]palmitate due to its reduced metabolism (*7*). Several ^{123}I-labeled fatty acid analogs have been extensively studied, i.e., 17-[^{123}I]iodoheptadecanoic acid, 15-(*p*-[^{123}I]iodophenyl)pentadecanoic acid (IPPA), 15-(*p*-[^{123}I]iodophenyl)-3-methylpentadecanoic acid (BMIPP), and 15-(*p*-[^{123}I]iodophenyl)-3,3-dimethylpentadecanoic acid (DMIPP) (*8*−*10*). [^{123}I]BMIPP and [^{123}I]DMIPP showed prolonged myocardial retention versus [^{123}I]IPPA, because methyl branching slowed their myocardial metabolism. Due to its lower liver uptake than [^{123}I]DMIPP, [^{123}I]BMIPP showed promise for the diagnosis of various myocardial diseases (*11*). 16-[^{18}F]Fluoropalmitic acid (FPA) and methyl-branched ω-[^{18}F]fluoroheptadecanoic acids at C3 (3-MFHA) or C5 (5-MFHA) have also been investigated, and 5-MFHA showed an initial myocardial uptake and a retention intermediate between those of FPA and 3-MFHA (*12*). 14-[^{18}F]Fluoro-6-thiaheptadecanoic acid, which was designed for prolonged myocardial retention, was found to be similar to [^{123}I]BMIPP in terms of myocardial uptake and retention (*13*, *14*).

^{99m}Tc-labeled fatty acid analogs are attractive due to ready availability and the nearly ideal physical properties of ^{99m}Tc (141 keV, $t_{1/2}$ = 6 h) (*15*, *16*). Early attempts to develop ^{99m}Tc-labeled long-chain fatty acid analogs included the preparation of ^{99m}Tc-labeled fatty acid analogs containing a strong chelating group, such as DTPA or EDTA (*17*, *18*). However, poor accumulation of these radiotracers in myocardium initiated the developments of more specific radiotracers for in vivo studies of fatty acid metabolism. During these developments, ^{99m}Tc cores were successfully coordinated to the ω-positions of fatty acid analogs, but radiolabeled fatty acid analogs showed poor myocardial uptake (*18*−*21*). Recently, the Magata group found that [^{99m}Tc]MAMA-hexadecanoic acid (HDA) shows high initial heart uptake and subsequent rapid clearance, and that it is metabolized to [^{99m}Tc]MAMA-butyric acid via β-oxidation in the body (*22*). Over the past decade, small ^{99m}Tc cores have been developed, including ^{99m}Tc(CO)$_3$-(cyclopentadienyl) (*23*−*25*), ^{99m}Tc(CO)$_3$-[*N*,*N*-(diacetyloxy)amino], ^{99m}Tc(CO)$_3$-[N^{α}-(histidinyl)], ^{99m}Tc(CO)$_3$-[*N*-(acetyloxy)-2-picolylamino] cores, and others (*26*−*28*). [^{99m}Tc(CO)$_3$(H$_2$O)$_3$]$^+$ is an attractive precursor for the introduction of the small [^{99m}Tc(CO)$_3$]$^+$ into biomolecules (*26*, *27*, *29*). As part of a strategy to develop ^{99m}Tc(CO)$_3$-labeled long-chain fatty acid analogs, the *N*-(hy-

* Corresponding author. Tel: +82-2-3410-2623. Fax: +82-2-3410-2639. E-mail: ysnm.choe@samsung.com.

[†] Inha University.

[‡] Sungkyunkwan University School of Medicine.

[§] Present address: Department of Nuclear Medicine, Seoul National University College of Medicine, Seoul, Korea.

10.1021/bc060299w CCC: $37.00 © 2007 American Chemical Society
Published on Web 05/16/2007

droxycarbonylmethyl)-2-picolylamino group can be labeled with $[^{99m}Tc(CO)_3(H_2O)_3]^+$ to form a $^{99m}Tc(CO)_3$-[*N*-(acetyloxy)-2-picolylamino] core, an ideal tridentate chelator.

In this work, we prepared $^{99m}Tc(CO)_3$-[*N*-(acetyloxy)-2-picolylamino]pentadecanoic acid (**1a**) by the facile incorporation of $[^{99m}Tc(CO)_3]^+$ into a *N*-(hydroxycarbonylmethyl)-2-picolylamino fatty acid analog and evaluated its potential as a substrate for fatty acid metabolism. The β-oxidation products of **1a** were compared with the proposed radioactive metabolite standards, $^{99m}Tc(CO)_3$-5-[*N*-(acetyloxy)-2-picolylamino]pentanoic acid (**1b**) and $^{99m}Tc(CO)_3$-3-[*N*-(acetyloxy)-2-picolylamino]propionic acid (**1c**).

EXPERIMENTAL SECTION

Materials and Methods. Chemicals and solvents were obtained from Sigma-Aldrich (St. Louis, MO), and HPLC solvents were obtained from J. T. Baker (Phillipsburg, NJ). ^1H NMR spectra were obtained using a Varian Unity Inova 500NB (500 MHz) spectrometer (Palo Alto, CA) at the Cooperative Center for Research Facilities, Sungkyunkwan University (Suwon, Korea), and a Varian Gemini-400 (Palo Alto, CA) at Inha University, and ^{13}C NMR spectra were obtained at 100 MHz. Chemical shifts (δ) are reported as parts per million (ppm) downfield of an internal tetramethylsilane standard. Fast atom bombardment (FAB) mass spectra were obtained using a JMS-700 Mstation (JEOL, Ltd., Tokyo, Japan) at the Korea Basic Science Institute (Seoul, Korea). HPLC was carried out using a Thermo Separation Products System (Fremont, CA) equipped with a semipreparative column (Alltech Econosil silica gel, 10 μ, 10 × 250 mm) or an analytical column (YMC-Pack C18, 5 μ, 4.6 × 250 mm). Eluant was simultaneously monitored using a UV detector (254 nm) and a NaI(Tl) radioactivity detector. TLC was performed on Merck F_{254} silica plates, which were analyzed using a Bioscan radio-TLC scanner (Washington, DC). $Na^{99m}TcO_4$ was eluted on a daily basis from a $^{99}Mo/^{99m}Tc$ generator (Samyoung Unitech, Co., Ltd., DuPont Pharmaceuticals Co., and Daiichi Radioisotope Labs). Radioactivity was measured in a dose calibrator (Biodex Medical Systems, Shirley, NY) and tissue radioactivity in a Wallac automated γ counter (Boston, MA). All animal experiments were performed in compliance with the rules of the Samsung Medical Center Laboratory Animal Care, which comply with NIH guidelines.

Synthesis of *tert*-Butyl 2-Picolylamino-*N*-acetate (3). 2-Picolylamine (946 μL, 9.25 mmol) was added to *tert*-butyl bromoacetate (1.7 mL, 12.03 mmol) in CH_3CN (10 mL). The reaction mixture was then stirred under N_2 at room temperature overnight. At the end of the reaction, solvent was removed in vacuo, and residue was extracted with dichloromethane (30 mL × 3), washed with water, and dried over anhydrous Na_2SO_4. Flash column chromatography (2:1 hexane−ethyl acetate) gave **3** (1.48 g) as a yellow oil in 72% yield: ^1H NMR ($CDCl_3$, 500 MHz) δ 8.57 (d, 1H, J = 5.0 Hz), 7.68−7.65 (m, 1H), 7.35 (d, 1H, J = 5.5 Hz), 7.19−7.17 (m, 1H), 3.96 (s, 2H), 3.39 (s, 2H), 1.48 (s, 9H); ^{13}C NMR ($CDCl_3$, 100 MHz) δ 171.2, 159.2, 149.1, 136.2, 121.8, 121.7, 80.8, 54.4, 51.0, 27.8; MS (FAB) *m*/*z* 223 (M^+ + H); HRMS calcd for $C_{12}H_{19}N_2O_2$ 223.1447, found 223.1451.

Synthesis of Methyl 15-[*N*-(*tert*-Butyloxycarbonylmethyl)-2-picolylamino]pentadecanoate (4a). Compound **3** (300 mg, 1.35 mmol) was dissolved in CH_3CN (12 mL), and to this solution was added DIEA (1.18 mL, 6.75 mmol). After stirring for 30 min at room temperature, methyl 15-bromopentadecanoate (543 mg, 1.62 mmol) was added dropwise. The reaction mixture was then stirred at 75 °C overnight, extracted with dichloromethane (30 mL × 3), washed with water, and dried over anhydrous Na_2SO_4. Flash column chromatography (4:1 hexane−ethyl acetate) afforded **4a** (521 mg) as a light yellow oil in 81% yield: ^1H NMR ($CDCl_3$, 400 MHz) δ 8.52 (dd, 1H, J = 2.0, 1.6 Hz), 7.65 (t, 1H, J = 8.0 Hz), 7.54 (d, 1H, J = 7.6 Hz), 7.14 (t, 1H, J = 6.0 Hz), 3.90 (s, 2H), 3.66 (t, 3H, J = 7.6 Hz), 3.29 (s, 2H), 2.62 (t, 2H, J = 7.6 Hz), 2.30 (t, 2H, J = 7.6 Hz), 1.64−1.58 (m, 2H), 1.51−1.41 (m, 9H), 1.31−1.18 (m, 22H); ^{13}C NMR ($CDCl_3$, 100 MHz) δ 174.0, 170.1, 160.0, 148.8, 136.1, 122.7, 121.6, 80.4, 60.3, 55.9, 54.1, 51.1, 33.9, 29.4; MS (FAB) *m*/*z* 477 (M^+ + H); HRMS calcd for $C_{28}H_{49}N_2O_4$ 477.3693, found 477.3697.

Synthesis of Methyl 5-[*N*-(*tert*-Butyloxycarbonylmethyl)-2-picolylamino]pentanoate (4b). Compound **3** (250 mg, 1.12 mmol) was dissolved in CH_3CN (7 mL), and to this solution was added DIEA (980 μL, 5.63 mmol). After stirring for 30 min at room temperature, methyl 5-bromopentanoate (240 μL, 1.69 mmol) was added dropwise. The remainder of the procedure was as described above. Flash column chromatography (2:1 hexane−ethyl acetate) gave **4b** (280 mg) as a light yellow oil in 74% yield: ^1H NMR ($CDCl_3$, 500 MHz) δ 8.55−8.53 (m, 1H), 7.67 (td, 1H, J = 8.0, 2.0 Hz), 7.55 (d, 1H, J = 7.6 Hz), 7.18−7.15 (m, 1H), 3.93 (s, 2H), 3.66 (s, 3H), 3.31 (s, 2H), 2.68 (t, 2H, J = 7.6 Hz), 2.30 (t, 2H, J = 7.6 Hz), 1.68−1.62 (m, 2H), 1.56−1.50 (m, 2H), 1.48 (s, 9H); MS (FAB) *m*/*z* 337 (M^+ + H); HRMS calcd for $C_{18}H_{29}N_2O_4$ 337.2128, found 337.2132.

Synthesis of Methyl 3-[*N*-(*tert*-Butyloxycarbonylmethyl)-2-picolylamino]propionate (4c). Compound **3** (400 mg, 1.75 mmol) was dissolved in CH_3CN (12 mL), and to this solution was added $NaHCO_3$ (453.6 mg, 5.40 mmol). After stirring for 30 min at room temperature, methyl 3-bromopropionate (257 μL, 2.34 mmol) was added dropwise. The mixture was then stirred at 60 °C overnight. Solvent was removed in vacuo, and the residue was extracted with dichloromethane (30 mL × 3), washed with water (30 mL × 3), and dried over anhydrous Na_2SO_4. Flash column chromatography (1:1 hexane−ethyl acetate) gave **4c** (320 mg) as a yellow oil in 58% yield: ^1H NMR ($CDCl_3$, 500 MHz) δ 8.55−8.54 (m, 1H), 7.67 (td, 1H, J = 8.0, 2.0 Hz), 7.50 (d, 1H, J = 8.0 Hz), 7.19−7.16 (m, 1H), 3.99 (s, 2H), 3.66 (s, 3H), 3.57 (s, 2H), 3.08 (t, 2H, J = 5.0 Hz), 2.53 (t, 2H, J = 7.0 Hz), 1.48 (s, 9H); MS (FAB) *m*/*z* 309 (M^+ + H); HRMS calcd for $C_{16}H_{25}N_2O_4$ 309.1815, found 309.1806.

Synthesis of Methyl 15-[*N*-(Hydroxycarbonylmethyl)-2-picolylamino]pentadecanoate (5a). Trifluoroacetic acid (2 mL) was added to **4a** (250 mg, 0.52 mmol) in dichloromethane (2 mL), and the reaction mixture was stirred for 2 h at room temperature. At the end of the reaction, solvent was removed in vacuo, and the residue was extracted with dichloromethane (30 mL × 3), washed with water, and dried over anhydrous Na_2SO_4. Flash column chromatography (15:1 dichloromethane−methanol) gave **5a** (188 mg) as a light yellow oil in 85% yield. Compounds **5b** and **5c** were synthesized in 79% and 62% yields, respectively, using the same procedure described for **5a**.

5a. ^1H NMR (CD_3OD, 500 MHz) δ 8.67−8.66 (m, 1H), 7.91 (td, 1H, J = 8.0, 1.5 Hz), 7.53 (d, 1H, J = 8.0 Hz), 7.47−7.44 (m, 1H), 4.56 (s, 2H), 3.76 (s, 2H), 3.66 (s, 3H), 3.27−3.23 (m, 2H), 2.32 (t, 2H, J = 7.0 Hz), 1.80−1.75 (m, 2H), 1.63−1.60 (m, 2H), 1.30 (s, 20H); ^{13}C NMR ($CDCl_3$, 100 MHz) δ 174.0, 170.1, 160.0, 148.8, 136.1, 122.7, 121.6, 80.4, 60.3, 55.9, 54.1, 51.1, 33.9, 29.4, 27.98, 27.4, 24.7; MS (FAB) *m*/*z* 421 (M^+ + H); HRMS calcd for $C_{24}H_{41}N_2O_4$ 421.3066, found 421.3066.

5b. ^1H NMR (CD_3OD, 500 MHz) δ 8.67−8.65 (m, 1H), 7.92 (td, 1H, J = 7.8, 2.0 Hz), 7.54 (d, 1H, J = 8.0 Hz), 7.53−7.45 (m, 1H), 4.55 (s, 2H), 3.78 (s, 2H), 3.67 (s, 3H), 3.27−3.24 (m, 2H), 2.38 (t, 2H, J = 2.0 Hz), 1.83−1.79 (m, 2H), 1.69−1.66 (m, 2H); MS (FAB) *m*/*z* 281 (M^+ + H); HRMS calcd for $C_{14}H_{21}N_2O_4$ 281.1502, found 281.1495.

5c. ^{1}H NMR (CD_3OD, 500 MHz) δ 8.62 (d, 1H, J = 4.0 Hz), 7.92 (td, 1H, J = 7.5, 1.5 Hz), 7.57 (d, 1H, J = 8.0 Hz), 7.46−7.44 (m, 1H), 4.43 (s, 2H), 3.70 (s, 2H), 3.42−3.39 (m, 2H), 3.36 (s, 3H), 2.76−2.74 (m, 2H); MS (FAB) m/z 253 (M^+ + H); HRMS calcd for $C_{12}H_{17}N_2O_4$ 253.1189, found 253.1192.

Synthesis of 15-[*N*-(Hydroxycarbonylmethyl)-2-picolylamino]pentadecanoic Acid (2a). Compound **5a** (40 mg, 0.10 mmol) was dissolved in a 1:1 mixture of 0.4 N NaOH and MeOH (3 mL) and stirred for 4 h at 70 °C. The solution was then cooled and neutralized with 1.5 mL of 0.1 N HCl in an ice bath. The reaction mixture was then extracted with dichloromethane, and the organic layer was dried over anhydrous Na_2SO_4 and concentrated. Flash column chromatography (9:1 CH_2Cl_2−MeOH) gave **2a** (22 mg) as light yellow solid in 54% yield. Compound **2b** was prepared in 46% yield using the procedure described for **2a** and C-18 Sep-Pak purification.

2a. ^{1}H NMR (CD_3OD, 500 MHz) δ 8.55 (d, 1H, J = 4.5 Hz), 7.84 (td, 1H, J = 7.8, 1.0 Hz), 7.61 (d, 1H, J = 7.5 Hz), 7.37−7.34 (m, 1H), 4.10 (s, 2H), 3.36 (s, 2H), 2.79 (t, 2H, J = 7.0 Hz), 2.17 (t, 2H, J = 7.5 Hz), 1.62−1.59 (m, 4H), 1.28 (s, 20H); MS (FAB) m/z 429 (M^+ + Na); HRMS calcd for $C_{23}H_{38}N_2O_4Na$ 429.2732, found 429.2729.

2b. ^{1}H NMR (CD_3OD, 500 MHz) δ 8.69−8.68 (m, 1H), 8.01−7.97 (m, 1H), 7.59−7.57 (m, 1H), 7.54−7.51 (m, 1H), 4.59 (d, 2H, J = 3.0 Hz), 4.06 (d, 2H, J = 6.0 Hz), 3.67−3.66 (m, 2H), 2.40−2.34 (m, 2H), 1.89−1.77 (m, 2H), 1.69−1.64 (m, 2H); MS (FAB) m/z 289 (M^+ + Na); HRMS calcd for $C_{13}H_{18}N_2O_4Na$ 289.1167, found 289.1169.

Synthesis of Re(CO)$_3$-15-[*N*-(Acetyloxy)-2-picolylamino]-pentadecanoic Acid (6a). $(NEt_4)_2[Re(CO)_3Br_3]$ was prepared as described in the literature (*30*). $(NEt_4)_2[Re(CO)_3Br_3]$ (187 mg, 0.24 mmol) was added to **2a** (60 mg, 0.16 mmol) in MeOH (1 mL) and stirred for 2 h at 65 °C. After reaction, solvent was removed in vacuo, and the resulting oily residue was purified by flash column chromatography (10:1 CH_2Cl_2−MeOH) to give **6a** (57 mg) as a light yellow solid in 53% yield. Compound **6b** was synthesized in 51% yield using the procedure described for **6a**.

6a. mp 221−225 °C; ^{1}H NMR ($CDCl_3$, 500 MHz) δ 8.85 (d, 1H, J = 5.5 Hz), 7.95 (td, 1H, J = 8.0, 1.5 Hz), 7.51 (d, 1H, J = 7.5 Hz), 7.44 (t, 1H, J = 6.0 Hz), 4.51−4.48 (m, 2H), 4.37−4.34 (m, 2H), 3.74−3.70 (m, 2H), 3.58−3.54 (m, 2H), 2.36−2.33 (m, 2H), 1.61−1.59 (m, 2H), 1.27 (s, 20H); MS (FAB) m/z 677 (M^+ + H); HRMS calcd for $C_{26}H_{38}N_2O_7{}^{187}Re$ 677.2237, found 677.2245.

6b. mp 237−240 °C; ^{1}H NMR (CD_3OD, 500 MHz) δ 8.83 (d, 1H, J = 5.5 Hz), 8.10 (td, 1H, J = 8.2, 1.0 Hz), 7.72 (d, 1H, J = 8.0 Hz), 7.55 (t, 1H, J = 6.0 Hz), 4.75−4.72 (m, 2H), 4.57−4.54 (m, 2H), 3.95−3.91 (m, 2H), 3.64−3.62 (m, 2H), 2.42 (t, 2H, J = 7.0 Hz), 1.71−1.69 (m, 2H); MS (FAB) m/z 537 (M^+ + H); HRMS calcd for $C_{16}H_{18}N_2O_7{}^{187}Re$ 537.0672, found 537.0668.

Synthesis of Re(CO)$_3$-3-[*N*-(Acetyloxy)-2-picolylamino]-propionic Acid (6c). $(NEt_4)_2[Re(CO)_3Br_3]$ (187 mg, 0.24 mmol) was added to **5c** (50 mg, 0.16 mmol) in MeOH (3 mL) and stirred for 2 h at 65 °C. After reaction, solvent was removed in vacuo, and the resulting oily residue was purified by flash column chromatography (20:1 CH_2Cl_2−MeOH) to give Re coordinated methyl ester (38 mg) as a light yellow solid in 46% yield: mp 187−192 °C; ^{1}H NMR ($CDCl_3$, 500 MHz) δ 8.86 (d, 1H, J = 5.0 Hz), 7.96 (td, 1H, J = 8.0, 1.5 Hz), 7.51 (d, 1H, J = 8.0 Hz), 7.46 (t, 1H, J = 6.5 Hz), 4.44−4.36 (m, 2H), 3.94−3.91 (m, 2H), 3.80 (s, 3H), 3.39−3.36 (m, 2H), 2.87 (t, 2H, J = 7.0 Hz); MS (FAB) m/z 523 (M^+ + H); HRMS calcd for $C_{15}H_{16}N_2O_7{}^{187}Re$ 523.0516, found 523.0522.

The methyl ester (30 mg, 0.057 mmol) was dissolved in a 1:1 mixture of 0.4 N NaOH and MeOH (1.5 mL) and stirred for 4 h at 70 °C. The solution was then cooled and neutralized with 1 mL of 0.1 N HCl in an ice bath. The reaction mixture was then extracted with dichloromethane, and the organic layer was dried over anhydrous Na_2SO_4 and concentrated. Sold-phase purification (C18 Sep-Pak cartridge) gave **6c** (9.3 mg) as a light yellow solid in 32% yield: mp 257−259 °C; ^{1}H NMR (CD_3OD, 500 MHz) δ 8.83 (d, 1H, J = 6.0 Hz), 8.10 (td, 1H, J = 8.0, 1.5 Hz), 7.72 (d, 1H, J = 8.0 Hz), 7.56 (t, 1H, J = 5.5 Hz), 4.84−4.76 (m, 2H), 4.58−4.55 (m, 2H), 3.93−3.90 (m, 2H), 2.92−2.87 (m, 2H); MS (FAB) m/z 509 (M^+ + H); HRMS calcd for $C_{14}H_{14}N_2O_7{}^{187}Re$ 509.0359, found 509.0359.

Radiochemical Synthesis of ^{99m}Tc(CO)$_3$-15-[*N*-(Acetyloxy)-2-picolylamino]pentadecanoic Acid (1a). *Kit Preparation of* $[^{99m}Tc(CO)_3(H_2O)_3]^+$. $^{99m}TcO_4^-$ (740 MBq, 300 μL) was added to a 10 mL sealed kit vial containing a lyophilized formulation (IsoLink). The vial was then shaken vigorously and placed in an oil bath for 30 min at 75 °C. It was then cooled to room temperature, and the mixture was neutralized with 0.1 N HCl (180 μL). The radio−TLC yield of $[^{99m}Tc(CO)_3(H_2O)_3]^+$ was greater than 95%.

In-House Preparation of $[^{99m}Tc(CO)_3(H_2O)_3]^+$. A mixture of Na_2CO_3 (4 mg, 38 μmol), NaK tartrate tetrahydrate (2 mg), and $NaBH_4$ (5 mg, 130 μmol) was placed in a 10 mL reaction vial and dissolved in water (500 μL), and the vial was then sealed. After bubbling CO in this solution for 10 min, $^{99m}TcO_4^-$ (370 MBq, 200 μL) was added, and the resulting solution was stirred for 30 min at 75 °C, cooled to room temperature, and then neutralized with 0.1 N HCl (180 μL). Radio−TLC yield was greater than 95%.

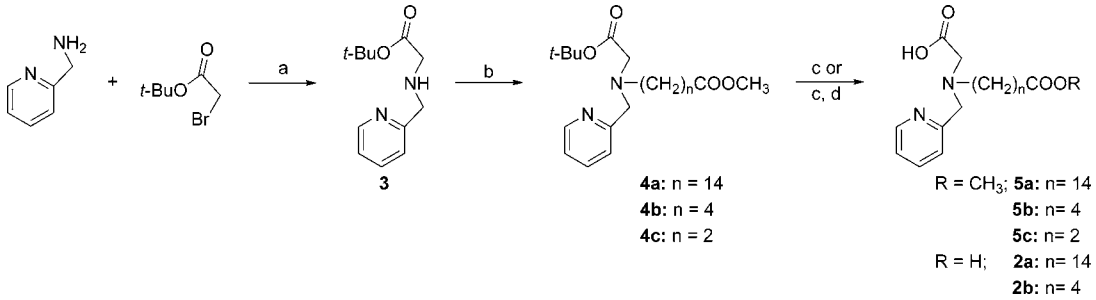
Radiochemical Synthesis of 1a. Compound **2a** (1.1 mg, 2.7 μmol) was dissolved in a 4:1 mixture of methanol and water (300 μL), and to this solution was added $[^{99m}Tc(CO)_3(H_2O)^3]^+$ (370 MBq, 250 μL). The reaction mixture was then stirred in a sealed vial for 30 min at 75 °C. The crude mixture was loaded onto a C18 Sep-Pak cartridge, which was washed with water (10 mL) and then with methanol (2 mL). The methanol layer was concentrated under N_2 and purified by HPLC using a 8:92 mixture of hexane and dichloromethane−2-propanol−acetic acid (88:12:0.3) at 4 mL/min. The desired fraction (t_R = 21.5−23.5 min) was collected, and solvents were removed under N_2. The residue was then passed through a C18 Sep-Pak cartridge that was washed with water (10 mL) and then with MeOH (2 mL). Methanol removal gave **1a** in 60−63% yield. Radiotracer **1b** was prepared in an identical manner and purified using a C18 Sep-Pak cartridge at yields of 48%.

In preparation of **1c**, methyl ester **5c** (1.3 mg, 4.64 μmol) was labeled with $[^{99m}Tc(CO)_3(H_2O)^3]^+$ (37 MBq, 25 μL) for 30 min at 75 °C. After solid-phase purification, the residue was redissolved in methanol (300 μL) and treated with 0.4 N NaOH (aq, 100 μL) for 10 min at 65 °C. The reaction mixture was then cooled, neutralized with 1 N HCl (40 μL), and purified using a C18 Sep-Pak cartridge and methanol as the eluant, which gave **1c** in 34% yield.

In Vitro Stability. An aliquot (9.7 MBq) of **1a** in saline was added to human plasma (1 mL) and incubated for 4 h at 37 °C, and the resulting solution was analyzed by radio−TLC using dichloromethane-methanol (9:1).

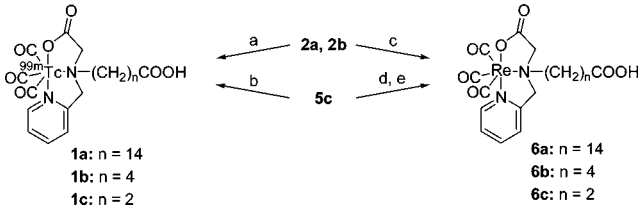
Tissue Distribution in Normal Mice. Radiotracer **1a** was dissolved in saline containing 1% bovine serum albumin (BSA) and 10% ethanol at 40 °C. ICR mice (male, 25−30 g, four mice per time point) were fasted for 12 h before injecting **1a** (1.11 MBq/mouse) via a tail vein. At the indicated time points (0.5, 1, 5, and 30 min), mice were sacrificed by cervical dislocation, and samples of blood were immediately obtained from the myocardial tissue via a syringe, and samples of whole organ (heart) and tissue (lung, liver, kidney, and

Scheme 1 [a]



[a] Reagents and conditions: (a) CH_3CN, room temperature, overnight, 72%; (b) methyl 15-bromopentadecanoate ($n = 14$), methyl 5-bromopentanoate ($n = 4$), or methyl 3-bromopropionate ($n = 2$), DIEA or $NaHCO_3$, CH_3CN, 60−75 °C, overnight, 58−81%; (c) CF_3COOH, CH_2Cl_2, room temperature, 2 h, 62−85%; (d) 0.4 N NaOH−MeOH, 70 °C, 4 h, 46−54%.

Scheme 2 [a]



[a] Reagents and conditions: (a) $[^{99m}Tc(CO)_3(H_2O)_3]^+$, MeOH, 75 °C, 30 min, 48−63%; (b) $[^{99m}Tc(CO)_3(H_2O)_3]^+$, MeOH, 75 °C, 30 min, 0.4 N NaOH−MeOH, 65 °C, 10 min, 34%; (c) $(NH_4)_2[Re(CO)_3Br_3]$, MeOH, 65 °C, 2 h, 51−53%; (d) $(NH_4)_2[Re(CO)_3Br_3]$, MeOH, 65 °C, 2 h, 46%; (e) 0.4 N NaOH−MeOH, 70 °C, 4 h, 32%.

stomach) were also removed, weighed, and counted. Data are expressed as the percent injected dose per gram of tissue (% ID/g).

Analysis of Metabolites. Radiotracer **1a** (18.5 MBq/mouse) was injected via a tail vein into 12 h-fasted ICR mice. At 30 min after injection, mice were sacrificed by cervical dislocation, and samples of the urine were collected, filtered through a membrane filter, and analyzed by HPLC at a flow rate of 1 mL/min using a combination of solution A (0.1% TFA−water) and solution B (methanol) and a linear gradient program from 60:40 A−B to 40:60 A−B over 20 min, followed by 40:60 A−B to 0:100 A−B over 20 min. A major radioactive metabolite was recovered from the HPLC column at a recovery efficiency of 71%. Radiotracers **1a**, **1b**, and **1c** were analyzed by HPLC using the same conditions.

RESULTS AND DISCUSSION

Chemistry. The precursor **2a** for $[^{99m}Tc(CO)_3]^+$ labeling was synthesized by reacting *tert*-butyl bromoacetate with 2-picolylamine, reacting the resulting compound **3** with methyl 15-bromopentadecanoate, and the subsequent removal of the *tert*-butyl group and the methyl ester group (Scheme 1). Reaction conditions for the synthesis of **4a**−**4c** depended on carbon chain length. Compound **2b** was synthesized using the procedure described for **2a**. Methyl ester **5c** was prepared from deprotection of *tert*-butyl group of **4c** and used directly for $[^{99m}Tc(CO)_3]^+$ labeling.

Radiotracer **1a** was prepared by labeling the precursor **2a** with $[^{99m}Tc(CO)_3(H_2O)_3]^+$ for 30 min at 75 °C (Scheme 2). Hydrolysis can be carried out after $[^{99m}Tc(CO)_3]^+$ labeling of methyl ester precursors **5a**−**5c**. This was the case for $[^{99m}Tc(CO)_3]^+$ labeling of methyl ester **5c**, due to limited isolation of its polar hydrolyzed product, 3-[*N*-(hydroxycarbonylmethyl)-2-picolylamino]propionic acid. No significant difference in the yields of $[^{99m}Tc(CO)_3(H_2O)_3]^+$ was apparent for kit and in-house preparations. The predicted β-oxidation metabolites, **1b** and **1c**, were prepared as shown in Scheme 2 and purified using a C-18 Sep-Pak cartridge.

Table 1. Tissue Distribution of 1a in Normal Mice[a]

	% ID/g			
tissue	0.5 min	1 min	5 min	30 min
blood	18.28 ± 3.32	7.54 ± 1.46	0.39 ± 0.14	0.17 ± 0.03
heart	12.67 ± 1.48	6.38 ± 0.69	0.73 ± 0.37	0.28 ± 0.08
lung	23.58 ± 1.16	15.98 ± 3.32	6.82 ± 1.77	1.36 ± 0.21
liver	27.60 ± 5.31	31.88 ± 2.51	30.33 ± 6.05	13.06 ± 3.24
kidney	16.06 ± 1.82	13.86 ± 2.24	6.63 ± 0.98	6.53 ± 0.90
stomach	1.24 ± 0.36	0.78 ± 0.16	2.27 ± 1.45	1.57 ± 0.44

[a] Values are given as mean ± SD for groups of four mice.

Re standards were also prepared using $(NH_4)_2[Re(CO)_3Br_3]$ as described for the synthesis of ^{99m}Tc-labeled fatty acids. ^{99m}Tc-fatty acid analogs had retention times that were similar to the Re standards on HPLC: 35.9 min vs 35.2 min, 16.7 min vs 15.7, and 11.8 min vs 11.3 min for **1a**−**1c** vs **6a**−**6c**. Although ^{99m}Tc and Re-fatty acid analogs were not coeluted on HPLC, the formers were identified on the basis of the similar chemical properties of ^{99m}Tc and Re complexes. The different HPLC retention times of ^{99m}Tc and Re complexes have also been reported for other cases (*24*, *25*).

In Vitro Stability. Radiotracer **1a** was incubated in human plasma for 4 h at 37 °C and analyzed by radio−TLC. The results showed that 97% of **1a** remained intact after 2 h and over 87% remained after 4 h, demonstrating its high chemical stability.

Tissue Distribution Studies. Since fatty acids are predominantly metabolized in the fasting state, mice were fasted for 12 h prior to experiments. High radioactivity accumulated in blood, heart, lung, liver, and kidneys, and the radioactivity washed out rapidly with time from all tissues except for liver and kidneys (Table 1). Heart uptake of **1a** (6.38% ID/g at 1 min and 0.73% ID/g at 5 min postinjection) was comparable to those of ^{99m}Tc-MAMA-HDA (5.46% ID/g at 2 min and 2.40% ID/g at 5 min postinjection) (*22*). ^{99m}Tc-BAT-pentadecanoic acid and HDA were evaluated in rats, and the results were expressed as % ID/organ (0.31−0.46% ID/organ at 5 min postinjection) (*19*). The maximum heart-to-blood uptake ratio of **1a** was 1.87 at 5 min postinjection, which appears higher than those obtained for other ^{99m}Tc-labeled fatty acid analogs (Table 2). Heart-to-liver uptake ratios of **1a** were similar to those of ^{99m}Tc-MAMA-HDA. ^{99m}Tc-[9,10-bis[*N*-(2′-methyl-2′-mercapto)propyl]aminooctadecanoic acid and ^{99m}Tc-[7,10-bis(2-mercapto-2-methyl)propyl]-7,10-diazapentadecanoic acid showed high heart-to-blood and heart-to-liver uptake ratios in rats (Table 2), probably due to the branching effect of the fatty acid analogs (*20*, *21*). Although direct comparisons in % ID/g of radiotracers may not be appropriate, due to different experiment conditions and animal species used for the studies, **1a** may be superior to other ^{99m}Tc-labeled fatty acid analogs in terms of its facile conjugation of $[^{99m}Tc(CO)_3]^+$ to a fatty acid analog, high heart uptake, and high heart-to-blood ratios. No significant uptake was observed

Table 2. Comparison of in Vivo Data of ^{99m}Tc-Labeled Fatty Acid Analogs[d]

radiotracer	heart	heart/blood[a]	heart/liver[a]	animal	metabolites
1a	12.67 (0.5 min)[b]	0.69	0.46	ICR mice	mainly **1b** (ICR mice)
	6.38 (1 min)	0.85	0.20		
	0.73 (5 min)	1.87	0.02		
	0.28 (30 min)	1.65	0.02		
^{99m}Tc-MAMA-HDA (*22*)	11.22 (0.5 min)[b]	1.14	0.53	ddY mice	^{99m}Tc-MAMA-BA
	5.46 (2 min)	1.51	0.21		(Wistar rats)
	2.40 (5 min)	0.82	0.09		
	0.60 (20 min)	0.77	0.03		
	0.32 (60 min)	0.86	0.02		
^{99m}Tc-BAT-PDA (*19*)	0.31 (5 min)[c]	1.39		SD rats	
	0.13 (15 min)	0.98			
	0.05 (30 min)	0.65			
^{99m}Tc-BAT-HDA (*19*)	0.46 (5 min)[c]	0.98		SD rats	
	0.16 (15 min)	0.59			
	0.10 (30 min)	0.46			
^{99m}Tc-[9,10-bis[*N*-(2′-methyl-2′-mercapto) propyl]amino-ODA (*20*)	1.30 (5 min)[b]	1.78	0.29	Fischer CD rats	
	0.50 (30 min)	1.67	0.11		
^{99m}Tc-[7,10-bis(2- mercapto-2-methyl)propyl] -7,10-diaza-PDA (*21*)	0.56 (15 min)[b]	0.71	0.21	Fischer CD rats	

[a] % ID/g ratio. [b] % ID/g. [c] % ID/organ. [d] HDA, hexadecanoic acid; PDA, pentadecanoic acid; ODA, octadecanoic acid; BA, butyric acid.

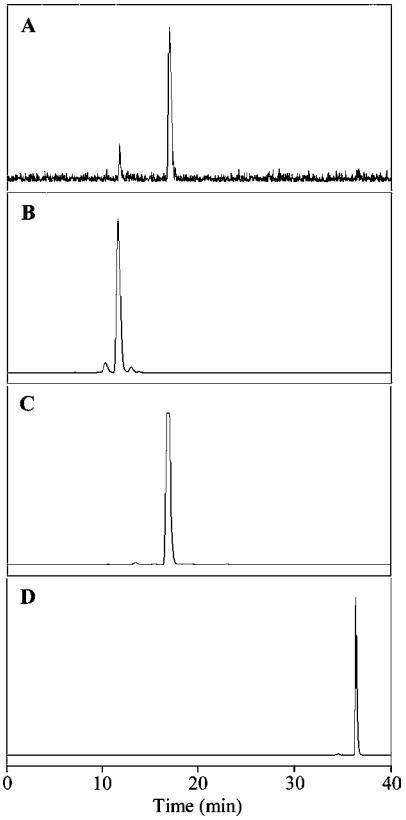


Figure 1. HPLC analysis of 30 min urine samples from mice injected via a tail vein with **1a** (A). HPLC profiles of radioactive metabolite standards: t_R = 11.8 min (**1c**) (B), t_R = 16.7 min (**1b**) (C), and t_R = 35.9 min (**1a**) (D). HPLC analysis was conducted using an analytical column (YMC-Pack C18, 5 μ, 4.6 × 250 mm) and a NaI(T1) radioactivity detector.

by the stomach, indicating that ^{99m}Tc pertechnetate was not regenerated during the study.

Analysis of Metabolites. When samples of urine were analyzed by HPLC, a 9.3:1 ratio of the radioactive metabolites at the retentions times of 16.7 and 11.8 min was observed, which were identified as **1b** and **1c**, respectively (Figure 1). Radioactive metabolite **1b**, which is produced by five cycles of **1a** β-oxidation, was the major metabolite (Figure 1A,C), which indicated that **1a** was metabolized to **1b** via β-oxidation and excreted to the kidneys. Although the metabolites were not analyzed in a time-dependent manner, it is believed that **1b** would be further metabolized to **1c** in time on the basis of the presence of a small portion of **1c** at 30 min postinjection on HPLC (Figure 1A). The metabolism of **1a** is similar to that of ^{99m}Tc-MAMA-HDA, which is metabolized to ^{99m}Tc-MAMA-butyric acid (BA) after six cycles of β-oxidation in rats (Table 2) (*22*). Although the metabolism of **1a** appears to be slower than ^{99m}Tc-MAMA-HDA, it is probable that metabolic rates are species-dependent (mice vs rats). Metabolite analysis has not been carried out for other ^{99m}Tc-labeled fatty acid analogs (Table 2).

CONCLUSION

A ^{99m}Tc-labeled fatty acid analog, **1a**, was prepared in high yield by incorporating $[^{99m}Tc(CO)_3]^+$ into a fatty acid analog, **2a**. An in vivo evaluation of **1a** demonstrated that high radioactivity accumulated in the heart and that the radiotracer is mainly metabolized to **1b** via β-oxidation in the body. Taken together, **1a** may be useful for evaluating the β-oxidation of fatty acids in myocardium.

ACKNOWLEDGMENT

We thank Hyun Jung Jeon for performing the tissue distribution studies and Iljung Lee and Byung Ho Ahn for their technical assistance. IsoLink kits were generous gifts from Mallinckrodt Medical B.V. (Petten, The Netherlands). This work was supported by the Korea Research Foundation Grant (MOEHRD) (KRF-2006-521-E00092).

LITERATURE CITED

(1) Corbett, J. R. (1999) Fatty acids for myocardial imaging. *Sem. Nucl. Med. 29*, 237−258.

(2) Bergmann, S. R., Weinheimer, C. J., Markham, J., and Herrero, P. (1996) Quantitation of myocardial fatty acid metabolism using PET. *J. Nucl. Med. 37*, 1723−1730.

(3) Wisneski, J. A., Gertz, E. W., Neese, R. A., and Mayr, M. (1987) Myocardial metabolism of free fatty acids. Studies with ^{14}C-labeled substrates in humans. *J. Clin. Invest. 79*, 359−366.

(4) Nellis, S. H., Liedtke, A. J., and Renstrom, B. (1992) Fatty acid kinetics in aerobic myocardium: characteristics of tracer carbon entry and washout and influence of metabolic demand. *J. Nucl. Med. 33*, 1864−1874.

(5) Tamaki, N., Morita, K., Kuge, Y., and Tsukamoto, E. (2000) The role of fatty acids in cardiac imaging. *J. Nucl. Med. 41*, 1525−1534.

(6) Lerch, R. A., Bergmann, S. R., Ambos, H. D., Welch, M. J., Ter-Pogossian, M. M., and Sobel, B. E. (1982) Effect of flow-independent reduction of metabolism on regional myocardial clearance of ^{11}C-palmitate. *Circulation 65*, 731−738.

(7) Buckman, B. O., VanBrocklin, H. F., Dence, C. S., Bergmann, S. R., Welch, M. J., and Katzenelenbogen, J. A. (1994) Synthesis and tissue biodistribution of [ω-^{11}C]palmitic acid: a novel PET imaging agent for cardiac fatty acid metabolism. *J. Med. Chem. 37*, 2481−2485.

(8) Freundlieb, C., Höck, A., Vyska, K., Feinendegen, L. E., Machulla, H.-J., and Stöcklin, G. (1980) Myocardial imaging and metabolic studies with [17-^{123}I]iodoheptadecanoic acid. *J. Nucl. Med. 21*, 1043−1050.

(9) Machulla, H. J., Marsmann, M., and Dutschka, K. (1980) Biochemical synthesis of a radioiodinated phenyl fatty acid for in vivo metabolic studies of the myocardium. *Eur. J. Nucl. Med. 5*, 171−173.

(10) Goodman, M. M., Kirsch, G., and Knapp, F. F., Jr. (1984) Synthesis of radioiodinated ω-(*p*-iodophenyl)-substituted methyl-branched long-chain fatty acids. *J. Med. Chem. 27*, 390−397.

(11) Sloof, G. W., Visser, F. C., van Lingen, A., Bax, J. J., Eersels, J., Teule, G. J., and Knapp, F. F., Jr. (1997) Evaluation of heart-to-organ ratios of ^{123}I-BMIPP and the dimethyl-substituted fatty acid analogue in humans. *Nucl. Med. Commun. 18*, 1065−1070.

(12) Takahashi, T., Nishimura, S. I., Ido, T., Ishiwata, K. I., and Iwata, R. (1996) Biological evaluation of 5-methyl-branched-chain ω-[^{18}F]-fluorofatty acid: A potential myocardial imaging tracer for positron emission tomography. *Nucl. Med. Biol. 23*, 303−308.

(13) DeGrado, T. R. (1991) Synthesis of 14(*R,S*)-[^{18}F]fluoro-6-thia-heptadecanoic acid (FTHA). *J. Labelled Compd. Radiopharm. 29*, 989−995.

(14) DeGrado, T. R., Coenen, H. H., and Stöcklin, G. (1991) 14(*R,S*)-[^{18}F]Fluoro-6-thia-heptadecanoic acid (FTHA): Evaluation in mouse of a new probe of myocardial utilization of long chain fatty acids. *J. Nucl. Med. 32*, 1888−1896.

(15) Schwochau, K. (1994) Technetium radiopharmaceuticals. Fundamentals, synthesis, structure, and development. *Angew. Chem., Int. Ed. Engl. 33*, 2258−2267.

(16) Jurisson, S., Berning, D., Jia, W., and Dangsche, M. (1993) Coordination compounds in nuclear medicine. *Chem. Rev. 93*, 1137−1156.

(17) Eckelman, W. C., Karesh, S. M., and Reba, R. C. (1975) New compounds: fatty acid and long chain hydrocarbon derivatives containing a strong chelating agent. *J. Pharm. Sci. 64*, 704−706.

(18) Karesh, S. M., Eckelman, W. C., and Reba, R. C. (1977) Biological distribution of chemical analogs of fatty acids and long chain hydrocarbons containing a strong chelating agent. *J. Pharm. Sci. 86*, 225−228.

(19) Mach, R. H., Kung, H. F., Jungwiwattanaporn, P., and Guo, Y. Z. (1991) Synthesis and biodistribution of a new class of ^{99m}Tc-labeled fatty acid analogs for myocardial imaging. *Nucl. Med. Biol. 18*, 215−226.

(20) Jones, G. S., Elmaleh, D. R., Strauss, H. W., and Fischman, A. J. (1994) Synthesis and biodistribution of new ^{99m}technetium fatty acid. *Nucl. Med. Biol. 21*, 117−123.

(21) Jones, G. S., Elmaleh, D. R., Strauss, H. W., and Fischman, A. J. (1996) 7,10-Bis(2-mercapto-2-methyl)propyl-7,10-diazapalmitic acid: A novel, N_2S_2 ligand for technetium-99m. *Bioorg. Med. Chem. Lett. 6*, 2399−2404.

(22) Magata, Y., Kawaguchi, T., Ukon, M., Yamamura, N., Uehara, T., Ogawa, K., Arano, Y., Temma, T., Mukai, T., Tadamura, E., and Saji, H. (2004) A Tc-99m-labeled long chain fatty acid derivative for myocardial imaging. *Bioconjugate Chem. 15*, 389−393.

(23) Spradau, T. W., and Katzenellenbogen, J. A. (1998) Preparation of cyclopentadienyltricarbonylrhenium complexes using a double ligand transfer reaction. *Organometallics 17*, 2009−2017.

(24) Skaddan, M. B., Wust, F. R., Jonson, S., Syhe, R., Welch, M. J., Spies, H., and Katzenellenbogen, J. A. (2000) Radiochemical synthesis and tissue distribution of Tc-99m-labeled 7α-substituted estradiol complex. *Nucl. Med. Biol. 27*, 269−278.

(25) Lee, B. C., Choe, Y. S., Chi, D. Y., Lee, K. H., Choi, Y., Kim, S. E., and Kim, B.-T. (2004) Cyclopentadieny tricarbonyl ^{99m}Tc octanoic acid: A novel radiotracer for evaluation of fatty acid metabolism in the liver. *Bioconjugate Chem. 15*, 121−127.

(26) Alberto, R., Schibli, R., Egli, A., Schubiger, A. P., Abram, U., and Kaden, T. A. (1998) A novel organometallic aqua complex of technetium for the labeling of biomolecules: Synthesis of [^{99m}Tc-$(OH_2)_3(CO)_3]^+$ from $[^{99m}TcO_4]^-$ in aqueous solution and its reaction with a bifunctional ligand. *J. Am. Chem. Soc. 120*, 7987−7988.

(27) Alberto, R., Schibli, R., Waibel, R., Abram, U., and Schubiger, A. P. (1999) Basic aqueous chemistry of $[M(OH_2)_3(CO)_3]^+$ (M = Re, Tc) directed towards radiopharmaceutical application. *Coord. Chem. Rev. 190−192*, 901−919.

(28) Alberto, R., Schibli, R., Schubiger, A. P., Abram, U., Pietzsch, H. J., and Johannsen, B. (1999) First application of fac-[^{99m}Tc$(OH_2)_3$-$(CO)_3]^+$ in bioorganometallic chemistry: Design, structure, and in vitro affinity of a 5-HT_{1A} receptor ligand labeled with ^{99m}Tc. *J. Am. Chem. Soc. 121*, 6076−6077.

(29) Schibli, R., Bella, R. L., Alberto, R., Garcia-Garayoa, E., Ortner, K., Abram, U., and Schubiger, A. P. (2000) Influence of the denticity of ligand systems on the in vitro and in vivo behavior of ^{99m}Tc(I)-tricarbonyl complexes: a hint for the future functionalization of biomolecules. *Bioconjugate Chem. 11*, 345−351.

(30) Hawkes, M. J., and Ginsberg, A. P. (1969) Dianionic rhenium carbonyl halides. *Inorg. Chem. 8*, 2189−2195.

BC060299W

Simplified Preparation via Streptavidin of Antisense Oligomers/Carriers Nanoparticles Showing Improved Cellular Delivery in Culture

Yi Wang,[†] Kayoko Nakamura,[‡] Xinrong Liu,[†] Naoto Kitamura,[‡] Atsushi Kubo,[‡] and Donald J. Hnatowich*[,†,‡]

Division of Nuclear Medicine, Department of Radiology, University of Massachusetts Medical School, Worcester, Massachusetts 01655, and Department of Radiology, Keio University School of Medicine, Tokyo 160-8582, Japan.
Received January 29, 2007; Revised Manuscript Received April 17, 2007

Objective: Carriers are increasingly now viewed as helpful or even essential to improve cellular uptake in connection with antisense tumor targeting and other applications requiring transmembrane delivery of oligomers. Evaluation of many of the large number of available and potentially useful carriers is limited only by the complexities of preparing the oligomer/carriers by covalent conjugation. However, using streptavidin as a linker between biotinylated carriers and biotinylated antisense oligomers would require only simple mixing for preparation. The goal of this study was to evaluate the preparation and cell accumulation in culture of carrier/streptavidin nanoparticle of an antisense phosphorodiamide morpholino (MORF) oligomer. Methods: The model carriers were cholesterol, a 10 mer HIV-tat peptide, and a 10 mer polyarginine, each having been reported elsewhere to improve cellular delivery of oligomers. The model antisense oligomer was the 25 mer MORF targeting the survivin mRNA. The accumulations of the antisense MORF/carrier nanoparticle were compared to the sense MORF/carrier, to the carrier-free nanoparticles, and to the naked antisense MORF in the survivin-expressing MCF-7 cells. The MORFs and peptides were purchased biotinylated, while the cholesterol was biotinylated in-house. In all cases, the ^{99m}Tc radiolabel was placed on the oligomers. Cell studies were performed at low nM concentration as required for antisense imaging applications and at 37 °C primarily in 1% FBS. Results: Each radiolabeled oligomer/streptavidin/carrier nanoparticle was successfully prepared by careful mixing at a 1:1 molar ratio. As evidence of carrier participation, the radiolabeled MORF showed increased accumulation in cells when incubated as the nanoparticle compared to the carrier-free nanoparticle and by as much as a factor of 11. Accumulation of the antisense MORF/streptavidin/tat nanoparticle was significantly higher than the sense MORF/streptavidin/tat nanoparticle as evidence of specific antisense targeting. Conclusions: The preparation of oligomer/carrier nanoparticles was greatly simplified over covalent conjugations by using streptavidin as a linker. Furthermore, our results suggest that the addition of streptavidin did not interfere with the cellular delivery function of the tat, polyarginine, or cholesterol carriers nor with the specific antisense mRNA binding function of the MORF oligomer.

INTRODUCTION

The results of recent investigations from these laboratories and elsewhere suggest that radiolabeled DNAs and other oligomers for in vivo antisense targeting of tumor may require carriers for improved transmembrane delivery. Fortunately, a large number of potential carriers have been identified primarily for use in cell culture but with increasing reports of successful in vivo use as well (*1*). However, many of the potentially useful carriers can only now be attached to oligomers by covalent conjugation usually requiring involved synthesis, a process that can be challenging (*2*). Two recent reports have described the use of streptavidin to alter the pharmacokinetics of the tat peptide (*3*) and an antisense peptide nucleic acid (PNA) (*4*). We considered that streptavidin could be used in this manner as a linker for radiolabeled antisense oligomer/carrier nanoparticles (*5*). A similar approach was recently described to improve RNA cellular transport in connection with RNAi (*6*). A large number of potential carriers are already available commercially with biotin groups attached, and others with primary amines may be readily biotinylated. In addition to a greatly simplified preparation stabilized by the high binding affinity of biotin for streptavidin, the advantages include the possibility of attaching up to four carriers or oligomers in any combination, since streptavidin possesses four biotin binding sites. This property is illustrated in the artist's conception presented as Figure 1. Toxicities, whether of the streptavidin, oligomer, or carrier, are unlikely to be evident given the low dosages that will be administered in connection with radioimaging, our application of interest. The potential disadvantages include the possibility that streptavidin may interfere with the transmembrane delivery properties of certain carriers and may encourage entrapment of the antisense oligomer in vesicles, thereby restricting its mRNA binding function. In addition, the possibility exists that the addition of streptavidin may unfavorably alter the pharmacokinetics of the oligomer. The goals of this investigation were first to evaluate the preparation of the 1:1 streptavidin nanoparticles and second to address the first two of the above concerns, namely, whether the presence of streptavidin in the nanoparticle will interfere with the ability of carriers to improve cellular accumulations and whether the presence of streptavidin interferes with target mRNA binding by an antisense mechanism.

The three model carriers selected for this initial investigation have each been reported to successfully increase cell membrane permeation in culture. The tat and polyarginine peptides are short cationic peptides with recognized effectiveness as carriers. The tat peptide is the 48−57 residues of the tat protein of HIV-1

* Address correspondence to Donald J. Hnatowich, Ph.D., Professor, Radiology, Division of Nuclear Medicine, Department of Radiology, H2-579, University of Massachusetts Medical School, 55 Lake Avenue North, Worcester, MA 01655,. Tel: (508) 856-4256; Fax: (508) 856-4572; E-mail: donald.hnatowich@umassmed.edu.

[†] University of Massachusetts Medical School.

[‡] Keio University School of Medicine.

10.1021/bc070032c CCC: $37.00 © 2007 American Chemical Society
Published on Web 07/03/2007

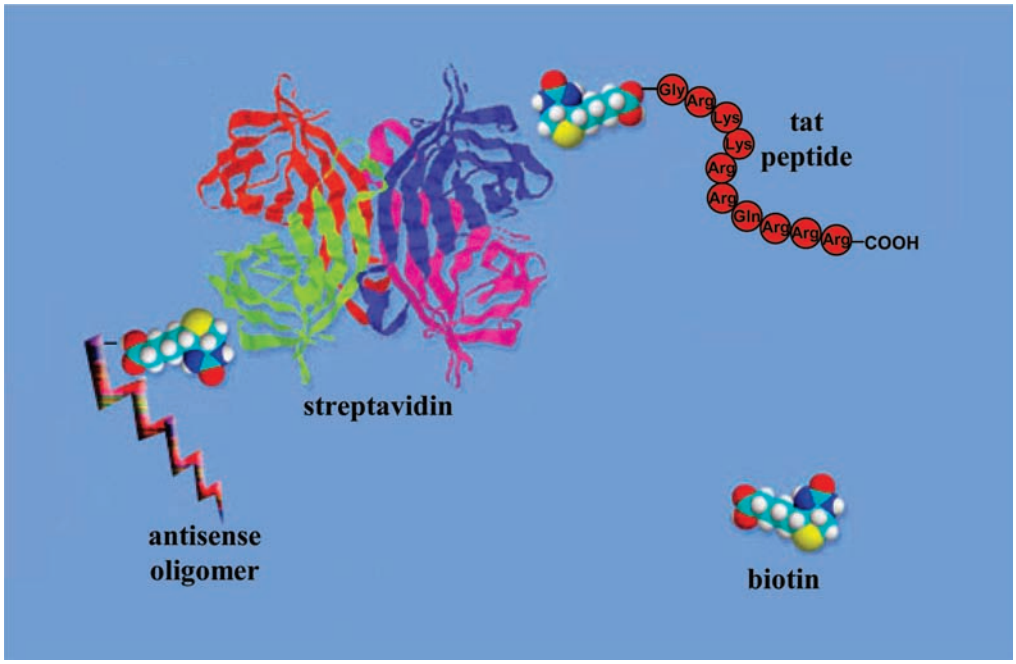


Figure 1. Artist's conception illustrating the composition of the nanoparticle in which the tat peptide and the antisense oligomer have been linked via streptavidin (modified from http://www.arrayit.com/Products/Substrates/SuperStreptavidin/superstreptavidin.html).

with the property of improving accumulations in possibly all cell types by an as yet unknown mechanism (*7*). It has been used as a delivery peptide for the intracellular transduction of large molecules such as proteins, peptides, and MRI contrast agents (*8*), as well as oligomers (*9*, *10*). A polyarginine peptide with similar properties to that of tat was included in this research because of recent reports of effectiveness (*11*−*14*). Finally, the charge neutral cholesterol was selected as a third carrier also because of recent reports of effectiveness (*15*). The model oligomers were both phosphorodiamide morpholinos (MORFs). The study MORF had a base sequence antisense to the 6−30 nucleotides within the survivin mRNA, while the control MORF had the sense sequence.

The influence of the carriers was evaluated by comparing the cell accumulations of the nanoparticle to the carrier-free nanoparticle and to the naked MORF (i.e., without the carrier or the streptavidin).

Determining the antisense properties of the nanoparticle in this investigation requires comment. Since the interest of these laboratories is in antisense imaging, the incubation concentration was fixed at low nanomolarity to avoid target mRNA saturation. While nanomolar concentrations of short double-stranded RNAs can decrease protein expression by RNAi mechanisms (*6*), concentrations in the micromolar range are generally required to decrease protein expression with antisense MORFs and other oligomers (*16*). Accordingly, in this investigation, evidence of antisense targeting was evaluated by comparing cellular accumulations of the antisense to the sense nanoparticles rather than by measurement of survivin protein concentration.

EXPERIMENTAL PROCEDURES

Chemicals and Oligomers. The 25 mer antisense MORF (5′-CCA-ACG-GGT-CCC-GCG-ATT-CAA-ATC-T) and the sense control MORF were obtained with a biotin group on the 3′ equivalent end via a 6-aminohexanoic acid linker and a primary amine on the opposite end (GeneTools, Philomath, OR). The S-acetyl NHS−MAG3 was synthesized in-house (*17*) and its structure confirmed by elemental analysis, proton nuclear magnetic resonance, and mass spectroscopy. The tat (biotin-linker-G-R-K-K-R-R-Q-R-R-R) and polyarginine peptide were both 10 mer and were purchased HPLC purified as the native L-isomer with the biotin attached to the amine end via a 6-aminohexanoic acid linker (21st Century Biochemicals, Marlboro, MA). The biotinylated cholesterol was synthesized by reacting biotinyl-3,6-dioxaoctanediamine (Pierce, Rockford, IL) with cholesteryl choloroformate (Aldrich, Milwaukee, WI). The human breast cancer cell line MCF-7 was a gift from Dr. Dario C. Altieri (Cancer Biology, University of Massachusetts Medical School). This cell line is reported to be a high-level expressor of the survivin mRNA (*18*), and the expression of the survivin mRNA was confirmed by RT-PCR (*19*). Standard chemicals were obtained from various suppliers and used without purification. The ^{99m}Tc-pertechnetate was eluted from a ^{99}Mo−^{99m}Tc generator (Bristol-Myers Squibb Medical Imaging Inc., North Billerica, MA).

Oligomer Conjugation and Radiolabeling. All oligomers were conjugated with S-acetyl NHS-MAG3 via the derivatized amine as previously described (*20*). A solution of 1 mg of oligomer in 200 μL of 0.3 M pH 8.0 HEPES buffer was added to a vial containing 0.7−1.0 mg S-acetyl NHS-MAG3. The vial was vortexed immediately to a clear solution and incubated for 1 h at room temperature. Thereafter, to the solution was added in order 50 μL of 2 M ammonium acetate, 120 μL of freshly prepared 20 mg/mL $SnCl_2 \cdot 2H_2O$/tartrate solution (100 mg/mL sodium tartrate in 0.5 M ammonium bicarbonate, 0.25 M ammonium acetate, and 0.18 M ammonium hydroxide, pH 9.2) with agitation. After heating at 100 °C for 25 min, the mixture was allowed to cool, and absolute ethanol was added to a concentration of 20% (v/v); then, the mixture was purified on a 1 × 20 cm P4 column (Bio-Rad, Hercules, CA) using 0.25 M ammonium acetate as eluant. The peak fractions were pooled and the oligomer concentration quantitated by UV absorbance at 265 nm according to the manufacturer's instructions. The purified samples were stored at refrigerator temperatures. All solutions were passed through a 0.22 μm filter to ensure sterility.

Radiolabeling of each oligomer was achieved by introducing about 0.5 to 1 mCi (20 μL) of ^{99m}Tc-pertechnetate generator eluant into a combined solution consisting of about 15 μL MAG3-conjugated oligomer (10 μg) in 0.25 M NH_4OAc, 45 μL of 0.25 M ammonium acetate, 15 μL of 50 μg/μL Na_2tartrate$\cdot 2H_2O$ in the pH 8.7 buffer, and 5 μL of fresh 4 μg/μL $SnCl_2 \cdot 2H_2O$ in 10 mM HCl containing 1 mg/mL ascorbate

(*20*). The final pH was about 8.5. After vortexing and then heating for 20 min in boiling water, the labeling was confirmed by size exclusion HPLC, or by C18 Sep-Pak (Waters, Milford, MA) in which the first elution with 0.2 M ammonium acetate removes radiolabeled pertechnetate and tartrate, the second elution with 40% acetonitrile removes radiolabeled oligomer while radiolabeled colloids are retained on the Sep-Pak.

Synthesis of Biotinylated Cholesterol. While both the tat and polyarginine peptides were biotinylated by the manufacturer, the biotinylated cholesterol was prepared in-house for this investigation. Briefly, 12 mg of cholesteryl choloroformate (26.7 μmol) in 60 μL anhydrous chloroform was added to a 1.5 mL microfuge tube containing 12 mg (32 μmol) biotinyl-3,6-dioxaoctanediamine in 200 μL anhydrous 1-methyl-2-pyrrolidinone (NMP). The mixture was vortexed to a clear solution. After adding 4 μL diisopropylethylamine (DIEA), the solution was agitated and placed at room temperature for 16 h. The raw product was precipitated as a white powder by addition of 1 mL ethyl ether. The white powder was dissolved in 200 μL NMP and reprecipitated by addition of ethyl ether two more times to remove diisopropylethylamine (DIEA) and unreacted cholesteryl choloroformate. The white powder was dissolved in 400 μL chloroform and washed with 400 μL 0.1 ammonium acetate four times to remove unreacted biotinyl-3,6-dioxaoctanediamine. The chloroform solution was collected, the solvent removed by evaporation over nitrogen, and the product lyophilized at a high vacuum to remove any remained ammonium acetate.

Nanoparticle Preparation and Testing. The streptavidin/tat was prepared by adding very slowly and with vigorous agitation 11.6 μL of tat at 0.5 μg/μL to 20 μL of streptavidin at 10.0 μg/μL both dissolved in 0.5 M NaCl and 0.2 M ammonium acetate solution (molar ratio 1:1). Although the addition was equimolar, the formation of significant concentrations of the 1:2 streptavidin/tat nanoparticle is possible. That the product was free of higher-order tat nanoparticles, i.e., two to four tat peptides per nanoparticle, was confirmed by adding tracer levels of ^{99m}Tc-labeled biotinylated tat peptide to the tat solution before the addition to streptavidin and analyzing the product by size exclusion HPLC with in-line UV and radioactivity detection using 20% acetonitrile in 1 M NaCl, 0.1 M ammonium acetate as eluant at a flow rate 0.6 mL/min. The appearance of a single peak in the UV trace at 280 nm corresponding to a single peak in the radioactivity trace was evidence of complete complexation, since this assay is capable of resolving 1:2 and higher-order nanoparticles (data not presented). Thereafter, the ^{99m}Tc-labeled biotinylated MORF was added to the streptavidin/tat nanoparticle in the identical fashion.

To confirm that the final product was also free of higher-order MORF nanoparticles, i.e., two or three MORFs per streptavidin/tat nanoparticle, the identical preparation was repeated with unlabeled antisense MORF and to the final product was added at tracer levels the complementary DNA (without biotin) radiolabeled with ^{99m}Tc. As before, the appearance by size exclusion HPLC of a single peak in the UV trace at 265 nm was evidence of a successful preparation. As further evidence against higher-order nanoparticles, the nanoparticle was intentionally prepared at a 1:1 tat/streptavidin molar ratio but at a 2:1 MORF/streptavidin molar ratio followed by agarose gel electrophoresis analysis. The complementary phosphodiester DNA was added to each nanoparticle before analysis so that ethidium bromide could be used for detection.

Both the radiolabeled polyarginine and cholesterol nanoparticles were prepared and tested in the identical fashion as was the carrier-free MORF/streptavidin nanoparticle. Radioactivity recoveries were routinely measured in all HPLC analyses and were in all cases 90% or better.

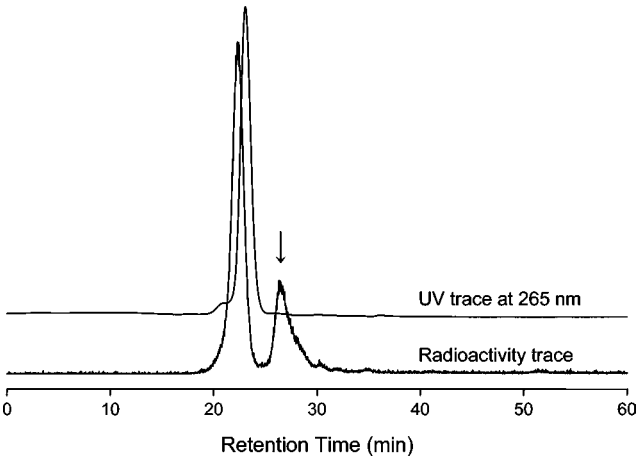


Figure 2. Size exclusion UV trace (265 nm) and radioactivity trace of the antisense MORF/streptavidin/tat nanoparticle radiolabeled by addition of trace ^{99m}Tc-sense DNA (without biotin). The smaller radioactivity peak (arrow) is due to free MORF in the nanoparticle preparation. The small difference in retention time between the UV and radioactivity traces is due to the hybridization of the sense DNA.

Cellular Accumulation Studies. The MCF-7 cells growing in monolayers were expected to be in log phase at the time of the study. Cells were seeded at $(3-4) \times 10^5$ cells per well in 12-well plates. In quadruplet, 1.0 mL of the ^{99m}Tc-labeled oligomer dissolved in 1% FBS DMEM medium was added to each well and the cells incubated at 37 °C in humidified 5% carbon dioxide for different times. The concentration of oligomer was at all times 8 nM to avoid mRNA saturation. The cells were harvested by lysis with 0.2 M NaOH and 1% SDS after removing the medium and washing twice with PBS.

RESULTS

Nanoparticle Preparation and Testing. Figure 2 presents both the UV (265 nm) and radioactivity traces obtained by size exclusion HPLC of the antisense MORF/streptavidin/tat nanoparticle to which trace ^{99m}Tc-labeled sense DNA (without biotin) was added. The radiolabeled sense DNA will hybridize with the antisense MORF in each of its forms and provide a radioactivity peak for each. As shown, only one peak corresponding to the antisense MORF/streptavidin/tat nanoparticles appears in the radioactivity profile and corresponds to the UV trace. Therefore, the result confirms the absence of higher-order MORF/streptavidin/tat nanoparticles. As shown in the figure, a second radioactivity peak is present with about 15% of the radioactivity. This peak is due to free antisense MORF in the preparation resulting from the absence of biotin on a fraction of the MORF provided by the manufacturer. Accordingly, the antisense MORF/streptavidin/tat nanoparticles also showed the same 15% impurity. Since the cellular accumulation of the uncharged naked MORFs is negligible (see below and ref 21), the accumulation of this radiocontaminant will lower the percent accumulations but may otherwise be ignored in the cell accumulations studies. By the same analysis method, biotin was missing on about 20% of the sense MORF.

Figure 3 presents the results of agarose gel electrophoresis of four nanoparticles prepared at 1- and 2-fold molar excess of MORF. The complementary phosphodiester DNA was added to each nanoparticle before analysis so that ethidium bromide could be used for visualization (thus, the nanoparticle with a 2-fold molar excess of MORF will also have twice the DNA therefore twice the charge). The obvious difference in migration of the nanoparticle with two MORFs per streptavidin compared to one (lanes 4 versus 2 without tat and lanes 5 versus 3 with tat) shows that preparation at an intentional 2-fold molar excess

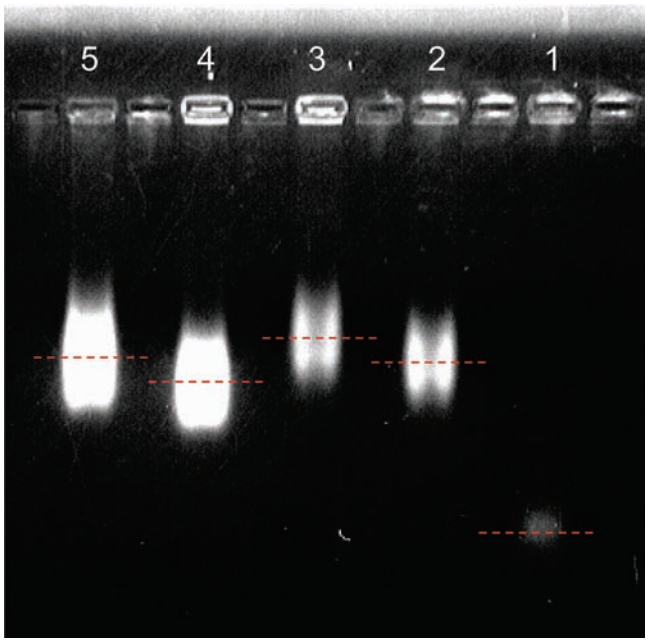


Figure 3. Agarose gel showing the relative positions of naked MORF (lane 1), MORF/streptavidin nanoparticle prepared at a 1:1 molar ratio (lane 2), MORF/streptavidin/tat prepared at a 1:1:1 molar ratio (lane 3), MORF/streptavidin prepared at a 2:1 molar ratio (lane 4), and MORF/streptavidin/tat prepared at a 2:1:1 molar ratio (lane 5). The dotted line in each lane defines the center of each band.

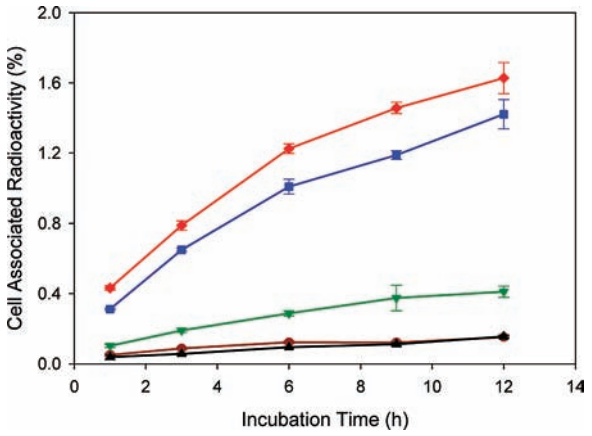


Figure 4. Percent accumulations in MCF-7 cells over time of radiolabeled antisense MORF when incubated as the tat (squares, ■), polyarginine (diamonds, ♦), or cholesterol (inverted triangles, ▼) streptavidin nanoparticles and as the carrier-free nanoparticle (circles, ●) and naked MORF (triangles, ▲) controls. ($N = 4$; error bars indicate one standard deviation).

provides a nanoparticle of higher order compared to nanoparticles prepared under the conditions of this investigation.

MORF Cellular Accumulation Studies. No evidence of cellular toxicity by growth delay was observed in any cell study of this investigation. Results are presented in Figure 4 as the average percent accumulation ($N = 4$) for each of three study MORF nanoparticles and both the carrier-free streptavidin nanoparticle and naked MORF controls in MCF-7 cells at 1, 3, 6, 9, and 12 h of incubation. As shown, adding the carrier increases the accumulations over controls by about 9-fold for tat and 11-fold for polyarginine and somewhat less for cholesterol. The identical accumulations for the MORF/streptavidin nanoparticle compared to the naked MORF suggest that the streptavidin was not responsible for these improved accumulations.

Figure 5 present accumulations in MCF-7 cells over time of the antisense and the sense control MORF/streptavidin/tat

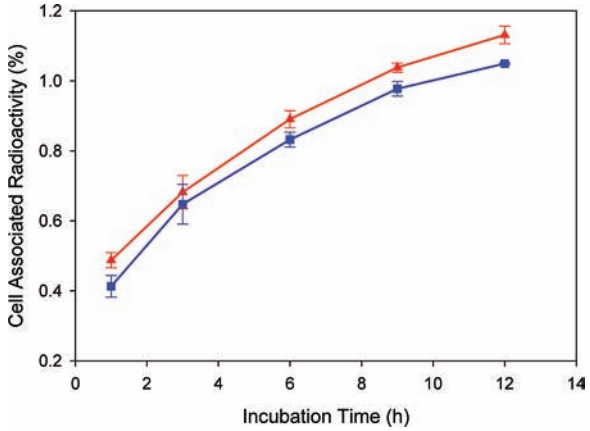


Figure 5. Percent accumulations over time of the antisense MORF/streptavidin/tat nanoparticle (triangles, ▲) compared to that of the control sense MORF/streptavidin/tat nanoparticle (squares, ■). The difference is significant (Student's t test, $p < 0.05$) at all times other than 3 h, providing evidence for specific binding to target mRNA of the nanoparticle and therefore escape from entrapment. ($N = 4$; error bars indicate one standard deviation).

nanoparticles. The differences are significant (Student's t test, $p < 0.05$) at all times other than 3 h, providing evidence for preserved antisense binding function of the nanoparticle and therefore escape from entrapment.

DISCUSSION

In general, all in vivo applications of radiolabeled DNAs and their analogues such as MORFs (collectively: oligomers) are currently characterized to varying degree by the same limitation: poor pharmacokinetic delivery to the target following intravenous administration and, in the case of applications with intracellular targets, poor delivery through cell membranes (*22*). Attempts to increase delivery are now often focused on the use of oligomer/carrier constructs in which the carrier is intended to improve pharmacokinetics, for example, by adding an antitumor antibody to direct the nanoparticle to its target, or more commonly, adding a carrier intended to improve cellular accumulations by chaperoning the oligomer through cellular membranes primarily in vitro but increasingly now in vivo as well.

Charged oligomers such as the DNAs have the advantage that they may be complexed to charged carriers such as cationic peptides or liposomes simply by electrostatic binding (*23*, *24*). While a number of cationic carriers for DNAs are commercially available, the vast majority of these have been designed for in vitro delivery in cell culture and are not recommended by the manufacturers for use in serum environments such as those experienced in vivo. We have achieved largely unfavorable in vivo results using two commercially available cationic carriers with DNAs prepared simply by electrostatic binding (*25*). In cases of uncharged oligomers such as peptide nucleic acids (PNAs) and MORFs, covalent conjugation is necessary at present for carrier attachment, and the synthesis of these nanoparticles can prove difficult (*2*). Even the solid-phase synthesis of PNA/peptide carrier nanoparticles is not without its own difficulties and in our hands has led to products of questionable quality.

In this investigation, the use of streptavidin to prepare the carrier and oligomer nanoparticles performed as anticipated. As shown in Figure 1, the slow addition at a 1:1 molar ratio with continuous agitation, first of the biotinylated carrier to streptavidin, and subsequently of the biotinylated MORF to the streptavidin/carrier, provided a product free of both 1:2 com-

plexes. Since the nanoparticle is expected to dissociate in situ, in all cases, the radiolabel was on the MORF rather than the carrier or streptavidin.

One potential drawback to the use of streptavidin as linker may be a susceptibility to dissociation by endogenous biotin. However, we do not expect endogenous biotin to interfere by displacing biotinylated agents from streptavidin. In preliminary studies, D-biotin at 56 mM was incubated with the streptavidin/tat or streptavidin/MORF used in this investigation at 0.028 mM for 1 h in 37 °C PBS with no evidence of displacement. Since the serum concentration of endogenous biotin in a mouse is about 10 nM (*26*), the displacement from streptavidin by endogenous biotin should be negligable for tat or other biotinylated agents.

In addition to evaluating the ease with which carriers and antisense oligomers may be joined via streptavidin as a convenient linker, a goal of this investigation was to evaluate whether the function of the carrier and the function of the antisense MORF was adversely influenced by the presence of the streptavidin. As shown in Figure 4, the presence of each of the carriers and the streptavidin significantly increased accumulations compared to that of both the naked MORF and the carrier-free nanoparticle and by as much as a factor of 11. Therefore, the streptavidin may not have adversely influenced the function of the carrier to increase cell permeation. As shown in Figure 5, the accumulation of the antisense MORF was statistically higher than the accumulation of the control sense MORF when both were incubated with the MCF-7 cells as the streptavidin/tat nanoparticles. Therefore, the streptavidin may not have adversely influenced the antisense binding properties of the MORF for its mRNA target.

This study is a more extensive evaluation of the use of streptavidin as a linker between biotinylated oligomers and carriers than earlier work from this laboratory (*5*). Recently, Chu et al. described their use of streptavidin as a bridge between a double-stranded siRNA and an RNA aptamer functioning as a cellular delivery agent (*6*). The streptavidin was found by PCR to have little or no effect on the ability of the siRNA to inhibit gene expression. Thus, both by gene expression analysis and by radioactivity accumulations in two difference cells in culture, the evidence is against an adverse influence of streptavidin on function.

CONCLUSION

In conclusion, an advantage to the use of streptavidin as linker is in the simplicity of nanoparticle preparation and therefore the ease with which different nanoparticles may be made and tested in contrast to covalent conjugation. Obviously, the same approach may be used to link tumor targeting agents such as antitumor antibodies as well as antitumor peptides to antisense oligomers with or without carriers. Finally, no evidence was obtained in this investigation that the presence of streptavidin in the nanoparticle interferes with the ability of carriers to improve cell membrane permeation nor with the antisense properties of the oligomers. Taken together, the results of this investigation suggest that further studies in tumored animals are justified to address the issue of whether the streptavidin adversely influences the pharmacokinetic properties of the oligomers.

ACKNOWLEDGMENT

The authors wish to thank Dr. Dario C. Altieri (Cancer Biology, University of Massachusetts Medical School, Massachusetts) for providing the MCF-7 cell line. This research was supported in part by the Office of Science (BER), U.S. Department of Energy, grant no. DE-FG02-03ER63602, the National Institute of Health, grant no. SR21CA100092-02, the Congressionally Directed Medical Research Programs (CDMRP), grant no. W81XWH-06-1-0649, and the 21st Century Center of Excellence (COE) Program entitled "Establishment of individualized cancer therapy based on comprehensive development of minimally invasive and innovative therapeutic methods (Keio University)" from the Japanese Ministry of Education, Science, Sports and Culture. The authors also thank Grant-in-Aid for Scientific Research (19591434, 17659374, 19659315).

LITERATURE CITED

(1) Hnatowich, D. J., and Nakamura, K. (2006) The influence of chemical structure of DNA and other oligomer radiopharmaceuticals on tumor delivery. *Curr. Opin. Mol. Ther. 8*, 136−143.

(2) Tung, C. H., and Stein, S. (2000) Preparation and applications of peptide-oligonucleotide conjugates. *Bioconjugate Chem. 112*, 605−618.

(3) Lee, H. J., and Partridge, W. H. (2001) Pharmacokinetics and delivery of tat and tat-protein conjugates to tissues in vivo. *Bioconjugate Chem. 12*, 995−999.

(4) Lee, H. J., Boado, R. J., Braasch, D. A., Corey, D. R., and Partridge, W. M. (2002) Imaging gene expression in the brain in vivo in a transgenic mouse model of Huntington's disease with an antisense radiopharmaceutical and drug-targeting technology. *J. Nucl. Med. 43*, 948−956.

(5) Nakamura, K., Wang, Y., Liu, X., Kubo, A. and Hnatowich, D. J. (2006) Addition of TAT, polyarginine and cholesterol carriers to MDR1 antisense DNA using streptavidin as linker. *J. Nucl. Med. 47 (Suppl.)*, 512 p.

(6) Chu, T. C., Twu, K. Y., Ellington, A. D., and Levy, M. (2006) Aptamer mediated siRNA delivery. *Nucleic Acids Res. 34*, e73.

(7) Vives, E., Richard, J. P., Rispal, C., and LeBleu, B. (2003) TAT peptide internalization: seeking the mechanism of entry. *Curr. Protein Pept. Sci. 4*, 125−132.

(8) Bhorade, R., Weissleder, R., Nakakoshi, T., Moore, A., and Tung, C. H. (2000) Macrocyclic chelaters with paramagnetic cations are internalized into mammalian cells via a HIV-tat derived membrane translocation peptide. *Bioconjugate Chem. 11*, 301−305.

(9) Astriab-Fisher, A., Sergueev, D. S., Fisher, M., Shaw, B. R., and Juliano, R. L. (2000) Antisense inhibition of P-glycoprotein expression using peptide-oligonucleotide conjugates. *Biochem. Pharmacol. 60*, 83−90.

(10) Moulton, H. M., Hase, M. C., Smith, K. M., and Iversen, P. L. (2003) HIV tat peptide enhances cellular delivery of antisense morpholino oligomers. *Antisense Nucleic Acid Drug Dev. 13*, 31−43.

(11) Chen, C. P., Zhang, L. R., Peng, Y. F., Wang, X. B., Wang, S. Q., and Zhang, L. H. (2003) A concise method for the preparation of peptide and arginine-rich peptide-conjugated antisense oligonucleotide. *Bioconjugate Chem. 14*, 532−538.

(12) Jiang, T., Olson, E. S., Nguyen, Q. T., Roy, M., Jennings, P. A., and Tsien, R. Y. (2004) Tumor imaging by means of proteolytic activation of cell-penetrating peptides. *Proc. Natl. Acad. Sci. U.S.A. 101*, 17867−17872.

(13) Shiraishi, T., and Nielsen, P. E. (2006) Photochemically enhanced cellular delivery of cell penetrating peptide-PNA conjugates. *FEBS Lett. 580*, 1451−1456.

(14) Noguchi, H., and Matsumoto, S. (2006) Protein transduction technology: a novel therapeutic perspective. *Acta Med. Okayama 60*, 1−11.

(15) Manoharan, M. (2002) Oligonucleotide conjugates as potential antisense drugs with improved uptake, biodistribution, targeted deliver, and mechanism of action. *Antisense Nucleic Acid Drug Dev. 12*, 103−128.

(16) Iversen P. I., Arora V., Acker A. J., Mason D. H., and Devi G. R. (2003) Efficacy of antisense morpholiono oligomer targeted to c-myc in prostate cancer xenograft murine model and a phase I safety study in humans. *Clin. Cancer Res. 9*, 2510−2519.

(17) Winnard, P. Jr., Chang, F., Rusckowski, M., Mardirossian, G., and Hnatowich, D. J. (1997) Preparation and use of NHS-MAG3 for technetium-99m labeling of DNA. *Nucl. Med. Biol. 24*, 425−432.

(18) Li, F., Ling, X., Huang, H., Brattain, L., Apontes, P., Wu, J., Binderup, L., and Brattain, M. G. (2005) Differential regulation of survivin expression and apoptosis by vitamin D3 compounds in two isogenic MCF-7 breast cancer cell sublines. *Oncogene 24*, 1385−1395.

(19) Wang, Y., Liu, X., Zhang, Y., Liu, G., Rusckowski, M., and Hnatowich, D. J. (2007) Nonspecific cellular accumulation of ^{99m}Tc-labeled oligonucleotides in culture is influenced by their guanine content. *Nucl. Med. Biol. 34*, 47−54.

(20) Wang, Y., Liu, G., and Hnatowich, D. J. (2006) Methods for MAG3 conjugation and ^{99m}Tc radiolabeling of biomolecules. *Nat. Protocols 1*, 1477−1480.

(21) Zhang, Y., Liu, C., Zhang, S., He, J., Rusckowski, M., and Hnatowich, D. J. (2002) Improved antisense vs. control accumulations in cells using ^{99m}Tc labeled morpholinos as alternatives to labeled DNAs when incubated naked. *J. Nucl. Med. 43 (Suppl.)*, 138 p.

(22) Behlke, M. A. (2005) Progress towards in vivo use of siRNAs. *Mol. Ther. 12*, 644−670.

(23) Zhang, Y., Rusckowski, M., Liu, N., Liu, C., and Hnatowich, D. J. (2001) Cationic liposomes enhance cellular/nuclear localization of ^{99m}Tc-antisense oligonucleotides in target tumor cells. *Cancer Biother. Radiopharm. 6*, 411−419.

(24) Zhang, Y., Liu, C., Liu, N., Ferro, Flores, G., Rusckowski, M., and Hnatowich, D. J. (2003) Electrostatic binding with tat and other cationic peptides increases cell accumulation of ^{99m}Tc-antisense DNAs without entrapment. *Mol. Imaging Biol. 5*, 240−247.

(25) Nakamura, K., Wang, Y., Liu, X., Kubo, A., and Hnatowich, D. J. (2006) Influence of two transfectors on delivery of 99mTc antisense DNA in tumor-bearing mice. *Mol. Imaging Biol. 8*, 188−192.

(26) Mock, D. M., and DuBois, D. B. (1986) A sequential, solid-phase assay for biotin in physiologic fluids that correlates with expected biotin status. *Anal. Biochem. 153*, 272−278.

BC070032C

Simple One-Pot Preparation of Water-Soluble, Cysteine-Reactive Cyanine and Merocyanine Dyes for Biological Imaging

Alexei Toutchkine,*,† Dan-Vinh Nguyen, and Klaus M. Hahn*

Department of Pharmacology and Lineberger Cancer Center, University of North Carolina at Chapel Hill, Chapel Hill, North Carolina 27599. Received December 3, 2006; Revised Manuscript Received February 16, 2007

A simple one-pot-procedure for preparation of protein-reactive, water-soluble merocyanine and cyanine dyes has been developed. The 1-(3-ammoniopropyl)-2,3,3-trimethyl-3*H*-indolium-5-sulfonate bromide **(1)** was used as a common starting intermediate. The method allows easy preparation of dyes with chloro- and iodoacetamide side chains for covalent attachment to cysteine. By placing a sulfonato group directly on the dye fluorophore system, dyes with high fluorescence quantum yields in water were generated. Both iodo- and chloroacetamido derivatives were shown to be useful in protein labeling. Less reactive chloroacetamides will be preferential for selective labeling of the most reactive cysteines.

INTRODUCTION

Cyanine and merocyanine dyes have been useful as fluorescent labels of proteins in many biological applications, because they have excellent photophysical properties, including high fluorescence quantum yields and extinction coefficients, photostability, and long fluorescence wavelengths that minimally overlap cellular autofluorescence (*1*). These dyes have been used in single molecule spectroscopy (*2*, *3*), in protein profiling (*4*), and for quantifying protein conformational changes in living cells (*5*, *6*). Site-specific protein labeling in these applications was accomplished through reaction with cysteine, introduced into proteins at the desired protein sites using molecular biology approaches.

Multiple different approaches have been used to prepare water-soluble, cysteine-reactive cyanine and merocyanine dyes. Gruber et al. produced cysteine-reactive cyanines by linking the succinimidyl ester of the lysine-reactive dyes to chains bearing different thiol-reactive groups (*7*). The dyes used as starting materials for this approach are expensive and available only in small quantities. In methods published by Wagoner et al. (*8*) and by our group (*9*), the unstable intermediate chloro- or iodoacetamido-indolenine is prepared and then condensed with the appropriate anyl to form the final dye (*9*). Alternately, our published synthesis of cysteine-reactive merocyanine dyes uses Fmoc-protection to mask amino functionality in the intermediate indolium or benzthiozolium salts. In the final steps of the synthesis, after assembling the fluorophore structure, the Fmoc group is removed and the amine linked to an iodoacetamido group (*6*).

Here we report a short synthesis of water-soluble, cysteine-reactive merocyanine and cyanine dyes from the same key intermediate, using a facile, one-pot reaction (Scheme 1). The reaction introduces chloroacetamido side chains into the dyes, which are shown to be cleanly converted into more reactive iodoacetamide derivates. Novel, highly fluorescent merocyanines and cyanine dyes are produced and their chloroacetamide and iodoacetamide derivates are used for protein derivatization.

* Corresponding authors. alexei.toutchkine@sial.com, khahn@med.unc.edu.

† Present address: Sigma-Aldrich Co., 1 Strathmore Rd., Natick, MA 01360-2447, phone: 774-290-1329.

EXPERIMENTAL PROCEDURES

Methods include preparation of the key intermediate 1-(3-ammoniopropyl)-2,3,3-trimethyl-3*H*-indolium-5-sulfonate **1** and its conversion to merocyanine and cyanine dyes. The reaction of this intermediate with hemicyanine **2** (*8*) or 3-methoxyprop-2-enyl-1-idene-2-thiobarbituric acid **3** (*6*) in dimethylformamide in the presence of sodium acetate and chloroacetic acid anhydride (CAA) gave the cyanine or merocyanine dyes, respectively. The pure dyes were obtained by chromatography of crude reaction mixtures on silica gel using acetone−methanol as eluent (Scheme 1). The chloroacetamides were cleanly converted into more reactive iodoacetamides by reaction with sodium iodide in methanol−chloroform.

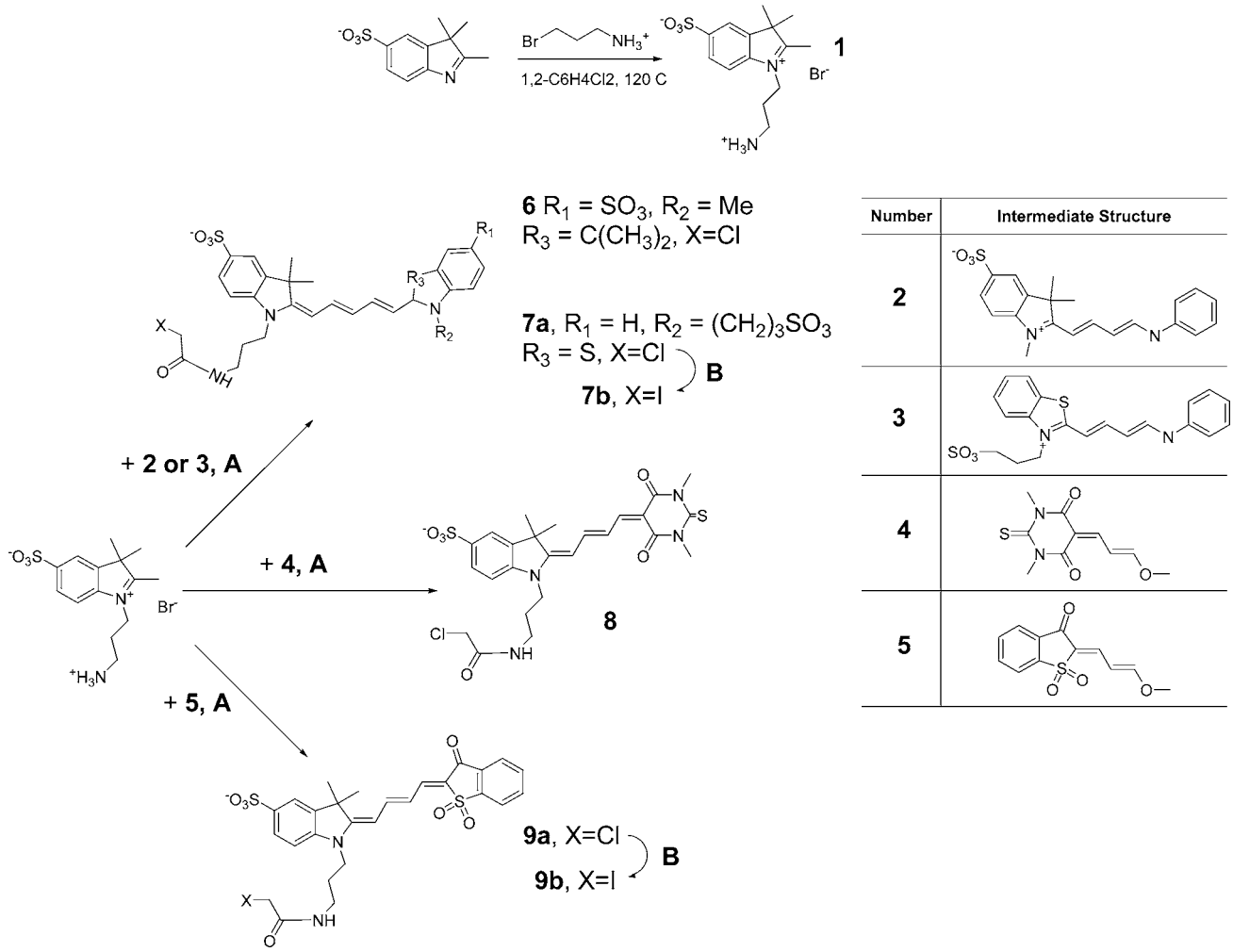
Materials. Analytical grade reagents were purchased from Sigma-Aldrich Co. Potassium 2,3,3-trimethyl-3*H*-indole-5-sulfonate (*10*), 3-{2-[(1*E*,3*E*)-4-anilinobuta-1,3-dien-1-yl]-1,3-benzothiazol-3-ium-3-yl}propane-1-sulfonate (**3**) (*11*), (2*Z*)-2-[(2*E*)-3-methoxyprop-2-en-1-ylidene]-1-benzothiophen-3(2*H*)-one 1,1-dioxide (**5**) (*6*), and 5-[(2*E*)-3-methoxyprop-2-en-1-ylidene]-1,3-dimethyl-2-thioxodihydropyrimidine-4,6(1*H*,5*H*)-dione (**4**) (*6*) were prepared as previously described.

Methods. Absorption spectra were recorded on a Hewlett-Packard UV−vis spectrophotometer, and fluorescence measurements were taken on a Spex Fluorolog 2 spectrofluorometer. NMR spectra were obtained on Varian Mercury 300 MHz or on a Bruker 500 MHz DRX 500 spectrometer. Mass spectra were obtained on a Hewlett-Packard 5890 gas chromatograph equipped with a 5971A mass selective detector (MS-EI). Quantum yields were measured using merocyanine 540 (*12*) or Cy5 (*7*) as an internal standards (*13*).

*Synthesis of Intermediate **1**: 1-(3-Ammoniopropyl)-2,3,3-trimethyl-3H-indolium-5-sulfonate Bromide (**1**).* To a suspension of 2.77 g of potassium 2,3,3-trimethyl-3*H*-indole-5-sulfonate in dichlorobenzene was added 2.18 g of 3-bromopropylamine hydrobromide. The mixture was stirred at 130 °C under nitrogen for 12 h. It was then cooled and the solid was filtered. The solid was stirred with 50 mL of hot methanol for 10 min, filtered, and dried. The yield was 2.45 g (65%). NMR (400 MHz, D_2O−DMSO-d_6) 1.48 (s, 6H, 2 × CH_3), 2.13 (p, $^3J_{H-H}$ = 6.2 Hz, 2H, $CH_2-CH_2CH_2$), 3.00 (t, $^3J_{H-H}$ = 6.2 Hz, 2H, $CH_2CH_2NH_3^+$), 4.45 (t, $^3J_{H-H}$ = 6.2 Hz, 2H, CH_2N), 7.81−7.87 (m, 2H), 7.94 (s, 1H). ESI-MS: 297 (M^+, positive ion detection).

10.1021/bc060376n CCC: $37.00 © 2007 American Chemical Society
Published on Web 06/02/2007

Scheme 1. Synthesis of Water-Soluble Dyes with Chloro- or Iodoacetamido Reactive Groups[a]



[a] Reagents and conditions: A. Chloroacetic anhydride, sodium acetate, DMF, rt, 1 h. B. NaI, MeOH−$CHCl_3$, reflux, 24 h.

General Method for the Preparation of the Chloroacetamido-Substituted Dyes. To a stirred suspension of 377 mg (1.00 mmol) of **1** in 10 mL of DMF were added 425 mg (2.50 mmol) chloroacetic anhydride (CAA), 1.20 mmol of acceptor intermediate (**2, 3, 4**, or **5**), and 200 mg (2.50 mmol) of sodium acetate. The mixture was stirred at room temperature for 1 h. The DMF was removed under vacuum, and the residue was purified by column chromatography on silica gel using acetone−methanol as eluent.

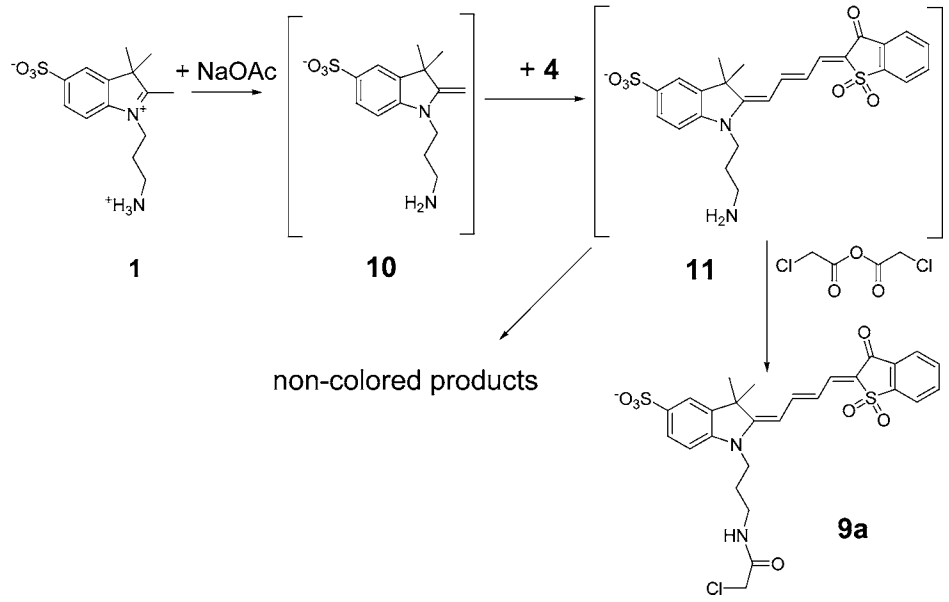
*Sodium (2-((1E,3E,5E)-5-(1-(3-(2-Chloroacetamido)propyl)-3,3-dimethyl-5-sulfonatoindolin-2-ylidene)penta-1,3-dienyl)-1,3,3-trimethyl-3H-indolium-5-sulfonate) or Cy5-CAA (**6**).* The yield was 369 mg (54%). NMR (300 MHz, DMSO-d_6): δ 1.69 (s, 12H, 4 × CH_3), 1.85 (p, $^3J_{H-H}$ = 6.8 Hz, 2H, CH_2CH_2-CH_2), 3.21 (q, $^3J_{H-H}$ = 6.8 Hz, 2H, CH_2CH_2NH), 3.61 (s, 3H, NCH_3), 4.08 (m, 4H, CH_2N and CH_2Cl), 6.27 (m, 2H), 6.54 (t, $^3J_{H-H}$ = 12.3 Hz, 1H), 7.30 (d, $^3J_{H-H}$ = 8.4 Hz, 1H), 7.33 (d, $^3J_{H-H}$ = 8.4 Hz, 1H), 7.60−7.66 (m, 2H), 7.80 (d, $^3J_{H-H}$ = 1.5 Hz, 1H), 7.82 (d, $^3J_{H-H}$ = 1.5 Hz, 1H), 8.30−8.41 (m, 3H). ESI-MS: 660 ((M − Na)$^-$, negative ion detection).

*(2-((1E,3E,5E)-5-(1-(3-(2-Chloroacetamido)propyl)-3,3-dimethyl-5-sulfonatoindolin-2-ylidene)penta-1,3-dienyl)-3-ethylbenzo-[d]thiazol-3-ium-6-sulfonate) or Cy5S-CAA (**7a**).* The yield was 369 mg (63%). NMR (300 MHz, DMSO-d_6): δ 1.64 (s, 6H, 2 × CH_3), 1.87 (p, $^3J_{H-H}$ = 6.8 Hz, 2H, $CH_2CH_2CH_2$), 2.03 (p, $^3J_{H-H}$ = 6.8 Hz, 2H, $CH_2CH_2CH_2$), 2.60 (t, $^3J_{H-H}$ = 6.8 Hz, 2H, CH_2SO_3) 3.25 (q, $^3J_{H-H}$ = 6.8 Hz, 2H, CH_2CH_2NH), 3.96 (t, $^3J_{H-H}$ = 6.8 Hz, 2H, CH_2N), 4.06 (2H, CH_2N, CH_2Cl), 4.67 (t, $^3J_{H-H}$ = 6.8 Hz, 2H, CH_2N), 6.07 (d, $^3J_{H-H}$ = 13.0 Hz, 1H), 6.51 (t, $^3J_{H-H}$ = 13.0 Hz, 1H), 6.98 (d, $^3J_{H-H}$ = 13.0 Hz, 1H), 7.15 (d, $^3J_{H-H}$ = 8.1 Hz, 1H), 7.50−7.70 (m, 4H), 7.98−8.15 (m, 4H), 8.42 (t, $^3J_{H-H}$ = 6.0 Hz, 1H, NH). ESI-MS: 678 ((M−Na)$^-$, negative ion detection).

*Sodium (E)-1-(3-(2-Chloroacetamido)propyl)-2-((E)-4-(1,3-dimethyl-4,6-dioxo-2-thioxotetrahydropyrimidin-5(6H)-ylidene)-but-2-enylidene)-3,3-dimethylindoline-5-sulfonate or I-TBA-CAA (**8**).* The yield was 308 mg (51%). NMR (500 MHz, DMSO-d_6): δ 1.64 (s, 6H, 2 × CH_3), 1.82 (p, $^3J_{H-H}$ = 7.0 Hz, 2H, $CH_2-CH_2CH_2$), 3.24 (q, 2H, $^3J_{H-H}$ = 7.0 Hz, CH_2CH_2NH), 3.60 (s, 6H, 2 × CH_3), 4.06 (s, 2H, CH_2Cl), 4.12 (t, $^3J_{H-H}$ = 7.0 Hz, 2H, CH_2N), 6.40 (d, $^3J_{H-H}$ = 14 Hz, 1H), 7.31 (d, $^3J_{H-H}$ = 8.5 Hz, 1H), 7.58 (d, $^3J_{H-H}$ = 8.5 Hz, 1H), 7.73 (d, $^3J_{H-H}$ = 1.5 Hz, 1H), 7.81 (t, $^3J_{H-H}$ = 13.0 Hz, 1H), 8.19 (d, $^3J_{H-H}$ = 13.5 Hz, 1H), 8.27 (t, $^3J_{H-H}$ = 13.5 Hz, 1H), 8.39 (t, $^3J_{H-H}$ = 6.0 Hz, 1H, NH). ESI-MS: 579 ((M − Na)$^-$, negative ion detection).

*Sodium (E)-1-(3-(2-Chloroacetamido)propyl)-3,3-dimethyl-2-((2E,4Z)-4-(3-oxobenzo[b]thiophen-1,1-dioxide-2(3H)-ylidene)-but-2-enylidene)indoline-5-sulfonate or I-SO-CAA (**9a**).* The yield was 313 mg (55%). NMR (300 MHz, DMSO-d_6): δ 1.64 (s, 6H, 2 × CH_3), 1.83 (p, $^3J_{H-H}$ = 6.5 Hz, 2H, $CH_2CH_2CH_2$), 3.24 (q, $^3J_{H-H}$ = 6.5 Hz, 2H, CH_2CH_2NH), 4.03 (t, $^3J_{H-H}$ = 6.5 Hz, 2H, CH_2N), 4.06 (s, 2H, CH_2Cl), 6.32 (d, 1H, $^3J_{H-H}$ = 13 Hz), 6.68 (t, 1H, $^3J_{H-H}$ = 13 Hz), 7.21 (d, 1H, $^3J_{H-H}$ = 8.5 Hz), 7.58 (d, 1H, $^3J_{H-H}$ = 8.5 Hz), 7.69 (s, 1H), 7.70−8.05

Scheme 2. Mechanism of One-Pot Dye Synthesis



(m, 5H), 8.25 (t, 1H, $^3J_{H-H}$ = 13 Hz), 8.39 (t, 1H, $^3J_{H-H}$ = 5.5 Hz, NH). ESI-MS: 589 ((M − Na)$^-$, negative ion detection).

General Method for the Preparation of the Iodoacetamido-Substituted Dyes. A solution of 0.5 mmol of chloro-substituted dye and 1 g of sodium iodide in 10 mL of 1:1 methanol−chloroform mixture was refluxed for 24 h under nitrogen. The mixture was filtered and evaporated. The iodoacetamides were purified on HPLC using a C18 column (VydacTP152022) with a water-acetonitrile gradient.

*Sodium (E)-1-(3-(2-Chloroacetamido)propyl)-3,3-dimethyl-2-((2E,4Z)-4-(3-oxobenzo[b]thiophen-1,1-dioxide-2(3H)-ylidene)-but-2-enylidene)indoline-5-sulfonate or I-SO-IAA (**9b**).* The yield was 211 mg (60%). NMR (300 MHz, DMSO-d_6): δ 1.64 (s, 6H, 2 × CH_3), 1.79 (p, $^3J_{H-H}$ = 6.5 Hz, 2H, $CH_2CH_2CH_2$), 3.21 (q, $^3J_{H-H}$ = 6.5 Hz, 2H, CH_2CH_2NH), 3.64 (s, 2H, CH_2I), 4.02 (t, $^3J_{H-H}$ = 6.5 Hz, 2H, CH_2N), 6.31 (d, $^3J_{H-H}$ = 13 Hz, 1H), 6.69 (t, $^3J_{H-H}$ = 13 Hz, 1H), 7.21 (d, $^3J_{H-H}$ = 8.5 Hz, 1H), 7.58 (d, $^3J_{H-H}$ = 8.5 Hz, 1H), 7.69 (s, 1H), 7.70−8.05 (m, 5H), 8.25 (t, $^3J_{H-H}$ = 13 Hz, 1H), 8.39 (t, $^3J_{H-H}$ = 5.5 Hz, 1H, NH). ESI-MS: 681 ((M−Na)$^-$, negative ion detection).

*(2-((1E,3E,5E)-5-(1-(3-(2-Iodooacetamido)propyl)-3,3-dimethyl-5-sulfonatoindolin-2-ylidene)penta-1,3-dienyl)-3-ethylbenzo[d]thiazol-3-ium-6-sulfonate) or Cy5S-IAA (**7b**).* The yield was 258 mg (76%). NMR (300 MHz, DMSO-d_6): δ 1.64 (s, 6H, 2 × CH_3), 1.85 (p, $^3J_{H-H}$ = 6.8 Hz, 2H, $CH_2CH_2CH_2$), 2.07 (p, $^3J_{H-H}$ = 6.8 Hz, 2H, $CH_2CH_2CH_2$), 2.60 (t, $^3J_{H-H}$ = 6.8 Hz, 2H, CH_2SO_3) 3.20 (q, $^3J_{H-H}$ = 6.8 Hz, 2H, CH_2CH_2-NH), 3.65 (2H, CH_2N, CH_2I), 3.96 (t, $^3J_{H-H}$ = 6.8 Hz, 2H, CH_2N), 4.67 (t, $^3J_{H-H}$ = 6.8 Hz, 2H, CH_2N), 6.07 (d, $^3J_{H-H}$ = 13.0 Hz, 1H), 6.51 (t, $^3J_{H-H}$ = 13.0 Hz, 1H), 6.98 (d, $^3J_{H-H}$ = 13.0 Hz, 1H), 7.15 (d, $^3J_{H-H}$ = 8.1 Hz, 1H), 7.50−7.70 (m, 4H), 7.98−8.15 (m, 4H), 8.42 (t, $^3J_{H-H}$ = 6.0 Hz, 1H, NH). ESI-MS: 770 ((M − Na)$^-$, negative ion detection).

Protein Labeling. A fusion protein of enhanced green fluorescent protein and extracellular regulated kinase 2 (EGFP-Erk2) was incubated with a 10-fold molar ratio of the **9a** or **9b** dye (Scheme 1) in 25 mM HEPES (pH 7.4), 50 mM NaCl (0.15 mL 20 μM EGFP-Erk2). To this protein solution was added 13.5 μL of 2 mM dye stock solution in DMSO. The mixture was incubated at room temperature with gentle agitation for 2 h and then was spun at 11750*g* (Eppendorf 5415C centrifuge) for 1 min to remove any precipitate that might have formed during labeling. The supernatant was then purified using a G25 sepharose gel filtration column, pre-equilibrated with 25 mM HEPES (pH 7.4). The dye−protein adduct was clearly separated from free dye during gel filtration. Purity of the conjugates was confirmed by SDS-PAGE electrophoresis. No free dye was seen in the purified protein conjugates. Control samples of free dye were clearly visible on the gel at lower MW than protein. Conjugates formed single, higly colored fluorescent protein bands with molecular weight corresponding to EGFP-Erk2. The degree of labeling D/P (dye-to-protein ratio) was calculated using the following formula:

$$\mathrm{D/P} = (A_{dye}/\epsilon_{dye})/(A_{prot}/\epsilon_{prot})$$

where A_{dye} is the absorbance at the absorption maximum of the dye, A_{prot} is the absorbance at the absorption maximum of EGFP (490 nm), ϵ_{dye} is the extinction coefficient of the dye in H_2O, and ϵ_{prot} is the extinction coefficient of EGFP (61000).

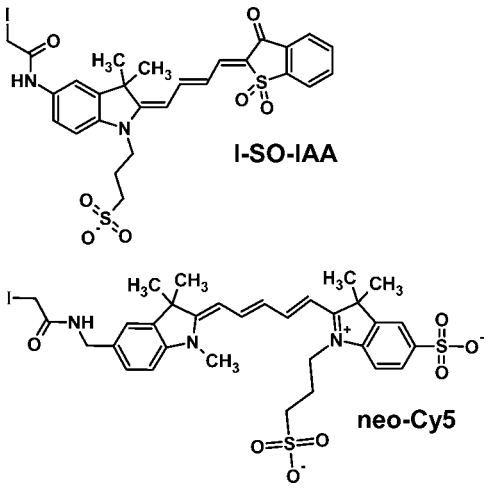
RESULTS AND DISCUSSION

Synthesis. As shown in Scheme 1, cyanine and merocyanine dyes were prepared using a facile one-pot procedure from the key intermediate, 1-(3-ammoniopropyl)-2,3,3-trimethyl-3*H*-indolium-5-sulfonate (intermediate **1**). This intermediate was prepared by reaction of potassium 2,3,3-trimethyl-3*H*-indole-5-sulfonate with 3-bromopropylamine hydrobromide in dichlorobenzene at 130 C. The intermediate **1** precipitates during the reaction and can be easily purified from unreacted starting compounds by simple washing with hot methanol, as the intermediate is practically insoluble in that solvent. The reaction of intermediate **1** with 3-methoxyprop-2-enyl-1-idene-2-thiobarbituric acid **4** or with 3-methoxyprop-2-enyl-1-idene-2-benzothiophen-3-one 1,1-dioxide **5** in the presence of sodium acetate and chloroacetic acid anhydride (CAA) resulted in the formation of merocyanine dyes bearing chloroacetamido reactive groups. Use of the same reaction conditions with hemicyanines **2** or **3** produced the cyanine dyes shown. The dyes were purified by chromatography of crude reaction mixtures on silica gel using acetone−methanol as an eluent. Iodoacetamides were prepared by the reaction of chloroacetamides with sodium iodide in methanol−chloroform mixture. The yields of both merocyanine and cyanine chloroacetamido dyes were in the range of 50−65%, and the substitution of iodide for chloride occurred with 60−80% yield.

The reaction mechanism likely proceeds by deprotonation of **1** by sodium acetate with formation of enamine **10** (Scheme 2).

The enamine then reacts with 3-methoxyprop-2-enyl-1-idene-2-benzothiophen-3-one 1,1-dioxide **4** to give amino-substituted dye **11**. The dye **11** is not stable, and its solution rapidly loses color, as Michael addition of the free amino group to the polymethine chain destroys the dye fluorophore system. In the presence of chloroacetic anhydride, the free amine is quickly trapped as the chloroacetamide (Scheme 2). This mechanism is supported by trapping of unstable dye intermediate **10** with amino-reactive compounds, including acetic anhydride or acetic acid succinimidyl ester.

Absorption and Fluorescence Properties. These reactions generated novel, bright merocyanine and cyanine dyes (Table 1). They had high extinction coefficients, in the range of 120,000−215,000 and moderate fluorescence quantum yields of 0.1−0.4. The absorption characteristics of dyes **6** and **9a** were very similar to those of the published analogues neoCy5 (*9*) and I-SO-IAA (*6*). Substitution with a sulfonato group ($-SO_3$) at the aromatic ring in the new merocyanine dye **9a** and in the new cyanine dye **6** significantly increased the fluorescence quantum yields in polar solvents (H_2O, MeOH) compared to I-SO-IAA and neo-Cy5. For the cyanine, the quantum yield in water more than doubled, and for the merocyanine it increased 5-fold. Similar increases in dye fluorescence upon ring-substitution with sulfonato-groups have been reported for rhodamines (*14*) and cyanines (*15*). Previously, it was thought that dye aggregation is the main reason for the significant drop in dye fluorescence quantum yields in aqueous solutions (*14*, *15*). The I-SO-IAA dye does not form H-aggregates (*6*), and its fluorescence is still significantly lower in water than the fluorescence of the dye **9a**. Although the mechanism of fluorescence quenching of I-SO-IAA in water is not clear, it likely includes either dynamic quenching of excited dye molecules through collision with dye in the ground state (*16*) or static quenching through association (other than H-aggregation) of ground state dye molecules (*17*). In both cases placement of negatively charged sulfonato groups directly on the dye fluorophore system (dyes **6**, **9a** in present study) rather than on alkyl side chains (I-SO-IAA and neoCy5) will reduce dye−dye interactions in water because of Coulombic repulsion and will lead to higher fluorescence quantum yields. Brightness in polar solvents is especially valuable for imaging applications, where dyes are conjugated to proteins and exposed to water.



Protein Labeling. The reactivity of the chloroacetamido and iodoacetamido derivates was compared by covalent derivatization of EGFP-Erk2 with the chloro- and iodoacetamido derivates of I-SO dye (**9a** and **9b)**. Chloroacetamido-reactive groups are not used in protein labeling because of their much lower reactivity toward thiols. In previous studies, chloroacetamides have been about 300 times less reactive than iodoacetamides

Table 1. Absoprption and Fluorescence Data for Merocyanine and Cyanine Dyes

dye	solvent	ϵ^a	λ_{max}(abs), nm[b]	λ_{max}(em), nm[c]	Φ^d
6	water	215000	644	660	0.24
	methanol	215000	646	658	0.27
	n-butanol	215000	656	671	0.39
7a	water	185000	636	662	0.11
	methanol	185000	643	668	0.22
	n-butanol	190000	652	676	0.34
8	water	160000	590	610	0.04
	methanol	180000	591	610	0.27
	n-butanol	180000	596	616	0.39
9a	water	140000	594	616	0.02
	methanol	120000	584	620	0.12
	n-butanol	120000	590	624	0.32
I-SO-AA[e]	water	143000	599	630	0.004
	methanol	138000	601	634	0.01
	n-butanol	150000	607	639	0.06
neo-Cy5[f]	PBS[g]	170000	643	660	0.10
	methanol	200000	648	665	0.22

[a] Extinction coefficient. [b] Absorption maximum. [c] Fluorescence maximum. [d] Fluorescence quantum yield. [e] From ref 6. [f] From ref 9. [g] Phosphate-buffered saline.

in reaction with mercaptoacetic acid (*18*). When EGFP-Erk2 was labeled with **9a** and **9b** under identical conditions (10:1 dye to protein ratio, 2 h, room temperature), the iodoacetamide **9b** produced conjugates with an average dye/protein (D/P) of 1.25, while labeling with chloroacetamide **9a** produced conjugates with D/P of 0.2 (Figure 1).

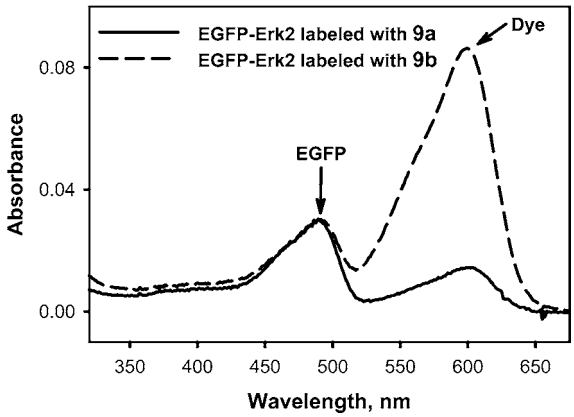


Figure 1. Labeling of EGFP-Erk2 with dyes **9a** and **9b**.

This protein has a total of nine free cysteines (two in EGFP and seven in Erk2) that can potentially react with halogenacetamido groups. The relatively low D/P produced by iodoacetamide labeling implies that there is only one reactive cysteine in EGFP-Erk2. Surprisingly, the reactivity of chloroacetamido-substituted dye was only six times lower than that of the iodoacetamido dye. The diminished difference between the two derivatives may be explained by a two-step reaction mechanism, in which slow formation of the dye−protein complex is followed by rapid reaction with a thiol group. In such a process the reactivity of the substrate will be determined by the rate of dye−protein complex formation, which should be similar for dyes with chloroacetamido and iodoacetamido side chains.

SUMMARY

A simple one-pot procedure for preparation of protein-reactive, water-soluble merocyanine and cyanine dyes has been developed. The method allows easy preparation of dyes with chloro- and iodoacetamide side chains for covalent attachement to cysteine. Novel bright dyes were generated, and both iodo-

and chloroacetamido derivatives were shown to be useful in protein labeling.

ACKNOWLEDGMENT

Financial support from the NIH (Grants GM57464 and GM64346) is gratefully acknowledged. We thank Dr. Frederique Gaits for assistance with EGFP-Erk2 expression and purification.

LITERATURE CITED

(1) Sturmer, D. M. (1977) Synthesis and properties of cyanine and related dyes. In *Special topics in heterocyclic chemistry* (Weissberger, A., and Taylor, E. C., Eds.) pp 441−587, John Wiley & Sons, New York.

(2) Tani, T., Miyamoto, Y., Fujimori, K. E., Taguchi, T., Yanagida, T., Sako, Y., and Harada, Y. (2005) Trafficking of a ligand-receptor complex on the growth cones as an essential step for the uptake of nerve growth factor at the distal end of the axon: a single-molecule analysis. *J. Neurosci. 25*, 2181−91.

(3) Borisenko, V., Lougheed, T., Hesse, J., Fureder-Kitzmuller, E., Fertig, N., Behrends, J. C., Woolley, G. A., and Schutz, G. J. (2003) Simultaneous optical and electrical recording of single gramicidin channels. *Biophys. J. 84*, 612−22.

(4) Redkar, R. J., Schultz, N. A., Scheumann, V., Burzio, L. A., Haines, D. E., Metwalli, E., Becker, O., and Conzone, S. D. (2006) Signal and sensitivity enhancement through optical interference coating for DNA and protein microarray applications. *J. Biomol. Technol. 17*, 122−30.

(5) Nalbant, P., Hodgson, L., Kraynov, V., Toutchkine, A., and Hahn, K. M. (2004) Activation of endogenous Cdc42 visualized in living cells. *Science 305*, 1615−9.

(6) Toutchkine, A., Kraynov, V., and Hahn, K. (2003) Solvent-sensitive dyes to report protein conformational changes in living cells. *J. Am. Chem. Soc. 125*, 4132−45.

(7) Gruber, H. J., Kada, G., Pragl, B., Riener, C., Hahn, C. D., Harms, G. S., Ahrer, W., Dax, T. G., Hohenthanner, K., and Knaus, H. G. (2000) Preparation of thiol-reactive Cy5 derivatives from commercial Cy5 succinimidyl ester. *Bioconjugate Chem. 11*, 161−6.

(8) Ernst, L. A., Gupta, R. K., Mujumdar, R. B., and Waggoner, A. S. (1989) Cyanine dye labeling reagents for sulfhydryl groups. *Cytometry 10*, 3−10.

(9) Toutchkine, A., Nalbant, P., and Hahn, K. M. (2002) Facile synthesis of thiol-reactive Cy3 and Cy5 derivatives with enhanced water solubility. *Bioconjugate Chem. 13*, 387−91.

(10) Mason, S. J., Hake, J. L., Nairne, J., Cummins, W. J., and Balasubramanian, S. (2005) Solid-phase methods for the synthesis of cyanine dyes. *J. Org. Chem. 70*, 2939−2949.

(11) Brooker, L. G. S., White, F. L., Keyes, G. H., Smyth, C. P., and Oesper, P. F. (1941) Color and constitution. II. Absorptions of some related vinylene-homologous series. *J. Am. Chem. Soc. 63*, 3192−203.

(12) Onganer, Y., Yin, M., Bessire, D. R., and Quitevis, E. L. (1993) Dynamical solvation effects on the cis−trans isomerization reaction: photoisomerization of merocyanine 540 in polar solvents. *J. Phys. Chem. 97*, 2344−2354.

(13) Demas, J. N., and Crosby, G. A. (1971) The Measurement of Photoluminescence Quantum Yields. A Review. *J. Phys. Chem. 75*, 991−1024.

(14) Panchuk-Voloshina, N., Haugland, R. P., Bishop-Stewart, J., Bhalgat, M. K., Millard, P. J., Mao, F., Leung, W. Y., and Haugland, R. P. (1999) Alexa dyes, a series of new fluorescent dyes that yield exceptionally bright, photostable conjugates. *J. Histochem. Cytochem. 47*, 1179−88.

(15) Mujumdar, S. R., Mujumdar, R. B., Grant, C. M., and Waggoner, A. S. (1996) Cyanine-Labeling Reagents: Sulfobenzindocyanine Succinimidyl Esters. *Bioconjugate Chem. 7*, 356−362.

(16) Kamal, P. V., and Lichtin, N. N. (1981) Electron Transfer in the Quenching of Protonated Triplet Methylene Blue by Ground-State Molecules of the Dye. *J. Phys. Chem. 85*, 814−818.

(17) Vaiana, A. C., Neuweiler, H., Shulz, A., Wolfrum, J., Sauer, M., and Smith, J. C. (2003) Fluorescence Quenching of Dyes by Tryptofan: Interactions of Atomic Detail from Combination of Experiment and Computer Stimulations. *J. Am. Chem. Soc. 125*, 14564−14572.

(18) Polgar, L. (1973) On the Mode of Activation of the Catalitically Essential Sulfhydryl Group of Papain. *Eur. J. Biochem. 33*, 104−109.

BC060376N

Alkyl Chain Moieties of Polyamidoamine Dendron-Bearing Lipids Influence Their Function as a Nonviral Gene Vector

Toshinari Takahashi, Chie Kojima, Atsushi Harada, and Kenji Kono*

Department of Applied Chemistry, Graduate School of Engineering, Osaka Prefecture University, 1-1 Gakuen-cho, Naka-ku, Sakai, Osaka 599-8531, Japan. Received October 6, 2006; Revised Manuscript Received February 21, 2007

We recently developed a novel family of cationic lipids consisting of a polyamidoamine (PAMAM) dendron and two dodecyl chains. Their transfection activity increases with increasing generation of the dendron moiety [Takahashi et al. (2003) *Bioconjugate Chem*. *14*, 764−773]. In the present study, to elucidate the effect of hydrophobic tail moieties of the dendron-bearing lipids, two kinds of PAMAM G3 dendron-bearing lipids were synthesized with different alkyl lengths, DL-G3-2C_{18} and DL-G3-2C_{12}. Their functions as gene vectors were compared. Irrespective of their different alkyl chain lengths, these dendron-bearing lipids formed complexes with plasmid DNA with similar efficiency. However, their complex sizes differed markedly: DL-G3-2C_{18} lipoplexes exhibited much smaller diameters than DL-G3-2C_{12} lipoplexes. Interaction of the lipoplexes with heparin revealed that the DL-G3-2C_{18} lipoplexes required more heparin than DL-G3-2C_{12} lipoplexes to cause dissociation of plasmid DNA from the lipoplexes. Although the DL-G3-2C_{12} lipoplexes and DL-G3-2C_{18} lipoplexes transfected CV1 cells with similar efficiency in the absence of serum, only the latter retained high transfection activity in the presence of serum. These results indicate that hydrophobic interaction of alkyl chain moieties plays an important role in the increment of stability and the serum-resistant transfection activity for dendron-bearing lipid lipoplexes.

INTRODUCTION

Preparation of nonviral vectors that deliver therapeutic genes to target cells has been demanded for efficient and safe gene therapy. Among these nonviral vectors, various types of cationic lipids have been studied intensively, but their activity requires improvement. These vectors can associate with plasmid DNA and form complexes, which are termed lipoplexes (*1*, *2*). Lipoplexes bind to the cell surface through electrostatic interactions and are taken up by cells mainly via endocytosis. Subsequently, some parts of plasmid DNA contained in the complexes reach the nucleus, where gene transcription occurs. Nevertheless, most complexes are likely to be trapped in the endosome and be eventually degraded in the lysosome. Therefore, avoidance of plasmid DNA degradation in the lysosome and its transfer into cytosol is considered to be a key process for efficient transfection (*3*).

Cationic polymers are another type of nonviral vector that has been studied intensively (*2*). Polyamidoamine (PAMAM) dendrimers have been shown to achieve efficient gene transfection of cells among cationic polymers: PAMAM dendrimers possess many tertiary amine groups, which become protonated under weakly acidic conditions (*4*−*6*). Those amine groups suppress the lowering of pH in endosomes and lysosomes by adsorbing protons and prohibiting degradation of DNA in the lysosome. In addition, the endosome buffering ability of PAMAM dendrimers is thought to induce osmotic swelling of the endosome interior, engendering rupture of the endosome and the subsequent release of DNA into the cytoplasm (*7*). Such a function of these tertiary amine groups of PAMAM dendrimers, the so-called proton sponge effect, is considered to contribute to their high transfection activity (*8*).

In a previous study (*9*), we developed a novel type of cationic lipid that consists of two dodecyl groups and a PAMAM dendron as a head group and showed that these dendron-bearing lipids are promising as a potent nonviral vector that exhibits higher transfection activity than the PAMAM dendrimer of the same generation. Their molecular structure, e.g., that of the head group of the dendron moiety and the tail moieties of alkyl chains, will influence their transfection activity. We showed in a previous study that their transfection activity increases concomitant with increasing generation of the head moiety (*9*). Nevertheless, it remains unclear how alkyl chains affect their transfection activity.

In this study, we synthesized the PAMAM dendron-bearing lipid with two octadecyl chains DL-G3-2C_{18} and compared its capability as a gene vector to that of DL-G3-2C_{12} (Figure 1). The importance of the alkyl chain moiety for stability and transfection activity of the dendron-bearing lipid lipoplexes is described.

EXPERIMENTAL PROCEDURES

General Methods. Dioctadecylamine was purchased from Fluka (Tokyo, Japan). Methyl acrylate, ethylenediamine, and tris(hydroxymethyl)aminomethane (Tris) were obtained from Kishida Chemical (Osaka, Japan). Sodium cyanide and ethidium bromide were supplied from Wako Pure Chemical Industries (Osaka, Japan). Merck Kieselgel 60 (230−400 mesh) was used for silica gel chromatography. Fetal calf serum (FCS) was obtained from PAA Laboratories GmbH (Pasching, Austria). Dulbecco's modified Eagle's medium (DMEM) was from Nissui Pharmaceutical (Tokyo, Japan). Heparin sodium salt was purchased from Sigma (St. Louis, MO). Agarose was purchased from nacalai tesque (Kyoto, Japan). DL-G3-2C_{12} was synthesized by the method previously reported (*9*). Plasmid DNA pCMV-Luc, which contains the cDNA of firefly luciferase driven by a human cytomegalovirus immediate-early promoter, was a gift from Dr. Kazuo Maruyama, Teikyo University, and amplified in *E. coli*, isolated, and purified using a QIAGEN plasmid Maxi Kit.

Synthesis of Dendron-Bearing Lipids. DL-G3-2C_{18} was synthesized by repetition of exhaustive Michael addition with

* Corresponding author. Kenji Kono, Department of Applied Chemistry, Graduate School of Engineering, Osaka Prefecture University, 1-1 Gakuen-cho, Naka-ku, Sakai, Osaka 599-8531, Japan. E-mail: kono@chem.osakafu-u.ac.jp. Tel: +81-722549330. Fax: +81-722549330.

10.1021/bc060311k CCC: $37.00 © 2007 American Chemical Society
Published on Web 05/09/2007

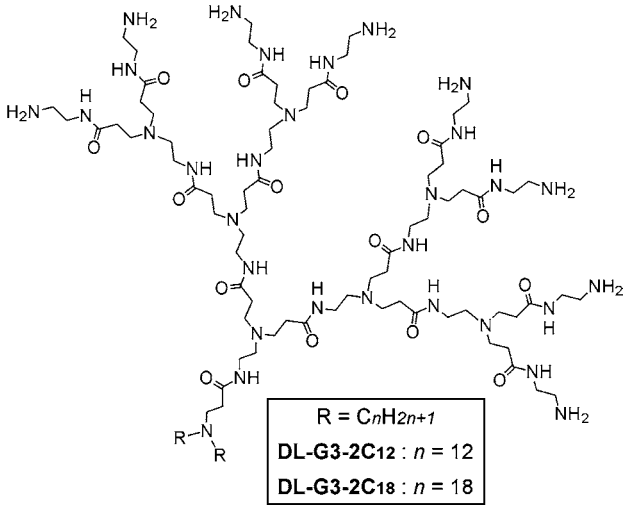


Figure 1. Structures of DL-G3-2C_{12} and DL-G3-2C_{18}.

methyl acrylate using dioctadecylamine as the core material and subsequent exhaustive amidation with ethylenediamine.

DL-G-0.5-2C_{18}. Dioctadecylamine (2.0 g, 3.8 mmol) was dissolved in methyl acrylate (35 mL, 0.39 mol), and the resultant solution was refluxed under nitrogen. After 18 h, unreacted methyl acrylate was removed under vacuum and the residue was chromatographed on silica gel using petroleum ether−diethyl ether (2/1, v/v) as eluent. Yield: 87.9%. ^{1}H NMR ($CDCl_3$): δ 0.88 (m, C*H*$_3$(CH$_2$)$_{15}$-), δ 1.26 (s, CH$_3$(C*H*$_2$)$_{15}$-), δ 1.41 (br, -C*H*$_2$CH$_2$N-), δ 2.35−2.46 (m, -C*H*$_2$COOCH$_3$, -C*H*$_2$N), δ 2.77 (t, -C*H*$_2$CH$_2$COOCH$_3$), δ 3.66 (s, -OC*H*$_3$).

DL-G0-2C_{18}. DL-G-0.5-2C_{18} (2.0 g, 3.4 mmol) was dissolved in methanol (40 mL). The resultant solution was added dropwise to distilled ethylenediamine (70 mL, 1.05 mol) containing sodium cyanide (33 mg, 0.67 mmol) and stirred at 50 °C under nitrogen. After 1 week, methanol and unreacted ethylenediamine were removed from the reaction mixture under vacuum. The obtained DL-G0-2C_{18} was chromatographed on silica gel using chloroform−methanol−water (60/35/5, v/v/v) as eluent. Yield: 53.2%. ^{1}H NMR ($CDCl_3$): δ 0.88 (m, C*H*$_3$(CH$_2$)$_{15}$-), δ 1.26 (s, CH$_3$(C*H*$_2$)$_{15}$-), δ 1.44 (br, -C*H*$_2$CH$_2$N-), δ 2.33−2.45 (m, -C*H*$_2$CONH-, -C*H*$_2$N-), δ 2.65 (t, -C*H*$_2$CH$_2$CONH-), δ 2.79 (t, -C*H*$_2$NH$_2$), δ 3.28 (q, -C*H*$_2$CH$_2$NH$_2$), δ 8.65 (m, -CON*H*-CONH). MALDI-TOF-MS *m*/*z* 636.5 ([M + H]$^+$).

DL-G0.5-2C_{18}. DL-G0-2C_{18} (1.2 g, 1.9 mmol) was dissolved in methanol (20 mL) and added to methyl acrylate (34 mL, 0.38 mol). The mixed solution was stirred at 35 °C for 50 h under nitrogen. The obtained material was chromatographed on silica gel using petroleum ether−diethyl ether (2/1, v/v) and then chloroform−methanol (9/1, v/v) as eluent. Yield: 97.7%. ^{1}H NMR ($CDCl_3$): δ 0.88 (m, C*H*$_3$(CH$_2$)$_{15}$-), δ 1.26 (s, CH$_3$-(C*H*$_2$)$_{15}$-), δ 1.44 (br, -C*H*$_2$CH$_2$N-), δ 2.35 (m, -C*H*$_2$CONH-), δ 2.43 (m, -C*H*$_2$COOCH$_3$, -C*H*$_2$N-), δ 2.54 (t, -CONHCH$_2$C*H*$_2$), δ 2.69−2.80 (m, -C*H*$_2$CH$_2$CONH-, -C*H*$_2$CH$_2$COOCH$_3$), δ 3.29 (q, -CONHC*H*$_2$-), δ 3.67 (s, -OC*H*$_3$), δ 7.76 (br, -CON*H*).

DL-G1-2C_{18}. DL-G0.5-2C_{18} (1.5 g, 1.8 mmol) was dissolved in methanol (50 mL) and added to ethylenediamine (65 mL, 0.92 mol) containing sodium cyanide (18 mg, 0.37 mmol). The mixed solution was stirred at 45 °C for 60 h under nitrogen. The obtained DL-G1-2C_{18} was purified with a Sephadex LH-20 column using chloroform as eluent. Yield: 94.3%. ^{1}H NMR ($CDCl_3$): δ 0.88 (m, C*H*$_3$(CH$_2$)$_{15}$-), δ 1.26 (s, CH$_3$(C*H*$_2$)$_{15}$-), δ 1.42 (br, -C*H*$_2$CH$_2$N-), δ 2.31 (m, -C*H*$_2$CONH-), δ 2.35−2.43 (m, -C*H*$_2$CONHCH$_2$CH$_2$NH$_2$, -C*H*$_2$N-), δ 2.51 (t, -CONHCH$_2$C*H*$_2$), δ 2.67 (t, -C*H*$_2$CH$_2$CONH-), δ 2.75 (t, -C*H*$_2$CH$_2$CONHCH$_2$-CH$_2$NH$_2$), δ 2.83 (t, -C*H*$_2$NH$_2$), δ 3.24−3.31 (m, -CONHC*H*$_2$), δ 7.37 and 8.65 (br, -CON*H*-). MALDI-TOF-MS *m*/*z* 862.9 ([M + H]$^+$).

DL-G1.5-2C_{18}. DL-G1-2C_{18} (1.3 g, 1.5 mmol) was dissolved in methanol (60 mL) and added to methyl acrylate (110 mL, 1.23 mol). The mixed solution was stirred at 35 °C for 52 h under nitrogen. The obtained material was chromatographed on silica gel using chloroform and then chloroform−methanol (9/1, v/v) as eluent. Yield: 71.9%. ^{1}H NMR ($CDCl_3$): δ 0.88 (m, C*H*$_3$(CH$_2$)$_{15}$-), δ 1.25 (s, CH$_3$(C*H*$_2$)$_{15}$-), δ 1.43 (br, -C*H*$_2$CH$_2$N), δ 2.37 (t, -C*H*$_2$CONH-), δ 2.43 (t, -C*H*$_2$COOCH$_3$, -C*H*$_2$N-), δ 2.52−2.58 (m, -CONHCH$_2$C*H*$_2$-), δ 2.75 (t, -C*H*$_2$CH$_2$CONH-, -C*H*$_2$CH$_2$COOCH$_3$), δ 2.82 (t, -C*H*$_2$CH$_2$CONH-), δ 3.30 (m, -CONHC*H*$_2$-), δ 3.68 (s, -OC*H*$_3$), δ 7.00 and 8.07 (br, -CON*H*).

DL-G2-2C_{18}. DL-G1.5-2C_{18} (1.3 g, 1.1 mmol) was dissolved in methanol (30 mL) and added to ethylenediamine (95 mL, 1.42 mol) containing sodium cyanide (21 mg, 0.43 mmol). The mixed solution was stirred at 45 °C for 50 h under nitrogen. The obtained DL-G2-2C_{18} was purified with a Sephadex LH-20 column using methanol as eluent. Yield: 92.2%. ^{1}H NMR ($CDCl_3$): δ 0.88 (m, C*H*$_3$(CH$_2$)$_{15}$-), δ 1.25 (s, CH$_3$(C*H*$_2$)$_{15}$-), δ 1.42 (br, -C*H*$_2$CH$_2$N-), δ 2.32−2.42 (m, -C*H*$_2$CONHCH$_2$CH$_2$-NH$_2$, -C*H*$_2$CONH-, -C*H*$_2$N-), δ 2.52 (m, -CONHCH$_2$C*H*$_2$-), δ 2.73 (m, -C*H*$_2$CH$_2$CONH-, -C*H*$_2$CH$_2$CONHCH$_2$CH$_2$NH$_2$), δ 2.83 (t, -C*H*$_2$NH$_2$), δ 3.25−3.30 (m, -CONHC*H*$_2$-), δ 7.73, 7.93, and 8.58 (br, -CON*H*-). MALDI-TOF-MS *m*/*z* 1320.6 ([M + H]$^+$).

DL-G2.5-2C_{18}. DL-G2-2C_{18} (0.94 g, 0.71 mmol) dissolved in methanol (60 mL) was added to methyl acrylate (55 mL, 0.61 mol). The mixed solution was stirred at 30 °C for 50 h under nitrogen. The obtained material was chromatographed on silica gel using chloroform−methanol (95/5 and then 8/2, v/v) as eluent. Yield: 67.4%. ^{1}H NMR ($CDCl_3$): δ 0.88 (m, C*H*$_3$-(CH$_2$)$_{15}$-), δ 1.25 (s, CH$_3$(C*H*$_2$)$_{15}$-), δ 1.47 (br, -C*H*$_2$CH$_2$N-), δ 2.37 (m, -C*H*$_2$CONH-), δ 2.44 (m, -C*H*$_2$COOCH$_3$, -C*H*$_2$N-), δ 2.55 (m, -CONHCH$_2$C*H*$_2$-), δ 2.74−2.81 (m, -C*H*$_2$CH$_2$CONH-, -C*H*$_2$CH$_2$COOCH$_3$), δ 3.29 (m, -CONHC*H*$_2$-), δ 3.67 (s, -OC*H*$_3$), δ 7.10, 7.65, and 8.09 (br, -CON*H*-).

DL-G3-2C_{18}. DL-G2.5-2C_{18} (0.92 g, 0.46 mmol) was dissolved in methanol (40 mL) and added to ethylenediamine (60 mL, 0.9 mol) containing sodium cyanide (8.9 mg, 0.18 mmol). The mixed solution was stirred at 45 °C for 55 h under nitrogen. The obtained DL-G3-2C_{18} was purified with a Sephadex LH-20 column using methanol as eluent. Yield: 90.7%. ^{1}H NMR ($CDCl_3$): δ 0.88 (m, C*H*$_3$(CH$_2$)$_{15}$-), δ 1.25 (s, CH$_3$(C*H*$_2$)$_{15}$-), δ 1.42 (br, -C*H*$_2$CH$_2$N-), δ 2.32−2.37 (m, -C*H*$_2$CONHCH$_2$CH$_2$-NH$_2$, -C*H*$_2$CONH-, -C*H*$_2$N-), δ 2.53 (m, -CONHCH$_2$C*H*$_2$-), δ 2.73 (br, -C*H*$_2$CH$_2$CONH-, -C*H*$_2$CH$_2$CONHCH$_2$CH$_2$NH$_2$), δ 2.83 (t, -C*H*$_2$NH$_2$), δ 3.24−3.30 (m, -CONHC*H*$_2$-), δ 7.82, 8.02, and 8.52 (br, -CON*H*-). MALDI-TOF-MS *m*/*z* 2234.3 ([M + H]$^+$).

Preparation of Lipoplexes. To a dry thin membrane of the dendron-bearing lipid, phosphate-buffered saline (PBS) was added and sonicated for 2 min using a bath-type sonicator to afford a lipid suspension. Plasmid DNA (1 μg) was dissolved in 20 mM Tris−HCl buffer (pH 7.4, 50 μL), mixed with the lipid suspension (50 μL), and incubated for 30 min at room temperature to afford a lipoplex with a given ratio of primary amine of DL-G3 to DNA phosphate (N/P ratio).

Agarose Gel Electrophoresis. The dendron-bearing lipid−DNA complexes with varying N/P ratios were prepared by mixing plasmid DNA (1 μg) dissolved in 20 mM Tris−HCl buffer (5 μL) and lipid suspension (5 μL). After 30 min incubation at room temperature, the samples (10 μL) were electrophoresed on 0.6 wt % agarose gel in 40 mM Tris, 20 mM sodium acetate, and 2 mM EDTA buffer (pH 8.0) containing 1 μg/mL ethidium bromide at 100 V for 30 min. The ethidium bromide stained bands were visualized using a

LAS-1000UVmini (Fujifilm, Tokyo, Japan) and analyzed with Science Lab 2003 Multi Gauge software (Fujifilm, Tokyo, Japan).

Dynamic Light Scattering (DLS) Measurement. The diameters of lipoplexes were estimated by DLS using an electrophoretic light scattering spectrometer ELS-8000F (Otuka Electronics Co, Ltd., Osaka, Japan). Lipoplexes with various N/P ratios were prepared by mixing plasmid DNA (20 μg) and a given amount of the dendron-bearing lipid and incubated for 30 min as described above. The data were obtained at a detection angle of 90° at 25 °C and were analyzed by the cumulant method.

Atomic Force Microscopy (AFM). AFM measurements were performed by SPI3800 probe station and SPA400 unit system of the scanning probe microscopy system (Seiko Instruments Inc., Chiba, Japan). The cantilever was made of silicon (SI-DF20; Seiko Instruments Inc., Chiba, Japan), and its spring constant was 14 N/m. Lipoplexes were formed at a total of 100 μg/mL of plasmid DNA concentration with N/P ratio of 4. Lipoplexes containing 0.5 μg of plasmid DNA were applied to freshly cleaved mica and incubated on it for 5 min. After incubation, excess fluid was dried under air flow. The measurements were performed in a dynamic force mode (noncontact mode). Raw AFM images have been processed only for background removal (flattening) using the microscope manufacturer's image-processing software.

Interaction of Lipoplexes with Heparin. The dendron-bearing lipid−DNA lipoplexes were prepared by mixing plasmid DNA (1 μg) dissolved in 20 mM Tris−HCl buffer (2.5 μL) and lipid suspension (2.5 μL). After 30 min incubation at room temperature, the lipoplexes were added to a given amount (0−2 μg) of heparin dissolved in PBS (5 μL) and incubated for 30 min at room temperature. The samples (10 μL) were electrophoresed on 0.6 wt % agarose gel in 40 mM Tris, 20 mM sodium acetate, and 2 mM EDTA buffer (pH 8.0) containing 1 μg/mL ethidium bromide at 100 V for 30 min. The ethidium bromide stained bands were visualized using a LAS-1000UVmini (Fujifilm, Tokyo, Japan) and analyzed with Science Lab 2003 Multi Gauge software (Fujifilm, Tokyo, Japan).

Transfection. Transfection of CV1 cells was done according to the following procedures unless otherwise noted in the text. The cells were seeded in 0.5 mL of DMEM supplemented with 10% FCS in 24-well culture plates at 5.0×10^4 cells per well the day before transfection. The cells were washed with PBS containing 0.36 mM $CaCl_2$ and 0.42 mM $MgCl_2$ [PBS(+)] and then covered with DMEM in the presence or absence of 10% FCS (1 mL). The lipoplexes containing plasmid DNA were added gently to the cells and incubated for 4 h at 37 °C. Then, the cells were rinsed with PBS(+), covered with DMEM containing 10% FCS, and incubated at 37 °C. After 40 h, the cells were lysed by adding 50 μL of Luc-PGC-50 detergent (Toyo Ink, Tokyo, Japan). A 20 μL aliquot was taken from each dish and used for one luciferase assay using a kit (Toyo Ink) and a Lumat LB9507 luminometer (Berthold, Bad Wildbad, Germany). The protein content of the lysate was measured by Coomassie protein assay reagent (Pierce, IL) using bovine serum albumin as the standard.

RESULTS AND DISCUSSION

Synthesis of Dendron-Bearing Lipid with Two Octadecyl Groups. In a previous study, we developed a new type of cationic lipids consisting of two dodecyl groups and PAMAM dendron of varying generations (*9*). Transfection activity of these dendron-bearing lipids was shown to increase with increasing dendron generation, demonstrating the importance of the head moiety of the dendron-bearing lipids. To elucidate the effect of the hydrophobic tail moiety of the lipids, a PAMAM G3 dendron-bearing lipid with two octadecyl chains DL-G3-2C_{18} was designed in this study (Figure 1). This lipid was synthesized through repetition of exhaustive Michael addition with methyl acrylate using dioctadecylamine as the core material and subsequent exhaustive amidation with ethylenediamine, as reported by Tomalia et al. (*10*−*12*). Characterization using ^{1}H NMR showed good correspondence between the theoretically expected and experimentally obtained values for the synthesized products, as shown in the Experimental Section.

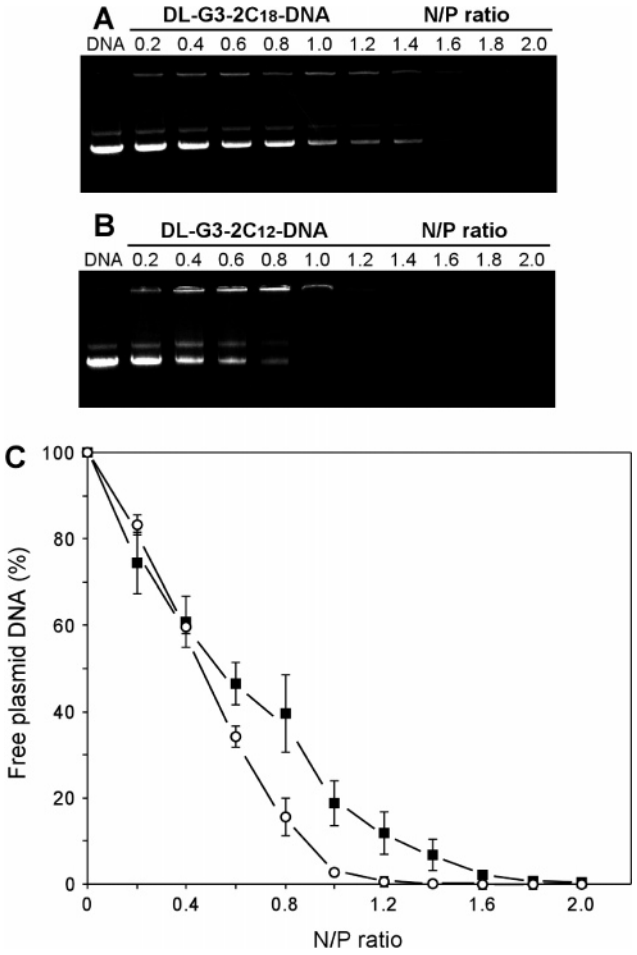


Figure 2. Agarose gel electrophoretic analysis for complexation of DL-G3-2C_{18} (A) and DL-G3-2C_{12} (B) with plasmid DNA at varying N/P ratios. Percent of free plasmid DNA was evaluated and plotted against N/P ratio (C) for complexation of DL-G3-2C_{18} (■) and DL-G3-2C_{12} (○) with plasmid DNA. Each point represents the mean ± SD ($n = 3$).

Lipoplex Formation with Plasmid DNA. The ability of the dendron-bearing lipid to form a lipoplex with plasmid DNA was investigated using gel retardation assay. The plasmid DNA (1 μg) was incubated with varying amounts of DL-G3-2C_{18} or DL-G3-2C_{12} for 30 min and electrophoresed on an agarose gel. Figure 2 shows that the amount of free plasmid DNA decreased with increasing N/P ratio, indicating that these lipids can form a lipoplex with plasmid DNA. In the case of DL-G3-2C_{18}, migration of plasmid DNA band was not observed for N/P ratios greater than 1.6 (Figure 2A), whereas migration of plasmid DNA was inhibited at N/P ratios greater than 1.0 for DL-G3-2C_{12} (Figure 2B). This result indicates that DL-G3-2C_{12} can form a lipoplex with plasmid DNA more efficiently than DL-G3-2C_{18}, even though their abilities of lipoplex formation are not markedly different. Their complex formation is driven by electrostatic interaction between the dendron moiety and DNA. Therefore, the difference of alkyl chains of these dendron-bearing lipids might only slightly affect their lipoplex formation.

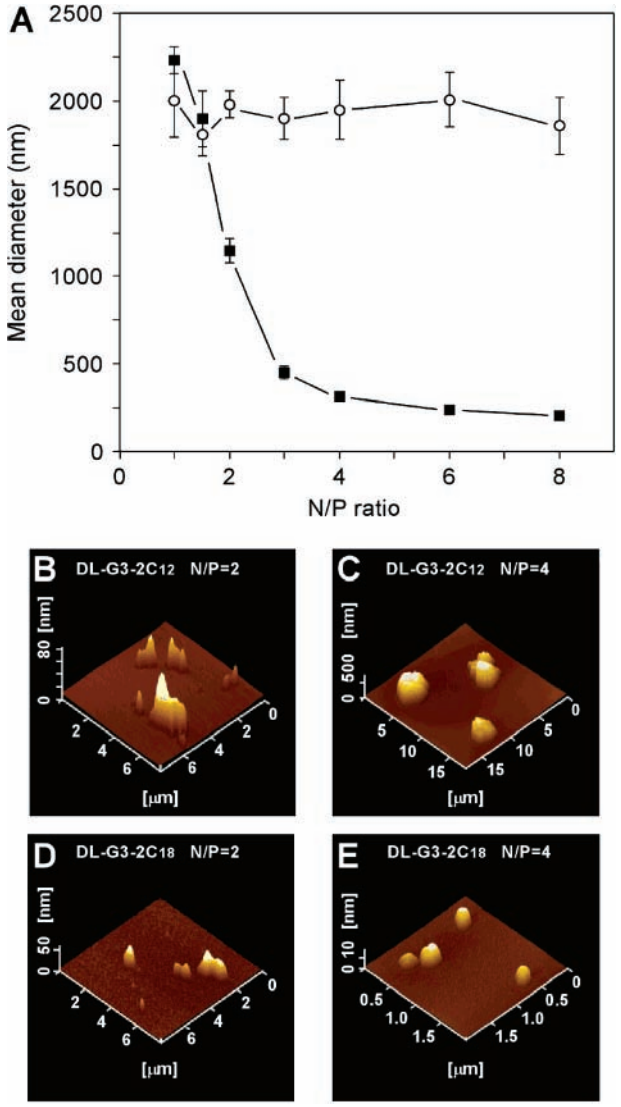


Figure 3. (A) Mean diameters of DL-G3-2C_{18} (■) and DL-G3-2C_{12} lipoplexes (○) as a function of N/P ratio. Mean diameters were estimated using DLS. Each point represents the mean ± SD (n = 3). AFM images of DL-G3-2C_{12} lipoplexes with N/P ratios of 2 (B) and 4 (C), and DL-G3-2C_{18} lipoplexes with N/P ratios of 2 (D) and 4 (E).

Particle Size and Morphology of Lipoplexes. Influence of the alkyl chain length of the dendron-bearing lipids on their lipoplex size was investigated using DLS. Figure 3A shows that the DL-G3-2C_{12} lipoplexes showed roughly the same diameter of about 2 μm, irrespective of the N/P ratio. In contrast, particle sizes of the DL-G3-2C_{18} lipoplexes depended greatly on the N/P ratio. Large particles of about 2 μm were observed at the N/P ratio of 1.0, but the lipoplex size decreased sharply with an increasing N/P ratio from 1 to 4 and became constant around 250 nm.

The lipoplexes particles were further characterized using AFM. Figure 3B,C shows that large particles with a diameter greater than 2 μm were observed for DL-G3-2C_{12} lipoplexes with N/P ratios of 2 and 4. These particles have irregular shapes and rough surfaces. Therefore, it seems that they might be formed by aggregation of smaller particles of the lipid−DNA complexes. Particles with similar morphology and diameter of ca. 1 μm were visible in the AFM image of the DL-G3-2C_{18} lipoplexes with the N/P ratio of 2 (Figure 3D). However, in the image of the DL-G3-2C_{18} lipoplexes with the N/P ratio of 4, spherical particles with 200−300 nm diameter were observed (Figure 3E). These sizes of lipoplexes, which were observed by AFM, were consistent with the DLS results (Figure 3A).

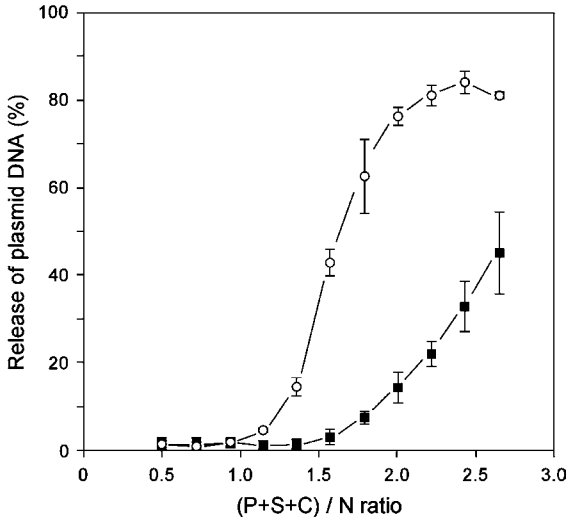


Figure 4. Release of plasmid DNA from DL-G3-2C_{18} (■) and DL-G3-2C_{12} (○) lipoplexes induced by the addition of heparin. Percent release of DNA was determined by agarose gel electrophoresis of DL-G3 lipoplexes with N/P ratio of 2 in the presence of varying amounts of heparin, and plotted against the charge ratio of phosphate (P) groups of DNA and sulfonate (S) and carboxylate (C) groups of heparin to primary amine groups (N) of dendron-bearing lipid. Each point represents the mean ± SD (n = 3).

Charge-neutralized lipoplexes with an N/P ratio around 1 are well-known to tend to form large aggregates because of their hydrophobic interaction (*13*). Therefore, both dendron-bearing lipids might form large lipoplexes at N/P ratio of 2, at which ratio their charge density was low. In contrast, at the N/P ratio of 4, the lipoplexes might possess sufficient net charge to suppress aggregation of small lipoplexes. In fact, we observed small particles with a diameter of 200−300 nm for the DL-G3-2C_{18} lipoplex. However, much larger particles appeared for the DL-G3-2C_{12} lipoplex with the N/P ratio of 4, although both lipoplexes possess the same charge density. Because of strong hydrophobic interaction of the long alkyl chains, the DL-G3-2C_{18} lipoplex particles might have a tightly packed interior and a positively charged surface, prohibiting aggregation and fusion of lipoplexes. However, because the DL-G3-2C_{12} has shorter alkyl chains, its lipoplex particles might be less stabilized than the DL-G3-2C_{18} lipoplex. Such low stability of the lipoplex particles might induce their aggregation and fusion, thereby generating larger particles.

Estimation of Lipoplex Stability. Some polyanions, such as heparin, are known to induce dissociation of DNA from lipoplexes by binding to cationic lipids of lipoplexes through electrostatic interaction (*14*, *15*). These polyanions have been used to estimate the lipoplexes' stability (*16*). Therefore, we examined the effect of addition of heparin on dissociation of plasmid DNA from the DL-G3-2C_{18} and DL-G3-2C_{12} lipoplexes to evaluate their stability. Lipoplexes with an N/P ratio of 2 were incubated for 30 min with various amounts of heparin; the amount of the liberated plasmid DNA was estimated using agarose gel electrophoresis.

Figure 4 shows the percentage of plasmid DNA released from the lipoplexes as a function of the charge balance of the lipoplex and added heparin, which is expressed as the ratio of negative charges of phosphate of DNA and sulfate and carboxylate of heparin and positive charges of primary amines of the dendron-bearing lipid [(P + S + C)/N]. The negative charges of heparin were calculated by assuming the structure of heparin as repeats of (1 → 4)-O-(α-L-idopyranosyluronic acid 2-sulfate)-(1→ 4)-(2-deoxyl-2-sulfamino-α-D-glucopyranosyl 6-sulfate) (*17*, *18*). Figure 4 shows that release of plasmid DNA from the DL-G3-2C_{12} lipoplex occurred at −/+ charge ratios greater than 1.15,

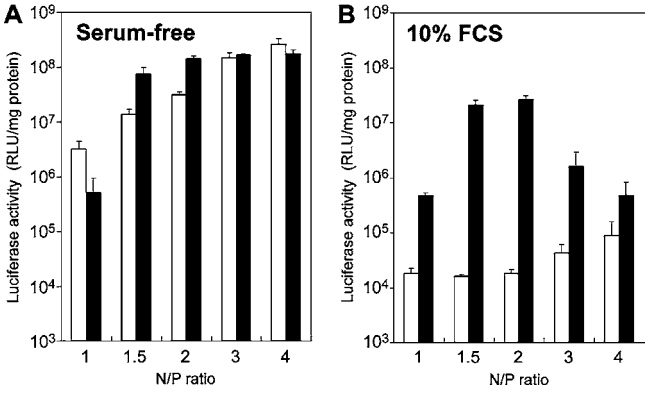


Figure 5. Luciferase activities of CV1 cells treated with DL-G3-2C_{12} lipoplexes (open bars) and DL-G3-2C_{18} lipoplexes (closed bars) in the absence (A) and presence (B) of 10% FCS. Each bar represents the mean ± SD (n = 3).

whereas the release of plasmid DNA was observed at −/+ charge ratios greater than 1.58 for the DL-G3-2C_{18} lipoplex, which indicates that 1.7 times more heparin was necessary to dissociate plasmid DNA from the DL-G3-2C_{18} lipoplexes than in the case of the DL-G3-2C_{12} lipoplex with the same N/P ratio. This result indicates clearly that hydrophobic interaction between the longer alkyl chains of DL-G3-2C_{18} increases the stability of the complex formed with plasmid DNA.

Transfection Activity of Dendron-Bearing Lipid-DNA Lipoplexes. Finally, we investigated the influence of the alkyl chain length of dendron-bearing lipids on their transfection activity. The transfection activity of lipoplexes varies depending on their N/P ratio (*19*). For that reason, we prepared lipoplexes consisting of the dendron-bearing lipid, DL-G3-2C_{12} or DL-G3-2C_{18}, and plasmid DNA containing luciferase gene at various N/P ratios and examined transfection of CV1 cells using these lipoplexes.

Figure 5A represents the expression of luciferase in the cells treated with these lipoplexes in the absence of serum. The transfection activity of these lipoplexes increased with increasing N/P ratio from 1 to 2 and reached an approximately constant level at N/P ratios greater than 2. Although the DL-G3-2C_{18} lipoplexes with the low N/P ratios seem to have a slightly higher activity than DL-G3-2C_{12} lipoplexes with the same N/P ratios, both lipoplexes exhibited similarly high transfection activities at higher N/P ratios.

However, marked differences were apparent when the transfection was performed in the presence of serum. Figure 5B shows that the DL-G3-2C_{12} lipoplexes with N/P ratios of 1−4 did not induce expression of luciferase in CV1 cells in the presence of FCS. In contrast, the DL-G3-2C_{18} lipoplexes caused transfection of CV1 cells efficiently. Especially, DL-G3-2C_{18} lipoplexes with N/P ratios of 1.5 and 2 induced a high level of luciferase expression, which is comparable to the level of transfection in the absence of serum (Figure 5A). In addition, we observed that viability of cells treated with the DL-G3-2C_{18} lipoplexes was about 100% under the experimental conditions, indicating that these lipoplexes were able to achieve efficient transfection without cellular damage (see Supporting Information).

Many studies have indicated that the transfection activity of lipoplexes is reduced dramatically in the presence of serum (*20*−*23*). As shown in Figure 5B, the DL-G3-2C_{12} lipoplexes also abolished their transfection activity in the presence of serum. It is likely that the DL-G3-2C_{12} lipoplexes are decomposed through strong interaction with serum proteins because these lipoplexes might be stabilized weakly by short alkyl chains. In contrast, the DL-G3-2C_{18} lipoplexes retained high transfection activity even in the presence of serum. Hydrophobic interaction of the long alkyl chains of DL-G3-2C_{18} might greatly improve the stability of the lipoplexes and impart a high serum-resistant property to them. In fact, we observed better stability of the DL-G3-2C_{18} lipoplex against interaction with heparin than that of the DL-G3-2C_{12} lipoplex (Figure 4). These results indicate the importance of hydrophobic tail moieties of the dendron-bearing lipid for retention of their high transfection activity in the presence of serum.

In conclusion, we demonstrated the importance of the hydrophobic tail moieties of dendron-bearing lipids for their lipoplex formation with plasmid DNA and their transfection activity. The newly synthesized dendron-bearing lipid DL-G3-2C_{18} produced highly potent, small lipoplexes with high transfection activity in the presence of serum. In a previous study, we showed that addition of dioleoylphosphatidylethanolamine, which increases fusion ability of lipoplexes, enhanced the transfection activity of the DL-G3-2C_{12} lipoplexes (*9*, *16*). Therefore, inclusion of this fusogenic lipid might further elevate transfection activity of the DL-G3-2C_{18} lipoplexes. For that reason, the DL-G3-2C_{18} might be a promising gene vector. We are currently examining the influence of addition of dioleoylphosphatidylethanolamine on transfection activity of the DL-G3-2C_{18} lipoplexes.

ACKNOWLEDGMENT

This work was partly supported by a Grant-in-aid for Scientific Research from the Ministry of Education, Science, Sports, and Culture in Japan. T. Takahashi thanks the Research Fellowships of the Japan Society for the Promotion of Science for Young Scientists (JSPS).

Supporting Information Available: Viability of CV1 cells treated with DL-G3-2C_{18} or DL-G3-2C_{12} lipoplexes. This material is available free of charge via the Internet at http://pubs.acs.org.

LITERATURE CITED

(1) de Lima, M. C. P., Simoes, S., Pires, P., Faneca, H., and Duzgunes, N. (2001) Cationic lipid-DNA complexes in gene delivery: from biophysics to biological applications. *Adv. Drug Delivery Rev. 47*, 277−294.

(2) Wagner, E., and Kloeckner, J. (2006) Gene delivery using polymer therapeutics. *Adv. Polym. Sci. 192*, 135−173.

(3) Pouton, C. W., and Seymour, L. W. (1998) Key issues in non-viral gene delivery. *Adv. Drug Delivery Rev. 34*, 3−19.

(4) Haensler, J., and Szoka, F. C., Jr. (1993) Polyamidoamine cascade polymers mediate efficient transfection of cells in culture. *Bioconjugate Chem. 4*, 372−379.

(5) Tang, M., Redemann, C. T., and Szoka, F. C., Jr. (1996) In vitro gene delivery by degraded polyamidoamine dendrimers. *Bioconjugate Chem. 7*, 703−714.

(6) Kukowska-Latallo, J. F., Bielinska, A. U., Johnson, J., Spindler, R., Tomalia, D. A., and Baker, J. R., Jr. (1996) Efficient transfer of genetic material into mamalian cells using Starburst polyamidoamine dendrimers. *Proc. Natl. Acad. Sci. U.S.A. 93*, 4897−4902.

(7) Sonawane, N. D., Szoka, F. C., Jr., and Verkman, A. S. (2003) Chloride accumulation and swelling in endosomes enhances DNA transfer by polyamine-DNA polyplexes. *J. Biol. Chem. 278*, 44826−44831.

(8) Boussif, O., Lezoualc'h, F., Zanta, M. A., Mergny, M. D., Scherman, D., Demeneix, B., and Behr, J. P. (1995) A versatile vector for gene and oligonucleotide transfer into cells in culture and in vivo: polyethylenimine. *Proc. Natl. Acad. Sci. U.S.A. 92*, 7297−7301.

(9) Takahashi, T., Kono, K., Itoh, T., Emi, N., and Takagishi, T. (2003) Synthesis of novel cationic lipids having polyamidoamine dendrons and their transfection activity. *Bioconjugate Chem. 14*, 764−773.

(10) Tomalia, D. A., Baker, H., Dewald, J., Hall, M., Kallos, G., Martin, S., Roeck, J., Ryder, J., and Smith, P. (1985) A new class of polymers: starburst-dendritic macromolecules. *Polym. J. 17*, 117−132.

(11) Esfand, R., and Tomalia, D. A. (2001) Laboratory synthesis of poly(amidoamine) (PAMAM) dendrimers. *Dendrimers and Other Dendritic Polymers* (Tomalia, D. A., and Fréchet, J. M. J., Eds.) pp 587−604, Chapter 25, John Wiley & Sons Ltd., West Sussex.

(12) Tomalia, D. A. (2004) Some Examples of Dendrimer Synthesis. *Polymer Chemistry - A Practical Approach* (Davis, F. J., Ed.) pp 188−200, Chapter 7, Oxford University Press, New York.

(13) Pitard, B., Aguerre, O., Airiau, M., Lachages, A. M., Boukhnikachvili, T., Byk, G., Dubertret, C., Herviou, C., Scherman, D., Mayaux, J. F., and Crouzet, J. (1997) Virus-sized self-assembling lamellar complexes between plasmid DNA and cationic micelles promote gene transfer. *Proc. Natl. Acad. Sci. U.S.A. 94*, 14412−14417.

(14) Zelphati, O., and Szoka, F. C., Jr. (1996) Mechanism of oligonucleotide release from cationic liposomes. *Proc. Natl. Acad. Sci. U.S.A. 93*, 11493−11498.

(15) Moret, I., Peris, J. E., Guillem, V. M., Benet, M., Revert, F., Dasi, F., Crespo, A., and Alino, S. F. (2001) Stability of PEI-DNA and DOTAP-DNA complexes: effect of alkaline pH, heparin and serum. *J. Controlled Release 76*, 169−181.

(16) Takahashi, T., Harada, A., Emi, N., and Kono, K. (2005) Preparation of efficient gene carriers using a polyamidoamine dendron-bearing lipid: improvement of serum resistance. *Bioconjugate Chem. 16*, 1160−1165.

(17) Casu, B. (1985) Structure and biological activity of heparin. *Adv. Carbohydr. Chem. Biochem. 43*, 51−134.

(18) Rabenstein, D. L. (2002) Heparin and heparin sulfate: structure and function. *Nat. Prod. Rep. 19*, 312−331.

(19) Sakurai, F., Inoue, R., Nishino, Y., Okuda, A., Matsumoto, O., Taga, T., Yamashita, F., Takakura, Y., and Hashida, M. (2000) Effect of DNA/liposome mixing ratio on the physicochemical characteristics, cellular uptake and intracellular trafficking of plasmid DNA/cationic liposome complexes and subsequent gene expression. *J. Controlled Release 66*, 255−269.

(20) Yang, J. P., and Huang, L. (1997) Overcoming the inhibitory effect of serum on lipofection by increasing the charge ratio of cationic liposome to DNA. *Gene Ther. 4*, 950−960.

(21) Yang, J. P., and Huang, L. (1998) Time-dependent maturation of cationic liposome-DNA complex for serum resistance. *Gene Ther. 5*, 380−387.

(22) Li, S., Tseng, W. C., Stolz, D. B., Wu, S. P., Watkins, S. C., and Huang, L. (1999) Dynamic changes in the characteristics of cationic lipidic vectors after exposure to mouse serum: implications for intravenous lipofection. *Gene Ther. 6*, 585−594.

(23) Crook, K., Stevenson, B. J., Dubouchet, M., and Porteous, D. J. (1998) Inclusion of cholesterol in DOTAP transfection complexes increases the delivery of DNA to cells in vitro in the presence of serum. *Gene. Ther. 5*, 137−143.

BC060311K

Function and Stability of Abscisic Acid Acyl Hydrazone Conjugates by LC-MS^2 of ex Vivo Samples

Timothy R. Smith,[†] Andrew J. Clark,[†] Richard Napier,[‡] Paul C. Taylor,[†] Andrew J. Thompson,[‡] and Andrew Marsh*[,†]

Department of Chemistry, University of Warwick, Coventry CV4 7AL, U.K., Warwick HRI, University of Warwick, Wellesbourne, Warwick, CV35 9EF, U.K. Received February 28, 2007; Revised Manuscript Received May 1, 2007

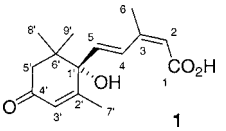
We prepare a biotinylated conjugate of the ubiquitous plant hormone (*S*)-(+)-abscisic acid via an acyl hydrazone linkage at the C4′ position and demonstrate in vivo cleavage of the otherwise stable acyl hydrazone linkage using LC-MS^2. As part of a wider chemical genomic study, biological activity of the conjugate was assessed using standard epidermal peel and gravimetric transpiration assays, showing significant activity but at a level lower than the unconjugated hormone. When deuterated samples of the conjugate were fed to the plant, however, it was apparent by LC-MS^2 experiments that significant levels of hydrolysis of the acyl hydrazone had taken place, contrary to in vitro stability assays in artificial sap. We conclude that abscisic acid is liberated in sufficient quantities to account for the observed physiological response and that LC-MS^2 monitoring of conjugates is a simple and practical method by which such events may be assessed, whether in plants or other organisms.

INTRODUCTION

The search for the biological targets of the ubiquitous plant hormone abscisic acid (ABA[1]) **1** (Figure 1) (*1*) has produced many sophisticated strategies for the preparation of analogues and conjugates (*2*). One favored tactic has been the use of bioconjugates such as 4′-hydrazones **2**−**5** (Figure 2) in order to identify anti-idiotypic monoclonal antibodies (*3*), to provide *in vivo* fluorophore reagents (*4*), and as ligands in affinity chromatography (*5*). Each relies on the bioconjugate or derived protein exhibiting demonstrable activity in order to be relevant to the process under investigation. An example of the bioconjugate strategy working well is the use of novel aromatic annelated abscisic acid derivatives (*6*) in order to identify the first (*7*) of two recently confirmed receptors (*8*). Conjugates that retain some activity but at a lower level may still offer useful material, because binding may occur, but with lower affinity. Reliable assays for both biological activity and chemical composition are hence critical components in the design of successful experiments using such bioconjugates. In this Technical Note, we demonstrate the use of LC-MS^2 on *in vitro* and *ex vivo* samples in conjunction with biological assays to determine the stability and biological activity of an acyl hydrazone conjugate of ABA. Significantly, we show that *in vivo* degradation of the conjugate released low levels of ABA that were sufficient to explain the apparent activity of our conjugate.

EXPERIMENTAL PROCEDURES

General Experimental. Unless otherwise noted, all materials were obtained from commercial sources and used without further purification. *S*-(+)-Abscisic acid (98%: purity confirmed by microanalysis) was purchased from Sichuan Lomon Bio Corporation, Chengdu Sichuan, China. Column chromatography was performed on Merck silica gel 60 H (230−400 mesh). Melting points were recorded on a Gallenkamp melting point apparatus and are uncorrected. Optical rotations (given in 10^{-1} deg cm^2 g^{-1}) were measured on an Optical Activity AA-1000 polarimeter. IR spectra were recorded on a Perkin-Elmer Paragon 1000 FT-IR instrument. ^{1}H and ^{13}C NMR spectra were recorded using a Bruker DPX300 at 300 and 75 MHz, respectively. NMR spectra were recorded in the indicated solvent, and chemical shifts (δ) are reported in parts per million (ppm) relative to residual nondeuterated solvent as an internal standard. *J* values are given in hertz (Hz). ^{2}D NMR spectra were recorded using a Bruker DRX500 at 77 MHz. LSIMS mass spectrometry was performed on a Micromass Autospec mass spectrometer. ESI mass spectrometry was performed on a Bruker micrOTOF instrument.



1

Figure 1. (*S*)-(+)-Abscisic acid with formal atom numbering.

Epidermal Peel Assay. Abaxial epidermal peels from *Commelina communis* L. were incubated at 25 °C under continuous white light (30 μmol m^{-2} s^{-1}) in Petri dishes containing aqueous buffer solution (25 mL) consisting of 8 mmol dm^{-3} MES·KOH pH 6.15 and 50 mmol dm^{-3} KCl. A needle inserted through the lid of the Petri dish allowed CO_2-free air to be bubbled through the buffer solution (100 cm^3 min^{-1}). After 2 h, the stomata were fully open. Solutions of ABA or conjugate were added and incubation continued for a further 2 h. The epidermal peels were then mounted on microscope slides, and stomatal aperture was immediately recorded digitally at 500× magnification. For each treatment, mean apertures were determined from 30 measurements made from 2 independent epidermal peels. Stomatal apertures were measured across the widest part of the opening and expressed as a percentage of an untreated control.

Gravimetric Transpiration Assay. Tomato (*Solanum lycoperiscum* L. cv Ailsa Craig) plants were grown in a glass house in 10 dm^3 pots of Levington M2 compost (Levington, Ipswich, U.K.), until they had produced approximately eight leaves. The youngest fully expanded leaf was cut from the plant, and the

* Corresponding author e-mail: a.marsh@warwick.ac.uk.
[†] Department of Chemistry.
[‡] Warwick HRI.

[1]Abbreviations: ABA, abscisic acid; AS, artificial sap; MES, 2-(*N*-morpholino)ethanesulfonic acid; MRM, multiple reaction monitoring; LCMS^2, liquid chromatography tandem mass spectrometry.

10.1021/bc070069x CCC: $37.00 © 2007 American Chemical Society
Published on Web 06/14/2007

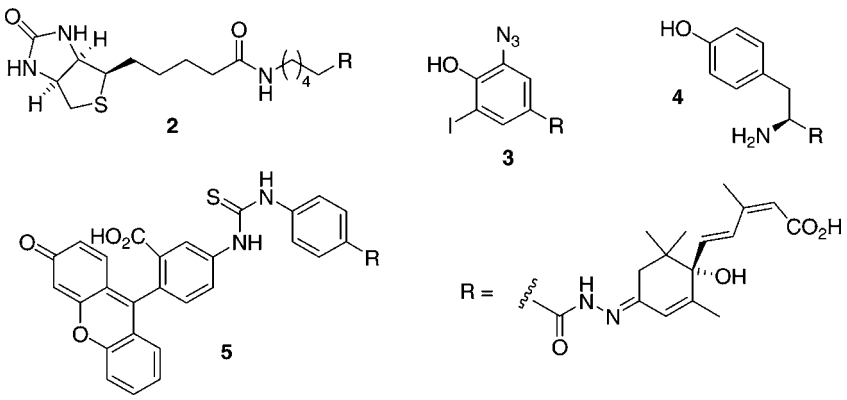


Figure 2. 4′-Acyl hydrazone conjugates of abscisic acid: biotinylated **2** (*9*), radio-iodinated **3** (*5*), tyrosyl **4** (*10*), and fluorescent **5** (*4*).

petiole was recut under degassed distilled water to avoid embolization and then immediately transferred to a 2.5 cm^3 glass vial containing 2 cm^3 of artificial sap (AS) consisting of 1.0 mmol dm^{-3} KH_2PO_4, 1.0 mmol dm^{-3} K_2HPO_4, 1.0 mmol dm^{-3} $CaCl_2$, 0.1 mmol dm^{-3} $MgSO_4$, 3.0 mmol dm^{-3} KNO_3, and 0.1 mmol dm^{-3} $MnSO_4$ (*11*). The sap was adjusted to pH 6.0 with aqueous HCl. Laboratory film was used to seal the petiole in the vial to reduce evaporation. Prepared leaf sets were randomized and placed on a laboratory bench under fluorescent lighting (37 μmol m^{-2} s^{-1}). Each vial was weighed every 20 min for 2 h to establish an untreated transpiration rate. After 30−90 min, the rate of transpiration was seen to reach a plateau. Each leaf set was then transferred to a new vial containing the same amount of AS in addition to the specified amount of either ABA or conjugate. The rate of transpiration was determined by weighing the vial every 20 min for 2 h and expressed as a percentage of the initial transpiration rate. Up to six replicates were performed for each assay at five different concentrations of ABA and conjugate.

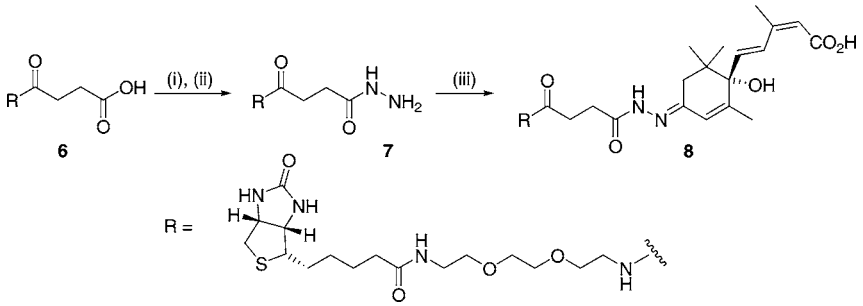
LC-MS^2 Analysis. *Sample Preparation.* On completion of the gravimetric transpiration assay, leaves fed with the most concentrated solution of conjugate were separated from the petiole and immediately homogenized in liquid nitrogen, lyophilized, and stored at −80 °C until required. Untreated leaves were collected and processed in a similar manner but were spiked with conjugate (75 μg) prior to homogenization as a control. Leaf material (100 mg) was extracted with 1 cm^3 of water by agitation on a whirly mix for 5 min. The sample was centrifuged (2880 g, 10 min at 4 °C) and the supernatant collected and filtered through a plug of glass wool into a centrifuge filter (Vivascience Vivaspin 2, 3000 MWCO). After centrifuging (2880 g, 30 min at 4 °C), the supernatant was collected and analyzed immediately.

LC-MS^2 Procedure. ESI mass spectrometry was performed on a Bruker HCTplus ion trap instrument. Parameters were optimized by direct infusion of d_6-abscisic acid (1 mg dm^{-3}) in water (70%), acetonitrile (30%), and formic acid (0.01%). The optimized conditions were as follows: negative ion polarity, trap drive 34.7 (arbitrary units), octopole RF amplitude 193.4 Vpp, capillary exit −111.5 V, HV capillary 4.5 kV, drying gas (N_2) temperature 320 °C, drying gas flow 9 dm^3 min^{-1}, and nebulizer 30 psi. Fragmentation parameters were handled automatically by the SmartFrag function. LC separation was performed on an Alltech Alltimer C18 column (100 mm × 2 mm, 3 μm) fitted with an Alltech C18 guard column (7.5 mm × 3.0 mm, 5 μm). For each run, 20 μL of the crude plant extract was injected onto the column. The sample was eluted using a binary solvent system comprising 0.01% formic acid in water (A) and 0.01% formic acid in acetonitrile (B). Solvents were mixed and delivered to the column by an integrated HPLC pump and autosampler (Agilent 1100 series) at a flow rate of 0.2 cm^3 min^{-1}. The sample was separated by gradient elution starting at 74% A and 26% B and changed linearly over a 15 min period to 70% A and 30% B.

Preparation of *N*-Succinamidylhydrazono-*N*′-biotinyl-3,6-dioxaoctane-1,8-diamine, 7. A solution of *N*-succinamidyl-*N*′-biotinyl-3,6-dioxaoctane-1,8-diamine **6** (*12*) (173 mg, 0.36 mmol, 1 equiv) in methanol (2 mL) was added dropwise to an ice-cooled solution of thionyl chloride (131 mg, 1.1 mmol, 3 equiv) in methanol (2 mL). The reaction was allowed to warm to room temperature and stirred for 24 h. The solvent was removed under reduced pressure before addition of a further portion of methanol (15 mL). This was removed once more under reduced pressure to yield a brown residue, which was dissolved in methanol (4 mL) and treated with hydrazine monohydrate (183 mg, 3.6 mmol, 10 equiv). The mixture was stirred at room temperature for 24 h, filtered, and then concentrated under reduced pressure. The crude product was purified by column chromatography (silica, 30% MeOH, and 3% concentrated aqueous ammonia solution in EtOAc) to yield a pale yellow solid (100 mg, 56%); R_f 0.10 (30% MeOH and 3% concentrated aqueous ammonia solution in EtOAc); mp 135−138 °C (EtOAc); $[\alpha]^{20}_D$ = +12.3 (*c* 0.65, DMSO); υ_{max}(solid) 3285, 2924, 1698, 1637, 1550, 1461, 1120 cm^{-1}; δ_H (300 MHz, DMSO-d_6) 1.22−1.37 (m, 2H), 1.40−1.69 (m, 4H), 2.06 (t, J = 7.4, 2H), 2.22−2.24 (m, 2H), 2.28−2.31 (m, 2H), 2.57 (d, J = 12.2, 1H), 2.82 (dd, J = 5.1, 12.2, 1H), 3.08−3.10 (m, 1H), 3.17−3.18 (m, 4H), 3.36−3.38 (m, 4H), 3.50 (s, 4H), 3.98 (s, 2H), 4.10−4.14 (m, 1H), 4.28−4.33 (m, 1H), 6.37 (s, 1H), 6.44 (s, 1H), 7.86 (t, J = 5.5, 1H), 7.92 (t, J = 5.3, 1H), 8.96 (s, 1H); δ_C (75 MHz, DMSO-d_6) 25.6 (CH_2), 28.6 (2 × CH_2), 29.3 (CH_2), 31.0 (CH_2), 35.4 (CH_2), 39.0 (2 × CH_2), 40.7 (CH_2), 55.7 (CH), 59.5 (CH), 61.4 (CH), 69.5 (2 × CH_2), 69.9 (2 × CH_2), 163.1 (C), 171.2 (C), 171.6 (C), 172.5 (C); HRMS (ESI): *m*/*z* requires ($C_{20}H_{37}N_6O_6S$) 489.2490, found 489.2489, 57% $[M + H]^+$.

Preparation of *S*-(+)-Abscisic acid 4′-(*N*-Succinamidyl acyl hydrazide-*N*′-biotinyl-3,6-dioxaoctane-1,8 diamine), 8. *N*-Succinamidylhydrazono-*N*′-biotinyl-3,6-dioxaoctane-1,8-diamine, **7**, (190 mg, 0.39 mmol, 1 equiv) and *S*-(+)-abscisic acid (206 mg, 0.78 mmol, 2 equiv) were dissolved in methanol (10 mL). Glacial acetic acid (50 μL) and crushed 4 Å molecular sieves (100 mg) were added and the reaction stirred in darkness at room temperature under a nitrogen atmosphere for 4 days. The mixture was filtered through Celite and the solvent removed under reduced pressure. The product was purified by preparative thin-layer chromatography (silica, 15% MeOH in DCM) to yield a pale yellow solid (177 mg, 62%); R_f 0.15 (15% MeOH in DCM); $[\alpha]^{20}_D$ = +267.2 (*c* 0.25, MeOH); υ_{max}(solid) 3266, 2929, 1653, 1546, 1400, 1119, 1026 cm^{-1}; δ_H (300 MHz, CD_3-OD) 1.06 (s, 3H), 1.09 (s, 3H), 1.40−1.56 (m, 2H), 1.58−1.83 (m, 4H), 1.87 (s, 3H), 2.06 (s, 3H), 2.26 (t, J = 7.4, 2H), 2.47−

Scheme 1. Preparation of Biotinylated Acyl Hydrazone-Linked Abscisic Acid[a]



[a] Reagents and conditions: (i) $SOCl_2$, MeOH, then (ii) hydrazine, MeOH, 56%, (iii) (*S*)-(+)-abscisic acid, AcOH, MeOH, 62%.

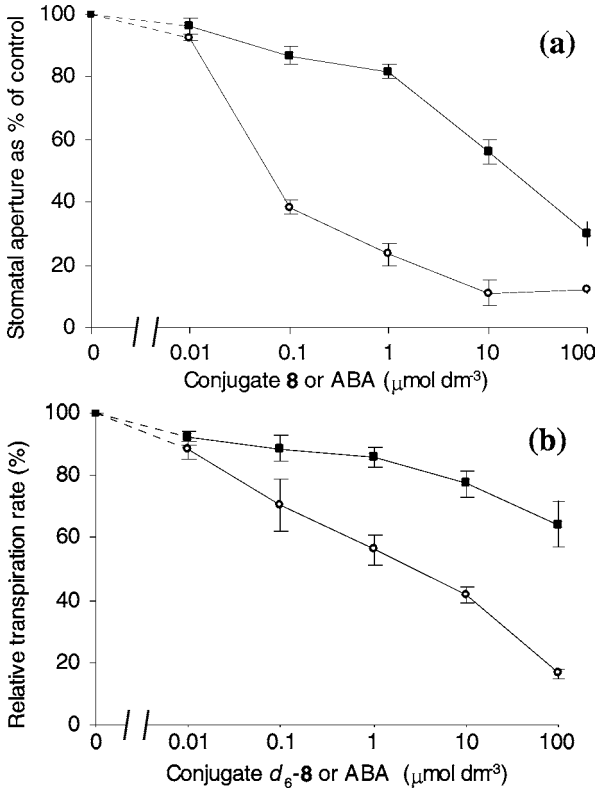


Figure 3. (a) The biological activity of conjugate **8** (■) compared to (*S*)-(+)-abscisic acid (○) in the stomatal closure of epidermal peels. Results are displayed as a percentage of the control with fully open stomata at 100%. Error bars indicate SE of means ($n = 10$). (b) The effect of feeding detached tomato leaves with AS containing conjugate d_6-**8** (■) or (*S*)-(+)-abscisic acid (○) on gravimetric transpiration. Results are displayed as a percentage of the transpiration rate of leaves that received AS alone. Error bars indicate SE of means ($n = 3$).

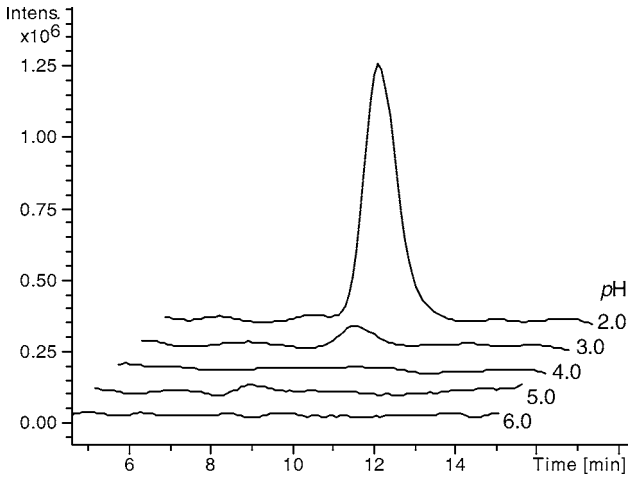


Figure 4. A 100 μmol dm^{-3} solution of d_6-**8** in artificial sap was acidified with HCl (aq) to a specific pH. The mixture was allowed to stand for 2 h, then immediately analyzed using LC-MS^2. Hydrolysis of d_6-**8** releases d_6-abscisic acid indicated by a peak at RT = 9.83 min. Chromatograms are offset.

2.70 (m, 6H), 2.74 (d, $J = 12.8$, 1H), 2.96 (dd, $J = 4.9$, 12.8, 1H), 3.21−3.28 (m, 1H), 3.39−3.42 (m, 4H), 3.55−3.63 (m, 4H), 3.66 (s, 4H), 4.33−4.37 (m, 1H), 4.52−4.56 (m, 1H), 5.75 (s, 1H), 6.19 (s, 1H), 6.19 (d, $J = 16.0$, 1H), 7.73 (d, $J = 16.0$, 1H); δ_C (75 MHz, CD_3OD) 19.7 (CH_3), 23.6 (CH_3), 24.4 (CH_3), 25.3 (CH_3), 27.3 (CH_2), 29.9 (CH_2), 30.2 (CH_2), 31.0 (CH_2), 32.3 (CH_2), 37.2 (CH_2), 38.7 (C), 40.7 (CH_2), 40.8 (CH_2), 41.5 (CH_2), 50.3 (CH_2), 57.4 (CH), 62.0 (CH), 63.8 (CH), 71.1 (2 × CH_2), 71.7 (2 × CH_2), 80.8 (C), 125.4 (CH), 125.7 (CH), 130.0 (CH), 136.4 (CH), 144.5 (C), 151.9 (C), 156.0 (C), 166.5 (C), 167.9 (C), 172.3 (C), 175.2 (C), 176.6 (C); HRMS (LSIMS): *m*/*z* requires ($C_{35}H_{54}N_6NaO_9S$) 757.3571, found 757.3564, 100% $[M + Na]^+$.

Preparation of *S*-(+)-d_6-Abscisic acid 4′-(*N*-Succinamidyl acyl hydrazide-*N*′-biotinyl-3,6-dioxaoctane-1,8 diamine), d_6-8. *S*-(+)-d_6-Abscisic acid, prepared from two successive rounds of deuterium exchange (*13*), was reacted with *N*-succinamidyl-hydrazono-*N*′-biotinyl-3,6-dioxaoctane-1,8-diamine **7**, in an identical manner to the preparation of **8**, yielding the title product (154 mg, 53%) as a pale yellow solid; $[\alpha]^{20}_D = +272.0$ (*c* 0.30, MeOH); υ_{max}(solid) 3282, 2933, 1655, 1534, 1458, 1127, 1026 cm^{-1}; δ_H (300 MHz, CD_3OD) 1.01 (s, 3H), 1.05 (s, 3H), 1.42−1.47 (m, 2H), 1.54−1.76 (m, 4H), 1.97 (s, 3H), 2.22 (t, $J = 7.6$, 2H), 2.58 (d, $J = 5.4$, 2H), 2.63 (d, $J = 5.4$, 2H), 2.70 (d, $J = 12.8$, 1H), 2.88 (dd, $J = 5.0$, 12.8, 1H), 3.17−3.23 (m, 1H), 3.36−3.38 (m, 4H), 3.54−3.56 (m, 4H), 3.63 (s, 4H), 4.29−4.32 (m, 1H), 4.48−4.51 (m, 1H), 5.75 (s, 1H), 6.05 (d, $J = 16.0$, 1H), 7.60 (d, $J = 16.0$, 1H); δ_D (77 MHz, CH_3OH) 0.88 (s, br, 3D), 1.63 (s, br, 2D), 7.71 (s, 1D); δ_C (125 MHz, CD_3OD) 19.4 (CH_3), 22.9 (CH_3), 23.6 (CH_3), 26.5 (CH_2), 28.5 (CH_2), 28.8 (CH_2), 29.7 (CH_2), 30.9 (CH_2), 36.0 (CH_2), 38.9 (C), 39.1 (CH_2), 39.3 (CH_2), 40.1 (CH_2), 56.0 (CH), 60.6 (CH), 62.4 (CH), 69.60 (CH_2), 69.63 (CH_2), 70.31 (CH_2), 70.34 (CH_2), 79.3 (C), 122.0 (CH), 128.4 (CH), 136.4 (CH), 146.4 (C), 150.0 (C), 154.4 (C), 165.1 (C), 170.7 (C), 170.8 (C), 173.7 (C), 175.2 (C); HRMS (ESI): *m*/*z* requires ($C_{35}H_{48}N_6O_9SD_6Na$) 763.3942, found 763.3957, 100% $[M + Na]^+$.

RESULTS AND DISCUSSION

Acyl hydrazones including **2**−**5** have been previously reported (*4*, *5*, *9*, *10*) and used in bioassays; hence, as part of a chemical genomic study on the action of abscisic acid requiring well-defined conjugates, related acyl hydrazone **8** was prepared (Scheme 1). A flexible and hydrophilic linker derived from 2-(2-(2-aminoethoxy)ethoxy)ethanamine was used for conjugating D-biotin to *S*-(+)-abscisic acid. Biotin hydrazide **7** was prepared from previously reported acid **6** (*12*) and then coupled to commercial *S*-(+)-abscisic acid, yielding **8** through a modifica-

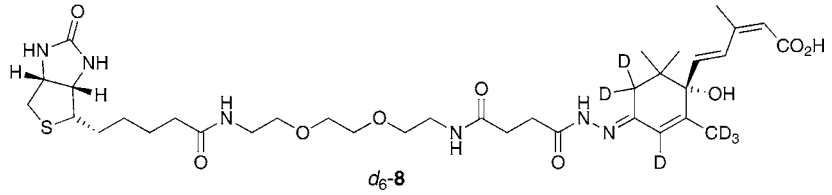


Figure 5. Deuterated ABA conjugate d_6-**8**.

tion of the method reported by Kohler et al. (*5*). Biological activity of this conjugate was observed in a stomatal aperture assay (Figure 3) and shows similar levels of activity to the biotinylated abscisic acid conjugate **2** reported by Yamazaki et al. (*9*). Conflicting reports concerning the stability of acyl hydrazones to hydrolysis led us to assay the purity of our new hydrazone by LC-MS before and after *in vitro* storage under a variety of conditions including in artificial sap (AS) (*11*) at a range of pH values (Figure 4), in addition to the usual methods used to confirm identity (see Experimental Section).

This data clearly showed that the acyl hydrazone was stable in acidic medium at pH ≥ 4.0, thus validating its use in the relatively less acidic *in vivo* plant environment but in line with a general acid-catalyzed hydrolysis mechanism, decomposed at pH ≤ 3.0. It has been proposed that acyl hydrazone conjugates of abscisic acid may hydrolyze *in vivo* (*14*), but this hypothesis has not been fully tested, so we extended this work to the study of their stabilities *in vivo* using a modification of the LC-MS^2 technique described by Gómez-Cadenas and co-workers (*15*). The detection of ABA in plant extracts by LC-MS^2 has been rigorously studied (*16*−*18*) and provides a rapid means of assessing whether *in vivo* hydrolysis has taken place. The labeled conjugate d_6-**8** (Figure 5) was prepared analogously to **8** using d_6-ABA, which allows the conjugated ABA to be distinguished from endogenous ABA in the plant. We were able to enrich the total deuterium content of our d_6-ABA to about 94% (determined by ^{1}H NMR) by submitting *S*-(+)-ABA to two successive rounds of deuterium exchange as described by Hirai and co-workers (*13*). The same authors demonstrated that the deuterium labels in this d_6-ABA were sufficiently stable for use as an internal standard for quantitative analysis. The deuterium content of conjugate d_6-**8** was similarly assessed and estimated at 92%. If *in vivo* hydrolysis of the deuterated biotinylated conjugate d_6-**8** occurs, then free abscisic acid would be released, indicating an apparent biological activity erroneously attributed to the conjugate. In the absence of *in vivo* hydrolysis, it is reasonable to assume that the intact conjugate is active.

ABA and the deuterated conjugate d_6-**8** was fed to detached tomato leaves in a solution of AS. The rate of uptake of the AS was determined gravimetrically and compared to the rate of untreated leaves. Since ABA and our nondeuterated conjugate reduce transpiration by effecting stomatal closure, the rate of AS uptake was, as expected, reduced (Figure 3).

The tomato leaves treated with d_6-**8** were homogenized, lyophilized, extracted with water, and immediately submitted to LC-MS^2 analysis. Although extraction of abscisic acid using water has been validated in previous work (*15*), it should be noted that these conditions may not be optimal for isolation of conjugate d_6-**8**. Spectrometric analysis of the extract was performed in negative-mode ESI to detect the well-characterized (*15*, *18*) fragmentation pattern of abscisic acid (263−153 Da) and our d_6-abscisic acid (269−159 Da). Multiple reaction monitoring (MRM) of the fragmentation to secondary ion peaks together with comparison of retention times of known samples provides unequivocal confirmation of the presence of these compounds. The ESI mass spectrometry parameters were optimized for d_6-abscisic acid by direct infusion of pure samples; however, a low level of d_6-**8** could also be detected. A pure sample of d_6-**8** gave fragments from 739 Da, $[M]^-$ to 455 and 409 Da. The exact nature of the latter fragment is unknown, but the 455 Da species is consistent with the elemental composition $C_{20}H_{31}N_4O_6S$, which we postulate to be the deprotonated ion of the structure shown in Figure 6. This fragment was the most intense, so we chose to monitor the 739−455 Da fragmentation as part of our MRM settings.

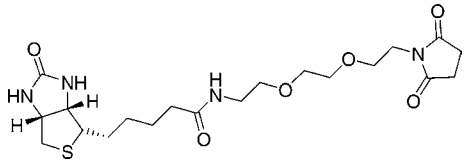


Figure 6.

The results (Figure 7) show the presence of a large peak representing endogenous abscisic acid and a small peak for the conjugate d_6-**8**. Crucially, d_6-abscisic acid was also detected with a peak area of about 15% of the endogenous abscisic acid (we found that d_6-abscisic acid and its fragments have similar ion intensity to those of nondeuterated abscisic acid, allowing comparison of these two peak areas). This result was observed in two biological replicates. A control experiment was performed to ensure that hydrolysis of d_6-**8** had not occurred in sample preparation or during the LC-MS^2 run. Plant cuttings were fed untreated AS, then prior to homogenization were spiked with d_6-**8**. After processing these cuttings in the manner described above, the plant extract was analyzed by LC-MS^2. Only endogenous abscisic acid and d_6-**8** were detected (data not shown), showing that decomposition of d_6-**8** had indeed occurred inside the living plant.

We conclude that the hydrolysis of acyl hydrazone conjugates takes place in living plant tissue at a rate sufficient to account for observed biological activity, although the mechanism and site of decomposition are presently unknown. The data support earlier reports of the inactivity of 4′-carbonyl conjugates (*14*, *19*). The exogenous ABA from the hydrolysis of d_6-**8** will be rapidly metabolized, making an accurate quantitative analysis

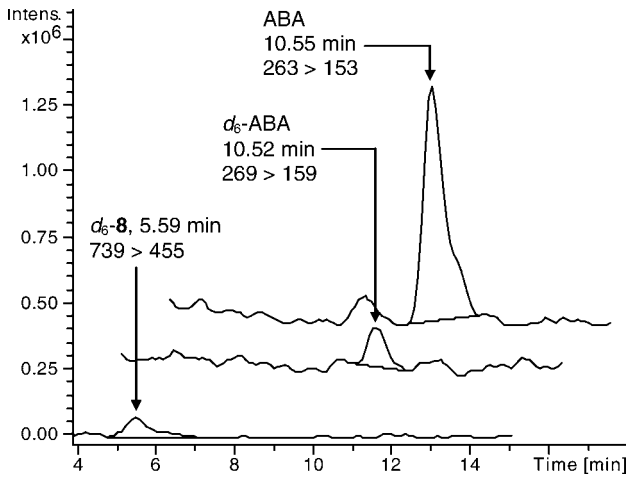


Figure 7. LC-MS^2 chromatograms of a plant extract from tomato leaves fed with conjugate d_6-**8** (100 μmol dm^{-3}) showing endogenous ABA (10.55 min), d_6-abscisic acid (10.52 min), and d_6-**8** (5.59 min). Chromatograms are offset.

of the extent of hydrolysis problematic. Quantification of deuterated ABA catabolites phaseic acid, dihydrophaseic acid, and abscisic acid glucose ester would need to be incorporated into any final quantitative analysis. Exogenous ABA is also likely to trigger increased biosynthesis and metabolism of endogenous ABA (*20*). In summary, knowledge of the *in vivo* stability of bioconjugates is important to the assessment of bioactivity: LC-MS^2 is widely available and ideally suited to such evaluations.

ACKNOWLEDGMENT

We thank the BBSRC for a BMS Committee Studentship (T.R.S.), and thank Dr. A. J. Clarke, Mr. J. C. Bickerton for technical assistance with NMR, mass spectrometry, respectively, and Dr. C. Corre for assistance with LC-MS experiments. We thank the reviewers for helpful comments.

LITERATURE CITED

(1) Schroeder, J. I., and Kuhn, J. M. (2006) Plant biology-abscisic acid in bloom. *Nature (London) 439*, 277−278.

(2) Zaharia, L. I., Walker-Simmon, M. K., Rodriguez, C. N., and Abrams, S. R. (2005) Chemistry of abscisic acid, abscisic acid catabolites and analogs. *J. Plant Growth Regul. 24*, 274−284.

(3) Quarrie, S. A., and Galfre, G. (1985) Use of different hapten-protein conjugates immobilised on nitrocellulose to screen monoclonal antibodies to abscisic acid. *Anal. Biochem. 151*, 389−399.

(4) Asami, T., Tao, L., Yamamoto, S., Robertson, M., Min, Y-K., Murofushi, N., and Yoshida, S. (1997) Fluorescence-labeled abscisic acid possessing abscisic acid-like activity in barley aleurone protoplasts. *Biosci. Biotechnol. Biochem. 61*, 1198−1199.

(5) Kohler, A. D., Beale, M. H., Rollason, R., Barratt, D. H. P., Lewis, M. J., Van der Meulen, R. M., and Wang, M. (1997) A radioiodinated abscisic acid photoaffinity probe. *J. Chem. Soc., Perkin Trans. 1* (*10*), 1543−1547.

(6) Nyangulu, J. M., Galka, M. M., Jadhav, A., Gai, Y., Graham, C. M., Nelson, K. M., Cutler, A. J., Taylor, D. C., Banowetz, G. M., and Abrams, S. R. (2005) An affinity probe for isolation of abscisic acid-binding proteins. *J. Am. Chem. Soc. 127*, 1662−1664. Nyangulu, J. M., Nelson, K. M., Rose, P. A., Gai, Y., Loewen, M., Lougheed, B., Quail, J. W., Cutler, A. J., and Abrams, S. R. (2006) Synthesis and biological activity of tetralone abscisic acid analogues. *Org. Biomol. Chem. 7*, 1400−1412.

(7) Razem, F. A., El-Kereamy, A., Abrams, S. R., and Hill, R. D. (2006) The RNA-binding protein FCA is an abscisic acid receptor. *Nature (London) 439*, 290−294.

(8) Shen, Y. Y., Wang, X. F., Wu, F. Q., Du, S. Y., Cao, Z., Shang, Y., Wang, X. L., Peng, C. C., Yu, X. C., Zhu, S. Y., Fan, R. C., Xu, Y. H., and Zhang, D. P. (2006) The Mg-chelatase H subunit is an abscisic acid receptor. *Nature (London) 443*, 823−826.

(9) Yamazaki, D., Yoshida, S., Asami, T., and Kuchitsu, K. (2003) Visualization of abscisic acid-perception sites on the plasma membrane of stomatal guard cells. *Plant J. 35*, 129−139.

(10) Hornberg, C., and Weiler, E. W. (1984) High-affinity binding sites for abscisic acid on the plasmalemma of *Vicia faba* guard cells. *Nature (London) 310*, 321−324.

(11) Wilkinson, S., and Davies, W. J. (1997) Xylem sap pH increase: a drought signal received at the apoplastic face of the guard cell that involves the suppression of saturable abscisic acid uptake by the epidermal symplast. *Plant Physiol. 113*, 559−573.

(12) Trester-Zedlitz, M., Kamada, K., Burley, S. K., Fenyö, D., Chait, B. T., and Muir, T. W. (2003) A modular cross-linking approach for exploring protein interactions. *J. Am. Chem. Soc. 125*, 2416−2425.

(13) Hirai, N., Kondo, S., and Ohigashi, H. (2003) Deuterium-labeled phaseic acid and dihydrophaseic acids for internal standards. *Biosci. Biotechnol. Biochem. 67*, 2408−2415.

(14) Hite, D. R. C., Outlaw, W. H., and Seavy, M. A. (1994) Substitution of hydrazones for the 4′ carbonyl on abscisic acid rendered it ineffective in a rapid stomatal-opening-inhibition bioassay. *Physiol. Plant. 92*, 79−84.

(15) Gómez-Cadenas, A., Pozo, O. J., García-Augustín, P., and Sancho, J. V. (2002) Direct analysis of abscisic acid in crude plant extracts by liquid chromatography-electrospray/tandem mass spectroscopy. *Phytochem. Anal. 13*, 228−234.

(16) López-Carbonell, M., and Jáuregui, O. (2005) A rapid method for analysis of abscisic acid (ABA) in crude extracts of water stressed *Arabidopsis thaliana* plants by liquid chromatography-mass spectrometry in tandem mode. *Plant Physiol. Biochem. 43*, 407−411.

(17) Durgbanshi, A., Arbona, V., Pozo, O., Miersch, O., Sancho, J. V., and Gómez-Cadenas, A. (2005) Simultaneous determination of multiple phytohormones in plant extracts by liquid chromatography-electrospray tandem mass spectroscopy. *J. Agric. Food Chem. 53*, 8437−8442.

(18) Ross, A. R. S., Ambrose, S. J., Cutler, A. J., Feurtado, J. A., Kermode, A. R., Nelson, K., Zhou, R., and Abrams, S. R. (2004) Determination of endogenous and supplied deuterated abscisic acid in plant tissue by high-performance liquid chromatography-electrospray ionization tandem mass spectrometry with multiple reaction monitoring. *Anal. Biochem. 329*, 324−333.

(19) Van der Meulen, R. M., Heidekamp, F., Jastorff, B., Horgan, R., and Wang, M. (1993) Effects of abscisic acid analogues on abscisic acid-induced gene expression in barley aleurone protoplasts: relationship between structure and function of the abscisic acid molecule. *J. Plant Growth Regul. 12*, 13−19.

(20) Lin, B., Wang, H., Wang, J., Zaharia, L. I., and Abrams, S. R. (2005) Abscisic acid regulation of heterophylly in *Marsilea quadrifolia* L.: effects of *R*-(-) and *S*-(+) isomers. *J. Exp. Bot. 56*, 2935−2948.

BC070069X

SEPTEMBER/OCTOBER 2007
Volume 18, Number 5

© *Copyright 2007 by the American Chemical Society*

Bioconjugate Chemistry

COMMUNICATIONS

Water-Soluble Contrast Agents Targeted at the Estrogen Receptor for Molecular Magnetic Resonance Imaging

Chidambaram Gunanathan,[†,‡] Adi Pais,[‡] Edna Furman-Haran,[‡] Dalia Seger,[‡] Erez Eyal,[‡] Sarbani Mukhopadhyay,[†] Yehoshoa Ben-David,[†] Gregory Leitus,[§] Hagai Cohen,[§] Ayelet Vilan,[§] Hadassa Degani,*[,‡] and David Milstein*[,†]

Department of Organic Chemistry, Department of Biological Regulation, and Unit of Chemical Research Support, Weizmann Institute of Science, Rehovot 76100, Israel. Received June 21, 2007; Revised Manuscript Received August 1, 2007

Novel estrogen-conjugated pyridine-containing Gd(III) and Eu(III) contrast agents (EPTA-Gd/Eu) were designed and effectively synthesized. Convenient to administration and MRI experiments, both EPTA-Gd and EPTA-Eu are soluble in water. The EPTA-Gd selectively binds with a micromolar affinity to the estrogen receptor and induces proliferation of human breast cancer cells. The EPTA-Gd is not lethal and does not cause any adverse effects when administrated intravenously. It enhances T_1 and T_2 nuclear relaxation rates of water and serves as a selective contrast agent for localizing the estrogen receptor by MRI.

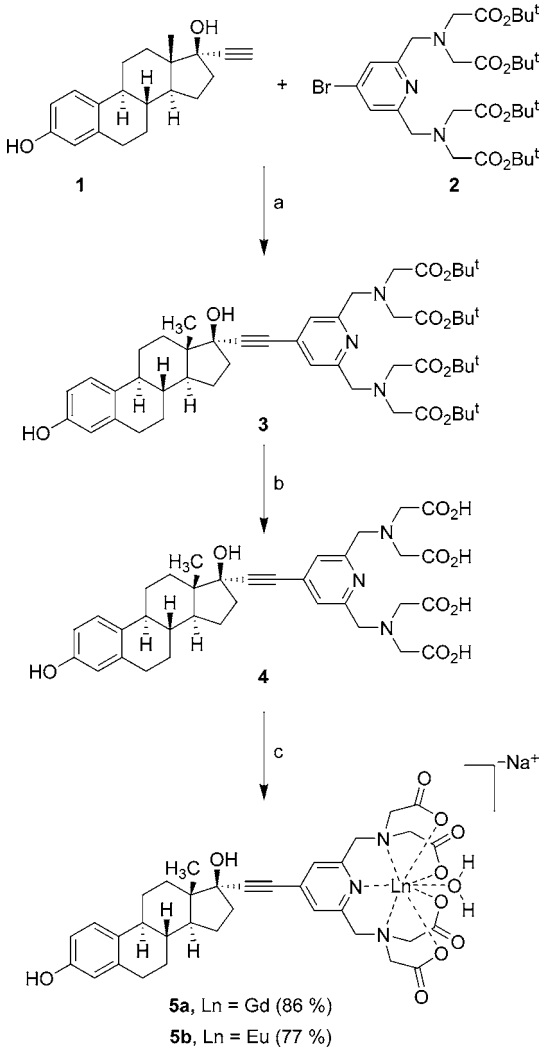
Targeting the delivery of hormones and drugs with a specific molecular recognition site and simultaneously monitoring their distribution and localization in the body is an important goal in pharmacology and medicinal chemistry, as well as in diagnostic molecular imaging. One such example (*1*) is targeting organs and tissues responsive to estrogen using a selective estrogen receptor modulator (SERM) that can be monitored *in vivo*. Estrogens are steroids that function as the primary sex hormones in females, regulating an assortment of activity in the female reproductive organs and the development and function of the mammary gland. 17β-Estradiol (E2), estriol, and estrone are the three naturally occurring estrogens, with the former being the most potent one. Estrogens enter freely the cells and bind with a very high affinity to nuclear estrogen receptors (ERs), α or β, which act as potent transcription factors regulating many cellular functions (*2*, *3*). The interaction of estrogen with its receptor also elicits ER degradation responsible for its cyclic activity (*2*). In breast cancer, specifically, evaluation of the ER level is a major and well-established tool for assessment of prognosis and for predicting response to endocrine therapy with antiestrogens such as tamoxifen (*4*, *5*). The levels of ERα in human breast cancer biopsies span a broad range reaching 1000 fmol/mg cytosol protein (*6*). However, the current clinical methods for determining ERα are semiquantitative and suffer from technical difficulties and analytical variations which may lead to inconsistent results (*7*). Furthermore, these techniques measure the level in a small fraction of the tumor, which may not reflect the actual distribution in the entire tumor.

Previous attempts to image ER *in vivo* were based on using positron emission tomography or single-photon emission computed tomography of $_{18}$F- or $_{123}$I-labeled ER ligands, respectively

* To whom the correspondence should be addressed. H.D.: E-mail hadassa.degani@weizmann.ac.il, Tel 972-8-9342017, Fax 972-8-9346154. D.M.: E-mail david.milstein@weizmann.ac.il, Tel 972-8-9342599, Fax 972-8-9344142.
† Department of Organic Chemistry.
‡ Department of Biological Regulation.
§ Unit of Chemical Research Support.

10.1021/bc700230m CCC: $37.00 © 2007 American Chemical Society
Published on Web 09/05/2007

Scheme 1. Synthesis of EPTA and EPTA−Lanthanide Complexes[a]



[a] Conditions: (a) *trans*-$PdCl_2(PPh_3)_2$, CuI, dry $^iPr_2NH$/THF, rt, 60 h, 89%. (b) CF_3CO_2H, rt, 3 h, 92%; (c) (i) pH 5−7, $GdCl_3{\cdot}3H_2O$, rt, 3 h, 86%; (ii) pH 5−7, $EuCl_3{\cdot}6H_2O$, rt, 3 h, 77%.

(*8*−*10*). Although the high-spin gadolinium(III) ion is extremely toxic for living cells, when complexed with suitable chelates it provides useful agents, for magnetic resonance imaging (MRI) (*11*, *12*). Potential target-directed contrast agents developed recently increase the scope of MRI experiments (*13*−*15*). We envision a novel method to detect ER in cancer patients using MRI by a new contrast agent derived from E2. As reported, upon introduction of bulky substituents at the 17α position of E2, a high affinity to ER was retained (*16*−*18*). Herein, we delineate the synthesis of a novel water-soluble, MRI contrast agent integrated SERM which binds to the estrogen receptor with high affinity and induces hormonal activity as well as contrast enhancement in human breast cancer cells.

The Pd-catalyzed reaction of 17α-ethynyl estradiol (**1**) with compound **2** (*19*, *20*) yielded E2-embedded pyridine tetracarboxylate **3**, which on ester deprotection provided the desired ligand, [estradiol-17α-ylethynyl(pyridin-2,6-diyl)bis(methylenenitrilo)] tetrakis(aceticacid) EPTA) **4** (Scheme 1). Complexation of **4** with hydrated $GdCl_3$ resulted in the formation of gadolinium chelate **5a**, EPTA-Gd, in 86% yield. The structure of EPTA-Gd was confirmed by HR/MS, ES/MS, IR, magnetic moment, and XPS studies (*21*). EPTA-Gd displays paramagnetic properties without any hysteresis phenomenon. The Curie constant *C* and effective magnetic moment *p* (for instance, for AC frequency $f = 74$ Hz and temperature $2\ K < T < 22\ K$, $C = 6.93(1)$ emu*K/mol and $p = 7.44\ \mu_B$/molecule; for DC ($2\ K < T < 300\ K$) FC, $C = 6.640(4)$ emu/mol*K and $p = 7.29\ \mu_B$/molecule) were well in accordance with the literature values (*22*). Complexation of **4** with $EuCl_3{\cdot}6H_2O$ provided EPTA-Eu **5b** in 77% yield (*21*).

Table 1. ERα Competitive Binding Affinities of EPTA and EPTA-Gd with 17β-Estradiol and Relaxivities (*24*) of EPTA-Gd[a]

compound	K_i, μM	r_1 (mM·s)$^{-1}$	r_2 (mM·s)$^{-1}$
EPTA (**4**)	0.40 ± 0.13	-	-
EPTA-Gd (**5a**)	0.97 ± 0.07	6.8 ± 0.05	25 ± 1.0

[a] K_i values were calculated using a dissociation constant for 17α-estradiol binding to ERα of 0.2 nM.

Binding affinities of EPTA **4** and EPTA-Gd **5a** to ER were determined by performing competitive radiometric binding assays using tritiated 17β-estradiol and human recombinant ER. Table 1 summarizes the values obtained for the competition constant, K_i (defined as the equilibrium concentration of the competing ligand that binds half of the ER binding sites) of both the metal-free ligand EPTA and the EPTA-Gd. Although the affinities of both EPTA and EPTA-Gd were about 3 orders of magnitude lower than that of 17β-estradiol, their effective concentration required for ER binding was within the micromolar range (*8*, *23*). The effectiveness of EPTA-Gd as a nuclear relaxation agent was demonstrated by the measurement of water proton T_1 and T_2 relaxivities (r_1 and r_2, respectively) at 4.7 T (Table 1).

The cellular hormonal-induced activities of both EPTA and EPTA-Gd were tested in ER+ MCF7 and T47D human breast cancer cells. Time- and dose-dependent growth curves of both cell lines in the presence of EPTA and EPTA-Gd proved a stimulating growth effect similar to that of E2 (Figure 1A). This stimulation was specific to the presence of ER in the cells, as neither EPTA nor EPTA-Gd exerted an effect on the growth of ER-negative MDA-MB-231 human breast cancer cells. In addition, EPTA and EPTA-Gd, like E2, induced ER degradation in the ER+ cells in a similar manner to that of E2, albeit at a slower rate, indicating their binding to ER (Figure 1B).

The ability of EPTA-Gd to specifically bind to the nuclear ER in living cells and consequently enhance the MRI signal in a distinct manner was tested in MDA-MB-231 human breast cancer cells, engineered to express ERα under tetracycline. Cells cultivated with a medium containing tetracycline (tet on) expressed high levels of ERα (ER+), as determined by Western blots, and served to detect the enhancement due to the binding of EPTA-Gd with this receptor. The same cells treated with tetracycline-free medium (tet off) did not express ERα (ER− control cells), as determined by Western blots, and served to determine the effect of nonspecific binding of EPTA-Gd to the cells and of possible decomposition of the contrast agent inside the cells (*25*). To maintain their viability throughout the experiments, the cells were cultivated on Biosilon beads to a density of ∼40 million cells/mL beads (Figure 1C). Enhancement and T_1 measurements by means of microscopic MRI of the cells on beads in the presence and absence of EPTA-Gd (6 μM) and after washout of EPTA-Gd indicated higher enhancement and difference in T_1 relaxation rates, ΔR_1, between EPTA-Gd-treated ER+ cells and the control ER+ cells as compared to the EPTA-Gd-treated ER− cells and the ER− control cells, specifically after removal of the free and nonbound EPTA-Gd from the cell system by washing with standard medium (Figure 1D). Macroscopic enhancement and T_1 measurements of the same cell systems in wells, in the presence and after washout of EPTA-Gd (Figure 1E), confirmed the above results obtained by microscopic MRI (Figure 1F). Although one expects a null ΔR_1 between EPTA-Gd-treated ER− cells and ER− control

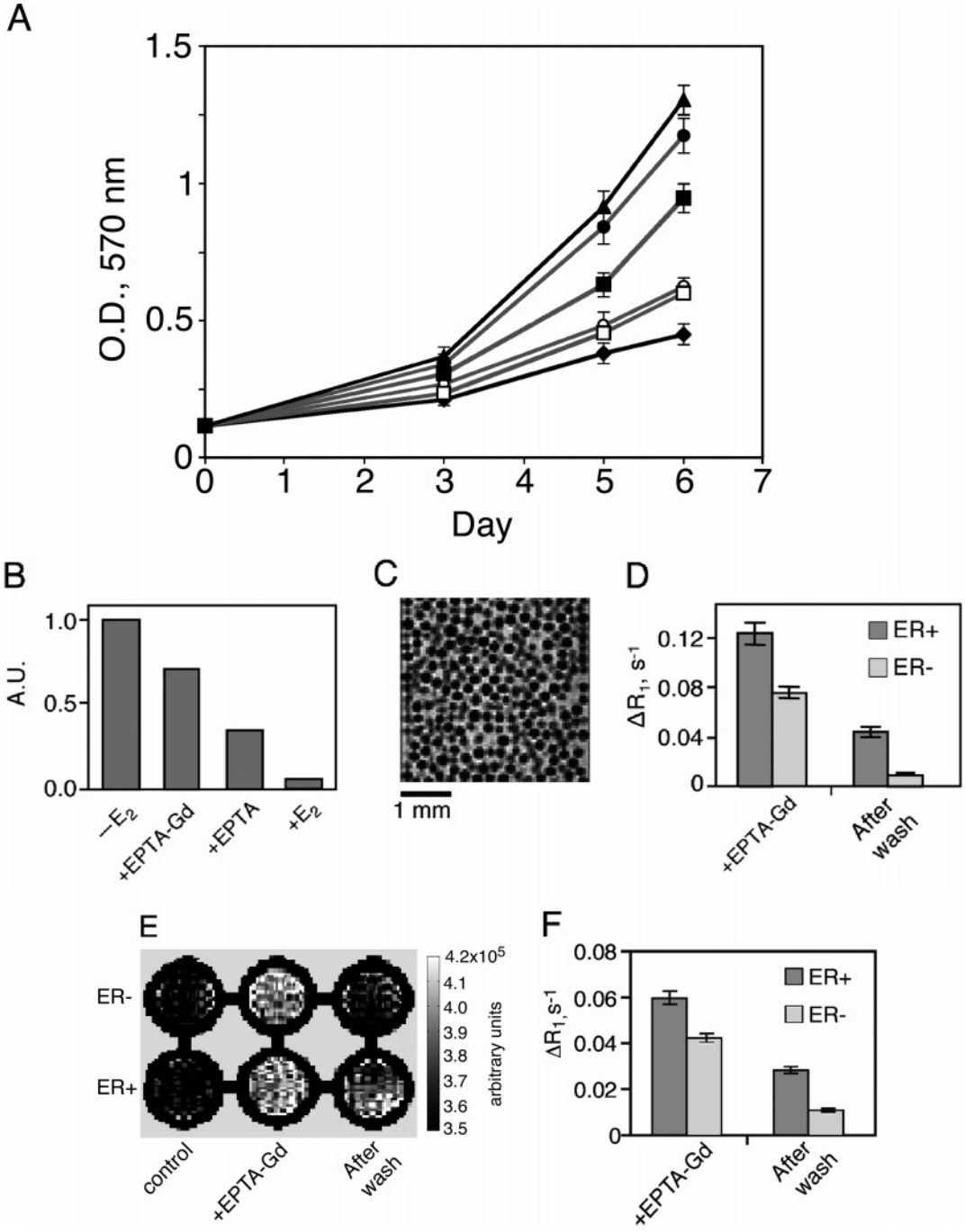


Figure 1. Biologic stimulation and MRI enhancement of EPTA-Gd in living human breast cancer cells. A. Growth curves of T47D cells in the presence of 17β-estradiol, 30 nM: ● EPTA, 2 μM; ○ EPTA, 0.1 μM; ■ EPTA-Gd, 2 μM; □ EPTA-Gd, 0.1 μM; ◆ Control, estrogen-free medium. B. Degradation of ER in MCF7 cells 6 h after treatment. C. High-resolution MR image of a tube containing tet-on MDA-MB-231 cells cultivated on Biosilon beads. D. The difference in T_1 relaxation rate of water (ΔR_1): +EPTA-Gd designates ΔR_1 between EPTA-Gd treated ER+ cells (incubated for 3 h with 6 μM EPTA-Gd) and ER+ control cells (incubated in standard medium) as compared to ΔR_1 between EPTA-Gd treated ER− cells (incubated for 3 h with 6 μM EPTA-Gd) and ER− control cells (incubated in standard medium); after wash designates ΔR_1 between EPTA-Gd treated ER+ cells (incubated for 3 h with 6 μM) after washout with standard medium and ER+ control cells as compared to ΔR_1 between EPTA-Gd treated ER− cells (incubated for 3 h with 6 μM EPTA-Gd) after washout with standard medium and ER− control cells. E. Low-resolution images of ER+ and ER− MDA-MB-231 cells cultivated on Biosilon beads using standard medium, in the presence of 6 μM EPTA-Gd, and after washout of EPTA-Gd with standard medium (spin echo with TE/TR = 15/300 ms). F. ΔR_1 obtained from experiments demonstrated in E with ΔR_1 defined as in D.

cells after washout, we found a small measurable value for this ΔR_1 (Figure 1D,F) but significantly lower than the comparable ΔR_1 for ER+ cells (Figure 1D,F) suggesting some nonspecific absorption of EPTA-Gd inside the cells. Thus, the difference between ΔR_1 of the ER+ cells and that of the ER− cells reflects the change due to the specific EPTA-Gd binding to ER in the ER+ cells.

Overall, targeting EPTA-Gd to ER in living breast cancer cells enabled us to detect differences in the intensity of T_1-weighted MR images, as well as in the T_1 relaxation rates between ER+ and ER− breast cancer cells. In general, the amount of ER in cells is controlled by a balance between its synthesis and degradation and is influenced by the nature of the bound ligand. For example, as shown in Figure 1A,B, estrogen induction of ER proliferating activity is strongly associated with its proteasomal degradation, leading to a marked decrease in ER within few hours. Temporal changes in ER level can therefore reflect the functional state of ER as well as the

presence or absence of SERMs. Hence, there is a strong scientific need to develop an *in vivo* imaging method that will provide us with knowledge of the ER signaling function and monitor temporal changes of receptor down-regulation and desensitization in the different estrogen-responsive organs.

The assessment of ER function is particularly important for the management of breast cancer. It has been well-established that the estrogen receptor has a pivotal role in prevention and treatment of breast cancer. Specifically, the ER level serves to select patients for adjuvant endocrine therapy, and together with the progesterone receptor, they serve as major prognostic factors predicting the likelihood of recurrence and survival. Assessment of the ER status in breast cancer patients by means of MRI is specifically advantageous, as it can be integrated with the unique diagnostic capabilities of MRI to record anatomical images, as well as produce parametric images that characterize tumor physiological and metabolic properties (*26*, *27*). In order to extend the *in vitro* measurements to *in vivo* conditions, several key experimental criteria must be reached: nontoxicity; high-affinity for ER; reasonable pharmacodynamics; ability to penetrate vascular walls, interstitial spaces, and cell membrane; and sufficient MRI sensitivity. The above *in vitro* results and preliminary *in vivo* experiments in rodents (not shown) have indicated that-indeed EPTA-Gd meets these criteria, particularly, it is not lethal and does not cause any adverse effects when administered intravenously even at a high dose. However, in order to achieve MRI sensitivity it is necessary to design protocols that overcome the heterogeneity of tumors. Further studies of breast cancer xenografts implanted in mice are underway to find out whether utilization of EPTA-Gd provides sufficient MRI sensitivity for the detection of ER down-regulation in the same tumor.

In conclusion, the first estrogen-conjugated Gd(III) contrast agent (EPTA-Gd) has been designed and synthesized. EPTA-Gd competes with E2 on binding to ERα, with a competition equilibrium constant $K_i = 0.97\ \mu M$, demonstrates like estrogens induced cell proliferation and down-regulation of ER level in ER+ breast cancer cells *in vitro*, both requiring binding to ER. Free EPTA-Gd displays a ∼50% higher relaxivity than the common Gd-based contrast agents and increases the T_1 relaxation rates of ER+ cells as compared to these rates in the same cells with null ER indicating a specific enhancement due to the binding to the ER. Structural modification studies aimed at enhancement of binding affinity are currently underway.

ACKNOWLEDGMENT

This work was supported by DOA/BC 044499 and NIH/CA 42238. We thank Tamar Kreizman for technical assistance. C.G. is the recipient of Deans of Faculties Postdoctoral Fellowship. D.M. is the Israel Matz Professor of Organic Chemistry. H.D. holds the Fred and Andrea Fallek Chair for Breast Cancer Research.

Supporting Information Available: Synthetic procedures, and spectral data of compounds **3**, **4**, and **5a**,**b**. Magnetic moment and XPS analyses of **5a**. ER competition binding assay, cell proliferation assay, assay for determination of ER protein level, and MRI experiments of living cells cultivated on beads. This material is available free of charge via the Internet at http://pubs.acs.org.

LITERATURE CITED

(1) Preliminary results of this study were presented as an abstract: Eyal, E., Milstein, D., Degani, H., Mukhopadhyay, S., Seger, D., Margalit, R., Hirsh, R., Ben-David, Y., and Furman-Haran, E. (2005) Molecular MR imaging of the estrogen receptor using a novel contrast agent. *Proc. Intl. Soc. Mag. Reson. Med. 13th Meeting*, Miami, U.S.A.

(2) Osborne, C. K., and Schiff, R. (2005) Estrogen-receptor biology: continuing progress and therapeutic implications. *J. Clin. Oncol. 23*, 1616−1622.

(3) Singh, R. R., and Kumar, R. (2005) Steroid hormone receptor signaling in tumor genesis. *J. Cell Biochem. 96*, 490−505.

(4) Katzenellenbogen, B. S., and Frasor, J. (2004) Therapeutic targeting in the estrogen receptor hormonal pathway. *Semin. Oncol. 31*, 28−38.

(5) Ikeda, K., and Inoue, S. (2004) Estrogen receptors and their downstream targets in cancer. *Arch. Histol. Cytol. 67*, 435−442.

(6) Struse, K., Audretsch, W., Rezai, M., Pott, G., and Bojar, H. (2000) The estrogen receptor paradox in breast cancer: association of high receptor concentrations with reduced overall survival. *Breast J. 6*, 115−125.

(7) Barnes, D. M., Millis, R. R., Beex, L. V. A. M., Thorpe, S. M., and Leake, R. E. (1998). Increased use of immunohistochemistry for estrogen receptor measurement in mammary carcinoma: the need for quality assurance. *Eur. J. Cancer 34*, 1677−1682.

(8) Katzenellenbogen, J. A., Coleman, R. E., Hawkins, R. A., Krohn, K. A., Larson, S. M., Mendelsohn, J., Osborne, C. K., Piwnica−Worms, D., Reba, R. C., Siegel, B. A., et al. (1995) Tumor receptor imaging: proceedings of the National Cancer Institute workshop, review of current work, and prospective for further investigations. *Clin. Cancer Res. 1*, 921−932.

(9) Mortimer, J. E., Dehdashti, F., Siegel, B. A., Katzenellenbogen, J. A., Fracasso, P., and Welch, M. J. (1996) Positron emission tomography with 2-[18F]Fluoro-2-deoxy-D-glucose and 16α-[18F]-fluoro-17β-estradiol in breast cancer: correlation with estrogen receptor status and response to systemic therapy. *Clin. Cancer Res. 2*, 933−939.

(10) Rijks, L. J., Bakker, P. J., van Tienhoven, G., Noorduyn, L. A., Boer, G. J., Rietbroek, R. C., Taat, C. W., Janssen, A. G., Veenhof, C. H., and van Royen, E. A. (1997) Imaging of estrogen receptors in primary and metastatic breast cancer patients with iodine-123-labeled Z-MIVE. *J. Clin. Oncol. 15*, 2536−2545.

(11) Raymond, K. N., and Pierre, V. C. (2005) Next generation, high relaxivity gadolinium MRI agents. *Bioconjugate Chem. 16*, 3−8.

(12) Caravan, P., Ellison, J. J., McMurry, T. J., and Lauffer, R. B. (1999) Gadolinium(III) chelates as MRI contrast agents: structure, dynamics, and applications. *Chem. Rev. 99*, 2293−2352.

(13) Weissleder, R. (2002). Scaling down imaging: molecular mapping of cancer in mice. *Nat. Rev. Cancer 2*, 11−18.

(14) Modo, M., Hoehn, M., and Bulte, J. W. (2005) Cellular MR imaging. *Mol. Imaging 4*, 143−164.

(15) Synthetic steroidal progesterone antagonist, RU-486, derived Gd-(III) contrast agent was reported which selectively binds a mutant of the progesterone receptor. See Lee, J., Zylka, M. J., Anderson, D. J., Burdette, J. E., Woodruff, T. K., and Meade, T. J. (2005) A steroid-conjugated contrast agent for magnetic resonance imaging of cell signaling. *J. Am. Chem. Soc. 127*, 13164−13166.

(16) el Amouri, H., Vessieres, A., Vichard, D., Top, S., Gruselle, M., and Jaouen, G. (1992) Syntheses and affinities of novel organometallic-labeled estradiol derivatives: a structure-affinity relationship. *J. Med. Chem. 35*, 3130−3135.

(17) Top, S., El Hafa, H., Vessieres, A., Quivy, J., Vaissermann, J., Hughes, D. W., McGlinchey, M. J., Mornon, J.-P., Thoreau, E., and Jaouen, G. (1995) Rhenium carbonyl complexes of β-estradiol derivatives with high affinity for the estradiol receptor: an approach to selective organometallic radiopharmaceuticals. *J. Am. Chem. Soc. 117*, 8372−8380.

(18) Ramesh, C., Bryant, B., Nayak, T., Revankar, C. M., Anderson, T., Carlson, K. E., Katzenellenbogen, J. A., Sklar, L. A., Norenberg, J. P., Prossnitz, E. R., and Arterburn, J. B. (2006) Linkage effects on binding affinity and activation of GPR30 and estrogen receptors ERα/β with tridentate pyridin-2-yl hydrazine tricarbonyl-Re/^{99m}Tc-(I) chelates. *J. Am. Chem. Soc. 128*, 14476−14476.

(19) Compound **2** is prepared by the literature procedures. (a) Takalo, H., and Kankare, J. (1987) Synthesis of dimethyl and dimethyl 4-(phenylethyl)-2,6-pyridinedicarboxylate. *Acta Chem. Scand. B41*, 219−221.

(20) Takalo, H., Pasanen, P., and Kankare, J. (1988) Synthesis of 4-(phenylethynyl)-2,6[*N*,*N*-bis-(carboxymethyl)aminomethyl]pyridine. *Acta Chem. Scand. B42*, 373−377.
(21) See Supporting Information for details.
(22) Kittel, C. *Introduction to Solid State Physics*, 4th ed., John-Wiley & Sons, Inc., New York, 1971.
(23) Similar affinities were demonstrated for other estrogen-derived steroidal *diamagnetic* metal complexes. See Jackson, A., Davis, J., Pither, R. J., Rodger, A., and Hannon, M. J. (2001) Estrogen-derived steroidal metal complexes: agents for cellular delivery of metal centers to estrogen receptor-positive cells. *Inorg. Chem. 40*, 3964−3973.
(24) The T1 and T2 relaxivities of EPTA-Gd is higher than those of GdDTPA, which is the common MRI contrast agent.
(25) Cabella, C., Crich, S. G., Corpillo, D., Barge, A., Ghirelli, C., Bruno, E., Lorusso, V., Uggeri, F., and Aime, S. (2006) Cellular labeling with Gd(III) chelates: only high thermodynamic stabilities prevent the cells acting as 'sponges' of $Gd3^{+}$ ions. *Contrast Med. Mol. Imaging 1*, 23−29.
(26) Furman-Haran, E., and Degani, H. (2002) Parametric analysis of breast MRI. *J. Comput. Assist. Tomogr. 26*, 376−386.
(27) Katz-Brull, R., Lavin, P. T., and Lenkinski, R. E. (2002) Clinical utility of proton magnetic resonance spectroscopy in characterizing breast lesions. *J. Natl. Cancer Inst. 94*, 1197−1203 and references cited therein.

BC700230M

Biomimetic Glycoliposomes as Nanocarriers for Targeting P-Selectin on Activated Platelets

Junmin Zhu,[†] Jie Xue,[‡] Zhongwu Guo,*[,‡] Linda Zhang,[†] and Roger E. Marchant*[,†]

Department of Biomedical Engineering, Case Western Reserve University, 10900 Euclid Avenue, Cleveland, Ohio 44106, and Department of Chemistry, Wayne State University, 5101 Cass Avenue, Detroit, Michigan 48202. Received June 14, 2007; Revised Manuscript Received July 2, 2007

The cell glycocalyx is an attractive model for surface modification of liposomes with the objectives of tissue targeting and prolonged circulation time. Here, we reported on glycocalyx-mimicking liposomes, prepared by incorporating a glycolipid of 3′-sulfo-Lewis a (SuLe^a)-PEG-DSPE with a headgroup of SuLe^a and a spacer of poly(ethylene glycol) (PEG) linked to two hydrophobic tails. This PEG spaced structure is used to mimic the extended structure of P-selectin glycoprotein ligand 1 (PSGL-1) on activated leukocytes, in order to facilitate the specific binding of liposomes to the receptor of P-selectin expressed on activated platelets. Our results indicate that SuLe^a-PEG-DSPE can form stable, narrowly distributed liposomes with 1,2-distearoyl-*sn*-glycero-3-phosphocholine (DSPC) and cholesterol, with a vesicle size of 113.3 nm. The resultant SuLe^a-PEG-liposomes can facilitate their binding to the receptor of P-selectin 22 times higher than SuLe^a-liposomes without a PEG spacer. Further studies by fluorescence microscopy show that SuLe^a-PEG-liposomes can bind to activated platelets *in vitro* effectively. It suggests that biomimetic SuLe^a-PEG-liposomes may be used as nanocarriers to target activated platelets for drug delivery to the injury sites of cardiovascular diseases.

The glycocalyx of cells like endothelial cells and erythrocytes is a membrane-bound carbohydrate-rich layer consisting of various glycoproteins, proteoglycans, and glycosaminoglycans. This carbohydrate-rich layer plays an important role in mediating cell-specific interactions and preventing nonspecific protein adsorption (*1*, *2*). Therefore, the cell glycocalyx is an attractive model for surface modification of liposomes with the objectives of tissue targeting and prolonged circulation time. Here, we report on glycocalyx-mimicking glycoliposomes, as shown in Figure 1, prepared by 1,2-distearoyl-*sn*-glycero-3-phosphocholine (DSPC) and cholesterol with incorporation of a glycolipid with a headgroup of 3′-sulfo-Lewis a (SuLe^a) and a spacer of poly(ethylene glycol) (PEG) linked to two hydrophobic tails. This PEG spaced structure is supposed to mimic the extended structure of P-selectin glycoprotein ligand 1 (PSGL-1) on activated leukocytes, in order to facilitate the specific binding of liposomes to the receptor of P-selectin expressed on activated platelets in the processes of thrombosis, inflammation, and atherosclerosis.

Platelets play a central role in thrombosis and atherosclerotic lesions (*3*−*5*), including angina, coronary artery disease, myocardial infarction, and ischemic stroke, which are main causes of death and disability in the Western countries (*6*, *7*). Platelets can be activated upon adhesion to extracellular matrix proteins in the vascular injury region, foreign material surface, or by thrombin generated in the coagulation process (*8*). A number of receptors have been recognized on activated platelets (*9*), including GPIIb/IIIa, GPIb, P-selectin, CD9, CD36, and CD63. P-selectin is one of the important receptors expressed on activated platelets with about 10 000 copies/cell (*10*). It is a member of the selectin family of adhesion molecules, which includes E-, L-, and P-selectin (*11*). P-selectin is stored in platelet α-granules, as well as endothelial Weibel−Palade bodies. After the activation of platelets, P-selectin is expressed on the platelet surface, which can bind to its receptor of PSGL-1, a dimeric membrane mucin on circulating leukocytes (*12*), as shown in Figure 2. P-selectin on activated platelets has a crucial function in the early phases of inflammation regulating

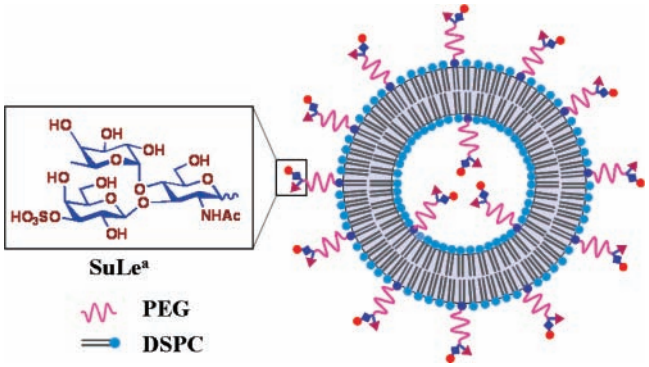


Figure 1. Model of glycocalyx-mimetic liposome with a PEG spacer between SuLe^a and the liposome surface. Cholesterol is not included in order to simply the liposome model.

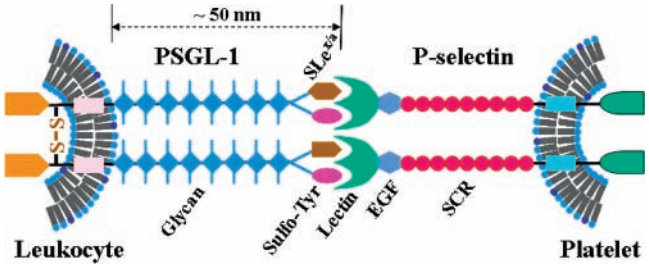


Figure 2. Model for interactions between P-selectin and PSGL-1. EGF, endothelial growth factor; SCR, short consensus repeat.

* Corresponding authors. R. E. Marchant, Tel: 216-368-3005, Fax: 216-368-4969, E-mail: roger.marchant@case.edu. Z. Guo, Tel: 313-577-2557, Fax: 313-577-8822, E-mail: zwguo@chem.wayne.edu.

[†] Case Western Reserve University.

[‡] Wayne State University.

10.1021/bc700212b CCC: $37.00 © 2007 American Chemical Society
Published on Web 08/11/2007

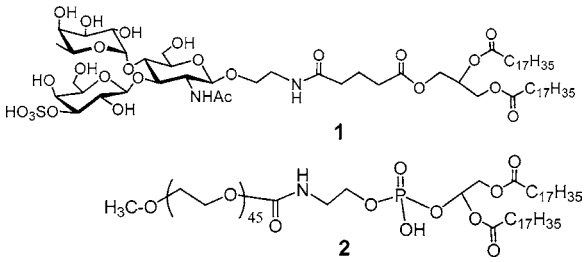


Figure 3. Structures of SuLe^a-DSGA (**1**) and PEG-DSPE (**2**, with PEG Mw of 2000).

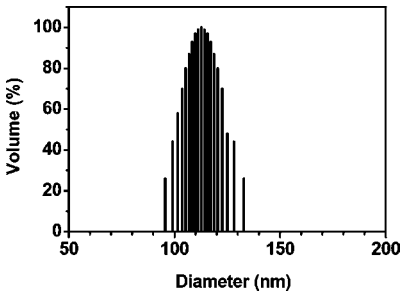


Figure 4. Vesicle size and distribution of liposomes with 5 mol % incorporation of SuLe^a-PEG-DSPE.

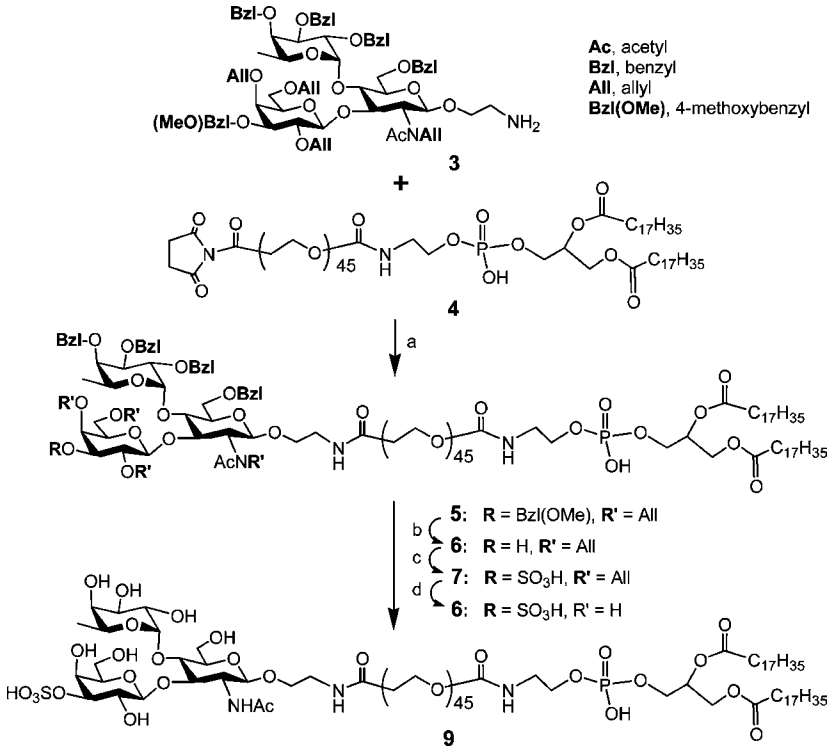
leukocyte−platelet interactions and mediating the recruitment of leukocytes and platelets to the sites of vascular injury (*13*−*15*). Therefore, P-selectin on activated platelets is an attractive candidate for targeted drug delivery to the sites of vascular injury.

P-selectin binds with high affinity to the extreme N-terminal extracellular region of mature PSGL-1, which begins at residue 42 (*12*). Specifically, tyrosine sulfate (Sulfo-Tyr) residues and sialylated O-glycans within this region have been considered essential for P-selectin binding (Figure 2). Much effort has been directed at identifying their carbohydrate mimetics as P-selectin ligands (*16*). One of the most important is Lewis x/a (Le$^{x/a}$) antigens, including sialyl Le$^{x/a}$ (SLe$^{x/a}$) (*17*), and sulfo-Le$^{x/a}$ (SuLe^{axa}) as found on epithelial mucins (*18*). To explore new therapeutic strategies for inflammatory diseases based on using biomimetic glycoliposomes, we have synthesized a SuLe^a glycolipid **1** (designated as SuLe^a-DSGA, Figure 3) by conjugating SuLe^a with 1,2-distearoyl-*rac*-glyceroglutaric acid (DSGA). SuLe^a-DSGA has been incorporated into liposomes for studying vesicle size and stability (*19*, *20*). However, PSGL-1 is a thin, highly extended molecule with an average length of 54 nm. From the natural interaction between PSGL-1 and P-selectin, the binding site for P-selectin is at the N-terminus of PSGL-1, which is about 50 nm away from the leukocyte surface (Figure 2) (*21*, *22*). Therefore, we propose that a spacer between SuLe^a and the liposome surfaces may better mimic the native PSGL-1 structure with enhanced binding affinity to P-selectin, compared with SuLe^a-liposomes without a spacer.

PEG is a good candidate for using as this kind of spacer due to its flexibility and biocompatibility (*23*). Also, it has another advantage to control the spacer length through adjusting its molecular weight. Here, we choose PEG with Mw of 2000 because it has been widely used for surface modification of liposomes (*24*, *25*). For example, PEG-1,2-distearoyl-*sn*-glycero-3-phosphoethanolamine (DSPE) (**2**, with PEG Mw of 2000) (Figure 3) has been incorporated into liposomes to enhance the circulation time of vesicles *in vivo*. Thus, a glycolipid, SuLe^a-PEG-DSPE **9** was designed and synthesized with a PEG spacer (Mw 2000) inserted between the headgoup of SuLe^a and two hydrophobic tails, as shown in Scheme 1.

The synthesis of **9** was based on the conjugation of our previously developed intermediate, a protected amino derivative of SuLe^a **3** with DSPE-PEG-NHS **4** (with PEG Mw of 2000 and an activated carboxylic group by *N*-hydroxylsuccinimide), followed by deprotection of *p*-methoxybenzyl [Bzl(OMe)] groups, 3′-sulfatation, and deprotection of allyl (All) and benzyl (Bzl) groups (*19*, *20*). In the natural form, Lewis antigens are attached through their reducing ends to lipids and/or proteins. If Lewis antigen conjugates have the lipids attached to the

Scheme 1. Synthesis of SuLe^a-PEG-DSPE[a]



[a] Reagents and conditions: (a) dichloromethane, RT, 36 h; (b) $(NH_4)_2Ce(NO_3)_6$, CH_3CN, $CHCl_3/H_2O$, RT, 2 h; (c) pyridine, $(CH_3)_3N.SO_3$, RT, 48 h; (d) $PdCl_2$, NaOAc, $HOAc/H_2O$, RT, 48 h; (e) H_2, 10% Pd/C, $CHCl_3/MeOH/H_2O$ (1:5:1), RT, 48 h.

Table 1. Properties of Liposomes with 5% Glycolipid Incorporation

lipid	D_v (nm)	PDI	ζ (mV)	IC_{50} (mM)
PEG-DSPE	108.5	0.12	0.41	N/A[a]
SuLe^a-PEG-DSPE	113.3	0.03	−5.66	0.13
SuLe^a-DSGA	105.8	0.19	−8.46	2.92
SuLe^a	N/A	N/A	N/A	5.61[b]

[a] Not applicable. [b] Using free SuLe^a as a positive control for IC_{50} measurements.

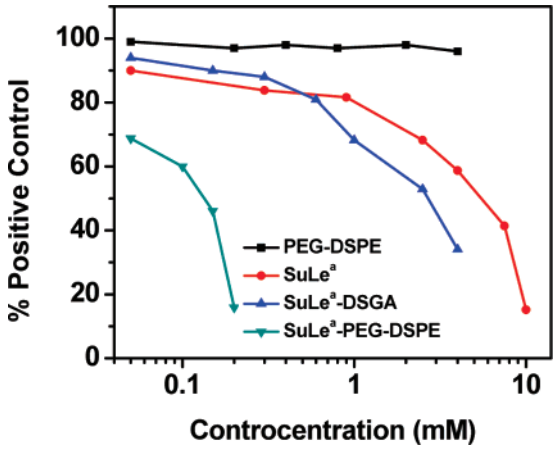


Figure 5. Inhibition of sPSGL-1 binding to recombinant rat P-selectin-IgG coated on plates by liposomes or carbohydrates.

2-amino group of the glucosamine residue with the reducing end capped by an unreactive group, it may affect the conformation of the antigen and their binding to selectins (*26*). SuLe^a-PEG-DSPE was synthesized with the lipid attachment through the reducing end of SuLe^a. Therefore, it has the advantage of stability under physiological conditions due to the lower susceptibility of the glycosyl ether linkage to glycosidases, compared with natural O-glycosides with reducing ends.

SuLe^a-PEG-DSPE (5 mol %) was used with DSPC (55 mol %) and cholesterol (40 mol %) to prepare glycoliposomes using a freeze−thraw and extrusion method through 100 nm membranes (*27*). The vesicle size and distribution was determined by photon correlation spectroscopy (PCS), as shown in Figure 4. The mean vesicle size for SuLe^a-PEG-liposomes is 113.3 nm after extrusion, which is close to the vesicle size of SuLe^a-liposomes (105.8 nm) and PEG-liposomes (108.5 nm) with 5 mol % incorporation of SuLe^a-DSGA **1** and PEG-DSPE **2** (with PEG Mw of 2000, Figure 3), respectively, as listed in Table 1. In addition, the vesicles of SuLe^a-PEG-liposomes were narrowly distributed with a polydispersity index (PDI) of 0.03, maybe due to the steric stabilization from PEG and the electrostatic effect from the charged head group of SuLe^a.

Zeta (ζ)-potential was measured to verify whether the negatively charged SuLe^a groups are on the liposome surface. The results (Table 1) show that the ζ-potential of SuLe^a-PEG-liposomes was −5.66 mV, which is comparable to that of SuLe^a-liposomes (−8.46 mV). It indicates that SuLe^a-PEG-DSPE was successfully incorporated into liposomes and the negatively charged headgroup of SuLe^a was present on the liposome surface. The stability of liposomes was determined by measuring the vesicle size change over time at room temperature. SuLe^a-PEG-liposomes with 5% of glycolipid incorporation maintained their vesicle size in the same range in storage over a 1 month period, comparable with results for PEG-liposomes. It demonstrates that SuLe^a-PEG-liposomes is stable enough for practical uses, and may maintain vesicle integrity while in the circulation.

Enzyme-linked immunosorbent assay (ELISA) was carried out to determine the binding affinity of the surface-modified liposomes to P-selectin. Briefly, recombinant rat P-selectin-IgG was coated on plates, followed by addition of human-soluble PSGL-1 (sPSGL-1) and glycoliposomes or carbohydrate ligands. After incubation, the plates were rinsed and the adherent sPSGL-1 was linked with horseradish peroxidase (HRP) through biotin−steptavidin interactions, followed by incubation with a substrate solution of tetramethylbenzidine (TMD). The absorbance of developed color was measured at 450 nm. The inhibition of sPSGL-1 binding to P-selectin by liposomes or carbohydrate ligands was expressed as the percentage of the sPSGL-1 control in the absence of any inhibitors, as shown in Figure 5. SuLe^a-PEG-liposomes show significant inhibition of sPSGL binding to P-selectin, while PEG-liposome shows no inhibition.

IC_{50} was used to compare the binding ability of liposomes, which was the concentration of carbohydrate ligands that inhibited sPSGL-1 binding to P-selectin by 50%. The IC_{50} values were obtained from Figure 5, as listed in Table 1. The results show that the free SuLe^a saccharide has an IC_{50} of 5.61 mM (Figure 4), but IC_{50} of SuLe^a-liposomes was 2.92 mM. The IC_{50} of SuLe^a-PEG-liposomes was 0.13 mM. That means the binding ability of the ligands on SuLe^a-PEG-liposomes was increased 43 and 22 times, compared to the free SuLe^a ligand and SuLe^a-liposomes, respectively. Therefore, the PEG spacer can increase the mobility of the ligands, and thereafter increase the binding ability.

To further confirm and visualize the specific binding of SuLe^a-PEG liposomes with P-selectin, liposomes were labeled by incorporating 1 mol % of nitrobenzodiazole-modified phosphatidylcholine (NBD−PC), and human platelets were activated and adsorbed on collagen-coated glass coverslips. The binding was studied by the fluorescence microscopy method (*28*). It was observed that the SuLe^a-PEG-liposomes had much higher binding to activated platelets (Figure 6b) than the control of PEG-liposomes (Figure 6a). The significantly increased binding of the former to activated platelets is attributed to the specific interactions between SuLe^a on the glycoliposome and the P-selectin on activated platelets.

In summary, we reported on novel glycocalyx-mimicking liposomes, SuLe^a-PEG-liposomes from a glycolipid, SuLe^a-PEG-DSPE with a headgroup of SuLe^a and a PEG spacer linked to two hydrophobic tails. Our results indicate that SuLe^a-PEG-

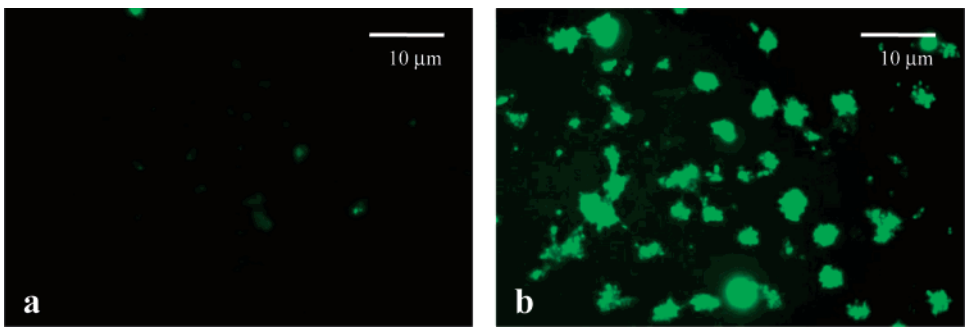


Figure 6. Fluorescence micrographs of platelet binding with NBD-labeled liposomes from PEG-DSPE (a) and SuLe^a-PEG-DSPE (b).

DSPE can form stable, narrowly distributed liposomes with DSPC and cholesterol, with a vesicle size of 113.3 nm. The resultant SuLe^a-PEG-liposomes can mimic the extended structure of PSGL-1 on activated leukocytes and facilitate their binding to the receptor of P-selectin 22 times higher than SuLe^a-liposomes without a PEG spacer. Further studies by fluorescence microscopy show that SuLe^a-PEG-liposomes can bind to activated platelets *in vitro* effectively. It suggests that biomimetic SuLe^a-PEG-liposomes may be used as nanocarriers to target activated platelets for drug delivery to the injury sites of cardiovascular diseases.

ACKNOWLEDGMENT

This project was supported by the National Institutes of Health (grant HL-70263-2). We gratefully thank the facilities provided by Center for Cardiovascular Biomaterials.

Supporting Information Available: Details of experimental section. This material is available free of charge via the Internet at http://pubs.acs.org.

LITERATURE CITED

(1) Tarbell, J. M., and Pahakis, M. Y. (2006) Mechanotransduction and the glycocalyx. *J. Clin. Med. 259*, 339−350.
(2) VanTeeffelen, J. W., Brands, J., Stroes, E. S., and Vink, H. (2007) Endothelial glycocalys: sweet shield of blood vessels. *Trends Cardiovasc. Med. 17*, 101−105.
(3) Steinhubl, S. R., and Moliterno, D. J. (2006) The role of the platelet in the pathogenesis of atherothrombosis. *Am. J. Cardiovasc. Drugs 5*, 399−408.
(4) Andrews, R. K., and Berndt, M. C. (2004) Platelet physiology and thrombosis. *Thromb. Res. 114*, 447−453.
(5) Becker, R. C. (1999) Thrombosis and the role of the platelet. *Am. J. Cardiol. 83*, 3E-6E.
(6) Madjid, M., Naghavi, M., Litovsky, S., and Casscells, S. W. (2003) Influenza and cardiovascular disease: a new opportunity for prevention and the need for further studies. *Circulation 108*, 2730−2736.
(7) Clemetson, K. J. (2001) Platelet glycoproteins and their role in diseases. *Transfus. Clin. Biol. 8*, 155−162.
(8) Kamath, S., Blann, A. D., and Yip, G. Y. H. (2001) Platelet activation: assessment and quantification. *Eur. Heart J. 22*, 1561−1571.
(9) Williams, M. J., Du, X., Loftus, J. C., and Ginsberg, M. H. (1995) Platelet adhesion receptors. *Semin. Cell Biol. 6*, 305−314.
(10) Shattil, S. J., Ginsberg, M. H., and Brugge, J. S. (1994) Adhesive signaling in platelets. *Curr. Opin. Cell Biol. 6*, 695−704.
(11) Crocker, P. R., and Feizi, T. (1996) Carbohydrate recognition systems: functional triads in cell-cell interactions. *Curr. Opin. Struc. Biol. 6*, 679−691.
(12) McEver, R. P., and Cummings, R. D. (1997) Cell adhesion in vascular biology. *J. Clin. Invest. 110*, 485−491.
(13) Blann, A. D., Nadar, S. K., and Lip, G. Y. H. (2003) The adhesion molecule P-selectin and cardiovascular disease. *Eur. Heart J. 24*, 2166−2179.
(14) Molenaar, T. J. M., Twisk, J., de Hass, S. A. M., Peterse, N., Vogelaar, B. J. C. P., van Leeuwen S. H., Michon, I. N., Van Berkel, T. J. C., Kuiper, J., and Biessen, E. A. L. (2004) P-selectin as a candidate target in atherosclerosis. *Biochem. Pharmacol. 66*, 859−866.
(15) Merten, M., and Thiagarajan, P. (2004) P-selectin in arterial thrombosis. *Zeit. Kardiol. 93*, 855−863.
(16) Van Kasteren, S. I., Kramer, H. B., Jensen, H. H., Campbell, S. J., Kirkpatrick, J., Oldham, N., Anthony, J. D. C., and Davis, B. G. (2007) Expanding the diversity of chemical protein modification allows post-translational mimicry. *Nature (London) 446*, 1105−1109.
(17) Varki, A. (1994) Selectin ligands. *Proc. Natl. Acad. Sci. U.S.A. 91*, 7390−7397.
(18) Yuen, C. T., Bezouska, K., O'Brien, J., Stoll, M., Lemoine, R., Lubineau, A., Kiso, M., Hasegawa, A., Bockovich, N. J., Nicolaou, K. C., and Feizi, T. (1994) Sulfated blood group Lewis^a. *J. Biol. Chem. 269*, 1595−1598.
(19) Zhu, J., Xue, J., Guo, Z., and Marchant, R. E. (2007) Vesicle size and stability of biomimetic liposomes for 3′-sulfo-Lewis a (SuLe^a) containing glycolipids. *Colloids Surf., B: Biointerf. 58*, 242−249.
(20) Xue, J., Zhu, J., Marchant, R. E., and Guo, Z. (2005) Pentaerythritol as the core of multivalent glycolipids: synthesis of a glycolipid with three SO_3Le^a ligands. *Org. Lett. 7*, 3753−3756.
(21) Li, F., Erickson, H. P., James, J. A., Moore, K. L., Cummings, R. D., and McEver, R. P. (1996) Visualization of P-selectin glycoprotein ligand-1 as a highly extended molecule and mapping of protein epitopes form monoclonal antibodies. *J. Biol. Chem. 271*, 6342−6348.
(22) Cummings, R. D. (1999) Structure and function of the selectin ligand PSGL-1. *Braz. J. Med. Biol. Res. 32*, 519−528.
(23) Lee, J. H., Lee, H. B., and Andrade, J. D. (1995) Blood compatibility of polyethylene oxide surfaces. *Prog. Polym. Sci. 20*, 1043−1079.
(24) Woodle, M. C. (1998) Controlling liposome blood clearance by surface-grafted polymers. *Adv. Drug Delivery Rev. 32*, 139−152.
(25) Allen, C., Santos, N. D., Gallagher, R., Chiu, G. N. C., Shu, Y., Li, W. M., Johnstone, S. A., Janoff, A. S., Mayer, L. D., Webb, M. S., and Bally, M. B. (2002) Controlling the physical behavior and biological performance of liposome formulations through use of surface grafted poly(ethylene glycol). *Biosci. Rep. 22*, 225−249.
(26) DeFrees, S. A., Phillips, L., Guo, L., and Zalipsky, S. (1996) Sialyl Lewis x liposomes as multivalent ligands and inhibitor of E-selectin mediated cellular adhesion. *J. Am. Chem. Soc. 118*, 6101−6104.
(27) Zhu, J., Yan, F., Guo, Z., and Marchant, R. E. (2005) Surface modification of liposomes by saccharides: vesicle size and stability of lactosyl liposomes studied by photon correlation spectroscopy. *J. Colloid Interface Sci. 289*, 542−550.
(28) Yan, F., Xue, J., Zhu, J., Marchant, R. E., and Guo, Z. (2005) Synthesis of a lipid conjugate of SO_3Le^a and its enhancement on liposomal binding to activated platelets. *Bioconjugate Chem. 16*, 90−96.

BC700212B

Bioimaging in the Mid-Infrared Using an Organometallic Carbonyl Tag

Kien Voon Kong,[†] Wee Chew,[‡] Lina Hsiu Kim Lim,[§] Wai Yip Fan,[†] and Weng Kee Leong*,[†]

Department of Chemistry, National University of Singapore, Kent Ridge, Singapore 119260, Institute of Chemical & Engineering Science, 1 Pesek Road, Jurong Island, Singapore 627833, and Department of Physiology, National University of Singapore, Kent Ridge, Singapore 117597. Received April 18, 2007; Revised Manuscript Received August 9, 2007

Two stable and water-soluble organometallic carbonyl cluster derivatives have been prepared and shown to enter the cell with ease. The CO stretching vibrations afford strong mid-infrared signals which have been demonstrated, for the first time, to be of utility in cell imaging via an IR microscope.

INTRODUCTION

The most highly developed imaging techniques currently employed in biological studies are probably those based on fluorescence spectroscopy. In comparison, there are far fewer reports on the IR and Raman imaging of cells (*1*−*4*). The use of IR-tagged molecules has been scant, and these have employed molecules absorbing in the near-IR (*5*−*8*). Part of the reason for the comparative scarcity of IR imaging is the high sensitivity that is achievable with current fluorescent detectors. However, IR imaging has its own advantages, which include narrower line-widths (which is important if it is to be used as a probe of the environment about the molecule) and lower energy content (hence less potential damage to the cell).

Organometallic carbonyl compounds show strong C═O stretching absorptions in the 2200−1650 cm^{-1} region, which is relatively devoid of interference from any functional groups in the cell. They can thus potentially be useful as spectroscopic tags for imaging in living systems. Organometallic compounds have already been employed in applications (*9*, *10*) such as the labeling of peptides (*11*−*15*) and enzymes (*16*) and in immunoassays (*17*−*23*). However, their use as spectroscopic imaging agents in cells appears to have been unexplored, although related work on the localization of organometallic compounds inside cells using XRF (*24*), fluorescence (*25*), and AAS (*26*) has been carried out. The organometallic clusters of osmium, in particular, offer the distinct advantages of relative inertness toward air and water and the availability of multiple sites for the attachment of various ligands as property modifiers.

EXPERIMENTAL PROCEDURES

Synthesis and Characterization of Compounds. Solvents were of AR grade, dried over the appropriate drying agents, distilled under nitrogen, and stored in containers fitted with a Teflon valve prior to use. All other starting materials were purchased from Aldrich. All synthetic steps were carried out under an atmosphere of nitrogen using standard Schlenk techniques. ^{1}H NMR spectra were recorded on a Bruker ACF300 NMR spectrometer as $CDCl_3$ solutions unless otherwise stated; chemical shifts reported are referenced against the residual proton signals of the solvents. Routine infrared spectra were recorded on a Shimadzu Prestige-21 FTIR spectrometer. All elemental analyses were performed by the microanalytical laboratory at NUS. The cluster $Os_3(CO)_{10}(\mu\text{-H})[\mu\text{-S}(CH_2)_{10}\text{COO}]$Na, **1**, its parent acid **1a** (*27*), and the monobenzylated triol $HOCH_2CH(OH)CH_2OBz$ were prepared according to the literature methods (*28*). All other reagents were from commercial sources and used without further purification.

Synthesis of $BzOCH_2CHCH_2$*-1,2-*$\{Os_3(CO)_{10}(\mu\text{-H})[\mu\text{-S}(CH_2)_{10}COO]\}_2$, ***3***. Cluster **1** (0.5734 g, 0.5399 mmol) was placed in a Carius tube, followed by dichloromethane (7 mL) and DCC (0.3251 g, 1.578 mmol). After stirring at room temperature for 24 h, DMAP (0.2241 g, 1.836 mmol) and $HOCH_2CH(OH)CH_2OBz$ (0.0491 g, 0.2699 mmol) were added and the mixture stirred for another 24 h. The white precipitate formed was removed by filtration; the filtrate was concentrated by rotary evaporation and then purified by preparative TLC (eluant 1:9 ethyl acetate/hexane, v/v). The third of four bands ($R_f = 0.56$) was identified as $BzOCH_2CHCH_2$-1,2-$\{Os_3(CO)_{10}(\mu\text{-H})[\mu\text{-S}(CH_2)_{10}COO]\}_2$, **3**. Yield = 0.3039 g (53%). IR (KBr): ν_{CO} 2110(s), 2062(s), 2031(s), 2015(s), 1973(s), 1700(s) cm^{-1}. ^{1}H NMR ($CDCl_3$): δ 1.27−1.62 (m, 32H, $CH_2(CH_2)_8CH_2$), 2.35 (m, 8H, CH_2S and $COCH_2$), 3.50−3.83 (m, 4H, $CH_2CH(O)CH_2$), 4.0 (m, 1H, CH_2CHCH_2), 4.55 (s, 2H, $OCH_2C_6H_5$), 7.22−7.36 (m, 5H, $CH_2C_6H_5$), −17.41(s, 2H, OsHOs). ^{13}C NMR ($CDCl_3$): δ 24.75, 24.78, 28.30, 29.53, 29.67, 29.72, 29.72, 29.83, 33.83, 33.96, 34.11, 55.33, 65.82, 68.23, 70.40, 73.56, 126.56, 126.56, 128.89, 129.12, 129.12, 136.86, 169.89, 170.86, 173.25, 173.68, 173.96, 176.53, 179.86, 180.12.

Deprotection of ***3***. Cluster **3** (46.1 mg, 19.9 μmol) was placed into a two-necked round-bottom flask. Absolute ethanol (15 mL) and 10% palladium on carbon (100 mg) were then added. The suspension was stirred at room temperature for 12 h with hydrogen gas bubbled through. The catalyst was then removed by filtration, and the solvent removed using a rotary evaporator. The crude product was purified by preparative TLC (eluant ethyl acetate/hexane, 2:8, v/v). The first of two bands ($R_f = 0.35$) was identified as $HOCH_2CHCH_2$-1,2-$\{Os_3(CO)_{10}(\mu\text{-H})[\mu\text{-S}(CH_2)_{10}COO]\}_2$, **4**. Yield = 13.8 mg (30%). IR (KBr): ν_{CO} 2110(s), 2062(s), 2031(s), 2015(s), 1973(s), 1700(s) cm^{-1}. ^{1}H NMR ($CDCl_3$): δ 1.25−1.59 (m, 32H, $CH_2(CH_2)_8CH_2$), 2.30 (m, 8H, CH_2S and $COCH_2$), 3.48−3.82 (m, 4H, CH_2CHCH_2), 4.0 (m, 1H, CH_2CHCH_2), −17.41(s, 2H, OsHOs). ^{13}C NMR ($CDCl_3$): δ 24.55, 24.68, 27.26, 28.56, 28.98, 29.23, 29.92, 33.32, 33.83, 33.83, 55.56, 62.28, 63.12, 70.56, 73.56, 169.90, 170.92, 173.28, 173.66, 173.82, 177.03, 180.02, 180.96.

* Corresponding author. Email: chmlwk@nus.edu.sg.
[†] Department of Chemistry, National University of Singapore.
[‡] Institute of Chemical & Engineering Science.
[§] Department of Physiology, National University of Singapore.

10.1021/bc070133a CCC: $37.00 © 2007 American Chemical Society
Published on Web 09/19/2007

FAB$^+$: *m*/*z* 2215 $[M + Na]^+$. Anal. Calcd: C, 24.50; H, 2.28; S, 2.92. Found: C, 24.29; H, 2.02; S, 2.78.

*Synthesis of **6***. To a thoroughly stirred solution of phosphorus oxychloride (2.0 g, 0.013 mol) in DCM (50 mL) was added 2-bromoethanol (0.95 g, 7.6 mmol) via a pressure-equalizing dropping funnel. A continuous stream of nitrogen was directed through the reaction mixture to remove the hydrogen chloride formed. After stirring for 12 h, toluene (50 mL) was added and the mixture rotary-evaporated to dryness with warming in a water bath set at 40 °C. The residue which contains bromoethylphosphoric acid dichloride was used without further purification. To a DCM (60 mL) solution of bromoethylphosphoric acid dichloride (4.86 g, 20.1 mmol) cooled in an ice bath was added triethylamine (8.30 mL, 82.1 mmol). With continuous stirring, a solution of cluster **4** (44.3 mg, 20.1 μmol) in DCM (30 mL) was added dropwise. The reaction was monitored by TLC, and was completed after 1 h. Toluene (120 mL) was added to the reaction mixture, and the precipitated triethylammonium chloride was removed by filtration. The filtrate was evaporated to dryness, the residue redissolved in THF (100 mL) and then hydrolyzed by stirring with aqueous sodium carbonate (0.5 M, 100 mL, pH 8.5) for 6 to 8 h. The pH of the solution was adjusted to 9.0 by the addition of aqueous sodium hydroxide, and then extracted with diisopropylether (100 mL); methanol (20−40 mL) was also added to facilitate phase separation. The ether phase was evaporated to dryness and then recrystallized from chloroform (20 mL) and acetone (200 mL). The crude precipitate of **5** (23.5 mg, 9.8 μmol) was dissolved in chloroform/2-propanol/ dimethylformamide (130 mL, 3:5:5, v/v/v), heated at 50 °C, and a solution of trimethylamine in water (70 mL, 40%, v/v) added. The reaction was completed after 4−6 h. Volatiles were removed by evaporation at 40 °C, and the residual water/dimethylformamide mixture was extracted with a chloroform/methanol (1:1, v/v) solvent mixture. The combined extracts were evaporated and the residue purified by silica gel chromatography to afford **6**. $R_f = 0.13$. Yield = 6.9 mg (15%). IR (KBr): ν_{CO} 2110(s), 2062(s), 2031(s), 2015(s), 1973(s), 1700(s) cm^{-1}. ^{1}H NMR ($CDCl_3$): δ 1.25−1.59 (m, 32H, CH_2-(CH_2)$_8$$CH_2$), 2.30 (m, 8H, CH_2S and COCH_2), 3.41 (s, 9H, N(CH_3)$_3$), 3.58−3.82 (m, 6H, POCH$_2$CH_2 and CH_2CHCH_2), 4.0 (m, 3H, CH_2CHCH$_2$ and POCH_2CH$_2$), −17.41(s, 2H, OsHOs). ^{13}C NMR ($CDCl_3$): δ 24.53, 24.62, 27.83, 29.01, 29.23, 29.62, 29.62, 29.96, 33.26, 33.78, 33.82, 54.00, 54.00, 54.00, 55.33, 58.96, 62.60, 63.54, 66.52, 70.58, 169.23, 171.03, 173.45, 173.56, 173.92, 177.02, 179.86, 180.92. MALDI-TOF$^+$: *m*/*z* 2356 (M^+). Anal. Calcd: C, 25.46: H, 2.54: S, 2.71. Found: C, 25.02: H, 2.16: S, 2.51.

Cell Studies. *Cell Culture and Viability Assay*. Cell culture medium, L-glutamine, and trypsin were purchased from Sigma-Aldrich. Phosphate buffered saline (PBS) was purchased from Fisher Scientific. Oral mucosa cells were scratched from the oral mucosa surface and washed twice in pure water before use. HL-60 cell lines were purchased from American Type Culture Collection (ATCC).

Cell viability under experimental conditions was assessed by the mitochondria-dependent reduction of 3-(4,5-dimethylthiazol-2-yl)-2,5-diphenyltetrazolium bromide (MTT) to formazan. HL-60 cells were treated with an equal amount of freshly prepared MTT solution (2−5 mg MTT reagent dissolved in plain media) per sample in triplicate in a 96-well plate. The plate was incubated for 2 h at 37 °C in the dark. After incubation, the plate was spun at 2000 rpm for 5 min. The supernatant was removed, and the crystals were dissolved in 200 μL of DMSO plus 10 μL of Sorenson's glycine buffer. The plate was then read at 570 nm using an ELISA plate reader. Group comparisons were made using the unpaired *t* test and *p*-values less than 0.05 were considered significant.

FT-IR Imaging Experiments. The IR mapping experiments were carried out with a Varian 7000 FT-IR spectrometer fitted with a Stingray infrared microscope and equipped with a 64 × 64 MCT focal plane array (FPA) detector. Oral mucosa cells were incubated using 0.32 mM stock solutions of the compounds for 24 h; the final concentration of the solutions used in the incubation was 0.032 mM. After incubation, the cells were washed with cool buffer solution, quickly transferred onto CaF_2 windows, and then dried under a flow of nitrogen or argon, before imaging. During infrared imaging, the average spatial resolution probed by each FPA pixel is ca. 5.5 μm, amounting to an average spatial field of view of 350 × 350 μm^2 for the entire 64 × 64 pixels of infrared image. FT-IR imaging was performed using 16 scans for co-add at 4 cm^{-1} resolution, and the acquisition time for each FT-IR image was ca. 2 min.

For single-point IR spectral acquisition of cells and cellular material, a Shimadzu Prestige-21 FTIR spectrometer equipped with an AIM-8800 IR microscope was used, with the aperture set to 10 × 10 μm^2 size and the resolution at 4 cm^{-1}.

Cell Fractional Assay. A Chemicon compartment separation kit was used for cell compartment separation. HL-60 cells were grown in culture flasks with modified IMDM containing 10% FBS in a 5% CO_2 incubator. The HL-60 cells were treated with compounds **1** or **6** (0.032 mM) for 24 h at 37 °C, and were then homogenized in sucrose gradient buffer at moderate speed and centrifuged at 20 000 × *g* at 4 °C for 20 min. The supernatant was saved as the cytoplasmic fraction. The pellet was washed with cold sucrose gradient buffer and centrifuged again as above. The supernatant was saved as the nuclear fraction. The procedure was repeated, and the supernatant now contained the membrane fraction, while the pellet contained organelles, granules and cytoskeleton, which was labeled the organelles fraction. Finally, all samples were characterized at a spectral resolution of 4 cm^{-1} as dry films on CaF_2 windows.

TEM Imaging. TEM images and the EDX spectra were recorded on a JEOL JEM 3010 transmission electron microscope at an accelerating voltage of 300 kV; a drop of the cells suspended in water was placed onto a carbon-coated Cu grid.

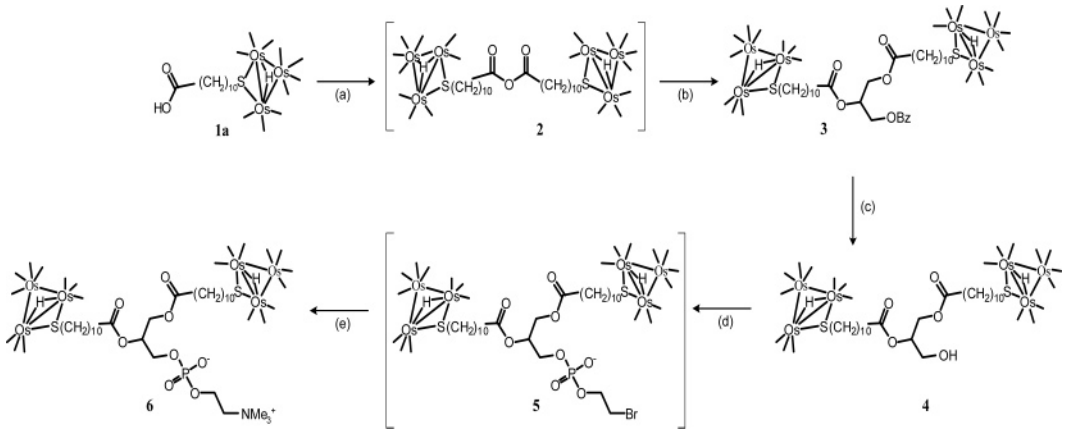
Washout Studies. HL-60 cells were treated with compound **1** or **6** (0.032 mM) for 24 h at 37 °C. At the end of the incubation period, the cells were rinsed in triplicate with medium at ambient temperature. The removed medium was digested with nitric acid and analyzed for osmium content using ICP−MS. Rinsing of the cells was then repeated as above.

ICP−MS Analysis. ICP−MS analyses were carried out on an ELAN 6100 instrument. Mucosa cells (total of 1000 cells each) were treated with an aqueous solution of **1** or **6** (0.032 mM) for 24 h at 37 °C. At the end of the incubation period, the cells were rinsed with buffer solution at ambient temperature. Mineralization was carried out with 65% HNO_3 at 120 °C, and the dried digested material was redissolved in 2% HNO_3. The osmium content was then determined by ICP−MS.

*Stability of **1** in Vivo*. A solution of **1** was incubated with HL-60 cells at 37 °C for 12, 24, and 48 h, respectively. After centrifugation, the cell pellets were place on CaF_2 and dried under nitrogen. The cells were characterized at a spectral resolution of 4 cm^{-1} on CaF_2 windows, and the stability was assessed by IR spectroscopy.

*Stability of **6** in Vivo*. A culture of (5−7) × 10^6 cells was incubated in a solution of **6** for 24 h. The cells were then collected by centrifugation (1500 rpm, 5 min), the media aspirated off, washed with PBS, then suspended in chloroform/methanol (3 mL, 1:2, v/v) and agitated until an even suspension was attained. Water (0.8 mL) was added, and the cells were transferred to a 15 mL tube and allowed to settle (30 min). The cellular debris was separated by centrifugation (3000 rpm, 5 min), chloroform (1 mL) and water (1 mL) were added to the

Scheme 1. Synthetic Pathway to 6[a]



[a] (a) DCC, CH_2Cl_2, 24 h; (b) $OHCH_2CH(OH)CH_2OBz$, DMAP, CH_2Cl_2, 24 h; (c) H_2, Pd/C, EtOH, 12 h; (d) i. $Br(CH_2)_2OPOCl_2$, Et_3N, CH_2Cl_2, 1 h; ii. aq. Na_2CO_3, THF, 6−8 h; (e) Me_3N/H_2O, $CHCl_3/^iPrOH/DMF$, 4−6 h.

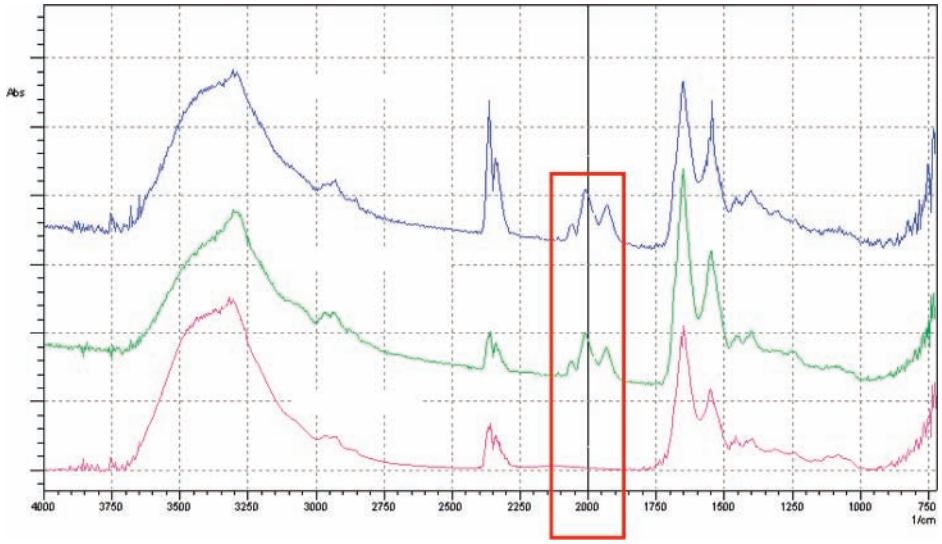


Figure 1. IR spectra recorded in absorbance mode of untreated mucosa cells (bottom), cells treated with **1** (middle), and cells treated with **6** (top). Boxed region shows carbonyl (CO) stretching vibrations of the organometallic fragments.

liquid material, and the suspension vortexed. Phase separation was obtained by allowing the mixture to stand for 15−30 min, followed by centrifuging (3000 rpm, 5 min); the lower organic phase was collected and then the solvent removed by evaporation. TLC analysis (silica gel, $CHCl_3/CH_3OH$, 3:1, v/v) of the residue showed the presence of only **6** but no **1** or **1a**.

Estimation of Cell Size. Mucosa cells were scratched from the oral mucosa surface, washed twice in pure water, and then quickly transferred onto CaF_2 windows. Cell surface area measurements of the dry cells were performed using the View program of the Shimadzu AIM 8800 microscope. The mucosa cells selected for measurements were flat in shape. The average cell surface area for 20 mucosa cells was measured, and the average cell volume estimated by assuming an average cell thickness of 2 μm. The average cell volume obtained was 1.78×10^{-11} L.

RESULTS AND DISCUSSION

We have recently synthesized the water-soluble cluster, $[Os_3(CO)_{10}(\mu\text{-H})(\mu\text{-S}(CH_2)_{10}COO)]Na$, **1** (*27*), which is essentially an inorganic salt of a fatty acid tagged with an organometallic cluster. This was also elaborated (via the acid precursor, **1a**) to a phosphotidylcholine analogue, **6** (Scheme 1). The synthetic route to **6** utilized synthetic steps similar to those employed in the synthesis of the related organic fragment (*29*−*34*).

Compounds **1** and **6** are air- and water-stable, so that no special handling is required. Cytotoxicity studies carried out showed that **1** does not significantly affect viability of an HL-60 leukemia cell line (89% of the control for 10−30 μM concentrations), although the viability of cells exposed to 30 μM of **6** showed a slight reduction (77% of the control) in viability (Supporting Information Figure S1). Thus, at the doses studied, the labeling method poses only a small effect on the viability of cells. For our chemical imaging, oral mucosa cells were incubated with aqueous solutions (0.032 mM) of **1** or **6** for 24 h, washed with cool buffer solution, quickly transferred onto CaF_2 windows, and dried under argon or nitrogen flow. Oral mucosa cells have been reported to have an average size of up to 100×100 μm^2 (*35*); in our case, we have found them to be closer to 60×60 μm^2. Typical (single-point) IR spectra of the treated and untreated cells are shown in Figure 1. The usual absorption bands due to the cell contents are clearly visible. They do not show unusual broadening and absence of a narrow band at 1730 cm^{-1} due to ester carbonyl groups, both of which have been reported to be associated with necrosis (*36*). There is a significant difference between the spectra for the treated and untreated cells in the 1900−2100 cm^{-1} region, which is due to the carbonyl (CO) stretching vibrations of the organometallic fragments. An EDX (energy-dispersive X-ray)

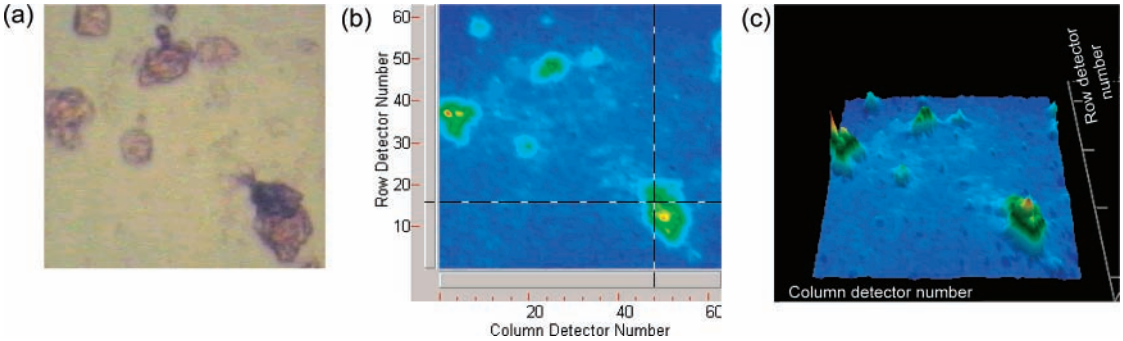


Figure 2. (a) Normal optical image; (b) false-color infrared image; (c) 3-D display of the image, of oral mucosa cells treated with **1**, taken at 2013 cm^{-1}.

spectrum taken of one of the cells treated with **1** also clearly showed the presence of osmium (Supporting Information Figure S2).

Figure 2 shows (a) a normal optical image, (b) a false-color infrared image, and (c) a 3-D display of the image of the oral mucosa cells treated with **1**, taken at 2013 cm^{-1}: one of the carbonyl vibration bands. The infrared images were obtained with a 64 × 64 pixel image plate detector; aperture size was set at 5.5 × 5.5 μm^2 and the signals were averaged over 16 scans. The chemical mapping images are closely correlated with the optical image. Similar images were obtained when different carbonyl vibrational bands, as well as some typical cellular vibrations (such as the amide I band, Supporting Information Figure S3) were chosen; the same was observed with **6** (Supporting Information Figure S4).

Cells that were soaked in an aqueous solution of **1** for different periods of time (*37*) showed a concentration profile of **1** which reached a plateau after ∼7 h of soaking time (Supporting Information Figure S5), consistent with internalization of **1** (*38*), since adsorption onto the outer surface of the cells would be expected to exhibit a profile that is more or less independent of the length of time that the cells were soaked. The profile also suggested delivery through passive diffusion; washout studies on both **1** and **6** support this and are consistent with studies on other modified phospholipids (*39*, *40*). Internalization of both **1** and **6** was confirmed by the fractionation of HL-60 cells incubated for 24 h with solutions of the compounds. Four major fractions (nuclear, cytoplasmic, organelles, and membrane) were obtained, and the IR spectra of the dried fractions clearly showed the presence of the compounds in the organelles and the membrane fractions, albeit with different distributions, but not in the other two (Supporting Information Figure S6).

While it may have been anticipated that the fatty acid-like **1** would stay in the cytoplasm and the more lipid-like **6** in the membrane, previous studies on labeled lipids have shown that they do accumulate in the internal apparatus, forming granules in the cell, or adsorb onto the cell membrane (*41*, *42*). The possible hydrolysis of **6** in the cell was also ruled out, as chromatographic analysis of the cell contents after 24 h incubation with **6** showed that there was no detectable amount of its hydrolysis product, *viz*., the fatty acid **1a**. This is also consistent with previous studies on modified phospholipids, which suggest that they are resistant to hydrolysis or metabolism by the cells (*42*). Thus, both compounds have indeed translocated into the cells and adsorbed onto the internal surface of the cell membrane. The IR spectra of HL-60 cells after incubation in a solution of **1** for various periods of time (up to 48 h) showed that **1** does not decompose to any spectroscopically detectable extent; any decomposition affecting the cluster core would show up clearly as a shift in the pattern of the carbonyl stretching region, and complete loss of carbonyl ligands in osmium clusters at ambient temperature is unknown.

The absorbance across a single mucosa cell showed similar intensities and profiles for both **1** and **6** (Supporting Information Figure S7). The extinction coefficients for the 2013 cm^{-1} bands of **1** and **6** in aqueous solutions have been determined to be 8.3 × 10^4 and 1.75 × 10^5 L mol^{-1} cm^{-1}, respectively. We have estimated the average volume of a mucosa cell to be 1.78 × 10^{-11} L, and together with an assumed cell thickness of 1 μm and an observed IR absorbance of ∼0.04, the osmium content in the cells was estimated to be ∼3 × 10^{-13} mol per cell; this is comparable to the 6 or 2 × 10^{-13} mol per cell obtained from ICP−MS on mucosa cells treated with **1** and **6**, respectively. Conversely, the ICP and IR results could be used to arrive at an estimated cell thickness of ∼0.4−1.3 μm. These values are quite close to the 1−2 μm reported (*35*).

CONCLUSION

This work serves to illustrate, for the first time, that bioimaging in the mid-infrared is possible and that it can be carried out with stable, water-soluble organometallic carbonyl compounds such as **1** and **6**.

ACKNOWLEDGMENT

This work was supported by the National University of Singapore (Research Grant No. R-143-000-267-112) and one of us (K.V.K.) thanks the University for a Research Scholarship.

Supporting Information Available: Additional experimental details. This material is available free of charge via the Internet at http://pubs.acs.org.

LITERATURE CITED

(1) Gazi, E., Dwyer, J., Lockyer, N. P., Miyan, J., Gardner, P., Hart, C., Brown, M., and Clarke, N. W. (2005) Fixation protocols for subcellular imaging by synchrotron-based Fourier transform infrared microspectroscopy. *Biopolymers 77*, 18−30.

(2) Raab, T. K., and Vogel, J. P. (2004) Ecological and agricultural applications of synchrotron IR microscopy. *Infrared Phys. Technol. 45*, 393−402.

(3) Gazi, E., Lockyer, N. P., Vickerman, J. C., Gardner, P., Dwyer, J., Hart, C. A., Brown, M. D., Clarke, N. W., and Miyan, J. (2004) Imaging ToF-SIMS and synchrotron-based FT-IR microspectroscopic studies of prostate cancer cell lines. *J. Appl. Surf. Sci. 452*, 231−232.

(4) Nakajima, R., Nakamura, T., Ogawa, M., Miyakawa, H., and Kudo, Y. (2004) Novel method for quantification of brain cell swelling in rat hippocampal slices. *J. Neurosci. Res. 76*, 723−734.

(5) Wu, S. P., Lee, I., Ghoroghchian, P. P., Frail, P. R., Zheng, G., Glickson, J. D., and Therien, M. J. (2005) Near-infrared optical imaging of B16 melanoma cells via low-density lipoprotein-mediated uptake and delivery of high emission dipole strength tris[(porphinato)zinc(II)] fluorophores. *Bioconjugate Chem. 16*, 542−550.

(6) Xing, B., Khanamiryan, A., and Rao, J. (2005) Cell-permeable near-infrared fluorogenic substrates for imaging β-lactamase activity. *J. Am. Chem. Soc. 127*, 4158−4159.
(7) Messerli, S. M., Prabhakar, S., Tang, Y., Shah, K., Cortes, M. L., Murthy, V., Weissleder, R., Breakefield, X. O., and Tung, C. T. (2004) A novel method for imaging apoptosis using a caspase-1 near-infrared fluorescent probe. *Neoplasia 6*, 95−105.
(8) Citrin, D., Lee, A. K., Scott, T., Sproull, M., Menard, C., Tofilon, P. J., and Camphausen, K. (2004) In vivo tumor imaging in mice with near-infrared labeled endostatin. *Mol. Cancer Ther. 3*, 481−488.
(9) Jaouen, G. (2006) *Bioorganometallics: Biomolecules, Labeling, Medicine*, Wiley-VCH, Weinheim.
(10) Simmoneaux, G. (2006) *Topics in Organometallic Chemistry: Bioorganometallic Chemistry*, Springer-Verlag, Berlin/Heidelberg.
(11) Barisic, L., Rapic, V., and Metzler-Nolte, N. (2006) Incorporation of the unnatural organometallic amino acid 1′-aminoferrocene-1-carboxylic acid (Fca) into oligopeptides by a combination of fmoc and boc solid-phase synthetic methods. *Eur. J. Inorg. Chem.* 4019−4021.
(12) Hoffmanns, U., and Metzler-Nolte, N. (2006) Use of the Sonogashira coupling reaction for the "two-step" labeling of phenylalanine peptide side chains with organometallic compounds. *Bioconjugate Chem. 17*, 204−213.
(13) Baldoli, C., Rigamonti, C., Maiorana, S., Licandro, E., Falciola, L., and Mussini, P. R. (2006) A new triferrocenyl-tris(hydroxymethyl)aminomethane derivative as a highly sensitive electrochemical marker of biomolecules: application to the labelling of PNA monomers and their electrochemical characterization. *Chem.—Eur. J. 12*, 4091−4100.
(14) Kirin, S. I., Wissenbach, D., and Metzler-Nolte, N. (2005) Unsymmetrical 1,1′-disubstituted ferrocenoyl peptides: convenient one pot synthesis and solution structures by CD and NMR spectroscopy. *New J. Chem. 29*, 1168−1173.
(15) Barisic, L., Dropucic, M., Rapic, V., Pritzkow, H., Kirin, S. I., and Metzler-Nolte, N. (2004) The first oligopeptide derivative of 1′-aminoferrocene-1-carboxylic acid shows helical chirality with antiparallel strands. *Chem. Commun*. 2004−2005.
(16) Anson, C. E., Creaser, C. S., Egyed, O., and Stephenson, G. R. (1997) FTIR studies of organometalcarbonyl-tagged enzymes. *Spectrochim. Acta 53A*, 1867−1877.
(17) Hromadová, M., Salmain, M., Fischer-Durand, N., Pospísil, L., and Jaouen, G. (2006) Electrochemical microbead-based immunoassay using an (η^5-cyclopentadienyl)tricarbonylmanganese redox marker bound to bovine serum albumin. *Langmuir 22*, 506−511.
(18) Mokhtari, M., Mousser, A., Salmain, M., and Jaouen, G. (2005) Labelling of biologically active molecules with a cyclohexadiene tricarbonyl iron unit. *C. R. Chim. 8*, 85−90.
(19) Alberto, R. (2005) New organometallic technetium complexes for radiopharmaceutical imaging. *Top. Curr. Chem. 252*, 1−44.
(20) Fischer-Durand, N., Salmain, M., Rudolf, B., Vessières, A., Zakrzewski, J., and Jaouen, G. (2004) Synthesis of metal-carbonyl-dendrimer-antibody immunoconjugates: towards a new format for carbonyl metallo immunoassay. *ChemBioChem 5*, 519−525.
(21) Heldt, J. M., Fischer-Durand, N., Salmain, M., Vessieres, A., and Jaouen, G. (2004) Preparation and characterization of poly(amidoamine) dendrimers functionalized with a rhenium carbonyl complex and PEG as new IR probes for carbonyl metallo immunoassay. *J. Organomet. Chem. 689*, 4775−4782.
(22) Salmain, M., Vessieres, A., Varenne, A., Brossier, P., and Jaouen, G. (1999) A new application of bioorganometallics: the first simultaneous triple assay by the carbonylmetalloimmunoassay (CMIA) method. *J. Organomet. Chem. 589*, 92−97.
(23) Cais, M. (1988) Metalloimmunoassay. *Nonisotopic Immunoassay*, Plenum, New York, pp 415−438.
(24) Waern, J. B., Harris, H. H., Lai, B., Cai, Z., Harding, M. M., and Dillon, C. T. (2005) Intracellular mapping of the distribution of metals derived from the antitumor metallocenes. *J. Biol. Inorg. Chem. 10*, 443−452.
(25) Gazi, E., Dwyer, J., Lockyer, N. P., Miyan, J., Gardner, P., Hart, C., Brown, M., and Clarke, N. W. (2005) Fixation protocols for subcellular imaging by synchrotron-based Fourier transform infrared microspectroscopy. *Biopolymers 77*, 18−30.
(26) Raab, T. K., and Vogel, J. P. (2004) Ecological and agricultural applications of synchrotron IR microscopy. *Infrared Phys. Technol. 45*, 393−402.
(27) Ahmed, M. O. E. and Leong, W. K. (2006) Colloidal silver nanoparticles stabilized by a water-soluble triosmium cluster. *J. Organomet. Chem. 691*, 1055−1060.
(28) Hanson, R. M. (1991) The synthetic methodology of nonracemic glycidol and related 2,3-epoxy alcohols. *Chem. Rev. 91*, 437−457.
(29) Bittman, R., and Witzke, N. M. (1989) Conversion of methylallyl alcohol into C2-methyl-1,2-di-O-hexadecylglycerophosphocholine, a conformationally restricted phospholipids. *Chem. Phys. Lipids 50*, 99−103.
(30) Patel, K. M., Morrisett, J. D., and Sparrow, J. T. (1979) A convenient synthesis of phosphatidylcholines: acylation of sn-glycero- 3-phosphocholine with fatty acid anhydride and 4-pyrrolidinopyridine. *J. Lipid Res. 20*, 674−677.
(31) Cubero Robles, E., and Van den Berg, D. (1969) Synthesis of lecithins by acylation of O-(sn-glycero-3-phosphoryl) choline with fatty acid anhydrides. *Biochim. Biophys. Acta 187*, 520−526.
(32) Selinger, Z., and Lapidot, Y. (1966) Synthesis of fatty acid anhydrides by reaction with dicyclohexylcarbodiimide. *J. Lipid Res. 7*, 174−175.
(33) Diembeck, W., and Eibl, H. (1979) Synthesis of phospholipid analogues. Variation of the P−N distance. *Chem. Phys. Lipids 24*, 237−244.
(34) Eibl, H., and Nicksch, A. (1978) The synthesis of phospholipids by direct amination. *Chem. Phys. Lipids 22*, 1−8.
(35) Lasch, P., Boese, M., Pacifico, A., and Diem, M. (2002) FT-IR spectroscopic investigations of single cells on the subcellular level. *Vib. Spectrosc. 28*, 147−157.
(36) Jamin, N., Dumas, P., Moncuit, J., Fridman, W.-H., Teillaud, J.-L., Carr, G. L., and Williams, G. P. (1998) Highly resolved chemical imaging of living cells by using synchrotron infrared microspectrometry. *Proc. Natl. Acad. Sci. U.S.A. 95*, 4837−4840.
(37) The cells were washed three times with distilled water after treatment with the aqueous solution of **1**, re-suspended in water for 30 min, and then deposited onto CaF_2 windows for imaging.
(38) Colangelo, D., Ghiglia, A., Ghezzi, A., Ravera, M., Rosenberg, E., Spada, F., and Osella, D. (2005) Water-soluble benzoheterocycle triosmium clusters as potential inhibitors of telomerase enzyme. *J. Inorg. Biochem. 99*, 505−512.
(39) Pagano, R. E., and Sleight, R. G. (1985) Defining lipid transport pathways in animal cells. *Science 229*, 1051−1057.
(40) Kasurinen, J., and Somerharju, P. (1995) Metabolism and distribution of intramolecular excimer-forming dipyrenebutanoyl glycerophospholipids in human fibroblasts. Marked resistance to metabolic degradation. *Biochemistry 34*, 2049−2057.
(41) Morand, O., Fibach, E., Dagan, A., and Gatt, S. (1982) Transport of fluorescent derivatives of fatty acids into cultured human leukemic myeloid cells and their subsequent metabolic utilization. *Biochim. Biophys. Acta 111*, 539−550.
(42) Morand, O., Fibach, E., Dagan, A., and Gatt, S. (1984) Induction of lipid storage in cultured leukemic myeloid cells by pyrene-dodecanoic acid. *Biochim. Biophys. Acta 793*, 95−104.

BC070133A

Osteotropic Peptide That Differentiates Functional Domains of the Skeleton

Dong Wang,[†,‡,⊥] Scott C. Miller,[§,⊥] Luda S. Shlyakhtenko,[†] Alexander M. Portillo,[†] Xin-Ming Liu,[†] Kongnara Papangkorn,[‡] Pavla Kopečková,[‡] Yuri Lyubchenko,[†] William I. Higuchi,[‡] and Jindřich Kopeček*[,‡,∥]

Department of Pharmaceutical Sciences, College of Pharmacy, University of Nebraska Medical Center, Omaha, Nebraska 68198-6025, Department of Pharmaceutics and Pharmaceutical Chemistry and Department of Bioengineering, University of Utah, Salt Lake City, Utah 84112, Department of Radiology/Radiobiology Division, University of Utah, Salt Lake City, Utah 84108. Received June 14, 2007; Revised Manuscript Received July 27, 2007

HPMA copolymer−D-aspartic acid octapeptide (D-Asp$_8$) conjugates have been found to target the entire skeleton after systemic administration. In a recent study using the ovariectomized rat model of osteoporosis, we surprisingly discovered that D-Asp$_8$ would favorably recognize resorption sites in skeletal tissues, while another bone-targeting moiety, alendronate (ALN), directs the delivery system to both formation and resorption sites. Atomic force microscopy (AFM) analyses reveal that ALN has a stronger binding force to hydroxyapatite (HA) than D-Asp$_8$. *In vitro* HA binding studies indicate that D-Asp$_8$ is more sensitive to change of HA crystallinity than ALN. Because the bone apatite in the newly formed bone (formation sites) usually has lower crystallinity than the resorption sites (mainly mature bone), we believe that the favorable recognition of D-Asp$_8$ to the bone resorption sites could be attributed to its relatively weak binding to apatite, when compared to bisphosphonates, and the different levels of crystallinity of bone apatite at different functional domains of the skeleton.

Bone is a specialized connective tissue, which provides mechanical support and participates in calcium homeostasis. It is continuously being resorbed and rebuilt to maintain its normal function. Disturbances of this resorption/formation balance are characteristic of most bone diseases (*1*−*3*). With ever-increasing understanding of bone biology, many new therapeutic agents have been identified for the treatment of bone diseases (*4*−*15*). However, most of them do not have tissue specificity to the skeleton (osteotropicity), which hampers their clinical application due to the side effects.

In order to overcome this problem, we have developed bone-targeting water-soluble polymeric drug delivery systems. In the initial study, alendronate and D-Asp$_8$ were used as the bone-targeting moieties and conjugated to fluorescein isothiocyanate (FITC)-labeled *N*-(2-hydroxypropyl)methacrylamide (HPMA) copolymers (Figure 1A). The administration of these polymers to young growing balb/c mice led to their strong deposition to the skeleton, especially at high turnover sites in bone as determined histologically (*16*). A later pharmacokinetics and biodistribution study confirmed that HPMA copolymer using D-Asp$_8$ as the bone-targeting moiety could recognize the skeleton, especially the high bone turnover sites, such as tibia and femur heads, lumbar vertebrae, and mandibular bone (*17*). To investigate whether the delivery system could deliver model drugs to the osteopenic skeleton, FITC-labeled HPMA copolymer−alendronate conjugate (P-ALN-FITC) and FITC-labeled HPMA copolymer−D-Asp$_8$ conjugate (P-D-Asp$_8$-FITC) were administered intravenously to ovariectomized (OVX) rats, a common model of postmenopausal osteoporosis. To allow the development of osteopenia, the OVX procedure was performed 3 months prior to the beginning of the study. To assist in the identification of different functional domains on bone surfaces, tetracycline (a fluorochrome marker of bone formation) (*18*) was administered intraperitoneally (20 mg/kg) 3 days prior to the administration of the conjugates. Twenty-four hours after administration of the conjugates, the OVX rats (three/group) were euthanized. Tibias, femurs, fifth lumbar vertebra, and mandibles were isolated, fixed, and processed for undecalcified histomorphometric analyses.

As shown in Figure 1B and C, both conjugates were found to bind well to some bone surfaces in the OVX rats, which agrees with a previous study using young balb/c mice (*16*). The tetracycline marker labeled bone formation surfaces permitted easier identification of both bone formation and bone resorption sites. The presence of osteoclasts on the resorption surface and osteoblasts on the formation surfaces was confirmed by histology. Surprisingly, P-D-Asp$_8$-FITC was found to preferentially bind to resorption surfaces, while P-ALN-FITC appeared to bind well at both formation and resorption surfaces. Such a result has never been reported before. As we examine the zone of dentine calcification, the binding of the P-ALN-FITC appeared to be stronger than P-D-Asp$_8$-FITC (Figure 1D and E) in the continuously erupting incisor in the mandible.

Because of this intriguing observation, we hypothesized that the binding strength of D-Asp$_8$ to bone apatite (a poorly crystallized, CO_3-containing, Ca-deficient hydroxyapatite analog) (*19*) may be weaker than that of alendronate. Therefore, it could be sensitive to the crystallinity of bone apatite. It is known that certain pathophysiological conditions such as Paget's disease (*20*) and osteoporosis (*21*) can result in changes of the size of hydroxyapatite crystals. It is also understood that the crystallinity of newly formed bone mineral at active bone

* Correspondence should be addressed to Jindřich Kopeček, Department of Pharmaceutics and Pharmaceutical Chemistry, University of Utah, 30 S. 2000 E. Rm. 201, Salt Lake City, Utah 84112-5820, USA; Phone: (801) 581-7211; Fax: (801) 581-7848. E-mail: Jindrich.Kopecek@utah.edu.

† Department of Pharmaceutical Sciences, College of Pharmacy, University of Nebraska Medical Center.

‡ Department of Pharmaceutics and Pharmaceutical Chemistry, University of Utah.

§ Department of Radiology/Radiobiology Division, University of Utah.

∥ Department of Bioengineering, University of Utah.

⊥ These authors contributed equally to this work.

10.1021/bc7002132 CCC: $37.00 © 2007 American Chemical Society
Published on Web 08/17/2007

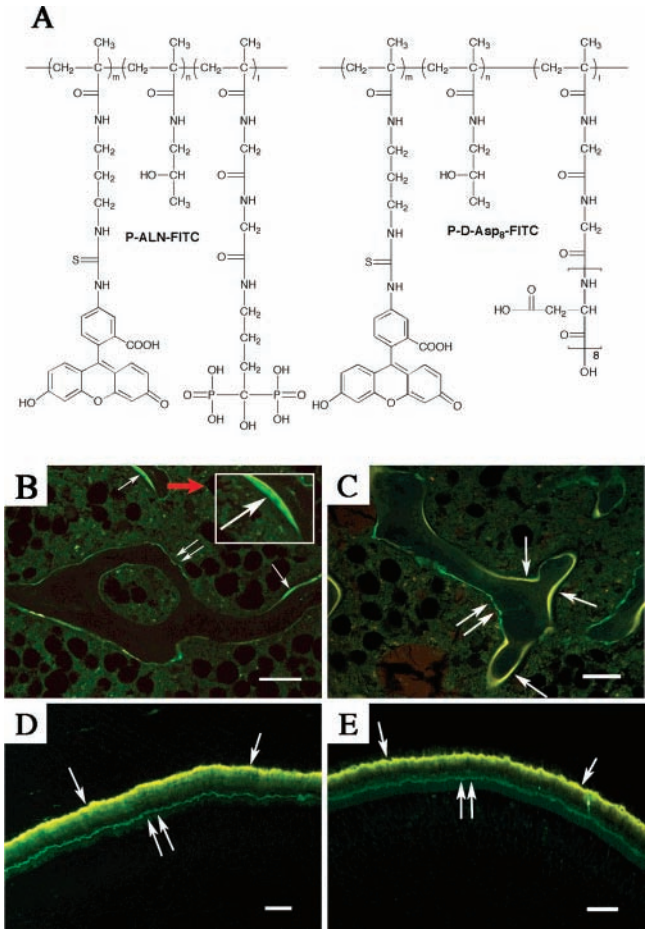


Figure 1. Different *in vivo* bone-binding abilities of HPMA copolymers conjugated with alendronate (P-ALN-FITC) and D-aspartic acid octapeptide (P-D-Asp$_8$-FITC). (A) Chemical structures of the osteotropic polymer conjugates. (B) Cancellous bone from an ovariectomized (OVX) rat injected with the bone formation marker tetracycline (TC) and the P-ALN-FITC. Both tetracycline (TC, yellow) and P-ALN-FITC (green) are seen on some surfaces (arrows) indicating uptake on bone-forming surfaces. A selected area is magnified (×2, insert) to show the double label of TC and P-ALN-FITC. P-ALN-FITC is also evident on some resorption surfaces (double arrows). Bar = 100 μm. (C) Cancellous bone from an OVX rat injected with TC and the P-D-Asp$_8$-FITC. Uptake of TC but little of P-D-Asp$_8$-FITC is evident on bone formation surfaces (arrows). P-D-Asp$_8$-FITC is evident on bone resorption surfaces (double arrows). Bar = 100 μm. (D) Cross sections of the forming mandibular incisor illustrating the uptake of the P-ALN-FITC. Bar = 50 μm. (E) Cross sections of the forming mandibular incisor illustrating the uptake of the P−D-Asp$_8$-FITC. Bar = 50 μm. The TC label (yellow) is clearly evident in both sections (arrows). There is more apparent uptake of P-ALN-FITC (green label, double arrows) in the mineralizing dentin than uptake of P-D-Asp$_8$-FITC.

formation sites is lower than that at the more mature sites where resorption occurs (*20*). This may help to explain the observed preferential binding of P-D-Asp$_8$-FITC to resorption surfaces in skeletal tissues.

To test this hypothesis, we employed force spectroscopy to directly measure the interaction of alendronate and D-Asp$_8$ with hydroxyapatite. Since the AFM force measurement requires a rather flat substrate, we chose tooth enamel (Figure 2) as a model of hydroxyapatite surface. Alendronate or D-Asp$_8$ was covalently attached to the AFM probes via glutaraldehyde cross-links (*22*−*24*). Force−distance measurements were performed in PBS buffer at room temperature at identical experimental conditions. Force curves were taken at various random locations on the surface in order to account for any heterogeneity on the surface. Although both modified tips clearly indicated the tip−surface interaction (Figure 3A and B), the most frequent force−

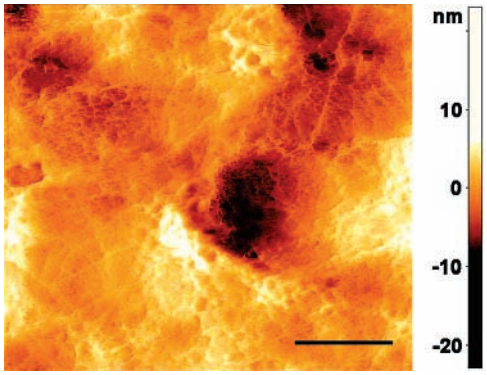


Figure 2. AFM amplitude image of tooth enamel surface taken in PBS buffer using nonmodified tip. Bar = 2 μm.

distance curves were different for alendronate and D-Asp$_8$. The force distance curves for the D-Asp$_8$-modified tip more often showed a single adhesion peak, whereas the alendronate-modified tip often had two clear peaks, including adhesion. Each individual force plot was analyzed one at a time. The rupture force and the distance for each peak were also measured. The results obtained for a series of measurements of adhesion forces for the tips modified with alendronate and D-Asp$_8$, respectively, are shown as histograms in Figure 3C and D. Both histograms demonstrate the interaction of modified tips with the tooth enamel surface, but they are clearly different. For alendronate, the distribution of forces is wide with majority of the forces recorded around 190 pN. For D-Asp$_8$, the distribution is narrower with the majority of the forces recorded around 105 pN. In addition to the analyses of adhesion forces at zero distances, secondary peaks at distances away from the adhesion peak were also analyzed and shown in Figure 3E and F. Clearly, the data reveal a more pronounced difference in the interaction patterns for alendronate and D-Asp$_8$. First, the number of secondary events was considerably larger for alendronate compared to D-Asp$_8$. Second, the values for rupture forces were higher for alendronate than for D-Asp$_8$. An additional difference was the position of the secondary peak. This effect is graphically illustrated in Figure 3G and H, on which the histograms for the distance distribution are plotted for alendronate and D-Asp$_8$, respectively. The positions for the secondary rupture events are centered around 40 nm for alendronate, whereas the secondary peaks for D-Asp$_8$ are scattered but with the majority of the events at distances of ∼10 nm. In spite of the heterogeneity in chemical composition and roughness of the enamel surface (Figure 2), which may widen the histograms for the interaction forces and distances, these AFM data strongly suggest that alendronate interacts more efficiently with the tooth enamel surface and has less sensitivity to the surface topography in comparison with D-Asp$_8$.

To further test the possibility that alendronate and D-Asp$_8$ will bind differently to hydroxyapatite with different crystallinity, we synthesized two hydroxyapatites (HA$_a$, high crystallinity, and HA$_b$, low crystallinity; Table 1) (*25*, *26*) for the *in vitro* binding test. Solubility studies and X-ray diffraction evaluation of these hydroxyapatites indicate that the lattice disorder of the bulk mineral phase (which is reflected by the crystallite microstrain parameter value) correlates well with the lattice disorder at the crystal-solution interface (to be published). So, it would be reasonable to expect that the binding behavior of molecules to apatite surfaces can be dependent upon the lattice disorder of the bulk mineral phase. PBS solutions of P-ALN-FITC and P-D-Asp$_8$-FITC were incubated with HA$_a$ and HA$_b$. After removal of HA powders from the solutions, the percentage of the FITC-labeled conjugates bound to HAs was calculated from the decreased UV absorbance of the polymer solutions. As shown in Figure 4, the higher absolute binding

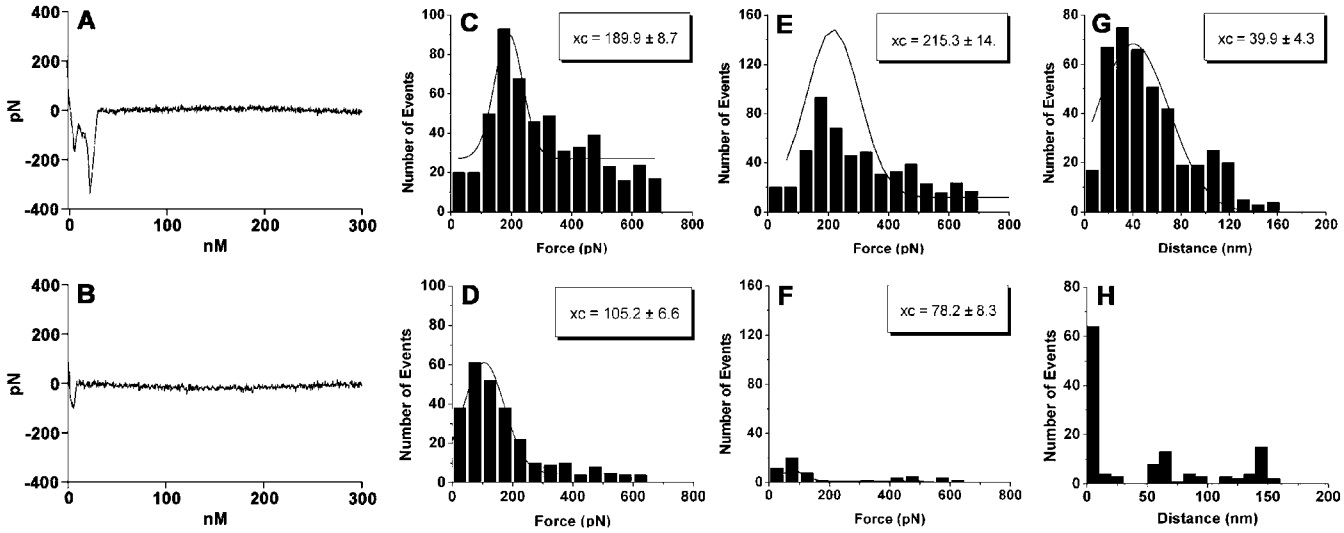


Figure 3. AFM analyses of different interaction between osteotropic compounds (alendronate and D-Asp$_8$) and tooth enamel surface. (A) Typical force−distance curve shows the interaction between alendronate modified tip and tooth enamel surface. (B) Typical force−distance curve shows the interaction between D-Asp$_8$ modified tip and tooth enamel surface. (C) Histogram for rupture forces obtained for the force spectroscopy measurements with the tips functionalized with alendronate. (D) Histogram for rupture forces obtained for the force spectroscopy measurements with the tips functionalized with D-Asp$_8$. (E) Histogram of the secondary rupture force events of Alendronate. (F) Histogram of the secondary rupture force events of D-Asp$_8$. (G) Histogram of the rupture events for all distances except at zero for alendronate. (H) Histogram of the rupture events for all distances except at zero for D-Asp$_8$. The most probable values obtained from the Gaussian fit for the histograms, which combine the analyses for more than 300 events are indicated in the inserts. No Gaussian fit could be obtained for (H).

Table 1. Characterization of Synthetic Hydroxyapatite with Different Crystallinity

sample	CO_3^{2-} (wt %)	PO_4^{3-} (wt %)	Ca^{2+} (wt %)	Na^+ (wt %)[a]	Ca/P	crystallite microstrain parameter (X)	specific surface area (m^2/g)
HA_a	0.5	53.9	38.1	0.23	1.68	0.17	26.7
HA_b	8.7	45.4	37.3	0.58	1.95	0.61	30.0

[a] The remaining contents in HA_a and Ha_b are mainly water, hydroxide, and trace elements (*27*).

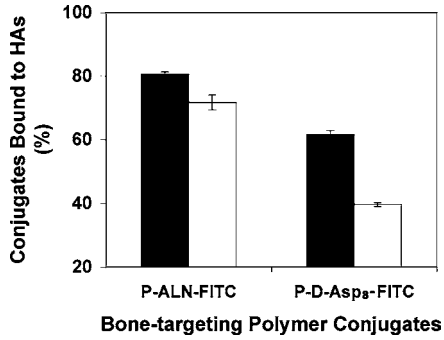


Figure 4. Binding ability of P-ALN-FITC and P-D-Asp$_8$-FITC to hydroxyapatites with different crystallinity. [ALN] = 3.2×10^{-5} mol/g for P-ALN-FITC; [D-Asp$_8$] = 7.0×10^{-5} mol/g for P-D-Asp$_8$-FITC. HA_a (■): microstrain = 0.05 ± 0.03 (high crystallinity). HA_b (□): microstrain = 0.61 ± 0.03 (low crystallinity). The different crystallinity of hydroxyapatites caused 9% difference in binding for P-ALN-FITC and 22% difference for P-D-Asp$_8$-FITC.

percentage of P-ALN-FITC to HAs, when compared to P-D-Asp$_8$-FITC, is probably confirming the stronger binding force of alendronate than D-Asp$_8$. Nevertheless, the binding of P-ALN-FITC to HAs is less sensitive to the change of apatite crystallinity compared to P-D-Asp$_8$-FITC.

Evidently, the AFM study suggests that alendronate has stronger binding to hydroxyapatite than D-Asp$_8$. Such differences in their ability to bind to hydroxyapatite coupled with their differences in binding with changes in apatite crystallinity would provide an explanation for the preferential binding of D-Asp$_8$ to hydroxyapatite with higher crystallinity. Though these experiments were not performed on bone apatite, the data support the hypothesis that it is the weak binding ability of D-Asp$_8$ to apatite that causes its *in vivo* selectivity to the bone resorption surface (containing bone apatite with relatively higher crystallinity) over formation surfaces (mainly amorphous calcium phosphate) (*19*). Incorporation of molecular structures (e.g., tetracycline, D-Asp$_8$) that could recognize different subtissue functional domains (osteolytic and osteoblastic) (*18*) into the new drug design and osteotropic drug delivery systems would greatly enhance the therapeutic index by delivering the drug directly to the desired cells and molecular targets.

ACKNOWLEDGMENT

We acknowledge financial support from the College of Pharmacy, University of Nebraska Medical Center (D.W., L.S.S., A.M.P., X.M.L., and Y.L.) and NIH Grant GM069847 (S.C.M., P.K., and J.K.).

Supporting Information Available: Detailed AFM procedures are described in the Supporting Information. This material is available free of charge via the Internet at http://pubs.acs.org.

LITERATURE CITED

(1) Marks, S. C., Jr., and Odgren, P. R. (2002) Structure and development of the skeleton. In *Principles of Bone Biology*, 2nd ed. (Bilezikian, J. P., Raisz, L. G., and Rodan, G. A., Eds.) pp 3−15, Chapter 1, Volume 1, Academic Press, San Diego.

(2) Rodan, G. A., and Martin, T. J. (2000) Therapeutic approaches to bone diseases. *Science 289*, 1508−1514.

(3) Taylor, D., Hazenberg, J. G., and Lee, T. C. (2007) Living with cracks: Damage and repair in human bone. *Nat. Mater. 6*, 263−268.

(4) Ducy, P., Zhang, R., Geoffroy, V., Ridall, A. L., and Karsenty, G. (1997) Osf2/Cbfa1: A transcriptional activator of osteoblast differentiation. *Cell 89*, 747−754.

(5) Takahashi, N., Udagawa, N., Takami, M., and Suda, T. (2002) Cells of bone: Osteoclast generation. In *Principles of Bone Biology*, 2nd ed. (Bilezikian, J. P., Raisz, L. G., and Rodan, G. A., Eds.) pp 109−126, Chapter 7, Volume 1, Academic Press, San Diego.

(6) Väänänen, K., and Zhao, H. (2002) Osteoclast function: Biology and mechanisms. In *Principles of Bone Biology*, 2nd ed. (Bilezikian, J. P., Raisz, L. G., and Rodan, G. A. Eds.) pp 127−139, Chapter 8, Volume 1, Academic Press, San Diego.
(7) Capparelli, C., Kostenuik, P. J., Morony, S., Starnes, C., Weimann, B., Van, G., Scully, S., Qi, M., Lacey, D. L., and Dunstan, C. R. (2000) Osteoprotegerin prevents and reverses hypercalcemia in a murine model of humoral hypercalcemia of malignancy. *Cancer Res. 60*, 783−787.
(8) Yamashita, D. S., and Dodds, R. A. (2000) Cathepsin K and the design of inhibitors of cathepsin K. *Curr. Pharm. Des. 6*, 1−24.
(9) Minkin, C., and Jennings, J. M. (1972) Carbonic anhydrase and bone remodeling: sulfonamide inhibition of bone resorption in organ culture. *Science 176*, 1031−1033.
(10) Engleman, V. W., Nickols, G. A., Ross, F. P., Horton, M. A., Griggs, D. W., Settle, S. L., Ruminski, P. G., and Teitelbaum, S. L. (1997) A peptidomimetic antagonist of the $\alpha v\beta 3$ integrin inhibits bone resorption *in vitro* and prevents osteoporosis *in vivo*. *J. Clin. Invest. 99*, 2284−2292.
(11) Shakespeare, W., Yang, M., Bohacek, R., Cerasoli, F., Stebbins, K., Sundaramoorthi, R., Azimioara, M., Vu, C., Pradeepan, S., Metcalf, C., III, Haraldson, C., Merry, T., Dalgarno, D., Narula, S., Hatada, M., Lu, X., van Schravendijk, M. R., Adams, S., Violette, S., Smith, J., Guan, W., Bartlett, C., Herson, J., Iuliucci, J., Weigele, M., and Sawyer, T. (2000) Structure-based design of an osteoclast-selective, nonpeptide src homology 2 inhibitor with *in vivo* antiresorptive activity. *Proc. Natl. Acad. Sci. U.S.A. 97*, 9373−9378.
(12) Miller, S. C., and Marks, S. C., Jr. (1994) Effects of prostaglandins on the skeleton. *Clin. Plast. Surg. 21*, 393−400.
(13) Yoshida, K., Oida, H., Kobayashi, T., Maruyama, T., Tanaka, M., Katayama, T., Yamaguchi, K., Segi, E., Tsuboyama, T., Matsushita, M., Ito, K., Ito, Y., Sugimoto, Y., Ushikubi, F., Ohuchida, S., Kondo, K., Nakamura, T., and Narumiya, S. (2002) Stimulation of bone formation and prevention of bone loss by prostaglandin E EP4 receptor activation. *Proc. Natl. Acad. Sci. U.S.A. 99*, 4580−4585.
(14) Mundy, G., Garrett, R., Harris, S., Chan, J., Chen, D., Rossini, G., Boyce, B., Zhao, M., and Gutierrez, G. (1999) Stimulation of bone formation *in vitro* and in rodents by statins. *Science 286*, 1946−1949.
(15) Lindsay, R., and Nieves, J. (1997) Randomised controlled study of effect of parathyroid hormone on vertebral-bone mass and fracture incidence among postmenopausal women on oestrogen with osteoporosis. *Lancet 350*, 550−555.
(16) Wang, D., Miller, S., Sima, M., Kopečková, P., and Kopeček, J. (2003) Synthesis and evaluation of water-soluble polymeric bone-targeted drug delivery systems. *Bioconjugate Chem. 14*, 853−859.
(17) Wang, D., Sima, M., Mosley, R. L., Davda, J. P., Tietze, N., Miller, S. C., Gwilt, P. R., Kopečková, P., and Kopeček, J. (2006) Pharmacokinetic and biodistribution studies of a bone-targeting drug delivery system based on *N*-(2-hydroxypropyl)methacrylamide copolymers. *Mol. Pharm. 3*, 717−725.
(18) Frost, H. M., Villaneuva, A. R., and Roth, H. (1960) Measurement of bone formation in a 57 year old man by means of tetracyclines. *Henry Ford Hosp. Med. Bull. 8*, 239−254.
(19) Posner, A. S., and Betts, F. (1975) Synthetic amorphous calcium phosphate and its relation to bone mineral structure. *Acc. Chem. Res. 8*, 273−281.
(20) Posner, A. S. (1969) Crystal chemistry of bone mineral. *Physiol. Rev. 49*, 760−792.
(21) Thompson, D. D., Posner, A. S., Laughlin, W. S., and Blumenthal, N. C. (1983) Comparison of bone apatite in osteoporotic and normal Eskimos. *Calcif. Tissue Int. 35*, 392−393.
(22) Limansky, A. P., Shlyakhtenko, L. S., Schaus, S., Henderson, E., and Lyubchenko, Y. L. (2002) Aminomodified probes for atomic force microscopy. *Probe Microsc. 2*, 227−234.
(23) McAllister, C., Karymov, M. A., Kawano, Y., Lushnikov, A. Y., Mikheikin, A., Uversky, V. N., and Lyubchenko, Y. L. (2005) Protein interactions and misfolding analyzed by AFM force spectroscopy. *J. Mol. Biol. 354*, 1028−1042.
(24) Shlyakhtenko, L. S., Gall, A. A., Filonov, A., Cerovac, Z., Lushnikov, A., and Lyubchenko, Y. L. (2003) Silatrane-based surface chemistry for immobilization of DNA, protein-DNA complexes and other biological materials. *Ultramicroscopy 97*, 279−287.
(25) Nelson, D. G., and Featherstone, J. D. (1982) Preparation, analysis, and characterization of carbonated apatites. *Calcif. Tissue Int. 34 Suppl. 2*, S69−81.
(26) Baig, A. A., Fox, J. L., Young, R. A., Wang, Z., Hsu, J., Higuchi, W. I., Chhettry, A., Zhuang, H., and Otsuka, M. (1999) Relationships among carbonated apatite solubility, crystallite size, and microstrain parameters. *Calcif. Tissue Int. 64*, 437−449.
(27) Markovic, M., Fowler, B. O., and Tung, M. S. (2004) Preparation and comprehensive characterization of a calcium hydroxyapatite reference material. *J. Res. Natl. Inst. Stand. Technol. 109*, 553−568.

BC7002132

On−Off Regulation of ^{19}F Magnetic Resonance Signals Based on pH-Sensitive PEGylated Nanogels for Potential Tumor-Specific Smart ^{19}F MRI Probes

Motoi Oishi,[†,‡,§] Shogo Sumitani,[†] and Yukio Nagasaki*[,†,‡,§,||]

Graduate School of Pure and Applied Sciences, Tsukuba Research Center for Interdisciplinary Materials Science (TIMS), Center for Tsukuba Advanced Research Alliance (TARA), and Master's School of Medical Sciences, Graduate School of Comprehensive Human, University of Tsukuba, 1-1-1 Ten-noudai, Tsukuba, Ibaraki 305-8573, Japan. Received June 17, 2007; Revised Manuscript Received August 11, 2007

The pH-sensitive PEGylated nanogels constructed from tethered PEG chains and a polyamine gel core containing ^{19}F compounds showed remarkable on−off regulation of ^{19}F MR (magnetic resonance) signals in response to the extracellular pH (6.5) of the tumor environment, even in the presence of 90% fetal bovine serum, due to the increase in the molecular motion of the ^{19}F compounds through the hydrophilic−hydrophobic (volume-phase) transition of the polyamine gel core. Eventually, an appreciably enhanced ^{19}F MR signal at an extremely low ^{19}F compound concentration (∼55 μM) was achieved, demonstrating the utility of these nanogels as solid tumor-specific smart ^{19}F MRI probes.

Magnetic resonance imaging (MRI[1]) based on ^{1}H has been recognized as a powerful and noninvasive methodology for cancer diagnosis (*1*, *2*). Nevertheless, the intense proton background causes insufficient discrimination of tumor tissues from normal tissues. An important advancement in this field is the ^{19}F MRI technique (*3*), which may be capable of producing high-contrast *in vivo* images, since there is no endogenous ^{19}F in the body that might be a source of background noise. Note that ^{19}F is 100% naturally abundant and has an MR (magnetic resonance) sensitivity nearly as high as that of protons. A variety of stimuli-sensitive ^{19}F probes have been developed so far; however, the tumor diagnostic value of such probes under *in vivo* conditions is still controversial due to their nonspecific accumulation in normal tissues, preferential renal clearance, and low sensitivity of the ^{19}F MR chemical shift ($\Delta\delta$) to tumor environments. Thus, nonspecific interaction between the ^{19}F probe and biological components such as serum proteins and cells often leads to a moderate chemical-shift imaging resolution (*4*). A major key to the success of cancer diagnosis is believed to be the development of nanosized (<100 nm) and nonfouling ^{19}F probes capable of complete on−off regulation of the ^{19}F MR signal in response to the tumor environment, enabling ^{19}F MR signal intensity imaging after smooth accumulation in solid tumor tissues through the enhanced permeability and retention (EPR) effect (*5*).

In this regard, we newly designed and prepared for the first time nanosized and pH-sensitive ("smart") ^{19}F probes based on PEGylated nanogels constructed from a cross-linked polyamine gel core containing ^{19}F compounds and tethered PEG chains bearing an acetal group as a platform moiety to install ligand molecules. Because of the core−shell structure of the nanogels, the pH-sensitive PEGylated nanogels (*6*, *7*) exhibited excellent solubility in aqueous media, minimum interaction with biological components, and significant hydrophilic−hydrophobic (volume-phase) transition of the polyamine gel core in response to the extracellular pH of solid tumor tissues where the pH is 0.4−1.0 units lower than the physiological pH of ∼7.4 (*8*, *9*). A unique finding, which we would like to describe here, is the remarkable on−off regulation of the ^{19}F MR signal based on the molecular motion of the ^{19}F compounds synchronizing with the hydrophilic−hydrophobic transition of the polyamine gel core of the pH-sensitive PEGylated nanogels (Figure 1a), thus achieving appreciably enhanced ^{19}F MR signal at an extremely low ^{19}F probe concentration and at the intracellular pH typical of tumor environments.

Our strategy of formulating pH-sensitive PEGylated nanogels as smart ^{19}F MRI probes is based on the emulsion copolymerization of 2-(*N*,*N*-diethylamino)ethyl methacrylate (DEAMA: pH-sensitive component) and 2,2,2-trifluoroethyl methacrylate (TFEMA: ^{19}F compound) at various molar ratios in the presence of heterobifunctional PEG bearing an acetal group (ligand installation moiety) at the α-end and a 4-vinylbenzyl group at the ω-end (acetal-PEG−Ph−CH=CH$_2$: M_n = 5030, M_w/M_n = 1.04), potassium persulfate (KPS: initiator), and 1.0 mol % of ethylene glycol dimethacrylate (EGDMA: cross-linker) (Figure 1b). The compositions of the PEGylated nanogels were determined as the feed ratio, since the polymerization proceeded smoothly with complete consumption of the DEAMA and TFEMA within 1 h (100% conversion). Figure 2a shows the pH dependency of the diameters of the PEGylated nanogels containing various amounts of TFEMA. As the TFEMA mol % increased in the nanogel, the size variation of the PEGylated nanogels with unimodal size distribution ($\mu_2/\Gamma^2 < 0.155$) became small due to the increase in hydrophobic and non-ionizable PTFEMA segment, leading to a decrease in the ion osmotic pressure of the PDEAMA-*co*-PTFEMA gel core. Note that pH-sensitive PEGylated nanogels containing TFEMA showed volume phase transition points in the pH range 7.3−6.8, strongly suggesting that the swelling of PEGylated nanogels will occur

* Corresponding author. Prof. Yukio Nagasaki (Phone: +81-29-853-5749. Fax: +81-29-853-5749. E-mail: nagasaki@nagalabo.jp).
† Graduate School of Pure and Applied Sciences.
‡ TIMS.
§ TARA.
|| Master's School of Medical Sciences.

[1] Abbreviations: MRI, magnetic resonance imaging; MR, magnetic resonance; EPR, enhanced permeability and retention; PEG, poly(ethylene glycol); DEAMA, 2-(*N*,*N*-diethylamino)ethyl methacrylate; TFEMA, 2,2,2-trifluoroethyl methacrylate; KPS, potassium persulfate; EGDMA, ethylene glycol dimethacrylate; FBS, fetal bovine serum.

10.1021/bc7002154 CCC: $37.00 © 2007 American Chemical Society
Published on Web 08/31/2007

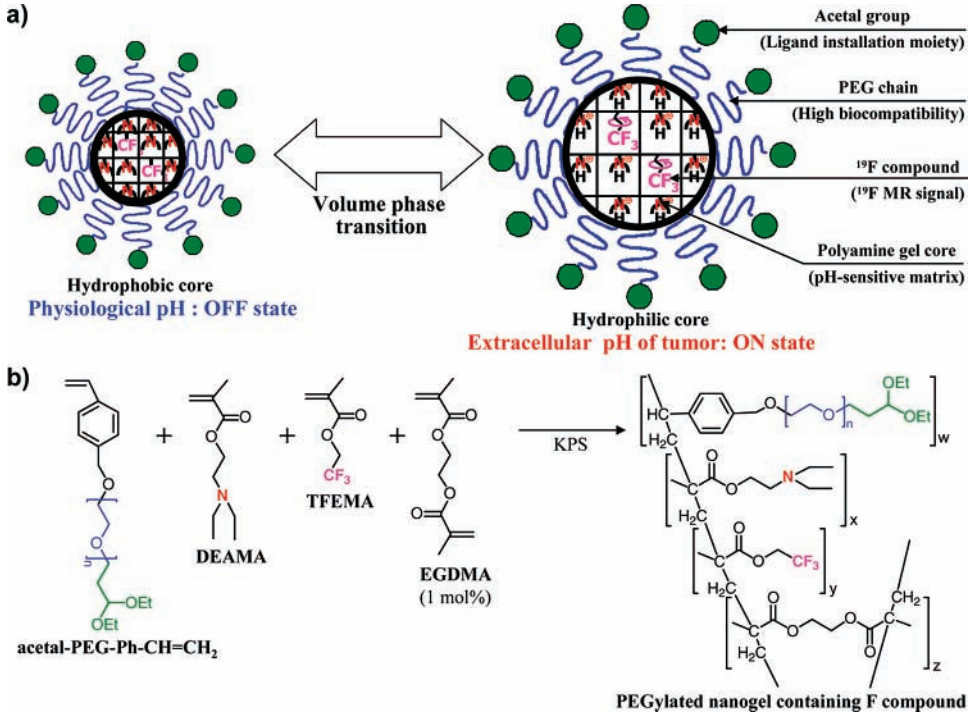


Figure 1. (a) Schematic illustration of the smart ^{19}F nanoprobe based on the pH-sensitive PEGylated nanogel. (b) Synthesis of the pH-sensitive PEGylated nanogel containing ^{19}F compounds.

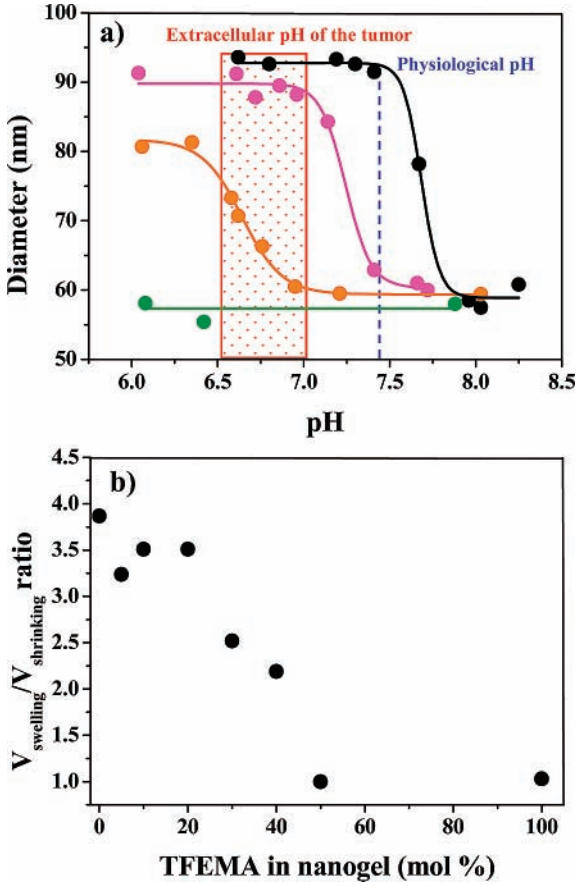


Figure 2. (a) pH dependency of the diameters of the PEGylated nanogels containing 0 (black), 10 (pink), 30 (orange), and 50 (green) mol % of TFEMA. (b) $V_{sweeling}/V_{shrinking}$ ratio of the PEGylated nanogels containing various amounts of TFEMA. (DLS measurement: angle, 90°; temperature, 37 °C; 10 mM phosphate buffer with 0.15 M NaCl).

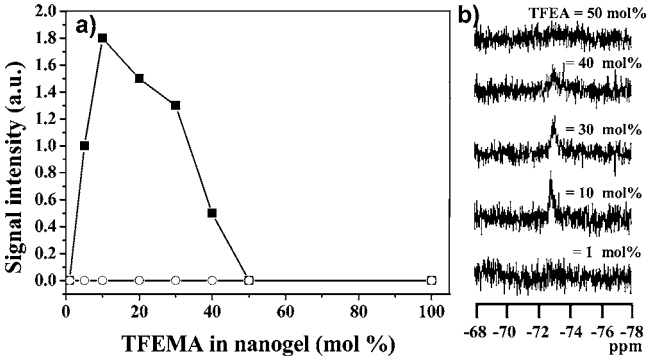


Figure 3. (a) Intensity of the ^{19}F MR signals of the PEGylated nanogels containing various amounts of TFEMA at pH 6.5 (■) and 7.4 (○). (b) ^{19}F NMR spectra of the pH-sensitive PEGylated nanogels containing various amounts of TFEMA at pH 6.5.

only at the extracellular pH of tumor tissues (7.0−6.5). In addition, there was a negligible change in the diameter (ca. 58 nm) of the PEGylated nanogels, because their highly hydrophobic core contains a TFEMA concentration of more than 50 mol %. The $V_{swelling}/V_{shrinking}$ ratio denotes the extent of hydrodynamic volume change at the volume phase transition point. Indeed, the $V_{swelling}/V_{shrinking}$ ratio for PEGylated nanogels containing the TFEMA component in the gel core was smaller than that of PEGylated nanogels without the TFEMA component (TFEMA = 0 mol %: $V_{swelling}/V_{shrinking}$ = 3.9), as shown in Figure 2b.

Figure 3a shows the intensity of the ^{19}F MR signal (ca. −73 ppm) from the ^{19}F compounds in the PEGylated nanogels (450 μg/mL), as measured by ^{19}F NMR spectroscopy at both the physiological pH (7.4) and the extracellular pH (6.5) of tumor environments. Note that almost no ^{19}F MR signal (background level) was observed at physiological pH (7.4), where the PDEAMA-*co*-PTFEMA gel core was hydrophobic owing to the deprotonation of the amino groups, *viz.*, the absence of ^{19}F MR signals is most likely due to the broadening effect caused by the limited molecular motion of the ^{19}F compounds in the hydrophobic (solid-state) gel core (*10*). In sharp contrast, the PEGylated nanogels in the TFEMA range 5−40 mol % showed

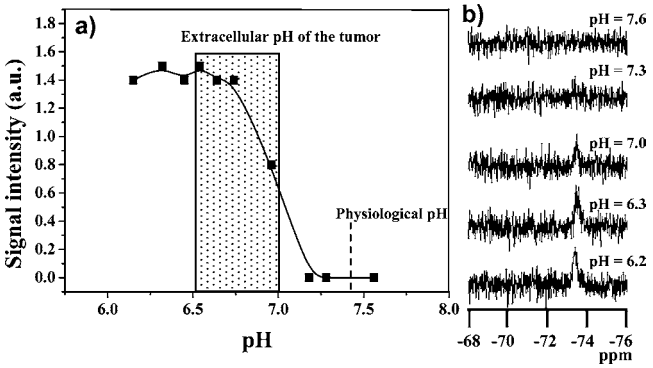


Figure 4. (a) pH dependency of the intensity of the ^{19}F MR signal from the PEGylated nanogel containing 10 mol % of TFEMA. (b) ^{19}F NMR spectra of the pH-sensitive PEGylated nanogels containing 10 mol % of TFEMA at various pH values.

clear ^{19}F MR signals at the extracellular pH (6.5) of tumor environments (Figure 3b). This complete on−off regulation of the ^{19}F MR signal by the pH-sensitive PEGylated nanogels is a remarkable characteristic of the tumor-specific ^{19}F MRI probe. Worth noting is that the signal intensity of the PEGylated nanogels in the TFEMA range 10−50 mol % is almost consistent with the $V_{swelling}/V_{shrinking}$ ratio of the PEGylated nanogels, as shown in Figure 2b. It should also be noted that the intensity of the ^{19}F MR signal of the PEGylated nanogels increased with decreasing TFEMA, *viz.*, the highest intensity of the ^{19}F MR signal was observed at TFEMA = 10 mol %. These findings strongly suggest that the PEGylated nanogels with a high $V_{swelling}/V_{shrinking}$ ratio have a more hydrophilic core and higher mobility than those with a low $V_{swelling}/V_{shrinking}$ ratio. On the other hand, the intensity of the ^{19}F MR signal of the PEGylated nanogels containing less than TFEMA = 5 mol % significantly decreased even though the $V_{swelling}/V_{shrinking}$ ratio was almost similar to that of PEGylated nanogels containing TFEMA = 10 mol %. This is most likely due to a lower TFEMA concentration ([TFEMA] = 83 μM) than that of PEGylated nanogel containing TFEMA = 10 mol % ([TFEMA] = 166 μM), because the weight concentration of all PEGylated nanogels was constant (450 μg/mL). Notably, the pH-sensitive PEGylated nanogel containing TFEMA = 10 mol % showed an increase in the intensity of the ^{19}F MR signal in synchronization with the decreasing pH as shown in Figure 4a,b; thus, this behavior is almost consistent with both the pH-dependent volume phase transition (Figure 2a) and the α/pH curve (Supporting Information Figure S2) of the PEGylated nanogel, indicating that the molecular motion of the ^{19}F compounds in the gel core plays a crucial role in the intensity of the ^{19}F MR signal in ^{19}F NMR spectroscopy.

The intensity of the ^{19}F MR signal of the pH-sensitive PEGylated nanogel containing TFEMA = 10 mol % was linearly correlated to the [TFEMA] concentration (in a dose-dependent manner) at the extracellular pH (=6.5) of tumor environments (Figure 5a), which could be related to the nanogel number, suggesting that it could be quantified by means of ^{19}F MRI *in vivo*. Notably, ^{19}F MR signal from the ^{19}F compounds in the PEGylated nanogel was observed at TFEMA concentration as low as ~55 μM. This finding is also remarkable because the ^{19}F probes (*11*) for ^{19}F MRI generally require concentrations in the millimolar range (~1 mM) in the buffer solution. Worth noting is that the pH-sensitive PEGylated nanogel containing TFEMA = 10 mol % was able to retain the on−off regulation of the ^{19}F MR signal even in the presence of 90% fetal bovine serum (FBS) (Figure 5b,c), which means that it can be used for *in vivo* applications.

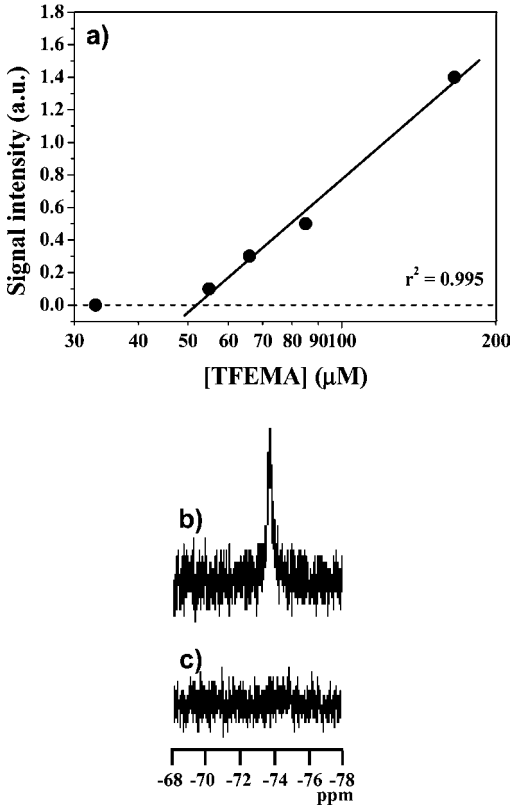


Figure 5. (a) Linear correlation of the intensity of the ^{19}F MR signal versus dilutions of the pH-sensitive PEGylated nanogel containing 10 mol % of TFEMA. ^{19}F NMR spectra of the pH-sensitive PEGylated nanogels containing 10 mol % of TFEMA in the presence of 90% FBS at (b) pH 6.5 and (c) pH 7.4. ([TEFMA] = 553 μM, at 37 °C; number of scans = 64).

In conclusion, the pH-sensitive PEGylated nanogels composed of a PDEAMA-*co*-PTFEMA gel core and tethered PEG chains exhibited significant ^{19}F MR signals at extremely low ^{19}F compound concentrations in response to the extracellular pH of tumor environments under ^{19}F NMR spectroscopy. Therefore, the construction of pH-sensitive PEGylated nanogel with appropriate ^{19}F compounds is a promising approach to the creation of tumor-specific smart ^{19}F MRI systems to be used *in vivo*. Furthermore, pH-sensitive PEGylated nanogels can also be utilized as pH-sensitive carriers in the anticancer drug delivery systems (*12*), *viz.*, the pH-sensitive PEGylated nanogel acts as a theranostic (therapeutic and diagnostic) nanodevice.

ACKNOWLEDGMENT

This work was partially supported by a Grant-in-Aid for Scientific Research (1800033) from the Ministry of Education, Culture, Sports, Science and Technology of Japan (MEXT).

Supporting Information Available: Information on the experimental details and materials. This material is available free of charge via the Internet at http://pubs.acs.org.

LITERATURE CITED

(1) Caravan, P., Ellison, J. J., McMurry, T. J., and Lauffer, R. B. (1999) Gadolinium (III) chelates as MRI contrast agents: structure, dynamics, and applications. *Chem. Rev. 99*, 2293−2352.

(2) Kobayashi, H., and Brechbiel, M. W. (2005) Nano-sized MRI contrast agents with dendrimer cores. *Adv. Drug Delivery Rev. 57*, 2271−2286.

(3) Yu, J-X., Kodibagkar, V. D., Cui, W., and Mason, R. P. (2005) ^{19}F: A versatile reporter for non-invasive physiology and pharmacology using magnetic resonance, *Curr. Med. Chem. 12*, 819−848.

(4) Mason, R. P. (1999) Transmembrane pH gradients in vivo: Measurements using fluorinated vitamin B6 derivatives. *Curr. Med. Chem. 6*, 481−499.

(5) Matsumura, Y., and Maeda, H. (1986) A new concept for macromolecular therapeutics in cancer chemotherapy: mechanism of tumoritropic accumulation of proteins and the antitumor agent smancs. *Cancer Res. 46*, 6387−6392.

(6) Hayashi, H., Iijima, M., Kataoka, K., and Nagasaki, Y. (2004) pH-Sensitive nanogel possessing reactive PEG tethered chains on the surface. *Macromolecules 37*, 5389−5396.

(7) Oishi, M., Hayashi, H., Itaka, K., Kataoka, K., and Nagasaki, Y. (2007) pH-Responsive PEGylated nanogels as targetable and low invasive endosomolytic agents to induce the enhanced transfection efficiency of nonviral gene vectors. *Colloid Polym. Sci. 285*, 1055−1060.

(8) Wike-Hooley, J. L., Haveman, J., and Reinhold, H. S. (1984) The relevance of tumour pH to the treatment of malignant disease. *Radiother. Oncol. 2*, 343−366.

(9) Gerweck, L. E., and Seetharaman, K. (1996) Cellular pH gradient in tumor versus normal tissue: potential exploitation for the treatment of cancer. *Cancer Res. 56*, 1194−1198.

(10) Butun, V., Billingham, N. C., and Armes, S. P. (1998) Unusual aggregation sehavior of a novel tertiary amine methacrylate-based diblock copolymer: formation of micelles and reverse micelles in aqueous solution. *J. Am. Chem. Soc. 120*, 11818−11819.

(11) Frenzel, T., Kossler, S., Bauer, H., Niedballa, U., and Weinmann, H. (1994) Noninvasive in vivo pH measurements using a fluorinated pH probe and fluorine-19 magnetic resonance spectroscopy. *Invest. Radiol. 29*, S220−222.

(12) Oishi, M., Hayashi, H., Iijima, M., and Nagasaki, Y. Endosomal release and intracellular delivery of anticancer drugs using pH-sensitive PEGylated nanogels. *J. Mater. Chem.* in press.

BC7002154

ARTICLES

Development of Poly(amino ester glycol urethane)/siRNA Polyplexes for Gene Silencing

S-ja Tseng and Shiue-Cheng Tang*

Department of Chemical Engineering, National Tsing Hua University, 101, Sec. 2, Kuang Fu Road, Hsinchu 300, Taiwan

Received December 11, 2006; Revised Manuscript Received April 2, 2007

Nonviral vectors, with their low immunogenicity and lack of pathogenicity, offer significant promise for siRNA therapy with fewer safety concerns. Nonviral vectors were also preferred in most transient siRNA delivery due to their ease of preparation. Previously, we incorporated tertiary amines and polyethylene glycol (PEG) into poly(ester urethane) to synthesize a soluble poly(amino ester glycol urethane), PaE_GU, as a novel DNA transfection reagent for transgene delivery. The aim of this study was to develop PaE_GU/siRNA polyplexes for gene silencing. We characterized the properties of PaE_GU/siRNA polyplexes and compared them with those of PaE_GU/DNA polyplexes. Using the Alexa Fluor 488-labeled, nonsilencing control siRNA as the reporter, we visualized cellular uptake of PaE_GU/siRNA polyplexes and optimized the mass ratio of PaE_GU/siRNA for delivery at 80/1. At this ratio, the average diameter of polyplexes was 540 nm, which was significantly larger than the average diameter of PaE_GU/DNA polyplexes at 155 nm for efficient DNA delivery. Using the optimized PaE_GU/siRNA polyplexes, transient silencing of constitutive luciferase expression (up to 92%) was achieved in our recombinant human HT-1080 fibroblast model via anti-luciferase siRNA delivery. In conclusion, PaE_GU/siRNA polyplexes were developed and optimized for cellular uptake to allow efficient gene silencing. Engineering of soluble biodegradable polymers to incorporate amino, ester, PEG, and urethane units in the backbone constitutes a useful approach for the future design of siRNA carriers.

INTRODUCTION

The emergence of small interfering RNA (siRNA) to inhibit gene expression in a sequence-specific fashion has initiated an industry of manufacturing synthetic RNA. However, a major challenge to the continued development and therapeutic application of siRNA is the design of suitable vectors for its delivery. Nonviral vectors are preferred over viral vectors for most transient studies due to their ease of preparation. More importantly, the low immunogenicity and lack of pathogenicity of nonviral vectors offer promise for siRNA therapy with fewer safety concerns (*1*−*4*).

Transfection reagents formulated by biodegradable polymers are good candidates for delivery of nucleic acids, including siRNA (*5*−*12*). These polymers can be modified with positively charged amine groups for electrostatic interaction with nucleic acids and bridged with hydrolytically unstable linkages, such as ester or urethane linkages, to induce biodegradability and generate nontoxic degraded compounds. In addition, cationic polymers have been shown to provide pH-buffering ability, allowing the formation of a "proton sponge" to assist in the escape of vectors from the endocytosis pathway and improve transfection efficiency (*13*−*15*).

Poly(ester urethane), PEU, is a class of biodegradable polymer that has been applied as a tissue-engineering scaffold with minimal cytotoxicity *in vitro* and *in vivo* (*16*−*20*). Previously, we developed a method of incorporating tertiary amines and polyethylene glycol (PEG) into PEU to synthesize a soluble poly(amino ester glycol urethane), PaE_GU (Figure 1A), as a novel DNA transfection reagent (*21*). Our study showed that PaE_GU exhibited faster hydrolysis kinetics than the control reagent poly(amino ester), half-lives of 19 h and 36 h for PaE_GU and poly(amino ester), respectively, in the phosphate buffer saline at 37 °C, which underscored PaE_GU's unique property of low cytotoxicity.

The aim of this study was to develop PaE_GU/siRNA polyplexes for gene silencing. Our previous results showed that PaE_GU was capable of mediating DNA transfection for transgene expression. For gene silencing, however, it is unclear whether PaE_GU remains effective in mediating siRNA delivery, because no reports have characterized the interaction of PEU-based vectors with siRNA. There are two important differences between siRNA and DNA transfection. First, the size of siRNA (21−23 base pairs) is significantly smaller than that of the gene-encoding DNA molecule by 2 orders of magnitude in molecular weight. Second, unlike the requirement for nuclear delivery in DNA transfection, siRNA is active within the cytoplasm, and therefore polymer/siRNA polyplexes cannot be too stable in withholding the RNA molecules (*6*, *22*). For instance, poly(ethylene imine) (PEI)-mediated siRNA delivery for gene silencing was observed only in a narrow window of conditions (*23*), in comparison to the efficiency and ease of use of PEI-mediated DNA delivery for transgene expression. We characterized and optimized PaE_GU/siRNA polyplexes for cellular uptake in this research. The results on developing PaE_GU/siRNA polyplexes for gene silencing and comparing the properties of PaE_GU/siRNA and PaE_GU/DNA polyplexes are presented and discussed.

* Corresponding author. Tel.: + 886-3-571-5131, ext. 33649; fax: + 886-3-571-5408; e-mail: sctang@che.nthu.edu.tw.

10.1021/bc060382j CCC: $37.00 © 2007 American Chemical Society
Published on Web 06/14/2007

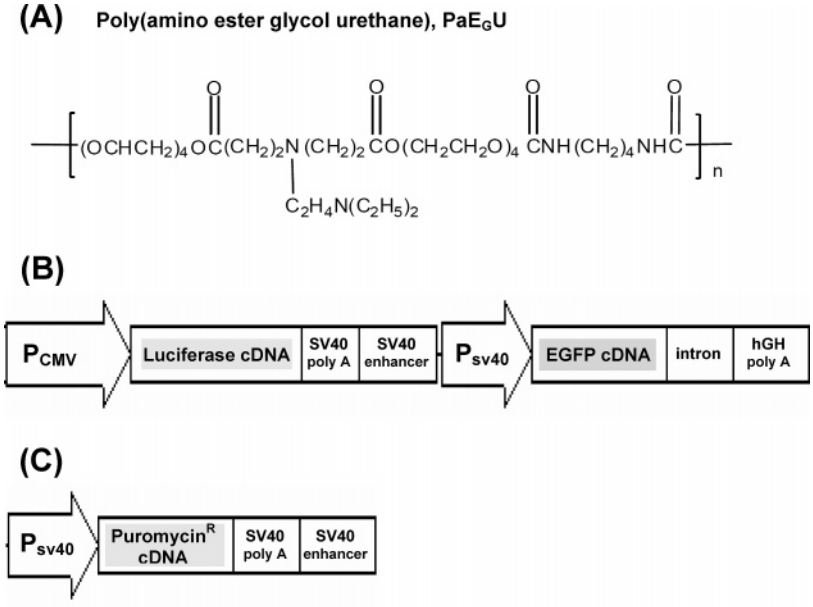


Figure 1. (A) Chemical structure of poly(amino ester glycol urethane), PaE$_G$U. (B and C) Schematics of the plasmids pAAV−luciferase−EGFP and pSV40−Puro, respectively, which were applied to generate recombinant HT-1080 fibroblasts with stable reporter gene expression. EGFP, enhanced green fluorescent protein. P_{cmv}, cytomegalovirus promoter. SV40 poly A, Simian Virus 40 late polyadenylation signal. P_{sv40}, Simian Virus 40 promoter. hGH poly A, human growth hormone polyadenylation signal.

EXPERIMENTAL PROCEDURES

Chemicals and siRNA. 2-Diethylaminoethylamine, 2-hydroxyethyl acrylate, dibutyltin dilaurate, tetrahydrofuran (THF), and *N*,*N*-dimethylformamide (DMF) were purchased from Fluka (Buchs, Switzerland) and were dried by passing them over calcium hydride and then distilled before use. Phosphate-buffered saline (PBS, pH 7.4) was purchased from Sigma Co. (St. Louis, MO). Poly(ethylene glycol) acrylate (MW = 375), 1,4-diisocyanatobutane, and poly(ethylene imine) (PEI, MW = 25 000) were purchased from Aldrich (Milwaukee, WI). The siRNA duplexes targeting luciferase (Luciferase GL3 siRNA) and EGFP (GFP-22 siRNA) and the Alexa Fluor 488, 5′-labeled siRNA with control scrambled sequence (Alexa Fluor 488-siRNA) were purchased from Qiagen (Deutschland, Germany). The siRNA sense sequences were luciferase, 5′-CUUACGCUGAGUACUUCGAdTdT-3′ and EGFP, 5′-GCAAGCUGACCCUGAAGUUCAUdTdT-3′; the control scrambled sequence was 5′-UUCUCCGAACGUGUCACGUdTdT-3′.

Cell Culture and Generation of Recombinant HT-1080 Fibroblasts with Constitutive Luciferase and EGFP Expression. Human HT-1080 fibroblasts (ATCC, Manassas, VA) were grown in Dulbecco's modified Eagle's medium (DMEM, Biosource, Rockville, MD) supplemented with 10% fetal bovine serum, 100 U/mL penicillin, and 100 μg/mL streptomycin at 37 °C in a humidified atmosphere of 5% CO_2. The plasmid pAAV−luciferase−EGFP, used to engineer HT-1080 cells into stable luciferase and EGFP expression cells, was constructed as previously described by Tang et al. (*24*). The dual expression cassettes of luciferase (CMV-driven) and EGFP (SV40-driven) are shown in Figure 1B. Plasmid pSV40−Puro, carrying the expression cassette of puromycin-resistant gene as a selection maker (Figure 1C), was constructed by cloning the 0.6-kb cDNA of puromycin-resistant gene (HindIII/XbaI fragment) from pIRESpuro (Clontech, Mountain View, CA) downstream of the SV40 promoter in pGL3-Control (Promega, Madison, WI) to replace the firefly luciferase cDNA and yield pSV40−Puro.

We applied a cotransfection of plasmids pAAV−luciferase−EGFP and pSV40−Puro to generate and select the recombinant HT-1080 fibroblasts which constitutively expressed puromycin, luciferase, and EGFP. When HT-1080 cells reached roughly 60−70% confluency, they were transfected using the FUGENE 6 reagent (Roche, Indianapolis, IN) according to the manufacturer's protocol. Cells were incubated for 24 h in a 40-mm culture dish with the culture medium (without penicillin and streptomycin) containing the plasmid pAAV−luciferase−EGFP (1 μg), plasmid pSV40−Puro (50 ng), and the FUGENE 6 reagent (3 μL). Cells were cultured for an additional 24 h for recovery after transfection. Cells were then trypsinized and split in 1:100 ratio into 100-mm culture dishes. During the selection process, which lasted over three weeks, cells were cultured in the presence of 1 μg/mL puromycin. Surviving cells formed colonies, which could be seen clearly under a microscope. Cells that expressed EGFP were identified, retrieved, and plated into the wells of a 24-well plate for expansion and later for tests of luciferase expression. Only cells that survived under puromycin selection and expressed both EGFP and luciferase were preserved for future use.

Synthesis and Characterization of Poly(amino ester glycol urethane), PaE$_G$U. PaE$_G$U was synthesized as previously described by Tseng and Tang (*21*). Briefly, poly(ethylene glycol) acrylate and 2-diethylaminoethylamine with a C═C/NH_2 molar ratio of 2/1.1 were mixed in anhydrous THF solvent under liquid nitrogen purge inside a reaction flask. The mixture was heated to 50 °C for reaction for 48 h to generate the monomer PEGamine-diol. In the second reaction, the synthesized PEGamine-diol and 1,4-diisocyanatobutane with a OH/NCO molar ratio of 1/1.1 were mixed in anhydrous DMF solvent in a three-necked reaction flask under dry nitrogen purge. The mixture was then heated to 70 °C for reaction for 6 h with 10 wt % dibutyltin dilaurate as the catalyst. An excess amount of methanol was slowly added into the reaction mixtures until no unreacted isocyanate groups were detected. After reaction, PaE$_G$U was precipitated in anhydrous ethyl ether and vacuum-dried at 40 °C.

The designated functional groups and polymer structure were confirmed by the FT-IR and the ^{1}H and ^{13}C NMR spectra. The molecular weight of PaE$_G$U was determined by high-performance liquid chromatography/gel permeation chromatography analysis (HPLC/GPC, Waters model LC-2410). The synthesized PaE$_G$U had a weight-average molecular weight of 17 500 and a polydispersity index of 1.4.

Preparation and Characterization of PaE$_G$U/siRNA Polyplexes. To prepare PaE$_G$U/siRNA polyplexes, 5.0 mg of PaE$_G$U was dissolved in PBS (pH 7.4) and mixed with Alexa Fluor 488-siRNA at mass ratios ranging from 10/1 to 100/1. The PaE$_G$U/siRNA mixture was incubated at room temperature for 30 min to allow self-assembly of polyplexes before further characterization. The hydrodynamic sizes of polyplexes were measured using a Zetasizer Nano ZS (3000HS, Malvern Instruments Ltd., Worcestershire, U.K.). The surface charges of polyplexes were determined by the electrophoretic mobility at 25 °C with a zeta-potential system (Nicomp Instrument, Santa Barbara, CA). The electrostatic interaction between PaE$_G$U and siRNA was evaluated by a gel retardation assay. In this assay, electrophoresis was carried out with different mass ratios of PaE$_G$U/siRNA polyplexes loaded into parallel wells of a 0.7% agarose gel in a Tris-acetate-EDTA (TAE) buffer. Polymer-free siRNA was used as the control. RNA duplexes ladder (Qiagen) with the smallest base pairs at 21 was used as a size reference. Electrophoresis was performed at 100 V for 35 min. The retardation of the polyplexes was visualized by staining with ethidium bromide.

Optimizing PaE$_G$U/siRNA Transfection. Prior to delivering the siRNA of interest for targeted gene silencing, we optimized transfection conditions using the Alexa Fluor 488-siRNA as the reporter. PaE$_G$U/siRNA polyplexes for transfection were prepared by incubating various amounts of PaE$_G$U (in PBS) with 1 μg of siRNA (in DMEM), with PaE$_G$U/siRNA mass ratios ranging from 40/1 to 200/1 for 30 min. In parallel, PEI/siRNA and Lipofectamine RNAiMAX (Lipofectamine, Invitrogen, Carlsbad, CA)/siRNA polyplexes were prepared as controls. PEI/siRNA polyplexes were prepared by incubating various amounts of PEI (in PBS) with 1 μg of siRNA (in DMEM), with PEI/siRNA mass ratios ranging from 0.5/1 to 5/1 for 30 min. Lipofectamine/siRNA polyplexes were prepared by incubating various volumes of Lipofectamine (μL) with 1 μg of siRNA (in DMEM), with Lipofectamine/siRNA ratios ranging from 2.5 μL/1 μg to 7.5 μL/1 μg for 30 min. Culture medium (without antibiotics) was then added to the mixture for adjusting the final volume to 1100 μL. Transfection was carried out by exposing cells on the 40-mm dish to the 1100-μL transfection cocktail. Approximately 24 h later, 2 mL of complete DMEM medium was added to the culture without removing the polymer/siRNA polyplexes, and cells were incubated for an additional 24 h before flow cytometry analysis.

Flow cytometry analysis of Alexa Fluor-488 positive cells was carried out using the FACSCalibur (Becton Dickinson) benchtop flow cytometer equipped with an argon laser at 488 nm excitation and a band-pass filter at 505−530 nm to detect the Alexa Fluor 488-labeled cells. Untransfected cells were used as the control. The cells were appropriately gated by forward and side scatters and 10 000 events per sample were collected. Additionally, transfected fibroblast monolayers were imaged by the Nikon ECLIPSE TS100-F fluorescence microscope for Alexa Fluor 488 detection with a Nikon GFP-L filter set (EX 480/40, DM 505, BA 510).

Silencing Luciferase and EGFP Expression. Recombinant HT-1080 cells, with constitutive luciferase and EGFP expression, were seeded in the wells of a 12-well plate overnight prior to transfection. Cells at various numbers, ranging from 2×10^4 to 5×10^5, were then treated with PaE$_G$U/siRNA (Luciferase GL3, Qiagen) polyplexes at 80/1 (μg/μg), PEI/siRNA polyplexes at 2/1 (μg/μg), or Lipofectamine/siRNA polyplexes at 5/1 (μL/μg) for silencing luciferase expression. At time = 0, 12, 24, 36, and 48 h, luciferase activity in transfected cells was measured with the luciferase assay system (Promega) according to the manufacturer's protocol and with a 20/20^n luminometer (Turner Biosystems, Sunnyvale, CA).

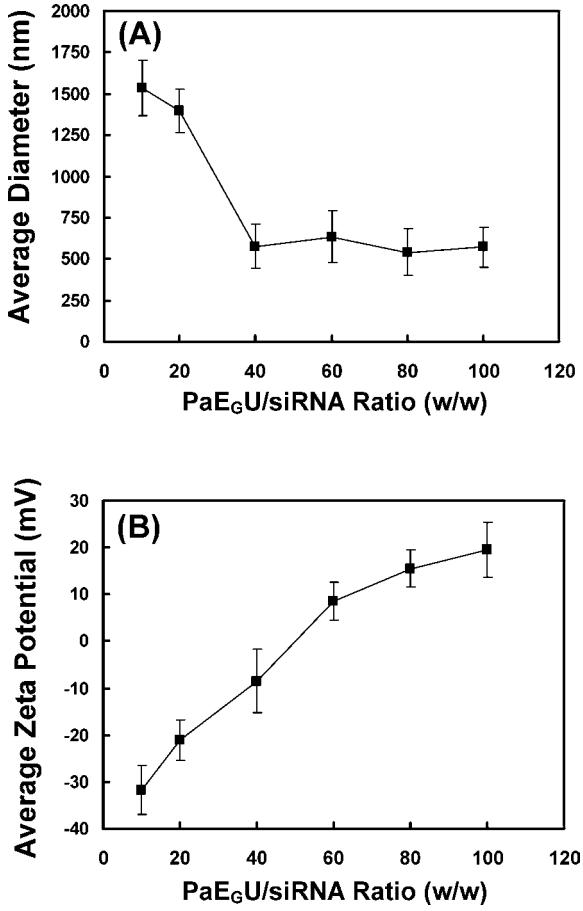


Figure 2. Size (A) and zeta-potential (B) of PaE$_G$U/siRNA polyplexes at different PaE$_G$U/siRNA mass ratios (w/w). Results are presented as mean ± standard deviation (n = 3).

We also evaluated the dose-dependent effect of PaE$_G$U/siRNA polyplexes on silencing luciferase expression. A half-million cells in each well of a 12-well plate were transfected with PaE$_G$U/siRNA polyplexes at different concentrations but at a fixed ratio of 80/1 (w/w). Luciferase activity was analyzed 36 h posttransfection. Silencing of EGFP using PaE$_G$U/GFP-22 siRNA polyplexes was performed in parallel with silencing of luciferase. The decrease in EGFP expression was visualized by the Nikon ECLIPSE TS100-F fluorescence microscope using the same settings as those for Alexa Fluor 488 detection. Untreated recombinant HT-1080 cells were used as the control.

Evaluation of PaE$_G$U/siRNA Cytotoxicity. The mitochondrial activity of PaE$_G$U/siRNA treated cells was measured using the CellTiter 96 AQueous one solution cell proliferation assay system (an MTS assay, Promega) according to the manufacturer's protocol. In this cell viability/proliferation assay, cells were treated with PaE$_G$U/siRNA or PEI/siRNA (control) polyplexes at various polymer/siRNA ratios for 36 h prior to the MTS assay. To compare the cytotoxicity of PaE$_G$U/siRNA (88 μg/1.1 μg) and Lipofectamine/siRNA polyplexes (3.3 μL/1 μg, following manufacturer's recommended dose), HT-1080 cells in 40-mm dishes were treated with polymer/siRNA polyplexes for 6 h and then replaced with polyplexes-free medium for another 30 h (a total of 36 h), or cells were treated with polyplexes for 36 h prior to the MTS assay. The methoxyphenyltetrazolium salt (MTS) compound was reduced by viable cells to form a colored formazan product, which was quantified colorimetrically at 490 nm using a spectrofluorometer (Sunrise/Tedan, Austria). GFP-22 siRNA (Qiagen) was used in this cytotoxicity experiment. Untreated HT-1080 cells were used as the control.

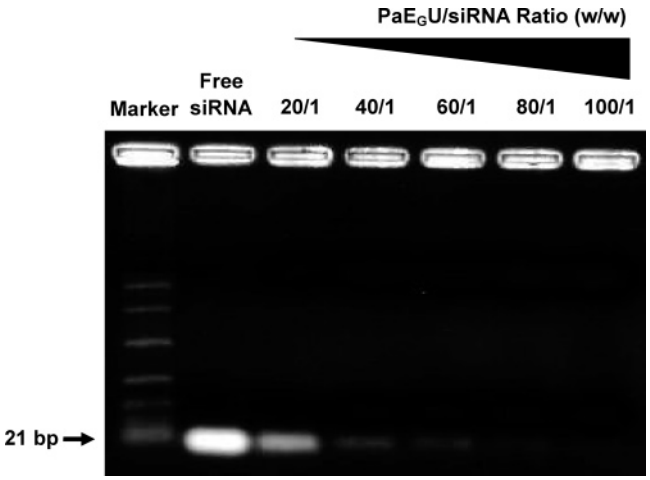


Figure 3. Gel retardation analysis of the PaE_GU/siRNA polyplexes. Migration of the PaE_GU/siRNA polyplexes in agarose gel at mass ratios varying from 20/1 to 100/1.

Dissociation Kinetics of Polymer/siRNA Polyplexes. Dissociation of polymer/siRNA polyplexes over time was assessed by measuring the fluorescence intensity generated from the Alexa Fluor 488-siRNA in PBS solution (pH 7.4) at 37 °C. PaE_GU/siRNA and PEI/siRNA polyplexes were prepared 80/1 (w/w) and 2/1 (w/w), respectively, and diluted to yield a concentration of 1-μg siRNA in a 200-μL solution. The 200-μL solution was then transferred to each well of an opaque black 96-well plate for analysis. The change of fluorescence intensity over time was recorded using the kinetic mode of the Molecular Devices SpectraMax M2^e microplate spectrofluorometer (Sunnyvale, CA) with settings of excitation wavelength at 485 nm and emission filter at 515 nm. Free Alexa Fluor 488-siRNA was used as the control.

RESULTS AND DISCUSSION

Characterization of PaE_GU/siRNA Polyplexes. We have previously developed PaE_GU/DNA polyplexes carrying the EGFP or β-galactosidase reporter gene for transfection (*21*). The sizes of DNA molecules were 5.4 and 7.8 kilobase pairs for EGFP and β-galactosidase-encoding genes, respectively, which were significantly larger than the size of siRNA at 21−23 base pairs by >230-fold in molecular weight. It was unclear whether siRNA would mimic DNA in forming polyplexes with PaE_GU in a similar fashion. We thus sought to characterize the particle size and zeta-potential of PaE_GU/siRNA polyplexes, and we compared them with those of PaE_GU/DNA polyplexes.

Figure 2A shows that the particle size decreased following an increase in the PaE_GU/siRNA (Alexa Fluor 488-labeled, nonsilencing control siRNA) mass ratio and reached a plateau when the ratio was larger than 40/1. We have previously observed a similar change in the size of PaE_GU/DNA polyplexes following an increase in the PaE_GU/DNA mass ratio (*21*). However, at the same PaE_GU/nucleic acids mass ratio, the sizes of PaE_GU/siRNA polyplexes were 3.4−6.5-fold larger than those of PaE_GU/DNA polyplexes in general. Figure 2B shows the zeta potential values of PaE_GU/siRNA polyplexes at the mass ratios ranging from 10/1 to 100/1 (w/w). The zeta potential steadily changed toward positive values associated with an increase in mass ratio. The values became larger than zero when the mass ratio was ≥60/1. Positively charged polyplexes were expected to bind to cellular membranes and to be taken up into cells by endocytosis.

We next studied the electrostatic interaction between PaE_GU and siRNA in the gel retardation assay. Figure 3 shows that the PaE_GU was able to partially retard siRNA in the agarose gel at the PaE_GU/siRNA mass ratio of 20/1 (lane 3) and efficiently retard siRNA at mass ratios ≥ 40/1 (lane 4), indicating that strong binding occurred between the negatively charged siRNA and the cationic PaE_GU and confirming the formation of PaE_GU/siRNA polyplexes.

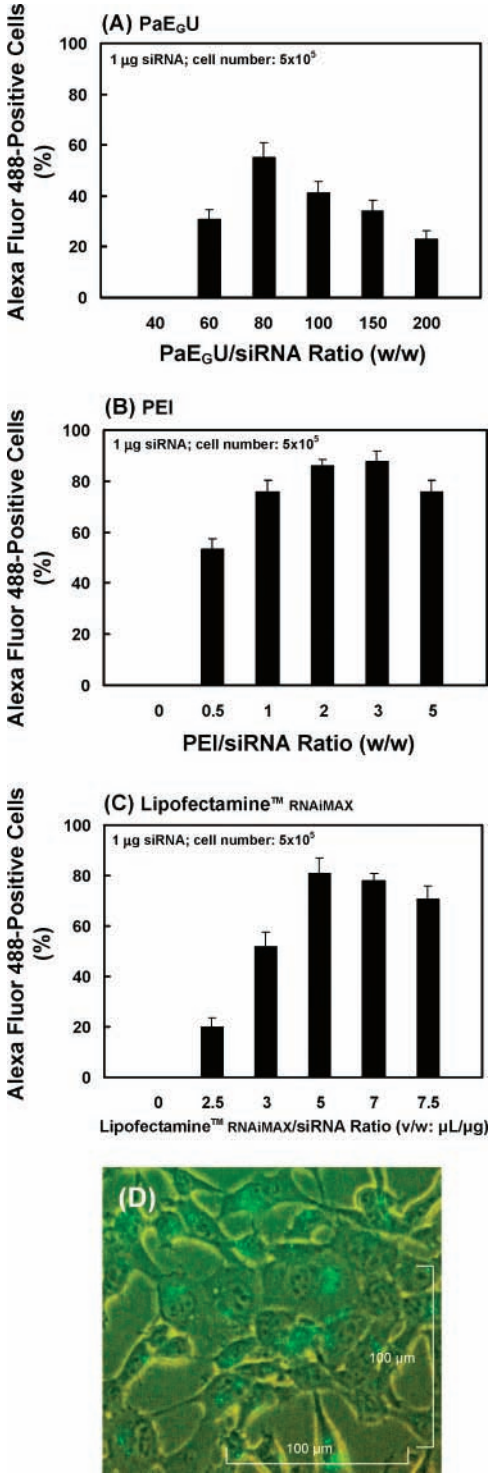


Figure 4. Alexa Fluor 488-positive cells (%) of PaE_GU (A), PEI (B), and Lipofectamine RNAiMAX (C)-mediated transfections. PEI and Lipofectamine transfections were used as controls. The percentage of positive cells was analyzed by fluorescence-activated flow cytometry. Results are presented as mean ± standard deviation (n = 3). (D) Fluorescence micrograph of PaE_GU-mediated transfection using Alexa Fluor 488-siRNA as the reporter. PaE_GU/siRNA polyplexes (80/1, w/w). The bar is 100 μm in length.

Optimization of PaE_GU/siRNA Polyplexes for Transfection. We applied the Alexa Fluor 488-labeled, nonsilencing

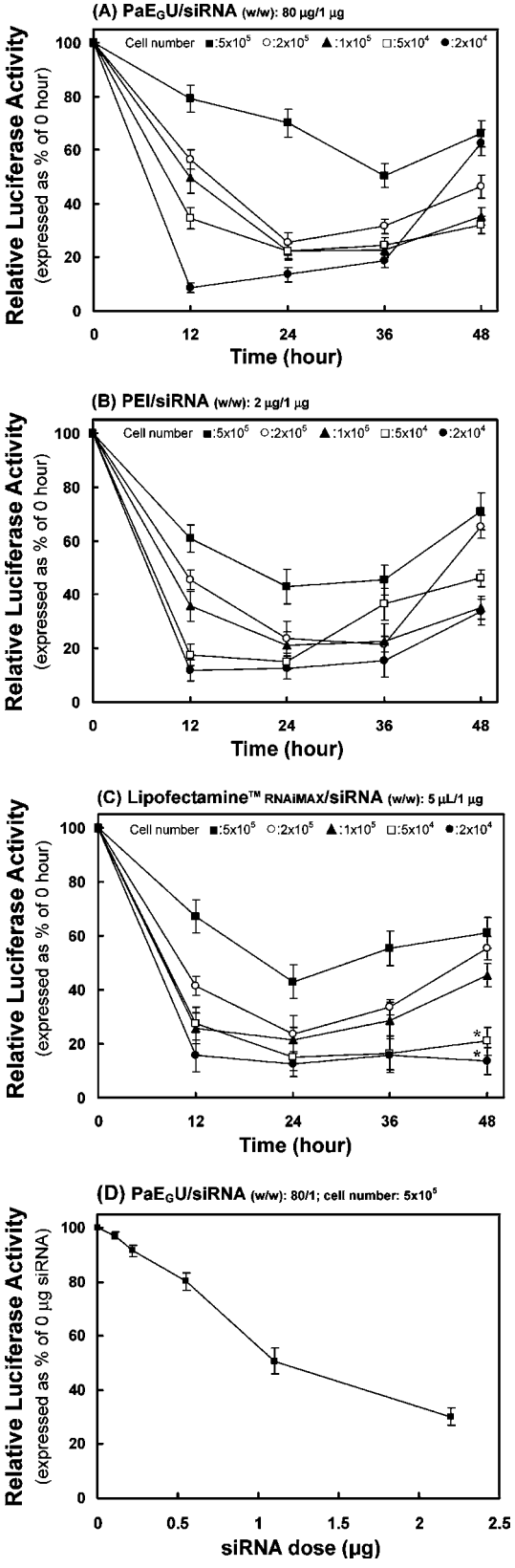


Figure 5. Kinetics of luciferase silencing via delivery of (A) PaE$_G$U/anti-luciferase siRNA polyplexes (80 μg/1 μg), (B) PEI/siRNA (2 μg/1 μg, control), and (C) Lipofectamine RNAiMAX/siRNA (5 μL/1 μg, control). In parts B and C, transfection cocktails were replaced with fresh, polymer-free media 12 h after the test. ∗indicates significant cell deformation, suggesting nonspecific, toxic effects of Lipofectamine on the treated cells. (D) Recombinant HT-1080 cells were transfected with PaE$_G$U/anti-luciferase siRNA polyplexes (80/1, w/w) at the indicated dose for luciferase silencing. Results are presented as mean ± standard deviation (n = 3).

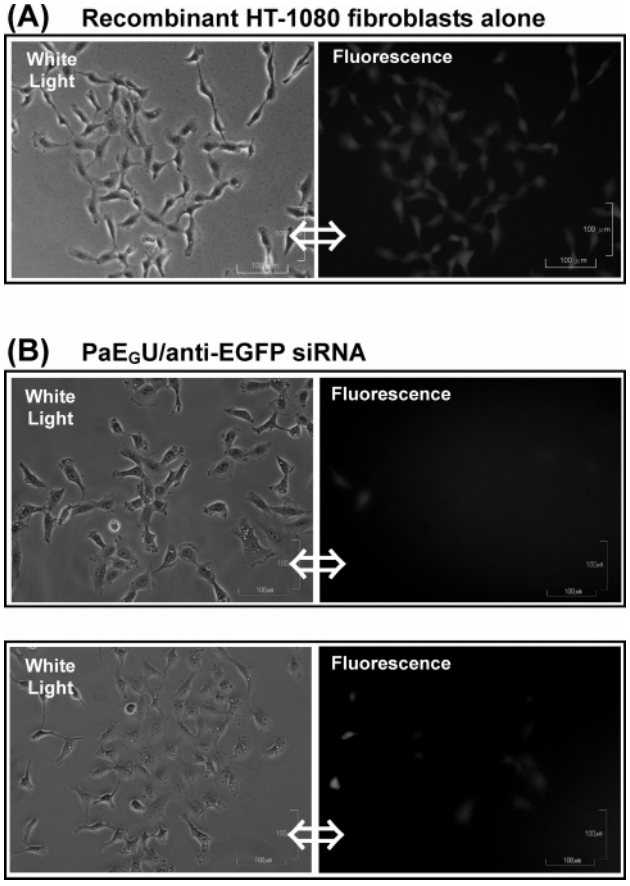


Figure 6. EGFP silencing via delivery of PaE$_G$U/anti-EGFP siRNA polyplexes. (A) Phase-contrast and fluorescence micrographs of untreated recombinant HT-1080 cells which constitutively expressed EGFP. (B) Two sets of micrographs of recombinant HT-1080 cells transfected with PaE$_G$U/anti-EGFP siRNA polyplexes (80/1, w/w) to suppress EGFP expression. Images were taken 36 h posttransfection. The bar is 100 μm in length.

control siRNA as the reporter to optimize the mass ratio of PaE$_G$U/siRNA for transfection and visualize the cellular uptake of polyplexes. Human HT-1080 fibroblasts grown as monolayers were transfected at various PaE$_G$U/siRNA mass ratios. Shortly after transfection (2−3 h), small amounts of Alexa Fluor 488-positive cells could be identified under the fluorescence microscope; six to 7 h after transfection, a significant number of fluorescent cells could be seen.

Fluorescence-activated flow cytometry was applied 48 h after transfection to quantify the percentage of fluorescence-positive cells, which can be considered as the average transfection efficiency (Figure 4A). The highest efficiency of PaE$_G$U-mediated transfection occurred at the polymer/siRNA mass ratio of 80/1, which generated 55% of Alexa Fluor 488-positive cells. In parallel, we applied PEI/siRNA and Lipofectamine/siRNA polyplexes as controls. Among the test conditions, the highest efficiency of PEI/siRNA and Lipofectamine/siRNA transfection generated 87% and 81% of fluorescence-positive cells (Figures 4B and 4C), respectively, indicating that PaE$_G$U was less efficient as a siRNA carrier in comparison to PEI and Lipofectamine.

Figure 4D shows a typical fluorescence micrograph of PaE$_G$U/siRNA (80/1) transfected cells 12 h posttransfection. A diffuse distribution of fluorescence-positive cells indicated a successful delivery of PaE$_G$U/siRNA polyplexes. The cellular uptake of PaE$_G$U/siRNA can be attributed to the polyplexes' positive surface charge (Figure 2B, when the mass ratio was ≥60/1), which facilitated their interaction with the negatively charged cellular membrane. On the other hand, when the surface charge

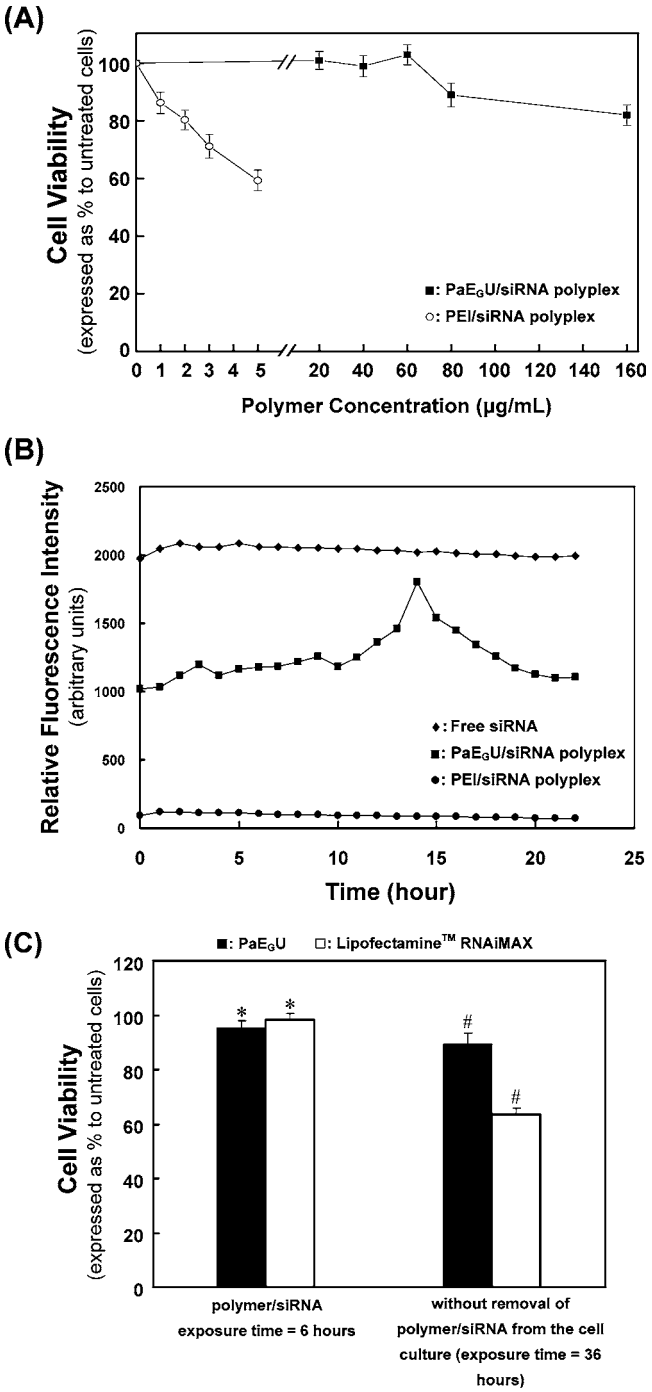


Figure 7. (A) Assessment of cell viability (MTS assay) after treatment with PaE_GU/siRNA or PEI/siRNA polyplexes. The viability of untreated HT-1080 cells was assigned a value of 100. Results are presented as mean ± standard deviation ($n = 3$). (B) Dissociation kinetics of PaE_GU/siRNA and PEI/siRNA polyplexes in PBS at 37 °C. The Alexa Fluor 488-siRNA was used as the reporter. Free Alexa Fluor 488-siRNA was used as the control. (C) Comparative cytotoxicity of PaE_GU/siRNA and Lipofectamine RNAiMAX/siRNA polyplexes. The viability of untreated HT-1080 cells was assigned a value of 100. ∗indicates $P = 0.18$. # indicates P value <0.002. P values were calculated using a two-tailed t test, assuming unequal variances. Results are presented as mean ± standard deviation ($n = 3$).

of PaE_GU/siRNA polyplexes was negative at the mass ratio of 40/1 (Figure 2B), the efficiency of siRNA delivery was zero (Figure 4A).

Interestingly, at the optimized ratio (80/1) for siRNA delivery, the average diameter of polyplexes was 540 nm (Figure 2A), which was 3.5-fold larger than the average diameter of PaE_GU/DNA polyplexes at 155 nm for efficient DNA delivery (*21*). Similar uptake of large fluorescent particles with an average size of 900 nm in diameter has been applied for endosomal labeling of mesenchymal stem cells, suggesting that PaE_GU/siRNA polyplexes could follow a similar endocytic pathway (*25*, *26*).

Gene Silencing via PaE_GU/siRNA Polyplexes Delivery. Cellular uptake of the labeled siRNA did not necessarily indicate that the internalized siRNA would be incorporated into the RNA-induced silencing complexes (RISCs) and in turn inhibit the target gene expression. Therefore, we sought to investigate RNA interference of endogenous protein expression. We created a model recombinant human HT-1080 fibroblast line, which stably expressed both luciferase and EGFP reporters, to evaluate target gene silencing. Detailed procedures were described in Experimental Procedures.

A transient suppression profile of luciferase expression was observed (Figure 5A) after the recombinant HT-1080 cells were transfected with PaE_GU/anti-luciferase siRNA polyplexes at the mass ratio of 80/1. The efficiency of gene silencing depended on the number of the targeted cells; the lower the cell number, the higher the siRNA dose per cell and the stronger the suppression. Among our test conditions, the highest efficiency of gene silencing occurred when 2×10^4 cells were transfected with PaE_GU/siRNA (80 μg/1 μg) for 12 h; in this situation, 92% of luciferase expression was suppressed relative to that in the untransfected recombinant HT-1080 cells. Under the same conditions, a similar efficiency of gene silencing, 88% and 84% for PEI/siRNA (2 μg/1 μg) and Lipofectamine/siRNA (5 μL/1 μg) transfections, were observed (Figures 5B and 5C) at 12 h posttransfection, respectively. However, unlike the mild PaE_GU transfection, PEI and Lipofectamine transfections were cytotoxic, especially toward the culture with fewer cell numbers. Thus, to avoid cell death, fresh culture media were used to replace the PEI and Lipofectamine transfection cocktails 12 h after the kinetics study. Figure 5D shows a dose-dependent suppression of PaE_GU-mediated siRNA delivery. Approximately 50% suppression of luciferase expression was achieved when 5×10^5 cells were transfected with the polyplexes consisting of 88 μg PaE_GU and 1.1 μg siRNA at the mass ratio of 80/1.

A similar result of gene silencing via PaE_GU/anti-EGFP siRNA delivery is illustrated in Figure 6, where the decrease in reporter EGFP expression was revealed by fluorescence micrographs. Figure 6A shows a typical fluorescence micrograph of EGFP expression in our model recombinant HT-1080 cells. Thirty-six hours after transfection, a decrease in fluorescence intensity of the transfected recombinant HT-1080 cells was observed (Figure 6B), in comparison to that of the untransfected control cells (Figure 6A). However, the turn-off of fluorescence from the recombinant cells was incomplete. This incomplete fluorescence suppression could be due to the long half-life of EGFP (>24 h, in comparison to 2 h for luciferase) leading to continuous emission of fluorescence from the residual EGFP molecules in the transfected cells, even when the EGFP mRNA was silenced by the anti-EGFP siRNA delivery (*27*, *28*).

Cytotoxicity of PaE_GU/siRNA Polyplexes. The cytotoxicity of PaE_GU/siRNA polyplexes was accessed in the HT-1080 cell culture by analyzing the mitochondrial activity (an MTS assay). As shown in Figure 7A, the cell viability of HT-1080 cells was at 89% when the PaE_GU concentration was at 80 μg/mL, after cells were incubated with PaE_GU/siRNA (80/1, w/w) for 36 h. Even when the concentration of PaE_GU reached 160 μg/mL, the cell viability was still approximately 82%, in contrast to 59% for 5 μg/mL of PEI (complexed with siRNA, 2/1, w/w), one of the commonly used cationic polymers for DNA and siRNA delivery (*29*−*33*).

Figure 7B shows the dissociation kinetics of polymer/siRNA polyplexes. The fluorescence intensity of PEI/Alexa Fluor 488-

siRNA polyplexes was low (1/20 of the intensity of free siRNA) and steady in PBS at 37 °C over a period of 22 h, suggesting a very stable PEI/siRNA structure. Cellular accumulation of nondegradable cationic polymer, such as PEI, could cause severe cytotoxicity, as indicated in Figure 7A and in other reports (*34*). On the other hand, the fluorescence intensity of PaE_GU/Alexa Fluor 488-siRNA polyplexes was higher than that of the PEI/siRNA polyplexes by 10-fold at time = 0 (1/2 of the intensity of free siRNA) and continuously increased and peaked at time = 14 h. This result suggested an unstable structure of the PaE_GU/siRNA polyplexes, underscoring the degradability of PaE_GU and its low cytotoxicity (*21*). The decline in fluorescence intensity after the peak could arise from the reassociation of Alexa Fluor 488-siRNA with the degraded PaE_GU to shed the absorption and/or emission of photons in the assay.

Figure 7C compares PaE_GU with the siRNA transfection reagent Lipofectamine in cytotoxicity. When cells were treated with polymer/siRNA for 6 h and then followed by reagent removal and another 30 h of cultivation in fresh medium, the viabilities of PaE_GU/siRNA (88 μg/1.1 μg)- and Lipofectamine/siRNA (3.3 μL/1 μg, recommended dose)-treated cells in 40-mm culture dishes were at 95% and 98%, respectively, and had no significant difference between them ($n = 3$; $P = 0.18$). However, when the administered polymer/siRNA polyplexes were left in the culture medium, mimicking an irretrievable situation of *in vivo* administration, the viability of Lipofectamine/siRNA-treated cells dropped to 63% from 98%, or by 35%. By contrast, PaE_GU/siRNA marginally decreased the viability to 89% from 95%, or by 6%, indicating that PaE_GU/siRNA was mild and exhibited little toxicity toward the target cells.

CONCLUSIONS

The present study constitutes an important step toward using poly(ester urethane (PEU)-based polymers to develop siRNA carriers while eliciting minimal cytotoxicity. We have demonstrated that PaE_GU, an engineered PEU with amine and PEG units in the backbone, was able to associate with siRNA through electrostatic interaction and led to self-assembly of polyplexes. Despite the average diameters of PaE_GU/siRNA polyplexes at 540 nm, 3.5-fold larger than the average diameters of PaE_GU/DNA polyplexes at 155 nm, efficient cellular uptake of PaE_GU/siRNA polyplexes was identified at the optimized PaE_GU/siRNA mass ratio of 80/1. At this ratio, transient silencing of constitutive luciferase expression (up to 92%) was achieved in the model recombinant human HT-1080 fibroblast line via anti-luciferase siRNA delivery. Our work thus provides a unique, PEU-based siRNA polyplex system for gene silencing, which is expected to be useful for the future design of siRNA carriers.

ACKNOWLEDGMENT

This work was supported in part by grants from the National Science Council, Taiwan (NSC 95-2120-M-007-010), and the Research Development Program, National Tsing Hua University, Taiwan.

LITERATURE CITED

(1) Uprichard, S. L. (2005) The therapeutic potential of RNA interference. *FEBS Lett. 579*, 5996−6007.
(2) Kennedy, D. (2002) Breakthrough of the year. *Science 298*, 2283−2283.
(3) Kiermer, V. (2006) Focus on RNA interference-A user's guide. *Nat. Methods 3*, 669−669.
(4) Behlke, M. A. (2006) Progress towards in vivo use of siRNAs. *Mol. Ther. 13*, 644−670.
(5) Yuan, X. D., Li, L., Rathinavelu, A., Hao, J. S., Narasimhan, M., He, M., Heitlage, V., Tam, L., Viqar, S., and Salehi, M. (2006) siRNA drug delivery by biodegradable polymeric nanoparticles. *J. Nanosci. Nanotechnol. 6*, 2821−2828.
(6) Read, M. L., Singh, S., Ahmed, Z., Stevenson, M., Briggs, S. S., Oupicky, D., Barrett, L. B., Spice, R., Kendall, M., Berry, M., Preece, J. A., Logan, A., and Seymour, L. W. (2005) A versatile reducible polycation-based system for efficient delivery of a broad range of nucleic acids. *Nucleic Acids Res. 33*, e86.
(7) Tseng, S. J., Tang, S. C., Shau, M. D., Zeng, Y. F., Cherng, J. Y., and Shih, M. F. (2005) Structural characterization and buffering capacity in relation to the transfection efficiency of biodegradable polyurethane. *Bioconjugate Chem. 16*, 1375−1381.
(8) Christensen, L. V., Chang, C. W., Kim, W. J., Kim, S. W., Zhong, Z. Y., Lin, C., Engbersen, J. F. J., and Feijen, J. (2006) Reducible poly(amido ethylenimine)s designed for triggered intracellular gene delivery. *Bioconjugate Chem. 17*, 1233−1240.
(9) Kloeckner, J., Bruzzano, S., Ogris, M., and Wagner, E. (2006) Gene carriers based on hexanediol diacrylate-linked oligoethylenimine: Effect of chemical structure of polymer on biological properties. *Bioconjugate Chem. 17*, 1339−1345.
(10) Lim, Y. B., Kim, S. M., Suh, H., and Park, J. S. (2002) Biodegradable, endosome disruptive, and cationic network-type polymer as a highly efficient and nontoxic gene delivery carrier. *Bioconjugate Chem. 13*, 952−957.
(11) Akinc, A., Anderson, D. G., Lynn, D. M., and Langer, R. (2003) Synthesis of poly(β-amino ester)s optimized for highly effective gene delivery. *Bioconjugate Chem. 14*, 979−988.
(12) Forrest, M. L., Koerber, J. T., and Pack, D. W. (2003) A degradable polyethylenimine derivative with low toxicity for highly efficient gene delivery. *Bioconjugate Chem. 14*, 934−940.
(13) Behr, J. P. (1997) The proton sponge: A trick to enter cells the viruses did not exploit. *Chimia 51*, 34−36.
(14) Akinc, A., Thomas, M., Klibanov, A. M., and Langer, R. (2005) Exploring polyethylenimine-mediated DNA transfection and the proton sponge hypothesis. *J. Gene Med. 7*, 657−663.
(15) Thomas, M., and Klibanov, A. M. (2002) Enhancing polyethylenimine's delivery of plasmid DNA into mammalian cells. *Proc. Natl. Acad. Sci. U.S.A. 99*, 14640−14645.
(16) Borkenhagen, M., Stoll, R. C., Neuenschwander, P., Suter, U. W., and Aebischer, P. (1998) In vivo performance of a new biodegradable polyester urethane system used as a nerve guidance channel. *Biomaterials 19*, 2155−2165.
(17) Marcos-Fernandez, A., Abraham, G. A., Valentin, J. L., and San Roman, J. (2006) Synthesis and characterization of biodegradable non-toxic poly(ester-urethane-urea)s based on poly(epsilon-caprolactone) and amino acid derivatives. *Polymer 47*, 785−798.
(18) Riboldi, S. A., Sampaolesi, M., Neuenschwander, P., Cossu, G., and Mantero, S. (2005) Electrospun degradable polyesterurethane membranes: potential scaffolds for skeletal muscle tissue engineering. *Biomaterials 26*, 4606−4615.
(19) Stankus, J. J., Guan, J. J., Fujimoto, K., and Wagner, W. R. (2006) Microintegrating smooth muscle cells into a biodegradable, elastomeric fiber matrix. *Biomaterials 27*, 735−744.
(20) Loh, X. J., Tan, K. K., Li, X., and Li, J. (2006) The in vitro hydrolysis of poly(ester urethane)s consisting of poly[(R)-3-hydroxybutyrate] and poly(ethylene glycol). *Biomaterials 27*, 1841−1850.
(21) Tseng, S. J., and Tang, S. C. (2006) Synthesis and Characterization of a Novel Transfection Reagent Poly(amino ester glycol urethane). *Biomacromolecules 8*, 50−58.
(22) Bettinger, T., Carlisle, R. C., Read, M. L., Ogris, M., and Seymour, L. W. (2001) Peptide-mediated RNA delivery: a novel approach for enhanced transfection of primary and post-mitotic cells. *Nucleic Acids Res. 29*, 3882−3891.
(23) Grayson, A. C. R., Doody, A. M., and Putnam, D. (2006) Biophysical and structural characterization of polyethylenimine-mediated siRNA delivery in vitro. *Pharm. Res. 23*, 1868−1876.
(24) Tang, S. C., Sambanis, A., and Sibley, E. (2005) Proteasome modulating agents induce rAAV2-mediated transgene expression in human intestinal epithelial cells. *Biochem. Biophys. Res. Commun. 331*, 1392−1400.
(25) Hinds, K. A., Hill, J. M., Shapiro, E. M., Laukkanen, M. O., Silva, A. C., Combs, C. A., Varney, T. R., Balaban, R. S., Koretsky, A. P., and Dunbar, C. E. (2003) Highly efficient endosomal labeling of progenitor and stem cells with large magnetic particles allows magnetic resonance imaging of single cells. *Blood 102*, 867−872.

(26) Hill, J. M., Dick, A. J., Raman, V. K., Thompson, R. B., Yu, Z. X., Hinds, K. A., Pessanha, B. S. S., Guttman, M. A., Varney, T. R., Martin, B. J., Dunbar, C. E., McVeigh, E. R., and Lederman, R. J. (2003) Serial cardiac magnetic resonance imaging of injected mesenchymal stem cells. *Circulation 108*, 1009−1014.

(27) Clontech Laboratories, Inc. (2001) *Living Colors User Manual. Properties of GFP and GFP Variants*, pp 5−13, Chapter 2, Mountain View, CA.

(28) Ignowski, J. M., and Schaffer, D. V. (2004) Kinetic analysis and modeling of firefly luciferase as a quantitative reporter gene in live mammalian cells. *Biotechnol. Bioeng. 86*, 827−834.

(29) Boussif, O., Lezoualch, F., Zanta, M. A., Mergny, M. D., Scherman, D., Demeneix, B., and Behr, J. P. (1995) A Versatile Vector for Gene and Oligonucleotide Transfer into Cells in Culture and in-Vivo-Polyethylenimine. *Proc. Natl. Acad. Sci. U.S.A. 92*, 7297−7301.

(30) Werth, S., Urban-Klein, B., Dai, L., Hobel, S., Grzelinski, M., Bakowsky, U., Czubayko, F., and Aigner, A. (2006) A low molecular weight fraction of polyethylenimine (PEI) displays increased transfection efficiency of DNA and siRNA in fresh or lyophilized complexes. *J. Controlled Release 112*, 257−270.

(31) Pun, S. H., Bellocq, N. C., Liu, A. J., Jensen, G., Machemer, T., Quijano, E., Schluep, T., Wen, S. F., Engler, H., Heidel, J., and Davis, M. E. (2004) Cyclodextrin-modified polyethylenimine polymers for gene delivery. *Bioconjugate Chem. 15*, 831−840.

(32) Mao, S. R., Neu, M., Germershaus, O., Merkel, O., Sitterberg, J., Bakowsky, U., and Kissel, T. (2006) Influence of polyethylene glycol chain length on the physicochemical and biological properties of poly(ethylene imine)-graft-poly(ethylene glycol) block copolymer/SiRNA polyplexes. *Bioconjugate Chem. 17*, 1209−1218.

(33) Grzelinski, M., Urban-Klein, B., Martens, T., Lamszus, K., Bakowsky, U., Hobel, S., Czubayko, F., and Aigner, A. (2006) RNA interference-mediated gene silencing of pleiotrophin through polyethylenimine-complexed small interfering RNAs in vivo exerts antitumoral effects in glioblastoma xenografts. *Hum. Gene Ther. 17*, 751−766.

(34) Lv, H. T., Zhang, S. B., Wang, B., Cui, S. H., and Yan, J. (2006) Toxicity of cationic lipids and cationic polymers in gene delivery. *J. Controlled Release 114*, 100−109.

BC060382J

Targeted Quantum Dot Conjugates for siRNA Delivery

Austin M. Derfus,[†,‡] Alice A. Chen,[§,▽] Dal-Hee Min,[§] Erkki Ruoslahti,[‡,#] and Sangeeta N. Bhatia*[,†,§]

Department of Bioengineering, University of California at San Diego, La Jolla, California 92093, Burnham Institute for Medical Research, La Jolla, California 92037, Health Sciences and Technology/Electrical Engineering and Computer Science, Massachusetts Institute of Technology, Cambridge, Massachusetts 02139, and School of Engineering and Applied Sciences, Harvard University, Cambridge, MA 02138. Received November 25, 2006; Revised Manuscript Received April 3, 2007

Treatment of human diseases such as cancer generally involves the sequential use of diagnostic tools and therapeutic modalities. Multifunctional platforms combining therapeutic and diagnostic imaging functions in a single vehicle promise to change this paradigm. in particular, nanoparticle-based multifunctional platforms offer the potential to improve the pharmacokinetics of drug formulations, while providing attachment sites for diagnostic imaging and disease targeting features. We have applied these principles to the delivery of small interfering RNA (siRNA) therapeutics, where systemic delivery is hampered by rapid excretion and nontargeted tissue distribution. Using a PEGlyated quantum dot (QD) core as a scaffold, siRNA and tumor-homing peptides (F3) were conjugated to functional groups on the particle's surface. We found that the homing peptide was required for targeted internalization by tumor cells, and that siRNA cargo could be coattached without affecting the function of the peptide. Using an EGFP model system, the role of conjugation chemistry was investigated, with siRNA attached to the particle by disulfide cross-linkers showing greater silencing efficiency than when attached by a nonreducible thioether linkage. Since each particle contains a limited number of attachment sites, we further explored the tradeoff between number of F3 peptides and the number of siRNA per particle, leading to an optimized formulation. Delivery of these F3/siRNA−QDs to EGFP-transfected HeLa cells and release from their endosomal entrapment led to significant knockdown of EGFP signal. By designing the siRNA sequence against a therapeutic target (e.g., oncogene) instead of EGFP, this technology may be ultimately adapted to simultaneously treat and image metastatic cancer.

INTRODUCTION

The development of multifunctional nanoparticles for treatment of focal disease is attractive for several reasons: they exhibit unique pharmacokinetics including minimal renal filtration, they have high surface to volume ratios enabling modification with surface functional groups that can be used to specifically target the delivery of therapeutic agents to sites of disease, and they can serve as vehicles for integration of diagnostic imaging and therapeutic drug delivery, a potentially transformative clinical paradigm. Use of a nanoparticle imaging core that is decorated with functional moieties provides a strategy that is particularly amenable to modular design of a multifunctional nanoparticle where features may be interchanged or combined to tailor formulations for a plethora of applications. In an attempt to move toward this goal, we have previously combined peptides derived from phage display- a powerful biological screening technique- with fluorescent semiconductor quantum dots to target multivalent nanoparticles to tumors (*1*). In this report, we further explore the feasibility of incorporating an oligonucleotide-based therapeutic cargo, siRNA. Short, double-stranded small-interfering-RNAs (siRNA) are one manifestation of a phenomenon known as RNA interference whereby translation of a target protein is inhibited. This type of therapeutic cargo is of particular interest in recent years because it has the potential to modulate so-called 'nondruggable' targets (*2*, *3*).

The *untargeted*, systemic delivery of siRNA has been explored by conglomeration of duplexes into nanosized complexes that reduce their renal filtration rates, extending the circulation half-life well beyond the ∼6 min observed for unmodified siRNA (*4*). For example, cholesterol−siRNA conjugates bind serum albumin after intravenous injection, forming long-circulating "natural" nanoparticles (*4*). Similarly, siRNA−carrier complexes can be formed ex vivo, prior to injection, by condensing the nucleic acid with a cationic protein (e.g., protamine (*5*)) or polymer (e.g., poly(ethylene imine) (PEI) (*6*), cyclodextrin-containing polycations (*7*), or PEG-based block catiomer (*8*)). In addition, targeted delivery of such agents has the potential to limit collateral toxicity and 'off-target' effects. Targeting has been explored through use of through the attachment of antibodies (*5*), small molecules (e.g., transferrin (*7*)), aptamers (*9*, *10*), or well-established peptide ligands (*6*)); however, these approaches are typically not modular nor multifunctional (i.e., do not incorporate imaging moieties). Addition of a nanoparticle-based imaging agent to siRNA delivery strategies may be particularly advantageous as protein knockdown by RNAi is delayed (>48 h or more after administration), and many fluorescent dyes are not stable for monitoring delivery over extended periods of time in vivo. In vitro, co-delivery of fluorescent reporter plasmid along with the siRNA is often utilized; however, this is unlikely to be used clinically given the potential risks associated with integration into host DNA.

Quantum dots offer the potential to serve as photostable beacons to track siRNA delivery. We have previously explored their utility for monitoring siRNA delivery in vitro by co-complexing QDs with cationic liposomes and siRNA (*11*, *12*); however, this approach is not amenable to either systemic delivery, because of their relatively large size and rapid uptake

* Author to whom correspondence should be addressed. Phone: (617) 324-0221, fax: (617) 324-0740, e-mail: sbhatia@mit.edu.
† University of California at San Diego.
‡ Burnham Institute for Medical Research.
§ M.I.T.
▽ Harvard University.
Burnham Institute for Medical Research, University of California, Santa Barbara, Santa Barbara, CA 93106-9610.

10.1021/bc060367e CCC: $37.00 © 2007 American Chemical Society
Published on Web 07/14/2007

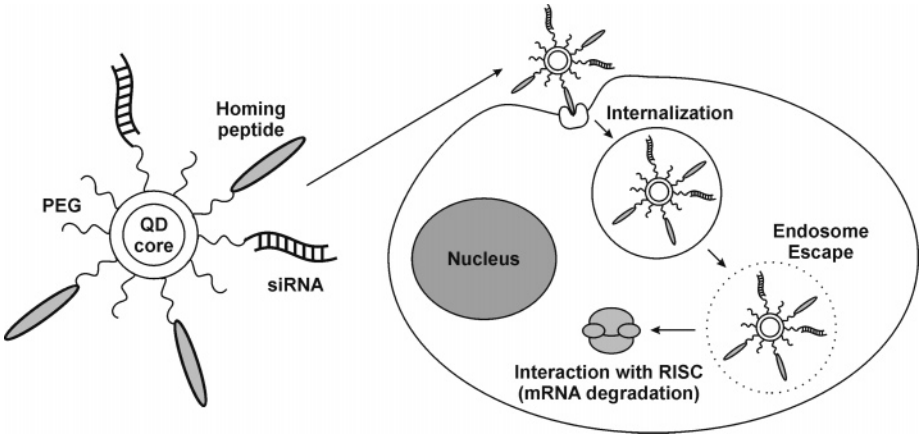


Figure 1. Design of a multifunctional nanoparticle for siRNA delivery. Because of their photostable fluorescence and multivalency, QDs are suitable vehicles for ferrying siRNA into live cells in vitro and in vivo. Conjugation of homing peptides (along with the siRNA cargo) to the QD surface allows targeted internalization in tumor cells. Once internalized, these particles must escape the endolysomal pathway and reach the cytoplasm to interact with the RNA-induced silencing complex (RISC), which leads to degradation of mRNA homologous to the siRNA sequence.

by macrophages, or targeted delivery, as they are ubiquitously internalized. In this report, we sought to generate multifunctional conjugates of a size compatible with eventual systemic delivery ($5 < d < 200$ nm) upon a quantum dot core that presented both targeting peptides and siRNA (Figure 1). A QD core with emission in the near-infrared (NIR) was chosen to allow greater imaging depth in tissue than that achieved with visible wavelengths. The siRNA was attached to the surface with a chemical cross-linker, rather than the electrostatic interactions used in many schemes. This strategy grants a smaller overall size than polymer-based particles, which may carry advantages in evading uptake by the reticuloendothelial system (*13*). As a proof-of-concept, the attached siRNA was designed against the enhanced green fluorescent protein (EGFP) gene, and complexes were delivered to EGFP-transfected HeLa cells in vitro. A tumor-homing peptide (F3), targeting cell-surface nucleolin (*14*), was attached to achieve cell uptake. F3 peptide has been shown to target tumor cells in vitro and in vivo when administered as a free peptide and also when coconjugated with poly(ethylene glycol) to quantum dots delivered systemically in mice bearing xenograft tumors(*15*).

Combining these components onto a single particle brings several engineering requirements and constraints that affect their design and fabrication. Accordingly, in this report we first investigate whether the attachment of the peptide is necessary and sufficient to achieve cell internalization. As particle surface area is limited (~100 surface amines on these QDs), the actual copy numbers of targeting peptide and siRNA required are also quantified. Increasing the number of peptides on the QDs lowers the siRNA dose per particle and vice versa. Next, because conjugation of siRNA to the particles must be stable in cell media yet also allow the duplex to interact with the RNA-induced silencing complex (RISC) in the cytosol, we test the efficacy of two different cross-linkers for this task. While RISC binding may be possible with the duplex attached to the particle, release of the siRNA from the particle's surface upon internalization proved advantageous to knockdown efficacy. Finally, cytoplasmic delivery, free of endosomes, is essential to allow siRNA to interact with cellular silencing machinery. While fluorophore-labeled F3 peptide has been shown to reach the nuclei of tumor cells (*15*), internalization of particles generally follows the endolysosomal pathway. In this report, the addition of endosome-disrupting agents was required to aid escape and increase siRNA-mediated knockdown.

EXPERIMENTAL SECTION

Materials. Quantum dots with emission maxima of 655 or 705 nm and modified with PEG and amino groups were obtained from Quantum Dot Corporation (ITK amino). QD concentrations were measured by optical absorbance at 595 nm, using extinction coefficients provided by the supplier. Cross-linkers used were sulfo-LC-SPDP (sulfosuccinimidyl 6-(3′-[2-pyridyldithio]-propionamido)hexanoate) (Pierce) and sulfo-SMCC (sulfosuccinimidyl 4-(*N*-maleimidomethyl)cyclohexane-1-carboxylate) (Sigma). Synthetic RNA duplexes directed against the EGFP mRNA were synthesized, with the sense strand modified to contain a 5′ thiol group (Dharmacon) (sense: 5′-Th-$(CH_2)_6$-GGC UAC GUC CAG GAG CGC ACC; antisense: 5′-UGC GCU CCU GGA CGU AGC CUU). The F3 peptide was synthesized with an aminohexanoic acid (Ahx) spacer and cysteine residue added for conjugation (final sequence: C[Ahx]-AKVK DEPQR RSARL SAKPA PPKPE PKPKK APAKK). A FITC-labeled F3 peptide was also synthesized, along with KAREC (Lys-Ala-Arg-Glu-Cys), a five amino acid control peptide. All peptides were synthesized by *N*-(9-fluorenylmethoxycarbonyl)-L-amino acid chemistry with a solid-phase synthesizer and purified by HPLC. The composition of the peptides was confirmed by MS.

Conjugation of Peptides and Nucleic Acid to QDs. Amino-modified QDs were conjugated to thiol-containing siRNA and peptides using sulfo-LC-SPDP and sulfo-SMCC cross-linkers. QDs were resuspended in 50 mM sodium phosphate, 150 mM sodium chloride, pH 7.2, using Amicon Ultra-4 (100 kDa cutoff) filters. Cross-linker (1000-fold excess) was added to QDs and allowed to react for 1 h. Samples were filtered on a NAP-5 gravity column (to remove excess cross-linker) into similar buffer supplemented with 10 mM EDTA. siRNA was treated with 0.1 M DTT for 1 h and filtered on a NAP-5 column into EDTA-containing buffer. Peptides were typically used from lyophilized powder. Peptide and/or siRNA was added to filtered QDs and allowed to react overnight at 4 °C. Using three Amicon filters, product was filtered twice with Dulbecco's phosphate-buffered saline (PBS), twice with a high salt buffer (1.0 M sodium chloride, 100 mM sodium citrate, pH 7.2), and twice again with PBS. High salt washes were required to remove electrostatically bound siRNA and peptide, which was not removed with PBS washes alone.

For siRNA−QDs, a 10-fold excess of siRNA was typically used for both cross-linkers. In the case of sulfo-LC-SPDP, the amount of conjugated siRNA was assayed using gel electro-

phoresis (20% TBE gel, Invitrogen), staining with SYBR Gold (Invitrogen). To confirm that similar amounts of siRNA (approximately two per QD) were conjugated to QDs using sulfo-SMCC, particles were stained with SYBR Gold and measured with a fluorimeter (SpectraMax Gemini XS, Molecular Devices).

For F3/siRNA−QDs and KAREC/siRNA−QDs, a molar ratio of 15:70:1 (siRNA:peptide:QDs) was found to be optimum, though a variety of ratios were attempted (Figure 4A). These conditions yielded approximately 20 F3 peptides and 1 siRNA duplex per particle.

Cell Culture. Internalization and knockdown experiments were performed using a HeLa cell line transfected with destabilized EGFP with a half-life of 1 h (courtesy of Phillip Sharp, MIT). Growth media was Dulbecco's modified Eagle's medium (DMEM) containing 4.5 g/L glucose and supplemented with 10% FBS, 100 units/mL penicillin, 100 ug/mL streptomycin, and 292 ug/mL L-glutamine. Cells were passaged into 24-well plates and used at 50−80% confluency for internalization experiments and 20−40% confluency for knockdown experiments.

For internalization experiments (Figure 2), QDs were added to cell monolayers in media without serum at a final concentration of 50 nM. After 4 h, cells were washed with media, treated with trypsin (0.25%) and EDTA, and resuspended in 1% BSA (in PBS) for flow cytometry (BD FACSort, FL1 for EGFP signal and FL3 for QD signal). Fluorescence data on 10 000 cells was collected for each sample, and the geometric mean of intensity was reported.

For knockdown experiments in Figure 3, siRNA−QDs (in 50 uL serum/antibiotic-free media) were added to Lipofectamine 2000 (1 μL in 50 μL media, Invitrogen) and allowed to complex for 20 min. Cell media was changed to 400 μL of serum/antibiotic-free per well, and QD solutions (100 μL) were added dropwise. Complete media was added 12−18 h later, and 48 h after the QD were added, cells were trypsinized and assayed for fluorescence by flow cytometry.

To assess EGFP knockdown, 50 nM or 10 nM concentrations of F3/siRNA−QDs or KAREC/siRNA−QDs were added to cell monolayers (20−40% confluent) in media with serum/antibiotics. To demonstrate specificity, irrelevant siRNA (designed against the Lamin A/C gene, as described in ref 12) was conjugated to QDs along with F3 and also delivered to cells. Four hours later, cells were washed with similar media. Some samples were then treated with 1 μL of Lipofectamine per well (added dropwise in 100 μL media) either immediately after washing or after a 90 min incubation at 37 °C (to allow membrane recycling). For all samples, media was changed to complete DMEM with serum/antibiotics ~16 h after the addition of QDs and assayed by flow cytometry 48 h from the start of the experiment. For imaging, cells were initially seeded on glass-bottom dishes (Mat-Tek) and observed 48 h after the addition of QDs using a 60× oil immersion objective. Images were captured with a SPOT camera mounted on a Nikon TE200 inverted epifluorescence microscope.

RESULTS AND DISCUSSION

Taking a modular approach, particle internalization and siRNA attachment were investigated separately before these functions were combined in a single particle. First, peptides were conjugated to QDs to improve tumor cell uptake. Addition of as-purchased PEGlyated QDs to HeLa cell monolayers led to minimal cell uptake, as quantified with flow cytometry (Figure 2A). Conjugation of siRNA or a control pentapeptide (KAREC) did not increase QD internalization, but addition of F3 peptide to the QDs improved the uptake significantly (2 orders of magnitude). To confirm the specificity of F3 uptake, free F3 peptide was added to cells along with 50 nM F3−QDs (Figure 2B). Dose-dependent inhibition of uptake was observed with F3 peptide concentrations from 1 μM to 1 mM. Inhibition of uptake by an irrelevant peptide, free KAREC, was minimal by comparison. The large excess of free peptide required for inhibition may be due to multiple copies of the F3 peptide on each QD and improved receptor binding as a result of multivalency.

To quantify the number of peptides added per particle, FITC-labeled F3 peptide was synthesized and attached to QDs using

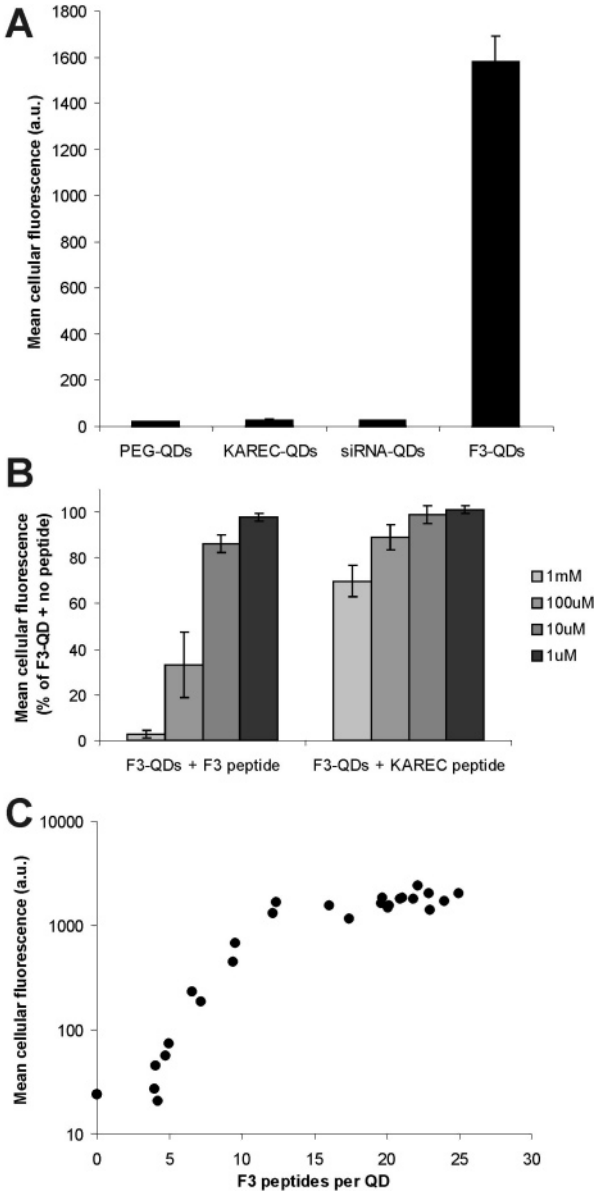


Figure 2. Attachment of F3 peptide leads to QD internalization in HeLa cells. Thiolated peptides (F3 and KAREC control) and siRNA were conjugated to PEG-amino QD705 particles using sulfo-SMCC. Particles were filtered to remove excess peptide or siRNA and incubated with HeLa cell monolayers for 4 h. Flow cytometry indicated the F3 peptide is required for cell entry (A). The addition of free F3 peptide inhibits F3−QD uptake, while KAREC peptide does not, suggesting the F3 peptide and F3-labeled particles target the same receptor (B). In part C, the relationship between the number of F3 peptides per QD and cell uptake was examined. In these experiments, FITC-labeled peptide was conjugated to QDs using sulfo-LC-SPDP. For each formulation (black circles), peptide:QD ratio was determined by measuring the QD concentration by absorbance and then treating the conjugate with 2-mercaptoethanol, filtering out the QDs, and measuring the FITC fluorescence. Cell uptake increases dramatically with peptide number but appears to saturate around 10−15 F3s per QD.

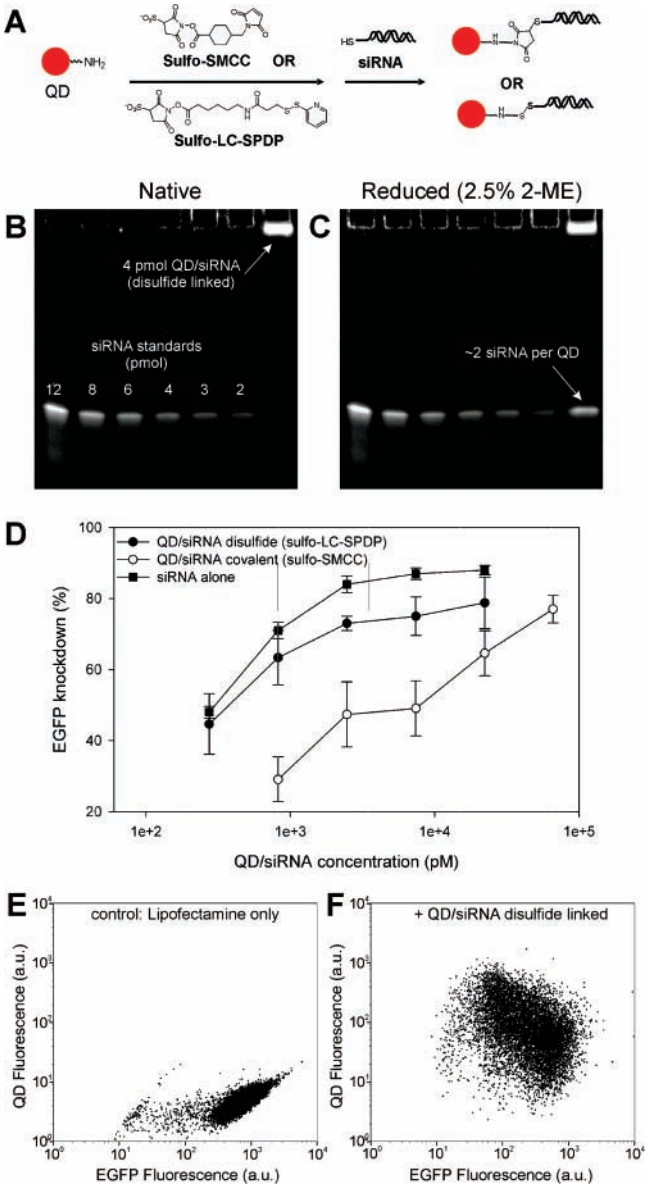


Figure 3. Conjugation of siRNA to QDs with cleavable or noncleavable cross-linkers. Thiol-modified siRNA was attached to PEG-amino QDs using the water-soluble heterobifunctional cross-linkers sulfo-SMCC and sulfo-LC-SPDP (A). The cross-link produced by SPDP is cleavable with 2-mercaptoethanol (2-ME), while SMCC yields a nonreducible linkage. Gel electrophoresis of the disulfide-linked conjugates indicated that no siRNA are electrostatically bound to the conjugate (B). Upon treatment with 2-ME, the QD/siRNA cross-link is reduced and the siRNA migrated down the gel alongside siRNA standards (C). QD/siRNA conjugates (or siRNA alone) were delivered to EGFP-expressing HeLa cells using Lipofectamine 2000 (cationic liposome reagent). Cells were trypsinized and assayed by flow cytometry 48 h later. Comparison with control cells (treated with Lipofectamine alone) indicated the disulfide bond leads to superior EGFP knockdown (% reduction in geometric mean fluorescence) (D). Comparing a dot-plot of cells treated with Lipofectamine alone (E) or disulfide-linked QD/siRNA (F) revealed a negative correlation between QD uptake and EGFP signal. Thus, the QD label can serve as a means of quantifying siRNA delivery and thus knockdown.

a cleavable cross-linker (sulfo-LC-SPDP). After unreacted peptide was removed by filtration, 2-mercaptoethanol (2-ME) was added to reduce the disulfide bond between peptide and QD. Using a 100 kDa cutoff filter, F3-FITC peptide was separated from the QDs and quantified by fluorescence. Several reactions were performed with various amounts of FITC-F3 and siRNA as reactants. For each formulation, the cellular uptake was quantified by flow cytometry and F3 number measured (Figure 2C, each point indicates a separate formulation). Attachment of a small number of peptides (0−5) did not lead to significant uptake (less than 10% of maximum). Uptake increases with peptide number but begins to saturate around 15 copies per QD.

The use of cleavable (sulfo-LC-SPDP) or noncleavable (sulfo-SMCC) cross-linkers for the attachment of F3 peptide did not significantly affect cell uptake. The choice of cross-linker, however, may affect the ability of the siRNA cargo to interact with RISC. The interior of the cell is a reducing environment, which would lead to cleavage of the disulfide bond generated by sulfo-LC-SPDP, freeing the siRNA. On the other hand, the amide bond produced by sulfo-SMCC is unaffected by reducing conditions (confirmed by treating the conjugates with 2.5% 2-ME for 30 min), leaving the intracellular QD/siRNA conjugate intact. We compared the efficiency of QD/siRNA conjugates prepared with both cross-linkers using an EGFP model system. Delivery of the conjugates to EGFP-labeled HeLa cells was performed by first complexing the particles with a cationic liposome transfection reagent (Lipofectamine 2000), to satisfy the functions of cell internalization and endosome escape, and knockdown efficiency was quantified by a reduction in EGFP fluorescence over controls (Lipofectamine only).

Using gel electrophoresis, the amount of siRNA conjugated per particle was quantified relative to double-stranded RNA standards. Particles conjugated using sulfo-LC-SPDP were first introduced under native (nonreduced) conditions (Figure 3B). The absence of a siRNA band in the QD/siRNA lanes indicates that no siRNA is noncovalently bound to the particles. Exposing the particles to 2-ME for 30 min led to the appearance of a siRNA band in the SPDP lane, which was quantified with RNA standards and ImageQuant software. Using this approach, approximately two siRNA duplexes were conjugated per QD under these conditions (Figure 3C). Cellular fluorescence was quantified 48 h after incubation with HeLa cells using flow cytometry. As hypothesized, the QD/siRNA formulation produced with the disulfide bond (using sulfo-LC-SPDP) led to greater EGFP knockdown (Figure 3D). The level of knockdown attained with disulfide-linked QD/siRNA, however, was less than observed when an equal concentration of free siRNA was delivered with Lipofectamine. On the basis of previous observations(*12*), one potential cause may be the limited surface area of the cationic liposomes, which is shared by QDs and siRNA. Additionally, the presence of the QDs in the endosome may reduce the efficiency of escape, or reduction of the disulfide bond may be incomplete, resulting in less efficient complexation with RISC.

The F3:siRNA reaction ratio was varied with the goal of generating a formulation capable of high cell uptake as well as the ability to carry a significant payload of siRNA. The cleavable cross-linker allowed the removal and quantification of both species after F3 peptide and siRNA coattachment. The results indicate a tradeoff between one siRNA per particle with high uptake (>15 peptides) and two duplexes but lower uptake (<10 peptides) (Figure 4A). Negatively charged siRNA may be electrostatically adsorbing to the surface of the aminated QDs, preventing the attachment of additional F3 peptides. Potentially, performing the reaction in high salt conditions, or in the presence of a surfactant, may allow higher loading. Since both high uptake efficiency and siRNA number are required for knockdown, particles with ~20 F3s and a single siRNA duplex were further investigated in cell studies.

When incubated with cells, these 20-F3/1−siRNA−QDs were shown to internalize significantly but did not lead to reduction in EGFP fluorescence 48 h later. Fluorescence microscopy revealed that the particles were intracellular, but they colocalized with an endosomal marker (LysoSensor, Molecular Probes).

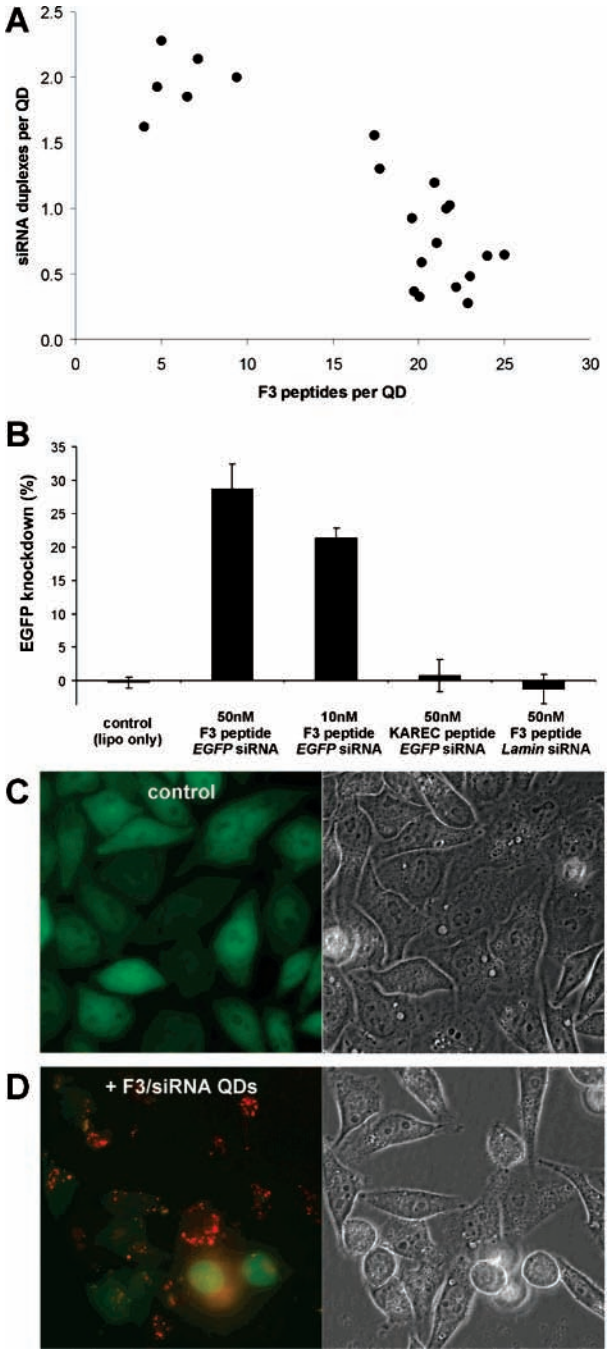


Figure 4. Co-attachment of F3 peptide and siRNA cargo allows EGFP knockdown upon delivery and endosome escape. Because of a limited number of attachment sites on the QDs, the goal of coattachment was to maximize siRNA loading while conjugating sufficient F3 peptides to allow internalization (>15). Varying the F3:siRNA ratio resulted in a number of QD formulations (black circles, A). We chose a formulation containing ~20 F3 peptides and ~1 siRNA per QD for knockdown studies in cell monolayers (B−D). EGFP-expressing HeLa cells were treated with 50 nM F3/siRNA−QDs for 4 h and then washed with cell media. When assayed for green fluorescence 48 h later, no knockdown was observed ("control", B). When these cells were treated with cationic liposomes (Lipofectamine 2000) immediately after removing the QDs and washing, a ~29% reduction in EGFP was observed. A lower concentration of QDs (10 nM) is less effective (21% knockdown). Incubation with KAREC-labeled particles followed by cationic liposomes leads to minimal particle internalization and thus no knockdown. Attachment of an irrelevant siRNA (directed against Lamin A/C) to QDs along with F3 peptide also results in no knockdown when delivered to cells followed by lipofectamine. Fluorescence imaging of cells incubated with F3/siRNA QDs (red dots) showed a reduced green fluorescence (D), compared with control cells incubated with Lipofectamine alone (C).

Addition of an endosome escape agent, therefore, was required to achieve knockdown. Specifically, after incubation of cells with F3/siRNA−QDs and washing, cationic liposomes were added for 12 h. Although cationic liposomes and polymers are typically used to form complexes with nucleic acids or particles, thereby ferrying the payload inside cells, in this case the reagent leads to endosomal escape of previously internalized QDs. We hypothesize that the cationic liposomes are internalized into new endosomes, which fuse with the endosomes carrying the QDs. As the pH of the vesicle is lowered by the cell, osmotic lysis leads to the release of both species into the cytoplasm. To assess the importance of the targeting ligand, particles carrying siRNA and a control peptide (KAREC) were used. These KAREC/siRNA particles were not internalized, and no EGFP knockdown was observed, despite endosome disruption. The specificity of knockdown was verified by delivery of F3/siRNA QDs containing an irrelevant siRNA (directed against Lamin A/C). Additionally, a time lag of 90 min between washing the cells free of QDs and cationic liposome addition did not lead to significant reduction in efficiency, indicating that endosomal degradation of the siRNA is not an issue on this time scale.

In addition to cationic liposomes, some chemotherapeutics, such as chloroquine have been shown to be capable of endosomal escape (*16*). While an endosome escape step could be a realistic part of a treatment regimen, there is also potential that this function could be built into each particle. Addition of fusogenic moieties to the QD surface, for example, may further improve delivery of the multifunctional particles described (*17*).

CONCLUSIONS

Decorating the surface of a fluorescent quantum dot with both a targeting ligand and siRNA duplex requires a tradeoff in the number of each species but can be used to generate a conjugate capable of knockdown in vitro. We found that multiple copies of the F3 targeting peptide were required for QD uptake, but that siRNA cargo could be co-attached without affecting the function of the peptide. Disulfide (sulfo-LC-SPDP) and covalent (sulfo-SMCC) cross-linkers were investigated for the attachment of siRNA to the particle, with the disulfide bond showing greater silencing efficiency. Finally, after delivery to cells and release from their endosomal entrapment, F3/siRNA−QDs produced significant knockdown of EGFP signal. By designing the siRNA sequence against a therapeutic target (e.g., oncogene) instead of EGFP, the technology explored in this study may be adapted to treat and image diseases such as cancer. This technology could also be readily adapted to other nanoparticle platforms, such as iron oxide or gold cores, which allow image contrast on magnetic resonance or X-ray imaging, respectively, and may therefore mitigate concerns over QD cytotoxicity and the limited tissue penetration of light. QDs, however, remain an attractive tool for in vitro and animal testing, where fluorescence is the most accessible and common imaging modality.

ACKNOWLEDGMENT

We thank Fernando Ferrer for peptide synthesis, Phillip Sharp for HeLa cell line and siRNA sequence, Joel Nielson for assistance with siRNA reagents and procedures, and we acknowledge financial support of the David and Lucile Packard Foundation, the National Cancer Institute of the National Institutes of Health (contract no. N01-C0-37117), the Centers for Cancer Nanotechnology Excellence at UCSD (U54 CA119335) and MIT (U54 CA119349-01), and a Bioengineering Research Partnership grant (1 R01 CA124427-01). A.M.D. thanks the UC Biotechnology Research and Education Program for a G.R.E.A.T. fellowship (no. 2004-16).

LITERATURE CITED

(1) Akerman, M. E., Chan, W. C., Laakkonen, P., Bhatia, S. N., and Ruoslahti, E. (2002) Nanocrystal targeting in vivo. *Proc. Natl. Acad. Sci. U.S.A. 99*, 12617−21.

(2) Dykxhoorn, D. M., Palliser, D., and Lieberman, J. (2006) The silent treatment: siRNAs as small molecule drugs. *Gene Ther. 13*, 541−552.

(3) Uprichard, S. L. (2005) The therapeutic potential of RNA interference. *FEBS Lett. 579*, 5996−6007.

(4) Soutschek, J., Akinc, A., Bramlage, B., Charisse, K., Constien, R., Donoghue, M., Elbashir, S., Geick, A., Hadwiger, P., Harborth, J., John, M., Kesavan, V., Lavine, G., Pandey, R. K., Racie, T., Rajeev, K. G., Rohl, I., Toudjarska, I., Wang, G., Wuschko, S., Bumcrot, D., Koteliansky, V., Limmer, S., Manoharan, M., and Vornlocher, H. P. (2004) Therapeutic silencing of an endogenous gene by systemic administration of modified siRNAs. *Nature 432*, 173−8.

(5) Song, E., Zhu, P., Lee, S. K., Chowdhury, D., Kussman, S., Dykxhoorn, D. M., Feng, Y., Palliser, D., Weiner, D. B., Shankar, P., Marasco, W. A., and Lieberman, J. (2005) Antibody mediated in vivo delivery of small interfering RNAs via cell-surface receptors. *Nat. Biotechnol. 23*, 709−17.

(6) Schiffelers, R. M., Ansari, A., Xu, J., Zhou, Q., Tang, Q., Storm, G., Molema, G., Lu, P. Y., Scaria, P. V., and Woodle, M. C. (2004) Cancer siRNA therapy by tumor selective delivery with ligand-targeted sterically stabilized nanoparticle. *Nucleic Acids Res. 32*, e149.

(7) Hu-Lieskovan, S., Heidel, J. D., Bartlett, D. W., Davis, M. E., and Triche, T. J. (2005) Sequence-specific knockdown of EWS-FLI1 by targeted, nonviral delivery of small interfering RNA inhibits tumor growth in a murine model of metastatic Ewing's sarcoma. *Cancer Res. 65*, 8984−92.

(8) Itaka, K., Kanayama, N., Nishiyama, N., Jang, W. D., Yamasaki, Y., Nakamura, K., Kawaguchi, H., and Kataoka, K. (2004) Supramolecular nanocarrier of siRNA from PEG-based block catiomer carrying diamine side chain with distinctive pK_a directed to enhance intracellular gene silencing. *J. Am. Chem. Soc. 126*, 13612−3.

(9) Chu, T. C., Twu, K. Y., Ellington, A. D., and Levy, M. (2006) Aptamer mediated siRNA delivery. *Nucleic Acids Res. 34*, e73.

(10) McNamara, J. O., 2nd, Andrechek, E. R., Wang, Y., Viles, K. D., Rempel, R. E., Gilboa, E., Sullenger, B. A., and Giangrande, P. H. (2006) Cell type-specific delivery of siRNAs with aptamer-siRNA chimeras. *Nat. Biotechnol. 24*, 1005−15.

(11) Derfus, A. M., Chan, W. C. W., and Bhatia, S. N. (2004) Intracellular Delivery of Quantum Dots for Live Cell Labeling and Organelle Tracking. *Adv. Mater 16*, 961−966.

(12) Chen, A. A., Derfus, A. M., Khetani, S. R., and Bhatia, S. N. (2005) Quantum dots to monitor RNAi delivery and improve gene silencing. *Nucleic Acids Res. 33*, e190.

(13) Moghimi, S. M., Hunter, A. C., and Murray, J. C. (2001) Long-circulating and target-specific nanoparticles: theory to practice. *Pharmacol. Rev. 53*, 283−318.

(14) Christian, S., Pilch, J., Akerman, M. E., Porkka, K., Laakkonen, P., and Ruoslahti, E. (2003) Nucleolin expressed at the cell surface is a marker of endothelial cells in angiogenic blood vessels. *J. Cell Biol. 163*, 871−8.

(15) Porkka, K., Laakkonen, P., Hoffman, J. A., Bernasconi, M., and Ruoslahti, E. (2002) A fragment of the HMGN2 protein homes to the nuclei of tumor cells and tumor endothelial cells in vivo. *Proc. Natl. Acad. Sci. U.S.A. 99*, 7444−9.

(16) Won, J., Kim, M., Yi, Y. W., Kim, Y. H., Jung, N., and Kim, T. K. (2005) A magnetic nanoprobe technology for detecting molecular interactions in live cells. *Science 309*, 121−5.

(17) Plank, C., Oberhauser, B., Mechtler, K., Koch, C., and Wagner, E. (1994) The influence of endosome-disruptive peptides on gene transfer using synthetic virus-like gene transfer systems. *J. Biol. Chem. 269*, 12918−12924.

BC060367E

N-Benzyl-2-(6,8-dichloro-2-(4-chlorophenyl)imidazo[1,2-*a*]pyridin-3-yl)-*N*-(6-(7-nitrobenzo[*c*][1,2,5]oxadiazol-4-ylamino)hexyl)acetamide as a New Fluorescent Probe for Peripheral Benzodiazepine Receptor and Microglial Cell Visualization†

Valentino Laquintana,‡ Nunzio Denora,‡ Angela Lopedota,‡ Hiromi Suzuki,§ Makoto Sawada,§ Mariangela Serra,# Giovanni Biggio,# Andrea Latrofa,‡ Giuseppe Trapani,*,‡ and Gaetano Liso‡

Dipartimento Farmaco-Chimico, Facoltà di Farmacia, Università degli Studi di Bari, Via Orabona 4, 70125 Bari, Italy, Department of Brain Function, Research Institute of Environmental Medicine, Nagoya University, Nagoya 464-8601, Japan, and Dipartimento di Biologia Sperimentale, Sezione di Neuroscienze, Università di Cagliari, Cittadella Universitaria Monserrato, SS 554 Km 4.5, Monserrato (Cagliari), Italy. Received December 20, 2006; Revised Manuscript Received July 17, 2007

The aim of this work was to develop new fluorescent probes for the localization and function of the peripheral benzodiazepine receptor (PBR). This receptor is primarily expressed on the mitochondria, and it is overexpressed in a variety of different states including glioma, breast cancer, Alzeheimer's disease, and activated microglia. For the mentioned purpose, imidazopyridine and imidazopyrimidine compounds **5**−**20** were synthesized, and their affinity for PBR was determined. Although some intrinsically fluorescent imidazopyrimidine compounds **12**−**20** possess good binding affinity, they cannot be used for visualizing PBR due to their unfavorable fluorescence characteristics. Among the imidazopyridine−7-nitrofurazan conjugates **5**−**11**, compound **10** was the most active, and it was found to stain live Ra2 microglial cells effectively. An in vivo biodistribution study carried out on compound **10** showed that this imidazopyridine derivative, injected in the carotid artery, is able to penetrate to liver parenchyma, whereas fluorescein isothiocyanate labeled dextran (FITC-dextran), used as a control dye, hardly penetrated from blood vessels to tissues. On the other hand, as for the distribution to brain, the patterns of staining with **10** and FITC-dextran are similar, indicating that both of them hardly penetrate into the brain because of the existence of the blood−brain barrier. The obtained results indicate that compound **10** represents a new useful fluorescent probe for visualization of activated microglia and PBR.

INTRODUCTION

The peripheral benzodiazepine receptor (PBR) is pharmacologically distinct from the central benzodiazepine receptor (CBR), which is coupled to GABA-regulated chloride channels in the central nervous system (CNS). CBR mediates the classical sedative, anxiolytic, anticonvulsant, and muscle relaxant properties of the benzodiazepines. On the other hand, the 18 kDa protein PBR, located in the outer mitochondrial membrane (*1*) and for which the name "translocator protein" has recently been proposed (*2*), plays an important role in stimulating the neurosteroids synthesis in glial cells, and it is involved in various neurological diseases such as Alzheimer's disease, Huntington's disease, and multiple sclerosis (*3*−*7*). In this regard, one useful index in delineating areas of active disease in the brain is the presence of activated microglia. In normal brain parenchyma, microglia are in a down-regulated state, but during disease or injury the microglia are activated and the expression of PBR in vivo is increased (*8*). Thus, the visualization of activated microglia is of relevant diagnostic value and suitable for monitoring of disease progression in the brain (*8*). There is also evidence showing that PBR expression is selectively increased in a wide variety of human tumors, including cancers of the colon, breast, ovary, liver, and especially the brain (*9*−*11*). Moreover, it has also been shown that PBR-specific ligands induce apoptosis and cell cycle arrest in cancer cells (*12*−*14*) and that appropriate PBR ligand−drug conjugates characterized by PBR affinity can be used as diagnostic imaging agents of solid tumors or to selectively release the linked anticancer drug to the target by a receptor-mediated mechanism (*15*−*18*). The synthesis and biological activity of compound **1** (Chart 1) have been reported by Kozikowski et al. (*19*), and this compound represents the first example of a fluorescent probe for PBR. Compound **1** was obtained by linking a fluorogenic 7-nitro-2,1,3-benzoxadiazol-4-yl moiety to the 2-phenylindole-3-acetic acid through a hexamethylenediamine spacer, and **1** was found to possess biological activity like other indoleacetamide PBR ligands at nanomolar levels (*19*). Moreover, by conjugation of different trifunctional lanthanide chelates to the isoquinoline PBR ligand PK11195 analogue, two conjugate compounds of general formula **2** (Chart 1) were prepared (*20*). For these conjugates, which may provide an optical or magnetic resonance (MR) signature depending on the involved lanthanide ion M (i.e., Eu^{3+} for optical or Gd^{3+} for MR), no affinity or selectivity data for PBR were provided. Subsequently, the same research group developed the molecular imaging agent **3** by conjugation of a PK11195 analogue with Lissamine−Rhodamine B dye, and the K_d of this conjugate to PBR was 1 μM (*21*). Chen et al. also reported that pyropheophorbides and their metal complexes **4** [M = In(III), Ni (II), and Zn(II)], characterized by PBR binding values at nano−micromolar levels, could be promising candidates as fluorescent probes for PBR and may have great potential as fluorophores to replace radioactive PBR probes (*22*). Further studies demonstrated that in addition to 2-phenylindole-3-acetic acid and isoquinoline derivatives (*23*, *24*), PBR binds with high affinity to other classes of compounds such as

† This work is dedicated to the memory of our colleague Prof. Gaetano Liso, recently deceased.

* Author to whom correspondence should be addressed [telephone (039) 080-5442764; fax (039) 080-5442754; e-mail trapani@farmchim.uniba.it.

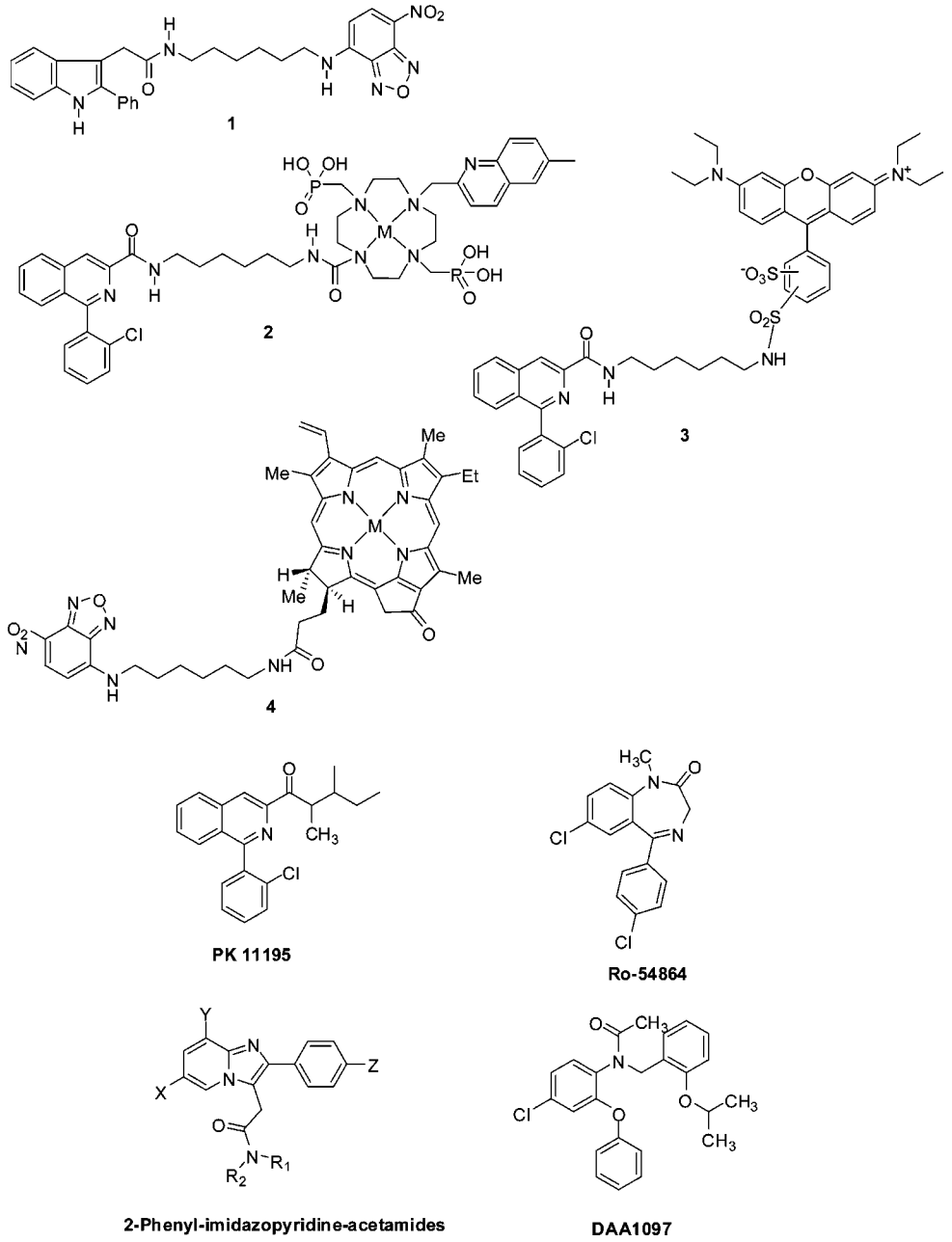
‡ Università degli Studi di Bari.

§ Nagoya University.

Università di Cagliari.

10.1021/bc060393c CCC: $37.00 © 2007 American Chemical Society
Published on Web 08/28/2007

Chart 1



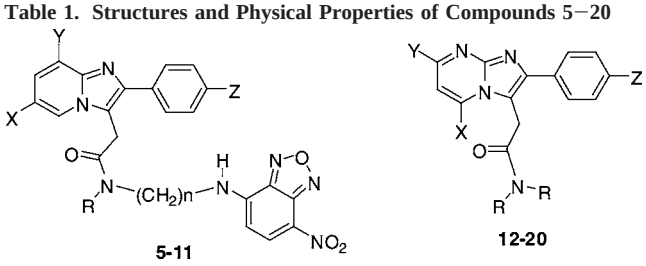
benzodiazepines (*25*) and *N*-phenoxyphenyl-*N*-isopropoxybenzyl-acetamides such as DAA1097 (*26*). We have shown that some 2-phenyl-imidazo[1,2-*a*]pyridine-3-acetamides (Chart 1) are potent and selective ligands for PBR and stimulate steroidogenesis both in the brain and at the periphery (*27*−29).

As part of our research program aimed at developing new probes for the localization and function of PBR in different tissues, we report the synthesis and biological evaluation of compounds **5**−**11** and **12**−**20** (Table 1). Compounds of the former set are characterized by a 7-nitro-2,1,3-benzoxadiazol-4-yl fluorophore linked through a diamine spacer to 2-phenylimidazo[1,2-*a*]pyridine-3-acyl moiety, whereas the other compounds may also be of interest because they are characterized by an imidazopyrimidine nucleus, which is intrinsically fluorescent (*30*) and are also analogues of imidazopyridine-3-acetamides with affinity and selectivity for PBR. Because the insertion of a bulky fluorescent group on a ligand is known to reduce binding affinity for the receptor, one might expect that compounds **12**−**20** would interact better than the conjugated compounds **5**−**11**. In this paper, the synthesis, binding data, fluorescence characteristics, and cell biology of these imidazopyridine and imidazopyrimidine compounds **5**−**20** are reported and discussed.

EXPERIMENTAL PROCEDURES

Chemistry. Melting points were determined in open capillary tubes with a Buchi apparatus and are uncorrected. IR spectra were obtained on a Perkin-Elmer 283 spectrophotometer (KBr pellets for solid or nujol for liquid). ^{1}H NMR spectra were determined on a Varian 390 or Bruker 300 MHz instrument. Chemical shifts are given in δ values downfield from Me_4Si as an internal standard. Mass spectra were recorded on a Hewlett-Packard 5995c GC-MS low-resolution spectrometer. All compounds showed appropriate IR, ^{1}H NMR, and mass spectra. Elemental analyses were performed on a Hewlett-Packard 185 C, H, N analyzer and agreed with theoretical values within ±0.40%. Silica gel 60 (Merck 70−230 mesh) was used for column chromatography. The starting 2-aminopyrimidine compounds, 4-chloro-7-nitrobenzofurazan (NBD chloride), alkyl-

Table 1. Structures and Physical Properties of Compounds 5−20



compd	R	X	Y	Z	*n*	mp (°C)	yield (%)
5	H	Cl	Cl	Cl	2	255−257	30
6	$CH_2C_6H_5$	Cl	Cl	Cl	2	250−253	35
7	H	Cl	Cl	Cl	4	155−160	44
8	$CH_2C_6H_5$	Cl	Cl	Cl	4	200−203	56
9	H	Cl	Cl	Cl	6	121−124	65
10	$CH_2C_6H_5$	Cl	Cl	Cl	6	213−215	55
11	H	Cl	Cl	H	4	212−217	45
12	C_2H_5	H	H	Cl		180−181	27
13	C_3H_7	H	H	H		115−117	20
14	C_3H_7	H	CH_3	Cl		126−128	10
15	C_3H_7	H	H	Cl		127−129	22
16	C_3H_7	H	CH_3	H		106−108	10
17	C_3H_7	CH_3	CH_3	Cl		111−113	20
18	C_4H_9	H	H	Cl		116−118	40
19	C_4H_9	H	H	H		121−123	39
20	C_6H_{13}	H	H	Cl		92−94	20

endiamines, triethylamine (TEA), ethyl 1,2-dihydro-2-ethoxy-1-quinolinecarboxylate (EEDQ), and anhydrous tetrahydrofuran (THF) were purchased from Sigma-Aldrich (Milan, Italy).

General Procedure for the Preparation of 2-Phenylimidazo[1,2-*a*]pyridineacetamide *N*-Alkylcarbamates 23a−g. To a stirred solution of the required imidazo[1,2-*a*]pyridin-3-acetic acid **21** (1 mmol) in anhydrous THF (20 mL) were added EEDQ (1.2 mmol), the appropriate mono-Boc-protected polymethylendiamine **22a−f** (1.1 mmol), and TEA (1.3 mmol) successively. Stirring was prolonged at room temperature for 6−12 h, and the resulting reaction mixture was poured into 20 mL of water (pH ∼4.5) and extracted with ethyl acetate (3 × 30 mL). The organic layer was separated, washed with water and brine, and dried over Na_2SO_4. Solvent was evaporated under reduced pressure, and the resulting residue was purified by silica gel column chromatography [light petroleum ether/ethyl acetate 6:4 (v/v) as eluent)] to give the corresponding compounds **23a−g**.

*tert-Butyl-2-(2-(6,8-dichloro-2-(4-chlorophenyl)imidazo[1,2-a]pyridin-3-yl)acetamido)ethylcarbamate (**23a**):* IR (KBr) 3340, 1681, 1640 cm^{-1}; ^1H NMR ($CDCl_3$) δ 1.36 (s, 9H, $C(CH_3)_3$), 3.2−3.3 (m, 2H, CH_2N-Boc), 3.3−3.4 (m, 2H, CH_2NCO), 3.92 (s, 2H, CH_2CO), 4.85 (br 1H, NH-Boc), 7.00 (br 1H, NH−CO), 7.35 (s, 1H, Ar), 7.43 (d, J = 8.2 Hz, 2H, Ar), 7.69 (d, J = 8.2 Hz, 2H, Ar), 8.22 (s, 1H, Ar); MS (ESI) *m/z* 497 $(M + H)^+$. Anal. ($C_{22}H_{23}Cl_3N_4O_3$) C, H, N.

*tert-Butyl-2-(N-benzyl-2-(6,8-dichloro-2-(4-chlorophenyl)imidazo[1,2-a]pyridin-3-yl)acetamido)ethylcarbamate (**23b**):* IR (KBr) 3345, 1710, 1631 cm^{-1}; ^1H NMR ($CDCl_3$) δ 1.44 (s, 9H, $C(CH_3)_3$), 3.1−3.6 (m, 4H, CH_2N-Boc and CH_2NCO), 4.01 (s, 1.4H, CH_2CO), 4.17 (s, 0.6H, CH_2CO), 4.55 (s, 1.4H, CH_2-Ar), 4.64 (s, 0.6H, CH_2Ar), 4.8−4.9 (br 1H, NH), 7.0−7.5 (m, 10H, Ar), 8.62 (m, 0.4H, Ar), 8.19 (m, 0.6H, Ar); MS (ESI) *m/z* 589 $(M + H)^+$. Anal. ($C_{29}H_{29}Cl_3N_4O_3$) C, H, N.

*tert-Butyl-4-(2-(6,8-dichloro-2-(4-chlorophenyl)imidazo[1,2-a]pyridin-3-yl)acetamido)butylcarbamate (**23c**):* IR (KBr) 3340, 3270, 1687, 1647 cm^{-1}; ^1H NMR (DMSO-d_6) δ 1.34 (s, 9H, $C(CH_3)_3$), 1.4−1.5 (m, 4H, CH_2CH_2), 2.8−3.0 (m, 2H, CH_2N-Boc) 3.0−3.1 (m, 2H, CH_2NCO), 4.00 (s, 2H, CH_2CO), 0.4.8 (br 1H, NH−CO), 6.80 (br 1H, NH-Boc), 7.53 (d, J = 8.5 Hz, 2H, Ar), 7.67 (d, J = 1.6 Hz, 1H, Ar), 7.79 (d, J = 8.5 Hz, 2H, Ar), 8.70 (d, J = 1.6 Hz, 1H, Ar); MS (ESI) *m/z* 525 $(M + H)^+$. Anal. ($C_{24}H_{27}Cl_3N_4O_3$) C, H, N.

*tert-Butyl-4-(N-benzyl-2-(6,8-dichloro-2-(4-chlorophenyl)imidazo[1,2-a]pyridin-3-yl)acetamido)butylcarbamate (**23d**):* IR (KBr) 3360, 1691, 1634 cm^{-1}; ^1H NMR ($CDCl_3$) δ 1.42 (s, 9H, $C(CH_3)_3$), 1.5−1.6 (m, 4H CH_2CH_2), 3.0−3.2 (m, 2H, CH_2N-Boc) 3.4−3.8 (m, 2H, CH_2NCO), 4.01 (s, 0.8H, CH_2-CO), 4.12 (s, 1.2H, CH_2CO), 4.45 (s, 0.8H, CH_2Ar), 4.59 (s, 1.2H, CH_2Ar), 6.9−7.7 (m, 10H, Ar), 8.11 (m, 0.9H, Ar), 8.24 (m, 0.1H, Ar); MS (ESI) *m/z* 617 $(M + H)^+$. Anal. ($C_{31}H_{33}Cl_3N_4O_3$) C, H, N.

*tert-Butyl-6-(2-(6,8-dichloro-2-(4-chlorophenyl)imidazo[1,2-a]pyridin-3-yl)acetamido)hexylcarbamate (**23e**):* IR (KBr) 3322, 3083, 1685, 1639 cm^{-1}; ^1H NMR ($CDCl_3$) δ 1.40 (s, 9H, $C(CH_3)_3$), 1.2−1.5 (m, 8H, CH_2), 3.0−3.1 (m, 2H, CH_2N-Boc) 3.2−3.3 (m, 2H, CH_2NCO), 3.93 (s, 2H, CH_2CO), 4.5 (br 1H, NH-Boc), 6.2 (br 1H, NH−CO), 7.33 (d, J = 1.6 Hz, 1H, Ar), 7.43 (d, J = 8.2 Hz, 2H, Ar), 7.69 (d, J = 8.2 Hz, 2H, Ar), 8.14 (d, J = 1.6 Hz, 1H, Ar); MS (ESI) *m/z* 555 $(M + H)^+$. Anal. ($C_{26}H_{31}Cl_3N_4O_3$) C, H, N.

*tert-Butyl-6-(N-benzyl-2-(6,8-dichloro-2-(4-chlorophenyl)imidazo[1,2-a]pyridin-3-yl)acetamido)hexylcarbamate (**23f**):* IR (KBr) 3350, 1705, 1639 cm^{-1}; ^1H NMR ($CDCl_3$) δ 1.43 (s, 9H, $C(CH_3)_3$), 1.2−1.4 (m, 4H CH_2) 1.6−1.8 (m, 4H CH_2), 3.0−3.2 (m, 2H, CH_2N-Boc) 3.4−3.5 (m, 2H, CH_2NCO), 4.00 (s, 1H, CH_2CO), 4.01 (s, 1H, CH_2CO), 4.43 (s, 1H, CH_2Ar), 4.57 (s, 1H, CH_2Ar), 4.5 (br, 1H, NH), 6.9−7.6 (m, 10H, Ar), 8.10 (m, 0.6H, Ar), 8.25 (m, 0.4H, Ar); MS (ESI) *m/z* 645 $(M + H)^+$. Anal. ($C_{33}H_{37}Cl_3N_4O_3$) C, H, N.

*tert-Butyl-4-(2-(6,8-dichloro-2-phenyl)imidazo[1,2-a]pyridin-3-yl)acetamido)butylcarbamate (**23g**):* IR (KBr) 3342, 1683, 1635 cm^{-1}; ^1H NMR ($CDCl_3$) δ 1.41 (s, 9H, $C(CH_3)_3$), 1.4−1.5 (m, 4H, CH_2CH_2), 3.0−3.2 (m, 2H, CH_2N-Boc) 3.2−3.4 (m, 2H, CH_2NCO), 3.95 (s, 2H, CH_2CO), 4.5−4.6 (br 1H, NH-Boc), 6.1−6.3 (br 1H, NH−CO), 7.32 (d, J = 1.6 Hz, 1H, Ar), 7.3−7.5 (m, 3H, Ar), 7.73 (d, J = 8.5 Hz, 2H, Ar), 8.15 (d, J = 1.6 Hz, 1H, Ar); MS (ESI) *m/z* 491 $(M + H)^+$. Anal. ($C_{24}H_{28}Cl_2N_4O_3$) C, H, N.

General Procedure for the Preparation of *N*-Aminoalkyl-2-phenylimidazo[1,2-*a*]pyridineacetamides 24a−g. In a stirred and ice-cooled solution of the appropriate carbamate **23** (0.5 mmol) in dichloromethane (20 mL) was bubbled HCl gas for 30 min. Evaporation of the solvent under reduced pressure gave the corresponding Boc-deprotected compound **24** as hydrochloride salt in good yield.

*N-(2-Aminoethyl)-2-(6,8-dichloro-2-(4-chlorophenyl)imidazo[1,2-a]pyridin-3-yl)acetamide (**24a**):* IR (KBr) 3285, 1685 cm^{-1}; ^1H NMR (DMSO-d_6) δ 2.8−2.9 (m, 2H, CH_2N), 3.3−3.4 (m, 2H, CH_2NCO), 4.06 (s, 2H, CH_2CO), 5.2 (br 2H, NH_2), 7.54 (d, J = 8.5 Hz, 2H, Ar), 7.70 (d, J = 1.6 Hz, 1H, Ar), 7.78 (d, J = 8.5 Hz, 2H, Ar), 8.44 (m, 1H, NHCO), 8.69 (d, J = 1.6 Hz 1H, Ar); MS (ESI) *m/z* 397 $(M + H)^+$. Anal. ($C_{17}H_{15}Cl_3N_4O$) C, H, N.

*N-(2-Aminoethyl)-2-(6,8-dichloro-N-benzyl-2-(4-chlorophenyl)imidazo[1,2-a]pyridin-3-yl)acetamide (**24b**):* IR (KBr) 3370, 1638 cm^{-1}; ^1H NMR ($CDCl_3$) δ 2.8−2.9 (m, 4H, CH_2N and NH_2), 3.3−3.4 (m, 2H, CH_2NCO), 3.72 (s, 2H, CH_2CO), 3.89 (s, 2H, CH_2Ar), 7.2−7.4 (m, 8H, Ar), 7.76 (d, J = 8.5 Hz, 2H, Ar), 8.17 (d, J = 1.4 Hz, 1H, Ar); MS (ESI) *m/z* 487 $(M + H)^+$. Anal. ($C_{24}H_{21}Cl_3N_4O$) C, H, N.

*N-(4-Aminobutyl)-2-(6,8-dichloro-2-(4-chlorophenyl)imidazo[1,2-a]pyridin-3-yl)acetamide (**24c**):* IR (KBr) 3444, 1662 cm^{-1}; ^1H NMR ($CDCl_3$) δ 1.4−1.6 (m, 6H, CH_2CH_2 and NH_2), 2.5−2.6 (m, 2H, CH_2NCO), 3.2−3.3 (m, 2H, CH_2N), 3.92 (s, 2H, CH_2CO), 7.33 (d, J = 1.6 Hz, 1H, Ar), 7.44 (d, J = 8.5 Hz, 2H, Ar), 7.3−7.4 (m, 1H, NHCO), 7.70 (d, J = 8.5 Hz, 2H,

Ar), 8.15 (d, $J = 1.6$ Hz 1H, Ar); MS (ESI) *m/z* 425 $(M + H)^+$. Anal. ($C_{19}H_{19}Cl_3N_4O$) C, H, N.

*N-(4-Aminobutyl)-2-(6,8-dichloro-N-benzyl-2-(4-chlorophenyl)imidazo[1,2-a]pyridin-3-yl)acetamide (**24d**):* IR (KBr) 3370, 1625 cm^{-1}; ^1H NMR ($CDCl_3$) δ 1.2−1.4 (m, 4H, CH_2CH_2), 1.5−1.8 (m, 2H, NH_2), 2.5−2.8 (m, 2H, CH_2N), 3.1−3.5 (m, 2H, CH_2NCO), 4.01 (s, 1.2H, CH_2CO), 4.12 (s, 0.8H, CH_2CO), 4.45 (s, 1.2H, CH_2Ar), 4.59 (s, 0.8H, CH_2Ar), 6.9−7.7 (m, 10H, Ar), 8.11 (d, $J = 1.6$ Hz, 0.6H, Ar), 8.27 (d, $J = 1.6$ Hz, 0.4H, Ar); MS (ESI) *m/z* 515 $(M + H)^+$. Anal. ($C_{26}H_{25}Cl_3N_4O$) C, H, N.

*N-(6-Aminohexyl)-2-(6,8-dichloro-2-(4-chlorophenyl)imidazo[1,2-a]pyridin-3-yl)acetamide (**24e**):* IR (KBr) 3442, 1636 cm^{-1}; ^1H NMR ($CDCl_3$) δ 1.2−1.6 (m, 10H, CH_2 and NH_2), 2.64 (t, $J = 6.4$ Hz, 2H, CH_2NCO), 3.24 (q, $J = 6.4$ Hz, 2H, CH_2N), 3.91 (s, 2H, CH_2CO), 5.8 (br, 1H, NHCO),7.34 (d, $J = 1.6$ Hz, 1H, Ar), 7.44 (d, $J = 8.2$ Hz, 2H, Ar), 7.68 (d, $J = 8.2$ Hz, 2H, Ar), 8.10 (d, $J = 1.6$ Hz 1H, Ar); MS (ESI) *m/z* 455 $(M + H)^+$. Anal. ($C_{21}H_{23}Cl_3N_4O$) C, H, N.

*N-(6-Aminohexyl)-2-(6,8-dichloro-N-benzyl-2-(4-chlorophenyl)imidazo[1,2-a]pyridin-3-yl)acetamide (**24f**):* IR (KBr) 3223, 1625 cm^{-1}; ^1H NMR ($CDCl_3$) δ 1.2−1.4 (m, 6H, CH_2 and NH_2), 1.6−1.8 (m, 4H, CH_2), 3.12 (m, 2H, CH_2N), 3.44 (m, 2H, CH_2NCO), 4.00 (s, 1H, CH_2CO), 4.10 (s, 1H, CH_2CO), 4.43 (s, 1H, CH_2Ar), 4.53 (s, 1H, CH_2Ar), 6.9−7.6 (m, 10H, Ar), 8.10 (d, $J = 1.6$ Hz, 0.6H, Ar), 8.25 (d, $J = 1.6$ Hz, 0.4H, Ar); MS (ESI) *m/z* 545 $(M + H)^+$. Anal. ($C_{28}H_{29}Cl_3N_4O$) C, H, N.

*N-(4-Aminobutyl)-2-(6,8-dichloro-2-phenylimidazo[1,2-a]pyridin-3-yl)acetamide (**24g**):* IR (KBr) 3471, 1641 cm^{-1}; ^1H NMR ($CDCl_3$) δ 1.2−1.6 (m, 4H, CH_2CH_2) 1.6−1.7 (br, 2H, NH_2), 2.55 (m, 2H, CH_2NCO), 3.25 (m, 2H, CH_2N), 3.96 (s, 2H, CH_2CO), 7.33 (d, $J = 1.6$ Hz, 1H, Ar), 7.4−7.5 (m, 3H, Ar), 7.74 (m, 2H, Ar), 8.18 (d, $J = 1.6$ Hz, 1H, Ar), 8.15 (d, $J = 1.6$ Hz 1H, Ar); MS (ESI) *m/z* 391 $(M + H)^+$. Anal. ($C_{19}H_{20}Cl_2N_4O$) C, H, N.

General Procedure for the Preparation of Benzooxadiazole-imidazopyridine Acetamides 5−11. To a stirred and ice-cooled solution of the appropriate compound **24a−g** (0.5 mmol) in anhydrous THF (20 mL) were added a solution of NBD chloride (0.5 mmol) in anhydrous THF (2 mL) and then TEA (0.7 mmol). Stirring was prolonged at room temperature for 1 h, and the resulting mixture was poured into 20 mL of water and then extracted with chloroform (3 × 30 mL). The organic layer was washed with water and brine and successively dried over Na_2SO_4. Solvent was evaporated under reduced pressure, and the resulting residue was purified by silica gel column chromatography [light petroleum ether/ethyl acetate 4:6 (v/v) as eluent)] to give the corresponding compounds **5−11**.

*2-(6,8-Dichloro-2-(4-chlorophenyl)imidazo[1,2-a]pyridin-3-yl)-N-(2-(7-nitrobenzo[c](1,2,5)oxadiazol-4-ylamino)ethyl)acetamide (**5**):* IR (KBr) 3250, 1656 cm^{-1}; ^1H NMR (acetone-d_6) δ 3.6−3.8 (m, 4H, NCH_2CH_2N), 4.18 (s, 2H, CH_2CO), 6.44 (d, $J = 8.8$ Hz, 1H, C(5)H NBD moiety), 7.4−7.5 (m, 3H, Ar), 7.87 (d, $J = 8.5$ Hz, 2H, Ar), 8.45 (d, $J = 8.8$ Hz, 1H, C(6)H of NBD moiety), 8.51 (d, $J = 1.6$ Hz 1H, Ar); MS (ESI) *m/z* 562 $(M + H)^+$. Anal. ($C_{23}H_{16}Cl_3N_7O_4$) C, H, N.

*N-Benzyl-2-(6,8-dichloro-2-(4-chlorophenyl)imidazo[1,2-a]pyridin-3-yl)-N-(2-(7-nitrobenzo[c](1,2,5)oxadiazol-4-ylamino)ethyl)acetamide (**6**):* IR (KBr) 3420, 1640 cm^{-1}; ^1H NMR (DMSO-d_6) δ 3.2−3.3 (m, 4H, NCH_2CH_2N), 3.6−4.9 (m, 4H, CH_2CO and CH_2Ar), 6.3−6.9 (m, 1H, C(5)H of NBD moiety), 7.1−7.8 (m, 10H, Ar), 8.2−8.9 (m, 2H, Ar and C(6)H of NBD moiety), 9.2−9.4 (m, 1H, NH); MS (ESI) *m/z* 652 $(M + H)^+$. Anal. ($C_{30}H_{22}Cl_3N_7O_4$) C, H, N.

*2-(6,8-Dichloro-2-(4-chlorophenyl)imidazo[1,2-a]pyridin-3-yl)-N-(4-(7-nitrobenzo[c](1,2,5)oxadiazol-4-ylamino)butyl)acetamide (**7**):* IR (KBr) 3280, 1658 cm^{-1}; ^1H NMR (DMSO-d_6) δ 1.4−1.5 (m, 2H, CH_2), 1.5−1.7 (m, 2H, CH_2), 3.1−3.4 (m, 4H, CH_2N), 3.73 (s, 2H, CH_2CO), 5.96 (d, $J = 9.1$ Hz, 1H, C(5)H NBD moiety), 7.08 (d, $J = 1.6$ Hz 1H, Ar), 7.22 (d, $J = 8.5$ Hz, 2H, Ar), 7.62 (d, $J = 8.5$ Hz, 2H, Ar), 7.7−7.8 (m, 1H, NH), 8.14 (d, $J = 1.6$ Hz 1H, Ar), 8.23 (d, $J = 9.1$ Hz, 1H, C(6)H of NBD moiety), 8−5-8.6 (m, 1H, NH); MS (ESI) *m/z* 586 $(M - H)^-$. Anal. ($C_{25}H_{20}Cl_3N_7O_4$) C, H, N.

*N-Benzyl-2-(6,8-dichloro-2-(4-chlorophenyl)imidazo[1,2-a]pyridin-3-yl)-N-(4-(7-nitrobenzo[c](1,2,5)oxadiazol-4-ylamino)butyl)acetamide (**8**):* IR (KBr) 3400, 1645 cm^{-1}; ^1H NMR (DMSO-d_6) δ 1.0−1.2 (m, 4H, CH_2CH_2), 3.0−3.3 (m, 2H CH_2N) 4.0−4.1 (m, 2H, CH_2NCO), 4.23 (s, 1H, CH_2CO), 4.41 (s, 1H, CH_2CO) 4.55 (s, 1.1H, CH_2Ar), 4.73 (s, 0.9H, CH_2Ar), 6.36 (d, 1H, C(5)H of NBD moiety), 7.1−7.7 (m, 10H, Ar), 8.2−8.7 (m 2H, Ar and C(6)H of NBD moiety), 9.5 (br, 1H, NH); MS (ESI) *m/z* 676 $(M - H)^-$. Anal. ($C_{32}H_{26}Cl_3N_7O_4$) C, H, N.

*2-(6,8-Dichloro-2-(4-chlorophenyl)imidazo[1,2-a]pyridin-3-yl)-N-(6-(7-nitrobenzo[c](1,2,5)oxadiazol-4-ylamino)hexyl)acetamide (**9**):* IR (KBr) 3373, 1656 cm^{-1}; ^1H NMR (DMSO-d_6) δ 1.2−1.5 (m, 6H, CH_2), 1.5−1.7 (m, 2H, CH_2), 3.0−3.1 (m, 2H, CH_2N), 3.2−3.3 (m, 2H, CH_2NCO), 4.01 (s, 2H, CH_2CO), 6.32 (d, $J = 9.3$ Hz, 1H, C(5)H NBD moiety), 7.49 (d, $J = 8.5$ Hz, 2H, Ar), 7.63 (d, $J = 1.6$ Hz 1H, Ar), 7.82 (d, $J = 8.5$ Hz, 2H, Ar), 8.3−8.4 (m, 1H, NH), 8.44 (d, $J = 9.3$ Hz, 1H, C(6)H of NBD moiety), 8.68 (d, $J = 1.6$ Hz 1H, Ar), 8.5 (br, 1H, NH); MS (ESI) *m/z* 614 $(M - H)^-$. Anal. ($C_{27}H_{24}Cl_3N_7O_4$) C, H, N.

*N-Benzyl-2-(6,8-dichloro-2-(4-chlorophenyl)imidazo[1,2-a]pyridin-3-yl)-N-(6-(7-nitrobenzo[c](1,2,5)oxadiazol-4-ylamino)hexyl)acetamide (**10**):* IR (KBr) 3223, 1643 cm^{-1}; ^1H NMR (DMSO-d_6) δ 1.2−1.4 (m, 4H, CH_2), 1.6−1.8 (m, 4H, CH_2), 3.0−3.2 (m, 2H CH_2N) 3.4−3.5 (m, 2H, CH_2NCO), 4.23 (s, 0.9H, CH_2CO), 4.37 (s, 1.1H, CH_2CO) 4.52 (s, 1.1H, CH_2Ar), 4.73 (s, 0.9H, CH_2Ar), 6.3−6.5 (m, 1H, C(5)H of NBD moiety), 6.9−7.6 (m, 10H, Ar), 8.43 (d, $J = 9.0$ Hz, 1H, C(6)H of NBD moiety), 8.56 (m, 0.4H, Ar), 8.66 (m, 0.6H, Ar), 9.5 (br, 1H, NH); MS (ESI) *m/z* 706 $(M + H)^+$. Anal. ($C_{34}H_{30}Cl_3N_7O_4$) C, H, N.

*2-(6,8-Dichloro-2-phenylimidazo[1,2-a]pyridin-3-yl)-N-(4-(7-nitrobenzo[c](1,2,5)oxadiazol-4-ylamino)butyl)acetamide (**11**):* IR (KBr) 3250, 1667 cm^{-1}; ^1H NMR (DMSO-d_6) δ 1.5−1.7 (m, 4H, CH_2CH_2), 3.3−3.5 (m, 2H, CH_2N), 4.02 (s, 2H, CH_2CO), 4.1−4.3 (m, 2H, CH_2NCO), 6.35 (d, $J = 8.9$ Hz, 1H, C(5)H NBD moiety), 6.6−6.7 (m, 1H, NH), 7.3−7.5 (m 4H, Ar), 7.61 (d, $J = 1.6$ Hz, 1H, Ar), 7.76 (d, $J = 8.5$ Hz, 2H, Ar), 8.3−8.4 (m, 1H, NH), 8.39 (d, $J = 9.1$ Hz, 1H, C(6)H of NBD moiety); MS (ESI) *m/z* 554 $(M + H)^+$; 552 $(M - H)^-$. Anal. ($C_{25}H_{21}Cl_2N_7O_4$) C, H, N.

General Procedure for the Preparation of *N,N*-Di-*n*-alkyl-(2-phenylimidazo[1,2-*a*]pyrimidin-3-yl)acetamides 12−20. To a stirred solution of the appropriate substituted 2-aminopyrimidine **27** (10 mmol) in 40 mL of DMF was added the required *N,N*-dialkyl-3-bromo-3-benzoylpropionamide **28** (10 mmol). The reaction mixture was refluxed for 6−9 h by monitoring the reaction progress on silica TLC plates [petroleum ether/ethyl acetate 1:1 (v/v) as eluent]. The solvent was removed by distillation under reduced pressure, and the resulting residue was purified by silica gel column chromatography [petroleum ether/ethyl acetate 1:1 (v/v) as eluent] to give the corresponding products **12−20**, which were crystallized from a petroleum ether/ethyl acetate mixture.

*N,N-Diethyl[2-(4-chlorophenyl)imidazo[1,2-a]pyrimidin-3-yl]-acetamide (**12**):* IR (KBr) 1645 cm^{-1}; ^1H NMR ($CDCl_3$) δ 0.9−1.2 (m, 6H, CH_3), 3.1−3.6 (m, 4H, CH_2), 4.15 (s, 2H, CH_2), 6.86 (m, 1H, Ar), 7.42 (d, $J = 8.5$ Hz, 2H, Ar), 7.70 (d, 2H,

Ar), 8.5−8.8 (m, 2H, Ar); MS *m*/*z* 342 (M^+ 25), 242 (base). Anal. ($C_{18}H_{19}ClN_4O$) C, H, N.

*N,N-Di-n-propyl(2-phenylimidazo[1,2-a]pyrimidin-3-yl)acetamide (**13**):* MS *m*/*z* 336 (M^+ 23), 208 (base). Anal. ($C_{20}H_{24}N_4O$) C, H, N.

*N,N-Di-n-propyl[2-(4-chlorophenyl)-7-methylimidazo[1,2-a]-pyrimidin-3-yl]acetamide (**14**):* IR (KBr) 1630 cm^{-1}; ^1H NMR ($CDCl_3$) δ 0.63 (t, J = 7.3 Hz, 3H, CH_3), 0.79 (t, 3H, CH_3), 1.3−1.5 (m, 4H, CH_2), 2.61 (s, 3H, CH_3), 2.9−3.0 (m, 2H, CH_2N), 3.1−3.2 (m, 2H, CH_2N), 4.08 (s, 2H, CH_2CO), 6.70 (d, J = 7.0 Hz, 1H, Ar), 7.42 (d, J = 8.6 Hz, 2H, Ar), 7.65 (d, J = 8.6 Hz, 2H, Ar),8.55 (d, 1H, Ar); MS *m*/*z* 384 (M^+ 18), 256 (base). Anal. ($C_{21}H_{25}ClN_4O$) C, H, N.

*N,N-Di-n-propyl[2-(4-chlorophenyl)imidazo[1,2-a]pyrimidin-3-yl]acetamide (**15**):* IR (KBr) 1650 cm^{-1}; ^1H NMR ($CDCl_3$) δ 0.65 (t, J = 7.3 Hz, 3H, CH_3), 0.79 (t, J = 7.3 Hz, 3H, CH_3), 1.3−1.5 (m, 4H, CH_2), 2.9−3.0 (m, 2H, CH_2N), 3.1−3.2 (m, 2H, CH_2N), 4.08 (s, 2H, CH_2CO), 6.7−6.9 (m, 1H, Ar), 7.4−7.7 (m, 4H, Ar), 8.48 (m, 1H, Ar), 8.61 (d, J = 6.6 Hz, 1H, Ar); MS *m*/*z* 370 (M^+ 28), 242 (base). Anal. ($C_{20}H_{23}ClN_4O$) C, H, N.

*N,N-Di-n-propyl(2-phenyl-7-methylimidazo[1,2-a]pyrimidin-3-yl)acetamide (**16**):* IR (KBr) 1655 cm^{-1}; ^1H NMR ($CDCl_3$) δ 0.59 (t, J = 7.4 Hz, 3H, CH_3), 0.78 (t, J = 7.4 Hz, 3H, CH_3), 1.3−1.5 (m, 4H, CH_2), 2.60 (s, 3H, CH_3), 2.9−3.0 (m, 2H, CH_2N), 3.2−3.3 (m, 2H, CH_2N), 4.15 (s, 2H, CH_2CO), 6.7−6.8 (m, 1H, Ar), 7.3−7.5 (m, 3H, Ar), 7.7 (d, J = 7.2 Hz, 2H, Ar), 8.67 (d, 1H, Ar); MS *m*/*z* 350 (M^+ 19), 222 (base). Anal. ($C_{21}H_{26}N_4O$) C, H, N.

*N,N-Di-n-propyl[2-(4-chlorophenyl)-5,7-dimethylimidazo[1,2-a]pyrimidin-3-yl]acetamide (**17**):* IR (KBr) 1645 cm^{-1}; ^1H NMR ($CDCl_3$) δ 0.8−1.0 (m, 6H, CH_3), 1.5−1.7 (m, 4H, CH_2), 2.52 (s, 3H, CH_3), 2.74 (s, 3H, CH_3), 3.2−3.4 (m, 4H, CH_2N), 4.12 (s, 2H, CH_2CO), 6.46 (s, 1H, Ar), 7.3−7.6 (m, 4H, Ar); MS *m*/*z* 398 (M^+ 10), 270 (base). Anal. ($C_{22}H_{27}ClN_4O$) C, H, N.

*N,N-Di-n-butyl[2-(4-chlorophenyl)imidazo[1,2-a]pyrimidin-3-yl]acetamide (**18**):* IR (KBr) 1627 cm^{-1}; ^1H NMR ($CDCl_3$) δ 0.8−1.0 (m, 6H, CH_3), 1.2−1.6 (m, 8H, CH_2), 3.1−3.5 (m, 4H, CH_2N), 4.20 (s, 2H, CH_2CO), 6.9−7.1 (m, 1H, Ar), 7.4−7.8 (m, 4H, Ar), 8.6−8.9 (m, 2H, Ar); MS *m*/*z* 398 (M^+ 31), 242 (base). Anal. ($C_{22}H_{27}ClN_4O$) C, H, N.

*N,N-Di-n-butyl(2-phenylimidazo[1,2-a]pyrimidin-3-yl)acetamide (**19**):* IR (KBr) 1630 cm^{-1}; ^1H NMR ($CDCl_3$) δ 0.7−1.0 (m, 6H, CH_3), 1.2−1.6 (m, 8H, CH_2), 2.9−3.4 (m, 4H, CH_2N), 4.15 (s, 2H, CH_2CO), 6.8−6.9 (m, 1H, Ar), 7.3−7.8 (m, 5H, Ar), 8.5−8.8 (m, 2H, Ar); MS *m*/*z* 364 (M^+ 24), 208 (base). Anal. ($C_{22}H_{28}N_4O$) C, H, N.

*N,N-Di-n-hexyl[2-(4-chlorophenyl)imidazo[1,2-a]pyrimidin-3-yl]acetamide (**20**):* IR (KBr) 1645 cm^{-1}; ^1H NMR ($CDCl_3$) δ 0.8−0.9 (m, 6H, CH_3), 1.1−1.5 (m, 16H, CH_2), 2.9−3.1 (m, 2H, CH_2N), 3.2−3.3 (m, 2H, CH_2N), 4.09 (s, 2H, CH_2CO), 6.8−6.9(m, 1H, Ar), 7.42 (d, J = 8.5 Hz, 2H, Ar), 7.63 (d, J = 8.5 Hz, 2H, Ar), 8.5−8.6 (m, 1H, Ar), 8.6−8.7 (m, 1H, Ar); MS *m*/*z* 454 (M^+ 21), 242 (base). Anal. ($C_{26}H_{35}ClN_4O$) C, H, N.

Stability Studies on Compound 10. *Chemical Hydrolysis.* Stability studies were carried out at controlled temperature (37 ± 0.2 °C) in a water bath shaken at 150 rpm. The hydrolysis of compound **10** was studied at pH 7.4 in isotonic 0.05 M phosphate buffer. The experiments were carried out by adding 35 μL of a stock solution in DMSO (1.0 mg/mL) to 1 mL of the buffer solution preheated at 37 °C. The final concentration of the resulting solutions was 50 μM. The test solutions were vortexed and maintained in a shaker water bath at a constant temperature of 37 ± 0.2 °C. At appropriate intervals, aliquots of 20 μL were removed and immediately analyzed by high-performance liquid chromatography (HPLC). Pseudo-first-order rate constants for the hydrolysis of the derivatives were determined from the slopes of linear plots of the logarithms of residual compound against time. HPLC analyses were performed with a Waters Associates model 600 pump equipped with a Waters 990 variable wavelength UV detector and a 20 μL loop injection valve. A reversed phase Symmetry C18 (25 cm × 3.9 mm; 5 μm particles) column in conjunction with a precolumn (Sentry Guard Symmetry C18, 20 × 3.9 mm) was eluted with mixtures of methanol/water 80:20 (v/v). The injected volume was 20 μL. The flow rate of 0.8 mL/min was maintained, and the column effluent was monitored continuously at 254 nm. The compounds were estimated by measuring the peak areas or peak heights in relation to those of standards chromatographed under the same conditions.

Stability in Physiological Medium. The stability of compound **10** in physiological medium was studied at 37 °C in 0.05 M phosphate buffer saline (0.14 M NaCl) at pH 7.4, containing 50% v/v of rat serum. The final concentration was 50 μM. The resulting test solution was maintained at 37 ± 0.2 °C in a shaking water bath. Aliquots of 100 μL were withdrawn at appropriate intervals and treated with 500 μL of cold acetonitrile to precipitate the serum proteins. After mixing and centrifugation for 5 min at 13200 rpm, the clear supernatant was analyzed by HPLC as described above.

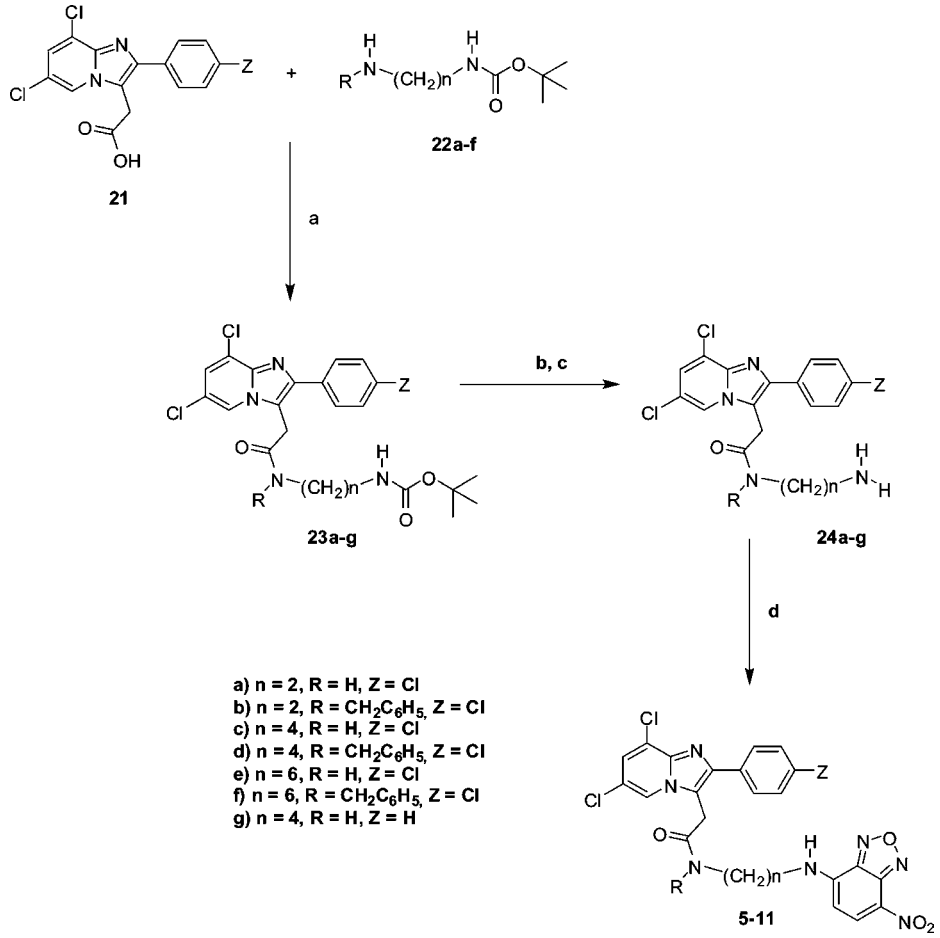
Biological Methods and Materials. Adult male or female Sprague−Dawley CD rats (Charles River, Como, Italy) with body masses of 200−250 g at the beginning of the experiments were maintained under an artificial 12-h light/dark cycle (light on from 8:00 a.m. to 8:00 p.m.) at a constant temperature of 23 ± 2 °C and 65% humidity. Food and water were freely available, and the animals were acclimated for >7 days before use. Experiments were performed between 8:00 a.m. and 2:00 p.m. Animal care and handling throughout the experimental procedure were performed in accordance with the European Communities Council Directive of 24 November 1986 (86/609/EEC). The experimental protocols were approved by the Animal Ethical Committee of the University of Cagliari.

In Vitro Receptor Binding Assays. After sacrifice, the brain was rapidly removed and the cerebral cortex was dissected; tissues were stored at −80 °C until assay.

[^{3}H]Flunitrazepam Binding. The tissues were thawed and homogenized with a Polytron PT 10 in 50 volumes of ice-cold 50 mM Tris-HCl buffer (pH 7.4) and centrifuged twice at 20000*g* for 10 min. The pellet was reconstituted in 50 volumes of Tris-HCl buffer and was used for the binding assay. Aliquots of 400 μL of tissue homogenate (0.4−0.5 mg of protein) were incubated in the presence of [^{3}H]flunitrazepam at a final concentration of 0.5 nM, in a total incubation volume of 1000 μL. The drugs were added in 100 μL aliquots. After a 60 min incubation at 0 °C, the assay was determined by rapid filtration through glass-fiber filter strips (Whatman GF/B). The filters were rinsed with 2−4 mL portions of ice-cold Tris-HCl buffer as described above. Radioactivity bound to the filters was quantitated by liquid scintillation spectrometry. Nonspecific binding was determined as binding in the presence of 5 μM diazepam and represented about 10% of total binding.

[^{3}H]PK11195 Binding. The tissues were thawed and homogenized in 50 volumes of Dulbecco's phosphate-buffered saline (PBS; pH 7.4) at 4 °C with a Polytron PT 10 (setting 5, for 20 s). The homogenate was centrifuged at 40000*g* for 30 min, and the pellet was resuspended in 50 volumes of PBS and recentrifuged. The new pellet was resuspended in 20 volumes of PBS and used for the assay. [^{3}H]PK11195 binding was determined in a final volume of 1000 μL of tissue homogenate (0.15−0.20 mg of protein), 100 μL of [^{3}H]PK11195 (specific activity = 85.5 Ci/mmol, New England Nuclear) at a final assay concentration of 1 nM, 5 μL of drug solution or solvent, and 795 μL

Scheme 1 [a]



[a] Reagents: (a) THF, TEA, EEDQ; (b) HCl gas, CH_2Cl_2; (c) Na_2CO_3, H_2O; (d) NBD-chloride, THF, TEA.

of PBS buffer (pH 7.4 at 25 °C). Incubations (25 °C) were initiated by the addition of membranes and were terminated 90 min later by rapid filtration through glass-fiber filter strips (Wathaman GF/B), which were rinsed five times with 4 mL of ice-cold PBS buffer using a Cell Harvester filtration manifold (Brandel). Filter-bound radioactivity was quantitated by liquid scintillation spectrometry. Nonspecific binding was defined as binding in the presence of 10 μM unlabeled PK11195 (Sigma-Aldrich, St. Louis, MO).

Cell Cultures. Ra2, an immortalized microglial clone, was established from a mouse primary microglial culture and maintained in Eagle's minimum essential medium (MEM) supplemented with 10% calf serum, 5 μg/mL bovine insulin, 0.2% glucose, and 1 ng/mL recombinant mouse granulocyte-macrophage colony stimulating factor (Genzyme, Cambridge, MA), which is essential for Ra2 growth in culture.

Ra2 cells were seeded at a density of 6500 cells/cm^2 on a glass cover slip and then cultured for 16 h. Compound **10** was added to the Ra2 culture at a final concentration of 1 μM followed by the addition of Mito Tracker Red after 10 min (a dye useful for staining mitochondria in live cells) (Molecular Probes, Eugene, OR) and was then incubated at 37 °C for 1 h. After treatment, Ra2 cells were observed by a fluorescent microscope and photographed. The Ra2 cells were then incubated for 24 h with 1 μg/mL lipopolysaccharide (LPS) (Sigma-Aldrich), which is an endotoxin from *Escherichia coli* and a potent activator of microglia.

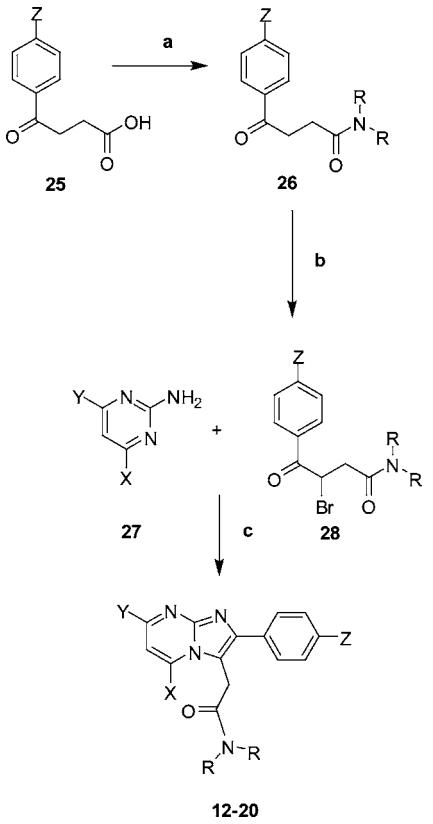
In Vivo Biodistribution Study on Compound 10. Adult male C57BL/6 mice were deeply anesthetized with sodium pentobarbital (25 mg/kg, ip) before surgery and remained under anesthesia throughout the entire procedure. When spinal reflexes were absent, a transverse incision was made and then the right carotid artery was exposed and dissected free of surrounding tissues. After the temporary occlusion of proximal site of the carotid artery with an aneurysm clip, a small hole was made in the distal site of the artery with a 27-gauge needle, and a polyethylene tube (Becton Dickinson) was inserted into the proximal site of the artery from the pole. After the aneurysm clip was released, 0.2 mL of compound **10** solution (1 μM in the final concentration) or the same volume of fluorescein isothiocyanate labeled dextran (FITC-dextran) (Sigma-Aldrich, average molecular weight over 250 000; 5 μM in the final concentration) were injected as a bolus over 30 s into the recipient's carotid artery through the polyethylene tube. The solution of compound **10** for injection was obtained from a stock solution (2.9 mM) in dimethyl sulfoxide in turn diluted to 1.0 μM with phosphate-buffered solution (pH 7.2).

Sampling for Fluorescence Observation. At 30 min after injection, animals were additionally anesthetized, and their blood was washed out by transcardial perfusion of isotonic saline solution. Then brains and livers were removed, frozen in liquid nitrogen, and embedded in OTC compound (Tissue Tek, Elkhart, IN). Coronal sections (8 μm) were cut in a cryostat and mounted on slides and dried. Then sections were fixed by 4% paraformaldehyde. Fluorescent observation was performed with a fluorescence microscope (Olympus BX50).

RESULTS AND DISCUSSION

The synthesis of compounds **5**−**11** was accomplished according to the procedure shown in Scheme 1. Synthesis involved the condensation of the suitably substituted imidazopyridineace-

Scheme 2 [a]



[a] Reagents: (a) R_2NH, TEA, EEDQ, THF; (b) Br_2/CCl_4; (c) DMF reflux.

tic acids **21** (*17*) with the appropriate mono-*N*-Boc-protected diamine compounds **22a**−**f** (*32, 33*) in anhydrous THF and in the presence of EEDQ to give the corresponding amides **23a**−**g**. The Boc deprotection of these last compounds yielded the corresponding compounds **24a**−**g**, which, in turn, by condensation with 7-nitro-2-oxa-1,3-diazole chloride (NBD-Cl) in anhydrous THF and in the presence of TEA afforded the desired compounds **5**−**11**. The synthesis of the imidazo[1,2-*a*]pyrimidines **12**−**20** was carried out as outlined in Scheme 2. Condensation of suitably substituted 2-aminopyrimidine **27** with the appropriate bromoketoamide **28** in refluxing DMF gave compounds **12**−**20** in moderate to good yield. In principle, by using 2-amino-4-methylpyrimidine in the condensation reaction, two regioisomeric compounds **14** and **14′** or **16** and **16′**, respectively, may be produced. The structural assignment of the isolated compounds is based on the analysis of 2D NOESY ^{1}H NMR spectra, which showed the presence of cross-peaks between the proton linked at C(5) and the protons of the methylene group at C(3) of the imidazopyrimidine nucleus, being consistent with the **14** and **16** structures only. The starting 2-aminopyrimidine **27** was commercially available, whereas compound **28** was prepared according to a two-step procedure and summarized in Scheme 2 (*28, 29*). This involved the condensation of the commercially available 3-benzoylpropionic acid **25** with the required dialkylamines in the presence of EEDQ as a dehydrating agent. Treatment of the resulting amide **26** with bromine in carbon tetrachloride afforded compound **28**. All compounds were fully characterized by IR, ^{1}H NMR, mass spectra, and elemental analyses. The yields and physical data for the final compounds are reported in Table 1.

Radioligand Binding Assays. The affinity of compounds **5**−**20** for CBR and PBR was assessed by measuring their ability to displace [^{3}H]flunitrazepam and [^{3}H]PK11195, respectively, from binding to membrane preparations from the cerebral cortex.

Table 2. Affinity for Rat Cerebrocortical CBR and PBR of Compounds 5−20 and Their Maximum Excitation and Emission Wavelengths

compd	CBR[a] IC_{50} (nM)	PBR[b] (cortex) IC_{50} (nM)	λ_{max} Ex (nm)	λ_{max} Em (nm)
5	(32)	(32)	465	522
6	(39)		465	522
7	(7)	(23)	465	522
8	(18.8)	(38)	465	522
9	(2)	(22)	465	522
10	(1.8)	6700	465	541
11	(15.8)	(18)	465	520
12	>10000	5200	336	350
13	11400	165		
14	9150		240	260
15	10300	82	336	350
16	24000	609	336	350
17		33.7		
18	19670	36	336	350
19	>10000	4700		
20	>10000	6900		
PK11195	24250	1.06		

[a] In parentheses are reported the percentages of [^{3}H]flunitrazepam inhibition at 10^{-5} M. [b] In parentheses are reported the percentages of [^{3}H]PK11195 inhibition at 10^{-5} M.

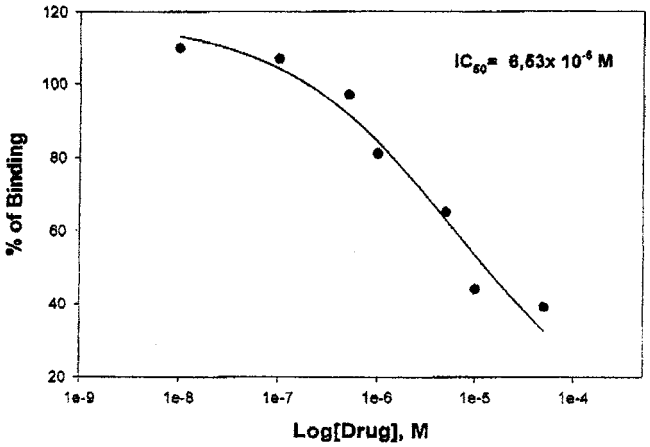


Figure 1. Inhibition of [^{3}H]PK11195 binding to rat cerebrocortical membranes by compound **10**.

Their effects were compared with those of unlabeled PK11195, and the results of these analyses are shown in Table 2. Compounds **5**−**11**, including both monoalkyl- and dialkylamides with *n* varying from 2 to 6, generally showed low affinity and selectivity for PBR. However, dialkylamides were more active and selective than monoalkylamides, and significant improvement in affinity and selectivity was observed by increasing the spacer chain length. In this subset of compounds, **10** ($n = 6$, R $= CH_2C_6H_5$) seemed to be the most interesting one, showing an IC_{50} value of 6.7 μM. Figure 1 shows the inhibition of [^{3}H]-PK11195 binding to rat cerebrocortical membranes by compound **10**. Analysis of the present binding data clearly demonstrates that imidazopyridine PBR ligands linked via a fluorogenic 7-nitro-2,1,3-benzoxadiazol- 4-yl spacer group give rise to new ligands with reduced affinity for the receptor, whereas this was not observed when the same fluorogenic group and spacer were linked to 2-phenylindole-3-acetic acid to give compound **1** (*19*). Thus, for example, compound **8** showed affinity and selectivity for PBR much lower than those of the previously described PBR ligand *N*-benzyl-*N*-*n*-butyl-(2-phenyl-6,8-dichloroimidazo[1,2-*a*]pyridin-3-yl)acetamide (*29*) (i.e., 18% of [^{3}H]PK11195 inhibition at 10^{-5} M versus IC_{50} 14 nM, respectively).

On the other hand, compounds **12**−**20** showed different affinities for the PBR ranging from the moderate (i.e., in the

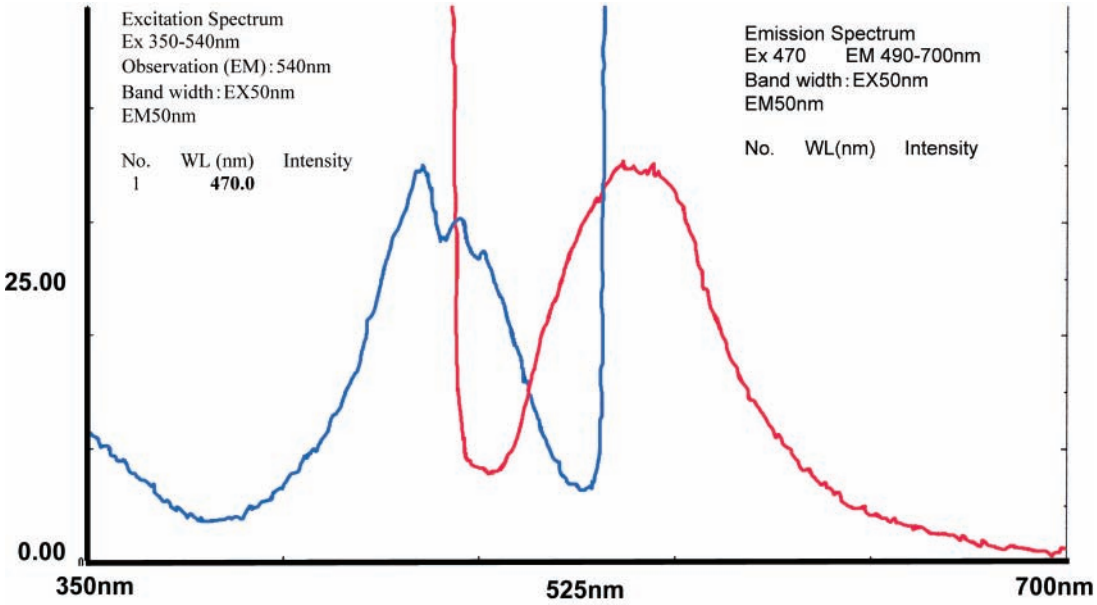


Figure 2. Fluorescence spectrum of compound **10** (excitation at λ 470 and 483 nm) recorded in phosphate-buffered saline (pH 7.2). Compound **10** in dimethyl sulfoxide at 10 mM was diluted to 100 nM in phosphate-buffered saline (pH 7.2) and then the fluorescence spectrum measured by fluorescent spectrophotometer (Shimadzu RF-5300, Shimadzu Co., Kyoto, Japan).

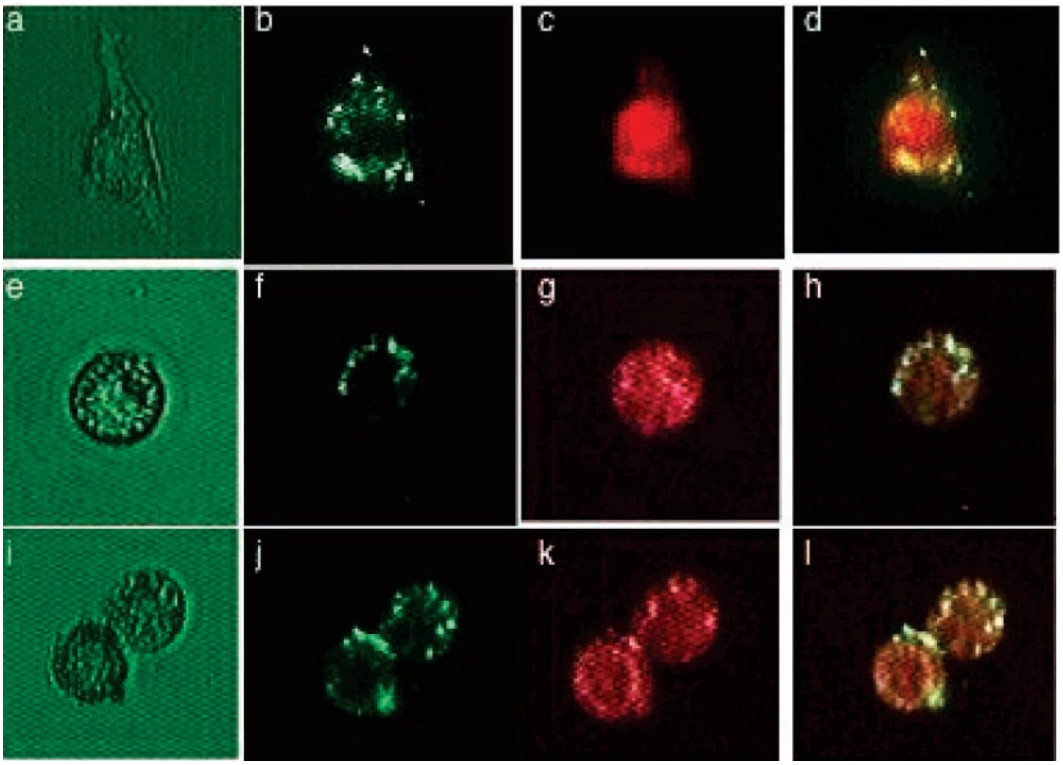


Figure 3. Fluorescent images of Ra2 microglia stimulated with (e−l) or without (a−d) LPS: (a, e, i) phase optics; (b, f, j) fluorescent optics of microglia stained with compound **10**; (c, g, k) fluorescent optics of microglia stained with Mito Tracker Red; (d, h, l) merged optics of fluorescence images of green (compound **10**) and red (Mito Tracker Red).

micromolar range, **12**, **19**, **20**) to high affinity (i.e., in the nanomolar range, **13**, **15**−**18**). Among the compounds of this subset, **17** and **18** were the most active and selective for the PBR, with selectivity indices (defined as the ratio IC_{50} CBR/IC_{50} PBR) of 278 and 546, respectively. From a structure−affinity relationship point of view, it can be pointed out in this subset that alkyl substituents of optimum length on the carboxamide nitrogen and substitution at the para position of the phenyl ring at C(2) of the imidazopyrimidine nucleus with a chlorine atom are crucial for high affinity and selectivity (compare the binding affinities of **15** and **16** as well as **18** and **19**, respectively).

Fluorescence Characteristics of Compounds 5−**20.** All of the examined compounds **5**−**20** showed a visible fluorescence, and the optimum excitation and emission wavelengths are summarized in Table 2. The data were recorded in methanol as solvent by using a Kontron UV−vis spectrometer and a Perkin-Elmer LS-50B spectrofluorometer. As can be seen from Table 2, the intrinsically fluorescent compounds **12**−**20** exhibited fluorescence emission maxima in the range of 260−350 nm,

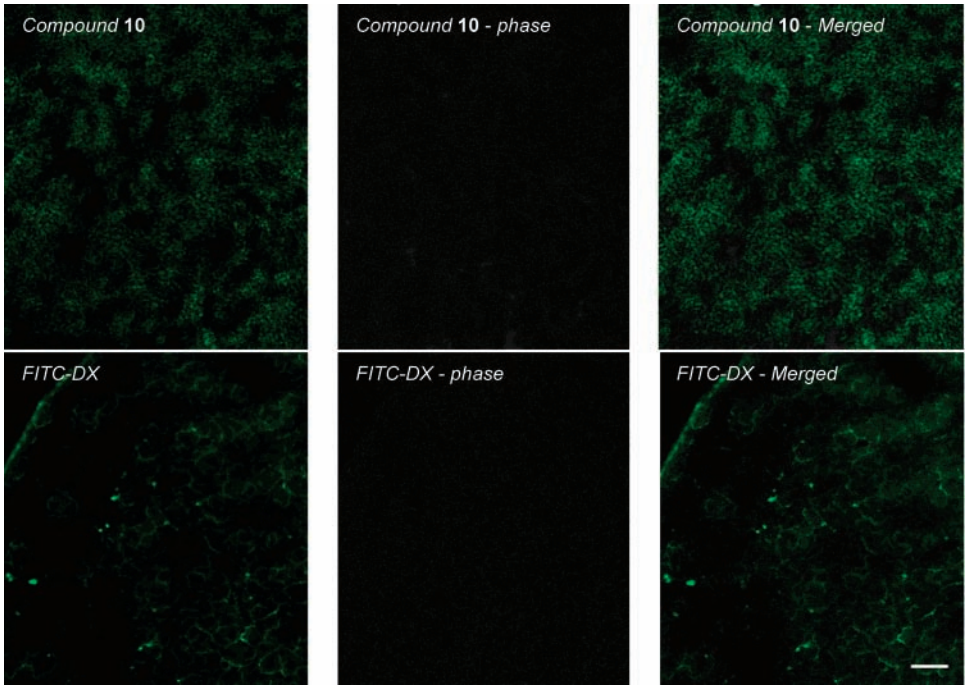


Figure 4. In vivo distribution of compound **10** and FITC-dextran in liver. Liver sections from mouse injected with **10** (upper panels) or FITC-dextran (lower panels) were observed with green fluorescence (left panels) and phase contrast (center panels). Right panels indicate the merged optics of green fluorescence and phase contrast. Bar = 20 μm.

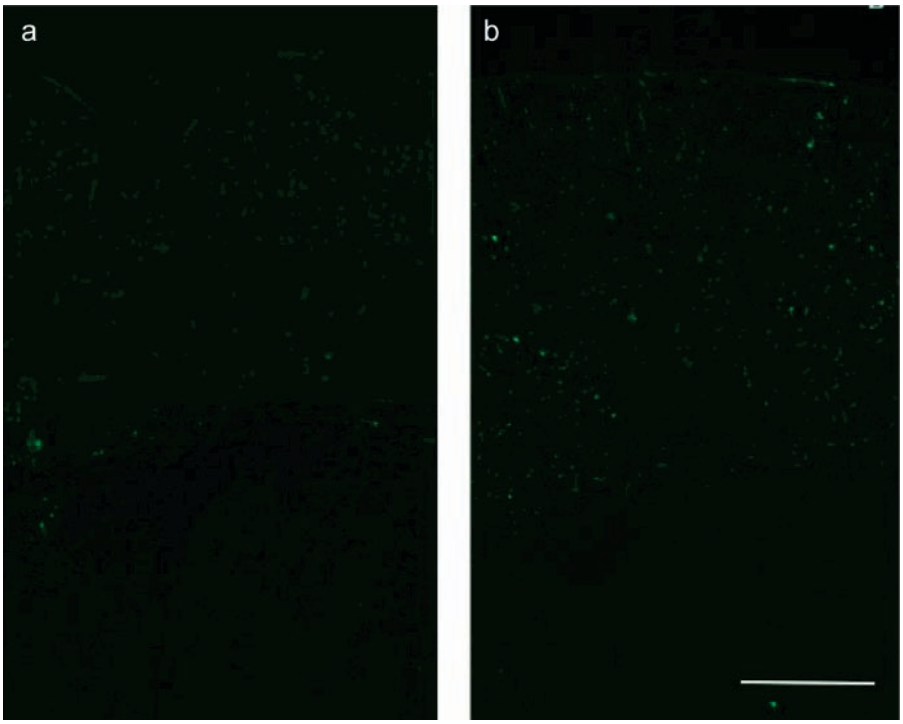


Figure 5. In vivo distribution of compound **10** and FITC-dextran in brain. Brain sections from mouse injected with **10** (a) or FITC-dextran (b) were observed with green fluorescence. Bar = 50 μm.

and thereby their use to successfully visualize PBR is restricted because these wavelengths correspond to those at which many cells and tissues autofluoresce. In contrast, compounds **5**−**11**, bearing the 7-nitrobenzofurazan probe, showed fluorescence emission at longer wavelengths (520−541 nm) and, hence, might be useful for visual imaging of PBR. Thus, in this subset, compound **10** as the most active and selective ligand for PBR was used in fluorescence microscopy studies. Figure 2 shows the fluorescence spectrum of compound **10** with the principal excitation and emission wavelengths at 470, 473, and 541 nm, respectively. Although compound **10** is characterized by a micromolar binding affinity to PBR, literature reports suggest (*21*, *22*) it still can be useful for cellular targeting applications.

Cell Biology, Fluorescence Microscopy, and in Vivo Biodistribution Study on Compound 10. Compound **10** was found to stain live Ra2 microglial cells effectively. Intense fluorescence was observed as a deposit-like pattern mainly distributed in cytosol. Some of the fluorescent deposits were observed to associate with the plasma membrane. Many compound **10**-positive deposits were also stained with Mito Tracker Red, suggesting that compound **10** binding sites may

exist on mitochondria. Large deposits that were not stained with Mito Tracker Red were sometimes observed.

Compound **10**-positive fluorescent deposits were translocated from cytosol to the plasma membrane by LPS stimulation. Some of the deposits were still positive for Mito Tracker Red staining (Figure 3).

The experiments showed that intracellular fluorescent labeling was obtained by using a concentration of 1 μM **10**, that is, a concentration about one-sixth lower than its IC_{50} value.

Compound **10** was used in a biodistribution study to evaluate its utility as a targeting moiety in vivo. Preliminarily, the stability of compound **10** was studied both in 0.05 M phosphate buffer at pH 7.4 and in diluted rat serum solution at 37 °C. Pseudo-first-order kinetics were always observed, and the half-lives were found to be >3 h.

After injection in the carotid artery of adult male C57BL/6 mice of compound **10** and FITC-dextran, used as a control dye, and successive brain and liver removal, it was found that in liver sections compound **10** penetrates to liver parenchyma and stains hepatocytes, whereas FITC-dextran was observed to remain in blood vessels (Figure 4). On the other hand, as for the distribution to brain, the patterns of staining with **10** and FITC-dextran are similar, indicating that both of them hardly penetrate into the brain because of the existence of the blood−brain barrier (BBB) (Figure 5).

In conclusion, some fluorescent imidazopyridine and imidazopyrimidine compounds **5**−**20** were synthesized, and their affinity for PBR was determined. Although members of the subset **12**−**20** possess good PBR binding affinity, they are characterized by a fluoroscence emission wavelength that prevents their use in successfully visualizing PBR. In contrast, compounds **5**−**11** fluoresce at a longer wavelength but possess a low to moderate affinity for PBR. Compound **10** was shown to be the most active derivative and represents a new fluorescent probe for visualization of activated microglia and PBR. It may have some significant advantages (structural simplicity, cost-effective, easy to handle) over the fluorescent or radioactive probes for PBR currently used. In particular, a comparison with compounds **1** [Kozikowski's compound, utilizing the same fluorophore (NBD)] and **3**, both characterized by simple structure and involving no linkages with transition metals, reveals that compound **10** should possess better BBB penetration properties on the basis of its log C_{brain}/C_{blood} (log BB) value (−0.54 compared with −1.06 of **1** and −1.78 of **3**) as estimated by using Clark's model (*34*), which relates log BB to polar surface area. This last descriptor was computed with a fragment-based approach, known as the topological PSA (TPSA) approach (*35*). It is generally accepted that compounds with log BB > 0.3 cross the BBB readily, whereas compounds with log BB < −1.0 are poorly distributed to the brain. On the basis of the predicted log BB values, compound **10** should be able to cross the BBB, whereas compounds **1** and **3** as such should be unable to. The observed in vivo poor BBB penetration of **10** might be due to the possibility that this compound is a substrate of Pglyco efflux protein (Pgp) or to extensive binding to serum proteins. From the results of cell culture and in vivo injection, it can be stated that compound **10** is a new useful tool of bioimaging for PBR and has potential to generate new information on the pathological role of this receptor in vivo. Further studies are in progress to synthesize additional compounds, particularly those that combine high affinity and selectivity for PBR and fluorescence emission at long wavelengths as well as good BBB penetration properties.

ACKNOWLEDGMENT

This work was supported by a grant from Ministero dell'Istruzione dell'Università e dellaRicerca (COFIN 2004 MIUR to G.T.). We thank Giovanni Dipinto for skillful technical assistance in recording mass spectra and determining microanalytical data. We also thank Dr. Kelly Desino (The University of Kansas) for helpful discussion.

LITERATURE CITED

(1) Anholt, R. R. H., Pedersen, P. L., De Souza, E. B., and Snyder, S. H. (1986) The peripheral benzodiazepine receptor: localization to the mitochondrial outer membrane. *J. Biol. Chem. 261*, 576−583.

(2) Papadopoulos, V., Baraldi, M., Guilarte, T. R., Knudsen, T. B., Lacapere, J. J., Lindemann, P., Norenberg, M. D., Nutt, D., Weizman, A., Zhang, M. R., and Gavish, M. (2006) Translocator protein (18 kDa): new nomenclature for the peripheral-type benzodiazepine receptor based on its structure and molecular function. *Trends Pharmacol. Sci. 27*, 402−409.

(3) Papadopulos, V., Guarneri, P., Krueger, K. E., Guidotti, A., and Costa, E. (1992) Pregnenolone biosynthesis in C6 glioma cell mitochondria: regulation by a mitochondrial diazepam binding inhibitor receptor. *Proc. Natl. Acad. Sci. U.S.A. 89*, 5113−5117.

(4) Messmer, K., and Reynolds, G. P. (1998) Increased peripheral benzodiazepine binding site in the brain of patients with Huntington's disease. *Neurosci. Lett. 241*, 53−56.

(5) Veenman, L., and Gavish, M. (2000) Peripheral-type benzodiazepine receptors: their implication in brain disease. *Drug Dev. Res. 50*, 355−370.

(6) Benveniste, E. N. (1997) Role of macrophages/microglia in multiple sclerosis and experimental allergic encephalomyelitis. *J. Mol. Med. 75*, 165−173.

(7) Cagnin, A., Brooks, D. J., Kennedy, A. M., Gunn, R. N., Myers, R., and Turkheimer, F. E. (2001) In-vivo measurement of activated microglia in dementia. *Lancet 358*, 461−467.

(8) Kassiou, M., Meikle, S. R., and Banati, R. B. (2005) Ligands for peripheral benzodiazepine binding sites in glial cells. *Brain Res. Rev. 48*, 207−210.

(9) Hardwick, M., Fertikh, D., Culty, M., Li, H., Vidic, B., and Papadopoulos, V. (1999) Peripheral-type benzodiazepine receptor (PBR) in human breast cancer: correlation of breast cancer cell aggressive phenotype with PBR expression, nuclear localization, and PBR-mediated cell proliferation and nuclear transport of cholesterol. *Cancer Res. 59*, 831−842.

(10) Katz, Y., Eitan, A., and Gavish, M. (1990) Increased density of peripheral benzodiazepine binding sites in ovarian carcinomas as compared with benign ovarian tumors and normal ovaries. *Clin. Sci. 78*, 155−158.

(11) Venturini, I., Zaneroli, M. L., Corsi, L., Avallona, R., Farina, F., Alho, H., Baraldi, C., Ferrarese, C., Pecora, N., Frigo, M., Ardizzone, G., Arrigo, A., Pellicci, R., and Baraldi, M. (1998) Up-regulation of peripheral benzodiazepine receptor system in hepatocellular carcinoma. *Life Sci. 65*, 1269−1280.

(12) Hirsch, T., Decaudin, D., Susin, S. A., Marchetti, P., Larochette, N., Resche-Rigon, M., and Kroemer, G. (1998) PK 11195, a ligand of the mitochondrial benzodiazepine receptor, facilitates the induction of apoptosis and reverses Bcl-2 mediated cytoprotection. *Exp. Cell Res. 241*, 426−34.

(13) Sutter, A. P., Maaser, K., Barthel, B., and Scherübl, H. (2003) Ligands of the peripheral benzodiazepine receptor induce apoptosis and cell cycle arrest in oesophageal cancer cells: involvement of the p38mapk signalling pathway. *Br. J. Cancer 89*, 564−572.

(14) Xia, W., Spector, S., Hardy, L., Zhao, S., Saluk, A., Alemane, L., and Spector, N. L. (2000) Tumor selective G2/M cell cycle arrest and apoptosis of epithelial and hematological malignancies by BBL22, a benzazepine. *Proc. Natl. Acad. Sci. U.S.A. 97*, 7494−7499.

(15) Galiegue, S., Tinel, N., and Casellas, P. (2003) The peripheral benzodiazepine receptors: a promising therapeutic drug target. *Curr. Med. Chem. 10*, 1563−1572.

(16) Kupczyk-Subotkowaka, L., Siahaan, T. J., Basile, A., Friedman, H. S., Higgins, P. E., Song, D., and Gallo, J. M. (1997) Modulation of melphalan resistance in glioma cells with a peripheral benzodiazepine receptor ligand−melphalan conjugate. *J. Med. Chem. 40*, 1726−1730.

(17) Trapani, G., Laquintana, V., Latrofa, A., Ma, J., Reed, K., Serra, M., Biggio, G., Liso, G., and Gallo, J. M. (2003) Peripheral

benzodiazepine receptor ligand−melphalan conjugates for potential selective drug delivery to brain tumors. *Bioconjugate Chem. 14*, 830−839.

(18) Guo, P., Ma, J., Li, S., Guo, Z., Adams, A. L., and Gallo, J. M. (2001) Targeted delivery of a peripheral benzodiazepine receptor ligand−gemcitabine conjugate to brain tumors in a xenograft model. *Cancer Chemother. Pharmacol. 48*, 169−176.

(19) Kozikowski, A. P., Kotoula, M., Ma, D., Boujrad, N., Tuckmantel, W., and Papadopoulos, V. (1997) Synthesis and biology of a 7-nitro-2,1,3-benzoxadiazol-4-yl derivative of 2-phenylindole-3-acetamide: a fluorescent probe for the peripheral-type benzodiazepine receptor. *J. Med. Chem. 40*, 2435−2439.

(20) Manning, H. C., Goebel, T., Thompson, R. C., Price, R. R., Lee, H., and Bornhop, D. J. (2004) Targeted molecular imaging agents for cellular-scale bimodal imaging. *Bioconjugate Chem. 15*, 1488−1495.

(21) Manning, H. C., Smith, S. M., Sexton, M., Haviland, S., Bai, M., Cederquist, K., Stella, N., and Bornhop, D. J. (2006) A peripheral benzodiazepine receptor targeted agent for in vitro imaging and screening. *Bioconjugate Chem. 17*, 735−740.

(22) Chen, Y., Zheng, X., Dobhal, M. P., Gryshuk, A., Morgan, J., Dougherty, T. J., Oseroff, A., and Pandey, R. K. (2005) Methyl pyrophorbide-α analogues: potential fluorescent probes for the peripheral-type benzodiazepine receptor. Effect of central metal in photosensitizing efficacy. *J. Med. Chem. 48*, 3692−3695.

(23) Romeo, E., Auta, J., Kozikowski, A. P., Ma, A., Papadopoulos, V., Puia, G., Costa, E., and Guidotti, A. (1992) 2-Aryl-3-indoleacetamides (FGIN-1): a new class of potent and specific ligands for the mitochondrial DBI receptor. *J. Pharmacol. Exp. Ther. 262*, 971−978.

(24) Le Fur, G., Perrier, M. L., Vaucher, N., Imbault, F., Flamier, A., Uzan, A., Renault, C., Dubroeucq, M. C., and Gueremy, C. (1983) Peripheral benzodiazepine binding sites: effect of PK11195, 1-(2-chlorophenyl)-*n*-(1-methylpropyl)-3-isoquinolinecarboxamide I. In vitro studies. *Life Sci. 32*, 1839−1847.

(25) Marangos, P. L., Pate, J., Boulenger, J. P., and Clark-Rosenberg, R. (1982) Characterization of peripheral-type benzodiazepine binding sites in brain using [3H]Ro 5-4864. *Mol. Pharmacol. 22*, 26−32.

(26) Okujama, S., Chaki, S., Yoshikawa, R., Ogawa, S., Suzuki, Y., Okubo, T., Nakazato, A., Nagamine, M., and Tomisawa, K. (1999) Neuropharmacological profile of peripheral benzodiazepine receptor agonists, DAA1097 and DAA1106. *Life Sci. 16*, 1455−1464.

(27) Trapani, G., Franco, M., Ricciardi, L., Latrofa, A., Genchi, G., Sanna, E., Tuveri, F., Cagetti, E., Biggio, and Liso, G. (1997) Synthesis and binding affinity of 2-phenyl-imidazo[1,2-*a*]pyridine derivatives for both central and peripheral benzodiazepine receptors. A new series of high-affinity and selective ligands for the peripheral type. *J. Med. Chem. 40*, 3109−3118.

(28) Trapani, G., Franco, M., Latrofa, A., Ricciardi, L., Carotti, A., Serra, M., Sanna, E., Biggio, G., and Liso, G. (1999) Novel 2-phenylimidazo[1,2-*a*]pyridine derivatives as potent and selective ligands for peripheral benzodiazepine receptors. synthesis, binding affinity, and *in vivo* studies. *J. Med. Chem. 42*, 3934−3941.

(29) Trapani, G., Laquintana, V., Denora, N., Trapani, A., Lopedota, A., Latrofa, A., Franco, M., Serra, M., Pisu, M. G., Floris, I., Sanna, E., Biggio, G., and Liso, G. (2005) Structure−activity relationships and effects on neuroactive steroids in a series of 2-phenylimidazo-[1,2-*a*]pyridineacetamide peripheral benzodiazepine receptors ligands. *J. Med. Chem. 48*, 292−305.

(30) Rackham, D. M. (1979) Spectroscopic studies of some imidazo-[1,2-*a*]pyridine and imidazo[1,2-*a*]pyrimidine derivatives. *Appl. Spectrosc. 33*, 561−563.

(31) Janssen, M. J., Ensing, K., and De Zeew, R. A. (2000) Fluorescent-labeled ligands for the benzodiazepine receptor. *Pharmazie 55*, 102−106.

(32) Muller, D., Zeltser, I., Bitan, G., and Gilon, C. (1997) Building units for N-backbone cyclic peptides. 3. Synthesis of protected N^{α}-(ω-aminoalkyl)amino acids and N^{α}-(ω-carboxyalkyl)amino acids. *J. Org. Chem. 62*, 411−416.

(33) Martin, B., Possémé, F., Le Barbier, C., Careaux, F., Carboni, B., Seiler, N., Moulinoux, J.-P., and Delcros, J.-G. (2001) *N*-Benzylpolyamines as vectors of boron and fluorine for cancer therapy and imaging: synthesis and biological evaluation. *J. Med Chem. 44*, 3653−3664.

(34) Clark, D. E. (1999) Rapid calculation of polar molecular surface area and its application to the prediction of transport phenomena. 2. Prediction of blood−brain barrier penetration. *J. Pharm. Sci. 88*, 815−821.

(35) Ertl, P., Rohde, B., and Selzer, P. (2000) Fast calculation of molecular polar surface area as a sum of fragment-based contributions and its application to the prediction of drug transport properties. *J. Med. Chem. 43*, 3714−3717.

BC060393C

PMMA Isocyanate-Modified Digital Discs as a Support for Oligonucleotide-Based Assays

María-José Bañuls, Victoria González-Pedro, Rosa Puchades, and Ángel Maquieira*

Instituto de Química Molecular Aplicada, Departamento de Química, Universidad Politécnica de Valencia, Camino de Vera s/n, Valencia, Spain. Received May 30, 2007; Revised Manuscript Received July 10, 2007

A mild chemical procedure for the derivatization of PMMA as the isocyanate on rigid supports is described. The proposal is based on spin-coating the support with a hydroxy-modified PMMA polymer, followed by treatment with (3-isocyanatopropyl)triethoxysilane, developing an isocyanate-ended PMMA. Oligonucleotide hybridization assays performed on this surface demonstrate that the process is simple and highly effective and agree with the results of other modified materials, including aminated PMMA, gold, and glass. As a demonstration, it has been applied to covalently attached aminated oligonucleotides on a modified audio−video compact disc (CD) surface to perform DNA probe hybridization assays. Measurements were carried out with a CD player, by detecting the solid microspots precipitated from an enzymatic reaction (HRP-TMB). This new approach, being a competitive technique, opens a broad horizon of applications for point of care or *in situ* needs.

INTRODUCTION

The concept of hybrid systems has become an active area of research. In them, a molecular event is detected by its ability to alter the transmission of a digital sequence; a true interaction between digits and molecules occurs (*1*).

Compact disc (CD)-based technology offer enormous possibilities as BioMEMS (Bio-micro-electromechanical systems) for molecular screening in biosensing (*2*). In 2000, Kido et al. demonstrated the potential of this technology, developing disc-based immunoassay microarrays (*3*). Other authors (*4*−*6*) have been working on polycarbonate (PC) surface modification of discs to attach proteins and nucleic acids. Also, Yu (*7*) has developed strategies for the preparation of high-quality SAMs for electrochemical analysis on gold-metalized CDs. Regarding the use of CD reader technology, Barathur et al. modified the standard CD drive to use a laser-scanning microscope for analysis of a biocompact disc assay (*8*). Potyrailo et al. (*9*) used conventional optical disc drives for quantitative detection of Ca^{2+} and other ionic species by sensitive films deposited on conventional CD and DVD optical discs.

Preliminary evidence displayed by our research team (*10*) illustrated the potential of using compact disc surfaces as high throughput screening platforms. The immobilization of biomolecules on the PC face of CDs was a suitable strategy to perform genomic analysis, providing good results in sensitivity and hybridization. These studies were performed employing avidin−biotin methodology and using fluorescence microarray scanning for detection. The challenge now was the use of the PMMA-modified compact discs as support and the CD player as detector.

The chemical derivatization of PMMA, a material employed as a protective layer for the metallic film of the CDs,[1] would allow covalent and oriented immobilization of DNA or protein for microarraying. Lacquering the metallic layer of the compact disc with a chemically modified polymer is an interesting alternative for developing surfaces with specific chemical moieties and physical properties to covalently attach nucleic acid probes; advantages arise from the possibility to derivatize the polymer in solution after application on metal and the facility to apply it by spin-coating, sputtering, etc., achieving well finished surfaces. The problem is that most of the methods employed for the chemical modification of PMMA surfaces (*11*, *12*) require use in fluidic structures, affecting the optical and mechanical properties of the polymer. So, the described approaches are not applicable for our purposes.

PMMA microspheres have been successfully used for the immobilization of enzymes by aldehyde oxidation of the hydroxyl groups introduced in the PMMA using poly(vinyl alcohol) (*13*), design of microfluidic devices, metal deposition (*14*), and immobilization of proteins and DNA. Henry et al. (*15*) showed that aminated PMMA sheets can be used for the immobilization of enzymes in the restriction digestion of dsDNA. Waddell et al. (*16*) have developed a method using *N*-lithiodiaminepropane-modified PMMA slides as substrate to test the immobilization and hybridization of oligonucleotides in a microarray format. Christensen et al. (*17*) also proposed a chemical procedure to functionalize PMMA in an easier and faster manner than that previously described, by using hexamethylenediamine and glutaraldehyde or sulfo-EMCS ([*N*-ϵ-maleimidocaproyloxy]sulfosuccinimide ester). The density of immobilized and hybridized DNA was similar to those obtained on other PMMA-modified surfaces and silanized glass.

Although isocyanates potentially represent an ideal covalent DNA or protein immobilization chemistry (*18*), none of the previously published modifications of PMMA employ the isocyanate moiety for the covalent attachment of biomolecules. Isocyanates can react with many functional groups including amines, hydroxyls, and carboxyls, using soft conditions and aqueous media. Their reactivity renders them highly versatile, since these groups are present in nucleic acids, proteins, and other biomolecules. All these reasons make isocyanate highly attractive to develop derivatized supports for the covalent immobilization of probes.

In this work, a new DNA covalent immobilization approach based on the isocyanate modification of PMMA and its application by spin-coating on the metallic layer of the CDs is proposed. The goal of this research also involves a demonstra-

* Corresponding author. Fax: +34 96 387 93 49; tel:+34 96 387 73 42, e-mail: amaquieira@qim.upv.es.

[1] Standard compact discs are made from a 1.2 mm thick disc of polycarbonate coated with a 100 Å reflective layer of aluminium, silver, or gold protected by a transparent polymeric layer, usually poly(methyl methacrylate) (PMMA).

10.1021/bc700194n CCC: $37.00 © 2007 American Chemical Society
Published on Web 09/19/2007

tion of the potential of our proposal by the development of microarray-based assays, reading the hybridization results with a CD player as detector.

EXPERIMENTAL PROCEDURES

Reagents. PMMA (ref 99530) sheets (1 mm thickness) were from Röhm (Darmstad, Germany). Ethanolamine and (3-isocyanatopropyl)triethoxysilane (ICPTS) were purchased from Acros (Barcelona, Spain) and Fluka (Madrid, Spain), respectively. Dowanol, Tween 20, streptavidin−horseradish peroxidase (strept-HRP) from *Streptomyces avidinii*, and 3,3′,5,5′-tetramethylbenzidine (TMB) substrate were purchased from Sigma-Aldrich (Madrid, Spain). Oligonucleotides (see Table 1) were from Sigma-Genosys (Suffolk, UK). All commercially available products were used without further purification. Oligonucleotide solutions were printed onto the desired surface by tip contact using a stamper, 6 × 4 pins, from V&P Scientific, Inc. (San Diego, CA).

Buffers employed were as follows: Saline sodium citrate (10 × SSC, 0.9 M sodium chloride, 0.09 M sodium citrate, pH 7); carbonate buffer (10 × CB, 0.5 M sodium carbonate, pH 11 and pH 9.6); phosphate buffer saline (10 × PBS, 0.08 M sodium phosphate dibasic, 0.02 M sodium phosphate monobasic, 1.37 M sodium chloride, 27 M potassium chloride pH 7.5); PBS-T (PBS containing 0.05% Tween 20); MES buffer (0.1 M 2-morpholinoethanesulfonic acid monohydrate, pH 3.5).

Apparatus. The Energy Dispersion Spectra (EDS) were obtained with a scattering electron microscope Jasco-SEM, resolution 59 eV (Easton, MD). Fluorescence scanner Genepix 4000B, from Axon Instruments (Union City, CA), was used to read fluorescent probes immobilized on chip.

Compact Discs. Golden CD-Rs, partially transparent (30% reflectivity), provided by U-Tech Media Corp. (Tau-Yuan Shien, China) were directly treated, keeping its original shape, or cut in chips of 55 × 25 mm size when necessary. These low reflectivity recordable compact discs (L-CD, 1.2 mm thick polycarbonate discs, with a gold reflective layer of 30 nm, 12 cm diameter) allow the laser (780 nm) to have two functions: (a) reflected light (30%) lets the laser follow the track, maintaining the rotation of the disc (autotracking), and (b) transmitted light (70%) reaches the microarray spots located on the upper side of the CD, detecting the hybridization intensities by the amount of precipitate produced by an enzymatic marker (HRP) and a substrate (TMB).

Disc Reader. A standard CD player from Plextor LLC (Fremont, CA) was used as detector. The drive uses the servo control system to center and focus the beam on the spiral data track across the whole disc surface. The CD reader uses the original design of the CD players, taking advantage of the CD driver optical system to accurately illuminate the polycarbonate face of the L-CD (partially reflecting the laser and transmitting the rest through the PMMA surface to the photodiode). The controlled parameters of the optical disc drive include positioning of the laser toward the disc, scanning the whole disc surface while controlling the spatial resolution, and the linear rotation velocity of the disc. A planar photodiode (SLSD-71N6, Silonex, Montreal, Canada), 25.4 mm long, with a spectral sensitivity of 0.55 A/W at 940 nm, and a spectral range between 400 and 1100 nm, transmitted laser light and converted it into an analog electrical signal.

A reflective photosensor (EE-SY125, Omron, Scahumburg) used to detect the analytical areas includes an infrared LED of 950 nm and a phototransistor with a sensing distance ranging from 0.5 mm to 2 mm. The operational principle of the photosensor is based on the detection of the different reflectivities between the sensing object and the disc. For that, the analytical areas are marked in the outer rim of the disc by low reflectivity trigger footprints of 3.5 cm size. Because the unmarked perimeter presents higher reflectivity, the photosensor detects the marked areas, providing a trigger signal to the data acquisition board in order to start capturing data exclusively from those zones.

A custom-built electronic board (DAB) incorporates the planar photodiode and the photosensor. The function of the board is 2-fold. First, the detection of analytical areas, and second the amplification of the analog signal. Both functions are carried out at the same time the CD drive performs its original function of reading and writing data. In this way, during the data acquisition process only the signals from the detection areas are digitized by the data acquisition board (DAQ), stored in the computer and deconvoluted into an image for further quantification. A scheme of the developed detection system is shown in Figure 1. The detector system is controlled by software running on a Windows-based computer connected to the PC through a universal serial bus interface (USB2.0) to become portable.

Custom software was written in Visual C++. The software provides the control for the CD/DVD driver to scan the surface of the disc, to modulate the disc linear rotation velocity to a specified spatial resolution, and to write data on the CD or DVD. Also, the software provides the control to the data acquisition board to configure the sampling frequency according to the disc rotation speed and desired angular resolution. To completely scan the surface of the L-CD, the software simulates the writing process of a 700 MB size file to a controlled disc rotation speed. The scan begins from the inner tracks of the disc, following the continuous spiral toward the outer tracks. The captured data of each detection area are represented within a sector that is formed by a set of arcs centered over a radial direction, starting from the inner toward the outer radial. The software collects the data of each area and stores them in independent files in uncompressed binary format and displays them into a graphical gray scale code image.

Because of the spatial difference between samples taken horizontally (each 13 μm) and vertically (each 1.6 μm), a graphical horizontal adjustment is done to display a proportional $x-y$ image. This software allows the image to be exported in a gray scale code to a compressed tif format or bitmap. Then, the images were processed with Photoshop 7.0 (Adobe Systems Inc., San Jose, CA), to map the lightest and darkest pixels into black and white before quantifying with GenePix software (Axon Inst., Union City, CA). Signal intensities of each spot were calculated by background subtraction.

Disc Surface Modification. *(a) PMMA Transamination.* PMMA (310 mg) was dissolved in THF (3 mL). Ethanolamine (1 mL) was added, and the mixture was refluxed for 5 h. After that, THF was removed under vacuum and the solid was dissolved in CH_2Cl_2. The organic phase was washed with MES buffer until the total removal of ethanolamine. The organic layer was dried with $MgSO_4$ and the solvent evaporated, providing the transaminated polymer as a colorless solid. The ^{1}H NMR spectrum showed 50% transaminated compound. ^{1}H NMR ($CDCl_3$): δ (ppm) 3.79 (t, CH_2OH), 3.57 (s+m, CH_3O and CH_2-NHCO), 1.87−1.78 (m, CH_2), 0.091 (s, CH_3), 0.806 (s, CH_3).

(b) Coating. The transaminated polymer was dissolved in Dowanol (5%). One milliliter of this solution was pipetted onto the metalized (gold) side of a standard L-CD for spin-coating at a centrifugal force of 47.33*g* (840 rpm). After that, the solvent was removed at 52 °C for 30 min.

(c) Isocyanate Treatment of Coated L-CD. Coated L-CDs were immersed into a solution of (3-isocyanatopropyl)triethoxysilane in 2-propanol (1%) for 10 min and cured at 62 °C for 15 min. Finally, they were washed with 2-propanol and dried at 62 °C.

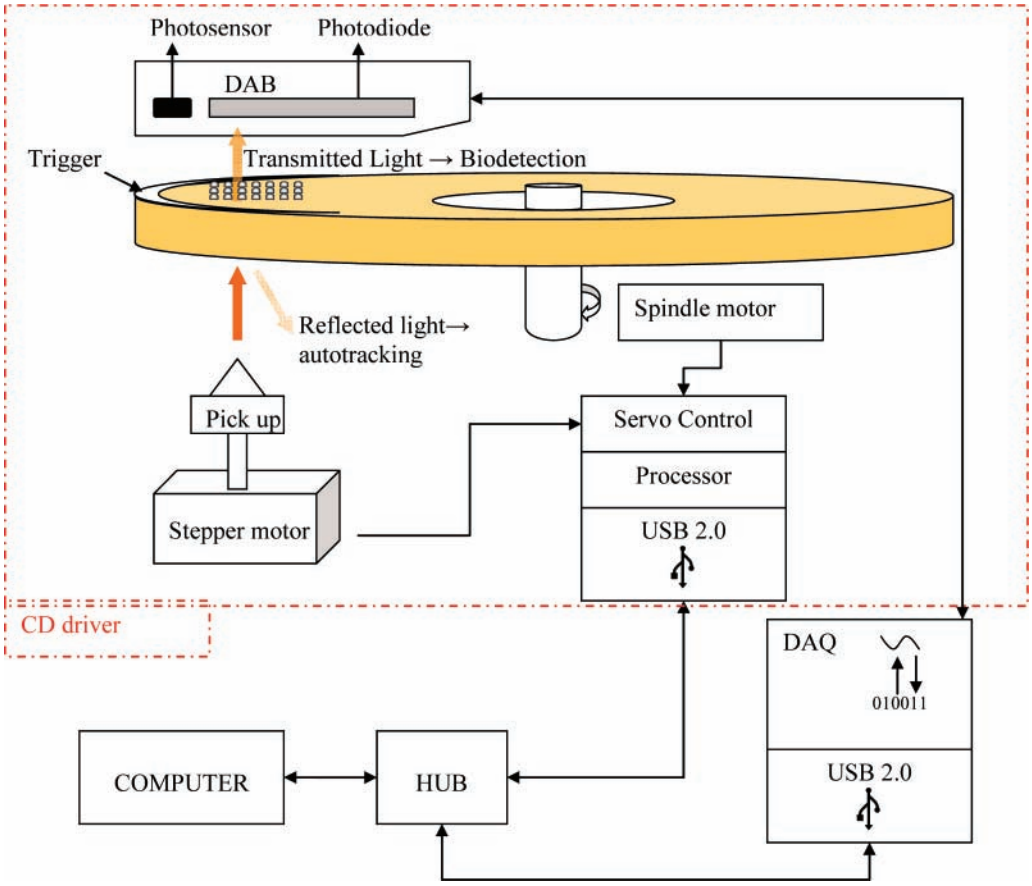


Figure 1. Schematic representation of the detection system. The set of servo systems (spindle and stepper motors) of the CD drive allows disc rotation and laser scanning. The transmitted light through the disc is transformed by the photodiode into an analog electrical signal (RF signal). At the same time, the photosensor detects the trigger footprints, starting the data collection on disc. The amplification/ detection board (DAB) is integrated into the CD drive unit and contains the planar photodiode and the photosensor. The data acquisition board (DAQ) digitizes the analog signals and transfers them to the computer for processing. On the disc, one detection area is represented.

Surface Behavior: DNA Immobilization and Hybridization Assays. Different 5′ Cy5-labeled and/or 3′ NH_2-ended oligonucleotides were employed for DNA immobilization and hybridization assays (Table 1). Amino-labeled DNA capture probes (SYM12 and SYM23) were serial diluted in carbonate buffer pH 11 ranging from 0.01 to 5 μM; 18 replicates (2 matrix of 3 × 3 spots) of each dilution were spotted on PMMA-modified chips. The fluorescence intensity of the spots was registered by the laser scanning detector to obtain a standard curve for the probes. Similar calibration curves for the Cy5-labeled target DNA were made. After immobilization and hybridization, the fluorescence signal of the spots was quantified and the amount of immobilized and hybridized DNA was calculated from the respective calibration curves.

Six 5′ Cy5-labeled, 3′ NH_2-ended oligonucleotide solutions (1 and 10 μM) were prepared employing different solvents: H_2O, 1 × PBS pH 7.5, and 1 × CB pH 11. Microarrays (3 × 3) of each solution were tip-contact-printed onto isocyanate-modified surfaces. L-CDs were then incubated for 2 h in a humid, dark chamber at room temperature. Then, the printed surfaces were washed with PBS-T and water and dried.

For the hybridization assays, the aminated probe SYM22 was covalently attached to the isocyanate surface as described above. Cy5-labeled target-DNA SYM8 was serial diluted between 0.1 and 1 μM in a mixture containing 6 × SSC, 0.6% SDS, 0.1% salmon sperm DNA, and 2% BSA. A 100 μL amount of the complementary oligonucleotide solution was dispensed on the microarrays and spread under a coverslip (22 × 22 mm). The temperature of hybridization was 37 °C, performing the incubation in a dark and humidified chamber for 1 h. After that, the slides were washed with 0.1 × SSC, 0.5% SDS for 15 min, and with 0.1 × SSC (5 min). Finally, the chips were rinsed with water and air-dried.

Table 1. Nucleotide Sequence of Probes and Targets Used

name	sequence (5′ to 3′)	5′ end	3′ end
SYM12	ACTGGTCGATCG	Cy5	C_6-NH_2
SYM23	TTACGATCGATTAGTTAGCCC-$(T)_{15}$	Cy5	C_7-NH_2
SYM8	AATGCTAGCTAATCAATCGGG	Cy5	none
SYM25	AATGCTAGCTAATCAATCGGG	biotin	none
SYM22	$(T)_{15}$-CCCGATTGATTAGCTAGCATT	none	C_7-NH_2

For hybridization assays on standard L-CDs, each disc was divided into eight printing zones and SYM22 was covalently attached as described above. Afterward, 35 μL of OVA in 1 × CB (pH 9.6) was dispensed on each printed area, spread under a coverslip, and incubated for 10 min at room temperature in a moist chamber. Then, L-CDs were washed 5 min with PBS-T and 5 min with water and air-dried. Biotin-ended target DNA (SYM25) was serial diluted between 0.001 and 0.2 μM in a mixture containing 6 × SSC, 0.6% SDS, 0.1% salmon sperm DNA, and 2% BSA. A 35 μL amount of the complementary oligonucleotide solution was dispensed on the microarrays and spread under a coverslip, performing the hybridization at 37 °C in a dark and humidified chamber, for 1 h. The discs were washed with PBS-T (15 min) and water (5 min) and air-dried. Following a similar procedure described by Cao et al. (*19*), 35 μL of 10 μg/mL streptavidin−HRP in 1 × PBS were deposited on each zone of the L-CD and incubated again for 20 min in a moist chamber at 37 °C. After rinsing with PBS-T (15 min) and water (5 min) and drying, 35 μL of TMB substrate solution was dispensed, causing a blue precipitate to appear on

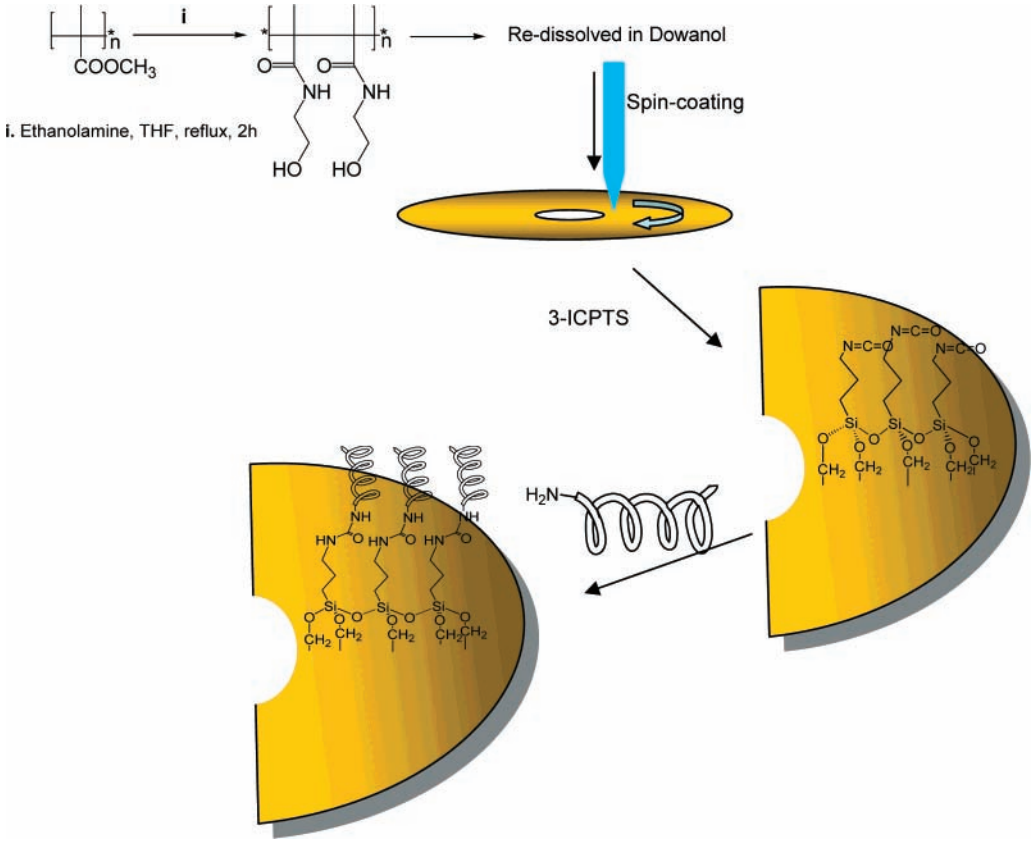


Figure 2. Scheme of the method for the covalent attachment of amino-ended oligonucleotides on L-CD surface.

the microarrays after 3 min. Results were read with the CD player as described above.

RESULTS AND DISCUSSION

L-CD Surface Modification. To achieve the covalent attachment of oligonucleotides onto the isocyanate-modified L-CD surface, the following three-step approach was investigated: (i) methyl ester transamination of PMMA employing ethanolamine in THF; (ii) spin-coating of the hydroxylated PMMA dissolved in Dowanol; (iii) introduction of the isocyanate moiety by the ether formation between the hydroxyl groups on PMMA and 3-isocyanatopropyltriethoxysilane (Figure 2).

The employment of organosilane allowed us to introduce a thin and homogeneous layer when working in a controlled manner. On the other hand, as isocyanate was chosen to attach the aminated oligomer, a urea bond was obtained. This bond is highly stable and easy to perform. The high reactivity of the isocyanate group results in a rapid coupling reaction and is particularly useful for covalent attachment of biomolecules such as nucleic acids, peptides, carbohydrates, lipooligosaccharides, etc.

The reaction of PMMA dissolved in THF with ethanolamine produced the aminolysis of the methyl ester, providing hydroxylated PMMA with a yield of around 50%, determined by NMR.

The modified polymer was dissolved in Dowanol for application of a thin layer onto the L-CD by spin coating and drying as described in the Experimental Section. The film thickness was 60 nm (measured by AFM and ellipsometry) with a high degree of homogeneity and reproducibility (tested by AFM and SEM).

For the organosilane treatment, selecting the proper solvent was a crucial point; thus, the mechanical and optical properties of the L-CDs must be unaltered in order to read the signals resulting from the hybridization assays. Most of the tested solvents (diethyl ether, tetrahydrofuran, dichloromethane, hexane) were promptly discarded; thus, they partially dissolved the base polymer (PC) and caused drastic alterations on the L-CD support. Finally, the selected solvent was 2-propanol. Also, different reaction concentrations, ranging from 0.1% to 5%, and times, between 10 min and 2 h, were studied.

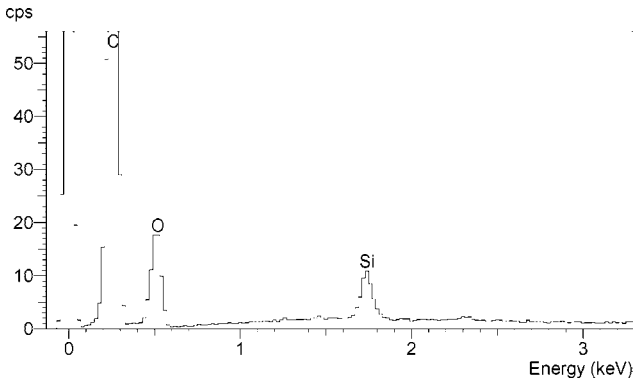


Figure 3. ED spectrum of the isocyanate-modified PMMA-L-CD surface.

To detect the effectiveness of ICPTS reaction onto hydroxylated PMMA-coated L-CDs, ED spectra were recorded; the presence of Si indicated that the organosilane reaction worked in a proper manner (Figure 3). Also, to examine the success of the reaction, the treated L-CDs were cut in chips (55 × 25 mm) and immersed into 4.5 mM fluoresceinamine dissolved in 2-propanol for 20 min. After washing, fluorescence was measured (λ_{exc} 485 nm; λ_{em} 580 nm), and the results were compared with different control chips to eliminate the solvent effect. This control is necessary, as the consecutive treatments produced an alteration of the surface and the fluorescein could swell the chip, resulting in high fluorescence signals. For that, treatment with fluoresceinamine was carried out for every step of the approach (raw L-CD, L-CD coated with hydroxylated PMMA, and isocyanate-treated L-CD) and compared.

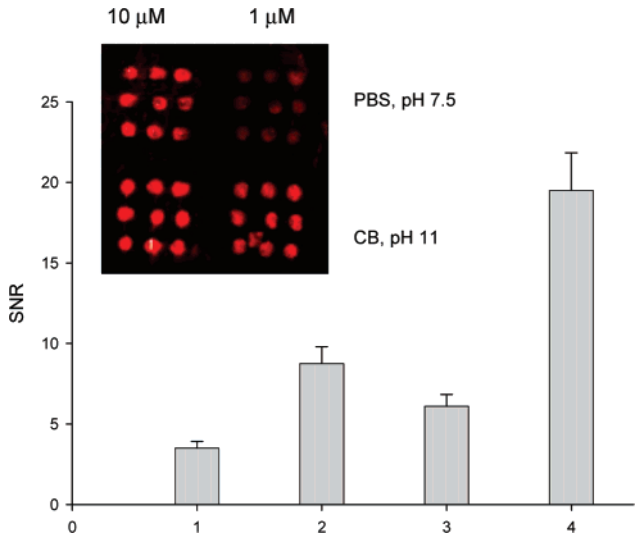


Figure 4. Results for oligomer immobilization on the isocyanate-modified L-CD surface using different buffers: (1) PBS, pH 7.5, 1 μM of probe; (2) PBS, pH 7.5, 10 μM of probe; (3) CB, pH 11, 1 μM of probe; (4) CB, pH 11, 10 μM of probe.

During the optimization process it was observed that the longer the treatment with organosilane the lower difference in fluorescence values with respect to the controls (similar conditions as for silanization but without the organosilane). This is explained considering that the solvent employed for the organosilane treatment did not alter the disc surface when short silanization times were applied, but prolonged exposure of PMMA to 2-propanol damaged the chip surface, lowering its transparency and producing a gummy texture.

Final conditions were chosen, limiting the time exposure to the organosilane solution (10 min, 1%) and curing the plastic after the treatment for 15 min at 62 °C. Oligomer immobilization was performed after the surface preparation.

DNA Immobilization. Under the chosen reaction conditions, L-CDs were prepared to assay the covalent attachment of oligonucleotides. For that, 1 μM and 10 μM 5′ Cy5-labeled, 3′ aminated oligonucleotide (SYM23) solutions were prepared in water, PBS buffer (pH 7.5), and carbonate buffer (pH 11). The oligonucleotide solutions were deposited onto the modified PMMA surfaces by tip-contact-printing. After immobilization, as explained in the Experimental Section, discs were cut in chips and the fluorescence of Cy5-labeled probes read using microarray laser scanning.

The best results were those employing CB, pH 11 (Figure 4), while results for water were far from that expected; the fluorescence at 1 μM and 10 μM was almost the same. This could be due to the unspecific adsorption and electrostatic forces. When working at pH values higher than 9, most of the amine groups in the oligomer exist as free amines and the nucleophilic attack of nitrogen to the isocyanate group is possible, providing a urea bond. However, at pH lower than 7, many of the amine groups exist as their ammonium salt and the covalent attachment is not possible, although it must be taken into account that this charged structure can adhere to the surface by electrostatic interactions as well as by hydrogen bonds.

In parallel, and in order to check the oligomer probe covalent attachment quality, several controls were performed employing raw L-CD, and hydroxyl-PMMA-coated L-CDs, raw and treated with 2-propanol. In all cases, the fluorescence signal was less than 10% of the fluorescence observed in isocyanate-modified L-CDs. Besides, to assess that all the attached oligomers were covalently bound to the disc surface, controls employing Cy5-labeled oligonucleotide without amine functionalization (SYM8) were printed on activated PMMA discs (blank assay), working in a way similar to that with amine-ended oligonucleotides. Again, the fluorescence signal was at the background level.

When the disc was inserted in the standard CD player and a recording simulation was done, the L-CD was read without presenting internal errors. It was concluded that the treatment proposed for oligomer immobilization on discs leave the L-CD available for further common use such as data recording, and the L-CD surface remained, to the naked eye, unaltered after the chemical treatment and oligomer attachment. This opens up an interesting application field of the developed methodology for performing chemical assays on the top of treated PMMA-L-CDs, using the bottom side (PC) to read it with the CD player laser, and for the registration of the analytical data and other management information. Another advantage of this methodology is the application of widely studied organosilane chemistry on CDs. By making use of these reagents, different ways of biomolecule covalent attachment are possible; for example, by employing a mercaptoorganosilane, thiol-ended biomolecules could be attached by formation of disulfide bridges.

To estimate the density of DNA single strands covalently attached to the surface, calibration assays were performed on treated L-CDs, employing SYM23 (analogous to SYM22, but Cy5-labeled). Considering the tip-contact dispensed volume (3 nL) and the averaged spot diameter, through the calibration curve, an immobilization density about 2 pmol/cm^2 for a 5 μM concentration of the spotted oligonucleotide was estimated. This value was in agreement with data found in the literature for glass (*20*) (2 pmol/cm^2), PMMA (*17*) (4 pmol/cm^2), and gold (*21*) (3 pmol/cm^2).

Hybridization on L-CD. One of the main concerns when preparing DNA microarrays is to achieve a good yield in hybridization assays. To check the performance of the developed approach, several experiments were conducted employing different concentrations of both DNA probe (1, 5, 10, and 20 μM) and Cy5-labeled complementary DNA strand (0.1, 0.2, 0.5, and 1 μM). The hybridization density (pmol/cm^2) was calculated from interpolation of the registered fluorescence value in the corresponding calibration curve.

Figure 5 shows the hybridization density reached at different sDNA probe concentrations, indicating that the best results correspond to 5 μM sDNA. Besides, it was observed that when probe concentration as high as 20 μM was assayed, the hybridization did not give good results; the spots were surrounded by a halo of fluorescence and presented a "black hole" at the center of the spot. This could be due to the high surface coverage with DNA probes that may cause a crowding effect, lowering the accessibility of the probes (*21*). Probably, repulsive electrostatic and steric interactions also increased with probe density. Likewise, by increasing the concentration of the complementary oligonucleotide solution, no significant improvement of hybridization efficiency was detected. Consequently, it was assumed that 0.1−0.2 μM hybridization solution and 5 μM DNA probe were the optimal for this assay. Related to immobilization density, the maximum hybridization efficiency was achieved between 2 and 4 pmol/cm^2. These results were in agreement with studies (*17*) performed on chemically modified PMMA, which provide oligonucleotide densities around 0.5 pmol/cm^2, employing similar hybridization conditions.

Finally, in order to demonstrate that the developed method is fully applicable to standard CD technology, discs were treated according to the described procedure, and different concentrations of SYM 22 probe (1, 5, 10, and 20 μM) were immobilized on the L-CD surface. After hybridization with serial dilutions of SYM 25 (0.2 to 0.001 μM), the L-CD was treated with HRP-conjugated streptavidin for 20 min, washed, and developed with

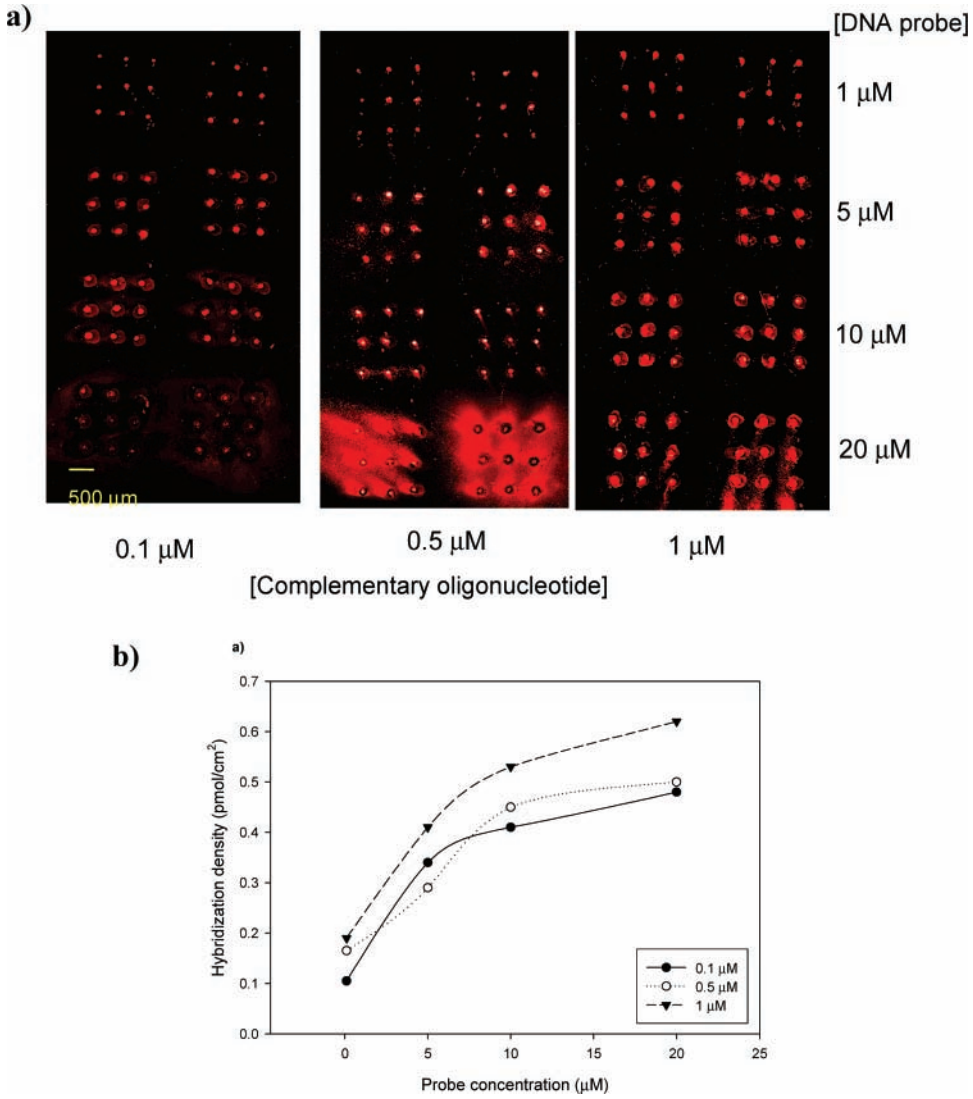


Figure 5. (a) Microarray picture of the hybridization assays performed on PMMA-modified L-CD employing Cy5-labeled complementary oligonucleotide and reading by microarray laser scanning. (b) Curves of hybridization density using different probe and target concentrations.

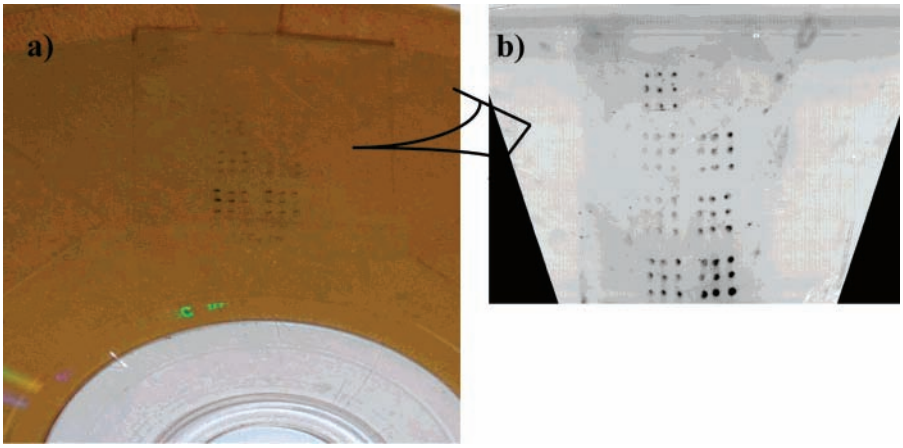


Figure 6. (a) Image of the microarray (blue spots) developed on modified L-CD after hybridization assay. (b) Magnification of the same image obtained with the CD player.

TMB for 3 min; the blue precipitate appeared in the matrixes where the hybridization happened (Figure 6) as read with the CD player.

Several controls were performed, avoiding the different working protocol steps: isocyanate treatment, covalent attachment of probe, OVA blocking of remaining isocyanate groups, hybridization solution and streptavidin−HRP incubation; none of them displayed blue points except when the OVA treatment was suppressed, as was expected.

Related to the detection system, similar trends where achieved employing conventional readers (Axon detector) or CD player. Thus, the best results were obtained for 5 μM of probe and 0.2 μM of hybridization solution although it was possible to detect concentrations of 0.005 μM hybridization solution (even by the

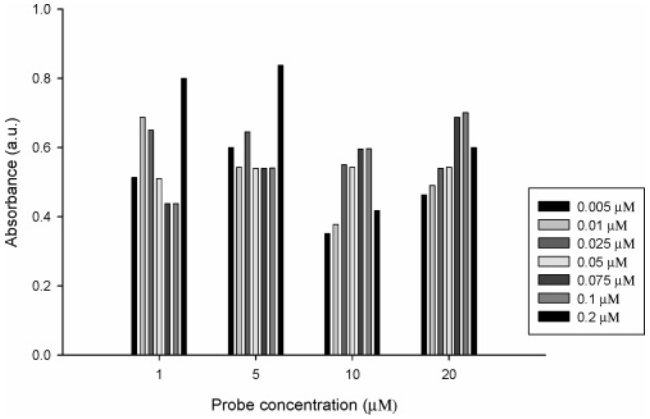


Figure 7. Signal intensity values read with the CD player for different probe and target concentrations.

naked eye). This is because of the higher sensitivity of the HRP labeling; thus, the developing procedure is based on an enzymatic reaction. The absorbance intensities of different concentrations of probe and target are shown in Figure 7. The most remarkable was that the highest signal is obtained for 5 μM probe and 0.2 μM target, as that which occurred in the assays with fluorescence detection. Also the high signal obtained for the lowest concentrations of hybridization solution provides an idea of the good sensitivity achieved from the disc isocyanate modification and CD player detection approach. These assays demonstrate that the proposed system works for qualitative detection; no quantification was intended, as the quantification protocol will depend on the application, but in general, intensity values can be converted into biologically relevant outputs by comparing the experimental and control elements present in a given microarray (*22*).

CONCLUSION

In this work a PMMA isocyanate modification is proposed for the covalent attachment of biomolecules, employing well established organosilane chemistry. The method retains the physical properties of the support, and its application is versatile and clean. The procedure is easily carried out and is compatible with aqueous media chemistry, which is crucial for its bioutility. Immobilization densities about 2 pmol/cm^2 were reached with oligonucleotides. The values were in agreement with other described methods for microarrays on modified PMMA, glass, and other surfaces.

The application on standard recordable compact discs opens an interesting field because of its potential advantages such as low fluorescent background, high quality materials at very low cost, high available surface (90 cm^2), and further use of laser technology found in the CD players as detectors, to be applied at point of need to health care or *in situ* environmental analysis.

ACKNOWLEDGMENT

We thank the MCYT (BIO 2000-0243-P4-03 and BQU 2003-02677) and Generalitat Valenciana (ACOMP06/12) for funding this project. D. Miguel García-Murillo, from Plexi S.A. (Valencia, Spain), is gratefully acknowledged for providing raw PMMA.

LITERATURE CITED

(1) Najmabadi, P., La Clair, J. J., and Burkart, M. D. (2007) A systems perspective to digital structures in molecular analysis. *Org. Biomol. Chem. 5*, 214−222.

(2) Hammock, B. D., Kido, H., and Maquieira, A. (Regents of the University of California). US Pat. 6 395 562, 1998. Larsson, A., and Almer, K. (Gyros AB). Eur. Pat. 1 077 771, 1998. La Clair, J. J. Eur. Pat. 1 189 062, 2000. La Clair, J. J. Eur. Pat. 1 215 613, 2000. Phan, B. C., Virtanen, J. A., Lam, A. H., Yeung, K. Y., and Coombs, J. H. (Burnstein Technologies Inc), US Pat. 6 342 349, 2000.

(3) Kido, H., Maquieira, A., and Hammock, B. (2000) Disc-based immunoassay microarrays. *Anal. Chim. Acta 411*, 1−11.

(4) Remacle, J., Alexandre, I., and Houbion, Y. *US Pat.* 177 144, 2001. Remacle, J. US Pat. 35 499, 1998. Alexandre, I., Houbion, Y., Collet, J., Demarteau, J., Gala, J. L., and Remacle, J. (2002) Compact Disc with both numeric and genomic information as DNA microarray platform. *Bio Techniques 33*, 435−439.

(5) La Clair, J. J., and Burkart, M. D. (2003) Molecular screening on a compact disc. *Org. Biol. Chem. 1*, 3244−3249. La Clair, J. J., and Burkart, M. D. (2006) Geometry in digital molecular arrays. *Org. Biomol. Chem. 4*, 3052−3055. La Clair, J. J. US Pat. 229 254, 2004.

(6) Li, Y., Wang, Z., Ou, L. M. L., and Yu, H-Y. (2007) DNA detection on plastic: Surface activation protocol to convert polycarbonate substrates to biochip platforms. *Anal. Chem. 79*, 426−433.

(7) Yu, H.-Z. (2004) New chemistry on old CDs. *Chem. Commun. 23*, 2633−2636.

(8) Barathur, R., Bookout, J., Sreevatsan, S., Gordon, J., Werner, M., Thor, G., and Worthington, M. (2002) New disc-based technologies for diagnostic and research applications. *Psychiatr. Genet. 12*, 193−206.

(9) Potyrailo, R. A., Morris, W. G., Leach, A. M., Sivavec, T. M., Wisnudel, M. B., and Boyette, S. (2006) Analog signal acquisition from computer optical disk drives for quantitative chemical sensing. *Anal. Chem. 78*, 5893−5899.

(10) Morais, S., Marco-Molés, A., Puchades, R., and Maquieira, A. (2006) DNA microarraying on compact disc surfaces. Application to the analysis of single nucleotide polymorphisms in Plum Pox virus. *Chem. Commun. 22*, 2368−2370.

(11) Iossifidis, D., Auroux, P. A., Reyes, D. R., and Manz, A. (2002) Micro Total Analysis Systems. Introduction, Theory, and Technology. *Anal. Chem. 74*, 2623−2652.

(12) Rossier, J., Reymond, F., and Michel, P. E. (2002) Polymer microfluidic chips for electrochemical and biochemical analyses. *Electrophoresis 23*, 858−867.

(13) Bulmus, V., Ayhan, H., and Piskin, E. (1997) Modified PMMA monosize microbeads for glucose oxidase immobilization. *Chem. Eng. J. 65*, 71−76.

(14) Henry, A. C., and McCarley, R. L. (2001) Selective deposition of metals on plastics used in the construction of microanalytical devices: photo-directed formation of metal features on PMMA. *J. Phys. Chem. B 105*, 8755−8761.

(15) Henry, A. C., Tutt, T. J., Galloway, M., Davidson, Y. Y., McWhorter, C. S., Soper, S. A., and McCarley, R. L. (2000) Surface modification of poly(methyl methacrylate) used in the fabrication of microanalytical devices. *Anal. Chem. 72*, 5331−5337.

(16) Waddell, E., Wang, Y., Stryjewski, W., McWhorter, S., Henry, A. C., Evans, D., McCarley, R. L., and Soper, S. A. (2000) High-resolution near-infrared imaging of DNA microarrays with time resolved acquisition of fluorescence lifetimes. *Anal. Chem. 72*, 5907−5917.

(17) Fixe, F., Dufva, M., Telleman, P., and Christensen, B. V. (2004) Functionalization of poly(methyl methacrylate) (PMMA) as a substrate for DNA microarrays. *Nucleic Acids Res. 32*, e9.

(18) Wong, S. S. (1991) Homobifunctional cross-linking reagents. In *Chemistry of protein conjugation and cross-linking*; pp 75, CRC Press Inc., Boca Raton, FL.

(19) Cao, X., Wang, Y. F., Zhang, C. F., and Gao, W. J. (2006) Visual DNA microarrays for simultaneous detection of *Ureaplasma urealyticum* and *Chlamydia trachomatis* coupled with multiplex asymmetrical PCR. *Biosens. Bioelectron. 22*, 393−398.

(20) Stillman, B. A., and Tonkinson, J. L. (2001) Expression microarray hybridization kinetics depend on length of the immobilized DNA but are independent of immobilization. *Anal. Biochem. 295*, 149−157.

(21) Peterson, A. W., Heaton, R. J., and Georgiadis, R. M. (2001) The effect of surface probe density on DNA hybridization. *Nucleic Acid Res. 29*, 5163−5168.

(22) Schena, M. (2003) Data quantitation. In *DNA Microarray Analysis*; pp 297−305, John Wiley and Sons, Inc., Hoboken, NJ.

BC700194N

Cyclic RGD Peptide-Conjugated Polyplex Micelles as a Targetable Gene Delivery System Directed to Cells Possessing $\alpha_v\beta_3$ and $\alpha_v\beta_5$ Integrins

Makoto Oba,[†] Shigeto Fukushima,[‡,§] Naoki Kanayama,[§,¶] Kazuhiro Aoyagi,[§] Nobuhiro Nishiyama,[#] Hiroyuki Koyama,[†] and Kazunori Kataoka*[,§,¶,#,⊥]

Department of Clinical Vascular Regeneration, Graduate School of Medicine, The University of Tokyo, 7-3-1 Hongo, Bunkyo, Tokyo 113-8655, Japan, R&D Division, Pharmaceuticals Group, Nippon Kayaku Co., Ltd., Department of Materials Engineering, Graduate School of Engineering, The University of Tokyo, 7-3-1 Hongo, Bunkyo, Tokyo 113-8656, Japan, CREST, Japan Science and Technology Agency, Japan, Center for Disease Biology and Integrative Medicine, Graduate School of Medicine, The University of Tokyo, 7-3-1 Hongo, Bunkyo, Tokyo 113-0033, Japan, and Center for NanoBio Integration, The University of Tokyo, 7-3-1 Hongo, Bunkyo, Tokyo 113-8656, Japan. Received January 15, 2007; Revised Manuscript Received May 11, 2007

A cyclic RGD peptide-conjugated block copolymer, cyclo[RGDfK(CX-)]−poly(ethylene glycol)−polylysine (c(RGDfK)−PEG−PLys), was synthesized from acetal-PEG−PLys under mild acidic conditions and spontaneously associated with plasmid DNA (pDNA) to form a polyplex micelle in aqueous solution. The cyclic RGD peptide recognizes $\alpha_v\beta_3$ and $\alpha_v\beta_5$ integrin receptors, which play a pivotal role in angiogenesis, vascular intima thickening, and the proliferation of malignant tumors. The c(RGDfK)−PEG−PLys/pDNA polyplex micelle showed a remarkably increased transfection efficiency (TE) compared to the PEG−PLys/pDNA polyplex micelle for the cultured HeLa cells possessing $\alpha_v\beta_3$ and $\alpha_v\beta_5$ integrins. On the other hand, in the transfection against the 293T cells possessing no $\alpha_v\beta_3$ and a few $\alpha_v\beta_5$ integrins, the TE of the c(RGDfK)−PEG−PLys/pDNA micelle showed no increase compared to the TE of the PEG−PLys/pDNA micelle. Flow cytometric analysis revealed a higher uptake of the c(RGDfK)−PEG−PLys/pDNA micelle than the PEG−PLys/pDNA micelle against HeLa cells, consistent with the transfection results. Furthermore, a confocal laser scanning microscopic observation revealed that the pDNA in the c(RGDfK)−PEG−PLys micelle preferentially accumulated in the perinuclear region of the HeLa cells within 3 h of incubation. No such fast and directed accumulation of pDNA to the perinuclear region was observed for the micelles without c(RGDfK) ligands. These results indicate that the increase in the TE induced by the introduction of the c(RGDfK) peptide ligand was due to an increase in cellular uptake as well as facilitated intracellular trafficking of micelles toward the perinuclear region via $\alpha_v\beta_3$ and $\alpha_v\beta_5$ integrin receptor-mediated endocytosis, suggesting that the cyclic RGD peptide-conjugated polyplex micelle has promising feasibility as a site-specifically targetable gene delivery system.

INTRODUCTION

With the increase in available information on various disease genes that has resulted from progress in the Human Genome Project, gene therapy is increasingly recognized as a promising therapy for many intractable diseases. Obviously, a major key to successful gene therapy is the development of gene vectors that are particularly effective for *in vivo* use. Nevertheless, there are many restrictions in the clinical application of viral vectors, which have played a pivotal role in gene therapy up to now, because of their safety issues, including antigenicity, as well as to the difficulty of formulating them with good quality control. These limitations of viral vectors have led to the recent trend in developing nonviral vectors with safety and high productivity as alternative systems to viral vectors.

One of the important challenges in the development of nonviral vectors is the system available for systemic injection, which must be stable enough to achieve longevity in the blood circulation but also be able to achieve high transfection efficiency (TE) in the target region with minimal toxicity. Lipoplex (*1*) and polyplex (*2*) systems based on cationic lipids and polymers, respectively, have been extensively studied as nonviral gene vectors for systemic administration. Nevertheless, there remain unresolved issues with these systems, because it is generally required that they contain excessive cationic lipids or polymers to increase solubility in an aqueous solution. Eventually, shifting their surface charge to a positive value induces nonspecific interaction with anionic components in the body such as plasma proteins and blood cells. This apparently hampers their applicability to systemic gene delivery. Polyplex micelles (*3*), characterized by the unique core−shell architecture of the hydrophilic shell layer surrounding their polyplex core, have the potential to acquire a so-called "stealth" property to minimize nonspecific interaction with biocomponents. Indeed, a polyplex micelle with poly(ethylene glycol) (PEG) as a hydrophilic shell layer achieved high stability in a medium containing serum compared to conventional lipoplexes and polyplexes and showed increased retention time in the bloodstream (*4*, *5*), suggesting that a polyplex micelle may be a promising candidate for a vector that can be used in systemic gene delivery. Nevertheless, in order to increase selective uptake into the target cells, appropriate ligands are preferably introduced into the surface of the polyplex micelles. In this way, surface-installed ligands are expected to enhance the uptake rate of the

* To whom correspondence should be addressed. Tel: +81-3-5841-7138, fax: +81-3-5841-7139, e-mail: kataoka@bmw.t.u-tokyo.ac.jp.
[†] Department of Clinical Vascular Regeneration, The University of Tokyo.
[‡] Nippon Kayaku Co., Ltd.
[§] Department of Materials Engineering, The University of Tokyo.
[¶] CREST.
[#] Graduate School of Medicine, The University of Tokyo.
[⊥] Center for NanoBio Integration, The University of Tokyo.

10.1021/bc0700133 CCC: $37.00 © 2007 American Chemical Society
Published on Web 06/27/2007

polyplex micelles into the target cells by receptor-mediated endocytosis, which may lead to higher gene TE compared to the ligand-free polyplex micelles taken up by the cells through adsorptive or fluid-phase endocytosis (*6*−*8*).

In this study, acetal-poly(ethylene glycol)−polylysine (acetal-PEG−PLys) was synthesized as a precursor for constructing ligand-installed polyplex micelles. PLys, which is one of the first polymers used and well studied as a nonviral vector, was chosen as a cationic segment of the block copolymer. PLys-based polyplexes are known to show a relatively low TE against cultured cell lines compared to those having the endosomal escape function, such as polyethylenimine (PEI)-based polyplexes, but they have an advantage in stability even in a diluted condition, and they have shown an appreciable level of gene transfection in animal models (*5*, *9*). A cyclic RGD peptide (c(RGDfK)), which selectively recognizes $\alpha_v\beta_3$ and $\alpha_v\beta_5$ integrin receptors (*10*), was chosen as a ligand and introduced into the PEG terminus of aldehyde-PEG−PLys, derived from acetal-PEG−PLys, through a thiazolidine ring formation, and the c(RGDfK)−PEG−PLys block copolymer was obtained. It is generally known that the $\alpha_v\beta_3$ and $\alpha_v\beta_5$ integrins are expressed on various cell types such as endothelial cells, osteoclasts, macrophages, platelets, and melanomas, and that they play a significant role in angiogenesis, vascular intima thickening, and the proliferation of malignant tumors (*11*). Therefore, gene delivery targeting the $\alpha_v\beta_3$ and $\alpha_v\beta_5$ integrins is expected to be useful in the treatment of cancer and vascular diseases. Indeed, the c(RGDfK)−PEG−PLys/pDNA polyplex micelle thus prepared showed a remarkably increased TE compared to ligand-free polyplex micelles against the HeLa cells expressing $\alpha_v\beta_3$ and $\alpha_v\beta_5$ integrins.

EXPERIMENTAL PROCEDURES

Materials. 3,3-Diethoxypropanol was purchased from Aldrich Chemical Co. Ltd. (Milwaukee, WI). Ammonia solution (25%), tetrahydrofuran (THF), *N*,*N*-dimethylformamide (DMF), *n*-hexane, methanesulfonyl chloride (MsCl), and triethylamine (TEA) were purchased from Wako Pure Chem. Co. Ltd. (Japan). Ethylene oxide (EO) was purchased from Sumitomo Seika Chemicals Co. Ltd. (Japan). THF was distilled according to the conventional procedure as previously reported (*12*). DMF was dehydrated using activated molecular sieves (4A) and distilled under reduced pressure. 3,3-Diethoxypropanol and *n*-hexane were distilled over sodium wire. MsCl, TEA, and EO were dried over calcium hydride followed by distillation. CXYGGRGDS (RGDS) and cyclo[RGDfK(CX-)] (c(RGDfK)) peptides (X = 6-aminocaproic acid; ϵ-Acp) were purchased from Peptide Institute, Inc. (Japan). The PEG−PLys block copolymer (PEG; 12 000 g/mol, polymerization degree of PLys segment; 73) was synthesized as previously reported (*13*). A micro BCA protein assay reagent kit was purchased from Pierce (Rockford, IL). The Luciferase assay kit was a product of Promega (Madison, WI). Plasmid pCAcc+Luc coding for firefly luciferase under the control of the CAG promoter was provided by the RIKEN Gene Bank (Japan), amplified in competent DH5α *Escherichia coli*, and then purified using a HiSpeed Plasmid MaxiKit purchased from QIAGEN Sciences Co., Inc. (Germany). FITC-labeled monoclonal antibodies against $\alpha_v\beta_3$ integrin, $\alpha_v\beta_5$ integrin, and mouse IgG were purchased from Cosmo Bio Co., Ltd. (Japan). QuantiLum recombinant luciferase was purchased from Promega (Madison, WI).

Measurements. Gel permeation chromatography (GPC) measurements were carried out using a TOSOH HLC-8220 equipped with TSKgel columns (G4000PWXL and G3000PWXL). The internal refractive index (RI) was used for detection of the polymer. DMF with 10 mM LiCl was used as an eluent at a flow rate of 0.8 mL min^{-1} at 40 °C. IR was measured with an IR Report-100 spectrometer (JASCO, Tokyo, Japan). ^{1}H NMR spectra were obtained with a JEOL EX300 spectrometer (JEOL, Tokyo, Japan). Chemical shifts are reported in ppm relative to the residual protonated solvent resonance.

Synthesis of RGDS−PEG−PLys 5a and c(RGDfK)−PEG−PLys 5b (Scheme 1). *Acetal-PEG-NH$_2$* ***2***. A THF solution of 3,3-diethoxypropanol (0.16 mL, 1 mmol) and potassium naphthalene (2.7 mL, 0.90 mmol) were mixed in THF (75 mL) to form potassium 3,3-diethoxypropanolate (PDP) as previously reported (*14*). After the mixture was stirred for 10 min, liquid EO (13.5 mL, 270 mmol) chilled below 0 °C was added to the solution with additional stirring at room temperature (r.t.) for 2 days. The reactant polymer was isolated by precipitation into diethyl ether and lyophilized from benzene to obtain acetal-PEG-OH (12.65 g, quant). Acetal-PEG-OH (6.01 g, 0.50 mmol) was then dissolved in THF (40 mL), followed by the addition of TEA (0.32 mL, 2.25 mmol). Subsequently, the solution was slowly added dropwise into MsCl (0.12 mL, 1.5 mmol) in THF (20 mL) and stirred at 0 °C for 2 h. The solution was poured into diethyl ether to precipitate acetal-PEG-OMs **1**. The recovered acetal-PEG-OMs **1** was dissolved in 25% ammonia solution (500 mL) and stirred at r.t. for 4 days. The volume of the solution was concentrated to 50 mL by evaporation and dialyzed sequentially against 0.125% ammonia solution and distilled water, followed by lyophilization to obtain acetal-PEG-NH$_2$ **2** (5.40 g, 90%).

Acetal-PEG−PLys(TFA) ***3***. N^{ϵ}-Trifluoroacetyl-L-lysine *N*-carboxyanhydride (Lys(TFA)-NCA) (3.59 g, 13.39 mmol, 80 equiv to **2**) prepared according to the protocol described in the literature (*15*) in DMF (40 mL) was added to acetal-PEG-NH$_2$ **2** (2.01 g, 167.5 μmol) in DMF (20 mL) and stirred at 40 °C for 2 days. The polymerization was monitored by IR. The reactant polymer was precipitated into AcOEt/hexane (4:6) and lyophilized in dioxane to obtain acetal-PEG−PLys(TFA) **3** (4.08 g, 73%).

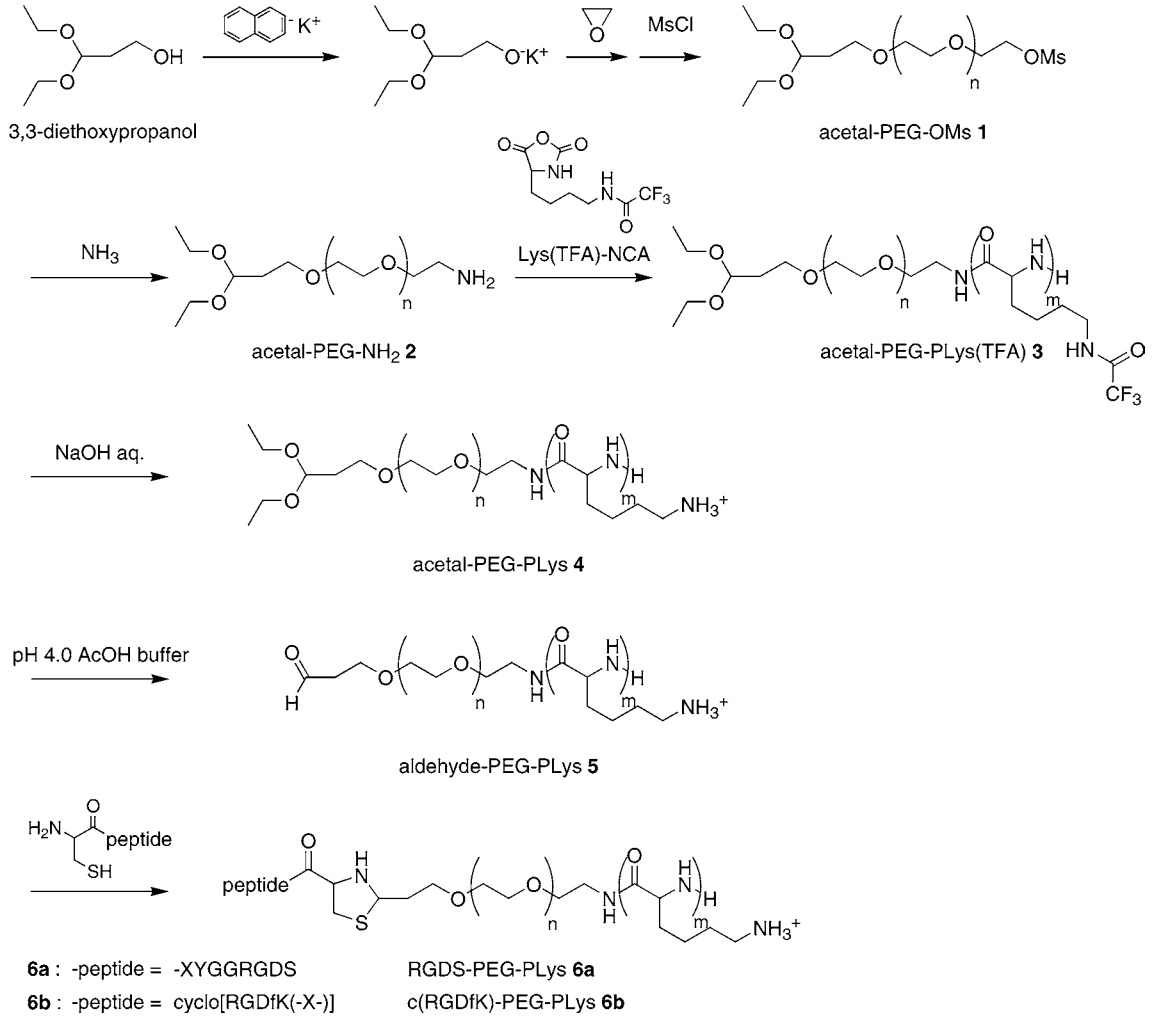
Acetal-PEG−PLys ***4***. NaOH solution (1 N, 4 mL) was added to acetal-PEG−PLys(TFA) **3** (500 mg, 17.77 μmol) in MeOH (40 mL) and stirred at 40 °C for 24 h. The reacted polymer was purified by dialysis sequentially against 10 mM PBS solution (pH 7.0) and distilled water and lyophilized to obtain acetal-PEG−PLys **4** (498 mg, quant).

RGDS−PEG−PLys ***6a*** *and c(RGDfK)−PEG−PLys* ***6b***. Conjugation of the peptide into the PEG terminus of PEG−PLys was performed through thiazolidine ring formation using RGDS or c(RGDfK) peptide. RGDS−PEG−PLys **6a** was synthesized according to the typical procedure, as follows: Acetal-PEG−PLys **4** (39.1 mg, 1.64 μmol) was added to RGDS (15.2 mg, 16.4 μmol) in 0.2 M AcOH buffer (pH 4.0, 8 mL) and stirred at room temperature for 5 days. The reacted polymer was purified by dialysis sequentially against 10 mM PBS solution (pH 7.0) and distilled water and lyophilized to obtain RGDS−PEG−PLys **6a** (35.4 mg, 86%). Conjugation of the c(RGDfK) to acetal-PEG−PLys **4** was carried out in a similar way, e.g., c(RGDfK) (7.4 mg, 9.03 μmol) and acetal-PEG−PLys **4** (30.0 mg, 1.26 μmol) were used to obtain c(RGDfK)−PEG−PLys **6b** (26.6 mg, 87%).

Preparation of Polyplex Micelles. Each block copolymer and pDNA was dissolved separately in 10 mM Tris-HCl buffer (pH 7.4). The polymer solution in varying concentrations was added to a twice-excess volume of pDNA solution to form polyplex micelles with different compositions. The final pDNA concentration was adjusted to 33.3 or 50 μg/mL. The resulting solution was kept at r.t. overnight. The N/P ratio was defined as the residual molar ratio of the amino groups of PLys units to the phosphate groups of pDNA.

Ethidium Bromide Exclusion Assay. Polyplex micelle solutions (50 μg pDNA/mL) prepared at various N/P ratios were

Scheme 1. Syntheses of RGDS−PEG−PLys 6a and c(RGDfK)−PEG−PLys 6b



adjusted to contain 10 μg pDNA/mL with 2.5 μg ethidium bromide (EtBr)/mL and 150 mM NaCl by adding 10 mM Tris-HCl solution (pH 7.4) containing EtBr and NaCl. The solutions were kept at r.t. overnight. The fluorescence intensity of the sample solutions at 590 nm (excitation wavelength: 365 nm) was measured at 25 °C using a spectrofluorometer (ND-3300, NanoDrop, Wilmington, DE). The fluorescence intensity of naked pDNA was set at 100% and measured against a background of EtBr without pDNA.

Dynamic Light Scattering Measurement. The size of the polyplex micelles was evaluated by dynamic light scattering (DLS) using Nano ZS (ZEN3600, Malvern Instruments, Ltd., UK). A He−Ne ion laser (633 nm) was used as the incident beam. Polyplex micelle solutions (50 μg pDNA/mL) with an N/P = 2 were adjusted to a concentration of 10 μg pDNA/mL. The data obtained at a detection angle of 173 ° at 25 °C were analyzed by a cumulant method to obtain the hydrodynamic diameters and polydispersity indices (μ/Γ^2) of the micelles. The results reported are expressed as the mean values (±SEM) of three experiments.

ζ-Potential Measurement. The ζ-potential of polyplex micelles was evaluated by the laser-doppler electrophoresis method using Nano ZS with a He−Ne ion laser (633 nm). Sample solutions similar to those used for the DLS measurements were prepared. The ζ-potential measurements were carried out at 25 °C. A scattering angle of 17° was used in these measurements. The results are expressed as the mean values (±SEM) of three experiments.

Detection of $\alpha_v\beta_3$ and $\alpha_v\beta_5$ Integrin Receptors. 293T cells and HeLa cells were detached by pipetting and by harvesting with trypsin, respectively. Both types of cells were washed twice with PBS. The 1×10^6 cells and FITC-labeled antibody against $\alpha_v\beta_3$ or $\alpha_v\beta_5$ integrin (2 μg) were resuspended in 100 μL of Dulbecco's Modified Eagle Medium (DMEM) (containing 10% serum) and incubated on ice for 1 h in the dark. The cells were washed three times with cold medium and, after being resuspended in PBS, were analyzed using a flow cytometer (EPICS XL, Beckman Coulter, Inc.). The cytometric data were analyzed using EXPO32 software (Beckman Coulter, Inc., Fullerton, CA).

Transfection. HeLa and 293T cells were respectively seeded on 24-well culture plates (10 000 cells/well) and incubated overnight in 500 μL of DMEM containing 10% serum. After the medium was replaced with fresh medium, 20 μL of polyplex solution (50 μg pDNA/mL, N/P = 2) was applied to each well. The amount of pDNA was adjusted to 1 μg per well. After incubation for various lengths of time, the medium was replaced with 500 μL of fresh medium, followed by reincubation. The reincubation time was adjusted so the total incubation time would be 48 h. The luciferase gene expression was then evaluated based on the intensity of the photoluminescence using the Luciferase assay kit and a Luminometer (Lumat LB9507, BERTHOLD, Germany). The amount of protein in each well was concomitantly determined using a Micro BCA protein assay reagent kit. The relative light units were converted into the absolute amount of luciferase (ng) using a standard curve calibrated with recombinant luciferase (QuantiLum, Promega). One nanogram of luciferase corresponded to 9.1×10^7 RLU in our experiments; this was defined as the conversion factor.

Analysis of Cellular Uptake of Polyplex Micelles. pDNA was labeled with fluorescein as previously reported (*4*). Briefly,

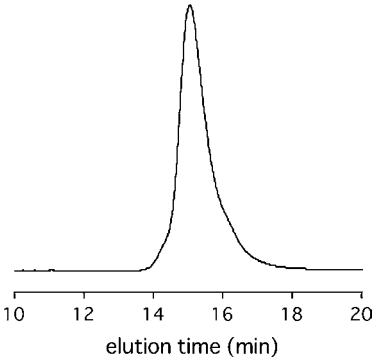


Figure 1. Gel permeation chromatogram of acetal-PEG−PLys(TFA) **3** (instrument TOSOH HLC-8220, detector RI, columns TSKgel G4000PWXL and G3000PWXL, eluent DMF with 10 mM LiCl, flow rate 0.8 mL min^{-1}, temperature 40 °C).

pDNA was labeled using a Label IT Nucleic Acid Labeling Kit (Mirus, Madison, WI). HeLa cells were seeded on six-well culture plates (100 000 cells/well) and incubated overnight in 1 mL of DMEM containing 10% serum. After the medium was replaced with fresh medium, 90 μL of polyplex solution (33.3 μg fluorescein-labeled pDNA/mL, N/P = 2) was applied to each well. The amount of fluorescein-labeled pDNA was adjusted to 3 μg per well. After various periods of incubation, the medium was removed and the cells were washed twice with PBS. After detachment by trypsin, the cells were resuspended in PBS and analyzed using the flow cytometer.

Confocal Laser Scanning Microscope (CLSM) Observation. pDNA was labeled with Cy5 in the same manner as fluorescein using the Label IT Nucleic Acid Labeling Kit. HeLa cells (30 000 cells) were seeded on a 35-mm glass base dish (Iwaki, Japan) and incubated overnight in 1 mL of DMEM containing 10% serum. After the medium was replaced with fresh medium, 90 μL of polyplex solution containing 3 μg Cy5-labeled pDNA (N/P = 2) was applied to a glass dish. After 3 h incubation, the medium was removed and the cells were washed twice with PBS. The intracellular distributions of the polyplex micelles were observed by CLSM following acidic late endosome and lysosome staining with LysoTracker Green (Molecular Probes, Eugene, OR) and nuclear staining with Hoechst 33342 (Dojindo Laboratories, Japan). The CLSM observation was performed using LSM 510 (Carl Zeiss, Germany) with a 63× objective (C-Apochromat, Carl Zeiss, Germany) at excitation wavelengths of 488 nm (Ar laser), 633 nm (He−Ne laser), and 710 nm (Mai Tai laser) for fluorescein, Cy5, and Hoechst 33342, respectively.

RESULTS

Synthesis of Peptide-Conjugated PEG−PLys (Scheme 1). The synthesis of acetal-PEG-OMs **1** has been previously reported (*14*). Briefly, PDP from 3,3-diethoxypropanol and potassium naphthalene initiated the anionic polymerization of EO to form acetal-PEG-OH (M_n 11 825, M_w 12 089, M_w/M_n 1.02), followed by the mesylation of alcohol using MsCl to obtain acetal-PEG-OMs **1**. Acetal-PEG-NH_2 **2** was then synthesized by amination of acetal-PEG-OMs **1** using ammonia solution and was confirmed to be unimodal with a narrow molecular weight distribution (M_w/M_n 1.03). Polymerization of Lys(TFA)-NCA using acetal-PEG-NH_2 **2** as an initiator led to the formation of acetal-PEG−PLys(TFA) **3**. A GPC of the obtained acetal-PEG−PLys(TFA) **3** showed a single peak with a narrow molecular weight distribution (M_w/M_n 1.12) (Figure 1). From the peak intensity ratio of the methylene protons of PEG (OCH_2CH_2, δ = 3.6 ppm) and the methylene protons of Lys(TFA) ($CH_2CH_2CH_2CH_2NH$, δ = 1.4, 1.5, 1.9, and 3.2 ppm) measured by ^{1}H NMR, the polymerization degree (DP) of Lys-(TFA) was calculated to be 70 (data not shown). Acetal-PEG−PLys **4** was then quantitatively obtained by the deprotection of acetal-PEG−PLys(TFA) **3** under basic conditions. From the ^{1}H NMR spectrum, the acetal group (CH_3CH_2O, δ = 1.2 ppm) was confirmed to be almost intact without converting to an aldehyde group (Figure 2). The DP of Lys was calculated to be 72 from the peak intensity ratio of the methylene protons of PEG (OCH_2CH_2, δ = 3.6 ppm) and the methylene protons of PLys ($CH_2CH_2CH_2CH_2NH_3$, δ = 1.4, 1.7, and 3.0 ppm) (Figure 2). The DP of acetal-PEG−PLys(TFA) **3** and acetal-PEG−PLys **4** were almost identical, indicating that main chain cleavage under the deprotection reaction was negligible.

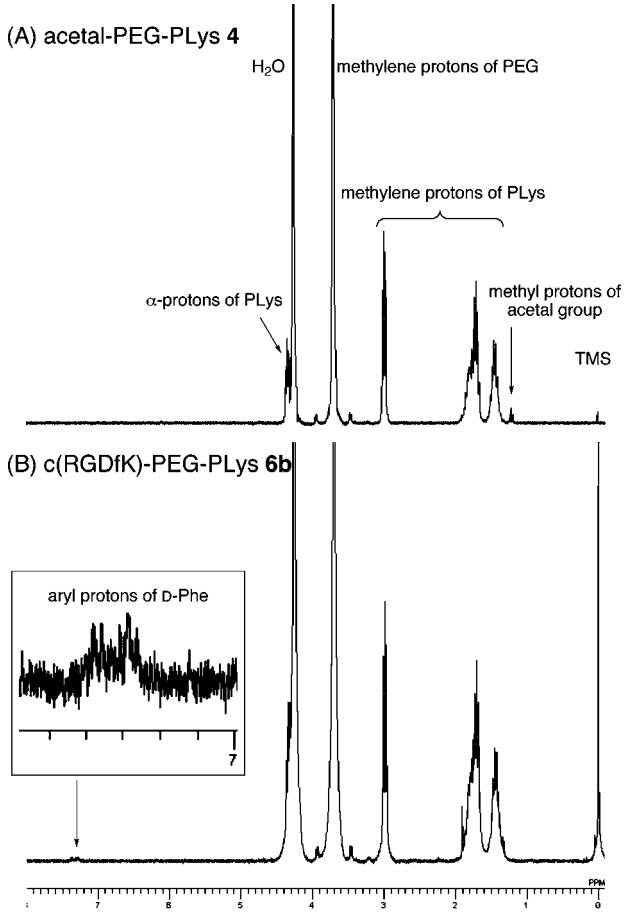


Figure 2. ^{1}H NMR spectra of acetal-PEG−PLys **4** (A) and c(RGDfK)−PEG−PLys **6b** (B) in D_2O at 80 °C.

Conjugation of peptide ligands into the PEG terminus of acetal-PEG−PLys **4** was achieved through the formation of a thiazolidine ring. The acetal group was deprotected under acidic conditions to an aldehyde group, giving aldehyde-PEG−PLys **5**. The aldehyde group is known to react with cysteine to form a stable thiazolidine ring (*16*). In this study, CXYGGRGDS (RGDS) and cyclo[RGDfK(CX-)] (c(RGDfK)), having an N-terminal cysteine residue (C: L-Cys), were reacted with acetal-PEG−PLys **4** under mild acidic conditions (pH 4.0) to prepare the peptide-conjugated PEG−PLys through thiazolidine formation. Note that Schiff base formation due to the reaction of the aldehyde and primary amino groups of the PLys segment was prohibited under the acidic conditions because of the complete protonation of the primary amino groups. The methyl protons of the acetal group (δ = 1.2 ppm) completely disappeared with the appearance of protons assigned to the aromatic rings of L-tyrosine (Y: L-Tyr:) (δ = 6.9 and 7.1 ppm) in the RGDS and D-phenylalanine (f: D-Phe) (δ = 7.3 and 7.4 ppm) in the c(RGDfK) (Figure 2). Based on the peak intensity ratios of the aromatic ring protons of peptide ligands and the methylene

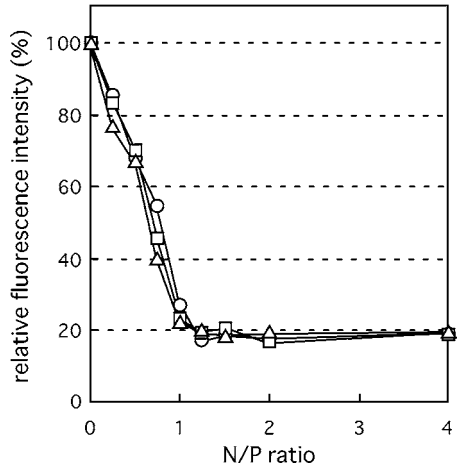


Figure 3. Ethidium bromide exclusion assays of PEG−PLys (open circle), RGDS−PEG−PLys (open square), and c(RGDfK)−PEG−PLys (open triangle). Fluorescence measurements were carried out as described in the Experimental Procedures.

Table 1. Size and ζ-Potentials of Polyplex Micelles

sample	cumulant diameter (nm)/ polydispersity index (μ/ Γ^2)	ζ-potential (mV)
PEG−PLys	124 ± 0.27/0.158 ± 0.014	−0.19 ± 0.195
RGDS−PEG−PLys	124 ± 0.88/0.177 ± 0.012	1.12 ± 0.349
c(RGDfK)−PEG−PLys	125 ± 1.00/0.166 ± 0.006	0.68 ± 0.238

protons of PEG (OCH_2CH_2, δ = 3.6 ppm), the introduction rates of peptide ligands were determined to be 100% in the RGDS−PEG−PLys **6a** and 66% in the c(RGDfK)−PEG−PLys **6b**.

Formation of Polyplex Micelles. Ethidium bromide (EtBr) is known to form an intercalating complex with double helical polynucleotides and subsequently show a striking enhancement of its fluorescence intensity (*17*). This enhancement is quenched by the formation of a complex between DNA and cationic components, because cationic components prevent EtBr from intercalating into the double-strand DNA. Thus, EtBr exclusion assay is frequently utilized to estimate the degree of pDNA condensation in the complex with a catiomer (*18*, *19*). As shown in Figure 3, as the N/P ratio increased, the fluorescence intensity in all the polyplex micelles decreased correspondingly and leveled off at around N/P = 1.25. This result indicates that the degree of pDNA condensation was not influenced by the introduction of peptide ligands. Table 1 summarizes the cumulant diameters and ζ-potentials of the polyplex micelles at N/P = 2. The cumulant diameters of all the micelles were approximately 125 nm with a moderate polydispersity index between 0.15 and 0.18. There was no change in the particle size because of the introduction of peptide ligands. Also, the ζ-potentials of all the polyplex micelles were approximately 0 mV. As previously reported (*5*, *18*), the PEG palisade surrounding the complex shields the charge of the micelles to maintain a very small absolute value in the ζ-potential even in the region of N/P > 1. All of the results of the EtBr assay, DLS analysis, and ζ-potential measurement suggest that the characteristics of the three types of polyplex micelles (PEG−PLys, RGDS−PEG−PLys, and c(RGDfK)−PEG−PLys) were quite similar regardless of the introduction of the peptide ligands.

Detection of $\alpha_v\beta_3$ and $\alpha_v\beta_5$ Integrin Receptors. To evaluate the expression of integrin receptors on the cell surface, flow cytometric analysis of 293T and HeLa cells was carried out using FITC-labeled antibodies (Figure 4). Flow cytometric analysis revealed that the 293T cells expressed almost no $\alpha_v\beta_3$ integrin and a slight amount of $\alpha_v\beta_5$ integrin, while the HeLa cells expressed a considerably higher amount of $\alpha_v\beta_3$ and $\alpha_v\beta_5$ integrins than the 293T cells. These results implied that HeLa cells might show a higher uptake of the cyclic RGD peptide-conjugated polyplex micelles than 293T cells through integrin-mediated endocytosis.

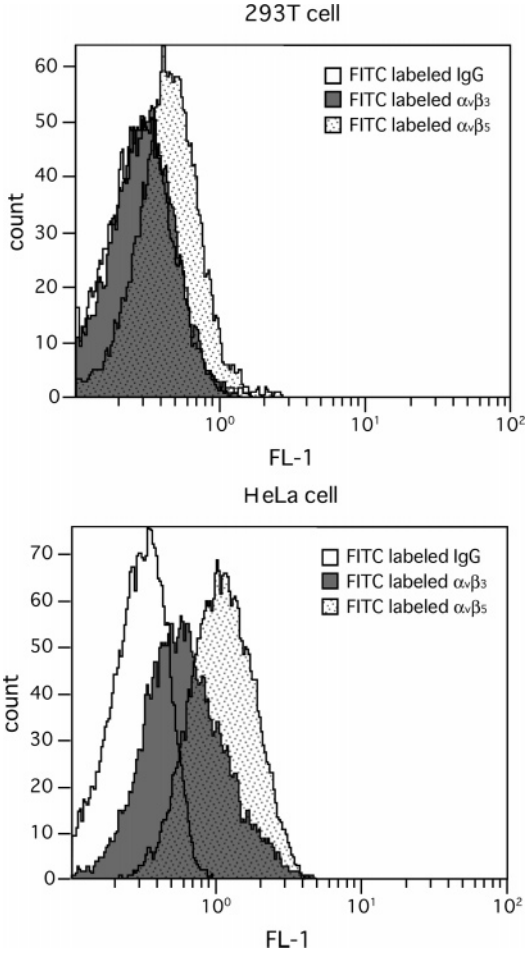


Figure 4. Flow cytometric analysis of integrin expression on 293T cells (left) and HeLa cells (right).

Transfection. *In vitro* TE of polyplex micelles was evaluated for 293T cells and HeLa cells at varying transfection times (Figure 5). PEG−PLys/pDNA micelles without the peptide ligand and RGDS−PEG−PLys/pDNA micelles with a linear RGD peptide ligand were used as controls. RGD peptide is the adhesion motif of extracellular matrix proteins for the various types of integrins (*20*, *21*). The linear RGD peptide showed a binding affinity for $\alpha_v\beta_3$ integrin approximately 1/1000 of that of the cyclic RGD peptide (*22*). In the transfection experiment using 293T cells, there were no differences in the TE of the three types of micelles at any of the transfection times. This finding is consistent with the observation that 293T cells showed low integrin expression (Figure 4). On the other hand, in the transfection experiment using HeLa cells, c(RGDfK)−PEG−PLys micelles achieved a significantly higher TE than PEG−PLys and RGDS−PEG−PLys micelles. It is reasonable to assume that HeLa cells might efficiently recognize c(RGDfK) ligands on the micelle through $\alpha_v\beta_3$ and $\alpha_v\beta_5$ integrins expressed on their surface. Nevertheless, the TE of linear RGD peptide-conjugated micelles toward HeLa cells was comparable to that of the micelles without any ligand, suggesting that the binding affinity of the linear RGD peptide for the integrins might be insufficient to increase the TE.

Analysis of Cellular Uptake of Polyplex Micelles. The cellular uptake of the micelles into the HeLa cells was evaluated by a flow cytometer using fluorescein-labeled pDNA-incorporated micelles with varying incubation times (Figure 6). The amount of the uptake was always higher for c(RGDfK)−PEG−

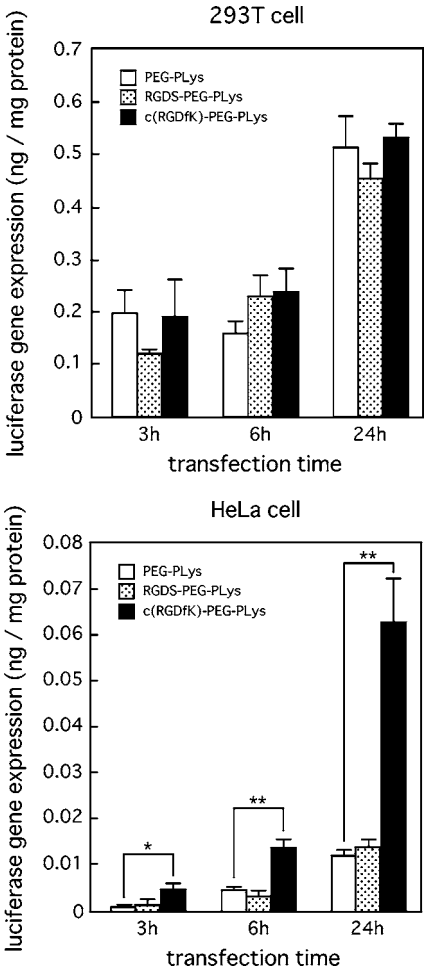


Figure 5. Effect of cell lines and transfection time on gene expression. 293T cells (left) and HeLa cells (right) were transfected with PEG−PLys, RGDS−PEG−PLys, and c(RGDfK)−PEG−PLys micelles prepared at N/P = 2 in a medium containing 10% serum. The data are the mean ± SEM, $n = 4$. $P^* < 0.05$ and $P^{**} < 0.01$.

PLys micelles than for PEG−PLys micelles at each incubation time, which suggests that the specific interaction of the cyclic RGD peptide with integrin receptors on the HeLa cells contributed to the uptake amount. In 24 h incubation, the amount of c(RGDfK)−PEG−PLys micelles that were taken up was 1.6 times the amount of PEG−PLys micelles taken up (Figure 6B). Nevertheless, c(RGDfK)−PEG−PLys micelles revealed an even higher TE of approximately 5 times that of the PEG−PLys micelles (Figure 5). This implied that other factors besides the enhanced uptake might also play a role in the enhanced TE observed for HeLa cells challenged with c(RGDfK)−PEG−PLys micelles.

Intracellular Distribution of Polyplex Micelles. The intracellular distribution of polyplex micelles was investigated by CLSM using Cy5-labeled pDNA-incorporated micelles with 3 h incubation, and typical images from this investigation are shown in Figure 7. A large fraction of the Cy5-labeled pDNA was still distributed near the cell membrane for the cells challenged with PEG−PLys polyplex micelles (Figure 7A). Alternatively, an appreciable accumulation of the Cy5-labeled pDNA in the perinuclear regions was observed for the cells challenged with c(RGDfK)−PEG−PLys polyplex micelles (Figure 7B). Further detailed observation using LysoTracker, which labels acidic late endosome and lysosome, revealed that the majority of c(RGDfK)−PEG−PLys polyplex micelles were localized in the acidic compartments as indicated by the yellow color in the merged fluorescence image of the Cy5-labeled pDNA (red) and LysoTracker (green), yet a fraction that did not co-localize with LysoTracker was also observed, suggesting that at least some of the polyplex micelles in the perinuclear regions may be located in a site other than the lysosomes.

DISCUSSION

There are many barriers to achieve effective transfection using nonviral gene vectors. Stability in the bloodstream and specific cellular uptake by the target tissues and organs are major obstacles, especially for *in vivo* gene delivery. Polyplex micelles with PEG as a hydrophilic shell layer have been shown to achieve an increased retention time in the bloodstream (*5*), and they are promising candidates for vectors that can be used for *in vivo* gene delivery. Also, the introduction of targetable ligands onto polyplex micelles has been reported, and some of the ligand-installed polyplex micelles have been demonstrated to be effective both in *in vivo* as well as *in vitro* transfection (*6*−*8*). The ligands on polyplex micelles may facilitate their internalization into the target cells, thus increasing the TE. A number of studies have aimed to find suitable ligands for this purpose (*23*), and cyclic RGD peptides have been highlighted as one of the promising candidates (*7*). Cyclic RGD peptides are well-known to selectively recognize $\alpha_v\beta_3$ and $\alpha_v\beta_5$ integrins, which are overexpressed in angiogenic endothelial cells in tumors. Therefore, a targetable gene delivery system equipped with a cyclic RGD peptide as the ligand may be useful for antiangiogenic therapy for tumors (*24*, *25*).

In this study, to construct polyplex micelles showing integrin-mediated gene transfection, the novel synthetic route of a block copolymer with a c(RGDfK) peptide ligand was exploited as summarized in Scheme 1. The acetal group may be converted to an aldehyde group under acidic conditions. Thus, the TFA group was selected to protect the primary amino group of the lysine units, because it can be removed under basic conditions without any conversion of acetal groups to aldehyde groups. The introduction of peptide ligands was then carried out under mild acidic conditions with good yields in a one-pot reaction involving the conversion of acetal groups to aldehyde groups and the subsequent conjugation of the ligand through the formation of a thiazolidine ring as seen in Scheme 1. In this way, various peptide ligands having a cysteine end group (Cys-peptide) may be readily introduced into the block copolymer. Moreover, this type of conjugation reaction between aldehyde and Cys-peptide occurs selectively even in the presence of primary amines, because the formation of a Schiff base between a primary amine and an aldehyde is reversible and thus sensitive to pH, while the thiazolidine ring formation between the N-terminal cysteine and aldehyde is an irreversible reaction. This reaction is available for the introduction of various ligands into the block copolymer, not only peptides but also other ligand molecules possessing an N-terminal cysteine.

Indeed, as confirmed by the NMR spectra shown in Figure 2, the c(RGDfK) peptide, which can peculiarly recognize $\alpha_v\beta_3$ and $\alpha_v\beta_5$ integrins, was successfully introduced into the PEG terminus of the PEG−PLys block copolymer as a targetable ligand molecule. The c(RGDfK)−PEG−PLys/pDNA micelle achieved a higher TE compared to nontargetable PEG−PLys and RGDS−PEG−PLys micelles against HeLa cells, which express an appreciable amount of $\alpha_v\beta_3$ and $\alpha_v\beta_5$ integrins. In contrast, there was no difference in TE among these three types of polyplex micelles against 293T cells, which show a limited expression of $\alpha_v\beta_5$ integrin, but no expression of $\alpha_v\beta_3$ integrin. This result is consistent with a previous report which found that the $\alpha_v\beta_3$ integrin has an approximately 10-times higher binding affinity for the cyclic RGD peptide than the $\alpha_v\beta_5$ integrin (*26*), which suggests that the $\alpha_v\beta_3$ integrin may be involved in an increased TE against HeLa cells by means of the c(RGDfK)−PEG−PLys/pDNA micelle. Flow cytometric analysis (Figure

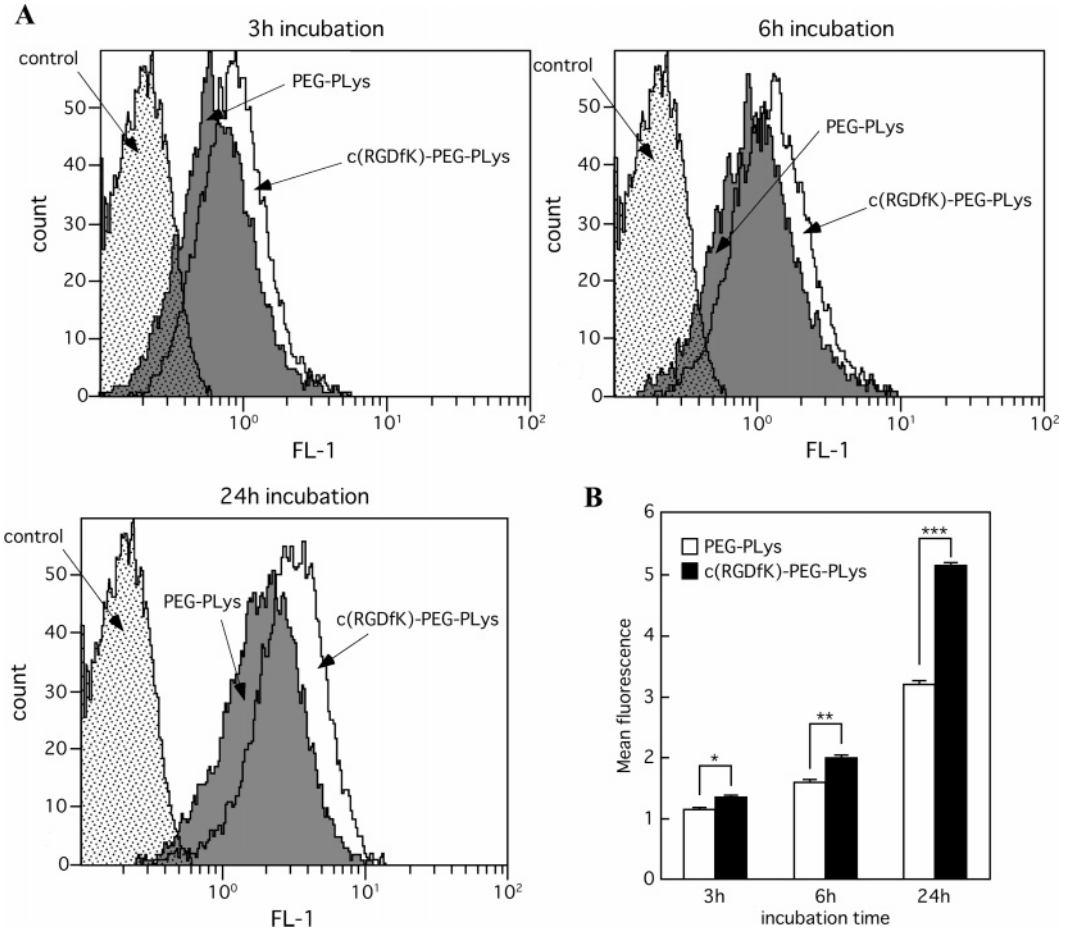


Figure 6. Cellular uptake of polyplex micelles. PEG−PLys and c(RGDfK)−PEG−PLys micelles loaded with fluorescein-labeled pDNA were applied to HeLa cells with varying incubation times. (A) Flow cytometric histogram profiles of time-dependent change in fluorescence intensity. (B) Mean fluorescence intensity at each incubation time. The data are the mean ± SEM, $n = 3$. $P^* < 0.05$, $P^{**} < 0.01$, and $P^{***} < 0.001$.

6) also suggests that the enhanced uptake of the c(RGDfK)−PEG−PLys/pDNA micelle might contribute to an increased TE against HeLa cells. Interestingly, the difference in the uptake ratio against the HeLa cells between the c(RGDfK) micelle and the ligand-free micelle became more significant with increased incubation time as seen in Figure 6. Integrin receptors are known to recycle to the plasma membrane through an endocytic cycle every 15−40 min (*27*). Consequently, this fast recycle of integrins might contribute to the facilitated uptake of the c(RGDfK) micelle into the HeLa cells in comparison with the ligand-free micelle. Nevertheless, as can be seen from Figures 5 and 6B, the uptake ratio is not simply correlated in a time-dependent manner with the TE. The ligand effect appeared to be more significant in the TE than in the uptake ratio, particularly after a prolonged time period such as 24 h. This result led us to assume that the c(RGDfK) ligand may also affect intracellular trafficking of the polyplex micelles. Indeed, a CLSM observation of HeLa cells challenged with polyplex micelles revealed a substantial difference in intracellular distribution between the PEG−PLys and c(RGDfK)−PEG−PLys micelles (Figure 7). In the cells challenged with the PEG−PLys polyplex micelle, a majority of pDNA was still distributed near the cell membrane, whereas in the same time frame of 3 h the cells with the c(RGDfK)−PEG−PLys polyplex micelle showed an appreciable accumulation of pDNA in the perinuclear region. It is noteworthy that a definite fraction of pDNA (colored red) in the perinuclear region did not co-localize with LysoTracker (colored green), suggesting that this fraction may be located in a compartment other than the acidic late endosome and lysosome. The $\alpha_v\beta_3$ integrin receptors have been reported to pass rapidly through the early endosomes, arriving at the perinuclear compartments approximately 30 min after internalization (*28*). Recent reports have shown an active transport pathway for a nonviral gene delivery system (*29*, *30*), in which microtubule-associated motor proteins have contributed to a rapid perinuclear accumulation of the polyplex within minutes after transfection. Also, recent studies have revealed that polyplexes in the perinuclear region but not in the acidic compartments significantly contribute to the effective transfection (*31*, *32*). These phenomena are consistent with our observation of a partial accumulation of the c(RGDfK)−PEG−PLys micelle in the perinuclear sites but outside of the acidic compartments, suggesting that the enhancement of the TE of the polyplex micelle by the introduction of cyclic RGD peptide ligands might be due not only to the enhanced uptake but also to the change in the intracellular trafficking route directed to the nucleus. It is likely that the micelle fraction distributed in nonacidic compartments near the nucleus may efficiently internalize into the nucleus when the cells are in the dividing phase, thus contributing to the increase in the transfection. Although the effective transport of the PLys-based polyplex micelles from the isolated compartment into the cytoplasm remains an issue because of inefficiency in the PLys function of facilitating the endosome-escaping step, the conjugation of c(RGDfK) ligands onto the polyplex micelle surface has great potential to improve the TE through modulated intracellular trafficking.

In conclusion, a successful synthetic route involving block copolymers conjugated with peptidyl ligands through thiazolidine ring formation was developed in this study. Cyclic RGD peptide-conjugated polyplex micelles showed an increased TE against HeLa cells possessing $\alpha_v\beta_3$ and $\alpha_v\beta_5$ integrins because

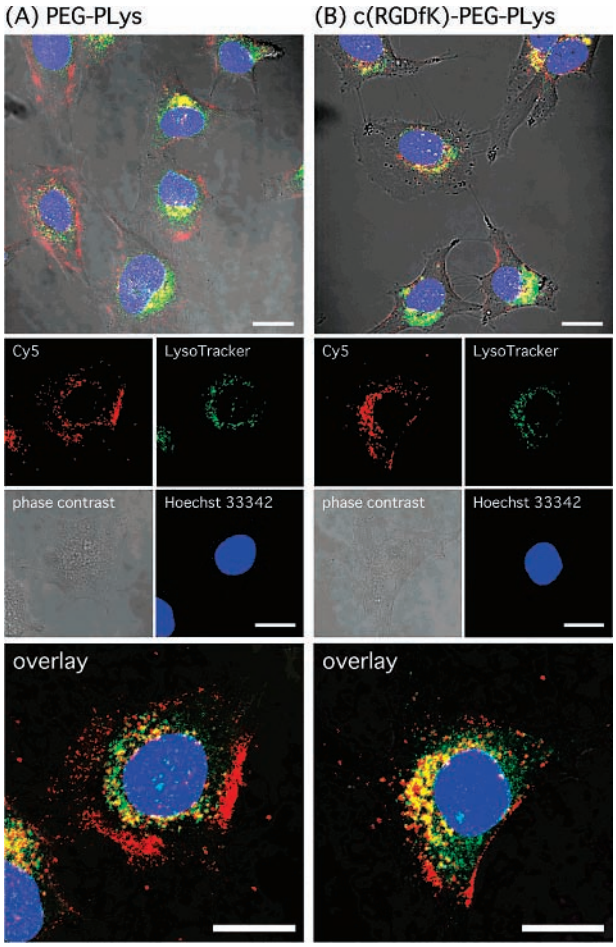


Figure 7. Intracellular distribution of pDNA challenged by the polyplex micelles. PEG−PLys and c(RGDfK)−PEG−PLys micelles loaded with Cy5-labeled pDNA (red) were incubated with HeLa cells for 3 h. The CLSM observation was performed using a 63× objective. The cell nuclei were stained with Hoechst 33342 (blue), and the acidic late endosome and lysosome were stained with LysoTracker Green (green). The scale bar represents 20 μm.

of enhanced uptake and a possible change in the route of intracellular trafficking. These results indicate that the introduction of various peptide ligands including c(RGDfK) peptide into the block copolymers is feasible and could eventually allow the construction of targetable polyplex micelles that are useful for site-specific gene therapy through a systemic route.

ACKNOWLEDGMENT

We thank Ms. K. Date (The University of Tokyo) and Ms. J. Kawakita (The University of Tokyo) for technical assistance. This work was financially supported in part by the Core Research Program for Evolutional Science and Technology (CREST) from Japan Science and Technology Corporation (JST) and the Project on the Materials Development for Innovative NanoDrug Delivery Systems from the Ministry of Education, Culture, Sports, Science and Technology (MEXT), Japan.

LITERATURE CITED

(1) Pedroso de Lima, M. C., Simoes, S., Pires, P., Faneca, H., and Düzgunes, N. (2001) Cationic lipid-DNA complexes in gene delivery: from biophysics to biological applications. *Adv. Drug Delivery Rev. 47*, 277−294.

(2) Merdan, T., Kopecek, J., and Kissel, T. (2002) Prospects for cationic polymers in gene and oligonucleotide therapy against cancer. *Adv. Drug Delivery Rev. 54*, 715−758.

(3) Kakizawa, Y., and Kataoka, K. (2002) Block copolymer micelles for delivery of gene and related compounds. *Adv. Drug Delivery Rev. 54*, 203−222.

(4) Itaka, K., Harada, A., Nakamura, K., Kawaguchi, H., and Kataoka, K. (2002) Evaluation by fluorescence resonance energy transfer of the stability of nonviral gene delivery vectors under physiological conditions. *Biomacromolecules 3*, 841−845.

(5) Harada-Shiba, M., Yamauchi, K., Harada, A., Takamisawa, I., Shimokado, K., and Kataoka, K. (2002) Polyion complex micelles as vectors in gene therapy-pharmacokinetics and in vivo gene transfer. *Gene Ther. 9*, 407−414.

(6) Wakebayashi, D., Nishiyama, N., Yamasaki, Y., Itaka, K., Kanayama, N., Harada, A., Nagasaki, Y., and Kataoka, K. (2004) Lactose-conjugated polyion complex micelles incorporating plasmid DNA as a targetable gene vector system: their preparation and gene transfecting efficiency against cultured HepG2 cells. *J. Controlled Release 95*, 653−664.

(7) Suh, W., Han, S.-O., Yu, L., and Kim, S. W. (2002) An angiogenic, endothelial-cell-targeted polymeric gene carrier. *Mol. Ther. 6*, 664−672.

(8) Ogris, M., Walker, G., Blessing, T., Kircheis, R., Wolschek, M., and Wagner, E. (2003) Tumor-targeted gene therapy: strategies for the preparation of ligand-polyethylene glycol-polyethylenimine/DNA complexes. *J. Controlled Release 91*, 173−181.

(9) Miyata, K., Kakizawa, Y., Nishiyama, N., Yamasaki, Y., Watanabe, T., Kohara, M., and Kataoka, K. (2005) Freeze-dried formulations for in vivo gene delivery of PEGylated polyplex micelles with disulfide crosslinked cores to the liver. *J. Controlled Release 109*, 15−23.

(10) Haubner, R., Gratias, R., Diefenbach, B., Goodman, S. L., Jonczyk, A., and Kessler, H. (1996) Structural and functional aspects of RGD-containing cyclic pentapeptides as highly potent and selective integrin $\alpha_v\beta_3$ antagonist. *J. Am. Chem. Soc. 118*, 7461−7472.

(11) Brooks, P. C., Clark, R. A. F., and Cheresh, D. A. (1994) Requirement of vascular integrin $\alpha_v\beta_3$ for angiogenesis. *Science 264*, 569−571.

(12) Akiyama, Y., Harada, A., Nagasaki, Y., and Kataoka, K. (2000) Synthesis of poly(ethylene glycol)-*block*-poly(ethylenimine) possessing an acetal group at the PEG end. *Macromolecules 33*, 5841−5845.

(13) Harada, A., and Kataoka, K. (1995) Formation of polyion complex micelles in an aqueous milieu from a pair of oppositely charged block copolymers with poly(ethylene glycol) segments. *Macromolecules 28*, 294−299.

(14) Nagasaki, Y., Kutsuna, T., Iijima, M., Kato, M., and Kataoka, K. (1995) Formyl-ended heterobifunctional poly(ethylene oxide): synthesis of poly(ethylene oxide) with a formyl group at one end and a hydroxyl group at the other end. *Bioconjugate Chem. 6*, 231−233.

(15) Poche, D. S., Moore, M. J., and Bowles, J. L. (1999) An unconventional method for purifying *N*-carboxyanhydride derivatives of γ-alkyl-L-glutamates. *Synth. Commun. 29*, 843−854.

(16) Zhang, L., Torgerson, T. R., Liu, X.-Y., Timmons, S., Colosia, A. D., Hawiger, J., and Tam, J. P. (1998) Preparation of functionally active cell-permeable peptides by single-step ligation of two peptide modules. *Proc. Natl. Acad. Sci. U.S.A. 95*, 9184−9189.

(17) LePecq, J.-B., and Paoletti, C. (1967) A fluorescent complex between ethidium bromide and nucleic acids. *J. Mol. Biol. 27*, 87−106.

(18) Itaka, K., Yamauchi, K., Harada, A., Nakamura, K., Kawaguchi, H., and Kataoka, K. (2003) Polyion complex micelles from plasmid DNA and poly(ethylene glycol)-poly(L-lysine) block copolymer as serum-tolerable polyplex system: physicochemical properties of micelles relevant to gene transfection efficiency. *Biomaterials 24*, 4495−4506.

(19) Wakebayashi, D., Nishiyama, N., Itaka, K., Miyata, K., Yamasaki, Y., Harada, A., Koyama, H., Nagasaki, Y., and Kataoka, K. (2004) Polyion complex micelles of pDNA with acetal-poly(ethylene glycol)-poly(2-(dimethylamino)ethyl methacrylate) block copolymer as the gene carrier system: physicochemical properties of micelles relevant to gene transfection efficiency. *Biomacromolecules 5*, 2128−2136.

(20) Pierschbacher, M. D., and Ruoslahti, E. (1984) Cell attachment activity of fibronectin can be duplicated by small synthetic fragments of the molecule. *Nature 309*, 30−33.

(21) Pierschbacher, M. D., and Ruoslahti, E. (1984) Variants of the cell recognition site of fibronectin that retain attachment-promoting activity. *Proc. Natl. Acad. Sci. U.S.A. 81*, 5985−5988.

(22) Dechantsreiter, M. A., Planker, E., Mathä, B., Lohof, E., Hölzemann, G., Jonczyk, A., Goodman, S. L., and Kessler, H. (1999) *N*-Methylated cyclic RGD peptides as highly active and selective $\alpha_v\beta_3$ integrin antagonists. *J. Med. Chem. 42*, 3033−3040.

(23) Allen, T. M. (2002) Ligand-targeted therapeutics in anticancer therapy. *Nat. Rev. 2*, 750−763.

(24) Kim, W. J., Yockman, J. W., Lee, M., Jeong, J. H., Kim, Y.-H., and Kim, S. W. (2005) Soluble *Flt-1* gene delivery using PEI-*g*-PEG-RGD conjugate for anti-angiogenesis. *J. Controlled Release 106*, 224−234.

(25) Kim, W. J., Yockman, J. W., Jeong, J. H., Christensen, L. V., Lee, M., Kim, Y.-H., and Kim, S. W. (2006) Anti-angiogenic inhibition of tumor growth by systemic delivery of PEI-*g*-PEG-RGD/pCMV-sFlt-1 complexes in tumor-bearing mice. *J. Controlled Release 114*, 381−388.

(26) Marinelli, L., Gottschalk, K.-E., Meyer, A., Novellino, E., and Kessler, H. (2004) Human integrin $\alpha_v\beta_5$: homology modeling and ligand binding. *J. Med. Chem. 47*, 4166−4177.

(27) Bretscher, M. S. (1996) Moving membrane up to the front of migrating cells. *Cell 85*, 465−467.

(28) Marnie, R., Simon, B., Alison, W., Peter, S., and Jim, N. (2001) PDGF-regulated rab4-dependent recycling of $\alpha_v\beta_3$ integrin from early endosomes is necessary for cell adhesion and spreading. *Curr. Biol. 11*, 1392−1402.

(29) Suh, J., Wirtz, D., and Hanes, J. (2003) Efficient active transport of gene nanocarriers to the cell nucleus. *Proc. Natl. Acad. Sci. U.S.A. 100*, 3878−3882.

(30) Kulkarni, R. P., Wu, D. D., Davis, M. E., and Fraser, S. E. (2005) Quantitating intracellular transport of polyplexes by spatio-temporal image correlation spectroscopy. *Proc. Natl. Acad. Sci. U.S.A. 102*, 7523−7528.

(31) Rejmna, J., Bragonzi, A., and Conese, M. (2005) Role of clathrin- and caveolae-mediated endocytosis in gene transfer mediated by lipo- and polyplexes. *Mol. Ther. 12*, 468−474.

(32) Gersdorff, K., Sanders, N. N., Vandenbroucke, R., Smedt, S. C., Wagner, E., and Ogris, M. (2006) The internalization route resulting in successful gene expression depends on both cell line and polyethylenimine polyplex type. *Mol. Ther. 14*, 745−753.

BC0700133

Surface Engineering of Quantum Dots for *In Vivo* Vascular Imaging

Ashwath Jayagopal, Patricia K. Russ, and Frederick R. Haselton*

Department of Biomedical Engineering, Vanderbilt University. Received January 21, 2007; Revised Manuscript Received July 22, 2007

Quantum dot−antibody bioconjugates (QD-mAb) were synthesized incorporating PEG cross-linkers and Fc-shielding mAb fragments to increase *in vivo* circulation times and targeting efficiency. Microscopy of endothelial cell cultures incubated with QD-mAb directed against cell adhesion molecules (CAMs), when shielded to reduce Fc-mediated interactions, were more specific for their molecular targets. *In vitro* flow cytometry indicated that surface engineered QD-mAb labeled leukocyte subsets with minimal Fc-mediated binding. Nontargeted QD-mAb nanoparticles with Fc-blockade featured 64% (endothelial cells) and 53% (leukocytes) lower nonspecific binding than non-Fc-blocked nanoparticles. Spectrally distinct QD-mAb targeted to the cell adhesion molecules (CAMs) PECAM-1, ICAM-1, and VCAM-1 on the retinal endothelium in a rat model of diabetes were imaged *in vivo* using fluorescence angiography. Endogenously labeled circulating and adherent leukocyte subsets were imaged in rat models of diabetes and uveitis using QD-mAb targeted to RP-1 and CD45. Diabetic rats exhibited increased fluorescence in the retinal vasculature from QD bioconjugates to ICAM-1 and VCAM-1 but not PECAM-1. Both animal models exhibited leukocyte rolling and leukostasis in capillaries. Examination of retinal whole mounts prepared after *in vivo* imaging confirmed the fluorescence patterns seen *in vivo*. Comparison of the timecourse of retinal fluorescence from Fc-shielded and non-Fc-shielded bioconjugates indicated nonspecific uptake and increased clearance of the non-Fc-shielded QD-mAb. This combination of QD surface design elements offers a promising new *in vivo* approach to specifically label vascular cells and biomolecules of interest.

INTRODUCTION

Inflammation is a complex process involving numerous cell types and surface proteins. It is characterized by leukocyte rolling and tethering along endothelial cells followed by transmigration into tissue, where their immunodefensive functions, such as phagocytosis, are elicited (*1*, *2*). Undesirable provocation of the inflammatory response is thought to be a detrimental feature of numerous diseases such as diabetes, atherosclerosis, and asthma (*3*−*6*). Treatment of inflammatory disease is challenging due to uncertainties associated with the roles of many of the cellular and biomolecular mediators. However, one developing strategy hinders inflammation by blockade of cell surface receptors either on the endothelium or on circulating leukocytes (*7*−*9*).

Detailed information about molecular mediators of inflammation might be acquired through *in vivo* imaging methods, since they can provide real-time data concerning the spatial and temporal dynamics of cellular activities and molecular expression throughout the time course of the disease. However, disadvantages of current imaging techniques include limited optical accessibility to tissue, invasiveness (*10*, *11*), low or unstable signal intensity due to the use of organic fluorophores (*12*−*14*), or low spatial and temporal resolution achieved by the use of radiolabeled antibodies (*15*). No available technique provides a framework for the simultaneous imaging of multiple molecular participants on moving leukocytes and stationary endothelium and leukocytes in real time.

Imaging inflammation is a difficult task, as the cell types of interest have one or more of the Fcγ receptor family (CD16, CD32, and CD64) which bind to Fc fragments of Immunoglobulin G (IgG) antibodies with variable affinity (*16*). Binding of bioconjugates to these receptors can yield false positive results when attempting to detect vascular cell surface targets. In addition, it is well-known that nanoparticulate probes are subject to rapid uptake by the tissues of the reticuloendothelial system, such as liver and spleen (*17*). These immunodefensive mechanisms serve to either rapidly clear the probe from the circulation or nonspecifically bind the probe. However, the many advantages afforded by nanoparticles as bioconjugates, particularly quantum dots (QD), which feature size-tunable visible-IR emission spectra, the need for only one excitation source, and high quantum efficiency, warrant new methods to facilitate their continued application (*18*, *19*). Recent work has indicated that the surface functionalization of PEG chains on the quantum dot surface can substantially reduce nonspecificity and clearance problems (*20*, *21*). In addition, many studies have established QD amenability to bioconjugation and ease of encapsulation in water-soluble coatings (*22*), and its incorporation within targeted *in vivo* imaging applications (*20*, *23*, *24*).

In this study, we selected spectrally distinct quantum dot (QD) nanocrystals to enable high-resolution, multispecies imaging using a previously developed, noninvasive *in vivo* retinal vascular imaging system (*25*). In this application, which pursues the detection of vascular targets, mitigation of nonspecific uptake and clearance mechanisms are essential. To address this, monoclonal antibodies (mAb) targeting leukocytes, neutrophils (*26*), or the cell adhesion molecules PECAM-1, ICAM-1, and VCAM-1 were site-specifically conjugated to PEG-maleimide-activated QD surfaces via 2-MEA to preserve mAb orientation and binding affinity (*27*). QD-mAb were then adsorbed with Fc-blocking $F(ab)_2$ fragments to reduce nonspecific immunorecognition. When incubated with endothelial cells or leukocytes *in vitro*, the shielded probes were found to be more specific for their targets relative to controls. *In vivo* retinal imaging of streptozotocin (STZ)-treated diabetic rats using QD-mAb revealed upregulation of ICAM-1 and VCAM-1 but not PECAM-1. Imaging of a rat model of endotoxin-induced uveitis (EIU)

* Corresponding author. Frederick R. Haselton, VU Station B Box 351510, Nashville, Tennessee 37235, Phone: 615-322-6622, Fax 615-343-7919, email: rick.haselton@vanderbilt.edu.

10.1021/bc070020r CCC: $37.00 © 2007 American Chemical Society
Published on Web 08/31/2007

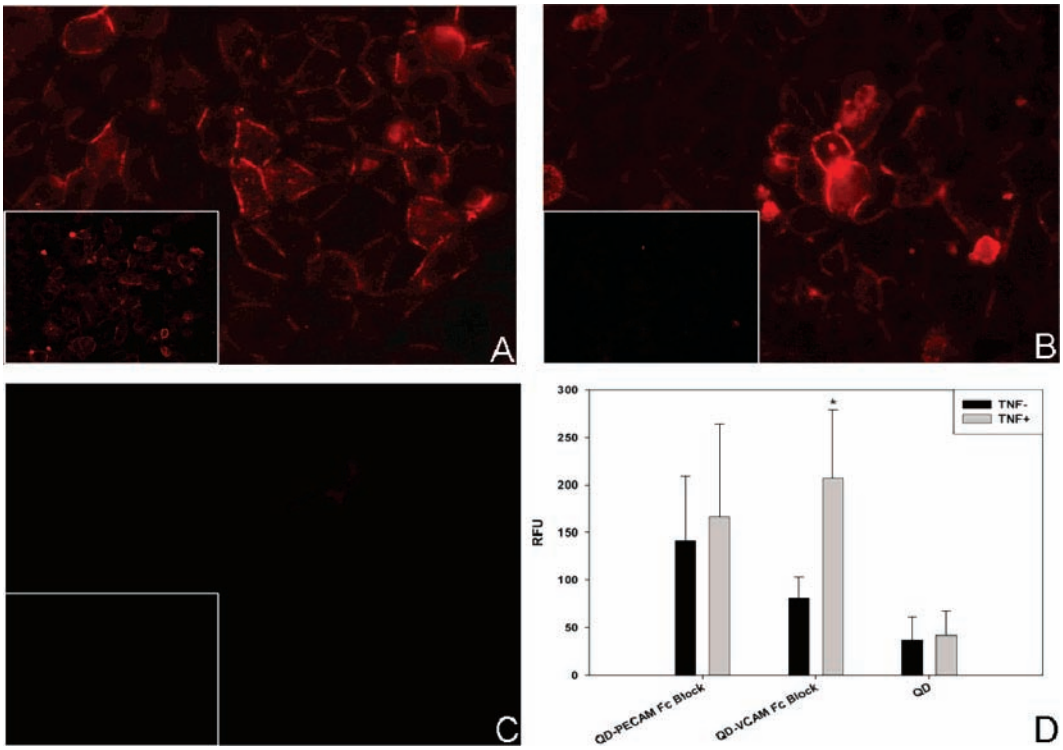


Figure 1. Evaluation of Fc-blocked QD-mAb conjugate specificity toward TNF-α stimulated (TNF+) or untreated (TNF−, image insets) rat endothelial cells (YPEN-1). (A−C) Fluorescence micrographs of QD655-anti-PECAM (A), QD655-anti-VCAM (B), and QD655 (C). Insets show incubation of TNF− YPEN-1 with matched bioconjugates. (D) Mean image intensities from immunofluorescence analysis of TNF ± YPEN-1 incubated with QD655-mAb bioconjugates (reported as mean + S.D., $n = 3$ images per sample). Intensities for each TNF+ and TNF− pair were compared by *t*-test for statistical significance ($P < 0.05$ indicated by asterisk).

Table 1. Quantum Dot-mAb Conjugates

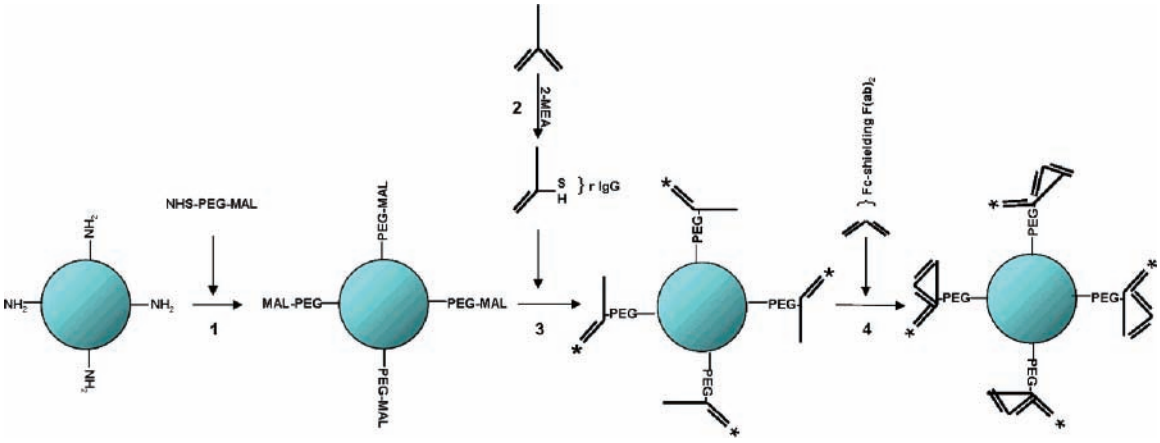
study target (function)	targeting monoclonal antibody	QD excitation	QD emission
PECAM-1, endothelial cell (transmigration)	Ms anti-rat CD31 IgG1 (BD)		525 nm, detection filter 525WB20
ICAM−1, endothelial cell (arrest)	Ms anti-rat CD54 IgG1 (BD)		605 nm, detection filter 605WB20
VCAM−1, endothelial cell (arrest)	Ms anti-rat CD106 IgG1 (BD)		655 nm, detection filter 655WB20
RP−1, neutrophil (unknown)	Ms anti-rat RP−1 IgG2a (BD)	excitation filter E460SPUV v2 peak emission 405 nm	585 nm, detection filter 585WB40 or 620WB90
CD45, leukocytes (multiple essential functions)	Ms anti-rat CD45 IgG1 (BD)		655 nm, detection filter 655WB20
nonspecific	Ms IgG1 or IgG2a isotype control (BD)		565 nm, detection filter 565WB20

showed the expected increase in stagnant leukocytes in the microcirculation. The high photostability of QD permitted post-experimental histological observations which confirmed the *in vivo* results. Real-time imaging of QD-IgG_1 conjugates indicated rapid clearance of conjugates lacking Fc-blocking $F(ab)_2$ fragments from the circulation. The distinct spectral emission characteristics of the QD enabled the simultaneous imaging of up to four biomarkers or cell types within the same animal with high specificity.

EXPERIMENTAL PROCEDURES

Synthesis and Characterization of Shielded Quantum Dot-Antibody Conjugates. QD nanocrystals with approximately 80 NH_2 groups/nanoparticle (ITK−NH_2, Invitrogen Corp.) were surface-functionalized with a heterobifunctional PEG-based cross-linker (NHS-PEG-MAL, Nektar Therapeutics) to couple reduced antibodies to the surface, followed by Fc-shielding $F(ab)_2$ surface adsorption as shown in Scheme 1. (**1**) 1 uM of QD-ITK-NH_2 (1.2×10^{14} nanoparticles in 200 uL solution) were maleimide-activated by incubation with a 20-fold molar excess of NHS-PEG-MAL (MW: 5218) for 2 h in PBS with 10 mM EDTA, pH = 7.4 (PBS-EDTA) at room temperature. Excess NHS-PEG-MAL was removed using two exchanges of PBS-EDTA on a 100K MWCO Amicon Ultra-4 column. The solution was analyzed qualitatively for the presence of large aggregates (>200 nm) using fluorescence microscopy, and was filtered through a 100 nm syringe filter if aggregates were observed. (**2**) mAb (Table 1) were buffer-exchanged in 500 μg amounts into PBS-EDTA, with two exchanges on a 100K MWCO spin column device (Amicon Ultra-4, Millipore) according to manufacturer-supplied instructions. The retentate was resuspended to 10 mg/mL concentration in PBS-EDTA. The antibodies were then reduced specifically in the hinge region to create two monovalent IgG (r IgG) bearing 1−2 free sulfhydryl groups using 2-mercaptoethylamine (2-MEA, Pierce) (*28*) according to manufacturer's instructions. Briefly, 6 mg of 2-MEA was dissolved in 100 μL of PBS-EDTA, and 1 μL of this solution was added to each 10 μL of mAb solution. The mixture was reacted for 120 min at 37 °C on a slowly rocking platform. Excess 2-MEA was removed from mAb using a NAP-5

Scheme 1 [a]



desalting column (GE Healthcare) pre-equilibrated with degassed PBS-EDTA buffer according to manufacturer's instructions. The presence of free sulfhydryl groups generated from 2-MEA reduction was confirmed using Ellman's reagent (Pierce)

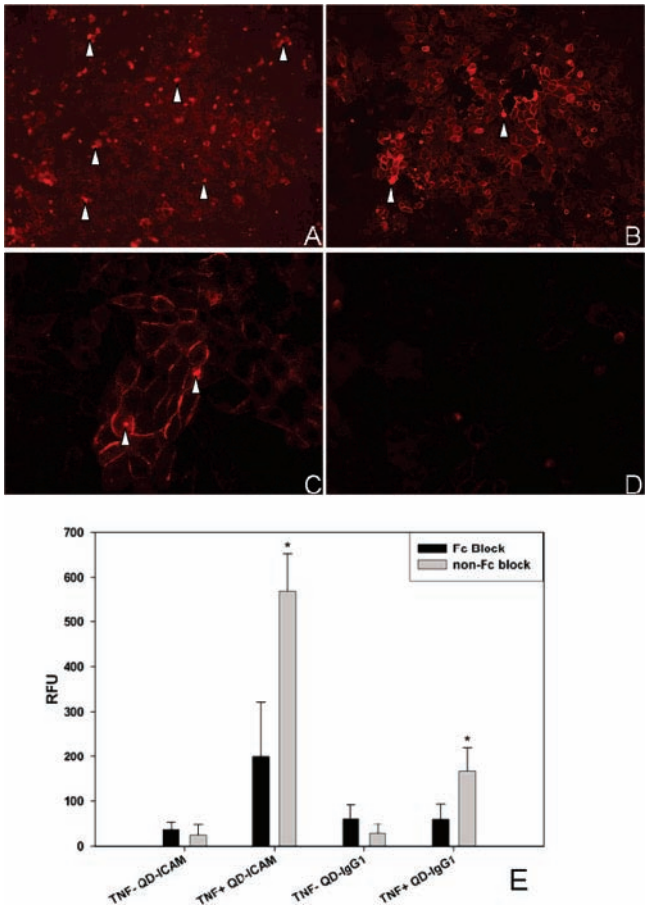


Figure 2. Comparison of Fc-blocked and non-Fc-blocked QD655-mAb conjugate specificity toward TNF-α-stimulated YPEN-1 (TNF+). (A−B) TNF+ YPEN-1 incubated with non-Fc-blocked (A) and Fc-blocked (B) QD655-anti-ICAM bioconjugates (magnification 100×). Arrowheads indicate possible Fc receptor capping, which was substantially reduced when using Fc-blocked conjugates. (C,D) TNF+ YPEN-1 incubated with non-Fc-blocked (C) and Fc-blocked (D) QD655-IgG_1 isotype control bioconjugates, with capping sites labeled with arrowheads (magnification 400×). (E) Mean image intensity analysis reveals lower nonspecific binding of bioconjugates featuring Fc blockade (reported as mean + S.D., $n = 3$ images per sample). Intensities for each matched Fc-blocked and non-Fc-blocked bioconjugate were compared by *t*-test for statistical significance ($P < 0.05$ indicated by asterisks).

on a Nanodrop ND-1000 spectrophotometer according to manufacturer's instructions. (**3**) The QD retentate from **1** was then added to the 2-MEA reduced and purified r IgG mixtures and incubated overnight at 4 °C. The following day, the reaction was terminated with 1 mg/mL L-cysteine (Sigma) to quench remaining maleimide groups. The QD-r IgG conjugates were purified by gel filtration chromatography according to manufacturer's instructions (Superdex 200, GE Healthcare). Fractions were eluted with PBS into 96-well microplates and evaluated by a UV−vis and fluorescence spectrophotometry (Nanodrop ND-1000 and ND-3300) or a fluorescence microplate spectrophotometer (Biotek Synergy HT) in order to identify appropriate QD-mAb fractions and to evaluate conjugation efficiency. In six separate conjugations of r IgG_{2a} to QD655, the average conjugation efficiency measured by UV−vis absorbance spectrophotometry on pooled QD-bound and unbound r IgG fractions was 59.33 ± 11.34%. This corresponds to 18 r IgG/QD. (**4**) The bioconjugate fraction was incubated with goat anti-mouse IgG (Fc-specific) blocking $F(ab)_2$ (Sigma) at molar concentrations equal to primary antibody concentrations for 1 h at room temperature, and the resulting mixture was filtered through a 0.22 μm syringe filter and stored at 4 °C until use. On the day of animal imaging, bioconjugates were briefly spun in an Eppendorf 5415R microcentrifuge for 10 min at 10 000 *g* to remove QD-mAb aggregates, reserving the supernatant for use. The supernatant was examined by fluorescence microscopy to ensure the absence of QD aggregates (>200 nm).

Flow Cytometry. Whole blood was collected in 2 × 3 mL aliquots from male Long-Evans rats into BD Vacutainer tubes spray-lined with K_3EDTA. Erythrocytes were lysed by incubation with BD PharMLyse at a 20:1 ratio of lysis buffer to whole blood for 15 min in the dark at room temperature to obtain a diffuse red suspension of white blood cells. The solution was then centrifuged at 400 *g* in an Allegra X-22R unit with swinging bucket rotor (Beckman) at room temperature. The leukocyte pellet was rinsed in 500 μL PBS (pH = 7.2) containing 0.5% BSA, and 0.1% sodium azide (staining buffer) to reduce shedding of membrane antigens. Each pellet was rinsed twice with staining buffer. The cells were resuspended to a 1×10^6 leukocytes/mL concentration, and were incubated for 45 min with one of the following in staining buffer: 50 nM each of QD585-anti-RP-1 conjugate, QD585-anti-CD45 conjugate, Fc-blocked QD585-isotype control IgG_1, maleimide-activated and L-cysteine quenched QD585, Fc-blocked QD585-isotype control IgG_{2a}, non-Fc-blocked QD585-IgG_{2a} isotype control, or 1 ug phycoerythrin (PE)-anti-RP-1 conjugate (BD Pharmingen). A separate unlabeled fraction was also retained for analysis. All samples were immediately analyzed (n =

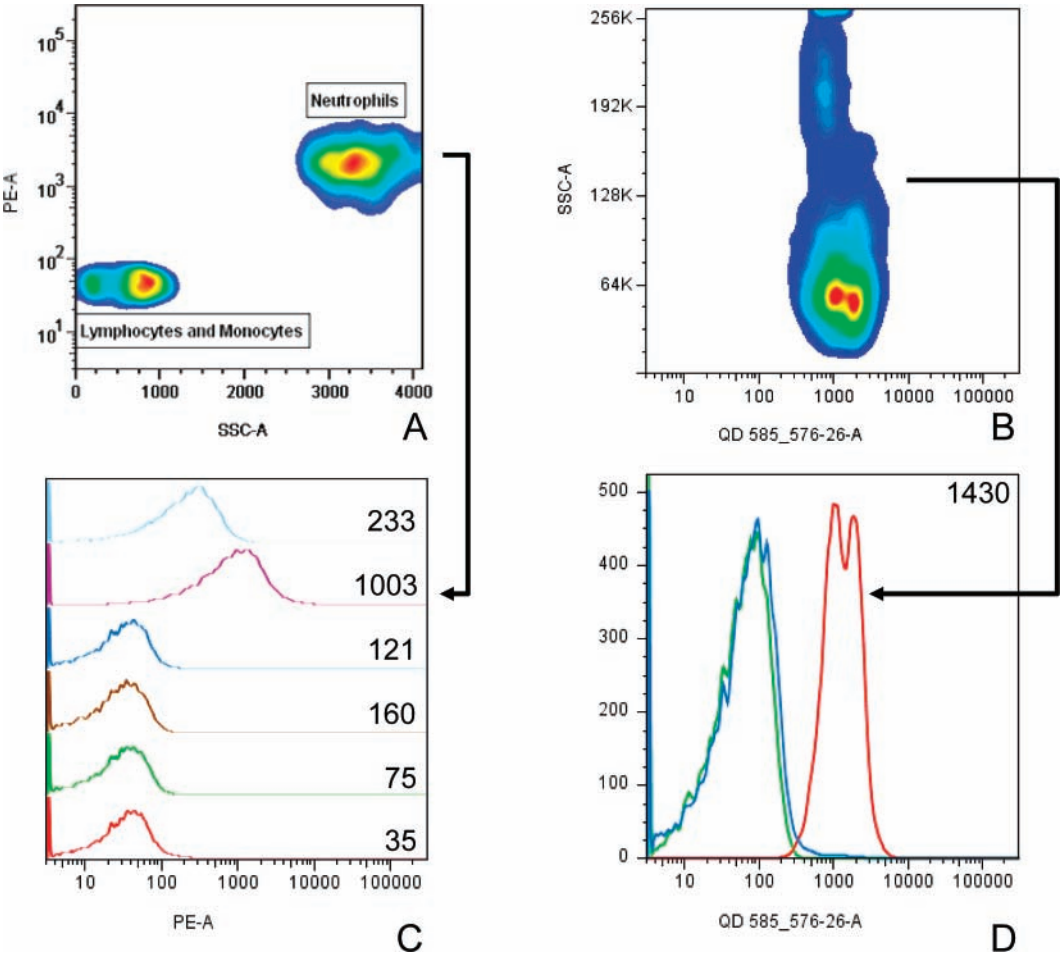


Figure 3. FACS analysis of leukocytes labeled with QD-mAb bioconjugates *in vitro*. (A) QD585-anti-RP-1 (Fc-blocked) specific labeling of neutrophils in peripheral blood. (B) QD585-anti-CD45 (Fc-blocked) labeling of all leukocyte subsets, with arrow from B to D indicating fluorescence histogram of gated leukocytes (D). (C) Gated neutrophil populations from rat peripheral blood (arrow from A to C shows a gated neutrophil population used for analysis of 1 sample), (488 nm Ar laser excitation, phycoerythrin (PE) emission filter (585/42 nm)), with mean fluorescence intensity of each sample indicated in bold. Light blue: PE-anti-RP-1 dye-labeled positive control mAb. Purple: QD585-anti-RP-1 (Fc-blocked). Blue: QD585 quenched with L-cysteine. Brown: QD-Ms-IgG2a isotype non-Fc blocked. Green: QD-Ms-IgG2a isotype Fc blocked. Red: Unlabeled rat peripheral blood. (D) Rat leukocytes labeled with QD585-anti-CD45 (red, gated leukocytes from (B)), QD585-Ms IgG1 Fc blocked isotype control (blue) or unlabeled (green).

20,000 gated events) using a BD LSR II multicolor flow cytometer equipped with a 488 nm Ar laser. Rat leukocyte subtypes could be readily resolved by forward and side scatter profiles as previously described (*29*). Band-pass emission filters were set at 585/42 nm to analyze QD or PE-labeled cells. Analysis was conducted using *Flowjo 7.0* (Treestar Software).

Cell Culture and Immunofluorescence Microscopy. YPEN-1 (CRL-2222, ATCC) rat prostate endothelial cells were cultured to confluency on Lab-Tek II 8-well chambered coverslips with media containing minimum essential medium (Eagle) with 2 mM L-glutamine and Earle's BSS adjusted to contain 1.5 g/L sodium bicarbonate, 0.1 mM nonessential amino acids, and 1.0 mM sodium pyruvate, supplemented with 0.03 mg/mL heparin; fetal bovine serum, 5%. YPEN-1 were stimulated with 30 ng/mL TNF-α in media overnight as previously described (*30*) to upregulate cell adhesion molecules, or incubated with media alone as a control. The next day, YPEN-1 were rinsed with one wash of media and incubated with 10 nM amounts of QD bioconjugates for 1 h at 37 °C as follows: QD655-anti-PECAM, QD655-anti-ICAM, QD655-anti-VCAM, QD655 (reactive maleimide group quenched with 1 mg/mL L-cysteine), and QD-isotype control IgG_1 in Fc-blocked forms as described above or as synthesized without the Fc-blocking step. Cells were then rinsed six times in Dulbecco's PBS containing Ca and Mg, pH = 7.4, and incubated with 4% paraformaldehyde in PBS for 15 min at 25 °C, followed by rinsing three times, 5 min each, with PBS with 50 mM glycine. Fixed cells were imaged using a Nikon TE2000U inverted fluorescence microscope with filter settings as shown in Table 1. These experiments were performed in triplicate. Images were acquired using a Hammamatsu C7780 12-bit color CCD in conjunction with *Image Pro Plus 5.1* (Media Cybernetics).

Preparation of Animal Subjects. All experimental procedures were approved by the Vanderbilt University Institutional Animal Care and Use Committee. Diabetes was induced in Long-Evans rats by intraperitoneal injection of 65 mg/kg streptozotocin (STZ, Sigma) in 0.1 mM sodium citrate, pH = 4.5, with the same number of rats remaining untreated as experimental controls ($n = 6$ per group). Elevated blood sugar (>250 mg/dL) was confirmed in STZ treated animals. Endotoxin-induced uveitis (EIU) was initiated in Long-Evans rats by intraperitoneal injection of 200 μg lipopolysaccharide. Controls were age-matched untreated rats ($n = 6$ per group). Animals were anesthetized with intraperitoneally administered 15/85% ketazine/xylazine prior to imaging. Tail vein catheterization was performed for injection of QD-mAb. Both eyes were dilated with 1 drop each of 2.5% phenylephrine hydrochloride and 1% tropicamide ophthalmic solutions (Alcon). The right eye was placed on the plano-concave lens previously filled with 2% methyl cellulose (Aqua Poly-Mount, Polysciences).

***In Vivo* Retinal Imaging.** Our imaging design is based on a previously published technique (*25*), in which an inverted

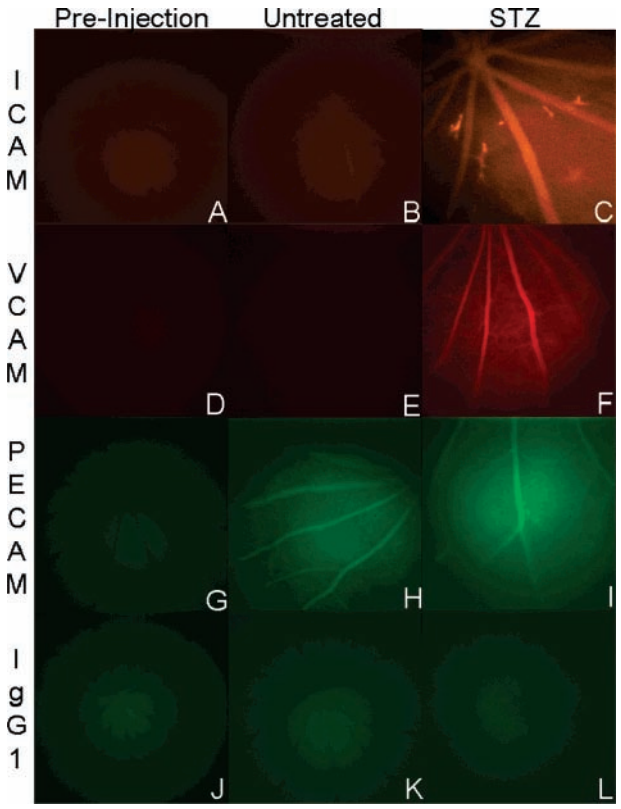


Figure 4. Frames from *in vivo* digital videos of STZ treated and untreated rat retinas. Pre-injection digital videos using the appropriate fluorescence filters for the spectrally distinct biomarkers of interest (left column; A, D, G, J) were acquired prior to bioconjugate injection. QD585-anti-ICAM, QD655-anti-VCAM, QD525-anti-PECAM, and QD565-Ms IgG_1 were systemically injected in STZ-treated rats. Untreated control rat fundi (middle column; B, E, H, K) and STZ-treated rat fundi (right column; C, F, I, L) were imaged either 30 min (ICAM) or 90 min (VCAM, PECAM, IgG_1) postinjection under identical acquisition settings used for background autofluorescence measurements for each biomarker channel. Fluorescence enhancement due to target binding in untreated controls (B, E, H, K) was primarily observed for PECAM (H). The retinal vasculature of STZ-treated rats (C, F, I, L) showed a marked increase in fluorescence due to binding of QD-mAb conjugates to ICAM (C) and VCAM (F), with at least 5-fold increases in fluorescence intensity over background measured for labeled vasculature. Injection of conjugates to PECAM (I) produced similar levels of fluorescence under both conditions (H, I). Fluorescence signal from nonspecific IgG_1 mAb bioconjugates (J−L) was not detected in either control or STZ retinas. Images shown were acquired at imaging intervals resulting in optimal signal-to-noise ratio.

fluorescence microscope (TE2000U Eclipse, Nikon) with 4× and 10× objectives and a plano-concave −6 D lens (Edmund Scientific) on the microscope stage were utilized to image the rat retinal circulation. In this study, this technique was modified to include a high sensitivity Andor Bioimaging iXon 885 EMCCD camera (Andor Bioimaging), Hamamatsu C7780 color camera, Exfo X-cite 120 metal halide lamp (Exfo Life Sciences), and a pulsed xenon arc flashlamp excitation source (FX 4400, Perkin-Elmer) triggered by a function generator configured for square wave output at 20 Hz (Tektronix). The metal halide lamp and flashlamp were utilized for the imaging of stationary endothelial targets and circulating leukocytes, respectively. Following measurements of pre-injection tissue autofluorescence levels in each QD-specific emission channel, QD-mAb were injected via the tail vein catheter. Injectate consisted of 200 μL of a 500 nM solution in PBS-EDTA. Initial digital sequences were acquired using exposures ranging from 20 to 200 ms (depending on the QD and the filter set, Table 1) at 110 ms intervals. Subsequent sequences were acquired at approximately 30 min intervals for 2.5 h. In four animals, a QD-IgG_1 isotype control was used as a negative control. Animals were sacrificed with 150 mg/kg sodium pentobarbital administered via tail vein catheter.

Immunofluorescence Microscopy of Retinal Tissue. Following euthanization of animals, both eyes were enucleated. Retinal flat mounts were prepared of the right eye, which was the eye imaged by our *in vivo* retinal imaging system. Eyes were fixed in 4% paraformaldehyde in PBS overnight and flat-mounted on a microscope slide mounted with fluorescence mounting media. The left eye was fixed in 4% paraformaldehyde and paraffin embedded for sectioning. Sections and flat mounts were analyzed by fluorescence microscopy (Nikon TE 2000U) using the same filters as those used in *in vivo* imaging (Table 1).

Image Analysis. For analysis of QD-mAb binding to YPEN-1, fluorescence micrographs acquired under identical settings and conditions (matched cell densities in field of view) were measured in the Red CCD channel (the chip with which QD655 emission is captured) for fluorescence intensity using *Image Pro Plus 5.1*. From these data, the mean Red channel fluorescence intensity was obtained and standard deviation determined. Background correction was performed on image intensities by subtracting the mean Red CCD channel intensity obtained from the same density of unlabeled YPEN-1. Intensities were analyzed for statistical significance using an unpaired two-tailed *t*-test (*SigmaStat 3.0*, SYSTAT). Background-corrected data was then plotted using *SigmaPlot 9.0* (SYSTAT). Statistical significance was interpreted by $P < 0.05$.

For *in vivo* image quantification of leukostasis, the area of image analysis of rat fundi was a circle of two optic disk diameters from the center, allowing for counts of stagnant leukocytes and observations of leukocyte trafficking and cell adhesion molecule expression within major arteries and veins as well as the microcirculation. A leukocyte was assumed to be stagnant if no displacement larger than one cell diameter was observed within 60 s of continuous imaging. The number of stagnant QD-labeled cells was quantified for STZ, EIU, and wild-type retinas postacquisition from digital video using *Andor iQ 1.6*, and compared using an unpaired two-tailed *t*-test in *SigmaStat 3.0*.

Quantitative analysis of Fc-blocked and non-Fc-blocked QD-IgG_1 bioconjugates was performed by analyzing 60 consecutive digital frames of wild-type rat retina before and after systemic injection of 500 nM (200 uL) of each probe. An observation area of 2 optic disc diameters from center was utilized for the analysis. Using *Andor iQ 1.6* image analysis software, the mean fluorescence intensity of 60 consecutive frames was plotted as a function of time. Data were plotted using *SigmaPlot 9.0*.

RESULTS

***In Vitro* Studies.** In cell culture studies, the QD655-mAb Fc-shielded conjugates specifically labeled CAMs on TNF-α-stimulated YPEN-1 rat endothelium (TNF+) (Figure 1A−D; Figure 2B,E). In order to simulate the *in vivo* environment, no traditional immunofluorescence blocking steps (e.g., serum, Fc receptor blocking mAbs) were utilized. Under TNF+ conditions, a statistically significant increase in Fc-blocked QD655-anti-VCAM binding to YPEN-1 (Figure 1B,D) was observed, whereas TNF+ conditions did not significantly affect QD655-anti-PECAM binding (Figure 1A). These observations were consistent with previous reports (*31, 32*). QD655-anti-ICAM bioconjugates bound TNF+ YPEN-1 by over 10-fold as compared to untreated cells (Figure 2E). A strong reduction in nonspecific binding was observed when comparing binding of Fc-blocked and non-Fc-blocked QD655-anti-ICAM bioconjugates (Figure 2A,B,E). A reduction in nonspecific binding was also observed when comparing measured intensities of YPEN-1 labeled with Fc-blocked or non-Fc-blocked QD655-isotype control IgG_1 nanoparticles (Figure 2C−E), suggesting that the

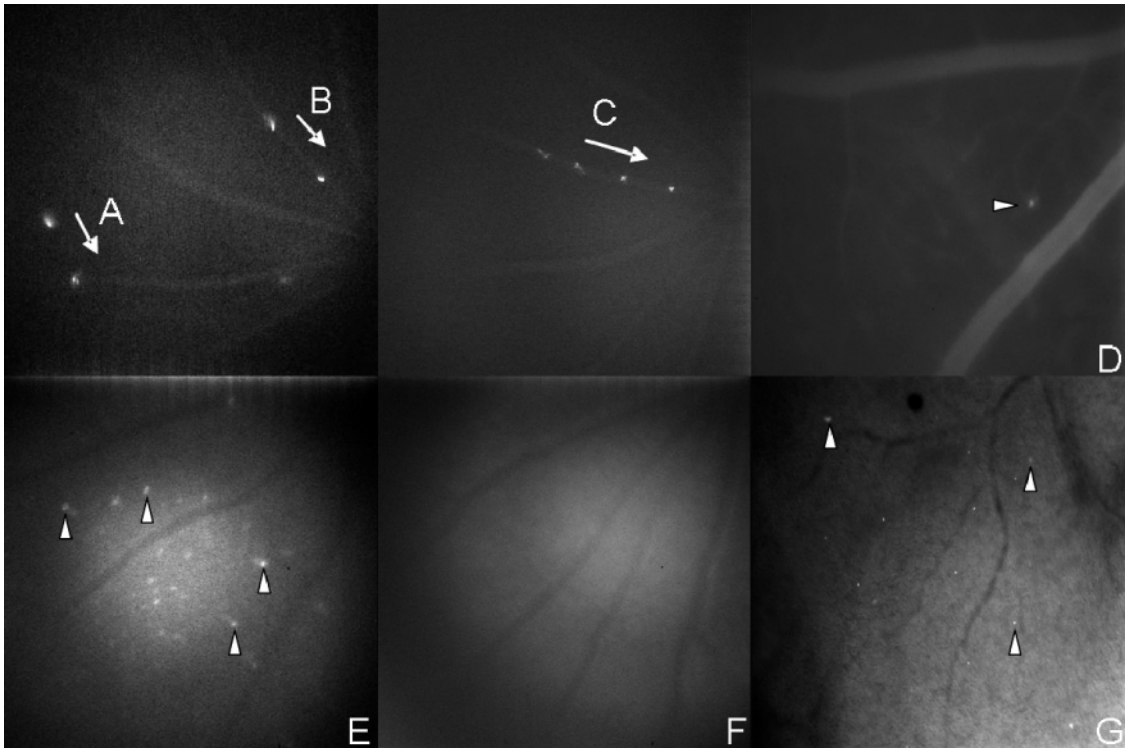


Figure 5. *In vivo* imaging of endogenously QD-mAb-labeled leukocyte trafficking in two rat models of inflammation. The CCD acquired images with exposure times ranging from 50 to 200 ms with 110 ms between exposures. Flowing of QD585-RP-1 labeled cells in vessels (A,B) or leukocyte rolling (C) in STZ model as detected by four pulses of a xenon flashlamp at 50 ms intervals within 30 min of probe injection. Leukostasis was frequently observed in the STZ-treated rat model (D in right panel). Stagnant neutrophil appears as a hyperfluorescent dot in the microcirculation. Stagnant neutrophils were continuously visible in the retinal vasculature for over 1 h of *in vivo* imaging. Stagnant leukocytes labeled *in vivo* with QD655-anti-CD45 were present at high densities in EIU rat models (E) relative to untreated controls (F). Stagnant neutrophils labeled in STZ-streated diabetic animals were visible in postmortem retinal flat mounts (G).

Fc fragment is responsible for a substantial percentage of QD-mAb nonspecific binding. Immunofluorescence analysis of YPEN-1 indicated that non-Fc-blocked QD655-mAb constructs were aggregated in focal locations along cell membranes, shown by arrowheads (Figure 2A−C). This observation may be due to two features: the upregulation of Fcγ receptors on endothelial cells following TNF-α stimulation, and the patching and capping effect observed previously for Fc receptor−ligand combinations (*33*). Specifically, patching and capping refers to the accumulation of surface-bound IgG-Fc receptor pairs at distinct, punctate locations at the membrane to form clumps of Fc receptor-IgG pairs. This incidence of cap formation was less evident in TNF+ YPEN-1 cells incubated with Fc-blocked bioconjugates (Figure 2B). Maleimide-quenched QD which were not conjugated to Mab (Figure 1C) did not bind appreciably to cell surfaces. These data collectively suggest that nonspecific binding of unshielded probe was likely due to the binding of mAb Fc fragment to endothelial Fc receptors.

Fc-blocked QD585-anti-RP-1 (neutrophils) and QD585-anti-CD45 (leukocyte common antigen) were shown to retain bioactivity and specificity *in vitro* (Figure 3). QD585-anti-RP-1 conjugates were shown to specifically bind to neutrophils and not other leukocyte subsets (Figure 3A), and QD585-anti-CD45 were shown to label the three main subclasses of leukocytes as shown by flow cytometric analysis of erythrocyte-lysed whole blood (Figure 3B,D). QD-anti-RP-1 was observed to have over 4-fold enhancement in fluorescence over PE-RP-1 (1003 vs 233), a positive control antibody coupled to phycoerythrin (Figure 3C). QD585-IgG2a (matching the isotype of QD585-anti-RP-1), when Fc-blocked with an anti-Fc $F(ab)_2$ fragment, featured 53% lower mean fluorescence levels than that due to the non-Fc-blocked conjugate (Figure 3C), indicative of reduced nonspecific binding of Fc-blocked bioconjugates. Fc-blocked QD585-anti-CD45 conjugates used to label leukocytes yielded a mean fluorescence of 1430, over 17-fold greater than cells labeled with Fc-blocked QD-IgG_1 isotype control (82) and 22-fold greater than unlabeled cells (65) (Figure 3D).

***In Vivo* Imaging.** Intravenous injection of QD bioconjugates targeted to ICAM-1 or VCAM-1 resulted in a maximum increase in vascular fluorescence in streptozotocin (STZ)-treated diabetic rats within 30 and 90 min, respectively (Figure 4). This increase in fluorescence was observed in major vessels as well as the microcirculation. Control rat retinas did not exhibit the same fluorescence intensity with either the ICAM (Figure 4A−C) or VCAM (Figure 4D−F) conjugates. Injection of QD anti-PECAM produced increases in fluorescence which were similar in both STZ-treated and untreated animals (Figure 4G−I). Injection of QD-IgG1, a nonspecific control, did not result in fluorescence signal accumulation in the retinal vasculature to any appreciable degree throughout the duration of imaging up to 2.5 h (Figure 4J−L).

Intravenous injection of QD585-anti-RP-1 conjugates enabled the fluorescence detection and long-term tracking of neutrophils in STZ-treated diabetic animals as shown in Figure 5A−D. Using a pulsed xenon flashlamp, we visualized individual free-flowing leukocytes (Figure 5A,B), leukocyte rolling along endothelial walls (Figure 5C), and leukostasis (Figure 5D) in major vessels as well as capillaries. Individual neutrophils were resolved in all vessels including arteries, and an increase in QD-anti-RP-1 positive stagnant neutrophils in the microcirculation was observed in the STZ-treated group (5.83 ± 2.86, $n = 6$) vs untreated animals (0.50 ± 0.55, $n = 6$) ($P < 0.01$). Fluorescence micrographs of stagnant neutrophils in flat-mounted STZ-treated rat retinas confirmed *in vivo* observations (Figure 5G).

Injection of the QD655-anti-CD45 bioconjugate in LPS-treated EIU rat models revealed a significant number of stagnant leukocytes in the microcirculation relative to untreated animals (Figure 5E,F). The number of QD-anti-CD45 positive stagnant

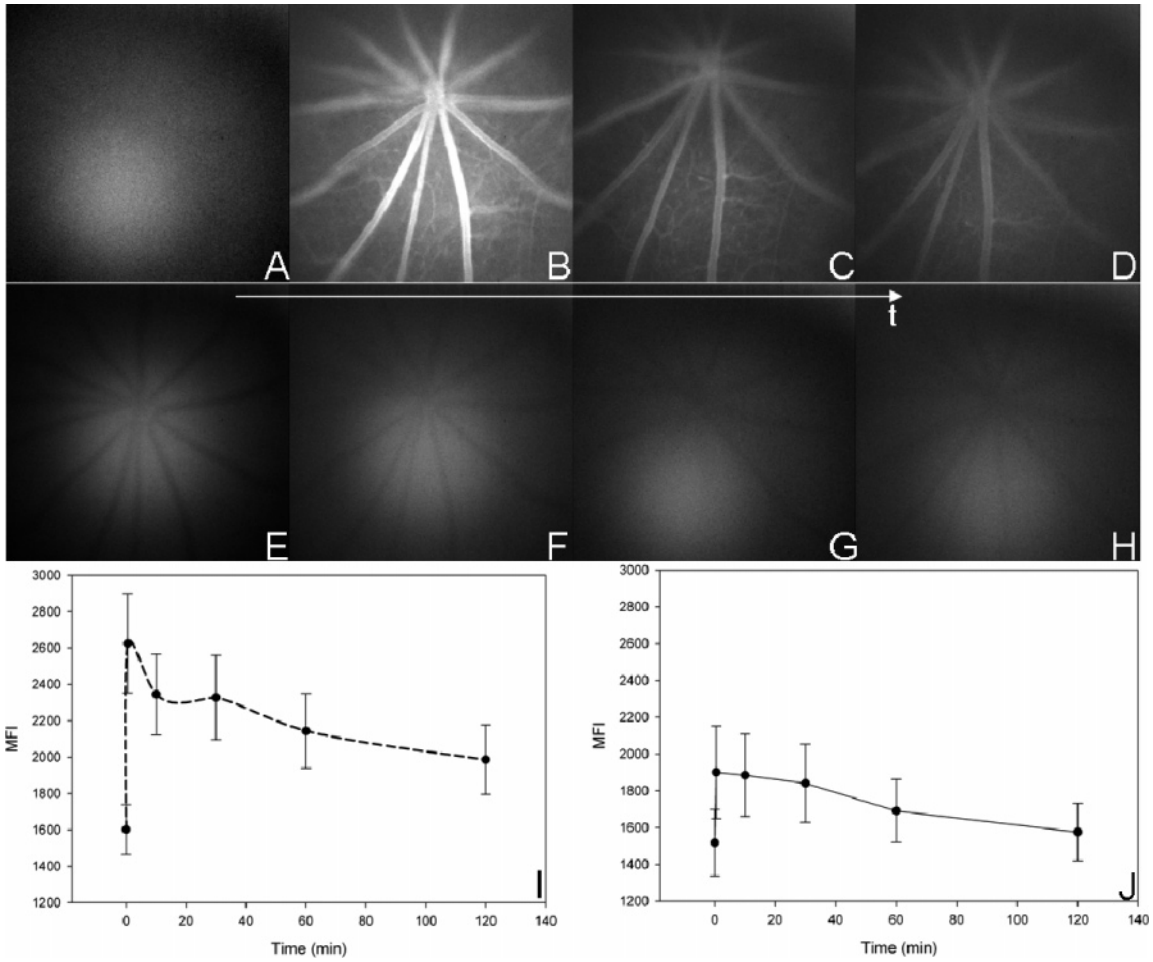


Figure 6. Comparison of Fc-blocked (A−D, I) and non-Fc-blocked (E−H, J) QD-IgG$_1$ mAb bioconjugates *in vivo*. (A) Pre-injection autofluorescence in QD655 emission channel. (B−D) Fc-blocked QD655-IgG$_1$ in retina observed 12 s postinjection (B) where the first pass of bolus through retinal circulation is observed, 1 h postinjection (C), and 2 h postinjection (D), by which time Fc-blocked QD655-induced fluorescence is still above background levels (I, dashed line). (E) Autofluorescence levels in QD565 channel. (F−H) non-Fc-blocked QD565-IgG$_1$ bolus was not qualitatively visible at 12 s postinjection (F), and subsequent image acquisitions at 1 h (G) and 2 h (H) revealed eventual return of image intensity to pre-injection levels (J, solid line), suggesting a relatively rapid clearance and/or uptake of non-Fc-blocked QD-mAb.

leukocytes in LPS-treated rat retinas (20.33 ± 8.73, $n = 6$) was elevated over control retinas (2.17 ± 1.17, $n = 6$) *in vivo* ($P < 0.01$).

Ten seconds after tail vein injection, comparison of the retinal fluorescence from Fc-shielded and non-Fc-shielded bioconjugates showed significantly less fluorescence from the non-shielded bioconjugate (Figure 6). Tracers injected intravenously into a tail vein travel through the hepatic circulation, heart, and lungs before the remainder reaches the eye. Our data indicate that non-Fc-blocked nonspecific QD-IgG$_1$ is cleared rapidly within 2 h of circulation, returning retinal fluorescence levels to pre-injection values (Figure 6E−H,J). For Fc-blocked non-specific QD-IgG$_1$, an apparent bolus is observed within 12 s of injection (Figure 6B), and fluorescence levels by 2 h have not returned to background values (Figure 6A−D,I). These results suggest that Fc blockade substantially enhances the circulation lifetime of the QD-mAb due to reduced uptake and clearance.

***Ex Vivo* Imaging of Retinal Tissue.** Immunofluorescence analysis of flat-mounted retinas showed correlation of *in vivo* features, such as enhanced CAM expression areas within the microcirculation, with *ex vivo* microscopy (Figure 7A,B). Analysis of postmortem retinal tissue also indicated low nonspecific binding of Fc-shielded bioconjugates (Figure 7C,D) within blood vessels. The microcirculation in a flat mount from an EIU rat featured leukocyte adhesions and extravasations similar to those observed *in vivo* (not shown), and similar to the result shown for the STZ-treated rat (Figure 5G).

DISCUSSION

Fc-blocked QD-mAb were found to be specific for CAM and leukocyte targets, as shown by immunofluorescence (Figures 1,2), flow cytometry (Figure 3), and *in vivo* and *ex vivo* retinal imaging (Figures 4−7). QD-IgG that were nonspecific in reactivity did not bind to retinal vasculature (Figure 6), which suggests that Fc-blocked QD-antibody bioconjugates feature reduced nonspecific binding tendencies while retaining the native binding affinity conferred by the mAb. Our technique, employing PEGylation, 2-MEA reduction, and Fc-blockade by Fc-specific F(ab)$_2$, is a rapid, cost-effective method for the site-specific bioconjugation and immune-shielding of mAb on nanoparticle surfaces. The 2-MEA reduction process was found to work equally well on mouse IgG$_1$ and IgG$_{2a}$ subclasses using the same protocol. As an alternative to removal of the Fc fragment from the antibody, we choose instead to adsorb it with an antibody fragment which itself has no Fc region. Nontargeted QD-IgG conjugates adsorbed with an Fc-blocking F(ab)$_2$ were less susceptible to nonspecific binding to leukocyte and endothelial cell surfaces compared to the same conjugates without Fc-blockade (Figures 1−3). This may be the result of steric inhibition conferred upon the bioconjugate by the F(ab)$_2$, which reduces Fc receptor access to its Fc fragment binding site on the IgG. Fc-blockade of CAM-targeted QD did not affect their binding affinities toward endothelial cell proteins *in vitro* or *in vivo* (Figures 1,2,4). Fc-blockade by itself also may potentially

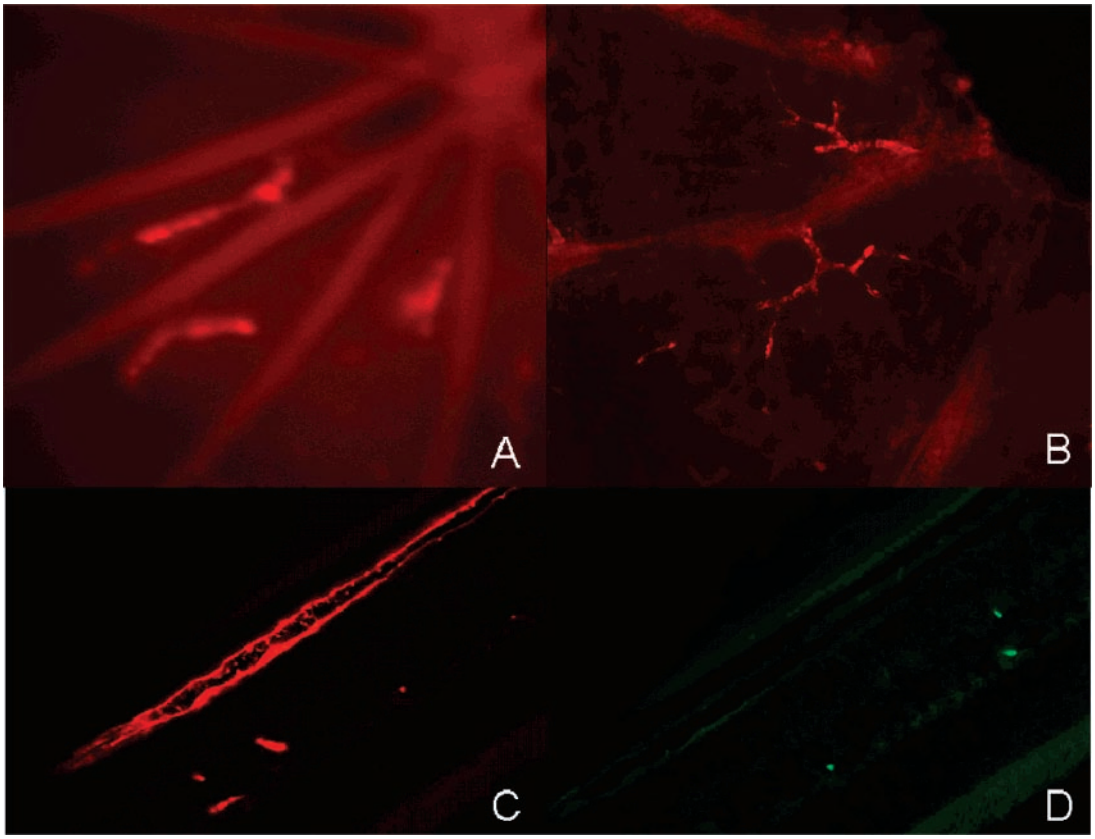


Figure 7. *In vivo* microcirculatory VCAM-1 expression (A) can be confirmed using immunofluorescence analysis postmortem (B), as shown for QD655-anti-VCAM-1 labeled vasculature. While QD655-VCAM-1 (Fc-blocked) conjugates were shown to specifically stain vasculature in retinal histological sections (C), no background staining due to QD-IgG_1 (Fc-blocked) was observed above background autofluorescence levels (D).

enhance the circulation half-life of QD-mAb when employed in conjunction with PEG. Fc-blocked, nontargeted QD-IgG were present in the retinal circulation in much higher fluorescence levels relative to the same dose of non-Fc-blocked constructs (Figure 6), suggesting that Fc-blockade of IgG may substantially reduce first-pass nonspecific clearance of probes due to liver and spleen immunorecognition. Therefore, our probe design features target selectivity with a reduced tendency for nonspecific binding.

Analogues of our strategy exist for reduction of nonspecific binding of bioconjugates for *in vitro* applications, and we have applied these *in vitro* techniques for the first time to *in vivo* imaging. For example, the commercial reagent FcBlock (anti-CD16, anti-CD32, BD Biosciences) has long been utilized to block Fc receptors on hematopoietic and endothelial cells prior to immunofluorescence (*34*) or flow cytometric (*35*) analysis for the reduction of background staining using cell surface protein antibodies. Direct blockade of the Fc *fragment* of antibodies rather than Fc receptors occurs often in biology. Blockade of the antibody Fc domain with streptococcal proteins has been found to reduce Fc-mediated nonspecific binding (*36*). Herpes Simplex Virus type 1 (HSV-1), when bound by an IgG, uses its Fcγ receptors to occupy the Fc fragment of the same IgG, thus preventing Fc-mediated immunodefensive mechanisms (*37*). By adsorption of the QD-IgG conjugate with an Fc-targeted $F(ab)_2$, it is likely that the adsorbed fragment makes the Fc binding site of the targeting antibody sufficiently inaccessible to immune surveillance, thus enhancing specificity and circulation time.

Other strategies to reduce Fc-mediated immune recognition of antibodies or antibody-based bioconjugates are reported in the literature. Specifically, antibody fragmentation techniques using papain, pepsin, or ficin require several reaction steps and much reagent quantity and time optimization for each antibody species and subclass, and generally do not yield a biomolecule with a site-specific cross-linking site suitable for nanoparticle conjugation. Instead, primary amines which reside in the antigen-binding site of the antibody could be cross-linked to the nanoparticle, obliterating its antigen binding affinity following bioconjugation. Protein engineering techniques now provide for a means of producing antibody fragments with engineered hinge region cysteines (Fab′) which allow for site-specific nanoparticle conjugation while preserving the antigen-binding region (*38*, *39*). However, this process is time-consuming and costly, and may not be suitable in applications where multiple IgGs are to be conjugated to nanoparticles for multiplexed imaging on a small scale, or where IgG targets are quickly examined and replaced for purposes of drug discovery or biology. Our process provides for the site-specific conjugation of antibodies to nanoparticles, without IgG subclass-specific optimization, with similar benefits of immune system evasion afforded by antibody fragmentation techniques.

Our *in vivo* imaging results are consistent with studies of ICAM and VCAM expression in diabetic and nondiabetic tissue, in which their upregulation is implicated in an inflammatory cascade that causes various complications of the disease (*6*, *40*, *41*). QD fluorescence due to ICAM and VCAM expression is apparent on major vessels as well as the microcirculation in disease models, which appears as an out of focus fluorescent background behind the major vessels (Figure 4A−F). QD targeted against PECAM, a panendothelial marker, produced increases in fluorescence which were similar in both STZ-treated and untreated animals (Figure 4G−I), thus suggesting its utility as an internal control or vascular counterstain in this imaging application. Our technique was found to be suitable for the long-term imaging of stagnant leukocytes commonly observed in both the STZ-treated rat model of diabetes (*6*, *9*) and the LPS-treated rat model of EIU (*42*).

Photobleaching is a problem with current techniques which probe leukocyte dynamics *in vivo*, such as acridine orange fluorography (*43*, *44*). Thus, long-term imaging of leukocytes is hindered. Using QD-based fluorography, we were able to continuously observe entrapped leukocytes in the circulation over an hour of continuous illumination without bleaching (Figure 5). Therefore, our QD-based imaging technique constitutes a potential alternative to current methods of imaging leukocytes due to the ability to simultaneously image multiple leukocyte subsets and stationary biomarkers with one excitation source with high specificity.

Our imaging technique provides noninvasive optical access to the *in vivo* retinal vasculature and continuous monitoring of vascular events. Spatial resolution on the order of a cell is achieved with this technique. QD have superior optical properties, such as high quantum efficiency and photostability, as well as distinct size-tunable emission wavelengths with the need for only one excitation source. By harnesseing these QD properties while immune-shielding the nanoparticle surface, it was readily possible to image three CAMs and one leukocyte subset within the same animal, without spectral overlap, using one blue excitation source to sufficiently illuminate QD-tagged species within the circulation. This feature enables detailed multiplexed studies of disease and biological processes. We used this approach to simultaneously observe the molecular expression of three different biomarkers, while also observing leukocyte-endothelial interactions. Other applications of this imaging strategy could readily be applied to studies in which multiple cellular and biomolecular vascular functions remain to be elucidated such as cancer, ocular angiogenesis, and atherosclerosis. While qualitative information was primarily presented in this initial application of our technique, we foresee the calculation of additional parameters including rolling velocities for various subtypes, relative fluorescence intensities of specific biomolecules along vascular walls, density of entrapped leukocytes, and important features of the inflammatory process *in vivo*.

ACKNOWLEDGMENT

We thank J.M. Higginbotham for assistance with flow cytometry, E.J. Dworska for assistance with tissue culture, and D.W. Piston for flash trigger equipment. This work was supported, in part, by grants from the National Institutes of Health (F.R. Haselton, PI, EY13451, EY017522), Vanderbilt University Discovery Grant Program, and Vanderbilt Vision Research Training Grant (J.D. Schall, PI, T32-EY07135-13).

LITERATURE CITED

(1) Kaneider, N. C., Leger, A. J., and Kuliopulos, A. (2006) Therapeutic targeting of molecules involved in leukocyte-endothelial cell interactions. *FEBS J. 273*, 4416−24.

(2) Cook-Mills, J. M., and Deem, T. L. (2005) Active participation of endothelial cells in inflammation. *J. Leukocyte Biol. 77*, 487−95.

(3) Frieri, M. (2005) Asthma concepts in the new millennium: update in asthma pathophysiology. *Allergy Asthma Proc. 26*, 83−8.

(4) Ulbrich, H., Eriksson, E. E., and Lindbom, L. (2003) Leukocyte and endothelial cell adhesion molecules as targets for therapeutic interventions in inflammatory disease. *Trends Pharmacol. Sci. 24*, 640−7.

(5) Wellen, K. E., and Hotamisligil, G. S. (2005) Inflammation, stress, and diabetes. *J. Clin. Invest. 115*, 1111−9.

(6) Joussen, A. M., Poulaki, V., Le, M. L., Koizumi, K., Esser, C., Janicki, H., Schraermeyer, U., Kociok, N., Fauser, S., Kirchhof, B., Kern, T. S., and Adamis, A. P. (2004) A central role for inflammation in the pathogenesis of diabetic retinopathy. *FASEB J. 18*, 1450−52.

(7) Miyamoto, K., Khosrof, S., Bursell, S. E., Rohan, R., Murata, T., Clermont, A. C., Aiello, L. P., Ogura, Y., and Adamis, A. P. (1999) Prevention of leukostasis and vascular leakage in streptozotocin-induced diabetic retinopathy via intercellular adhesion molecule-1 inhibition. *Proc. Natl. Acad. Sci. U.S.A. 96*, 10836−10841.

(8) Gotoh, R., Suzuki, J., Kosuge, H., Kakuta, T., Sakamoto, S., Yoshida, M., and Isobe, M. (2004) E-selectin blockade decreases adventitial inflammation and attenuates intimal hyperplasia in rat carotid arteries after balloon injury. *Arterioscler. Thromb. Vasc. Biol. 24*, 2063−2068.

(9) Barouch, F. C., Miyamoto, K., Allport, J. R., Fujita, K., Bursell, S. E., Aiello, L. P., Luscinskas, F. W., and Adamis, A. P. (2000) Integrin-mediated neutrophil adhesion and retinal leukostasis in diabetes. *Invest. Ophthalmol. Vis. Sci. 41*, 1153−1158.

(10) Baez, S. (1973) An open cremaster muscle preparation for the study of blood vessels by in vivo microscopy. *Microvasc. Res. 5*, 384−94.

(11) Conway, R. S., Factor, S. M., Sonnenblick, E. H., and Baez, S. (1987) Microvascular reactivity of the myopathic Syrian hamster cremaster muscle. *Cardiovasc. Res. 21*, 796−803.

(12) Nishiwaki, H., Ogura, Y., Kimura, H., Kiryu, J., and Honda, Y. (1995) Quantitative evaluation of leukocyte dynamics in retinal microcirculation. *Invest. Ophthalmol. Vis. Sci. 36*.

(13) Nishiwaki, H., Ogura, Y., Kimura, H., Kiryu, J., Miyamoto, K., and Matsuda, N. (1996) Visualization and quantitative analysis of leukocyte dynamics in retinal microcirculation of rats. *Invest. Ophthalmol. Vis. Sci. 37*.

(14) Tsujikawa, A., Kiryu, J., Nonaka, A., Yamashiro, K., Nishiwaki, H., Honda, Y., and Ogura, Y. (2000) Leukocyte-endothelial cell interactions in diabetic retina after transient retinal ischemia. *Am. J. Physiol. Regul. Integr. Comp. Physiol. 279*, 980−989.

(15) McHale, J. F., Harari, O. A., Marshall, D., and Haskard, D. O. (1999) Vascular endothelial cell expression of ICAM-1 and VCAM-1 at the onset of eliciting contact hypersensitivity in mice: evidence for a dominant role of TNF-alpha. *J. Immunol. 162*, 1648−55.

(16) Ivan, E., and Colovai, A. I. (2006) Human Fc receptors: Critical targets in the treatment of autoimmune diseases and transplant rejections. *Human Immunol. 67*, 479−491.

(17) Berry, C., and Curtis, A. (2003) Functionalisation of magnetic nanoparticles for applications in biomedicine. *J. Phys. D 36*, R198−R206.

(18) Gao, X., Yang, L., Petros, J. A., Marshall, F. F., Simons, J. W., and Nie, S. (2005) In vivo molecular and cellular imaging with quantum dots. *Curr. Opin. Biotechnol. 16*, 63−72.

(19) Smith, A. M., Gao, X., and Nie, S. (2004) Quantum dot nanocrystals for in vivo molecular and cellular imaging. *Photochem. Photobiol. 80*, 377−85.

(20) Ballou, B., Lagerholm, B. C., Ernst, L. A., Bruchez, M. P., and Waggoner, A. S. (2004) Noninvasive imaging of quantum dots in mice. *Bioconjugate Chem. 15*, 79−86.

(21) Bentzen, E. L., Tomlinson, I. D., Mason, J., Gresch, P., Warnement, M. R., Wright, D., Sanders-Bush, E., Blakely, R., and Rosenthal, S. J. (2005) Surface modification to reduce nonspecific binding of quantum dots in live cell assays. *Bioconjugate Chem. 16*, 1488−94.

(22) Dubertret, B., Skourides, P., Norris, D. J., Noireaux, V., Brivanlou, A. H., and Libchaber, A. (2002) In vivo imaging of quantum dots encapsulated in phospholipid micelles. *Science 298*, 1759−62.

(23) Akerman, M. E., Chan, W. C., Laakkonen, P., Bhatia, S. N., and Ruoslahti, E. (2002) Nanocrystal targeting in vivo. *Proc. Natl. Acad. Sci. U.S.A. 99*, 12617−21.

(24) Gao, X. H., Cui, Y. Y., Levenson, R. M., Chung, L. W. K., and Nie, S. M. (2004) In vivo cancer targeting and imaging with semiconductor quantum dots. *Nat. Biotechnol. 22*, 969−976.

(25) Russ, P. K., Gaylord, G. M., and Haselton, F. R. (2001) Retinal vascular permeability determined by dual-tracer fluorescence angiography. *Ann Biomed. Eng. 29*, 638−47.

(26) Gotoh, S., Itoh, M., Fujii, Y., Arai, S., and Sendo, F. (1986) Enhancement of the expression of a rat neutrophil-specific cell-surface antigen by activation with phorbol-myristate acetate and concanavalin-A. *J. Immunol. 137*, 643−650.

(27) Karyakin, A. A., Presnova, G. V., Rubtsova, M. Y., and Egorov, A. M. (2000) Oriented immobilization of antibodies onto the gold surfaces via their native thiol groups. *Anal. Chem. 72*, 3805−11.

(28) Yoshitake, S., Yamada, Y., Ishikawa, E., and Masseyeff, R. (1979) Conjugation of glucose oxidase from Aspergillus niger and rabbit antibodies using N-hydroxysuccinimide ester of N-(4-carboxycyclohexylmethyl)-maleimide. *Eur. J. Biochem. 101*, 395−9.

(29) Li, W., and Chung, S. C. (2003) Flow cytometric evaluation of leukocyte function in rat whole blood. *In Vitro Cell Dev. Biol. Anim. 39*, 413−9.
(30) Barouch, F. C., Miyamoto, K., Allport, J. R., Fujita, K., Bursell, S. E., Aiello, L. P., Luscinskas, F. W., and Adamis, A. P. (2000) Integrin-mediated neutrophil adhesion and retinal leukostasis in diabetes. *Invest. Ophthalmol. Vis. Sci. 41*, 1153−8.
(31) Romer, L. H., McLean, N. V., Yan, H. C., Daise, M., Sun, J., and DeLisser, H. M. (1995) IFN-gamma and TNF-alpha induce redistribution of PECAM-1 (CD31) on human endothelial cells. *J. Immunol. 154*, 6582−92.
(32) Zou, Y., Yoon, S., Jung, K. J., Kim, C. H., Son, T. G., Kim, M. S., Kim, Y. J., Lee, J., Yu, B. P., and Chung, H. Y. (2006) Upregulation of aortic adhesion molecules during aging. *J. Gerontol. A Biol. Sci. Med Sci. 61*, 232−44.
(33) Pan, L. F., Kreisle, R. A., and Shi, Y. D. (1998) Detection of Fcgamma receptors on human endothelial cells stimulated with cytokines tumour necrosis factor-alpha (TNF-alpha) and interferon-gamma (IFN-gamma). *Clin. Exp. Immunol. 112*, 533−8.
(34) Llodra, J., Angeli, V., Liu, J. H., Trogan, E., Fisher, E. A., and Randolph, G. J. (2004) Emigration of monocyte-derived cells from atherosclerotic lesions characterizes regressive, but not progressive, plaques. *Proc. Natl. Acad. Sci. U.S.A. 101*, 11779−11784.
(35) Flano, E., Husain, S. M., Sample, J. T., Woodland, D. L., and Blackman, M. A. (2000) Latent murine gamma-herpesvirus infection is established in activated B cells, dendritic cells, and macrophages. *J. Immunol. 165*, 1074−1081.
(36) Woof, J. M. (2002) The human IgA-Fc alpha receptor interaction and its blockade by streptococcal IgA-binding proteins. *Biochem. Soc. Trans. 30*, 491−4.
(37) Lin, X. Q., Lubinski, J. A., and Friedman, H. M. (2004) Immunization strategies to block the herpes simplex virus type 1 immunoglobulin G Fc receptor. *J. Virol. 78*, 2562−2571.
(38) Chapman, A. P. (2002) PEGylated antibodies and antibody fragments for improved therapy: a review. *Adv. Drug Delivery Rev. 54*, 531−45.
(39) Filpula, D. (2007) Antibody engineering and modification technologies. *Biomol. Eng. 24*, 201−15.
(40) Meleth, A. D., Agron, E., Chan, C. C., Reed, G. F., Arora, K., Byrnes, G., Csaky, K. G., Ferris, F. L., and Chew, E. Y. (2005) Serum inflammatory markers in diabetic retinopathy. *Invest. Ophthalmol. Vis. Sci. 46*, 4295−4301.
(41) Ludwig, R., Kretschmer, M., Caspar, G., Bojunga, J., Oldenburg, A., Schumm-Draeger, P., Stegmuller, M., Von Minckwitz, G., Usadel, K. H., and Kusterer, K. (1999) In vivo microscopy of murine islets of Langerhans: increased adhesion of transferred lymphocytes to islets depends on macrophage-derived cytokines in a model of organ-specific insulitis. *Immunology 98*, 111−115.
(42) Rosenbaum, J. T., McDevitt, H. O., Guss, R. B., and Egbert, P. R. (1980) Endotoxin-induced uveitis in rats as a model for human disease. *Nature (London) 286*, 611−3.
(43) Hossain, P. (1999) Scanning laser ophthalmoscopy and fundus fluorescent leucocyte angiography. *Br. J. Ophthalmol. 83*, 1250−3.
(44) Kimura, H., Kiryu, J., Nishiwaki, H., and Ogura, Y. (1995) A new fluorescent imaging procedure in vivo for evaluation of the retinal microcirculation in rats. *Curr. Eye Res. 14*, 223−8.

BC070020R

Coupling into the Base Pair Stack Is Necessary for DNA-Mediated Electrochemistry

Alon A. Gorodetsky, Omar Green, Eylon Yavin, and Jacqueline K. Barton*

Division of Chemistry and Chemical Engineering, California Institute of Technology, Pasadena, California 91125. Received February 12, 2007; Revised Manuscript Received April 24, 2007

The electrochemistry of DNA films modified with different redox probes linked to DNA through saturated and conjugated tethers was investigated. Experiments feature two redox probes bound to DNA on two surfaces: anthraquinone (AQ)-modified uridines incorporated into thiolated DNA on gold (Au) and 2,2,6,6-tetramethylpiperidine 1-oxyl (TEMPO)-modified uridines in pyrene-labeled DNA on highly oriented pyrolytic graphite (HOPG). The electrochemistry of these labels when incorporated into DNA has been examined in DNA films containing both well matched and mismatched DNA. DNA-mediated electrochemistry is found to be effective for the TEMPO probe linked with an acetylene linker but not for a saturated TEMPO connected through an ethylenediamine linker. For the AQ probe, DNA-mediated electrochemistry is found with an acetylene linker to uridine but not with an alkyl chain to the 5′ terminus of the oligonucleotide. Large electrochemical signals and effective discrimination of intervening base mismatches are achieved for the probes connected through the acetylene linkages, while probes connected through saturated linkages exhibit small electrochemical signals associated only with direct surface to probe charge transfer and poor mismatch discrimination. Thus DNA electrochemistry with these probes is dramatically influenced by the chemical nature of their linkage to DNA. These results highlight the importance of effective coupling into the π-stack for long-range DNA-mediated electrochemistry.

INTRODUCTION

Numerous studies in solution have shown that the DNA duplex can serve as an effective medium to transport charge (*1*−*5*). DNA-mediated charge transport (CT) in solution exhibits exquisite sensitivity to perturbations in the intervening base stack such as single base mismatches (*6*), bulges (*7*, *8*), and protein binding (*9*−*11*). Previous work has shown that self-assembled DNA monolayers on both gold and graphite can also mediate charge transport over significant distances (*12*−*14*). In particular, electrochemistry at DNA-modified electrodes has been demonstrated in both a chip-based format for mismatch detection (*15*, *16*, *17*) and as a tool for monitoring protein/DNA interactions (*18*−*23*).

Assays based on DNA CT have frequently made use of solution-borne substrates that interact with duplex DNA at the electrode surface (*12*−*15*). To further develop electrochemical detection strategies based on DNA CT, it is necessary to explore electroactive probes that are covalently tethered to duplex DNA. Electrochemistry of DNA monolayers modified with daunomycin, ferrocene, methylene blue, and anthraquinone has shown that these redox-active reporters covalently linked to DNA can function as DNA-bound electrochemical probes (*24*−*34*). However, important questions remain regarding the nature of charge transfer to these probes, which may proceed either via the base pair stack of DNA or by direct contact of the probe with the surface.

Daunomycin has displayed particularly large electrochemical signals when used as a covalently attached probe (*24*−*26*). The size of the signals associated with this probe likely reflect its intimate intercalation within the base pair stack (*35*, *36*), as can be seen in crystal structures of daunomycin bound to DNA. Furthermore, breaks in the sugar phosphate backbone were shown to have no significant effect on the electrochemistry of covalently attached daunomycin (*26*); base mismatches, on the other hand, cause a dramatic attenuation of the signal (*24*). These observations are consistent with DNA CT occurring through the base pair stack rather than through the sugar−phosphate backbone.

Ferrocene/DNA conjugates have been employed in DNA electrochemistry experiments and, in particular, to examine the importance of the linkage between DNA and the redox active probe (*27*). Interrupting conjugation of the ferrocene label with the base pair stack results in an almost complete loss of the electrochemical signal. Furthermore, the location of the ferrocene label within a DNA monolayer was found to affect dramatically the magnitude of the electrochemical signals (*29*, *31*). A well coupled ferrocene−uridine derivative exhibited a larger electrochemical signal at the top of the DNA monolayer than in close proximity to the surface (*29*). However, the opposite effect was observed for a poorly coupled ferrocene; an alkyl chain-derivatized ferrocene connected to the top of a DNA monolayer exhibited a smaller signal than the same ferrocene moiety incorporated in close proximity to the surface (*31*).

There remains some controversy about the effects of DNA conformation on electrochemical behavior of ferrocene, however. Recently, Anne and Demaille explored the electrochemistry of a ferrocene label attached to the 5′ terminus of duplex DNA (*37*). These ferrocene labels were not conjugated into the base pair stack but still afforded strong electrochemical signals. Elastic bending of 5′ ferrocene-labeled DNA was suggested as the cause of the electrochemical signals observed. It was concluded that bending of the DNA could account for the electrochemistry of all DNA bound probes. This conclusion was in direct contrast to those based upon the ferrocene data already described (*29*, *31*). Further, these investigations did not account for the role of the linkage between DNA and ferrocene, nor the effect of sequence context on electrochemical signals.

* Author to whom correspondence should be addressed. E-mail: jkbarton@caltech.edu.

10.1021/bc0700483 CCC: $37.00 © 2007 American Chemical Society
Published on Web 06/20/2007

Experiments with covalently tethered methylene blue have underscored the importance of intercalative stacking for DNA-mediated electrochemistry (*28*). In low salt buffers, intercalation is detected electrochemically in DNA films containing methylene blue tethered distally at the top of the film. Simply changing to a high ionic strength buffer leads to the complete loss of electrochemical signal in the DNA film; methylene blue, though still covalently attached, cannot bind by intercalation under these conditions. Thus intercalative stacking appears necessary for efficient reduction of the attached probe by DNA-mediated CT. Notably, recent studies have also demonstrated the effectiveness of methylene blue in assays based on surface to probe charge transfer without DNA mediation (*38, 39*).

In this work we focus on two established probes of DNA CT to explore in more detail how the linkage to DNA affects the efficiency of DNA-mediated electrochemistry. We have utilized two different redox active markers that can be covalently attached to DNA. Anthraquinone (AQ) has been extensively studied in electrochemical assays based on DNA-mediated CT. For example, AQ has been applied to the electrochemical monitoring of primer extension reactions at Au surfaces (*29*). Additionally, AQ-modified uridines have been used for detection of single nucleotide polymorphisms (*32, 33*) and of duplex to triplex conversions at DNA-modified Au surfaces (*34*). Recent studies in our group have also examined uridine modified with 2,2,6,6-tetramethyl-3,4-dehydro-piperidine-N-oxyl (3,4-dehydro-TEMPO) as a probe of DNA CT from a redox-active protein to DNA (*40*). Notably, the acetylene linkage connecting the probe to the uridine was shown to be crucial for determining its effectiveness as an electron trap for DNA CT using electron paramagnetic resonance (EPR) spectroscopy.

Here we present the electrochemistry of DNA duplexes featuring AQ-modified uridines on Au and TEMPO-modified uridines on highly oriented pyrolytic graphite (HOPG). The observations reported for the AQ and TEMPO probes make them particularly well suited for establishing a correlation between the linkage connecting the probe to the DNA and the effectiveness of the probe in assays based on DNA-mediated electrochemistry. On DNA-modified HOPG, we examine the difference between a modified 3,4-dehydro-TEMPO moiety connected to the base pair stack via an acetylene linker and a saturated TEMPO connected via an ethylenediamine linker. On DNA-modified Au, we examine the difference between an AQ moiety connected to the base pair stack via an acetylene linker and an AQ linked via an alkyl chain to the 5′ terminus of the DNA. Electrochemistry with these probes is dramatically influenced by the chemical nature of their linkage to DNA.

EXPERIMENTAL SECTION

Materials. All phosphoramidites and reagents for DNA synthesis were purchased from Glen Research with the exception of the 5-ethynyluracil phosphoramidite, which was purchased from Berry and Associates. All organic reagents (acetonitrile, dichloromethane, *N*,*N*-dimethylformamide, pyridine, tetrahydrofuran, triethylamine, and 40% aqueous methylamine solution) were purchased from Aldrich in the highest available purity and used as received. All buffers were freshly prepared and filtered using a 0.45 μm filter prior to use. Tetrakis(triphenylphosphine)-Pd(0) was purchased from Strem Chemicals. Technical grade 2-aminoanthraquinone was obtained from Aldrich, and anthraquinone-2-carbonyl chloride was purchased from TCI America. The synthesis of 2-iodoanthraquinone has been previously described (*41*). TEMPO was purchased from Aldrich. The preparation of 4-diamoethylene-2,2,6,6-tetramethyl-3,4-dehydropiperidine-*N*-oxyl (ethylenediamine TEMPO) (*42*) and 4-ethynyl-2,2,6,6-tetramethyl-3,4-dehydropiperidine-*N*-oxyl (acetylene-3,4-dehydro-TEMPO) (*40, 43*) followed established literature procedures.

Oligonucleotide Synthesis. Oligonucleotides were prepared using standard phosphoramidite chemistry on an ABI 392 DNA Synthesizer. DNA was purified by HPLC on a reverse phase C18 column with acetonitrile and ammonium acetate as the eluents. Unless otherwise noted, all oligonucleotides were cleaved from the resin with concentrated ammonium hydroxide (NH_4OH) prior to purification. The desired products were characterized by UV−visible spectroscopy and MALDI-TOF mass spectrometry.

Synthesis of Pyrene-Modified Oligonucleotides. DNA was modified with pyrene at the 5′ terminus by following a previously reported procedure (*13*). In brief, oligonucleotides were prepared by solid-phase synthesis with an unprotected hydroxyl group at the 5′ terminus. The 5′-OH was treated with a 120 mg/mL solution of carbonyldiimidazole in dioxane for 2 h followed by an 80 mg/mL solution of 1,6-diaminohexane for 30 min. Subsequently, the free amine was treated with 1-pyrenebutyric acid, *N*-hydroxysuccinimide ester, resulting in the desired pyrene moiety linked to the 5′ terminus. The oligonucleotides were deprotected with concentrated NH_4OH at 60 °C for 6 h.

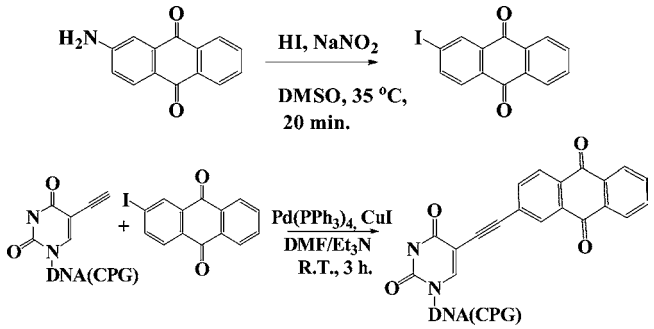
Synthesis of Thiol-Modified Oligonucleotides. The synthesis of DNA featuring a thiol at the 5′ terminus followed previously established procedures (*44*). In brief, oligonucleotides were prepared by solid-phase synthesis with the commercially available C6 S−S linker phosphoramidite incorporated at the 5′ terminus. The oligonucleotides were deprotected in NH_4OH at 60 °C for 12 h. Dithiothreitol (100 mM) was subsequently added to reduce the disulfide, leaving a free thiol at the 5′ terminus.

Synthesis of TEMPO-Modified Oligonucleotides. The synthesis of acetylene 3,4-dehydro-TEMPO-modified DNA has been previously described (*40*). The 5′ DMT-protected 5-iodouridine was Pd coupled to the acetylene-modified 3,4-dehydro-TEMPO in THF. The 3′-OH of the product of this reaction was subsequently converted to its phosphoramidite form. The phosphoramidite was dissolved in acetonitrile and used immediately for DNA synthesis.

The synthesis of the ethylenediamine TEMPO-modified DNA was carried out according to a protocol adapted from the literature (*42*). DNA featuring a 5-bromouridine at the position targeted for modification was synthesized on a solid support. A ∼0.5 M aqueous solution of the ethylenediamine TEMPO was added to the 5-bromouridine-modified DNA on solid support with the resulting slurry incubated at 60 °C overnight. This incubation resulted in the ethylenediamine TEMPO replacing the bromine, and in cleaving the DNA from the bead and deprotecting the bases. Prior to HPLC purification, the aqueous phase was washed with dichloromethane to remove excess ethylenediamine TEMPO.

Synthesis of Anthraquinone-Modified Oligonucleotides. The modification of DNA with anthraquinone was carried out as shown in Scheme 1. 2-Iodoanthraquinone was synthesized according to literature precedent (*41*) DNA containing a 5-ethynyluracil at the position targeted for modification was synthesized on a solid support. The beads were placed in an oven-dried flask which had been charged with 2.5 mL of DMF/Et_3N (3.5:1.5). 2-Iodoanthraquinone (60 mmol) and CuI (60 mmol) were added to the flask, and the solution was flushed with argon. $Pd(PPh_3)_4$ (30 mmol) was then added to the flask, and the solution was again flushed with argon. The mixture was allowed to stir at ambient temperature for 3 h under argon. Subsequently, the beads were washed with a 5% (w/v) EDTA solution, DMF, CH_3CN, and CH_2Cl_2 in succession to remove excess reagents. The DNA was cleaved from the resin and deprotected at 60 °C for 20 min with a 1:1 mixture of 40%

Scheme 1. Conditions for Synthesis of 2-Iodoanthraquinone and Its Coupling to Ethynyluracil-Modified DNA[a]



[a] The synthesis of 2-iodoanthraquinone was performed according to literature procedure (*41*). The coupling of the 2-iodoanthraquinone to the ethynyluracil-modified DNA was performed while the DNA was still attached to controlled pore glass (CPG) solid support.

aqueous methylamine and a saturated ammonium hydroxide solution. *m/z* calculated 5417, found 5416. λ_{max}nm (M^{-1} cm^{-1}) 260 ($\in$ 158 400), 320 ($\in$ 58 000), 394 ($\in$ 43 800).

Attachment of AQ at the 5′ terminus of DNA was carried out using procedures modified from the literature and Glen Research protocols (*44*−*47*). DNA with a six-methyl carbon chain terminated with a monomethoxytrityl (MMT)-protected amine was incorporated at the 5′ terminus on the solid support. The MMT-protecting group was removed from the 5′ amine with 3% trichloroacetic acid in CH_2Cl_2. A 0.5 M solution of anthraquinone-2-carbonyl chloride in CH_2Cl_2/Et_3N (10:1) was added to the amine-modified DNA on a solid support. The resulting slurry was incubated overnight. The beads were subsequently washed with copious amounts of CH_2Cl_2 to remove excess reagents. The DNA was cleaved from the resin at 60 °C for 20 min with a 1:1 mixture of 40% aqueous methylamine and a saturated ammonium hydroxide solution. *m/z* calculated 5615, found 5614.

Formation of DNA Monolayers. DNA films were formed on SPI-1 grade HOPG electrodes (SPI, Inc.) with a surface area of 0.08 cm^2, or on commercially available Au electrodes (BAS, Inc.) with a surface area of 0.02 cm^2, as previously described (*12, 13*). Duplex DNA (in 5 mM sodium phosphate, 50 mM NaCl, pH 7.1) was formed by combining equimolar amounts of the pyrene or thiol-modified strand with TEMPO or AQ-labeled complements, respectively. Duplex DNA (25−50 μM) was deposited onto HOPG or Au over a period of 24−48 h. Mg^{2+} was included to minimize electrostatic repulsion between the duplexes and ensure well packed monolayers on both HOPG and Au (*12, 13*). Longer incubation times (48 h) and lower incubation temperatures (4 °C) generally improved film formation. Electrodes being compared were prepared under equivalent conditions. Also, electrodes were brought to ambient temperature prior to electrochemical analysis.

Electrochemical Measurements. Electrochemical data were collected using a CH Instruments 760B potentiostat. Electrochemical experiments were performed at ambient temperature in 5 mM sodium phosphate, 50 mM NaCl, pH 7.1, under anaerobic conditions. All measurements reported for working electrodes were taken versus a platinum (Pt) auxiliary. Either a saturated calomel electrode or a silver/silver chloride electrode (Ag/AgCl) was used as the reference electrode. Square wave voltammetry was performed at 15 Hz, and cyclic voltammetry was performed at 50 mV/s.

Surface Characterization. All atomic force microscopy (AFM) measurements were performed using an MFP-3D atomic force microscope from Asylum Research, Inc. (Santa Barbara, CA). The HOPG block was mounted in a custom designed glass chamber before being modified with DNA as described. AFM

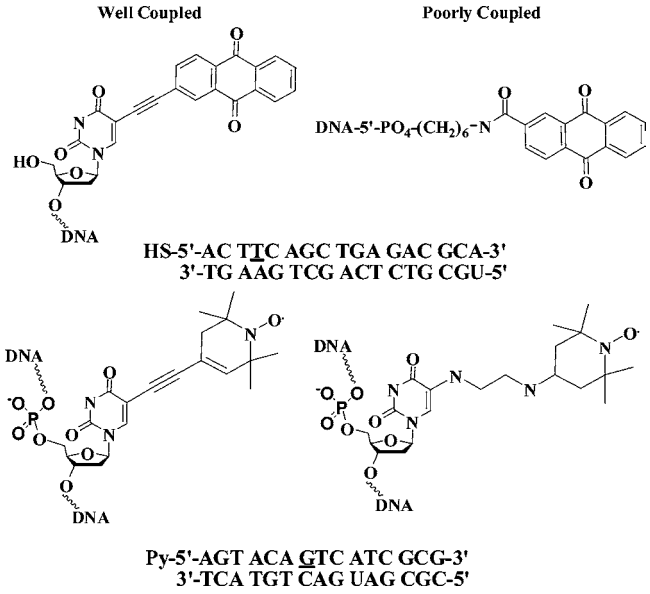


Figure 1. Sequences and probes used during the course of these studies. The DNA sequence used for each electrochemical marker is shown below the structures of the markers. Top: structures of well and poorly coupled AQ; -SH indicates the position of thiol modification on DNA. Bottom: structures of well and poorly coupled TEMPO and its derivative; Py- indicates the position of pyrene modification on DNA. The location of the mismatch is underlined, and the location of the electrochemical probe is indicated by uracil (U).

measurements were performed in buffer containing 5 mM sodium phosphate, 50 mM NaCl, pH 7.1, either in contact (constant force) or tapping mode. Commercially available silicon tips were utilized for all experiments.

RESULTS

Electrochemical Probes and DNA Sequences. The electrochemical probes and sequences examined are illustrated in Figure 1. Two redox active probes were tested, AQ and TEMPO-based moieties, and the probes were each linked to the base pair stack in two ways. The AQ was attached to a modified uridine via an acetylene linker and to the 5′ phosphate terminus via a six-carbon alkane linker. The synthesis of the acetylene-linked AQ moiety involved coupling of 2-iodoanthraquinone to ethylnyl-modified DNA (Scheme 1). Although DNA has previously been modified via Sonogashira conditions (*48, 49*), these syntheses involved halogenated bases incorporated into DNA coupled to ethynyl-containing molecules. 3,4-Dehydro-TEMPO was attached to a modified uridine by an acetylene linker, and TEMPO was connected via an ethylenediamine linker. The acetylene linkage and the 3,4-dehydro-TEMPO probe were designed to allow for efficient coupling of the probe into the base pair stack, whereas the alkane linkage was intended to insulate the probe electronically from the base pair stack. TEMPO experiments were performed with a 15-mer sequence modified with a pyrene on the complementary strand. The 15-mer sequence selected to compare the acetylene and saturated TEMPO probes is that utilized extensively by our laboratory (*12, 15*) and others (*27*) in characterizing different redox probes for DNA-mediated redox chemistry. Many experiments have been used to demonstrate, however, for a variety of probes that DNA-mediated electrochemistry is independent of DNA sequence and length (<30 bp) (*12, 13, 15, 18, 24*−*26*). It should be noted that electrochemistry experiments were also carried out on the 10-mer TEMPO probes that had been utilized in solution experiments with similar results (data not shown) (*40*). Anthraquinone experiments are described using a 17-mer oligonucleotide sequence containing a 5′-thiolate on the

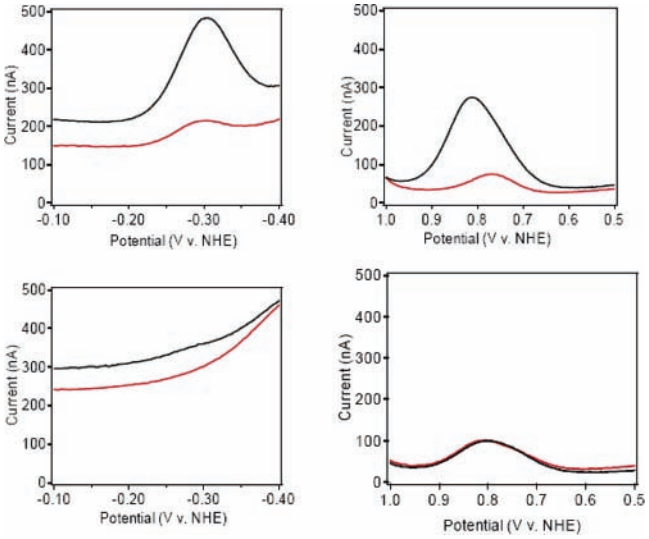


Figure 2. Square wave voltammetry of AQ and TEMPO-modified DNA. Voltammograms for DNA modified with the acetylene-linked AQ (top left), the acetylene-linked 3,4-dehydro-TEMPO (top right), the alkane-linked AQ (bottom left), and the alkane-linked TEMPO (bottom right) are shown. Voltammograms of well matched DNA are shown in black, and voltammograms of DNA featuring a CA mismatch are shown in red. All experiments were performed in 5 mM sodium phosphate, 50 mM NaCl, pH 7.1.

strand complementary to that modified with AQ. Several different AQ-modified DNA sequences 14−17 base pairs in length were prepared with comparable results obtained (data not shown). Since neither of these redox probes intercalate directly into the DNA base stack, they depend upon their links to the stacked uridine within the helix for π-coupling. Hence parallel experiments with these assemblies should give insight into the effect of DNA−probe linkages on DNA-mediated electrochemistry.

Two different surfaces, Au and graphite, are utilized for these electrochemical experiments. Studies involving AQ-modified DNA were performed on standard Au electrodes since the aromatic AQ moiety may directly adsorb to the graphite surface, impeding proper formation of DNA monolayers. Experiments utilizing TEMPO-modified DNA take advantage of the extended potential range afforded by HOPG. Since thiols are known to undergo oxidation at the large positive biases necessary for oxidation of TEMPO, HOPG is more suitable for exploring the electrochemistry of this marker.

Electrochemical measurements were used to assess the CT yields from the surface to the redox active probe. The efficiency of DNA CT was determined by direct comparison of peak currents and integrated charge obtained using square wave and cyclic voltammetry. Peak potentials reported were obtained using SWV and are reported versus NHE.

Electrochemistry of the Acetylene-Linked Probes. Large electrochemical signals are observed for probes linked to the DNA via an acetylene unit. Figure 2 shows the SWV of the acetylene-linked AQ and TEMPO moieties. A reversible electrochemical signal is found at −301 (±7) mV versus NHE for AQ-modified DNA on Au, and the signal is stable for a minimum of two hundred scans under anaerobic conditions. The magnitudes and potentials of the AQ signals are similar to those previously reported (*29*−*34*). As expected for a surface-bound species, a plot of peak current as a function of scan rate is linear for the DNA-bound AQ (*50*), and the electron-transfer rate was estimated to be approximately 30 s^{-1} (Supporting Information). This electron-transfer rate is consistent with previous electrochemical studies of DNA-modified surfaces using similar alkylthiol linkages to bind the DNA to the Au surface (*24*, *26*). A reversible electrochemical signal is also observed at 810 (±20) mV versus NHE for the 3,4-dehydro-TEMPO-modified DNA on graphite. The potential of the signal observed for the 3,4-dehydro-TEMPO-modified DNA is similar to that previously reported for the free label in solution (*40*). It is important to note that the TEMPO signal is electrochemically unstable and rapidly decays upon repeated scanning when attached to an electrode or to graphite felt (*51*, *52*). Therefore, a plot of peak current as a function of scan rate could not be easily obtained for this marker. As expected, controls run with well matched, unmodified DNA reveal no electrochemical signals at the potentials reported for the 3,4-dehydro-TEMPO and AQ-modified DNA (data not shown).

The introduction of a mismatch below the two labels causes a significant attenuation of the electrochemical signal (Figure 2 and Table 1). For AQ-modified DNA, the peak current is reduced from 160 (±50) nA for well matched DNA to 40 (±20) nA for DNA featuring a CA mismatch. For the 3,4-dehydro-TEMPO-modified DNA, the peak current is reduced from 250 (±100) nA for well matched DNA to 30 (±15) nA for DNA featuring a CA mismatch below the probe. It is noteworthy that the introduction of a CA mismatch above the 3,4-dehydro-TEMPO probe has little effect on the magnitude of the peak current (Supporting Information).

Electrochemistry of the Poorly Coupled Probes. Small electrochemical signals are observed for probes connected to the DNA via an alkane linkage. Figure 2 also shows SWVs for the alkane-linked AQ and TEMPO moieties. A small signal centered at −330 (±60) mV vs NHE, whose reversibility cannot be judged, is observed for the AQ-modified DNA on Au. The size of this signal makes it difficult to obtain a plot of peak current as a function of scan rate. The signal is reduced by almost 2 orders of magnitude in comparison to the acetylene-linked AQ probe (Table 1) with a drop in peak current from 160 (±50) nA to 9 (±4) nA. For the ethylenediamine-linked TEMPO label, a reversible signal is found at 800 (±10) mV vs NHE. Unlike the AQ, the magnitude of the TEMPO signal is reduced by only 4-fold upon altering the linkage from an acetylene to an alkane; the peak current drops from 250 (±100) nA for the acetylene-linked 3,4-dehydro-TEMPO to 60 (±20) nA for the ethylenediamine-linked TEMPO. As with the AQ case, the smaller size and instability of the TEMPO signal make it difficult to plot peak current as a function of scan rate.

In contrast to that seen for the acetylene-linked probes, the introduction of a mismatch below the alkane-linked AQ and TEMPO labels does not lead to substantial reductions in the electrochemical signals (Figure 2). Incorporation of a CA mismatch below the alkane AQ has virtually no effect on the electrochemical signal. The electrochemical signals are small for both well matched and mismatched DNA making quantitative evaluation difficult. Similarly, incorporation of a CA mismatch below the ethylenediamine-linked TEMPO does not lead to a diminution in the electrochemical signal. Well-defined electrochemical signals are observed with and without the mismatches for these ethylenediamine-linked, TEMPO-modified DNAs. Peak currents of 60 (±20) nA are found for well matched TEMPO-modified DNA, and peak currents of 70 (±10) nA are found for DNA featuring a CA mismatch below the TEMPO.

Surface Characterization. To aid in the proper interpretation of electrochemical data, surface characterization is necessary. DNA monolayers on both HOPG and Au have previously been examined using scanning probe microscopy, radioactive labeling, and electrochemical techniques (*13*, *53*, *54*, *55*). Previous AFM measurements found smooth films with depths corresponding to duplexes oriented at a ∼45° angle with respect to the surface. As a complement to our electrochemical studies, we also examined DNA monolayers with or without appended

Table 1. Electrochemical Characteristics of DNA Modified with Electroactive Moieties

	AQ[a]		TEMPO[a]	
DNA sequence[a]	peak current[b] (nA)	potential[c] (mV)	peak current[b] (nA)	potential[c] (mV)
well coupled	160 (±50)	−301 (±7)	250 (±100)[d]	810 (±20)[d]
CA mismatch	40 (±20)	−302 (±8)	34 (±15)[d]	800 (±50)[d]
poorly coupled	9 (±4)	−330 (±60)	64 (±17)	800 (±11)

[a] See Figure 1 for structures and sequences. Well coupled and CA mismatch DNA sequences contain sequences with marker moieties attached to the DNA through an ethynyl linkage. Well coupled DNA strands are fully complementary, and CA mismatch strands contain a CA mismatch at the position indicated in Figure 1. Poorly coupled DNA sequences have the electroactive molecule coupled through a saturated linkage, as shown in Figure 1. [b] Peak currents are reported from square wave voltammetry (SWV). SWV was performed at 15 Hz in 5 mM sodium phosphate, 50 mM NaCl, pH 7.1, under anaerobic conditions. Electrochemical data were compiled over a minimum of five trials. Experiments were performed with a SCE reference electrode and a Pt wire auxiliary electrode. [c] All electrochemical potentials are reported vs NHE. [d] DNA modified with 3,4-dehydro-TEMPO.

electrochemical markers on HOPG (Supporting Information). These monolayers were found to be indistinguishable from those previously examined.

DISCUSSION

Electrochemical Reduction of the Acetylene-Linked Probes Is Mediated by DNA Duplex. For efficient DNA-mediated CT, it is necessary for the electrochemical probe to be directly coupled into the base pair stack. Our data provide strong evidence that the acetylene-linked probes are reduced in a DNA-mediated fashion. The largest signals are found for 3,4-dehydro-TEMPO and AQ moieties connected to the DNA by an acetylene linker. The inclusion of a CA mismatch below either of these probes significantly attenuates the electrochemical signal, a hallmark of DNA-mediated CT.

Interestingly, previous reports of DNA modified with AQ-labeled uridines allow for a strong correlation to be drawn between the nature of the DNA−probe linkage and the size of the electrochemical signal. The signals obtained here for an unsaturated tether integrate to current densities of 7900 nA/cm^2. Gooding and co-workers have previously reported the electrochemistry of a partially saturated tether whose current densities integrate to a value of ∼1500 nA/cm^2 (*29, 30*). Further, Okamoto and co-workers have found current densities on the order of ∼300 nA/cm^2 for a fully saturated linkage (*32, 33*). A clear trend emerges from these values: a linkage which allows for conjugation of the probe into the base pair stack leads to larger redox signals and more effective electrochemistry.

DNA-mediated electrochemistry is observed for the acetylene-linked probes at both positive and negative potentials. DNA is expected to be repelled from the surface at negative potentials and attracted to the surface at positive potentials (*53, 56*). Assays based on DNA-mediated electrochemistry rely on DNA maintaining an upright orientation; CT can then take place through the base pair stack. However, at positive potentials direct contact of the probe with the surface is possible if sufficient space surrounding each duplex is available. It has been shown that in a close packed monolayer, the DNA is not able to make direct contact with the surface (*56*). Therefore, assays based on DNA CT may be possible even for probes which are reduced at positive potentials.

Electrochemical Reduction of Alkane-Linked Probes Do Not Depend on DNA Mediated Electrochemistry. Electrochemical experiments with alkane-tethered TEMPO and AQ labels support the notion of direct surface to probe charge transfer for these assemblies. Changing from an acetylene linkage to an alkane linkage minimizes electronic coupling, and the signals observed for such linkages are associated with pathways of charge-transfer that are not DNA-mediated. The lack of mismatch discrimination observed for either of these probes strongly supports the notion of direct surface to probe CT for these cases. Since there is no effect upon inclusion of a mismatch in the DNA sequence, this electrochemistry cannot be mediated by the base pair stack.

The current densities obtained for the alkane-linked TEMPO and AQ labels are much smaller than those of the acetylene-linked probes. The peak current densities obtained from SWV are 400 nA/cm^2 and 200 nA/cm^2 for the TEMPO and AQ, respectively. Anthraquinone is a poor intercalator which should not interact strongly with the base pair stack, and TEMPO does not intercalate. Therefore the smaller signals for these probes are reasonable since the CT pathway to each of these probes involves poor electronic coupling. Furthermore, it is not unexpected that the TEMPO label exhibits larger current densities compared to the AQ label. The AQ is reduced at negative potentials, where DNA is repelled from the surface, making reduction of the probe by direct CT from the surface less likely (*53, 56*). On the other hand, the TEMPO is oxidized at positive potentials where the DNA can electrostatically contact the surface, making direct surface to probe charge-transfer more likely (*53, 56*).

Electronic Coupling into the Base Pair Stack Governs the Size of the Electrochemical Signal. Electrochemical signals that are far smaller than expected based on surface coverage are observed for the acetylene-linked probes versus that expected when compared to the electrochemical signal of intercalated daunomycin (*24*). Previous reports for daunomycin have revealed surface coverages of 35−45 pmol/cm^2 based upon charge integration (*24, 25*). These values are similar to the theoretical maximum coverage of the surface by a DNA monolayer. However, far lower apparent surface coverages are obtained for the two acetylene-linked probes presented here; cathodic waves give peak currents (Table 1) which roughly translate to surface coverages of 6 and 8 pmol/cm^2 for the AQ and TEMPO-modified DNA, respectively.

How can the dramatic difference in signal intensities be reconciled? Covalently attached daunomycin has a particularly intimate association with the base pair stack and raises the melting temperature of the duplex by 20 °C upon crosslinking (*35, 36*). On the other hand, the bulky AQ moiety only raises the melting temperature of the DNA duplex by 4 °C compared to unmodified DNA (Supporting Information). Therefore, it is reasonable to assume that the AQ is not as well coupled into the DNA base stack. This lack of electronic coupling would account for the smaller electrochemical signals observed relative to daunomycin.

In order to investigate if the apparent discrepancy in surface coverage is due to the AQ and TEMPO moieties interfering with surface formation, the monolayers were examined by scanning probe microscopy. Previous work has shown that even subtle structural variations in the DNA monolayer can be easily detected with a high-resolution AFM tip (*54*). However, we observed no obvious differences between the morphology of monolayers formed with acetylene-TEMPO-modified DNA and unmodified, well matched DNA (Supporting Information).

DNA Charge Transfer with Acetylene and Alkane-Linked Probes. The two linkages may provide different electron-transfer pathways from the electrode to the marker, as illustrated

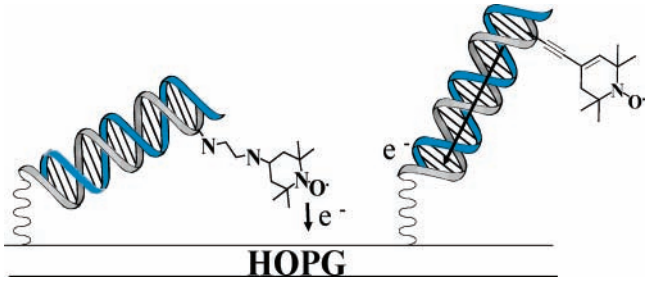


Figure 3. Schematic representation of two possible modes of charge transfer from an electroactive label incorporated into DNA. Direct interaction of the diaminoethane-linked TEMPO probe with the surface is shown on the left, and DNA-mediated electrochemistry to the well coupled probe is shown on the right.

schematically in Figure 3. When the probes are effectively coupled into the base pair stack through an acetylene linkage, the yield of DNA-mediated electrochemistry is high and charge transfer through the DNA base pair stack takes place. Large electrochemical signals result, and perturbations within the base pair stack can be easily detected. When the probes are insulated from the base pair stack through a σ-bonded alkane linkage, the yield of DNA-mediated electrochemistry is low and alternative charge-transfer pathways are dominant. Small electrochemical signals are observed and perturbations within the base pair stack are not easily detected.

These results can now be used to reexamine some of the data obtained from experiments involving long-range oxidative damage to DNA. Adequate sensitivity to mismatches or lesions can only be achieved with probes that are well coupled into the DNA base pair stack. Consequently, solution studies with covalently attached anthraquinone provide a particularly interesting example of the necessity of coupling into the DNA base pair stack. For example, in direct agreement with the electrochemical data presented here, anthraquinone linked to the 5′ terminus of DNA by an alkane chain has exhibited poor mismatch sensitivity in some contexts (*46*). Additionally, a direct comparison of the ability of various photooxidants to promote DNA-mediated CT showed that even changing the length of the linker connecting the anthraquinone had a significant effect on the yields of oxidative damage. In the same study, significant differences were found between poorly coupled probes that bind by an end-capping mode and well coupled probes that bind by an intercalative mode. Therefore, it is important to note that DNA CT reveals the characteristics not only of the DNA sequence employed but also of the redox probe.

Consideration of the inherent sensitivity of DNA CT to the linkage of the redox probe to the DNA base pair stack can also be extended to solution studies of protein/DNA interactions. A uridine modified with the TEMPO moiety was utilized as an electron trap for DNA bound repair enzymes (*40*). Notably, the linkage connecting the TEMPO to the uridine was shown to be crucial for determining its effectiveness as an electron trap in EPR experiments. When the TEMPO moiety is connected to a uridine by an unsaturated acetylene linkage, large EPR signals result, consistent with the larger electrochemical signals observed for this probe. On the other hand, when the TEMPO probe is connected by a saturated linkage, small EPR signals result, consistent with the smaller electrochemical signals observed.

Implications. Subtle structural changes can have a significant effect on the sensitivity of redox active reporters in DNA-mediated electrochemistry. Clearly, the utility of labels that are covalently attached to DNA depends upon their interaction with the base pair stack of DNA. Assays based on DNA-mediated CT necessitate well coupled probes that are highly sensitive to even subtle perturbations in the base pair stack.

This need is clearly illustrated by the electrochemical characteristics of AQ and TEMPO when coupled to DNA via a saturated linker versus being conjugated into the base stack. The electrochemistry of the acetylene-linked 3,4-dehydro-TEMPO and AQ is shown to be DNA-mediated. In contrast, charge transfer to the alkane TEMPO on HOPG and the alkane AQ on Au must proceed through an alternate direct surface-to-marker pathway. The data presented makes it clear that linkers conjugated into the base pair stack afford larger electrochemical signals, revealing a direct connection between the electronic structures of DNA-bound probes and their electrochemical properties.

DNA-modified electrodes are a powerful tool for directly comparing the electrochemistry of various redox active probes that are bound to DNA. DNA-mediated electrochemistry clearly allows the base pair stack to be probed directly. However, surface to probe charge transfer, while useful in other contexts, does not allow for the DNA base pair stack to be interrogated. In fact, the impressive sensitivity of DNA CT chemistry allows for the transduction of small structural changes into large electrochemical differences. As observed in the current study, the linkage directly governs the electrochemical characteristics of the probe. For electrochemical assays to be successful, it is crucial to tailor the probe to the desired application.

ACKNOWLEDGMENT

We thank the National Institutes of Health (GM61077) for their financial support of this research.

Supporting Information Available: Figure S1 contains AFM characterization of DNA modified and bare HOPG. Figure S2 shows melting point determinations of DNA modified with ethynylanthraquinone and unmodified DNA composed of the same sequence. Figure S3 shows the correlation of the current displayed by DNA modified with ethynylanthraquinone as a function of scan rate. Figure S4 shows the peak splitting as compared to the log of scan rate. This material is available free of charge via the Internet at http://pubs.acs.org/BC.

LITERATURE CITED

(1) Boon, E. M., and Barton, J. K. (2002) Charge Transport in DNA. *Curr. Opin. Struct. Biol. 12*, 320−329.

(2) Delaney, S., and Barton, J. K. (2003) Long-Range DNA Charge Transport. *J. Org. Chem. 68*, 6475−6483.

(3) O'Neill, M. A., and Barton, J. K. (2005) Sequence-Dependent DNA Dynamics: The Regulator of DNA-Mediated Charge Transport. In *Charge Transfer in DNA: From Mechanism to Application* (H.-A. Wagenknecht, Ed.) pp 27−75, Wiley-VCH, Hoboken.

(4) Giese, B. (2000) Long-Distance Charge Transport in DNA: The Hopping Mechanism. *Acc. Chem. Res. 33*, 631−636.

(5) Schuster, G. B. (2000) Long-Range Charge Transfer in DNA: Transient Structural Distortions Control the Distance Dependence. *Acc. Chem. Res. 33*, 253−260.

(6) Bhattacharya, P. K., and Barton, J. K. (2001) The Influence of Intervening Mismatches on Long-range Guanine Oxidation in DNA Duplexes. *J. Am. Chem. Soc. 123*, 8649−8656.

(7) Hall, D. B., and Barton, J. K. (1997) Sensitivity of DNA-mediated Electron Transfer to the Intervening π-Stack: A Probe for the Integrity of the DNA Base Stack. *J. Am. Chem. Soc. 119*, 5045−5046.

(8) Dandliker, P. J., Holmlin, R. E., and Barton, J. K. (1997) Oxidative Thymine Dimer Repair in the DNA Helix. *Science 275*, 1465−1468.

(9) Rajski, S. R., Kumar, S., Roberts, R. J., and Barton, J. K. (1999) Protein-Modulated DNA Electron Transfer. *J. Am. Chem. Soc. 121*, 5615−5616.

(10) Rajski, S. R., and Barton, J. K. (2001) How Different DNA-Binding Proteins Affect Long-Range Oxidative Damage to DNA. *Biochemistry 40*, 5556−5564.

(11) Boon, E. M., Pope, M. A., Williams, S. D., David, S. S., and Barton, J. K. (2002) DNA-Mediated Charge Transport as a Probe of MutY/DNA Interaction. *Biochemistry 41,* 8464−8470.
(12) Kelley, S. O., Boon, E. M., Barton, J. K., Jackson, N. M., and Hill, M. G. (1999) Single-Base Mismatch Detection Based on Charge Transduction Through DNA. *Nucl. Acids Res. 27,* 4830−4837.
(13) Gorodetsky, A. A., and Barton, J. K. (2006) Electrochemistry Using Self-Assembled DNA Monolayers on Highly Oriented Pyrolytic Graphite. *Langmuir 22,* 7917−7922.
(14) Li, X., Song, H., Nakatani, K., and Kraatz, H.-B. (2007) Exploiting Small Molecule Binding to DNA for the Detection of Single-Nucleotide Mismatches and Their Base Environment. *Anal. Chem. 79,* 2552−2555.
(15) Boon, E. M., Ceres, D. M., Drummond, T. G., Hill, M. G., and Barton, J. K. (2000) Mutation Detection by Electrocatalysis at DNA-Modified Electrodes. *Nature Biotechnol. 18,* 1096−1100.
(16) Li, X., Lee, J. S., and Kraatz, H.-B. (2006) Electrochemical Detection of Single-Nucleotide Mismatches Using an Electrode Microarray. *Anal. Chem. 78,* 6096−6101.
(17) Drummond, T. G., Hill, M. G., and Barton, J. K. (2003) Electrochemical DNA Sensors. *Nature Biotechnol. 21,* 1192−1199.
(18) Boon, E. M., Salas, J. E., and Barton, J. K. (2002) An Electrical Probe of Protein-DNA Interactions on DNA-modified Surfaces. *Nature Biotechnol. 20,* 282−286.
(19) Derosa, M. C., Sancar, A., and Barton, J. K. (2005) Electrochemically Monitoring DNA Repair by Photolyase. *Proc. Natl. Acad. Sci. U.S.A. 102,* 10788−10792.
(20) Boal, A. K., Yavin, E., Lukianova, O. A., O'Shea, V. L., David, S. S., and Barton, J. K. (2005) DNA-Bound Redox Activity of DNA Repair Glycosylases Containing [4Fe-4S] Clusters. *Biochemistry 44,* 8397−8407.
(21) Gorodetsky, A. A., Boal, A. K., and Barton, J. K. (2006) Direct Electrochemistry of Endonuclease III in the Presence and Absence of DNA. *J. Am. Chem. Soc. 128,* 12082−12083.
(22) Li, C. Z., Long, Y. T., Lee, J. S., and Kraatz, H. B. (2004) Protein-DNA Interaction: Impedance Study of MutS Binding to a DNA mismatch. *Chem. Commun. 7,* 574−575.
(23) Masarik, M., Cahova, K., Kizek, R., Palecek, E., Fojta, Label-free, M. (2007) Voltammetric Detection of Single-Nucleotide Mismatches Recognized by the Protein MutS. *Anal. Bioanal. Chem. 388,* 259−270.
(24) Kelley, S. O., Jackson, N. M., Hill, M. G., and Barton, J. K. (1999) Long Range Electron Transfer Through DNA Films. *Angew. Chem., Int. Ed. 38,* 941−945.
(25) Drummond, T. G., Hill, M. G., and Barton, J. K. (2004) Electron Transfer Rates in DNA Films as a Function of Tether Length. *J. Am. Chem. Soc. 126,* 15010−15011.
(26) Liu, T., and Barton, J. K. (2005) DNA Electrochemistry through the Base Pairs Not the Sugar-Phosphate Backbone. *J. Am. Chem. Soc. 127,* 10160−10161.
(27) Inouye, M., Ikeda, R., Takase, M., Tsuri, T., and Chiba, J. (2005) Single-nucleotide polymorphism detection with "wire-like" DNA probes that display quasi "on-off" digital action. *Proc. Natl. Acad. Sci. U.S.A. 102,* 11606−11610.
(28) Boon, E. M., Jackson, N. M., Wightman, M. D., Kelley, S. O., Barton, J. K., and Hill, M. G. (2003) Intercalative Stacking: A Critical Feature of DNA Charge Transport Electrochemistry. *J. Phys. Chem. B 107,* 11805−11812.
(29) Di Giusto, D. A., Wlasoff, W. A., Giesebrecht, S., Gooding, J. J., and King, G. C. (2004) Multipotential Electrochemical Detection of Primer Extension Reactions on DNA Self-Assembled Monolayers. *J. Am. Chem. Soc. 126,* 4120−4121.
(30) Di Giusto, D. A., Wlasoff, W. A., Giesebrecht, S., Gooding, J. J., and King, G. C. (2004) Enzymatic Synthesis of Redox-Labeled RNA and Dual-Potential Detection at DNA-Modified Electrodes. *Angew. Chem., Int. Ed. 43,* 2809−2812.
(31) Zuo, X., Song, S., Zhang, J., Pan, D., Wang, L., and Fan, C. (2007) Target-Responsive Electrochemical Aptamer Switch (TREAS) for Reagentless Detection of Nanomolar ATP. *J. Am. Chem. Soc. 129,* 1042−1043.
(32) Okamoto, A., Kamei, T., Tanaka, K., and Saito, I. (2004) Photostimulated Hole Transport Through a DNA Duplex Immobilized on a Gold Electrode. *J. Am. Chem. Soc. 126,* 14732−14733.
(33) Okamoto, A., Kamei, T., and Saito, I. (2006) DNA Hole Transport on an Electrode: Application to Effective Photoelectrochemical SNP Typing. *J. Am. Chem. Soc. 128,* 658−662.
(34) Tanabe, K., Iida, H., Haruna, K., Kamei, T., Okamoto, A., and Nishimoto, S. (2006) Electrochemical Evaluation of Alternating Duplex-Triplex Conversion Effect on the Anthraquinone-Photoinjected Hole Transport through DNA Duplex Immobilized on a Gold Electrode. *J. Am. Chem. Soc. 128,* 692−693.
(35) Wang, A. H.-J., Gao, Y.-G., Liaw, Y.-C., and Li, Y.-K. (1991) Formaldehyde Crosslinks DNA and Daunorubicin Efficiently: HPLC and X-Ray Diffraction Studies. *Biochemistry 30,* 3812−3815.
(36) Leng, F., Savkur, R., Fokt, I, Przewloka, T, Priebe, W., and Chaires, J. B. (1996) Base Specific and Regioselective Chemical Cross-Linking of Daunorubicin to DNA. *J. Am. Chem. Soc. 118,* 4731−4738.
(37) Anne, A., and Demaille, C. (2006) Dynamics of Electron Transport by Elastic Bending of Short DNA Duplexes. Experimental Study and Quantitative Modeling of the Cyclic Voltammetric Behavior of 3′-Ferrocenyl DNA End-Grafted on Gold. *J. Am. Chem. Soc. 128,* 542−557.
(38) Lai, R. Y., Lagally, E. T., Lee, S.-H., Soh, H. T., Plaxco, K. W., and Heeger, A. J. (2006) Rapid, Sequence Specific Detection of Unpurified PCR Amplicons via a Reusable, Electrochemical Sensor. *Proc. Natl. Acad. Sci. U.S.A. 103,* 4017−4021.
(39) Xiao, Y., Lubin, A. A., Baker, B. R., Plaxco, K. W., and Heeger, A. J. (2006) Single Step Electronic Detection of Femtomolar DNA by Target-induced Strand Displacement in an Electrode Bound Duplex. *Proc. Natl. Acad. Sci. U.S.A. 103,* 16677−16680.
(40) Yavin, E., Stemp, E. D. A., O'Shea, V. L., David, S. S., and Barton, J. K. (2006) Electron Trap for DNA-bound Repair Enzymes: A Strategy for DNA-mediated Signaling. *Proc. Natl. Acad. Sci. U.S.A. 103,* 3610−3614.
(41) Baik, W., Luan, W., Lee, H. J., Yoon, C. H., Koo, S., and Kim, B. H. (2005) Efficient One-pot Transformation of Aminoarenes to Haloarenes Using Halodimethylisulfonium Halides Generated in Situ. *Can. J. Chem. 83,* 213−219.
(42) Bondarev, G. N., Burzina, T. S., Krasotskaya, G. I., Kachurin, A. M., Kleiner, A. R. (1985) Synthesis of 2,2,6,6-tetramethyl-4-[(aminoalkyl)amino]-1-oxylpiperidines. *Izvestiya Akademii Nauk SSSR: Seriya Khimicheskaya.* 1850−1855.
(43) Gannett, P. M., Darian, E., Powell, J. H., and Johnson, E. M. (2001) A Short Procedure for Synthesis of 4-Ethynyl-2, 2, 6, 6-Tetramethyl-3,4-Dehydro-Piperidine-1-Oxyl-Nitroxide. *Synth. Commun. 31,* 2137−2141.
(44) Kelley, S. O., Barton, J. K., Jackson, N. M., and Hill, M. G. (1997) Electrochemistry of Methylene Blue Bound to a DNA Modified Electrode. *Bioconjugate Chem. 8,* 31−37.
(45) Gasper, S. M., and Schuster, G. B. (1997) Intramolecular Photoinduced Electron Transfer to Anthraquinones Linked to Duplex DNA: The Effect of Gaps and Traps on Long-Range Radical Cation Migration. *J. Am. Chem. Soc. 119,* 12762−12771.
(46) Williams, T. T., Dohno, C., Stemp, E. D. A., and Barton, J. K. (2004) Effects of the Photooxidant on DNA-Mediated Charge Transport. *J. Am. Chem. Soc. 126,* 8148−8158.
(47) Shao, F., Augustyn, K., and Barton, J. K. (2005) Sequence Dependence of Charge Transport Through DNA Domains. *J. Am. Chem. Soc. 127,* 17445−17452.
(48) Rist, M., Amann, N., and Wagenknecht, H.-A. (2003) Preparation of 1-Ethynylpyrene-Modified DNA via Sonogashira-Type Solid Phase Couplings and Characterization of the Fluorescence Properties for Electron Transfer Studies. *Eur. J. Org. Chem. 13,* 2498−2504.
(49) Abou-Elkhair, R. A. I., and Netzel, T. L. (2005) Synthesis of Two 8-[(Anthraquinone-2-yl)-Linked]-2′-Deoxyadenosine 3′-Benzyl Hydrogen Phosphates for Studies of Photoinduced Hole Transport in DNA. *Nucleosides Nucleotides Nucleic Acids 24,* 85−110.
(50) Bard, A. J., and Faulkner, L. R. (2001) *Electrochemical Methods,* 2nd ed., John Wiley & Sons: New York.
(51) Geneste, F., and Moinet, C. (2005) Electrochemically Linking TEMPO to Carbon Via Amine Bridges. *New J. Chem. 29,* 269−271.
(52) Geneste, F., Moinet, C., Ababou-Girard, S., and Solal, F. (2005) Covalent Attachment of TEMPO onto a Graphite Felt Electrode and Application in Electrocatalysis. *New J. Chem. 29,* 1520−1526.

(53) Kelley, S. O., Barton, J. K., Jackson, N. M., McPherson, L. D., Potter, A. B., Spain, E. M., Allen, M. J., and Hill, M. G. (1998) Orienting DNA Helices on Gold Using Applied Electric Fields. *Langmuir 14*, 6781−6784.

(54) Boon, E. M., Sam, M., Barton, J. K., Hill, M. G., and Spain, E. M. (2001) Morphology of 15-mer Duplexes Tethered to Au(111) Probed Using Scanning Probe Microscopy. *Langmuir 17*, 5727−5730.

(55) Oliveira Brett, A. M., and Chiorcea, A.-M. (2003) Atomic Force Microscopy of DNA Immobilized onto a Highly Oriented Pyrolytic Graphite Surface. *Langmuir 19*, 3830−3839.

(56) Rant, U., Arinaga, K., Fujita, S., Yokoyama, N., Abstreiter, G., and Tornow, M. (2004) Dynamical Electrical Switching of DNA Layers on a Metal Surface. *Nano Lett. 4*, 2441−2445.

BC0700483

Supporting Information

Coupling Into the Base Pair Stack is Necessary for DNA-mediated Electrochemistry

Alon A. Gorodetsky, Omar Green, Eylon Yavin, and Jacqueline K. Barton*

Division of Chemistry and Chemical Engineering

California Institute of Technology,

Pasadena, California 91125

*to whom correspondence should be addressed

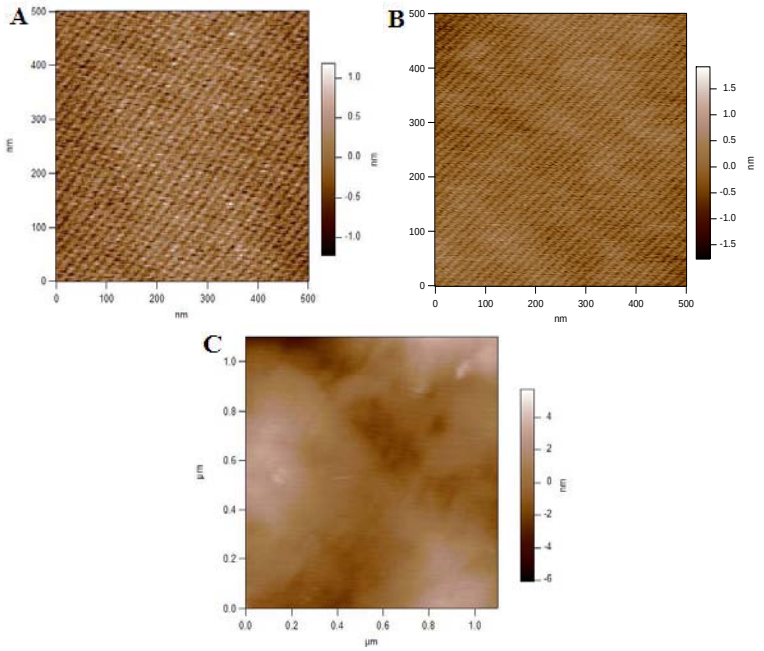


Figure S1. AFM characterization of DNA-modified and bare HOPG. Data were collected in 5 mM sodium phosphate, 50 mM NaCl, pH 7.1 (tapping mode). Typical AFM image of A: well matched DNA on HOPG, B: DNA featuring an acetylene-TEMPO modified uridine, and C: unmodified HOPG. Sequences for A are pyrene-$(CH_2)_3CONH(CH_2)_6$ NHCO-5'-CTACAGTCGT-3' pluswell matched complement and for B are pyrene-$(CH_2)_3CONH(CH_2)_6$NHCO-5'-CTACAGTCGT-3' plus TEMPO modified complement.

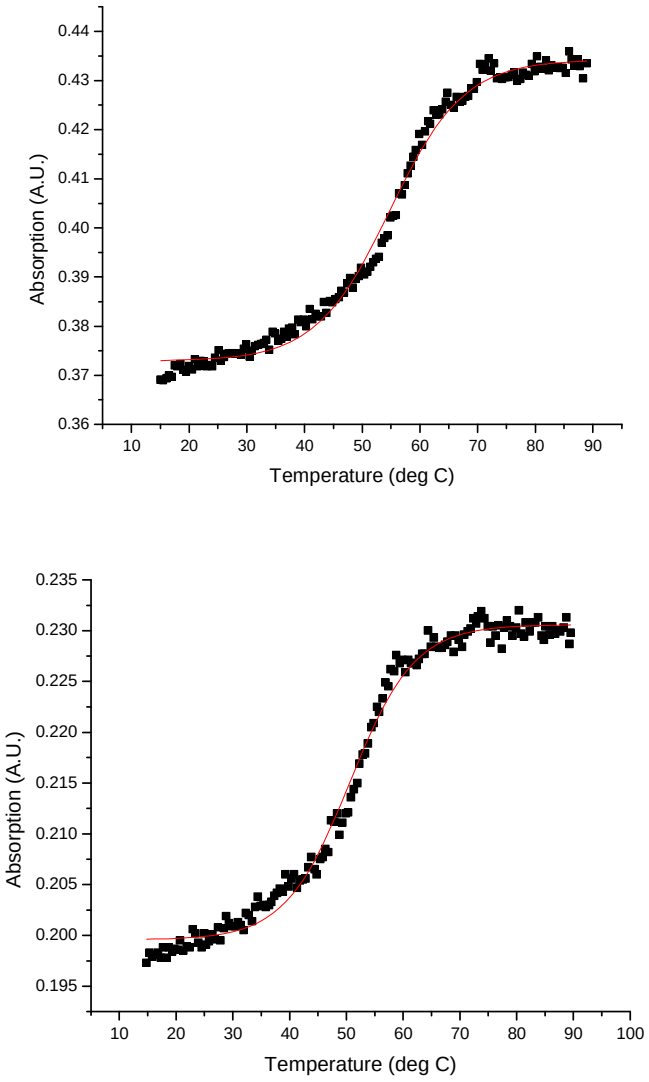


Figure S2. Melting temperature determinations of DNA modified by AQ through an acetylene linkage (top) and unmodified DNA with the same sequence (bottom). The melting temperature was determined through application of a sigmoidal fit (red), revealing a melting point of 55°C for AQ modified DNA, and 51°C for unmodified DNA. Data were collected in 5 mM sodium phosphate, 50 mM NaCl, pH 7.1.

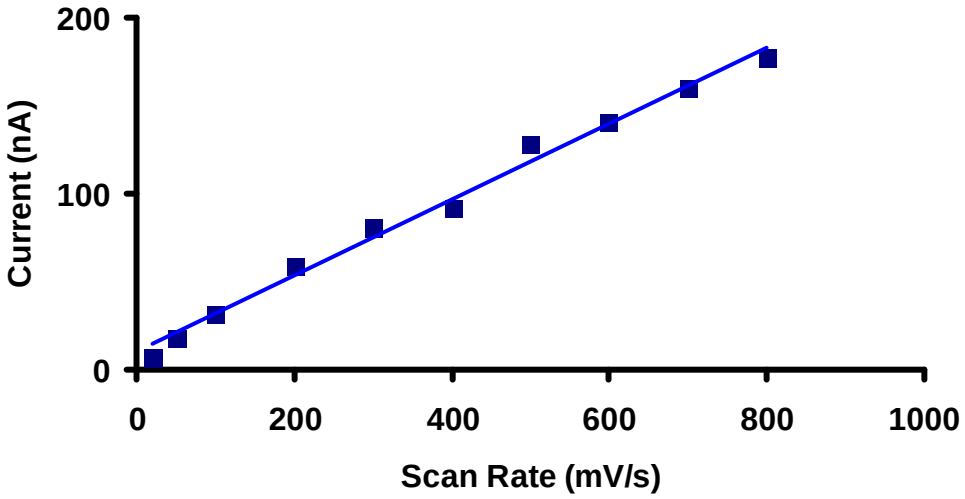


Figure S3. Scan rate dependence of DNA modified by AQ through an acetylene linkage. Data were collected in 5 mM sodium phosphate, 50 mM NaCl, pH 7.1.

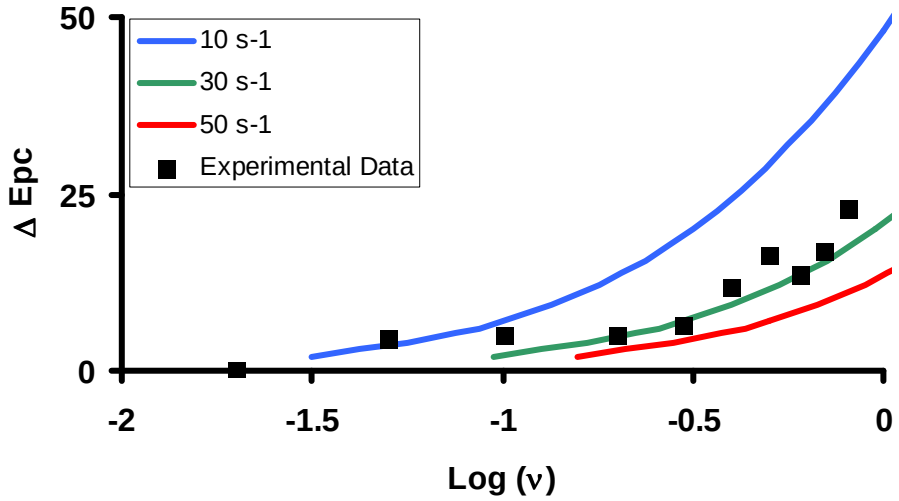


Figure S4. Plot of peak splitting ΔE_{pc} ($\Delta E_{pc} = E_{pc}-E°$) versus log (ν) (where ν = scan rate) for DNA modified by AQ through an acetylene linkage. Simulated curves corresponding to k_s values of 10 s^{-1} (blue), 30 s^{-1} (green) and 50 s^{-1} (red) are shown for comparison.[1]

[1]Tender, L., Carter, M.T., Murray, R.W., *Anal. Chem.*, **1994**, *66*, 3173-3181

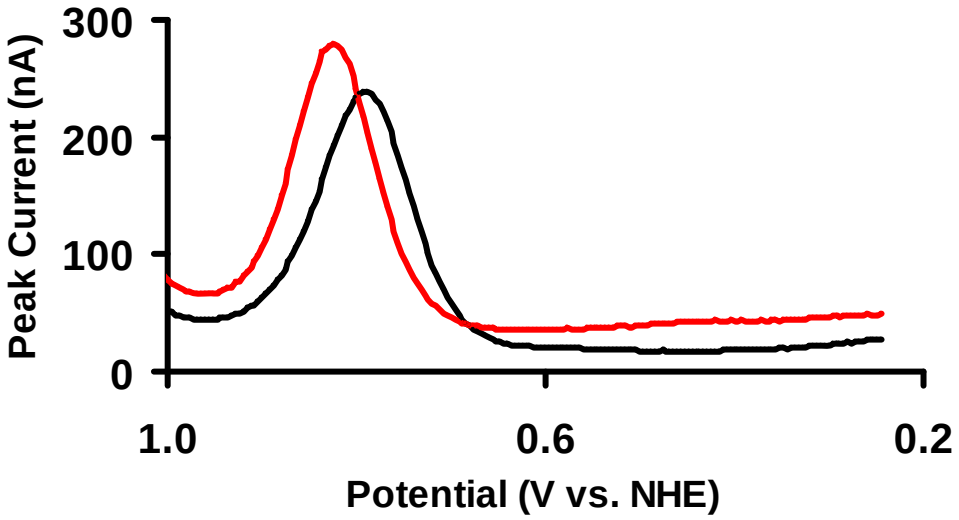


Figure S5. Square wave voltammetry of a DNA-modified surface featuring well matched DNA (black) and DNA with a CA mismatch above the TEMPO label (red). The sequence was pyrene-$(CH_2)_3CONH(CH_2)_6$ NHCO-5'-CTA C*A*G **T**CG T-3' plus TEMPO modified complement The italicized base indicates the location of the TEMPO, and the bold base indicates the location of the mismatch.

Supporting Information

Coupling Into the Base Pair Stack is Necessary for DNA-mediated Electrochemistry

Alon A. Gorodetsky, Omar Green, Eylon Yavin, and Jacqueline K. Barton*

Division of Chemistry and Chemical Engineering

California Institute of Technology,

Pasadena, California 91125

*to whom correspondence should be addressed

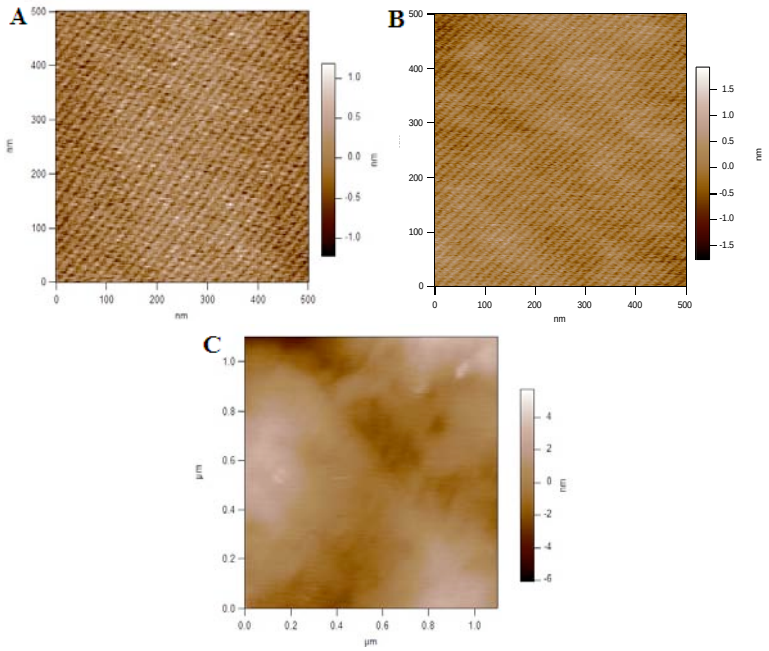


Figure S1. AFM characterization of DNA-modified and bare HOPG. Data were collected in 5 mM sodium phosphate, 50 mM NaCl, pH 7.1 (tapping mode). Typical AFM image of A: well matched DNA on HOPG, B: DNA featuring an acetylene-TEMPO modified uridine, and C: unmodified HOPG. Sequences for A are pyrene-$(CH_2)_3CONH(CH_2)_6$ NHCO-5'-CTA CAGTCGT-3' plus well matched complement and for B are pyrene-$(CH_2)_3CONH(CH_2)_6$NHCO-5'-CTACAGTCGT-3' plus TEMPO modified complement.

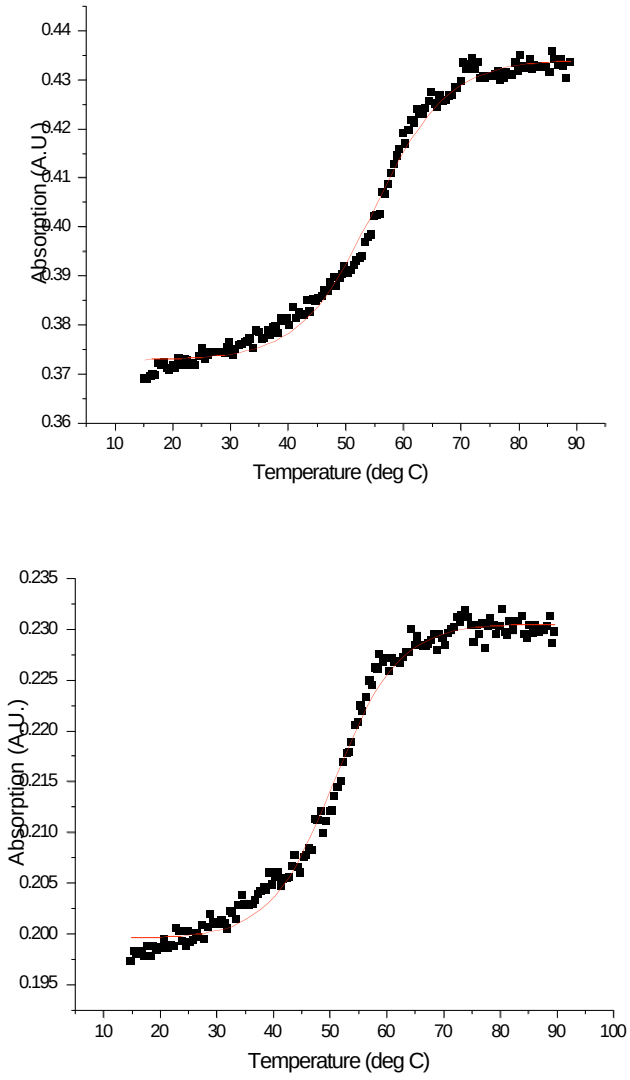


Figure S2. Melting temperature determinations of DNA modified by AQ through an acetylene linkage (top) and unmodified DNA with the same sequence (bottom). The melting temperature was determined through application of a sigmoidal fit (red), revealing a melting point of 55°C for AQ modified DNA, and 51°C for unmodified DNA. Data were collected in 5 mM sodium phosphate, 50 mM NaCl, pH 7.1.

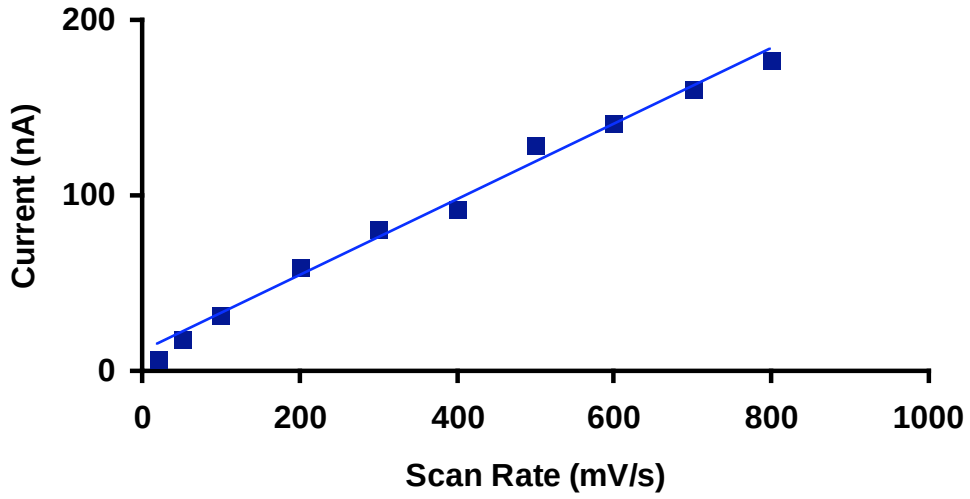


Figure S3. Scan rate dependence of DNA modified by AQ through an acetylene linkage. Data were collected in 5 mM sodium phosphate, 50 mM NaCl, pH 7.1.

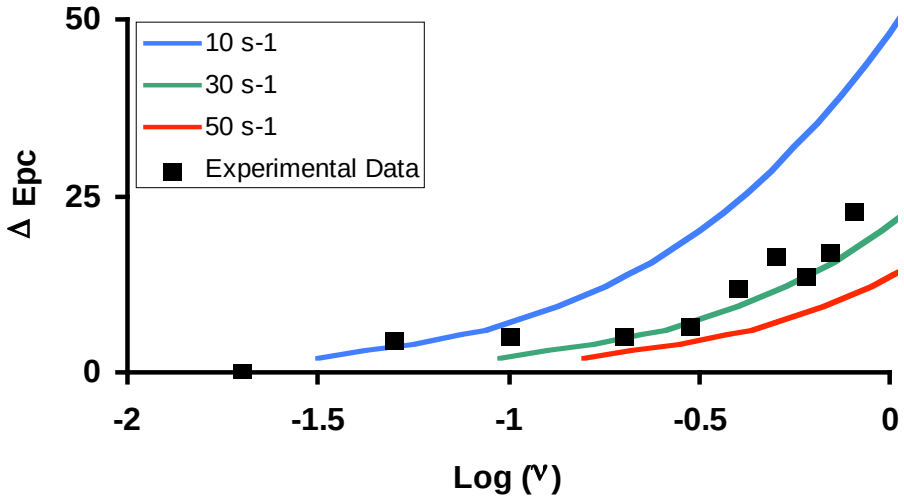


Figure S4. Plot of peak splitting ΔE_{pc} ($\Delta E_{pc} = E_{pc}-E°$) versus log (ν) (where ν = scan rate) for DNA modified by AQ through an acetylene linkage. Simulated curves corresponding to k_s values of 10 s^{-1} (blue), 30 s^{-1} (green) and 50 s^{-1} (red) are shown for comparison.[1]

[1]Tender, L., Carter, M.T., Murray, R.W., *Anal. Chem.*, **1994**, *66*, 3173-3181

Biofunctionalized Surfactant Mesophases as Polyvalent Inhibitors of Cholera Toxin

Anastasios Polyzos,*,† Malcolm R. Alderton,‡ Raymond M. Dawson,‡ and Patrick G. Hartley†

CSIRO Molecular and Health Technologies, Bayview Avenue, Clayton South, Victoria 3169, Australia, and DSTO Melbourne, Defence Science and Technology Organisation, P.O. Box 4331, Melbourne, Victoria 3001, Australia. Received February 25, 2007; Revised Manuscript Received July 9, 2007

The cubic lyotropic mesophase composed of the ganglioside G_{M1} and the synthetic surfactant phytantriol has been employed as a scaffold to prepare a polyvalent inhibitor of cholera toxin (CT). Surfactant mixtures containing up to 20% (w/w) G_{M1}/phytantriol afforded a hydrated insoluble gel-like material, which retained an inverse cubic phase (Q) structure in excess water and at 22 °C, as confirmed using small-angle X-ray scattering. The G_{M1}-functionalized mesophases bind up to 98.8% of CT from solution containing 100 ng/mL of CT with a dissociation constant (K_d) of 67−73 nM. The estimated IC_{50} values for the mesophase systems were 0.1−0.27 μM. The inhibitory effect of the mesophases may be enhanced through the high internal surface area of the inverse cubic phase in addition to the optimal self-orientation of G_{M1} ligand to match the distribution of binding sites on the toxin surface. As a result, polyvalent inhibitor materials manufactured using these mesophase structures do not require precise control of ligand distribution, which offers advantages with respect to complexity of synthesis and formulation when compared to more rigid and conformationally restricted materials. This approach provides a route to a unique class of polyvalent inhibitors, which should be broadly applicable to a range of bacterial and plant toxins.

INTRODUCTION

Cholera toxin (CT) is a heterohexameric protein which is secreted by the Gram-negative bacteria *Vibrio cholerae* (*1*) and is the agent responsible for the diarrheal disease cholera. The toxin architecture consists of a catalytic A subunit that is surrounded by an axisymmetric arrangement of five identical B subunits (*2*), and it therefore belongs to the AB_5 class of toxins. Within the lumen of the gastrointestinal tract, toxin endocytosis is mediated by the polyvalent recognition of the cell surface receptor lipid, ganglioside G_{M1} (Figure 1) (*2*), by the B pentamer (*3*). The enzymatic A subunit then separates from the B-pentamer and translocates into the cytosol, where it effects the stimulation of cyclic adenosine monophosphate (cAMP) production. This results in an active efflux of salts and water from the lumen, an accumulation of intestinal fluids in the gut, and diarrhea. An attractive approach to developing cholera prophylactics or therapeutics involves the development of receptor-binding antagonists that interfere with B-subunit recognition of the cell surface receptor. Crystallographic elucidation of the structure of CT has led to the extensive characterization of the recognition of G_{M1} by the binding epitopes in the pentameric B-subunits (*4*, *5*). These studies reveal that the terminal galactose of the G_{M1} oligosaccharide binds to a shallow binding epitope on each B subunit (*6*). Hence, the development of molecular mimics of the terminal galactose and sialic acid groups on the G_{M1} oligosaccharide are of interest (*7*).

CT receptor-binding antagonists, or inhibitors, fall into two classes. The first class comprises low molecular weight galactose derivatives, such as *m*-nitrophenyl galactose (MNPG) (*8*), that reversibly bind to one or more binding sites on the B-pentamer of CT. This class of inhibitor, also known as a monovalent inhibitor, has proven only moderately successful due to their relatively low affinity (*9*), which can be attributed to the weak binding interaction with the receptor site. The second class of inhibitors are known as polyvalent inhibitors. Polyvalent inhibitors, which are generally macromolecules, employ multiple binding moieties (typically galactose functionalities) to take advantage of the pentameric nature of the B subunit-cell surface receptor interaction. Structure-based inhibitors that incorporate five or ten single-site inhibitors covalently coupled to a central core have been reported (*10*, *11*), resulting in remarkable gains in CT inhibitor activity compared to the monovalent analogues (*7*, *12*−*15*). A variety of polyvalent scaffolds using generic backbones have been developed including random-coil and cyclic polypeptide-based glycopolymers (*16*). Further, oligosaccharide-derivatized dendrimers (glycodendrimers), which are hyperbranched polymers with a narrow size distribution, have been used as polyvalent scaffolds (*17*, *18*). The polyvalent display of mono- and oligosaccharides at the glycodendrimer surface has resulted in binding enhancements of up to 3 orders of magnitude compared with the monovalent analogue (*19*). The limitation associated with the rational design of polyvalent CT inhibitors is that their design is heavily reliant on crystallographic information, where the geometry and the dimensions of the polyvalent macromolecules must match the spatial distributions of binding epitopes on the B pentamer. As such, in pentameric and decameric inhibitors, the spacer length between the central core and pendant galactose groups must be optimized, using numerous structural derivatives to achieve optimal binding. Further, the display of galactose derivatives on polymeric scaffolds may not contain the requisite complimentary geometry to match the CT epitope surface, and these restrictions may often lead to modest binding affinities.

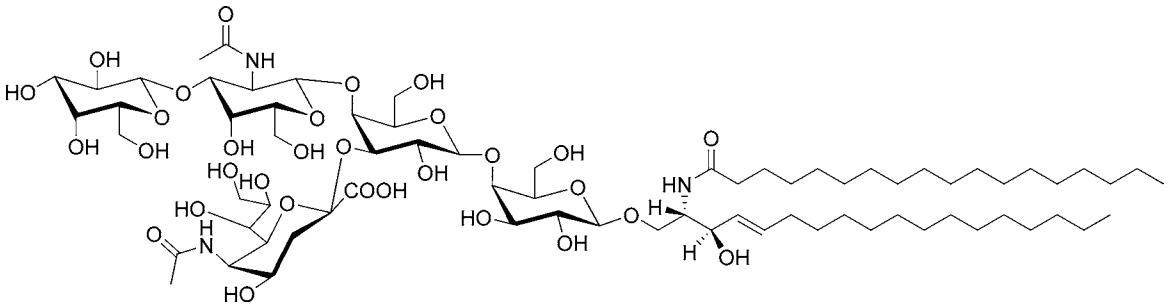
We have recently introduced a new class of polyvalent scaffold based on lyotropic (solvent containing) mesophases (*20*). In the presence of water, these systems develop from the

* Author to whom correspondence should be addressed. E-mail: tash.polyzos@csiro.au.

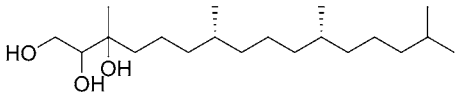
† CSIRO Molecular and Health Technologies.

‡ Defence Science and Technology Organisation.

10.1021/bc0700640 CCC: $37.00 © 2007 American Chemical Society
Published on Web 08/24/2007



1



2

Figure 1. The structures of G_{M1} (1) and phytantriol (2).

aggregation of lipid molecules into a liquid crystalline phase, forming a three-dimensional bilayer structure with a high degree of internal order and structural uniformity. These self-assembled structures include the lamellar phase (L_α), which is comprised of sheets of stacked bilayer sheets and the inverse hexagonal phase (H_{II}) which can be conceptualised as infinitely packed cylindrical rods with an aqueous interior. Of particular interest is the bicontinuous inverse cubic phase in which a surfactant bilayer is folded onto an infinitely periodic minimal surface (IPMS) (*21*) consisting of infinite interwoven arrays of saddle surfaces with zero mean curvature and constant negative Gaussian curvature (*22*, *23*). The middle of the bilayer, defined by the terminal methyl groups of the intersecting hydrophobic moieties, forms the IPMS and the hydrophilic parts interface with the bulk water. This molecular architecture affords distinct aqueous regions that form two continuous water networks (or channels) throughout the cubic phase. Long-range crystallographic periodicity is found in such structures, with crystallographic space groups including the *Im*3*m*, *Pn*3*m*, and *Ia*3*d* having been reported (*24*, *25*).

The inverse cubic mesophase is thermodynamically stable and coexists in equilibrium with excess water over a broad temperature range. The resulting self-assembled material, in contrast to other aggregate systems such as micelles, is stable to dilution in water. These properties, and in particular the internal three-dimensional cubic nanostructure, have been exploited in biological applications such as protein entrapment and crystallization (*26*, *27*) as well as drug delivery (*28*−*33*). We reasoned that the cubic mesophase provides the appropriate hydrophilic and hydrophobic microenvironments reminiscent of the cell membrane, which should be favorable for biological ligand-receptor recognition (*31*). We further reasoned that owing to the high surface area of the internal mesophase structure (up to 400 m^2/g) (*34*), the inverse cubic phase provides an excellent scaffold for the immobilization of a high concentration of mobile monomeric antagonists which might facilitate self-arrangement of the ligands resulting in a polyvalent interaction. Such self-arrangement mitigates the requirement of a rigid molecular architecture currently employed in the design of polyvalent inhibitors. We have recently demonstrated the utility of this approach by incorporating synthetic galactose-functionalized surfactants within cubic phases for the sequestration of the plant toxin ricin (*20*). Here, we demonstrate for the first time a cubic phase toxin inhibitor based on the naturally derived lipid receptor for cholera toxin, ganglioside G_{M1} (Figure 1). The interaction between G_{M1} and CT is well characterized and involves a very strong binding interaction (K_d, 0.7−7 nM) (*35*).

The matrix we have employed for supporting the bioactive G_{M1} is the bicontinuous cubic phase of the inverse type formed by the surfactant 3,7,11,15-tetramethyl-1,2,3-hexadecanetriol or 'phytantriol' (Figure 1). The inverse cubic phase of phytantriol exists over a broad temperature range (*36*) and importantly, is not susceptible to hydrolysis that other surfactants such as glycerol monoolein (GMO) may undergo. We have studied both the physical chemistry and binding efficacy of G_{M1} functionalized cubic phases. We believe that this approach demonstrates the potential for inverse cubic phases in either bulk or dispersed forms to act as generic scaffolds for the design of polyvalent inhibitors which target a large class of biotoxins (*37*).

EXPERIMENTAL PROCEDURES

Preparation of G_{M1}/Phytantriol Mixtures. Monosialoganglioside (G_{M1}) (95%) obtained from bovine brain was purchased from Sigma Aldrich. 3,7,11,15-tetramethyl-1,2,3-hexadecanetriol (phytantriol) (96%) was purchased from Aldrich and was used without further purification. Dichloromethane was HPLC grade and used without further purification. The required quantity of G_{M1} was suspended in phytantriol and dissolved in a solution of 10 mL of 20% methanol/dichloromethane. The mixture was thoroughly dissolved until an optically transparent solution resulted. The solvent was then removed using rotary evaporation at a temperature of 40 °C for 25 min @ −68 kPa to afford a clear viscous oil.

Phase Behavior Observations by Polarizing Microscopy. Each sample mixture was placed between a microscope slide and coverslip and placed into the slide holder of a Mettler FP82HT hot stage controlled by a FP90 central processor. Water was dispersed at the edge of the coverslip, and capillary action drew the water between the two glass surfaces to surround the surfactant mixture. The sample was heated from room temperature (20 to 22 °C) at 2 °C/min or less. The interaction of water with the G_{M1}/phytantriol mixtures was viewed using an Olympus IX-70 microscope equipped with crossed polarizing lenses. Images were captured using a Canon EOS 300D digital camera. These 'water penetration scans' were usually performed in the temperature range 22−100 °C ± 0.5 °C.

Small-Angle X-ray Scattering (SAXS). The lipid phases in the presence of excess water were used for SAXS. Samples were analyzed at 22 °C. The hydrated mesophase systems did not exhibit any signs of instability under the conditions described. All small-angle X-ray scattering analyses were performed using a Bruker Nanostar SAXS camera equipped with a position sensitive 2-D "Hi-Star" detector using point collimated copper K_α radiation. Experiments were performed under a low-pressure

helium atmosphere to minimize background scattering. The gels were prepared with excess water and placed between two mica windows taped to a 1 mm stainless steel spacer. This was clamped to the analysis geometry by a stainless steel plate. Data acquisition was performed at a sample-to-detector distance of 23 cm which facilitated analysis of intensity behavior over the wavevector range: $0.0498\ \text{Å}^{-1} \leq q \leq 0.950\ \text{Å}^{-1}$. The scattering profiles of the empty sample geometries were subtracted from the final scattering profile of the sample (per-pixel subtraction) after first correcting for the intensity of the X-ray beam.

Assay for Cholera Binding by Lyotropic Mesophases. Nunc-Immuno 96-microwell flat-bottom plates with a Maxisorp surface were obtained through Medos Company, Melbourne, Australia. Phosphate-buffered saline (PBS) was prepared by dissolving a tablet from Sigma-Aldrich in 200 mL of deionized distilled water. The resultant solution comprised 0.01 M phosphate, 0.137 M NaCl, and 0.0027 M KCl, pH 7.4 at 25 °C. PBS-Tween was prepared by dissolving the contents of a sachet from Sigma-Aldrich in 1 L of deionized distilled water. This gave a solution of 0.01 M phosphate, 0.138 M NaCl, 0.0027 M KCl, 0.05% Tween 20, pH 7.4, at 25 °C. Cholera toxin from *Vibrio cholerae* Inaba 569B (azide free) was obtained from List Biological Laboratories, Campbell, CA. The toxin was received as a powder, dissolved in 1.0 mL of deionized distilled water, and then stored at 2 °C. The reconstituted cholera toxin contained 1 mg of protein in 1.0 mL of 0.05 M Tris, 0.2 M NaCl, and 0.001 M Na_2EDTA at pH 7.5. The solution was diluted with PBS-Tween immediately prior to assays. Purified polyclonal goat anti-cholera toxin was a product of Biogenesis, Poole, UK. All other materials were obtained from Sigma-Aldrich, Sydney, Australia. Monosialoganglioside G_{M1} from bovine brain was obtained as 1 mg of powder. It was dissolved in 1 mL of methanol, stored at −20 °C, and diluted just before use. The substrate solution for alkaline phosphatase was prepared by dissolving two *p*-nitrophenyl phosphate tablets and two TRIS buffer tablets from Sigma-Aldrich in 11 mL of deionized distilled water.

Stock solutions (50 mg/mL or 23 mg/mL) of the surfactant mixtures were prepared in methylene chloride. Serial dilutions of the mixtures in dichloromethane were prepared to give the appropriate concentration. Ten-microliter aliquots of the serial dilutions were placed in glass test tubes, and the solvent was allowed to evaporate for 1−2 h in a fume cupboard at room temperature (20 °C). The movement of air in the fume cupboard facilitated the rapid evaporation of the solvent. Cholera toxin solution, of a concentration between 1.0 and 100 ng/mL in blocking buffer (PBS-Tween with 0.25% bovine serum albumin; 130 μL), was added to the tubes, and they were placed on a rocker platform and gently oscillated for 24 h at room temperature. Aliquots (100 μL) of the supernatants from these tubes were then added to immobilized G_{M1} in Nunc microtiter plates, and the cholera toxin assay was performed as described below. Additional runs were performed both without the mesophase solution and in the presence of pure phytantriol (without G_{M1}) as controls.

In the standard cholera toxin assay, all incubations were at room temperature (20−22 °C), with a volume per well of 0.1 mL except for the incubation with blocking buffer (0.36 mL). After each incubation, the microtiter plate was emptied and washed three times with PBS-Tween. An additional wash with distilled water was performed before addition of the alkaline phosphatase substrate. The wells of a microtiter plate received 100 ng/mL of G_{M1} in PBS and were left overnight (ca. 16 h) before rinsing with PBS-Tween and sequential treatment with blocking buffer, cholera toxin from the assay supernatant (100 μL in blocking buffer), goat anti-cholera toxin antibody (1:8000 dilution in blocking buffer), rabbit anti-goat alkaline phosphatase conjugate (1:2000 dilution in blocking buffer), and substrate (*p*-nitrophenyl phosphate solution). Incubation times were 1 h for the blocking buffer, antibody, and conjugate and 1.5−3 h for the cholera toxin. The microtiter plate was shaken on a plate shaker (Ratek Instruments, Melbourne, Australia) during incubations with cholera toxin and the two antibody solutions. After addition of substrate, the absorbance was read at 405 nm at 2.5-min intervals for 17.5 min in an ICN Titertek-Plus MS212 plate reader, and the steady-state rate of increase of absorbance was calculated. Each experiment was performed at least twice.

A calibration curve for solution cholera toxin (CT) concentration (1.0−100 ng/mL) *versus* rate of change of absorbance per minute (abs/min) for each ELISA assay was constructed. The data was conveniently fit using a logarithmic relationship (*20*).

$$\text{abs/min} = A + B.\ln[\text{CT}] \quad (1)$$

The *A* and *B* factors in the above relationship were obtained from the linear plot of ln[CT] *versus* abs/min. These factors were then used to derive a residual CT concentration (final [CT]) and % binding in solutions which were exposed to mesophase test samples. The data are plotted in Figures S1 and S2 (Supporting Information) for the G_{M1}/phytantriol mesophase formulations. For each mesophase mixture, six concentrations of G_{M1}/phytantriol were submitted to binding assay ($0.13-1.3 \times 10^4$ ng/mL and $0.065-6.5 \times 10^3$ ng/mL for 10% G_{M1}/phytantriol and 20% G_{M1}/phytantriol, respectively), as described above. The percentage binding of CT by the mesophase mixtures for the highest concentration of CT studied (100 ng/mL) is reported in Figure 5.

Equilibrium dissociation constants (K_d) for the binding of CT by mesophase components were calculated using the relationship (eq 2), where the reciprocal of the equilibrium association constant (K_a) gives K_d. The K_a value was calculated from the estimated equilibrium concentration of the G_{M1}−CT complex (MT), the equilibrium concentration of unbound G_{M1} (M) and cholera toxin (T), (eq 3).

$$K_d = 1/K_a \quad (2)$$

$$K_a = [\text{MT}]/[\text{M}].[\text{T}] \quad (3)$$

The model assumes a 1:1 stoichiometry for (MT), since unambiguous determination of polyvalent binding equilibria introduces significant complexity into equilibrium binding analysis.

Table 1. G_{M1}/Phytantriol Liquid Crystalline Phases Assigned in the Presence of Excess Water

	temperature regime of phases (°C)			
mixture	L_α	Q	H_{II}	L_{II}
100% phytantriol	-	<23−54	54−67	68−100
10% G_{M1}/phytantriol	-	<23−60	60−85	85−100
20% G_{M1}/phytantriol	-	<23−46	<46−70	70−100
30% G_{M1}/phytantriol	<22−28	<28−29	-	30−60
40% G_{M1}/phytantriol	<26−30	<30−33	-	35−52

RESULTS AND DISCUSSION

We focused our initial studies on obtaining mesophase mixtures in which a high concentration of G_{M1} could be incorporated into phytantriol, while retaining the inverse cubic phase structure. Four mixtures were prepared each with a loading of G_{M1} between 10 and 40% w/w. The structure and presence of phases for the G_{M1}/phytantriol mixtures was qualitatively identified by light polarizing microscopic observation as excess water diffused into the surfactant mixture ('water penetration scans'). Table 1 compares the temperature for the first appearance of phases at the surfactant-water interface and the tem-

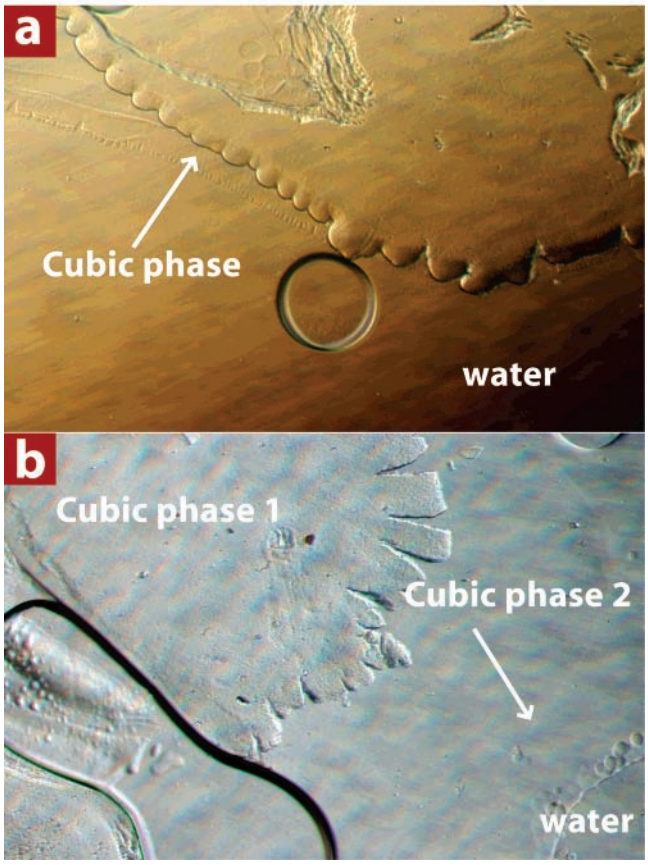


Figure 2. Polarized optical microscopy images of representative mesophase mixtures. (A) 10% G_{M1}/phytantriol ($T = 37.0$ °C) and **(B)** 20% G_{M1}/phytantriol ($T = 40.0$ °C) in excess water.

perature range over which they are present for the G_{M1}/phytantriol mixtures. The microscopy data shows that a cubic phase (Q) was exhibited by all mesophase mixtures at ambient temperature. Figure 2 shows representative light polarizing microscope images for the 10% G_{M1}/phytantriol and 20% G_{M1}/phytantriol, respectively. The inverse cubic phase behavior of each phase was characterized by non-birefringence and irregular morphologies (indicating high viscosity) at the aqueous interface. For the 10% and 20% G_{M1}/phytantriol mixtures, the phase behavior in excess water follows the sequence of cubic (Q) to inverse hexagonal (H_{II}), followed by a mobile isotropic phase ($H_{II} \rightarrow L$) with increasing temperature. The mobile isotropic phase was characterized by a non-birefringent optical property and low viscosity, detailed by the flow of air bubbles in the isotropic phase close to the bulk aqueous region. This phase was assigned as reversed micellar (L_{II}), which are the expected phase transitions with decreasing water content (*38*). This is similar to the phase sequence recently reported by Barauskas and Landh (*36*) for phytantriol in excess water ($Q \rightarrow H_{II} \rightarrow L_{II}$). It is important to note however, that the $Q \rightarrow H_{II}$ phase transition temperature of the phytantriol used in the present study occurred at 54 °C, while Barauskas and Landh report a lower temperature of 44 °C. Other groups have also observed a higher temperature for this phase transition (*39*).

When the ganglioside G_{M1} concentration was increased to 30−40% in phytantriol, the resemblance to the pure phytantriol phase behavior was lost. At these higher loadings of ganglioside, the phase transitions followed the order of lamellar (L_α) to cubic phase (Q) followed by a transition to a reversed micellar (L_{II}), ($L_\alpha \rightarrow Q \rightarrow L$). Thus, unlike the 10% and 20% G_{M1}/phytantriol mixtures, the higher loading of ganglioside appeared to destabilize the Q phase, which also appeared over a very narrow temperature range (25−33 °C). A plausible reason for the observed instability of the Q phase, in addition to the appearance of the L_α at higher G_{M1} concentrations, is the modification of mesophase curvature derived from the difference in molecular packing geometry of the ganglioside and phytantriol. We assume that that G_{M1} is homogeneously distributed within the phytantriol matrix and the mode of insertion involves the occupation of the pentasaccharide at the aqueous interface, with the ceramide hydrophobe embedded into the interior of the surfactant bilayer, packing with the terpenoid chains of phytantriol. The packing of each lipid is described by the critical packing parameter, S, which is described by the relationship $S = \nu(\alpha_0 l_C)^{-1}$, where ν is the molecular volume of the chains, l_C is the molecular length of the chains, and α_0 is the optimal headgroup area for each amphiphile monomer. When the packing parameter is less than unity ($S < 1$), the resulting aggregate is curved toward the hydrophobic region as in normal micellar aggregates (L_I), while for molecules where $S \approx 1$, a cylindrical molecular geometry is suggested, resulting in the formation of a flat bilayer (lamellar phase). On the other hand, if the amphiphile contains a hydrophobic moiety that occupies a large volume and correspondingly small headgroup, then $S > 1$ and the aggregate is curved toward the polar region, as observed with cubic or inverse hexagonal phases. Qualitatively, phytantriol displays an inverted cone-shaped molecular geometry derived from the small triol-containing headgroup and terpenoid tail that occupies a large molecular volume (*40*), thus $S > 1$. An inspection of the structure of G_{M1} reveals a wedge-shaped molecular geometry based on relative cross-sectional area of 40 Å^2 (*41*) for the ceramide and 95 Å^2 (*42*) for the hydrated G_{M1} pentasaccharide headgroup, affording a critical packing parameter of less than unity ($S < 1$). In general, negative interfacial curvature increases, with respect to water, in proceeding from a lamellar to cubic to an inverse hexagonal phase transition ($L_\alpha \rightarrow Q \rightarrow H_{II}$) (*38*). Thus, the incorporation of an increased mole fraction of G_{M1} into the bilayer of phytantriol forces a reduction in the net negative curvature relative to water, owing to the geometric incompatibility of the two lipids. Moreover, the formation of a lamellar phase (L_α) observed at room-temperature suggests that a 30−40% w/w G_{M1} loading completely disrupts (flattens) the interfacial curvature. Accordingly, the highest concentration of ganglioside that could be incorporated into phytantriol, while retaining mesophase structure, was 20% w/w, and the compositions reported here represent the upper limit of G_{M1} loading within the phytantriol mesophase matrix. Accordingly, the 10% G_{M1}/phytantriol and 20% G_{M1}/phytantriol mesophase mixtures were examined in greater detail as potential cholera toxin (CT) inhibitors.

A detailed structural analysis for the 10% G_{M1}/phytantriol and 20% G_{M1}/phytantriol mesophase mixtures was performed using SAXS. The SAXS diffraction patterns for each of these mixtures, as shown in Figure 3, verified cubic phase structures in excess water at room temperature (22 °C). This study evidence a periodic (cubic) structure for both samples, supporting the cross-polarizer microscopic observations. The Bragg reflections for each sample gave reciprocal spacings in the ratio $1{:}\sqrt{2},\sqrt{4},\sqrt{6}$, etc., which was consistent with the cubic phase with a $Im3m$ (Q^{229}) spacer group (*22*). The allowed Bragg reflections for an $Im3m$ space group correspond to $h\ k\ l = 110$, 200, 211, 220, 310, 222, 321, etc. The intense 110, 200, and 211 reflections were conclusively assigned as the first three reflections for the $Im3m$ (Q^{229}) space group observed for each mesophase mixture. The higher order reflections (220, 310, 222, 321, etc.) exhibited a weak intensity and could not be unambiguously assigned. Figure 4 shows the plot of q ($= 2\pi/d$) for the observed reflections as a function of $(h^2 + k^2 + l^2)^{1/2}$. The plot generated a straight line, passing through the origin, which is the expected trend behavior for the cubic phase (*43*). The

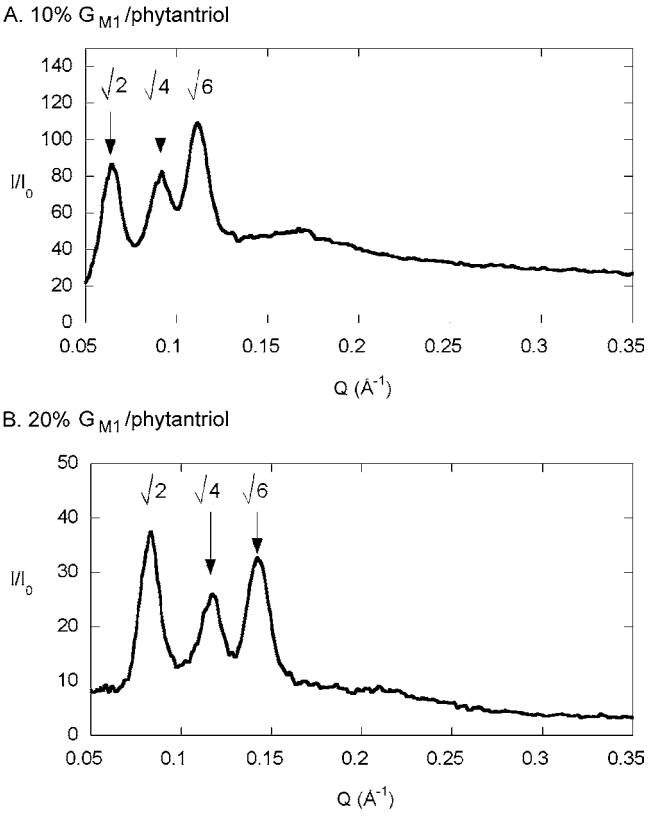


Figure 3. SAXS diffraction patterns obtained from the cubic phases of the **(**A**)** 10% G_{M1}/phytantriol and **(**B**)** 20% G_{M1}/phytantriol in excess water at 22 °C. The Bragg reflections gave higher order reciprocal spacings in the ratio 1:√2,√4,√6.

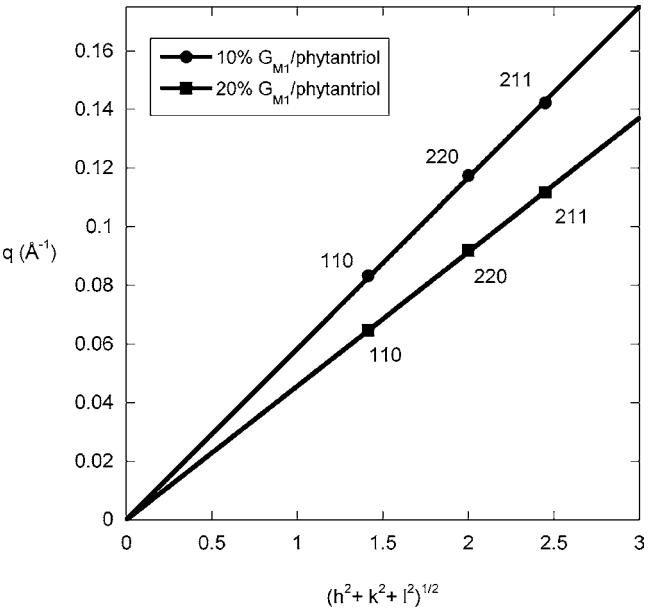


Figure 4. Plots of the reciprocal *d*-spacings (*q*) as a function of the Miller indices, $(h^2 + k^2 + l^2)^{1/2}$ from the observed reflections in the SAXS diffraction patterns for the 10% and 20% G_{M1}/phytantriol mixtures in excess water. The linearity of the plots and the intercept through the origin is consistent with the cubic phase with a *Im*3*m* (Q^{229}) spacer group. From the slope of the plots, the calculated lattice parameters (α) were 107.1 Å and 137.3 Å for 10% G_{M1}/phytantriol and 20% G_{M1}/phytantriol, respectively.

graph shows a good fit to data for the indexing of the observed diffraction peaks, confirming *Im*3*m* symmetry for both phases. Interestingly, pure phytantriol adopts a cubic phase with a *Pn*3*m* (Q^{224}) space group in the presence of excess water (*36*). Thus, in excess water and at room temperature, the addition of 10−20% G_{M1} to pure phytantriol induces a phase transition from *Pn*3*m* symmetry to the *Im*3*m* space group. For different cubic phases (Q), interfacial curvature of the polar region decreases in moving from *Ia*3*d* → *Pn*3*m* → *Im*3*m* (*44*), again indicating that introduction of the G_{M1} lipid induces a reduction in negative interfacial curvature of the phytantriol mesophase. This behavior is consistent with the light polarizing microscopic observations of increased lamellar tendency on addition of G_{M1} described earlier. A similar *Pn*3*m* → *Im*3*m* phase transition was demonstrated by Engblom et al. (*45*, *46*) for the related inverse system, monoolein, with the addition of the lipid, distearoylphosphatidylglycerol (DSPG). We reason that the addition of the G_{M1} lipid increases the effective headgroup area (α_0) within the mesophase, thereby decreasing the critical packing parameter value (*S*), leading to an overall reduction in negative interfacial curvature, as described earlier.

Further structural analysis of the G_{M1}/phytantriol mixtures revealed that the phytantriol liquid crystalline phase swells with the addition of ganglioside. From the slope of the plot of q (= $2\pi/d$) *versus* $(h^2 + k^2 + l^2)^{1/2}$ (Figure 4), the lattice parameters (α) for each cubic unit cell were estimated. Thus, the calculated lattice parameters (α) were 107.1 Å and 137.3 Å for 10% G_{M1}/phytantriol and 20% G_{M1}/phytantriol, respectively. The dimension of the cubic unit cell for pure phytantriol, as described by the lattice parameter (α), has been reported to be 64−66 Å (*36*). This represents an increase in α of approximately 54%, under the given conditions. The swelling of the related liquid crystalline (cubic) phase of monoolein (*45*−*48*) with the addition of sodium cholate or cationic surfactants has also been observed (*49*). The uptake of solvent by the ternary monoolein systems is due to the long-range electrostatic repulsion of the charged bilayers as the concentration of the cationic component is increased. The swelling of the liquid crystalline phase in the G_{M1}/phytantriol systems is most likely a result of the reduced negative curvature of the cubic phase due to addition of ganglioside G_{M1} to phytantriol, as discussed earlier. The reduction of the negative curvature of the lipid/water interface of G_{M1}/phytantriol systems is accompanied with an affiliated increase of the surface area of the aqueous interface which promotes the diffusion of additional water into the mesophase structure. An important implication of this effect is that the expansion or 'tuning' of aqueous pore channels of the phytantriol (*Im*3*m*) cubic phase can be controlled by increasing the fraction of G_{M1}.

Cholera toxin uptake by mesophase formulations using an enzyme linked immunosorbent assay (ELISA) were performed. The ELISA assay results for the residual CT in solution, following exposure to 100 ng/mL of cholera toxin to G_{M1}/phytantriol mesophases samples, are shown in Figure 5. The data shows that the toxin has a very high affinity for each of the mesophase preparations and demonstrates that approximately 13 ng/mL of the 10%, and 6.5 ng/mL of the 20% G_{M1}/phytantriol mixtures, respectively, is capable of removal of 95−99% CT. To facilitate comparison with other polyvalent inhibitors of CT, we calculated the IC_{50} values for each of the mesophase mixtures (IC_{50} is the molar concentration of an antagonist that produces 50% maximal inhibitory response). An IC_{50} of 0.27 μM and 0.10 μM was determined for the 10% and 20% G_{M1}/phytantriol mixtures, respectively (Table 2). The estimated IC_{50} compared favorably with the IC_{50} for pentavalent and decavalent inhibitors, which have generally micromolar activity (*10*, *11*, *18*). The authors do acknowledge that the literature IC_{50} values were obtained with water soluble inhibitors, and therefore direct comparison with IC_{50} values from water insoluble mesophase inhibitors reported herein may not reflect the differences in inhibitory activity. Accordingly, the comparison between IC_{50}s are indicative of inhibitor activity, and

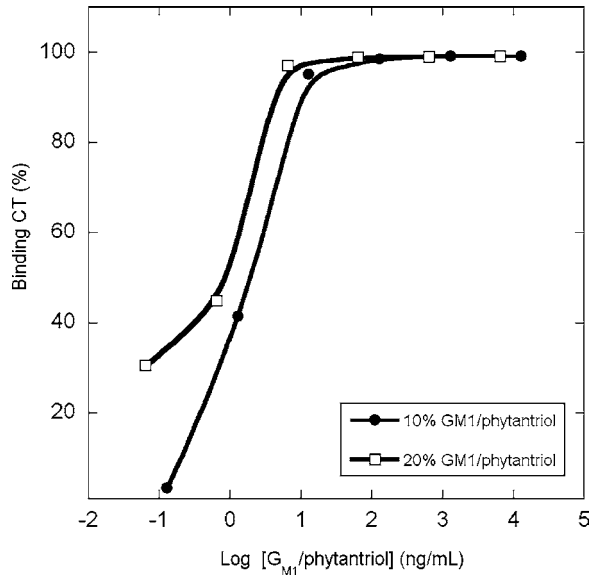


Figure 5. Percent binding of cholera toxin (CT) (100 ng/mL) as a function of mesophase concentration (ng/mL) by the 10% and 20% G_{M1}/phytantriol mesophase systems.

Table 2. Estimated Binding Parameters and IC_{50} Values

mesophase	IC_{50} (μM)	K_d (nM)
10% G_{M1}/phytantriol	0.27	73
20% G_{M1}/phytantriol	0.10	67
phytantriol	-	5.64×10^7

the preparation of a water soluble dispersion of the mesophase will generate IC_{50} values *via* a classical competitive inhibition binding assay.

The equilibrium dissociation constant, K_d, which is a measure of the affinity of the interaction, was calculated to be 73 nM for the 10% G_{M1}/phytantriol mesophases and 67 nM for the 20% G_{M1}/phytantriol mixture. The reported K_d is the average value obtained from a range of K_d values estimated for the different samples. The estimated K_d is reported on the basis of a 1:1 G_{M1}/CT binding interaction. Although the binding of G_{M1}/CT involves a 1:5 stoichiometry, the estimation of K_d *via* a 1:1 interaction simplifies the binding affinity calculation and facilitates direct comparison with literature values, which also assume an equimolar reaction (*35*, *50*). The similar K_d values suggest a comparable affinity of CT for each mesophase. However, the difference in absolute value may be attributed to incomplete equilibrium between toxin and mesophase. This may also account for the considerably higher dissociation constants than those recently estimated for G_{M1} immobilized in liposomes ($K_d = 0.26$ nM) using surface plasmon resonance (SPR) (*50*). An important consideration with the comparison of K_d values with those obtained from G_{M1}-functionalized liposomes, is that the mesophases are bulk gel-like materials and not dispersed particles. It is reasonable to assume that the liposomal systems have a large surface area for the presentation of G_{M1} for binding with the toxin. This facilitates rapid diffusion and binding of the CT to surface G_{M1}, leading to the establishment of equilibrium between toxin and receptor. The diffusion kinetics of CT within the bulk mesophase gel studied here may be limited compared to these dispersed liposome systems. Work is continuing to prepare cubic mesophase nanoparticles to optimize surface area and binding kinetics (*51*).

The pure phytantriol control shows that nonspecific binding to the mesophases is minimal at the concentrations studied, as demonstrated by the performance of the gels relative to the phytantriol. Referring to Table 2, the low affinity of pure phytantriol is evidenced by a large dissociation constant (K_d, 5.64×10^7 nM), which is approximately 8×10^5-fold greater than the G_{M1}-functionalized mesophases. This data suggests that the mechanism of CT immobilization by the mesophase mixtures involves the specific interaction of G_{M1} and CT. In addition to the absence of a specific binding interaction for the pure phytantriol systems, the geometric constraints of the *Pn*3*m* space group for pure phytantriol may reduce CT diffusion within the aqueous channels compared with the G_{M1}/phytantriol mixtures (which have a more 'open' *Im*3*m* space group). The *Im*3*m* has a higher water content than the *Pn*3*m* cubic phase and the higher levels of hydration (*38*) favor protein diffusion within the (G_{M1}/phytantriol) phase structure.

We further reason that the polyvalent recognition of CT by the immobilized G_{M1} is aided by the lateral diffusion of the ganglioside within the phytantriol bilayer to promote alignment of the B-subunit binding epitope with the G_{M1} pentasaccharide group. The reorganization of G_{M1} provides an additional favorable entropic contribution that promotes B-subunit-G_{M1} interaction. Supporting this hypothesis is the observed mobility of G_{M1} in monolayer or vesicle bilayers (*52*, *53*) and the lateral diffusion of lipids within inverse cubic mesophases (*22*, *54*). By virtue of the possible lateral mobility of G_{M1} within the mesophase bilayer, the requirement for ligands to be incorporated into rigid molecular architectures with precise spatial arrangement, such as dendrimers, is mitigated. It must be noted that the accurate location of bound toxin within the aqueous regions of the mesophase structure is unknown. We speculate that the protein adhesion to the mesophase must involve a combination of diffusion at the periphery, penetration of the aqueous channels of the surfactant assembly (*31*), and binding at the exterior surface. Further experimental evidence is required to confirm this postulate.

CONCLUSION

The demonstration of cholera toxin binding by a ganglioside-functionalized cubic mesophase is a significant advance in the development of cubic mesophase polyvalent inhibitors of AB_x-type toxins. To our knowledge this is the first example of the functionalization of an inverse cubic mesophase with lipid receptors to selectively bind cholera toxin. We have shown that phytantriol provides an excellent inert surfactant scaffold for inhibitor immobilization due to the retention of cubic phase behavior at high loadings of glycolipid and at physiological temperature, as shown by SAXS and water penetration studies. Furthermore, control measurements demonstrated that the phytantriol matrix shows minimal nonspecific binding of cholera toxin, demonstrating the tuneable specificity of these systems. A key feature of the mesophases is that the requirement for the incorporation of toxin structural data into inhibitor design is mitigated because of the possible lateral mobility of the toxin antagonists with the mesophase bilayer. The reorganization of ligands within the bilayer with toxin recognition is a unique mechanism that is unavailable to conformationally restricted polyvalent inhibitors. These results support our novel approach for the use of lyotropic mesophase systems as a new class of polyvalent affinity ligands in the development of new antitoxin prophylactics and therapeutics. Work is presently continuing to prepare cubic phase nanoparticles that will enable evaluation of mesophase particles as antitoxins by classical inhibition assay.

Supporting Information Available: The plots of the ELISA data showing the final concentration of cholera toxin (final [CT])

following incubation with a given concentration of mesophase sample. This material is available free of charge via the Internet at http://pubs.ac.org/BC.

ACKNOWLEDGMENT

We thank Dr. Jamie Booth and Prof. Suresh Bhargava of RMIT, Melbourne, for assistance with SAXS measurements.

LITERATURE CITED

(1) Haan, L., and Hirst, T. (2004) Cholera Toxin: a paradigm for multifunctional engagement of cellular mechanism. *Mol. Membr. Biol. 21*, 77−92.

(2) Zhang, R. G., Scott, D. L., Westbrook, M. L., Nance, S., Spangler, B. D., Shipley, G. G., and Westbrook, E. M. (1995) The three-dimensional crystal structure of cholera toxin. *J. Mol. Biol. 251*, 563−573.

(3) van Heyningen, W. A., Carpenter, W. E., Pierce, N. F., and Greenough, W. B. (1971) Deactivation of cholera toxin by ganglioside. *J. Infect. Dis. 124*, 415−418.

(4) Merritt, E. A., Sixma, T. K., Kalk, K. H., van Zanten, B. A. M., and Hol, W. G. J. (1994) Galactose-binding site in Escherichia coli heat-labile enterotoxin (LT) and cholera toxin (CT). *Mol. Microbiol. 13*, 745−753.

(5) Zhang, R. G., Westbrook, M. L., Westbrook, E. M., Scott, D. L., Otwinowski, Z., Maulik, P. R., Reed, R. A., and Shipley, G. G. (1995) The 2.4 Å crystal structure of cholera toxin B subunit pentamer: choleragenoid. *J. Mol. Biol. 251*, 550−562.

(6) Merritt, E. A., Sarfaty, S., Akker, F., L'Hoir, C., Martial, J. A., and Hol, W. (1994) Crystal structure of cholera toxin B-pentamer bound to receptor G(M1) pentasaccharide. *Protein Sci. 3*, 166−175.

(7) Fan, E., O'Neal, C. J., Mitchell, D. D., Robien, M. A., Zhang, Z., Pickens, J. C., Tan, X. J., Korotkov, K., Roach, C., Krumm, B., Verlinde, C., Merritt, E. A., and Hol, W. G. J. (2004) Structural biology and structure-based inhibitor design of cholera toxin and heat-labile enterotoxin. *Int. J. Med. Microbiol. 294*, 217−223.

(8) Mitchell, D. D., Pickens, J. C., Korotkov, K., Fan, E., and Hol, W. G. J. (2004) 3,5-Substituted phenyl galactosides as leads in designing effective cholera toxin antagonists. *Bioorg. Med. Chem. 12*, 907−920.

(9) Minke, W. E., Roach, C., Hol, W. G. J., and Verlinde, C. (1999) Structure-based exploration of the ganglioside GM1 binding sites of Escherichia coli heat-labile enterotoxin and cholera toxin for the discovery of receptor antagonists. *Biochemistry 38*, 5684−5692.

(10) Merritt, E. A., Zhang, Z., Pickens, J. C., Ahn, M., Hol, W. G. J., and Fan, E. (2002) Characterization and crystal structure of a high-affinity pentavalent receptor-binding inhibitor for cholera toxin and E. coli heat-labile enterotoxin. *J. Am. Chem. Soc. 124*, 8818−8824.

(11) Zhang, Z., Merritt, E. A., Ahn, M., Roach, C., Hou, Z., Verlinde, C., Hol, W. G. J., and Fan, E. (2002) Solution and crystallographic studies of branched multivalent ligands that inhibit the receptor-binding of cholera toxin. *J. Am. Chem. Soc. 124*, 12991−12998.

(12) Liu, J., Zhang, Z., Tan, X., Hol, W. G. J., Verlinde, C., and Fan, E. (2005) Protein heterodimerization through ligand-bridged multivalent pre-organization: Enhancing ligand binding toward both protein targets. *J. Am. Chem. Soc. 127*, 2044−2045.

(13) Fan, E., and Merritt, E. A. (2002) Combating infectious diseases through multivalent design. *Curr. Drug Targets−Infect. Disord. 2*, 161−167.

(14) Mammen, M., Choi, S. K., and Whitesides, G. M. (1998) Polyvalent interactions in biological systems: Implications for design and use of multivalent ligands and inhibitors. *Angew. Chem., Int. Ed. 37*, 2754−2794.

(15) Roy, R. (1996) Syntheses and some applications of chemically defined multivalent glycoconjugates. *Curr. Opin. Struct. Biol. 6*, 692−702.

(16) Polizzotti, B. D., and Kiick, K. L. (2006) Effects of polymer structure on the inhibition of cholera toxin by linear polypeptide-based glycopolymers. *Biomacromolecules 7*, 483−490.

(17) Vrasidas, I., De Mol, N., Liskamp, R., and Pieters, R. (2001) Synthesis of lactose dendrimers and multivalency effects in binding to the cholera toxin B subunit. *Eur. J. Org. Chem. 2001*, 4685−4692.

(18) Arosio, D., Vrasidas, I., Valentini, P., Liskamp, R. M. J., Pieters, R. J., and Bernardi, A. (2004) Synthesis and cholera toxin binding properties of multivalent GM1 mimics. *Org. Biomol. Chem. 2*, 2113−2124.

(19) Thompson, J. P., and Schengrund, C. L. (1997) Oligosaccharide-derivatized dendrimers: Defined multivalent inhibitors of the adherence of the cholera toxin B subunit and the heat labile enterotoxin of E. coli to GM1. *Glycoconjugate J. 14*, 837−845.

(20) Hartley, P. G., Alderton, M. R., Dawson, R. M., and Wells, D. (2007) Ricin antitoxins based on lyotropic mesophases containing galactose amphiphiles. *Bioconjugate Chem. 18*, 152−159.

(21) Scriven, L. E. (1976) Equilibrium bicontinuous structure. *Nature 263*, 123−125.

(22) Lindblöm, G., and Rilfors, L. (1989) Cubic phases and isotropic structures formed by membrane lipids-possible biological relevance. *Biochim. Biophys. Acta 988*, 221−256.

(23) Templer, R. H. (1998) Thermodynamic and theoretical aspects of cubic mesophases in nature and biological amphiphiles. *Curr. Opin. Colloid Interface Sci. 3*, 255−263.

(24) Delacroix, H., Gulik-Krzywicki, T., and Seddon, J. M. (1996) Freeze fracture electron microscopy of lyotropic lipid systems: Quantitative analysis of the inverse micellar cubic phase of space group fd3m (Q227). *J. Mol. Biol. 258*, 88−103.

(25) Seddon, J. M., Robins, J., Gulik-Krzywicki, T., and Delacroix, H. (2000) Inverse micellar phases of phospholipids and glycolipids. *Phys. Chem. Chem. Phys. 2*, 4485−4493.

(26) Landau, E. M., and Rosenbusch, J. P. (1996) Lipidic cubic phases: A novel concept for the crystallization of membrane proteins. *Proc. Natl. Acad. Sci. U.S.A. 93*, 14532−14535.

(27) Caffrey, M. (2003) Membrane protein crystallization. *J. Struct. Biol. 142*, 108−132.

(28) Drummond, C. J., and Fong, C. (1999) Surfactant self-assembly objects as novel drug delivery vehicles. *Curr. Opin. Colloid Interface Sci. 4*, 449−456.

(29) Boyd, B. J., Whittaker, D. V., Khoo, S. M., and Davey, G. (2006) Lyotropic liquid crystalline phases formed from glycerate surfactants as sustained release drug delivery systems. *Int. J. Pharm. 309*, 218−226.

(30) Clogston, J., Craciun, G., Hart, D. J., and Caffrey, M. (2005) Controlling release from the lipidic cubic phase by selective alkylation. *J. Controlled Release 102*, 441−461.

(31) Clogston, J., and Caffrey, M. (2005) Controlling release from the lipidic cubic phase. Amino acids, peptides, proteins and nucleic acids. *J. Controlled Release 107*, 97−111.

(32) Cherezov, V., Yamashita, E., Liu, W., Zhalnina, M., Cramer, W. A., and Caffrey, M. (2006) In meso structure of the cobalamin transporter, BtuB, at 1.95 A resolution. *J. Mol. Biol. 364*, 716−734.

(33) Liu, W., and Caffrey, M. (2006) Interactions of tryptophan, tryptophan peptides, and tryptophan alkyl esters at curved membrane interfaces. *Biochemistry 45*, 11713−11726.

(34) Lawrence, M. J. (1994) Surfactant systems: their use in drug delivery. *Chem. Soc. Rev. 23*, 417−423.

(35) MacKenzie, C. R., Hirama, T., Lee, K. K., Altman, E., and Young, N. M. (1997) Quantitative analysis of bacterial toxin affinity and specificity for glycolipid receptors by surface plasmon resonance. *J. Biol. Chem. 272*, 5533−5538.

(36) Barauskas, J., and Landh, T. (2003) Phase behavior of the phytantriol/water system. *Langmuir 19*, 9562−9565.

(37) Falnes, P., and Sandvig, K. (2000) Penetration of protein toxins into cells. *Curr. Opin. Cell Biol. 12*, 407−413.

(38) Hyde, S., Andersson, S., Larsson, K., Blum, Z., Landh, T., Lidin, S., and Ninham, B. W. (1997) *The language of shape. The role of curvature in condensed matter: physics, chemistry and biology*; Elsevier, Amsterdam.

(39) Dong, Y.-D., Larson, I., Hanley, T., and Boyd, B. J. (2006) Bulk and dispersed aqueous phase behavior of phytantriol: Effect of vitamin E acetate and F127 polymer on liquid crystal nanostructure. *Langmuir 22*, 9512−9518.

(40) Fong, C., Wells, D., Krodkiewska, I., Hartley, P. G., and Drummond, C. J. (2006) New role for urea as a surfactant headgroup promoting self-assembly in water. *Chem. Mater. 18*, 594−597.
(41) Majewski, J., Kuhl, T. L., Kjaer, K., and Smith, G. S. (2001) Packing of ganglioside-phospholipid monolayers: An x-ray diffraction and reflectivity study. *Biophys. J. 81*, 2707−2715.
(42) Corti, M., Boretta, M., Cantù, L., Del Favero, E., and Lesieur, P. (1996) Dependence of the form factor of ganglioside micelles on a conformational change with temperature. *J. Mol. Struct. 383*, 91−98.
(43) Alexandridis, P., Olsson, U., and Lindman, B. (1998) A record nine different phases (four cubic, two hexagonal, and one lamellar lyotropic liquid crystalline and two micellar solutions) in a ternary isothermal system of an amphiphilic block copolymer and selective solvents (water and oil). *Langmuir 14*, 2627−2638.
(44) Shearman, G. C., Ces, O., Templer, R. H., and Seddon, J. M. (2006) Inverse lyotropic phases of lipids and membrane curvature. *J. Phys.: Condens. Matter 18*, S1105−S1124.
(45) Engblom, J., Miezis, Y., Nylander, T., Razumas, V., and Larsson, K. (2000) On the swelling of monoolein liquid-crystalline aqueous phases in the presence of distearoylphosphatidylglycerol. *Prog. Colloid Polym. Sci. 116*, 9−15.
(46) Lindell, K., Engblom, J., Jonstroemer, M., Carlsson, A., and Engstroem, S. (1998) Influence of a charged phospholipid on the release pattern of timolol maleate from cubic liquid crystalline phases. *Prog. Colloid Polym. Sci. 108*, 111−118.
(47) Cherezov, V., Clogston, J., Misquitta, Y., Abdel-Gawad, W., and Caffrey, M. (2002) Membrane protein crystallization in meso: Lipid type-tailoring of the cubic phase. *Biophys. J. 83*, 3393−3407.
(48) Gustafsson, J., Nylander, T., Almgren, M., and Ljusberg-Wahren, H. (1999) Phase behaviour and aggregate structure in aqueous mixtures of sodium cholate and glycerol monooleate. *J. Colloid Interface. Sci. 211*, 326−335.
(49) Gustafsson, J., Orädd, G. N. M., Hansson, P., and Almgren, M. (1998) Defective lamellar phases and micellar polymorphism in mixtures of glycerol monooleate and ceytltrimethylammonium bromide in aqueous solution. *Langmuir 14*, 4987−4996.
(50) Cooper, M. A., Hansson, A., LöFåS, S., and Williams, D. H. (2000) A vesicle capture sensor chip for kinetic analysis of interactions with membrane-bound receptors. *Anal. Biochem. 277*, 196−205.
(51) Fong, C., Krodkiewska, I., Wells, D., Boyd, B. J., Booth, J., Bhargava, S., Mcdowall, A., and Hartley, P. G. (2005) Submicron dispersions of hexosomes based on novel glycerate surfactants. *Aust. J. Chem. 58*, 683−687.
(52) Menke, M., Künneke, S., and Janshoff, A. (2002) Lateral organization of GM1 in phase-separated monolayers visualized by scanning force microscopy. *Eur. Biophys. J. 31*, 317−322.
(53) Wang, R., Shi, J., Parikh, A. N., Shreve, A. P., Chen, L., and Swanson, B. I. (2004) Evidence for cholera aggregation on GM1-decorated lipid bilayers. *Colloid Surface B 33*, 45−51.
(54) Barauskas, J., Raumas, V., and Nylander, T. (1999) Solubilisation of ubiquinone-10 in the lamellar and bicontinuous cubic phases of aqueous monoolein. *Phys. Lipids 97*, 167−179.

BC0700640

Lung Delivery Studies Using siRNA Conjugated to TAT(48−60) and Penetratin Reveal Peptide Induced Reduction in Gene Expression and Induction of Innate Immunity

Sterghios Athanasios Moschos,*,† Simon Wyn Jones,‡ Mark Michael Perry,† Andrew Evan Williams,† Jonas Sten Erjefalt,§ John James Turner,|| Peter John Barnes,† Brian Stephen Sproat,⊥ Michael John Gait,|| and Mark Andrew Lindsay†

Biopharmaceutics Research Group, Airways Disease, National Heart and Lung Institute, Imperial College, London, UK, AstraZeneca R&D, Respiratory and Inflammation Research Area, Alderley Park, Macclesfield, Cheshire, UK, Department of Experimental Medical Science, Division of Vascular and Airway Research, Lund University, Lund, Sweden, Medical Research Council Laboratory of Molecular Biology, Cambridge, UK, and Integrated DNA Technologies, BVBA, Leuven, Belgium .
Received March 8, 2007; Revised Manuscript Received May 31, 2007

The therapeutic application of siRNA shows promise as an alternative approach to small-molecule inhibitors for the treatment of human disease. However, the major obstacle to its use has been the difficulty in delivering these large anionic molecules *in vivo*. In this study, we have investigated whether siRNA-mediated knockdown of p38 MAP kinase mRNA in mouse lung is influenced by conjugation to the nonviral delivery vector cholesterol and the cell penetrating peptides (CPP) TAT(48−60) and penetratin. Initial studies in the mouse fibroblast L929 cell line showed that siRNA conjugated to cholesterol, TAT(48−60), and penetratin, but not siRNA alone, achieved a limited reduction of p38 MAP kinase mRNA expression. Intratracheal administration of siRNA resulted in localization within macrophages and scattered epithelial cells and produced a 30−45% knockdown of p38 MAP kinase mRNA at 6 h. As with increasing doses of siRNA, conjugation to cholesterol improved upon the duration but not the magnitude of mRNA knockdown, while penetratin and TAT(48−60) had no effect. Importantly, administration of the penetratin or TAT(48−60) peptides alone caused significant reduction in p38 MAP kinase mRNA expression, while the penetratin−siRNA conjugate activated the innate immune response. Overall, these studies suggest that conjugation to cholesterol may extend but not increase siRNA-mediated p38 MAP kinase mRNA knockdown in the lung. Furthermore, the use of CPP may be limited due to as yet uncharacterized effects upon gene expression and a potential for immune activation.

INTRODUCTION

The discovery of RNA interference (RNAi) and the application of short interference RNA (siRNA) for the knockdown of protein expression through mRNA degradation has revolutionized the area of functional genomics (*1*, *2*). Thus, siRNA macromolecules composed of double-stranded RNA 21−23 nucleotides in length are now commonly used in cell-based studies to investigate gene function. Furthermore, a number of academic groups and biotechnology companies are investigating the utility of siRNA as a therapeutic approach in the treatment of diseases such as macular degeneration, hepatitis C infection, and cancer (*3*−*6*).

Compared with small molecule inhibitors, the relatively large size and anionic charge of siRNA means that one of the key barriers to their *in vivo* use is the availability of effective approaches for delivery both to specific tissues and across the plasma membrane. Since intravenous siRNA administration is subject to first-pass metabolism, unless a liver condition is being targeted (i.e., hepatitis C infection), therapeutic application is limited to tissues where siRNA localization for extended periods is possible, e.g., following intra-ocular injection for the treatment of macular degeneration. In the case of the lung, the structure of the tissue permits direct access to large numbers of cells within the branching airways and alveoli, an estimated surface area of 400 m^2 in man. Importantly, the facility of topical delivery via intranasal, intratracheal, or aerosol administration suggests the lung as an ideal target organ for siRNA-based therapeutics. Indeed, studies have shown that siRNA-mediated attenuation of cytokine (*7*) and heme oxygenase-1 expression (*8*) during acute lung injury. Similarly, intranasal and intratracheal siRNA administration have been shown to prevent parainfluenza and respiratory syncytial virus (PIV and RSV, respectively) infection in mice (*9*−*12*) and severe acute respiratory syndrome (SARS) infection in rhesus monkeys (*13*).

In the majority of these studies, cationic lipids (e.g., lipofectin) and polymers (e.g., PEI and dendrimers) have been employed to package and deliver the siRNA to the lung. However, generic application of these strategies is limited by drawbacks such as toxicity and siRNA-mediated induction of immune responses through Toll-like receptors (TLR) (*14*−*16*). In an attempt to circumvent these problems, we examined the utility of chemical conjugation of siRNA to the nonviral delivery vector cholesterol and the cell-penetrating peptides (CPP) penetratin and TAT-(48−60) to improve siRNA-mediated mRNA knockdown in the mouse lung. Specifically, we attempted to target the constitutively expressed p38 mitogen-activated protein (MAP) kinase (also known as MAPK14). Activation of this protein is known

* Author to whom correspondence should be addressed: Sterghios A. Moschos, Ph.D., Biopharmaceutics Research Group, Airways Disease, National Heart and Lung Institute, Imperial College, Dovehouse Street, London, SW3 6LY, UK Tel: +44 2073528121 ext 3061; Fax: +44 2073528127; E-mail: s.moschos@imperial.ac.uk.

† Imperial College.

‡ AstraZeneca R&D.

§ Lund University.

|| Medical Research Council Laboratory of Molecular Biology.

⊥ Integrated DNA Technologies.

10.1021/bc070077d CCC: $37.00 © 2007 American Chemical Society
Published on Web 08/21/2007

to be important in the release of multiple pro-inflammatory mediators including tumor necrosis factor (TNF)-α and interleukin (IL)-1. Indeed, many pharmaceutical companies are developing small-molecule inhibitors that target p38 MAP kinase to be used in the treatment of a host of inflammatory diseases including rheumatoid arthritis, Crohn's disease, chronic obstructive pulmonary disease, and psoriasis (*17*, *18*).

Chemical conjugation of siRNA to cholesterol has been shown to facilitate intracellular siRNA uptake *in vitro* (*19*) and *in vivo* (*20*). In the latter case, intravenous administration of cholesterol-conjugated siRNA was shown to silence endogenous apolipoprotein B (ApoB) gene expression in the liver and jejunum, resulting in decreased plasma levels of apoB protein and total cholesterol (*20*). Interestingly, a recent study has shown that the delivery of siRNA targeted to ApoB can be further increased ~20-fold compared to cholesterol conjugation by formulation in stabilized nucleic acid lipid particles (SNALP) (*21*). Additional evidence of the utility of cholesterol for oligonucleotide delivery is provided in a recent report showing cholesterol-mediated delivery of 2′-O-methyl- and phosphorothioate-modified single-stranded RNA for the knockdown of microRNA expression in the liver, lung, kidney, heart, intestine, fat, skin, bone marrow, muscle, ovaries, and adrenal glands following intravenous injection (*22*).

The CPP TAT(48−60) and penetratin are short cationic peptides derived from the HIV-1 TAT *trans*-activator protein (*23*, *24*) and the insect *Antennaedia* homeoprotein (*25*) that have been extensively used for the *in vitro* and *in vivo* delivery of biologically active peptides and proteins (*26*, *27*). Significantly, CPP have been shown to mediate uptake of a range of biological and nonbiological cargos, which has led to the suggestion that they may represent a universal, nontoxic approach for the delivery of oligonucleotides (*28*−*31*). Interestingly, although no studies have examined the utility of CPP for the *in vivo* delivery of siRNA, this possibility is supported by reports showing penetratin-mediated delivery of siRNA and antisense into isolated neurons (*32*−*34*) and TAT(48−60)−siRNA conjugate-mediated knockdown of eGFP and CDK9 expression in HeLa cells (*35*).

In this report, we demonstrate that intratracheal administration of siRNA achieved a limited attenuation of mRNA expression in the lung for an endogenous, constitutively expressed target, p38 MAP kinase. However, although conjugation to cholesterol, TAT(48−60), or penetratin facilitated knockdown of p38 MAP kinase mRNA in a mouse cell line, only cholesterol−siRNA conjugates were found to influence target gene mRNA levels *in vivo*. Importantly, since both CPP inhibited p38 MAP kinase mRNA expression *in vivo*, but not *in vitro*, we document the existence of as yet uncharacterized CPP bioactivity. Moreover, the detection of innate immune response induction by penetratin−siRNA but not TAT(48−60)−siRNA conjugates suggests differential cellular uptake mechanisms between the two CPP.

EXPERIMENTAL METHODS

siRNA Conjugation and Annealing. Initial screening studies were performed with pre-annealed and PAGE-purified siRNA obtained from Dharmacon, Inc. (Lafayette, USA), using the following sequences: A—sense, 5′-GCACACUGAUGAUGAGAUGUU-3′; antisense, 5′-CAUCUCAUCAUCAGUGUGCUU-3′; B—sense, 5′-ACAUUCGGCUGACAUAAUUUU-3′; antisense, 5′-AAUUAUGUCAGCCGAAUGUUU-3′; C—sense, 5′-GGGAGGUGCCCGAACGAUAUU-3′; antisense, 5′-UAUCGUUCGGGCACCUCCCUU-3′; mismatch 1 (MM1)—sense, 5′-CCGAGGUGGCGGAACGAUAUU; antisense, 5′-UAUCGUUCCGCCACCUCGGUU-3′; mismatch 2 (MM2)—sense, 5′-GCGAGCUGCGCGAAGGAUAUU-3′; antisense, 5′-UAUCCUUCGCGCAGCUCGCUU-3′.

The synthesis of disulfide-linked constructs was performed by Dr. Brian Sproat at Integrated DNA Technologies (Leuven, Belgium). Npys-activated C-terminal Cys containing TAT(48−60 − grkkrrqrrrpppqc) and penetratin (rqikiwfqnrrmkwkkc) peptides with N-terminal acetyl and C-terminal amide functions were obtained from American Peptide Company Inc. (Sunnyvale, USA) and conjugated to the 5′-end of the sense strand of sequence C (HS-$(CH_2)_6$-OP(O_2^-)-GGGAGGUGCCCGAACGAUAUidT) via disulfide exchange under denaturing conditions in the presence of urea. The two peptide−RNA conjugates were purified by preparative anion-exchange HPLC under denaturing conditions, desalted, and supplied as lyophilized sodium salts. The purity of the final products was determined by analytical anion-exchange HPLC and electrospray mass spectroscopy with deconvolution. For analytical HPLC, constructs were eluted through MonoQ 5/5 columns (Amersham Biosciences, Piscataway, NJ) with a linear gradient from 10% to 50% buffer B in buffer A + B during 30 min at a flow rate of 1 mL/min, with the effluent monitored by UV spectroscopy at 260 and 280 nm. For HS-$(CH_2)_6$-OP(O_2^-)-GGGAGGUGCCCGAACGAUAUidT, analytical HPLC buffer A consisted of 10 mM $LiClO_4$, 20 mM Tris−HCl, 50 μM EDTA, and 8 M urea, pH 7.4; and buffer B was as buffer A with a [$LiClO_4$] of 600 mM. For the penetratin and TAT(48−60) peptide−RNA conjugates, $LiClO_4$ was substituted with NaCl at 10 mM and 1 M for buffers A and B, respectively. For Chol-$(CH_2)_6$-S-S-$(CH_2)_6$-O-P(O_2^-)-O-GGGAGGUGCCCGAACGAUAUidT, a linear gradient of 10% to 100% buffer B in A + B over 40 min elution at 1 mL/min was used, with buffers prepared in 20% v/v acetonatrile, pH 7.4, in the absence of urea, and 10 mM or 1 M NaCl (buffers A and B, respectively). The cholesterol-conjugated sense strand RNA was synthesized directly in solid phase using the commercially available cholesterol phosphoramidite coupled to a $(CH_2)_6$-S-S-$(CH_2)_6$ linker at the 5′-end of the RNA. Mismatch studies in animals were performed with MM2-5′- H_2N-CO-CH_2-S-$(CH_2)_6$-OP(O_2)-GCGAGCUGCGCGAAGGAUAUidT-3′; antisense, 5′-UAUCCUUCGCGCAGCUCGCUidT-3′.

For annealing, 240 nmol of lyophilized siRNA−sense strand or sense strand conjugates were resuspended at 240 μM concentrations in sterile Dulbecco's phosphate buffered saline (PBS; Sigma, Poole, UK) and then mixed by pipetting with an equal volume of antisense strand (5′-UAUCGUUCGGGCACCUCCCUidT-3′) resuspended in PBS at equimolar concentrations, to give a final siRNA concentration of 1 nmol/μl. Annealing was performed by heating to 95 °C for 5 min on a Peltier element thermal cycler block followed by slow cooling over a period of 1 h.

siRNA Construct Analysis and Quality Control. Annealing products were examined upon a precast 20% polyacrylamide Tris borate ethylenedinitrilotetraacetic acid (EDTA) gel (Invitrogen, Carlsbad, CA), RNA visualized by SybrGold staining as recommended by the manufacturer (Invitrogen), and documented using a computer-controlled UVP GelDoc-It Imagining System (Fisher) fitted with an ethidium bromide filter. Image analysis was performed using the *UVP Labworks Image Acquisition and Analysis* software version 4.6.00.0 (Media Cybernetics, Inc., Atlanta, GA). LPS content in dosing preparations was determined using the PyroGene Recombinant Factor C Endotoxin Detection System according to the manufacturer's instructions (Cambrex Bio Science Wokingham Ltd, Wokingham, UK).

To assess siRNA and siRNA conjugate susceptibility to RNases in a simulated lung microenvironment, stability studies were carried out in murine bronchoalveolar lavage (BAL) fluid. This was collected from three terminally anaesthetized male BALB/c mice (20−25 g) following exposure of the lungs by

three repeat lavages of 0.3 mL of RPMI media (Invitrogen). All collected media was pooled and stored at −20 °C. To assess siRNA stability in BAL fluid, annealed siRNA and siRNA constructs were incubated in excess volumes of 95% v/v murine BAL fluid at 37 °C. 20 μL volumes were removed at set time points, gel loading buffer II (Invitrogen) was quickly added to a final 1× concentration, and the mixture was snap-frozen in liquid nitrogen. Samples were thawed on ice, and 10 pmol quantities were analyzed by polyacrylamide gel electrophoresis (PAGE).

***In Vitro* Cell Culture Studies.** L929 cells were grown to 70% confluence in DMEM (Sigma) supplemented with 10% fetal calf serum, 1% penicillin/strepavidin/glutamine, and 5 mM nonessential amino acids (Invitrogen). On the day of transfection, cells were trypsinised and resuspended at 2×10^5 in media. siRNA, siRNA−Lipofectamine 2000 (Invitrogen) complexes prepared to the manufacturer's instructions, or siRNA conjugates were diluted to 2× the final indicated concentration in OptiMEM (Invitrogen) and mixed with an equal volume of cell suspension to give a final serum concentration of 5% FCS. The cells were then plated into a 96-well plate in triplicate in a volume of 100 μL (1×10^4 cells/well) and incubated for 24 h at 37 °C before either RNA extraction or measurement of cell viability using the MTT assay (Sigma) was carried out.

***In Vivo* Procedures.** All *in vivo* procedures were carried out under local ethics approval and in strict accordance to the 1986 Animals (Scientific Procedures) Act. Groups of 6−18 male BALB/c mice (20−25 g) were sedated with 4% Halothane in O_2 and given the indicated dose of siRNA, mismatch, siRNA conjugates, TAT(48−60), penetratin, polyinosinic/polycytidylic acid (poly(I:C); Sigma), or LPS from *Escherichia coli* 0111: B4 (Sigma) in 20 μL volumes by intratracheal administration. Animals were sacrificed at the indicated time points using an overdose of pentobarbitone (200 mg/kg intraperitoneally).

RNA Extraction and Determination of p38 MAP Kinase mRNA Expression. Cell culture samples were extracted using the Qiagen RNeasy mini kits according to the manufacturer's instructions (Qiagen, Crawley, UK). Animal tissues were gently removed immediately after confirmation of death and stored in RNA*later* according to the manufacturers' instructions (Sigma). Total RNA was extracted by rotor/stator homogenization in Tri Reagent (Sigma) using an Ultraturrax T18 homogenizer (Fisher Scientific), followed by isopropanol precipitation of the aqueous phase and reconstitution in RNase-free water (Promega, Southampton, UK). Yield and purity were determined by spectrophotometric measurement of the absorbance at 260 nm and 280 nm.

For the determination of p38 MAP kinase mRNA expression, mouse-specific Taqman primers and probes were obtained from the "Assay on Demand" service provided by Applied Biosystems (assay no. Mm00442497_m1, Applied Biosystems, Applera Corp., Warrington, UK). Real-time PCR was performed using the one-step Quanti-Tect RT-PCR Kit (Qiagen) in a MicroAmp 96-well reaction plate (Applied Biosystems). Each well contained 25 ng total RNA, 300 nM of forward and reverse transcription primers, and 125 nM Taqman probe in a reaction volume of 25 μL. All sample and nontemplate control reactions were performed in the ABI Prism 7700 Sequence Detection System (Applied Biosystems) in triplicate. Comparative slopes of the relationship between log[RNA] and C_t (gradient = −3.3) for both the gene of interest and the endogenous control 18S (Applied Biosystems) indicated that the comparative C_t method ($\Delta\Delta C_t$) could be used for the relative quantification of gene expression. Data were analyzed on the *Prism* version 4.03 statistic analysis package (GraphPad Software, Inc., San Diego, CA) using nonparametric analysis of variance followed by Tukey post-tests where appropriate.

Measurement of Cytokine Protein Expression. Lungs were gently removed immediately after confirmation of death and snap-frozen in liquid nitrogen, then stored at −80 °C. Frozen lung was homogenized in ice-cold RIPA buffer (25 μg/mL aprotinin, 10 μg/mL leupeptin, 10 μg/mL pepstatin A, 5 mM dithithreitol, 0.5 mM phenylmethylsulphonyl fluoride, 2 mM sodium orthovanadate, 1.25 mM sodium fluoride, 1 mM sodium pyrophosphate; Sigma) at a ratio of 1 mL per 100 mg tissue, using an Ultraturrax T18 homogenizer. The homogenates were then spun in a refrigerated (4 °C) tabletop microcentrifuge at 21 000 *g* for 20 min. The supernatants were removed and stored at −20 °C. Total protein content was determined by Bradford Assay (Bio-Rad, Hertfordshire, UK) according to the manufacturer's instructions. Tissue tumor necrosis factor (TNF)-α, interleukin (IL)-12 p40 (DuoSet ELISA kits; R&D Systems Europe, Abingdon, UK), and interferon (IFN)-α (PBL laboratories, Piscataway, NJ) were measured by sandwich ELISA and normalized for total protein content.

Histology. The 5′-end Cy3-labeled antisense strand (Dharmacon) was annealed to the appropriate sense strand, and 10 nmol of the resulting Cy3-labeled siRNA, penetratin−siRNA, TAT−siRNA, or cholesterol−siRNA or equimolar amounts of Cy3 alone were given by intratracheal administration. Whole lungs were collected 3 h later and fixed in 4% formaldehyde−supplemented phosphate buffered saline (Sigma). After fixation, the samples were rinsed in 70% EtOH, dehydrated, and embedded in paraffin. Paraffin sections (3 μm, Leica microtome, Leica Microsystems, Milton Keynes, UK) were rehydrated, rinsed in Tris−buffered saline pH 7.6 (Sigma), and stained with the DNA-binding fluorochrome Hoechst 33342 (Sigma). After mounting in Aqua Perm mountant (484975 Life Sci. International), Cy3 (red channel) and Hoechst 33342 (green channel) were visualized on an epifluoresence microscope (Olympus BX10, Olympus Sveridge AB, Solna, Sweden) equipped with a high-resolution Olympus DP-50 digital camera (Olympus Sveridge AB) linked to a computerized image analysis system (Viewfinder Lite, v1, Pixera Co, and Image-Pro Plus v 4.5, Media Cybernetics). Cy3−siRNA positive cell phenotypes in the lung parenchyma alveolar macrophages were distinguished from structural alveolar cells by immunohistochemical visualization of the macrophage marker F4/80 (*36*). Briefly, after rehydration the slides were subjected to antigen retrieval through mild proteinase K digestion (Sigma). After blocking the nonspecific binding sites, sections were incubated with a monoclonal rat anti-murine F40/80 (dilution 1:50, clone CI: A3−1, Serotec Ltd, Oxford, UK) for 1 h. After repeated rinsing, the immunoreactivity was detected by an Alexa 448 conjugated goat anti-rat antibody (green channel).

RESULTS

TAT(48−60), Penetratin, and Cholesterol-Mediated siRNA Knockdown of p38 MAP Kinase mRNA in a Mouse Cell Line. Initial studies were focused upon the identification of an optimum siRNA sequence for p38 MAP kinase mRNA knockdown. To this end, the concentration-dependent knockdown achieved by three siRNAs was determined in the L929 mouse fibroblast cell line at 24 h (Supporting Information Figure S1) following reverse transfection with Lipofectamine 2000. Thus, an efficacious sequence (C) was selected that gave a maximal knockdown of 87% and an EC_{50} of 139 pM when transfected into the cells with lipofectamine (Figure 1). As a negative control, we identified a four mismatch siRNA sequence that gave no significant knockdown except at the highest concentration of 100 nM, where we observed a p38 MAP kinase mRNA reduction of ∼20% (Figure 1). To facilitate the conjugation of TAT(48−60), penetratin, or cholesterol upon siRNA, the 5′-end of the siRNA sense strand was modified with a C6-thiol

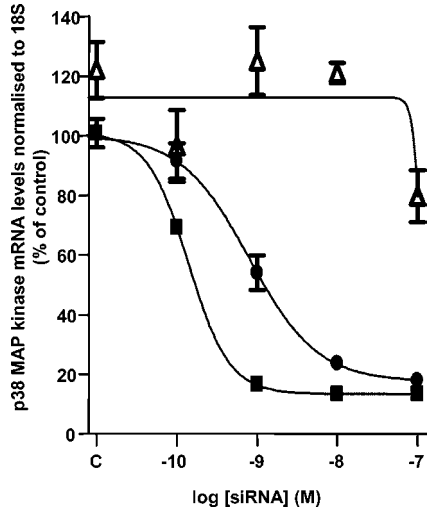


Figure 1. Addition of the C6 linker to a p38 MAP kinase siRNA causes a shift in EC_{50} without affecting maximal knockdown. L929 cells were reverse-transfected with the indicated concentrations of siRNA (square), C6 linker modified siRNA (circle), or mismatch control (open triangle) using Lipofectamine 2000; the RNA was extracted at 24 h; p38 MAP kinase mRNA levels were determined by TaqMan RT-PCR, normalized against 18S, and plotted as the percentile expression of lipofectamine-treated controls (means ± SEM of three independent experiments).

linker, providing a thiol group for disulfide conjugation with a cysteine residue on the CPP (Analytical HPLC and electrospray mass spectrograms available in Supporting Information Figure S2). C6-thiol linker-modified sense strands and CPP−sense strand conjugates were then annealed to the antisense strand to yield siRNA duplexes. To evaluate the impact of the conjugation of the C6-thiol linker group on the biological action of the siRNA, C6-thiol modified siRNA duplexes were transfected using lipofectamine 2000 in cultured L929 fibroblasts. Addition of the C6-thiol linker to the siRNA had no significant effect upon the magnitude of knockdown but caused a shift in the EC_{50} to 798 pM (Figure 1). Visual examination of CPP−siRNA constructs showed no precipitation, while separation on 20% polyacrylamide gels demonstrated the formation of discrete annealed products (Figure S2). In contrast, annealing of the cholesterol−siRNA gave a higher molecular weight product, suggesting the formation of higher-order structures.

The biological action of siRNAs conjugated to TAT(48−60), penetratin, or cholesterol was then examined *in vitro* following a 24 h incubation in the absence of any transfection reagent (i.e., Lipofectamine 2000). Figure 2 shows that equimolar concentrations of siRNA incubated in the absence of Lipofectamine 2000, TAT(48−60) peptide, or penetratin peptide had no effect upon p38 MAP kinase mRNA levels. In contrast, the TAT(48−60)−, penetratin−, and cholesterol−siRNA conjugates produced a small but significant knockdown of 36% ± 6%, 20% ± 3%, and 28% ± 7%, respectively, at 10 μM (Figure 2). Examination of all the constructs showed no significant cellular toxicity at 24 h (Supporting Information Figure S4).

siRNA-Mediated mRNA Knockdown of p38 MAP Kinase in Mouse Lung. Examination of the relative levels of p38 MAP kinase expression in mouse tissues indicated constitutive expression in the lung (Supporting Information Figure S5). To ascertain the capacity of siRNA to down-regulate p38 MAP kinase mRNA levels, increasing doses of the C6-thiol linker-modified siRNA were administered intratracheally, and the effect upon p38 MAP kinase mRNA expression was determined over a 24 h period. From Figure 3, it can be seen that all doses of the linker-modified siRNA (50 nmol, 10 nmol, or 1 nmol siRNA) produced a significant (∼30−45%) mRNA knockdown at 6 h. However, this effect appeared transient, and only animals dosed with 50 nmol showed significantly attenuated gene expression at 12 h (30 ± 5%) and 24 h (20 ± 6%). Administration of 10 nmol mismatch control produced no significant down-regulation of p38 MAP kinase expression over the 24 h period (Figure 4).

Effect of Conjugation to TAT(48−60), Penetratin and Cholesterol upon siRNA-Mediated mRNA Knockdown of p38 MAP Kinase in the Mouse Lung. We next investigated whether the duration and magnitude of p38 MAP kinase mRNA knockdown could be influenced by conjugation of the siRNA to TAT(48−60), penetratin, or cholesterol (Figure 4). TAT(48−60)−siRNA showed 20−30% knockdown at all time points, although this was only significant at 12 h. However, though this knockdown was comparable to that achieved by equimolar doses of unconjugated siRNA, administration of the TAT(48−60) peptide alone produced a comparable and statistically significant knockdown at all time points examined, suggesting the CPP as a modulator of p38 MAP kinase expression. Similarly, although the penetratin−siRNA conjugate appeared to show increased knockdown (47 ± 9%) at 6 h, the peptide alone also caused significant reduction (30 ± 7%) of p38 MAP kinase mRNA levels. In contrast, cholesterol-conjugated siRNA increased the duration but not the magnitude of the response: significant reduction of p38 MAP kinase mRNA expression was seen both at 6 h (28 ± 9%) and at 12

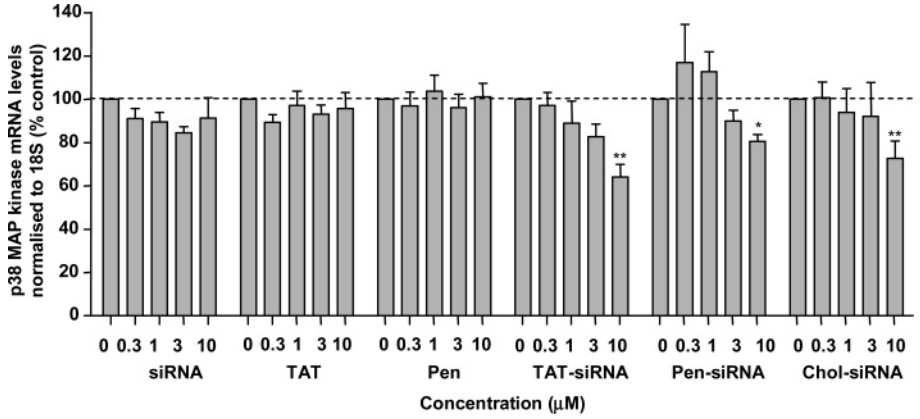


Figure 2. Conjugation of cell penetrating peptides or cholesterol facilitates siRNA-mediated p38 MAP kinase knockdown *in vitro* in the absence of transfection reagents. L929 cells were incubated for 24 h with the indicated concentrations of siRNA without Lipofectamine 2000, TAT(48−60) peptide (TAT), penetratin peptide (Pen), or siRNA conjugated to TAT(48−60), (TAT-siRNA), penetratin (Pen-siRNA) or cholesterol (Chol-siRNA) in the absence of transfection reagents; RNA was extracted; p38 MAP kinase mRNA levels were determined by Taqman RT-PCR, normalized to 18S, and plotted as the percentile expression of lipofectamine treated controls (means ± SEM of three independent experiments; *p* vs nontreated controls: * <0.05; ** <0.01).

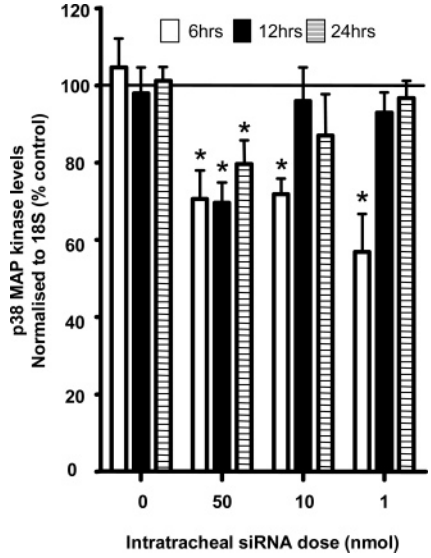


Figure 3. Intratracheal administration of a p38 MAP kinase siRNA in mice results in acute (6 h) but limited (<45%) mRNA knockdown in the whole lung, with the duration of knockdown dependent on the siRNA dose. Mice were dosed intratracheally under halothane anaesthesia with increasing amounts of siRNA in 20 μL PBS volumes; the lungs were removed at the indicated timepoints; RNA was extracted; p38 MAP kinase mRNA levels were determined by TaqMan RT-PCR normalized against 18S and plotted as the percentile expression of vehicle-treated (PBS) controls (values are means ± SEM of 6−18 animals; *p* vs time-matched PBS-treated controls: * <0.05).

h (42 ± 13%), at levels comparable to those achieved by the 50 nmol dose of unconjugated siRNA. Because of the highly lipophilic nature of cholesterol and the resultant low solubility in water, we were unable to determine if this was a direct result of the administration of cholesterol to the lung.

Histological Studies of siRNA and siRNA Conjugate Distribution. To determine the distribution of the siRNA and siRNA conjugates in the lung, the 5′-end of the antisense strand was labeled with the fluorochrome Cy3. At 3 h post-administration, histological analysis showed intense staining of macrophages within the parenchyma and sub-epithelial tissue of bronchi and bronchioles, which suggested that these might represent the principal target cell population (Figure 5). In addition, we observed intense and scattered staining of epithelial cells within the bronchi and bronchioles, which appeared to be an all-or-nothing response. Only rarely were positively stained alveolar epithelial cells detected. siRNA conjugation to penetratin or cholesterol did not influence the cellular labeling pattern (results not shown); however, conjugation to TAT(48−60) appeared to cause a small increase in the staining intensity and number of Cy3-positive cells, with some increase in nuclear staining (Figure 5). In contrast, dosing with equimolar amounts of Cy3 dissolved in PBS produced diffuse staining around the large bronchi and blood vessels (data not shown).

Examination of siRNA and siRNA Conjugate Stability *in Vivo.* To determine whether our observations might have been influenced by siRNA and siRNA conjugate stability, we examined the degradation profile following exposure to mouse BAL fluid. Although BAL fluid incubation resulted in the appearance of a single double-stranded cleavage product, full-length siRNA could still be detected at >7 h (Figure 6). Identical stability and cleavage patterns were seen with the TAT(48−60)−siRNA, penetratin−siRNA, and cholesterol−siRNA, implying that conjugation of such delivery moieties has no significant effect upon siRNA stability, nor were the higher-order structures observed in annealed chol-siRNA gels capable of improving siRNA stability (Supporting Information Figure S3). Importantly, as the shift in gel mobility appears to be entirely due to siRNA cleavage, both the TAT(48−60) and penetratin peptides and the conjugation chemistry are stable in BAL fluid over this time range. Examination of the breakdown product using MALDI-TOF mass spectral analysis showed that the AUidT was cleaved from the 3′-end of the sense strand while the U residue was cleaved from the 5′-end of the antisense strand, most probably by the action of an RNase A-like activity, to produce a blunt-ended siRNA (*37*).

Examination of the Effect of siRNA, CPP, and siRNA Conjugates upon the Innate Immune Response *in Vivo.* Previous reports have suggested that siRNAs are capable of stimulating the innate immune response through binding to Toll-like receptors (TLR)-3, -7, and -8 within the endosomes (*38*).

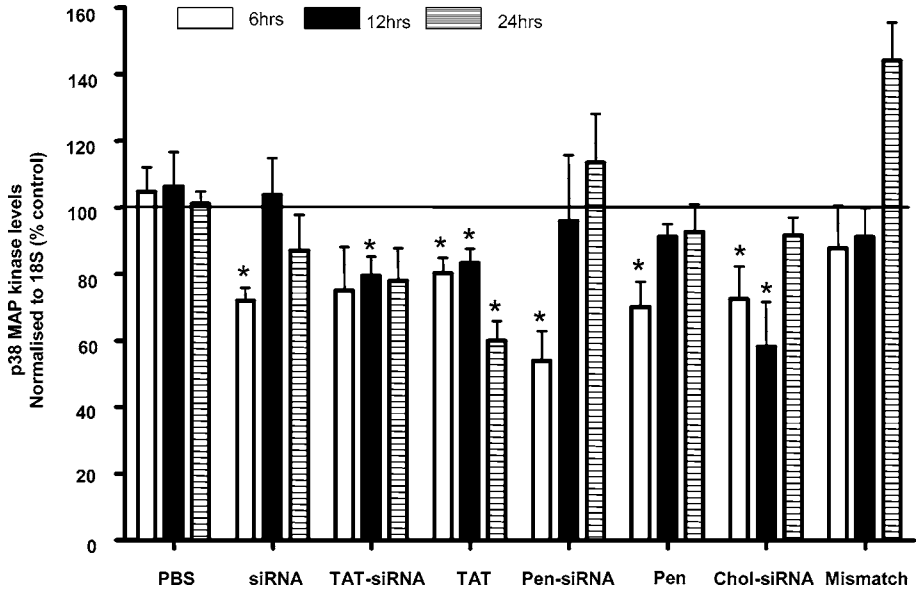


Figure 4. Intratracheal administration of a single 10 nmol dose of the cell penetrating peptides TAT(48−60) (TAT) or penetratin (Pen) causes p38 MAP kinase mRNA downregulation in the whole lung, without improving p38 MAP kinase siRNA (siRNA) knockdown efficiency when conjugated to the siRNA (TAT−siRNA and Pen−siRNA, respectively), whereas cholesterol conjugation extends the duration but not magnitude of knockdown achieved by the siRNA. Mice were dosed under halothane anaesthesia in 20 μL PBS volumes; the lungs were removed at the indicated timepoints; RNA was extracted; p38 MAP kinase mRNA levels were determined by TaqMan RT-PCR normalized against 18S and plotted as the percentile expression of vehicle-treated (PBS) controls (values are means ± SEM of 6−18 animals; *p* vs time-matched vehicle-treated controls: * <0.05).

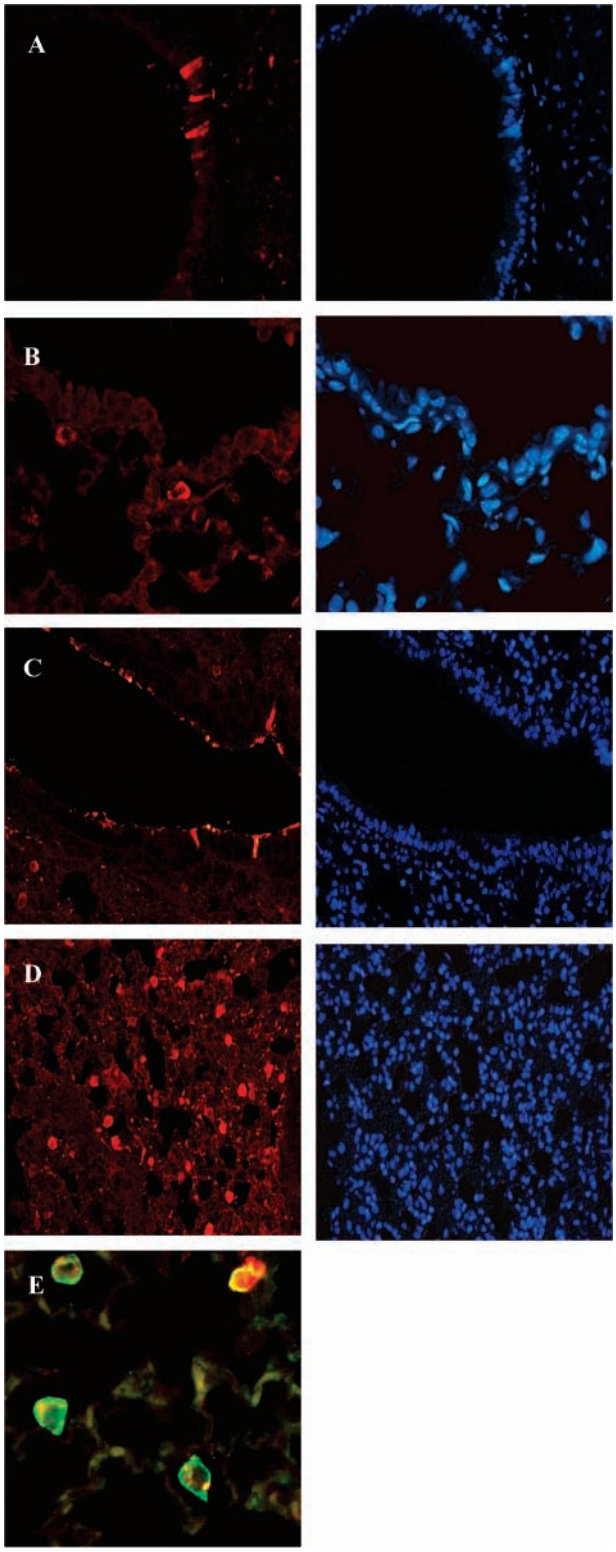


Figure 5. Histological analysis of the lung distribution of intratracheally dosed Cy3 (red) labeled siRNA (panels A, B, and E) and Cy3 labeled siRNA conjugated to the cell penetrating peptide TAT(48−6) (panels C and D) indicates scattered uptake in bronchial epithelial cells (panels A and C), as well as peribronchial (panel B) and parenchymal (panel D) macrophages, as confirmed by use of a macrophage specific marker, F4/80 (panel E), with TAT conjugation conferring limited increases in staining density and nuclear uptake. Mice were dosed with 10 nmol doses under halothane anaesthesia in 20 μL PBS volumes; the lungs were removed after 3 h, fixed, paraffin embedded, sectioned, and counterstained for DNA with Hoechst 33342 (blue) or the macrophage specific marker F4/80 by immunofluorescence (Alexa 448 − green; magnification: panels A, C, D, 5×; panel B, 20×; panel E, 40×).

To eliminate the possibility that the observed reductions in p38 MAP kinase mRNA expression might have resulted from the activation of this response, we measured the levels of the immune markers IFN-α, TNF-α, and IL-12 p40 in whole lung. As expected, the positive controls lipopolysaccharide (LPS) and poly(I:C), known activators of the immune response through of TLR4 and TLR3, respectively, induced a robust increase in IFNα production at 6 h while LPS increased TNFα at 1 h (Figure 7). Interestingly, with the exception of penetratin−siRNA, none of the experimental agents induced an immune response following intratracheal administration; in the case of penetratin−siRNA, we observed a significant increase in the expression of TNF-α and IL-12p40, as well as elevated release of IFN-α (Figure 7). As a control for contaminating LPS in the dosing preparations, potentially influencing p38 MAP kinase expression, or inducing immune activation, measurement of LPS content was included in our siRNA quality control process. Crucially, LPS levels were <0.01 EU among all preparations, significantly below the concentration believed to activate TLR-4-mediated responses (*14*).

DISCUSSION

In this paper, we have investigated the utility of the cell-penetrating peptides TAT(48−60) and penetratin and the lipidic carrier cholesterol in improving siRNA-mediated knockdown of endogenous mRNA expression in the mouse lung. The chosen target was p38 MAP kinase, a key component of inflammatory signal transduction pathways whose inhibition can ameliorate inflammatory responses (*17*, *18*), constitutively expressed in a variety of lung-associated cell types including epithelial, endothelial, macrophage, eosinophil, fibroblast, and smooth muscle cell types. The quantities of siRNA employed in our investigation, which were approximately 37.5 mg/kg (50 nmol), 7.5 mg/kg (10 nmol), and 0.75 mg/kg (1 nmol), are comparable to those reported as efficacious in lung. Thus, a 2 mg/kg siRNA dose was employed to attenuate heme oxygenase 1 (HO-1) expression (*8*) and a 5 mg/kg dose was found to reduce RSV and PIV titer in the lung (*12*). Following intratracheal administration, sequence-specific siRNA-mediated p38 MAP kinase mRNA knockdown was observed as early as 6 h, implying rapid uptake and action of naked siRNA upon the target gene mRNA levels. However, the short duration of knockdown observed with 1 nmol and 10 nmol doses, quickly reversed within 12 h, suggested that naked siRNA might be rapidly degraded and that its action might be extended through chemical stabilization. Indeed, BAL fluid stability studies showed that, even though full-length siRNA could still be recovered at 7 h, cleavage did indeed occur, detectable as early as 15 min.

An alternative hypothesis might be the existence of feedback mechanisms that maintain the mRNA level of the constitutively expressed p38 MAP kinase through increased transcription. Failure to detect this *in vitro* could be ascribable to the cell line used; however, our *in vitro* studies allowed the identification of a potent and selective siRNA sequence. Insofar as the utility of siRNA in the regulation of gene expression in the lung has been pursued, to our knowledge we are the first to report an attempt to manipulate an endogenous, constitutively expressed gene. Indeed, little is known about the biochemistry of p38 MAP kinase mRNA level homeostasis, as research has focused on phosphorylation of the protein, a key part of the inflammatory signal transduction process (*17*, *18*). In this respect, we have observed no significant change in p38 MAP kinase mRNA expression in the mouse lung 4 h after a 30 min challenge with 0.1 mg/mL aerosolized LPS (0.88 ± 0.29-fold p38 MAP kinase relative mRNA levels to saline-challenged controls (Moschos, unpublished data). Therefore, MAPK14 mRNA levels are either not affected by cellular stress signals such as LPS-induced

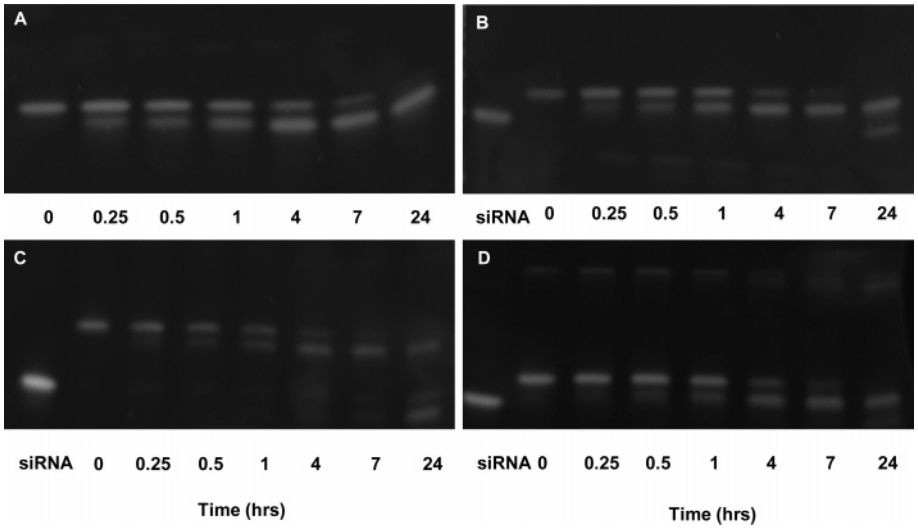


Figure 6. Stability of p38 MAP kinase siRNA (A) and siRNA conjugated to the cell penetrating peptides TAT(48−60) (B) and penetratin (C), as well as cholesterol (D) in mouse lung bronchoalveolar lavage fluid. siRNA and constructs were incubated in 95% v/v mouse lung BAL fluid at 37 °C for the indicated times, and 10 pmol quantities were analyzed by 20% TBE PAGE using the SybrGold stain.

inflammation or are closely monitored and strictly maintained at specific levels. Our findings of an apparent limit on the maximal mRNA knockdown achievable *in vivo* lends further weight to this hypothesis; we were unable to overcome this threshold, since increasing the siRNA dose to 50 nmol improved the duration but not the magnitude of the response. Notwithstanding homeostasis, additional contributors to the limited knockdown could be uneven lung distribution, localization in the immediate epithelial cell layer, or poor cellular uptake. We therefore examined the distribution of Cy3-labeled siRNA by histology and showed uptake into macrophages and scattered airway epithelial cells. However, the total tissue mRNA down-regulation by about 30−45% was comparable to that seen in the liver following intravenous administration of cholesterol-linked *and* stabilized siRNA (*20*).

To improve upon the duration and magnitude of p38 MAP kinase mRNA knockdown, we examined the effect of chemical conjugation of siRNA to a number of nonviral molecular delivery vectors, including cholesterol and the cell-penetrating peptides TAT(48−60) and penetratin. Since a free hydroxyl group at the 5′-end of the antisense strand is thought to be crucial to the mechanism of RNA interference (*39, 40*), these delivery moieties were conjugated to the 5′-end of the sense strand via a C6-thiol linker. To dissociate the sense strand from the delivery vector in the cytosol, we included a disulfide bond within our conjugation chemistry, believed to be cleaved intracellularly. Examination of the biological action of this modified siRNA *in vitro* showed that conjugation of the C6-thiol linker increased the EC_{50} but did not affect the maximal level of mRNA knockdown (∼85%). This magnitude of efficacy in cell culture is similar to that reported for other siRNAs that have been successfully used *in vivo* (*41*), thus ratifying our choice of conjugation chemistry.

Unlike the mouse studies, examination of the p38 MAP kinase knockdown in cells showed no effect of naked siRNA at concentrations up to 10 μM. In contrast, the cholesterol, penetratin, and TAT(48−60) constructs produced a small (20−40%) but significant mRNA knockdown without inducing toxicity. Importantly, this was determined to be siRNA-specific, as no effect was observed by equimolar quantities of the two unconjugated CPP. However, the uptake mechanism appears highly inefficient, since these concentrations were >100 000× higher than those effective with Lipofectamine 2000. Surprisingly, previous cell-based studies using siRNA conjugated to cholesterol, penetratin, or TAT(48−60) (*35*) gave values reportedly in the sub-micromolar range. The reason for these differences is presently unknown, although they could be related to the gene target, cell type, and/or the type of synthetic construct. The majority of investigators have, like ourselves, attached the delivery vector to the 5′-end of the sense strand *via* a disulfide bond (*19, 32−34*), although Chiu et al. (*35*) attached TAT(48−60) to the 3′-end of the antisense strand, and in the report by Soutschek et al. (*20*), the cholesterol moiety was conjugated to the 3′-end of the sense strand via a pyrrolidone linker. Crucially, unlike ourselves, many investigators do not report post-conjugation HPLC purification in the presence of denaturing agents to remove excess, unconjugated cationic CPP from CPP−siRNA conjugates. As with electrostatically based delivery systems such as cationic lipids and polymers, omission of this purification step is likely to result in the formation of complexes between excess CPP and CPP−siRNA conjugates that might increase the efficacy of uptake (*42*).

Despite the low potency of our conjugates in culture, we proceeded to *in vivo* investigations, since we were administrating solutions of 500 μM (20 μL of 10 nmol), concentrations 50× greater than those effective *in vitro*. Significantly, these studies failed to show an effect of conjugation to the cell-penetrating peptides TAT(48−60) or penetratin upon lung distribution, magnitude, or duration of p38 MAP kinase mRNA knockdown. Strikingly, penetratin peptide alone induced a significant down-regulation in p38 MAP kinase mRNA expression at 6 h and, in the case of TAT(48−60), this was also observed at 12 and 24 h. These data therefore document a biological action of these peptides upon gene expression, or associated regulatory processes. The mechanism underlying this response is not currently known, nor is the extent or consequence of the gene modulation enacted by CPP *in vivo*. The lack of adverse reactions or behavior at 24 h following peptide administration implies that this does not involve lung toxicity in the form of necrosis or apoptosis. Indeed, in associated studies in our laboratory using the lung epithelial cell line A549 exposed to TAT(48−60) and penetratin, we have been unable to detect toxicity at concentrations up to 30 μM (*43*). Alternatively, down-regulation of p38 MAP kinase mRNA expression might occur following the interaction of CPP with extracellular or intracellular targets. Indeed, extracellular CPP−protein interactions are likely as Fotin-Mleczek *et al.* (*44*) have shown that both TAT(48−60) and penetratin induce clathrin-dependent uptake of the TNF-α and EGF receptors without their activation, though the exact

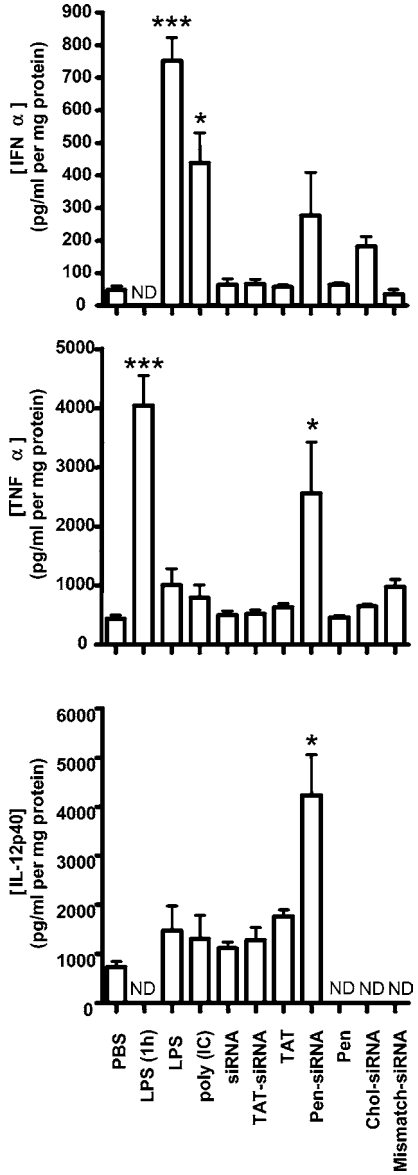


Figure 7. Intratracheal administration of a single 10 nmol dose of the cell penetrating peptides TAT(48−60) (TAT) or penetratin (Pen), a p38 MAP kinase siRNA (siRNA), or conjugates of this siRNA to TAT-(48−60) (TAT-siRNA) or cholesterol (Chol-siRNA) but not a penetratin−siRNA conjugate (pen-siRNA), do not elicit inflammatory cytokine release in murine lung tissue. Mice were dosed under halothane anaesthesia in 20 μL PBS volumes; the lungs were removed at 6 h, protein extracted; interferon α (IFN-α), tumor necrosis factor α (TNF-α), and interleukin 12 p40 (IL-12 p40) content was determined by sandwich ELISA and expressed as pg/mL per mg total protein (p vs PBS-treated controls: * <0.05; *** <0.001; ND = not determined due to lack of sample).

mechanism is unknown. Also, given the fact that CPP are derived from the DNA binding domains of transcription factors and are highly positively charged, it might be envisaged that, once taken up into cells at high concentrations, these peptides directly interfere with gene transcription. Interestingly, the high-affinity binding of CPP to both plasma membranes and genomic DNA has previously been shown to result in erroneous conclusions about the mechanism of CPP uptake (*45*, *46*). Interpretation of our findings as an indication of global gene expression perturbation by CPP is restricted by the lack of effect of CPP on the expression of MAPK14 *in vitro* even at concentrations as high as 10 μM. In terms of a direct effect of CPPs in the regulation of MAPK14 gene expression, lack of specific effects on the MAPK14 locus by means of CPP−DNA interactions can be postulated only under the assumption that no significant sequence differences exist between the genome of the BALB/c mice used in our *in vivo* experiments and that of the L929 cell line (derived from C3H/An mice). Instead, a more likely scenario would favor CPP targeting the signal transduction pathways or transcriptional regulators of MAPK14 gene expression. Alternatively, the viral origin of some CPP coupled to the internalization of cytokine receptors might be expected to activate the antiviral innate response, resulting in inhibition of transcription. However, such a mechanism would appear unlikely, as associated pro-inflammatory marker release *in vivo* was not detected.

Investigation of the immunological response *in vivo* showed that penetratin−siRNA but not TAT(48−60) or cholesterol conjugate administration induced an innate immune response, possibly through activation of TLR-3, -7, and/or -8 (*38*). Liposomal delivery of siRNA containing immunostimulatory sequences has been shown to be necessary for activation of these Toll-like receptors, underscoring the importance of the uptake mechanism in TLR-mediated immune activation by siRNA. Significantly, none of the currently known immunostimulatory siRNA motifs are found in the siRNA sequence we administered *in vivo*, nor did siRNA, TAT, or penetratin alone induce an innate immune response. Thus, our data suggest that either penetratin-mediated siRNA delivery is accomplished in a different manner from that of the TAT and cholesterol conjugates or the individual conjugates are subject to different biochemical fates once in the cytosol.

In contrast to the CPP, although cholesterol conjugation failed to increase the magnitude of p38 MAP kinase knockdown, it extended the duration of mRNA knockdown. However, although gel electrophoresis indicated the formation of higher molecular weight complexes in cholesterol siRNA conjugates, this did not improve upon siRNA stability in BAL fluid, nor was it found to improve upon lung distribution according to our histological investigations.

Overall, these studies have demonstrated siRNA-mediated knockdown of the endogenous, constitutively expressed gene, p38 MAP kinase, in the mouse lung. Although cholesterol increased the duration of the knockdown, the fact that the magnitude of the responses was unaffected following conjugation to cholesterol, TAT(48−60), or penetratin suggests that either these CPP are unable to increase cellular delivery and distribution or , under these circumstances, maximal responses can be achieved with naked siRNA alone. However, since both TAT and penetratin alone induced changes in gene expression, we believe that, despite the widespread success of CPP for the delivery of biologically active peptides and proteins *in vivo* (*26*, *27*), these results highlight a need to continue to elucidate the mechanisms of CPP bioactivity in order to determine their application in the delivery of biopharmaceuticals. This contention is further supported by our findings that penetratin−siRNA but not TAT(48−60)−siRNA conjugates caused activation of the innate immune response, which implies that these have different intracellular fates.

ACKNOWLEDGMENT

Sterghios Moschos is supported by BBSRC (BB/C508234/1); Simon W. Jones and John J. Turner are supported by a grants from the EU framework 5 program; Mark M. Perry and Mark A. Lindsay are supported by the Wellcome Trust (076111). Jonas Erjefelt is supported by the Swedish Heart and Lung Foundation. We would like to thank Prof. Maria Belvisi and Dr. Mark A. Birrell, Department of Respiratory Pharmacology, National Heart and Lung Institute, Imperial College, for their advice on using mice models.

Supporting Information Available: Figure S1, dose-dependent percentile p38 MAP kinase mRNA levels *in vitro* following lipofection with three mouse p38 MAP kinase siRNA or two mismatch controls; Figure S2, analytical HPLC and electrospray mass spectrograms of peptide− and cholesteryl−RNA constructs; Figure S3, analytical gels of CPP and cholesterol conjugate annealing products; Figure S4, cell viability following incubation with siRNA, CPP, or siRNA conjugates; Figure S5, p38 MAP kinase expression across a mouse tissue panel. This material is available free of charge via the Internet at http://pubs.acs.org.

LITERATURE CITED

(1) Dorsett, Y., and Tuschl, T. (2004) siRNAs: applications in functional genomics and potential as therapeutics. *Nat. Rev. Drug Discovery 3*, 318−329.

(2) Elbashir, S. M., Harborth, J., Lendeckel, W., Yalcin, A., Weber, K., and Tuschl, T. (2001) Duplexes of 21-nucleotide RNAs mediate RNA interference in cultured mammalian cells. *Nature (London) 411*, 494−498.

(3) Jones, S. W., Souza, P. M., and Lindsay, M. A. (2004) siRNA for gene silencing: a route to drug target discovery. *Curr. Opin. Pharmacol. 4*, 522−527.

(4) Mahanthappa, N. (2005) Translating RNA interference into therapies for human disease. *Pharmacogenomics 6*, 879−883.

(5) Whelan, J. (2005) First clinical data on RNAi. *Drug Discovery Today 10*, 1014−1015.

(6) Karagiannis, T. C., and El Osta, A. (2005) RNA interference and potential therapeutic applications of short interfering RNAs. *Cancer Gene Ther. 12*, 787−795.

(7) Ambros, V., Bartel, B., Bartel, D. P., Burge, C. B., Carrington, J. C., Chen, X., Dreyfuss, G., Eddy, S. R., Griffiths-Jones, S., Marshall, M., Matzke, M., Ruvkun, G., and Tuschl, T. (2003) A uniform system for microRNA annotation. *RNA 9*, 277−279.

(8) Zhang, X., Shan, P., Jiang, D., Noble, P. W., Abraham, N. G., Kappas, A., and Lee, P. J. (2004) Small interfering RNA targeting heme oxygenase-1 enhances ischemia-reperfusion-induced lung apoptosis. *J. Biol. Chem. 279*, 10677−10684.

(9) Ge, Q., Filip, L., Bai, A., Nguyen, T., Eisen, H. N., and Chen, J. (2004) Inhibition of influenza virus production in virus-infected mice by RNA interference. *Proc. Natl. Acad. Sci. U.S.A. 101*, 8676−8681.

(10) Tompkins, S. M., Lo, C. Y., Tumpey, T. M., and Epstein, S. L. (2004) Protection against lethal influenza virus challenge by RNA interference in vivo. *Proc. Natl. Acad. Sci. U.S.A. 101*, 8682−8686.

(11) Zhang, W., Yang, H., Kong, X., Mohapatra, S., Juan-Vergara, H. S., Hellermann, G., Behera, S., Singam, R., Lockey, R. F., and Mohapatra, S. S. (2005) Inhibition of respiratory syncytial virus infection with intranasal siRNA nanoparticles targeting the viral NS1 gene. *Nat. Med. 11*, 56−62.

(12) Bitko, V., Musiyenko, A., Shulyayeva, O., and Barik, S. (2005) Inhibition of respiratory viruses by nasally administered siRNA. *Nat. Med. 11*, 50−55.

(13) Li, B. J., Tang, Q., Cheng, D., Qin, C., Xie, F. Y., Wei, Q., Xu, J., Liu, Y., Zheng, B. J., Woodle, M. C., Zhong, N., and Lu, P. Y. (2005) Using siRNA in prophylactic and therapeutic regimens against SARS coronavirus in Rhesus macaque. *Nat. Med. 11* (9), 944−951.

(14) Kariko, K., Bhuyan, P., Capodici, J., and Weissman, D. (2004) Small interfering RNAs mediate sequence-independent gene suppression and induce immune activation by signaling through toll-like receptor 3. *J. Immunol. 172*, 6545−6549.

(15) Hornung, V., Guenthner-Biller, M., Bourquin, C., Ablasser, A., Schlee, M., Uematsu, S., Noronha, A., Manoharan, M., Akira, S., de Fougerolles, A., Endres, S., and Hartmann, G. (2005) Sequence-specific potent induction of IFN-alpha by short interfering RNA in plasmacytoid dendritic cells through TLR7. *Nat. Med. 11*, 263−270.

(16) Judge, A. D., Sood, V., Shaw, J. R., Fang, D., McClintock, K., and MacLachlan, I. (2005) Sequence-dependent stimulation of the mammalian innate immune response by synthetic siRNA. *Nat. Biotechnol. 23*, 457−462.

(17) O'Neill, L. A. (2006) Targeting signal transduction as a strategy to treat inflammatory diseases. *Nat. Rev. Drug Discovery 5*, 549−563.

(18) Saklatvala, J. (2004) The p38 MAP kinase pathway as a therapeutic target in inflammatory disease. *Curr. Opin. Pharmacol. 4*, 372−377.

(19) Lorenz, C., Hadwiger, P., John, M., Vornlocher, H. P., and Unverzagt, C. (2004) Steroid and lipid conjugates of siRNAs to enhance cellular uptake and gene silencing in liver cells. *Bioorg. Med. Chem. Lett. 14*, 4975−4977.

(20) Soutschek, J., Akinc, A., Bramlage, B., Charisse, K., Constien, R., Donoghue, M., Elbashir, S., Geick, A., Hadwiger, P., Harborth, J., John, M., Kesavan, V., Lavine, G., Pandey, R. K., Racie, T., Rajeev, K. G., Rohl, I., Toudjarska, I., Wang, G., Wuschko, S., Bumcrot, D., Koteliansky, V., Limmer, S., Manoharan, M., and Vornlocher, H. P. (2004) Therapeutic silencing of an endogenous gene by systemic administration of modified siRNAs. *Nature (London) 432*, 173−178.

(21) Judge, A. D., Bola, G., Lee, A. C., and MacLachlan, I. (2006) Design of noninflammatory synthetic siRNA mediating potent gene silencing in vivo. *Mol. Ther. 13*, 494−505.

(22) Krutzfeldt, J., Rajewsky, N., Braich, R., Rajeev, K. G., Tuschl, T., Manoharan, M., and Stoffel, M. (2005) Silencing of microRNAs in vivo with 'antagomirs'. *Nature (London) 438*, 685−689.

(23) Frankel, A. D., and Pabo, C. O. (1988) Cellular uptake of the tat protein from human immunodeficiency virus. *Cell 55*, 1189−1193.

(24) Green, M., and Loewenstein, P. M. (1988) Autonomous functional domains of chemically synthesized human immunodeficiency virus tat trans-activator protein. *Cell 55*, 1179−1188.

(25) Berlose, J. P., Convert, O., Derossi, D., Brunissen, A., and Chassaing, G. (1996) Conformational and associative behaviours of the third helix of antennapedia homeodomain in membrane-mimetic environments. *Eur. J. Biochem. 242*, 372−386.

(26) Lindsay, M. A. (2002) Peptide-mediated cell delivery: application in protein target validation. *Curr. Opin. Pharmacol. 2*, 587−594.

(27) Dietz, G. P., and Bahr, M. (2004) Delivery of bioactive molecules into the cell: the Trojan horse approach. *Mol. Cell Neurosci. 27*, 85−131.

(28) Snyder, E. L., and Dowdy, S. F. (2001) Protein/peptide transduction domains: potential to deliver large DNA molecules into cells. *Curr. Opin. Mol. Ther. 3*, 147−152.

(29) Schwarze, S. R., and Dowdy, S. F. (2000) In vivo protein transduction: intracellular delivery of biologically active proteins, compounds and DNA. *Trends Pharmacol. Sci. 21*, 45−48.

(30) Gait, M. J. (2003) Peptide-mediated cellular delivery of antisense oligonucleotides and their analogues. *Cell Mol. Life Sci. 60*, 844−853.

(31) Zatsepin, T. S., Turner, J. J., Oretskaya, T. S., and Gait, M. J. (2005) Conjugates of oligonucleotides and analogues with cell penetrating peptides as gene silencing agents. *Curr. Pharm. Des. 11*, 3639−3654.

(32) Muratovska, A., and Eccles, M. R. (2004) Conjugate for efficient delivery of short interfering RNA (siRNA) into mammalian cells. *FEBS Lett. 558*, 63−68.

(33) Davidson, T. J., Harel, S., Arboleda, V. A., Prunell, G. F., Shelanski, M. L., Greene, L. A., and Troy, C. M. (2004) Highly efficient small interfering RNA delivery to primary mammalian neurons induces MicroRNA-like effects before mRNA degradation. *J. Neurosci. 24*, 10040−10046.

(34) Schratt, G. M., Tuebing, F., Nigh, E. A., Kane, C. G., Sabatini, M. E., Kiebler, M., and Greenberg, M. E. (2006) A brain-specific microRNA regulates dendritic spine development. *Nature (London) 439*, 283−289.

(35) Chiu, Y. L., Ali, A., Chu, C. Y., Cao, H., and Rana, T. M. (2004) Visualizing a correlation between siRNA localization, cellular uptake, and RNAi in living cells. *Chem. Biol. 11*, 1165−1175.

(36) Lee, S. H., Starkey, P. M., and Gordon, S. (1985) Quantitative analysis of total macrophage content in adult mouse tissues. Immunochemical studies with monoclonal antibody F4/80. *J. Exp. Med. 161*, 475−489.

(37) Turner, J. J., Jones, S. W., Moschos, S. A., Lindsay, M. A., and Gait, M. J. (2007) MALDI-TOF mass spectral analysis of siRNA degradation in serum confirms an RNAse A-like activity. *Molecular Biosystems 3* (1), 43−50.

(38) Sioud, M. (2006) Innate sensing of self and non-self RNAs by Toll-like receptors. *Trends Mol. Med. 12*, 167−176.

(39) Khvorova, A., Reynolds, A., and Jayasena, S. D. (2003) Functional siRNAs and miRNAs exhibit strand bias. *Cell 115*, 209−216.

(40) Schwarz, D. S., Hutvagner, G., Du, T., Xu, Z., Aronin, N., and Zamore, P. D. (2003) Asymmetry in the assembly of the RNAi enzyme complex. *Cell 115*, 199−208.

(41) Morrissey, D. V., Lockridge, J. A., Shaw, L., Blanchard, K., Jensen, K., Breen, W., Hartsough, K., Machemer, L., Radka, S., Jadhav, V., Vaish, N., Zinnen, S., Vargeese, C., Bowman, K., Shaffer, C. S., Jeffs, L. B., Judge, A., MacLachlan, I., and Polisky, B. (2005) Potent and persistent in vivo anti-HBV activity of chemically modified siRNAs. *Nat. Biotechnol. 23*, 1002−1007.

(42) Turner, J. J., Arzumanov, A. A., and Gait, M. J. (2005) Synthesis, cellular uptake and HIV-1 Tat-dependent trans-activation inhibition activity of oligonucleotide analogues disulphide-conjugated to cell-penetrating peptides. *Nucleic Acids Res. 33*, 27−42.

(43) Jones, S. W., Christison, R., Bundell, K., Voyce, C. J., Brockbank, S. M. V., Newham, P., and Lindsay, M. A. (2005) Characterisation of cell-penetrating peptide-mediated peptide delivery. *Br. J. Pharmacol. 145* (8), 1093−1102.

(44) Fotin-Mleczek, M., Welte, S., Mader, O., Duchardt, F., Fischer, R., Hufnagel, H., Scheurich, P., and Brock, R. (2005) Cationic cell-penetrating peptides interfere with TNF signalling by induction of TNF receptor internalization. *J. Cell Sci. 118*, 3339−3351.

(45) Green, I., Christison, R., Voyce, C. J., Bundell, K. R., and Lindsay, M. A. (2003) Protein transduction domains: are they delivering? *Trends Pharmacol. Sci. 24*, 213−215.

(46) Richard, J. P., Melikov, K., Vives, E., Ramos, C., Verbeure, B., Gait, M. J., Chernomordik, L. V., and Lebleu, B. (2003) Cell-penetrating peptides. A reevaluation of the mechanism of cellular uptake. *J. Biol. Chem. 278*, 585−590.

BC070077D

Comparative *in Vitro* and *in Vivo* Studies on Long-Wavelength Photosensitizers Derived from Bacteriopurpurinimide and Bacteriochlorin p_6: Fused Imide Ring Enhances the *in Vivo* PDT Efficacy

Yihui Chen,[†] William R. Potter,[†] Joseph R. Missert,[†] Janet Morgan,[‡] and Ravindra K. Pandey*,[†]

Medicinal Chemistry Division, PDT Center, and Department of Dermatology, Roswell Park Cancer Institute, Buffalo, New York 14263. Received March 15, 2007; Revised Manuscript Received June 22, 2007

In situ conversion of bacteriochlorophyll-a, present in *Rhodobacter sphaeroides* (*Rb. sphaeroides*) gave bacteriopurpurin-18 in modest yield, which in a sequence of reactions was converted into two series of bacteriochlorins: bacteriopurpurinimide and bacteriopurpurin p_6 with and without a fused imide ring system, respectively. To determine the effect of overall lipophilicity in photosensitizing efficacy, these bacteriochlorins were independently reacted with HBr gas and subsequently treated with various alkyl alcohols to afford the corresponding alkyl ether derivatives as diastereomeric mixtures (the R- and S-isomers were obtained in almost equal ratios). Between the two series of bacteriochlorins, the bacteriopurpurinimides containing a fused imide ring system were found to be more effective *in vivo* (C_3H mice bearing RIF tumors). To investigate the effect of the presence of the chiral center at position 3 of the most effective purpurinimide **9** [3(1′-heptyloxy)ethyl-3-deacetyl-bacteriopurpurin-18-*N*-hexylimide propyl ester], the acetyl group was replaced with a hydroxymethyl substituent and converted into 3(1′-decyloxy)methyl-3-deacetyl-purpurin-18-*N*-hexylimide methyl ester **26** with a similar lipophilicity. Interestingly, compared to **26**, the bacteriopurpurinimide **9** was found to be more effective, suggesting that the chiral center at position 3 certainly plays an important role in photosensitizing activity. Among a series of alkyl ether analogues, between the PDT efficacy and the lipophilicity (log *P* and log *D*) calculated by computational methods (*PALLAS* program), a parabolic relationship was observed to some extent. However, it was limited to a particular series, e.g., compounds with similar log *P* values between bacteriopurpurinimides and bacteriochlorin e_6 did not produce similar *in vivo* efficacy. As expected, within a series, a linear relationship was observed between the log *P* values and the HPLC retention times of the photosensitizers. Some of the mitochondrial localized photosensitizers showed a significant peripheral benzodiazepine binding (PBR) affinity. However, limited correlation between PBR binding affinity and *in vivo* PDT efficacy was observed. Compared to the naturally occurring bacteriochlorophyll-a, the bacteriopurpurinimides with fused imide ring system showed higher *in vitro/in vivo* stability. In contrast to methyl pyropheophorbide-a, the ester functionalities in bacteriopurpurinimide did not convert into the corresponding carboxylic acid by the enzyme esterases.

INTRODUCTION

Photodynamic therapy (PDT) is a relatively new modality for the treatment of various forms of cancer (*1*−*16*). PDT requires three elements: a photosensitizer, light, and oxygen. Following the absorption of light (*17*), the photosensitizer is transformed from its ground singlet state (S_0) into an electronically excited triplet state (T_1, $\sim 10^{-2}$ s) via a short-lived excited singlet state (S_1, $\sim 10^{-6}$ s). The photosensitizer at the excited triplet state can undergo a photochemical process (a type II reaction), which results in the conversion of stable triplet oxygen ($^3O_2$) to the short-lived but highly reactive singlet oxygen ($^1O_2$), the putative cytotoxic agent. In water, the lifetime of $^1O_2$ is approximately 1−3 μs, whereas in most organic solvents, the lifetime is 4−50 times longer. However, the lifetime of $^1O_2$ is considerably shorter in cellular systems, ranging from 100 ns in the lipid regions of membranes to 250 ns in the cytoplasm. Therefore, the diffusion range of $^1O_2$ is predicted to be limited to approximately 45 nm in cellular media. Because the diameter of human cells ranges from approximately 10 to 100 μm, they cannot diffuse more than a single cell length. Thus, the site of the primary generation of $^1O_2$ determines which subcellular structures may be accessed and attacked (*1*). Therefore, the tissue-penetration distance of light is a very important consideration for PDT when targeting tissues far from the light source. It is well-established that both the absorption and scattering of light by tissue increases as the wavelength decreases (*1*). Heme protein in tissue accounts for most of the absorption of light in the visible region. Light penetration drops off rapidly below 550 nm. However, it doubles from 550 to 630 nm and doubles again up to 700 nm, and then tissue penetration increases a further 10% as the wavelength moves toward 800 nm. Light wavelengths of 700−800 nm light therefore provide the optimum tissue penetration depth together with sufficient energy for singlet oxygen formation. To take advantage of this to treat more deeply seated tumors, it becomes necessary to develop photosensitizers exhibiting long-wavelength absorptions in this range.

The porphyrins and related tetrapyrrolic systems are among the most widely studied of all macrocyclic compounds (*17*). Porphyrins are 22π-electron aromatic macrocycles that exhibit characteristic optical spectra with a strong $\pi-\pi^*$ transition around 400 nm (Soret band) and usually four Q bands in the visible region. In the porphyrin system, two of the peripheral double bonds in opposite pyrrolic rings are cross-conjugated and are not required to maintain aromaticity. Thus, reduction

* Address for correspondence: Ravindra K. Pandey, Ph.D., Distinguished Professor, PDT Center, Director, Pharmaceutical Chemistry, Roswell Park Cancer Institute, Buffalo, NY 14263, Phone 716-845-3203, Phone 716-845-8920, E-mail: ravindra.pandey@roswellpark.org.

[†] PDT Center.

[‡] Department of Dermatology.

10.1021/bc070092i CCC: $37.00 © 2007 American Chemical Society
Published on Web 08/17/2007

of one or both of these cross-conjugated double bonds (to give chlorins and bacteriochlorins, respectively) maintains much of the aromaticity, but the change in symmetry results in bathochromically shifted Q bands with higher extinction coefficients. Most bacteriochlorins exhibit long-wavelength absorptions between 740 and 800 nm, so they could be potentially useful for deeply seated tumors.

During the past decade, several naturally occurring bacteriochlorins have been evaluated for *in vitro* and *in vivo* efficacy. Some of them have shown significant *in vivo* photosensitizing efficacy. Unfortunately, these compounds were found to be quite unstable under PDT protocols and decomposed into the corresponding chlorins or porphyrin systems.

Therefore, the synthesis of stable bacteriochlorins with appropriate photochemical properties has been an important goal to obtain long-wavelength photosensitizers for PDT. In our previous studies with several chlorins, we observed that the five-member isocyclic ring (λ_{max} 660 nm) in methyl pheophorbide-a could be converted into the related chlorins bearing either a fused six-member anhydride or imide ring systems and named purpurin-18 and purpurinimide, respectively. The presence of such fused ring systems extended their long-wavelength absorptions from 660 to 700 nm (*18*). In spite of their high stability *in vitro*, results obtained from *in vivo* reflectance spectroscopy indicated that compounds containing the six-member imide ring system were more stable *in vivo* than the photosensitizers with anhydride and isoimide ring systems (*19*). Among these alkyl ether analogues, the purpurinimides were found to be quite effective for photodynamic therapy. Due to a close structural relationship between the purpurinimide and bacteriopurpurinimide moieties, our objective was to translate those parameters which were most efficacious in the purpurinimides to the bacteriopurpurinimide systems and compare their photosensitizing efficacy. To investigate the impact of the fused imide ring system, a series of open-chain bacteriochlorins (bacteriochlorin p_6) with variable lipophilicity were also prepared. The bacteriochlorins evaluated in our present study were derived from bacteriopurpurin-18, which in turn was isolated from *Rb. sphaeroides* by following the methodology developed in our laboratory.

EXPERIMENTAL PROCEDURES

Chemistry. ^{1}H NMR spectra were recorded in $CDCl_3$ solutions at 400 MHz on a Bruker instrument. Chemical shifts are reported in ppm with $CDCl_3$ as internal standard (for ^{1}H, 7.26 ppm). Mass spectral analysis was performed in the Biopolymer Facility, Roswell Park Cancer Institute, Buffalo, and Michigan State University, East Lansing, Michigan. UV−vis spectra were recorded on a Varian (Cary-50 Bio) spectrophotometer. Column chromatographic separations were performed over silica gel 60 (70−230 mesh) or neutral alumina (Brockmann grade III, ∼150 mesh). Preparative TLC was performed on silica 20 × 20 cm^2 TLC plates (Analtech). *Rb. sphaeroides* was purchased from Porphyrin Products (Frontier Scientific Inc., Logan, Utah).

3-Acetylbacteriopurpurin-18 Propyl Ester (1). 350 mL (∼440 g) *Rb. sphaeroides* (purchased from Frontier Scientific Inc., Logan, UT) was dissolved in 800 mL 1-propanol. It was filtered, and 20 g KOH was added to the filtrate. The reaction mixture was stirred at room temperature for 1 h under a stream of air bubbled through the solution. It was then extracted with CH_2Cl_2/THF after adjusting the pH to 2−3. The organic layer was dried over sodium sulfate. Evaporation of the solvent gave a purple residue, which was dissolved in THF, and the solvent was evaporated. This process was repeated several times until there was no absorption at 756 nm and a strong peak appeared at 813 nm. The residue was chromatographed on a silica column eluting first with *n*-hexane, then with 1% v/v acetone/CH_2Cl_2, and finally with 2% v/v acetone/CH_2Cl_2. The appropriate eluates were combined and the solvent was evaporated and precipitated as purple−red crystals from CH_2Cl_2/*n*-hexane. Yield: 200 mg. Mp: 245 °C. UV−vis λ_{max} (nm, CH_2Cl_2): 364 (ϵ 8.91 × 10^4), 412 (ϵ 5.36 × 10^4), 545 (ϵ 3.4 × 10^4), 815 (ϵ 5.53 × 10^4). ^{1}H NMR (400 MHz, $CDCl_3$, δ ppm): 9.21 (s, 1H, 5-H), 8.78 (s, 1H, 10-H), 8.62 (s, 1H, 20-H), 5.18−5.12 (m, 1H, 17-H), 4.39−4.26 (m, 2H, 1H for 7-H, 1H for 18-H), 4.14−4.06 (m, 1H, 8-H), 3.99−3.91 (m, 2H, COOC*H*$_2$CH$_2$CH$_3$), 3.63 (s, 3H, 12-CH$_3$), 3.54 (s, 3H, 2-CH$_3$), 3.15 (s, 3H, CH$_3$C), 2.76−2.67 (m, 1H, -C*H*HCH$_2$COOC$_3$H$_7$), 2.50−2.40 (m, 2H, 8-C*H*$_2$CH$_3$), 2.40−2.31 (m, 1H, -CH*H*CH$_2$COOC$_3$H$_7$), 2.13−1.95 (m, 2H, -CH$_2$C*H*$_2$COOC$_3$H$_7$), 1.80 (d, J = 7.17 Hz, 3H, 7-CH$_3$), 1.70 (d, J = 6.82 Hz, 3H, 18-CH$_3$),1.65−1.50 (m, 2H, COOCH$_2$C*H*$_2$-CH$_3$), 1.1 (t, J = 6.46 Hz, 3H, 8-CH$_2$C*H*$_3$), 0.85(t, J = 7.30H$_z$, 3H, -COOCH$_2$CH$_2$C*H*$_3$), −0.30 (s, 1H, NH), −0.65 (s, 1H, NH). Anal. Calcd for $C_{36}H_{40}N_4O_6$: C, 69.21; H, 6.45; N, 8.97. Found: C, 69.54; H, 6.74; N, 8.67. Mass Calcd for $C_{36}H_{40}O_6N_4$: 624.3. Found: 625.6 (M + 1). HRMS, Calcd: 624.2948. Found: 624.2916.

Note: The purple residue obtained after adjusting the pH to 2−3 mainly contained the 3-acetylbacteriopurpurin-18 carboxylic acid and the corresponding propyl ester, which on refluxing with THF for 1 h hydrolyzed the ester functionality and the 3-acetylbacteriopurpurin-18 carboxylic acid was obtained as a major product.

3-Acetylbacteriopurpurin-18-*N*-hexylimide Propyl Ester (4). 3-Acetylbacteriopurpurin-18 propyl ester **1** (180 mg) dissolved in CH_2Cl_2 (20 mL) was treated with a large excess of hexylamine (0.5 mL) at room temperature for 24 h. The disappearance of the 813 nm band and the appearance of a new 753 nm absorption indicated the formation of the intermediate amide system. The solvent and the excess amine were then evaporated under high vacuum (<25 °C) to give a residue, which was dissolved in CH_2Cl_2 and treated with diazomethane to convert the carboxylic acid to the corresponding methyl ester (about 45 min); a catalytic amount of methanolic KOH was added and the mixture was stirred for 1−2 min. The disappearance of the absorption band at 753 nm and appearance of a new peak 822 nm indicated the completion of the reaction. Following the standard workup, the residue was chromatographed over a silica column eluting with acetone/CH_2Cl_2 (2% v/v). The appropriate fractions were combined. The residue obtained after removing the solvents was crystallized from CH_2Cl_2/*n*-hexane as purple−red crystals in 58.5% yield (120 mg). Mp: 200 °C. UV−vis λ_{max} (nm, CH_2Cl_2): 364 nm (ϵ 6.06 × 10^4), 413 (ϵ 3.64 × 10^4), 545 (ϵ 2.57 × 10^4), 822 (ϵ 4.85 × 10^4). ^{1}H NMR (400 MHz, $CDCl_3$, δ ppm): 9.23 (s, 1H, 5-H), 8.80 (s, 1H, 10-H), 8.62 (s, 1H, 20-H), 5.35−5.29 (m, 1H, 17-H), 4.43 (t, J = 6.03 Hz, 2H, -NC*H*$_2$(CH$_2$)$_4$CH$_3$), 4.33−4.27 (m, 2H, 1H for 7-H, 1H for 18-H), 4.13−4.07 (m, 1H, 8-H), 3.93−3.87 (m, 2H, COOC*H*$_2$CH$_2$CH$_3$), 3.71 (s, 3H,12-CH$_3$), 3.54 (s, 3H, 2-CH$_3$), 3.16 (s, 3H, CH$_3$C), 2.68−2.62 (m, 1H, -C*H*HCH$_2$COOC$_3$H$_7$), 2.39−2.33 (m, 3H, 1H for -CH*H*CH$_2$-COOC$_3$H$_7$, 2H for 8-C*H*$_2$CH$_3$), 2.00−1.94 (m, 2H, -NCH$_2$C*H*$_2$-(CH$_2$)$_3$CH$_3$), 1.82 (d, J = 6.90 Hz, 3H, 7-CH$_3$), 1.74 (d, J = 6.91 Hz, 3H, 18-CH$_3$), 1.63−1.57 (m, 2H, -CH$_2$C*H*$_2$COOC$_3$H$_7$), 1.53−1.47 (m, 2H, -COOCH$_2$C*H*$_2$CH$_3$), 1.45−1.37 (m, 4H, -NCH$_2$CH$_2$C*H*$_2$ C*H*$_2$CH$_2$CH$_3$), 1.33−1.26 (m, 2H, -(CH$_2$)$_4$C*H*$_2$-CH$_3$), 1.10 (t, J = 6.89 Hz, 3H, 8-CH$_2$C*H*$_3$), 0.95 (t, J = 7.60 Hz, 3H, N(CH$_2$)$_5$C*H*$_3$), 0.85 (t, J = 7.30H$_z$, 3H, -COOCH$_2$-CH$_2$C*H*$_3$), −0.5 (s, 1H, NH), −0.72 (s, 1H, NH). Mass Calcd for $C_{42}H_{53}O_5N_5$: 707.4. Found 707.9 (M + 1). HRMS, Calcd: 707.4046. Found: 707.4051.

3-(1-Hydroxy)ethyl-3-deacetylbacteriopurpurin-18-N-hexylimide Propyl Ester (5). Bacteriochlorin **4** 200 mg (0.283

mmol) was dissolved in 5 mL CH_2Cl_2. Sodium borohydride (500 mg) and 1 mL methanol were added to the reaction mixture. The reaction was monitored by TLC and UV−vis spectrophotometry. The disappearance of the 822 nm band and the appearance of a new band at 787 nm indicated the completion of the reaction (reaction time: 20 min). Following the standard workup, the residue was chromatographed on a silica column eluting with acetone/CH_2Cl_2 (2% v/v), and the title compound was obtained after crystallizing from CH_2Cl_2/*n*-hexane as purple−red crystals in almost quantitative yield. Mp: >300 °C. UV−vis λ_{max} (nm, CH_2Cl_2): 367 (ϵ 1.11 × 10^5), 417 (ϵ 5.82 × 10^4), 536 (ϵ 4.02 × 10^4), 787 (ϵ 4.73 × 10^4). ^{1}H NMR (400 MHz, $CDCl_3$, δ (ppm): 8.81 and 8.79 (two singlets, 5-H), 8.62 (s, 1H, 10-H), 8.33 (s, 1H, 20-H), 6.23−6.17 (m, 1H, 3-CH_3C*H*(OH)-), 5.28−5.23 (m, 1H, 17-H), 4.43−4.37 (m, 2H, -NC*H*$_2$(CH_2)$_4$$CH_3$), 4.23−4.15 (m, 2H, 1H for 7-H, 1H for 18-H), 4.05−3.99 (1H, m, 8-H), 3.96−3.90 (m, 2H, -COOC*H*$_2$-CH_2CH_3), 3.65−3.59 (s, 3H, 12-CH_3), 3.28−3.21 (s, 3H, 2-CH_3), 2.63−2.57 (m, 1H, -C*H*HC$H_2$$COOC_3H_7$), 2.51−2.45 (m, 1H, -CH*H*C$H_2$$COOC_3H_7$), 2.33−2.27 (m, 2H, 8-C*H*$_2$$CH_3$), 2.06−2.00 (d, J = 6.63 Hz, 3H, 3-C*H*$_3$CH(OH)-), 1.96−1.90 (m, 2H, NCH_2C*H*$_2$ (CH_2)$_3$$CH_3$), 1.78 (2d overlapped, each d for one isomer, J = 7.06 Hz, 3H, 7-CH_3), 1.68 (2d overlapped, each d for one isomer, J = 7.21 Hz, 3H, 18-CH_3), 1.58−1.52 (m, 4H, 2H for -CH_2C*H*$_2$$COOC_3H_7$, 2H for -$COOCH_2$C*H*$_2$$CH_3$), 1.43−1.38 (m, 6H, -NC$H_2$$CH_2$(C*H*$_2$)$_3$$CH_3$), 1.09 (t, 3H, J = 7.53 Hz, 8-CH_2C*H*$_3$), 0.913 (t, 3H, J = 7.08HZ, -N(CH_2)$_5$C*H*$_3$), 0.82 (t, J = 7.30H$_z$, 3H, -$COOCH_2CH_2$C*H*$_3$), −0.05 (s, 1H, NH), −0.39 (s, 1H, NH). Mass Calcd for $C_{42}H_{55}O_5N_5$: 709.4. Found: 09.9 (M + 1). HRMS, Calcd: 709.4203. Found: 709.4222.

3-Vinyl-3-deacetylbacteriopurpurin-18-*N*-hexylimide Propyl Ester (6). The bacteriochlorin **5** (40 mg) was dissolved in 5 mL dry dichloromethane. HBr gas was bubbled through the solution for 2 min, and the reaction mixture was stirred at room temperature under an argon atmosphere for 5 min. The solvent and the excess hydrogen bromide were then evaporated under high vacuum (at or below 30 °C) to give a residue. Another 40 mg **5** in dichloromethane solution and then 200 mg potassium carbonate were added. The reaction mixture was stirred for an additional 30 min. Following the standard workup, the residue was chromatographed on a silica column with acetone/CH_2Cl_2 (2% v/v), and the title compound was obtained in 85% yield (33 mg). UV−vis λ_{max} (nm, CH_2Cl_2): 366 (ϵ 1.02 × 10^5), 417 (ϵ 4.53 × 10^4), 538 (ϵ 3.91 × 10^4), 796 (ϵ 5.55 × 10^4). ^{1}H NMR (400 MHz, $CDCl_3$, δ ppm): 8.622 (s 1H, 5-H), 8.50 (s, 1H, 10-H), 8.395 (s, 1H, 20-H), 7.77 (dd, J_1 = 11.92 Hz, J_2 = 18.3 Hz, 1H, 3-C*H*═CH_2), 6.185 (d, J = 18.3 Hz, 1H, 3-CH═C*H*H), 6.075 (d, J = 11.92 Hz, 1H, 3-CH═CH*H*), 5.33−5.27 (m, 1H, 17-H), 4.48−4.42 (m, 2H, -NCH_2(CH_2)$_4$$CH_3$), 4.23−4.17 (m, 2H, 1H for 7-H, 1H for 18-H), 4.06−3.99 (m, 1H, 8-H), 3.96−3.91 (m, 2H, -COOC$H_2$$CH_2CH_3$), 3.68−3.61 (s, 3H, 12-$CH_3$), 3.27 (s, 3H, 2-$CH_3$), 2.68−2.63 (m, 1H, -C*H*HCH_2-$COOC_3H_7$), 2.36−2.29 (m, 3H, 1H for-CH*H*C$H_2$$COOC_3H_7$, 2H for 8-C*H*$_2$$CH_3$), 2.03−1.96 (m, 2H, -NC$H_2$C*H*$_2$($CH_2$)$_3$$CH_3$), 1.80 (d, J = 7.09 Hz, 3H, 7-CH_3), 1.73 (d, J = 7.70 Hz, 3H, 18-CH_3), 1.60 (t, J = 7.4 Hz, 2H, CH_2C*H*$_2$$COOC_3H_7$), 1.51−1.46 (m, 4H, 2H for -N(CH_2)$_2$C*H*$_2$(CH_2)$_2$$CH_3$, 2H for -$COOCH_2$C*H*$_2$-$CH_3$), 1.46−1.39 (m, 4H, -N($CH_2$)$_3$C*H*$_2$C*H*$_2$$CH_3$), 1.11 (t, J = 7.21 Hz, 3H, 8-CH_2C*H*$_3$), 0.96 (t, J = 6.91 Hz, 3H, -N(CH_2)$_5$C*H*$_3$), 0.85 (t, J = 7.30 Hz, 3H, -$COOCH_2CH_2$C*H*$_3$), −0.01 (s, 1H, NH), −0.354 (s, 1H, NH). Mass Calcd for $C_{42}H_{53}O_4N_5$: 691.4. Found: 691.8 (M + 1). HRMS, Calcd: 691.4097. Found: 691.4090.

3-(1-Methoxy)ethyl-3-deacetylbacteriopurpurin-18-*N*-hexylimide Propyl Ester (7) Bacteriochlorin **5** (40 mg) was dissolved in dry dichloromethane (5.0 mL). HBr gas was bubbled through the solution for 2 min, and stirred at room temperature under an argon atmosphere for 5 min. The solvent and the excess hydrogen bromide were then evaporated under anhydrous high vacuum (at or below 30 °C) to give a residue, which was not characterized, but immediately redissolved in dry dichloromethane (5.0 mL) and reacted with methanol (1.0 mL) in the presence of anhydrous potassium carbonate (200 mg). The reaction mixture was stirred for 30 min. After the standard workup, the residue was chromatographed on a silica column, eluting with acetone/CH_2Cl_2 (2% v/v), and the title compound was obtained in 86.5% yield (41 mg) as a viscous oil. UV−vis λ_{max} (nm, CH_2Cl_2): 367 (ϵ 1.12 × 10^5), 417 (ϵ 5.81 × 10^4), 536 (ϵ 4.04 × 10^4), 787 (ϵ 4.75 × 10^4). ^{1}H NMR (400 MHz, $CDCl_3$, δ ppm): 8.78 and 8.73 (two singlets, 5-H), 8.61 (s, 1H, 10-H), 8.33 (s, 1H, 20-H), 5.63−5.57 (m, 1H, 3-CH_3C*H*(OCH_3)), 5.29−5.24 (m, 1H, 17-H), 4.45−4.40 (m, 2H, -NCH_2(CH_2)$_4$$CH_3$), 4.23−4.16 (m, 2H, 1H for 4-H, 1H for 18-H), 4.05−3.99 (m, 1H, 8-H), 3.94−3.87 (m, 2H, -COOCH_2-CH_2CH_3), 3.63 (s, 3H, 12-CH_3), 3.50 (s, 3H, -OCH_3), 3.25 (s, 3H, 2-CH_3), 2.63−2.58 (m, 1H, -C*H*HC$H_2$$COOC_3H_7$), 2.36−2.29 (m, 3H, 1H for-CH_2CH*H*$COOC_3H_7$, 2H for 8-C*H*$_2$$CH_3$), 1.99 (d, J = 6.58 Hz, overlapped like a quaterlet, 3H, 3-C*H*$_3$-CH(OCH_3)), 2.04−1.97 (m, 2H, -NCH_2C*H*$_2$(CH_2)$_3$$CH_3$), 1.78 (t, J = 7.4 Hz, 2H, -$COOCH_2$C*H*$_2$$CH_3$), 1.70 (2d, J = 7.15, 3H, 7-CH_3), 1.53−1.47 (m, 11H, 2H for -CH_2C*H*$_2$$COOC_3H_7$, 3H for 18-$CH_3$, 6H for NCH_2CH_2C*H*$_2$C*H*$_2$C*H*$_2$$CH_3$,), 1.13 (t, J = 7.21 Hz, 3H, 8-CH_2C*H*$_3$), 0.94 (t, J = 6.91 Hz, 3H, -N(CH_2)$_5$C*H*$_3$), 0.82 (t, J = 7.30 Hz, 3H, -$COOCH_2CH_2$C*H*$_3$), 0.05 (s, 1H, NH), −0.33 (s, 1H, NH). Mass Calcd for $C_{43}H_{57}O_5N_5$: 723.4. Found: 724.1 (M + 1). HRMS, Calcd: 723.4359. Found: 723.4395.

3-(1-Propyloxy)ethyl-3-deacetylbacteriopurpurin-18-*N*-hexylimide Propyl Ester (8). Bacteriochlorin **5** (45 mg) was reacted with 1-propanol following the procedure of preparing bacteriochlorin **7**, The title compound was obtained in 86.5% yield (41 mg) as a viscous oil. UV−vis λ_{max} (nm, CH_2Cl_2): 367 (ϵ 1.12 × 10^5), 417 (ϵ 5.81 × 10^4), 536 (ϵ 4.04 × 10^4), 787 (ϵ 4.75 × 10^4). ^{1}H NMR (400 MHz, $CDCl_3$, δ ppm) 8.83 and 8.78 (two singlets, 5-H), 8.59 (s, 1H, 10-H), 8.31 (s, 1H, 20-H), 5.68−5.62 (m, 1H, 3-CH_3C*H*(OCH_3)), 5.28−5.21 (m, 1H, 17-H), 4.44−4.40 (m, 2H, -NCH_2(CH_2)$_4$$CH_3$), 4.22−4.16 (m, 2H, 1H for 4-H, 1H for 18-H), 4.03−3.96 (m, 1H, 8-H), 3.94−3.88 (m, 2H, -COOC$H_2$$CH_2CH_3$), 3.63 (s, 3H, 12-$CH_3$), 3.53−3.47 (m, 2H, 3′-OC$H_2$$CH_2$ CH_3), 3.25 (s,1.5H,1/2 × 2-CH_3), 3.23 (s, 1.5H, ,1/2 × 2-CH_3), 2.63−2.57 (m, 1H, -C*H*HCH_2-$COOC_3H_7$), 2.33−2.27 (m, 3H, 1H for-CH*H*C$H_2$$COOC_3H_7$, 2H for 8-C*H*$_2$$CH_3$), 1.99 (d, J = 6.58 Hz, 3H, 3-C*H*$_3$CH(OC_3H_7)), 1.98−1.91 (m, 2H, NCH_2C*H*$_2$(CH_2)$_3$$CH_3$), 1.78 (t, J = 7.4 Hz, 2H, -CH_2C*H*$_2$ $COOC_3H_7$), 1.70 (d, J = 7.15, 3H, 7-CH_3), 1.53−1.47 (m, 13H, 2H for -$COOCH_2$C*H*$_2$$CH_3$, 3H for 18-$CH_3$, 6H for NCH_2CH_2C*H*$_2$C*H*$_2$C*H*$_2$$CH_3$, 2H for 3′-$OCH_2$C*H*$_2$$CH_3$), 1.10 (two triplets overlapped, J = 7.21 Hz, 3H, 8-CH_2C*H*$_3$), 0.94 (two triplets overlapped, 3H for -N(CH_2)$_5$C*H*$_3$, 3H for 3′-OCH_2-CH_2C*H*$_3$), 0.82 (t, J = 7.30 Hz, 3H, -$COOCH_2CH_2$C*H*$_3$), 0.05 (s, 1H, NH), −0.30 (s, 1H, NH). Mass Calcd for $C_{45}H_{61}O_5N_5$: 751.5. Found: 752.3 (M + 1). HRMS, Calcd: 751.4672. Found: 751.4697.

3-(1-Heptyloxy)ethyl-3-deacetylbacteriopurpurin-18-*N*-hexylimide Propyl Ester (9). Bacteriochlorin **5** (45 mg) was reacted with 1-heptanol following the procedure described for bacteriochlorin **7** (residual heptanol was removed by the azeotropic method with water); the title compound was obtained in 81% yield (41 mg) as a viscous oil. UV−vis λ_{max} (nm, CH_2Cl_2): 367 (ϵ 1.12 × 10^5), 417 (ϵ 5.81 × 10^4), 536 (ϵ 4.04 × 10^4), 787 (ϵ 4.75 × 10^4). ^{1}H NMR (400 MHz, $CDCl_3$, δ ppm): 8.85 and 8.81 (two singlets, 5-H), 8.61 (s, 1H, 10-H), 8.33 (s, 1H, 20-H), 5.69−5.62 (m, 1H, 3′-CH_3C*H*($O(CH_2)_6CH_3$)-),

5.31−5.24 (m, 1H, 17-H), 4.46−4.40 (m, 2H, -NC*H*$_2$(CH$_2$)$_4$-CH$_3$), 4.23−4.17 (m, 2H, 1H for 4-H, 1H for 18-H), 4.06−4.00 (m, 1H, 8-H), 3.95−3.89 (m, 2H, -COOCH$_2$CH$_2$CH$_3$), 3.62 (s, 3H, 12-CH$_3$), 3.62−3.56 (m, 2H, -COOC*H*$_2$CH$_2$CH$_3$), 3.59−3.53 (m, 2H, 3′-OC*H*$_2$(CH$_2$)$_5$CH$_3$), 3.250 (s, 1.5H, 1/2 × 2-CH$_3$), 3.239 (s, 1.5H, 1/2 × 2-CH$_3$), 2.65−2.59 (m, 1H, -C*H*HCH2C-OOC$_3$H$_7$), 2.35−2.29 (m, 3H, 1H for-CH*H* CH2COOC$_3$H$_7$, 2H for 8-C*H*$_2$CH$_3$), 1.99 (d, *J* = 6.58 Hz, 3H, 3′-C*H*$_3$CH(OC$_7$H$_{15}$)), 2.01−1.95 (m, 2H, -NCH$_2$C*H*$_2$(CH$_2$)$_3$CH$_3$), 1.80 (2d, *J* = 7.15, overlapped like a triplet, 3H, 7-CH$_3$), 1.689 (4H, d, *J* = 7.02 Hz,1H for -CH$_2$C*H*HCOOC$_3$H$_7$, 3H for 18-CH$_3$,), 1.64−1.56 (3H, m, 1H for -CH$_2$CH*H*COOC$_3$H$_7$, 2H for -OCH$_2$C*H*$_2$(CH$_2$)$_4$-CH$_3$), 1.47−1.41 (m, 6H, 4H for NCH$_2$CH$_2$C*H*$_2$C*H*$_2$CH$_2$CH$_3$, 2H for -COOCH$_2$C*H*$_2$CH$_3$), 1.32−1.18 (m, 13H, 2H for -N(CH$_2$)$_4$C*H*$_2$CH$_3$, 3H for 8-CH$_2$C*H*$_3$, 8H for -OCH$_2$CH$_2$(C*H*$_2$)$_4$-CH$_3$), 1.15 (two triplets overlapped, *J* = 7.21 Hz, 3H, 8-CH$_2$C*H*$_3$), 0.95 (t, 3H, *J* = 6.81 Hz, -N(CH$_2$)$_5$C*H*$_3$), 0.82 (6H, two triplets overlapped, 3H for -O(CH$_2$)$_6$C*H*$_3$, 3H for -COOCH$_2$-CH$_2$C*H*$_3$), 0.10 (s, 1H, NH), −0.30 (s, 1H, NH). Mass Calcd for C$_{49}$H$_{69}$O$_5$N$_5$: 807.5. Found: 808.3 (M + 1). HRMS, Calcd: 807.5298. Found: 807.5348.

3-(1-Decyloxy)ethyl-3-deacetylbacteriopurpurin-18-*N*-hexylimide Propyl Ester (10). Compound **5** (42 mg**)** was reacted with 1-decanol following the procedure of making bacteriochlorin **7** (decanol was removed by the azeotropic method with water); the title compound was obtained in 82% yield (41 mg) as a viscous oil. UV−vis λ_{max} (nm, in CH$_2$Cl$_2$): 367 (ϵ 1.12 × 10^5), 417 (ϵ 5.81 × 10^4), 536 (ϵ 4.04 × 10^4), 787 (ϵ 4.75 × 10^4). ^{1}H NMR (400 MHz, CDCl$_3$, δ ppm): 8.83 and 8.81 (two singlets, 5-H), 8.61 (s, 1H, 10-H), 8.34 (s, 1H, 20-H), 5.69−5.63 (m, 1H, 3′-CH$_3$C*H*(O(CH$_2$)$_6$CH$_3$)-), 5.33−5.27 (m, 1H, 17-H), 4.47−4.41 (m, 2H, -NC*H*$_2$(CH$_2$)$_4$CH$_3$), 4.25−4.19 (m, 2H, 1H for 4-H, 1H for 18-H), 4.06−4.00 (m, 1H, 8-H), 3.95−3.89 (m, 2H, -COOCH$_2$CH$_2$CH$_3$), 3.63 (s, 3H, 12-CH$_3$), 3.62−3.56 (m, 2H, -COOC*H*$_2$CH$_2$CH$_3$), 3.59−3.52 (m, 2H, 3′-OC*H*$_2$(CH$_2$)$_8$-CH$_3$), 3.250 (s, 3H, 2-CH$_3$), 2.66−2.60 (m, 1H, -C*H*HCH$_2$-COOC$_3$H$_7$), 2.35−2.29 (m, 3H, 1H for-CH*H* CH$_2$COOC$_3$H$_7$, 2H for 8-C*H*$_2$CH$_3$), 1.99 (d, *J* = 6.58 Hz, 3H, 3′-C*H*$_3$CH-(OC$_{10}$H$_{21}$)), 1.98−1.92 (m, 2H, -NCH$_2$C*H*$_2$(CH$_2$)$_3$CH$_3$), 1.80 (2d, *J* = 7.15, overlapped like a triplet, 3H, 7-CH$_3$), 1.70 (4H, d, *J* = 7.02 Hz, 1H for -CH$_2$C*H*HCOOC$_3$H$_7$, 3H for 18-CH$_3$,), 1.63−1.57 (m, 3H, 1H for -CH$_2$CH*H*COOC$_3$H$_7$, 2H for -OCH$_2$C*H*$_2$(CH$_2$)$_4$CH$_3$), 1.47−1.41 (m, 6H, 4H for NCH$_2$-CH$_2$C*H*$_2$C*H*$_2$CH$_2$CH$_3$, 2H for -COOCH$_2$C*H*$_2$CH$_3$), 1.35−1.10 (m, 22H, 2H for -N(CH$_2$)$_4$C*H*$_2$CH$_3$, 3H for 8-CH$_2$C*H*$_3$, 14H for -OCH$_2$CH$_2$(C*H*$_2$)$_7$CH$_3$, 3H for 8-CH$_2$C*H*$_3$), 0.95 (t, 3H, *J* = 6.81 Hz, -N(CH$_2$)$_5$C*H*$_3$), 0.82 (6H, two triplet overlapped, 3H for -O(CH$_2$)$_6$C*H*$_3$, 3H for -COOCH$_2$CH$_2$C*H*$_3$), 0.10 (s, 1H, NH), −0.30 (s, 1H, NH). Mass Calcd for C$_{52}$H$_{75}$O$_5$N$_5$: 849.6. Found: 849.6. HRMS, Calcd: 849.5768. Found: 849.5748.

3-Acetylbacteriopurpurin-18-methyl Ester (11). When preparing bacteriochlorin **1** starting from *Rb. sphaeroids*, 350 mL (about 440 g) as described as above, 3-acetyl-purpurin-18 carboxylic acid (**2**) was also obtained in the crude product. After treating crude **2** with diazomethane, the corresponding methyl ester (**11**) was obtained. To purify **11**, it was chromatographed on a silica column eluting with acetone/CH$_2$Cl$_2$ (2% v/v), and the title compound was obtained as purple−red crystals after crystallizing from CH$_2$Cl$_2$/*n*-hexane. Yield: 650 mg. Mp: 272 °C. UV−vis λ_{max} (nm, in CH$_2$Cl$_2$): 364 (ϵ 8.91 × 10^4), 418 (ϵ 5.36 × 10^4), 545 (ϵ 3.4 × 10^4), 815 (ϵ 5.53 × 10^4). ^{1}H NMR (400 MHz, CDCl$_3$, δ ppm): 9.21 (s, 1H, 5-H), 8.78 (s, 1H, 10-H), 8.62 (s, 1H, 20-H), 5.16−5.10 (m,1H, 17-H), 4.33−4.27 (m, 2H, 1H for 7-H, 1H for 18-H), 4.11−4.05 (m, 1H, 8-H), 3.63 (s, 3H, 12-CH$_3$), 3.57 (s, 3H, -COOCH$_3$), 3.52 (s, 3H, 2-CH$_3$), 3.15 (s, 3H, CH$_3$C), 2.73−2.67 (m, 1H, -C*H*HCH$_2$-COOCH$_3$), 2.45−2.39 (m, 2H, 8-C*H*$_2$CH$_3$), 2.38−2.32 (m, 1H, -CH*H*CH$_2$ COOCH$_3$), 2.03−1.97 (m, 2H, -CH$_2$C*H*$_2$COOCH$_3$), 1.80 (d, *J* = 7.17 Hz, 3H, 7-CH$_3$), 1.70 (d, *J* = 6.82 Hz, 3H, 18-CH$_3$), 1.1 (t, *J* = 6.46 Hz, 3H, 8-CH$_2$C*H*$_3$), −0.30 (s, 1H, NH), −0.65 (s, 1H, NH). Mass Calcd for C$_{34}$H$_{36}$N$_4$O$_6$·H$_2$O: C, 66.42; H, 6.24; N, 9.12. Found: C, 66.30; H, 5.90; N, 8.99. Mass Calcd for C$_{34}$H$_{36}$N$_4$O$_6$: 596.3. Found: *m*/*e* 596.8 (M + 1). HRMS, Calcd: 596.2635. Found: 596.2615.

3-Acetylbacteriopurpurin-18-*N*-hexylimide Methyl Ester (12): Following the procedure described for the preparation of compound **4**, compound **11** (180 mg) was first reacted with hexylamine, which on subsequent cyclization gave the title compound as a crude residue. The residue was purified by silica column chromatography, eluting with acetone/CH$_2$Cl$_2$ (2% v/v). The residue obtained after evaporating the solvent was crystallized from CH$_2$Cl$_2$/*n*-hexane; the title compounds were achieved as purple−red crystals in 58.5% yield (120 mg). Mp: 260 °C. UV−vis λ_{max} (nm, CH$_2$Cl$_2$): 364 nm (ϵ 6.06 × 10^4), 413 nm (ϵ 3.64 × 10^4), 545 nm (ϵ 2.57 × 10^4), 822 (ϵ 4.85 × 10^4). ^{1}H NMR (400 MHz, CDCl$_3$, δ ppm): 9.24 (s, 1H, 5-H), 8.80 (s, 1H, 10-H), 8.64 (s, 1H, 20-H), 5.36−5.30 (m,1H, 17-H), 4.43 (t, *J* = 6.03 Hz, 2H, -NC*H*$_2$(CH$_2$)$_4$CH$_3$), 4.33−4.27 (m, 2H, 1H for 7-H, 1H for 18-H), 4.13−4.07 (m, 1H, 8-H), 3.71 (s, 3H,12-CH$_3$), 3.58 (s, 3H, -COOCH$_3$), 3.54 (s, 3H, 2-CH$_3$), 3.16 (s,3H, CH$_3$C), 2.71−2.65 (m, 1H, -C*H*HCH$_2$COOCH$_3$), 2.41−2.35 (m, 3H, 1H for -CH*H*CH$_2$COOH$_3$, 2H for 8-C*H*$_2$CH$_3$), 2.00−1.94 (m, 2H, -NCH$_2$C*H*$_2$(CH$_2$)$_3$CH$_3$), 1.82 (d, *J* = 6.90 Hz, 3H, 7-CH$_3$), 1.74 (d, *J* = 6.91 Hz, 3H, 18-CH$_3$), 1.60 (m, 2H, -CH$_2$C*H*$_2$COOCH$_3$), 1.45−1.39 (m, 4H, -NCH$_2$CH$_2$C*H*$_2$C*H*$_2$-CH$_2$CH$_3$), 1.31−1.25 (m, 2H, -(CH$_2$)$_4$C*H*$_2$CH$_3$), 1.10 (t, *J* = 6.89 Hz, 3H, 8-CH$_2$C*H*$_3$), 0.95 (t, *J* = 7.60 Hz, 3H, N(CH$_2$)$_5$C*H*$_3$), −0.5 (s, 1H, NH), −0.72 (s, 1H, NH). Mass Calcd for C$_{40}$H$_{49}$N$_5$O$_5$: 679.3 Found: *m*/*e* 680.5 (M + 1). HRMS, Calcd: 679.3733. Found: 679.3729.

3-(1-Hydroxy)ethyl-3-deacetylbacteriopurpurin-18-*N*-hexylimide Methyl Ester (13) Following the procedure described for the preparation of **5**, compound **12** (50 mg) was reacted with sodium borohydride, and the title compound was obtained after crystallizing from CH$_2$Cl$_2$/*n*-hexane as purple−red crystals in almost quantitative yield (50 mg). Mp: 185 °C. UV−vis λ_{max} (in CH$_2$Cl$_2$): 367 nm (ϵ 1.11 × 10^5), 417 nm (ϵ 5.82 × 10^4), 536 nm (ϵ 4.02 × 10^4), 787 nm (ϵ 4.73 × 10^4). ^{1}H NMR (400 MHz, CDCl$_3$, δ ppm): 8.795 and 8.78 (two singlets, 5-H), 8.60 (s, 1H, 10-H), 8.318 (s, 1H, 20-H), 6.23−6.17 (m, 1H, 3-CH$_3$C*H*(OH)-), 5.26−5.20 (m, 1H, 17-H), 4.46−4.40 (m, 2H, -NC*H*$_2$(CH$_2$)$_4$CH$_3$), 4.21−4.15 (m, 2H, 1H for 7-H, 1H for 18-H), 4.03−3.97 (1H, m, 8-H), 3.60 (s, 3H, 12-CH$_3$), 3.544 (s, 1.5H, 1/2×-COOCH$_3$), 3.540 (s, 1.5H, 1/2×-COOCH$_3$), 3.25 (s, 3H, 2-CH$_3$), 2.65−2.59 (m, 1H, -C*H*HCH$_2$COOCH$_3$), 2.49−2.43 (m, 1H, -CH*H*CH$_2$COOCH$_3$), 2.33−2.27 (m, 2H, 8-C*H*$_2$-CH$_3$), 2.03 (d, *J* = 6.63 Hz, 3H, 3-C*H*$_3$CH(OH)-), 1.96−1.90 (m, 2H, NCH$_2$C*H*$_2$(CH$_2$)$_3$CH$_3$), 1.76 (2d overlapped, each d for one isomer, *J* = 7.06 Hz, 3H, 7-CH$_3$), 1.66 (2d overlapped, each d for one isomer, *J* = 7.21 Hz, 3H, 18-CH$_3$), 1.58−1.51 (m, 2H, -CH$_2$C*H*$_2$COOCH$_3$), 1.43−1.37 (m, 6H, -NCH$_2$CH$_2$-(C*H*$_2$)$_3$CH$_3$), 1.09 (t, 3H, *J* = 7.53 Hz, 8-CH$_2$C*H*$_3$), 0.913 (t, 3H, *J* = 7.08HZ, -N(CH$_2$)$_5$C*H*$_3$), −0.05 (s, 1H, NH), −0.42 (s, 1H, NH). Mass Calcd for C$_{40}$H$_{51}$N$_5$O$_5$: 681. Found: *m*/*e* 682 (M + 1). HRMS, Calcd: 681.3890. Found: 681.3870.

3-(1-Heptyloxy)ethyl-3-deacetylbacteriopurpurin-18-*N*-hexylimide Methyl Ester (14): Following the procedure described for the preparation of **7**, bacteriochlorin **13** (40 mg) was reacted with 1-heptanol. Excess 1-heptanol was removed under a high vacuum by azotropic distillation. The title compound was obtained in 87% (40 mg) yield as a viscous oil. UV−vis λ_{max} (nm, CH$_2$Cl$_2$): 367 (ϵ 1.12 × 10^5), 417 (ϵ 5.81 × 10^4), 536 (ϵ 4.04 × 10^4), 787 (ϵ 4.75 × 10^4). ^{1}H NMR (400 MHz, CDCl$_3$, δ ppm): 8.86 and 8.82 (two singlets, 5-H), 8.62

(s, 1H, 10-H), 8.34 (s, 1H, 20-H), 5.69−5.63 (m, 1H, 3-$CH_3CH(O(CH_2)_6CH_3)$-), 5.31−5.25 (m, 1H, 17-H), 4.46−4.40 (m, 2H,-$NCH_2(CH_2)_4CH_3$), 4.25−4.19 (m, 2H, 1H for 4-H, 1H for 18-H), 4.06−3.99 (m, 1H, 8-H), 3.65 (s, 3H, 12-CH_3), 3.62−3.56 (m, 2H, -$CH_2(CH_2)_5CH_3$), 3.56 (s, 3H, -$COOCH_3$), 3.24 (s,3H, 2-CH_3), 2.68−2.61 (m, 1H, -$CHHCH_2$ $COOCH_3$), 2.38−2.32 (m, 3H, 1H for-$CH_2CHHCOOCH_3$, 2H for 8-CH_2CH_3), 2.02 (d, J = 6.58 Hz, 3H, 3-$CH_3CH(OC_7H_{15})$), 2.03−1.97 (m, 2H, -NCH_2CH_2 $(CH_2)_3CH_3$), 1.788 (2d, J = 7.15, overlapped to be like triplet, 3H, 7-CH_3), 1.72 (4H, 1H for -CH_2 CHH-$COOCH_3$, 3H for 18-CH_3, d, J = 7.02 Hz), 1.65−1.59 (3H, m, 1H for -$CH_2CHHCOOCH_3$, 2H for -$OCH_2CH_2(CH_2)_4CH_3$, 1.48−1.42 (m, 4H, NCH_2CH_2 $CH_2CH_2CH_2CH_3$), 1.40−1.10 (m, 13H, 2H for -$N(CH_2)_4CH_2CH_3$, 3H for 8-CH_2CH_3, 8H for -$OCH_2CH_2(CH_2)_4CH_3$), 0.95 (t, 3H, J = 6.81 Hz, -$N(CH_2)_5CH_3$), 0.85−0.79 (m, 3H, -$O(CH_2)_8CH_3$), 0.08 (s, 1H, NH), −0.28 (s, 1H, NH). Mass Calcd for $C_{47}H_{65}N_5O_5$: 779.5. Found: *m*/*e* 780.8 (M + 1). HRMS, Calcd: 779.4985. Found: 779.4944.

3-(1-Nonyloxy)ethyl-3-deacetylbacteriopurpurin-18-*N*-hexylimide Methyl Ester (15): Following the procedure described for the preparation of **7**, bacteriochlorin **13** (40 mg) was reacted with 1-nonanol, and the title compound was isolated in 87% yield (41 mg) as a viscous oil. UV−vis λ_{max} (nm, CH_2Cl_2): 367 (ϵ 1.12 × 10^5), 417 (ϵ 5.81 × 10^4), 536 (ϵ 4.04 × 10^4), 787 (ϵ 4.75 × 10^4). ^{1}H NMR (400 MHz, $CDCl_3$, δ ppm): 8.86 and 8.82 (two singlets, 5-H), 8.62 (s, 1H, 10-H), 8.33 (s, 1H, 20-H), 5.69−5.63 (m, 1H, 3-$CH_3CH(O(CH_2)_8CH_3)$-), 5.31−5.25 (m, 1H, 17-H), 4.46−4.40 (m, 2H,-$NCH_2(CH_2)_4CH_3$), 4.23−4.17 (m, 2H, 1H for 4-H, 1H for 18-H), 4.06−4.00 (m, 1H, 8-H), 3.62 (s, 3H, 12-CH_3), 3.62−3.56 (m, 2H, -$CH_2(CH_2)_7CH_3$), 3.56 (s, 3H, -$COOCH_3$), 3.224 (s, 1.5H, 1/2 × 2-CH_3), 3.218 (s, 1.5H, 1/2 × 2-CH_3), 2.66−2.60 (m, 1H, -$CHHCH_2COOCH_3$), 2.35−2.29 (m, 3H, 1H for-$CH_2CHHCOOCH_3$, 2H for 8-CH_2CH_3), 1.99 (d, J = 6.58 Hz, 3H, 3-$CH_3CH(OC_9H_{19})$), 2.01−1.95 (m, 2H, -NCH_2CH_2 $(CH_2)_3CH_3$), 1.788 (2d, J = 7.15, overlapped to be like triplet, 3H, 7-CH_3), 1.689 (4H, 1H for -CH_2 $CHHCOOCH_3$, 3H for 18-CH_3, d, J = 7.02 Hz), 1.63−1.57 (3H, m, 1H for -$CH_2CHHCOOCH_3$, 2H for -$CH_2CH_2(CH_2)_6CH_3$, 1.47−1.41 (m, 4H, $NCH_2CH_2CH_2CH_2CH_2CH_3$), 1.36−1.08 (m, 17H, 2H for -$N(CH_2)_4CH_2CH_3$, 3H for 8-CH_2CH_3, 12H for -$OCH_2CH_2(CH_2)_6CH_3$), 0.931 (t, 3H, J = 6.81 Hz, -$N(CH_2)_5CH_3$), 0.783 (m, 3H, -$O(CH_2)_8CH_3$), 0.10 (s, 1H, NH), −0.30 (s, 1H, NH). Mass Calcd for $C_{49}H_{69}N_5O_5$: 807.5. Found: *m*/*e* 808.9 (M + 1). HRMS, Calcd: 807.5294. Found: 807.5303.

3-Acetylbacteriochlorin p_6 Trimethyl Ester (17). Bacteriochlorin **11** (110 mg) was dissolved in tetrahydrofuran (5 mL). A catalytic amount of 0.1 N KOH/methanol was added. The reaction was monitored by UV−visible spectrophotometer. After approximately 5 min, all the starting material (813 nm) was consumed (monitored by TLC). The reaction mixture was acidified with 10% aqueous acidic acid. The intermediate product was washed with water before reacting with diazomethane. The residue obtained after removing the solvent was chromatographed on a silica column with methanol/CH_2Cl_2 (2% v/v), and the title compound was obtained in 80% overall yield (97 mg). Mp: 285 °C. UV−vis λ_{max} (nm, CH_2Cl_2): 354 (ϵ 7.69 × 10^4), 390 (ϵ 6.23 × 10^4), 522 (ϵ 2.01 × 10^4), 768 (ϵ 5.03 × 10^4). ^{1}H NMR (400 MHz, $CDCl_3$, δ ppm): 9.28 (s, 1H, 5-H), 8.74 (s, 1H, 10-H), 8.67 (s, 1H, 20-H), 5.00−4.94 (m, 1H, 17-H), 4.31−4.25 (m, 2H, 1H for 7-H, 1H for 18-H), 4.18 (s, 3H, -$COOCH_3$), 4.20−4.14 (m, 1H, 8-H), 4.15 (s, 3H, -$COOCH_3$), 3.58 (s, 3H, 12-CH_3), 3.54 (s, 3H, -$CH_2CH_2COOCH_3$), 3.46 (s, 3H, 2-CH_3), 3.18 (s, 3H, CH_3C), 2.38−2.32 (m, 1H, -$CHHCH_2COOCH_3$), 2.08−2.02 (m, 1H, -$CHHCH_2COOCH_3$), 1.85 (d, J = 7.17 Hz, 3H, 7-CH_3), 1.70 (d, J = 6.82 Hz, 3H, 18-CH_3), 1.58−1.52 (m, 2H, 8-CH_2CH_3), 1.33−1.27 (m, -CH_2CH_2-$COOCH_3$), 1.1 (t, J = 6.46 Hz, 3H, 8-CH_2CH_3), −0.108 (s, 1H, NH), −0.112 (s, 1H, NH). Mass Calcd for $C_{36}H_{42}N_4O_7$: 642.3. Found: *m*/*e* 642.5. HRMS, Calcd: 642.3053. Found: 642.3032.

3-(1-Hydroxyethyl)-bacteriochlorin p_6 Trimethyl Ester (18). Following the procedure described for the preparation of bacteriochlorin **5**, bacteriochlorin **17** (100 mg) was reacted with sodium borohydride. After the standard workup, the residue was chromatographed on a silica column with acetone/CH_2Cl_2 (2% v/v), and the title compound was obtained in 96% yield (98 mg). Mp: 180−183 °C. UV−vis λ_{max} (nm, CH_2Cl_2): 352 (1.32 × 10^5), 385 (ϵ 1.05 × 10^5), 509 (ϵ 2.85 × 10^4), 663 (ϵ 1.97 × 10^4), 737 (5.24 × 10^4). ^{1}H NMR (400 MHz, $CDCl_3$, δ ppm): 8.74 and 8.72 (two singlets, 5-H), 8.53 (s, 1H, 10-H), 8.28 and 8.26 (two singlets, 20-H), 6.16 (m, 1H, 3-$(CH_3)CHOH$), 4.97 (m, 1H, 17-H), 4.15 (m, 2H, 1H for 7-H, 1H for 18-H), 4.14 (s, 3H, -$COOCH_3$), 4.10 (s, 3H, -$COOCH_3$), 4.0 (m, 1H, 8-H), 3.51 and 3.50 (two singlets, 12-CH_3), 3.38 (s, 3H, -CH_2CH_2-$COOCH_3$), 3.22 and 3.19 (two singlets, 2-CH_3), 2.75 (s, broad, 3-$(CH_3)CHOH$, 2.37−2.17 (m, 2H, -$CH_2CH_2COOCH_3$), 2.10−1.90 (m, 5H, 3H for 3-$CH_3CH(OH)$, 2H for 8-CH_2CH_3), 2.05−1.99 (2 m, 2H, -$CH_2CH_2COOCH_3$), 1.82−1.72 (m, 6H, 3H for 7-CH_3, 3H for 18-CH_3), 1.05 (t, J = 6.46 Hz, 3H, 8-CH_2CH_3), −0.30 (s, 1H, NH), −0.65 (s, 1H, NH). Mass Calcd for $C_{36}H_{44}N_4O_7$·1/2H_2O: C, 66.14; H, 6.94; N, 8.57. Found: C, 66.51; H, 7.06; N, 8.29. Mass Calcd for $C_{36}H_{44}N_4O_7$: 644.3. Found: *m*/*e* 645.6 (M + 1). HRMS, Calcd: 644.3210. Found: 644.3198.

3-(1-Methyloxyethyl)-bacteriochlorin p_6 Trimethyl Ester (19). Following the procedure described for the preparation of **7,** bacteriochlorin **18** (50 mg) reacted with methanol and the title compound was obtained in 85% (43 mg) yield as viscous oil. UV−vis λ_{max} (nm, CH_2Cl_2): 352 (ϵ 1.34 × 10^5), 385 (ϵ 1.07 × 10^5), 509 (ϵ 2.87 × 10^4), 663 (ϵ 1.95 × 10^4), 737 (5.23 × 10^4). ^{1}H NMR (400 MHz, $CDCl_3$, δ ppm): 8.71 and 8.67 (two singlets, 5-H), 8.53 (s, 1H, 10-H), 8.29 (s, 1H, 20-H), 5.63−5.57 (m, 1H, 3-$(CH_3)CHOCH_3$), 4.99−4.93 (m, 1H, 17-H), 4.15 (s, 3H, -$COOCH_3$), 4.14−4.08 (m, 2H, 1H for 7-H, 1H for 18-H), 4.10 (s, 3H, -$COOCH_3$), 4.07−4.01 (m, 1H, 8-H), 3.55 (s, 3H, 12-CH_3), 3.50 (s, 3H, 3^1-OCH_3), 3.40 (s, 3H, -$CH_2CH_2COOCH_3$), 3.25 (s, 3H, 2-CH_3), 2.29−2.23 (m, 2H, -$CH_2CH_2COOCH_3$), 2.09−2.03 (m, 2H, -$CH_2CH_2COOCH_3$), 1.98 (d, J = 6.58 Hz, 3H, 3-$CH_3CH(OCH_3)$), 1.78 (d, J = 6.54 Hz, 6H, 3H for 7-CH_3, 3H for 18-CH_3), 1.73−1.50 (m, 2H, 8-CH_2CH_3), 1.07 (t, J = 6.46 Hz, 3H, 8-CH_2CH_3), −0.38 (s, 1H, NH), −0.59 (s, 1H, NH). HRMS for $C_{37}H_{46}N_4O_7$ Calcd: 658.3366. Found: 658.3367.

3-(1-Propyloxyethyl)-bacteriochlorin p_6 Trimethyl Ester (20). Following the procedure as described for the preparation of **7,** bacteriochlorin **18** (50 mg) was reacted with 1-propanol and the title compound was obtained in 86% yield (46 mg) as viscous oil. UV−vis λ_{max} (nm, CH_2Cl_2): 352 (ϵ 1.32 × 10^5), 385 (ϵ 1.09 × 10^5), 509 (ϵ 2.88 × 10^4), 663 (ϵ 1.96 × 10^4), 737 (5.21 × 10^4). ^{1}H NMR (400 MHz, $CDCl_3$, δ ppm): 8.76 and 8.71 (two singlets, 5-H), 8.52 (s, 1H, 10-H), 8.27 (s, 1H, 20-H), 5.71−5.65 (m, 1H, 3-$(CH_3)CHOC_3H_7$), 5.00−4.94 (m, 1H, 17-H), 4.17 (s, 3H, -$COOCH_3$), 4.18−4.12 (m, 2H, 1H for 7-H, 1H for 18-H), 4.12 (s, 3H, -$COOCH_3$), 4.07−4.01 (m, 1H, 8-H), 3.53 (s, 3H, 12-CH_3), 3.50 (2H, -$OCH_2CH_2CH_3$), 3.40 (s, 3H, -$CH_2CH_2COOCH_3$), 3.24 (s, 3H, 2-CH_3), 2.29−2.22 (m, 2H, -$CH_2CH_2COOCH_3$), 2.09−2.03 (m, 2H, -$CH_2CH_2COOCH_3$), 1.98 (d, J = 6.58 Hz, 3H, 3-$CH_3CH(OC_3H_7)$), 1.78 (6H, 3H for 7-CH_3, 3H for 18-CH_3), 1.73−1.67 (m, 2H, 8-CH_2CH_3), 1.56 (2H, -$OCH_2CH_2CH_3$), 1.06 (3H, t, J = 6.9 Hz, 8-CH_3), 0.90 (3H, t, J = 6.9 Hz, -$OCH_2CH_2CH_3$), −0.35 (s, 1H, NH), −0.55 (s, 1H, NH). HRMS for $C_{39}H_{50}N_4O_7$ Calcd: 686.3679. Found: 686.3681.

3-(1-Heptyloxyethyl)-bacteriochlorin p_6 Trimethyl Ester (21). Following the procedure described for the preparation of **7,** bacteriochlorin **18** (50 mg) was reacted with 1-heptanol and the title compound was obtained in 85% yield (48 mg) as viscous oil. UV−vis λ_{max} (nm, CH_2Cl_2): 352 (ϵ 1.32 × 10^5), 385 (ϵ 1.09 × 10^5), 509 (ϵ 2.85 × 10^4), 663 (ϵ 1.96 × 10^4), 737 (5.25 × 10^4). ^{1}H NMR (400 MHz, $CDCl_3$, δ ppm): 8.77 and 8.72 (two singlets, 5-H), 8.52 (s, 1H, 10-H), 8.27 (s, 1H, 20-H), 5.71−5.65 (m, 1H, 3-(CH_3)C*H*OC_7H_{15}), 4.98−4.92 (m, 1H, 17-H), 4.15 (s, 3H, -$COOCH_3$), 4.14−4.08 (m, 2H, 1H for 7-H, 1H for 18-H), 4.10 (s, 3H, -$COOCH_3$), 4.06−4.00 (m, 1H, 8-H), 3.53 (t, J = 6.0 Hz, 2H, -OC*H*$_2$$(CH_2)_5CH_3$), 3.52 (s, 3H, 12-$CH_3$), 3.40 (s, 3H, -$CH_2CH_2COOCH_3$), 3.23 (s, 3H, 2-$CH_3$), 2.26 (m, 2H, -C*H*$_2$$CH_2COOCH_3$), 2.09−2.03 (2 m, 2H, -$CH_2$C*H*$_2$-$COOCH_3$), 1.98 (d, J = 6.58 Hz, 3H, 3-C*H*$_3$$CH(OC_7H_{15})$), 1.76 (d, J = 6.58 Hz, 6H, 3H for 7-CH_3, 3H for 18-CH_3), 1.73−1.67 (m, 2H, 8-C*H*$_2$$CH_3$), 1.59−1.53 (m, 2H, -$OCH_2$C*H*$_2$$(CH_2)_4$-$CH_3$), 1.35−1.15 (8H, -$O(CH_2)_2$(C*H*)$_4$$CH_3$), 1.06 (t, 3H, J = 6.9 Hz, 8-CH_3), 0.80 (t, J = 7.8 Hz, 3H, -$O(CH_2)_6$C*H*$_3$), −0.35 (s, 1H, NH), −0.55 (s, 1H, NH). HRMS for $C_{43}H_{58}N_4O_7$ Calcd: 742.4305. Found: 742.4310.

3-(1-Undecyloxyethyl)-bacteriochlorin p_6 Trimethyl Ester (22). Following the procedure described for the preparation of **7,** bacteriochlorin **18** (50 mg) was reacted with 1-undecanol and the title compound was obtained in 85% yield (51 mg) as viscous oil. UV−vis λ_{max} (nm, CH_2Cl_2): 352 (ϵ 1.32 × 10^5), 385 (ϵ 1.05 × 10^5), 509 (ϵ 2.85 × 10^4), 663 (ϵ 1.97 × 10^4), 737 (5.24 × 10^4). ^{1}H NMR (400 MHz, $CDCl_3$, δ ppm): 8.78 and 8.73 (two singlets, 5-H), 8.54 (s, 1H, 10-H), 8.28 (s, 1H, 20-H), 5.71−5.65 (m, 1H, 3-(CH_3)C*H*O$C_{11}H_{23}$), 5.00−4.94 (m, 1H, 17-H), 4.15 (s, 3H, -$COOCH_3$), 4.14−4.06 (m, 2H, 1H for 7-H, 1H for 18-H), 4.10 (s, 3H, -$COOCH_3$), 4.04 (m, 1H, 8-H), 3.64 (t, J = 6.0 Hz, 2H, -OC*H*$_2$$(CH_2)_9CH_3$), 3.53 (s, 3H, 12-$CH_3$), 3.40 (s, 3H, -$CH_2CH_2$ $COOCH_3$), 3.24 (s, 1.5H, 1/2 × 2-CH_3), 3.23 (s, 1.5H, 1/2 × 2-CH_3), 2.29−2.21 (m, 2H, -C*H*$_2$ CH_2COOCH_3), 2.09−2.02 (2 m, 2H, -CH_2C*H*$_2$$COOCH_3$), 1.98 (d, J = 6.58 Hz, 3H, 3-C*H*$_3$$CH(OC_{11}H_{23})$), 1.78 (d, J = 6.58 Hz, 6H, 3H for 7-CH_3, 3H for 18-CH_3), 1.73−1.67 (m, 2H, 8-C*H*$_2$$CH_3$), 1.59−1.53 (m, 2H, -$OCH_2$C*H*$_2$ $(CH_2)_8CH_3$), 1.56 (t, J = 6.9 Hz, 8-CH_3), 1.44−1.12, 1.12−1.02, 0.92−0.86 (altogether 16H, -$O(CH_2)_2$(C*H*)$_8$$CH_3$), 0.84 (t, overlapped with other peaks, J = 7.8 Hz, 3H, -$O(CH_2)_{10}$C*H*$_3$), −0.35 (s, 1H, NH), −0.55 (s, 1H, NH). Mass Calcd for $C_{47}H_{66}N_4O_7$: 798.5. Found: *m*/*e* 799.7 (M + 1). HRMS, Calcd: 798.4931. Found: 798.4966.

3-Vinyl-3-deacetylbacteriopurpurin-18-*N*-hexylimide Methyl Ester (23). Starting from compound **13**, following the similar procedure for preparing bacteriochlorin **6**, the title compound was obtained in 85% yield (33 mg). Mp: 245 °C. UV−vis λ_{max}(nm, CH_2Cl_2): 366 (ϵ 1.02 × 10^5), 417 (ϵ 4.53 × 10^4), 538 (ϵ 3.91 × 10^4), 791 (ϵ 5.55 × 10^4). ^{1}H NMR (400 MHz, $CDCl_3$, δ ppm): 8.579 (s 1H, 5-H), 8.457 (s, 1H, 10-H), 8.346 (s, 1H, 20-H), 7.75 (dd, J_1 = 11.92 Hz, J_2 = 18.3 Hz, 1H, 3-C*H*═CH_2), 6.157 (d, J = 18.3 Hz, 1H, 3-CH═C*H*H), 6.047 (d, J = 11.92 Hz, 1H, 3-CH═CH*H*), 5.28−5.22 (m, 1H, 17-H), 4.44−4.37 (m, 2H, -NC*H*$_2$$(CH_2)_4CH_3$), 4.22−4.16 (m, 2H, 1H for 7-H, 1H for 18-H), 4.03−3.97 (m, 1H, 8-H), 3.616 (s, 3H, 12-CH_3), 3.554 (s, 3H, -$COOCH_3$), 3.259 (s, 3H, 2-CH_3), 2.66−2.60 (m, 1H, -C*H*CH_2COOCH_3), 2.36−2.30 (m, 3H, 1H for-CH*H*CH_2COOCH_3, 2H for 8-C*H*$_2$$CH_3$), 1.98−1.90 (m, 2H, -$NCH_2$C*H*$_2$$(CH_2)_3CH_3$), 1.771 (d, J = 7.09 Hz, 3H, 7-CH_3), 1.689 (d, J = 7.70 Hz, 3H, 18-CH_3), 1.61−1.56 (m, 4H, 2H for -N$(CH_2)_2$C*H*$_2$$(CH_2)_2CH_3$, 2H for CH_2C*H*$_2$$COOCH_3$), 1.45−1.39 (m, 4H,-N$(CH_2)_3$C*H*$_2$C*H*$_2$$CH_3$), 1.09 (t, J = 7.21 Hz, 3H, 8-CH_2C*H*$_3$), 0.924 (t, J = 6.91 Hz, 3H, -N$(CH_2)_5$C*H*$_3$), −0.01 (s, 1H, NH), −0.354 (s, 1H, NH). Mass Calcd for $C_{40}H_{49}N_5O_4$: 663.4. Found: *m*/*e* 663.6 HRMS, Calcd: 663.3784. Found: 663.3766.

3-Formylbacteriopurpurin-18-*N*-hexylimide (24). The bacteriochlorin **23** (100 mg) was dissolved in THF (20 mL). Osmium tetroxide (300 mg) dissolved in CCl_4 (3 mL) and sodium periodate (2000 mg) in water (10 mL) were added. The reaction mixture was stirred for 20 h and monitored by UV−vis spectrophotometry. The disappearance of the long-wavelength absorption band at 796 nm and appearance of a new peak at 830 nm indicated the completion of the reaction. The reaction mixture was then extracted with dichloromethane, washed with 2% acetic acid/water solution and then with water (3 × 200 mL). After the standard workup, the residue was purified by preparative chromatography, and the title compound was obtained in 50% yield (50 mg). Mp: 265 °C. UV−vis λ_{max} (nm, CH_2Cl_2): 364 (ϵ 8.04 × 10^4), 412 (ϵ 4.32 × 10^4), 548 (ϵ 3.64 × 10^4), 829 (ϵ 8.16 × 10^4). ^{1}H NMR (400 MHz, $CDCl_3$, δ ppm): 11.28 (s, 1H, -CHO), 9.383 (s, 1H, 5-H), 8.801 (s, 1H, 10-H), 8.626 (s, 1H, 20-H), 5.33−5.27 (m, 1H, 17-H), 5.03−4.97 (m, 2H, -NC*H*$_2$$(CH_2)_4CH_3$), 4.45−3.39 (m, 2H, 1H for 7-H, 1H for 18-H), 4.15−3.09 (m, 1H, 8-H), 3.71 (s, 3H, 12-CH_3), 3.616 (s, 3H, $COOCH_3$), 3.565 (s, 3H, 2-CH_3), 2.70−2.63 (m, 1H, C*H*HCH_2COOCH_3), 2.39−2.33 (m, 3H, 1H for CH*H*CH_2-$COOCH_3$, 2H for 8-C*H*$_2$$CH_3$), 1.99−1.91 (m, 2H, NCH_2C*H*$_2$-$(CH_2)_3CH_3$), 1.84 (d, J = 7.07 Hz, 3H, 7-CH_3), 1.725 (d, J = 7.59 Hz, 3H, 18-CH_3), 1.60−1.53 (m, 2H, CH_2C*H*$_2$$COOCH_3$), 1.46−1.40 (m, 4H, N$(CH_2)_2$C*H*$_2$C*H*$_2$$CH_2CH_3$), 1.29−1.22 (m, 2H, N$(CH_2)_4$C*H*$_2$$CH_3$), 1.11 (t, J = 7.20, 3H, 8-CH_2C*H*$_3$), 0.937 (t, J = 7.04, 3H, N$(CH_2)_5$C*H*$_3$), −0.508 (s, 1H, NH), −0.651 (s, 1H, NH). Mass Calcd for $C_{39}H_{47}N_5O_5$: 665.4. Found: *m*/*e* 665.6. HRMS, Calcd: 665.3577. Found: 665.3566.

3-(Hydroxy)methyl-3-deacetyl-bacteriopurpurin-18-*N*-hexylimide Methyl Ester (25). Following the procedure described for the preparation of **5**, bacteriochlorin **24** (*30*) reacted with sodium borohydride. The title compound was obtained in 93% yield (47 mg) as viscous oil. UV−vis λ_{max} (nm, CH_2Cl_2): 369 (ϵ 9.12 × 10^4), 417 (ϵ 4.25 × 10^4), 536 (ϵ 3.49 × 10^4), 798 (ϵ 4.52 × 10^4). ^{1}H NMR (400 MHz, $CDCl_3$, δ ppm): 8.66 (s, 1H, 5-H), 8.60 (s, 1H, 10-H), 8.40 (s, 1H, 20-H), 5.70 (s, 2H, 3-C*H*$_2$-OH), 5.29−5.22 (m, 1H, 17-H), 4.45−4.39 (m, 2H, -NC*H*$_2$$(CH_2)_4$-$CH_3$), 4.25−4.18 (m, 2H, 1H for 7-H, 1H for 18-H), 4.07−4.01 (1H, m, 8-H), 3.63 (s, 3H, 12-CH_3), 3.56 (s, 3H, -$COOCH_3$), 3.28 (s, 3H, 2-CH_3), 2.68−2.61 (m, 1H, -C*H*HCH_2-$COOCH_3$), 2.42−2.27 (m, 3H, 1H for -CH*H*CH_2COOCH_3, 2H for 8-C*H*$_2$$CH_3$), 2.01−1.95 (m, 4H, NCH_2C*H*$_2$ C*H*$_2$$(CH_2)_2CH_3$), 1.84−1.74 (d, J = 7.06 Hz, 3H, 7-CH_3), 1.69 (d, J = 7.21 Hz, 3H, 18-CH_3), 1.58−1.51 (m, 2H, -CH_2C*H*$_2$$COOCH_3$), 1.46−1.39 (m, 4H, -$NCH_2(CH_2)_2$ (C*H*$_2$)$_2$$CH_3$), 1.10 (t, 3H, J = 7.53 Hz, 8-CH_2C*H*$_3$), 0.93 (t, 3H, J = 7.08 Hz, -N$(CH_2)_5$C*H*$_3$), −0.19 (s, 1H, NH), −0.48 (s, 1H, NH). HRMS for $C_{39}H_{49}N_5O_5$, Calcd: 667.3733. Found: 667.3733.

3-(Decyloxy)methyl-3-deacetyl-purpurin-18-*N*-hexylimide Methyl Ester (26). Following the procedure described for the preparation of **7**, bacteriochlorin **25** (50 mg) was reacted with 1-decanol. The title compound was obtained in 85% yield (51 mg) as viscous oil. UV−vis λ_{max} (nm, CH_2Cl_2): 368 (ϵ 9.12 × 10^4), 417 (ϵ 4.25 × 10^4), 536 (ϵ 3.49 × 10^4), 798 (ϵ 4.52 × 10^4). ^{1}H NMR (400 MHz, $CDCl_3$, δ ppm): 8.61 (s, 1H, 5-H), 8.57 (s, 1H, 10-H), 8.35 (s, 1H, 20-H), 5.48 (s, 2H, 3-C*H*$_2$-OH), 5.28−5.21 (m, 1H, 17-H), 4.43−4.35 (m, 2H, -NC*H*$_2$$(CH_2)_4$-$CH_3$), 4.21−4.13 (m, 2H, 1H for 7-H, 1H for 18-H), 4.04−4.37 (1H, m, 8-H), 3.72 (t, J = 7.1 Hz, 2H, -OC*H*$_2$$(CH_2)_8CH_3$), 3.62 (s, 3H, 12-$CH_3$), 3.53 (s, 3H, -$COOCH_3$), 3.24 (s, 3H, 2-$CH_3$), 2.67−2.60 (m, 1H, -C*H*HCH_2COOCH_3), 2.40−2.25 (m, 3H, 1H for -CH*H*CH_2COOCH_3, 2H for 8-C*H*$_2$$CH_3$), 1.98−1.91 (m, 4H, NCH_2C*H*$_2$ C*H*$_2$$(CH_2)_2CH_3$), 1.78 (d, J = 7.06 Hz, 3H,

Table 1. Tumor vs Skin Uptake of Bacteriopurpurinimides by *in Vivo* Reflectance Spectroscopy[a]

compound	log *P* value[b]	tumor uptake (μmolar) (std dev)	skin uptake (μmolar) (std dev)	tumor/skin ratio	retention time[c] (min)	singlet oxygen yield
4	7.88	2.64 (0.51)	0.542 (0.13)	4.87	14.3	0.40
5 (*R/S*)	7.55	5.80 (1.09)	2.04 (0.47)	2.84	7.5	0.53
6	8.84	2.732 (0.51)	0.759 (0.15)	3.61	21.2	0.45
7 (*R/S*)	8.18	13.25 (1.54)	4.84 (0.65)	2.74	14.8/15.3	0.42
8 (*R/S*)	9.16	8.74 (1.05)	2.92 (0.55)	2.99	20.2/21.6	0.41
9 (*R/S*)	11.19	9.4 (1.13)	3.35 (0.64)	2.80	35.6/37.9	0.46
10 (*R/S*)	12.72	12.38 (2.01)	2.54 (0.46)	4.87	57.0/62.9	0.43
14 (*R/S*)	10.22	15.87 (3.01)	1.61 (0.22)	9.85	28.4/30.1	0.50
15 (*R/S*)	11.24	18.07 (2.67)	3.22 (0.55)	5.61	36.7/39.6	0.45
19	6.18	0.521 (0.10)	0.13 (0.04)	4.00	3.4	0.44
20 (*R/S*)	7.16	0.626 (0.13)	0.18 (0.03)	3.48	4.2/4.4	0.42
21 (*R/S*)	9.17	12.16 (2.2)	4.52 (0.89)	2.69	6.8/7.2	0.40
22 (*R/S*)	11.19	15.78 (1.06)	2.845 (0.82)	5.55	11.3/12.4	0.41
26	11.22	10.68 (0.93)	7.13 (0.90)	1.50	33.0	0.42

[a] Drug uptake was measured in mice (C_3H) bearing RIF tumors, dose 5.0 mmol/kg at 24 h postinjection, and the data are the average of three replicates. [b] The computed log *P* and log *D* values was quite close. [c] Setup for the HPLC analysis: Waters Symmetry C-18 analytical column, 4.6 × 150 mm dimensions, 5 μm particle size; solvent, methanol; flow rate, 1.0 mL/min

7-CH_3), 1.72−1.64 (m, 5H, 3H for 18-CH_3, d, J = 7.21 Hz; 2H for -$OCH_2CH_2(CH_2)_7CH_3$), 1.58−1.51 (m, 2H, -CH_2CH_2-$COOCH_3$), 1.44−1.37 (m, 4H, -$NCH_2(CH_2)_2(CH_2)_2CH_3$), 1.30−1.12 (m, 14H, -$O(CH_2)_2(CH_2)_7CH_3$), 1.09 (t, 3H, J = 7.53 Hz, 8-CH_2CH_3), 0.92 (t, 3H, J = 7.08 Hz, -$N(CH_2)_5CH_3$), 0.82(m, 3H, -$O(CH_2)_9CH_3$), −0.19 (s, 1H, NH), −0.48 (s, 1H, NH). HRMS for $C_{49}H_{69}N_5O_5$, Calcd: 807.5298. Found: 807.5348.

HPLC Analysis. The photosensitizers' purity was determined using an HPLC system consisting of a Waters 600 controller, Waters 996 diode array detector, and a Waters Delta 600 fluid delivery system, equipped with a Waters Symmetry C18 column (5 μm, 100 Å, of dimensions 4.6 × 150 mm, Waters part #WAT 045905). The solvent was 100% methanol at a flow rate of 1.0 mL/min. Peak detection was set to the wavelengths corresponding to the absorption peaks of each compound. The retention times (RT) of all the compounds are listed in Table 1.

Method for Determine Singlet-Oxygen Generating Efficacy. A SPEX 270M Spectrometer (Jobin Yvon) equipped with an InGaAs photodetector (Electro-Optical Systems Inc., U.S.A.) was utilized for acquisition of $^1O_2$ emission spectra. A diode pumped solid-state laser (Verdi, Coherent) at 532 nm was used to excite the photosensitizers and reference samples (Rose Bengal purchased from Fisher Scientific, Hampton, NH) at room temperature. The $^1O_2$ yield for Rose Bengal in methanol solution is $Q_\Delta = 0.80$. All samples were dissolved in methanol solution purchased from J. T. Baker (Phillipsburg, NJ), which was used without purification. Once dissolved in methanol, the sample was transferred into a quartz cuvette where it was placed directly in front of the entrance slit of the spectrometer, and the exciting laser beam was directed at 90° relative to the collection of emission. Long-pass filters, 538AELP and 950 LP (Omega Optical, U.S.A.), were used to attenuate the excitation laser light and fluorescence from dyes as a means of studying singlet oxygen phosphorescence, which peaked at around 1270 nm.

Formulation of Photosensitizers. Similar to most of the porphyrin-based compounds, the photosensitizers discussed in this study were insoluble in water and were formulated in 1% Tween 80/water solution. In a typical experiment, 3 mg of a photosensitizer was taken in a mortar and 100 μL Tween 80 was added. It was mixed with a pestle until it turned into a viscous paste and was left overnight in the dark for 12 h. The next day, 10 mL 5% D5W (5% dextrose solution in water) was added to it slowly with continuous mixing and filtered *via* a 0.2 μm cellulose acetate sterile syringe filter. 100 μL of the solution was taken in a cuvette and diluted 30-fold with methanol to disaggregate the compound, and the OD was measured, which in addition to the extinction coefficient values was used for determining the concentrations of the photocensitizers by following the Beer−Lambert law.

Biological Studies. *Tumor vs Skin Uptake by in Vivo Reflectance Spectroscopy.* The *in vivo* reflection data were collected by delivering monochromatic light through a quartz fiber in contact with the tissue in question. At a measured distance (typically ∼5 mm) from the delivery fiber, a pickup fiber was placed in contact with the surface. Both fibers were perpendicular to the tissue surface. Very low optical power levels (about 1 μW) are necessary in these experiments to avoid PDT effects during measurement. Light that entered the pickup fiber was conducted to a silicon photodiode detector. The detector circuit measured the photocurrent that was linear in power over 7−8 orders of magnitude. Because of the optical properties of tissue, the spectral range of greatest utility is the region between 600 and 1000 nm. In this spectral range, the probability of diffuse scattering of photons by tissue is greater than the probability of absorption. The wavelength of light was varied by scanning the monochromator, and a spectrum of diffusely scattered photons was recorded. To calculate the concentration, we used the longest absorption wavelength. The drug concentration C is calculated by eq 1.

$$C = \frac{1}{2\cdot\epsilon}\left\{-\sqrt{\mu_s{}^2 + \frac{4}{3}\alpha_0{}^2} + \sqrt{\mu_s{}^2 + \frac{4}{3}\left(\frac{\mathrm{OD}}{r} + \alpha_0\right)^2}\right\} \quad (1)$$

In this equation, ϵ is the molar extinction coefficient, α_0 is the intrinsic tissue attenuation, OD is the diffuse optical density, μ_s is the reduced scattering coefficient, and r is the distance from the detector to the tissue in question (5 mm). For a specific compound, we measured its molar extinction coefficient (ϵ) by the Beer−Lambert Law, eq 2.

$$A = \epsilon l c \quad (2)$$

In this equation, A is the absorbance, ϵ is the molar extinction coefficient, l is the distance that the light travels through the material, and c is the concentration. We measured α_0 and μ_s by another method: C^{14} drug labeling and chemical dissolution of the tissue. It was found that, for RIF tumor in C3H mice, the value of α_0 was 3.3 cm^{-1} and the value of μ_s was 4.9 cm^{-1}.

Intracellular Localization of Photosensitizers. To determine subcellular localization, photosensitizers were coincubated with organelle-specific fluorescent probes. RIF cells were seeded at 2×10^5 on poly(L-lysine)-coated coverslips in 6-well plates and cultured for 24 h to allow attachment and spreading. Photosensitizers at appropriate concentrations (typically 0.5−2 μM) were

added to cells in culture medium, and the cells incubated for 24 h at 37 °C, 5% CO_2, in the dark. To determine subcellular localization, cells were coincubated with fluorescent probes (Molecular Probes, Invitrogen Carlsbad, CA) known to target mitochondria (Rhodamine 123, 1 μM) or lysosomes (yellow−green Fluospheres 0.1 μm diameter, 1:10 000 dilution). Photosensitizers and Fluospheres were added 24 h prior to microscopy, the latter with gently rocking, and the R-123 was added during the final 30 min of incubation. The cells were then rinsed briefly with phosphate-buffered saline (PBS) and examined immediately by fluorescence microscopy (Zeiss Axiovert 35, Carl Zeiss, Inc., Germany) with a 200 W mercury arc lamp light source.

Fluorescence was imaged with a CCD camera and intensifier and processed with Metamorphose 4.5 (Universal Imaging Corp., Downington, PA). Images of photosensitizers and colocalizing dyes in the same field were taken in rapid succession. Photosensitizers were detected using a combination of 530−580 nm excitation and 600 nm dichroic/615 nm long-pass emission filters. R-123 and Fluospheres were detected using 445−490 nm excitation and 510 dichroic/520−560 nm long-pass/emission filters. The results obtained by using Fluospheres as a counterstain did not show any lysosomal colocalization, so they are not shown in the Results section.

Method for Determining in Vitro Efficacy (MTT Assay). RIF cells were grown in α-DMEM with 10% fetal calf serum, and penicillin and streptomycin (*20*). Cells were maintained in 5% CO_2 and 95% air at 100% humidity. For phototoxicity studies, RIF cells were plated in 96-well plates at a density of 1×10^4 cells well, in complete medium. 24 h later, compounds were added to a final concentration of 1.5 μM. After 24 h incubation in the dark at 37 °C, the cells were irradiated with laser light from an argon pumped dye laser using fluences of 0−12 J/cm^2 at a dose rate of 5.6 mW/cm^2. After PDT, the cells were washed once, placed in complete medium, and incubated for 48 h. Cells were incubated with 10 μL/well of 4 mg/mL MTT for the final 4 h. The MTT-containing medium was removed, and 100 μL DMSO was added to solubilize the formazan crystals. The absorbance of the wells was read on a microtiter plate reader at a wavelength of 560 nm. The results were plotted as percent growth vs days after treatment.

Evaluation of in Vivo Photosensitizing Efficacy. C3H mice (10 mice/group) were injected subcutaneously on the shoulder with 3×10^5 RIF-1 cells in 40 μL of complete α-MEM. Tumors were permitted to grow to treatment size (4−5 mm) The day before light treatment, the mice were injected intravenously (*via* lateral tail vein) with photosensitizers in 1% Tween-80/D5W at the selected dose in approximately 0.2 mL. At 24 h postinjection, mice were restrained without anesthesia in Plexiglas holders, designed to expose to light only the tumor and a 2−4 mm margin of skin. The mice were treated with laser light (135 J/cm^2 at 75 mW/cm^2). The animal experiments were conducted under the animal protocol approved by the Institute IACUC committee.

Following treatment, the tumor dimensions (orthogonal diameters) were measured by caliper every other day for tumor growth/regrowth assays. The tumor volume, *V*, was calculated with the formula $V = (lw^2/2)$, were *l* is the longest axis of the tumor and *w* is the axis perpendicular to *l*. Mice were euthanized when tumors reached the endpoint volume of 400 mm^3. Mice were considered cured if there was no palpable tumor by day 90.

Procedure for Competitive Binding to the Peripheral-Type Benzodiazopine Receptor. To labeled 5 mL disposable glass borosilicate tubes were added 1×10^6 cells in 50 μL Tris buffer (25 mM, pH 7.4), 50 μL ^{3}H-PK11195 (45 nM final concentration), and 50 μL competitor (cold PK11195 or photosensitizers). Final concentrations (molar) of the competitors were 1×10^9, 1×10^{-8}, 1×10^{-7}, 5×10^{-7}, 1×10^{-6}, 5×10^{-6}, 1×10^{-5}, 5×10^{-5}, and 1×10^{-4} diluted in Tris buffer. The background control contained no cells, 50 μL ^{3}H-PK11195, and 100 μL Tris buffer, and the maximum binding control contained 50 μL Tris buffer instead of competitor. Samples were incubated for 1 h at 4 °C, and then the incubation was inhibited by dilution with 3 mL of Tris buffer. The cells were filtered by vacuum on GF/C Whatman filters presoaked in Tris buffer containing 0.5% polyethyleneimine to prevent nonspecific binding to the filter. The filters were washed 3 times each with 4 mL of Tris buffer. The filters were transferred to scintillation vials and 4 mL of scintillation fluid (Universol, ICN) was added. The vials were shaken to dissolve ^{3}H-PK11195 and left in the dark to equilibrate, and the radioactivity of the samples was counted in a beta counter. The concentration of competitor at which 50% of ^{3}H-PK11195 binding was inhibited (IC50) was calculated to determine the binding of competitors compared to PK11195.

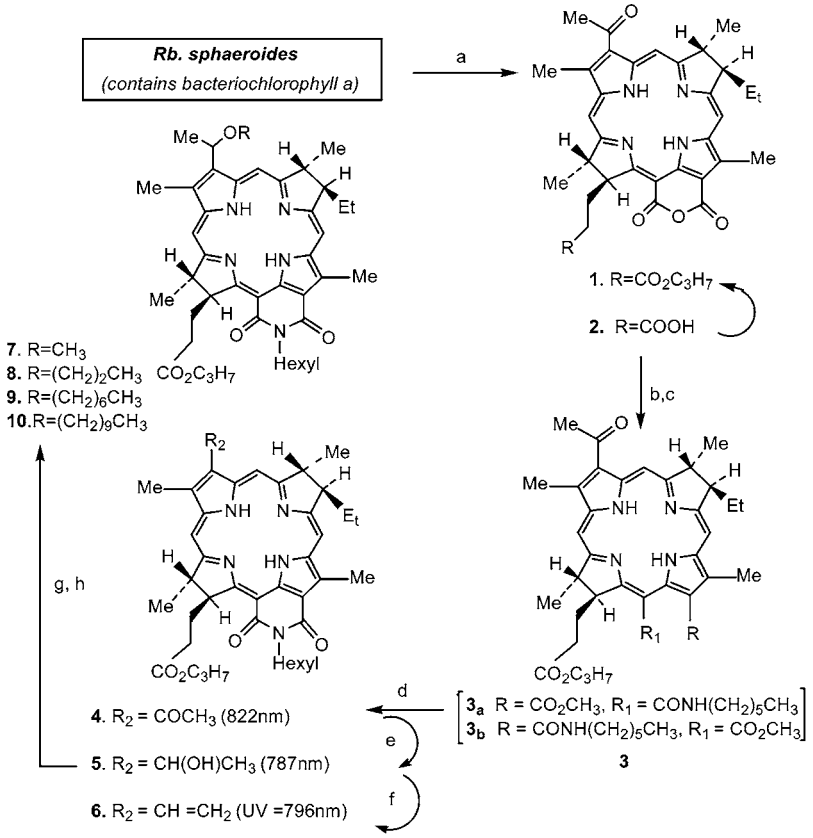
RESULTS AND DISCUSSION

Chemistry. *Alkyl Ether Analogues of N-Substituted Bacteriopurpurinimides. Rb. sphaeroides* enriched with bacteriochlorophyll-a (*21, 22*) was converted into bacteriopurpurin propyl ester **1** by following the methodology developed in our laboratory (Scheme 1). Reaction of **1** (λ_{max} 813 nm) with hexylamine produced an isomeric mixture of amides $\mathbf{3_a}$ and $\mathbf{3_b}$, which under base-catalyzed intramolecular cyclization afforded the corresponding *N*-hexylimide **4** with a strong long-wavelength absorption at 822 nm (in CH_2Cl_2). In our previous studies with a series of alkyl ether analogues of purpurinimides, we observed a linear correlation between the overall lipophilicity and PDT efficacy. To investigate the effect of such substitutions in the bacteriopurpurinimide system, two different approaches were used.

In our first approach, purpurinimide **4** was initially reacted with sodium borohydride and the corresponding (1-hydroxyethyl)purpurinimide **5** (λ_{max} 787 nm) was isolated in almost quantitative yield. Dehydration of **5** with *o*-dichlorobenzene at 140 °C for 2−3 min produced the corresponding 3-vinyl analogue **6** in ∼60% yield (λ_{max} 796 nm). Further reaction of **6** with 30% HBr/AcOH and then with dry methanol generated a mixture of the desired 3-(1-methoxy)ethyl-*N*-hexylpurpurinimide **7**, the related 3-(1′-hydroxy)ethyl analogue **5**, and the corresponding dehydration product **6**. In our second approach, HBr gas was bubbled through a solution of 3-(1-hydroxy)ethylpurpurin-*N*-hexylimide **5** in dry dichloromethane for 2 min. The solvent was evaporated under high vacuum, and the residue so obtained was redissolved in dry dichloromethane and reacted with dry methanol for 40 min in the presence of anhydrous potassium carbonate. After the standard workup, the desired methyl ether derivative **7** was obtained in about 90% yield. Compared to the HBr/AcOH method, the HBr gas method was found to be more efficient for the synthesis of **7** and other related purpurinimides **8**−**10** with fewer decomposition products. The resulting bacteriopurpurinimides exhibited long-wavelength absorptions at 787 nm (ϵ = 47 300 in dichloromethane). Thus, when compared to Photofrin, hematoporphyrin derivative (630 nm, ϵ = 5000), HPPH [3-(1-hexyloxyethyl) pyropheophorbide-a, 660 nm, ϵ = 47 500), and the alkyl ether analogues of purpurin-18-*N*-alkylimide (700 nm, ϵ = 45 000), significant red shifts of 157, 127, and 87 nm respectively were observed.

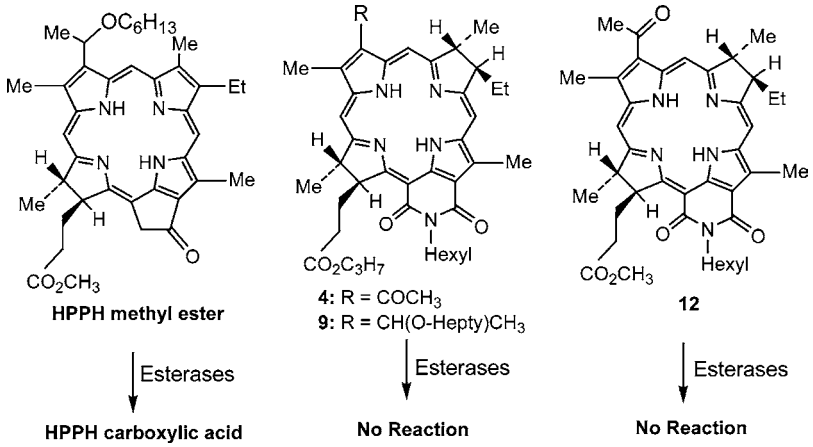
Although all the imide analogues shown in Scheme 1 were obtained in good yield, the starting bacteriopurpurin-18 was always isolated as a mixture of the propyl ester **1** and the corresponding carboxylic acid **2**. The overall yield was consistent; however, the individual components were isolated in variable yields from the different batches of *Rb. sphaeroides*. Several methods were followed to convert the carboxylic

Scheme 1. Synthesis of the Alkyl Ether Analogs of Bacteriopurpurin-18-*N*-hexylimide Propyl Ester



Reagents: a. KOH/1-propanol, H_2SO_4; b. $NH_2N(CH_2)_5CH_3$; c. CH_2N_2; d. KOH/M_eOH; e. N_aBH_4; f. o-dichlorobenzene(140°C, 2min); g. HBr/AcOH or HBr gas; h. ROH.

Scheme 2. Specificity of *in Vitro* and *in Vivo* Esterase Hydrolysis



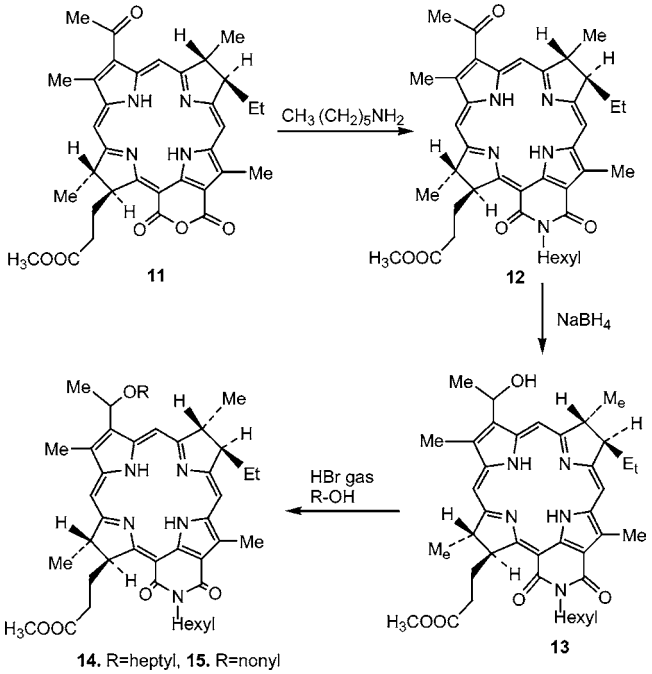
analogue **2** to the corresponding propyl ester **1**, but in general, the yield at the esterification step was low. Therefore, the bacteriopurpurin-18 was left refluxing in THF for a longer period of time until all the bacteriopurpurin-18 propyl ester was converted into the corresponding carboxylic acid, which upon diazomethane treatment afforded the corresponding methyl ester **11**.

Our next step was to prepare a series of the alkyl ether analogues of bacteriopurpurinimide methyl ester **15** with lipophilicity similar to that of the corresponding propyl ester **9** and to compare their photosensitizing efficacy under similar treatment conditions. Before synthesizing a series of alkyl ether analogues, we thought it necessary to look at the *in vivo* stability of the bacteriopurpurinimides containing the methyl or propyl ester substituents.

Previously, in a related study we observed that the methyl ester analogue of 3-devinyl-3(1′-hexyloxyethyl)-pyropheophorbide-a (HPPH), which is currently in phase I/II human clinical trials, was quite stable *in vivo*, except the methyl ester group was converted into the corresponding carboxylic acid (Scheme 2).

The *in vivo* conversion of the methyl ester to the corresponding carboxylic acid was possibly due to the presence of certain esterases specific for ester hydrolysis. To our surprise in an *in vitro* experiment, in contrast to the results obtained from the methyl ester of HPPH, no ester hydrolysis was observed in the bacteriopurpurinimides containing either the methyl or propyl ester functionality, which suggests that the presence of the fused imide ring system might inhibit the activity of the enzyme. The extraction of the photosensitizer **9** from RIF tumors in mice at

Scheme 3. Synthesis of a Series of Bacteriopurpurin-18-*N*-hexylimide Methyl Ester



24 h postinjection also showed no ester hydrolysis, which demonstrated the *in vivo* stability of the methyl and propyl ester functionalities in the bacteriopurpurinimide system. The log *P* values (a measure of the lipophilicity of the molecules) of the various alkyl ether analogues of bacteriopurpurinimide methyl ester were determined with the computer program module of the *PALLAS* system. The objective was to compare the *in vivo* biological efficacy of bacteriopurpurinimides (methyl ester vs propyl ester) with similar lipophilicity. Among the bacteriopurpurinimides containing propyl or methyl ester functionalities, compounds **7**−**10**, **14**, and **15** with *P* values ranging from 8.18 to 12.72 were synthesized (Scheme 3).

Alkyl Ether Derivatives of Bacteriopurpurin p_6. Among the chlorin-based photosensitizers derived from chlorophyll-a, certain chlorin p_6 analogues are reported to be effective PDT agents (*23*). However, in our own *in vivo* study with a series of chlorin analogues, the open-chain compounds were found to be less effective than those containing the fused isocyclic and imide ring systems. To investigate the structural requirements of the effective photosensitizers in the bacteriochlorin system, we synthesized a series of alkyl ether derivatives of bacteriochlorin p_6 and compared their efficacy with the alkyl ether analogues of *N*-hexylbacteriopurpurinimide.

To investigate a possible correlation between lipophilicity and PDT efficacy, the alkyl ether derivatives of bacteriochlorin p_6 **19**−**22** with log *P* values ranging from 6.18 to 11.19 were prepared by following the methodology depicted in Scheme 4. In brief, the six-member anhydride ring of bacteriopurpurin-18 methyl ester under basic conditions was cleaved into the corresponding bacteriochlorin p_6 dicarboxylic acid **16**, which upon treatment with diazomethane yielded bacteriochlorin p_6 trimethyl ester **17** in 80% overall yield. The hydroxy analogue **18** obtained from **17** by sodium borohydride reduction was converted into the corresponding alkyl ether analogues **19**−**22** by following the standard methodology.

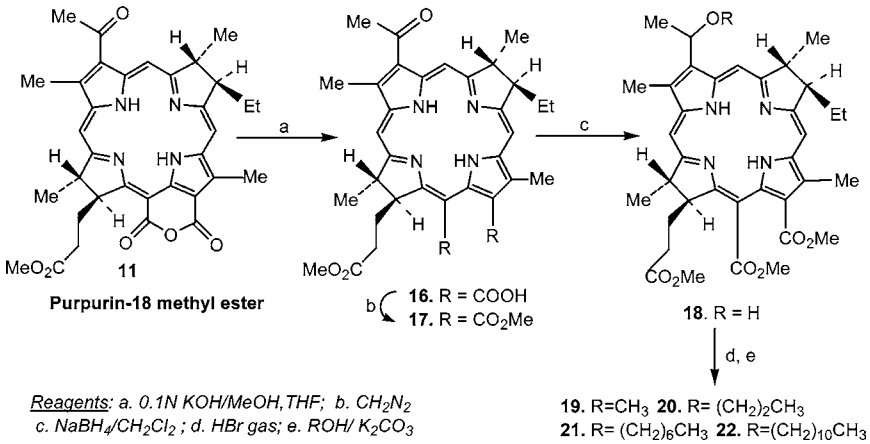
Synthesis of Bacteriopurpurinimide without Introducing any Chirality at Position-3[1]. Among all the alkyl ether analogues of purpurinimide and bacteriochlorin p_6, the 3-(1-heptyloxy)-ethyl-3-deacetylbacteriopurpurin-18-*N*-hexylimide propyl ester **9** tested as a mixture of R- and S-isomers was found to be the most effective (see the biological results). For investigating the importance of the chirality (position 3) in photosensitizing efficacy, bacteriochlorin **26** without any chirality at this partcular position was prepared. For compound **26** to have a similar lipophilicity as that of **9** (log $P = 11.19$), a decyl ether group was introduced at position 3 by following the reaction sequences illustrated in Scheme 5. In brief, the 3-vinyl bacteriochlorin **23** (the dehydration product of **13**) was first converted into the corresponding formyl derivative **24** in good yield by reacting **23** with a mixture of OsO_4 and sodium periodate ($NaIO_4$). Reduction of **24** by sodium borohydride and subsequent treatment with HBr gas/*n*-decyl alcohol produced the corresponding alkyl ether derivative **26** in 94% yield.

Photophysical Properties. All bacteriochlorins showed high singlet-oxygen producing efficiency (>40%) (see Table 1) and exhibited a strong long-wavelength absorption >750 nm. However, compared to bacteriopurpurinimides, the bacteriochlorin p_6 analogues exhibited a slight blue shift in their electronic absorption spectra (see Figure 1).

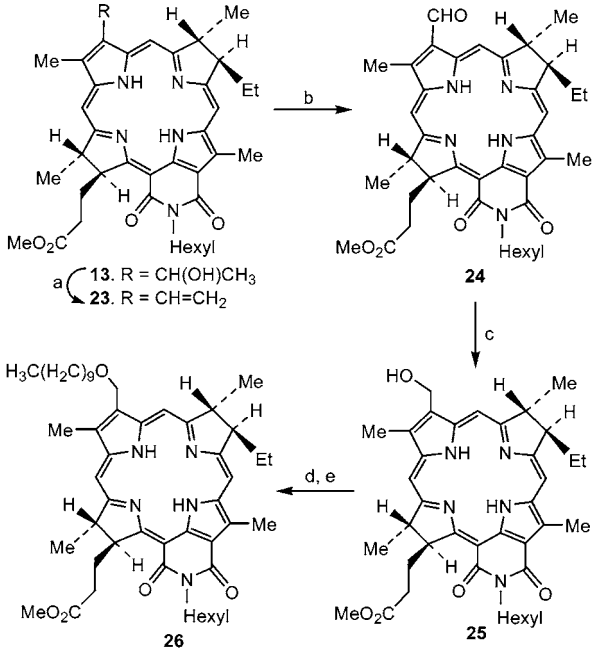
Biological Studies. *Determination of Tumor vs Skin Uptake by in Vivo Reflectance Spectroscopy.* The tumor and skin uptake of each compound was determined by *in vivo* reflectance spectroscopy (*24*, *25*), which measures transmittance of light through tissue in anesthetized C3H mice bearing RIF tumors. The optical transmittance as a function of wavelength was recorded before and after the i.v. injection of the photosensitizer at a dose of 5.0 μmol/kg.

The *in vivo* drug absorption spectrum is best displayed by taking the ratio of the postinjection spectrum to the preinjection spectrum. The tumor vs skin ratio of the bacteriopurpurinimides and their log *P* values calculated by *PALLAS* are summarized in Table 1. All photosensitizers showed a greater uptake in tumor vs skin at 24 h postinjection, indicating some degree of tumor

Scheme 4. Synthesis of the Alkyl Ether Analogues of Bacteriopurpurin p_6



Scheme 5. Synthesis of Isomerically Pure Bacteriopurpurinimide 31



Reagents: a. o-dichlorobenzene (140°C, 2min); b.OsO_4/$NaIO_4$; c. $NaBH_4$; d. HBr gas; e: $C_{10}H_{21}OH$

selectivity; varying from less than 2 (compound **26**) to almost 10 (compound **14**). Similar to the bacteriopurpurinimides, the bacteriochlorin p_6 analogues were also found to be quite stable both *in vitro* and *in vivo*. This might be due to its two ester groups being directly linked to the bacteriochlorin ring. Tumor and skin concentrations at different time points postinjection for the representative bacteriopurpurinimides **9** and **26** and bacteriochlorin p_6 **22** are plotted in Figure 2.

In Vitro Photosensitizing Efficacy. The *in vitro* photoactivity of the synthetic bacteriochlorins was determined in RIF cells by MTT assay (*26*) (see Experimental Procedures). To determine the optimum drug concentration, One of the bacteriochlorins, **9**, was initially tested at three different concentrations (1.5, 2.0, and 2.5 μM) producing good phototoxicity with no dark toxicity at 1.5 μM, with a light dose of 12 J/cm^2, The other photosensitizers (bacteriopurpurinimides **7**, **8**, **10**, **14**, **15**, and **26** and bacteriopurpurins p_6 **19**−**22**) were evaluated under similar experimental conditions and demonstrated similar phototoxity (Figure 3). The IC_{50} values of these compounds are summarized in Table 2.

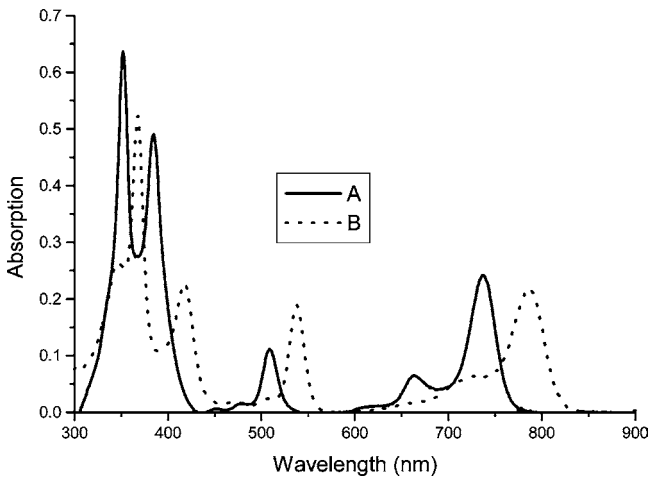


Figure 1. The electronic absorption spectra of compound **22** (A) and **9** (B) in dichloromethane at equimolar concentration (4.6 μM).

In Vivo Photosensitizing Efficacy of Bacteriopurpurinimides. To relate the molecular structure of the photosensitizers to their *in vivo* therapeutic response, the photosensitizing efficacies of four propyl ester analogues **7**−**10** were determined in C3H mice bearing RIF tumors (10 mice/group). Groups of mice with tumors of 4−5 mm diameter were treated at 0.4 μmol/kg and 135 J/cm^2 at 790 nm (*in vivo* absorption) at 24 h postinjection, and the tumor response (reappearance of tumor) was recorded. Among the alkyl ether analogues, the 3-(1-methoxy)ethyl **7** (log $P = 8.18$) and 3-(1-propyloxy)ethyl **8** (log $P = 9.16$) produced limited activity. Bacteriochlorin **9** containing a heptyl ether group with log $P = 11.19$ showed excellent PDT efficacy with 5/10 mice tumor-free at day 90. The corresponding bacteriochlorin **10** with a decyl ether group (log $P = 12.72$) showed similar activity: 4/10 mice tumor-free on day 90 (Figure 4). The photosensitizers **7** and **8**, which were found to be quite effective *in vitro*, showed limited *in vivo* photosensitizing ability suggesting that, in addition to tumor uptake, other factors such as intracellular localization of the drug may also be playing an important role in the final outcome of the therapy.

For preliminary screening, each compound was evaluated in mice (10 mice/group) bearing RIF tumors at variable drug doses and a fixed light dose. However, further studies with a larger group of mice, necessary for selecting the best photosensitizer, showed similar efficacy, and these studies are currently in progress. At lower doses (e.g., 0.1 μmol/kg; see Figure 5), none of these compounds showed any significant long-term efficacy.

The photosensitizing ability of bacteriopurpurinimide **26** was compared with compounds **9** and **15** possessing similar overall lipophilicity. As can be seen from the data summarized in Figures 4 and 5, compared to compound **26** (2/10 mice tumor-free on day 90), both purpurinimides **9** and **15** showed increased activity. These results suggest that the chiral center in position 3^1 is not indispensable, but plays an important role to achieve enhanced efficacy. Interestingly, photosensitizers **9** and **14** with propyl and methyl ester functionality, respectively, bearing the heptyl and nonyl ether groups at position 3 showed similar efficacy. However, it should be realized that, while the *in vivo* results discussed in this paper are important to relate the structure−activity relationships, they are very preliminary. Extensive *in vivo* study with larger group of mice is required for selecting the best compound from the most promising candidates.

In Vivo Photosensitizing Efficacy of Bacteriochlorin p_6. Bacteriochlorins p_6 **19**−**22** were evaluated for *in vivo* PDT efficacy at two different doses. At a dose of 1.0 μmol/kg, both **21** and **22** showed some photosensitizing efficacy with cure rates of 20% and 10%, respectively. However, at a reduced dose (0.4 μmol/kg, an effective dose for certain bacteriopurpurinimides including compound **9**), these analogues produced limited photosensitivity (Figures 6). Even though the calculated log P values for bacteriochlorin **22** and bacteriopurpurinimide **9** were quite close (log $P = 11.19$), a significant difference in long-term cure between these photosensitizers was observed.

Intracellular Localization. Many porphyrin-based compounds can be observed intracellularly with a fluorescence microscope (*27*). Most photosensitizers localize to cytosolic targets such as the Golgi, endoplasmic reticulum, mitochondria, lysosomes, and membranes. It has been reported that intracellular localization of the photosensitizers could be an important determinant for photosensitizing activity. In general, most of the photosensitizers that localize in mitochondria (primary or secondary targets) were found to be quite effective. Therefore, the effective bacteriopurpurinimides **9** and **26** and the bacteriopurpurin p_6 **22** with limited efficacy were evaluated for intracellular localization by routine methods. As can be seen in Figure 7, both

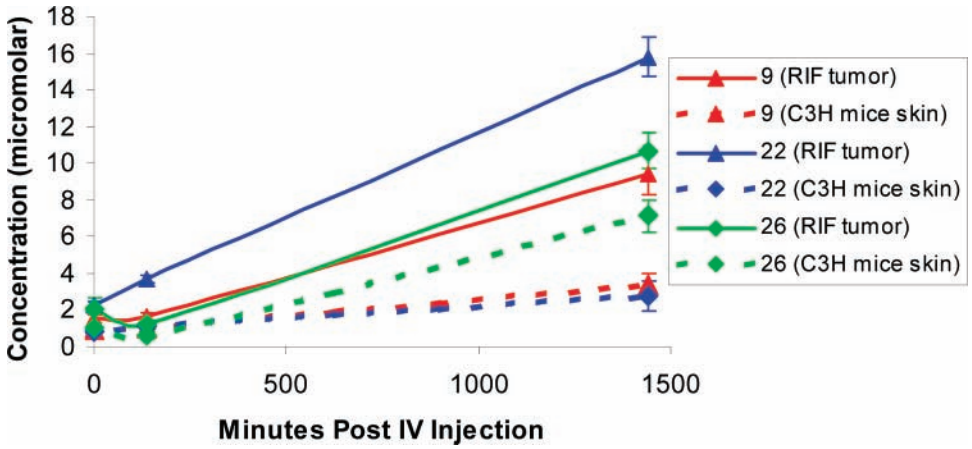


Figure 2. Tumor vs skin uptake for compounds **9**, **22**, and **26**.

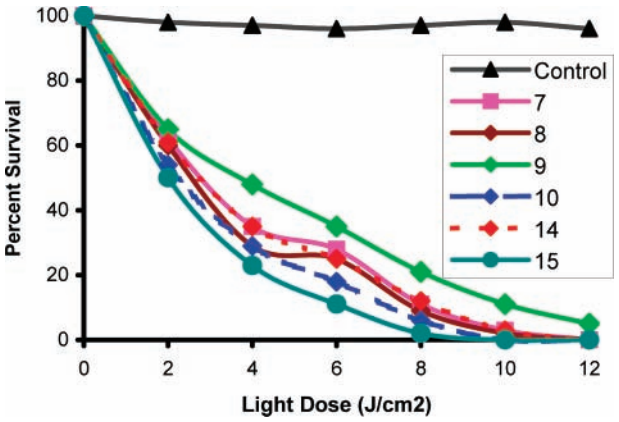


Figure 3. *In vitro* PDT efficacy of bacteriochlorins **7**−**10**, **14**, and **15** in RIF cells at a dose of 1.5 μM at 48 h MTT assay. The cells were treated with a laser light (λ_{max} 790 nm) after 24 h incubation. Control: Exposed to light without photosensitizer.

Table 2. IC_{50} Values of Bacteriochlorin Analogues

compound	7	8	9	10	14	15	19	20	21	22	26
IC_{50}(J/cm^2)	2.8	2.56	3.81	2.25	2.68	2.05	4.12	3.95	5.0	3.28	2.86

bacteriochlorins derived either from bacteriopurpurinimide or bacteriochlorin p_6 localized primarily in mitochondria.

Comparative Peripheral Benzodiazepine Receptor (PBR) Binding Affinity. Peripheral benzodiazepine receptor (PBR) is an 18 kDa protein of the outer mitochondrial membrane, and one intriguing aspect of this protein is its possible role as a target for PDT (*27*). Therefore, using the labeled high-affinity PBR ligand PK11195 as a tool, we measured the ability of

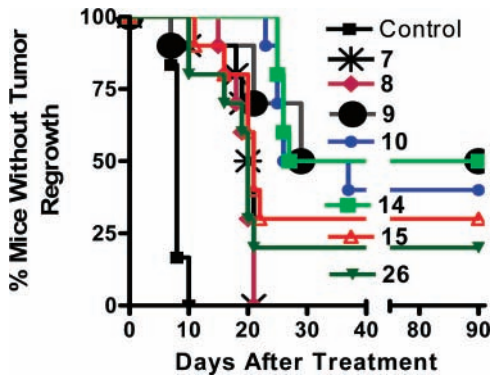


Figure 4. *In vivo* photosensitizing efficacy of photosensitizers **7**−**10**, **14**, **15**, and **26** in C3H mice (10 mice/group) bearing RIF tumors at a dose of 0.4 μmol/kg. The mice were treated with laser light (790 nm, 135 J/cm^2) at 24 h postinjection of the drug.

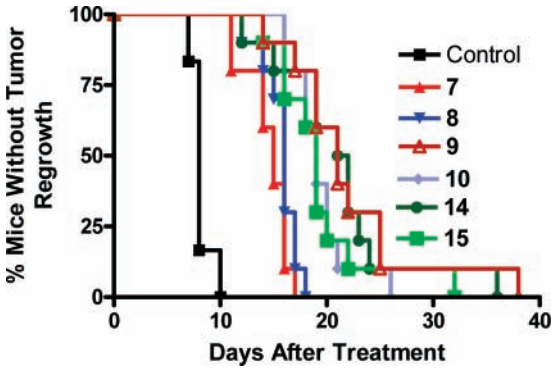


Figure 5. *In vivo* photosensitizing efficacy of photosensitizers **7**−**10**, **14**, and **15** in C3H mice (10 mice/group) bearing RIF tumors at a dose of 0.1 μmol/kg. The mice were treated with laser light (790 nm, 135 J/cm^2) at 24 h postinjection of the drug.

compounds **19**−**22** to displace ^{3}H-PK11195 from its specific cellular binding site, the isoquinoline (IQ) site on PBR, using known methodology (*27, 28*). Significant displacement of ^{3}H-PK11195 by compounds **19**−**22** was observed (Figure 8). For example, compounds **19**, **20**, and **21** displaced more than 70% ^{3}H-PK11195 at 10^{-4} M, while bacteriochlorin p_6 **22** displaced about 51% ^{3}H-PK11195. However, under similar experimental conditions, the most effective bacteriopurpurinimide **9** did not show any significant binding affinity (*28*) (see Table 3). The IC_{50} displacement values of these compounds are listed in Table 3. These results suggest that there is no direct correlation between the photosensitizing efficacy and the PBR binding affinity of the photosensitizers discussed in our present study.

CONCLUSION

Unstable bacteriochlorophyll-a was converted into a series of highly stable bacteriochlorins (related bacteriopurpurinimide and bacteriochlorin p_6) with strong long-wavelength absorptions at 787 and 737 nm, respectively. Among photosensitizers with high log *P* values and higher molecular weights (>500), the regular octanol/water method to determine the overall lipophilicity was not a practical approach. Therefore, for drug design the computational methods in determining log *P* and log *D* values, which are quite common in drug development, was used. Log *D*, a pH-dependent version of log *P*, is a descriptor of the octanol−water distribution coefficient for partitioning of ionizable species in biphasic media and accounts for mixtures of species that may exist at any given pH. In order to compare the *in vivo* efficacy of photosensitizers derived from bacteriopurpurinimide and bacteriochlorin p_6 with overall lipophilicity, both log *P* and log *D* values were calculated (the octanol/water

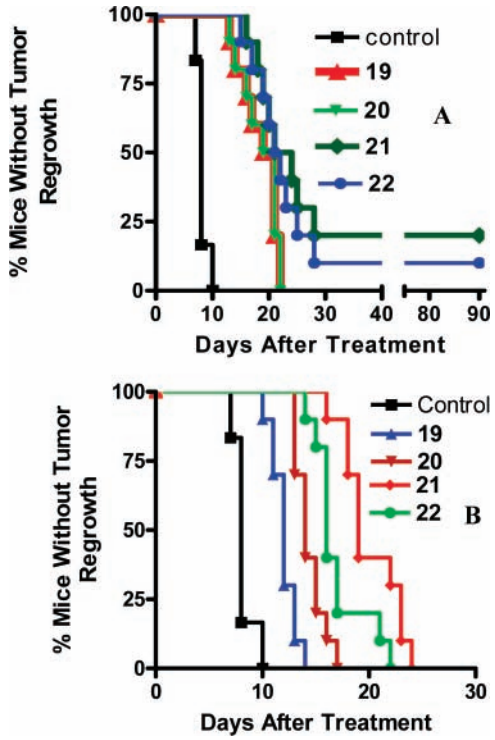


Figure 6. *In vivo* photosensitizing efficacy of bacteriochlorin p_6 **19**−**22** in C3H mice (10 mice/group) bearing RIF tumors at doses of (A) 1.0 μmol/kg and (B) 0.4 μmol/kg. The mice were treated with laser light (790 nm, 135 J/cm^2) at 24 h postinjection of the drug.

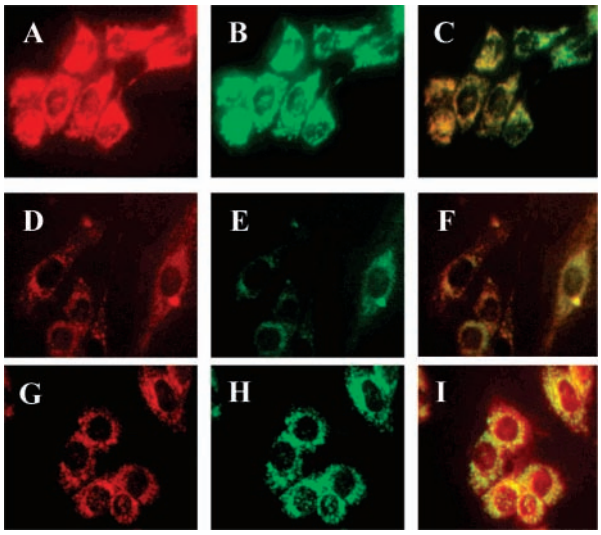


Figure 7. Comparative intracellular localization of **9**, **22**, and **26** with Rhodamine 123: (A) **9**; (B) Rhodamine 123; (C) overlap of **9** and Rhodamine 123; (D) **22**; (E) Rhodamine 123; (F) overlap of **22** and Rhodamine 123; (G) **26**; (H) Rhodamine 123; and (I) overlap of **26** and Rhodamine123.

method is not suitable for compounds with molecular weight of >500). At physiological pH, the calculated values of log *P* and log *D* for both series of photosensitizers were quite close. In a homologous series of the alkyl ether derivatives of both purpurinimide and bacteriopurpurinimide, a parabolic relationship between the overall lipophilicity and PDT was observed to some extent. However, compounds with the same log *P* value in two independent series did not show similar efficacy. These observations were similar to those reported previously by us in SAR and QSAR studies of a series of pyropheophorbide-a analogues (*29*, *30*). As expected, a linear correlation between the calculated log *P*/*D* values and HPLC retention times of a particular series of compounds was observed. Interestingly, compared to more effective bacteriopurpurinimide analogues, bacteriochlorin p_6 derivatives with limited PDT efficacy showed significant PBR binding affinity. These results further confirm that the PBR binding affinity of a photosensitizer has no direct correlation with photosensitizing efficacy as reported previously by us (*28*) and others (*31*) in other studies.

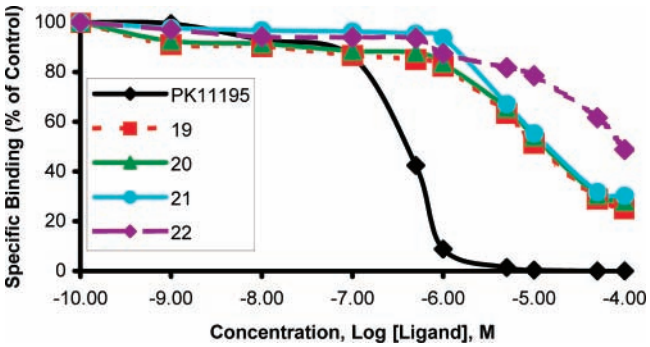


Figure 8. Displacement of ^{3}H-PK11195 with PK11195 and bacteriochlorin p_6 **19**−**22**.

Table 3. Displacement (IC_{50}) of ^{3}H-labeled PK11195 from PBR by Various Photosensitizers

compound	PK11195	**9**	**19**	**20**	**21**	**22**	**26**
IC_{50} ($\times 10^{-7}$)	4	1540	100	138	158	890	29000

ACKNOWLEDGMENT

We are thankful to the NIH (CA 55791 and CA 114053) and the shared resources of the RPCI support grant (P30CA16056).

Supporting Information Available: Copies of the NMR spectra are included. This material is available free of charge via the Internet at http://pubs.acs.org.

LITERATURE CITED

(1) Dougherty, T. J., Gomer, C. J., Henderson, B. W., Jori, G., Kessel, D., Korbelik, M., Moan, J., and Peng, Q. (1998) Phtodynamic therapy. *J. Natl. Cancer I 90* (12), 889−905.

(2) Sol, V., Chaleix, V., Champavier, Y., Granet, R., Huang, Y. M., and Krausz, P. (2006) Glycosyl bis-porphyrin conjugates: Synthesis and potential application in PDT. *Biorg. Med. Chem. 14* (23), 7745−7760.

(3) Luguya, R., Jensen, T. J., Smith, K. M., and Vicente, M. G. H. (2006) Synthesis and cellular studies of a carboranylchlorin for the PDT and BNCT of tumors. *Bioorg. Med. Chem. 14* (17), 5890−5897.

(4) Campo, M. A., and Lange, N. (2006) Fluorescence diagnosis using enzyme-related metabolic abnormalities of neoplasia. *J. Environ. Pathol. Toxicol. Oncol. 25* (1−2), 341−372.

(5) Sharman, W. M., and van Lier, J. E. (2005) Synthesis and photodynamic activity of novel asymmetrically substituted fluorinated phthalocyanines. *Bioconjugate Chem. 16* (5), 1166−1175.

(6) Paolesse, R., Jaquinod, L., Della, S. F., Nurco, D. J., Prodi, L., Montalti, M., Di Natale, C., D'Amico, A., Di Carlo, A., Lugli, P., and Smith, K. M. (2000) beta-fused oligoporphyrins: A novel approach to a new type of extended aromatic system. *J. Am. Chem. Soc. 122* (46), 11295−11302.

(7) Kessel, D., Vicente, M. G. H., and Reiners, J. J. (2006) Initiation of apoptosis and autophagy by photodynamic therapy. *Laser Surg. Med. 38* (5), 482−488.

(8) Sharman, W. M., van Lier, J. E., and Allen, C. M. (2004) Targeted photodynamic therapy via receptor mediated delivery systems. *Adv. Drug Delivery Rev. 56* (1), 53−76.

(9) Paolesse, R., Marini, A., Nardis, S., Froiio, A., Mandoj, F., Nurco, D. J., Prodi, L., Montalti, M., and Smith, K. M. (2003) Novel routes

to substituted 5,10,15-triarylcorroles. *J. Porphyrins Phthalocyanines 7* (1), 25−36.
(10) Zeisser-Labouebe, M., Lange, N., Gurny, R., and Delie, F. (2006) Hypericin-loaded nanoparticles for the photodynamic treatment of ovarian cancer. *Int. J. Pharm. 326* (1−2), 174−181.
(11) Sol, V., Lamarche, F., Enache, M., Garcia, G., Granet, R., Guilloton, M., Blais, J. C., and Krausz, P. (2006) Polyamine conjugates of meso-tritolyiporphyrin and protoporphyrin IX: Potential agents for photodynamic therapy of cancers. *Bioorg. Med. Chem. 14* (5), 1364−1377.
(12) Vargas, A., Pegaz, B., Debefve, E., Konan-Kouakou, Y., Lange, N., Ballinj, J. P., van den Bergh, H., Gurny, R., and Delie, F. (2004) Improved photodynamic activity of porphyrin loaded into nanoparticles: An in vivo evaluation using chick embryos. *Int. J. Pharm. 286* (1−2), 131−145.
(13) Sibrian-Vazquez, M., Jensen, T. J., Hammer, R. P., and Vicente, M. G. H. (2006) Peptide-mediated cell transport of water-soluble porphyrin conjugates. *J. Med. Chem. 49* (4), 1364−1372.
(14) Allen, C. M., Langlois, R., Sharman, W. M., La Madeleine, C., and van Lier, J. E. (2002) Photodynamic properties of amphiphilic derivatives of aluminum tetrasulfophthalocyanine. *Photochem. Photobiol. 76* (2), 208−216.
(15) Lamarche, F., Sol, V., Huang, Y. M., Granet, R., Guilloton, M., and Krausz, P. (2002) Synthesis and biological evaluation of polyamine-porphyrin conjugates as potential agents in photodynamic therapy (PDT). *J. Porphyrins Phthalocyanines 6* (2), 130−134.
(16) Pervaiz, S., and Olivo, M. (2006) Frontiers in research review: Cutting-edge molecular approaches to therapeutics. Art and science of photodynamic therapy. *Clin. Exp. Pharmacol. Physiol. 33* (5−6), 551−556.
(17) Pandey, R. K., and Zheng, G. (2000) Porphyrins as photosensitizers in photodynamic therapy. In *The Porphyrin Handbook* (Kadish, Smith, and Guilard, Eds.) Vol. 6, pp 157−230, Academic Press, New York.
(18) Schermann, G., Schmidt, R., Volcker, A., Brauer, H. D., Mertes, H., and Franck, B. (1990) Potential photosensitizers for photodynamic therapy. 2. Photophysical properties of [26]porphyrin. *Photochem. Photobiol. 52* (4), 741−744.
(19) Grahn, M. F., McGuinness, A., Benzie, R., Boyle, R., DeJode, M. L., Dilkes, M. G., Abbas, B., and Williams, N. S. (1997) Intracellular uptake, absorption spectrum and stability of the bacteriochlorin photosensitizer 5,10,15,20-tetrakis(m-hydroxyphenyl) bacteriochlorin (mTHPBC). Comparison with 5,10,15,20-tetrakis-(m-hydroxyphenyl) chlorin (mTHPC). *J. Photochem. Photobiol., B 37* (3), 261−266.
(20) Morgan, J., Whitaker, J. E., and Oseroff, A. R. (1998) GRP78 induction by calcium ionophore potentiates photodynamic therapy using the mitochondrial targeting dye Victoria Blue BO. *Photochem. Photobiol. 67* (1), 155−164.
(21) Hashimoto, H., Fujii, R., Yanagi, K., Kusumoto, T., Gardiner, A. T., Cogdell, R. J., Roszak, A. W., Issacs, N. W., Pendon, Z., Niedzwiedski, D., and Frank, H. A. (2006) Structures and functions of carotenoids bound to reaction centers from purple photosynthetic bacteria. *Pure Appl. Chem. 78* (8), 1505−1518.
(22) Biebl, H., and Wagner-Dobler, I. (2006) Growth and bacteriochlorophyll a formation in taxonomically diverse aerobic anoxygenic phototrophic bacteria in chemostat culture: Influence of light regimen and starvation. *Process Biochem. 41* (10), 2153−2159.
(23) Leach, M. W., Higgins, R. J., Boggan, J. E., Lee, S. J., Autry, S., and Smith, K. M. (1992) Effectiveness of a lysyl chlorin p_6/chlorin p_6 mixture in photodynamic therapy of the subcutaneous 9L glioma in the rat. *Cancer Res. 52*, 1235−1239.
(24) Zheng, G., Potter, W. R., Sumlin, A., Dougherty, T. J., and Pandey, R. K. (2000) Photosensitizers related to purpurin-18-N-alkylimides: A comparative in vivo tumoricidal ability of ester versus amide functionalities. *Bioorg. Med. Chem. Lett. 10* (2), 123−137.
(25) Locsmandi, L., Kover, G., Bazar, G., Szabo, A., and Romvari, R. (2006) Development of a model using near-infrared reflectance spectroscopy for the determination of the chemical composition of fatty goose liver. *Acta Aliment. Hung. 35* (4), 455−463.
(26) Morgan, J., Lottman, H., Abbou, C. C., and Chopin, D. K. (1994) A comparison of direct and liposomal antibody conjugates of sulfonated aluminum phthalocyanines for selective photoimmunotherapy of human bladder-carcinoma. *Photochem. Photobiol. 60* (5), 486−496.
(27) (a) Kessel, D., Antolovich, M., and Smith, K. M. (2001) The role of the peripheral benzodiazepine receptor in the apoptotic response to photodynamic therapy. *Photochem. Photobiol. 74* (2), *346*−349. (b) Chen, Y. H., Zheng, X., Dobhal, M. P., Gryshuk, A., Morgan, J., Dougherty, T. J., Oseroff, A., and Pandey, R. K. (2005) Methyl pyropheophorbide-a analogues: Potential fluorescent probes for the peripheral-type benzodiazepine receptor. Effect of central metal in photosensitizing efficacy. *J. Med. Chem. 48* (11), 3692−3695.
(28) Chen, Y. H., Graham, A., Potter, W., Morgan, J., Vaughan, L., Bellnier, D. A., Henderson, B. W., Oseroff, A., Dougherty, T. J., and Pandey, R. K. (2002) Bacteriopurpurinimides: Highly stable and potent photosensitizers for photodynamic therapy. *J. Med. Chem. 45* (2), 255−258.
(29) Pandey, R. K., Sumlin, A. B., Constantine, S., Aoudia, M., Potter, W. R., Bellnier, D. A., Henderson, B. W., Rodgers, M. A., Smith, K. M., and Dougherty, T. J. (1996) Alkyl ether analogs of chlorophyll-a derivatives. 1. Synthesis, photophysical properties and photodynamic efficacy. *Photochem. Photobiol. 64* (1), 194−204.
(30) Henderson, B. W., Bellnier, D. A., Greco, W. R., Sharma, A., Pandey, R. K., Vaughan, L. A., Weishaupt, K. R., and Dougherty, T. J. (1997) An in vivo quantitative structure-activity relationship for a congeneric series of pyropheophorbide derivatives as photosensitizers for photodynamic therapy. *Cancer Res. 57* (18), 4000−4007.
(31) Morris, R. L., Varnes, M. E., Kenney, M. E., Li, Y. S., Azizuddin, K., McEnery, M. W., and Oleinick, N. L. (2002) The peripheral benzodiazepine receptor in photodynamic therapy with the phthalocyanine photosensitizer Pc 4. *Photochem. Photobiol. 75* (6), 652−661.

BC070092I

Preparation and Preliminary Evaluation of a Biotin-Targeted, Lectin-Targeted Dendrimer-Based Probe for Dual-Modality Magnetic Resonance and Fluorescence Imaging

Heng Xu,[†] Celeste A. S. Regino,[†] Yoshinori Koyama,[‡] Yukihiro Hama,[‡] Andrew J. Gunn,[‡,§] Marcelino Bernardo,[||] Hisataka Kobayashi,[‡] Peter L. Choyke,[‡] and Martin W. Brechbiel*[,†]

Radiation Oncology Branch, and Molecular Imaging Program, Center for Cancer Research, National Cancer Institute, National Institutes of Health, 10 Center Drive, Bethesda, Maryland 20892-1088, Howard Hughes Medical Institute, 4000 Jones Bridge Road, Chevy Chase, Maryland 20815-6789, and Research Technology Program, SAIC-Frederick, Inc., NCI-Frederick, Frederick, Maryland 21702. Received March 26, 2007; Revised Manuscript Received June 1, 2007

A novel approach for the preparation of a biotinylated dendrimer-based MRI agent **5** is described, in which a unique disulfide bond in the core of the Gd(III)-1B4M-DTPA chelated G2 PAMAM dendrimer was reduced and then attached to a maleimide-functionalized biotin. The new MRI agent **5** features a well-defined dendron structure and a unique biotin functionality. Immobilization of up to four copies of biotinylated dendrimer **5** to fluorescently labeled avidin yields a supramolecular avidin−biotin−dendrimer-Gd(III) complex. Validation of the complex in mice bearing ovarian cancer tumors demonstrates that the avidin−biotin−dendrimer targeting system efficiently targets and delivers sufficient amounts of chelated Gd(III) and fluorophores (e.g., Rhodamine green) to ovarian tumors to produce visible changes in the tumors by both MRI and optical imaging, respectively. Thus, the avidin−biotin−dendrimer complex may be used as a tumor-targeted probe for dual-modality magnetic resonance and fluorescence imaging.

INTRODUCTION

Diffuse peritoneal metastasis, or "seeding", is a common and often fatal complication of ovarian cancer (*1*). While detection of metastatic disease is essential for proper surgical cytoreduction and improved survival of the patient (*2*−*4*), the current imaging modalities for peritoneal disease using intravenously administered iodinated contrast media for computed tomography (CT) or gadolinium (Gd(III)) chelates for magnetic resonance imaging (MRI) are nonspecific, insensitive, and unable to provide the surgeon with intraoperative guidance. The surgical removal of peritoneal disease is complicated by poor visual contrast between the tumor and normal tissue under white light, making the identification of small peritoneal implants difficult. Therefore, it is of interest to improve the detection of small foci of peritoneal metastasis. A desirable agent would be targeted to cancer but also allow dual labeling such that the probe could be used as an MRI contrast agent in the preoperative setting for surgical planning purposes and as an optical contrast agent in the operative setting to guide the surgeon to small lesions.

MRI is widely used in both diagnostic and clinical medicine as well as biomedical research, because it offers high spatial resolution without ionizing radiation. The addition of targeted intraperitoneal MR contrast media potentially could increase the conspicuity of lesions within the peritoneum compared with intravenously injected contrast media (*5*, *6*). Dendrimers, highly branched synthetic polymers (*7*), can serve as an excellent scaffold for the basis of multimodal contrast media. Dendrimer-based contrast agents have a higher molar relaxivity than simple Gd(III) complexes such as Gd(III)-diethylenetriaminepentaacetic acid (Gd(III)-DTPA, Magnevist) and Gd(III)-*N*,*N*′,*N*″,*N*‴-tetracaroxymethyl-1,4,7,10-tetraazacyclododecane (Gd(III)-DOTA, Dotarem) because they bind multiple Gd(III) chelates (*8*−*10*) (which increases local Gd(III) concentrations), and slow the molecular tumbling time (*11*), thus increasing the magnetic relaxivity of individual Gd(III) ions (*5*). Newer families of dendrimers (*12*) possess a disulfide function (cystamine) core (Figure 1) which, when treated with traditional redox chemistry, provides a site for the introduction of the highly specific and efficient maleimide and sulfhydryl coupling reaction. This in turn permits the half-dendrimer to form a conjugate with peptides, monoclonal antibodies, biotin, or other targeting moieties.

Targeted agents are preferred over nontargeted methods, since they not only increase the target-to-background ratio but provide much more tissue specificity than nontargeted agents. An example of a targeting moiety is the 68 kDa tetrameric glycoprotein, avidin, which binds with high capacity to lectins differentially expressed on the surface of many cancer cells such as ovarian cancer (*13*−*16*). These lectins are surface proteins that specifically binds to carbohydrate moieties on glycolipids and glycoproteins such as avidin and other galactosylated proteins (*13*−*16*). Avidin is an excellent targeting moiety, because once bound, the protein and its conjugates are internalized into the cell while unbound avidin reenters the circulation, is absorbed to the liver, and is eventually eliminated via the hepatobiliary system, effectively reducing the background signal (*13*−*16*). Biotinylated dendrimers provide an exceptional structure to which the molecular targeting agent, avidin, could be attached; the biotin−avidin interaction is among the strongest known ($K_{ass} = 1.7 \times 10^{15}\ M^{-1}$) (*17*). Previous work has shown that the biotin−avidin targeting system efficiently targets and increases the delivery of avidin-conjugated-biotinylated dendrimer-Gd(III) complexes to the ovarian cancer cell line, SHIN3 (*18*−*20*). Moreover, the biotin−avidin targeting system coupled

* Martin W. Brechbiel, Ph.D., Radioimmune & Inorganic Chemistry Section, Radiation Oncology Branch, NCI, NIH, Building 10, Room 1B40, 10 Center Drive, Bethesda, Maryland 20892-1088, Fax: (301) 402-1923. E-mail: martinwb@mail.nih.gov.

[†] Radiation Oncology Branch, National Cancer Institute.

[‡] Molecular Imaging Program, Center for Cancer Research, National Cancer Institute.

[§] Howard Hughes Medical Institute.

[||] Research Technology Program, SAIC-Frederick, Inc.

10.1021/bc0701085 CCC: $37.00 © 2007 American Chemical Society
Published on Web 08/21/2007

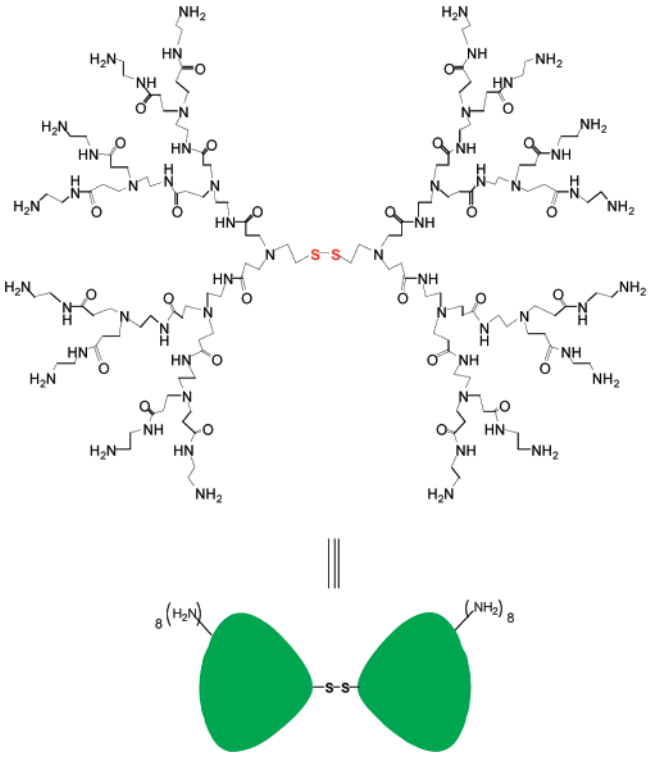


Figure 1. Structure of a poly(amidoamine) (PAMAM) dendrimer possessing a disulfide cystamine core.

to MRI contrast agents has been successfully exploited to investigate blood volume and vascular permeability (*21*). Avidin also possesses the added benefit of having sites to which an optical fluorophore agent can be attached, thus providing the opportunity for dual-modality imaging.

Herein, we describe the synthesis and testing of an intraperitoneally delivered dendrimer-based, avidin−biotin targeted, dual-reporter probe to detect peritoneal tumors in mice using the SHIN3 ovarian cancer model.

MATERIALS AND METHODS

2-Methyl-6-(*p*-aminobenzyl-*N*-[5-oxopentanoic acid])diethylene-*N*,*N*,*N*′,*N*″,*N*″-penta-*tert*-butylacetate hydroxysuccinimidyl ester (NHS-1B4M-DTPA) was prepared as previously described (*22*). *N*-hydroxysuccinimide (NHS), 1-[3-(dimethylamino)propyl]-3-ethylcarbodiimide hydrochloride (EDCI), peptide sequence grade trifluoroacetic acid, and $Gd(OAc)_3 \cdot xH_2O$ were purchased from Sigma-Aldrich Co. (St. Louis, MO) and were used as received. Generation 2 cystamine core PAMAM dendrimer was obtained from Dendritic Nanotech, Inc. (Midland, MI) as a 15.35% w/w solution in MeOH. *N*-(2-Aminoethyl)-aminomethyl polystyrene was purchased from Novabiochem (Laüfelfingen, Switzerland). Maleimide-PEO_2-biotin and immobilized TCEP disulfide reducing gel were purchased from Pierce Biotechnology, Inc. (Rockford, IL).

Avidin was purchased from Pierce Biochemical, Inc. (Milwaukee, WI). Rhodamine green-succinimidyl ester (RhodG) was purchased from Invitrogen/Molecular Probes, Inc. (Eugene, OR).

All experiments with moisture- and/or air-sensitive compounds were carried out under a dried N_2 or Ar atmosphere. Column chromatography was conducted using Merck 60 Silica Gel (70−230 mesh). Thin-layer chromatography (TLC) was performed on silica gel 60 F-254 plates from EM Reagents (Gibbstown, NJ). Water was purified using a Hydro Ultrapure Water Purification system (Rockville, MD) prior to all experiments.

Proton and ^{13}C NMR data were obtained using a Varian Gemini 300 MHz instrument and chemical shifts are reported in ppm on the δ scale relative to TMS, TSP, or residual solvent. Proton chemical shifts are annotated as follows: ppm (multiplicity, coupling constant (Hz), integration). Low- and high-resolution mass spectra (HRMS) were obtained on a Waters' LCT Premier time-of-flight mass spectrometer using electrospray ionization (ESI/TOF/MS) in positive ion mode operated at a resolution of 10 000. The electrospray capillary voltage was 3 kV, and the sample cone voltage was 60 V. Desolvation temperature was 225 °C, and the desolvation gas was nitrogen at 300 L/h. Accurate masses were obtained using the lock spray mode with Leu-Enkephalin as the external reference compound. Elemental analyses were performed in duplicate by Desert Analytics (Tucson, AZ) using the combustion analysis method for C, H, N and S, and the inductively coupled plasma-atomic emission spectroscopy (ICP-AES) method for determining the percentage of Gd. MALDI-TOF mass spectral data were obtained by the Scripps Center for Mass Spectrometry (La Jolla, CA).

Dendrimer conjugation and purity was assessed by size exclusion HPLC (SE-HPLC) using a Beckman System Gold (Fullerton, CA) equipped with a Model 126 solvent delivery module and a Model 168 UV detector (λ 254 and 280 nm) controlled by *32 Karat* software. Size exclusion chromatography was performed on a Tosohaas G2000SW, 10 μm, 7.8 mm × 30 cm column (Montgomeryville, PA) using phosphate buffered saline (PBS) solution as the eluent (0.5 mL/min).

Cystamine Core Dendrimer 1B4M-DTPA Conjuate (2). Typical procedure: Cystamine core PAMAM G2-dendrimer **1** (0.31 g, 0.093 mmol) was added to a solution of NHS-1B4M-DTPA (3.00 g, 2.98 mmol) in DMSO (15 mL). The mixture was stirred at room temperature for 24 h and then treated with *N*-(2-aminoethyl)aminomethyl polystyrene (0.60 g, loading ≥2.00 mmol/g). After stirring an additional 24 h, the reaction mixture was filtered, diluted with CH_2Cl_2 (50 mL), and washed with H_2O (50 mL). The organic layer was concentrated under reduced pressure to afford crude **2**. The crude product was then treated with pure trifluoroacetic acid (10 mL) and stirred for 18 h. The solution was then evaporated and the residue was washed with hexane (2 × 30 mL) and dissolved in H_2O (30 mL). The dendrimer solution was adjusted to pH = 5 with 1 N aqueous NaOH, exchanged to H_2O using a Centriprep 3 (MW cutoff 3000 Da), and lyophilized to give **2** as a white solid (0.76 g, 62% yield).

MALDI-TOF: *m*/*z* 9304, calcd for $[G2(1B4M)_{10}(CF_3COOH)_2Na_{23}(H_2O)_{412})^{2+}]$ 9431; found 9429. SE-HPLC: R_t = 14.8 min. Elemental Analysis calcd for $[G2(1B4M)_{12}(CF_3COO)_5Na_{23}(H_2O)_{52}]$: C, 45.10; H, 6.37; N, 11.72;, S, 0.51; found: C, 44.93, 44.78; H, 5.87, 5.46; N, 11.65, 11.76; S, 0.85, 0.75.

Cystamine Core Dendrimer 1B4M-DTPA Gd(III) (3). To a solution of **2** (100 mg, ∼11 μmol) in 0.3 M citrate buffer (10 mL, pH = 4.5) was added $Gd(OAc)_3 \cdot xH_2O$ (56.8 mg, 0.17 mmol). The solution was stirred at room temperature for 12 h and then transferred to a Centriprep 3 centrifugal filter device with a 3000 Da cutoff membrane and subjected to exhaustive ultrafiltration with deionized water while monitoring with SE-HPLC. The retentate was lyophilized and product **3** was obtained as a yellow solid (89 mg, ∼72%).

MALDI-TOF: *m*/*z* 11249, calcd for $[G2(Gd\text{-}1B4M)_{11}(1B4M)(C_6H_7O_3)_4Na_{32}(H_2O)_{446}]$ 10961; found 10957. SE-HPLC: R_t = 15.3 min. Elemental Analysis calcd for $[G2(Gd\text{-}1B4M)_{11}(1B4M)(C_6H_7O_3)_4Na_{32}(H_2O)_{43}]$: C, 40.22; H, 5.39; N, 10.16; S, 0.44; Gd, 11.83. Found: C, 40.05, 40.18; H, 4.45, 4.45; N, 10.52, 10.51; S, 0.61, 0.49; Gd, 11.47, 11.48.

Cleavage of Cystamine Core Dendrimer 1B4M-DTPA Conjugate and Preparation of Biotin Conjugate (4). An aqueous solution of **2** (0.1 g, ∼11.1 μmol) in 10 mL was added to the immobilized TCEP reducing gel solution (2 mL) and the

reaction mixture was gently stirred for 2 h. The reducing gel was filtered through a glass wool plugged glass pipet. Maleimide-PEO_2-biotin was added (17.5 mg, 33.3 μmol) and the mixture was stirred under N_2 atmosphere for 18 h. The reaction solution was then transferred to a Centriprep 3 (MWCO 3000 Da) and subjected to exhaustive filtration with deionized water, monitored by SE-HPLC. Finally, the retentate was lyophilized and the product **4** was obtained as a white solid (68 mg, ~51%).

^{1}H NMR (D_2O, 300 Hz) δ 7.42 (d, J = 7.2 Hz, aromatic protons of 1B4M chelates), 7.27 (d, J = 6.6 Hz, aromatic protons of 1B4M chelates), 4.58 (m, SCHC*H* of biotin), 4.32 (m, SCH_2CH of biotin), 3.95−3.60 (m), 3.40 (br), 3.22 (s), 2.69 (m), 2.47 (m), 2.37 (br), 2.19 (m), 1.88 (br), 1.56 (m), 1.27 (m), 1.25−1.00 (br). MALDI-TOF: *m*/*z* 4837, 5482, 5952, 6597, 7139, calcd for [G1Biotin(1B4M)$_4$, $C_{203}H_{326}N_{50}O_{69}S_2$; G1Biotin(1B4M)$_5$, $C_{230}H_{362}N_{54}O_{81}S_2$; G1Biotin(1B4M)$_6$, $C_{257}H_{398}N_{58}O_{93}S_2$; G1Biotin(1B4M)$_7$, $C_{284}H_{434}N_{62}O_{105}S_2$; G1Biotin(1B4M)$_8$, $C_{311}H_{470}N_{66}O_{117}S_2$]: 4632, 5241, 5849, 6457, 7065. SE-HPLC: R_t = 15.8 min. Elemental Analysis calcd for [G1(1B4M)$_6$($C_{23}H_{35}N_5O_7S$)Na_5(H_2O)$_{25}$]: C, 47.81; H, 7.17; N, 12.64; S, 1.00. Found: C, 47.88, 47.65; H, 7.17, 7.05; N, 12.56, 12.42; S, 0.91, 0.92.

Cleavage of Cystamine Core Dendrimer 1B4M-DTPA Gd(III) Conjugate (5). *Method A.* An aqueous solution of **3** (80 mg, ~7.2 μmol) in 5 mL was added to the immobilized TCEP reducing gel solution (1 mL) and the reaction mixture was gently stirred for 2 h. The reducing gel was filtered through a glass wool plugged glass pipet. Maleimide-PEO_2-biotin was added (7.9 mg, 15 μmol) and the mixture was stirred under N_2 atmosphere for 18 h. The reaction solution was then transferred to a Centriprep 3 (MWCO 3000 Da), exchanged to deionized water, and the completion of the filtration was monitored by SE-HPLC. The retentate was lyophilized and the product **5** was obtained as a white solid (46 mg, ~49%).

Method B. To a solution of **4** (20 mg, ~3.3 μmol) in 0. 3M citrate buffer (10 mL, pH = 4.5) was added $Gd(OAc)_3{\cdot}xH_2O$ (10.0 mg, 30.0 μmol). The solution was stirred at room temperature for 12 h and then transferred to a Centriprep 3 (MWCO 3000 Da) and subjected to exhaustive filtration with deionized water while monitoring with UV spectrometer at 650 nm using arsenazo III as an indicator (*23*). The retentate was lyophilized and the product **5** was obtained as a yellow solid (10 mg, ~47%).

MALDI-TOF: *m*/*z* 5475, 6243, 6902, 7666, 8328, calcd for [G1Biotin(Gd-1B4M)$_4$(CH_3COO^-)$_3{\cdot}$(H_2O)$_3$, $C_{209}H_{322}Gd_4N_{50}O_{78}S_2$; G1Biotin(Gd-1B4M)$_5$($CH_3COO^-$)$_3{\cdot}$($H_2O$)$_2$ Na, $C_{236}H_{350}Gd_5N_{54}O_{89}S_2Na$; G1Biotin(Gd-1B4M)$_6$($CH_3COO^-$)$_2H_2O$, $C_{261}H_{377}Gd_6N_{58}O_{98}S_2$; G1Biotin(Gd-1B4M)$_7$($CH_3COO^-$)$_2H_2O$, $C_{288}H_{407}Gd_7N_{62}O_{110}S_2$; G1Biotin(Gd-1B4M)$_8$$NaH_2O$, $C_{311}H_{432}Gd_8N_{66}O_{118}S_2Na$]: 5476, 6241, 6903, 7664, 8328. SE-HPLC: R_t = 16.4 min. Elemental Analysis calcd for [G1(1B4M)$_6$$Gd_{5.4}$($C_{23}H_{35}N_5O_7S$)($C_6H_7O_3$)$_2$$Na_{18}$($H_2O$)$_{32}$]: C, 39.81; H, 5.85; N, 10.06; S, 0.79; Gd, 10.51. Found: C, 39.57; H, 5.25; N, 10.50; S, 0.74; Gd, 10.55.

Cleavage of Cystamine Core Dendrimer Conjugate (6). An aqueous solution of **1** (60.6 mg, 18.1 μmol) in 5 mL was added to the immobilized TCEP reducing gel solution (2 mL) and the reaction mixture was gently stirred for 1 h. The reducing gel was filtered through a 50 mL tube top filter (Corning). Maleimide-PEO_2-biotin was added (19.0 mg, 36.2 μmol) and the mixture was stirred under N_2 atmosphere for 2.5 h. The reaction solution was lyophilized and the product **6** was obtained as an oil (66.0 mg, ~83%). ^{1}H NMR (D_2O, 300 Hz) δ 4.58 (m, 1H), 4.40 (m, 1H), 3.66 (s, 4H), 3.60 (m, 6H), 3.48 (t, J = 6.3 Hz, 16H), 3.38 (m, 8H), 3.30 (t, J = 6.9 Hz, 12H), 3.12 (t, J = 6.3 Hz, 16H), 2.98 (dd, J = 12.6, 6.0 Hz, 1H), 2.84 (t, J = 6.9 Hz, 28H), 2.76 (d, J = 12.6 Hz, 1H), 2.62 (t, J = 6.9 Hz, 12H), 2.50 (t, J = 6.9 Hz, 2H), 2.42 (t, J = 6.9 Hz, 28H), 2.23 (t, J = 6.9 Hz, 2H), 1.60 (m, 4H), 1.41 (m, 2H). ESI: *m*/*z* 2199.8, calcd for $C_{95}H_{183}N_{34}O_{21}S_2$ $[M + H]^+$, 2200.4.

Synthesis of Avidin Rhodamine Green Conjugate. Avidin (2 mg, 29 nmol) in Na_2HPO_4 (pH = 8.5, 495 μL, 0.1 M) was reacted with Rhodamine green-succinimidyl ester in DMSO (50 nmol, 5 μL, 10 mM) and was incubated at room temperature for 15 min. The mixture was then purified and the buffer changed to PBS (pH = 7.4) with Sephadex G50 (PD-10; GE Healthcare, Milwaukee, WI). The avidin-conjugated Rhodamine green (Av-RhodG) stock solution was stored at 4 °C.

The protein concentration of the Av-RhodG stock solution was determined with the Coomassie Plus Protein Assay Kit (Pierce Chemical Co., Rockford, IL) by comparing the absorption of the stock solution at 595 nm with a UV−vis system (8453 Value UV-Bis System, Agilent Technologies, Palo Alto, CA) against the absorption of solutions with known concentrations of avidin (100, 200, and 400 μg/mL). The final concentration of avidin in the Av-RhodG stock solution was determined to be ~0.022 mM. The stock solution concentration of RhodG was determined by the absorption at 504 nm measured after avidin was attached to the biotinylated dendrimer with a UV−vis system (8453 Value UV-Bis System, Agilent Technologies, Palo Alto, CA) to confirm the average number of RhodG molecules conjugated to each avidin molecule. The stock solution concentration of Rhodamine green dye was 0.033 mM. Thus, the ratio of RhodG to Avidin was determined to be ~1.5.

Reaction of Biotinylated Dendrimer 5 with the Avidin−Rhodamine Green. Avidin (800 μL, 0.15 mM in PBS) was mixed with Av-RhodG stock solution (200 μL, 0.022 mM in 1X PBS) at room temperature. Biotinylated dendrimer **5 (**2.98 mg) was added to this 1 mL solution at room temperature. Following the addition of unconjugated avidin, the final Av-RhodG concentration of the solution was 0.0044 mM, and through elemental analysis, the final Gd(III) concentration of the solution was found to be ~2 mM. This reaction was characterized by the HABA binding assay (*24*). In summary, HABA-avidin reagent was prepared according to the manufacturer's instructions by adding 300 μL of 10 mM HABA solution and 5 mg of avidin to 9.7 mL of PBS. HABA-avidin-biotinylated dendrimer sample was prepared by mixing 100 μL of biotinylated dendrimer solution (1 mg/mL PBS) with the 900 μL of HABA-avidin reagent. Afterward, the UV absorbance at 500 nm was recorded as 0.992 and 0.508 for 900 μL of HABA-avidin reagent and 1000 μL of HABA-avidin-biotinylated dendrimer solution, respectively. Using the calculation method described by the vendor ((Pierce Chemicals), approximately 0.75 biotin was conjugated to each dendrimer molecule.

Molar Relaxivity Measurements. Stock solutions of the biotinylated dendrimer **5** (5.0 Mm in Gd), biotinylated dendrimer-avidin-RhodG conjugate (1.25 mM in Gd), and native G2 dendrimer **1** (5.0 mM in Gd) were diluted to concentrations of 0.25 mM, 0.5 mM, 0.75 mM, and 1 mM in PBS. Solutions of Gd(III)-DTPA (Magnevist) at 1.97 mM, 0.99 mM, and 0.18 mM were prepared in PBS and used as a reference standard. Relaxivity measurements were obtained at ~22 °C using a 3-Tesla clinical scanner (Signa Excite, GE Medical System, Waukesha, WI) equipped with a rectangular single loop receiver coil (84 × 126 × 6 mm^3). A series of single-slice 2D multiple spin echo images of all the solutions were acquired at the same time with a TE around 9 ms and using different repetition times (TR = 167, 312, 625, 1250, 2500, and 5000 ms). The R_1 map was calculated from the averaged image of the 8 echo images at each TR and the R_2 map was calculated from the TR = 5000 ms image in *ImageJ* ((http://rsb.info.nih.gov/ij) using the MRI analysis plug-in (http://rsb.info.nih.gov/ij/plugins/mri-analysis.html). The T_1 and T_2 relaxivities, r_1 and r_2, were determined

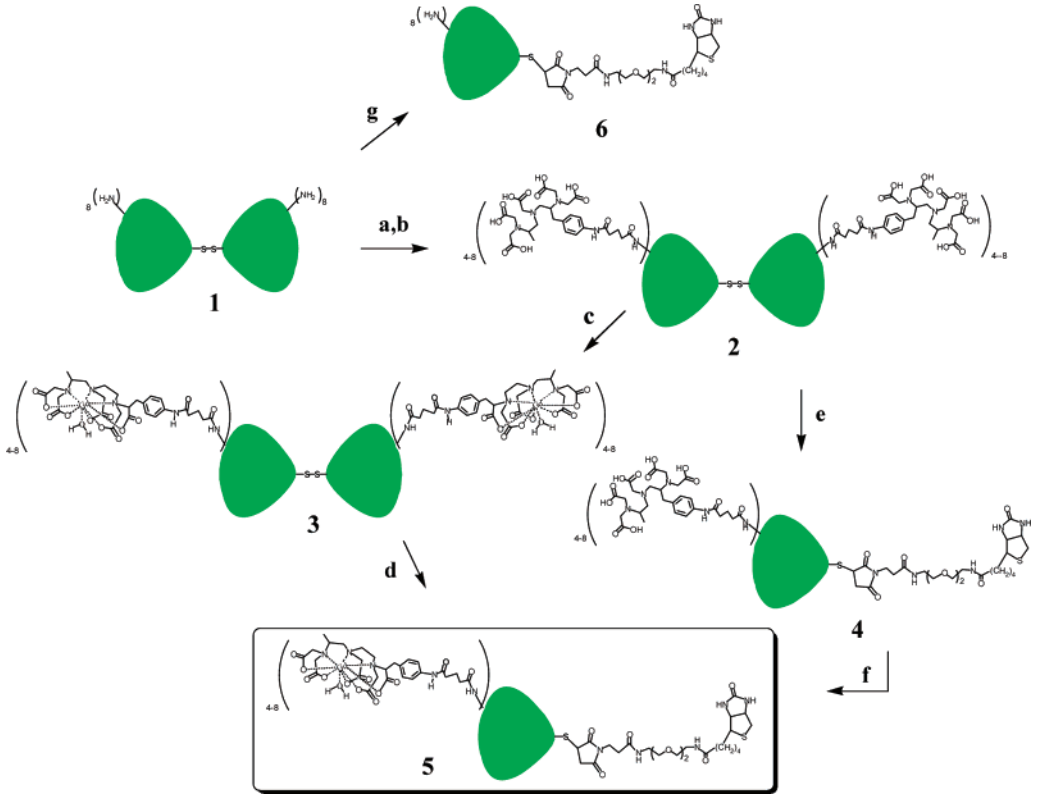


Figure 2. Synthesis of the monobiotinylated dendron for use as an MRI contrast agent. Reagents and conditions: (a) NHS-1B4M-DTPA, DMSO; (b) trifluroacetic acid, overall 62%; (c) $Gd(OAc)_3 \cdot xH_2O$, citrate buffer, 72%; (d) immoblizing TCEP gel, maleimide-PEO_2-biotin, 49%; (e) immobilizing TCEP gel, maleimide-PEO_2-biotin, 51%; (f) $Gd(OAc)_3 \cdot xH_2O$, citrate buffer, 47%; (g) immobilizing TCEP reducing gel, maleimide-PEO_2-biotin, 83%.

from the slope of R_1 or R_2 vs [Gd(III)] determined from region of interest measurements.

Cell Line and Cell Culture. SHIN3, an established ovarian cancer cell line (provided by Dr. Imai, Nara, Japan) (*20*), was used for generating intraperitoneal disseminated tumors. SHIN3 cell lines were grown in RPMI 1640 medium (Gibco, Gaithersburg, MD) containing 10% fetal bovine serum (Gibco), 0.03% L-glutamine at 37 °C, 100 U/mL penicillin, and 100 μg/mL streptomycin in 5% CO_2.

Tumor Model. All procedures were carried out in compliance with the Guide for the Care and Use of Laboratory Animal Resources (1996), the National Research Council, and were approved by the National Cancer Institute Animal Care and Use Committee. Xenografts of intraperitoneal (i.p.) tumor were introduced by an i.p. injection of 2×10^6 SHIN3 cells suspended in 200 μL of PBS in 6−8 week old female athymic nude mice (National Cancer Institute Animal Production Facility, Frederick, MD). Mice were used at 21 days post-implantation of the tumor cells.

Magnetic Resonance Imaging (MRI). All images for this study were obtained using a 3T clinical scanner (Signa Excite, GE Medical System, Waukesha, WI) equipped with a modified Alderman-Grant receive-only mouse coil (38 mm in diameter × 70 mm in length).

Mice were anesthetized using gas mixtures of 1.5−2.5% isofluorane in O_2 to maintain a respiration rate of ∼30 bpm during the acquisition of all images. Each mouse was given an i.p. injection of 300 μL of a 2 mM [Gd(III)] (600 nmol of Gd(III)) solution. A T_1-weighted 3D-fast spoiled gradient echo image (matrix size of 256 × 512 pixels, slice thickness of 0.6 mm, repetition time of 11.2 ms, echo time of 3.9 ms, and 4 averages; total scan time of 3 min 41 s.) and a T_2-weighted multislice fast spin echo short time inversion recovery (FSE-STIR) fat suppressed image (matrix size of 192 × 384 pixels, slice thickness of 1.0 mm, repetition time of 5000 ms, echo time of 46.3 ms, 2 averages, and inversion time of 175 ms; total scan time of 5 min 30 s) were obtained prior to injection of the imaging agent ($t = 0$ h), at 2 h postinjection ($t = 2$ h), at 4 h postinjection ($t = 4$ h), and 6.5 h postinjection ($t = 6.5$ h). The mice were allowed to recover from anesthesia in between imaging time points.

Fluorescence Imaging. After the final MR image was acquired for each mouse, the mouse was sacrificed by CO_2 inhalation. The abdominal wall was then incised and the abdominal cavity was exposed for spectral fluorescence imaging using the Maestro *In Vivo* Imaging System (CRi, Inc., Woburn, MA). Whole abdominal images were obtained using a 445−490 nm band-pass excitation filter and a 515 nm long-pass emission filter. The tunable filter was automatically stepped in 10 nm increments from 500 to 800 nm, while the camera captured images at each wavelength interval with constant exposure. Spectral unmixing was performed using the Maestro software (CRi, Inc., Woburn, MA) to create unmixed and composite images of RhodG and autofluorescence spectra.

Histological Studies of Tumor Tissue. SHIN3 tumor xenografts were confirmed by histological methods as previously reported (*16*). In summary, every fluorescent nodule produced through avidin−fluorophore binding contained cancer cells as visualized by standard hematoxylin and eosin stain; no false positives were found.

RESULTS AND DISCUSSION

Biotin is a small, naturally occurring vitamin that binds with high specificity and affinity ($K_{ass} = 1.7 \times 10^{15}$ M^{-1}) to avidin (*17*). The "avidin chase-biotin" system has been coupled to MRI contrast agents to rapidly clear blood pool agents to the liver in order to investigate blood volume and vascular permeability (*21*). In the present experiment, our goal was to use the binding

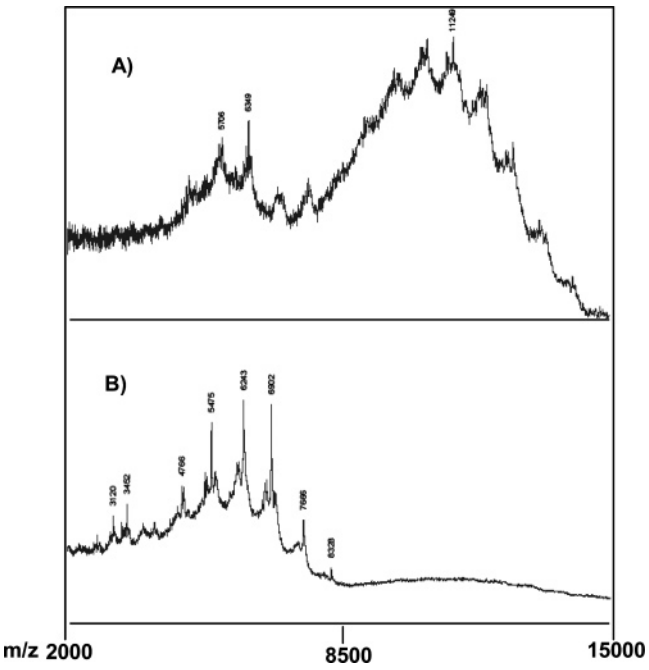


Figure 3. MALDI-TOF mass spectra of (A) cystamine core dendrimer chelated Gd(III) conjugate **3** and (B) biotinylated dendrimer **5**.

affinity of avidin for cell surface lectins found on ovarian cancer cells to provide targeted imaging using dendrimers to amplify the MR signal. To synthesize a single biotinylated dendrimer **5**, dendrimer **1** was reacted with 2 equiv of NHS-1B4M-DTPA (*22*) per each primary amine available on the surface of the dendrimer at pH = 7 in DMSO (Figure 2). After the reaction mixture was stirred under N_2 atmosphere for 24 h, *N*-(2-aminoethyl)aminomethyl polystyrene resin was added as a reactive scavenger to remove excess NHS-1B4M-DTPA. After stirring for 18 h, the resin was removed by filtration; the resulting mixture was diluted with CH_2Cl_2 and then washed with H_2O. The organic layer was concentrated and treated with pure trifluoroacetic acid (TFA) to cleave the *tert*-butyl protecting group esters on the 1B4M-DTPA for future complexation of Gd(III) ions. To purify dendrimer **2**, the TFA was first evaporated and the residue was then dissolved in deionized water. The aqueous solution was transferred to a Centriprep 3 with a 3000 Da cutoff membrane and subjected to exhaustive filtration with deionized water while monitoring with SE-HPLC. The retentate was lyophilized, and the product was obtained as a white solid with an overall 62% yield.

Last, the 1B4M-DTPA moieties on the functionalized dendrimer **2** were used to complex Gd(III) by addition of a solution of $Gd(OAc)_3$ in 0.3 M citrate buffer at pH = 4.5. Excess Gd(III) was removed by exhaustive filtration. Product **3** was isolated as a white powder after lyophilization in 72% yield. A single peak with a retention time of 14 min by SE-HPLC indicated the excellent purity of agent **3**.

Dendrimer **2** was also analyzed by MALDI-TOF mass spectrometry. The mass spectra give rather broad signals; however, the mass peak pattern was consistent with previous dendrimer MALDI-TOF mass analysis (*22*). In the case of 1B4M-DTPA modified dendrimer **2**, a mixture of functionalized dendrimers was actually observed, corresponding to 8−16 chelators being covalently attached to the dendrimer. Among them, the dendrimer with 12 conjugated 1B4M-DTPA chelators gave the highest-intensity mass signals. For Gd(III)-complexed dendrimer **3**, the mass peak pattern was very similar to that of **2**. However, each mass signal was shifted ~157 × *n* (*n* = number of chelators) higher mass units, indicating each 1B4M-DTPA moiety on the dendrimer **2** fully complexed Gd(III).

Reducing the disulfide bond within the dendrimer core was critical for attaching biotin or other promising targeting moieties. Several disulfide reducing agents such as dithiotreitol (DTT), tris(2-carboxyethyl)phosphine (TCEP), and immobilized TCEP were evaluated for this step. All were able to reduce the disulfide bond and produce a free sulfhydryl dendron product as determined by both an Ellman's test and SE-HPLC. However, immobilized TCEP was finally chosen because its use eliminated the need for exhaustive dialysis to separate the reduced dendrimer from the reducing agent and thus minimize potential reoxidation of the sulfhydryl dendron back to the disulfide dendrimer. Thus, immobilized TCEP reducing gel was added to an aqueous solution of dendrimer **3** and gently stirred for 2 h. Thereafter, the reducing gel was filtered off by using a glass pipet with a glass wool plug. The filtrate was used for the

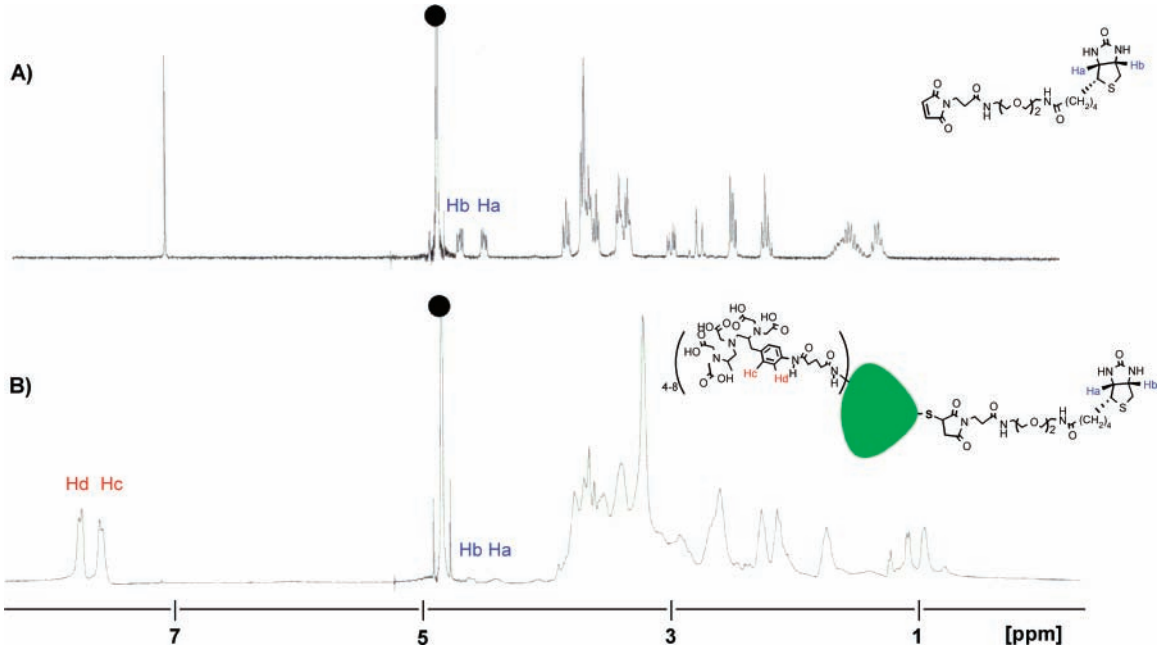


Figure 4. ^1H NMR spectra (300 MHz, 295 ± 1 K, D_2O) of (A) maleimide-PEO_2-biotin and (B) biotinylated cystamine core dendrimer chelated conjugate **4**. The residual solvent signals are marked as ●.

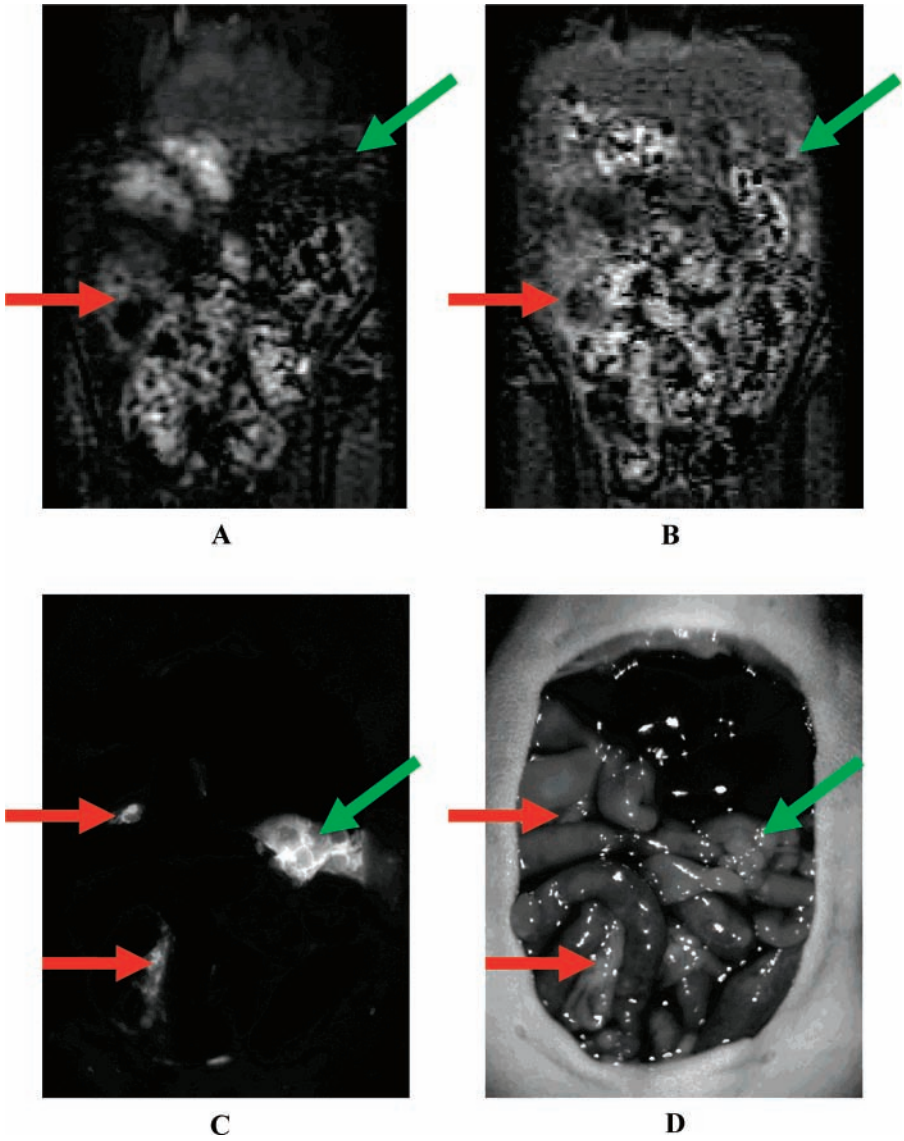


Figure 5. (a) T_1-weighted MR image obtained prior to contrast agent injection ($t = 0$) reveals an area of tumor growth (low signal intensity) below the liver, stomach, and spleen in the left abdomen (blue arrow) and adjacent to the gastrointestinal tract in the lower right abdomen (orange arrow). (b) T_1-weighted MR image obtained at 6.5 h after i.p. injection of the dual contrast agent reveals signal enhancement on the surface of the tumors (blue and orange arrows). (c) Spectrally unmixed optical image demonstrates fluorescence corresponding to sites of tumor (arrows). (d) White-light photo of the exposed abdomen confirms the presence of tumor in the locations predicted by MR and optical imaging although they are considerably more difficult to see.

coupling reaction with maleimide-PEG-biotin. The average number of the sulfhydryls was determined using Ellman's reagent, and thus, the concentration of the free thiol-bearing dendrimer was calculated to be twice as much as dendrimer **3**, indicating that the disulfide bonds inside the dendrimer were reduced quantitatively.

A 1.1 equiv quantity of maleimide-PEG-biotin was used for the conjugation to sulfhydryl dendrons, and the reaction mixture was then stirred under N_2 atmosphere overnight. The resulting mono-biotin-functionalized dendrimer **5** was separated from low molecular weight impurities by dialysis as described above and lyophilized. SE-HPLC, CHN elemental analysis, and MALDI-TOF mass spectra were employed to characterize agent **5**. Typically, SE-HPLC spectra showed a new peak with a retention time of ~16 min, ~1 min later compared to its precursor. As expected, MALDI-TOF mass spectra showed a mixture of single biotinylated dendrimers bearing ~5 Gd(III)-1B4M-DTPA moieties, respectively, while mass signals of dendrimers with 5 and 6 chelators have much higher intensity than others (Figure 3). Notably, the most distinct mass signal for each biotinylated dendrimer is not $M^+ + H$ but molecular ion plus several counter-ions (e.g., acetate ions) and H_2O molecules. One possible explanation is that each Gd(III)-DTPA moiety on the dendrimer **5** has one open coordination site for H_2O molecule and also 3 positive charges that electronically attract counter-ions (i.e., acetate ions). In terms of the number of chelators, this analytical result of 4−8 chelators on the biotinylated dendrimer **5** was consistent with that of its precursor dendrimer **3** attaining 8−16 1B4M-DTPA moieties.

The extent of biotinylation and ratio of biotin to dendrimer were determined by the HABA-avidin assay (*24*). Upon addition of biotinylated dendrimer **5** (100 μL, ~1.54×10^{-4} mM) to a solution of avidin (900 μL, ~7.35×10^{-3} mM in PBS buffer) containing 10 equiv of HABA per binding site, HABA was displaced by biotinylated dendrimer, resulting in a decrease in the UV absorption at 500 nm from 1.01 to 0.53. By using an extinction coefficient of 34 000 M^{-1} cm^{-1} for HABA/avidin samples at 500 nm, 0.73 biotin structures per dendrimer were calculated. This binding assay confirmed that avidin could be successfully employed as a supramolecular scaffold to carry multiple copies (up to four) of Gd(III)-DTPA biotin-functionalized dendrons.

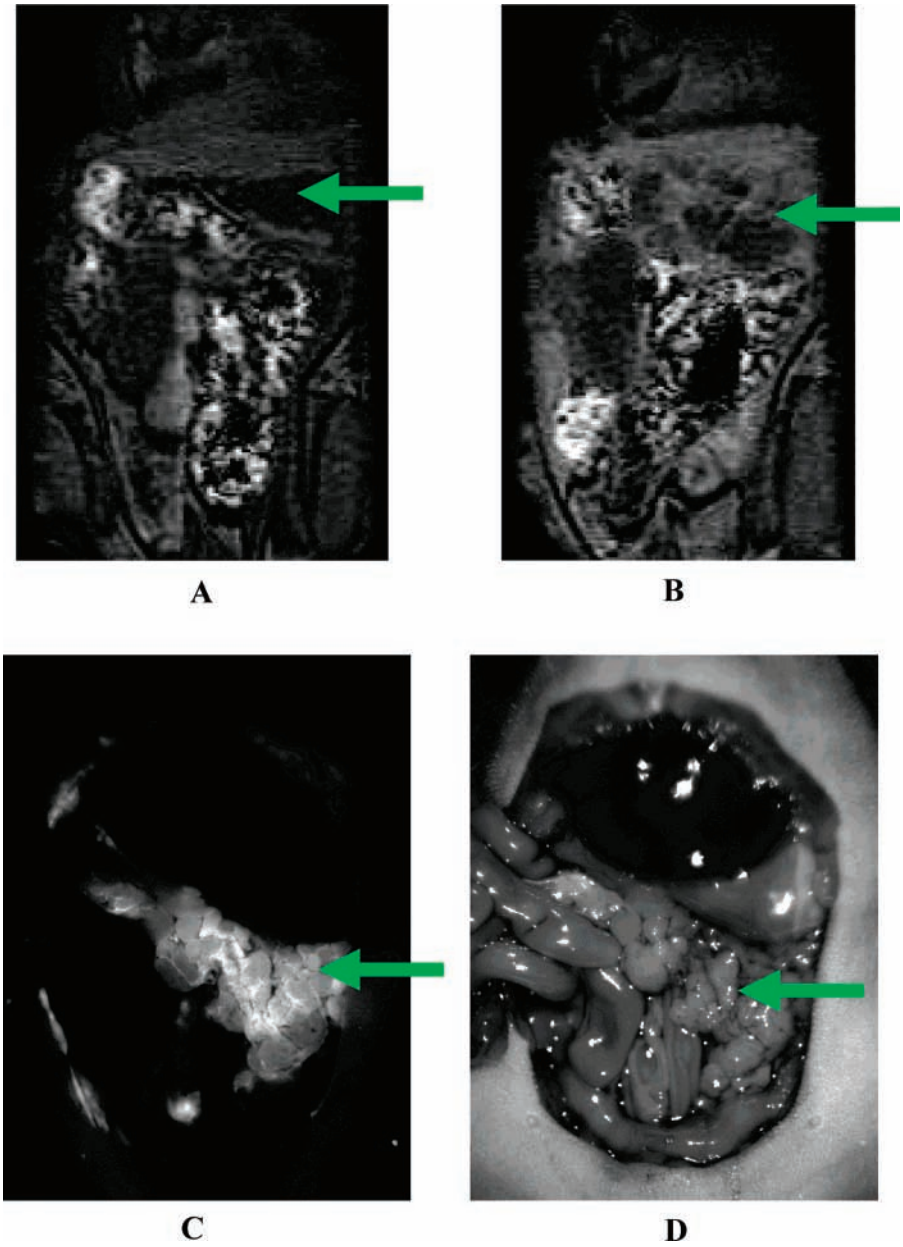


Figure 6. (a) T_1-weighted MR image obtained prior to contrast agent injection ($t = 0$) reveals a tumor (low signal intensity) below the liver and stomach in the left abdomen (blue arrow). (b) T_1-weighted MR image obtained at 6.5 h reveals signal enhancement from the edge of the tumor (blue arrow). (c) Spectrally unmixed optical image demonstrates fluorescence within the tumor. (d) White-light photo of the exposed abdomen confirms the presence of tumor in the locations predicted by MR and optical imaging.

Using the above conditions, dendrimers **1** and **2** could also be reduced to produce a unique sulfhydryl group and then coupled with maleimide-PEO_2-biotin to generate **6** and **4**, respectively, which were characterized by ^{1}H NMR, ESI-MS, and SE-HPLC. Typically, in ^{1}H NMR spectra of **4** and **6** (Figure 4), two diagnostic signals at ~4.38 and 4.56 ppm from the SCHC*H* and SCH_2CH protons of the biotin moiety were evident, while disappearance of the signal for the maleimide protons at ~6.90 ppm indicated complete removal of unbound biotin compounds after purification by exhaustive filtration. For compound **4**, a ~1:5 ratio of biotin/chelate was obtained by comparing the integrals of the signals from the biotin SCHC*H* and SCH_2CH protons (4.20−4.60 ppm) and the characteristic aromatic protons (7.15−7.60 ppm) from the 1B4M-DTPA. SE-HPLC spectra showed that reduced dendrimer **4** had a retention time ~0.8 min longer than **2**, supportive of the decreased size of **4**. For **6**, the $[M + H]^+$ peak (theoretical, 2200.4; found, 2199.8) on ESI-MS spectra confirmed this compound's identity.

Saturation of amino-terminated dendrimer 6 with NHS-1B4M-DTPA, following by deprotection of *tert*-butyl ester and incorporation of Gd(III), provides an alternative approach to generate biotinylated agent **5**. Additionally, other imaging labels can be also envisioned, for example, fluorescence dyes, being combined with 1B4M-DTPA (e.g., MRI agents) by attachment with 8 amino groups in the periphery of **6** for targeted multimodality imaging purposes.

Attempts were made to react biotinylated dendrimer **6** directly with NHS-1B4M-DTPA and then remove the *tert*-butyl esters with TFA for preparation of **4**. However, in our hands, isolation of the desired product **4** from excess 1B4M-DTPA chelators using the 3000 cutoff membrane Centriprep was not successful due to the ~6000 molecular weight dendrimer agent **4** significantly passing through the membrane during the extensive

dialysis process. Alternate isolation methods are currently being pursued to provide for the flexibility of alternate agent preparations that this route might permit.

Biotinylated-Dendrimer Conjugated to Avidin-Rhodamine Green. The avidin−biotin targeting system can be a carrier biomolecule to deliver imaging and/or therapeutic agents into cancer cells that express β-D-galactose receptors, namely, ovarian and colorectal adenocarcinoma cells (*13*−*16*). Previous studies have demonstrated the efficacy of the avidin−biotin targeting system. For example, while a G4 dendrimer conjugated with radioactive antisense oligo-DNA was able to independently increase delivery of the antisense oligo-DNA to SHIN3 cells, this delivery was further enhanced through avidin−biotin targeting (*18*). Additionally, avidin−biotin targeting of optical fluorophores to SHIN3 cells improved the ability to detect tiny foci of peritoneal implants (*16*). The avidin−biotin targeting system has also been employed as an internalizing tumor-targeting reagent in ovarian cancer to potentially deliver large quantities of Gd(III) (in the form of biotinylated Gd(III)-1B4M functionalized G6 dendrimers) for Gd-neutron capture therapy (*19*). However, inability to accurately control the 1:1 biotin−dendrimer ratio compromised the reproducibility of the avidin−biotin−dendrimer complex. In the current study, the design strategy takes advantage of a new family of dendrimers that possess a cystamine core (*12*). A single biotin moiety was attached to a reduced dendron using well-established sulfhydryl and maleimide chemistry. Through this approach, it is likely that the control of the incorporation of dendrimer moieties into the avidin complex will be more accurate.

Furthermore, avidin has the added benefit of being able to be conjugated to an optical fluorophore, thus allowing for dual-modality imaging. A dual-reporter probe has a distinct clinical advantage over a single-reporter probe in that a dual-reporter probe can be used in both preoperative planning and during the surgical debulking procedure for peritoneal metastases. However, the different sensitivities of the two types of imaging reporters require different amounts of each type of reporter to be employed to assemble the complex. In this case, to account for the much higher sensitivity of optical fluorescence compared to MR, the number of optical fluorophores required to produce an acceptable fluorescence image is much smaller when compared to the number of Gd(III) complexes required for an MR image. Using 100% Rhodamine green-conjugated avidin as the targeting vector will result in an overwhelming amount of Rhodamine green being delivered to the ovarian cancer cells and would potentially increase self-quenching of that signal. For this reason, preparation of the biotin−dendrimer agent included the addition of unlabeled avidin (nonfluorescent) to effectively dilute the concentration of Rhodamine green-conjugated avidin molecules to 0.0044 mM as compared to the ~2 mM concentration of Gd(III) ions on the surface of the dendrons. This method of preparation corrected for the sensitivity differences between the two modalities generating a solution that would deliver sufficient amount of Gd(III) complexes for an acceptable MR image while maintaining an adequate concentration of Rhodamine green to provide an acceptable optical image with the added benefit of limiting possible fluorescence self-quenching.

Relaxivity. The T_1 relaxivity measurements for the native G2 dendrimer (**1**), the biotinylated dendron (**5**), biotinylated dendrimer-avidin-RhodG conjugate, and Gd(III)-DTPA (Magnevist) were 14.7 mM^{-1} s^{-1} ($R^2 = 1$), 11.0 mM^{-1} s^{-1} ($R^2 = 0.99$), 12.4 mM^{-1} s^{-1} ($R^2 = 1$), and 5.3 mM^{-1} s^{-1} ($R^2 = 1$), respectively. These results confirm previous reports (*5*, *8*−*11*) that dendrimers have higher relaxivity compared to low-molecular-weight contrast agents such as Gd(III)-DTPA (Magnevist) and demonstrate that the biotinylation of the dendron and the conjugation of avidin to the biotinylated dendron do not adversely affect this enhancement.

Magnetic Resonance Images and Optical Fluorescent Images. The T_1-weighted MR images obtained prior to injection of the biotinylated dendrimer-avidin-RhodG conjugate (Figures 5a and 6a) failed to detect tumors (which are low in signal intensity) in the abdomen. The images acquired at 2 and 4 h (not shown) demonstrated that free contrast agent remained within the peritoneal cavity, making it impossible to identify specific tumor binding. However, images acquired at 6.5 h were clear of excess unbound conjugate. The T_1-weighted MR images (Figures 5b and 6b) showed areas of enhancement on the surface of the tumors as confirmed by spectral fluorescence imaging (Figures 5c and 6c), white-light photos (Figures 5d and 6d), and histology (*16*). In all cases, the areas of signal enhancement in the T_1-weighted images corresponded to hyperintense areas in T_2-weighted STIR images. The spectral fluorescence imaging (Figures 5c and 6c) demonstrated intense RhodG fluorescence while minimizing background fluorescence which, in combination with all images obtained, suggests that biotinylated dendrimer-avidin-RhodG conjugate was in fact targeting and enhancing visualization of SHIN3 tumor cells.

In conclusion, a novel synthetic approach for the preparation of a single biotinylated dendrimer-based MRI agent conjugated to fluorescently labeled avidin has been presented. Higher-generation dendrimers (e.g., G3−G8) with cystamine cores are currently being explored for this application. Additionally, in principle, any interesting biological targeting groups bearing a maleimide moiety can be now attached to a Gd(III)-DTPA functionalized dendrimer in a site-specific operation. Thus, this synthetic route provides a versatile strategy for designing and synthesizing targeted dendrimer-based MRI agents. Ongoing research is focused on constructing dendrimer−monoclonal antibody and dendrimer−peptide conjugates for use in targeted radiation therapy and imaging.

ACKNOWLEDGMENT

This research was supported by the Intramural Research Program of the NIH, National Cancer Institute, Center for Cancer Research.

LITERATURE CITED

(1) Chan, J. K., Cheung, M. K., Husain, A., Teng, N. N., West, D., Whittemore, A. S., Berek, J. S., and Osann, K. (2006) Patterns and progress in ovarian cancer over 14 years. *Obstet. Gynecol. (New York 1953*) *108*, 521−528.

(2) Griffiths, C. T. (1975) Surgical resection of tumor bulk in the primary treatment of ovarian carcinoma. *Natl. Cancer Inst. Monogr. 42*, 101−104.

(3) Tingulstad, S., Skjeldestad, F. E., Halvorsen, T. B., and Hagen, B. (2003) Survival and prognostic factors in patients with ovarian cancer. *Obstet. Gynecol. (New York 1953*) *101*, 885−891.

(4) Bristow, R. E., Tomacruz, R. S., Armstrong, D. K., Trimble, E. L., and Montz, F. J. (2002) Survival effect of maximal cytoreductive surgery for advanced ovarian carcinoma during the platinum era: a meta-analysis. *J. Clin. Oncol. 20*, 1248−1259.

(5) Caravan, P., Ellison, J. J., McMurry, T. J., and Lauffer, R. B. (1999) Gadolinium(III) chelates as MRI contrast agents: structure, dynamics, and applications. *Chem. Rev. 99*, 2293−2352.

(6) Raymond, K. N., and Pierre, V. C. (2005) Next generation, high relaxivity gadolinium MRI agents. *Bioconjugate Chem. 16*, 3−8.

(7) Tomalia, D. A., Naylor, A. M., and Goddard, W. A., III (1990) Starburst dendrimers: Molecular-level control of size, shape, surface chemistry, topology, and flexibility from atoms to macroscopic matter. *Angew. Chem., Int. Ed. 29*, 138−175.

(8) Langereis, S., de Lussanet, Q. G., van Genderen, M. H. P., Meijer, E. W., Beets-Tan, R. G. H., Griffioen, A. W., van Engelshoven, J. M. A., and Backes, W. H. (2006) Evaluation of Gd(III)DTPA-

terminated poly(propylene imine) dendrimers as contrast agents for MR imaging. *NMR Biomed. 19*, 133−141.
(9) Weiner, E. C., Brechbiel, M. W., Brothers, H., Magin, R. L., Gansow, O. A., Tomalia, D. A., and Lauterbur, P. C. (1994) Dendrimer-based metal chelates: a new class of magnetic resonance imaging contrast agents. *Magn. Reson. Med. 31*, 1−8.
(10) Kobayashi, H., Kawamoto, S., Jo, S.-K., Bryant, L. H., Jr., Brechbiel, M. W., and Star, R. A. (2003) Macromolecular MRI contrast agents with small dendrimers: Pharmocokinetics differences between sizes and cores. *Bioconjugate Chem. 14*, 388−394.
(11) Rudovsky, J., Botta, M., Hermann, P., Hardcastle, K. I., Lukes, I., and Aime, S. (2006) PAMAM dendrimeric conjugates with a Gd-DOTA phosphinate derivative and their adducts with polyaminoacids: The interplay of global motion, internal rotation, and fast water exchange. *Bioconjugate Chem. 17*, 975−987.
(12) Tomalia, D. A., Huang, B., Swanson, D. R., Brothers, H. M., and Klimash, J. W. (2003) Structure control within poly(amindoamine) dendrimers: size, shape and regio-chemical mimicry of globular proteins. *Tetrahedron 59*, 3799−3813.
(13) Yao, Z., Zhang, M., Sakahara, H., Saga, T., Arano, Y., and Konishi, J. (1998) Avidin targeting of intraperitoneal tumor xenografts. *J. Natl. Cancer Inst. 90*, 25−29.
(14) Yao, Z., Zhang, M., Sakahara, H., Saga, T., Nakamoto, Y., Sato, N., Zhao, S., Arano, Y., and Konishi, J. (1998) Imaging of intraperitoneal tumors with technetium-99m GSA. *Ann. Nucl. Med. 12*, 115−118.
(15) Lotan, R., and Raz, A. (1988) Lectins in cancer cells. *Ann. N. Y. Acad. Sci. 551*, 385−398.
(16) Hama, Y., Urano, Y., Koyama, Y., Kamiya, M., Bernardo, M., Paik, R., Krishna, M. C., Choyke, P. L., and Kobayashi, H. (2006) In vivo spectral fluorescence imaging of submillimeter peritoneal cancer implants using a lectin-targeted optical agent. *Neoplasia 8*, 607−612.
(17) Green, N. M. (1990) Avidin and streptavidin. *Methods Enzymol. 184*, 51−67.
(18) Sato, N., Kobayashi, H., Saga, T., Nakamoto, Y., Ishimori, T., Togashi, K., Fujibayashi, Y., Konishi, J., and Brechbiel, M. W. (2001) Tumor targeting and imaging of intraperitoneal tumors by use of antisense oligo-DNA complexed with dendrimers and/or avidin in mice. *Clin. Cancer Res. 7*, 3606−3612.
(19) Kobayashi, H., Kawamoto, S., Saga, T., Sato, N., Ishimori, T., Konishi, J., Ono, K., Togashi, K., and Brechbiel, M. W. (2001) Avidin-dendrimer-(1B4M-Gd)$_{254}$: A tumor-targeting therapeutic agent for gadolinium neutron capture therapy of intraperitoneal disseminated tumor which can be monitored by MRI. *Bioconjugate Chem. 12*, 587−593.
(20) Imai, S., Kiyozuka, Y., Maeda, H., Noda, T., and Hosick, H. L. (1990) Establishment and characterization of a human ovarian serous adenocarcinoma cell line that produces the tumor markers CA-125 and tissue polypeptide antigen. *Oncology 47*, 177−184.
(21) Kobayashi, H., Kawamoto, S., Star, R. A., Waldmann, T. A., Brechbiel, M. W., and Choyke, P. L. (2003) Activated clearance of a biotinylated macromolecular MRI contrast agent from the blood pool using an avidin chase. *Bioconjugate Chem. 14*, 1044−1047.
(22) Xu, H., Regino, C. A. S., Bernardo, M., Koyama, Y., Kobayashi, H., Choyke, P. L., and Brechbiel, M. W. (2007) Towards improved syntheses of dendrimer-based MR contrast agents: new bifunctional DTPA ligands and non-aqueous conjugation chemistry. *J. Med. Chem. 50*, 3185−3193.
(23) Savvin, S. B. (1961) Analytical use of Arsenazo III. Determination of thorium, zirconium, uranium and rare earth elements. *Talanta 8*, 673−685.
(24) Green, N. M. (1965) A spectrometric assay for avidin and biotin based on binding of dyes by avidin. *Biochem. J 94*, 23c−24c.

BC0701085

Antisense Oligodeoxynucleotide-Conjugated Hyaluronic Acid/Protamine Nanocomplexes for Intracellular Gene Inhibition

Hyejung Mok, Ji Won Park, and Tae Gwan Park*

Department of Biological Sciences, Korea Advanced Institute of Science and Technology, Daejeon 305-701, South Korea.
Received April 3, 2007; Revised Manuscript Received May 17, 2007

Green fluorescent protein (GFP) antisense oligodeoxynucleotide (ODN) was covalently conjugated to hyaluronic acid (HA) via a reducible disulfide linkage, and the HA−ODN conjugate was complexed with protamine to increase the extent of cellular uptake and enhance the gene inhibition efficiency of GFP expression. The HA−ODN conjugate formed more stable polyelectrolyte complexes with protamine as compared to naked ODN, probably because of its increased charge density. The higher cellular uptake of protamine/HA−ODN complexes than that of protamine/naked ODN complexes was attributed to the formation of more compact nanosized complexes (∼200 nm in diameter) in aqueous solution. Protamine/HA−ODN complexes also showed a comparable level of GFP gene inhibition to that of cytotoxic polyethylenimine (PEI)/ODN complexes. Since both HA and protamine are naturally occurring biocompatible materials, the current formulation based on a cleavable conjugation strategy of ODN to HA could be potentially applied as safe and effective nonviral carriers for ODN and siRNA nucleic acid therapeutics.

INTRODUCTION

Recently, efficient and specific down-regulation of therapeutically important genes has received special attention to treat various genetic and infectious diseases, including cancer (*1*−*3*). Nucleic acid-based drugs, such as antisense oligodeoxynucleotide (ODN), ribozyme, and small interfering RNA (siRNA), have been shown to inhibit expression of target proteins at post-transcriptional level. While they show highly sequence-specific gene silencing behaviors, critical delivery problems such as poor intracellular uptake and severe enzymatic degradation still remain to be solved for successful in vivo therapeutic applications (*4*−*6*). To improve their intracellular uptake and nuclease-resistant stability, a variety of cationic agents including polymers, polypeptides, and lipids were complexed with anionic nucleic acid drugs to produce nanosized polyplexes and lipoplexes. The nanoscale complexes can readily be transported into cells via an endocytic pathway while protecting the genetic drugs from degradation by nucleases. Among the cationic synthetic polymers, poly(ethylenimine) (PEI) and poly L-lysine (PLL) have been widely used to form nanosized polyelectrolyte complexes to deliver plasmid DNA, ODN, and siRNA (*7*−*12*). It is generally known that high molecular weight (MW) PEI and PLL produce more stable polyplexes with plasmid DNA than low MW polyplexes, generally resulting in increased gene transfection efficiency (*13*). This is because the charge density (the number of charges per polymer chain) of cationic polymers plays an utmost important role in maintaining the colloidal structural stability of polyelectrolyte nanocomplexes, especially in the transfection medium containing high salt concentration. The charge density effect on complex stability is closely related to inter- and intramolecular chain entanglement and mixing degree of two oppositely charged polyelectrolytes upon complexation. However, using high MW PEI and PLL as nonviral gene carriers has often elicited harmful cytotoxic effects, adversely influencing gene transfection efficiency. For producing stable and compact polyplexes, two oppositely charged polyelectrolytes (cationic polymer and DNA) must have sufficient charge densities for complexation. To form stable and non-cytotoxic polyplexes with ODN, reducible or self-degradable cationic polymers have been used to increase charge density for improved complex stability without compromising the cytotoxicity problem (*14*−*17*). The immediate degradation of reducible or self-degradable cationic polymers after cellular uptake produced less cytotoxic low MW fragments tolerable to the cells.

Antisense ODN is a single strand DNA composed of about 20 nucleotides with MW of around 5000, which has very low charge density compared to plasmid DNA with MW of a few million. Accordingly, when ODN was complexed with cationic polymers, the resultant ODN polyplexes often exhibited much reduced colloidal stability than that of the plasmid DNA polyplexes, mainly because of insufficient charge density of ODN.

Protamine is a nontoxic, cationic, and naturally occurring polypeptide which is known to provide unique membrane-translocating and nuclear-localizing activities because of its arginine-rich sequence (*18*−*22*). Although protamine has been used as a condensing agent for ODN, the transfection efficiency of protamine/ODN polyelectrolyte complexes was far less than that of high MW PEI or PLL (*23*, *24*). This was probably because both protamine and ODN did not have sufficient MW and charge density to form stable colloidal complexes, in addition to the presence of weak basic guanidine groups in protamine.

In this study, antisense GFP ODN was conjugated to anionic and biocompatible HA via a cleavable disulfide linkage to increase the charge density of ODN. HA, composed of *N*-acetyl-D-glucosamine and D-glucuronic acid, was expected to provide enough charge density to the conjugated ODN. The HA−ODN conjugate was complexed with clinically acceptable low MW protamine to improve the stability of HA−ODN/protamine polyelectrolyte complexes and increase gene inhibition efficiency. Anti-sense GFP ODN was used for conjugation to HA. HA−ODN/protamine complexes were physically characterized,

* Corresponding author. Tel: +82-42-869-2621, fax: +82-42-869-2610, e-mail: tgpark@kaist.ac.kr.

10.1021/bc070111o CCC: $37.00 © 2007 American Chemical Society
Published on Web 06/28/2007

and their inhibition extent of GFP expression was evaluated using HEK293 cells.

MATERIALS AND METHODS

Materials. Hyaluronic acid (sodium salt form, MW 17 000) was obtained from Lifecore Biomedical (Chaska, MN). Dialysis membrane (MW cutoff, 50 000) was a product from Spectrum (Houston, TX). GFP Antisense ODN (GAGCTGCACGCTGCCGTC, 5′ amine modification, MW 5656) was purchased from Bioneer (Daejeon, Korea). Plasmid DNA (pEGFP-C1) was extracted from transformed *Escherichia coli* by a standard alkaline lysis technique and purified by a DNA-purification column which was obtained from QIAGEN (Valencia, CA) according to the manufacturer's instruction. The purity and concentration of plasmid DNA was determined by measuring the absorbance ratio at 260/280 nm using a spectrophotometer (UV-1601, Shimadzu, Japan). *N*-Succinimidyl 3-(2-pyridyldithio)-propionate (SPDP) was purchased from Pierce (Rockford, IL). Dulbecco's phosphate-buffered saline (PBS), fetal bovine serum (FBS), and DMEM were purchased from Gibco BRL (Grand Island, NY). A pEGFP-C1 vector was obtained from BD Bioscience Clontech (Palo Alto, CA). Protamine, [1-ethyl-3-(dimethylamino)propyl]carbodiimide hydrochloride (EDC), PEI (branched, MW 25 K), cystamine, and dithiothreitol (DTT) were purchased from Sigma (St. Louis, MO). Cell counting kit-8 (CCK-8) was obtained from Dojindo Laboratories (Kumamoto, Japan). All other chemicals and reagents were of analytical grade.

Methods. *Synthesis and Characterization of ODN-Conjugated Hyaluronic Acid.* For preparation of thiol-modified hyaluronic acid (HA, MW 17 000), HA (200 mg) dissolved in PBS solution (pH 7.0) was added into 4 mL of dimethyl sulfoxide (DMSO)/deionized water mixture (50/50 (v/v)) containing EDC (194 mg) and HOBt (138 mg). To the solution was added cystamine (229 mg) for conjugation overnight. After treating with DTT (DTT:cystamine molar ratio = 4:1), the whole solution was dialyzed against deionized water using a membrane (MW cutoff: 3500) for 2 days and lyophilized. ^{1}H NMR spectra were taken with a Brucker DRX 300 NMR operating at 300.13 MHz by using D_2O to determine the degree of cystamine modification. The degree of thiol substitution in HA was calculated based on the molar ratio of thiol groups in thiolated HA to the total carboxylic acid groups in unmodified HA. The amount of thiol groups per HA chain was also quantified by the Ellman's assay.

To prepare the HA−SS−ODN conjugate (HA−ODN), 2-pyridyl disulfide-activated ODN was first synthesized by adding SPDP (275 μg) in DMSO to the PBS solution (pH 7.4) containing 5′-amine-modified antisense ODN (500 μg). After reaction for 5 h at room temperature, the unreacted SPDP was removed by using a desalting column (D-Salt dextran desalting column, Pierce, Rockford, IL). The activated ODN (340 μg) was reacted with 2.4 mg of thiol-modified HA in PBS solution at room temperature for 2 days. The unreacted antisense ODN was removed by dialysis against deionized water (MWCO 10 000). The resulting product, HA−ODN conjugate, was analyzed by polyacrylamide gel (20%) electrophoresis. The electrophoresis was carried out at a voltage of 120 V for 1 h in TAE buffer solution (40 mM Tris-HCl, 1% (v/v) acetic acid, 1 mM EDTA). Antisense ODN was visualized by ethidium bromide (EtBr) staining. HA−ODN conjugate was also analyzed by gel permeation chromatography (GPC) using a Waters 510 HPLC pump system (Waters 486, Waters, Milford, MA) equipped with a refractive index detector (Shodex RI-71, Kawasaki, Japan). GPC analysis was performed on a column (Ultrahydrogel 250, 7.8 × 300 mm, Waters) using distilled water as an eluant with a flow rate of 1 mL/min. To evaluate cleavability of the disulfide linkage for HA−ODN conjugate, the sample was incubated in 50 mM of glutathione solution for 1 h or 2 h and injected to the GPC system to separate the fraction of cleaved ODN from the HA−ODN conjugate.

Preparation and Characterization of Protamine/HA−ODN Complexes. Naked ODN or HA−ODN conjugate (4 μg) dissolved in 100 μL of PBS (pH 7.4) solution was mixed with various amounts of desalted protamine (0.4, 2, 4, and 64 μg) dissolved in 100 μL of PBS solution. After incubation for 15 min at room temperature, 2.8 mL of PBS solution was added to the mixture. To determine the hydrodynamic diameter of nanocomplexes formed from ODN or HA−ODN with protamine, the resulting complex solutions were analyzed by a dynamic light scattering instrument (Zeta-Plus, Brookhaven, NY). To evaluate stability of the protamine/HA−ODN complexes, a polyanion competition assay was done as previously reported (*25*). After preparation of nanocomplexes from ODN or HA−ODN (nucleotide 1 μg) with protamine (16 μg) by incubation in 20 μL of PBS solution for 15 min, different amounts of heparin (0, 4, 10, 50, and 100 μg) were added to the solution and incubated for 15 min. The mixture solution was subjected to 1% agarose gel electrophoresis running at 100 V for 20 min. The fraction of decomplexed ODN by heparin was visualized in the gel by staining with EtBr.

Intracellular Uptake Assay. HEK293 cells were maintained in DMEM medium supplemented with 10% FBS, 100 units/mL penicillin, and 100 μg/mL streptomycin at 37 °C in a humidified atmosphere of 5% CO_2. Cells were regularly passaged at subconfluence and plated on a four-well chamber slide at 24 h before transfection. On the next day, the cells were transfected with protamine/ODN or protamine/HA−ODN complexes formulated at a protamine/ODN weight ratio of 7.5. To visualize antisense ODN, a FITC-labeled sense ODN having a complementary sequence to antisense GFP ODN (FITC-sense ODN) was hybridized with either naked ODN or HA−ODN conjugate. After 5 h incubation, cells were washed three times with cold PBS solution and fixed with 1% (w/v) paraformaldehyde solution for 30 min at 4 °C. The nucleus was stained with DAPI (4′,6-diamidino-2-phenylindole) dye, a double strand DNA specific marker. Uptake of antisense ODN within the HEK293 cells was visualized by confocal microscopy (Carl Zeiss, Germany).

Cell Culture and Transfection. For GFP gene silencing experiments, GFP plasmid DNA was cotransfected with protamine/ODN or protamine/HA−ODN complexes to HeLa cells (human cervical cancer cell line), according the previously published method with minor modifications (*26*). Briefly, the cells were cotransfected in serum free medium with pEGFP-C1 plasmid (1 μg) using Lipofectamine 2000 reagent (2 mg/mL, Invitrogen, Carlsbad, CA) and protamine/ODN or protamine/HA−ODN complexes formulated at a protamine/ODN weight ratio of 1.5 and 6 (ODN amount: 1 μg). Polyelectrolyte complexes formed from PEI and naked ODN (1 μg) formulated at an N/P ratio of 8 were used as a positive control. After 5 h incubation, medium was replaced with new DMEM medium containing 10% FBS. After 48 h, transfected cells were harvested by treating with a cell lysis solution (1% Triton X-100 in PBS solution) and centrifuged to remove cell debris. The supernatant was analyzed to determine the amount of GFP protein expression using a spectrofluorophotometer (SLM-AMINCO 8100, SLM Instruments Inc., Rochester, NY) with an excitation and emission wavelength at 488 and 507 nm, respectively. All values were normalized by the cellular protein amount which was determined by the Micro-BCA protein assay (Pierce, Rockford, IL). Relative GFP expression level was then calculated as relative percentage using that of pEGFP-C1 transfected HeLa cells as 100% (*26*).

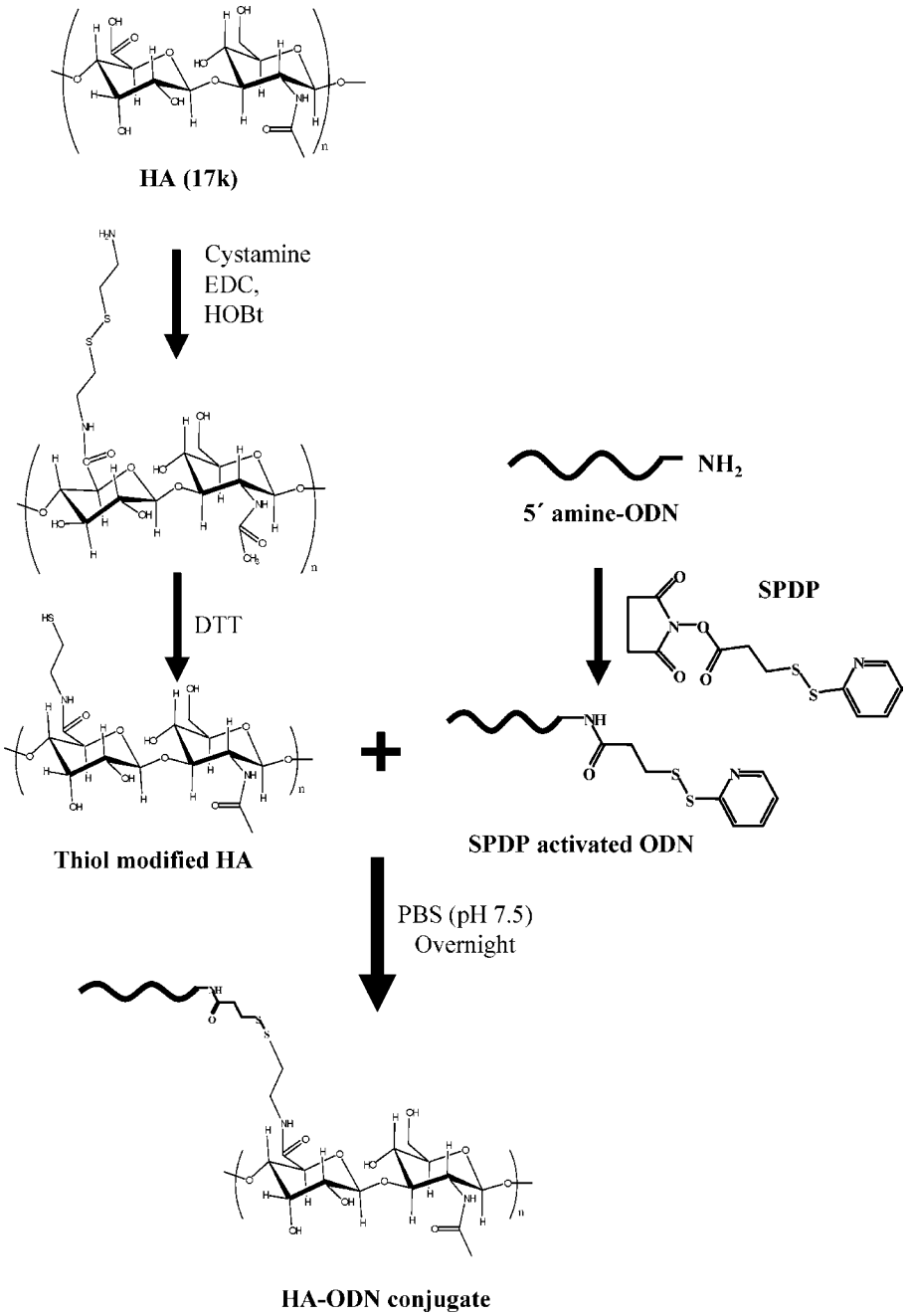


Figure 1. Synthetic scheme of thiolated HA and HA−ODN conjugate.

The cytotoxicity of the two cationic polymers, protamine and PEI, was evaluated by the CCK-8 cell viability assay which depends on the mitochondrial dehydrogenase activity of the cells. HEK 293 cells were seeded in a 96-well plate at a density of 1×10^4 cells per well and grown in DMEM medium supplemented with 10% (v/v) fetal bovine serum for 24 h at 37 °C. On the next day, protamine or PEI was added to the culture medium to give a final concentration of 0 to 160 μg/mL. After further incubation for 24 h, the number of viable cells was determined by the CCK-8 cell viability assay according to the manufacturer's protocol.

RESULTS AND DISCUSSION

Synthetic schemes of thiol-modified hyaluronic acid (HA) and HA−ODN conjugate are shown in Figure 1. The degree of cystamine substitution in the total carboxylic acid group in HA was 27.4 ± 3.4% as quantified by ^{1}H NMR (data not shown). The conjugation extent of cystamine was determined by relating the relative peak area of $NHCH_2CH_2SH$ (2.55 ppm) protons of cystamine to that of $COCH_3$ (1.86 ppm) protons of HA. The degree thiol substitution in HA was 20.8 ± 9.2%, and the number of thiol group in HA after DTT treatment was 8.8 ± 3.9 per HA chain, as quantified by Ellman's assay.

The primary amine group at the 5′-end of antisense ODN was first reacted with an active NHS group of a hetero-bifunctional cross-linker, SPDP (*N*-succinimidyl 3-(2-pyridyldithio)propionate), to produce 2-pyridyl disulfide-activated ODN. Thiol-modified HA was then added to the 2-pyridyl disulfide-activated ODN to obtain the HA−SS−ODN conjugate (HA−ODN) via a sulfhydryl exchange reaction. The HA−ODN conjugate was purified by using a gel elution method and analyzed by gel electrophoresis. Figure 2a shows the 20% polyacrylamide gel electrophoresis result, indicating that HA−ODN conjugate was successfully synthesized.

To calculate the number of ODN molecules conjugated onto the HA backbone, naked ODN and HA−ODN conjugate were

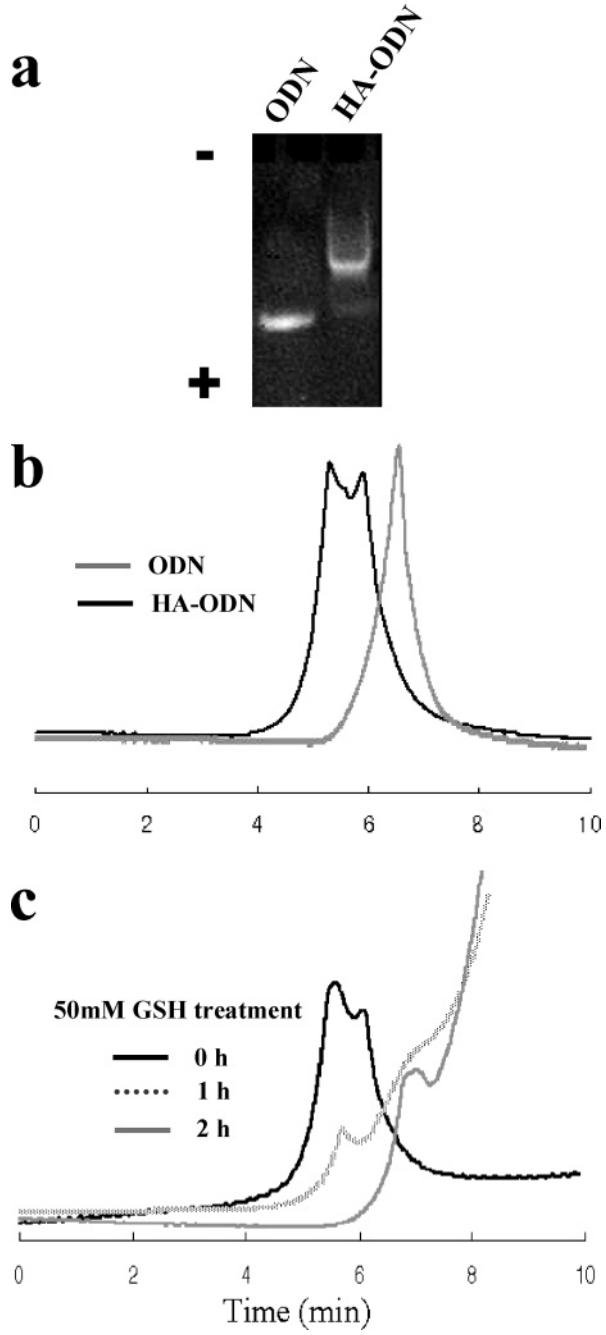


Figure 2. (a) Migration profiles of unconjugated ODN and HA−ODN conjugate in 20% polyacrylamide gel. (b) GPC result of unmodified ODN and HA−ODN conjugate. (c) Time-dependent cleavage of disulfide linkage in the HA−ODN conjugate when incubated in the medium containing 50 mM glutathione.

analyzed by GPC, using a series of dextran molecules with different molecular weights as standards (Figure 2b). The HA−ODN conjugate eluted earlier at a retention time corresponding to MW 22 700, while the naked ODN was eluted later at a peak position of MW 5656. From the GPC results, the number of ODN per HA chain was 0.83 ± 0.15, which was simply calculated based on the difference in elution times between HA−ODN conjugate and naked ODN. The calculation for the number of ODN molecules on the HA chain based on the MW difference, however, was somewhat misleading, because highly charged HA−ODN conjugate and ODN had different hydrodynamic volumes from neutral dextran molecules that were used as standards in the GPC analysis. It should be noted that the HA−ODN conjugate was eluted as doublet peaks in the chromatogram, implying that roughly one or two ODN chains

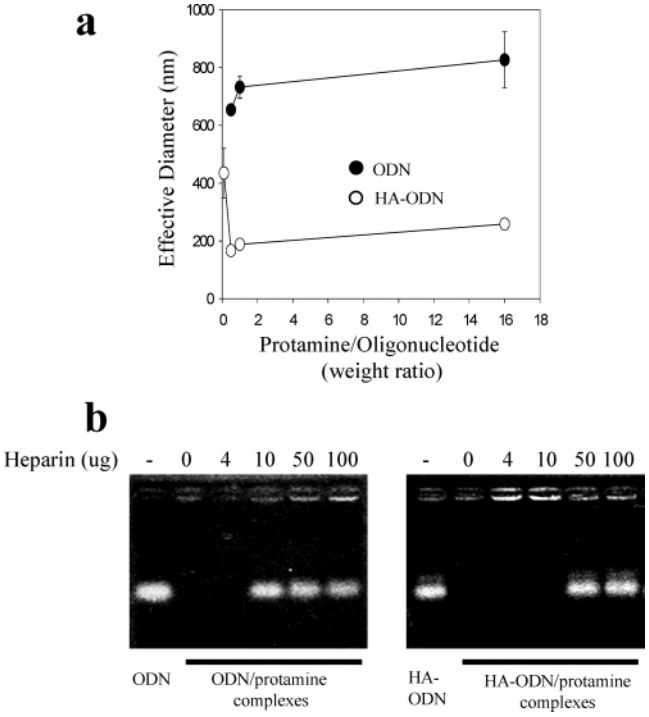


Figure 3. (a) Effective diameter of protamine/ODN and protamine/HA−ODN polyelectrolyte complexes as determined by dynamic light scattering. (b) Stability of polyelectrolyte complexes in the presence of competing polyanion, heparin. Protamine/ODN and protamine/HA−ODN complexes were incubated with various amount of heparin prior to loading on 1% agarose gel.

were conjugated onto the HA backbone. To verify that the disulfide linkage of HA−ODN conjugate could be cleaved in reducing condition, the HA−ODN conjugate was incubated in a solution containing 50 mM glutathione (GSH). Figure 2c shows that free ODN is liberated from the conjugate as a result of cleavage of the disulfide linkage between HA and ODN. The doublet peak for the HA−ODN conjugate disappeared progressively, and a new peak for the released free ODN fraction appeared gradually with increasing incubating time. The sharply increasing signal observed in the late elution time was due to the nonspecific effect of GSH present in the sample. After 2 h incubation in reductive condition, a free form of ODN was completely regenerated from the conjugated form. The main reason for the introduction of a cleavable disulfide linkage in the HA−ODN conjugate was to release an intact form of antisense ODN into the cytosol. It is known that the cytoplasmic space maintains a reductive microenvironment mainly by the presence of high GSH concentrations of up to 10 mM (*27*). It was postulated that the free form of ODN might have a better gene silencing activity than the conjugated form of HA−ODN because the steric hindrance effect of adjacent HA on binding to a target mRNA sequence was likely to be minimized (*28*).

Dynamic light scattering (DLS) analysis revealed that the HA−ODN conjugate could form much smaller complexes than the unconjugated ODN (Figure 3a). The hydrodynamic sizes of protamine complexes with ODN and HA−ODN conjugate were 653.5 ± 5.1 nm and 166.0 ± 13.9 nm at a protamine/ODN weight ratio of 0.5, respectively. This suggests that HA−ODN conjugate could produce more stable and compact complexes with protamine primarily because of the increased charge density. The conjugated HA provided additional anionic charges for the formation of complexes between protamine and ODN. When increasing the protamine/ODN weight ratio, the diameters of protamine/HA−ODN conjugate complexes were still around 200 nm, while those of protamine/ODN complexes were about 800 nm. Gel retardation assay was also performed

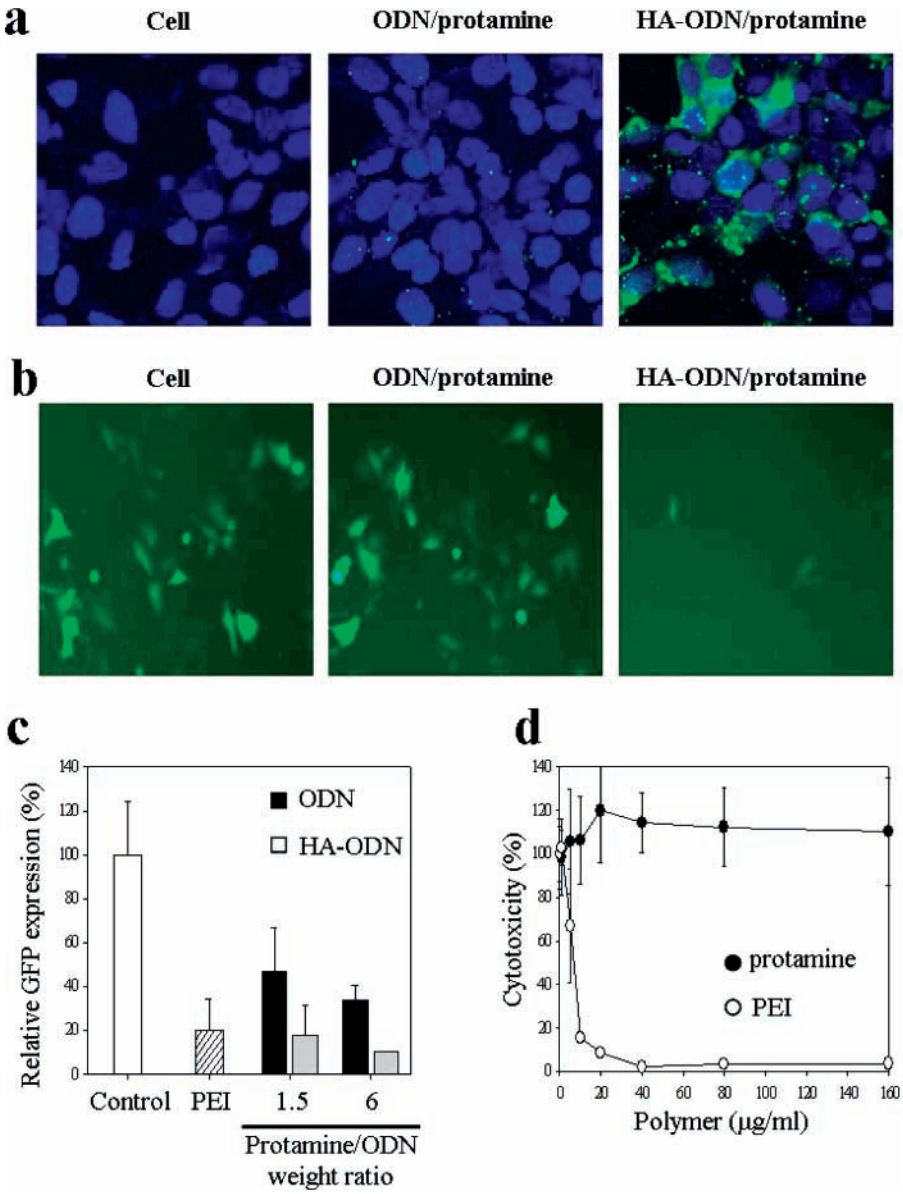


Figure 4. (a) Intracellular uptake protamine/ODN (middle panel) and protamine/HA−ODN/(right panel) complexes in HEK293 cells. FITC-labeled sense ODN was annealed to antisense ODN to visualize the cellular uptake. PBS treated cells were used as a control (left panel). (b) Inhibition degree of GFP gene expression in HeLa cells treated with protamine/ODN and protamine/HA−ODN complexes as observed by fluorescence microscopy. (c) The extent of GFP expression was quantitatively analyzed by determining intracellular fluorescence intensity after cell lysis. Protamine/ODN weight ratio was adjusted at 1.5 and 6 in the serum free condition. (d) Comparative cytotoxicities of protamine and PEI for HEK293 cells.

to confirm that ODN and HA−ODN conjugate could form nanoscale complexes with protamine by electrostatic interactions. Complete gel retardation of ODN and HA−ODN conjugate complexes was observed at a protamine/ODN weight ratio of 1 (data not shown).

To evaluate the relative structural stability of protamine/ODN and protamine/HA−ODN complexes, a competing polyanion, heparin, at various concentrations was added to induce decomplexation. After incubation with heparin, the fraction of decomplexed ODN was visualized in the gel (Figure 3b). Protamine/ODN and protamine/HA−ODN complexes were completely decomplexed at heparin concentrations of 10 μg and 50 μg, respectively. A 5-fold higher heparin concentration was required to destabilize the protamine/HA−ODN complexes than for the protamine/ODN complexes. It should be noted in Figure 3b that both ODN and HA−ODN conjugate bands appeared at the same migration position in the gel. This was because of the fact that 1% agarose gel electrophoresis did not provide sufficient resolution to separate the two species having a MW difference of around 20 000−30 000. From the above results, it is reasonable to say that HA−ODN conjugate formed more stable polyelectrolyte complexes than naked ODN. The stability and size of DNA polyplexes play an important role in promoting cellular uptake and enhancing gene transfection efficiency. It was reported that the size of polyplexes should be less than or around 200 nm for facile intracellular transport by an endocytic pathway (*29*). The DLS and heparin-induced decomplexation assay clearly indicate that more stable and compact polyplexes can be produced by conjugating ODN molecules to a highly charged HA chain backbone by increasing the charge density of HA−ODN conjugate for electrostatic interactions with protamine.

Figure 4a represents confocal images of HEK 293 cells incubated with protamine/ODN and protamine/HA−ODN complexes, respectively. The nuclei of cells were stained with the DAPI dye, which appeared blue. To visualize intracellular uptake of ODN and HA−ODN, an FITC-labeled sense ODN strand was used to hybridize an antisense ODN strand. The annealed FITC-labeled double strand ODN was used for complex formulation. Protamine/HA−ODN complexes appeared

scattered as green fluorescent dots within the cytosolic space of cells (Figure 4a right panel). They were likely to be preferentially located within the endosomal and lysosomal vesicles after cellular uptake. On the other hand, cells treated with PBS (left panel), protamine/ODN complexes (middle panel), and sense-FITC ODN only (data not shown) showed no measurable green fluorescent intensities. The confocal images evidently suggest that the conjugation of ODN to HA could greatly enhance the extent of intracellular uptake by producing more stable nanosized polyelectrolyte complexes suitable for intracellular endocytosis.

Protamine/HA−ODN and protamine/ODN complexes (formulated with a single strand GFP antisense ODN) were cotranfectected with GFP plasmid formulated with Lipofectamine to HeLa cells. Their GFP gene inhibition degrees were comparatively evaluated by fluorescence microscopy as shown in Figure 4b. In the fluorescent images, it can be seen that protamine/HA−ODN complexes formulated at a protamine/ODN weight ratio of 1.5 inhibit expression of GFP to a greater extent (right panel), compared to protamine/ODN complexes (middle panel). The extent of GFP inhibition was quantitatively analyzed by measuring intracellular GFP fluorescence intensity after cell lysis. Protamine/HA−ODN conjugate complexes prepared at a protamine/ODN weight ratio of 1.5 and 6 showed more significant inhibition of GFP gene expression than the protamine/ODN complexes (Figure 4c). It is also noticeable that increasing the weight ratio of protamine/ODN enhances the extent of GFP expression. High molecular weight PEI (25 k) was used as a control in this study. PEI/ODN complexes exhibited 19.7 ± 14.5% of GFP gene expression at an N/P ratio of 8, which is known to be an optimal condition for gene transfection (*30*). Protamine/ODN and protamine/HA−ODN complexes prepared at a protamine/ODN weight ratio of 1.5 showed 46.9 ± 19.5% and 17.5 ± 13.7% of GFP expression levels, respectively. The results imply that the greater extent of gene silencing effect observed for protamine/HA−ODN complexes was mostly because of enhanced complex stability and compact complex size without causing any cytotoxic effects. Furthermore, the reductive cleavage of the disulfide linkage between HA and ODN released out unconjugated and intact ODN species into the cytoplasm, which additionally contribute to the effective inhibition of GFP expression. Although protamine/HA−ODN and PEI complexes showed similar gene silencing levels, PEI was very cytotoxic in contrast to protamine at the same weight ratio, as measured by the CCK8 assay (Figure 4d). Thus, the more biocompatible protamine compared to any other cationic synthetic polymers such as PEI and PLL could be used as an effective condensing agent for the HA−ODN conjugate.

Last, it is worthwhile to note that low MW HA fraction is known to be internalized into cancer cells overexpressing HA receptors such as CD44 via receptor-mediated endocytosis. It was recently reported that HA conjugated chemical drugs including paclitaxel showed higher intracellular uptake and better therapeutic efficiency compared to unconjugated ones (*31*−*33*). Various water insoluble drugs could be conjugated in a cleavable or noncleavable manner to HA. HA−conjugated drugs could be solubilized in aqueous solution as self-assembling micelles, enabling intravenous administration. Moreover, HA-based prodrugs were expected to show target-specific cellular uptake against HA receptor-positive cells. In this study, we introduced the HA−ODN conjugation approach to increase the stability of nanosized complexes with protamine. It cannot be ruled out that protamine/HA−ODN conjugate polyplexes could possibly be internalized within cells via HA−receptor mediated endocytosis to some extent, in addition to the nonspecific endocytic mechanism. Quite recently, we reported that siRNA-encapsulated HA nanogels could be delivered into cells by HA receptor-mediated endosytosis (*34*). Thus, more detailed studies will be necessary to elucidate the cellular uptake mechanism.

In conclusion, antisense ODN was conjugated to HA, a negatively charged natural polysaccharide, to increase the charge density of the resultant conjugate for facile complexation with another naturally occurring polypeptide, protamine. Stable and non-cytotoxic protamine/HA−ODN complexes were formed, which exhibited a comparable gene silencing level to a cytotoxic PEI-based ODN formulation. The current novel ODN formulations prepared only from naturally occurring and clinically safe materials would have potential applications for siRNA delivery in the future.

ACKNOWLEDGMENT

This study was supported by the grants from the National Research Laboratory project from the Ministry of Science and Technology and the National Cancer Center, Republic of Korea.

LITERATURE CITED

(1) Jeong, J. H., Kim, S. W., and Park, T. G. (2003) Novel intracellular delivery system of antisense oligonucleotide by self-assembled hybrid micelles composed of DNA/PEG conjugate and cationic fusogenic peptide. *Bioconjugate Chem. 14*, 473−479.

(2) Vinogradov, S. V., Batrakova, E. V., Li, S., and Kabanov, A. V. (2004) Mixed polymer micelles of amphiphilic and cationic copolymers for delivery of antisense oligonucleotides. *J. Drug Targeting 12*, 517−526.

(3) Kim, S. H., Jeong, J. H., Cho, K. C., Kim, S. W., and Park, T. G. (2005) Target-specific gene silencing by siRNA plasmid DNA complexed with folate-modified poly(ethylenimine). *J. Controlled Release 104*, 223−232.

(4) Kim, D. H., and Rossi, J. J. (2007) Strategies for silencing human disease using RNA interference. *Nat. Rev. Genet. 8*, 173−184.

(5) Zhao, X. B., and Lee, R. J. (2004) Tumor-selective targeted delivery of genes and antisense oligodeoxyribonucleotides via the folate receptor. *Adv. Drug Delivery Rev. 56*, 1193−1204.

(6) Park, T. G., Jeong, J. H., and Kim, S. W. (2006) Current status of polymeric gene delivery systems. *Adv. Drug Delivery Rev. 58*, 467−486.

(7) Oishi, M., Hayama, T., Akiyama, Y., Takae, S., Harada, A., Yamasaki, Y., Nagatsugi, F., Sasaki, S., Nagasaki, Y., and Kataoka, K. (2005) Supramolecular assemblies for the cytoplasmic delivery of antisense oligodeoxynucleotide: polyion complex (PIC) micelles based on poly(ethylene glycol)-SS-oligodeoxynucleotide conjugate. *Biomacromolecules 6*, 2449−2454.

(8) Oishi, M., Nagasaki, Y., Itaka, K., Nishiyama, N., and Kataoka, K. (2005) Lactosylated poly(ethylene glycol)-siRNA conjugate through acid-labile beta-thiopropionate linkage to construct pH-sensitive polyion complex micelles achieving enhanced gene silencing in hepatoma cells. *J. Am. Chem. Soc. 127*, 1624−1625.

(9) Sagara, K., and Kim, S. W. (2002) A new synthesis of galactose-poly(ethylene glycol)-polyethylenimine for gene delivery to hepatocytes. *J. Controlled Release 79*, 271−281.

(10) Lee, H., Jeong, J. H., and Park, T. G. (2002) PEG grafted polylysine with fusogenic peptide for gene delivery: high transfection efficiency with low cytotoxicity. *J. Controlled Release 79*, 283−291.

(11) Lee, M., and Kim, S. W. (2005) Polyethylene glycol-conjugated copolymers for plasmid DNA delivery. *Pharm. Res. 22*, 1−10.

(12) Putnam, D., Zelikin, A. N., Izumrudov, V. A., and Langer, R. (2003) Polyhistidine-PEG:DNA nanocomposites for gene delivery. *Biomaterials 24*, 4425−4433.

(13) Choosakoonkriang, S., Lobo, B. A., Koe, G. S., Koe, J. G., and Middaugh, C. R. (2003) Biophysical characterization of PEI/DNA complexes. *J. Pharm. Sci. 92*, 1710−1722.

(14) Christensen, L. V., Chang, C. W., Yockman, J. W., Conners, R., Jackson, H., Zhong, Z., Feijen, J., Bull, D. A., and Kim, S. W. (2007) Reducible poly(amido ethylenediamine) for hypoxia-inducible VEGF delivery. *J. Controlled Release 118*, 254−261.

(15) Read, M. L., Bremner, K. H., Oupicky, D., Green, N. K., Searle, P. F., and Seymour, L. W. (2003) Vectors based on reducible polycations facilitate intracellular release of nucleic acids. *J. Gene Med. 5*, 232−245.

(16) Gosselin, M. A., Guo, W., and Lee, R. J. (2001) Efficient gene transfer using reversibly cross-linked low molecular weight polyethylenimine. *Bioconjugate Chem. 12*, 989−994.

(17) Read, M. L., Singh, S., Ahmed, Z., Stevenson, M., Briggs, S. S., Oupicky, D., Barrett, L. B., Spice, R., Kendall, M., Berry, M., Preece, J. A., Logan, A., and Seymour, L. W. (2005) A versatile reducible polycation-based system for efficient delivery of a broad range of nucleic acids. *Nucleic Acids Res. 33*, e86.

(18) Meistrich, M. L., Mohapatra, B., Shirley, C. R., and Zhao, M. (2003) Roles of transition nuclear proteins in spermiogenesis. *Chromosoma 111*, 483−488.

(19) Reynolds, F., Weissleder, R., and Josephson, L. (2005) Protamine as an efficient membrane-translocating peptide. *Bioconjugate Chem. 16*, 1240−1245.

(20) Park, Y. J., Chang, L. C., Liang, J. F., Moon, C., Chung, C. P., and Yang, V. C. (2005) Nontoxic membrane translocation peptide from protamine, low molecular weight protamine (LMWP), for enhanced intracellular protein delivery: in vitro and in vivo study. *FASEB J. 19*, 1555−1557.

(21) Tsui, B., Singh, V. K., Liang, J. F., and Yang, V. C. (2001) Reduced reactivity towards anti-protamine antibodies of a low molecular weight protamine analogue. *Thromb. Res. 101*, 417−420.

(22) Liang, J. F., Zhen, L., Chang, L. C., and Yang, V. C. (2003) A less toxic heparin antagonist−low molecular weight protamine. *Biochemistry (Mosc.) 68*, 116−120.

(23) Masuda, T., Akita, H., and Harashima, H. (2005) Evaluation of nuclear transfer and transcription of plasmid DNA condensed with protamine by microinjection: the use of a nuclear transfer score. *FEBS Lett. 579*, 2143−2148.

(24) Dinauer, N., Lochmann, D., Demirhan, I., Bouazzaoui, A., Zimmer, A., Chandra, A., Kreuter, J., and von Briesen, H. (2004) Intracellular tracking of protamine/antisense oligonucleotide nanoparticles and their inhibitory effect on HIV-1 transactivation. *J. Controlled Release 96*, 497−507.

(25) Glodde, M., Sirsi, S. R., and Lutz, G. J. (2006) Physiochemical properties of low and high molecular weight poly(ethylene glycol)-grafted poly(ethylene imine) copolymers and their complexes with oligonucleotides. *Biomacromolecules 7*, 347−356.

(26) Kim, S. H., Mok, H., Jeong, J. H., Kim, S. W., and Park, T. G. (2006) Comparative evaluation of target-specific GFP gene silencing efficiencies for antisense ODN, synthetic siRNA, and siRNA plasmid complexed with PEI-PEG-FOL conjugate. *Bioconjugate Chem. 17*, 241−244.

(27) Wang, W., and Ballatori, N. (1998) Endogenous glutathione conjugates: occurrence and biological functions. *Pharmacol. Rev. 50*, 335−356.

(28) Jeong, J. H., Kim, S. W., and Park, T. G. (2003) Novel intracellular delivery system of antisense oligonucleotide by self-assembled hybrid micelles composed of DNA/PEG conjugate and cationic fusogenic peptide. *Bioconjugate Chem. 14*, 473−479.

(29) Cherng, J. Y., van de Wetering, P., Talsma, H., Crommelin, D. J., and Hennink, W. E. (1996) Effect of size and serum proteins on transfection efficiency of poly ((2-dimethylamino)ethyl methacrylate)-plasmid nanoparticles. *Pharm. Res. 13*, 1038−1042.

(30) Kunath, K., von Harpe, A., Fischer, D., Petersen, H., Bickel, U., Voigt, K., and Kissel, T. (2003) Low-molecular-weight polyethylenimine as a non-viral vector for DNA delivery: comparison of physicochemical properties, transfection efficiency and in vivo distribution with high-molecular-weight polyethylenimine. *J. Controlled Release 89*, 113−125.

(31) Luo, Y., Ziebell, M. R., and Prestwich, G. D. (2000) A hyaluronic acid-taxol antitumor bioconjugate targeted to cancer cells. *Biomacromolecules 1*, 208−218.

(32) Jaracz, S., Chen, J., Kuznetsova, L. V., and Ojima, I. (2005) Recent advances in tumor-targeting anticancer drug conjugates. *Bioorg. Med. Chem. 13*, 5043−5054.

(33) Takei, Y., Maruyama, A., Ferdous, A., Nishimura, Y., Kawano, S., Ikejima, K., Okumura, S., Asayama, S., Nogawa, M., Hashimoto, M., Makino, Y., Kinoshita, M., Watanabe, S., Akaike, T., Lemasters, J. J., and Sato, N. (2004) Targeted gene delivery to sinusoidal endothelial cells: DNA nanoassociate bearing hyaluronan-glycocalyx. *FASEB J. 18*, 699−701.

(34) Lee, H., Mok, H., Lee, S., Y-K Oh, and Park T. G. (2007) Hyaluronic acid nanogels for target-specific intracellular delivery of siRNA. *J. Controlled Release 119*, 245−252.

BC070111O

Peptide-Conjugated Gold Nanorods for Nuclear Targeting

Adegboyega K. Oyelere,*[,†] Po C. Chen,[†] Xiaohua Huang,[‡] Ivan H. El-Sayed,[§] and Mostafa A. El-Sayed*[,‡]

Parker H. Petit Institute for Bioengineering and Biosciences, Laser Dynamics Laboratory, School of Chemistry and Biochemistry, Georgia Institute of Technology, 901 Atlantic Drive, Atlanta, Georgia 30332, Otolaryngology-Head and Neck Surgery, Comprehensive Cancer Center, University of California, San Francisco, 400 Parnassus Avenue, California 94143-0342.
Received April 18, 2007; Revised Manuscript Received June 6, 2007

Resonant electron oscillations on the surface of noble metal nanoparticles (Au, Ag, Cu) create the surface plasmon resonance (SPR) that greatly enhances the absorption and Rayleigh (Mie) scattering of light by these particles. By adjusting the size and shape of the particles from spheres to rods, the SPR absorption and scattering can be tuned from the visible to the near-infrared region (NIR) where biologic tissues are relatively transparent. Further, gold nanorods greatly enhance surface Raman scattering of adsorbed molecules. These unique properties make gold nanorods especially attractive as optical sensors for biological and medical applications. In the present work, gold nanorods are covalently conjugated with a nuclear localization signal peptide through a thioalkyl-triazole linker and incubated with an immortalized benign epithelial cell line and an oral cancer cell line. Dark field light SPR scattering images demonstrate that nanorods are located in both the cytoplasm and nucleus of both cell lines. Single cell micro-Raman spectra reveal enhanced Raman bands of the peptide as well as molecules in the cytoplasm and the nucleus. Further, the Raman spectra reveal a difference between benign and cancer cell lines. This work represents an important step toward both imaging and Raman-based intracellular biosensing with covalently linked ligand−nanorod probes.

INTRODUCTION

Nanobiotechnology and nanomedicine are emerging fields engendered by the convergence of multiple scientific fields for biologic applications and the recently discovered novel properties of materials at the nanoscale. Nanoparticles, because of their small sizes and unique properties, have been widely used in drug delivery (*1*−*4*), cellular imaging (*5*−*9*), and biomedical diagnostics and therapeutics (*10*−*13*). Plasmonic nanoparticles are especially useful for these applications because of their enhanced resonant absorption and scattering properties as well as strong Raman scattering, which are essential properties for their applications in photothermal therapy (*14*−*25*), optical imaging (*26*−*31*), and Raman probe design (*32*−*38*).

Nuclear targeting of nanoparticles in live cells is generating widespread interest because of the prospect of developing novel diagnostic and therapeutic strategies such as gene therapy. However, nuclear delivery of the nanoparticles requires bypassing the formidable barriers of the cellular membrane and the nuclear membrane. The cellular membrane endocytoses nonspecific particles on the cell surface, enveloping them with a phopholipid membrane and restricting interaction with the general cell cytoplasm. The nuclear membrane is a double-layer membrane marked with nuclear pores that allow diffusion of molecules and selective uptake into the nucleus. One common approach to targeted nuclear delivery is the conjugation of drug molecules and nanoparticles to nuclear membrane-penetrating peptides.

Gold nanoparticles are examples of extremely attractive candidates for attachment to such carrier peptides due to their small sizes, ease of preparation and bioconjugation (*39*, *40*), strong absorbing and scattering properties (*41*−*44*), as well as their well-known biocompatibility (*45*). Tkachenko et al. (*46*, *47*), using video-enhanced color differential interference contrast microscopy, have demonstrated nuclear entry of 20 nm gold nanospheres indirectly conjugated to various nuclear localization signal (NLS) peptides through a shell of bovine serum albumin (BSA) protein. However, these gold nanospheres only absorb in the visible region, thus limiting their use in *in vivo* applications such as in photothermal therapy, which requires near-infrared region where the light penetration is optimal.

Unlike gold nanospheres, gold nanorods possess unique optical properties ideal for *in vivo* applications. They have two surface plasmon absorption bands, a strong long-wavelength band due to longitudinal oscillation of their electrons and a weak short wavelength band around 520 nm due to the transverse electronic oscillation (*42*, *43*, *48*−*51*). The longitudinal absorption band is very sensitive to the size of the nanorods. By increasing the aspect ratio (length divided by width), the longitudinal absorption maximum red-shifts with an increase in the absorption intensity. This provides the opportunity for their applications as near-infrared photoabsorbers and scatterers (*23*).

Gold nanorods also provide a scaffold for observing surface-enhanced Raman scattering (SERS) (*52*−*59*). The well-developed synthesis of nanorods with different aspect ratios provides the opportunity to tune the surface plasmon band to the excitation laser to obtain the largest enhancement. It has been shown that the enhancement factors on the order of 10^4−10^5 could be observed for the adsorbed molecules on gold nanorods, while no such enhancement was observed on nanospheres (*52*). Biological species are known to have small Raman scattering cross section and sensitivity toward photochemical damage and interference from fluorescence when UV or visible laser excitation is used. In order to overcome these difficulties, the size of gold nanorods can be adjusted to have its enhancement in the near-infrared region away from the biomolecular

* To whom correspondence may be addressed. Adegboyega K. Oyelere. Phone: 404-894-4047. Fax: 404-894-7452. E-mail: aoyelere@gatech.edu, Mostafa A. El-Sayed. Phone: 404-894-0292. Fax: 404-894-0294. E-mail: melsayed@gatech.edu.

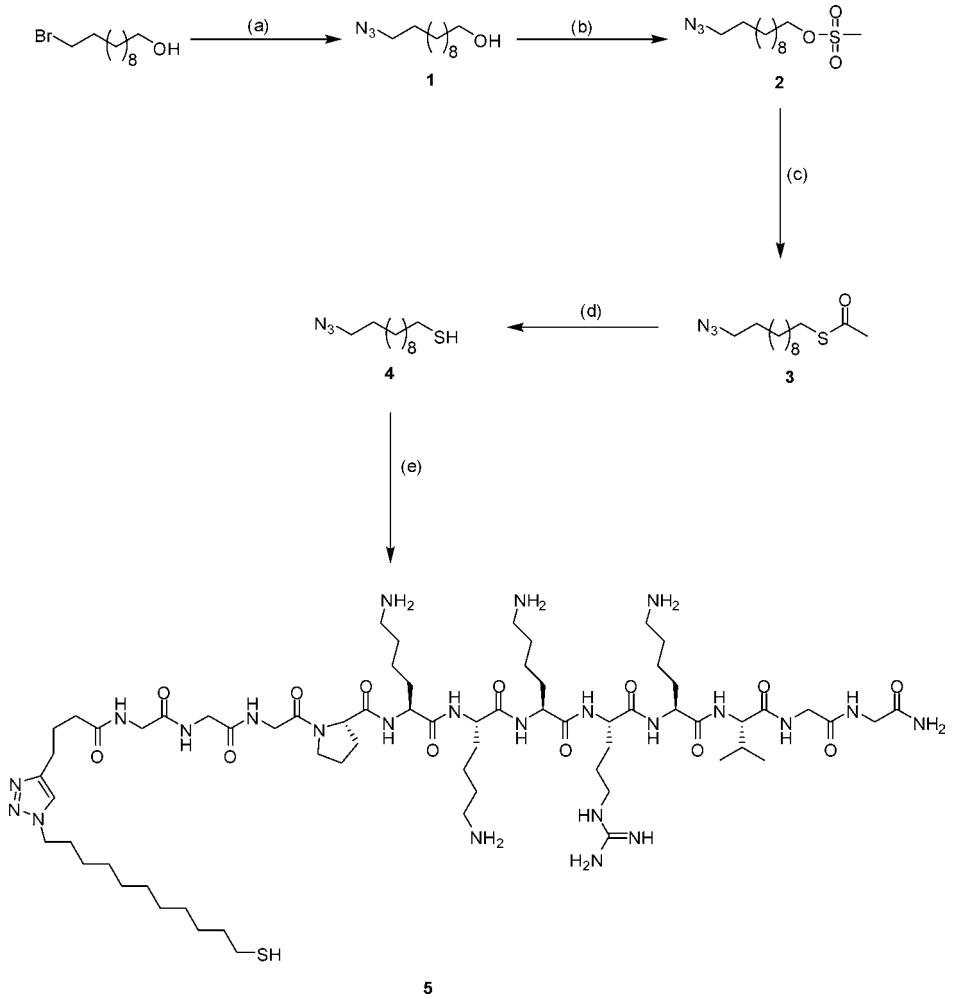
† Parker H. Petit Institute for Bioengineering and Biosciences, Georgia Institute of Technology.

‡ Laser Dynamics Laboratory, Georgia Institute of Technology.

§ University of California, San Francisco.

10.1021/bc070132i CCC: $37.00 © 2007 American Chemical Society
Published on Web 07/13/2007

Scheme 1. Synthesis of Thiolalkyl-Triazole Linked NLS Peptide[a]



[a] Conditions: (a) NaN_3, DMF, 110 °C; (b) MsCl, Et_3N, CH_2Cl_2, rt; (c) potassium thioacetate, THF, reflux; (d) conc. HCl, methanol, reflux; (e) alkyne-modified NLS (PC-37044-PI), TBTA, CuI, DMF, rt. Abbreviations: MsCl, methanesulfonyl chloride; TBTA, Tris-(benzyltriazolylmethyl)amine.

excitation transitions that could lead to fluorescence or photochemical decomposition. Moreover, the surface chemistry of gold nanorods allows for multiple functionalization so that the capping molecules, such as cetyltrimethylammonium bromide (CTAB), could be replaced or conjugated with many functional groups (*60*−*63*).

In the present work, we describe the preparation of gold nanorods directly conjugated to a simian virus (SV40) NLS peptide through a thioalkyl-triazole linker. Using a simple conventional microscope in the dark field, we are able to image the intracellular localization of these nanorods. Furthermore, cellular components are observed by surface-enhanced Raman scattering of these gold nanorod−peptide conjugates. Our results demonstrate that these nanorods are useful for cellular delivery applications, especially nuclear targeting and cellular components sensing.

EXPERIMENTAL PROCEDURES

Materials. 11-Bromoundecan-11-ol and all chemicals used for the synthesis of gold nanorods are purchased from Sigma Aldrich. Anhydrous solvents and other reagents are purchased and used without purification. Analtech silical gel plate (60 F_{254}) is used for analytical TLC, and UV light is used to examine the spots. Tris-(benzyltriazolylmethyl)amine (TBTA) is prepared by using the procedure described by Chan et al. (*64*). Alkyne-modified NLS (PCS-37044-PI) is synthesized by the solid-phase method at Peptide International, Louisville, Kentucky. NMR spectra are recorded on a Varian-Gemini 400 magnetic resonance spectrometer. ^{1}H NMR spectra are recorded in parts per million (ppm) relative to the peak of $CDCl_3$, (7.24 ppm). Mass spectra are recorded at the Georgia Institute of Technology mass spectrometry facility in Atlanta.

Synthesis of Thiolalkyl-Triazole Linked NLS Peptide (Scheme 1). *1. Synthesis of 1-Azidoundecan-11-ol (**1**).* This compound is synthesized by adapting the method of Shon et al. (*65*). Briefly, sodium azide (1.2 g, 18.5 mmol) is added to a solution of 1-bromoundecan-11-ol (2.0 g, 7.96 mmol) anhydrous DMF (20 mL). The reaction mixture is heated to 110 °C in a pressure tube and stirred continuously for 24 h. The reaction mixture is then cooled to room temperature and quenched with distilled water (30 mL). The cooled reaction mixture is extracted with anhydrous diethyl ether (3 × 20 mL), and the combined organic layers are washed with distilled water (3 × 20 mL) and dried over Na_2SO_4. The solvent is removed and concentrated *in vacuo* to give 1.275 g (75%) of **1** as pale yellowish oil. ^{1}H NMR ($CDCl_3$, 400 MHz) δ 1.25−1.38 (14H, m), δ 1.50−1.60 (4H, m), δ 3.22 (2H, t, J = 7.2 Hz), δ 3.61 (2H, t, J = 7.2 Hz).

*2. Synthesis of 1-Azidoundecan-11-methylsulfonate (**2**).* Triethylamine (4.35 mL, 31.2 mmol) is added to a solution of 1-azidoundecan-11-ol **1** (2.42 g, 11.3 mmol) in anhydrous CH_2Cl_2 (100 mL). The reaction mixture is stirred for 15 min at 0 °C, and then methanesulfonyl chloride (2.41 mL, 31.2 mmol) is added. The reaction mixture is allowed to warm up to room temperature and stirring continued for 2 h. The reaction mixture is quenched with ice-cold distilled water (35 mL) and extracted

with anhydrous diethyl ether (2 × 35 mL). The combined organic layer is washed in succession with 1 N HCl, distilled water, saturated $NaHCO_3$, and again with distilled water. The organic layer is dried over Na_2SO_4 and concentrated *in vacuo* to give 2.934 g (89%) of **2** as pale yellowish oil. ^{1}H NMR ($CDCl_3$, 400 MHz) δ 1.25−1.40 (14H, m), δ 1.53−1.60 (2H, m), δ 1.68−1.75 (2H, m), δ 2.97 (3H, s), δ 3.22 (2H, t, J = 6.8 Hz), δ 4.19 (2H, t, J = 6.8 Hz).

*3. Synthesis of 1-Azidoundecan-11-thioacetate (**3**).* Potassium thioacetate (2.02 g, 6.79 mmol) is added to a solution of 1-azidoundecan-11-sulfonate **2** (1.00 g, 3.43 mmol) in anhydrous THF (10 mL). The reaction mixture is degassed, refilled with argon, and heated under reflux for 3 h. The reaction mixture is quenched with ice-cold distilled water (30 mL) and extracted with anhydrous diethyl ether (3 × 30 mL). The combined organic layer is dried over Na_2SO_4 and concentrated *in vacuo* to give 856 mg (87%) of **3** as yellowish oil. ^{1}H NMR ($CDCl_3$, 400 MHz) δ 1.23−1.38 (14H, m), δ 1.50−1.60 (4H, m), δ 2.29 (3H, s), δ 2.83 (2H, t, J = 7.6 Hz), δ 3.22 (3H, t, J = 7.6 Hz).

*4. Synthesis of 1-Azidoundecane-11-thiol (**4**).* A solution of 1-azidoundecane-11-thiolacetate **3** (0.1 g. 0.369 mmol) in anhydrous methanol (7.0 mL) is first degassed and refilled with argon. Concentrated HCl (0.4 mL) is added to the solution, and the resulting mixture is refluxed for 3 h. The reaction mixture is quenched with distilled water (10 mL) and extracted with anhydrous diethyl ether (2 × 10 mL). The organic layer is dried over Na_2SO_4 and concentrated *in vacuo* to give 85 mg (100%) of **4** as yellowish oil. ^{1}H NMR ($CDCl_3$, 400 MHz) δ 1.25−1.38 (14H, m), δ 1.53−1.62 (4H, m), δ 2.50 (2H, q, J = 15.2 Hz, 7.2 Hz), δ 3.23 (2H, t, J = 5.6 Hz).

*5. Synthesis of Thiolalkyl-Triazole Linked NLS Peptitde (**5**).* Anhydrous CuI (0.003 g, 0.011 mmol) and tris-(benzyltriazolylmethyl)amine (0.007 g, 0.011 mmol) is added to a solution of 1-azidoundecane-11-thiol **4** (0.02 g, 0.079 mmol) and alkyne-modified NLS peptides PC-37044-PI (0.05 g, 0.039 mmol) in anhydrous DMF (2 mL). The solution is stirred at room temperature under argon for 48 h. Excess DMF is removed *in vacuo*, and the residue is quenched with distilled water (5 mL). The resulting mixture is extracted with dichloromethane (2 × 10 mL) to remove unreacted 1-azidoundecane-11-thiol **4**. The remaining aqueous layer is frozen in an acetone−dry ice bath and concentrated *in vacuo* to give 50 mg (43%) of **5** as a brown solid. ^{1}H NMR (DMSO-d_6, 400 MHz) δ 0.83 (2H, t, J = 6.0 Hz), δ 1.23−1.36 (6H, m), δ 1.42−1.54 (3H, m), δ 1.56−1.68 (1H, m), δ 2.13−2.24 (2H, m), δ 2.40−2.50 (5H, m), δ 2.66−2.80 (2H, m), δ 2.87 (1H, s), δ 3.29 (1H, t, J = 8.0 Hz), δ 3.34−3.54 (1H, m), δ 3.62−3.78 (1H, m), δ 4.10−4.30 (1H, m), δ 7.26−7.36 (1H, m), δ 7.64−7.88 (3H, m), δ 7.94 (1H, s), δ 8.10−8.32 (2H, m). MS (MALDI, CHCA) calcs for $[C_{67}H_{123}N_{23}O_{13}S + H]^+$ 1490.9, found 1491.0.

Synthesis of Gold Nanorods and Peptide Conjugation. The gold nanorods are synthesized according to the seed-mediated growth method (*66*). Briefly, 600 uL 0.01 M ice-cold sodium borohydride is quickly added into a 10 mL 0.5 mM stirring auric acid, which is dissolved in 0.2 M CTAB solution. 2−5 nm gold nanoparticles are formed after 2 min as a seed solution. In a separate flask, 1 mL of 4 mM silver citrate is added to 50 mL growth solution, which contains 0.2 M CTAB, 0.15 M benzyldimethylammonioum chloride hydrate (BDAC), and 1 mM auric acid. 0.07 mL of 0.0788 M ascorbic acid is added to the growth solution to reduce the auric acid to form $HAuCl_2$ solution. 0.08 mL seed solution is injected into the growth solution to initiate the rod formation and growth. In this procedure, gold nanorods with absorption maximum at 650 nm (aspect ratio of 2.4) are obtained overnight. For the conjugation of peptide **5** to gold nanorods, 100 μL 1 mM peptide **5** is added to 10 mL gold nanorod solution (OD_{650} = 1.0), and the mixture is left to react for 72 h. The unbound peptide is separated by centrifugation at 5000 rpm for 10 min.

Cell Culture and Cellular Delivery of Peptide-Conjugated Gold Nanorod. One nonmalignant epithelial cell line, HaCaT (human keratinocytes), and one malignant epithelial cell lines, HSC 3 (human oral squamous cell carcinoma), are cultured on coverslips in DMEM (Dulbecco's Modification of Eagle's Medium, Cellgro) plus 10% FBS (fetal bovine serum, Gem Cell) at 37 °C under 5% CO_2 for 24 h. The DMEM medium is then taken out and rinsed with PBS buffer. Fresh DMEM medium containing 1 nM thioalkyl-triazole peptide/Au nanorod conjugates is added, and the cells are put back in the incubator for 2 h. After the incubation of the nanorods, the cells are rinsed with PBS buffer, fixed with paraformaldehyde, coated with glycerol, and sealed with another coverslip.

Dark Field Imaging. The dark field images are taken under an inverted Olympus IX70 microscope. A dark field condenser (U−DCW) with a numerical aperture between 0.9 and 1.2 is used to deliver a very narrow beam of white light from a tungsten lamp to the sample. A 100×/1.35 oil Iris objective (UPLANAPO) is used to collect only the scattered light from samples. In this mode, the samples with highly scattering properties are shown as a bright object in a dark background.

Raman Measurements. The Raman spectra are obtained with a Holoprobe series 5000 Micro-spectrometer (Kaiser Optical Systems, Inc., Ann Arbor, MI) in a 180° reflective configuration with a 50× objective. The excitation wavelength is 785 nm from a diode laser. The spectral resolution is 5 cm^{-1}, and the laser power is 25 mW. Each spectrum is obtained in 10 s collection time with six accumulations.

RESULTS AND DISCUSSION

Peptide Conjugation to Gold Nanorods. The use of NLS for targeting of proteins, peptides, nucleic acids, and small organic molecules to the cell nucleus has been extensively investigated (*46, 47, 67−72*). One of the most studied is the NLS of SV40 large T antigen, which has been shown to act as a "Trojan horse", efficiently distributing appended payloads into the cell nucleus (*68*). However, the chemical syntheses of NLS-conjugated payloads are very difficult, often requiring technically challenging compound purification and characterization protocols. In the case of nanoparticle−peptide conjugates, an alternative synthetic approach has been to indirectly couple these nanoparticles to carrier peptides through a secondary protein, such as bovine serum albumin (BSA) protein (*46, 47*). The resulting conjugates are large and possess highly branched polypeptides that are very difficult to characterize.

We observe in this study that thiol-terminated NLS peptides incorporating appropriate spacer groups could be easily accessed by Cu(I)-catalyzed cycloaddition reaction (click chemistry) (*71*) between an alkyne-terminated NLS, such as PC-37044-PI, and an appropriate azidothiols (Scheme 1). Subsequent reaction of the resulting thioalkyl-triazole linked NLS **5** with gold nanorods which are stabilized with CTAB molecules yields peptide-conjugated gold nanorods by forming Au−S bonds between the peptide and the gold surface. There are some other previous reports of bioconjugation to gold nanoparticles through Au−S bonds. For example, HS-mPEG has been reported to rapidly assemble onto gold nanoshells through Au−S bonds within 1 h (*14*). In this case, there are no capping molecules on the surface of the gold layer. In comparison to a bare gold surface, it takes a longer time to assemble thiolated molecules to the surface of gold nanorods. The adsorption of HS-mPEG onto gold nanorods requires stirring for 24 h (*61*), while thiolated DNA is bound to gold nanorods after 72 h of incubation (*73*). Gold nanorods are capped with CTAB surfactants, which form a bilayer structure around the gold surface (*74*). The inner layer

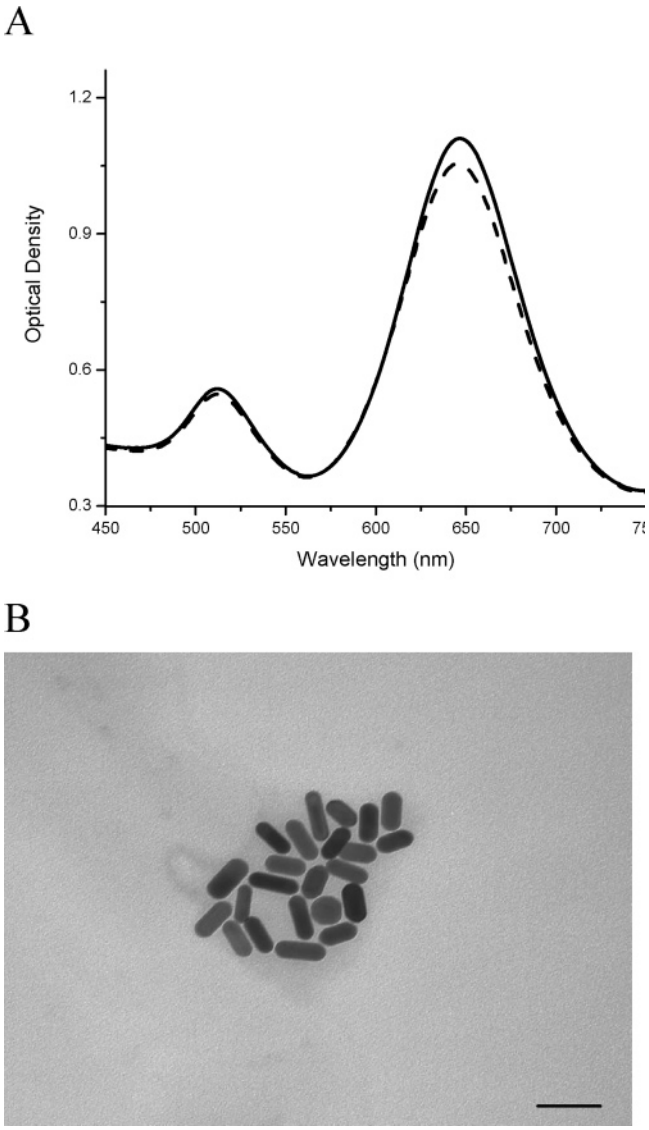


Figure 1. A. Absorption spectra of gold nanorods (solid line) and peptide conjugated gold nanorods (dashed line). B. TEM image of gold nanorods. Scale bar: 50 nm.

of the surfactants is bound to the gold surface via the surfactant headgroups. In our work, the thiolated peptide and gold nanorod solution are left for up to 72 h. The absorption spectra in Figure 1 show that there is no change in the peak position after CTAB replacement, but the peak intensity decreases slightly. This intensity damping is due to the increase of the positive charge on the capping molecules when positive CTAB is replaced by more positively charged peptide molecules.

SERS of the Peptide-Conjugated Gold Nanorods. Figure 2 shows a comparison of the Raman spectrum of the peptide-conjugated gold nanorods with that of the pure peptide and CTAB-capped gold nanorods. It can be seen that the Raman spectrum of the peptide-conjugated gold nanorods show some signals from CTAB molecules, which indicates that a small proportion of the CTAB molecules remained on the rod surface. It is very interesting to note that the amide I C═O stretching vibration of the peptide at 1665 cm^{-1} is not enhanced when it is bound to the nanorod surface. The CH bending at 1432 cm^{-1} for the peptide is shifted to 1440 cm^{-1} on the rod surface. The amide III C−N stretching at 1240 cm^{-1} is the same for peptide and peptide bound to gold nanorods. The amide II N−H vibrations (1500−1570 cm^{-1} region) are not observed in both the peptide powder and the peptide bound onto gold nanorods. The thioalkyl-triazole linker shows a strong CH_2 rocking

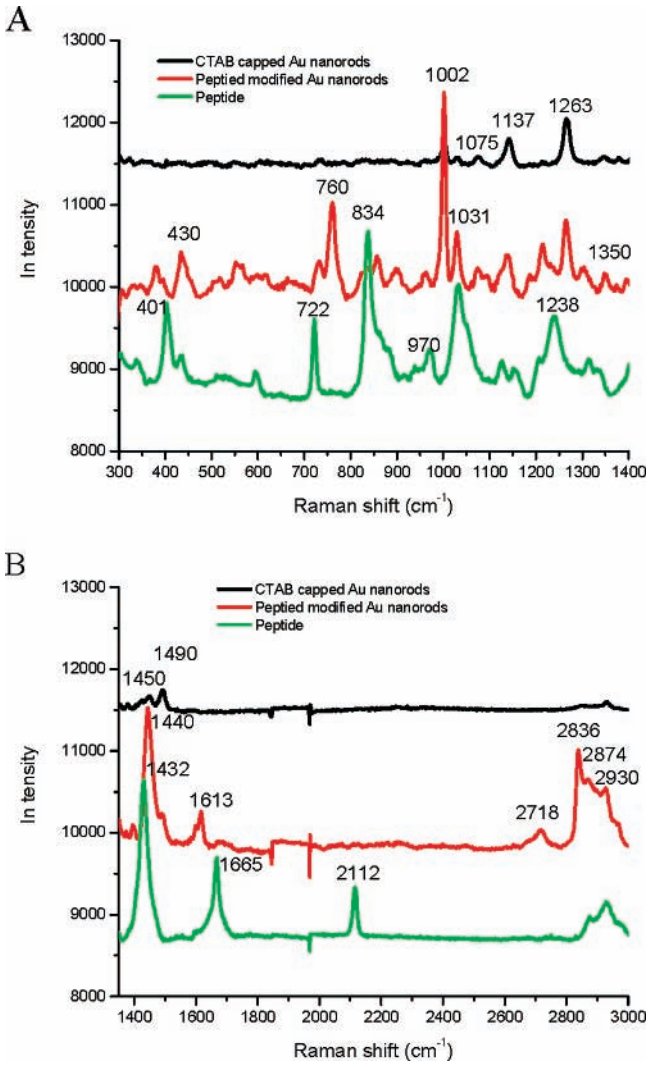


Figure 2. SERS of CTAB capping molecules on gold nanorods, thioalkyl−triazole−peptide on gold nanorods and Raman spectrum of peptide. A. 300−1400 cm^{-1} region. B. 1400−3000 cm^{-1} region.

vibration at 760 cm^{-1} (*75*) and C−C stretch at 1092 cm^{-1} (*75*, *76*). The CH bending is found to overlap with the CH bending in the peptide at 1440 cm^{-1} (*52*). The C−N stretch in CTAB molecules overlaps with C−N stretch in the thioalkyl-triazole to give a strong peak at 1002 cm^{-1} (*52*). The C−H stretching vibrations of the peptide, the thioalkyl-triazole, and the CTAB are at 2836 cm^{-1} and 2930 cm^{-1} (*52*, *76*). The peptide residues show their strong COO^- deformation at 722 cm^{-1} (*77*). The signal at 831 cm^{-1} is assigned to the proline and valine C−C stretch, and the 1031 cm^{-1} signal is assigned to C−N stretch vibrations from glycine and proline (*77*).

The CTAB capping molecules show strong Raman bands at 1137 cm^{-1} for the C−C stretch vibrations, 1267 cm^{-1} for δ (CH) of the $CH_2-N+(CH_3)_3$ groups and 1450 cm^{-1} and 1490 cm^{-1} for CH_2 bending vibrations (*52*). From Figure 2, it can be seen that these bands are still observed in the Raman spectrum of the peptide-conjugated gold nanorods due to the incomplete replacement of the CTAB molecules. In comparison to the Raman spectrum of the antibody-conjugated gold nanorods in which CTAB molecules are not replaced (*78*), the intensity of these bands in the peptide-conjugated gold nanorods are much weaker due to the replacement of the capping molecules with the thiolated peptide.

Light Scattering Images of Peptide-Conjugated Gold Nanorods Inside Cells. Figure 3 shows the dark field light scattering images of cells after incubation with 1nM CTAB

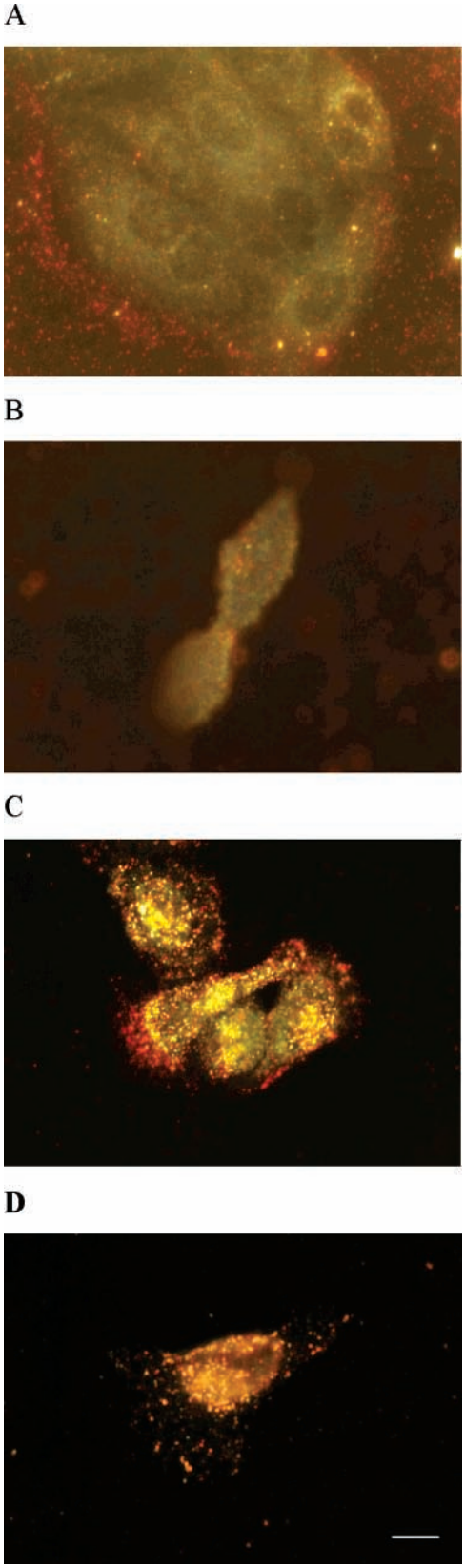


Figure 3. Dark field light scattering images of cells after incubation with gold nanorods and peptide-conjugated gold nanorods for 2 h. A. HaCat normal cells incubated with gold nanorods. B. HSC cancer cells incubated with gold nanorods. C. HaCat normal cells incubated with peptide-conjugated gold nanorods. D. HSC cancer cells incubated with peptide-conjugated gold nanorods. Peptide conjugation promotes the cellular uptake of gold nanorods. Scale bar: 10 μm.

capped nanorods and 1nM thioalkyl−triazole−peptide conjugated gold nanorods for 2 h. It can be seen clearly that, while the CTAB-capped gold nanorods are not efficiently absorbed by the cells, the thioalkyl−triazole−peptide conjugated gold nanorods enter into both cell lines with much higher efficiency. This result indicates that peptide conjugation enhances the cellular uptake of the gold nanorods. Importantly, it is worth noting that the observed enhancement of gold nanorod uptake took place in medium containing a very low concentration of peptide-conjugated nanorods (~1 nM) within a very short incubation time (2 h). This enhanced gold nanorod uptake may be due to the receptor-mediated endocytosis. Moreover, we observed that the thioalkyl−triazole−peptide conjugated nanorods are distributed into both nucleus and cytoplasm in either normal or cancer cells. However, the nanorods are more concentrated in the nucleus of the cancer cells. Reasons for increased nuclear distribution particles in the malignant cells could reflect increased specific and active uptake of the NLS peptide or decreased regulation of passive uptake of cytoplasmic components due to the disruption of the normal cellular process. It is quite possible that the nuclear pores of the nuclear membrane which routinely restrict entrance into the nucleus may be faulty and thereby facilitate the penetration of the peptide-conjugated nanorods into the nucleus. Identification of alterations in cellular pathways, such as nuclear pore function, by this multimodal method suggests further avenues of investigation that may yield novel methods of exploiting cellular defects of carcinogenesis for therapeutic applications.

SERS of Peptide-Conjugated Gold Nanorods Inside Cells. The Raman spectra of cells incubated with the peptide-conjugated gold nanorods are also measured (Figure 4). The Raman laser spot covers the major part of a single cell. Statistically, over twenty cells for each cell line are measured. They gave similar spectra with slight differences in some peak intensities. Shown in Figure 4A,B are five typical spectra for both normal and cancer cells. Figure 4C compares a typical spectrum of a normal and cancer cell as well as the spectrum when the peptide-conjugated nanorods are outside the cells. Spectra of the peptide-conjugated gold nanorods reveal a difference pre- and post-cellular uptake. New bands at 620, 655, and 1158 cm^{-1} are observed after cellular translocation of the conjugates. The 620 cm^{-1} band is due to protein COO^- wag vibrations and tyrosine δ (ring) vibrations (*79*). The 655 cm^{-1} band is due to an overlapping of a strong tyrosine vibration and the guanine bands (*36*, *80*). The DNA backbone vibrations are reflected most likely at bands in the region between 1030 and 1137 cm^{-1}, such as 1058 cm^{-1} for the DNA C−O stretch (*76*) and 1094 cm^{-1} for O−P−O vibrations (*81*). The 1155 cm^{-1} band could be assigned to chromatin and histone octamer Raman signals (*80*). The intensities around 820 and 850 cm^{-1} bands are greatly increased inside the cells. This indicates that such residues as phenylalanine (830 cm^{-1}, CH_2 rock) and tyrosine (850 cm^{-1}, ring breath) in cell proteins (*77*) are probably enhanced. The lysine Raman signal at 900 cm^{-1} (*77*) in the peptide is shifted to 914 cm^{-1} when it is present inside the cells, suggesting interaction of this residue with the cell components. The Raman intensity of the thioalkyl-triazole C−N stretch band at 760 cm^{-1} inside the cell is greatly decreased in comparison to that outside the cells. This suggests a change in linker conformation upon nanorod translocation into the cells.

The normal and cancer cells show some differences in their Raman signals as well. The 731 cm^{-1} line which is assigned to adenine (*82*) is stronger in the cancer cells than that in the normal cells. In addition, a peak at 398 cm^{-1} is observed only in cancer cells. All these spectral differences might be useful for cancer diagnostics.

Feld, Kneipp, and some other groups have demonstrated that individual and aggregated gold nanospheres could be useful for single cell micro-Raman spectroscopy (*32*−*38*). However, the

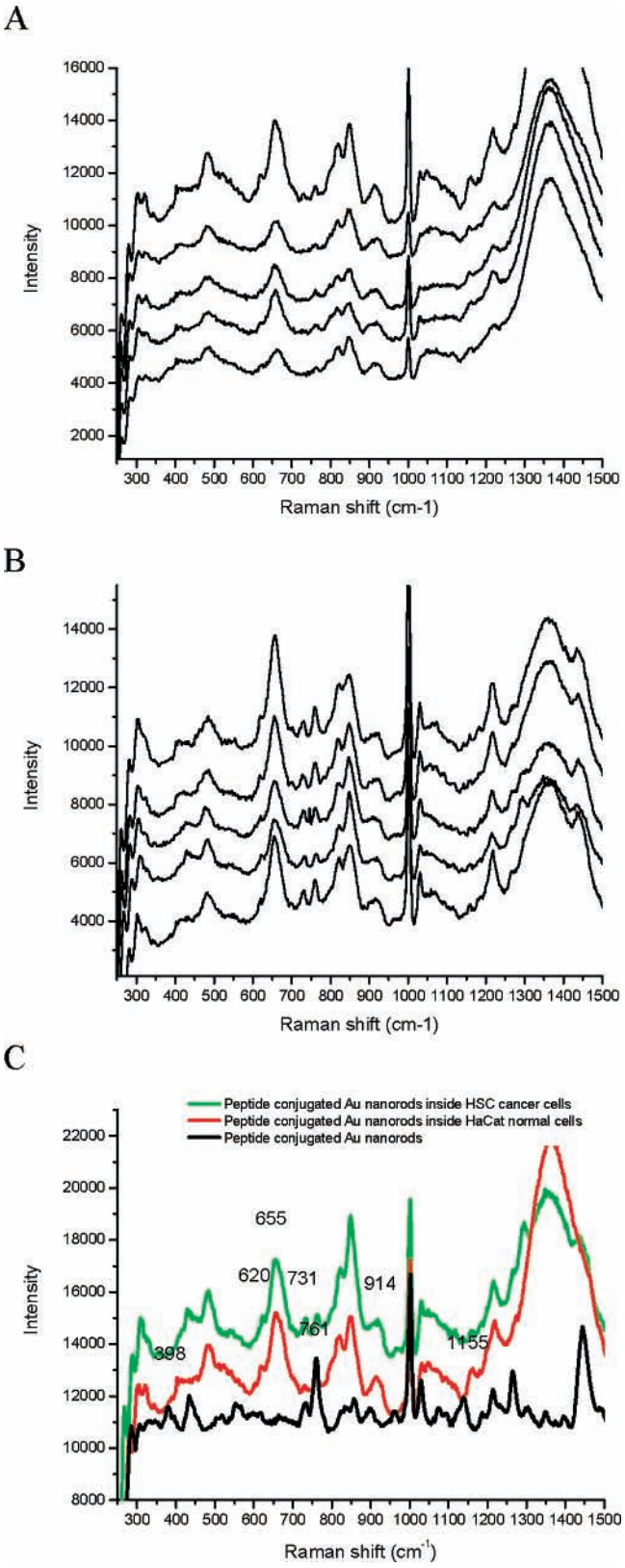


Figure 4. Raman spectra of peptide-conjugated gold nanorods inside HaCat normal cells (A) and HSC cancer cells (B). The Raman spectrum of the peptide-conjugated gold nanorods outside cells is shown in (C) as the bottom curve for comparison. Raman spectra from five cells for each cell line are shown.

inability of controlled delivery of the particles within the cell has limited their applications. The data in this project suggest that the intracellular distribution of the particles inside the cell can be controlled and simultaneously provides information regarding the local biochemical environment. Identification of spectral differences, such as an increased adenine signal within the cancer cell nucleus, provides detailed biochemical information at the molecular level with concurrent imaging of the particles in subcellular compartments. This multiomodal and ultrasensitive probe has a significant potential for a range of investigative and medical diagnostic applications.

CONCLUSIONS

We have demonstrated in this work that gold nanorods, directly conjugated to a SV40 virus NLS peptide through a thioalkyl-triazole linker, could be efficiently delivered into cells within a very short time. Multimodal optical sensing is available with Raman spectroscopy and dark field light scattering imaging. The peptide-conjugated gold nanorods are translocated into both the cytoplasm and the nucleus portion. Raman spectra reveal an enhanced signal of the NLS peptide as well as molecules from both the cytoplasm and the nucleus. In addition, in this pilot study, the Raman signal distinguishes the malignant from nonmalignant cells. This study demonstrates that gold nanorods can be used for nuclear targeting as a novel type of imaging-based contrast agents and an ultrasensitive Raman probe for intracellular molecular sensing as well.

ACKNOWLEDGMENT

M.A.E. thanks the Miller Foundation at the University of California at Berkeley for their hospitality during his tenure as a Miller visiting professor. We thank Professor Paul Edmonds for the use of his cell culture facilities. We also like to thank the support of NCI Center of Cancer Nanotechnology Excellence (CCNE) Award (U54CA119338).

Supporting Information Available: ^{1}H NMR spectra of compounds **1**−**5** and LSMS spectra of compound **5**. This material is available free of charge via the Internet at http://pubs.acs.org.

LITERATURE CITED

(1) Rawat, M., Singh, D., Saraf, S., and Saraf, S. (2006) Nanocarriers: promising vehicle for bioactive drugs. *Biol. Pharm. Bull. 29* (9), 1790−1798.

(2) Petrak, K. (2006) Nanotechnology and site-targeted drug delivery. *J. Biomater. Sci. Polym. Ed. 17* (11), 1209−1219.

(3) Rabinow, B., and Chaubal, M. V. (2006) Injectable nanoparticles for efficient drug delivery. *Drugs Pharm. Sci. 159*, 199−229.

(4) Chavanpatil, M. D., Khdair, A., and Panyam, J. (2006) Nanoparticles for cellular drug delivery: mechanisms and factors influencing delivery. *J. Nanosci. Nanotechnol. 6* (9/10), 2651−2663.

(5) Hayat, M. A. (1970) Principles and techniques of electron microscopy: biological applications. Van Nostrand Reihold, New York.

(6) Bruchez, M., Jr., Moronne, M., Gin, P., Weiss, S., and Alivisatos, A. P. (1998) Semiconductor nanocrystals as fluorescent biological labels. *Science 281*, 2013−2016.

(7) Chan, W. C. W., and Nie, S. (1998) Quantum dot bioconjugates for ultrasensitive nonisotopic detection. *Science 281,* 2016−2018.

(8) Wu, X., Liu, H., Liu, J., Haley, K. N., Treadway, J. A., Larson, J. P., Ge, N., Peale, F., and Bruchez, M. P. (2003) Immunofluorescent labeling of cancer marker Her2 and other cellular targets with semiconductor quantum dots. *Nat. Biotechnol. 21*, 41−46.

(9) Santra, S., Dutta, D., Walter, G. A., and Moudgil, B. M. (2005) Fluorescent nanoparticle probes for cancer imaging. *Technol. Cancer Res. Treat. 4* (6), 593−602.

(10) Brigger, I., Dubernet, C., and Couvreur, P. (2002) Nanoparticles in cancer therapy and diagnosis. *Adv. Drug Delivery Rev. 54* (5), 631−651.

(11) Holm, B. A., Bergey, E. J., De, T., Rodman, D. J., Kapoor, R., Levy, L., Friend, C. S., and Prasad, P. N. (2002) Nanotechnology in biomedical applications. *Mol. Cryst. Liq. Cryst. 374*, 589−598.

(12) Moghimi, S. M., Hunter, A. C., and Murray, J. C. (2005) Nanomedicine: current status and future prospects. *FASEB J. 19* (3), 311−330.
(13) Jain, K. K. (2005) Nanotechnology in clinical laboratory diagnostics. *Clin. Chim. Acta 358* (1−2), 37−54.
(14) Hirsch, L. R., Stafford, R. J., Bankson, J. A., Sershen, S. R., Rivera, B., Rrice, R. E., Hazle, J. D., Halas, N. J., and West, J. L. (2003) Nanoshell-mediated near-infrared thermal therapy of tumors under magnetic resonance guidance. *Proc. Natl. Acad. Sci. U.S.A. 100*, 13549−13554.
(15) O'Neal, D. P., Hirsch, L. R., Halas, N. J., Payne, J. D., and West, J. L. (2004) Photo-thermal tumor ablation in mice using near infrared-absorbing nanoparticles. *Cancer Lett. 209* (2), 171−176.
(16) Loo, C., Lin, A., Hirsch, L., Lee, M. H., Barton, J., Halas, N., West, J., and Drezek, R. (2004) Nanoshell-enabled photonics-based imaging and therapy of cancer. *Technol. Cancer Res. Treat. 3* (1), 33−40.
(17) Loo, C., Lowery, A., Halas, N., West, J., and Drezek, R. (2005) Immunotargeted nanoshells for integrated cancer imaging and therapy. *Nano Lett. 5* (4), 709−711.
(18) Hainfeld, J. F., Slatkin, D. N., and Smilowitz, H. M. (2004) The use of gold nanoparticles to enhance radiotherapy in mice. *Phys. Med. Biol. 49*, N309−N315.
(19) Zharov, V. P., Galitovskaya, E. N., Johnson, C., and Kelly, T. (2005) Synergistic enhancement of selective nanophotothermolysis with gold nanoclusters: potential for cancer therapy. *Lasers Surg. Med. 37*, 219−226.
(20) El-Sayed, I. H., Huang, X., and El-Sayed, M. A. (2006) Selective laser photo-thermal therapy of epithelial carcinoma using anti-EGFR antibody conjugated gold nanoparticles. *Cancer Lett. 239* (1), 129−135.
(21) Khlebtsov, B., Zharov, V., Melnikov, A., Tuchin, V., and Khlebtsov, N. (2006) Optical amplification of photothermal therapy with gold nanoparticles and nanoclusters. *Nanotechnology 17*, 5167−5179.
(22) Pissuwan, D., Valenzuela, S., and Cortie, M. B. (2006) Therapeutic possibilities of plasmonically heated gold nanoparticles. *Trends Biotechnol. 24* (2), 62−67.
(23) Huang, X., El-Sayed, I. H., and El-Sayed, M. A. (2006) Cancer cell imaging and photothermal therapy in the near-infrared region by using gold nanorods. *J. Am. Chem. Soc. 128* (6), 2115−2120.
(24) Takahashi, H., Niidome, T., Nariai, A., Niidome, Y., and Yamada, S. (2006) Gold nanorod-sensitized cell death: microscopic observation of single living cells irradiated by pulsed near-infrared laser light in the presence of gold nanorods. *Chem. Lett. 35* (5), 500−501.
(25) Huff, T. B., Tong, L., Zhao, Y., Hansen, M. N., Cheng, J. X., and Wei, A. (2007) Hyperthermic effects of gold nanorods on tumor cells. *Nanomedicine 2* (1), 125−132.
(26) Sokolov, K., Robinson, C., Collier, T., Richards-Kortum, R., Follen, M., and Lotan, R. (2002) Metal nanoparticles as biospecific contrast agents for cancer imaging. *Trends Opt. Photonics 71*, 376−378.
(27) Sokolov, K., Follen, M., Aaron, J., Pavlova, I., Malpica, A., Lotan, R., and Richards-Kortum, R. (2003) Real-time vital optical imaging of precancer using anti-epidermal growth factor receptor antibodies conjugated to gold nanoparticles. *Cancer Res. 63* (9), 1999−2004.
(28) El-Sayed, I. H., Huang, X., and El-Sayed, M. A. (2005) Surface plasmon resonance scattering and absorption of anti-EGFR antibody conjugated gold nanoparticles in cancer diagnostics: Applications in oral cancer. *Nano Lett. 5* (5), 829−834.
(29) Loo, C., Hirsch, L., Lee, M. H., Chang, E., West, J., Halas, N., and Drezek, R. (2005) Gold nanoshell bioconjugates for molecular imaging in living cells. *Opt. Lett. 30* (9), 1012−1014.
(30) Stoeva, S. I., Lee, J. S., Smith, J. E., Rosen, S. T., and Mirkin, C. A. (2006) Multiplexed detection of protein cancer markers with biobarcoded nanoparticle probes. *J. Am. Chem. Soc. 128* (26), 8378−8379.
(31) Hainfeld, J. F., Slatkin, D. N., Focella, T. M., and Smilowitz, H. M. (2006) Gold nanoparticles: a new X-ray contrast agent. *Br. J. Radiol. 79* (939), 248−253.
(32) Manfait, M., Morjani, H., Millot, J. M., Debal, V., Angiboust, J. F., and Nabiev, I. (1990) Drug-target interactions on a single living cell. An approach by optical microspectroscopy. *Proc. SPIE Int. Soc. Opt. Eng. 1403*, 695−707.
(33) Nabiev, I., Morjani, H., and Manfait, M. (1991) Selective analysis of antitumor drug interaction with living cancer cells as probed by surface-enhanced Raman spectroscopy. *Eur. Biophys. J. 19*, 311−316.
(34) Manfait, M., Morjani, H., and Nabiev, I. J. (1992) Molecular events on single living cancer cells as studied by microspectrofluorometry and micro-SERS Raman spectroscopy. *J. Cell. Pharmacol. 3*, 120−125.
(35) Morjani, H., Riou, J. F., Nabiev, I., Lavelle, F., and Manfait, M. (1993) Molecular and cellular interactions between intoplicine, DNA, and Topoisomerase II studied by surface-enhanced Raman scattering spectroscopy. *Cancer Res. 53*, 4784−4790.
(36) Kneipp, K., Haka, A. S., Kneipp, H., Badizadegan, K., Yoshizawa, N., Boone, C., Shafer-Peltier, K. E., Motz, J. T., Dasari, R. R., and Feld, M. S. (2002) Surface-enhanced Raman spectroscopy in single living cells using gold nanoparticles. *Appl. Spectrosc. 56* (2), 150−154.
(37) Kneipp, J., Kneipp, H., Rice, W. L., and Kneipp, K. (2005) Optical probes for biological applications based on surface-enhanced Raman scattering from indocyanine green on gold nanoparticles. *Anal. Chem. 77*, 2381−2385.
(38) Schluecker, S., Kuestner, B., Punge, A., Bonfig, R., Marx, A., and Stroebel, P. (2006) Immuno-Raman microspectroscopy: in situ detection of antigens in tissue specimens by surface-enhanced Raman scattering. *J. Raman Spectrosc. 37* (7), 719−721.
(39) Turkevich, J., Stevenson, P. C., and Hillier, J. (1951) The nucleation and growth processes in the synthesis of colloidal gold. *Discuss. Faraday Soc.* (11), 55−75.
(40) Hayat, M. A. (1989) Colloidal gold: principles, methods and applications, Vol 1, Academic Press, San Diego.
(41) Mie, G. (1908) Contributions to the optics of turbid media, especially colloidal metal solutions. *Ann. Phys. 25*, 377−445.
(42) Link, S., and El-Sayed, M. A. (2000) Shape and size dependence of radiative, non-radiative and photothermal properties of gold nanocrystals. *Int. Rev. Phys. Chem. 19* (3), 409−453.
(43) Link, S., and El-Sayed, M. A. (2003) Optical properties and ultrafast dynamics of metallic nanocrystals. *Annu. Rev. Phys. Chem. 54*, 331−366.
(44) Lee, K. S., and El-Sayed, M. A. (2006) Gold and silver nanoparticles in sensing and imaging: sensitivity of plasmon response to size, shape, and metal composition. *J. Phys. Chem. B 110*, 19220−19225.
(45) Connor, E. E., Mwamuka, J., Gole, A., Murphy, C. J., and Wyatt, M. D. (2005) Gold nanoparticles are taken up by human cells but do not cause acute cytotoxicity *Small 1* (3), 25−327.
(46) Tkachenko, A. G., Xie, H., Coleman, D., Glomm, W., Ryan, J., Anderson, M. F., Franzen, S., and Feldheim., D. L. (2003) Multifunctional gold nanoparticle-peptide complexes for nuclear targeting. *J. Am. Chem. Soc. 125*, 4700−4701.
(47) Tkachenko, A. G., Xie, H., Liu, Y., Coleman, D., Ryan, J., Glomm, W. R., Shipton, M. K., Franzen, S., and Feldheim, D. L. (2004) Cellular trajectories of peptide-modified gold particle complexes: comparison of nuclear localization signals and peptide transduction domains. *Bioconjugate Chem. 15*, 482−490.
(48) Gans, R. (1915) Form of ultramicroscopic particles of silver. *Ann. Phys. 47*, 270−284.
(49) Link, S., Mohamed, M. B., and El-Sayed, M. A. Simulation of the optical absorption spectra of gold nanorods as a function of their aspect ratio and the effect of the medium dielectric constant. *J. Phys. Chem. B 103*, 3073−3077.
(50) Link, S., and El-Sayed, M. A. (2005) Additions and corrections to "Simulation of the optical absorption spectra of gold nanorods as a function of their aspect ratio and the effect of the medium dielectric constant". *J. Phys. Chem. B 109*, 10531−10532.
(51) Link, S., and El-Sayed, M. A. (1999) Spectral properties and relaxation dynamics of surface plasmon electronic oscillations in gold and silver nanodots and nanorods. *J. Phys. Chem. B 103*, 8410−8426.
(52) Nikoobakht, B., Wang, J., and El-Sayed, M. A. (2002) Surface-enhanced Raman scattering of molecules adsorbed on gold nanorods: off-surface plasmon resonance condition. *Chem. Phys. Lett. 366*, 17−23.
(53) Nikoobakht, B., and El-Sayed, M. A. (2003) Surface-enhanced Raman scattering studies on aggregated gold nanorods. *J. Phys. Chem. A 107* (18), 3372 -3378.

(54) Gole, A., Orendorff, C. J., and Murphy, C. J. (2004) Immobilization of gold nanorods onto acid-terminated self-assembled monolayers via electrostatic interactions. *Langmuir 20* (17), 7117−7122.
(55) Suzuki, M., Niidome, Y., Terasaki, N., Inoue, K., Kuwahara, Y., and Yamada, S. (2004) Surface-enhanced nonresonance Raman scattering of rhodamine 6G molecules adsorbed on gold nanorod films. *Jpn. J. Appl. Phys. 43* (4B), L554−L556.
(56) Laurent, G., Félidj, N., Aubard, J., Lévi, G., Krenn, J. R., Hohenau, A., Schider, G., Leitner, A., and Aussenegg, F. R. (2005) Evidence of multipolar excitations in surface enhanced Raman scattering. *Phys. Rev. B 71*, 045430−045436.
(57) Laurent, G., Félidj, N., Aubard, J., Lévia, G., Krenn, J. R., Hohenau, A., Schider, G., Leitner, A., and Aussenegg, F. R. (2005) Surface enhanced Raman scattering arising from multipolar plasmon excitation. *J. Chem. Phys. 122*, 011102−011104.
(58) Félidj, N., Laurent, G., Grand, J., Aubard, J., Lévi, G., Hohenau, A., Aussenegg, F. R., and Krenn, J. R. (2006) Far-field Raman imaging of short-wavelength particle plasmons on gold nanorods. *Plasmonics 1* (1), 35−39.
(59) Orendorff, C. J., Gearheart, L., Jana, N. R., and Murphy, C. J. (2006) Aspect ratio dependence on surface enhanced Raman scattering using silver and gold nanorod substrates. *Phys. Chem. Chem. Phys. 8*, 165−170.
(60) Liao, H., and Hafner, J. H. (2005) Gold nanorod bioconjugates. *Chem. Mater. 17*, 4636−4641.
(61) Niidome, T., Yamagata, M., Okamoto, Y., Akiyama, Y., Takahashi, H., Kawano, T., Katayama, Y., and Niidome, Y. (2006) PEG-modified gold nanorods with a stealth character for in vivo applications. *J. Controlled Release 114*, 343−347.
(62) Takahashi, H., Niidome, Y., Niidome, T., Kaneko, K., Kawasaki, H., and Yamada, S. (2006) Modification of gold nanorods using phosphatidylcholine to reduce cytotoxicity. *Langmuir 22*, 2−5.
(63) Chen, C. C., Lin, Y. P., Wang, C. W., Tzeng, H. C., Wu, C. H., Chen, Y. C., Chen, C. P., Chen, L. C., and Wu, Y. C. (2006) DNA-gold nanorod conjugates for remote control of localized gene expression by near infrared irradiation. *J. Am. Chem. Soc. 128*, 3709−3715.
(64) Chan, T. R., Hilgraf, R., Sharpless, K. B., and Fokin, V. V. (2004) Polytriazoles as copper(I)-stabilizing ligands in catalysis. *Org. Lett. 6*, 2853−2855.
(65) Shon, Y., Kelly, K. F., Halas, N. J., and Lee, T. R. (1999) Fullerene-terminated alkanethiolate SAMs on gold generated from unsymmetrical disulfides. *Langmuir 15*, 5329−5332.
(66) Nikoobakht, B., and El-Sayed, M. A. (2003) Preparation and growth mechanism of gold nanorods (NRs) using seed-mediated growth method. *Chem. Mater. 15*, 1957−1962.
(67) Kalderon, D., Roberts, B. L., Richardson, W. D., and Smith, A. E. (1984) A short amino acid sequence able to specify nuclear location. *Cell 39*, 499−509.
(68) Kalderon, D., Richardson, W. D., Markham, A. F., and Smith, A. E. (1984) Sequence requirements for nuclear location of simian virus 40 large-T antigen. *Nature (London) 311*, 33−38.
(69) Goldfarb, D. S., Gariepy, J., Schoolnik, G., and Kornberg, R. D. (1986) Synthetic peptides as nuclear localization signals. *Nature (London) 322*, 641−644.
(70) Feldherr, C. M., Lanford, R. E., and Akin, D. (1992) Signal-mediated nuclear transport in simian virus 40-transformed cells is regulated by large tumor antigen. *Proc. Natl. Acad. Sci. U.S.A. 89*, 11002−11005.
(71) Dietz, G. P., and Bahr, M. (2004) Delivery of bioactive molecules into the cell: the Trojan horse approach. *Mol. Cell. Neurosci. 27*, 85−131.
(72) Numerous examples of click chemistry have appeared in the literature (a comprehensive list is available at www.scripps.edu/chem/sharpless/click.html). Cited here are two pioneering examples: (i) Rostovtsev, V. V., Green, L. G., Fokin, V. V., and Sharpless, K. B. (2002) A stepwise Huigsen cycloaddition process: copper (I)-catalyzed regioselective "ligation" of azides and terminal alkynes. *Angew. Chem., Int. Ed.* 41, 2596−2599. (ii) Tornoe, C. W., Christensen, C., and Meldal, M. (2002) Peptidotriazoles on solid phase: [1,2,3]-triazoles by regiospecific copper (I)-catalyzed 1,3-dipolar cycloadditions of terminal alkynes to azides. *J. Org. Chem. 67*, 3057−3064.
(73) Dujardin, E., Hsin, L. B., Wang, C. R. C., and Mann. S. (2001) DNA-driven self-assembly of gold nanorods. *Chem. Commun.* 1264−1265.
(74) Nikoobakht, B., and El-Sayed, M. A. (2001) Evidence for bilayer assembly of cationic surfactants on the surface of gold nanorods. *Langmuir 17*, 6368−6374.
(75) Bryant, M. A., and Pemberton, J. E. (1991) Surface Raman scattering of self-assembled monolayers formed from 1-alkanethiols: behavior of films at gold and comparison to films at silver. *J. Am. Chem. Soc. 113* (22), 8284−8293.
(76) Shafer-Peltier, K. E., Haynes, C. L., Glucksberg, M. R., and Van Duyne, R. P. (2003) Toward a glucose biosensor based on surface-enhanced raman scattering. *J. Am. Chem. Soc. 125* (2), 588−593.
(77) Stewart, S., and Fredericks, P. M. (1999) Surface-enhanced Raman spectroscopy of amino acids adsorbed on an electrochemically prepared silver surface. *Spectrochim. Acta, Part A 55*, 1641−1660.
(78) Huang, X., El-Sayed, I. H., Qian, W., and El-Sayed, M. A. Cancer cells assemble and align gold nanorods *conjugated* to *antibodies to* produce highly enhanced, sharp and polarized surface Raman spectra: a potential cancer diagnostic marker. *Nano Lett*. in press.
(79) Grabbet, E. S., and Buck, R. P. (1989) Surface-enhanced Raman spectroscopic investigation of human immunoglobulin G adsorbed on a silver electrode. *J. Am. Chem. Soc. 111* (22), 8362−8366.
(80) Peticolas, W. L., Patapoff, T. W., Thomas, G. A., Postlewait, J., and Powell, J. W. (1996) Laser Raman microscopy of chromosomes in living eukaryotic cells: DNA polymorphism in vivo. *J. Raman Spectrosc. 27*, 571−578.
(81) Puppels, G. J., Olminkhof, J. H. F., Segers-Nolten, G. M. J., Otto, C., Demul, F. F. M., and Greve, J. (1991) Laser irradiation and Raman spectroscopy of single living cells and chromosomes: sample degradation occurs with 514.5 nm but not with 660 nm laser light. *Exp. Cell Res. 195* (2), 361−367.
(82) Nabie, I. R., Sokolov, K. V., and Voloshin, O. N. (1990) Surface-enhanced Raman spectroscopy of biomolecules. Part III: Determination of the local destabilization regions in the double helix. *J. Raman Spectrosc. 21*, 333−335.

BC070132I

A Macrophage−Nanozyme Delivery System for Parkinson's Disease

Elena V. Batrakova,*[,†,‡] Shu Li,[†,‡] Ashley D. Reynolds,[§] R. Lee Mosley,[§] Tatiana K. Bronich,[†,‡] Alexander V. Kabanov,[†,‡,⊥] and Howard E. Gendelman[†,§,∥]

Center for Drug Delivery and Nanomedicine, Department of Pharmaceutical Sciences, Center for Neurovirology and Neurodegenerative Disorders, and Department of Pharmacology and Experimental Neuroscience, University of Nebraska Medical Center, Omaha, Nebraska, and Department of Chemistry, M.V. Lomonosov Moscow State University, Moscow, Russia. Received May 23, 2007; Revised Manuscript Received July 16, 2007

Selective delivery of antioxidants to the substantia nigra pars compacta (SNpc) during Parkinson's disease (PD) can potentially attenuate oxidative stress and as such increase survival of dopaminergic neurons. To this end, we developed a bone-marrow-derived macrophage (BMM) system to deliver catalase to PD-affected brain regions in an animal model of human disease. To preclude BMM-mediated enzyme degradation, catalase was packaged into a block ionomer complex with a cationic block copolymer, polyethyleneimine-poly(ethylene glycol) (PEI-PEG). The self-assembled catalase/PEI-PEG complexes, "nanozymes", were ca. 60 to 100 nm in size, stable in pH and ionic strength, and retained antioxidant activities. Cytotoxicity was negligible over a range of physiologic nanozyme concentrations. Nanozyme particles were rapidly, 40−60 min, taken up by BMM, retained catalytic activity, and released in active form for greater than 24 h. In contrast, "naked" catalase was rapidly degraded. The released enzyme decomposed microglial hydrogen peroxide following nitrated alpha-synuclein or tumor necrosis factor alpha activation. Following adoptive transfer of nanozyme-loaded BMM to 1-methyl 4-phenyl 1,2,3,6-tetrahydropyridine-intoxicated mice, ca. 0.6% of the injected dose were found in brain. We conclude that cell-mediated delivery of nanozymes can reduce oxidative stress in laboratory and animal models of PD.

INTRODUCTION

The need for delivery of therapeutic polypeptides to affected brain tissues in Alzheimer's and Parkinson's diseases, AD and PD) (*1*−*3*), infectious (meningitis, encephalitis, prion disease, and HIV-related dementia) (*4*, *5*), stroke (*6*, *7*), lysosomal storage (*8*, *9*), obesity (*10*, *11*), and other metabolic and inflammatory diseases of the central nervous system (CNS) is of immediate need and cannot be overstated.

An important component of metabolic and degenerative diseases of the nervous system involves inflammation (*12*). Such inflammatory activities are profound, as they lead to excessive production of pro-inflammatory products and reactive oxygen species (ROS) that lead in part, to cell death and neurodegeneration. We posit that by affecting neuroinflammatory activities during disease, such as through the use of targeted antioxidants or drugs that inhibit the production or formation of pro-inflammatory cytokines and eicosanoids, the levels of ROS as well as other neurotoxins could be reduced, resulting in improved disease outcomes (*13*). However, such approaches have been limited, as drugs must not only penetrate the BBB but also find themselves in sufficient concentrations to affect ongoing disease mechanisms. Moreover, as inflammatory mechanisms are a likely early event for disease, therapeutic modalities must be used early and frequently. The limitation of drug delivery is one major obstacle confronting the development of new treatment paradigms for nervous system disorders.

One such disease is PD, the second most prevalent neurodegenerative disorder in people over 65. This disease is characterized by lack of the neurotransmitter dopamine due to a loss of dopaminergic neurons within the SNpc and their innervations to the striatum. PD neuropathology involves brain inflammation, microglia activation, and subsequent secretory neurotoxic activities, including ROS production, that play crucial roles in cell damage and death (*14*−*17*). PD brains show reduced levels of antioxidant enzymes and antioxidants (*18*−*20*) resulting in a reduced capacity to manage oxidative stress and associated neurodegeneration. Mounting evidence supports the notion that antioxidants can inhibit inflammatory responses and protect dopaminergic neurons in laboratory and animal models of PD (*21*−*27*). Catalase catalyzes the conversion of hydrogen peroxide, a known ROS, to water and molecular oxygen with one of the highest turnover rates for all known enzymes. In an *in vitro* model of PD, catalase was shown to rescue primary cultured cerebellar granule cells from ROS toxic effects (*13*, *28*). Furthermore, a low molecular mass catalase activator, rasagiline, induced neuroprotection in a mouse model of PD (*29*). Few clinical trials have been performed using low molecular mass antioxidants, of which the most extensive used is α-tocopherol and deprenyl to inhibit the rate of PD progression (*30*). However, and as described above, most of the trials failed to show significant improvements because of restricted transport of α-tocopherol across the blood−brain barrier (BBB) and the time following the disease the drugs were used (*31*).

Recent works from our laboratories demonstrate that bone-marrow derived monocytes (BMM) can be used as carriers of nanoformulated drugs, both in the periphery and across the BBB (*32*, *33*). Entry into the brain occurs as a consequence of the establishment of a chemokine gradient induced through neuroinflammatory responses (*34*, *35*). Thus, we have sought to develop replicate PD-like model systems for testing the utility

* Corresponding author. Tel: (402) 559-9364; fax (402) 559-9365; ebatrako@unmc.edu.

† Center for Drug Delivery and Nanomedicine, University of Nebraska Medical Center

‡ Department of Pharmaceutical Sciences, University of Nebraska Medical Center.

§ Center for Neurovirology and Neurodegenerative Disorders, University of Nebraska Medical Center.

∥ Department of Pharmacology and Experimental Neuroscience, University of Nebraska Medical Center.

⊥ M.V. Lomonosov Moscow State University.

10.1021/bc700184b CCC: $37.00 © 2007 American Chemical Society
Published on Web 08/31/2007

of cell-based delivery. First, divergent inflammatory cues were used to stimulate ROS production from microglia and included nitrated alpha synuclein (N-α-syn), thought to be released extracellularly in PD and elicit immune activation (*36*−*38*). Second, 1-methyl-4-phenyl-1,2,3,6-tetrahydropyridine (MPTP)-induced inflammation served as a gradient for BMM ingress into the brain. It is well-documented that following inflammatory cues, leukocytes are recruited to the brain through diapedesis and chemotaxis (*39*−*43*). Monocyte-macrophages can migrate across the brain paracellular spaces crossing junctional complexes of brain endothelial cells (*44*, *45*). Their combat arsenal consists of engulfing foreign particles and liberating engulfed substances by exocytosis. All together, these features make it possible to exploit macrophages as carriers to affect neuroinflammatory processes (*46*−*49*).

Here we used BMM as a vehicle for carriage of therapeutic concentrations of catalase to the brain. We found that a major obstacle for success in this approach is that macrophages efficiently disintegrate engulfed particles (*49*). Therefore, it is crucial to protect the activity of the enzyme inside of the cell-carrier. Incorporation into polymeric nanocarries (nanospheres, liposomes, micelles, nanoparticles) can provide such protection (*50*−*60*). Early work by V.A. Kabanov et al. demonstrated that use of interpolyelectrolyte complexes can immobilize enzymes (*61*−*63*). The enzyme polyelectrolyte complexes can be prepared at the nanoscale by self-assembly of enzymes with oppositely charged block polyelectrolytes containing ionic and nonionic water soluble blocks (*64*, *65*). The resulting nanoparticles contain a core of protein−polyelectrolyte complex surrounded by a shell of water soluble nonionic polymer such as polyethylene glycol (PEG). In the current work, we immobilized catalase by reacting it with a cationic block copolymer, polyethyleneimine-poly(ethylene glycol) (PEI-PEG), previously used for delivery of polynucleotides (*66*). The resulting block ionomer complexes of catalase ("nanozymes") are taken up by BMM. We present evidence that such modification protects catalase against degradation in BMM, that BMM release nanozymes in the external medium for at least 4−5 days, and that BMM can carry nanozymes to the brain in the MPTP model of PD.

EXPERIMENTAL PROCEDURES

Materials. Catalase from bovine liver, polyethylenimine (PEI) (2K, branched, 50% aq solution), sulforhodamine-B (SRB), sodium dodecylsulfate (SDS), Sephadex G-25, and Triton X-100 were purchased from Sigma-Aldrich (St-Louis, MO). Methoxypoly(ethylene glycol) epoxy (Me-PEG-epoxy) was purchased from Shearwater Polymer Inc., Huntsville, AL (custom synthesis).

BMM. Bone marrow cells extracted from murine femurs (C57BL/6, female mice) as described (*32*) were cultured for 10 days in the media supplemented with 1000 U/mL macrophage colony-stimulating factor (MCSF) (a generous gift from Wyeth Pharmaceutical, Cambridge, MA). The purity of monocyte culture was determined by flow cytometry using FACSCalibur (BD Biosciences, San Jose, CA).

Microglia. Brains from C57BL/6 neonates (1−3 days old) were removed, washed with ice-cold HBSS, and mashed into small pieces. Supernatant was replaced for 2.5% trypsin and DNAse solution (1 mg/mL) and incubated for 30 min at 37 °C, and then 1 mL of ice cold FBS with 10 mL HBSS was added. The mixture was centrifuged (5 min, 1500 rpm, 4 °C), and complete media with MCSF was added to the pellet. The cells were cultured until maturation (typically 10 days).

MPTP. For MPTP-intoxication recipient C57BL/6, mice were treated as described (*67*). After 12 h, MPTP-treated mice were injected i.v. with the 50 μCi/mouse of ^{125}I-labeled nanozyme alone or nanozyme loaded into BMM (10×10^6 cells/mouse, 4 mice/group). After 24 h mice were sacrificed and the amount of radioactivity in major organs (brain, spleen, liver, lungs, and kidney) was detected by 1480 gamma-counter Wizard 3 (Perkin-Elmer Life Sciences, Shelton, CT). The amount of the delivered enzyme was expressed as a percent of the injected dose for the whole organ.

PEI-PEG Conjugates. The copolymer was synthesized using a modified procedure (*68*) by conjugation of PEI and Me-PEG-epoxy. Briefly, Me-PEG-epoxy water solution was added to 5% PEI in water and incubated overnight at RT. To purify from the excess of PEI (as well as from low molecular weight residuals), the obtained conjugates were dialyzed in SpectraPore membrane tubes with cutoff 6000−8000 Da against water (twice replaced) for 48 h and then concentrated *in vacuo*. For final purification, the conjugate was dissolved in 20 mL of 100% methanol and then added dropwise to 400 mL of ether. The precipitate was centrifuged (400*g*, 5 min), washed twice with ether, and dried in an exicator. Detailed characterization of the product was performed by spectrophotometry and mass spectrometry as reported (*68*).

Block Ionomer Complexes. Given amounts of the catalase (1 mg/mL) and the block copolymer (2 mg/mL) were separately dissolved in phosphate-buffered saline (PBS) at RT. A solution of the enzyme was added dropwise to the block copolymer solution at constant stirring. The +/− charge ratio (Z) was calculated by dividing the amount of amino groups of PEI-PEG protonated at pH 7.4 (*66*) by the total amount of Gln and Asp in catalase. A combination of physicochemical methods (electrophoretic retention, dynamic light scattering (DLS), and transmission electron microscopy (TEM)) was used to characterize composition, size, dispersion stability, morphology, shape, and structure of the obtained nanoparticles, as described previously (*69*−*72*).

Electrophoretic Retention. The formation of polyion complexes was examined by acrylamide gel shift assay. Enzyme complexes at various Z were loaded in a 7.5% acrylamide gel with 5 mM Tris, 50 mM glycine, pH 8.3, under nondenaturizing conditions (in the absence of SDS) to preserve the complex. The protein bands were visualized with rabbit polyclonal anti-catalase (Ab 1877, Abcam Inc, Cambridge, MA; 1:6000) and secondary horseradish peroxidase anti-rabbit Ig Ab (Amersham Life Sciences, Cleveland, OH; 1:1500). The specific protein bands were visualized using a chemiluminescence kit (Pierce, Rockford, IL).

Light Scattering Measurements. Effective hydrodynamic diameter and zeta-potential of nanozymes was measured by photon correlation spectroscopy using 'ZetaPlus' Zeta Potential Analyzer (Brookhaven Instruments, Santa Barbara, CA) as described previously (*73*, *74*).

TEM. A drop of catalase/PEI-PEG dispersion ($Z = 1$) in PBS was placed on Formvar-coated copper grid (150 mesh, Ted Pella Inc., Redding, CA). The dried grid containing nanozymes was stained with vanadyl sulfate and visualized using a Philips 201 transmission electron microscope (Philips/FEI Inc., Briarcliff Manor, NY).

Catalase and Catalase Activity. The activity of the enzyme in polymer nanoparticles (*75*) was studied using the reaction rate of hydrogen peroxide decomposition by catalase or nanozymes at various charge ratios and was determined by monitoring the change in absorbance at 240 nm (the extinction coefficient of H_2O_2 is 44×10^6 M^{-1} cm^1).

Labeling Catalase with Alexa Fluor 594 and Rhodamine Isothiocyanate (RITC). For loading and release studies, the enzyme was labeled with Alexa Fluor 594 Protein Labeling Kit (A10239, Molecular probes, Inc., Eugene, OR) according to the manufacturers protocol. For confocal microscopy studies, cata-

lase was labeled with RITC. Briefly, catalase was dissolved in 0.1 M sodium carbonate buffer, pH 8.5 (1 mg/mL), and treated with RITC (10 mg/mL) in DMSO for 2 h at RT. Labeled catalase was purified from low molecular weight residuals by gel filtration on a Sephadex G-25 column (1 × 20 cm) in PBS at elution rate 0.5 mL min^{-1} and lyophilized.

Accumulation and Release of Nanozymes in BMM. BMM grown on 24-well plates (2.5 × 10^6cells/plate) (*76*, *77*) were preincubated with assay buffer (122 mM NaCl, 25 mM $NaHCO_3$, 10 mM glucose, 3 mM KCl, 1.2 mM $MgSO_4$, 0.4 mM K_2HPO_4, 1.4 mM $CaCl_2$, and 10 mM HEPES) for 20 min. Following preincubation, the cells were treated with the Alexa-Fluor 594 labeled enzyme (0.7 mg/mL) in assay buffer alone or nanozyme for various time points. After incubation, the cells were washed three times with ice-cold PBS and solubilized in Triton X 100 (1%). For measures of nanozyme released from BMM, loaded BMM were incubated with fresh media at various time points. Fluorescence in each sample was measured by a Shimadzu RF5000 fluorescent spectrophotometer (λ_{ex} = 580 nm, λ_{em} = 617 nm). The amount of nanozyme was normalized for protein content and expressed in μg of enzyme per mg of the protein for loading experiments and μg enzyme per mL media as mean ± SEM (n = 4).

Intracellular Localization of Nanozymes. Monocytes grown in the chamber slides (*77*) were exposed to RITC-labeled nanozyme (Z = 1) for 24 h at 37 °C. Following incubation, the cells were fixed in 4% paraformaldehyde and stained with F-actin-specific Oregon Green 488 phalloidin and a nuclear stain, ToPro-3 (Molecular Probes, Inc., Eugene, OR). Labeled cells were examined by a confocal fluorescence microscopic system ACAS-570 (Meridian Instruments, Okimos, MI) with argon ion laser (excitation wavelength, 488 nm) and corresponding filter set. Digital images were obtained using the CCD camera (Photometrics) and Adobe Photoshop software.

Antioxidant Activity Measures. Mature mouse BMM were loaded with the enzyme alone or nanozymes (Z = 1) for 1 h and washed with PBS, and fresh media was added to the cells. Following various time intervals, the media was collected and antioxidant activity of the enzyme released from BMM was assayed by the rate of hydrogen peroxide decomposition.

Ampex Red Dye Fluorescence Assay. Murine microglial cells seeded in 96-well plates (0.1 × 10^6 cells/well) were either stimulated with tumor necrosis factor alpha (TNF-α) (200 ng/mL) for 48 h or with nitrated alpha-synuclein (N-α-syn) (0.5 μM) to induce ROS production. In parallel, BMM grown in 24-well plates were loaded with "naked" catalase (1 mg/mL) or nanozyme for 1 h and then incubated with Krebs-Ringer buffer (145 mM NaCl, 4.86 mM KCl, 5.5 mM glucose, 5.7 mM NaH_2PO_4, 0.54 mM $CaCl_2$, 1.22 mM $MgCl_2$, pH 7.4) for 2 h to collect catalase released from the cells into the supernatant (Figure 5A). Following incubation, the supernatants collected from BMM loaded with "naked" catalase or nanozyme were supplemented with Ampex Red Dye stock solution (10 U/mL HRP, 10 mM Ampex Red). For N-α-syn stimulation of microglia, supernatants were also supplemented with 0.5 μM aggregated N-α-syn. Obtained solutions were added to the activated microglial cells, and the decomposition of ROS by "naked" catalase or nanozyme was measured by fluorescence at λ_{ex} = 563 nm, λ_{em} = 587 nm. The effect of the supernatants collected from nonloaded BMM or loaded with PEI-PEG alone on ROS decomposition was evaluated in comparison to the control experiments.

^{125}I-Labeling of Catalase Nanozyme. To obtain ^{125}I-labeled catalase nanozyme, the protein solution in PBS (1 mg/mL) was incubated for 15 min with Na^{125}I (1 mCi) in the presence of IODO-BEADS Iodination Reagent (Pierce, Rockford, IL) and then purified from nonconjugated label using D-salt Desalting Columns (Pierce, Rockford, IL). ^{125}I-labeled catalase (400 μCi/mL, 0.7 mg/mL) was supplemented with PEI-PEG block copolymer (Z = 1) and loaded into mature monocytes (80 × 10^6 BMM in 1 mL of medium) for 2 h at 37 °C. After incubation, the loaded monocytes were washed three times with ice-cold PBS.

Statistical Analysis. For the all experiments, data are presented as the mean ± SEM. Tests for significant differences between the groups were done using one-way ANOVA with multiple comparisons (Fisher's pairwise comparisons) using GraphPad Prism 4.0 (GraphPad software, San Diego, CA). A minimum p value of 0.05 was estimated as the significance level for all tests.

RESULTS

Manufacture and Testing of Nanozymes. Block ionomer complexes spontaneously form by mixing block ionomers with either oppositely charged surfactants or polyelectrolytes (*64*, *78*−*80*). Neutralization of the polyion charges leads to formation of hydrophobic domains, which segregate in aqueous media into a core of polyion complex micelles. Water-soluble nonionic segments of block ionomers (for example, PEG) prevent aggregation and macroscopic phase separation. As a result, these complexes self-assemble into particles of nanoscale size and form stable aqueous dispersions (Figure 1A). Catalase has a net negative charge under physiological conditions. Therefore, the polyion complexes were obtained in phosphate buffer (pH 7.4) by mixing the enzyme (1 mg/mL) and PEI-PEG (2 mg/mL), which is positively charged.

Catalase and PEI-PEG complexes were obtained at various +/− charge ratios (Z = from 0 to 4). They were subjected to electrophoresis under nondenaturizing conditions and then transferred to nitrocellulose membranes. The protein bands were visualized with antibodies to catalase (Figure 1B). The band intensity decreased as the copolymer increased. This suggested that complexes formed that were unable to enter the gel and was confirmed by DLS. Addition of PEI-PEG to catalase solution (1 mg/mL) resulted in particles of nanoscale size with relatively low polydispersity index (about 0.1−0.2), while no particles were detected for catalase alone.

Particle size depended on the charge ratio, ionic strength, and pH (Figure 1, parts C, D, and E). In PBS, the effective diameter increased as the charge ratio increased and then stabilized at ca. 90 to 100 nm at the charge ratio (Z) of 1 and above (Figure 1C). The zeta-potential was increased upon increasing the amount of the block copolymer (Figure 1C). At a constant charge ratio (Z = 1) large aggregates over 600 nm were formed in the absence of salt (Figure 1D). Addition of salt decreased the particle size which stabilized at ca. 90 nm as the NaCl concentration reached 0.15 M. It is likely that large nonequilibrium polyelectrolyte complex aggregates form upon mixing the catalase and PEI-PEG solutions. In the absence of salt these aggregates could not equilibrate and remained "frozen" due to a low rate of polyion interchange (*81*, *82*). As salt was added the polyion interchange was accelerated, resulting in formation of small (equilibrium) particles. These particles were stable in an approximate range of pH 7.4 to 11.5 but irreversibly aggregated when pH was decreased below or increased above this range (Figure 1E). Within this range the catalase and PEI-PEG were oppositely charged. The aggregation of the complexes was linked to protonation and charge inversion of catalase (pI = 6.5) at low or deprotonation of PEI at high pH. Overall, nanozyme particles were stable under physiological pH and ionic strength. Under these conditions the particles were close to spherical (Figure 1D). No changes in the enzymatic activity of catalase were observed at charge ratios used for subsequent cell loading, delivery, and release experiments (Supporting Information, Figure S-1).

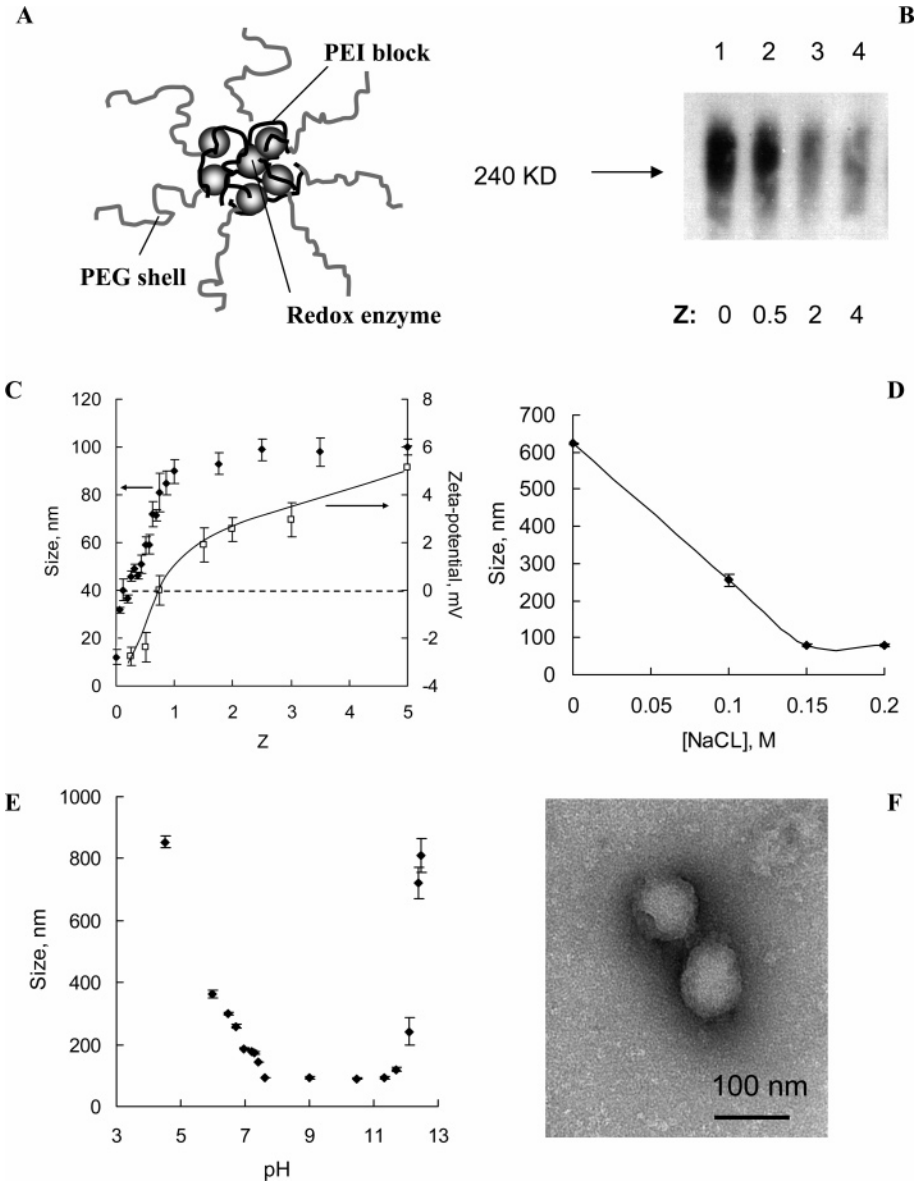


Figure 1. Characterization of catalase nanozyme. A: Schematic presentation of the enzyme-polyion complex structure. B: Gel retardation assay of the enzyme/polyion complexes at various Z. Samples were subjected to gel electrophoresis in polyacrylamide gel (7.5%) under nondenaturing conditions (without SDS). Line 1: enzyme alone; lines 2−4: enzyme/PEI-PEG complexes with progressive increasing of *Z* (0.5, 2, 4). C−E: Characterization of catalase/polyion complex by DLS. Changes in cumulant diameter (C−E) and zeta-potential (C) of catalase nanozyme with various: C: *Z* in PBS solutions; D: ionic strength ($Z = 1$, pH 7.4); E: pH ($Z = 1$, [NaCl] = 0.15M). F: TEM images of catalase nanozyme ($Z = 1$). Bar represents 100 nm.

Loading of Catalase Nanozymes in BMM. Initially, using the sulforhodamine-B (SRB) cell viability assay, we demonstrated that nanozymes (as well as catalase or copolymer alone) did not induce BMM cytotoxicity over a wide range of concentrations (0.03 to 1000 μg catalase per mL) (Supporting Information, Figure S-2). The accumulation kinetics suggested a rapid uptake of both free catalase and nanozyme in BMM (Figure 2A). Notably the free enzyme was taken up in BMM almost twice as fast as the nanozyme. At 60 min time point the loading of BMM with nanozyme was ca. 30 μg catalase/10^6 cells. The uptake of the nanozyme at the 60 min time point decreased as the charge ratio increased (Figure 2B), which may be due to the effect of the PEG corona. The confocal microscopy data suggested vesicular and/or cytoplasmic localization of RITC-labeled catalase administered to BBM in nanozyme (Figure 2C).

Nanozyme Release from BMM. Mature BMM were preloaded with Alexa Fluor 594-labeled catalase nanozyme (60 min) and then cultured in the fresh media for different time intervals. The loaded BMM released catalase in the external media for at least 4−5 days (Figure 3). During the same period, the amount of the enzyme associated with the cells was proportionally decreased. Exposure of nanozyme-loaded BMM to 10 μM phorbol myristate acetate (PMA), a potent activator of the protein kinase C pathway and ROS generation (*83*), enhanced enzyme release in the media by ca. 50% (Supporting Information, Figure S-3). This suggested that release of nanozyme from BMM may be dependent on cell activation.

BMM Released Nanozyme Activity. BBM loaded with "naked" catalase or nanozyme were placed in a fresh media, and the activity of the enzyme released in the media was determined at different incubation time intervals. Contrary to BMM loaded with free catalase that was practically inactive after the release, the nanozyme-loaded cells released active enzyme for at least 24 h (Figure 4A). The maximal activity of the released enzyme was observed for BMM loaded with nanozyme prepared at the stoichiometric ratio, $Z = 1$ (Figure 4B). All together, this suggests that incorporation of catalase

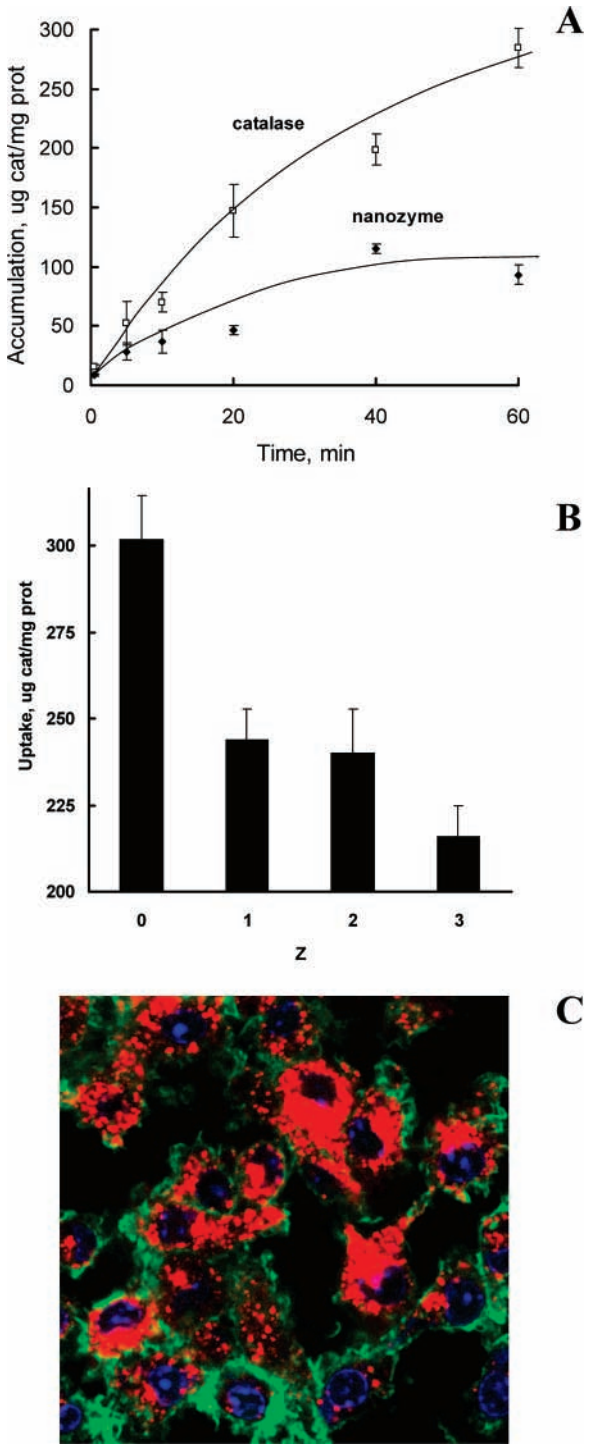


Figure 2. A: Kinetics of "naked" catalase and nanozyme ($Z = 1$) accumulation in monocytes. Cells were treated with the Alexa Fluor 594 labeled enzyme or nanozyme at various time points. Following incubation, the cellular content was collected, and the amount of fluorescence was measured by fluorescent spectrophotometer ($\lambda_{ex} =$ 580 nm, $\lambda_{em} = 617$ nm). Data represent means ± SEM ($n = 4$); B: Accumulation of catalase nanozymes in BMM at various Z. C: Intracellular localization of RITC-labeled catalase nanozyme in BMM. Cells grown on cover slips were loaded with catalase/PEI-PEG complex ($Z = 1$) (red staining) for 24 h. Following the incubation, the cells were fixed and stained with F-actin−specific Oregon Green 488 phalloidin (green) and a nuclear stain, ToPro-3 (blue). Images were obtained by confocal fluorescence microscopic system ACAS-570.

in a block ionomer complex with PEI-PEG results in protection and sustained release of active catalase from BMM.

Modulation of ROS Released by Activated Microglia. To assess the antioxidant capacity of the catalase nanoformulations

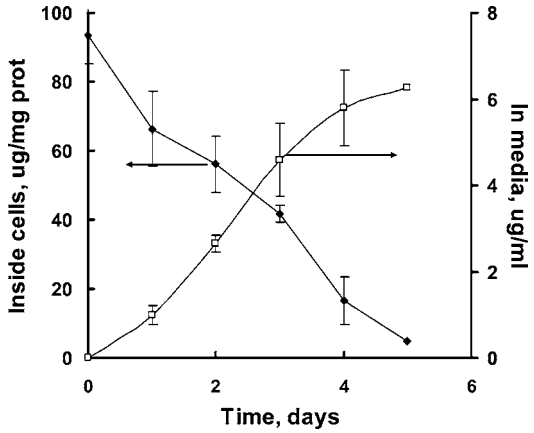


Figure 3. Release profile of catalase nanozyme from BMM. Cells were loaded with catalase/PEI-PEG complex ($Z = 1$) for 1 h, washed with PBS, and incubated with catalase-free media for various time intervals. Amount of catalase released into the media and retained in the cells was accounted by fluorescent spectrophotometry. Data represent means ± SEM ($n = 4$).

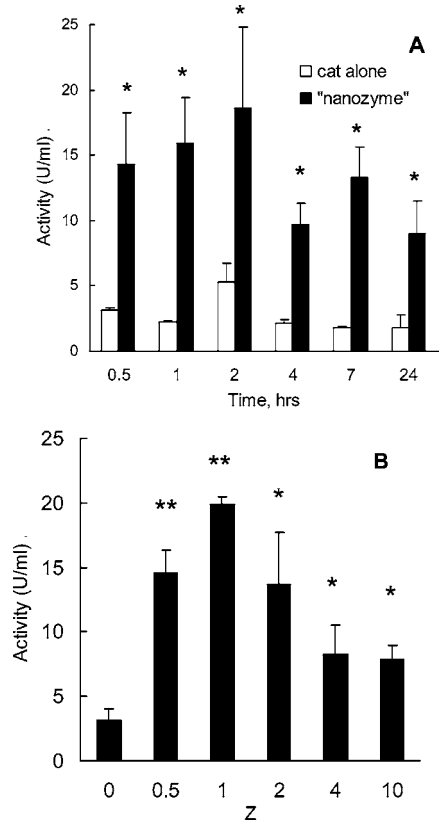


Figure 4. Preservation of enzymatic activity of catalase against degradation in BMM. A: "Naked" catalase or nanozyme ($Z = 1$) were loaded into BMM, and cells were washed and incubated with catalase-free media for various time intervals. The activity of catalase released from BMM was determined by spectrophotometry. B: Catalase polyion complexes with various compositions (Z) were loaded into the cells and incubated in catalase-free media for 2 h. Then, the media was collected and assessed for catalase activity by spectrophotometry. Data represent means ± SEM ($n = 4$). Statistical significance of nanozyme activity compared to catalase alone is shown by asterisks: (*) $p < 0.05$, (**) $p < 0.005$.

on microglial ROS production, BMM loaded with "naked' catalase or nanozyme were incubated for 2 h in Krebs-Ringer buffer, and the reluctant supernatant was then collected and added to TNF-α (200 ng/mL)-stimulated microglial cells. The catalase in the supernatants collected from the catalase- or nanozyme-loaded BMM decomposed hydrogen peroxide by

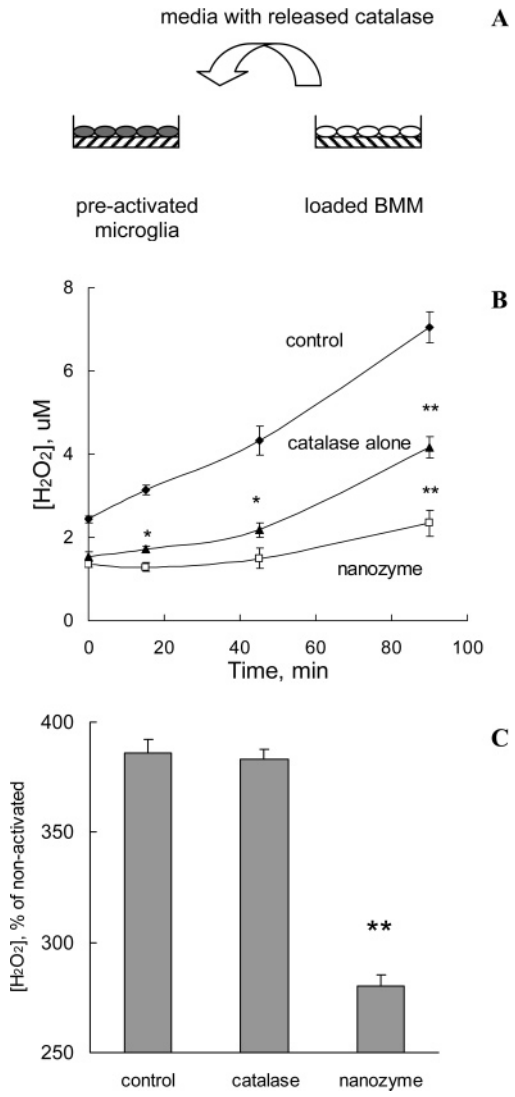


Figure 5. Modulation of microglial-derived ROS by catalase nanozyme released from BMM (A: overall scheme). "Naked" catalase or catalase nanozyme ($Z = 1$) were loaded into BMM. Then, cells were washed and incubated in Kreb's Ringer buffer for 2 h. In parallel, murine microglial cells were either stimulated with (B) 200 ng/mL TNF-α (48 h), or (C) 0.5 μM N-α-syn. Then, supernatants collected from BMM with the released enzyme were supplemented with Amplex Red and HRP solutions and added to the activated microglial cells. Control activated microglia was incubated with fresh media (B) or 0.5 μM aggregated N-α-syn (C). The amount of H_2O_2 produced by microglial cells and decomposed by catalase released from BMM was detected by fluorescence. Data represent mean ± SEM ($n = 6$). Statistical significance of the amount of H_2O_2 decomposed by released from BMM nanozyme or catalase, compared to activated microglia (control) is shown by asterisks: (*) $p < 0.05$, (**) $p < 0.005$.

microglia (Figure 5A). A greater effect was observed by nanozyme, which was consistent with its ability to preserve enzyme activity in carrier cells. Furthermore the supernatants collected from unloaded BMM (Figure 5B) or from BMM loaded with PEI-PEG alone (Supporting Information, Figure S-4) had little, if any, effect on the hydrogen peroxide level. To determine whether these findings could be reproduced in microglia activated by stimuli typically found in PD, cells were stimualted with 0.5 μM N-α-syn. Aggregated N-α-syn present as cytoplasmic bodies in PD are released following the death of dopaminergic neurons and are a major component of Lewy bodies (*84*) . These aggregated proteins are hypothesized to serve as a stimulus for microglial activation (*36*, *85*). Once again, the level of hydrogen peroxide was significantly reduced with

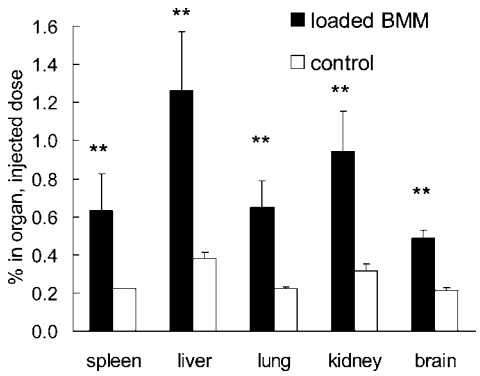


Figure 6. Biodistribution of ^{125}I-labeled nanozyme in MPTP-treated mice. Mice were injected with BMM (10×10^6 cells/mouse) loaded with catalase nanozyme ($Z = 1$, 50 μCi/mouse) or with nanozyme alone (control group). Twenty-four hours later mice were sacrificed and the amount of radioactivity was measured in various organs. Data represent mean ± SEM ($n = 4$). Statistical significance of the BMM-loaded nanozyme transport compared to the nanozyme alone group is shown by asterisks: (**) $p < 0.005$.

the addition of supernatants from nanozyme loaded BMM (Figure 5C). All together this study suggests that nanozyme released from BMM can attenuate oxidative stress resulting from activation of microglia.

Biodistribution of ^{125}I-labeled Catalase in MPTP-treated Mice. To determine if BMM carrying nanozyme could reach brain subregions with active neuroinflammatory disease reflective of human PD, we used the MPTP model. Two groups of MPTP-intoxicated C57Bl/6 mice were either injected intravenously with free nanozyme containing ^{125}I-labeled catalase or received adoptively transferred nanozyme-loaded BMM. Twenty four hours after injection there were significant increases in the radioactivity levels in spleen, liver, lung, kindney, and brain in the groups receiving adoptive transfer compared to groups treated with nanozyme alone (Figure 6). Noteworthy, after the adoptive transfer about 0.6% of the injected dose was found in the brain which was twice what was found in animals injected with free nanozyme. All together these data provide initial evidence that adoptive transfer of nanozyme loaded BMM can increase the delivery of the enzyme to the brain as well as other peripheral tissues known to be sites of macrophage tissue migration.

DISCUSSION

Efficient transport of therapeutic polypeptides to the brain is required for successful therapies for neurodegenerative and neuroinflammatory diseases. To this end, we examined whether BMM could be used as vehicles for delivery of a potent antioxidant, catalase. Indeed, it has long been known that macrophages and microglia as well as other mononuclear phagocytes can endocytose colloidal nanomaterials, for example, liposomes or nanosuspensions, and subsequently carry and release the drug to site of tissue injury, infection, or disease (*32*, *33*, *35*, *46*, *86*).

Moreover, the abilities of BMM to cross BBB was also investigated (*87*−*94*). In particular, it was demonstrated that monocytes infiltrate the brain in the MPTP mouse model of PD (*91*−*93*). Indeed, MPTP toxicity stimulated transient and global increases in the rate of monocyte infiltration into the midbrain, stratum, septum, and hippocampus. In these prior studies, the maximal accumulation of the monocyte-macrophages in the brain was observed 1 day after the MPTP treatment. On the basis of these data, we hypothesize that catalase-loaded monocytes adoptively transferred in MPTP-treated mice can deliver enzyme to regions of the brain most affected in PD and including the substantia nigra and striatum.

To protect against catalase degradation inside the BMM, the protein was immobilized in the block ionomer complex with a cationic block copolymer, PEI-PEG. The resulting nanoparticles, nanozymes, were ca. 60 to 100 nm in size and stable in physiological conditions (pH, ionic strength). We optimized the composition and structure of nanozymes to achieve high loading in BMM and preserve catalase activity. Internalization of foreign particles, as well as the exocytotic secretion, is one of the most basic functions in macrophages (*95*). This study demonstrated that BMM can accumulate a significant amount of nanozyme (ca. 30 μg catalase/10^6 cells) in a relatively short time period (about 40−60 min), followed by its sustained release during 4−5 days into the external media. This also suggested that nanozyme-loaded cells after adoptive transfer may have sufficient time to reach the brain and release catalase. Moreover, it was reported (*96*−*98*) that exocytosis can be stimulated by activation of monocytes and macrophages. Our experiment shows that release of nanozyme by BMM can be enhanced by stimulation with PMA.

We also demonstrate that block ionomer complex protects activity of catalase inside the host cells. Notably, the nanozyme-loaded BMM released active enzyme in the media for at least 24 h. Furthermore, the culture supernatants collected from nanozyme-loaded BMM had potent antioxidant effects in our assay for ROS produced by microglia activated with either N-α-syn or TNF-α. Thus, these cell culture models suggest that nanozyme-loaded BMM can mitigate oxidative stress that may be associated with the neurodegenerative process. Finally, we provide initial *in vivo* evidence that adoptive transfer of nanozyme-loaded BMM can increase delivery of labeled enzyme into the tissues including 2-fold increase in the amount of the enzyme in the brain in MPTP-treated mice. Interestingly, considerable amount of the labeled enzyme was also found in the brain after injection of the nanozyme alone. We cannot exclude that in this case the nanozyme may be taken up by circulating monocytes, which then carry the enzyme to the brain. Our further experiments will examine the possibilities for increasing nanozyme transport specifically to the areas of neurodegeneration and evaluate neuroprotective effects in PD models.

Overall, we demonstrate that BMM loaded with catalase incorporated into a protective polymer container and has therapeutic potential. We are cautiously optimistic that these studies will lead to development of new technologies based on cell-mediated delivery of therapeutic polypeptides that can attenuate oxidative stress and elicit anti-inflammatory responses that may be widely useful in the treatment of neurodegenerative disorders.

ACKNOWLEDGMENT

This study was supported by Tobacco Settlement Funds awarded to University of Nebraska, NSF DMR-0071682 to A.V.K. and 2 R37 NS36126, 1 P01 NS043985-01, 5 P01 MH64570-03, and P20 RR15635 to H.E.G. We would like to thank Dr. Sergey Vinogradov for assistance in synthesis of PEI-PEG and Drs. Jonathan Kipnis and Mark Thomas for valuable discussions.

Supporting Information Available: Experimental results of (1) enzymatic activity of catalase in polyion complexes, (2) cytotoxicity of nanozyme in BMM, (3) triggered release of catalase from BMM in the media, and (4) modulation of microglial-derived ROS by media collected from BMM loaded with PEI-PEG. This material is available free of charge via the Internet at http://pubs.acs.org.

LITERATURE CITED

(1) Brinton, R. D. (1999) A women's health issue: Alzheimer's disease and strategies for maintaining cognitive health. *Int. J. Fertil. Womens Med. 44*, 174−85.

(2) Gozes, I. (2001) Neuroprotective peptide drug delivery and development: potential new therapeutics. *Trends Neurosci. 24*, 700−5.

(3) Kroll, R. A., and Neuwelt, E. A. (1998) Outwitting the blood-brain barrier for therapeutic purposes: osmotic opening and other means. *Neurosurgery 42*, 1083−99; discussion 1099−100.

(4) Bachis, A., and Mocchetti, I. (2005) Brain-Derived Neurotrophic Factor Is Neuroprotective against Human Immunodeficiency Virus-1 Envelope Proteins. *Ann. N. Y. Acad. Sci. 1053*, 247−57.

(5) Ying Wang, J., Peruzzi, F., Lassak, A., Del Valle, L., Radhakrishnan, S., Rappaport, J., Khalili, K., Amini, S., and Reiss, K. (2003) Neuroprotective effects of IGF-I against TNFalpha-induced neuronal damage in HIV-associated dementia. *Virology 305*, 66−76.

(6) Koliatsos, V. E., Clatterbuck, R. E., Nauta, H. J., Knusel, B., Burton, L. E., Hefti, F. F., Mobley, W. C., and Price, D. L. (1991) Human nerve growth factor prevents degeneration of basal forebrain cholinergic neurons in primates. *Ann. Neurol. 30*, 831−40.

(7) Dogrukol-Ak, D., Banks, W. A., Tuncel, N., and Tuncel, M. (2003) Passage of vasoactive intestinal peptide across the blood-brain barrier. *Peptides 24*, 437−44.

(8) Desnick, R. J., and Schuchman, E. H. (2002) Enzyme replacement and enhancement therapies: lessons from lysosomal disorders. *Nat. Rev. Genet. 3*, 954−66.

(9) Urayama, A., Grubb, J. H., Sly, W. S., and Banks, W. A. (2004) Developmentally regulated mannose 6-phosphate receptor-mediated transport of a lysosomal enzyme across the blood-brain barrier. *Proc. Natl. Acad. Sci. U.S.A. 101*, 12658−63.

(10) Banks, W. (2003) Is obesity a disease of the blood-brain barrier? Physiological, pathological, and evolutionary considerations. *Curr. Pharm. Des. 9*, 801−809.

(11) Banks, W., and Lebel, C. (2002) Strategies for the delivery of leptin to the CNS. *J. Drug Target. 10*, 297−308.

(12) Perry, V. H., Bell, M. D., Brown, H. C., and Matyszak, M. K. (1995) Inflammation in the nervous system. *Curr. Opin. Neurobiol. 5*, 636−41.

(13) Prasad, K. N., Cole, W. C., Hovland, A. R., Prasad, K. C., Nahreini, P., Kumar, B., Edwards-Prasad, J., and Andreatta, C. P. (1999) Multiple antioxidants in the prevention and treatment of neurodegenerative disease: analysis of biologic rationale. *Curr. Opin. Neurol. 12*, 761−70.

(14) McGeer, P. L., Itagaki, S., Boyes, B. E., and McGeer, E. G. (1988) Reactive microglia are positive for HLA-DR in the substantia nigra of Parkinson's and Alzheimer's disease brains. *Neurology 38*, 1285−91.

(15) Busciglio, J., and Yankner, B. A. (1995) Apoptosis and increased generation of reactive oxygen species in Down's syndrome neurons in vitro. *Nature 378*, 776−9.

(16) Ebadi, M., Srinivasan, S. K., and Baxi, M. D. (1996) Oxidative stress and antioxidant therapy in Parkinson's disease. *Prog. Neurobiol. 48*, 1−19.

(17) Wu, D. C., Teismann, P., Tieu, K., Vila, M., Jackson-Lewis, V., Ischiropoulos, H., and Przedborski, S. (2003) NADPH oxidase mediates oxidative stress in the 1-methyl-4-phenyl-1,2,3,6-tetrahydropyridine model of Parkinson's disease. *Proc. Natl. Acad. Sci. U.S.A. 100*, 6145−50.

(18) Ambani, L. M., Van Woert, M. H., and Murphy, S. (1975) Brain peroxidase and catalase in Parkinson disease. *Arch. Neurol. 32*, 114−8.

(19) Riederer, P., Sofic, E., Rausch, W. D., Schmidt, B., Reynolds, G. P., Jellinger, K., and Youdim, M. B. (1989) Transition metals, ferritin, glutathione, and ascorbic acid in parkinsonian brains. *J. Neurochem. 52*, 515−20.

(20) Abraham, S., Soundararajan, C. C., Vivekanandhan, S., and Behari, M. (2005) Erythrocyte antioxidant enzymes in Parkinson's disease. *Indian J. Med. Res. 121*, 111−5.

(21) Wu, D. C., Jackson-Lewis, V., Vila, M., Tieu, K., Teismann, P., Vadseth, C., Choi, D. K., Ischiropoulos, H., and Przedborski, S. (2002) Blockade of microglial activation is neuroprotective in the 1-methyl-4-phenyl-1,2,3,6-tetrahydropyridine mouse model of Parkinson disease. *J. Neurosci. 22*, 1763−71.

(22) Du, Y., Ma, Z., Lin, S., Dodel, R. C., Gao, F., Bales, K. R., Triarhou, L. C., Chernet, E., Perry, K. W., Nelson, D. L., Luecke, S., Phebus, L. A., Bymaster, F. P., and Paul, S. M. (2001) Minocycline prevents nigrostriatal dopaminergic neurodegeneration in the MPTP model of Parkinson's disease. *Proc. Natl. Acad. Sci. U.S.A. 98*, 14669−74.
(23) Kurkowska-Jastrzebska, I., Babiuch, M., Joniec, I., Przybylkowski, A., Czlonkowski, A., and Czlonkowska, A. (2002) Indomethacin protects against neurodegeneration caused by MPTP intoxication in mice. *Int. Immunopharmacol. 2*, 1213−8.
(24) Teismann, P., and Ferger, B. (2001) Inhibition of the cyclooxygenase isoenzymes COX-1 and COX-2 provide neuroprotection in the MPTP-mouse model of Parkinson's disease. *Synapse 39*, 167−74.
(25) Ferger, B., Teismann, P., Earl, C. D., Kuschinsky, K., and Oertel, W. H. (1999) Salicylate protects against MPTP-induced impairments in dopaminergic neurotransmission at the striatal and nigral level in mice. *Naunyn Schmiedebergs Arch. Pharmacol. 360*, 256−61.
(26) Ferger, B., Spratt, C., Earl, C. D., Teismann, P., Oertel, W. H., and Kuschinsky, K. (1998) Effects of nicotine on hydroxyl free radical formation in vitro and on MPTP-induced neurotoxicity in vivo. *Naunyn Schmiedebergs Arch. Pharmacol. 358*, 351−9.
(27) Peng, J., Stevenson, F. F., Doctrow, S. R., and Andersen, J. K. (2005) Superoxide dismutase/catalase mimetics are neuroprotective against selective paraquat-mediated dopaminergic neuron death in the substantial nigra: implications for Parkinson disease. *J. Biol. Chem. 280*, 29194−8.
(28) Gonzalez-Polo, R. A., Soler, G., Rodriguezmartin, A., Moran, J. M., and Fuentes, J. M. (2004) Protection against MPP+ neurotoxicity in cerebellar granule cells by antioxidants. *Cell Biol. Int. 28*, 373−80.
(29) Maruyama, W., Akao, Y., Carrillo, M. C., Kitani, K., Youdium, M. B., and Naoi, M. (2002) Neuroprotection by propargylamines in Parkinson's disease: suppression of apoptosis and induction of prosurvival genes. *Neurotoxicol. Teratol. 24*, 675−82.
(30) Group, T. P. S. (1993) Effects of tocopherol and deprenyl on the progression of disability in early Parkinson's disease. *N. Engl. J. 328*, 176−183.
(31) Pappert, E. J., Tangney, C. C., Goetz, C. G., Ling, Z. D., Lipton, J. W., Stebbins, G. T., and Carvey, P. M. (1996) Alpha-tocopherol in the ventricular cerebrospinal fluid of Parkinson's disease patients: dose-response study and correlations with plasma levels. *Neurology 47*, 1037−42.
(32) Dou, H., Destache, C. J., Morehead, J. R., Mosley, R. L., Boska, M. D., Kingsley, J., Gorantla, S., Poluektova, L., Nelson, J. A., Chaubal, M., Werling, J., Kipp, J., Rabinow, B. E., and Gendelman, H. E. (2006) Development of a macrophage-based nanoparticle platform for antiretroviral drug delivery. *Blood 108*, 2827−35.
(33) Dou, H., Morehead, J. R., Destache, C., Kingsley, J., Shlyakhtenko, L., Zhou, Y., Chaubal, M., Werling, J., Kipp, J., Rabinow, B., and Gendelman, H. (2007) Laboratory investigations for the morphologic, pharmacokinetic, and anti-retroviral properties of indinavir nanoparticles in human nomocyte-derived macrophages. *Virology 358*, 148−158.
(34) Kadiu, I., Glanzer, J. G., Kipnis, J., Gendelman, H. E., and Thomas, M. P. (2005) Mononuclear phagocytes in the pathogenesis of neurodegenerative diseases. *Neurotox. Res. 8*, 25−50.
(35) Gorantla, S., Dou, H., Boska, M., Destache, C., Nelson, J., Poluektova, L., Rabinow, B., Gendelman, H., and Mosley, R. (2006) Quantitative magnetic resonance and SPECT imaging for macrophage tissue migration and nanoformulated drug delivery. *J. Leukocyte Biol. 80*, 1165−1174.
(36) Gendelman, H. (2006) Synuclein-linked neuroimmunity and the pathogenesis of Parkinson's disease. *Neurotoxicology 27*, 1162−1162.
(37) Mosley, R., Benner, E., Kadiu, I., Thomas, M., Boska, M., Hasan, K., Laurie, C., and Gendelman, H. (2006) Neuroinflammation, oxidative stress, and the pathogenesis of Parkinson's disease. *Clin. Neurosci. Res. 6*, 261−281.
(38) El-Agnaf, O. M., Salem, S. A., Paleologou, K. E., Cooper, L. J., Fullwood, N. J., Gibson, M. J., Curran, M. D., Court, J. A., Mann, D. M., Ikeda, S., Cookson, M. R., Hardy, J., and Allsop, D. (2003) Alpha-synuclein implicated in Parkinson's disease is present in extracellular biological fluids, including human plasma. *FASEB J. 17*, 1945−7.
(39) Anthony, D. C., Bolton, S. J., Fearn, S., and Perry, V. H. (1997) Age-related effects of interleukin-1 beta on polymorphonuclear neutrophil-dependent increases in blood-brain barrier permeability in rats. *Brain 120 (Pt 3)*, 435−44.
(40) Anthony, D. C., Blond, D., Dempster, R., and Perry, V. H. (2001) Chemokine targets in acute brain injury and disease. *Prog. Brain Res. 132*, 507−24.
(41) Blamire, A. M., Anthony, D. C., Rajagopalan, B., Sibson, N. R., Perry, V. H., and Styles, P. (2000) Interleukin-1beta -induced changes in blood-brain barrier permeability, apparent diffusion coefficient, and cerebral blood volume in the rat brain: a magnetic resonance study. *J. Neurosci. 20*, 8153−9.
(42) Persidsky, Y., Ghorpade, A., Rasmussen, J., Limoges, J., Liu, X. J., Stins, M., Fiala, M., Way, D., Kim, K. S., Witte, M. H., Weinand, M., Carhart, L., and Gendelman, H. E. (1999) Microglial and astrocyte chemokines regulate monocyte migration through the blood-brain barrier in human immunodeficiency virus-1 encephalitis. *Am. J. Pathol. 155*, 1599−611.
(43) Kuby, J. (1994) *Immunology*; Freeman, WH. and Co., New York.
(44) Pawlowski, N. A., Kaplan, G., Abraham, E., and Cohn, Z. A. (1988) The selective binding and transmigration of monocytes through the junctional complexes of human endothelium. *J. Exp. Med. 168*, 1865−82.
(45) Lossinsky, A. S., and Shivers, R. R. (2004) Structural pathways for macromolecular and cellular transport across the blood-brain barrier during inflammatory conditions. Review. *Histol. Histopathol. 19*, 535−64.
(46) Daleke, D. L., Hong, K., and Papahadjopoulos, D. (1990) Endocytosis of liposomes by macrophages: binding, acidification and leakage of liposomes monitored by a new fluorescence assay. *Biochim. Biophys. Acta 1024*, 352−66.
(47) Lee, K. D., Hong, K., and Papahadjopoulos, D. (1992) Recognition of liposomes by cells: in vitro binding and endocytosis mediated by specific lipid headgroups and surface charge density. *Biochim. Biophys. Acta 1103*, 185−97.
(48) Nishikawa, K., Arai, H., and Inoue, K. (1990) Scavenger receptor-mediated uptake and metabolism of lipid vesicles containing acidic phospholipids by mouse peritoneal macrophages. *J. Biol. Chem. 265*, 5226−31.
(49) Fujiwara, M., Baldeschwieler, J. D., and Grubbs, R. H. (1996) Receptor-mediated endocytosis of poly(acrylic acid)-conjugated liposomes by macrophages. *Biochim. Biophys. Acta 1278*, 59−67.
(50) Aoki, H., Kakinuma, K., Morita, K., Kato, M., Uzuka, T., Igor, G., Takahashi, H., and Tanaka, R. (2004) Therapeutic efficacy of targeting chemotherapy using local hyperthermia and thermosensitive liposome: evaluation of drug distribution in a rat glioma model. *Int. J. Hypertherm. 20*, 595−605.
(51) Calvo, P., Gouritin, B., Chacun, H., Desmaele, D., D'Angelo, J., Noel, J., Georgin, D., Fattal, E., Andreux, J., and Couvreur, P. (2001) Long-circulating PEGylated polycyanoacrylate nanoparticles as new drug carrier for brain delivery. *Pharm. Res. 18*, 1157−1166.
(52) Gref, R., Minamitake, Y., Peracchia, M., Trubetskoy, V., Torchilin, V., and Langer, R. (1994) Biodegradable long-circulating polymeric nanospheres. *Science 263*, 1600−1603.
(53) Harada, A., and Kataoka, K. (1999) Chain length recognition: core-shell supramolecular assembly from oppositely charged block copolymers. *Science 283*, 65−7.
(54) Jaturanpinyo, M., Harada, A., Yuan, X., and Kataoka, K. (2004) Preparation of bionanoreactor based on core-shell structured polyion complex micelles entrapping trypsin in the core cross-linked with glutaraldehyde. *Bioconjugate Chem. 15*, 344−8.
(55) Kabanov, A., Batrakova, E., and Alakhov, V. (2002) Pluronic block copolymers as novel polymer therapeutics for drug and gene delivery. *J. Controlled Release 82*, 189−212.
(56) Kwon, G. S. (2003) Polymeric micelles for delivery of poorly water-soluble compounds. *Crit. Rev. Ther. Drug Carrier Syst. 20*, 357−403.
(57) Mora, M., Sagrista, M. L., Trombetta, D., Bonina, F. P., De Pasquale, A., and Saija, A. (2002) Design and characterization of liposomes containing long-chain N-acylPEs for brain delivery: penetration of liposomes incorporating GM1 into the rat brain. *Pharm. Res. 19*, 1430−8.
(58) Rousseau, V., Denizot, B., Le Jeune, J. J., and Jallet, P. (1999) Early detection of liposome brain localization in rat experimental allergic encephalomyelitis. *Exp. Brain Res. 125*, 255−64.

(59) Torchilin, V. P. (2000) Drug targeting. *Eur. J. Pharm. Sci. 11 Suppl 2*, S81−91.
(60) Vinogradov, S. V., Batrakova, E. V., and Kabanov, A. V. (2004) Nanogels for oligonucleotide delivery to the brain. *Bioconjugate Chem 15*, 50−60.
(61) Kabanov, V. A., Evdakov, V. P., Mustafaev, M. I., and Antipina, A. D. (1977) A cooperative interaction of serum albumin with quaternized poly-4-vinyl pyridine and structure of the complexes. *Mol. Biol. (Russian) 11*, 582−596.
(62) Kabanov, V. (1994) Physicochemical basis and the prospects of using soluble interpolyelectrolyte complexes. *Polym. Sci. 36*, 183−197.
(63) Kabanov, V., Skobeleva, V., Rogacheva, V., and Zezin, A. (2004) Sorption of proteins by slightly cross-linked polyelectrolyte hydrogels: Kinetics and mechanism. *J. Phys. Chem. B 108*, 1485−1490.
(64) Harada, A., and Kataoka, K. (2001) Pronounced activity of enzymes through the incorporation into the core of polyion complex micelles made from charged block copolymers. *J. Controlled Release 72*, 85−91.
(65) Harada, A., and Kataoka, K. (2003) Switching by pulse electric field of the elevated enzymatic reaction in the core of polyion complex micelles. *J. Am. Chem. Soc. 125*, 15306−7.
(66) Vinogradov, S., Bronich, T., and Kabanov, A. (1998) Self-assembly of polyamine-poly(ethylene glycol) copolymers with phosphorothioate oligonucleotides. *Bioconjugate Chem. 9*, 805−812.
(67) Benner, E. J., Mosley, R. L., Destache, C. J., Lewis, T. B., Jackson-Lewis, V., Gorantla, S., Nemachek, C., Green, S. R., Przedborski, S., and Gendelman, H. E. (2004) Therapeutic immunization protects dopaminergic neurons in a mouse model of Parkinson's disease. *Proc. Natl. Acad. Sci. U.S.A. 101*, 9435−40.
(68) Nguyen, H. K., Lemieux, P., Vinogradov, S. V., Gebhart, C. L., Guerin, N., Paradis, G., Bronich, T. K., Alakhov, V. Y., and Kabanov, A. V. (2000) Evaluation of polyether-polyethyleneimine graft copolymers as gene transfer agents. *Gene Ther. 7*, 126−38.
(69) Vinogradov, S., Batrakova, E., Li, S., and Kabanov, A. (1999) Polyion complex micelles with protein-modified corona for receptor-mediated delivery of oligonucleotides into cells. *Bioconjugate Chem. 10*, 851−60.
(70) Lemieux, P., Vinogradov, S. V., Gebhart, C. L., Guerin, N., Paradis, G., Nguyen, H. K., Ochietti, B., Suzdaltseva, Y. G., Bartakova, E. V., Bronich, T. K., St-Pierre, Y., Alakhov, V. Y., and Kabanov, A. V. (2000) Block and graft copolymers and NanoGel copolymer networks for DNA delivery into cell. *J. Drug Target. 8*, 91−105.
(71) Vinogradov, S. V., Batrakova, E. V., Li, S., and Kabanov, A. V. (2004) Mixed polymer micelles of amphiphilic and cationic copolymers for delivery of antisense oligonucleotides. *J. Drug Target. 12*, 517−26.
(72) Vinogradov, S. V., Zeman, A. D., Batrakova, E. V., and Kabanov, A. V. (2005) Polyplex Nanogel formulations for drug delivery of cytotoxic nucleoside analogs. *J. Controlled Release 107*, 143−57.
(73) Bronich, T., Nguyen, H., Eisenberg, A., and Kabanov, A. (2000) Recognition of DNA topology in reactions between plasmid DNA and cationic copolymers. *J. Am. Chem. Soc. 122*, 8339−8343.
(74) Vinogradov, S., Batrakova, E., and Kabanov, A. (1999) Poly(ethylene glycol)-polyethyleneimine NanoGel (TM) particles: novel drug delivery systems for antisense oligonucleotides. *Colloids Surf. B-Biointerfaces 16*, 291−304.
(75) Beckman, J. S., Minor, R. L., Jr., White, C. W., Repine, J. E., Rosen, G. M., and Freeman, B. A. (1988) Superoxide dismutase and catalase conjugated to polyethylene glycol increases endothelial enzyme activity and oxidant resistance. *J. Biol. Chem. 263*, 6884−92.
(76) Batrakova, E., Han, H., Miller, D., and Kabanov, A. (1998) Effects of pluronic P85 unimers and micelles on drug permeability in polarized BBMEC and Caco-2 cells. *Pharm. Res. 15*, 1525−1532.
(77) Batrakova, E. V., Vinogradov, S. V., Robinson, S. M., Niehoff, M. L., Banks, W. A., and Kabanov, A. V. (2005) Polypeptide point modifications with fatty acid and amphiphilic block copolymers for enhanced brain delivery. *Bioconjugate Chem. 16*, 793−802.
(78) Kabanov, A., Vinogradov, S., Suzdaltseva, Y., and Alakhov, V. (1995) Water-soluble block polycations as carriers for olygonucleotide delivery. *Bioconjugate Chem. 6*, 639−643.
(79) Harada, A., and Kataoka, K. (1995) Formation of polyion complex micelles in an aqueous milieu from a pair of oppositely charged block-copolymers with poly(ethylene glycol) segments. *Macromolecules 28*, 5294−5299.
(80) Bronich, T., Kabanov, A., Kabanov, V., Yu, K., and Eisenberg, A. (1997) Soluble complexes from poly(ethylene oxide)-block-polymethacrylate anions and N-alkylpyridinium cations. *Macromolecules 30*, 3519−3525.
(81) Kabanov, V. (1994) Physicochemical basis and the prospects of using soluble interpolyelectrolyte complexes. *Polym. Sci. 36*, 143−156.
(82) Kabanov, V. (2003) Fundamentals of Polyelectrolyte Complexes in Solution and the Bulk. In *Multilayer Thin Films* (Decher, G., and Schlenoff, J., Eds.) pp 47−86, Wiley-VCH Verlag GmbH & Co. KGaA, Weinheim.
(83) Chang, Z., and Beezhold, D. (1993) Protein-kinase-C activation in human monocytes - regulation of PKC isoforms. *Immunology 80*, 360−366.
(84) Zhang, W., Wang, T., Pei, Z., Miller, D. S., Wu, X., Block, M. L., Wilson, B., Zhou, Y., Hong, J. S., and Zhang, J. (2005) Aggregated alpha-synuclein activates microglia: a process leading to disease progression in Parkinson's disease. *FASEB J. 19*, 533−42.
(85) Thomas, M. P., Chartrand, K., Reynolds, A., Vitvitsky, V., Banerjee, R., and Gendelman, H. E. (2007) Ion channel blockade attenuates aggregated alpha synuclein induction of microglial reactive oxygen species: relevance for the pathogenesis of Parkinson's disease. *J. Neurochem. 100*, 503−19.
(86) Jain, S., Mishra, V., Singh, P., Dubey, P. K., Saraf, D. K., and Vyas, S. P. (2003) RGD-anchored magnetic liposomes for monocytes/neutrophils-mediated brain targeting. *Int. J. Pharm. 261*, 43−55.
(87) Lawson, L. J., Perry, V. H., and Gordon, S. (1992) Turnover of resident microglia in the normal adult mouse brain. *Neuroscience 48*, 405−15.
(88) Simard, A. R., and Rivest, S. (2004) Bone marrow stem cells have the ability to populate the entire central nervous system into fully differentiated parenchymal microglia. *FASEB J. 18*, 998−1000.
(89) Male, D., and Rezaie, P. (2001) Colonisation of the human central nervous system by microglia: the roles of chemokines and vascular adhesion molecules. *Prog. Brain Res. 132*, 81−93.
(90) Streit, W. J., Walter, S. A., and Pennell, N. A. (1999) Reactive microgliosis. *Prog. Neurobiol. 57*, 563−81.
(91) Kokovay, E., and Cunningham, L. A. (2005) Bone marrow-derived microglia contribute to the neuroinflammatory response and express iNOS in the MPTP mouse model of Parkinson's disease. *Neurobiol. Dis. 19*, 471−8.
(92) Kurkowska-Jastrzebska, I., Wronska, A., Kohutnicka, M., Czlonkowski, A., and Czlonkowska, A. (1999) MHC class II positive microglia and lymphocytic infiltration are present in the substantia nigra and striatum in mouse model of Parkinson's disease. *Acta Neurobiol. Exp. (Wars) 59*, 1−8.
(93) Kurkowska-Jastrzebska, I., Wronska, A., Kohutnicka, M., Czlonkowski, A., and Czlonkowska, A. (1999) The inflammatory reaction following 1-methyl-4-phenyl-1,2,3, 6-tetrahydropyridine intoxication in mouse. *Exp. Neurol. 156*, 50−61.
(94) Simard, A. R., and Rivest, S. (2006) Neuroprotective properties of the innate immune system and bone marrow stem cells in Alzheimer's disease. *Mol. Psychiatry 11*, 327−35.
(95) Stout, R. D., and Suttles, J. (1997) T cell signaling of macrophage function in inflammatory disease. *Front. Biosci. 2*, d197−206.
(96) Schorlemmer, H. U., Edwards, J. H., Davies, P., and Allison, A. C. (1977) Macrophage responses to mouldy hay dust, Micropolyspora faeni and zymosan, activators of complement by the alternative pathway. *Clin. Exp. Immunol. 27*, 198−207.
(97) Allison, A. C., and Davies, P. (1974) Mechanisms of endocytosis and exocytosis. *Symp. Soc. Exp. Biol*. 419−46.
(98) Cardella, C. J., Davies, P., and Allison, A. C. (1974) Immune complexes induce selective release of lysosomal hydrolases from macrophages. *Nature 247*, 46−8.

BC700184B

New Noninvasive Methodology for Real-Time Monitoring of Lipid Flip

Christine A. Winschel,[†] Vivek Kaushik,[†] Galya Abdrakhmanova,[‡] Sheena M. Aris,[†] and Vladimir Sidorov[†,*]

Department of Chemistry, Virginia Commonwealth University, Richmond, Virginia 23284-2006, and Department of Pharmacology and Toxicology, Virginia Commonwealth University, Richmond, Virginia 23298. Received May 25, 2007; Revised Manuscript Received July 4, 2007

A new methodology for the detection of lipid flip was developed. This methodology relies on the quenching of the fluorescence of the cascade-blue-labeled lipid through complex formation with a membrane-impermeable cyclen-tetranaphthalenethiourea synthetic receptor for this dye. The high affinity of the receptor to cascade-blue label allows the use of micromolar concentrations of this receptor during the experiment. At these low concentrations, the receptor does not interfere with the membrane integrity and, therefore, renders this new methodology less invasive to the model and cell membranes than commonly utilized 7-nitro-1,2,3-benzoxadiazol-4-yl (NBD)-dithionite methodology. Unlike with the NBD-dithionite assay, where the fluorescence quenching of the NBD group is achieved through its chemical modification, this new assay relies on the noncovalent interactions between cascade-blue label and the receptor. Therefore, the quenching can be reverted by either competitive displacement of the lipid-attached label with a water-soluble substrate or by enzymatic degradation of the receptor leading to the label release and fluorescence dequenching. We demonstrate that this new methodology is suitable for the study of lipid flip in both model spherical bilayer membranes and in-vitro experiments.

INTRODUCTION

Lipid flip detection assays allow monitoring of the activity of enzymes known as flippases, floppases, and scramblases (*1*) and their fully synthetic (*2*−*5*) or peptide analogues (*6*, *7*). These enzymes control the transmembrane distribution of lipids in cells and are responsible for membrane asymmetry. Lipid translocation mediated by these enzymes is associated with apoptosis (*8*−*12*) and blood clotting (*13*, *14*). The synthetic molecules capable of lipid flipping can be considered as developmental therapeutics for several disorders (*15*, *16*), such as Scott syndrome and vascular complications in Alzheimer's disease (*17*, *18*). Furthermore, flip of cationic lipids may greatly improve the efficiency of nonviral gene delivery systems (*19*). To date, three major assays are utilized for the monitoring of lipid flip in model spherical bilayers (liposomes). The first method relies on the flip of transferable fluorescent 7-nitro-1,2,3-benzoxadiazol-4-yl (NBD)-labeled lipid from the donor liposomes to the acceptor liposomes containing nontransferable rhodamine-labeled lipid that serves as a fluorescence quencher (*20*). The second methodology is based on removal of the fluorescent lipid (*21*) from the bilayer outer leaflet by incubation with serum albumin (*22*). The most conventional way for detection of flippase activity is based on the irreversible quenching of the fluorescence of NBD-labeled lipids in cells (*23*) or liposomes (*24*, *25*) with 10−60 mM sodium dithionite ($Na_2S_2O_4$, Scheme 1A). The extent of lipid flip is assessed from the residual fluorescence of liposomes after the application of the quencher. Because of its anionic character, dithionite exhibits low permeability to the hydrophobic bilayer membrane and therefore does not rapidly quench the fluorescence of the lipid located on the inner bilayer leaflet but quickly quenches the fluorescence of lipid residing on the outer leaflet. The assay has numerous intrinsic deficiencies arising from the high concentration of the quencher required for the assay, the reductive nature of this reagent, and some permeability of the quencher to the bilayer membrane. Thus, it has been shown recently that sodium dithionite diffusion through the bilayer is similar or faster than that of unfacilitated lipid flip (*26*). Potentially, dithionite can reduce the disulfide cross-links found in some flippases. For example, wild type human P-glycoprotein (Pgp), which is a known flippase (*27*), facilitates the lipid flip to a lesser extent than Pgp treated with the reducing agent because of inhibitory disulfide cross-links between nucleotide binding sites (*28*). In contrast, the activity of human scramblase protein is suppressed by reducing reagents because of the reduction of disulfide cross-links (*29*). These examples demonstrate that dithionite may affect the flipping activity of enzymes in a dual way and, therefore, cannot be used in the real time monitoring experiments.

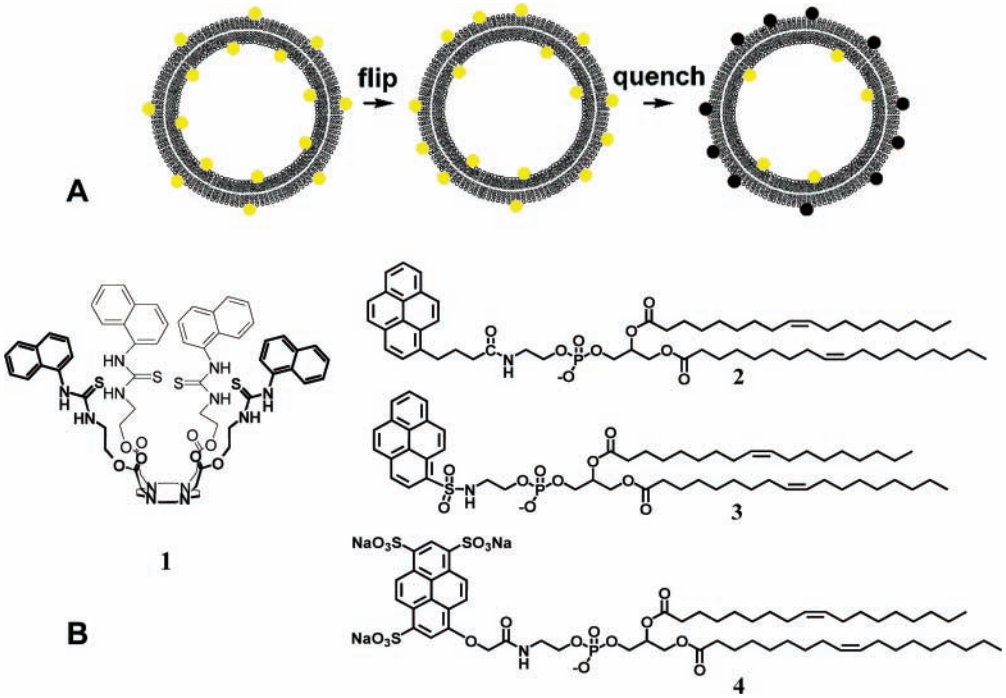
EXPERIMENTAL PROCEDURES

General. The ^{1}H NMR spectra were recorded on a Varian AS400 instrument operating at 400.130 MHz or Varian Mercury instrument operating at 299.865 MHz. Chemical shifts are reported in ppm relative to the residual protonated solvent peak. The mass spectra were recorded on a Micromass Q-TOF 2 instrument (Manchester, UK) using the electrospray technique (positive and negative modes were used). The samples were introduced into the mass spectrometer using a flow rate of 10 μL/min, the needle voltage was set at 3500 V with ion source at 110 °C, and the cone voltage was set at 35 V. All spectrophotometric experiments were carried out on a Fluoromax 3 (Jobin-Yvon/Horriba) spectrophotometer. The pH of solutions was monitored with a Corning 350 pH/ion analyzer, using a Ag/AgCl pH-sensitive electrode (Accumet). Chromatography was performed using 60−200 mesh silica purchased from Baker and 40−120 μm Sephadex G-75 purchased from Aldrich. Thin layer chromatography was performed on Kieselgel 60 F254 and Uniplate Silica Gel GF silica-coated glass plates and visualized by UV and I_2. High-pressure extrusion was performed on the Avanti miniextruder with a 0.1 μm polycarbonate membrane. All chemicals, solvents, and dyes were purchased from Aldrich, Sigma, Fluka, and Invitrogen. Egg yolk phosphatidylcholine, L-α-dioleoylphosphatidylethanolamine

* Corresponding author. E-mail: vasidorov@vcu.edu.
[†] Department of Chemistry.
[‡] Department of Pharmacology and Toxicology.

10.1021/bc700189n CCC: $37.00 © 2007 American Chemical Society
Published on Web 09/07/2007

Scheme 1. Schematic Representation of Lipid-Flip Detection Assay and Structures of the Compounds Used in the Present Study[a]



[a] A. Liposomes containing fluorescently labeled lipids are treated with membrane-impermeable quencher. Alterations in the residual fluorescence of the lipids from inner bilayer leaflet serve as the measure of lipid flip. B. Structures of the receptor **1** and fluorescently labeled lipids used in the present study.

(DOPE), *N*-(7-nitro-2−1,3-benzoxadiazol-4-yl)-(1,2-dioleoyl-sn-glycero-3)-phosphoethanolamine (NBD-PE), and *N*-(1-pyrenesulfonyl)-(1,2-dioleoyl-sn-glycero)-3-phosphoethanolamine (lipid **3**) were purchased from Avanti Polar Lipids.

Synthesis. Cyclen **1** was synthesized as reported (*30*).

Lipid **2** was synthesized in a one-step procedure as follows: 1,2-Dioleoyl-sn-glycero-3-phosphoetyanolamine (DOPE) (33 mg, 0.044 mmol) and 1-pyrenebutyric acid (68 mg, 0.177 mmol, 4-fold excess) were dissolved in 2 mL of DMF. A 1 mL solution of N,N′-dicyclohexylcarbodiimide (DCC) (37 mg, 0.177 mmol, 4-fold excess) and 4-dimethylaminopyridine (22 mg, 0.177 mmol, 4-fold excess) was added dropwise at 0 °C. The reaction was allowed to come to room temperature and was stirred for 12 h. The solution was removed under reduced pressure and purified by column chromatography (silica gel, gradient of $CHCl_3$ and MeOH) yielding 9 mg of pure product (0.009 mmol, 20%). ^{1}H NMR ($CDCl_3$, δ): 8.18 (br s, 1H), 7.82−8.10 (m, 7H), 7.72 (br s, 1H), 5.28 (br s, 4H), 4.34 (br s, 1H), 4.12 (br s, 2H), 4.02 (br s, 2H), 3.94 (br s, 2H), 3.50 (s, 8H), 3.28 (br s, 3H) 2.50−0.80 (br m, 59H). MS (ESI, high-resolution) $[M]^-$: 1012.5525 calculated for $C_{61}H_{91}NO_9P^-$ 1012.644.

Lipid **4** was synthesized in a two-step procedure:

(i) 1,2-Dioleoyl-sn-glycero-3-phosphoethanolamine (50 mg, 0.067 mmol) was dissolved in 5 mL of CH_2Cl_2, and diisopropylethylamine(20 μL, 0.115 mmol, 1.7-fold excess) was added. A solution of bromoacetyl bromide (20 μL in 1 mL of CH_2Cl_2, 0.23 mmol, 3.4-fold excess) was added to the reaction mixture dropwise. The reaction mixture was stirred for 12 hrs at room temperature, and the solvent and excess reagents were removed under reduced pressure to afford crude *N*-(2-bromoacetyl)-1,2-dioleoyl-sn-glycero-3-phosphoethanolamine. The crude product was purified by column chromatography (silica gel, methanol: CH_2Cl_2 6:94) to give 53 mg of the pure product (0.061 mmol, 91%). ^{1}H NMR ($CDCl_3$, δ): 10.36 (br s, 2H), 5.33 (app p, 2H, J = 2.4 Hz), 4.39 (br s, 1H), 4.13 (br s, 1H), 3.93 (br s, 2H), 3.79−3.65 (m, 4 H), 3.18−3.05 (m, 4H), 2.38−2.30 (m, 2H), 2.00 (app q, 4 H, J = 5.7 Hz), 1.73 (m, 2H), 1.65−1.15 (m, 48 H), 0.87 (app t, 6 H, J = 5.7 Hz). MS (ESI, high-resolution) $[M]^-$: 862.5907, calcd for $C_{43}H_{78}BrNO_9P^-$ 862.4598.

(ii) *N*-(2-Bromoacetyl)-1,2-dioleoyl-sn-glycero-3-phosphoethanolamine (10 mg, 0.011 mmol) was dissolved in 2 mL of acetone, potassium carbonate (10 mg, 0.072 mmol, 6.5-fold excess) was added, and the reaction mixture was stirred for 40 min at room temperature. Then, 8-hydroxypyrene-1,3,6-trisulfonic acid sodium salt (10 mg, 0.019 mmol, 1.7-fold excess) was added, and the reaction mixture was stirred for 48 h under reflux. The solvent was evaporated under reduced pressure, and the residual solid was partitioned in chloroform−water. The organic layer was separated, and the solvent was removed under reduced pressure. The crude product was purified by the size exclusion chromatography (Sephadex G-75 as solid phase, Millipore water as mobile phase) to afford 4 mg of pure lipid **4** (potassium salt, 0.0029 mmol, 26%). ^{1}H NMR ($CDCl_3$, δ): 7.70 (m, 1H), 7.51 (m, 1H), 7.10 (br s, 1H), 6.96 (br s, 1H); 6.82−6.73 (m, 2H), 5.37 (app s, 2H), 4.69 (app s, 1H), 4.38−4.33 (m, 4 H), 4.15 (br s, 2H), 3.89 (s, 1H), 3.62 (br s, 2H), 2.36−2.25 (m, 2H), 2.0 (m, 4H), 1.66−1.10 (m, 48H), 0.72 (app t, 6H, J = 5.7 Hz). (ESI) $[M]^{2-}$: 658.4895, calcd for $C_{59}H_{85}K_2NO_{19}PS_3^{2-}$ 658.1948.

Preparation of Symmetric Liposomes for Lipid-Flip Monitoring Assays. Egg yolk L-α-phosphatidylcholine (EYPC ethanol solution, 60 μL, 79 μmol) and chloroform solution of labeled lipid (NBD-PE, lipid **2**, **3**, or **4**, 20−50 μL, 79 nmol) were dissolved in a $CHCl_3$/MeOH mixture to give a 1:1000 mixture of labeled lipid:EYPC, the solution was evaporated under reduced pressure, and the resulting thin film was dried under high vacuum for 2 h. The lipid film was hydrated for 40 min in 1.2 mL of sodium phosphate buffer (10 mM sodium phosphate, pH = 6.4, 100 mM NaCl). During hydration, the suspension was submitted to three freeze−thaw cycles (dry ice/acetone, water at room temperature). The resulting suspension of large multilamellar vesicles (1 mL) was submitted to high-pressure extrusion at room temperature. The LUV suspension was purified by size exclusion chromatography (SEC) (stationary

phase: Sephadex G-75, mobile phase: sodium phosphate buffer of the same composition) and diluted with the same sodium phosphate buffer to give a stock suspension with the total lipid concentration of 33 mM (assuming 100% of lipid was incorporated into liposomes).

Preparation of Asymmetric Liposomes with Excess of Lipid 4 in the Outer Bilayer Leaflet. The stock suspension of liposomes (30 μL), symmetrically labeled with lipid **4** (see above), was diluted with 2 mL of phosphate buffer (10 mM sodium phosphate, pH = 6.4, 100 mM NaCl), and a solution of lipid **4** in DMSO (10 μL, 0−100 μM) was added. This suspension was preincubated for 10 min prior the experiments. The immediate fluorescence monitoring resulted in lower initial fluorescence levels, probably due to the slow incorporation of lipid **4** into the liposomal exterior from the individual lipid **4**-formed liposomes and self-quenching of the lipid **4** fluorescence in these liposomes due to high local concentration of the cascade-blue label (*31*).

Kinetic Fluorescence Quenching Experiments with Symmetrically Labeled LUVs. In a typical experiment, 50 μL of LUVs labeled with lipid **2**, **3**, **4**, or NBD-PE (stock solution) was suspended in 1.95 mL of the phosphate saline buffer (10 mM sodium phosphate, pH = 6.4, 100 mM NaCl) and placed into a thermostated spectrophotometric cell. The suspension of liposomes was gently stirred throughout the entire course of experiment. The emission of labeled lipid (397 nm for lipids **2** and **3**, 434 nm for lipid **4**, and 534 nm for NBD-PE) was monitored with the excitations at 317, 354, 402, and 460 nm, respectively. The emission and excitation slits of the spectrophotometer were set at 5 nm, time increments were set at 1 s, and the integration time was set at 1 s. The temperature of the spectrophotometric cell was set at 25 °C. During the experiment, 20 μL of a 0−5 mM DMSO solution of cyclen **1** or 1 M aqueous solution of sodium dithionite was added through the injection port. At the end, the experiments were terminated by the injection of 40 μL of 20% aqueous solution of Triton X-100. In the case of experiments with variable amounts of Triton-X-100, 40 μL injections of the corresponding Triton X-100 aqueous solutions were performed. Binding constant and the maximum emission loss with the confidence interval values were computed using the homemade nonlinear regression curve-fitting program. The 1:1 binding model was used.

Kinetic fluorescence quenching experiments with asymmetrically labeled LUVs were carried out analogously, except that the suspension of asymmetric LUVs described above were used without further dilution.

Cell Culture. HEK 293 cells were obtained from ATCC (Manassas, VA) and maintained at 37 °C with 5% CO_2 in an incubator. The culture medium used was minimum essential medium (MEM) supplemented with 10% fetal bovine serum (FBS), 100 U/mL penicillin, and 100 μg/mL streptomycin (all from Invitrogen Corp, Carlsbad, CA). A2780 human ovarian carcinoma cells were a generous gift from Dr. Stephen Williams, Ovarian Cancer Program, Fox Chase Cancer Center, Philadelphia, PA. A2780 cells were cultured in Roswell Park Memorial Institute (RPMI) (Gibco: Invitrogen, Carlsbad, CA) in 5% FBS, 5% BCS (bovine calf serum), 0.25% penicillin/streptomycin. Cells were routinely passaged at 80−90% confluency.

Confocal Imaging. The activity of the compounds tested was evaluated using confocal microscopy. HEK 293 cells were plated on 12-mm round glass cover slips pretreated with poly-D-lysine (BD Biosciences, Bedford, MA). Prior to experiment, the cover slips with the cells were washed with PBS, transferred to a small experimental chamber (Warner Instruments, Hamden, CT) mounted on the stage of an Olympus confocal microscope (Olympus FV 300, Tokyo, Japan) equipped with a ×40/0.95 water immersion objective and cooled, charge-coupled device camera. Bath solution (in mM): 140 NaCl, 3 KCl, 2 $MgCl_2$, 25 D-glucose, 10 HEPES, and 2 $CaCl_2$, with pH adjusted to 7.4 with NaOH (all from Sigma Aldrich (Atlanta, GA)). Cells were visualized and selected for an experiment using the brightfield system. The excitation light to the preparation was supplied from a 405 nM diode laser, LD-405 (Olympus). The ultraviolet excitation wavelength was controlled by a mirror unit that filtered the excitation at 360−370 nm and the emission at 420−460 nm levels. Digital images (640 × 480 pixels) were obtained and processed using Fluoview v.5.0 software (Olympus), and preset settings for DAPI (4,6-diamidino-2-phenylindole) were acquired. Experiments were performed at room temperature (22−25 °C). During the experiment, 10 μL of 300 μM DMSO solution of lipid **4** or **2** was added to the bath solution (1 mL), followed by the addition of 10 μL of 2.5 mM DMSO solution of cyclen **1**.

Cell Growth Inhibition Assays. For the MTT (3-(4,5-dimethyl-2-thiazolyl)-2,5-diphenyl-2*H*-tetrazolium bromide) assay, A2780 human ovarian carcinoma cells were plated at a density of 6500 cells per well in a 96-well plate and incubated overnight at 37 °C in a 5% CO_2 atmosphere. Stock solutions of sodium dithionite, 100 mM in media, and cyclen **1** compound, 5 mM in DMSO, were made fresh prior to each use. Cells were treated at 10 mM and 25 μM concentrations of sodium dithionite and cyclen **1**, respectively, for 72 h. After medium removal, cells were washed twice with cold PBS and incubated with MTT (2 mg/mL in PBS) for 3 h. The excess MTT (Sigma, St. Louis, MO) was then removed, the dye dissolved in 100 μL of DMSO (Sigma, St. Louis, MO), and absorbance read on a Molecular Devices Vmax kinetic microplate reader at 540 nm. Transmission images of the cells were obtained on an Olympus IX70 microscope, using 20× magnification.

RESULTS AND DISCUSSION

Identification of Appropriate Components for the Lipid-Flip Detection Assay. We have recently developed a synthetic receptor, cyclen thiourea **1**, which is capable of selective binding of anionic pyrene-based dyes with submicromolar affinity under near physiological conditions (*30*). This receptor is impermeable to the bilayer membrane and quenches 90−99% of the fluorescence of pyrene-based dyes. We hypothesized that this type of receptor should be able to quench the fluorescence of the accessible portion of pyrene-labeled phospholipids residing on the outer leaflet of the bilayer membrane of liposomes upon its exogenous application. Such quenching of the fluorescence of the outer portion of the labeled lipid should provide the basis for a new lipid-flip detection assay. The high affinity of cyclen **1** to the anionic pyrene-based dyes should warrant the low micromolar concentration range required for the fluorescence quenching and therefore provide less invasive conditions for the lipid-flip detection than in the otherwise analogous NBD-dithionite assay.

In order to verify the validity of such an approach we synthesized two pyrene-labeled phospholipids: dioleoylphosphatidylethanolamine-pyrenebutyric acid **2** and dioleoylphosphatidylethanolamine-hydroxypyrene trisulfonate **4**, and also tested the commercially available dioleoylphosphatidylethanolamine-pyrene-sulfonamide **3**. Previously, we identified the hydrophobic effect rather than electrostatic or hydrogen-bonding interactions as the major driving force for the complex formation between pyrene-based dyes and cyclen **1**. Therefore, it was reasonable to expect that neutral pyrene labels of phospholipids **2** and **3** will also bind to cyclen **1**.

Phospholipids **2** and **3** feature a neutral pyrene label tethered by linkers of variable length. Phospholipid **2** was the most hydrophobic lipid among three probes because of nonpolar nature of pyrene group and substantially higher hydrophobicity

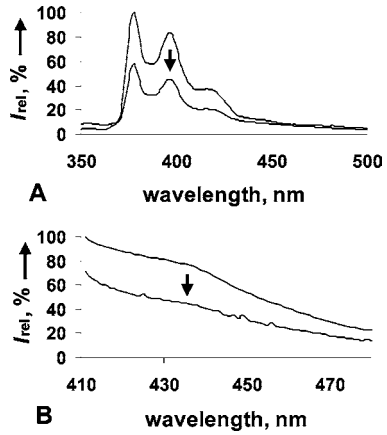


Figure 1. Fluorimetric characterization of interactions of cyclen **1** with fluorescently labeled LUVs. A. Emission spectra (ex = 317 nm) of LUVs labeled with lipid **2** in the absence (top spectrum) and in the presence (bottom spectrum) of 20 μM cyclen **1**. B. Emission spectra (ex = 402 nm) of LUVs labeled with lipid **4** in the absence (top spectrum) and in the presence (bottom spectrum) of 20 μM cyclen **1**. LUVs in all experiments were suspended in 1% DMSO in the phosphate saline buffer.

of amide linker than that of sulfonamide linker of lipid **3** (*32*). Therefore, lipid **2** was expected to diffuse across bilayer membranes with the highest rate, whereas the trianionic character of the cascade-blue label (*33*) in the phospholipid **4** was expected to prevent any unmediated diffusion of this lipid across the membrane.

First, we prepared three sets of large unilamellar liposomes (LUVs) from egg yolk phosphatidylcholine (EYPC) containing 0.1 mol % of the pyrene-labeled lipids **2**−**4** evenly distributed between the inner and outer leaflets of the bilayer. The emission spectra for the suspensions of these three sets of liposomes were recorded in the presence (20 μM) and in the absence of cyclen **1.** No apparent changes in the fluorescent spectrum were observed upon addition of cyclen **1** to the LUVs labeled with lipid **3**. This is probably because the short length of the linker connecting the pyrene label to the phospholipids caused the immersion of the pyrene moiety into the hydrophobic region of the bilayer, thus making this label inaccessible to cyclen **1**.

The identical experiments with LUVs containing phospholipids **2** and **4** revealed 46% and 41% fluorescence intensity loss, respectively, upon addition of 20 μM cyclen **1** (Figure 1). However, the kinetic experiments, where the maximum fluorescence intensity was monitored as a function of time, revealed that the fast loss of 46% of fluorescence by LUVs containing lipid **2** was followed by a somewhat slower phase of quenching, resulting in the overall 80% loss of the fluorescence in only 20 min (not shown). These results can be explained by the high rate of unmediated diffusion of lipid **2** across the bilayer membrane and subsequent quenching of the fluorescence of the exposed lipid by extravesicular cyclen **1**. However, the secondary phase of the fluorescence quenching in LUVs labeled with polar phospholipid **4** was negligibly slow, consistent with the expected slow unmediated flipping rate for this lipid. The kinetic quenching experiments were terminated by application of 0.5% of the detergent Triton X-100, which resulted in a complete lysis of LUVs and exposure of the inaccessible portion of the fluorescent lipids to cyclen **1**.

Application of cyclen **1** to LUVs labeled with lipid **4** and lysis of these LUVs with the detergent Triton X-100 gave 87% of the fluorescence quenching. However, the fluorescence of the LUVs labeled with lipid **2** increased upon application of Triton X-100 and even exceeded the original fluorescence of the cyclen **1**-free suspension of LUVs. This is most likely because of repartitioning of nonpolar pyrene headgroup of lipid **2** into the hydrophobic core of the Triton X-100 micelles, accompanied by the decomposition of the complex formed from lipid **2** and cyclen **1**. This observation made lipid **2** a less attractive probe for lipid-flip monitoring, and most of the further work was carried out with the polar lipid **4**.

Kinetic Experiments under Lipid-Flip Mimicking Conditions. In order to find the optimal concentration of cyclen **1** required for the quenching of the fluorescence of lipid **4**, we carried out a series of kinetic titration experiments, where the emission intensity of LUVs treated with variable amounts of cyclen **1** was monitored as a function of time (Figure 2A). Application of variable amounts of cyclen **1** resulted in various degrees of fluorescence quenching; however, the apparent saturation was observed at cyclen **1** concentrations above 10 μM.

The extent of fluorescence quenching by cyclen **1** can be interpreted in terms of complex formation between lipid **4** and cyclen **1**; therefore, the fluorescence data were fitted into the binding isotherm (Figure 2B, 1:1 stoichiometry was assumed). The kinetics of fluorescence quenching clearly consisted of two phases, where the primary fast phase was likely due to the interactions of the outer leaflet portion of lipid **4**, and the slower phase was due to the lipid flipping from the inner leaflet into the outer leaflet, followed by complex formation. The secondary phase was almost linear for all traces; therefore, linear fit of the data points in the secondary phase time interval (300−800 s for all traces) and extrapolation to the time of the cyclen **1** injection (60 s in all traces) allowed us to assess the extent of lipid quenching in the primary phase accurately. These data were fitted into the binding isotherm, and the maximum fluorescence quenching and apparent binding constant K_a were assessed. The found values for these two parameters were 46 ± 2% and 4.8-($\pm$1.5) × 10^5 M^{-1}, respectively. A similar data fit was performed for the fluorescence intensity values after lysis of LUVs by Triton X-100. The corresponding values for the maximum fluorescence quenching and binding constant K_a were assessed as 92 ± 4% and 2.1($\pm$1.5) × 10^5 M^{-1}, respectively. The maximum fluorescence quenching by cyclen **1** before and after the lysis of liposomes is consistent with the hypothesis that the membrane-impermeable receptor quenches 50% of the fluorescence in the symmetrically labeled LUVs, whereas the similar values of K_a before and after the lysis suggest that the detergent produced little effect on the complex formation. The assessed binding constant for the lipid **4**−cyclen **1** complex was approximately 10 times lower than that assessed for the complex of a water-soluble dye 8-hydroxypyrene-1,3,6-trisulfonic acid (HPTS) reported previously (*30*); however, the affinity of cyclen **1** to the dye attached to the lipid remained high enough to allow the detection of lipid flip with micromolar concentrations of cyclen **1**.

Next, we performed experiments with LUVs exhibiting asymmetry in the distribution of the labeled lipid between the inner and outer bilayer leaflets. The residual fluorescence at the end of experiments increased as the total concentration of cyclen **1**−lipid **4** complex increased. However, the ratio between fluorescence quenching upon application of 20 μM cyclen **1** and fluorescence quenching upon application of Triton X-100 changed proportionally to the excess of labeled lipid in the outer leaflet of the bilayer (Figure 2C). Subtraction of the residual fluorescence and normalization of the fluorescence intensity to 100% of symmetrical LUVs gave a set of traces with the extent of cyclen **1**-induced fluorescence quenching proportional to the amount of labeled lipid in the outer leaflet (Figure 2D). At the same time, the extent of fluorescence quenching upon application of the detergent remained constant, consistent with the unchanged amount of labeled lipid residing on the inner leaflet of the bilayer. These observations suggest that the proposed

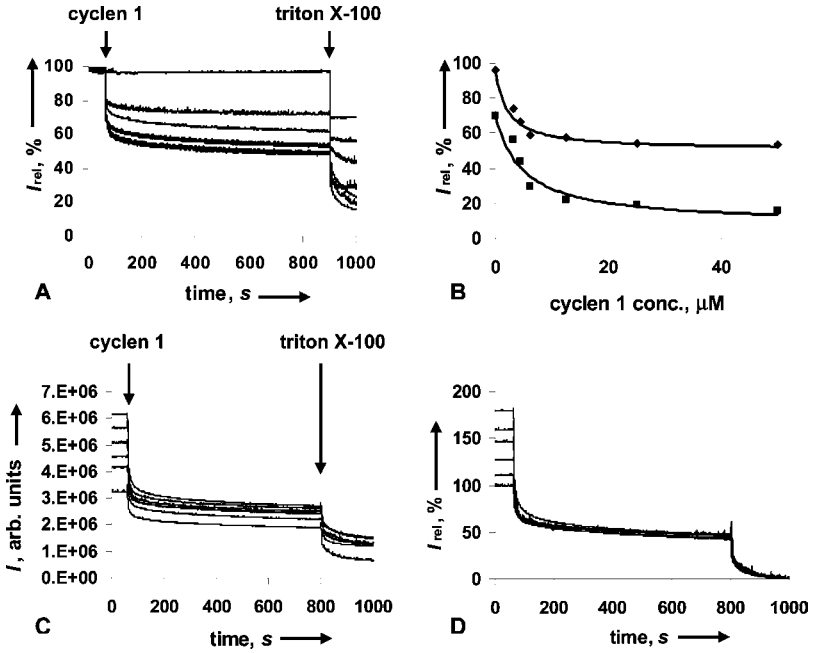


Figure 2. Kinetic monitoring of the fluorescence (ex = 402 nm, em = 434 nm) of LUVs labeled with lipid **4** in the presence of cyclen **1.** A. Fluorescence of symmetrically labeled LUVs in the presence of variable amounts of cyclen **1.** From top to bottom the traces at 500 s denote fluorescence of LUVs in the presence of 0, 3.1, 4.5, 6.3, 12.5, 25, and 50 (μM) cyclen **1**. Time events: 60 s: 20 μL of 0−5 mM DMSO solution of cyclen **1** was injected into 2 mL of LUVs suspension; 900 s: 40 μL of aqueous 25% solution of Triton X-100 was injected. B. Points in the upper trace correspond to the fluorescence intensity values from (A) extrapolated to the maxima of the fast quenching (see main text for explanation). Points in the bottom trace correspond to the fluorescence intensity values after the lysis of LUVs with Triton X-100. Continuous lines in both traces represent best fits to a 1:1 binding model. **C**. Kinetic monitoring of the fluorescence of LUVs asymmetrically labeled with lipid **4**. From bottom to top at 30 s traces denote LUVs containing 0.25, 0.31, 0.38, 0.5, 0.68, and 0.75 μM (bulk concentration) lipid **4** in the outer leaflet and 0.25 μM lipid **4** in the inner leaflet. Time events: 60 s*:* 20 μL of 2 mM DMSO solution of cyclen **1** was injected into 2 mL of LUVs suspension; 900s: 40 μL of aqueous 25% solution of Triton X-100 was injected. D. Data from (C) after subtraction of the residual fluorescence and normalization to 100% of the fluorescence of symmetrical LUVs.

methodology is indeed suitable for the assessment of the lipid distribution between the inner and outer leaflets of liposomal membranes.

In the envisioned mode of interaction between lipid **4** and cyclen **1,** cyclen **1** binds to the cascade-blue label of lipid **4** at the surface of the bilayer membrane. Therefore, it was possible that the receptor bound to the membrane was perturbing the integrity of this membrane, thus affecting the rate of the lipid flip. In order to find whether this was the case, we performed an additional experiment with symmetrically labeled LUVs containing 0.5 mol % of lipid **4**. This five times higher concentration of lipid **4** would introduce five times more of cyclen **1** upon binding. If cyclen **1** interferes with the integrity of the bilayer membrane, a different rate of lipid **4** quenching in the secondary slow phase would be observed. However, the kinetic trace obtained in the experiment with these new LUVs was identical (except the absolute fluorescence intensity) to that obtained for the LUVs labeled with 0.1 mol % of lipid **4**, including the extent of fluorescence quenching in the fast phase and the slope of the fluorescence quenching in the secondary slow phase. Therefore, we concluded that cyclen **1** does not perturb the integrity of the bilayer membrane in the range of concentrations of cascade-blue label used in these experiments, and it does not affect the rate of the lipid flip.

Reversibility of Binding. The NBD-dithonite lipid flip assay relies on the irreversible covalent modification of the NBD label by reduction of the nitro group to an amino group, which leads to the loss of fluorescence. In contrast, the pyrene-cyclen **1**-based assay relies on the noncovalent and, therefore, potentially reversible interactions of the fluorescent label with the receptor. Two independent methods can be considered for such binding reversal: first, a competitive displacement

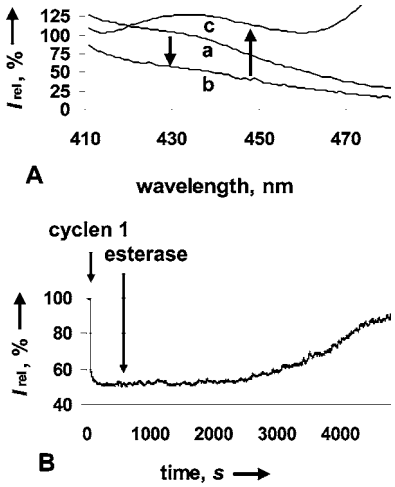


Figure 3. Reversibility of cyclen **1**−lipid **4** complexation. A. Emission spectra of the LUVs labeled with lipid **4** (ex = 402 nm): (a) spectrum of LUVs in the presence of 1% DMSO (blank experiment); (b) spectrum of LUVs in the presence of 5 μM cyclen **1** and 1% DMSO; (c) spectrum of LUVs in the presence of 5 μM cyclen **1**, 1% DMSO, and 5 μM HPTS. The intensities were normalized to 100% of the emission intensity of cyclen **1**-free set of LUVs (trace a) at 434 nm. B. Kinetic monitoring of the fluorescence intensity of LUVs labeled with lipid **4** upon application of 10 μM cyclen **1**, followed by the application of porcine liver esterase (150 U).

of the fluorescent label, attached to the lipid with the water-soluble substrate for the same receptor and, second, degradation of the receptor leading to the release of the phospholipid label.

The first method has a disadvantage where all the identified substrates for the receptor cyclen **1** are fluorescent dyes with spectral characteristics similar to that of cascade-blue label of

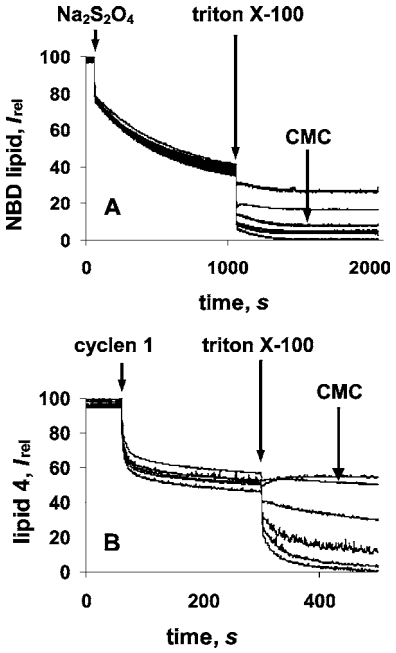


Figure 4. Comparison of NBD-dithionite and cyclen **1**−lipid **4**−lipid flip monitoring assay in the presence of variable amounts of Triton X-100**.** A. Kinetic monitoring of the fluorescence of NBD-labeled LUVs treated with 60 mM $Na_2S_2O_4$ and varying amounts of Triton X-100. From top to bottom the traces at 1500 s denote application of 0.12, 0.17, 0.22, 0.36, 0.72, 1.45, and 2.9 (mM) Triton X-100. Please note a significant fluorescence quenching at 0.17 mM (below CMC) concentration of Triton X-100 (second trace from top). B. Kinetic monitoring of the fluorescence of lipid **4**-labeled LUVs treated with 20 μM cyclen **1** and varying amounts of Triton X-100. From top to bottom the traces at 400 s denote 0.12, 0.22, 0.36, 0.72, 1.45, 2.9 (mM) Triton X-100. Please note that the application of submicellar and micellar concentrations of Triton X-100 (two upper traces) resulted in a little loss of the fluorescence quenching. In both figures, the traces were normalized by the subtraction of the residual fluorescence observed in the sample with highest amount of Triton X-100, and adjustment to 100% of the initial fluorescence values.

lipid **4**. The largest spectral window, however, was found for the cascade-blue label of lipid **4** (ex = 402 nm, em = 434 nm) and its synthetic precursor, HPTS (ex = 405 nm, em = 510 nm). The displacement experiments, where a suspension of LUVs labeled with lipid **4** was originally treated with 5 μM cyclen **1** and then with 0−10 μM HPTS, demonstrated an increase of the fluorescence intensity at 434 nm (ex = 402 nm) upon addition of HPTS (Figure 3A). Yet, a substantial contribution of the HPTS emission to the total intensity of the fluorescence at this wavelength made this approach nonpractical. We are currently screening other potential candidate molecules that might form strong complexes with cyclen **1** and displace cascade-blue label of lipid **4**.

To demonstrate the possibility for the second approach, we decided to enzymatically degrade cyclen **1**. The thiourea units of cyclen **1** are tethered to the cyclen scaffold via ester-type linkers, making cyclen **1** a suitable substrate for a variety of esterases. In the course of the kinetic experiment, the fluorescence of LUVs labeled with lipid **4** was monitored as a function of time. The application of 10 μM cyclen **1** resulted in the loss of 43% fluorescence. Application of 150 U of porcine liver esterase resulted in a gradual increase of the fluorescence, which reached 90% of the original intensity in approximately 1.5 h (Figure 3B). This example demonstrates that the bound portion of lipid **4** can be released if required during the lipid-flip monitoring experiment.

Comparative Invasiveness of Cyclen 1 and Sodium Dithionite. Another potential disadvantage of the NBD-dithionite assay can arise from the fact that dithionite is the anion of inorganic

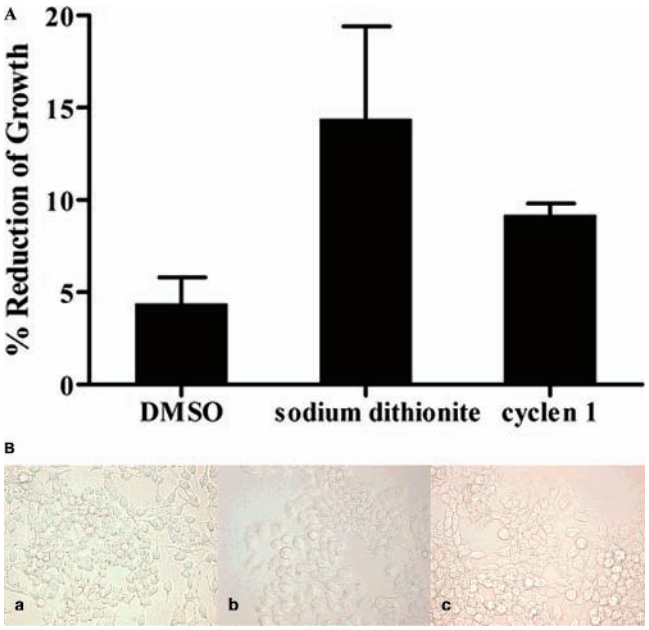


Figure 5. Relative nontoxicity of cyclen **1**. A. Results of growth inhibition assay (A2780 cell line) relative to untreated cells. B. Images of A2780 cells from the growth inhibition assays: (a) untreated cells, (b) cells in the presence of 0.5% DMSO; (c) cells in the presence of 25 μM cyclen **1** and 0.5% DMSO.

salt and can therefore be taken up by cellular transporters, for example sulfate-anion exchangers (*34*). Such internalization of dithionite would result in the reduction of the NBD-label residing on the inner leaflet of the bilayer and may lead to the false-positives in the in vitro experiments. A large molecule of cyclen **1** will unlikely be a substrate for cellular transporters; therefore, no such false positive identification of lipid-flip activity should be expected. We demonstrated this potential advantage of cyclen **1**-based assay in an experiment with LUVs under ion-transport mimicking conditions. It has been shown that detergents at sublytic (below CMC) concentrations form transient pores in the bilayer membranes that may allow passage of small molecules (*35*−*37*). Specifically, sublytic concentrations of Triton X-100 were shown to increase permeability of erythrocyte membranes to small ions (Na^+, Cl^-) but not to the relatively large molecules (glucose) (*38*). We performed a parallel series of kinetic experiments with LUVs containing NBD-labeled phospholipid and LUVs labeled with lipid **4** (Figure 4). The slope of the secondary quenching phase was substantially higher for the LUVs labeled with NBD-PE than with lipid **4**. This is probably because of a higher rate of unmediated transmembrane diffusion of sodium dithionite than that of cyclen **1** at their operating concentrations. As can be seen, the fluorescence decay upon injection of Triton X-100 to LUVs labeled with lipid **4** and treated with 20 μM cyclen **1** was observed only at Triton X-100 concentration exceeding CMC (0.22 mM) (*39*). However, in similar experiments with NBD-labeled LUVs, treated with 60 mM $Na_2S_2O_4$, a substantial decrease in the fluorescence was observed after application of submicellar concentrations of the detergent.

Physiological Compatibility of Cyclen 1. To demonstrate the relative nontoxicity of cyclen **1**, we performed a series of cell growth inhibition assays in the presence of cyclen **1** and sodium dithionite at concentrations relevant to the lipid-flip monitoring assays.

These assays revealed 10% inhibition of cell growth in the presence of 25 μM cyclen **1**, compared to untreated cells, and approximately 5% cell growth inhibition compared to the cells treated with relevant amounts of DMSO (0.5%), consistent with physiological compatibility of this receptor (Figure 5A). Treat-

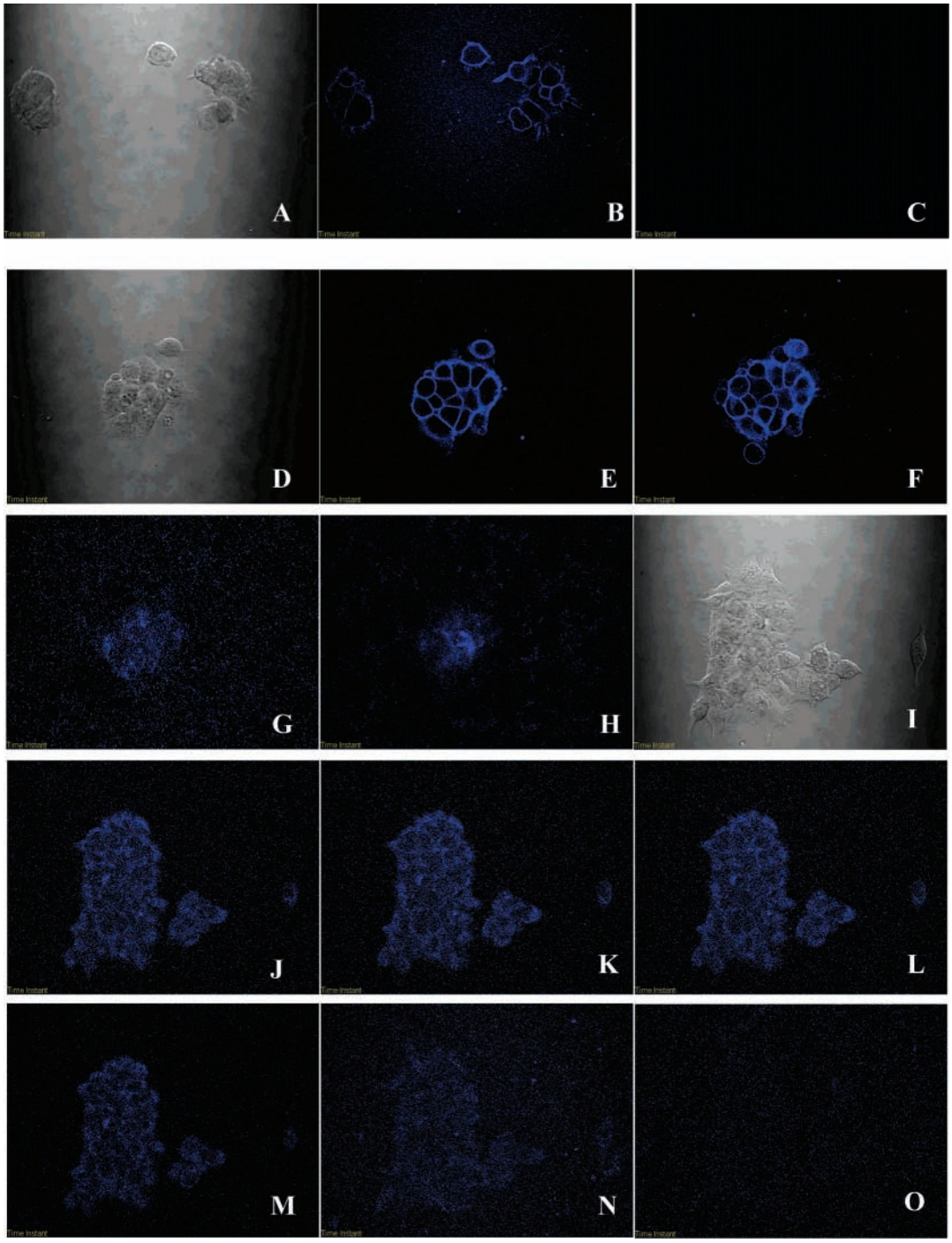


Figure 6. Confocal microscopy images of HEK-293 cell clusters. Images A−C, D−H, and I−O correspond to three distinct sets of cell clusters. A. Brightfield image of the first set of cell clusters. Consequent fluorescence images of the first set of clusters immediately after addition of lipid **4** (B) and upon addition of the quencher cyclen **1** (C, the time interval between additions of lipid **4** and cyclen **1** was less than 5 min). D**.** Brightfield image of the second set of cell clusters. Consequent fluorescence images of the second set of clusters immediately after addition of the lipid **4** (E), after 1 h of incubation with the lipid **4** (F), immediately (G) and 20 min (H) after the addition of the quencher cyclen **1**. I. Brightfield image of the third set of cell clusters. Consequent fluorescence images of the third set of clusters immediately after the addition of lipid **2** (J), after 30 min (K) and 1 h (L) incubation with the lipid **2**; immediately (M**),** 10 min (N), and 20 min (O) after the addition of the quencher cyclen **1**.

ment of the cells with the smallest concentration of sodium dithionite used in the lipid-flip monitoring assays (10 mM) resulted in 15% growth inhibition. No morphological signs of cell damage or death was observed upon treatment with cyclen **1** (Figure 5B).

Applicability of New Methodology to the in Vitro Studies. Finally, we demonstrated that the cyclen **1**-based lipid flip monitoring assay can be utilized for in vitro studies. A series of confocal microscopy imaging experiments on HEK-293 cells showed that the application of lipid **4** resulted in its rapid partitioning into the outer membranes of the cells (Figure 6A−C). Immediate application of cyclen **1** (20 μM) resulted in a complete fluorescence quenching consistent with the fact that all lipid **4** was accessible to the receptor. However, the incubation of the cells with lipid **4** for 1 h resulted in partial diffusion of lipid **4** into the internal membranes of cellular organelles. Application of 20 μM cyclen **1** in this case resulted in the fluorescence quenching of the outer cell membranes, but some residual fluorescence of the cell interior was still observed (Figure 6D−H). Finally, we performed staining of the cells with

lipid **2**, which has high permeability to the membrane barriers (Figure 6I−O). Unlike with lipid **4**, no preferential staining of the outer membranes was observed but rather even distribution of the fluorescent lipid within the cellular interior. A subsequent application of lipid **1** resulted in the fluorescence quenching, which was complete after 15 min of incubation.

These experiments demonstrate that a lipid **4**−cyclen **1** pair provide a suitable pair for the lipid flip monitoring in in-vitro experiments. The focus of our future studies will be a real-time monitoring of the flippase activity of Pgp, using a lipid **4**−cyclen **1** lipid flip monitoring assay.

As with any other fluorimetric methodology, the interpretation of the results obtained through the lipid **4**−cyclen **1** lipid-flip detection assay requires some care because of the possible effects of the non-natural cascade-blue label attached to the lipid molecule. However, the highly anionic character of the cascade-blue label makes a flip of such conjugated lipids more difficult than that of the less polar natural lipids, and therefore no false-positive flippase activity should be detectable by this new methodology. As an alternative, the hydrophobic lipid **2** in place of lipid **4** can be utilized, although with some limitations, to test the flip of less polar substrates.

CONCLUSION

In conclusion, we developed a new methodology for monitoring of lipid flip in both model and cell membranes. This methodology relies on the micromolar concentrations of the fluorescence quencher cyclen **1** and therefore has better compatibility with the physiological conditions than the commonly utilized NBD-dithionite methodology which relies on high millimolar concentrations of sodium dithionite. Unlike with NBD-dithionite assay, where the dithionite causes the irreversible quenching of the fluorescence of NBD-labeled lipid, cyclen **1** forms a noncovalent complex with cascade-blue labeled lipid. The noncovalent nature of such interactions provides a possibility for the reversal of binding through the displacement of the cascade-blue labeled lipid by a water-soluble substrate for cyclen **1**. Alternatively, the complex between cyclen **1** and lipid **4** can be decomposed through the enzymatic degradation of cyclen **1**. The focus of our future studies will be a real-time monitoring of the flippase activity of Pgp, using a lipid **4**−cyclen **1** lipid flip monitoring assay.

ACKNOWLEDGMENT

This work was supported by VCU, NSF (grant ECS-0508381) and the Jeffress Memorial Trust (grant J-764). We thank Prof. Nicholas Farrell for consultations regarding cell proliferation assays, Prof. Sarah Rutan for critical reading and John B. Mangrum for high-resolution MS analysis. The authors thank Prof. Leslie Satin and Dr. Min Zhang from the Department of Pharmacology and Toxicology at VCU for their expertise in confocal imaging.

LITERATURE CITED

(1) Daleke, D. L. (2003) Regulation of transbilayer plasma membrane phospholipid asymmetry. *J. Lipid Res. 44*, 233−242.

(2) Smith, B. D., Lambert, T. N. (2003) Molecular ferries: membrane carriers that promote phospholipid flip-flop and chloride transport. *Chem. Commun.* 2261−2268.

(3) Forbes, C. C., DiVittorio, K. M., and Smith, B. D. (2006) Bolaamphiphiles promote phospholipid translocation across vesicle membranes. *J. Am. Chem. Soc. 128*, 9211−9218.

(4) Shukla, R., Sasaki, Y., Krchnak, V., and Smith, B. D. (2004) Identification of synthetic phosphatidylserine translocases from a combinatorial library prepared by directed split-and-pool synthesis. *J. Comb. Chem. 6*, 703−709.

(5) Yaroslavov, A. A., Melik-Nubarov, N. S., and Menger, F. M. (2006) Polymer-induced flip-flop in biomembranes. *Acc. Chem. Res. 39*, 702−710.

(6) Powers, J. P. S., Tan, A., Ramamoorthy, A., and Hancock, R. E. W. (2005) Solution structure and interaction of the antimicrobial polyphemusins with lipid membranes. *Biochemistry 44*, 15504−15513.

(7) Li, W. J., Nicol, F., and Szoka, F. C. (2004) GALA: a designed synthetic pH-responsive amphipathic peptide with applications in drug and gene delivery. *Adv. Drug Delivery Rev. 56*, 967−985.

(8) Castegna, A., Lauderback, C. M., Mohmmad-Abdul, H., and Butterfield, D. A. (2004) Modulation of phospholipid asymmetry in synaptosomal membranes by the lipid peroxidation products, 4-hydroxynonenal and acrolein: implications for Alzheimer's disease. *Brain Res. 1004*, 193−197.

(9) Fadok, V. A., Voelker, D. R., Campbell, P. A., Cohen, J. J., Bratton, D. L., and Henson, P. M. (1992) Exposure of phosphatidylserine on the surface of apoptotic lymphocytes triggers specific recognition and removal by macrophages. *J. Immunol. 148*, 2207−2216.

(10) Williamson, P., and Schlegel, R. A. (2002) Transbilayer phospholipid movement and the clearance of apoptotic cells. *Biochim. Biophys. Acta 1585*, 53−63.

(11) Borisenko, G. G., Matsura, T., Liu, S. X., Tyurin, V. A., Jianfei, J., Serinkan, F. B., and Kagan, V. E. (2003) Macrophage recognition of externalized phosphatidylserine and phagocytosis of apoptotic Jurkat cells−existence of a threshold. *Arch. Biochem. Biophys. 413*, 41−52.

(12) Hamon, Y., Chambenoit, O., and Chimini, G. (2002) ABCA1 and the engulfment of apoptotic cells. *Biochim. Biophys. Acta 1585*, 64−71.

(13) Zwaal, R. F. A., and Schroit, A. J. (1997) Pathophysiologic implications of membrane phospholipid asymmetry in blood cells. *Blood 89*, 1121−1132.

(14) Chung, S. M., Bae, O. N., Lim, K. M., Noh, J. Y., Lee, M. Y., Jung, Y. S., and Chung, J. H. (2007) Lysophosphatidic acid induces thrombogenic activity through phosphatidylserine exposure and procoagulant microvesicle generation in human erythrocytes. *Arterioscler. Thromb. Vasc. Biol. 27*, 414−421.

(15) DiVittorio, K. M., Lambert, T. N., and Smith, B. D. (2005) Steroid-derived phospholipid scramblases induce exposure of phosphatidylserine on the surface of red blood cells. *Bioorg. Med. Chem. 13*, 4485−4490.

(16) Boon, J. M., Lambert, T. N., Sisson, A. L., Davis, A. P., and Smith, B. D. (2003) Facilitated phosphatidylserine (PS) flip-flop and thrombin activation using a synthetic PS scramblase. *J. Am. Chem. Soc. 125*, 8195−8201.

(17) Nicolay, J. P., Gatz, S., Liebig, G., Gulbins, E., and Lang, F. (2007) Amyloid induced suicidal erythrocyte death. *Cell Physiol. Biochem. 19*, 175−184.

(18) Zwaal, R. F. A., Comfurius, P., and Bevers, E. M. (2005) Surface exposure of phosphatidylserine in pathological cells. *Cell Mol. Life Sci. 62*, 971−988.

(19) Uhl, R. G., Stevenson, A., and Sidorov, V. (2007) Towards improved gene delivery: Flip of cationic lipids in highly polarized liposomes. *Chem. Commun.* 383−385.

(20) Fattal, E., Nir, S., Parente, R. A., and Szoka, F. C. (1994) Pore-forming peptides induce rapid phospholipid flip-flop in membrane. *Biochemistry 33*, 6721−6731.

(21) Estronca, L. M. B. B., Moreno, M. J., Laranjinha, J. A. N., Almeida, L. M., and Vaz, W. L. C. (2005) Kinetics and thermodynamics of lipid amphiphile exchange between lipoproteins and albumin in serum. *Biophys. J. 88*, 557−565.

(22) Pomorski, T., Herrmann, A., Zimmermann, B., Zachowski, A., and Muller, P. (1995) An improved assay for measuring the transverse redistribution of fluorescent phospholipids in plasma membranes. *Chem. Phys. Lipids 77*, 139−146.

(23) Pomorski, T., Muller, P., Zimmermann, B., Burger, K., Devaux, P. F., and Herrmann, A. (1996) Transbilayer movement of fluorescent and spin-labeled phospholipids in the plasma membrane of human fibroblasts: a quantitative approach. *J. Cell Sci. 109*, 687−698.

(24) McIntyre, J. C., and Sleight, R. G. (1991) Fluorescence assay for phospholipid membrane asymmetry. *Biochemistry 30*, 11819−11827.

(25) Armstrong, V. T., Brzustowicz, M. R., Wassall, S. R., Jenski, L. J., and Stillwell, W. (2003) Rapid flip-flop in polyunsaturated

(docosahexaenoate) phospholipid membranes. *Arch. Biochem. Biophys. 414*, 74−82.
(26) Moreno, M. J., Estronca, L. M. B. B., and Vaz, W. L. C. (2006) Translocation of phospholipids and dithionite permeability in liquid-ordered and liquid-disordered membranes. *Biophys. J. 91*, 873−881.
(27) Eckford, P. D. W., and Sharom, F. J. (2005) The reconstituted P-glycoprotein multidrug transporter is a flippase for glucosylceramide and other simple glycosphingolipids. *Biochem. J. 389*, 517−526.
(28) Urbatsch, I. L., Gimi, K., Wilke-Mounts, S., Lerner-Marmarosh, N., Rousseau, M. E., Gros, P., and Senior, A. E. (2001) Cysteines 431 and 1074 are responsible for inhibitory disulfide cross-linking between the two nucleotide-binding sites in human P-glycoprotein. *J. Biol. Chem. 276*, 26980−26987.
(29) Kamp, D., Sieberg, T., and Haest, C. W. M. (2001) Inhibition and stimulation of phospholipid scrambling activity. Consequences for lipid asymmetry, echinocytosis, and microvesiculation of erythrocytes. *Biochemistry 40*, 9438−9446.
(30) Winschel, C. A., Kalidindi, A., Zgani, I., Magruder, J. L., and Sidorov, V. (2005) Receptor for anionic pyrene derivatives provides the basis for new biomembrane assays. *J. Am. Chem. Soc. 127*, 14704−14713.
(31) Kwak, E. S., and Vanden Bout, D. A. (2003) Fully time-resolved near-field scanning optical microscopy fluorescence imaging. *Anal. Chim. Acta 496*, 259−266.
(32) Obreza, A., and Gobec, S. (2004) Recent advances in design, synthesis and biological activity of aminoalkylsulfonates and sulfonamidopeptides. *Curr. Med. Chem. 11*, 3263−3278.
(33) Whitaker, J. E., Haugland, R. P., Moore, P. L., Hewitt, P. C., Reese, M., and Haugland, R. P. (1991) Cascade blue derivatives: Water soluble, reactive, blue emission dyes evaluated as fluorescent labels and tracers. *Anal. Biochem. 198*, 119−130.
(34) Markovich, D., Bissig, M., Sorribas, V., Hagenbuch, B., Meier, P. J., and Murer, H. (1994) Expression of rat renal sulfate transport systems in *Xenopus laevis* oocytes. Functional characterization and molecular identification. *J. Biol. Chem. 269*, 3022−3026.
(35) Lin, H.-Y., and Thomas, J. L. (2003) PEG-lipids and oligo-(ethylene glycol) surfactants enhance the ultrasonic permeabilizability of liposomes. *Langmuir 19*, 1098−1105.
(36) Strupp, W., Weidinger, G., Scheller, C., Ehret, R., Ohnimus, H., Girschick, H., Tas, P., Flory, E., Heinkelein, M., and Jassoy, C. (2000) Treatment of cells with detergent activates caspases and induces apoptotic cell death. *J. Membr. Biol. 175*, 181−189.
(37) Lesieur, S., Grabielle-Madelmont, C., Menager, C., Cabuil, V., Dadhi, D., Pierrot, P., and Edwards, K. (2003) Evidence of surfactant-induced formation of transient pores in lipid bilayers by using magnetic-fluid-loaded liposomes. *J. Am. Chem. Soc. 125*, 5266−5267.
(38) Shalel, S., Streichman, S., and Marmur, A. (2002) The mechanism of hemolysis by surfactants: Effect of solution composition. *J. Colloid Interface Sci. 252*, 66−76.
(39) Tiller, G. E., Mueller, T. J., Dockter, M. E., and Struve, W. G. (1984) Hydrogenation of triton X-l00 eliminates its fluorescence and ultraviolet light absorption while preserving its detergent properties. *Anal. Biochem. 141*, 262−266.

BC700189N

Radiolabeling of Bombesin-Like Peptide with ^{99m}Tc: ^{99m}Tc-Litorin and Biodistribution in Rats†

Kubra Durkan, Fatma Yurt Lambrecht,* and Perihan Unak

Department of Nuclear Applications, Institute of Nuclear Sciences, Ege University, Bornova 35100, Izmir, Turkey. Received December 26, 2006; Revised Manuscript Received July 19, 2007

Bombesin-like peptides are related to several human cancer receptors, including small cell lung, prostate, breast, colon, and pancreatic cancers. Litorin, an amphibian bombesin peptide derivative, is found to stimulate the contraction of smooth muscle, to stimulate gastrin, gastric acid, and pancreatic secretion, and to suppress the nutriment in in vivo experiments. In the present study, litorin was labeled with ^{99m}Tc by the stannous chloride procedure. Labeling yield is 95 ± 1.4%, as determined by radio thin layer chromatography (RTLC) and radio high performance chromatography (RHPLC). Results of in vitro studies demonstrated a high stability in serum and cysteine solutions. In vivo biodistribution was investigated with normal male Albino Wistar rats. Biodistribution data showed fast clearance, low intestinal accumulation, and significant uptake in bombesin/gastrin releasing peptide (BN/GRP) receptor rich tissues such as the pancreas (23.56 ± 0.01 %ID/g 30 min pi). It can be blocked partially by previous administration of 'cold' litorin. The results showed specificity of the uptake. As ^{99m}Tc-litorin displays good radiolabeling and biodistribution, it is a potentially useful radiopharmaceutical for detection of bombesin receptor-expressing cancers.

INTRODUCTION

Radiolabeled peptides have exhibited great potential for imaging and therapy of tumors in recent years. Peptides have some favorable characteristics: they are readily synthesized, are inexpensive, and can withstand rigid chemical conditions for modifications and radiolabeling. Furthermore, because of their low molecular weight, small peptides are expected to efficiently penetrate into tumor tissue, exhibit a faster clearance, and thus lead to better tumor-to-background ratios than high molecular weight compounds such as monoclonal antibodies and their constructs (*1*−*7*).

The amphibian 14-amino acid peptide bombesin (BN) is part of the super family of bombesin-like peptides that also includes the mammalian homologue gastrin relasing peptide (GRP) and the related neuromedin B (NMB) (*1*). The gastrin releasing peptide has been found to produce a wide range of biological responses in peripheral tissues as well as in the central nervous system, for instance stimulation of gastrointestinal hormone release, exocrine secretion, and maintenance of circadian rhythms (*1*, *2*, *8*−*11*).

Bombesin-like peptides exert their effects on target cells by binding to surface G protein-coupled receptors characterized by the typical configuration of seven transmembrane domains (*12*). They have a wide range of physiological activities, including stimulation of the release of numerous gastrointestinal hormones, stimulation of pancreatic enzyme secretion effects on the central nervous system, such as thermoregulation, and inhibition of thyroid-stimulating hormone (*13*). In addition to these physiological effects, it also plays an important role in cancer. Initiation of its interaction with the GRP receptor promotes tumor growth in a number of normal and human cancer cells both in culture and in nude mice xenografts (*12*, *14*). On the other hand, it has been established that BN/GRP receptors are expressed in resected human biopsy specimens of mainly small lung cancers, prostate carcinomas, gastric, pancreatic, colon cancer, and breast carcinomas often at much higher densities than in normal surrounding tissue; this provides at molecular basis for GRP-R-targeted diagnostic imaging and/or internal radiotherapy of malignant lesions with radiolabeled bombesin analogues. In addition, the high frequency of these tumors has had a synergic effect in stimulating research on novel bombesin-like radiotracers for effective in vivo targeting of GRP-R-positive neoplastic disease (*12*−*15*). Furthermore, the use of BN/GRP antagonists as carrier molecules for targeting cytotoxic drugs to tumor cells has recently been proposed (*12*).

Some peptides structurally related to bombesin were discovered from amphibian skin and divided into three groups: (1) bombesin family that includes bombesin and alytesin; (2) ranatensin family that includes ranatensin, litorin; (3) their derivatives and the phyllolitorin family (*16*). Litorin (pGlu-Gln-Trp-Ala-Val-Gly-His-Phe-Met-NH_2) has an amino acid sequence similar to that of bombesin.

Rapid pharmacokinetics is ideal for labeling peptides with a radioisotope that has a short half-life, such as technetium-99m. Among all radioisotopes used in nuclear medicine, Tc-99m is still the most widely applied for diagnostic purposes, mainly because of ready availability, low cost, excellent imaging properties, favorable dosimetry, and high specific activity.

The development of ^{99m}Tc-labeled BN/GRP analogues for cancer imaging would be even more promising. For this reason, various ^{99m}Tc- or ^{111}In-labeled bombesin analogues could probably allow early noninvasive diagnosis of GRP receptor-positive tumors by SPECT in nuclear medicine (*1*, *2*, *8*, *10*−*15*, *17*−*23*). The aim of the present work is to develop a ^{99m}Tc-labeled bombesin-like peptide for tumor imaging. Litorin was labeled with Tc-99m, and its radiopharmaceutical potential was investigated with biodistribution studies in normal male Albino Wistar rats.

* To whom correspondence should be addressed. Fax: 90 2323886466; e-mail: fatma.yurt.lambrecht@ege.edu.tr.

† A part of radiolabeling of this study was presented at a poster session of the Technetium, Rhenium and Other Metals in Chemistry and Nuclear Medicine 7, 7th International Symposium on Technetium in Chemistry and Nuclear Medicine, 329-330, Bressanone (BZ), Italy, September 6−9, 2006.

10.1021/bc060400x CCC: $37.00 © 2007 American Chemical Society
Published on Web 08/31/2007

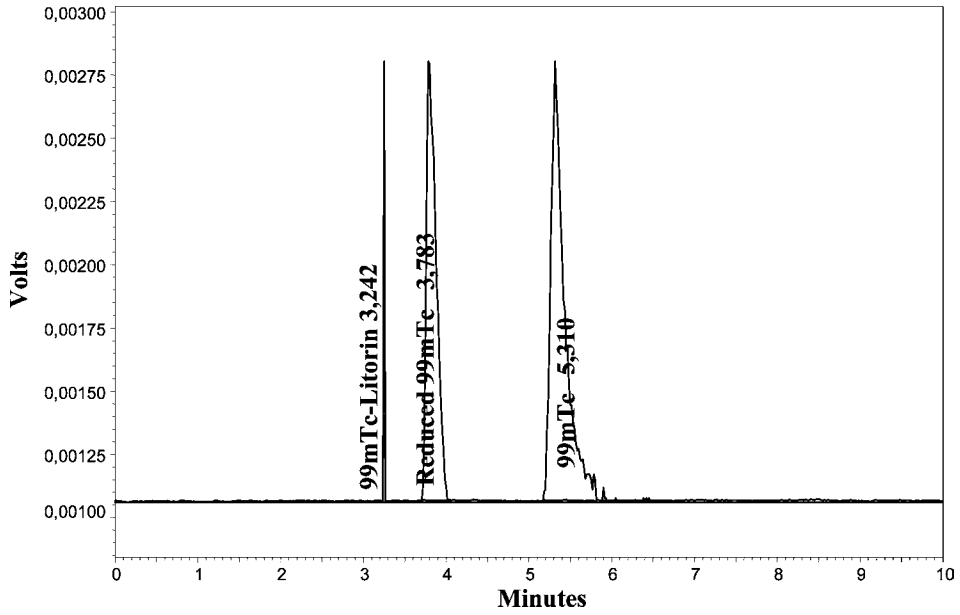


Figure 1. RHPLC chromatograms from radioactivity detection.

EXPERIMENTAL PROCEDURES

Materials. $Na^{99m}TcO_4$ was supplied by the Department of Nuclear Medicine of Ege University, as $^{99}Mo/^{99m}Tc$ generator eluent (Monrol, Istanbul-Turkey). Litorin was obtained from Phoenix Pharmaceuticals Inc., Germany. All other chemicals were from Merck Chemical Co.

Radiolabeling with ^{99m}Tc. Radiolabeling of litorin with Tc-99m was performed via the stannous (II) chloride method. Litorin was dissolved in distilled water at 1 mg/50 mL concentration. The solution of peptide was distributed in 10 μg/500 μL aliquots in eppendorf vials that were stored at −20 °C. $SnCl_2{\cdot}2H_2O$ (1 mg) was freshly prepared by dissolving in 1 mL distilled water and 25 μL of stannous chloride solution was added to the eppendorf vial containing 5 μg/250 μL litorin solutions. pH was adjusted to 3 by using HCI (0.1N) or NH_3 (0.1N). After the $SnCl_2{\cdot}H_2O$ solution was added to the vial, about 55.5 MBq $Na^{99m}TcO_4$ was added. It was left to incubate for 25 min at room temperature.

Radiochemical Analysis. Effects of pH, amount of stannous chloride on labeling percentage, and serum stability time were investigated.

Radio-TLC Analysis. RTLC was done with a Sigma ITLC chamber using 10 × 1.5 cm^2 RTLC-SG strips. After development, they were dried, covered by sellotape, and cut into 0.5 cm strips. These were counted with a Cd(Te) detector equipped with a RAD 501 single channel analyzer (Isin Electronic Co., Izmir, Turkey). Two different solution systems were used as a developing solution: ACD [citrate-dextrose buffer solution (Eczacibasi-Baxter)] and acetone.

Radio-HPLC Analysis. HPLC analysis was performed on a low-pressure gradient HPLC system with LC-10 ATvp quaternary pump, UV detector (Shimadzu SPD-10ATvp, Macherey-Nagel, EC 250/4.6 Nucleodur 100-5 C18 column) and 20 μL loop and equipped with a Cd(Te) detector equipped with a RAD-501 single channel analyzer. HPLC was run using a gradient of 0.1% TFA in H_2O (solvent A) and 0.1% TFA in CH_3CN (solvent B) at a flow rate of 1 mL/min. The HPLC gradient system was begun with a solvent composition of 95% A and 5% B and reached to 60% A and 40% B in 20 min. The UV detector was settled at 240 and 280 nm.

Serum Stability of ^{99m}Tc-Litorin. ^{99m}Tc-Litorin (300 μL) was incubated with fresh human serum (600 μL) in duplicate at 37 °C through 24 h. During incubation, the sample was analyzed at 15 min, 1, 2, 3, 4, and 24 h. The amount of free pertechnetate in the samples was determined by RTLC using ACD and acetone as medium.

Partition Coefficient. A 100 μL aliquot of radiolabeled peptide was added to a test tube containing 3 mL of each of n-octanol and water. The tube was vortexed, for 1 h at room temperature, and then centrifuged at 3000 rpm for 5 min. Aliquots (0.5 mL) of each phase were taken for counting. The partition coefficient was determined by the function: Partition coefficient = $\log_{10}$(counts in n-octanol layer/ counts in aqueous layer) (*15*).

Cysteine Challenge. ^{99m}Tc-Litorin was tested for instability toward cysteine. A fresh cysteine solution was prepared (0.5 mg mL^{-1} in 0.1 M PBS, pH 7.0) and diluted to different concentrations. A known amount of the radiolabeled peptides was incubated with an excess amount of cysteine (100 fold molar excess compared to the peptide) at 37 °C for 1 h. Radiochemical purity was determined by RTLC.

Biodistribution in Normal Rats. The institutional Animal Review Committee of Ege University approved the animal experiments. Male, 24 weeks rat Albino Wistar rats (average weight 150−200 g) were used for the biodistribution in the groups of three per time point. The pH of ^{99m}Tc-litorin (0.1 μg litorin, specific activity 401 GBq/μmol) was adjusted to 7, using 0.1 N NH_3. The solution was then passed through a 0.22 μm Millipore filter. ^{99m}Tc-Litorin was injected into the tail vein. Animals were sacrificed under intense ether atmosphere at 30, 90, 180, and 300 min postinjection and main organs and blood were removed, weighed, and counted. Biodistribution data were calculated as the percent injected dose per gram tissue (%ID/g).

In Vivo Blocked Experiments. Receptor blocking studies were also carried out where cold litorin was administered to the animals for *in vivo* saturation of GRP receptors prior to an injection of ^{99m}Tc-litorin. In this study, each animal received 1 μg of cold litorin i.v., 30 min prior to the injection of ^{99m}Tc-litorin (specific activity 401 GBq/μmol). They were sacrificed at 30 min postinjection, the main tissues were removed, the radioactivity was counted, and %ID/g tissue was calculated.

Statistical Analysis. Differences in the mean values of measured activities were evaluated statistically by SPSS 10 program (Univariate Variance Analyses and Pearson Correlation). Probability values <0.05 were considered to be significant.

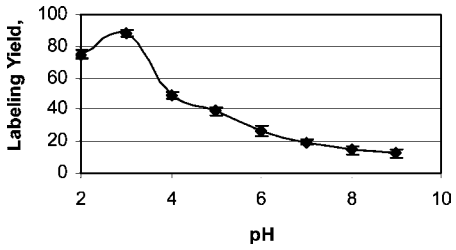


Figure 2. Effect of pH on radiolabeling yield of ^{99m}Tc-litorin.

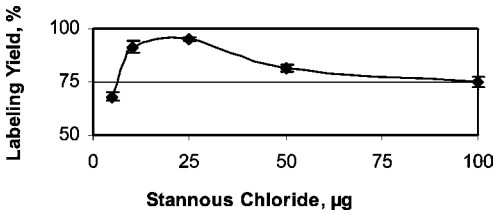


Figure 3. Effect of stannous chloride concentration on radiolabeling yield of ^{99m}Tc-litorin.

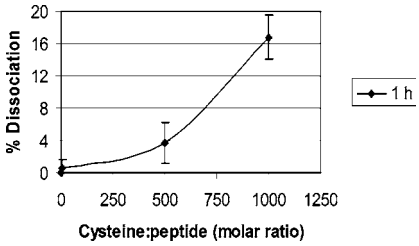


Figure 4. Dissociation of ^{99m}Tc from ^{99m}Tc-litorin following incubation with cysteine at different molar ratios (mean ± SD, $n = 3$).

A Pearson Correlation between the organs of blocked and unblocked animals, testing for ^{99m}Tc-litorin, was obtained.

RESULTS AND DISCUSSION

Radiolabeling. By RTLC, reduced-Tc-99m ($R_f = 0.08$) and ^{99m}Tc-litorin ($R_f = 0.07$) are separated from free $^{99m}TcO_4^-$ ($R_f = 1.00$) using acetone as medium. With ACD solution, reduced Tc-99m ($R_f = 1.00$) and $^{99m}TcO_4^-$ ($R_f = 0.72$) moved to the front, whereas ^{99m}Tc-litorin ($R_f = 0.07$) is almost immobile. In radio-HPLC analysis (Figure 1) retention time values of ^{99m}Tc-litorin, reduced Tc-99m, and pertechnetate are 3.24, 3.78, and 5.31 min, respectively.

Influence of pH on radiolabeling yields was examined in the pH range 2−9 (Figure 2), the optimum being pH 3. Experiments with 5−100 μg of $SnCl_2$ indicated a maximum at 25 μg (Figure 3). On the other hand, the labeling yield decreased with high levels of $SnCl_2$.

Serum stability results showed that *in vitro* stability of the radiolabeled peptide was quite high. Labeling percentage was found 87.4 ± 1.1 and 67.5 ± 5.0 at 4 and 24 h, respectively.

Partition coefficient results show that the partition coefficient of litorin was calculated as theoretical partition coefficient = −2.33 ± 0.96, and the experimental partition coefficient of ^{99m}Tc-litorin was found as −1.12 ± 0.8. Radiolabeled peptide also exhibits low lipophilicity.

Cysteine challenge study shows that the incubation of ^{99m}Tc-litorin with excess cysteine did not produce any significant transchelation to cysteine. A maximum of 16.8 ± 2.7% radioactivity was displaced to cysteine, which indicates that the bond strength of the radiolabeled peptide is high (Figure 4).

Biodistribution in Normal Animals. The biodistribution evaluation of ^{99m}Tc-litorin in normal male Albino Wistar rats at 30, 90, 180, and 300 min is shown in Figure 5.

Maximum uptake of radioactivity was observed in the pancreas ($p = 0.01$), spleen ($p = 0.02$), prostate ($p = 0.08$), and kidneys ($p = 0.01$) as 23.56 ± 0.01, 4.73 ± 0.83, 0.41 ± 0.01, and 11.93 ± 0.8 %ID/g, 30 min postinjection, respectively. On the other hand, that in liver and small intestine was 0.36 ± 0.08 and 0.38 ± 0.02 %ID/g at 30 min. While the uptake of ^{99m}Tc-litorin increased in kidneys, liver, and small intestine to 46.01 ± 2.0, 1.28 ± 0.5,and 0.80 ± 0.06 %ID/g, the uptake in pancreas was almost same (24.41 ± 0.5 %ID/g) at 90 min. That in kidneys, small intestine, and liver still increased to 90 min. Excretion of the radioactivity from the body is high by the renal pathway (46.01 ± 2.0 %ID/g in kidney, 90 min) and low by the hepatobiliary pathway (1.28 ± 0.5 %ID/g in liver and 0.80 ± 0.06 %ID/g in small intestine, 90 min). Karra et al. found similar results when $^{99m}Tc-P_2S_2-BBN(7-14)$ analogue (*23*) was used. They showed that the labeled compound was eliminated mainly through the kidneys to the urinary tract, without any significant retention in the kidneys (*14*). The radiolabeled peptide has a tendency to accumulate in kidneys as a result of its low lipophilicity (*2*, *11*, *15*, *21*). ^{99m}Tc-Litorin has low hepatobiliary clearance and predominantly renal excretion. Accumulation of radioactivity in the liver is also low: 0.36 ± 0.08 %ID/g at 30 min postinjection.

Only small amounts of radioactivity remain in kidneys, liver, and spleen at 180 min: 0.17 ± 0.02, 0.008 ± 0.001, and 0.08 ± 0.01 %ID/g, respectively. Therefore, the labeled peptide exhibits rapid clearance from nontarget tissues.

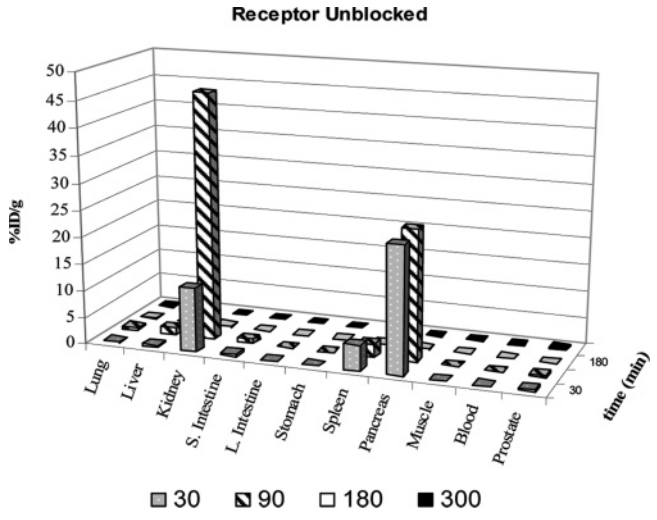


Figure 5. Organs biodistribution data at 30, 90, 180, and 300 min after injection of ^{99m}Tc-litorin in normal male Albino wistar rats.

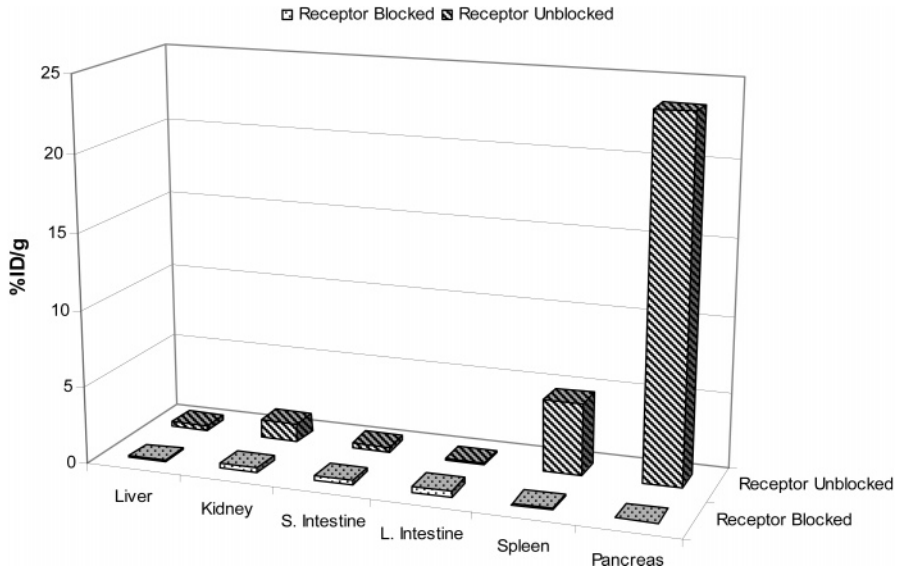


Figure 6. Blocked biodistribution data at 30 min after injection of ^{99m}Tc-litorin in normal male Albino wistar rats (SD: ±0.01−0.03).

In this study, a significant uptake (23.56 ± 0.01 %ID/g, 30 min postinjection) of the radioactivity was found for the pancreas. This demonstrates the ability of ^{99m}Tc-litorin to target BN/GRP receptor-expressing cells in vivo. The pancreas, which expresses BN receptors, has been used as a target by other investigators for the biological evaluation of newly developed radiolabeled BN analogues (*21*, *23*, *13*). The highest pancreas/blood and pancreas/muscle ratios were 472 and 2356, respectively, at 30 min postinjection. The ratios are higher than in another study in which the ratios (23 and 74, 2 h postinjection) were obtained by Lin et al. using [DTPA^1, Lys^3 (^{99m}Tc-Hx-DADT),Tyr^4]BN (*13*). On the other hand, in the study performed by Karra et al., the pancreas/muscle and pancreas/blood ratios were found to be 80 and 22, respectively, at 4 h postinjection (*23*).

Results of receptor-blocked experiments with litorin confirmed the specificity of ^{99m}Tc-litorin toward the BN/GRP receptor (Figure 6). The difference in the uptake of labeled peptide with and without subcutaneous injection of 1 μg of litorin are significant in the pancreas (0.01 ± 0.01, 23.56 ± 0.01) at 30 min. Little additional uptake was observed in the small intestine (0.38 ± 0.02 %ID/g at 30 min). In animals pretreated with cold litorin, this uptake was significantly reduced (0.28 ± 0.02 %ID/g at 30 min), implying an at least partially specific GRP-R process. 'Cold' peptide is able to reduce uptake in rich tissues, such as the pancreas by 98% and small intestine, by 27%. Acini cells of the pancreas, submucosal layer of the small intestine, circular muscle, and submucosal layer of the colon, as well as the circular muscle of gastric fundus and antrum, all have been shown to express BN/GRP receptors (*12*, *13*) and corresponding accumulation of Tc-99m peptide.

Receptor-blocked results showed that the uptake also decreased in prostate (the uptake in unblocked and blocked 0.41 ± 0.01, 0.19 ± 0.03 %ID/g at 30 min, respectively). Bombesin is a specific growth factor for prostate cancer (*22*), but ^{99m}Tc-litorin uptake is definitely less than with the pancreas. Equally, it is hampered by administration of 'cold' litorin.

The uptake in the stomach was small: 0.01 ± 0.008 %ID/g, 30 min, 0.04 ± 0.01 %ID/g, 90 min. This implies the absence of considerable in vivo decomposition and re-formation of pertechnetate (*2*, *15*).

CONCLUSION

Although, the molecular structure of our labeled complex is unknown, ^{99m}Tc-litorin is assumed to be a complex with litorin attached to reduced Tc-99m. Radiolabeling yield of ^{99m}Tc-litorin is over 95% by using of 5 μg of litorin and 25 μg of $SnCl_2$ at pH 3 in 25 min reaction time at room temperature.

In conclusion, the biodistribution of ^{99m}Tc-litorin in normal animals features high and specific pancreas uptake. The results of the present study are sufficiently encouraging to justify further evaluation of the radiolabeled peptide as a possible GRP-based tumor imaging agent.

ACKNOWLEDGMENT

The authors gratefully acknowledge the financial support received from the Ege University Department of Scientific Projects and T. R Prime Ministry State Planning Organization.

LITERATURE CITED

(1) La Bella, R., Garcia-Garayoa, E., Bahler, M., Blauenstein, P., Schibli, R., Conrath, P., Tourwe, D., and Schubiger, P. A. (2002) A ^{99m}Tc(I)-Postlabeled high affinity bombesin analogue as a potential tumor imaging agent. *Bioconjugate Chem. 13*, 599−604.

(2) La Bella, R., Garcia-Garayoa, E., Langer, M., Blauenstein, P., Beck-Sickinger, A. G., and Schubiger, P. A. (2002) In vitro and in vivo evaluation of a ^{99m}Tc(I)-labeled bombesin analogue for imaging of gastrin releasing peptide receptor-positive tumors. *Nucl. Med. Biol. 29*, 553−560.

(3) Decristoforo, C., and Mather, S. J. (1999) ^{99m}Technetium-labelled peptide-HYNIC conjugates: effects of lipophilicity and stability on biodistribution. *Nucl. Med. Biol. 26*, 389−396.

(4) Stalteri, M. A., Bansal, S., Hider, R., and Mather, S. J. (1999) Comparison of the stability of technetium-labeled peptides to challenge with cysteine. *Bioconjugate Chem. 10*, 130−136.

(5) Heppeler, A., Froidevaux, S., Eberle, A. N., and Maecke, H. R. (2000) Receptor targeting for tumor localisation and therapy with radiopeptides. *Curr. Med. Chem. 7*, 971−994.

(6) Okarvi, S. M. (2002) Peptide-based radiopharmaceuticals: future tools for diagnostic imaging of cancers and other diseases. *Med. Res. Rev. 24*, 357−397.

(7) Mihael, J. W., and Carol, S. R. (2003) *Handbook of Radiopharmaceuticals Radiochemistry and Applications*; pp 643−664, John Wiley and Sons, Chichester, England.

(8) Breeman, W. A. P., Jong, M. D., Bernard, B. F., Kwekkeboom, D. J., Srinivasan, A., Pululim, M. E., Hofland, L. J., Visser, T. J., and Krenning, E. P. (1999) Pre-clinical evaluation of [^{111}In-DTPA-Pro^1, Tyr^4]bombesin, a new radioligand for bombesin-receptor scintigraphy. *Int. J. Cancer. 83*, 657−663.

(9) Breeman, W. A. P., Hofland, L. J., Jong, M. D., Bernard, B. F., Srinivasan, A., Kwekkeboom, D. J., Visser, T. J., and Krenning, E.

P. (1999) Evaluation of radiolabelled bombesin analogues for receptor-targeted scintigraphy and radiotherapy. *Int. J. Cancer. 81*, 658−665.

(10) Breeman, W. A. P., Jong, M. D., Erion, J. L., Bugaj, J. E., Srinivasan, A., Bernard, B. F., Kwekkeboom, D. J., Visser, T. J., and Krenning, E. P. (2002) Preclinical comparison of ^{111}In-labeled DTPA-or DOTA-bombesin analogs for receptor-targeted scintigraphy and radionuclide therapy. *J. Nucl. Med. 43*, 1650−1656.

(11) Ferro-Flores, G., Arteaga de Murphy, C., Rodriguez-Cortes, J., Pedraza-Lopez, M., and Ramirez-Iglesias, M. T. (2006) Preparation and evaluation of ^{99m}Tc-EDDA/HYNIC-[Lys^3]-bombesin for imaging gastrin-releasing peptide receptor-positive tumours. *Nucl. Med. Com. 27*, 371−376.

(12) Nock, B., Nikolopoulou, A., Chiotellis, E., Loudos, G., Maintas, D., Reubi, J. C., and Maina, T. (2002) [^{99m}Tc]Demobesin 1, a novel potent bombesin analogue for GRP receptor-targeted tumour imaging. *Eur. J. Nucl. Med. 30*, 247−258.

(13) Lin, K. S., Luu, A., Baidoo, K. E., Hashemzadeh-Gargari, H., Chen, M. K., Pili, R., Pomper, M., Carducci, M., and Wagner, H. N. (2004) A new high affinity technetium analogue of bombesin containing DTPA as a pharmacokinetic modifier. *Bioconjugate Chem. 15*, 1416−1423.

(14) Gourni, E., Bouziotis, P., Zikos, C., Loudos, G., Xanthopoulos, S., Fani, M., Archimandritis, S. C., and Varvarigou, A. D. (2006) Comparative in vivo evaluation of two novel ^{99m}Tc labelled bombesin derivatives. *Nucl. Instrum. Methods Phys. Res., Sect. A 569*, 518−521.

(15) Okarvi, S. M., and Al-Jammaz, I. (2003) Synthesis, radiolabeling and biological characteristics of a bombesin peptide analog as a tumor imaging agent. *Anticancer Res. 23*, 2745−2750.

(16) Ohki-Hamazaki, H., Iwabuchi, M., and Maekawa, F. (2005) Development and function of bombesin-like peptides and their receptors. *Int. J. Dev. Biol. 49*, 293−300.

(17) Baidoo, K. E., Lin, K. S., Zhan, Y., Finley, P., Scheffel, U., and Wagner, H. N. (1998) Design, synthesis, and initial evaluation of high-affinity technetium bombesin analogues. *Bioconjugate Chem. 9*, 218−225.

(18) Scopinaro, F., Paschali, E., Di Santo, G., Antonellis, T., Massari, R., Trotta, C., Gourni, H., Bouziotis, P., David, V., Soluri, A., and Varvarigou, A. D. (2006) Bombesin receptors and transplanted stem cells in rat brain: high-resolution scan with ^{99m}Tc BN1.1. *Nucl. Instrum. Methods Phys. Res., Sect. A 569*, 525−528.

(19) Scopinaro, F., Varvarigou, A. D., Ussof, W., De Vincentis, G., Sourlingast, T. G., Evangelatos, G. P., Datsteris, J., and Archimandritis, S. C. (2002) Technetium labeled bombesin-like peptide: preliminary report on breast cancer uptake in patients. *Can. Biother. Radiopharm. 17*, 327−335.

(20) Presti-Torres, J., Lima, M. N., Scalco, F. S., Caldana, F., Garcia, V. A., Guimaraes, M. R., Schwartsmann, G., Roesler, R., and Schröder, N. (2007) Impairments of social behavior and memory after neonatal gastrin-releasing peptide receptor blockade in rats: implications for an animal model of neurodevelopmental disorders. *Neuropharmacology 52* (3), 724−32.

(21) Garayoa, E. G., Rüegg, D., Blauenstein, P., Zwimpfer, M., Khan, I. U., Maes, V., Blanc, A., Beck-Sickinger, A. G., Tourwe, D. A., and Schubiger, P. A. (2007) Chemical and biological characterization of new Re(CO)$_3$/ [^{99m}Tc](CO)$_3$ bombesin analogues. *Nucl. Med. Biol. 34* (1), 17−28.

(22) Scopinaro, F., De Vincentis, G., Varvarigou, A. D., Laurenti, C., Iori, F., Remediani, S., Chiarini, S., and Stella, S. (2003) ^{99m}Tc-bombesin detects prostate cancer and invasion of pelvic lymph nodes. *E. J. Nucl. Mol. Imag. 30*, 1378−1382.

(23) Karra, S. R., Schibi, R., Gali, H., Kati, K. V., Hoffman, T. J., Higginbotham, C., Sieckman, G. L., and Volkert, W. A. (1999) ^{99m}-Tc-Labeling and in vivo studies of a bombesin analogue with a novel water-soluble dithiadiphosphine-based bifunctional chelating agent. *Bioconjugate Chem.10*, 254−260.

BC060400X

Surface Modification of Poly(L-lactic acid) Membrane via Layer-by-Layer Assembly of Silver Nanoparticle-Embedded Polyelectrolyte Multilayer

Da-Guang Yu,*[,†] Wen-Ching Lin,*[,‡] and Ming-Chien Yang[‡]

Department of Textile Science, Nanya Institute of Technology, Chung-Li, Tao-Yuan, Taiwan, and Department of Polymer Engineering, National Taiwan University of Science and Technology, Taipei, Taiwan. Received April 20, 2006; Revised Manuscript Received October 13, 2006

The improvement of hydrophilicity, antibacterial activity, hemocompatibility, and cytocompatibility of poly(L-lactic acid) (PLLA) membrane was developed via polyelectrolyte multilayer (PEM) immobilization. Colloidal silver nanoparticles were prepared by using dextran sulfate (DS) as a stabilizer to precede chemical reduction by dextrose. The polysaccharide PEMs, including chitosan (CH) and dextran sulfate (DS)-stabilized silver nanosized colloid (DSS), were successfully deposited on the aminolyzed PLLA membrane in a layer-by-layer (LBL) self-assembly manner. The obtained results showed that the contact angle of PLLA membranes decreased with PEMs grafting layers and reached a steady value after four bilayers of coating, hence suggesting that full coverage was achieved. The PLLA−PEM membranes with DSS as the outermost layer could resist platelet adhesion and human plasma fibrinogen (HPF) adsorption, while prolonging the blood coagulation time. The PLLA−PEM membranes could possess antibacterial activity against Methicilin-resistant *Staphylococus aureus* (MRSA). In addition, the proliferation and viability of human endothelial cells (ECs) on PLLA−PEM membranes could be significantly improved. Overall results demonstrated that such a fast, easy processing and shape-independent method for an antithrombogenic coating can be used for applications in hemodialysis devices.

1. INTRODUCTION

Nowadays, great efforts are being devoted to the development of biodegradable materials in potential applications such as waste management, agriculture, tissue engineering, and clinical treatment (*1*−*3*). Biodegradable polyesters have the excellent water-resistance properties of synthetic polymers as well as the biocompatibility and biodegradability of agricultural-based raw materials. Recently, Poly(L-lactic acid) (PLLA) displayed better processability, improved breaking elongation, lower cost, and improved fabrication ability into compositescompared to other biodegradable synthetic polymers (*4*−*6*) and are complementary to other renewable resource-based materials. However, surface-induced thrombosis and protein fouling of biodegradable polymers should be the most serious problems in applications as blood-contacting materials (*7*, *8*). It is well-known that endothelialization (*9*, *10*) is one approach to solve this problem. Incomplete coverage of endothelial cells (ECs) on the vascular graft surfaces and the subsequent myointimal hyperplasia are the main reasons for the long-term failure of the small-diameter vascular graft (*11*, *12*). Due to the lack of bioactive functionality, PLLA commonly used in tissue engineering is not always suitable for cell adhesion. In consequence, attempts have been engaged to chemically modify the PLLA surface to favor polymer−cell interaction.

The layer-by-layer (LBL) self-assembly of polycations and polyanions into multilayers has emerged as an efficient, versatile, yet easy technique to develop biologically active surfaces. The method depends on the sequential charge inversion of a polymeric surface upon successive immersions of this surface in solutions of oppositely charged polyelectrolytes. Recently, application of the electrostatic LBL self-assembly technique in biomedical engineering was widely developed in artificial tissues (*13*−*18*). Herein, we describe the preparation and properties of a new bioactive immobilization on a PLLA membrane for hemodialysis or endovascular devices based on the LBL self-assembly of polysaccharides, chitosan (CH), and dextran sulfate (DS).

During the past few decades, silver nanoparticles have attracted considerable interest because of their potential applications, such as electromagnetic interference shielding, antibiocidal medical device, and surface-enhanced Raman scattering (*19*, *20*). However, widely used reducing agents in chemical reduction, such as sodium borohydride, hydrazine, and formamide, should be toxic with high risk. In the present study, $AgNO_3$ was the chosen as precursor for the chemical reduction process. Some forms of inorganic silver have been demonstrated to be effective against burns, severe chronic osteomyelitis, urinary tract infections, and central venous catheter infections (*21*). It has been reported that silver contents show an antibacterial property, even at low concentrations in the parts per billion range (*22*). Silver nanoparticles have been reported recently as antibacterial agents against *E. coli*, *S. epidermidis*, and methicillin-resistant *S. aureus* (MRSA) (*23*). In general, colloidal silvers selectively bind to thiol groups, which are widely distributed in bacterial cell wall proteins, and may also bind to bacterial DNA. The pathogens suffocate and die, and are cleared out of the body by the immune, lymphatic, and elimination systems (*24*). Colloidal silver can be taken indefinitely, because it is unlikely to provoke much bacterial resistance as there are a variety of mechanisms of toxicity. Unlike pharmaceutical antibiotics, which destroy beneficial enzymes, colloidal silver leaves these beneficial enzymes intact. Thus, colloidal silver is absolutely safe for humans, plants, and all multicelled living matter (*25*).

We report here novel coatings for PLLA substrates created by the formation of insoluble interpolymeric complexes generated by depositing oppositely charged polyelectrolytes in an LBL

* Corresponding author. Tel: +886-3-4361070; Fax: +886-3-465-9253; E-mail address: hollow.yu@msa.hinet.net.

† Nanya Institute of Technology.

‡ National Taiwan University of Science and Technology.

10.1021/bc060098s CCC: $37.00 © 2007 American Chemical Society
Published on Web 08/10/2007

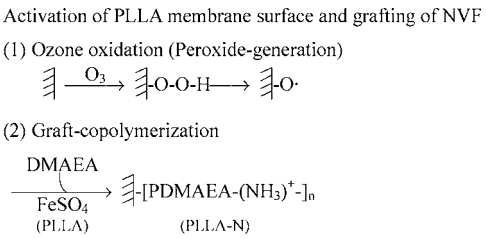


Figure 1. The chemical scheme of PDMAEA immobilization on PLLA membrane via ozone treatment and graft copolymerization.

assembly manner. The polysaccharide PEMs included chitosan (CH) and dextran sulfate (DS)-stabilized silver nanosized colloid (DSS). The non-cytotoxic dextran sulfate (DS) and dextrose served as stabilizer and reducing agent, respectivel,y to form well-distributed silver nanosized colloid (DSS). To characterize the as-fabricated PLLA membranes, measurements of X-ray photoelectron spectroscopy (XPS), field-emission scanning electron microscopy (FE-SEM) and atomic force microscopy (AFM) were performed. The hemocomptibility was evaluated by the plasma protein adsorption, platelet adhesion, and surface-induced thrombogenicity. The in vitro antibacterial activity and cytocompatibility of the resultant PLLA membrane was also accessed. We hope the method of surface modification can contribute to the progress in development of PLLA-related medical devices.

2. EXPERIMENTAL SECTION

2.1. Materials. PLLA chips were purchased from Eastman Corp, Taiwan. Chitosan (M_w = 390 kD, about 85% deacetylation) was obtained from the Taiwan Textile Research Institute, Taiwan. Human plasma fibrinogen (HPF) was purchased from Calbiochem Co., U.S.A. Dextran sulfate (M_w = 500 kD, sulfation degree 16−19%) was supplied by MDBio, Inc., Taiwan. Anticoagulant citrate dextrose (ACD) human blood was provided from the Blood Center in Taiwan. 2-(Dimethylamino)-ethyl methacrylate (DMAEA) was purchased from Aldrich. These chemicals were reagent grade and used without further purification.

2.2. Preparation of DS-Stabilized Silver Nanoparticles. $AgNO_3$ (purity ≥ 99%, Aldrich) was used as a precursor in the preparation of the silver nanoparticles. Dextran sulfate (DS) was used as the stabilizer under chemical reduction by dextrose. The reaction scheme was similar to the silver mirror reaction. Briefly, 0.01 M $AgNO_3$, 0.01 M NaOH, and 0.02 M NH_4OH were mixed thoroughly together for 1 h. Then, 1 mL of the silver alkali solution was added into a 2 wt % DS solution for 30 min, and subsequently added to 10 wt % of dextrose (Sigma). The reaction temperature was maintained at 60 °C by a water bath in the dark. The morphology of nanosized silver colloids was observed using a transmission electron microscope (Philips CM 200) after 20× dilution with ethanol and ultrasonic treatment.

2.3. Surface Modification. Chloroform solutions containing 10 wt % PLLA polymer were stirred for 6−8 h at 25 °C and cast on a glass plate. The solution was allowed to evaporate slowly at 25 °C for 6 h. The resulting membranes with about 0.1 mm thickness were then dried at 50 °C for 24 h. The aminolyzed PLLA membrane was prepared in accordance with the chemical scheme, as shown in Figure 1. The extruded PLLA membranes were ultrasonically cleaned in isopropyl alcohol (IPA) for 15 min prior to surface grafting. Subsequently, as-cleaned membranes were cut into pieces of 2 × 2 cm^2 and treated with 10 g/m^3 of ozone density. The ozone was generated using an ozone generator (Kang I Ozone Enterprise Co., Ltd., Taiwan), and the ozone concentration was controlled by an Ozone UV Photometric Analyzer (SOZ-6000, SKEI Electronics Co., Ltd., Japan). After ozone oxidation for a determined time, the membranes were degassed under vacuum for 5 min to remove ozone adsorbed on the membranes. Afterward, the membranes were immersed in 20 mL of 20 wt % NVF in a glass tube purged with nitrogen, adding 0.1 mL of 0.015 M $FeSO_4$/0.005 M H_2SO_4 to carry out graft polymerization at 60 °C for 120 min. The aminolyzed PLLA (PLLA−N) was rinsed with phosphate buffer solution (PBS, pH 7.4) and double-distilled water to remove the unreacted monomer and homopolymers.

Solutions of DSS, 1 mg/mL in 0.14 M aqueous NaCl, and CH, 1 mg/mL in 0.1 M acetic acid (pH 3.8) containing 0.14 M NaCl, were prepared separately. Ultrapure water was used in all experiments (Milli-Q system, Millipore). The multilayer buildup was accomplished by sequential dipping of the substrate in the polysaccharide solution (alternating between DSS and CH), followed by a 15 min adsorption and a wash with a flow of 0.14 M NaCl. Finally, the samples were extensively cleaned with ultrapure water and freeze-dried at −52 °C using a freeze-dryer (model ZDG, vacuum Freeze Drier, China) for 24 h. The PLLA membranes modified with CH/DSS polyelectrolyte multilayers (PEMs) were defined as PLLA−DSS(CH−DSS)$_n$, where n represented the number of PEMs.

2.4. Determination of Surface Grafting Density. According to our previous work (*26*−*30*), the peroxide groups were tested by a 1,1-diphenyl-2-picrylhydrazyl (DPPH) method. Briefly, ozone-treated TPU membranes were placed in 20 mL of benzene containing 2.5 × 10^{-5} M 1,1-diphenyl-2-picrylhydrazyl (DPPH, Sigma) and kept at 70 °C for 24 h to decompose the peroxides. The DPPH molecules binding to the free radicals formed were quantified from the difference in absorbance at 520 nm between the original and the residual DPPH solutions. The surface density of sulfate groups of DS and amino groups was determined by dyeing with toluidine blue O (Sigma, U.S.A.) and C.I. Acid Orange 7 (Tokyo Kaseo Kogyo Co., Japan), respectively. The dye concentration was determined using an ultraviolet (UV) spectrometer (Ultrospec 1100 pro, Biochrom, Ltd., Cambridge, U.K.).

2.5. Surface Characterization Analysis. Elemental analysis of PEMs on modified PLLA membranes was performed using XPS (ESCALAB 250, Thermo VG Scientific, West Sussex, U.K.) equipped with Mg Kα at 1253.6 eV and 150 W power at the anode. The contact angles of the membranes were evaluated using a contact angle goniometer (DSA 100, Krüss GmbH, Hamburg, Germany) at 25 °C (*28*). The streaming potential (ΔE_{str}) and ζ potential were determined with a tester (EKA088, Austria) using 0.01 M KCl, 8 × 10^{-4}M Na_2HPO_4, and 2 × 10^{-4}M NaH_2PO_4 as the testing solution (pH 7.4). The relationship between ζ potential and streaming potential could be denoted as follows

$$\zeta = 4\pi\eta k_b \Delta E_{str}/\epsilon \Delta P$$

where ζ is ζ potential, ΔE_{str} is streaming potential, ΔP is driving pressure, η is solution viscosity, ϵ is the dielectric constant, and k_b is bulk conductivity.

The surface morphology was further examined using FE-SEM (JSM-6500F, JEOL, Japan) and AFM (MMAFM-2, Santa Barbara, CA).

2.6. Protein Adsorption. The 2 × 2 cm^2 pieces of as-fabricated samples were immersed in 1 mg/mL of HPF (M_w = 341 000, clottable proteins > 95%; Calbiochem, U.S.A.) PBS 7.4 solution with shaking at 100 rpm and 37 °C for 24 h. The membrane was gently taken out and rinsed 5 times with PBS. The sample was placed in a glass bottle with 1 wt % aqueous solution of sodium dodecyl sulfate (SDS) and shaken for 60 min at room temperature to remove the protein adsorbed on the surface. The protein contents of the individual samples were measured colorimetrically using the BCA reagents (Pierce

Chemical Company, U.S.A.) (*31*). The absorption at 570 nm was measured using an ultraviolet spectrometer. The calibration curve was preset by measuring varying protein concentrations in SDS solution.

2.7. Blood Coagulation. To obtain platelet-rich plasma (PRP), the ACD blood was centrifuged at 100 *g* for 20 min at 4 °C to separate the blood corpuscles. Subsequently, a portion of the PRP was further centrifuged at 2000 *g* for 20 min at 4 °C to obtain the platelet-poor plasma (PPP). The in vitro determination of platelet adhesion and coagulation times was in accordance with our previous study (*28*), including activated partial thrombin time (APTT); prothrombin times (PT) were determined using an automated blood coagulation analyzer (CA-50, Sysmex Corp., Kobe, Japan).

2.8 Cytocompatibility evaluation (*32*). The human endothelial cells (ECs) were isolated from human umbilical cord veins of a new bornbaby with 1.0 mg/mL collagenase (type I, Sigma)/phosphate buffer solution (PBS, pH 7.4) for 20−25 min at room temperature. The as-prepared PLLA membranes were fixed with vacuum grease to the bottom of six 15 mm polystyrene Petri dishes without biomaterial deposit to prevent them from floating in the growth media. The human EC cell suspension (100 μL) with a cell density of 2.5×10^5 cell/disk of isolated ECs were routinely seeded on the beds prelaid with native or modified PLLA membranes as well as on tissue culture polystyrene (TCPS) (Nunc, Denmark) as a control. The ECs were incubated in a culture medium consisting of 10% (v/v) fetal calf serum (FCS, Sijiqing Biotech Co., China) in humidified air containing 5% CO_2 at 37 °C. After incubation for 24 h, the culture medium was changed, and then changed again every 2 days. The cell attachment and proliferation ratio were averaged from five parallel measurements at 12 h and 4 days, respectively, by trypsinization of the human ECs using a Neubauer hemacytometer on an inverted light microscope to count the number of cells. The cell proliferation ratio was defined as $(N_2 - N_1)/N_1$, where N_1 and N_2 represent the cell number per well at 12 h and 4 days, respectively. The MTT (3-[4,5-dimethylthiazol-2-yl]-2,5-diphenyltetrasodium bromide; Sigma) assay was used to measure the viability of the fibroblasts (*33*). In addition, after 3 days culture in the 6 well plate, in which 100 μL of the MTT assay (5 mg/mL) was added to each well and incubated at 37 °C for 4 h, the blue formazan reaction product was dissolved by adding 0.5 mL DMSO and diluting to 2 mL with PBS. The absorbance was measured at 490 nm using a microplate autoreader. The relative viability ratio was defined as $(A_{sample} - A_{blank})/A_{control} - A_{blank}$, where A_{sample}, $A_{control}$, and A_{blank} represent the absorption at 490 nm per well of specimen and TCPS at incubation time (68−72 h), and blank disk, respectively.

2.9. Antibacterial Activity Evaluation. Bactericidal activity was evaluated on the basis of the killing rate by the viable cell counting technique against Methicilin-resistant *Staphylococus aureus* (MRSA). One loopful of the bacteria was inoculated in 10 mL of nutrient agar and incubated at 37 °C for 18−24 h; then, 20 mL PBS (composed of 0.2 M Na_2HPO_4, 0.2 M NaH_2PO_4, 0.5 g NaCl, and 2 g/L Tween 80 to 1000 mL) was added. After mixing, 1 mL of the solution was transferred into 9 mL of nutrient broth, and mixed with a vortex mixer. The bacteria solution was diluted with PBS to 1.5×10^5 cells/mL and placed in flasks (6 samples of 0.4 g/sample for each group). After incubating at 37 °C for 0−24 h, 20 mL of PBS was added and stirred for 30 s. Consecutive dilutions were made by taking 1 mL of the previous solution and mixing with 9 mL of PBS. From the diluted solution, the surviving bacteria were determined by the spread plate method. After inoculation, the plates were kept at 37 °C, and the colonies were counted after 18−24 h (*30*).

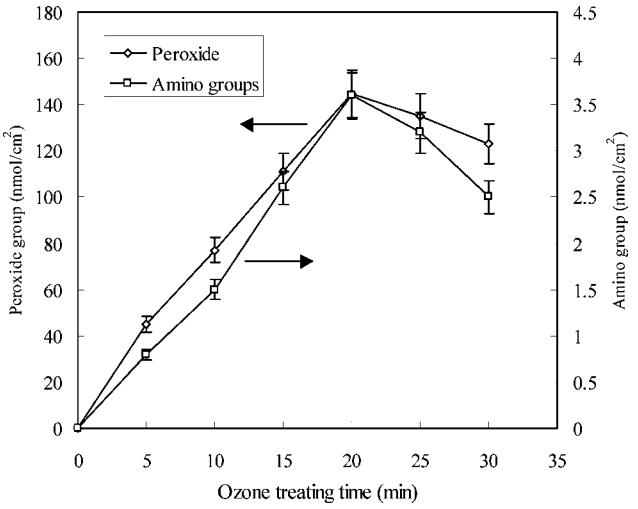


Figure 2. Peroxide and amino group graft density vs ozone treating time determined by DPPH method and dye assay.

3. RESULTS AND DISCUSSION

3.1. The Ozone Treatment of PLLA Membranes. Surface modification of the polymer membrane becomes important when polymeric material is in contact with a physiological component such as blood and living tissue. Zhu et al. (*6*) have developed a novel technique to introduce free amino groups onto polyester scaffolds via aminolyzing the ester groups with diamine. Positively charged chitosan was then deposited onto the aminolyzed poly(L-lactic acid) (PLLA) membrane surface in an LBL assembly manner using poly(styrene sulfonate) sodium salt (PSS) as a negatively charged polyelectrolyte. In the present study, the surface modification was based on the chemical schemes described in Figure 1. By inducing oxidization to modify the PLLA surface with ozone, peroxide groups were easily generated on the surface. The maximum amount (144.8 nmol/cm^2) of peroxide groups appeared at 20 min of ozone exposure and leveled off to a constant value, as shown in Figure 2. The amount of peroxide groups decreased with prolonged treatment time. This was probably attributed to the increase in cross-linking between those peroxide groups or free radicals on the surface of the membrane after prolonged ozone attack. In other words, those peroxides were partially converted into inactive species and thus reduced the free radicals.

Those peroxides were broken by redox-polymerization and provided active species to initiate poly(DMAEA) on the surface of the PLLA membrane. Hence, the aminolyzed PLLA membrane was fabricated. It could be found that the grafting density of the amino group (3.21 nmol/cm^2) was inducted at 20 min of ozone exposure. The multilayer coating procedure was initiated by the immobilization of an aminolyzed PLLA substrate (PLLA−N), yielding a positively charged surface, subsequently placed in contact alternating with a solution of the polyanion DSS and a solution of the polycation CH.

3.2. Formation of DS-Stabilized Silver Nanosized Colloid. To prepare nanosized silver colloid via the chemical reduction method, it is very important to choose an appropriate stabilizer and reducing agent. Generally speaking, a stabilizer agent absorbs on the solid−liquid interface and forms a layer of molecular membrane to hinder contact between the particles. At the same time, it will reduce surface tension, thereby reducing the absorption capability of the capillary. In this work, the water-soluble polymer stabilizer, namely, dextran sulfate (DS), was employed as a stabilizer agent. Colloidal silver nanoparticles were prepared by using dextran sulfate (DS) as a stabilizer to precede chemical reduction by non-cytotoxic dextrose. Because of having moderate reduction power, dextrose was chosen as the reducing agent in this work.

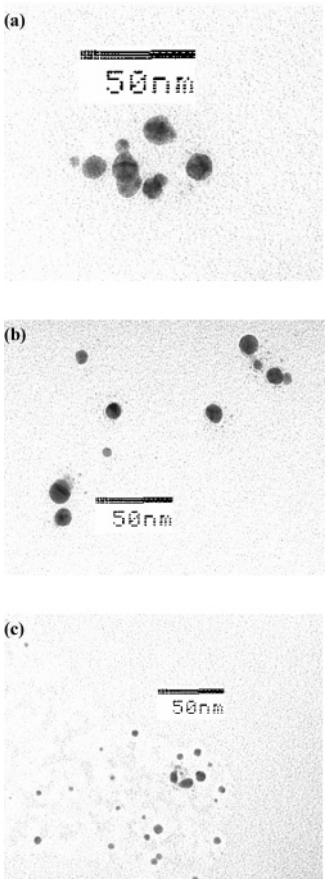


Figure 3. TEM image and corresponding particle analysis of DS-stabilized nanosized silver colloid: (a) 0.5 wt % DS, (b) 1 wt % DS, (c) 2 wt % DS-stabilized silver colloid.

When NaOH was used to promote the reduction reaction, the precursor solution $AgNO_3$ would quickly turn the dark color of pure Ag_2O precipitate. When the NH_4OH was added, the solution became clear, due to the formation of $[Ag(NH_3)_2]^+$. It is possible that at the very beginning of this synthesis process some Ag_2O was formed by the following reaction:

$$2Ag^+ + 2OH^- \rightarrow Ag_2O + H_2O$$

$$Ag_2O + 4NH_3 + H_2O \rightarrow 2[Ag(NH_3)_2]^+ + 2OH^-$$

Subsequently, when adding into DS solution and dextrose, the complex solution gradually changed into a yellowish green color as the reaction was completed. Presumably, it suggested that silver ion was reduced into extremely fine silver particles, which then gradually agglomerated into a stable size distribution. A longer DS molecule chain might provide a physical barrier to slow down the agglomeration process, thus enabling the stabilization process to those silver colloids. No aggregation or decomposition of the silver nanoparticles occurred even after six months storage.

During this process, DS is expected to inhibit the further aggregation of silver nanoparticles and to stabilize the dispersed silver nanoparticles in solution. Figure 3 showed the TEM image of silver nanosized colloid with DS as a stabilizer at the different concentration. The average size of 2 wt % DS-capped silver nanoparticles (7−10 nm) is less than that of 0.5 wt % DS-capped particles (15−20 nm). Using DS as a stabilizer in the chemical reduction process resulted in smaller and more uniform silver nanosized colloids. However, the colloidal silver solution turned turbid after 30 min stirring in the absence of DS. Shin et al. (*33*) proposed that silver nanoparticles were prepared by using poly(vinylpyrrolidone) (PVP) as a stabilizer and γ-irradiation with a size range of 10 to 30 nm. Zhao et al. (*34*) reported that spherical silver nanoparticles capped by mercaptosulfonic acid with a diameter of about 8 nm were prepared by chemical reaction.

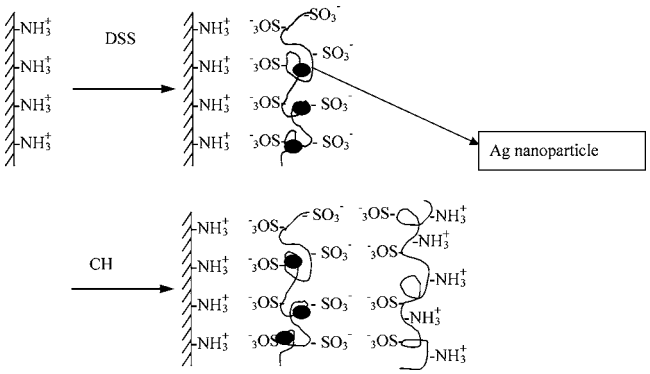


Figure 4. The schematic representation of LBL self-assembly process with oppositely charged PEMs on an aminolyzed PLLA membrane surface. Colloidal silver nanoparticles were prepared by using DS as a stabilizer to precede chemical reduction by dextrose.

Table 1. Characterization of PEM-Modified PLLA Membranes (n = 6, mean ± std)

sample	surface density: amino group[a]	surface density: sulfate group[b]
PLLA−N	3.21 ± 0.01	
PLLA−DSS	0.07 ± 0.01	0.24 ± 0.02
PLLA−DSS−CH	0.87 ± 0.04	0.11 ± 0.04
PLLA−DSS(CH−DSS)$_1$	0.49 ± 0.04	1.37 ± 0.04
PLLA−DSS(CH−DSS)$_2$	0.67 ± 0.05	1.87 ± 0.04
PLLA−DSS(CH−DSS)$_3$	0.74 ± 0.04	2.15 ± 0.04
PLLA−DSS(CH−DSS)$_4$	0.95 ± 0.06	2.27 ± 0.05
PLLA−DSS(CH−DSS)$_5$	0.96 ± 0.07	2.29 ± 0.07

[a] Amino groups (μmol/cm^2), determined with dye staining of C.I. Acid Orange 7. [b] DS (μg/cm^2), determined with dye staining of toluidine blue O.

3.3. Monitoring the LBL Deposition Process onto PLLA Surface. In principle, the adsorption of DSS carrying more than one equal charge allows for charge reversal on the surface, which has two important consequences: (1) repulsion of equally charged molecules and thus self-regulation of the adsorption and restriction to a single layer (2). The ability of oppositely charged molecules to be adsorbed is a second step on top of the first one. The alternative LBL deposition was fabricated by CH and DSS electrostatic adsorption, as described in Figure 4. Chitosan, a polycationic repeating monosaccharide may be combined with the polyanionic DSS such that ionic cross-linking results in hydrogel formation. They appeared to be polyelectrolyte complexes obtained by the formation of polyanion−polycation interactions held between ammonium functions of chitosan and sulfate groups of DSS. The multilayer buildup procedure was monitored next by measuring the dye-staining assay. As listed in Table 1, the amount of CH and DSS in the coating increased with the number of PEMs, showing that the two polyelectrolytes follow a typical multilayer construction mechanism.

3.4. Surface Characterization. Figure 5 and Table 2 showed the XPS survey wide-range spectra of PLLA and PLLA−DSS-(CH−DSS)$_5$ from binding energies 100−600 eV. As illustrated, from the PLLA−PEM membrane was found the additional Ag_{3d} (395 eV), N_{1s} (400 eV), and S_{2p} peaks (167 eV) in comparison with that of native PLLA. These spectra showed the success of Ag-nanoparticle-embedded PEM immobilization on the surface of the PLLA membrane.

The evolution of surface topography throughout the PEM construction process was assessed using FE-SEM, as shown in

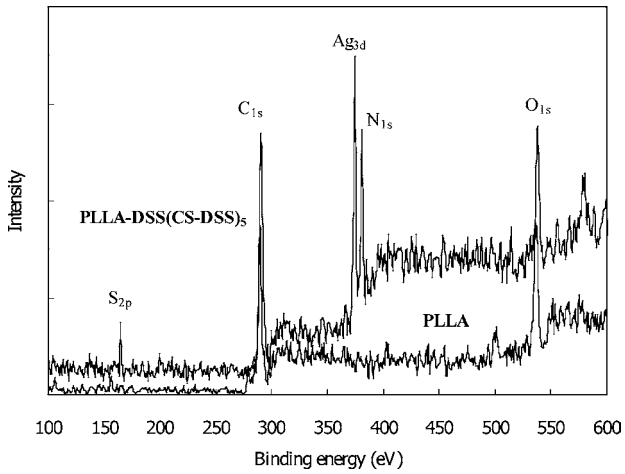


Figure 5. The XPS survey scan spectra of as-fabricated PLLA membranes, which represented relative intensity vs binding energy (100−600 eV).

Table 2. Elemental Compositions of the Modified PLLA Membrane Surfaces with CH−DSS PEM Immobilization

	atomic %				
membrane type	C%	O%	N%	S%	Ag%
PLLA	79.1	20.9	0	0	0
PLLA−DM	77.34	20.86	1.8	0	0
PLLA−DSS−CH	75.4	22.5	1.9	0.13	0.07
PLLA−DSS(CH−DSS)$_3$	74.2	23.2	2.3	0.17	0.13
PLLA−DSS(CH−DSS)$_5$	72.7	24.1	2.7	0.27	0.21

Figure 6. It was worth noting that the more PEM layers deposited the rougher the PLLA membrane was. These surface features were gradually masked in the coated surfaces and replaced by PEM clusters. These structures increase in size with the number of layers, reaching a layer height on the scale of hundred of nanometers to micrometers. It is understood in the assembly that membranes grow homogeneously when the roughness and size of the pores is far greater than the molecular size of CH or DS. It was found that the three-dimensional and porous structure layer onto PEM-deposited PLLA membrane. After four bilayers are deposited, the surface became smoother (Figure 6d).

Table 3 illustrated the contact angle of PEMs immobilized on PLLA membranes. Deposition of PEMs on the PLLA membrane resulted in a sharp decrease of the contact angle (31.2 ± 3.2° for PLLA−DSS(CH−DSS)$_4$ vs 69.4 ± 4.1° for PLLA). This result suggested that the CH/DSS PEM deposition apparently improves the hydrophilicity of PLLA membrane. Note that the contact angle further decreased with an increasing number of layers, reaching an angle of about 31° upon deposition of four bilayers and remaining constant upon further polyelectrolyte layer deposition. There were no further changes in the contact angle, thus indicating that at least four bilayers were necessary to mask the substrate with respect to the properties of the multilayer/water interface. The contact angles displayed a distinct oscillation as the outermost layer changed from DS to chitosan, demonstrating the greater hydrophilicity of samples containing DS as the outermost layer than those with chitosan as the outermost layer. However, the same outermost layer did not present the same contact angle. This may be due to the layer interpenetration between neighboring DSS and CH molecules where the segments of the underlying layer are able to influence the surface hydrophilicity. This is likely the main reason for the slow growth of the layer thickness after assembling some layers due to the weakening of surface charge. These results were similar to those of Thierry et al. (*18*) and Zhu et al. (*6*). Figure 7 illustrated the ζ potential of PEM-immobilized PLLA membranes. Deposition of a layer of

Table 3. Contact Angle Data as a Function of the Layer Number of DS and CS, where 1−5 Number Membranes Have DS as the Outermost Layer[a]

sample	contact angle (°)
PLLA	69.4 ± 4.6
PLLA−N	58.2 ± 2.6
PLLA−DSS	54.3 ± 3.2
PLLA−DSS−CH	63.2 ± 2.1
PLLA−DSS(CH−DSS)$_1$	52.7 ± 2.5
PLLA−DSS(CH−DSS)$_1$CH	58.3 ± 1.7
PLLA−DSS(CH−DSS)$_2$	43.2 ± 2.5
PLLA−DSS(CH−DSS)$_2$CH	53.6 ± 1.9
PLLA−DSS(CH−DSS)$_3$	37.4 ± 2.5
PLLA−DSS(CH−DSS)$_3$CH	44.2 ± 2.1
PLLA−DSS(CH−DSS)$_4$	34.8 ± 1.9
PLLA−DSS(CH−DSS)$_4$CH	44.2 ± 2.1
PLLA−DSS(CH−DSS)$_5$	33.5 ± 1.5

[a] (n = 6, mean ± std).

PLLA-N resulted in a sharp increase of the contact angle (+24 mV for PLLAT-N vs 0 for PLLA). The ζ potential of PLLA−DSS and PLLA−DSS−CH was −34 mV and +18 mV, respectively. It may be due to the layer interpenetration between neighboring DS and CH membranes where the segments of the underlying layer are able to influence the surface charge. However, we found that the ζ potentials were −37 mV and −36 mV for PLLA−DSS(CH−DSS)$_4$ and PLLA−DSS(CH−DSS)$_5$, respectively, in other words, deposition of four bilayers and remaining constant upon further polyelectrolyte layer deposition, thus indicating that at least four bilayers were necessary to mask the substrate. The results were consistent with contact angle values.

3.5. Protein Adsorption and Platelet Adhesion of Surface-Modified PLLA. Figure 8 showed the relationship of HPF adsorption and platelet adhesion onto the surface-modified PLLA membranes. It was clear that the adsorbed amount decreased on PLLA−PEMs with DSS as the outermost layer, but increased with CH as the outermost layer. The reason is probably the electrostatic effect. The isoelectric point of HPF in the blood is 4−6; thus, these proteins normally carry a negative charge in the blood (pH 7.4). Considering chitosan alone, it is possible to evaluate the percentage of amino groups at pH 7.2−7.4. Because the pK_a of chitosan is 6.5 (*35*), it still carried a positive charge at pH between 7.2 and 7.4 (12% < $[NH_3^+]/[NH_2]$ < 20%). Owing to the electrical attraction, the adsorption of proteins was promoted. On the other hand, when PLLA−chitosan was linked with DS, it showed that HPF had no binding affinity to DS, due to the electrostatic repulsive interaction between SO_3^- groups of DS and HPF. Similarly, the platelets carry a negative charge; therefore, the adhesion behavior corresponded to HPF adsorption. As mentioned above, the ζ potential was influenced by the PEM structure; the HPF adsorption and platelet adhesion of PLLA−DSS(CH−DSS)$_4$ would reach the steady state (33μg/cm^2 and 14%). Nevertheless, the adsorbed amounts were significantly curtailed in comparison with that of native PLLA (110μg/cm^2 and 32%). Baumann et al. (*8*) studied the reduced adsorption of plasma proteins, such as fibrinogen and albumin onto heparin-immobilized surfaces. They demonstrated that immobilization of the CH/DSS PEMs might exert a heparin-like efficiency.

3.6. Blood Anticoagulation of Surface-Modified PLLA. It is well-known that protein adsorption and platelet adhesion should be a critical index for evaluating compatibility of blood with artificial surfaces. The blood coagulation cascade includes the intrinsic pathway, the extrinsic pathway, and the common pathway. The activated partial thromboplastin time (APTT) and plasma recalcification time (PT) are used to examine mainly the extrinsic and intrinsic pathways, respectively. Figure 9 shows that the clotting times of the native and PLLA-N membranes

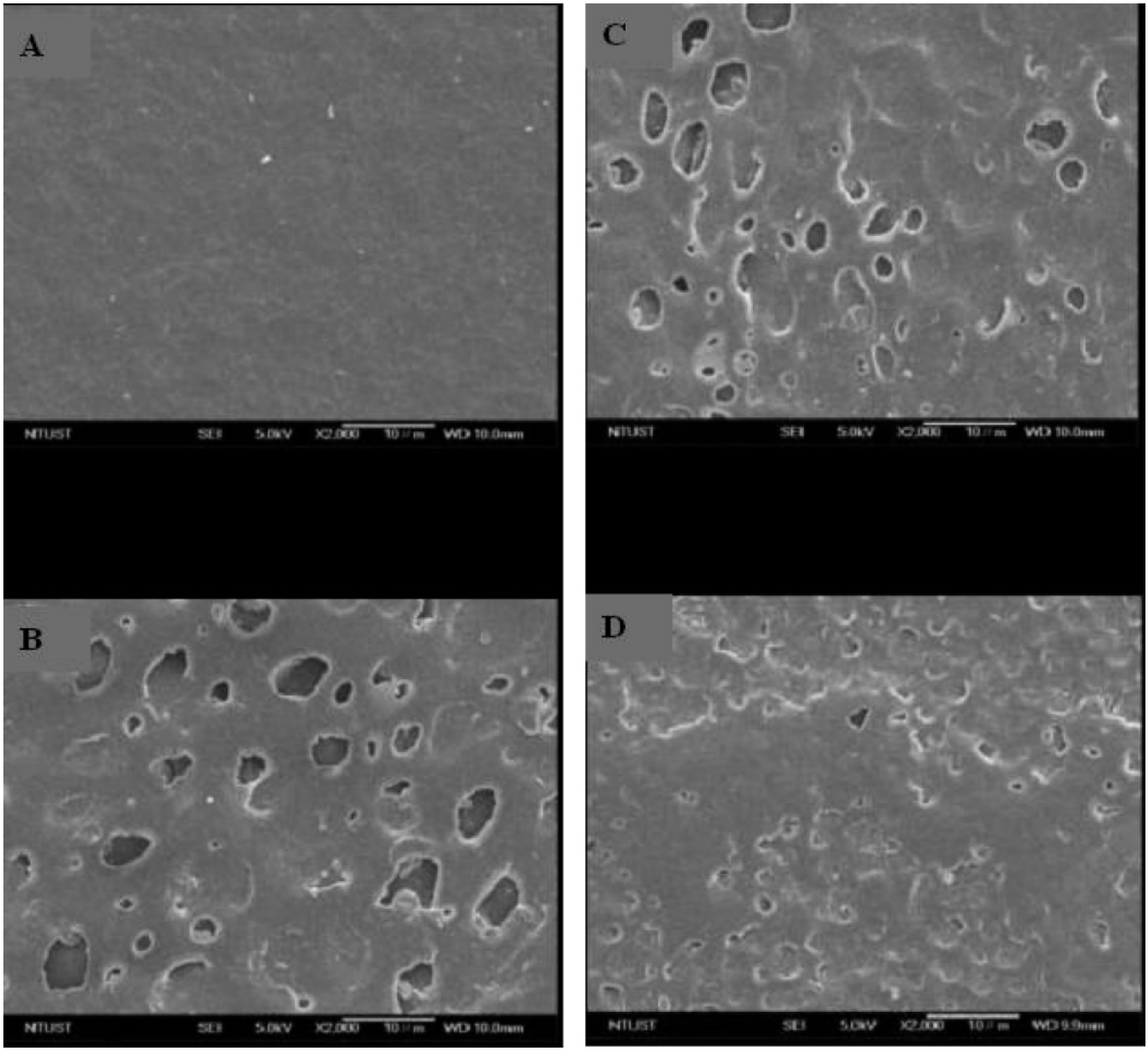


Figure 6. FE-SEM images of the PLLA membrane surface: (A) native PLLA control, (B) three bilayer (PLLA−DSS(CH−DSS)$_3$), (C) four bilayers (PLLA−DSS(CH−DSS)$_4$), and (D) five bilayers PLLA−DSS(CH−DSS)$_5$).

were nearly the same as that of human plasma (the negative control), whereas the clotting times of PEM-immobilized PLLA membranes were longer. This suggested that dextran sulfate should be an effective agent in prolonging the blood clotting time (*36*). Besides, it was also confirmed that positively charged surfaces (CH-grafted) are generally thromobogenic, while uniformly negatively charged surfaces tend to be antithrombogenic (DS-grafted). This result demonstrated that the PEMs with dextran sulfate as the outmost layer provided the PLLA membrane with heparin-like activity in terms of antithrombogenic properties. Serizawa et al. (*37*) have studied the alternating anti- vs procoagulant activity of ultrathin polymer films prepared by the LBL assembly technique against human blood. Dextran sulfate and chitosan were selected as polymers with anti- and procoagulant activities, respectively. They also concluded that the outermost surface was the key factor in the anticoagulant activity observed, rather than the total film thickness.

3.7. Cytocompatibility. Figure 10 displays the cell attachment of native and surface-modified PLLA membranes on the growth of human ECs.

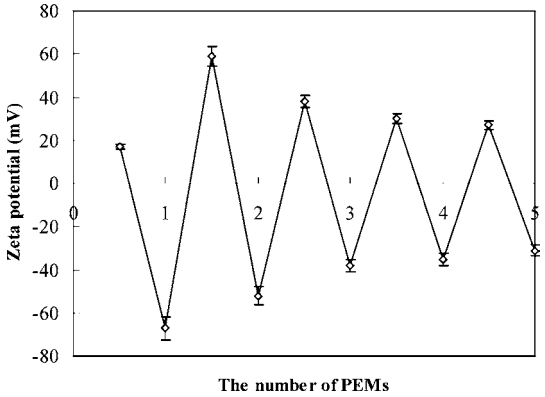


Figure 7. ζ-Potential data as a function of the layer number of DS and CH. 0.5 values represent membranes with CH as the outermost layer, whereas 1−5 number membranes have DS as the outermost layer (PLLA−N, +24 mV; PLLA−DSS, −44 mV) (n = 6).

The order of the amount of cell attachment was PLLA−DSS-(CH−DSS)$_3$ > PLLA−DSS(CH−DSS)$_4$ > PLLA−DSS(CH−

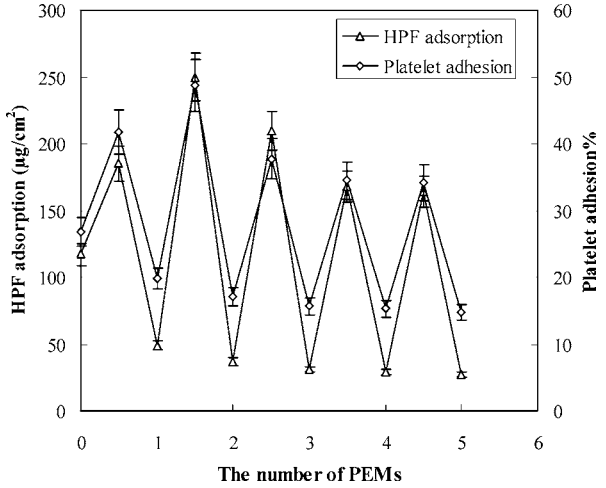


Figure 8. The comparison of HPF and platelet adhesion as a function of the number of layers of PEM (PLLA: HPF adsorption (μg/cm^2)/ platelet adhesion % = 110/32).

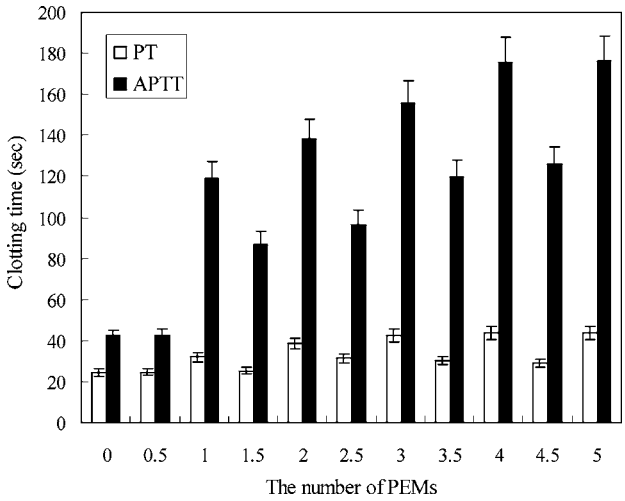


Figure 9. APTT and PT as a function of the number of layers of CH/ DSS PEMs (plasma control: APTT/PT = 47/32 s).

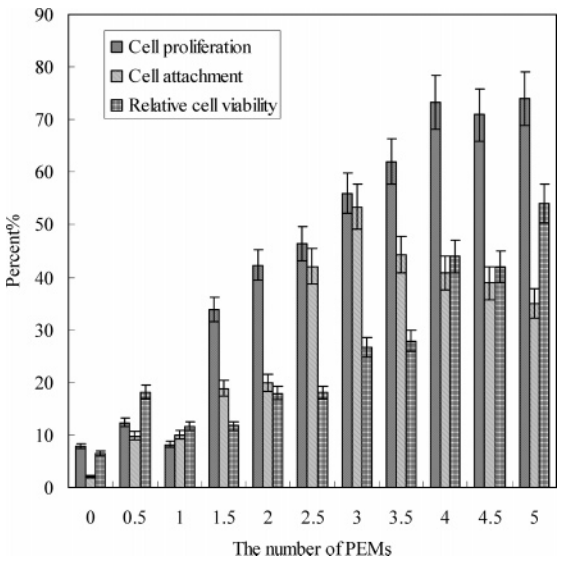


Figure 10. The comparison of cell attachment, proliferation, and relative viability of human ECs on as-prepared PLLA membranes (n = 6). The TCPS acted as the100% control.

DSS)$_5$ > PLLA−DSS(CH−DSS)$_2$ > PLLA−DSS(CH−DSS)$_1$ > PLLA. It suggested that the cell attachment depended apparently on the morphology of the PEM layers on the PLLA membranes. According to the results of FE-SEM (Figure 6), it was found that PLLA−DSS(CH−DSS)$_3$ had the roughest and most porous structure; therefore, cells were easy to immerse or embed into the PEM layer. The cell activity on PLLA assembled with three bilayers of PEMs was apparently better than that on native PLLA. However, it was found that the ECs represented higher viability (52.2%) and proliferation (73.2%) on PLLA−DSS(CH−DSS)$_5$ than on PLLA−DSS(CH−DSS)$_3$ (26.4% and 54.5%). It suggested that higher cell attachment could not lead to higher cell viability and proliferation. Besides, deposition of only one DSS layer on PLLA-N resulted in lower cell activity and proliferation compared with one bilayer of DSS/chitosan. Relative cell viability of 8.2% and proliferation ratio of 11.6% were measured for the PLLA−DSS(CH−DSS)$_1$, while 12.4% and 18.2% were obtained for the one PLLA−DSS−CH. However, cell viability and proliferation showed no obvious difference between PLLA−DSS(CH−DSS)$_4$ (43.2%/72.2%) and PLLA−DSS(CH−DSS)$_1$CH (42.2%/71.6%). These results demonstrate that the negatively charged DSS is not as effective as CH in enhancement of cytocompatibility due to either the charge repulsion or disadvantageous surface chemistry at lower bilayer immobilization number. As pointed out above, defects may exist on the one bilayer-modified PLLA surface in the manner of LBL deposition, whereas those were fully covered by more than four bilayers of modified PLLA. Richert et al. (*38*) have studied the short-term interactions of chondrosarcoma cells with polyelectrolyte multilayer films built up by the alternate adsorption of poly(L-lysine) (PLL) and poly(L-glutamic acid) (PGA). They proposed that PGA-ending films were found to prevent the adsorption of serum proteins, whereas important protein adsorption was always observed on PLL-ending films. These results show that cell interactions with polyelectrolyte films can be tuned by the type of outermost layer and the number of layers in the film.

Furthermore, appropriate electronic equilibrium of PEMs should be considered. It is well-known that the higher surface density of the amino group has led to more cell attachment (*39*, *40*). These cationic charges of chitosan could certainly improve the cell attachment through the interaction with the negatively charged cell surface. However, they suggested that chitosan seems to be cytostatic toward fibroblasts: it is not cytotoxic, but inhibits cell proliferation. It suggests that an extremely high level of adhesion of fibroblasts on chitosan-based materials would alter their growth, thereby reducing fibroblast migration and resulting in inhibition of cell proliferation. Thus, it is the inhibition of human EC cell migration that inhibits cell proliferation. In the present study, the positive charges of the amino groups of chitosan were being shielded by the negatively charged sulfate of DSS. Therefore, chitosan alone cannot be considered a suitable biomaterial for in vitro human ECs cell cultivation. In a word, the cell attachment, proliferation, and viability depended on the polyelectrolyte equilibrium of immobilized CH/DSS PEMs on the PLLA surface via LBL assembly technique.

3.8. Antibacterial Activity Assessment. Figure 11 showed the effect of silver nanoparticles on the log plots of viable growth curves against methicillin-resistant *S. aureus* (MRSA). After soaking for 24 h, the silver content in the bulk was too little to determine using an inductively coupled plasma atomic emission spectrometer (ICP) (S-35, Kontron, Germany) at a wavelength of 328.068 nm (data no show). When in contact with native PLLA, the bacteria grew from 1×10^5 to 2.5×10^7 CFU/mL. However, when in contact with PLLA−PEMs, the concentration of bacteria reduced rapidly and died out after incubating at 37 °C for 12 h. In particular, it was observed that the significant reduction in the number of MRSA began to occur at 3 h for

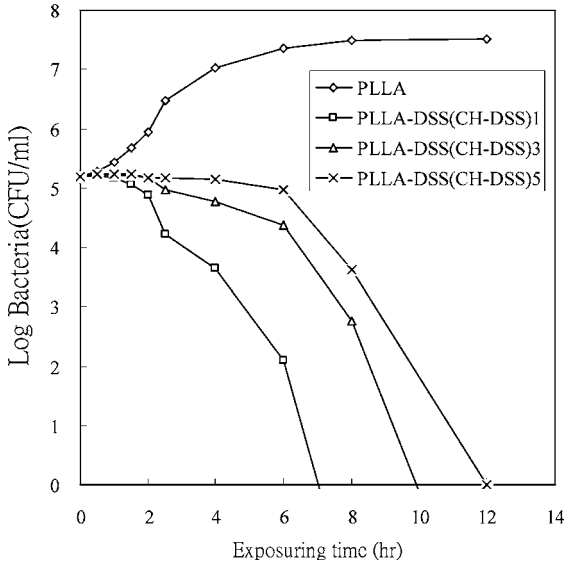


Figure 11. Antibacterial activity was expressed as a measure of MRSA in PEM-modified PLLA membranes.

silver-embedded PLLA−DSS(CH−DSS)$_5$. This suggested that the antibacterial activity was enhanced with the increase of PEM layer.

Lee et al. (*41*) reported that, when Ag nanoparticles existed within the multilayers, the Ag ions that were produced at the surfaces of the nanoparticles are the source of antibacterial activity. Furthermore, the oxidation of zerovalent Ag to Ag ions would occur to a greater extent in the nanocomposite thin films. The diffusion of Ag ions out of the multilayers is rapid compared to the ionization process. Therefore, in the present study, the formation of Ag nanoparticles would reduce the amount of Ag ion released from the nanocomposite films. In view of the results, the Ag nanoparticle-embedded PEM-immobilized PLLA membranes possessed effective and long-tern antibacterial activity.

4. CONCLUSIONS

In conclusion, herein it was ascertained that the versatile CH/DSS PEMs have been successfully immobilized onto the aminolyzed PLLA membrane surface in a LBL assembly manner. The PLLA membranes deposited with four bilayers with DSS as the outermost layer can suppress the protein adsorption and platelet adhesion and greatly prolong blood coagulation time. The human endothelial cell (EC) attachment, proliferation, and viability depended on the polyelectrolyte equilibrium and morphology of immobilized CH/DSS PEM layers on the PLLA surface. Besides, the as-prepared PLLA membranes exhibited antibacterial activity against MRSA. Overall, results demonstrated that the current research explores the construction of CH/DSS multilayers on biomedical PLLA membrane via LBL method, developing a fast, simple-to-process, and shape-independent method for antithrombogenic coating in the application of hemodialysis devices.

LITERATURE CITED

(1) Hu, Y., Zhang, C., Zhang, S., Xiong, Z., and Xu, J. (2003) Development of a porous poly(L-lactic acid)/hydroxyapatite/collagen scaffold as a BMP delivery system and its use in healing canine segmental bone defect. *J. Biomed. Mater. Res. 67A*, 591−8.

(2) Hutmacher, D. W. (2000) Scaffolds in tissue engineering bone and cartilage. *Biomaterials 21*, 2529−43.

(3) Na, Y. H., He, Y., Shuai, X., Kikkawa, Y., Doi, Y., and Inoue, Y. (2002) Compatibilization effect of poly(ϵ-caprolactone)-β-poly(ethylene glycol) block copolymers and phase morphology analysis in immiscible poly(lactide)/poly(ϵ-caprolactone) blends. *Biomacromolecules 3*, 1179−86.

(4) Jiang, L., Wolcott, M. P., and Zhang, J. (2006) Study of biodegradable polylactide/poly(butylene adipate-co-terephthalate) blends. *Biomacromolecules 7*, 199−207.

(5) Pan, J., Wang, Y., Qin, S., Zhang, B., Luo, Y. (2005) Grafting reaction of poly(D,L)lactic acid with maleic anhydride and hexanediamine to introduce more reactive groups in its bulk. *J. Biomed. Mater. Res., Part B 74*, 476−80.

(6) Zhu, Y., Gao, C., Liu, Y., and Shen J. (2004) Endothelial cell functions in vitro cultured on poly(L-lactic acid) membranes modified with different methods. *J. Biomed. Mater. Res., Part A 69*, 436−43.

(7) Winterton, L. C., Andrade, J. D., Feijen, J., and Kim, S. W. (1986) Heparin interaction with protein with protein-adsorbed surfaces. *J. Colloid Interface Sci. 111*, 314−42.

(8) Baumann, H., and Kokott, A. (2000) Surface modification of the polymers present in a polysulfone hollow fiber hemodialyzer by covalent binding of heparin or endothelial cell surface heparan sulfate: Flow characteristics and platelet adhesion. *J. Biomater. Sci., Polym. Ed. 11*, 245−72.

(9) Ito, Y., Zheng, J., and Imanishi, Y. (1997) Enhancement of cell growth on a porous membrane co-immobilized with cell-growth and cell adhesion factors. *Biomaterials 18*, 197−202.

(10) Deutsch, M., Meinhart, J., Fischlein, T., Preiss, P., and Zilla, P. Clinical autologous in vitro endothelialization of infrainguinal ePTFE grafts in 100 patients: a 9-year experience. *Surgery 126*, 847−55.

(11) Meinhart, J., Deutsch, M., and Zilla, P. (1997) Eight years of clinical endothelial cell transplantation. Closing the gap between prosthetic grafts and vein grafts. *ASAIO J. 43*, M515−21.

(12) Liu, Y., He, T., and Gao, C. (2005) Surface modification of poly(ethylene terephthalate) via hydrolysis and layer-by-layer assembly of chitosan and chondroitin sulfate to construct cytocompatible layer for human endothelial cells. *Colloids Surf., B 46*, 117−26.

(13) Ye, S., Wang, C., Liu, X., and Tong, Z. (2005) Deposition temperature effect on release rate of indomethacin microcrystals from microcapsules of layer-by-layer assembled chitosan and alginate multilayer films. *J. Controlled Release 106*, 319−28.

(14) Ren, K., Wang, Y., Ji, J., and Lin, Q. (2005) Shen construction and deconstruction of PLL/DNA multilayered films for DNA delivery: Effect of ionic strength. *Colloids Surf., B 46*, 63.

(15) Liu, X., Gao, C., Shen, J., and Ohwald, H. M. (2005) Multilayer microcapsules as anti-cancer drug delivery vehicle: Deposition, sustained release, and in vitro bioactivity. *Macromol. Biosci. 5*, 1209−19.

(16) Khademhosseini, A., Suh, K. Y., Yang, J. M., Eng, G., Yeh, J., Levenberg, S., and Langer, R. (2004) Layer-by-layer deposition of hyaluronic acid and poly-l-lysine for patterned cell co-cultures. *Biomaterials 25*, 3583−92.

(17) Boura, C., Menu, P., Payan, E., Picart, C., Voegel, J. C., Muller, S., and Stoltz, J. F. (2003) Endothelial cells grown on thin polyelectrolyte mutlilayered films: an evaluation of a new versatile surface modification. *Biomaterials 24*, 3521−30.

(18) Thierry, B., Winnik, F. M., Merhi, Y., Silver, J., and Tabrizian, M. (2003) Bioactive coatings of endovascular stents based on polyelectrolyte multilayers. *Biomacromolecules 4*, 1564−71.

(19) Alt, V., Bechert, T., Steinrücke, P., Wagener, M., Seidel, P., Dingeldein, E., Domann, E., and Schnettler, R. (2004) An in vitro assessment of the antibacterial properties and cytotoxicity of nanoparticulate silver bone cement. *Biomaterials 25*, 4383−91.

(20) Yoshida, K., Tanagawa, M., and Atsuta, M. (1999) Characterization and inhibitory effect of antibacterial dental resin composites incorporating silver-supported materials. *J. Biomed. Mater. Res. 47*, 516−22.

(21) Jansen, B., Rinck, M., Wolbring, P., Strohmeier, A., and Jahns, T. (1994) In vitro evaluation of the antimicrobial efficacy and biocompatibility of a silver-coated central venous catheter. *J. Biomater. Appl. 9*, 55−70.

(22) Kawashita, M., Toda, S., Kim, H. M., Kokubo, T., and Masuda, N. (2003) Preparation of antibacterial silver-doped silica glass microspheres. *J. Biomed. Mater. Res., Part A 66*, 266−74.

(23) Balogh, L., Swanson, D. R., Tomalia, D. A., Hagnauer, G. L., and McManus, A. T. (2001) Dendrimer-silver complexes and nanocomposites as antimicrobial agents. *Nano Lett. 1*, 18−21.

(24) Klueh, U., Wagner, V., Kelly, S., Johnson, A. J., and Bryers, D. (2000) Efficacy of silver-coated fabric to prevent bacterial colonization and subsequent device-based biofilm formation. *J. Biomed. Mater. Res. 53*, 621−31.

(25) Melaiye, A., Sun, Z., Hindi, K., Milsted, A., Ely, D., Reneker, D. H., Tessier, C. A., and Youngs, W. J. (2005) Silver(I)-imidazole cyclophane gem-diol complexes encapsulated by electrospun tecophilic nanofibers: formation of nanosilver particles and antimicrobial activity. *J. Am. Chem. Soc. 27*, 2285−91.

(26) Lin, W. C., Yu, D. G., and Yang, M. C. (2005) Blood compatibility of thermoplastic polyurethane membrane immobilized with water-soluble chitosan/dextran sulfate. *Colloids Surf., B 44*, 82−92.

(27) Lin, W. C., Liu, T. Y., and Yang, M. C. (2004) Hemocompatibility of polyacrylonitrile dialysis membrane immobilized with chitosan and heparin conjugate. *Biomaterials 25*, 1947−57.

(28) Liu, T. Y., Lin, W. C., Huang, L. Y., Chen, S. Y., and Yang, M. C. (2005) Hemocompatibility and anaphylatoxin formation of protein-immobilizing polyacrylonitrile hemodialysis membrane. *Biomaterials 26*, 1437−44.

(29) Lin, W. C, Tseng, C. H., and Yang, M. C. (2005) In-vitro hemocompatibility evaluation of a thermoplastic polyurethane membrane with surface-immobilized water-soluble chitosan and heparin. *Macromol. Biosci. 5*,1013−21.

(30) Hu, S. G., Jou, C. H., and Yang, M. C. (2003) Protein adsorption, fibroblast activity and antibacterial properties of poly(3-hydroxybutyric acid-co-3-hydroxyvaleric acid) grafted with chitosan and chitooligosaccharide after immobilized with hyaluronic acid. *Biomaterials 24*, 2685−93.

(31) Smith, P. K., Krohn, R. I., Hermanson, A. K., Mallia, A. K., Gartner, F. H., Provenzano, M. D., Fujimoto, E. K., Goeke, N. M., Olson, B. J., and Klenk, D. C. (1985) Measurement of protein using bicinchoninic acid. *Anal. Biochem. 150*, 76−85.

(32) Ciapetti, G., Stea, S., Cenni, E., Sudanese, A., Marraro, D., Toni, A., and Pizzoferrato, A. (1994) Toxicity of cyanoacrylates in vitro using extract dilution assay on cell cultures. *Biomaterials 15*, 92−6.

(33) Shin, H. S., Yang, H. J., Kim, S. B., and Lee, M. S. (2004) Mechanism of growth of colloidal silver nanoparticles stabilized by polyvinyl pyrrolidone in γ-irradiated silver nitrate solution. *J. Colloid Interface Sci. 274*, 89−94.

(34) Zhao, S., Zhang, K., Sun, A. J., and Sun, C. (2006) Synthesis and layer-by-layer self-assembly of silver nanoparticles capped by mercaptosulfonic acid. *Mater. Lett. 60*, 1215−1218

(35) Uchida, Y., Izume, M., and Ohtakara, A. (1988) *Chitin and Chitosan*, p 373, Elsevier Applied Science, London and New York.

(36) Amiji, M. M. (1996) Surface modification of chitosan films by complexation-interpenetrating of anionic polysaccharides for improved blood compatibility in hemodialysis. *J. Biomed. Sci., Polym. Ed. 8*, 281−98.

(37) Serizawa, T., Yamaguchi, M., and Akashi, M. (2002) Alternating bioactivity of polymeric layer-by-layer assemblies: anticoagulation vs procoagulation of human blood. *Biomacromolecules 3*, 724−31.

(38) Richert, L., Lavalle, Rh., Vautier, D., Senger, B., Stoltz, J. F., Schaaf, P., Voegel, J. C., and Picart, C. (2002) Cell interactions with polyelectrolyte multilayer films. *Biomacromolecules 3*, 1170−8.

(39) Freier, T., Koh, H. S., Kazazian, K., and Shoichet, M. S. (2005) Controlling cell adhesion and degradation of chitosan films by N-acetylation. *Biomaterials 26*, 5872−8.

(40) **(40)** Amaral, I. F., Sampaio, P., and Barbosa, M. A. (2006) Three-dimensional culture of human osteoblastic cells in chitosan sponges: the effect of the degree of acetylation. *J. Biomed. Mater. Res., Part A 76*, 335−46.

(41) Lee, D., Cohen, R. E., and Rubner, M. F. (2005) Antibacterial properties of Ag nanoparticle loaded multilayers and formation of magnetically directed antibacterial microparticles. *Langmuir 21*, 9651−59.

BC060098S

Preactivated Carboxyl Linker for the Rapid Conjugation of Alkylamines to Oligonucleotides on Solid Support

Alexandre V. Lebedev,* David Combs, and Richard I. Hogrefe

Trilink Biotechnologies, Inc., San Diego, California 92121. Received December 18, 2006; Revised Manuscript Received July 9, 2007

A C_{10} linker phosphoramidite reagent terminated with a succinimidyl-activated carboxyl group was prepared and used to couple to the 5′-end of an oligonucleotide synthesized on a solid support. The succinimidyl-activated carboxyl functionality can be used for rapid conjugation of amines to oligonucleotides on solid support or it can be hydrolyzed to form a carboxylic acid functionality. The activated linker was successfully used for conjugation of several primary and secondary aliphatic amine derivatives (including biotin and fluorescein cadaverine) onto a solid support-bound 12-mer DNA oligonucleotide at scales ranging from 0.15 to 1.0 μmol. The overall yields of the conjugation products after AMA deprotection and cleavage from the solid support ranged from 43 to 75% of the total oligonucleotide product. This value is significant, as it includes oligonucleotide synthesis, coupling of the linker, and conjugation of the amine. In addition, the entire process of oligonucleotide synthesis, linker coupling, amine conjugation, deprotection, and cleavage of the oligonucleotide from solid support can be accomplished in 1 day.

INTRODUCTION

The preparation of 5′- or 3′-modified oligonucleotides containing conjugated functionalities, such as biotin, fluorescent dyes, or hydrophobic groups, is often accomplished through the use of an oligonucleotide end modified with a primary amino group (*1*, *2*). In most cases, the 5′-alkylamino group of a deprotected (and typically purified) oligonucleotide is coupled with compounds containing an activated carboxyl or isothiocyanate functionality to form amide or thiourea bonds. We considered the plausibility of reversing the coupling partners by placing an activated carboxyl group directly on the 5′-end of the oligonucleotide for reaction with an alkylamine derivative.

An ideal modifying reagent for oligonucleotides would be a phosphoramidite linker terminated with an activated carboxyl group. Furthermore, the activated carboxyl group of the linker would need to be compatible with the conditions of oligonucleotide synthesis including linker coupling and oxidation (or sulfurization). The ability of such functionality to survive these conditions has not been reported. Because the activated carboxyl group cannot survive treatment with strong base, the conjugation reaction with alkylamine derivative must be performed on support-bound, linker-modified oligonucleotide prior to oligonucleotide deprotection and cleavage. However, we saw a number of advantages to solid-phase conjugation, such as high throughput preparation and a combinatorial chemistry approach to oligonucleotide conjugation chemistry.

Herein we describe the synthesis of a novel heterobifunctional C_{10}-linker containing an activated carboxyl group (succinimidyl ester) on one end and a 2-cyanoethylphosphoramidite on the other end. The linker is coupled to the 5′-end of the oligonucleotide on solid support via efficient P(III) phosphoramidite chemistry and oxidized using standard protocols. The resulting succinimidyl-modified oligonucleotide is very stable on solid support and can be stored at low temperature until needed. Direct conjugation of the alkylamine derivative to the succinimidyl activated carboxyl function can be done under mild conditions. The synthesized oligonucleotide 5′-conjugate can then be cleaved from solid support and deprotected using the versatile AMA (ammonium hydroxide/methylamine) treatment procedure. While providing a convenient way for 5′-conjugation of amines to oligonucleotides on solid support, the approach is compatible with preparation of the oligonucleotide conjugates containing alkylamino linkers in other locations, such as the 3′-terminus, offering a more convenient way to prepare unusual double conjugates.

* Corresponding author. Tel: (858)546-0004; fax: (858)546-0020; e-mail: alebedev@trilinkbiotech.com.

EXPERIMENTAL PROCEDURES

All oligonucleotide synthesis reagents were obtained from Glen Research Corporation (Sterling, VA). Oligonucleotide synthesis was done on a ABI Expedite 8909 DNA synthesizer using standard manufacturer-suggested procedures. The alkylamine derivatives and other chemicals used in this study were commercial products (Fisher Scientific, Sigma-Aldrich, Pierce, Molecular Probes). DMF should be free of amine contaminants. HPLC was accomplished on a Beckman, Inc. (Fullerton, CA) System Gold Nouveau Model 126 with Model 168 photodiode array detector. NMR spectra were recorded on a Bruker Model AX 500 spectrometer (NuMega, San Diego, CA). Electrospray and FAB mass spectrometry analyses were done by HT Laboratories (San Diego, CA).

Succinimidyl 10-Hydroxydecanoate (**2**). To a solution of 10-hydroxydecanoic acid (20 g, 106 mmol) in dioxane (200 mL) at room temperature was added *N*-hydroxysuccinimide (12.2 g, 106 mmol) followed by *N*,*N*′-dicyclohexylcarbodiimide (22.8 g, 106 mmol). After 45 min, the precipitate was removed by filtration, and the solvent was evaporated. The resulting solid was dissolved in ethyl acetate (500 mL), and the organic solution was washed with 5% $NaHCO_3$ (2 × 100 mL) and brine (100 mL), dried over anhydrous $MgSO_4$, filtered, and concentrated in vacuo. Crude compound **2** was purified by silica gel chromatography (hexane−ethyl acetate) to afford the desired succinimidyl ester (20.8 g; 69% yield). ^{1}H NMR ($CDCl_3$): 3.46 (t, 2H, J = 7 Hz), 2.75 (s, 4H), 2.59 (t, 2H, J = 7 Hz), 1.62−1.72 (m, 2H), 1.29−1.47 (s+m, 12H). Mass spectrum (FAB^+): m/z 286 $(M + H)^+$, (Electrospray$^-$): m/z 284 $(M - H)^-$; calculated mass: 285.

10.1021/bc0603891 CCC: $37.00 © 2007 American Chemical Society
Published on Web 09/19/2007

Succinimidyl 10-(2-Cyanoethyl-*N*,*N*′-diisopropylphosphoramidyl)-decanoate (3). Succinimydyl 10-hydroxydecanoic acid **2** (3.7 g; 13.0 mmol) was dissolved in 100 mL of anhydrous dichloromethane, cooled to 0 °C, and 3.40 mL (1.5equiv, 19.5 mmol) of diisopropylethylamine added, followed by 3.48 mL (1.2 equiv, 15.6 mmol) of 2-cyanoethyl *N*,*N*′-diisopropylchlorophosphoramidite. After 1 h of stirring at room temperature, the solvent was evaporated. Purification was done by silica gel chromatography with heptane−ethyl acetate 1:1 with 1% triethylamine, yielding 44% of pure product (2.76 g). ^{1}H NMR ($CDCl_3$): 3.8 (m, 2H), 3.6 (m, 4H), 2.8 (s, 4H), 2.6 (m, 4H), 1.7 (m, 2H), 1.5 (m, 2H), 1.2 (s, 10H), 1.1 (m, 12H). ^{31}P NMR ($CDCl_3$): 147.0 ppm. Mass spectrum (electrospray): *m*/*z* 486 (MH^+), calculated mass: 485.

Coupling of Linkers to Oligonucleotides. The phosphoramidite linker **3** was dissolved in anhydrous acetonitrile (<30 ppm of water) to a concentration of 0.1 M and stored over molecular seives (3 Å) overnight prior to use. One micromol scale coupling and oxidation was performed on an Expedite 8900 using standard parameters for solid-phase oligonucleotide synthesis.

For manual 1.0 μmol scale couplings of the linker **3** on column, the detritylated oligonucleotide synthesized on solid support was washed with 30 mL of anhydrous acetonitrile using a syringe and dried using a stream of argon gas. The linker **3** (20 equiv; 200 μL) was drawn into a 1 mL syringe. The activator (0.45 M tetrazole in acetonitrile, 200 μL) was drawn into another 1 mL syringe. The syringes were placed on opposite ends of the column and the reagent passed back and forth for exactly 1 min, at which time the reagent was completely drawn into a syringe. The phosphite triester intermediate **5** was then oxidized immediately for 1 min using (1*S*)-(+)-(10-camphorsulfonyl)-oxaziridine (0.1 M in acetonitrile; 2 mL) using the two-syringe method as described in this paragraph. The column was washed with 2 × 10 mL of acetonitrile and dried with a stream of argon gas.

Conjugation of Alkylamines to an Oligonucleotide with Activated Carboxyl Group. The alkylamine derivative was dissolved at 0.15 M concentration in dry *N*,*N*-dimethylformamide containing 0.4 M triethylamine (best if used within 1 day).

For 0.15 μmol scale syntheses, 4.0 mg of the support with bound 12-mer oligonucleotide intermediate **6** was transferred from the column into a 1.5 mL screw cap plastic tube, and 100 μL of alkylamine solution (15 μmol, 100 equiv) was added. The tube was placed on a shaker for 30 min at room temperature, then centrifuged and the alkylamine solution removed by pipet. The support was then sequentially washed with 1000 μL of DMF containing 0.4 M triethylamine, 1000 μL of DMF, and 1000 μL of acetonitrile, with vortex mixing to ensure completed rinsing of the support.

For 1.0 μmol scale syntheses, the support (ca. 25 mg) with bound 12-mer oligonucleotide intermediate **6** was transferred from the column into a 1.5 mL screw cap plastic tube, and 500 μL of alkylamine solution (75 μmol, 75 equiv) was added. The remainder of the procedure is identical to the 0.15 μmol scale conjugation described above. Alternatively, the 1.0 μmol scale conjugation was performed in the column using the manual two-syringe technique similar to that described above for the coupling of the activated linker. Reagent concentration/equivalent and incubation time are similar to the 1.0 μmol scale conjugation described in the preceding paragraph for 0.15 μmol scale conjugation. After the reaction, the alkylamine solution is drawn into one syringe and the support in the column is washed sequentially with 10 mL of DMF containing 0.4M TEA, 10 mL of DMF, and 10 mL of acetonitrile, followed by drying of the column with a stream of argon gas.

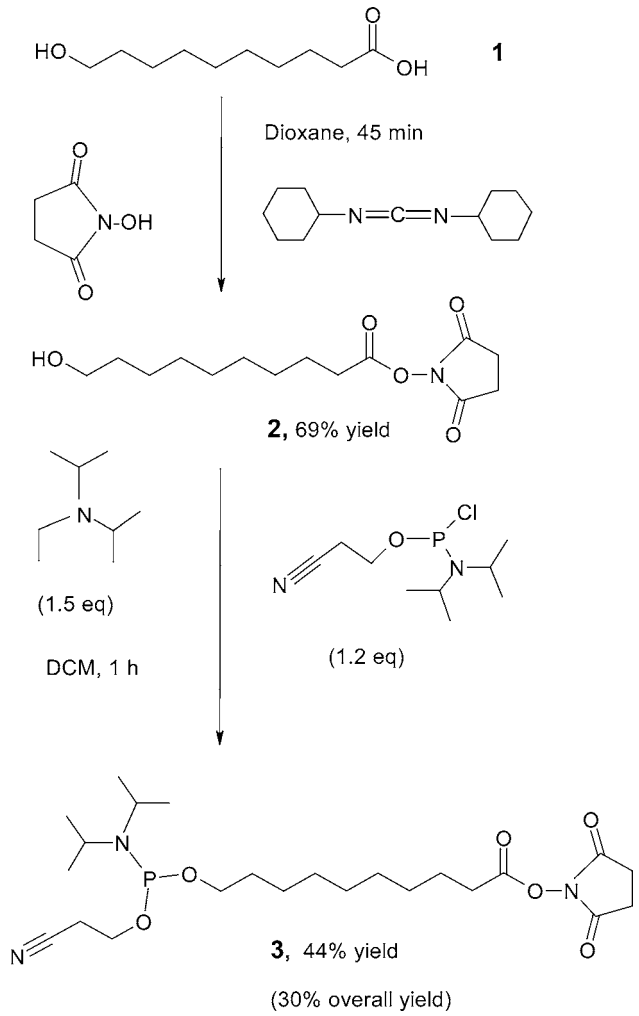
Deprotection and Cleavage of Oligonucleotide Conjugate (7). For 1.0 μmol scale reaction, 1 mL of AMA (1:1 mixture of 28% concentrated ammonium hydroxide and 40% methylamine in water) was added to a 4 mL glass vial containing the solid support obtained from conjugation step (see above). The vial was capped and incubated for 10 min at 65 °C. The solution was removed with a pipet, and the solid support was washed sequentially with 1 mL of AMA and 1 mL of water. The deprotection solution and washes were combined, concentrated in a SpeedVac concentrator, and analyzed by either anion-exchange or reverse-phase HPLC. For the 0.15 μmol scale the AMA solution (200 μL) was added to 1.5 mL screw cap plastic tube containing support with oligonucleotide conjugate and treated as above.

HPLC Analysis of Oligonucleotide Conjugate (8). The crude material was analyzed using a Waters μBondapak analytical column (15 μm, C18 3.9 × 30 mm) with linear gradient of acetonitrile in 100 mM TEAA, pH 7.2 (0−50% over 40 min, 1 mL/min). Anion exchange HPLC analyses were performed using a Dionex DNAPac PA-100 column (4 × 250 mm) with a gradient of 1M LiCl in 25 mM Tris base, pH 10.0 (0−50% over 40 min, 1 mL/min).

Example of Preparation of 5-[(5-Aminopentyl)thioureidyl]-fluorescein Oligonucleotide Conjugate (8) at 1 μmol Scale. Fluorescein cadaverine was dissolved in *N*,*N*-dimethylformamide containing 0.4M triethylamine to a concentration of 23.5 mM. A 300 μL (7.0 μmol of fluorescein cadaverine) amount of this solution was drawn into a 1 mL syringe and attached to the column containing support-bound oligonucleotide **6** with an activated carboxyl group. Conjugation was performed using the two-syringe method (see above) for 30 min at room temperature, at which time the reagent was completely expelled into a glass vial. The solid support in column was washed sequentially with DMF (10 mL), acetonitrile (2 × 10 mL), and a 1:1 mixture of acetonitrile/water (8 × 10 mL) until no color was noted in the washes. The final wash was with methanol (10 mL), followed by DCM (10 mL), and the support was dried on the column under a flow of argon. The deprotection and cleavage of the conjugate from the support was performed with AMA procedure as described above. The product was isolated by anion exchange HPLC, and the yield of isolated compound was estimated to be greater than 0.70 μmol of the 12-mer DNA conjugate as calculated by the UV measurements at 260 nm. The molecular mass of the conjugate was confirmed by mass spectrometry (electrospray): mass found 4368 ($M - H^+$); mass calculated 4368 ($M - H^+$).

Preparation of Carboxylic Acid Derivative of Oligonucleotide (9). Method 1. For a 1.0 μmol scale synthesis ca. 25 mg of support-bound oligonucleotide intermediate **6** was transferred into a 1.5 mL screw cap plastic tube, and 800 μL of aqueous 0.5 M sodium hydroxide was added. The mixture was incubated at room temperature for 24 h, neutralized by 1 M monobasic sodium phosphate (400 μL), and transferred to a 4 mL cap screw glass vial containing 2.4 mL of concentrated ammonium hydroxide. After incubation for 4 h at 55 °C, the mixture was centrifuged, and the supernatant was collected, evaporated, and redissolved in 100 mM TEAA (20 mL, pH 7.2). The resulting mixture was centrifuged, and the supernatant was loaded onto a Waters μBondapak C18 column (19 × 300 mm, 15 μm) equilibrated with 100 mM TEAA pH 7.2. Elution was performed with a gradient of acetonitrile from 0 to 50% over 50 min (10 mL/min). The major peak was collected and dried in a SpeedVac concentrator and the resulting product **9** desalted on a SepPak cartridge (Waters) using water−acetonitrile (1:1) as an eluent. The molecular mass of the conjugate was confirmed by mass spectrum (electrospray): mass found 3896 ($M - H^+$); mass

Scheme 1. Preparation of the C_{10}-Linker 3



(calcd) = 3896 ($M - H^+$). The isolated yield: 47% (54 OD units at 260 nm).

Method 2. For a 1.0 μmol scale synthesis ca. 25 mg of support-bound oligonucleotide intermediate **6** was transferred into a 1.5 mL screw cap plastic tube, and 800 μL of 0.4M sodium hydroxide solution (methanol−water = 4:1) was added. The mixture was incubated at elevated temperature (48 h at 30 °C) to complete the reaction and neutralized by 1 M monobasic sodium phosphate (350 μL). The mixture was diluted with 15 mL of 100 mM TEAA (pH 7.2), and the carboxylic acid oligonucleotide derivative **9** was isolated and purified as described above.

RESULTS

Preparation of Linker 3. The heterobifunctional C_{10}-linker was prepared in two steps (Scheme 1). First, *N*-hydroxysuccinimide was coupled to 10-hydroxydecanoic acid **1** in the presence of *N*,*N*′-dicyclohexylcarbodiimide. Next, 2-cyanoethyl phosphoramidite was attached to the hydroxyl function of the intermediate **2** using chloro-*N*,*N*-diisopropylamino-2-cyanoethoxyphosphine and *N*,*N*-diisopropylethylamine mixture in dichloromethane resulting in a 30% overall isolated yield of the heterobifunctional linker **3** after silica gel chromatography.

Coupling of the Linker 3 to the Oligonucleotide on Solid Support. Solid-phase coupling of linker **3** to solid-bound oligonucleotide **4** is illustrated in Scheme 2. First, the 12-mer oligonucleotide d(GAT CTG CGA ACT) was synthesized on an Expedite 8909 DNA synthesizer using standard phosphoramidite chemistry on a solid support. The 5′-DMT-group was removed, and coupling of the linker **3** to the support-bound oligonucleotide was accomplished either on an Expedite 8909 Synthesizer or using a two-syringe manual procedure as described in Experimental Procedures. The manual procedure is appropriate when linker **3** is to be coupled to one or a few oligonucleotides in order to save reagents, while the Expedite 8909 Synthesizer is normally utilized when linker **3** is to be coupled to a larger set of oligonucleotides. The coupling efficiency of both automated and manual procedures was identical.

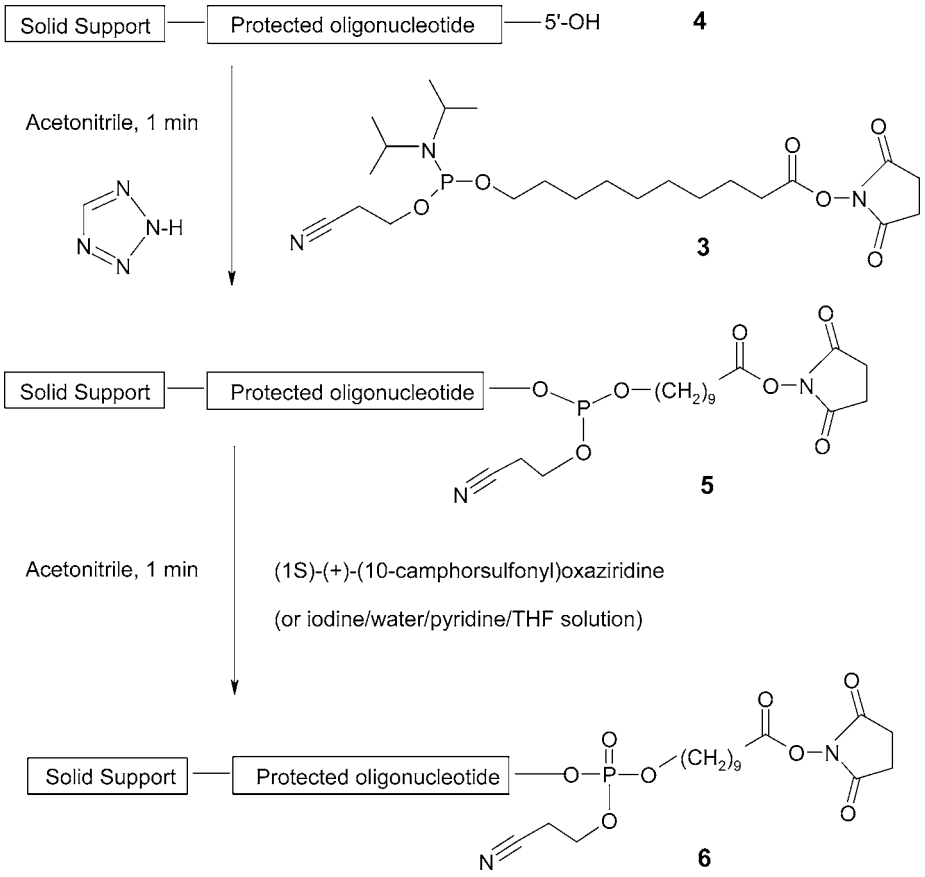
The oxidation of the phosphite triester intermediate **5** during fully automated synthesis was performed immediately after coupling the linker with standard oxidizing reagent (I_2/water/pyridine/THF). Alternatively, manual oxidation could be performed with either the standard iodine oxidizing reagent or with (1*S*)-(+)-(10-camphorsulfonyl)oxaziridine (Scheme 2). The latter is preferred because it does not require the presence of base or water (as does the iodine-based oxidation reagent) and yields a cleaner product compared to iodine oxidation (determined by HPLC analyses, data not shown). Although the oxaziridine reagent performs better, it is currently too expensive to replace I_2/water/pyridine/THF mixture in standard automated syntheses.

Conjugation of Alkylamines to an Oligonucleotide with an Activated Carboxyl Group. The solid support carrying 12-mer oligonucleotide intermediate **6** with an attached activated linker after oxidation can be used immediately for conjugation of alkylamines or can be stored for future use. Our experiments showed that the oligonucleotide intermediate **6** is stable for at least one week at room temperature or up to 6 months at −20 °C without significant loss of activated carboxyl function. A typical conjugation procedure involved reaction of support bound 12-mer oligonucleotide intermediate **6** with the corresponding alkylamine derivative in dry *N*,*N*-dimethylformamide containing 0.4M triethylamine at room temperature (Scheme 3). The reactions were performed at 1.0 μmol scale directly in the column, using the manual two-syringe technique, or at a 0.15 to 1.0 μmol scale after transferring the support to either a glass vial or plastic tube. Both approaches gave similar results.

Since the alkylamine derivatives are normally stable in DMF (in contrast to traditional compounds with activated carboxyl acids, which degrade rapidly), any recovered excess reagent can be re-used "as is" in subsequent reactions without any change to the conjugation protocol. (For multiple reuses of the alkylamine solutions, the reaction time may be elongated to compensate for the decrease in the concentration of the consumed alkylamine derivative.) This was tested experimentally, and two subsequent conjugations resulted in similar yields of the conjugate **8**. By comparison, the activated carboxyl acid derivatives, which are used to couple with amine-derivatized oligonucleotides, are normally used in aqueous buffers. A total loss of the activated carboxyl function occurs by unavoidable hydrolysis, preventing reuse of solutions of activated carboxylic acid derivatives.

Deprotection of Nucleoside Bases and Removal of the Oligonucleotide Conjugate 7 from Solid Support. For deprotection of the conjugate **7** we used the AMA procedure introduced by Reddy and co-workers to deprotect DNA and RNA oligonucleotides (*3*, *4*). Our findings suggest that AMA is a very versatile and clean way to deprotect many oligonucleotide conjugates, including methylphosphonate and phosphorothioate oligonucleotide derivatives (data not shown). At room temperature, AMA deprotection is complete in less than 90 min, and at 65 °C it takes only 10 min to complete deprotection and to cleave the oligonucleotide product (**8**) from solid support (1 h AMA treatment at 65 °C does not reduce the yield). Combined solution, supernatant, and solid support washes were concentrated on a SpeedVac concentrator and can be directly purified

Scheme 2. Attachment of C_{10}-Linker to a Solid-Support-Bound Oligonucleotide



by HPLC. As an important note, we found that AMA treatment of an activated carboxylic acid oligonucleotide intermediate **6** leads to formation of methylamide conjugate **8**, while treatment with concentrated ammonium hydroxide gives an amide derivative **8**. Therefore, amine conjugations need to be performed prior to deprotection of the oligonucleotide; otherwise the activated carboxyl functionality will be lost.

Analysis and Purification of the Conjugate 8. The crude material was analyzed and purified using either anion exchange or reverse phase HPLC. Typically, the product was retained on reverse phase (and anion exchange) columns, eluting several minutes after the starting oligonucleotide with the linker only and other failure products. Integration of the HPLC profile of the crude mixture after deprotection allows estimation of the overall yield of the 12-mer oligonucleotide conjugate **8**.

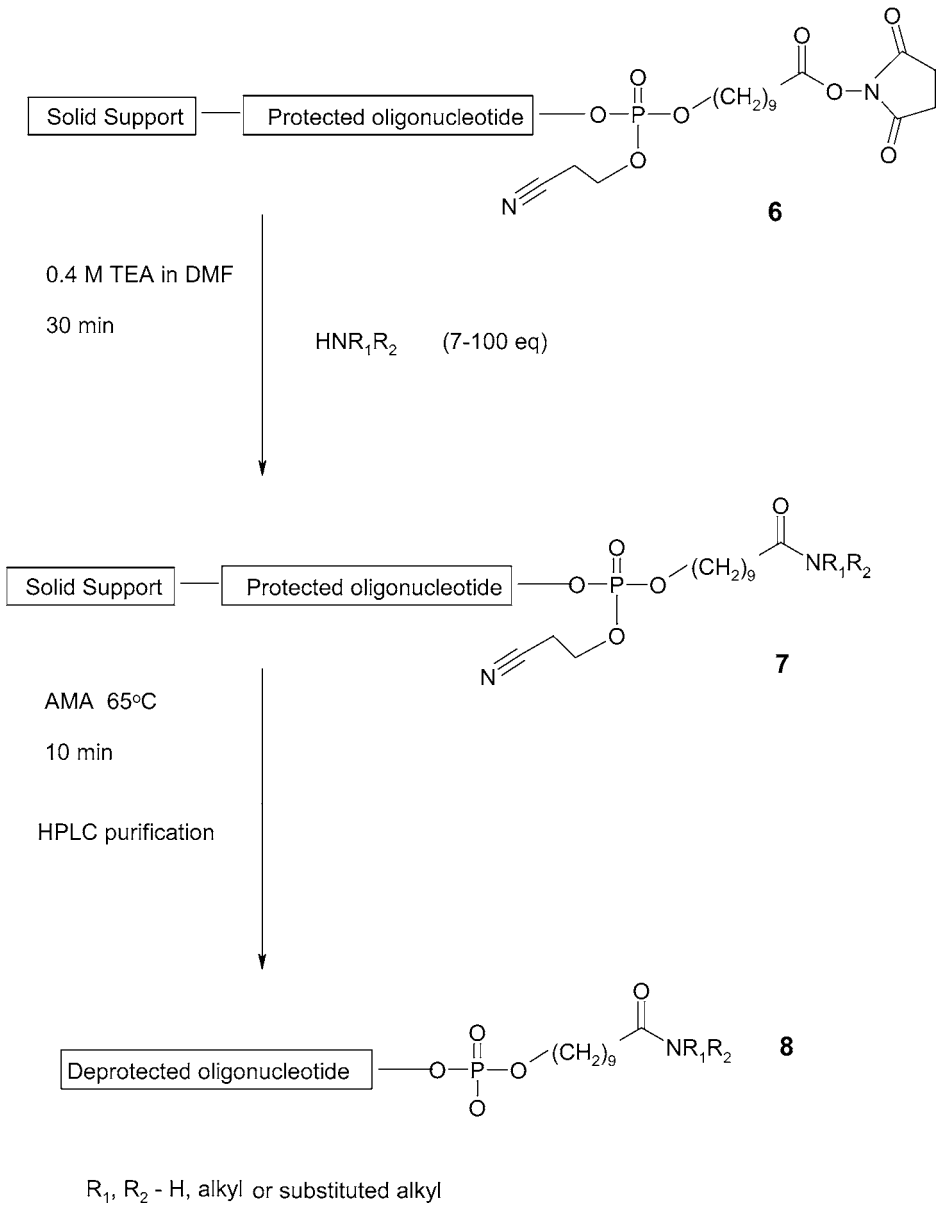
Model Study of Conjugation of Alkylamine Derivatives. A number of different alkylamine derivatives were conjugated to the support-bound oligonucleotide intermediate **6**. Those derivatives included primary and secondary amines with linear or branched alkyl chains containing different substituents such as a hydroxyl group, a carboxyl group, an aliphatic amine, an aromatic amine, biotin, and fluorescein.

The complete results of the RP HPLC analyses of the crude mixtures of all synthesized amide oligonucleotide derivatives are presented in Table 1. The estimated yields of the final product were 43−75%, as determined by the integrated area of the HPLC profiles at 260 nm. When the yield of final conjugate **8** was normalized to the area of methylamine-conjugated oligonucleotide (after AMA treatment of the intermediate **6**), the overall efficiency of the conjugation step in most cases is estimated to be in the range 78−98%. In these studies, there were few exceptions. The yield of conjugate **8** was lower for 1,4-diaminobutane and 1,6-diaminohexane reactions because of formation of byproducts. In both cases the major byproduct observed was a compound with a longer RP HPLC retention time compared to that for a respective conjugate **8** (1−3 min longer). Although the structure of the major byproduct was not investigated, we speculate that it could be a molecule consisting of two oligonucleotides attached to one diamine. For 4-aminobutyric acid reaction less efficient conversion of the intermediate **6** to conjugate **7** was observed in parallel with a formation of several unidentified byproducts with shorter and longer HPLC retention times. When intermediate **6** was reacted with 2-carboxymethyl-1-aminobenzene, no conjugation product was detectable after 1.5 h of incubation at room temperature.

The synthesis of the fluorescein cadaverine conjugate was performed with a lower molar excess of the dye−alkylamine (7.0 vs 100 equiv used above, Table 1) over oligonucleotide intermediate **6**. Nevertheless, the HPLC analysis of the crude mixture (Figure 1, Table 1) shows that there was no loss in the efficiency of the conjugation of fluorescein cadaverine in comparison to other conjugations. By HPLC analysis, the estimated yield of the dye-conjugated oligonucleotide (Figure 1b) was >70%, while the yield of the precursor oligonucleotide (before coupling of the linker and conjugation of fluorescein cadaverine (Figure 1a) was >75%. Therefore, the coupling of the activated carboxyl linker and subsequent conjugation of the fluorescein cadaverine was accomplished with better than 90% conversion. Moreover, the recovered fluorescein cadaverine solution from that synthesis was used for conjugation to another portion of the oligonucleotide intermediate **6** giving nearly the same yield of fluorescein cadaverine conjugate as in the previous conjugation.

Preparation of Carboxylic Acid Derivatives of Oligonucleotides. The succinimidyl ester group of the linker attached to the oligonucleotide intermediate **6** can be converted directly to a carboxylic acid function (Scheme 4). A typical procedure

Scheme 3. Conjugation of Alkylamine to Succinimidyl-Activated Oligonucleotide 6 on Solid Support



involves a treatment of solid-bound oligonucleotide intermediate **6** with 0.4 M sodium hydroxide in methanol−water (4:1) solution. The reaction is incubated at elevated temperature (~ 40 °C) overnight or at 30 °C for 2 days (monitoring the reaction progress by HPLC) and neutralized by monobasic sodium phosphate buffer. The nucleoside base protecting groups are removed during this procedure. The product **9** is isolated by reverse phase HPLC. Notably, LiOH may be substituted for NaOH in this procedure (0.1M LiOH in methanol−water = 1:2).

Alternatively, the intermediate **6** can be converted to carboxylic acid derivative **9** by a treatment with 0.5 M sodium hydroxide in water. However, the additional treatment of that mixture with concentrated ammonium hydroxide (or AMA) is required to complete deprotection of the nucleoside bases.

DISCUSSION

This novel heterobifunctional C_{10}-linker has several outstanding properties. The reagent is made in two steps, is relatively inexpensive, and can be utilized for automated solid-support coupling. The precursor phosphoramidite reagent has been stable for more than 2 years when stored in the freezer at −70 °C. Furthermore, 0.1 M acetonitrile solution of the reagent **3** stored over molecular sieves in the refrigerator is stable for at least 10 days.

The main advantage of the activated carboxyl function is an opportunity to use alkylamine-derivatized compounds for conjugation reaction rather than the corresponding active ester or isothiocyanate compounds. The alkylamine derivatives are easier synthetic targets for a variety of reasons, and many potential candidates for conjugation to oligonucleotides are already available commercially as amines.

The alkylamine derivative is typically stable during the conjugation reaction, and the recovered alkylamine solution can be used in subsequent conjugation reactions without further manipulation. The oligonucleotide intermediate **6** with attached activated carboxyl linker on dry CPG-support is stable for at least a week at room temperature and for several months at −20 °C, thus allowing preparation of a stock supply of precursor oligonucleotide **6**. Because of these advantages, it is possible to rapidly screen combinations of alkylamine derivatives and oligonucleotide sequences using this technology. In addition, the activated carboxylic function of the oligonucleotide intermediate **6** can be hydrolyzed with sodium hydroxide or lithium

Scheme 4. Conversion of Succinimidyl-Activated Oligonucleotide 6 on Solid Support to a Carboxylic Acid Oligonucleotide Derivative 9

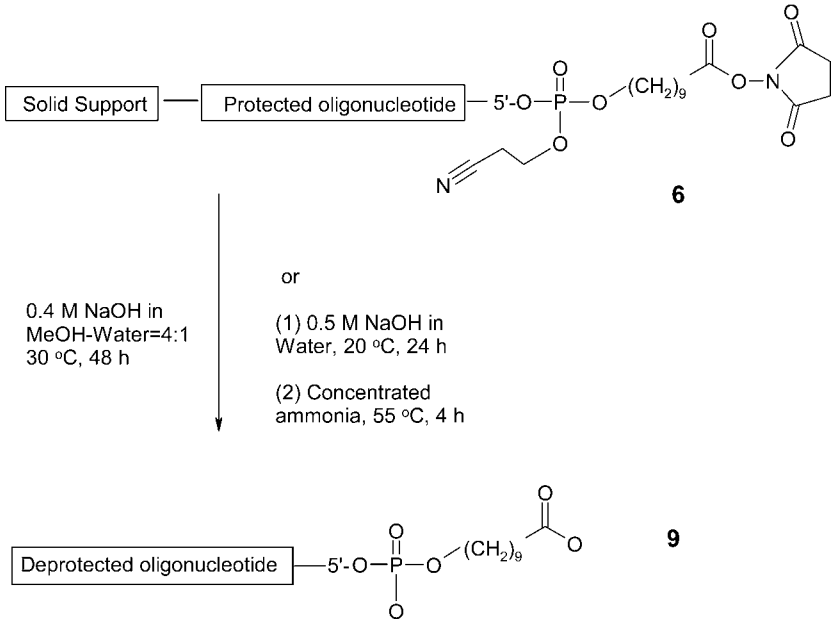


Table 1. Results of RP HPLC Analyses of Crude Reaction Mixtures after Alkylamine Conjugation to the Oligonucleotide Intermediate 6 and AMA Deprotection

amine compound	conjugate yield, % [a]	conversion, %[b]	retention time, min
n-butylamine	68−71	92−96	20.9
tert-butylamine	58−68	81−89	23.0
sec-butylamine	65−71	92−94	21.0
isobutylamine	66−74	92−97	21.4
n-propylamine	66−73	93−95	19.8
3-aminopropanol	67−75	94−98	17.9
dibutylamine	59−65	82−86	31.9
morpholine	61−67	85−88	19.8
allylamine	63−71	89−93	20.2
benzylamine	63−71	88−93	22.4
N-(naphthyl)ethylene-diamine	69−70	91−97	27.7
1,4-diaminobutane	45−53	64−70	17.0
1,6-diaminohexane	43−51	61−67	17.8
biotin-LC-amine	55−62	78−81	20.4
fluorescein cadaverine[c]	70−75	91−95	23.0[d]
4-Aminobutyric acid	44−49	58−60	17.7
2-aminobenzoic acid methyl ester	no product detected	no product detected	−
AMA	72−76[e]	100[b]	17.2
28% NH_4OH	72−77[f]	98−100	16.4
0.4 M NaOH in MeOH−H_2O (4:1)	68−70[g]	92−94	15.8

[a] Calculated from HPLC profile of crude reaction mixtures. [b]Relative to formation of methylamide (as determined with control treatment of intermediate **6** with AMA). [c]Conjugation was performed with 7 equiv of fluorescein cadaverene. [d]Anion-exchange HPLC. [e]Methylamide derivative formed. [f]Amide derivative formed. [g]Carboxylic acid derivative formed.

hydroxide to an oligonucleotide derivative **9** containing a terminal carboxylic acid group.

The conjugation technology on solid support has several inherent advantages. It is very efficient and gives good yield with minimal effort. The entire process of oligonucleotide synthesis, linker coupling, conjugation, and deprotection requires minimal postsynthetic chemistry and can be accomplished on an automated synthesizer within 1 day. The approach is adaptable up to a 15 μmol scale synthesis and is expected to readily scale-up for production of therapeutically relevant oligonucleotide conjugates.

However, one major consideration is whether the oligonucleotide conjugate moiety is stable to standard conditions of nucleoside base deprotection. If the conjugate is not expected to be stable to the concentrated ammonium hydroxide conditions required to deprotect oligonucleotides under normal circum-

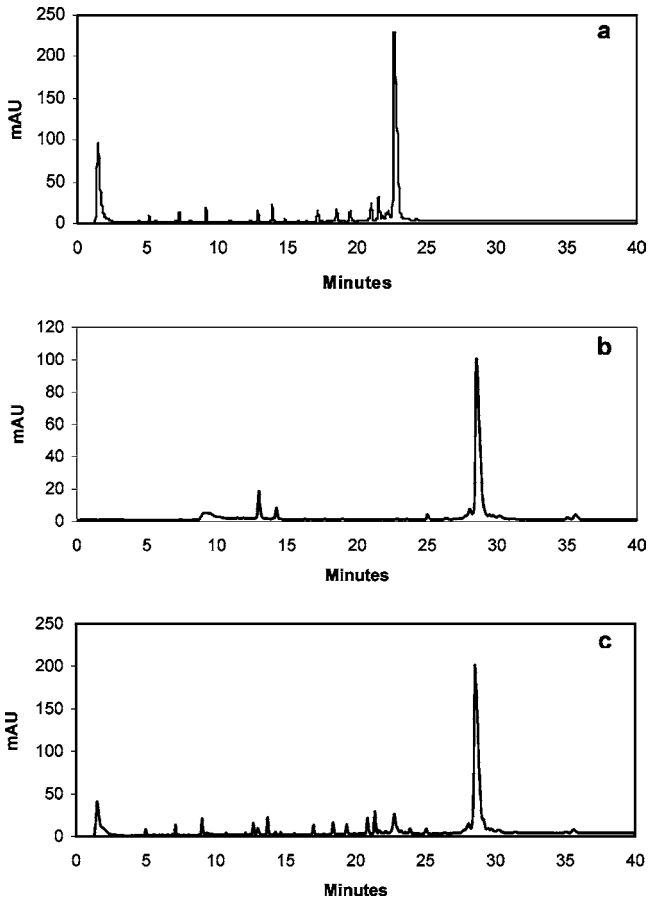


Figure 1. Anion exchange HPLC analyses on the crude mixture after AMA deprotection and cleavage from solid support: (a) d(GAT CTG CGA ACT) precursor **4**; (b and c) fluorescein cadaverine conjugate **8** of d(GAT CTG CGA ACT). Detection: at 260 nm (a, c) or at 500 nm (b).

stances, we suggest utilizing AMA for deprotection. Using AMA deprotection is completed within 90 min at room temperature or in 10 min at 65 °C. In very sensitive cases, we recommend using fast deprotecting phenoxyacetyl phosphoramidite monomers for oligonucleotide synthesis in combination with mild deprotection/cleavage conditions such as 50 mM potassium carbonate in methanol at room temperature (*5*).

The synthesis of DNA−oligonucleotide conjugates on solid support described above has been tested for a series of different alkylamine derivatives (Table 1) as well as for oligonucleotides with different sequences and backbones (data not shown). In all cases the results are very similar to those reported in this manuscript.

ACKNOWLEDGMENT

The technical assistance provided by Katelyn Hanesana, Paul Imperial, Kristin Aquino in oligonucleotide synthesis, and Sean Ahearn in organic synthesis, is highly appreciated. Authors are thankful to Dr. Natasha Paul for helpful discussions and proofreading the manuscript.

LITERATURE CITED

(1) Agrawal, S. (1994) Functionalization of oligonucleotides with amino groups and attachment of amino specific reporter groups. *Methods Mol. Biol. 26*, 73−92.

(2) Meyers, R. (1994) Incorporation of Modified Bases into Oligonucleotides. *Methods Mol. Biol. 26*, 93−120.

(3) Reddy, M. P., Hanna, N. B., and Farooqui, F. (1994) Fast Cleavage and Deprotection of Oligonucleotides. *Tetrahedron Lett. 35*, 4311−4314.

(4) Reddy, M. P., Farooqui, F., and Hanna, N. B. (1995) Methylamine Deprotection Provides Increased Yield of Oligoribonucleotides. *Tetrahedron Lett. 36*, 8929−8932.

(5) Schnetz-Boutaud, N. C., Mao, H., Stone, M. P., and Marnett, L. J. (2000) Synthesis of Oligonucleotides Containing the Alkali-Labile Pyrimidopurinone Adduct, M_1G. *Chem. Res. Toxicol. 13*, 90−95.

BC0603891

Synthesis and Gene Transfer Activities of Novel Serum Compatible Cholesterol-Based Gemini Lipids Possessing Oxyethylene-Type Spacers

Avinash Bajaj,[†] Paturu Kondaiah,[‡] and Santanu Bhattacharya*[,†,§]

Department of Organic Chemistry and Department of Molecular Reproduction, Development and Genetics, Indian Institute of Science, Bangalore 560 012, and Chemical Biology Unit of JNCASR, Bangalore 560 064, India. Received January 11, 2007; Revised Manuscript Received March 26, 2007

Four novel cholesterol-based gemini cationic lipids differing in the length of oxyethylene-type spacers [$-CH_2-(CH_2-O-CH_2)_n-CH_2-$] between each ammonium headgroup have been synthesized. These formed stable suspensions in aqueous media. Cationic liposomes were prepared from each of these lipids individually and as mixtures of cationic lipid and DOPE. These were used as nonviral gene delivery agents. All the cholesterol-based gemini lipids induced better transfection activity than their monomeric counterpart. Inclusion of DOPE in co-liposomal formulation of the cationic gemini lipid potentiates their gene transfer activity significantly. A major characteristic feature of these oxyethylene spacer based cholesterol gemini lipids was that serum does not inhibit the transfection activity of these gemini lipids, whereas the transfection activity of their monomeric counterpart decreased drastically in the presence of serum. One of the cholesterol-based gemini lipids **2a** possessing a $-CH_2-CH_2-O-CH_2-CH_2-$ spacer showed the highest transfection activity.

INTRODUCTION

Viral vectors, although capable of ensuring high levels of transgene expression, suffer from many disadvantages like generation of toxic inflammatory responses, possibility of random integration into host chromosome, limited insert size of virally packaged therapeutic gene, possibility of generating replication-competent virus through recombination with host genome, and so forth (*1*−*4*). Therefore, the development of effective and safe genetic carriers is the key to achieving clinical success for gene therapy.

Major nonviral gene delivery reagents mainly comprises two types: polymers and cationic lipids (*5*). Cationic polymers like polyethyleneimines (PEI) (*6*), polylysines (*7*, *8*), have already been studied in detail for gene transfection. Cationic liposomes are promising tools for delivery of genes, because of their lower toxicity, very low immunogenicity, convenient preparation, and so forth, as compared to their viral counterparts. Among cationic lipids, various structure−activity investigations have been reported using different types of cationic lipids with variation of hydrophobic parts, linker region, headgroups, and others (*9*−*17*).

We have been investigating the role of various molecular modifications in different synthetic lipids on their membrane level properties and their further influence on gene delivery (*18*−*20*). The functional group that links the polar head group and the hydrocarbon chains of such lipid molecules plays a crucial role in their utilization in gene transfer events. Thus, *N*-[1-(2,3-dioleyloxy)propyl]-*N*,*N*,*N*-trimethylammonium chloride (DOTMA[1]), which contains an ether linkage between the headgroup and the long alkyl chains shows greater *in vivo* transfection efficiency than the corresponding ester analogue *N*-[1-(2,3-dioleyl)]-*N*,*N*,*N*-trimethylammonium chloride (DOTAP) (*21*, *22*). We have shown the effect of this linkage functionality on the gene transfection efficiencies of cholesterol-based amphiphiles. It was observed that cholesterol-based cationic lipids bearing ether linkages between cholesterol backbone and headgroup possessed greater transfection capability as compared to other linkages (*23*, *24*).

Gemini (dimeric) surfactants have also been found to possess transfecting abilities. The effect of the nature of the spacer, hydrocarbon chains, and headgroups on the aggregation and transfection properties has been studied in detail in the case of gemini surfactants (*16*, *25*−*30*). The gemini analogue of the lipid is also known to exist in natural cell membranes. For instance, cardiolipin, a glycerol-bridged phosphatidic acid, is a dimeric lipid that occurs in the heart and skeletal muscles (*31*). Taking inspiration from the cardiolipins, we reported for the first time the synthesis and membrane-forming properties of pseudoglyceryl gemini lipids with polymethylene spacers (*32*). The aggregation properties of these gemini lipids were found to depend on the length of the spacer (*33*). Later on, Ahmad et al. showed the transfection activities of cardiolipin-based gemini lipids (*34*, *35*). Recently, we reported that the properties of cationic gemini lipids were quite different when oxyethylene-based spacers were employed in place of polymethylene chains (*36*). We also described the gene transfection properties of gemini lipids where the monomeric cholesterol based units are connected by polymethylene spacer (*37*). Herein, we present the synthesis and transfection properties of cholesterol-based biscationic (**2a**−**2d**) gemini lipids, where each lipid monomer is connected at the level of headgroup via oxyethylene-based spacer chains of variable length (Figure 1).

In this paper, we describe the detailed, optimized synthetic procedures and transfection activities of these new biologically active compounds. To put our results into appropriate perspective, we compared the transfection activities of these new gemini cationic lipids with that of monomeric lipid **1**. We have observed

* Corresponding author. E-mail: sb@orgchem.iisc.ernet.in. Phone: (91)-80-2293-2664. Fax: (91)-80-2360-0529.

[†] Department of Organic Chemistry, Indian Institute of Science.

[‡] Department of Molecular Reproduction, Development and Genetics, Indian Institute of Science.

[§] Chemical Biology Unit of JNCASR.

[1] Abbreviations: DOPE, 1,2-dioleoyl-L-α-glycero-3-phosphatidylethanolamine; DOTMA, *N*-[1-(2,3-dioleyloxy)propyl]-*N*,*N*,*N*-trimethylammonium chloride; DOTAP, *N*-[1-(2,3-dioleyl)]-*N*,*N*,*N*-trimethylammonium chloride; MFI, mean fluorescence intensity; FACS, fluorescence activated cell sorting.

10.1021/bc070010q CCC: $37.00 © 2007 American Chemical Society
Published on Web 07/28/2007

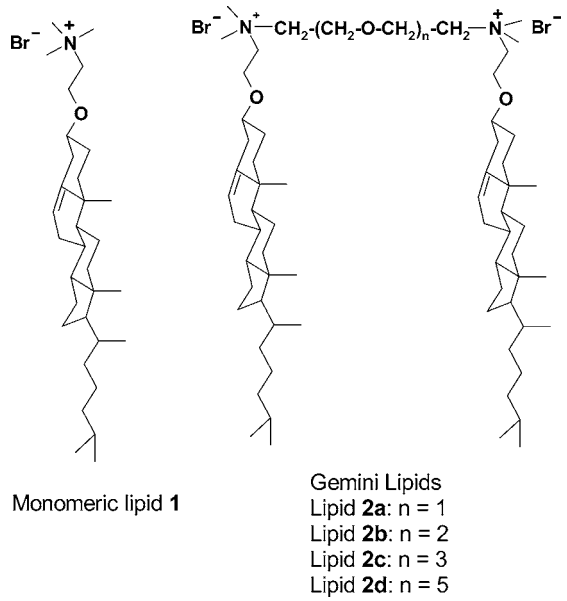


Figure 1. Molecular structures of cholesterol-based cationic monomeric lipid **1** and gemini lipids (**2a**−**2d**) synthesized and used for transfection studies.

significantly enhanced gene transfection activities of these gemini lipids as compared to the monomeric counterpart. Serum is known to inhibit the transfection efficiency of cationic liposomes, whereas the major distinguishing feature of these gemini lipids is that they are able to transfect the mammalian cell lines even in the presence of serum.

EXPERIMENTAL PROCEDURES

Materials and Methods. All reagents, solvents, and chemicals used in this study were of the highest purity available. The solvents were dried prior to use. Column chromatography was performed using 60−120 mesh silica gel. NMR spectra were recorded using Jeol JNM λ-300 (300 MHz for ^{1}H and 75 Hz for ^{13}C) spectrometer. The chemical shifts (δ) are reported in ppm downfield from the internal standard: TMS, for ^{1}H NMR and ^{13}C NMR. Mass spectra were recorded on a Kratos PCKompact SEQ V1.2.2 MALDI-TOF spectrometer or on a MicroMass ESI-TOF spectrometer or Shimadzu table-top GC-MS or ESI-MS (HP1100LC-MSD). Infrared (IR) spectra were recorded on a Jasco FT-IR 410 spectrometer either using KBr pellets or neat. Gemini lipids were synthesized as described below and were characterized fully by their ^{1}H NMR, ^{13}C NMR, mass spectra, and elemental analysis.

General Method for Synthesis of Gemini Lipids (2a−2e). A mixture of cholest-5-en-3β-oxyethan-*N*,*N*-dimethyl amine (*24*) (0.2 mmol) and an appropriate α,ω-dibromoalkoxyalkanes (0.07 mmol) in dry MeOH−EtOAc (4 mL, v/v 1/1) was refluxed over a period of 48−72 h in a screw-top pressure tube, after which TLC indicated complete disappearance of the starting dibromide. After that, the reaction mixture was cooled and solvent was evaporated to furnish a crude solid. It was repeatedly washed with ethyl acetate to remove any cholest-5-en-3β-oxyethan-*N*,*N*-dimethyl amine, and the residue was finally subjected to repeated crystallization from a mixture of MeOH and EtOAc. The product yields ranged from 50% to 60%. The purities of the individual lipids were ascertained from TLC; the R_f ranged from 0.2 to 0.3 in 10:1 $CHCl_3$/MeOH. All the new gemini lipids were fully characterized by ^{1}H NMR, ^{13}C NMR, mass spectrometry, and C, H, N analysis. Pertinent spectroscopic and analytical data are given below.

*Lipid **2a***. ^{1}H NMR (300 MHz, $CDCl_3$): δ 0.67 (s, 6H), 0.85−2.29 (m, 82H), 3.19 (m, 2H), 3.49 (s, 12H), 3.93 (br m, 8H), 4.01 (br s, 4H), 4.29 (br s, 4H), 5.35 (d, J = 4.5 Hz, 2H). ^{13}C NMR ($CDCl_3$, 75 MHz): δ 11.65, 18.50, 19.13, 20.87, 22.34, 22.58, 23.65, 24.08, 27.73, 27.80, 27.93, 28.01,31.65, 31.70, 35.60, 35.99, 36.57, 36.75, 38.54, 39.31, 39.53, 42.11, 49.89, 52.59, 55.98, 56.50, 61.57, 64.60, 65.25, 79.80, 121.17, 139.64. ESI-MS: 1067.4 [M^{+2} + Br^-], 493.4 [M^{+2}/2]. Anal. ($C_{66}H_{120}O_3N_2Br_2 \cdot H_2O$) C, H, N.

*Lipid **2b***. ^{1}H NMR (300 MHz, $CDCl_3$): δ 0.67 (s, 6H), 0.85−2.37 (m, 82H), 3.19 (m, 2H), 3.47 (s, 12H), 3.78 (br s, 4H), 3.93 (br s, 12 H), 4.09 (br s, 4H), 5.35 (d, J = 4.5 Hz, 2H). ^{13}C NMR ($CDCl_3$, 75 MHz): δ 11.76, 18.62, 19.28, 20.96, 22.45, 22.70, 23.79, 24.20, 27.90, 28.05, 28.11, 30.83, 31.75 31.81, 35.69, 36.09, 36.65, 36.83, 38.67, 39.40, 39.63, 42.19, 49.94, 52.85, 56.08, 56.59, 61.92, 64.70, 64.88, 70.22, 79.73, 122.22, 139.79. ESI-MS: 1110.2 [M^{+2} + Br^-]. Anal. ($C_{68}H_{122}O_4N_2Br_2 \cdot H_2O$) C, H, N.

*Lipid **2c***. ^{1}H NMR (300 MHz, $CDCl_3$): δ 0.67 (s, 6H), 0.85−2.35 (m, 82H), 3.19 (m, 2H), 3.49 (s, 12H), 3.65 (br s, 4H), 3.72 (br s, 4H), 3.94 (br s, 12 H), 4.06 (br s, 4H), 5.35 (d, J = 4.5 Hz, 2H). ^{13}C NMR ($CDCl_3$, 75 MHz): δ 11.68, 18.52, 19.21, 20.89, 22.39, 22.63, 23.70, 24.11, 27.82, 27.98, 28.05, 31.66, 31.73, 35.61, 36.01, 36.58, 36.76, 38.59, 39.31, 39.54, 42.13, 49.86, 52.69, 55.99, 56.50, 61.88, 64.65, 64.88, 70.06, 70.22, 79.62, 122.09, 139.76. ESI-MS: 1155.5 [M^{+2} + Br^-], 537.5 [M^{+2}/2] Anal. ($C_{70}H_{128}O_5N_2Br_2 \cdot 3H_2O$) C, H, N.

*Lipid **2d***. ^{1}H NMR (300 MHz, $CDCl_3$): δ 0.67 (s, 6H), 0.85−2.35 (m, 82H), 3.19 (m, 2H), 3.49 (s, 12H), 3.63 (br s, 12H), 3.73 (br s, 4H), 3.95 (br s, 12 H), 4.06 (br s, 4H), 5.35 (d, J = 4.5 Hz, 2H). ^{13}C NMR ($CDCl_3$, 75 MHz): δ 11.83, 18.69, 19.34, 21.04, 22.53, 22.78, 23.82, 24.26, 27.98, 28.14, 28.19, 31.83, 31.88, 35.76, 36.16, 36.75, 36.90, 38.75, 39.48, 39.69, 42.29, 49.86, 52.69, 55.99, 56.50, 61.88, 64.74, 65.06, 70.14, 70.35, 70.45, 70.54, 79.88, 122.35, 139.87. ESI-MS: 1206.1 [M^{+2} + Br^-]. Anal. ($C_{64}H_{134}O_7N_2Br_2 \cdot 3H_2O$) C, H, N.

Liposome Preparation. Each lipid or its mixture with DOPE in the desired mole ratio was dissolved in dry chloroform in autoclaved Wheaton glass vials. Thin films were made by evaporation of the organic solvent under a steady stream of dry nitrogen. Last traces of organic solvent were removed by keeping these films under high vacuum overnight. Freshly autoclaved Milli-Q water was added to individual film such that the final concentration of the cationic lipid was maintained at 0.5 mM. The mixtures were kept for hydration at 4 °C for 10−12 h and were subjected to repeated freeze−thaw cycles (ice-cold water to 60 °C) with intermittent vortexing to ensure hydration. Sonication of these suspensions for 15 min in a bath sonicator at 60 °C afforded closed cationic liposomes, as evidenced from transmission electron microscopy. Liposomes were prepared and kept under sterile conditions. Formulations were stable, and no precipitation was observed within 3 months if stored at 4 °C.

Transmission Electron Microscopy. Freshly prepared aqueous suspensions of lipid−DNA complexes were examined under transmission electron microscopy by negative staining using 1% uranyl acetate. A 10 μL sample of the suspension was loaded onto Formvar-coated, 400 mesh copper grids and allowed to remain for 1 min. Excess fluid was wicked off the grids by touching their edges to filter paper, and 10 μL of 1% uranyl acetate was applied on the same grid, after which the excess stain was similarly wicked off. The grid was air-dried for 30 min, and the specimens were observed under TEM (JEOL 200-CX) operating at an acceleration voltage of 120 keV. Micrographs were recorded at a magnification of 5000−20 000×.

Plasmid DNA. pEGFP-c3 (Clontech, USA), which encodes for an enhanced green fluorescence protein (GFP) under a CMV promoter, was amplified in *Escherichia coli* (DH5α) and purified using Qiagen Midi Prep Plasmid Purification protocol

(Qiagen, Germany). Purity of the plasmid was checked by electrophoresis on 1.0% agarose gel. Concentration of the DNA was estimated spectroscopically by measuring the absorption at 260 nm and confirmed by gel electrophoresis. The plasmid preparations showing a value of $OD_{260}/OD_{280} > 1.8$ were used.

Cell culture. Cells (HeLa) were cultured in Dulbecco's Modified Eagle's Medium (DMEM; Sigma) supplemented with 10% fetal bovine serum (FBS) in T25 culture flasks (Nunc, Denmark) and were incubated at 37 °C in a humidified atmosphere containing 5% CO_2. Cells were regularly passaged by trypsinization with 0.1% trypsin (EDTA 0.02%, dextrose 0.05%, and trypsin 0.1%) in PBS (pH 7.2).

Cytotoxicity. Toxicity of each cationic lipid formulation toward HeLa cells was determined using 3-(4,5-dimethyl thiazole-2-yl)-2,5-diphenyltetrazolium bromide (MTT) reduction assay following literature procedures (*38*, *39*). MTT gets converted to an insoluble blue dye, formazan, in actively respiring cells. The assay estimates the concentration of the formazan formed, which in turn gives a measure of the population of cells that are metabolically active.

A range of liposomal concentrations 5−30 μM were investigated for toxicity studies. Cytotoxicity of the lipid formulations optimal for transfection experiments was determined under conditions exactly the same as transfection conditions. Nearly 12 000 cells/well were plated in 96 well plates. After 24 h, optimized lipid/DOPE formulations were complexed with 0.2 μg of the DNA at various N/P ratios for 30 min. DNA−lipid complexes were added to the cells in the absence of serum. After 6 h of incubation, lipoplexes were removed, and 200 μL of media with 10% FBS was added. After 42 h, 20 μL of MTT solution was added, and the cells were incubated further for 4 h. Blue formazan crystals were seen when checked under the microscope. Media was removed, and 200 μL of DMSO was added per well. The absorbance was measured using a microtiter plate reader. The % viability was then calculated as [{A590-(treated cells) − background]/[A590(untreated cells) − background}] × 100.

Transfection Procedure. All transfection experiments were carried out in HeLa cells in antibiotic-free media unless specified otherwise. In a typical experiment, 24 well plates were seeded with 45 000 cells/well in antibiotic-free media 24 h before transfection such that they were at least ∼70% confluent at the time of transfection. For transfection, lipid formulation and DNA were serially diluted separately in DMEM containing no serum to have the required working stocks. DNA was used at a concentration of 0.8 μg/well unless specified otherwise. The lipid and DNA were complexed in a volume of 200 μL by incubating the desired amount of lipid formulation and DNA together at room temperature for about 30 min. The lipid concentrations were varied so as to obtain the required lipid/DNA (N/P) charge ratios. Charge ratios here represent the ratio of charge on cationic lipid (in mol) to nucleotide base molarity and were calculated by considering the average nucleotide mass of 330. After 30 min of complexation, 200 μL of media were added to the complexes (final DNA concentration = 12.12 μM). Old medium was removed from the wells, cells were washed with DMEM, and lipid−DNA complexes in 200 μL media were added to the cells. The plates were then incubated for 6 h at 37 °C in a humidified atmosphere containing 5% CO_2. At the end of the incubation period, medium was removed, and cells were washed with DMEM; 500 μL of DMEM containing 10% FBS was added per well. Plates were further incubated for a period of 42 h before checking for the reporter gene expression. Green fluorescent protein (GFP) expression was examined by fluorescence microscopy and was quantified by flow cytometry analysis. All the experiments were done in duplicate, and results presented are the average of at least two such independent experiments done on two different days. For comparison, transfections using lipid **1** were performed using optimized lipid/DOPE ratio (*24*) of 1:1 at N/P ratio of 1.0, using 0.8 μg of plasmid DNA.

For transfections in the presence of serum, lipid and DNA were separately diluted in serum-free media as already mentioned, and the complexation was done in serum-free media (200 μL) for 30 min. The complex was then diluted to 400 μL with DMEM containing 20% FBS so as to achieve a final serum concentration of 10%. The cells were then incubated with this complex for 6 h. At the end of the incubation period, medium was removed, and cells were washed with DMEM; 500 μL of DMEM containing 10% FBS was added per well. For transfections at 30% and 50% of serum concentrations, complexes were diluted to 400 μL with DMEM containing 60% FBS or with neat FBS, respectively.

Gel Electrophoresis. To examine the complexation of DNA with cationic lipid suspensions at different lipid−DNA ratios, we prepared lipid−DNA complexes at different lipid−DNA charge ratios in an identical manner as was done with transfection experiments using 0.2 μg of the plasmid DNA. After 30 min of incubation, these complexes were electrophoretically run on a 1.0% agarose gel. The uncomplexed DNA moved out of the well, but the DNA that was complexed with lipid remained inside the well (*40*).

Flow Cytometry. The reporter gene expression was examined by fluorescence microscopy at regular intervals and was quantified 48 h post-transfection by flow cytometry. The percentages of transfected cells were obtained by determining the statistics of cells fluorescing above the control level wherein nontransfected cells were used as the control. Approximately 10 000 cells were analyzed to obtain the statistical data, which have been presented as the average of at least two independent measurements. For flow cytometry analysis, ∼48 h post-transfection, old medium was removed from the wells; cells were washed with PBS and trypsinized by adding 100 μL of 0.1% trypsin. To each well, 200 μL of PBS containing 20% FBS was added. Duplicate cultures were pooled and analyzed by flow cytometry immediately using a Becton and Dickinson flow cytometer equipped with a fixed laser source at 488 nm.

FACS Analysis. FACS data were analyzed by public domain *WinMDI* software to eliminate data from cell debris (particles smaller than cells), dead cells, and clumps of two or more cells. Subcellular debris and clumps can be distinguished from single cells by size (estimated by the intensity of low-angle forward-scatter). Dead cells have lower forward-scatter and higher side-scatter than living cells. The FACS scans had been configured to display the fluorescence signals only from those particles with a specified set of scatter properties, namely, living single cells. This is called a scatter-gated fluorescence analysis. Therefore, the data from dead cells had been eliminated by gating out brightly fluorescent cells.

RESULTS AND DISCUSSION

Chemistry. Four cholesterol-based gemini lipids possessing oxyethylene-based spacer chains have been synthesized. Each lipid differed from the others based on the spacer lengths [$-CH_2-(CH_2-O-CH_2)_n-CH_2-$]. These gemini lipids have been synthesized from the precursor cholest-5-en-3β-oxyethan-*N*,*N*-dimethyl amine by Menshutkin reaction with the corresponding α,ω-dibromoalkoxyalkanes. The synthesis of precursor cholest-5-en-3β-oxyethan-*N*,*N*-dimethyl amine and monomeric lipid **1** has already been reported (*24*). All the gemini lipids have been purified by repeated precipitation with MeOH, EtOAc, and acetone. All the gemini lipids were fully characterized by ^{1}H NMR, ^{13}C NMR, ESI-MS, and C, H, N analysis.

Aggregate Formation from Cationic Gemini Cholesterol Lipids. Upon hydration, each of the gemini cholesterol lipids

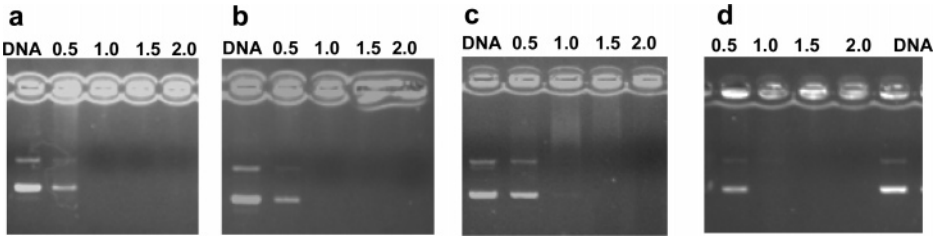


Figure 2. Electrophoretic gel patterns for lipoplex-associated DNA in gel retardation for gemini cholesterol lipids: (a) **2a**; (b) **2b**; (c) **2c**; (d) **2d**. The N/P ratios are indicated at the top of each lane. 0.2 μg of the DNA was complexed with liposomes at various N/P ratios for 30 min, and lipoplexes were run electrophoretically on 1% agarose gel.

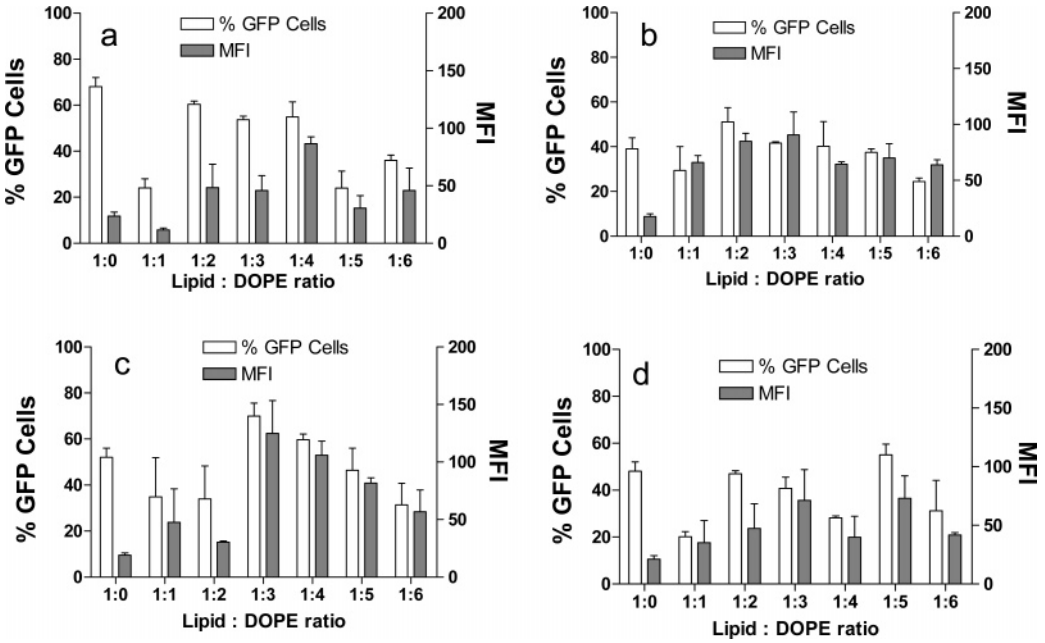


Figure 3. Transfection efficiencies of cholesterol-based gemini lipids with various mole ratios of DOPE: (a) **2a**; (b) **2b**; (c) **2c**; (d) **2d**. Concentration of the DNA = 0.8 μg/well, and lipids were used at N/P ratio of 0.5. Lipoplexes were incubated with cells for 6 h. Data are expressed as the number of transfected cells and MFI as obtained from flow cytometry analysis after 48 h of transfection.

was found to disperse easily in water. All the lipid molecules mentioned here formed stable suspensions in water. The suspensions formed from lipids were found to be translucent. Generally, TEM examination of air-dried, aqueous suspensions revealed the existence of closed vesicle-like aggregate structures for all the gemini lipids (not shown). The aggregates formed from all the gemini lipids ranged from 30 to 80 nm in size. When compared, all gemini lipid aggregates were generally found to be smaller in size as compared to the aggregates of monomeric lipid **1**, which ranged ~100 ± 30 nm in size (not shown).

Mixed Liposome Formation with 1,2-Dioleoyl-L-α-glycero-3-phosphatidyl Ethanolamine (DOPE). Liposomes could be conveniently prepared from a mixture of gemini lipid with helper lipid 1,2-dioleoyl-L-α-glycero-3-phosphatidyl ethanolamine (DOPE) by first subjecting the films of lipid mixtures to hydration, repeated freeze−thaw cycles, and followed by sonication at 60 °C for 15 min. All the gemini lipid/DOPE formulations formed optically transparent suspensions. Liposomes were prepared under sterile conditions and were resonicated for 5 min at room temperature before transfection experiments. The vesicular suspensions were sufficiently stable, and no precipitation was observed within 3 months if stored at 4 °C.

Gel Electrophoresis. To characterize the electrostatic binding interactions between the plasmid DNA and the mixed cationic liposomes as a function of different N/P charge ratios (or lipid/DNA mole ratios), we performed conventional electrophoretic gel retardation assays (Figure 2). All gemini lipid suspensions were able to retard the plasmid DNA from the well at N/P ratio of 1.0. It should be noted that every gemini molecule possesses two hard charges, which indicates that the whole plasmid DNA gets retarded at a lipid/DNA mol ratio of 0.5. Significant retardation of DNA was also observed at an N/P ratio of 0.5 (or lipid/DNA mole ratio of 0.25) as well.

Transfection Biology. To find out the optimized transfection efficiency, both the number of transfected cells and the mean fluorescence intensity (MFI) have been considered. The MFI defined for GFP-positive cells reveal that the level of GFP expression with a higher MFI value correlates positively with high GFP expression (*41*). These data were obtained from flow cytometric analysis. Figure 3 clearly indicates that individual lipid formulations were able to transfect the high number of cells, but the MFI observed was very low. When cells transfected with individual lipids were observed under the fluorescence microscope (not shown), very few green fluorescent cells were visible. This is confirmed by FACS analysis, which showed very low MFI.

Optimization of Lipid/DOPE Ratio. Naturally occurring lipid such as DOPE has been known to increase the efficiency of transfection in lipid-mediated gene transfer applications. In order to see the most effective formulations, transfections with identical lipid/DNA mole ratios (or N/P ratio), varying the mole ratio of gemini lipids (**2a**−**2d**) in DOPE, were performed (Figure 3). FACS analysis (Supporting Information) indicates that incorporation of DOPE enhances the transfection efficacy of gemini lipids dramatically, especially in terms of MFI. When cells transfected with lipid−DOPE co-liposomes were observed

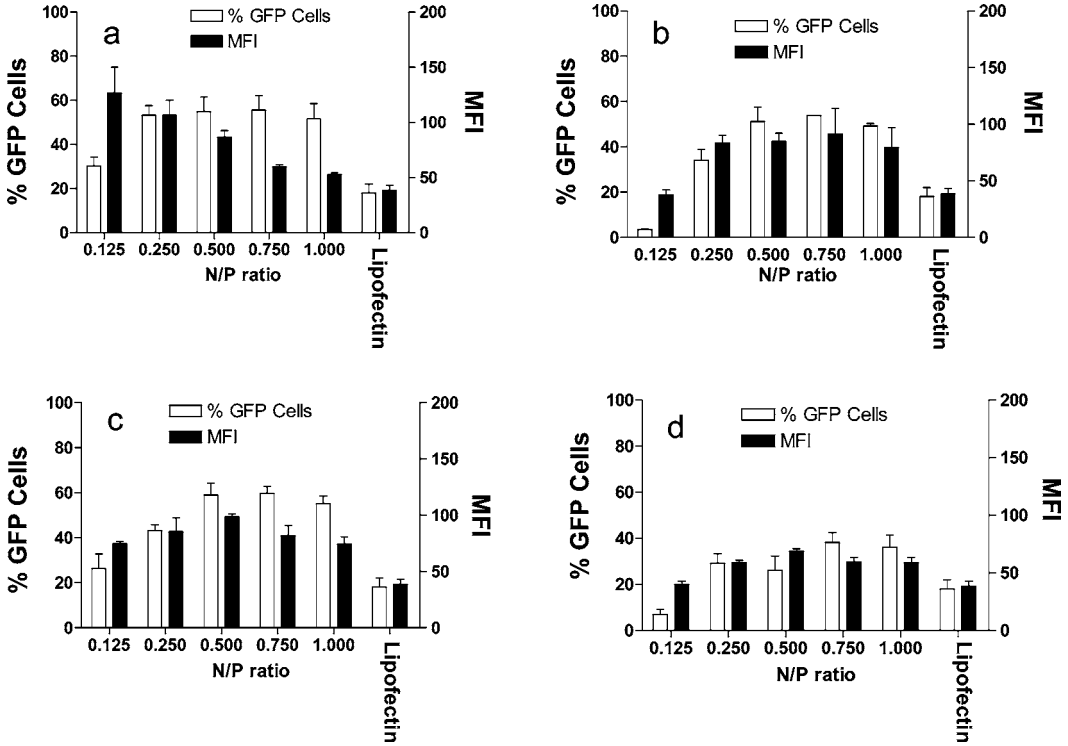


Figure 4. Transfection efficiencies of gemini lipids using optimized lipid/DOPE formulations at various N/P ratios in the absence of serum (−FBS−FBS). (a) **2a**; (b) **2b**; (c) **2c**; (d) **2d**. Concentration of the DNA = 0.8 μg/well. Lipoplexes were incubated with cells for 6 h. Data are expressed as the number of transfected cells and MFI as obtained from flow cytometry analysis after 48 h of transfection.

under the fluorescence microscope, we observed highly fluorescent cells which were confirmed by the increase in MFI observed from FACS analysis. In our studies, we had considered both the number of transfected cells and the MFI for optimizing the transfection efficacies of gemini lipids, both as the number of transfected cells and the amount of gene expression matter for successful gene therapy.

The optimized lipid/DOPE ratio was found to vary with the length of the oxyethylene spacer of gemini lipids. Lipid **2a** showed maximum gene transfection activity at a lipid/DOPE ratio of 1:4, whereas **2b** showed maximum activity at a lipid/DOPE ratio of 1:2, and with further increase in DOPE mole ratio, transfection activity started to decrease. Gemini lipid **2c** showed maximum activity at a lipid/DOPE mol ratio of 1:3. Lipid **2a** at a lipid/DOPE ratio of 1:4 was able to transfect nearly 50% of the cells with MFI of 100, whereas **2b** was able to show the same activity at a lipid/DOPE mole ratio of 1:2. Lipid **2c** at a lipid/DOPE mole ratio of 1:3 was found to be most effective, transfecting nearly 60% of cells with MFI greater than 100, and with further increase in the DOPE mole ratio, transfection efficiency decreased. Lipid **2d** was not found to be highly effective at any of the lipid/DOPE ratios, although maximum transfection activity was observed at a lipid/DOPE mol ratio of 1:5. While comparing all the gemini lipids, lipid **2c** was found to be the most effective gemini lipid and even required a lower mole percentage of DOPE as compared to other gemini lipids. Each gemini lipid required different amounts of DOPE for optimized transfection efficiency; this may be because of the change in the balance between hydrophilicity and hydrophobicity of the gemini lipids.

Optimization of N/P Ratio. After optimization of the lipid/DOPE mole ratio for each gemini lipid, all the gemini lipids were tested by taking the identical amount of DNA (0.8 μg) and varying the amount of lipid using the respective optimized lipid/DOPE ratio. Lipid **2a** was able to transfect a maximum of 50% of the cells with an MFI of 100 at N/P ratio of 0.25, whereas lipid **2b** formulations could transfect approximately the same number of cells but with low MFI at N/P ratio of 0.5 (Figure 4). Transfection efficiency of the lipid **2a** formulation decreased at higher N/P ratios, especially in terms of MFI. Gemini lipid **2c** was able to transfect more than 60% of the cells at N/P ratio of 0.5 with MFI of ∼100. While comparing the transfection efficiencies, the lipid **2b** formulation induced a lower transfection efficiency than lipid **2a**, whereas the transfection efficiency of the lipid **2c** formulation was greater than that of lipid **2b** and was comparable to that of **2a**. The lipid **2d** formulation was found to be the least effective gene delivery agent in this series of gemini cholesterol lipids. All the gemini lipids followed a bell-shaped graph when transfection efficiencies were plotted against N/P ratio. When all the gemini lipids were compared at N/P ratio of 0.5, lipid **2a** and **2c** formulations were found to be the best transfecting agents.

Effect of Serum. One of the serious shortcomings of the cationic lipid-mediated gene delivery, especially involving *in vivo* trials, is that the transfection is inefficient particularly in the presence of serum proteins. Serum proteins that are negatively charged are known to interact with cationic lipids, thereby competing with DNA for cationic lipids, leading to inhibition of transfection. To have better potential especially in gene therapy, it is important to have reagents that are capable of delivering and expressing an external gene inside a cell in the presence of serum. There are very few reports of cationic lipids, including our own, which induce transfection activity even in the presence of serum (*19*, *42*, *43*). Therefore, we planned to study the efficiencies of these cholesterol-based gemini lipids in the presence of serum as well and compared the transfection activities of these lipid formulations against a commercially available reagent, Lipofectin. To our pleasant surprise, serum did not inhibit the transfection efficiency of any of the gemini lipids; an enhancement in transfection efficiency was even observed in the presence of 10% serum conditions (Figure 5). Gemini lipid **2a** showed better transfection efficiency in the presence of serum. Nearly 60−70% of the cells were found to be transfected with MFI of 100−135 using the lipid

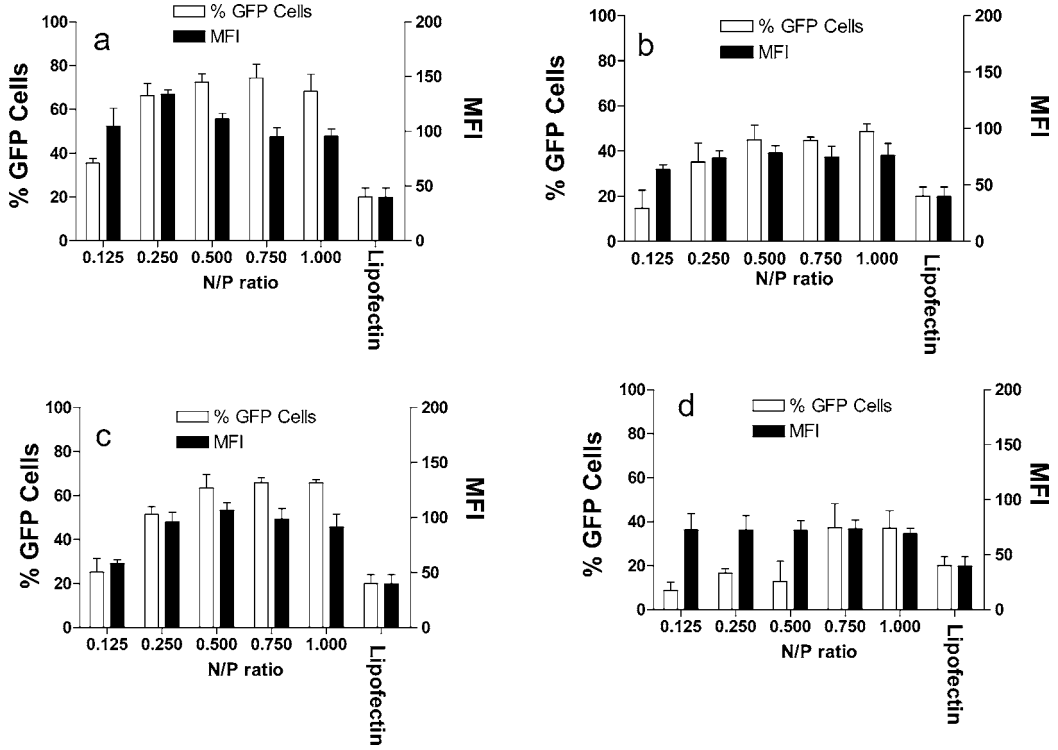


Figure 5. Transfection efficiencies of gemini lipids using optimized lipid/DOPE formulations at various N/P ratios in the presence of 10% FBS (−FBS+FBS). (a) **2a**; (b) **2b**; (c) **2c**; (d) **2d**. Concentration of the DNA = 0.8 μg/well. Lipoplexes were incubated with cells for 6 h. Data are expressed as the number of transfected cells and MFI as obtained from flow cytometry analysis after 48 h of transfection.

2a formulation at N/P ratio of 0.25 in the presence of 10% serum conditions. Serum also did not affect the transfection efficiency of gemini lipid **2b**, although efficiency was lower than that of the lipid **2a** formulation. The transfection efficiency of lipid **2c** was nearly 60−70% of cells with MFI of 100−110 at N/P ratio of 0.5. Gemini lipid **2d** was much less efficient in the presence of 10% serum as compared to other gemini lipids. Therefore, all the gemini lipids (except **2d**) were found to show high transfection activity in the presence of serum.

Gemini Lipids vs Monomeric Lipid. To put our results into proper perspective, we compared the transfection activities of the cholesterol gemini lipid formulations with those of their corresponding monomer. Figure 6 shows the transfection efficiencies of the gemini lipids (**2a**−**2d**) in comparison with that of monomeric lipid **1** formulation.

Although the monomeric lipid **1** showed transfection efficiency of ∼60%, but the mean fluorescence intensity in the case of monomeric lipid **1** was much lower as compared to any of the gemini lipids tested (Figure 6). MFI indirectly tells the amount of the protein expressed in the cells, which gives the number of copies of the plasmids delivered inside the cell. It is clear that each gemini lipid shows enhanced mean fluorescence intensity as compared to the monomeric lipid counterpart **1.** Figure 6b shows that there is a dramatic decrease in the transfection efficiency of the monomeric lipid **1** in the presence of 10% serum conditions, whereas in the case of gemini lipids, there is hardly any effect on the transfection activity in the presence of serum. The lipid **2a** formulation was found to transfect nearly 70% of the cells with MFI of ∼100, whereas formulations based on monomeric lipid **1** transfected only nearly 20% of cells with very low MFI of ∼40.

Therefore, in conclusion, all gemini lipids were much better transfecting agents as compared to the monomeric lipid **1**. Among gemini lipids, the lipid **2a** formulation was found to be the best transfecting agent in the presence of serum, whereas the lipid **2d** formulation was least effective.

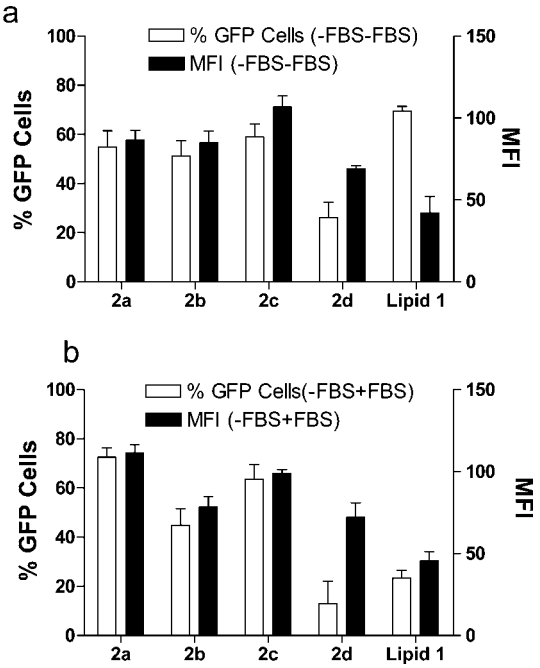


Figure 6. Comparative transfection efficiencies of gemini lipids (**2a**−**2d**) and monomeric lipid **1** in the absence (−FBS−FBS) and presence of 10% serum (−FBS+FBS). Concentration of the DNA = 0.8 μg/well. Lipoplexes were incubated with cells for 6 h. Data are expressed as the number of transfected cells and MFI as obtained from flow cytometry analysis after 48 h of transfection.

GFP Assay at High Serum Concentrations. To see the effect of high concentrations of serum on the gene transfection efficiencies, we performed the gene transfection efficiencies using optimized lipid/DOPE formulations at 30% and 50% serum concentrations (Figures 7 and 8). The lipid **2a**/DOPE formulation was able to transfect ∼50% of cells at 30% and

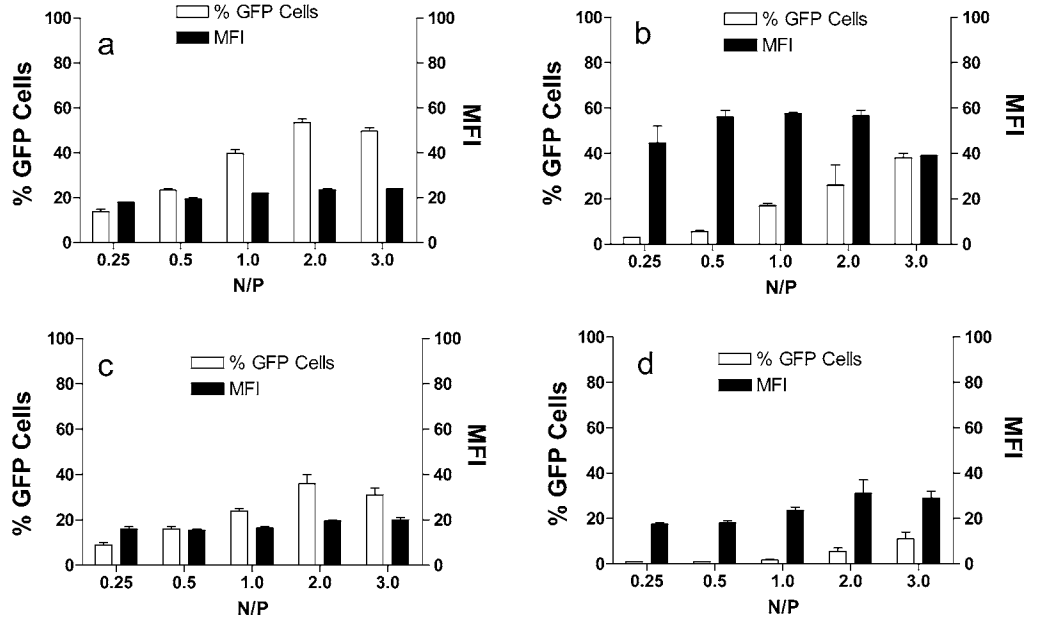


Figure 7. Transfection efficiencies of gemini lipids using optimized lipid/DOPE formulations at various N/P ratios in the presence of 30% FBS. (a) **2a**; (b) **2b**; (c) **2c**; (d) **2d**. Concentration of the DNA = 0.8 μg/well. Lipoplexes were incubated with cells for 6 h. Data are expressed as the number of transfected cells and MFI as obtained from flow cytometry analysis after 48 h of transfection.

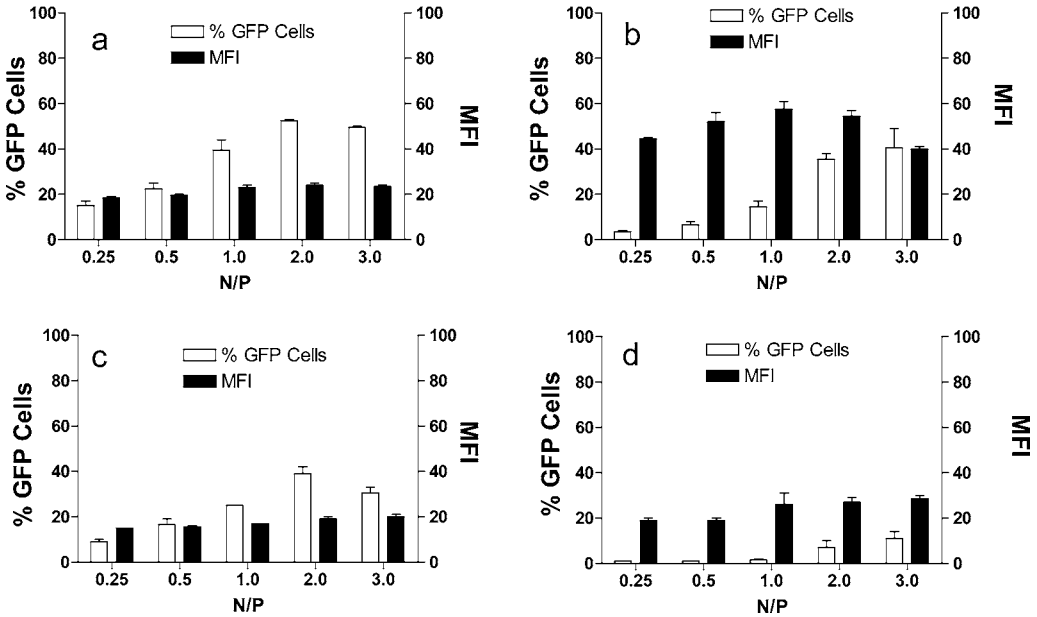


Figure 8. Transfection efficiencies of gemini lipids using optimized lipid/DOPE formulations at various N/P ratios in the presence of 50% FBS. (a) **2a**; (b) **2b**; (c) **2c**; (d) **2d**. Concentration of the DNA = 0.8 μg/well. Lipoplexes were incubated with cells for 6 h. Data are expressed as the number of transfected cells and MFI as obtained from flow cytometry analysis after 48 h of transfection.

50% serum concentrations, although there was a decrease in the MFI at higher serum conditions and maximum transfections were observed at N/P ratio of 2.0. This is expected, because at such higher serum conditions, negatively charged serum proteins start to compete with DNA for complexation with cationic lipids. One major characteristic feature of the lipid **2a** formulation is that there is no effect on the number of cells getting transfected even in the presence of high concentrations of serum. Therefore, it indicates that serum does not inhibit the number of transfected cells but reduces the amount of the DNA delivered inside the cells as indicated by FACS analysis. Lipid **2b** is able to transfect nearly 40% of the cells at N/P ratio of 3.0 at 30% and 50% serum conditions. The MFI observed in the case of lipid **2b** formulations was nearly twice that of the lipid **2a** formulation, which indicates that lipid **2b** was able to deliver double the amount of DNA into the cells as compared to the lipid **2a** formulation, whereas the transfection efficacy of commercially available Lipofectin diminished completely at higher serum concentrations. Lipid **2c** was able transfect 30% of cells with low MFI at N/P ratios 2.0−3.0. Lipid **2d** was not able to transfect at high serum concentrations.

Effect of Variation of the Amount of DNA. To see whether the varying the amount of DNA affects the transfection efficiency of gemini lipids, we have performed transfection experiments with all gemini lipids at N/P ratios of 0.25 and 0.5, varying the amount of DNA from 0.4 to 2.0 μg. We did not observe any increase in gene transfection activity by varying the amount of DNA in all cases of gemini lipids, except gemini lipid **2a**, which showed an enhancement in gene delivery when 0.4 μg of DNA was used (Figure 9). This indicates that lipid **2a** is more efficient at low DNA concentrations. Lipid **2a** was able to transfect nearly 70% of cells with MFI of ∼170 at an

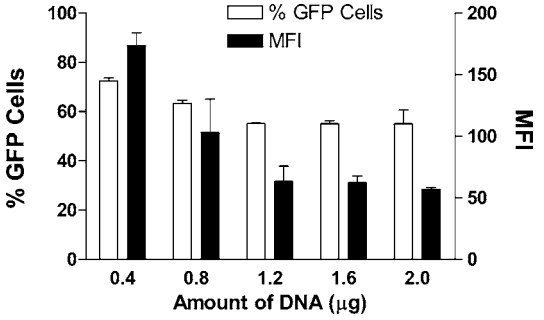


Figure 9. Effect of the variation of the amount of the DNA on gene transfection efficiency of gemini lipid **2a**/DOPE (1:4 mol ratio) formulation at N/P ratio of 0.5. Lipoplexes were incubated with cells for 6 h. Data are expressed as the number of transfected cells and MFI as obtained from flow cytometry analysis after 48 h of transfection.

N/P ratio of 0.5. Therefore, among all gemini lipids, the lipid **2a** formulation was found to be the best, transfecting nearly 70% of cells using 0.4 μg of DNA at an N/P ratio of 0.5.

Cytotoxicity. The cytotoxic effects of the cationic lipids toward HeLa cells had been examined in detail, as shown in Figure 10. First, all the liposome formulations of lipids had been tested at different concentrations of 5, 10, 15, 20, and 30 μM, as the maximum amount of lipid used in all transfection is 18.8 μM. All the lipid formulations were found to be nontoxic at all lipid concentrations, except lipid **2d** formulation, where 80% cell viability was found at 20 μM concentration and 70% cell viability at 30 μM concentration (Figure 10a). To see the effect of the DOPE on cell viability, we also investigated the cell viability assays on HeLa cells using optimized lipid/DOPE formulations at different concentrations of 5, 10, 15, 20, and 30 μM (Figure 10b). Lipid/DOPE formulations were also found be nontoxic at all concentrations, except lipid **2d** where nearly 80% cell viability was found. The lipid **2d** formulation was also found to be the least efficient transfecting agent among the series of lipids studied herein. Lipid−DNA lipoplexes using optimized lipid/DOPE formulations were studied for cell viability assays. More than 80% cell viability was observed with all formulations at all N/P ratios (Figure 10c).

Characterization of Lipid−DNA Complexes. Morphology of lipid/plasmid complexes was visualized under a transmission electron microscope after negative staining using uranyl acetate. The complexes formed with the best gemini lipids (**2a** and **2c**) at their optimized transfection ratios with plasmid DNA revealed some distinct morphological changes depending on the length of the spacer in between the cationic ammonium headgroups of the gemini cholesterol lipid molecules (Figure 11). The lipoplexes formed from gemini lipid **2a**/DNA showed a tendency to form "elongated" structures (Figure 11a). It appears the lipid vesicles are organized on the templates of plasmid DNA surface. In contrast, the lipid **2c**/DNA complexes showed aggregation during such complexation, leading to the formation of irregular morphologies.

CONCLUSIONS

We have presented here the syntheses of four cholesterol-based gemini cationic lipids, which bear oxyethylene-based spacers in between the headgroups. These gemini lipids are dimers of the monomeric lipid **1**, which also possess a nonhydrolyzable ether-type linkage between the cationic headgroup and cholesterol backbone. The gemini lipids differ from each other in the number of oxyethylene groups present between the headgroups. The gemini lipids have been synthesized in a single step from cholest-5-en-3β-oxyethan-*N*,*N*-dimethylamine, by reacting with appropriate α,ω-dibromoalkoxyalkanes.

Electron micrographs showed the presence of vesicle-like aggregates formed from the aqueous suspensions of these gemini

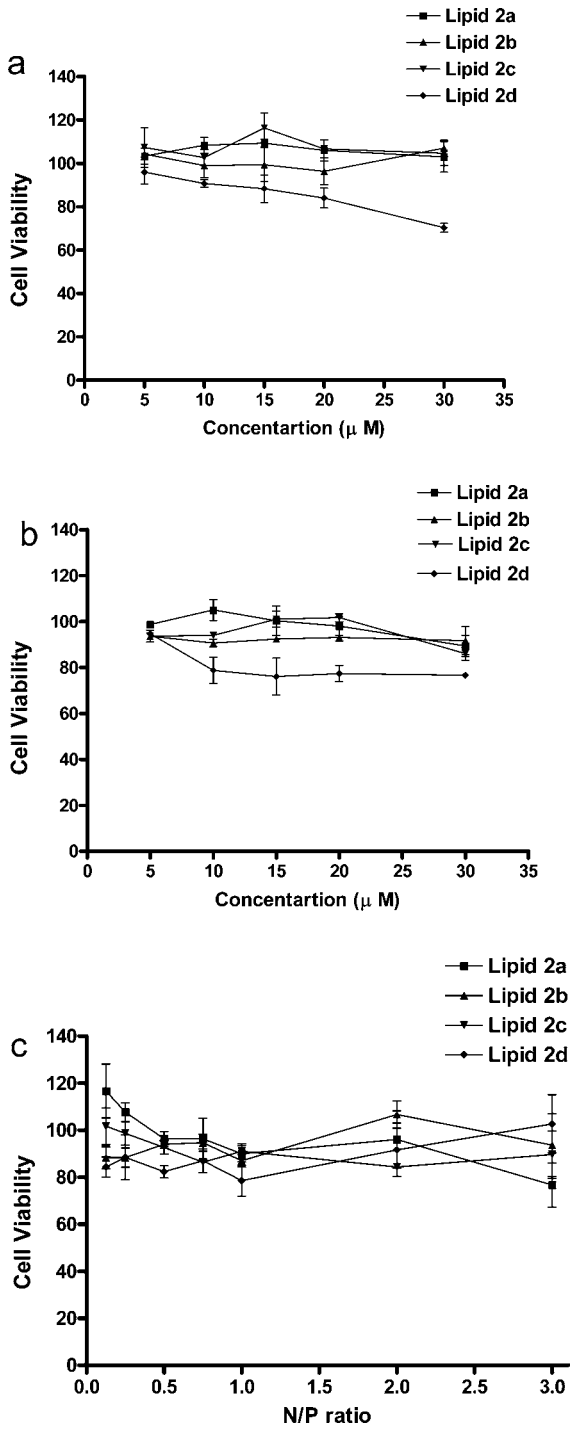


Figure 10. (a) Cytotoxicity exhibited toward HeLa cells by liposomes. (b) Cytotoxicity exhibited toward HeLa cells by optimized lipid/DOPE co-liposomes. (c) Cytotoxicity toward HeLa cells by lipoplexes at different N/P ratios using optimized lipid/DOPE formulations. All the experiments were performed in triplicate in 96-well plates. The % viability was then calculated as [{A590(treated cells) − background]/[A590(untreated cells) − background}] × 100.

lipids. All gemini cholesterol lipids were able to transfect the mammalian cells. Incorporation of an oxyethylene spacer between the cationic ammonium headgroups dramatically increased the transfection activities of the gemini cholesterol lipids as compared to their monomeric counterparts.

Serum is known to be a major impediment for *in vivo* applications of cationic liposomes. All the gemini lipid formulations were, however, able to transfect the mammalian cells even in the presence of serum, in contrast to their monomeric lipid counterparts, where a dramatic decrease in transfection efficacy

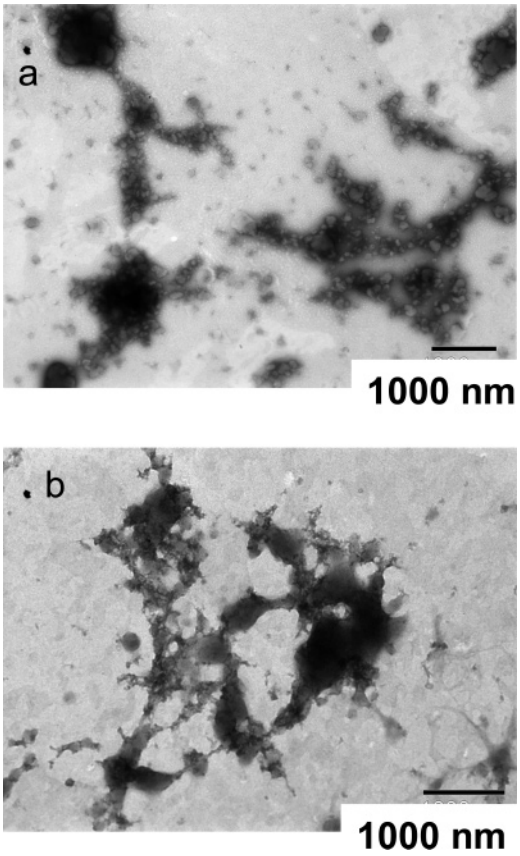


Figure 11. Transmission electron micrographs for the lipoplexes prepared from most effective gemini lipid/DOPE liposome/DNA complexes at the optimized N/P ratio. (a) **2a**; (b) **2c**.

was observed. The transfection efficiency of gemini lipid **2a** was in fact enhanced in the presence of 10% serum conditions. The lipid **2a** formulation was able to transfect nearly 70% of the cells with high MFI. A characteristic feature of the lipid **2a** formulation is that highest transfection efficiency was achieved using only 0.4 μg of the DNA at an N/P ratio of 0.5. The lipid **2c** formulation was found to be effective at a lipid/DOPE ratio of 1:2 and also compatible in the presence of serum. The lipid **2d** formulation was found to be the least effective.

Maximum transfection efficacies of gemini lipids were observed at N/P ratios of 0.5−0.75 in the absence of serum, whereas we observed the complete complexation of DNA at N/P ratios higher than 1.0. Similar observations have also been reported by others. Complete retardation of the plasmid DNA is not essential for maximum gene transfection efficacy. There are many interactions including hydrophobic interactions between liposomes and DNA and between lipoplexes and cell membranes, other than electrostatic interactions, that may be responsible for enhanced gene transfection activities at low N/P ratios.

Although the precise molecular mechanism for their compatibility in the presence of serum is beyond the scope of this presentation, these results indicate that gemini cholesterol lipids with proper design may afford new carriers which may be useful in the field of gene therapy. Cytotoxicity assay shows nearly 80% of the cell viability at the optimum lipid/DNA concentrations. Since the resulting gemini lipids and their liposomes with DOPE are stable both chemically and as colloidal suspensions, these could be used for more practical applications.

ACKNOWLEDGMENT

This work was supported by Department of Biotechnology, Government of India, New Delhi, India. Avinash Bajaj thanks CSIR for a senior research fellowship.

Supporting Information Available: Elemental analysis and FACS details. This material is available free of charge via the Internet at http://pubs.acs.org.

LITERATURE CITED

(1) Yang, Y., Nunes, F. A., Berencsi, K., Furth, E. E., Gonczol, E., and Wilson, J. M. (1994) Cellular immunity to viral antigens limits E1-deleted adenoviruses for gene therapy. *Proc. Natl. Acad. Sci. U.S.A. 91*, 4407−4411.

(2) Knowles, M. R., Hohneker, K. W., Zhou, Z., Olsen, J. C., Noah, T. L., Hu, P. C., Leigh, M. W., Engelhardt, J. F., Edwards, L. J., and Jones, K. R. (1995) A controlled study of adenoviral-vector-mediated gene transfer in the nasal epithelium of patients with cystic fibrosis. *New Engl. J. Med. 333*, 823−831.

(3) Crystal, R. G., McElvaney, N. G., Rosenfeld, M. A., Chu, C.-S., Mastrangeli, A., Hay, J. G., Brody, S. L., Jaffe, H. A., Eissa, N. T., and Danel, C. (1994) Administration of an adenovirus containing the human CFTR cDNA to the respiratory tract of individuals with cystic fibrosis. *Nat. Genet. 8*, 42−51.

(4) Yang, Y., Nunes, F. A., Berencsi, K., Goenczoel, E., Engelhardt, J. F., and Wilson, J. M. (1994) Inactivation of E2a in recombinant adenoviruses improves the prospect for gene therapy in cystic fibrosis. *Nat. Genet. 7*, 362−369.

(5) Gao, X., and Huang, L. (1995) Cationic liposome-mediated gene transfer. *Gene Ther. 2*, 710−22.

(6) Boussif, O., Lezoualc'h, F., Zanta, M. A., Mergny, M. D., Scherman, D., Demeneix, B., and Behr, J.-P. (1995) A versatile vector for gene and oligonucleotide transfer into cells in culture and in vivo: polyethylenimine. *Proc. Natl. Acad. Sci. U.S.A. 92*, 7297−7301.

(7) Wagneer, E., Ogris, M., and Zauner, W. (1999) Polylysine-based transfection systems utilizing receptor mediated delivery. *Adv. Drug Delivery Rev. 30*, 97−113.

(8) Kabanov, A. V., and Kabanov, V. A. (1995) DNA Complexes with Polycations for the delivery of genetic material into cells. *Bioconjugate Chem. 6*, 7−20.

(9) Miller, A. D. (2003) The problem with cationic liposome/micelle-based non-viral vector systems for gene therapy. *Curr. Med. Chem. 10*, 1195−1211.

(10) Nakanishi, M. (2003) New strategy in gene transfection by cationic transfection lipids with a cationic cholesterol. *Curr. Med. Chem. 10*, 1289−1296.

(11) Nicolazzi, C., Garinot, M., Mignet, N., Scherman, D., and Bessodes, M. (2003) Cationic lipids for transfection. *Curr. Med. Chem. 10*, 1263−1277.

(12) Niculescu-Duvaz, D., Heyes, J., and Springer, C. J. (2003) Structure-activity relationship in cationic lipid mediated gene transfection. *Curr. Med. Chem. 10*, 1233−1261.

(13) Ilies, M. A., Seitz, W. A., Ghiviriga, I., Johnson, B. H., Miller, A., Thompson, E. B., and Balaban, A. T. (2004) Pyridinium cationic lipids in gene delivery: a structure-activity correlation study. *J. Med. Chem. 47*, 3744−3754.

(14) Karmali, P. P., Kumar, V. V., and Chaudhuri, A. (2004) Design, syntheses and in vitro gene delivery efficacies of novel mono-, di- and tri-lysinated cationic lipids: a structure-activity investigation. *J. Med. Chem. 47*, 2123−2132.

(15) Majeti, B. K., Karmali, P. P., Reddy, B. S., and Chaudhuri, A. (2005) In vitro gene transfer efficacies of *N*,*N*-dialkylpyrrolidinium chlorides: a structure-activity investigation. *J. Med. Chem. 48*, 3784−3795.

(16) Ilies, M. A., Seitz, W. A., Johnson, B. H., Ezell, E. L., Miller, A. L., Thompson, E. B., and Balaban, A. T. (2006) Lipophilic pyrylium salts in the synthesis of efficient pyridinium-based cationic lipids, gemini surfactants, and lipophilic oligomers for gene delivery. *J. Med. Chem. 49*, 3872−3887.

(17) Gardner, R. A., Belting, M., Svensson, K., and Phanstiel, O., IV (2007) Synthesis and transfection efficiencies of new lipophilic polyamines. *J. Med. Chem. 50*, 308−318.
(18) Bhattacharya, S., and Mandal, S. S. (1998) Evidence of interlipidic ion-pairing in anion-induced DNA release from cationic amphiphile-DNA complexes. mechanistic implications in transfection. *Biochemistry 37*, 7764−7777.
(19) Dileep, P. V., Antony, A., and Bhattacharya, S. (2001) Incorporation of oxyethylene units between hydrocarbon chain and pseudoglyceryl backbone in cationic lipid potentiates gene transfection efficiency in the presence of serum. *FEBS Lett. 509*, 327−331.
(20) Bhattacharya, S., and Dileep, P. V. (2004) Cationic oxyethylene lipids. Synthesis, aggregation, and transfection properties. *Bioconjugate Chem. 15*, 508−519.
(21) Felgner, J. H., Kumar, R., Sridhar, C. J., Wheeler, Y. J., Tsai, R., Border, P., Ramsey, M., Martin, C. N., and Felgner, P. L. (1994) Enhanced gene delivery and mechanism studies with a novel series of cationic lipid formulations. *J. Biol. Chem. 269*, 2550−2561.
(22) Song, Y. K., Liu, F., Chu, S., and Liu, D. (1997) Characterization of cationic liposome-mediated gene transfer in vivo by intravenous administration. *Hum. Gene Ther. 8*, 1585−1594.
(23) Ghosh, Y. K., Visweswariah, S. S., and Bhattacharya, S. (2000) Nature of linkage between the cationic headgroup and cholesteryl skelton controls gene transfection efficiency. *FEBS Lett. 473*, 341−344.
(24) Ghosh, Y. K., Visweswariah, S. S., and Bhattacharya, S. (2002) Advantage of the ether linkage between the positive charge and the cholesteryl skeleton in cholesterol-based amphiphiles as vectors for gene delivery. *Bioconjugate Chem. 13*, 378−384.
(25) McGregor, C., Perrin, C., Monck, M., Camilleri, P., and Kirby, A. J. (2001) Rational approaches to the design of cationic gemini surfactants for gene delivery. *J. Am. Chem. Soc. 123*, 6215−6220.
(26) Bell, P. C., Bergsma, M., Dolbnya, I. P., Bras, W., Stuart, M. C. A., Rowan, A. E., Feiters, M. C., and Engberts, J. B. F. N. (2003) Transfection mediated by gemini surfactants: engineered escape from the endosomal compartment. *J. Am. Chem. Soc. 125*, 1551−1558.
(27) Kirby, A. J., Camilleri, P., Engberts, J. B. F. N., Feiters, M. C., Nolte, R. J. M., Soderman, O., Bergsma, M., Bell, P. C., Fielden, M. L., Garcia, Rodriguez, C. L., Guedat, P., Kremer, A., McGregor, C., Perrin, C., Ronsin, G., and van Eijk, M. C. P. (2003) Gemini surfactants: New synthetic vectors for gene transfection. *Angew. Chem., Int. Ed. 42*, 1448−1457.
(28) Prata, C. A. H., Zhao, Y., Barthelemy, P., Li, Y., Luo, D., McIntosh, T. J., Lee, S. J., and Grinstaff, M. W. (2004) Charge-reversal amphiphiles for gene delivery. *J. Am. Chem. Soc. 126*, 12196−12197.
(29) Chittimalla, C., Zammut-Italiano, L., Zuber, G., and Behr, J.-P. (2005) Monomolecular DNA Nanoparticles for Intravenous Delivery of Genes. *J. Am. Chem. Soc. 127*, 11436−11441.
(30) Paul, B., Bajaj, A., Indi, S. S., and Bhattacharya, S. (2006) Synthesis of novel dimeric cationic lipids based on an aromatic backbone between the hydrocarbon chains and headgroup. *Tetrahedron Lett. 47*, 8401−8405.
(31) Hubner, W., Mantsch, H. H., and Kates, M. (1991) Intramolecular hydrogen bonding in cardiolipin. *Biochim. Biophys. Acta 1066*, 166−174.
(32) Bhattacharya, S., De, S., and George, S. K. (1997) Synthesis and vesicle formation from novel pseudoglyceryl dimeric lipids. Evidence of formation of widely different membrane organizations with exceptional thermotropic properties. *Chem. Commun.* 2287−2288.
(33) Bhattacharya, S., and De, S. (1999) Synthesis and vesicle formation from dimeric pseudoglyceryl lipids with $(CH_2)_m$ spacers: pronounced m-value dependence of thermal properties, vesicle fusion, and cholesterol complexation. *Chem.—Eur. J. 5*, 2335−2347.
(34) Kasireddy, K., Ali, S. M., Ahmad, M. U., Choudhury, S., Chien, P.-Y., Sheikh, S., and Ahmad, I. (2005) Synthesis of cationic cardiolipin analogs. *Bioorg. Chem. 33*, 345−362.
(35) Chien, P.-Y., Wang, J., Carbonaro, D., Lei, S., Miller, B., Sheikh, S., Ali, S. M., Ahmad, M. U., and Ahmad, I. (2005) Novel cationic cardiolipin analog-based liposome for efficient DNA and small interfering RNA delivery in vitro and in vivo. *Cancer Gene Ther. 12*, 321−328.
(36) Bhattacharya, S., and Bajaj, A. (2007) Membrane forming properties of pseudoglyceryl backbone based gemini lipids possessing oxyethylene spacers. *J. Phys. Chem. B 111*, 2463−2472.
(37) Bajaj, A., Kondiah, P., and Bhattacharya, S. (2007) Design, synthesis, and in vitro gene delivery efficacies of novel cholesterol-based gemini cationic lipids and their serum compatibility: a structure-activity investigation. *J. Med. Chem. 50*, 2432−2442.
(38) Mosmann, T. (1983) Rapid colorimetric assay for cellular growth and survival: application to proliferation and cytotoxicity assays. *J. Immunol. Methods 65*, 55−63.
(39) Hansen, M. B., Nielsen, S. E., and Berg, K. (1989) Re-examination and further development of a precise and rapid dye method for measuring cell growth/cell kill. *J. Immunol. Methods 119*, 203−210.
(40) Choi, J. S., Lee, E. J., Jang, H. S., and Park, J. S. (2001) New cationic liposomes for gene transfer into mammalian cells with high efficiency and low toxicity. *Bioconjugate Chem. 12*, 108−113.
(41) Chabaud, P., Camplo, M., Payet, D., Serin, G., Molreau, L., Barthelemy, P., and Grinstaff, M. W. (2006) Cationic nucleoside lipids for gene delivery. *Bioconjugate Chem. 17*, 466−472.
(42) Matsui, K., Sando, S., Sera, T., Aoyama, Y., Sasaki, Y., Komatsu, T., Terashima, T., and Kikuchi, J.-I. (2006) Cerasome as an infusible, cell-friendly, and serum-compatible transfection agent in a viral size. *J. Am. Chem. Soc. 128*, 3114−3115.
(43) Karmali, P. P., Majeti, B. K., Sreedhar, B., and Chaudhuri, A. (2006) In vitro gene transfer efficacies and serum compatibility profiles of novel mono-, di-, and tri-histidinylated cationic transfection lipids: a structure-activity investigation. *Bioconjugate Chem. 17*, 159−171.

BC070010Q

Synthesis of Glycocluster−Tumor Antigenic Peptide Conjugates for Dendritic Cell Targeting

Oruganti Srinivas,[†] Pierre Larrieu,[‡,#] Eric Duverger,[†] Claire Boccaccio,[§] Marie-Thérèse Bousser,[†] Michel Monsigny,[†] Jean-François Fonteneau,[‡] Francine Jotereau,*[,‡,#] and Annie-Claude Roche*[,†]

Glycobiologie, Vectorologie et Traffic Intracellulaire, Centre de Biophysique Moléculaire CNRS, Rue Charles-Sadron, 45071 Orléans, Cedex 2, France, INSERM, Unité 601, 44093 Nantes, France, Faculté des Sciences, Université de Nantes, 44322 Nantes, France and IDM Research Laboratory, LUTI, Bat.F, Institut de Recherches Biomédicales des Cordeliers, 15 rue de l'Ecole de Médecine, 75006 Paris, France. Received January 23, 2007; Revised Manuscript Received May 14, 2007

The use of dendritic cells (DC) for the development of therapeutic cancer vaccines is attractive because of their unique ability to present tumor epitopes *via* the MHC class I pathway to induce cytotoxic $CD8^+$ T lymphocyte responses. C-Type membrane lectins, DC-SIGN and the mannose receptor (MR), present on the DC surface, recognize oligosaccharides containing mannose and/or fucose and mediate sugar-specific endocytosis of synthetic oligolysine-based glycoclusters. We therefore asked whether a glycotargeting approach could be used to induce uptake and presentation of tumor antigens by DC. To this end, we designed and synthesized glycocluster conjugates containing a $CD8^+$ epitope of the Melan-A/Mart-1 melanoma antigen. These glycocluster−Melan-A conjugates were obtained by coupling glycosynthons: oligosaccharyl-pyroglutamyl-β-alanine derivatives containing either disaccharides, a dimannoside (Manα-6Man) or lactoside, or a Lewis oligosaccharide, to Melan-A 16−40 peptide comprising the 26−35 HLA-A2 restricted T cell epitope, extended with an oligolysine stretch at the C-terminal end. We showed by confocal microscopy and flow cytometry that fluorescent-labeled Melan-A glycoclusters containing either dimannoside or Lewis oligosaccharide were taken up by DC and concentrated in acidic vesicles; conversely lactoside glycopeptides were not at all taken up. Furthermore, using surface plasmon resonance, we showed that dimannoside and Lewis−Melan-A conjugates bind MR and DC-SIGN with high affinity. DC loaded with these conjugates, but not with the lactose−Melan-A conjugate, led to an efficient presentation of the Melan-A epitope eliciting a $CD8^+$ T-lymphocyte response. These data suggest that synthetically designed glycocluster−tumor antigen conjugates may induce antigen cross-presentation by DC and represent a promising tool for the development of tumor vaccines.

INTRODUCTION

Dendritic cells (DC) are antigen-presenting cells critical for the induction of adaptive immune responses (*1*, *2*). After capturing and internalizing antigen in peripheral organs, they efficiently associate antigenic peptides derived by limited proteolysis to nascent MHC class I protein and expose these MHC class I peptide complexes on their surface, a process termed cross-presentation. Cross-presentation of tumor epitopes to cytotoxic T cell (CTL) precursors in peripheral lymphoid organs (*1*) contributes to the induction of cytotoxic responses to microbes and tumors (*3*). Several C-type lectins and lectin-like receptors, abundantly expressed on the surface of DC, bind sugars in a calcium-dependent manner using highly conserved carbohydrate-recognition domains (CRDs) (*4*). Among these, the mannose specific receptor (MR, CD206) binds and internalizes glycoproteins containing terminal mannose, *N*-acetylglucosamine, or fucose (*5*, *6*), and the dendritic-cell-specific ICAM-3 grabbing nonintegrin (DC-SIGN, CD209) (*7*) binds mannose oligosaccharides (*8*) and fucose-containing glycans (*9*−*11*). The sugar specificity was determined by using oligolysine-based Lewis type oligosaccharide clusters (*9*) and synthetic glycoconjugates (*10*) and by screening an extensive glycan array (*11*). While DC-SIGN and MR act similarly in mediating endocytosis and receptor recycling, they may differ in routing their ligands to distinct intracellular compartments. It was reported that DC-SIGN ligand complexes are targeted to late endosomes/lysosomes (*12*), while MR is preferentially targeted to early endosomes (*13*).

DC membrane lectins which mediate efficient sugar-specific endocytosis could be potentially exploited for glycotargeting tumor antigens to enhance cross-presentation. It is known that sugar−lectin interactions depend on the density of the partners (see for reviews, refs *14*, *15*), so that there is a stringent requirement of clustered patches of carbohydrate ligands for high binding to the protein receptors (*16*, *17*). High affinity binding ligands for membrane lectins have therefore been produced such as neoglycoproteins, prepared by covalent attachment of sugars to a protein, (see for reviews, refs *15*, *18*, *19*); multivalent glycosylated peptides were obtained by coupling monosaccharides derivatives to polylysine (*20*, *21*), as well as to oligolysine (*22*, *23*). Glycoclusters were recently synthesized in our laboratory by coupling glycosynthons to small oligolysine-based peptides (*24*). Glycosynthons (*25*, *26*) were prepared by an original two-step one-pot procedure involving the oligosaccharide reducing sugar and a peptide with a glutamyl residue in the N-terminal position. We previously showed that oligolysine substituted with dimannosides or Lewis oligosaccharides were taken up by dendritic cells (*9*, *27*).

In this study, we asked whether glycoclusters, specific for either DC-SIGN or MR and able to be internalized by DC, might

* To whom correspondence should be addressed. (A.-C.R) Tel: +33-(0)238255537, fax: +33(0)238255557, e-mail: roche@cnrs-orleans.fr. (F.J.) (for immunological data) Tel: +33(0)240084720, e-mail: joterau@nantes.inserm.fr.

[†] Centre de Biophysique Moléculaire CNRS.

[‡] INSERM.

[#] Université de Nantes.

[§] Institut de Recherches Biomédicales des Cordeliers.

10.1021/bc070026g CCC: $37.00 © 2007 American Chemical Society
Published on Web 06/29/2007

represent efficient vectors to induce the cross-presentation by DC of a tumor epitope. We designed glycoclusters containing a 25 amino acid long peptide of the Melan-A/Mart-1 protein (a melanoma tumor antigen): Melan-A 16−40 peptide, containing the A27L analogue of the HLA-A*0201 restricted Melan-A epitope (26−35) (*28*−*30*). This epitope is a good model for developing vaccine targets for melanoma patients, as it is highly expressed by about half of melanoma tumors (*31*).

We report here the synthesis and characterization of glycocluster−Melan-A peptide conjugates containing the Melan-A (26−35) A27L epitope and either Manα-6Man (DiMan) or a mixture of Lewis^a and Lewis^x oligosaccharides (Lewis) chosen on the basis of their affinity for MR and DC-SIGN, or Galβ-4Glc (lactose or Lac) selected as a negative control, based on the fact that the lactose glycocluster is not recognized by DC (*9*). The capacity of DC to internalize fluorescent-labeled Melan-A glycopeptides was checked by confocal microscopy and flow cytometry. The kinetic constants for the binding of the glycocluster−Melan-A conjugates to MR and DC-SIGN were measured by surface plasmon resonance. Interestingly, DC loaded with DiMan− and Lewis−Melan-A glycopeptides allowed activation of a specific $CD8^+$ T cell clone. On the basis of present results, these glycopeptides are discussed as a putative new cellular vaccination approach.

EXPERIMENTAL PROCEDURES

Materials. Chemicals were purchased from Sigma-Aldrich (Saint-Quentin Fallavier, France) unless otherwise mentioned. Benzotriazol-1-yloxy-tris(dimethylamino)phosphonium hexafluorophosphate (BOP) and 2-(1*H*-benzotriazol-1-yl)-1,1,3,3-tetramethyluronium hexafluorophosphate (HBTU) were from Richelieu Biotechnologies (Saint-Hyacinthe, QC, Canada). *N*-Methylpyrrolidone (NMP) was from Applied Biosytems (Foster City, CA). Triethylammonium phosphate (TEAP), 1-hydroxybenzotriazole (HOBt), *N*,*N*-diisopropylethylamine (DIEA), and *tert*-butyl methyl ether (TBME) were from Senn Chemical AG (Dieslldorf, Switzerland). Lactose and *N*,*N*-diisopropylethlamine (DIEA) were from Janssen Chimica (Beerse, Belgium). Manα-6Man disaccharide was from Dextra laboratories (Reading, UK). A mixture of Lewis^a and Lewis^x oligosaccharides isolated from human milk were a kind gift from Dr. Gérard Strecker (Lille, France). L-Glu-βAla-OBn was purchased from CNH Technologies (Woburn, MA). Melan-A (16−40)−oligo K containing the promiscuous $CD8^+$ (26−35) A27L analogue epitope, Ac-GHGHSYTTAE*ELAGIGILTV*ILGV-LKKKK, was synthesized by NeoMPS systems (Strasbourg, France). Spectra/Por regenerated cellulose membrane (cutoff M_r 1000) was used for the dialysis. Mannosylated serum albumin and fucosylated serum albumin (Man−BSA and Fuc−BSA, respectively) were prepared as previously described (*18*) and contained 25 ± 3 sugar residues per molecule.

Chromatography. Conjugates were purified by gel filtration on a Biogel P-4 (Bio-Rad, Oxfordshire, England) column (2 × 45 cm) stabilized and eluted with 50 mM acetic acid. The flow rate was 0.5 mL/min. Analytical reverse-phase high performance liquid chromatography (RP-HPLC) separations were performed with a Waters 2690 (Milford, MA) system linked to a Waters 996 photodiode array detector, using an Alltech C18 column (5 μm, 4.6 mm × 250 mm) at a flow rate of 1 mL/min, with detection at 254 nm (or 280 nm) at 25 °C (solvent A: 0.1% TEAP in H_2O; solvent B: 0.1% TEAP in acetonitrile; gradient from 70% A/30% B to 2% A/98% B in 20 min).

Mass Spectrometry. MALDI-TOF mass spectra were recorded on a Biflex III instrument (Bruker, Wissembourg, France), in positive mode using α-cyano-4-hydroxycinnamic acid as a matrix.

Synthesis of Glycocluster−Antigenic Peptide Conjugates. *General Procedure for Coupling Glycosynthons and Melan-A−Oligo K (Scheme 1).* The glycosynthons (glycosyl-pyroglutamyl-β-alanine derivatives) were obtained according to (*25*). Briefly, an oligosaccharide was allowed to react with α-glutamyl-β-alanyl benzyl ester in the presence of imidazole, and the glycosylamine derivative obtained was stabilized by an *in situ* intramolecular acylation using BOP. Then, the hydrogenolysis of the benzyl ester afforded the expected glycosynthons in high yields.

The coupling of glycosynthons to the peptide-oligo K was carried out using amide coupling reagents. A mixture of glycosynthon (0.01 mmol), 2-(1*H*-benzotriazol-1-yl)-1,1,3,3-tetramethyluronium hexafluorophosphate (HBTU, 0.01 mmol), 1-hydroxybenzotriazole (HOBt, 0.01mmol), and 4 Å molecular sieve beads (25 mg) in *N*-methylpyrrolidone (NMP, 1 mL) was stirred for 20 min under N_2 atmosphere. A solution of Melan-A (16−40)-oligo K peptide (0.0015 mmol) in *N*-methylpyrrolidone (200 μL) and 2 M *N*,*N*-diisopropylethylamine in *N*-methylpyrrolidone (20 μL) were added, and the mixture was stirred for another 6 h. The molecular sieve beads were removed, and 10 volumes of *tert*-butyl methyl ether (TBME) was added: the precipitated crude product was collected upon centrifugation. The pellet was dissolved in water (1 mL) and passed through a Biogel P-4 column with 50 mM acetic acid as an eluent, and the fast eluting sugar-containing fractions identified by a microscale resorcinol−H_2SO_4 assay (*32*) were pooled, dialyzed (cutoff M_r 1000), and lyophilized to obtain the glycocluster−Melan-A conjugate as a white fluffy powder (yield ≈ 55%).

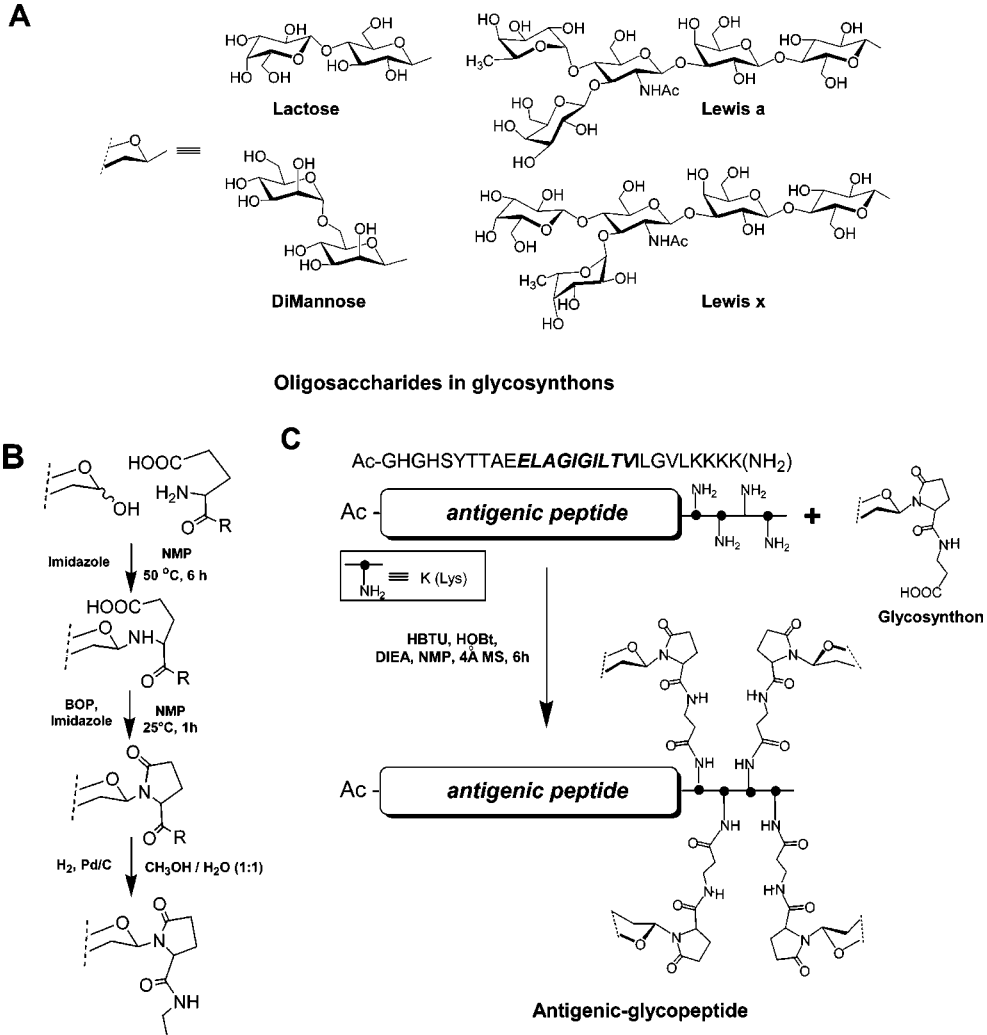
The glycocluster−peptide conjugates were analyzed by HPLC: Lac−Melan-A, DiMan−Melan-A, and Lewis−Melan-A have a retention times of 7.50, 7.51, and 6.48 min, respectively, as compared to 6.98 min for Melan-A. These glycocluster−peptide conjugates were analyzed by MALDI-TOF mass spectrometry; the glycocluster−peptide derivatives appeared to be predominantly the trivalent derivatives. DiMan−Melan-A, Lac−Melan-A, and Lewis−Melan-A conjugates gave molecular ion peaks at $m/z = 4640.94$, 4639.08, and 6165.24, respectively, corresponding to their $[M + K]^+$ ions. In addition, $[M + K]^+$ adducts at $m/z = 5147.48$ and 5145.49 for DiMan−Melan-A and Lac−Melan-A, respectively, were also observed, corresponding to the tetravalent derivatives.

General Procedure To Add Fluorescent Probe on Glycocluster−Melan-A Conjugates. A solution of iodoacetamido-fluorescein (2 μmol in 15 μL of NMP) was added to the glycocluster−Melan-A conjugate (1 μmol) in 500 μL of carbonate buffer (pH 8.5) and stirred at room temperature for 2 h in darkness. The reaction mixture was purified by gel chromatography, Ultrogel GF05 (1.5 cm × 20 cm) column; the fluorescent glycopeptide was eluted with 10 mM acetic acid and was lyophilized. The concentration was determined by absorbance measurement at 495 and 280 nm, assuming that fluorescein $\epsilon_M^{1\,cm}$ at 488 nm is 80 000 and at 475 nm is 26 000 and tyrosine $\epsilon_M^{1\,cm}$ at 488 nm is 1400.

Cells. DC-IL-13 were provided by IDM (Immuno Designed Molecules, Paris) in frozen vials; they were obtained from monocytes isolated by elutriation from peripheral blood mononuclear cells differentiated in the presence of GM-CSF and IL-13 (*33*). These DC were used immediately upon thawing or plated and cultured in Aim-V medium supplemented with 500 units/mL GM-CSF and 50 ng/mL IL-13 before use.

For cross-presentation experiments, DC-IL-4 were used. Briefly, healthy HLA-A*0201 donor PBMC was obtained by Ficoll separation. Monocytes and lymphocytes were isolated by elutriation (Aventi J-20, Beckman Coulter) and frozen. DC (DC-IL-4) were generated by culturing the monocyte-enriched fraction in six-well plates using 3×10^6 cells/well in 3 mL of RPMI containing 1% nonautologous plasma, 100 IU/mL GM-CSF (Abys), and 300 U/mL IL-4 (AbCys). The cytokines were

Scheme 1.[a] **Panel A: Oligosaccharides Used To Prepare Glycosynthons. Panel B: Preparation of a Typical Glycosynthon: A Reducing Oligosaccharide Is Allowed To React with a Dipeptide Having a Glutamyl Moiety in the N-Terminal Position and with R = $NHCH_2CH_2CO_2Bn$. The Glycosylamine Derivative Is Stabilized by Formation of a Pyroglutamyl Ring, and Then the Benzyl Group Is Removed by Catalytic Reduction, Leading to the Desired Glycosynthon. Panel C: Preparation of an Antigenic Glycopeptide: A Peptide (including the CD 8^+ Melan-A epitope and an oligolysine tail) Is Substituted with Glycosynthons**



[a] Abbreviations: NMP, *N*-methylpyrrolidone; BOP, benzotriazol-1-yloxy-tris(dimethylamino)phosphonium hexafluorophosphate; Pd/C, palladium on charcoal; CD 8^+ epitope, *ELAGIGILTV*; HBTU, 2-(1*H*-benzotriazol-1-yl)-1,1,3,3-tetramethyluronium hexafluorophosphate; HOBt, 1-hydroxybenzotriazole; DIEA, *N*,*N*-diisopropylethylamine; MS, molecular sieves; Lactose, Galβ4Glc; Lewis a, Galβ3(Fucα4)GlcNAcβ3Galβ4Glc; Lewis x, Galβ4(Fucα3)GlcNAcβ3Galβ4Glc; DiMannose, Manα6Man.

added to the cultures at day 0 and 2. On day 5, DC were harvested and used in antigen cross-presentation experiments. M77−84 is a HLA-A2 restricted Melan-A (26−35) specific $CD8^+$ T cell clone obtained from tumor-infiltrating lymphocytes (TIL) of a melanoma patient (*34*).

Cell Reagents. A soluble fragment of the human MR consisting of the eight C-type CRDs (MMR1−8) and the extracellular domain of DC-SIGN were kindly provided respectively by Maureen Taylor and Kurt Drickamer (London, UK).

Flow Cytometry Analysis of Endocytosis. Freshly thawed DC-IL-13 (10^6 cells in 100 μL of Aim-V medium) were incubated for 2 h at 37 °C in the presence of 10 μM fluorescein-labeled glycopeptides. After being washed in PBS, DC were further incubated for 30 min at 4 °C in the absence or in the presence of 50 μM monensin. Monensin is a proton/sodium ionophore which transports monovalent cations (Na^+ and H^+) across membranes and, thereby, equilibrates the external and internal pH of organelles in intact cells. Therefore, monensin neutralizes intracellular acidic compartments, allowing the recovery of fluorescein fluorescence quenched in acidic environment; a higher fluorescence intensity of the monensin-treated cells compared to that of untreated cells demonstrate that the conjugate had reached acidic compartments upon endocytosis (*35*). Cell-associated fluorescence was assessed using a BD-LSR flow cytometer, and the data were analyzed with the Cell Quest software (BD Biosciences).

Confocal Microscopy Analysis. DC-IL-13 plated on cover slip after thawing and overnight incubation in complete medium were incubated for 2 h at 37 °C with 1 μM fluorescein-labeled glycopeptides, washed, and either fixed immediately 20 min in PBS containing 4% formaldehyde at room temperature or further incubated 2 h in medium before fixation. Coverslips were mounted on slides in a PBS/glycerol mixture (1:1 v/v) containing 1% 1,4-diazabicyclo[2.2.2]octane (DABCO) as an antifading agent and fixed 20 min in PBS containing 4% formaldehyde at room temperature. Cell fluorescence was analyzed with a confocal imaging system MRC-1024 (Bio-Rad) equipped with

a Nikon Optiphot epifluorescence microcope and a ×60 planapo objective (numerical aperture 1.4). The krypton/argon laser was tuned to produce a 488 nm beam. Images were recorded with a Kalman filter average of 5−10 images.

Surface Plasmon Resonance. Surface plasmon analyses (see for a review, ref *36*) were performed on a BIAcore 2000 biosensor system (BIAcore Inc., Uppsala, Sweden). The carboxymethyl dextran CM-5 research grade sensor chip and ethanolamine-HCl solution (pH 8.5) were obtained from BIAcore Inc.; the immobilization reagents (*N*-ethyl-*N*′-(dimethylaminopropyl)carbodiimide, (EDC) and *N*-hydroxysuccinimide, (NHS) were purchased from Sigma. All solutions were filtered using a 0.22 μm of polytetrafluoroethylene membrane syringe filter and degassed prior use. Extracellular soluble fragments (MMR1−8) of the human MR (*37*−*39*) and of the human DC-SIGN (*8*) were immobilized on a CM5 sensor chip. The fragment of MR (MMR1−8) contains all the domains necessary for Ca^{2+}-dependent binding of mannose, *N*-acetylglucosamine, and fucose-terminated glycoconjugates and binds such ligands as the whole receptor does. These soluble extracellular fragments containing the CRDs of human MMR1−8 (45 μg/mL) and DC-SIGN (20 μg/mL) in 10 mM sodium acetate at pH 4.5 were covalently immobilized using a standard amine coupling procedure according to the immobilization wizard. In a typical procedure, the carboxymethyl dextran surface was activated using freshly mixed 100 mM NHS and 400 mM EDC solutions, followed by lectin coupling (immobilization time of 8 min and a constant flow rate of 20 μL/min). The remaining activated groups were blocked with 1 M ethanolamine at pH 8.5, and efficient fixation was indicated by a large increase in the refractive index, in both cases, about 5000 RU (relative units, RU). The control flow cell was also activated by EDC-NHS and then blocked by using 1 M ethanolamine. The biosensor experiments were carried out in the running buffer (pH 7.4, 10 mM HEPES, 1 mM $CaCl_2$, 1 mM $MgCl_2$, 150 mM, NaCl, 17 mM NaN_3, 0.005% P20 BIAcore surfactant). For binding studies, the temperature was kept at 25 °C and the flow rate was 20 μL/min for both the association and dissociation steps during 5 and 10 min, respectively. The binding capacity of the immobilized lectin fragments was ascertained by using Man−BSA and Fuc−BSA neoglycoproteins; then, binding experiments with glycocluster−antigenic peptide conjugates at concentrations from 0.1 μM to 5 μM were carried out. The glycocluster−peptide conjugate solutions were prepared in the running buffer containing 1 mg/mL BSA (99% purity). Regeneration was carried out using two consecutive pulses of 30 μL of the running buffer containing 1 M NaCl and 0.3 M methyl α-mannopyranoside and 1 mg/mL BSA.

Dendritic Cell Cross-Presentation to MelanA/MART-1 Specific T Cells. Immature DC (DC-IL-4) were incubated at 37 °C with various concentrations of Melan-A-glycopeptide. Maturation stimuli, 100 μg/mL poly I/C (Sigma) and 10 ng/mL TNF-α (Abcys) were added 3 h later. After an 18 h incubation at 37 °C, DC were washed and 10^5 loaded DC were co-incubated with 10^5 M77−84 cells in the presence of 10 μg/mL Brefeldin A (Sigma). After 6 h at 37 °C, cells were fixed and intracellular IFN-γ was stained as described (*40*). Briefly, cells were fixed in 4% paraformaldehyde for 10 min at room temperature and then stained with phycoerythrin (PE)-conjugated monoclonal antibody (mAb) specific for IFN-γ (Pharmingen BD). Antibody dilutions and washes were performed with PBS containing 1 mg/mL BSA and 1 mg/mL saponin at room temperature. After staining, cells were suspended in PBS and analyzed on a FACScan (BD Biosciences) with a gate set on T cells (on the FSC−SSC dot plot).

RESULTS

Design and Synthesis of Glycocluster−Melan-A Conjugates. The Melan-A peptide stands for Melan-A (16−40) A27L with the sequence: Ac-G[16]HGHSYTTAE*E*[26]*LAGIGILTV*[35]-ILGVL[40]KKKK, (Ac, for acetyl) containing a variant of the HLA-A2-restricted $CD8^+$ epitope (26−35) *ELAGIGILTV* instead of EAAGIGILTV, ended by a tetralysine tail. The *ELAGIGILTV*, A27L analogue binds to HLA-A2 better than the natural peptide because of an altered anchor residue (*29*, *30*).

The synthesis of the glycocluster−antigenic peptide conjugates involved the synthesis of glycosynthons containing Galβ-4Glc (lactose, Lac), Manα-6Man (DiMan), or Lewis oligosaccharides (a mixture of Lewis[a] and Lewis[x] oligosaccharides). The coupling of glycosynthons: Galβ-4Glc-βGlp-Ala-OH, Manα-6Man-βGlp-Ala-OH, and Lewis-βGlp-Ala-OH to Melan-A was carried out using amide coupling reagents HBTU/HOBT, to afford Lac−Melan-A, DiMan−Melan-A, and Lewis−Melan-A, respectively (Scheme 1). After purification on a Biogel column, the glycopeptides were analyzed by MALDI-TOF mass spectroscopy, showing a high proportion of trivalent conjugates and a small proportion of tetravalent derivatives.

Uptake of Fluorescent-Labeled Melan-A Glycopeptides by Dendritic Cells (DC-IL-13). Dendritic cells were incubated 2 h at 37 °C with fluorescent glycopeptides and analyzed by confocal microscopy. As expected, DiMan−Melan-A and Lewis−Melan-A were efficiently internalized and were found in numerous vesicles (Figure 1A) after 2 h pulse chase (lower panel) as well as immediately upon incubation (upper panel); conversely, Lac−Melan-A was not internalized by DC (data not shown) in agreement with our previous data (*9*), showing that DC are devoid of galactose or lactose-binding proteins. The cell-associated fluorescence was analyzed by flow cytometry. Monensin treatment was used to increase the fluorescence intensity of the endocytosed material (Figure 1B). The enhancement of cell fluorescence intensity, 1.5-fold upon addition of monensin, is proof that upon endocytosis, the fluorescein-labeled glycopeptide was contained in acidic compartments.

Surface Plasmon Resonance Analysis. The extracellular moieties of DC-SIGN and MR (MMR1−8) were immobilized on chips, leading to ΔRU values of 5200 and 5700 for DC-SIGN and MR, respectively. In preliminary experiments, we confirmed the binding activity of the immobilized lectins by evaluating their capacity to bind Man−BSA and Fuc−BSA neoglycoproteins. The binding profiles and the kinetic constants were in good agreement with our earlier results (*9*), indicating that the immobilized lectins did retain their binding activity (data not shown).

Solutions of DiMan−Melan-A, Lewis−Melan-A, and Lac−Melan-A were injected over a period of 5 min, followed by a dissociation time of 10 min with a glycopeptide-free buffer. It is noteworthy to mention that upon the injection of glycocluster−Melan-A conjugates on the SPR chips, the regeneration of the lectin-immobilized surface with methyl-α-mannoside solutions was inefficient. To circumvent this problem, the glycocluster−Melan-A conjugates were injected in the presence of 1 mg/mL BSA; the regeneration solution contained 1 mg/mL BSA and 1 M NaCl in addition to methyl-α-mannoside. The presence of BSA efficiently prevents nonspecific hydrophobic interactions derived from the presence of a large number of aliphatic amino acid residues in the antigenic Melan-A peptide.

Both DiMan−Melan-A and Lewis−Melan-A conjugates, injected onto the flow cell containing immobilized DC-SIGN, elicited a clear concentration-dependent response indicative of their binding; this is illustrated in Figure 2 for DiMan−Melan-A. During the binding of Lewis−Melan-A to MMR1−8, the slope (k_{bind})of the association curve was quite small and the

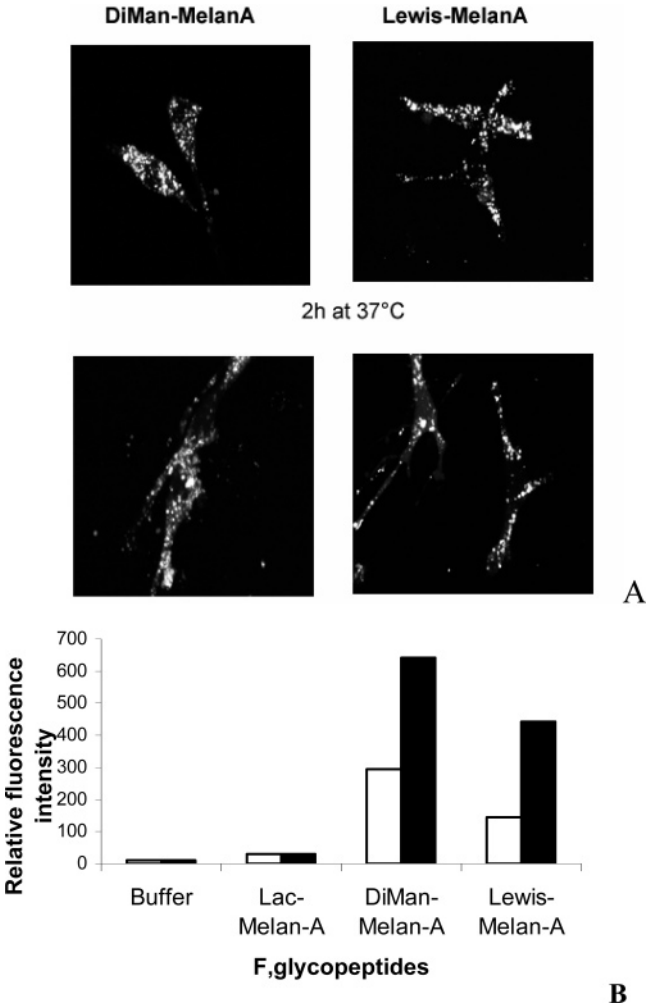


Figure 1. A. Confocal microscopy analysis of glycopeptide uptake by dendritic cells. DC plated on glass coverslips were incubated 2 h at 37 °C with F-DiMan-Melan-A or F-Lewis−Melan-A and fixed before mounting (*upper panels);* alternatively, DC were incubated 2 h at 37 °C with the glycosylated antigens and further chased 2 h without them before fixation (*lower panels).* B. Flow cytometry analysis of the uptake of F-glycopeptides by dendritic cells. DC were incubated for 2 h at 37 °C in the presence of either F-DiMan−Melan-A or F-Lewis−Melan-A, or F-Lac−Melan-A. Fluorescence intensity was measured by flow cytometry following postincubation in the absence (open bars) or in the presence (closed bars) of monensin.

RU signal linearly increased along with the duration of the Lewis−Melan-A injection (data not shown).

In a SPR binding study, the slope of the curve corresponding to the association phase depends on (k_{bind}), the experimental kinetic constant with a value of:

$$k_{bind} = k_{ass}\, g_0 + k_{diss}$$

where $k_{bind} = k_{ass}g_0 + k_{diss}k_{ass}$ stands forthe kinetic association constant, k_{diss} for the kinetic dissociation constant, and g_0 for the free ligand (i.e., the free glycopeptide) concentration. The dissociation profiles from immobilized DC-SIGN were characteristic for each of the two conjugates: that of Lewis−Melan-A was more than 10 times slower ($k_{diss} = 6.8 \times 10^{-5}$ s^{-1}) compared to that of DiMan−Melan-A ($k_{diss} = 8.8 \times 10^{-4}$ s^{-1}). In the binding to immobilized DC-SIGN, the calculated equilibrium association constants K_a ($K_a = k_{ass}/k_{diss}$) were 6.2×10^6 and 5.3×10^7 L mol^{-1} for DiMan−Melan-A and Lewis−Melan-A, respectively (Table 1).

It was previously shown from inhibition experiments that the mannose-based glycoclusters have a high affinity for MR (*9*).

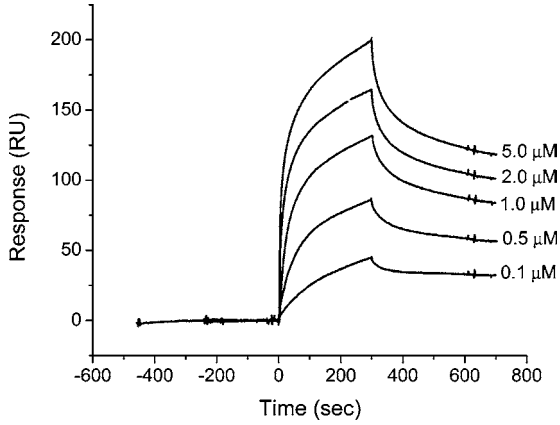


Figure 2. Surface plasmon resonance analysis of the concentration-dependent binding of DiMan−Melan-A conjugate with the immobilized extracellular domain of DC-SIGN. Solutions of DiMan−Melan-A (0.1 μM to 5 μM concentration range) were prepared in the running buffer containing 1 mg/mL BSA (pH 7.4) and were injected over a period of 5 min, with a dissociation interval of 5 min.

Table 1. SPR Derived Kinetic Constants for the Binding of Glycocluster−Peptide Conjugates to Immobilized DC-SIGN and MR Lectins

	K_a (L mol^{-1})	k_{diss} (s^{-1})
	DC-SIGN Extracellular	
DiMan−Melan-A	6.2×10^6	8.8×10^{-4}
Lewis−Melan-A	5.3×10^7	6.8×10^{-5}
Lac−Melan-A	NB[a]	NB[a]
	MMR1−8	
DiMan−Melan-A	2.5×10^7	6.7×10^{-4}
Lewis−Melan-A	*b*	*b*
Lac−Melan-A	NB[a]	NB[a]

[a] NB: No binding observed. [b] The kinetic constants could not be calculated.

This was confirmed with the binding of DiMan−Melan-A ($K_a = 2.5 \times 10^7$ L mol^{-1}) to immobilized MR. Lewis−Melan-A showed a poor association with MR and a very slow dissociation precluding the determination of the kinetic constants. Lac−Melan-A did not give any detectable response, in agreement with the failure of lactoside-based glycoconjugates to bind DC lectins (Table 1).

Glycocluster−Melan-A Conjugate Uptake by DC Induces Melan-A Epitope Presentation. In order to evaluate the capacity of glycocluster−Melan-A conjugates to serve as agents for antigen vectorization into DC, DC were incubated with the various glycocluster Melan-A conjugates and the presentation of the Melan-A (27−35) A27L peptide on DC was analyzed by measuring the activation of a specific T cell clone by intracellular IFN-γ labeling. As shown in Figure 3, DC incubated with DiMan−Melan-A and Lewis−Melan-A, but not with Lac−Melan-A conjugates, induced a clone response. The level of this response, shown by the fraction of IFN-γ labeled lymphocytes, was correlated with the glycocluster dose. When DC were incubated at 4 °C with DiMan−Melan-A and Lewis−Melan-A peptide, the clone activation was negligible (data not shown).

DISCUSSION

DC-SIGN or MR-specific antibody−antigen conjugates (*43*−*46*) have been used for the induction of tumor antigen cross-presentation by DC. Glycosylated antigen targeting to macrophages or DC lectin receptors was already used, but only to induce antigen presentation by MHC class II molecules. Indeed, glycoside-clustered tetanus toxoid (among other antigens) conjugates were shown to induce MR dependent antigen

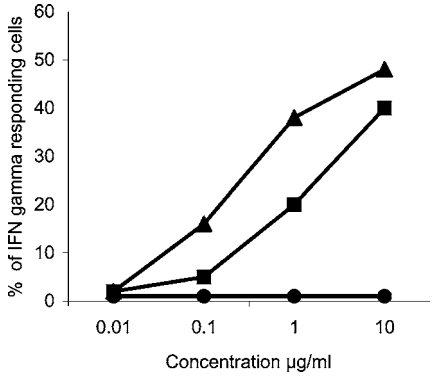


Figure 3. Response of Melan-A (26−35) specific $CD8^+$ T cell clone upon glycocluster−Melan-A conjugate uptake by DC. HLA-A*0201+ DC were incubated 18 h with various doses of DiMan−Melan-A (▲), Lewis−Melan-A (■) or Lac−Melan-A (●). Poly I/C and TNF-α were added 3 h after the beginning of the incubation. DC were then washed and cultured with HLA-A*0201 restricted Melan-A (26−35) specific $CD8^+$ T cell clone, in the presence of brefeldin-A to inhibit secretion. After 6 h, cells were fixed and intracytoplasmic staining of IFN-γ was performed and analyzed by flow cytometry.

presentation by macrophages on MHC class II molecules (*47*); mannosylated tetanus toxoid or proinsulin was shown to induce the uptake and targeting of these antigens to the MHC class II pathway (*48*). So far, there has been no report of glycotargeting of human DC lectins for the induction of tumor antigen presentation *via* the MHC class I pathway, a process called cross-presentation.

The aim of this study was to investigate whether glycotargeting of MR and DC-SIGN is a promising strategy to induce tumor antigen uptake by DC and to favor the MHC class I cross-presentation pathway. Our aim was to design a general route to synthesize glycocluster−tumor antigen conjugates with the flexibility of varying either the sugar moieties or the peptide epitope. In order to synthesize glycocluster−tumor antigenic peptide conjugates, two strategies were considered: (i) coupling of glycosynthons to an oligolysine template added to one of two ends of the antigenic peptide and (ii) synthesis of an oligolysine-based glycocluster (*24*) followed by an attachment to an antigenic peptide. The former strategy was selected, and four lysine residues were appended at the C-terminal end of the antigenic peptide Melan-A chosen for the study in order to allow attachment of up to four glycosynthons per molecule. Along this line, glycocluster−Melan-A peptide conjugates were prepared in a one-pot reaction involving the coupling of pyroglutamyl-based glycosynthons to ϵ-amino groups of lysine residues present at the C-terminal end of the peptide. This approach allowed an efficient attachment of DiMan-, Lewis-, and Lac-glycosynthons to the Melan-A 16−40 sequence and an efficient recovery of the glycocluster−Melan-A conjugates. In previous papers (*9*, *27*), we showed that DiMan-glycoclusters and Lewis-glycoclusters were taken up by DC. In order to monitor the cell uptake of the glycocluster−Melan-A conjugates, they were substituted with a fluorescent probe. The glycocluster−Melan-A, being devoid of any cysteine residue, has two histidine resisues (H^{17},H^{19}) that were fluoresceinylated by allowing iodoacetamido fluorescein to react at neutral pH; this procedure is based on the fact that iodoacetamide leads to carboxymethylation of the imidazole moiety of histidine as previously described (*41*, *42*). Here, we report that glycosylated antigenic peptides bearing DiMan- and Lewis-oligosaccharides were efficiently taken up in slightly acidic compartments, while the lactose-based glycopeptides were not.

A series of SPR experiments were carried out to evaluate the apparent binding of glycocluster−Melan-A conjugates to the DC membrane lectins, MR and DC-SIGN. Owing to the relatively high molecular weight of the glycocluster−Melan-A conjugates, in the present work, we were able to determine the association constants of the glycocluster−Melan-A conjugates by direct surface plasmon resonance measurements of their binding to the immobilized lectins, while in our earlier report (*9*), by using low molecular weight glycoclusters, the binding constants were deduced from their ability to inhibit the binding of neoglycoproteins (Man−BSA or Fuc−BSA). Here, we showed that DiMan−Melan-A and Lewis−Melan-A exhibited a high apparent affinity for DC-SIGN and MR (MMR1−8) lectins. However, their binding behavior differed. The binding constant K_a of DiMan−Melan-A to MMR1−8 was 4 fold higher than that to DC-SIGN; this difference is related to the association rate, not to the dissociation rate. In contrast, the binding constant K_a of Lewis−Melan-A to DC-SIGN was 10 times higher than that of DiMan−Melan-A; this difference is related to the dissociation rate of Lewis−Melan-A from this lectin, which is 10 times slower than that of DiMan−Melan-A. The binding of DiMan−Melan-A to DC-SIGN and MMR1−8, and that of Lewis−Melan-A to DC-SIGN, being within the 10^{-7} L mol^{-1} range clearly shows that these glycopeptides benefit from an avidity effect similar to that shown with the glycoclusters themselves (*9*). In the case of the interaction between Lewis−Melan-A and MMR1−8, no kinetic constant could be obtained, precluding any determination of the binding parameters. This result sheds light onto our previous negative results, when, by using a competitive approach, we were not able to show any interaction (*9*) between Lewis glycoclusters and immobilized MR. As expected, Lac−Melan-A did not exhibit any significant binding to either DC-SIGN or MMR1−8 lectins, in agreement with the fact that the lactose-based glycocluster is not a ligand for either DC-SIGN or MR. Therefore, in the present study, by direct SPR measurements with glycocluster peptide conjugates, we were able to demonstrate a binding of DiMan−Melan-A to DC-SIGN and to determine the binding parameters, while with small glycoclusters used as inhibitors of a neoglycoprotein binding, we were not able to detect interaction between DiMan glycoclusters and DC-SIGN (*9*).

In addition, glycocluster−Melan-A conjugates were clearly shown to serve as agents for antigen vectorization into DC. The fact that DC incubated with DiMan−Melan-A and Lewis−Melan-A allowed activation of specific CTL clones, and that DC incubated with Lac−Melan-A did not induce such a peptide presentation, strongly suggest that glycocluster−Melan-A conjugates induce Melan-A epitope cross-presentation through a sugar-specific mediated uptake, a subsequent intracellular routing, and an epitope processing through the MHC class I presentation pathway. As stated above, the efficacy of this antigen cross-presentation, as well as its time-course and dose−ligand dependency, is being investigated to ascertain the putative interest of glycotargeting tumor antigens to DC lectins for the stimulation of tumor specific T cell responses in cancer patients.

Having assessed the binding affinities of DiMan−Melan-A and Lewis−Melan-A to DC membrane lectins, their uptake by DC, their capacity to induce the presentation by DC of the epitope ELAGIGILTV of Melan-A (26−35) A27L on HLA-A2, inducing CTL specific clones activation, we find that such glycoconjugates are promising for DC-mediated *ex vivo* and/or *in vivo* cellular vaccination.

ACKNOWLEDGMENT

This work was supported by grants from la Ligue Nationale Contre le Cancer (AC.R, Commité du Loiret and F. J Labellisation 05), Fondation pour la Recherche Médicale (FRM), Cancéropôle Grand Ouest, and Institut National du Cancer (INCA, projet libre 2005, F. Jotereau). We are grateful to Maureen Taylor and Kurt Drickamer (Imperial College, London)

for kindly providing us with fibroblasts expressing MR and DC-SIGN and with MMR1−8 and DC-SIGN lectins, and for critical reading of the manuscript. We thank Prof. Gérard Stecker (University of Lille, France) for providing Lewis oligosaccharides, and Dr. Natacha Frison for the synthesis of fluorescent glycoclusters. We thank Margarita Salcedo (IDM, Paris) for kindly providing us with the DC-IL-13 and for critical reading of the manuscript, and C. Buré for her skillful help with MALDI, CBM-CNRS, Orléans). O.S. thanks La Ligue Nationale Contre le Cancer for the postdoctoral fellowship. ED is Assistant Professor (Université d'Orléans), ACR is Research Director (Inserm), MM is Emeritus Professor (Université d'Orléans).

NOTE ADDED IN PROOF

A recently published paper (Burgdorf et al. (2007) Distinct pathways of antigen uptake and intracellular routing in CD4 and CD8 T cell activation. *Science 216*, 612−616) clearly demonstrates that mannose receptor-mediated endocytosis of ovalbumin (OVA), used as a soluble model antigen, targets early endosomes and enables its cross-presentation to $CD8^+$ T cells. In the conclusion they suggest that "targeting antigen to the MR may represent an avenue for improving vaccines aimed at inducing $CD8^+$ T cells mediated immunity against viruses or tumors".

LITERATURE CITED

(1) Bevan, M. J. (1976) Cross-priming for a secondary cytotoxic response to minor H antigens with H-2 congenic cells which do not cross-react in the cytotoxic assay. *J. Exp. Med. 143*, 1283−1288.

(2) Mellman, I., and Steinman, R. M. (2001) Dendritic cells: specialized and regulated antigen processing machines. *Cell 106*, 255−258.

(3) Banchereau, J., and Steinman, R. M. (1998) Dendritic cells and the control of immunity. *Nature 392*, 245−252.

(4) Figdor, C. G., van Kooyk, Y., and Adema, G. J. (2002) C-type lectin receptors on dendritic cells and Langerhans cells. *Nat. Rev. Immunol. 2*, 77−84.

(5) Stahl, P. D., Rodman, J. S., Miller, M. J., and Schlesinger, P. H. (1978) Evidence for receptor-mediated binding of glycoproteins, glycoconjugates, and lysosomal glycosidases by alveolar macrophages. *Proc. Natl Acad. Sci., U.S.A. 75*, 1399−1403.

(6) Taylor, P. R., Gordon, S., and Martinez-Pomares, L. (2005) The mannose receptor: linking homeostasis and immunity through sugar recognition. *Trends Immunol. 26*, 104−110.

(7) Geijtenbeek, T. B., Kwon, D. S., Torensma, R., van Vliet, S. J., van Duijnhoven, G. C., Middel, J., Cornelissen, I. L., Nottet, H. S., KewalRamani, V. N., Littman, D. R., Figdor, C. G., and van Kooyk, Y. (2000) DC-SIGN, a dendritic cell-specific HIV-1-binding protein that enhances trans-infection of T cells. *Cell 100*, 587−597.

(8) Mitchell, D. A., Fadden, A. J., and Drickamer, K. (2001) A novel mechanism of carbohydrate recognition by the C-type lectins DC-SIGN and DC-SIGNR. Subunit organization and binding to multivalent ligands. *J. Biol. Chem. 276*, 28939−28945.

(9) Frison, N., Taylor, M. E., Soilleux, E., Bousser, M. T., Mayer, R., Monsigny, M., Drickamer, K., and Roche, A. C. (2003) Oligolysine-based oligosaccharide clusters: selective recognition and endocytosis by the mannose receptor and dendritic cell-specific intercellular adhesion molecule 3 (ICAM-3)-grabbing nonintegrin. *J. Biol. Chem. 278*, 23922−23929.

(10) Appelmelk, B. J., van Die, I., van Vliet, S. J., Vandenbroucke-Grauls, C. M., Geijtenbeek, T. B., and van Kooyk, Y. (2003) Cutting edge: carbohydrate profiling identifies new pathogens that interact with dendritic cell-specific ICAM-3-grabbing nonintegrin on dendritic cells. *J. Immunol. 170*, 1635−1639.

(11) Guo, Y., Feinberg, H., Conroy, E., Mitchell, D. A., Alvarez, R., Blixt, O., Taylor, M. E., Weis, W. I., and Drickamer, K. (2004) Structural basis for distinct ligand-binding and targeting properties of the receptors DC-SIGN and DC-SIGNR. *Nat. Struct. Mol. Biol. 11*, 591−598.

(12) Engering, A., Geijtenbeek, T. B., van Vliet, S. J., Wijers, M., van Liempt, E., Demaurex, N., Lanzavecchia, A., Fransen, J., Figdor, C. G., Piguet, V., and van Kooyk, Y. (2002) The dendritic cell-specific adhesion receptor DC-SIGN internalizes antigen for presentation to T cells. *J. Immunol. 168*, 2118−2126.

(13) Engering, A. J., Cella, M., Fluitsma, D. M., Hoefsmit, E. C., Lanzavecchia, A., and Pieters, J. (1997) Mannose receptor mediated antigen uptake and presentation in human dendritic cells. *Adv. Exp. Med. Biol. 417*, 183−187.

(14) Lee, Y. C., and Lee, R. T. (1995) Carbohydrate-protein interactions: basis of glycobiology. *Acc. Chem. Res. 28*, 321−327.

(15) Monsigny, M., Mayer, R., and Roche, A. C. (2000) Sugar-lectin interactions: sugar clusters, lectin multivalency and avidity. *Carbohydr. Lett. 4*, 35−52.

(16) Drickamer, K. (1995) Multiplicity of lectin-carbohydrate interactions. *Nat. Struct. Biol. 2*, 437−439.

(17) Crocker, P. R., and Feizi, T. (1996) Carbohydrate recognition systems: functional triads in cell-cell interactions. *Curr. Opin. Struct. Biol. 6*, 679−691.

(18) Monsigny, M., Roche, A. C., and Midoux, P. (1984) Uptake of neoglycoproteins via membrane lectin(s) of L1210 cells evidenced by quantitative flow cytofluorometry and drug targeting. *Biol. Cell 51*, 187−196.

(19) Lee, Y. C., and Lee, R. T. (1994) in Neoglycoconjugates: Preparation and Application (Lee, Y. C., Lee, R. T., Eds.), pp. 23−50, Academic Press, San Diego, CA.

(20) Derrien, D., Midoux, P., Petit, C., Negre, E., Mayer, R., Monsigny, M., and Roche, A. C. (1989) Muramyl dipeptide bound to poly-L-lysine substituted with mannose and gluconoyl residues as macrophage activators. *Glycoconjugate J. 6*, 241−255.

(21) Midoux, P., Mendes, C., Legrand, A., Raimond, J., Mayer, R., Monsigny, M., and Roche, A. C. (1993) Specific gene transfer mediated by lactosylated poly-L-lysine into hepatoma cells. *Nucleic Acids Res. 21*, 871−878.

(22) Biessen, E. A., Noorman, F., van Teijlingen, M. E., Kuiper, J., Barrett-Bergshoeff, M., Bijsterbosch, M. K., Rijken, D. C., and van Berkel, T. J. (1996) Lysine-based cluster mannosides that inhibit ligand binding to the human mannose receptor at nanomolar concentration. *J. Biol. Chem. 271*, 28024−28030.

(23) Grandjean, C., Rommens, C., Gras-Masse, H., and Melnyk, O. (2000) One-Pot Synthesis of Antigen-Bearing, Lysine-Based Cluster Mannosides Using Two Orthogonal Chemoselective Ligation Reactions. *Angew. Chem., Int. Ed. 39*, 1068−1072.

(24) Frison, N., Marceau, P., Roche, A. C., Monsigny, M., and Mayer, R. (2002) Oligolysine-based saccharide clusters: synthesis and specificity. *Biochem. J. 368*, 111−119.

(25) Quétard, C., Bourgerie, S., Normand-Sdiqui, N., Mayer, R., Strecker, G., Midoux, P., Roche, A. C., and Monsigny, M. (1998) Novel glycosynthons for glycoconjugate preparation: oligosaccharylpyroglutamylanilide derivatives. *Bioconjugate Chem. 9*, 268−276.

(26) Monsigny, M., Quetard, C., Bourgerie, S., Delay, D., Pichon, C., Midoux, P., Mayer, R., and Roche, A. C. (1998) Glycotargeting: the preparation of glyco-amino acids and derivatives from unprotected reducing sugars. *Biochimie 80*, 99−108.

(27) Bédouet, L., Bousser, M. T., Frison, N., Boccaccio, C., Abastado, J. P., Marceau, P., Mayer, R., Monsigny, N., and Roch, A. C. (2001) Uptake of dimannoside clusters and oligomannosides by human dendritic cells. *Biosci. Rep. 21*, 839−855.

(28) Romero, P., Gervois, N., Schneider, J., Escobar, P., Valmori, D., Pannetier, C., Steinle, A., Wolfel, T., Lienard, D., Brichard, V., van Pel, A., Jotereau, F., and Cerottini, J. C. (1997) Cytolytic T lymphocyte recognition of the immunodominant HLA-A*0201-restricted Melan-A/MART-1 antigenic peptide in melanoma. *J. Immunol. 159*, 2366−2374.

(29) Valmori, D., Gervois, N., Rimoldi, D., Fonteneau, J. F., Bonelo, A., Lienard, D., Rivoltini, L., Jotereau, F., Cerottini, J. C., and Romero, P. (1998) Diversity of the fine specificity displayed by HLA-A*0201-restricted CTL specific for the immunodominant Melan-A/MART-1 antigenic peptide. *J. Immunol. 161*, 6956−6962.

(30) Valmori, D., Fonteneau, J. F., Lizana, C. M., Gervois, N., Lienard, D., Rimoldi, D., Jongeneel, V., Jotereau, F., Cerottini, J. C., and Romero, P. (1998) Enhanced generation of specific tumor-reactive CTL in vitro by selected Melan-A/MART-1 immunodominant peptide analogues. *J. Immunol. 160*, 1750−1758.

(31) Chen, Y. T., Stockert, E., Jungbluth, A., Tsang, S., Coplan, K. A., Scanlan, M. J., and Old, L. J. (1996) Serological analysis of

Melan-A(MART-1), a melanocyte-specific protein homogeneously expressed in human melanomas. *Proc. Natl Acad. Sci., U.S.A. 93*, 5915−5919.
(32) Monsigny, M., Petit, C., and Roche, A. C. (1988) Colorimetric determination of neutral sugars by a resorcinol sulfuric acid micromethod. *Anal. Biochem. 175*, 525−530.
(33) Goxe, B., Latour, N., Chokri, M., Abastado, J. P., and Salcedo, M. (2000) Simplified method to generate large quantities of dendritic cells suitable for clinical applications. *Immunol. Invest. 29*, 319−336.
(34) Pandolfino, M. C., Viret, C., Gervois, N., Guilloux, Y., Davodeau, F., Diez, E., and Jotereau, F. (1992) Specificity, T cell receptor diversity and activation requirements of CD4+ and CD8+ clones derived from human melanoma-infiltrating lymphocytes. *Eur. J. Immunol. 22*, 1795−1802.
(35) Midoux, P., Roche, A. C., and Monsigny, M. (1987) Quantitation of the binding, uptake, and degradation of fluoresceinylated neoglycoproteins by flow cytometry. *Cytometry 8*, 327−334.
(36) Duverger, E., Frison, N., Roche, A. C., and Monsigny, M. (2003) Carbohydrate-lectin interactions assessed by surface plasmon resonance. *Biochimie 85*, 167−179.
(37) Simpson, D. Z., Hitchen, P. G., Elmhirst, E. L., and Taylor, M. E. (1999) Multiple interactions between pituitary hormones and the mannose receptor. *Biochem. J. 343 Pt 2*, 403−411.
(38) Napper, C. E., Dyson, M. H., and Taylor, M. E. (2001) An extended conformation of the macrophage mannose receptor. *J. Biol. Chem. 276*, 14759−14766.
(39) Taylor, M. E., and Drickamer, K. (1993) Structural requirements for high affinity binding of complex ligands by the macrophage mannose receptor. *J. Biol. Chem. 268*, 399−404.
(40) Jung, T., Schauer, U., Heusser, C., Neumann, C., and Rieger, C. (1993) Detection of intracellular cytokines by flow cytometry. *J. Immunol. Methods 159*, 197−207.
(41) Parsons, S. M., Jao, L., Dahlquist, F. W., Borders, C. L., Jr., Racs, J., Groff, T., and Raftery, M. A. (1969) The nature of amino acid side chains which are critical for the activity of lysozyme. *Biochemistry 8*, 700−712.
(42) Takahashi, K. (1976) The structure and function of ribonuclease T1. XXI. Modification of histidine residues in ribonuclease T1 with iodoacetamide. *J. Biochem.* (Tokyo) *80*, 1267−1275.
(43) Ramakrishna, V., Treml, J. F., Vitale, L., Connolly, J. E., O'Neill, T., Smith, P. A., Jones, C. L., He, L. Z., Goldstein, J., Wallace, P. K., Keler, T., and Endres, M. J. (2004) Mannose receptor targeting of tumor antigen pmel17 to human dendritic cells directs anti-melanoma T cell responses via multiple HLA molecules. *J. Immunol. 172*, 2845−2852.
(44) Keler, T., Ramakrishna, V., and Fanger, M. W. (2004) Mannose receptor-targeted vaccines. *Expert Opin. Biol. Ther. 4*, 1953−1962.
(45) Tacken, P. J., de Vries, I. J., Gijzen, K., Joosten, B., Wu, D., Rother, R. P., Faas, S. J., Punt, C. J., Torensma, R., Adema, G. J., and Figdor, C. G. (2005) Effective induction of naive and recall T-cell responses by targeting antigen to human dendritic cells via a humanized anti-DC-SIGN antibody. *Blood 106*, 1278−1285.
(46) Dakappagari, N., Maruyama, T., Renshaw, M., Tacken, P., Figdor, C., Torensma, R., Wild, M. A., Wu, D., Bowdish, K., and Kretz-Rommel, A. (2006) Internalizing antibodies to the C-type lectins, L-SIGN and DC-SIGN, inhibit viral glycoprotein binding and deliver antigen to human dendritic cells for the induction of T cell responses. *J. Immunol. 176*, 426−440.
(47) Gras-Masse, H. (2001) Chemoselective ligation and antigen vectorization. *Biologicals 29*, 183−188.
(48) Narendran, P., Elsegood, K., Leech, N. J., Macindoe, W. M., Boons, G. J., and Dayan, C. M. (2004) Dendritic cell-based assays, but not mannosylation of antigen, improves detection of T-cell responses to proinsulin in type 1 diabetes. *Immunology 111*, 422−429.

BC070026G

Self-Assembled Nano-Bioreactor from Block Ionomers with Elevated and Stabilized Enzymatic Function

Akifumi Kawamura,[†] Atsushi Harada,*[,†] Kenji Kono,[†] and Kazunori Kataoka*[,‡,§]

Department of Applied Chemistry, Graduate School of Engineering, Osaka Prefecture University, 1-1 Gakuen-cho, Naka-ku, Sakai, Osaka 599-8531, Japan, Department of Materials Engineering, Graduate School of Engineering, and Center for NanoBio Integration, The University of Tokyo, 7-3-1 Hongo, Bunkyo-ku, Tokyo 113-8656, Japan. Received January 24, 2007; Revised Manuscript Received July 7, 2007

Core-cross-linked polyion complex (PIC) micelles entrapping trypsin in the core were prepared by mixing trypsin and poly(ethylene glycol)-*block*-poly(α,*β*-aspartic acid) in aqueous medium, followed by the introduction of glutaraldehyde cross-linkages. Trypsin incorporated into the core-cross-linked micelles showed high storage stabilities, and the initial enzymatic activity of trypsin was maintained even after standing for one week at ambient temperature. Further, stable compartmentalization of trypsin into the core-cross-linked micelles led to a unique modulation in the enzymatic functions including an improved thermal tolerability with an increased maximum reaction rate compared to native trypsin.

INTRODUCTION

Immobilized enzymes have been utilized in numerous applications including bioreactors, biosensors, and therapeutics (*1*−*5*). The major advantage of immobilized enzymes is an improvement in the storage and operational stabilities, which is especially crucial for proteolytic enzymes showing autolysis reaction. Conventionally, solid and porous matrices, including agarose, cellulose, and silica, have been used to immobilize enzymes through physical adsorption or covalent attachment. Also, water-soluble conjugates of enzymes with various polymers have been prepared (*6*−*9*). A novel approach to the immobilization of enzymes at the nanometric scale is the supramolecular assembly of nanoreactors. Noteworthy in this regard is the core−shell-type polyion complex (PIC) micelles formed from block ionomers. Charged enzymes can be incorporated into PIC micelles driven by electrostatic interaction in aqueous medium (*10*−*13*). Indeed, egg white lysozyme with cationic character was successfully incorporated into the core of PIC micelles through complexation with poly(ethylene glycol)-*block*-poly(α,*β*-aspartic acid) (PEG-PAA). Lysozyme-incorporated PIC micelles showed unique features including the on−off switching of an elevated enzymatic reaction synchronized with an external electric field. However, in the case of entrapping proteolytic enzymes (e.g., trypsin) in the micelles, autolysis was facilitated due to an increase in the local concentration of the enzyme. This problem has been recently overcome by the introduction of cross-linking into the core of PIC micelles (*14*). The tolerability of trypsin in PIC micelles, which is a typical proteolytic enzyme that selectively cleaves the bond adjacent to Lys and Arg, was dramatically improved by introducing cross-linking in the core of the micelles. Glutaraldehyde was used as a cross-linking reagent of the PIC micelles prepared by mixing trypsin and PEG-PAA. The core-cross-linked PIC micelles had a hydrogel core of nanoscopic size, formed by the cross-linking of trypsin and PAA, and an outer PEG shell layer. The core-cross-linked micelles might provide unique features in the field of nanoscopic enzymatic reactions.

Here, we studied in detail the enzymatic function of the core-cross-linked PIC micelles entrapping trypsin. Note that the Schiff base linkages in the cross-linked PIC micelles may undergo reductive amination to form alkylamine linkages. The amidase activity of entrapped trypsin in the micelle was evaluated by colorimetric assays using L-lysine *p*-nitroanilide as a substrate, both before and after the reductive amination. A remarkable improvement in the storing stability of trypsin was observed as a result of the compartmentalization of the enzyme into the cross-linked core of the PIC micelles. Further, an appreciable increase in the optimal temperature as well as a significantly improved tolerance to urea in the enzymatic reaction were achieved in the cross-linked micelles.

EXPERIMENTAL PROCEDURES

Materials. Poly(ethylene glycol)-poly(α,*β*-aspartic acid) block copolymer [PEG-PAA; 12 000 g/mol of PEG Mw; 68 of polymerization degree in PAA segment] was synthesized as described previously (*10*). Bovine pancreas trypsin, L-lysine *p*-nitroanilide and 3-methyl-2-benzothiazolinone hydrazone were purchased from Sigma (St. Louis, MO) and used without further purification. Sodium cyanotrihydroborate ($NaBH_3CN$), $Na_2HPO_4 \cdot 12H_2O$, $NaH_2PO_4 \cdot 2H_2O$, and 70% glutaraldehyde were reagent grade and were purchased from Wako Pure Chemical Industries (Osaka, Japan).

Preparation of Core-Cross-Linked PIC Micelles Entrapping Trypsin in the Core. Given amounts of trypsin and PEG-PAA were separately dissolved in sodium phosphate buffer (10 mM; pH 7.4) at 4 °C. The solutions were mixed at the optimum mixing ratio for PIC micelle formation, i.e., the ratio of the number of Asp residues in PEG-PAA against the total number of Lys and Arg residues in trypsin to be 0.75. The mixed

* To whom corresponding should be addressed. Prof. Kazunori Kataoka, Department of Materials Engineering, Graduate School of Engineering, The University of Tokyo, 7-3-1 Hongo, Bunkyo-ku Tokyo 113-8656, Japan, Tel: +81-3-5841-7138, Fax: +81-3-5841-7139, e-mail: kataoka@bmw.t.u-tokyo.ac.jp. Dr. Atsushi Harada, Department of Applied Chemistry, Graduate School of Engineering, Osaka Prefecture University, 1-1 Gakuen-cho, Naka-ku, Sakai, Osaka 599-8531, Japan, Tel & Fax: +81-72-254-9328, e-mail: harada@chem.osakafu-u.ac.jp.

[†] Osaka Prefecture University.

[‡] Graduate School of Engineering, The University of Tokyo.

[§] Center for NanoBio Integration, The University of Tokyo.

10.1021/bc070029t CCC: $37.00 © 2007 American Chemical Society
Published on Web 08/14/2007

solution was stored at 4 °C for 30 min, and then 70% glutaraldehyde solution was added to prepare cross-linked micelles with varying cross-linking ratios (GR). The cross-linking ratio (GR) was defined as the residual molar ratio of aldehyde group to lysine in the solution. The cross-linked PIC micelle solution was then kept at 4 °C for 30 min. In order to remove excess glutaraldehyde, the cross-linked PIC micelle solution was dialyzed against buffer. The removal of free glutaraldehyde was confirmed from the absence of aldehyde species in the dialysate, as determined by colorimetric assay using 3-methyl-2-benzothiazolinone hydrazone. Then, $NaBH_3$-CN was added to the solution to convert the Schiff base linkages to alkylamine linkages by reductive amination. The reductive amination step was also confirmed by colorimetric assay using 3-methyl-2-benzothiazolinone hydrazone.

Dynamic Light Scattering Measurements. Dynamic light scattering (DLS) measurements were carried out using a DLS-700 spectrometer (Otsuka Electronics Co., Ltd., Japan) equipped with an Ar ion laser (λ = 488 nm) at 25 °C. The detection angle was fixed at 90°. The average diameter and polydispersity index were obtained by the cumulant method, and the size distribution was obtained by histogram analysis.

Evaluation of Amidase Activity of Trypsin. The amidase activity of trypsin was evaluated using L-lysine *p*-nitroanilide as a substrate. The reaction rates of the native trypsin and trypsin incorporated into the core-cross-linked micelles were determined by monitoring the change in the absorbance at 410 nm, where the wavelength for the extinction coefficient of *p*-nitroaniline after mixing of the trypsin solution and substrate solution is 8800 cm^{-1} M^{-1}. The initial reaction rate was determined from the slope of the change in the absorbance at 410 nm during the period between 150 and 250 s after mixing.

RESULTS AND DISCUSSION

The cross-linkages in the core of PIC micelles, which were prepared from trypsin and PEG-PAA, were introduced using glutaraldehyde as cross-linking reagent for the stabilization of the micellar structure. There is known to be two types of cross-linkages in the cross-linking reaction of amine compounds by glutaraldehyde: One is the Schiff base linkage formed between the primary amino group of the Lys residue in trypsin and the aldehyde group of glutaraldehyde, and the other cross-linkage involves the formation of a quaternary pyridinium structure (see Supporting Information). We have recently confirmed the formation of the quaternary pyridinium structure for lysozyme-entrapped PIC micelles cross-linked using glutaraldehyde by spectroscopic analysis (*15*). Further, the quaternary pyridinium structure might also be formed in trypsin-entrapped PIC micelles cross-linked by glutaraldehyde. Reduction of the Schiff base and pyridinium structure using $NaBH_3CN$ as a reductant results in the formation of saturated alkylamines, further stabilizing the micelle structure due to the formation of the stable covalent bonds. The nonreacted aldehyde groups in the core-cross-linked PIC micelles were also reduced to hydroxyl groups by $NaBH_3$-CN treatment, which was confirmed by using 3-methyl-2-benzothiazolinone hydrazone as an aldehyde-detecting reagent. Figure 1 shows the size distribution of PIC micelles before and after the reductive amination. Unimodal size distribution was maintained even after this treatment. Also, the reduction process induced no change in the average diameter and polydispersity index (μ_2/Γ^2), which were determined by the cumulant analysis of dynamic light scattering measurements (69.6 nm, μ_2/Γ^2 = 0.04 for the original sample; and 68.9 nm, μ_2/Γ^2 = 0.06 for the sample after the treatment).

As an evaluation of the stabilized enzymatic function, the storage stability of the amidase activity of trypsin was studied by using L-lysine *p*-nitroanilide as a substrate. Figure 2 shows

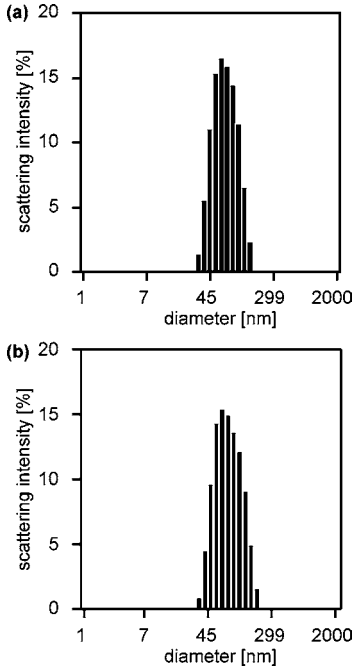


Figure 1. Size distributions of core-stabilized micelles before (a) and after (b) reductive amination, as measured by dynamic light scattering (GR = 100; detection angle 90°; temperature 25 °C).

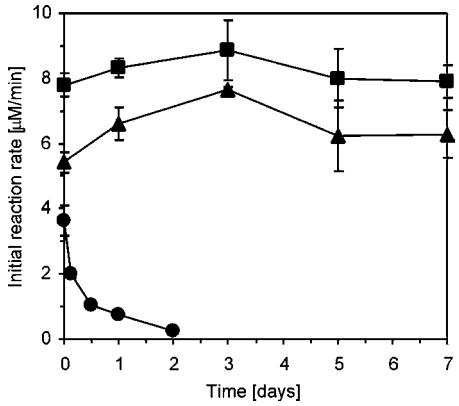


Figure 2. Time course of the enzymatic reaction rate of native trypsin (●) and trypsin incorporated into nonreduced (▲) and reduced (■) micelles at 25 °C. (Trypsin concentration 16.8 μM; substrate concentration 5 mM. The plots are presented as the average of three experiments ± SD.)

the time-dependent change in the initial reaction rate for both native trypsin and trypsin incorporated into the nonreduced and reduced micelles. The initial reaction rate of native trypsin immediately decreased due to autolysis, and there was no detectable activity after 2 days incubation. On the other hand, the trypsin incorporated into the nonreduced and reduced core-cross-linked micelles maintained a constant reaction rate even after 1 week incubation at 25 °C, indicating that the autolysis of trypsin was effectively prevented due to being incorporated into the core-cross-linked micelles. In the cross-linked core, the migration of trypsin molecules was highly restricted, thereby inhibiting their mutual contact. As a result, the autolysis of trypsin was effectively inhibited. There was no difference in the storage stability of trypsin activity between the nonreduced and reduced micelles. This effect will be discussed later on the basis of the enzymatic reaction constants. Further, it should be noted that the reaction rate of the trypsin incorporated into the core-cross-linked micelles was appreciably higher than that of native trypsin, suggesting that the amidase activity of trypsin might increase through the entrapment into the core of the

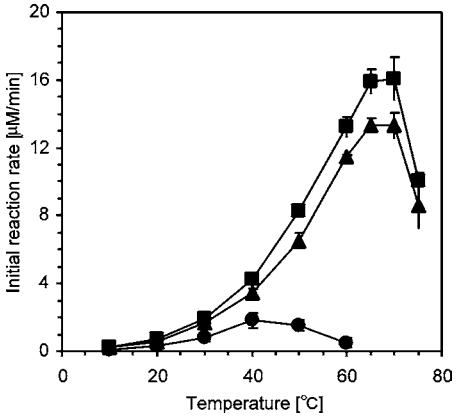


Figure 3. Temperature dependence of the enzymatic reaction of native trypsin (●) and trypsin incorporated into nonreduced (▲) and reduced (■) micelles. (Trypsin concentration 4.2 μM; substrate concentration 1.25 mM. The plots are presented as the average of three experiments ± SD.)

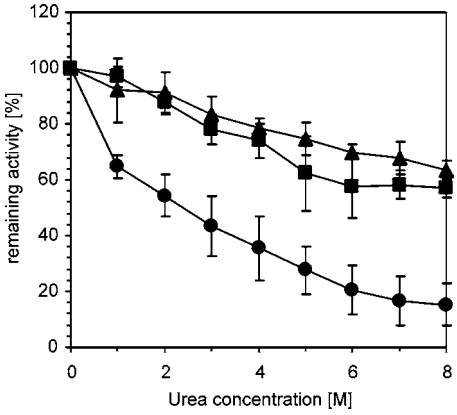


Figure 4. Change in relative remaining activity with urea concentration for native trypsin (●) and trypsin incorporated into nonreduced (▲) and reduced (■) micelles. (Trypsin concentration 16.8 μM; substrate concentration 5.0 mM; The initial reaction rates of native trypsin and trypsin incorporated into nonreduced and reduced micelles were 4.3 ± 0.1, 7.3 ± 0.7, and 8.9 ± 0.9 μM/min, respectively. The plots are presented as the average of three experiments ± SD.)

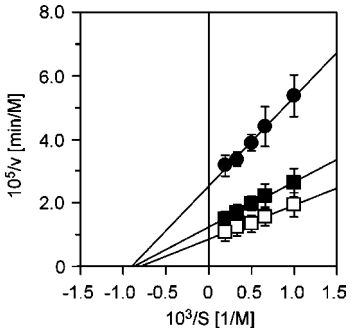


Figure 5. Lineweaver−Burk plots of native trypsin (●) and trypsin incorporated into the nonreduced (■) and reduced (□) micelles. (Trypsin concentration 16.8 μM; temperature 25 °C; $n = 3$.)

micelle. For the stabilized enzymes physically or chemically immobilized in polymer networks, the decreased enzymatic activity through the immobilization was often observed, which was induced by the restriction of the mobility of enzyme as well as by the limited solute transfer (*16*, *17*). No decrease in enzymatic activity of trypsin in the micelles might be due to the unique characteristics of core-cross-linked micelles including small size and core−shell structure with enzyme molecules stably entrapping into the core surrounded by a biocompatible and hydrophilic shell layer, providing a uniform distribution of stabilized enzymatic nanoreactor and maintenance of substrate diffusion.

The entrapment of trypsin into the micellar cross-linked core induced a substantial shift in the optimal temperature of the enzymatic reaction, as compared to native trypsin. Figure 3 shows the temperature dependence of the enzymatic reaction rate of both the native trypsin and the trypsin incorporated into the nonreduced and reduced micelles. In the case of native trypsin, a maximum reaction rate was observed at 40 °C, and this reaction rate gradually decreased in the higher-temperature region due to thermal denaturation. Obviously, the optimal temperature of the trypsin activity increased from 40 to 65 and 70 °C, respectively, for the nonreduced and reduced micelles. Various types of trypsin stabilized by polymers have been evaluated on their thermal stability, and the highest optimal temperature of stabilized trypsin in such a way was 65 °C reported by Fernandez et al. (*18*, *19*). In their study, trypsin conjugated with the derivatives of cyclodextrin showed an increased optimal temperature of trypsin, but the autolysis reaction was not completely prevented. The significant increase in the optimal temperature up to 70 °C obtained in the present study of the PIC micelle system might be due to the effective stabilization of the trypsin molecule by the introduction of the cross-linked structure in the matrix of the micellar core. In the core of the cross-linked micelles, cross-linkages were formed not only between the trypsin−trypsin molecules, but also between the primary amino groups at the ω-end of the PAA segments and the aldehyde groups in glutaraldehyde, i.e., trypsin−trypsin and trypsin−polymer cross-linkages, forming a hybrid nanogel structure. Consequently, the thermal-denaturing temperature of trypsin shifted to a higher temperature through the immobilization into the nanogel network, thus avoiding the thermal unfolding of the protein structure. It is worth noting that, in the immobilized trypsin in the micellar core, the spatial arrangement of the Asp-His-Ser catalytic triad in the trypsin molecule should be maintained even at 70 °C.

The stabilized spatial arrangement of the catalytic triad in the core-cross-linked micelles was also supported by the results of the tolerated trypsin activity against urea addition. Figure 4 shows the change in the relative remaining activity, defined as the ratio of the initial enzymatic reaction rate in the presence and absence of urea. Urea is well-known as a strong breaker of hydrogen bonding, as well as a disruptor of hydrophobic interaction, including enzyme denaturation in a concentration dependent manner. Indeed, the relative remaining activity of native trypsin gradually decreased with increasing urea concentration, and became lower than 50% at 3.0 M urea. On the other hand, even at 8.0 M urea, the trypsin incorporated into the core-cross-linked micelles maintained more than 60% of its relative remaining activity, indicating that the spatial arrangement of the catalytic triad in the cross-linked micelles was preserved even at high urea concentration. These results shown in Figures 3 and 4 suggest that the original tertiary structure of the trypsin molecule in the micelles might be effectively stabilized through chemical cross-linking.

As seen in Figures 2 and 3, the trypsin incorporated into the core-cross-linked micelles always showed higher initial reaction rates compared with native trypsin, suggesting that the enzyme incorporated into core-cross-linked micelles exhibits apparently enhanced activity. In order to evaluate the difference in the amidase activity of native trypsin and trypsin in the nonreduced and the reduced micelles, enzymatic reaction constants were determined by preparing Lineweaver−Burk plots (Figure 5). The good linear relations observed between the reciprocals of the initial reaction rate and the substrate concentration in the Lineweaver−Burk plots was confirmed not only for native

Table 1. Enzymatic Reaction Constants of Native Trypsin and Trypsin Incorporated into the Core-Cross-Linked Micelles

	k_{cat} [min^{-1}]	K_m [mM]	k_{cat}/K_m [M^{-1} min^{-1}]
native trypsin	0.236 (1.0)[a]	1.11 (1.0)[a]	213 (1.0)[a]
trypsin in nonreduced micelle	0.482 (2.0)[a]	1.14 (1.0)[a]	423 (2.0)[a]
trypsin in reduced micelle	0.689 (2.9)[a]	1.23 (1.1)[a]	560 (2.6)[a]

[a] These values were relative values against the values of native trypsin.

trypsin, but also for the trypsin incorporated into the reduced and nonreduced micelles. This linear relation indicates that the enzymatic function of trypsin incorporated into the core-cross-linked micelles can be kinetically analyzed on the basis of the Michaelis−Menten equation. The obtained enzymatic reaction constants, the catalytic rate constant (k_{cat}), the Michaelis constant (K_m), and k_{cat}/K_m, were summarized in Table 1. It was observed that the K_m values remained almost unchanged following the incorporation of trypsin into the core-cross-linked micelles, indicating that the affinity between trypsin and the substrate did not change. On the other hand, the k_{cat} values of the core-cross-linked micelles were approximately two to three times higher than that of native trypsin. The higher reaction rates of trypsin in the core-cross-linked micelles, as compared to those of native trypsin, were ascribed to an increase in the k_{cat} values. It is well-known that trypsin has a catalytic site constituted of the Asp-His-Ser triad (*20*−*22*). In this catalytic site, the nucleophilicity of the hydroxyl group of Ser increases through a proton-transfer process in the Asp-His dyad, in which the carboxylate group of Asp stabilizes the imidazolium ion of the His residue. We recently found that a part of the carboxylate group of the Asp residue in PEG-PAA stabilized an imidazolium ion of the His residue in the catalytic triad, thus accelerating the catalytic reaction of trypsin (*23*). This effect might also be induced in the core-cross-linked micelles as a means to increase the catalytic constant, as compared to native trypsin.

CONCLUSION

Core-cross-linked PIC micelles, prepared from trypsin and PEG-PAA, were effectively formed in both a reduced and a nonreduced state, both entrapping trypsin in the core. Both a remarkable improvement in the storing stability and a significant increase in the optimal temperature of the trypsin activity, as well as the marked resistance to denaturation by urea, were all confirmed as effects of the incorporation of trypsin into the core-cross-linked micelles. Note that there were few reports on the immobilization method of enzymes which attained increases in both the enzymatic activity and the optimal temperature. Most of the conventional enzyme-immobilized systems showed an apparent decrease in enzymatic activity due to the mass-transfer effect attributed to the restricted mobility of the enzyme as well as to the limited diffusion of the solute molecules (*16*, *17*). In the case of the core-cross-linked micelles, the enzymes were fixed to each other by the cross-linking reagent to form a nanoscopic hydrogel domain consisting of several tens of enzyme molecules. Since the size of the domain was sufficiently small, the diffusion of the substrate might not be the rate-determining step of the enzyme reaction. As a result, the mass-transfer effect was not significant for the core-cross-linked micelles. This is also an advantage of the cross-linked PIC micelle systems when compared to the conventional immobilization of enzymes in gel matrices with significantly larger dimensions. These core-cross-linked micelles incorporating enzymes represent a new entity of supramolecular nanobioconjugates, which are expected to find significant application in both the medical and bioengineering fields.

ACKNOWLEDGMENT

This study was supported by the Industrial Technology Research Grant Program of the New Energy and Industrial Technology Development Organization (NEDO) of Japan.

Supporting Information Available: The quaternary pyridinium structure in the core-cross-linked micelle. This material is available free of charge via the Internet at http://pubs.acs.org.

LITERATURE CITED

(1) Griffith, L. G. (2000) Polymeric biomaterials. *Acta Mater. 48*, 263−277.

(2) Sakiyama-Elbert, S. E., and Hubbell, J. A. (2001) Functional biomaterials: design of novel biomaterials. *Annu. Rev. Mater. Res. 31*, 183−201.

(3) Vandermeulen, G. W. M., and Klok, H. A. (2004) Peptide/protein hybrid materials: enhanced control of structure and improved performance through conjugation of biological and synthetic polymers. *Macromol. Biosci. 4*, 383−398.

(4) Vriezema, D. M., Aragonès, M. C., Elemans, J. A. A. W., Cornelissen, J. J. L. M., Rowan, A. E., and Nolte, R. J. M. (2005) Self-assembled nanoreactor. *Chem. Rev. 105*, 1445−1489.

(5) Girelli, A. M., and Mattei, E. (2005) Application of immobilized enzyme reactor in on-line high performance liquid chromatography: a review. *J. Chromatogr., B 819*, 3−16.

(6) Duncan, R. (2006) Polymer conjugates as anticancer nanomedicine. *Nat. Rev. Cancer 6*, 688−701.

(7) EI-Sayed, M. E. H., Hoffman, A. S., and Stayton, P. S. (2005) Smart polymeric carriers for enhanced intracellular delivery of therapeutic macromolecules. *Exp. Opin. Biol. Ther. 5*, 23−32.

(8) Alarcon, C. D. H., Pennadam, S., and Alexander, C. (2005) Stimuli responsive polymers for biomedical applications. *Chem. Soc. Rev. 34*, 276−285.

(9) Harada, A., and Kataoka, K. (2006) Supramolecular assemblies of block copolymers in aqueous media as nanocontainers relevant to biological applications. *Prog. Polym. Sci. 31*, 949−982.

(10) Harada, A., and Kataoka, K. (1998) Novel polyion complex micelles entrapping enzyme molecules in the core: preparation of narrowly-distributed micelles from lysozyme and poly(ethylene glycol)-poly(aspartic acid) block copolymer in aqueous medium. *Macromolecules 31*, 288−294.

(11) Harada, A., and Kataoka, K. (1999) On-off control of enzymatic activity synchronizing with reversible formation of supramolecular assembly from enzyme and charged block copolymers. *J. Am. Chem. Soc. 121*, 9241−9242.

(12) Harada, A., and Kataoka, K. (2001) Pronounced activity of enzymes through the incorporation into the core of polyion complex micelles made from charged block copolymers. *J. Controlled Release 72*, 85−91.

(13) Harada, A., and Kataoka, K. (2003) Switching by pulse electric field of the elevated enzymatic reaction in the core of polyion complex micelles. *J. Am. Chem. Soc. 125*, 15306−15307.

(14) Jaturanpinyo, M., Harada, A., Yuan, X., and Kataoka, K. (2004) Preparation of bionanoreactor based on core-shell structured polyion complex micelles entrapping trypsin in the core cross-linked with glutaraldehyde. *Bioconjugate Chem. 15*, 344−348.

(15) Yuan, X., Yamasaki, Y., Harada, A., and Kataoka, K. (2005) Characterization of stable lysozyme-entrapped polyion complex (PIC) micelles with crosslinked core by glutaraldehyde. *Polymer 46*, 7749−7758.

(16) Tischer, W., and Kasche, V. (1999) Immobilized enzymes: crystals of carriers? *Trends Biotechnol. 17*, 326−335.

(17) Cao, L., Langen, L., and Sheldon, R. A. (2003) Immobilized enzymes: carrier-bound of carrier-free? *Curr. Opin. Biotechnol. 14*, 387−394.

(18) Fernandez, M., Villalonga, M. L., Caballero, J., Fragoso, A., Cao, R., and Villalonga, R. (2003) Effect of beta-cycolodextrin-dextran polymer on stability properties of trypsin. *Biotechnol. Bioeng. 83*, 743−747.

(19) Fernandez, M., Villalonga, M. L., Fragoso, A., Cao, R., and Villalonga, R. (2004) Effect of beta-cyclodextrin-polysucrose poly-

mer on the stability properties of soluble trypsin. *Enzyme Microb. Technol. 34*, 78−82.
(20) Hunkapiller, M. W., Smallcombe, S. H., Whitaker, D. R., and Richards, J. H. (1973) Ionization behavior of the histidine residue in the catalytic triad of serine proteases. Mechanistic implications. *J. Biol. Chem. 248*, 8306−8308.
(21) Scheiner, S., and Lipscomb, W. N. (1976) Molecular orbital studies of enzyme activity: catalytic mechanism of serine proteinases. *Proc. Natl. Acad. Sci. U.S.A. 73*, 432−436.
(22) Craik, C. S., Roczniak, S., Largman, C., and Rutter, W. J. (1987) The catalytic role of the active site aspartic acid in serine proteases. *Science 237*, 909−913.
(23) Kawamura, A., Yoshioka, Y., Harada, A., and Kono, K. (2005) Acceleration of enzymatic reaction of trypsin through the formation of water-soluble complexes with poly(ethylene glycol)-block-poly-(α,*β*-aspartic acid). *Biomacromolecules 6*, 627−631.

BC070029T

Synthesis of Oxytocin HYNIC Derivatives as Potential Diagnostic Agents for Breast Cancer

Alma D. Miranda-Olvera,[†] Guillermina Ferro-Flores,[‡] Martha Pedraza-López,[§] Consuelo Arteaga de Murphy,[§] and Luis M. De León-Rodríguez*[,†]

Instituto de Investigaciones Científicas, Universidad de Guanajuato, Guanajuato, Gto. Mexico, Gerencia de Aplicaciones Nucleares en la Salud, Instituto Nacional de Investigaciones Nucleares, Ocoyoacac, Edo. Mex., Mexico, and Instituto Nacional de Ciencias Médicas y Nutrición Salvador Zubirán, Mexico City, Mexico. Received February 12, 2007; Revised Manuscript Received April 11, 2007

Two synthetic procedures for HYNIC oxytocin labeling were developed: one based on an orthogonal protection approach and the other with prelabeled (Boc)HYNIC-(Fmoc) amino acids. Both procedures were compared and applied to the preparation of several HYNIC−oxytocin derivatives where ligand position and amino acid (lysine and phenylalanine) were varied. Additionally, an oxytocin derivative labeled with HYNIC in the α-amino group of the Cys^1 residue was also prepared. ^{99m}Tc-ethylendiaminediacetic acid (EDDA) labeling efficiencies were examined for all the derivatives, resulting in two candidates which showed affinity for the oxytocin receptor. Further biochemical experiments demonstrated that ^{99m}Tc-EDDA/HYNIC-Cys^1-OT-$CONH_2$ could be used as a potential radiopharmaceutical for breast cancer diagnosis.

INTRODUCTION

Recently, the development of target-specific diagnostic pharmaceuticals (TSP) has heightened the interest in studying the different chemical aspects involved in the production of these agents. In general, diagnostic TSP consist of a specific vector, a linker, a ligand, and a metal ion. The vector is the moiety acting as a carrier to the specific target. The usage of vectors such as organic compounds, antibodies, proteins, and peptides has been widely reported in the literature (*1*). However, peptides are of particular interest, given that sequence target specificity can be easily monitored by techniques such as phage display (*2*), and peptide synthesis and modification can be chemically accomplished by solid-phase peptide synthesis (SPPS). The linker is the intermediate group connecting the ligand with the vector and selection depends on either the metabolic characteristics desired for the TSP or the maintenance of the ligand as far as possible from the vector to minimize activity modification of the vector due to the proximity of the ligand. The ligand is the molecule in charge of forming a thermodynamically and kinetically stable complex with the metal ion of interest. The selection of the metal ion depends on its nuclear, physical, and magnetic properties, given a particular application. For instance, ^{99m}Tc is used in radiodiagnostics, and Gd^{3+} is used in contrast agents for magnetic resonance imaging (MRI). In particular, ^{99m}Tc is used in nearly 80% of all single-photon emission computed tomography (SPECT) diagnostic radiopharmaceuticals currently used in nuclear medicine (*3*), given its optimal half-life time (6 h), wide availability, and low-energy particle emission (*4*). Therefore, peptides labeled with ligands that form stable metal complexes with ^{99m}Tc are thoroughly studied as diagnostic tools (*5*). Among the chelators, HYNIC (2-hydrazinnicotinic acid) (*6*) (Figure 1a) is of particular interest, because

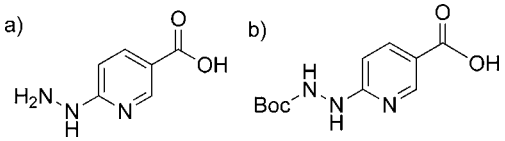


Figure 1. (a) HYNIC and (b) Boc-HYNIC.

it shows a high labeling efficiency (rapid and high yield radiolabeling) and its usage with various co-ligands (e.g., ethylendiaminediacetic acid, tricine, and glucoheptonate) allows for easy modification of the hydrophilicity and pharmacokinetics of the ^{99m}Tc -labeled small peptides (*7*). Given the implications of chelate-labeled peptides, the study of the influence of ligand position within a peptide sequence on targeting specificity and properties of the peptide is of great interest. The most common way to attach a ligand to a peptide has been through the N-terminus or the ϵ-amino group of lysine by means of protected derivatives of the ligand for SPPS (Figure 1b). However, this limits the possibilities of creating peptide libraries for screening purposes. Additionally, several lysine-protected derivatives have been prepared (*8*, *9*) and are commercially available (e.g., Bachem Bioscience Inc. USA, Advanced ChemTech Inc. USA, Merck KGaA, Germany) to specifically attach ligands to peptides through lysine residues by orthogonal protection procedures (*10*). Recently, a chemical procedure for introducing DOTA-lysine (DOTA-Lys) or DOTA-phenylalanine (DOTA-Phe) within a peptide sequence using standard SPPS was reported, and thus, a small peptide library was created and monitored for peptide activity (*11*). Similarly, a HYNIC-Lys derivative (Scheme 1, compound **6**) was reported for site-specific labeling of a calcitonin salmon peptide (*12*). In that work, the synthesis was accomplished by reacting Boc-HYNIC succinimide with Nα-Fmoc lysine. However, the desired product was obtained in moderate yields after purification by HPLC, given the formation of a Boc-HYNIC-(Nα-Fmoc $Lys)_2$ subproduct. Thus, although the procedure is simple and partially works with amino acids and its derivatives containing a free aliphatic amino group (lysine), it has not been proven to work for amino aromatic amino acid derivatives, given its low nucleophilicity. Additionally, the moderate yields of the HYNIC-Lys and

* Corresponding author. Instituto de Investigaciones Científicas. Cerro de la Venada s/n. Guanajuato, Gto., C.P. 36040. México. Tel., Fax: +52-4737326252; E-mail: lmdeleon@quijote.ugto.mx.

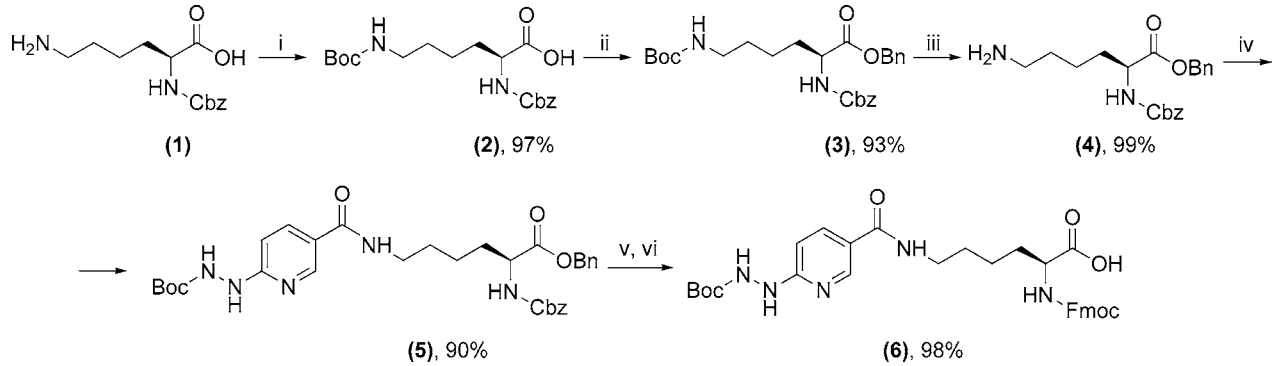
[†] Universidad de Guanajuato.

[‡] Instituto Nacional de Investigaciones Nucleares.

[§] Instituto Nacional de Ciencias Médicas y Nutrición Salvador Zubirán.

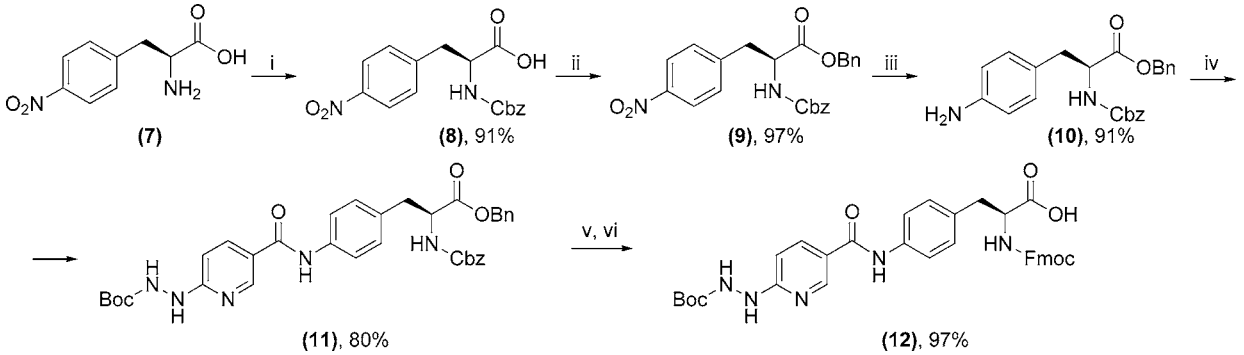
10.1021/bc070047a CCC: $37.00 © 2007 American Chemical Society
Published on Web 08/01/2007

Scheme 1. Synthesis of HYNIC-Lys Derivative[a]



[a] (i) $(Boc)_2O$, water-dioxane, TEA; (ii) BnBr, DIPEA, ACN; (iii) CH_2Cl_2, TFA; (iv) Boc-HYNIC, HBTU, DIPEA; (v) EtOH, H_2, Pd/C; (vi) Fmoc-Succinimide, DMSO.

Scheme 2. Synthesis of HYNIC-Phe Derivative[a]



[a] (i) BnOCOCl, water-dioxane, Na_2CO_3; (ii) BnBr, DIPEA, ACN; (iii) Zn, EtOH, AcOH; (iv) Boc-HYNIC, HBTU, DIPEA, MW 100W; (v) EtOH, H_2, Pd/C; (vi) Fmoc-Succinimide, DMSO.

subproduct formation are fully attributed to the free carboxylic acid of the Nα-Fmoc amino acid. In spite of the existence of different chemical procedures for generating ligand−peptide libraries based on solid-phase peptide synthesis, there have been few reports related to the generation of these libraries for screening purposes of diagnostic or therapeutic agents. Therefore, in this work, we present a generalized procedure for the synthesis of HYNIC Lys (**6**) and Phe (**12**) (Schemes 1 and 2, respectively) derivatives based on functional group protection. To demonstrate the utility of these derivatives, a small library of the bioactive peptide oxytocin (OT) labeled with HYNIC was prepared. Additionally, the procedure was compared with an orthogonal protection approach for the controlled positioning of HYNIC in OT. Oxytocin is an important hypothalamic cyclic neurononapeptide (NH_2-$Cys^1Tyr^2Ile^3Gln^4Asn^5Cys^6Pro^7Leu^8Gly^9$-$CONH_2$) that plays an important role in many reproductive and behavioral functions. OT structure−activity relationships have been widely studied, and the following characteristics may be noted: (a) The cyclic part of the peptide (Cys^1-Cys^6) is more important in conferring binding selectivity for the OT receptor (OTR) compared to the linear tripeptidic part ($Pro^7Leu^8Gly^9$) (*13*); (b) the replacement of the $CONH_2$ terminal group for COOH leads to less active OT derivatives; (c) the tripeptide tail of OT is important for binding, and Pro^7Leu^8 can be replaced by a variety of residues (moreover, OT derivatives with reduced potency are obtained when Pro^7 is substituted by a residue that induces conformational constraints) (*14*); and (d) the deaminoCys^1−oxytocine derivative is more active than OT (*15*) and has higher stability to oxytocinase degradation (*16*). However, structure−activity relationships for OT−ligand conjugates are unknown.

Recently, novel sites for OT receptor expression have been detected, including breast cancer cells, bone cells, myoblasts, cardiomyocytes, endothelial cells, and in ovarian carcinoma (*17*, *18*). Although the mechanism is not completely understood, in tumors, OT acts as a growth regulator, and it has been demonstrated that in some cases it has an growth-inhibiting effect (mammarian carcinomas, neoplastic epithelial, nervous or bone cells, and ovarian carcinoma cells), while in others, it promotes cell proliferation (trophoblast and endothelium neoplastic cells) (*19*). Additionally, it has been recently recognized that the placental leucine aminopeptidase (P-LAP) acts as an OT-degrading aminopeptidase (oxytocinase) in endometrial adenocarcinoma tissues and ovarian cancer, and it has been suggested that the system OT-OTR-P-LAP might be involved in cellular growth for this type of cancers (*18*). Thus, we hypothesized that the presence of P-LAP might counterattack the growth-inhibiting effect of the OT degrading it. If such a mechanism exists, then it is important to consider that OT-radiolabeled derivatives stable to P-LAP might serve as diagnostic or therapeutic agents for different cancer cells.

As for OT−ligand conjugates, there are scarce reports (*20*, *21*), and no OT libraries with different ligand position and nature have been reported specifically for HYNIC derivatives.

EXPERIMENTAL PROCEDURES

General Procedures. ^1H and ^{13}C nuclear magnetic resonance spectra were taken using a JEOL Eclipse 200 MHz spectrometer and referenced to a tetramethylsilane standard. Chemical shifts are reported as parts per million (δ), with splitting patterns designated as singlet (s), doublet (d), triplet (t), multiplet (m), or double of doublets (dd). Coupling constants are reported in hertz. Melting points were taken in a Fisher Johns melting point apparatus. HPLC peptide analysis and purification were performed on a HP1050 instrument equipped with a 1050 series diode array UV−vis detector, while quantitative analysis was carried out on a C18 Jupiter column 5 μm, 250 × 4.6 mm 300

Å, and purification was done on a C18 Jupiter column 10 μm, 250 × 10 mm 300 Å, both from Phenomenex. Products were eluted at a flow rate of 1 mL/min (4.8 mL/min for semipreparative HPLC) using a linear gradient [(100:0) to (0:100) in 35 min] of H_2O/TFA (0.1%) and acetonitrile/H_2O/TFA (90/10/0.1). MS-ESI analysis was performed in an Agilent 1100 series instrument LC-MSD trap. Peptides were lyophilized in a FreeZone 2.5 Labconco lyophilizer.

Microwave-assisted solid-phase peptide synthesis was carried out following Fmoc standard protocols. Microwave-assisted reactions were carried out in a Microwave Accelerated Reaction System, Mars X, version 047928, CEM corporation. Reaction conditions were as follows: swelling, 1 pulse of 120 s at 15 W; coupling, 4 pulses of 15 s at 100 W; capping, 3 pulses of 30 s at 75 W; deprotection, 3 pulses of 30 s at 75 W. To avoid racemization, cooling was applied after each pulse to keep reaction temperature below 60 °C. Peptides were synthesized on a 0.1 mmol scale using single-step couplings of 2 equiv Fmoc-amino acids, 2 equiv coupling agent and HOBt, and 6 equiv DIPEA in DMF and capping of free, unreacted amino groups with a 4.75 % v/v acetic anhydride solution in NMP. Coupling and capping completion was monitored with the ninhydrin test. Following linear peptide assembly, cleavage from the resin and final deprotection were carried out with TFA/thioanisole/1,2-ethanedithiol/anisole (9:0.5:0.3:0.2) at 25 °C for 2 h. The resin was filtered off and the filtrate dried with a gentle nitrogen flow, and peptides were precipitated with cold diethyl ether (−20 °C). Precipitate was filtered, washed with cold ether, and dried. Into the resulting residue, a 10 mM solution of 2,2′-bispyridyl disulfide in methanol was added. The resultant solution was stirred at room temperature, and peptide oxidation completion was monitored by HPLC. The solvent was removed, and the residue was redisolved in 10% acetic acid. Peptides were purified by reverse-phase HPLC, lyophilized, and characterized by MS-ESI.

2-(1*H*-Benzotriazole-1-yl)-1,1,3,3-tetramethyluronium hexafluorophosphate (HBTU), *N*-Hydroxybenzotriazole (HOBT), Fmoc-L-amino acids, and resins (Wang resin for −COOH peptides and Rink amide for $-CONH_2$ peptides) were obtained from Novabiochem (San Diego, CA). All other chemicals and solvents were purchased from commercial sources and were used without further purification.

Synthesis. Compounds **2**, **3**, **4**, **7**, **8**, **9**, and **10** were prepared following procedures reported in the literature, and the characterization data (^{1}H and ^{13}C NMR, MS-ESI, elemental analysis) were in agreement with the proposed structure and what is reported (*11*).

Nα-(Carbobenzyloxy)-Nϵ[6-*(tert-butoxycarbonylhydrazinpyridyn)-3-carboxyl]*-L-*Lysine Benzyl Ester (**5**).* 6-Boc-hydrazinpyridyn-3-carboxylic acid (248 mg, 0.98mmol), HBTU (371 mg, 0.98 mmol), and DIPEA (0.88 g, 6.8 mmol) were dissolved, followed by the addition of compound **4** (362 mg, 0.98 mmol). The resultant solution was stirred at room temperature for 1 day, and reaction completion was monitored by HPLC (Gemini polymeric column, 5 μm, 250 × 4.6 mm, Phenomenex, linear gradient from 85% DI−H_2O/15% MeCN to 10% DI−H_2O/90% MeCN in 20 min, at a flow of 1.0 mL/min and spectrophotometric detection at 254 and 275 nm). After reaction completion, the solvent was removed by rotary evaporation, and the product was purified by chromatography column in silica gel 60 (70−230 mesh), using ether as eluent. The fractions containing the product were collected, and the solvent was removed, yielding 0.53 g (90%) of colorless oil. R_f = 0.36 (SiO_2, ethyl acetate). ^{1}H NMR (200 MHz, $CDCl_3$, 25 °C, TMS) δ 8.4(s, 1H), 7.8 (d, J = 8.8 Hz, 1H), 7.3 (s, 10H), 7.1 (s, 1H), 6.8 (s, 1H), 6.5 (d, J = 8.8 Hz, 1H), 5.8 (s, 1H), 5.0 (m, 4H), 4.3 (m, 1H), 3.2 (m, 2H), 1.9−1.4 (m, 6H), 1.5 (s, 9H). ^{13}C NMR (50 MHz, $CDCl_3$, 25 °C, TMS) δ 171, 165, 160, 155, 154, 146, 136, 134, 127, 121, 104, 81, 66, 65, 52, 38, 30, 28, 27, 21. MS-ESI: *m*/*z* 605 (calcd. 605) $[M]^+$; Anal. ($C_{32}H_{39}N_5O_7$) C, H, N.

*Nϵ[6-(tert-butoxycarbonylhydrazinpyridyn)-3-carboxyl]-Nα-(fluorenilmethoxycarbonyl)-*L-*lysine (**6**).* Compound **5** (300 mg, 0.49 mmol) was dissolved in ethanol (15 mL), and 10% Pd/C catalyst (40 mg) was added. The reaction mixture was set in a Parr hydrogenation apparatus and was purged with H_2 (10×), and pressure was set to 40 psi for 2 days. At the end of the reaction, the solution was filtered to remove the catalyst, and the solvent was removed by rotary evaporation. The residue was vacuum-dried, yielding 180 mg (97%) of a white solid. R_f = 0.9 (SiO_2, MeOH) corresponding to the nonprotected amino acid derivative. mp = 220 °C. ^{1}H NMR (200 MHz, 25 °C, DMSO-d_6) δ 8.9 (s, 1H), 8.6 (s, 1H), 8.5 (d, J = 2.4 Hz, 1H), 7.9 (dd, J = 2.4 Hz, 8.8 Hz, 1H), 7.3 (s, 1H), 6.5 (d, J = 8.8 Hz, 1H), 3.5 (s, 2H), 3.2 (m, 2H), 1.8−1.2 (m, 6H), 1.4 (s, 9H). ^{13}C NMR (50 MHz, 25 °C, DMSO-d_6) δ 171, 166, 156, 148, 136, 121, 104, 80, 46, 44, 30, 28, 27, 23. MS-ESI: *m*/*z* 381 (calcd. 381) $[M]^+$, 404 (calcd. 404) $[M + Na]^+$; Anal. ($C_{17}H_{27}N_5O_5$) C, H, N.

The obtained intermediate (50 mg, 0.13 mmol) was dissolved in DMSO (2 mL) and was set under inert atmosphere and 0 °C in an ice bath. Fmoc-succinimide (40 mg, 0.13 mmol) in DMSO (2 mL) was slowly added under inert atmosphere. The reaction mixture was allowed to stand at RT overnight, and the reaction completion was monitored by HPLC and MS-ESI. Reaction conversion was quantitative, and therefore the reaction mixture can be used without purification for SPPS. The solvent was removed by rotary evaporation, and the product was purified by column chromatography in silica gel 60 (70−230 mesh) using as eluents $CHCl_3$, $CHCl_3$/MeOH (50/50), and $CHCl_3$/MeOH (15/85) successively. The fractions containing the product were collected, and the solvent was removed, yielding 77 mg (98%) of off-white solid. R_f = 0.74 (SiO_2, $CHCl_3$/MeOH 15/85). ^{1}H NMR (200 MHz, 25 °C, DMSO-d_6) δ 8.8 (s, 1H, -CH^6-, arom. pyridine), 8.6 (s, 1H, Boc-NH-N*H*-), 8.5 (d, J = 2.4 Hz, 1H, Boc-N*H*-NH-), 8.3 (s, 1H, -CH_2−N*H*CO-pyridine), 7.9 (d, J = 8.8 Hz, 1H, -CH^4-, arom. pyridine), 7.8 (m, 2H, arom. Fmoc), 7.7 (d, J = 7.2 Hz, 2H, arom. Fmoc), 7.5 (m, 2H, arom. Fmoc), 7.3 (m, 2H, arom. Fmoc), 6.5 (d, J = 8.8 Hz, 1H, -CH^3-, arom. pyridine), 4.3−4.2 (m, 3H, -C*H*-CH_2-OCO-, Fmoc), 3.9 (m, 1H, -C*H*-COOH), 3.2 (m, 2H, -CH_2-NHCO-pyridine), 1.8−1.5 (m, 4H, -$(CH_2)_2$-), 1.4 (s, 11H, -$C(CH_3)_3$, -CH_2-). ^{13}C NMR (50 MHz, 25 °C, DMSO-d_6) δ 173 (-COOH), 165 (-NHCO-pyridine), 156 (-NHCOO-Fmoc and Boc), 148 (-C^{6}H-, arom. pyridine), 143 (arom. Fmoc), 141 (arom. Fmoc), 139 (-C^{4}H-, arom. pyridine), 129 (arom. Fmoc), 128 (arom. Fmoc), 127 (arom. Fmoc), 124 (-C^{5}H-, arom. pyridine), 110 (-C^{3}H-, arom. pyridine), 79 (-*C*$(CH_3)_3$), 66 (-CH_2-, Fmoc), 54 (-*C*H-COOH), 47 (-CH-, Fmoc), 31 (-CH_2-), 28 (-CH_2-), 25 (-C(*C*$H_3)_3$), 22 (-CH_2-). MS-ESI: *m*/*z* 627 (calcd. 627) $[M + Na]^+$; Anal. ($C_{32}H_{37}N_5O_7$) C, H, N.

*Nα-(carbobenzyloxy)-Nϵ[6-(tert-butoxycarbonylhydrazinpyridyn)-3-carboxyl]-*L-*Phenylalanine Benzyl Ester (**11**).* 6-Boc-hydrazinpyridyn-3-carboxylic acid (0.177 g, 0.7 mmol), HBTU (0.7 mmol, 0.266 g), and DIPEA (0.636 g, 4.9 mmol) were dissolved in acetonitrile (3 mL), followed by compound **10** (0.28 g, 0.7 mmol). The resultant mixture was irradiated by MW 100 W for 20 min. Solvent was removed by rotary evaporation, and the product was purified by chromatography in silica using ethyl ether as eluent. Fractions containing the product were collected, the solvent was removed by rotary evaporation, and the residue was dried under reduced pressure, yielding 0.35 g (80%) of a yellow oil. R_f = 0.66 (SiO_2, Et_2O). ^{1}H NMR (200 MHz, $CDCl_3$, 25 °C, TMS) δ 8.6 (s, 1H), 7.9 (d, J = 8.8 Hz, 1H), 7.5 (d, J = 7.8 Hz, 2H), 7.2 (s, 10H), 6.9 (d, J = 7.8 Hz, 2H), 6.6 (d, J

= 8.8 Hz, 1H), 5.2 (m, 4H), 4.6 (m, 1H), 3.0 (s, 2H), 1.5 (s, 9H). ^{13}C NMR (50 MHz, $CDCl_3$, 25 °C, TMS) δ 170, 164, 160, 155, 154, 146, 135, 133, 130, 128, 127, 121, 120, 104, 81, 66, 65, 54, 36, 28. MS-ESI: *m/z* 639 (calcd.) 639 $[M]^+$; Anal. ($C_{35}H_{37}N_5O_7$) C, H, N.

Nα-(fluorenylmethoxycarbonyl)-Nϵ[6-*(tert-butoxycarbonylhydrazinpyridyn)-3-carboxyl]*-L-*Phenylalanine* (**12**). Compound **11** (0.2 g, 0.31 mmol) was dissolved in ethanol (15 mL), and 10% Pd/C catalyst was added (20 mg). The reaction mixture was set in a Parr hydrogenation apparatus and purged with H_2 (10×), and the pressure was set to 40 psi for 2 days. At the end of the reaction, the solution was filtered to remove the catalyst, and the solvent was removed by rotary evaporation. The residue was vacuum-dried, yielding 125 mg (98%) of a yellow solid. R_f = 0.9 (SiO_2, MeOH), corresponding to the nonprotected amino acid derivative. mp = 250 °C. ^{1}H NMR (200 MHz, 25 °C, DMSO-d_6) δ 11.0 (s, 1H), 8.9 (s, 1H), 8.8 (s, 1H), 8.7 (d, J = 2.4 Hz, 1H), 8.2 (dd, J = 2.4 Hz, 8.8 Hz, 1H), 7.7 (d, J = 8.6 Hz, 2H), 7.6 (s, 1H), 7.2 (d, J = 8.6 Hz, 2H), 6.5 (d, J = 8.8 Hz, 1H), 3.9 (m, 1H), 3.1 (m, 2H), 2.1 (s, 2H), 1.4 (s, 9H). ^{13}C NMR (50 MHz, 25 °C, DMSO-d_6) δ 170, 164, 161, 156, 148, 139, 138, 130, 129, 128, 120, 105, 79, 54, 28. MS-ESI: *m/z* 415 (calcd. 415) $[M]^+$; Anal. ($C_{20}H_{25}N_5O_5$) C, H, N.

The obtained intermediate (50 mg, 0.13 mmol) was dissolved in DMSO (2 mL) and was set under inert atmosphere and 0 °C in an ice bath. Fmoc-succinimide (40 mg, 0.13 mmol) in DMSO (2 mL) was slowly added under inert atmosphere. The reaction mixture was allowed to stand at RT overnight, and reaction completion was monitored by HPLC and MS-ESI. Reaction conversion was quantitative, and therefore the reaction mixture can be used without purification for SPPS. The solvent was removed by rotary evaporation, and the product was purified by column chromatography in silica gel 60 (70−230 mesh) using as eluents $CHCl_3$, $CHCl_3$/MeOH (50/50), and $CHCl_3$/MeOH (15/85) successively. The fractions containing the product were collected, and the solvent was removed, yielding 74 mg (97%) of light yellow solid. R_f = 0.58 (SiO_2, $CHCl_3$/MeOH 15/85). ^{1}H NMR (200 MHz, 25 °C, DMSO-d_6) δ 9.0 (s, 1H, -CH^6-, arom. pyridine), 8.8 (s, 1H, Boc-NH-N*H*-), 8.7 (d, J = 2.4 Hz, 1H, Boc-N*H*-NH-), 8.0 (d, J = 8.6 Hz, 1H, -CH^4-, arom. pyridine), 7.8 (m, 2H, arom. Fmoc), 7.7−7.6 (m, 4H, arom. Fmoc), 7.5 (m, 2H, arom. Fmoc), -CH-, arom.), 7.3 (m, 2H, arom. Fmoc), 7.2 (d, J = 8.0 Hz, 2H), 6.5 (d, J = 8.6 Hz, 1H, -CH^3-, arom. pyridine), 4.3−4.0 (m, 4H, -C*H*-COOH, -C*H*-C*H*$_2$-OCO-, Fmoc), 3.0 (m, 2H, -C*H*$_2$-CH-COOH), 1.4 (s, 9H, -C(CH$_3$)$_3$). ^{13}C NMR (50 MHz, 25 °C, DMSO-d_6) δ 174 (-COOH), 165 (-NHCO-pyridine), 156 (-NHCOO-Fmoc and Boc), 145 (-C^{6}H-, arom. pyridine), 143 (arom. Fmoc), 141 (arom. Fmoc), 139 (-C^{4}H- arom. pyridine), 136 (-CH- arom.), 131 (-CH- arom.), 129 (arom. Fmoc), 128 (arom. Fmoc and arom.), 127 (arom. Fmoc), 125 (-C^{5}H- arom. pyridine), 120 (arom.), 110 (-C^{3}H- arom. pyridine), 80 (-*C*(CH$_3$)$_3$), 49 (-CH-, Fmoc), 37(-CH$_2$-), 26 (-C(*C*H$_3$)$_3$). MS-ESI: *m/z* 638 (calcd. 638) $[M + H]^+$; Anal. ($C_{35}H_{35}N_5O_7$) C, H, N.

Peptide Characterization. NH_2-**C**YIQN**C**PLG-$CONH_2$, MS-ESI: *m/z* 1007 (calcd. 1007) $[M + H]^+$.

NH_2-**C**YIQN**C**PLG-COOH, MS-ESI: *m/z* 1008 (calcd. 1006) $[M + H]^+$.

HYNIC-NH-**C**YIQN**C**PLG-$CONH_2$, MS-ESI: *m/z* 1142 (calcd. 1142) $[M + H]^+$.

HYNIC-NH-**C**YIQN**C**PLG-COOH, MS-ESI: *m/z* 1143 (calcd. 1141) $[M + H]^+$.

NH_2-**C**YIQN**C**P(K-HYNIC)G-$CONH_2$, MS-ESI: *m/z* 1157 (calcd. 1157) $[M + H]^+$.

NH_2-**C**YIQN**C**P(K-HYNIC)G-COOH, MS-ESI: *m/z* 1158 (calcd. 1156) $[M + H]^+$.

NH_2-**C**YIQN**C**P(F-HYNIC)G-$CONH_2$, MS-ESI: *m/z* 1191 (calcd. 1192) $[M + H]^+$.

NH_2-**C**YIQN**C**P(F-HYNIC)G-COOH, MS-ESI: *m/z* 1192 (calcd. 1190) $[M + H]^+$.

Peptide Conjugates Technetium-99m Labeling. Radiolabeling was carried out in a glass vial by adding 10 μL (10 μg) of each HYNIC−OT derivative, 0.5 mL of tricine/ethylendiaminediacetic acid (EDDA) solution (40 mg of tricine plus 20 mg of EDDA in 1 mL of 0.2 M phosphate buffer), 25 μL of $SnCl_2$ solution (1 mg/mL of stannous chloride in 10 mM HCl), and 740−1110 MBq (0.5 mL) of ^{99m}Tc-pertechnetate (^{99}Mo/^{99m}Tc generator system, GETEC-Mexico), followed by incubation at 90 °C for 30 min in a dry block heater.

Evaluation of Radiochemical Purity. Radiochemical purity analyses were performed by instant thin-layer chromatography on silica gel (ITLC-SG, Gelman Sciences), solid-phase extraction (Sep-Pak C-18 cartridges), and reverse-phase high-performance liquid chromatography (HPLC).

ITLC-SG analysis was accomplished using three different mobile phases: 2-butanone to determine the amount of free $^{99m}TcO_4^-$ (R_f = 1), 0.1 M sodium citrate pH 5 to determine ^{99m}Tc-coligand and $^{99m}TcO_4^-$ (R_f = 1), and methanol/1 M ammonium acetate (1:1 v/v) for ^{99m}Tc-colloid (R_f = 0). R_f values of the radiolabeled peptide in each system were 0.0, 0.0, and 0.7−1.0, respectively.

The Sep-Pak cartridges were preconditioned with 5 mL of ethanol, followed by 5 mL of 1 mM HCl and 5 mL of air. An aliquot of 0.1 mL of the labeled peptide was loaded on the preconditioned Sep-Pak cartridge, followed by 5 mL of 1 mM HCl to elute free $^{99m}TcO_4^-$. The radiolabeled peptide was eluted with 3 mL of ethanol/saline (1:1), and the hydrolyzed−reduced ^{99m}Tc or ^{99m}Tc-colloid remained in the cartridge.

HPLC analyses were carried out with a Waters instrument running Millenium software with both radioactivity and UV-photodiode array in-line detectors, and YMC ODS-AQ S5 column (5 μm, 4.6 × 250 mm) at a flow rate of 1 mL/min using the gradient system described above. In this system, retention times for free $^{99m}TcO_4^-$, ^{99m}Tc-coligand, and ^{99m}Tc-EDDA/HYNIC-OT were 3 min, 3.5−4.5 min, and 12 min, respectively.

Plasma Stability. A volume of 10 μL of the labeled peptide solution (0.8 μg/10 μL) was incubated at 37 °C with 1 mL of fresh normal female human plasma, and also with 1 mL of phosphate buffer as a control. Radiochemical stability was determined by taking samples of 50 μL at different times from 30 min to 24 h for analysis. The plasma protein in 50 μL of the sample was precipitated with acetonitrile and centrifuged at 1000 *g* for 5 min; the supernatant was removed, diluted 1:7 with saline solution, and analyzed by reverse-phase HPLC.

Competition Assay. In order to evaluate the biological integrity of the labeled peptides, a radioimmunoassay (RIA) was carried out comparing the competition of the labeled peptides and the unlabeled peptide binding to a limited quantity of specific antibody (Oxytocin radioimmunoassay kit, Peninsula Laboratories Inc., Bachem). ^{125}I-OT was used as the "gold" standard (IC_{50} = 0.05 nM), and the unlabeled peptide (oxytocin) was used in the range 1−128 pg/100 μL (0.01−1.28 nM). ^{99m}Tc-EDDA/HYNIC-Lys^8-OT-$CONH_2$ and ^{99m}Tc-EDDA/HYNIC-Cys^1-OT-$CONH_2$ (both obtained with radiochemical purities higher than 96%) were purified by reverse-phase HPLC in order to eliminate the cold peptide and to obtain a radioligand concentration less than 1 pg/100 μL useful for the competition assay.

A plot of % B (binding)/Bo (total binding less nonspecific binding) versus the log of the unlabeled OT concentrations was generated for each labeled peptide: ^{125}I-OT, ^{99m}Tc-EDDA/HYNIC-Lys^8-OT-$CONH_2$, and ^{99m}Tc-EDDA/HYNIC-Cys^1-OT-

$CONH_2$. The IC_{50} was calculated as the concentration of competitor (unlabeled OT) inhibiting 50% of the radioligand binding.

Cell Lines. Human breast carcinoma cell MCF7 line was originally obtained from ATCC (USA). The cells were routinely grown at 37 °C, with 5% CO_2 atmosphere and 100% humidity in RPMI medium supplemented with 10% newborn calf serum and antibiotics (100 μg/mL streptomycin).

Internalization Assay and Nonspecific Binding. MCF7 cells (1×10^6) supplied with fresh medium were incubated in 6-well plates with about 200 000 cpm of ^{99m}Tc-EDDA/HYNIC-Lys^8-OT-$CONH_2$ or ^{99m}Tc-EDDA/HYNIC-Cys^1-OT-$CONH_2$ (0.2 nmol total peptide) for 2 h at 4 °C. Afterward, the preincubation cells were washed three times with ice-cold culture medium. Warmed culture medium was added to the plates, which were incubated in triplicate at 37 °C for 2, 4, 6, and 24 h in order to allow internalization. Cell-surface bound radioligand was removed in two steps of 5 min acid wash (50 mM glycine−HCl/100 mM NaCl, pH 2.8) at room temperature. Cells were solubilized by incubation with 1 N NaOH at 37 °C to determine internalized radioligand. Results were expressed as the percentage of total activity internalized. The nonspecific binding was determined in parallel but in the presence of 10 μM cold OT (Bachem-USA) to block OT receptor cells. Differences in the obtained cell binding data were evaluated with the Student *t* test.

Imaging. Tumor uptake studies in mice were carried out according to the rules and regulations of the Official Mexican Norm 062-ZOO-1999.

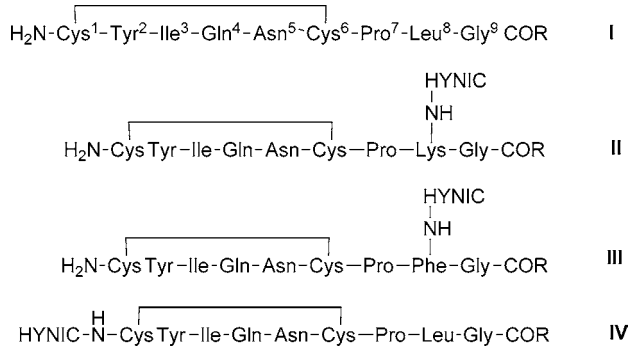
Athymic male mice (20−22 g) were kept in sterile cages with sterile wood-shavings bed; constant temperature, humidity, and noise; and 12:12 light periods. Water and feed (standard PMI 5001 feed) were given ad libitum. Tumors were induced by subcutaneous injection of MCF7 cells (1×10^6) resuspended in 0.2 mL of phosphate-buffered saline, into the backside of 6−7 week old nude mice. The sites of injection were observed at regular intervals for the appearance of tumor formation and progression.

Athymic mice with induced tumors were used for imaging studies. ^{99m}Tc-EDDA/HYNIC-Cys^1-OT-$CONH_2$ or ^{99m}Tc-EDDA/HYNIC-Lys^8-OT-$CONH_2$ (~1.11 MBq) in 0.04 mL was injected in the tail vein. The nude mice ($n = 4$) with the implanted tumors were scanned with a gamma camera with a pinhole collimator 2 h after the radiopharmaceutical was injected in the tail vein.

RESULTS

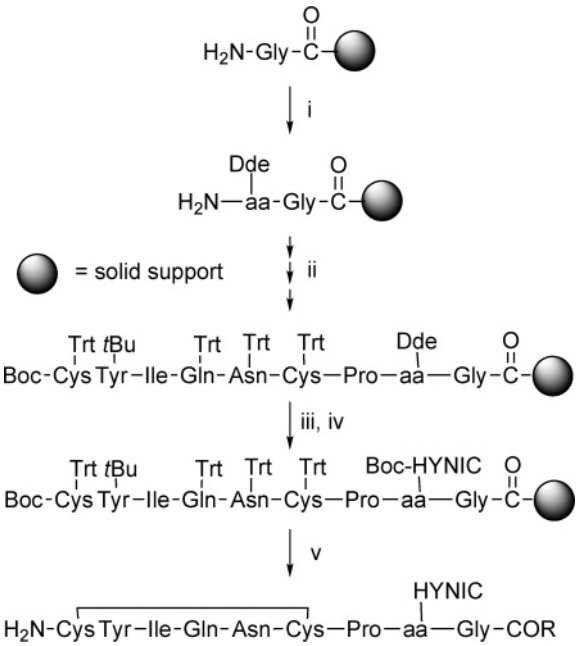
An orthogonal protection strategy was followed to prepare HYNIC-Lys and HYNIC-Phe as shown in Schemes 1 and 2. Thus, intermediates **4** and **10** were obtained in excellent yields. The later derivatives have the α-amino and carboxylic acid groups protected with Cbz and Bn, respectively. Intermediates **4** and **10** were reacted with Boc-HYNIC (Figure 1b) using HBTU as activating agent, to generate intermediates **5** and **11**. While this stage was smooth for the lysine derivative, ligand conjugation with **10** was not completed even after several days of reaction. In a first attempt to drive to completion the ligand coupling step with **10**, a succinimide active ester of Boc-HYNIC was used, giving similar results to those obtained with HBTU. Further attempts varying reaction conditions were also unsuccessful. As an alternative, microwave-assisted coupling was carried out, and thus, product **11** was obtained in high yield after 20 min irradiation at 100 W. The next steps for both amino acids proceeded without further complications, obtaining compounds **6** and **12** in good overall yields (76% and 61%, respectively) and enantiopurity.

Scheme 3 [a]



[a] (**I**) Oxytocin, (**II**) HYNIC-Lys^8-oxytocin, (**III**) HYNIC-Phe^8-oxytocin, and (**IV**) HYNIC-Cys^1-oxytocin. R = −OH or $-NH_2$.

Scheme 4. Synthesis of Oxytocin-HYNIC Peptides by SPPS Following an Orthogonal Protection Approach[a]



[a] (i) Dde-Lys or Dde-Phe (aa) coupling followed by Fmoc removal; (ii) succesive amino acid coupling; (iii) Dde removal with 2% hydrazine; (iv) Boc-HYNIC coupling; (v) protecting groups and peptide removal from solid support, cysteine oxidation, purification, and characterization.

The nanopeptide neurohypophysial hormone oxytocin (Scheme 3, **I**, R = $-NH_2$) was chosen as a model to demonstrate the utility of usage of derivatives **6** and **12** for the controlled HYNIC positioning of peptides during SPPS and henceforth for generating HYNIC−peptide libraries to screen specific activity.

The linear part of OT was chosen as one of the targets to place HYNIC within the peptide based on previous knowledge. For this work, the Leu^8 residue was selected as the point to be substituted by the HYNIC-Lys (Phe) residues (Scheme 3, **II** and **III**). Additionally, for comparison, the synthesis of **II** and **III** was also carried out following an orthogonal protection approach (Scheme 4) using a *N*-2-(4,4-dimethyl-2,6-dioxocyclohexylidene)ethylamine (Dde)-protected lysine derivative (Figure 2a) commercially available or a *p*-aminophenylalanine derivative protected with Dde in the *p*-amino group recently prepared by our group (unpublished results) (Figure 2b). A HYNIC-α-amide-Cys^1 derivative was also synthesized despite the fact that the ligand stays inside the cyclic part of the peptide (Scheme 3, **IV**). In all cases, peptides were prepared with both carboxylic and amide groups by using different solid supports. Synthesis of these derivatives and the OT native peptide was

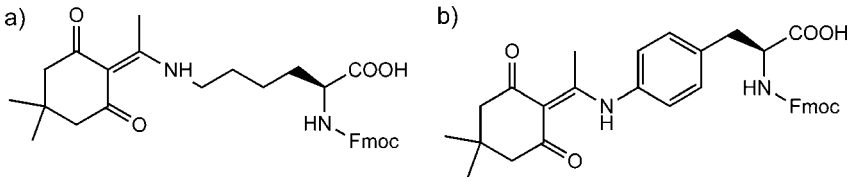


Figure 2. (a) Nϵ-Dde-Nα-Fmoc-lysine and (b) pN-Dde-Nα-Fmoc-phenylalanine.

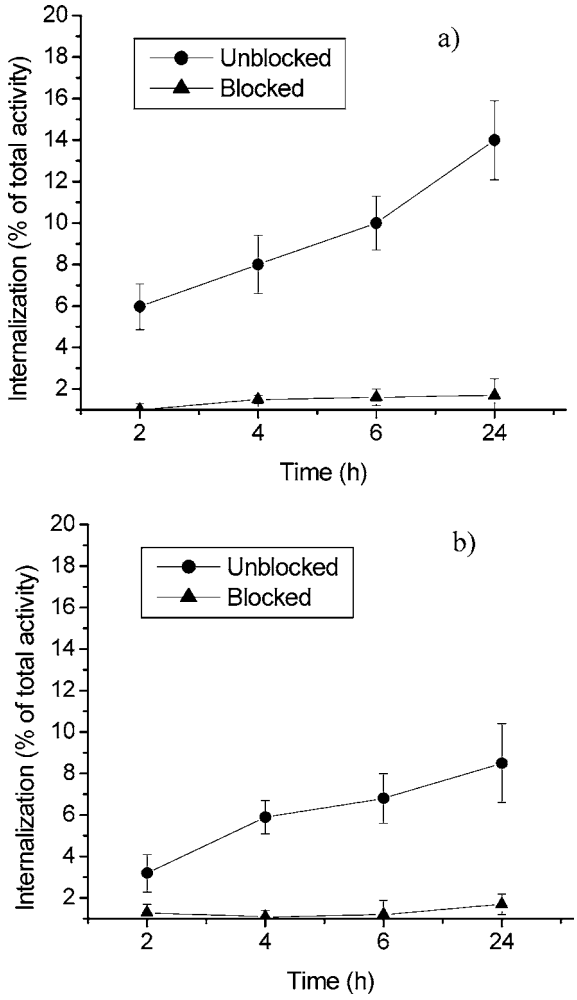


Figure 3. Time-dependent internalization of (a) ^{99m}Tc-EDDA/HYNIC-Lys^8-OT-CONH$_2$ and (b) ^{99m}Tc-EDDA/HYNIC-Cys^1-OT-CONH$_2$ in unblocked and blocked MCF7 cells expressed as % of total activity (mean ± sd, $n = 3$). Blocked cells were incubated with an additional receptor blocking dose of unlabeled OT in order to determine the nonspecific binding of radioactivity.

carried out using commercially available reagents following standard Fmoc SPPS protocols, and step reactions were assisted by microwave radiation in order to minimize reaction times and to demonstrate the suitability of using this procedure for the quick generation of peptide-ligand libraries. The microwave-assisted synthesis of the full peptides was accomplished very rapidly (ca. 40 min per peptide, not considering purification), which compared to classical SPPS protocols (ca. 30 h, not considering purification) is very attractive for generating peptide conjugate libraries. Following cleavage from the resin and total deprotection, cysteine oxidation for the crude peptides was obtained quantitatively in 5 min using 2,2′-bispyridyl disulfide. Crude cyclic peptides were purified by semipreparative HPLC yielding peptides **I**−**IV**. The global yield for peptides **II** and **III** prepared via the HYNIC prelabeled amino acids **6** and **12** was approximately 20% in both cases and 40% when the same peptides were prepared by an orthogonal protection approach, all carried out under the same nonoptimized reaction conditions

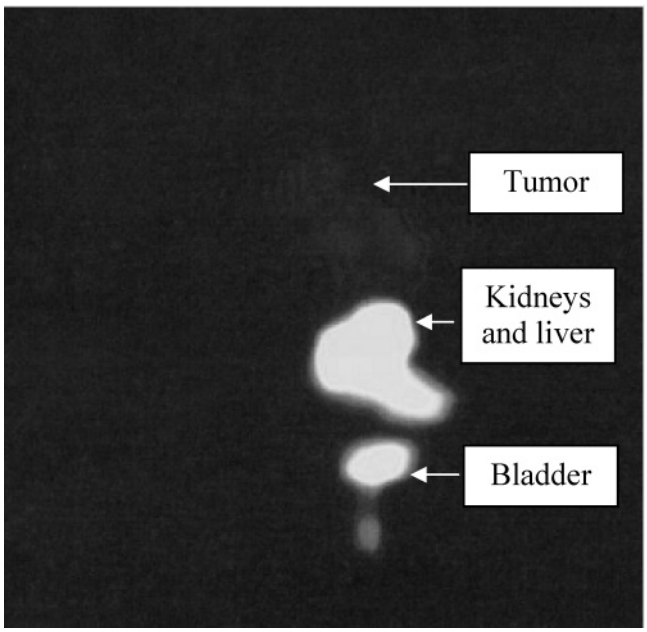


Figure 4. Uptake of ^{99m}Tc-EDDA/HYNIC-Lys^8-OT-CONH$_2$ in tumor MCF7 cells in athymic mouse (whole mouse).

(reaction time, reactant equivalents, temperature, etc.). On the other hand, yields were not dependent on the type of resin used for the synthesis. Furthermore, higher global yields can be obtained when reaction conditions are independently optimized for each peptide for a given procedure.

Peptide labeling efficiencies of these peptides with ^{99m}Tc and EDDA were tested, and the results showed low labeling yields for **I** and **III** (10% and 40%, respectively), while for **II** and **IV**, yields above 96% were obtained. In addition, a 40% ^{99m}Tc-EDDA labeling efficiency for a Boc,Fmoc-deprotected HYNIC-Phe derivative of **12** was observed. Biological integrity of the labeled OT peptides ^{99m}Tc-EDDA/HYNIC-Cys^1-OT-CONH$_2$ and ^{99m}Tc-EDDA/HYNIC-Lys^8-OT-CONH$_2$ was determined by a radioimmunocompetition binding assay. Thus, it was found that a ^{125}I-OT peptide has an IC_{50} value of 0.05 nM, while peptides ^{99m}Tc-EDDA/HYNIC-Cys^1-OT-CONH$_2$ and ^{99m}Tc-EDDA/HYNIC-Lys^8-OT-CONH$_2$ have IC_{50} values of 0.2 and 1 nM, respectively. Therefore, IC_{50} values less than 10 nM indicate that both peptides maintain an important biological recognition. After 24 h in human plasma, the radiochemical purity of ^{99m}Tc-EDDA/HYNIC-Cys^1-OT-CONH$_2$ remained higher than 90%, while the radiochemical purity of ^{99m}Tc-EDDA/HYNIC-Lys^8-OT-CONH$_2$ decreased to 15%.

Results of the in vitro assays showed a rapid internalization and a specific receptor binding of ^{99m}Tc-EDDA/HYNIC-Lys^8-OT-CONH$_2$ and ^{99m}Tc-EDDA/HYNIC-Cys^1-OT-CONH$_2$ to MCF7 cells, since there were significant differences in the percentage of uptake between blocked receptor and unblocked receptor cells at different times ($p < 0.05$) (Figure 3). In vivo images of ^{99m}Tc-EDDA/HYNIC-Lys^8-OT-CONH$_2$ and ^{99m}Tc-EDDA/HYNIC-Cys^1-OT-CONH$_2$ showed that the highest non-specific uptake was found in the kidneys and in lower amounts in the liver (Figures 4 and 5). However a clear tumor uptake

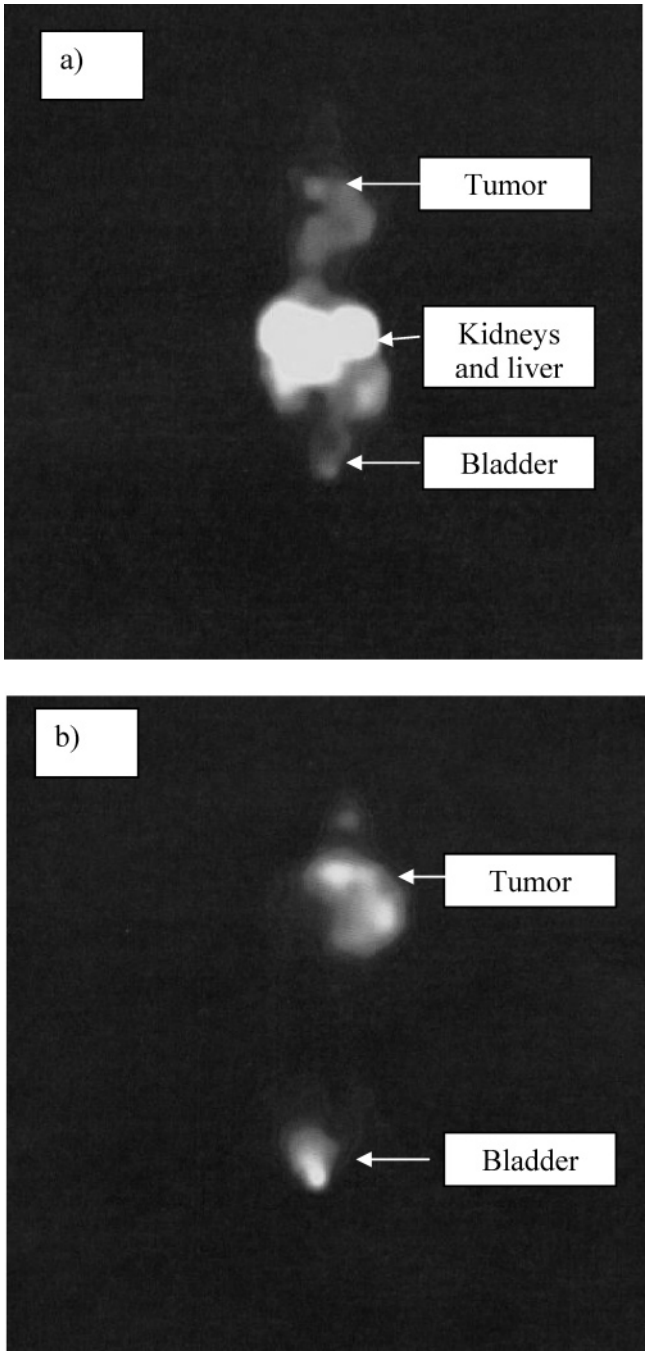


Figure 5. Uptake of ^{99m}Tc-EDDA/HYNIC-Cys^1-OT-CONH$_2$ in tumor MCF7 cells in athymic mouse: (a) whole mouse; (b) mouse with dissection of internal viscera to highlight tumor uptake.

was only observed for ^{99m}Tc-EDDA/HYNIC-Cys^1-OT-CONH$_2$ (Figure 5).

DISCUSSION

In this work, unlike the report indicated above for the synthesis of the lysine derivative **6** (*12*), blocking the carboxylic acid group was done to minimize side reactions such as mixed ligand−amino acid anhydride formation, and thus, **6** was prepared in a good overall yield. Moreover, as for the phenylalanine derivative, the observed lack of reactivity of **10** can be explained by the weaker nucleophilicity of the *p*-amino group in Phe when compared to the ϵ-amino aliphatic group of the lysine derivative. Furthermore, the MW-assisted ligand coupling with **10** gives an alternative for the future efficient synthesis of Phe−ligand peptide libraries when either an orthogonal protection or a prelabeled amino acid approach is followed.

The lower peptide yields obtained for the prelabeled amino acid approach when compared to the orthogonal protection procedure can be attributed to an increase in peptide aggregation in the resin, given the higher probability of hydrogen bonding formation due to the HYNIC unit being readily attached to the solid support.

The HYNIC−OT radiolabeling results show that ^{99m}Tc is complexed to the peptide through HYNIC and also that labeling efficiency depends on the nature of the amino acid where HYNIC is attached. The poor ^{99m}Tc labeling efficiency for **III** can be attributed to a lower electron-donation ability of the hydrazine group of HYNIC toward the metal, provoked by the conjugation of the ligand to the *p*-amino aromatic amino acid and not by the conjugate−peptide structure.

As previously mentioned, it has been shown that OT receptors have weak selectivity to peptides sharing the same cyclic part (from Cys^1 to Cys^6). This indicates that the cyclic part of OT is more important in conferring binding affinity for the OT receptor compared with the linear tripeptidic part of the hormone (from Pro^7 to Gly^9) (*13*). However, our results showed that peptide−ligand conjugation in the tripeptide part diminishes binding affinity to a higher extent than when the peptide is labeled in the Cys^1 residue. This is opposite to what has been hypothesized previously on the basis of what is known of the nonconjugated peptide (*18*, *19*).

^{99m}Tc-EDDA/HYNIC-Lys^8-OT-CONH$_2$ degradation in plasma and its poor in vivo tumor uptake might be caused by the effect of the oxytocinase enzyme, which acts on the N-terminal Cys^1 residue (*16*). Furthermore, the plasma stability and in vivo tumor uptake of ^{99m}Tc-EDDA/HYNIC-Cys^1-OT-CONH$_2$ could support the hypothesis that the introduction of HYNIC-Cys^1 produces a protective steric effect on the amide bond susceptible to hydrolysis by P-LAP, which acts on the N-terminal Cys^1 residue.

These results justify further in vitro and in vivo evaluations of ^{99m}Tc-EDDA/HYNIC-Cys^1-OT-CONH$_2$ as a potential radiopharmaceutical for diagnosis of OT receptor overexpressing tumors and might be useful for further understanding of the OT cancer regulation mechanisms, particularly where OT has shown to have an inhibitory growth effect.

Finally, we can conclude that, when designing peptide-based ligand conjugates for diagnostic or therapeutic applications and determining the best ligand position, the use of conventional wisdom (such as known structure−activity relationships for the nonconjugated peptide) as prescribed by numerous studies may be a time-saving, and on occasion convenient, approach. However, as this work has demonstrated, challenging conventional wisdom—while time-consuming and seemingly foolhardy—can also lead to exciting possibilities. This research has provided and demonstrated the utility of different chemical tools to generate ligand−peptide libraries when searching for that metal−peptide conjugate that can have the desired characteristics.

ACKNOWLEDGMENT

This work was supported by CONCYTEG Mexico grants no. GTO-2002-C01-6029 and GTO-2003-C02-11517.

APPENDIX. ELEMENTAL ANALYSES

Compound **5**: Anal. ($C_{32}H_{39}N_5O_7$) C, H, N calcd. 63.46, 6.49, 11.56; found 63.53, 6.51, 11.60.

Intermediate before compound **6**: Anal. ($C_{17}H_{27}N_5O_5$) C, H, N calcd. 53.53, 7.13, 18.36; found 53.61, 7.10, 18.39.

Compound **6**: Anal. ($C_{32}H_{37}N_5O_7$) C, H, N calcd. 63.67, 6.18, 11.60; found 63.79, 6.20, 11.58.

Compound **11**: Anal. ($C_{35}H_{37}N_5O_7$) C, H, N calcd. 65.71, 5.83, 10.95; found 65.43, 5.84, 10.96. MS-ESI: *m*/*z* 639, (calcd.) 639 $[M]^+$.

Intermediate before compound **12**: Anal. ($C_{20}H_{25}N_5O_5$) C, H, N calcd. 57.82, 6.07, 16.86; found 57.88, 6.05, 16.84.

Compound **12**: Anal. ($C_{35}H_{35}N_5O_7$) C, H, N calcd. 65.92, 5.53, 10.98; found 65.69, 5.50, 10.95.

LITERATURE CITED

(1) Griffiths, G. L., Goldenberg, D. M., Jones, A. L., and Hansen, H. J. (1992) Radiolabeling of monoclonal antibodies and fragments with technetium and rhenium. *Bioconjugate Chem. 3*, 91−99.

(2) Smith, G. P. (1985) Filamentous fusion phage: novel expression vectors that display cloned antigens on the virion surface. *Science 228*, 1315−1317.

(3) Chilton, H. M., and Witcofski, R. L. (1990) *Pharmaceuticals in Medical Imaging*. Macmillan Publishing Co., New York.

(4) Jurisson, S., Berning, D., Jia, W., and Ma, D. (1993) Coordination Compounds in Nuclear Medicine. *Chem. Rev. 93*, 1137−1156.

(5) Liu, S., and Edwards, D. S. (1999) ^{99m}Tc-Labeled Small Peptides as Diagnostic Radiopharmaceuticals. *Chem. Rev. 99*, 2235−2268.

(6) Abrams, M. J., Juweid, M., tenKate, C. I., Schwartz, D. A., Hauser, M. M., Gaul, F. E., Fuccello, A. J., Rubin, R. H., Strauss, H. W., and Fischman, A. J. (1990) Technetium-99m-human polyclonal IgG radiolabeled via the hydrazino nicotinamide derivative for imaging focal sites of infection in rats. *J. Nucl. Med. 31*, 2022−2028.

(7) Decristoforo, C., and Mather, S. J. (1999) 99m-Technetium-labelled peptide-HYNIC conjugates: effects of lipophilicity and stability on biodistribution. *Nucl. Med. Biol. 26*, 389−396.

(8) Dangles, O., Guibe, F., Balavoine, G., Lavielle, S., and Marquet, A. (1987) Selective cleavage of the allyl and (allyloxy)carbonyl groups through palladium-catalyzed hydrostannolysis with tributyltin hydride. Application to the selective protection-deprotection of amino acid derivatives and in peptide synthesis. *J. Org. Chem. 52*, 4984−4993.

(9) Bycroft, B. W., Chan, W. C., Chharbra, S. R., and Hone, N. D. (1993) A novel lysine-protecting procedure for continuous flow solid phase synthesis of branched peptides. *J. Chem. Soc.: Chem. Commun. 9*, 778−779.

(10) Bhorade, R., Weissleder, R., Nakakoshi, T., Moore, A., and Tung, C. H. (2000) Macrocyclic chelators with paramagnetic cations are internalized into mammalian cells via a HIV-Tat derived membrane translocation peptide. *Bioconjugate Chem. 11*, 301−305.

(11) De Leon-Rodriguez, L. M., Kovacs, Z., Dieckmann, G. R., and Sherry, A. D. (2004) Solid-phase synthesis of DOTA-peptides. *Chem.—Eur. J. 10*, 1149−1155.

(12) Greenland, W. E., Howland, K., Hardy, J., Fogelman, I., and Blower, P. J. (2003) Solid-phase synthesis of peptide radiopharmaceuticals using Fmoc-N-epsilon-(hynic-Boc)-lysine, a technetium-binding amino acid: application to Tc-99m-labeled salmon calcitonin. *J. Med. Chem. 46*, 1751−1757.

(13) Gimpl, G., and Fahrenholz, F. (2001) The oxytocin receptor system: structure, function, and regulation. *Physiol. Rev. 81*, 629−683.

(14) Hruby, V. J., Chow, M. S., and Smith, D. D. (1990) Conformational and structural considerations in oxytocin-receptor binding and biological activity. *Annu. Rev. Pharmacol. Toxicol. 30*, 501−534.

(15) Wood, S. P., Tickle, I. J., Treharne, A. M., Pitts, J. E., Mascarenhas, Y., Li, J. Y., Husain, J., Cooper, S., Blundell, T. L., Hruby, V. J., et al. (1986) Crystal structure analysis of deamino-oxytocin: conformational flexibility and receptor binding. *Science 232*, 633−636.

(16) Luciani, N., Marie-Claire, C., Ruffet, E., Beaumont, A., Roques, B. P., and Fournie-Zaluski, M. C. (1998) Characterization of Glu350 as a critical residue involved in the N-terminal amine binding site of aminopeptidase N (EC 3.4.11.2): insights into its mechanism of action. *Biochemistry 37*, 686−692.

(17) Zingg, H. H., and Laporte, S. A. (2003) The oxytocin receptor. *Trends Endocrinol. Metab. 14*, 222−227.

(18) Morita, T., Shibata, K., Kikkawa, F., Kajiyama, H., Ino, K., and Mizutani, S. (2004) Oxytocin inhibits the progression of human ovarian carcinoma cells in vitro and in vivo. *Int. J. Cancer 109*, 525−532.

(19) Cassoni, P., Sapino, A., Marrocco, T., Chini, B., and Bussolati, G. (2004) Oxytocin and oxytocin receptors in cancer cells and proliferation. *J. Neuroendocrinol. 16*, 362−364.

(20) Bussolati, G., Chinol, M., Chini, B., Nacca, A., Cassoni, P., and Paganelli, G. (2001) 111In-labeled 1,4,7,10-tetraazacyclododecane-N,N′,N″,N‴-tetraacetic acid-Lys8-vasotocin: a new powerful radioligand for oxytocin receptor-expressing tumors. *Cancer Res. 61*, 4393−4397.

(21) Chini, B., Chinol, M., Cassoni, P., Papi, S., Reversi, A., Areces, L., Marrocco, T., Paganelli, G., Manning, M., and Bussolati, G. (2003) Improved radiotracing of oxytocin receptor-expressing tumors using the new [111In]-DOTA-Lys8-deamino-vasotocin analogue. *Br. J. Cancer 89*, 930−936.

BC070047A

Self-Organized Nanogels Responding to Tumor Extracellular pH: pH-Dependent Drug Release and *in Vitro* Cytotoxicity against MCF-7 Cells

Kun Na,[†] Eun Seong Lee,[‡] and You Han Bae*[,‡]

Division of Biotechnology, The Catholic University of Korea, 43-1 Yeokgok 2-dong, Wonmi-gu, Bucheon-si, Gyeonggi-do 420-743, Korea, and Department of Pharmaceutics and Pharmaceutical Chemistry, University of Utah, Salt Lake City, 421 Wakara Way, Suite 315, Utah 84108. Received February 14, 2007; Revised Manuscript Received June 8, 2007

The principal objective of this study was to fabricate doxorubicin-loaded self-organized nanogels composed of hydrophobized pullulan (PUL)-N_α-Boc-L-histidine (bHis) conjugates. Their responses to tumor extracellular pH (pH_e) were determined, and they were also evaluated with regard to their anticancer efficacy against breast cancer cell lines (MCF-7). bHis was grafted to a PUL-deoxycholic acid (DO) conjugate (PUL−DO) via an ester linkage. PUL−DO/bHis conjugates with two different degrees of bHis substitutions (PUL−DO/bHis36 and PUL−DO/bHis78) were synthesized. PUL−DO/bHis nanogels formed via dialysis at a pH of 8.5 evidenced larger particle sizes (<140 nm) and lower critical aggregation concentrations (CACs) than did the PUL−DO nanogels (90 nm). The pH-dependent CAC of PUL−DO/bHis78 changed dramatically, from 1.2 μg/mL at pH 8.5, to 10 at 7.0, and to 660 at 6.2. A similar tendency in pH-dependent size was also noted. The ionization of the imidazole ring in bHis is principally responsible for pH dependency. The bHis moieties function as a switching tool responding to external pH. Doxorubicin (DOX)-loaded nanogels were assessed for pH-dependent releasing kinetics. The release rate of DOX from the PUL−DO/bHis78 nanogels increased significantly with reductions in pH. This resulted in increased cytotoxicity (30% cell viability at a dose of 10 μg/mL DOX equivalent) against sensitive MCF-7 cells at a pH of 6.8 and low cytotoxicity at pH 7.4 (65% cell viability at an identical dose). The results show that PUL−DO/bHis nanogels may potentially be employed as anti-tumor drug carriers.

INTRODUCTION

The switching of release kinetics in nanocarriers of anticancer drugs, from a slow rate during circulation to a fast rate at tumor sites, has been hypothesized to benefit chemotherapy, as the dose−response relationship (log[dose] vs cell viability) of most anticancer drugs evidence a typical sigmoidal curve, where the viability sharply decreases as drug concentration increases above a certain threshold value (*1*−*4*). It is believed that slow release prior to the reaching of the target tumor site reduces drug-induced side effects, while fast release kinetics tend to improve tumor treatment (*5*−*7*).

To realize such switching properties of release kinetics, a variety of approaches have been attempted, including the construction of thermoresponsive polymeric micelle systems that respond to hyperthermic conditions (42 °C) (*2*), and pH-sensitive systems that respond to endosomal pH via the cleavage of pH-labile chemical bonds (*8*). This research group has reported novel pH-responsive nanosystems predicated on acidic sulfonamide (*1*, *4*, *9*−*11*) and basic histidine chemistries (*3*, *12*−*14*) which effect the switching of a variety of physicochemical properties of nanocarriers, including surface hydrophobicity, drug release rates, and stability, by lowering the pH from 7.4 to 6.8. Among these systems, it was shown that mixed micelles constructed from poly(L-histidine) (polyHis)-*b*-PEG and polylactide-*b*-PEG evidenced a destabilization pH that was tunable to the tumor extracellular pH (around pH 6.8) and early endosomal pH, via alterations in the micelle composition (*12*, *13*). The imidazole ring of histidine harbors lone electron pairs on the unsaturated nitrogen that confers pH-dependent amphoteric properties (*15*−*17*). In addition, the dissociated block copolymer of polyHis and PEG evidence a profound endosomolytic property, which might facilitate drug escape from endosomal sequestration. This micelle system was shown to be effective in the treatment of sensitive and drug-resistant tumors in both *in vitro* and animal experiments (*14*). One of the disadvantages of this micelle system is its time- and labor-intensiveness, coupled with the high cost of polymer preparation, including synthesis, purification, and the relatively limited yields possible.

To devise a more practical method for the preparation of nanosystems with equivalent or similar pH sensitivity to polyHis-based micelles, the nanogel approach was adopted in this study, in place of the polymeric micelles. Hydrophobized polysaccharides self-assemble via the appropriate methods into nanogels consisting of multicores and a hydrophilic shell, allowing for the achievement of low Gibb's energy in water. The nanogels enclose water-insoluble drugs within their cores, thus minimizing interactions with biological components (*18*, *19*). The nanogels can be further functionalized as the result of the abundance of hydroxyl groups along the polymer chain.

Pullulan (PUL; Scheme 1a) is a linear polysaccharide which harbors an α-(1-6)-linked maltotriosyl repeating unit, and is known to be biocompatible. Its derivatives have been evaluated with regard to their potential use in the pharmaceutical industry and the biomedical field (*19*, *20*). Deoxycholic acid (DO; Scheme 1b), a bile acid, can function as a noncovalent cross-linking moiety, forming polycores in the nanogel. *N*-Boc-histidine (bHis; Scheme 1d) was introduced as a pH-sensitive moiety into a PUL/DO conjugate. All conjugation occurred via the formation of an ester linkage between the hydroxyl group of PUL and the carboxyl group on DO and bHis. Doxorubicin-loaded PUL−DO/bHis nanogels were evaluated via the monitoring of pH-dependent drug release behavior and cytotoxicity against sensitive breast tumor cells (MCF-7).

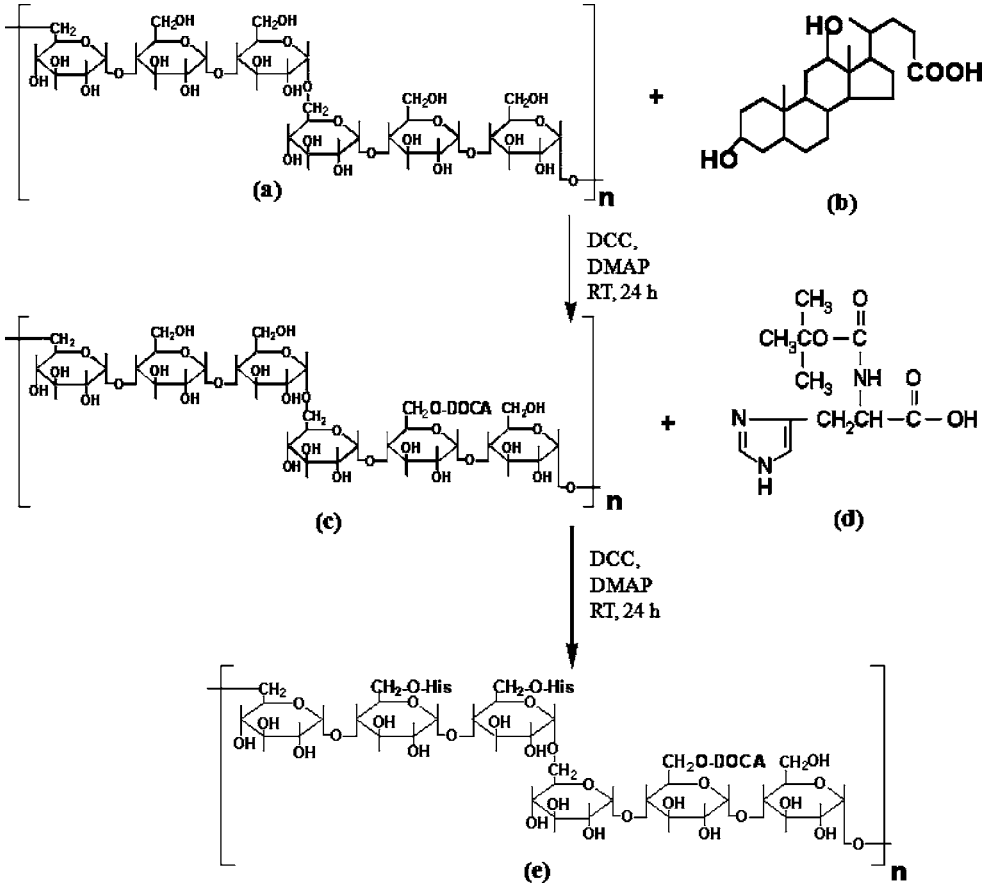
* To whom correspondence should be addressed. Tel: +(801)-585-1518; Fax: +(801)-585-3614; E-mail: you.bae@utah.edu.

[†] The Catholic University of Korea.

[‡] University of Utah.

10.1021/bc070052e CCC: $37.00 © 2007 American Chemical Society
Published on Web 08/10/2007

Scheme 1. Chemical Structures of Pullulan (PUL) (a), Deoxycholic Acid (DOCA) (b), N_α-Boc-L-histidine (bHis) (d), and Synthesis Schemes of PUL−DO (c) and PUL−DO/bHis Conjugates (e)



EXPERIMENTAL PROCEDURES

Materials. Pullulan (PUL) (MW: 200 000 kDa) was acquired from Hayashibara (Okayama, Japan). Deoxycholic acid (DO), N_α-Boc-L-histidine (bHis), folate (Fol), dicyclohexyl carbodiimide (DCC), 4-dimethylaminopyridine (DMAP), doxorubicin (DOX), and pyrene were obtained from the Sigma Chemical Company (St. Louis, Mo, USA). All other chemicals utilized in this study were of reagent grade.

Synthesis of PUL−DO and PUL−DO/bHis Conjugates. All conjugations between the PUL hydroxyl group and the DO and His carboxyl groups were conducted via the conventional carbodiimide reaction. First, PUL−DO was synthesized via DCC- and DMAP-mediated ester formation. 12 mM of DO was added to dried DMSO containing 0.1 mM of PUL, 15 mM of DCC, and 12 mM of DMAP, and maintained at room temperature for 24 h. The reactant mixture was then filtered and dialyzed for 2 days against distilled water using a dialysis tube (molecular cutoff: 12 000 kDa). The distilled water was changed every 3 to 6 h. The PUL−DO conjugate (Scheme 1c) was recovered via filtration and thoroughly washed with diethyl ether and distilled water, after which it was lyophilized. In order to completely remove the nonreactants, the lyophilized sample was again dissolved in DMSO and dialyzed against distilled water. This process was repeated 3 times. The conjugation of His into PUL−DO was conducted via a similar method for PUL−DO. 50 and 100 mM quantities of His were added to dried DMSO containing 700 mg of PUL−DO, DCC (55 and 110 mM), and DMAP (40 and 80 mM), respectively, and maintained for 24 h at room temperature (Scheme 1e). The other steps were similar to the PUL−DO conjugation method.

The degree of substitution (DS), which is defined as the number of DO and His groups per 100 anhydroglucose units of PUL, was determined via nuclear magnetic resonance (^{1}H NMR, 300 MHz). The NMR measurements were obtained with all samples dissolved in DMSO-d_6 (Aldrich, Milwakee, WI). The ^{1}H NMR spectra of PUL−DO (Supporting Information Figure S-1): δ 0.6 to δ 2.3 (−CO−C***H***$_2$− on DO) for DO and broad multiple peaks in the range 3−5.5 ppm for PUL. The degree of substitution (DS) was calculated at a ratio of δ 5.0 (proton peak of −O−C***H***$_2$−O− on the glucose of PUL) to δ 2.3 (−CO−C***H***$_2$− on DO). The number of DO units per 100 PUL glucose units DS was 8.36. The ^{1}H NMR spectra of PUL−DO/His was as follows: δ 0.8−1.0 (−C***H***$_3$− on Boc group) and δ 6.8 and δ 7.6 (−C***H***− on imidazole ring) for His. The degree of substitution (DS) was calculated at the ratio of δ 5.0 (proton peak of −O−C***H***$_2$−O− on the glucose of PUL) to δ 4.7 (−C***H***− on His). DS of PUL−DO/bHis36 and PUL−DO/bHis78 were 36 and 78, respectively.

Preparation of Self-Organizing Nanogels from the Conjugates. Self-organizing nanogels were prepared via the dialysis method (molecular cutoff: 2000 kDa). Each 50 mg portion of conjugate was dissolved in 20 mL of DMSO. The solutions were then stirred at room temperature and dialyzed for 3 days against distilled water. The solution was filtered with a 0.45 μm filter in order to remove the precipitated material.

Measurement of the pK_a Values of PUL−DO/bHis Conjugates. The pK_a values of PUL−DO/bHis conjugates were determined via classical acid−base titration. The conjugates were dissolved in deionized water, and then the solution was adjusted to a pH of 2 with 1 M HCl. The diluted solution was then titrated with 1 M NaOH solution in a stepwise manner in order to obtain the titration profiles. NaCl solution (identical concentration) was employed as a control and compared with the buffering effects of the conjugates.

Light Transmittance of Nanogel Solution. The optical transmittance of the nanogel solution (1 g/L) at various pHs

was measured at 500 nm using a Varian Cary 1E UV/vis spectrometer. The pH was lowered gradually via the addition of 0.01 M HCl solution, and the relative transmittances (%) at differing pH values were expressed relative to the transmittance at pH 9.0 (100%).

Particle Size Analysis. The particle size was determined via dynamic light scattering (DLS; Zetasizer 3000, Malvern Instruments LTD, UK), using an argon ion laser at a wavelength of 488 nm and a scattering angle of 90°. Each of the samples was filtered through a 0.45 μm filter directly into a precleaned cylindrical cell (diameter: 10 mm). The sample concentration was maintained at 1.0 mg/mL.

Measurement of Critical Aggregation Concentration (CAC). A stock solution of pyrene (6.0×10^{-2} M) in acetone was prepared and stored at 5 °C until use. In order to measure the steady-state fluorescence spectra, this solution was added to distilled water, yielding a pyrene concentration of 12.0×10^{-7} M. The solution was then distilled under vacuum at 60 °C for 1 h in order to remove the acetone from the solution. The acetone-free pyrene solution was mixed together with solutions containing self-organized nanogels at a range of concentrations from 1×10^{-4} mg/mL to 1.0 mg/mL. The final pyrene concentration in each sample solution was 6.0×10^{-7} M, which is nearly equal to its solubility in water at 25 °C (*21*).

Morphological Observations of the PUL−DO/bHis Nanogels. In order to observe the nanoparticles in a dried state, a drop of the self-organized nanogels was dissolved in water and positioned on a carbon-coated copper grid, then dried under vacuum at 30 °C. The samples were observed without staining via transmission electron microscopy (TEM; Philips CM 30, Philips Electron Optics, Eindhoven, The Netherlands) at 80 kV.

DOX Loading and Release. DOX·HCl (0.1 mM) and 1.3 molar equiv triethylamine were allowed to react in dimethylsulfoxide (DMSO) (3 mL) to form the DOX basic adduct. Each of the conjugates (50 mg) was added to the DOX solution, and the mixture was stirred overnight at 4 °C in darkness. The conjugate/DOX solution was then transferred to dialysis tubing (Spectra/Por; molecular weight cutoff: 1000 kDa) and dialyzed against a 0.01 M phosphate buffered saline (PBS) solution (pH = 8.5) for 3 days at 25 °C. The buffer was exchanged with fresh solution every 3 h for the first 24 h, and then daily. The solution was then filtered through a 0.45 μm filter in order to remove any polymer or drug that had precipitated out of solution, and was freeze-dried in order to obtain the DOX-loaded nanogels. To evaluate the drug-loading capacity of these nanogels, a freeze-dried sample was added to DMF, stirred vigorously for 2 h, then sonicated for 3 min. The resultant solution was centrifuged for 30 min at 20 000 × *g*, and the supernatant was analyzed with an ultraviolet (UV) spectrophotometer at 490 nm. Using a linear standard curve out of free DOX in *N*,*N*-dimethylacetamide (DMAc), the loading amounts could be calculated and were determined to be 13 ± 4.4%, 19 ± 6.1%, and 24 ± 6.9% (w/w) for PUL−DO, PUL−DO/bHis36, and PUL−DO/bHis78, respectively.

The release rate was measured at various pHs (7.8, 7.4, 6.8, and 6.2) as follows: 2 mL of the drug-loaded nanogel solution (1 g/L) was transferred in 10 mL of PBS to a dialysis tube. The release medium was stirred at 100 rpm at 37 °C. PBS buffer was used at the same ionic strength. At the predetermined sampling time, all of the media were removed and replaced with fresh solution in order to maintain a sink condition. The amount of DOX in the solution was determined via UV spectroscopy at 490 nm.

Cytotoxicity of DOX-Loaded Nanogels at Different pH. MCF-7 cells (5×10^4 cells/mL) harvested as a monolayer from growing cells were seeded in a 96-well plate in 200 μL of RPMI 1640 medium 24 h prior to the cytotoxicity test. Free DOX or DOX-loaded nanogels in RPMI 1640 medium (in PBS pH 7.4 or 6.8 and adjusted with 0.1 N NaOH or 0.1 N HCl) were prepared immediately prior to use, as in the previously described report (*12*), added to the medium-removed 96-well plates with different DOX concentrations, and incubated for 48 h. Chemosensitivity was assessed via the tetrazolium salt MTT assay. 100 μL of PBS at a pH of 7.4 containing 20 μL of MTT (1.2 mM) solution was added to each well. The plate was incubated for an additional 4 h, and then 100 μL of DMSO was added to each well. The absorbance of each well was read on a microplate reader using a test wavelength of 570 nm and a reference wavelength of 630 nm.

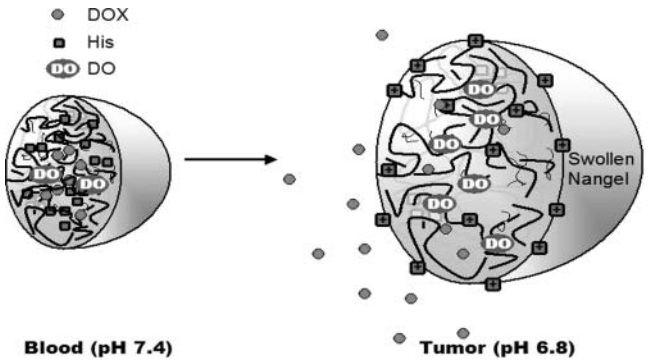


Figure 1. Schematic representation of pH-dependent anti-cancer drug release from proposed pH-sensitive PUL−DO/bHis nanogels. At normal pH (7.4), the nanogels are stable, and so the drug release rate is slower. However, at tumor acidic pH (6.8), the nanogels evidence swelling or disruption behavior as the result of changes in internal structure, resulting in accelerated drug release.

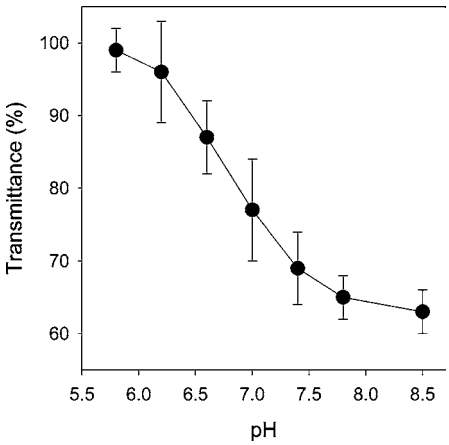


Figure 2. Change in transmittance of PUL-His66 nanogels (1 g/L) on decreasing pH. Data represent a mean ± SD; $n = 3$.

Statistical Analysis. Statistical analyses were conducted using the *SPSS* software package (version 11.0, SPSS Inc., Chicago). The descriptive data are presented as the means ± standard deviations. The cytotoxicities of the three groups (PUL−DO, PUL−DO/bHis78, and free DOX) against the MCF-7/DOX cells were compared via ANOVA tests. The differences were considered significant if the p value was less than 0.05.

RESULTS AND DISCUSSION

In order to develop an easy process for the acquisition of self-organized nanogels responding to tumor pH_e, we synthesized PUL−bHis conjugates with ester linkages between OH in PUL and COOH in His (degree of substitution of N_α-Boc-L-histidine (His) per 100 anhydroglucose unit of pullulan: 66). The conjugates evidenced a pH-sensitive dissociation in the pH range 7.8−6.2 (Figure 2). After dialysis for the preparation of the nanogel from PUL−His conjugate at pH 8.5, a considerable

Table 1. Physicochemical Characterization of Self-Assembled Nanogels on the pK_a, Critical Aggregation Concentrations (CAC), and Particle Sizes at pH 8.5

sample name	DS[a−1] of DO	DS[a−2] of bHis	pK_a[b]	CAC[c] (μg/mL)	d[d] ± SD (nm)
PUL−DO	8.36			5.6	85 ± 68
PUL−DO/bHis36	8.36	35.88	6.7	3.6	109 ± 84
PUL−DO/bHis78	8.36	78.39	6.4	1.2	130 ± 94

[a] DS indicates the degree of substitution in conjugates based on the ^{1}H NMR results. [a−1]Degree of substitution of deoxycholic acid (DO) per 100 anhydroglucose units of pullulan. [a−2]Degree of substitution of N_α-Boc-L-histidine (bHis) per 100 anhydroglucose units of pullulan. [b] pK_a values of bHis in the conjugates were determined via classical acid−base titration. The conjugates were dissolved in deionized water, and the solution was adjusted to pH 10 with 1 M NaOH. The diluted solution was then titrated via a stepwise decrease of 0.1 N HCl solution in order to determine the titration profiles. NaCl solution (identical concentration) was used as a control for comparison of the buffering effects with those of the conjugates. [c] Critical aggregation concentration (CAC) in aqueous solution (pH 8.5) as determined by fluorescence spectroscopy. [d] Mean diameter in aqueous solution (pH 8.5) measured by DLS.

reduction in the transmittance of the solution was observed, which is indicative of the formation of nanogels in aqueous media (pH 8.5). As the pH decreased, the transmittance increased continuously until a pH of 6.2 was reached. In particular, at pH values below 7.4, the change was more dramatic. Unfortunately, the nanogels evidenced neither sufficient loading efficiency for an anti-tumor drug (DOX, below 6 wt %) nor good drug loading capacity at a pH of 7.4 (Supporting Information Figure S-2). This result is quite similar to our previous result (*21*). Thus, we elected to employ a hydrophobically modified polysaccharide in order to improve drug loading and holding. DO was selected as a hydrophobic moiety, as its potential has already been established in a variety of reports (*22*, *23*).

Physicochemical Characterization of PUL−DO/bHis Nanogels. The pK_a of imidazole in PUL−DO/bHis36 and PUL−DO/bHis78 was estimated via classical acid−base titration, in order to define their ionization patterns. The value of PUL−DO/bHis78 was found to be lower than that of PUL−DO/bHis36 (Table 1). In general, as monomers with cationic groups are coupled to polymers with hydrophobic segments, the pK_a of the groups normally shifts toward a lower range of pH. As the hydrophobic and chargeable groups are in close proximity (*24*), the hydration of the chargeable groups is reduced as the result of influence from the hydrophobic segment. Thus, it appears that this tendency resulted in different pK_a values between PUL−DO/bHis36 and PUL−DO/bHis78.

The size of self-organized nanogels and size distributions at pH 8.5 were assessed by DLS. Both PUL−DO/bHis nanogels prepared via the dialysis method at pH 8.5 evidenced particle sizes below 140 nm (Table 1). In order to trace the self-organizing behavior of PUL−DO/bHis conjugates in PBS buffer (pH 8.5), the CACs of PUL−DO/bHis36 and PUL−DO/bHis78 were measured using pyrene as a fluorescence probe. The CACs of PUL−DO/bHis nanogels, determined from the change of the intensity ratio (I_{338}/I_{335}) of pyrene according to the concentration of the conjugates, were lower than that of PUL−DO. These results indicate that the His groups in the conjugate contributed to the increase in hydrophobicity. Their lower CAC values may result in the maintenance of the stability of nanogels in the bloodstream.

In order to elucidate the effects of pH on the organization of the nanogels, various dialysis pH values (pH_{dia}) in the range 8.5−5.8 were employed for the preparation. Changes in the CAC values of PUL−DO/bHis36 and PUL−DO/bHis78 nanogels prepared at various pH_{dia} values are shown in Figure 3a. Although the change in CAC was negligible with decreasing pH_{dia} from 8.5 to 7.4, at pH_{dia} 6.8 the CACs increased drastically.

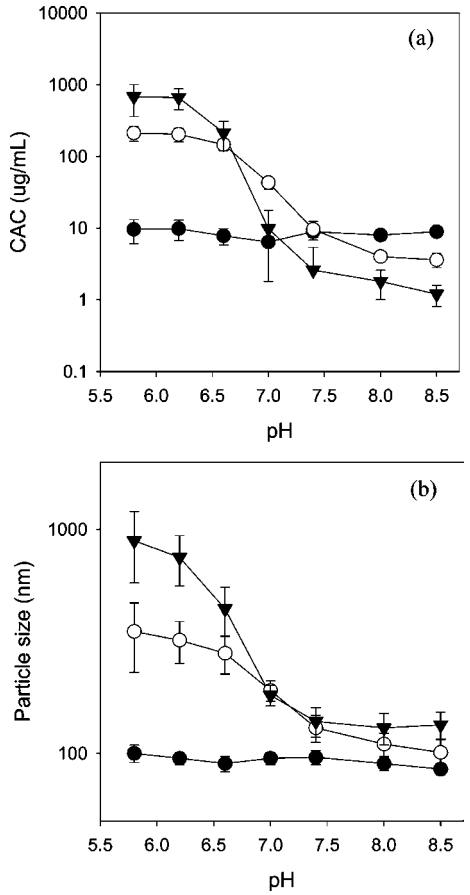


Figure 3. Changes in critical aggregation concentration (CAC) (a) and particle size (b) of self-organized nanogels on decreasing pH: PUL−DO (●), PUL−DO/bHis36 (○), and PUL−DO/bHis78 (▼) nanogels. Data are expressed as the means ± SD; $n = 3$.

PUL−DO/bHis78 evidenced a sharper transition with pH; up to a pH_{dia} of 7.0, the CACs were in the range 1−10 μg/mL, but at a pH_{dia} of 6.2, the CAC increased by approximately 600 times. This result was attributable to the fact that the imidazole in the His group was altered from hydrophobicity to hydrophilicity as the result of ionization. At pH_{dia} values below 7.0, the imidazoles of the His groups are well-ionized and contribute to inter- or intramolecular electrostatic repulsions for the dissociation of the nanogels, while at pH_{dia} values above 7.0, deionized imidazole enhanced the hydrophobic interactions. Of course, the CAC of the PUL−DO nanogel evidenced no dramatic difference. The pH-sensitive behavior of the PUL−DO/bHis nanogel was also verified via particle size analysis at various pHs (Figure 3b). The sizes of the nanogels in the pH range 8.5−7.8 remained similar. However, the sizes of PUL−DO/bHis78, in particular, increased to 750 nm at pH 6.2, from 140 nm measured at pH 7.4. Many investigations into the size of tumor vascular pores have reported gap openings significantly larger than those observed along vessels in normal tissues (*25*, *26*). The average size of tumor vascular pores is generally 400−600 nm (*25*). This fact and the particle size results suggest the possibility of prolonged retention of PUL−DO/bHis nanogels in tumors. Gels of smaller size may pass into normal blood vessels (pH 7.4), and accumulate at tumor sites (lower pH) by virtue of their enhanced permeability and retention (EPR) effects (*26*). The retention time of entrapped nanogels at tumor sites may be prolonged by these larger tumor vascular pores.

The changes in particle size were induced via particle disruption or swelling of the gel as the result of the imidazole ionization in the His group. In order to define the mechanism, the morphology of PUL−DO/bHis78 was observed at a pH of

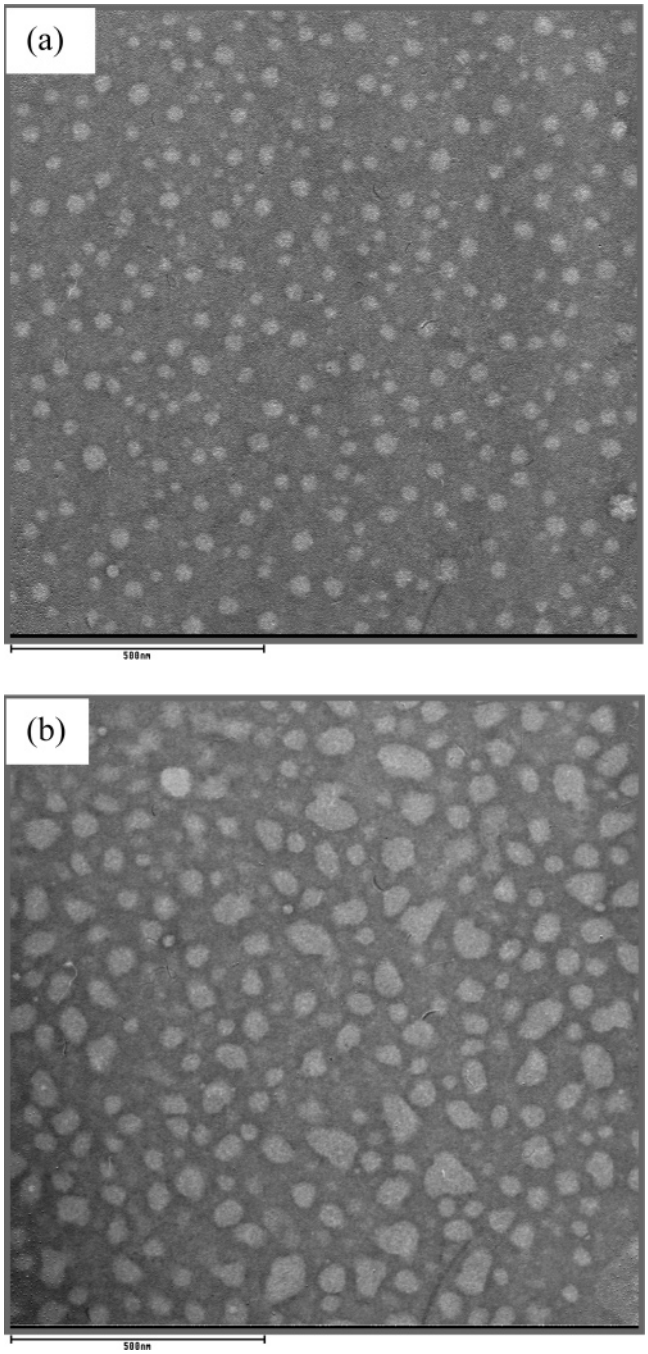


Figure 4. Transmittance electron microscopic (TEM) images of PUL−DO/bHis78 nanogels (scale bar = 500 nm) at pH 8.5 (a) and 6.2 (b). Bar means 500 nm.

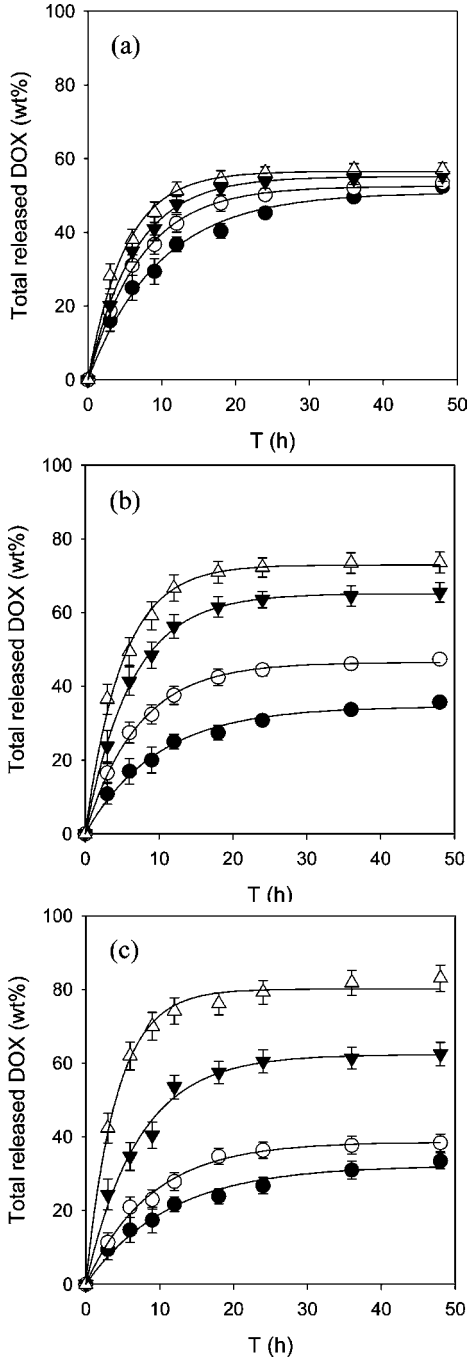


Figure 5. DOX release kinetics from PUL−DO (a), PUL−DO/bHis36 (b), and PUL−DO/bHis78 (c) self-organized nanogels loaded around physiological pH values: pH 8.0 (●), 7.4 (○), 6.8 (▼), and 6.2 (△). Data are expressed as the means ± SD; $n = 3$.

8.5 and 6.2 by TEM (Figure 4). The nanogel at pH 8.5 evidenced well-dispersed "irregular polygons" of 30−50 nm (Figure 4a), which is not consistent with the DLS results. We already reported that the differences in size between the dried and swollen nanogels resulted from the huge hydrodynamic volume of the nanogels (*21*). At a pH of 6.2, PUL−DO/bHis nanogel size increased to 100−300 nm and its morphology was not maintained (Figure 4b). This result shows that the nanogel at slightly acidic pH values was disrupted as a result of the alternation of internal structures by imidazole ionization in the His group.

pH-Sensitive DOX Release Behavior of PUL−DO/bHis Nanogel. The *in vitro* release profiles of DOX from PUL−DO/bHis36 and PUL−DO/bHis78 at various pHs (8.0, 7.4, 6.8, and 6.2) were examined, and the results are shown in Figure 5. The release of DOX from PUL−DO evidenced some slight pH-dependent behavior; i.e., the amount of DOX released increased with decreasing medium pH as the result of the pH-dependent solubility of DOX (a weak base, $pK_b = 8.22$) (Figure 5a). In cases of PUL−DO/bHis36 and PUL−DO/bHis78, DOX release also evidenced pH dependency (Figure 5b,c). The pH dependency of PUL−DO/bHis78 was more profound than that of PUL−DO/bHis36. Graphs from the release test were analyzed by the exponential rise model equation, $y = a(1 - e^{-bx})$. Here, the equation elucidates the pH-sensitive DOX release. Slope "a" in the equation indicates pH sensitivity in drug release. The

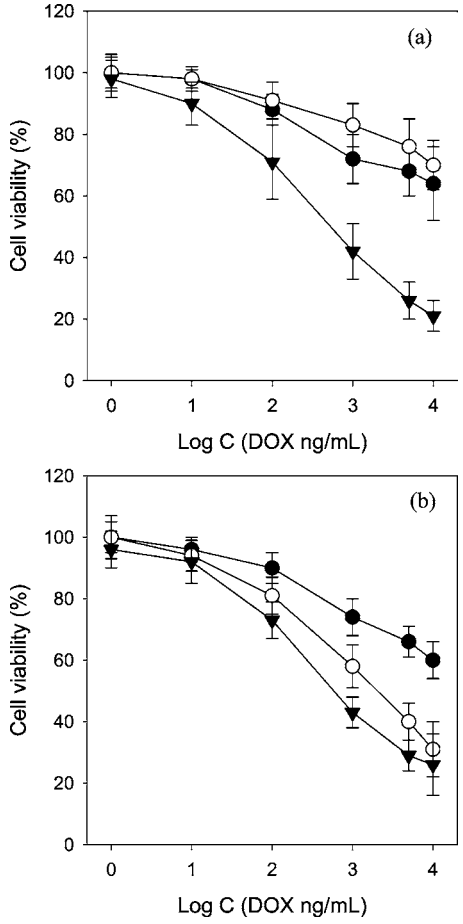


Figure 6. Cytotoxicity of DOX-loaded PUL−DO and PUL−DO/bHis78 nanogels against MCF-7 cells, as a function of drug concentration at (a) pH 7.4 and (b) 6.8: PUL−DO (●), PUL−DO/bHis78 (○), and free DOX (▼). Data are expressed as the means ± SD; $n = 7$.

model was predominantly predicated on diffusivity, whereas the drug solubility also affects the model. We developed this equation to determine the "pH-sensitivity DOX release behavior". The regression equations for PUL-DO/bHis78 at various pHs were as follows: $y = 32.2137(1 - e^{-0.0891x})$, $y = 38.5969(1 - e^{-0.1142x})$, $y = 62.3356(1 - e^{-0.1400x})$, and $y = 80.0910(1 - e^{-0.2410x})$ for pH 8.0, 7.4, 6.8, and 6.2. The equation evidenced a good correlation factor, in that the R^2 values were 0.9983, 0.9994, 0.9991, and 0.9997, respectively. It is known that the release rate of a drug incorporated in a hydrophobic domain depends on the solubility and diffusivity of the drug (*21*). However, studies of polymeric nanogels prepared from stimuli-sensitive amphiphilic polymers have demonstrated that the drug release rate can be altered rapidly via the deformation of the inner core induced by changes in environmental conditions (Figure 1). Therefore, pH-accelerated DOX release from PUL−DO/bHis nanogels may be consistent with pH-induced structural changes. The ionized imidazole in the gel at lower pH values may create charge−charge repulsions between His-grafted chains or the swelling of the core by the hydrophilization of His, resulting in interior structural changes of the PUL−DO/bHis nanogels. This phenomenon may accelerate DOX release rates at pH values below 6.8.

Cytotoxicity of PUL−DO/bHis Nanogels to MCF-7 Cells. The majority of solid tumors have been shown to evidence lower extracellular pH (around 6.8) than the surrounding tissues and blood (pH 7.4) (*27*−*29*). The vasculature of tumors is frequently inadequate to provide sufficient oxygen and nutrients for the expanding tumor cell population. The production of lactic acid under hypoxic conditions and the hydrolysis of ATP in an energy-deficient environment contribute to an acidic microenvironment, which has been detected in many tumor types. Therefore, the *in vitro* cytotoxicity of PUL−DO/bHis78 nanogels to MCF-7 cells at two different pH values (7.4 and 6.8) were compared in Figure 6. A method for the maintenance of a given pH in the medium during experiment was previously reported (*12*). In addition, for the maintenance of the pH of RPMI 1640 medium during cell culture, we utilized RPMI 1640 medium containing PBS (1 M) solution and checked for changes in the pH of the culture medium prior to the tests. Although a negligible change in pH in the culture medium was detected after 2 days of incubation, this did not affect the cell cytotoxicity results.

At a pH of 7.4, we noted no significant differences in the cytotoxicity of PUL−DO and PUL−DO/bHis78 nanogels at the DOX concentration range of 1.0 ng/mL to 10 μg/mL (Figure 6a). However, at a pH of 6.8, the DOX-loaded PUL−DO/bHis78 evidenced significantly enhanced cytotoxicity, whereas the DOX-loaded PUL−DO nanogels (as a control) evidenced no pH effects on cytotoxicity (Figure 6b). The pronounced cytotoxicity of PUL−DO/bHis78 at pH 6.8 may be attributed to the enhanced release rate of DOX in Figure 5. After our group reported a potential way to effectively deliver anti-cancer drugs using polyHis-based micelles (*13*, *14*), His-based nanocarriers have received a great deal of attention as an anti-tumor drug carrier (*30*, *31*). Yang et al. reported the direct conjugation of histidine to poly(2-hydroxyethyl aspartamide) (PHEA) and octadecylamine-grafted PHEA via an ester linkage (*30*). However, this system may be quite difficult to construct as compared to the polyHis system, as the polymer was predicated on poly(2-hydroxyethyl aspartamide) (PHEA-His) and C18-grafted PHEA (PHEA-g-C18-His). In particular, the nanocarrier did not evidence significant differences in drug release with pH, unlike the polyHis-based polymeric micelles due to the lack of flexibility, which is instrumental in the swelling and compressing properties of the nanocarrier. Park et al. also demonstrated the use of *N*-acetyl histidine-conjugated glycol chitosan self-assembled nanoparticles for intracytoplasmic drug delivery (*31*). The nanoparticles were synthesized in PBS buffer via the EDC reaction, resulting in a lower rate of the conjugation of *N*-acetyl histidine to glycol chitosan. Thus, their nanoparticles did not evidence pH-sensitive behavior such as pH-dependent dissociation and drug release as compared to polyHis-based micelles. Therefore, the cytotoxicity of PUL−DO/bHis 78 nanogel indicates that the nanogel is a very superior carrier for anti-cancer drug delivery.

CONCLUSIONS

In order to develop a self-organized nanogel responsive to tumor extracellular pH on the basis of histidine chemistry via a conjugation approach, a self-organized nanogel from PUL−DO/bHis conjugates was investigated with regard to its efficacy as an anti-tumor carrier. Nanogels prepared at pH 8.5 were smaller than 140 nm. The CAC of the PUL−DO/bHis78 nanogel dropped sharply with increasing pH_{dia}. Its size also significantly increased to 750 nm at pH 6.2 from 130 nm at pH 8.5 as a result of the particle destabilization induced by the ionization of imidazole in bHis moieties at lower pH values. Moreover, lower pH enhanced the rate of release of the loaded DOX from PUL−DO/bHis nanogels. At tumor pH_e (pH 6.8), the PUL−DO/bHis78 nanogels evidenced drastically augmented cytotoxicity as compared to that observed at normal pH, resulting from the enhanced release rate. The continuous study of polymeric nanogels harboring bHis may prove the efficacy of tumor targeting on the basis of tumor pH_e.

ACKNOWLEDGMENT

This work was supported by NIH CA101850.

Supporting Information Available: Supplementary figures. This material is available free of charge via the Internet at http://pubs.acs.org.

LITERATURE CITED

(1) Na, K., and Bae, Y. H. (2002) Self-assembled hydrogel nanoparticles responsive to tumor extracelluar pH from hydrophobized pullulan and sulfonamide conjugate; Characterization, aggregation and adriamycin release in vitro. *Pharm. Res. 19*, 681−688.

(2) Chung, J. E., Yokoyama, M., and Okano, T. (2000) Inner core segment design for delivery control of thermo-responsive polymeric micelles. *J. Controlled Release 65*, 93−103.

(3) Lee, E. S., Shin, H., Na, K., and Bae, Y. H. (2003) Poly(L-histidine)/PEG block copolymer micelle and pH-induced destabilization. *J. Controlled Release 90*, 363−374.

(4) Na, K., Lee, E. S., and Bae, Y. H. (2003) Adriamycin loaded pullulan acetate/sulfonamide conjugate nanoparticles responding to tumor pH: pH-dependent cell interaction, internalization and cytotoxicity in vitro. *J. Controlled Release 87*, 3−13.

(5) Leroux, J. C., Roux, E., Garrec, D. L., Hong, K., and Drummond, D. C. (2001) N-Isopropylacrylamide copolymers for the preparation of pH-sensitive liposomes and polymeric micelles. *J. Controlled Release 72*, 71−84.

(6) Cammas, S., Suzuki, K., Sone, C., Sakurai, Y., Kataoka, K., and Okano, T. (1997) Thermo-responsive polymer nanoparticles with a core-shell micelle structure as site-specific drug carriers. *J. Controlled Release 48*, 157−164.

(7) Na, K., Lee, K. H., Lee, D. H., and Bae, Y. H. (2006) Biodegradable temperature-sensitive nanoparticles from poly(ethylene glycol)(PEG)/poly(L-lactic acid)(PLLA) alternating multiblock copolymer for anticancer drug delivery. *Eur. J. Pharm. Sci. 27*, 115−122.

(8) Bae, Y., Nishiyama, N., Fukushima, S., Koyama, H., Yasuhiro, M., and Kataoka, K. (2005) Preparation and biological characterization of polymeric micelle drug carriers with intracellular pH-triggered drug release property: tumor permeability, controlled subcellular drug distribution, and enhanced in vivo antitumor efficacy. *Bioconjugate Chem. 16*, 122−130.

(9) Na, K., Lee, K. H., and Bae, Y. H. (2005) pH-Sensitivity and pH-dependent interior structure change of Self-assembled hydrogel nanoparticles of pullulan acetate/oligo(methacryloyl sulfadimethoxine) (PA/OSDM) conjugates. *J. Controlled Release 97*, 513−525.

(10) Han, S. K., Na, K., and Bae, Y. H. (2003) Sulfonamide based pH-sensitive polymeric micelles: Physicochemical characteristics and pH-dependent aggregation. *Colloids Surf., A 214*, 49−59.

(11) Sethuraman, V. A., Na, K., and Bae, Y. H. (2006) pH-responsive sulfonamide/PEI system for tumor specific gene delivery: an in vitro study. *Biomacromolecules 7*, 64−70.

(12) Lee, E. S., Na, K., and Bae, Y. H. (2003) Polymeric micelle for tumor pH and folate mediated targeting. *J. Controlled Release 91*, 103−113.

(13) Lee, E. S., Na, K., and Bae, Y. H. (2005) Doxorubicin loaded smart polymeric micelles for reversal of resistant MCF-7 tumor. *J. Controlled Release 103*, 405−418.

(14) Lee, E. S., Na, K., and Bae, Y. H. (2005) Super pH-sensitive multifunctional polymeric micelle. *Nano Lett. 5* (2) 325−329.

(15) Pack, D. W., Putnam, D., and Langer, R. (2000) Design of imidazole-containing endosomolytic biopolymers for gene delivery. *Biotechnol. Bioeng. 67*, 217−223.

(16) General, S., and Thunemann, A. F. (2001) pH-sensitive nanoparticles of poly(amino acid) dodecanoate complexes. *Int. J. Pharm 230*, 11−24.

(17) Mccurdie, M. P., and Belfiore, L. A. (1999) Solid-state complexes of poly(L-histidine) with metal chlorides from the first row of the d-block. *J. Polym. Sci., Part B: Polym. Phys. 37*, 301−310.

(18) Nishikawa, T., Akiyoshi, K., and Sunamoto, J. (1997) Microscopic structure and thermoresponsiveness of hydrogel nanoparticle by self-assembly of a hydrophobized polysaccharide. *Macromolecules 30*, 857−861.

(19) Nishikawa, T., Akiyoshi, K., and Sunamoto, J. (1996) Macromolecular complexation between bovine serum albumin and self-assembled hydrogel nanoparticle of hydrophobized polysaccharide. *J. Am. Chem. Soc. 118*, 6110−6115.

(20) Gupta, M., and Gupta, A. K. (2004) Hydrogel pullulan ananoparticles encapsulating pBUDLacZ plasmid as an efficient gene delivery carrier. *J. Controlled Release 99*, 157−166.

(21) Na, K., Park, K-.H., Kim, S., and Bae, Y. H. (2000) Self-aggregated hydrogel nanoparticles from curdlan derivatives: characterization, anti-cancer drug release and interaction with a hepatoma cell line (HepG2). *J. Controlled Release 69*, 225−236.

(22) Lee, K. Y., Jo, W. H., Kwon, I. C., Kim, Y. H., and Jeong, S. Y. (1998) Physicochemical characteristics of self-aggregates of hydrophobically modified chitosans. *Langmuir 14*, 2329−2332.

(23) Lee, K. Y., Jo, W. H., Kwon, I. C., Kim, Y. H., and Jeong, S. Y. (1998) Structural determination and interior polarity of self-aggregates prepared from deoxycholic acid-modified chitosan in water. *Macromolecules 31*, 378−383.

(24) Urry, D. W., Peng, S. Q., Parker, T. M., Gowda, D. C., and Harris, R. D. (1993) Relative significance of electrostatic and hydrophobic-induced pK_a shifts in a model protein: the aspartic acid residue. *Angew. Chem., Int. Ed. Engl. 32*, 1440−1442.

(25) Campbell, R. B. (2006) Tumor physiology and delivery of nanopharmaceuticals. *Anti-cancer agents in medical chemistry 6*, 503−512.

(26) Maeda, H., Wu, J., Sawa, T., Matsumura, Y., and Hori, K. (2000) Tumor vascular permeability and the EPR effect in macromolecular therapeutics: a review. *J. Controlled Release 65*, 271−284.

(27) Kong, G., Braun, R. D., and Dewhirst, M. W. (2001) Characterization of the effect of hyperthermia on nanoparticle extravasation from tumor vasculature. *Cancer Res. 61*, 3027−3032.

(28) Tannock, I. F., and Rotin, D. (1989) Acid pH in tumors and its potential for therapeutic exploitation. *Cancer Res. 49*, 4373−4384.

(29) Stubbs, M., McSheehy, P. M. J., Griffiths, J. R., and Bashford, C. L. (2000) Causes and consequences of tumor acidity and implications for treatment. *Mol. Med. Today 6*, 15−19.

(30) Yang, S. R., Lee, H. J., and Kim, J.-D. (2006) Histidine-conjugated poly(amino acid) derivatives for the novel endosomolytic delivery carrier of doxorubicin. *J. Controlled Release 114*, 60−68.

(31) Park, J., Han, T. H., Lee, K. Y., Han, S. S., Hwang, J. J., Moon, D. H., Kim, S. Y., and Cho, Y. U. (2006) N-Acetyl histidine-conjugated glycol chitosan self-assembled nanoparticles for intracytoplasmic delivery of drugs: endocytosis, exocytosis and drug release. *J. Controlled Release 115*, 37−45.

BC070052E

Lipophosphoramidates as Lipidic Part of Lipospermines for Gene Delivery

François Lamarche,[†] Mathieu Mével,[†] Tristan Montier,[‡] Laure Burel-Deschamps,[†] Philippe Giamarchi,[†] Raphaël Tripier,[†] Pascal Delépine,[‡] Tony Le Gall,[‡] Dominique Cartier,[†] Pierre Lehn,[‡] Paul-Alain Jaffrès,[†] and Jean-Claude Clément*,[†]

UMR CNRS 6521, Université de Bretagne Occidentale, UFR Sciences, 6, Avenue Le Gorgeu, C.S. 93837, F-29238 Brest cedex 3, France, and INSERM U 613, Université de Bretagne Occidentale, C.S. 2653, F-29275 Brest cedex, France.
Received March 2, 2007; Revised Manuscript Received May 30, 2007

The DNA compacting properties of polyamines (especially spermine) are well-known, hence the use of spermine as the cationic part in several synthetic DNA carriers. Here, we describe the synthesis of modified spermines, with a "lipophosphoramidate" as the lipidic part, and their use for efficient *in vitro* transfection. Physicochemical measurements (particle size, zeta potentials, pK_a determination) and gel retardation assays were also performed. Theoretical membrane-disrupting ability was established by FRET. Taken together, our results indicate that lipophosphoramidates constitute an interesting alternative to "classical" lipidic parts of cationic lipids used as DNA carriers.

INTRODUCTION

Together with polymers, cationic lipids hold the most important place among synthetic carriers for gene delivery. In these vectors, the lipidic part generally consists of a cholesteryl group or two $C_{12}-C_{20}$ saturated or unsaturated hydrocarbon chains. To the first category belong, for instance, the commercial DC-Chol (*1*), BGTC (a bis-guanidinium cholesterol derivative) (*2*), and Lipid 67 (a spermine cholesterol derivative) (*3*) (Scheme 1).

Chronologically, DOTMA (*4*) is the first representative of the second category, and since 1987, several dozen cationic lipids bearing two hydrocarbon chains, with various spacers and polar heads, have been published (*5*, *6*). Some representative examples are given in Scheme 2.

Because of its compacting properties, the naturally occurring spermine was used as the polar head in several carriers, and among them, apart from Lipid 67 already quoted, appear DOGS (*7*) and DOSPA, the cationic part of Lipofectamine (*8*). Since lipophosphoramidates proved to be efficient for *in vivo* gene delivery when associated with ammonium, phosphonium, or arsonium cations (*9*), we wondered about their efficiency when associated to spermine as the cationic part.

EXPERIMENTAL PROCEDURES

Syntheses of Lipidic Spermines. Solvents were freshly distilled on appropriate driers and reactions run under nitrogen atmosphere. All compounds were fully characterized by ^{1}H (400 MHz), ^{13}C (100 MHz), and ^{31}P (121.49 MHz) NMR spectroscopy (Bruker AC 300 and Advance DRX 400 spectrometers). Coupling constants *J* are given in hertz. The following abbreviations were used: s for singlet, d doublet, t triplet, q quadruplet, qt quintuplet, and m for multiplet. When needed, ^{13}C heteronuclear HMQC and HMBC were used to unambiguously establish structures.

N^4-(3-Phtalimidopropyl)-N^1,N^8,N^{12}-tris-tert-butyloxycarbonyl−Spermine ***6***. SpermineBoc$_3$ (1 g, 2 mmol, 1 equiv) and *N*-(3-bromopropyl)phthalimide (666 mg, 2.48 mmol, 1.25 equiv) were dissolved in dry acetonitrile (30 mL) with an excess of K_2CO_3 (1.37 g, 9.95 mmol, 5 equiv). The mixture was stirred for 18 h under reflux. Then, acetonitrile was evaporated under vacuum, and the crude product was dissolved in methylene chloride (50 mL). The organic layer was washed with $NaHCO_3$ (2 × 50 mL) and water (50 mL), dried with $MgSO_4$, and evaporated to give after purification by column chromatography ($CHCl_3$/EtOH 100:0 to 80:20) 910 mg of compound **6** (66%). R_f = 0.50 ($CHCl_3$/EtOH 90:10). ^{1}H NMR (DMSO-d_6): 7.84 (m, 2H), 7.82 (m, 2H), 6.70 (m, 2H), 3.57 (t, *J* = 7.2, 2H), 3.07 (m, 4H), 2.89 (m, 2H), 2.87 (m, 2H), 2.37 (t, *J* = 6.6, 2H), 2.30 (t, *J* = 6.8, 2H), 2.29 (t, *J* = 6.8, 2H), 1.68 (qt, *J* = 7.2, *J* = 14.1, 2H), 1.53 (m, 2H), 1.44 (qt, *J* = 6.7, *J* = 13.2, 2H), 1.37 (m, 2H), 1.34 (m, 27H), 1.27 (qt, *J* = 6.7, *J* = 13.9, 2H). ^{13}C NMR (DMSO-d_6): 167.9, 155.5, 154.6, 134.3, 131.6, 122.9, 78.2, 77.4, 77.2, 52.9, 51.1, 50.9, 44.3, 38.3, 37.6, 36.0, 28.4, 28.2, 28.1, 28.0, 26.8, 25.7, 23,7.

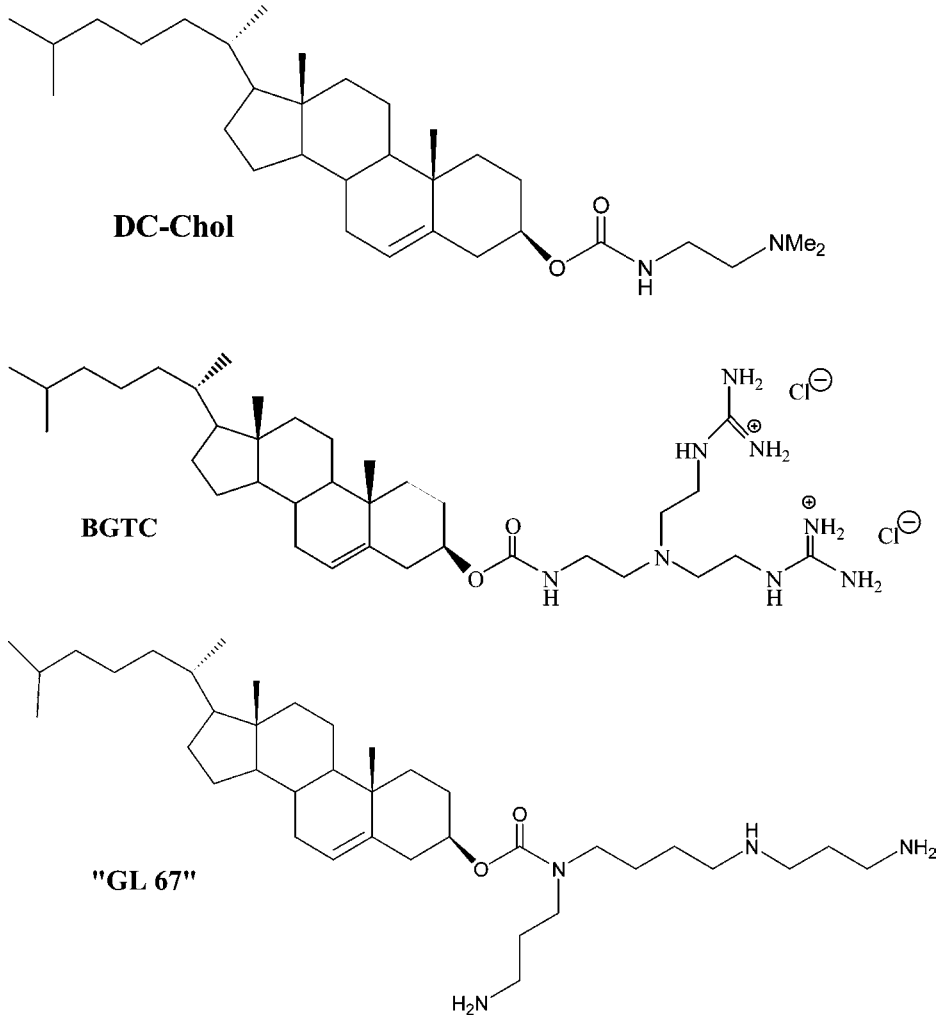
N^4-(3-Aminopropyl)-N^1,N^8,N^{12}-tris-tert-butyloxycarbonyl−Spermine ***7***. Compound **6** (880 mg, 1.28 mmol, 1 equiv) and an excess of hydrazine monohydrate (1.98 mL, 64 mmol, 50 equiv) were dissolved in THF/EtOH (80:20; 20 mL). The mixture was stirred 5 h at 80 °C and then 18 h at 50 °C. After evaporation under reduced pressure, the residue was dissolved in $CHCl_3$ (50 mL) and washed with 5% sodium hydroxide solution (2 × 50 mL). The organic phase was separated, dried over anhydrous magnesium sulfate, filtered, concentrated, and subjected to flash chromatography using 3% NH_4OH/MeOH to give the desired amine **7** (573 mg, 80%). R_f = 0.42 (MeOH + 5% NH_4OH). ^{1}H NMR (DMSO-d_6): 6.70 (m, 2H), 3.08 (m, 4H), 2.90 (m, 2H), 2.87 (m, 2H), 2.53 (m, 2H), 2.35 (m, 2H), 2.30 (m, 2H), 2.29 (m, 2H), 1.58 (m, 2H), 1.51 (m, 2H), 1.44 (m, 2H), 1.37 (m, 2H), 1.35 (m, 27H), 1.29 (m, 2H). ^{13}C NMR (DMSO-d_6): 155.5, 154.6, 78.2, 77.4, 77.2, 53.1, 51.5, 51.1, 48.6, 48.6, 39.8, 38.4, 37.6, 28.9, 28.7, 28.2, 28.0, 27.0, 26.2, 23.8.

General Procedure for the Synthesis of Phosphoramidate−Spermines ***3*** *and* ***9***. Fatty phosphites (1 equiv) and 1 equiv of triprotected spermine **1** or 3-aminopropylspermine **7** were dissolved in anhydrous CH_2Cl_2. Then, 10 equiv of CCl_4 and 1.5 equiv of DIPEA were added. The reaction was carried out under a nitrogen atmosphere and stirred for 1 h at 0 °C and

* To whom correspondence should be addressed. E-mail: jean-claude.clement@univ-brest.fr.
[†] UMR CNRS 6521.
[‡] INSERM U 613.

10.1021/bc070070w CCC: $37.00 © 2007 American Chemical Society
Published on Web 08/03/2007

Scheme 1. Some Structures of Cationic Lipids with a Cholesteryl Lipidic Moiety



then for 18 h at room temperature. After evaporation under reduced pressure, the residue was dissolved in $CHCl_3$ (50 mL) and washed with water (2 × 50 mL). The organic phase was separated, dried over anhydrous magnesium sulfate, filtered, and evaporated to give after purification by column chromatography ($CHCl_3$/EtOH 100:0 to 50:50) the desired compounds **2** (**2a**, R = $C_{14}H_{29}$; **2b**, R = $C_{18}H_{35}$) and **8** (**8a**, R = $C_{14}H_{29}$; **8b**, R = $C_{18}H_{35}$).

NMR data for **2a**: ^{1}H ($CDCl_3$) 5.28 (s, 2H), 3.95 (m, 4H), 3.22−2.94 (m, 12H), 1.80−1.25 (m, 12H), 1.44 (m, 27H), 1.30−1.25 (m, 44H), 0.80 (t, J = 6.7, 6H). ^{31}P ($CDCl_3$) 11.25.

NMR data for **2b**: ^{1}H ($CDCl_3$) 5.32 (s, 4H), 4.05 (m, 4H), 3.25−2.93(m, 12H), 1.99 (m, 8H), 1.57−1.64 (m, 12H), 1.44 (m, 27H), 1.29−1.20 (m, 44H), 0.88 (t, J = 6.7, 6H). ^{31}P ($CDCl_3$) 11.85.

NMR data for **8a**: ^{1}H ($CDCl_3$) 5.28 (s, 2H), 3.95 (m, 4H) 3.42−2.94 (m, 10H), 2.42 (m, 6H), 1.80−1.64 (m, 14H) 1.44 (m, 27H), 1.30−1.25 (m, 44H) 0.80 (t, J = 6.7, 6H). ^{31}P ($CDCl_3$) 9.71.

NMR data for **8b**: ^{1}H ($CDCl_3$) 5.34 (s, 4H), 3.98 (m, 4H), 3.15−2.95 (m, 10H), 2.43 (m, 6H), 1.99 (m, 8H), 1.80−1.64 (m, 14H), 1.43 (m, 27H), 1.29−1.20 (m, 44H), 0.89 (t, J = 6.7, 6H). ^{31}P ($CDCl_3$) 9.70.

Protected phosphoramidates (**2a**,**b** or **8a**,**b**) were then deprotected into a CH_2Cl_2−CF_3CO_2H (1/1 v/v) mixture during 2 h at room temperature (RT). After washing with water, then drying ($MgSO_4$), solvent was split off. Phosphoramidates−spermines **3** (**3a**, R = $C_{14}H_{29}$; **3b**, R = $C_{18}H_{35}$) and **9** (**9a**, R = $C_{14}H_{29}$; **9b**, R = $C_{18}H_{35}$) were obtained quantitatively as their trifluoroacetic salts.

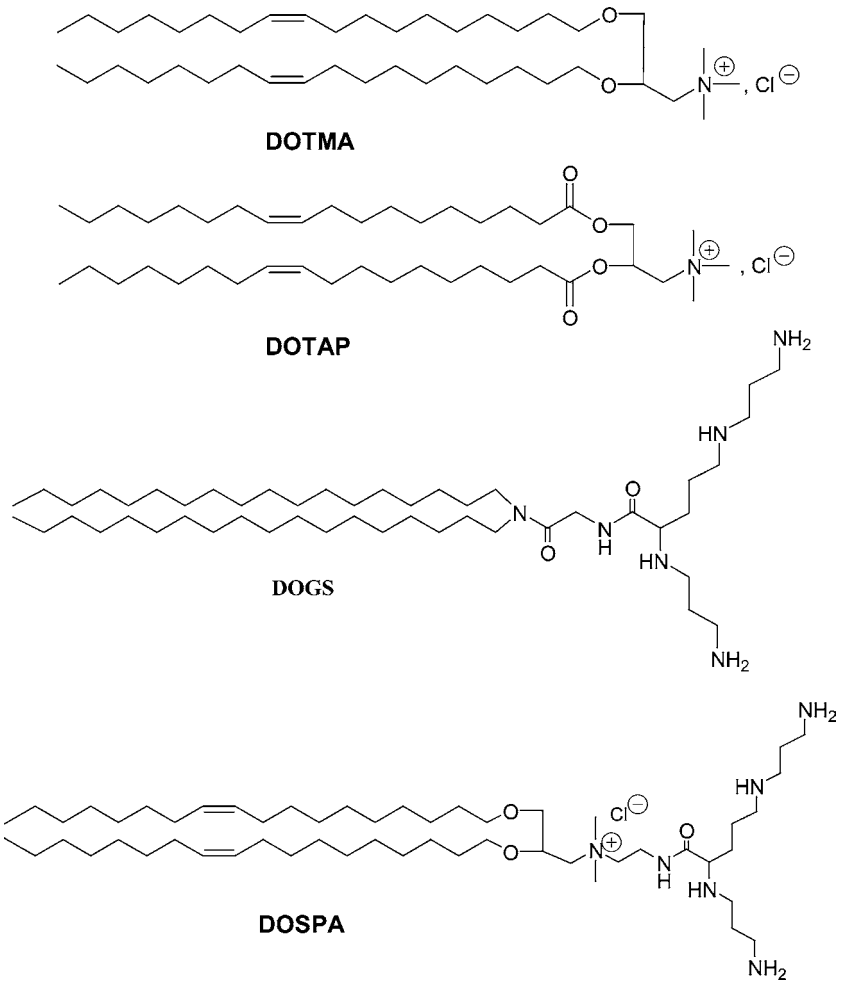
NMR data for **3a**: ^{1}H (DMSO-d_6) 3.83 (m, 4H), 2.99 (m, 2H), 2.96 (m, 2H), 2.89 (m, 2H), 2.87 (m, 2H), 2.86 (m, 2H), 2.76 (t, J = 7.5, 2H), 1.98 (q, J = 7.3, 2H), 1.75 (q, J = 6.9, 2H), 1.59 (m, 2H), 1.55 (m, 4H), 1.53 (m, 2H), 1.22 (m, 44H), 0.80 (t, J = 6,7, 6H). ^{13}C (DMSO-d_6) 65.9, 47.1, 45.5, 44.3, 43.7, 37.1, 36.7, 26.9, 24, 23.3, 30.5, 30−20, 13.9. ^{31}P (DMSO-d6) 11.21.

NMR data for **3b**: ^{1}H (DMSO-d_6) 5.3 (m, 4H), 3.81 (m, 4H), 2.98 (m, 2H), 2.85 (m, 2H), 2.83 (m, 2H), 2.75 (m, 2H), 2.63 (m, 2H), 2.60 (m, 2H), 1.96 (m, 8H), 1.72 (m, 2H), 1.70 (m, 2H), 1.55 (m, 4H), 1.46 (m, 2H), 1.38 (m, 2H), 1.22 (m, 44H), 0.84 (t, J = 6.9, 6H). ^{13}C (DMSO-d_6) 129.6, 65.5, 48.2, 46.2, 45.1, 42.2, 39.7, 36.7, 29.7, 27.5, 27.1, 26.5, 25.1, 24.7, 30−20, 13.8. ^{31}P (DMSO-d_6) 10.87.

NMR data for **9a**: ^{1}H (DMSO-d_6) 5.74 (m, 1H), 3.81 (m, 4H), 2.85 (t, J = 7.2, 2H), 2.77 (t, J = 7.4, 2H), 2.74 (m, 2H), 2.72 (m, 2H), 2.63 (m, 2H), 2.38 (t, J = 6.5, 2H), 2.36 (t, J = 6.5, 2H), 2.33 (t, J = 6.8, 2H), 1.70 (m, 2H), 1.61 (m, 2H), 1.53 (m, 2H), 1.48 (m, 2H), 1.40 (m, 2H), 1.37 (m, 2H), 1.22 (m, 44H), 0.84 (t, J = 6.6, 6H). ^{13}C (DMSO-d_6) 65.8, 52.7, 50.5, 50.2, 48.5, 45.7, 39.5, 37.5, 37.2, 29.7, 28.9, 28.8, 28.7, 26.1, 24.7, 30−20, 14. ^{31}P (DMSO-d_6) 10.20.

NMR data for **9b**: ^{1}H (DMSO-d_6) 5.3 (m, 4H), 4.81 (m, 1H), 3.80 (m, 4H), 2.85 (m, 2H), 2.82 (m, 2H), 2.76 (m, 2H), 2.74 (m, 2H), 2.72 (m, 2H), 2.40 (m, 2H), 2.38 (m, 2H), 2.33 (m, 2H), 1.96 (m, 8H), 1.78 (m, 2H), 1.62 (m, 2H), 1.55 (m, 2H), 1.49 (m, 2H), 1.48 (m, 2H), 1.39 (m, 2H), 1.22 (m, 44H), 0.84 (t, J = 6.6, 6H). ^{13}C (DMSO-d_6) 129.6, 65, 52.6, 50.7, 47.5, 44.9, 39, 37.3, 37, 29.9, 28.9, 28.8, 28.7, 26.5, 25, 24.4, 30−20, 13.8. ^{31}P (DMSO-d_6) 10.72.

Scheme 2. Some Cationic Lipids with a Double-Tailed Hydrocarbon Chain



*N^4-Chlolesteryl−Spermine **5***. To a mixture of 0.688 g of triBocSpermine **1** (1.37 mmol) and 0.360 mL (2.06 mmol) of diisopropylethylamine (DIPEA) into CH_2Cl_2 (10 mL) at 0 °C is added a solution of 0.614 g of cholesterylchloroformate (1.37 mmol) into CH_2Cl_2 (10 mL). The mixture is kept 1 h at 0 °C, then 18 h at RT under nitrogen atmosphere. After washing (H_2O) and drying ($MgSO_4$), the solvent is split off. Purification was accomplished by column chromatography (silica gel), eluting with a gradient of 5−20% EtOH in CH_2Cl_2, and led to 0.8 g (64%) of the triprotected compound **4** as white crystals. ^{1}H NMR ($CDCl_3$) 5.37 (s, 1H), 5.29 (s, 2H), 4.50 (m, 1H), 3.40−3.05 (m, 12H), 2.38−2.20 (m, 2H), 2.10−1.05 (m, 61H), 1.01 (s, 3H), 0.91 (m, 3H), 0.86 (d, J = 6.5, 6H), 0.68 (s, 3H).

Compound **4** was then deprotected as described above, and the cholesterylspermine **5** was thus obtained quantitatively. ^{1}H NMR ($CDCl_3$) 5.37 (s, 1H), 4.50 (m, 1H), 3.40−3.05 (m, 12H), 2.32−2.15 (m, 2H), 2.10−0.94 (m, 34H) 0.99 (s, 3H), 0.91 (m, 3H) 0.86 (d, J = 7, 6H), 0.67 (s, 3H).

*N^4-Chlolesteryl-(4-amidopropyl)−Spermine **11***. From 0.874 g of cholesterylchloroformate (1.95 mmol), 1.09 g of triprotected 4-aminopropylspermine **7** (1.95 mmol), and 0.5 mL of DIPEA (2.92 mmol) into 30 mL of CH_2Cl_2, with the same conditions as for the synthesis of **5**, 1.23 g (1.26 mmol, 65%) of the triprotected derivative **10** is obtained as white crystals after purification by column chromatography (silica gel, eluting with a gradient of 5−50% EtOH in CH_2Cl_2). ^{1}H NMR ($CDCl_3$) 5.37 (s, 1H), 5.29 (s, 2H), 4.48 (m, 1H), 3.22−2.95 (m, 10H), 2.43−2.20 (m, 8H), 2.05−1.01 (m, 63H), 1.01 (s, 3H), 0.91 (m, 3H), 0.86 (d, J = 6.5, 6H), 0.68 (s, 3H).

Deprotection in a CF_3CO_2H/CH_2Cl_2 mixture as described above led quantitatively to cholesteryl derivative **11**. ^{1}H NMR ($CDCl_3$) 5.37 (s, 1H), 4.48 (m, 1H), 3.22−2.90 (m, 10H), 2.43−2.15 (m, 8H), 2.05−1.01 (m, 36H), 1.01 (s, 3H), 0.91 (m, 3H), 0.86 (d, J = 6.5, 6H), 0.68 (s, 3H).

***In Vitro* Experiments.** *Cell Culture.* Two different cell lines (A549 and HeLa) were used. The alveolar type II epithelial cell line A549 (*19*) and the human adenocarcinoma epithelial cell line HeLa were obtained from the American Type Culture Collection (respectively, cat. no. CCL-185 and ccl-2, ATCC, Rockville, MD). These cells were grown in D-MEM (Gibco-BRL, UK) and supplemented with 10% fetal calf serum (FCS) (Gibco-BRL, UK) and 100 U/mL of penicillin/streptomycin. All the cells were maintained in a humidified incubator with 5% CO_2 at 37 °C.

Complex Formulation. Each cationic lipid was prepared alone or in combination with the neutral colipid DOPE (w/w = 1:1). Lipids were kept and formulated in chloroform solutions; then, chloroform was removed by rotary evaporation to produce dried lipid films. A total of 1 mL of sterile pyrogen-free DI water per milligram of lipid was added, and the vials were sealed and stored at 4 °C overnight. Vesicles were then prepared by sonicating the aqueous suspension for 10 min in a bath sonicator.

Cationic lipid/DNA complexes were formed as follows: plasmid DNA (1 μg) was diluted with sterile pyrogen-free deionized water and added to the lipid solution in a polystyrene tube. Lipoplexes were kept at room temperature for 30 min before being used for transfection.

Determination of the Lipoplex Charge Ratio. The charge ratio was calculated theoretically as the molar ratio of the cationic lipids to DNA. In order to study the impact of the formulation on gene expression, various charge ratios (±) were prepared with a constant amount of pDNA (1 μg). As a control, 2 μL of

Lipofectamine (Invitrogen) was used, accordingly to manufacturer's instructions, and in these conditions, for 1 μg of delivered DNA, the N/P ratio is equal to 2.

Transfection Protocol. Cells were seeded 24 h before transfection onto a 24-well plate at a density of 100 000 cells per well and incubated overnight in a humidified 5% CO_2 atmosphere at 37 °C. Transfection was performed as described by Felgner et al. (*4*) with the following modifications. Appropriate amounts of the cationic lipids and the plasmid vector in OptiMem were complexed, and about 200 μL was added to each well. After 2 h 30 min incubation at 37 °C, the medium was removed, and fresh medium was added. Following a further 48 h at 37 °C, the cells were assayed for luciferase expression using a chemiluminescent assay (Promega). Assays were carried out as described by the manufacturer. The total protein concentration of the cell culture was determined using the BC assay kit (Uptima). Luciferase activity of each condition was expressed as total relative light units (Total RLU) per mg of total protein. Results are reported as means ± SEM.

DNA Binding Ability. To 1 μg of plasmid DNA in Optimem (Gibco) were added cationic lipids at concentrations corresponding to an N/P charge ratio ranging from 0.5 to 8. The mixture was incubated for 30 min at room temperature. The complexes were subjected to electrophoresis in 1% agarose gel at 100 V, 90 mA. The gel was stained with ethidium bromide (10 mg/mL) and visualized on an UV illuminator (Fischer Bioblock).

FRET Experiments. The FRET method described by Pagano et al. (*10*) was used for assaying membrane fusion. In this method, membranes labeled with a combination of fluorescence energy transfer donor and acceptor lipid probes, respectively, NBD-PE and Rhod-PE (both from Molecular Probes), are mixed with unlabeled cationic lipids.

As the labeled membrane, we used liposomes made with L-α-phosphatidylcholine (PC) and fluorescent probes, or liposomes made with PC, L-α-phosphatidylethanolamine (PE), L-α-phosphatidyl-L-serine (PS), cholesterol (Chol), and fluorescent probes, (PC/PE/PS/Chol/NBD-PE/Rhod-PE approximately 44/25/10/20/0.8/0.2 m/m), a lipid composition close to that of the plasma membrane. All lipids were from Sigma. Stock solutions of each lipid were prepared in chloroform and stored in the dark, at 4 °C. Aliquots of these solutions were mixed and dried under reduced pressure. The dried lipid film formed was hydrated with a 5 mM Hepes buffer (pH 7 or pH 5.5) containing NaCl (150 mM). Suspensions were vigorously vortexed for 5 min and sonicated at 40 °C for 10 min.

Stock solutions of each cationic lipid were prepared in chloroform (5 $g.L^{-1}$). An aliquot was dried under reduced pressure, and liposome suspensions (1 $g.L^{-1}$) were prepared as described before.

Labeled and unlabeled liposomes were added in a buffer solution and vortexed. The final Rhod-PE and NBD-PE concentrations were 6.10^{-8} $mol.L^{-1}$ and 3.10^{-7} $mol.L^{-1}$. The labeled membrane final concentration was 15 $mg.L^{-1}$, corresponding approximately to 2.10^{-5} M for PC.

The Rhod-PE/lipid ratio was chosen after determination of the FRET efficiency versus Rhod-PE/PC molar ratio. A ratio close to 0.003 was chosen so that lipid fusion undergoes a significant decrease of FRET efficiency. NBD-PE concentrations did not affect the FRET efficiency as described before (*10*).

Fluorescence measurements were performed 1 h later, at room temperature, by exciting the sample at 450 nm. A Varian Cary Eclipse Fluorescence spectrophotometer was used. Following each measurement, liposomes were disrupted with Triton X-100 (1% final concentration) in order to eliminate energy transfer and to allow the determination of the concentration of NBD-PE from its emission intensity.

Table 1. Potentiometric Determination of the pK_a of Phosphoramidate−Spermines

	3b	**9b**	spermine [18]
pK_1	10.60	11.10	10.8
pK_2	9.80	10.78	10.0
pK_3	7.00	8.62	8.8
pK_4	< 2	6.78	7.90

The efficiency of energy transfer was calculated from the fluorescence emission intensity of NBD-PE at 530 nm by using eq 1

$$E = 1 - F/F_0 \quad (1)$$

Fluorescence intensities were recorded in the presence (F_0) and absence (F) of Triton X-100. Values obtained in the presence of Triton X-100 were corrected for sample dilution and for the effect of Triton-X on the quantum yield of NBD-PE.

The relative fluorescence intensity, E_R (in %), is calculated using relation 2

$$E_R = (E_{mix}/E_{lab}) \times 100 \quad (2)$$

where E_{mix} and E_{lab} are the FRET efficiency calculated in the presence (E_{mix}) or absence (E_{lab}) of unlabeled liposomes for a same labeled liposome concentration.

pK_a Determinations. Potentiometric measurements were performed in a jacketed cell thermostated at 25.0 °C, kept under inert atmosphere of purified argon, using an automatic titrator (Metrohm, DMS Titrino 716) connected to a microcomputer. The free hydrogen concentrations were measured with a glass−Ag/AgCl combined electrode (Metrohm) filled with 0.1 M NaCl. The electrode was calibrated in order to read $-\log[H^+]$, designated as p[H], by titration of a small quantity of diluted HCl by standardized NaOH at 0.02 M ionic strength and 25 °C (and determining the equivalent point by the Gran's method) followed by adjustment of the meter by using the program GLEE so as to minimize the calculated p[H] vs observed values. log K_w for the system, defined in terms of $\log([H^+][OH^-])$, was found to be −13.78 at the ionic strength employed and was maintained fixed during refinements (*11*, *12*). NaCl was employed as the supporting electrolyte to maintain the ionic strength at 0.10 M.

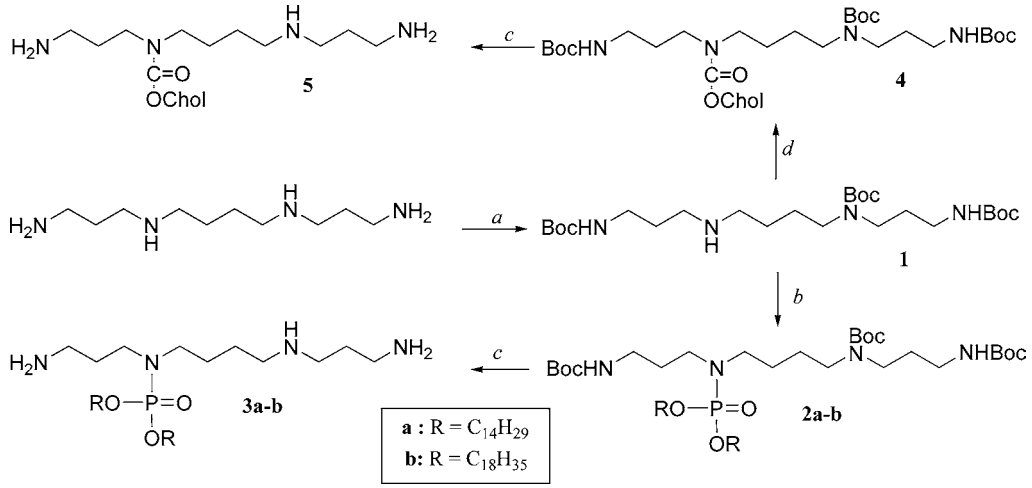
Potentiometric measurements obtained from NaOH titration of protonated polyamines were made at about 1 mM in concentration and ionic strength μ = 0.10 M (NaCl). Each titration makes use of at least 10 points per neutralization of a hydrogen ion equivalent, and titrations were repeated until a satisfactory agreement was reached. A minimum of three sets of data was used in each case to calculate the overall stability constants and their standard deviations. The standard deviations obtained for the different recognition constants were ±0.02 of the last significant digit reported in Table 1. The range of accurate p[H] measurements was considered to be 2−12. Equilibrium constants and species distribution diagrams were calculated by using the program *HYPERQUAD 2003* (*13*).

The stability constants K_{lh} were noted with respect to ternary species L_lH_h where l and h are, respectively, the stoichiometric number of L (ligand) and H (proton).

RESULTS AND DISCUSSION

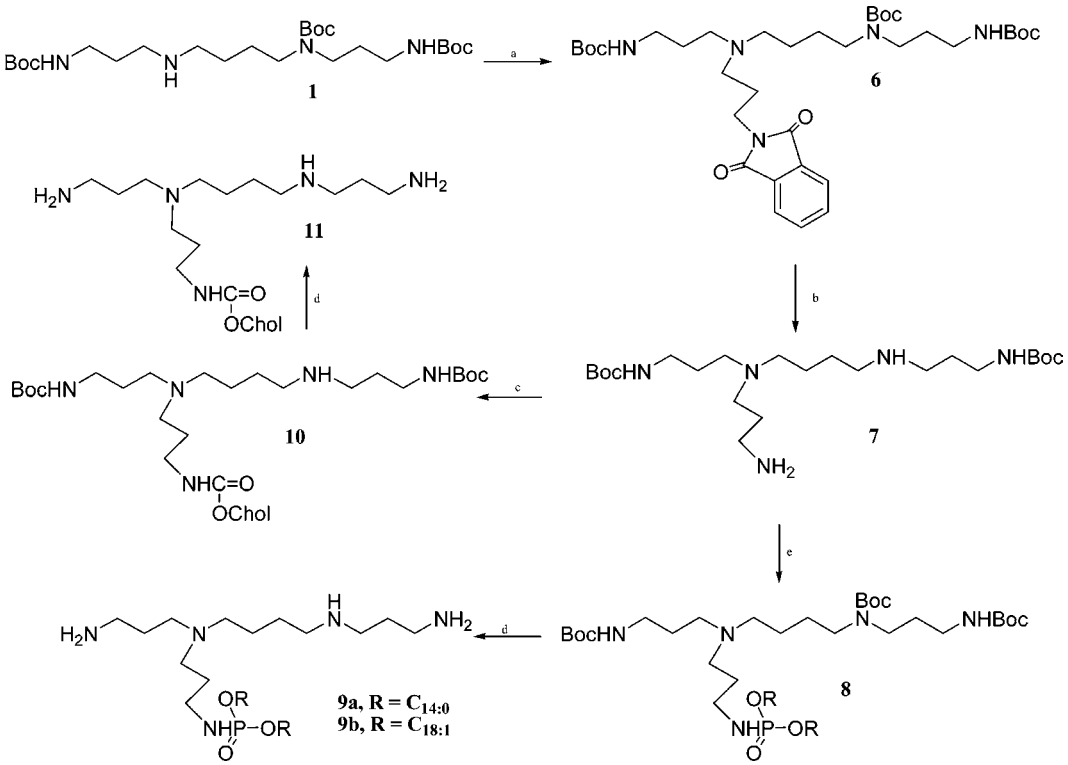
Syntheses of Lipidic Spermines. One of the most popular routes to phosphoramidates is the reaction of a hydrogen phosphite with an amine, in the presence of carbon tetrachloride (*14*). We adapted this procedure for reacting lipidic phosphites with spermine, first triprotected with Boc-ON (*15*), thus leading to lipophosphorylated spermines **3a** (R = $C_{14:0}$) or **3b** (R = $C_{18:1}$), after TFA deprotection (lipidic phosphites were obtained

Scheme 3. Syntheses of Lipophosphoramidate−Spermines 3 and Cholesteryl Spermine 5[a]



[a] (a) Boc-ON (3 equiv)/THF, 18 h, RT, 72%; (b) $(RO)_2P(O)H/CCl_4$ (10 equiv)/DIPEA (1.5 equiv), RT, 18 h; (c) TFA/CH_2Cl_2 (1:1), RT, 3 h; (d) CholOC(O)Cl, DIPEA (1.5 equiv), RT, 18 h.

Scheme 4. Syntheses of Lipophosphoramidate−Propylspermines 9 and Cholesteryl−Propylspermine 11[a]



[a] (a) 3-Bromopropylphthalimide (1.25 equiv), K_2CO_3 (5 equiv), CH_3CN, reflux, 18 h, 66%; (b) hydrazine monohydrate (50 equiv), THF/EtOH (80:20), 80 °C, 5 h; then 50 °C, 18 h, 80%; (c) cholOC(O)Cl, DIPEA (1.5 equiv), RT, 18 h; (d) TFA/CH_2Cl_2 (1:1), RT, 3 h; (e) $(RO)_2P(O)H/CCl_4$ (10 equiv)/DIPEA (1.5 equiv), RT, 18 h.

by reaction of fatty alcohols with diphenyl phosphite). For the purpose of comparison with other lipidic parts, the cholesteryl derivative of spermine **5** was synthesized and obtained unambiguously by reaction of cholesteryl chloroformate with Boc-triprotected spermine **1** and TFA deprotection (Scheme 3).

During our previous work on phosphonolipids as DNA carriers, we noticed that, when an ammonium cation was replaced by a phosphonium or arsonium (i.e., a more bulky polar head), a good transfection efficiency required a longer spacer between the cationic part and the phosphoryl group (*16*, *17*). So, we also designed and synthesized analogues of lipids **3** and **5** including a longer spacer between spermine and the lipidic part. For that purpose, the Boc-triprotected spermine with a pendant aminopropyl arm was first synthesized from Boc-triprotected spermine **1** and 3-bromopropylphtalimide, then hydrazinolysis of the phtalimide protecting group. Subsequent reaction with fatty phosphites or cholesteryl chloroformate led to phosphoramidates **9a** and **9b** or cholesteryl derivative **11,** after deprotection (Scheme 4).

***In Vitro* Biological Tests.** *In Vitro Transfection Efficiency.* Two different cell lines (A549 and HeLa) were used to compare the efficiency of the different lipidic parts, without (**3b**, **5**) or with a spacer (**9b**, **11**), and with (+D) or without DOPE added. The efficacy of each lipid (expressed as luciferase activity) was established for an increasing N/P charge ratio from 0.5 to 8, according to routinely used and previously described procedures (*4*, *9*, *16*). As an example, Chart 1 shows the values of total RLU/mg of protein for HeLa cells, according to increasing N/P

Chart 1. Comparison of Charge Ratio and DOPE Influence on the Transfection Efficiency for HeLa Cell Line

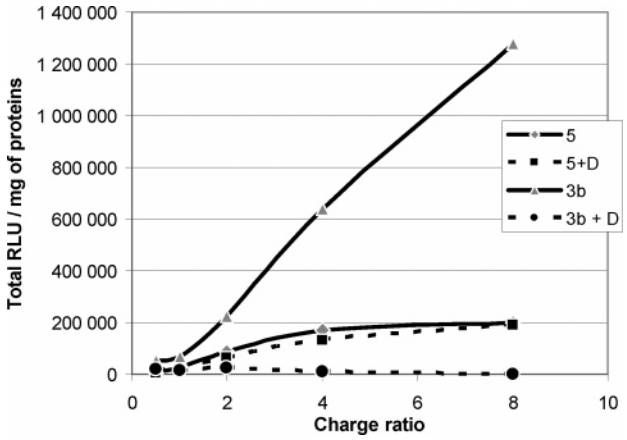


Chart 2. Luciferase Activity for HeLa Cells[a]

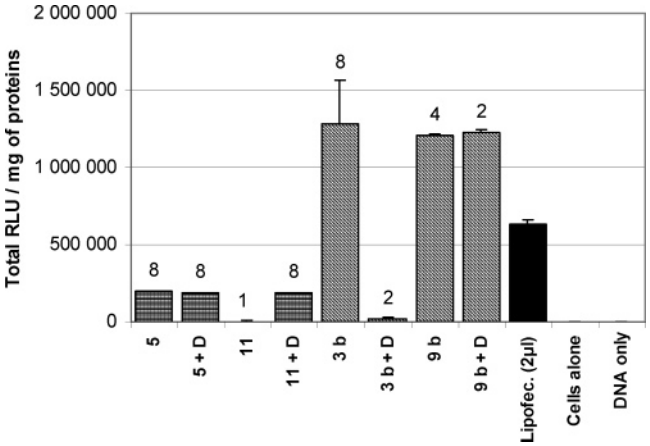
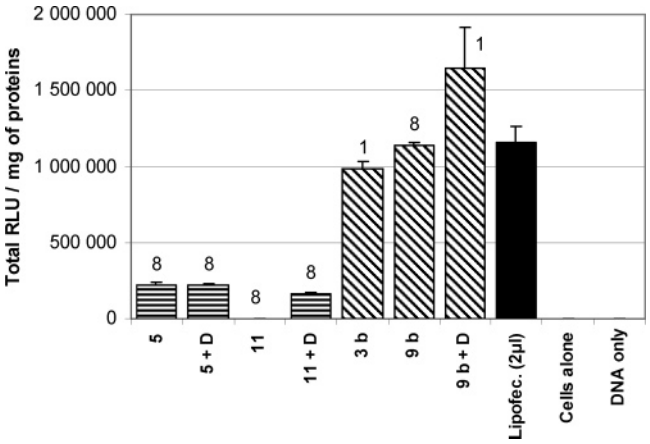


Chart 3. Luciferase Activity for A549 Cells[a]



ratios. Charts 2 and 3 indicate the average efficiencies of each lipid at its better N/P ratio (marked on top of each bar). Using the above-mentioned protocols and formulations, the efficacy of the phosphoramidates has the same magnitude as lipofectamine or slightly higher, whereas the cholesteryl derivatives were about ten times lower. But, insofar as the lipid/DOPE ratio used was the same (1:1) in all our experiments, these results have not a comparative but only an indicative value, since formulations were not optimized for each lipid. Compound **5**, for instance, was reported as most efficient at a 1:2 lipid/DOPE ratio (*3*).

DNA Binding Ability. Electrophoretic mobility of plasmid DNA was examined with increasing N/P ratios (0.5−8) using 1% agarose gel (DNA was visualized by ethidium bromide staining). Complete binding of DNA was observed at an N/P ratio lower than 2 for phosphoramidate **9b**, for instance, whereas binding was not complete at a N/P ratio of 8 for cholesteryl spermine **5** (Figure 1).

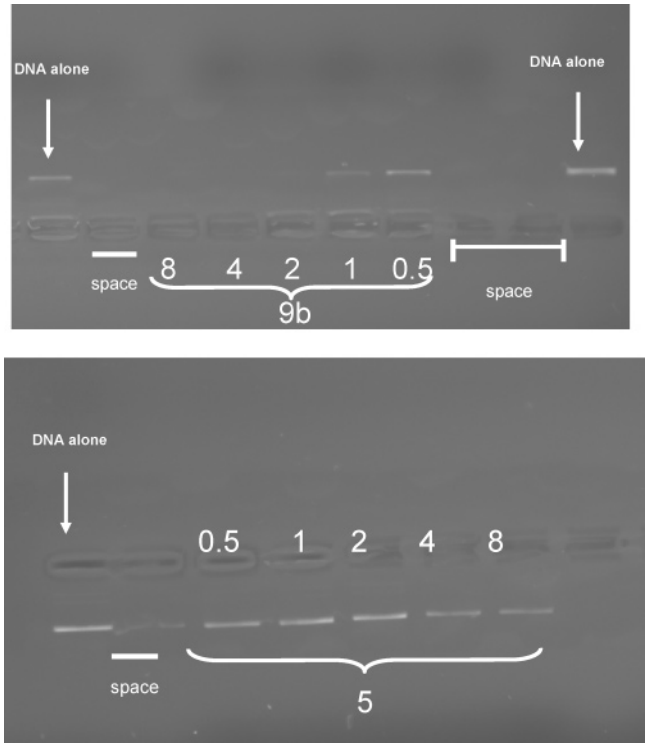


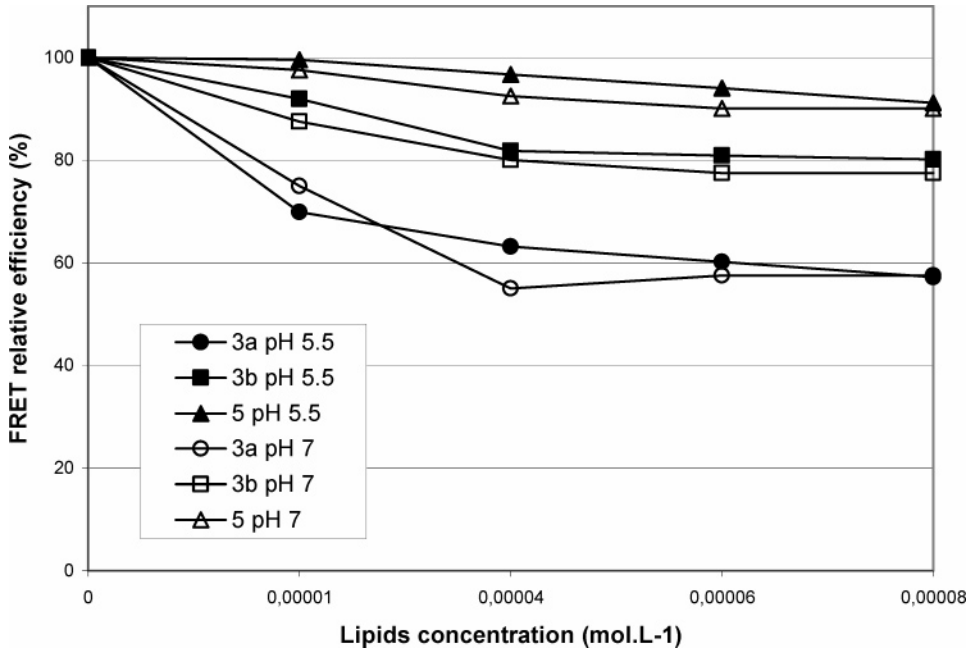
Figure 1. DNA binding ability of phosphoramidate **9b** and cholesteryl **5**.

FRET Experiments. In an attempt to explain these results, we undertook a comparative study toward the ability of these lipidic spermines to disrupt an artificial membrane with a lipid composition close to that of the plasma membrane. We exploited the widely used fluorescence resonance energy transfer (FRET) technique (*10*). Briefly, this technique depends upon the interactions that occur between two fluorophores when the emission band of one (the energy donor) overlaps with the excitation band of the second (the energy acceptor) when the probes are in close proximity. If a couple of two lipidic fluorophores, one energy donor (NBD-PE, for instance) and one energy acceptor (Rho-PE, for instance) is introduced into a liposome, any fusion event of such a doubly labeled liposome with a second liposome (devoid of any fluorophore) will decrease the efficiency of resonance energy transfer. Thus, any decrease in FRET efficiency provides evidence for membrane fusion.

The model membrane was made with PC, L-α-phosphatidylethanolamine (PE), L-α-phosphatidyl-L-serine (PS), cholesterol (Chol), and fluorescent probes (PC/PE/PS/Chol/NBD-PE/Rhod-PE approximately 44/25/10/20/0.8/0.2 m/m). To that membrane were added the different lipidic spermines at increasing concentrations from 10^{-6} to 10^{-4} mol/L, with DOPE added (1:1 m/m) or not, in each case. Chart 4 (no DOPE added) is a representative example of the observed differences between cholesteryl spermine **5** (90% average efficacy) and phosphoramidates **3a** and **3b** (60% and 80% average efficacy, respectively).

From this example, a correlation between FRET and *in vitro* efficacies seems to appear, since phosphoramidates **3a** and **3b** exhibited lower FRET values than cholesteryl derivative **5**, thus indicating a theoretical greater membrane-disrupting ability, at a pH of 7 (extracellular) or 5.5 (endosomal). However, as the curves were practically merged for the two pH values, there is

Chart 4. Comparative FRET Efficiency of Phosphoramidates 3 and Cholesteryl 5 at pH 5.5 and 7



no obvious endosomal acidity-induced advantage for lipophosphoramidates. The same experiments conducted with compounds **9a**, **9b**, and **11** gave rather similar results, but the lack of reproducibility to get homogeneous vesicles, notably with cholesteryl derivative **11**, made those results (and therefore a comparison) inconclusive (data not shown).

Sizes and pK_a. Another difference lies in the behavior of these lipids in water: after 5 min in an ultrasonic bath, the average sizes of the particles of each suspended lipid (1 mg/mL) were 2800 and 640 nm for cholesteryl derivatives **5** and **11**, compared to 290 and 770 nm for phosphoramidates **3b** and **9**.

The pK_a values of the two phosphoramidates **3b** and **9b** were determined by potentiometric titration (see Experimental Procedures for details) and quoted in Table 1. When compared to the pK_a of spermine, the presence of the lipidic phosphoramidate obviously leads to a decrease of the basicity of the third amine in the case of **3b** (7.0 vs 8.8 for spermine) and of the fourth for **9b** (6.78 vs 7.9 for spermine).

CONCLUSION

As previously observed in the case of monocationic lipids (*9*), the use of a lipophosphoramidate group, as linker between the lipidic part and the cationic head, is a very attractive approach to design synthetic vectors for DNA delivery. In this study, the lipophosphoramidate lipidic group has been attached either directly or *via* a short spacer on a spermine unit. In a will of comparison, the spermine has been also functionalized with a cholesterol unit, acting as the lipidic part, *via* a carbamate group. We observed that the influence of the lipid part on the transfection efficiency is important. Notably, the spermine−lipid vectors having two oleoyl chains attached on a phosphoramidate group are the most efficient. Also, the addition of DOPE as a neutral helper lipid in the formulation has no effect in the case of compound **9b** or a dramatically negative effect in the case of compound **3b**. When the spermine−phospholipid is formulated alone, the presence or absence of a spacer between the spermine unit and the phosphoramidate group has only a low influence on the transfection results. As in the case of DOGS (*7*), the introduction of a lipidic group close to the third amine of spermine lowers the value of its pK_a, thus widening the field of basicity, hence, probably, an increased "buffer effect". This explanation could be one of the reasons for the efficiency of compounds **3b** and **9b**.

However, the standard formulations used were not optimized, with regard to the optimal cationic lipid/DOPE ratios (which, of course, are not necessarily the same for each compound) or concerning the sizes of lipidic vesicles in water. Since liposomes have sizes from 290 nm for lipid **3b** to 2800 nm for cholesteryl **5** (and no attempt was made to reduce these sizes), comparisons must be taken cautiously and have only an indicative value.

Since the last pK_a values of **3b** and **9b** are 7.0 and 6.78, respectively, these tri- and tetraamines can be considered polycationic species at the physiological pH despite the fact that a local variation of pH could modify the cationic state of these vectors. In another work (*20*), we examined the transfection efficacies of lipophosphoramidates bearing a couple of cations (N^+/P^+ or N^+/As^+), permanent regardless of the pH. Transfection assays with these dicationic compounds, performed on the same cell lines (HeLa and A549), with the same experimental conditions, systematically resulted in luciferase levels twice as high.

Nevertheless, the lipophosphoramidate group constitutes an interesting alternative to the "classical" cholesteryl or double aliphatic chains generally used as the lipidic part in cationic lipids. As lipophosphoramidates were found especially efficient for *in vivo* experiments when associated to an ammonium, a phosphonium, or an arsonium cation, the *in vivo* activity of lipids **3** and **9** will be evaluated in the near future.

ACKNOWLEDGMENT

"Brest Métropole Océane" is gratefully acknowledged for a grant to M.M. The authors thank also the "Conseil Régional de Bretagne" and "Vaincre La Mucoviscidose" for financial support and the CNRS for a postdoctoral grant to F.L.

LITERATURE CITED

(1) Gao, X., and Huang, L. (1991) A novel cationic liposome reagent for efficient transfection of mammalian cells. *Biochem. Biophys. Res. Commun. 179*, 280.

(2) Vigneron, J. P., Oudrhiri, N., Fauquet, M., Vergely, L., Bradley, J. C., Basseville, M., Lehn, P., and Lehn, J. M. (1996) Guanidinium-

cholesterol cationic lipids: efficient vectors for the transfection of eukaryotic cells. *Proc. Natl. Acad. Sci. U.S.A. 93*, 9682−9686.
(3) Lee, E. R., Marshall, J., Siegel, C. S., Jiang, C., Yew, N. S., Nichols, M. R., Nietupsky, J. B., Ziegler, R. J., Lane, M. B., Wang, K. X., Wan, N. C., Scheule, R. K., Harris, D. J., Smith, A. E., and Cheng, S. H. (1996) Detailed analysis of structures and formulations of cationic lipids for efficient gene transfer to the lung. *Hum. Gene Ther. 7*, 1701−1717.
(4) Felgner, P. L., Gadek, T. R., Holm, M., Roman, R., Chan, H. W., Wenz, M., Northrop, J. P., Ringold, G. M., and Danielsen, M. (1987) A highly efficient, lipid-mediated DNA-transfection procedure. *Proc. Natl. Acad. Sci. U.S.A. 84*, 7413−7417.
(5) Miller, A. D. (1998) Cationic liposomes for gene therapy. *Angew. Chem., Int. Ed. 37*, 1768−1785.
(6) Martin, B., Sainlos, M., Aissaoui, A., Oudrhiri, N., Hauchecorne, M., Vigneron, J. P., Lehn, J. M., and Lehn, P. (2005) The design of cationic lipids for gene delivery. *Curr. Pharm. Des. 11*, 375−394.
(7) Behr, J. P., Demeneix, B., Loeffer, J. P., and Perez-Mutul, J. (1989) Efficient gene transfert into mammalian primary endocrine cells with lipopolyamine-coated DNA. *Proc. Natl. Acad. Sci. U.S.A. 86*, 6982−6986.
(8) Hawley-Nelson, P., Ciccarone, V., Geheyehu, G., Jesee, J., and Felgner, P. L. (1993) Lipofectamine reagent: a new, higher efficiency polycationic liposome transfection reagent. *Focus 15*, 73.
(9) Picquet, E., Le Ny, K., Delépine, P., Montier, T., Yaouanc, J. J., Cartier, D., Des Abbayes, H., Férec, C., and Clément, J. C. (2005) Cationic lipophosphoramidates and lipophosphoguanidines are very efficient for in vivo DNA delivery. *Bioconjugate Chem. 16*, 1051−1053.
(10) Struck, D. K., Hoeckstra, D., and Pagano, R. E. (1981) Use of resonance energy transfer to monitor membrane fusion. *Biochemistry 20*, 4093−4099.
(11) Gran, G. (1952) Determination of the equivalence point in potentiometric titrations. *Analyst (London) 77*, 661.
(12) Martell, A. E., and Motekaitis, R. J. (1992) *Determination and Use of Stability Constants*, 2nd ed., John Wiley and Sons, New York.
(13) Gans, P., Sabatini, A., and Vacca, A. (1996) Investigation of equilibria in solution. Determination of equilibrium constants with the HYPERQUAD suite of programs. *Talanta 43*, 1739.
(14) Atherton, F. R., Openshaw, H. T., and Todd, A. R. (1945) Studies on phosphorylation. Part I. Dibenzylchlorophosphonate as a phosphorylating agent. *J. Chem. Soc*. 382−385.
(15) Cohen, G. M., Cullis, P. M., Hartley, J. A., Marther, A., Symons, C. R., and Wheelhouse, R. T. (1992) Targeting of cytotoxic agents by polyamines: synthesis of chlorambucil-spermidine conjugate. *J. Chem. Soc.: Chem. Commun.* 298−306.
(16) Floch, V., Loisel, S., Guénin, E., Hervé, A. C., Clément, J. C., Yaouanc, J. J., des Abbayes, H., and Férec, C. (2000) Cation substitution in cationic phosphonolipids: a new concept to improve transfection activity and decrease cellular toxicity. *J. Med. Chem. 43*, 4617−4628.
(17) Guénin, E., Hervé, A. C., Floch, V., Loisel, S., Yaouanc, J. J., Clément, J. C., Férec, C., and des Abbayes, H. (2000) Cationic phosphonolipids containing quaternary phosphonium and arsonium groups for DNA transfection with good efficiency and low cellular toxicity. *Angew. Chem., Int. Ed. 39*, 629−631.
(18) Bergeron, R. J., McManis, J. S., Weimar, W. R., Porter, C., and Vinson, J. R. T. (1995) The role of charge in polyamine analogue recognition. *J. Med. Chem. 38*, 2278−2285.
(19) Cushion, M. T., Ruffolo, J. J., and Walzer, P. D. (1988) Analysis of the developmental stages of *Pneumocystis carinii*, in vitro. *Lab Invest. 58*, 324−331.
(20) Mével, M., Montier, T., Lamarche, F., Delépine, P., Le Gall, T., Yaouanc, J. J., Jaffrès, P. A., Cartier, D., Lehn, P., and Clément, J. C. Dicationic lipophosphoramidates as DNA carriers. *Bioconjugate Chem.*, in press.

BC070070W

Di(azacrown) Conjugates of 2′-*O*-Methyl Oligoribonucleotides as Sequence-Selective Artificial Ribonucleases

Teija Niittymäki, Pasi Virta, Kaisa Ketomäki, and Harri Lönnberg*

Department of Chemistry, University of Turku, FIN-20014 Turku, Finland. Received March 2, 2007; Revised Manuscript Received July 5, 2007

Functionalized 2′-*O*-methyl oligoribonucleotides bearing two 3-(3-hydroxypropyl)-1,5,9-triazacyclododecane ligands attached via a phosphodiester linkage to a single non-nucleosidic building block have been prepared on a solid-support by conventional phosphoramidite chemistry. The branching units employed for the purpose include 2,2-bis(3-hydroxypropylaminocarbonyl)propane-1,3-diol, 2-hydroxyethyl 3′-*O*-(2-hydroxyethyl)-*β*-D-ribofuranoside, and 2-hydroxyethyl 2′-*O*-(2-hydroxyethyl)-*β*-D-ribofuranoside. Each of these has been introduced as a phosphoramidite reagent either into the penultimate 3′-terminal site or in the middle of the oligonucleotide chain. The dinuclear Zn^{2+} complexes of these conjugates have been shown to exhibit enhanced catalytic activity over their monofunctionalized counterpart, the 3′-terminal conjugate derived from 2-hydroxyethyl 3′-*O*-(2-hydroxyethyl)-*β*-D-ribofuranoside being the most efficient cleaving agent. This conjugate cleaves an oligoribonucleotide target at a single phosphodiester bond and shows turnover and 1000-fold cleaving activity compared to the free monomeric Zn^{2+} chelate of 1,5,9-triazacyclododecane.

INTRODUCTION

Development of artificial ribonucleases, i.e., agents able to cleave RNA phosphodiester bonds sequence-selectively, has been the subject of numerous studies during the past decade (*1*−*6*). Such man-made catalysts are believed to find applications as artificial restriction enzymes with which large RNA molecules could be tailored in a predesign manner *in vitro* (*7*−*11*) and hopefully also as chemotherapeutic agents capable of silencing an overexpressed gene by recognizing and destroying the respective mRNA (*12*−*16*). Although recent advances in gene silencing by short double-stranded RNAs (siRNA) (*17*−*21*) has diminished the interest in conventional antisense approaches, the recognition of multiple roles of RNA in gene regulation has simultaneously made RNA an object of extensive studies. Accordingly, development of tools useful in chemical manipulation of RNA, such as artificial ribonucleases, still appears worthwhile.

Most of the artificial ribonucleases described so far consist of a metal ion chelate tethered to an oligonucleotide or PNA-oligomer that serves as a sequence-recognizing moiety (*1*−*6*), although some purely organic conjugates have recently been introduced (*22*−*24*). Among the metal-ion-dependent conjugates, those derived from lanthanide ion chelates exhibit the highest cleaving activity (*25*−*31*), followed by nucleases based on intracellularly occurring Cu^{2+} (*32*−*36*) and Zn^{2+} ions (*37*−*41*). The most efficient lanthanide ion conjugates, *viz.* the 5′-tethered Dy^{3+}-texaphyrin oligonucleotide conjugates (*28*), exhibit a half-life of 2 h at pH 7.5 and 37 °C, when used in a stoichiometric amount compared to the oligoribonucleotide target. The best Cu^{2+}- and Zn^{2+}-based cleaving agents, *viz.* the Cu^{2+} (*34*) and Zn^{2+} complexes (*39*) of intrachain 2,9-dimethyl-5-aminophenanthroline−oligonucloeotide conjugates, in turn, show under the same conditions half-lives of 8 and 9 h, respectively. A comparable cleaving activity, but at a lower Zn^{2+} concentration, has been obtained with a dinuclear Zn^{2+} complex of a conjugate bearing a 5′-terminal 3,5-bis[di(pyridin-2-ylmethyl)aminomethyl]phenoxy group (*38*). By simultaneous use of 3′- and 5′-tethered Cu^{2+}-terpyridine conjugates that hybridize to the target leaving no gap between them, the half-life is reduced to 5 h (*36*) and by covalent 3′,5′-bridging of the two oligonucleotide conjugates to 2.5 h (*35*). With the most efficient metal-ion-independent oligonucleotide conjugates, the 5′-tris(2-aminobenzimidazole) conjugates, a half-life of 12 h at pH 8 and 37 °C has been achieved (*22*).

We have previously reported on synthesis of 1,5,7-triazacyclododecane conjugates of 2′-*O*-methyloligoribonucleotides (*42*) and on studies of the cleaving activity of their 3d transition metal chelates (*40*). The advantage of such conjugates is that they bind 3d transition metal ions more tightly than 2,9-dimethylphenanthroline conjugates, but unfortunately they cleave the target RNA 1 order of magnitude more slowly than the phenanthroline conjugates. We now report on synthesis of difunctionalized oligonucleotides bearing two 3-(3-hydroxypropyl)-1,5,9-triazacyclododecane ligands attached via a phosphodiester linkage to a single non-nucleosidic building block, either to 2,2-bis(3-hydroxypropylaminocarbonyl)propane-1,3-diol (**1a**,**b**), 2-hydroxyethyl 3′-*O*-(2-hydroxyethyl)-*β*-D-ribofuranoside (**2a**,**b**), or 2-hydroxyethyl 2′-*O*-(2-hydroxyethyl)-*β*-D-ribofuranoside (**3a**,**b**). Interestingly, the Zn^{2+} complex of conjugate **3a**, bearing the azacrown ligands close to the 3′-terminus, exhibits a 15-fold enhanced catalytic activity over its monofunctionalized counterpart. The catalytic activity of this conjugate is equal to that of the most efficient Zn^{2+}- or Cu^{2+}-based artificial ribonucleases described so far.

EXPERIMENTAL PROCEDURES

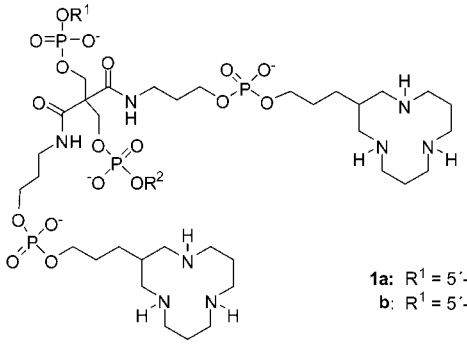
General Methods and Materials. The NMR spectra were recorded at 500 MHz. The chemical shifts are given in ppm from internal TMS and the coupling constants in hertz. The mass spectra of small molecular compounds were recorded by EI ionization and those of oligonucleotides and their conjugates by ESI ionization. For details, see the Supporting Information.

The chimeric 2′-*O*-methylribo/ribo oligonucleotides (**4**−**6**) used as targets for the artificial ribonucleases and as reference material for identification of the cleavage site (**7**−**9**) were

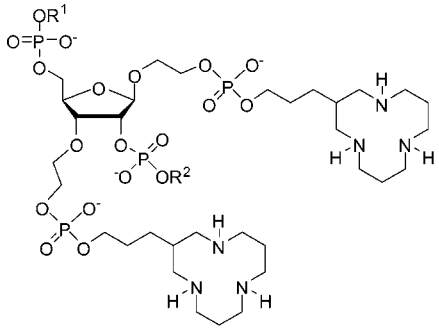
* Corresponding author. E-mail: harlon@utu.fi; tel.: +358-2-333 6770; fax: +358-2-333 6776.

10.1021/bc070071o CCC: $37.00 © 2007 American Chemical Society
Published on Web 08/21/2007

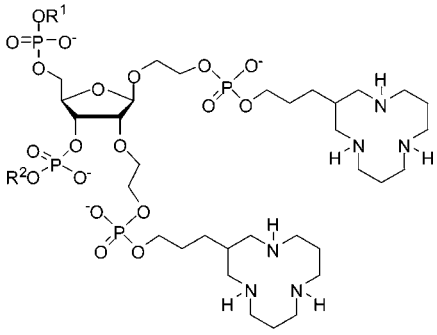
Chart 1. Structures of Cleaving Agents (1−3), Targets (4−6), and Potential Product Oligonucleotides (7−9)[a]



1a: R^1 = 5′-ACACAGCAACGCC-; R^2 = -C-3′
b: R^1 = 5′-CUCUCC-; R^2 = -GCAAGCUUCG-3′



2a: R^1 = 5′-ACACAGCAACGCC-; R^2 = -C-3′
b: R^1 = 5′-CUCUCC-; R^2 = -GCAAGCUUCG-3′



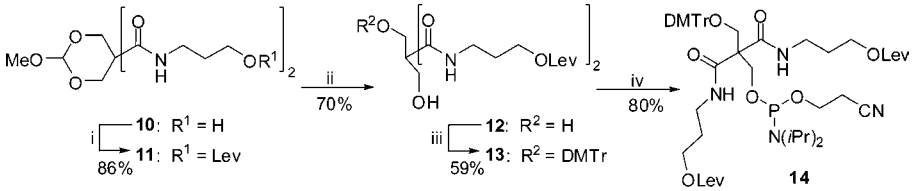
3a: R^1 = 5′-ACACAGCAACGCC-; R^2 = -C-3′
b: R^1 = 5′-CUCUCC-; R^2 = -GCAAGCUUCG-3′

Targets: **4:** 3′-UGUGUCGUU**GCGGACAACAA**-5′
5: 3′-GAGAG**GAAACG**UUCGAAGC-5′
6: 3′-GAGAG**GAAAAACG**UUCGAAGC-5′

Potential cleavage products: **7**: 3′-UGUGUCGUU**GCGG**-5′
8: 3′-UGUGUCGUU**GCGGA**-5′
9: 3′-UGUGUCGUU**GCGGAC**-5′

[a] Bold letters refer to ribonucleotides, the rest to 2′-*O*-methylribonucleotides.

Scheme 1 [a]



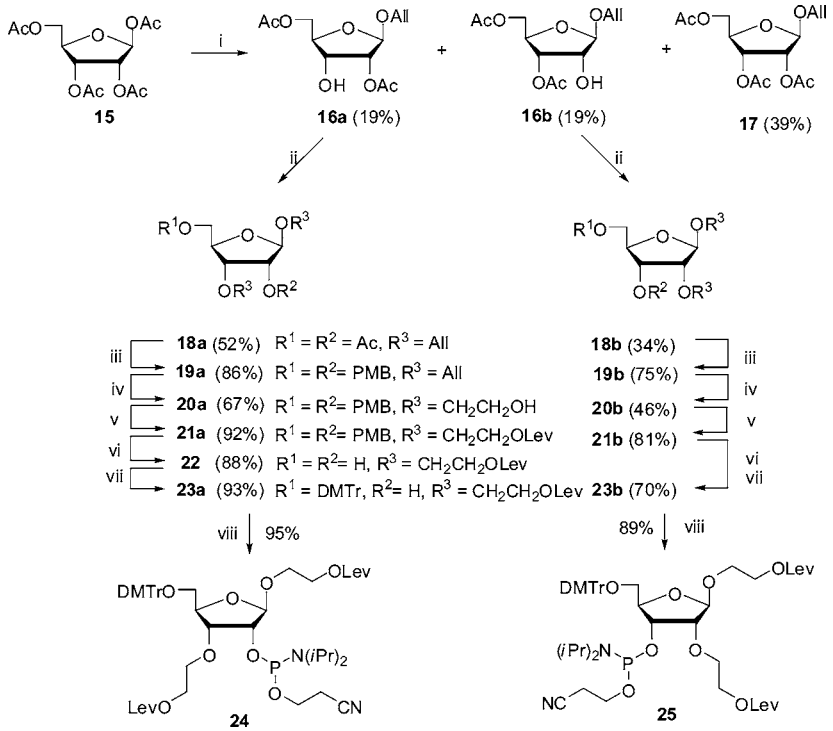
[a] Reagents and conditions: (i) levulinic anhydride, DMAP, pyridine, (ii) aq 80% AcOH, (iii) DMTrCl, pyridine, (iv) 2-cyanoethyl *N*,*N*,*N*′,*N*′-tetraisopropylphosphorodiamidite, tetrazole, acetonitrile.

assembled from commercially available 2′-*O*-methyl- and 2′-*O*-triisopropylsilyloxymethyl-protected 2-cyanoethyl-*N*,*N*-diisopropylphosphoramidite building blocks (Glen Research) by conventional phosphoramidite strategy using a 1.0 μmol scale and following the standard RNA-coupling protocol of Applied Biosystems 3400 DNA synthesizer. The artificial ribonucleases **1**−**3** were prepared as described below. The buffer reagents and salts employed were of reagent grade. All buffer solutions were prepared in sterilized water, and sterilized equipment was used for their handling.

***N*,*N*′-Bis[3-(levulinoyloxy)propyl]-2-methoxy-1,3-dioxane-5,5-dicarboxamide (11).** *N*,*N*′-Bis(3-hydroxypropyl)-2-methoxy-1,3-dioxane-5,5-dicarboxamide (**10**, Scheme 1) was synthesized as described earlier (*43*). A mixture of **10** (4.0 g, 12 mmol), levulinic anhydride (62 mmol) and a catalytic amount of 4-dimethylaminopyridine in pyridine (30 mL) was stirred overnight at room temperature and evaporated to dryness. The residue was dissolved in dichloromethane and washed with 5% aqueous $NaHCO_3$. The organic phase was dried with Na_2SO_4 and evaporated to dryness. Purification of the crude product by silica gel chromatography (first 50% EtOAc in dichloromethane and then 5% MeOH in dichloromethane) yielded 5.7 g (86%) of **11** as brownish oil. ^{1}H NMR ($CDCl_3$, 500 MHz): δ 7.69 (br s, 2H), 5.31 (s, 1H), 4.51 (d, 2H, J = 12.0 Hz), 4.16−4.12 (m, 6H), 3.41 (s, 3H), 3.41−3.33 (m, 4H), 2.77 (m, 4H), 2.63 (t, 4H, J = 6.8 Hz), 2.20 (s, 6H), 1.87 (m, 4H); ^{13}C NMR ($CDCl_3$, 125 MHz): δ 206.8, 175.9, 169.5, 169.0, 109.6, 65.1, 62.1, 53.1, 50.8, 38.0, 36.9, 35.1, 29.8, 28.4, 28.0; MS (EI): M^+ requires 516.2, found 515.

2,2-Bis(hydroxymethyl)-*N*,*N*′-bis[3-(levulinoyloxy)propyl]-malondiamide (12). A mixture of **11** (2.7 g, 5.3 mmol) in 80% aqueous AcOH (50 mL) was stirred for 2 h at room temperature

Scheme 2 [a]



[a] Reagents and conditions: (i) allyl alcohol, $BF_3{\cdot}Et_2O$, dichloromethane, (ii) allyl methyl carbonate, $Pd(OAc)_2$, PPh_3, THF, reflux for 15 min, (iii) (1) NaOMe/MeOH, (2) NaH, 4-methoxybenzyl chloride, DMF, (iv) (1) OsO_4, $NaIO_4$, H_2O, dioxane, (2) $NaBH_4$, EtOH, dichloromethane, (v) levulinic anhydride, DMAP, pyridine, (vi) H_2, Pd/C, EtOH, (vii) DMTrCl, pyridine, (viii) 2-cyanoethyl *N*,*N*-diisopropylphosphonamidic chloride, NEt_3, dichloromethane.

and evaporated to dryness. The residue was coevaporated several times with water and then subjected to a silica gel column. Chromatographic purification (0 to 10% MeOH in dichloromethane) afforded 1.8 g (70%) of **12** as a colorless oil. ^{1}H NMR ($CDCl_3$, 500 MHz): δ 7.74 (t, 2H, J = 5.6 Hz), 4.11 (t, 4H, J = 6.1 Hz), 3.90 (s, 4H), 3.36 (m, 4H), 2.76 (dd, 4H, J = 6.7 Hz, 6.3 Hz), 2.58 (dd, 4H, J = 6.7 Hz, 6.3 Hz), 2.19 (s, 6H), 1.85 (m, 4H); ^{13}C NMR ($CDCl_3$, 125 MHz): δ 207.0, 173.0, 171.5, 64.1, 61.8, 58.1, 37.9, 36.4, 35.1, 29.8, 28.3, 27.9; MS (EI): M^+ requires 474.2, found 474.

2-(4,4′-Dimethoxytrityloxymethyl)-2-hydroxymethyl-*N*,*N*′-bis[3-(levulinoyloxy)propyl]malondiamide (13). 4,4′-Dimethoxytrityl chloride (1.3 g, 3.7 mmol) was slowly added to a mixture of **12** (1.8 g, 3.7 mmol) in dry pyridine (10 mL), and the mixture was then stirred overnight at room temperature. After evaporation, the residue was dissolved in dichloromethane and washed with 5% aq $NaHCO_3$. The organic phase was dried with Na_2SO_4 and evaporated to dryness. The residue was coevaporated with toluene and purified by silica gel chromatography (0 to 10% MeOH in dichloromethane) to give 1.71 g (59%) of **13** as a colorless oil. ^{1}H NMR ($CDCl_3$, 500 MHz): δ 7.51 (t, 2H, J = 5.8 Hz), 7.40−7.16 (m, 9H), 6.84 (m, 4H), 4.14 (t, 1H, J = 6.0 Hz), 4.09 (t, 4H, J = 6.1 Hz), 3.90 (m, 2H), 3.81 (s, 6H), 3.47 (s, 2H), 3.39 (m, 4H), 2.76 (m, 4H), 2.58 (m, 4H,), 2.20 (s, 6H), 1.84 (m, 4H); ^{13}C NMR ($CDCl_3$, 125 MHz): δ 206.7, 173.0, 172.8, 170.6, 158.6, 144.3, 135.2, 130.1, 129.1, 127.7, 126.9, 112.9, 86.4, 65.3, 64.2, 63.9, 62.0, 61.8, 58.5, 57.6, 55.3, 55.2, 37.9, 36.6, 36.3, 29.9, 28.4, 28.3, 27.9; MS (ESI): $[M+Na]^+$ requires 799.3, found 799.7.

2-Cyanoethyl 3-(4,4′-Dimethoxytrityloxy)-2,2-bis[*N*-(3-levulinoyloxypropyl)carbamoyl]propyl *N*,*N*-Diisopropylphosphoramidite (14). Compound **13** (1.6 g, 2.0 mmol) was dried by repeated coevaporations with dry acetonitrile and dissolved in dry acetonitrile (2.0 mL). 2-Cyanoethyl *N*,*N*,*N*′,*N*′-tetraisopropylphosphorodiamidite (0.83 mL, 2.6 mmol) and tetrazole (4.5 mL of 0.45 M solution in acetonitrile, 2.01 mmol) were added to the mixture, and the reaction was then allowed to stir at room temperature for 2 h. Acetonitrile was removed in vacuo, saturated aq $NaHCO_3$ was added to the residue, and the product was then extracted with dichloromethane. The organic phase was separated, dried with Na_2SO_4, and evaporated to dryness. The residue was purified by silica gel chromatography (1% triethylamine in EtOAc) to yield 1.6 g (80%) of the product (**14**) as a colorless oil. ^{1}H NMR ($CDCl_3$, 500 MHz): δ 7.51 (t, 1H, J = 5.8 Hz), 7.44 (m, 2H), 7.34−7.29 (m, 7H), 7.23 (m, 1H), 4.14−4.02 (m, 4H), 3.81 (s, 6H), 3.75−3.71 (m, 2H), 3.66 (s, 2H), 3.56−3.50 (m, 2H), 3.37−3.24 (m, 4H), 2.77−2.74 (m, 4H), 2.59−2.54 (m, 4H), 2.19 (s, 6H), 1.83−1.77 (m, 4H), 1.18, 1.16, 1.10 and 1.10 (each s, each 3H); ^{13}C NMR ($CDCl_3$, 125 MHz): δ 206.6, 172.7, 169.9, 169.7, 158.6, 144.2, 135.2, 130.0, 128.0, 127.9, 127.0, 113.2, 86.6, 64.9, 64.8, 63.5, 62.0, 61.9, 58.6, 58.5, 55.2, 53.5, 45.4, 45.3, 43.3, 37.9, 36.5, 29.9, 28.4, 27.9, 24.5, 23.5, 23.0, 20.3, 19.3; ^{31}P NMR ($CDCl_3$, 200 MHz): δ 149.2; HRMS (ESI) $[M + Na]^+$ requires 999.4491, found 999.4461.

Allyl 2,5-Di-*O*-acetyl-3-*O*-allyl-β-D-ribofuranoside (18a) and Allyl 3,5-Di-*O*-acetyl-2-*O*-allyl-β-D-ribofuranoside (18b). An equimolar mixture of isomeric allyl di-*O*-acetyl-β-D-ribofuranosides (**16a**,**b**, each 19%) and allyl tri-*O*-acetyl-β-D-ribofuranoside (**17**; 39%) was obtained by boron trifluoride-promoted glycosidation of 1,2,3,5-tetra-*O*-acetyl-β-ribofuranose (**15**) with allyl alcohol in dichloromethane (*44*) (Scheme 2). The di-*O*-acetylated products (**16a**,**b**; 5.0 g, 18 mmol), allyl methyl carbonate (4.1 mL, 36 mmol), $Pd(OAc)_2$ (80 mg, 0.36 mmol, 0.02 equiv), and Ph_3P (0.48 g, 0.18 mmol, 0.1 equiv) were dissolved in THF (50 mL), and the mixture was refluxed for 15 min and then evaporated to dryness (*45*). The residue was purified by silica gel chromatography (20% EtOAc in petroleum ether) to yield 3.0 g (52%) of allyl 2,5-di-*O*-acetyl-3-*O*-allyl-β-D-ribofuranoside (**18a**) and 2.0 g (34%) of allyl 3,5-bis-*O*-acetyl-2-*O*-allyl-β-D-ribofuranoside (**18b**). The isomers were obtained as colorless oils. **18a**: ^{1}H NMR ($CDCl_3$, 500 MHz) δ

5.90−5.81 (m, 2H), 5.28 (m, 2H, 5.25 (d, 1H, J = 4.4 Hz), 5.01 (s, 1H), 4.86 (dd, 1H, J = 11.4, 2.9 Hz), 4.24−4.04 (m, 5H), 3.99−3.94 (m, 2H), 2.14 (s, 3H), 2.10 (s, 3H); ^{13}C NMR ($CDCl_3$, 125 MHz) δ 170.8, 169.9, 133.9, 133.6, 118.0, 117.7, 104.3, 78.9, 77.6, 73.8, 72.1, 68.3, 64.8, 20.9, 20.8; HRMS (ESI) $[M + Na]^+$ requires 337.1258, found 337.1257. **18b**: ^{1}H NMR ($CDCl_3$, 500 MHz) δ 5.91−5.83 (m, 2H), 5,31−5.27 (m, 2H), 5.22−5.20 (m, 2H), 5.13 (dd, 1H, J = 6.1 Hz, 5.3 Hz), 5.06 (d, 1H, J = 0.6 Hz), 4.37−4.32 (m, 2H), 4.23 (m, 1H), 4.13−4.03 (m, 4H), 3.98 (m, 1H), 2.13 (s, 3H), 2.09 (s, 3H); ^{13}C NMR ($CDCl_3$, 125 MHz) δ 170.7, 170.3, 134.0, 133.8, 117.6, 117.3, 104.9, 80.5, 78.8, 73.1, 72.0, 68.5, 64.5, 20.9, 20.8; HRMS (ESI) $[M + Na]^+$ requires 337.1258, found 337.1255.

Allyl 2,5-Di-*O*-(4-methoxybenzyl)-3-*O*-allyl-*β*-D-ribofuranoside (19a). Compound **18a** (2.3 g, 7.2 mmol) was dissolved in 0.1 mol L^{-1} methanolic sodium methoxide (25 mL). The mixture was stirred at ambient temperature for 1 h, neutralized by addition of strongly acidic cation-exchange resin, and filtered. The filtrate was evaporated to dryness, and the residue was dissolved in dry DMF (7.0 mL) and cooled to 0 °C. NaH (60% dispersion in mineral oil, 0.63 g, 16 mmol) and 4-methoxybenzyl chloride (2.4 mL, 18 mmol) were added, and the mixture was then stirred overnight at ambient temperature. Water (20 mL) was added, and the product was extracted by diethyl ether (2 × 20 mL). The organic phases were combined, dried with Na_2SO_4, and evaporated to dryness. The residue was purified by silica gel chromatography (20% EtOAc in petroleum ether) to yield 2.9 g (86%) of the product (**19a**) as a colorless oil. ^{1}H NMR ($CDCl_3$, 500 MHz) δ 7.33−7.27 (m, 4H), 6.91−6.87 (m, 4H), 5.94−5.82 (m, 2H), 5.28−5.22 (m, 2H), 5.19−5.16 (m, 2H), 5.04 (s, 1H), 4.66 (d, 1H, J = 11.8 Hz), 4.61 (d, 1H, J = 11.8 Hz), 4.56 (d, 1H, J = 11.8 Hz), 4.52 (d, 1H, J = 11.8 Hz), 4.30 (ddd, 1H, J = 7.0 Hz, 6.3 Hz, 3.7 Hz), 4.19 (m, 1H), 4.03−3.90 (m, 4H), 3.83 (s, 3H), 3.82 (s, 3H), 3.64 (dd, 1H, J = 10.6 Hz, 3.6 Hz), 3.54 (dd, 1H, J = 10.6 Hz, 6.1 Hz); ^{13}C NMR ($CDCl_3$, 125 MHz) δ 159.4, 159.1, 134.5, 134.2, 130.5, 129.9, 129.7, 129.3, 117.4, 117.3, 113.8, 113.7, 104.5, 80.5, 79.2, 78.5, 72.8, 71.9, 71.5, 71.2, 68.2, 55.3, 55.3; HRMS (ESI) $[M + Na]^+$ requires 493.2197, found 493.2200.

Allyl 3,5-Di-*O*-(4-methoxybenzyl)-2-*O*-allyl-*β*-D-ribofuranoside (19b). 19b was obtained from **18b** (1.0 g, 3.3 mmol) as described for **19a**. The product (**19b**) was a colorless oil in a 75% yield (1.2 g). ^{1}H NMR ($CDCl_3$, 500 MHz) δ 7.29−7.26 (m, 4H), 6.90−6.86 (m, 4H), 5.97−5.83 (m, 2H), 5.35−5.16 (m, 4H), 5.07 (s, 1H), 4.56 (d, 1H, J = 11.6 Hz), 4.53 (d, 1H, J = 11.7 Hz), 4.49 (d, 1H, J = 11.7 Hz), 4.48 (d, 1H, J = 11.6 Hz), 4.30 (ddd, 1H, J = 6.3 Hz, 6.3 Hz, 3.9 Hz), 4.20 (m, 1H), 4.17−4.08 (m, 2H), 4.04 (dd, 1H, J = 7.0 Hz, 4.7 Hz), 3.96 (m, 1H), 3.84 (d, 1H, J = 4.8 Hz), 3.83 (s, 3H), 3.82 (s, 3H), 3.59 (dd, 1H, J = 10.7 Hz, 3.8 Hz), 3.49 (dd, 1H, J = 10.6 Hz, 6.0 Hz); ^{13}C NMR ($CDCl_3$, 125 MHz) δ 159.3, 159.1, 134.5, 134.2, 130.5, 130.0, 129.6, 129.3, 117.6, 117.3, 113.8, 113.7, 104.5, 80.5, 79.9, 78.2, 72.8, 72.1, 71.5, 71.1, 68.3, 55.3, 55.3; HRMS (ESI) $[M + Na]^+$ requires 493.2197, found 493.2182.

(2-Hydroxyethyl) 3-*O*-(2-hydroxyethyl)-2,5-di-*O*-(4-methoxybenzyl)-*β*-D-ribofuranoside (20a). Osmium tetroxide (2.5 wt. % solution in 2-methyl-2-propanol, 1.0 mL, 80 μmol) was added to a mixture of **19a** (2.9 g, 6.1 mmol) in water−dioxane (1:4 *v*/*v*, 20 mL) (*46*). After 1 h stirring, the mixture was cooled to 0 °C, the solvent volume was increased to 80 mL, and $NaIO_4$ (6.6 g, 31 mmol) was slowly added. The reaction was then stirred at ambient temperature for 5 h. The resulted aldehyde intermediate was extracted with ethyl acetate (3 × 20 mL). The organic phases were combined, dried with Na_2SO_4, and evaporated to dryness. The residue was dissolved in a mixture of dichloromethane−ethanol (1:2, *v*/*v*, 30 mL), and then $NaBH_4$ (1.2 g, 31 mmol) was added. After 5 h stirring, the excess $NaBH_4$ was destroyed by addition of saturated ammonium chloride (20 mL) and the product was extracted with dichloromethane (3 × 15 mL). The organic phases were combined, dried with Na_2SO_4, and evaporated to dryness. The residue was purified by silica gel chromatography (10% MeOH in dichloromethane) to yield 1.8 g (60%) of **20a** as a colorless oil. ^{1}H NMR ($CDCl_3$, 500 MHz) δ 7.32−7.27 (m, 4H), 6.92−6.88 (m, 4H), 5.02 (s, 1H), 4.66 (d, 1H, J = 11.5 Hz), 4.59 (d, 1H, J = 11.9 Hz), 4.59 (d, 1H, J = 11.5 Hz), 4.48 (d, 1H, J = 11.9 Hz), 4.21 (m, 1H), 4.13 (dd, 1H, J = 7.6 Hz, 4.6 Hz), 3.94 (d, 1H, J = 4.6 Hz), 3.82 (s, 6H), 3.77−3.63 (m, 7H), 3.58 (m, 1H), 3.54−3.50 (m, 2H), 3.19 (dd, 1H, J = 6.7 Hz, 5.7 Hz), 2.47 (t, 1H, J = 6.2 Hz); ^{13}C NMR ($CDCl_3$, 125 MHz) δ 159.5, 159.4, 129.8, 129.6, 129.4, 113.9, 113.8, 105.5, 80.1, 79.6, 78.4, 72.9, 72.1, 71.9, 71.3, 68.9, 61.9, 61.7, 55.3, 55.3; HRMS (ESI) $[M + Na]^+$ requires 501.2095, found 501.2087.

(2-Hydroxyethyl) 2-*O*-(2-Hydroxyethyl)-3,5-di-*O*-(4-methoxybenzyl)-*β*-D-ribofuranoside (20b). 20b was synthesized from **19b** (1.1 g, 2.4 mmol) as described for **20a**. The product (**20b**) was obtained as a colorless oil in a 46% yield (0.52 g). ^{1}H NMR ($CDCl_3$, 500 MHz) β 7.29−7.22 (m, 4H), 6.91−6.87 (m, 4H), 5.00 (s, 1H), 4.53 (d, 1H, J = 11.8 Hz), 4.51 (d, 1H, J = 11.2 Hz), 4.44 (d, 1H, J = 11.2 Hz), 4.41 (d, 1H, J = 11.8 Hz), 4.23 (dd, 1H, J = 7.6 Hz, 4.3 Hz), 4.19 (m, 1H), 3.82 (s, 3H), 3.81 (s, 3H), 3.82−3.60 (m, 10H), 3.45 (dd, 1H, J = 10.7 Hz, 3.6 Hz), 3.32 (t, 1H, J = 6.5 Hz), 2.62 (t, 1H, J = 6.2 Hz); ^{13}C NMR ($CDCl_3$, 125 MHz) β 159.5, 159.3, 129.7, 129.7, 129.6, 129.5, 113.9, 113.8, 105.9, 81.4, 80.0, 77.1, 72.9, 72.5, 72.4, 71.5, 68.5, 61.9, 61.8, 55.3, 55.3; HRMS (ESI) $[M + Na]^+$ requires 501.2095, found 501.2072.

(2-Levulinoyloxyethyl) 3-*O*-(2-Levulinoyloxyethyl)-2,5-di-*O*-(4-methoxybenzyl)-*β*-D-ribofuranoside (21a). Levulinic anhydride (0.90 g, 4.2 mmol) was added to a mixture of **20a** (0.56 g, 1.2 mmol) in pyridine (10 mL). After 3 h stirring, saturated $NaHCO_3$ (20 mL) was added to the mixture and then the product was extracted with ethyl acetate (3 × 20 mL). The organic phases were combined, dried with Na_2SO_4, and evaporated to dryness. The residue was purified by silica gel chromatography to yield 0.73 g (92%) of the product (**21a**) as a colorless oil. ^{1}H NMR ($CDCl_3$, 500 MHz) δ 7.33−7.26 (m, 4H), 6.91−6.87 (m, 4H), 5.02 (d, 1H, J = 0.8 Hz), 4.66 (d, 1H, J = 11.7 Hz), 4.62 (d, 1H, J = 11.7 Hz), 4.55 (d, 1H, J = 11.7 Hz), 4.51 (d, 1H, J = 11.7 Hz), 4.27 (ddd, 1H, J = 6.9 Hz, 5.9 Hz, 3.8 Hz), 4.23−4.19 (m, 3H), 4.10 (ddd, 1H, J = 12.0 Hz, 7.0 Hz, 3.4 Hz), 3.98 (dd, 1H, J = 7.0 Hz, 4.7 Hz), 3.92 (dd, 1H, J = 4.7 Hz, 0.8 Hz), 3.84 (ddd, 1H, J = 11.4 Hz, 5.7 Hz, 3.4 Hz), 3.82 (s, 3H), 3.82 (s, 3H), 3.70−3.57 (m, 4H), 3.53 (dd, 1H, J = 10.7 Hz, 5.8 Hz), 2.76−2.70 (m, 4H), 2.60−2.53 (m, 4H), 2.20 (s, 3H), 2.18 (s, 3H); ^{13}C NMR ($CDCl_3$, 125 MHz) δ 206.5, 206.5, 172.7, 172.6, 159.4, 159.2, 130.3, 129.9, 129.5, 129.3, 113.8, 113.7, 105.2, 80.5, 79.6, 79.3, 72.8, 72.0, 71.0, 68.4, 65.2, 63.7, 63.5, 55.3, 55.3, 37.8, 37.8, 29.9, 29.8, 27.8, 27.8; HRMS (ESI) $[M + Na]^+$ requires 697.2831, found 697.2860.

(2-Levulinoyloxyethyl) 2-*O*-(2-Levulinoyloxyethyl)-di-*O*-(4-methoxybenzyl)-*β*-D-ribofuranoside (21b). 21b was synthesized from **20b** (0.50 g, 1.0 mmol) as described for **21a**. The product (**21b**) was obtained as a colorless oil in an 81% yield (0.57 g). ^{1}H NMR ($CDCl_3$, 500 MHz) δ 7.29−7.24 (m, 4H), 6.90−6.86 (m, 4H), 5.03 (s, 1H), 4.56 (d, 1H, J = 11.5 Hz), 4.51 (d, 1H, J = 11.7 Hz), 4.48 (d, 1H, J = 11.5 Hz), 4.47 (d, 1H, J = 11.7 Hz), 4.29−4.20 (m, 4H), 4.10 (ddd, 1H, J = 11.9 Hz, 7.1 Hz, 3.4 Hz), 4.04 (dd, 1H, J = 7.1 Hz, 4.7 Hz), 3.86−3.79 (m, 4H), 3.82 (s, 3H), 3.82 (s, 3H), 3.61 (ddd, 1H, J = 11.3 Hz, 7.0 Hz, 3.4 Hz), 3.59 (dd, 1H, J = 10.6 Hz, 3.7 Hz), 3.48 (dd, 1H, J = 10.6 Hz, 5.9 Hz), 2.76−2.73 (m, 4H), 2.60−2.54 (m, 4H), 2.20 (s, 3H), 2.19 (s, 3H); ^{13}C NMR

($CDCl_3$, 125 MHz) δ 206.5, 206.5, 172.7, 172.6, 159.3, 159.2, 130.3, 130.0, 129.5, 129.3, 113.8, 113.7, 105.2, 81.1, 80.6, 78.2, 72.8, 72.2, 70.9, 68.5, 65.2, 63.8, 63.5, 55.3, 55.3, 37.9, 37.8, 29.9, 29.8, 27.9, 27.9; HRMS (ESI) $[M + Na]^+$ requires 697.2831, found 697.2851.

(2-Levulinoyloxyethyl) 5-*O*-(4,4′-Dimethoxytrityl)-3-*O*-(2-levulinoyloxyethyl)-β-D-ribofuranoside (23a). Compound **21a** (0.65 g, 0.96 mmol) was dissolved in ethanol (10 mL). Pd/C (10% Pd/C, 50% wet with water, 0.13 g) was added, and then hydrogen was bubbled through the mixture for 2 h at ambient temperature. The mixture was filtered, the filtrate was evaporated to dryness, and the residue was purified by silica gel chromatography to yield 0.37 g (88%) of the (2-levulinoyloxyethyl) 3-*O*-(2-levulinoyloxyethyl)-β-D-ribofuranoside (**22**) as a colorless oil. HRMS (ESI) $[M + Na]^+$ requires 457.1680, found 457.1699. Compound **22** was dissolved in pyridine (5 mL), and then DMTrCl[1] (0.29 g, 0.86 mmol) was slowly added. The reaction was stirred overnight at ambient temperature. Saturated $NaHCO_3$ (20 mL) was added to the mixture, and the product was extracted with dichloromethane (3×20 mL). The organic phases were combined, dried with Na_2SO_4, and evaporated to dryness. The residue was purified by silica gel chromatography (80% EtOAc in petroleum ether) to yield 0.54 g (93%, 82% from **21a**) of the product (**23a**) as a colorless oil. ^{1}H NMR ($CDCl_3$, 500 MHz) δ 7.50−7.47 (m, 2H), 7.38−7.35 (m, 4H), 7.32−7.29 (m, 3H), 7.23 (m, 1H), 6.86−6.83 (m, 4H), 5.03 (s, 1H), 4.27 (ddd, 1H, J = 12.1 Hz, 5.1 Hz, 2.9 Hz), 4.20−4.15 (m, 4H), 4.13−4.08 (m, 2H), 3.83 (ddd, 1H, J = 11.4 Hz, 5.2 Hz, 3.4 Hz), 3.81 (s, 6H), 3.72 (ddd, 1H, J = 11.2 Hz, 5.2 Hz, 3.0 Hz), 3.68−3.60 (m, 2H), 3.32 (dd, 1H, J = 10.0 Hz, 4.5 Hz), 3.19 (dd, 1H, J = 10.0 Hz, 5.0 Hz), 3.00 (d, 1H, J = 3.1 Hz), 2.77−2.74 (m, 2H), 2.71−2.69 (m, 2H), 2.57−2.54 (m, 2H), 2.52−2.49 (m, 2H), 2.20 (s, 3H), 2.18 (s, 3H); ^{13}C NMR ($CDCl_3$, 125 MHz) δ 206.7, 206.5, 172.6, 172.6, 158.5, 144.9, 136.1, 136.0, 130.0, 130.0, 128.2, 127.8, 126.8, 113.1, 107.4, 85.9, 80.6, 80.2, 73.4, 68.7, 65.5, 64.2, 63.5, 63.4, 55.2, 37.9, 37.9, 29.8, 29.8; HRMS (ESI) $[M + Na]^+$ requires 759.2987, found 759.3007.

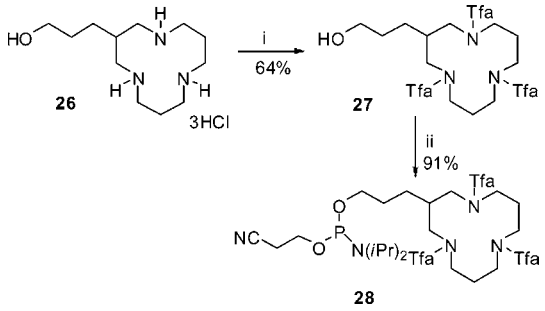
(2-Levulinoyloxyethyl) 5-*O*-(4,4′-Dimethoxytrityl)-2-*O*-(2-levulinoyloxyethyl)-β-D-ribofuranoside (23b). 23b was synthesized from **21b** (0.55 g, 0.82 mmol) as described for **23a**, except that the 2-levulinoyloxyethyl 2-*O*-(2-levulinoyloxyethyl)-β-D-ribofuranoside intermediate was used without chromatographic purification. The product (**23b**) was obtained as a colorless oil in a 70% overall yield (0.42 g). ^{1}H NMR ($CDCl_3$, 500 MHz) δ 7.51−7.49 (m, 2H), 7.40−7.36 (m, 4H), 7.31−7.27 (m, 2H), 7.22 (m, 1H), 6.85−6.82 (m, 4H), 5.08 (d, 1H, J = 1.4 Hz), 4.34−4.21 (m, 4H), 4.14−4.08 (m, 2H), 3.94 (ddd, 1H, J = 11.4 Hz, 5.3 Hz, 3.4 Hz), 3.88 (ddd, 1H, J = 11.3 Hz, 5.6 Hz, 3.3 Hz), 3.86 (dd, 1H, J = 4.8 Hz, 1.4 Hz), 3.81 (s, 6H), 3.80 (ddd, 1H, J = 11.3 Hz, 6.6 Hz, 3.4 Hz), 3.66 (ddd, 1H, J = 11.4 Hz, 7.1 Hz, 3.3 Hz), 3.34 (dd, 1H, J = 10.0 Hz, 3.6 Hz), 3.15 (dd, 1H, J = 10.0 Hz, 5.5 Hz), 2.80−2.77 (m, 2H), 2.72 (d, 1H), J = 8.4 Hz), 2.70−2.67 (m, 2H), 2.63−2.60 (m, 2H), 2.50−2.46 (m, 2H), 2.21 (s, 3H), 2.16 (s, 3H); ^{13}C NMR ($CDCl_3$, 125 MHz) δ 206.7, 206.5, 172.7, 172.6, 158.4, 145.0, 136.1, 136.1, 130.1, 130.1, 128.2, 127.8, 126.7, 113.1, 104.8, 85.9, 83.6, 83.1, 71.6, 68.9, 65.6, 64.7, 63.4, 55.2, 37.9, 37.8, 29.8, 29.8, 27.9, 27.8; HRMS (ESI) $[M + Na]^+$ requires 759.2987, found 759.3015.

2-Cyanoethyl [(2-Levulinoyloxyethyl) 5-*O*-(4,4′-dimethoxytrityl)-3-*O*-(2-levulinoyloxyethyl)-β-D-ribofuranoside-2-yl] *N,N*-Diisopropylphosphoramidite (24). 2-Cyanoethyl *N,N*-diisopropylphosphonamidic chloride (91 μL, 0.41 mmol) was added to a mixture of **23a** (0.25 g, 0.34 mmol) and triethylamine (0.24 mL, 1.7 mmol) in dichloromethane (3.0 mL) under nitrogen. The mixture was stirred for 1 h at ambient temperature and then subjected directly to a silica gel column. Elution with 1% triethylamine in EtOAc yielded 0.30 g (95%) of the product (**24**) as a colorless oil. ^{1}H NMR ($CDCl_3$, 500 MHz) δ 7.51−7.49 (m, 2H), 7.40−7.36 (m, 4H), 7.31−7.28 (m, 2H), 7.24−7.20 (m, 1H), 6.86−6.82 (m, 4H), 5.15 and 5.01 (s 0.48H and s 0.52H), 4.30−4.10 (m, 7H), 3.96−3.87 (m, 2H), 3.81 and 3.80 (s and s, 6H), 3.82−3.53 (m, 8H), 3.41−3.37 (m, 1H), 3.15−3.12 (m, 1H), 2.73−2.64 (m, 6H), 2.55−2.43 (m, 4H), 2.18 (s, 6H), 2.17 (s, 3H), 2.17 (s, 3H), 1.23−1.19 (m, 12H); ^{13}C NMR ($CDCl_3$, 125 MHz) δ 206.5, 206.5, 172.6, 172.6, 158.4, 145.0, 145.0, 136.2, 136.1, 130.1, 130.1, 128.2, 128.2, 127.8, 126.7, 117.9, 117.7, 113.1, 106.5, 106.4, 85.7, 85.7, 80.3, 80.3, 79.2, 78.8, 75.0, 74.8, 73.5, 73.4, 68.5, 68.0, 65.5, 65.4, 63.9, 63.7, 63.6, 63.5, 63.4, 59.0, 58.9, 58.0, 57.8, 55.2, 43.4, 43.3, 43.2, 43.0, 37.8, 37.8, 29.8, 27.8, 27.8, 24.7, 24.6, 24.6, 24.5, 20.4, 20.4; ^{31}P NMR ($CDCl_3$, 200 MHz) δ 150.6, 149.8; HRMS (ESI) $[M + H]^+$ requires 937.4246, found 937.4290.

2-Cyanoethyl [(2-Levulinoyloxyethyl) 5-*O*-(4,4′-dimethoxytrityl)-2-*O*-(2-levulinoyloxyethyl)-β-D-ribofuranoside-3-yl] *N,N*-Diisopropylphosphoramidite (25). 25 was synthesized from **23b** (0.19 g, 0.26 mmol) as described for **24**. The product (**25**) was obtained as a colorless oil in an 89% yield (0.24 g). ^{1}H NMR ($CDCl_3$, 500 MHz) δ 7.54−7.50 (m, 2H), 7.41−7.30 (m, 6H), 7.27−7.22 (m, 1H), 6.91−6.88 (m, 4H), 5.05 (m, 1H), 4.43−4.10 (m, 7H), 3.95−3.52 (m, 10H), 3.79 and 3.79 (s and s, 6H), 3.39 (dd, 0.63H, J = 10.4 Hz, 2.5 Hz), 3.29 (dd, 0.37H, J = 10.2 Hz, 2.7 Hz), 3.09−3.05 (m, 1H), 2.77−2.74 (m, 2H), 2.69−2.66 (m, 3H), 2.55−2.52 (m, 2H), 2.49−2.46 (m, 1H), 2.44−2.35 (m, 2H), 2.15, 2.14 and 2.11 (each s, 6H), 1.17, 1.16, 1.15, 1.15, 1.14, 1.13, 1.00, 0.99 (each s, 12H); ^{13}C NMR (CD_3CN, 125 MHz) δ 206.8, 206.8, 206.7, 172.6, 172.6, 172.5, 172.5, 158.6, 145.3, 136.2, 136.1, 130.1, 130.1, 130.1, 128.1, 128.0, 127.8, 127.8, 126.8, 118.6, 118.3, 113.1, 113.0, 105.6, 105.2, 85.8, 85.7, 82.3, 82.3, 82.2, 82.2, 81.5, 81.5, 81.4, 73.0, 72.9, 72.3, 72.2, 68.7, 68.5, 65.4, 65.4, 64.3, 63.9, 63.7, 63.6, 63.1, 58.6, 58.4, 54.9, 54.9, 43.0, 43.0, 42.9, 42.9, 37.5, 37.4, 29.0, 28.9, 27.7, 27.7, 27.6, 24.1, 24.1, 24.0, 23.9, 23.9, 23.8, 20.0, 20.0, 19.9, 19.9; ^{31}P NMR ($CDCl_3$, 200 MHz) δ 149.6, 149.1; HRMS (ESI) $[M + H]^+$ requires 937.4246, found 937.4283.

1,5,9-Tris(2,2,2-trifluoroacetyl)-3-(3-hydroxypropyl)-1,5,9-triazacyclododecane (27). The 3-(3-hydroxypropyl)-1,5,9-triazacyclododecane trihydrochloride (**26**, Scheme 3) was synthesized as earlier described (*42*). Freshly distilled methyl trifluoroacetate (7.1 mL, 71 mmol) was added in two portions to a mixture of **26** (1.0 g, 3.0 mmol) and NaOMe (0.96 g, 18 mmol) in MeOH (10 mL). The reaction was stirred at ambient temperature for 48 h, and then ethyl acetate (200 mL) and 1 mol L^{-1} aqueous hydrogen chloride (20 mL) were added to the

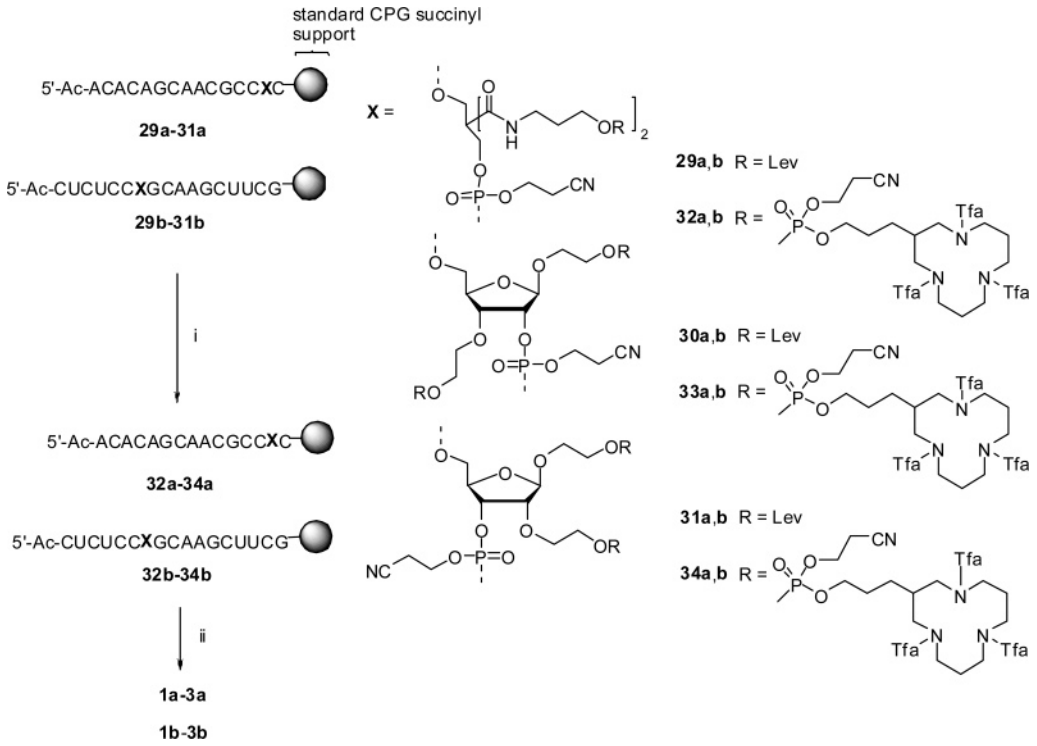
Scheme 3 [a]



[a] Reagents and conditions: (i) methyl trifluoroacetate, NaOMe, MeOH, (ii) 2-cyanoethyl *N,N*-diisopropylphosphonamidic chloride, NEt_3, dichloromethane.

[1] Abbreviations: All, allyl; CPG, controlled pore glass; DMAP, 4-dimethylaminopyridine; DMTr, 4,4′-dimethoxytrityl; HEPES, 4-(2-hydroxyethyl)-1-piperazineethanesulfonic acid; Lev, levulinoyl (4-oxopentanoyl); PMB, 4-methoxybenzyl; Tfa, trifluoroacetyl.

Scheme 4 [a]



[a] Reagents and conditions: (i) (1) hydrazine hydrate, pyridine, AcOH (0.124/4/1, v/v/v, 1h at 25 °C) (2) two consecutive standard phosphoramidite couplings with **28** (600 s coupling time, 0.1 mol L^{-1} solution of **28** in acetonitrile), (ii) aq NH_3, 15 h at 55 °C.

mixture. The organic phase was separated, washed with saturated $NaHCO_3$ and NaCl solutions, dried with Na_2SO_4, and evaporated to dryness. The residue was purified by silica gel chromatography (70% EtOAc in petroleum ether) to yield 0.98 g (64%) of the product (**19**) as white foam. ^{1}H NMR (MeOD, 500 MHz) δ 4.10−3.15 (m, 14H), 2.64−1.92 (m, 5H), 1.72−1.28 (m, 4H); HRMS (ESI) $[M + H]^+$ requires 518.1696, found 518.1717.

2-Cyanoethyl 3-[1,5,9-Tris(2,2,2-trifluoroacetyl)-1,5,9-triazacyclododecan-3-yl]propyl *N*,*N*-Diisopropylphosphoramidite (28). Cyanoethyl *N*,*N*-diisopropylphosphonamidic chloride (0.49 mL, 2.2 mmol) was added to a mixture of **27** (0.94 g, 1.8 mmol) and triethylamine (1.27 mL, 9.0 mmol) in dichloromethane (10 mL) under nitrogen. The mixture was stirred for 1 h at room temperature and then directly applied onto a silica gel column (0.4% triethylamine and 80% EtOAc in petroleum ether as an eluent). The chromatographic purification yielded 1.2 g (91%) of the product (**28**) as white foam. ^{1}H NMR (CD_3-CN, 500 MHz) δ 4.05−3.00 (m, 18H), 2.65 (t, 2H, J = 6.0 Hz), 2.50−1.90 (m, 5H), 1.75−1.25 (m, 4H), 1.19−1.15 (m, 12H); ^{31}P NMR ($CDCl_3$, 200 MHz) δ 148.0, 147.7, 147.6, 147.5, 147.4; HRMS (ESI) $[M + Na]^+$ requires 740.2594, found 740.2594.

Synthesis of the 2′-*O*-Methyl Oligoribonucleotide Conjugates (1a−3a, 1b−3b). The 2′-*O*-methyl oligoribonucleotide conjugates (**1a**−**3a**, **1b**−**3b**, Chart 1) were assembled on an Applied Biosystems 3400 DNA synthesizer in 1.0 μmol scale using conventional phosphoramidite chemistry and following the standard RNA coupling protocol (Scheme 4). Coupling efficiency of branching units **24** and **25** was equal to that of the commercially available 2′-*O*-methylnucleoside phosphoramidites (0.1 mol L^{-1} solutions of **24** and **25** in acetonitrile, 600 s coupling time). Building block **1** was somewhat less reactive, requiring two consecutive coupling cycles (0.1 mol L^{-1} solutions of **1** in acetonitrile, 600 s coupling time, twice) and prolonged detritylation time [three consecutive standard detritylation treatments (3% DCA in dichloromethane)]. Once the 2′-*O*-methyl oligoribonucleotide chains were assembled to obtain **29a**−**31a** and **29b**−**31b**, the levulinoyl protections were manually removed by 0.5 mol L^{-1} hydrazine acetate solution (0.124/4/1 $NH_2NH_2 \cdot H_2O$/pyridine/AcOH *v*/*v*/*v*, 1 h at 25 °C). The deprotected resin-bound oligonucleotides were washed with pyridine, MeOH, and acetonitrile, dried, and reset to the DNA synthesizer. The azacrown phosphoramidite reagent (**28**) was then coupled using two consecutive standard couplings (0.1 mol L^{-1} solution of **4** in dry acetonitrile, 600 s coupling time, twice). Fully protected resin-bound 2′-*O*-methyl oligoribonucleotide conjugates (**32a**−**34a**, **32b**−**34b**) were released from the support and deprotected by concentrated ammonia (15 h at 55 °C). The crude product mixtures were filtered, and the filtrates were evaporated to dryness, dissolved in water, and then subjected to RP HPLC purification. Purity of the crude conjugates (**1a**−**3a**, **1b**−**3b**) ranged from 20 to 30% (according to RP HPLC chromatograms). Isolated yields of the conjugates were 10 to 15% [according to UV absorbances of dissolved **1a**−**3a**, **1b**−**3b**]. The authenticity of the conjugates was verified by MS(ESI) and MS(MALDI) spectroscopy. Three main multiply charged peaks in the MS(ESI) spectra are listed below. **1a**: MS(ESI) $[(M - nH)/n]^{-n}$, n = 6, 7, and 8 requires 690.4, 789.1, and 920.8, found 690.2, 789.0, and 920.6, **2a**: MS(ESI) $\{[M + Na - (n + 1)H]/n\}^{-n}$, n = 6, 7, and 8 requires 918.2, 786.8 and 688.4, found 920.0, 788.6 and 690.0, **3a**: MS(ESI) $[(M - nH)/n]^{-n}$, n = 7, 8, and 9 requires 783.4, 685.4, and 609.1, found 784.9, 686.4, and 610.3. **1b**: MS(ESI) $\{[M + Na - (n + 1)H]/n\}^{-n}$, n = 7, 8, and 9 requires 879.7, 769.6, and 684.0, found 881.3, 771.2, and 685.5, **2b**: MS(ESI) $[(M - nH)/n]^{-n}$, n = 7, 8, and 9 requires 870.6, 761.6, and 676.9, found 870.4, 761.6, and 676.9, **3b**: MS(MALDI) $(M + H)^+$ requires 6102, found 6103.

Kinetic Measurements. The reactions were carried out in Eppendorf tubes immersed in a water bath, and the temperature of which was maintained at 35.0 ± 0.1 °C. pH was adjusted to 7.3 with a HEPES buffer (0.1 mol L^{-1}) prepared in sterilized water. The Zn^{2+} ion was added as a nitrate salt to give the overall metal ion concentration of 90 or 180 μmol L^{-1}. The

ionic strength was adjusted to 0.1 mol L^{-1} with sodium nitrate. The concentration of the artificial nuclease (**1a**−**3a**, **1b**−**3b**) was 9 or 18 μmol L^{-1} and that of the target (**4**−**6**) 18 or 36 μmol L^{-1}. 4-Nitrobenzenesulfonate ion was used as an internal standard. The total volume of the reaction mixture was 200 μL in each kinetic run. Aliquots of 20 μL were withdrawn at suitable intervals and cooled immediately to 0 °C, and the reaction was quenched by adding aqueous hydrogen chloride (1.0 μL of 1.0 mol L^{-1} solution). This results in release of the Zn^{2+} ion from the azacrown ligand and markedly decelerates the reaction, since the metal ion-catalyzed cleavage of RNA is known to be first-order in hydroxide ion concentration at pH < 7 (*47*). After this, the composition of the samples was quantified by capillary zone elctrophoresis (Beckman Coulter P/ACE MDQ CE System) using a fused silica capillary (inner diameter 50 μm, effective length 50 cm). Inverted polarity, citrate buffer (0.2 mol L^{-1}, pH 3.1) and −30 kV voltage were used. The temperature of the capillary was kept at 25 °C. Hydrodynamic injection at 2 psi for 8 s was applied. Between each analytical run, the capillary was flushed for 3 min with water, 10 mmol L^{-1} aqueous hydrogen chloride, and the background electrolyte buffer. The quantification of the target and product oligonucleotides was based on comparison of their UV absorption at 254 nm to that of the internal standard. The peak area was first normalized by dividing it by the migration time and then by the similarly normalized peak area of the internal standard. First-order rate constants for the cleavage of the target oligonucleotides (**4**−**6**) by the artificial nucleases (**1a**−**3a**, **1b**−**3b**) were obtained by applying the integrated first-order rate law to the disappearance of the target oligonucleotide.

The site of cleavage within target **4** was determined by spiking with reference oligonucleotides **7**−**9**. Each of these was added one after another to a sample containing the cleaved target and the sample was then subjected to capillary electrophoresis. Oligonucleotide **8** comigrated with the product obtained by cleaving **4** with either **1a** or **2a**, while addition of **7** or **9** resulted in appearance of a new peak in the electropherogram.

RESULTS AND DISCUSSION

Synthesis of the Phosphoramidite Reagents (14, 24, 25, 28). Preparation of the artificial nucleases (**1a**−**3a**, **1b**−**3b**) bearing two azacrown ligands attached to a single non-nucleosidic building block was based on standard solid-supported phosphoramidite chemistry. For this purpose, three different non-nucleosidic branching units were prepared and converted to 4,4′-dimethoxytritylated 2-cyanoethyl *N*,*N*-diisopropylphosphoramidite building blocks (**14**, **24**, **25**) as outlined in Schemes 1 and 2. In each building block, the two hydroxy functions aimed at allowing subsequent attachment of the azacrown ligands were protected as levulinic acid esters. As shown previously (*43*, *48*, *49*), this group may be conveniently removed on a solid-support by brief treatment with hydrazinium acetate in pyridine.

The precursor of the bis(hydroxymethyl)malondiamide-derived building-block, *N*,*N*′-bis(3-hydroxypropyl)-2-methoxy-1,3-dioxane-5,5-dicarboxamide (**10** in Scheme 1), was synthesized as described earlier (*43*). The hydroxypropyl arms of this precursor were esterified with levulinic anhydride (**11**) and the orthoester protection was removed (**12**). One of the exposed hydroxy groups was then protected as a DMTr ether (**13**), and the other one was phosphitylated to obtain **14**.

The ribose-based branching units (**24**, **25**) were prepared from commercially available 1,2,3,5-tetra-*O*-acetyl-β-D-ribofuranose (**15** in Scheme 2). A mixture of allyl 2,5- and 3,5-di-*O*-acetyl-β-D-ribofuranosides (**16a** and **16b**), together with allyl 2,3,5-tri-*O*-acetyl-β-D-ribofuranoside, was obtained in one step by BF_3 promoted glycosidation with allylic alcohol (*44*). The exposed hydroxyl group was then allylated under neutral condition with allyl methyl carbonate in the presence of $Pd(OAc)_2$ and triphenylphosphine (*45*). After this step, the isomers, *viz.* allyl 2,5-di-*O*-acetyl-3-*O*-allyl-β-D-ribofuranoside (**18a**) and allyl 3,5-di-*O*-acetyl-2-*O*-allyl-β-D-ribofuranoside (**18b**), were separated, and the base-labile acetyl protections were removed and replaced with 4-methoxybenzyl (PMB) groups (**19a**,**b**). OsO_4 hydroxylation and concomitant $NaIO_4$ oxidation converted the allyl groups to 2-oxoethyl groups, which were subsequently reduced to 2-hydroxyethyl groups with $NaBH_4$ (**20a**,**b**) (*50*). The hydroxyl groups were esterified with levulinic anhydride (**21a**,**b**), the PMB protections were removed by Pd/C-catalyzed hydrogenolysis, and the 5-hydroxy group was protected with a DMTr-group (**23a**,**b**). Phosphitylation of the remaining secondary hydroxy function gave **24** and **25**.

Previously prepared (*42*) 3-(3-hydroxypropyl)-1,5,9-triazacyclododecane (**26**) was converted to trifluoroacetyl-protected phosphoramidite reagent (**28**) as outlined in Scheme 3, i.e., by acylation of the nitrogen atoms with methyl trifluoroacetate in the presence sodium methoxide (**27**) and subsequent phosphitylation of the hydroxypropyl tether (**28**).

Synthesis of the Artificial Ribonucleases (1a−3a, 1b−3b). To verify the applicability of the branching building blocks (**14**, **24**, **25**) to the standard automated oligoribonucleotide synthesis, the coupling of these blocks was first followed by DMTr-cation assay and RP HPLC analysis of the released oligonucleotide aliquots. The coupling efficiency of the ribose-based building blocks (**24**, **25**) turned out to be equal to that of the commercially available 2′-*O*-methylribonucleoside building blocks: the coupling was quantitative in 600 s (standard RNA-coupling protocol, 0.1 mol L^{-1} phosphoramidite solution used). By contrast, two consecutive coupling cycles (2 × 600 s, 0.1 mol L^{-1} solution of **14** in acetonitrile) had to be used with the malondiamide-derived block (**14**) to achieve a satisfactory 95% coupling. For this building block, a prolonged detritylation time (three consecutive standard detritylation cycles) was also needed, consistent with previous observations (*43*, *51*, *52*). These exceptions apart, the 2′-*O*-methyloligoribonucleotides incorporating one of the branching units (**14**, **24**, or **25**) close to the 3′-terminus (**29a**−**31a**) or in the middle of the chain (**29b**−**31b**) were assembled in 1 μmol scale, using conventional phosphoramidite chemistry and following the standard RNA coupling protocol (Scheme 4). After chain assembly, the levulinoyl protections were removed by 1 h treatment with 0.5 mol L^{-1} hydrazinium acetate in pyridine and then the trifluoroacetyl-protected azacrown phosphoramidite (**28**) was coupled. Two consecutive coupling cycles (2 × 600 s, 0.1 mol L^{-1} solution of **28** in acetonitrile) were used for this simultaneous phosphorylation of the two hydroxyalkyl branches to obtain the support-anchored conjugates **32a**−**34a** and **32b**−**34b**. These fully protected conjugates were released into solution and deprotected by a slightly prolonged ammonolytic treatment (concd aq NH_3, 15 h at 55 °C) and purified by RP HPLC (Figure 1). Purity of the crude conjugates (**1a**−**3a**, **1b**−**3b**) ranged from 20 to 30%. The isolated yields varied from 10 to 15%. Authenticity of the conjugates was verified by MS(ESI) and MS(MALDI) spectroscopy.

Cleavage by the 3′-Tethered Conjugates (1a−3a). The cleaving activity of conjugates **1a**−**3a**, bearing the two azacrown moieties close to the 3′-terminus of a 15-mer 2′-*O*-methyl oligoribonucleotide, was determined by using a 20-mer chimeric ribo/2′-*O*-methylribo oligonucleotide (**4**) as a target. Within this target, the 3′-terminus consisted of 9 2′-*O*-methylribonucleotides, ensuring efficient hybridization with the fully complementary artificial nuclease, and the 11 non-methylated nucleotides at the 5′-terminus constituted the actual target sequence incorporating scissile ribonucleoside 3′-phosphodiester bonds. The artificial

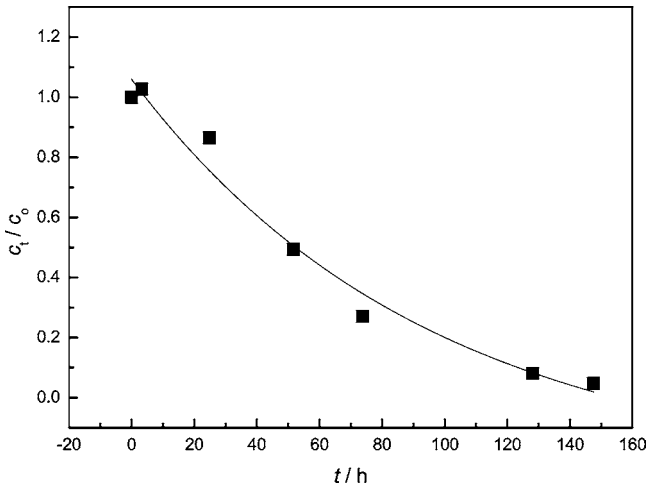


Figure 1. Cleavage of chimeric ribo/2′-*O*-methylribo oligonucleotide **4** by the Zn^{2+} complex of artificial nuclease **1a** in HEPES buffer (0.1 mol L^{-1}, I = 0.1 mol L^{-1} with $NaNO_3$) at pH 7.3 and 35 °C. The concentration of **4** and the initial concentration of **1a** (c_o) was 18 μmol L^{-1} and that of Zn^{2+} 90 μmol L^{-1}.

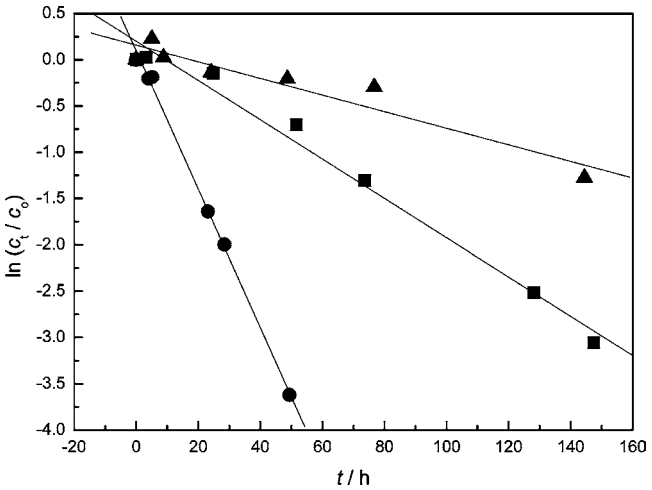
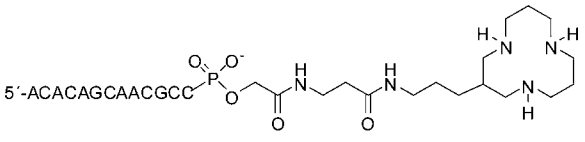


Figure 2. Cleavage of chimeric ribo/2′-*O*-methylribo oligonucleotide **4** by the Zn^{2+} complex of artificial nucleases **1a**−**3a**, using the target and cleaving agent at equimolar concentration. The logarithmic concentration of **4** plotted against time. For the conditions, see the legend of Figure 1. Notation: **1a** (■), **2a** (●), **3a** (▲).

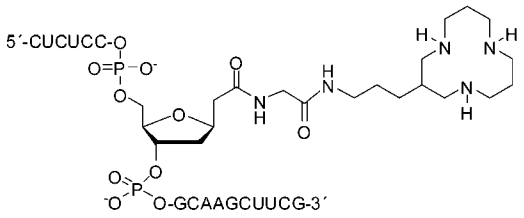
nuclease and target were incubated at equimolar concentration (18 μmol L^{-1}) and 35 °C in a HEPES buffer (0.1 mol L^{-1}, pH 7.3, I = 0.1 mol L^{-1} with $NaNO_3$) containing 90 μmol L^{-1} $Zn(NO_3)_2$. Aliquots were withdrawn at appropriate intervals, and their composition was determined by zone capillary electrophoresis. The progress of the cleavage of **4** by nuclease **1a** is shown in Figure 1 as an illustrative example. As seen from Figure 2, the breakdown of target **4** obeyed first-order kinetics with all the cleaving agents studied (**1a**−**3a**). Spiking of the product mixture with oligonucleotides **7**−**9** revealed that **1a**−**3a** all cleaved the target at the 5′-C(6)pA(7)-3′ bond, i.e., at 5′-side of the nucleoside (A7) opposite to the non-nucleosidic unit bearing the azacrown ligands.

Interestingly, the catalytic activity of **1a**−**3a** differs considerably in spite of structural similarity of the cleaving agents. We have shown previously (*40*) that monofunctionalized oligonucleotide conjugate **35** (Chart 2), having the same base sequence as **1a**−**3a**, cleaves target **4** at the 5′-A(7)pG(8)-3′ bond, the first-order rate constant being $(1.4 \pm 0.1) \times 10^{-6}$ s^{-1} under the experimental conditions of the present study. The rate constants obtained now with **1a**, **2a**, and **3a** are $(5.9 \pm 0.3) \times 10^{-6}$ s^{-1}, $(2.08 \pm 0.05) \times 10^{-5}$ s^{-1}, and $(2.5 \pm 0.3) \times 10^{-6}$ s^{-1}, respectively (Table 1). In other words, all the di(azacrown) conjugates are better catalysts than their mono(azacrown) counterpart, the increase in the catalytic activity being most remarkable with **2a**, 15-fold compared to **35**. The cleaving ability of **2a** is equal to that reported (*39*) for 2,9-dimethyl-5-aminophenanthroline−oligonucloeotide conjugates. Compared to the Zn^{2+} chelate of monomeric 1,5,9-triazacyclododecane at the same concentration (18 μmol L^{-1}), the rate acceleration is 1000-fold (*53*).

Chart 2. Structures of Previously (*40*) Studied Monofunctionalized Azacrown Conjugates of 2′-*O*-methyl Oligoribonucleotides



35



36

Table 1. First-order Rate Constants for the Cleavage of Target 4 by the Zn^{2+} Complexes of Oligonucleotide Di(azacrown) Conjugates 1a−3a and Targets 5 and 6 with Conjugates 1b−3b in 0.10 mol L^{-1} HEPES Buffer at pH 7.3 and 35 °C (I = 0.1 mol L^{-1} with $NaNO_3$)

cleaving agent	target	c(cleaving agent), μmol L^{-1}	c(target), μmol L^{-1}	$c(Zn^{2+})$, μmol L^{-1}	k, 10^{-6} s^{-1}
1a	**4**	18	18	90	5.9 ± 0.3
2a	**4**	18	18	90	20.8 ± 0.5
3a	**4**	18	18	90	2.5 ± 0.3
1a	**4**	18	18	180	6.3 ± 0.3
2a	**4**	18	18	180	20.7 ± 0.9
1a	**4**	9	36	90	0.27 ± 0.01
2a	**4**	9	36	90	0.76 ± 0.08
1b	**5**	18	18	90	0.9 ± 0.3
2b	**5**	18	18	90	1.7 ± 0.1
3b	**5**	18	18	90	1.1 ± 0.2
1b	**6**	18	18	90	1.2 ± 0.1
2b	**6**	18	18	90	1.7 ± 0.1
3b	**6**	18	18	90	1.0 ± 0.1

The effect of metal ion concentration on the cleavage rate was studied with conjugates **1a** and **2a**. The concentration of Zn^{2+} was increased to 180 μmol L^{-1} keeping the other conditions unchanged. The rate constants obtained were within the limits of experimental errors equal to those obtained at $[Zn^{2+}]$ = 90 μmol L^{-1} (Table 1), suggesting that the binding of Zn^{2+} to **1a** and **2a** is virtually quantitative. The reaction shows turnover in spite of the fact that the cleavage site is outside the complementary region between the cleaving agent and the target. As seen from Figure 3, the breakdown of target **4** at least roughly obeys first-order kinetics when present in 4-fold excess compared to the cleaving agent.

Artificial ribonucleases **1b** and **2b**, incorporating two azacrown ligands in the middle of the chain, cleaved targets **5** and **6**, forming upon hybridization a 3- and 5-nucleotide bulge, respectively, opposite to the azacrown moieties (Table 1). The cleavage was, however, less efficient than with **1a**−**3a**. Again the cleaving agent derived from the 1-*O*,3-*O*-funtionalized ribofuranosyl building block (**2b**) was most efficient, but the catalytic activity was more than 1 order of magnitude lower than with its 3′-terminal counterpart, **2a**. In fact, the catalytic

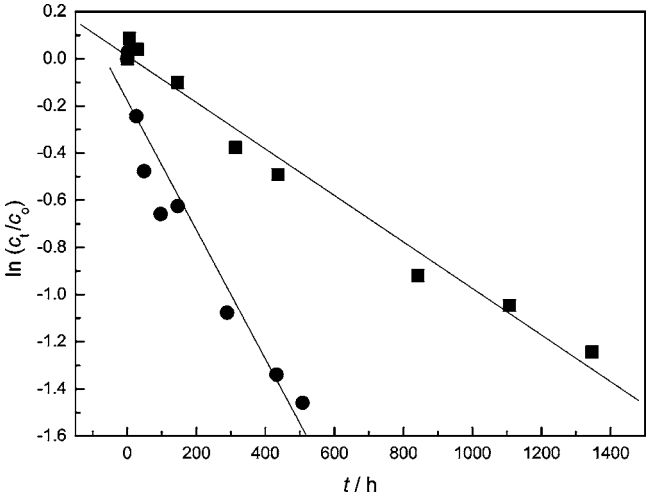


Figure 3. Cleavage of chimeric ribo/2′-*O*-methylribo oligonucleotide **4** by the Zn^{2+} complex of artificial nucleases **1a** and **2a** on using the target in 4-fold excess compared to the cleaving agent. The logarithmic concentration of **4** plotted against time. For the conditions, see Table 1. Notation: **1a** (■), **2a** (●).

activity was only double compared to that of the monofunctionalized azacrown conjugate **36** (*40*). The other two intrachain conjugates, **1b** and **3b**, cleaved **5** and **6** approximately as readily as the monofunctionalized **36**.

The origin of the high catalytic activity of the 1-*O*,3-*O*-tethered di(azacrown) conjugate (**2a**) compared to its 1-*O*,2-*O*-tethered isomer (**3a**) or mono(azacrown) counterpart (**35**) remains obscure. Either the two azacrown moieties of **2a** act in a cooperative manner, or the orientation of the 3-*O*-tethered group is optimal for the cleavage. Of these two alternative explanations, the latter appears more attractive. Cleavage of dinucleoside-3′,5′-monophosphates by a number of dinuclear Zn^{2+} bis(azacrown) chelates has been previously studied (*54*). Enhanced catalytic activity over the mononuclear Zn^{2+} chelate is observed only when one of the chelate moieties anchors the cleaving agent to a neighboring uracil base and, hence, brings the other chelate moiety in the proximity of the phosphodiester bond. This kind of rate-acceleration by additional anchoring to a base moiety in the vicinity of the scissile bond cannot be strictly excluded in the present case, but for the following reasons it appears less probable. First, there is no uracil base in the 5′-terminal ribo sequence of target **4** that would allow efficient anchoring (*55*). Second, the di(azacrown) unit in **2a** is so flexible that binding of one of the chelate moieties to any base or phosphate moiety near the cleavage site hardly increases the local concentration of the catalytic chelate moiety much more than already reached by hybridization.

In summary, the present study shows that tethering of two azacrown ligands to the 3′-terminus of a 2′-*O*-methyl oligoribonucleotide increases the catalytic efficiency by more than 1 order of magnitude compared to the corresponding monoazacrown-derivatized oligonucleotide. Half-lives shorter than 10 h are achieved at equimolar concentration of the target and cleaving agent under physiological conditions. The cleavage shows turnover. The efficiency of the cleaving agent, however, depends on the site of attachment of the azacrown moieties, in spite of marked overall flexibility of such constructs. Di(azacrown)-functionalized intrachain conjugates also cleave their bulged complementary sequences, but the catalytic activity is not much higher than that of their mono(azacrown) counterparts.

ACKNOWLEDGMENT

The financial support from the Academy of Finland is gratefully acknowledged.

Supporting Information Available: Experimental details and spectral data for phosphoramidites **14**, **24**, **25**, and **28**, and the precursor glycosides **23a**,**b**, and the RP HPLC data for the 2′-*O*-methyl oligoriboucleotide conjugates **1a**−**3a** and **1b**−**3b**. The material is available free of charge via the Internet at http://pubs.acs.org.

LITERATURE CITED

(1) Niittymäki, T., and Lönnberg, H. (2006) Artificial ribonucleases. *Org. Biomol. Chem. 4*, 15−25.
(2) Morrow, J. R., and Iranzo, O. (2004) Synthetic metallonucleases for RNA cleavage. *8*, 192−200.
(3) Häner, R. (2001) Artificial ribonucleases. *Chimia 55*, 1035−1037.
(4) Cowan, J. A. (2001) Chemical nucleases. *Curr. Opin. Chem. Biol. 5*, 634−642.
(5) Komiyama, M., Sumaoka, J., Kuzuya, A., and Yamamoto, Y. (2001) Sequence-selective artificial ribonucleases. *Methods Enzymol. 341*, 455−468.
(6) Travick, B. N., Daniher, A. T., and Bashkin, J. K. (1998) Inorganic mimics of ribonucleases and ribozymes: from random cleavage to sequence-specific chemistry to catalytic antisense drugs. *Chem. Rev. 98*, 939−960.
(7) Whitney, A., Gavory, G., and Balasubramanian, S. (2003) Site-specific cleavage of human telomerase RNA using PNA-neocuproine•Zn(II) derivatives. *Chem. Commun.*, 36−37.
(8) Kuzuya, A., Mizoguchi, R., Morisawa, F., and Komiyama, M. (2003) Site-selective RNA scission at two sites for precise genotyping of SNPs by mass spectrometry. *Chem. Commun.*, 770−771.
(9) Canaple, L., Hüsken, D., and Häner, R. (2002) Artificial ribonucleases: efficient and specific in vitro cleavage of human *c-raf-1* RNA. *Bioconjugate Chem. 13*, 945−951.
(10) Beloglazova, N. G., Fabani, M. M., Zenkova, M. A., Bichenkova, E. V., Polushin, N. N., Silnikov, V. V., Douglas, K. T., and Vlassov, V. V. (2004) Sequence-specific artificial ribonucleases. I. *Bis*-imidazole-containing oligonucleotide conjugates prepared using precursor-based strategy. *Nucleic Acids Res. 32*, 3887−3897.
(11) Mironova, N. L., Pyshnyi, D. V., Ivanova, E. M., Zarytova, V. F., Zenkova, M. A., Gross, H. J., and Vlassov, V. V. (2002) Sequence-specific RNA cleavage by oligonucleotide-peptide conjugates. *Russ. Chem. Bull. 51*, 1177−1186.
(12) Sasaki, S., and Nagatsugi, F. (2006) Application of unnatural oligonucleotides to chemical modification of gene expression. *Curr. Opin. Chem. Biol. 10*, 615−621.
(13) Wilson, C., and Keefe, A. D. (2006) Building oligonucleotide therapeutics using non-natural chemistries. *Curr. Opin. Chem. Biol. 10*, 607−614.
(14) Crooke, S. T. (2004) Progress in antisense technology. *Annu. Rev. Med. 55*, 61−95.
(15) Crooke, S. T. (2004) Antisense strategies. *Curr. Mol. Med. 4*, 465−487.
(16) Manoharan, M. (2002) Oligonucleotide conjugates as potential antisense drugs with improved uptake, biodistribution, targeted delivery, and mechanism of action. *Antisense Nucleic Acid Drug Dev. 12*, 103−128.
(17) Bumcrot, D., Manoharan, M., Koteliansky, V., and Sah, D. W. Y. (2006) RNAi therapeutics: a potential new class of pharmaceutical drugs. *Nat. Chem. Biol. 2*, 711−719.
(18) Dykxhoorn, D. M., Palliser, D., and Lieberman, J. (2006) The silent treatment: siRNA as small molecule drugs. *Gene Ther. 13*, 541−552.
(19) Leung, R. K. M., and Whittaker, P. A. (2005) RNA interference: from gene silencing to gene-specific therapeutics. *Pharm. Ther. 107*, 222−239.
(20) Mittal, V. (2004) Improving the efficiency of RNA interference in mammals. *Nat. Rev. Gen. 5*, 355−365.
(21) Dorsett, Y., and Tuschl, T. (2004) siRNA: applications in functional genomics and potential as therapeutics. *Nat. Rev. Drug Discovery 3*, 318−329.
(22) Gnaccarini, C., Peter, S., Scheffer, U., Vonhoff, S., Klussmann, S., and Göbel, M. W. (2006) Site-specific cleavage of RNA by a metal-free artificial nuclease attached to antisense oligonucleotides. *J. Am. Chem. Soc. 128*, 8063−8067.

(23) Riguet, E., Tripathi, S., Chaubey, B., Desire, J., Pandey, V. N., and Decout, J.-L. (2004) A peptide nucleic acid−neamine conjugate that targets and cleaves HIV-1 TAR RNA inhibits viral replication. *J. Med. Chem. 47*, 4806−4809.

(24) Verheijen, J. C., Deiman, B. A. L. M., Yeheskiely, E., van der marel, G. A., and van Boom, J. H. (2000) Efficient hydrolysis of RNA by a PNA-diethylenetriamine adduct. *Angew. Chem., Int. Ed. 39*, 369−372.

(25) Matsumura, K., Endo, M., and Komiyama, M. (1994) Lanthanide complex-oligo-DNA hybrid for sequence-selective hydrolysis of RNA. *J. Chem. Soc., Chem. Commun.* 2019−2020.

(26) Hall, J., Hüsken, D., Pieles, U., Moser, H. E., and Häner, R. (1994) Efficient sequence-specific cleavage of RNA using novel europium complexes conjugated to oligonucleotides. *Chem. Biol. 1*, 185−190.

(27) Magda, D., Miller, R. A., Sessler, J. L., and Iverson, B. L. (1994) Site-specific hydrolysis of RNA by europium(III) texapyrin conjugated to a synthetic oligodeoxyribonucleotide. *J. Am. Chem. Soc. 116*, 7439−7440.

(28) Magda, D., Crofts, S., Lin, A., Miles, M., Wright, M., and Sessler, J. L. (1997) Synthesis and Kinetic Properties of Ribozyme Analogues Prepared Using Phosphoramidite Derivatives of Dysprosium(III) Texaphyrin. *J. Am. Chem. Soc. 119*, 2293−2294.

(29) Magda, D., Wright, M., Crofts, S., Lin, A., and Sessler, J. L. (1997) Metal complex conjugates of antisense DNA which display ribozyme-like activity. *J. Am. Chem. Soc. 119*, 6947−6948.

(30) Hall, J., Hüsken, D., and Häner, R. (1996) Towards artificial ribonucleases: the sequence specific cleavage of RNA in a duplex. *Nucleic Acids Res. 24*, 3522−3526.

(31) Häner, R., and Hall, J. (1997) The sequence-specific cleavage of RNA by artificial chemical ribonucleases. *Antisense Nucleic Acid Drug Dev. 7*, 423−430.

(32) Bashkin, J. K., Frolova, E. I., and Sampath, U. (1994) Sequence-specific cleavage of HIV mRNA by a ribozyme mimic. *J. Am. Chem. Soc. 116*, 5981−5982.

(33) Trawick, B. N., Osiek, T. A., and Bashkin, J. K. (2001) Enhancing sequence-specific cleavage of RNA within a duplex region: incorporation of 1,3-propanediol linkers into oligonucleotide conjugates of serinol-terpyridine. *Bioconjugate Chem. 12*, 900−905.

(34) Putnam, W. C., Daniher, A. T., Trawick, B. N., and Bashkin, J. K. (2001) Efficient new ribozyme mimics: direct mapping of molecular design principles from small molecules to macromolecular, biomimetic catalysis. *Nucleic Acids Res. 29*, 2199−2204.

(35) Sakamoto, A., Tamura, T., Furukawa, T., Komatsu, Y., Ohtsuka, E., Kitamura, M., and Inoue, H. (2003) Highly efficient catalytic RNA cleavage by the cooperative action of two Cu(II) complexes embodied within an antisense oligonucleotide. *Nucleic Acids Res. 31*, 1416−1425.

(36) Inoue, H., Furukawa, T., Shimizu, M., Tamura, T., Matsui, M., and Ohtsuka, E. (1999) Efficient site-specific cleavage of RNA using a terpyridine−copper(II) complex joined to a 2′-*O*-methyloligonucleotide by a non-flexible linker. *Chem. Commun.*, 45−46.

(37) Hovinen, J., Guzaev, A., Azhayeva, E., Azhayev, A., and Lönnberg, H. (1995) Imidazole tethered oligodeoxyribonucleotides: synthesis and RNA cleaving activity. *J. Org. Chem. 60*, 2205−2209.

(38) Matsuda, S., Ishikubo, A., Kuzuya, A., Yashiro, M., and Komiyama, M. (1998) Conjugates of a dinuclear zinc(II) complexes and DNA oligomers as novel sequence-selective artificial ribonucleases. *Angew. Chem., Int. Ed. 37*, 3284−3286.

(39) Åström, H., Williams, N. H., and Strömberg, R. (2003) Oligonucleotide based artificial nuclease (OBAN) systems. Bulge size dependence and positioning of catalytic group in cleavage of RNA-bulges. *Org. Biomol. Chem. 1*, 1461−1465.

(40) Niittymäki, T., and Lönnberg, H. (2004) Sequence-selective cleavage of oligoribonucleotides by 3d transition metal complexes of 1,5,9-triazacyclododecane-functionalized 2′-*O*-methyl oligoribonucleotides. *Bioconjugate Chem. 15*, 1275−1280.

(41) Åström, H., and Strömberg, R. (2004) Synthesis of new OBAN's and further studies on positioning of the catalytic group. *Org. Biomol. Chem. 2*, 1901−1907.

(42) Niittymäki, T., Kaukinen, U., Virta, P., Mikkola, S., and Lönnberg, H. (2004) Preparation of azacrown-functionalized 2′-*O*-methyl oligoribonucleotides, potential artificial RNases. *Bioconjugate Chem. 15*, 174−184.

(43) Katajisto, J., Virta, P., and Lönnberg, H. (2004) Solid-phase synthesis of multiantennary oligonucleotide glycoconjugates utilizing on-support oximation. *Bioconjugate Chem. 15*, 890−896.

(44) Liu, M.-Z., Fan, H.-N., Guo, Z.-W., and Hui, Y.-Z. (1996) One-step glycosylation and selective deprotection of peracetylated monosaccharides for facile syntheses of allyl glycosides with a free C-2 hydroxyl group. *Carbohydrate Res. 290*, 233−237.

(45) Guibe, F., and Saint M'Leux, Y. (1981) The allyloxycarbonyl group for alcohol protection: quantitative removal or transformation into allyl protecting group via π-allyl complexes of palladium. *Tetrahedron Lett. 22*, 3591−3594.

(46) Buskas, T., Söderberg, E., Konradson, P., and Fraser-Reid, B. (2000) Use of n-pentenyl glycosides as precursors to various spacer functionalities. *J. Org. Chem. 65*, 958−963.

(47) Kuusela, S., and Lönnberg, H. (1994) Metal-ion-promoted hydrolysis of polyuridylic acid. *J. Chem. Soc., Perkin Trans. 2*, 2301−2306.

(48) Guzaev, A., Azhayeva, E., Hovinen, J., Azhayev, A., and Lönnberg, H. (1994) Synthesis and primer properties of oligonucleotides containing 3′-deoxypsicothymidine units labeled with fluorescein at the 1′-position. *Bioconjugate Chem. 5*, 501−503.

(49) Azhayev, A., Guzaev, A., Hovinen, J., Azhayeva, E., and Lönnberg, H. (1993) Analogues of oligonucleotides containing 3′-deoxy-β-D-psicothymidine. *Tetrahedron Lett. 34*, 6435−6438.

(50) Jin, S., Miduturu, C. V., McKinney, D. C., and Silverman, S. K. (2005) Synthesis of amine- and thiol-modified nucleoside phosphoramidites for site-specific introduction of biophysical probes into RNA. *J. Org. Chem. 70*, 4284−4299.

(51) Katajisto, J., Heinonen, P., and Lönnberg, H. (2004) Solid-phase synthesis of oligonucleotide glycoconjugates bearing three different glycosyl groups: orthogonally protected bis(hydroxymethyl)-*N*,*N*-bis(3-hydroxypropyl)malondiamide phosphoramidite as key building block. *J. Org. Chem. 69*, 7609−76154.

(52) Guzaev, A., Salo, H., Azhayev, A., and Lönnberg, H. (1996) Novel non-nucleosidic building blocks for the preparation of multilabeled oligonucleotides. *Bioconjugate Chem. 7*, 240−248.

(53) Kaukinen, U., Bielecki, L., Mikkola, S., Adamiak, R. W., and Lönnberg, H. (2001) The cleavage of phosphodiester bonds within small RNA bulges in the presence and absence of metal ion catalysts. *J. Chem. Soc., Perkin Trans. 2*, 1024−1031.

(54) Wang, Q., and Lönnberg, H. (2006) Simultaneous interaction with base and phosphate moieties modulates the phosphodiester cleavage of dinucleoside-3′,5′-monophosphates by dinuclear Zn^{2+} complexes of di(azacrown) ligands. *J. Am. Chem. Soc. 128*, 10716−10728.

(55) Aoki, S., and Kimura, E. (2004) Zinc-nucleic acid interaction. *Chem. Rev. 104*, 769−787.

BC070071O

Biotinylated Anisomycin: A Comparison of Classical and "Click" Chemistry Approaches

Iain A. Inverarity,[†] Romain F. H. Viguier,[†] Philip Cohen,[‡] and Alison N. Hulme*[,†]

The School of Chemistry, University of Edinburgh, Kings Buildings, West Mains Road, Edinburgh, EH9 3JJ, United Kingdom, and MRC Protein Phosphorylation Unit, School of Life Sciences, University of Dundee, Dow Street, Dundee, DD1 5EH, United Kingdom. Received March 13, 2007; Revised Manuscript Received June 14, 2007

Two approaches to the synthesis of biotinylated derivatives of the stress-activated protein kinase (SAPK) pathway activator anisomycin have been investigated. Attachment of the biotin moiety to the central core was achieved either through the use of a classical displacement reaction on α-halo carbonyl derivatives of biotin or through a copper(I)-catalyzed 1,3-dipolar Huisgen cycloaddition ("click") coupling of biotinylated azides to propargyl-marked analogues of anisomycin. In each case, the resultant *N*-linked molecular probes were found to be active in SAPK pathway immunoblot assays, while their *O*-linked counterparts were inactive. However, in sharp contrast to the classical coupling approach which results in low coupling yields, the aqueous "click" coupling process was found to deliver high yields of biotinylated probes, making it the conjugation method of choice. A survey of the available methods for the addition of a propargyl marker onto a range of chemical functionalities strongly suggests that this copper(I)-catalyzed 1,3-dipolar Huisgen cycloaddition approach to biotinylation may be generally applied.

INTRODUCTION

Despite rapid advances in the generation and testing of small molecule libraries in recent years (*1*−*3*), current strategies for the identification of the biological targets of library members in forward chemical genetics screens still require the synthesis of an appropriate molecular probe. The structure of this molecular probe is typically based on an active library member, which has been modified by introduction of a tag (biotin, photoactive, or fluorescent label) (*4*−*7*). Selective biotinylation has been widely used over the last 30 years as a method for purification and identification of a range of targets (*8*). The popularity of this strategy stems from the peculiarly tight binding of biotin to (strept)avidin (K_d of 10^{-15} M) (*9*), which means that affinity chromatography methods based around this partnership are particularly useful for the identification of the binding partners of high-affinity small molecules where there is an abundant protein receptor. A notable recent example of this strategy includes the identification of the biological target of L-685,485 (a potent γ-secretase inhibitor) as the PS1 protein (*10*), while further examples of this approach encompass the biotinylation of a range of biologically active molecules including carbohydrates (*11*), steroids (*12*), and a number of drugs such as ezetimibe (a cholesterol inhibitor) (*13*), and paclitaxel (an anti-cancer compound) (*14*).

The pyrrolidine antibiotic anisomycin **1a** was first isolated from *Streptomyces roseochromogenes* and *S. griseolus* in 1954 (*15*). Over subsequent years, a series of studies have confirmed the structure and absolute stereochemistry as 2*R*,3*S*,4*S* for the three stereocentres around the pyrrolidine ring (*16*−*19*). Since its discovery, anisomycin has been found to generate many interesting biological responses including anti-fungal activity (*20*), protein synthesis inhibition (*21*), and anti-tumor activity in the nanomolar region (*22*). In addition, over the past fifteen years anisomycin has been used as a chemical stimulant of the stress-activated protein kinase (SAPK) pathways at subinhibitory levels (Figure 1) (*23*−*28*). The SAPK pathway is a distinct signaling branch within the mitogen activated protein kinase (MAPK) superfamily. The core unit of the MAPK pathways is a three-membered protein kinase cascade whose components are highly conserved in structure and organization. In this cascade, the MAPKs are phosphorylated and activated by a MAPK kinase (MAPKK/MKK). The MAPKK are "dual-specific" kinases that catalyze the phosphorylation of MAPKs at Thr and Tyr sites, specifically targeting a Thr-X-Tyr motif on MAPK (where X is proline and glycine for the JNK/SAPK1 and p38/SAPK2 modules, respectively) (*29*, *30*). Regulation of these pathways results in controlled activation of downstream kinases and transcription factors including c-Jun, ATF-2, and MAPKAP-K2. Regulation of the SAPK pathways is of interest across a broad range of fields, as it is thought to play a role in a range of conditions such as ischemic brain injury resulting from stroke episodes (*31*), cancer (*32*), and Alzheimer's disease (*33*). Although the precise target of anisomycin is unknown, the downstream effects on the SAPK pathways have been well-documented (*29*−*30*). The treatment of mammalian, yeast, and insect cells with anisomycin is known to strongly activate both the JNK/SAPK1 and p38/SAPK2 pathways, resulting in phosphorylation of their substrates, such as JNK and MAPKAP-K2, respectively.

Previous structure−activity relationship (SAR) studies for activation of the JNK/p38 pathways by anisomycin gave us an insight into the core functionality required to stimulate this phenotypic response, and hence allowed us to hypothesize potential sites for biotinylation. Principally, these studies showed that the presence of an ester functionality at the C(3) position on the pyrrolidine ring was essential for activity, with both the C(3) acetate (anisomycin, **1a**) and C(3) propionate ester **1b** shown to be active compounds (Figure 2) (*34*). In addition, both the C(4)-H **2a** and C(4)-Me **2b** analogues were found to activate the SAPK pathways, with the C(4)-H analogue exhibiting similar levels of activation to that of anisomycin (*34*). More recent work has shown that, while the N(1)-Bn analogue **1c** generates a strong activation of the SAPK pathways (*35*), simultaneous

* Corresponding author. E-mail: Alison.Hulme@ed.ac.uk. Phone: +44 131 6504711. Fax: +44 131 6506453.

[†] University of Edinburgh.

[‡] University of Dundee.

10.1021/bc070085u CCC: $37.00 © 2007 American Chemical Society
Published on Web 08/17/2007

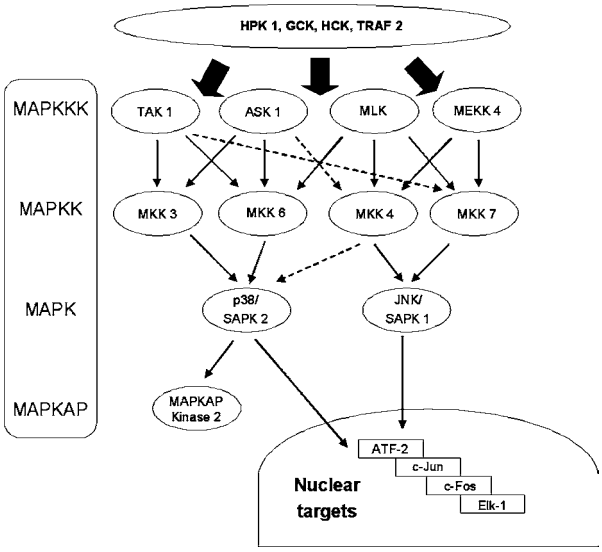
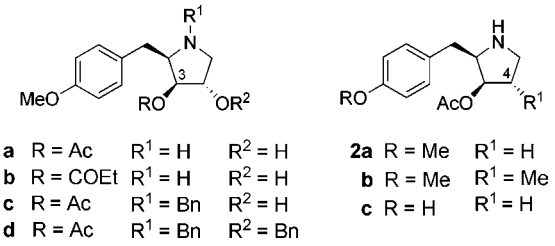


Figure 1. Stress-activated protein kinase (SAPK) pathways.



1a R = Ac R^1 = H R^2 = H
b R = COEt R^1 = H R^2 = H
c R = Ac R^1 = Bn R^2 = H
d R = Ac R^1 = Bn R^2 = Bn

2a R = Me R^1 = H
b R = Me R^1 = Me
c R = H R^1 = H

Figure 2. Anisomycin and analogues used to determine the structure−activity relationships (SAR) for activation of the SAPK pathways.

dibenzylation of N(1) and C(4)-OH, analogue **1d**, is not tolerated. These results suggest that the C(3) and C(4) sites are unsuitable for conjugation as biotinylated probes. However, the N(1) position is tolerant of relatively bulky functionalization, particularly as an amino- rather than an amido/carbamate-type linkage (*36*). Furthermore, a survey of the literature relating to the bioactivity of anisomycin in other cellular assays led us to postulate that conjugation of the phenolic oxygen might also be possible (*22*). We therefore set out to synthesize a series of biotinylated molecular probes coupling to the anisomycin scaffold through either the pyrrolidine nitrogen or the phenolic oxygen.

EXPERIMENTAL SECTION

General Methods. All reactions involving air- or water-sensitive reagents were carried out under an atmosphere of nitrogen using flame- or oven-dried glassware. Unless otherwise noted, starting materials and reagents were obtained from commercial suppliers and were used without further purification. CH_2Cl_2 and Et_3N were distilled from calcium hydride. Anhydrous methanol, DMF, and acetonitrile were used as supplied. Unless otherwise indicated, organic extracts were dried over anhydrous sodium sulfate and concentrated under reduced pressure using a rotary evaporator. Purification by flash column chromatography was carried out using Merck Kieselgel 60 silica gel as the stationary phase. IR spectra were measured on a Perkin-Elmer Paragon 1000 FT-IR spectrometer as thin films unless otherwise stated. ^{1}H and ^{13}C NMR spectra were measured on Bruker DPX360 and Bruker AVA600 instruments; *J*-values are in hertz. Fast atom bombardment (FAB) mass spectra were obtained using a Kratos MS50TC mass spectrometer at The University of Edinburgh.

Complete Protease Inhibitor tablet was obtained from Roche (Lewes, Sussex, UK), cell culture media from Gibco (Paisley, UK), precast Bis-Tris gradient SDS-polyacrylamide gels, running buffer, and transfer buffer from Invitrogen (Paisley, UK), and enhanced chemiluminescence (ECL) reagents from Amersham (Bucks, UK). Phospho-specific antibodies that recognize JNK1/2 phosphorylated at Thr183 or unphosphorylated JNK1/2 were purchased from Biosource (Nivelles, Belgium), while horseradish peroxidase-conjugated secondary antibodies were from Pierce (Cheshire, UK).

Coupling to C_2 Biotinylated Iodoacetamide 4. *2′-N-Biotinylamino-eth-1-yl 4′-(2″-acetoxyeth-1″-yl)phenyloxyacetamide 5*. To biotinylated iodoacetamide **4** (20.0 mg, 40.0 μmol) in DMF (1.5 mL) was added phenol **3** (10.0 mg, 40.0 μmol), followed by K_2CO_3 (6.00 mg, 40.0 μmol). The solution was stirred for 48 h at 80 °C. The solution was concentrated *in vacuo*, and the residue was purified by flash chromatography [10% MeOH/CH_2Cl_2] to give phenol ether **5** as a colorless solid (17.0 mg, 34.4 μmol, 86%). R_f [10% MeOH/CH_2Cl_2] = 0.30. ^{1}H NMR δ (360 MHz, DMSO) 8.12 (1H, t, *J* 5.2, $N_{17}H$), 7.87 (1H, t, *J* 5.2, $N_{14}H$), 7.17 (2H, d, *J* 8.7, Ar*H*), 6.89 (2H, d, *J* 8.7, Ar*H*), 6.42 (1H, br s, N_6H), 6.36 (1H, br s, N_4H), 4.42 (2H, s, $C_{19}H_2$), 4.30−4.27 (1H, m, C_3H), 4.15 (2H, t, *J* 7.0, $C_{26}H_2$), 4.12−4.08 (1H, m, C_7H), 3.15 (4H, dt, *J* 9.9, 5.6, $C_{15}H_2$, $C_{16}H_2$), 3.10−3.04 (1H, m, C_8H), 2.81 (2H, t, *J* 7.0, $C_{25}H_2$), 2.80 (1H, dd, *J* 12.3, 5.2, $C_2H_AH_B$), 2.56 (1H, d, *J* 12.3, $C_2H_AH_B$), 2.04 (2H, t, *J* 7.3, $C_{12}H_2$), 1.97 (3H, s, OA*c*), 1.64−1.23 (6H, m, C_9H_2, $C_{10}H_2$, $C_{11}H_2$). ^{13}C NMR δ (90.7 MHz, DMSO) 172.3 (1C, C_{13}, Q), 170.2 (1C, OA*c*, Q), 167.8 (1C, C_{18}, Q), 162.6 (1C, C_5, Q), 156.6 (1C, Ar, Q), 130.4 (1C, Ar, Q), 129.5 (2C, *Ar*H, CH), 114.4 (2C, *Ar*H, CH), 66.7 (1C, C_{19}, CH_2), 64.2 (1C, C_{26}, CH_2), 60.7 (1C, C_7, CH), 59.0 (1C, C_3, CH), 55.1 (1C, C_8, CH), 39.6 (1C, C_2, CH_2), 38.3 (1C, C_{16}, CH_2), 37.8 (1C, C_{15}, CH_2), 34.9 (1C, C_{12}, CH_2), 33.2 (1C, C_{25}, CH_2), 28.0 (1C, C_{10}, CH_2), 27.8 (1C, C_9, CH_2), 24.9 (1C, C_{11}, CH_2), 20.5 (1C, OA*c*, CH_3). *m/z* (FAB, THIOG) 507 ([M + H]$^+$, 29%), 91 (75). HRMS (FAB, THIOG) (found: [M + H]$^+$, 507.2281. $C_{24}H_{35}N_4O_6S$ requires *m/z*, 507.2277).

C_2-Classical O-Linked Boc C(4)-H Anisomycin Biotin Molecular Probe 7a. To biotinylated iodoacetamide **4** (50.0 mg, 111 μmol) in DMF (2.5 mL) was added C(4)-H analogue **6** (37.0 mg, 111 μmol), followed by K_2CO_3 (18.0 mg, 130 μmol). The solution was stirred for 48 h at 80 °C. The solution was concentrated *in vacuo*, and the residue was purified by flash chromatography [5% to 15% MeOH/CH_2Cl_2] to give carbamate **7a** as a colorless solid (23.0 mg, 34.0 μmol, 31%). R_f [20% MeOH/CH_2Cl_2] = 0.27. ^{1}H NMR δ (600 MHz, $CDCl_3$, 323 K) 7.23 (1H, br t, *J* 4.6, $N_{17}H$), 7.14 (2H, d, *J* 8.0, Ar*H*), 6.85 (2H, d, *J* 8.0, Ar*H*), 6.80 (1H, br s, $N_{14}H$), 6.35 (1H, br s, N_6H), 5.45 (1H, br s, N_4H), 5.11 (1H, br q, *J* 6.6, $C_{27}H$), 4.52−4.45 (3H, br s, C_3H, $C_{19}H_2$), 4.31−4.29 (1H, m, C_7H), 4.24 (1H, br q, *J* 6.1, C_{26}H), 3.48−3.43 (5H, m, $C_{15}H_2$, $C_{16}H_2$, $C_{29}H_MH_N$), 3.35−3.31 (1H, m, $C_{29}H_MH_N$) 3.14−3.12 (1H, m, C_8H), 2.95−2.92 (1H, m, $C_{25}H_SH_T$), 2.89 (1H, dd, *J* 12.7, 4.4, $C_2H_AH_B$), 2.82 (1H, dd, 13.5, 5.5, $C_{25}H_SH_T$), 2.71 (1H, d, *J* 12.7, $C_2H_AH_B$), 2.21 (2H, br q, *J* 6.5, $C_{12}H_2$), 2.10−2.05 (1H, m, $C_{28}H_EH_F$), 2.00 (3H, s, OA*c*), 1.82−1.65 (5H, m, C_9H_2, $C_{11}H_2$, $C_{28}H_EH_F$), 1.46 (9H, s, ^{t}*Bu*O), 1.30−1.27 (2H, m, $C_{10}H_2$). ^{13}C NMR δ (151.1 MHz, $CDCl_3$, 323 K) 174.3 (1C, *CO*^{t}*Bu*, Q), 174.2 (1C, C_{13}, Q), 170.3 (1C, OA*c*, Q), 169.9 (1C, C_{18}, Q), 164.1 (1C, C_5, Q), 156.2 (1C, *Ar*, Q), 132.7 (1C, *Ar*, Q), 130.9 (2C, *Ar*H, CH), 114.9 (2C, *Ar*H, CH), 80.1 (1C, ^{t}*Bu*, Q), 73.3 (1C, C_{27}, CH), 67.7 (1C, C_{19}, CH_2), 61.9 (1C, C_7, CH), 60.4 (1C, C_3, CH), 59.5 (1C, C_{26}, CH), 55.7 (1C, C_8, CH), 43.3 (1C, C_{29}, CH_2), 40.7 (1C, C_2, CH_2), 39.6 (1C, C_{16}, CH_2), 39.6 (1C, C_{15}, CH_2), 35.9 (1C, C_{12}, CH_2), 34.4 (1C, C_{25}, CH_2), 29.8 (1C, C_{10}, CH_2), 29.0 (1C, C_{28}, CH_2), 28.4 (3C, ^{t}*Bu*, CH_3), 28.4 (1C, C_9, CH_2), 25.5 (1C, C_{11}, CH_2), 21.0 (1C, OA*c*, CH_3). *m/z* (FAB, THIOG) 662 ([M + H]$^+$, 3%), 562 (27) 91 (22). HRMS (FAB,

THIOG) (found: $[M + H]^+$, 662.3229. $C_{32}H_{48}N_5O_8S$ requires *m/z*, 662.3224).

*C_2-Classical O-Linked C(4)-H Anisomycin Biotin Molecular Probe **7b***. To a solution of carbamate **7a** (19.0 mg, 31.0 μmol) in CH_2Cl_2 (2 mL) was added trifluoroacetic acid (23.0 μL, 310 μmol), and the solution was stirred for 3 h at RT. The reaction was concentrated *in vacuo* to give *O*-linked probe **7b** (20.0 mg, 29.0 μmol, 94%) as a colorless foam. R_f [20% MeOH/CH_2Cl_2] = 0.36. ^{1}H NMR δ (360 MHz, DMSO) 8.16 (1H, t, *J* 5.3, $N_{17}H$), 7.90 (1H, t, *J* 5.3, $N_{14}H$), 7.19 (2H, d, *J* 8.6, Ar*H*), 6.93 (2H, d, *J* 8.6, Ar*H*), 6.45 (1H, br s, N_6H), 6.38 (1H, br s, N_4H), 5.15 (1H, t, *J* 3.7, $C_{27}H$), 4.43 (2H, s, $C_{19}H_2$), 4.31−4.28 (1H, m, C_3H), 4.14−4.10 (1H, m, C_7H), 3.88−3.82 (1H, m, $C_{26}H$), 3.33−3.23 (2H, m, $C_{29}H_2$), 3.20−3.10 (4H, m, $C_{15}H_2$, $C_{16}H_2$), 3.08 (1H, ddd, *J* 8.7, 6.2, 4.5, C_8H), 2.98−2.86 (2H, m, $C_{25}H_2$), 2.80 (1H, dd, *J* 12.4, 5.0, $C_2H_AH_B$), 2.57 (1H, d, *J* 12.4, $C_2H_AH_B$), 2.29−2.18 (1H, m, $C_{28}H_EH_F$), 2.12 (3H, s, OA*c*), 2.05 (2H, t, *J* 7.4, $C_{12}H_2$), 2.02−1.97 (1H, m, $C_{28}H_EH_F$), 1.65−1.25 (6H, m, C_9H_2, $C_{10}H_2$, $C_{11}H_2$). ^{13}C NMR δ (90.7 MHz, DMSO) 172.2 (1C, C_{13}, Q), 169.4 (1C, O*Ac*, Q), 167.7 (1C, C_{18}, Q), 162.5 (1C, C_5, Q), 156.4 (1C, *Ar*, Q), 129.7 (2C, *Ar*H, CH), 128.9 (1C, *Ar*, Q), 114.8 (2C, *Ar*H, CH), 72.6 (1C, C_{27}, CH), 66.8 (1C, C_{19}, CH_2), 63.1 (1C, C_{26}, CH), 60.8 (1C, C_7, CH), 59.0 (1C, C_3, CH), 55.2 (1C, C_8, CH), 42.5 (1C, C_{29}, CH_2), 39.6 (1C, C_2, CH_2), 38.3 (1C, C_{16}, CH_2), 37.8 (1C, C_{15}, CH_2), 35.0 (1C, C_{12}, CH_2), 30.8 (1C, C_{25}, CH_2), 30.2 (1C, C_{28}, CH_2), 28.1 (1C, C_{10}, CH_2), 27.9 (1C, C_9, CH_2), 25.0 (1C, C_{11}, CH_2), 20.6 (1C, O*Ac*, CH_3). *m/z* (FAB, THIOG) 562 ($[M + H]^+$, 80%), 91 (100). HRMS (FAB, NOBA) (found: $[M + H]^+$, 562.2705. $C_{27}H_{40}N_5O_6S$ requires *m/z*, 562.2699).

*C_2-Classical N-Linked Anisomycin Biotin Molecular Probe **8***. To biotinylated iodoacetamide **4** (25.0 mg, 55.0 μmol) in DMF (5 mL) was added anisomycin **1a** (15.0 mg, 55.0 μmol), followed by K_2CO_3 (7.60 mg, 55.0 μmol). The solution was stirred for 48 h at 80 °C. The solution was concentrated *in vacuo*, and the residue was purified by flash chromatography [5% to 15% MeOH/CH_2Cl_2] to give *N*-linked probe **8** as a colorless solid (11.0 mg, 18.7 μmol, 34%). R_f [14% MeOH/CH_2Cl_2] = 0.33. ^{1}H NMR δ (360 MHz, DMSO) 7.87 (2H, br s, $N_{14}H$, $N_{17}H$), 7.08 (2H, d, *J* 8.6, Ar*H*), 6.81 (2H, d, *J* 8.6, Ar*H*), 6.43 (1H, br s, N_6H), 6.38 (1H, br s, N_4H), 4.60 (1H, dd, *J* 4.2, 1.5, $C_{23}H$), 4.31−4.28 (1H, m, C_3H), 4.13−4.09 (1H, m, C_7H), 3.95−3.90 (1H, m, $C_{22}H$), 3.70 (3H, s, O*Me*), 3.49−3.35 (2H, m, $C_{19}H_XH_Y$, $C_{21}H_MH_N$), 3.17−3.05 (5H, m, C_8H, $C_{15}H_2$, $C_{16}H_2$,), 3.00−2.85 (3H, m, $C_{19}H_XH_Y$, $C_{21}H_MH_N$), 2.80 (1H, dd, *J* 12.5, 5.0, $C_2H_AH_B$), 2.77−2.71 (1H, m, $C_{25}H_SH_T$), 2.66−2.60 (1H, m, $C_{25}H_SH_T$), 2.57 (1H, d, *J* 12.5, $C_2H_AH_B$), 2.08 (3H, s, O*Ac*), 2.06 (2H, t, *J* 7.6, $C_{12}H_2$), 1.76−1.22 (6H, m, C_9H_2, $C_{10}H_2$, $C_{11}H_2$). ^{13}C NMR δ (151.1 MHz, DMSO) 172.5 (1C, C_{13}, Q), 171.1 (1C, C_{18}, Q), 169.7 (1C, O*Ac*, Q), 162.8 (1C, C_5, Q), 157.7 (1C, *Ar*, Q), 130.2 (1C, *Ar*, Q), 129.7 (2C, *Ar*H, CH), 113.5 (2C, *Ar*H, CH), 78.5 (1C, C_{23}, CH), 72.5 (1C, C_{22}, CH), 69.6 (1C, C_{24}, CH), 60.8 (1C, C_7, CH), 60.8 (1C, C_{21}, CH_2), 59.0 (1C, C_3, CH), 58.2 (1C, C_{19}, CH_2), 55.2 (1C, C_8, CH), 54.7 (1C, O*Me*, CH_3), 39.5 (1C, C_2, CH_2), 38.2 (1C, C_{16}, CH_2), 37.8 (1C, C_{15}, CH_2), 35.1 (1C, C_{12}, CH_2), 32.4 (1C, C_{25}, CH_2), 28.2 (1C, C_{10}, CH_2), 27.8 (1C, C_9, CH_2), 25.0 (1C, C_{11}, CH_2), 20.7 (1C, O*Ac*, CH_3). *m/z* (FAB, THIOG) 592 ($[M + H]^+$, 52%), 91 (100). HRMS (FAB, THIOG) (found: $[M + H]^+$, 592.2804. $C_{28}H_{42}N_5O_7S$ requires *m/z*, 592.2805).

Coupling to C_6 Biotinylated Iodoacetamide 9. *6′-N-Biotinylamino-hex-1-yl 4′-(2″-acetoxyeth-1″-yl)phenyloxyacetamide **10**.* To biotinylated iodoacetamide **9** (20.0 mg, 47.0 μmol) in DMF (5.0 mL) was added **3** (8.60 mg, 47.0 μmol), followed by K_2CO_3 (6.60 mg, 47.0 μmol). The solution was stirred for 48 h at 80 °C. The solution was concentrated *in vacuo*, and the residue was purified by flash chromatography [5% to 15% MeOH/CH_2Cl_2] to give phenol ether **10** as a colorless solid (20.0 mg, 33.8 μmol, 72%). R_f [10% MeOH/CH_2Cl_2] = 0.16. ^{1}H NMR δ (600 MHz, DMSO) 8.03 (1H, t, *J* 5.7, $N_{21}H$), 7.72 (1H, t, *J* 5.7, $N_{14}H$), 7.17 (2H, d, *J* 8.5, Ar*H*), 6.88 (2H, d, *J* 8.5, Ar*H*), 6.41 (1H, br s, N_6H), 6.35 (1H, br s, N_4H), 4.42 (2H, s, $C_{23}H_2$), 4.31−4.29 (1H, m, C_3H), 4.15 (2H, t, *J* 6.9, $C_{30}H_2$), 4.13−4.11 (1H, m, C_7H), 3.10 (2H, br q, *J* 6.8, $C_{20}H_2$), 3.09−3.07 (1H, m, C_8H), 3.00 (2H, br q, *J* 6.7, $C_{15}H_2$), 2.60 (1H, dd, *J* 12.5, 5.0, $C_2H_AH_B$), 2.81 (2H, t, *J* 6.7, $C_{29}H_2$), 2.57 (1H, d, *J* 12.5, $C_2H_AH_B$), 2.04 (2H, t, *J* 7.4, $C_{12}H_2$), 1.97 (3H, s, O*Ac*), 1.64−1.21 (14H, m, C_9H_2, $C_{10}H_2$, $C_{11}H_2$, $C_{16}H_2$, $C_{17}H_2$, $C_{18}H_2$, $C_{19}H_2$). ^{13}C NMR δ (151.5 MHz, DMSO) 171.6 (1C, C_{13}, Q), 170.1 (1C, O*Ac*, Q), 167.3 (1C, C_{22}, Q), 162.5 (1C, C_5, Q), 156.2 (1C, Ar, Q), 130.4 (1C, Ar, Q), 129.7 (2C, *Ar*H, CH), 114.5 (2C, *Ar*H, CH), 66.9 (1C, C_{23}, CH_2), 64.4 (1C, C_{30}, CH_2), 60.9 (1C, C_7, CH), 59.0 (1C, C_3, CH), 55.2 (1C, C_8, CH), 39.7 (1C, C_2, CH_2), 38.1 (1C, C_{15}, CH_2), 38.0 (1C, C_{20}, CH_2), 35.1 (1C, C_{12}, CH_2), 33.3 (1C, C_{29}, CH_2), 29.0, 28.9, 28.8, 28.1, 27.9, 25.9, 25.2 (7C, C_9, C_{10}, C_{11}, C_{16}, C_{17}, C_{18}, C_{19}, CH_2), 20.6 (1C, O*Ac*, CH_3). *m/z* (FAB, THIOG) 563 ($[M + H]^+$, 49%), 91 (70). HRMS (FAB, NOBA) (found: $[M + H]^+$, 563.2907. $C_{28}H_{43}N_4O_6S$ requires *m/z*, 563.2903).

*C_6-Classical N-Linked Anisomycin Biotin Molecular Probe **11**.* To biotinylated iodoacetamide **9** (20.0 mg, 47.0 μmol) in DMF (5.0 mL) was added anisomycin **1a** (12.6 mg, 47.0 μmol), followed by K_2CO_3 (6.60 mg, 47.0 μmol). The solution was stirred for 48 h at 80 °C. The solution was concentrated *in vacuo*, and the residue was purified by flash chromatography [5% to 15% MeOH/CH_2Cl_2] to give *N*-linked probe **11** as a colorless solid (11.0 mg, 16.5 μmol, 35%). R_f [10% MeOH/CH_2Cl_2] = 0.19. ^{1}H NMR δ (360 MHz, DMSO) 7.74 (1H, t, *J* 5.6, $N_{14}H$), 7.68 (1H, t, *J* 5.6, $N_{21}H$), 7.06 (2H, d, *J* 8.6, Ar*H*), 6.80 (2H, d, *J* 8.6, Ar*H*), 6.43 (1H, br s, N_6H), 6.36 (1H, br s, N_4H), 5.29 (1H, d, *J* 4.8, O*H*), 4.59 (1H, dd, *J* 4.9, 2.2, $C_{27}H$), 4.32−4.28 (1H, m, C_3H), 4.14−4.10 (1H, m, C_7H), 3.89−3.85 (1H, m, $C_{26}H$), 3.70 (3H, s, O*Me*), 3.42−3.38 (1H, m, $C_{25}H_MH_N$), 3.26 (1H, d, *J* 15.9, $C_{23}H_XH_Y$), 3.19−3.13 (1H, m, $C_{28}H$), 3.11−2.98 (5H, m, C_8H, $C_{15}H_2$, $C_{20}H_2$), 2.97 (1H, d, *J* 15.9, $C_{23}H_XH_Y$), 2.81 (1H, dd, *J* 12.3, 5.1, $C_2H_AH_B$), 2.75−2.72 (1H, m, $C_{29}H_SH_T$), 2.59−2.57 (1H, m, $C_{29}H_SH_T$), 2.57 (1H, d, *J* 12.3, $C_2H_AH_B$), 2.31 (1H, dd, *J* 10.4, 3.5, $C_{25}H_MH_N$), 2.06 (3H, s, O*Ac*), 2.04 (2H, t, *J* 7.4, $C_{12}H_2$), 1.49−1.25 (14H, m, C_9H_2, $C_{10}H_2$, $C_{11}H_2$, $C_{16}H_2$, $C_{17}H_2$, $C_{18}H_2$, $C_{19}H_2$). ^{13}C NMR δ (90.7 MHz, DMSO) 171.7 (1C, C_{13}, Q), 169.9 (1C, C_{22}, Q), 169.6 (1C, O*Ac*, Q), 162.5 (1C, C_5, Q), 157.4 (1C, *Ar*, Q), 130.7 (1C, *Ar*, Q), 129.7 (2C, *Ar*H, CH), 113.6 (2C, *Ar*H, CH), 78.9 (1C, C_{27}, CH), 72.9 (1C, C_{26}, CH), 65.6 (1C, C_{28}, CH), 60.8 (1C, C_7, CH), 60.1 (1C, C_{25}, CH_2), 59.0 (1C, C_3, CH), 57.1 (1C, C_{23}, CH_2), 55.2 (1C, C_8, CH), 54.7 (1C, O*Me*, CH_3), 39.7 (1C, C_2, CH_2), 38.2 (1C, C_{20}, CH_2), 37.9 (1C, C_{15}, CH_2), 35.0 (1C, C_{12}, CH_2), 32.8 (1C, C_{29}, CH_2), 29.2, 28.9, 28.0, 27.8, 25.9, 25.5, 25.2 (7C, C_9, C_{10}, C_{11}, C_{16}, C_{17}, C_{18}, C_{19}, CH_2), 20.9 (1C, O*Ac*, CH_3). *m/z* (FAB, NOBA) 648 ($[M + H]^+$, 5%), 307 (50), 77 (70). HRMS (FAB, THIOG) (found: $[M + H]^+$, 648.3435. $C_{32}H_{50}N_5O_7S$ requires *m/z*, 648.3431).

*Synthesis of Biotinylated Azides **15** and **16**.* Safety in the handling of sodium azide and other azides: (*37*) Sodium azide is toxic (LD_{50} oral (rats) = 27 mg kg^{-1}) and can be absorbed through the skin. It decomposes explosively upon heating to above 275 °C; hence, its use in airbags in the automotive industry. Sodium azide reacts vigorously with CS_2, bromine, nitric acid, dimethyl sulfate, and a series of heavy metals, including copper and lead. In reaction with water or Brønsted acids, the highly toxic and explosive hydrogen azide is released. It has been reported that sodium azide and polymer-bound azide reagents form explosive di- and triazidomethane with CH_2Cl_2 and $CHCl_3$, respectively.

Heavy-metal azides that are highly explosive under pressure or shock are formed when solutions of NaN_3 or HN_3 vapors come into contact with heavy metals or their salts. Heavy-metal azides can accumulate under certain circumstances, for example, in metal pipelines and on the metal components of diverse equipment (rotary evaporators, freeze drying equipment, cooling traps, water baths, waste pipes), and thus lead to violent explosions. Some organic and other covalent azides are classified as toxic and highly explosive, and appropriate safety measures must be taken at all times.

*2-Azido-1-ethylamine **17***. To a solution of 2-chloro-1-ethylamine (500 mg, 4.31 mmol) in water (5 mL) was added sodium azide (840 mg, 12.9 mmol), and the reaction mixture was heated at 80 °C for 15 h. The solution was basified with KOH (solid) and extracted with ether. The organics were dried and concentrated to give amino azide **17** as a volatile colorless oil (371 mg, 4.31 mmol, 100%). ν_{max}(neat)/cm^{-1} 3375, 2104. ^{1}H NMR δ (360 MHz, $CDCl_3$) 3.30 (2H, t, *J* 5.7, C*H*$_2$), 2.79−2.74 (2H, m, C*H*$_2$), 1.43 (2H, s, N*H*$_2$). ^{13}C NMR δ (90.7 MHz, $CDCl_3$) 54.2 (1C, CH_2), 40.9 (1C, CH_2). *m*/*z* (ESI+) 194 ([2M + H]$^+$). All spectroscopic data were in good agreement with that of the literature (*38*).

*6-Azido-1-hexylamine **18***. A solution of 6-amino-hexan-1-ol (1.17 g, 10.0 mmol) and $SOCl_2$ (3.28 mL, 45.0 mmol) in toluene (10 mL) was heated at reflux for 1 h. The solvent was removed *in vacuo*, and the intermediate 6-chloro-1-hexylamine was obtained as a hygroscopic solid. *m*/*z* (ESI+, MeOH) 136 ([M + H]$^+$, 100), 138 ([M + H]$^+$, 33). To a solution of sodium azide (1.95 g, 30.0 mmol) in water (10 mL) was added 6-chloro-1-hexylamine and the reaction was stirred at 90 °C for 2 h. The solution was basified (pH 12−14) with KOH (solid), extracted with CH_2Cl_2, dried ($MgSO_4$), and concentrated *in vacuo*. The amino azide **18** was obtained as a colorless solid (1.28 g, 9.01 mmol, 90% over two steps). ^{1}H NMR δ (360 MHz, DMSO) 3.40−3.20 (4H, m, C*H*$_2$NH$_2$, C*H*$_2$N$_3$), 1.75−1.45 (4H, m, 2CH$_2$), 1.41−1.22 (4H, m, 2CH$_2$). ^{13}C NMR δ (90.6 MHz, DMSO) 51.0 (1C, CH_2), 39.4 (1C, CH_2), 29.6 (1C, CH_2), 29.5 (1C, CH_2), 27.2 (1C, CH_2), 26.8 (1C, CH_2). *m*/*z* (ESI+, MeOH) 143.0 ([M + H]$^+$, 100%). HRMS (FAB, NOBA) (found: [M + H]$^+$, 143.1297. $C_6H_{15}N_4$ requires *m*/*z*, 143.1297).

*N-Biotinyl-2-azido-1-ethylamine **15***. To a solution of biotin succinimidyl ester **19** (60.0 mg, 170 μmol) in methanol (2 mL) was added triethylamine (73.0 μL, 530 μmol) and 1-azidoethylamine **17** (90.0 mg, 1.06 mmol). The reaction mixture was stirred at RT for 6 h. The solution was concentrated *in vacuo*, and the residue was purified by flash chromatography [8% to 12% MeOH/CH_2Cl_2] to give biotinylated azide **15** as a colorless solid (48.0 mg, 160 μmol, 94%). R_f [8% MeOH/CH_2Cl_2] = 0.19. ν_{max}(neat)/cm^{-1} 3286, 2103, 1694, 1651. ^{1}H NMR δ (360 MHz, DMSO) 8.06 (1H, t, *J* 5.8, N$_{14}$*H*), 6.44 (1H, br s, N$_6$*H*), 6.38 (1H, br s, N$_4$*H*), 4.31−4.28 (1H, m, C$_3$*H*), 4.16−4.12 (1H, m, C$_7$*H*), 3.32 (2H, t, *J* 5.8, C$_{16}$*H*$_2$), 3.23 (2H, t, *J* 5.8, C$_{15}$*H*$_2$), 3.09−3.07 (1H, m, C$_8$*H*), 2.87 (1H, dd, *J* 12.5, 5.1, C$_2$*H*$_A$H$_B$), 2.56 (1H, d, *J* 12.5, C$_2$H$_A$*H*$_B$), 2.07 (2H, t, *J* 7.4, C$_{12}$*H*$_2$), 1.52−1.28 (6H, m, C$_9$*H*$_2$, C$_{10}$*H*$_2$, C$_{11}$*H*$_2$). ^{13}C NMR δ (90.7 MHz, DMSO) 172.7 (1C, *C*$_{13}$, Q), 163.0 (1C, *C*$_5$, Q), 61.2 (1C, *C*$_7$, CH), 59.4 (1C, *C*$_3$, CH), 55.7 (1C, *C*$_8$, CH), 50.2 (1C, *C*$_{16}$, CH$_2$), 40.1 (1C, *C*$_2$, CH$_2$), 38.4 (1C, *C*$_{15}$, CH$_2$), 35.4 (1C, *C*$_{12}$, CH$_2$), 28.4 (1C, *C*$_{10}$, CH$_2$), 28.3 (1C, *C*$_9$, CH$_2$), 25.4 (1C, *C*$_{11}$, CH$_2$). *m*/z (FAB, THIOG) 313 ([M + H]$^+$, 48%), 45 (100). HRMS (FAB, THIOG) (found: [M + H]$^+$, 313.1445. $C_{12}H_{21}N_6O_2S$ requires *m*/*z*, 313.1447).

*N-Biotinyl-6-azido-1-hexylamine **16***. To a solution of 6-azido-1-hexylamine **18** (316 mg, 1.46 mmol) and triethylamine (202 μL, 1.46 mmol) in methanol (20 mL) was slowly added a solution of biotin succinimidyl ester **19** (500 mg, 1.46 mmol) in methanol (10 mL). The reaction was stirred overnight at RT. The solution was concentrated *in vacuo*, and the residue was purified by flash chromatography [5% MeOH/CH_2Cl_2] to give biotinylated azide **16** as a pale yellow solid (479 mg, 1.30 mmol, 89%). R_f [10% MeOH/CH_2Cl_2] = 0.11. ν_{max}(neat)/cm^{-1} 3301, 2099, 1704, 1638. ^{1}H NMR δ (360 MHz, DMSO) 7.76 (1H, t, *J* 5.5, N$_{14}$*H*), 6.44 (1H, br s, N$_6$*H*), 6.38 (1H, br s, N$_4$*H*), 4.32−4.29 (1H, m, C$_3$*H*), 4.15−4.11 (1H, m, C$_7$*H*), 3.31 (2H, t, *J* 6.9, C$_{20}$*H*$_2$), 3.12−3.06 (1H, m, C$_8$*H*), 3.01 (2H, dt, *J* 12.5, 6.7, C$_{15}$*H*$_2$), 2.82 (1H, dd, *J* 12.5, 5.1, C$_2$*H*$_A$H$_B$), 2.58 (1H, d, *J* 12.5, C$_2$H$_A$*H*$_B$), 2.04 (2H, t, *J* 7.4, C$_{12}$*H*$_2$), 1.54−1.25 (14H, m, C$_9$*H*$_2$, C$_{10}$*H*$_2$, C$_{11}$*H*$_2$, C$_{16}$*H*$_2$, C$_{17}$*H*$_2$, C$_{18}$*H*$_2$, C$_{19}$*H*$_2$,). ^{13}C NMR δ (90.7 MHz, DMSO) 172.1 (1C, *C*$_{13}$, Q), 163.0 (1C, *C*$_5$, Q), 61.3 (1C, *C*$_7$, CH), 59.4 (1C, *C*$_3$, CH), 55.7 (1C, *C*$_8$, CH), 50.8 (1C, *C*$_{20}$, CH$_2$), 39.9 (1C, *C*$_2$, CH$_2$), 38.5 (1C, *C*$_{15}$, CH$_2$), 35.5 (1C, *C*$_{12}$, CH$_2$), 29.3, 28.5, 28.3, 26.2, 26.1, 25.6, 25.5 (7C, *C*$_9$, *C*$_{10}$, *C*$_{11}$, *C*$_{16}$, *C*$_{17}$, *C*$_{18}$, *C*$_{19}$, CH$_2$). *m*/z (FAB, THIOG) 369 ([M + H]$^+$, 58%), 258 (46). HRMS (FAB, THIOG) (found: [M + H]$^+$, 369.2074. $C_{16}H_{29}N_6O_2S$ requires *m*/*z*, 369.2073).

Coupling to C_2 Biotinylated Azide 15. *1-(N-Biotinyl-2-aminoeth-1-yl)-4-[4′-(2″-acetoxyeth-1″-yl)phenyloxymethyl]-1H-[1,2,3]triazole **20***. To biotinylated azide **15** (30.0 mg, 90.0 μmol) in H_2O/^{t}BuOH (2 mL, 1:1) was added propargyl ether **12** (24.0 mg, 100 μmol), followed by copper(II) sulfate (2.00 mg, 10 mol %) and sodium ascorbate solution (20.0 μL, 1 M solution, 20 mol %). The solution was stirred for 15 h at RT. The solution was concentrated *in vacuo*, and the residue was purified by flash chromatography [8% to 15% MeOH/CH_2Cl_2] to give probe **20** as a colorless solid (41.0 mg, 77.4 μmol, 86%). R_f [20% MeOH/CH_2Cl_2] = 0.30. ^{1}H NMR δ (600 MHz, DMSO) 8.18 (1H, s, C$_{18}$*H*), 8.00 (1H, t, *J* 5.9, N$_{14}$*H*), 7.17 (2H, d, *J* 8.6, Ar*H*), 6.96 (2H, d, *J* 8.6, Ar*H*), 6.44 (1H, br s, N$_6$*H*), 6.38 (1H, br s, N$_4$*H*), 5.09 (2H, s, C$_{20}$*H*$_2$), 4.42 (2H, t, *J* 5.9, C$_{16}$*H*$_2$), 4.28−4.27 (1H, m, C$_3$*H*), 4.16 (2H, t, *J* 7.0, C$_{27}$*H*$_2$), 4.14−4.09 (1H, m, C$_7$*H*), 3.48 (2H, br q, *J* 5.9, C$_{15}$*H*$_2$), 3.10−3.05 (1H, m, C$_8$*H*), 2.81 (2H, t, *J* 7.0, C$_{26}$*H*$_2$), 2.79 (1H, dd, *J* 12.2, 5.2, C$_2$*H*$_A$H$_B$), 2.54 (1H, d, *J* 12.2, C$_2$H$_A$*H*$_B$), 2.03 (2H, t, *J* 7.4, C$_{12}$*H*$_2$), 1.98 (3H, s, O*Ac*), 1.56−0.86 (6H, m, C$_9$*H*$_2$, C$_{10}$*H*$_2$, C$_{11}$*H*$_2$). ^{13}C NMR δ (151.1 MHz, DMSO) 173.5 (1C, *C*$_{13}$, Q), 171.2 (1C, *C*$_{29}$, Q), 163.6 (1C, *C*$_5$, Q), 157.6 (1C, *Ar*, Q), 143.4 (1C, *C*$_{19}$, Q), 131.0 (1C, *Ar*, Q), 130.6 (2C, *Ar*H, CH), 125.6 (1H, *C*$_{18}$, CH), 115.5 (2C, *Ar*H, CH), 65.6 (1C, *C*$_{27}$, CH$_2$), 62.1 (1C, *C*$_{20}$, CH$_2$), 61.9 (1C, *C*$_7$, CH), 60.2 (1C, *C*$_3$, CH), 56.3 (1C, *C*$_8$, CH), 49.8 (1C, *C*$_{16}$, CH$_2$), 40.8 (1C, *C*$_2$, CH$_2$), 38.7 (1C, *C*$_{15}$, CH$_2$), 36.0 (1C, *C*$_{12}$, CH$_2$), 34.4 (1C, *C*$_{26}$, CH$_2$), 29.3 (1C, *C*$_{10}$, CH$_2$), 28.0 (1C, *C*$_9$, CH$_2$), 26.0 (1C, *C*$_{11}$, CH$_2$), 21.6 (1C, O*Ac*, CH$_3$). *m*/z (FAB, THIOG) 531 ([M + H]$^+$, 27%), 270 (22) 227 (16), 45 (100). HRMS (FAB, THIOG) (found: [M + H]$^+$, 531.2390. $C_{25}H_{35}N_6O_5S$ requires *m*/*z*, 531.2387).

*C_2-Click O-Linked Boc-Protected C(4)-H Anisomycin Biotin Molecular Probe **21a***. To biotinylated azide **15** (50.0 mg, 160 μmol) in H_2O/^{t}BuOH (3 mL, 1:1) was added *O*-propargyl analogue **13** (60.0 mg, 170 μmol), followed by copper(II) sulfate (3.5 mg, 10 mol %) and sodium ascorbate solution (37.0 μL, 1 M solution, 20 mol %). The solution was stirred for 15 h at RT. The solution was concentrated *in vacuo*, and the residue was purified by flash chromatography [5% to 15% MeOH/CH_2Cl_2] to give carbamate **21a** as a colorless oil (76.0 mg, 111 μmol, 70%). R_f [10% MeOH/CH_2Cl_2] = 0.19. ^{1}H NMR δ (360 MHz, $CDCl_3$, 323 K) 7.71 (1H, s, C$_{18}$*H*), 7.11 (2H, d, *J* 8.4, Ar*H*), 6.89 (2H, d, *J* 8.4, Ar*H*), 5.14 (2H, s, C$_{20}$*H*$_2$), 5.10 (1H, br q, *J* 7.0, C$_{28}$*H*), 4.54−4.57 (3H, m, C$_3$*H*, C$_{16}$*H*$_2$), 4.36−4.31 (1H, m, C$_7$*H*), 4.26−4.21 (1H, m, C$_{27}$*H*), 3.70−3.76 (2H, q, *J* 5.8, C$_{15}$*H*$_2$), 3.48−3.41 (1H, m, C$_{30}$*H*$_M$H$_N$), 3.35−3.28 (1H, m, C$_{30}$H$_M$*H*$_N$), 3.16−3.11 (1H, m, C$_8$*H*), 3.03−2.96 (1H, m, C$_{26}$*H*$_S$H$_T$), 2.89 (1H, dd, *J* 13.0, 4.9, C$_2$*H*$_A$H$_B$), 2.80 (1H, dd, *J* 13.8, 8.6, C$_{26}$H$_S$*H*$_T$), 2.70 (1H, d, *J* 13.0, C$_2$H$_A$*H*$_B$), 2.18 (2H, t, *J* 6.5, C$_{12}$*H*$_2$), 2.09−2.01 (1H, m, C$_{29}$*H*$_E$H$_F$), 1.97 (3H, s, OA*c*),

1.85−1.76 (1H, m, $C_{29}H_EH_F$), 1.72−1.38 (6H, m, C_9H_2, $C_{10}H_2$, $C_{11}H_2$), 1.45 (9H, s, ^tBuO). ^{13}C NMR δ (90.7 MHz, $CDCl_3$, 323 K) 174.3 (1C, CO^tBu, Q), 172.7 (1C, C_{13}, Q), 170.3 (1C, O*Ac*, Q), 156.9 (1C, C_5, Q), 155.5 (1C, *Ar*, Q), 144.3 (1C, C_{19}, Q), 131.7 (1C, *Ar*, Q), 130.7 (2C, *Ar*H, CH), 124.1 (1C, C_{18}, CH), 115.1 (2C, *Ar*H, CH), 80.0 (1C, ^tBu, Q), 73.5 (1C, C_{28}, CH), 62.3 (1C, C_7, CH), 62.2 (1C, C_{20}, CH_2), 60.7 (1C, C_3, CH), 59.6 (1C, C_{27}, CH), 55.7 (1C, C_8, CH), 49.8 (1C, C_{16}, CH_2), 43.7 (1C, C_{30}, CH_2), 40.6 (1C, C_2, CH_2), 39.5 (1C, C_{15}, CH_2), 35.8 (1C, C_{12}, CH_2), 34.3 (1C, C_{26}, CH_2), 29.8 (1C, C_{29}, CH_2), 28.7 (3C, ^tBu, CH_3), 27.9 (1C, C_{10}, CH_2), 27.8 (1C, C_9, CH_2), 25.1 (1C, C_{11}, CH_2), 20.0 (1C, O*Ac*, CH_3). *m*/z (FAB, THIOG) 686 ($[M + H]^+$, 16%), 586 (60). HRMS (FAB, THIOG) (found: $[M + H]^+$, 686.3336. $C_{33}H_{48}N_7O_7S$ requires *m/z*, 686.3336).

*C_2-Click O-Linked C(4)-H Anisomycin Biotin Molecular Probe **21b***. To a solution of carbamate **21a** (25.0 mg, 36.0 μmol) in CH_2Cl_2 (2 mL) was added trifluoroacetic acid (27.0 μL, 360 μmol), the solution was stirred for 4 h at RT. The reaction was concentrated *in vacuo* to give *O*-linked probe **21b** (23.0 mg, 32.9 μmol, 91%) as a colorless foam. R_f [20% MeOH/CH_2Cl_2] = 0.16. ^{1}H NMR δ (360 MHz, DMSO) 8.19 (1H, s, $C_{18}H$), 8.01 (1H, t, *J* 5.6, $N_{14}H$), 7.20 (2H, d, *J* 8.6, Ar*H*), 7.02 (2H, d, *J* 8.6, Ar*H*), 6.76 (1H, br s, N_6H), 6.44 (1H, br s, N_4H), 5.16 (1H, t, *J* 3.7, $C_{28}H$), 5.10 (2H, s, $C_{20}H_2$), 4.42 (2H, t, *J* 6.0, $C_{16}H_2$), 4.31−4.28 (1H, m, C_3H), 4.13−4.10 (1H, m, C_7H), 3.87−3.84 (1H, m, $C_{27}H$), 3.49 (2H, q, *J* 5.8, $C_{15}H_2$), 3.33−3.23 (2H, m, $C_{30}H_2$), 3.11−3.06 (1H, m, C_8H), 2.98−2.85 (2H, m, $C_{26}H_2$), 2.80 (1H, dd, *J* 12.4, 5.0, $C_2H_AH_B$), 2.57 (1H, d, *J* 12.4, $C_2H_AH_B$), 2.30−2.20 (1H, m, $C_{29}H_EH_F$), 2.12 (3H, s, O*Ac*), 2.03 (2H, t, *J* 7.4, $C_{12}H_2$), 2.01−1.97 (1H, m, $C_{29}H_EH_F$), 1.64−1.21 (6H, m, C_9H_2, $C_{10}H_2$, $C_{11}H_2$). ^{13}C NMR δ (90.7 MHz, DMSO) 172.1 (1C, C_{13}, Q), 169.3 (1C, O*Ac*, Q), 162.1 (1C, C_5, Q), 157.1 (1C, *Ar*, Q), 142.1 (1C, C_{19}, Q), 129.7 (2C, *Ar*H, CH), 128.3 (1C, *Ar*, Q), 124.5 (1C, C_{18}, CH), 114.5 (2C, *Ar*H, CH), 72.5 (1C, C_{28}, CH), 63.0 (1C, C_{27}, CH), 60.7 (1C, C_{20}, CH_2), 60.7 (1C, C_7, CH), 58.9 (1C, C_3, CH), 55.1 (1C, C_8, CH), 48.7 (1C, C_{16}, CH_2), 42.5 (1C, C_{30}, CH_2), 39.6 (1C, C_2, CH_2), 38.5 (1C, C_{15}, CH_2), 34.9 (1C, C_{12}, CH_2), 30.7 (1C, C_{26}, CH_2), 30.1 (1C, C_{29}, CH_2), 27.9 (1C, C_{10}, CH_2), 27.7 (1C, C_9, CH_2), 24.8 (1C, C_{11}, CH_2), 20.5 (1C, O*Ac*, CH_3). *m*/z (FAB, THIOG) 586 ($[M + H]^+$, 29%). HRMS (FAB, THIOG) (found: $[M + H]^+$, 586.2812. $C_{28}H_{40}N_7O_5S$ requires *m/z*, 586.2812).

*C_2-Click N-Linked Anisomycin Biotin Molecular Probe **22***. To biotinylated azide **15** (27.0 mg, 90.0 μmol) in H_2O/^{t}BuOH (2 mL, 1:1) was added *N*-propargyl anisomycin **14** (17.0 mg, 50 μmol), followed by copper(II) sulfate (2.0 mg, 10 mol %) and sodium ascorbate solution (20.0 μL, 1 M solution, 20 mol %). The solution was stirred for 15 h at RT. The solution was concentrated *in vacuo*, and the residue was purified by flash chromatography [8% to 15% MeOH/CH_2Cl_2] to give *N*-linked probe **22** as a colorless solid (22.0 mg, 35.5 μmol, 71%). R_f [20% MeOH/CH_2Cl_2] = 0.35. ^{1}H NMR δ (360 MHz, DMSO) 7.98 (1H, t, *J* 5.4, $N_{14}H$), 7.96 (1H, s, $C_{18}H$), 7.11 (2H, d, *J* 8.6, Ar*H*), 6.82 (2H, d, *J* 8.6, Ar*H*), 6.43 (1H, br s, N_6H), 6.38 (1H, br s, N_4H), 5.10 (1H, d, J 3.9, O*H*), 4.48 (1H, dd, *J* 4.5, 1.8, $C_{24}H$), 4.39 (2H, t, *J* 6.0, $C_{16}H_2$), 4.32−4.28 (1H, m, C_3H), 4.15−4.10 (1H, m, C_7H), 3.92 (1H, d, *J* 14.1, $C_{20}H_XH_Y$), 3.81−3.78 (1H, m, $C_{23}H$), 3.71 (3H, s, O*Me*), 3.63 (1H, d, *J* 14.1, $C_{20}H_XH_Y$), 3.48 (2H, br q, *J* 5.8, $C_{15}H_2$), 3.18 (1H, dd, *J* 10.3, 6.2, $C_{22}H_MH_N$), 3.09 (1H, ddd, *J* 8.2, 6.1, 4.5, C_8H), 3.01−2.93 (2H, m, $C_{25}H$, $C_{26}H_SH_T$), 2.81 (1H, dd, *J* 12.4, 5.0, $C_2H_AH_B$), 2.60−2.53 (2H, m, $C_2H_AH_B$, $C_{26}H_SH_T$), 2.24 (1H, dd, *J* 10.3, 4.5, $C_{22}H_MH_N$), 2.04 (3H, s, O*Ac*), 2.02 (2H, t, *J* 7.4, $C_{12}H_2$), 1.48−0.80 (6H, m, C_9H_2, $C_{10}H_2$, $C_{11}H_2$). ^{13}C NMR δ (90.7 MHz, DMSO) 173.5 (1C, C_{13}, Q), 169.7 (1C, O*Ac*, Q), 162.7 (1C, C_5, Q), 157.5 (1C, *Ar*, Q), 143.0 (1C, C_{19}, Q), 131.0 (1C, *Ar*, Q), 129.8 (2C, *Ar*H, CH), 123.8 (1C, C_{18}, CH), 113.7 (2C, *Ar*H, CH), 79.5 (1C, C_{24}, CH), 72.9 (1C, C_{23}, CH), 64.8 (1C, C_{25}, CH), 61.0 (1C, C_7, CH), 59.2 (1C, C_3, CH), 55.4 (1C, C_{22}, CH_2), 49.9 (2C, CH, CH_3, C_8, C_{32}), 48.7 (1C, C_{16}, CH_2), 47.0 (1C, C_{20}, CH_2), 39.8 (1C, C_2, CH_2), 38.7 (1C, C_{15}, CH_2), 35.0 (1C, C_{12}, CH_2), 32.2 (1C, C_{26}, CH_2), 28.1 (1C, C_{10}, CH_2), 28.0 (1C, C_9, CH_2), 25.1 (1C, C_{11}, CH_2), 20.8 (1C, O*Ac*, CH_3). *m*/z (FAB, THIOG) 615 ($[M]^+$, 19%). HRMS (FAB, THIOG) (found: $[M + H]^+$, 616.2916. $C_{29}H_{42}N_7O_6S$ requires *m/z*, 616.2917).

Coupling to C_6 Biotinylated Azide 16. *1-(N-Biotinyl-6-aminohex-1-yl)-4-[4′-(2″-acetoxyeth-1″-yl)phenyloxymethyl]-1H- [1,2,3] triazole **23***. To biotinylated azide **16** (50.0 mg, 140 μmol) in H_2O/^{t}BuOH (5 mL, 1:1) was added *O*-propargyl analogue **12** (30.0 mg, 140 μmol), followed by copper(II) sulfate (4.0 mg, 15 mol %) and sodium ascorbate solution (28.0 μL, 1 M solution, 20 mol %). The solution was stirred for 24 h at RT. The solution was concentrated *in vacuo*, and the residue was purified by flash chromatography [2% to 5% MeOH/CH_2Cl_2] to give probe **23** as a colorless solid (62.0 mg, 105 μmol, 75%). R_f [10% MeOH/CH_2Cl_2] = 0.08. ^{1}H NMR δ (360 MHz, DMSO) 8.30 (1H, s, $C_{22}H$), 7.72 (1H, br s, $N_{14}H$), 7.16 (2H, d, *J* 8.5, Ar*H*), 6.95 (2H, d, *J* 8.5, Ar*H*), 6.40 (1H, br s, N_6H), 6.35 (1H, br s, N_4H), 5.09 (2H, s, $C_{24}H_2$), 4.34 (2H, t, *J* 7.1, $C_{20}H_2$), 4.32−4.30 (1H, m, C_3H), 4.15 (2H, t, *J* 6.9, $C_{31}H_2$), 4.14−4.10 (1H, m, C_7H), 3.12−3.06 (1H, m, C_8H), 3.01 (2H, dt, *J* 12.5, 6.7, $C_{15}H_2$), 2.81 (2H, t, *J* 6.9, $C_{30}H_2$), 2.80 (1H, dd, *J* 12.2, 5.1, $C_2H_AH_B$), 2.58 (1H, d, *J* 12.2, $C_2H_AH_B$), 2.04 (2H, t, *J* 7.3, $C_{12}H_2$), 1.97 (3H, s, O*Ac*), 1.80 (2H, qn, *J* 6.9, $C_{19}H_2$), 1.66−1.16 (12H, m, C_9H_2, $C_{10}H_2$, $C_{11}H_2$, $C_{16}H_2$, $C_{17}H_2$, $C_{18}H_2$). ^{13}C NMR δ (90.7 MHz, DMSO) 171.7 (1C, C_{13}, Q), 170.1 (1C, O*Ac*, Q), 162.6 (1C, C_5, Q), 156.6 (1C, Ar, Q), 142.5 (1C, C_{23}, Q), 130.2 (1C, Ar, Q), 129.6 (2C, *Ar*H, CH), 124.2 (1C, C_{22}, CH), 114.5 (2C, *Ar*H, CH), 64.4 (1C, C_{31}, CH_2), 61.0 (1C, C_{24}, CH_2), 60.8 (1C, C_7, CH), 59.0 (1C, C_3, CH), 55.3 (1C, C_8, CH), 49.0 (1C, C_{20}, CH_2), 39.6 (1C, C_2, CH_2), 38.1 (1C, C_{15}, CH_2), 35.0 (1C, C_{12}, CH_2), 33.2 (1C, C_{30}, CH_2), 29.4 (1C, C_{19}, CH_2), 28.8, 28.0, 25.8, 25.7, 25.2, 25.1 (6C, C_9, C_{10}, C_{11}, C_{16}, C_{17}, C_{18}, CH_2), 20.5 (1C, O*Ac*, CH_3). *m*/z (FAB, THIOG) 587 ($[M + H]^+$, 18%), 91 (78). HRMS (FAB, THIOG) (found: $[M + H]^+$, 587.3020. $C_{29}H_{43}N_6O_5S$ requires *m/z*, 587.3016).

*C_6-Click O-Linked Boc-Protected C(4)-H Anisomycin Biotin Molecular Probe **24a***. To biotinylated azide **16** (41.0 mg, 111 μmol) in H_2O/^{t}BuOH (2 mL, 1:1) was added *O*-propargyl analogue **13** (45.0 mg, 120 μmol), followed by copper(II) sulfate (3.0 mg, 10 mol %) and sodium ascorbate solution (25.0 μL, 1 M solution, 20 mol %). The solution was stirred for 18 h at RT. The solution was concentrated *in vacuo*, and the residue was purified by flash chromatography [5% to 15% MeOH/CH_2Cl_2] to give carbamate **24a** as a colorless oil (62.0 mg, 84.0 μmol, 76%). R_f [10% MeOH/CH_2Cl_2] = 0.24. ^{1}H NMR δ (360 MHz, $CDCl_3$, 323 K), 7.60 (1H, s, $C_{22}H$), 7.10 (2H, d, *J* 8.5, Ar*H*), 6.88 (2H, d, *J* 8.5, Ar*H*), 5.16 (2H, s, $C_{24}H_2$), 5.11 (1H, dt, *J* 6.5, 14.1, $C_{32}H$), 4.52−4.46 (1H, m, C_3H), 4.34 (2H, t, *J* 7.0, $C_{20}H_2$), 4.33−4.29 (1H, m, C_7H), 4.29−4.21 (1H, m, $C_{31}H$), 3.47−3.27 (2H, m, $C_{34}H_2$), 3.25−3.14 (3H, m, C_8H, $C_{15}H_2$), 3.01−3.92 (1H, m, $C_{30}H_SH_T$), 2.89 (1H, dd, *J* 12.6, 4.3, $C_2H_AH_B$), 2.81 (1H, dd, *J* 13.8, 8.4 $C_{30}H_SH_T$), 2.72 (1H, d, *J* 12.6, $C_2H_AH_B$), 2.19 (2H, t, *J* 6.9, $C_{12}H_2$), 2.09−2.00 (1H, m, $C_{33}H_EH_F$), 1.97 (3H, s, OAc), 1.91 (2H, br t, *J* 6.6, $C_{19}H$), 1.84−1.74 (1H, m, $C_{33}H_EH_F$), 1.71−1.56 (4H, m, C_9H_2, $C_{11}H_2$), 1.44 (9H, s, ^tBuO), 1.49−1.27 (8H, m, $C_{10}H_2$, $C_{16}H_2$, $C_{17}H_2$, $C_{18}H_2$). ^{13}C NMR δ (90.7 MHz, $CDCl_3$, 323 K) 173.1 (1C, C_{13}, Q), 170.7 (1C, CO^tBu, Q), 169.7 (1C, O*Ac*, Q), 162.1 (1C, C_5, Q), 156.8 (1C, Ar, Q), 144.0 (1C, C_{23}, Q), 131.4 (1C, Ar, Q), 130.3 (2C, *Ar*H, CH), 122.5 (1C, C_{22}, CH), 114.7 (2C, *Ar*H, CH),

79.7 (1C, *^{t}Bu*, Q), 73.0 (1C, *C_{32}*, CH), 62.1 (1C, *C_{24}*, CH_2), 61.8 (1C, *C_7*, CH), 60.2 (1C, *C_3*, CH), 59.1 (1C, *C_{31}*, CH), 55.4 (1C, *C_8*, CH), 50.1 (1C, *C_{20}*, CH_2), 43.0 (1C, *C_{34}*, CH_2), 40.3 (1C, *C_2*, CH_2), 39.1 (1C, *C_{15}*, CH_2), 35.8 (1C, *C_{12}*, CH_2), 33.9 (1C, *C_{30}*, CH_2), 29.8 (1C, *C_{19}*, CH_2), 29.4, 29.2, 28.5, 28.3, 28.3, 28.1, 25.8, 25.4 (10C, *C_9*, *C_{10}*, *C_{11}*, *C_{16}*, *C_{17}*, *C_{18}*, *C_{33}* all CH_2's and *^{t}Bu* CH_3's), 20.7 (1C, O*Ac*, CH_3). *m/z* (FAB, THIOG) 742 ($[M + H]^+$, 20%), 642 (57), 91 (61). HRMS (FAB, THIOG) (found: $[M + H]^+$, 742.3960. $C_{37}H_{56}N_7O_7S$ requires *m/z*, 742.3962).

*C_6-Click O-LinkedC(4)-H Anisomycin Biotin Molecular Probe **24b***. To a solution of carbamate **24a** (41.0 mg, 55.0 μmol) in CH_2Cl_2 (2 mL) was added trifluoroacetic acid (41.0 μL, 550 μmol), the solution was stirred for 4 h at RT. The reaction was concentrated *in vacuo* to give *O*-linked probe **24b** (40.0 mg, 52.9 μmol, 96%) as a colorless foam. R_f [20% MeOH/CH_2Cl_2] = 0.38. ^{1}H NMR δ (360 MHz, DMSO) 8.23 (1H, s, $C_{22}H$), 7.76 (1H, t, *J* 5.6, $N_{14}H$), 7.19 (2H, d, *J* 8.6, Ar*H*), 7.00 (2H, d, *J* 8.6, Ar*H*), 6.44 (1H, br s, N_6H), 6.38 (1H, br s, N_4H), 5.16 (1H, t, *J* 3.8, $C_{32}H$), 5.10 (2H, s, $C_{24}H_2$), 4.42 (2H, t, *J* 7.0, $C_{20}H_2$), 4.31−4.28 (1H, m, C_3H), 4.13−4.10 (1H, m, C_7H), 3.87−3.81 (1H, m, $C_{31}H$), 3.34−3.22 (2H, m, $C_{34}H_2$), 3.08 (1H, ddd, 8.5, 6.1, 4.8, C_8H), 2.99 (2H, br q, *J* 6.0, $C_{15}H_2$), 3.33−3.23 (2H, m, $C_{30}H_2$), 2.80 (1H, dd, *J* 12.5, 5.1, $C_2H_AH_B$), 2.57 (1H, d, *J* 12.5, $C_2H_AH_B$), 2.30−2.18 (1H, m, $C_{33}H_EH_F$), 2.12 (3H, s, OA*c*), 2.03 (2H, t, *J* 7.3, $C_{12}H_2$), 2.01−1.97 (1H, m, $C_{33}H_EH_F$), 1.80 (2H, qn, *J* 7.1, $C_{19}H$), 1.65−1.19 (12H, m, C_9H_2, $C_{10}H_2$, $C_{11}H_2$, $C_{16}H_2$, $C_{17}H_2$, $C_{18}H_2$). ^{13}C NMR δ (90.7 MHz, DMSO) 172.0 (1C, *C_{13}*, Q), 169.8 (1C, O*Ac*, Q), 162.9 (1C, *C_5*, Q), 157.3 (1C, Ar, Q), 142.9 (1C, *C_{23}*, Q), 130.3 (2C, *Ar*H, CH), 128.8 (1C, Ar, Q), 124.8 (1C, *C_{22}*, CH), 115.1 (2C, *Ar*H, CH), 73.0 (1C, *C_{32}*, CH), 63.5 (1C, *C_{31}*, CH), 61.2 (1C, *C_7*, CH), 61.2 (1C, *C_{24}*, CH_2), 59.4 (1C, *C_3*, CH), 55.7 (1C, *C_8*, CH), 49.5 (1C, *C_{20}*, CH_2), 42.8 (1C, *C_{34}*, CH_2), 40.0 (1C, *C_2*, CH_2), 38.4 (1C, *C_{15}*, CH_2), 35.5 (1C, *C_{12}*, CH_2), 31.1 (1C, *C_{30}*, CH_2), 30.6 (1C, *C_{33}*, CH_2), 29.9 (1C, *C_{19}*, CH_2), 29.1, 28.5, 28.3, 26.0, 25.7, 25.6 (6H, *C_9*, *C_{10}*, *C_{11}*, *C_{16}*, *C_{17}*, *C_{18}*, CH_2), 21.0 (1C, O*Ac*, CH_3). *m/z* (FAB, THIOG) 642 ($[M + H]^+$, 30%), 91 (69). HRMS (FAB, THIOG) (found: $[M + H]^+$, 642.3437. $C_{32}H_{48}N_7O_5S$ requires *m/z*, 642.3438).

*C_6-Click N-Linked Anisomycin Biotin Molecular Probe **25***. To biotinylated azide **16** (47.0 mg, 130 μmol) in H_2O/^{t}BuOH (3 mL, 1:1) was added *N*-propargyl anisomycin **14** (42.0 mg, 140 μmol), followed by copper(II) sulfate (3.0 mg, 10 mol %) and sodium ascorbate solution (28.0 μL, 1 M solution, 20 mol %). The solution was stirred for 15 h at RT. The solution was concentrated *in vacuo*, and the residue was purified by flash chromatography [8% to 15% MeOH/CH_2Cl_2] to give *N*-linked probe **25** as a colorless solid (64.0 mg, 95.0 μmol, 73%). R_f [20% MeOH/CH_2Cl_2] = 0.35. ^{1}H NMR δ (360 MHz, 323 K, DMSO) 8.13 (1H, br s, $C_{22}H$), 7.58 (1H, t, *J* 5.6, $N_{14}H$), 7.09 (2H, d, *J* 8.6, Ar*H*), 6.83 (2H, d, *J* 8.6, Ar*H*), 6.26 (1H, br s, N_6H), 6.23 (1H, br s, N_4H), 5.06 (1H, br s, O*H*), 4.58 (1H, dd, *J* 4.9, 2.1, $C_{28}H$), 4.33 (2H, t, *J* 7.0, $C_{20}H_2$), 4.32−4.28 (1H, m, C_3H), 4.15−4.12 (1H, m, C_7H), 3.98 (1H, br d, *J* 13.9, $C_{24}H_XH_Y$), 3.90−3.86 (1H, m, $C_{27}H$), 3.75 (1H, br d, *J* 13.9, $C_{24}H_XH_Y$), 3.72 (3H, s, O*Me*), 3.25−3.10 (2H, m, $C_{26}H_MH_N$, $C_{29}H$), 3.08 (1H, ddd, *J* 8.1, 6.6, 4.8, C_8H), 2.98 (2H, br q, *J* 6.6, $C_{15}H$), 2.91 (1H, dd, *J 13.3, 4.6*, $C_{30}H_SH_T$), 2.83 (1H, dd, *J* 12.4, 5.1, $C_2H_AH_B$), 2.60 (1H, d, *J 13.3*, $C_{30}H_SH_T$), 2.81 (1H, d, *J* 12.4, $C_2H_AH_B$), 2.41−2.32 (1H, m, $C_{26}H_MH_N$), 2.05 (2H, t, *J* 7.3, $C_{12}H_2$), 2.04 (3H, s, O*Ac*), 1.82 (2H, qn, *J* 7.0, $C_{19}H_2$), 1.70−1.20 (12H, m, C_9H_2, $C_{10}H_2$, $C_{11}H_2$, $C_{16}H_2$, $C_{17}H_2$, $C_{18}H_2$). ^{13}C NMR δ (90.7 MHz, DMSO) 171.8 (1C, *C_{13}*, Q), 169.5 (1C, O*Ac*, Q), 162.6 (1C, *C_5*, Q), 157.6 (1C, Ar, Q), 142.3 (1C, *C_{23}*, Q), 130.4 (1C, Ar, Q), 129.6 (2C, *Ar*H, CH), 123.4 (1C, *C_{22}*, CH), 113.5 (2C, *Ar*H, CH), 78.9 (1C, *C_{28}*, CH), 72.3 (1C, *C_{27}*, CH), 64.7 (1C, *C_{29}*, CH), 60.9 (1C, *C_7*, CH), 59.0 (1C, *C_3*, CH), 58.8 (1C, *C_{26}*, CH_2), 55.0 (1C, *C_8*, CH), 54.7 (1C, O*Me*, CH_3), 49.0 (1C, *C_{20}*, CH_2), 47.3 (1C, *C_{24}*, CH_2), 39.5 (1C, *C_2*, CH_2), 38.0 (1C, *C_{15}*, CH_2), 34.9 (1C, *C_{12}*, CH_2), 31.9 (1C, *C_{30}*, CH_2), 29.4 (1C, *C_{19}*, CH_2), 28.6, 27.9, 27.8, 25.5, 25.2, 25.0 (6H, *C_9*, *C_{10}*, *C_{11}*, *C_{16}*, *C_{17}*, *C_{18}*, CH_2), 20.4 (1C, O*Ac*, CH_3). *m/z* (FAB, THIOG) 672 ($[M + H]^+$, 38%), 91 (88). HRMS (FAB, THIOG) (found: $[M + H]^+$, 672.3540. $C_{33}H_{50}N_7O_6S$ requires *m/z*, 672.3543).

Immunoblot Assays. (*34*, *35*, *39*) *Cell Culture and Stimulation.* Human embryonic kidney (HEK) 293 cells were cultured at 37 °C, 95% air/5% CO_2, in Dulbecco's modified Eagle's medium (DMEM) supplemented with 10% foetal bovine serum, 100 U/mL penicillin, 100 μg/mL streptomycin, and 2 mM L-glutamine. Anisomycin **1a** was dissolved at 10 mg/mL (38 mmol L^{-1}) in DMSO, while the other compounds (**5**, **7b**, **8**, **10**, **11**, **20**, **21b**, **22**, **23**, **24b**, **25**) were dissolved in DMSO at 38 mmol L^{-1}. Cells (9 mL of cell culture) were incubated with the library members by addition of 9 μL of anisomycin solution, anisomycin analogue in DMSO, or DMSO as a control.

Cell Lysis. After stimulation for 30 min, the media was aspirated and the cells lysed in 50 mM Tris/HCl, pH 7.5, containing 1 mM EDTA, 1 mM EGTA, 1 mM sodium orthovanadate, 10 mM sodium β-glycerophosphate, 5 mM sodium pyrophosphate, 50 mM sodium fluoride, 0.27 M sucrose, 1% (v/v) Triton X-100, 0.1% (v/v) 2-mercaptoethanol, and Complete Protease Inhibitor cocktail (one tablet per 50 mL). Lysates were centrifuged at 13 000 *g* for 10 min at 4 °C and the supernatants (termed "cell extract") were removed. Protein concentrations were determined according to the method of Bradford (*40*).

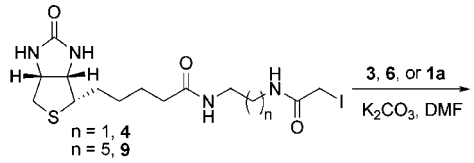
Immunoblotting. Samples were denatured in SDS, run on polyacylamide gels, and transferred to nitrocellulose membranes. The membranes were incubated for 1 h at room temperature in 50 mM Tris−HCl pH 7.5, 150 mM NaCl, 0.2% (v/v) Tween, and 5% (w/v) skimmed milk powder. Primary antibodies were added to 10 mL of the previous buffer and incubated at 4 °C overnight. The membranes were then washed four times with buffer (5 min per wash) to remove the excess primary antibody. The membranes were then incubated with the secondary antibody at room temperature for 1 h. After washing six times with buffer to remove the excess secondary antibody (5 min per wash), immunoreactive proteins were visualized *via* enhanced chemiluminescence reagent according to the manufacturer's instructions.

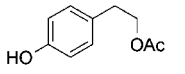
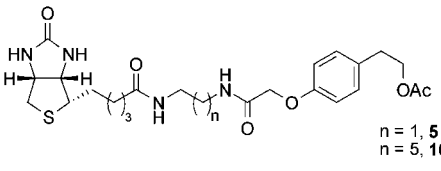
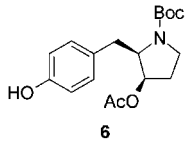
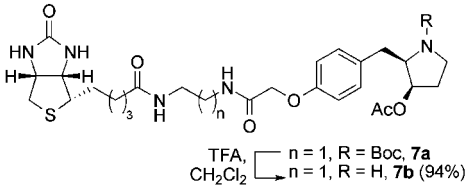
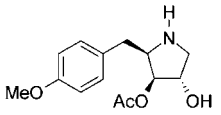
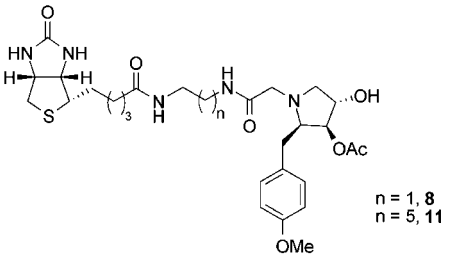
RESULTS AND DISCUSSION

Traditional approaches to the design of functional biotin molecular probes are often based on the formation of peptide and ester bonds (*8*). However, for biotinylation of anisomycin at either the pyrrolidine nitrogen (*N*-linked) or phenolic oxygen (*O*-linked), this approach was ruled out first due to the SAR data, which suggests that only amine derivatives are able to activate the SAPK pathways, and second due to the known poor stability of phenolic esters. We therefore turned our attention to the classical nucleophilic displacement reaction of α-halo carbonyl derivatives of biotin by each of these functionalities. In designing appropriate biotin derivatives for coupling, two linker lengths were identified for the carbon chain between the active small molecule (anisomycin) and the functional tag (biotin): a short commercially available C_2 linker, and a longer C_6 linker. To allow us to establish whether any false positives were caused in the immunoblot assays from activation by these linkers, the synthesis of a series of structurally related, but SAPK-inactive, control probes was also envisaged.

The monoacetate of 2-(4-hydroxyphenyl)ethanol **3** was chosen as a simple model of the anisomycin core (*41*), allowing initial

Table 1. Classical Nucleophilic Displacement Reactions of Anisomycin and Analogues to Give *O*-Linked and *N*-Linked Biotinylated Molecular Probes

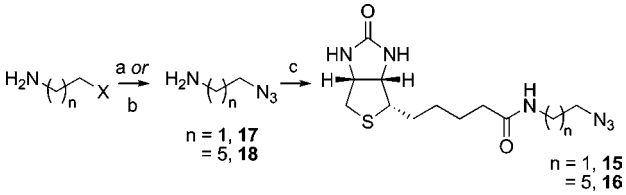


Substrate	Coupled Product	Yield
 **3**	 n = 1, **5** n = 5, **10**	**5** 86% **10** 72%
 **6**	 TFA, CH_2Cl_2 n = 1, R = Boc, **7a** n = 1, R = H, **7b** (94%)	**7a** 31%
 **1a**	 n = 1, **8** n = 5, **11**	**8** 34% **11** 35%

investigations into the conditions required for the nucleophilic displacement coupling to give *O*-linked biotinylated probes. Promising initial results were obtained in the reaction of **3** with commercially available iodoacetyl biotin **4**, which occurred readily upon heating at 80 °C in DMF in the presence of potassium carbonate, to give the desired product **5** in 86% yield (Table 1). However, rather disappointingly, heating the analogous Boc-protected C(4)-H analogue of anisomycin **6** (*35*) gave only a low yield of coupled material **7a** (31%), while *N*-alkylation of anisomycin **1a** under the same conditions was found to be only marginally more successful, giving 34% of the C_2-biotinylated probe **8** (Table 1). The longer C_6-linked iodoacetyl biotin derivative **9** was shown to exhibit a similar pattern of reactivity when coupled to the simple model **3** (72%) and anisomycin **1a** (35%) under identical conditions (Table 1) to give biotin-conjugated analogues **10** and **11**, respectively. With these more-complex substrates, the highly polar nature of the starting materials and resultant biotinylated products, combined with low conversions, gave rise to difficult separation procedures. Thus, while the coupling of simple substrates can be achieved in good yield using this classical nucleophilic displacement methodology, on more complex substrates it was found to be highly unsatisfactory.

In a contrasting approach, the synthesis of a number of biotinylated probes was envisaged using an extension of our recent marked library strategy (*35*). In this strategy, a biocompatible marker is attached onto the small molecule's scaffold; this marker plays no role in the screening process itself, but facilitates the formation of a range of molecular probes from active marked library members. Having previously utilized the highly popular copper(I) catalyzed Huisgen 1,3-dipolar cycloaddition reaction as a means of formation of fluorescent molecular probes from marked library members (*35*), we sought to extend this strategy to the synthesis of biotinylated probes (*42*). To this end, propargylation of the monoacetate of 2-(4-hydroxyphenyl)ethanol **3**, the Boc-protected C(4)-H analogue of anisomycin **6**, and anisomycin **1a** was carried out in DMF to give the *O*-linked (**12**, **13**) and *N*-linked (**14**) "click" precursors in excellent yield (77%, 99% (*35*), and 99% (*35*), respectively). The C_2 **15** and C_6 **16** biotinylated azides required by this approach are readily prepared by coupling alkylamino azides **17** or **18** to biotin *N*-hydroxy succinimidyl ester **19** in high yield (94% and 89%, respectively; Scheme 1).

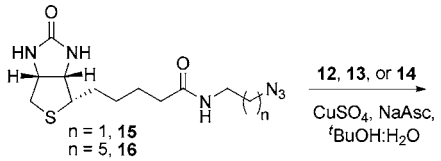
Scheme 1. Preparation of C_2 and C_6 Biotinylated Azides[a]

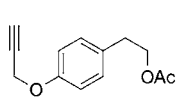
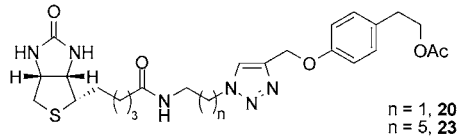
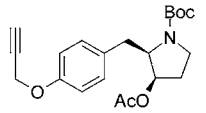
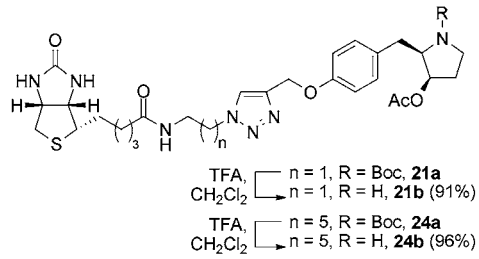
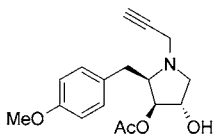
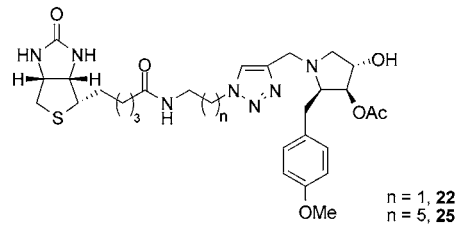


[a] Reagents and Conditions: (a) NaN_3, H_2O, 80 °C, 15 h (n = 1, X = Cl; 100%); (b) (i) $SOCl_2$, $PhCH_3$, 110 °C, 1 h; (ii) NaN_3, H_2O, 90 °C, 2 h (n = 5, X = OH; 90% over two steps); (c) biotin NHS (**19**), MeOH, Et_3N, rt, 6−15 h (n = 1, 94%; n = 5, 89%).

Using standard coupling conditions [10 mol % $CuSO_4$, 20 mol % NaAsc, ^{t}BuOH/H_2O (1:1)] for the copper(I)-catalyzed Huisgen 1,3-dipolar cycloaddition reaction (*43*−*44*), the propargyl derivative of the model of the anisomycin core **12** was coupled to the C_2 biotinylated azide **15** to give **20** in high yield (Table 2). Applying the same reaction conditions to the *O*-linked (**13**) and *N*-linked (**14**) precursors resulted in gratifyingly high yields of products (**21a** and **22**, Table 2). When the linker chain length was extended through coupling to the related C_6 azide

Table 2. Copper(I) Catalyzed Huisgen 1,3-Dipolar Cycloaddition Coupling Reactions of *O*-Linked and *N*-Linked Propargyl Anisomycin Derivatives to Give Biotinylated Molecular Probes



Substrate	Coupled Product	Yield
 **12**	 n = 1, **20** n = 5, **23**	**20** 86% **23** 75%
 **13**	 TFA, CH_2Cl_2 → n = 1, R = Boc, **21a** → n = 1, R = H, **21b** (91%); TFA, CH_2Cl_2 → n = 5, R = Boc, **24a** → n = 5, R = H, **24b** (96%)	**21a** 70% **24a** 76%
 **14**	 n = 1, **22** n = 5, **25**	**22** 71% **25** 73%

16, comparable reactivity was observed, and the control **23**, *O*-linked **24a**, and *N*-linked **25** probes were also isolated in excellent yields (Table 2). In all cases, the products were isolated as discreet chemical entities which could be fully characterized using a range of spectroscopic techniques (1D and 2D NMR experiments, including COSY, HSQC, and HMBC), and which were shown to be single regioisomers around the triazole core. The high purity and high yields of conjugation that are possible using this "click" methodology, combined with the relative ease of production of a range of linker lengths and functionalities for the biotinylated azide, make this an extremely attractive synthetic approach to biotinylation.

The relative levels of activation of the SAPK1 pathway by the classical and "click" biotinylated probes generated in this study were screened using an immunoblot assay for phosphorylation of JNK1/2 in HEK-293 cells (Figure 3). For this study, Boc-protected pyrrolidines **7a**, **21a**, and **24a** were deprotected (TFA, CH_2Cl_2) in high yield (91−96%) to give the corresponding pyrrolidines **7b**, **21b**, and **24b** (Tables 1 and 2) which were used in the SAPK pathway activation assays. The observed activation levels were scaled against anisomycin and DMSO (strong activator and control respectively). These assays showed that, independent of the coupling strategy used, the *O*-linked biotinylated probes (C_2: **5**, **7b**, **20**, **21b**; C_6: **10**, **23**, **24b**) were inactive, whereas their *N*-linked counterparts (C_2: **8**, **22**; C_6: **11**, **25**) were found to be comparable in the levels of activation they induced to anisomycin **1a**. Levels of SAPK1 activation also appear to be relatively unaffected by the length of linker (C_2 or C_6) in both classical and "click" series; although we anticipate that the nature (all-carbon, PEG, etc.) and length (C_2, C_6, etc.) of linker is likely to be of far greater significance in future affinity chromatography studies using these biotinylated molecular probes. Overall, these results were in good accord with our previous studies into the synthesis of fluorescent molecular probes (*35*).

A survey of the methods available for the selective derivatization of a range of chemical functionalities (Table 3), suggests that this "click"-based approach to biotinylation might be applicable to a wide range of substrates. Chemical coupling of a propargyl marker to small molecules may be readily achieved using commercially available (or easily prepared) reagents, and can be tailored to fit diverse synthetic strategies. By matching the chemical reactivity of the propargyl reagent to the known SAR profile of a small molecule, both in terms of site of attachment (*e.g.*, *O*-linked or *N*-linked probes in this study) and resultant functionality (*e.g.*, amine, amide, or carbamate formation; see Table 3), a series of propargyl derivatives may be readily synthesized. Subsequent coupling of these propargyl derivatives with a biotinylated azide under standard "click" coupling conditions allows the rapid and high-yielding synthesis of biotinylated probes.

CONCLUSIONS

The attachment of a propargyl group (or "marker") to a small molecule core may be achieved using a wide range of reagents to common chemical functionalities. Through examining the known SAR of the SAPK pathway activator anisomycin, two potential sites for the rapid development of molecular probes were identified. In these, phenolic methyl and pyrrolidine *N*-benzyl groups were replaced by the propargyl marker to give small molecules which retain comparable activity to their parent

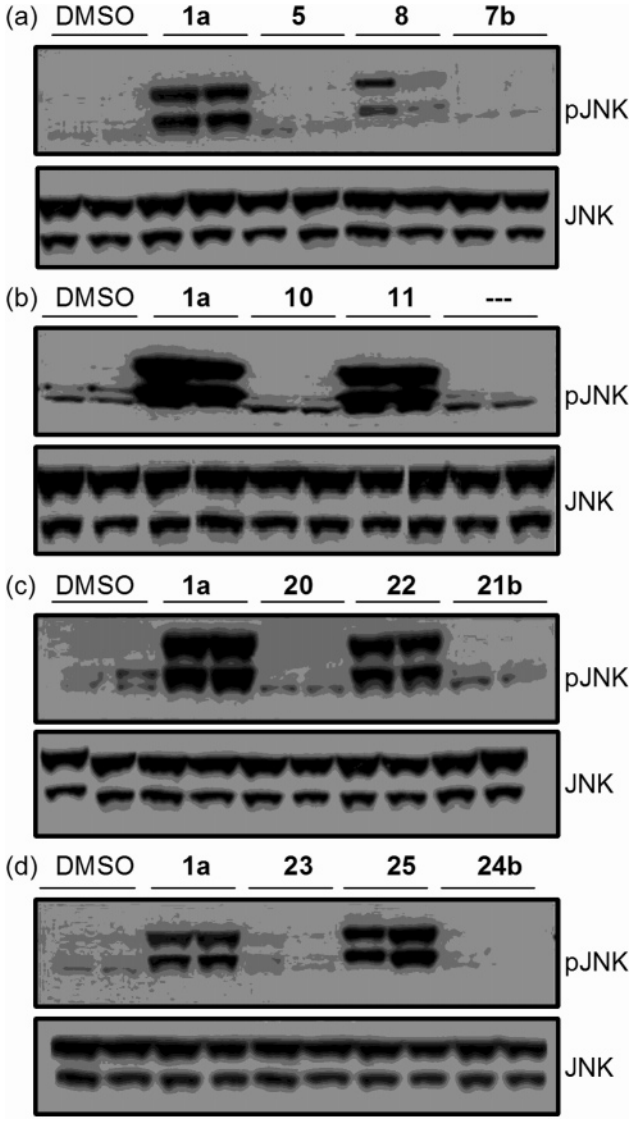


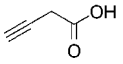
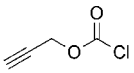
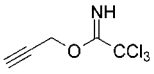
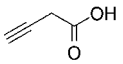
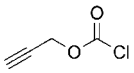
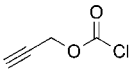
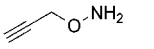
Figure 3. Effect of anisomycin and biotinylated conjugates on the phosphorylation of JNK1/2 isoforms in HEK-293 cells. The cells were exposed to DMSO (lanes 1 and 2), anisomycin **1a** (lanes 3 and 4), and the analogues indicated (lanes 5−10), each dissolved in DMSO: (a) classical C_2 probes; (b) classical C_6 probes; (c) click C_2 probes; (d) click C_6 probes. The cells were lysed and an aliquot (20 μg of lysate protein) was denatured in SDS, subjected to electrophoresis on a 10% polyacrylamide gel, transferred to a nitrocellulose membrane, and immunoblotted with an antibody that recognized JNK1/2 phosphorylated at Thr183 or with an antibody that recognized phosphorylated and unphosphorylated JNK1/2 equally well.

structures. Of these two lead compounds, the *N*-linked precursor was found to allow the development of active biotinylated probes, while derivatization of the *O*-linked precursor led to a loss of phenotypic response. Although these assay results were mirrored by molecular probes formed using classical nucleophilic displacement coupling strategies, low reaction yields were shown to be inherent to this alternate methodology. Thus, the versatility of precursor synthesis, mild coupling conditions, high yields, and excellent regioselectivity found using the "click"-based strategy renders it the method of choice in conjugative routes to biotinylated molecular probes.

ACKNOWLEDGMENT

We thank the BBSRC (Studentship to IAI), and MRC for financial support of this work; and the Scottish Executive/Royal Society of Edinburgh (Research Fellowship to ANH). We thank Dr. Ian Sadler and Juraj Bella for assistance with NMR studies and Dr. Simon Morton for technical assistance with the immunoassays.

Table 3. Survey of Propargylation Methodologies for the Selective Functionalization of Alcohol, Amine, Thiol, Ketone/Aldehyde, and Acid Functionalities

	Reagent	Conditions	Refs
R−OH		Base, DMF	35, 45
		DIC, DMAP, CH_2Cl_2	46
		Base, CH_2Cl_2	47-49
		TfOH, ROH	50-52
R−NHR' or R−NH_2		K_2CO_3, DMF	35, 53, 54
		DCC, THF *or* HBTU, DMF	55, 56
		Base, CH_2Cl_2	57, 58
R−SH		K_2CO_3, KI, Acetone	59
		BuLi, THF *or* Py, Et_2O	60, 61
		MeOH	62, 63
R−COOH		DCC, DMAP, CH_2Cl_2	64-66
		As above *or* TBTU, HOBt, NMO, DMF	66, 67

Supporting Information Available: Experimental for the preparation of C_6 biotinylated iodoacetamide **9**; synthesis of compound **12**; NMR spectra for *N*-linked molecular probes **8**, **11**, **22**, and **25**; NMR spectra for biotinylated azides **15** and **16**. This information is available free of charge via the Internet at http://pubs.acs.org.

LITERATURE CITED

(1) Schreiber, S. L. (1998) Chemical genetics resulting from a passion for synthetic organic chemistry. *Bioorg. Med. Chem. 6*, 1127−1152.
(2) Spring, D. R. (2005) Chemical genetics to chemical genomics: small molecules offer big insights. *Chem. Soc. Rev. 34*, 472−482.
(3) Walsh, D. P., and Chang, Y.-T. (2006) Chemical genetics. *Chem. Rev. 106*, 2476−2530.
(4) Peterson, B. R., and Muddana, S. S. (2004) Facile synthesis of CIDs: Biotinylated estrone oximes efficiently heterodimerize estrogen receptor and streptavidin proteins in yeast three hybrid systems. *Org. Lett. 6*, 1409−1412.
(5) Nesnas, N., Robert, R. R., and Nakanishi, K. (2002) Synthesis of biotinylated retinoids for cross-linking and isolation of retinol binding proteins. *Tetrahedron 58*, 6577−6584.
(6) Musachio, J. L., and Lever, J. R. (1992) Vinylstannylated alkylating-agents as prosthetic groups for radioiodination of small molecules-

design, synthesis, and application to iodoallyl analogs of spiperone and diprenorphine. *Bioconjugate Chem. 3*, 167−175.
(7) Alexander, M. D., Burkart, M. D., Leonard, M. S., Portonovo, P., Liang, B., Ding, X., Joullie, M. M., Gulledge, B. M., Aggen, J. B., Chamberlin, A. R., Sandler, J., Fenical, W., Cui, J., Gharpure, S. J., Polosukhin, A., Zhang, H.-R., Evans, P. A., Richardson, A. D., Harper, M. K., Ireland, C. M., Vong, B. G., Brady, T. P., Theodorakis, E. A., and La Clair, J. J. (2006) A central strategy for converting natural products into fluorescent probes. *ChemBioChem 7*, 409−416.
(8) Means, G., and Feeney, R. (1990) Chemical modifications of proteins: history and applications. *Bioconjugate Chem. 1*, 2−12.
(9) Bayer, E. A., and Wilchek, M. (1990) Application of avidin-biotin technology to affinity-based separations. *J. Chromatogr., A 510*, 3−11.
(10) Li, Y. M., Xu, M., Lai, M. T., Huang, Q., Castro, J. L., DiMuzio-Mower, J., Harrison, T., Lellis, C., Nadin, J. L., Neduvelil, J. G., Register, R. B., Sardana, M. K., Shearman, M. S., Smith, A. L., Shi, X. P., Yin, K. C., Shafer, J. A., and Gardell, S. J. (2000) Photoactivated gamma-secretase inhibitors directed to the active site covalently label presenilin 1. *Nature (London) 405*, 689−694.
(11) Kalovidouris, S. A., Gama, C. I., Lee, L. W., and Hsieh-Wilson, L. C. (2005) A role for fucose alpha(1−2)galactose carbohydrates in neuronal growth. *J. Am. Chem. Soc. 127*, 1340−1341.
(12) Honda, T., Janosik, T., Honda, Y., Han, J., Liby, K. T., Williams, C. R., Couch, R. D., Anderson, A. C., Sporn, M. B., and Gribble, G. W. (2004) Design, synthesis, and biological evaluation of biotin conjugates of 2-cyano-3,12-dioxooleana-1,9(11)-dien-28-oic acid for the isolation of the protein targets. *J. Med. Chem. 47*, 4923−4932.
(13) Frick, W., Bauer-Schafer, A., Bauer, J., Girbig, F., Corsiero, D., Heuer, H., and Kramer, W. (2003) Synthesis of a biotin-tagged photoaffinity probe of 2-azetidinone cholesterol absorption inhibitors. *Bioorg. Med. Chem. 11*, 1639−1642.
(14) Sambaiah, T., King, K. Y., Tsay, S. C., Mei, N. W., Hakimclahi, S., Lai, Y. K., Lieu, C. H., and Hwu, J. R. (2002) Synthesis and immunofluorescence assay of a new biotinylated paclitaxel. *Eur. J. Med. Chem. 37*, 349−353.
(15) Sobin, B. A., and Tanner, F. W. (1954) Anisomycin, a new anti-protozoan antibiotic. *J. Am. Chem. Soc. 76*, 4053−4053.
(16) Beereboom, J. J., Butler, K., Pennington, F. C., and Solomons, I. A. (1965) Anisomycin. I. Determination of structure and stereochemistry of anisomycin. *J. Org. Chem. 30*, 2334−2342.
(17) Schaefer, J. P., and Wheatley, P. J. (1967) Structure of anisomycin. *Chem. Commun.* 578−579.
(18) Schaefer, J. P., and Wheatley, P. J. (1968) Structure of anisomycin. *J. Org. Chem. 33*, 166−169.
(19) Butler, K. (1968) Anisomycin. III. Conformational studies of the pyrrolidine ring. *J. Org. Chem. 33*, 2136−2141.
(20) Lynch, J. E., English, A. R., Bauck, H., and Deligianis, H. (1954) Studies on the *in vitro* activity of anisomycin. *Antibiot. Chemother. 4*, 844−848.
(21) Hansen, J. L., Moore, P. B., and Steitz, T. A. (2003) Structures of five antibiotics bound at the peptidyl transferase center of the large ribosomal subunit. *J. Mol. Biol. 330*, 1061−1075.
(22) Schwardt, O., Veith, U., Gaspard, C., and Jager, V. (1999) Stereoselective synthesis and biological evaluation of anisomycin and 2-substituted analogues. *Synthesis* 1473−1490.
(23) Cano, E., Hazzalin, C. A., and Mahadevan, L. C. (1994) Anisomycin-activated protein kinase-P45 and kinase-P55 but not mitogen-activated protein kinase-Erk-1 and kinase-Erk-2 are implicated in the induction of C-Fos and C-Jun. *Mol. Cell Biol. 14*, 7352−7362.
(24) Kyriakis, J. M., Banerjee, P., Nikolakaki, E., Dai, T. A., Rubie, E. A., Ahmad, M. F., Avruch, J., and Woodgett, J. R. (1994) The stress-activated protein-kinase subfamily of c-Jun kinases. *Nature (London) 369*, 156−160.
(25) Cano, E., Doza, Y. N., BenLevy, R., Cohen, P., and Mahadevan, L. C. (1996) Identification of anisomycin-activated kinases p45 and p55 in murine cells as MAPKAP kinase-2. *Oncogene 12*, 805−812.
(26) Chen, D., Waters, S. B., Holt, K. H., and Pessin, J. E. (1996) SOS phosphorylation and disassociation of the Grb2-SOS complex by the ERK and JNK signaling pathways. *J. Biol. Chem. 271*, 6328−6332.
(27) Hazzalin, C. A., Cano, E., Cuenda, A., Barratt, M. J., Cohen, P., and Mahadevan, L. C. (1996) p38/RK is essential for stress-induced nuclear responses: JNK/SAPKs and c-Jun/ATF-2 phosphorylation are insufficient. *Curr. Biol. 6*, 1028−1031.
(28) Meier, R., Rouse, J., Cuenda, A., Nebreda, A. R., and Cohen, P. (1996) Cellular stresses and cytokines activate multiple mitogen-activated-protein kinase kinase homologues in PC12 and KB cells. *Eur. J. Biochem. 236*, 796−805.
(29) Tibbles, L. A., and Woodgett, J. R. (1999) The stress-activated protein kinase pathways. *Cell Mol. Life Sci. 55*, 1230−1254.
(30) Chen, Z., Gibson, T. B., Robinson, F., Silvestro, L., Pearson, G., Xu, B. E., Wright, A., Vanderbilt, C., and Cobb, M. H. (2001) MAP kinases. *Chem. Rev. 101*, 2449−2476.
(31) Mitsios, N., Gaffney, J., Kumar, P., Krupinski, J., Kumar, S., and Slevin, M. (2006) Pathophysiology of acute ischaemic stroke: An analysis of common signalling mechanisms and identification of new molecular targets. *Pathobiology 73*, 159−175.
(32) Chen, Y.-R., and Tan, T.-H. (2000) The c-Jun N-terminal kinase pathway and apoptotic signaling (Review). *Int. J. Oncol. 16*, 651−662.
(33) Zhu, X., Raina, A. K., Lee, H., Casadesus, G., Smith, M. A., and Perry, G. (2004) Oxidative stress signalling in Alzheimer's disease. *Brain Res. 1000*, 32−39.
(34) Rosser, E. M., Morton, S., Ashton, K. S., Cohen, P., and Hulme, A. N. (2004) Synthetic anisomycin analogues activating the JNK/SAPK1 and p38/SAPK2 pathways. *Org. Biomol. Chem. 2*, 142−149.
(35) Inverarity, I. A., and Hulme, A. N. (2007) Marked small molecule libraries: A truncated approach to molecular probe design. *Org. Biomol. Chem. 5*, 636−643.
(36) Goard, M., Aakalu, G., Fedoryak, O. D., Quinonez, C., St. Julien, J., Poteet, S. J., Schuman, E. M., and Dore, T. M. (2005) Light-mediated inhibition of protein synthesis. *Chem. Biol. 12*, 685−693.
(37) Brase, S., Gil, C., Knepper, K., and Zimmermann, V. (2005) Organic azides: An exploding diversity of a unique class of compounds. *Angew. Chem., Int. Ed. 44*, 5188−5240.
(38) Benalil, A., Carboni, B., and Vaultier, M. (1991) Synthesis of 1,2-aminoazides-Conversion to unsymmetrical vicinal diamines by catalytic-hydrogenation or reductive alkylation with dichloroboranes. *Tetrahedron 47*, 8177−8194.
(39) Morton, S., Davis, R. J., McLaren, A., and Cohen, P. (2003) A reinvestigation of the multisite phosphorylation of the transcription factor c-Jun. *EMBO J. 22*, 3876−3886.
(40) Bradford, M. M. (1976) A rapid and sensitive method for the quantitation of microgram quantities of proteins utilising the principles of protein-dye binding. *Anal. Biochem. 72*, 248−254.
(41) Sun, C., and Bittman, R. (2006) A photoreactive analogue of the immunosuppressant FTY720. *J. Org. Chem. 71*, 2200−2202.
(42) A related approach has very recently been published using alkynyl biotin derivatives. Bonnet, D., Ilien, B., Galzi, J.-L., Riché, S., Antheaune, C., and Hibert, M. (2006) A rapid and versatile method to label receptor ligands using "click" chemistry: Validation with the muscarinic M1 antagonist pirenzepine. *Bioconjugate Chem. 17*, 1618−1623.
(43) Kolb, H. C., Finn, M. G., and Sharpless, K. B. (2001) Click chemistry: Diverse chemical function from a few good reactions. *Angew. Chem., Int. Ed. 40*, 2004−2021.
(44) Kolb, H. C., and Sharpless, K. B. (2003) The growing impact of click chemistry on drug discovery. *Drug Discovery Today 8*, 1128−1137.
(45) Xiong, Y. F., Xia, H. J., and Moore, H. W. (1995) Ring expansion of 4-alkynylcyclobutenones−Synthesis of enantiomerically pure pyranoquinones from 4-(4-oxo-1,6-enynyl)-4-hydroxycyclobutenones and 4-(4-oxo-1,6-dialkynyl)-4-hydroxycyclobutenones. *J. Org. Chem. 60*, 6460−6467.
(46) Inverarity, I. A. (2007) Marked small molecule libraries: A new approach to molecular probe design. Ph.D. Thesis, The University of Edinburgh.
(47) Ramesh, R., Bhat, R. G., and Chandrasekaran, S. (2005) Highly selective deblocking of propargyl carbonates in the presence of propargyl carbamates with tetrathiomolybdate. *J. Org. Chem. 70*, 837−840.
(48) Sridhar, P. R., and Chandrasekaran, S. (2002) Propargyloxycarbonyl (Poc) as a protective group for the hydroxyl function in carbohydrate synthesis. *Org. Lett. 4*, 4731−4733.

(49) Gouault-Bironneau, S., Deprèle, S., Sutor, A., and Montchamp, J.-L. (2005) Radical reaction of sodium hypophosphite with terminal alkynes: Synthesis of 1,1-bis-*H*-phosphinates. *Org. Lett. 7*, 5909−5912.

(50) Overman, L. E., Clizbe, L. A., Freerks, R. L., and Marlowe, C. K. (1981) Thermal rearrangements of propargylic trichloroacetimidates−Synthesis of (trichloroacetamido)-1,3-dienes and (trichloroacetamido)-1,2-dienes. *J. Am. Chem. Soc. 103*, 2807−2815.

(51) Overman, L. E., Marlowe, C. K., and Clizbe, L. A. (1979) Preparation of *N*-trichloroacetamido-1,2-dienes. *Tetrahedron Lett. 43*, 599−600.

(52) Fanning, K. N., Jamieson, A. G., and Sutherland, A. (2006) Stereoselective *β*-hydroxy-α-amino acid synthesis *via* an ether-directed, palladium-catalysed aza-Claisen rearrangement. *Org. Biomol. Chem. 3*, 3749−3756.

(53) Sterling, J., Herzig, Y., Goren, T., Finkelstein, N., Lerner, D., Goldenberg, W., Miskolczi, I., Molnar, S., Rantal, F., Tamas, T., Toth, G., Zagyva, A., Zekany, A., Lavian, G., Gross, A., Friedman, R., Razin, M., Huang, W., Krais, B., Chorev, M., Youdim, M. B., and Weinstock, M. (2002) Novel dual inhibitors of AChE and MAO derived from hydroxy aminoindan and phenethylamine as potential treatment for Alzheimer's disease. *J. Med. Chem. 45*, 5260−5279.

(54) Gee, K. R., Barmettler, P., Rhodes, M. R., McBurney, R. N., Reddy, N. L., Hu, L.-Y., Cotter, R. E., Hamilton, P. N., Weber, E., and Keana, J. F. W. (1993) 10,5-(Iminomethano)-10,11-dihydro-5*H*-dibenzo[a,d]cycloheptene and derivatives. Potent PCP receptor ligands. *J. Med. Chem. 36*, 1938−1946.

(55) Wu, C. Y., Chang, C. F., Chen, J. S. Y., Wong, C. H., and Lin, C. H. (2003) Rapid diversity-oriented synthesis in microtiter plates for in situ screening: Discovery of potent and selective alpha-fucosidase inhibitors. *Angew. Chem., Int. Ed. 42*, 4661−4664.

(56) Casaschi, A., Grigg, R., Sansano, J. M., Wilson, D., and Redpath, J. (2000) Palladium catalysed tandem cyclisation-anion capture. Part 5: Cascade hydrostannylation-bis-cyclisation-intramolecular anion capture. Synthesis of bridged- and spiro-cyclic small and macrocyclic heterocycles. *Tetrahedron 56*, 7541−7551.

(57) Gong, B. Q., Hong, F., Kohm, C., Bonham, L., and Klein, P. (2004) Synthesis and SAR of 2-arylbenzoxazoles, benzothiazoles and benzimidazoles as inhibitors of lysophosphatidic acid acyltransferase-beta. *Bioorg. Med. Chem. Lett. 14*, 1455−1459.

(58) Bhat, R. G., Sinha, S., and Chandrasekaran, S. (2002) Propargyloxycarbonyl (Poc) amino acid chlorides as efficient coupling reagents for the synthesis of 100% diastereopure peptides and resin bound tetrathiomolybdate as an effective deblocking agent for the Poc group. *Chem. Commun.* 812−813.

(59) Chen, Y., Zhang, Q., Zhang, B., Xia, P., Xia, Y., Yang, Z. Y., Kilgore, N., Wild, C., Morris-Natschke, S. L., and Lee, K. H. (2004) Anti-AIDS agents. Part 56: Synthesis and anti-HIV activity of 7-thia-di-O-(-)-camphanoyl-(+)-cis-khellactone (7-thia-DCK) analogs. *Bioorg. Med. Chem. 12*, 6383−6387.

(60) Behloul, C., Guijarro, D., and Yus, M. (2005) Deallyloxy- and debenzyloxycarbonylation of protected alcohols, amines and thiols *via* a naphthalene-catalyzed lithiation reaction. *Tetrahedron 61*, 9319−9324.

(61) Wiesler, W. T., and Caruthers, M. H. (1996) Synthesis of phosphorodithioate DNA *via* sulfur-linked, base-labile protecting groups. *J. Org. Chem. 61*, 4272−4281.

(62) Cerri, A., Almirante, N., Barassi, P., Benicchio, A., Fedrizzi, G., Ferrari, P., Micheletti, R., Quadri, L., Ragg, E., Rossi, R., Santagostino, M., Schiavone, A., Serra, F., Zappavigna, M. P., and Melloni, P. (2000) 17 beta-*O*-aminoalkyloximes of 5 beta-androstane-3 beta,14 beta-diol with digitalis-like activity: Synthesis, cardiotonic activity, structure-activity relationships, and molecular modeling of the Na^+,K^+-ATPase receptor. *J. Med. Chem. 43*, 2332−2349.

(63) Ide, H., Akamatsu, K., Kimura, Y., Michiue, K., Makino, K., Asaeda, A., Takamori, Y., and Kubo, K. (1993) Synthesis and damage specificity of a novel probe for the detection of abasic sites in DNA. *Biochemistry 32*, 8276−8283.

(64) Trost, B. M., and Rudd, M. T. (2005) Ruthenium-catalyzed cycloisomerizations of diynols. *J. Am. Chem. Soc. 127*, 4763−4776.

(65) Ott, I., Schmidt, K., Kircher, B., Schumacher, P., Wiglenda, T., and Gust, R. (2005) Antitumor-active cobalt-alkyne complexes derived from acetylsalicylic acid: Studies on the mode of drug action. *J. Med. Chem. 48*, 622−629.

(66) Yamamoto, Y., Kinpara, K., Saigoku, T., Nishiyama, H., and Itoh, K. (2004) Synthesis of benzo-fused lactams and lactones *via* Ru(II)-catalyzed cycloaddition of amide- and ester-tethered alpha, omega-diynes with terminal alkynes: electronic directing effect of internal conjugated carbonyl group. *Org. Biomol. Chem. 2*, 1287−1294.

(67) Zhu, L., Lynch, V. M., and Anslyn, E. V. (2004) FRET induced by an 'allosteric' cycloaddition reaction regulated with exogenous inhibitor and effectors. *Tetrahedron 60*, 7267−7275.

BC070085U

Dicationic Lipophosphoramidates as DNA Carriers

Mathieu Mével,[†] Tristan Montier,[‡] François Lamarche,[†] Pascal Delépine,[‡] Tony Le Gall,[‡] Jean-Jacques Yaouanc,[†] Paul-Alain Jaffrès,[†] Dominique Cartier,[†] Pierre Lehn,[‡] and Jean-Claude Clément*[,†]

UMR CNRS 6521, Université de Bretagne Occidentale, UFR Sciences, 6, Avenue Le Gorgeu, C.S. 93837, F-29238 Brest cedex 3, France, and INSERM U 613, Université de Bretagne Occidentale, C.S. 2653, F-29275 Brest cedex, France. March 14, 2007; Revised Manuscript Received May 30, 2007

Lipophosphoramidates with two different permanent cations as polar heads were synthesized and evaluated for their gene transfer activity. Physicochemical measurements (particle size, zeta potentials) and gel retardation assays were also performed. *In vitro* biological evaluation was conducted with A542 and HeLa cell lines, and cytotoxicity determined by a chemiluminescent assay. The set of results indicates that, on the whole, dicationic lipophosphoramidates constitute an interesting alternative to their monocationic analogues.

INTRODUCTION

The use of cationic lipids for mediating DNA transfection has become widespread. Since the pioneering work of Felgner et al. (*1*), this trend has grown rapidly, so that now a variety of such compounds have been described and asserted as DNA carriers for future applications to gene therapy (*2*, *3*). Mixing an anionic plasmid DNA with variable amounts of cationic lipids (in terms of ± charge ratio) results in a "lipoplex", whose transfection efficiency will generally vary according to that ratio. In our previous *in vitro* experiments with phosphonolipids (*4*, *5*) or lipophosphoramidates (*6*), optimal ± ratios were in the range 2−4. Lower ratios exhibited lower efficiency and higher, generally, an increased cytotoxicity.

A possible way to lower the proportion of cationic lipid to DNA is to increase twofold (or more) the number of cations of the lipid. Moreover, additional cations could increase the strength of the interaction with DNA. Indeed, many examples of polycationic lipids are reported, notably lipidic polyamines. Their different amino groups are protonated at variable pH, leading to multicationic species, especially once internalized into cells (*2*). Permanently polycationic compounds are less numerous. Apart from polymers or bis-guanidinium derivatives (*7*), most of them are recorded as "gemini" (*8*). Some examples of gemini compounds used as DNA carriers are described, and in all quoted compounds, the cations are quaternary ammoniums (*9*−*15*).

We have previously shown that monocationic "phosphonolipids" (*4*, *5*) and "lipophosphoramidates" (*6*) had good transfection efficacy, together with moderate cytotoxicity. Moreover, the replacement of the ammonium by a phosphonium or arsonium head group was generally beneficial in terms of efficiency and cytotoxicity. So, we wondered about the behavior of such phosphorylated derivatives including two cations, identical or different, e.g., an ammonium plus a phosphonium, or an ammonium plus an arsonium, for instance. Furthermore, one can suppose that the arrangement of the two cations and the lipidic part (e.g., in single file or T-shaped) would lead to different interactions with DNA, hence a different efficacy. That is the case for cholesteryl polyamines, for instance, where the T-shaped arrangement was found to be more efficient than the linear one (*16*).

EXPERIMENTAL PROCEDURES

1. Materials and Reagents. Diisopropylethylamine (DIPEA) was dried and distilled over KOH. Fatty phosphites were synthesized by heating diphenyl phosphite (1 equiv) with tetradecanol or oleoyl alcohol (2 equiv) for 3 h at 120 °C and elimination of the produced phenol by distillation under vacuum. Bromopropyltrimethylammonium bromide **2** was purchased from Aldrich. Solvents were freshly distilled on appropriate driers and reactions run under nitrogen atmosphere. All compounds were fully characterized by ^{1}H (400 MHz), ^{13}C (100 MHz) and ^{31}P (121.49 MHz) NMR spectroscopy (Bruker AC 300 and Advance DRX 400 spectrometers). Coupling constants *J* are given in hertz. The following abbreviations were used: s for singulet, d doublet, t triplet, q quadruplet, qt quintuplet, and m for multiplet. High-resolution mass spectroscopy (HRMS) (ESI) was performed at the "Centre Régional des Mesures Physiques de l'Ouest", Rennes, France.

O,*O*-Ditetradecyl-*N*-(dimethylaminopropyl)phosphoramidate **1a** and *O*,*O*-dioleoyl-*N*-(dimethylaminopropyl)phosphoramidate **1b** Ditetradecyl phosphite (2.37 g, 5 mmol) or dioleoyl phosphite (2.91 g, 5 mmol), dimethylaminopropylamine (0.63 mL, 5 mmol), CH_2Cl_2 (15 mL), and $CBrCl_3$ (0.55 mL, 5.5 mmol) were mixed and cooled at 5 °C. DIPEA (0.96 mL, 5.5 mmol) was then added and the temperature kept 1 h at 5 °C, then 1 h at room temperature (RT). Solvent was discarded under reduced pressure, then DIPEA halides were precipitated in diethyl ether and filtered off. Purification of crude products was accomplished by column chromatography (silica gel), eluting with a chloroform/methanol (9/1) mixture. Compound **1a** ($C_{14:0}$) is a white solid (80% yield), and **1b** ($C_{18:1}$) a pale yellow oil (80% yield).

NMR data for **1a**: ^{1}H ($CDCl_3$) 0.86 (t, $^{3}J_{H-H}$ = 6.6, 6H), 1.26 (m, 44H), 1.65 (m, 4H), 1.66 (q, $^{3}J_{H-H}$ = 6.7, 2H), 2.22 (s, 6H), 2.35 (t, $^{3}J_{H-H}$ = 6.9, 2H), 2.98 (m, 2H), 3.47 (m, 1H), 3.98 (m, $^{3}J_{H-H}$ = $^{3}J_{P-H}$ = 6.4, 4H). ^{13}C ($CDCl_3$) 14.1, 22.6−32.0, 25.5, 30.3 (d, $^{3}J_{P-C}$ = 6.2), 40.3, 45.2, 57.2, 66.1 (d, $^{2}J_{P-C}$ = 6.6). ^{31}P ($CDCl_3$) 9.76.

NMR data for **1b**: ^{1}H ($CDCl_3$) 0.86 (t, $^{3}J_{H-H}$ = 6.6, 6H), 1.26 (m, 44H), 1.65 (m, 4H), 1.68 (m, 2H), 1.99 (m, 8H), 2.21 (s, 6H), 2.34 (m, 2H), 3.01 (m, 2H), 3.52 (m, 1H), 3.98 (m, $^{3}J_{H-H}$ = $^{3}J_{P-H}$ = 6.4, 4H), 5.32 (m, 4H). ^{13}C ($CDCl_3$) 14.1,

* To whom correspondence should be addressed. E-mail: jean-claude.clement@univ-brest.fr.

[†] UMR CNRS 6521.

[‡] INSERM U 613.

10.1021/bc070089z CCC: $37.00 © 2007 American Chemical Society
Published on Web 08/03/2007

22.6−32.0, 25.4, 30.3 (d, $^3J_{P-C}$ = 6.2), 40.1, 45.4, 57.1, 66.1 (d, $^2J_{P-C}$ = 6.6), 129.6, 129.7. ^{31}P ($CDCl_3$) 9.77.

*3-Iodopropyltrimethylphosphonium Iodide **3***. Into 50 mL of degassed toluene were added under nitrogen atmosphere diiodopropane (1.32 mL, 12 mmol) and 10 mL of a 1 M solution of trimethylphosphine in THF (Aldrich). The mixture was then heated for 3 days at 40 °C. After cooling at RT, the white precipitate was washed twice with 10 mL of pentane and dried under vacuum (82% yield).

NMR data: ^{1}H (DMSO-d_6) 1.85 (d, 9H), 2.03 (q, 2H), 2.24 (m, 2H), 3.33 (t, 2H). ^{13}C (DMSO-d_6) 7.3, 7.4, 23.8, 24.9. ^{31}P (DMSO-d_6) 28.4.

HRMS (ESI): *m*/*z* calcd (*z* = 1) 244.9956; found 244.9953 (an ionization cluster [2C$^+$, I$^-$] was also observed at *m*/*z* 617).

*3-Iodopropyltrimethylarsonium Iodide **4***. Into 50 mL of degassed toluene were added under nitrogen atmosphere diiodopropane (2.27 mL, 20.7 mmol) and trimethylarsine (1.95 mL, 18.4 mmol). After heating for 6 days at 70 °C and cooling at RT, the white precipitate was washed twice with 10 mL of pentane and dried under vacuum (86% yield).

NMR data: ^{1}H (CD_3CN) 1.86 (s, 9H), 2.08 (q, $^3J_{H-H}$ = 6.9, 2H), 2.42 (m, 2H), 3.28 (t, $^3J_{H-H}$ = 6.8, 2H). ^{13}C (CD_3CN) 5.7, 7.7, 26.0, 27.1.

HRMS (ESI): *m*/*z* calcd (*z* = 1) 288.9434; found 288.9441 (an ionization cluster [2C$^+$, I$^-$]$^+$ was also observed at *m*/*z* = 705.

*Dicationic Lipophosphoramidates **5**, **6**, And **7***. Into 2 mL of CH_3CN were added **1a** (632 mg, 1.1 mmol) or **1b** (751 mg, 1.1 mmol) and 1 mmol of the "oniums" **2** (261 mg), **3** (372 mg), or **4** (416 mg). The mixture was heated at 70 °C for 3 days, then the solvent discarded under reduced pressure. The residues were precipitated and washed in ethyl acetate, then dried under vacuum. Ditetradecyl dicationic compounds **5a**, **6a**, and **7a** are off-white powders. Dioleoyl **5b**, **6b**, and **7b** are yellow to orange waxes. All yields were in the range 90−92%.

NMR data for **5a**: ^{1}H (DMSO-d_6) 0.85 (t, $^3J_{H-H}$ = 6.6, 6H), 1.24 (m, 44H), 1.57 (m, 4H), 1.80 (m, 2H), 2.19 (m, 2H), 2.82 (m, 2H), 3.07 (s, 6H), 3.12 (s, 9H), 3.27 (m, 2H), 3.34 (m, 4H), 3.95 (m, $^3J_{H-H}$ = $^3J_{P-H}$ = 6.4, 4H), 5.01 (m). ^{13}C (DMSO-d_6) 13.9, 16.5, 20.1−31.3, 24.1, 29.0 (d, $^3J_{P-C}$ = 6.2), 37.7, 50.0, 52.4, 59.6, 61.5, 61.9, 66.1 (d, $^2J_{P-C}$ = 6.6). ^{31}P (DMSO-d_6) 9.34.

NMR data for **5b**: ^{1}H (DMSO-d_6) 0.85 (t, $^3J_{H-H}$ = 6.6, 6H), 1.24 (m, 44H), 1.57 (m, 4H), 1.80 (m, 2H), 1.97 (m, 8H), 2.19 (m, 2H), 2.84 (m, 2H), 3.06 (s, 9H), 3.11 (s, 9H), 3.27 (m, 2H), 3.34 (m, 4H), 3.95 (m, $^3J_{H-H}$ = $^3J_{P-H}$ = 6.4, 4H), 5.01 (m, 1H), 5.31 (m, 4H). ^{13}C (DMSO-d_6) 13.9, 16.8, 20.1−31.3, 25.1, 29.0 (d, $^3J_{P-C}$ = 6.2), 36.3, 51.0, 53.4, 59.6, 61.8, 62.1, 66.1 (d, $^2J_{P-C}$ = 6.6). ^{31}P (DMSO-d_6) 9.40.

NMR data for **6a**: ^{1}H (DMSO-d_6) 0.87 (t, $^3J_{H-H}$ = 6.6, 6H), 1.27 (m, 44H), 1.57 (m, 4H), 2.10 (m, 2H), 2.27 (d, 9H), 2.48 (m, 2H), 2.80 (m, 2H), 3.08 (m, 2H), 3.39 (s, 6H), 3.70 (m, 2H), 3.77 (m, 2H), 3.84 (m, $^3J_{H-H}$ = $^3J_{P-H}$ = 6.4, 4H), 4.17 (m, 1H). ^{13}C (DMSO-d_6) 10.0 (d), 14.1, 17.7, 20.5, 22.7−32.1, 25.7, 30.5 (d, $^3J_{P-C}$ = 6.2), 37.9, 52.3, 62.8, 63.2, 67.1 (d, $^2J_{P-C}$ = 6.6). ^{31}P (DMSO-d_6) 9.01, 27.9.

NMR data for **6b**: ^{1}H (DMSO-d_6) 0.87 (t, $^3J_{H-H}$ = 6.6, 6H), 1.27 (m, 44H), 1.57 (m, 4H), 1.99 (m, 2H), 2.11 (m, 2H), 2.27 (d, 9H), 2.46 (m, 2H), 2.80 (m, 2H), 3.07 (m, 2H), 3.38 (s, 6H), 3.70 (m, 2H), 3.78 (m, 2H), 3.95 (m, $^3J_{H-H}$ = $^3J_{P-H}$ = 6.4, 4H), 4.18 (m, 1H), 5.45 (m, 4H). ^{13}C (DMSO-d_6) 10.0 (d), 14.1, 17.0, 20.5, 22.7−32.1, 25.7, 30.5 (d, $^3J_{P-C}$ = 6.2), 38.0, 52.4, 62.9, 63.3, 67.0 (d, $^2J_{P-C}$ = 6.6), 129.7, 130.0. ^{31}P (DMSO-d_6) 9.1, 28.1.

HRMS (ESI): *m*/*z* calcd (with *z* = 2) 400.3526; found 400.3533 (an ionization cluster [2C$^+$, I$^-$]$^+$ was also observed at *m*/*z* 927).

NMR data for **7a**: ^{1}H (DMSO-d_6) 0.87 (t, $^3J_{H-H}$ = 6.6, 6H), 1.27 (m, 44H), 1.57 (m, 4H), 2.11 (m, 2H), 2.30 (s, 9H), 2.60 (m, 2H), 2.90 (m, 2H), 3.08 (m, 2H), 3.35 (s, 6H), 3.66 (m, 2H), 3.72 (m, 2H), 3.84 (m, $^3J_{H-H}$ = $^3J_{P-H}$ = 6.4, 4H), 4.24 (m, 1H). ^{13}C (DMSO-d_6) 9.0, 13.6, 14.1, 22.7−32.1, 29.5, 25.4, 30.5 (d, $^3J_{P-C}$ = 6.2), 37.8, 51.1, 63.0, 67.1 (d, $^2J_{P-C}$ = 6.6). ^{31}P (DMSO-d_6) 9.11.

NMR data for **7b**: ^{1}H (DMSO-d_6) 0.87 (t, $^3J_{H-H}$ = 6.6, 6H), 1.27 (m, 44H), 1.57 (m, 4H), 1.99 (m, 2H), 2.06 (m, 2H), 2.32 (s, 9H), 2.55 (m, 2H), 2.86 (m, 2H), 3.08 (m, 2H), 3.37 (s, 6H), 3.68 (m, 2H), 3.74 (m, 2H), 3.95 (m, $^3J_{H-H}$ = $^3J_{P-H}$ = 6.4, 4H), 4.11 (m, 1H), 5.45 (m, 4H). ^{13}C (DMSO-d_6) 9.7, 14.1, 14.8, 19.3, 22.7−32.1, 25.8, 30.5 (d, $^3J_{P-C}$ = 6.2), 38.1, 52.3, 63.8, 67.0 (d, $^2J_{P-C}$ = 6.6), 129.7, 130.0. ^{31}P (DMSO-d_6) 9.05.

*O,O-Dioleoyl-N-(3-(N-imidazolyl)propyl)phosphoramidate **10***. Into 15 mL of CH_2Cl_2 were added $CBrCl_3$ (0.55 mL, 5.5 mmol), 3-aminopropylimidazole (0.59 mL, 5 mmol), and dioleoyl phosphite (2.91 g, 5 mmol). After cooling at 5 °C, DIPEA (0.96 mL, 5.5 mmol) was added and the mixture kept at this temperature for 1 h, then 1 h at RT. Solvent was evaporated and DIPEA halides filtered off, after precipitation from diethylether. Purification of crude product was accomplished by column chromatography (silica gel), eluting with a chloroform/methanol (9/1) mixture. Dioleoyl phosphoramidate **10** was isolated as a yellow wax (80% yield).

NMR data for **10**: ^{1}H ($CDCl_3$) 0.86 (t, $^3J_{H-H}$ = 6.6, 6H), 1.26 (m, 44H), 1.65 (m, 4H), 1.94 (q, $^3J_{H-H}$ = 6.7, 2H), 1.99 (m, 8H), 2.89 (m, 2H), 3.61 (m, 1H), 3.98 (m, $^3J_{H-H}$ = $^3J_{P-H}$ = 6.4, 4H), 4.03 (t, $^3J_{H-H}$ = 6.9, 2H), 5.32 (m, 4H), 6.92 (s, 1H), 7.04 (s, 1H), 7.49 (s, 1H). ^{13}C ($CDCl_3$) 13.2, 21.8−31.0, 24.7, 29.7 (d, $^3J_{P-C}$ = 6.2), 37.1, 43.0, 65.4 (d, $^2J_{P-C}$ = 6.6), 117.9, 128.4, 128.8, 129.1, 136.4. ^{31}P ($CDCl_3$) 9.57.

*Dicationic Lipophosphoramidates **11** And **12***. To 2 mL of CH_3CN were added 0.781 mg (1.1 mmol) of phosphoramidate **10** and 372 mg (1 mmol) of onium **3** or 416 mg (1 mmol) of onium **4**. The mixture was heated at 70 °C for 3 days, then the solvent evaporated. After precipitation from ethyl acetate, dicationic phosphoramidates **11** (P^+) and **12** (As^+) were isolated as yellow to orange waxes (90−95% yield).

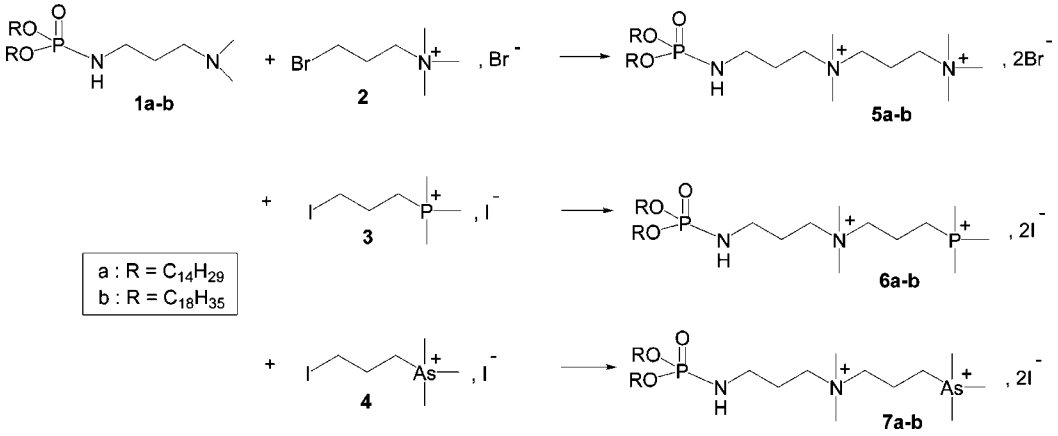
NMR data for **11**: ^{1}H ($CDCl_3$) 0.87 (t, $^3J_{H-H}$ = 6.6, 6H), 1.27 (m, 44H), 1.57 (m, 4H), 1.99 (m, 8H), 2.15 (d, 9H), 2.18 (m, 2H), 2.62 (m, 2H), 2.99 (m, 2H), 3.05 (m, 2H), 3.93 (m, 1H), 3.95 (m, $^3J_{H-H}$ = $^3J_{P-H}$ = 6.4, 4H), 4.41 (m, 2H), 4.66 (m, 2H), 5.45 (m, 4H), 7.37 (s, 1H), 7.97 (s, 1H), 9.89 (s, 1H). ^{13}C ($CDCl_3$) 10.0 (d), 14.1, 20.5, 22.7−32.1, 24.0, 30.5 (d, $^3J_{P-C}$ = 6.2), 30.7, 38.0, 47.8, 49.0, 67.0 (d, $^2J_{P-C}$ = 6.6), 129.7, 130.0, 122.0, 123.4, 136.7. ^{31}P ($CDCl_3$) 9.52, 27.89. ^{15}N ($CDCl_3$) 201.7, 203.4, 341.5.

NMR data for **12**: ^{1}H ($CDCl_3$) 0.87 (t, $^3J_{H-H}$ = 6.6, 6H), 1.27 (m, 44H), 1.57 (m, 4H), 1.99 (m, 8H), 2.19 (m, 2H), 2.25 (d, 9H), 2.66 (m, 2H), 2.99 (m, 2H), 3.03 (m, 2H), 3.86 (m, 1H), 3.95 (m, $^3J_{H-H}$ = $^3J_{P-H}$ = 6.4, 4H), 4.42 (m, 2H), 4.60 (m, 2H), 5.45 (m, 4H), 7.53 (s, 1H), 7.94 (s, 1H), 9.85 (s, 1H). ^{13}C ($CDCl_3$) 9.2, 14.1, 21.8, 22.7−32.1, 24.1, 30.5 (d, $^3J_{P-C}$ = 6.2), 31.2, 37.7, 47.5, 49.4, 67.0 (d, $^2J_{P-C}$ = 6.6), 129.7, 130.0, 121.7, 123.1, 137.0. ^{31}P ($CDCl_3$) 9.52. ^{15}N ($CDCl_3$) 201.7, 203.4, 341.5.

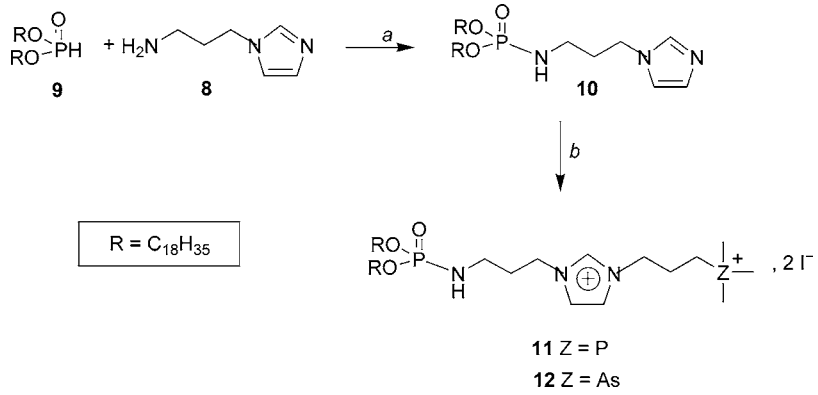
*O,O-Dioleoyl-N-(N,N-bis-(3-(dimethylamino)propyl)))phosphoramidate **14***. Dioleoylphosphite (2.91 g, 5 mmol), 3,3′iminobis-(*N*,*N*-dimethylpropylamine) **13**, CH_2Cl_2 (15 mL), and CCl_4 (2 mL, 10 mmol) were mixed at 5 °C. DIPEA (0.96 mL, 5.5 mmol) was then added and the mixture kept for 1 h at 5 °C, then 1 h at RT. Solvents were discarded and DIPEA halides precipitated and filtered from diethyl ether. Dioleoyl phosphoramidate **14** was isolated as a yellowish oil (88% yield).

NMR data for **14**: ^{1}H ($CDCl_3$) 0.87 (t, $^3J_{H-H}$ = 6.6, 6H), 1.25 (m, 44H), 1.63 (m, 4H), 1.70 (m, 4H), 1.99 (m, 8H), 2.25

Scheme 1. Synthesis of "in Single File" Dicationic Lipophosphoramidates

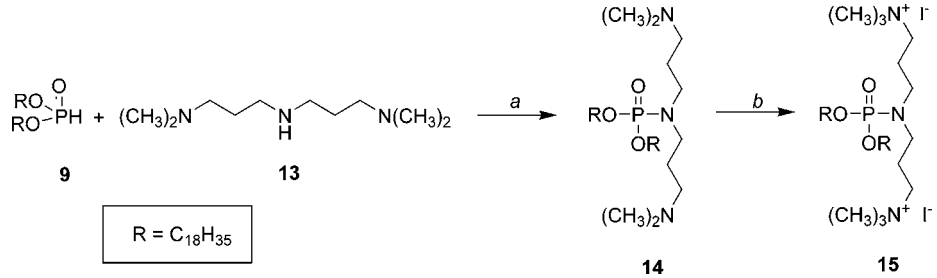


Scheme 2. Synthesis of Mixed Imidazolium-Onium Dicationic Lipophosphoramidates[a]



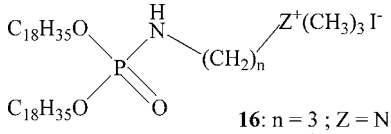
[a] (*a*) $CBrCl_3$ (1.1 equiv), DIPEA (1.1 equiv), 5 °C, 1 h, then RT, 1 h. (*b*) $I(CH_2)_3Z^+(CH_3)_3$, I^- (0.9 equiv), CH_3CN, 70 °C, 3 days.

Scheme 3. Synthesis of a T-shaped Dicationic Phosphoramidate[a]



[a] (*a*) CCl_4 (2 equiv), DIPEA (2.2 equiv), 5 °C, 1 h, then RT, 1 h. (*b*) CH_3I (6 equiv), RT, 12 h.

Scheme 4. Monocationic Lipophosphoramidates Used for Comparison Tests



16: n = 3 ; Z = N
17: n = 3 ; Z = P
18: n = 2 ; Z = As
19 n = 3 ; Z = As

(s, 12H), 3.06 (m, 4H), 3.83 (m, 4H), 3.95 (m, $^3J_{H-H} = {}^3J_{P-H}$ = 6.4, 4H), 5.34 (m, 4H). ^{13}C ($CDCl_3$) 14.0, 22.6−32.0, 25.6, 30.2 (d, $^3J_{P-C}$ = 6.5), 44.0, 45.3, 56.8, 66.4 (d, $^2J_{P-C}$ = 5.9), 129.7, 129.9. ^{31}P ($CDCl_3$) 10.6.

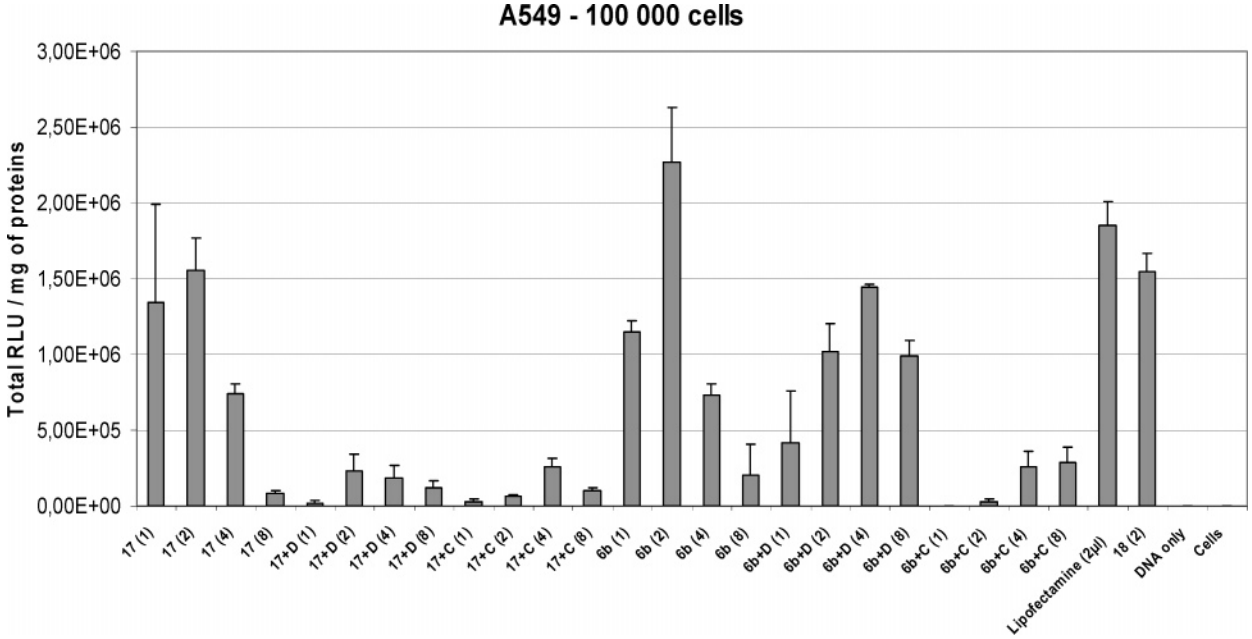
*O,O-Dioleoyl-N-(N,N-bis-(3-(trimethylamonium)propyl)))-phosphoramidate, diiodide **15.*** Compound **14** was shaken with an excess of CH_3I for 24 h at RT. Excess of CH_3I was evaporated and the diammonium **15** isolated as a yellow wax (94% yield).

NMR data for **15**: ^1H ($CDCl_3$) 0.86 (t, $^3J_{H-H}$ = 6.6, 6H), 1.25 (m, 44H), 1.66 (m, 4H), 1.99 (m, 8H), 2.21 (m, 4H), 3.23 (m, 4H), 3.46 (s, 18H), 3.70 (m, 4H), 3.96 (m, $^3J_{H-H} = {}^3J_{P-H}$ = 6.4, 4H), 5.34 (m, 4H). ^{13}C ($CDCl_3$) 14.0, 22.8−32.0, 24.0, 29.8 (d, $^3J_{P-C}$ = 6.6), 42.6, 53.6, 64.0, 66.6 (d, $^2J_{P-C}$ = 5.9), 129.1, 129.3. ^{31}P ($CDCl_3$) 10.0.

***2. In Vitro* Experiments.** *Cell Culture.* Two different cell lines (A549 and HeLa) were used. The alveolar type II epithelial cell line A549 and the human adenocarcinoma epithelial cell line HeLa were obtained from the American Type Culture Collection (respectively, cat. nos .CCL-185 and ccl-2, ATCC, Rockville, MD). These cells were grown in D-MEM (Gibco-BRL, UK) and supplemented with 10% fetal calf serum (FCS) (Gibco-BRL, UK) and 100 U/mL of penicillin/streptomycin. All the cells were maintained in a humidified incubator with 5% CO_2 at 37 °C.

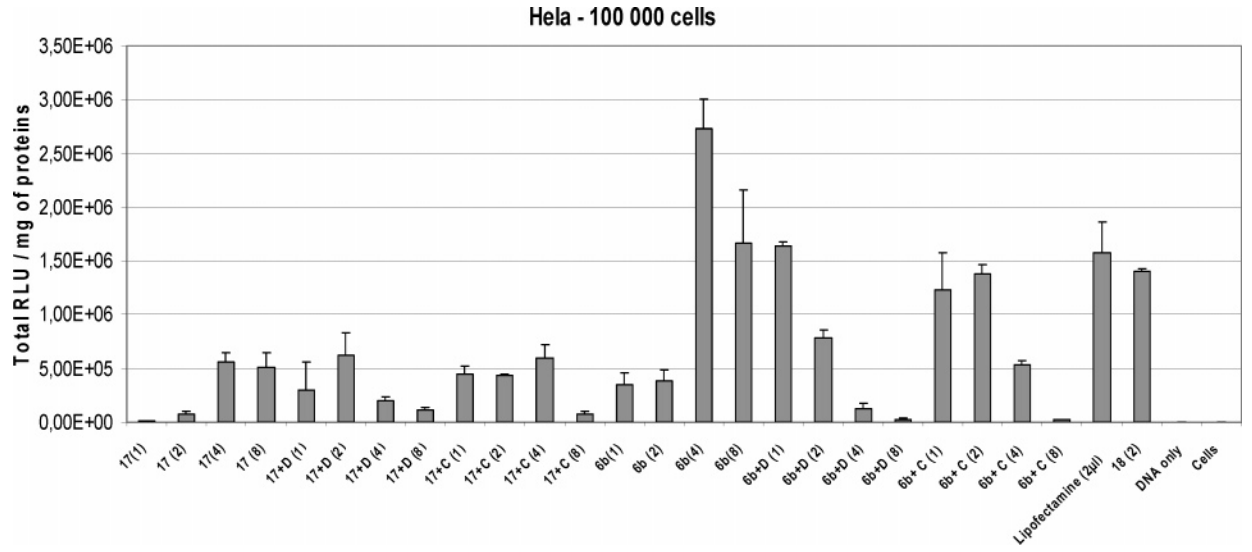
Complex Formulation. Each cationic lipid was prepared alone or in combination with the neutral co-lipid DOPE (w/w = 1:1). Lipids were kept and formulated in chloroform solutions; then, chloroform was removed by rotary evaporation to produce dried lipid films. A total of 1 mL of sterile pyrogen-free DI

Chart 1. *In Vitro* Transfection Efficiency of Dicationic 6b with A549 cells, in Comparison with Monocationic Compounds 17 and 18 and Lipofectamine[a]



[a] Numbers in brackets correspond to the charge ratio ±. The letter D indicates a formulation with DOPE (vector/ DOPE ratio: 1/1). The letter C indicates a formulation with cholesterol (vector/ DOPE ratio: 1/1).

Chart 2. *In Vitro* Transfection Efficiency of Dicationic 6b with HeLa cells, in Comparison with Monocationic Compounds 17 and 18 and Lipofectamine[a]



[a] Numbers in brackets correspond to the charge ratio ±. The letter D indicates a formulation with DOPE (vector/ DOPE ratio: 1/1). The letter C indicates a formulation with cholesterol (vector/ DOPE ratio: 1/1).

water per milligram of lipid was added, and the vials were sealed and stored at 4 °C overnight. Vesicles were then prepared by sonicating the aqueous suspension for 10 min in a bath sonicator.

Cationic lipid/DNA complexes were formed as follows: plasmid DNA (1 μg) was diluted with sterile pyrogen-free deionized water and added to the lipid solution in a polystyrene tube. Lipoplexes were kept at room temperature for 30 min before being used for transfection.

Determination of the Lipoplex Charge Ratio. The charge ratio was calculated theoretically as the molar ratio of the cationic lipids to DNA. In order to study the impact of the formulation on gene expression, various charge ratios (±) were prepared with a constant amount of pDNA (1 μg). As a control, 2 μL of Lipofectamine (Invitrogen) was used, accordingly to manufacturer's instructions, and in these conditions, for 1 μg of delivered DNA, the N/P ratio is equal to 2.

Transfection Protocol. Cells were seeded 24 h before transfection onto a 24-well plate at a density of 100 000 cells per well and incubated overnight in a humidified 5% CO_2 atmosphere at 37 °C. Transfection was performed as described by Felgner et al. (*1*), with the following modifications. Appropriate amounts of the cationic lipids and the plasmid vector in OptiMem were complexed, and about 200 μL was added to each well. After 2 h 30 min incubation at 37 °C, the medium was removed, and fresh medium was added. Following a further 48 h at 37 °C, the cells were assayed for luciferase expression using a chemiluminescent assay (Promega). Assays were carried out as described by the manufacturer. The total protein concentration of the cell culture was determined using the BC assay kit (Uptima). Luciferase activity of each condition was expressed to total relative light units (Total RLU) per milligram of total protein. Results are reported as means ± SEM.

Table 1. Luciferase Activity of Dicationic Lipids and Comparison with Monocationic Lipids

dicationic lipid no./lipid alone/etc.	cells	DOPE[a]	±[b] ratio	TRLU ×10^6
5b	HeLa	-	2	1.1
		+	2	0.8
6b	HeLa	-	4	2.7
		+	1	1.6
	A549	-	2	2.3
		+	4	1.45
7b	HeLa	-	4	2.0
		+	2	0.55
	A549	-	4	7.5
		+	4	1.6
11b[c]	HeLa	-	4	0.10
		+	1	0.12
	A549	-	8	0.08
		+	1	0.13
12b[c]	HeLa	-	8	0.17
		+	2	0.01
	A549	-	8	0.5
		+	4	0.07
15	HeLa	-	2	1.1
		+	8	0.3
	A549	-	8	1.3
		+	4	0.3
16		-	4	0.9
		+	8	0.4
17		-	4	0.55
		+	2	0.6
18		-	2	1.4
17		-	2	1.55
		+	2	0.3
18		-	2	1.55
19		-	2	1.2
		+	2	0.9
19		-	4	2.1
		+	4	2.1

[a] Without (−) or with (+) DOPE (1:1) added. [b] The better ± ratio in the range 1−8 is quoted. [c] Because of values about a decade lower, no comparison was made with monocationic lipids.

Determination of Cell Toxicity. The toxicity of the different lipid/DNA complexes was determined by using a chemiluminescent assay (TOXILIGHT − Cambrex, Liège, Belgium). Twenty-four hours before the assay, the cells were plated in a 24-well plate (100 000 cells per well). Transfections were performed as described above, and the cells were incubated for 48 h at 37 °C. The toxicity assay was then carried out as specified by the manufacturer. This kit quantitatively measures the release of adenylate kinase (AK) from damaged cells into the surrounding medium. The reaction involves two steps. The first one involves the addition of ADP as a substrate for AK. In the presence of AK, the ADP is converted to ATP for assay by bioluminescence. Then, the bioluminescence method utilizes an enzyme Luciferase, which catalyzes the emission of photons from ATP and luciferin. By combining both reactions, the emitted light intensity is directly related to the AK concentration. The relative light units (RLU) were conversely proportional to the number of living cells. Untransfected cells were used as a reference.

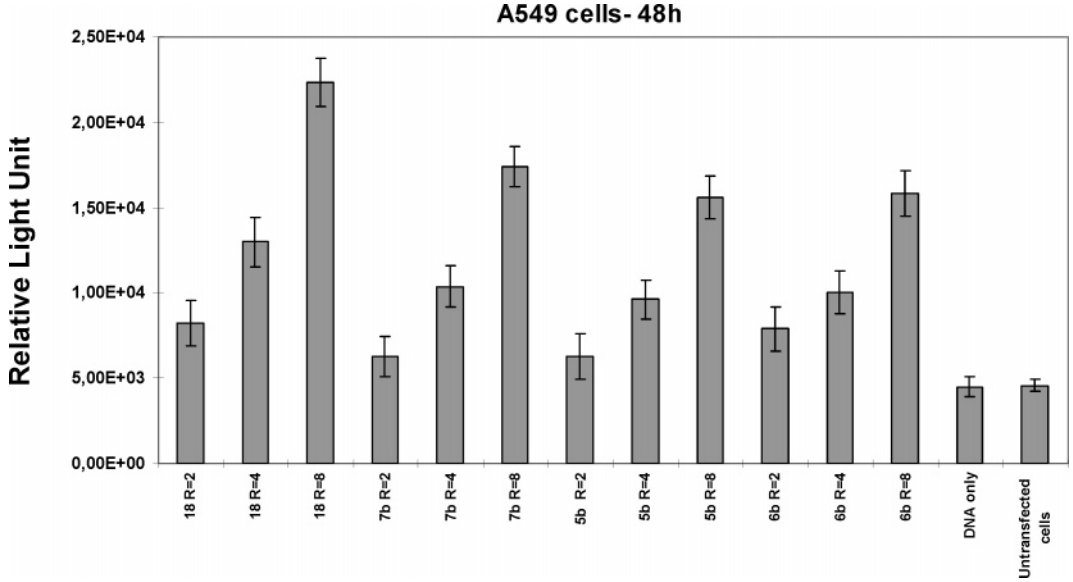
3. DNA Binding Ability. To 1 μg of plasmid DNA in Optimem (Gibco) were added cationic lipids at concentrations corresponding to an N/P charge ratio ranging from 0.5 to 8. The mixture was incubated for 30 min at room temperature. The complexes were subjected to electrophoresis in 1% agarose gel at 100 V, 90 mA. The gel was stained with ethidium bromide (10 mg/mL) and visualized on an UV illuminator (Fischer Bioblock).

4. Sizes and ζ Potential Determination. Particle size and ζ potentials were determined using a Malvern Zetasizer 3000 HAS. For lipids alone, 2.7 mM (about 3 mg/mL) solutions in 10 mM Hepes buffer were prepared. Then, 0.2 mL of the solution was put into the cuvette and diluted up to 4 mL with Hepes. For lipoplexes, plasmidic DNA (2.5 μg) in Optimem (20 μL) was added to 5.5 μL (± ratio = 4) or 11 μL (± ratio = 8) of the above lipid 2.7 mmol solution diluted in 0.2 mL of Optimem, and left at RT for 30 min. The solution was then diluted to 4 mL with 10 mM Hepes buffer into the cuvette for measurement.

RESULTS AND DISCUSSION

1. Synthesis of Dicationic Lipophosphoramidates. We thus sought a synthetic route to "dicationic lipophosphoramidates". For the "in single file" ones, since the phosphoramidate **1** is easily accessible by a Todd-Atherton reaction (*17*), a subsequent quaternarization by haloalkyl "onium" salts **2**, **3**, or **4** would lead directly to dicationic phosphoramidates **5**, **6**, or **7**, respectively. Bromopropyltrimetylammonium **2** is commercially available, whereas iodopropyltrimethylphosphonium **3** and arsonium **4** were synthesized by adapting a procedure described for bromopropyltrimethylphosphonium (*18*). Indeed, heating

Chart 3. Cell Toxicity of Monocationic 18 and Dicationic 5b, 6b, and 7b



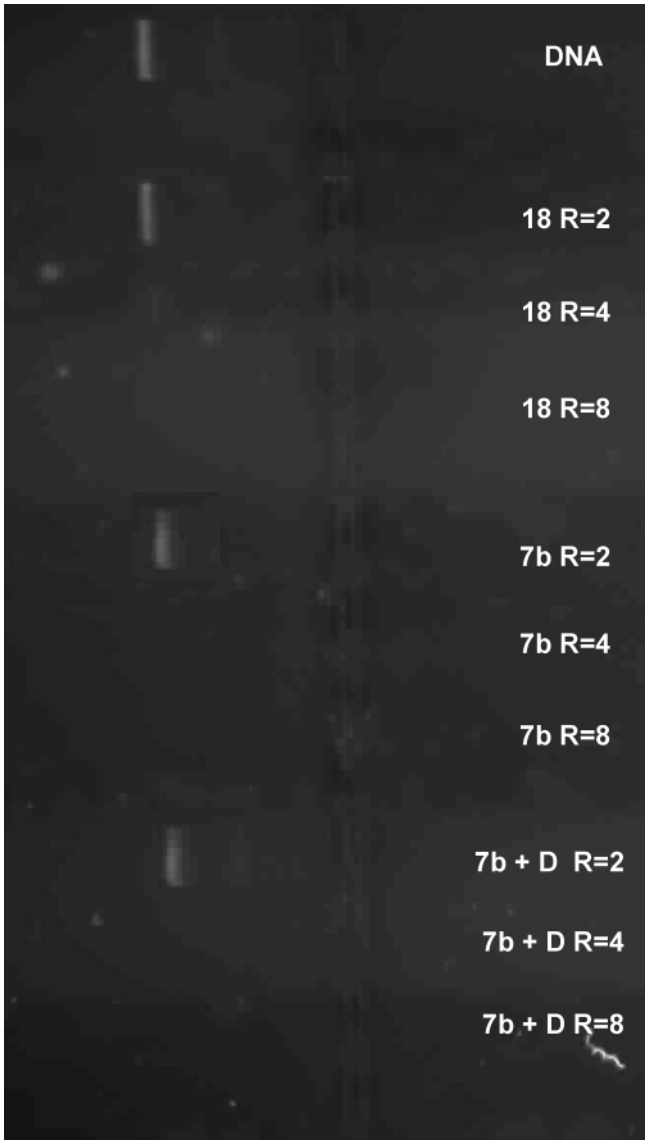


Figure 1. DNA binding ability of monocationic lipid **18** and dicationic **7b**.

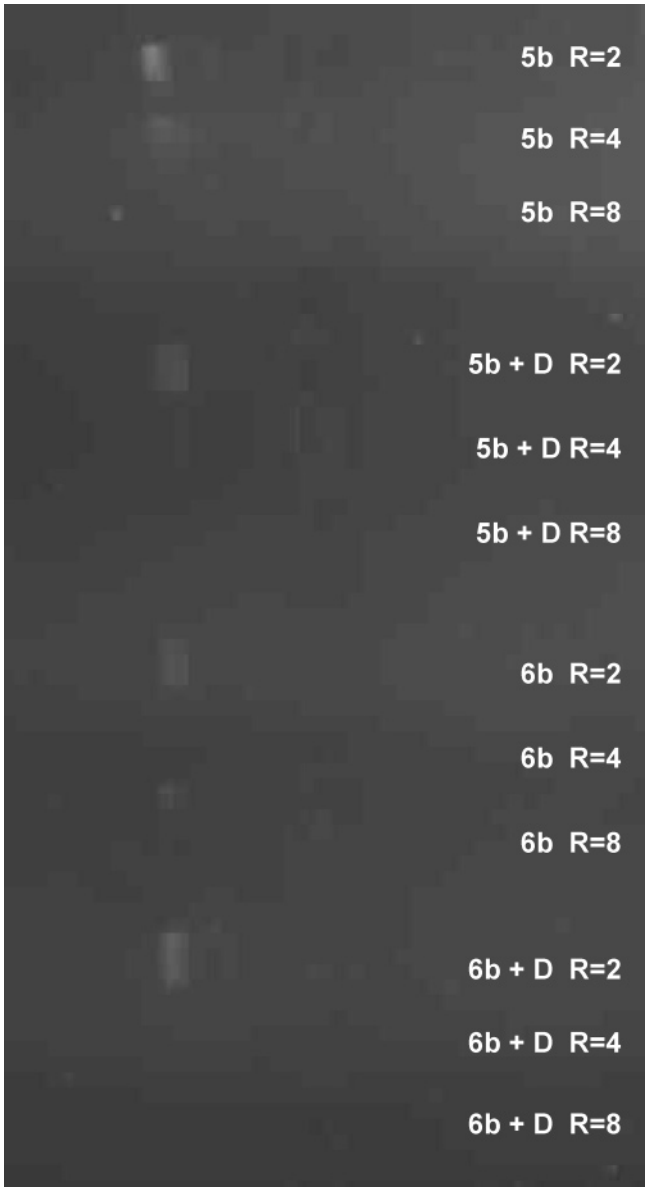


Figure 2. DNA binding ability of dicationic lipids **5b** and **6b**.

salts **2**, **3**, and **4** with an equivalent quantity of dimethylamino phosphoramidate **1** in acetonitrile at 70 °C for 3 days led to the wanted dicationic compounds **5**, **6**, and **7** in a 90−92% yield range (Scheme 1).

Then, we considered synthesizing imidazolium cations too, since some DNA carriers with such polar heads have been described (*19*). Propylimidazole phosphoramidate **10** was easily accessible from aminopropylimidazole **8** and fatty phosphite **9**. Quaternarization by the same onium salts **3** or **4** led to dicationic compounds **11** and **12** with excellent yields (90−95%) (Scheme 2).

A T-shaped dicationic phosphoramidate **15** was also synthesized from triamine **13** and fatty phosphite **9**, followed by a quaternarization of the resulting diamino compound **14** with methyl iodide (Scheme 3). However, its *in vitro* efficiency was lower than the corresponding "in single file" diammonium **5** (see below), and that way was not continued further.

In comparison with the already described (*6*) very efficient monocationic lipophosphoramidates **16**−**19** (Scheme 4), these dicationic compounds were then evaluated for their transfection efficiency, their cytotoxicity, and their DNA binding ability. Some physicochemical parameters (lipoplexes size, zeta potentials) were also established.

2. Transfection Efficiency and Cytotoxicity. Transfection efficiency (expressed as luciferase activity) of dicationic compouds was performed on two different cell lines (A549 and HeLa), in comparison with monocationic phosphoramidates **16**−**19**, according to routinely used and previously described procedures (*5*, *20*). Each lipid was tested at increasing ± charge ratios (*1*−*8*). Charts 1 and 2 show an example of the superiority of dicationic **6b** (ammonium/phosphonium) vs monocationic **17** (phosphonium) or **18** (arsonium).

Table 1 recapitulates the observed efficiencies for each dicationic lipid described above. As a general rule, dicationic lipids **5**, **6**, and **7** exhibit slightly greater values than the corresponding monocationic ones, at the same ± charge ratio, and are more efficient without DOPE added. On the other hand, dicationic lipids **11b** and **12b** with a central imidazolium core exhibit rather disappointing lower values. T-shaped diammonium **15** shows less efficiency than the corresponding "in single file" **5b**.

Insofar as at the same ± charge ratio dicationic lipids require half the material as the monocationic ones, a lower cytotoxicity was expected. To that effect, the toxicity of the different lipoplexes was determined by using a chemiluminescent assay (see the Experimental Procedures for details).

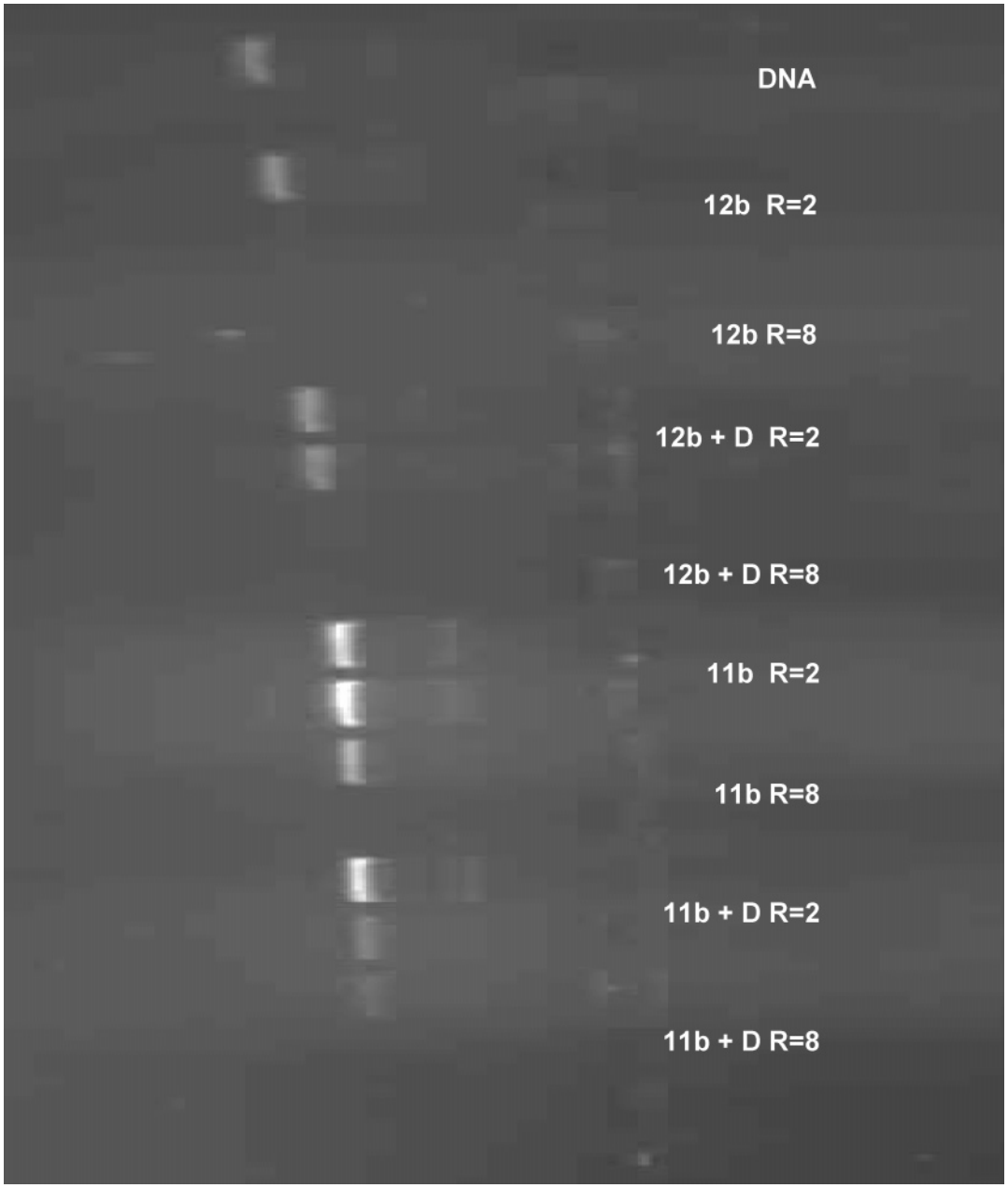


Figure 3. DNA binding ability of dicationic lipids **11b** and **12b**.

Chart 3 presents a comparison among dicationic lipids **5b**, **6b**, and **7b** and monocationic **18** (more RLUs are detected, more the cytoxicity increases correlated to the toxicity of the tested cationic lipid formulations). For each ± charge ratio (2, 4, or 8), the cytotoxicity of dicationic compounds is about one-third lower than that of **18**.

3. DNA Binding Ability. Electrophoretic mobility of plasmid DNA was examined with increasing N/P ratios (*2*−*8*) using 1% agarose gel (DNA was visualized by ethidium bromide staining). Complete binding of DNA was observed at an N/P ratio lower than 4 for phosphoramidates **5b**, **6b**, **7b**, and **18**, whereas binding was not complete at an N/P ratio of 4 for imidazolium compound **12b** or 8 for **11b** (Figures 1−3). This difference may explain the lower values quoted above.

4. Lipoplex Sizes and ζ Potentials. On the basis of purely electrostatic interactions, dicationic lipids were anticipated to be better DNA-condensing amphiphiles than their monocationic analogues. In other words, the hydrodynamic diameters for lipoplexes prepared from lipids **5**−**7** and **11**−**12** were expected to be smaller than those prepared from monocationic lipids.

Table 2. Sizes and ζ Potentials of Lipids and Their Lipoplexes (formulation without neutral co-lipid)

	size (μm)			ζ potential (mV)		
		lipoplex			lipoplex	
lipid no	lipid alone	$r = 4$	$r = 8$	lipid alone	$r = 4$	$r = 8$
5b	175	240	235	69	26	33
6b	176	268	249	80	19	46
7b	146	187	175	79	30	43
11b	100	328	344	90	20	24
12b	140	332	328	85	20	26
15	259	-	-	89	26	39
18	210	247	229	62	44	60

Table 2 recapitulates sizes and ζ potentials for lipids alone and their lipoplexes (at a ± charge ratio of 4 and 8) (see Experimental Procedures for details).

Indeed, average diameters of dicationic lipids are in the 100−175 range, compared to 210 for monocationic **18**, for lipids alone, but the lipoplex of **18** appears in the same range as dicationics. Changing lipid for lipoplex is accompanied by a 35−50 mV downshift of the ζ potentials for dicationic lipids,

whereas the same change keeps the values basically unchanged for **18**, at the same ± charge ratio. From these data, a correlation between size, ζ potentials, and transfection efficacies of lipoplexes is not obvious. The same conclusions were made by Chaudhuri et al., from a series of cationic amphiphiles containing mono-, di-, and trilysine headgroups (*21*).

CONCLUSION

The synthesis of permanently charged dicationic phosphoramidates was reported. The new vectors were readily obtained in good yield by using as a key reaction a Todd-Atherton coupling followed by a quaternarization step involving a halogeno-alkane ω-functionalized by either an ammonium, a phosphorinum, or an arsonium. The central cationic charge is either an ammonium or an imidazolium. Moreover, the synthesis of a T-shaped diammonium phosphoramidate was reported in high yield. These dicationic lipophosphoramidates are slightly more efficient than their monocationic analogues for *in vitro* gene delivery. The best vector for the transfection of the two cell lines studied (A549 and Hela) is compound **6b**, which is characterized, on the polar head, by the presence of a central ammonium and a terminal phosphonium. Furthermore, its cytotoxicity is about one-third lower than that of the monocationic vector **18**. In another work (*22*), we have examined the transfection efficacies of lipophosphoramidates bearing a spermine as the polar head. Biological evaluation was performed on the same cell lines as above and in the same experimental conditions. Spermine derivatives expressed luciferase levels one-half the values of permanently dicationic compounds described here. Since monocationic phosphoramidates exhibit interesting *in vivo* activity (*6*), their dicationic analogues are currently under investigation to this end.

ACKNOWLEDGMENT

"Brest Métropole Océane" is gratefully acknowledged for a grant to M.M. The authors thank also the "Conseil Régional de Bretagne" and "Vaincre La Mucoviscidose" for financial support and the CNRS for a postdoctoral grant to F.L.

LITERATURE CITED

(1) Felgner P. L., Gadek T. R., Holm M., Roman R., Chan H. W., Wenz M., Northrop J. P., Ringold G. M., and Danielsen M. (1987) Lipofection: a highly efficient, lipid-mediated DNA-transfection procedure. *Proc. Natl. Acad. Sci. U.S.A. 84*, 7413−7417.

(2) Miller, A .D. (1998) Cationic liposomes for gene therapy. *Angew. Chem., Int. Ed. 37*, 1768−1785.

(3) Martin, B., Sainlos, M., Aissaoui, A., Oudrhiri, N., Hauchecorne, M., Vigneron, J. P., Lehn, J. M., and Lehn, P. (2005) The design of cationic lipids for gene delivery. *Curr. Pharm. Des. 11*, 375−394.

(4) Guénin, E., Hervé, A. C., Floch, V., Loisel, S., Yaouanc, J. J., Clément, J. C., Férec, C., and Des Abbayes, H. (2000) Cationic phosphonolipids containing quaternary phosphonium and arsonium groups for DNA transfection with good efficiency and low cellular toxicity. *Angew. Chem., Int. Ed. 39*, 629−631.

(5) Floch, V., Loisel, S., Guénin, E., Hervé, A. C., Yaouanc, J. J., Clément, J. C., Férec, C., and Des Abbayes, H. (2000) Cation substitution in cationic phosphonolipids: A new concept to improve transfection activity and decrease cellular toxicity. *J. Med. Chem. 43*, 4617−4628.

(6) Picquet, E., Le Ny, K., Delépine, P., Montier, T., Yaouanc, J. J., Cartier, D., Des Abbayes, H., Férec, C. and Clément, J. C. (2005) Cationic lipophosphoramidates and lipophosphoguanidines are very efficient for in vivo DNA delivery. *Bioconjugate Chem. 16*, 1051−1053.

(7) Vigneron, J. P., Oudrhiri, N., Fauquet, M., Vergely, L., Bradley, J. C., Basseville, M., Lehn, P., and Lehn, J. M. (1996) Guanidinium-cholesterol cationic lipids: efficient vectors for the transfection of eukaryotic cells. *Proc. Natl. Acad. Sci. U.S.A. 93*, 9682−9686.

(8) Menger, F. M., and Keiper, J. S. (2000) Gemini surfactants. *Angew. Chem., Int. Ed. 39*, 1907−1920.

(9) Kirby, A. J., Camilleri, P., Engberts, J. B. F. N., Feiters, M. C., Nolte, R. J. M., Söderman, O., Bergsma, M., Bell, P. C., Fielden, M. L., Garcia Rodriguez, C. L., Guédat, P., Kremer, A., Mc Gregor, C., Perrin, C., Ronsin, G., and Van Eijk, M. C. P. (2003) Gemini surfactants: new synthetic vectors for gene tranfection. *Angew. Chem., Int. Ed. 42*, 1448−1457.

(10) Meekel, A. P., Wagenaar, A., Smisterova, J., Kroeze, J. E., Haadsma, P., Bosgraaf, B., Stuart, M. C. A., Brisson, A., Ruiters, M. H. J., Hoekstra, D. and Engberts, J. B. F. N. (2000) Synthesis of pyridinium amphiphiles used for transfection and some characteristics of amphiphile/DNA complex formation. *Eur. J. Org. Chem.* 665−673.

(11) Rosenzweig, H. S., Rakhmanova, V. A., and MacDonald, R. C. (2001) Diquaternary ammonium compounds as transfection reagents. *Bioconjugate Chem. 12*, 258−263.

(12) Gaucheron, J., Wong, T., Wong, K. F., Maurer, N., and Cullis, P. R. (2002) *Bioconjugate Chem. 13*, 671−675.

(13) Kasireddy, K., Ahmad, M. U., Ali, S. M. and Ahmad, I. (2004) Synthesis of novel cationic cardiolipin analogues for the optimal delivery of therapeutic agents. *Tetrahedron Lett.* 2743−2746.

(14) Bombelli, C., Faggioli, F., Luciani, P., Mancini, G., and Sacco, M. G. (2005) Efficient transfection of DNA by liposomes formulated with cationic gemini amphiphiles. *J. Med. Chem. 48*, 5378−5382.

(15) Paul, B., Bajaj, A., Indi, S. S., and Bhattacharya, S. (2006) Synthesis of novel dimeric cationic lipid based on an aromatic backbone between the hydrocarbon chains and headgroup. *Tetrahedron Lett. 47*, 8401−8405.

(16) Lee, E. R., Marshall, J., Siegel, C. S., Jiang, C., Yew, N. S., Nichols, M. R., Nietupski, J. B., Ziegler, R. J., Lane, M., Wang, K. X., Scheule, R. K., Harris, D. J., Smith, A. E., and Cheng, S. H. (1996) Detailed analysis of structure and formulations of cationic lipids for efficient gene transfer to the lung. *Human Gene Ther. 7*, 1701−1717.

(17) Atherton, F. R., Openshaw, H. T., and Todd, A. R. (1945) Studies on phosphorylation. Part II. The reaction of dialkyl phosphates with polyhalogen compounds in presence of bases. A new method for the phosphorylation of amines. *J. Chem. Soc.* 660.

(18) Schmidbaur, H. and Scherm, H. P. (1976) 1-Methyl-1-methylen-1λ^5-phosphorinan und cyclopropyl-(dimethyl)methylenphosphoran: Zwei verschiedene Ylid-typen aus einer analogreaktion und ihre Komplexbildung. *Chem. Ber.* 1576−1585.

(19) Solodin, I., Brown, C. S., Bruno, M. S., Chow, C-Y., Jang, E-H., Debs, R. J., and Heath, T. D. (1995) A novel series of amphiphilic imidazolium compounds for in vitro and in vivo gene delivery. *Biochemistry 34*, 13537−13544.

(20) Montier, T., Delépine, P., Le Ny, K., Fichou, Y., Le Bris, M., Hardy, E., Picquet, E., Clément, J. C., Yaouanc, J. J., and Férec, C. (2004) KLN-5: a safe monocationic lipophosphoramidate to transfect efficiently haematopoietic cell lines and human $CD34^+$ cells. *Biochim. Biophys. Acta 1665*, 118−133.

(21) Karmali, P. P., Kumar, V. V., and Chaudhuri, A. (2004) Design, syntheses and in vitro gene delivery efficacies of novel mono-, di- and trilysinated cationic lipids: a structure-activity investigation. *J. Med. Chem. 47*, 2123−2132.

(22) Lamarche, F., Mével, M., Montier, T., Burel-Deschamps, L., Giamarchi, P., Tripier, R., Delépine, P., Le Gall, T., Cartier, D., Lehn, P., and Clément, J. C. Lipophosphoramidates as lipidic part of lipospermines for gene delivery. *Bioconjugate Chem.*, in press.

BC070089Z

3-Amino-4-(2-((4-[^{18}F]fluorobenzyl)methylamino)methylphenylsulfanyl)benzonitrile, an F-18 Fluorobenzyl Analogue of DASB: Synthesis, *in Vitro* Binding, and *in Vivo* Biodistribution Studies

Sudha Garg, Shankar R. Thopate,§ Richard C. Minton, Kimberly W. Black, Andrew J. H. Lynch, and Pradeep K. Garg*

PET Center, Department of Radiological Sciences, Wake Forest University Medical Center, Winston Salem, North Carolina 27157. Received April 3, 2007; Revised Manuscript Received July 10, 2007

3-Amino-4-(2[^{11}C]methylaminomethylphenylsulfanyl)benzonitrile (C-11 DASB) exhibits excellent *in vitro* and *in vivo* properties toward the serotonin transporter. If labeled with a longer physical half-life radioisotope, this ligand could be more attractive to research groups lacking an on-site cyclotron or lacking C-11 synthesis capabilities. We produce *p*-[^{18}F]fluorobenzyl iodide on a routine basis to synthesize several neuroimaging agents. Therefore, it was straightforward for us to substitute the DASB precursor with this prosthetic group and assess its biological properties. We designed a different synthesis strategy to obtain the DASB precursor (desmethyl DASB). Herein we report an efficient and facile synthetic route that provides higher chemical yields of 3-amino-4-(2-aminomethylphenylsulfanyl)benzonitrile and related analogues. In addition, we report our results from incorporating *p*-[^{18}F]fluorobenzyl iodide in DASB precursor and its affect on the *in vitro* and *in vivo* biological properties of the DASB.

INTRODUCTION

The neurotransmitter serotonin (5-hydroxytryptamine, 5HT) plays an important role in the regulation of a variety of brain functions such as mood, appetite, sleep, behavioral traits, anxiety, depression, sexual disorders, and pain (*1*, *2*). The serotonin transporter (SERT) is located presynaptically on the cell bodies and terminals of the 5-HT neurons. The SERT are distributed throughout the brain in varying densities with the highest density in the raphe and thalamus. The main function of SERT is to regulate serotonin in the synaptic cleft via the reuptake mechanism. SERT transfers 5HT from the synapse into the nerve terminals, thus terminating the 5-HT signal. Diminished synaptic 5HT in turn leads to depression and related disorders. Chemicals that block SERT action have found utility in the treatment of depression, panic disorder, post-traumatic stress disorder, and obsessive compulsive disorder (*3*−*5*). Therefore, accurate quantification of SERT density is critical in understanding the role of SERT on serotonin neurotransmission.

Noninvasive *in vivo* imaging of the SERT with positron emission tomography (PET) would provide accurate quantitative information. PET imaging has been quite effective in assessing drug occupancy on SERT and dopamine transporter (DAT) to evaluate efficacy of novel drugs in humans using specific ligands (*6*, *7*). (+)-[^{11}C]McN5652 was the first PET probe to interrogate SERT in humans (*8*). A variety of psychiatric disorders including mood disorder, alcoholism, and patients with drug abuse problems were studied using this probe (*9*, *10*). Unfortunately, slow kinetics of this tracer in the brain (*11*) limited its utility. Therefore, developing another generation of more effective SERT probes became the goal of various laboratories. To achieve that goal, several PET ligands were developed over the past decade (*12*, *13*). An F-18 analogue of McN5652 (FMe-McN5652) was also developed showing higher target to nontarget tissue ratio and faster tracer kinetics than the parent (+)-[^{11}C]McN5652 (*14*, *15*). Unfortunately, quantification capabilities using FMe-McN5652 and other biological factors limited the utility of this ligand (*14*). To obtain a probe with higher affinity and potency, several investigators explored another series of compounds incorporating a diaryl sulfide motif (*12*, *16*, *17*). One of the lead compounds from this series, 3-amino-4-(2-[^{11}C]methylaminomethylphenylsulfanyl)benzonitrile (C-11 DASB) showed a higher signal-to-noise ratio and faster brain uptake kinetics than (+)-[^{11}C]McN5652. C-11 DASB was further assessed for its imaging characteristics and found to be a preferred ligand to study SERT (*18*, *19*).

Despite excellent specificity and sensitivity of C-11 DASB to SERT, the short half-life of C-11 (20 min) remains an obstacle for many PET groups to utilize this ligand who lack an on-site cyclotron facility. Introducing an F-18 isotope with a longer half-life ($t_{1/2}$ 110 min) while maintaining the DASB template would facilitate its use for longer scanning sessions and more importantly at remote centers without an on-site cyclotron facility. Although previous attempts to incorporate F-18 in a DASB motif were somewhat successful (*13*), the results were less than convincing to replace C-11 DASB with the newly developed ligands. This kept the search for an effective F-18-labeled DASB analogue open. In our laboratories, we routinely synthesize [^{18}F]fluorobenzyl iodide to synthesize various ligands for neuroimaging applications (*20*−*22*). It was important for us to assess the feasibility of incorporating the [^{18}F]fluorobenzyl iodide in DASB precursor and study its affect on *in vitro* and *in vivo* characteristics. Toward that goal, we designed an F-18-labeled analogue by replacing one of the *N*-methyl groups with a *p*-fluorobenzyl group. During the synthesis of the DASB precursor, 3-amino-4-(2-aminomethylphenylsulfanyl)benzonitrile, we also developed a more efficient and facile synthesis to prepare the intermediate 3-amino-4-(2-aminomethylphenylsulfanyl)benzonitrile and related compounds in higher yields. In addition, we report the synthesis of 3-amino-4-(2-[(4-fluoroben-

* Author to whom correspondence should be addressed. Tel: 336-716-5624; fax: 336-716-5639; e-mail: pgarg@wfubmc.edu.

§ Current address: Dr. Shankar R. Thopate, Department of Chemistry, 102 Vasant Vihar; Balikashram Road, Ahmednagar 414 001; Maharashtra, India.

10.1021/bc070112g CCC: $37.00 © 2007 American Chemical Society
Published on Web 08/18/2007

zyl)methylamino]methylphenylsulfanyl)benzonitrile (FBASB), its *in vitro* binding, and *in vivo* biodistribution studies in normal rats and mice.

EXPERIMENTAL PROCEDURES

All reactions were carried out under an inert atmosphere with dry solvents, under anhydrous conditions, unless otherwise stated. Reagents and solvents were purchased from commercial suppliers and were used without further purification. Melting points were determined on an Electrothermal "MEL-TEMP" melting point apparatus and are uncorrected. Flash column chromatography was carried out over silica gel (60 Å, Mallinckrodt, Baker). ^{1}H NMR data was acquired on a Bruker Advance 300 DPX spectrometer. All chemical shift values are reported in ppm (δ). Elemental analyses (C, H, N) were determined by Atlantic Microlab, Inc., and the analytical results were within $\pm$0.4% of the theoretical values for the formula given.

Radioactivity levels in tissues were assessed with a Packard Cobra γ-counter. High-pressure liquid chromatography (HPLC) was performed in isocratic mode with a Varian 9010 LC pump, a variable wavelength 9050UV VIS detector (*23*) (Varian Corp, Palo Alto, CA) set at 254 λ, and a radioisotope detector (Bioscan Inc, Washington, D.C.) attached to Varian's chromatography software package (Varian Corp, Palo Alto, CA). The HPLC system used for purification of ^{18}F-labeled FBASB was a C-18 reverse-phase ODS, 10 $\times$ 250 mm 5μ column (Phenomenex, Torrence, CA) eluted with MeOH: 0.1 M ammonium formate (80:20) at 5 mL/min. The desired peak was eluted at 16 min using this system. Quality control of purified product was performed using a Varian HPLC system and a microsorb reverse phase C-18 column 250 $\times$ 4.6 mm eluted with MeOH:0.1 M ammonium formate (80:20) at 1 mL/min and was eluted at 14 min.

Preparation of 4-(2-Hydroxymethylphenylsulfanyl)-3-nitrobenzonitrile (1). A mixture of 2-mercaptobenzyl alcohol (2.00 g, 14.28 mmol), 4-chloro-3-nitrobenzonitrile (3.12 g, 17.13 mmol), K_2CO_3 (3.13 g, 22.64 mmol), and copper powder (0.272 g, 4.28 mmol) was added to DMF (20 mL), and the reaction mixture was stirred under argon for 1 h. Afterward, the reaction mixture was diluted with water (50 mL), and the desired compound was extracted in ethyl acetate (3 $\times$ 50 mL). The combined extracts were washed with water (2 $\times$ 50 mL) and dried (Na_2SO_4), and the solvent was removed using a rotary evaporator. A yellow foamy residue thus obtained was purified by flash chromatography using a silica gel column and eluting it with dichloromethane. The yellow solid powder was recrystallized from CH_2Cl_2/hexane to furnish the desired compound **1** as a yellow solid (3.52 g, 86%): mp 126−130 °C, lit. (*23*). 120−126 °C, ^{1}H NMR (300 MHz, $CDCl_3$) δ 8.54 (d, J = 1.8 Hz, 1H, Ar-*H*), 7.74 (dd, J = 0.9, 7.8 Hz, 1H, Ar-*H*), 7.64 (dt, J = 1.5, 7.5 Hz, 1H, Ar-*H*), 7.57 (dd, J = 1.2, 7.8 Hz, 1H, Ar-*H*), 7.51 (dd, J = 1.8, 8.4 Hz, 1H, Ar-*H*), 7.47 (dt, J = 1.5 and 7.5, Hz, 1H, Ar-*H*), 6.81 (d, J = 8.4 Hz, 1H, Ar-*H*), 4.76 (d, J = 5.7 Hz, 2H, C*H*$_2$OH), 1.95 (t, J = 5.7 Hz, 1H, CH$_2$O*H*).

Preparation of 3-Amino-4-(2-hydroxymethylphenylsulfanyl)benzonitrile (2). Compound **1** (4.10 g, 14.33 mmol) was dissolved in methanol (40 mL), and 12 N HCl (30 mL) was added. The suspension was cooled to 0 °C, and $SnCl_2$ (10.351 g, 45.87 mmol) was added. The reaction mixture was stirred overnight at room temperature. The mixture was diluted with H_2O (50 mL), and the compound was extracted in ethyl acetate (3 $\times$ 50 mL). The combined organic layers were washed with a saturated aqueous solution of $NaHCO_3$ (2 $\times$ 10 mL), followed by water (2 $\times$ 20 mL), dried, and concentrated. The yellow solid was purified using flash column chromatography and eluting with ethyl acetate/hexanes (1:2). Further recrystallization of this product in CH_2Cl_2/hexane yielded the desired compound **2** as a yellow solid (3.11 g, 85%): mp 122−125 °C, lit. (*23*) mp 121−124 °C; ^{1}H NMR (300 MHz, $CDCl_3$) δ 7.47 (dd, J = 1.5, 7.2 Hz, 1H, Ar-*H*), 7.18−7.31 (m, 3H, Ar-*H*), 7.03 (dd, J = 1.2, 7.5 Hz, 1H, Ar-*H*), 6.92−6.96 (m, 2H, Ar-*H*), 4.82 (d, J = 6.0 Hz, 2H, C*H*$_2$OH), 4.44 (bs, 2H, Ar-N*H*$_2$), 2.06 (t, J = 6.0 Hz, 1H, CH$_2$O*H*).

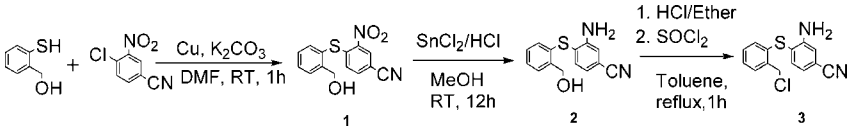
Preparation of 3-Amino-4-(2-chloromethylphenylsulfanyl)benzonitrile (3). To a solution of **2** (2.00 g, 7.81 mmol) in diethyl ether (5 mL + few drops of MeOH) was added a solution of HCl in diethyl ether (5 mL, 2.0 N). After 10 min, the ether was evaporated, and toluene (20 mL) was added followed by a slow addition of thionyl chloride (1.71 mL). After refluxing for 1 h (clear solution) under argon atmosphere, the reaction mixture was cooled to room temperature. The compound was extracted in ethyl acetate (20 mL), the organic layer was washed with a saturated solution of $NaHCO_3$ (5 mL) and dried over Na_2SO_4. The solvent was removed under vacuum to give solid material **3** in 93% yields. This crude product was used for the next reaction without further purification.

Preparation of 3-Amino-4-(2-isoindole-1,3-dionemethylphenylsulfanyl)benzonitrile (4). A mixture of **3** (0.50 g. 1.82 mmol) and potassium phtalimide (0.675 g, 3.64 mmol) in DMF (20 mL) was heated at 100 °C for 1 h. The reaction mixture was cooled to room temperature, and water (20 mL) was added. The product was extracted in ethyl acetate (3 $\times$ 25 mL), and the combined organic layer was dried over Na_2SO_4. After removing the solvent, the yellow solid residue was recrystallized from ethyl acetate/hexanes to yield **4** in 76% yield as a yellowish crystalline solid. Mp 180−183 °C, ^{1}H NMR (300 MHz, $CDCl_3$) δ 7.85−7.89 (m, 2H, Phth-*H*), 7.73−7.78 (m, 2H, Phth-*H*), 7.32 (m, 1H, Ar-*H*), 7.26 (m, 1H, Ar-*H*), 7.15−7.24 (m, 3H, Ar-*H*), 7.08 (dd, J = 1.8, 7.8 Hz, 1H, Ar-*H*), 6.9 (m, 1H, Ar-*H*), 5.06 (s, 2H, C*H*$_2$N), 4.55 (bs, 2H, Ar-N*H*$_2$). Anal. ($C_{22}H_{15}N_3O_2S$) C, H, N.

Preparation of 3-Amino-4-(2-aminomethylphenylsulfanyl)benzonitrile (5). A solution of **4** (0.350 g, 0.909 mmol) and hydrazine (0.062 mL, 1.99 mmol) in anhydrous ethanol (15.00 mL) was refluxed for 2 h under argon atmosphere. The reaction mixture was cooled to room temperature, and volatiles were removed using a rotary evaporator. The white residue thus obtained was dissolved in 40% aq KOH (50 mL) and extracted in ether (3 $\times$ 25 mL), and the combined organic layer was dried over Na_2SO_4. After removal of the solvents, the oily residue was purified with flash column chromatography using acetone/ethyl acetate (1:9) as the solvent to give a thick yellow syrup in 98% yields. Treatment with HCl in ether yielded the desired compound **5** as a white crystalline material. mp 133−137 °C, ^{1}H NMR (300 MHz, DMSO) δ 13.40 (bs, 1H, N*H*), 8.60 (bs, 1H, N*H*), 7.50−7.60 (m, 1H, Ar-*H*), 7.30−7.38 (m, 2H, Ar-*H*), 7.20−7.25 (m, 1H, Ar-*H*), 7.13 (d, J = 1.5 Hz, 1H, Ar-*H*), 6.93−7.02 (m, 2H, Ar-*H*), 4.98 (s, 2H, C*H*$_2$NH$_2$). Anal. ($C_{14}H_{13}N_3S\cdot HCl\cdot 0.5H_2O$) C, H, N.

Preparation of 3-Amino-4-(2-(4-fluorobenzyl)aminomethylphenylsulfanyl)benzonitrile (6). To a solution of **3** (0.800 g, 2.91 mmol) in acetonitrile (10 mL) were added 4-fluorobenzylamine (0.667 mL, 5.83 mmol) and triethylamine (1.22 mL, 8.75 mmol). After refluxing for 1 h, the reaction mixture was cooled to room temperature and the solvent was removed under vacuum. The oily residue was further purified using flash column chromatography on silica gel and eluting with ethyl acetate/hexane (1:4). The compound thus obtained was further recrystallized from CH_2Cl_2/hexanes to yield **6** as a white fluffy solid in 90% yield. mp 98−99 °C, ^{1}H NMR (300 MHz, $CDCl_3$). δ 7.12−7.36 (m, 6H, Ar-*H*), 6.98−7.04 (m, 3H, Ar-*H*), 6.92−6.95 (m, 2H, Ar-*H*), 4.59 (bs, 2H, Ar-N*H*$_2$), 3.92 (s, 2H, benzylic *CH*$_2$), 3.81 (s, 2H, benzylic *CH*$_2$), 1.60 (bs, 1H, N*H*). Anal. ($C_{21}H_{18}FN_3S$) C, H, N.

Scheme 1. Synthesis of Substituted Benzyl Chloride 3, a Key Intermediate in the Preparation of Various Substituted Benzyl Amines



Preparation of 3-Amino-4-(2-methylaminomethylphenylsulfanyl)benzonitrile (8). To a solution of **3** (0.400 g, 1.45 mmol) in acetonitrile (5 mL) was added 40% aqueous methylamine (1.132 mL, 14.59 mmol), followed by triethylamine (0.610 mL, 4.37 mmol). After the reaction mixture was refluxed for 1 h, it was cooled to room temperature and the solvent was removed. The residue was dissolved in ethyl acetate (20 mL), and the organic layer was washed with water (3 × 5 mL) and dried over Na_2SO_4. The solvent was removed *in vacuo*, and the oily residue was further purified using flash column chromatography and eluting with acetone as a thick viscous oil. Recrystallation of this oily residue using CH_2Cl_2/hexanes yielded **8** as a white crystalline compound in 72% yields. mp 93−96 °C, ^{1}H NMR (300 MHz, $CDCl_3$) δ 7.32−7.37 (m, 2H, Ar-*H*), 7.21−7.27 (m, 1H, Ar-*H*), 7.12−7.19 (m, 1H, Ar-*H*), 7.00 (dd, J = 1.5, 7.8 Hz, 1H, Ar-*H*), 6.91−6.94 (m, 2H, Ar-*H*), 4.73 (bs, 2H, Ar-N*H*$_2$), 3.89 (s, 2H, C*H*$_2$NHMe), 2.47 (s, 3H, CH$_2$-NH*Me*), 1.53 (bs, 1H, CH$_2$N*H*Me). Anal. ($C_{15}H_{15}N_3S$) C, H, N.

Preparation of 3-Amino-4-(2-(4-fluorobenzyl)methylaminomethylphenylsulfanyl)benzonitrile FBASB (9). To a solution of **8** (0.025 g, 0.092 mmol) and DBU (0.042 mL, 0.278 mmol) in dry acetonitrile (2 mL) was added 4-fluorobenzyl bromide (0.014 mL, 0.111 mmol). The reaction mixture was stirred at room temperature for 12 h under argon. The solvent was removed, and the oily residue was purified using column chromatography and eluting with ethyl acetate/hexane (1:6) to yield colorless oil in 72% yields. Compound **9** was obtained as an HCl salt by treating the oily residue with HCl in ether. Mp 166−170 °C, ^{1}H NMR (300 MHz, $CDCl_3$) δ 7.44 (d, J = 7.8 Hz, 1H, Ar-*H*), 7.30−7.35 (m, 3H, Ar-*H*), 7.12−7.18 (m, 2H, Ar-*H*), 6.92−7.02 (m, 5H, Ar-*H*), 4.61 (bs, 2H, Ar-N*H*$_2$), 3.67 (s, 2H, benzylic *CH*$_2$), 3.56 (s, 2H, benzylic *CH*$_2$), 2.10 (s, 3H, NC*H*$_3$). Anal. for HCl salt. ($C_{22}H_{20}FN_3S\cdot HCl\cdot H_2O$) C, H, N.

Radiochemical Synthesis of [^{18}F]FBASB. The F-18 FBASB was obtained via N-alkylation of 3-amino-4-(2-methylaminomethylphenylsulfanyl)benzonitrile (**8**) using [^{18}F]fluorobenzyl iodide ([^{18}F]FBI) as the intermediate. The alkylating group [^{18}F]-FBI was prepared as previously described (*24*). Briefly, [^{18}F]-FBI was reacted with 3-amino-4-(2-methylaminomethylphenylsulfanyl)benzonitrile in DMF and triethylamine at 106 °C for 10 min followed by HPLC purification using a C-18 column eluted with MeOH: 0.1 M ammonium formate (80:20) to yield the desired product in 36 ± 8% radiochemical yields (EOS) and >99% radiochemical purity. The specific activity of FBASB was 4900 ± 1100 Ci/mmol (n = 7).

***In Vitro* Binding.** Affinity of FBASB to 5-HT transporter sites was determined using cortical membranes from rat brains as described (*25*). The binding affinity was determined from binding of 0.4 nM [^{3}H]paroxetine with 50 mg of the rat cortical membrane. The nonspecific binding was determined from binding of 10 μM fluoxetine to the membrane. Potencies were calculated from displacement curves using 7−10 concentrations of unlabeled compound. The K_i values were calculated using the Cheng−Prusoff (*26*).

Biodistribution Studies. *In vivo* biodistribution of [^{18}F]-FBASB was performed in normal rats and mice. A group of animals was injected with 20 μCi of [^{18}F]FBASB each via a tail vein injection. At 30, 60, and 120 min postinjection, groups of five animals were killed and the tissue of interest excised, weighed, and counted for radioactivity on a gamma counter. Radioactivity uptake in various tissues was calculated as a percent-injected dose per gram of tissue (%ID/g tissue) by counting the dose standard of appropriate count rate along with the tissues.

RESULTS AND DISCUSSION

In order to synthesize the desired compound **9**, we prepared several intermediate compounds. Another compound of interest for us was compound **3** since this would provide a convenient route to place a variety of radiolabeled prosthetic groups. Compound **4** would provide a convenient single step route to synthesize a wide array of substituted amines. In addition, compound **8** (3-amino-4-(2-methylaminomethylphenylsulfanyl)-benzonitrile) was also of special interest since this compound is widely used as a precursor to serotonin transporter ligand DASB and is commonly known as MASB.

Our first goal was to obtain compound **3**. This would be a common intermediate to obtain several compounds of our interest. The synthetic strategy is shown in Scheme 1. To accomplish this, we started our synthesis with commercially available 2-thiobenzyl alcohol. Copper-catalyzed coupling of thiobenzyl alcohol with 4-chloro-3-nitrobenzonitrile using K_2CO_3 as a base and DMF as a reaction solvent provided product **1** in 86% yields (Scheme 1).

The next step was to reduce the nitro group on the benzonitrile ring (Figure 1, ring B) to the corresponding amine. Wilson et al. reported such reduction by heating a corresponding nitro compound with hydrazine hydrate and ferric chloride in ethanol for 3 days to obtain the desired compound in 49% yield (*23*). In an effort to improve chemical yields and to reduce the overall reaction time, we explored various other reduction methods. We found that a reduction of nitro compound **1** by using tin(II) chloride in HCl and stirring the reaction mixture at room temperature overnight was a simple, fast, and high yielding

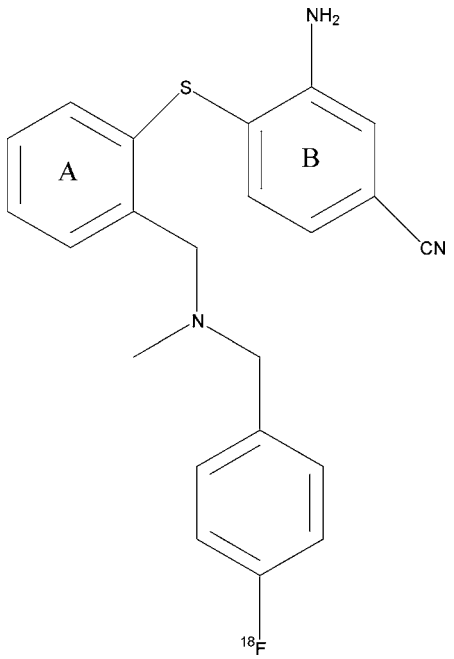
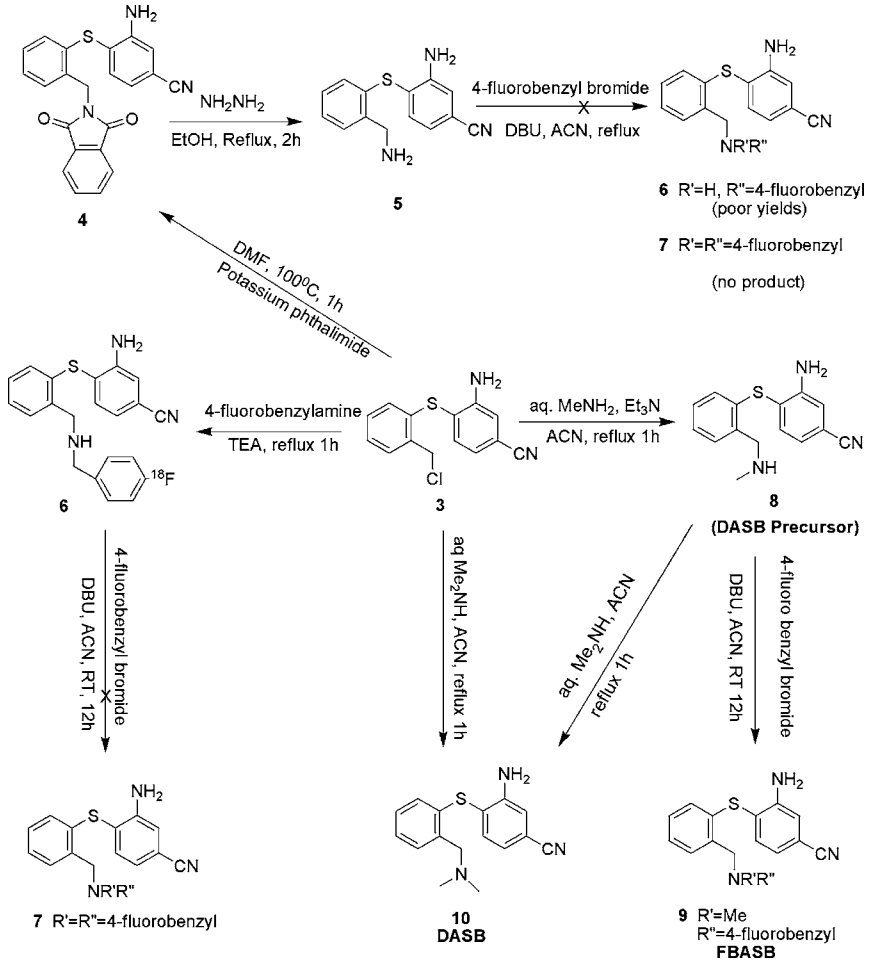


Figure 1. Structure of FBASB. The designation of rings A and B represent the assignments referred to in the discussion section.

Scheme 2. Synthesis of FBASB, DASB, and Precursor of DASB[a]



[a] This scheme depicts an improved synthesis of precursor to DASB, and FBASB. this scheme highlights the significance of compound **3** as a key intermediate in the synthesis of various dialkylamines. It also shows the utility of compounds **6** and **8** as important intermediates to synthesize a variety of substituted amines.

procedure. Using this procedure, followed by a routine workup of the reaction mixture, we obtained the desired compound **2** in 85% yields. Others have also successfully used tin chloride for facile reduction of the nitro groups while use of hydrazine hydrate resulted in incomplete reduction of nitro compound (*27*). Benzyl alcohol **2** was refluxed with thionyl chloride in toluene to provide corresponding benzyl chloride **3** in 93% yields. Our next goal was to synthesize compound **5** with a methylamine group at 2-position on the phenyl ring A.

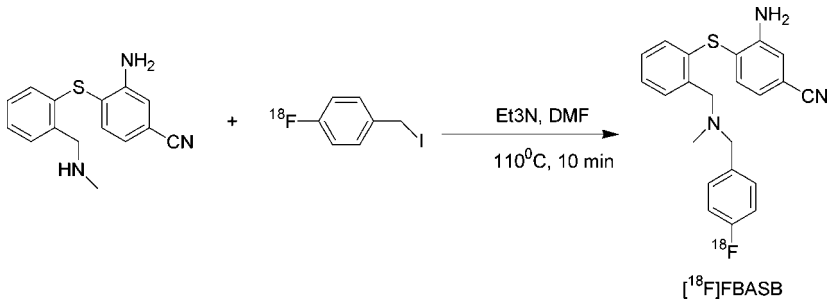
A previously reported method (*28*) used coupling of thiosalicylic acid with chlorobenzenes followed by reaction with thionyl chloride to produce acid chloride. Subsequent reaction with ammonia yielded the corresponding amide. Reduction of this amide with BH_3/THF complex delivered the desired benzylamine (*28*). To simplify and improve the reaction conditions and overall scheme, we adopted a different synthetic route. We explored conversion of benzyl chloride to a thalimide intermediate. As shown in Scheme 2, heating benzyl chloride **3** with potassium thalimide at 100 °C in DMF for 1 h gave 76% of thalimide **4** which on refluxing with hydrazine in ethanol for 2 h produced the target compound **5** in 98% yield. For our synthetic scheme, we found the use of thalimide as a free amine synthon to be a rapid, efficient, and high yielding intermediate. Reacting **3** with substituted amines yielded a wide selection of analogues of **5** viz. compounds **6, 8, 9, 10**.

Reaction of compound **5** in acetonitrile with excess *p*-fluorobenzyl bromide and DBU as a base did not yield the expected *N*,*N*-bis(4-fluorobenzyl)amino compound **7**. Instead, a small amount of compound **6** (a monobenzylated derivative) was detected with the majority of the recovered compound as the starting material. Thereafter, we decided to synthesize compound **6** and **7** in a step by step manner using an alternate strategy as depicted in Scheme 2.

Reaction of the benzyl chloride **3** with *p*-fluorobenzyl amine in refluxing acetonitrile using Et_3N as the base provided compound **6** in 90% yields (Scheme 2). Our subsequent efforts to react compound **6** with *p*-fluorobenzyl bromide and DBU or Et_3N as a base in acetonitrile failed to yield compound **7** (Scheme 2). One possible explanation for this failed reaction could be the presence of bulky functionality (i.e. *p*-fluorobenzyl group on benzylic nitrogen) causing steric hindrance that in turn hampered the second *p*-fluorobenzyl group substitution. The other factor responsible for these failed attempts could be due to a highly electronegative fluorine atom (Pauling scale of electronegativity: $F = 4.0$, $H = 2.1$) rendering benzylic nitrogen less basic through negative inductive effect, this in turn preventing benzylation. These factors may have been also responsible for our previous failed attempts in synthesizing compound **7** from compound **5** (Scheme 2), where only a small quantity of compound **6** was obtained instead.

Refluxing compound **3** with 40% aqueous methylamine in acetonitrile for 1 h produced compound **8** in 74% yields. Compound **8** is an important compound since this is used as a precursor to synthesize C-11-labeled DASB. Wilson et al. (*23*) reported synthesizing compound **8** by directly reacting the corresponding benzyl alcohol (compound **2**, Scheme 2) first with thionyl chloride to generate **3** in situ and then reacting it with 40% aqueous methylamine for 24 h at room temperature. The

Scheme 3. Radiochemical Synthesis of [^{18}F]FBASB Using [^{18}F]FBI as a Synthon



yields for the desired product remained modest (37%). We preferred isolating compound **3** and purifying this product before its subsequent reaction with methyl amine. Using this approach, we obtained **8** in higher purity and yields. Despite isolating and purifying benzyl chloride **3** followed by reaction with methylamine, our method remains a convenient and high yielding procedure to synthesize compound **8** (precursor for DASB). Following this procedure, it is simple to perform a large-scale synthesis of DASB precursor.

Compound **9** was obtained in 72% yield by reacting compound **8** with *p*-fluorobenzyl bromide using DBU as a base. Reacting **3** or **8** with aqueous dimethylamine and refluxing in acetonitrile provided compound **10**. Using this strategy, we were able to synthesize compounds **6**, **8**, **9**, and **10** in high overall yields. In addition, we synthesized compound **4** that serves as a useful intermediate to synthesize various substituted amines.

In vitro binding of FBASB, i.e., **9**, to SERT as assessed by rat membrane homogenate was 0.51 ± 0.11 μM. Although the *in vitro* binding of FBASB was significantly lower than that for the DASB (*19*), the *in vitro* binding for the desmethyl analogue of FBASB, i.e., compound **6** was 4.04 ± 0.95 nM, a value several fold higher than the N-methylated analogue **9**. Similarly, binding for the unsubstituted benzylamine **5** was 0.070 ± 0.015 μM, a 7-fold higher binding affinity toward SERT than the substituted analogue **9**. These *in vitro* results further echo earlier findings on compounds with a tropane template that the N-substitution reduces 5HT potency and a reduced 5HT affinity for methylated analogues of compounds with similar motif as ours (*25*). Although demethylation of compound **9** lead to reduced affinity toward SERT, we did not screen this compound against other receptors and transporters.

Radiochemical synthesis of [^{18}F]FBASB was accomplished as shown in Scheme 3. Reaction of [^{18}F]FBI with compound **8** provided [^{18}F]FBASB in 36 ± 8% radiochemical yield (EOS). These radiochemical yields are comparable to other radiotracers routinely synthesized in our laboratory using the [^{18}F]FBI synthon. After HPLC purification, the radiochemical purity of this product was >99%. The total synthesis time to produce [^{18}F]FBASB was ~140 ± 20 min including the reformulation and quality control assays on the final product. The entire synthesis was a remote operated process and required minimal intervention from the production staff.

In our earlier attempts to modify chemical structure of a routinely used dopamine transporter ligand FCT by replacing the chloro group on the phenyl ring with alkyl, despite a high *in vitro* binding affinity of the newer analogue, we observed a complete blockade of brain penetration (*29*). Therefore, for the current study, our interest was to first ascertain if this compound penetrates into the rat brain. The results from the biodistribution studies show 0.34 ± 0.02% of the injected dose in rat brain at 30 min. In comparison, [^{11}C]DASB uptake was 0.89 ± 0.39% and 0.33 ± 0.07% injected dose per gram of brain at 30 and 60 min, respectively (*30*). These results swayed us to investigate if there is any preferential distribution of this ligand between target and nontarget sites within the brain. In addition, we wanted to investigate if this compound exhibits resistance to *in vivo* dehalogenation. Therefore, we performed biodistribution studies in mice to ascertain F-18 distribution in the whole body as well as differential distribution in various brain tissues. The results from these *in vivo* biodistribution studies are shown in Figure 2.

Although the radioactivity accumulation in all organs remained low, the major sites of retention of F-18 at 60 and 120 min were the kidneys, liver, and muscles. Each of these organs showed less than 0.9% of the injected dose per gram of tissue. The F-18 uptake in the next highest uptake organ was the lung with 0.37 ± 0.09% and 0.23 ± 0.08% injected dose per gram of tissue at 60 and 120 min, respectively. F-18 uptake in the muscles was 0.32 ± 0.09% ID/g at 120 min, and muscle remained the tissue with the third highest uptake of radioactivity, perhaps from increased lipophilicity of FBASB due to the fluorobenzyl group in the molecule. Similar to that seen from our rat studies, [^{18}F]FBASB showed resistance to *in vivo* dehalogenation in mice. At 120 min, the F-18 uptake in the bones was 0.14 ± 0.07 %ID/g.

Further studies were performed to assess a differential distribution pattern of F-18 within brain tissues. In these studies, cerebellum was chosen as tissue with nonspecific binding (*30*). As seen from F-18 uptake data, the radioactivity distribution remained quite homogeneous throughout the brain with slightly higher uptake in the thalamus when compared to that for the cerebellum. For example, at 60 min the F-18 uptake in the rat cerebellum was 0.16 ± 0.03 %ID/g as compared to 0.21 ± 0.08, %ID/g in the hypothalamus.

Specific to nonspecific ratio in the mouse brain at 60 min time points is shown in Figure 3. Although, at 60 min, the specific to nonspecific uptake ratio remained higher than 1 for most SERT rich tissue, the amplitude of this ratio was significantly lower than DASB and other related SERT specific compounds. While all tissues show specific to nonspecific ratios better than 1 at 60 min, cerebellum to tissue ratio for the cortex, thalamus, and hypothalamus improved slightly with time.

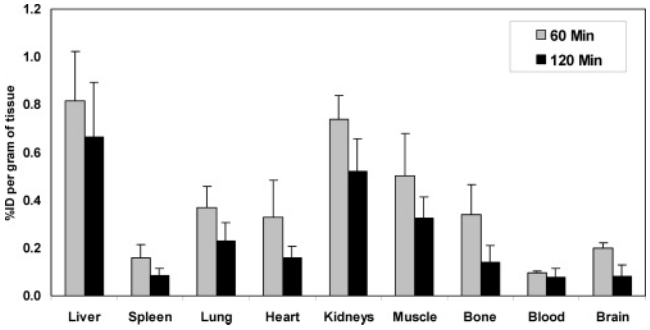


Figure 2. Tissue distribution of F-18 in mice at 60 and 120 min after injecting F-18 FBASB via the tail vein injection. An overall low radioactivity in all normal tissue and further reduction in accumulation at a 2 h time point supports rapid clearance of radiotracer from the body. Low bone uptake at 1 and 2 h further supports its resistance to dehalogenation.

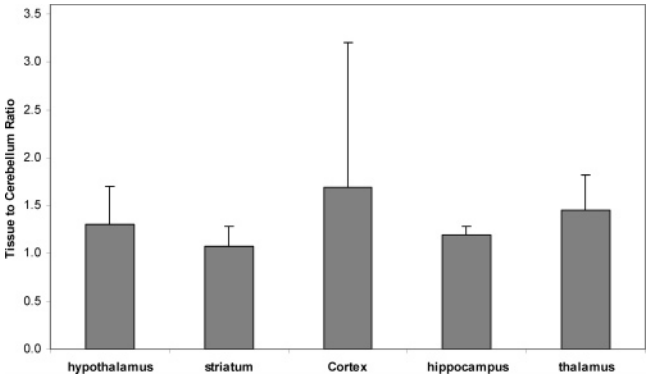


Figure 3. Tissue to cerebellum ratio for the F-18 FBASB at 60 min as derived from F-18 uptake in the mouse brain.

Despite slightly better ratios in SERT specific tissues, the properties of this ligand remained marginal for the imaging application. Nonetheless, *in vivo* results are in agreement with *in vitro* binding affinity results toward the SERT. Owing to its higher *in vitro* affinity, the desmethyl analogue **8** may exhibit better biodistribution properties and selectivity toward SERT than that seen with the [^{18}F]FBASB. It is also likely that the substitution of less bulky prosthetic groups, such as fluoromethyl or fluoroethyl would yield a more promising SERT ligand.

In summary, we synthesized an F-18 analogue of DASB using a simple and facile radiochemical synthesis procedure. Low binding affinity of this compound resulted in low brain uptake along with low selectivity toward SERT rich tissues, resulting in a poor specific to nonspecific uptake ratio.

In conclusion, we herein describe a rapid and high yielding synthesis to prepare a key intermediate precursor necessary to synthesize [^{11}C]DASB. In addition, this paper describes a facile and high yielding synthesis of another key intermediate that could aid in the synthesis of a wide array of compounds with application in PET and SPECT.

ACKNOWLEDGMENT

We thank Jessica Stukes for her assistance with tissue biodistribution studies and the cyclotron staff for providing help with obtaining F-18 radioisotope. We are thankful to Drs. Steve Childers and Li Wu for their help with performing the *in vitro* binding assay. This research was supported in part through a grant from National Institutes of Health (CA105382 to P.K.G.).

LITERATURE CITED

(1) Lucki, I. (1998) The spectrum of behaviors influenced by serotonin. *Biol. Psychiatry 44*, 151−162.

(2) Frazer, A., Maayani, S., and Wolfe, B. B. (1990) Subtypes of receptors for serotonin. *Annu. Rev. Pharmacol. Toxicol. 30*, 307−348.

(3) Sturpe, D. A., and Weissman, A. M. (2002) Clinical inquiries. What are effective treatments for panic disorder? *J. Fam. Pract. 51*, 743.

(4) Stein, D. J. (2002) Obsessive-compulsive disorder. *Lancet 360*, 397−405.

(5) Albucher, R. C., and Liberzon, I. (2002) Psychopharmacological treatment in PTSD: a critical review. *J. Psychiatr. Res. 36*, 355−367.

(6) Meyer, J. H., Wilson, A. A., Sagrati, S., Hussey, D., Carella, A., Potter, W. Z., Ginovart, N., Spencer, E. P., Cheok, A., and Houle, S. (2004) Serotonin transporter occupancy of five selective serotonin reuptake inhibitors at different doses: an [11C]DASB positron emission tomography study. *Am. J. Psychiatry 161*, 826−835.

(7) Volkow, N. D., Wang, G. J., Fowler, J. S., Learned-Coughlin, S., Yang, J., Logan, J., Schlyer, D., Gatley, J. S., Wong, C., Zhu, W., Pappas, N., Schueller, M., Jayne, M., Carter, P., Warner, D., Ding, Y. S., Shea, C., and Xu, Y. (2005) The slow and long-lasting blockade of dopamine transporters in human brain induced by the new antidepressant drug radafaxine predict poor reinforcing effects. *Biol. Psychiatry 57*, 640−646.

(8) Szabo, Z., Kao, P. F., Scheffel, U. A., Suehiro, M., Mathews, W. B., Ravert, H. T., Musachio, J. L., Marenco, S., Kim, S. E., Ricaurte, G. A., Wong, D. F., Wagner, H. N., Jr., and Dannals, R. F. (1995) PET imaging of serotonin transporters in the human brain using [^{11}C]-(+)McN 5652. *Synapse 20*, 37−43.

(9) Buchert, R., Thomasius, R., Nebeling, B., Petersen, K., Obrocki, J., Jenicke, L., Wilke, F., Wartberg, L., Zapletalova, P., and Clausen, M. (2003) Long-term effects of "ecstasy" use on serotonin transporters of the brain investigated by PET. *J. Nucl. Med. 44*, 375−384.

(10) Szabo, Z., Owonikoko, T., Peyrot, M., Varga, J., Mathews, W. B., Ravert, H. T., Dannals, R. F., and Wand, G. (2004) Positron emission tomography imaging of the serotonin transporter in subjects with a history of alcoholism. *Biol. Psychiatry 55*, 766−771.

(11) Szabo, Z., Scheffel, U., Mathews, W. B., Ravert, H. T., Szabo, K., Kraut, M., Palmon, S., Ricaurte, G. A., and Dannals, R. F. (1999) Kinetic analysis of [^{11}C]McN5652: A serotonin transporter radioligand. *J. Cereb. Blood Flow Metab. 19*, 967−981.

(12) Huang, Y., Hwang, D. R., Narendran, R., Sudo, Y., Chatterjee, R., Bae, S. A., Mawlawi, O., Kegeles, L. S., Wilson, A. A., Kung, H. F., and Laruelle, M. (2002) Comparative evaluation in nonhuman primates of five PET radiotracers for imaging the serotonin transporters: [11C]McN 5652, [11C]ADAM, [11C]DASB, [11C]-DAPA, and [11C]AFM. *J. Cereb. Blood. Flow Metab. 22*, 1377−1398.

(13) Shiue, G. G., Choi, S. R., Fang, P., Hou, C., Acton, P. D., Cardi, C., Saffer, J. R., Greenberg, J. H., Karp, J. S., Kung, H. F., and Shiue, C. Y. (2003) N,N-dimethyl-2-(2-amino-4-(18)F-fluorophenylthio)-benzylamine (4-(18)F-ADAM): an improved PET radioligand for serotonin transporters. *J. Nucl. Med. 44*, 1890−1897.

(14) Brust, P., Hinz, R., Kuwabara, H., Hesse, S., Zessin, J., Pawelke, B., Stephan, H., Bergmann, R., Steinbach, J., and Sabri, O. (2003) In vivo measurement of the serotonin transporter with (S)-([18F]-fluoromethyl)-(+)-McN5652. *Neuropsychopharmacology 28*, 2010−2019.

(15) Zessin, J., Eskola, O., Brust, P., Bergman, J., Steinbach, J., Lehikoinen, P., Solin, O., and Johannsen, B. (2001) Synthesis of *S*-[^{18}F]fluoromethyl-(+)-McN5652 as a potential PET radioligand for the serotonin transporter. *Nucl. Med. Biol. 28*, 857−863.

(16) Zessin, J., Deuther-Conrad, W., Kretzschmar, M., Wust, F., Pawelke, B., Brust, P., Steinbach, J., and Bergmann, R. (2006) [11C]-SMe-ADAM, an imaging agent for the brain serotonin transporter: synthesis, pharmacological characterization and microPET studies in rats. *Nucl. Med. Biol. 33*, 53−63.

(17) Oya, S., Choi, S. R., Kung, M. P., and Kung, H. F. (2007) 5-Chloro-2-(2′-((dimethylamino)methyl)-4′-iodophenylthio)benzenamine: a new serotonin transporter ligand. *Nucl. Med. Biol. 34*, 129−139.

(18) Frankle, W. G., Narendran, R., Huang, Y., Hwang, D. R., Lombardo, I., Cangiano, C., Gil, R., Laruelle, M., and Abi-Dargham, A. (2005) Serotonin transporter availability in patients with schizophrenia: a positron emission tomography imaging study with [11C]-DASB. *Biol. Psychiatry 57*, 1510−1516.

(19) Lundquist, P., Wilking, H., Hoglund, A. U., Sandell, J., Bergstrom, M., Hartvig, P., and Langstrom, B. (2005) Potential of [11C]DASB for measuring endogenous serotonin with PET: binding studies. *Nucl. Med. Biol. 32*, 129−136.

(20) Blurton, A. M., Bounds, M. C., Garg, S., Tobin, J., Staab, E., Smith, H. C., Black, K., and Garg, P. K. (2006) Radiation dosimetry of chollinergic imaging agent F-18 fluorobenzyltrozamicol. *Mol. Imaging Biol. 8*, 117.

(21) Clark, P., Kraas, J., Burbank, N., Gage, H. D., Buchheimer, N., Black, K., Smith, H. C., Rideout, S., and Calles, J. S. (2005) Pancreatic uptake of 18F-(+)-4-Fluorobenzyltrozamicol in diabetic mice: A potential surrogate marker for beta cell mass. *J. Nucl. Med. 46*, 226P.

(22) Bounds, M. C., Nader, M. A., Czoty, P. W., Garg, P. K., and Gage, H. D. (2006) Application of the Reference Tissue Method to a Longitudinal Positron Emission Tomography Study: A Non-Invasive Approach to Quantitation. *Mol. Imaging. Biol. 8*, 79.

(23) Wilson, A. A., Ginovart, N., Schmidt, M., Meyer, J. H., Threlkeld, P. G., and Houle, S. (2000) Novel radiotracers for imaging the serotonin transporter by PET: synthesis, radiosynthesis, and in vitro

and ex vivo evaluation of ^{11}C-labeled 2-(phenylthio)araalkylamines. *J. Med. Chem. 43*, 3103−3110.

(24) Mach, R. H., Elder, S. T., Morton, T. E., Nowak, P. A., Evora, P. H., Scripko, J. G., Luedtke, R. R., Unsworth, C. D., Filtz, T., Rao, A. V., and et al. (1993) The use of [18F]4-fluorobenzyl iodide (FBI) in PET radiotracer synthesis: model alkylation studies and its application in the design of dopamine D1 and D2 receptor-based imaging agents. *Nucl. Med. Biol. 20*, 777−794.

(25) Davies, H. M., Kuhn, L. A., Thornley, C., Matasi, J. J., Sexton, T., and Childers, S. R. (1996) Synthesis of 3 beta-aryl-8-azabicyclo-[3.2.1]octanes with high binding affinities and selectivities for the serotonin transporter site. *J. Med. Chem. 39*, 2554−2558.

(26) Cheng, Y., and Prusoff, W. H. (1973) Relationship between the inhibition constant (K_i) and the concentration of inhibitor which causes 50 per cent inhibition (I_{50}) of an enzymatic reaction. *Biochem. Pharmacol. 22*, 3099−3108.

(27) Hahn, F. E., Garcia Plumed, C., Munder, M., and Lugger, T. (2004) Synthesis of benzannulated N-heterocyclic carbene ligands by a template synthesis from 2-nitrophenyl isocyanide. *Chemistry 10*, 6285−6293.

(28) Huang, Y., Bae, S. A., Zhu, Z., Guo, N., Roth, B. L., and Laruelle, M. (2005) Fluorinated diaryl sulfides as serotonin transporter ligands: synthesis, structure-activity relationship study, and in vivo evaluation of fluorine-18-labeled compounds as PET imaging agents. *J. Med. Chem. 48*, 2559−2570.

(29) Garg, P. K., Garg, S., Black, K., Liu, Q., Childers, S., and Davies, H. M. (2006) Synthesis, in vitro binding, rodent biodistribution, and non-human primate PET imaging using F-18 FIPPT. *Mol. Imaging Biol. 8*, 114.

(30) Wilson, A. A., Ginovart, N., Hussey, D., Meyer, J., and Houle, S. (2002) In vitro and in vivo characterisation of [^{11}C]DASB: a probe for in vivo measurements of the serotonin transporter by PET. *Nucl. Med. Biol. 29*, 509−515.

BC070112G

Design of a Thermocontrollable Protein Complex

Yoshihiko Fujita, Hisakage Funabashi, Masayasu Mie, and Eiry Kobatake*

Department of Biological Information Graduate School of Bioscience and Biotechnology, Tokyo Institute of Technology, 4259 Nagatsuta-cho, Midori-ku, Yokohama, Kanagawa 226-8501, Japan. Received April 11, 2007; Revised Manuscript Received June 27, 2007

It is widely recognized that stimuli-responsive nanostructures play a promising role in nanodevices for medical treatments and experimental tools. We have designed and constructed a basic structure which controls the distance between two termini domains through temperature reversibility. Our structure, shaped like a bouquet, is composed of two proteins, α-helix and elastin-like protein (ELP). α-Helices align and bundle the ELP while ELP twists and forms a fiber-like structure at warm temperatures. This ELP conformational change alters the distance between the structure termini at the site opposite the α-helix. We connected enhanced yellow fluorescent protein (EYFP) and enhanced cyan fluorescent protein (ECFP) at the structure's two termini to evaluate the distance using fluorescence resonance energy transfer (FRET) efficiency. These proteins spontaneously formed a complex which decreased the distance between the two fluorescent proteins located at its termini, at physiologically relevant temperatures. This change was repeated with complete reversibility ($n = 5$).

INTRODUCTION

External modification of nanomachine function and conformation is essential. In the past, chemically based, simple molecular machines were constructed (*1*−*3*). These machines could change structural conformation in response to an external chemical or physical stimulation with complete reversibility. Natural biomotor molecules also have been discovered (*4*−*6*). However, few artificial biomaterial-based molecular machines have been constructed due to the unpredictable nature of biomaterials.

To create these biomaterial-based machines, one approach was to position a new stimuli-responsive tag on existing biomaterials (*7*, *8*). The characteristics of these biomaterials are constantly controlled by external chemical or physical stimulation. Modification of the existing natural biomolecule, by exploiting its original conformation and function, can create highly functional machines. However, the degree of design freedom is limited, as this approach highly depends on the original biomolecule conformation. An alternate approach is to design biomaterial building blocks that form biomachines using a bottom-up strategy. Many structures composed of nucleic acids (*9*) or peptides (*10*, *11*) have been constructed using this technique; however, few can be controlled by external stimulation.

A temperature-responsive protein complex we designed in this article contains artificial α-helices and ELP. Three artificial α-helices, A, B, and C (*12*, *13*) (we call them helixA, helixB, and helixC, respectively, in this paper), served as self-assembly domains along with ELP, since they are small and assemble into a highly stable heterotrimer coiled coil up to approximately 80 °C. The amino acids sequence $(GVGVP)_n$, which is one of the ELPs derived from the hydrophobic region of elastin (*14*, *15*), shrinks under warm conditions to form fibril structures (*16*) and aggregations called coacervation. Since its conformational change is well-characterized and completely reversible with temperature change, we adopted $(GVGVP)_n$ as the temperature-responsive domain. A model of the structure at high temperature is proposed as a β-spiral structure composed of three twisted $(GVGVP)_n$ (*17*). On the basis of this model, we expected that, when the opposite sites were bundled, the two domains fused to $(GVGVP)_n$ individually could be approximated at high temperature. Then, we constructed helixA−$(GVGVP)_n$, helixB−$(GVGVP)_n$, and helixC−$(GVGVP)_n$ recombinant proteins, which contain the α-helix in order to align the termini of the $(GVGVP)_n$. These proteins were expected to spontaneously form a trimer, aligning the termini by α-helices, bringing the opposite termini together at high temperatures and subsequently releasing them at low temperatures. In this study, we fused ECFP and EYFP to the helixA−$(GVGVP)_n$ and helixB−$(GVGVP)_n$, respectively, and were able to control the distance between the ECFP and EYFP (Figure 1). This study demonstrates future possibilities of this structure becoming a thermoresponsive part for complete biomaterial-based machines which can be expressed and assembled in cells.

EXPERIMENTAL PROCEDURES

Plasmid Construction. The ELP, helixA, helixB, and helixC genes were obtained by elongating partially hybridized two DNA oligonucleotides. About 20 bases at the 3′ end of one oligonucleotide were hybridized with a region at the 5′ end of another oligonucleotide, followed by a polymerase reaction. Enhanced cyan fluorescent protein (ECFP) and enhanced yellow fluorescent protein (EYFP) genes were amplified by PCR, from pECFP-N1 (BD Biosciences, Clontech) and pEYFP-actin (BD Biosciences, Clontech), respectively. All the genes were cloned on pBluescriptII SK (+) (Stratagene) and then sequenced (Beckman; CEQ2000XL). ELP tandem repeats (×18, 36, and 72) were constructed by recursive directional ligation (*18*) between *Bam*HI and *Bgl*II sites. The expression plasmids for the helices (helixA, helixB, and helixC) and fluorescent proteins (ECFP and EYFP) were constructed by ligating the cloned coding DNA fragments with a modified pET28b (Novagen) vector and digested with *Nco*I and *Xho*I or *Bam*HI and *Bgl*II, respectively. The expression plasmids for helixA−$(GVGVP)_n$−ECFP, helixB−$(GVGVP)_n$−EYFP, helixC−$(GVGVP)_n$, $(GVGVP)_n$−ECFP, and $(GVGVP)_n$−EYFP fusion proteins were constructed by inserting each cloned gene fragment into the modified pET28b in the order described.

* ekobatak@bio.titech.ac.jp.

10.1021/bc070120x CCC: $37.00 © 2007 American Chemical Society
Published on Web 08/28/2007

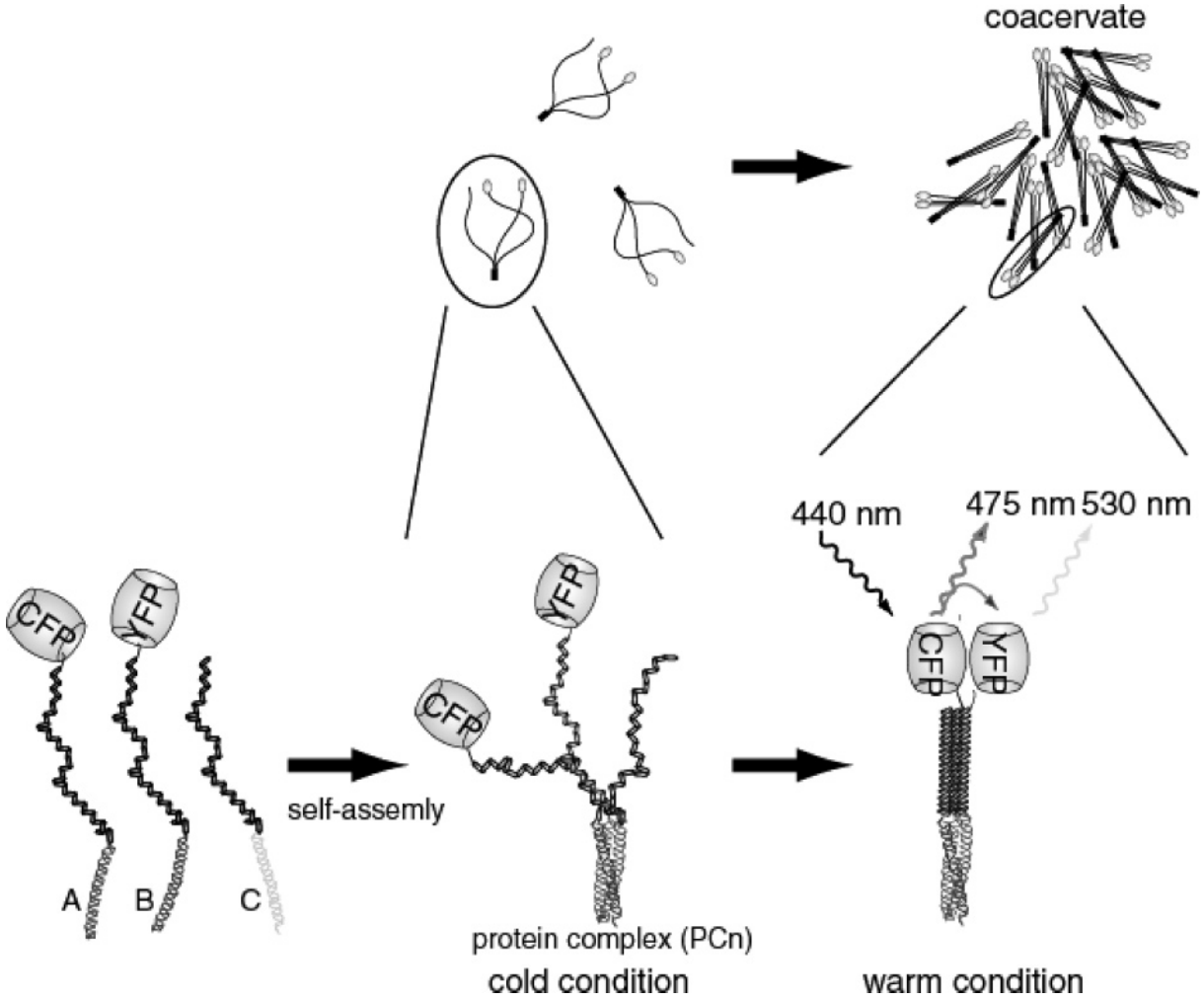


Figure 1. Schematic diagram of PC_n. Upper illustration indicates a macroscopic view; lower is a microscopic view. The helix parts assemble independently and form a protein complex (PC_n). Under cold conditions, the fluorescent proteins at the termini of $(GVGVP)_n$ reside away from each other due to the relaxed nature of the $(GVGVP)_n$ components. As the temperature increases and the $(GVGVP)_n$ components stabilize, the two fluorescent proteins come close together. The distance between them then decreases due to its inverse temperature transition.

Protein Expression and Purification. The expression vectors were transformed into the *E. coli* strain BL21(DE3). LB medium, supplemented with 20 μg/mL kanamycin, was inoculated with transformed cells from confluent precultures and incubated with shaking at 37 °C. When the OD660 reached between 0.5 and 0.6, expression was induced by adding IPTG, reaching a final concentration of 1 mM. The cells containing pET28b-helixA, pET28b-helixB, pET28b-helixC, pET28b-ECFP, pET28b-EYFP, pET28b-helixA-$(GVGVP)_n$-ECFP, pET28b-helixB-$(GVGVP)_n$-EYFP, or pET28b-helixC-$(GVGVP)_n$ were harvested after induction for 16 h at 16 °C, and centrifuged at 2000 *g* for 3 min at 4 °C. The cells with pET28b-$(GVGVP)_n$-ECFP, and pET28b-$(GVGVP)_n$-EYFP were harvested after induction for 6 h at 30 °C. Next, the pellets were lysed by 1×BugBuster (Novagen) including benzonase nuclease (Novagen), and the cell lysates were centrifuged at 16 000 *g*, for 15 min at 4 °C, to remove insoluble cellular debris. The proteins with $(GVGVP)_n$ ($n \geq 36$) were purified using the modified method of inverse transition cycling (*19*) and then dissolved in PBS. Other proteins were purified according to the standard metal affinity chromatography protocol of His-Select Nickel Affinity Gel (Sigma) and dialyzed with PBS using a Slide-A-Lyzer Dialysis Cassette (Pierce). The purified protein concentrations were determined using the BCA Protein Assay Kit (Pierce) and then stored at −80 °C. The purified proteins are listed in Figure 2.

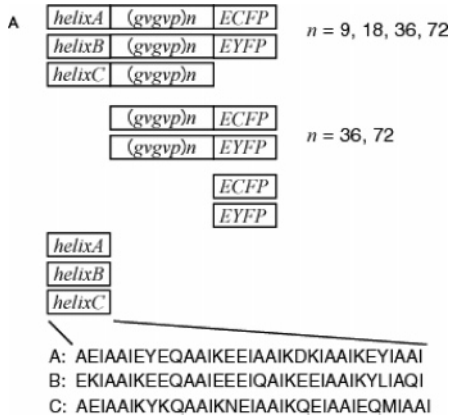


Figure 2. Constructed proteins. helixA, helixB, and helixC are the artificial helices. The repetitive number of the GVGVP (*n*) was indicated at the right. Proteins are fused with polyhistidine tag. The amino acids sequences are indicated at the bottom.

Protein Complex Preparation. A protein complex with various lengths of $(GVGVP)_n$ was prepared by incubating a mixture containing equal amounts of helixA−$(GVGVP)_n$−ECFP, helixB−$(GVGVP)_n$−EYFP, and helixC−$(GVGVP)_n$ in PBS for 30 min at 4 °C. Mixtures of fluorescent proteins (ECFP and EYFP) only, without helixA and helixB ($(GVGVP)_n$−ECFP, $(GVGVP)_n$−EYFP, and helixC−$(GVGVP)_n$), were also prepared as above and served as negative controls. The protein

complex consisting of helixA−$(GVGVP)_n$−ECFP, helixB−$(GVGVP)_n$−EYFP, and helixC−$(GVGVP)_n$ is named PC_n (*n* indicates the number of the repeated GVGVP peptapeptide) in this article.

Estimation of FRET Efficiency. The PC_{72} was prepared in 700 μL of PBS and incubated at 4 °C for 20 min. The fluorescent spectra excitation under cold conditions was measured at 425 nm excitation immediately after transfer to the spectrofluorometer (Jasco, FP-777). The sample was heated with a dryer and immediately measured in the same manner to obtain the fluorescent spectra under warm conditions. The spectra measurements were then normalized by dividing intensity from 450 to 600 nm by that at 475 nm.

To estimate fluorescence resonance energy transfer (FRET) efficiency, the fluorescence of the purified protein was determined using the CYTOFLUOR Multi-Well Plate Reader series 4000 (PerSeptive Biosystems). The PC_n solutions were prepared directly on a 96-well ELISA plate (Sumilon) in 200 μL of PBS and gently vortexed. After a 20 min incubation at each preset temperature, the fluorescent signal was obtained using 440/40 nm, 485/20 nm, and 530/10 nm filters for excitation, ECFP emission, and EYFP emission, respectively. At each temperature, FRET efficiency was defined as the fluorescent intensity ratio $I(530 \pm 10\ nm)/I(485 \pm 20\ nm)$. Sequential measurements of the same sample were taken at low through to high temperatures.

To test temperature reversibility, protein complexes were prepared as described above. The fluorescent signals were obtained first at 37 °C, followed by at 4 °C sequentially. This measurement was repeated five times on the same sample.

Protein Complex Coacervation. The inverse phase transition temperature was determined by monitoring absorbance to quantify the turbidity of the solution as a function of temperature at 350 nm, using a UV−visible spectrophotometer DU-7500 (Beckman) equipped with a multicell thermal controller. The protein solutions were heated 1 °C every minute, from 25 °C to 55 °C. Turbidity was calculated by subtracting the absorbance at 25 °C from each absorbance reading. The inverse phase transition temperature was defined as the temperature where the liquid absorbance is midway between the two parallel lines, tangent to the slope of the data at the beginning and end of the analysis.

Complex Disruption Test. Protein self-assembly was inhibited by blocking the helix region in the components (helixA−$(GVGVP)_n$−ECFP, helixB−$(GVGVP)_n$−EYFP, and helixC−$(GVGVP)_n$) of the PC_n using the respective counterpart helices, i.e., helixA and helixB for helixC−$(GVGVP)_n$, helixB and helixC for helixA−$(GVGVP)_n$−ECFP, and helixC and helixA for helixB−$(GVGVP)_n$−EYFP. Aliquots of components (0.4 μM) with counterparts, whose concentrations were 0.1, 0.2, 0.4, 0.8, or 1.6 μM, were prepared and incubated for 1 h at room temperature in order to block the helix regions. Next, the blocked components were mixed in 200 μL of PBS to obtain the solutions containing 0.1 μM of each blocked component. The final concentrations of the α-helix counterparts in prepared samples were 0.075, 0.15, 0.3, 0.6, and 1.2 μM.

RESULTS AND DISCUSSION

Temperature Control of the Distance between Proteins. First, we investigated the change in distance between ECFP and EYFP at various temperatures by measuring the fluorescent spectra of assembled PC_{72} (Figure 3A), which consists of helixA−$(GVGVP)_{72}$−ECFP, helixB−$(GVGVP)_{72}$−EYFP, and helixC−$(GVGVP)_{72}$ as described in the Experimental Section. At low temperatures (approximately 4 °C), the fluorescent light derived from EYFP was undetected. In contrast, at high temperatures, a remarkable peak occurred around 530 nm, suggesting that FRET from ECFP to EYFP had occurred. These

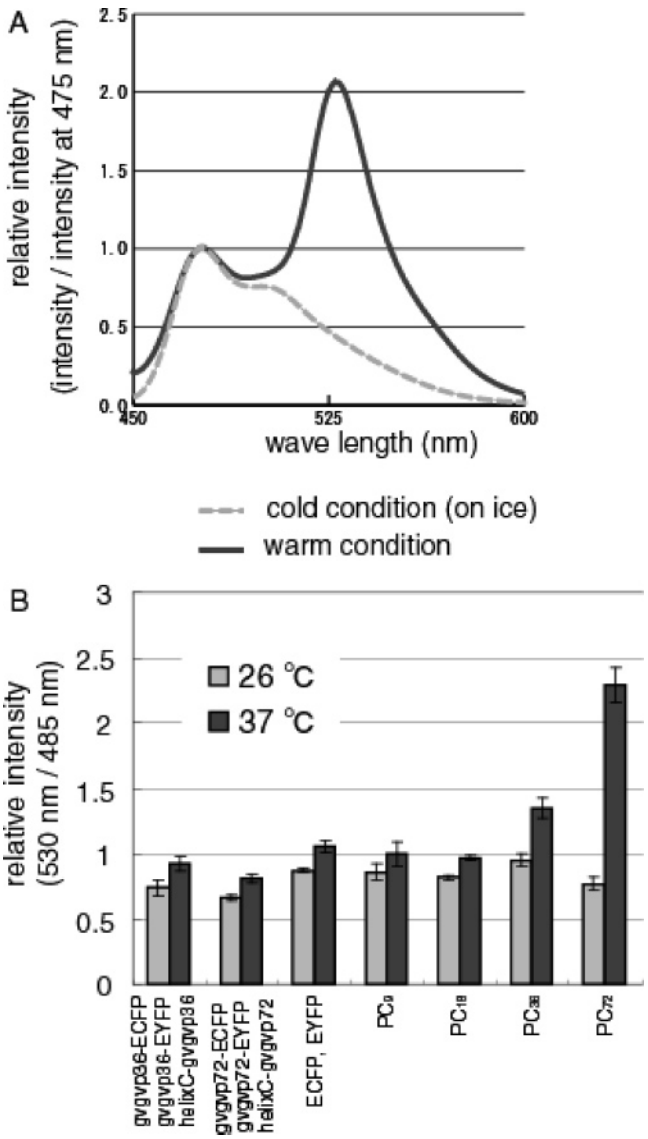


Figure 3. (A) The normalized fluorescent spectra of PCs (helixA-$(GVGVP)_{72}$-ECFP, helixB-$GVGVP)_{72}$-EYFP, and helixC-$(GVGVP)_{72}$) under cold conditions (broken line) and warm conditions (solid line). (B) Complex FRET efficiencies at various lengths of (GVGVP), at 26 °C (open bar) and 37 °C (filled bar). The fluorescence data are the mean ± SD from four separate samples.

results indicate that the two fluorescent proteins came close at the warm temperature, as illustrated in Figure 1. The shapes of the relative fluorescent intensity did not change significantly except for the intensity at 530 nm which was emission maxima of EYFP, at low or high temperatures. That is, the FRET signal can be detected even if the light scattering of coacervation might affect the emission light from the fluorescent proteins.

To optimize fluorescent protein approximation by temperature, the FRET efficiencies of PC_n having various lengths of $(GVGVP)_n$ with or without the helix were tested (Figure 3B). The PC_n's ($n = 9, 18$), which have a short $(GVGVP)n$, caused only a slight increase in FRET efficiency at 37 °C, and reached control levels. This slight increasing in FRET efficiency is due to the inactivation of the ECFP by temperature. The apparent FRET efficiency increased because both ECFP and EYFP indicated the thermal inactivation with heating, but the intensity of ECFP more rapidly decreased over that of EYFP. In contrast, an obvious FRET signal was detected in the PC_n ($n = 36, 72$) samples. This is not a false FRET signal due to the decrease of ECFP fluorescence light depending on the inactivation of the ECFP by temperature, because the control, which is a mixture

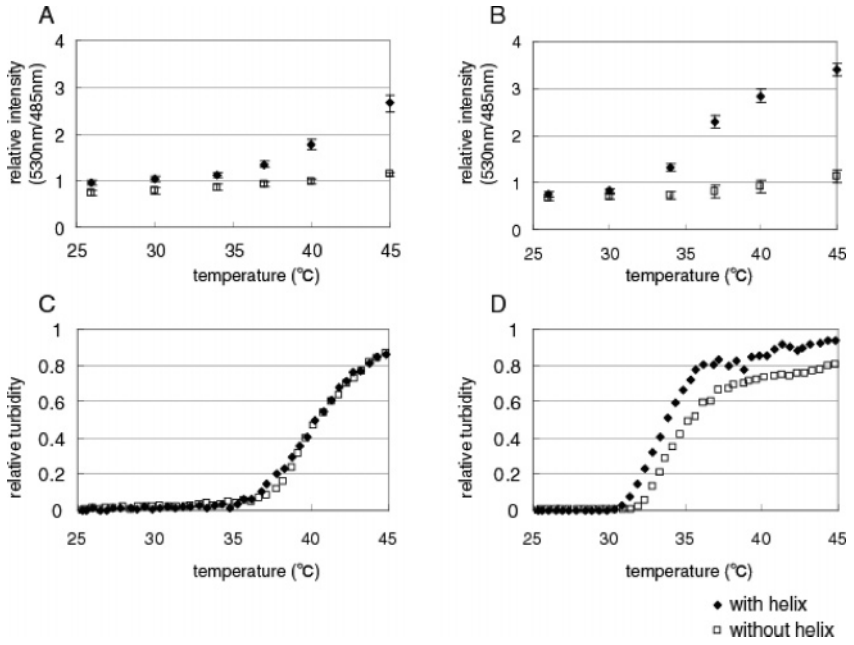


Figure 4. The FRET and turbidity profiles of the PC_{36} or PC_{72} with (filled diamond) or without (open square) helixA and helixB regions. (A) FRET profiles under the same conditions as (C). (B) FRET profiles under the same conditions as (D). The fluorescence data are the mean ± SD from four separate samples. (C) Turbidimetric profiles of the PBS solutions containing 0.1 μM PC_{36} with or without helixA and helixB regions. (D) Similar data as (C) but in a PC_{72} solution.

of ECFP and EYFP, did not cause an obvious increase of the signal. The effect of thermal inactivation of fluorescent proteins on the FRET signal may exist, but only slightly. In addition, FRET efficiency of the PC_{72} was higher than PC_{36}. This result suggests that long $(GVGVP)_n$s twist and form more stable fiber structures at 37 °C than shorter sequences. This coincides with research on the relationship between coacervation transition temperature and length of $(GVGVP)_n$ (*20*).

Comparison of FRET with Turbidity Profiles. When coacervation occurs, FRET increases derived from intercomplex proximity must be taken into account. To determine whether the increase of FRET is due to the intercomplex proximity by coacervation or intracomplex proximity due to a protein complex conformational change, we compared FRET and the turbidity of solutions containing 0.1 μM of helixA−$(GVGVP)_n$−ECFP, helixB−$(GVGVP)_n$−EYFP, and helixC−$(GVGVP)_n$ (PC_n, n = 36 or 72) with solutions containing 0.1 μM of $(GVGVP)_n$−ECFP, $(GVGVP)_n$−EYFP, and helixC−$(GVGVP)_n$ (nonhelix-PC_n, n = 36 or 72). The former protein group contains the α-helix region that self-assembles, while the $(GVGVP)_n$−ECFP and $(GVGVP)_n$−EYFP in the latter group do not contain these helices.

Improvements in FRET efficiency have been detected in PC_n solutions, while no changes have been detected in non-helix-PC_n (Figure 4A,B). Although differences in FRET efficiency have been observed in solutions with or without helixA and helixB, only small differences in the turbidimetric profiles have been detected (Figure 4C,D). The FRET derived from intercomplex proximity by the coacervation was expected to be dependent on the turbidity regardless of the helices. Thus, these results suggest that increases in FRET efficiency were derived from intracomplex proximity, since increased FRET efficiency was not detected in the samples without an α-helix that formed coacervates. The fact that FRET efficiency of PC_{72} with helixA and helixB increased throughout the higher temperature (>35 °C), despite the turbidity, increased a little supports the hypothesis. Presumably, the FRET efficiency is mainly dependent on the stability of the microscopic structure formed by $(GVGVP)_n$. It is notable that the temperature at which the FRET signal rises shifts to lower when the longer $(GVGVP)_n$ is used. This indicates that the distance between ECFP and EYFP can be controlled at various temperatures by changing the length of (GVGVP).

The small difference between the turbidity profiles of PC_{72} with or without helixA and helixB was speculated as follows. ELP molecules including GVGVP need three steps before coacervation (*21*). First, ELP changes from random structure into a β-turn-like structure. Second, ELPs associate with each other and form a microscopic structure which includes just a few ELP molecules. Third, the microscopic structures assemble into macroscopic aggregation. They suggest that the process from step 1 to step 2 is stoichiometric; that is, this process is dependent on the concentration of ELP. In the case of a protein complex with helixA and helixB, the microscopic concentration of $(GVGVP)_n$ was high because a helix put one $(GVGVP)_n$ close to other $(GVGVP)_n$'s conjugated with counterpart helices. This proximity effect promoted the process from step 1 to step 2 of $(GVGVP)_{72}$. Consequently, the temperature of the coacervation decreased, and intensity increased more rapidly. On the other hand, the microscopic structure of $(GVGVP)_{36}$ is less stable than that of $(GVGVP)_{72}$ because the free energy difference between the monomeric state and the associated state is dependent on the length of ELP (longer ELP indicates larger free energy difference). Thus, even if the microscopic concentration increases by proximity effect, $(GVGVP)_{36}$ could form fewer microscopic structures than $(GVGVP)_{72}$, and we could not detect the small change as turbidity.

Complex Disruption by Counterparts. To confirm whether the FRET signal disappeared when the complex was inhibited, the α-helix region in the PC_{72} was blocked by monomer α-helice binding. FRET efficiencies of the mixed solutions containing the components of PC_{72} and α-helices decreased with increasing concentrations of α-helices at 37 °C (Figure 5).

FRET efficiency attenuation at low counterpart concentrations (0−0.1 μM) was greater than high concentrations (>0.2 μM). This nonlinear inhibition can be explained through interactions between the counterpart helices. Counterpart helices' binding to the helix regions of the PC_n components was nearly complete

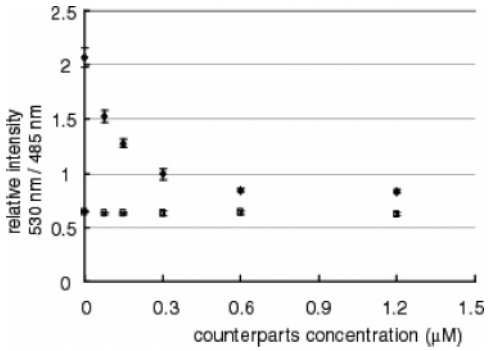


Figure 5. FRET efficiencies of the PC_{72} containing various concentrations of the counterpart α-helices. FRET efficiencies at 37 °C (filled diamond) and 4 °C (open square) as indicated, where each component of the PC_{72} was 0.1 μM.

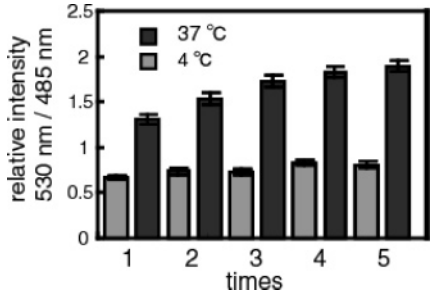


Figure 6. Reversibility of 0.1 μM of PC_{72}. FRET efficiencies of PC_{72} were sequentially measured at 4 °C (open bar) and 37 °C (filled bar) five times.

at low concentrations. In contrast, when there were many counterpart helices, they bound with other monomeric helices and formed stable complexes which were not capable of blocking the components. Thus the exceeded helices could not block the components efficiently. This inhibition indicates that domain proximity at the PC_n termini requires helices that permit individual protein bundling.

Reversibility Test. To control PC_n termini domain function, conformational reversibility is necessary. Therefore, we repeatedly measured FRET efficiencies, alternating between 4 °C and 37 °C as illustrated in Figure 6. FRET efficiency increased at 37 °C and decreased at 4 °C in all cycles. Even after four cooling and warming cycles, FRET efficiency consistently decreased at 4 °C. This result suggests that changing temperature could control the distance between the domains positioned at the PC_{72} termini in a reversible manner. An upward trend in the FRET efficiency is explained by two possibilities. The first is the difference between thermal inactivation rates of ECFP and EYFP described above. The second is the incorrect homocomplex of helices. Some protein complexes might contain only ECFP or EYFP, such as a complex containing helixA−$(GVGVP)_n$−ECFP, helixA−$(GVGVP)_n$−ECFP, and helixC−$(GVGVP)_n$, at the start condition, because the same helix can form a homodimer or trimer coiled coil (*12*, *13*). During thermal cycling, these incorrect complexes were substituted to assemble correct heterotrimer complexes. Thus, the upward trend of the FRET efficiency should have been observed.

CONCLUSION

Our designed recombinant proteins, helix-$(GVGVP)_n$, spontaneously formed a trimeric complex. The FRET signal from EYFP indicated that its temperature-induced conformational change promoted ECFP and EYFP proximity. Moreover, this conformational change was reversible. This complex, although composed of amino acids, behaved much like a machine. Thus, this complex has the potential to function as basic components in the construction of future biomaterial-based machines. In this study, fluorescent proteins modeled the functional domain. Alternate proteins could be used in their place, which are activated by multimerizaton or complementation. Thus, we have the ability to control multimeric proteins as typified by DNA binding proteins or split enzymes by altering the external temperature.

A problem of the undesirable coacervation between complexes must be solved to use it in liquid because the steric hindrance is expected. This problem may be overcome by modifying the $(GVGVP)_n$ or fixing complexes on a solid structure, such as a cell membrane. Although a simple heterotrimer coiled coil was used in this paper in order to distinguish between ECFP and EYFP, and indicate whether proximity occurs or not, we can replace them with not only multimeric helices but also transmembrane helices (*22*). We also have to consider undesirable effects on cells when this thermal control is applied to cells. It is impossible to completely remove the effects on cells in principle as long as the thermal control is used; the effects, however, will reduce when the activity-controllable temperature is set around 37 °C by an appropriate length of $(GVGVP)_n$. Therefore, this approach has an advantage in the situation where the effects on cells are well-known or simplicity, speed, or reversibility is required.

Our adjustable protein complexes can be expressed and formed in cells, since they are composed of amino acids. Once the plasmids coding this protein complex were introduced into cells, the additional harmful injection is unnecessary every time we would like to activate the interest function. Therefore, this proposed method may control cellular function without causing additional damage.

LITERATURE CITED

(1) Badjic, J. D., Balzani, V., Credi, A., Silvi, S., and Stoddart, J. F. (2004) A molecular elevator. *Science 303*, 1845−1849.

(2) Muraoka, T., Kinbara, K., Kobayashi, Y., and Aida, T. (2003) Light-driven open-close motion of chiral molecular scissors. *J. Am. Chem. Soc. 125*, 5612−5613.

(3) Norikane, Y., and Tamaoki, N. (2004) Light-driven molecular hinge: a new molecular machine showing a light-intensity-dependent photoresponse that utilizes the trans-cis isomerization of azobenzene. *Org. Lett. 6* (15), 2595−2598.

(4) Noji, H., Yasuda, R., Yoshida, M., and Kinosita, K. (1997) Direct observation of the rotation of F1-ATPase. *Nature (London) 386*, 299−302.

(5) Finer, J. T., Simmons, R. M., and Spudich, J. A. (1994) Single myosin molecule mechanics: piconewton forces and nanometer steps. *Nature (London) 368*, 113−119.

(6) Suzuki, H., Yonekura, K., and Namba, K. (2004) Structure of the rotor of the bacterial flagellar motor revealed by electron cryomicroscopy and single-particle image analysis. *J. Mol. Biol. 337*, 105−113.

(7) Liu, H., Schmidt, J. J., Bachand, G. D., Rizk, S. S., Looger, L. L., Hellinga, H. W., and Montemagno, C. D. (2002) Control of a biomolecular motor-powered nanodevice with an engineered chemical switch. *Nat. Mater. 1*, 173−177.

(8) Reiersen, H., and Rees, A. R. (1999) An engineered minidomain containing an elastin turn exhibits a reversible temperature-induced IgG binding. *Biochemistry 38*, 14897−14905.

(9) Yan, H., Park, S. H., Finkelstein, G., Reif, J. H., and LaBean, T. H. (2003) DNA-templated self-assembly of protein arrays and highly conductive nanowires. *Science 301*, 1882−1884.

(10) Holowka, E. P., Pochan, D. J., and Deming, T. J. (2005) Charged polypeptide vesicles with controllable diameter. *J. Am. Chem. Soc. 127*, 12423−12428.

(11) Ellerby, H. M., Lee, S., Ellerby, L. M., Chen, S., Kiyota, T., del Rio, G., Sugihara, G., Sun, Y., Bredesen, D. E., Arap, W., and Pasqualini, R. (2003) An artificially designed pore-forming protein with anti-tumor effects. *J. Biol. Chem. 278*, 35311−35316.

(12) Nautiyal, S., Woolfson, D. N., King, D. S., and Alber, T. (1995) A designed heterotrimeric coiled coil. *Biochemistry, 34*, 11645−11651.

(13) Nautiyal, S., and Alber, T. (1999) Crystal structure of a designed, thermostable, heterotrimeric coiled coil. *Protein Sci. 8*, 84−90.

(14) Sciortino, F., Prasad, K. U., Urry, D. W., and Palma, M. U. (1993) Self-assembly of bioelastomeric structures from solutions: mean-field critical behavior and Flory-Huggins free energy of interactions. *Biopolymers 33*, 743−752.

(15) Urry, D. W., and Parker, T. M. (2002) Mechanics of elastin: molecular mechanism of biological elasticity and its relationship to contraction. *J. Muscle Res. Cell Motil. 23*, 543−559.

(16) Bressan, G. M., Pasquali-Ronchetti, I., Fornieri, C., Mattioli, F., Castellani, I., and Volpin, D. (1986) Relevance of aggregation properties of tropoelastin to the assembly and structure of elastic fibers. *J. Ultrastruct. Mol. Struct. Res. 94*, 209−216.

(17) Urry, D. W. (1997) Physical chemistry of biological free energy transduction as demonstrated by elastic protein-based polymers. *J. Phys. Chem. B 101*, 11007−11028.

(18) Meyer, D. E., and Chilkoti, A. (2002) Genetically encoded synthesis of protein-based polymers with precisely specified molecular weight and sequence by recursive directional ligation: examples from the elastin-like polypeptide system. *Biomacromolecules 3*, 357−367.

(19) Meyer, D. E., Trabbic-Carlson, K., and Chilkoti, A. (2001) Protein purification by fusion with an environmentally responsive elastin-like polypeptide: effect of polypeptide length on the purification of thioredoxin. *Biotechnol. Prog. 17*, 720−728.

(20) Meyer, D. E., and Chilkoti, A. (1999) Purification of recombinant proteins by fusion with thermally-responsive polypeptides. *Nat. Biotechnol. 17*, 1112−1115.

(21) Yamaoka, T., Tamura, T., Seto, Y., Tada, T., Kunugi, S., and Tirrell, D. A. (2003) Mechanism for the phase transition of a genetically engineered elastin model peptide $(VPGIG)_{40}$ in aqueous solution. *Biomacromolecules 4*, 1680−1685.

(22) Bilgiçer, B., and Kumar, K. (2004) De novo design of defined helical bundles in membrane environments. *Proc. Natl. Acad. Sci. U.S.A. 101*, 15324−15329.

BC070120X

A Robust and Convergent Synthesis of Dipeptide−DOTAM Conjugates as Chelators for Lanthanide Ions: New PARACEST MRI Agents

Filip Wojciechowski,[†] Mojmir Suchy,[†,‡] Alex X. Li,[‡] Hassan A. Azab,[§] Robert Bartha,[‡] and Robert H. E. Hudson*[,†]

Department of Chemistry, The University of Western Ontario, London, Ontario, Canada N6A 5B7. Received April 16, 2007; Revised Manuscript Received July 11, 2007

A generally applicable synthetic approach to dipeptide−DOTAM conjugates has been developed which is based on the peralkylation of 1,4,7,10-tetraazacyclododecane (cyclen) with protected *N*-iodoacetyl dipeptides. Standardized procedures were used for the alkylation, metalation, and purification of the resultant lanthanide complexes. Using this approach, we have been able to rapidly and reliably prepare and screen five different ligands each with up to six lanthanide ions. This preliminary investigation has identified several paramagnetic compounds with strong chemical exchange saturation transfer (PARACEST) properties in water at physiological temperature and pH. Extension of the synthetic approach to a wide variety of amino acids is possible.

INTRODUCTION

Over the course of the past decade, there have been dramatic developments in the use of chelated lanthanide metals as contrast agents in magnetic resonance imaging (MRI). The recognition that chemical exchange saturation transfer (CEST) via proton exchange (*1*) could be exploited for generating MR contrast has led to new ligand designs. Subsequently, it has been shown that paramagnetic lanthanide ions induced a large hyperfine shift of the bound water protons and exchangeable protons in the ligand framework, and that MR signal modulation could be generated if the exchange rate of the spins with bulk water was slow (*2*). Selective saturation of these exchangeable spins led to a new method of generating MRI contrast now referred to as PARACEST: paramagnetic chemical exchange saturation transfer (*2*). The PARACEST effect has been exploited to image or otherwise detect biologically important metabolites, such as glucose (*3*) and lactate (*4*), and to measure physiologic parameters such as temperature (*5*) and pH by a ratiometric method (*6*, *7*). A further advantage of employing the PARACEST effect is that one ligand may be endowed with different magnetic properties by the use of different lanthanide(III) ions (*7*, *8*).

The syntheses of tetra-substituted 1,4,7,10-tetraazacyclododecanes (cyclens) has been well-documented in the literature. The reaction of the cyclic polyamine with electrophiles is the most common route for the synthesis of tetra-substituted cyclen. Even so, there exists little by way of standard procedures for enabling systematic variation of the periphery of a derivatized cyclen. It has been established previously that the tetraamide derivatives of cyclen are an important structural feature for the slow exchange of bound water with bulk water in the sample and also provide a pool of exchangeable protons in the ligand (*6*, *7*, *9*−*11*). Therefore, a straightforward and reliable synthetic route to a variety of peptide-decorated cyclens may produce interesting ligands with potential to be used as PARACEST MRI agents. The compounds described herein are structurally related to the lanthanide chelators 1,4,7,10-tetraazacyclododecane-*N*,*N*′,*N*″,*N*‴-tetraacetic acid (DOTA) and 1,4,7,10-tetraazacyclododecane-1,4,7,10-tetraacetamide (DOTAM) (*12*), as shown in Figure 1.

To access peptide-decorated cyclens, there are two obvious routes to consider: the coupling of appropriately protected amino acids to DOTA, which has been reported to give a low yield (*13*), or the alkylation of cyclen with N-terminal haloacetyl amino acids, which can proceed in very good yields (*14*−*18*). The latter approach is shown herein to provide a robust and flexible route to a diverse selection of dipeptide-conjugated DOTAM derivatives (Scheme 1).

In this synthetic scheme, the DOTAM−ligand framework is preserved while the nature of the periphery is readily varied. This approach has proven to be very efficient and convenient, permitting the synthesis of ligands possessing neutral (N-Gly-Phe-C), basic (N-Gly-Lys-C), and acidic (N-Asp-Glu-C) amino acids with minimal protecting group manipulations. We also describe a convenient and reproducible size-exclusion purification method for the isolation of metalated compounds. The MR behavior of the metalated ligands has been determined. It is shown that Eu^{3+}-DOTAM-(Gly-Phe)$_4$ possesses a large CEST effect at physiological temperature and pH while Nd^{3+}-DOTAM-(Gly-Lys)$_4$ and Yb^{3+}-DOTAM-(Gly-Lys-OMe)$_4$ possess CEST effect associated with amide protons.

EXPERIMENTAL SECTION

General Experimental Procedures. All amino acids (naturally occurring L-isomers) and reagents were commercially available, unless otherwise stated. All solvents were HPLC grade and used as such, except for CH_2Cl_2 and THF (dried over Al_2O_3, in a solvent purification system) and water (18.2 MΩ/cm). Organic extracts were dried with Na_2SO_4, and solvents were removed under reduced pressure by rotary evaporation. Flash column chromatography (FCC) was carried out using silica gel, mesh size 230−400 Å. Size exclusion chromatography (SEC) was carried out on Bio-Gel P2, 45−90 μm mesh resin (20 g, column size 15 × 2 cm per 0.1 mmol of compound). Ten fractions (10 mL each) were collected. Fractions were identified by 5% solution of ninhydrin in AcOH/EtOH (tetraacetyl-Gly-Lys-OH and Gly-Lys-OMe cyclen derivatives); by I_2 vapors (tetraacetyl-Asp-Glu-OH derivatives); or by UV/I_2 vapors (tetraacetyl-Gly-Phe-OH and Asp-Phe-OH derivatives). Meta-

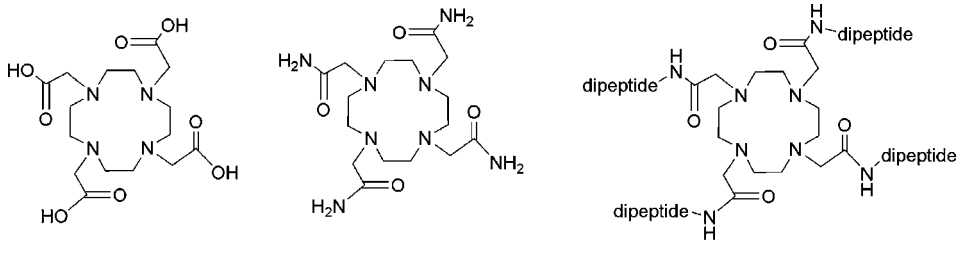
* E-mail address: rhhudson@uwo.ca.

[†] The University of Western Ontario.

[‡] Centre for Functional and Metabolic Mapping, Robarts Research Institute, Department of Medical Biophysics, University of Western Ontario, London, Ontario, Canada, N6A 5K8.

[§] Chemistry Department, Faculty of Science, Suez Canal University, Ismailia 41522, Egypt.

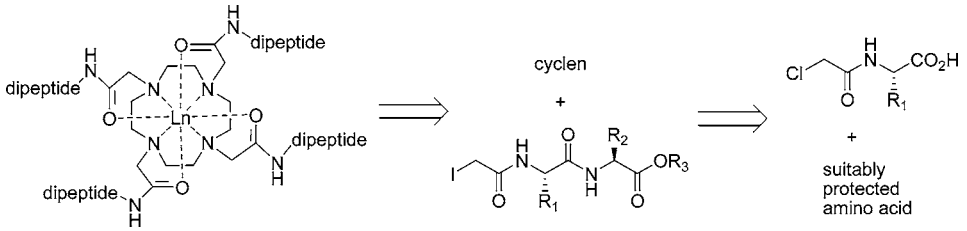
10.1021/bc0701287 CCC: $37.00 © 2007 American Chemical Society
Published on Web 08/22/2007



compound		R_1	R_2	R_3
7	Gly-Phe-OH	H	CH_2Ph	H
8	Gly-Lys-OMe	H	$(CH_2)_4NH_2$	CH_3
9	Gly-Lys-OH	H	$(CH_2)_4NH_2$	H
10	Asp-Glu-OH	CH_2CO_2H	$(CH_2)_2CO_2H$	H
11	Asp-Phe-OH	CH_2CO_2H	CH_2Ph	H

Figure 1. Structural comparison of the known chelators DOTA and DOTAM to the dipeptide conjugates of DOTAM.

Scheme 1. Retrosynthetic Analysis of Lanthanide(III) Complexes of Cyclen−Oligopeptide Conjugates



lation of the ligands was confirmed by inspection of the ^1H NMR spectra (Supporting Information), MS (ESI-TOF) spectrograph, or by HPLC analysis of the reaction mixture and fractionated products. Effective separation of the metalated ligand from free metal by SEC was confirmed by MS (ESI-TOF) analysis of the fractions. Thin layer chromatography (TLC) was carried out on Al-backed silica gel plates; compounds were visualized by UV light or I_2 vapors. Melting points were obtained on a Fisher−Johns apparatus and are uncorrected. Specific rotations $[\alpha]_D$ were determined at ambient temperature using a 5 mL, 10 cm path length cell; the units are 10^{-1} deg cm^2 g^{-1} and the concentrations are reported in g/100 mL. NMR spectra of the synthetic intermediates were recorded on 400 MHz spectrometer for ^1H; δ values were referenced as follows: $CDCl_3$ (7.23 ppm); DMSO-d_6 (2.49 ppm); D_2O (4.75 ppm) for ^{13}C (125 MHz) $CDCl_3$ (77.0 ppm); DMSO-d_6 (39.5 ppm). Chemical exchange saturation transfer (CEST) spectra were acquired on a 400 MHz (9.4 T) Varian INOVA AS400 spectrometer. The CEST effect was measured by recording the bulk water signal intensity as function of presaturation frequency. The basic pulse sequence consisted of a 10 s presaturation pulse (B_1 = 14 μT) followed by a hard (13.8 μs) 90° pulse and a 3 s data acquisition (receiver bandwidth = 6400 Hz, repetition time = 13 s). All CEST spectra were recorded at a ligand concentration of 10 mM in a NaH_2PO_4 (10 mM), pH 7.0, buffer at near-physiologic temperature (37 or 38 °C). Mass spectra (MS) were obtained using electron impact (EI) and electrospray (ES) for ionization. Peptide sequences are denoted in the conventional way from left-to-right, N-to-C terminus.

Synthesis. *N-Chloroacetylglycine (**1a**).* Glycine (30 g, 0.4 mol) was dissolved in 2.5 N NaOH (400 mL, 1.0 mol), and diethyl ether (200 mL) was added. The mixture was cooled (0 °C), and the solution of chloroacetyl chloride (32 mL, 0.4 mol) in 150 mL of ether was added dropwise over 30 min. The mixture was stirred for 45 min at 0 °C, then allowed to gradually warm up to rt while stirring for further 2 h. The organic layer was separated, and the aqueous layer was extracted with Et_2O (100 mL). The aqueous layer was acidified (pH 2) and extracted with EtOAc (4 × 250 mL). The combined ethyl acetate extracts were washed with 100 mL of brine, dried, and concentrated to afford a colorless oil. Hexanes (200 mL) were added to the obtained oil, and the solvent was removed to give a white solid. The crude product was recrystallized from EtOAc to give the title compound in 43% yield. mp 105−106 °C. ^1H NMR (DMSO-d_6) δ 12.68 (br s, 1H); 8.51 (t, J = 5.0 Hz, 1H); 4.13 (s, 2H); 3.79 (d, J = 5.9 Hz, 2H).

*O-Chloroacetyl-N-hydroxysuccinimide (**5**).* DCC (15.5 g, 75.0 mmol) was dissolved in a minimum amount of THF and added dropwise to a solution (cooled to 0 °C) of NHS (8.7 g, 75.0 mmol) and chloroacetic acid (7.1 g, 75.0 mmol) in THF (200 mL). The reaction was stirred for 5 h at 0 °C, the precipitate (*N*,*N*′-dicyclohexylurea) was filtered off, and the filtrand was washed with 50 mL of THF. Hexanes (50 mL) were added and the filtrate was set aside for 12 h at 5 °C. Additional amounts of *N*,*N*′-dicyclohexylurea were filtered off, and the filtrate was concentrated in vacuo. The product was triturated with 100 mL of hexanes, set aside at 5 °C for 2 h, and the product collected by filtration. White solid, 11.9 g (83%); mp 109−110 °C (lit. 120 °C (*19*)). ^1H NMR ($CDCl_3$) δ 4.36 (s, 2H); 2.86 (s, 4H).

*Aspartic Acid β-Methyl Ester Hydrochloride (**4**).* Methanol (MeOH, 100 mL) was placed in a round-bottom flask (**I**) and cooled to 0 °C. Acetyl chloride (AcCl, 33.4 g, 0.42 mol) was added dropwise over a period of 30 min (caution: the reaction is exothermic and dropwise addition is necessary), and the mixture was stirred for a further 30 min at 0 °C. A solution of aspartic acid (40.0 g, 0.3 mol) in MeOH (100 mL) in a separate round-bottom flask (II) was cooled to 0 °C, and the cold (0 °C) methanolic HCl generated in the flask I was added to the flask II. After 3 h at 0 °C, the ice bath was removed and stirring continued for a further 8 h at rt. The reaction mixture was concentrated to approximately $^1/_3$ of its original volume (bath temperature not exceeding 25 °C). Diethyl ether (Et_2O, 500 mL)

was added and the solution was set aside for 12 h at 0 °C. The white precipitate was filtered off to give 47.7 g (87%) of methyl ester **4**, mp 190−193 °C (lit. 191−193 °C (*20*)). ^{1}H NMR (D_2O) δ 4.30 (t, J = 5.5 Hz, 1H); 3.67 (s, 3H); 3.05 (m, 2H).

*N-Chloroacetyl-Asp(OMe)-OH (**1b**).* Aspartic acid β-methyl ester (**4**) (10.9 g, 50 mmol) was dissolved in dioxane/H_2O (1:1, 250 mL), and the solution was cooled to 0 °C. Na_2CO_3 (5.3 g, 50 mmol) was added to the solution, followed by stirring (at 0 °C) for 30 min. Another portion of Na_2CO_3 (5.3 g, 50 mmol) was added, followed by portionwise addition of *O*-chloroacetyl-*N*-hydroxysuccinimide (**5**) (9.58 g, 50 mmol). The mixture was stirred for 2 h at 0 °C, and for 12 h at rt. Organic impurities were removed by extraction with EtOAc (200 mL); the aqueous phase was acidified (pH 2) with HCl (36%) and was extracted with EtOAc (4 × 100 mL). The combined organic extracts (obtained after adjusting the pH to 2) were dried and concentrated to afford a colorless oil (9.10 g, 81%); the product was partially contaminated with NHS (approximately 15 mol %). ^{1}H NMR ($CDCl_3$) δ 10.48 (br s, 1H); 7.68 (br d, J = 7.5 Hz, 1H); 4.87 (m, 1H); 4.10 (m, 1H); 3.71 (s, 3H); 3.10 (dd, J = 17.5 Hz, 3.5 Hz, 1H); 2.89 (dd, J = 17.5 Hz, 3.5 Hz, 1H); 2.74 (s, 1H). ^{13}C NMR 173.0, 172.8, 171.4, 167.1, 52.2, 48.7, 42.1, 35.4, 25.3. HRMS (EI) *m/z*: found 224.0321, calcd 224.0278 for $C_7H_{11}ClNO_5$ $[M + H]^+$. LRMS (EI) *m/z* (rel abundance): 224 $[M + H^+]$ (100), 192 (9), 178 (10), 116 (48).

*Coupling of N-Chloroacetylglycine (**1a**) with H-Phe-OEt·HCl and H-Lys(Boc)-OMe·HCl to Give **2a** and **2b**.* General procedure: To a stirred suspension of *N*-chloroacetylglycine (**1a**, 455 mg, 3 mmol) in dry CH_2Cl_2 (25 mL), NHS (345 mg, 3 mmol) and DCC (805 mg, 3.9 mmol) were added (at 0 °C). Separate suspensions of H-Phe-OEt·HCl (687 mg, 3 mmol) and H-Lys-(Boc)-OMe·HCl (890 mg, 3 mmol) in dry CH_2Cl_2 (5 mL) were treated with Et_3N (840 μL, 6 mmol) and were stirred for 10 min at rt before addition to the mixture containing NHS, DCC, and *N*-chloroacetylglycine. The mixtures were stirred for 18 h at rt; the precipitate (*N*,*N*′-dicyclohexylurea and Et_3N·HCl) was filtered off; the filtrates were consecutively washed with 1 M HCl and brine (30 mL each) and were dried to afford white solids, purified by trituration in Et_2O (*N*-chloroacetyl-Gly-Phe-OEt, 882 mg, 90%) or by crystallization using CH_2Cl_2/hexane solution (*N*-chloroacetyl-Gly-Lys(Boc)-OMe, 1.08 g, 91%).

N-Chloroacetyl-Gly-Phe-OEt (**2a**), amorphous white solid; $[\alpha]^{25}_D$ +20 (c 0.50, CH_2Cl_2). ^{1}H NMR (DMSO-d_6) δ 8.44 (br d, D_2O exch., J = 7.5 Hz, 1H); 8.37 (br t, D_2O exch., J = 5.5 Hz, 1H); 7.27 (m, 2H); 7.20 (m, 3H); 4.43 (ddd, J = 6 Hz, 6 Hz, 1 Hz, 1H); 4.10 (s, 2H); 4.02 (q, J = 7 Hz, 2H); 3.73 (m, 2H); 2.99 (dd, J = 6 Hz, 6 Hz, 1H); 2.90 (dd, J = 8.5 Hz, 8.5 Hz, 1H); 1.08 (t, J = 7 Hz). ^{13}C NMR (DMSO-d_6) δ 171.3, 168.4, 166.1, 137.0, 129.1, 128.3, 126.6, 60.6, 53.7, 42.5, 41.8, 36.8, 13.9. HRMS (EI) *m/z*: found 326.1035 (326.1033 calcd for $C_{15}H_{19}ClN_2O_4$). LRMS (EI) *m/z* (rel abundance): 326 $[M]^+$ (5), 224 (16), 176 (100), 120 (55), 91 (37).

N-Chloroacetyl-Gly-Lys(Boc)-OMe (**2b**), white crystals, mp 83−84 °C; $[\alpha]^{25}_D$ −11 (c 0.47, CH_2Cl_2). ^{1}H NMR ($CDCl_3$) δ 7.42 (br s, D_2O exch., 1H); 6.94 (br d, D_2O exch., J = 7 Hz, 1H); 4.71 (br t, D_2O exch., J = 5.5 Hz, 1H); 4.56 (ddd, J = 7.5 Hz, 7.5 Hz, 1 Hz, 1H); 4.08 (s, 2H); 4.04 (d, J = 5.5 Hz, 2H); 3.73 (s, 3H); 3.08 (ddd, 6 Hz, 6 Hz, 1 Hz, 2H); 1.85 (m, 1H); 1.72 (m, 1H); 1.47 (m, 2H); 1.42 (s, 9H); 1.31 (m, 2H). ^{13}C NMR ($CDCl_3$) δ 172.5, 167.9 , 166.6, 156.2, 79.2, 52.5, 52.2, 43.0, 42.3, 39.9, 31.5, 29.5, 28.4, 22.3. HRMS (EI) *m/z*: found 394.1745 (394.1745 calcd for $C_{16}H_{29}ClN_3O_6$). LRMS (EI) *m/z* (rel abundance): 394 $[M + H]^+$ (53), 360 (27), 338 (60), 294 (100), 225 (51), 100 (30).

*Coupling of N-Chloroacetyl-Asp(OMe)-OH (**1b**) with H-Glu-(OMe)-OMe·HCl or H-Phe-OEt·HCl to give **2c** and **2d**.* General procedure: To a stirred suspension of *N*-chloroacetyl-Asp-(OMe)-OH (**1b**, 4.47 g, 20.0 mmol) in dry THF (50 mL), NHS (2.30 g, 20.0 mmol) and DCC (4.54 g, 22.0 mmol) were added (at 0 °C) and the suspension was stirred for 1 h at 0 °C. Separate suspensions of H-Glu(OMe)-OMe·HCl (4.66 g, 22.0 mmol) or H-Phe-OEt·HCl (4.30 g, 22.0 mmol) in dry THF (50 mL) were treated with Et_3N (3.2 mL, 22.0 mmol) and were stirred for 1 h at 0 °C, followed by the addition to the mixture containing NHS, DCC, and *N*-chloroacetyl-Asp(OMe)-OH. The ice baths were removed and separate mixtures were stirred for 12 h at rt, and the precipitate (*N*,*N*′-dicyclohexylurea and Et_3N·HCl) was filtered off. The filtrates were concentrated and were extracted with EtOAc (150 mL). The organic extracts were consecutively washed with 1 M NaH_2PO_4 (pH 2.0, adjusted with H_3PO_4) (2 × 50 mL), a saturated aqueous solution of $NaHCO_3$ (2 × 50 mL), and brine (50 mL); were dried over Na_2SO_4 and concentrated to give oils. The obtained oils were dissolved in EtOAc (75 mL), the solutions were set aside for 5 h at 5 °C, and more of the precipitated *N*,*N*′-dicyclohexylurea was filtered off. The filtrates were concentrated. Compound **2c** was purified by trituration with Et_2O/hexanes (1:1, 100 mL) to afford an off-white solid which was further triturated with MeOH/Et_2O/hexanes (1:1:4, 150 mL) to give *N*-chloroacetyl-Asp(OMe)-Glu(OMe)-OMe (**2c,** 5.8 g, 76%). Compound **2d** was triturated with Et_2O/hexanes (1:1, 100 mL) to obtain an off-white solid, recrystallized form acetone/hexanes (1:3, 65 mL) to give *N*-chloroacetyl-Asp(OMe)-Phe-OEt (**2d**, 6.19 g, 81%).

N-Chloroacetyl-Asp(OMe)-Glu(OMe)-OMe (**2c**), white solid; $[\alpha]^{25}_D$ −37 (c 0.54, MeOH). ^{1}H NMR ($CDCl_3$) δ 7.79 (d, J = 8 Hz, 1H); 7.29 (d, J = 8 Hz, 1H); 4.82 (m, 1H); 4.51 (m, 1H); 4.08 (m, 2H) 3.69 (s, 3H); 3.69 (s, 3H); 3.64 (s, 3H); 2.99 (dd, J = 17 Hz, 4.5 Hz, 1H); 2.66 (dd, J = 17 Hz, 6.5 Hz, 1H); 2.36 (m, 2H); 2.17 (m, 1H); 1.97 (m, 1H). ^{13}C NMR ($CDCl_3$) δ 173.2, 172.2, 171.5, 169.7, 166.3, 52.4, 52.2, 52.0, 51.8, 49.3. 42.4, 35.5, 29.8, 26.6. HRMS (EI) *m/z*: found 381.1056 $[M + H^+]$ (calcd 381.1065 for $C_{14}H_{22}ClN_2O_8$). LRMS: *m/z* (rel. abundance): 381 $[M + H]^+$ (100), 225 (25).

N-Chloroacetyl-Asp(OMe)-Phe-OEt (**2d**), white solid, mp 115−116 °C; $[\alpha]^{25}_D$ −18 (c 0.56, MeOH). ^{1}H NMR ($CDCl_3$) δ 7.88; (d, J = 7.8 Hz, 1H); 7.29 (m, 3H); 7.13; (d, J = 7.0 Hz, 2H); 6.92; (d, J = 7.8 Hz, 1H); 4.78 (m, 2H); 4.17 (q, J = 7.2 Hz, 2H); 3.98 (m, 2H); 3.72 (s, 3H); 3.17 (dd, J = 13.9 Hz, 5.7 Hz, 1H); 3.17 (dd, J = 13.9 Hz, 6.6 Hz, 1H); 3.0 (dd, J = 17.3 Hz, 3.6 Hz, 1H); 2.63 (dd, J = 17.3 Hz, 6.9 Hz, 1H); 1.25 (t, J = 7.2 Hz, 3H). ^{13}C NMR ($CDCl_3$) δ 172.0, 170.7, 169.2, 166.1, 135.5, 129.1, 128.3, 126.9, 61.4, 53.3, 52.0, 49.1, 42.1, 37.3, 35.0, 13.9. HRMS (EI) *m/z*: found 398.1252 $[M^+]$ (calcd 398.1243 for $C_{18}H_{23}ClN_2O_6$). LRMS (EI) *m/z* (rel. abundance): 398 $[M^+]$ (10), 176 (100), 120 (35), 102 (33).

*Conversion of N-Chloroacetyldipeptides **2a** and **2b** to N-Iodoacetyldipeptides **3a** and **3b.*** Sodium iodide (2.25 g, 15 mol) was added to separate solutions of *N*-chloroacetyl-Gly-Phe-OEt (**2a**, 817 mg, 2.5 mmol) or *N*-chloroacetyl-Gly-Lys(Boc)-OMe (**2b**, 985 mg, 2.5 mmol) in acetone (15 mL). The mixtures were stirred for 18 h at rt, concentrated to ca. $^1/_4$ of their original volumes, diluted with EtOAc (25 mL), and finally washed with 10% solution of Na_2SO_3 (25 mL). The aqueous layers were extracted with EtOAc (20 mL), and the combined organic extracts were dried and concentrated to afford white solids, purified by trituration in Et_2O (*N*-iodoacetyl-Gly-Phe-OEt, 816 mg, 78%) or by crystallization using 1:1 acetone/hexane solution (*N*-iodoacetyl-Gly-Lys(Boc)-OMe, 1.01 g, 83%).

N-Iodoacetyl-Gly-Phe-OEt (**3a**), amorphous white solid; $[\alpha]^{25}_D$ +30 (c 0.50, CH_2Cl_2). ^{1}H NMR (DMSO-d_6) δ 8.42 (br m, D_2O exch., 2H); 7.27 (m, 2H); 7.20 (m, 3H); 4.43 (ddd, J = 8 Hz, 8 Hz, 1 Hz, 1H); 4.02 (q, J = 7 Hz); 3.70 (m, 2H); 3.68 (s, 2H); 2.98 (dd, J = 6 Hz, 6 Hz, 1H); 2.90 (dd, J = 8.5 Hz, 8.5 Hz, 1H); 1.08 (t, J = 7 Hz). ^{13}C NMR (DMSO-d_6) δ 171.3,

168.5, 167.8, 136.9, 129.1, 128.2, 126.6, 60.5, 53.7, 42.0, 36.9, 33.3, 13.9. HRMS (EI) *m/z*: found 418.0347 [M^+] calcd (418.0390 for $C_{15}H_{19}IN_2O_4$). LRMS (EI) *m/z* (rel abundance): 418 [$M]^+$ (5), 225 (20), 176 (100), 120 (41), 91 (19).

N-Iodoacetyl-Gly-Lys(Boc)-OMe (**3b**), white crystals, mp 101−102 °C; $[\alpha]^{25}_D$ −11 (c 0.45, CH_2Cl_2). ^{1}H NMR ($CDCl_3$) δ 7.12 (br s, D_2O exch., 1H); 6.87 (br d, D_2O exch., J = 7.5 Hz, 1H); 4.72 (br t, D_2O exch., J = 6 Hz, 1H); 4.56 (ddd, J = 7 Hz, 7 Hz, 1 Hz, 1H); 4.01 (m, 2H); 3.75 (s, 2H); 3.74 (s, 3H); 3.10 (ddd, 6 Hz, 6 Hz, 1 Hz, 2H); 1.87 (m, 1H); 1.74 (m, 1H); 1.50 (m, 2H); 1.44 (s, 9H); 1.36 (m, 2H). ^{13}C NMR ($CDCl_3$) δ 172.5, 168.5, 168.2, 156.2, 79.3, 52.5, 52.3, 43.6, 40.0, 39.9, 31.4, 29.5, 28.4, 22.4. HRMS (EI) *m/z*: found 486.1086 (486.1056 calcd for $C_{16}H_{28}IN_3O_6$). LRMS (EI) *m/z* (rel abundance): 394 [$M]^+$ (5), 385 (36), 187 (21), 142 (100), 128 (14), 84 (36).

*Conversion of N-Chloroacetyldipeptides **2c** and **2d** to N-Iodoacetyldipeptides **3c** and **3d***. Sodium iodide (9.0 g, 60 mmol) was added to separate solutions of *N*-chloroacetyl-Asp(OMe)-Glu(OMe)-OMe (**2c**, 3.81 g, 10.0 mmol) or *N*-chloroacetyl-Asp-(OMe)-Phe-OEt (**2d**, 3.84 g, 10.0 mmol) in acetone (50 mL). The mixtures were stirred for 1 h at rt and for 2 h at 45 °C, cooled to rt, concentrated to ca. $^1/_4$ of their original volumes, diluted with EtOAc (100 mL), and finally washed with 10% solution of Na_2SO_3 (4 × 25 mL). The aqueous layers were extracted with EtOAc (25 mL), and the combined organic extracts were dried and concentrated to afford white solids which were purified by trituration in acetone/hexanes (1:10 v/v, 100 mL) to give *N*-chloroacetyl-Asp(OMe)-Glu(OMe)-OMe (**3c**, 3.89 g, 82%) or *N*-chloroacetyl-Asp(OMe)-Phe-OEt (**3d**, 4.31 g, 90%).

N-Iodoacetyl-Asp(OMe)-Glu(OMe)-OMe (**3c**), white solid; $[\alpha]^{25}_D$ −27 (c 0.56, MeOH). ^{1}H NMR ($CDCl_3$) δ 7.57 (d, J = 7.8 Hz, 1H); 7.32 (d, J = 7.6 Hz, 1H); 4.81 (m, 1H); 4.48 (m, 1H); 3.70 (m, 2H) 3.64 (s, 6H); 3.59 (s, 3H); 2.85 (dd, J = 17.0 Hz, 4.7 Hz, 1H); 2.69 (dd, J = 16.8 Hz, 6.4 Hz, 1H); 2.34 (m, 2H); 2.12 (m, 1H), 1.94 (m, 1H). ^{13}C NMR ($CDCl_3$) δ 173.0, 171.7, 171.4, 170.0, 167.9, 52.3, 52.0, 51.8, 51.7, 49.6, 35.5, 29.8, 26.7. HRMS (EI) found 472.0339 [M^+] (calcd 472.0343 for $C_{14}H_{21}IN_2O_8$) LRMS *m/z* (%): 472 [M^+] (5), 440 (5), 345 (5), 270 (20), 144 (100).

N-Iodoacetyl-Asp(OMe)-Phe-OEt (**3d**), white solid; $[\alpha]^{25}_D$ −19 (c 0.54, MeOH). ^{1}H NMR ($CDCl_3$) δ 7.29 (m, 3H); 7.14; (d, J = 7.2 Hz, 2H); 6.94; (d, J = 8.0 Hz, 1H); 4.75 (m, 2H); 4.15 (q, J = 7.2 Hz, 2H); 3.70 (s, 3H); 3.63 (m, 2H); 3.14 (dd, J = 13.9 Hz, 6.0 Hz, 1H); 3.07 (dd, J = 13.9 Hz, 6.6 Hz, 1H); 2.96 (dd, J = 17.2 Hz, 3.9 Hz, 1H); 2.61 (dd, J = 17.3 Hz, 6.9 Hz, 1H); 1.25 (t, J = 7.2 Hz, 3H). ^{13}C NMR ($CDCl_3$) δ 171.4, 170.6, 169.6, 167.7, 135.6, 129.0, 128.2, 126.8, 61.2, 53.5, 51.9, 49.5, 37.4, 35.4, 13.8. HRMS (EI) *m/z*: found 490.0597 [M^+] (calcd 490.0598 for $C_{18}H_{23}IN_2O_6$). LRMS (EI) *m/z* (rel. abundance): 490 [M^+] (10), 270 (20), 176 (100), 102 (50).

*Alkylation of Cyclen with Iodoacetyl Dipeptides **3a**, **3b**, **3c**, and **3d***. *N*-Iodoacetyl-Gly-Phe-OEt (**3a**, 836 mg, 2 mmol), *N*-iodoacetyl-Gly-Lys(Boc)-OMe (**3b**, 971 mg, 2 mmol), *N*-iodoacetyl-Asp(OMe)-Glu(OMe)-OMe (**3c**, 950 mg, 2 mmol), and *N*-iodoacetyl-Asp(OMe)-Phe-OEt (**3d**, 985 mg, 2 mmol) were added (at rt) to a stirred solution of cyclen (86 mg, 0.5 mmol) and diisopropylethylamine (350 μL, 2 mmol) in acetonitrile (7 mL). The mixtures were stirred for 18 h at 50 °C (**3a** and **3b**) or 70 °C (**3c** and **3d**), cooled to rt, diluted with EtOAc (25 mL), and washed with 10% solution of Na_2SO_3 (25 mL). The aqueous layers were extracted with EtOAc (20 mL), and the combined organic extracts were dried and concentrated to afford white solids, purified by repeated (twice) trituration with hexanes.

Tetraacetyl-Gly-Phe-OEt cyclen (**6a**, 653 mg, 98%), white solid; $[\alpha]^{25}_D$ −10 (c 0.50, CH_2Cl_2). ^{1}H NMR ($CDCl_3$) δ 7.40−7.08 (m, D_2O exch., 7H); 4.74−4.62 (m, 1H); 4.14−3.79 (br m, 4H); 3.30−3.01 (br m, 4H); 2.82−2.26 (br m, 4H); 1.24−1.11 (m, 3H). ^{13}C NMR ($CDCl_3$) δ 171.9, 171.4, 171.3, 169.4, 167.8, 136.2, 129.3, 128.5, 126.9, 61.6, 61.4, 56.5, 54.6, 54.0, 53.7, 42.8, 42.4, 37.7, 37.6, 14.0. HRMS (ESI) *m/z*: found 1355.6617 [M + Na]$^+$ (calcd 1355.6652 for $C_{68}H_{92}N_{12}O_{16}Na$).

Tetraacetyl-Gly-Lys(Boc)-OMe cyclen (**6b**, 777 mg, 97%), white solid, $[\alpha]^{25}_D$ −30 (c 0.50, CH_2Cl_2). ^{1}H NMR ($CDCl_3$) δ 7.79 (br s, D_2O exch., 1H); 7.45 (br s, D_2O exch., 1H); 4.98 (br s, D_2O exch., 1H); 4.46−4.43 (br m, 1H); 4.05−3.95 (br m, 2H); 3.71 (s, 3H); 3.52−2.62 (br m, 4H); 3.07 (ddd, J = 6.5 Hz, 6.5 Hz, 1 Hz); 2.05−1.98 (br m, 2H); 1.85−1.76 (br m, 2H); 1.51−1.34 (br m, 2H); 1.41 (s, 9H). ^{13}C NMR ($CDCl_3$) δ 173.1, 172.7, 172.0, 156.9, 79.0, 52.5, 52.4, 50.6, 49.0, 41.1, 40.1, 33.8, 29.4, 28.4, 25.6, 24.9. HRMS (ESI) *m/z*: found 1623.9191 [M + Na]$^+$ (calcd 1623.9185 for $C_{72}H_{128}N_{16}O_{24}$-Na).

Tetraacetyl-Asp(OMe)-Glu(OMe)-OMe cyclen (**6c**, 670 mg, 87%), white solid; $[\alpha]^{25}_D$ −7 (c 0.69, CH_2Cl_2). ^{1}H NMR ($CDCl_3$) δ 7.88 (m, 2H); 7.34 (m, 2H); 7.17 (m, 2H); 4.51 (m, 4H); 4.19 (m, 4H); 3.79 (m, 3H); 3.36 (m, 36H); 2.77 (m, 10H); 2.60 (m, 12H); 2.10 (m, 8H); 1.86 (m, 4H); 1.71 (m, 4H). ^{13}C NMR ($CDCl_3$) δ 173.0, 172.8, 171.8, 171.7, 171.6, 171.4, 171.2, 170.3, 170.1, 52.2, 52.1, 51.7, 51.6, 51.4, 49.5, 49.1, 35.4, 29.6, 26.3. HRMS (ESI) found 1571.6516 [M + Na]$^+$ (calcd 1571.6446 for $C_{64}H_{100}N_{12}O_{32}Na$).

Tetraacetyl-Asp(OMe)-Phe-OEt cyclen (**6d**, 800 g, 98%), white solid; $[\alpha]^{25}_D$ −8 (c 0.61, CH_2Cl_2). ^{1}H NMR ($CDCl_3$) δ 7.37−7.07 (m, D_2O exch., 7H); 4.78−4.66 (m, 1H); 4.20−4.08 (m, 3H); 3.62 (s, 3H); 3.49−2.38 (m, 8H); 1.35−1.18 (m, 3H). ^{13}C NMR ($CDCl_3$) δ 171.9, 171.8, 171.2, 170.1, 135.8, 129.2, 128.2, 128.1, 126.6, 61.3, 61.2, 55.7, 53.3, 53.2, 51.8, 51.6, 49.0, 37.0, 34.7, 13.8. HRMS (ESI) *m/z*: found 1643.7426 [M+Na]$^+$ (calcd 1643.7497 for $C_{80}H_{108}N_{12}O_{24}Na$).

*Hydrolysis of Tetraacetyl-Gly-Phe-OEt Cyclen (**6a**)*. A solution of NaOH (384 mg, 9.6 mmol) in water (2.5 mL) was added to a stirred solution of tetraacetyl-Gly-Phe-OEt cyclen (**6a**, 800 mg, 0.6 mmol) in THF (2.5 mL). The mixture was stirred for 2 h at rt, then cooled to 0 °C, and the pH was adjusted to 4 (2.5 M HCl), after which an oil spontaneously separated. The water was decanted and the oil which deposited on the flask walls was triturated with Et_2O (twice) to afford tetraacetyl-Gly-Phe-OH cyclen (**7**) as a white solid (550 mg, 75%); $[\alpha]^{25}_D$ −10 (c 0.50, EtOH). ^{1}H NMR (DMSO-d_6) δ 12.80 (br s, D_2O exch., 1H); 8.46−8.30 (br m, D_2O exch., 2H); 7.26−7.16 (m, 5H); 4.45−4.40 (br m, 1H); 3.80−3.64 (br m, 2H); 3.24−2.65 (br m, 4H); 3.05−3.00 (m, 2H); 2.90−2.84 (m, 2H). ^{13}C NMR (DMSO-d_6) δ 172.8, 170.8, 170.7, 137.5, 129.2, 128.3, 126.5, 56.07, 53.7, 41.7, 41.5, 36.8, 33.4. HRMS (ESI) *m/z*: found 1222.6270 [M + H]$^+$ (calcd 1222.3242 for $C_{60}H_{77}N_{12}O_{16}$).

*Deprotection of Tetraacetyl-Gly-Lys(Boc)-OMe Cyclen (**6b**)*. Tetraacetyl-Gly-Lys(Boc)-OMe cyclen (**6b**, 150 mg, 0.094 mmol) was dissolved in TFA (1.5 mL), and the mixture was stirred for 15 min at rt. It was concentrated to afford tetraacetyl Gly-Lys-OMe cyclen tetratrifluoroacetate (**8**, 155 mg, 100%) as a slightly yellow oil which was used directly for further reactions.

*Hydrolysis of Tetraacetyl-Gly-Lys-OMe Cyclen Tetratrifluoroacetate (**8**)*. A solution of NaOH (2.5 M, 940 μL) was added to a solution of tetraacetyl-Gly-Lys-OMe cyclen tetratrifluoroacetate **8** (155 mg, 0.094 mmol) in MeOH (900 μL). The mixture was stirred for 2 h at 60 °C, MeOH was evaporated, and the mixture was neutralized (using 2 M HCl). It was subjected to size exclusion chromatography; fractions containing the product were combined and were freeze-dried to afford

tetraacetyl-Gly-Lys-OH cyclen (**9**) as a colorless oil (97 mg, 90%), $[\alpha]^{25}_D$ −167 (c 0.27, H_2O). ^{1}H NMR (D_2O) δ 3.83 (br s, 1H); 3.69 (s, 2H); 3.62−3.58 (m, 2H); 3.13−2.62 (br m, 4H); 2.89−2.83 (m, 2H); 1.90−1.72 (m, 2H); 1.67−1.52 (m, 2H); 1.41−1.20 (m, 2H). ^{13}C NMR (D_2O) δ 178.9, 170.5, 55.2, 50.9, 49.3, 42.2, 39.4, 31.3, 26.5, 22.1. HRMS (ESI) *m/z*: found 1145.6628 $[M + H]^+$ (calcd 1145.6642 for $C_{48}H_{89}N_{16}O_{16}$).

*Hydrolysis of Tetraacetyl-Asp(OMe)-Glu(OMe)-OMe Cyclen (**6c**).* A solution of NaOH (2.5 M, 2 mL) was added to a solution of tetraacetyl-Asp(OMe)-Glu(OMe)-OMe cyclen (**6c**, 155 mg, 0.1 mmol) in MeOH (2 mL). The mixture was stirred for 2 h at 60 °C, MeOH was evaporated, and the mixture was neutralized (using 4 M HCl). It was subjected to size exclusion chromatography; fractions containing the product were combined and were freeze-dried to afford tetraacetyl-Asp-Glu-OH cyclen (**10**) as a colorless solid (103 mg, 75%); $[\alpha]^{25}_D$ +7 (c 0.62, H_2O). ^{1}H NMR (D_2O) δ 4.39−4.36 (m, 1H); 3.98−3.93 (m, 1H); 3.71−3.57 (m, 2H); 3.24−3.02 (m, 4H); 2.07−2.03 (m, 2H); 1.89−1.83 (m, 1H); 1.74−1.64 (m, 1H). ^{13}C NMR (D_2O) δ 181.9, 181.8, 179.0, 55.4, 52.3, 34.0, 28.8, 28.5. HRMS (ESI) *m/z*: found 1381.4708 $[M + H]^+$ (calcd 1381.4767 for $C_{52}H_{77}N_{12}O_{32}$).

*Hydrolysis of Tetraacetyl-Asp(OMe)-Phe-OEt Cyclen (**6d**).* A solution of NaOH (2.5 M, 7.5 mL) was added to a solution of tetraacetyl-Asp(OMe)-Phe-OEt cyclen (**6d**, 610 mg, 0.38 mmol) in MeOH (7.5 mL). The mixture was stirred for 20 min at 60 °C, MeOH was evaporated, and the mixture was cooled to 0 °C and was acidified (pH 2, using 4 M HCl). The oily product deposited on the flask wall and the water was decanted. The residue was triturated with Et_2O (twice) to afford tetraacetyl-Asp-Phe-OH cyclen (**11**) as a colorless solid (530 mg, 95%); $[\alpha]^{25}_D$ +7 (c 0.73, DMSO). ^{1}H NMR (DMSO-d_6) δ 12.74 (br s, D_2O exch., 2H); 8.85 (br s, D_2O exch., 1H); 8.42 (br s, D_2O exch., 1H); 7.32−7.17 (m, 5H); 4.63−4.37 (m, 2H); 3.78−3.73 (m, 1H); 3.45−2.55 (m, 9H); ^{13}C NMR (DMSO-d_6) δ 172.8, 172.6, 172.1, 169.1, 137.6, 129.2, 128.3, 126.5, 65.0, 56.1, 53.8, 48.9, 36.8, 36.5, 36.4, 18.6, 15.2. HRMS (ESI) *m/z*: found 1453.5862 $[M + H]^+$ (calcd 1453.5800 for $C_{68}H_{85}N_{12}O_{24}$).

*Treatment of Tetraacetyl-Gly-Phe-OH Cyclen (**7**), Tetraacetyl-Gly-Lys-OH Cyclen (**9**), Tetraacetyl-Asp-Glu-OH Cyclen (**10**), and Tetraacetyl-Asp-Phe Cyclen (**11**) with Lanthanide(III) Chlorides.* Separate solutions of tetraacetyl-Gly-Phe-OH cyclen (**7**, 114 mg, 0.094 mmol), tetraacetyl-Gly-Lys-OH cyclen (**9**, 107 mg, 0.094 mmol), tetraacetyl-Asp-Glu-OH cyclen (**10**, 130 mg, 0.094 mmol), and tetraacetyl-Asp-Phe-OH cyclen (**11**, 137 mg, 0.094 mmol) in water (3 mL) were treated with lanthanide(III) chlorides (0.094 mmol) as follows: tetraacetyl-Gly-Phe-OH cyclen ($EuCl_3 \cdot 6H_2O$, $NdCl_3 \cdot H_2O$, $TmCl_3 \cdot 6H_2O$, and $YbCl_3 \cdot 6H_2O$); tetraacetyl-Gly-Lys-OH cyclen ($DyCl_3 \cdot 6H_2O$, $EuCl_3 \cdot 6H_2O$, $NdCl_3 \cdot H_2O$, $TbCl_3 \cdot 6H_2O$, $TmCl_3 \cdot 6H_2O$, and $YbCl_3 \cdot 6H_2O$); tetraacetyl-Asp-Glu-OH cyclen ($EuCl_3 \cdot 6H_2O$, $NdCl_3 \cdot H_2O$, $TmCl_3 \cdot 6H_2O$, and $YbCl_3 \cdot 6H_2O$); tetraacetyl-Asp-Phe-OH cyclen ($EuCl_3 \cdot 6H_2O$). Reaction mixtures were treated with NaOH (2.5 M solution) to adjust the pH to 9 and were stirred for 18 h at rt followed by size exclusion chromatography. The fractions containing the lanthanide(III) complexes were combined and were isolated as dry solids by lyophilization.

Eu^{3+} tetraacetyl-Gly-Phe-OH cyclen (**12**), white solid; ^{1}H NMR (D_2O) δ 24.44 (s); 21.93 (s); 8.50 (s); 7.83 (s); 7.47 (s); 7.36 (s); 7.10−6.80 (m); 6.59−6.58 (m); 6.38 (s); 6.22 (s); 6.04 (s); 3.57−2.05 (m); 1.50 (s); −3.08 (s); −3.78 (s); −4.49 (s); −5.04 (s); −8.03 (s); −8.91 (s); −9.20 (s); −9.91 (s); −11.66 (s); −12.05 (s); −13.06 (s). HRMS (ESI) *m/z*: found 1369.4544 $[M - 2H]^+$ (calcd 1369.4597 for $C_{60}H_{74}N_{12}O_{16}Eu$).

Nd^{3+} tetraacetyl-Gly-Phe-OH cyclen (**13**), white solid; ^{1}H NMR (D_2O) δ 15.00 (s); 13.34 (s); 9.31 (s); 7.44−6.37 (m); 5.76 (s); 5.19 (s); 4.91 (s); 4.18−2.60 (m); −14.68 (s); −16.55 (s). HRMS (ESI) *m/z*: found 1360.4401 $[M - 2H]^+$ (calcd 1360.4423 for $C_{60}H_{74}N_{12}O_{16}Nd$).

Tm^{3+} tetraacetyl-Gly-Phe-OH cyclen (**14**), white solid; ^{1}H NMR (D_2O) δ 29.42 (s); 14.79 (s); 13.18 (s) 7.49 (s); 7.09−7.00 (m); 5.09 (s); 4.86 (s); 4.20−4.11 (m); 3.54−3.38 (m); 2.94−1.43 (m); 1.16−0.94 (m); −3.41 (s); −4.69 (s); −14.15 (s); −15.76 (s); −16.54 (s). HRMS (ESI) *m/z*: found 1387.4661 $[M - 2H]^+$ (calcd 1387.4688 for $C_{60}H_{74}N_{12}O_{16}Tm$).

Yb^{3+} tetraacetyl-Gly-Phe-OH cyclen (**15**), white solid; ^{1}H NMR (D_2O) δ 91.49 (s); 16.96 (s); 14.04 (s); 10.89 (s); 9.23 (s); 7.95 (s); 7.69−6.81 (m); 5.71 (s); 3.93−1.00 (m); 0.52 (s); 0.41 (s); −2.59 (s); −2.91 (s); −24.02 (s); −29.20 (s); −53.19 (s). HRMS (ESI) *m/z*: found 1392.4300 $[M - 2H]^+$ (calcd 1392.4688 for $C_{60}H_{74}N_{12}O_{16}Yb$).

Dy^{3+} tetraacetyl-Gly-Lys-OH cyclen (**22**), colorless oil; ^{1}H NMR (D_2O) δ 36.98 (s); 34.01 (s); 13.58 (s); 11.01 (s); 10.70 (s); 10.09 (s); 9.72 (s); 8.11−7.92 (m); 4.29−4.14 (m); 3.60−2.84 (m); 1.87−1.58 (m). HRMS (ESI) *m/z*: found 1306.5760 $[M - 2H]^+$ (calcd 1306.5700 for $C_{48}H_{86}N_{16}O_{16}Dy$).

Eu^{3+} tetraacetyl-Gly-Lys-OH cyclen (**23**), colorless oil; ^{1}H NMR (D_2O) δ 25.10 (s); 15.13 (s); 13.37 (s); 9.36 (s); 6.54 (s); 5.55 (s); 3.21−0.68 (m); −2.89 (s); −5.06 (s); −10.18 (s); −13.14 (s); −16.60 (s). HRMS (ESI) *m/z*: found 1361.5056 $[M - 5H + 3Na]^+$ (calcd 1361.5078 for $C_{48}H_{83}N_{16}O_{16}EuNa_3$).

Nd^{3+} tetraacetyl-Gly-Lys-OH cyclen (**24**), colorless oil; ^{1}H NMR (D_2O) δ 15.24 (s); 13.40 (s); 9.45 (s); 6.63 (s); 5.58 (s); 3.78 (s); 3.07 (s); 2.84−2.80 (m); 2.63 (s); 2.54 (s); 2.27 (s); 2.02 (s); 1.84−1.51 (m); 1.22−1.16 (m); −16.81 (s). HRMS (ESI) *m/z*: found 1287.5600 $[M - 2H]^+$ (calcd 1287.5587 for $C_{48}H_{86}N_{16}O_{16}Nd$).

Tb^{3+} tetraacetyl-Gly-Lys-OH cyclen (**25**), colorless oil; ^{1}H NMR (D_2O) δ 41.68 (s); 31.21 (s); 3.89−3.62 (m); 3.10−2.90 (m); 2.78−2.10 (m); 1.63−1.39 (m); 1.11 (s); −0.46 (s); −0.52 (s); −2.79 (s); −3.26 (s); −4.35 (s); −5.05 (s); −6.09 (s); −14.76 (s); −16.31 (s); −75.61 (s). HRMS (ESI) *m/z*: found 1301.5658 $[M - 2H]^+$ (calcd 1301.5661 for $C_{48}H_{86}N_{16}O_{16}Tb$).

Tm^{3+} tetraacetyl-Gly-Lys-OH cyclen (**26**), colorless oil; ^{1}H NMR (D_2O) δ 30.65 (s); 4.66 (s); 3.91−3.38 (m); 3.16−2.11 (m); 1.44−0.84 (m); −0.46 to −0.74 (m); −2.74 to −3.55 (m); −4.30 to −4.57 (m); −4.98 to −5.25 (m); −6.00 to −6.28 (m); −14.63 to −14.93 (m); −16.06 to −16.33 (m). HRMS (ESI) *m/z*: found 1311.5773 $[M - 2H]^+$ (calcd 1311.5750 for $C_{48}H_{86}N_{16}O_{16}Tm$).

Yb^{3+} tetraacetyl-Gly-Lys-OH cyclen (**27**), colorless oil; ^{1}H NMR (D_2O) δ 17.29 (s); 14.34 (s); 3.94−3.90 (m); 3.71 (s); 3.32 (s); 2.78−2.74 (m); 2.59 (s); 2.54 (s); 2.48 (s); 1.61−1.41 (m); 1.20−1.10 (m); −0.12 (s); −0.26 (s); −0.60 (s); −0.85 (s); −1.11 (s); −1.20 (s); −3.17 (s); −3.43 (s); −24.97 (s); −30.13 (s); −55.19 (s). HRMS (ESI) *m/z*: found 1316.5853 $[M - 2H]^+$ (calcd 1316.5796 for $C_{48}H_{86}N_{16}O_{16}Yb$).

Eu^{3+} tetraacetyl-Asp-Glu-OH cyclen (**28**), white solid; ^{1}H NMR (D_2O) δ 23.75 (s); 3.88−2.57 (m); 1.41−0.72 (m); −2.49 to −3.26 (m); −4.58 to −5.28 (m); −8.69 to −8.93 (m); −12.72 to −13.43 (m). HRMS (ESI) *m/z*: found 1529.3807 $[M - 2H]^+$ (calcd 1529.3731 for $C_{52}H_{74}N_{12}O_{32}Eu$).

Nd^{3+} tetraacetyl-Asp-Glu-OH cyclen (**29**), white solid; ^{1}H NMR (D_2O) δ 15.47 (s); 13.65 (s); 8.18−6.81 (m); 4.44−3.73 (m); 3.20−2.05 (m); 1.70−0.70 (m); −2.80 to −3.28 (m); −8.63 to −9.19 (m); −12.78 to −13.40 (m); −16.75 (s). HRMS (ESI) *m/z*: found 1522.3549 $[M - 2H]^+$ (calcd 1522.3633 for $C_{52}H_{74}N_{12}O_{32}Nd$).

Tm^{3+} tetraacetyl-Asp-Glu-OH cyclen (**30**), white solid; ^{1}H NMR (D_2O) δ 1.52 (s); −3.32 (s); −7.36 (s); −14.08 (s). HRMS (ESI) *m/z*: found 1547.3875 $[M - 2H]^+$ (calcd 1547.3874 for $C_{52}H_{74}N_{12}O_{32}Tm$).

Yb^{3+} tetraacetyl-Asp-Glu-OH cyclen (**31**), white solid; ^1H NMR (D_2O) δ 19.17−13.45 (m); 1.32 to −6.21 (m); −23.84 to −34.64 (m). HRMS (ESI) *m/z*: found 1552.3845 $[M - 2H]^+$ (calcd 1552.3921 for $C_{52}H_{74}N_{12}O_{32}Yb$).

Eu^{3+} tetraacetyl-Asp-Phe-OH cyclen (**32**), white solid; ^1H NMR (D_2O) δ 24.99−23.14 (m); 7.25−6.58 (m); 4.26−4.09 (m); 3.19−1.09 (m); −2.59 to −5.03 (m); −8.17 to −9.43 (m); −12.07 to −13.13 (m). HRMS (ESI) *m/z*: found 1604.4856 $[M - 2H]^+$ (calcd 1604.4916 for $C_{68}H_{83}N_{12}O_{24}Eu$).

*Treatment of Tetraacetyl-Gly-Lys-OMe Cyclen Tetratrifluoroacetate (**8**) with Lanthanide(III) Chlorides.* Solutions of tetraacetyl-Gly-Lys-OMe cyclen tetratrifluoroacetate (**8**, 155 mg, 0.094 mmol) in water (3 mL) were treated with lanthanide(III) chlorides ($DyCl_3 \cdot 6H_2O$, $EuCl_3 \cdot 6H_2O$, $NdCl_3 \cdot H_2O$, $TbCl_3 \cdot H_2O$, $TmCl_3 \cdot 6H_2O$, and $YbCl_3 \cdot 6H_2O$, 0.094 mmol). Reaction mixtures were treated with NaOH (2.5 M solution) to adjust the pH to 9 and were stirred for 18 h at rt. The reaction mixtures were subjected to size exclusion chromatography. The fractions containing the lanthanide(III) complexes were combined and were freeze-dried to afford colorless oils.

Dy^{3+} tetraacetyl-Gly-Lys-OMe cyclen (**16**), colorless oil; ^1H NMR (D_2O) δ 35.31 (s); 26.08 (s); 13.01 (s); 10.42 (s); 9.19 (s); 8.78 (s); 8.61 (s); 6.82 (s); 6.45 (s); 6.29 (s); 4.08−4.00 (m); 3.80 (s); 3.49−3.42 (m); 3.28 (s); 3.14 (s); 3.05−2.66 (m); 2.04−1.69 (m); 1.47−1.32 (m). HRMS (ESI) *m/z*: found 1362.6381 $[M - 2H]^+$ (calcd 1362.6326 for $C_{52}H_{94}N_{16}O_{16}Dy$).

Eu^{3+} tetraacetyl-Gly-Lys-OMe cyclen (**17**), colorless oil; ^1H NMR (D_2O) δ 24.19 (s); 12.56 (s); 6.06 (s); 3.86 (s); 3.60 (s); 3.11−2.45 (m); 1.74−0.85 (m); −3.17 (s); −4.63 (s); −8.80 (s); −9.62 (s); −12.80 (s). HRMS (ESI) *m/z*: found 1351.6251 $[M - 2H]^+$ (calcd 1351.6246 for $C_{52}H_{94}N_{16}O_{16}Eu$).

Nd^{3+} tetraacetyl-Gly-Lys-OMe cyclen (**18**), colorless oil; ^1H NMR (D_2O) δ 14.97 (s); 13.25 (s); 9.41−9.01 (m); 6.69 (s); 5.85−5.54 (m); 4.04−3.86 (m); 3.05−3.04 (m); 2.83 (s); 2.64 (s); 2.55 (s); 2.25−1.53 (m); 1.26−1.16 (m); −16.27 (s). HRMS (ESI) *m/z*: found 1343.5500 $[M - 2H]^+$ (calcd 1343.6213 for $C_{52}H_{94}N_{16}O_{16}Nd$).

Tb^{3+} tetraacetyl-Gly-Lys-OMe cyclen (**19**), colorless oil; ^1H NMR (D_2O) δ 31.81 (s); 22.90 (s); 12.26−11.52 (m); 9.35 (s); 8.15 (s); 7.98 (s); 7.71 (s); 6.88 (s); 6.15 (s); 6.02 (s); 5.71 (s); 4.14 (s); 3.89−3.86 (m); 3.61−3.60 (m); 3.11−3.05 (m); 3.00 (s); 2.90 (s); 2.80 (s) 2.03−1.56 (m). HRMS (ESI) *m/z*: found 1357.6310 $[M - 2H]^+$ (calcd 1357.6287 for $C_{52}H_{94}N_{16}O_{16}Tb$).

Tm^{3+} tetraacetyl-Gly-Lys-OMe cyclen (**20**), colorless oil; ^1H NMR (D_2O) δ 39.76 (s); 29.66 (s); 3.71 (s); 3.27 (s); 2.51 (s); 1.20−0.40 (m); −0.22 to −0.40 (m); −1.62 (s); −1.94 (s); −2.72 to −3.02 (m); −3.43 to −3.80 (m); −4.29 to −4.61 (m); −5.36 to −5.61 (m); −9.56 to −10.44 (m); −13.56 to −14.81 (m); −72.82 (s); −83.14 (s). HRMS (ESI) *m/z*: found 1367.6353 $[M - 2H]^+$ (calcd 1367.6376 for $C_{52}H_{94}N_{16}O_{16}Tm$).

Yb^{3+} tetraacetyl-Gly-Lys-OMe cyclen (**21**), colorless oil; ^1H NMR (D_2O) δ 90.91 (s); 16.82 (s); 14.02 (s); 4.20 (s); 3.79−3.74 (m); 3.52 (s); 3.22−2.49 (m); 1.94 (s); 1.68 (s); 1.55−1.45 (m); 1.32 (s); 1.20 (s); 0.37−0.26 (m); −0.05 (s); −0.23 (s); −0.44 (s); −0.59 (s); −0.84 (s); −2.59 (s); −24.01 (s); −28.93 (s); −53.35 (s). HRMS (ESI) *m/z*: found 1371.6310 $[M - 2H]^+$ (calcd 1371.6476 for $C_{52}H_{94}N_{16}O_{16}Yb$).

*Selective Deprotection of di-Cbz-His-OMe (**33**).* A suspension of di-Cbz-His-OMe (*21*) (**33,** 1.65 g, 3.77 mmol) in 30% HBr in AcOH (25 mL) was stirred until a clear solution was obtained (ca. 90 min) at rt. The mixture obtained was cooled to 0 °C, Et_2O (50 mL) was added, and the mixture was set aside for 30 min at 0 °C. Separated precipitate was filtered off, was washed with Et_2O, and was dried to afford H-His(Cbz)-OMe·2HBr (1.42 g, 81%) of sufficient purity for the next reaction.

H-His(Cbz)-OMe·2HBr (**34**), white solid, mp 166−68 °C (167−167.5 °C lit. (*22*)); $[\alpha]^{25}_D$ +13 (c 0.39, H_2O). ^1H NMR (DMSO-d_6) δ 8.37 (s, 1H); 8.30 (br s, D_2O exch., 2H); 7.48 (m, 3H); 7.40 (m, 3H); 5.43 (s, 2H); 4.33 (m, 1H); 3.71 (s, 3H); 3.04 (m, 2H). ^{13}C NMR (DMSO-d_6) δ 168.5, 164.7, 137.4, 134.5, 129.2, 128.6, 128.4, 126.5, 118.2, 53.2, 52.8, 51.1, 34.5. HRMS (EI) *m/z*: found 303.1223 (free amine) (calcd 303.1219 for $C_{15}H_{17}N_3O_4$). LRMS (EI) *m/z* (rel abundance): 303 $[M]^+$ (10), 152 (23), 110 (24).

*Chloroacetyl-Gly-His(Cbz)-OMe (**35**).* To a stirred solution of *N*-chloroacetylglycine (277 mg, 1.5 mmol) in dry THF (15 mL) were added NHS (173 mg, 1.5 mmol) and EDC·HCl (863 mg, 4.5 mmol). The mixture was stirred for 18 h at rt and then was concentrated. The residue was dissolved in water (30 mL) and was extracted with EtOAc (30 mL + 3 × 20 mL). The combined organic extracts were dried and concentrated to afford 257 mg (70%) of *O*-hydroxysuccinimidyl *N*-chloroacetylglycinate. This was dissolved in dry THF (10 mL), H-His(Cbz)-OMe·2HBr (481 mg, 1.03 mmol) and Et_3N (580 μL, 4.13 mmol) were added, and the mixture was stirred for 2 h at rt. The solvent was evaporated; the residue was dissolved in EtOAc (30 mL) and was washed with water (30 mL). The aqueous phase was extracted with EtOAc (20 mL), combined organic extract was dried and was concentrated, and the residue was subjected to flash column chromatography (FCC) on 20 g SiO_2 (hexane/acetone, 1:1) to afford 203 mg (45%, based on *O*-hydroxysuccinimidyl *N*-chloroacetylglycinate, 31%, based on *N*-chloroacetylglycine) of chloroacetyl-Gly-His(Cbz)-OMe (**35**).

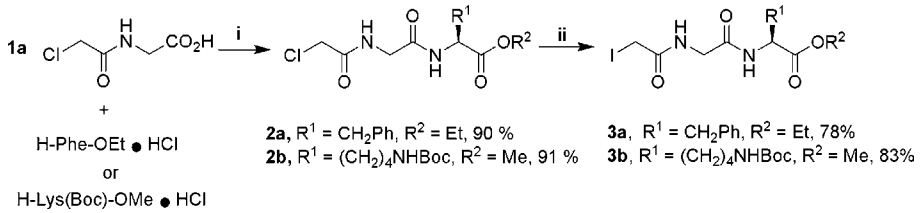
Chloroacetyl-Gly-His(Cbz)-OMe, colorless oil; $[\alpha]^{25}_D$ −35 (c 0.29, DMSO). ^1H NMR ($CDCl_3$) δ 8.03 (s, 1H); 7.58 (br d, D_2O exch., J = 7.5 Hz, 1H); 7.41 (m, 5H); 7.34 (br m, D_2O exch., 1H); 7.20 (s, 1H); 5.38 (s, 2H); 4.84 (m, 1H); 4.07 (d, J = 1.5 Hz, 2H); 4.03 (m, 2H); 3.68 (s, 3H); 3.08 (dd, J = 9.5 Hz, 5.5 Hz, 1H); 3.00 (dd, J = 11 Hz, 4.5 Hz, 1H). ^{13}C NMR ($CDCl_3$) δ 171.2, 167.8, 166.3, 148.2, 138.8, 137.0, 133.8, 129.2, 128.8, 128.7, 114.7, 70.0, 52.5, 51.9, 42.9, 42.4, 29.2. HRMS (ESI) *m/z*: found 459.1057 $[M + Na]^+$ (calcd 459.1047 for $C_{19}H_{21}ClN_4O_6Na$).

*Iodoacetyl-Gly-His(Cbz)-OMe (**36**).* Sodium iodide (415 mg, 2.79 mmol) was added to a solution of chloroacetyl-Gly-His-(Cbz)-OMe (**35**, 203 mg, 0.46 mmol) in acetone (6 mL). The mixture was stirred for 18 h at rt, the solvent was then evaporated, and the residue was dissolved in EtOAc (30 mL). The organic phase was washed with 10% $NaHSO_3$ solution (30 mL) and the aqueous wash was back-extracted with EtOAc (20 mL). The combined organic extracts were dried and concentrated. The residue was subjected to FCC on 25 g SiO_2 (hexane/acetone, 1:1) to afford 204 mg (83%) of unstable iodoacetyl-Gly-His(Cbz)-OMe (**36**).

Iodoacetyl-Gly-His(Cbz)-OMe, colorless solid; ^1H NMR ($CDCl_3$) δ 8.05 (s, 1H); 7.42 (br m, D_2O exch., 6H); 7.21 (s, 1H); 6.90 (br m, D_2O exch., 1H); 5.40 (s, 2H); 4.85 (m, 1H); 4.01 (d, J = 5 Hz, 2H); 3.72 (s, 2H); 3.69 (s, 3H); 3.11 (dd, J = 10 Hz, 5.5 Hz, 1H); 3.02 (dd, J = 10.5 Hz, 4.5 Hz, 1H). HRMS (ESI) *m/z*: found 551.0419 $[M + Na]^+$ (calcd 551.0404 for $C_{19}H_{21}IN_4O_6Na$).

*Iodoacetyl-Gly-Arg(NO_2)-OMe (**39**).* To a solution of *N*-chloroacetylglycine (**1a**, 303 mg, 2 mmol) in dry THF (20 mL) was added NHS (230 mg, 2 mmol). The mixture was cooled to 0 °C, DCC (536 mg, 2.6 mmol) was added, and the mixture was stirred for 1 h at 0 °C, followed by the addition of H-Arg(NO_2)-OMe·HCl (**37**, 539 mg, 2 mmol) and Et_3N (560 μL, 4 mmol). The cooling bath was removed and the mixture was stirred for 18 h at rt. The solvent was evaporated and the residue was subjected to FCC on 75 g SiO_2 (CH_2Cl_2/MeOH/NH_4OH, 80:20:1). Evaporation of the eluate afforded 615 mg of chloroacetyl-Gly-Arg(NO_2)-OMe (**38**), containing ca. 20% of *N*,*N*′-dicyclohexylurea, as determined by analysis of the ^1H NMR spectrum. The impure *N*-chloroacetyl-dipeptide **38** was

Scheme 2. Synthesis of *N*-Iodoacetyl-Gly-Phe-OEt (3a) and *N*-Iodoacetyl-Gly-Lys(Boc)-OMe (3b)[a]



[a] Reagents and conditions: (i) NHS/DCC, Et_3N, CH_2Cl_2, 18 h, rt; (ii) NaI (6.0 equiv), acetone, 18 h, rt.

dissolved in acetone (15 mL), and NaI (736 mg, 4.91 mmol) was added. The mixture was stirred for 18 h at rt, a small amount of SiO_2 was added, the solvent was evaporated, and the residue was subjected to FCC on 50 g SiO_2 (CH_2Cl_2/MeOH/NH_4OH, 80:20:1). Evaporation of the eluate afforded 583 mg (64%, based on *N*-chloroacetylglycine) of iodoacetyl-Gly-Arg(NO_2)-OMe (**39**).

Iodoacetyl-Gly-Arg(NO_2)-OMe, colorless solid; $[\alpha]^{25}_D$ −12 (c 0.41, MeOH). ^{1}H NMR (DMSO-d_6) δ 8.46 (br m, D_2O exch., 2H); 8.32 (br d, D_2O exch., J = 7.5 Hz, 1H); 7.81 (br d, D_2O exch., J = 7.5 Hz, 2H); 4.25 (m, 1H); 3.73 (m, 2H); 3.68 (s, 2H); 3.61 (s, 3H); 3.13 (m, 2H); 1.60 (m, 4H). ^{13}C NMR (DMSO-d_6) δ 172.2, 172.1, 168.6, 168.0, 56.7, 52.0, 51.6, 42.1, 28.1. HRMS (ESI) *m/z*: found 481.0285 $[M + Na]^+$ (481.0309 calcd for $C_{11}H_{19}IN_6O_6Na$).

*Alkylation of Cyclen with Iodoacetyl-Gly-Arg(NO_2)-OMe (**39**).* To a solution of cyclen (15 mg, 0.086 mmol) in acetonitrile (6 mL), ethyldiisopropylamine (60 μL, 0.34 mmol) was added. The mixture was stirred for 30 min at rt followed by the addition of iodoacetyl-Gly-Arg(NO_2)-OMe (**39**, 158 mg, 0.34 mmol). The stirring continued for 18 h at rt, at which time the product had separated from solution. Conveniently, the solvent was decanted and the residue was washed with acetonitrile (2 × 5 mL) and was dried to afford 46 mg (46%) of triacetyl-Gly-Arg(NO_2)-OMe cyclen (**40**).

Triacetyl-Gly-Arg(NO_2)-OMe cyclen (**40**), colorless solid; $[\alpha]^{25}_D$ −53 (c 0.38, MeOH). ^{1}H NMR (D_2O) δ 4.40 (m, 3H); 3.92 (m, 6H); 3.68 (3, 9H); 3.29−3.06 (m, 12H); 2.98−2.67 (m, 16H); 1.87 (m, 3H); 1.72−1.56 (m, 9H). ^{13}C NMR (DMSO-d_6) δ 172.3, 172.2, 171.7, 171.2, 170.8, 169.6, 169.3, 168.9, 159.3, 52.0, 51.7, 49.2, 41.5, 41.4, 40.3, 38.8, 38.5, 33.4, 28.2, 25.3, 24.9, 24.8, 24.7, 24.6, 24.5. HRMS (ESI) *m/z*: found 1163.5588 $[M + H]^+$ (calcd 1163.5630 for $C_{41}H_{75}N_{22}O_{18}$).

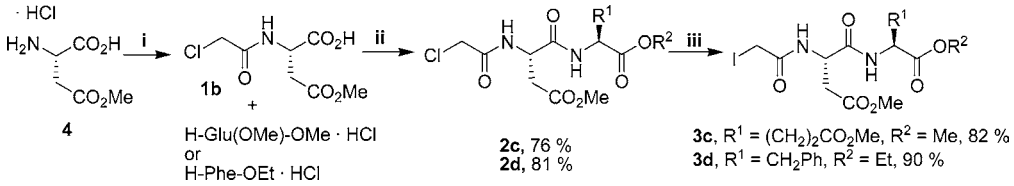
RESULTS AND DISCUSSION

Our synthetic scheme required the alkylation of cyclen with the appropriate reactive dipeptide derivatives. Our initial approach to *N*-haloacetyl-dipeptides involved the synthesis of fully protected, side chain and C-terminus, α-*N*-Boc-dipeptides. After *t*-butyloxycarbonyl (Boc) removal, the N-terminus of an otherwise fully protected dipeptide was further reacted with bromoacetyl bromide to give the required *N*-bromoacetyl-dipeptide. This approach proved to be difficult to execute as the success of the reaction was highly dependent on the dipeptide sequence. Additionally, we also attempted, without much success, to couple partially protected (free N-terminus) dipeptides to DOTA. Although these approaches may be successful in certain cases, we did not consider either of them to be a generally applicable route to cyclen−tetra(oligopeptide) conjugates. We decided to pursue an alternative convergent strategy in order to circumvent the above-mentioned problems and also avoid the tedious synthesis of individual α-*N*-Boc-dipeptides and eliminate a step that involved a protecting group manipulation. Our strategy involved first preparing *N*-chloroacetylglycine as a convenient precursor to a variety of *N*-chloroacetylglycyl−(amino acid) compounds. Schotten-Baumann acylation of glycine with chloroacetyl chloride gave *N*-chloroacetylglycine (**1a**) in 43% yield after recrystallization from ethyl acetate, similar to the reported procedure (*23*). Unlike more reactive α-haloacetamides that may not tolerate the presence of nucleophiles, the *N*-chloroacetylglycine was stable to handling, storage, and amide bond forming reactions. Therefore, next, a straightforward *N*-hydroxysuccinimide (NHS)/dicyclohexylcarbodiimide (DCC) promoted coupling (*24*) of *N*-chloroacetylglycine (**1a**) with H-Phe-OEt·HCl or H-Lys(Boc)-OMe·HCl afforded *N*-chloroacetyl-Gly-Phe-OEt (**2a**) and *N*-chloroacetyl-Gly-Lys(Boc)-OMe (**2b**) in excellent yield (Scheme 2).

In our experience, the alkylation of cyclen proceeded quite slowly with the *N*-chloroacetylamino acids. The alkylation reaction generally required halide exchange to a more active derivative to be high-yielding. Although cyclen may be reacted in a one-pot procedure with *N*-chloroacetyl-dipeptides **2a** and **2b** in the presence of excess NaI and K_2CO_3, we have found that the success of peralkylation was variable. Therefore, we decided to perform the Finkelstein reaction and isolate the *N*-iodoacetyl-dipeptides prior to their use. This permitted us to conveniently monitor the consumption of the *N*-iodoacetyl-dipeptides during its use by TLC analysis of the reaction mixture. Thus, treatment of **2a** and **2b** with NaI in acetone proceeded smoothly, and *N*-iodoacetyl-dipeptides **3a** and **3b** were obtained in approximately 80% yield (Scheme 2). An upfield shift of the methylene peak in the ^{1}H NMR is observed upon conversion of *N*-chloroacetyl-dipeptides **2** to *N*-iodoacetyl-dipeptides **3**. The *N*-iodoacetyl-dipeptides are stable and easily isolable solids that may be stored for prolonged periods without deterioration.

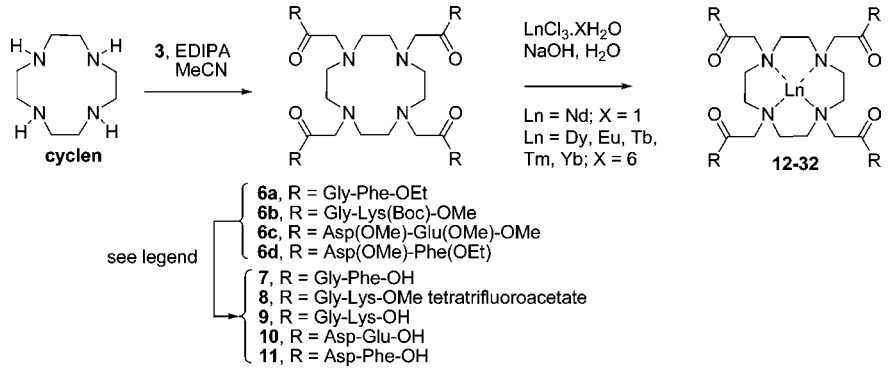
The above strategy was also extended to the synthesis of cyclen containing aspartic acid as the second amino acid; the key compound toward the synthesis of such molecules is *N*-chloroacetyl-Asp(OMe)-OH (**1b**). This compound was prepared by first monoesterification of aspartic acid to its β-methyl ester (**4**) with methanolic HCl (*20*). Initial attempts at acylating **4** involved neutralization of the hydrochloride salt with 1 equiv of sodium hydroxide followed by the addition of 1 equiv of sodium carbonate and dropwise addition of chloroacetyl chloride. Although this procedure gave **1b** in 56% yield as an oil, it was contaminated with the side product chloroacetic acid, which proved difficult to remove. In order to improve the acylation yield and to avoid hydrolysis of the β-methyl ester, we decided to react **4** with *O*-chloroacetyl-*N*-hydroxysuccinimide (**5**). Using sodium carbonate and a 1:1 mixture of dioxane/H_2O, this reaction gave **1b** in a crude yield of 81%, slightly contaminated with NHS as judged by ^{1}H NMR. Without purification, **1b** was condensed with H-Glu(OMe)-OMe·HCl or H-Phe-OEt·HCl to give *N*-chloroacetyl-Asp(OMe)-Glu(OMe)-OMe (**2c**) and *N*-chloroacetyl-Asp(OMe)-Phe-OEt (**2d**), using NHS/DCC. At this point, NHS was easily eliminated by extraction against aqueous sodium bicarbonate. Treatment of **2c** and **2d** with NaI in acetone gave *N*-iodoacetyl-Asp(OMe)-Glu(OMe)-OMe (**3c**), and *N*-iodoacetyl-Asp(OMe)-Phe-OEt (**3d**) in very good yields (Scheme 3).

Scheme 3. Synthesis of *N*-Iodoacetyl-Asp(OMe)-Glu(OMe)-OMe (3c) and *N*-Iodoacetyl-Asp(OMe)-Phe-OEt (3d)[a]



[a] Reagents and conditions: (i) $ClCH_2CONHS$ (**5**), Na_2CO_3, dioxane/H_2O, 14 h, (ii) NHS/DCC, Et_3N, THF, 12 h, (iii) NaI (6.0 equiv), acetone, rt 1 h.

Scheme 4. Synthesis of Cyclen−Oligopeptide Conjugates 7−11 and Their Treatment with Lanthanide(III) Chlorides[a]



[a] Reagents and Conditions. **6a** → **7**: NaOH, THF/H_2O. **6b** → **8**: TFA. **6b** → **9**: (i) TFA, (ii) NaOH, MeOH/H_2O. **6c** → **10**: NaOH, MeOH/H_2O. **6d** → **11**: NaOH, MeOH/H_2O.

With *N*-iodoacetyl-dipeptides **3a**−**3d** in hand, we investigated the alkylation of cyclen (Scheme 4). The use of potassium carbonate did not give satisfactory conversion as judged by TLC, and we turned to ethyldiisopropylamine (EDIPA, Hünig's base), which gave acceptable results. The alkylation reactions were carried out at 50 °C in MeCN, using 4 equiv of *N*-iodoacetyl-dipeptides **3a** or **3b** and EDIPA. Slightly higher temperatures (70 °C) were used for the alkylation of cyclen with the more bulky compounds **3c** and **3d**. Tetraalkylated cyclen−oligopeptide conjugates **6** were obtained in excellent yields (>90%). To obtain the desired ligands for the complexation with lanthanides, protecting groups were removed as described in Scheme 4. Saponification of **6a**, **6c**, and **6d** afforded compounds **7** (Gly-Phe-OH), **10** (Asp-Glu-OH), and **11** (Asp-Phe-OH), respectively. Treatment of compound **6b** with TFA gave **8** (Gly-Lys-OMe tetratrifluoroacetate), which without further purification under the conditions of basic hydrolysis gave **9** (Gly-Lys-OH). Cyclen−oligopeptide conjugates **7** and **11** were purified by trituration with Et_2O, while conjugates **9** and **10** were purified by size exclusion chromatography on desalting gel with an exclusion limit of 1800 Da.

Currently, there are numerous literature reports describing the synthesis of lanthanide(III) complexes derived from cyclen. Various reaction conditions (elevated temperatures (*25*, *26*), slightly acidic pH (*27*−*29*), and slightly basic pH (*6*)) have been employed in order to prepare lanthanide(III) cyclen complexes. As described in the literature, the workup usually involves filtration of insoluble particles followed by the concentration of the filtrate without any further purification (*30*, *31*). Alternatively, the reaction mixtures are sometimes centrifuged, and the supernatant is concentrated as described above (*32*). Less water-soluble complexes are purified by precipitation of their methanolic solutions with Et_2O (*25*) or by trituration with Et_2O (*33*). Oftentimes, the crude material obtained after concentration is used directly, without any form of purification (*7*, *16*). To the best of our knowledge, a general procedure for the purification of cyclen derived lanthanide(III) complexes has not been described. Taking into account this lack of consistent purification of lanthanide(III) complexes, and the fact that compounds **12**−**32** are very water-soluble and resist precipitation, we have decided to establish a widely applicable method for the purification of lanthanide(III) complexes of cyclen−oligopeptide conjugates and test its scope. Ligands **7**−**11** have been treated with 1 equiv of various lanthanide(III) chlorides in water under slightly basic conditions (pH 9) (Scheme 4). The conditions for introducing the metal are gentle enough to retain the C-terminal ester, e.g., **16**−**21**. This was also true in the case of DOTAM-(Gly-Phe-OEt)$_4$ (**6a**), which was metalated; however, the complexes were not sufficiently soluble in water and they were abandoned.

Once the ligands were metalated, the resulting complexes were isolated and purified by size exclusion chromatography (SEC) in deionized water (*34*). The SEC gel that was used had an exclusion limit of 1800 Da and was found to be widely applicable for the purification of water-soluble lanthanide(III) complexes with a molecular weight of approximately 1000−1800 Da—i.e., most conceivable dipeptide DOTAM conjugates. Compounds with a molecular weight well in excess of 1800 Da would be better purified using a desalting gel with a higher exclusion limit. The fractions containing the compounds were identified by UV/I_2 vapors (Gly-Phe-OH and Asp-Phe-OH complexes), ninhydrin test (Gly-Lys-OH and Gly-Lys-OMe complexes), or I_2 vapors (Asp-Glu-OH complex). Chemical yields for the purified complexes varied from 44% to 98%, as listed in Table 1. All the prepared complexes were characterized by HR MS (ESI- TOF) and ^{1}H NMR spectroscopy.

The synthetic approach reported herein is convenient and robust because it reliably works for a number of diverse dipeptides without modification and utilizes known or commercially available amino acid derivatives. Two notable exceptions were found in the attempted preparation of tetraacetyl-Gly-His-OMe and tetraacetyl-Gly-Arg-OMe. These compounds are potentially interesting targets due to the presence of additional exchangeable protons in the ligand periphery and the nature of the side chain functional groups.

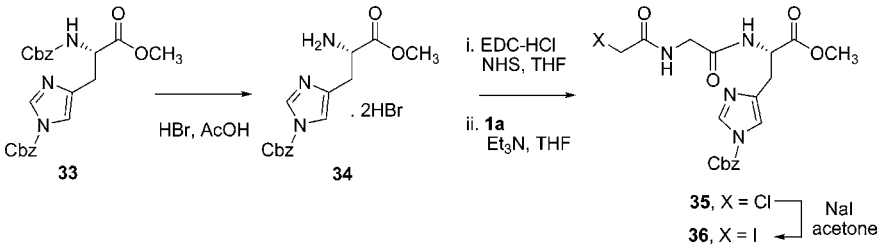
We approached the tetraacetyl-Gly-His-OMetarget by first preparing the bis(Cbz)-protected-histidine methyl ester (**33**) as described in the literature (*21*). Treatment of **33** with 30% HBr in AcOH (*22*) resulted in selective removal of Cbz group from the amino group, while the protecting group on the imidazole

Table 1. Yields and HRMS ESI Data of Lanthanide(III) Complexes of Cyclen−Oligopeptide Conjugates 12−32[a]

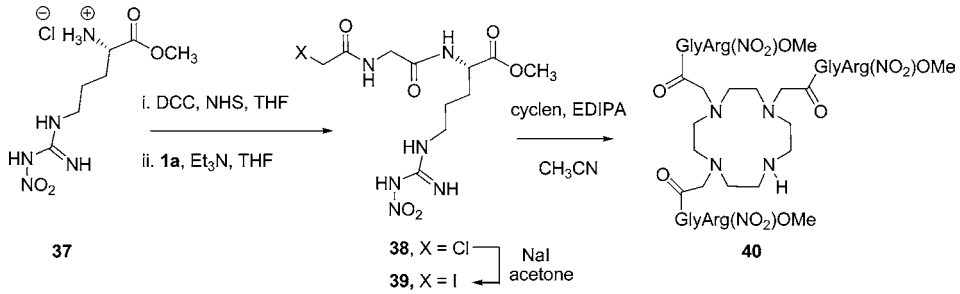
	compound number yield (mass, percent)[a]			
metal	**12−15** R = Gly-Phe-OH	**16−21** R = Gly-Lys-OMe	**22−27** R = Gly-Lys-OH	**28−31** R = Asp-Glu-OH
Dy(III)		(**16**)	(**22**)	
mass (yield)		94 mg, 73%	120 mg, 98%	
Eu(III)	(**12**)	(**17**)	(**23**)	(**28**)
mass (yield)	57 mg, 44%	120 mg, 94%	119 mg, 98%	115 mg, 80%
Nd(III)	(**13**)	(**18**)	(**24**)	(**29**)
mass (yield)	56 mg, 44%	112 mg, 96%	102 mg, 85%	71 mg, 49%
Tb(III)		(**19**)	(**25**)	
mass (yield)		100 mg, 79%	92 mg, 75%	
Tm(III)	(**14**)	(**20**)	(**26**)	(**30**)
mass (yield)	55 mg, 42%	118 mg, 96%	88 mg, 72%	125 mg, 86%
Yb(III)	(**15**)	(**21**)	(**27**)	(**31**)
mass (yield)	64 mg, 49%	104 mg, 81%	107 mg, 86%	89 mg, 59%

[a] Eu(III) Asp-Phe-OH (**32**) was achieved in 71 mg, 47%.

Scheme 5. Synthesis of Haloacetyl-Gly-His(Cbz)-OMe 35 and 36



Scheme 6. Synthesis of Triacetyl-Gly-Arg(NO$_2$)-OMe Cyclen (40)



ring remained intact (Scheme 5). The possibility of coupling of dihydrobromide **34** with *N*-chloroacetylglycine was then investigated. The reaction was troublesome and low-yielding. The best conditions proved to be EDC·HCl and NHS in the presence of Et_3N (Scheme 5), which afforded chloroacetyl-Gly-His(Cbz)-OMe (**35**) in 40% yield. Application of the Finkelstein reaction gave the rather unstable iodoacetyl-Gly-His(Cbz)-OMe (**36**) (Scheme 5). This compound underwent massive decomposition in solution in less than 1 h, as observed by ^{1}H NMR in $CDCl_3$ or DMSO-d_6. Nonetheless, the alkylation of cyclen was attempted; however, no product of alkylation was detected which was likely due to instability of *N*-iodoacetyl-dipeptide **36**. Attempts to prepare *N*-iodoacetyl-dipeptide **36** *in situ* were unsuccessful. The reactivity of chloroacetyl-Gly-His(Cbz)-OMe (**35**) toward the alkylation of cyclen appeared to be insufficient even at elevated temperatures.

The synthesis of the required dipeptide electrophile to approach tetraacetyl-Gly-Arg-OMe was achieved much more readily. The NHS/DCC mediated coupling of *N*-chloroacetylglycine with H-Arg(NO$_2$)-OMe (**37**) afforded chloroacetyl-Gly-Arg(NO$_2$)-OMe (**38**) (Scheme 6), containing a small amount of *N*,*N*′-dicyclohexylurea. The Finkelstein reaction of **38** proceeded smoothly, and iodoacetyl-Gly-Arg(NO$_2$)-OMe (**39**) was isolated in 64% overall yield (Scheme 6). Alkylation of cyclen was carried out in acetonitrile using EDIPA as a base. Surprisingly, the trialkylated cyclen **40** formed exclusively and was found to deposit on the flask walls at room temperature. Metalation of **40** (using $EuCl_3 \cdot 6H_2O$ and $NdCl_3 \cdot H_2O$) could not be achieved even at elevated temperatures and slightly basic pH. The origin of the lack of chelation by this ligand is not understood at this time. Since ligand **40** could not be metalated, no studies were carried out toward the tetraalkylation of cyclen with iodoacetyl-Gly-Arg(NO$_2$)-OMe (**39**) nor on removal of guanidine protecting group.

With the intention of the discovery of new MRI PARACEST agents that generate signal variation by the CEST effect, we have acquired CEST spectra (*2*) of the metalated ligands under conditions of near-physiological temperature and pH. The results of this survey are presented in Figure 2. The observed CEST effects are the result of the intrinsic properties of the compound as well as the experimental conditions. Since all CEST spectra were measured under identical experimental conditions, the differences in the observed CEST effects were likely due to alterations in the exchangeable proton lifetimes. For example, a CEST effect was observed from bound water protons when the exchange rate of bound water with bulk water was slow (M = Eu^{3+}, Nd^{3+}). Conversely, no bound water CEST effect was observed for metal complexes when the exchange between bound and bulk water was relatively fast (M = Dy^{3+}, Tb^{3+}, Tm^{3+}, Yb^{3+}). However, for the latter metals, it is possible in some instances to observe the CEST effect from the protons bound to the amide nitrogen. This phenomenon may be exploited to measure the pH of the environment if the signal intensity is observably sensitive to pH and reasonably resolved from the

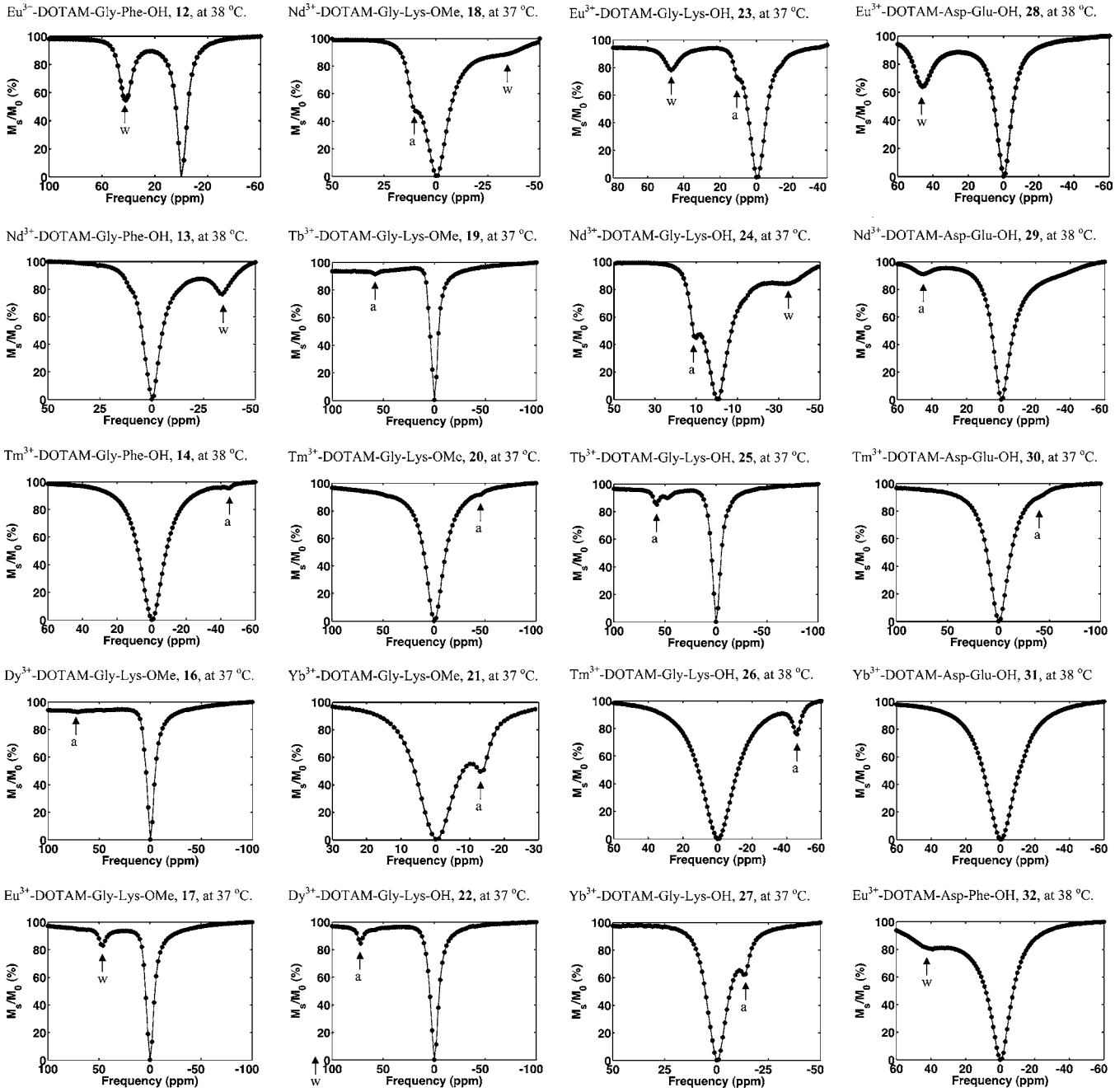


Figure 2. CEST spectra for compounds **12**−**32** determined at 10 mM concentration, pH 7.0. All spectra were collected using a 9.4 T NMR spectrometer with saturation power of 14 μT (saturation time = 10 s) at the temperature indicated. CEST signals due to bound water and amide protons are marked by an arrowhead and denoted (w) or (a), respectively.

bulk water signal, e.g., **24**. In limited circumstances, it is possible to simultaneously observe the signal due to bound water and amide protons under conditions close to physiological pH and temperature (M = Nd^{3+}). One compound did not produce an observable CEST effect (**31**), while another compound could not be measured under the conditions employed due to limited solubility (**15**).

Our methodology can be used to readily prepare a number of ligated metals to examine their potential utility as MRI PARACEST agents. The most strongly bound water signals are found for ligands containing Eu^{3+}. For example, the Eu^{3+}-DOTAM-Gly-Phe-OH complex **12** clearly exhibits bound water saturation at approximately 43 ppm from bulk water. This compound has a large CEST effect (∼45%) at physiological temperature and pH (Figure 2). The chemical shift of the bound water is also sensitive to temperature (0.3 ppm/°C, data not shown), and will be investigated for its ability to measure temperature *in vivo*. The CEST spectrum of Eu^{3+}-DOTAM-Asp-Glu-OH **28** is qualitatively similar to that of Eu^{3+}-DOTAM-Gly-Phe-OH **12**, but with a slightly smaller CEST effect. The bound water signals for the Eu^{3+}-containing complexes **17** and **23** are evident at approximately the same chemical shift (43 ppm) but with weaker intensity, as compared to the aforementioned compounds. Since both Eu^{3+}-DOTAM-Gly-Phe-OH **12** and the Eu^{3+}-DOTAM-Asp-Glu-OH **28** exhibited a large CEST effect from the bound water, we were interested in the effect of combining the nature of the dipeptide; thus, Eu^{3+}-DOTAM-Asp-Phe-OH **32** was prepared and studied. Rather than increasing the CEST effect, this complex only showed a small CEST effect due to the bound water at 43 ppm.

Many of the complexes, especially those containing Tm^{3+}, Tb^{3+}, or Dy^{3+}, exhibit very small CEST effects due to the amide protons (e.g., **14**, **16**, **19**, **20**, **22**, **25**, **30**), yet this is not always the case—a clear CEST signal is observed for **26** (*cf.* **20** and

26). The two complexes, Tm^{3+}-DOTAM-Gly-Lys-OMe **20** and Tm^{3+}-DOTAM-Gly-Lys-OH **26**, highlight the impact of subtle structural changes on the MR properties of the complex. Ligands **8** and **9** differ by the nature of the peripheral groups, the former being a neutral methyl ester and the latter an anionic carboxylate (under the conditions of measurement), but curiously the CEST effect contributed by the amide protons is greater for complexes of **9** for M = Tm^{3+}, Tb^{3+}, and Dy^{3+}. The ytterbium (Yb^{3+}) complex of both **8** and **9**, i.e., Yb^{3+}-DOTAM-Gly-Lys-OMe **21** and Yb^{3+}-DOTAM-Gly-Lys-OH **27**, possesses amide protons that produce a CEST effect at −15 ppm and −18 ppm, respectively. For these complexes, the amide proton saturation is better resolved from the bulk water saturation compared to Nd^{3+}-DOTAM-Gly-Lys-OME **18** and Nd^{3+}-DOTAM-Gly-Lys-OH **24**, making the observation of changes with pH easier. However, saturation of the bound water pool was not detected in the Yb^{3+}-containing complexes. Simultaneous observation of the CEST effect produced by the amide and bound water protons may be an advantage for pH measurement using ratiometric methods (*6*, *7*). A CEST effect was observed simultaneously for bound water and amide protons in several compounds. The Nd^{3+}-DOTAM-Gly-Lys-OMe complex **18** showed a broad CEST signal due to bound water at approximately −35 ppm and an amide CEST effect a 11 ppm, not fully resolved from the bulk water signal. Upon hydrolysis of the terminal ester groups of the ligand and subsequent metalation, the Nd^{3+}-DOTAM-Gly-Lys-OH complex **24** exhibited more clearly resolved CEST effects from bound water (−34 ppm) and amide protons (11 ppm). Both signals are clearly observed under the same experimental conditions. The CEST effect from amide protons is very sensitive to pH (data not shown), which potentially may be used to measure the pH of the environment of the complex (*5*, *6*).

In summary, we have demonstrated a reliable and convergent synthesis of several new dipeptide−DOTAM conjugates. This approach relies largely on available commercial reagents and a minimum of protecting group manipulations. It is easy to imagine extending this approach of diversification of the ligand periphery by incorporating other natural or unnatural amino acids. Each ligand was used to chelate a variety of lanthanide(III) ions, and the resulting complexes were examined for MR-CEST effects. A number of the compounds produced interesting CEST spectra, validating this approach for the discovery of new lead compounds. Currently, we are extending this synthetic approach to the screening of a variety of amino acids for useful PARACEST properties.

ACKNOWLEDGMENT

The authors thank the Natural Sciences and Research Council of Canada (RHEH), the Ontario Research and Development Challenge Fund, and the Canadian Institutes of Health Research Strategic Training Program in Cancer Research and Technology Transfer for supporting this work. Ms. Paula Pittock of the Biological Mass Spectrometry Laboratory at the University of Western Ontario and Mr. Doug Hairsine of the Department of Chemistry Mass Spectral Facility are thanked for expert assistance with collection and analysis of mass spectral data.

Supporting Information Available: Selected molecular characterization is provided by way of ^{1}H NMR spectra for compounds **1b**, **2**, **3**, **6**, **7**, **9**−**32**, **34**−**36**, **39**, and **40** and ^{13}C NMR spectra of compounds **1b**, **2**, **3**, **34**, **35**, and **39**. This material is available free of charge via the Internet at http://pubs.acs.org.

LITERATURE CITED

(1) Ward, K. M., Aletras, A. H., and Balaban, R. S. (2000) A new class of contrast agents for MRI based on proton chemical exchange dependent saturation transfer (CEST). *J. Magn. Reson. 143*, 79−87.

(2) Zhang, S., Merritt, M., Woessner, D. E., Lenkinski, R. E., and Sherry, A. D. (2003) PARACEST agents: modulating MRI contrast via water and proton exchange. *Acc. Chem. Res. 36*, 783−790.

(3) Zhang, S., Trokowski, R., and Sherry, A. D. (2003) A paramagnetic CEST agent for imaging glucose by MRI. *J. Am. Chem. Soc. 125*, 15288−15289.

(4) Aime, S., Delli Castelli, D., Fedeli, F., and Terreno, E. (2002) A paramagnetic MRI-CEST agent responsive to lactate concentration. *J. Am. Chem. Soc. 124*, 9364−9365.

(5) Zhang, S., Malloy, C. R., and Sherry, A. D. (2005) MRI thermometry based on PARACEST agents. *J. Am. Chem. Soc. 127*, 17572−17573.

(6) Aime, S., Delli Castelli, D., and Terreno, E. (2002) Novel pH-reporter MRI contrast agents. *Angew. Chem., Int. Ed. 41*, 4334−4336.

(7) Aime, S., Barge, A., Delli Castelli, D., Fedeli, F., Mortillaro, A., Nielsen, F. U., and Terreno, E. (2002) Paramagnetic lanthanide (III) complexes as pH-sensitive chemical exchange saturation transfer (CEST) contrast agents for MRI applications. *Magn. Reson. Med. 47*, 639−648.

(8) Aime, S., Carrera, C., Delli Castelli, D., Crich, S., and Terreno, E. (2005) Tunable imaging of cells labeled with MRI-PARACEST agents. *Angew. Chem., Int. Ed. 44*, 1813−1815.

(9) Aime, S., Barge, A., Botta, M., De Sousa, A. S., and Parker, D. (1998) Direct NMR spectroscopic observation of a lanthanide-coordinated water molecule whose exchange rate is dependent on the conformation of the complexes. *Angew. Chem., Int. Ed. 37*, 2673−2675.

(10) Aime, S., Barge, A., Bruce, J. I., Botta, M., Howard, J. A. K., Moloney, J. M., Parker, D., de Sousa, A. S., and Woods, M. (1999) NMR, relaxometric, and structural studies of the hydration and exchange dynamics of cationic lanthanide complexes of macrocyclic tetraamide ligands. *J. Am. Chem. Soc. 121*, 5762−5771.

(11) Zhang, S., Wu, K., Biewer, M. C., and Sherry, A. D. (2001) ^{1}H and ^{17}O NMR detection of lanthanide-bound water molecule at ambient temperatures and in pure water as solvent. *Inorg. Chem. 40*, 4284−4290.

(12) Caravan, P., Ellison, J. J., McMurry, T. J., and Lauffer, R. B. (1999) Gadolinium(III) chelates as MRI contrast agents: structure, dynamics, and applications *Chem. Rev. 99*, 2293−2352.

(13) Govenlock, L. J., Howard, J. A. K., Moloney, J. M., Parker, D., Peacock, R. D., and Siligardi, G. (1999) Chiroptical features and luminescence behavior of macrocyclic tetra(4-quinolyl)-complexes: surprising absence of exciton coupling. *J. Chem. Soc., Perkin Trans. 2 11*, 2415−2418.

(14) Gunnlaugsson, T., O'Brien, J. E., and Mulready, S. (2002) Glycine-alanine conjugated macrocyclic lanthanide ion complexes as artificial ribonucleases. *Tetrahedron Lett. 43*, 8493−8497.

(15) De Leon-Rodriquez, L. M., Kovacs, Z., Diekmann, G. R., and Sherry, A. D. (2004) Solid-phase synthesis of DOTA-peptides. *Chem.—Eur. J. 10*, 1149−1155.

(16) Zhang, S., Winter, P., Wu, K., and Sherry, A. D. (2001) A novel europium (III)-based MRI contrast agent. *J. Am. Chem. Soc. 123*, 1517−1518.

(17) Kataky, R., Matthes, K. E., Nicholson, P. E., Parker, D., and Bushmann, H.-J. (1990) Synthesis and binding properties of amide-functionalized polyaza macrocycles. *J. Chem. Soc., Perkin Trans. 2* 1424−1432.

(18) Amin, S., Morrow, J. R., Lake, C. H., and Churchill, M. R. (1994) Lanthanide (III) tetraamide macrocyclic complexes as synthetic ribonucleases: structure and catalytic properties of $[La(tcmc)CF_3SO_3)(EtOH)](CF_3SO_3)_2$. *Angew. Chem., Int. Ed. Engl. 33*, 772−775.

(19) Salmain, M., Gunn, M., Gorfti, A., Top, S., and Jaouen, G. (1993) Labeling of proteins by organometallic complexes of rhenium(I). Synthesis and biological activity of the conjugates. *Bioconjugate Chem. 4*, 425−433.

(20) Gmeiner, P., Feldman, P. L., Chu-Moyer, M., and Rapoport, H. (1990) An efficient and practical total synthesis of (+)-vincamine from *L*-aspartic acid. *J. Org. Chem. 55*, 3068−3074.

(21) Aurelio, L., Box, J. S., Brownlee, R. T. C., Hughes, A. B., and Sleebs, M. M. (2003) An efficient synthesis of *N*-methyl amino acids by way of intermediate 5-oxazolidinones. *J. Org. Chem. 68*, 2652−2667.

(22) Inouye, K., and Otsuka, H. (1961) New method for synthesis of peptides containing histidine. *J. Org. Chem. 26*, 2613−2614.

(23) Nakane, M., Reid, J. A., Han, W. C., Das, J., Truc, V. C., Haslanger, M. F., Garber, D., Harris, D. N., Hedberg, A., Ogletree, M. L., and Hall, S. A. (1990) 7-Oxabicyclo[2.2.1]heptyl carboxylic acids as thromboxane A_2 antagonists: aza ω-chain analogues. *J. Med. Chem. 33*, 2465−2476.

(24) Anderson, G. W., Zimmermann, J. E., and Callahan, F. M. (1964) The use of esters of *N*-hydroxysuccinimide in peptide synthesis. *J. Am. Chem. Soc. 86*, 1839−1842.

(25) Fanning, A. M., Plush, S. E., and Gunnlaugsson, T. (2006) Tuning the properties of cyclen based lanthanide complexes for phosphodiester hydrolysis; the role of basic cofactors. *Chem. Commun.* 3791−3793.

(26) Yoo, B., and Pagel, M. D. (2006) A facile synthesis of α-amino-DOTA as versatile molecular imaging probe. *Tetrahedron Lett. 47*, 7327−7330.

(27) Costa, J., Balogh, E., Turcry, V., Tripier, R., LeBaccon, M., Chuburu, F., Handel, H., Helm, L., Toth, E., and Merbach, A. E. (2006) Unexpected aggregation of neutral, xylene-cored dinuclear Gd(III) chelates in aqueous solution. *Chem.—Eur. J. 12*, 6841−6851.

(28) Tremblay, M. S., and Sames, D. (2006) Synthesis of luminiscent heterometallic bis-lanthanide complexes *via* selective, sequential metallation. *Chem. Commun*. 4116−4118.

(29) Viguier, R. F. H., and Hulme, A. N. (2006) A sensitized europium complex generated by micromolar concentrations of copper(I): toward the detection of copper(I) in biology. *J. Am. Chem. Soc. 128*, 11370−11371.

(30) Trokowski, R., Zhang, S., and Sherry, A. D. (2004) Cyclen-based phenylboronate ligands and their Eu^{3+} complexes for sensing glucose by MRI. *Bioconjugate Chem. 15*, 1431−1440.

(31) Yoo, B., and Pagel, M. D. (2006) A PARACEST MRI contrast agent to detect enzyme activity. *J. Am. Chem. Soc. 128*, 14032−14033.

(32) Crich, S. G., Cabella, C., Barge, A., Belfiore, S., Ghirelli, C., Lattauda, L., Lanzardo, S., Mortillaro, A., Tei, L., Visigalli, M., Forni, G., and Aime, S. (2006) In vitro and in vivo magnetic resonance detection of tumor cells by targeting glutamine transporters with Gd-based probes. *J. Med. Chem. 49*, 4926−4936.

(33) Poole, R. A., Bobba, G., Cann, M. J., Frias, J. C., Parker, D., and Peacock, R. D. (2005) Synthesis and characterization of highly emissive and kinetically stable lanthanide complexes suitable for usage "*in Cellulo*". *Org. Biomol. Chem. 3*, 1013−1024.

(34) Que, E. L., and Chang, C. J. (2006) A smart magnetic resonance contrast agent for selective copper sensing. *J. Am. Chem. Soc. 128*, 15942−15943.

BC0701287

Fucosylated Pentaerythrityl Phosphodiester Oligomers (PePOs): Automated Synthesis of DNA-Based Glycoclusters and Binding to *Pseudomonas aeruginosa* Lectin (PA-IIL)

François Morvan,*,† Albert Meyer,† Anne Jochum,‡ Charles Sabin,§ Yann Chevolot,|| Anne Imberty,§ Jean-Pierre Praly,‡ Jean-Jacques Vasseur,† Eliane Souteyrand,|| and Sébastien Vidal*,‡

Institut des Biomolécules Max Mousseron, UMR 5247 CNRS - Université Montpellier I - Université Montpellier II, LACAN, CC008, Place E. Bataillon, 34095 Montpellier Cedex 5, France, Institut de Chimie et Biochimie Moléculaires et Supramoléculaires, UMR 5246 CNRS - Université Claude Bernard Lyon 1 - CPE, Laboratoire de Chimie Organique 2 - Glycochimie, 43 Boulevard du 11 Novembre 1918, 69622 Villeurbanne, France, CERMAV-CNRS (affiliated with Université Joseph Fourier), BP 53, 38041 Grenoble Cedex 9, France, and Institut des Nanotechnologies de Lyon, UMR 5512 CNRS - Ecole Centrale de Lyon - INSA Lyon - Université Claude Bernard Lyon 1, Equipe Chimie et Nanobiotechnologies, 36 Avenue Guy-de-Collongue, 69134 Ecully, France. Received April 17, 2007; Revised Manuscript Received May 29, 2007

The synthesis of propargylated pentaerythrityl phosphodiester oligomers (PePOs) was achieved using a DNA synthesizer with a bis-propargylated pentaerythritol-based phosphoramidite. An azido fucose derivative was reacted under "click" chemistry conditions activated by microwaves to construct a series of glycosylated PePOs bearing 4, 6, 8, and 10 L-fucose residues. Binding to the fucose-specific bacterial lectin (PA-IIL) was determined for the fucosylated PePOs through an enzyme-linked lectin amplification competition assay. The IC_{50} values measured are 10−20 times better than for monovalent L-fucose and denotate for a "macromolecular" effect rather than a "cluster" effect.

INTRODUCTION

Carbohydrates are involved in numerous biological events such as cell-to-cell communication, signal transduction, and viruses or bacterial infection (*1*−*4*). Lectins are carbohydrate receptors with typically weak affinities for monovalent interactions with K_d values in the millimolar range (*5*−*12*). Multivalency (*13*−*17*) is often required in order to overcome the low affinity observed between carbohydrates and lectins, according to the so-called "cluster effect" (*18*−*26*).

Synthetic organic chemists and biochemists have designed a series of strategies to mimic the "cluster effect" by preparing and studying the binding of glycoclusters (*27*−*59*) to lectins based on various scaffolds such as peptides (*37*, *38*, *57*), glycosides (*34*, *60*), cyclodextrins (*29*, *39*, *43*), pentaerythritol (*28*, *53*), cyclic peptides (*41*, *48*, *51*), or calix[4]arenes (*31*, *35*). Other multivalent carbohydrate macromolecules such as glycopolymers (*61*−*68*) and glycodendrimers (*19*, *69*−*72*) have also been studied for their improved binding to lectins in comparison to monovalent species.

In each family, glycoclusters display a specific geometry and a controlled number of carbohydrate moieties at their surface and appear as promising multivalent carbohydrate structures for studying lectin−carbohydrate interactions. The synthesis of glycoclusters remains rather complicated particularly due to the difficulty of their purification. Nevertheless, there are no examples of glycocluster based on an oligonucleotidic or pseudo-oligonucleotidic scaffold, even though a few examples of glycoconjugates with oligonucleotides (*27*, *44*, *45*, *50*, *73*) have been reported, but these compounds display only a limited number of carbohydrates and do not display a phosphodiester backbone.

We present herein a flexible synthetic approach to afford rapidly and easily fucosylated pentaerythrityl phosphodiester oligomers (PePOs) based on a bis-2,2-saccharidyl-1,3-propanediol phosphodiester scaffold (Figure 1). Their synthesis was based on a combination of oligonucleotide phosphoramidite chemistry on solid support and microwave-assisted click chemistry. The PePOs exhibited only one nucleotide at the pseudo-3′-end as a tag for the determination of glycosylated PePOs concentration by UV analysis. The propargylated PePOs were conveniently prepared using a phosphoramidite dialkyne building block, which was coupled several times using a DNA-like synthesis on solid support. Carbohydrate moieties were then introduced from their azide derivatives by 1,3-dipolar cycloaddition (*74*−*82*) according to our previously reported procedure (*83*−*85*) leading to the desired PePOs glycoclusters. The solid-supported oligonucleotidic automated synthesis allows for a rapid and efficient preparation of propargylated PePOs with control of the number of propargyl residues. An excess of reagents can be used to reach quantitative yields for each cycle with washings to remove them. Click chemistry on a solid support is an efficient method for the rapid and efficient multiple labeling with azido carbohydrate derivatives. Finally, the cleavage from the solid support was achieved with concomitant deprotection of the glycosylated PePOs which were used without further purification. The thymidine residue introduced at the pseudo-3′-end allows for the determination of the quantity of material present in the final solution.

Fucosylated PePOs bearing 4, 6, 8, and 10 carbohydrate residues were synthesized as potential ligands for *Pseudomonas aeruginosa* lectin (PA-IIL). Recently, a series of bacterial lectins

* Corresponding authors. S. Vidal: Phone, +33/688 71 72 03; Fax, +33/472 44 83 49. F. Morvan: Phone, +33/467 14 49 61; Fax, +33/467 04 20 29.

† Institut des Biomolécules Max Mousseron, CNRS - Université Montpellier I/II.

‡ Laboratoire de Chimie Organique 2 - Glycochimie - CNRS - Université Claude Bernard Lyon 1.

§ CERMAV - CNRS.

|| Institut des Nanotechnologies de Lyon - CNRS - Ecole Centrale de Lyon - INSA Lyon - Université Claude Bernard Lyon 1.

10.1021/bc070129z CCC: $37.00 © 2007 American Chemical Society
Published on Web 07/21/2007

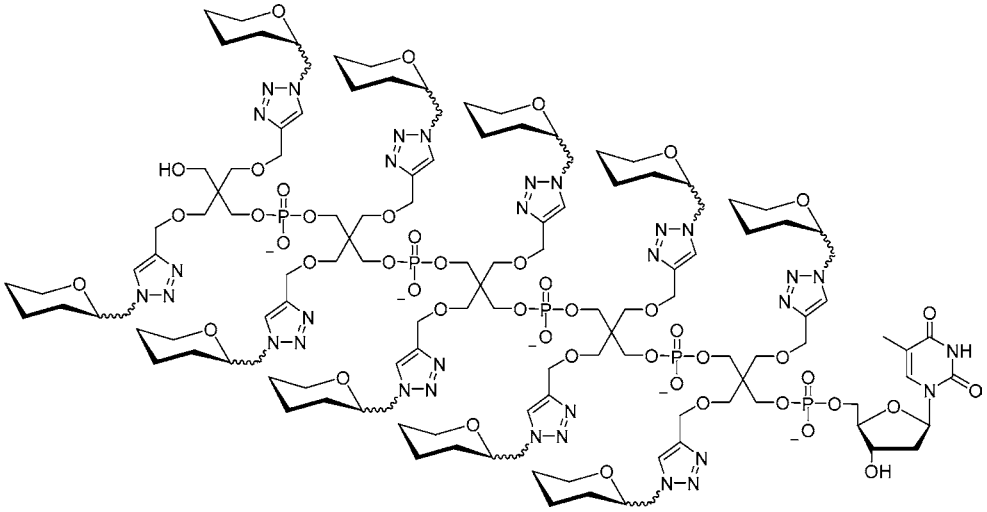


Figure 1. Schematic representation of a decaglycosylated PePO (waves represents triethylene glycol chains).

have been identified that display micromolar affinities for their ligands (*86*). Among them, PA-IIL has been identified in *Pseudomonas aeruginosa*, an opportunistic bacterium that is life-threatening for immunosuppressed and cystic fibrosis patients and that displays increasing resistance to antibiotics. PA-IIL is a fucose-binding lectin that has been well-characterized for its high affinity for fucose (*87*, *88*) and its interaction with other monosaccharides (*89*) and oligosaccharides (*90*). The lectin is a tetramer, and the high avidity provided by multivalent ligands could make these compounds of interest for anti-adhesive therapy against bacterial infection.

EXPERIMENTAL PROCEDURES

Material and Methods. Thin-layer chromatography (TLC) was carried out on aluminum sheets coated with silica gel 60 F_{254} (Merck). TLC plates were inspected by UV light ($\lambda = 254$ nm) and developed by treatment with a mixture of 10% H_2SO_4 in EtOH/H_2O (1/1 v/v) followed by heating. Silica gel column chromatography was performed with Geduran silica gel Si 60 (40−63 μm) purchased from Merck (Darmstadt, Germany). ^{1}H and ^{13}C NMR spectra were recorded at 23 °C using Bruker Advance DRX300 or DRX500 spectrometers with the residual solvent as the internal standard. The following abbreviations are used to explain the observed multiplicities: s, singlet; d, doublet; dd, doublet of doublet; ddd, doublet of doublet of doublet; t, triplet; td, triplet of doublet; q, quadruplet; m, multiplet; br, broad; p, pseudo. Structure elucidation was deduced from 1D and 2D NMR spectroscopy which allowed, in most cases, complete signal assignments based on COSY, HSQC, and HMBC correlations. NMR solvents were purchased from Euriso-Top (Saint Aubin, France). HRMS (LSIMS) mass spectra were recorded in the positive mode using a Thermo Finnigan Mat 95 XL spectrometer. MS (ESI) mass spectra were recorded in the positive mode using a Thermo Finnigan LCQ spectrometer. Optical rotations were measured using a Perkin-Elmer polarimeter. MALDI-ToF spectra were recorded on a PerSeptive Biosystem Voyager DE apparatus using 2′,4′,6′-trihydroxyacetophenone as a matrix.

***O*-(4,4′-Dimethoxytrityl)-Pentaerythritol 1**. Pentaerythritol (2.7 g, 20 mmol) was dried by coevaporation in dry pyridine (3 × 10 mL) and then dissolved in dry pyridine (120 mL). Dimethoxytrityl chloride (5.42 g, 16 mmol) was added to the solution, and the reaction was stirred at room temperature for 16 h. The reaction was quenched with methanol (2 mL), stirred for 10 min, and then poured into aqueous saturated $NaHCO_3$ (300 mL). The aqueous layer was extracted with CH_2Cl_2 (3 × 150 mL). The organic layers were combined, dried (Na_2SO_4), filtered, and evaporated. The residue was purified by chromatography on silica gel (CH_2Cl_2/MeOH 99:1 to 94:6, v/v) affording the monotritylated pentaerythritol **1** (2.2 g, 30%) as a pale yellow foam. $R_f = 0.50$ (CH_2Cl_2/MeOH, 9:1, v/v). ^{1}H NMR ($CDCl_3$, 400 MHz): δ 2.36 (br s, 3H), 3.10 (s, 2H), 3.65 (br s, 6H), 3.71 (s, 6H), 6.74−7.31 (m, 13H). ^{13}C NMR ($CDCl_3$, 100 MHz): δ 45.3, 53.5, 55.2, 63.9, 64.6, 86.5, 113.3, 127.0, 128.0, 130.0, 135.6, 144.6, 158.6.

1-*O*-(4,4′-Dimethoxytrityl)-2,2-bis-propargyloxymethyl-1,3-propanediol 2. Sodium hydride (1.16 g, 29.1 mmol, 60% in oil) was added at 0 °C to a solution of monotritylated pentaerythritol **1** (2.2 g, 4.8 mmol) in dry THF (30 mL). The reaction was stirred for 10 min before adding propargyl bromide (3.3 mL, 29.1 mmol, 80% in toluene) at room temperature (rt). The resulting milky solution was stirred for an additional 3 h at rt. The solution was diluted with CH_2Cl_2 (80 mL), and the organic layer was washed with cold water (50 mL), brine (50 mL), and then dried (Na_2SO_4), filtered, and evaporated. The residue was purified by chromatography on silica gel (CH_2Cl_2/MeOH 99.5:0.5 to 97:3, v/v) affording the bis-propargylated pentaerythritol **2** (2.2 g, 89%) as pale yellow foam. $R_f = 0.45$ (cyclohexane/CH_2Cl_2/Et_3N, 7:2:1, v/v/v). ^{1}H NMR ($CDCl_3$, 400 MHz): δ 2.35 (m, 3H), 3.05 (s, 2H), 3.48−3.60 (m, 6H), 3.70 (s, 6H), 4.02 (s, 4H), 6.73−7.26 (m, 13H). ^{13}C NMR ($CDCl_3$, 100 MHz): δ 11.7, 45.1, 46.3, 53.5, 55.2, 58.7, 62.3, 65.3, 70.3, 74.5, 86.0, 113.0, 113.1, 126.7, 127.8, 128.2, 129.2, 130.1, 136.0, 145.0, 158.4. HRFABMS (positive mode, nitrobenzylic alcohol) *m/z*: calcd for $C_{32}H_{34}O_6$ $[M + H]^+$ 514.2355, found 514.2365.

3-(4,4′-Dimethoxytrityloxy)-2,2-bis(propargyloxymethyl)-propyl (2-cyanoethyl *N*,*N*-diisopropyl)-phosphoramidite 3. Alcohol **2** (680 mg, 1.32 mmol) and diisopropylammonium tetrazolide (113 mg, 0.66 mmol) were dried three times by coevaporation with anhydrous acetonitrile, then dissolved in anhydrous CH_2Cl_2 (8 mL) before addition of 2-cyanoethyl tetraisopropylphosphorodiamidite (503 μL, 1.58 mmol) at rt. The resulting mixture was stirred at room temperature for 3 h, then diluted with EtOAc (50 mL). The organic layer was washed with brine (2 × 100 mL), dried (Na_2SO_4), filtered, and evaporated. The residue was purified by chromatography on silica gel (cyclohexane/CH_2Cl_2 100/0 to 80/20 with 4% Et_3N) affording the phosphoramidite **3** (800 mg, 85%) as an oil. $R_f =$ 0.60 (cyclohexane/CH_2Cl_2/Et_3N, 7:2:1, v/v/v). ^{1}H NMR ($CDCl_3$, 200 MHz): δ 1.15−1.24 (m, 12H), 2.40 (m, 2H), 2.54 (t, 2H, $J = 6.5$ Hz), 3.15 (br s, 2H), 3.45−3.74 (m, 10H), 3.81 (s, 6H), 4.09−4.12 (m, 4H), 6.76−7.49 (m, 13H). ^{13}C NMR ($CDCl_3$,-100 MHz): δ 20.3, 20.4, 24.6, 24.6, 26.92, 26.93, 29.7, 30.2,

30.3, 43.0, 43.1, 43.5, 45.5, 45.6, 46.3, 53.4, 55.2, 58.2, 58.4, 58.6, 58.7, 61.2, 62.2, 62.4, 69.4, 74.1, 74.2, 80.0, 85.6, 112.9, 117.7, 126.6, 127.6, 128.3, 130.3, 136.3, 145.3, 158.3. ^{31}P NMR ($CDCN_3$, 80 MHz): δ 148.6. HRFABMS (positive mode, nitrobenzylic alcohol) *m/z*: calcd for $C_{41}H_{52}O_7N_2P_1$ $[M + H]^+$ 715.3512, found 715.3522.

8-Azido-3,6-dioxapent-1-yl 2,3,4-tri-*O*-acetyl-α-L-fucopyranoside 5. A solution of L-fucose (1 g, 6.1 mmol) and 2-[2-(2-chloroethoxy)ethoxy]ethanol (3 mL, 20.6 mmol) was stirred at rt for 5 min, followed by the dropwise addition of BF_3·Et_2O (1.54 mL, 12.2 mmol). The reaction mixture was stirred at 100 °C for 5 h, and the solution turned yellow then dark brown. The crude mixture was then poured into pyridine (35 mL), and acetic anhydride (7 mL) was then added at 0 °C. The solution was stirred at rt for 48 h, then poured into iced water (100 mL), and the aqueous layer was extracted with EtOAc (150 mL). The organic layer was washed with water (100 mL), then saturated aqueous $NaHCO_3$ (100 mL), and then dried (Na_2SO_4), filtered, evaporated to dryness, and coevaporated with toluene (4 × 30 mL). The oily residue was purified by flash silica gel column chromatography (CH_2Cl_2 then CH_2Cl_2/EtOAc 4:1) to afford the intermediate 1-chloro-3,6-dioxapent-8-yl 2,3,4-tri-*O*-acetyl-L-fucopyranoside **4** (718 mg) as a colorless oil and as an α/β (3:1) mixture of anomers. A solution of **4** (718 mg, 1.63 mmol), sodium azide (1.06 g, 16.3 mmol), and *n*-tetrabutylammonium iodide (300 mg, 0.81 mmol) in DMF (20 mL) was stirred at 90 °C for 16 h. The solution was diluted with water (100 mL) and the aqueous layer extracted with CH_2Cl_2 (2 × 150 mL). The organic layers were combined, dried (Na_2SO_4), filtered, and evaporated to dryness. The oily residue was purified by flash silica gel column chromatography (hexane/$CHCl_3$ then hexane/$CHCl_3$/acetone 2:1:1) to afford **5** (441 mg, 16%) as a pale yellow oil. A first crop of the α anomer (113 mg) was obtained, followed by two additional crops of 226 mg and 102 mg of α/β mixture of anomers in 4:1 and 1:1 ratios, respectively. ^{1}H NMR ($CDCl_3$, 300 MHz): δ 1.13 (d, 3H, $J_{6,5}$ = 6.6 Hz, H-6), 1.98, 2.07, 2.16 (3s, 3 × 3H, 3 × C*H*$_3$CO), 3.40 (t, 2H, J = 5.2 Hz, C*H*$_2$N$_3$), 3.60−3.85 (m, 11H, OC*H*$_2$, H-5), 4.23 (q, 1H, $J_{5,6}$ = 6.6 Hz, H-5), 5.10−5.17 (m, 2H), 5.30 (dd, 1H, $J_{2,1}$ = 1.1 Hz, $J_{2,3}$ = 3.4 Hz, H-2), 5.34−5.40 (m, 1H).

General Procedure for the Automated Synthesis of Propargylated PePOs 6a−d. The syntheses of propargylated PePOs **6a−d** were performed on a DNA synthesizer (381A, ABI) on 1 μ molar scale using standard phosphoramidite chemistry with commercial LCAA-CPG solid-supported 5′-*O*-dimethoxytrityl-thymidine (500 Å) and phosphoramidite **3**. The pseudo-oligonucleotidic chain elongation cycle was as follows: Dedimethoxytritylation was performed with trichloroacetic acid (3% in CH_2Cl_2) for 60 s; coupling was performed with **3** (0.09 M in acetonitrile, 18 molar eq) activated with benzylthiotetrazole (0.3 M in acetonitrile) for 60 s; oxidation was performed with I_2 (0.1 M in THF/pyridine/water 90:5:5, v/v/v) for 20 s; and capping was performed with a 1:1 solution of Cap A (Ac_2O in pyridine/THF 1:1:8, v/v/v) and Cap B (10% *N*-methylimidazole in THF) for 16 s. An average yield of phosphoramidite coupling of >98.5% was obtained.

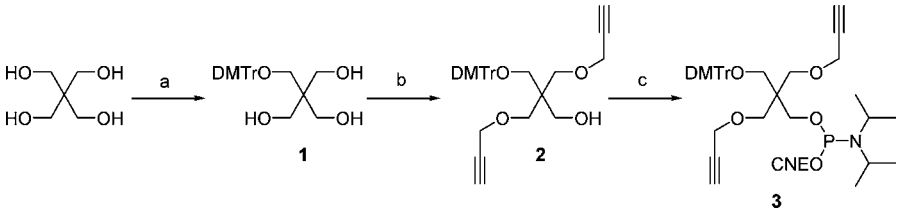
Table 1. Quantities and MALDI-ToF Data Obtained for PePOs 8a−d

glycosylated PePOs	quantity obtained (mg)	number of moles (μmol)	$[M - H]^-$ calcd	$[M - H]^-$ found
8a	0.88	0.43	2074.99	2075.29
8b	1.89	0.63	2991.87	2992.12
8c	2.43	0.62	3908.75	3908.22
8d	2.77	0.57	4825.63	4825.43

General Procedure for the Synthesis of Fucosylated PePOs 8a−d. Solid-supported propargylated PePOs **6a−d** were transferred into a microwave vial; and azido fucose derivative **5** (0.6 M in MeOH, 5 molar equiv per alkyne), $CuSO_4$ (0.1 M in water, 0.2 molar equiv per alkyne), and sodium ascorbate (0.25 M in water, 1 molar equiv per alkyne) were added, and the solution was completed with water and MeOH to obtain a final volume of 200 μL water/MeOH (1/1). The vial was sealed, then irradiated with microwaves for 30 min at 60 °C to afford **7a−d**. Treatment of the beads with concentrated aqueous ammonia for 2 h at rt afforded the fucosylated PePOs **8a−d**. The concentration of the glycosylated PePOs was determined by UV measurement at 260 nm based on the extinction coefficient of thymidine (ϵ^{260nm} = 8700 L.mol^{-1}.cm^{-1}) and characterized by MALDI-ToF mass spectrometry (Table 1).

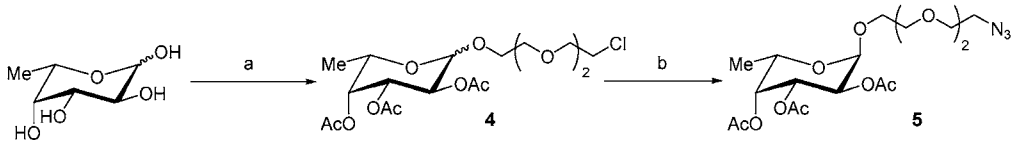
ELLA (Enzyme-Linked Lectin Assay) Experiments. ELLA experiments were conducted using 96-well microtiter plates (Nunc Maxisorb) coated with polymeric α-L-fucose (5 μg/mL; Lectinity Holding, Inc., Moscow) diluted in carbonate buffer, pH 9.6 (100 μL), for 1 h at 37 °C. After blocking at 37 °C for 1 h with 100 μL per well of 3% (w/v) BSA in PBS (pH 7.4), plates were incubated at 37 °C for 1 h with 100 μL of biotinylated PA-IIL at 0.1 μg/mL in the presence of an increasing amount of competitors **8a−d**. After washing with T−PBS (PBS containing 0.05% Tween), 100 μL of streptavidin−peroxidase conjugate (dilution 1:10 000; Boehringer-Mannheim) was added and left for 1 h at 37 °C. The color was

Scheme 1[a]



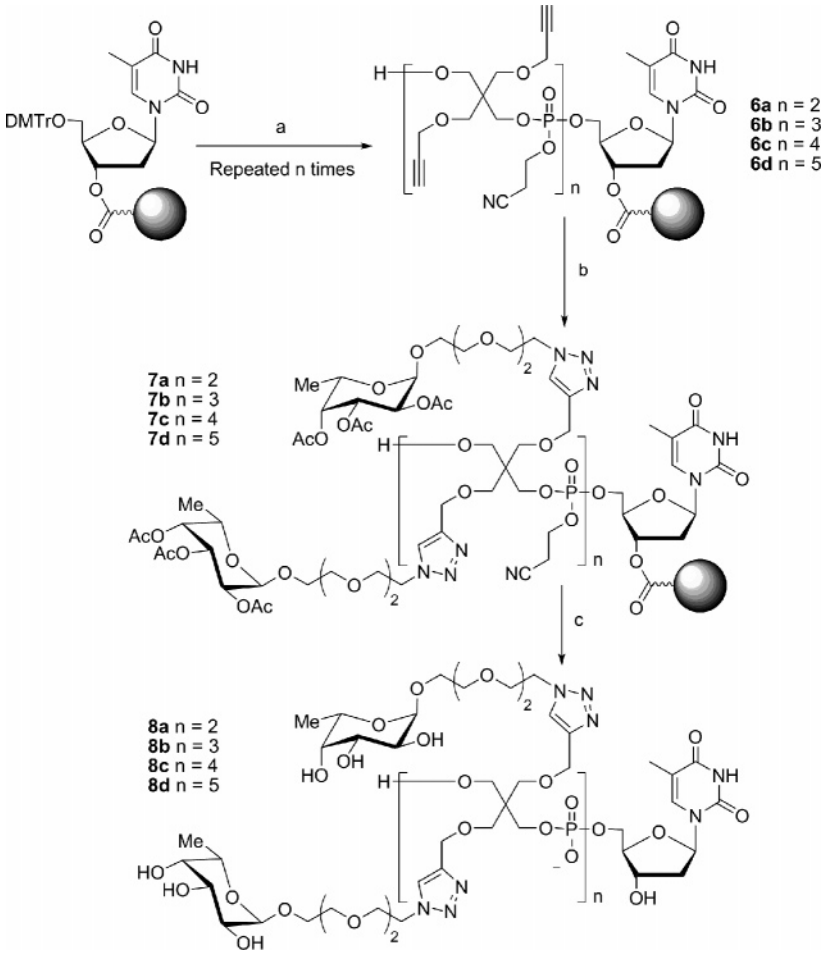
[a] Reagents and conditions: (a) DMTrCl, C_5H_5N, 30%; (b) propargyl bromide, NaH, THF, 89%; (c) diisopropylammonium tetrazolide, 2-cyanoethyl tetraisopropylphosphorodiamidite, CH_2Cl_2, 85%.

Scheme 2[a]



[a] Reagents and conditions: (a) (i) $HOCH_2(CH_2OCH_2)_2CH_2Cl$, BF_3•Et_2O, 100 °C, (ii) Ac_2O, C_5H_5N; (b) NaN_3, nBu$_4$NI, DMF, 90 °C.

Scheme 3[a]



[a] Reagents and conditions: (a) automated synthesis on solid support: (i) Cl_3CCO_2H, CH_2Cl_2, (ii) **3**, benzylthiotetrazole, MeCN, (iii) I_2, H_2O, C_5H_5N, THF, (iv) Ac_2O, C_5H_5N (cycle repeated *n* times); (b) **5**, $CuSO_4$, sodium ascorbate, H_2O, MeOH, MW (100 W, 60 °C, 30 min); (c) NH_4OH.

developed using 100 μL per well of 0.05 M phosphate/citrate buffer containing *O*-phenylenediamine dihydrochloride (0.4 mg/mL) and urea hydrogen peroxide (0.4 mg/mL) (Sigma-Aldrich). The reaction was stopped by the addition of 50 μL of 30% H_2SO_4. Absorbance was read at 490 nm using a microtiter plate reader (Bio-Rad; model 680).

RESULTS AND DISCUSSION

The PePOs display a pentaerythritol residue between each phosphodiester linkage providing two functional groups with a high geometrical flexibility for an optimal arrangement of the ligands through space in order to reach high affinities. A triethylene glycol linker between the saccharide and the triazole was selected for its hydrophilic properties for a better display of the carbohydrate moieties on the periphery of the glycocluster.

Preparation of the Building Blocks. Automated synthesis requires orthogonally protected multifunctional scaffolds where each functional group can be activated selectively for reacting with the next entity. Pentaerythritol was selected as a tetrafunctional molecule which can be easily desymmetrized through simple reaction schemes. Monoprotection of pentaerythritol with dimethoxytrityl chloride provided the triol **1** (Scheme 1) (*91*). Alkylation of **1** using a large excess of propargyl bromide yielded the bis-propargylated alcohol **2** in good yield. Reaction of alcohol **2** with 2-cyanoethyl tetraisopropylphosphorodiamidite activated with diisopropylammonium tetrazolide provided the expected phosphoramidite **3**. This molecule is presenting a masked alcohol and a phosphoramidite moiety for the DNA-like chain elongation, as well as two propargyl residues for a further conjugation with carbohydrate azide derivatives using a [3+2]-cycloaddition reaction (*83*, *85*).

The synthesis of azido-carbohydrates is required for their conjugation by click chemistry on the propargyl residues. The control of the anomeric configuration of sugars is often crucial for optimal and selective binding to lectins. The *O*-acyl or Fischer stereoselective glycosylation methods were selected for the preparation of the α-L-fucoside derivative (Scheme 2). Glycosylation of L-fucose with chlorotriethylene glycol under Fischer conditions afforded a mixture of anomers (α/β 3/1), which was directly peracetylated to obtain L-fucoside **4**. The separation of each anomer was unsuccessful at that point. Subsequent azidation of **4** afforded the corresponding azide derivative **5** (*92*) with the same α/β distribution. Each anomer was isolated pure after a flash silica gel column chromatography.

Solid-Supported Synthesis of PePOs. The dialkyne phosphoramidite building block **3** was coupled starting from a commercial solid-supported thymidine applying a phosphoramidite elongation cycle on a DNA synthesizer. The thymidine present at the pseudo-3′-end of the polyglycosyl nucleic acid was used as a UV tag for HPLC analyses, as well as for the determination of concentrations in material in solution. The thymidine functionalized beads were subjected to a standard sequence of detritylation, phosphoramidite coupling under benzylthiotetrazole activation, oxidation, and capping used for the synthesis of oligonucleotides (Scheme 3). This cycle was repeated 2, 3, 4, and 5 times to obtain the oligoalkyne nucleic acids **6a**−**d**, respectively. After elongation, 1,3-dipolar cycloaddition was achieved on solid support (*83*, *85*) using the α-L-

Table 2. Competition of Binding of PA-IIL to Polymeric α-L-Fucose with the Fucosylated PePOs 8a−d

fucosylated PePOs	valency	IC_{50} (μM)	relative potency[a]	potency per fucose residue[b]
L-fucose[c]	1	5.60	1	1.0
8a	4	0.70	8	2.0
8b	6	0.40	14	2.3
8c	8	0.35	16	2.0
8d	10	0.25	22.4	2.2

[a] Calculated as the ratio of L-fucose to glycosylated PePOs IC_{50} values. [b] Calculated as the ratio of relative potency to the number of fucose residues. [c] L-Fucose was selected as the monovalent reference for the comparison of IC_{50} values.

fucoside azide derivative **5** to obtain the fully protected glycosylated PePOs **7a−d**. Aminolysis of the protecting groups (i.e., acetates and cyanoethyls) and concomitant cleavage from the solid support using concentrated aqueous ammonia afforded the fully deprotected glycosylated PePOs **8a−d** in solution with high purity and good yield. Each glycocluster was analyzed by HPLC and characterized by MALDI-ToF mass spectrometry (see Supporting Information). The quantities of available materials in solution were determined by UV measurements at 260 nm based on the extinction coefficient of thymidine.

Binding Studies. The affinity of the glycosylated PePOs for PA-IIL was studied using an enzyme-linked lectin assay (ELLA). The fucosylated PePOs **8a−d** were evaluated for binding to PA-IIL. A clear inhibition of the fixation of the lectin on the polymeric α-L-fucose was observed. The results obtained show that multivalency is responsible for an improved binding to the lectin (Table 2). The negative charges present on the phosphodiester linkages of the fucosylated PePOs **8a−d** did not prevent binding to the lectin. PA-IIL is a tetramer in solution, with each monomer requiring two calcium ions for binding fucose (*93*). These multivalent structures are good ligands of PA-IIL, since the IC_{50} values measured for the fucosylated PePOs are in the submicromolar range (0.25−0.70 μM) in comparison with the value observed for L-fucose of 5.6 μM. The higher affinity observed for these multivalent scaffolds in comparison to monovalent species (L-fucose) may also be explained by a relatively high flexibility and a good distribution of the L-fucose moieties on the PePOs due to a good solubility of the phosphodiester and ethylene glycol linkages in aqueous media, providing large freedom of movement to the ligands in solution. The number of carbohydrate residues displayed on the nucleic acid-like backbone is slightly influencing the binding to the lectin, and 6 to 8 fucose residues appear to be sufficient for a high interaction with PA-IIL, since a plateau was almost reached.

The enhancement observed cannot be attributed to a "cluster" effect, since the potency per carbohydrate is only of 2 for every multivalent ligand **8a−d**, regardless of the number of fucose residues. The increased binding of these multivalent carbohydrate ligands is more likely to be attributed to the recently described "macromolecular" effect (*36*).

ACKNOWLEDGMENT

The authors wish to thank the financial support from the CNRS, INSERM, Université Claude Bernard Lyon 1, Université Montpellier 2, Ecole Centrale de Lyon and Vaincre la Mucoviscidose.

Supporting Information Available: ^1H and ^{13}C NMR data for compounds **1−3**; HPLC and MALDI-ToF data for PePOs **8a−d**. This material is available free of charge via the Internet at http://pubs.acs.org.

LITERATURE CITED

(1) Varki, A., Cummings, R., Esko, J., Freeze, H., Hart, G., and Marth, J. (1999) *Essentials of Glycobiology*, Spring Harbor Laboratory Press, New York.
(2) Bertozzi, C. R., and Kiessling, L. L. (2001) Chemical glycobiology. *Science 291*, 2357−2364.
(3) Dwek, R. A. (1996) Glycobiology: toward understanding the function of sugars. *Chem. Rev. 96*, 683−720.
(4) Varki, A. (1993) Biological roles of oligosaccharides: all of the theories are correct. *Glycobiology 3*, 97−130.
(5) Angata, T., and Brinkman-Van der Linden, E. C. M. (2002) I-type lectins. *Biochim. Biophys. Acta 1572*, 294−316.
(6) Brewer, C. F. (2002) Binding and cross-linking properties of galectins. *Biochim. Biophys. Acta 1572*, 255−262.
(7) Dahms, N. M., and Hancock, M. K. (2002) P-type lectins. *Biochim. Biophys. Acta 1572*, 317−340.
(8) East, L., and Isacke, C. M. (2002) The mannose receptor family. *Biochim. Biophys. Acta 1572*, 364−386.
(9) Gabius, H.-J., Andre, S., Kaltner, H., and Siebert, H.-C. (2002) The sugar code: functional lectinomics. *Biochim. Biophys. Acta 1572*, 165−177.
(10) Kilpatrick, D. C. (2002) Animal lectins: a historical introduction and overview. *Biochim. Biophys. Acta 1572*, 187−197.
(11) Lis, H., and Sharon, N. (1998) Lectins: carbohydrate-specific proteins that mediate cellular recognition. *Chem. Rev. 98*, 637−674.
(12) Loris, R. (2002) Principles of structures of animal and plant lectins. *Biochim. Biophys. Acta 1572*, 198−208.
(13) Gargano, J. M., Ngo, T., Kim, J. Y., Acheson, D. W. K., and Lees, W. J. (2001) Multivalent inhibition of AB5 toxins. *J. Am. Chem. Soc. 123*, 12909−12910.
(14) Lee, R. T., and Lee, Y. C. (2000) Affinity enhancement by multivalent lectin-carbohydrate interaction. *Glycoconjugate J. 17*, 543−551.
(15) Mammen, M., Choi, S.-K., and Whitesides, G. M. (1998) Polyvalent interactions in biological systems: implications for design and use of multivalent ligands and inhibitors. *Angew. Chem., Int. Ed. 37*, 2754−2794.
(16) Mulder, A., Huskens, J., and Reinhoudt, D. N. (2004) Multivalency in supramolecular chemistry and nanofabrication. *Org. Biomol. Chem. 2*, 3409−3424.
(17) Wolfenden, M. L., and Cloninger, M. J. (2005) Mannose/glucose-functionalized dendrimers to investigate the predictable tunability of multivalent interactions. *J. Am. Chem. Soc. 127*, 12168−12169.
(18) Badjic, J. D., Nelson, A., Cantrill, S. J., Turnbull, W. B., and Stoddart, J. F. (2005) Multivalency and cooperativity in supramolecular chemistry. *Acc. Chem. Res. 38*, 723−732.
(19) Cloninger, M. J. (2002) Biological applications of dendrimers. *Curr. Opin. Chem. Biol. 6*, 742−748.
(20) Fan, J.-Q., Quesenberry, M. S., Takegawa, K., Iwahara, S., Kondo, A., Kato, I., and Lee, Y. C. (1995) Synthesis of neoglycoconjugates by transglycosylation with arthrobacter protophormiae N-acetylglucosaminidase. *J. Biol. Chem. 270*, 17730−17735.
(21) Lee, R. T., Ichikawa, Y., Kawasaki, T., Drickamer, K., and Lee, Y. C. (1992) Multivalent ligand binding by serum mannose-binding protein. *Arch. Biochem. Biophys. 299*, 129−136.
(22) Lee, Y. C., and Lee, R. T. (1995) Carbohydrate-protein interactions: basis of glycobiology. *Acc. Chem. Res. 28*, 321−327.
(23) Lee, Y. C., Lee, R. T., Rice, K., Ichikawa, Y., and Wong, T.-C. (1991) Topography of binding sites of animal lectins: ligand's view. *Pure Appl. Chem. 63*, 499−506.
(24) Lindhorst, T. K. (2002) Artificial multivalent sugar ligands to understand and manipulate carbohydrate-protein interactions. *Top. Curr. Chem. 218*, 201−235.
(25) Lundquist, J. J., and Toone, E. J. (2002) The cluster glycoside effect. *Chem. Rev. 102*, 555−578.
(26) Turnbull, W. B., and Stoddart, J. F. (2002) Design and synthesis of glycodendrimers. *Rev. Mol. Biotechnol. 90*, 231−255.
(27) Akhtar, S., Routledge, A., Patel, R., and Gardiner, J. M. (1995) Synthesis of mono- and dimannoside phosphoramidite derivatives for solid-phase conjugation to oligonucleotides. *Tetrahedron Lett. 36*, 7333−7336.
(28) Al-Mughaid, H., and Grindley, T. B. (2006) Synthesis of a nonavalent mannoside glycodendrimer based on pentaerythritol. *J. Org. Chem. 71*, 1390−1398.

(29) Andre, S., Kaltner, H., Furuike, T., Nishimura, S. I., and Gabius, H. J. (2004) Persubstituted cyclodextrin-based glycoclusters as inhibitors of protein-carbohydrate recognition using purified plant and mammalian lectins and wild-type and lectin-gene-transfected tumor cells as targets. *Bioconjugate Chem. 15*, 87−98.

(30) Andre, S., Liu, B., Gabius, H.-J., and Roy, R. (2003) First demonstration of differential inhibition of lectin binding by synthetic tri- and tetravalent glycoclusters from cross-coupling of rigidified 2-propynyl lactoside. *Org. Biomol. Chem. 1*, 3909−3916.

(31) Arosio, D., Fontanella, M., Baldini, L., Mauri, L., Bernardi, A., Casnati, A., Sansone, F., and Ungaro, R. (2005) A synthetic divalent cholera toxin glycocalix[4]arene ligand having higher affinity than natural GM1 oligosaccharide. *J. Am. Chem. Soc. 127*, 3660−3661.

(32) Autar, R., Khan, A. S., Schad, M., Hacker, J., Liskamp, R. M. J., and Pieters, R. J. (2003) Adhesion inhibition of F1C-fimbriated *Escherichia coli* and *Pseudomonas aeruginosa* PAK and PAO by multivalent carbohydrate ligands. *ChemBioChem 4*, 1317−1325.

(33) Carpenter, C., and Nepogodiev, S. A. (2005) Synthesis of αMan-(1−3)αMan(1−2)αMan glycocluster presented on β-cyclodextrin scaffold. *Eur. J. Org. Chem. 2005*, 3286−3296.

(34) Danishefsky, S. J., and Allen, J. R. (2000) From the laboratory to the clinic: a retrospective on fully synthetic carbohydrate-based anticancer vaccines. *Angew. Chem., Int. Ed. 39*, 836−863.

(35) Dondoni, A., and Marra, A. (2006) *C*-Glycoside clustering on calix[4]arene, adamantane, and benzene scaffolds through 1,2,3-triazole linkers. *J. Org. Chem. 71*, 7546−7557.

(36) Dubber, M., Sperling, O., and Lindhorst, T. K. (2006) Oligomannoside mimetics by glycosylation of 'octopus glycosides' and their investigation as inhibitors of type 1 fimbriae-mediated adhesion of *Escherichia coli*. *Org. Biomol. Chem. 4*, 3901−3912.

(37) Frison, N., Marceau, P., Roche, A.-C., Monsigny, M., and Mayer, R. (2002) Oligolysine-based saccharide clusters: synthesis and specificity. *Biochem. J. 368*, 111−119.

(38) Frison, N., Taylor, M. E., Soilleux, E., Bousser, M.-T., Mayer, R., Monsigny, M., Drickamer, K., and Roche, A.-C. (2003) Oligolysine-based oligosaccharide clusters: selective recognition and endocytocis by the mannose receptor and dendritic cell-specific intracellular adhesion molecule 3 (ICAM-3)-grabbing nonintegrin. *J. Biol. Chem. 278*, 23922−23929.

(39) Fulton, D. A., and Stoddart, J. F. (2001) Synthesis of cyclodextrin-based carbohydrate clusters by photoaddition reactions. *J. Org. Chem. 66*, 8309−8319.

(40) Furuike, T., Sadamoto, R., Niikura, K., Monde, K., Sakairi, N., and Nishimura, S.-I. (2005) Chemical and enzymatic synthesis of glycocluster having seven sialyl lewis X arrays using β-cyclodextrin as a key scaffold material. *Tetrahedron 61*, 1737−1742.

(41) Grigalevicius, S., Chierici, S., Renaudet, O., Lo-Man, R., Deriaud, E., Leclerc, C., and Dumy, P. (2005) Chemoselective assembly and immunological evaluation of multiepitopic glycoconjugates bearing clustered Tn antigen as synthetic anticancer vaccines. *Bioconjugate Chem. 16*, 1149−1159.

(42) Kalovidouris, S. A., Blixt, O., Nelson, A., Vidal, S., Turnbull, W. B., Paulson, J. C., and Stoddart, J. F. (2003) Chemically defined sialoside scaffolds for investigation of multivalent interactions with sialic acid binding proteins. *J. Org. Chem. 68*, 8485−8493.

(43) Kassab, R., Felix, C., Parrot-Lopez, H., and Bonaly, R. (1997) Synthesis of cyclodextrin derivatives carrying bio-recognisable saccharide antennae. *Tetrahedron Lett. 38*, 7555−7558.

(44) Katajisto, J., Heinonen, P., and Lonnberg, H. (2004) Solid-phase synthesis of oligonucleotide glycoconjugates bearing three different glycosyl groups: orthogonally protected bis(hydroxymethyl)-*N*,*N*′-bis(3-hydroxypropyl)malondiamide phosphoramidite as key building block. *J. Org. Chem. 69*, 7609−7615.

(45) Katajisto, J., Virta, P., and Lonnberg, H. (2004) Solid-phase synthesis of multiantennary oligonucleotide glycoconjugates utilizing on-support oximation. *Bioconjugate Chem. 15*, 890−896.

(46) Kolomiets, E., Johansson, E. M. V., Renaudet, O., Darbre, T., and Reymond, J. L. (2007) Neoglycopeptide dendrimer libraries as a source of lectin binding ligands. *Org. Lett. 9*, 1465−1468.

(47) Nelson, A., Belitsky, J. M., Vidal, S., Joiner, C. S., Baum, L. G., and Stoddart, J. F. (2004) A self-assembled multivalent pseudopolyrotaxane for binding galectin-1. *J. Am. Chem. Soc. 126*, 11914−11922.

(48) Renaudet, O., and Dumy, P. (2004) Chemoselectively template-assembled glycopeptide presenting clustered cancer related T-antigen. *Tetrahedron Lett. 45*, 65−68.

(49) Roy, R., and Kim, J. M. (2003) Cu(II)-self-assembling bipyridyl-glycoclusters and dendrimers bearing the Tn-antigen cancer marker: syntheses and lectin binding properties. *Tetrahedron 59*, 3881−3893.

(50) Sheppard, T. L., Wong, C.-H., and Joyce, G. F. (2000) Nucleoglycoconjugates: design and synthesis of a new class of DNA-carbohydrate conjugates. *Angew. Chem. 39*, 3660−3663.

(51) Singh, Y., Renaudet, O., Defrancq, E., and Dumy, P. (2005) Preparation of a multitopic glycopeptide-oligonucleotide conjugate. *Org. Lett. 7*, 1359−1362.

(52) Tosin, M., Muller-Bunz, H., and Murphy, P. V. (2004) Synthesis and X-ray single crystal structure of a bivalent glycocluster. *Chem. Commun.* 494−495.

(53) Touaibia, M., Shiao, T. C., Papadopoulos, A., Vaucher, J., Wang, Q., Benhamioud, K., and Roy, R. (2007) Tri- and hexavalent mannoside clusters as potential inhibitors of type 1 fimbriated bacteria using pentaerythritol and triazole linkages. *Chem. Commun.* 380−382.

(54) Turnbull, W. B., Kalovidouris, S. A., and Stoddart, J. F. (2002) Large oligosaccharide-based glycodendrimers. *Chem.—Eur. J. 8*, 2988−3000.

(55) Virta, P., Karskela, M., and Lonnberg, H. (2006) Orthogonally protected cyclo-β-tetrapeptides as solid-supported scaffolds for the synthesis of glycoclusters. *J. Org. Chem. 71*, 1989−1999.

(56) von der Lieth, C.-W., Frank, M., and Lindhorst, T. K. (2002) Molecular dynamics simulations of glycoclusters and glycodendrimers. *Rev. Mol. Biotechnol. 90*, 311−337.

(57) Wan, Q., Chen, J., Chen, G., and Danishefsky, S. J. (2006) A potentially valuable advance in the synthesis of carbohydrate-based anticancer vaccines through extended cycloaddition chemistry. *J. Org. Chem. 71*, 8244−8249.

(58) Woller, E. K., and Cloninger, M. J. (2002) The lectin-binding properties of six generations of mannose-functionalized dendrimers. *Org. Lett. 4*, 7−10.

(59) Woller, E. K., Walter, E. D., Morgan, J. R., Singel, D. J., and Cloninger, M. J. (2003) Altering the strength of lectin binding interactions and controlling the amount of lectin clustering using mannose/hydroxyl-functionalized dendrimers. *J. Am. Chem. Soc. 125*, 8820−8826.

(60) Wu, P., Malkoch, M., Hunt, J. N., Vestberg, R., Kaltgrad, E., Finn, M. G., Fokin, V. V., Sharpless, K. B., and Hawker, C. J. (2005) Multivalent, bifunctional dendrimers prepared by click chemistry. *Chem. Commun.* 5775−5777.

(61) Flitsch, S. L. (2000) Chemical and enzymatic synthesis of glycopolymers. *Curr. Opin. Chem. Biol. 4*, 619−625.

(62) Gardiner, J. M. (1998) The therapeutic potential of synthetic multivalent carbohydrates. *Exp. Opin. Invest. Drugs 7*, 405−411.

(63) Ladmiral, V., Melia, E., and Haddleton, D. M. (2004) Synthetic glycopolymers: an overview. *Eur. Polym. J. 40*, 431−449.

(64) Leeuwenburgh, M. A., van der Marel, G. A., and Overkleeft, H. S. (2003) Olefin metathesis in glycobiology: new routes towards diverse neoglycoconjugates. *Curr. Opin. Chem. Biol. 7*, 757−765.

(65) Nishimura, S. I., and Lee, Y. C. (1998) Synthetic glycopolymers: new tools for glycobiology, in *Polysaccharides* (Dimitriu, S., Ed.) pp 523−537, Marcel Dekker, New York.

(66) Roy, R. (1996) Syntheses and some applications of chemically defined multivalent glycoconjugates. *Curr. Opin. Struct. Biol. 6*, 692−702.

(67) Roy, R. (1998) The chemistry of neoglycoconjugates, in *Carbohydrate Chemistry* (Boons, G.-J., Ed.) pp 243−321, Blackie, London.

(68) Roy, R., and Baek, M.-G. (2002) Glycodendrimers: novel glycotope isosteres unmasking sugar coding. Case study with T-antigen markers from breast cancer MUC1 glycoprotein. *Rev. Mol. Biotechnol. 90*, 291−309.

(69) Bezouska, K. (2002) Design, functional evaluation and biomedical applications of carbohydrate dendrimers (glycodendrimers). *Rev. Mol. Biotechnol. 90*, 269−290.

(70) Boas, U., and Heegaard, P. M. H. (2004) Dendrimers in drug research. *Chem. Soc. Rev. 33*, 43−63.

(71) Kim, Y., and Zimmerman, S. C. (1998) Applications of dendrimers in bio-organic chemistry. *Curr. Opin. Chem. Biol. 2*, 733−742.

(72) Rockendorf, N., and Lindhorst, T. K. (2001) Glycodendrimers. *Top. Curr. Chem. 217*, 201−238.
(73) Dubber, M., and Frechet, J. M. J. (2003) Solid-phase synthesis of multivalent glycoconjugates on a DNA synthesizer. *Bioconjugate Chem. 14*, 239−246.
(74) Calvo-Flores, F. G., Isac-Garcia, J., Hernandez-Mateo, F., Perez-Balderas, F., Calvo-Asin, J. A., Sanchez-Vaquero, E., and Santoyo-Gonzalez, F. (2000) 1,3-Dipolar cycloadditions as a tool for the preparation of multivalent structures. *Org. Lett. 2*, 2499−2502.
(75) Chen, Q., Yang, F., and Du, Y. (2005) Synthesis of a C_3-symmetric (1→6)-N-acetyl-β-D-glucosamine octadecasaccharide using click chemistry. *Carbohydr. Res. 340*, 2476−2482.
(76) Chittaboina, S., Xie, F., and Wang, Q. (2005) One-pot synthesis of triazole-linked glycoconjugates. *Tetrahedron Lett. 46*, 2331−2336.
(77) Dedola, S., Nepogodiev, S. A., and Field, R. A. (2007) Recent applications of the CuI-catalysed Huisgen azide-alkyne 1,3-dipolar cycloaddition reaction in carbohydrate chemistry. *Org. Biomol. Chem. 5*, 1006−1017.
(78) Fernandez-Megia, E., Correa, J., Rodriguez-Meizoso, I., and Riguera, R. (2006) A click approach to unprotected glycodendrimers. *Macromolecules 39*, 2113−2120.
(79) Giguere, D., Patnam, R., Bellefleur, M.-A., St-Pierre, C., Sato, S., and Roy, R. (2006) Carbohydrate triazoles and isoxazoles as inhibitors of galectins-1 and -3. *Chem. Commun.* 2379−2381.
(80) Kolb, H. C., Finn, M. G., and Sharpless, K. B. (2001) Click chemistry: diverse chemical function from a few good reactions. *Angew. Chem., Int. Ed. 40*, 2004−2021.
(81) Perez-Balderas, F., Ortega-Munoz, M., Morales-Sanfrutos, J., Hernandez-Mateo, F., Calvo-Flores, F. G., Calvo-Asin, J. A., Isac-Garcia, J., and Santoyo-Gonzalez, F. (2003) Multivalent neoglycoconjugates by regiospecific cycloaddition of alkynes and azides using organic-soluble copper catalysts. *Org. Lett. 5*, 1951−1954.
(82) Tejler, J., Tullberg, E., Frejd, T., Leffler, H., and Nilsson, U. J. (2006) Synthesis of multivalent lactose derivatives by 1,3-dipolar cycloadditions: selective galectin-1 inhibition. *Carbohydr. Res. 341*, 1353−1362.
(83) Bouillon, C., Meyer, A., Vidal, S., Jochum, A., Chevolot, Y., Cloarec, J. P., Praly, J. P., Vasseur, J. J., and Morvan, F. (2006) Microwave assisted "click" chemistry for the synthesis of multiple labeled-carbohydrate oligonucleotides on solid support. *J. Org. Chem. 71*, 4700−4702.
(84) Chevolot, Y., Bouillon, C., Vidal, S., Morvan, F., Meyer, A., Cloarec, J.-P., Jochum, A., Praly, J.-P., Vasseur, J.-J., and Souteyrand, E. (2007) DNA-based carbohydrate biochips: a platform for surface glyco-engineering. *Angew. Chem., Int. Ed. 46*, 2398−2402.
(85) Meyer, A., Bouillon, C., Vidal, S., Vasseur, J.-J., and Morvan, F. (2006) A versatile reagent for the synthesis of 5′-phosphorylated, 5′-thiophosphorylated or 5′-phosphoramidate-conjugated oligonucleotides. *Tetrahedron Lett. 47*, 8867−8871.
(86) Imberty, A., Mitchell, E. P., and Wimmerova, M. (2005) Structural basis of high-affinity glycan recognition by bacterial and fungal lectins. *Curr. Opin. Struct. Biol. 15*, 525−534.
(87) Mitchell, E. P., Houles, C., Sudakevitz, D., Wimmerova, M., Gautier, C., Perez, S., Wu, A. M., Gilboa-Garber, N., and Imberty, A. (2002) Structural basis for oligosaccharide-mediated adhesion of *Pseudomonas aeruginosa* in the lungs of cystic fibrosis patients. *Nat. Struct. Biol. 9*, 918−921.
(88) Mitchell, E. P., Sabin, C., Najdrová, L., Pokorná, M., Perret, S., Gautier, C., Gilboa-Garber, C. H. N., Koccaron, J., Wimmerová, M., and Imberty, A. (2005) High affinity fucose binding of *Pseudomonas aeruginosa* lectin PA-IIL: 1.0 Å resolution crystal structure of the complex combined with thermodynamics and computational chemistry approaches. *Proteins: Struct. Funct. Bioinf. 58*, 735−746.
(89) Sabin, C., Mitchell, E. P., Pokorna, M., Gautier, C., Utille, J.-P., Wimmerova, M., and Imberty, A. (2006) Binding of different monosaccharides by lectin PA-IIL from Pseudomonas aeruginosa: thermodynamics data correlated with X-ray structures. *FEBS Lett. 580*, 982−987.
(90) Perret, S., Sabin, C., Dumon, C., Pokorna, M., Gautier, C., Galanina, O., Ilia, S., Bovin, N., Nicaise, M., Desmadril, M., Gilboa-Garber, N., Wimmerova, M., Mitchell, E. P., and Imberty, A. (2005) Structural basis for the interaction between human milk oligosaccharides and the bacterial lectin PA-IIL of *Pseudomonas aeruginosa*. *Biochem. J. 389*, 325−332.
(91) Kim, S. J., Bang, E.-K., and Kim, B. H. (2003) Synthesis of novel phosphoramidite building blocks from pentaerythritol. *Synlett* 1838−1840.
(92) Sanki, A., and Mahal, L. (2006) A one-step synthesis of azide-tagged carbohydrates: versatile -intermediates for glycotechnology. *Synlett* 0455−0459.
(93) Imberty, A., Wimmerova, M., Mitchell, E. P., and Gilboa-Garber, N. (2004) Structures of the lectins from *Pseudomonas aeruginosa*: insights into the molecular basis for host glycan recognition. *Microb. Infect. 6*, 221−228.

BC070129Z

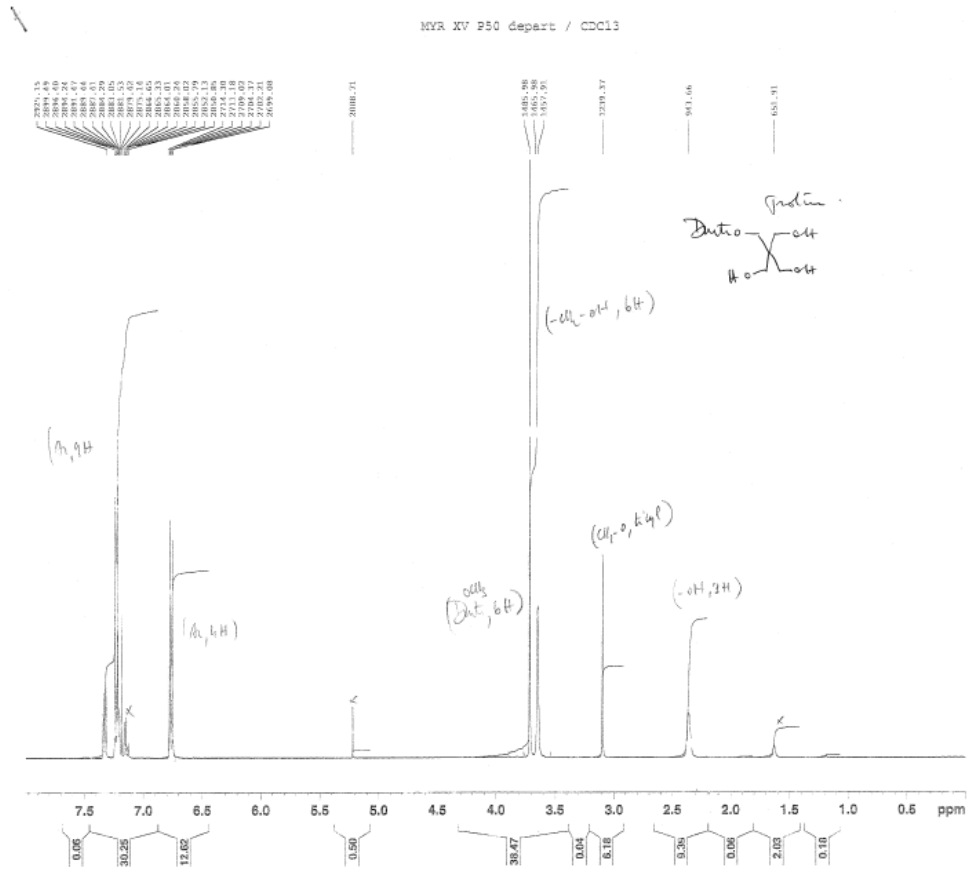
Fucosylated Pentaerythrityl Phosphodiester Oligomers (PePOs): Automated synthesis of DNA-based glycoclusters and binding to *Pseudomonas aeruginosa* lectin (PA-IIL)

François Morvan, Albert Meyer, Anne Jochum, Charles Sabin, Yann Chevolot, Anne Imberty, Jean-Pierre Praly, Jean-Jacques Vasseur, Eliane Souteyrand, and Sébastien Vidal**

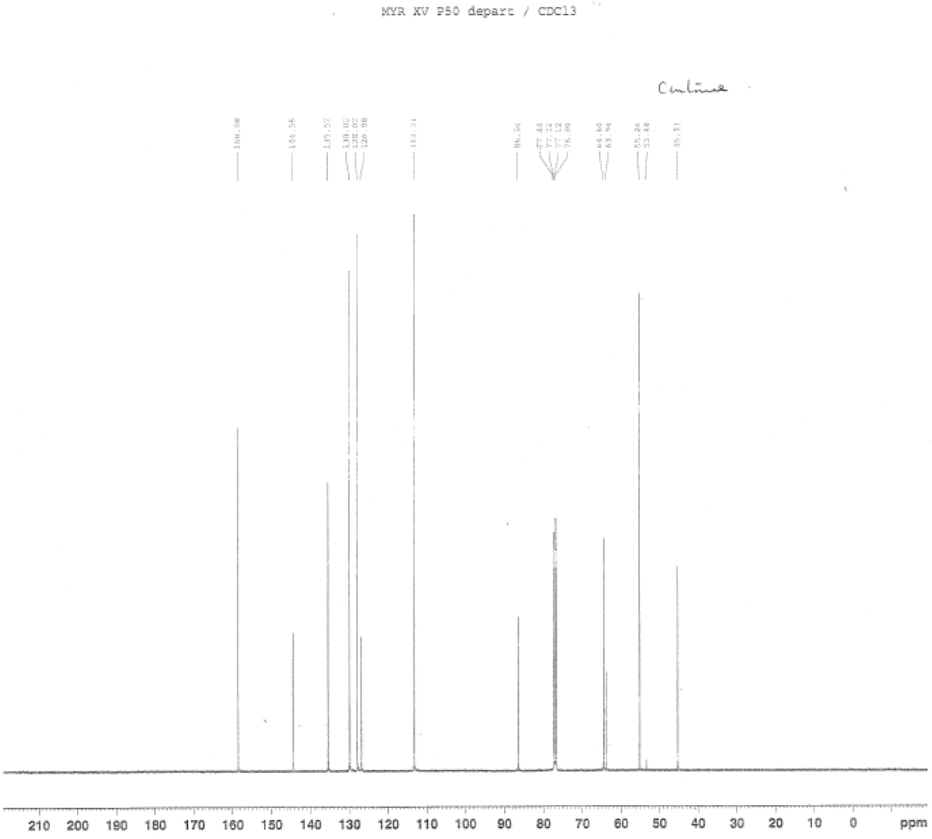
Supporting Information

^{1}H-NMR of **1**	S2
^{13}C-NMR of **1**	S2
^{1}H-NMR of **2**	S3
^{13}C-NMR of **2**	S3
^{1}H-NMR of **3**	S4
^{13}C-NMR of **3**	S4
^{31}P-NMR of **3**	S5
HPLC profiles of fucosylated PePOs **8a-d**	S5
MALDI-ToF profiles of fucosylated PePOs **8a-d**	S6-S9

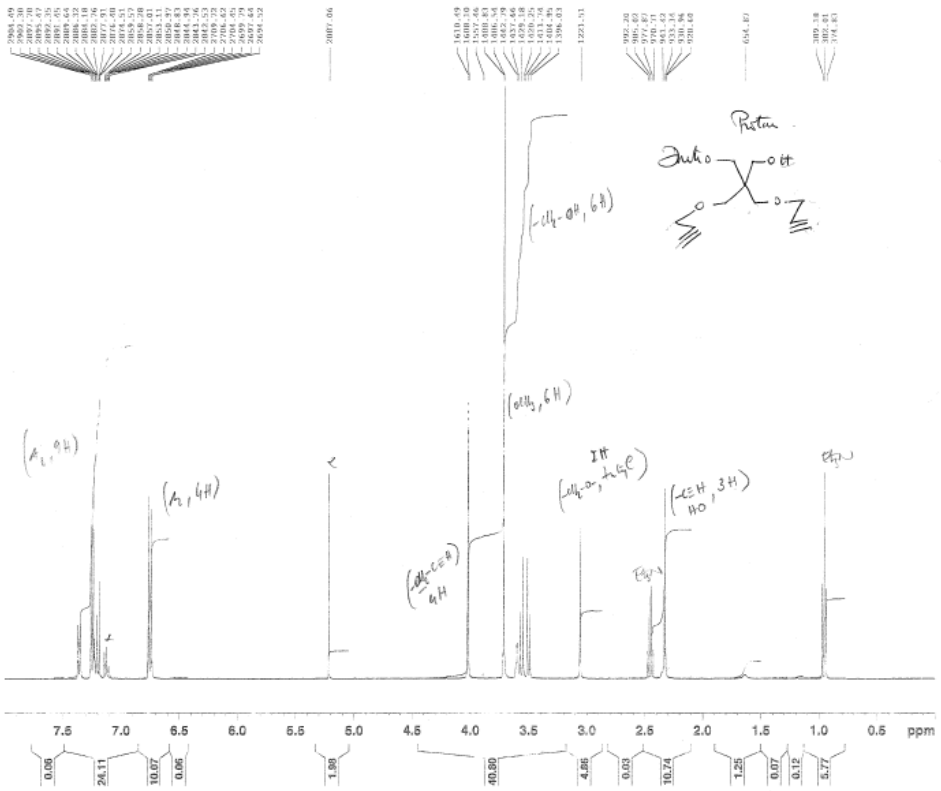
^{1}H-NMR of **1** ($CDCl_3$, 400 MHz, 298 K)



^{13}C-NMR of **1** ($CDCl_3$, 100 MHz, 298 K)

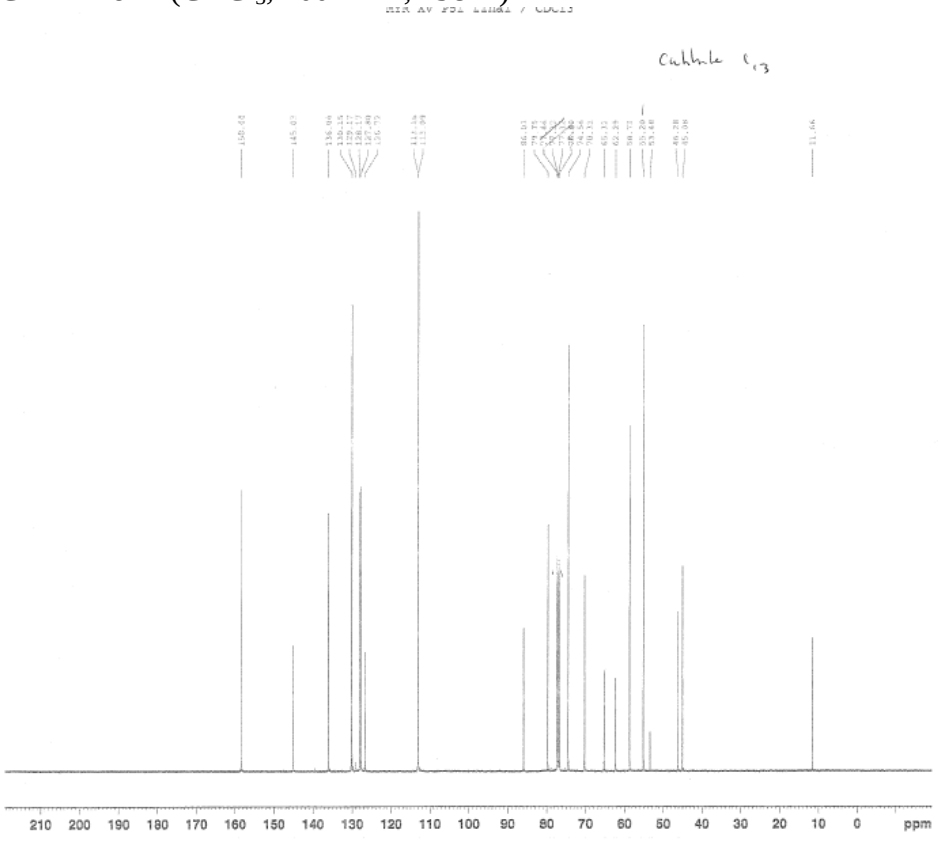


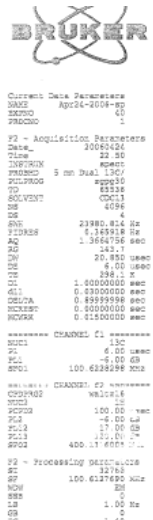
^{1}H-NMR of **2** ($CDCl_3$, 400 MHz, 298 K)



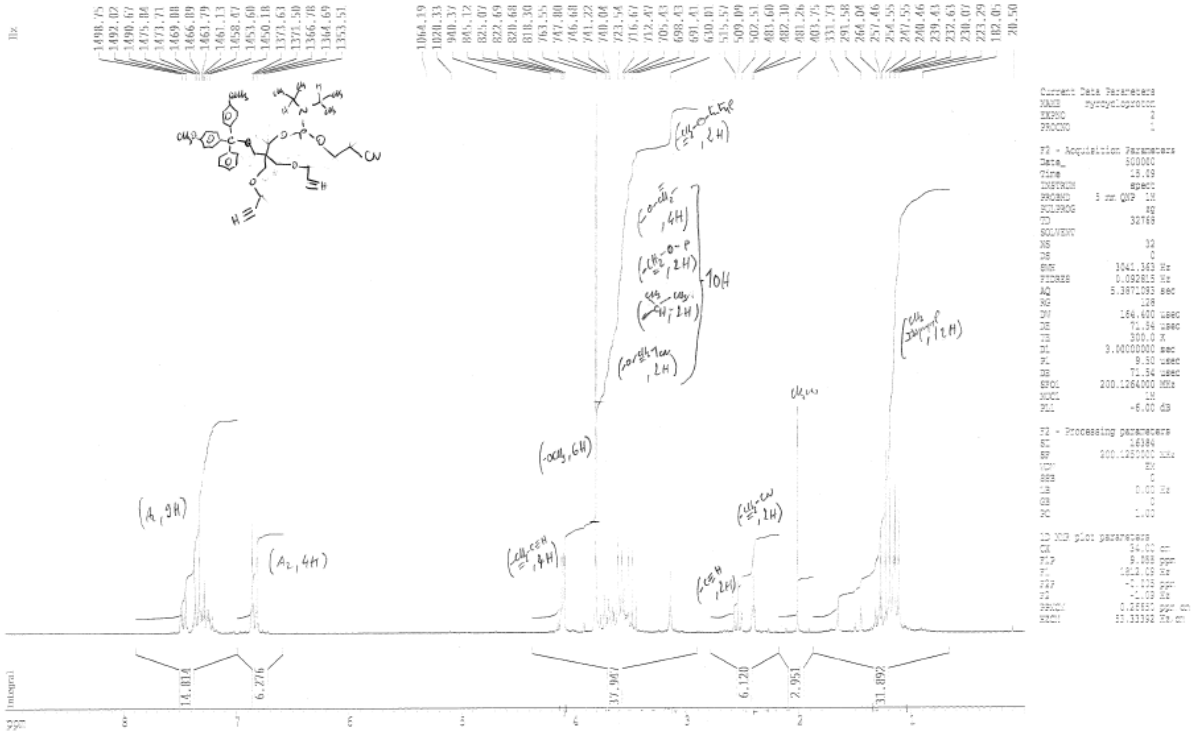


^{13}C-NMR of **2** ($CDCl_3$, 100 MHz, 298 K)

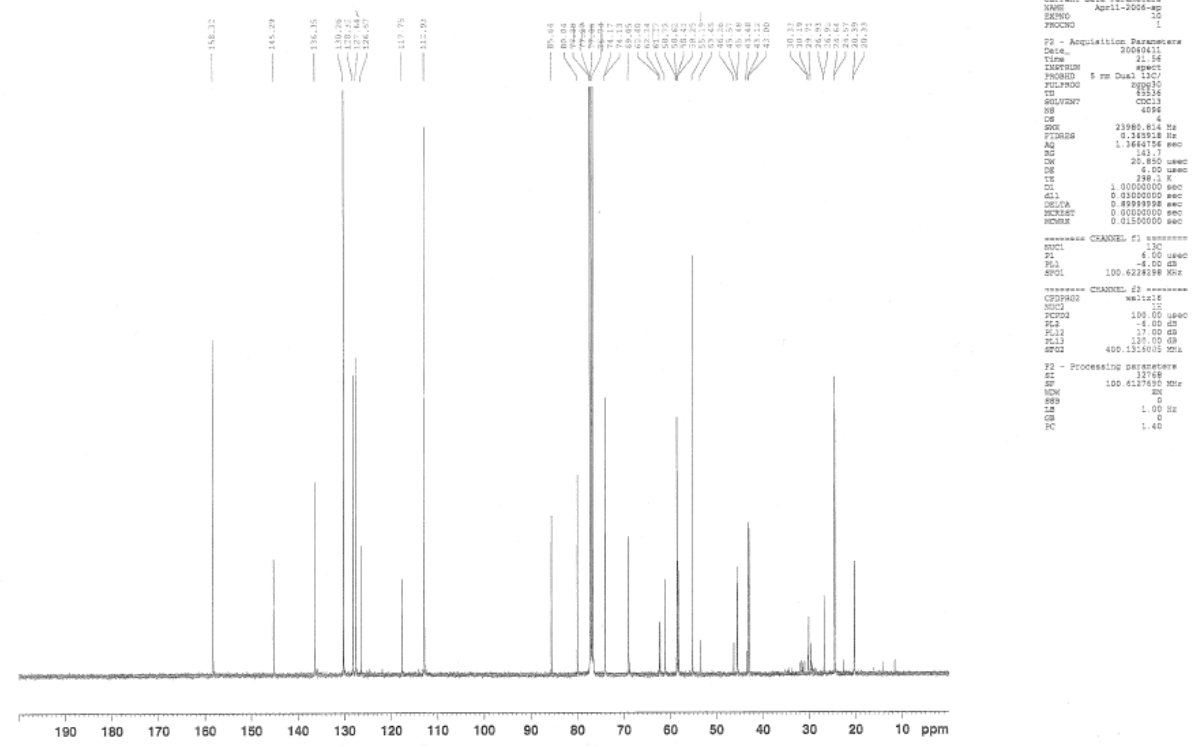




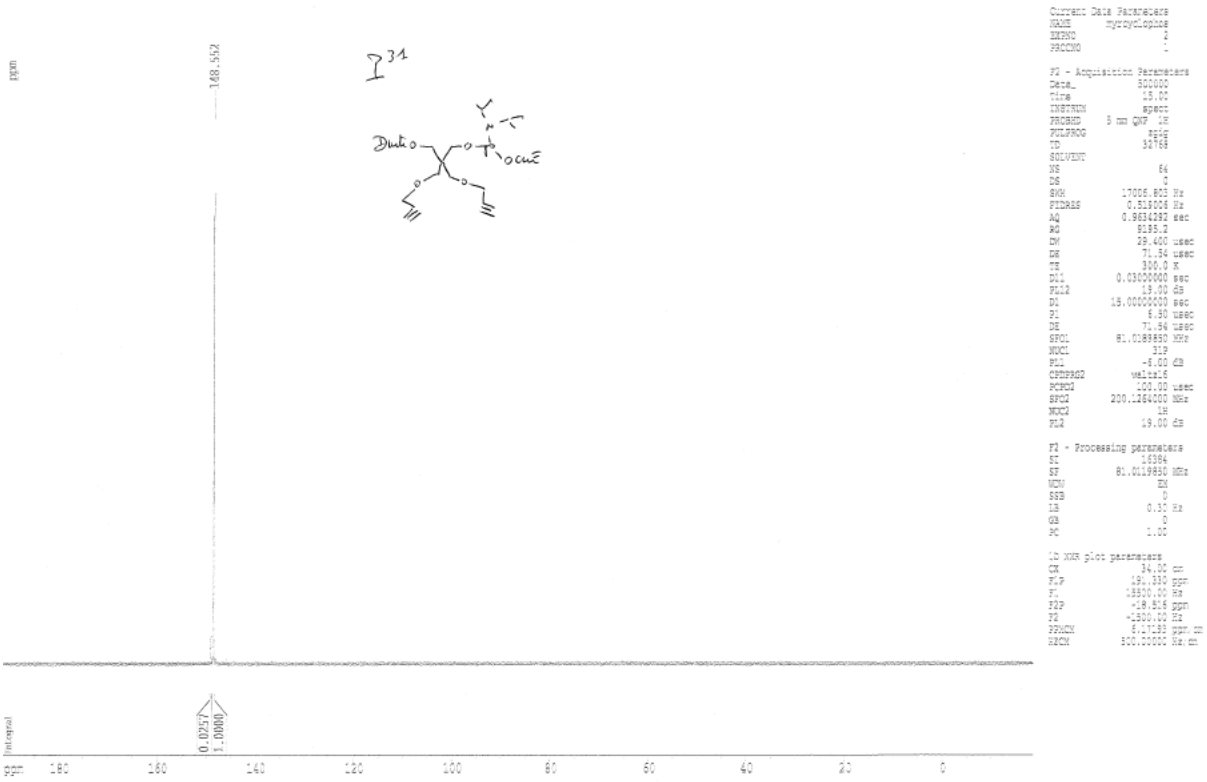
^{1}H-NMR of **3** ($CDCl_3$, 400 MHz, 298 K)



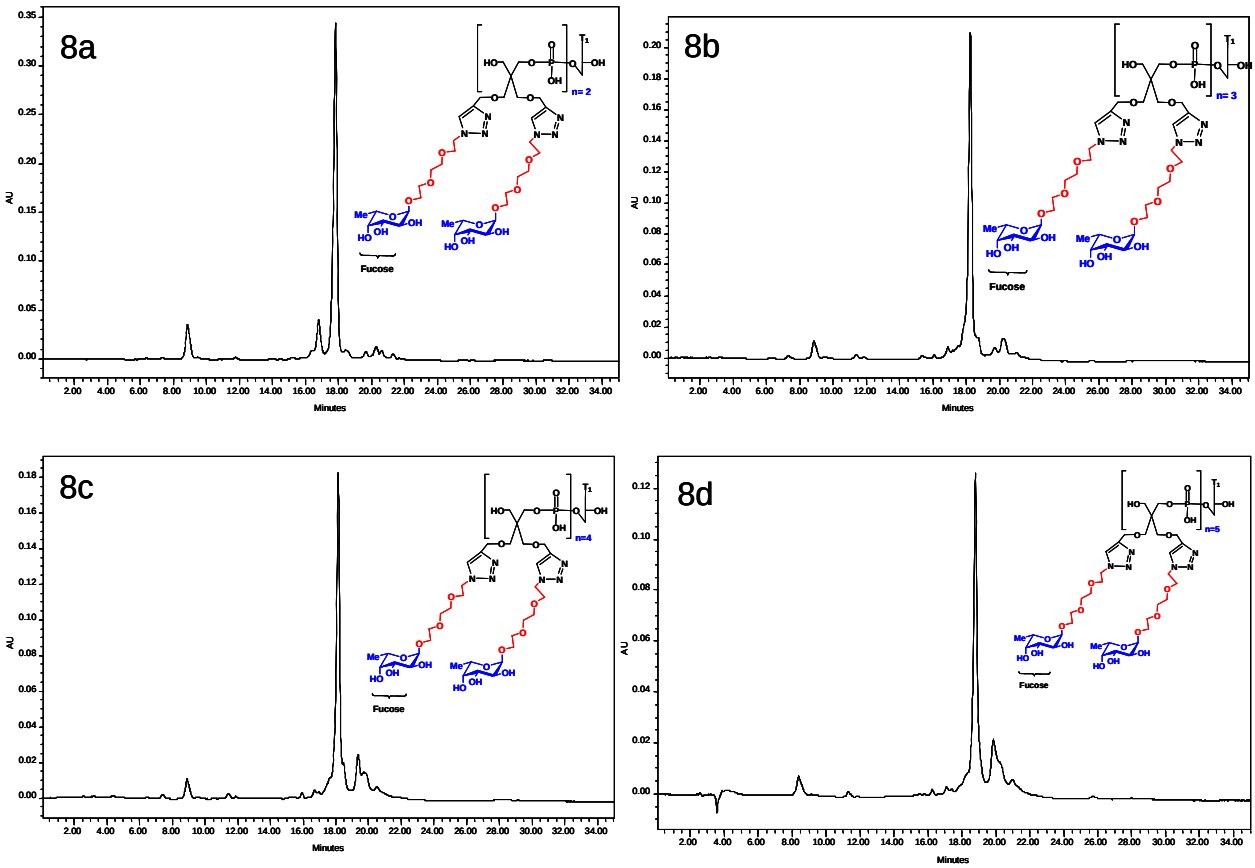
^{13}C-NMR of **3** ($CDCl_3$, 100 MHz, 298 K)

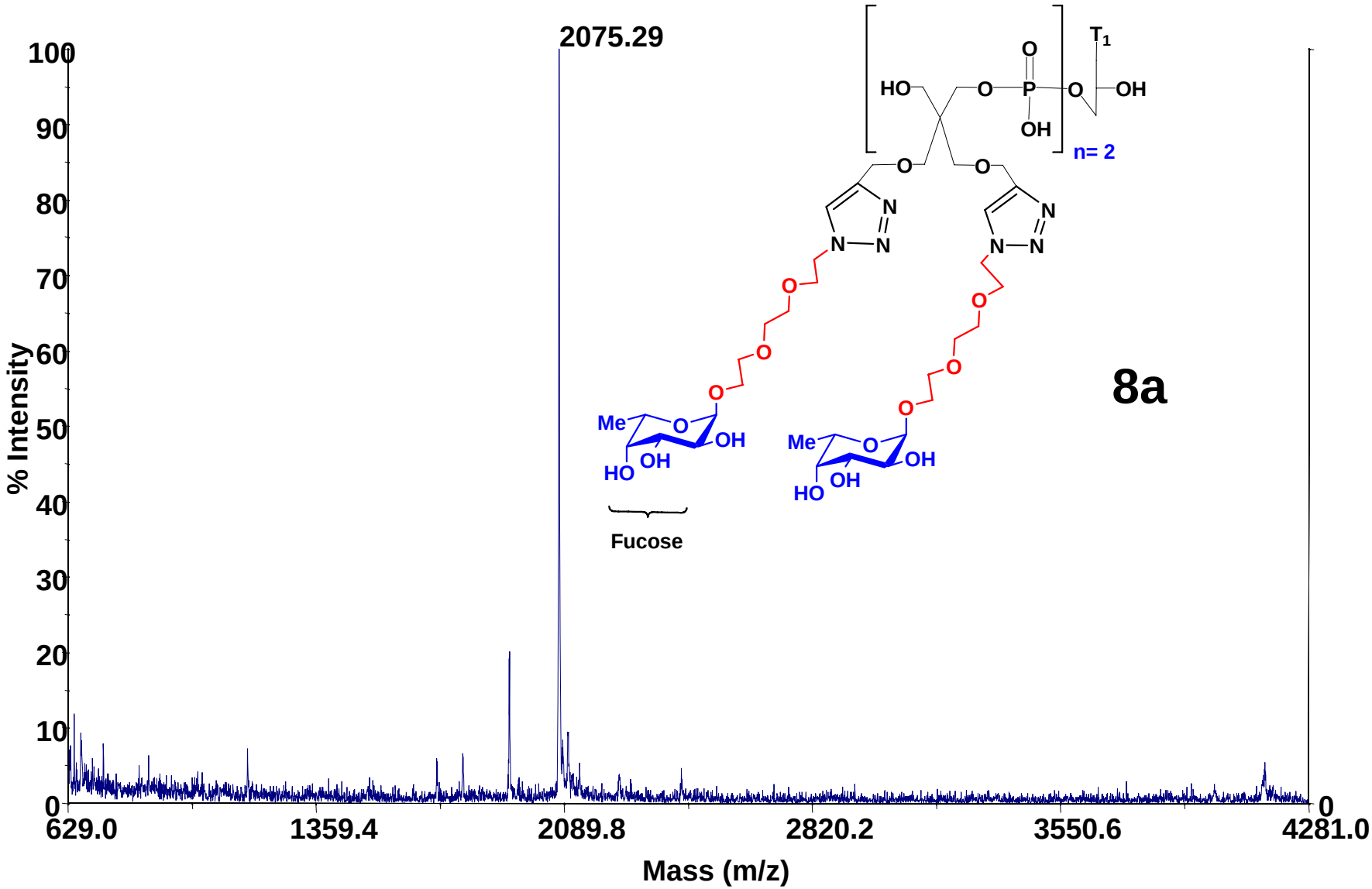


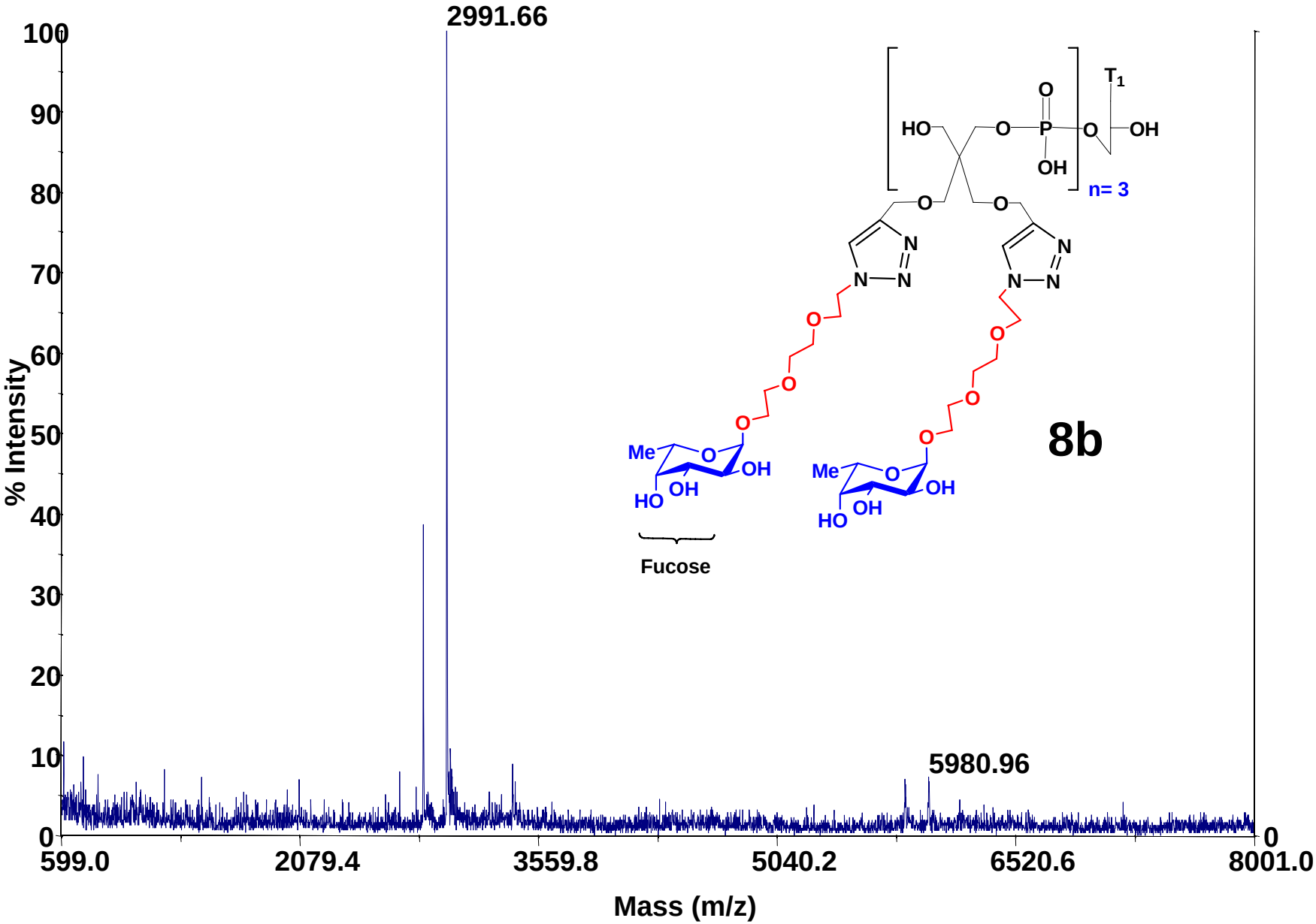
^{31}P-NMR of **3** ($CDCl_3$, 80 MHz, 298 K)



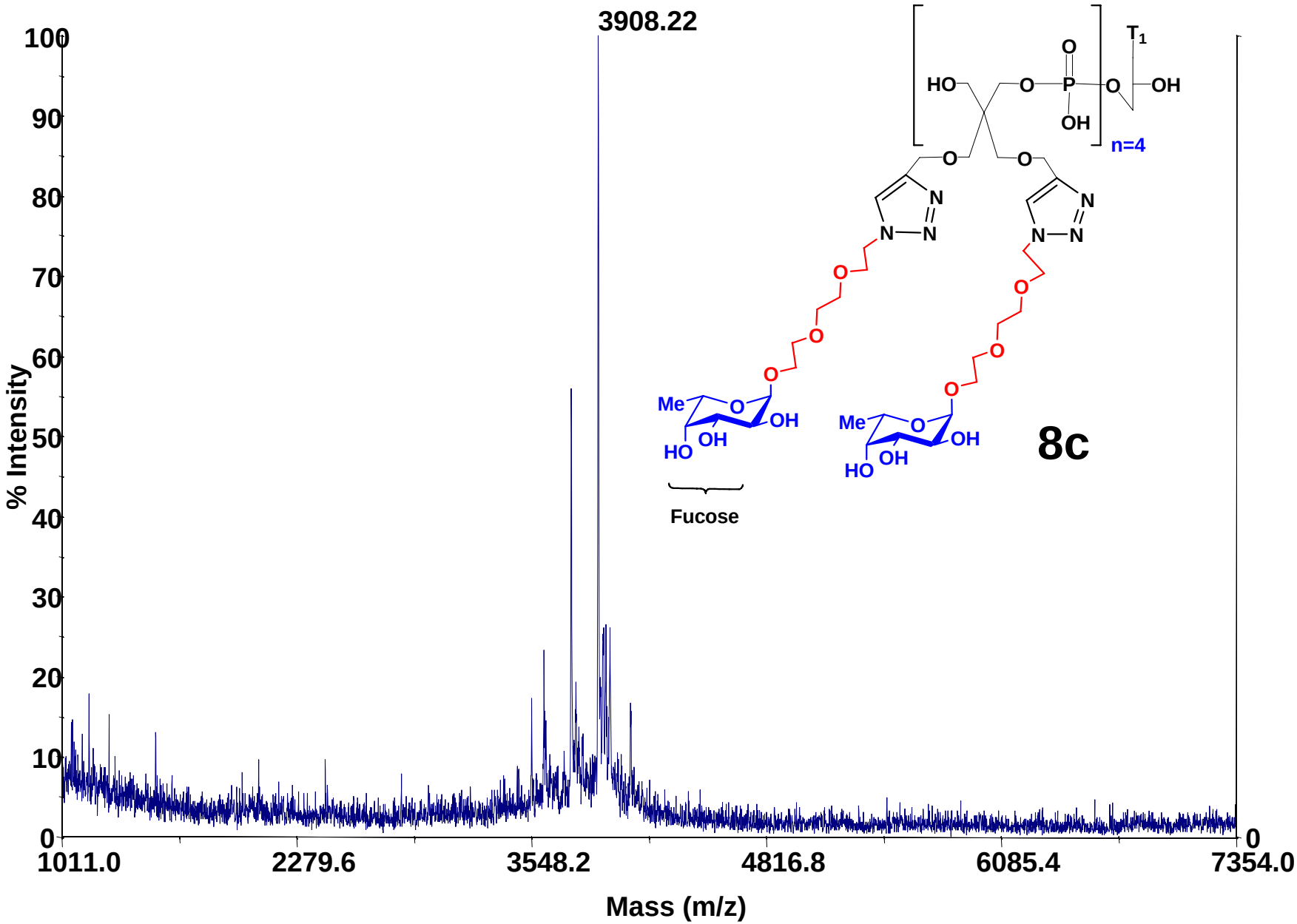
HPLC profiles of fucosylated PePOs **8a-d**

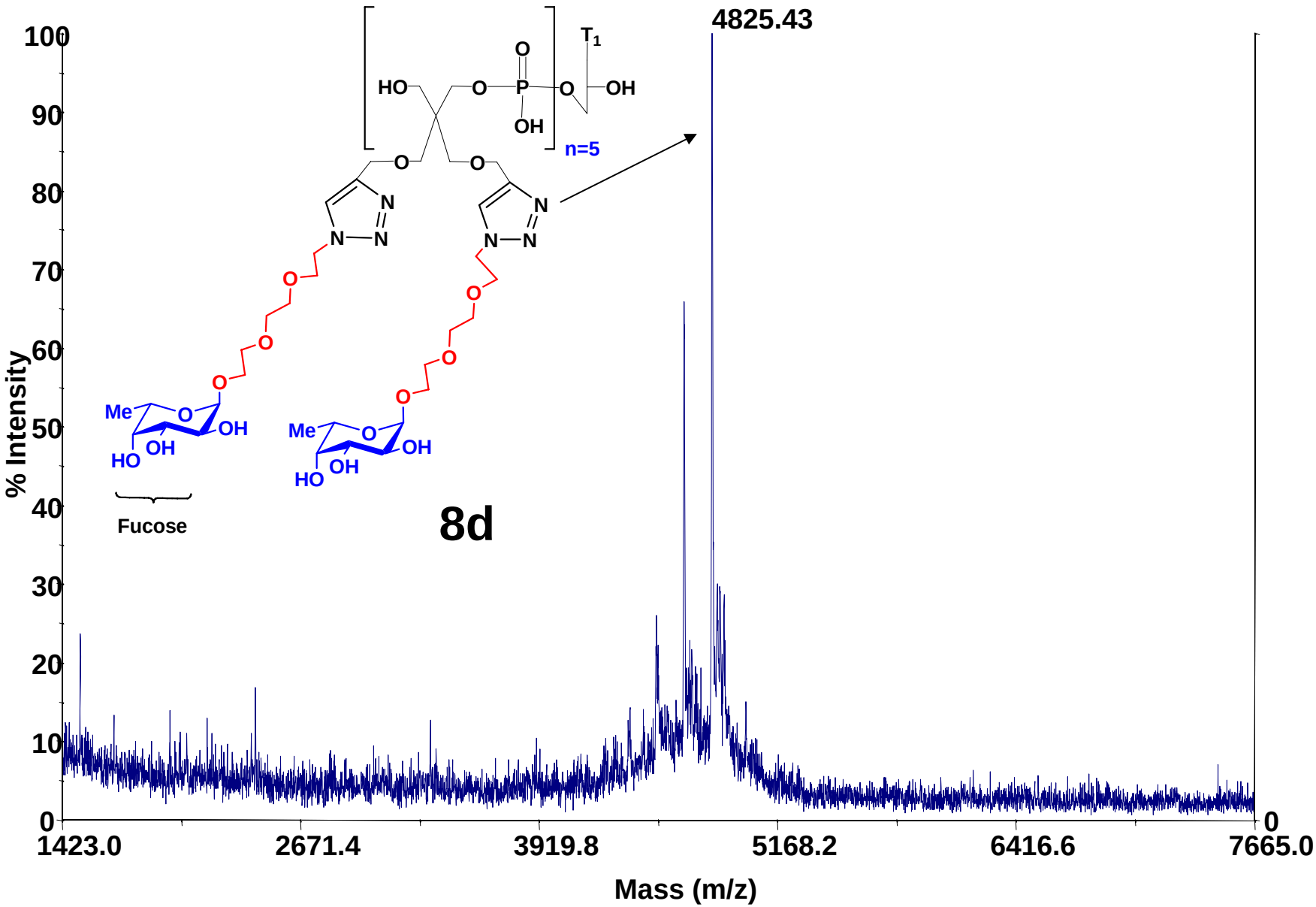



2075.29
100
90
80
70
60
50
40
30
20
10
0
% Intensity
629.0
1359.4
2089.8
2820.2
3550.6
4281.0
Mass (m/z)
HO
O
P
OH
T1
n= 2
N
Me
Fucose
8a


2991.66
5980.96
100
90
80
70
60
50
40
30
20
10
0
% Intensity
599.0
2079.4
3559.8
5040.2
6520.6
8001.0
Mass (m/z)
HO
O
P
OH
T1
n= 3
N
Me
Fucose
8b

S8


3908.22
100
90
80
70
60
50
40
30
20
10
0
% Intensity
1011.0
2279.6
3548.2
4816.8
6085.4
7354.0
Mass (m/z)
HO
O
P
OH
T1
n=4
N
Me
Fucose
8c


4825.43
100
90
80
70
60
50
40
30
20
10
0
% Intensity
1423.0
2671.4
3919.8
5168.2
6416.6
7665.0
Mass (m/z)
HO
O
P
OH
T1
n=5
N
Me
Fucose
8d

Avidin−Biotin−PEG−CPA Complexes as Potential EPR-Directed Therapeutic Protein Carriers: Preparation and Characterization

Shan Ke,[†,‡] John C. Wright,[†] and Glen S. Kwon*[,‡]

Department of Chemistry, University of Wisconsin−Madison, 1101 University Avenue, Madison, Wisconsin 53706-1322, and Division of Pharmaceutical Sciences, School of Pharmacy, University of Wisconsin−Madison, 777 Highland Avenue, Madison, Wisconsin 53705-2222. Received May 21, 2007; Revised Manuscript Received July 10, 2007

Bovine carboxypeptidase A (CPA) conjugated with biotinylated poly(ethylene glycol) (PEG) has been synthesized and characterized in terms of stoichiometry and half-life of the avidin−biotin−PEG(s)−CPA complex. The half-lives for dissociation are 3.34 days for the avidin−biotin−PEG(3400)−CPA 1:1 complex, 3.65 days for the avidin−biotin−PEG(5000)−CPA 1:1 complex, 3.91 days for the avidin−biotin−PEG(3400)−CPA−PEG(2000) 1:1 complex, and 2.74 days for the avidin−biotin−PEG(5000)−CPA−PEG(2000) 1:1 complex. The slow dissociation demonstrates the stability of complexes using a PEGylated biotin terminus as a linker with avidin. The stoichiometry of the biotin−PEGylated CPA with avidin was determined by the 2,6-ANS method, and the results are consistent with measurements of the stoichiometry using size exclusion chromatography. The stoichiometries are 1:2 for the avidin−biotin−PEG(3400)−CPA complex and the avidin−biotin−PEG(3400)−CPA−PEG(2000) complex, 1:1 for the avidin−biotin−PEG(5000)−CPA complex, and 1:4 for the avidin−biotin−PEG(5000)−CPA−PEG(2000) complex. These findings stress both the importance of the length of a PEG chain as an appropriate spacer between the biotin terminus and a functional group, and the great potential of the avidin−biotin−PEGylated-protein complex as a therapeutic protein delivery system for solid tumor prodrug targeting.

INTRODUCTION

Successful applications of chemotherapy for clinical cancer treatments are limited by deficient drug cytotoxic concentration and systemic toxicity arising from low selectivity for tumors over the normal cells (*1*). Antibody-directed enzyme prodrug therapy (ADEPT) has been explored as an answer to the challenge of delivering sufficient cytotoxic reagents to tumor tissues in the monoclonal antibody therapies for solid tumors (*2*−*4*). The benefit from the ADEPT is based on a catalytic conversion of a large number of prodrug molecules into cytotoxins by each targeted enzyme. However, even though monoclonal antibodies recognize certain proteins that are found on the surface of some cancer cells, so far the most striking understanding in monoclonal antibody therapy is that only 1 to 10 parts per 100 000 of the administered monoclonal antibodies can reach the target in vivo (*1*, *5*).

The enhanced permeability and retention (EPR) effect is another important method in antitumor drug delivery. This method exploits the ineffective tumor lymphatic drainage, and the defective vessels within and between the endothelium and basement membranes of various tumors, where the macromolecules can extravasate more easily and localize in the tissue intrastitial space. Through the EPR effect, the prolonged plasma circulation of macromolecules such as the polymer-conjugated drugs leads to significant passive tumor targeting (*6*−*8*).

We propose a new EPR-directed enzyme prodrug therapy (EDEPT) based on the EPR effect of macromolecules. Bovine carboxypeptidase A (CPA) was chosen as the prototype of our series of targeted enzymes. The capacity of CPA to hydrolyze the first peptide or amide bond at the carboxyl or C-terminal end of proteins and peptides offers an important way to generate the active methotrexate (MTX) from the inactive prodrug of MTX, such as Phe-MTX (*9*, *10*). Ideally, the release of the cytotoxic MTX only occurs in the vicinity of tumor cells, thereby sparing normal cells from concomitant destruction. This type of drug release might be accomplished by pretargeting CPA to the tumors through the EPR effect.

In the field of polymer-conjugated drugs, poly(ethylene glycol) (PEG) is a highly investigated polymer. PEG's importance in pharmaceutical and biotechnical applications originates from its modification of biological macromolecules, such as peptides and proteins. The potential benefits include shielding these macromolecules from being uptaken by the reticuloendothelial system (RES), decreasing the protein immunogenicity, and preventing recognition and degradation by proteolytic enzymes (*11*−*13*). Moreover, PEG modification also increases the apparent size of an enzyme and thus reduces the renal filtration of the enzyme (*14*).

Previous research on PEGylated CPA has demonstrated that CPA conjugated with two PEG chains has a much higher accumulation in a tumor than CPA conjugated with one PEG chain because the former's plasma circulation time is longer (*15*). Also, positive tumor accumulation of a non-biodegradable poly(vinylpyrrolidone) polymer occurs when it is administered using a molecular weight greater than the glomerular filtration threshold of ∼87 000 Da (*16*, *17*). Therefore, we attempted to increase the molecular weight of CPA above the glomerular filtration threshold by PEGylation to prolong the plasma circulation time. However, to achieve a high tumor-to-blood ratio, the concentration of a PEGylated CPA in the circulation system must be kept as low as possible. Since the removal of PEG or PEGylated proteins depends primarily on the renal filtration, it is necessary to keep the molecular weight of PEGylated CPA smaller than the glomerular filtration threshold. To solve this dilemma, we propose using an avidin−biotin−PEG−CPA complex system as a potential drug delivery system (DDS) for EDEPT. We hypothesize that the ideal avidin−

* Corresponding author. Tel: 608-265-5183; fax: 608-262-5345; e-mail: gskwon@pharmacy.wisc.edu.

[†] Department of Chemistry.

[‡] Division of Pharmaceutical Sciences.

10.1021/bc700182t CCC: $37.00 © 2007 American Chemical Society
Published on Web 08/18/2007

biotin−PEG−CPA complex with a molecular weight higher than the glomerular filtration threshold might dissociate avidin and biotin−PEG−CPA in the circulation system and be cleared by the renal system, but also that the half-life of the avidin−biotin−PEG−CPA complex might be sufficiently long for significant tumor accumulation.

The avidin−biotin system has an extremely high binding affinity and has been explored as a molecular linker apparatus in biosensors, purifications, and syntheses of important molecules for biotechnology (*18*, *19*). Yet such strong avidin−biotin binding interaction also limits the applications of the system in some fields requiring facile capture and release (*20*). Research on the effects of biotinylated derivatives on the binding constant has been reported (*21*). For example, PEGylated biotin has a lower affinity with avidin than biotin (*22*). Our previous research on intermolecular interactions of avidin and PEGylated biotin demonstrates that a PEG chain can alter not only the affinity but also the stoichiometry of the avidin−biotin complex system. Following these findings, in this work we focused our research on (i) increasing the molecular weight of CPA by biotin−PEGylation and successive formation of the avidin−biotin−PEG−CPA complexes, and (ii) adjusting the stoichiometry and the half-life of the avidin−biotin−PEG−CPA complex systems by the PEG chains. The aim is for novel, reversible, and nonimmunogenic complexes as a DDS for EDEPT.

EXPERIMENTAL PROCEDURES

Materials. Commercially available analytical grade or higher materials were used, except for the aqueous crystalline suspension of bovine carboxypeptidase A (CPA) and the PEGylated biotins. Bovine CPA, D-biotin, and hippuryl-L-phenylananine (hipp-L-phe) were obtained from Sigma (St. Louis, MO). Avidin was purchased from Pierce (Rockford, IL). PEG(2000)-SPA, biotin−PEG(3400)-NHS, and biotin−PEG(5000)-NHS were obtained from Nektar (Huntsville, AL). 2,6-Anilinonaphthalenesulfonate (2,6-ANS) was obtained from Molecular Probes (Carlsbad, CA).

PEGylation of CPA. CPA was obtained as an aqueous crystalline suspension and purified as described elsewhere (*23*). Briefly, the crystals were washed with Millipore pure water and centrifuged three times. The protein pellet was collected. Bicarbonate buffer with a high salt concentration (0.5 M $NaHCO_3$/0.5M NaCl, pH 8.0) was added until the entire protein pellet dissolved. This CPA bicarbonate buffer solution was then sterile-filtered with a 0.4 μm filtration disc from Millipore to remove the insoluble impurities. The concentration of the CPA solution was determined by the absorption at 278 nm using the molar absorptivity of 6.41×10^4 M^{-1} cm^{-1}. The CPA solution was stored at 4 °C until use.

Biotin−PEG(3400)−CPA was prepared by conjugating CPA with the *N*-hydroxysuccinamide ester of biotinylated PEG 3.4 kDa (biotin−PEG(3400)-NHS). Biotin−PEG(3400)-NHS solution was prepared in the same bicarbonate buffer and immediately added dropwise into a 0.20 mM stirred CPA solution, which was cooled by incubation in an ice bath. A sufficient yield of biotin−PEG(3400)−CPA was achieved using a 1.25:1 reaction molar ratio of biotin−PEG(3400)-NHS to CPA with a 120 min PEGylation time. PEGylation of CPA with biotin−PEG(5000)-NHS was performed using the same reaction conditions.

Biotin−PEG(3400)−CPA−PEG(2000) and biotin−PEG(5000)−CPA−PEG(2000) were prepared in two steps. First, CPA was PEGylated using a succinimidyl propionate derivative of PEG, PEG(2000)-SPA, by the same PEGylation conditions described above. After CPA−PEG(2000) was separated and collected through SEC (the concentration of CPA−PEG(2000) decreased to $\sim 10^{-6}$ M), we PEGylated CPA−PEG(2000) immediately with biotin−PEG(3400)-NHS or biotin−PEG(5000)-NHS at a 2:1 reaction molar ratio of PEG-NHS/CPA−PEG.

Purification of Biotin−PEGylated CPA. The purification of biotin−PEGylated CPA was achieved by size-exclusion chromatography (SEC) on an ÄKTA fast protein liquid chromatograph (FPLC) system (Pharmacia, Piscataway, NJ). The PEGylation mixtures were loaded directly into a Superose 12/30 HR column preequilibrated by PBS buffer. The elution buffer was also PBS buffer (pH 7.4) with a flow rate 0.50 mL/min, and the UV detector measured the absorbance at 280 nm. The fractions of the targeted biotin−PEGylated CPAs were collected and stored at 4 °C until use.

Because the ultraviolet−visible spectra of biotin−PEG(3400)−CPA, biotin−PEG(5000)−CPA, biotin−PEG(3400)−CPA−PEG(2000), and biotin−PEG(5000)−CPA−PEG(2000) are the same as that of native CPA, the concentrations of these four biotin−PEGylated CPAs were first roughly determined by the absorption at 278 nm using the molar absorptivity of native CPA. After determining the stoichiometry of the binding of their avidin complexes, their concentrations were measured using a displacement titration where a standard D-biotin or a biotin−PEGylated CAP titrant displaced weakly bound 2,6-ANS from the fluorescent 2,6-ANS-avidin complex.

The molecular weight and the degree of the PEGylation of the purified biotin−PEGylated CPA were determined by MALDI−TOF mass spectroscopy using a Bruker REFLEX II (Billirica, MA), equipped with a reflectron, a 337 nm nitrogen laser, and delayed extraction. Native CPA was used as the external calibrant, and the matrix chosen for this study was a freshly prepared, saturated sinapic acid solution in acetonitrile/water (50% V/V). Briefly, the sample solutions were prepared before measurement with a typical concentration of 1 mg/mL. A 1 μL amount of the matrix and sample were mixed in a spot plate, and then a 0.5 μL sample of the mixture was deposited on the target. Analysis was performed using the reflectron mode, and the results were averaged over at least 50 shots with the laser power just above the threshold of ion formation/desorption. In particular, the samples of biotin−PEGylated CPAs for MALDI−TOF mass spectroscopy were specially purified by SEC using the volatile ammonium acetate buffer as the elution solution (*24*).

Quantitative Assay for Stoichiometry of Biotin−PEGylated CPA with Avidin. Two biotin-binding assays were exploited to determine the stoichiometry of the binding of biotin−PEG(s)−CPA with avidin. The first was based on the use of the dye 2,6-anilinonaphthalene sulfonate (ANS), which binds to avidin and can be removed by the addition of biotin or biotinylated derivatives (*25*). D-Biotin solution was prepared as the primary standard to titrate the avidin solution. The standardized avidin solution was then used as the secondary standard to titrate the unknown biotin−PEG(s)−CPA solutions. Generally, we added the primary standard D-biotin solution or the unknown biotin−PEGylated CPA solution in increments to 20 mL of a PBS buffer containing about 0.50 nmol of avidin and 10 nmol of 2,6-ANS. After each addition, the fluorescence was excited at 328 nm (bandwidth of 10 nm) and measured at 408 nm (bandwidth of 10 nm), using a Shimadzu RF-1501 spectrofluorophotometer (Shimadzu, Tokyo 101-8448, Japan). A typical titration required ~1.5 h.

The second assay was based on the SEC chromatography of the avidin−biotin−PEG−CPA complexes. Briefly, 0.50 mL 1×10^{-6} M avidin PBS solutions were added with various amounts of biotin−PEG(s)−CPAs that the ratios of the two mixture components ranged from 0.5 to 6. After 24 h incubation at room temperature to ensure the equilibrium, these mixture solutions were loaded into a Superose 12/30 HR column in the

ÄKTA FPLC system to perform the SEC chromatography. A quantitative evaluation of the biotin/avidin stoichiometry was achieved from the presence of the peaks of 1:1, 1:2, 1:3, or 1:4 avidin−biotin−PEG(s)−CPA complexes in the SEC chromatography against the molar ratio of avidin/biotin−PEG−CPA. PBS buffer (pH 7.4) was employed as the elution buffer with a flow rate 0.50 mL/min and the absorbance was measured at 280 nm.

Quantitative Assay for Half-Life of Avidin−Biotin−PEG(s)−CPA Complex. Of the four avidin−biotin−PEG(s)−CPA complexes, the 1:1 avidin−biotin−PEG(s)−CPA complex has the longest half-life and was chosen for our dissociation rate constant investigation. The 1:1 avidin−biotin−PEG(s)−CPA complex was purified and collected by SEC separation after biotin−PEG(s)−CPA and avidin were mixed with a 1:1 molar ratio in PBS buffer for ∼2 h at room temperature. Once a 1:1 complex was collected, the kinetic dissociation rate constant k_{off} was immediately analyzed from the active ligand displacement by adding D-biotin (∼500 mol/mol of avidin) to 30 mL ∼5 × 10^{-7} M 1:1 avidin−biotin−PEG(s)−CPA complex solution. Since a large excess of D-biotin prevented reassociation of biotin−PEG(s)−CPA with avidin, the dissociation became first order with respect to the concentration of the 1:1 avidin−biotin−PEG(s)−CPA complex. Aliquots of 300 μL mixture were loaded to a Superose 12/30 HR column in the FPLC ÄKTA system to monitor the relative concentrations of 1:1 avidin−biotin−PEG(s)−CPA complexes after the indicated incubation times (recorded from the introduction of excess D-biotin) at room temperature. The hydrolysis product of PEG(3400)-NHS or NHS was utilized as the internal standard to remove any effects of drift in the FPLC system during the long measurement period. The natural logarithm of the relative peak height of the avidin−biotin−PEG(s)−CPA complex compared with the internal standard was plotted against the incubation times. From the slope of the plot, k_{off} and the half-life were determined. Since the peaks of 1:1 avidin−biotin−PEG(s)−CPA complexes overlap with the peaks of avidin and biotin−PEG(s)−CPAs in SEC chromatography, OriginPro 7.0 Gaussian peak fitting software was applied to deconvolute these overlapped peaks.

Surface Plasmon Resonance (SPR) for Half-Life of Streptavidin-Biotin−PEG(s)−CPA Complex. SPR analysis was performed using a Biacore 2000 with a streptavidin (SA) sensor chip. The SA sensor chips were docked into the instrument and were preconditioned by applying three consecutive 1-min injections of 1.0 M NaCl in 50 mM NaOH solution with running PBS buffer at 20 μL/min. After that, the flow rate was adjusted to 10 μL/min, and 10 μL of biotin−PEGylated CPA solution with the concentration on the order ∼10^{-6} M in PBS buffer was injected. SPR measurements were made using standard procedures.

Previous research shows that the binding between avidin and PEGylated biotin is temperature dependent (*26*), and all data in the present study were specifically collected at 24 °C.

RESULTS

PEGylation of CPA. Because none of both the fifteen lysine groups and C-terminal carboxylic acid on CPA is involved in its enzymatic hydrolysis of the peptide bond, PEGylation was performed using biotin−PEG-NHS to conjugate lysine ϵ-NH_2 groups or C-terminal carboxylic acid on CPA (*27*). PEGylated CPAs with one biotin terminus were chosen for study to delete the unwanted cross-linked products when we formulated the avidin−biotin−PEG(s)−CPA complexes. After various reactions were tested, the PEGylation conditions to yield biotin−PEG−CPA with one biotin terminus were optimized as 1.25:1.0 molar ratio of biotin−PEG-NHS per CPA in 0.50 M $NaHCO_3$/0.50 M NaCl buffer (pH 8.0) with 2 h reaction time in the ice bath. The PEGylation reaction stoichiometry might increase to 2:1 of PEG-NHS/CPA because of self-hydrolysis of PEG-NHS with water during storage. Although it was not necessary to site-specifically PEGylate the lysine groups on CPA, PEGylation generated a highly heterogeneous distribution of m-biotin−PEG−CPA products where m indicates the number of PEG chains coupled on CPA such as di-biotin−PEG−CPA and tri-biotin−PEG−CPA (Figure 1). Purification of biotin−PEG−CPA was necessary and was achieved through SEC chromatography. Hydrophobic interaction chromatography was also tried but worked poorly for this application because PEGs also bind to chromatography media that have hydrophobic interactions (*28*).

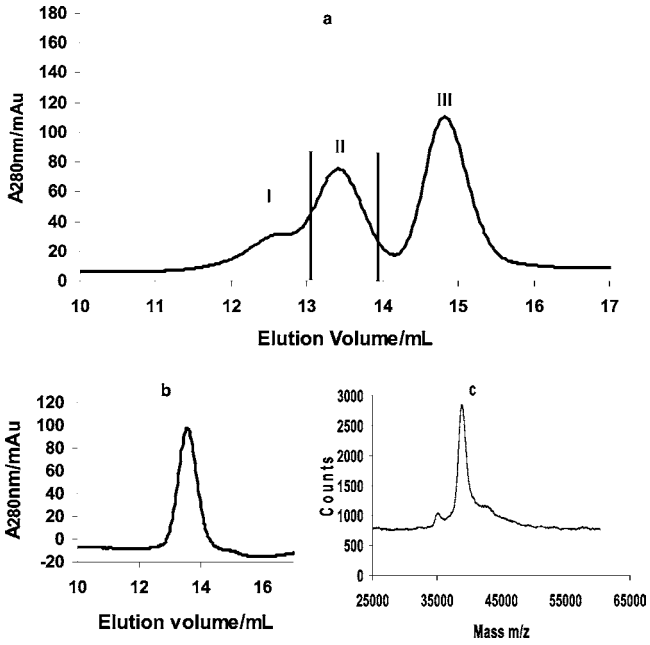


Figure 1. (a) Fractionation of biotin−PEG(3400)−CPA conjugates after PEGylation, using a Superose 12/30 HR column on an ÄKTA FPLC system. Peak I is from the tri- and di-biotin−PEG(3400)−CPA mixture, Peak II is from mono-biotin−PEG(3400)−CPA and Peak III is from unmodified native CPA. The elution buffer was PBS buffer (pH 7.4), with a flow rate of 0.50 mL/min. (b) SEC chromatogram of Fraction II. (c) MALDI-TOF mass spectroscopy of Fraction II.

Previous research shows that di- or tri−PEG−CPA has a longer circulatory half−life than mono−PEG−CPA (*15*). We prepared biotin−PEG−CPA−PEG′, in which there are two conjugated PEG chains to protect CPA during circulation and only one of them has a biotin terminus that acts as a linker and a spacer with avidin. Such PEGylation was achieved by two steps as shown in Figure 2. The PEGylation conditions and purification procedure were the same as those for the biotin−PEG−CPA preparation, except that PEG-SPA(2000) was used for the first PEGylation and that the reaction stoichiometry increased to 2:1 of PEG-NHS/PEG−CPA in the secondary PEGylation.

Stoichiometry of Avidin−Biotin−PEG−CPA Complex. Although avidin has four binding sites for biotin/biotinylated derivatives, PEG can alter the stoichiometry. For example, a 1:1 stoichiometry was found for the avidin−biotin−PEG(5000) complex in our previous work. The 2,6-ANS fluorometric analysis was performed to measure the stoichiometry of biotin−PEGylated CPA with avidin and the results are shown in Figure 3. Biotin−PEG(3400)−CPA and biotin−PEG(3400)−CPA−PEG(2000) accessed two sites on avidin while biotin−PEG(5000)−CPA accessed only one. In contrast, it was surprising to find that biotin−PEG(5000)−CPA−PEG(2000) accessed all

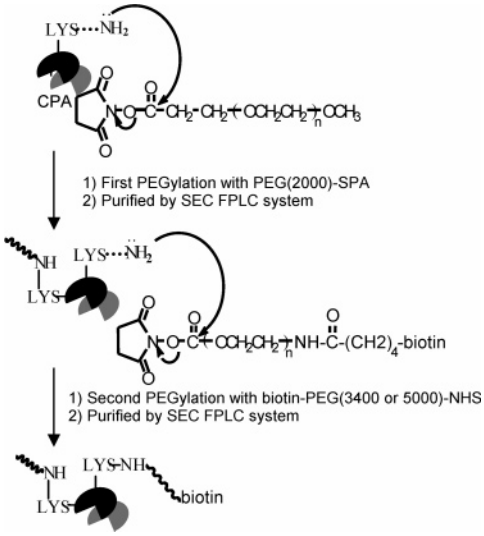


Figure 2. Scheme for the synthesis of biotin−PEG−CPA−PEG′.

four sites on avidin. It appears that biotin−PEG(5000)−CPA bound on avidin sterically hinders the binding to both the adjacent and the oppositely located biotin binding sites on avidin, while biotin−PEG(5000)−CPA−PEG(2000) does not have such steric hindrance.

To obtain independent evidence of the binding stoichiometry, we also investigated the avidin−biotin−PEG−CPA complex system using size exclusion chromatography (SEC). The peak positions in SEC indicate the size of the complex and therefore the stoichiometry. As shown in Figure 4a, three identifiable peaks corresponding to avidin (Peak A), biotin−PEG(5000)−CPA (Peak B), and the avidin−biotin−PEG(5000)−CPA complex (Peak C) were present in the chromatogram. No free biotin−PEG(5000)−CPA was seen when it was mixed with avidin at molar ratio 0.5:1, while excess avidin appeared as Peak A and the avidin−biotin−PEG(5000)−CPA complex appeared as Peak C. When the molar ratio was increased to 1:1, Peak A almost vanished whereas the area of Peak C doubled. After mixing avidin with a 2-fold and 4-fold molar excess of biotin−PEG(5000)−CPA, the elution position and the area of Peak C did not change significantly, except that Peak B from excess biotin−PEG(5000)−CPA began to appear. On the basis of this information, we conclude the avidin−biotin−PEG(5000)−CPA complex stoichiometry is 1:1. In contrast, except for the excess avidin and biotin−PEG(5000)−CPA−PEG(2000) that appeared as peaks A and B in Figure 4b, there were four other peaks labeled C, D, E, and F. If the biotin−PEG−CPA/avidin ratio increased from 1:1.5 to 2:1, the areas of Peak E and F increased while the areas of Peak A, C, and D decreased. When the ratio was larger than 4:1, the A, C, D, and E peaks disappeared while Peak B appeared. Peak F in the 6:1 mixture did not change significantly compared with that from the 4:1 mixture. Accordingly, the stoichiometry for the avidin−biotin−PEG(5000)−CPA−PEG(2000) complex must be 1:4, and peaks C, D, E, and F must correspond to the 1:1, 1:2, 1:3, and 1:4 avidin−biotin−PEG−CPA complexes, respectively. The same strategy was applied for the avidin−biotin−PEG(3400)−CPA complex and the avidin−biotin−PEG(3400)−CPA−PEG(2000) complex, and the stoichiometries for both systems were determined to be 1:2.

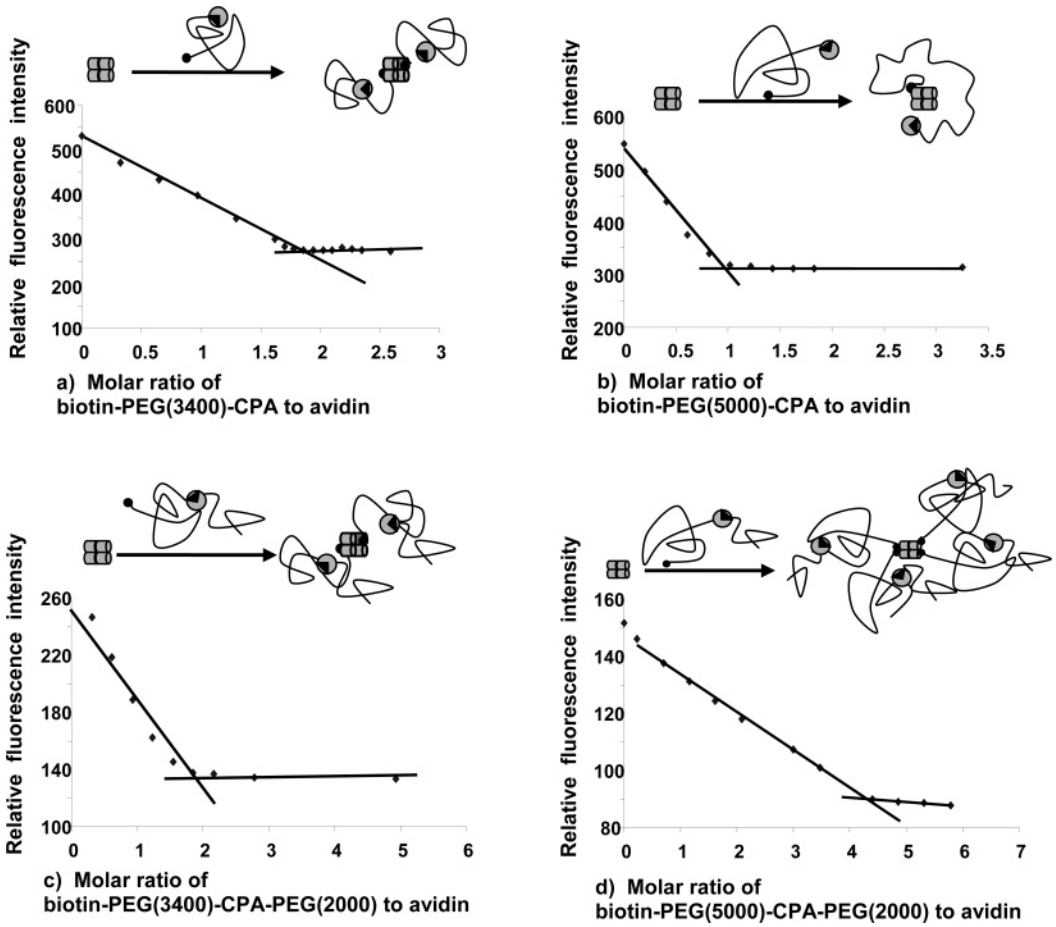


Figure 3. Titration curves of 2,6-ANS fluorometric assay for stoichiometry of the avidin−biotin−PEG−CPA complex are (a) biotin−PEG-(3400)−CPA, (b) biotin−PEG(5000)−CPA, (c) biotin−PEG(3400)−CPA−PEG(2000), and (d) biotin−PEG(5000)−CPA−PEG(2000) with avidin/2,6-ANS in PBS buffer (pH: 7.4).

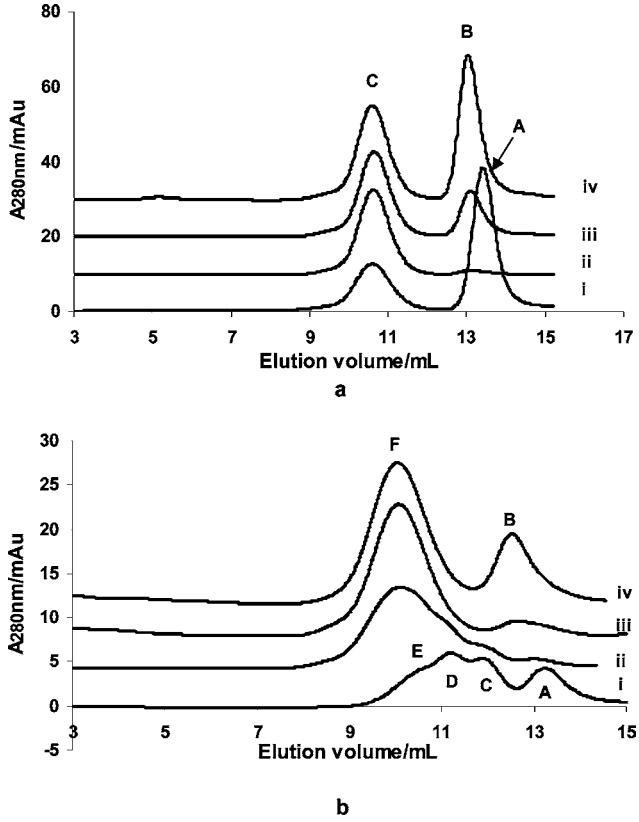


Figure 4. SEC elution profiles of (a) the avidin−biotin−PEG(5000)−CPA complex vs molar ratio of avidin to biotin−PEG(5000)−CPA, i, 1:0.5; ii, 1:1; iii, 1:2; iv, 1:4; and (b) the avidin−biotin−PEG(5000)−CPA−PEG(2000) complex vs molar ratio of avidin to biotin−PEG(5000)−CPA−PEG(2000), i, 1.5:1; ii, 1:2; iii, 1:4; iv, 1:6. Chromatograms were obtained using a Superose 12/30 HR column on an ÄKTA FPLC system. Eluting buffer was PBS buffer (pH 7.4) with a flow rate of 0.50 mL/min.

Table 1. Stoichiometry and Half-Life of Avidin−Biotin−PEG−CPA Complexes at 24 °C

	stoichiometry with avidin	MW (kDa)	$t_{1/2}$ (day)[b] from SEC	$t_{1/2}$ (day)[c] from SPR
biotin−PEG(3400)−CPA	1:2	142.3	3.34	2.09
biotin−PEG(5000)−CPA	1:1	105.7	3.65	2.60
biotin−PEG(3400)−CPA−PEG(2000)	1:2	146.3	3.91	4.14
biotin−PEG(5000)−CPA−PEG(2000)	1:4	233.0	2.74	1.26

[a] MW, molecular weight of the avidin−biotin−PEG−CPA complex with the maximum stoichiometry. [b] $t_{1/2,}$ half-life of the 1:1 avidin−biotin−PEG−CPA complex from SEC chromatography analysis. [c] $t_{1/2,}$ half-life of the 1:1 avidin−biotin−PEG−CPA complex from SPR analysis.

Half-Life of Avidin−Biotin−PEG(s)−CPA Complex. Because the tailing factors of avidin, biotin−PEG−CPA and their complexes are almost equal to one in SEC, their overlapped peaks were deconvoluted with the OriginPro 7.0 Gaussian peak fitting illustrated in Figure 5. The natural logarithm of the relative peak height of the 1:1 avidin−biotin−PEG(5000)−CPA complex decreased linearly with time so the dissociation of the biotin−PEG(5000)−CPA from avidin followed pseudo-first-order kinetics (*29*). The pseudo-first-order dissociation rate constants (k_{off}) are the slopes of the temporal decay and have the following values: 1.32×10^{-4} min^{-1} for the 1:1 avidin−biotin−PEG(5000)−CPA complex, 1.44×10^{-4} min^{-1} for the 1:1 avidin−biotin−PEG(3400)−CPA complex, 1.76×10^{-4} min^{-1} for the 1:1 avidin−biotin−PEG(5000)−CPA−PEG(2000) complex, and 1.23×10^{-4} min^{-1} for the 1:1 avidin−biotin−PEG(3400)−CPA−PEG(2000) complex. The corresponding half-lives are 3.6 days, 3.3 days, 2.7 days, and 3.9 days.

The dissociation rate constant (k_{off}) of biotin−PEGylated CPA on the SA sensor chip was determined to be on the order of 10^{-6} s^{-1} from SPR analysis. The data, together with the stoichiometries, are summarized in Table 1

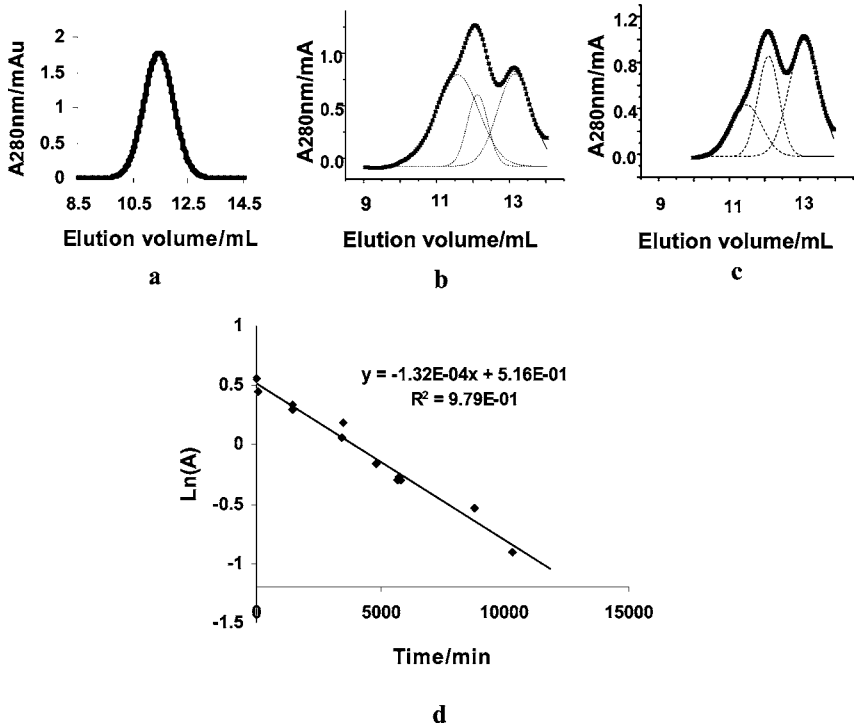


Figure 5. Elution profile of dissociation of the 1:1 avidin−biotin−PEG(5000)−CPA complex using a Superose 12/30 HR column on an ÄKTA FPLC system. (a) incubation time = 0; (b) incubation time = 7059 min; (c) incubation time = 10276 min; (d) 1:1 avidin−biotin−PEG(5000)−CPA complex dissociation rate at 24 °C. The peak at elution position ~11.45 mL is from the 1:1 avidin−biotin−PEG(5000)−CPA complex and A in Ln(A)is the relative peak height of the complex in SEC chromatography. The elution buffer was PBS buffer (pH 7.4) with a flow rate of 0.50 mL/min. The dash lines (-----) stand for the deconvoluted peaks using OriginPro 7.0 Gaussian peak fitting.

DISCUSSION

Stoichiometry. The stoichiometries of avidin binding with biotin−PEG(3400)−CPA (1:2), biotin−PEG(5000)−CPA (1:1), and biotin−PEG(3400)−CPA−PEG(2000) (1:2) support our previous conclusion that, as a spacer, PEG can block the further binding of biotin derivatives with avidin. But it was also surprising to find that biotin−PEG(5000)−CPA−PEG(2000) accesses all four binding sites on avidin.

While the avidin−biotin−PEG(3400) complex has a 1:4 stoichiometry, biotin−PEG(3400)−CPA only accesses two oppositely located biotin binding sites on avidin. This 1:2 stoichiometry is attributed to the increased steric hindrance from PEG and CPA, as well as to the electrostatic repulsion among CPAs (*9*). The hindrance and repulsion also result in a 1:2 stoichiometry for the avidin−biotin−PEG(3400)−CPA−PEG-(2000) complex.

The 1:1 stoichiometry with avidin shows that the biotin−PEG(5000)−CPA hinders the binding to not only adjacent but also oppositely located biotin binding sites on avidin, as observed in biotin−PEG(5000) (to be published). We speculate that the attractive interaction between PEG and avidin should be stronger than that between PEG and CPA; thus, the PEG-(5000) chain surrounds avidin instead of CPA, even though CPA is first conjugated with PEG(5000). It is also possible that PEG-(5000) is large enough to surround avidin while it is not for CPA. PEG(5000) has a Flory radius of 60 Å (*30*), avidin has dimensions of approximately 56 Å × 50 Å × 40 Å (*31*), and CPA has dimensions of approximately 51 Å × 60 Å × 47 Å (*32*).

In contrast, avidin is not surrounded by the PEG chain in the avidin−biotin−PEG(5000)−CPA−PEG(2000) complex since biotin−PEG(5000)−CPA−PEG(2000) is able to access all four binding sites of avidin. This inability to surround avidin may occur because the PEG−PEG repulsion between PEG(2000) and PEG(5000) prevents PEG(5000) from surrounding avidin. Moreover, the release of biotin−PEG(5000)−CPA from avidin by introduction of biotin also indicates the flexibility of such a surrounding. The observed 1:2 stoichiometry of the avidin−biotin−PEG(3400)−CPA−PEG(2000) complex and the 1:4 stoichiometry of the avidin−biotin−PEG(5000)−CPA−PEG-(2000) complex may mean that the longer PEG can relieve more electrostatic repulsion among CPAs and that the electrostatic repulsion among CPAs may be stronger than PEG−PEG steric repulsion.

Half-Life. The duration of efficacy of a protein ligand complex cannot be determined by the in vitro measured equilibrium dissociation constant but rather depends on the complex dissociation rate constants (k_{off}) or half-life (*33*). As we proposed, the ideal avidin−biotin−PEG(s)−CPA complexes would dissociate but still have a prolonged plasma circulation for the sufficient accumulation in tumor tissues through the EPR effect. Optimization of the half-life of the complex is therefore crucial for such a drug delivery. The results show that the dissociation half-life and the stoichiometry of the complex can be adjusted by the lengths of the PEG chains, and the half-lives of these 1:1 complexes are about 3−4 days, which is very promising (Table 1). In addition, since the 1:4 complex dissociates to 1:3 and 1:2 and finally 1:1, the 1:4 complex can be explored for a drug release with a relatively constant concentration over a long period.

We also obtained the dissociation rate constant (k_{off}) of these biotin−PEGylated CPAs with streptavidin using the surface plasmon resonance (SPR) analysis. A streptavidin sensor chip was used because an avidin chip was not available through Biacore. The dissociation rate constants determined from the SPR analysis are different than those determined by the solution-based method (see Table 1). This result reflects the difference between avidin and streptavidin, as well as a variety of potential artifacts in surface-based measurements (*34*, *35*). It signals the advantage of the solution-based method, which is closer to the physical environment involved in drug delivery applications. Although it is simpler to obtain the data by SPR, we use the data from the solution-based method in all of our work.

It was reported that PEG could create attractive interactions among proteins and cause protein crystallization or aggregation (*36*). To investigate the stability of our system, we kept biotin−PEG(3400)−CPA, biotin−PEG(3400)−CPA−PEG(2000), biotin−PEG(5000)−CPA, biotin−PEG(5000)−CPA−PEG(2000), avidin−biotin−PEG(3400)−CPA complex, avidin−biotin−PEG(5000)−CPA complex, avidin−biotin−PEG(3400)−CPA−PEG(2000) complex, and avidin−biotin−PEG(5000)−CPA−PEG(2000) complex in a refrigerator at 4 °C. We did not find any precipitation or any obvious SEC peak from the aggregated proteins over three weeks. This observation means that these complexes can be kept at least for three weeks without precipitation and aggregation.

The study on PEGylated CPA shows that the attachment of up to three PEG to CPA improves CPA catalytic properties (*15*). Following the same strategy using hipp-L-phe, we simply evaluated the enzymatic hydrolysis capacity of CPA in a 1:4 complex of avidin−biotin−PEG(5000)−CPA−PEG(2000) and in a 1:2 complex of avidin−biotin−PEG(3400)−CPA−PEG-(2000) by comparison with native CPA. It appears that CPA in both complexes has similar catalytic properties to those of native CPA. Even though these preliminary findings show that CPA does not lose its enzymatic capacity during the PEGylation and formation of the avidin−biotin−PEG(s)−CPA complexes, the systemic investigation of the enzymatic ability, bioactivity, and pharmacokinetic properties of these complexes will definitely be our next approach in this field.

CONCLUSIONS

The aim of the present study is to investigate the practical potential of the avidin−biotin−PEG−CPA complex as a novel DDS for MTX prodrug EPR-directed pretargeting. Basic steps include synthesis of biotin−PEG(s)−CPA, formation of the avidin−biotin−PEG(s)−CPA complexes, and analytical procedures to measure the stoichiometries and half-lives of the complexes. The results show (i) the molecular weights of the avidin−biotin−PEG−CPA complexes are in the same order as that of an antibody, (ii) the stoichiometries of avidin−biotin−PEG−CPA complexes are 1:4 for avidin−biotin−PEG(5000)−CPA−PEG(2000), 1:2 for avidin−biotin−PEG(3400)−CPA and avidin−biotin−PEG(3400)−CPA−PEG(2000), and 1:1 for avidin−biotin−PEG(5000)−CPA, and (iii) the half-lives of these 1:1 complexes are around 3−4 days at 24 °C so the dissociation kinetics are slow enough for typical tumor accumulations through EPR. On the basis of the half-life and stoichiometry, the avidin−biotin−PEG−CPA complexes or their analogues have potential as a new protein drug delivery system, in which the avidin−biotin−PEG−CPA complex acts as both the transporting device and the targeting device, while CPA is the drug moiety for the prodrug pretargeting strategy.

In addition, the data in the present study provides information on four interactions that can alter the binding of avidin with biotin in avidin-biotin-PEG(s)-CPA complexes: (i) the steric repulsion between PEG−PEG; (ii) the interaction among the attached functional groups on the second terminus of PEG, such as the electrostatic repulsion among the conjugated CPAs; (iii) the interaction between the attached functional group and PEG, such as that PEG chains relieve the interaction among CPAs; (iv) the surrounding of PEG around avidin. Both the length of a PEG chain and the interactions of the attached functional

groups on PEG should be considered when a PEG chain is chosen as an appropriate spacer.

ACKNOWLEDGMENT

We thank Dr. McClain for his assistance in fluorometric assay for the stoichiometry quantitative evaluation and helpful discussion of the paper.

LITERATURE CITED

(1) Ferrari, M. (2005) Cancer nanotechnology: opportunities and challenges. *Nat. Rev. Cancer 5*, 161−171.
(2) Begent, R. H. J., and Bagshawe, K. D. (1996) Biodistribution studies. *Adv. Drug Delivery Rev. 22*, 325−329.
(3) Niculescu-Duvaz, I., and Springer, C. J. (1995) Antibody-directed enzyme prodrug therapy (ADEPT): a targeting strategy in cancer chemotherapy. *Curr. Med. Chem. 2*, 687−706.
(4) Bagshawe, K. D. (1995) Antibody-directed enzyme prodrug therapy: a review. *Drug Dev. Res. 34*, 220−30.
(5) Li, K. C. P., Pandit, S. D., Guccione, S., and Bednarski, M. D. (2004) Molecular imaging applications in nanomedicine. *Biomed. Microdevices 6*, 113−116.
(6) Peterson, H. I. (1979) Tumor blood flow compared with normal tissue blood flow. *Tumor Blood Circulation: Angiogenesis, Vascular Morphology and Blood Flow of Experimental and Human Tumors* (Peterson, H. I., Ed.) pp 103−114, CRC Press, Boca Raton, FL.
(7) Maki, S., Konno, T., and Maeda, H. (1985) Image enhancement in computerized tomography for sensitive diagnosis of liver cancer and semiquantitation of tumor selective drug targeting with oily contrast medium. *Cancer 56*, 751−757.
(8) Ulbrich, K., and Subr, V. (2004) Polymeric anticancer drugs with pH-controlled activation. *Adv. Drug Delivery Rev. 56*, 1023−1050.
(9) Christianson, D. W., and Lipscomb, W. N. (1989) Carboxypeptidase A. *Acc. Chem. Res. 22*, 62−69.
(10) Vitols, K. S., Haag-Zeino, B., Baer, T., Montejano, Y. D., and Huennekens, F. M. (1995) Methotrexate-α-Phenylalanine: Optimization of methotrexate prodrug for activation by carboxypeptidase A-monoclonal antibody conjugate. *Cancer Res. 55*, 478−481.
(11) Yuji, I., Ayako, M., Yoh, K., and Hiroyuki, N. (1990) Review: polyethylene glycol (PEG)-protein conjugates: application to biomedical and biotechnological processes. *J. Bioact. Compat. Polym. 5*, 343−364.
(12) Veronese, F. M. (2001) Peptide and protein PEGylation: a review of problems and solutions. *Biomaterials 22*, 405−17.
(13) Tsutsumi, Y., Onda, M., Nagata, S., Lee, B., Kreitman, R. J., and Pastan, Ira. (2000) Site-specific chemical modification with polyethylene glycol of recombinant immunotoxin anti-Tac(Fv)-PE38 (LMB-2) improves antitumor activity and reduces animal toxicity and immunogenicity. *Proc. Natl. Acad. Sci. U.S.A. 97*, 8548−8553.
(14) Yamaoka, T., Tabata, Y., and Ikada, Y. (1994) Distribution and tissue uptake of poly(ethylene glycol) with different molecular weights after intravenous administration to mice. *J. Pharm. Sci. 83*, 601−606.
(15) Ton, G. N., Weichert, J. P., Longino, M. A., and et al. (2005) Methoxypoly(ethylene glycol)-conjugated carboxypeptidase A for solid tumor targeting, Part II: Pharmacokinetics and iodistribution in normal and tumor-bearing rodents. *J. Controlled Release 104*, 155−166.
(16) Ruth, D. (2003) The dawning era of polymer therapeutics. *Nat. Rev. Drug Discovery 5*, 347.
(17) Robinson, B. V., Sullivan, F. M., Borzelleca, J. F., and Schwartz, S. L. (1990) Excretion and metabolism of PVP. *PVP: A critical review of the kinetics and toxicologyof polyvinylpyrrolidone (povidone*) (Robinson, B. V., Sullivan, F. M., Borzelleca, J. F., and Schwartz, S. L., Eds.) pp 55−68, Lewis Publishers, Chelsea, MI.
(18) Wilchek, M., and Bayer, E. A. (1990) Avidin-biotin technology. *Methods Enzymology* (Wilchek, M., and Bayer, E. A., Eds.) Vol. 184, Academic Press, San Diego, CA.
(19) Diamandis, E. P., and Christopoulos, T. K. (1991) The biotin-(strept) avidin system: principles and applications in biotechnology. *Clin. Chem. 37*, 625−636.
(20) Jung, L. S., Nelson, K. E., Stayton, P. S., and et al. (2000) Binding and dissociation kinetics of wild-type and mutant streptavidins on mixed biotin-containing alkylthiolate monolayers. *Langmuir 16*, 9421−9432.
(21) Wilbur, D. S., Chyan, M. K., Pathare, P. M., and et al. (2000) Biotin reagents for antibody pretargeting. 4. Selection of biotin conjugates for in vivo application based on their dissociation rate from avidin and streptavidin. *Bioconjugate Chem. 11*, 569−583.
(22) Kaiser, K., Marek, M., Haselgruebler, T., Schindler, H., and Gruber, H. J. (1997) Basic studies on heterobifunctional biotin−PEG conjugates with a 3-(4-pyridyldithio)propionyl marker on the second terminus. *Bioconjugate Chem. 8*, 545−551.
(23) Sebastian, J. F., Liang, G. Q., Jabarin, A., and et al. (1996) Effect of enzyme-substrate interactions away from the reaction site on carboxypeptidase A catalysis. *Bioorg. Chem. 3*, 290−303.
(24) Gruic-Sovulj, I., Ludemann, H. C., Hillenkamp, F., and et al. (1997) Detection of noncovalent tRNA-aminoacyl-tRNA synthetase complexes by matrix-assisted laser desorption/ionization mass spectrometry. *J. Biol. Chem. 272*, 32084−32091.
(25) Mock, D. M., and Horowitz, P. (1990) Fluorometric assay for avidin-biotin interaction. *Method. Enzymol. 184*, 234−40.
(26) Ding, Z., Shimoboji, T., Stayton, P. S., and Hoffman, A. S. (2001) A smart polymer shield that controls the binding of different size biotinylated proteins to streptavidin. *Nature 411*, 59−62.
(27) Bradshaw, R. A., Walsh, K. A., and Neurath, H. (1969) The amino acid sequence of bovine carboxypeptide A. *Proc. Natl. Acad. Sci. U.S.A. 63*, 1389−1394.
(28) Seely, J. E., and Richey, C. W. (2001) Use of ion-exchange chromatography and hydrophobic interaction chromatography in the preparation and recovery of polyethylene glycol-linked proteins. *J. Chromatogr. A 908*, 235−241.
(29) Sidorova, N. Y., and Rau, D. C. (2000) The dissociation rate of the EcoR1-DNA-specific complex is linked to water activity. *Biopolymers 53*, 363−368.
(30) Jeppesen, C., Wong, J. Y., Kuhl, T. L., Israelachvili, J. N., Mullah, N., and Marques, C. M. (2001) Impact of polymer tether length on multiple ligand-receptor bond formation. *Science 293*, 465−468.
(31) Pugliese, L., Coda, A., Malcovati, M., and Bolognesi, M. (1993) Three-dimensional structure of the tetragonal crystal from egg-white avidin in its functional complex with biotin at 2.7 A resolution. *J. Mol. Biol. 231*, 698−710.
(32) Ludwig, M. L., Paul, I. C., Pawley, G. S., and. Lipscomb, W. N. (1963) The Structure of Carboxypeptidase A, I. A two-dimensional superposition function. *Proc. Natl. Acad. Sci. U.S.A. 50*, 282−285.
(33) Copeland, R. A., Pompliano, D. L., and Meek, T. D. (2006) Opinion Drug-target residence time and its implications for lead optimization. *Nat. Rev. Drug Discovery 5*, 730−739.
(34) O'Shannessy, D. J., and Winzor, D. J. (1996) Interpretation of deviations from pseudo-first-order kinetic behavior in the characterization of ligand binding by biosensor technology. *Anal. Biochem. 236*, 275−283.
(35) Myszka, D. G. (1997) Kinetic analysis of macromolecular interactions using surface plasmon resonance biosensors. *Curr. Opin. Biotechnol. 8*, 50−57.
(36) Kulkarni, A. M., Chatterjee, A. P., Schweizer, K. S., and et al. (2000) Effects of polyethylene glycol on protein interactions. *J. Chem. Phys. 113*, 9863−9873.

BC700182T

Organometallic ^{99m}Tc(III) '4 + 1' Bombesin(7−14) Conjugates: Synthesis, Radiolabeling, and *in Vitro*/*in Vivo* Studies

Jens-Uwe Kunstler,[†] Bhadrasetty Veerendra,[‡] Said D. Figueroa,[‡] Gary L. Sieckman,[||] Tammy L. Rold,[⊥] Timothy J. Hoffman,[||,⊥] Charles J. Smith,*[,‡,§,||] and Hans-Jurgen Pietzsch*[,†]

Institute of Radiopharmacy, Forschungszentrum Dresden-Rossendorf, 01314 Dresden, Germany, Department of Radiology and Department of Internal Medicine, University of Missouri−Columbia School of Medicine, Columbia, Missouri 65211, University of Missouri Research Reactor Center, University of Missouri−Columbia, Columbia, Missouri 65211, and Research Division, Harry S. Truman Memorial Veterans' Hospital, Columbia, Missouri 65201. Received May 31, 2007

Bombesin (BBN) peptide exhibits high selectivity and affinity for the gastrin-releasing peptide receptor (GRPr). The GRPr is overexpressed on many human cancer cell types, thus making BBN a potent delivery vehicle for radionuclide targeting. In this study, the biologically active minimal sequence BBN(7−14) was labeled using the novel Tc '4 + 1' mixed-ligand system, [Tc(NS_3)(CN−R)], in which Tc(III) is coordinated by a monodentate isocyanide linker bearing the peptide and the tetradentate, tripodal chelator, 2,2′,2″-nitrilotriethanethiol (NS_3). BBN(7−14) was N-terminally modified with Gly-Gly-Gly, βAla, and Ser-Ser-Ser spacer groups (X) and functionalized with 4-(isocyanomethyl)benzoic acid (L1) or 4-isocyanobutanoic acid (L2), resulting in a series of [M(NS_3)(L−X−BBN(7−14))] conjugates (M = ^{99m}Tc, Re). The isocyanide ligand frameworks were introduced using novel bifunctional coupling agents. The spacer groups (X), the monodentate isocyanide units, and a tetradentate NS_3 chelator bearing a pendant carboxylic acid (NS_3COOH) were proposed as pharmacological modifiers. ^{99m}Tc-labeling was performed in a two-step procedure by first preparing ^{99m}Tc-EDTA/mannitol followed by reactions with the isocyanides and NS_3 or NS_3COOH ligand frameworks. The ^{99m}Tc complexes were obtained with a radiochemical yield of 30−80% depending on the amount of the isocyanide (20−100 nmol) used. These new conjugates were purified by reversed-phased high-performance liquid chromatography (RP-HPLC) to give a radiochemical purity of ≥95%. The ^{99m}Tc conjugates exhibited high *in vitro* stability (>90%, 24 h). Analogous nonradioactive Re conjugates were synthesized and characterized by electrospray ionization mass spectrometry (ESI-MS). RP-HPLC analyses of the Re conjugates indicated that they exhibited identical retention times to the corresponding ^{99m}Tc conjugates under identical HPLC conditions, demonstrating structural similarity between the two metalated species. The [Re(NS_3)(L−X−BBN(7−14))] conjugates exhibited GRPr affinity in the nanomolar range as demonstrated by *in vitro* competitive binding assays using PC-3 human prostate cancer cells. *In vitro* internalization/externalization assays indicated that ∼65% of [^{99m}Tc(NS_3)(L2−βAla−BBN(7−14))] conjugate was either surface-bound or internalized in PC-3 cells. Cell-associated activity for all other ^{99m}Tc conjugates was below 20%. Biodistribution studies of [^{99m}Tc(NS_3)(L−βAla−BBN(7−14))], L = L1 or L2, in normal, CF-1 mice showed minimal accumulation in normal pancreas (a tissue expressing the GRPr in high density in rodent models) and rapid hepatobiliary elimination. Introduction of a carboxyl group onto the NS_3 ligand framework had only minimal effects to increase renal excretion. Activity distribution and accumulation was highly dominated by the relatively lipophilic '4 + 1' complex unit.

INTRODUCTION

The development of radiotracers based upon peptides as targeting moieties for tumors has been a focus of research over the past decade. Design and development of specific radiotracers of this type vary broadly by type of peptide and the radiolabeling approach used (*1*−*5*). The pharmacological properties of radiometal-labeled peptides are highly dependent on the conjugated metal complex. Therefore, it would be useful to have as wide a spectrum of alternative labeling systems as possible. As part of our ongoing research to establish a new labeling system for peptides, we have developed '4 + 1' mixed-ligand complexes of Tc and Re, [M(NS_3)(CN−R)], where Tc/Re(III) is coordinated by a monodentate isocyanide or phosphine ligand framework and a tetradentate tripodal chelator. The '4 + 1' mixed-ligand approach features high stability, mild labeling conditions, well-defined complexes, and the possibility of varying the chelator and monodentate ligand. '4 + 1' complexes have been studied under various structural−chemical aspects and assessed on the labeling of some biomolecules. For example, there are studies on '4 + 1' conjugates of serotonin receptor ligands and fatty acids, but only exemplary studies on neurotensin (*8*−*13*) as a peptide have been reported (*6*−*11*). Herein, bombesin was selected as biomolecule to further study '4 + 1' complexes for the ^{99m}Tc-labeling of peptides.

Among the peptides for tumor targeting, bombesin (BBN), a tetradecapeptide binding with high affinity to the gastrin-releasing peptide receptor (GRPr), has recently gained increasing

* Authors to whom correspondence should be addressed: Dr. Hans-Jurgen Pietzsch, Forschungszentrum Dresden-Rossendorf, Institute of Radiopharmacy, PF 510 119, D-01314 Dresden, Germany. E-mail: h.j.pietzsch@fzd.de. Phone: +49-351-260-2706. Fax: +49-351-260-3232. Dr. Charles J. Smith, Harry S. Truman Memorial VA Hospital, Research Service Room A005, 800 Hospital Drive, Columbia, Missouri 65201. E-mail: smithcj@health.missouri.edu. Phone: (573) 814-6000 ext. 3683. Fax: (573) 882-1663.

[†] Institute of Radiopharmacy, Forschungszentrum Dresden-Rossendorf.

[‡] Department of Radiology, University of Missouri−Columbia School of Medicine.

[§] University of Missouri Research Reactor Center, University of Missouri−Columbia.

[||] Harry S. Truman Memorial Veterans' Hospital.

[⊥] Department of Internal Medicine, University of Missouri−Columbia School of Medicine.

10.1021/bc700197m CCC: $37.00 © 2007 American Chemical Society
Published on Web 07/31/2007

attention. The GRPr is overexpressed on a variety of tumors including commonly diagnosed breast and prostate cancers and rarer pancreatic and small-cell lung cancers (*1*, *12*, *13*). Many radiolabeled bombesin derivatives have been designed showing varying pharmacokinetic behavior depending on the radiolabeling approach, the pharmacokinetic modifier or spacer between the radiometal-chelate and the N-terminus, and specific modifications in the peptide sequence. Research investigations have examined BBN derivatives radiolabeled with ^{64}Cu (*14*−*17*), ^{18}F (*18*−*20*), ^{68}Ga (*19*, *20*), ^{125}I (*21*−*23*), ^{111}In (*24*−*26*), ^{177}Lu (*25*, *27*−*29*), ^{188}Re (*30*−*32*), and ^{90}Y (*25*).

Many studies have focused on radiolabeling of BBN peptide with ^{99m}Tc as well, exploiting favorable physical characteristics/nuclear properties, ready availability, and simple handling of this radioisotope. For example, ^{99m}Tc has a $t_{1/2}$ of 6 h, emits an imageable γ photon of 140 keV (89% abundance), is readily available from a ^{99}Mo/^{99m}Tc generator, and is used in more than 85% of all diagnostic patient applications in nuclear medicine (*33*). Radiolabeld BBN conjugates containing the Tc(V) monooxo $[Tc{=}O]^{3+}$ core coordinated by N_3S (*34*−*37*), N_2S_2 (*37*−*40*), or Tc(V) dioxo $[O{=}Tc{=}O]^{+}$ core chelated by N_4 (*41*, *42*) and P_2S_2 ligands (*43*), as well as organometallic Tc(I) conjugates containing the $[^{99m}Tc(CO)_3]^{+}$ metal fragment (*44*−*48*), have been extensively investigated. Various limitations are associated with some labeling concepts, such as low radiochemical yield, extended reaction time, high temperature, high pH values, and high lipophilicity of the radiometal chelate. In the series of the applied labeling systems so far, the novel '4 + 1' concept might be an alternative.

The ^{99m}Tc complexes were generally coupled directly to the N-terminus of BBN(7−14) (*36*, *42*, *47*) or *via* spacer groups to BBN-derived peptides. For example, Gly-Gly-Gly (*48*), Ser-Ser-Ser (*46*), βAla, and 5-aminovaleric, 8-aminooctanoic, and 11-aminoundecanoic acid (*36*, *43*) have been studied as spacers or pharmacokinetic modifying linker groups. ^{99m}Tc-tricarbonyl complexes conjugated to [DPhe^6, βAla^{12}, Nle^{14}]BBN(6−14) or [Cha^{13}]BBN(7−14) have been exclusively studied by Bläuenstein and co-workers (*47*). ^{99m}Tc(V)−N_4 complexes have been conjugated to [Pro^1, Tyr^4]BBN or [Pro^1, Tyr^4, Nle^{14}]BBN as well as *via* the *p*-[(carboxymethoxy)acetyl]aminobenzyl group to BBN(7−14), [Nle^{14}]BBN(7−14) or [DPhe^6, Leu-NHEt^{13}, *des*-Met^{14}]BBN(6−14) (*26*, *41*, *42*). Gourni et al. have studied ^{99m}Tc conjugates of BBN(2−14) using Xaa-Gly-Gly (Xaa = Gly, methylglycine, dimethylglycine, mercaptoacetic acid) as the chelating ligand frameworks and 6-aminohexanoic acid as the pharmacokinetic modifier (*49*). Baidoo et al. have extensively investigated ^{99m}Tc(V)−N_2S_2 complexes conjugated *via* Lys^3 to [Lys^3]BBN or [DTPA^1, Lys^3, Tyr^4]BBN (*38*−*40*). All of the aforementioned ^{99m}Tc conjugates exhibited affinity for the GRPr and a biodistribution behavior that is influenced specifically by the choice of metal center, chelator, linking substituent, or peptide targeting vector. The best biodistribution results have been achieved by conjugates consisting of BBN(7−14) or an analog of them and a hydrophilic ^{99m}Tc complex placed at a certain distance from the BBN(7−14) sequence.

To study the potential of '4 + 1' complexes for bombesin labeling, we herein report on the synthesis and characterization of novel Tc/Re(III) BBN(7−14) conjugates where the metal (M = ^{99m}Tc, Re) is coordinated by a monodentate isocyanide-functionalized BBN derivative and a tetradentate, tripodal chelator, 2,2′,2″-nitrilotriethanethiol (NS_3), resulting in a series of [M(NS_3)(L−X−BBN(7−14))] conjugates. BBN(7−14) was N-terminally modified with Gly-Gly-Gly, βAla, and Ser-Ser-Ser spacer groups (X) and functionalized with 4-(isocyanomethyl)benzoic acid (L1) or 4-isocyanobutanoic acid (L2). The peptides X−BBN(7−14) were selected from our previous studies where their ^{99m}Tc conjugates containing a N_3S or tricarbonyl framework showed promising *in vitro* and *in vivo* characteristics (*36*, *46*, *48*). Radiolabeling studies, *in vitro* cell binding affinity studies, internalization/externalization assays, and biodistributions in normal CF-1 mice are reported.

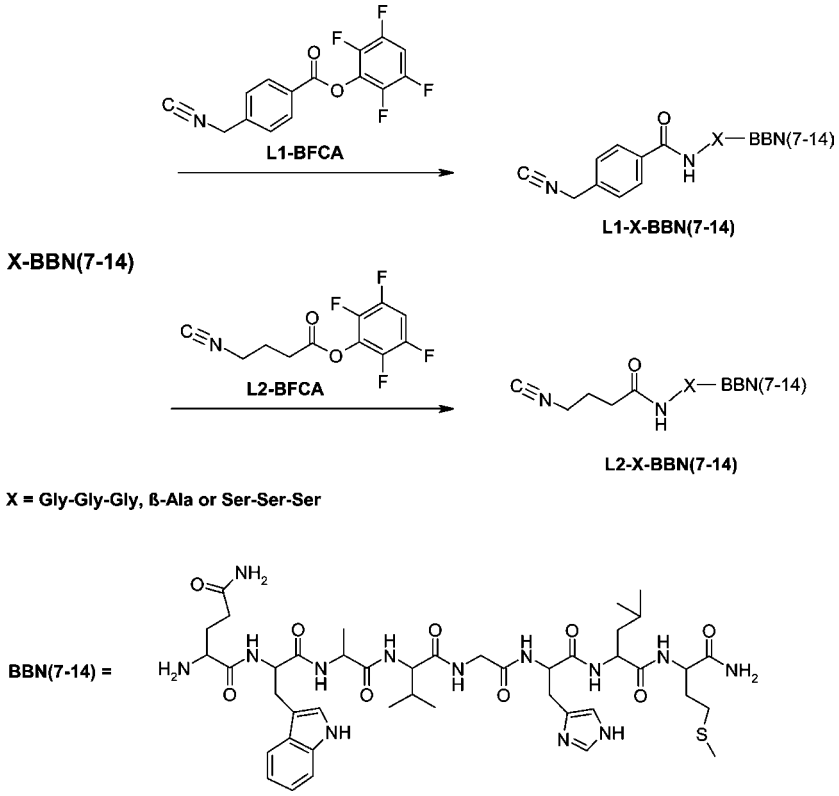
EXPERIMENTAL PROCEDURES

Materials. The tetradentate ligand 2,2′,2″-nitrilotriethanethiol (NS_3) was synthesized as previously described (*6*). 2,2′,2″-Nitrilotriethanethiol was precipitated as the oxalate and applied as such. *N*,*N*-bis(2-mercaptoethyl)cysteine (NS_3COOH) and 2,3,5,6-tetrafluorophenyl 4-(isocyanomethyl)benzoate (L1-BFCA) were synthesized according to previously published procedures (*9*). [Re(NS_3)(PMe_2Ph)] was prepared according to the methods of Pietzsch et al. (*7*). Na$^{99m}TcO_4$ was eluted from a commercial ^{99}Mo/^{99m}Tc generator (Mallinckrodt). RP-HPLC analyses and purification were performed on a Waters 600E system equipped with a Varian 2550 variable absorption detector and a solid sodium iodide crystal radiometric detector. Solvents were of HPLC grade and purchased from Fisher Scientific (Chicago, IL). The gradient and HPLC conditions were as follows: eluent A, 0.1% (v/v) trifluoroacetic acid (TFA) in acetonitrile; eluent B, 0.1% (v/v) TFA in water; eluent C, 0.1 M NH_3 in acetonitrile, eluent D, 0.1 M NH_3 in water. System 1: Jupiter 5 μ C18 300 Å (Phenomenex), 250 × 10 mm, gradient elution using eluents A and B: 5−70% A in 25 min, 3 mL/min. System 2: Jupiter 5 μ C18 300 Å (Phenomenex), 250 × 4.6 mm, gradient elution using eluents A and B: 5−70% A in 25 min, 1.5 mL/min. System 3: Gemini 5 μ C18 (Phenomenex), gradient elution using eluents C and D: 20−80% C in 20 min, 3 mL/min. System 4: Jupiter 4 μ Proteo 90 Å (Phenomenex), 250 × 10 mm, gradient elution using eluents A and B: 20−80% A in 20 min, 3 mL/min. System 5: Jupiter 4 μ Proteo 90 Å (Phenomenex), 250 × 4.6 mm, gradient elution using eluents A and B: 20−80% A in 20 min. Elemental analyses were performed on a LECO elemental analyzer CHNS-932. Electrospray ionization mass spectrometry (ESI-MS) was performed using a Micromass Tandem Quadropole Mass Spectrometer (Quattro LC) or by Synpep Corporation (Dublin, CA). Nuclear magnetic resonance spectra were recorded on a 400 MHz Varian Inova 400 spectrometer. IR spectra were measured on the FTIR spectrometer IR 2000 (Perkin-Elmer) using KBr pellets. TLC strips were scanned using a Raytest Rita radioanalyzer. ^{125}I-[Tyr^4]BBN was obtained from NEN Life Sciences Products, Inc. (Boston, MA). All other compounds and solvents were purchased from Sigma-Aldrich (St. Louis, MO) and used without further purification.

Methods. *1. Solid-Phase Peptide Synthesis (SPPS).* GGG−BBS(7−14), βAla−BBS(7−14), and SSS−BBS(7−14) were synthesized on an automated solid-phase peptide synthesizer (Perkin-Elmer Applied Biosystem model 432) using traditional Fmoc chemistry and Rink amide resin (25 μmol). Each coupling step was performed using HBTU and appropriate Fmoc-protected amino acids (75 μmol) including the following side-chain protecting groups: Gln(Trt), Trp(Boc), His(Trt), and Ser(tBu). The final products were cleaved by a standard procedure using a cocktail containing thioanisol, water, ethanedithiol, and trifluoroacetic acid. Typical yields of the crude peptides were 75−85%. The crude materials were purified by RP-HPLC (system 1) and the solvent removed on a SpeedVac concentrator. ESI-MS was used to determine the molecular mass of the prepared peptides. HPLC (system 2): t_R = 12.2 min for GGG−BBN(7−14), t_R = 12.2 min for βAla−BBN(7−14), t_R = 12.3 min for SSS−BBN(7−14). ESI-MS (*m*/*z*) found (calcd): 1111.4 (1111.5) for $[GGG{-}BBN(7{-}14)]^{+}$, 1011.5 (1011.5) for $[\beta Ala{-}BBN(7{-}14)]^{+}$, 1201.5 (1201.6) for $[SSS{-}BBN(7{-}14)]^{+}$.

2. Synthesis of 2,3,5,6-Tetrafluorphenyl 4-Isocyanobutanoate (L2-BFCA). The bifunctional coupling agent L2-BFCA was

Scheme 1. Introduction of Isocyanides onto Bombesin Derivatives (BFCA = Bifunctional Coupling Agent)



prepared from 4-aminobutanoic acid *via* 4-(formylamino)-butanoic acid and 2,3,5,6-tetrafluorphenyl 4-(formylamino)-butanoate.

2.1. Synthesis of 4-(Formylamino)butanoic Acid. 194 mmol of 4-aminobutanoic acid were dissolved in 1 mL of acetic anhydride and 150 mL formic acid and refluxed at 100 °C. After a period of time, the temperature was increased to 115 °C and maintained for 8 h. The solvent was removed and the precipitate stirred in a solvent mixture of diethyl ether, acetonitrile, and ethyl acetate (30/5/5, v/v/v). After decanting and repeating the procedure, a white granular product was collected, washed with diethyl ether, and dried *in vacuo*. Yield: 35% white powder. Anal. ($C_5H_9NO_4$) found (calcd): C 44.9 (45.7), H 6.9 (6.9), N 10.5 (10.7).

2.2. Synthesis of 2,3,5,6-Tetrafluorphenyl 4-(Formylamino)-butanoate. 15.2 mmol of 4-(formylamino)butanoic acid and 15.2 mmol of *N*-hydroxysuccinimide were dissolved in 10 mL of anhydrous dimethylformamide. A solution of 15.2 mmol dicyclohexylcarbodiimide in 10 mL dimethylformamide was added and the reaction mixture stirred for 12 h at room temperature. After filtering, the solution was concentrated, filtered once again, and the solvent removed *in vacuo*. The residue was dissolved in acetonitrile/trichloromethane (1/1, v/v), precipitated by addition of diethyl ether, and dried *in vacuo*. Yield: 45% white powder. Anal. ($C_{11}H_9F_4NO_4$), found (calcd): C 44.1 (44.8), H 3.3 (3.1), N 4.9 (4.7).

2.3. Synthesis of L2-BFCA. 2.2 mmol of 2,3,5,6-tetrafluorphenyl 4-(formylamino)butanoate and 2.6 mmol of triphenylphosphine were mixed in a solution of 2.2 mmol of tetrachloromethane, 5 mL of trichloromethane, and 2.2 mmol of triethylamine. The reaction mixture was stirred at 50 °C for 3 h and the solvent removed *in vacuo*. The residue was washed with diethyl ether. The product was purified by column chromatography on silica gel 60 using a mixture of acetonitrile/trichloromethane/*n*-hexane (15/10/5, v/v/v) as the eluents. The product was collected and evaporated *in vacuo*. Yield: 35% pale yellow oil. Anal. ($C_{11}H_7F_4NO_2$), found (calcd): C 50.3 (50.6), H 2.7 (2.7), N 5.2 (5.4). ESI-MS (*m*/*z*) found (calcd) $[M + H]^+$: 262.1 (262.0). IR (KBr, cm^{-1}): 1790 (st, C=O), 2152 (m, C≡N). ^1H NMR (CD_3CN): 2.07 (m, 2H, CH_2CH_2-CH_2), 2.87 (t, J = 7.4 Hz, 2H, $CH_2C(O)$), 3.56 (tt, $^2J_{NH}$ = 2.0 Hz, $^3J_{HH}$ = 6.6 Hz, 2H, CH_2NC), 7.31 (m, 1H, H_{arom}). ^{13}C NMR (CD_3CN): 24.11 (s, $CH_2CH_2CH_2$), 29.83 (s, $CH_2C(O)$), 40.54 (t, J = 6.1 Hz, $CNCH_2$), 103.98 (m, $C_{arom}H$), 130−150 (very small signals not evaluated, $C_{arom}F$), 157.19 (s, CN), 169.04 (s, C(O)).

3. Synthesis of [L−X−BBN(7−14)], L = L1, L2, X = GGG, βAla, SSS. The isocyanides were introduced onto BBN(7−14) by conjugation with active esters L1-BFCA and L2-BFCA as depicted in Scheme 1. Briefly, 5 μmol of GGG−BBN(7−14), βAla−BBN(7−14), or SSS−BBN(7−14) were dissolved in 1 mL of dimethylformamide containing 15 μmol triethylamine. 5 μmol of either L1-BFCA or L2-BFCA were added. After being stirred for 6 h at room temperature, the solvent was removed *in vacuo*. The residues were dissolved in a mixture of acetonitrile and water (∼1/1) and then purified by RP-HPLC (system 3). The collected fractions were lyophilized to yield final conjugates as white powders. Yield: 20−30%. ESI-MS (*m*/*z*) found (calcd): 1255.0 (1254.6) for [L1−GGG−BBN(7−14)]$^+$, 1154.8 (1154.6) for [L1−βAla−BBN(7−14)]$^+$, 1344.6 (1344.6) for [L1−SSS−BBN(7−14)]$^+$, 1206.9 (1206.6) for [L2−GGG−BBN(7−14)]$^+$, 1107.9 (1106.6) for [L2−βAla−BBN(7−14)]$^+$, 1296.7 (1296.6) for [L2−SSS−BBN(7−14)]$^+$.

4. Preparation of ^{99m}Tc '4 + 1' Radiolabeled Bombesin Derivatives. ^{99m}Tc-labeled bombesin derivatives and the corresponding Re analogues are depicted in Figure 1. ^{99m}Tc labeling was performed in a two-step procedure similar to that described in ref *9*. Eluate of a ^{99}Mo/^{99m}Tc generator (0.2−1.5 GBq) was added to a kit formulation containing 1 mg Na_2EDTA, 5 mg mannitol, and 0.1 mg $SnCl_2$ in freeze-dried form under nitrogen. The solution was allowed to stand at room temperature for 20 min. The radiochemical purity was checked using TLC silica gel 60 W strips (Merck). ^{99m}Tc-EDTA/mannitol migrates to the solvent front in water and remains at the origin in acetone. The

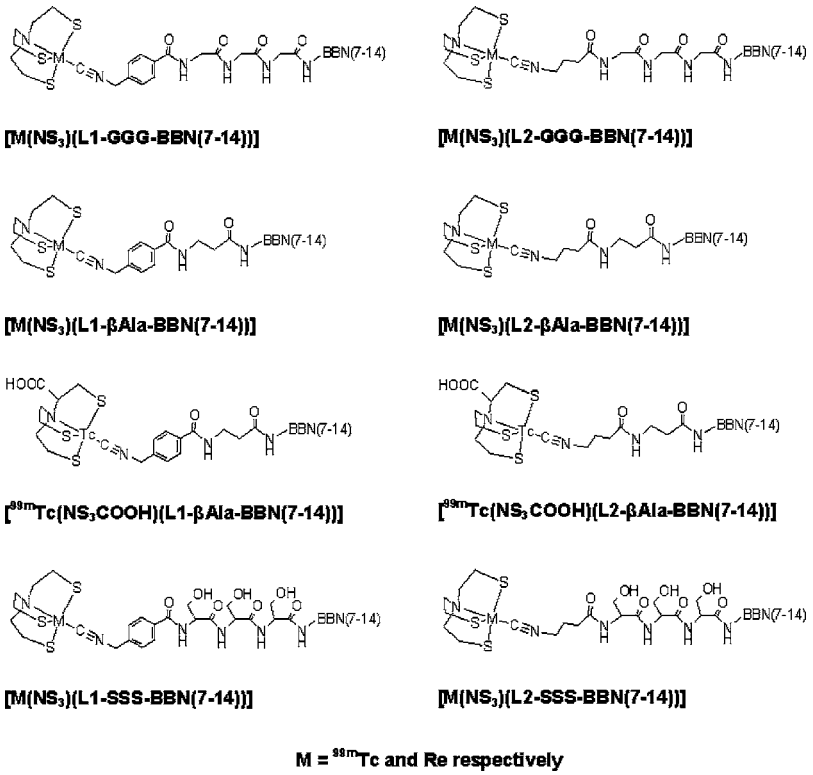


Figure 1. ^{99m}Tc and Re '4 + 1' complex-bearing bombesin derivatives.

radiochemical yield is usually >90%. 0.3 mg of NS_3 or NS_3-COOH were added to ^{99m}Tc-EDTA/mannitol, and the solution was transferred to a vial containing 0.05−0.2 mg isocyanide-modified BBN(7−14). Methanol was added so that it constituted $^1/_3$ of the volume of the labeling mixture. After flushing the space above the solution with argon, the vial was heated at 50 °C for 2 h. The radiolabeled conjugates were purified by RP-HPLC (system 4). For *in vitro* and *in vivo* studies, product fractions were collected and HPLC solvents evaporated under a nitrogen stream. The conjugates were dissolved in a solution of 1 mg bovine serum albumin in 1 mL water. Bovine serum albumin was used to minimize adhesion on vial surfaces for conjugates of this general type. HPLC (system 5): coelution with the analogous Re conjugates; for t_R of the Re conjugates, see below.

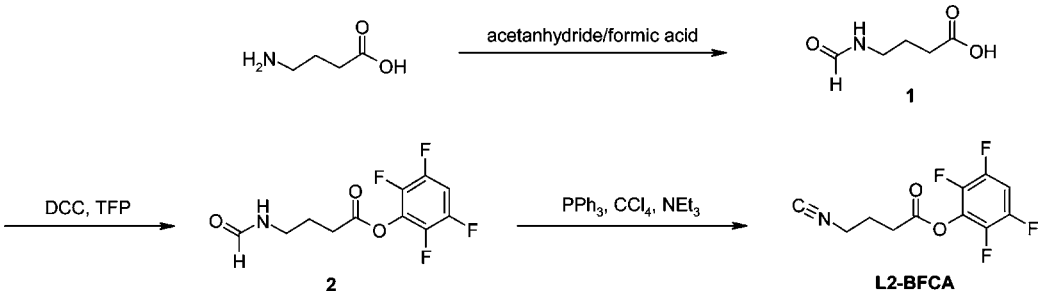
5. Synthesis of [Re(NS3)(L2−BFCA)]. L2−BFCA (0.22 mmol), dissolved in 3 mL trichloromethane, was added to 0.2 mmol [Re(NS_3)(PMe_2Ph)] dissolved in 3 mL trichloromethane. The mixture was stirred at room temperature for 1 h, evaporated, and the residues washed with diethyl ether. The product was precipitated from trichloromethane after adding methanol and diethyl ether. Yield: 90% olive-brown powder. Anal. ($C_{17}H_{19}F_4NO_2ReS_3$), found (calcd): C 32.0 (31.8), H 3.1 (3.0), N 4.3 (4.4). ESI-MS (*m*/*z*) found (calcd) $[M + Na]^+$: 665.1 (665.0). IR (KBr, cm^{-1}): 1783 (st, C═O), 1982 (st, C≡N). ^{1}H NMR (CD_3CN): 2.15 (m, 2H, $CH_2CH_2CH_2$), 2.6−3.2 (bs, 12H, CH_2CH_2SH), 3.04 (t, J = 3.9 Hz, 2H, $CH_2C(O)$), 4.77 (t, J = 6.2 Hz, 2H, CH_2NC), 7.30 (m, 1H, H_{arom}). ^{13}C NMR (CD_3CN): 28.70 (s, $CH_2CH_2CH_2$), 30.52 (s, $CH_2C(O)$), 43.79 (s, CN_2S), 44.69 (s, $CNCH_2$), 58.72 (s, NCH_2CH_2S), 103.98 (m, $C_{arom}H$), 169.04 (s, C(O)).

6. Synthesis of [Re(NS3)(L−X−BBN(7−14))], L = L1, L2, X = GGG, βAla, SSS. The Re '4 + 1' complexes were introduced onto BBN(7−14) by conjugation with the active esters [Re(NS_3)(L1−BFCA)] and [Re(NS_3)(L2−BFCA)]. The formulas of the products are depicted in Figure 1. 5 μmol of GGG−BBN(7−14), βAla−BBN(7−14), or SSS−BBN(7−14) was dissolved in 1 mL of dimethylformamide containing 15 μmol triethylamine. 5 μmol [Re(NS_3)(L1−BFCA)] or [Re(NS_3)-(L2−BFCA)] was added. After being stirred for 6 h at room temperature, the solvent was removed *in vacuo*. The residues were dissolved in a mixture of acetonitrile and water (1/1) and purified by semipreparative HPLC (system 4). Fractions were collected and lyophilized. Yield: 20−30% green powder. ESI-MS (*m*/*z*) found (calcd) $[M + H]^+$: 1636.1 (1635.5) for [Re(NS_3)(L1−GGG-BBN(7−14))], 1536.5 (1535.5) for [Re(NS_3)-(L1−βAla−BBN(7−14))], 1727.6 (1725.6) for [Re(NS_3)(L1−SSS−BBN(7−14))], 1588.1 (1587.5) for [Re(NS_3)(L2−GGG−BBN(7−14))], 1488.8 (1487.5) for [Re(NS_3)(L2−βAla−BBN(7−14))], and 1678.6 (1677.6) for [Re(NS_3)(L2−SSS−BBN(7−14))]. HPLC (system 5): t_R = 13.3 min for [Re(NS_3)(L1−GGG−BBN(7−14))], t_R = 14.0 min for [Re(NS_3)(L1−βAla−BBN(7−14))], t_R = 12.2 min for Re(NS_3)(L1−SSS−BBN(7−14)), t_R = 12.3 min for [Re(NS_3)(L2−GGG−BBN(7−14))], t_R = 12.9 min for [Re(NS_3)(L2−βAla−BBN(7−14))], and t_R = 11.8 min for [Re(NS_3)(L2−SSS−BBN(7−14))].

7. Receptor Binding Assays for [Re(NS3)(L−X−BBN(7−14))], L = L1, L2, X = GGG, βAla, SSS. The IC_{50} (inhibitory concentration 50%) values of [Re(NS_3)(L−X−BBN(7−14))] conjugates were determined by a competitive displacement cell binding assay using ^{125}I-Tyr^4-bombesin as the radiolabeling displacement ligand. Approximately 3×10^4 cells (suspended in D-MEM/F-12K media containing 0.01 M MEM and 2% BSA, pH = 5.5) were incubated at 37 °C for 1 h in the presence of 20 000 cpm ^{125}I-Tyr^4-bombesin (8.2×10^{-15} mol, 2200 Ci/mmol) and increasing concentrations of [Re(NS_3)(L−X−BBN-(7−14))] conjugate. Upon completion of the incubation, the reaction medium was aspirated, and the cells were washed four times with media. Cell-associated radioactivity was determined by counting in a Packard Riastar γ counting system. IC_{50} values were calculated using *Sigma Plot* graphing software.

8. In Vitro Evaluation of the Internalization and Externalization Properties of 99mTc Conjugates in Human, PC-3, Prostate Cancer Cells: *In vitro* internalization analyses of [^{99m}Tc(NS_3)(L−X−BBN(7−14))] conjugates were carried out by incubation of ~3×10^4 cells (in D-MEM/F-12K media

Scheme 2. Reaction Route to L2-BFCA



containing 0.01 M MEM and 2% BSA, pH = 5.5) in the presence of ~20 000 cpm [^{99m}TcNS$_3$)(L−X−BBN(7−14))] at 37 °C for selected time points of 15, 30, 45, 60, 90, and 120 min. Upon completion of the incubation, the reaction medium was aspirated, and the cells were washed four times with media. Surface-bound radioactivity was removed by washing the cells with 0.2 N acetic acid/0.5 M NaCl (pH = 2.5). The percent of internalized, cell-associated radioactivity as a function of time was determined by counting in a Packard Riastar γ counting system. Externalization studies were performed after a 45 min internalization period. The cellular medium was washed (3×) with buffer (room temperature) and resuspended for further incubation. Selected sampling at 0, 15, 30, 45, 60, and 90 min post-internalization was performed by an initial cold buffer wash of the cells, followed by washing with acetic acid/saline (pH = 2.5 at 4 °C). The percent of externalized radioactivity as a function of time was determined by counting in a Packard Riastar γ counting system. Internalization and externalization curves (least-squares best-fit line) were generated by *D-plot* graphing software.

9. Biodistribution of [^{99m}Tc(NS$_3$)(L1−βAla−BBN(7−14))], [^{99m}Tc(NS$_3$)(L2−βAla−BBN(7−14))], [^{99m}Tc(NS$_3$COOH)(L1−βAla−BBN(7−14))], and [^{99m}Tc(NS$_3$COOH)(L2−βAla−BBN-(7−14))] in Normal, CF-1 Mice. Mice were housed five animals per cage in sterile micro-isolator cages in a temperature- and humidity-controlled room with a 12 h light/12 h dark schedule. The animals were fed autoclaved rodent chow (Ralston Purina Company, St. Louis, MO) and water *ad libitum*. All animal studies were conducted in accordance with the highest standards of care as outlined in the NIH guide for Care and Use of Laboratory Animals and the Policy and Procedures for Animal Research at the Harry S. Truman Memorial Veterans' Hospital. The biodistribution studies of the [^{99m}Tc(NS$_3$)(L−X−BBN(7−14))] conjugates were determined in normal CF-1 mice. The mice were injected with 0.2 MBq (~0.5 × 10^{-10} g) of the ^{99m}Tc conjugate in 100 μL of isotonic saline *via* the tail vein. The mice were euthanized, and tissues and organs were excised from the animals at 1 h postinjection (p.i.). Subsequently, the tissues and organs were weighed and counted in a NaI well counter, and the percent injected dose (% ID) and % ID/g of each organ or tissue was calculated. The % ID in whole blood was estimated assuming a whole-blood volume of 6.5% of the total body weight. The animals were sacrificed at 1 h p.i. The tissues were removed, weighed, and counted as previously described.

RESULTS AND DISCUSSION

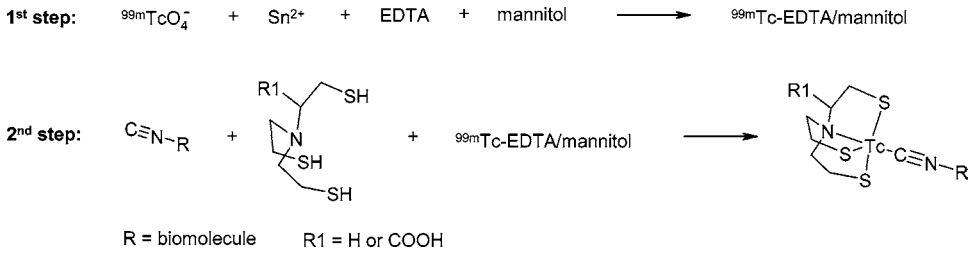
To couple the '4 + 1' complexes, BBN(7−14) bearing N-terminal βAla, Ser-Ser-Ser, and Gly-Gly-Gly as spacer groups X to serve as pharmacokinetic modifiers for the radiolabeled '4 + 1' conjugate were selected on the basis of previously published results: ^{99m}Tc-labeling using the N_3S chelator linked via βAla as spacer group to BBN(7−14) did not affect receptor affinity and showed a remarkable pancreatic uptake as well as the highest degree of renal excretion compared to analogous compounds containing a 5-, 8-, or 11-carbon spacer (*36*). ^{99m}Tc-tricarbonyl-labeled BBN(7−14) conjugates containing Ser-Ser-Ser as the spacer were similar regarding receptor affinity and pancreatic uptake while exhibiting a more extensive urinary excretion (*46*). BBN(7−14) conjugated to a ^{99m}Tc-tricarbonyl complex via a Gly-Gly-Gly spacer showed predominant urinary excretion but only low uptake into the pancreas (*48*).

The X−BBN(7−14) derivatives were conveniently synthesized by standard solid-phase peptide synthesis and characterized by ESI-MS. The isocyanides 4-(isocyanomethyl)benzoic acid (L1) and the smaller and more flexible 4-isocyanobutanoic acid (L2) may also serve as a modifier of the pharmacokinetic properties of the radiolabeled peptides. For the preparation of isocyanide-modified peptides, the isocyanide-containing active esters L1-BFCA (*9*) and L2-BFCA were designed to serve as bifunctional coupling agents (BFCA). L2-BFCA was prepared as described in Scheme 2. Briefly, formylation of 4-aminobutanoic acid produced product **1**. Esterification of **1** with 2,3,5,6-tetrafluorophenol to produce **2**, followed by reduction using PPh_3 in CCl_4 and triethylamine, afforded the final product L2-BFCA. Conversion of the formylamino derivative **2** to the isocyanide was performed according to a previously published procedure (*50*). The novel L2-BFCA was characterized by elemental analysis, ESI-MS, IR, and ^{1}H and ^{13}C NMR.

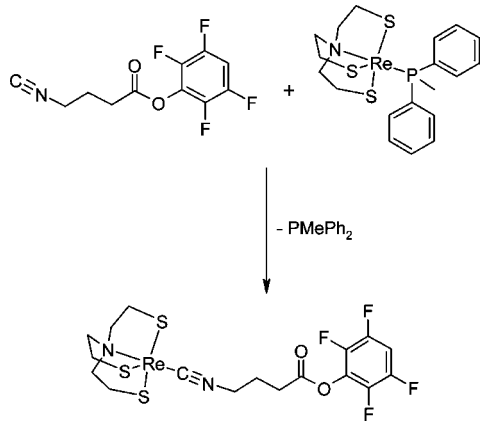
L1-BFCA and L2-BFCA allow for convenient coupling of the isocyanide group to peptides. However, it is not possible to use L1-BFCA and L2-BFCA in standard solid-phase peptide synthesis due to conversion of the isocyanide group to an N-formyl amino derivative in acidic media. Furthermore, acidic HPLC eluents comprising acetonitrile, water, and TFA, as normally used for purification of peptides on silica-based, reverse-phase columns, are not recommended. Conversion of isocyanide-modified BBN(7−14) to the N-formyl amino derivative was not immediately observed in the chromatographic profiles when analyzing conjugates by RP-HPLC using a TFA-containing mobile phase. However, purification in this way with subsequent neutralization after collection of the product resulted in a considerable amount of the N-formyl amino derivative. Therefore, purification of the isocyanide BBN(7−14) conjugates was performed using a mobile phase containing 0.1 M ammonia and a polymer-based RP column. The obtained ESI-MS data were consistent with the molecular weights calculated for each compound.

Preparation of ^{99m}Tc-labeled conjugates was performed in a similar manner to a previously published labeling procedure (*9*). The protocol is a two-step procedure and is outlined in Scheme 3. The radiochemical yields were around 30−80% (RP-HPLC) and were dependent upon the amount of isocynaide (20−100 nmol) in the reaction mixture. Methanol was added to the labeling mixture so that it constituted approximately $^1/_3$ of the volume. This was done to prevent precipitation development during the labeling reaction, which would inherently decrease the radiochemical yield. The lipophilic precipitation product was formed by the NS_3 ligand, tin, and ^{99m}Tc species. The labeled compounds were purified by HPLC to give a radiochemical purity of higher than 95%. The ^{99m}Tc conjugates eluted with

Scheme 3. ^{99m}Tc-Labeling Reaction



Scheme 4. Synthesis of [Re(NS$_3$)(L2-BFCA)]



retention times approximately 3 min longer than the nonmetalated isocyanide derivatives, allowing for collection of compounds of very high specific activity. The HPLC elution profiles of the labeling mixture and of the purified compound [^{99m}Tc(NS$_3$)(L1−βAla−BBN(7−14))] are shown in Figure 2. The peak at t_R = 8.4 min is a complex containing ^{99m}Tc and the NS$_3$ ligand but no isocyanide. The identity of the formed [^{99m}Tc(NS$_3$)(L−X−BBN(7−14))] conjugates were revealed by comparing their HPLC profiles with chromatograms of the analogous Re compounds which eluted at the same retention times (Figure 2). The stability of the [^{99m}Tc(NS$_3$)(L−X−BBN-(7−14))] conjugates in the HPLC eluate and in PBS were higher than 90% after 24 h.

Instabilities of a peptide labeled *via* a radiometal chelate can be caused by decomposition of the metal complex and/or the peptide. Previous studies have examined the stability of ^{99m}Tc '4 + 1' complexes showing that there was no decomposition of the ^{99m}Tc chelate in plasma, rat blood, and *in vivo*, as well as no transchelation by glutathione (*7*, *9*). A limitation of the ^{99m}Tc-labeled BBN conjugates presented here could be seen in the proteolytic instability of the peptide sequence. However, there are several examples in the literature of nonstabilized bombesin derivatives exhibiting *in vivo* results as outlined in the Introduction which indicate that BBN(7−14) might be sufficiently stable for *in vivo* imaging applications.

For a convenient synthesis of Re '4 + 1' complex-conjugated peptides, active esters containing Re '4 + 1' complexes analogous to the complex structure of the ^{99m}Tc conjugates were prepared. They were obtained from [Re(NS$_3$)(PMe$_2$Ph)] by exchanging the monodentate phosphine with L1-BFCA or L2-BFCA (Scheme 4). In contrast to the free isocyanide-bearing peptides, standard RP-HPLC using TFA containing mobile phases is possible. The organometallic Re/Tc−C bond exhibits a high stability in strongly acidic media (*6*). The purity (≥95%) of the [Re(NS$_3$)(L−X−BBN(7−14))] conjugates was confirmed by HPLC. ESI-MS data obtained were consistent with the calculated molecular weights.

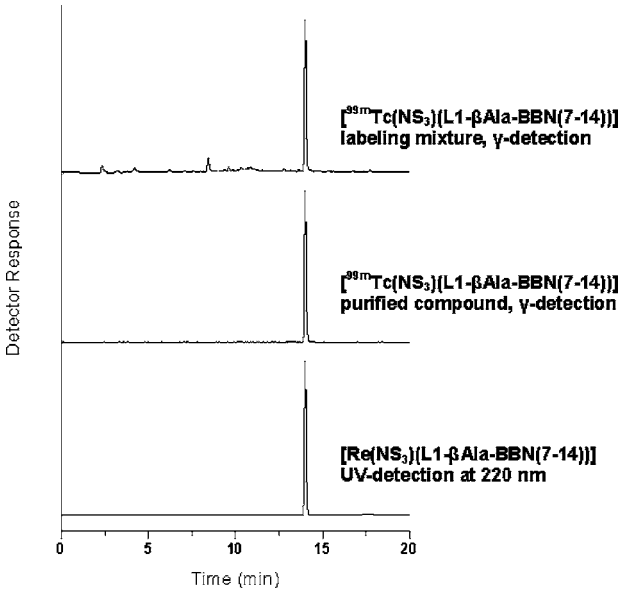


Figure 2. RP-HPLC (system 5) elution profiles of [^{99m}Tc(NS$_3$)(L1−βAla−BBN(7−14))] and [Re(NS$_3$)(L1−βAla−BBN(7−14))].

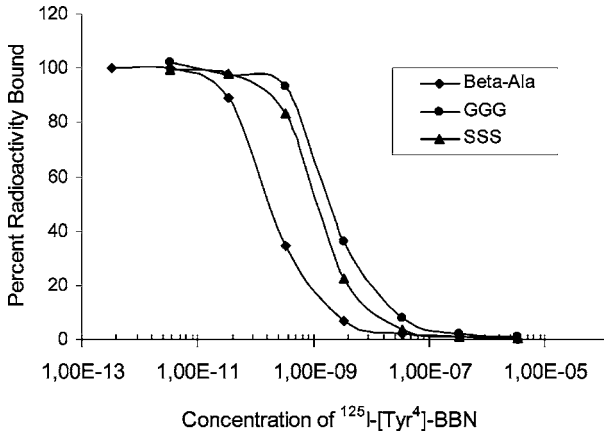


Figure 3. Displacement of ^{125}I-[Tyr^4]BBN by [Re(NS$_3$)(L1−X−BBN-(7−14))], X = βAla, GGG, SSS, from PC3 cells, n = 3.

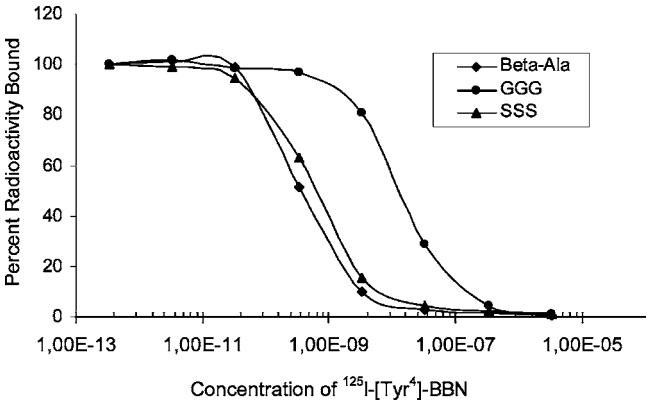


Figure 4. Displacement of ^{125}I-[Tyr^4]BBN by [Re(NS$_3$)(L2−X−BBN-(7−14))], X = βAla, GGG, SSS, from PC3 cells, n = 3.

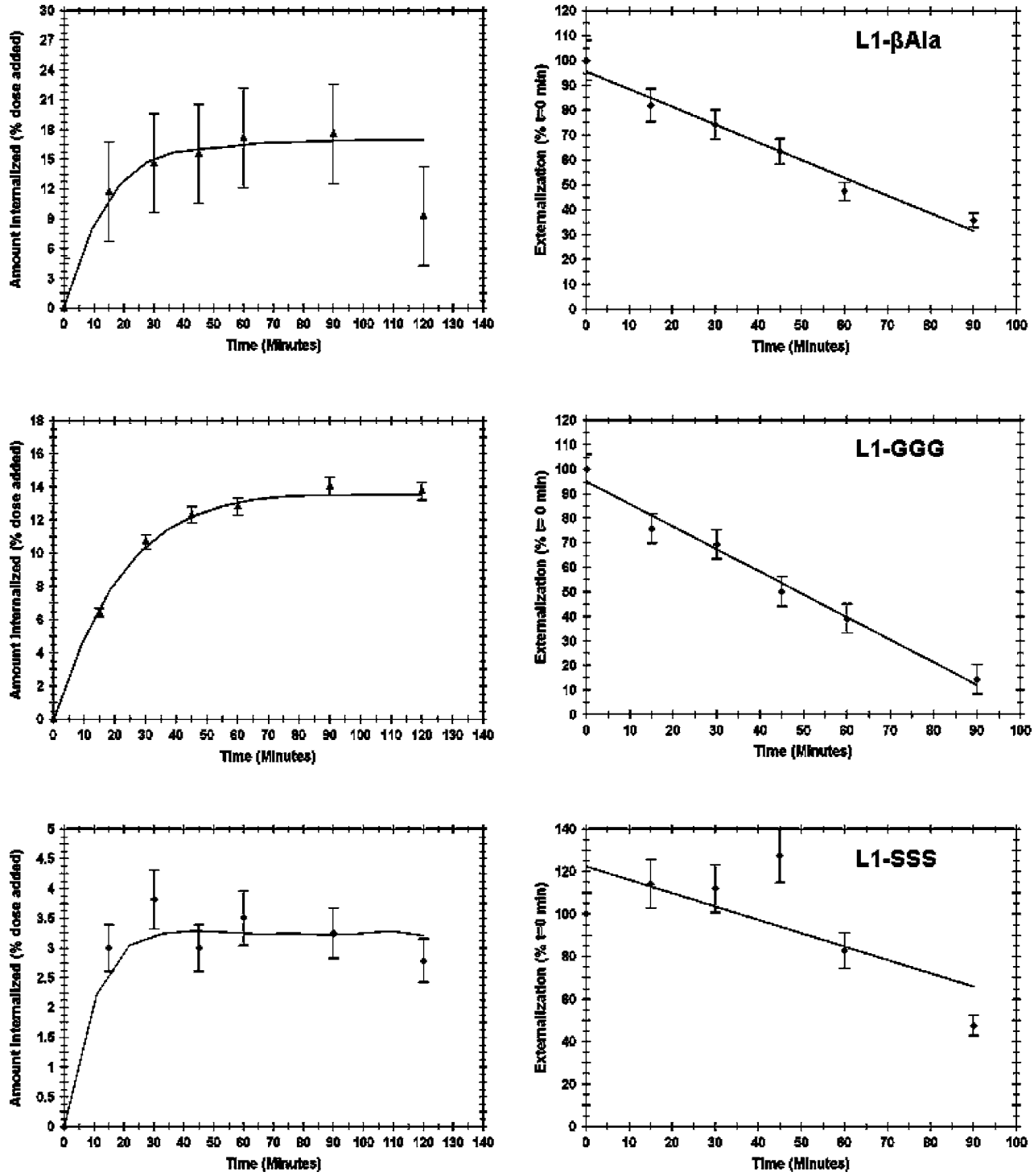


Figure 5. Internalization and externalization studies of [^{99m}Tc(NS$_3$)(L1−X−BBN(7−14))], X = βAla, GGG, SSS, using PC-3 cells.

Table 1. IC_{50} Values of [Re(NS$_3$)(L−X−BBN(7−14))] Obtained by Displacement of ^{125}I-[Tyr^4]BBN from PC-3 Cells, $n = 3$

Re '4 + 1' Conjugates	IC_{50} (nM)
[Re(NS$_3$)(L1-GGG-BBN(7−14))]	1.9 ± 0.4
[Re(NS$_3$)(L1-βAla-BBN(7−14))]	0.20 ± 0.04
[Re(NS$_3$)(L1-SSS−BBN(7−14))]	1.2 ± 0.1
[Re(NS$_3$)(L2-GGG-BBN(7−14))]	1.4 ± 0.1
[Re(NS$_3$)(L2-βAla-BBN(7−14))]	0.35 ± 0.03
[Re(NS$_3$)(L2-SSS−BBN(7−14))]	0.65 ± 0.32

Affinity of the [Re(NS$_3$)(L−X−BBN(7−14))] conjugates to GRP receptors overexpressed on PC-3 cells was determined by a competitive binding displacement assay (Figures 3 and 4). IC_{50} values, ranging from 0.20 ± 0.04 to 1.9 ± 0.4 nM, show low variation and indicate a high affinity for the GRPr for all of the new conjugates (Table 1). The spacer group βAla, in comparison with Gly-Gly-Gly or Ser-Ser-Ser, resulted in the highest receptor affinity. The aromatic or aliphatic isocyanides L1 or L2 did not cause a significant difference in receptor binding. The determined IC_{50} values are highly comparable to those previously reported for X−BBN(7−14), X = Gly-Gly-Gly, βAla, Ser-Ser-Ser, N-terminally bearing $[Re(CO)_3]^+$ moieties, or Re−N$_3$S complexes (*36*, *46*, *48*).

Figures 5 and 6 summarize the results of studies to assess the degree of uptake (internalization) and efflux (externalization) of the [^{99m}Tc(NS$_3$)(L−X−BBN(7−14))] conjugates in PC-3 cells. The significance of the internalization experiments was to demonstrate the agonist activity of the ^{99m}Tc conjugates.

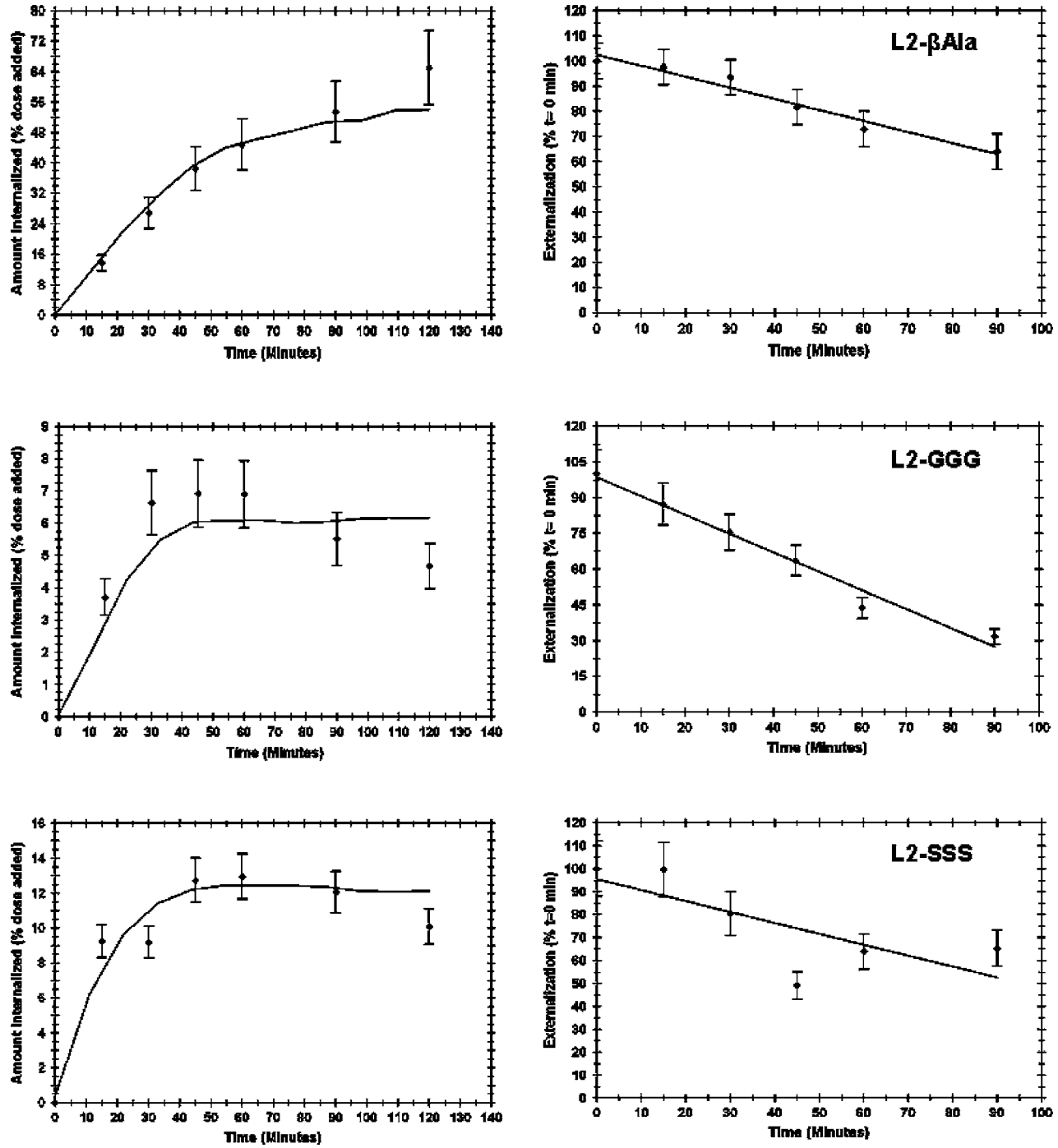


Figure 6. Internalization and externalization studies of [^{99m}Tc(NS$_3$)(L2−X−BBN(7−14))], X = βAla, GGG, SSS, using PC-3 cells.

Radioligands acting as agonists are inherently internalized into the cell, often resulting in prolonged activity within the cell. Of all the conjugates evaluated in this series, [^{99m}Tc(NS$_3$)(L2−βAla−BBN(7−14))] exhibited the highest degree of cellular uptake. Up to ∼65% of the total activity administered was internalized at 120 min. For all of the other conjugates, the maximum of internalized activity ranged from approximately 10% to 20% of the total activity administered between 60 and 80 min post incubation. The amount of internalized activity for these conjugates is comparable to (or slightly lower than) other metalated X−BBN(7−14) conjugates previously reported (*36*, *46*, *48*). To assess the externalization of ^{99m}Tc activity from PC-3 cells, at time point 45 min incubation, cells were washed with the pH 2.5 buffer to remove any surface-bound activity and then incubated in pH 7.4 media. Measurements up to 90 min incubation showed that ∼70% of the ^{99m}Tc activity for [^{99m}Tc(NS$_3$)(L2−βAla−BBN(7−14))] and ∼60% for [^{99m}Tc(NS$_3$)(L2−SSS−BBN(7−14))] remained trapped in the cells, whereas about 20−40% of the internalized ^{99m}Tc activity remained in the cells for the other [^{99m}Tc(NS$_3$)(L−X−BBN-(7−14))] conjugates. The externalization data for [^{99m}Tc(NS$_3$)-(L2−βAla−BBN(7−14))] and [^{99m}Tc(NS$_3$)(L2−SSS−BBN(7−14))] is comparable with previous studies of similar BBN(7−14) conjugates (*36*, *46*, *48*), whereas a lesser amount of ^{99m}Tc activity remained trapped in PC-3 cells for all of the other [^{99m}Tc(NS$_3$)(L−X−BBN(7−14))] conjugates as compared to previously published reports (*36*, *46*, *48*).

[^{99m}Tc(NS$_3$)(L−βAla−BBN(7−14))], L = L1 or L2, showed favorable *in vitro* receptor binding and cellular uptake/internalization in PC-3 cells and were selected as candidates from a [^{99m}Tc(NS$_3$)(L−X−BBN(7−14))] series for biodistribution studies in normal CF-1 mice. Analogous conjugates were

Table 2. Biodistribution of [^{99m}Tc(NS$_3$)(L1−βAla−BBN(7−14))], A; [^{99m}Tc(NS$_3$)(L2−βAla−BBN(7−14))], B; [^{99m}Tc(NS$_3$COOH)(L1−βAla−BBN(7−14))], C; [^{99m}Tc(NS$_3$COOH)(L2−βAla−BBN(7−14))], D; in Normal Mice (% ID/g ± SD, 1 h p.i., n = 4 or 5)

tissue/organ	A	B	C	D
blood	1.5 ± 0.3	1.4 ± 0.4	0.5 ± 0.4	1.7 ± 1.2
heart	1.2 ± 0.3	1.3 ± 0.5	0.2 ± 0.2	0.7 ± 0.2
lungs	2.4 ± 0.4	2.0 ± 0.6	0.4 ± 0.3	1.3 ± 0.6
liver	7.2 ± 1.8	8.3 ± 2.7	7.3 ± 4.0	9.4 ± 1.7
spleen	1.0 ± 0.4	0.8 ± 0.2	0.2 ± 0.1	0.9 ± 0.6
stomach	2.8 ± 1.4	1.0 ± 0.4	1.6 ± 0.6	3.3 ± 1.9
intestines	44.3 ± 6.4	39.3 ± 5.8	46.7 ± 10.0	40.5 ± 7.4
kidneys	3.0 ± 0.6	4.6 ± 1.7	1.8 ± 1.3	6.3 ± 3.5
pancreas	0.8 ± 0.1	1.9 ± 0.5	0.8 ± 0.18	1.6 ± 0.8
muscle	0.3 ± 0.2	0.4 ± 0.2	0.1 ± 0.1	0.2 ± 0.1

also evaluated where the NS_3 coligand was replaced by NS_3-COOH. The selection of the tetradentate coligand NS_3COOH bearing a pendant carboxyl group in comparison to NS_3 based on our previously published results showed that the introduction of the carboxyl group decreases the lipophilicity and the liver uptake of small '4 + 1' model complexes (*9*). Decreasing the lipophilicity of a ^{99m}Tc-labeled BBN derivative by introducing carboxyl groups via coupling of DTPA as a pharmacokinetic modifier was demonstrated by Lin et al. (*40*).

Results of the biodistribution studies in normal CF-1 mice are summarized in Table 2. There is minimal ^{99m}Tc activity uptake in the stomach, indicating that there is little or no *in vivo* dissociation of ^{99m}Tc from the ligands to produce $^{99m}TcO_4^-$. After 1 h i.v. administration, the compounds rapidly accumulated in the liver and were excreted *via* the intestines. Accumulation in the pancreas, an accessible tissue expressing the GRPr in high density, was very low. This can probably be attributed to rapid accumulation in liver and hepatobiliary excretion that decreases the concentration of the ^{99m}Tc conjugates in the blood pool, lessening the concentration of radiolabeled conjugate available for receptor uptake. Rapid hepatobilary excretion and the fact that there are only minimal differences between the biodistribution profiles for all of the compounds indicates that the biodistribution profiles are highly dominated by the '4 + 1' complex unit. These findings compared with the pharmacokinetic behavior of other ^{99m}Tc conjugates of the general type X−BBN(7−14), X = Gly-Gly-Gly, βAla, Ser-Ser-Ser (*36*, *46*, *48*), where renal/urinary excretion is the primary mode of elimination of conjugate from the body, suggests that the radiometal complex unit is significant for the biodistribution of these radiolabeled ^{99m}Tc conjugates. ^{99m}Tc conjugates of X−BBN(7−14), where X = βAla and 5-aminovaleric, 8-aminooctanoic, and 11-aminoundecanoic acid (*36*), have demonstrated a rise in lipophilic character associated with the increasing length of the linker. This results in an increased hepatobiliary elimination, whereas pancreatic uptake decreases. High lipophilic ^{99m}Tc conjugates of this series containing the 8- and 11-carbon atom spacer have a similar degree of hepatobiliary excretion compared to the ^{99m}Tc '4 + 1' conjugates described herein.

CONCLUSION

The work presented herein describes the preparation and characterization of novel BBN(7−14) conjugates bearing ^{99m}Tc/Re '4 + 1' complexes, so far only exemplarily assessed on peptides (*9*). The concept of isocyanide modification by bifunctional coupling agents as well as conjugation using Re '4 + 1' complex-bearing active esters proved to be very convenient for peptide modification. The '4 + 1' complex units conjugated *via* spacers to the BBN(7−14) N-terminus were well-tolerated by the GRP receptor. Using βAla as spacer compared to Gly-Gly-Gly and Ser-Ser-Ser resulted in slightly higher receptor binding affinity. In contrast to receptor binding assays, the '4 + 1' complex BBN(7−14) conjugates described herein showed greater variation with regard to PC-3 cell uptake and externalization. Here, only [^{99m}Tc(NS$_3$)(L2−βAla−BBN(7−14))] exhibited characteristics roughly comparable to previously reported BBN(7−14) conjugates (*36*, *46*, *48*). Biodistribution studies showed rapid hepatobiliary excretion of the conjugates, a likely cause of the low uptake in target-specific pancreatic tissue. The biodistribution profile is dominated by the '4 + 1' complex unit. In order to decrease the lipophilicity of the ^{99m}Tc complex unit, a carboxyl group was introduced onto the NS_3 chelate. This only slightly changed the biodistribution behavior of the conjugates, further indicating that more wide-ranging modifications of the '4 + 1' complex unit are necessary to produce site-directed conjugates of this general type. This should be facilitated by the bulk tolerance shown when attaching metal units *via* the N-terminus of BBN(7−14).

ACKNOWLEDGMENT

The authors would like to thank the University of Missouri−Columbia School of Medicine, Department of Radiology, for funding a working stay of J.-U. Kunstler at the University of Missouri−Columbia and the Harry S. Truman Memorial Veterans' Hospital. We would also like to acknowledge the University of Missouri−Columbia School of Medicine and the Harry S. Truman Memorial Veterans' Hospital for providing laboratory space and resources for completion of this work.

LITERATURE CITED

(1) Reubi, J. C. (2003) Peptide receptors as molecular targets for cancer diagnosis and therapy. *Endocr. Rev. 24*, 389−427.

(2) Reubi, J. C., Maecke, H. R., and Krenning, E. P. (2005) Candidates for peptide receptor radiotherapy today and in the future. *J. Nucl. Med. 46*, 67S−75S.

(3) Weiner, R. E., and Thakur, M. L. (2005) Radiolabeled peptides in oncology: role in diagnosis and treatment. *BioDrugs 19*, 145−163.

(4) Giblin, M. F., Veerendra, B., and Smith, C. J. (2005) Radiometallation of receptor-specific peptides for diagnosis and treatment of human cancer. *in vivo 19*, 9−30.

(5) Pietzsch, H.-J., Künstler, J.-U., and Spies, H. (2006) Technetium Coupled to Biologically Active Molecules. Technetium-99m Pharmaceuticals. *Preparation and Quality Control in Nuclear Medicine* (Zolle, I., Ed.) Chapter 2.3, pp 40−58, Springer, Berlin.

(6) Spies, H., Glaser, M., Pietzsch, H.-J., Hahn, F. E., and Lügger, T. (1995) Synthesis and reactions of trigonal-bipyramidal rhenium and technetium complexes with a tripodal, tetradentate NS_3 ligand. *Inorg. Chim. Acta 240* 465−478.

(7) Pietzsch, H.-J., Gupta, A., Syhre, R., Leibnitz, P., and Spies, H. (2001) Mixes-ligand technetium(III) complexes with tetradentate/monodentate NS_3/isocyanide coordination: a new nonpolar technetium chelate system for the design of neutral and lipophilic complexes stable in vivo. *Bioconjugate Chem. 12*, 538−544.

(8) Drews, A., Pietzsch, H.-J., Syhre, R., Seifert, S., Varnäs, K., Hall, H., Halldin, C., Kraus, W., Karlsson, P., Johnssom, C., Spies, H., and Johannsen, B. (2002) Synthesis and biological evaluation of technetium(III) mixed-ligand complexes with high affinity for the cerebral 5-HT_{1A} receptor and the alpha1-adrenergic receptor. *Nucl. Med. Biol. 29*, 389−398.

(9) Seifert, S., Künstler, J.-U., Schiller, E., Pietzsch, H.-J., Pawelke, B., Bergmann, R., and Spies, H. (2004) Novel procedures for preparing ^{99m}Tc(III) complexes with tetradentate/monodentate coordination of varying lipophilicity and adaptation to ^{188}Re analogues. *Bioconjugate Chem. 15*, 856−863.

(10) Schiller, E., Seifert, S., Tisato, F., Refosco, F., Kraus, W., Spies, H., and Pietzsch, H.-J. (2005) Mixed-ligand rhenium-188 complexes with tetradentate/monodentate NS_3/P ('4+1') coordination: relation of structure with antioxidation stability. *Bioconjugate Chem. 16*, 634−643.

(11) Walther, M., Jung, C. M., Bergmann, R., Pietzsch, J., Rode, K., Fahmy, K., Mirtschink, P., Stehr, S., Heintz, A., Wunderlich, G., Kraus, W., Pietzsch, H.-J., Kropp, J., Deussen, A., and Spies, H. (2007) Synthesis and biological evaluation of a new type of ^{99m}technetium-labeled fatty acid for myocardial metabolism imaging. *Bioconjugate Chem. 18*, 216−230.

(12) Smith, C. J., Volkert, W. A., and Hoffman, T. J. (2003) Gastrin releasing peptide (GRP) receptor targeted radiopharmaceuticals: A concise update. *Nucl. Med. Biol. 30*, 861−868.

(13) Smith, C. J., Volkert, W. A., and Hoffman, T. J. (2005) Radiolabeled peptide conjugates for targeting of the bombesin receptor superfamily subtypes. *Nucl. Med. Biol. 32*, 733−740.

(14) Rogers, B. E., Bigott, H. M., McCarthy, D. W., Manna, D. D., Kim, J., Sharp, T. L., and Welch, M. J. (2003) MicroPET Imaging of a gastrin-releasing peptide receptor-positive tumor in a mouse model of human prostate cancer using a ^{64}Cu-labeled bombesin analogue. *Bioconjugate Chem. 14*, 756−763.

(15) Chen, X., Park, R., Hou, Y., Tohme, M., Shahinian, A. H., Bading, J. R., and Conti, P. S. (2004) MicroPET and autoradiographic imaging of GRP receptor expression with ^{64}Cu-DOTA-[Lys^3]-bombesin in human prostate adenocarcinoma xenografts. *J. Nucl. Med. 45*, 1390−1397.

(16) Parry, J. J., Andrews, R., and Rogers, B. E. (2007) MicroPET imaging of breast cancer using radiolabeled bombesin analogs targeting the gastrin-releasing peptide receptor. *Breast Cancer Res. Treat. 101*, 175−183.

(17) Yang, Y.-S., Zhang, X., Xiong, Z., and Chen, X. (2006) Comparative in vitro and in vivo evaluation of two ^{64}Cu-labeled bombesin analogs in a mouse model of human prostate adenocarcinoma. *Nucl. Med. Biol. 33*, 371−380.

(18) Zhang, X., Cai, W., Cao, F., Schreibmann, E., Wu, Y., Wu, J. C., Xing, L., and Chen, X. (2006) ^{18}F-labeled bombesin analogs for targeting GRP receptor-expressing prostate cancer. *J. Nucl. Med. 47*, 492−501.

(19) Meyer, G.-J., Mäcke, H., Schuhmacher, J., Knapp, W. H., and Hofmann, M. (2004) ^{68}Ga-labelled DOTA-derivatised peptide ligands. *Eur. J. Nucl. Med. 31*, 1097−1104.

(20) Schuhmacher, J., Zhang, H., Doll, J., Mäcke, H. R., Matys, R., Hauser, H., Henze, M., Haberkorn, U., and Eisenhut, M. (2005) GRP receptor-targeted PET of rat pancreas carcinoma xenograft in nude mice with a ^{68}Ga-labeled bombesin(6−14) analog. *J. Nucl. Med. 46*, 691−699.

(21) Rogers, B. E., Rosenfeld, M. E., Khazaeli, M. B., Mikheeva, G., Stackhouse, M. A., Liu, T., Curiel, D. T., and Buchsbaum, D. J. (1997) Localization of iodine-125 mIP-Des-Met14-bombesin(7−13) NH_2 in ovarian carcinoma induced to express the gastrin releasing peptide receptor by adenoviral vector-mediated gene transfer. *J. Nucl. Med. 38*, 1221−1229.

(22) Rogers, B. E., Curiel, D. T, Mayo, M. S., Laffoon, K. K., Bright, S. J., and Buchsbaum, D. J. (1997) Tumor localization of a radiolabeled bombesin analogue in mice bearing human ovarian tumors induced to express the gastrin-releasing peptide receptor by an adenoviral vector. *Cancer 89* (12 Suppl), 2419−2424.

(23) Reubi, J. C., Wenger, S., Schmuckli-Maurer, J., Schaer, J. C., and Gugger, M. (2002) Bombesin receptor subtypes in human cancers: detection with the universal radioligand ^{125}I-[D-TYR^6, β-ALA^{11}, PHE^{13}, NLE^{14}] bombesin(6−14). *Clin. Cancer Res. 8*, 1139−1146.

(24) Hoffman, T. J., Gali, H., Smith, C. J., Sieckman, G. L., Hayes, D. L., Owen, N. K., and Volkert, W. A. (2003) Novel series of ^{111}In-labeled bombesin analogs as potential radiopharmaceuticals for specific targeting of gastrin-releasing peptide receptors expressed on human prostate cancer cells. *J. Nucl. Med. 44*, 823−831.

(25) Zhang, H., Chen, J., Waldherr, C., Hinni, K., Waser, B., Reubi, J. C., and Maecke, H. R. (2004) Synthesis and evaluation of bombesin derivatives on the basis of pan-bombesin peptides labeled with indium-111, lutetium-177, and yttrium-90 for targeting bombesin receptor-expressing tumors. *Cancer Res. 64*, 6707−6715.

(26) Maina, T., Nock, B. A., Zhang, H., Nikolopoulou, A., Waser, B., Reubi, J.-C., and Maecke, H. R. (2005) Species differences of bombesin analog interactions with GRP-R define the choice of animal models in the development of GRP-R-targeting drugs. *J. Nucl. Med. 46*, 823−830.

(27) Smith, C. J., Gali, H., Sieckman, G. L., Hayes, D. L., Owen, N. K., Mazuru, D. G., Volkert, W. A., and Hoffman, T. J. (2003) Radiochemical investigations of ^{177}Lu-DOTA-8-Aoc-BBN[7−14]-NH_2: an in vitro/in vivo assessment of the targeting ability of this new radiopharmaceutical for PC-3 human prostate cancer cells. *Nucl. Med. Biol. 30*, 101−109.

(28) Waser, B., Eltschinger, V., Linder, K., Nunn, A., and Reubi, J. C. (2007) Selective in vitro targeting of GRP and NMB receptors in human tumours with the new bombesin tracer ^{177}Lu-AMBA. *Eur. J. Nucl. Med. 34*, 95−100.

(29) Lantry, L. E., Cappelletti, E., Maddalena, M. E., Fox, J. S., Feng, W., Chen, J., Thomas, R., Eaton, S. M., Bogdan, N. J., Arunachalam, T., Reubi, J. C., Raju, N., Metcalfe, E. C., Luttuada, L., Linder, K. E., Swenson, R. E., Tweedle, M. F., and Nunn, A. D. (2006) ^{177}Lu-AMBA: synthesis and characterization of a selective ^{177}Lu-Labeled GRP-R agonist for systemic radiotherapy of prostate cancer. *J. Nucl. Med. 47*, 1144−1152.

(30) Safavy, A., Khazaeli, M. B., Qin, H., and Buchsbaum, D. J. (1997) synthesis of bombesin analogues for radiolabeling with rhenium-188. *Cancer 89* (12 Suppl), 2354−2359.

(31) Smith, C. J., Sieckman, G. L., Owen, N. K., Hayes, D. l., Mazuru, D. G., Volkert, W. A., and Hoffman, T. J. (2003) Radiochemical Investigation of [^{188}Re(H_2O)(CO)$_3$-diaminopropionic acid-SSS-bombesin(7−14)NH_2]: syntheses, radiolabeling and *in vitro/ in vivo* grp receptor targeting studies. *Anticancer Res. 23*, 63−70.

(32) Moustapha, M. E., Ehrhardt, G. J., Smith, C. J., Szajek, L. P., Eckelman, W. C., and Jurisson, S. S. (2006) Preparation of cyclotron-produced ^{186}Re and comparison with reactor-produced ^{186}Re and generator-produced ^{188}Re for the labeling of bombesin. *Nucl. Med. Biol. 33*, 81−89.

(33) Jurisson, S. S., and Lydon, J. D. (1999) Potential technetium small molecule radiopharmaceuticals. *Chem. Rev. 99*, 2205−2218.

(34) Van de Wiele, C., Dumont, F., Broecke, R. V., Oosterlinck, W., Cocquyl, V., Serreyn, R., Peers, S., Thornback, J., Slegers, G., and Dierckx, R. A. (2000) Technetium-99m RP527, a GRP analogue for visualisation of GRP receptor-expressing malignancies: a feasibility study. *Eur. J. Nucl. Med. 27*, 1694−1699.

(35) Van de Wiele, C., Dumont, F., Dierckx, R. A., Peers, S. H., Thornback, J. R., Slegers, G., and Thierens, H. (2001) Biodistribution and dosimetry of ^{99m}Tc-RP527, a gastrin-releasing peptide (GRP) agonist for the visualization of GRP receptor-expressing malignancies. *J. Nucl. Med. 42*, 1722−1727.

(36) Smith, C. J., Gali, H., Sieckman, G. L., Higginbotham, C., Volkert, W. A., and Hoffman, T. J. (2003) Radiochemical investigations of ^{99m}Tcc-N_3S-X-BBN[7−14]NH_2: an in vitro/in vivo structure-activity relationship study where X = 0-, 3-, 5-, 8-, and 11-carbon tethering moieties. *Bioconjugate Chem. 14*, 93−102.

(37) Block, D., Feitsma, H. I. J., Kooy, Y. M. C., Welling, M. M., Ossendorp, F., Vermeij, P., and Drijfhout, J. W. (2004) New chelation strategy allows for quick and clean ^{99m}Tc-labeling of synthetic peptide. *Nucl. Med. Biol. 31*, 815−820.

(38) Baidoo, K., E., Lin, K.-S., Zhan, Y., Finley, P., Scheffel, U., and Wagner, H. N., Jr. (1998) Design, synthesis, and initial evaluation of high-affinity technetium bombesin analogues. *Bioconjugate Chem. 9*, 218−225.

(39) Lin, K.-S., Luu, A., Baidoo, K. E., Hashemzadeh-Gargari, H., Chen, M.-K., Pili, R., Pomper, M., Carducci, M., and Wagner, H. N., Jr. (2004) A new high affinity technetium analogue of bombesin containing DTPA as a pharmacokinetic modifier. *Bioconjugate Chem. 15*, 1416−1423.

(40) Lin, K.-S., Luu, A., Baidoo, K. E., Hashemzadeh-Gargari, H., Chen, M.-K., Brenneman, K., Pili, R., Pomper, M., Carducci, M. A., and Wagner, H. N., Jr. (2005) A new high affinity technetium-99m-bombesin analogue with low abdominal accumulation. *Bioconjugate Chem. 16*, 43−50.

(41) Nock, B., Nikolopoulou, A., Chiotellis, E., Loudos, G., Maintas, D., Reubi, J. C., and Maina, T. (2003) [^{99m}Tc]Demobesin 1, a novel potent bombesin analogue for GRP receptor-targeted tumour imaging. *Eur. J. Nucl. Med. 30*, 247−258.

(42) Nock, B. A., Nikolopoulou, A., Galanis, A., Cordopatis, P., Waser, B., Reubi, J.-C., and Maina, T. (2005) Potent bombesin-like peptides for GRP-receptor targeting of tumors with ^{99m}Tc: a preclinical study. *J. Med. Chem. 48*, 100−110.

(43) Karra, S. R., Schibli, R., Gali, H., Katti, K. V., Hoffman, T. J., Higginbotham, C., Sieckman, G. L., and Volkert, W. A. (1999) ^{99m}Tc-labeling and in vivo studies of a bombesin analogue with a

novelwater-soluble dithiadiphosphine-based bifunctional chelating agent. *Bioconjugate Chem. 10,* 254−260.

(44) La Bella, R., Garcia-Garayoa, E., Bähler, M., Bläuenstein, P., Schibli, R., Conrath, P., Tourwé, D., and Schubiger, P. A. (2002) A ^{99m}Tc(I)-postlabeled high affinity bombesin analogue as a potential tumor imaging agent. *Bioconjugate Chem. 13,* 599−604.

(45) La Bella, R., Garcia-Garayoa, E., Langer, M., Bläuenstein, P., Beck-Sickinger, A. G., and Schubiger, P. A. (2002) *In vitro* and *in vivo* evaluation of a ^{99m}Tc(I)-labeled bombesin analogue for imaging of gastrin releasing peptide receptor-positive tumors. *Nucl. Med. Biol. 29,* 553−560.

(46) Smith, C. J., Sieckman, G. L., Owen, N. K., Hayes, D. L., Mazuru, D. G., Kannan, R., Volkert, W. A., and Hoffman, T. J. (2003) Radiochemical investigations of gastrin-releasing peptide receptor-specific [^{99m}Tc(X)$(CO)_3$-Dpr-Ser-Ser-Ser-Gln-Trp-Ala-Val-Gly-His-Leu-Met-(NH_2)] in PC-3, tumor-bearing, rodent models: syntheses, radiolabeling, and *in vitro/in vivo* studies where Dpr = 2,3-diaminopropionic acid and X = H_2O or $P(CH_2OH)_3$. *Cancer Res. 63,* 4082−4088.

(47) Bläuenstein, P., García-Garayoa, E. G., Rüegg, D., Blanc, A., Tourwé. D., Beck-Sickinger, A., and Schubiger, P. A. (2004) Improving the tumor uptake of ^{99m}Tc-labeled neuropeptides using stabilized peptide analogues. *Cancer. Biother. Radiopharm. 19,* 181−188.

(48) Alves, S., Paulo, A., Correia, J. D. G., Gano, L., Smith, C. J., Hoffman, T. J., and Santos, I. (2005) Pyrazolyl derivatives as bifunctional chelators for labeling tumor-seeking peptides with the *fac*-$[M(CO)_3]^+$ moiety (M= ^{99m}Tc, Re): synthesis, characterization, and biological behavior. *Bioconjugate Chem. 16,* 438−449.

(49) Gourni, E., Paravatou, M., Bouziotis, P., Zikos, C., Fani, M., Xanthopoulos, S., Archimandritis, S. C., Livaniou, E., and Varvarigou, A. D. (2006) Evaluation of a series of new ^{99m}Tc-labeled bombesin-like peptides for early cancer detection. *Anticancer Res. 26,* 435−438.

(50) Appel, R., Kleinstück, R., and Ziehn, K.-D. (1971) New preparation of isocyanides. *Angew. Chem., Int. Ed. 10,* 132.

BC700197M

Design of Aminated Poly(1-vinylimidazole) for a New pH-Sensitive Polycation To Enhance Cell-Specific Gene Delivery

Shoichiro Asayama,* Takashi Sekine, Hiroyoshi Kawakami, and Shoji Nagaoka

Department of Applied Chemistry, Tokyo Metropolitan University, 1-1 Minami-Osawa, Hachioji, Tokyo 192-0397, Japan
Received June 7, 2007; Revised Manuscript Received July 24, 2007

Poly(1-vinylimidazole) (PVIm) with aminoethyl groups has been synthesized as a new pH-sensitive polycation to enhance cell-specific gene delivery. The resulting aminated PVIm (PVIm-NH_2) was water-soluble despite deprotonation of the imidazole groups at physiological pH, as determined by acid−base titration and solution turbidity measurement. Hemolysis assay showed that PVIm-NH_2 enhanced membrane disruptive ability at endosomal pH, owing to the protonation of the imidazole groups with a pK_a value around 6.0. Agarose gel retardation assay proved that the introduced aminoethyl groups worked as anchor groups to retain DNA. Furthermore, the ternary complex of DNA, PVIm-NH_2, and a poly(L-lysine) conjugated with lactose molecules, PLL-Lac, at pH 7.4 dissociated the PLL-Lac polycation by protonation of the imidazole groups of PVIm-NH_2 at pH 6.0. The resulting PVIm-NH_2/DNA binary complexes easily released DNA, as compared with the PLL-Lac/PVIm-NH_2/DNA ternary complex, which was examined by competitive exchange with dextran sulfate. By using PVIm-NH_2 as a pH-sensitive DNA carrier, as well as PLL-Lac as a cell-targeting DNA carrier, the resulting ternary complex specifically mediated the gene expression, which depended on the protonation of the imidazole groups, on human hepatoma HepG2 cells with asialoglycoprotein receptors. These results suggest that the cell-specific gene delivery mediated by PLL-Lac was enhanced by PVIm-NH_2 as a new pH-sensitive polycation.

INTRODUCTION

In gene delivery systems, the formation of DNA−carrier polyion complexes is a key factor for new designs of efficient delivery (*1*−*3*). The carrier design typically focuses on the ability of a ligand to bind tightly to its target. The ligand−receptor complexes on the cell plasma membrane are internalized into acidic endosomal vesicles, where they are subjected to a significant pH change from pH 7 to 5 (*4*). Subsequently, the targeting ligands are routed to the degradation in the acidic compartment following endosomal vesicles or are recycled to the cell surface (*5*). Such fate of ligands leads us to create the DNA−polyion complexes dissociating ligand molecules in response to pH. In general, targeting ligands are unnecessary to make DNA complexes escape from endosomal vesicles. The endosomal escape is one of the critical factors for efficient gene delivery. If the carrier stably retains DNA during the delivery to the target site and easily releases DNA after the escape from endosomal vesicles, gene delivery is expected to be more efficient. Therefore, we have designed a DNA ternary complex, with a pH-sensitive and ligand polycation, that stably retains DNA at physiological pH and dissociates the ligand polycation in response to endosomal pH. The resulting DNA binary complex is expected to promote the endosomal escape by the physicochemical/biochemical properties of the pH-sensitive polycation and the DNA release by the easier competitive exchange with anionic biomacromolecules than shown by the ternary complex.

Recently, pH-sensitive polymers such as poly(ethylenimine) (PEI[1]), which is able to capture protons entering an endosome, have been used to achieve efficient release of the delivered material from endosomes (*6*−*8*). PEI induces swelling of the endosomes that leads to membrane disruption, that is, the proton sponge effect. On the other hand, we have already reported the biphasic polycation (*9*) consisting of a poly(1-vinylimidazole) (PVIm) backbone and lactosylated poly(L-lysine) (PLL-Lac) side chains as a DNA carrier with a proton-buffering effect at endosomal pH (*10*). Furthermore, we have already synthesized poly(L-histidine) with several aminoethyl groups, that is, aminated poly(L-histidine) (PLH-NH_2), to make complexes with DNA (*11*, *12*). The protonation of imidazole groups of the resulting PLH-NH_2 at pH 6.0 has triggered the dissociation of PLL-Lac from the PLL-Lac/PLH-NH_2/DNA ternary complex (*13*). Although pH-sensitive ternary complexes such as imidazole-containing polyhistidine/polylysine-transferrin/DNA complexes (*14*) are reported (*15*), our concept that DNA ternary complexes dissociate ligand polycations in response to endosomal pH, resulting in DNA binary complexes, has no precedent, to the best of our knowledge. However, neither biphasic polycation nor PLH-NH_2 exhibited significant transfection activity.

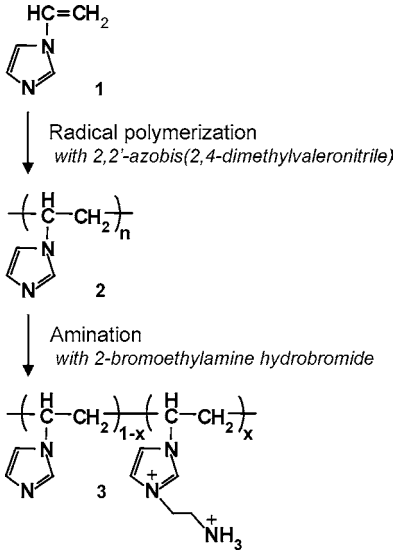
In this study, to realize efficient gene expression, we have designed PVIm with several aminoethyl groups, that is, "aminated PVIm" (PVIm-NH_2), by extracting the advantages of both the biphasic polycation and PLH-NH_2. PVIm is a water-soluble homopolymer possessing many imidazole groups with a pK_a around 6.0. Despite a large capacity for H^+ buffering at endosomal pH, PVIm has difficulty in forming complexes with DNA at physiological pH because its imidazole groups are negligibly charged at pH 7.4. The introduced aminoethyl groups with a pK_a around 10 are expected to work as anchor groups to retain DNA. The DNA ternary complex with the resulting

* Author to whom correspondence should be addressed (telephone +81-426-77-1111, ext. 4975; fax +81-426-77-2821; e-mail asayama-shoichiro@c.metro-u.ac.jp).

[1] Abbreviations: PEI, poly(ethylenimine); PVIm, poly(1-vinylimidazole); PLL-Lac, lactosylated poly(L-lysine); PLH-NH_2, aminated poly(L-histidine); PVIm-NH_2, aminated poly(1-vinylimidazole); ASGP-R, asialoglycoprotein receptor; VIm, 1-vinylimidazole; V-65, 2,2′-azobis(2,4-dimethylvaleronitrile); FITC, fluorescein isothiocyanate; GFC, gel filtration chromatography; FBS, fetal bovine serum; EtBr, ethidium bromide; PLL, poly(L-lysine); RLU, relative light unit; DS, dextran sulfate.

10.1021/bc700205t CCC: $37.00 © 2007 American Chemical Society
Published on Web 08/25/2007

Scheme 1. Synthesis of Aminated Poly(1-vinylimidazole)



PVIm-NH_2 and PLL-Lac, the β-galactose residues of which are ligands for an asialoglycoprotein receptor (ASGP-R) expressed on hepatocytes or hepatoma cells (*16*), is therefore expected to dissociate the PLL-Lac ligand polycation at endosomal pH. Consequently, PVIm-NH_2 as a pH-sensitive polycation promises to enhance the cell-specific gene delivery mediated by the PLL-Lac as a ligand polycation.

EXPERIMENTAL PROCEDURES

Materials. 1-Vinylimidazole (VIm) was purchased from Aldrich Chemical Co. (Milwaukee, WI) and was distilled under reduced pressure. 2,2′-Azobis(2,4-dimethylvaleronitrile) (V-65) was purchased from Wako Pure Chemical Industries, Ltd. (Osaka, Japan) and was recrystallized from ethanol. 2-Bromoethylamine hydrobromide was purchased from Kanto Chemical Co., Inc. (Tokyo, Japan). PEI solution, salmon testis deoxyribonucleic acid (DNA) sodium salt, and fluorescein isothiocyanate (FITC) isomer I were from Sigma Chemical Co. (St. Louis, MO). All other chemicals of a special grade were used without further purification.

Synthesis of PVIm-NH_2. The synthetic route to PVIm-NH_2 is shown in Scheme 1. VIm (**1**) (300 μL) and V-65 (15.8 mg) as an initiator were dissolved in 2.7 mL of *N*,*N*-dimethylformamide. Radical polymerization reaction was carried out for 2 h at 45 °C. After the reaction, the content was poured into a large excess of acetone, and the precipitate was dried in vacuo. The resulting polymer (**2**) (25 mg) and 2-bromoethylamine hydrobromide (3.75 g) were dissolved in 12.5 mL of dimethyl sulfoxide. The reaction mixture was incubated at 40 °C for 5 days, followed by dialysis against distilled water using a Spectra/Por 7 membrane (molecular weight cutoff = 10^3) to remove unreacted 2-bromoethylamine. The resulting polymer (**3**) was obtained by freeze-drying.

Gel Filtration Chromatography (GFC). GFC was carried out using a JASCO PU-980 pumping system (Tokyo, Japan) at the flow rate of 1.0 mL/min with a Shodex OHpak SB-804 HQ column (Showa Denko K.K., Tokyo, Japan). The aqueous solution containing 0.5 M CH_3COOH and 0.2 M $NaNO_3$ was used as a mobile phase. One hundred microliters of a 1 mg/mL sample was injected into the column. Eluate was detected by a refractive index detector (RI-1530, JASCO). Calibration was made with polyethylene glycol standards.

^{1}H NMR Spectroscopy. Each polymer (3 mg) was dissolved in 700 μL of D_2O (99.8 atom % deuterium; Acros). The ^{1}H NMR spectra (400 MHz) were obtained by a JEOL JNM-AL400 spectrometer (Tokyo, Japan).

Acid−Base Titration and Turbidity Measurement of PVIm-NH_2. To 1.5 mL of an aqueous solution of the polymer (3.3 mg/mL) was added a 1 M NaOH solution, and the basic polymer solution (pH 10) was titrated with a 1 M HCl solution. The pH value was checked with a pH-meter (model F-52T, Horiba, Kyoto, Japan). The titration was carried out by the stepwise addition of 1 M HCl and stopped at pH 3.5. The turbidity of the solution during the titration was measured by monitoring the absorbance at 500 nm with a spectrophotometer (model Ubest-55, JASCO, Tokyo, Japan).

Assay for the Interaction between PVIm-NH_2 and Serum Protein. The mixture of PVIm-NH_2 (0.5 mg/mL) and 50% heat-inactivated fetal bovine serum (FBS) was incubated at 37 °C. As a control, PEI (0.5 mg/mL) was used. The turbidity of the solution during the incubation was measured by monitoring the absorbance at 700 nm.

Hemolysis Assay. The stock solution (10 mg/mL) of PVIm-NH_2 was diluted to 670 μg/mL with 10 mM sodium phosphate buffer (pH 7.4, 6.0, or 5.0) containing 130 mM NaCl. Then, 150 μL of the polymer solution was incubated with 20 μL of sheep preserved blood (Cosmo Bio Co., Ltd., Tokyo, Japan) for 90 mim at 37 °C. After centrifugation (13000 rpm, 1 min, 4 °C), the released hemoglobin was determined by measuring the absorbance at 577 nm of the 10-fold diluted supernatant.

Agarose Gel Retardation Assay. Salmon testis DNA was dissolved in PBS (−) at 0.9 mg/mL. The resulting DNA stock solution was added to the polymer solutions in 50 mM sodium phosphate buffer (pH 7.5 or 6.0) at various polymer/DNA ratios. The final diluted concentration of DNA was adjusted to 60 μg/mL. After 30 min of incubation at room temperature, each sample (corresponding to 0.6 μg of DNA) was mixed with a loading buffer and loaded onto a 1% agarose gel containing 1 μg/mL of ethidium bromide (EtBr). Gel electrophoresis was run at room temperature in 50 mM sodium phosphate buffer (pH 7.5 or 6.0) at 50 V for 15 min. The DNA bands were visualized under UV irradiation.

Synthesis of PLL-Lac. Poly(L-lysine) (PLL) hydrobromide (50 mg; number-average degree of polymerization = 266) and lactose monohydrate (288 mg) were preincubated at 37 °C for 3 days in 7.5 mL of sodium borate buffer (0.1 M, pH 8.5) (*17*). Then, a reducing agent, $NaBH_3CN$, was added to the mixture of PLL and lactose in 10 mL of the sodium borate buffer at a final concentration of 0.3 M. The reaction mixture was incubated at 37 °C for 3 days. The degree of amino group modification (approximately 100 mol %) was examined by the primary amino group determination with fluorescamine (*18*). The reaction mixture was dialyzed against distilled water using a Spectra/Por 7 membrane (molecular weight cutoff = 10^3) to remove unreacted lactose, followed by freeze-drying. For fluorescent labeling, the resulting PLL-Lac (10 mg) and FITC isomer I (1 mg) were dissolved in 1.1 mL of 10 mM K_2CO_3. The reaction mixture was incubated at room temperature for 2 h, followed by dialysis against distilled water using a Spectra/Por 7 membrane (molecular weight cutoff = 10^3) to remove unreacted FITC. The resulting polypeptide was obtained by freeze-drying.

Cell Viability Assay. HepG2 cells (a gift from the Japan Health Sciences Foundation), human hepatoma cell line, were cultured in tissue culture flasks containing Dulbecco's modified Eagle's medium supplemented with 10% heat-inactivated FBS. The cells were seeded at 1×10^4 cells/well in a 96-well plate and incubated overnight at 37 °C in a 5% CO_2 incubator. The cells were treated with each polymer (0−400 μg/mL) and incubated for 24 h at 37 °C. By further incubation for 4 h, the cell viability was measured using the Alamar Blue assay (*19*) in triplicate.

Transfection Procedure. In a typical 96-well plate experiment, 1×10^4 cells/well HepG2 cells were transfected in

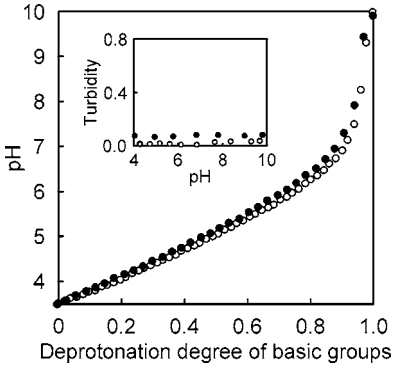


Figure 1. Acid−base titration curves of polymers: (●) PVIm-NH_2; (○) PVIm. Basic polymer solutions were titrated with the stepwise addition of 1 M HCl. The horizontal axis is normalized as the deprotonation degree based on the total basic groups of each polymer. The deprotonation degree indicates the ratio of the amount of deprotonated basic groups to that of total basic groups at the indicated pH. (Inset) Effect of pH on the solubility of the polymers in water (3.3 mg/mL): (●) PVIm-NH_2; (○) PVIm. The turbidity was measured by monitoring the absorbance at 500 nm of the polymer aqueous solution during the acid−base titration.

Dulbecco's modified Eagle's medium supplemented with 10% heat-inactivated FBS by the addition of 15 μL of PBS (−) containing 200 ng of plasmid DNA encoding the modified firefly luciferase (pGL3-Control Vector; from Promega Co.) and complexed with polycations. After 1 day of incubation in the presence or absence of chloroquine at a 100 μM final concentration, the medium was removed and the cells were further incubated for 3 days in the Dulbecco's modified Eagle's medium supplemented with 10% FBS. Then, the cells were subjected to the luciferase assay (Promega kit) according to the manufacturer's instruction. Luciferase activities were normalized by protein concentrations and are presented as relative light units (RLU). Protein concentrations were determined by BCA protein assay kit (Pierce) according to the manufacturer's instruction.

RESULTS AND DISCUSSION

Synthesis of PVIm-NH_2. As shown in Scheme 1, PVIm (**2**) was reacted with 2-bromoethylamine hydrobromide for one-step introduction of amino groups. The GFC profile (results not shown) of the resulting polymer (**3**) indicated that unreacted 2-bromoethylamine reagents were removed by the purification process, including dialysis. The number-average molecular weight of the isolated polymer determined by GFC was about 8.1×10^3. The ^{1}H NMR spectrum of the resulting polymer showed the characteristic signals of both PVIm (*20*) [δ 1.8−2.2 (methylene), 2.3−3.7 (methine), 6.4−7.2 (imidazole)] and aminoethyl (δ 3.2−4.0) moieties. To examine whether the properties of imidazole and amino groups were preserved, we carried out the acid−base titration of the polymer solution, as shown in Figure 1. The imidazole protons of PVIm were gently dissociated around pH 6, whereas the resulting polymer exhibited slight dissociation around pH 10 as well as gentle dissociation around pH 6. The proton dissociation around pH 6 and 10 was attributed to that of imidazole and amino groups, respectively, of the resulting polymer. The slight dissociation of amino protons was almost consistent with the content (approximately 2.5 mol %) of introduced aminoethyl groups determined by the primary amino group determination with fluorescamine (*18*). Thus, we have synthesized PVIm with aminoethyl groups, that is, "PVIm-NH_2."

Physicochemical and Biochemical Properties of PVIm-NH_2. It should be noted that the aqueous solution of PVIm-NH_2 as well as that of PVIm exhibited no significant turbidity above pH 6 (Figure 1, inset). On the other hand, in our previous study, PLH-NH_2 exhibited precipitation above pH 6.0 owing to the deprotonation of the imidazole groups (*11*, *12*). In this study, PVIm-NH_2 was water-soluble despite the deprotonation of the imidazole groups. Therefore, we examined how the water solubility of PVIm-NH_2 influenced the solution stability in serum protein (FBS). No significant turbidity is observed during the incubation of PVIm-NH_2 with serum protein (results not shown). The aqueous solution of PEI as a control of pH-sensitive polymer (*6*−*8*), on the other hand, exhibits turbidity during the incubation with the serum. Because the water solubility of PVIm-NH_2 was probably sufficient, the polymers dispersed in the medium as colloidal particles without undergoing particle aggregation despite the possession of the cationic amino groups. However, the cationic PEI interacting with anionic serum protein presumably reduced the electrostatic repulsion among the colloidal particles, inducing particle aggregation to exhibit turbidity (*21*). These results suggest that no significant effect on a rapid aggregate formation of serum proteins is induced by PVIm-NH_2.

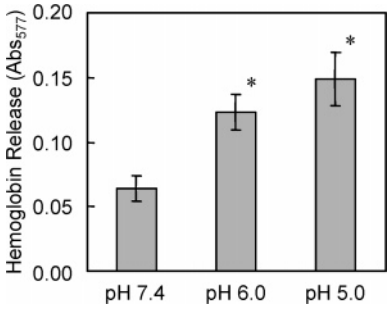


Figure 2. Effect of pH on the hemolytic activity of PVIm-NH_2. Erythrocytes were incubated with PVIm-NH_2 for 90 min at 37 °C in 10 mM sodium phosphate buffer (pH 7.4, 6.0, or 5.0) containing 130 mM NaCl. The released hemoglobin was determined by measuring the absorbance at 577 nm (Abs_{577}). The Abs_{577} at 100% hemolysis achieved with hypotonic treatment is 0.453 ± 0.065. Symbols and error bars represent the mean and standard deviation of the measurements made in paired samples ($n = 3$). ∗ indicates statistical significance ($p < 0.002$) when compared to the pH 7.4 value.

To examine the interaction of PVIm-NH_2 with real cell membranes, the effects on the hemolytic activity were investigated. As shown in Figure 2, PVIm-NH_2 caused negligible hemolysis at pH 7.5, whereas the hemolytic activity significantly increased at pH 6.0 as well as pH 5.0. These results suggest that the membrane disruptive ability of PVIm-NH_2 increased at endosomal pH. It is therefore expected that PVIm-NH_2 enhances the ability to escape from acidic endosomal vesicles.

Then, we examined whether PVIm-NH_2 formed the polyion complex with DNA by agarose gel electrophoresis. As shown in Figure 3, DNA was stained by EtBr, which was intercalated between base pairs of duplex DNA. The intercalation of EtBr increases the fluorescence, so that EtBr is effective for the detection of DNA (*22*). Each lane contains the same amount of DNA, and lanes 2−6 and lanes 2′−6′ contain increasing amounts of the unmodified PVIm (**2**) and the PVIm-NH_2 (**3**), respectively. Even in the presence of an excess amount of the unmodified PVIm at pH 7.4, most of the DNA migrated into the plus pole of the gel, which suggested that the DNA and PVIm exhibited no complex formation owing to the almost complete deprotonation of the imidazole groups (see Figure 1). In the case of PVIm-NH_2, on the other hand, the bands were retained at the origin when the DNA was mixed with an excess of PVIm-NH_2 (lanes 4′−6′). In particular, almost no free DNA was observed at the imidazole/phosphate ratio of 40 (lane 6′), which almost corresponded to the amino/phosphate ratio of 1. These results suggest that the PVIm-NH_2 formed the DNA complex at the stoichiometric charge ratio of DNA to introduced aminoethyl groups; that is, the introduced aminoethyl groups

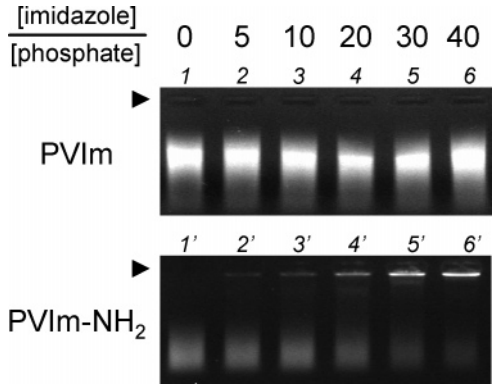


Figure 3. Analysis of the formation of the complex between DNA and the polymers by agarose gel electrophoresis; interaction of PVIm (lanes 1−6) or PVIm-NH_2 (lanes 1′−6′) with DNA: lanes 1 and 1′, DNA alone; lanes 2−6 and 2′−6′, DNA/polymer mixtures at different unit ratios relative to imidazole groups of polymer per phosphate group of DNA ([imidazole]/[phosphate]); lanes 2 and 2′, 5×; lanes 3 and 3′, 10×; lanes 4 and 4′, 20×; lanes 5 and 5′, 30×; lanes 6 and 6′, 40×. Solid arrowhead indicates the well where each sample was loaded.

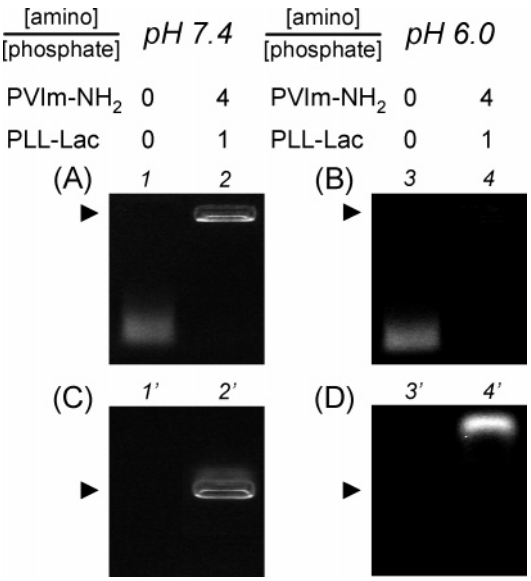


Figure 4. Analysis of the pH-dependent formation of PLL-Lac/PVIm-NH_2/DNA ternary complexes in the presence (A, B) or absence (C, D; where PLL-Lac was labeled with FITC) of EtBr: lanes 1, 1′, 3, and 3′, DNA alone; lanes 2, 2′, 4, and 4′, PLL-Lac/PVIm-NH_2/DNA mixtures, where the unit ratios relative to amino groups of PVIm-NH_2 and PLL-Lac per phosphate group of DNA ([amino]/[phosphate]) are 4 and 1, respectively. PLL-Lac/PVIm-NH_2/DNA mixtures were loaded at pH 7.4 (A, C) or pH 6.0 (B, D). Solid arrowhead indicates the well where each sample was loaded.

worked as anchor groups to retain DNA. Furthermore, the resulting complexes showed a significant fluorescence owing to EtBr staining. These results suggest that the DNA in the complex was not completely compacted (*23*). A similar observation was previously reported in the case of the soluble complexes between DNA and the polycation grafted with water-soluble polymer chains such as dextran (*24*). In this study, the nonionic PVIm backbone seems to solubilize the DNA complexes and to reduce DNA compaction at physiological pH.

pH-Dependent Dissociation of Carbohydrate Ligand Polycations from DNA Ternary Complexes. We have already reported the concept that DNA ternary complexes dissociate ligand polycations in response to endosomal pH (*13*). In this study, as shown in Figure 4, we examined the pH-dependent dissociation of PLL-Lac from the DNA ternary complexes with PLL-Lac and PVIm-NH_2 by agarose gel electrophoresis. At pH 7.4, the band was retained at the origin when DNA was mixed with PLL-Lac and PVIm-NH_2 ($[\text{amino group}]_{\text{PLL-Lac}}/[\text{phosphate group}]_{\text{DNA}} = 1$; $[\text{amino group}]_{\text{PVIm-NH2}}/[\text{phosphate group}]_{\text{DNA}} = 4$) (Figure 4A). It should be noted that the band retained at the origin at pH 7.4 disappeared at pH 6.0 (Figure 4B). These results suggest that the protonation of imidazole groups of PVIm-NH_2 at pH 6.0 induced the coil−globule transition of DNA and inhibited the EtBr intercalation (*22*, *25*).

In the above experiments, however, the formation of the polyion complex with PLL-Lac was unclear. Therefore, we labeled PLL-Lac with FITC and examined whether PLL-Lac formed the polyion complex with DNA by agarose gel electrophoresis in the absence of EtBr. At pH 7.4, the band was also retained at the origin (Figure 4C). It is therefore confirmed that PLL-Lac formed the polyion complex with DNA at pH 7.4; that is, DNA, PVIm-NH_2, and PLL-Lac formed ternary complexes at pH 7.4. At pH 6.0, on the other hand, it is worth noting that PLL-Lac migrated into the minus pole of the gel (Figure 4D). The migration into the minus pole suggests that the PLL-Lac polycation was dissociated from the DNA complex. Taking these results into account, PLL-Lac/PVIm-NH_2/DNA ternary complexes at pH 7.4 have dissociated the PLL-Lac polycations by the protonation of the imidazole groups of PVIm-NH_2 at pH 6.0, resulting in PVIm-NH_2/DNA binary complexes.

Stability of PVIm-NH_2/DNA Binary or PLL-Lac/PVIm-NH_2/DNA Ternary Complexes. The interaction between oppositely charged polyelectrolytes (polyions) is very strong, and the dissociation of the polyion complexes is unlikely under physiological ionic strength conditions. However, the DNA ternary complexes successfully dissociate ligand polycations in response to endosomal pH, resulting in DNA binary complexes. Therefore, the stability of the PVIm-NH_2/DNA binary or PLL-Lac/PVIm-NH_2/DNA ternary complexes was examined. To examine the complex stability, we attempted to release DNA from the polyion complex by competitive exchange with other polyanions (*26*). For effective transfection, the release of DNA should not happen outside the target cell, whereas that must occur somewhere inside to allow binding of the transcription machinery. In biological fluids, the proteins borne by various anionic polysaccharides circulate. As an extreme case, dextran sulfate was used as a polyanion; that is, agarose gel electrophoresis was carried out after the binary or ternary complex was incubated with dextran sulfates. The results are shown in Figure 5. As the concentration of the dextran sulfate increased, the DNA increasingly migrated (lanes 3−6) in the case of the PVIm-NH_2/DNA binary complex. On the other hand, in the case of the PLL-Lac/PVIm-NH_2/DNA ternary complex, almost no DNA migrated even in the presence of the higher concentration of the dextran sulfate (lane 6′). These results suggest that the PVIm-NH_2/DNA binary complex released the DNA by exposure to polyanions and that the PLL-Lac/PVIm-NH_2/DNA ternary complex stably retained the DNA. We have therefore expected the PLL-Lac/PVIm-NH_2/DNA ternary complex, which results in the PVIm-NH_2/DNA binary complex by the pH-dependent dissociation of the PLL-Lac, to lead effective gene expression.

Cell-Specific Gene Delivery by the PLL-Lac/PVIm-NH_2/DNA Ternary Complex. To confirm the required property as gene carrier, we first carried out a cytotoxicity assay (additional results not shown). The cell viability of HepG2 hepatoma cells did not significantly decrease when the PVIm-NH_2 was added up to the concentration of 400 μg/mL, which was higher than the transfection conditions. The PLL-Lac exhibited the same tendency as the PVIm-NH_2. On the other hand, little viability was observed when the control PEI was added up to 200 μg/mL. Furthermore, the PLL-Lac/PVIm-NH_2/DNA ternary complex also had no apparent cytotoxicity (results not shown). These results suggest that the PVIm-NH_2, as well as PLL-Lac, with no apparent cytotoxicity promises to be an effective gene carrier.

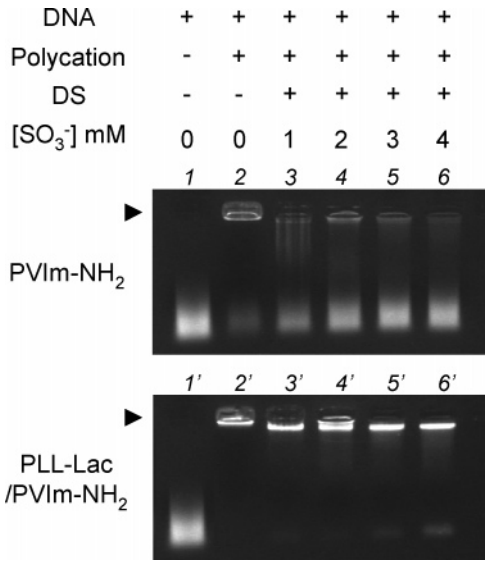


Figure 5. Release of DNA from PVIm-NH_2/DNA binary or PLL-Lac/PVIm-NH_2/DNA ternary complexes by dextran sulfates (DS) as assessed by agarose gel electrophoresis: lanes 1 and 1′, DNA alone; lanes 2 and 2′, 0 mM; lanes 3 and 3′, 1 mM; lanes 4 and 4′, 2 mM; lanes 5 and 5′, 3 mM; lanes 6 and 6′, 4 mM. The PVIm-NH_2/DNA ($[amino]_{PVIm-NH2}/[phosphate]_{DNA} = 4$; lanes 2−6) or PLL-Lac/PVIm-NH_2/DNA ($[amino]_{PVIm-NH2}/[phosphate]_{DNA} = 4$, $[amino]_{PLL-Lac}/[phosphate]_{DNA} = 1$; lanes 2′-6′) mixtures were incubated for 10 min at room temperature in the presence (lanes 3−6 and 3′−6′) or absence (lanes 2 and 2′) of DS (0−4 mM as sulfate group), followed by loading into the gel. Solid arrowhead indicates the well where each sample was loaded.

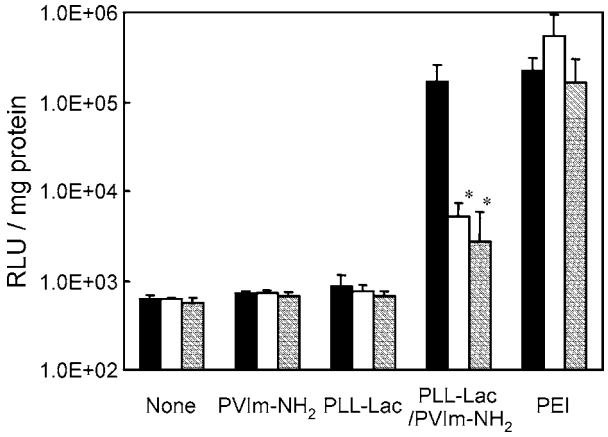


Figure 6. Transfection of luciferase gene to HepG2 (black bars), FR (white bars), or MC3T3-E1 (slashed bars) cells by the PLL-Lac/PVIm-NH_2/DNA ternary complex ($[amino]_{PVIm-NH2}/[phosphate]_{DNA} = 4$, $[amino]_{PLL-Lac}/[phosphate]_{DNA} = 1$). PLL-Lac/DNA and PVIm-$NH_2$/DNA binary complexes were prepared at an [amino]/[phosphate] ratio of 5, and the PEI/DNA complex was prepared at the N/P ratio of 15. The cells (1×10^4 cells/well) were transfected by adding 200 ng of plasmid DNA complexed with the polycations for 1 day in the presence of 10% FBS. Gene expression was determined 3 days later as RLU normalized by protein concentrations. Symbols and error bars represent the mean and standard deviation of the measurements made in paired samples ($n = 3$). $*$ indicates statistical significance ($p < 0.02$) when compared to the HepG2 value.

As a result of no apparent cytotoxicity, we finally examined the gene expression mediated by the PLL-Lac/PVIm-NH_2/DNA ternary complex. HepG2 cells are a human hepatoma cell line, so that ASGP-Rs are expressed on the cell surface (*16*). As shown in Figure 6, the PLL-Lac/PVIm-NH_2/DNA ternary complex mediated remarkable gene expression, which was almost the same level as that mediated by the control PEI, on HepG2 cells. On both skin fibroblast (FR) and immature osteoblast-like (MC3T3-E1) cell line with no ASGP-R on the cell surface, on the other hand, the ternary complex mediated little gene expression, which was significantly lower than the expression on the HepG2 cells. The control PEI preserved remarkable gene expression even on both FR and MC3T3-E1 cells. Furthermore, the gene expression mediated by the PLL-Lac/PVIm-NH_2/DNA ternary complex on HepG2 cells decreased in the presence of not free maltose but free lactose as a competitor (*27*) (additional results not shown). Although it is unclear if only a small percentage of cells took up the complexes and then had high expression or if a large percentage of these cells were transfected, as is implied, which is the topic of our future investigation, these results suggest that the PLL-Lac/PVIm-NH_2/DNA ternary complex with β-galactose residues recognized the HepG2 cells via ASGP-Rs on the cell surface.

It is worth noting that the PLL-Lac/PVIm-NH_2/DNA ternary complex showed gene expression values 200 and 230 times higher than that of the PLL-Lac/DNA and PVIm-NH_2/DNA, respectively, binary complex. Furthermore, gene expression mediated by the PLL-Lac/PVIm-NH_2/DNA ternary complex was significantly decreased by the treatment of HepG2 cells with chloroquine (additional results not shown), which is a weak base known to inhibit lysosomal hydrolases by reducing the acidification of the endosomal/lysosomal compartments (*28*, *29*). The chloroquine is a diprotic weak base that accumulates in acidic organelles as a function of the pH gradient present between the organelle and the external medium (*30*). Because the incubation of target cells with chloroquine blocks the acidification of the endosomes and lysosomes, the PVIm-NH_2 should encounter a less acidic pH during endocytosis, resulting in less protonation of the imidazole group. In the presence of chloroquine, therefore, gene expression mediated by the ternary complex with the imidazole groups of PVIm-NH_2 was decreased. However, because there was less degradation at a less acidic pH during endocytosis, gene expression increased in the case of the PLL used as a control polycation with no pH sensitivity. These results suggest that the gene delivery mediated by PVIm-NH_2 is dependent on the protonation of the imidazole groups of the PVIm backbone leading to the membrane disruptive ability at endosomal pH (see Figure 2 as well as Figure 1) as well as the proton sponge effect (*6*, *8*) and to the pH-dependent dissociation of PLL-Lac (see Figures 4 and 5). Taking these results into account, although an intercellular colocalization study of labeled PLL-Lac, PVIm-NH_2, and DNA is now in progress for more detail investigation, the synergistic effect of the PLL-Lac and PVIm-NH_2 is considered to succeed in cell-specific efficient gene delivery and to depend on the protonation of the imidazole groups of PVIm-NH_2.

CONCLUSION

We have synthesized the new pH-sensitive polycation PVIm-NH_2 and evaluated the physicochemical and biochemical properties of the pH-sensitive gene carrier. The resulting PVIm-NH_2 was water-soluble despite deprotonation of the imidazole groups at physiological pH and exhibited membrane disruptive ability at endosomal pH. By using PVIm-NH_2 as a pH-sensitive DNA carrier, as well as PLL-Lac as a cell-targeting DNA carrier, the resulting DNA ternary complex at pH 7.4 dissociated PLL-Lac by the protonation of the imidazole groups of PVIm-NH_2 at pH 6.0. The resulting PVIm-NH_2/DNA binary complexes easily released DNA, as compared with the PLL-Lac/PVIm-NH_2/DNA ternary complex. The ternary complex mediated the cell-specific gene delivery attributed to the PLL-Lac, and the gene expression depended on the protonation of the imidazole groups of PVIm-NH_2. Consequently, PVIm-NH_2 as a new pH-sensitive polycation enhanced cell-specific gene delivery by PLL-Lac. The synergistic effect of the cell-targeting PLL-Lac

and the pH-sensitive PVIm-NH_2 in this study is expected to offer unique design for gene delivery systems.

ACKNOWLEDGMENT

This work was supported by Grant-in-Aid 17700400 from the Japan Society for the Promotion of Science.

Supporting Information Available: Additional figures. This information is available free of charge via the Internet at http://pubs.acs.org.

LITERATURE CITED

(1) Fukushima, S., Miyata, K., Nishiyama, N., Yamasaki, Y., and Kataoka, K. (2005) PEGylated polyplex micelles from triblock catiomers with spatially ordered layering of condensed pDNA and buffering units for enhanced intracellular gene delivery. *J. Am. Chem. Soc. 127*, 2810−2811.

(2) Zugates, G. T., Anderson, D. G., Little, S. R., Lowhorn, I. E. B., and Ranger, R. (2006) Synthesis of poly(β-amino ester)s with thiol-reactive side chains for DNA delivery. *J. Am. Chem. Soc. 128*, 12726−12734.

(3) Liu, Y., and Reineke, T. M. (2007) Poly(glycoamidoamine)s for gene delivery. Structural effects on cellular internalization, buffering capacity, and gene expression. *Bioconjugate Chem. 18*, 19−30.

(4) Steinman, R. M., Mellman, I. S., Muller, W. A., and Cohn, Z. A. (1983) Endocytosis and the recycling of plasma membrane. *J. Cell Biol. 96*, 1−27.

(5) Sarkar, C. A., Lowenhaupt, K., Horan, T., Boone, T. C., Tidor, B., and Lauffenburger, D. A. (2002) Rational cytokine design for increased lifetime and enhanced potency using pH-activated "histidine switching". *Nat. Biotechnol. 20*, 908−913.

(6) Boussif, O., Lezoualc'h, F., Zanta, M. A., Margny, M. D., Scherman, D., Demeneix, B., and Behr, J. P. (1995) A versatile vector for gene and oligonucleotide transfer into cells in culture and *in vivo*: polyethylenimine. *Proc. Natl. Acad. Sci. U.S.A. 92*, 7297−7301.

(7) Thomas, M., and Klibanov, A. M. (2002) Enhancing polyethylenimine's delivery of plasmid DNA into mammalian cells. *Proc. Natl. Acad. Sci. U.S.A. 99*, 14640−14645.

(8) Sonawane, N. D., Szoka, F. C., Jr., and Verkman, A. S. (2003) Chloride accumulation and swelling in endosomes enhances DNA trandfer by polyamine−DNA polyplexes. *J. Biol. Chem. 278*, 44826−44831.

(9) Asayama, S., Maruyama, A., Cho, C. S., and Akaike, T. (1997) Design of comb-type polyamine copolymers for a novel pH-sensitive DNA carrier. *Bioconjugate Chem. 8*, 833−838.

(10) Asayama, S., Akaike, T., and Maruyama, A. (2001) Bi-phasic polycation for the DNA carrier responding to endosomal pH. *Colloids Surf. B: Biointerfaces 22*, 183−191.

(11) Asayama, S., Kawakami, H., and Nagaoka, S. (2003) Facile chemical modification of the poly(L-histidine) for a new pH-sensitive polypeptide. *Chem. Lett. 32*, 1152−1153.

(12) Asayama, S., Sekine, T., Hamaya, A., Kawakami, H., and Nagaoka, S. (2005) Poly(L-histidine) with several aminoethyl groups for a new pH-sensitive DNA carrier. *Polym. Adv. Technol. 16*, 567−570.

(13) Asayama, S., Sekine, T., Kawakami, H., and Nagaoka, S. (2006) pH-Dependent dissociation of carbohydrate ligand polycations from DNA ternary complexes. *Chem. Lett. 35*, 100−101.

(14) Pack, D. W., Putnam, D., and Langer, R. (2000) Design of imidazole-containing endosomolytic biopolymers for gene delivery. *Biotechnol. Bioeng. 67*, 217−223.

(15) Zeng, J., Wang, X., and Wang, S. (2007) Self-assembled ternary complexes of plasmid DNA, low molecular weight polyethylenimine and targeting peptide for nonviral gene delivery into neurons. *Biometerials 28*, 1443−1451.

(16) Chiu, M. H., Tamura, T., Wadhwa, M. S., and Rice, K. G. (1994) *In vivo* targeting function of *N*-linked oligosaccharides with terminating galactose and *N*-acetylgalactosamine residures. *J. Biol. Chem. 269*, 16195−16202.

(17) Martinez-Fong, D., Mullersman, J. E., Purchio, A. F., Armendariz-Borunda, J., and Martinez-Hernandez, A. (1994) Nonenzymatic glycosylation of poly-L-lysine: a new tool for targeted gene delivery. *Hepatology 20*, 1602−1608.

(18) Udenfriend, S., Stein, S., Bohlen, P., Dairman, W., Leimgruber, W., and Weigele, M. (1972) Fluorescamine: a reagent for assay of amino acids, peptides, proteins, and primary amines in the picomole range. *Science 24*, 871−872.

(19) Unsworth, J. M., Rose, F. R. A. J., Wright, E., Scotchford, C. A., and Shakesheff, K. M. (2003) Seeding cells into needled felt scaffolds for tissue engineering applications. *J. Biomed. Mater. Res. 53*, 617−620.

(20) Henrichs, P. M., Whitlock, L. R., Sochor, A. R., and Tan, J. S. (1980) Conformational behavior of poly(*N*-vinylimidazole). Potentiometric titration, viscosity, and proton nuclear magnetic resonance studies. *Macromolecules 13*, 1375−1381.

(21) Asayama, S., Nogawa, M., Takei, Y., Akaike, T., and Maruyama, A. (1998) Synthesis of novel polyampholyte comb-type copolymer consisting of a poly(L-lysine) backbone and hyaluronic acid side chains for a DNA carrier. *Bioconjugate Chem. 9*, 476−481.

(22) Shuai, X., Merdan, T., Unger, F., and Kissel, T. (2005) Supramolecular gene delivery vectors showing enhanced transgene expression and good biocompatibility. *Bioconjugate Chem. 16*, 322−329.

(23) Yamagata, M., Kawano, T., Shiba, K., Mori, T., Katayama, Y., and Niidome, T. (2007) Structural advantage of dendritic poly(L-lysine) for gene delivery into cells. *Bioorg. Med. Chem. 15*, 526−532.

(24) Maruyama, A., Watanabe, H., Ferdous, A., Katoh, M., Ishihara, T., and Akaike, T. (1998) Characterization of interpolyelectrolyte complexes between double-stranded DNA and polylysine comb-type copolymers having hydrophilic side chains. *Bioconjugate Chem. 9*, 292−299.

(25) Pouton, C. W., Lucas, P., Thomas, B. J., Uduehi, A. N., Milroy, D. A., and Moss, S. H. (1998) Polycation−DNA complexes for gene delivery: a comparison of the biopharmaceutical properties of cationic polypeptides and cationic lipids. *J. Controlled Release 53*, 289−299.

(26) Chittimalla, C., Zammut-Italiano, L., Zuber, G., and Behr, J. P. (2005) Monomolecular DNA nanoparticles for intravenous delivery of genes. *J. Am. Chem. Soc. 127*, 11436−11441.

(27) Asayama, S., Mizushima, K., Nagaoka, S., and Kawakami, H. (2004) Design of metalloporphyrin−carbohydrate conjugates for a new superoxide dismutase mimic with cellular recognition. *Bioconjugate Chem. 15*, 1360−1363.

(28) Ohkuma, S., and Poole, B. (1978) Fluorescence probe measurement of the intralysosomal pH in living cells and the perturbation of pH by various agents. *Proc. Natl. Acad. Sci. U.S.A. 75*, 3327−3331.

(29) Wittmar, M., Ellis, J. S., Morell, F., Unger, F., Schumacher, J. C., Roberts, C. J., Tendler, S. J. B., Davies, M. C., and Kissel, T. (2005) Biophysical and transfection studies of an amine-modified poly(vinyl alcohol) for gene delivery. *Bioconjugate Chem. 16*, 1390−1398.

(30) Martiney, J. A., Cerami, A., and Slater, A. F. G. (1995) Verapamil reversal of chloroquine resistance in the malaria parasite *Plasmodium falciparum* is specific for resistant parasites and independent of the weak base effect. *J. Biol. Chem. 270*, 22393−22398.

BC700205T

TECHNICAL NOTES

Multiple Labeling of Antibodies with Dye/DNA Conjugate for Sensitivity Improvement in Fluorescence Immunoassay

Qin Zhang and Liang-Hong Guo*

State Key Laboratory of Environmental Chemistry and Ecotoxicology, Research Center for Eco-environmental Sciences, Chinese Academy of Sciences, P.O. Box 2871, 18 Shuangqing Road, Beijing 100085, China. Received September 17, 2006; Revised Manuscript Received June 27, 2007

Fluorescence immunoassays are widely used in life science research, medical diagnostics, and environmental monitoring due to the intrinsically high specificity, simplicity, and versatility of immunoassays, as well as the availability of a large variety of fluorescent labeling molecules. However, the sensitivity needs to be improved to meet the ever-increasing demand in the new proteomics era. Here, we report a simple method of attaching multiple fluorescent labels on an antibody with a dye/DNA conjugate to increase the immunoassay sensitivity. In the work, mouse IgG adsorbed on the surface of a 96-well plate was detected by its immunoreaction with biotinylated goat anti-mouse antibody. A 30 base pair double-stranded oligonucleotide terminated with biotin was attached to the antibody through the biotin/streptavidin/biotin interaction. Multiple labeling of the antibody was achieved after a fluorescent DNA probe was added into the solution and bound to the oligonucleotide at high ratios. By comparison with fluorescein-labeled streptavidin, the assay with the dye/DNA label produced up to 10-fold increase in fluorescence intensity, and consequently about 10-fold lower detection limit. The multiple labeling method uses readily available reagents, and is simple to implement. Further sensitivity improvement can be obtained by using longer DNAs for antibody labeling, which can incorporate more fluorescent dyes on each DNA.

INTRODUCTION

Immunoassays are widely used in life science research, drug discovery, clinical diagnostics, and environmental monitoring due to their high specificity, simplicity, and versatility. In general, in order to detect and quantify the formed antibody−antigen complex in the immunoassay, a label is attached to the antibody to generate a detectable signal. Since Berson and Yalow (*1*) first introduced radioisotope-labeled immunoassays in 1959, a variety of labels have been developed (*2*), including fluorescent dyes and metal complexes (*3*), enzymes for colorimetric (*4*), chemiluminescent (*5*), and amperometric detection (*6*), and metal chelates for electrochemiluminescent assays (*7*). Among them, fluorescence immunoassay perhaps offers one of the best combinations in terms of label stability, assay robustness, detection sensitivity, and multiplexity. As such, it has become the standard detection platform for protein microarrays (*8*).

However, the sensitivity of the current fluorescence immunoassay technology needs to be improved substantially to meet the demand in the proteomics study. Unlike gene detection in which the nucleic acid target can be amplified by PCR by orders of magnitude, currently there is no amplification technique for proteins. Therefore, sensitivity improvement for protein detection relies on signal amplification. In 1992, Sano et al. established the immuno-PCR method by using nucleic acids as immunoassay labels and amplifying them by PCR after the immunoreaction (*9*). As a result of nucleic acid amplification, the detection limit is improved by 100- to 10 000-fold (*10*). The limitation of immuno-PCR is that it employs gel electrophoresis, PCR-ELISA, or real-time PCR for assay readout, which adds a substantial amount of time and reagent cost. In addition, it is difficult to implement the method in the protein microarray technology.

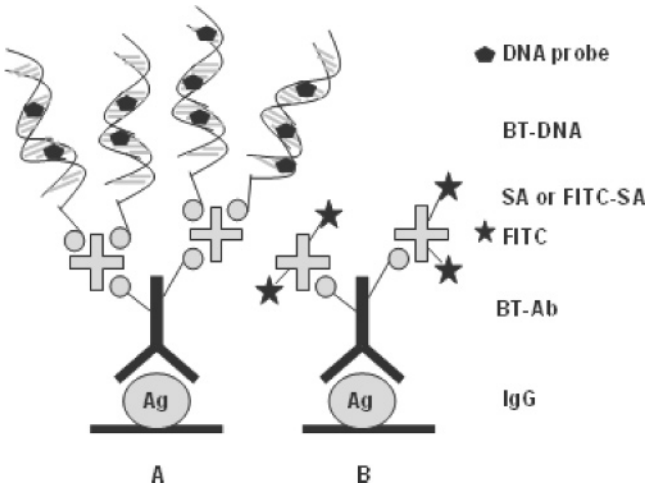
An alternative approach for signal amplification in fluorescence immunoassay is to increase the number of labels conjugated to each antibody. This can be done by either attaching multiple labels at multiple sites of the antibody with only one label at each site or attaching multiple labels at one site with a macromolecular carrier. Due to the finite size and hydrophobic nature of most fluorescent dyes, the multiple-site approach suffers from reduced immunoreactivity and increased nonspecific binding of the labeled antibody. In the single-site approach, an organic dendrimer (*11*, *12*) or protein loaded with a large number of fluorescent dyes (*13*) is linked covalently or noncovalently (e.g., through biotin−streptavidin interaction) to the antibody at a single site. The single-site linkage minimizes structural alteration of the antibody, thus maintaining its native immunoreactivity. The challenge of this approach is the synthesis and purification of dye-conjugated macromolecules.

More recently, fluorescent micro- and nanometer-sized particles have drawn much attention as a new type of nonisotopic immunoassay labels. Because each particle contains hundreds or even thousands of fluorescent entities, its emission is substantially brighter than the most efficient organic dyes. In 1998, Alivisatos (*14*) and Nie's group (*15*) described separately the application of semiconductor nanocrystals (quantum dots) in biological detections. The new label exhibited such advantageous features as single excitation wavelength, tunable emission wavelength, and improved photostability. Immunoassay sensitivity can also be improved by using fluorophore-doped silica (*16*) and latex beads (*17*). As with the quantum dots, the

* Corresponding author. Phone & Fax: (86)-10-62849685. E-mail: LHGuo@rcees.ac.cn.

10.1021/bc060289v CCC: $37.00 © 2007 American Chemical Society
Published on Web 08/08/2007

Scheme 1. Illustration of the Two Immunoassay Labeling Formats for the Detection of Goat Anti-Mouse Antibody Using the Conjugate Label (A) and Dye Label (B)[a]



[a] Mouse IgG of various concentrations is coated on a 96-well plate. Biotinylated goat anti-mouse antibody is reacted with mouse IgG. (A) The dye/DNA conjugate with multiple DNA probes is attached to the antibody through the biotin-streptavidin-biotin linkage. (B) The molecular label fluorescein is attached to the antibody by the biotin−streptavidin interaction.

difficulties include the uniformity of the particle, conjugation of biomolecules, dispersion in aqueous solution, and reaction kinetic.

In the work described below, we employed a 30 base pair biotinylated double-stranded oligonucleotide as a carrier for the conjugation of multiple fluorescent dyes. It was attached to a biotin-modified goat anti-mouse antibody through the high-specificity, high-affinity biotin−streptavidin interaction. A highly fluorescent DNA probe, SYBR Green I, binds in situ to the oligonucleotide at high ratios by the specific binding interaction with DNA. Because the free (unbound) probe does not emit fluorescence, measurement can be performed without a wash step. A direct comparison was made with fluorescein-labeled streptavidin in the immunological detection of goat anti-mouse antibody on a mouse IgG-coated 96-well plate (Scheme 1). The dye/DNA conjugate labeled immunocomplex produced up to 10-fold increase in the fluorescence intensity.

EXPERIMENTAL PROCEDURES

Fluorescein isothiocyanate (FITC) was purchased from Amresco (Solon, OH), and SYBR Green I from Invitrogen (Carlsbad, CA). Biotinyl-*N*-hydroxysuccinimide (BT-NHS) was from Sigma (St. Louis, MO). Streptavidin was obtained from Promega (Madison, WI). Bovine serum albumin fraction V (BSA), mouse IgG, and goat anti-mouse IgG were from Xinjingke Corp. (Beijing, China). All buffers were prepared in high-purity water from a Millipore Milli-Q (Biocel) purification system. Unless specified, all antibodies were dissolved in phosphate buffered saline (PBS, 137 mM NaCl, 2.7 mM KCl, 10 mM Na_2HPO_4, 1.5 mM KH_2PO_4, pH 7.4) containing 0.1% BSA and 0.1% NaN_3.

Biotinylated goat anti-mouse antibody (BT-Ab) was obtained by mixing the antibody with BT-NHS at a molar ratio of 5.6 BT-NHS: 1 antibody in 0.1 M sodium bicarbonate, pH 9.15, for 4 h at room temperature with stirring. After the reaction, the remaining free BT-NHS was separated from the antibody by gel filtration on a D-Salt polyacrylamide desalting column from Pierce (Rockford, IL). The antibody concentration was determined by its absorbance at 280 nm on a UNICO UV-2800 visible spectrophotometer (Shanghai, China). The biotin content was determined with the HABA/avidin reagent from Sigma (St. Louis, MO), and was found to be 1.9 biotins per antibody. Mouse IgG, goat anti-mouse IgG, and streptavidin were labeled with FITC by following the same procedure. The protein and FITC concentration of the labeled biomolecules were determined by absorbance at 280 nm and 495 nm, respectively, and the label ratios were 2.0, 4.0, and 3.5 per protein, respectively. They were stored at 4 °C in the dark until use.

A 30 base pair biotinylated double-stranded oligonucleotide (BT-DNA) was obtained by hybridizing two complementary single-stranded oligonucleotides purchased from Invitrogen (Shanghai, China): strand A, biotin-5′-TTT TTT TTT GCG GGT AAC GTC AAT ATT AAC TTT ACT CCC-3′; strand B, 5′-GGG AGT AAA GTT AAT ATT GAC GTT ACC CGC-3′. The nine thymine nucleotides on strand A are designed to minimize possible spatial hindrance to binding with streptavidin. The two oligonucleotides were mixed in 2 × SSC buffer (0.3 M NaCl, 30 mM sodium citrate, pH 7.0), denatured at 95 °C for 5 min on a Biometra T-Gradient thermocycler (Goettingen, Germany), and then naturally cooled down to room temperature. The concentration of the oligonucleotide was determined by absorbance at 260 nm.

The following is an optimized immunoassay protocol for the detection of mouse IgG using the dye/DNA conjugate labels. First, a white 96-well plate was coated with 100 μL mouse IgG of various concentrations (in 50 mM $NaHCO_3$, pH 9.6, with 0.01% rabbit IgG) by incubating overnight at 4 °C. The plate was washed three times with 300 μL of washing buffer (50 mM Tris, 50 mM NaCl, 0.1% Tween 20, pH 8.0). The plate was then blocked overnight at 4 °C with 300 μL of 1% BSA in PBS, pH 7.4. The plate was washed as above. In the second step, 100 μL of 784 μg/mL BT-Ab in dilution buffer (0.1% BSA, 50 mM Tris, 50 mM NaCl, pH 8.0) was added into the coated well and incubated at 37 °C for 2 h with shaking. The plate was again washed. In the third step, 100 μL of 7.4 μg/mL streptavidin was added into the well and reacted at 37 °C for 2 h with shaking, then washed. In the fourth step, BT-DNA was added and reacted at 37 °C for 1 h with shaking, and washed again. Finally, SYBR Green I was added into the plate and incubated for 10 min at room temperature with shaking. The fluorescence intensity was measured on a Thermo Electron Varioskan Flash luminescence spectrometer (Waltham, MA) with 495 nm excitation, 520 nm emission, 5 nm slit width, and 515 nm cutoff filter. In the dye-labeled immunoassay, fluorescence of fluorescein was measured with 495 nm excitation, 525 nm emission, 5 nm slit width, and 515 nm cutoff filter.

RESULTS AND DISCUSSION

As described above, our strategy is to use a strand of DNA as a carrier to attach multiple fluorescent dyes to an antibody at a single site. The dye/DNA conjugate is not presynthesized, but rather formed in situ as part of the immunoassay. For this strategy to work, there are a few requirements for the fluorescent label. First of all, it must bind to DNA only, not to proteins or immunoglobulins. And the binding stoichiometry is preferably high to ensure a high labeling ratio. Second, the quantum yield of the DNA-bound probe should be comparable to that of the commonly used fluorescent dyes such as fluorescein, Cy-3, Cy-5, and rhodamine, which is in the range 0.1−0.9 (*18*). Third, fluorescence of the unbound probe should be minimal so that the immunoassay can be quantified without wash.

Among the commercially available fluorescent DNA probes, PicoGreen, SYBR Green I, SYBR Gold, and YOYO-1 fulfill the above requirements (*19*). SYBR Green I was selected in our work because its fluorescence excitation and emission maximum wavelengths are close to that of fluorescein, to which the SYBR Green/DNA conjugate is going to be compared. To characterize the binding interaction between SYBR Green and

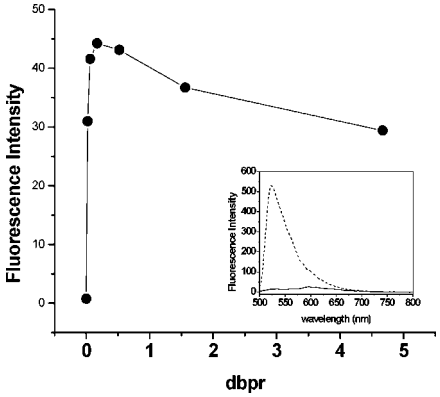


Figure 1. Fluorescence intensity of SYBR Green as a function of the dye to base pair ratio (dbpr). The DNA probe is titrated from 0 to 2.1 μM into a 0.15 μM (base pair) solution of the biotinylated oligonucleotide in 50 mM Tris/50 mM NaCl, pH 8.0. Inset shows the fluorescence emission spectra of the free (solid line) and oligonucleotide-bound dye at 0.02 dbpr (dotted line).

BT-DNA, the probe was titrated into the BT-DNA solution at increasing dye to base pair ratios (dbpr). As illustrated in Figure 1, the fluorescence intensity increased rapidly from 0 to 0.17 dbpr, reached a plateau between 0.17 and 0.52 dbpr, and started to drop at higher ratios. Vitzthum and co-workers have investigated the fluorescent response of SYBR Green I after binding with double-stranded (ds-) and single-stranded (ss-) plasmid DNA (heat-denatured) (*20*). In ds-DNA, the fluorescence increased gradually with the dye concentration until 2 dbpr, after which it became constant. In ss-DNA, however, the response increased more rapidly with the dye concentration, reached the maximum at 0.2 dbpr, and then dropped with further increase of dbpr. The reduction in fluorescence at high dbpr was attributed to self-quenching. The dependence of fluorescence on dbpr with BT-DNA in our work resembles more closely that of ss-DNA in Vitzhum's investigation. This can be explained by the fact there are nine unpaired thymine bases in BT-DNA that bear the characteristics of ss-DNA. Due to the quenching effect, binding constant and stoichiometry between the probe and BT-DNA cannot be determined from the fluorescence titration curve. Cosa et al. revealed (*19*) that the quantum yield of SYBR Green I was 0.69 when bound to double-stranded calf thymus DNA, an increase of more than 1500-fold over the free dye. The drastic enhancement was also observed for the dye/BT-DNA conjugate, as shown in the inset of Figure 1. Furthermore, at the same dye concentration of 20 nM, the emission intensity of SYBR Green/BT-DNA conjugate with 0.22 dbpr is 88% of that of fluorescein-labeled streptavidin (FITC-SA), indicating that the quantum yields of the two fluorescent dyes are similar. All the experimental data obtained above support our notion that the SYBR Green/BT-DNA conjugate can be used effectively to attach multiple fluorescent labels in immunoassays.

After the fluorescence property of the SYBR Green/BT-DNA conjugate was investigated, a 96-well plate based immunoassay for the detection of mouse IgG was carried out. The assay protocol described in the Experimental Section was established after a series of optimization experiments were performed to determine the optimal concentration, reaction time, and temperature for IgG/BT-Ab immunoreaction and biotin/streptavidin binding. The results of the optimization experiments are described in the Supporting Information.

The optimal condition for the binding of BT-DNA/SYBR Green conjugate to the surface-attached IgG/BT-Ab/SA immunocomplex was investigated as follows. The concentrations of the reagents for the formation of the immunocomplex were 30

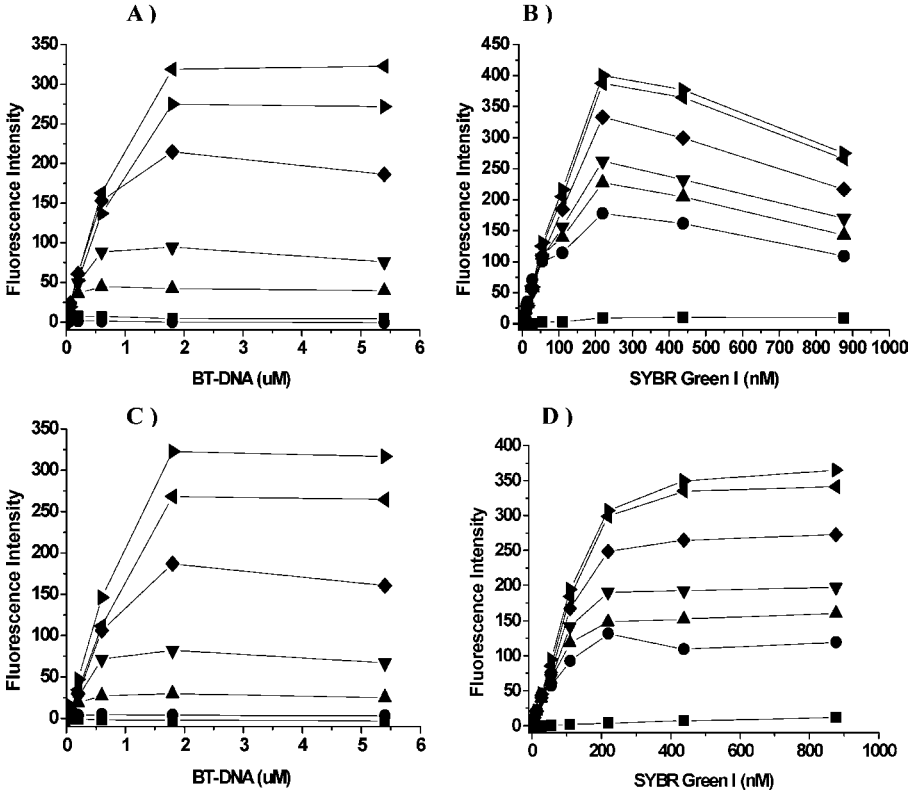


Figure 2. Fluorescence intensity of the SYBR Green/BT-DNA conjugate attached to the IgG/BT-Ab/SA complex formed on a 96-well plate as a function of BT-DNA (A,C) and SYBR Green (B,D) concentration. Different curves in (A) and (C) correspond to 0 nM (●), 14 nM (■), 27 nM (▲), 55 nM (▼), 110 nM (◆), 219 nM (right-facing solid triangle), and 438 nM (left-facing solid triangle) SYBR Green. Different curves in (B) and (D) correspond to 0 μM (■), 0.04 μM (●), 0.12 μM (▲), 0.37 μM (▼), 1.11 μM (◆), 3.33 μM (left-facing solid triangle), and 10 μM (right-facing solid triangle) BT-DNA. Fluorescence was measured before (A,B) and after (C,D) plate wash to remove unbound dyes.

μg/mL IgG for plate coating, 784 μg/mL BT-Ab for immunoreaction, and 7.4 μg/mL (114 nM) SA for BT-Ab binding. BT-DNA of various concentrations was then added to the plate. After binding of BT-DNA to SA on the surface, SYBR Green I was added into the plate from 0 to 876 μM at approximately 2-fold increments for each BT-DNA concentration. Fluorescence intensity was measured, first without wash (in the presence of excessive SYBR Green), then after wash to remove unbound dye molecules. From Figure 2A,C, it is apparent that the binding site for BT-DNA on the plate surface is saturated when the DNA concentration exceeds 1.8 μM. An increase in the dye concentration only enhanced the detection signal, and had no effect on the saturation concentration of BT-DNA. In the unwashed measurement, the light intensity reached its maximum with 219 nM SYBR Green in solution, and decreased at higher concentrations (Figure 2B). This is similar to the trend observed in the solution study of the dye/BT-DNA binding reaction illustrated in Figure 1. The fact that the signal starts to decrease at the same dye concentration but is independent of BT-DNA concentration suggests the reduction is due to quenching by the free dye molecules in solution. This notion is further supported by the results displayed in Figure 2D for the washed measurement. Once excessive SYBR Green molecules were removed from the plate, there was no loss of fluorescence at high dye concentrations. Therefore, a combination of 1.8 μM BT-DNA and 219 nM dye produced the most intense signal in the unwashed measurement, whereas the intensity was slightly lower for the washed assay.

After all the reaction parameters were optimized, a direct comparison was made between the dye label and the dye/DNA conjugate label format in the immunoassay for mouse IgG. The experiment is illustrated in Scheme 1. IgG coating and BT-Ab reaction were performed in the same way for the two labeling formats, with the IgG concentration varied from 0 to 30 μg/mL. In the conjugate-labeled assay, 120 nM unlabeled SA was reacted with BT-Ab on the plate. BT-DNA (1.8 μM) and SYBR Green (219 nM for the nonwashed assay and 438 nM for the washed assay) were then added sequentially to the plate and reacted. The fluorescence was measured first without wash, then with wash. In the dye-labeled assay, 120 nM FITC-SA was reacted with the biotin group on the antibody and its fluorescence measured after wash. A more preferred way for carrying out the single-label assay would be to use a biotin−dye conjugate to bind to the unlabeled SA. Unfortunately, most of the conjugates lose their fluorescence upon binding to streptavidin (*17*), and cannot be used. The results obtained in the comparison experiment are shown in Figure 3. The signal is subtracted by the background, which was found to be caused by the scattered light, not by nonspecific binding of the DNA probe. In both assays, the fluorescence signal is progressively higher with increasing IgG concentration, suggesting that both methods can be used for quantitative detection of immunoassays. However, in the whole range of the IgG concentration examined, the intensity of the SYBR Green/DNA labeled assay is persistently higher than the dye-labeled assay by about 8-fold. The calculated limit of lower detection (3 times the standard deviation above the blank) is 1.7 μg/mL for the dye-labeled assay and 0.14 μg/mL for the dye/DNA conjugate-labeled assay, respectively. Obviously, the dye/DNA multiple labeling strategy improved the detection sensitivity for IgG by 10-fold.

To evaluate the specificity of the assay for mouse IgG, an experiment was carried out in which the surface-adsorbed protein was replaced with either rabbit IgG or BSA, while keeping the protein concentration the same as mouse IgG. The subsequent assay procedure was also the same as for mouse IgG. As illustrated in Figure 4, at a protein concentration of 30 μg/mL, the fluorescence intensity of either rabbit IgG or BSA

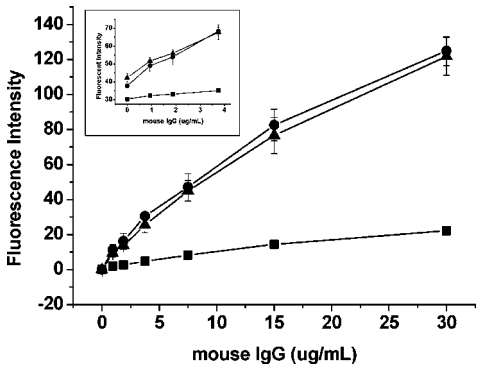


Figure 3. Fluorescence immunoassay for the detection of mouse-IgG on a 96-well plate using the SYBR Green/BT-DNA conjugate label and fluorescein molecular label. Mouse-IgG was dissolved in 50 mM $NaHCO_3$, pH 9.6, with 0.01% rabbit IgG. The concentrations of the reagents used in the assay were 4.9 μM BT-Ab for the immunoreaction, 120 nM FITC-SA (filled square) in the dye-labeled assay, or 120 nM unlabeled SA/1.8 μM BT-DNA/438 nM SYBR Green (filled triangle) in the washed conjugate labeled assay, or 120 nM unlabeled SA/1.8 μM BT-DNA/219 nM SYBR Green (filled circle) in the unwashed conjugate-labeled assay. Inset is an expanded view.

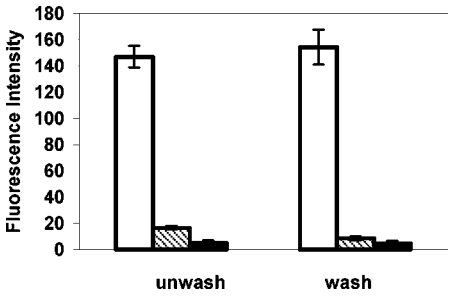


Figure 4. Comparison of fluorescence immunoassay for mouse-IgG (open column), rabbit IgG (hatched column), and BSA (filled column) on a 96-well plate using the SYBR Green/BT-DNA conjugate label. The concentrations of the reagents used in the assay are the same as in Figure 3 for the unwashed (left) and washed (right) assay.

sample is very low by comparison with that of mouse IgG. The result indicates that the immunoassay is highly specific for mouse IgG.

As discussed in the Introduction, although there are a few approaches reported in the literature of employing the multiple-label strategy for signal amplification in immunoassays, none of them can be readily adopted for the sensitive detection of protein microarrays, which is highly sought after due to the low concentration in biological samples and lack of target amplification method. While chemiluminescence has been proven to be a very sensitive detection method, it is very difficult to implement the method on microarrays, since the light-emitting species are not confined to the surface (*22*). Immuno-PCR has been reported to improve the immunoassay sensitivity by 100- to 10 000-fold (*11*), but requires a separate set of assay for DNA quantitation. The covalent labeling approach using organic polymers or proteins as the label carrier faces a severe challenge in chemical synthesis and post-labeling purification. By comparison, the dye/DNA conjugate approach reported in this paper uses all the common reagents such as biotin, streptavidin, oligonucleotides, and fluorescent DNA probes. Multiple labeling of antibodies is achieved in situ by reacting with the oligonucleotide and DNA probe on a 96-well plate. There is even no need to remove the unbound dyes before measurement. If one is concerned about the assay time, the BT-Ab/SA/BT-DNA can be premixed at a controlled ratio to save time. Furthermore, the signal amplification efficiency can potentially be enhanced substantially by using longer DNAs to carry more fluorescent

dyes. DNA markers of 150 to 300 base pairs are commonly used in immuno-PCR (*23*). By simple extrapolation, such a long DNA sequence would increase the fluorescent signal by 50−100 fold over the dye-labeled assays, and probably with similar improvement in detection sensitivity. The improved sensitivity would be very attractive for protein microarray detection.

ACKNOWLEDGMENT

This work was supported by the National Basic Research Program of China (grant number 2006CB403303) and the Knowledge Innovation Program of the Chinese Academy of Sciences (grant number KZCX2-YW-420-1).

Supporting Information Available: Details of the experiments in determining the optimal concentration, reaction time, and temperature for IgG/BT-Ab immunoreaction and biotin/streptavidin binding. This material is available free of charge via the Internet at http://pubs.acs.org.

LITERATURE CITED

(1) Berson, S. A., and Yalow, R. S. (1959) Assay of plasma insulin in human subjects by immunological methods. *Nature (London) 184*, 1648−1649.

(2) Kricka, L. J. (1994) Selected strategies for improving sensitivity and reliability of immunoassays. *Clin. Chem. 40*, 347−357.

(3) Li, T. M., and Parrish, R. F. (2002) Fluorescence and Immunodiagnostic Methods. *Topics in Fluorescence Spectroscopy. Volume 3*: *Biochemical Applications* (Lakowicz, J. R., Ed) Chapter 6, pp 273−287, Springer, New York.

(4) Marquette, C. A., and Blum, L. J. (2006) State of the art and recent advances in immunoanalytical systems. *Biosens. Bioelectron. 21*, 1424−1433.

(5) Kricka, L. J. (1999) Chemiluminescence and bioluminescence. *Anal. Chem. 71*, 305−308.

(6) Bange, A., Halsall, H. B., and Heineman, W. R. (2005) Microfluidic immunosensor systems. *Biosens. Bioelectron. 20*, 2488−2503.

(7) Blackburn, G. F., Shah, H. P., Kenten, J. H., Leland, J., Kamin, R. A., Link, J., Peterman, J., Powell, M. J., Shah, A., and Talley, D. B. (1991) Electrochemiluminescence detection for development of immunoassays and DNA probe assays for clinical diagnostics. *Clin. Chem. 37*, 1534−1539.

(8) Zhu, H., and Snyder, M. (2003) Protein chip technology. *Curr. Opin. Chem. Biol. 7*, 55−63.

(9) Sano, T., Smith, C. L., and Cantor, C. R. (1992) Immuno-PCR: very sensitive antigen detection by means of specific antibody-DNA conjugate. *Science 258*, 120−122.

(10) Alder, M., Wacker, R., and Niemeyer, C. M. (2003) A real-time immuno-PCR assay for routine ultrasensitive quantification of proteins. *Biochem. Biophys. Res. Commun. 308*, 240−250.

(11) Ong, K. K., Jenkins, A. L., Cheng, R., Tomalia, D. A., Durst, H. D., Jensen, J. L., Emanuel, P. A., Swim, C. R., and Yin, R. (2001) Dendrimer enhanced immunosensors for biological detection. *Anal. Chim. Acta 444*, 143−148.

(12) Zhou, M., Roovers, J., Robertson, G. P., and Grover, C. P. (2003) Multilabeling biomolecules at a single site. 1. synthesis and characterization of a dendritic label for electrochemiluminescence assays. *Anal. Chem. 75*, 6708−6717.

(13) Diamandis, E. P. (1991) Multiple labeling and time-resolvable fluorophores. *Clin. Chem. 37*, 1486−1491.

(14) Bruchez, M., Jr, Moronne, M., Gin, P., Weiss, S., and Alivisatos, A. P. (1998) Semiconductor nanocrystals as fluorescent biological labels. *Science. 281*, 2013−2016.

(15) Chan, W. C. W., and Nie, S. (1998) Quantum dot bioconjugates for ultrasensitive nonisotopic detection. *Science 281*, 2016−2018.

(16) Wang, L., Wang, K., Santra, S., Zhao, X., Hilliard, L. R., Smith, J. E., Wu, Y., and Tan, W. (2006) Watching silica nanoparticles glow in the biological world. *Anal. Chem. 78*, 646−654.

(17) Bangs, L. B. (1996) New developments in particle-based immunoassays: Introduction. *Pure Appl. Chem. 68*, 1873−1879.

(18) Schena, M. (2002) *Microarray Analysis*. p 215, John Wiley & Sons, New Jersey.

(19) Cosa, G., Focsaneanu, K. S., McLean, J. R., McNamee, J. P., and Scaiano, J. C. (2001) Photophysical properties of fluorescent DNA-dyes bound to single- and double-stranded DNA in aqueous buffered solution. *Photochem. Photobio. 73*, 585−599.

(20) Zipper, H., Brunner, H., Bernhagen, J., and Vitzthum, F. (2004) Investigations on DNA intercalation and surface binding by SYBR Green I, its structure determination and methodological implications. *Nucleic Acids Res. 32*, e103.

(21) Kada, G., Kaiser, K., and Gruber, H. J. (1999) Rapid estimation of avidin and streptavidin by fluorescence quenching or fluorescence polarization. *Biochim. Biophys. Acta 1427*, 44−48.

(22) Schweitzer, B., Predki, P., and Snyder, M. (2003) Microarrays to characterize protein interactions on a whole-proteome scale. *Proteomics 3*, 2190−2199.

(23) Niemeyer, C. M., Adler, M., and Wacker, R. (2005) Immuno-PCR: high sensitivity detection of proteins by nucleic acid amplification. *Trends Biotechnol. 23*, 208−216.

BC060289V

O_2-Binding Albumin Thin Films: Solid Membranes of Poly(ethylene glycol)-Conjugated Human Serum Albumin Incorporating Iron Porphyrin

Akito Nakagawa,[†] Teruyuki Komatsu,[†,‡,*] Yubin Huang,[†] Gang Lu,[†] and Eishun Tsuchida[†,*]

Research Institute for Science and Engineering, Waseda University, 3-4-1 Okubo, Shinjuku-ku, Tokyo 169-8555 Japan, and PRESTO, Japan Science and Technology Agency (JST), 4-1-8 Honcho, Kawaguchi-shi, Saitama 332-0012, Japan.
Received March 14, 2007; Revised Manuscript Received July 7, 2007

Poly(ethylene glycol) (PEG)-conjugated human serum albumin (HSA) incorporating the tetrakis(α,α,α,α-*o*-amidophenyl)porphinatoiron(II) derivative (FeP) [PEG(HSA−FeP)] is a unique plasma protein-based O_2 carrier as a red blood cell substitute. The aqueous solution of PEG(HSA−FeP) [mw of PEG: 2-kDa (PEG_2) or 5-kDa (PEG_5)] was evaporated on a glass surface to produce a red-colored solid membrane. Scanning electron microscopy observations revealed that the PEG_2(HSA−FeP) membrane consisted of two parts: (i) a surface layer made of a fibrous component (10 μm thickness), and (ii) a bottom layer of an amorphous phase (5 μm thickness). The condensed solution provided a thick membrane (70 μm), which also has the amorphous bottom layer. On the other hand, the PEG_5(HSA−FeP) produced homogeneous membrane made of the fibrous component. The FeP active sites in the solid membrane formed very stable O_2-adduct complexes at 37 °C with a half-lifetime of 40 h. The O_2-binding affinity of the PEG_2(HSA−FeP) membrane ($P_{1/2}$ = 40 Torr, 25 °C) was 4-fold lower than that in aqueous solution, which is kinetically due to the low association rate constant. The membrane was soluble again in water and organic solvents (ethanol and chloroform) without deformation of the secondary structure of the protein. The addition of hyaluronic acid gave a free-standing flexible thin film, and it can also bind and release O_2 as well. These O_2-carrying albumin membranes with a micrometer-thickness would be of significant medical importance for a variety of clinical treatments.

INTRODUCTION

Covalently surface-modified proteins with poly(ethylene glycol) (PEG) show a number of unique properties that make them of interest in a range of practical applications (*1*−*6*). The most beneficial effect of the PEG conjugation from a biological aspect is to confer a nonimmunogenicity to the proteins, rendering them invisible in the body (*7*−*10*). Several classes of protein drugs, such as enzymes and cytokines, have already been approved by the FDA (*4*, *5*), and one of the expected compounds is a PEG-conjugated hemoglobin (PEG-Hb) for use as artificial blood (*11*, *12*). The optimized product has completed a phase I trial and is currently undergoing a phase II safety study (*13*). Second, the PEG modification allows the proteins to be soluble in nonaqueous solvents (benzene, ethanol, and chloroform, etc.) (*14*−*16*). In organic solutions, the proteins exhibited new characteristics, for example, a high thermal stability and a different substrate selectivity. Third, the aqueous PEGylated proteins can be dried on a flat surface to produce solid membranes without any loss of their original activities. However, only limited characterization has been performed on the PEG-conjugated proteins in the solid state.

Recombinant human serum albumin (HSA) incorporating the tetrakis{α,α,α,α-*o*-(1-methylcyclohexanamido)phenyl}-porphinatoiron(II) derivative (FeP, Figure 1) (HSA−FeP) is a unique plasma protein-based O_2 carrier (*17*, *18*). This entirely synthetic hemoprotein can reversibly bind and release O_2 under physiological conditions (pH 7.4, 37 °C) in a fashion similar to Hb. It has also been demonstrated that the surface decoration of HSA−FeP by PEG improved its circulation persistence in the bloodstream (*19*). The PEG(HSA−FeP) is now the most promising material for an entirely synthetic red blood cell substitute.

We have recently found that the aqueous PEG(HSA−FeP) solution cast on the glass surface produces a very smooth solid membrane. The spectroscopic measurements revealed that a reversible O_2 binding to FeP took place in the red-colored membrane. We now report our new findings on the layered film structures of the PEG-conjugated artificial hemoprotein and their O_2-binding behavior.

EXPERIMENTAL PROCEDURES

Materials and Apparatus. All reagents were purchased from commercial sources as special grades and used without further purification. 2-{8-(2-Methylimidazolyl-1-yl)octanoyloxymethyl}-5,10,15,20-tetrakis{α,α,α,α-o-(1-methylcyclohexanamido)-phenyl}porphinatoiron(II) (FeP) was synthesized according to our previously reported procedures (*17*, *20*). Recombinant HSA was provided by the NIPRO Corp. (Osaka, Japan). 2-Iminothiolane hydrochloride (IMT) was purchased from Wako Pure Chemical Industries, Ltd. (Osaka, Japan). α-[3-(3-Maleimido-1-oxopropyl)amino]propyl-ω-methoxy PEG [averaged mw: 2333, Sunbright ME-020MA, PEG_2, and averaged mw: 5207, Sunbright MEMAL-50H, PEG_5) was purchased from the NOF Corp. (Tokyo, Japan). Hyaluronic acid sodium salt (HA, mw: 1.9−2.7 × 10^3 kDa) was a gift from Shiseido Co., Ltd. (Tokyo, Japan). The water was deionized using Millipore Elix and Simpli Lab-UV. The UV−vis absorption spectra were recorded using an Agilent 8453 UV−visible spectrophotometer fitted with an Agilent 89090A temperature control unit. The circular dichroism (CD) spectra were obtained using a JASCO J-820 spectropolarimeter over the range of 200−250 nm.

* Corresponding author. (E.T.) Tel: +81-3-5286-3120, fax: +81-3-3205-4740, e-mail: eishun@waseda.jp. (T.K.) E-mail: teruyuki@waseda.jp.

[†] Waseda University.

[‡] Japan Science and Technology Agency.

10.1021/bc070086m CCC: $37.00 © 2007 American Chemical Society
Published on Web 08/16/2007

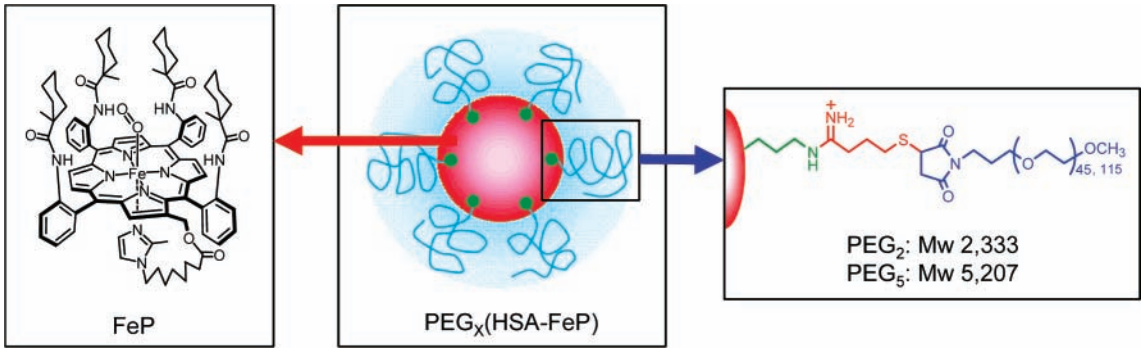


Figure 1. Structure of the PEG$_X$(HSA−FeP) molecule.

Preparation of PEG$_X$(HSA−FeP) Solid Membranes. The phosphate-buffered saline (PBS) solutions of PEG$_X$(HSA−FeP) (X = 2 or 5) were prepared with IMT and PEG$_X$ (pH 7.4, [HSA] = 5 wt %, FeP/HSA = 4/1 (mol/mol)) according to our previously reported methods (*19*). The binding number of the PEG$_X$ chain on the HSA−FeP surface was determined by the MALDI-TOF MS spectra (*19*). The PBS solution was dialyzed using a Spectra/Por 1 regenerated cellulose dialysis membrane (MWCO: 6−8 kDa, Spectrum Labratories, Inc.) against the pure water to remove any included electrolytes. The obtained aqueous solution of PEG$_X$(HSA−FeP) (CO adduct complex, 0.5 mL) was spread on a glass plate [30 × 40 mm, thickness: 0.12−0.17 mm, Matsunami Glass Ind., Ltd. (Osaka, Japan)] and evaporated at an ambient temperature in the dark for 12 h, which produced a red-colored transparent solid membrane.

For the scanning electron microscopy measurements, the samples on the glass plate were sputtered with Pd−Pt using a Hitachi E-1030 ion sputter. The SEM observations were performed using a Hitachi S-4500S field emitted scanning electron microscope.

Furthermore, 0.5 mL of an aqueous solution of hyaluronic acid (HA, 0.2, 0.4, 0.6, 0.8, 1.0 wt %) was added to the PEG$_2$-(HSA−FeP) solution (CO adduct complex, 0.5 mL, [HSA] = 5 wt %). The mixture was poured into a poly(styrene) balance dish (44 × 44 × 15 mm) and dried at room temperature in the dark. After 12 h, the formed membrane was gently peeled off and characterized.

The water content of the solid membrane was measured by thermogravimetric-differential thermal analysis using a Rigaku TG8120 instrument at a hearing rate of 10 °C/min.

O_2-Binding Parameters. The O_2 binding to PEG$_X$(HSA−FeP) is expressed by eq 1,

$$\text{PEG}_X(\text{HSA}-\text{FeP}) + \text{O}_2 \underset{k_{\text{off}}}{\overset{k_{\text{on}}}{\rightleftharpoons}} \text{PEG}_X(\text{HSA}-\text{FeP}(\text{O}_2)) \quad (1)$$

where the O_2 binding equilibrium constant $K = k_{on}/k_{off}$.

The PEG$_X$(HSA−FeP) membrane or PEG$_2$(HSA−FeP)/HA hybrid membrane on the glass plate was placed in a 1-cm quartz cuvette for the spectral measurements, which was sealed tightly with a rubber septa. The O_2-binding affinity (gaseous partial pressure at which 50% of FeP was dioxygenated, $P_{1/2} = 1/K$) was determined by the spectral changes at various O_2/N_2 pressures (*17*, *19*, *20*). The UV−vis absorption spectra were recorded within the range of 350−700 nm. The half-lifetime of the autoooxidation of the FeP(O_2) complex was determined by the time-course of the absorption change at 426 nm. The association and dissociation rate constants for O_2 (k_{on}, k_{off}) to the PEG$_X$(HSA−FeP) membrane or PEG$_2$(HSA−FeP)/HA hybrid membrane were measured by a competitive rebinding technique using a Unisoku TSP-1000WK laser flash photolysis instrument (*17*, *19*, *20*).

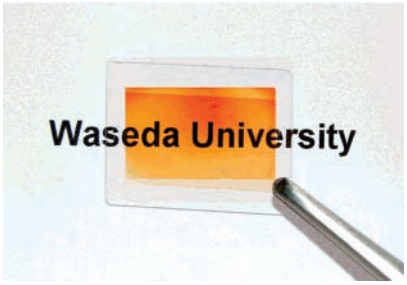


Figure 2. Photograph of the PEG$_2$(HSA−FeP) solid membrane on the glass plate.

RESULTS AND DISCUSSION

Structure of PEG$_X$(HSA−FeP) Membrane. The PEGylation of HSA−FeP (FeP/HSA = 4/1 (mol/mol)) was readily accomplished under mild conditions using the commercially available IMT and maleimide-terminated PEG (*19*). The average number of the PEG chain on the HSA−FeP surface was modulated to 6.0; the viscosity and colloid osmotic pressure of the PBS solution of this molecule ([HSA] = 5 wt %) satisfied the clinical requirements of a red blood cell substitute (*19*). The solution was subsequently desalted by dialysis against pure water and spread on the glass plate. After drying overnight at room temperature, a red-colored transparent solid membrane was formed (Figure 2). The HSA−FeP without the PEG modification did not produce such a homogeneous thin film, only affording a brittle membrane with many cracks.

Scanning electron microscopy observations of the PEG$_2$-(HSA−FeP) membrane showed a uniform thickness of 15 μm and a very smooth surface [Figure 3a,b)]. From a careful inspection of the side-view, we found that the membrane consists of two parts: (i) the surface layer with a thickness of 10 μm made of a highly oriented fibrous component, and (ii) the bottom layer with a thickness of 5 μm made of an amorphous phase (Figure 3b). Cutting the glass plate with a lateral force, the PEG$_2$-(HSA−FeP) membrane was extended and produced long fibers with a width of 350 nm (Figure 3c). The condensed solution ([HSA] = 15 wt %) provided a thick membrane with a thickness of 70 μm, which also has the amorphous bottom layer of 5 μm (Figure 3d). Interestingly, the membrane prepared on the poly-(styrene) dish was mainly composed of the amorphous layer; the surface fibrous phase was less than 20% (Figure 3e). On the other hand, water evaporation of the PEG$_5$(HSA−FeP) solution ([HSA] = 5 wt %) on the glass surface provided a homogeneous membrane, which is made of the fibrous component. The precise mechanism of the fiber formation during the water evaporation process is still not clear, but our results show that the structure of the PEG$_X$(HSA−FeP) membrane is very dependent on the surface feature of the substrate and the chain length of the PEG.

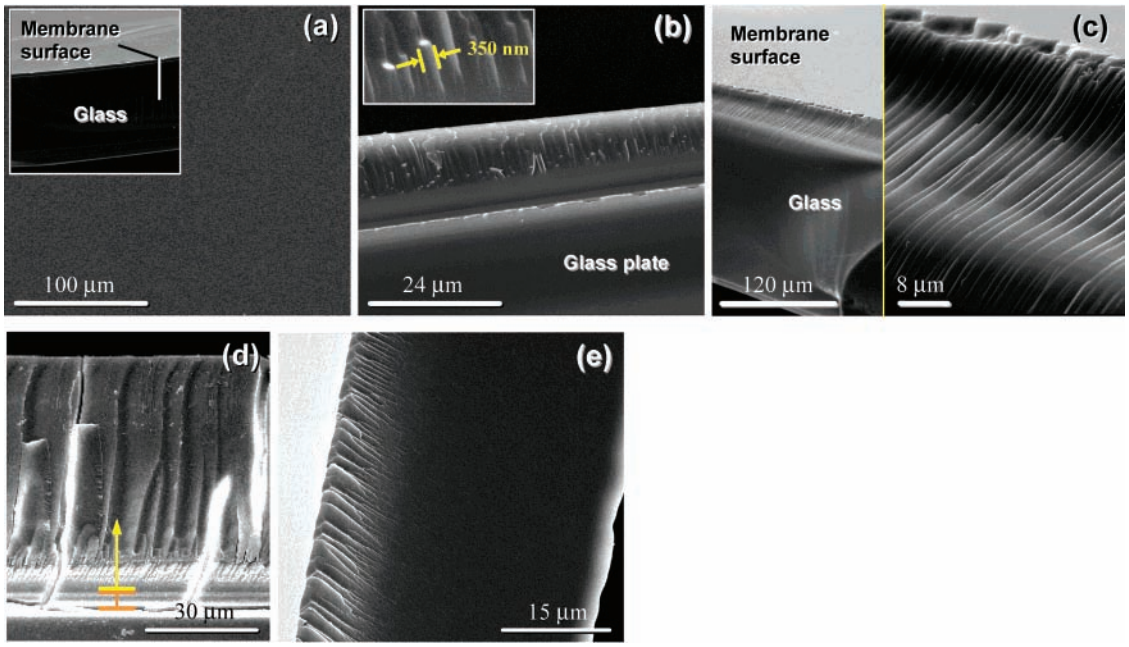


Figure 3. SEM images of the PEG_2(HSA−FeP) membrane on the glass plate. (a) Top-view of the very smooth surface without any crack. (b) Side-view of the membrane section, showing a surface layer made of fibrous component and a bottom layer made of an amorphous phase. (c) Extended nanofiber structure of the surface layer. (d) Thick membrane with a 5 μm amorphous bottom layer (indicated by orange bars) on the glass surface. (e) Membrane prepared on the poly(styrene) surface.

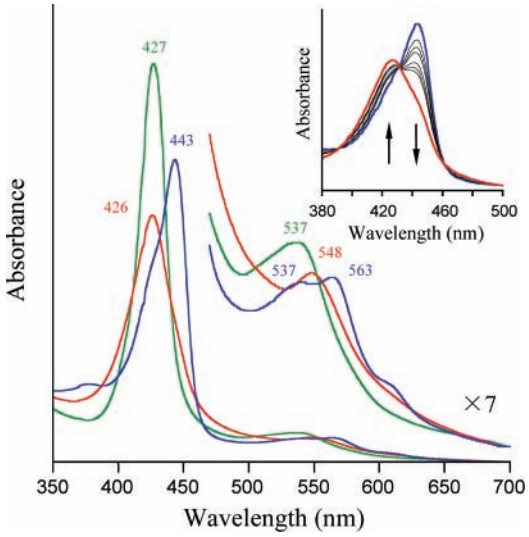


Figure 4. UV−vis absorption spectral changes of the PEG_2(HSA−FeP) membrane on the glass plate at 25 °C (blue line: under N_2, red line: under O_2, green line: under CO). The inset shows the spectral changes at various O_2-partial pressures (P_{O_2}: 0, 10, 19, 30, 76, 114, 152, 760 Torr from blue to red line).

O_2-Binding Properties. The UV−vis absorption spectrum of the PEG_X(HSA−FeP) membrane showed an absorption maxima (λ_{max}) at 427 and 537 nm, indicating the formation of the CO-coordinate low-spin state of FeP (Figure 4) (*17*, *19*−21). This suggested that the ferrous carbonyl complex was retained during the water evaporation for 12 h at an ambient temperature. Light irradiation to the membrane using a 500-W halogen lamp under a 100% O_2 for 20 min led to the CO dissociation and O_2-adduct complex formation of FeP (λ_{max}: 426, 548 nm). By flowing N_2 to the membrane in the quartz cuvette, the UV−vis absorption spectrum shifted to that of a high-spin ferrous complex with an intramolecularly coordinated 2-methylimidazolyl group (λ_{max}: 443, 537, 563 nm). These spectral changes were repeatedly observed and found dependent on the O_2-partial pressure (0 Torr ↔ 760 Torr), which demonstrated that the reversible dioxygenation of FeP took place in the membrane. The half-lifetime of the autoxidation ($\tau_{1/2}$) of the FeP(O_2) to Fe^{3+}P was 40 h at 37 °C, which is 3-fold longer than the value in the PBS solution.

The O_2-binding affinity of the PEG_2(HSA−FeP) membrane ($P_{1/2}$ = 40 Torr, 25 °C) determined from the UV−vis absorption spectral changes at various O_2/N_2 pressures (Figure 4 inset) was 4-fold lower (high $P_{1/2}$) than that of the monomeric PEG_2(HSA−FeP) in water (Table 1). Since the O_2 coordination to the Fe porphyrin is an exothermic reaction, the O_2-binding affinity of the membrane decreased at 37 °C ($P_{1/2}$ = 61 Torr). In contrast, PEG_5(HSA−FeP) membrane showed the identical O_2-bidnig affinity to that in aqueous PBS solution ($P_{1/2}$ = 11 Torr, 25 °C).

In order to elucidate the O_2-binding kinetics of the PEG_X-(HSA−FeP) membrane, flash photolysis experiments were carried out. The time course of the absorption change after the laser pulse irradiation to the PEG_2(HSA−FeP) membrane in the quartz cuvette exhibited two first-order kinetics. We previously reported that the binding processes of O_2 to HSA−FeP and PEG_X(HSA−FeP) in aqueous media were fitted to a double-exponential expression, giving two different association rate constants for the fast and slow reactions (k_{on} and k'_{on}) (*19*, *22*). It has been interpreted that the O_2 recombination to FeP in the protein could be affected by the each nanoscopic environment around the accommodation site, for example, a steric hindrance of the amino acid residue and difference in polarity. The k'_{on} was used to be approximately one-third of the k_{on} (*17*, *19*, *22*). Nevertheless, the ratio of k'_{on}/k_{on} observed in the PEG_2-(HSA−FeP) membrane was less than one-tenth (Table 1). We then theorized that this can be attributed to the O_2 diffusion in the two parts of the membrane. In the major surface layer of the fibrous component, the diffusion of the O_2 could be slower than in water, and it could be much slower in the amorphous bottom phase. The following results support our assumption. (i) The thickness ratio of the two layers (10 μm/5 μm = 2.0) corresponds well to the molar ratio of the k_{on} and k'_{on} (= 2.1). (ii) The absorption decay accompanied with the O_2 rebinding

Table 1. O_2-Binding Parameters of Solid Membranes of PEG_X(HSA−FeP) at 25 °C

system	k_{on} (Torr^{-1} s^{-1})	k'_{on} (Torr^{-1} s^{-1})	k_{off} (s^{-1})	k'_{off} (s^{-1})	$P_{1/2}$ (Torr)[a]
PEG_2(HSA−FeP) solution[b]	20	7.5	1.7×10^2	70	11 [32]
PEG_5(HSA−FeP) solution[b]	20	10	1.7×10^2	90	11 [31]
PEG_2(HSA−FeP) membrane	5.7	0.54	2.3×10^2	22	40 [61]
PEG_5(HSA−FeP) membrane	3.1		34		11 [33]
PEG_2(HSA−FeP)/HA membrane	4.3	0.22	1.4×10^2	7	32 [60]
Hb solution (T-state)[c]	4.8		1.8×10^2		40
Hb/maltose membrane[d]	1.2×10^{-13}		8.3×10^{-11}		760

[a] At 37 °C in brackets [ ]. [b] In PBS solution (pH 7.4), ref 19. [c] In 50 mM potassium phosphate buffer (pH 7.0) at 20 °C, ref 24. [d] Reference 23.

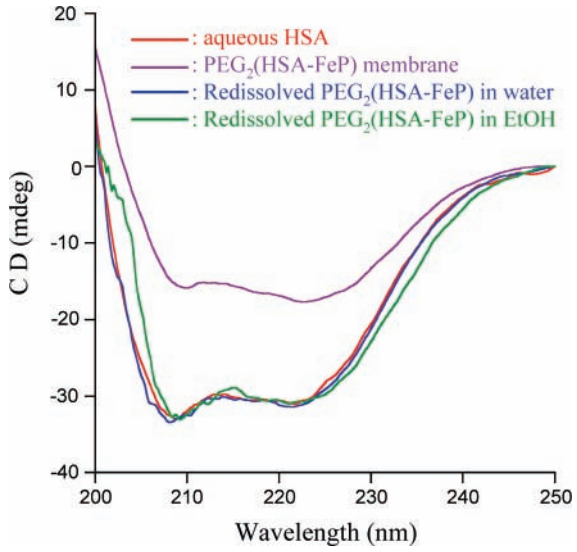


Figure 5. CD spectra of PEG_2(HSA−FeP) at various conditions at 25 °C.

to the PEG_5(HSA−FeP) membrane, which consists of the homogeneous fibrous layer, was fitted by single exponential, giving only one association rate constant k_{on}.

The low O_2-binding affinity of the solid membrane of PEG_2-(HSA−FeP) compared to that in the PBS solution is kinetically due to the low association rate constants (Table 1). Even though this result was in significant contrast to the fact that the similar solid membrane of human Hb with maltose (Hb/maltose = 6/4, wt/wt) could not bind O_2 under the same conditions, its O_2-binding affinity was extremely low ($P_{1/2}$ = 760 Torr) (*23*). Since the quaternary structure of Hb was restrained in the solid form, its tense-state conformation cannot change to a relaxed-state with a high O_2-binidng affinity (*24*). In the PEG_X(HSA−FeP) membrane, the protein scaffold was solidified by a bulk water evaporation; however, it would not dramatically influence the dioxygenation of FeP, because the O_2-binding equilibrium is not synchronized with the quaternary structure of the HSA matrix.

PEG_X(HSA−FeP) in Organic Solutions. We have found that the PEG modification enables HSA−FeP to dissolve in organic solvents. The red-colored PEG_X(HSA−FeP) membrane was homogeneously soluble not only in water but also in ethanol and chloroform. The CD spectrum of the membrane showed a different pattern compared to that in aqueous media (Figure 5). The intensity ratio of the double minimum peaks at 208 and 222 nm (I_{208}/I_{222}) of rHSA or PEG_X(HSA−FeP) is normally 1.1 (*25*, *26*), while the membrane showed 0.9. Interestingly, the redissolved aqueous and ethanol solutions both showed the same spectra as the original aqueous HSA. This result implies that the change of the secondary structure in the protein in the solid and liquid states is reversible. The ethanolic PEG_X(HSA−FeP) also exhibited the same absorption changes upon exposure to O_2 and N_2. These organic solutions can also be cast on a glass surface to form identical PEG_X(HSA−FeP) membranes.

PEG_2(HSA−FeP) Membrane with Hyaluronic Acid. An attempt to isolate the PEG_X(HSA−FeP) membrane from the glass surface unfortunately failed, because it was rather fragile, when peeled off. We then added a supporting polymer to the protein solution and prepared the solid membrane on a glass plate or a poly(styrene) dish. Hyaluronic acid (HA), which is known as a glycosaminoglycan component of connective tissues, hyaline body and extracellular matrix, was selected as the biocompatible polymer support (*27*). We also expected that the high water retention capability of HA may have a positive effect on retarding the proton-driven oxidation of the FeP(O_2) complex. Water evaporation of the PEG_2(HSA−FeP)/HA mixture [0.5 mL/0.5 mL, total [HSA] = 2.5 wt %, total [HA] = 0.2 wt %] on the glass plate or poly(styrene) dish produced the red-colored uniform solid membranes. It could not be isolated from the glass plate but was easily peeled off from the poly(styrene) surface, providing a free-standing thin film of the PEG_2(HSA−FeP)/HA hybrid [Figure 6a]. The formation of the flexible film was quite dependent on the HA content. When the total concentration of HA is 0.2−0.5 wt %, we could readily obtain the membrane from the plastic surface. The SEM observations of the film showed that it was made of a homogeneous layer with a relatively coarse structure (Figure 6b). In contrast, the film cast on the glass plate consists of the two-layered form: a major course phase and bottom dense phase (Figure 6c). This implies

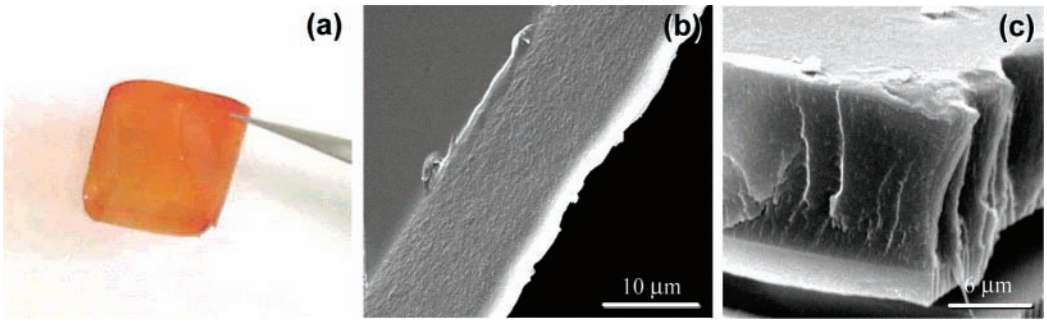


Figure 6. PEG_2(HSA−FeP)/HA membrane. (a) Photograph of the free-standing flexible film, which is prepared on the poly(styrene) surface. (b) SEM of the isolated film. (c) SEM of the membrane prepared on the glass surface.

that the membrane structure of the PEG_2(HSA−FeP)/HA is also influenced by the surface properties of the substrate.

The UV−vis absorption spectral pattern reversibly changed from that of the five-N-coordinate high-spin ferrous complex under an N_2 atmosphere (λ_{max}: 445, 540, 566 nm) to that of the O_2-adduct complex under an O_2 atmosphere (λ_{max}: 426, 545 nm). The O_2-binding parameters of the PEG_2(HSA−FeP)/HA membrane showed a tendency similar to the PEG_2(HSA−FeP) film; the low O_2-binding affinity ($P_{1/2}$ = 32 Torr, 25 °C) is mainly due to the slow association rate constant (Table 1). The half-life of the O_2-adduct complex was 40 h at 37 °C; we could not see any water retention effect of HA that could prolong the stability of FeP(O_2). The water content of the PEG_2(HSA−FeP) membrane and PEG_2(HSA−FeP)/HA membrane were determined by the differential thermal analyses to be 6.5 wt % and 6.6 wt %, respectively.

CONCLUSIONS

The stable solid membranes of a PEGylated artificial hemoprotein have been prepared, and their O_2-binding properties were physicochemically characterized in relation to the layer morphology. The red-colored thin film is soluble again in water and organic solvents (ethanol, chloroform) without any deformation of the secondary structure of the protein. The addition of hyaluronic acid as the polymer support gave the free-standing flexible film. These O_2-binding albumin membranes are a red blood cell substitute with a micrometer-thickness that can be preserved anywhere (e.g., on a shelf and in an ambulance) and reproduced as a saline solution at anytime (e.g., at the scene of a disaster). Furthermore, it would be of great medical importance for a variety of clinical treatments, such as O_2-enriched coating agents for medical devices or artificial organs and an O_2-transporting adhesive plaster for wound healing.

ACKNOWLEDGMENT

This work was partially supported by a Grant-in-Aid for Scientific Research (No. 16350093, No. 18750156) from JSPS, PRESTO, and from JST, and Health Science Research Grants from MHLW, Japan.

LITERATURE CITED

(1) Harris, J. M., Martin, N. E., and Modi, M. (2001) Pegylation—a novel process for modifying pharmacokinetics. *Clin. Pharmacokinet. 40*, 539−551.

(2) Veronese, F. M., and Harris, J. M. (2002) Introduction and overview of peptide and protein PEGylation. *Adv. Drug Delivery Rev. 54*, 453−456.

(3) Roberts, M. J., Bentley, M. D., and Harris, J. M. (2002) Chemistry for peptide and protein PEGylation. *Adv. Drug Delivery Rev. 54*, 459−476.

(4) Veronese, F. M. (2001) Peptide and protein PEGylation: a review of problems and solutions. *Biomaterials 22*, 405−417.

(5) Veronese, F. M., and Pasut, G. (2005) PEGylation, successful approach to drug delivery. *Drug Discovery Today 10*, 1451−1455.

(6) Nucci, M. L., Shorr, R., and Abuchowski, A. (1991) The therapeutic value of poly(ethylene glycol) modified proteins. *Adv. Drug Delivery Rev. 6*, 133−151.

(7) Abuchowski, A., van Es, T., Palzuk, N. C., and Davis, F. F. (1977) Alteration of immunological properties of bovine serum albumin by covalently attachment of polyethylene glycol. *J. Biol. Chem. 252*, 3578−3581.

(8) Abuchowski, A., McCoy, J. R., Palczuk, N. C., van Es, T., and Davis, F. F. (1977) Effect of covalently attachment of polyethylene glycol on immunogenicity and circulating life of bovine liver catalase. *J. Biol. Chem. 252*, 3582−3586.

(9) He, X. H., Shaw, P. C., and Tam, S. C. (1999) Reducing the immunogenicity and improving the in vivo activity of trichosanthin by site-directed PEGylation. *Life Sci. 65*, 355−368.

(10) Hinds, K. D., and Kim, S. W. (2002) Effects of PEG conjugation on insulin properties. *Adv. Drug Delivery Rev. 54*, 505−530.

(11) Vandegriff, K. M., Malavalli, A., Wooldbridge, J., Lohman, J., and Winslow, R. M. (2003) MP4, a new nonvasoactive PEG-Hb conjugate. *Transfusion 43*, 509−516.

(12) Manjula, B. M., Tsai, A., Upadhya, R., Perumalsamy, K., Smith, P. K., Malavalli, A., Vandegriff, K., Winslow, R. M., Intaglietta, M., Prabhakaran, M., Friedman, J. M., and Acharya, A. S. (2003) Site-specific PEGylation of hemoglobin at Cys-93(β): correlation between the colligative properties of the PEGylated protein and the length of the conjugated PEG chain. *Bioconjugate Chem. 14*, 464−472.

(13) Olofsson, C., Ahl, T., Johansson, T., Larsson, S., Nellgard, P., Ponzer, S., Fagrell, B., Przybelski, R., Keipert, P., Winslow, N., and Winslow, R. M. (2006) A multicenter clinical study of the safety and activity of maleimide-polyethylene glycol-modified hemoglobin (hemospan) in patients undergoing major orthopedic surgery. *Anesthesiology 105*, 1153−1163.

(14) Takahashi, K., Ajima, A., Yoshimoto, T., and Inada, Y. (1984) Polyethylene glycol-modified catalase exhibits unexpectedly high activity in benzene. *Biochem. Biophys. Res. Commun. 125*, 761−766.

(15) Kawahara, N. Y., and Ohno, H. (1997) Induced thermostability of poly(ethylene oxide)-modified hemoglobin in glycols. *Bioconjugate Chem. 8*, 643−648.

(16) Wiwatchaiwong, S., Nakamura, N., and Ohno, H. (2006) Spectroscopic characterization and electrochemistry of poly(ethylene oxide)-modified myoglobin in organic solvents. *Biotechnol. Prog. 22*, 1276−1281.

(17) Komatsu, T., Matsukawa, Y., and Tsuchida, E. (2002) Effect of heme structure on O_2-binding properties of human serum albumin−heme hybrids: intramolecular histidine coordination provides a stable O_2-adduct complex. *Bioconjugate Chem. 13*, 397−402.

(18) Komatsu, T., Yamamoto, H., Huang, Y., Horinouchi, H., Kobayashi, K., and Tsuchida, E. (2004) Exchange transfusion with synthetic oxygen-carrying plasma protein "albumin-heme" into an acute anemia rat model after seventy-percent hemodilution. *J. Biomed. Mater. Res. A 71A*, 644−651.

(19) Huang, Y., Komatsu, T., Wang, R.-M., Nakagawa, A., and Tsuchida, E. (2006) Poly(ethylene glycol)-conjugated human serum albumin including iron porphyrins: surface modification improves the O_2-transporting ability. *Bioconjugate Chem. 17*, 393−398.

(20) Tsuchida, E., Komatsu, T., Kumamoto, S., Ando, K., and Nishide, H. (1995) Synthesis and O_2-Binding properties of tetraphenylporphyrinatoiron(II) derivatives bearing a proximal imidazole covalently bound at the β-pyrrolic position. *J. Chem. Soc., Perkin Trans. 2*, 747−753.

(21) Collman, J. P., Brauman, J. I., Iverson, B. L., Sessler, J. L., Morris, R. M., and Gibson, Q. H. (1983) O_2 and CO binding to iron(II) porphyrins: a comparison of the "picket fence" and "pocket" porphyrins. *J. Am. Chem. Soc. 105*, 3052−3064.

(22) Komatsu, T., Matsukawa, Y., and Tsuchida, E. (2000) Kinetics of CO and O_2 binding to human serum albumin−heme hybrid. *Bioconjugate Chem. 11*, 772−776.

(23) Chung, J. E., Sakai, H., Takeoka, S., Nishide, H., and Tsuchida, E. (1995) Coordination behavior of O_2 and CO in a solid film consisting of hemoglobin and maltose. *Bull. Chem. Soc. Jpn. 68*, 1006−1011.

(24) Sawicki, C. A., and Ginson, Q. H. (1977) Properties of the T state of human oxyhemoglobin studied by laser photolysis. *J. Biol. Chem. 252*, 7538−7547.

(25) Nakajou, K., Watanabe, H., Kragh-Hansen, U., Maruyama, T., and Otagiri, M. (2003) The effect of glycation on the surface on the structure, function and biological fate of human serum albumin as revealed by recombinant mutants. *Biochim. Biophys. Acta 1623*, 88−97.

(26) Peters, T. (1996) *All about albumin: biochemistry, genetics and medical applications*; Academic Press, San Diego.

(27) Goa, K. L., and Benfield, P. (1994) Hyaluronic-acid −a review of its pharmacology and use as a surgical and in ophthalmology, and its therapeutic potential in joint disease and wound-healing. *Drugs 47*, 536−566.

BC070086M

Reaction of the Indole Group with Malondialdehyde: Application for the Derivatization of Tryptophan Residues in Peptides

Alexandra Foettinger,† Michael Melmer, Alexander Leitner, and Wolfgang Lindner*

Department of Analytical Chemistry and Food Chemistry, University of Vienna, Währinger Strasse 38, 1090 Vienna, Austria.
Received January 2, 2007; Revised Manuscript Received June 14, 2007

A method for the selective modification of tryptophan residues based on the reaction of malondialdehyde with the indole nitrogen of the tryptophan side chain at acidic conditions is presented. The condensation reaction is quantitative and leads to a substituted acrolein moiety with a remaining reactive aldehyde group. As is shown, this group can be further converted to a hydrazone using hydrazide compounds, but if hydrazine or phenylhydrazine are used, release of the free indole group is observed upon cleavage of the substitution. Alternatively, secondary amines such as pyrrolidine may also act as cleavage reagents. This general reaction scheme has been adapted and optimized for the derivatization of tryptophan-containing peptides and small N-heterocyclic compounds. It serves as the basis of a reversible tagging scheme for Trp-peptides or molecules of interest carrying indole structures as it allows the specific attachment and removal of a reactive group that may be used for a variety of purposes such as affinity tagging.

INTRODUCTION

Chemical labeling strategies in the field of peptide and protein analysis play an increasingly important role not only for structure elucidation, but also for quantitative purposes. In this context, derivatization reactions are used to introduce stable isotopes that enable relative quantification or to enrich certain classes of peptides and proteins via affinity tags (*1*, *2*). Furthermore, labeling and cross-linking reactions can be used for protein conformation studies, especially in combination with mass spectrometry (*3*−*5*). Moreover, for the determination of residues contributing to active sites of, e.g., receptor proteins or enzymes, dedicated derivatization reactions can be applied (*6*, *7*).

Tryptophan is an interesting target for the development of chemical tagging strategies. It is a low abundance amino acid with 1.1% frequency (*8*), but approximately 90% of proteins contain at least one tryptophan residue in their sequence (*9*). There are several well-known methods for the derivatization of tryptophan residues in peptides and proteins, most of them targeting the C-2 or C-3 position of the indole ring (see Figure 1). 2-Hydroxy-5-nitrobenzylbromide, for example, finds broad application for the investigation of the role of Trp in active sites of enzymes (*6*, *7*) for the estimation of the tryptophan content in proteins (*10*, *11*) and has recently been used for the determination of the surface accessibility of Trp residues in proteins (*12*). Another frequently used group of reagents are sulfenyl halides. Compounds like 2-nitro- and 2,4-dinitrophenylsulfenylchloride reacting at the 2-position of the indole group can be used for studying active sites of enzymes (*13*). Applications in the field of proteomics, including relative quantification studies employing stable isotope-labeled analogues, were reported (*14*−*16*); *N*-bromosuccinimide is a derivatizing reagent used for similar applications (*17*). Another method, selectively targeting the indole nitrogen, uses rhodium carbenoids for the derivatization of tryptophan residues in proteins as recently reported by Antos et al. (*18*).

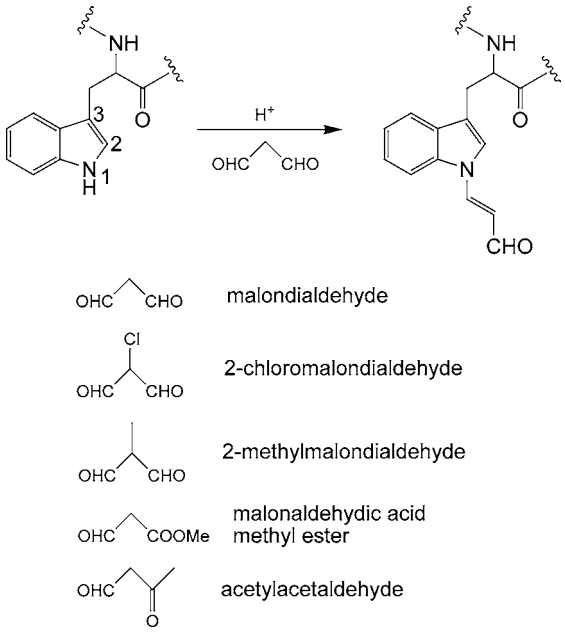


Figure 1. Reaction of the indole group of tryptophan in a peptide with malondialdehyde (MDA) and alternative reagents used in the study.

The principal reaction of the indole ring of the tryptophan side-chain with dicarbonyl compounds like acetylacetaldehyde or malondialdehyde (MDA) has already been briefly described in the 1960s by Teuber et al. (*19*, *20*) but was not followed up since then. The authors investigated the reaction on a synthetic scale for carbazole- and indole-type compounds in concentrated hydrochloric acid. Under these conditions, malondialdehyde also reacts with the guanidine group of arginine forming a pyrimidine (*21*) as reported by King and recently followed by work in our group (*22*).

We have investigated this reaction for the purpose of labeling arginine residues in peptides and observed a side reaction with tryptophan residues during optimization not observed by King.

* Correspondence to: Wolfgang Lindner, Department of Analytical Chemistry and Food Chemistry, University of Vienna, Währinger Strasse 38, 1090 Vienna, Austria. Phone: +43 1 4277 52300. Fax: +43 1 3196312. E-mail: wolfgang.lindner@univie.ac.at.

† Current address: Baxter AG, Biomedical Research Center, Uferstrasse 15, 2304 Orth/Donau, Austria.

10.1021/bc070001h CCC: $37.00 © 2007 American Chemical Society
Published on Web 08/17/2007

Further studies have now revealed that the modification corresponds to a condensation product with the indole nitrogen as shown in Figure 1, in accordance with Teuber's previous work. Here, we report how this reaction scheme can be adapted for the selective derivatization of tryptophan residues in peptides and can be applied for the introduction of functional tags.

EXPERIMENTAL PROCEDURES

Materials. The derivatization reagents, 1,1,3,3-tetramethoxypropane (TMP) and 1,1,3,3-tetraethoxypropane (TEP), were from Aldrich (Steinheim, Germany). 1,1,3,3-tetraisopropoxypropane (*22*), 2-methylmalondialdehyde (*23*), and the sodium salt of MDA (*24*) were synthesized in-house.

All other chemicals and reagents were from Fluka (Buchs, Switzerland), Sigma (Deisenhofen, Germany), Aldrich, or Acros Organics (Geel, Belgium). All model peptides were acquired from Bachem and used as received (Weil am Rhein, Germany).

Instrumentation. Liquid chromatography−mass spectrometry was performed on an Agilent 1100 HPLC system coupled to an Agilent MSD Trap SL quadrupole ion trap mass spectrometer (Agilent Technologies, Waldbronn, Germany) equipped with a standard electrospray source. Chromatographic separations were performed on a BetaBasic-18 column (150 × 4.6 mm, 3 μm, Thermo Electron Corporation, Runcorn, UK) equipped with a guard column containing the same material. The mobile phases for gradient elution were (A) 0.1% (v/v) formic acid in water and (B) 0.1% (v/v) formic acid in acetonitrile. The gradient was as follows: 0−5 min 5% B, 5−25 min 5−50% B, 25−30 min 50% B, 30−35 min 50−5% B, and 35−40 min 5% B. The flow rate was set to 0.7 mL min^{-1} and the column temperature to 25 °C. UV absorption was monitored at 230 nm using an Agilent 1100 variable wavelength detector.

For direct infusion experiments, samples were introduced with a syringe pump (kd scientific, Holliston, MA) at a flow rate of 5 μL min^{-1}.

Preparation and Characterization of the MDA Derivative of *N*-Acetyltryptophan (N-Ac-Trp) as Model/Reference Compound. Approximately 100 mg of N-Ac-Trp (400 μmol) was dissolved in 10 mL of 80% aqueous TFA and 800 μL of TMP (~10-fold molar excess) was added dropwise. The solution was stirred at room temperature for 1 h. Then, the solvent was evaporated in vacuo, and the product was taken up in ethyl acetate and purified by flash chromatography on silica with the mobile phase consisting of ethyl acetate, methanol, and acetic acid (40/1/1, v/v/v). Following removal of the solvents in vacuo, an intensively yellowish colored product was obtained in 72% yield.

^{1}H NMR (d_6-DMSO, 400 MHz): 9.49 (d, 1H), 8.55 (d, 1H), 8.09 (d, 1H), 7.90 (d, 1H), 7.77 (s, 1H), 7.62 (d, 1H), 7.35 (t, 1H), 7.26 (t, 1H), 6.4 (m, 1H), 4.56 (m, 1H), 3.18 (q, 1H), 3.08 (q, 1H), 1.83 (s, 3H) ppm.

^{13}C NMR (d_6-DMSO, 100 MHz): 191.95 (aldehyde C═O), 173.46 (carboxyl C═O), 169.58 (N-acetyl C═O), 145.84 (Ar CH), 136.45 (Ar), 130.26 (Ar), 124.31 (Ar CH), 123 (Ar CH), 122.92 (Ar CH), 119.84 (Ar CH), 119.68 (Ar), 112.58 (Ar CH), 111.09 (Ar CH), 52.76 (N-acetyl CH_3), 27.31 (CH_2), 22.81 (CH) ppm.

MS (ESI-quadrupole): $[M + H]^+ = 301.4$.

UV spectrum (methanol): 209, 272, 332 nm (ϵ 2.81 × 10^{-5}, 1.63 × 10^{-5}, 2.36 × 10^{-5} L mol^{-1} cm^{-1}).

Fluorescence spectrum (methanol): $\lambda_{exc.,max} = 230$ nm, $\lambda_{em.,max} = 380$ nm.

Analytical-Scale Derivatization Procedure for Trp-Containing Peptides. Typically, 50 μg of peptide was dissolved in 50 μL of aqueous acidic solution (hydrochloric acid, TFA, or acetic acid), and a 100-fold molar excess of TMP (0.9 μL) or TEP (1.2 μL) was added. After a reaction time of 1 h (at room temperature), the reaction mixture was diluted with water (1:10 for TFA and 1:100 for HCl conditions, respectively) and purified by solid-phase extraction on reversed-phase C_{18} material (100 mg sorbent, Phenomenex, Torrence, CA) to remove the acid and excess reagents. The elution solution was either used directly for infusion experiments or evaporated to dryness with nitrogen and redissolved in mobile phase for LC-MS analysis.

Formation of the Hydrazones. Typically, 50 μg of MDA-labeled peptide was dissolved in 200 μL ammonium acetate buffer (pH adjusted to 5 with acetic acid) containing 10 to 20 mM of hydrazide reagent (50−100 fold molar excess). Usually, the reaction proceeded for 1−2 h.

Cleavage Reaction Using Hydrazine Dihydrochloride. 50 μg of labeled peptide was incubated in 200 μL of a 20 mM aqueous hydrazine dihydrochloride solution with the pH adjusted to approximately 3 with acetic acid. The reaction mixture was incubated for 1 h at 50 °C to achieve complete cleavage.

Cleavage Reaction Using Pyrrolidine. 50 μg of labeled peptide was incubated in 200 μL of a water/acetonitrile mixture (50:50, v/v) containing 500 mM pyrrolidine. The reaction mixture was left for 1 h at room temperature to achieve complete cleavage.

Hazardous Substances Statement. Hydrazine dihydrochloride is a toxic and potentially carcinogenic reagent and should be handled with special care. Appropriate safety precautions should be taken when handling concentrated acids and bases.

RESULTS AND DISCUSSION

Reaction of the Indole Group of Tryptophan Residues with MDA−Reaction Conditions and Specificity. As mentioned in the Introduction, a side reaction with tryptophan residues was observed during MDA-labeling of arginine residues in peptides (*22*). To investigate this phenomenon further, dedicated studies were carried out using *N*-acetyltryptophan as a model compound. Using conditions comparable to the analytical-scale reaction for arginine labeling (12 M hydrochloric acid, room temperature), the N-Ac-Trp MDA-derivative was isolated in preparative scale (see Experimental Procedures for details). Characterization by ^{1}H and ^{13}C NMR as well as mass spectrometry allowed us to assign a structure like that shown in Figure 1, corresponding to a condensation product of MDA with the indole nitrogen in the form of an acrolein-type derivative.

To explore the possibility of applying this reaction for the modification of Trp-containing peptides, we studied whether lower concentrations of HCl or other organic acids can also be used for this reaction in order to avoid side reactions with arginine residues in peptides. Throughout this optimization procedure, N-Ac-Trp and the standard peptides PTHIK**W**GD, HPKRP**W**IL, L**W**MR, KG**W**K, and A**W** were used as model analytes. The reactivity was evaluated by means of mass spectrometry using an ion trap mass spectrometer with electrospray ionization either by direct infusion of the sample solution or by LC-MS.

First, we elucidated whether analyte-friendly conditions for a complete derivatization reaction can be achieved in reasonable time, avoiding degradation of the analytes and the occurrence of side reactions. Therefore, kinetic studies were performed with N-Ac-Trp at different concentrations of aqueous HCl (0.1, 1, 3, 6, and 12 M in water), TFA (20%, 50%, and 80% in water and 100%, v/v), and acetic acid (50% and 80% in water and 100%, v/v), and the reaction was followed by LC-MS and LC-UV. As a reagent, malondialdehyde may be applied in its commercially available acetal form (as tetramethoxy- or tetraethoxypropane) from which MDA is formed in situ during the reaction. Selected results illustrating the reaction kinetics in HCl

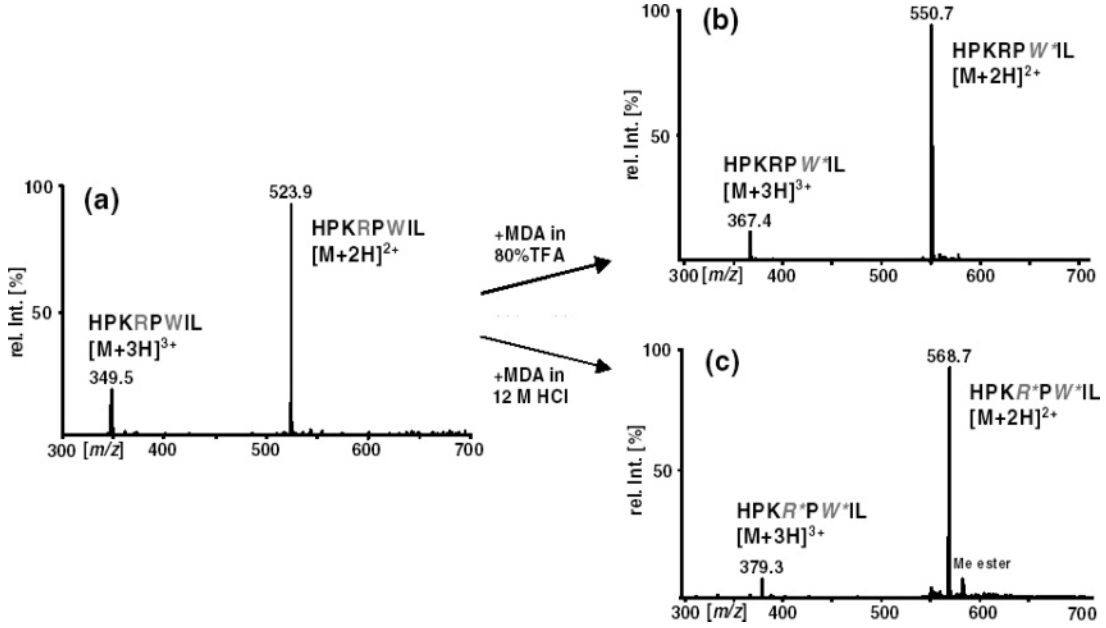


Figure 2. Mass spectra of the peptide HPKRPWIL (a) in the free form ($[M + 2H]^{2+} = 523.9$, $[M + 3H]^{3+} = 349.5$), (b) after MDA derivatization of Trp-residues in 80% TFA ($[M + 2H]^{2+} = 550.7$, $[M + 3H]^{3+} = 367.4$), and (c) after MDA derivatization of Trp and Arg residues in 12 M HCl ($[M + 2H]^{2+} = 568.7$, $[M + 3H]^{3+} = 379.3$). Modified residues are marked with asterisks.

and TFA solutions are shown as Supporting Information (Figures S1−S3).

Generally, the reaction proceeds in the presence of all three acids, but in acetic acid, even at a very high concentration, the reaction is not quantitative after 1 h (data not shown). When using smaller amounts of acid such as 1 M HCl or 20% TFA or less in aqueous solution, the formation of Schiff bases with amino groups that are usually present in amino acids and peptides (N-terminus, lysine) is observed and the yield of the desired reaction product is reduced. Consequently, we found that at least 3 M HCl or 50% of TFA in water are necessary to achieve complete indole group reaction within 1 h at room temperature and to avoid Schiff base formation. Using aqueous TFA (usually 80%), no side reactions such as Schiff base formation or conversion of the guanidine group of arginine (*22*) are observed. In contrast, when using HCl the reaction with arginine residues has to be considered, which always proceeds to some extent in the presence of HCl but completely only at 12 M HCl (*22*). An example of the derivatization reaction at different conditions is given in Figure 2 for the model peptide HPKRPWIL.

Additionally, ester formation with the alcohol released from the MDA−acetal is observed under hydrochloric acid conditions which could be minimized by using the isopropyl−acetal of MDA or the sodium salt of MDA (*24*) which are, however, not commercially available. Reaction yields (>98% for 80% TFA and ∼40% for 12 M HCl) were determined by using the synthetically prepared N-Ac-Trp MDA adduct as external standard for quantification by HPLC-UV, again favoring TFA conditions. Therefore, for all further experiments, 80% TFA was used unless otherwise stated.

Expansion of the Reaction Concept toward Other Analytes and Reagents. In order to elucidate the broader applicability of the MDA-based reaction, we tested various compounds at the optimized reaction conditions. These were, on one hand, various indole and tryptophan derivatives, but also other N-heterocyclic compounds. As already found by Teuber (*19*, *20*), carbazoles react in the same way as the indole group under the conditions we applied. Additionally, 3-chloroindazole and 3-indazolinone also reacted, whereas indazole itself did not react. Pyrrole was found to give the corresponding product at least partially. For pyrazole, benzotriazole, and benzimidazole derivatives, no reaction product was observed.

To explore the full potential of the reaction type outlined in Figure 1, reagents structurally related to malondialdehyde were also tested, and the reaction products were again evaluated by LC-MS. The 2-substituted derivatives of MDA, 2-chloromalondialdehyde and 2-methylmalondialdehyde, were found to react, but much more slowly than MDA itself. In TFA, almost no product was detected, and with hydrochloric acid as the medium even after a reaction time of 2 h, conversion was not complete for Trp−peptides, as could be judged from the underivatized analytes still present. Malonaldehydic acid methyl ester (applied as 3,3-dimethoxypropionic acid methyl ester), carrying one aldehyde and one ester group, does also react with the indole nitrogen in TFA as well as HCl. LC-MS experiments revealed that the reaction proceeds quantitatively with tryptophan and Trp-containing peptides, as no unmodified analytes were observed, but it turned out that the product is chromatographically not homogeneous (whereas the MDA derivative is). Another disadvantage of this reagent is that side products formed by the reagent itself were observed which interfere with the analysis of the derivatized peptides (e.g., as coeluting peaks during LC-MS analysis). Acetylacetaldehyde (used as the dimethylacetal) also reacts according to the general reaction scheme shown in Figure 1 as observed previously by Teuber et al. (*19*, *20*) but establishes the same problem concerning disturbing side products.

Reagents having only keto groups, but no aldehyde functionalities such as acetylacetone and acetoacetateic acid methyl ester, did not show any reactivity toward the indole group. Using dichloroacetaldehyde (applied as the diethylacetal) as the reagent, no condensation product was observed, and monoaldehydes like propionaldehyde and butyraldehyde did not react in a defined way as well. Although formation of a double bond is possible in principle, this has not been observed, and a mixture of different products was observed by MS analysis. These were not characterized in detail, although evidence for cross-linking processes (i.e., aminal formation) was obtained from LC-MS/MS experiments.

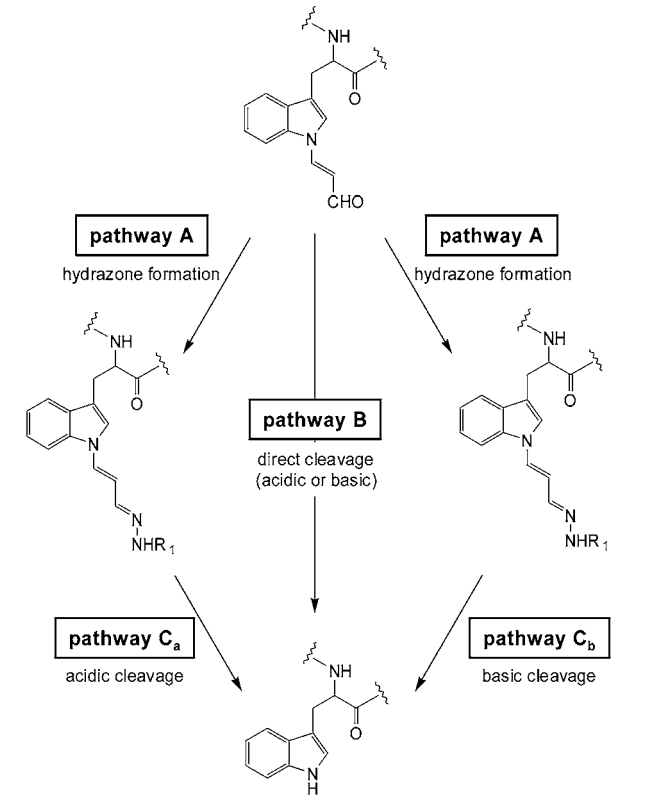


Figure 3. Reaction pathways of the tryptophan−MDA condensates (N-acroleinyl derivatives) that were evaluated in this study. For details, see text.

Further Reactions of the α,β-Unsaturated Aldehyde Derivatives. The α,β-unsaturated aldehyde group resulting from the reaction of the tryptophan side chain with malondialdehyde, which de facto corresponds to a 3-substituted acrolein moiety, opens up the possibility for further reactions. Such carbonyl groups typically react with amino groups or hydrazines or carbazides to Schiff base-type products (see Figure 3). Dinitrophenylhydrazine, for instance, is a classical reagent used for the analysis of small aldehydes often applied in environmental chemistry (*25*), and also for studying protein oxidation (*26*).

Hydrazone formation (pathway A in Figure 3) was successfully tested with 2,4-dinitrophenylhydrazine and semicarbazide using the peptide PTHIKWGD as model analyte (see Figure 4). Using phenylhydrazine, however, we noticed the removal of the initially present acroleinyl label, resulting in the unlabeled indole moiety of the peptide being observed (reaction pathway B in Figure 3). Instability of the condensation product upon addition of excess phenylhydrazine was already noticed by Teuber in the 1960s (*19*). To investigate this in more detail, different hydrazines (phenylhydrazine, benzylhydrazine, hydrazine) and hydrazides (benzylhydrazide, acethydrazide, semicarbazide) were tested for their reactivity, and we observed that hydrazides, with a carbonyl group next to the hydrazine group, form stable adducts with the aldehyde (pathway A), while hydrazines lead to cleavage of the whole MDA adduct resulting in the free indole group (pathway B). 2,4-Dinitrophenylhydrazine seems to be an exception, but the explanation might be that the electron withdrawing nitro groups significantly influence

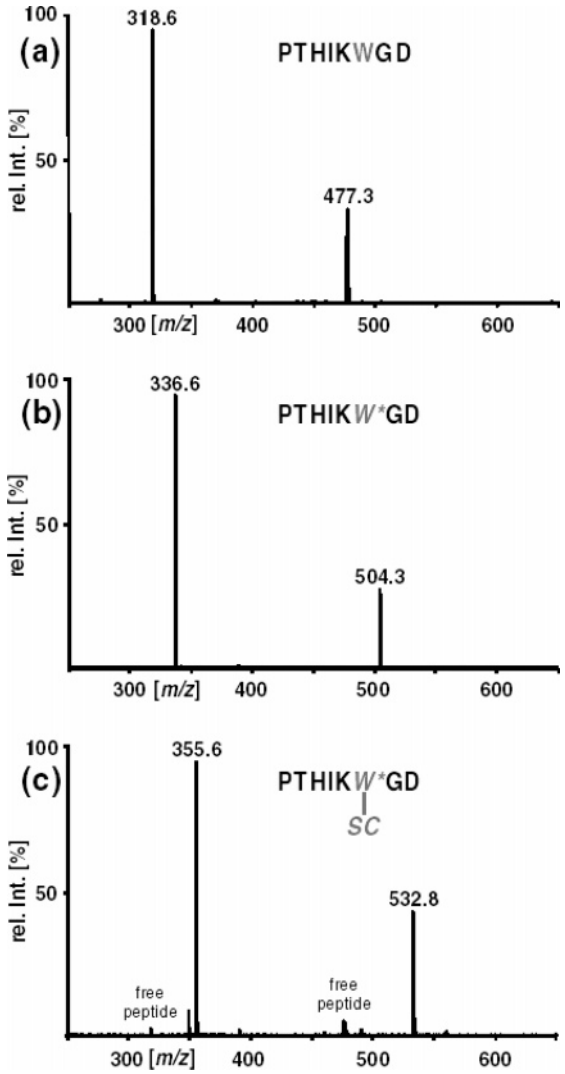


Figure 4. Mass spectra of the peptide PTHIKWGD (a) in the free form ($[M + 2H]^{2+} = 477.3$, $[M + 3H]^{3+} = 318.6$), (b) after reaction with MDA ($[M + 2H]^{2+} = 504.3$, $[M + 3H]^{3+} = 336.6$), and (c) after further reaction of the acroleinyl moiety (free aldehyde) to the semicarbazone ($[M + 2H]^{2+} = 532.8$, $[M + 3H]^{3+} = 355.6$).

the properties of the molecule. As a third option, we incubated a hydrazone-labeled peptide with hydrazine under acidic conditions, also resulting in the parent compound (see pathway C in Figure 3).

The conditions for both reactions, the hydrazone formation and the cleavage of the MDA derivative with hydrazine, were optimized concerning pH, buffer, temperature, and reagent excess followed by LC-MS analysis. Acetate and phosphate buffers were tested at different pH values. For hydrazone formation (pathway A), approximately 50-fold molar reagent excess at a pH of 5−7 was found to be the optimum. A slight increase in reaction speed can be achieved by increasing the temperature from room temperature to 50 °C. At acidic pH conditions, the hydrazones are unstable when the reagent excess is removed. In contrast, the hydrazone bond remains stable in alkaline milieu (pH > 9). The optimal results for the cleavage reaction (pathways B and C_a) were found using hydrazine (applied as the dihydrochloride salt) in ammonium acetate solution at a pH of approximately 3. Increasing the temperature during the cleavage step to 50 °C makes the reaction significantly faster. Using N-Ac-Trp as a model analyte, the individual yields of the three reaction steps (MDA adduct formation, conversion to a hydrazide using acethydrazide, cleavage using hydrazine) were evaluated under optimized conditions. Accord-

ing to LC-MS data, all reactions proceeded with yields in excess of 90%. Furthermore, these reaction conditions were found to be fully compatible with the integrity of a number of model peptides covering all proteinogenic amino acids, as no degradation products were observed in noticeable amounts.

The release of the free indole moiety upon addition of hydrazine is only observed at acidic or neutral pH. Incubation under alkaline conditions, for example, with hydrazine or phenylhydrazine in methanol, leads to formation of a stable hydrazone that can be detected by HPLC-MS, but upon acidification, the whole label is released, leading to the free indole moiety. This very specific cleavage reaction is only possible for the malondialdehyde adduct but not for products resulting from the reaction with the other reagents such as malonaldehydic acid methyl ester (see Figure 1). This led us to the assumption that cleavage of the N-linked acroleinyl substituent only occurs after intermediate formation of the hydrazone, which seems to activate the cleavage reaction. When this process cannot be promoted, the cleavage reaction according to Figure 3 (pathways B and C_a) does not occur.

As an alternative route for the removal of the MDA adduct, we investigated an amine-mediated nucleophilic cleavage. A similar strategy was employed by Villarasa and co-workers (*27*) for the cleavage of N-substituted nucleosides resulting from the reaction with methyl propynoate (other bases may be used as well (*28*, *29*)). Several primary and secondary amines were studied, including ammonium hydroxide, diethylamine, pyrrolidine, and piperidine. Removal of the acroleinyl group from the indole nitrogen was possible with all reagents to some extent, but pyrrolidine consistently gave the best results in terms of reaction speed and clean reaction. Even at room temperature, quantitative cleavage was observed in 1 h upon incubation with 500 mM pyrrolidine in aqueous or hydroorganic medium (water/acetonitrile, 50:50, v/v). Pyrrolidine-mediated cleavage is possible both directly from the MDA adduct (pathways B) and via the hydrazone (pathway C_b).

Conclusions and Outlook; Potential Applications of the Reversible MDA Tag on Tryptophan Residues. In this contribution, we have described the adaptation and optimization of the condensation reaction of malondialdehyde (MDA) with the indole nitrogen of tryptophan residues in peptides under strongly acidic conditions. The resulting acroleinyl label at the indole nitrogen can be used for further reactions, e.g., Schiff base formation, as we have shown for the formation of hydrazides. Cleavage of these MDA labels to the free indole group was found to be possible with reagents such as hydrazine (at acidic conditions) and pyrrolidine (at alkaline conditions).

This highly chemoselective cascade of reactions, including the cleavage of the MDA "tag" resulting in the release of the free intact indole group, opens up the possibility for various highly interesting applications. For instance, we have now developed a solid-phase capture strategy for tryptophan-containing peptides involving a solid support carrying hydrazide groups (*30*). This protocol can be used for the selective enrichment of other analytes of interest that carry indole moieties from complex samples such as biofluids. Furthermore, labels for specific fluorescence detection or isotope labels and so forth could be introduced via the acroleinyl group, always with the possibility of complete cleavage of the label at a later stage, resulting in the unlabeled, intact starting analytes. This could be important for further MS analysis, because high molecular mass labels or tags may be problematic when LC-MS and MS/MS analysis is performed if they show decreased sensitivity or unfavorable fragmentation properties (*31*). This has also been observed for some MDA-labeled Trp−peptides that show dominant cleavage of water during MS/MS, but can be overcome by release of the free indole group before MS analysis.

ACKNOWLEDGMENT

The authors would like to thank the FWF (Austrian Science Fund, project #P15482) for financial support.

Supporting Information Available: LC-MS and LC-UV chromatograms illustrating the reaction kinetics of N-Ac-Trp with MDA in 1, 3, and 6 M HCl as well as 80% TFA (Figures S1 and S2, respectively); overview of reaction kinetics (% yield in dependence of reaction time) for the MS and UV assays (Figure S3). This material is available free of charge via the Internet at http://pubs.acs.org.

LITERATURE CITED

(1) Leitner, A., and Lindner, W. (2004) Current chemical tagging strategies for proteome analysis by mass spectrometry. *J. Chromatogr., B 813*, 1−26.

(2) Leitner, A., and Lindner, W. (2006) Chemistry meets proteomics: The use of chemical tagging reactions for mass spectrometry-based proteomics. *Proteomics 6*, 5418−5434.

(3) Ethier, M., Lambert, J.-P., Vasilescu, J., and Figeys, D. (2006) Analysis of protein interaction networks using mass spectrometry compatible techniques. *Anal. Chim. Acta 564*, 10−18.

(4) Sinz, A. (2003) Chemical crosslinking and mass spectrometry for mapping three-dimensional structures of proteins and protein complexes. *J. Mass Spectrom. 38*, 1225−1237.

(5) Winston, R. L., and Fitzgerald, M. C. (1997) Mass spectrometry as a readout of protein structure and function. *Mass Spectrom. Rev. 16*, 165−179.

(6) Wink, M. R., Buffon, A., Bonan, C. D., Valenzuela, M. A., Sarkis, J. J. F., and Battastini, A. M. O. (1999) Effect of protein-modifying reagents on ecto-apyrase from rat brain. *Int. J. Biochem. Cell Biol. 32*, 105−113.

(7) Bell, J. E., Castellino, F. J., Trayer, I. P., and Hill, R. L. (1975) Modification of bovine alpha-lactalbumin with N-bromosuccinimide and 2-hydroxy-5-nitrobenzylbromide. *J. Biol. Chem. 250*, 7579−7585.

(8) Gilis, D., Massar, S., Cerf, N. J., and Rooman, M. (2001) Optimality of the genetic code with respect to protein stability and amino-acid frequencies. *Genome Biol. 2*, research0049.1-0049.12. (DOI:10.1186/gb-2001-2-11-research0049).

(9) Gevaert, K., Van Damme, P., Martens, L., and Vandekerckhove, J. (2005) Diagonal reverse-phase chromatography applications in peptide-centric proteomics: Ahead of catalogue-omics? *Anal. Biochem. 345*, 18−29.

(10) Horton, H. R., and Koshland, D. E., Jr. (1965) A highly reactive colored reagent with selectivity for the tryptophan residue in proteins. 2-Hydroxy-5-nitrobenzyl bromide. *J. Am. Chem. Soc. 87*, 1126−1132.

(11) Barman, T. E., and Koshland, D. E., Jr. (1967) A colorimetric procedure for the quantitative determination of tryptophan residues in proteins. *J. Biol. Chem. 242*, 5771−5776.

(12) Strohalm, M., Santrucek, J., Hynek, R., and Kodicek, M. (2004) Analysis of tryptophan surface accessibility in proteins by MALDI-TOF mass spectrometry. *Biochem. Biophys. Res. Commun. 323*, 1134−1138.

(13) Scoffone, E., Fontana, A., and Rocchi, R. (1968) Sulfenyl halides as modifying reagents for polypeptides and proteins. I. Modification of tryptophan residues. *Biochemistry 7*, 971−979.

(14) Kuyama, H., Watanabe, M., Toda, C., Ando, E., Tanaka, K., and Nishimura, O. (2003) An approach to quantitative proteome analysis by labeling tryptophane residues. *Rapid Commun. Mass Spectrom. 17*, 1642−1650.

(15) Ou, K., et al. (2006) Quantitative profiling of drug-associated proteomic alterations by combined 2-nitrobenzenesulfenyl chloride (NBS) isotope labeling and 2DE/MS identification. *J. Proteome Res. 5*, 2194−2206.

(16) Li, C., Gawandi, V., Protos, A., Phillips, R. S., and Amster, I. J. (2006) A matrix-assisted laser desorption/ionization compatible reagent for tagging tryptophen residues. *Eur. J. Mass Spectrom. 12*, 213−221.

(17) Spande, T. F., Green, N. M., and Witkop, B. (1966) The reactivity toward N-bromosuccinimide of tryptophan in enzymes, zymogens, and inhibited enzymes. *Biochemistry 5*, 1926−1933.

(18) Antos, J. M., and Francis, M. B. (2004) Selective tryptophan modification with rhodium carbenoids in aqueous solution. *J. Am. Chem. Soc. 126*, 10256−10257.

(19) Teuber, H. J., Cornelius, D., and Pfaff, H. (1963) N-Substitution of indoles with hydroxymethylene ketones. *Chem. Ber. 96*, 2617−2631.

(20) Teuber, H. J., Glosauer, O., and Hochmuth, U. (1964) Syntheses of heterocycles with hydroxymethylene ketones. IV. A new condensation product from tryptamine and acetoacetaldehyde. *Chem. Ber. 97*, 557−562.

(21) King, T. P. (1966) Selective chemical modification of arginyl residues. *Biochemistry 5*, 3454−3459.

(22) Foettinger, A., Leitner, A., and Lindner, W. (2006) Derivatisation of arginine residues with malondialdehyde for the analysis of peptides and protein digests by LC-ESI-MS/MS. *J. Mass Spectrom. 41*, 623−632.

(23) Arnold, Z., and Sorm, F. (1958) Synthetical reactions of dimethylformamide I. General synthesis of β-dialdehydes. *Coll. Czech. Chem. Commun. 23*, 452−461.

(24) Slatter, D. A., Murray, M., and Bailey, A. J. (1998) Formation of a dihydropyridine derivative as a potential cross-link derived from malondialdehyde in physiological systems. *FEBS Lett. 421*, 180−184.

(25) Vogel, M., Buldt, A., and Karst, U. (2000) Hydrazine reagents as derivatizing agents in environmental analysis-a critical review. *Fresenius J. Anal. Chem. 366*, 781−791.

(26) Levine, R. L., Williams, J. A., Stadtman, E. R., and Shacter, E. (1994) Carbonyl assays for determination of oxidatively modified proteins. *Methods Enzymol. 233*, 346−357.

(27) Faja, M., Ariza, X., Gálvez, C., and Villarasa, J. (1995) Reaction of uridines and thymidines with methyl propynoate. A new N-3 protecting group. *Tetrahedron Lett. 36*, 3261−3264.

(28) Sun, L.-P., and Dai, W.-M. (2006) An engineered linker capable of promoting on-resin reactions for microwave-assisted solid-phase organic synthesis. *Angew. Chem., Int. Ed. 45*, 7255−*7258.*

(29) Dai, W.-M., Guo, D.-S., and Sun, L.-P. Chemistry of aminophenols. Part 1: Remarkable additive effect on Sonogashira cross-coupling of 2-carboxamidoaryl triflates and application to novel synthesis of indoles. *Tetrahedron Lett. 42*, 5275−5278.

(30) Foettinger, A., Leitner, A., and Lindner, W. (2007) Selective enrichment of tryptophan-containing peptides from protein digests employing a reversible derivatization with malondialdehyde and solid-phase capture on hydrazide beads. *J. Proteome Res.*, in press, DOI:10.1021/pr0702767.

(31) Borisov, O. V., Goshe, M. B., Conrads, T. P., Rakov, V. S., Veenstra, T. D., and Smith, R. D. (2002) Low-energy collision-induced dissociation fragmentation analysis of cysteinyl-modified peptides. *Anal. Chem. 74*, 2284−2292.

BC070001H

Fixed Bed Reactor for Solid-Phase Surface Derivatization of Superparamagnetic Nanoparticles

Benedikt Steitz,[†,‡] Jatuporn Salaklang,[†] Andrija Finka,[†] Conlin O'Neil,[§] Heinrich Hofmann,[†] and Alke Petri-Fink*[,†]

Laboratory of Powder Technology, Ecole Polytechnique Fédérale de Lausanne, Lausanne, Switzerland, Microsystems Laboratory 4, Ecole Polytechnique Fédérale de Lausanne, Lausanne, Switzerland, and Regenerative Medicine and Pharmacobiology Laboratory, Ecole Polytechnique Fédérale de Lausanne, Lausanne, Switzerland. Received March 21, 2007; Revised Manuscript Received June 27, 2007

The functionalization of nanoparticles is *conditio sine qua non* in studies of specific interaction with a biological target. Often, their biological functionality is achieved by covalent binding of bioactive molecules on a preexisting single surface coating. The yield and quality of the resulting coated and functionalized superparamagnetic iron oxide nanoparticles (SPIONs) can be significantly improved and reaction times reduced by using solid-phase synthesis strategies. In this study, a fixed bed reactor with a quadrupole repulsive arrangement of permanent magnets was assayed for SPION surface derivatization. The magnet array around the fixed bed reactor creates very high magnetic field gradients that enables the immobilization of SPIONs with a diameter as low as 9 nm. The functionalization on the surface of immobilized 25 nm 3-(aminopropyl)trimethoxysilane-coated SPIONs (APS-SPIONs) was performed using fluorescein-isothiocyanate directly, and by the SV40 large T-antigen nuclear localization signal peptide (PKKKRKVGC) conjugated to acryloylpoly(ethylene glycol)-*N*-hydroxysuccinimide, where the PEG reagent is conjugated first to create a functionalized nanoparticle and the peptide is added to the acryloyl group. We show that the yield of reactant grafted on the surface of the APS-coated SPIONs was higher in solid-phase within the fixed bed reactor compared to conventional liquid-phase chemistry. In summary, the functionalization of SPIONs using a magnetically fixed bed reactor was superior to the liquid-phase reaction in terms of the yield, reaction times required for derivatization, size distribution, and scalability.

INTRODUCTION

In recent years, functionalized superparamagnetic iron oxide nanoparticles (SPIONs) have found applications in magnetic resonance imaging (*1*), hyperthermia (*2*), the study of molecular interactions (*3*), and in drug (*4*) and gene delivery (*5*). In order to improve the biological targeting capability and therefore the pharmacodynamics, chemical or biological reagents having a strong affinity for target cells and high efficiency for nanoparticle internalization must be conjugated to the SPION surface (*6*).

The bottom up approach of building nanoparticles from the superparamagnetic core to an outer functional layer of bioactive molecules offers flexibility when designing drug or gene delivery carriers. Recent research on the attachment of these bioactive molecules and handling of these particles has been focused on synthesis, purification, and biofunctionalization of the SPIONs with synthesis routes in liquid-phase (*7*). Multistep liquid-phase synthesis is time-consuming and laborious because each addition reaction on the SPION surface is followed by a purification step such as magnetic sedimentation (*8*), size exclusion chromatography (*7*), or dialysis. In addition, repeated magnetic sedimentation of the SPIONs may cause irreversible agglomeration of the nanoparticles (*9*). Although ultrasonication is often applied to dissociate the bead agglomerations, it may cause damage to the bound active molecules, resulting in an overall decrease of their biological activity. The use of size exclusion chromatography in repeated multistep modification results in dilution of the particles upon each purification step and in a loss of particles after each purification step on the column.

In order to bypass the need for repeated purification and to ensure a continuous working process, we immobilized SPIONs as a stationary solid phase in a column using a high gradient permanent magnetic field. For functionalization of the immobilized particles during solid-phase synthesis, the chemical reagent is conducted over the SPIONs as a solid support. Although solid-phase synthesis on a polymer support is widely described (*10*), to our knowledge the solid-phase multistep biofunctionalization of SPIONs in a magnetic fixed bed reactor has not been shown.

In this magnetic fixed bed reactor the immobilization of the magnetic particles is based on the attractive force exerted on the magnetized particles by a magnetic field gradient. This force, F_{mag}, on the SPION with inducible magnetization, M, on an external flux density, B, perpendicular to a magnet (z-direction) with the magnetic volume V_{mag} can be described by the following relation:

$$F_{mag} = \frac{1}{2} \cdot V_{mag} M \frac{\partial B}{\partial z} \quad (1)$$

This equation shows that the force on a particle is depending on the magnetic field gradient. As well, the magnetic volume of the particles and the magnetization of the particles play an important role on the force. According to this equation a higher force is exerted onto larger particles compared to particles with a smaller magnetic volume. Therefore, especially for magnetic trapping of small particles, the creation of high magnetic field gradients is important.

In this study, we used a fixed bed reactor with a quadrupole arrangement of magnets for the (bio)-modification of SPIONs.

* Corresponding author. Tel.: +41 (0)21 693 5107, fax.: +41 (021) 693 3089; e-mail: alke.fink@epfl.ch.

[†] Laboratory of Powder Technology.

[‡] Microsystems Laboratory 4.

[§] Regenerative Medicine and Pharmacobiology Laboratory.

10.1021/bc070100v CCC: $37.00 © 2007 American Chemical Society
Published on Web 08/25/2007

The immobilization of SPIONs onto the fixed bed reactor and the subsequent functionalization of SPIONs are shown by different examples. We demonstrated that surface derivatization of SPIONs can be produced directly with this instrument configuration. Our data indicates that the efficiencies, product qualities, and recovery rates of the functionalized nanoparticles produced by solid-phase synthesis were superior to those obtained using conventional liquid-phase methods.

MATERIALS AND METHODS

Fixed Bed Reactor. A model fixed bed reactor was build from Inox as the solid support for the 20 FeNdB magnets (Maurer Magnets, M662056, 40/10/5 mm (l/w/h)) assembled to four stacks containing five magnets each, a Teflon tube (Semadeni 4.8 mm outer diameter, 3 mm inner diameter), and a soft magnetic iron-nickel alloy (Goodfellow; 52% Fe, 48% Ni; diameter 0.5 mm; $H_C = 20$ A/m, $M_S = 1.6$ T, permeability 25 000). The Fe−Ni-alloy wire is used to increase the magnetized surface area for efficient magnetic immobilization. In general, iron-nickel alloys exhibit a wide range of magnetic properties in relation to their nickel content. The high nickel alloys have high initial permeability but low saturation, whereas the low nickel alloys are lower in initial permeability but higher in saturation induction. All tubing was connected to two pumps (Knauer K 1001) which were also made of Teflon. UV and conductivity measurements of the efflux were performed online by the detectors of an Äkta prime FPLC chromatography system connected directly to the outlet of the fixed bed reactor.

Particle Synthesis. All chemicals were of analytical reagent grade and used without further purification. Ultrapure deionized water (Seralpur delta UV/UF setting, 0.055 μS/cm) was used in all synthesis steps. Dialysis tubing with a molecular weight cut off at 12 000 Da was used for purification (D-9527 Sigma, cellulose membrane). Superparamagnetic nanoparticles were prepared by alkaline coprecipitation of ferric and ferrous chlorides in aqueous solution (*11*−*13*). A 185 mL amount of a 0.086 M $FeCl_3 \cdot 6H_2O$ solution and 185 mL of a 0.043 M $FeCl_2 \cdot 4H_2O$ solution were mixed and precipitated with concentrated ammonia (volume fraction 30%) while stirring vigorously. The black precipitate, which immediately formed, was washed several times with ultrapure water until the pH decreased from 10 to 7. The solid fraction was collected and refluxed in a mixture of 2 M nitric acid (40 mL) and 0.27 M aqueous $Fe(NO_3)_3 \cdot 9H_2O$ (60 mL) for 1 h. During this step the initial black slurry turned brown and the formation of nitric oxide could be observed. The system was allowed to cool to room temperature, the magnetic nanoparticles were sedimented on a permanent magnet, the supernatant was discarded, and 100 mL of ultrapure water was added to the slurry, which immediately dispersed. The brown suspension was dialyzed for 2 days against 0.01 M nitric acid and stored at 4 °C.

3-(Aminopropyl)triethoxysilane Coating of SPIONs. Superparamagnetic iron oxide nanoparticles were coated with 3-(aminopropyl)triethoxysilane (APS) via a sonochemical route. A 400 μL amount of ferrofluid (from concentrations ranging from 12 mg to 0.6 mg iron/mL) were added to 9.6 mL of ethanol in a 50 mL polystyrene vessel. Subsequently 1.5 mL of aqueous ammonia (volume fraction 25%) and 1 mL of APS were added, and the mixture was continuously sonicated for 1 h in an ultrasound horn (Ultrasons Annemasse, Sonimasse S20). The reaction was carried out at a molar ratio of 1:35:15 APS/ethanol/H_20. After sonication the sample was centrifuged at 30 000 g for 25 min (Jouan, GR2022). The supernatant was discarded, and the pellet was resuspended in ultrapure water. This process was repeated three times. The magnetic particles were sedimented overnight on a permanent magnet (Maurer Magnets, Switzerland, $B_r = 300$ mT), and the clear supernatant was removed and the particles were re-dispersed in water (*14*). The particles having a mean diameter of 25 ± 2 nm consisted of 94% of γ-Fe_2O_3 (w/w) and 6% aminopropyl silica (w/w) as determined by atomic emission spectroscopy and had a saturation magnetization of 58 emu/g, which reflects the composition of the beads as the uncoated SPIONs showed a saturation magnetization of 61 emu/g (*14*).

Iron Determination (Prussian Blue colorimetric assay). A 50 μL amount of various concentrations (0.25 to 50 μg) of APS-coated particles before and after modification were dissolved for 1 h in 6 N HCl (100 μL/well of a 96-well plate), 100 μL of a 5% solution of $K_4[Fe(CN)_6]$ (Merck) in H_2O was added, and the absorbance at was read after 10 min at 690 nm in a multiwell plate reader (Infinite M200, Tecan). Each experiment was repeated in triplicate at least three times.

Determination of Immobilization Efficiency onto the Fixed Bed Reactor. APS-SPIONs (8 mg of iron) dispersed in 16 mL of 20 mM borate buffer at pH 7.5 were injected at a flow rate 0.2 mL/min and the amount of immobilized iron was determined by Prussian Blue colorimetric assay after continuous washing of the reactor with 10 mL of buffer at the same flow rate. A Teflon tube (Semadeni 4.8 mm outer diameter, 3 mm inner diameter) without and with one and two Fe−Ni-alloy wires (Goodfellow; 52% Fe, 48% Ni; diameter 0.5 mm; $H_C = 20$ A/m, $M_S = 1.6$ T, permeability 25 000) with a length of 70 mm were inserted.

Labeling of APS-Coated SPIONs with FITC. The coupling of fluorescein-isothiocyanate (FITC, Fluka) in a polystyrene vessel (50 mL) was carried out by adding 6 mL at 0.1 mg/mL of FITC in 20 mM borate buffer at pH 7.5 to 500 μg of APS-coated SPIONs. The mixture was allowed to react for 1 h at room temperature (with and without mixing). After the reaction, the dispersion was washed six times with 6 mL of 20 mM borate buffer at pH 7.5 by using a magnet to sediment the particles followed by aspiration of the supernatant using a pipet.

Parallel to the reaction in the liquid phase, 500 μg of APS-coated SPIONs was loaded onto the fixed bed reactor. The flow was stopped for 20 min so all the SPIONs were attached to the fixed bed column. After the reactor was loaded with APS-SPIONs, 6 mL of 0.1 mg/mL of FITC in 20 mM borate buffer at pH 7.5 was circulated over the immobilized particles for 1 h at a flow rate of 3.5 mL/min, which corresponds to a flow speed of 50 cm/min. After the reaction, the particles were washed with 150 mL of 20 mM borate buffer pH 7.5.

The amount of FITC immobilized onto the surface of the particles was determined in a Tecan Infinite M200 microplate reader using a 96-well plate (Falcon Microtest 96). Each well contained 250 μL of sample. Three fluorescence standard curves were generated using either pure FITC (from 1 ng/mL to 500 ng/mL) or FITC (from 1 ng/mL to 500 ng/mL) with APS-SPIONs added at concentrations of 5 μg/mL and 50 μg/mL, respectively. Fluorescence was measured at an excitation wavelength of 490 ± 9 nm and an emission wavelength of 520 ± 20 nm. The amount of immobilized FITC onto the surface of the nanoparticles was finally estimated using a concentration of 5 μg/mL APS-coated SPIONs for both reaction types (solid- and liquid-phase). Because of the high absorption coefficient of APS-SPIONs, the fluorescence was determined at SPION concentrations of 5 μg/mL of iron. Using higher APS-SPION concentrations, e.g., 50 μg/mL iron the amount of FITC is underestimated. However, because of possible quenching effects, these measurements should be considered as a comparison of the fluorescence between the two synthetic methods rather than absolute FITC loading (*15*, *16*).

Synthesis of Nuclear Targeting Peptide. For the fabrication of the nuclear targeting peptide with the sequence PKKKRKVGC, the following protected amino acids were used: Fmoc-Pro-OH,

Fmoc-Lys(Boc)-OH, Fmoc-Arg(Pbf)-OH, Fmoc-Val-OH, Fmoc-Gly-OH and Fmoc-Cys(Trt)-OH, (Novabiochem). The NovaSyn TGR resin (loading: 0.23 mmol/g) was used as the solid-phase support. All solvents were dried over molecular sieves 3A (Fluka). Peptide syntheses were performed using a PSW1100 peptide synthesizer (Chemspeed AG) according to the manufacturer's instructions. After completion, the resin was recovered and the cleavage was carried out with trifluoroacetic acid (TFA)/triisopropylsilane (TIS)/H_2O (94:5:1) for 4 h at room temperature with shaking. The peptide was precipitated directly from the cleavage cocktail into cold diethyl ether (800 mL), collected using a filter, dried under vacuum, and stored at −20 °C. The peptide was dissolved in 0.1% TFA in water just prior to purification. The peptide was purified via preparative scale reverse-phase HPLC using a Waters Ultrapurification system with a preparative Atlantis dC18 column (19 × 150 mm) and mobile phases of acetonitrile and 0.1% (v/v) TFA in water. The peptide was sequenced using ESI+ MS/MS in a Thermo Scientific LTQ Linear Ion Trap mass spectrometer equipped with an Advion Biosciences electrospray source.

The resulting PKKKRKVGC peptide was labeled with Alexa Fluor 568 carboxylic acid, succinimidyl ester (Invitrogen) according to the manufacturers instructions and is referred to as Alexa Fluor 568-PKKKRKVGC in this work. The labeled peptide was purified using a Waters 2695 Alliance system with fluorescence detector and a Waters Atlantis dC18 column (4.6 × 150 mm). The final product displayed a molecular weight of 2005.96 Da as measured using a Waters ZQ single quadropole mass spectrometer in ESI+ mode, which corresponds precisely to a 1 dye one peptide conjugate plus charge (M + H).

Nuclear Targeting Peptide and PEG Functionalization of APS Coated SPIONS. APS-coated SPIONs were functionalized in a first step with acryloylpoly(ethylene glycol)-*N*-hydroxysuccinimide (acryl-PEG-NHS, 3400 Da; Nektar Therapeutics, Huntsville, AL). To 1 mg of APS-coated SPIONs, 3 mg of acryl-PEG-NHS (6 mg/mL) was added and mixed for 20 min (control experiment in beaker) or recirculated for 20 min at a flow rate 3.5 mL/min (50 cm/min) over the immobilized particles in the fixed bed reactor. After the reaction of the N-hydroxysuccinimide site of the acryl-PEG-NHS to the amino groups of the APS-SPIONs, the particles were washed by sedimenting the modified particles three times for 1 h on a FeNdB (Maurer Magnets, M695.8) magnet and subsequently adding 1 mL of 20 mM borate buffer at pH 7.5 each time. The particles derivatized in the fixed bed reactor were washed by continuously flushing the immobilized particles with 150 mL of 20 mM borate buffer at pH 7.5.

After completion of the washing, 1.85 mg of Alexa Fluor 568-PKKKRKVGC in 6 mL of 20 mM borate buffer at pH 7.5 was added to both the fixed bed reactor and the beaker and were either recirculated or shaken for 1 h. Next, an additional washing step was performed as described previously. Following the wash, active acrylate groups were quenched by adding 1 mL of 4 mg/mL cysteine (Acros Organics) to both reactions and allowed to react for 2 h again with either recirculation (fixed bed) or shaking of the mixture (beaker). After quenching, the mixture was again washed as described previously.

For the quantification of the fluorescence in the supernatant and on the SPION surfaces of both reaction types, fluorescence standard curves with the Alexa Fluor 568 were measured at an excitation wavelength of 578 ± 9 nm and an emission wavelength of 605 ± 20 nm.

Centrifugal Filters and Size-Exclusion Chromatography for Particle Purification. A 2.5 mL amount of APS-coated SPIONs (500 μg/mL) dispersed in 20 mM borate buffer (pH 7.5) was loaded into a size exclusion column (GE Healthcare, disposable PD-10 desalting columns) pre-equilibrated with 30 mL of 20 mM borate buffer (pH 7.5). The eluent was collected according to the supplier's instructions, and the amount of iron was measured with the Prussian Blue colorimetric assay. As well, 2.5 mL of APS-coated SPIONs (500 μg/mL) dispersed in 20 mM borate buffer (pH 7.5) was loaded into a centrifugal filter (Millipore, Amicon Ultra - 4, Ultracel − 30k). The filter was centrifuged (Jouan, GR2022) at 4000*g* for 20 min. The amount of iron in the recovered sample from the filter was determined by Prussian Blue colorimetric assay.

Phase Transfer of SPIONs in Solid-Phase. A 2 mL amount of APS-coated SPIONs (500 μg/mL) dispersed in 20 mM borate buffer (pH 7.5) was loaded in the reactor. The phase transfer from aqueous phase to organic phase was achieved by applying a solvent gradient. Therefore, ethanol in water (volume fraction 50%) was introduced in the reactor for 10 min (1 mL/min), followed by ethanol (volume fraction 99.8%) for another 10 min with the same flow rate using a HPLC-pump (Waters 515). Then, dry *N*,*N*-dimethylformamide (DMF, VWR Prolabor) was introduced in the reactor for 20 min (1 mL/min). The exchange of DMF solution was controlled via Masslynx software and was run by means of preparative HPLC-MS system (Waters 2695 Alliance).

Size and Zeta Potential Determination. Light-scattering measurements were carried out at 90° on a photon correlation spectrometer (PCS) from Brookhaven equipped with a BI-9000AT digital autocorrelator. The CONTIN method was used for data processing. The concentration of iron oxide nanoparticles was set to 0.025 mg iron/mL for all measurements. The theoretical refractive index of magnetite (2.42) was used to calculate the number-weighted distribution from the raw-intensity weighted data (*17*). Zeta-potential measurements were performed using the same setting, equipped with a platinum electrode. The electrode was cleaned for 10 min in an ultrasonic bath prior to each measurement and pre-equilibrated for 2 min in an aliquot of the sample. For size and zeta-potential the nanoparticles were diluted in a 20 mM borate buffer solution, pH 7.5. Viscosity, refractive index, and dielectric constant of pure water were used to characterize the solvent.

Atomic Emission Spectroscopy. Atomic emission spectroscopy with inductive coupled plasma (PerkinElmer, ICP-Plasma 2000) was used for the analysis of the iron and silica content of the APS-SPION beads.

Transmission Electron Microscopy. Transmission electron microscopy (TEM) was performed using a Phillips CM-20 microscope operating at 200 kV. For sample preparation, dilute drops of suspensions were allowed to dry slowly on carbon-coated copper grids.

Magnetic Measurements. Magnetic field strengths were measured with an M-Test MK IV Maurer Magnetic AG.

REACTOR SET-UP AND RESULTS

Description of the Fixed Bed Reactor. A protocol for the immobilization and enhanced surface modification of SPIONs in a magnetic fixed bed reactor was developed. In order to create a high magnetic field gradient, four magnet assemblies, each consisting of a stack of 5 FeNdB magnets with a resulting surface remanence magnetization of 0.66 T, were placed repulsive to each other. An INOX bloc was used as the support for the magnet arrangement (Figure 1A). The distance between the magnets was controlled by screws leaving space for the insertion of a tube in the core of the reactor. High gradients of several hundred T m^{-1} were generated with this magnetic arrangement (Figure 1B). Within 10 mm of distance from a single stack of five single magnets a gradient of 55 T/m was measured. For 2 stacks of magnets the magnetic field at half distance between them was always zero. The magnetic field gradient increased to 250 T/m for 2 stacks of magnets at a

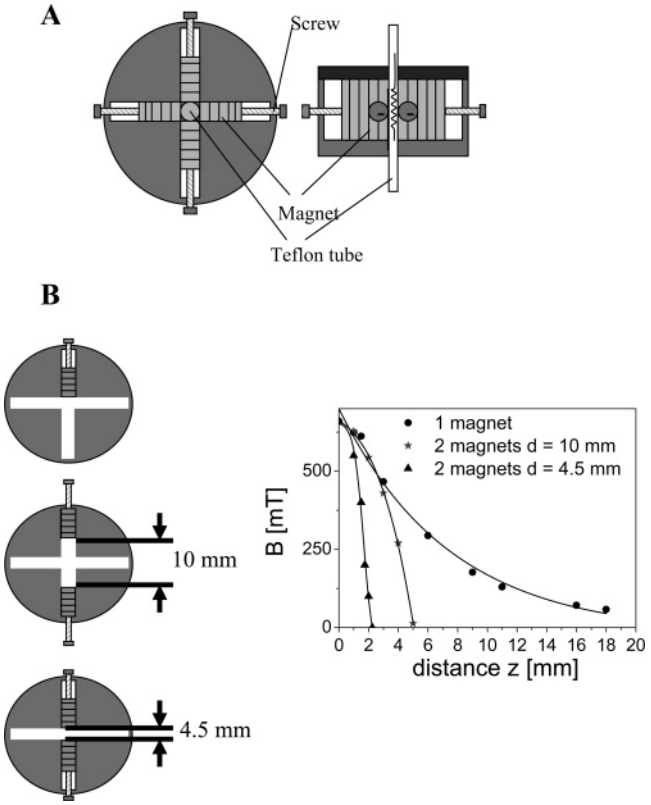


Figure 1. (A) Schematic view of the fixed bed reactor with a quadropole arrangement of magnets. Four stacks of five FeNdB magnets are inserted repulsive to each other into a support and are screwed to small distances. (B) Magnetic field, *B* [mT], as a function of the distance from the magnet using different magnetic assemblies. For simplification, only half of the distance between the magnets (when using two magnets) is shown in Figure B.

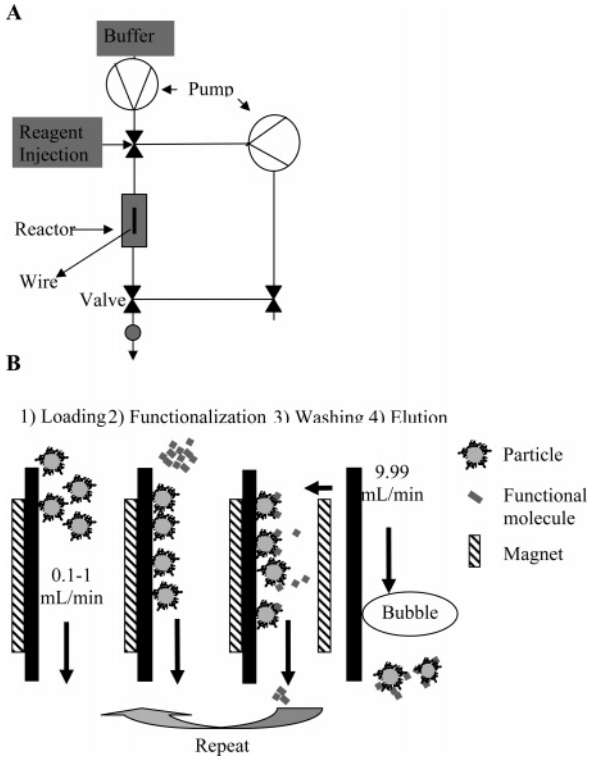


Figure 2. (A) Schematic representation of the fixed bed reactor for nanoparticle modification connected to two pumps. (B) Functionalization scheme for SPIONs in the fixed bed reactor. Particles are loaded at low flow rates onto the surface (1) and are subsequently functionalized by passing the reactive species over the immobilized nanoparticles in the bypass loop at high flow rates (2). Particles can be washed by running the washing buffer through the column (3). After functionalization of the particles, they can be eluted by removing the magnetic field and introducing bubbles at high flow rates (4).

distance of 10 mm (Figure 1B). The gradient was only determined for two stacks of magnets and could not be measured for shorter distances between the magnets and more stacks (three and four stacks of magnets) because of the geometry of the measuring device.

A Teflon tube with 4.5 mm outer and 3 mm inner diameter was inserted into the hole in the middle of the magnet arrangement. The magnets were placed in the vicinity of each other so that the outer diameter of the Teflon tube wall determined the distance between the magnets and hence the magnetic field gradient.

Immobilization experiments with 3-(aminopropyl)triethoxysilane-coated SPIONs (APS-SPIONs) with a mean diameter of 25 ± 2 nm were performed onto the magnetic reactor. The amounts of immobilized APS-SPIONs into the reactor with and without Fe−Ni-alloy magnetic wires were measured by Prussian Blue colorimetric assay. Within the Teflon tube without wire 677 ± 118 μg, with one wire 1285 ± 95 μg, and with two wires 1582 ± 77 μg of Fe was immobilized. When using only one magnet in the fixed bed reactor, 70 ± 11 mg of Fe was immobilized onto the tube without the wire. Therefore, the immobilization efficiency is dependent on the available area and the magnetic field gradient. One way to locally increase the gradient of the magnetic field is to place a ferromagnetic wire in the region of the magnetic field; in fact, the higher the curvature of this wire (i.e., the smaller the diameter), the larger the gradient of the magnetic field and hence the greater the force acting on the SPIONs (*18*), which explains the loading efficiency data with and without the Fe−Ni-alloy coils inserted into the tube.

The fixed bed reactor was connected to two pumps, one of which was solely used for circulating the reagents in a closed circuit over the immobilized sample (Figure 2A). The other pump was used for washing and injecting the sample and reagents.

The flow scheme for a general functionalization of APS-SPIONs is shown (Figure 2B). The SPIONs were either loaded onto the support at flow rates of 0.1−1 mL/min (1.4−14.1 cm/min) or preincubated for several minutes with zero flow for higher immobilization efficiency of the particles. Further functionalization was performed by injecting a functional molecule onto the fixed bed reactor in a closed circuit at a flow rate of 3.5 mL/min (50 cm/min) that allowed for passing the molecule several times over the immobilized particles. In addition, this minimized the diffusion limiting reaction by convection especially for large molecules and highly viscous solution (e.g., proteins, polymers). After reaction with the particles, the unbound molecules were washed away with a washing buffer. For elution of the particles from the fixed bed reactor, the magnet is removed and bubbles are injected at flow rates of 9.99 mL/min (maximal flow rate of pump). Using this procedure the particles can be completely recovered from the magnetic reactor.

Different pumps were used for washing and recirculation of the buffer and reagents. The pump type employed was important with respect to the resistance of the immobilized nanoparticles in the flow. Low pulse HPLC pumps, Knauer K 1001, and an annular gear pump, mzr-S05 from HNP Microsysteme GmbH, showed better performance than an Äkta prime system (Amersham), or different peristaltic pumps which eluted the particles at flow rates of only 0.1 mL/min.

Biofunctionalization of Coated Superparamagnetic Iron Oxide Nanoparticles. The derivatization of the particle surface

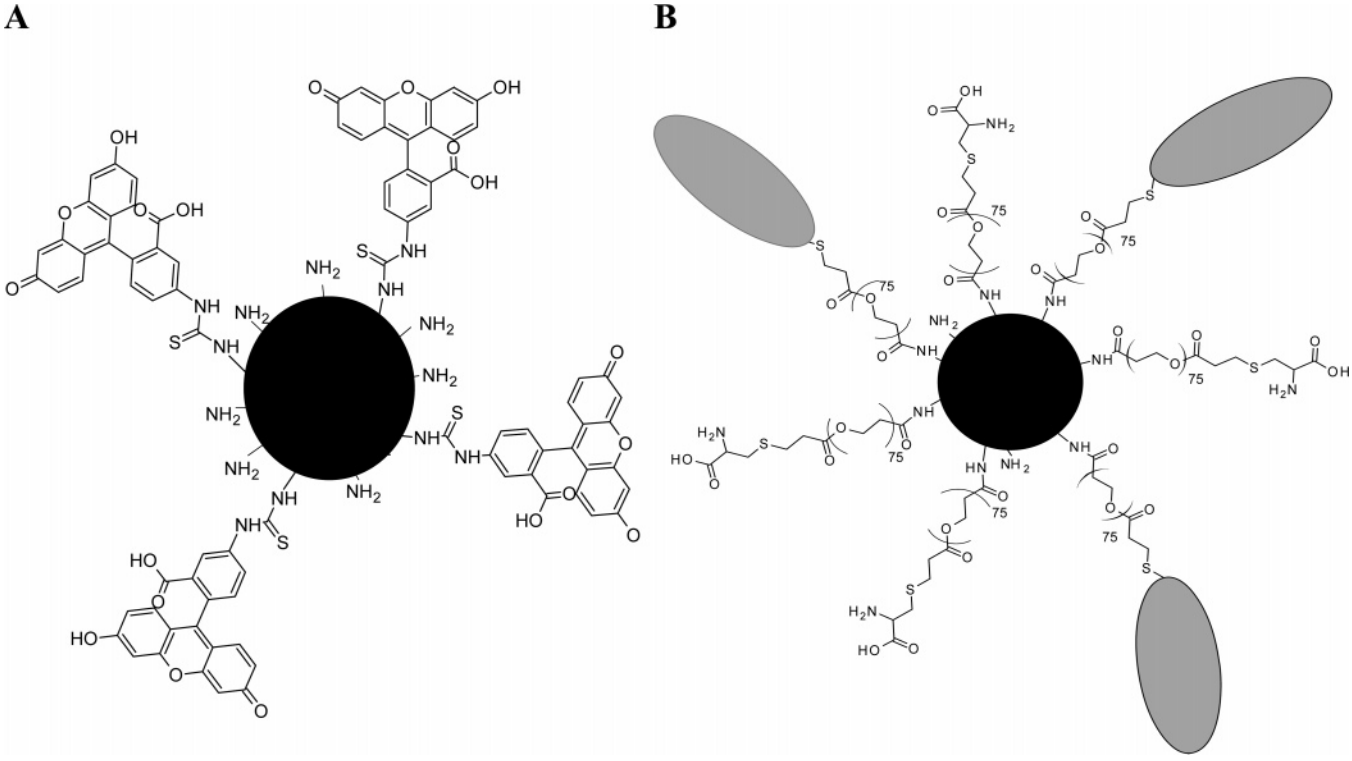


Figure 3. Biofunctionalized particles created by the modification of APS-coated nanoparticles. (A) Modification of APS-SPIONs with fluorescein-isothiocyanate (FITC) and (B) immobilization of an acryl-PEG-NHS polymer followed by the polymer modification with an Alexa Fluor 568 dye labeled nuclear targeting peptide (simplified as gray ovals) were performed. Unreacted acrylate was quenched with cysteine.

Table 1. Summary of Data Obtained for the Functionalization of APS-SPIONs in the Liquid- and Solid-Phase Synthesis

		solid-phase synthesis	liquid-phase synthesis
APS-SPIONs	mean size [nm]	25 ± 2	
	zeta-potential [mV]	33 ± 0.9	
FITC-APS-SPIONs	mean size [nm]	96 ± 15	1047 ± 180
	zeta-potential [mV]	−21.9 ± 0.9	−10.8 ± 0.5
	Fe recovery [%]	98	96
	fluorescence (ratio)	2.5	1
PEG-APS-SPIONs	mean size [nm]	75 ± 13	107 ± 29
	zeta-potential [mV]	−20.7 ± 0.7	−11.07
	Fe recovery [%]	91	61
Alexa Fluor 568-peptide-PEG-APS-SPIONs	mean size [nm]	78.7 ± 0.7	210 ± 109
	zeta-potential [mV]	−11.2 ± 0.48	−15.4 ± 0.28
	Fe recovery [%]	91	62
	fluorescence (ratio)	2.9	1

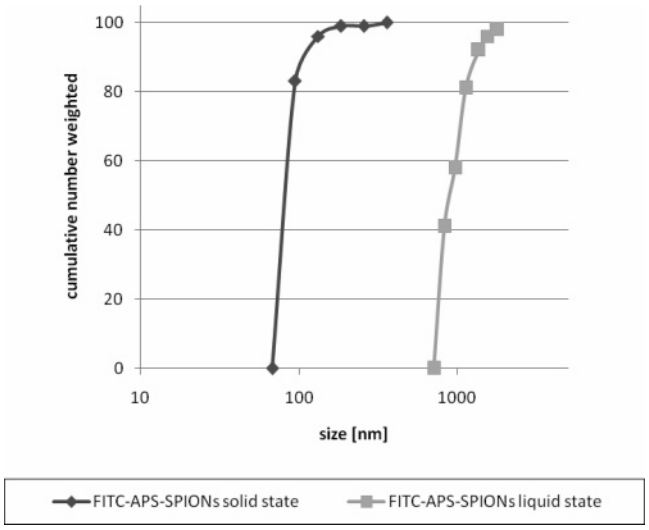


Figure 4. Cumulative number weighted size distribution determined by photon correlation spectroscopy of FITC-functionalized SPIONs as synthesized in solid phase and liquid phase.

was achieved using different compounds and was characterized by means of fluorescence, zeta-potential, and size measurements. These derivatizations included the immobilizations of a small chemically activated molecule, fluorescein-isothiocyanate (FITC), and a heterobifunctional poly(ethylene glycol) followed by peptide conjugation (Figure 3). All experiments were performed in the aforementioned fixed bed reactor in parallel to typical optimized surface chemistry protocols in the liquid phase for a comparison between solid- and liquid-phase synthesis. A summary of the obtained data can be found in Table 1.

FITC was coupled directly to the amino groups of APS-SPIONs. The amount of FITC immobilized during the solid-phase synthesis in the fixed bed reactor was determined to be 466 ng/mg iron, whereas in the liquid-phase synthesis 184 ng/mg of FITC was determined to be on the surface of the APS-SPIONs. Therefore, 2.5 times more dye was immobilized onto the same amount of particles in the fixed bed reactor. The zeta-potential and size of the FITC-APS-SPION surface from the particles produced in both synthesis routes was also determined. The zeta-potential decreased from 33.3 ± 0.9 mV for APS-SPIONs to −21.9 ± 0.9 mV in the solid-phase synthesis and to −10.8 ± 0.5 mV in the liquid-phase. These data corroborate that more FITC can be immobilized onto the APS-SPION surface in the fixed bed reactor. Also, the size of the APS-coated particles and the functionalized APS-SPIONs as obtained after synthesis was determined by photon correlation spectroscopy (PCS). The size of the FITC-APS-SPIONs obtained by the solid-phase synthesis was smaller with a mean diameter of 96 ± 15 nm compared to the agglomerates of 1047 ± 180 nm obtained for particles from the liquid-phase synthesis in 20 mM borate buffer at pH 7.5 (Figure 4).

The synthesis of the PEG-APS-SPIONs (Figure 3B) included the conjugation of the heterobifunctional PEG (*19*) via the N-hydroxysuccinimidyl ester (NHS) with the amino groups on

the surface of the APS-SPIONs. The coating of the APS-SPIONs by PEG can be qualitatively shown by monitoring the zeta-potential of the PEG-APS-SPION composites. Upon pegylation of the surface in the fixed bed reactor the zeta-potential decreased from 33.3 ± 0.9 mV for the APS-SPIONs to −20.7 ± 0.7 mV when recirculating the acryl-PEG-NHS over the immobilized nanoparticles at a flow rate of 3.5 mL/min as the amount of positively charged amino groups decreased on the surface of the APS-SPIONs. Upon coating of the APS-SPIONs with PEG using the liquid-phase method, the positive zeta-potential decreased from 33.3 ± 0.9 mV to −11.2 ± 0.7 mV (Table 1) at pH 7.5. The pegylated surfaces in both cases were therefore negatively charged and the particles were well electrostatically and sterically stabilized for use in biological buffers and cell media (data not shown).

Recirculation of the acryl-PEG-NHS over the immobilized APS-SPIONs resulted in a significantly lower zeta-potential compared to vigorously shaking (1000 min^{-1}) in the liquid-phase reaction. This lower zeta-potential reveals that the surface coupling chemistry was more efficient in the fixed bed reactor compared to the liquid-phase synthesis. Without recirculation, the zeta-potential did not decrease significantly and remained positive at 30.1 ± 0.5 mV, indicating that only small quantities of PEG were bound to the surface of the SPIONs. The acryl-PEG-NHS solution was very viscous, and the data shows that the diffusion of the acryl-PEG-NHS to the surface of the particles is the rate-limiting step for the reaction, as the diffusion time for this relatively large molecule is relatively long.

In addition, upon coating of the APS-SPIONs with PEG, the mean diameter of the nanoparticles increased from 25 ± 2 nm for the APS-coated SPIONs to either 75 ± 13 nm ($n = 6$) in the solid-phase synthesis or to 107 ± 29 nm ($n = 4$) for the PEG-APS-SPIONs as measured after modification in the beaker, respectively.

Given the data from the previous experiments, a sophisticated multistep functionalization of the APS-SPION bead surface was undertaken. This included the peptide modification of the APS-coated SPIONs for the nuclear targeting of cells. The nuclear targeting peptide PKKKRKVGC was coupled onto the surface of the modified SPIONs via the cysteine terminal site. The peptide was labeled with an Alexa Fluor 568 fluorescent probe as previously described for the determination of the immobilization efficiency. This peptide sequence contains the 7-mer functional site PKKKRKV (*20*) derived from the SV40 large T antigen nuclear localization signal that is responsible for nuclear targeting.

The coupling of the Alexa Fluor 568 nuclear targeting peptide was done by the reaction of the cysteine thiol group on the peptide with the acrylate group of the heterobifunctional PEG (acryloylpoly(ethylene glycol)-*N*-hydroxysuccinimide, acryl-PEG-NHS) via Michael addition. The fluorescence of the particles and the supernatant was measured for the quantification of the bound peptide. The functionalization of the PEG-APS-SPIONs with this peptide had no influence on the size of the composite particles as produced in the reactor (78.7 nm), whereas the mean size of the particles produced in the liquid phase increased significantly from 107 to 210 nm. These significantly larger compounds consisted of agglomerates of individual nanoparticles, which could not be redispersed. This is a major result of our study which proves the superior properties of solid-phase compared to liquid-phase derivatized particles. Because of quenching effects of the surface-bound peptide, the fluorescence in the washing solution from the reactor and the supernatant of the liquid-phase synthesis were analyzed. This showed that 99% of the peptide was bound onto the surface of the PEG-APS-SPIONs in the reactor.

The iron recovery rate determined by Prussian Blue assay of the particles was higher when using the fixed bed reactor compared to liquid-phase synthesis. When modifying APS-SPIONs batches equivalent to 500 μg of Fe to peptide-PEG-APS-SPIONs, 91% of the iron could be recovered from the solid-phase synthesis whereas only 62% were recovered from the liquid-phase particle modification route. This high loss of particles is mainly due to incomplete sedimentation of the particles when washing after each modification step. For complete sedimentation of the particles in the liquid-phase reaction, 8 h per washing step in the given PEG solution was required.

This incomplete washing of the particles may also be a reason for obtaining higher sizes for the liquid-phase modified particles, as larger particles with a higher magnetic content tend to sediment faster than smaller particles which are therefore easier lost during the washing steps. Again this result showed that there was less agglomeration of the particles and a better stabilization of the SPIONs upon coating with the heterobifunctional polymer in the fixed bed reactor.

All these results for the functionalization of APS-coated SPIONs showed that immobilization efficiencies of the different molecules to the particle surface were better in the solid-phase synthesis compared to the liquid-phase synthesis. This showed that the mass transport of the small molecules, peptide, and polymer through the immobilized layer of particles is given. Less agglomerated particles after immobilization of the protein were obtained in the magnetic reactor.

Other methods for particle purification such as size exclusion chromatography and centrifugal filtration were tested, too. However, APS-SPIONs could not be recovered from the size exclusion resin (Sephadex G-25) of the PD-10 column. The use of centrifugal filters for purification and concentration of the particles led to very low yields, because 89% of the SPIONs stuck to the filter wall. Therefore, these commonly used methods were not useful as purification and/or concentration methods for these particles after surface derivatization.

In other experiments, this reactor setup proved as well suitable for phase transfer of uncoated SPION particles dissolved in water to organic solvents. Immiscibility problems were overcome by running a gradient of the respective solvents over the column. Particle agglomeration of the eluted SPIONs was not observed. This allows for easy solvent exchange compared to liquid-phase synthesis, where the most rapid option for solvent exchange is the sequential washing the SPIONs by centrifugation of the particles at speeds over 30 000 g for at least 1 h. This new fixed bed technology opens a large processing window for further chemistry on the SPIONs.

DISCUSSION

The fixed bed reactor system for solid-phase surface modification of superparamagnetic nanoparticles displayed various advantages compared to the modification of particles performed using conventional liquid-phase chemistry. Comparing the amount of molecules on the surface of the particles, the main advantage of this reactor is that the surface derivatization of APS-coated SPIONs in the fixed bed reactor was more efficient than the surface modification done in liquid phase. The recovery rate of the injected SPIONs was very high (91−98%) compared to liquid-phase synthesis where a lot of particles are lost because of incomplete settling of the particles during washing.

The modification of particles within the magnetic reactor was less time-consuming because of faster and more efficient purification steps which can be performed by a continuous washing of the product at high flow rates. This was especially observed when modifying the particles with high viscosity polymers such as PEG. This is advantageous for multistep

reactions when high product purity and fast sequential reactions are required.

It was also observed that the polydispersity of the functionalized particles in the reactor was lower compared to surface modifications carried out in the liquid phase. This indicates that particle−particle interactions during the coating process in the solid phase are minimized.

SPIONs and the APS-coated SPIONs used in these experiments have a low colloidal stability in most of the buffers used during a typical chemical modification procedure. Therefore, very low concentrations of particles need to be used to minimize flocculation. In addition, high concentrations of buffer cannot be used (data not shown). Much higher amounts of SPIONs can be functionalized in the magnetic reactor therefore minimizing high costs or difficulties to manufacture reagents (e.g., proteins). With the fixed bed reactor the scale-up of the reaction is easier than in liquid phase. Scale-up can be relatively simple by augmenting the amount of magnetic support or increasing the size of the inserted magnets.

The surface derivatization process of the SPIONs in the fixed bed reactors can be automated, which will allow for functionalization of SPIONs in an efficient way. This also allows for more reproducibility of the functionalization and better quality control of the end product: the production of cell-specific magnetic resonance imaging (*21*) and targeted drug delivery agents (*22*) at a low-cost using an automated production process. These functional SPION materials can then be readily scaled-up using a system that can be operated by nonexpert users.

CONCLUSION AND OUTLOOK

This proof-of-principle fixed bed reactor presented in this paper was satisfactory for carrying out single and multiple step chemistry on immobilized superparamagnetic iron oxide nanoparticles. In addition to the well-known advantages of solid-phase synthesis such as ease of purification, all functionalizations done in this reactor were superior to the liquid-phase synthesis in terms of recovery rate of particles, size distribution, and yield. Next generation reactors will be built totally automated and equipped with online measurement devices for more advanced multistep modifications on the particle surface.

The peptide modifications of the APS-SPIONs showed potential in further experiments for the biological localization of functionalized SPIONs and isolation of cell compartments (personal communication). Yielding sizes of particles smaller 150 nm was therefore important, as these particle systems were efficiently taken up by cells via endocytotic pathways (*23*).

ACKNOWLEDGMENT

This work was supported by the Swiss National Science Foundation (SNF 200020-109490 and SNF 205321-111908) and the Competence Centre of Materials Science of the Swiss Federal Institute of Technology, Education and Research Unit "Surface, Coating and Particle Engineering", Project PAPA-MOD.

Supporting Information Available: Absorbance and fluorescence standard curves of pure FITC and FITC with APS-SPIONs added at concentrations of 5 μg/mL and 50 μg/mL, respectively. This information is available free of charge via the Internet at http://pubs.acs.org.

LITERATURE CITED

(1) Rudin, M., and Weissleder, R. (2003) Molecular Imaging in Drug Discovery and Development. *Nat. Rev. Drug Discovery. 2*, 123−131.

(2) Hergt, R., Dutz, S., Müller, R., and Zeisberger, M. (2006) Magnetic Particle Hyperthermia: Nanoparticle Magnetism and Materials Development for Cancer Therapy. *J. Phys.: Condens. Matter 18*, S2919−S2934.

(3) Won, J., Kim, M., Yi, Y.-W., Kim, Y. H., Jung, N., and Kim, T. K. (2005) A Magnetic Nanoprobe Technology for Detecting Molecular Interactions in Live Cells. *Science 309*, 121−125.

(4) Jurgons, R., Seliger, D., Hilpert, A., Trahms, L., Odenbach, S., and Alexiou, C. (2006) Drug Loaded Magnetic Nanoparticles for Cancer Therapy. *J. Phys.: Condens. Matter 18*, S2893−S2902.

(5) Kamau, S. W., Hassa, P. O., Steitz, B., Petri-Fink, A., Hofmann, H., Hofmann-Amtenbrink, M., von Rechenberg, B., and Hottiger, M. O. (2006) Enhancement of the Efficiency of Non-viral Gene Delivery by Application of Pulsed Magnetic Field. *Nucleic Acids Res. 34* (5), e40.

(6) Neuberger, T., Schöpf, B., Hofmann, H., Hofmann, M., and von Rechenberg, B. (2005) Superparamagnetic Nanoparticles for Biomedical Applications: Possibilities and Limitations of a new Drug Delivery System. *J. Magn. Magn. Mater. 293*, 483−496.

(7) Pittet, M. J., Swirski, F. K., Reynolds, F., Josephson, L., and Weissleder, R. (2006) Labeling of Immune Cells for *in vivo* Imaging using Magnetofluorescent Nanoparticles. *Nat. Protoc. 1* (1), 73−79.

(8) Khng, H. P., Cunliffe, D., Davies, S., Turner, N. A., and Vulfson, E. N. (1998) The Synthesis of Sub-Micron Magnetic Particles and their use for Preparative Purification of Proteins. *Biotechnol. Bioeng. 60* (4), 419−424.

(9) Wang, J., Wu, J., Zhang, Z., Zhang, X., Pan, Z., Wang, L., and Xu, L. (2006) Sonocatalytic Damage of Bovine Serum Albumin (BSA) in the Presence of Nanometer Anatase Titanium Dioxide (TiO_2). *Ultrasound Med. Biol. 32* (1), 147−152.

(10) Chan, W. C., and White, P. D. (2000) *Fmoc Solid Phase Peptide Synthesis - A Practical Approach*, Oxford University Press, Cary, NC.

(11) Bee, A., and Massart, R., and Neveu, S. (1995) Synthesis of very fine Maghemite Particles. *J. Magn. Magn. Mater. 149*, 6−9.

(12) van Ewijk, G. A., Vroege, G. J., and Philipse, A. P. (1999) Preparation and Magnetisation of a Silica-Magnetite Inverse Ferrofluid. *J. Magn. Magn. Mater. 201*, 31−33.

(13) Chastellain, M., Petri, A., and Hofmann, H. (2004) Particle Size Investigations of a Multistep Synthesis of PVA Coated Superparamagnetic Nanoparticles. *J. Colloid Interface Sci. 278* (2), 353−360.

(14) Steitz, B., Hofmann, H., and Petri-Fink, A. (2007) Production and Biofunctionalization of Magnetic Nanobeads for Magnetic Separation of Messenger RNA. *Biophys. Rev. Lett. 2* (1), 109−122.

(15) Mandal, S. K., Lequeux, N., Rotenberg, B., Tramier, M., Fattaccioli, J., Bibette, J., and Dubertret, B. (2005) Encapsulation of Magnetic and Fluorescent Nanoparticles in Emulsion Droplets. *Langmuir 21*, 4175−4179.

(16) Simberg, D., Duza, T., Park, J. H., Essler, M., Pilch, J., Zhang, L., Derfus, A. M., Yang, M., Hoffman, R. M., Bhatia, S., Sailor, M. J., and Ruoslahti, E. (2007) Biomimetic amplification of nanoparticle homing to tumors. *P. Natl. Acad. Sci. U.S.A. 104* (3), 932−936.

(17) Cornell, M., and Schwertmann, U. (1996) *The Iron Oxides*; VCH, Weinheim.

(18) Ritter, J. A., Ebner, A. D., Daniel, K. D., and Stewart, K. L. (2004) Application of High Gradient Magnetic Separation Principles to Magnetic Drug Targeting. *J. Magn. Magn. Mater. 280*, 184−201.

(19) Oishi, M., Sasaki, S., Nagasaki, Y., and Kataoka, K. (2003) pH-Responsive Oligodeoxynucleotide (ODN)-Poly(Ethylene Glycol) Conjugate through Acid-Labile Thiopropionate Linkage: Preparation and Polyion Complex Micelle. *Biomacromolecules 4* (5), 1426−1432.

(20) Kalderon, D., Roberts, L., Richardson, W. D., and Smith, A. E. (1984) A Short Amino acid Sequence Able to Specify Nuclear Location. *Cell 39* (4), 499−509.

(21) Dijkhuizen, R. M, and Nicolay K. (2003) Magnetic Resonance Imaging in Experimental Models of Brain Disorders. *J. Cereb. Blood Flow Metab. 23*, 1383−1402.

(22) Kumar, C. S. S. R. (2007) *Nanomaterials for Medical Diagnosis and Therapy. Nanotechnologies for the Life Sciences (Band 10)*, Wiley-VCH, Weinheim.

(23) Petri-Fink, A., Steitz, B., Finka, A., Salaklang, J., and Hofmann, H. (2007) Effect of Cell Media on Polymer Coated Superparamagnetic Iron Oxide Nanoparticles (SPIONs): Colloidal Stability, Cytotoxicity, and Cellular Uptake Studies. *Eur. J. Pharm. Biopharm.*, DOI:10.1016/j.ejpb.2007.02.024.

BC070100V

5(6)-Carboxyfluorescein Revisited: New Protecting Group, Separation of Isomers, and their Spectral Properties on Oligonucleotides

Maksim V. Kvach,[†] Dmitry A. Tsybulsky,[†] Alexey V. Ustinov,[‡] Irina A. Stepanova,[‡] Stanislav L. Bondarev,[§] Sergey V. Gontarev,[†] Vladimir A. Korshun,*[,‡] and Vadim V. Shmanai*[,†]

Institute of Physical Organic Chemistry, Surganova 13, 220072 Minsk, Belarus, Shemyakin-Ovchinnikov Institute of Bioorganic Chemistry, Miklukho-Maklaya 16/10, 117997 Moscow, Russia, and Institute of Molecular and Atomic Physics, Nezavisimosti av. 70, 220072 Minsk, Belarus. Received May 25, 2007; Revised Manuscript Received July 12, 2007

Pentafluorophenyl esters of 5- and 6-carboxyfluorescein-3′,6′-*O*-dipivalate can be easily separated in multigram quantities by column chromatography. The individual isomers were converted into stable phosphoramidites suitable for oligonucleotide synthesis. The use of the cyclohexylcarbonyl (Chc) protecting group instead of pivaloyl (Piv) facilitates the separation of isomers. The fluorescence spectra of 5- and 6-carboxyfluoresceins on oligonucleotides were compared.

INTRODUCTION

Carboxy derivatives of fluorescein (*1*) are widely used for labeling of biomolecules (*2*), e.g., in DNA biotechnology applications (*3*−*7*). The mixture of 5- and 6-isomers of carboxyfluorescein **1** can be easily obtained by condensation of 1,2,4-benzenetricarboxylic anhydride and resorcinol (*1*, *8*). However, the individual isomers are highly preferred as labels because of physicochemical and spectral homogeneity of labeled species. The separation of 5- and 6-isomers of fluorescein derivatives was reported by fractional crystallization (*9*−*15*) or extensive chromatography (*16*−*18*). The fluorescence of fluorescein is determined by the xanthene moiety, but can be finely modulated by various substituents in the benzene ring (*19*). Thus, it was of interest to compare the spectral properties of individual regioisomers of carboxyfluorescein when attached to an oligonucleotide. Surprisingly, we were unable to find any literature precedent for this.

The pivaloyl group is a convenient protection for fluorescein hydroxyls in phosphoramidite reagents for the synthesis of labeled oligonucleotides (*17*, *20*−*23*). Oligonucleotides containing carboxyfluorescein as an amide derivative (FAM) in the 5′-terminal position are the most useful conjugates applicable as DNA probes or PCR primers (the nonmodified 3′ terminus is suitable for elongation by DNA polymerases). There is no need to introduce multiple FAMs into an oligonucleotide because fluorescein is prone to self-quenching (*8*). Although both 5- and 6-FAM phosphoramidites for 5′-terminal labeling are commercially available (*24*, *25*), they are (a) rather expensive and (b) derived from primary alcohols, thus reducing their stability during storage as acetonitrile solutions in a DNA synthesizer (*26*).

EXPERIMENTAL PROCEDURES

General. Reagents and solvents obtained from commercial suppliers were used without further purification. CH_2Cl_2 was used freshly distilled from CaH_2. HPLC-grade DMF was distilled under reduced pressure and stored over 4 Å molecular sieves under argon. Other solvents were used as received. *N*,*N*-Diisopropylamino-2-cyanoethoxychlorophosphine was prepared as described (*27*, *28*).

500 MHz ^{1}H, 125.7 MHz ^{13}C, and 202.4 MHz ^{31}P NMR spectra were recorded on a Bruker DRX-500 spectrometer and referenced to $CDCl_3$ (7.26 ppm for ^{1}H and 77.1 ppm for ^{13}C), DMSO-d_6 (2.50 ppm for ^{1}H and 39.5 ppm for ^{13}C) (*29*), and 85% aq H_3PO_4 (0.00 ppm for ^{31}P). 564.4 MHz ^{19}F NMR spectra were recorded on a Varian Unity NMR spectrometer and referenced to $PhCF_3$ as the internal standard (−63.72 ppm for ^{19}F). ^{1}H−^{13}C gradient-selected HMQC and HMBC spectra were obtained by using 2048 (t_2) × 256 (t_1) complex point data sets, zero-filled to 2048 (F_2) × 1024 (F_1) points. The spectral widths were 13 and 200 ppm for ^{1}H and ^{13}C dimensions, respectively. HMBC spectra were measured with a 50 ms delay for the evolution of long-range couplings. ^{1}H NMR coupling constants are reported in hertz (Hz) and refer to apparent multiplicities. High-resolution mass spectra (HRMS) were recorded in positive-ion mode using an IonSpec FT ISR mass spectrometer (MALDI) or PE SCIEX QSTAR pulsar mass spectrometer (ESI). Melting points were determined using a Boetius heating table and are uncorrected. Analytical thin-layer chromatography was performed on Kieselgel 60 F_{254} precoated aluminum plates (Merck); spots were visualized under UV light (254 nm). Silica gel column chromatography was performed using Merck Kieselgel 60 0.040−0.063 mm. The oligonucleotide synthesis was carried out on a BiosSet ASM-700 instrument on a 200 nmol scale using standard manufacturer's protocols. Oligonucleotides were isolated using electrophoresis in 20% denaturing (7 M urea) PAGE in Tris−borate buffer, pH 8.3, and desalted by gel filtration on a Sephadex G-25 column in saltless buffer. MALDI-TOF mass spectra of oligonucleotide conjugates were recorded in positive-ion mode on a Bruker Ultraflex spectrometer. UV absorption spectra were recorded using a Varian Cary-500 spectrophotometer in a 0.1 M carbonate buffer pH 8.3−9.5. Fluorescence studies in the same buffer were performed using a large-aperture apparatus described earlier (*30*). The fluorescence quantum yields Φ_f were measured by the relative method using a standard of fluorescein in 0.1 M NaOH ($\Phi_f = 0.95 \pm 0.03$) (*31*). The measurements were performed at an angle of 90° to the exciting light beam. The optical density of the solutions in the 1 cm quartz cell at the excitation wavelength

* Corresponding authors. V.A.K.: E-mail: korshun@mail.ibch.ru, Tel/Fax: +7-495-330-6738. V.V.S.: E-mail: shmanai@ifoch.basnet.by, Tel: +375-17-284-2055, Fax: +375-17-284-2539.

[†] Institute of Physical Organic Chemistry.

[‡] Shemyakin-Ovchinnikov Institute of Bioorganic Chemistry.

[§] Institute of Molecular and Atomic Physics.

10.1021/bc7001874 CCC: $37.00 © 2007 American Chemical Society
Published on Web 08/16/2007

did not exceed 0.1. The values of Φ_f were corrected with the refractive index of the solvent; the measured refractive indexes of 0.1 M NaOH and carbonate buffer were 1.3335 and 1.3340 at 20 °C, respectively. Fluorescence lifetimes were determined by the method of time-correlated single-photon counting using a PRA 3000 nanosecond lifetime fluorometer. The parameters of the fluorescence decays were analyzed using T900 software (Edinburgh Instruments). The samples used in quantum yield and fluorescence lifetime measurements were not degassed.

Cyclohexanecarboxylic anhydride (*32*) was prepared as follows. A mixture of cyclohexanecarboxylic acid (1 equiv) and $SOCl_2$ (1.5 equiv) was heated for 4 h at 60 °C, then evaporated and distilled under reduced pressure to give cyclohexanecarbonyl chloride (91%, bp 71−73 °C/10 Torr). The chloride (50.7 g, 0.346 mol) was dissolved in benzene (350 mL); pyridine (56 mL, 0.69 mol) and cyclohexanecarboxylic acid (44.9 g, 0.35 mmol) were added subsequently; and the mixture was stirred for 2.5 h at 60 °C, then cooled, filtered, and evaporated. The residue was distilled *in vacuo* to afford Chc_2O as a colorless liquid (68.8 g, 91%, bp 125−135 °C/1 Torr). ^{1}H NMR ($CDCl_3$) δ = 2.38 (tt, 2H, $J_{a,a}$ = 11.2 Hz, $J_{a,e}$ = 3.7 Hz, H-1*a*), 1.94 (m, 4H, H-2*e*,6*e*), 1.76 (m, 4H, H-3*e*,5*e*), 1.63 (m, 2H, H-4*e*), 1.46 (m, 4H, H-2*a*,6*a*), 1.25 (m, 6H, H-3*a*,4*a*,5*a*). ^{13}C NMR ($CDCl_3$) δ = 171.9 (2C, *C*O), 44.0 (2C, C1), 28.4 (4C, C2,6), 25.6 (2C, C4), 25.2 (4C, C3,5).

5(6)-Carboxy-3′,6′-*O*-diacylfluoresceins, Pentafluorophenyl Esters (4a−d); General Procedure. To the magnetically stirred, ice-cooled solution of 5(6)-carboxyfluorescein **1** (20.00 g, 53.2 mmol) in DMF (100 mL) was added dropwise diisopropylethylamine (36.3 mL, 213 mmol) followed by trimethylacetic or cyclohexylcarbonic anhydride (117 mmol). The reaction solution was stirred at room temperature for 72 h, protected from light. The solvent was rotary-evaporated, and residue was dissolved in CH_2Cl_2 (170 mL) and EtOAc (350 mL), washed with 1 M phosphate buffer (3 × 300 mL, pH 7.0), and dried over $MgSO_4$. After evaporation of solvents, the remaining residue was dried in high vacuum overnight. Then, it was dissolved in EtOAc (400 mL), ice-cooled, and pentafluorophenol (11.75 g, 63.9 mmol) in EtOAc (50 mL), followed by dropwise addition of the solution of DCC (13.15 g, 63.8 mmol) in EtOAc (150 mL) within 1 h. After 2 h, the cooling was removed, and the mixture was stirred overnight at room temperature. The precipitate of dicyclohexylurea was filtered off, and the solution was concentrated to dryness. The residue was purified by column chromatography on silica gel eluting with $CHCl_3$; desired fractions were combined and evaporated to dryness. The resultant foam was dissolved in toluene (55 mL), and hexane (400 mL) was added. After crystallization at −20 °C overnight, the precipitate formed was filtered off and dried *in vacuo* to give the mixture of isomers as a white crystalline solid (25.28 g, 67% of **4a** + **4c** or 28.73 g, 71% of **4b** + **4d**). The solids were separated by chromatography on a silica gel column (850 g) with a step gradient of EtOAc in toluene (toluene → 0.1% EtOAc → 1% EtOAc in toluene) as the mobile phase to afford pure individual isomers **4a** (15.57 g, 62%) and **4c** (9.55 g, 38%) or **4b** (17.09 g, 59%) and **4d** (11.40 g, 40%) as white foams.

3′,6′-*O*-Bis(2,2-dimethyl-1-oxopropyl)-3-oxo-spiro[isobenzofuran-1(3*H*),9′-[9*H*]xanthene]-5-carboxylic acid, Pentafluorophenyl Ester (4a). R_f 0.12 (toluene); mp 233−234 °C (toluene−hexane). ^{1}H NMR ($CDCl_3$) δ = 8.88 (br. s, 1H, H-4), 8.47 (dd, 1H, $J_{6,7}$ = 8.0 Hz, $^4J_{4,6}$ = 1.5 Hz, H-6), 7.37 (d, 1H, $J_{6,7}$ = 8.0 Hz, H-7), 7.10 (d, 2H, $J_{3',4'} = J_{5',6'}$ = 1.8 Hz, H-4′,5′), 6.87−6.79 (m, 4H, H-1′,2′,7′,8′), 1.37 (s, 18H, C*H*$_3$). ^{13}C NMR ($CDCl_3$) δ = 176.5 (2C, *C*OBu^t), 167.6 (C3), 161.2 (*C*$O_2C_6F_5$), 158.4 (C7a), 153.1 (2C, C4a′,10a′), 151.6 (2C, C3′,6′), 141.3 (m, 2C, $^1J_{CF}$ = 253 Hz, $^2J_{CF}$ = 12 Hz, C2″,6″), ∼140 (m, $^1J_{CF}$ ∼ 240 Hz, C4″), ∼138 (m, 2C, $^1J_{CF}$ ∼ 240 Hz, C3″,5″), 137.1 (C6), 129.4 (C5), 128.7 (2C, C1′,8′), 128.2 (C4), 127.2 (C3a), ∼125 (m, C1″), 125.1 (C7), 118.1 (2C, C2′,7′), 115.2 (2C, C8a′, 9a′), 110.7 (2C, C4′,5′), 82.2 (C1), 39.3 (2C, *C*CH$_3$), 27.2 (6C, *C*H$_3$). ^{19}F NMR ($CDCl_3$) δ = −11.51 (d, 2F, $J_{2'',3''} = J_{5'',6''}$ = 18.3 Hz, F-2″,6″), −16.11 (t, 1F, $J_{3'',4''} = J_{4'',5''}$ = 21.4 Hz, F-4″), −20.89 (m, 2F, F-3″,5″). HRMS (MALDI+): *m*/*z* [M + H]$^+$ calcd for $C_{37}H_{28}F_5O_9^+$ 711.1648; found 711.1642.

3′,6′-*O*-Bis(cyclohexylcarbonyl)-3-oxo-spiro[isobenzofuran-1(3*H*),9′-[9*H*]xanthene]-5-carboxylic acid, Pentafluorophenyl Ester (4b). R_f 0.14 (toluene); mp 147−148 °C (toluene−hexane). ^{1}H NMR ($CDCl_3$) δ 8.88 (m, 1H, H-4), 8.47 (dd, 1H, $J_{6,7}$ = 8.0 Hz, $^4J_{4,6}$ = 1.4 Hz, H-6), 7.37 (d, 1H, $J_{6,7}$ = 8.0 Hz, H-7), 7.11 (m, 2H, H-4′,5′), 6.83 (m, 4H, H-1′,2′,7′,8′), 2.57 (tt, 2H, $J_{a,a}$ = 11.2 Hz, $J_{a,e}$ = 3.6 Hz, H-1*a*‴), 2.05 (m, 4H, H-2*e*‴,6*e*‴), 1.82 (m, 4H, H-3*e*‴,5*e*‴), 1.70 (m, 2H, H-4*e*‴), 1.59 (m, 4H, H-2*a*‴,6*a*‴), 1.33 (m, 6H, H-3*a*‴,4*a*‴,5*a*‴). ^{13}C NMR ($CDCl_3$) δ 174.0 (2C, *C*OCH), 167.6 (C3), 161.2 (*C*$O_2C_6F_5$), 158.4 (C7a), 152.8 (2C, C4a′,10a′), 151.6 (2C, C3′,6′), ∼141.5 (m, 2C, $^1J_{CF}$ ∼ 247 Hz, *C*2″,6″), ∼140 (m, $^1J_{CF}$ ∼ 240 Hz, C4″), ∼138 (m, 2C, $^1J_{CF}$ ∼ 240 Hz, C3″,5″), 137.1 (C6), 129.4 (C5), 128.8 (2C, C1′,8′), 128.2 (C4), 127.2 (C3a), 125.4 (m, C1″), 125.1 (C7), 118.2 (2C, *C*2′,7′), 115.2 (2C, C8a′,9a′), 110.8 (2C, C4′,5′), 82.2 (C1), 43.3 (2C, C1‴), 29.0 (4C, *C*2‴,6‴), 25.7 (2C, C4‴), 25.4 (4C, C3‴,5‴). ^{19}F NMR ($CDCl_3$) δ = −11.52 (d, 2F, $J_{2'',3''} = J_{5'',6''}$ = 18.3 Hz, F-2″,6″), −16.12 (t, 1F, $J_{3'',4''} = J_{4'',5''}$ = 21.4 Hz, F-4″), −20.90 (m, 2F, F-3″,5″). HRMS (MALDI+): *m*/*z* [M + Na]$^+$ calcd for $C_{41}H_{31}F_5NaO_9^+$ 785.1780; found 785.1799.

3′,6′-*O*-Bis(2,2-dimethyl-1-oxopropyl)-3-oxo-spiro[isobenzofuran-1(3*H*),9′-[9*H*]xanthene]-6-carboxylic acid, Pentafluorophenyl Ester (4c). R_f 0.05 (toluene); mp 202−203 °C (toluene−hexane). ^{1}H NMR ($CDCl_3$): δ = 8.45 (dd, 1H, $J_{4,5}$ = 8.0 Hz, $^4J_{5,7}$ = 1.4 Hz, H-5), 8.21 (d, 1H, $J_{4,5}$ = 8.0 Hz, H-4), 7.96 (br. s, 1H, H-7), 7.10 (br. s, 2H, H-4′,5′), 6.84 (m, 4H, H-1′,2′,7′,8′), 1.36 (s, 18H, C*H*$_3$). ^{13}C NMR ($CDCl_3$) δ = 176.5 (2C, *C*OBu^t), 167.7 (C3), 161.2 (*C*$O_2C_6F_5$), 153.6 (C7a), 153.0 (2C, C4a′,10a′), 151.6 (2C, C3′,6′), 141.2 (m, 2C, $^1J_{CF}$ = 257 Hz, *C*2″,6″), 140.0 (m, $^1J_{CF}$ = 240 Hz, C4″), 138.0 (m, 2C, $^1J_{CF}$ = 241 Hz, C3″,5″), 133.4 (C6), 132.3 (C5), 131.0 (C3a), 128.8 (2C, C1′,8′), 126.4 (C7), 125.9 (C4), 124.8 (m, C1″), 118.1 (2C, *C*2′,7′), 115.2 (2C, C8a′,9a′), 110.7 (2C, C4′,5′), 82.3 (C1), 39.3 (2C, *C*CH$_3$), 27.1 (6C, *C*H$_3$). ^{19}F NMR ($CDCl_3$) δ = −11.15 (d, 2F, $J_{2'',3''} = J_{5'',6''}$ = 18.3 Hz, F-2″,6″), −16.09 (t, 1F, $J_{3'',4''} = J_{4'',5''}$ = 21.9 Hz, F-4″), −21.00 (m, 2F, F-3″,5″). HRMS (MALDI+): *m*/*z* [M + H]$^+$ calcd for $C_{37}H_{28}F_5O_9^+$ 711.1648; found 711.1655.

3′,6′-*O*-Bis(cyclohexylcarbonyl)-3-oxo-spiro[isobenzofuran-1(3*H*),9′-[9*H*]xanthene]-6-carboxylic acid, Pentafluorophenyl Ester (4d). R_f 0.05 (toluene); mp 124−126 °C (toluene−hexane). ^{1}H NMR ($CDCl_3$) δ 8.45 (dd, 1H, $J_{4,5}$ = 8.0 Hz, $^4J_{5,7}$ = 1.2 Hz, H-5), 8.20 (d, 1H, $J_{4,5}$ = 8.0 Hz, H-4), 7.96 (br. s, 1H, H-7), 7.11 (br. s, 2H, H-4′,5′), 6.84 (m, 4H, H-1′,2′,7′,8′), 2.57 (tt, 2H, $J_{a,a}$ = 11.2 Hz, $J_{a,e}$ = 3.6 Hz, H-1*a*‴), 2.05 (m, 4H, H-2*e*‴,6*e*‴), 1.82 (m, 4H, H-3*e*‴,5*e*‴), 1.69 (m, 2H, H-4*e*‴), 1.59 (m, 4H, H-2*a*‴,6*a*‴), 1.33 (m, 6H, H-3*a*‴,4*a*‴, 5*a*‴). ^{13}C NMR ($CDCl_3$) δ 174.0 (2C, *C*OCH), 167.7 (C3), 161.2 (*C*$O_2C_6F_5$), 153.6 (C7a), 152.8 (2C, C4a′,10a′), 151.6 (2C, C3′,6′), ∼141.5 (m, 2C, $^1J_{CF}$ ∼ 249 Hz, *C*2″,6″), ∼140 (m, $^1J_{CF}$ = 240 Hz, C4″), ∼138 (m, 2C, $^1J_{CF}$ = 241 Hz, C3″,5″), 133.4 (C6), 132.3 (C5), 131.1 (C3a), 128.8 (2C, C1′,8′), 126.5 (C7), 126.0 (C4), 125.4 (m, C1″), 118.2 (2C, *C*2′,7′), 115.2 (2C, C8a′,9a′), 110.7 (2C, C4′,5′), 82.4 (C1), 43.3 (2C, C1‴), 29.0 (4C, *C*2‴,6‴), 25.7 (2C, C4‴), 25.4 (4C, C3‴,5‴). ^{19}F NMR ($CDCl_3$) δ = −11.16 (d, 2F, $J_{2'',3''} = J_{5'',6''}$ = 18.3 Hz, F-2″,6″), −16.10 (t, 1F, $J_{3'',4''} = J_{4'',5''}$ = 22.0 Hz, F-4″), −20.98 (m, 2F,

F-3″,5″). HRMS (MALDI+): *m/z* [M + H]$^+$ calcd for $C_{41}H_{32}F_5O_9^+$ 763.1961; found 763.1979.

Amides 5a−d; General Procedure. To a solution of activated ester **4a−d** (5.0 mmol) in CH_2Cl_2 (60 mL), *trans*-4-aminocyclohexanol hydrochloride (0.76 g, 5.0 mmol) and DIEA (1.74 mL, 10.0 mmol) were added. The suspension was diluted with DMF (60 mL) and stirred overnight at room temperature to give a homogeneous solution. The latter was diluted with $CHCl_3$ (200 mL), washed with water (4 × 200 mL), dried over Na_2SO_4, and evaporated to dryness. The residue was purified by chromatography on a silica gel column (100 g) with a step gradient of MeOH (0 → 5%) in toluene as the mobile phase to give amides **5a−d** as white amorphous foams.

3′,6′-*O*-Bis(2,2-dimethyl-1-oxopropyl)-5-(4-hydroxycyclohexylaminocarbonyl)-3-oxo-spiro[isobenzofuran-1(3*H*),9′-[9*H*]xanthene] (5a). Yield 3.17 g (quant.) R_f 0.30 (MeOH−toluene 15:85 v/v). ^{1}H NMR (DMSO-d_6): δ = 8.57 (d, 1H, $J_{4'',NH}$ = 7.9 Hz, N*H*), 8.55 (br. s, 1H, H-4), 8.28 (d, 1H, $J_{6,7}$ = 8.2 Hz, H-6), 7.48 (d, 1H, $J_{6,7}$ = 8.2 Hz, H-7), 7.27 (s, 2H, H-4′,5′), 6.93 (s, 4H, H-1′,2′,7′,8′), 4.56 (d, 1H, J = 4.0 Hz, O*H*), 3.78 (m, 1H, H-4″), 3.42 (m, 1H, H-1″), 1.92−1.80 (m, 4H, H-2*e*″,3*e*″,5*e*″,6*e*″), 1.48−1.20 (m, 22H, H-2*a*″,3*a*″, 5*a*″,6*a*″, C*H*$_3$). ^{13}C NMR (DMSO-d_6) δ = 175.8 (2C, *C*OBu^t), 167.8 (C3), 163.5 (*C*ONH), 154.0 (C7a), 152.3 (2C, C4a′,10a′), 150.7 (2C, C3′,6′), 136.7 (C6), 135.0 (C5), 129.1 (2C, C1′,8′), 125.6 (C3a), 124.1 (C4), 123.6 (C7), 118.4 (2C, *C*2′,7′), 115.6 (2C, C8a′,9a′), 110.2 (2C, C4′,5′), 81.0 (C1), 68.2 (C1″), 48.1 (C4″), 38.5 (2C, *C*CH$_3$), 34.0 (2C, *C*2″,6″), 30.0 (2C, C3″,5″), 26.5 (6C, *C*H$_3$). HRMS (MALDI+): *m/z* [M + H]$^+$ calcd for $C_{37}H_{40}NNaO_9^+$ 642.2698; found 642.2709.

3′,6′-*O*-Bis(cyclohexylcarbonyl)-5-(4-hydroxycyclohexylaminocarbonyl)-3-oxo-spiro[isobenzofuran-1(3*H*),9′-[9*H*] xanthene] (5b). Yield 3.42 g (quant). R_f 0.34 (MeOH−toluene 1:9 v/v). ^{1}H NMR (DMSO-d_6) δ 8.57 (d, 1H, $J_{4'',NH}$ = 7.8 Hz, N*H*), 8.55 (br. s, 1H, H-4), 8.28 (dd, 1H, $J_{6,7}$ = 8.0 Hz, $^4J_{4,6}$ = 1.4 Hz, H-6), 7.49 (d, 1H, $J_{6,7}$ = 8.0 Hz, H-7), 7.26 (br. s, 2H, H-4′,5′), 6.92 (s, 4H, H-1′,2′,7′,8′), 4.56 (d, 1H, J = 4.3 Hz, O*H*), 3.79 (m, 1H, H-4″), 3.42 (m, 1H, H-1″), 2.61 (tt, 2H, $J_{a,a}$ = 11.0 Hz, $J_{a,e}$ = 3.6 Hz, H-1*a*‴), 1.99 (m, 4H, H-2*e*‴,6*e*‴), 1.87 (m, 4H, H-2*e*‴,3*e*‴,5*e*″,6*e*″), 1.72 (m, 4H, H-3*e*‴,5*e*‴), 1.61 (m, 2H, H-4*e*‴), 1.55−1.18 (m, 14H, H-2*a*″,3*a*″,5*a*″,6*a*″,2*a*‴, 3*a*‴,4*a*‴,5*a*‴,6*a*‴). ^{13}C NMR (DMSO-d_6) δ 173.2 (2C, *C*OCH), 167.8 (C3), 163.5 (*C*ONH), 153.9 (C7a), 152.1 (2C, C4a′,10a′), 150.7 (2C, C3′,6′), 136.7 (C6), 135.0 (C5), 129.1 (2C, C1′,8′), 125.7 (C3a), 124.1 (C4), 123.6 (C7), 118.4 (2C, *C*2′,7′), 115.5 (2C, C8a′,9a′), 110.2 (2C, C4′,5′), 81.1 (C1), 68.2 (C1″), 48.1 (C4″), 41.9 (2C, C1‴), 34.0 (2C, *C*2″,6″), 30.0 (2C, C3″,5″), 28.2 (4C, *C*2‴,6‴), 25.1 (2C, C4‴), 24.5 (4C, C3‴,5‴). HRMS (MALDI+): *m/z* [M + Na]$^+$ calcd for $C_{41}H_{43}NNaO_9^+$ 716.2830; found 716.2808.

3′,6′-*O*-Bis(2,2-dimethyl-1-oxopropyl)-6-(4-hydroxycyclohexylaminocarbonyl)-3-oxo-spiro[isobenzofuran-1(3*H*),9′-[9*H*]xanthene] (5c). Yield 3.06 g (95%). R_f 0.24 (MeOH−toluene 15:85 v/v). ^{1}H NMR (DMSO-d_6) δ = 8.37 (d, 1H, $J_{4'',NH}$ = 7.8 Hz, N*H*), 8.22 (d, 1H, $J_{4,5}$ = 8.2 Hz, H-5), 8.14 (d, 1H, $J_{4,5}$ = 8.2 Hz, H-4), 7.79 (s, 1H, H-7), 7.28 (s, 2H, H-4′,5′), 6.94 (s, 4H, H-1′,2′,7′,8′), 4.51 (br. s, 1H, O*H*), 3.67 (m, 1H, H-4″), 3.32 (m, 1H, H-1″), 1.83−1.72 (m, 4H, H-2*e*″,3*e*″,5*e*″,6*e*″), 1.31 (s, 18H, C*H*$_3$), 1.30−1.14 (m, 4H, H-2*a*″,3*a*″,5*a*″,6*a*″). ^{13}C NMR (DMSO-d_6) δ = 175.8 (2C, *C*OBu^t), 167.6 (C3), 163.4 (NH*C*O), 152.3 (2C, C4a′,10a′), 152.1 (C7a), 150.7 (2C, C3′,6′), 141.2 (C6), 130.0 (C5), 129.3 (2C, C1′,8′), 127.3 (C3a), 125.1 (C4), 122.0 (C7), 118.4 (2C, *C*2′,7′), 115.6 (2C, C8a′,9a′), 110.2 (2C, C4′,5′), 81.1 (C1), 68.1 (C1″), 48.1 (C4″), 38.5 (2C, *C*CH$_3$), 34.0 (2C, *C*2″,6″), 29.9 (2C, C3″,5″), 26.5 (6C, *C*H$_3$). HRMS (MALDI+): *m/z* [M + Na]$^+$ calcd for $C_{37}H_{39}NNaO_9^+$ 664.2517; found 664.2498.

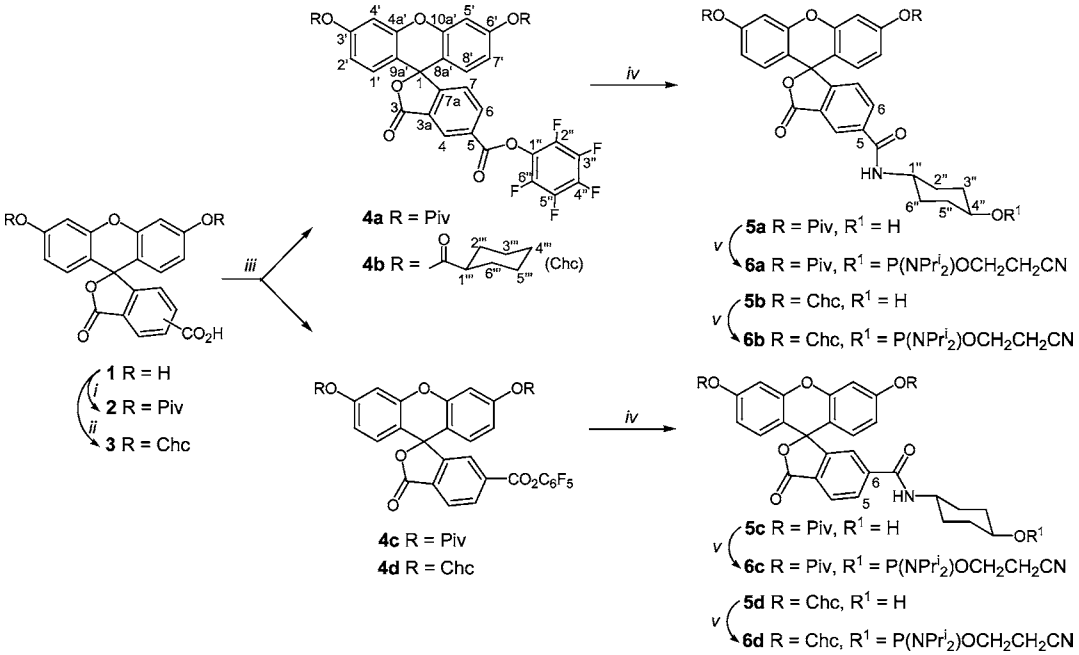
3′,6′-*O*-Bis(cyclohexylcarbonyl)-6-(4-hydroxycyclohexylaminocarbonyl)-3-oxo-spiro[isobenzofuran-1(3*H*),9′-[9*H*]-xanthene] (5d). Yield 3.26 g (94%). R_f 0.20 (MeOH−toluene 1:9 v/v). ^{1}H NMR (DMSO-d_6) δ 8.38 (d, 1H, $J_{4'',NH}$ = 7.6 Hz, N*H*), 8.22 (dd, 1H, $J_{4,5}$ = 8.1 Hz, $^4J_{5,7}$ = 1.0 Hz, H-5), 8.14 (d, 1H, $J_{4,5}$ = 8.1 Hz, H-4), 7.81 (s, 1H, H-7), 7.28 (s, 2H, H-4′,5′), 6.93 (s, 4H, H-1′,2′,7′,8′), 4.51 (d, 1H, J = 4.4 Hz, O*H*), 3.67 (m, 1H, H-4″), 3.29 (m, 1H, H-1″), 2.61 (tt, 2H, $J_{a,a}$ = 11.0 Hz, $J_{a,e}$ = 3.6 Hz, H-1*a*‴), 1.97 (m, 4H, H-2*e*‴,6*e*‴), 1.84−1.65 (m, 8H, H-2*e*″,3*e*″,5*e*″,6*e*″,3*e*‴,5*e*‴), 1.61 (m, 2H, H-4*e*‴), 1.54−1.43 (m, 4H), 1.38−1.14 (m, 10H) (H-2*a*″, 3*a*″,5*a*″,6*a*″,2*a*‴,3*a*‴,4*a*‴,5*a*‴,6*a*‴). ^{13}C NMR (DMSO-d_6) δ 173.2 (2C, *C*OCH), 167.6 (C3), 163.4 (NH*C*O), 152.1 (2C, C4a′,10a′), 152.0 (C7a), 150.7 (2C, C3′,6′), 141.1 (C6), 130.0 (C5), 129.2 (2C, C1′,8′), 127.4 (C3a), 125.1 (C4), 122.0 (C7), 118.5 (2C, *C*2′,7′), 115.6 (2C, C8a′,9a′), 110.2 (2C, C4′,5′), 81.1 (C1), 68.1 (C1″), 48.1 (C4″), 41.9 (2C, C1‴), 34.0 (2C, *C*2″,6″), 29.9 (2C, C3″,5″), 28.2 (4C, *C*2‴,6‴), 25.1 (2C, C4‴), 24.5 (4C, C3‴,5‴). HRMS (MALDI+): *m/z* [M + Na]$^+$ calcd for $C_{41}H_{43}NNaO_9^+$ 716.2830; found 716.2817.

Phosphoramidites 6a−d; General Procedure. Amide **5a−d** (4.0 mmol) was evaporated with dry CH_2Cl_2 (2 × 50 mL), dissolved in dry CH_2Cl_2 (50 mL) and DIEA (4.4 mmol, 0.765 mL), followed by addition of *N*,*N*-diisopropylamino-2-cyanoethoxychlorophosphine (1.04 g, 4.4 mmol), and the mixture was stirred under argon for 1 h. After conversion of the starting compound was complete (monitoring by TLC, Me_2CO−toluene 3:7 + 1% pyridine v/v/v), the mixture was washed with 5% $NaHCO_3$ (50 mL) and sat NaCl (60 mL). The organic layer was dried over Na_2SO_4 during 1 h, evaporated to dryness, and the residue was purified by chromatography on a silica gel column (100 g) with 5% acetone in toluene + 1% pyridine (v/v/v) as the mobile phase. Fractions containing product were combined and evaporated. The resulting phosphoramidite was dissolved in dry toluene (25 mL) and precipitated into hexane (350 mL). The obtained compound was filtered, dissolved in CH_2Cl_2, and evaporated to dryness to afford compounds **6a−d** as white amorphous solids.

3′,6′-*O*-Bis(2,2-dimethyl-1-oxopropyl)-5-[4-(*N*,*N*-diisopropylamino-2-cyanoethoxyphosphinyloxy)cyclohexylaminocarbonyl]-3-oxo-spiro[isobenzofuran-1(3*H*),9′-[9*H*]xanthene] (6a). Yield 2.60 g (77%). R_f 0.68 (Me_2CO−toluene 3:7 + 1% pyridine v/v/v). ^{1}H NMR (DMSO-d_6) δ 8.58 = (d, 1H, $J_{4'',NH}$ = 7.6 Hz, N*H*), 8.55 (br. s, 1H, H-4), 8.28 (dd, 1H, $J_{6,7}$ = 7.9 Hz, $^4J_{4,6}$ = 1.2 Hz, H-6), 7.49 (d, 1H, $J_{6,7}$ = 7.9 Hz, H-7), 7.27 (s, 2H, H-4′,5′), 6.93 (s, 4H, H-1′,2′,7′,8′), 3.87−3.65 (m, 4H, H-1″,4″, POC*H*$_2$), 3.63−3.52 (m, 2H, PNC*H*), 2.77 (t, 2H, J = 6.0 Hz, C*H*$_2$CN), 2.04 (m, 1H), 1.96 (m, 1H), 1.90 (m, 2H) (H-2*e*″,3*e*″,5*e*″,6*e*″), 1.47 (m, 4H, H-2*a*″,3*a*″,5*a*″,6*a*″), 1.31 (m, 18H, CC*H*$_3$), 1.15 (d, 12H, J = 6.7 Hz, CHC*H*$_3$). ^{13}C NMR (DMSO-d_6) δ = 175.8 (2C, *C*OBu^t), 167.8 (C3), 163.6 (*C*ONH), 154.0 (C7a), 152.3 (2C, C4a′,10a′), 150.7 (2C, C3′,6′), 136.7 (C6), 135.0 (C5), 129.1 (2C, C1′,8′), 125.6 (C3a), 124.1 (C4), 123.6 (C7), 118.9 (*C*N), 118.4 (2C, *C*2′,7′), 115.6 (2C, C8a′,9a′), 110.2 (2C, C4′,5′), 81.0 (C1), 71.7 (d, $^2J_{P,C}$ = 19.2 Hz, C1″), 57.8 (d, $^2J_{P,C}$ = 19.2 Hz, POC*H*$_2$), 47.6 (C4″), 42.4 (d, $^2J_{P,C}$ = 13.0 Hz, PNC*H*), 38.5 (2C, *C*CH$_3$), 32.6, 32.5 (*C*2″,6″), 29.7 (2C, C3″,5″), 26.5 (6C, C*C*H$_3$), 24.2 (d, 2C, $^3J_{P,C}$ = 8.0 Hz), 24.1 (d, 2C, $^3J_{P,C}$ = 8.0 Hz) (CH*C*H$_3$), 19.7 (d, $^3J_{P,C}$ = 7.4 Hz, *C*H$_2$CN). ^{31}P NMR (DMSO-d_6) δ = 144.96. HRMS (ESI+): *m/z* [M + Na]$^+$ calcd for $C_{46}H_{56}N_3NaO_{10}P^+$ 864.3595; found 864.3556.

3′,6′-*O*-Bis(cyclohexylcarbonyl)-5-[4-(*N*,*N*-diisopropylamino-2-cyanoethoxyphosphinyloxy)cyclohexylaminocarbonyl]-3-oxo-spiro[isobenzofuran-1(3H),9′-[9H]xanthene] (6b). Yield 2.73 g (76%). R_f 0.69 (Me_2CO−toluene 3:7 + 1% pyridine v/v/v). ^{1}H NMR (DMSO-d_6) δ 8.58 (d, 1H, $J_{4'',NH}$ = 7.8 Hz,

Scheme 1[a]



[a] Reagents and conditions: *i*, Piv_2O, DIEA, DMF, 72 h; *ii*, Chc_2O, DIEA, DMF, 72 h; *iii*, C_6F_5OH, DCC, EtOAc, overnight; *iv*, *trans*-4-aminocyclohexanol, DIEA, CH_2Cl_2, DMF, overnight; *v*, $Pr^i_2N(Cl)POCH_2CH_2CN$, CH_2Cl_2, 1 h.

N*H*), 8.55 (br. s, 1H, H-4), 8.28 (dd, 1H, $J_{6,7}$ = 8.1 Hz, $^4J_{4,6}$ = 1.2 Hz, H-6), 7.49 (d, 1H, $J_{6,7}$ = 8.1 Hz, H-7), 7.26 (br. s, 2H, H-4′,5′), 6.92 (s, 4H, H-1′,2′,7′,8′), 3.88−3.67 (m, 4H, H-1″,4″, POCH_2), 3.63−3.54 (m, 2H, C*H*CH$_3$), 2.77 (t, 2H, J = 6.0 Hz, CH_2CN), 2.61 (tt, 2H, $J_{a,a}$ = 11.0 Hz, $J_{a,e}$ = 3.6 Hz, H-1*a*‴), 2.07−1.88 (m, 8H, H-2*e*″,3*e*″,5*e*″,6*e*″,2*e*‴,6*e*‴), 1.72 (m, 4H, H-3*e*‴,5*e*‴), 1.60 (m, 2H, H-4*e*‴), 1.54−1.21 (m, 14H, H-2*a*″,3*a*″,5*a*″,6*a*″,2*a*‴,3*a*‴,4*a*‴,5*a*‴,6*a*‴), 1.15 (d, 12H, J = 6.7 Hz, CH_3). ^{13}C NMR (DMSO-d_6) δ 173.2 (2C, *C*OCH), 167.7 (C3), 163.6 (*C*ONH), 153.9 (C7a), 152.1 (2C, C4a′,10a′), 150.7 (2C, C3′,6′), 136.7 (C6), 135.0 (C5), 129.1 (2C, C1′,8′), 125.7 (C3a), 124.1 (C4), 123.6 (C7), 118.9 (*C*N), 118.4 (2C, *C*2′,7′), 115.5 (2C, C8a′,9a′), 110.2 (2C, C4′,5′), 81.0 (C1), 71.7 (d, $^2J_{P,C}$ = 17.8 Hz, C1″), 57.8 (d, $^2J_{P,C}$ = 17.8 Hz, PO*C*H$_2$), 47.6 (C4″), 42.4 (d, $^2J_{P,C}$ = 12.6 Hz, PN*C*H), 41.9 (2C, C1‴), 32.6, 32.5 (*C*2″,6″), 29.7 (2C, C3″,5″), 28.2 (4C, *C*2‴,6‴), 25.1 (2C, C4‴), 24.5 (4C, C3‴,5‴), 24.2 (d, 2C, $^3J_{P,C}$ = 7.4 Hz), 24.1 (d, 2C, $^3J_{P,C}$ = 7.4 Hz) (CH*C*H$_3$), 19.7 (d, $^3J_{P,C}$ = 6.9 Hz, *C*H$_2$-CN). ^{31}P NMR (DMSO-d_6) δ 144.97. HRMS (ESI+): *m*/*z* [M + Na]$^+$ calcd for $C_{50}H_{60}N_3NaO_{10}P^+$ 916.3908; found 916.3892.

3′,6′-*O*-Bis(2,2-dimethyl-1-oxopropyl)-6-[4-(*N*, *N*-diisopropylamino-2-cyanoethoxyphosphinyloxy)cyclohexylaminocarbonyl]-3-oxo-spiro[isobenzofuran-1(3*H*),9′-[9*H*]xanthene] (6c). Yield 2.51 g (74%). R_f 0.60 (Me$_2$CO−toluene 3:7 + 1% pyridine v/v/v). ^{1}H NMR (DMSO-d_6) δ = 8.39 (d, 1H, $J_{4'',NH}$ = 7.8 Hz, N*H*), 8.22 (d, 1H, $J_{4,5}$ = 8.0 Hz, H-5), 8.14 (d, 1H, $J_{4,5}$ = 8.0 Hz, H-4), 7.79 (s, 1H, H-7), 7.28 (s, 2H, H-4′,5′), 6.94 (s, 4H, H-1′,2′,7′,8′), 3.76−3.60 (m, 4H, H-1″,4″, POCH_2), 3.58−3.50 (m, 2H, PNC*H*), 2.74 (t, 2H, J = 6.0 Hz, CH_2CN), 1.95 (m, 1H), 1.87 (m, 1H), 1.81 (m, 2H) (H-2*e*″,3*e*″,5*e*″,6*e*″), 1.42−1.29 (m, 22H, H-2*a*″,3*a*″,5*a*″,6*a*″, CCH_3), 1.12 (m, 12H, CHCH_3). ^{13}C NMR (DMSO-d_6) δ = 175.8 (2C, *C*OBu^t), 167.6 (C3), 163.4 (NH*C*O), 152.3 (2C, C4a′,10a′), 152.1 (C7a), 150.7 (2C, C3′,6′), 141.1 (C6), 129.9 (C5), 129.2 (2C, C1′,8′), 127.3 (C3a), 125.1 (C4), 122.0 (C7), 118.8 (*C*N), 118.4 (2C, *C*2′,7′), 115.6 (2C, C8a′,9a′), 110.2 (2C, C4′,5′), 81.1 (C1), 71.85 (d, $^2J_{P,C}$ = 17.8 Hz, C1″), 57.8 (d, $^2J_{P,C}$ = 17.8 Hz, PO*C*H$_2$), 47.6 (C4″), 42.3 (d, $^2J_{P,C}$ = 12.6 Hz, PN*C*H), 38.5 (2C, *C*CH$_3$), 32.6 (d, $^3J_{P,C}$ = 3.4 Hz), 32.5 (d, $^3J_{P,C}$ = 3.4 Hz) (*C*2″,6″), 29.7, 29.6 (C3″,5″), 26.71 (6C, C*C*H$_3$), 24.2 (d, 2C, $^3J_{P,C}$ = 7.4 Hz), 24.1 (d, 2C, $^3J_{P,C}$ = 6.9 Hz) (CH*C*H$_3$), 19.7 (d, $^3J_{P,C}$ = 6.9 Hz, *C*H$_2$CN). ^{31}P NMR (DMSO-d_6) δ = 144.88. HRMS (ESI+): *m*/*z* [M + Na]$^+$ calcd for $C_{46}H_{56}N_3NaO_{10}P^+$ 864.3595; found 864.3565.

3′,6′-*O*-Bis(cyclohexylcarbonyl)-6-[4-(*N*,*N*-diisopropylamino-2-cyanoethoxyphosphinyloxy)cyclohexylaminocarbonyl]-3-oxo-spiro[isobenzofuran-1(3*H*),9′-[9*H*]xanthene] (6d). Yield 2.84 g (79%). R_f 0.62 (Me$_2$CO−toluene 3:7 + 1% pyridine v/v/v). ^{1}H NMR (DMSO-d_6) δ 8.39 (d, 1H, $J_{4'',NH}$ = 7.6 Hz, N*H*), 8.22 (d, 1H, $J_{4,5}$ = 8.0 Hz, H-5), 8.14 (d, 1H, $J_{4,5}$ = 8.0 Hz, H-4), 7.80 (s, 1H, H-7), 7.28 (s, 2H, H-4′,5′), 6.93 (s, 4H, H-1′,2′,7′,8′), 3.75−3.60 (m, 4H, H-1″,4″, POCH_2), 3.59−3.50 (m, 2H, C*H*CH$_3$), 2.74 (t, 2H, J = 5.8 Hz, CH_2CN), 2.62 (tt, 2H, $J_{a,a}$ = 11.0 Hz, $J_{a,e}$ = 3.6 Hz, H-1*a*‴), 2.02−1.68 (m, 12H, H-2*e*″,3*e*″,5*e*″,6*e*″,2*e*‴,3*e*‴,5*e*‴,6*e*‴), 1.61 (m, 2H, H-4*e*‴), 1.52−1.19 (m, 14H, H-2*a*″,3*a*″,5*a*″,6*a*″,2*a*‴,3*a*‴, 4*a*‴,5*a*‴,6*a*‴), 1.12 (d, 6H, J = 6.4 Hz), 1.11 (d, 6H, J = 6.4 Hz) (CH_3). ^{13}C NMR (DMSO-d_6) δ 173.2 (2C, *C*OCH), 167.6 (C3), 163.4 (NH*C*O), 152.1 (2C, C4a′,10a′), 152.0 (C7a), 150.7 (2C, C3′,6′), 141.1 (C6), 130.0 (C5), 129.2 (2C, C1′,8′), 127.4 (C3a), 125.1 (C4), 122.0 (C7), 118.8 (*C*N), 118.5 (2C, *C*2′,7′), 115.6 (2C, C8a′,9a′), 110.2 (2C, C4′,5′), 81.1 (C1), 71.7 (d, $^2J_{P,C}$ = 17.8 Hz, C1″), 57.8 (d, $^2J_{P,C}$ = 17.8 Hz, PO*C*H$_2$), 47.6 (C4″), 42.3 (d, $^2J_{P,C}$ = 12.6 Hz, PN*C*H), 41.9 (2C, C1‴), 32.6 (d, $^2J_{P,C}$ = 4.0 Hz), 32.5 (d, $^2J_{P,C}$ = 4.0 Hz) (*C*2″,6″), 29.7, 29.6 (C3″,5″), 28.2 (4C, *C*2‴,6‴), 25.1 (2C, C4‴), 24.5 (4C, C3‴,5‴), 24.2 (d, 2C, $^3J_{P,C}$ = 7.4 Hz), 24.1 (d, 2C, $^3J_{P,C}$ = 6.9 Hz) (CH*C*H$_3$), 19.7 (d, $^3J_{P,C}$ = 6.9 Hz, *C*H$_2$CN). ^{31}P NMR (DMSO-d_6) δ 144.89. HRMS (ESI+): *m*/*z* [M + Na]$^+$ calcd for $C_{50}H_{60}N_3NaO_{10}P^+$ 916.3908; found 916.3886.

RESULTS AND DISCUSSION

Our aim was to prepare stable and inexpensive 5- and 6-FAM phosphoramidites and to study the fluorescence of the regioisomers on an oligonucleotide. The synthesis of phosphoramidite reagents is given in Scheme 1. First, we found that 5(6)-carboxyfluorescein-3′,6′-*O*-dipivalate **2** (*17*) can be converted into pentafluorophenyl (Pfp) ester (similar as described for isobutyryl derivatives (*8*)) and the resulting mixture (**4a** + **4c**) is easily resolved by column chromatography on silica gel in

Chart 1. Structures of 5′-(5-FAM) and 5′-(6-FAM) Oligonucleotide Conjugates

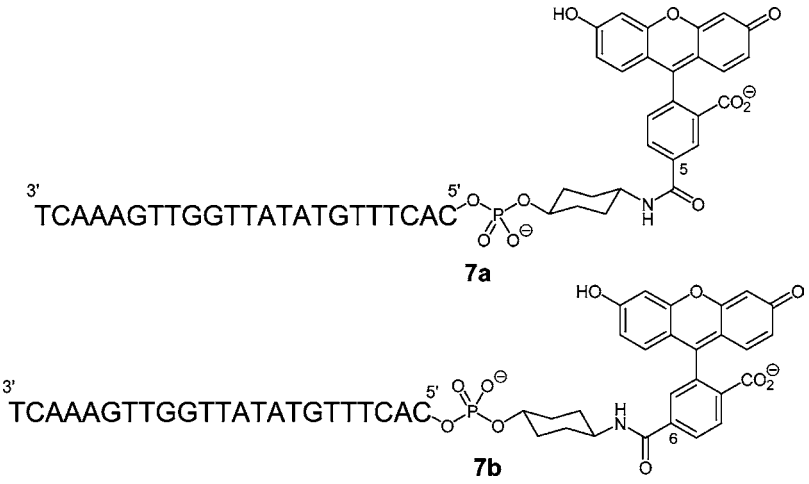


Table 1. Spectroscopic (λ^{abs}_{max}, λ^{abs}_{max}, $\Delta\nu^{fl}_{1/2h}$)[a] and Photophysical (Φ_f, τ_f, k_f)[b] Characteristics of Fluorescent Oligonucleotide Conjugates 7a (5-FAM) and 7b (6-FAM) at Various pH (20 °C)

	data for conjugates **7a**/**7b**					
pH	λ^{abs}_{max}, nm	λ^{fl}_{max}, nm	$\Delta\nu^{fl}_{1/2h}$, [c] cm^{-1}	$\Phi_f \pm 0.05$	$\tau_f \pm 0.02$, ns	$k_f \times 10^{-8} \pm 0.1$, s^{-1}
8.35	494/494	521/518	1990/1440	0.58/0.48	4.22/4.21	1.4/1.1
8.50	494/494	521/517	1710/1430	0.48/0.53	4.19/4.18	1.1/1.3
9.00	494/494	521/517	1730/1440	0.53/0.58	4.21/4.18	1.3/1.4
9.50	494/494	522/517	1715/1435	0.51/0.56	4.23/4.20	1.2/1.3

[a] $\lambda^{abs}_{max}$and λ^{fl}_{max} − absorbance and fluorescence wavelength maxima; $\Delta\nu^{fl}_{1/2h}$− half-width of the emission spectrum. [b] Φ_f − fluorescence quantum yield; τ_f − average fluorescence lifetime; $k_f = \Phi_f/\tau_f$ − emission rate constant. [c] Error limits are ±40 cm^{-1} (**7a**) and ±30 cm^{-1} (**7b**).

toluene in multigram quantities. Then, we examined the cyclohexylcarbonyl (Chc) as a protecting group for fluorescein. It was found that 3′,6′-*O*-diacylation of 5(6)-carboxyfluorescein with Chc_2O proceeds smoothly and gives similar yields (71% for two-step one-pot procedure **1** → **3** → (**4b** + **4d**) compared to 67% for **1** → **2** → (**4a** + **4c**)). However, the more pronounced difference in chromatographic mobility between **4b** and **4d** (ΔR_f 0.09) in toluene makes their separation easier than Piv derivatives **4a** and **4c** (ΔR_f 0.07). The small difference in mobility ($\Delta\Delta R_f$ 0.02) can be felt strongly while separating decigram quantities of these isomer derivatives.

The structures of compounds **4a**−**d** were assigned using 2D $^1H-^{13}C$ HMQC and HMBC NMR spectra.

trans-4-Aminocyclohexanol was reported as an achiral precursor for phosphoramidites which are more stable in acetonitrile solution than phosphoramidites derived from primary alcohols (*26*). The individual regioisomers of pentafluorophenyl esters **4a**−**d** were reacted with *trans*-4-aminocyclohexanol to give amides **5a**−**d** in high yields. The following phosphitylation with *N*,*N*-diisopropylamino-2-cyanoethoxychlorophosphine furnishes the desired phosphoramidites **6a**−**d** (Scheme 1).

Reagents **6a**−**d** were used in the last coupling step of machine-assisted solid-phase DNA synthesis for the preparation of 5′-labeled 23-mer 5′-**X**CACTTTGTATATTGGTTGAAACT-3′. The conjugates prepared were cleaved from their supports, deprotected by conc aq ammonia treatment at 55 °C overnight, analyzed by reversed-phase HPLC and MALDI-TOF MS, and purified by PAGE for fluorescence studies. Reagents **6a** and **6b** gave conjugate 5′-(5-FAM)-CACTTTGTATATTGGTTGAAACT-3′ (**7a**) (Chart 1); the products from two syntheses were identical by HPLC and MALDI-TOF MS and showed the same electrophoretic mobilities. There was no substantial difference in the amounts of isolated products. In a similar manner, the use of reagents **6c** or **6d** gave one labeled oligonucleotide−5′-(6-FAM)-CACTTTGTATATTGGTTGAAACT-3′ (**7b**). Conjugates **7a** and **7b** were characterized by UV−vis and fluorescence spectra (Figure 1, Table 1).

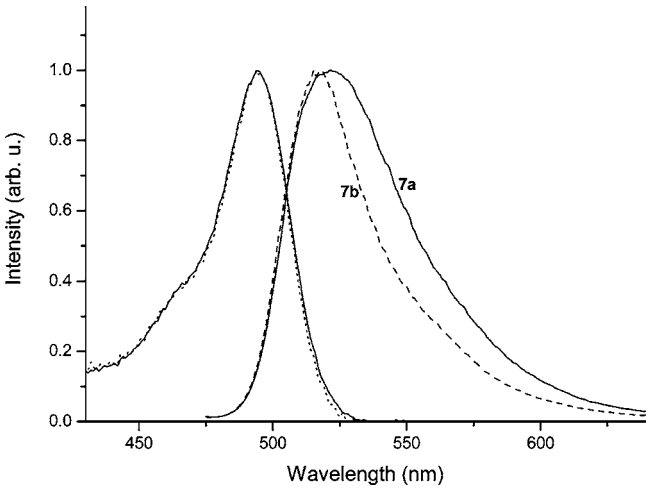


Figure 1. Normalized absorption (left) and fluorescence (right) spectra of labeled oligonucleotides **7a** (straight lines) and **7b** (doted and dashed lines) in sodium carbonate buffer, pH 8.35, excitation at λ = 470 nm.

There is no difference between UV−vis absorbances of 5- and 6-FAM attached to an oligonucleotide (Figure 1). The study of fluorescent properties of 5- and 6-FAM isomers in the usual pH range for fluorescein (8.35−9.5) showed that the differences in their photophysical characteristics depending on the pH are within error limits. In contrast, spectroscopic characteristics of 5- and 6-FAM are not essentially similar: 5-isomer displays a 3−5 nm red shift of the fluorescence maximum against 6-isomer (Figure 1, Table 1). The emission band in the spectrum of 5-FAM is substantially broader.

The obvious consequences from the presented data for 5- and 6-FAM are that these dyes in aqueous solutions within the pH range 8.35−9.5 have similar absorbance and fluorescence quantum yields, and, therefore, similar fluorescence brightness.

However, in the case of multiplex detection of several fluorochromes, the sharper emission band of 6-FAM could be an advantage.

To conclude, we have shown that 5- and 6-carboxyfluoresceins can be easily separated as Pfp esters of 3′,6′-*O*-diacyl derivatives, and Chc is the acyl protecting group of choice for this procedure; inexpensive phosphoramidite reagents can be easily prepared from the above esters in two steps; spectroscopic and photophysical data for 5- and 6-FAM on oligonucleotide were collected and compared.

ACKNOWLEDGMENT

We thank Marina Zhilinskaya and Youri Habrus for the oligonucleotides synthesis, BFBR (project B06R-004) and RFBR (projects 06-04-81019 and 06-03-32426) for the financial support; Z. Shenkarev, K. Nadezhdin, A. Paramonov, and Shemyakin-Ovchinnikov Institute NMR Spectrometry Facility (registry no. 98-03-08) for NMR spectra. We are also grateful to A.P. Stupak and V.N. Knyukshto for help in fluorescence measurements.

LITERATURE CITED

(1) Drechsler, G., and Smagin, S. (1965) Zur Darstellung von Trimelliteinen und 5′-Carboxyfluoresceinen. *J. Prakt. Chem. 28*, 315−324.

(2) *The Handbook − A Guide to Fluorescent Probes and Labeling Technologies* (2005) 10th ed., Invitrogen/Molecular Probes (web edition: http://probes.invitrogen.com/handbook/).

(3) Wojczewski, C., Stolze, K., and Engels, J. W. (1999), Fluorescent oligonucleotides-versatile tools as probes and primers for DNA and RNA analysis. *Synlett* 1667−1678.

(4) Davies, M. J., Shah, A., and Bruce, I. J. (2000) Synthesis of fluorescently labelled oligonucleotides and nucleic acids. *Chem. Soc. Rev. 29*, 97−107.

(5) *Topics in Fluorescence Spectroscopy, V. 7: DNA Technology* (2003) (Lakowicz, J. R., Ed.) Kluwer Academic/Plenum Publishers, New York.

(6) Ranasinghe, R. T., and Brown, T. (2005) Fluorescence based strategies for genetic analysis. *Chem. Commun.* 5487−5502.

(7) Asseline, U. (2006) Development and applications of fluorescent oligonucleotides. *Curr. Org. Chem. 10*, 491−518.

(8) Haralambidis, J., Angus, K., Pownall, S., Duncan, L., Chai, M., and Tregear, G. W. (1990) The preparation of polyamide-oligonucleotide probes containing multiple non-radioactive labels. *Nucl. Acids Res. 18*, 501−505.

(9) Öberg, C. T., Carlsson, S., Fillion, E., Leffler, H., and Nilsson, U. J. (2003) Efficient and expedient two-step pyranose-retaining fluorescein conjugation of complex reducing oligosaccharides: galectin oligosaccharide specificity studies in a fluorescence polarization assay. *Bioconjugate Chem. 14*, 1289−1297.

(10) Rossi, F. M., and Kao, J. P. Y. (1997) Practical method for the multigram separation of the 5- and 6-isomers of carboxyfluorescein. *Bioconjugate Chem. 8*, 495−497.

(11) Sun, W.-C., Gee, K. R., Klaubert, D. H., and Haugland, R. P. (1997) Synthesis of fluorinated fluoresceins. *J. Org. Chem. 62*, 6469−6475.

(12) Lyttle, M. H., Carter, T. G., and Cook, R. M. (2001) Improved synthetic procedures for 4,7,2′,7′-tetrachloro- and 4′,5′-dichloro-2′,7′-dimethoxy-5(and 6)-carboxyfluoresceins. *Org. Proc. Res. Dev. 5*, 45−49.

(13) Jiao, G.-S., Han, J. W., and Burgess, K. (2003) Syntheses of regioisomerically pure 5- or 6-halogenated fluoresceins. *J. Org. Chem. 68*, 8264−8267.

(14) Ueno, Y., Jiao, G.- S., and Burgess K. (2004) Preparation of 5- and 6-carboxyfluorescein. *Synthesis 15*, 2591−2593.

(15) Woodroofe, C. C., Lim, M. H., Bu, W., and Lippard, S. J. (2005) Synthesis of isomerically pure carboxylate- and sulfonate-substituted xanthene fluorophores. *Tetrahedron 61*, 3097−3105.

(16) Adamczyk, M., Fishpaugh, J. R., and Heuser, K. J. (1997) Preparation of succinimidyl and pentafluorophenyl active esters of 5- and 6-carboxyfluorescein. *Bioconjugate Chem. 8*, 253−255.

(17) Adamczyk, M., Chan, C. M., Fino, J. R., and Mattingly, P. G. (2000) Synthesis of 5- and 6-hydroxymethylfluorescein phosphoramidites. *J. Org. Chem. 65*, 596−601.

(18) Mattingly, P. G. (1992) Preparation of 5- and 6-(aminomethy1)-fluorescein. *Bioconjugate Chem. 3*, 430−431.

(19) Ueno, Y., Urano, Y., Setsukinai, K., Takakusa, H., Kojima, H., Kikuchi, K., Onkubo, K., Fukuzumi, S., and Nagano, T. (2004) Rational principles for modulating fluorescence properties of fluorescein. *J. Am. Chem. Soc. 126*, 14079−14085.

(20) Theisen, P., McCollum, C., Upadhya, K., Jacobson, K., Vu, H., and Andrus, A. (1992) Fluorescent dye phosphoramidite labelling of oligonucleotides. *Tetrahedron Lett. 33*, 5033−5036.

(21) Nelson, P. S., Kent, M., and Muthini, S. (1992) Oligonucleotide labeling methods 3. Direct labeling of oligonucleotides employing a novel, non-nucleosidic, 2-aminobutyl-1,3-propanediol backbone. *Nucleic Acids Res. 20*, 6253−6259.

(22) McKeen, C. M., Brown, L. J., Nicol, J. T. G., Mellor, J. M., and Brown, T. (2003) Synthesis of fluorophore and quencher monomers for use in Scorpion primers and nucleic acid structural probes. *Org. Biomol. Chem. 1*, 2267−2275.

(23) Griesang, N., Kervio, E., and Richert, C. (2005) Linker-free fluorophore-labeled oligonucleotides: synthesis of 3′-fluoresceinylthymidine building blocks and their coupling reactions. *Synthesis* 2327−2334.

(24) Glen Research − http://www.glenres.com/.

(25) Biosearch Technologies − http://www.biosearchtech.com/.

(26) Morocho, A. M., Karamyshev, V. N., and Polushin, N. N. (2004) Methoxyoxalamido chemistry in the synthesis of novel amino linker and spacer phosphoramidites: A robust means for stability, structural versatility, and optimal tether length. *Bioconjugate Chem. 15*, 569−575.

(27) Sinha, N. D., Biernat, J., and Köster, H. (1983) β-Cyanoethyl N,N-dialkylamino/N-morpholinomonochlorophosphoamidites, new phosphitylating agents facilitating ease of deprotection and work-up of synthesized oligonucleotides. *Tetrahedron Lett. 24*, 5843−5846.

(28) Smith, L. M., Kaiser, R. J., Sanders, J. Z., and Hood, L. E. (1987) The synthesis and use of fluorescent oligonucleotides in DNA sequence analysis. *Methods Enzymol. 155*, 260−301.

(29) Gottlieb, H. E., Kotlyar, V., and Nudelman, A. (1997) NMR chemical shifts of common laboratory solvents as trace impurities. *J. Org. Chem. 62*, 7512−7515.

(30) Borisevich, E. A., Knyukshto, V. N., Kozyrev, A. N., and Solov'ev, K. N. (1993) The influence of external bromine atoms on photophysical processes and NH-shift in porphyrine macrocycle. *Opt. Spectrosc. 74*, 129−135.

(31) Brannon, J. H., and Magde, D. (1978) Absolute quantum yield determination by thermal blooming. Fluorescein. *J. Phys. Chem. 82*, 705−709.

(32) Gerchuk, M. P., and Katsnel'son, M. M. (1936) The synthesis of naphthenic anhydrides. *Dokl. Acad. Nauk SSSR 13*, 417−418.

BC7001874

Bioconjugate Chemistry

NOVEMBER/DECEMBER 2007
Volume 18, Number 6

© Copyright 2007 by the American Chemical Society

COMMUNICATIONS

Use of a Genetically Engineered Protein for the Design of a Multivalent MRI Contrast Agent

Lindsay S. Karfeld,[†,‡] Steve R. Bull,[†,§] Nicolynn E. Davis,[‡] Thomas J. Meade,[§,||,#] and Annelise E. Barron*[,⊥,‡,§]

Departments of Chemical and Biological Engineering, Chemistry, and Biochemistry and Molecular and Cell Biology, and Feinberg School of Medicine, Northwestern University, Evanston, Illinois 60208. Received April 25, 2007; Revised Manuscript Received July 26, 2007

The majority of clinically used contrast agents (CAs) for magnetic resonance imaging have low relaxivities and thus require high concentrations for signal enhancement. Research has turned to multivalent, macromolecular CAs to increase CA efficiency. However, previously developed macromolecular CAs do not provide high relaxivities, have limited biocompatibility, and/or do not have a structure that is readily modifiable to tailor to particular applications. We report a new family of multivalent, biomacromolecular, genetically engineered protein polymer-based CAs; the protein backbone contains evenly spaced lysines that are derivatized with gadolinium (Gd(III)) chelators. The protein's length and repeating amino acid sequence are genetically specified. We reproducibly obtained conjugates with an average of 8–9 Gd(III) chelators per protein. These multivalent CAs reproducibly provide a high relaxivity of 7.3 mM^{-1} s^{-1} per Gd(III) and 62.6 mM^{-1} s^{-1} per molecule. Furthermore, they can be incorporated into biomaterial hydrogels via chemical cross-linking of the remaining free lysines, and provide a dramatic contrast enhancement. Thus, these protein polymer CAs could be a useful tool for following the evolution of tissue engineering scaffolds.

One significant barrier to the development of new generations of biocompatible materials, particularly tissue engineering hydrogels, is the inability to noninvasively evaluate the properties and performance of the biomaterial over time (*1–6*). Magnetic resonance imaging (MRI) is capable of whole animal or human imaging at high spatial and temporal resolution and is an ideal modality for evaluating tissue engineering scaffolds *in vivo* (*7–11*). Exogenous contrast agents (CAs) increase the relaxation rate ($1/T_1$) of water protons and therefore improve image contrast. However, current clinically used CAs have low relaxivities (3–7 mM^{-1} s^{-1}) (*12*) and thus must be used at high concentrations for useful MRI signal enhancement (*12*).

T_1 CAs provide positive contrast by employing a paramagnetic ion (typically gadolinium, Gd(III)). The efficacy of a contrast agent is dominated by three parameters: q, the number of coordinated water molecules; τ_m, the residence lifetime; and τ_R, the rotational correlation time (*13*). Current clinically used small-molecule CAs are limited by their fast τ_R. More recently, these small-molecule CAs have been attached via covalent or noncovalent interactions to a number of macromolecules, including albumin (*14*), carbohydrates (*15*), linear polymers such

* Corresponding author. Annelise E. Barron, Department of Bioengineering, Stanford University, W300B James H. Clark Center, 318 Campus Drive, Stanford, CA 94305-5440; Phone (650) 725-7665; Fax (650) 723-8544; Email aebarron@stanford.edu.

[†] Both authors contributed equally.

[‡] Department of Chemical and Biological Engineering.

[§] Department of Chemistry.

[||] Department of Biochemistry and Molecular and Cell Biology.

[#] Feinberg School of Medicine.

[⊥] Present address: Department of Bioengineering, Stanford University, W300B James H. Clark Center, 318 Campus Drive, Stanford, CA 94305-5440; Phone (650) 725-7665; Fax (650) 723-8544; E-mail aebarron@stanford.edu.

10.1021/bc700149u CCC: $37.00 © 2007 American Chemical Society
Published on Web 10/10/2007

as polylysine (*16*), dendrimers (*17*), viral capsids (*18*), and liposomes (*19*). These multivalent CA designs are advantageous because they increase τ_R, Gd(III) concentration, and CA retention *in vivo*. Previously, researchers have tracked tissue engineering scaffolds *in vivo* by MRI without using any exogenous CAs (*20, 21*) or using soluble small-molecule CAs with a single Gd(III) chelator (*22, 23*). Recently, Bull et al. synthesized a self-assembled peptide amphiphile (PA)-based biomaterial scaffold, in which an MRI CA was incorporated, creating the first biomaterial designed for subsequent MRI-based *in vivo* fate mapping (*11*).

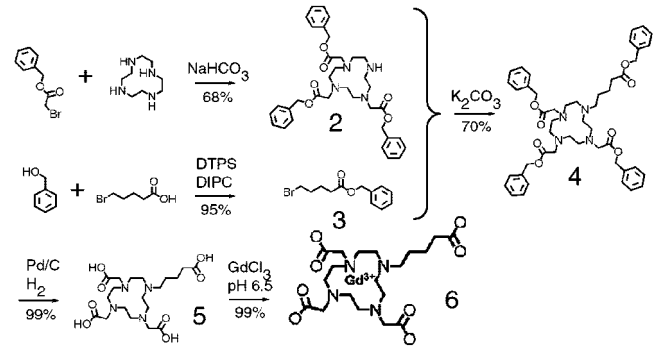
Here, we report the design, synthesis, and characterization of a novel family of multivalent, macromolecular CAs based on genetically engineered proteins with repetitive sequences that form the backbone for subsequent chemical modification with Gd(III) chelators. These "protein polymer" CAs have high relaxivities in aqueous solution. Moreover, they provide a dramatic contrast enhancement when covalently cross-linked into protein-based hydrogels. The artificial protein polymers were generated by controlled cloning and recombinant protein expression in *E. coli* and were designed to satisfy the specific criteria of water solubility, controlled reactivity, and ability to be cross-linked into hydrogels that could be useful for tissue engineering applications. In contrast to other biocompatible polymers such as dextran and other chemically synthesized and/or modified polymers, we can control the precise monomer composition, sequence, and chain length of these protein scaffolds. Affinity chromatography affords pure, monodisperse biopolymers with evenly spaced, primary amine reactive sites, which serve as an ideal scaffold for CA modification.

The protein polymer backbone we used comprises 30 repeats of the amino acid sequence G**K**AGTGSA, providing 30 reactive primary amines (ϵ-amino groups of lysines) that are available for derivatization (*24*). The 21 825 Da protein polymer (molar mass confirmed by MALDI; see Supporting Information (SI)) is water-soluble and can be produced in high yield. Circular dichroism spectroscopy shows that the protein adopts a random-coil (unfolded) configuration in aqueous solution (see SI) (*25*), thereby avoiding particular secondary structures that could potentially lead to decreased τ_R (such as a cylindrical α-helix). The macrocyclic chelate that coordinates the Gd(III) ion is a chemically synthesized derivative of 1,4,7,10-tetraazacyclododecane-1,4,7,10-tetraacetic acid (DOTA) (*26*). The three acetate arms chelate the Gd(III), while the carboxylate group on the 5-carbon arm is used for covalent attachment to the primary amine of the lysine residues via amide bond formation.

A multistep controlled cloning method was used to create the 720 base pair gene that encodes the protein polymer (*25*), and standard transformation and expression protocols were used to produce the 264 amino acid–protein polymer, **1** (see SI) (*27*). The pET19b expression vector into which the gene was ligated contains an N-terminal histidine fusion tag, GH_{10}SSGHIDDDDKHM, enabling protein purification via Ni-NTA affinity chromatography under denaturing conditions (*27*). In a typical expression, up to ~60 mg/L of culture medium are obtained after purification. Further details are given in the SI.

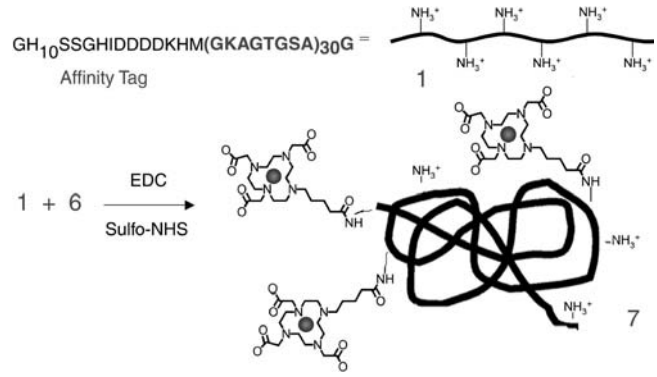
The Gd(III) chelator was synthesized using a hydrogenation-labile protection scheme with benzyl 2-bromoacetate and benzyl 5-bromopentanoate as the chelating arms of the macrocycle (Scheme 1). The addition of three benzyl 2-bromoacetate arms to cyclen was followed by the addition of benzyl 5-bromopentanoate. Global deprotection by hydrogenation of the chelator and subsequent metalation with $GdCl_3$ afforded **6,** which subsequently was conjugated to the protein polymer. The synthesis and characterization of the chelator is described in the SI.

Scheme 1. Synthesis of Gd(III) Chelator Using a Hydrogenation-Labile Global Deprotection Scheme [a]



[a] Gd(III) was chelated before conjugation to the protein to ensure that all chelators contained Gd(III).

Scheme 2. Conjugation of Gd(III) Chelator to Protein Polymer Backbone through Amide Bond Formation Using EDC and Sulfo-NHS, where ~8–9 Chelators Per Protein Molecule Are Available for Conjugation



The coupling reaction between the lysine residues of **1** and **6** was carried out in aqueous 0.1 M 4-morpholineethanesulfonic acid (MES), 0.5 M NaCl buffer with 1-ethyl-3-carbodiimide hydrochloride (EDC), and *N*-hydroxysulfosuccinimide (sulfo-NHS), which are water-soluble peptide bond-forming agents (Scheme 2) (*28*). We chose to conjugate premetallated chelators to the protein polymer in order to simplify the synthetic process, avoid solubility issues, and guarantee that each chelator contains a Gd(III) ion. MALDI-MS analysis of the conjugate confirmed that an average of ~8–9 out of a possible 31 lysines per molecule are typically derivatized using this procedure ($n = 4$), but we have achieved up to 15 Gd(III)-conjugated sites per protein molecule in some cases. The conjugation efficiency of this reaction is limited by a competing hydrolysis reaction involving water molecules. The derivatization with Gd(III) chelators introduces a small degree of polydispersity, since the positions of the chelators along the backbone are different in each individual CA, but these CAs can still be well-characterized by MALDI due to the monodispersity of the protein polymer backbone. As determined through relaxivity and inductively coupled plasma (ICP)-MS measurements, the CAs display relaxivities of 7.3 ± 0.4 mM^{-1} s^{-1} per Gd(III) ion ($n = 4$) and 62.6 ± 3.5 mM^{-1} s^{-1} per protein molecule complex, which is the product of the number of Gd(III) chelators per protein backbone times the relaxivity per Gd(III). Synthetic polymers such as dendrimers and metallofullerenes display molecular relaxivities of ~35 mM^{-1} s^{-1} (*29*) and ~60 mM^{-1} s^{-1} (*30*), respectively. There are a few examples of natural protein-based CAs that display greater molecular relaxivities (cowpea chlorotic mottle virus, ~200–400 mM^{-1} s^{-1} per viral conjugate (*31*), apoferritin, ~800 mM^{-1} s^{-1} per protein complex (*32*), MS2

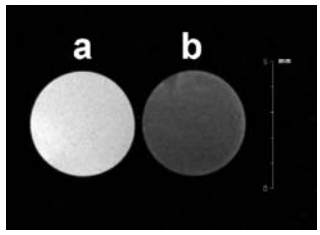


Figure 1. MR images acquired at 14.1 T with TR 250.0 ms, TE 10.2 ms. (a) Glutaraldehyde-cross-linked hydrogel doped with **7** with an added Gd(III) concentration of 0.8 mmol. (b) Control hydrogel without contrast agent.

viral capsid, ~7200 mM^{-1} s^{-1} (*18*)). Even though some of these CAs have shown higher relaxivities per molecule, our new protein polymer CAs avoid some disadvantages associated with these other CAs. As compared with synthetic polymers, protein polymers consist of amino acids, so they are biodegradable and should not have any toxic byproducts (chelated Gd(III) is nontoxic). The above-mentioned natural protein CAs are less easily tunable and modifiable, so the relaxivity, size of the CAs, toxicity, *in vivo* circulation time, and mode of excretion cannot be as easily modulated. On the other hand, protein polymers can be precisely designed for the particular application and point of use; they can be customized to vary protein lengths and the spacing and number of lysines for conjugation to Gd(III) chelators. Additionally, these protein polymer CAs can be derivatized with other biological moieties for additional functionality, such as targeting and intracellular translocation.

To demonstrate one useful application of these new protein polymer-based CAs, tracking the evolution of tissue engineering hydrogels over time, we prepared 5.8% (w/v) protein-based hydrogels in aqueous solution in 5 mm NMR tubes for MR imaging experiments. The protein–CA conjugate, **7**, was doped into a solution of unconjugated protein polymer, **1**, and the free amines were cross-linked with 45 μL of 25% glutaraldehyde to form a gel (see SI). One advantage of these protein polymer-based CAs is that at least 50% of the primary amines on the backbone remain underivatized and are available for covalent cross-linking to form the hydrogel, as well as assisting in water solubility. Thus, once cross-linked to other proteins within a hydrogel, the multivalent CAs can only be removed from the hydrogel as a result of hydrolysis of the scaffold and not as a result of diffusion. The MR images show that the hydrogel incorporating **7** is homogenous and exhibits dramatically higher MRI contrast than the hydrogel formed from a protein polymer control (Figure 1).

In conclusion, a combination of biosynthetic and chemical methods has been used to create high-contrast, multivalent, protein polymer-based MRI CAs. We have demonstrated a reliable synthetic protocol that allows conjugates to be characterized by MALDI and provides reproducible relaxivity results, both per molecule and per Gd(III). As shown in MR images, this protein polymer-based CA can be incorporated into a hydrogel and yields dramatic contrast enhancement, which could be a useful tool for following the evolution of tissue engineering scaffolds *in vivo*. We plan to employ other cross-linking mechanisms and hydrogel media to create a family of biocompatible tissue engineering scaffolds that can be fate-mapped *in vivo* by MRI, enabling tracking of both the cellular ingrowth and the scaffold degradation over time.

ACKNOWLEDGMENT

This work was supported by NIH/NIBIB grant nos. 1-R01 EB003806, RFA-CA-05-024, and 1-R01 EB005866, and the NIH/NRSA Biotechnology Training Grant (2-T32-GM008449). This work made use of the Analytical Services Laboratory of Northwestern University. We thank Keith Macrenaris for his assistance with ICP and MR image acquisition. We thank Dr. Jong-In Won for helpful discussions.

Supporting Information Available: Procedures on protein polymer, chelator, and CA synthesis and characterization including SDS-PAGE, MALDI, circular dichroism, and NMR data. This material will be available free of charge via the Internet at http://pubs.acs.org.

LITERATURE CITED

(1) Yang, S. F., Leong, K. F., Du, Z. H., and Chua, C. K. (2001) The design of scaffolds for use in tissue engineering. Part 1. Traditional factors. *Tissue Eng. 7*, 679–689.
(2) Langer, R., and Tirrell, D. A. (2004) Designing materials for biology and medicine. *Nature (London) 428*, 487–492.
(3) Liu, W., and Chen, C. (2005) Engineering biomaterials to control cell function. *Mater. Today 8*, 28–35.
(4) Discher, D. E., Janmey, P., and Wang, Y. L. (2005) Tissue cells feel and respond to the stiffness of their substrate. *Science 310*, 1139–1143.
(5) Pihlajamaki, H., Kinnunen, J., and Bostman, O. (1997) In vivo monitoring of the degradation process of bioresorbable polymeric implants using magnetic resonance imaging. *Biomaterials 18*, 1311–1315.
(6) Neves, A. A., Medcalf, N., Smith, M., and Brindle, K. M. (2006) Evaluation of engineered meniscal cartilage constructs based on different scaffold geometries using magnetic resonance imaging and spectroscopy. *Tissue Eng. 12*, 53–62.
(7) Bull, S., Guler, M., Bras, R., Venkatasubramanian, P., Stupp, S., and Meade, T. (2005) Magnetic resonance imaging of self-assembled biomaterial scaffolds. *Bioconjugate Chem. 16*, 1343–1348.
(8) Cheery, S. (2004) In vivo molecular and genomic imaging: new challenges for imaging physics. *Phys. Med. Biol. 49*, R13–R48.
(9) Huber, M., Staubli, A., Kustedjo, K., Gray, M., Shih, J., Fraser, S., Jacobs, R., and Meade, T. (1998) Fluorescently detectable magnetic resonance imaging agents. *Bioconjugate Chem. 9*, 242–249.
(10) Watanabe, T. (2002) Recent topics in NMR imaging and MRI. *Magn. Reson. Med. Sci. 1*, 38–49.
(11) Bull, S. R., Guler, M. O., Bras, R. E., Meade, T. J., and Stupp, S. I. (2005) Self-assembled peptide amphiphile nanofibers conjugated to MRI contrast agents. *Nano Lett. 5*, 1–4.
(12) Artemov, D., Bhujwalla, Z., and Bulte, J. (2004) Magnetic resonance imaging of cell surface receptors using targeted contrast agents. *Curr. Pharm. Biotechnol. 5*, 485–494.
(13) Merbach, A. E., and Toth, E. (2001) *The Chemistry of Contrast Agents in Medical Magnetic Resonance Imaging.* John Wiley & Sons, Inc., West Sussex, England.
(14) Caravan, P., Ellison, J., McMurry, T., and Lauffer, R. (1999) Gadolinium(III) chelates as MRI contrast agents: structure, dynamics, and applications. *Chem. Rev. 99*, 2293–2352.
(15) Sirlin, C., Vera, D., Corbell, J., Caballero, M., Buxton, R., and Mattrey, R. (2004) Gadolinium-DTPA-dextran: a macromolecular MR blood pool contrast agent. *Acad. Radiol. 11*, 1361–1169.
(16) Opsahl, L., Uzgiris, E., and Vera, D. (1995) Tumor imaging with a macromolecular paramagnetic contrast agent: gadopentetate dimeglumine-polylysine. *Acad. Radiol. 2*, 762–767.
(17) Langereis, S., de Lussanet, Q., van Genderen, M., Meijer, E., Beets-Tan, R., Griffioen, A., van Engelshoven, J., and Backes, W. (2006) Evaluation of Gd(III)DTPA-terminated poly(propylene imine) dendrimers as contrast agents for MR imaging. *NMR Biomed. 19*, 133–141.
(18) Anderson, E. A., Isaacman, S., Peabody, D. S., Wang, E. Y., Canary, J. W., and Kirshenbaum, K. (2006) Viral nanoparticles donning a paramagnetic coat: Conjugation of MRI contrast agents to the MS2 capsid. *Nano Lett. 6*, 1160–1164.
(19) Strijkers, G., Mulder, W., van Heeswijk, R., Frederik, P., Bomans, P., Magusin, P., and Nicolay, K. (2005) Relaxivity of

liposomal paramagnetic MRI contrast agents. *Magma 18*, 186–192.
(20) Stroman, P. W., Dorvil, J. C., Marois, Y., Poddevin, N., and Guidoin, R. (1999) In vivo time course studies of the tissue responses to resorbable polylactic acid implants by means of MRI. *Magn. Reson. Med. 42*, 210–214.
(21) Traore, A. S., Woerly, S., Doan, V. D., Marois, Y., and Guidoin, R. (2000) In vivo magnetic resonance imaging and relaxometry study of a porous hydrogel implanted in the trapezius muscle of rabbits. *Tissue Eng. 6*, 265–278.
(22) Barbash, I. M., Leor, J., Feinberg, M. S., Tessone, A., Aboulafia-Etzion, S., Orenstein, A., Ruiz-Cabello, J., Cohen, J. S., and Mardor, Y. (2004) Interventional magnetic resonance imaging for guiding gene and cell transfer in the heart. *Heart 90*, 87–91.
(23) Cheng, H. L. M., Chen, J., Babyn, P. S., and Farhat, W. A. (2005) Dynamic Gd-DTPA enhanced MRI as a surrogate marker of angiogenesis in tissue-engineered bladder constructs: A feasibility study in rabbits. *J. Magn. Reson. Imaging 21*, 415–423.
(24) Davis, N., Ding, S., Karfeld, L., and Barron, A. (2007). Synthesis and characterization of a new class of cationic protein polymers for multivalent display and biomaterial applications. Unpublished results.
(25) Won, J., and Barron, A. (2002) A new cloning method for the preparation of long repetitive polypeptides without a sequence requirement. *Macromolecules 35*, 8281–8287.
(26) Artemov, D., Mori, N., Okollie, B., and Bhujwalla, Z. (2003) MR molecular imaging of the Her-2/neu receptor in breast cancer cells using targeted iron oxide nanoparticles. *Magn. Reson. Med. 49*, 403–408.
(27) Ausbel, F. (2001) *Current Protocols in Molecular Biology*, J. Wiley & Sons, Inc., New York.
(28) Hermanson, G. (1996) *Bioconjugate Chemistry*, Academic Press, San Diego.
(29) Kobayashi, H., and Brechbiel, M. W. (2004) Dendrimer-based nanosized MRI contrast agents. *Curr. Pharm. Biotechnol. 5*, 539–549.
(30) Mikawa, M., Kato, H., Okumura, M., Narazaki, M., Kanazawa, Y., Miwa, N., and Shinohara, H. (2001) Paramagnetic water-soluble metallofullerenes having the highest relaxivity for MRI contrast agents. *Bioconjugate Chem. 12*, 510–514.
(31) Allen, M., Bulte, J., Liepold, L., Basu, G., Zywicke, H., Frank, J., Young, M., and Douglas, T. (2005) Paramagnetic viral nanoparticles as potential high-relaxivity magnetic resonance contrast agents. *Magn. Reson. Med. 54*, 807–812.
(32) Aime, S., Frullano, L., and Crich, S. G. (2002) Compartmentalization of a gadolinium complex in the apoferritin cavity: A route to obtain high relaxivity contrast agents for magnetic resonance imaging. *Angew. Chem., Int. Ed. 41*, 1017–1019.

BC700149U

Protease-Sensitive Fluorescent Nanofibers

Benedict Law,[†] Ralph Weissleder, and Ching-Hsuan Tung*

Center for Molecular Imaging Research, Massachusetts General Hospital, Harvard Medical School, Charlestown, Massachusetts 02129. Received February 16, 2007; Revised Manuscript Received September 17, 2007

We report the design and synthesis of enzyme-responsive nanofibers. The fibers are composed of self-assembled hydrophobic β-sheet peptides incorporating protease-sensitive domains, fluorescent reporters, and hydrophilic poly(ethylene glycol) (PEG) units. Using urokinase plasminogen activator (uPA) as a model system, nanofibers were developed to release fluorescent fragments upon uPA incubation. These protease-sensitive nanofibers may have considerable biomedical applications as diagnostic sensors or for protease-assisted drug deliveries.

INTRODUCTION

A variety of nanomaterials have shown promise in biomedical applications (*1*–*3*). Over the past few years, several synthetic materials have emerged from biological systems and have been developed as sensors or for drug delivery. Self-assembly peptides can provide a high degree of flexibility and smartness when constructed into bioresponsive materials (*4*). For instance, self-complementary nanofibers have been proposed as scaffolds for tissue engineering, drug delivery, and imaging agent development (*5*, *6*). These fibers are typically assembled from simple building blocks driven by noncovalent interactions. Peptide nanofibers have been designed, by using the biotin-sandwich approach, to provide specific and prolonged local myocardial delivery of survival factor, ICF-1 in cell-based therapies (*7*). Another study designed heparin-tagged nanofibers as sustained release system for grow factors such as FGF-2 or VEGF to promote angiogenesis (*8*). Importantly, these assemblies are often quite stable and homogenous in biological conditions.

One of the approaches to fine-tune bioresponsiveness is to incorporate environmentally sensitive chemical moieties into nanomaterials. For example, we have previously demonstrated that protease-responsive matrices composed of multiple peptide substrates (kldlkl-SGRSANA-dlkldlkl-NH_2, lowercase letters indicated D-amino acid, and upper-case letters indicated L-amino acid) could be synthesized (*9*). Here, the self-assembly nature of β-sheets was adapted to develop highly stable nanofibers. The core sequences were designed to incorporate the following (Figure 1): (1) a hydrophobic β-sheet segment, $[kldl]_3$ (*10*), which consisted of D-amino acids to avoid nonspecific proteolytic digestion at the C-terminus, (2) an α-methyl-substituted poly(ethylene glycol) (mPEG) hydrophilic polymer attached at the N-terminus to prevent potential aggregation, (3) a specific peptide substrate (SGRSANA) positioned in the middle of the hydrophobic and hydrophilic segments that has been employed previously for in vivo protease imaging (*11, 12*). The substrate is highly degradable by uPA (*13*), an enzyme known to have distinct roles in tumor growth, invasion, migration, and angiogenesis by facilitating the breakdown of extracellular matrix (ECM)[1] through proteolytic cascades (*14*–*16*), and finally (4) a conjugated fluorescein derivative, 5(6)-fluorescein isothiocyanate (FITC), as an optical reporter.

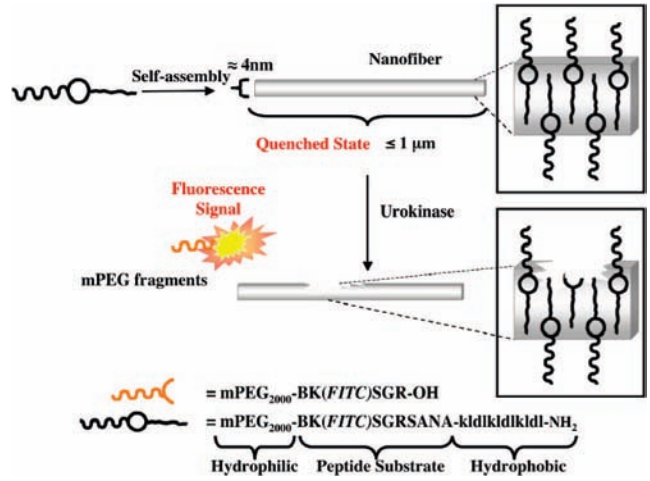


Figure 1. Design of uPA sensitive nanofibers. The fibers are composed of multiple PEG2000–peptide conjugates ($mPEG_{2000}$-BK(*FITC*)SGR-SANA-$[kldl]_3$-NH_2, where B = β-alanine). Each conjugate consists of a uPA peptide substrate (SGRSANA, L-amino acid) inserted in between the hydrophilic ($mPEG_{2000}$) and hydrophobic ($[kldl]_3$, D-amino acid) fractions. In addition, a fluorescein isothiocyanate (FITC) is introduced onto individual peptides as the optical reporter. In 10 mM of PBS buffer (pH 7.4), the mPEG2000–peptide conjugates self-assemble spontaneously to form filaments with organized structures, so that the fluorophores are arranged in close proximity and result in fluorescence quenching. Upon addition of uPA, the substrate site is cleaved, leading to release of the fluorescent hydrophilic fragments ($mPEG_{2000}$-BK(*FITC*)SGR) and resulting in fluorescence recovery.

EXPERIMENTAL PROCEDURES

Chemicals. All solvents were purchased from Fisher Scientific (Fair Lawn, NJ). All D- and L-amino acids were supplied by Novabiochem (San Diego, CA). α-Methyl-substituted poly-

* Corresponding author. Ching H. Tung, Ph.D. The Methodist Hospital Research Institute, Weill Cornell Medical College, 6565 Fannin Street, #B5-022, Houston, TX 77030, Tel: 713-441-8682, e-mail: ctung@tmhs.org.

[†] Current address: Department of Pharmaceutical Sciences, North Dakota State University, 116 Sudro, Fargo, ND 58105, Tel: 701-231-7906, e-mail: Shek.Law@NDSU.edu.

[1] Abbreviations: beta-alanine (B), *N*,*N*-diisopropylethylamine (DIEPA), extracellular matrix (ECM), 5(6)-fluorescein isothiocyanate (FITC), 2(1*H*-benzotriazole-1-yl)-1,1,3,3-tetramethyluronium hexafluorophosphate (HBTU), *N*-hydroxybenzotriazole (HOBt), 4,4-dimethyl-2,6-dioxocyclohexylidene)3-methylbutyl (ivDde), α-methyl substituted poly(ethylene glycol) (mPEG), *N*-methylpyrrolidone (NMP), poly(ethylene glycol) (PEG), urokinase plasminogen activator (uPA).

10.1021/bc070054z CCC: $37.00 © 2007 American Chemical Society
Published on Web 10/05/2007

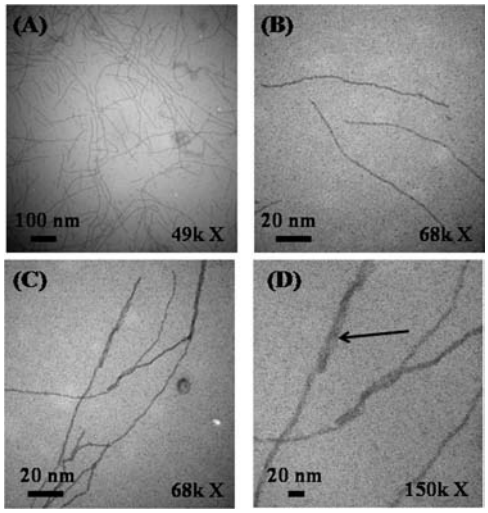


Figure 2. TEM images of protease-sensitive nanofibers. Images of fibers are shown at different magnifications (A,B). All samples were negatively stained with uranyl formate to provide contrast. Some fibers self-assemble to form supercoil networks (black arrow, C,D).

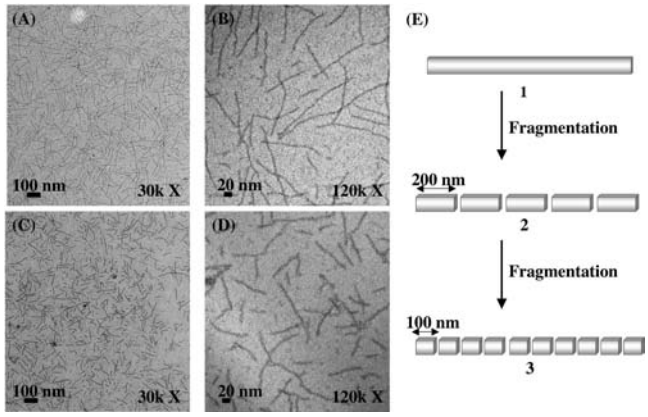


Figure 3. Size control of nanfibers. TEM images of 200 nm nanofiber **2** (A,B) and 100 nm nanofiber **3** (C,D). All samples were negatively stained with uranyl formate to provide contrast. (E) Schematic presentation indicates the synthesis of nanofiber **3**.

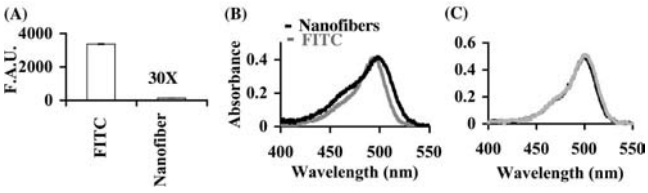


Figure 4. Optical properties of 100 nm nanofiber **3**. (A) Relative fluorescence intensities of FITC and fibers in PBS buffer (10 μM). The nanofiber was 30× less fluorescent than free FITC. The absorption spectra of FITC and nanofiber **3** in (B) PBS buffer and (C) methanol. The spectra were normalized at 494 nm.

(ethylene glycol) *N*-hydroxysuccinimide ester ($mPEG_{2000}$-NHS ester) was purchased from Nektar Therapeutics (San Carlos, CA). Amiloride, anisole, ethandithiol, 5(6)-fluorescein isothiocyanate (FITC), thioanisole, urokinase (EC: 3.4.21.73), and all other chemicals were obtained from Sigma-Aldrich (St. Louis, MO).

Peptide Synthesis. Peptide synthesis was performed on an automated solid-phase peptide synthesizer (ABI-433A, Applied Biosystems, Foster City, CA) employing the traditional Nα-Fmoc methodology on Rink amide resin (280 mg, 0.1 mmol). Side-chain protections were Arg(Pbf), Asn(Trt), Lys(Boc), and Ser(tBu). Lys(ivDde) was used for selective deprotection on solid phase prior to FITC conjugation. All amino acids (10 equiv) were attached to the resin by stepwise elongation using 2(1*H*-benzotriazole-1-yl)-1,1,3,3-tetramethyluronium hexafluorophosphate (HBTU)/*N*-hydroxybenzotriazole (HOBt)/*N*,*N*-diisopropylethylamine (DIEPA) as the coupling reagent in *N*-methylpyrrolidone (NMP). mPEG-NHS (avg MW = 2470, 500 mg, 0.2 mmol) in DMSO (4 mL) was coupled to the peptide resin (140 mg, 0.05 mmol), initiated with the addition of DIEPA (1 mL), and subjected to further gentle shaking for 3 h at room temperature. The resulting resin was washed three times with 2% (v/v) hydrazine monohydrate in DMF (10 mL) for 5 min to selectively remove ivDde (4,4-dimethyl-2,6-dioxocyclohexylidene)-3-methylbutyl) side-chain amino protecting group. FITC (151 mg, 0.4 mmol) and DIEPA (1 mL) were dissolved in DMSO (4 mL). The solution was then added to the resin and further shaken for 3 h at room temperature. After drying with methanol, the peptide was cleaved from the resin with addition of a cleavage cocktail containing TFA/thioanisole/ethandithiol/anisole 90/5/3/2 (5 mL) for 3 h at room temperature. The filtrate was collected and precipitated into methyl-*tert*-butyl ether at 4 °C. Crude mPEG–peptide conjugates were purified by high-performance liquid chromatography (HPLC) (Ranin, Worburn, MA). MALDI-TOF mass spectrometry (Tufts Medical School, Core Facility, Boston, MA) confirmed the average mass ions for all synthetic conjugates. The concentrations of all peptides were determined by UV absorbance for their attached FITC moieties ($\varepsilon = 65 \times 10^{-3}$ M^{-1} cm^{-1} at 490 nm) in methanol.

Synthesis of Nanofibers 1, 2, and 3. The peptide ($mPEG_{2000}$−BK(*FITC*)SGRSANA-[kldl]$_3$, 20 mg) or the control sequence ($mPEG_{2000}$−BK(*FITC*)SGASNRA-[kldl]$_3$, 20 mg) was dissolved in 50% (v/v) acetonitrile in water (5 mL). The solution mixtures were stirred vigorously overnight inside a fume hood to evaporate the solvent. The resulting fibers **1** were then purified by size-exclusion chromatography (P-10 Biogel, Bio-Rad, Hercules, CA). Concentrations were determined by UV absorbance for their attached FITC moieties in methanol. To control the lengths of the preparations, the nanofiber solutions were passed through a mini-extruder (Avanti Polar Lipids Ltd., Alabaster, AL) using polycarbonate membranes (Whatman, Florham Park, NJ) with 0.4 μm and 0.2 μm pore sizes for the synthesis of 200 nm **2** and 100 nm **3** fibers, respectively. After 10 passages, the solutions were collected and further purified by size-exclusion chromatography to remove the smaller fragments. The amounts were determined by UV absorbance for their attached FITC concentrations in methanol.

Transmission Electron Microscopy. All images were recorded by transmission electron microscopy (Tecnai G^2 Spirit BioTWIN, Hillsboro, OR) equipped with an AMT 2k CCD camera at Harvard Medical School (Department of Cell Biology, Boston, MA). All samples were negatively stained with uranyl formate (*17*). Briefly, the samples were diluted with water and absorbed onto the formvar/carbon coated grids. Excess samples were blotted off on a filter paper. The grids were then floated on small drops (5 μL) of uranyl formate solutions 2% (v/v) for a few minutes and then blotted off. The samples were dried and examined in the TEM.

Enzyme Digestion Study by Fluorescence Imaging. Fluorescence imaging was performed by a reflectance fluorescence imaging system that has been described previously. Band-pass filters (Omega Optical, Brattleboro, VT) were employed to adjust the corresponding excitation wave bands for FITC. Stock nanofibers **3** (400 μM) in PBS buffer (10 mM, pH 7.4, 50 μL) or control fibers (400 μM) containing a scrambled uPA substrate sequence (SGASNRA) in PBS buffer (10 mM, pH 7.4, 50 μL) were loaded onto individual wells of a clear-bottom 96-well

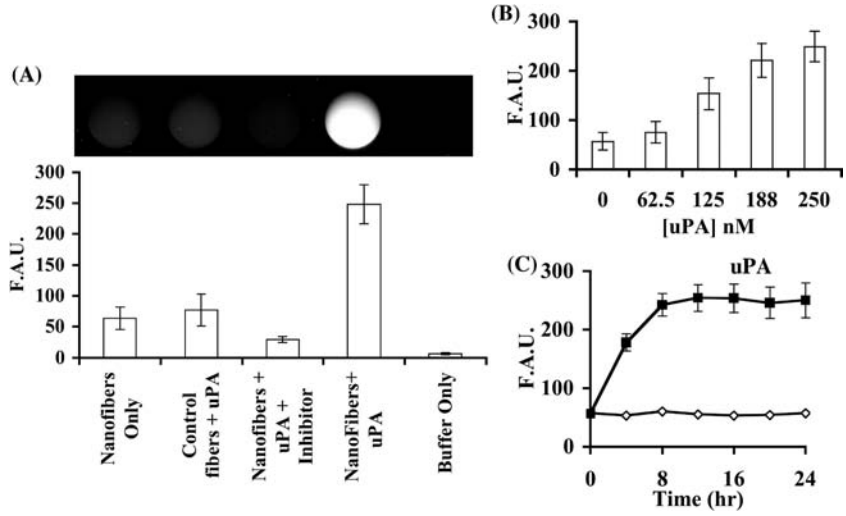


Figure 5. Enzyme responsiveness. (A) Activation of 100 nm nanofiber **3** (100 μM) in different conditions at 24 h after incubation with uPA (250 nM) in 10 mM of PBS buffer (pH 7.4) at room temperature. No enzyme was added in the negative control. Nanofibers containing a scrambled uPA substrate sequence (SGASNRA) were synthesized as control fibers. Amiloride (1 mM) was used as the inhibitor to coincubate with enzyme. The concentrations of nanofibers or the controls were 100 μM. All samples were imaged in a 96-well plate by a reflectance imaging system. Individual wells were chosen as the region of interest (R.O.I.). (B) Fluorescence intensities of nanofibers (100 μM) at 24 h after incubation with various uPA concentrations (0–250 nM). (C) Fluorescence intensities plotted against time (hr) following activation of nanofiber **3** (100 μM) with (■) or without uPA (250 nM) (◇).

plate (Corning, Corning, NY). PBS (10 mM, pH 7.4, 50 μL) or amiloride (4 mM) dissolved in PBS (10 mM, pH 7.4, 50 μL) was added to the corresponding wells. After 24 h incubation at room temperature, the plates were imaged with the exposure time of 10 min per image for four images. The entire wells were chosen as the region of interest (R.O.I.), and the relative fluorescence intensities were further analyzed by using computer software (Kodak Digital Science 1D software, Rochester, NY). To investigate whether the fluorescence activation of **3** was uPA-dependent, stock nanofibers **3** (400 μM) in PBS buffer (10 mM, pH 7.4, 50 μL) were loaded onto the wells of a clear-bottom 96-well plate. Different concentrations of urokinase (from 0 to 250 nM, 0–9.45 units, 150 μL) were then added to the corresponding wells. After 24 h incubation at room temperature, the plates were imaged as described above. For kinetic experiments, the enzyme-treated and -untreated samples were imaged every 4 h over a period of 24 h.

RESULTS AND DISCUSSION

The complete peptide–polymer conjugate ($mPEG_{2000}$−BK-(*FITC*)SGRSANA-$[kldl]_3$) was synthesized in solid phase employing the standard Fmoc chemistry on Rink amide resins. Following peptide synthesis, mPEG-NHS with average molecular weight of 2470 Da was attached at the N-terminus. To introduce the fluorescein reporter group, Lys(ivDde) was employed as the amino acid building block. The protecting group, ivDde, was selectively removed by hydrazine prior to fluorophore conjugation. The cleaved peptides were purified by HPLC, and the average molecular mass ($[M + H]^+ = 4755$) was confirmed by MALDI-TOF.

The morphology of any designed assemblies can be influenced by modifying hydrophobic/hydrophilic ratios (*18*). The employed hydrophobic β-sheet segment ($[kldl]_3$) (*10*) and several similar ionic self-complementary peptides are known to form amyloid-type fibers (*19, 20*). Nanofibers were assembled by dissolving pegylated peptides in a mixture of acetonitrile and water, followed by solvent evaporation. Nanofibers assembled spontaneously into unique structures of homogenous width and length (Figure 2A and B). The widths of fiber **1** observed by TEM were extremely narrow (approx. 4 nm). In contradiction to previous reports (*19, 21*), we did not observe cylindrical tubes (approx. 50 nm in diameter). Intermediate helical ribbons with the longer fibers (>1 μm), indicating an early sign of lamination, were found infrequently (Figure 2C and D). The nanofibers did not fuse into nanotubes (*20*), presumably because the conjugated mPEG2000 in **1** sterically prevents aggregation.

To prepare homogenous nanofibers, the assembled samples were physically disrupted into shorter fragments by passing them through a mini-extruder. This procedure is similar to routinely used methods for producing homogenous liposomes. Depending on the pore sizes of the employed polycarbonate membranes, nanofibers with approximate lengths of 200 nm for **2** and 100 nm for **3** were obtained (Figure 3). The fragmented fibers (2 μM) had similar physical properties as the original fibers **1**, and there was no aggregation or cross-linking between fibers. Further experiments are underway to study the long-term stability of these fibers.

The conjugated FITC fluorophores of **3** positioned in close proximity resulted in nearly complete quenching (96%) of fluorescence in intact nanofibers (Figure 4A). When compared to the same concentrations of free FITC, the normalized (at 494 nm) absorption spectrum in PBS buffer was broadened and had an increased peak maximum (at 460 nm) (Figure 4B). In contrast, when **3** was completely dissociated in methanol, the absorption overlapped with the free FITC (Figure 4C), thus providing evidence that fluorescence quenching of **3** is caused by structural orientations of the nanofiber assemblies.

The core nanofiber peptide was designed to contain a uPA cleavage site (SGRSANA) for proteolytic digestion. We hypothesized that the assembled nanofibers could thus respond to uPA by releasing FITC-conjugated fragments ($mPEG_{2000}$-BK(*FITC*)SGR) when cleaved (Figure 1). To study enzymatic activation, the nanofibers **3** (100 μM) were incubated with uPA (250 nM) for 24 h. We observed an up to 4-fold increase in fluorescence intensity (Figure 5A), which was uPA-concentration dependent (Figure 5B). In the presence of amiloride (1 mM), an inhibitor of uPA, fluorescence remained at the baseline level. Enzyme selectivity was further confirmed by using control nanofibers. Here, the substrate cleavage site was substituted with a scrambled peptide sequence (SGASRNA). As expected, in the presence of uPA, there was no activation of the control

nanofibers. To study digestion kinetics, nanofibers **3** were analyzed serially over time. In the absence of uPA, the fluorescence baseline remained constant with time, suggesting that the formulations were stable. The fluorescence increases reached a plateau after 8 h using 250 nM of uPA. Further experiments are underway to analyze the morphological changes of the nanofibers after enzymatic digestion.

In summary, using hydrophobic β-sheet peptides as core materials, we have developed a new type of protease-sensitive nanofiber. The materials are easy to synthesize and self-assemble into fibers with homogeneous nanometer diameters. The lengths of these fibers can be controlled by membrane filtration. Proof-of-principle experiments demonstrated that these nanofibers could be made protease-sensitive and biodegradable. These novel materials could have important applications in in vivo protease imaging or as enzyme-responsive biopolymers for systemic drug delivery.

ACKNOWLEDGMENT

The authors would like to thank Maria Ericsson (Department of Cell Biology, Harvard Medical School) for technical support on TEM. This research was supported in part by NIH P50-CA86355, RO1 CA099385, and R33 CA114149.

LITERATURE CITED

(1) Duncan, R. (2006) Polymer conjugates as anticancer nanomedicines. *Nat Rev Cancer 6*, 688–701.
(2) Schatzlein, A. G. (2006) Delivering cancer stem cell therapies - a role for nanomedicines? *Eur. J. Cancer 42*, 1309–15.
(3) Weissleder, R., and Mahmood, U. (2001) Molecular imaging. *Radiology 219*, 316–33.
(4) Fairman, R., and Akerfeldt, K. S. (2005) Peptides as novel smart materials. *Curr Opin Struct Biol 15*, 453–63.
(5) Nagai, Y., Unsworth, L. D., Koutsopoulos, S., and Zhang, S. (2006) Slow release of molecules in self-assembling peptide nanofiber scaffold. *J. Controlled Release 115*, 18–25.
(6) Bull, S. R., Guler, M. O., Bras, R. E., Meade, T. J., and Stupp, S. I. (2005) Self-assembled peptide amphiphile nanofibers conjugated to MRI contrast agents. *Nano Lett 5*, 1–4.
(7) Davis, M. E., Hsieh, P. C., Takahashi, T., Song, Q., Zhang, S., Kamm, R. D., Grodzinsky, A. J., Anversa, P., and Lee, R. T. (2006) Local myocardial insulin-like growth factor 1 (IGF-1) delivery with biotinylated peptide nanofibers improves cell therapy for myocardial infarction. *Proc Natl Acad Sci U S A 103*, 8155–60.
(8) Rajangam, K., Behanna, H. A., Hui, M. J., Han, X., Hulvat, J. F., Lomasney, J. W., and Stupp, S. I. (2006) Heparin binding nanostructures to promote growth of blood vessels. *Nano Lett 6*, 2086–90.
(9) Law, B., Weissleder, R., and Tung, C. H. (2006) Peptide-based biomaterials for protease-enhanced drug delivery. *Biomacromolecules 7*, 1261–5.
(10) Kisiday, J., Jin, M., Kurz, B., Hung, H., Semino, C., Zhang, S., and Grodzinsky, A. J. (2002) Self-assembling peptide hydrogel fosters chondrocyte extracellular matrix production and cell division: implications for cartilage tissue repair. *Proc Natl Acad Sci U S A 99*, 9996–10001.
(11) Law, B., Curino, A., Bugge, T. H., Weissleder, R., and Tung, C. H. (2004) Design, synthesis, and characterization of urokinase plasminogen-activator-sensitive near-infrared reporter. *Chem Biol 11*, 99–106.
(12) Law, B., Hsiao, J. K., Bugge, T. H., Weissleder, R., and Tung, C. H. (2005) Optical zymography for specific detection of urokinase plasminogen activator activity in biological samples. *Anal. Biochem. 338*, 151–8.
(13) Ke, S. H., Coombs, G. S., Tachias, K., Corey, D. R., and Madison, E. L. (1997) Optimal subsite occupancy and design of a selective inhibitor of urokinase. *J. Biol. Chem. 272*, 20456–62.
(14) Lee, M., Fridman, R., and Mobashery, S. (2004) Extracellular proteases as targets for treatment of cancer metastases. *Chem Soc Rev 33*, 401–9.
(15) Koblinski, J. E., Ahram, M., and Sloane, B. F. (2000) Unraveling the role of proteases in cancer. *Clin. Chim. Acta 291*, 113–35.
(16) Blasi, F., and Carmeliet, P. (2002) uPAR: a versatile signalling orchestrator. *Nat Rev Mol Cell Biol 3*, 932–43.
(17) Isaacs, A. M., Senn, D. B., Yuan, M., Shine, J. P., and Yankner, B. A. (2006) Acceleration of amyloid beta-peptide aggregation by physiological concentrations of calcium. *J. Biol. Chem. 281*, 27916–23.
(18) Discher, D. E., and Eisenberg, A. (2002) Polymer vesicles. *Science 297*, 967–73.
(19) Zhang, S., Marini, D. M., Hwang, W., and Santoso, S. (2002) Design of nanostructured biological materials through self-assembly of peptides and proteins. *Curr Opin Chem Biol 6*, 865–71.
(20) Lu, K., Jacob, J., Thiyagarajan, P., Conticello, V. P., and Lynn, D. G. (2003) Exploiting amyloid fibril lamination for nanotube self-assembly. *J. Am. Chem. Soc. 125*, 6391–3.
(21) Vauthey, S., Santoso, S., Gong, H., Watson, N., and Zhang, S. (2002) Molecular self-assembly of surfactant-like peptides to form nanotubes and nanovesicles. *Proc Natl Acad Sci U S A 99*, 5355–60.

BC070054Z

Energy Transfer between CdSe/ZnS Core/Shell Quantum Dots and Fluorescent Proteins

Vitor R. Hering,*[,†] Gary Gibson,[‡] Robert I. Schumacher,[†] Adelaide Faljoni-Alario,[†] and Mário J. Politi[†]

Departamento de Bioquímica, Instituto de Química, Universidade de São Paulo, São Paulo, SP 05513-970, Brazil, and Hewlett-Packard Laboratories, Palo Alto, California 94304. Received April 25, 2007; Revised Manuscript Received September 11, 2007

Fluorescent proteins from the green fluorescent protein (GFP) family interact strongly with CdSe/ZnS quantum dots. Photoluminescence of GFP5 is suppressed by red-emitting CdSe/ZnS quantum dots with high efficiency in a pH-dependent manner. The elevated degree of quenching, around 90%, makes it difficult to analyze the remaining signal, and it is not clear yet whether FRET is the reason behind the quenching. When the donor is a green-emitting CdSe/ZnS quantum dot and the acceptor is the HcRed1 protein, it is possible to detect quenching of the donor and sensitized emission from the acceptor. It was verified that the sensitized emission has the low anisotropy characteristic of FRET. The present characterization identifies donor–acceptor pairs formed by fluorescent proteins and CdSe/ZnS quantum dots that are suitable for the exploration of cellular events. These donor–acceptor pairs take advantage of the exceptional photochemical properties of quantum dots allied with the unique ability of fluorescent proteins to act as gene-based fluorescent probes.

INTRODUCTION

CdSe/ZnS core/shell quantum dots and fluorescent proteins belonging to the green fluorescent protein (GFP) family provide components among which Förster resonance energy transfer (FRET) is possible. The emission and absorption profiles of these elements can be matched to optimize FRET, and the distances can be kept below 10 nm. The occurrence of FRET in such system suggests a great diversity of possible donor–acceptor pairs and, because both components play important roles as biological labels, potential usefulness in cell biology experiments that make use of donor–acceptor labels.

CdSe/ZnS core/shell quantum dots have large absorption cross sections, high photoluminescence (PL) quantum yields (QY), size-tunable PL spectra covering the region from blue to red, exceptional photochemical stability (*1*, *2*), and good dispersibility in biological fluids (*3–6*). The GFP family is composed of a group of homologous, colored, compact proteins that spontaneously generate their own fluorophore (*7–9*). These proteins also cover the visible spectrum and have been extensively used as gene-based probes in molecular and cell biology (*10*).

Förster resonance energy transfer (*11*) between two fluorophores is typically observed over distances of less than 10 nm. Because FRET efficiency is strongly dependent on the distance separating the FRET pair and the relative orientation of the fluorophores, FRET can be used to analyze molecular interaction with high precision (*11–14*).

In this letter, we describe some aspects of the interaction between quantum dots and fluorescent proteins, with particular emphasis on the evidence for FRET between these components.

Our interest in the interaction between fluorescent proteins and semiconducting nanocrystals was piqued by the observation that GFP5 binds to 2-mercaptoethanol-covered ZnS nanocrystals, synthesized in accordance to Kosravi et al. (*15*). This was accomplished by cloning the gene coding for GFP5 into the HIS-tagging vector pET28a (Qiagen) and expressing it in *E. coli*. GFP5 contains three mutations from wild-type GFP aimed at improving bacterial expression (*16*). After purification, GFP5 was poured into a suspension of ZnS nanocrystals, and it was observed that it coprecipitates with them. GFP5 bound to these nanocrystals retains its photoluminescence. Following this first evidence, a further step was given by substituting the ZnS nanocrystals by red-emitting CdSe/ZnS core/shell quantum dots coated with mercaptoundecanoic acid (MUA), henceforth denoted QD-R. The quantum dots were purchased from NN-Laboratories and had a photoluminescence peak at 638 nm. Once the carboxylic end groups of MUA are exposed over the surfaces of the QDs, and given the usual pK_a of carboxylic acids (~4.5) of isolated molecules or even attached as surface groups (pK_{app} ~4.5 – 6.0), negatively charged particles will predominate at pH's ≥ 6.0. (*17*). The photoluminescence of GFP5 overlaps with the absorption spectrum of the QDs, as can be seen in Figure 1.

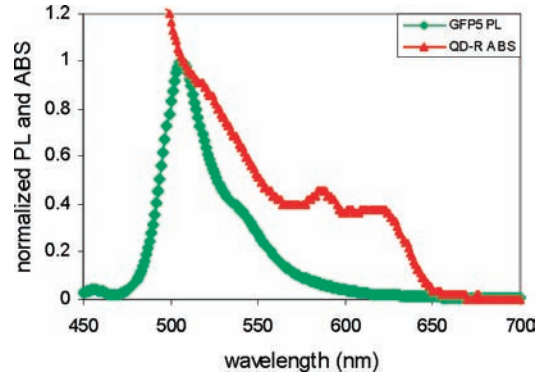


Figure 1. Normalized photoluminescence (PL) spectrum of GFP5 and absorption (ABS) spectrum of red-emitting CdSe/ZnS core/shell QD solutions.

Using the measured spectral overlap and a value of 79% for the quantum yield of GFP5 (*10*), we calculated a Förster radius (*12*) of 4.2 nm for the pair GFP5-QD-R. Because the diameter of the GFP5 barrel is 2.4 nm and its height is 4.2 nm (*8*) and the MUA coating thickness of the QDs is around 1 nm (data

* Corresponding author. E-mail: vrhering@uol.com.br. Phone number: 55 11 8335 5536.
† Universidade de São Paulo.
‡ Hewlett-Packard Laboratories.

10.1021/bc700147j CCC: $37.00 © 2007 American Chemical Society
Published on Web 09/28/2007

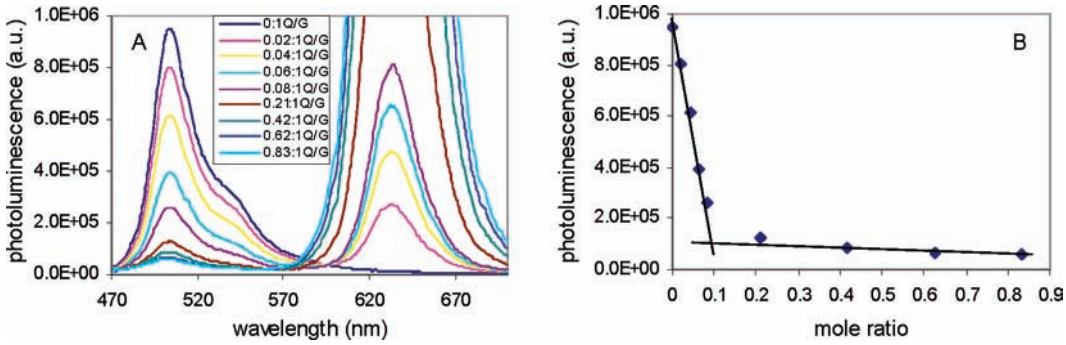


Figure 2. (A) Evolution of the photoluminescence spectra of GFP5 in GFP5-QD-R assemblies vs increasing QD-R (Q) to GFP5 (G) molar ratio. (B) Photoluminescence of GFP5 at 505 nm as a function of GFP5:QD-R mole ratio.

provided by NN-Laboratories), the central fluorophore of GFP5 may be sufficiently close to the quantum dot to allow FRET. In fact, the titration of red-emitting CdSe/ZnS quantum dots in a solution containing GFP5 results in quenching of the photoluminescence of GFP5 (see Figure 2A). The concentration of GFP5 was kept fixed at 24 nM, and the concentration of QD-R was increased from 0 to 20 nM. The GFP5-QD-R assemblies were prepared in dilute aqueous solutions where the effects of absorption of the incident light, reabsorption of PL, and aggregation of nanoparticles were negligible. The solutions also contained 5 mM NaCl and 5 mM NaH_2PO_4, and the pH was adjusted to 6 with NaOH. The excitation was performed at 395 nm, which coincides with the first absorption peak of GFP5 (*16*). There is no wavelength where GFP5 could be selectively excited, because the broad absorption of the QD-Rs covers the entire GFP5 absorption spectrum. The overlap of absorption spectra made it difficult to verify that the quenching of the PL of GFP5 resulted in any sensitized emission of the quantum dots. The stoichiometry for the GFP5-QD-R complex formation at pH 6 and room temperature were determined by the mole ratio method (*18*) using the quenching of the photoluminescence of GFP5 as the property to map the complexation. From the plot of photoluminescence quenching versus mole ratio (see Figure 2B), a stoichiometry of 10:1 for the GFP5-QD-R complex was established. It is important to note that the hydrodynamic radius of QD-R (nanocrystal plus MUA) is 10 nm (data provided by NN-Laboratories), which provides a surface area large enough to accommodate 10 GFP5 molecules.

The formation of the GFP5-QD-R complexes is driven by electrostatic interactions, as shown by the pH dependence of the GFP5 PL quenching. At a pH of 6, 90% of the GFP5 emission is quenched at a 0.5:1 molar ratio of QD-R to GFP5. At pH 8, 75% of the GFP5 emission is quenched, while at pH 10, there is only a 10% quenching of the PL of GFP5. There are no major variations in PL intensities of GFP5 and QD-R as the pH is raised from 6 to 10, as can be seen in the control experiments demonstrating the pH dependence of PL intensities for the quantum dots and fluorescent proteins (see Supporting Information). In the Supporting Information is also presented the reversibility of the GFP5 PL quenching as the pH is raised from 6 to 10.

Circular dichroism (CD) measurements verified that the suppression of the PL of GFP5 did not result from denaturing of its secondary structure (see Figure 3). At pH 6 and with a QD-R/GFP5 molar ratio of 0.4, where the PL quenching is near maximum, the secondary structure of GFP5 appears substantially unchanged when exposed to QD-Rs.

To verify that FRET is occurring between the GFP5 and QD-R elements, anisotropy and nanosecond time-resolved fluorimetry measurements were undertaken. FRET would be expected to increase GFP5 anisotropy and reduce its fluorescence lifetime (*12–14*). Unfortunately, these measurements were

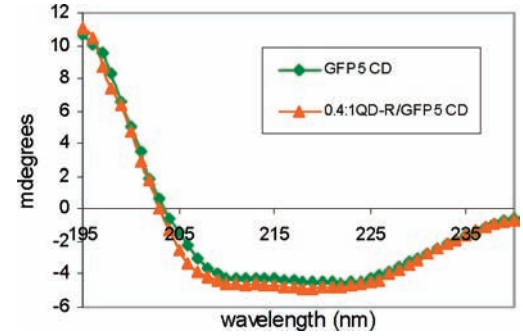


Figure 3. Circular dichroism spectra of GFP5 and GFP5 assembled to quantum dots are nearly identical, suggesting that the quantum dots do not denature the secondary structure of GFP5.

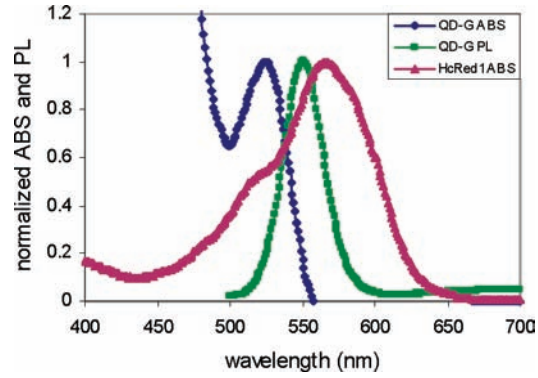


Figure 4. Normalized absorption and photoluminescence spectra of green-emitting CdSe/ZnS core/shell QDs and absorption spectrum of HcRed1 protein solutions.

inconclusive, because the strong GFP5 PL quenching, coupled with the need to keep the QD-R concentration low to avoid aggregation, resulted in poor signal-to-noise ratios. One explanation for these results is the possibility that the fraction of GFP5 complexed to the QD-Rs was completely quenched so that the remaining emission due to the uncomplexed fraction dominated the signal (*19*). Also, it is possible that charge transfer to the QD-R (in addition to energy transfer) contributes to the GFP5 PL quenching (*20*), despite the fact that GFP5 fluorophore is buried inside a proteic barrel that surrounds and protects it (*7, 21*).

Alternative ways to determine whether the observed PL quenching is due to FRET are under investigation. One possibility would be to selectively excite the GFP5 through a chemiluminescent reaction and then observe the eventual sensitized emission from the QD-Rs. GFP has a chemiluminescent resonance energy transfer pair *in vivo*, the protein aequorin (*10, 22*), that could be used for such finality.

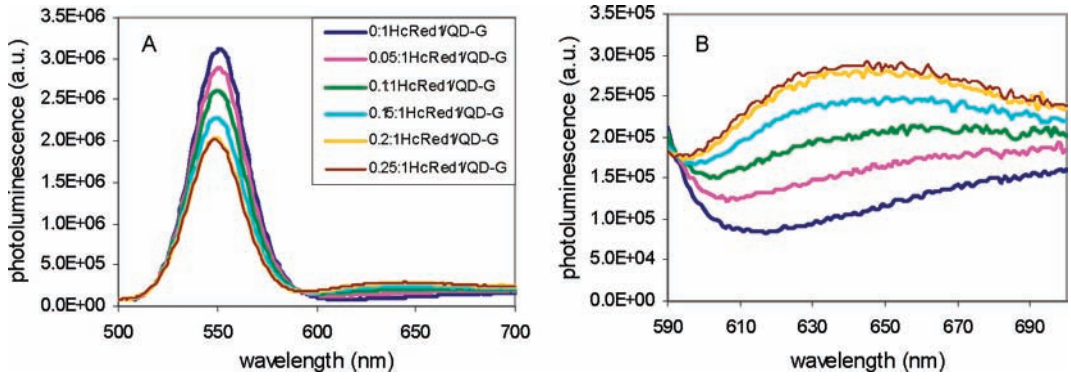


Figure 5. (A) Evolution of the photoluminescence spectra of HcRed1 protein in QD-G-HcRed1 assemblies vs increasing HcRed1 to QD-G molar ratio. (B) Amplified view of the 590–700 nm region of part A enables us to better observe HcRed1-sensitized emission.

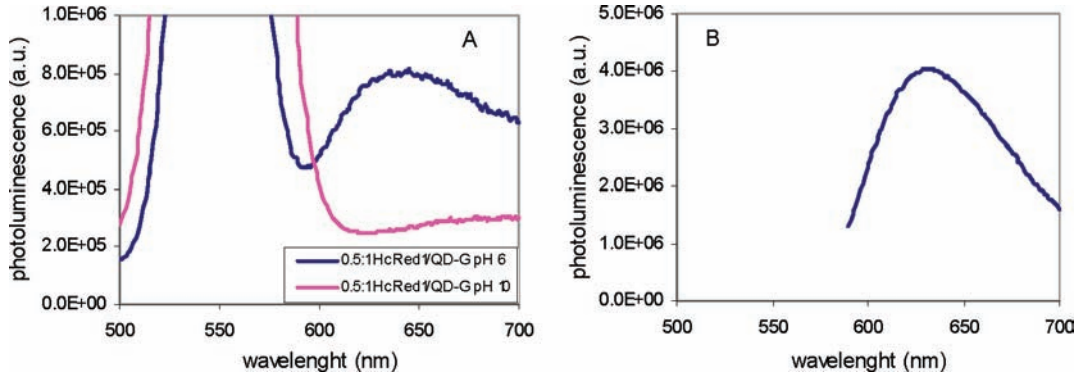


Figure 6. (A) pH dependency of the sensitized emission from HcRed1 complexed with green-emitting quantum dots. (B) PL of HcRed1 directly excited at 545 nm.

Alternatively, the larger two-photon cross section of GFP in comparison to the that of the QDs (*23, 24*) could be used to selectively excite this protein with 800 nm radiation and then try to observe the sensitized emission from the QD-Rs. The possibility of increasing the distance between GFP5 and the QD-Rs by the incorporation of an additional capping layer over the QD-Rs (*25*) is also being considered, aiming to reduce the efficiency of the quenching and make the remaining PL intensity of GFP5 appropriate for anisotropy and time resolved analysis.

In the meantime, an inverted approach was investigated where a GFP homologous red-emitting protein, HcRed1, has been used together with a green-emitting CdSe/ZnS mercaptoundecanoic acid coated quantum dot (henceforth denoted QD-G), forming a pair where the QD-G is the donor and HcRed1 is the acceptor. The overlap between QD-Gs emission and HcRed1 absorption can be seen in Figure 4. The broad absorption spectrum of the quantum dots enabled us to find a wavelength interval, around 425 nm, where the quantum dots are selectively excited.

Excited at 425 nm, the PL intensity of the quantum dots is partially suppressed by the titration of HcRed1 (see Figure 5A). The suppression is not intense as in the case of GFP5 and QD-R, but the selective excitation enabled us to observe a subtle sensitized emission from HcRed1 (see Figure 5B). The concentration of QD-Gs was kept fixed at 33 nM, and the concentration of HcRed1 was augmented from 0 to 8 nM. The assemblies were prepared in dilute aqueous solutions where the effects of absorption of the incident light, reabsorption of PL, and aggregation of nanoparticles were negligible. The solutions also contained 5 mM NaCl and 5 mM NaH_2PO_4, and the pH was adjusted to 6 with NaOH.

The formation of the HcRed1–QD-G complexes is also driven by electrostatic interactions, as shown by the pH dependence of the sensitized emission. At a pH of 6, it is possible to observe the sensitized emission at a 0.5:1 molar ratio of HcRed1 to QD-G excited at 425 nm. At pH 10, no sensitized emission is observed (see Figure 6A) in spite of an increase in the PL intensity of HcRed1 when excited with 545 nm and no major variation in the PL intensity of the QD-G (see Supporting Information). The PL spectrum of HcRed1 excited at 545 nm has the same profile of the sensitized emission (see Figure 6B).

Detection of sensitized emission anisotropy is a technique that enables the characterization of FRET with high contrast (*13, 26*). Sensitized emission is highly depolarized, because the orientation of emitted light is not wholly constrained by the excitation polarization (*27*). Due to the relatively large size and slow rotational diffusion, PL emission from fluorescent proteins is highly anisotropic (*26, 27*). In the case of HcRed1, the anisotropy of the PL obtained by direct excitation is nearly 0.4. The anisotropy of the sensitized emission of HcRed1, measured in the excitation interval from 400 to 470 nm, is below 0.1. The low anisotropy of the sensitized emission contrasting with the elevated anisotropy of the direct PL emission provides strong evidence that FRET occurs between QD-Gs and HcRed1.

Other pairs of QD and fluorescent proteins are under present consideration. The protein HcRed1 may be substituted by other red-emitting fluorescent proteins with higher quantum yields to be the acceptors with green- or yellow-emitting quantum dot donors. Actually, HcRed1 has a quantum yield of only 0.05 (*28*), which may account for the low intensity of its sensitized emission. The proteins mCherry, tdTomato, and mStrawberry (*29*) would be attractive acceptor candidates, due to their elevated quantum yield and brightness. tdTomato (*29*), in particular, has a quantum yield of 0.69 and brightness superior to that of fluorescein. An optimized donor–acceptor pair would be convenient for in-depth characterization and quantification of FRET parameters and for high-contrast *in vivo* investigations.

ACKNOWLEDGMENT

The authors thank Dr. Jim Haseloff for providing the gene coding for GFP5. V.R.H. was supported by a grant from Numina Nanotecnologia Ltda. The authors wish to express their gratitude to the Brazilian funding agencies CNPQ, FAPESP, and CAPES, being also thankful for the support from the Biochemistry Department of the Chemistry Institute of the University of São Paulo, Brazil.

Supporting Information Available: PL intensity variation for quantum dots and fluorescent proteins as a function of pH and reversibility of PL quenching of GFP5 by raising the pH from 6 to 10. This material is available free of charge via the Internet at http://pubs.acs.org.

LITERATURE CITED

(1) Wagnier, R., Baranov, A. V., Maslov, V. G., Stsiapura, V., Artemyev, M., Pluot, M., Sukhanova, A., and Nabiev, I. (2004) Energy transfer in aqueous solutions of oppositely charged CdSe/ZnS core/shell quantum dots and in quantum dot-nanogold assemblies. *Nano Lett. 4*, 451–457.

(2) Dabbousi, B. O., Rodriguez-Viejo, J., Mikulec, F. V., Heine, J. R., Mattoussi, H., Ober, R., Jensen, K. F., and Bawendi, M. G. (1997) (CdSe)ZnS core-shell quantum dots: synthesis and characterization of a size series of highly luminescent nanocrystallites. *J. Phys. Chem. B 101*, 9463–9475.

(3) Ma, J., Chen, J., Guo, J., Wang, C. C., Yang, W. L., Xu, L., and Wang, P. N. (2006) Photostability of thiol-capped CdTe quantum dots in living cells: the effect of photo-oxidation. *Nanotechnology 17*, 2083–2089.

(4) Sukhanova, A., Devy, J., Venteo, L., Kaplan, H., Artemyev, M., Oleinikov, V., Klinov, D., Pluot, M., Cohen, J. H. M., and Nabiev, I. (2004) Biocompatible fluorescent nanocrystals for immunolabeling of membrane proteins and cells. *Anal. Biochem. 324*, 60–67.

(5) Wenhua, L., Haiyan, X., Zhixiong, X., Zhexue, L., Jianhong, O., Xiangdong, C., and Ping, S. (2004) Exploring the mechanism of competence development in Escherichia coli using quantum dots as fluorescent probes. *J. Biochem. Biophys. Methods 58*, 59–66.

(6) Dubertret, B., Skourides, P., Norris, D. J., Noireaux, V., Brivanlou, A. H., and Libchaber, A. (2002) In vivo imaging of quantum dots encapsulated in phospholipid micelles. *Science 298*, 1759–1762.

(7) Wachter, R. M. (2006) The family of GFP-like proteins: structure, function, photophysics and biosensor applications. Introduction and perspective. *Photochem. Photobiol. 82*, 339–344.

(8) Ormo, M., Cubitt, A. B., Kallio, K., Gross, L. A., Tsien, R. Y., and Remington, S. J. (1996) Crystal structure of the Aequorea victoria green fluorescent protein. *Science 273*, 1392–1395.

(9) Yang, F., Moss, L. G., and Phillips, G. N. (1996) The molecular structure of green fluorescent protein. *Nat. Biotechnol. 14*, 1246–1251.

(10) Tsien, R. Y. (1998) The green fluorescent protein. *Annu. Rev. Biochem. 67*, 509–544.

(11) Förster, T. (1948) Zwischenmolekulare energiewanderung und fluoreszenz. *Ann. Phys. 2*, 55–75.

(12) Lakowicz, J. R. (2006) *Principles of Fluorescence Spectroscopy*, 3rd ed., pp 443–475, Springer, Berlin.

(13) Rizzo, M. A., Springer, G., Segawa, K., Zipfel, W. R., and Piston, D. W. (2006) Optimization of pairings and detection conditions for measurement of FRET between cyan and yellow fluorescent proteins. *Microsc. Microanal. 12*, 238–254.

(14) Jares-Erijman, E. A., and Jovin, T. M. (2003) FRET imaging. *Nat. Biotechnol. 21*, 1387–1395.

(15) Khosravi, A. A., Kundu, M., Kuruvilla, B. A., Shekhawat, G. S., Gupta, R. P., Sharma, A. K., Vyas, P. D., and Kulkarni, S. K. (1995) Manganese doped zinc sulphide nanoparticles by aqueous method. *Appl. Phys. Lett. 67*, 2506–2508.

(16) Siemering, K. R., Golbik, R., Sever, R., and Haseloff, J. (1996) Mutations that suppress the thermosensitivity of green fluorescent protein. *Curr. Biol. 6*, 1653–1663.

(17) Hiemenz, P. C. and Rajagopolan, R. (1997) *Principles of Colloid and Surface Chemistry*, 3rd ed., Marcel Dekker Inc., New York.

(18) Meyer, A. S., and Ayres, G. H. (1957) The mole ratio method for spectrophotometric determination of complexes in solution. *J. Am. Chem. Soc. 79*, 49–53.

(19) Song, L., Jares-Erijman, E. A., and Jovin, T. M. (2002) A photochromic acceptor as a reversible light-driven switch in fluorescence resonance energy transfer (FRET). *J. Photochem. Photobiol., A 150*, 177–185.

(20) Nikobaakht, B., Burda, C., Braun, M., Hun, M., and El-Sayed, M. A. (2002) The quenching of CdSe quantum dots photoluminescence by gold nanoparticles in solution. *Photochem. Photobiol. 75*, 591–597.

(21) Herberhold, H., Marchal, S., Lange, R., Scheyhing, C. H., Vogel, R. F., and Winter, R. (2003) Characterization of the pressure-induced intermediate and unfolded state of red-shifted green fluorescent protein - a static and kinetic FTIR, UV/VIS and fluorescence spectroscopy study. *J. Mol. Biol. 330*, 1153–1164.

(22) Shimomura, O., Musicki, B., and Kishi, Y. (1988) Semi-synthetic aequorin. An improved tool for the measurement of calcium ion concentration. *Biochem. J. 251*, 405–410.

(23) Hao, Z., Gong, H., Han, J., Zhai, Y., and Wang, Q. (2006) One- and two-photon excited fluorescence of CdSe and CdSe/ZnS quantum dots in n-hexane. *Chin. Phys. Lett. 23*, 2859–2862.

(24) Kirkpatrick, S. M., Naik, R. R., and Stone, M. O. (2001) Nonlinear saturation and determination of the two-photon absorption cross section of green fluorescent protein. *J. Phys. Chem. B 105*, 2867–2873.

(25) Jafaar, S., Nam, K. T., Khademhosseini, A., Xing, J., Langer, R. S., and Belcher, A. M. (2004) Layer-by-layer surface modification and patterned electrostatic deposition of quantum dots. *Nano Lett. 4*, 1421–1425.

(26) Rizzo, M. A., and Piston, D. W. (2004) High-contrast imaging of fluorescent protein FRET by fluorescence polarization microscopy. *Biophys. J.: Biophys Lett.* L14–L16.

(27) Lakowicz, J. R. (2006) *Principles of Fluorescence Spectroscopy*, 3rd ed., pp 353–382, Springer, Berlin.

(28) Wilmann, P. G., Petersen, J., Pettikiriarachchi, A., Buckle, A. M., Smith, S. C., Olsen, S., Perugini, M. A., Devenish, R. J., Prescott, M., and Rossjohn, J. (2005) The 2.1 A crystal structure of the far-red fluorescent protein HcRed: inherent conformational flexibility of the chromophore. *J. Mol. Biol. 349*, 223–237.

(29) Shaner, N. C., Steinbach, P. A., and Tsien, R. Y. (2005) A guide to choosing fluorescent proteins. *Nat. Meth. 2*, 905–909.

BC700147J

Novel Arylhydrazone-Conjugated Gold Nanoparticles with DNA-Cleaving Ability: The First DNA-Nicking Nanomaterial

Ming-Hua Hsu,[†] Thainashmuthu Josephrajan,[†] Chen-Sheng Yeh,[‡] Dar-Bin Shieh,[§] Wu-Chou Su,[||] and Jih Ru Hwu*,[†]

Department of Chemistry, National Tsing Hua University, Hsinchu, Taiwan 300, Republic of China, and Department of Chemistry, Department of Dentistry and Institute of Oral Medicine, and Department of Internal Medicine, National Cheng Kung University, Tainan, Taiwan 701, Republic of China. Received June 20, 2007; Revised Manuscript Received September 20, 2007

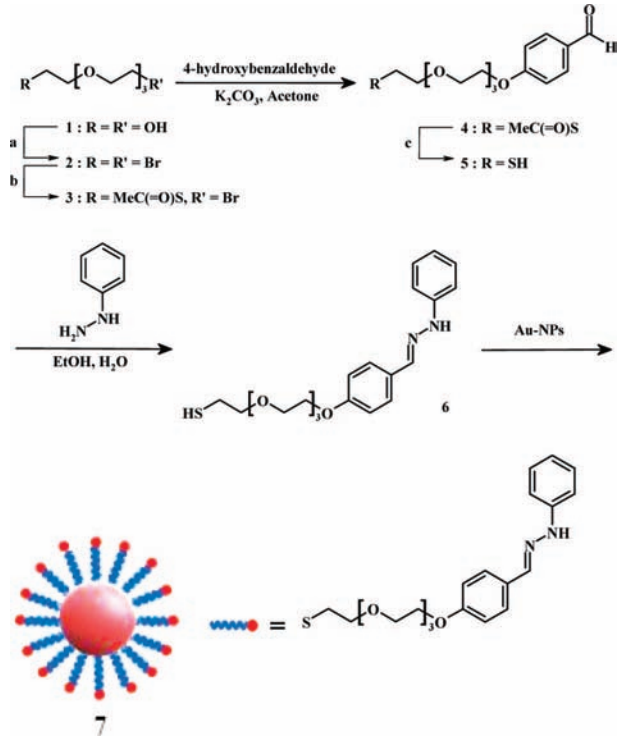
Arylhydrazones were linked onto gold nanoparticles through the poly(ethylene glycol) spacer to produce a new type of photoinduced DNA-cleaving nanomaterials with great potency.

INTRODUCTION

Nanobioscience and technology possess enormous potential, as their development could lead to new materials beneficial to human life. Prominent progress has been observed in various fields, including drug delivery, DNA sequencing, biosensor, biomolecular separation, magnetic resonance imaging, and so forth (*1–6*). Among various nanoparticles (NPs), gold nanoparticles (Au-NPs) are most stable and, thus, suitable for biological systems. Their inert surface prevents undesired reactions from taking place with different functional groups of biomolecules (*7*); yet, Au-NPs can still be capped with water-soluble organic compounds (*8, 9*) or biomolecules through thiols (*10*). For example, Mirkin (*11–13*), Yeh (*14*), and co-workers functionalized Au-NPs with 3′- and/or 5′-thiol oligonucleotides. Russell et al. (*15*) used a thiolated ethylene glycol anchor chain with various lengths to link lactose derivatives to preformed Au-NPs.

We planned to develop nanoparticles that bear multi-DNA cleaving "warheads". It is necessary for the warheads to be controlled by a trigger, which can be used to initiate the DNA-nicking process. These new functional nanoparticles may possess the following features and advantages: 1. The DNA-cleaving potency could be enhanced dramatically because of the high local density of warheads, many of which are attached to one nanoparticle nucleus. 2. The warheads as "soft" moieties are attached onto the "hard" core of nanoparticles, which could serve as bullets of a gene gun (*16–18*). Consequently, the DNA-cleaving warheads can be delivered to a specific location by mechanical force. 3. The solubility of the hybrids can be adjusted by spacers, which link the warheads to nanoparticles. Our research group has been developing new artificial agents for cleaving nucleic acids under control conditions (*19–22*). Among these agents, arylhydrazones were found stable and can nick DNA by use of UV light as the trigger (*22*). Herein, we report our success in the attachment of arylhydrazones onto gold nanoparticles to form a new class of DNA-cleaving materials. Being water-soluble, these hybrid nanomaterials were manipulated without difficulty in aqueous solutions for nicking DNA upon UV irradiation.

Scheme 1. Synthesis of Arylhydrazone-Conjugated Au-NPs[a]



[a] Reagents and conditions: (a) PBr_3, 60 °C, 4.0 h; (b) thioacetic acid, NaOH, THF, 25 °C, 6.0 h; (c) NaOH, MeOH, 25 °C, 5.0 h.

RESULTS

Our synthetic strategy for incorporation of an arylhydrazone onto Au-NPs is shown in Scheme 1. The starting material Au-NPs with diameters of 13 ± 1.8 nm were prepared by reduction of $HAuCl_4$ with sodium tricitrate according to the established procedure (*23, 24*); meanwhile, poly(ethylene glycol) (PEG) was used as the spacer. Thus, we treated tetraethylene glycol (**1**) with PBr_3 in ether to give the corresponding dibromide **2**. Protection of one terminal in **2** with a stoichiometric amount of thioacectic acid in the presence of NaOH in THF led to thioacetate **3**. Coupling of **3** with *p*-hydroxybenzaldehyde in the presence of K_2CO_3 in acetone provided PEG-containing

* E-mail: jrhwu@mx.nthu.edu.tw. Fax: 886 35 721 594. Tel: 886 35 725 813.
[†] National Tsing Hua University.
[‡] Department of Chemistry, National Cheng Kung University.
[§] Department of Dentistry and Institute of Oral Medicine, National Cheng Kung University.
[||] Department of Internal Medicine, National Cheng Kung University.

10.1021/bc700222n CCC: $37.00 © 2007 American Chemical Society
Published on Web 10/23/2007

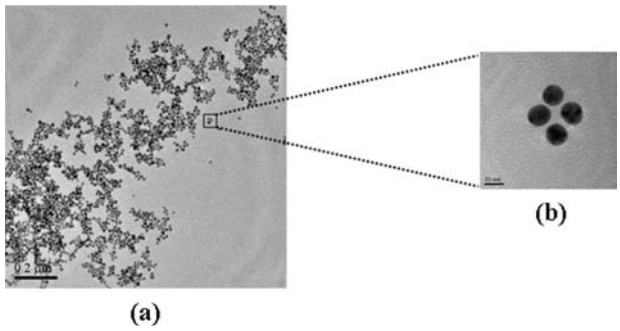


Figure 1. TEM images of gold nanoparticles conjugated with arylhydrazones through PEG spacers (i.e., **7**).

benzaldehyde **4**, in which the acetyl group was deprotected with methanolic NaOH under carefully controlled conditions (*25*). The desired free thiol **5** was isolated in 77% yield by flash chromatography packed with silica gel. Its characteristic SCH_2 protons appeared at 2.72 ppm with $J = 7.2$ Hz and the benzaldehydic singlet proton at 9.85 ppm in the ^1H NMR spectrum. A downfield resonance for the benzylic carbon exhibited at 190.63 ppm in its ^{13}C NMR spectrum. Furthermore, a strong absorption at 1692 cm^{-1} associated with the conjugated C═O stretch also appeared in its IR spectrum. Condensation of this benzaldehyde **5** with phenylhydrazine gave the corresponding phenylhydrazone **6** with $m/z = 404.1765$. In its ^{13}C NMR spectrum, eight peaks showed up between 112.85 and 159.39 ppm for the aromatic carbons; meanwhile, the newly generated benzylic N═C carbon shifted to 159.39 ppm. The N═CH proton resonated at 7.62 ppm in its ^1H NMR spectrum.

To obtain conjugated target materials, we treated the ~13 nm Au-NPs with a large excess (500–1000 equiv) of phenylhydrazone **6** (2.0 mL, 10 mM) in water at 25 °C for 4.0 h. The desired hybrid **7** was produced and isolated by centrifuge; a red solution of its colloids in water was attributed to their surface plasmon resonance (*26*, *27*). The centrifuge process assured the following DNA-cleaving results coming from hybrid nanoparticles **7** instead of the organic molecule **6**. Because the Au-NPs were attached by the HS-PEG-arylhydrazone ligand through the sulfide terminal, we observed a hyperchromic and bathochromic shift by 5 nm in the UV spectra in situ. These results are consistent with reports on spectral surface plasmon resonance shifts for the thiols on Au-NPs (*28*). By using the displacement method with mercaptoethanol reported by Nie et al. (*29*), we determined the number of ligands **6** per particle as 55–60 on average. In this experiment, the concentration of displaced hydrazone-containing thiol **6** from hybrid **7** was compared with that from freshly synthesized **6** at λ 345 nm of UV spectrometry.

Furthermore, the transmission electron microscopy (TEM) was used for determination of the nanoscale structures. We dropped a casting solution of nanoparticles onto carbon-coated copper grids. The distribution of gold cores of hybrid **7** is shown in Figure 1a, which indicates that the nanoparticles were well-dispersed. The amplified TEM in Figure 1b reveals that spherically shaped particles were obtained; of which the diameter of 13 ± 1.9 nm as the average was estimated on the basis of 120 sampled arylhydrazone–PEG-capped nanoparticles (*30*, *31*).

To investigate the DNA-cleaving ability, we dissolved the water-soluble Au-PEG–arylhydrazone colloids **7** (2.0 nM) in a sodium phosphate buffer (pH 7.4) and 10% ethanol containing the supercoiled circular φX174 RFI DNA (form I; 50 μM/base pair). These solutions were irradiated with UV light (312 nm, 1.43 mW/cm^2) under aerobic conditions at room temperature for 2.0 h. By analyzing the results from gel electrophoresis on 1.0% agarose gel with ethidium bromide staining, we found

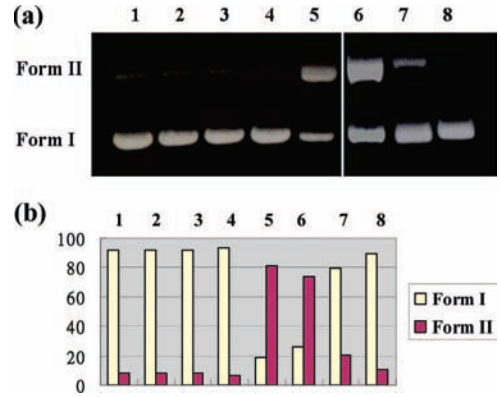


Figure 2. (a) Single-strand cleavages of supercoiled circular φX 174 RFI DNA: lane 1, DNA alone; lane 2, 13 nm gold nanoparticles in the dark; lane 3, 13 nm gold nanoparticles under UV light; lane 4, Au-NPs hybrid **7** in the dark; lanes 5–8, 2.0 nM, 500 pM, 100 pM, and 20 pM of Au-NPs hybrid **7** under UV light. (b) Percentages of form II/form I for lanes 1–8.

that the hybrid **7** caused single-strand cleavages of DNA efficiently to give the relaxed circular DNA (i.e., form II; see lane 6 of Figure 2). Our results shown in lane 7 indicate that hybrid **7** was able to cleave DNA at a concentration as low as 1.00×10^2 pM.

To seek for the essential factors of the DNA nicking, we performed two control experiments. The first was to carry out the experiment under the same conditions except in the dark (see lane 4). The second involved UV irradiation; however, we replaced Au-PEG–arylhydrazone hybrid (**7**) by Au-NPs (see lane 3). These results indicate that the DNA were not damaged; thus, both the UV light and the integrated Au-PEG–arylhydrazone were essential for DNA nicking. Moreover, the positive results shown in lanes 5 and 6 clearly indicate that the Au-NP cores did not significantly inhibit UV light to activate arylhydrazones on the shell, although they showed UV absorption at 520 nm.

DISCUSSION

There are three reasons to tether arylhydrazones onto the shell of Au-NPs by use of the PEG strands. First, an alkoxy substitutent can enhance the DNA-cleaving ability of arylhydrazones, which generate aminyl (R_2N) and iminyl (R_2C═N) radicals upon UV irradiation (*22*). A terminal oxygen atom of triethylene glycol for its connection to the arylhydrazone serves this purpose. Moreover, the great enhancement of DNA-cleaving potency may also indicate that the oxygen-containing PEG spacers prevented the nitrogen-containing radicals absorbed by gold surface, as reported by Meisel et al. (*32*). Second, the citrate anions were coordinated to the Au^I shell, although the core of our Au-NPs was Au^0 (*13*). When we treated the Au-NPs with salts, aggregations often took place among particles, and color changed from red to dark blue. This problem was circumvented after we attached the PEG spacers onto Au-NPs. The stability came from the steric repulsion effect of the tethered PEG spacers, which improved the dispersion of the Au-NPs–PEG–arylhydrazone particles in aqueous media. Third, the PEG strands on the surface of the functionalized Au-NPs improved their hydrophilicity. This effect enabled the hybrid nanoparticles of **7** to approach and, thus, to cleave the DNA target with ease.

Our previous findings indicate that the hydrophobic organic compound, *p*-methoxylbenzaldehyde *p*-methoxylphenylhydrazone (PMBH), can cleave DNA at a concentration as low as 50 μM (*22*). The current findings indicate that arylhydrazone-containing Au-NPs **7** cleaved DNA at a much lower concentration (i.e., 2.0 nM). In comparison with PMBH, the efficacy of the hybrid **7** was improved by a factor of $>10^4$ despite each

nanoparticle containing 55–60 warheads. Although the total warhead number on each nanoparticle could be increased, we tried not to keep it overcrowded. This design is on the basis of our speculation that, otherwise, coupling reactions might take place among the radical warheads after their generation upon UV irradiation.

Our results shown in lanes 5–7 of Figure 2 indicate that only form II DNA (open-circular product) was generated through single-strand breaks; meanwhile, the formation of form III DNA (i.e., linear product) resulting from double-strand breaks was not observed. The generation of form III DNA has to come from two separate single-stand cleavage events in close proximity. Therefore, we consider that the high efficiency of DNA single-strand breaks may be derived from the nanoparticles bearing multiradical warheads toward all directions on their spherical surface. When these hydrophilic "maces" with a high local density of radicals bumped into DNA, the chance for nicking a single strand would be much higher than individual organic radicals, such as the aminyl (R_2N) and the iminyl ($R_2C{=}N$) radicals. The efficiency resulting from the mace, however, may not be necessarily extendable to the double-strand break event. Further works will be in due course in order to have good insight into this intriguing issue.

Recently, Mirkin et al. (*33*) reported a novel strategy for intracellular gene regulation with oligonucleotide-modified Au-NPs. They demonstrate that nanoparticle-bound antisense oligodexoyonucleotides can be degraded by DNase. On the other hand, Liu and Lu (*34*) developed colorimetric biosensors on the basis of DNAzyme-assembled Au-NPs. In the presence of Pb^{2+}, the DNAzyme catalyzes specific hydrolytic cleavage of the substrate strand, which disrupts the formation of the nanoparticle assembly. Up to the present date, these two approaches are likely to be the only published examples that involve cleavage of nanoparticles conjugated with DNA or oligonucleotides. In both examples, the cleaving "warheads" are not attached to the nanoparticles. In contrast, the currently developed conjugate materials **7** possessed warheads on their shells and can be regarded as a new type of DNase.

In conclusion, gold nanoparticles conjugated with arylhydrazones through thiol-based PEG ligands (i.e., **7**) were successfully synthesized. The diameters of these new nanoparticles with spherical shape were 13 ± 1.9 nm as observed by TEM. Upon triggering by 312-nm UV light, hybrid **7** cleaved supercoiled DNA to give a relaxed circular shape at a concentration as low as 2.0 nM. To the best of our knowledge, this is the first example of nanoparticles with the DNA-cleaving property.

ACKNOWLEDGMENT

This work was supported by the National Science Council of Republic of China.

Supporting Information Available: Details of synthetic and experimental procedures, and spectroscopic data of compounds. This material is available free of charge via the Internet at http://pubs.acs.org.

LITERATURE CITED

(1) Niemeyer, C. M., and Mirkin, C. A. (2004) *Nanobiotechnology concepts, applications and perspectives*, pp 288–307, Wiley-VCH, Weinheim.

(2) Rosi, N. L., and Mirkin, C. A. (2005) Nanostructures in biodiagnostics. *Chem. Rev. 105*, 1547–1562.

(3) Hans, M. L., and Lowman, A. M. (2006) *Nanomaterials Handbook*, pp 637–664, CRC Press LLC, Boca Raton, FL.

(4) Lin, T.-J., Huang, K.-T., and Liu, C.-Y. (2006) Determination of organophosphorous pesticides by a novel biosensor based on localized surface plasmon resonance. *Biosens. Bioelectron. 22*, 513–518.

(5) Hormes, J., Leuschner, C., and Kumar, C. S. S. R. (2005) *Nanofabrication towards biomedical applications: techniques, tools, applications, and impact*, pp 227–245, Wiley-VCH, Weinheim.

(6) Lagerqvist, J., Zwolak, M., and Ventra, M. D. (2006) Fast DNA sequencing via transverse electronic transport. *Nano Lett. 6*, 779–782.

(7) Ge, Z., Kang, Y., Taton, T. A., Braun, P. V., and Cahill, D. G. (2005) Thermal transport in Au-core polymer-shell nanoparticles. *Nano Lett. 5*, 531–535.

(8) Foos, E. E., Snow, A. W., Twigg, M. E., and Ancona, M. G. (2002) Thiol-terminated di-, tri-, and tetraethylene oxide functionalized gold nanoparticles: A water-soluble, charge-neutral cluster. *Chem. Mater. 14*, 2401–2408.

(9) Kanaras, A. G., Kamounah, F. S., Schaumburg, K., Kiely, C. J., and Brust, M. (2002) Thioalkylated tetraethylene glycol: a new ligand for water soluble monolayer protected gold clusters. *Chem. Commun.* 2294–2295.

(10) For a recent review, see Katz, E., and Willner, I. (2004) Integrated nanoparticle-biomolecule hybrid systems: synthesis, properties, and applications. *Angew. Chem., Int. Ed. 43*, 6042–6108.

(11) Mirkin, C. A., Letsinger, R. L., Mucic, R. C., and Storhoff, J. J. (1996) A DNA-based method for rationally assembling nanoparticles into macroscopic materials. *Nature (London) 382*, 607–609.

(12) Storhoff, J. J., Lazarides, A. A., Mucic, R. C., Mirkin, C. A., Letsinger, R. L., and Schatz, G. C. (2000) What controls the optical properties of DNA-linked gold nanoparticle assemblies? *J. Am. Chem. Soc. 122*, 4640–4650.

(13) Mirkin, C. A. (2000) Programming the assembly of two- and three-dimensional architectures with DNA and nanoscale inorganic building blocks. *Inorg. Chem. 39*, 2258–2272.

(14) Tsai, C.-Y., Shiau, A.-L., Cheng, P.-C., Shieh, D.-B., Chen, D.-H., Chou, C.-H., Yeh, C.-S., and Wu, C.-L. (2004) A biological strategy for fabrication of Au/EGFP nanoparticle conjugates retaining bioactivity. *Nano Lett. 4*, 1209–1212.

(15) Reynolds, A, J., Haines, A. H., and Russell, D. A. (2006) Gold glyconanoparticles for mimics and measurement of metal ion-mediated carbohydrate-carbohydrate interactions. *Langmuir 22*, 1156–1163.

(16) For a review, see Lin, M. T. S., Pulkkinen, L., Uitto, J., and Yoon, K. (2000) The gene gun: current applications in cutaneous gene therapy. *Int. J. Dermatol. 39*, 161–170.

(17) Helenius, E., Boije, M., Teeri, V. N., Palva, E. T., and Teeri, T. H. (2000) Gene delivery into intact plants using the helios™ gene gun. *Plant Mol. Biol. Rep. 18*, 287a–287l.

(18) Roizenblatt, R., Weiland, J. D., Carcieri, S., Qiu, G., Behrend, M., Humayun, M. S., and Chow, R. H. (2006) Nanobiolistic delivery of indicators to the living mouse retina. *J. Neurosci. Meth. 153*, 154–161.

(19) Nozoe, T., Lin, C. C., Tsay, S.-C., Yu, S.-F., Lin, L. C., Yang, P. W., and Hwu, J. R. (1997) Single-strand cleavage of DNA with site-specificity by photolysis of azulenequinones. *Bioorg. Med. Chem. Lett. 7*, 975–978.

(20) Tsai, F.-Y., Lin, S.-B., Tsay, S.-C., Lin, W.-C., Hsieh, C.-L., Chuang, S. H., Kan, L.-S., and Hwu, J. R. (2001) Photochemical cleavage of single- and double-stranded oligonucleotides by 3-(*p*-tolylamino)-1,5-azulenequinone. *Tetrahedron Lett. 42*, 5733–5735.

(21) Hwu, J. R., Tsay, S.-C., Hong, S. C., Leu, Y.-J., Liu, C.-F., and Chou, S.-S. P. (2003) Oxime esters of anthraquinone as photo-induced DNA-cleaving agents for single- and double-strand scissions. *Tetrahedron Lett. 44*, 2957–2960.

(22) Hwu, J. R., Lin, C. C., Chuang, S. H., King, K. Y., Su, T.-R., and Tsay, S.-C. (2004) Aminyl and iminyl radicals from arylhydrazones in the photo-induced DNA cleavage. *Bioorg. Med. Chem. 12*, 2509–2515.

(23) Frens, G. (1973) Controlled nucleation for the regulation of the particle size in monodisperse gold suspensions. *Nat. Phys. Sci. 241*, 20–22.

(24) Grabar, K. C., Freeman, R. G., Hommer, M. B., and Natan, M. J. (1995) Preparation and characterization of Au colloid monolayers. *Anal. Chem. 67*, 735–743.

(25) Keana, J. F. W., Wu, Y., and Wu, G. (1987) Di-, tri-, tetra-, and pentacationic alkylammonium salts. Ligands designed to prevent the nonspecific electrostatic precipitation of polyanionic, functionalized cyclopentadienyltitanium-substituted heteropolytungstate electron microscopy labels with cationic biomolecules. *J. Org. Chem. 52*, 2571–2576.

(26) Elghanian, R., Storhoff, J. J., Mucic, R. C., Letsinger, R. L., and Mirkin, C. A. (1997) Selective colorimetric detection of polynucleotides based on the distance-dependent optical properties of gold nanoparticles. *Science 277*, 1078–1081.

(27) Link, S., and El-Sayed, M. A. (1999) Size and temperature dependence of the plasmon absorption of colloidal gold nanoparticles. *J. Phys. Chem. B 103*, 4212–4217.

(28) Mangeney, C., Ferrage, F., Aujard, I., Marchi-Artzner, V., Jullien, L., Ouari, O., Rekai, E. D., Laschewsky, A., Vikholm, I., and Sadowski, J. W. (2002) Synthesis and properties of water-soluble gold colloids covalently derivatized with neutral polymer monolayers. *J. Am. Chem. Soc. 124*, 5811–5821.

(29) Maxwell, D. J., Taylor, J. R., and Nie, S. (2002) Self-assembled nanoparticle probes for recognition and detection of biomolecules. *J. Am. Chem. Soc. 124*, 9606–9612.

(30) Wuelfing, W. P., Gross, S. M., Miles, D. T., and Murray, R. W. (1998) Nanometer gold clusters protected by surface-bound monolayers of thiolated poly(ethylene)glycol) polymer electrolyte. *J. Am. Chem. Soc. 120*, 12696–12697.

(31) Otsuka, H., Akiyama, Y., Nagasaki, Y., and Kataoka, K. (2001) Quantitative and reversible lectin-induced association of gold nanoparticles modified with α-lactosyl-ω-mercapto-poly(ethylene glycol). *J. Am. Chem. Soc. 123*, 8226–8230.

(32) Zhang, Z., Berg, A., Levanon, H., Fessenden, R. W., and Meisel, D. (2003) On the interactions of free radicals with gold nanoparticles. *J. Am. Chem. Soc. 125*, 7959–7963.

(33) Rosi, N. L., Giljohann, D. A., Thaxton, C. S., Lytton-Jean, A. K. R., Han, M. S., and Mirkin, C. A. (2006) Oligonucleotide-modified gold nanoparticles for intracellular gene regulation. *Science 312*, 1027–1030.

(34) Liu, J., and Lu, Y. (2004) Colorimetric biosensors based on DNAzyme-assembled gold nanoparticles. *J. Fluoresc. 14*, 343–354.

BC700222N

Surface Re-engineering of Pancreatic Islets with Recombinant azido-Thrombomodulin

Cherie L. Stabler,[†] Xue-Long Sun,[‡] Wanxing Cui, John T. Wilson, Carolyn A. Haller, and Elliot L. Chaikof*

Departments of Surgery and Biomedical Engineering, Emory University, Atlanta, Georgia 30322, and School of Chemical and Biomolecular Engineering, Georgia Institute of Technology, Atlanta, Georgia 30332. Received July 25, 2007; Revised Manuscript Received October 2, 2007

Chemoselective conjugation of an azido-functionalized thrombomodulin to pancreatic islets was achieved by Staudinger ligation to a surface-bound bifunctional poly(ethylene glycol) linker. The presence of the tethered thrombomodulin resulted in a significant increase in the production of activated protein C with a reduction in islet-mediated thrombogenicity. This report highlights the potential of tissue-targeted chemistry to reduce donor cell mediated procoagulant and proinflammatory responses.

Type 1 diabetes results from the autoimmune destruction of insulin-producing pancreatic beta cells and inevitably leads to dependence upon exogenous insulin for control of blood glucose. The transplantation of donor human islets into the liver of diabetic recipients is a promising treatment strategy, but remains limited by a high rate of early islet destruction due to the instant blood-mediated inflammatory reaction (IBMIR) triggered by the interaction of infused islets with blood (*1–3*). IBMIR is initiated by the activation of the coagulation and complement systems, which promotes rapid leukocyte infiltration of the donor islet graft (*4*). Heparin, low-molecular-weight dextran sulfate, melagatran, and activated protein C have been used to minimize IBMIR (*5–8*). Systemic delivery of these anticoagulants at therapeutic doses, however, substantially increases the risk of bleeding. We have postulated that biochemically re-engineering the islet surface with constituents that serve to inhibit the activation of the coagulation cascade would provide a novel strategy to reduce IBMIR (Figure 1A). Specifically, we have developed a scheme to conjugate human recombinant thrombomodulin (*r*TM) to the islet surface through bifunctional poly(ethylene glycol) (PEG) linkers in a chemo-and bioorthogonal fashion (Figure 1B). Thrombomodulin (TM), an endothelial cell transmembrane protein, binds thrombin and inactivates its known procoagulant–proinflammatory properties (*9*). In addition, the TM–thrombin complex rapidly activates circulating protein C (APC), which inactivates clotting factors **Va** and **VIIIa**, thereby serving as a negative feedback system by reducing new thrombin generation (*10, 11*). In this regard, re-engineering islet surfaces with TM and localizing the activation of protein C may provide a novel strategy to reduce IBMIR.

Recent innovations in protein engineering and bioorganic synthesis facilitate incorporation of special tags into recombinant proteins for site-specific modification and immobilization through selective chemical reactions that are orthogonal to the diverse functionality of biological systems (*12*). For example, using a biosynthetic approach, we have recently created a short TM construct containing the thrombin and protein C binding

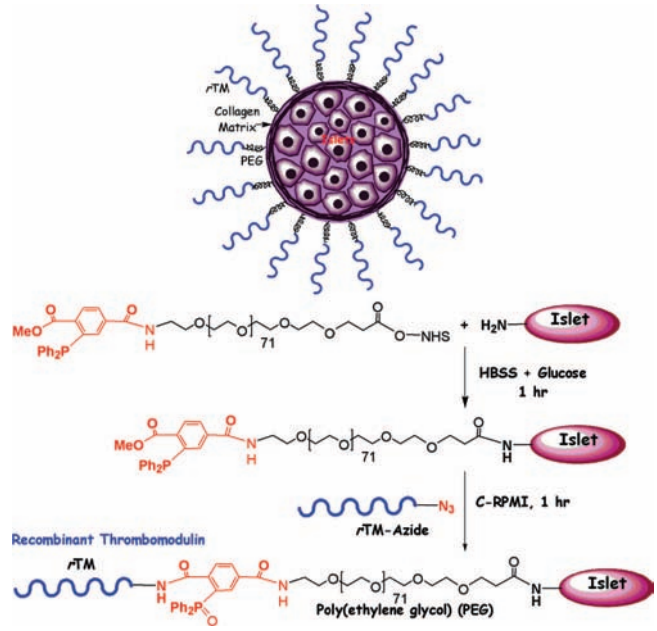


Figure 1. PEGylation and subsequent Staudinger ligation between recombinant azido-thrombomodulin and the PEG–phosphine linker.

regions and terminated with an artificial "non-natural" amino acid, azido (N_3)-alanine, at the C-terminus of the protein (*13*). The azide has secured a prominent role as a unique chemical handle for bioconjugation. We have made extensive use of the azide as a chemical handle for site-specific PEGylation in solution via Staudinger ligation and immobilization of proteins on artificial surfaces via azide-alkyne [3 + 2] cycloaddition (*13, 14*). The Staudinger ligation is particularly advantageous, as it can be performed in living systems without physiological harm, in high yield, and within short time periods offering the potential to re-engineer a variety of cell and tissue surfaces (*15*).

PEG has been widely used to functionalize solid surfaces for inert and biocompatible surface engineering, as well as to limit immunogenicity and prolong the circulating half-life of proteins and peptides for drug delivery. Recently, it has been suggested that PEG grafted onto the collagen matrix of isolated islets could inhibit pathways leading islet xenograft rejection (*16*). Specifically, PEGylation leads to a reduction in antibody/complement-mediated cytotoxicity (*16*). Under this premise, we utilized a

* Address correspondence to Elliot L. Chaikof, M.D., Ph.D., Emory University, 101 Woodruff Circle, Rm 5105, Atlanta, GA 30322. Tel: (404) 727-8413. Fax: (404) 727-3660. E-mail: echaiko@emory.edu.

[†] Current address: Department of Biomedical Engineering, University of Miami.

[‡] Current address: Department of Chemistry, Cleveland State University.

10.1021/bc7002814 CCC: $37.00 © 2007 American Chemical Society
Published on Web 10/26/2007

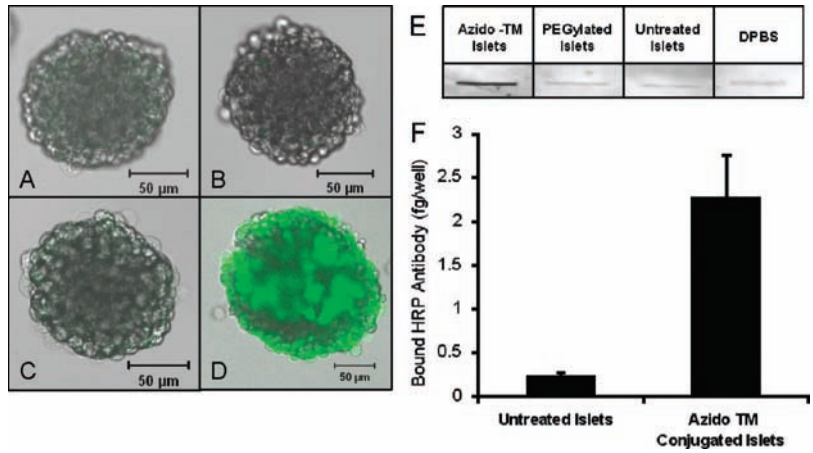


Figure 2. Confocal images (10×) after staining with anti-S-tag antibody of (A) native mouse islets; (B) islets treated with PEG linker; (C) azido-thrombomodulin; or (D) both PEG and azido-thrombmodulin. (E) Slot blot of cell lysate of mouse islets stained with sheep antihuman thrombomodulin antibody, followed by an antisheep HRP. (F) ELISA assay using antihuman thrombomodulin–HRP antibody to measure islet-bound human thrombomodulin. Data points represent the mean ± SD, for a minimum of three independent measurements.

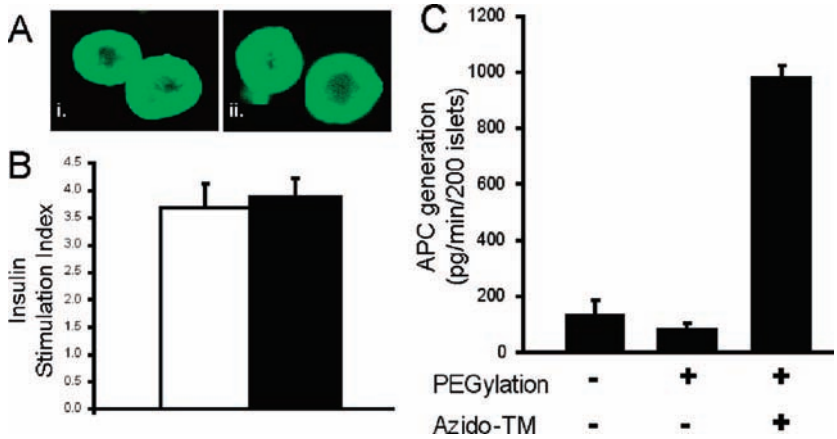


Figure 3. (A) Confocal images (10×) of untreated (i) and TM-conjugated islets using live/dead staining assay (ii). (B) Insulin stimulation index for native (open bars) and thrombomodulin-treated (solid bars) islets. Data points represent the mean ± SD, for a minimum of six independent measurements ($p > 0.05$). (C) Activated protein C (APC) generation by native islets or those treated with PEG linker alone or both linker and azido-TM. Data points represent the mean ± SD, for a minimum of three independent measurements (*$p < 0.05$).

bifunctional PEG linker to chemoselectively target recombinant azido-TM to the surface of living islets in a two-step process with the goal of creating a localized anti-inflammatory environment and reducing islet thrombogenicity.

The bifunctional PEG linker, with a triphenylphosphine (phosphine-PEG-NHS) at one end and a succinimidyl active ester at the other, was synthesized from commercially available amino-PEG-carboxylic acid, as described in Supporting Information. Pancreatic islets were isolated and purified from B10.BR mice using standard techniques by intraductal injection of rodent collagenase (Sigma, MO) (*17*). After culturing islets for 48 h, islets were transferred to a 12 μm plate insert (Millipore, MA) within a 24 well plate. RPMI media was flushed from the islets using PBS (Mediatech, VA). Following washes, the mouse islets were incubated for 1 h with 4 mM phosphine-PEG-NHS in PBS supplemented with 11 mM glucose solution. After a PBS wash, the islets were incubated for 1 h with recombinant azido-TM in fully supplemented RPMI. To elucidate the specificity of the reaction, confocal imaging, slot blot analysis, and ELISA were performed on several test groups, including (i) islets receiving no treatment; (ii) islets undergoing PEGylation alone; (iii) islets incubated solely with azido-TM; and (iv) islets treated sequentially with PEGylation and azido-TM. Since the recombinant azido-TM was expressed as fusion protein bearing a unique N-terminal S-Tag, a FITC-labeled anti-S-Tag antibody was used to detect islet bound TM (Figure 2).

The sequential two-step reaction with both linker and TM led to significant islet labeling, which was not observed on islets exposed solely to azido-TM or PEG linker alone (Figure 2A–D). Slot blot analysis of cell lysates confirmed the presence of human recombinant TM only on mouse islets treated with both linker and azido-TM (Figure 2E). Moreover, an ELISA assay performed with a horseradish peroxidase (HRP) conjugated antihuman TM antibody demonstrated a 10-fold increase in antibody binding to remodeled islet surfaces when compared to untreated islets or to those treated with linker alone ($p < 0.05$; Figure 2F).

Confocal fluorescence imaging using a live/dead staining protocol confirmed preservation of islet viability after surface treatment with linker and Staudinger ligation of azido-TM (Figure 3A). Likewise, glucose-stimulated insulin secretion, as a measure of islet function, was unchanged after surface treatment (Figure 3B). Significantly, a 7-fold increase in protein C activation was observed for islets conjugated with the recombinant azido-TM compared to untreated or pegylated islets (Figure 3C). Moreover, TM conjugation substantially delayed clot formation upon incubation of untreated islets in human plasma. The calculated half-maximal clotting times were 8.15 ± 0.67 min for untreated islets, 9.88 ± 0.49 min for pegylated islets, and 14.08 ± 2.07 min for TM-treated islets ($p < 0.05$).

To date, traditional coating techniques have focused on passive barrier methods that either immunoisolate or immuno-

camouflage transplanted cells from the host. The generation of a bioactive coating through tissue-targeted chemistry serves not only to mask cell surface proteins, but also to provide a means to alter the local microenvironment of the islet graft. In the process, islet-mediated procoagulant and proinflammatory responses are reduced, which may lead to a substantial improvement in clinical outcomes. In principle, the chemical scheme illustrated in this report highlights the potential to immobilize a wide array of functionally complex constituents onto the islet surface in order to actively manipulate the donor–host tissue interface.

ACKNOWLEDGMENT

This work was supported by grants from the NIH and JDRF.

Supporting Information Available: Detail synthetic procedures and spectral data for intermediates and final PEG linker, procedures for islet isolation, assays for islet viability, function, APC generation, and in vitro clotting time (PDF). This material is available free of charge via the Internet at http://pubs.acs.org.

LITERATURE CITED

(1) Bennet, W., Sundberg, B., Groth, C. G., Brendel, M. D., Brandhorst, D., Brandhorst, H., Bretzel, R. G., Elgue, G., Larsson, R., Nilsson, B., and Korsgren, O. (1999) Incompatibility between human blood and isolated islets of Langerhans: a finding with implications for clinical intraportal islet transplantation? *Diabetes 48*, 1907–1914.

(2) Johansson, H., Lukinius, A., Moberg, L., Lundgren, T., Berne, C., Foss, A., Felldin, M., Kallen, R., Salmela, K., Tibell, A., Tufveson, G., Ekdahl, K., Elgue, G., Korsgen, O., and Nilsson, B. (2005) Tissue factor produced by the endocrine cells of the islets of langerhans is associated with a negative outcome of clinical islet transplantation. *Diabetes 54*, 1755–1762.

(3) Johansson, U., Olsson, A., Gabrielsson, S., Nilsson, B., and Korsgen, O. (2003) Inflammatory mediators expressed in human islets of Langerhans: implications for islet transplantation. *Biochem. Biophys. Res. Commun. 308*, 474–479.

(4) Moberg, L., Johansson, H., Lukinius, A., Berne, C., Foss, A., Kallen, R., Ostraat, O., Salmela, K., Tibell, A., Tufveson, G., Elgue, G., Ekdahl, K., Korsgen, O., and Nilsson, B. (2002) Productions of tissue factor by pancreatic islet cells as a trigger of detrimental thrombotic reactions in clinical islet transplantation. *Lancet 360*, 2039–2045.

(5) Bennet, W., Groth, C. G., Larsson, R., Nilsson, B., and Korsgren, O. (2000) Isolated human islets trigger an instant blood mediated inflammatory reaction: implications for intraportal islet transplantation as a treatment for patients with type 1 diabetes. *Ups. J. Med. Sci. 105*, 125–133.

(6) Contreras, J., Eckstein, C., Smyth, C., Bilbao, G., Vilatoba, M., Ringland, S., Young, C., Thompson, J., Fernandez, J., Griffin, J., and Eckhoff, D. (2004) Activated protein C preserves functional islet mass after intraportal transplantation. A novel link between endothelial cell activation, thrombosis, inflammation, and islet cell death. *Diabetes 53*, 2804–2814.

(7) Goto, M., Johansson, H., Maeda, A., Elgue, G., Korsgen, O., and Nilsson, B. (2004) Low-molecular weight dextran sulfate abrogates the instant blood-mediated inflammatory reaction induced by adult porcine islets both in vitro and in vivo. *Transplant Proc. 36*, 1186–1187.

(8) Ozmen, L., Ekdahl, K. N., Elgue, G., Larsson, R., Korsgren, O., and Nilsson, B. (2002) Inhibition of thrombin abrogates the instant blood-mediated inflammatory reaction triggered by isolated human islets: possible application of the thrombin inhibitor melagatran in clinical islet transplantation. *Diabetes 51*, 1779–84.

(9) Esmon, C. (2004) Crosstalk between inflammation and thrombosis. *Maturitas 47*, 305–314.

(10) Esmon, C., Gu, J.-M., Xu, J., Qu, D., Sterns-Kurosawa, D., and Kurosawa, S. (1999) Regulation and functions of the protein C anticoagulation pathway. *Haematologica 84*, 363–368.

(11) Esmon, N., Owen, W., and Esmon, C. (1982) Isolation of a membrane-bound cofactor for thrombin-catalyzed activation of protein C. *J. Biol. Chem. 257*, 859–864.

(12) Link, A. J., Mock, M. L., and Tirrell, D. A. (2003) Non-canonical amino acids in protein engineering. *Curr. Opin. Biotechnol. 14*, 603–609.

(13) Cazalis, C. S., Haller, C. A., Sease-Cargo, L., and Chaikof, E. L. (2004) C-terminal site-specific PEGylation of a truncated thrombomodulin mutant with retention of full bioactivity. *Bioconjugate Chem. 15*, 1005–1009.

(14) Sun, X. L., Stabler, C. L., Cazalis, C. S., and Chaikof, E. L. (2006) Carbohydrate and protein immobilization onto solid surfaces by sequential Diels-Alder and azide-alkyne cycloadditions. *Bioconjugate Chem. 17*, 52–57.

(15) Prescher, J., Dube, D., and Bertozzi, C. (2004) Chemical remodeling of cell surfaces in living animals. *Nature (London) 430*, 873–877.

(16) Xie, D., Smyth, C., Eckstein, C., Bilbao, G., Mays, J., Eckhoff, D., and Contreras, J. (2005) Cytoprotection of PEG-modified adult porcine pancreatic islets for improved xenotransplantation. *Biomaterials 26*, 403–412.

(17) Kaufman, D. B., Platt, J. L., Rabe, F. L., Dunn, D. L., Bach, F. H., and Sutherland, D. E. (1990) Differential roles of Mac-1+ cells, and CD4+ and CD8+ T lymphocytes in primary nonfunction and classic rejection of islet allografts. *J. Exp. Med. 172*, 291–302.

BC7002814

ARTICLES

Synthesis and Characterization of a New Bioactivated Paramagnetic Gadolinium(III) Complex [Gd(DOTA-FPG)(H_2O)] for Tracing Gene Expression

Yu-Ton Chang,[†] Chiu-Min Cheng,[‡] Yu-Zheng Su,[†] Wei-Thung Lee,[†] Jui-Sheng Hsu,[§] Gin-Chung Liu,[||] Tian-Lu Cheng,*[,‡] and Yun-Ming Wang*[,†]

Faculty of Medicinal and Applied Chemistry, Faculty of Biomedical Science and Environmental Biology, Department of Radiology, Kaohsiung Municipal Hsiao-Kang Hospital, Department of Medical Imaging, Kaohsiung Medical University Hospital, and Department of Radiology, Kaohsiung Medical University, and 100 Shih-Chuan 1st Road, Kaohsiung 807, Taiwan.
Received January 18, 2007; Revised Manuscript Received June 7, 2007

A smart contrast agent for magnetic resonance imaging (MRI) can be used to exploit an enzymatic activity specific to the tissue or disease state signified by converting an MRI-inactivated agent to an activated MRI agent. In this study, a β-galactopyranose-containing gadolinium(III) complex [Gd(DOTA-FPG)(H_2O)] was designed, synthesized, and characterized as being potentially suitable for a bioactivated MRI contrast agent. The ^{17}O NMR experiments were conducted to estimate the water exchange rate k_{ex}^{298} and rotational correlation time τ_R^{298}. The k_{ex}^{298} value of [Gd(DOTA-FPG)(H_2O)] is similar to that of [Gd(DO3A-bz-NO_2)(H_2O)]. The rotational correlation time value of [Gd(DOTA-FPG)(H_2O)] is dramatically longer than that of [Gd(DOTA)(H_2O)]$^-$ Relaxometric studies show that the percentage change in the T_1 value of [Gd(DOTA-FPG)(H_2O)] decreases dramatically in the presence of β-galactosidase and human serum albumin. The T_1 change percentage of [Gd(DOTA-FPG)(H_2O)] (60%) is significantly higher than those of Egad and gadolinium(III)-1-(4-(2-(1-(4,7,10-triscarboxymethyl-(1,4,7,10-tetraazacyclododecyl)))-ethylcarbamoyloxymethyl)-2-nitrophenyl)-β-D-glucopyronuronate. The signal intensity of the MR image for [Gd(DOTA-FPG)(H_2O)] in the presence of human serum albumin and β-galactosidase (2670 $\pm$ 210) is significantly higher than that of [Gd(DOTA-FPG)(H_2O)] in the sodium phosphate buffer solution (1490 $\pm$ 160). In addition, the MR images show a higher-intensity enhancement in CT26/β-gal tumor with β-galactosidase gene expression but not for the CT26 tumor without β-galactosidase gene expression. We conclude that [Gd(DOTA-FPG)(H_2O)] is a suitable candidate for a bioactivated MRI contrast agent in tracing gene expression.

INTRODUCTION

Molecular imaging is providing a sensitive and specific method for the detection and localization of the biochemical appearance *in vivo*. Magnetic resonance imaging (MRI) offers several advantages over other clinical diagnostic techniques for molecular imaging, including high spatial resolution, noninvasiveness, high anatomical contrast, and lack of harmful radiation. However, sensitivity of MRI to depicting a small molecule is constrained by the ubiquitous protons in the body, resulting in a high background and low signal to noise ratio (SNR). Hence, the alternative amplification strategies using smart contrast agents are required to yield a higher sensitivity (*1*).

Nonspecific contrast agents such as [Gd(DTPA)(H_2O)]$^{2-}$ (H_5DTPA = 3,6,9-tri(carboxymethyl)-3,6,9-triazaundecanedioic acid) (Magnevist, gadopentetate), [Gd(DTPA-BMA)(H_2O)] (H_3DTPA-BMA = 1,7-bis[(*N*-methylcarbamoyl)methyl]-1,4,7-tris(carboxymethyl)-1,4,7-triazaheptane) (Omniscan, gadodiamide), and [Gd(DOTA)(H_2O)]$^-$ (H_4DOTA = 1,4,7,10-tetraazacyclododecane-1,4,7,10-tetraacetic acid) (Dotarem, gadoterate) are widely available for clinical use. They provide a nonspecific distribution pattern that allows measurement of tissue profusion, vascular permeability, or vascular volume. These parameters can be fitted by fast pharmacologic modeling and imaging techniques or steady-state imaging techniques (*2*, *3*). However, the true molecular targets cannot be ideally displayed with these approaches. Different signal characteristics upon interacting with the specific target by smart contrast agents could provide new ways for detecting the stages of biological molecules. Theoretically, smart contrast agents exhibit a strong signal alteration upon target interaction whether there is a bioactivated effect or not. This makes them ideal candidates for molecular imaging because they have the highest SNR for molecular target identification.

* Corresponding authors. Dr. Yun-Ming Wang, Kaohsiung Medical University, Faculty of Medicinal and Applied Chemistry, 100 Shih-Chuan 1st Road, Kaohsiung 807, Taiwan, Tel 886-7-3121101ext. 2218, Fax 886-7-3125339, E-mail address ymwang@kmu.edu.tw; Dr. Tian-Lu Cheng, Kaohsiung Medical University, Faculty of Biomedical and Environmental Biology, 100 Shih-Chuan 1st Road, Kaohsiung 807, Taiwan, Tel 886-7-3121101ext. 2697, Fax 886-7-3227508, E-mail tlcheng@kmu.edu.tw.

[†] Faculty of Medicinal and Applied Chemistry.

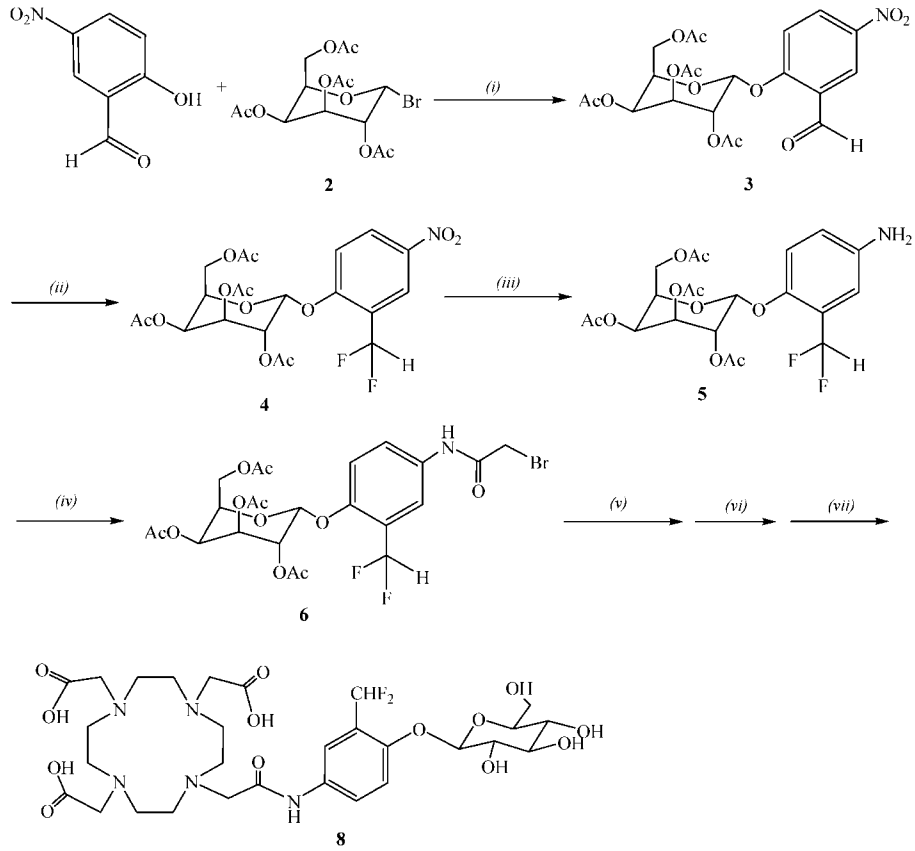
[‡] Faculty of Biomedical Science and Environmental Biology.

[§] Department of Radiology, Kaohsiung Municipal Hsiao-Kang Hospital.

[||] Department of Medical Imaging, Kaohsiung Medical University Hospital, and Department of Radiology, Kaohsiung Medical University.

10.1021/bc070019s CCC: $37.00 © 2007 American Chemical Society
Published on Web 10/13/2007

Scheme 1. Synthetic Scheme of DOTA-FPG[a]



[a] Reagents and conditions: (i) NaOH, TBAB, H_2O, CH_2Cl_2, 73%; (ii) DAST, CH_2Cl_2, 94%; (iii) H_2, Pd/C, ethyl acetate, 85% (*35*); bromoacetyl bromide, dimethylamine, CH_2Cl_2, 32%; (v) DO3A-tris-^{t}butyl ester (**7**), triethylamine, CH_2Cl_2 (*36*); $NaOCH_3$, CH_3OH; (vii) TFA, 45% for three steps.

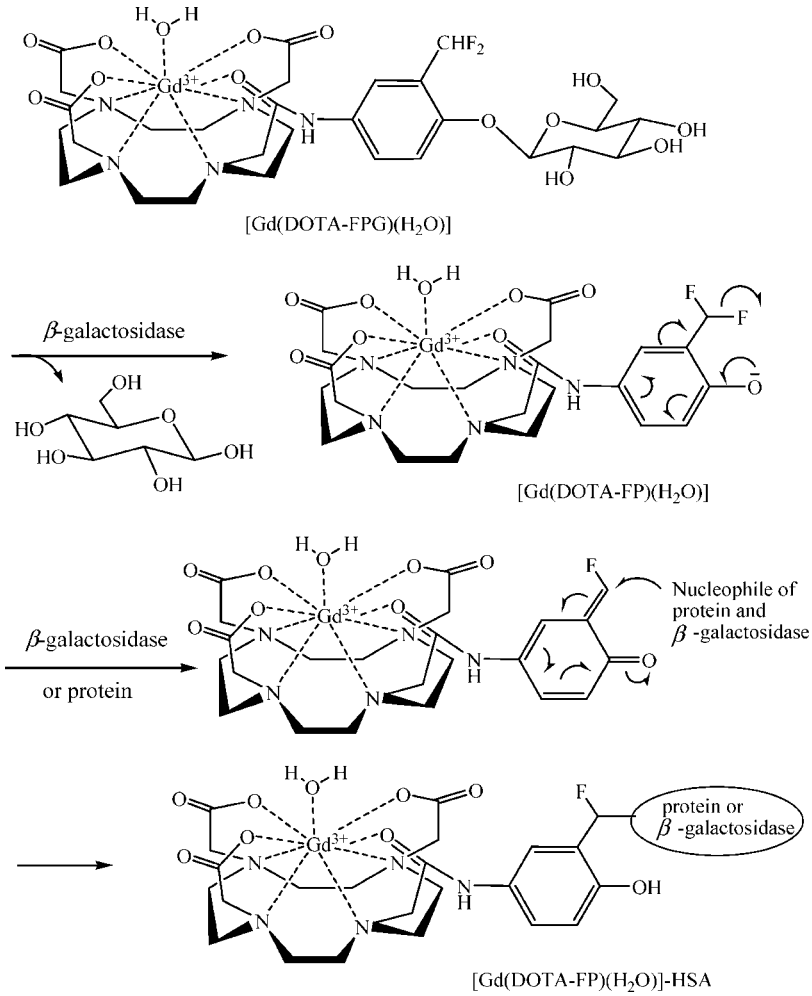
The smart MR contrast agents carry out structural changes upon target interaction, which significantly change their signal properties (e.g., increasing the number of inner-sphere water molecules, *q*) (*4*). Enzyme-activated contrast agents for MRI have been developed and characterized (*1, 5*). These gadolinium(III) chelates developed an MR signal amplification strategy based on oxidoreductase-mediated polymerization of paramagnetic monomer into oligomers of higher relaxivity. Other enzyme motifs such as β-galactosidase, often used as a reporter gene in molecular biology, have been explored for a smart contrast agent for MRI (*4, 6, 7*). In this system, the route of water exchange to the gadolinium chelate is blocked by an enzymatically cleavable galactopyranoside substrate. β-Galactosidase activity results in an increase in T_1 relaxivity, and thus, the signal intensity increased in the T_1-weighted image. The feasibility of detecting β-galactosidase expression in *Xenopus laevis* embryos has been evaluated (*6, 8*).

The synthesis and characterization of Gd(III) complexes with poly(amino carboxylate) had been investigated in our previous studies (*9–12*). In this study, we design, synthesize (Scheme 1), and characterize the enzymatic contrast agent [Gd(DOTA-FPG)(H_2O)] (H_3DOTA-FPG = 1-(2-difluoromethyl-4-(1-(4,7,10-triscarboxymethyl-(1,4,7,10-tetraazacyclodecyl))acetamido)phenyl)-β-D-galactopyranose), which can be activated by β-galactosidase. In an attempt to achieve improvements in enzyme-mediated relaxivity enhancement, we decided to link a bioactivated residue onto gadolinium(III) chelate in order to achieve conjugation and, therefore, a higher molecular weight of the final product obtained. This chelate consists of a gadolinium(III) complex and an enzymatic moiety, 2-difluoromethylphenyl-β-galactopyranoside, which can be cleaved when there is the existence of β-galactosidase. The nucleophile of human serum albumin (HSA) and β-galactosidase will attack [Gd(DOTA-FP)(H_2O)] (H_3DOTA-FP = 1-(6-fluoromethylene-4-(1-(4,7,10-triscarboxymethyl(1,4,7,10-tetraazacyclodecyl)) acetamido)cyclohexa-2,4-dienone) complex to form biomacromolecules (*13*) [Gd(DOTA-FP)(H_2O)]-HSA and [Gd(DOTA-FP)(H_2O)]-β-galactosidase. The higher relaxivity (r_1) of the [Gd(DOTA-FP)(H_2O)]-HSA is achieved as a result of the larger rotational correlation time value of the macromolecule [Gd-(DOTA-FP)(H_2O)]-HSA as shown in Scheme 2. ^{17}O NMR relaxation rates and angular frequencies of the free Gd(III) complex in the presence and absence of HSA and β-galactosidase at variable temperatures will be reported. Furthermore, the effect of β-galactosidase on the longitudinal relaxation time (T_1) of Gd(III) complex will be investigated. Finally, the MR images of Gd(III) chelate in the presence and absence of β-galactosidase and HSA, animal model with and without β-galactosidase expression will be performed.

EXPERIMENTAL PROCEDURES

Materials. 1-(2-Difluoromethyl-4-aminophenyl)-2,3,4,6-tetraacetyl-β-D-galactopyranose (*13*) and 4,7,10-(tris-^{t}butylcarboxymethyl)-(1,4,7,10-tetraazacyclodecane) (DO3A-tris-^{t}butyl ester) (*14, 15*) were prepared by the previously published method. D(+)-Galactose was purchased from Acros. 2-Hydroxy-5-nitrobenzaldehyde, tetra-*N*-butylammonium bromide (TBAB), and diethylaminosulfur trifluoride (DAST) were purchased from Lancaster. All other reagents used for the synthesis of the ligand were purchased from commercial sources, unless otherwise noted. ^{17}O-enriched water (20.3%) was purchased from Isotec Inc. Human serum albumin (HSA, product no. A-1653, fraction V powder 96–99%) and β-galactosidase (product no. G5635–5KU, grade VIII from *Escherichia coli*) were purchased from Sigma

Scheme 2. Proposed Mechanism of HSA to Bind to [Gd(DOTA-FPG)(H_2O)]



and used without any further purification. The molecular weights were assumed to be 66.5 kDa (HSA) and 465 kDa (β-galactosidase). β-Gal Staining Kit was purchased from Invitrogen. The 100 mM sodium phosphate buffer solution was used to maintain the pH of all solutions (pH = 7.4) containing HSA. ^{1}H (400 MHz) and ^{13}C (100 MHz) NMR spectra were recorded on a Varian Gemini-400 spectrometer with 5 mm sample tubes. The ^{13}C NMR spectra were referenced internally relative to 3-(trimethylsilyl)-1-propanesulfonic acid for D_2O. The concentration of Gd(III) complex was determined by ICP-MS with a Perkin-Elmer OPTIMA 2000.

Synthesis. *1-(2-Formyl-4-nitrophenyl)-2,3,4,6-tetraacetyl-β-D-galactopyranose (**3**).* A solution of 2-hydroxy-5-nitrobenzaldehyde (8.29 g, 49.61 mmol) in CH_2Cl_2 (100 mL) was stirred at room temperature with an aqueous solution of 1 N NaOH (50 mL) and tetra-*N*-butylammonium bromide (TBAB) (10.99 g, 33.1 mmol). A solution of 2,3,4,6-aceto-α-D-bromogalactopyranose (13.60 g, 33.07 mmol) was added to this stirred mixture at room temperature. The synthesis of 2,3,4,6-aceto-α-D-bromogalactopyranose was prepared by the previously published method. The mixture solution was stirred for 3 days. The mixture solution was evaporated and yielded a bright yellow oil. Then, the oil was dissolved in CH_2Cl_2 and washed with 2 N NaOH solution (4 × 250 mL) and water several times. After collecting the organic phase, the goal compound was obtained by evaporating the solvent. Purification by chromatography (silica, CH_2Cl_2) gave a yellow viscous solid. The yellow solid was crystallized in diethyl ether, and this led to the production of a white solid. Collected solid and evaporated to dryness, yield 11.98 g (72.82%). ^{1}H NMR (400 MHz, $CDCl_3$): δ 10.31 (s, 1H, -CHO), 8.66 (dd, 1H, ArH), 8.38 (dd, 1H, ArH), 7.27 (d, 1H, ArH), 5.60 (dd, 1H, sugar, -CH-), 5.50 (d, 1H, sugar, -CH-), 5.30 (d, 1H, sugar, -CH-), 5.18 (dd, 1H, sugar, -CH-), 4.20 (m, 3H, sugar, -C*H*- and -CH_2OAc), 2.06 (m, 12H, -OAc). ^{13}C NMR (100 MHz, $CDCl_3$): δ 20.47, 20.56, 20.61, 61.26, 66.56, 68.06, 70.23, 71.76, 98.77, 115.76, 124.34, 125.75, 130.10, 143.28, 162.04, 169.29, 169.94, 170.03, 170.23, 187.02. ESI-MS: calcd *m*/*z* 497.4, found 498.8 $[M + H]^+$. Anal. Calcd for $C_{21}H_{23}NO_{13}$: C 50.71, H 4.66, N 2.82. Found: C 50.33, H 4.78, N 2.90.

*1-(2-Difluoromethyl-4-nitrophenyl)-2,3,4,6-tetraacetyl-β-D-galactopyranose (**4**).* Diethylaminosulfur trifluoride (DAST) (3.81 mL) was added to a solution of 1-(2-formyl-4-nitrophenyl)-2,3,4,6-tetraacetyl-β-D-galactopyranose (11.98 g, 24.08 mmol) in dry CH_2Cl_2 (300 mL). The reaction was stirred at ambient temperature under N_2 for 6.5 h. The reaction mixture was quenched by the addition of ice and extracted twice with CH_2Cl_2 (100 mL). The combined organic layers were washed successively with water and brine and dried over $MgSO_4$. The above solution was filtered and concentrated by rotary evaporation, which yielded a yellow crude compound. Purification by chromatography (silica, CH_2Cl_2) collected the first point and gave a yellow solid (11.82 g, 94.49%). ^{1}H NMR (400 MHz, $CDCl_3$): δ 8.47 (dd, 1H, ArH), 8.32 (dd, 1H, ArH), 7.23 (d, 1H, ArH), 6.70–6.98 (t, 1H, -CF_2H), 5.56 (dd, 1H, sugar, -CH-), 5.50 (d, 1H, sugar, -CH-), 5.15(m, 2H, sugar, -CH-), 4.20 (m, 3H, sugar, -C*H*- and -CH_2OAc), 2.06 (m, 12H, -OAc). ^{13}C NMR (100 MHz, $CDCl_3$): δ 20.49, 20.56, 20.61, 30.88, 61.31, 66.58, 67.74, 70.18, 71.72, 99.25, 107.54, 109.91, 112.28, 114.91, 122.73, 122.77, 122.81, 122.86, 127.68, 143.07, 158.65, 158.72, 169.50, 169.95, 170.03, 170.23. ESI-MS: calcd *m*/*z* 519.4, found

520.0 $[M + H]^+$. Anal. Calcd for $C_{21}H_{23}F_2NO_{12}$: C 48.56, H 4.46, N 2.70. Found: C 48.36, H 4.55, N 2.71.

*1-(2-Difluoromethyl-4-aminophenyl)-2,3,4,6-tetraacetyl-β-D-galactopyranose (***5***).* Pd/C (10% Pd, 0.22 g) was added to a stirring solution of 1-(2-difluoromethyl-4-nitro-phenyl)-2,3,4,6-tetraacetyl-β-D-galactopyranose (11.23 g, 21.62 mmol) in ethyl acetate under 1.5 atm H_2. This step was repeated until the pressure stopped decreasing. Purification by chromatography (silica, CH_2Cl_2) can produce a yellow solid (8.98 g, 84.86%) and concentrated the pure compound in a vacuum. ^{1}H NMR (400 MHz, $CDCl_3$): δ 6.66–6.97 (m, 4H, ArH and -CF_2H), 5.45 (m, 2H, sugar, -CH_2-), 5.09 (dd, 1H, sugar, -CH-), 4.87 (d, 1H, sugar, -CH-), 4.24 (dd, 1H, sugar, -CH-), 4.16 (dd, 1H, sugar, -CH-), 4.02 (t, 1H, sugar, -CH-), 2.06 (m, 12H, -OAc). ^{13}C NMR (100 MHz, $CDCl_3$): δ 20.54, 20.61, 20.63, 61.31, 66.82, 68.34, 70.69, 71.01, 101.04, 108.75, 111.10, 112.51, 112.54, 112.58, 112.62, 113.45, 117.81, 118.35, 141.99, 169.60, 170.09, 170.21, 170.34. ESI-MS: calcd *m/z* 489.4, found 490.8 $[M + H]^+$. Anal. Calcd for $C_{21}H_{25}F_2NO_{10}$: C 51.54, H 5.15, N 2.86. Found: C 51.34, H 5.28, N 2.75.

*1-(2-Difluoromethyl-4-(1-bromoacetamido)phenyl)-2,3,4,6-tetraacetyl-β-D-galactopyranose (***6***).* 1-(2-Difluoromethyl-4-aminophenyl)-2,3,4,6-tetraacetyl-β-D-galactopyranose (8.94 g, 18.27 mmol) was dissolved in CH_2Cl_2 (60 mL) and treated with 40% dimethylamine (2.31 mL, 18.30 mmol). Bromoacetyl bromide (1.59 mL, 18.30 mmol) was dissolved in CH_2Cl_2 (40 mL) and dropped into the above solution in an ice bath overnight. Then, the reaction was treated with dilute HCl, dilute $NaHCO_3$ solution, and water. The organic solution was evaporated and washed with diethyl ether to give a pure white solid (3.61 g, 32.38%). ^{1}H NMR (400 MHz, $CDCl_3$): δ 8.19 (s, 1H, ArH), 7.79 (d, 1H, ArH), 7.58 (s, 1H, -NH-), 7.13 (d, 1H, ArH), 6.98–6.70 (t, 1H, -CF_2H), 5.50 (m, 2H, sugar, -CH_2-), 5.12 (dd, 1H, sugar, -CH-), 5.01 (d, 1H, sugar, -CH-), 4.24 (dd, 1H, sugar, -CH-), 4.16 (dd, 1H, sugar, -CH-), 4.02 (t, 1H, sugar, -CH-), 4.03 (s, 2H, -CH_2Br), 2.06 (m, 12H, -OAc). ^{13}C NMR (100 MHz, $CDCl_3$): δ 20.55, 20.64, 20.67, 29.24, 61.37, 66.73, 68.04, 70.48, 71.27, 100.13, 108.31, 110.67, 113.02, 116.17, 118.26, 118.30, 118.34, 124.00, 132.55, 132.54, 163.51, 169.61, 170.06, 170.17, 170.34. ESI- MS: calcd *m/z* 610.4, found 611.7 $[M + H]^+$. Anal. Calcd for $C_{23}H_{26}BrF_2NO_{11}$: C 45.26, H 4.29, N 2.29. Found: C 45.02, H 4.44, N 2.36.

1-(2-Difluoromethyl-4-(1-(4,7,10-triscarboxymethyl-(1,4,7,10-tetraazacyclodecyl))-acetamido)phenyl)-β-D-galactopyranose (DOTA-FPG, **8***).* DO3A-tris-^{t}butyl ester (1.05 g, 2.04 mmol), KI (0.0354 g, 0.21 mmol), and triethylamine (0.545 mL, 3.93 mmol) were dissolved in CH_3CN (50 mL); 1-(2-difluoromethyl-4-(1-bromoacetamido)phenyl)-2,3,4,6-tetraacetyl-β-D-galactopyranose (1.18 g, 1.93 mmol) was added to the solution, and the mixture was stirred for 2 h. The synthesis of DO3A-tris-^{t}butyl ester was prepared by the previously published method. After 2 h, the mixture was warmed to 50 °C and stirred for 24 h. The solvent was removed by rotary evaporation. The acetyl group was removed by reaction with $NaOCH_3$ and dry CH_3OH (50 mL) for 2 h. Deprotection of *tert*-butyl ester group was achieved by stirring at room temperature in trifluoroacetic acid (TFA) (20 mL) for 12 h. After 12 h, the solution was quenched with water and adjusted to pH 11 with ammonium hydroxide. Next, this compound was purified by AG 1 × 8 anion exchange resin column (200–400 mesh, HCO_2^- form, eluted first with H_2O (2 L) and then with a gradient of formic acid) and then collected and concentrated 0.02–0.03 N formic acid solution to give major product. The trace of formic acid was removed by coevaporation with water (200 mL) five times, yielding 0.65 g (45.02%) of DOTA-FPG as a yellow viscous oil. ^{1}H NMR (400 MHz, D_2O): δ 7.61 (s, 1H, ArH), 7.48 (d, 1H, ArH), 7.18 (d, 1H, ArH), 7.03 (t, 1H, -CF_2H), 4.98 (d, 1H, sugar, -O-CH-O), 3.92 (d, 1H, sugar, -CH-), 3.61 (m, 9H, sugar and DOTA, -CH- and -CH_2-), 3.35 (s, 8H, DOTA, -N-CH_2-CO-), 3.02 (m, 12H, DOTA, -CH_2-). ^{13}C NMR (100 MHz, D_2O): δ 7.40, 22.43, 18.01, 48.16, 50.90, 51.32, 53.30, 55.25, 55.56, 56.40, 60.67, 61.31, 68.39, 70.37, 72.53, 75.46, 101.11, 109.43, 111.76, 114.10, 116.33, 117.48, 19.04, 120.53, 123.49, 123.71, 125.38, 125.81, 129.78, 130.94, 132.14, 151.37, 156.84, 169.85, 170.17, 174.33, 197.37. HRMS (FAB^+): *m/z* 708.0 $[M + H]^+$. Anal. Calcd for $C_{29}H_{43}F_2N_5O_{13}$: C 49.22, H 6.12, N 9.90. Found: C 49.42, H 6.08, N 9.95.

Preparation of Lanthanide Complexes. The Gd(III) and Eu(III) complexes were prepared by dissolving the DOTA-FPG (0.58 mmol) in H_2O (10 mL) and adjusting the pH of the solution to 6.5 with dilute NaOH. $LnCl_3$ (0.57 mmol, dissolved in 5 mL H_2O and brought to pH = 6.5 with NaOH) was added dropwise, maintaining pH at 5.5–6.0 with dilute NaOH periodically. The mixture solution was stirred at room temperature. After 2–3 days, the pH showed no change and the formation of Ln(III) chelate was considered complete. The pH was brought to 8.0, and the solution was centrifuged to remove excess lanthanide ions as $Ln(OH)_3$ and verified by the xylenol orange test. The trace $Ln(OH)_3$ was removed by filtration through a 200 nm nylon filter, and the solution was then evaporated under reduced pressure. The purity of [Gd(DOTA-FPG)(H_2O)] and [Eu(DOTA-FPG)(H_2O)] was determined by HPLC and identified by mass. The HPLC chromatograms of these complexes were deposited as Supporting Information (Figures 1S–2S).

Reversed-Phase High-Performance Liquid Chromatography (HPLC) Method. The HPLC experiments were performed on an Amersham ÄKTAbasic 10 instrument equipped with an Amersham UV-900 detector and Amersham Frac-920 fraction collector. Supelco RP-C18 column (5 μm, 4.6 × 250 mm; and 5 μm, 10 × 250 mm) were used.

^{17}O NMR Measurements. For the variable-temperature ^{17}O NMR measurements of [Gd(DOTA-FPG)(H_2O)], [Gd(DOTA-FP)(H_2O)], and [Gd(DOTA-FP)(H_2O)]-HSA, the components and pH values of the utilized solutions were as follows: 20 mM [Gd(DOTA-FPG)(H_2O)] in 100 mM sodium phosphate buffer solution, 5.5% ^{17}O isotope, pH = 7.4; 20 mM [Gd(DOTA-FPG)(H_2O)] in 100 mM sodium phosphate buffer solution, 2 μM β-galactosidase, 5.5% ^{17}O isotope, pH = 7.4; 20 mM [Gd(DOTA-FPG)(H_2O)] in 100 mM sodium phosphate buffer solution, 2 μM β-galactosidase, 4.5% (w/v) human serum albumin (HSA), 5.5% ^{17}O isotope, pH = 7.4. The measurement of the ^{17}O longitudinal, transverse relaxation rates and chemical shift were carried out with a Varian Gemini-400 (9.4 T, 54.2 MHz) spectrometer equipped with a 10 mm probe using an external D_2O lock. The Varian 600 temperature control unit was used to stabilize the temperature in the range 278–323 K. The samples were sealed in glass spheres adapted into 10 mm NMR tubes to eliminate susceptibility corrections to the chemical shift.

Data Analysis. The simultaneous least-squares fitting of ^{17}O NMR data was determined by fitting the experimental data using the program *SCIENTIST* for WINDOWS by Micromath, version 2.0.

MR Experiments. Relaxation Time Measurement. The longitudinal relaxation times (T_1) in different buffer solutions of Gd(III) complex were measured to determine relaxivity (r_1). The measurements were made using a NMR relaxometer operating at 20 MHz and 37.0 ± 0.1 °C (NMR-120 Minispec, Bruker). Before each measurement, the relaxometer was tuned and calibrated. The values of r_1 were determined from five data points generated by an inversion–recovery pulse sequence. To study the effect of β-galactosidase enzyme on the r_1 value of [Gd(DOTA-FPG)(H_2O)] solutions, β-galactosidase isolated from *Escherichia coli* was used. The *Escherichia coli* enzyme was reconstituted with 0.1 M sodium phosphate buffer, pH = 7.4 at

25.0 ± 0.1 °C, and proved its activity with *p*-nitrophenyl-β-D-galactopyranoside (PNPG). For the longitudinal relaxation time (T_1) measurements of [Gd(DOTA-FPG)(H_2O)] in the presence and absence of β-galactosidase and HSA, the components of the utilized solutions were as follows: (a) 0.5 mM [Gd(DOTA-FPG)(H_2O)] in 100 mM sodium phosphate buffer solution; (b) 0.5 mM [Gd(DOTA-FPG)(H_2O)] and 2 μM β-galactosidase in 100 mM sodium phosphate buffer solution; (c) 0.5 mM [Gd(DOTA-FPG)(H_2O)] and 0.5 mM HSA in 100 mM sodium phosphate buffer solution; (d) 0.5 mM [Gd(DOTA-FPG)(H_2O)], 0.5 mM HSA and 2 μM β-galactosidase in 100 mM sodium phosphate buffer solution. The percentage change of T_1 value in these solutions was plotted against the incubation time. These measurements were made in triplicate to reduce systematic error in the relaxation time (T_1) measurements.

Cells and Animal Model. CT26 colon carcinoma cells were obtained from American type Culture Collection (Manassas, VA). Recombinant β-galactosidase retrovirus was packaged by cotransfection of pVSVG with pLNCX-LacZ into GP2-293 cells (Clontech, BD Biosciences, USA). After 48 h, the culture medium was filtered, mixed with 8 μg/mL polybrene, and added to CT26 colon carcinoma cells. The cells were selected in G418 and reclone to generate CT26/β-gal cells. Cells were grown in Dulbecco's Minimal Essential Medium (Sigma, St Louis, MO, USA) supplemented with 10% heat-inactivated bovine calf serum, 100 units/mL penicillin and 100 μg/mL streptomycin at 37 °C in an atmosphere of 5% CO_2. 6–8 week old female Balb/c mice were purchased from National Laboratory Animal Center, Taipei, Taiwan. Animal experiments were performed in accordance with institutional guidelines.

The CT26 and CT26/β-gal tumors were conducted with three Balb/c mice via subcutaneous injection of 100 μl (10^6 cells) phosphate buffer solution suspension into the right or left shoulder regions of mouse. The CT26 and CT26/β-gal tumors took one to three weeks to reach a predetermined size. The experiment was performed three weeks after implantation, at which time the tumors measured at least 0.5 cm in diameter.

Functional β-galactosidase in Vitro. Functional expression of β-galactosidase in cells was measured by staining CT26 or CT26/β-gal cells with β-galactosidase activity by the β-Gal Staining Kit according to the manufacturer's instructions. Cells were grown in 6 well plates and fixed with 3 mL fixation solution at room temperature for 10 min. The plate was washed twice with phosphate buffer solution, and 2 mL staining solution (1 mg/mL X-gal) was added at room temperature until the cell stained blue. Cells were examined on an upright microscope (Olympus BX41, Japan).

Cytotoxicity of Gd(III) Chelate. CT-26 cells were seeded overnight in 96-well plates. Graded concentrations of [Gd-(DOTA-FPG)(H_2O)] were added into CT-26 cells in the presence and absence β-galactosidase (2 μg/well) in triplicate for 24 h at 37 °C. The cells were subsequently incubated for 48 h in fresh medium. Cell viability was determined by the ^{3}H-thymidine incorporation assay. Cells were harvested with a filtermate apparatus and incorporated radioactivity was determined on a Top-Count scintillation counter. Results are expressed as percent inhibition of ^{3}H-thymidine incorporation as compared to untreated cells by the following formula:

$$\% \text{ inhibition} = (\text{cpm}_{\text{sample}} - \text{cpm}_{\text{background}})/(\text{cpm}_{\text{control}} - \text{cpm}_{\text{background}}) \times 100$$

Histological Analysis of Functional β-galactosidase in Vivo. CT26 and CT26/β-gal tumors were excised and embedded in Tissue-Tek OCT in liquid nitrogen and sectioned into 10 μm slices. The tumor sections were stained for β-galactosidase activity by the β-Gal Staining Kit as described above and counterstained with nuclear fast red. All sections were examined under phase contrast microscope.

In Vitro MR Studies of [Gd(DOTA-FPG)(H_2O)]. For the MR images of [Gd(DOTA-FPG)(H_2O)] and its enzymatic cleavage, the components and pH values of the utilized solutions were as follows: (a) 0.8 mM [Gd(DOTA-FPG)(H_2O)], 2 μM β-galactosidase, and 0.8 mM HSA in 100 mM sodium phosphate buffer solution pH = 7.4; (b) 0.8 mM [Gd(DOTA-FPG)(H_2O)] and 0.8 mM HSA in 100 mM sodium phosphate buffer solution pH = 7.4; (c) 0.8 mM [Gd(DOTA-FPG)(H_2O)] in 100 mM sodium phosphate buffer solution pH = 7.4; (d) 0.8 mM [Gd(DOTA-FPG)(H_2O)] and 2 μM β-galactosidase in 100 mM sodium phosphate buffer solution pH = 7.4; (e) sodium phosphate buffer solution. The solutions were transferred to 1.5 mL test tubes for MR imaging. MR imaging was performed with a clinical 1.5T superconductive MR scanner (Gyroscan ACS-NT; Philips Medical Systems, Best, The Netherlands) and a knee coil. MR pulse sequence included T1-weighted (TR/TE 100/10 ms) two-dimensional spin–echo sequence. Mean signal intensities for the test tubes were measured in the central section of the imaging volume with use of operator-defined regions of interest with a minimum of 10 pixels per region. To compare differences in SI data among various test tubes, analysis of variance for repeated measurements was used. Mean data were compared with the Scheffe test. A P value of less than 0.05 was considered to indicate a statistically significant difference.

In Vivo MR Studies of [Gd(DOTA-FPG)(H_2O)] for Animal Model. The Balb/c mice ($n = 3$) established CT26 and CT26/β-gal tumors in the left and right shoulder regions, respectively, were anesthetized with 40–50 mg/kg intraperitoneal sodium pentobarbital. The mouse was then placed in an animal coil. MR imaging was performed using a clinical 3.0 T superconductive MR scanner (Signa; GE Medical Systems, Milwaukee, WI). T1-weighted (TR/TE 100/13 ms) transaxial images were obtained before and after intravenous injection of 0.3 mmol/kg [Gd(DOTA-FPG)(H_2O)]. The following parameters were used: two excitation, slice thickness = 3 mm, matrix = 256 × 224, field of view = 8 cm, one signal acquisition, and imaging time = 1.6 min. Postcontrast scans were obtained every 5 min for half an hour.

RESULTS

Synthesis of the Ligand. The starting material 2,3,4,6-aceto-α-D-bromogalactopyranose was synthesized by methods in the literature (*4*). The ligand DOTA-FPG was prepared as follows. First, 2-hydroxy-5-nitrobenzaldehyde was successfully alkylated on the hydroxyl group with 2,3,4,6-aceto-α-D-bromogalactopyranose. Second, the aldehyde group was fluorinated, and the nitro group was hydrogenated to the amino group. Then, the bromoacetyl group was used as a linker to bind DO3A-tris-^{t}butyl ester and 2-difluoromethylphenyl-β-galactopyranose. Finally, the ligand DOTA-FPG underwent hydrolysis with $NaOCH_3$ and TFA. The ligand DOTA-FPG was analyzed by HPLC and showed one peak, which was identified by ESI-MS to confirm its purity. The HPLC chromatogram of this ligand is deposited as Supporting Information (Figure 3S).

Luminescence Method for Establishing Solution Hydration States. Luminescence lifetime data have been obtained for the complex [Eu(DOTA-FPG)(H_2O)] to determine the number of inner-sphere water molecules in the aqueous solution (*16–18*). The luminescence lifetime (τ) has been determined in both H_2O and D_2O ($\tau_{H_2O} = 0.590$ ms and $\tau_{D_2O} = 1.90$ ms). The [Eu(DOTA-FPG)(H_2O)] complexes containing 1.23 and 1.10 inner-sphere water (Table 1) were calculated by eqs 1 and 2 as follows

$$q = 1.05[\tau_{H_2O}^{-1} - \tau_{D_2O}^{-1}] \quad (1)$$

$$q = 1.2\,[(\tau_{H_2O}^{-1} - \tau_{D_2O}^{-1}) - 0.25] \quad (2)$$

Table 1. Relaxivity r_1 of [Gd(DOTA-FPG)(H_2O)], [Gd(DOTA-FPG)(H_2O)]/β-gal, [Gd(DOTA-FPG)(H_2O)]/HSA, [Gd(DOTA-FPG)(H_2O)]/β-gal + HSA, [Gd(HP-DO3A)(H_2O)], [Gd(DOTA)(H_2O)]$^-$, and [Gd(DTPA)(H_2O)]$^{2-}$ in 100 mM sodium phosphate buffer solution at 37.0 ± 0.1 °C and 20 MHz

complex	pH	relaxivity r_1/mM^{-1} s^{-1}
[Gd(DOTA-FPG)(H_2O)]	7.4 ± 0.1	3.96 ± 0.04
[Gd(DOTA-FPG)(H_2O)]/β-gal [a]	7.4 ± 0.1	3.77 ± 0.09
[Gd(DOTA-FPG)(H_2O)]/HSA [b]	7.4 ± 0.1	7.58 ± 0.06
[Gd(DOTA-FPG)(H_2O)]/β-gal + HSA [c]	7.4 ± 0.1	15.5 ± 0.2
[Gd(HP-DO3A)(H_2O)][d]	7.5 ± 0.1	3.65
[Gd(DOTA)(H_2O)]$^-$[e]	7.3 ± 0.1	3.56
[Gd(DTPA)(H_2O)]$^{2-}$[f]	7.6 ± 0.1	3.89 ± 0.03

[a] [Gd(DOTA-FPG)(H_2O)] in the presence of β-galactosidase (2 μM). [b] [Gd(DOTA-FPG)(H_2O)] in the presence of human serum albumin (HSA) (0.5 mM). [c] [Gd(DOTA-FPG)(H_2O)] in the presence of β-galactosidase (2 μM) and human serum albumin (HSA) (0.5 mM). [d] Data obtained from ref (*23*). [e] ref (*22*). [f] ref (*24*).

where q is the number of water molecules bound to metal ions, τ_{H_2O} is the luminescence half-life in H_2O solution and τ_{D_2O} is the luminescence half-life in D_2O solution. The q value is obtained from the luminescence study.

Relaxometric Studies of the Gd(III) Complex. The longitudinal water proton relaxivity (r_{1p}) results from the contribution arising from water molecules in the inner and outer coordination spheres as in eq 3

$$r_{1p} = R_{1p}^{is} + R_{1p}^{os} \quad (3)$$

The outer sphere term, R_{1p}^{os} , describes the contribution arising from the water molecules diffusing near the paramagnetic chelate (*19*). For compounds of similar size, it can be assumed that the outer-sphere mechanism makes a similar contribution at high magnetic flux densities (>0.1 T). Therefore, the small differences in relaxivity can be ascribed to differences in R_{1p}^{is} . The contribution arising from the exchange of the water molecules directly coordinated to the paramagnetic metal ion is obtained by eq 4 as follows (*20, 21*)

$$R_{1p}^{is} = [C]q/[55.6(T_{1M} + \tau_M)] \quad (4)$$

where [*C*] represents the molar concentration of the gadolinium(III) complex, τ_{1M} is the longitudinal relaxation time of the inner-sphere water protons and τ_M is the residence lifetime of the bound water. The longitudinal relaxivity (r_1) value of [Gd(DOTA-FPG)(H_2O)] in the presence and absence of β-galactosidase and HSA compared with [Gd(DOTA)(H_2O)]$^-$ (*22*), [Gd(HP-DO3A)(H_2O)] (*23*) (H_3HP-DO3A = 1,4,7,10-tetraazacyclododecane-1-(2-hydroxylpropyl)-4,7,10-triacetic acid), and [Gd(DTPA)(H_2O)]$^{2-}$ (*24*) (the structural formula shown in Chart 1) are shown in Table 1. The relaxivity (r_1) of [Gd(DOTA-FPG)(H_2O)] is slightly higher than those of [Gd(DOTA)(H_2O)]$^-$, [Gd(HP-DO3A)(H_2O)], and [Gd(DTPA)(H_2O)]$^{2-}$. It is quite clear that introducing 2-difluoromethylphenyl-β-galactopyranoside into DOTA increases the relaxivity value. The relaxivity of [Gd(DOTA-FPG)(H_2O)]/β-gal is slightly lower than that of [Gd(DOTA-FPG)(H_2O)] because of the β-galactopyranoside residue removed from [Gd(DOTA-FPG)(H_2O)] by β-galactosidase. The relaxivity of [Gd(DOTA-FP)(H_2O)]/β-gal + HSA (15.5 ± 0.2 mM^{-1} s^{-1}) is about 4-fold higher than that of [Gd(DOTA-FPG)(H_2O)]. This is due to cleavage of [Gd(DOTA-FPG)(H_2O)] by β-galactosidase and subsequent conjugation to proteins to form the macromolecules [Gd(DOTA-FP)(H_2O)]-β-gal and [Gd(DOTA-FP)(H_2O)]-HSA.

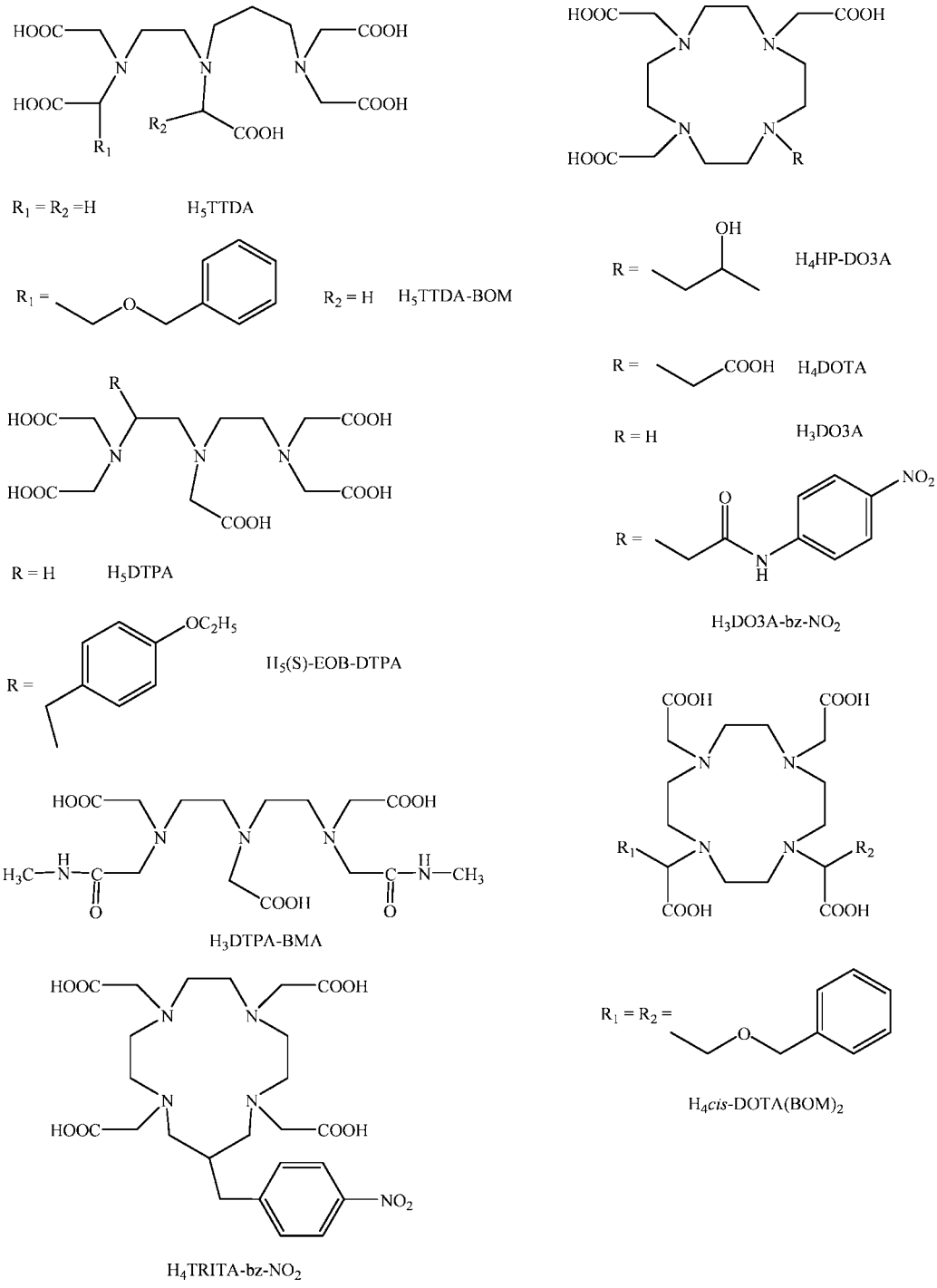
The presence of proteins, small molecules, or ions in Gd(III) chelate solution can affect the relaxivity of the Gd(III) complex. Relaxivity (r_1) measurements obtained in solutions of varying species not only describe how the Gd(III) complex responds to that composition but also provide coordinate information occurring at the Gd(III) center. The native lysosomal environment of β-galactosidase is acidic, with maximum activity observed between pH 4 and 5. The relaxivity values of [Gd(DOTA-FPG)(H_2O)] in two different buffer solutions were thus measured at pH = 5.0. The [Gd(DOTA-FPG)(H_2O)] chelate under 10 mM pyridine and 100 mM sodium chloride buffer solution at pH = 5.0 has a relaxivity (r_1) of 3.88 ± 0.02 mM^{-1} s^{-1}. However, for this chelate in 100 mM acetate buffer solution at pH = 5.0, the r_1 value is 3.63 ± 0.01. The slight difference between these buffer solutions may be attributed to the coordinating ability of the buffer constituents. The coordinating ability of pyridine is weaker than that of acetate buffer (*7*). The r_1 values at pH = 5.0 in different buffer solutions are only slightly lower than that of sodium phosphate buffer solution at pH = 7.4, which indicates that [Gd(DOTA-FPG)(H_2O)] is still stable in a native lysosomal environment.

In this study, the [Gd(DOTA-FPG)(H_2O)] under the sodium phosphate buffer solution in the absence or presence of β-galactosidase and HSA, the longitudinal relaxation time (T_1) change percentage was investigated under different incubation times as shown in Figure 1. The relaxation time (T_1) of [Gd(DOTA-FPG)(H_2O)] under the sodium phosphate buffer solution maintains constant T_1 values over 45 min. This result implicates that the [Gd(DOTA-FPG)(H_2O)] chelate is cleaved by β-galactosidase to form macromolecules [Gd(DOTA-FP)(H_2O)]-β-gal and [Gd(DOTA-FP)(H_2O)]-HSA in the presence of β-galactosidase and HSA. The bound relaxivity (r_1^b) (25.0 mM^{-1} s^{-1}) for the noncovalent [Gd(DOTA-FPG)(H_2O)]/HSA adduct was also obtained by the proton relaxation enhancement method (*25, 26*) and ultrafiltration studies. (*27–29*) The studies of [Gd(DOTA-FPG)(H_2O)] noncovalently bound to HSA were deposited as Supporting Information (Figures S2–S4).

Proof of the Proposed Mechanism by LC/MS. In order to mimic HSA or enzyme proteins to bind to the Gd(III) chelate, L-lysine was used to prove this proposed mechanism. The HPLC chromatograms of (a) 1.0 mM [Gd(DOTA-FPG)(H_2O)] alone, (b) 1.0 mM [Gd(DOTA-FPG)(H_2O)] in the presence of 2 μM β-galactosidase, and (c) 1.0 mM [Gd(DOTA-FPG)(H_2O)] in the presence of 2 μM β-galactosidase and excess L-lysine in pH 7.4 Tris buffer were shown in Figure 2a–c, respectively. From Figure 2a, [Gd(DOTA-FPG)(H_2O)] was detected at 19.9 min and confirmed by LC-MS (ESI$^+$): calcd *m*/*z* 861.9, found *m*/*z* 862.6 [M + H]$^+$. A peak of [Gd(DOTA-FP)(H_2O)] at 24.6 min as shown in Figure 2b was obtained when [Gd(DOTA-FPG)(H_2O)] was incubated with β-galactosidase and was proven by LC-MS (ESI$^+$): calcd *m*/*z* 679.75, found *m*/*z* 680.22 [M + H]$^+$. From Figure 2c, a peak of [Gd(DOTA-FP)(H_2O)]-L-lysine was detected at 30.2 min and confirmed by LC-MS (ESI$^+$): calcd *m*/*z* 825.94, found *m*/*z* 827.28 [M + H]$^+$. These results indicate that [Gd(DOTA-FPG)(H_2O)] can bind generally to protein in the presence of β-galactosidase and HSA.

Water-Exchange Rate and Rotational Correlation Time Studies of Gd(III) Complexes. The experimental ^{17}O NMR data for [Gd(DOTA-FPG)(H_2O)] complex in the presence and absence of β-galactosidase and HSA is deposited as Supporting Information (Tables 1S–3S); that is, the ^{17}O NMR chemical shifts ($\Delta\omega$, longitudinal ($1/T_{1r}$) and transverse ($1/T_{2r}$) relaxation rates were analyzed simultaneously (eqs 1S–9S used in Supporting Information S1). The results are plotted in Figure 3 with the corresponding curve representing the results of the best fitting of the data according to the equations. As illustrated by Table 2, there are a large number of parameters influencing the data obtained by the different techniques. The ^{17}O NMR technique has the advantage that the outer-sphere contributions

Chart 1



to the relaxation rates are negligibly small, which is a consequence of the oxygen nucleus being closer to the paramagnetic center when bound to the inner-sphere.

Cytotoxicity of Gd(III) Chelate. The cytotoxicity of [Gd(DOTA-FPG)(H_2O)] was also investigated by incubating various concentrations of [Gd(DOTA-FPG)(H_2O)] with CT-26 cells. After 72 h, cell viability was examined by the ^{3}H-thymidine incorporation into cellular DNA. Figure 4 shown that the IC_{50} value of [Gd(DOTA-FPG)(H_2O)] to CT26 cells was larger than 100 μM, demonstrating that [Gd(DOTA-FPG)(H_2O)] displayed low-cytotoxicity to CT26 cells after β-galactosidase activation.

MR Imaging Studies of Enzymatic Activation of Gd(III) Chelate. The percentage change in r_1 generated by enzymatic conversion of [Gd(DOTA-FPG)(H_2O)] can be visualized by MR images. The MR images of [Gd(DOTA-FPG)(H_2O)] solution placed in 1.5 mL (11 mm $\times$ 39 mm) microtubes in the presence and absence of β-galactosidase and HSA were shown in Figure 5 ($p < 0.05$). The signal intensity values of the MR images for these Gd(III) complex solutions were also given in Figure 5, indicating that a high signal intensity of [Gd(DOTA-FPG)(H_2O)] in the presence of β-galactosidase and HSA was obtained.

Characterization of Functional β-Galactosidase in Vitro and in Vivo. To verify the enzymatic activity of the β-galactosidase in cells, CT26 and CT26/β-gal cells were stained with X-gal and the cells examined under a microscope as shown in Figure 6. The results indicated that CT26/β-gal cells, but not the parental CT26 cells, converted X-gal to a blue color, demonstrating that β-galactosidase on the CT26/

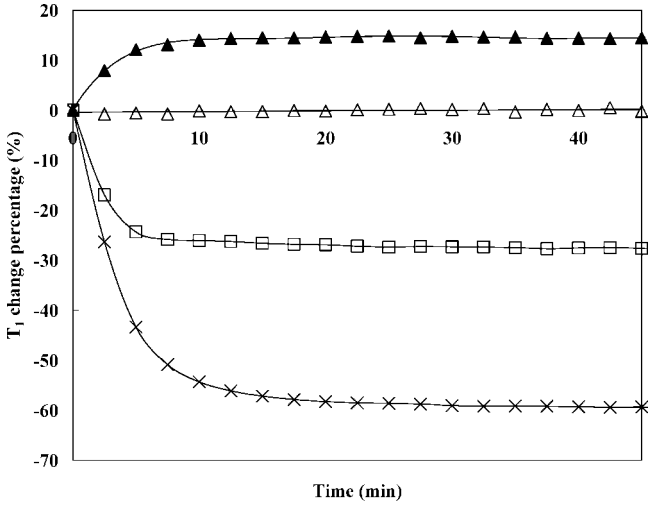


Figure 1. Change in T_1 (%) of enzyme-catalyzed hydrolysis of [Gd(DOTA-FPG)(H_2O)] measured at 20 MHz 37.0 ± 0.1 °C. (□) 0.5 mM [Gd(DOTA-FPG)(H_2O)] in 100 mM sodium phosphate buffer solution; (▲) 0.5 mM [Gd(DOTA-FPG)(H_2O)] and 2 μM β-galactosidase in 100 mM sodium phosphate buffer solution; (□) 0.5 mM [Gd(DOTA-FPG)(H_2O)] and 0.5 mM HSA in 100 mM sodium phosphate buffer solution; (□) 0.5 mM [Gd(DOTA-FPG)(H_2O)], 2 μM β-galactosidase, and 0.5 mM HSA in 100 mM sodium phosphate buffer solution.

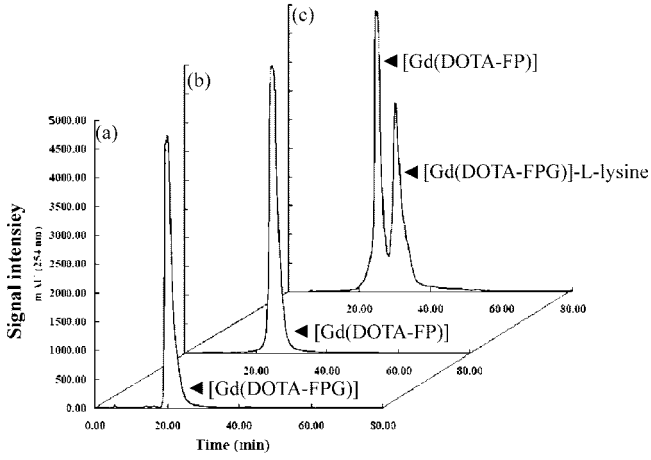


Figure 2. The HPLC chromatograms of [Gd(DOTA-FPG)] incubated with 2 μM β-galactosidase and bound to L-lysine. (a) 1.0 mM [Gd(DOTA-FPG)(H_2O)] alone, (b) 1.0 mM [Gd(DOTA-FPG)(H_2O)] in the presence of 2 μM β-galactosidase, and (c) 1.0 mM [Gd(DOTA-FPG)(H_2O)] in the presence of 2 μM β-galactosidase and excess L-lysine in pH 7.4 Tris buffer and 298 K. HPLC conditions: gradient of 100% to 0% water in CH_3OH as organic phase; flow rate 0.5 mL/min; wavelength set at 254 nm; reverse-phase C18 column used.

β-gal cells was functionally active. To investigate whether the β-galactosidase activity was still functionally active in vivo, the tumor sections were also stained with X-gal and the sections examined under a microscope as shown in Figure 7. Histological staining for β-galactosidase activity revealed a strong blue color in CT26/β-gal tumors but not in parental CT26 tumors. This result shows that β-galactosidase on the CT26/β-gal tumors was functionally active in vivo.

MR Images Studies in Vivo. To investigate whether sites of β-galactosidase expression could be noninvasively imaged, Balb/c mice bearing established CT26 and CT26/β-gal tumors in their left and right shoulder regions, respectively, were intravenously injected with 0.3 mmol/kg [Gd(DOTA-FPG)(H_2O)]. The MR images of the animal and time-signal intensity change of the tumor were shown in Figure 8, indicating that [Gd(DOTA-FPG)(H_2O)] can act as a MRI contrast agent for noninvasive imaging of gene expression in vivo.

DISCUSSION

As shown in Figure 1, the [Gd(DOTA-FPG)(H_2O)] complex is cleaved to form a smaller molecular weight [Gd(DOTA-FP)(H_2O)] under the sodium phosphate buffer solution at pH = 7.4 in the presence of β-galactosidase, and then conjugated to the β-galactosidase to form the macromolecule [Gd(DOTA-FP)(H_2O)]-β-galactosidase. However, there is only a small amount of cleaved [Gd(DOTA-FPG)(H_2O)] conjugated to β-galactosidase due to the concentration of β-galactosidase (2 μM) being significantly lower than that of [Gd(DOTA-FPG)(H_2O)] (0.5 mM). Thus, the percentage change in longitudinal relaxation time (T_1) increases about 15%. Furthermore, for the [Gd(DOTA-FPG)(H_2O)] in human serum albumin under sodium phosphate buffer solution at pH = 7.4 in the presence of β-galactosidase, the percentage change in longitudinal relaxation time (T_1) significantly decreased by about 60%. The reason is that [Gd(DOTA-FPG)(H_2O)] is cleaved to form a small molecule [Gd(DOTA-FP)(H_2O)], and then conjugated to β-galactosidase and human serum albumin to form the macromolecules [Gd(DOTA-FP)(H_2O)]-HSA and [Gd(DOTA-FP)(H_2O)]-β-galactosidase. Therefore, the relaxation time (T_1) is dramatically lower than those of the above two conditions. In comparison with the bioactivated contrast agent 4,7,10-tri(acetic acid)-1-(2-β-galactopyranosylethoxy)-1,4,7,10-tetraazacyclododecane gadolinium (Egad) (*4*) and gadolinium(III)-1-(4-(2-(1-(4,7,10-triscarboxymethyl-(1,4,7,10-tetraazacyclododecyl)))ethylcarbamoyloxymethyl)-2-nitrophenyl)-β-D-glucopyronuronate (*7*), the T_1 change percentages were 20% and 15%, respectively. Therefore, the T_1 change percentage of [Gd(DOTA-FPG)(H_2O)] is significantly higher than those of the above two bioactivated contrast agents. In addition, for the [Gd(DOTA-FPG)(H_2O)] and human serum albumin in sodium phosphate buffer solution at pH = 7.4 in the absence of β-galactosidase as a control experiment, longitudinal relaxation time is slightly decreased by about 25%, which is a result of the liphophilic [Gd(DOTA-FPG)(H_2O)] noncovalently bound to human serum albumin. The lower binding constant (K_A) (9.0 ± 0.1 × 10^2 M^{-1} and bound fraction (33.8%) of [Gd(DOTA-FPG)(H_2O)] to HSA were obtained by E and M titrations (*25, 26*) and used to explain the result of the percentage change in relaxation time (T_1) of [Gd(DOTA-FPG)(H_2O)] chelate in HSA without β-galactosidase decreasing by only 25%.

As shown in Table 2, the scalar coupling constant values of [Gd(DOTA-FPG)(H_2O)] only and [Gd(DOTA-FPG)(H_2O)] in the presence and absence of β-galactosidase and HSA, $A/\hbar$, are very similar to those obtained for other Gd(III) complexes (−3.4 × 10^6 and −3.8 × 10^6 rad s^{-1} for [Gd(DOTA)(H_2O)]$^-$ (*30*) and [Gd(DO3A-bz-NO_2)(H_2O)] (H_3DO3A-bz-NO_2 = 1-(4-nitrobenzyl)methylcarbamoyl-4,7,10-tri(acetic acid)tetraazacyclododecane) (*31*), respectively) with one inner-sphere water molecule. Over the whole temperature range, the transverse ^{17}O relaxation rates ($1/T_{2r}$) increase with increasing temperature, indicating that this system is in the slow exchange regime. However, there is degradation of the protein at temperatures higher than 50 °C for the [Gd(DOTA-FPG)(H_2O)] in the presence of β-galactosidase and [Gd(DOTA-FPG)(H_2O)] in the presence of β-galactosidase and HSA in ^{17}O NMR experiments. Therefore, the temperatures of these ^{17}O NMR experiments are in the range 278–323 K. $1/T_{2r}$ is determined by the relaxation rate of the coordinated water molecule ($1/T_{2m}$), which is influenced by the water residence lifetime ($\tau_M = 1/k_{ex}$), the longitudinal electronic relaxation rate ($1/T_{1e}$), and the scalar coupling constant ($A/\hbar$). The k_{ex}^{298} (2.54 × 10^6 s^{-1}) value of

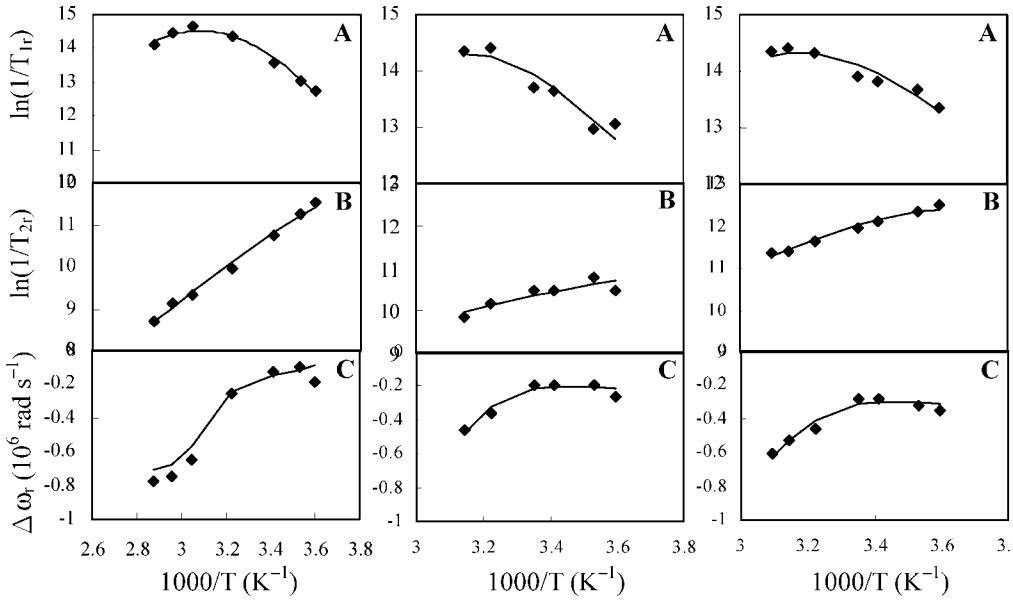


Figure 3. Temperature dependence of (A) transverse and (B) longitudinal ^{17}O relaxation rates; (C) ^{17}O chemical shifts at $B = 9.4$ T for 20 mM [Gd(DOTA-FPG)(H_2O)] under 100 mM sodium phosphate, 5.5% ^{17}O isotope (left); 20 mM [Gd(DOTA-FPG)(H_2O)] under 100 mM sodium phosphate, 2 μM β-galactosidase, 5.5% ^{17}O isotope (middle); 20 mM [Gd(DOTA-FPG)(H_2O)] under 100 mM sodium phosphate, 2 μM β-galactosidase, 4.5% (w/v) HSA, 5.5% ^{17}O isotope (right). The lines represent simultaneous least-squares fits to all data points displayed.

Table 2. Parameters Obtained from Simultaneous Fitting of ^{17}O NMR Relaxation Time and Chemical Shift Data[a]

parameter	[Gd(DOTA-FPG)(H_2O)][b]	[Gd(DOTA-FP)(H_2O)][c]	[Gd(DOTA-FP)(H_2O)]-HSA[d]	[Gd(DOTA)(H_2O)]$^-$ [e]	[Gd(TRITA-bz-NO_2)(H_2O)]$^-$ [f]	[Gd(DO3A-bz-NO_2)(H_2O)][g]	[Gd(DTPA-*N*-MA)(H_2O)]$^-$ [h]
k_{ex}^{298} (10^6 s^{-1})	2.54 ± 0.1	1.32 ± 0.8	1.64 ± 0.4	4.8 ± 0.4	120 ± 20	1.6 ± 0.1	1.3 ± 0.1
$\Delta H\ddagger$ (kJ mol^{-1})	53.4 ± 0.7	41.8 ± 1.5	31.4 ± 4.0	48.8 ± 1.6	35.5 ± 1.9	40.9 ± 2.5	48.6 ± 1.1
$\Delta S\ddagger$ (J $mol^{-1}k^{-1}$)	57.0 ± 1.4	12.6 ± 5.6	−20.6 ± 6.9	46.6 ± 6.0	21 ± 5	11.1 ± 8	35.7 ± 4
$A/\hbar$ (10^6 rad s^{-1})	−3.8 ± 0.1	−3.8 ± 0.1	−3.8 ± 0.1	−3.4 ± 0.3	−3.7 ± 0.1	−3.8 ± 0.2	−4.2 ± 0.2
τ_R^{298} (ps)	228 ± 13	188 ± 6	1068 ± 39	90 ± 15	225 ± 7	210 ± 10	143 ± 4
C_{os}	**0**	**0.23**	**0.23**	0.25 ± 0.08		0.06 ± 0.04	0.16 ± 0.03
E_R (kJ mol^{-1})	24.2 ± 3.8	15.1 ± 5.8	26.5 ± 1.2	17 ± 3	23.3 ± 1	17.7 ± 0.1	19.8 ± 0.6
method	^{17}O	^{17}O	^{17}O	^{17}O	NMRD, ^{17}O	^{17}O	^{17}O, EPR

[a] The bold values were fixed in the fitting procedure. [b] 20 mM [Gd(DOTA-FPG)(H_2O)] under 100 mM sodium phosphate buffer solution, 5.5% ^{17}O isotope. [c] 20 mM [Gd(DOTA-FPG)(H_2O)] under 100 mM sodium phosphate buffer solution, 2 μM β-galactosidase, 5.5% ^{17}O isotope. [d] 20 mM [Gd(DOTA-FPG)(H_2O)] under 100 mM sodium phosphate buffer solution, 2 μM β-galactosidase, 4.5% (w/v) HSA, 5.5% ^{17}O isotope. [e] Data obtained from ref (*30*). [f] ref (*33*). [g] ref (*31*). [h] ref. (*32*).

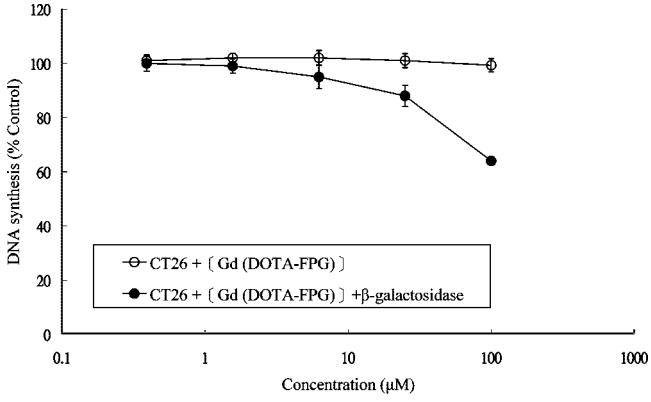


Figure 4. Cytotoxicity of [Gd(DOTA-FPG)(H_2O)] to CT26 cells. CT-26 (○) or CT-26 in the presence of β-galactosidase (•) was incubated with graded concentrations of [Gd(DOTA-FPG)(H_2O)]. Cellular DNA synthesis was measured 72 h later. Results represent the mean of results from three separate wells. Error bars show the standard error of the mean.

[Gd(DOTA-FPG)(H_2O)] is similar to those of [Gd(DOTA-FPG)(H_2O)] in the presence of β-galactosidase ([Gd(DOTA-FP)(H_2O)]) (1.32×10^6 s^{-1}) and [Gd(DOTA-FPG)(H_2O)] in the presence of β-galactosidase and HSA ([Gd(DOTA-FP)(H_2O)]-HSA) (1.64×10^6 s^{-1}) These k_{ex}^{298} values are also similar to those of the Gd(III) complexes with DO3A- and DTPA-monoamide derivatives ([Gd(DO3A-bz-NO_2)(H_2O)] (1.6×10^6 s^{-1}) (*31*) and [Gd(DTPA-*N*′-MA)(H_2O)]$^-$ (H_4DTPA-*N*′-MA = *N*-(methylcarbamoylmethyl)diethylenetriamine-*N*,*N*′,*N*-tetraacetic acid) (1.9×10^6 s^{-1}) (*32*).

As has been observed above, the water exchange rate decreases from [Gd(TRITA-bz-NO_2)(H_2O)]$^-$ (H_4TRITA-bz-NO_2 = 12-(*p*-nitrobenzyl)-1,4,7,10-tetraazacyclo-tridecane-1,4,7,10-tetraacetic acid) (120×10^6 s^{-1}) (*33*) to the [Gd(DOTA-FPG)(H_2O)] (2.54×10^6 s^{-1}) with one inner-sphere water molecule. This rate of decrease is accompanied by an increase in $\Delta H\ddagger$. Since the result for the Gd(III) complex with DOTA-FPG obeyed this trend, we conclude that water exchange on the [Gd(DOTA-FPG)(H_2O)] complex takes place most probably via a limiting dissociative D mechanism (*34*).

At 298 K, the τ_R^{298} value of [Gd(DOTA-FPG)(H_2O)] (228 ps) shown in Table 2 is significantly higher than that of [Gd(DOTA)(H_2O)]$^-$ (90 ps) (*30*) but is similar to [Gd(DO3A-bz-NO_2)(H_2O)] (210 ps) (*31*). It indicates that the introduction of the 2-difluoromethylphenyl-β-galactopyranoside in DOTA increases the τ_R^{298} value and causes the relatively high relaxivity of the [Gd(DOTA-FPG)(H_2O)] complex, compared to the previous results for [Gd(DOTA)(H_2O)]$^-$ and [Gd(HP-DO3A)(H_2O)]. A similar relationship between the τ_R^{298} value and the relaxivity (r_1) was observed in Gd(III) complexes with TTDA

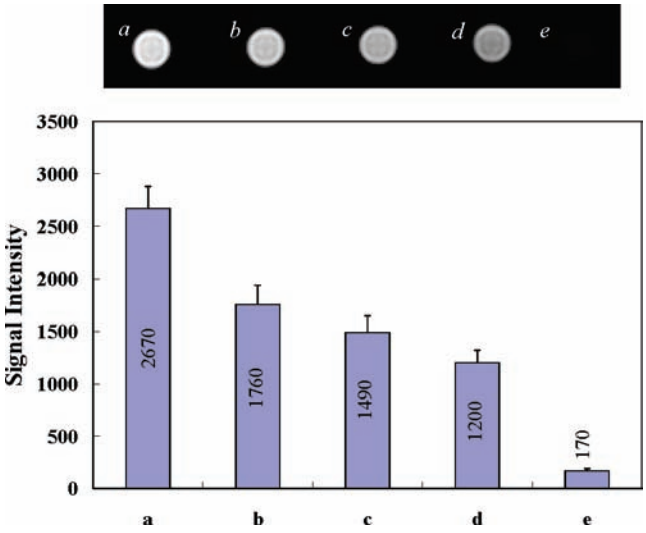


Figure 5. Representative T_1-weighted (TR/TE 100/10 ms) MR images of solutions and the signal intensity in test tubes at 1.5 T MR scanner: (a) sodium phosphate buffer solution with [Gd(DOTA-FPG)(H_2O)], β-galactosidase and HSA; (b) sodium phosphate buffer solution with [Gd(DOTA-FPG)(H_2O)] and HSA; (c) sodium phosphate buffer solution with [Gd(DOTA-FPG)(H_2O)]; (d) sodium phosphate buffer solution with [Gd(DOTA-FPG)(H_2O)] and β-galactosidase; (e) sodium phosphate buffer solution.

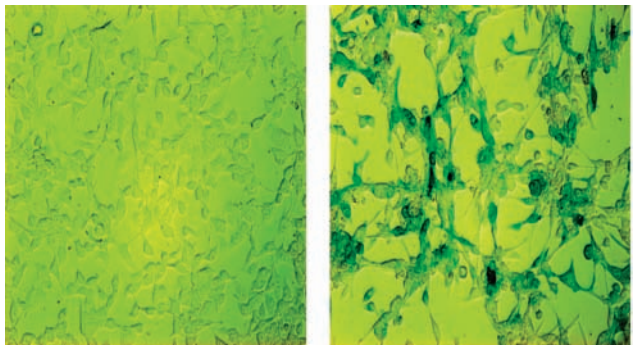


Figure 6. Cell display of functional β-galactosidase. CT26 cells (left) and CT26/β-gal cells (right) were stained with β-galactosidase activity by the β-Gal Staining Kit (1 mg/mL X-gal) before examination under an upright microscope.

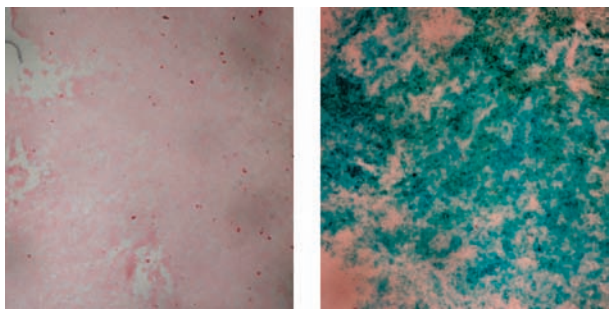


Figure 7. Histological analysis of functional β-galactosidase in vivo. Sections of CT26 (left) and CT26/β-gal (right) tumor were stained with β-galactosidase activity by the β-Gal Staining Kit and viewed under phase contrast microscope.

(H_5TTDA = 3,6,10-tri(carboxymethyl)-3,6,10-triazadodecanedioic acid) (*11*) and TTDA-BOM (H_5TTDA-BOM = 6-carboxymethyl-benzyloxymethyl-3,10-di(carboxymethyl)-3,6,10-triazadodecanedioic acid) (*12*). The attainment of high relaxivities can be expected when the molecular reorientational correlation time of the complexes is lengthened to the nanosecond range

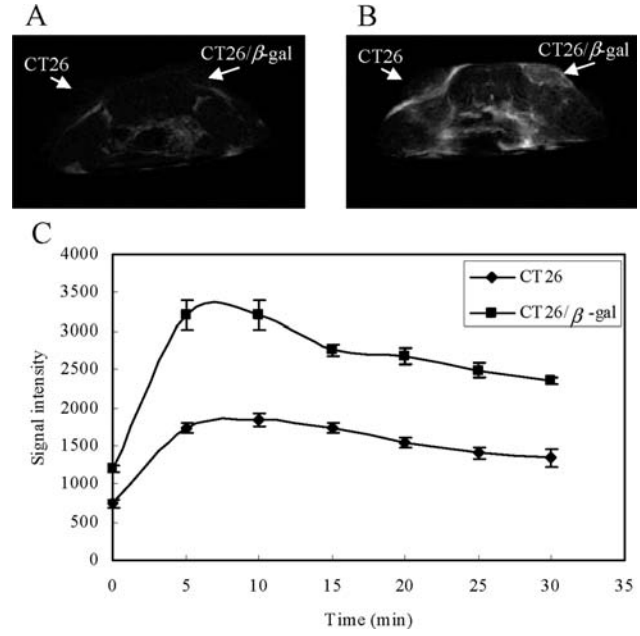


Figure 8. Representative T_1-weighted (TR/TE 100/13 ms) MR images of animal model at 3.0 T MR scanner: (A) precontrast images; (B) at 10 min after intravenous injection of 0.3 mmol/kg [Gd(DOTA-FPG)(H_2O)] intensity enhancement of CT26/β-gal tumor; (C) time-signal intensity change of the CT26 and CT26/β-gal tumors after injection of 0.3 mmol/kg [Gd(DOTA-FPG)(H_2O)].

(*25*). At 298 K, the τ_R^{298} value of [Gd(DOTA-FPG)(H_2O)] is higher than that of [Gd(DOTA-FPG)(H_2O)] in the presence of β-galactosidase, but is significantly lower than that of [Gd-(DOTA-FPG)(H_2O)] in the presence of β-galactosidase and HSA. These results can be employed to explain the percentage change in T_1 values of Gd(III) chelate increasing by 15% in the presence of β-galactosidase and decreasing by 60% in the presence of β-galactosidase and HSA.

The signal intensity of [Gd(DOTA-FPG)(H_2O)] only in 100 mM sodium phosphate buffer solution (1490 $\pm$ 160) is higher than that of [Gd(DOTA-FPG)(H_2O)] in the presence of β-galactosidase enzyme (1200 $\pm$ 120) (Figure 5) attributed to the molecular reorientational correlation time (τ_R^{298}) decreasing after the galactopyranoside residue was removed as shown in Table 2. The nucleophile of β-galactosidase attacks the Gd(III) chelate after the galactopyranoside residue is removed; however, the concentration of β-galactosidase is significantly lower than that of the Gd(III) complex. In addition, the signal intensity of [Gd(DOTA-FPG)(H_2O)] in the presence of β-galactosidase and HSA (2670 $\pm$ 210) is significantly higher than that of [Gd-(DOTA-FPG)(H_2O)] in the sodium phosphate buffer solution. The nucleophile of the higher molecular weight HSA (66.5 kDa) mainly attacks the Gd(III) chelate and the high relaxivity of the Gd(III) chelate conjugate is obtained. The T_1-mediated enhancement of [Gd(DOTA-FPG)(H_2O)] was altered by the action of β-galactosidase yielding the expected high signal intensity for MR imaging. These results are in agreement with the previous percentage change in relaxation time (T_1) decreasing by 60%. The [Gd(DOTA-FPG)(H_2O)] complex under the sodium phosphate buffer solution in the presence of HSA was conducted as a control experiment. The signal intensity of its MR imaging is slightly higher than that of [Gd(DOTA-FPG)(H_2O)] in sodium phosphate buffer solution but is significantly lower than that of [Gd(DOTA-FPG)(H_2O)] in the presence of HSA and β-galactosidase. Therefore, the expected high signal intensity of [Gd(DOTA-FPG)(H_2O)] in the presence of β-galactosidase and HSA obtained is attributed to HSA and β-galactosidase conjugated to Gd(III) chelate.

The signal intensity of the CT26/β-gal tumor (3210 ± 190) is significantly higher than CT26 tumor (1830 ± 80) ($p < 0.05$) at 10 min (Figure 8). This intense enhancement clearly indicates that [Gd(DOTA-FPG)(H_2O)] can be activated by CT26/β-gal tumors. These results are consistent with the previous percentage change in T_1 significantly decreasing in the presence of β-galactosidase and HSA. The main reason is attributed to its higher rotational correlation time (τ_R^{298}) of [Gd(DOTA-FP)(H_2O)]-HSA after the galactopyranoside residue is removed and conjugated to protein. Therefore, [Gd(DOTA-FPG)(H_2O)] may be a potential MRI contrast agent for imaging gene expression.

In conclusion, a novel bioactivated magnetic resonance imaging contrast agent containing galactopyranoside residue, [Gd(DOTA-FPG)(H_2O)], was designed and synthesized. The percentage change in longitudinal relaxation time (T_1) decreased to 60% of enzymatic cleavage of [Gd(DOTA-FPG)(H_2O)] in the presence of β-galactosidase and HSA. This indicates that the HSA and β-galactosidase conjugate to the Gd(III) chelate after the galactopyranoside residue is removed. A significant signal intensity enhanced by MR images was also observed for [Gd(DOTA-FPG)(H_2O)] solution in the presence of β-galactosidase and HSA. Moreover, the signal intensities of tumors with β-galactosidase gene expression are significantly higher than those of tumors without β-galactosidase gene expression in vivo. Therefore, [Gd(DOTA-FPG)(H_2O)] possesses enzymatic cleavage and a longer rotational correlation time, as well as higher percentage change in relaxation time (T_1) and higher signal intensity of the MR image in the presence of β-galactosidase and protein. This might result in a new type of contrast agent to trace gene expression by MRI.

ACKNOWLEDGMENT

We are grateful to the National Science Council of the Republic of China for financial support under Contract Nos. NSC 95-2627-M-037-001 and NSC 95-2623-7-037-001-NU. This research was also supported in part by grants from National Health Research Institutes under Contract No. NHRI-EX-95-9424EI.

Supporting Information Available: Additional experimental data and spectra as outlined in the text. This material is available free of charge via the Internet at http://pubs.acs.org.

LITERATURE CITED

(1) Bogdanov, A. J., Matuszewski, L., Bremer, C., Petrovsky, A., and Weissleder, R. (2002) Oligomerization of paramagnetic substrates result in signal amplification and can be used for MR imaging of molecular targets. *Mol. Imaging 1*, 16–23.

(2) Brasch, R. C., Li, K. C., and Husband, J. E. (2000) In vivo monitoring of tumor angiogenesis with MR imaging. *Acad. Radiol. 7*, 812–823.

(3) Bremer, C., Mustafa, M., Bogdanov, A. J., Vasilis, N., Alexander, P., and Weissleder, R. (2003) Steady-state blood volume measurements in experimental tumors with different angiogenic burdens-a study in mice. *Radiology 226*, 214–220.

(4) Moat, R. A., Fraser, S. E., and Meade, T. J. (1997) A "smart" magnetic resonance imaging agent that reports on specific enzymatic activity. *Angew. Chem., Int. Ed. Engl. 36*, 729–728.

(5) Querol, M., Chen, J. W., Weissleder, R., and Bogdanov, A. J. (2005) DTPA-bisamide-based MR sensor agents for peroxidase imaging. *Org. Lett. 7*, 1719–1722.

(6) Louie, A. Y., Huber, M. M., and Ahrens, E. T. (2000) In vivo visualization of gene expression using magnetic resonance imaging. *Nat. Biotechnol. 18*, 321–325.

(7) Duimstra, J. A., Femia, F. J., and Meade, T. J. (2005) A gadolinium chelate for detection of b-glucuronidase: a self-immolative approach. *J. Am. Chem. Soc. 127*, 12847–12855.

(8) Alauddin, M. M., Louie, A. Y., Shahinian, A., Meade, T. J., and Conti, P. S. (2003) Receptor mediated uptake of a radiolabeled contrast agent sensitive to b-galactosidase activity. *Nucl. Med. Biol. 30*, 261–265.

(9) Wang, Y. M., Lee, C. H., Liu, G. C., and Sheu, R. S. (1998) Synthesis and complexation of Gd^{3+}, Ca^{2+}, Cu^{2+} and Zn^{2+} by 3,6,10-tri(carboxymethyl)-3,6,10-triazadodecanedioic acid. *J. Chem. Soc., Dalton Trans.* 4113–4118.

(10) Cheng, T. H., Lee, T. M., Ou, M. H., Li, C. R., Liu, G. C., and Wang, Y. M. (2002) Thermodynamic stability and physicochemical characterization of ligand (4S)-4-benzyl-3,6,10-tris(carboxymethyl)-3,6,10-triazadodecanedioic acid (H5[(S)-4-Bz-ttda]) and its complexes formed with lanthanides, calcium(II), zinc(II), and copper(II) ions. *Helv. Chim. Acta 85*, 1033–1050.

(11) Wang, Y. M., Li, C. R., Huang, Y. C., Ou, M. H., and Liu, G. C. (2005) Synthesis and characterization of the novel monoamide derivatives of Gd-TTDA. *Inorg. Chem. 44*, 382–392.

(12) Ou, M. H., Tu, C. H., Tsai, S. C., Lu, W. K., Lee, W. T., Liu, G. C., and Wang, Y. M. (2006) Synthesis and physicochemical characterization of two gadolinium(III) TTDA-like complexes and their interaction with human serum albumin. *Inorg. Chem. 45*, 244–254.

(13) Janda, K. D., Lo, L. C., Lo, C. H. L., Sim, M. M., Wang, R., Wong, C. H., and Lerner, R. A. (1997) Chemical selection for catalysis in combinatorial antibody libraries. *Science 275*, 945–948.

(14) Gai, H. Z., and Kaden, T. A. (1994) Metal complexes with macrocyclic ligands. Part XXXVI. Thermodynamic and kinetic studies of bivalent and trivalent metal ions with 1,4,7,10-tetraazacyclododecane-1,4,7-triacetic acid. *Helv. Chim. Acta 77*, 383–398.

(15) Kumar, K., Chang, C. A., and Tweedle, M. F. (1993) Equilibrium and kinetic studies of lanthanide complexes of macrocyclic polyamino carboxylates. *Inorg. Chem. 32*, 587–593.

(16) Beeby, A., Clarkson, I. M., Dickins, R. S., Faulkner, S., Parker, D., Royle, L., Sousa, A. S. d., Williams, J. A. G., and Woods, M. (1999) Non-radiative deactivation of the excited states of europium, terbium and ytterbium complexes by proximate energy-matched OH, NH and CH oscillators: an improved luminescence method for establishing solution hydration states. *J. Chem. Soc., Perkin Trans. 2*, 493–504.

(17) Horrocks, W. D., Jr., and Sudnick, D. R. (1979) Lanthanide ion probes of structure in biology. Laser-induced luminescence decay constants provide a direct measure of the number of metal-coordinated water molecules. *J. Am. Chem. Soc. 101*, 334–340.

(18) Horrocks, W. D., Jr., and Sudnick, D. R. (1981) Lanthanide ion luminescence probes of the structure of biological macromolecules. *Acc. Chem. Res. 14*, 384–392.

(19) Hwang, L. P., and Freed, J. H. (1975) Dynamic effects of pair correlation functions on spin relaxation by translational diffusion in liquids. *J. Chem. Phys. 63*, 4017–4025.

(20) Luz, Z., and Meiboom, S. (1964) Nuclear magnetic resonance study of the solvation of Co^{2+} in methanol and methanol-water mixtures. *J. Chem. Phys. 40*, 1058–1066.

(21) Swift, T. J., and Connick, R. E. (1962) NMR-relaxation mechanisms of O^{17} in aqueous solutions of paramagnetic cations and the lifetime of water molecules in the first coordination sphere. *J. Chem. Phys. 37*, 307–320.

(22) Aime, S., Anelli, P. L., Botta, M., Fedeli, F., Grandi, M., Paoli, P., and Uggeri, F. (1992) Synthesis, characterization, and $1/T_1$ NMRD profiles of gadolinium(III) complexes of monoamide derivatives of DOTA-like ligands. X-ray structure of the 10-[2-[[2-hydroxy-1-(hydroxymethyl)ethyl]amino]-1-[(phenylmethoxy)methyl]-2-oxoethyl]-1,4,7,10-tetraazacyclododecane-1,4,7-triacetic acid-gadolinium(III) complex. *Inorg. Chem 31*, 2422–2428.

(23) Zhang, X., Chang, C. A., Brittain, H. G., Garrison, J. M., Telser, J., and Tweedle, M. F. (1992) pH Dependence of relaxivities and hydration numbers of gadolinium(III) complexes of macrocyclic amino carboxylates. *Inorg. Chem. 31*, 5597–5600.

(24) Weinmann, H. J., Brasch, R. C., Press, W. R., and Wesbey, G. E. (1984) Characteristics of gadolinium-DTPA complex: a potential NMR contrast agent. *Am. J. Roentgenol. 142*, 619–624.

(25) Aime, S., Botta, M., Fasano, M., and Terreno, E. (1998) Lanthanide(III) chelates for NMR biomedical applications. *Chem. Soc. Rev. 27*, 19–29.

(26) Aime, S., Botta, M., Fasano, M., Crich, S. G., and Terreno, E. (1996) Gd(III) complexes as contrast agents for magnetic resonance imaging: a proton relaxation enhancement study of the interaction with human serum albumin. *J. Biol. Inorg. Chem. 1*, 312–319.

(27) Caravan, P., Cloutier, N. J., Greenfield, M. T., McDermid, S. A., Dunham, S. U., Bulte, T. W. M., Jr., Looby, R. J., Supkowski, R. M., Jr, and Lauffer, R. B. (2002) The interaction of MS-325 with human serum albumin and its effect on proton relaxation rates. *J. Am. Chem. Soc. 124*, 3152–3162.

(28) Caravan, P., Greenfield, M. T., Li, X., and Sherry, A. D. (2001) The Gd^{3+} complex of a fatty acid analogue of DOTP binds to multiple albumin sites with variable water relaxivities. *Inorg. Chem. 40*, 6580–6587.

(29) Klotz, I. M. (1987) *Ligand Receptor Energetics-A Guide for the Perplexed*, John Wiley & Sons, New York.

(30) Micskei, K., Helm, L., Brucher, E., and Merbach, A. E. (1993) ^{17}O NMR study of water exchange on $[Gd(DTPA)(H_2O)]^{2-}$ and $[Gd(DOTA)(H_2O)]^{-}$ related to NMR imaging. *Inorg. Chem. 32*, 3844–3850.

(31) Toth, E., Pubanz, D., Vauthey, S., Helm, L., and Merbach, A. E. (1996) The role of water exchange in attaining maximum relaxivities for dendrimeric MRI contrast agents. *Chem. Eur. J. 2*, 1607–1615.

(32) Toth, E., Burai, L., Brucher, E., and Merbach, A. E. (1997) Tuning water-exchange rates on (carboxymethyl)iminobis-(ethylenenitrilo)tetraacetate (dtpa)-type gadolinium(III) complexes. *J. Chem. Soc., Dalton Trans.* 1587–1594.

(33) Ruloff, R., Toth, E., Scopelliti, R., Tripier, R., Handelb, H., and Merbach, A. E. (2002) Accelerating water exchange for GdIII chelates by steric compression around the water binding site. *Chem. Commun. 9*, 2630–2631.

(34) Aime, S., Barge, A., Borel, A., Botta, M., Chemerisov, S., Merbach, A. E., Muller, U., and Pubanz, D. (1997) A multinuclear NMR study on the structure and dynamics of lanthanide(III) complexes of the poly(amino carboxylate) $EGTA^{4-}$ in aqueous solution. *Inorg. Chem. 36*, 5104–5112.

(35) Nivorozhkin, A. L., Kolodziej, A. F., Caravan, P., Greenfield, M. T., Lauffer, R. B., and McMurry, T. J. (2001) *Angew. Chem., Int. Ed. 15*, 2903.

(36) Bruce, J. I., Dickins, R. S., Govenlock, L. J., Gunnlaugsson, T., Lopinski, S., Lowe, M. P., Parker, D., Peacock, R. D., Perry, J. J. B., Aime, S., and Botta, M. (2000) The selectivity of reversible oxy-anion binding in aqueous solution at a chiral europium and terbium center: signaling of carbonate chelation by changes in the form and circular polarization of luminescence emission. *J. Am. Chem. Soc. 122*, 9674–9684.

BC070019S

Solid-Phase PEGylation of Recombinant Interferon α-2a for Site-Specific Modification: Process Performance, Characterization, and *in Vitro* Bioactivity

Byung Kook Lee,[†] Jin Sook Kwon,[†] Hyung Jin Kim,[†] Shuichi Yamamoto,[‡] and E. K. Lee*,[†]

Bioprocessing Research Laboratory, Department of Chemical Engineering, Hanyang University, Ansan, Korea 426-791, and Department of Chemical Engineering, Yamaguchi University, Tokiwadai, Ube 755-8611, Japan. Received August 7, 2006; Revised Manuscript Received August 1, 2007

'Solid-phase' PEGylation, in which a conjugation reaction attaches proteins to a solid matrix, has distinct advantages over the conventional, solution-phase process. We report a case study in which recombinant interferon (rhIFN) α-2a was adsorbed to a cation-exchange resin and PEGylated at the N-terminus by 5, 10, and 20 kDa mPEG aldehydes through reductive alkylation. After PEGylation, a salt gradient elution efficiently purified the mono-PEGylate of unwanted species such as unmodified IFN and unreacted PEG. Mono-PEGylation and purification were integrated into a single, chromatographic step. Depending on the molecular weight of the mPEG aldehyde, the mono-PEGylation yield ranged from 50 to 65%. Major problems associated with the solution-phase process such as random or uncontrollable multi-PEGylation and post-PEGylation purification difficulties were overcome. N-terminus sequencing and MALDI-TOF mass spectrophometry confirmed that the PEG molecule was conjugated only to the N-terminus. A cell proliferation study indicated reduced antiviral activity of the mono-PEGylate compared to that of the unmodified IFN. As higher molecular weight PEG was conjugated, *in vitro* bioactivity and antibody binding activity, as measured by a surface plasmon resonance biosensor, decreased. Nevertheless, trypsin resistance and thermal stability were considerably improved .

INTRODUCITON

Recombinant interferon (rh-INF) α-2a was developed as an antiviral immunostimulator and is clinically used for the treatment of chronic hepatitis B and C as well as cancers, such as Kaposi's sarcoma and hairy-cell leukemia (*1*). Several disadvantages of parenteral administration include frequent injections, that is, 3 times a week, because of a short lifetime in blood circulation (*2–4*), high immunogenicity causing fever, vomiting, and so forth (*5, 6*), and poor solution stability causing a significant drop in *in vitro* bioactivity (*7–9*). To overcome these drawbacks, the cytokine surface is chemically modified by conjugation with a water-soluble synthetic polymer, poly-(ethylene glycol) (PEG). The improvements in half-life by PEGylation are well documented (*10, 11*) and PEGylated interferon-α is currently on the market (e.g., PEGASYS, PEG-Intron[c]).

PEGylation is a reaction between a functional group of an activated PEG molecule and specific amino acid residues, such as lysine, on a protein surface. Frequently, PEGylation results in nonsite-specificity and multiple attachments, which might mask or interfere with the receptor binding sites, causing a dramatic decrease in *in vitro* bioactivity (*12–14*). To solve this problem, site-specific PEGylation has been employed. Specifically, reductive alkylation of the N-terminus amine was achieved by conjugating a methoxy PEG (mPEG) molecule under acidic conditions (*15–17*) and was reported to maintain bioactivity (*18*). However, the current practice of reductive alkylation occurs in the solution phase, and three to four purification steps are required to remove undesired species, such as the reducing agent, unreacted PEG, and multi-PEGylates (*19*).

In this study, we propose solid-phase PEGylation for the modification of interferon α-2a. Monkarsh et al. used CM-52 cellulose resin for the solid-phase PEGylation of interferon α-2a to generate various positional isomers of interferon α-2a mono-PEGylates (*20*). PEGylation with pyridyl PEG was performed at a high pH, and site-specificity was not achieved. In our study, the protein is first adsorbed to the surface of an ion exchange matrix through electrostatic interactions. mPEG aldehyde with different molecular weights (MW 5, 10, and 20 kDa) were introduced at an acidic pH to a reducing agent. The mPEG reacts primarily with the α-amine at the N-terminus for reductive alkylation. The process is called solid-phase PEGylation because the protein is PEGylated while attached to a solid phase, and only the desired PEGylate can be eluted from the matrix with the proper technique. This process reproducibly yielded N-terminus mono-PEGylate (*21, 22*). Various characterization methods, such as Edman degradation, trypsin-digested peptide mapping, and MALDI-TOF, were used to confirm mono-PEGylation. Two-dimensional (2-D) electrophoresis was performed to investigate the changes in molecular weight and the isoelectric point of the mono-PEGylate. Cationic exchange chromatography was used to reveal the separation behavior of the unmodified and mono-PEGylated proteins. Gel permeation chromatography (GPC) was used to recover the mono-PEGylate in a purified form. Antiviral activities were evaluated by cell proliferation, and immunoreactivity was assessed by antibody binding activity using a surface plasmon resonance biosensor. In addition, antitrypsin and thermal stability were evaluated.

MATERIALS AND METHODS

Materials. Purified rhIFN-α-2a was a gift from Korean GreenCross Corp. (YongIn, Korea). mPEG aldehydes of 5, 10, and 20 kDa (nominal MW) were purchased from Sun Bio, Inc. (Anyang, Korea). Sodium cyanoborohydride ($NaBH_3CN$) and other buffers of reagent grade were purchased from Sigma (St.

* Corresponding author. Phone: +82 31 400 5275. Fax: +82 31 408 3779. E-mail: eklee@hanyang.ac.kr.
[†] Hanyang University.
[‡] Yamaguchi University.

10.1021/bc060245m CCC: $37.00 © 2007 American Chemical Society
Published on Web 10/18/2007

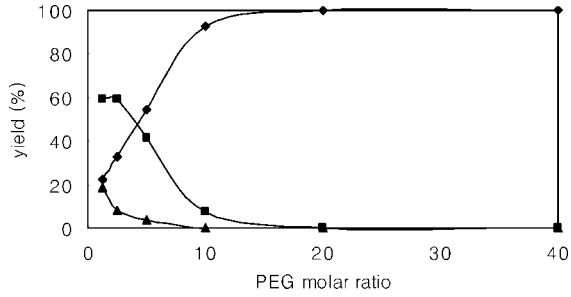


Figure 1. Solution phase PEGylation yield of multi-PEGylated (♦), mono-PEGylated (■), and unPEGylated IFN (▲) in 20 mM $NaBH_3CN$.

Louis, MO, U.S.A.) The chromatographic resins, CM-Sepharose and SP-Sepharose, for the solid-phase PEGylation, were purchased from Amersham Biosciences (Uppsala, Sweden). Bradford dyes and SDS–PAGE chemicals were from Bio-Rad, Inc. (Hercules, CA, U.S.A.) Superose 12HR 10/30 (Amersham Biosciences, Uppsala, Sweden) was used for GPC. Ettan IPGphor IEF system (Amersham Biosciences, Uppsala, Sweden) was used for 2-D electrophoresis.

Solution-Phase PEGylation of rhIFN-α-2a with mPEG Aldehydes. Solution-phase PEGylation of rhIFN-α-2a with 5 kDa mPEG-aldehyde was performed for 2 h at room temperature with 0.1 M sodium phosphate buffer (SPB, pH 4.0) in the presence of 20 mM $NaBH_3CN$. The PEG-to-protein molar ratio was 1.25, 2.5, 5, 10, and 20.

Solid-Phase PEGylation of rhIFN-α-2a with mPEG Aldehydes. The basic process was as follows: One milliliter of a 2 mg/mL solution of rhIFN-α-2a in 50 mM acetate buffer (pH 4.0) was fed at 1 mL/min through a CM-Sepharose Hi-Trap column (1 mL bed volume). The column was pre-equilibrated with 0.1 M SPB at pH 4.0. Unadsorbed IFN was removed with 6 mL of SPB at 1 mL/min. Fifteen milliliters of the mPEG aldehyde solution containing 20 times the IFN molar ratio and 25 mM $NaBH_3CN$ was circulated at 0.01 mL/min for 120 min. Ten milliliters of equilibrium buffer (0.1 M SPB, pH 4.0) was circulated to wash the unreacted mPEG. The PEGylate was eluted by applying a linear salt gradient from 0.1 M to 0.6 M of 1 M NaCl SPB from 5 to 40 min at a rate of 0.5 mL/min.

To calculate the PEGylation yield, the mono-PEGylate was collected from the appropriate fractions of the cation exchange and GPC. The protein content of the mono-PEGylate was analyzed by a Bradford assay.

The eluate mixture was further purified using a GPC column (approximately 23.6 mL bed volume). After 1 mL sample loading, the column was eluted with 0.1 M SPB (pH 4.0) at 0.4 mL/min.

2-D Electrophoresis. To measure the pI values of the PEGylate, 2-D electrophoresis was performed using an Ettan IPGphor (Amersham Biosciences, Uppsala, Sweden). Each sample was prepared to a protein concentration of 15–20 μg/mL, dialyzed to reduce the salt concentration below 10 mM, and freeze-dried. The protein was rehydrated in a buffer (8 M urea, 2% (w/w) CHAPS, 0.002% (w/v) bromophenol blue, and 50 mM dithiothreitol) at 20 °C for 12 h before feeding it to a 2-D electrophoresis strip (pH 3–10). For primary electrophoresis, a total of 32,000 V/h was applied. The 2-D electrophoresis strip was added to an equilibration buffer (50 mM tris-HCl, 6 M urea, 30% (v/v) glycerol, 2% (w/v) SDS, and 0.002% (w/v) bromophenol blue at pH 8.8) and equilibrated for 30 min before secondary electrophoresis. The gel was silver stained.

Analysis of N-Terminal Mono-PEGylation. The degree and site of PEGylation of the recovered fraction of mono-PEGylate from cation exchange and GPC were analyzed. First, the mass increase due to PEGylation was checked by mass analysis using a MALDI-TOF mass spectrometer. The samples were desalted with Poros R2 resins (Applied Biosystems, CA, U.S.A.) using a narrow GELoader tip (Eppendorf, Germany). One microliter of the PEGylate solution was mixed with 1 μL of the matrix solution (sinapinic acid saturated in 0.1% TFA/acetonitrile, 7:3). One microliter of the mixture was deposited on a MALDI target plate. Mass spectra of positively charged ions were recorded on a Bruker Ultraflex instrument (Bruker Daltonik, Germany) operated in linear mode, with a 337 nm nitrogen laser, 39 ns pulse duration, and 25 kV acceleration voltage (*18*).

The native and mono-PEGylate were exposed to tryptic digestion, and the peptide fragment containing the N-terminus (1313.6 Da) was identified from the database and the mass spectra of the native IFN digestion. Edman degradation was performed on the PEGylate to confirm that the modified N-terminus did not have a terminal amino acid, as the covalently modified amine was known to resist peptide cleavage by 1-fluoro-2,4-dinitrobenzene (FDNB).

Purity Analysis by RP-HPLC. A C4 RP-HPLC column (Phenomenox, Torrance, CA, U.S.A.) was used to separate the PEGylate from the unmodified protein and assess the purity. The equilibrium buffer was 0.1% trifluoracetic acid (TFA) in deionized water, and the elution buffer was 0.1% TFA in 80% acetonitrile. Twenty microliters of the sample was injected into the column, after which the equilibration buffer was circulated for 10 min at 1 mL/min. For elution, a mixture of the equilibrium buffer and the elution buffer was fed by applying a gradient from 0% to 100% of the elution buffer.

Far-UV Circular Dichloism Analysis. A spectropolarimeter (Model J-715, Jasco, Japan) was used to determine if the secondary protein structures were disrupted by the PEGylation reaction. The spectrum and excitation wavelength were 190–250 nm and 200–230 nm, respectively, and the path length was 0.5 mm.

Bioassays for Antiviral Activity and Immunoreactivity. Antiviral activity of the PEGylated IFN was compared to unmodified IFN by quantifying the surviving Madin–Darby bovine kidney (MDBK) cells after being infected with the vesicular stomatitis virus (VSV) (*23*, *24*). The molecules were compared by quantifying the binding activity of a monoclonal antibody (product # 21100-2, R&D Systems, Minneapolis, MN, U.S.A.) using a surface resonance plasmon (SPR) system (Biacore 3000, Biacore AB, Uppsala, Sweden) equipped with a CM5 chip. The antibody was immobilized on the chip as a ligand, and the binding with PEGylated IFN was compared to that of the control, unmodified IFN. The *in vitro* immunoassay based on the SPR technique was reported to provide reliable information on immunoreactivity (*25–27*).

Proteolytic and Thermal Stability Analysis. The in-serum stability of the IFN PEGylate was indirectly evaluated by comparing antitrypsin stability with unmodified IFN. Purified IFN PEGylate from the GPC eluate was freeze-dried. Trypsin from Promega, Inc. (Madison, WI, U.S.A.) was dissolved at 100 mg/mL in 50 mM ammonium bicarbonate buffer (pH 7.8). Freeze-dried IFN or IFN PEGylate was added to the trypsin solution at a mass ratio of 30:1 protein to trypsin. The mixture was incubated at 37 °C for 12 h. Samples were taken every 30 min, and 50 μL of 20% TFA was added to stop the trypsin reaction. The change in IFN peak height was measured. Assuming the reaction rate was a first-order reaction, the constant could be calculated and compared. Thermal stability was evaluated by monitoring the turbidity increase at 340 nm caused by thermal aggregation when the protein solution was exposed to 50 °C (*28*).

RESULTS AND DISCUSSION

Solution-Phase PEGylation. To compare with solid-phase PEGylation, solution-phase PEGylation experiments were per-

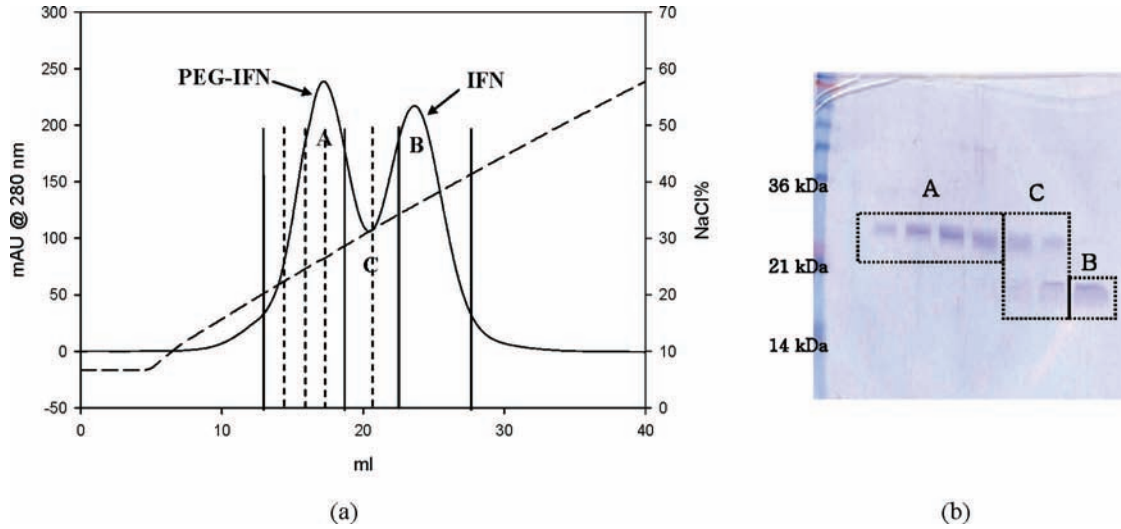


Figure 2. Elution chromatogram from CM-Sepharose. The column was eluted by feeding SPB containing 1 M NaCl at 0.5 mL/min with a salt gradient from 0.1 M to 0.6 M NaCl for 35 min.

formed at a pH of 4.0 for 2 h using 20 mM $NaBH_3BN$ as a reducing agent. The PEG-to-protein molar ratio was varied (1.25, 2.5, 5, 10, 20, and 40) to investigate its effect on the degree of PEGylation. The mono-PEGylate yield was determined by scanning PAGE with a densitometer, as shown in Figure 1. The multi-PEGylation yield increased at molar ratios higher than 10, such that nearly all of the PEGylates were multi-PEGylates. At a lower molar ratio (1.25 and 2.5), the mono-PEGylation yield was ca. 60%, and the multi-PEGylation was 20–30%. The mono-PEGylation decreased to nearly zero at a molar ratio of 20. The higher yield of multi-PEGylation and lower yield of mono-PEGylation would require more post-PEGylation purification steps. Monkarsh et al. performed solution-phase PEGylation at pH 10 at a molar ratio of 1 to obtain 11 isomers and used SP-HPLC to purify the isomers (*20*).

Solid-Phase PEGylation. The effects of resin and reaction pH on the mono-PEGylate yield were investigated with CM- and SP-Sepharose at pH 3.0, 3.5, 4.0, and 4.5. CM-Sepharose at pH 4.0 produced the highest PEGylation yield. In this condition, the effects of the PEG-to-protein molar ratio and the $NaBH_3CN$ concentration were studied by varying the molar ratio from 10, 20, 30, to 40, and the reductant concentration from 10, 20 to 40 mM. The best result was obtained at a 20:1 PEG-to-protein ratio at 20 mM $NaBH_3CN$ concentration (data not shown). As the reaction time increased, the PEGylate yield increased, and after 100 min, the reaction reached a plateau. To this end, the reaction time was set at 120 min for subsequent experiments.

Solid-Phase Mono-PEGylate and Separation Behavior. Figure 2 shows the elution profile from the CM-Sepharose column after PEGylation. Mono-PEGylated IFN predominantly eluted in the first peak (A) at 0.15–0.28 M NaCl and the unreacted, native IFN in the second peak (B) at 0.34–0.39 M NaCl. PEGylated IFN eluted earlier because of masking or shielding of the N-terminus amine group by PEGylation, resulting in the weakened interaction of the protein with the resin. Corroborating the results of Figure 2, Seely suggested the PEG-to-protein molar ratio of the PEGylates determined the elution order from an ion exchange column, regardless of cationic or anionic exchange type (*30*). Fee and Mason observed a significant change in pI after PEGylation (*32*). However, when the isoelectric points and molecular weights of the 5, 10, and 20 kDa mono-PEGylates were measured by 2-D electrophoresis, the PEGylation did not alter the pI value, only increased the molecular weights, as shown in Figure 3. The identical pI values

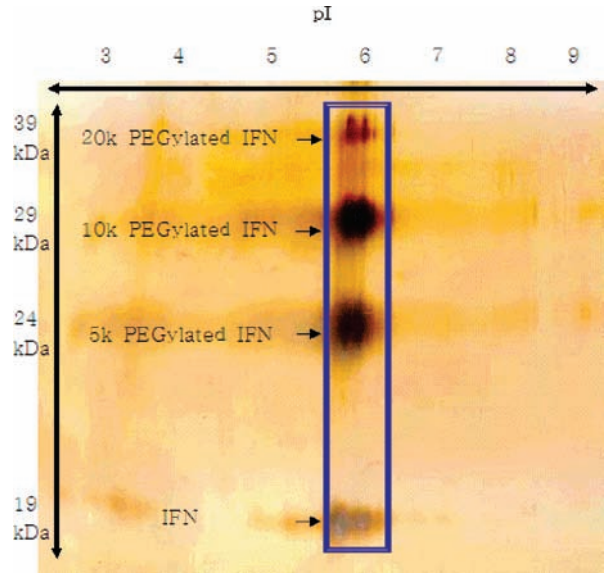


Figure 3. 2-D electrophoresis of the mono-PEGylated IFNs with 5, 10, and 20 kD mPEG aldehydes.

indicate identical electrostatic interactions with the cation exchange resin, resulting in the same column retention time. To this end, the retention time difference, shown in Figure 2, was likely due to the shielding effect by conjugated 5 kDa PEGs.

The separation between the two peaks was not definitive, requiring analysis of the overlapped fraction by GPC (Superose 12 HR). Figure 4 shows that the mono-PEGylate (with 5 kDa mPEG aldehyde) and unmodified IFN were nearly completely separated approximately 5 min apart in retention time. Furthermore, Figure 5 shows that the 10 and 20 kDa PEG PEGylates could also be well separated, suggesting that GPC could serve as a powerful separation step to recover the desired PEGylate (*33*). Figure 6 shows that the native and mono-PEGylate (with 5 kDa PEG) separated by RP-HPLC with C4 resin. The mono-PEGylate eluted after the native protein, indicating that the surface hydrophobicity increased by PEGylation. Additionally, circular dichloism analysis revealed that the secondary structure changed little by mono-PEGylation (data not shown).

Multi-PEGylation, often seen in solution-phase PEGylation, was avoided by solid-phase PEGylation for several different reasons. First, the reactivity of the lysine residues was sup-

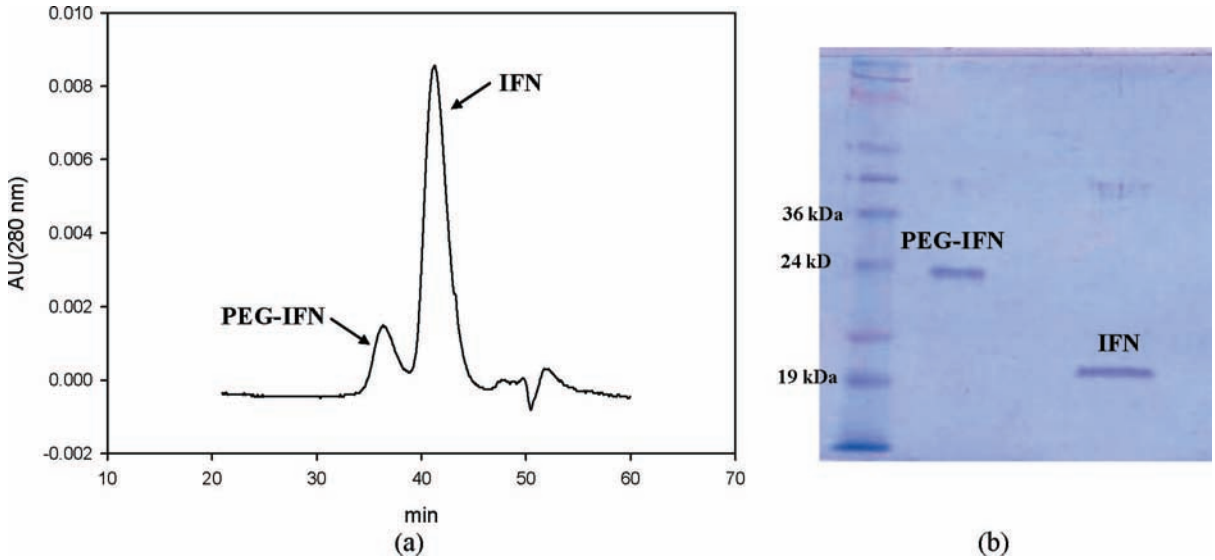


Figure 4. Resolution of the PEGylation mixture by GPC (Superose 12HR 10/30). The column was eluted isocratically by 0.1 M SPB (pH 4.0) at 0.4 mL/min.

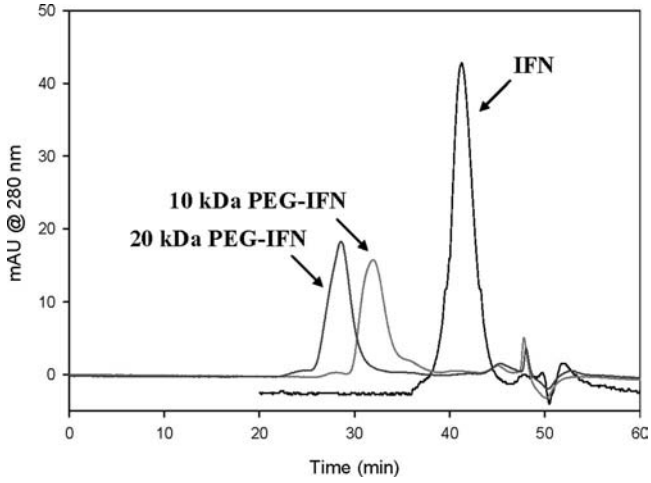


Figure 5. GPC chromatogram for the mono-PEGylates with various MW PEGs.

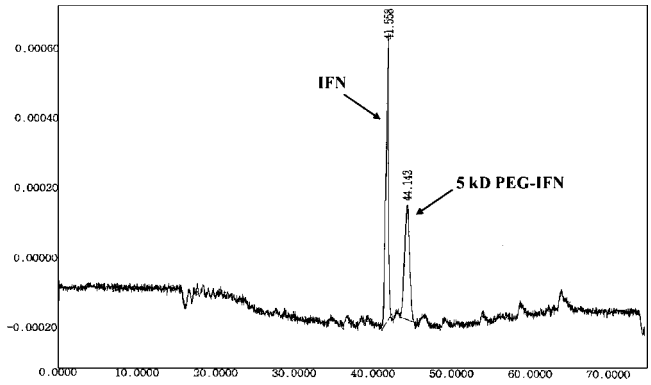


Figure 6. RP-HPLC (C4) separation of the native and mono-PEGylated IFNs.

pressed by the reductive alkylation condition (e.g., a low pH) (*12*). Second, certain lysine residues might be buried by the electrostatic interactions between the protein and the resin (*13*). Third, the frequency of protein contact with the PEG molecules was reduced because the protein was attached to a solid surface.

The reduced reactivity may be responsible for the relatively lower yield of solid-phase PEGylation. The mono-PEGylate yield in the recovered eluate was 62, 58, and 51% with 5, 10, and 20 kDa PEG, respectively (approximately 32% of the IFNs were not modified). However, Kinstler et al. achieved a 92% yield of N-terminus, mono-PEGylated rh-GCSF (granulocyte colony stimulating factor) by the solution-phase method using aldehyde PEG at an acidic pH for reductive alkylation (*17*). However, the yield with the rh-IFN (consensus) was about 66%, which was comparable to our data. Solid-phase PEGylation generated a small amount of multi-PEGylate (24%), and about 32% of the IFNs were not PEGylated.

The mono-PEGylate and the unmodified IFN could be easily separated, as shown in Figure 2, and the unmodified IFN could be recycled for an additional PEGylation to improve the yield. The geometrical interference of the CM-Sepharose resin micropores with the PEG molecules and the associated diffusional problems could be responsible for the lower yield, as witnessed by the increasing PEG molecular weight.

These results suggest that several potential advantages of solid-phase PEGylation could be realized. First, site-specific, mono-PEGylation was achieved. Second, impurity removal and isolation of the desired PEGylate was integrated into one unit operation. Third, the burden of post-PEGylation purification could be much reduced, as at least 3 to 4 purification steps were required to purify the desired PEGylate from solution-phase PEGylation (*34*).

Site Specificity of N-Terminus Mono-PEGylate. To verify the conjugation of single molecule of PEG to the N-terminus, we performed both mass spectrometry of the digests before and after PEGylation and Edman degradation of the N-terminus amino acid of the PEGylate. From the mass spectra of the PEGylate digests, we confirmed that the peptide fragment containing the N-terminus of the native digest disappeared and that a new peak emerged, reflecting the mass increase due to PEG conjugation (*29*). Figure 7 shows that the mass of the peptide fragment (1313 Da) increased by conjugated PEG molecular weight, that is, 6314 for 5 kDa of PEG, indicating that the PEG was indeed conjugated to the N-terminus. However, the MW of the PEGylated N-terminus peptide fragments showed broader peaks due to a wider PEG MW distribution than that of the nominal MW. In addition, the N-terminus sequencing by Edman degradation revealed that the N-terminus could not be degraded after four cycles (data not shown), as the covalently modified α-amine resisted peptide cleavage by FDNB because the N-terminus was conjugated by

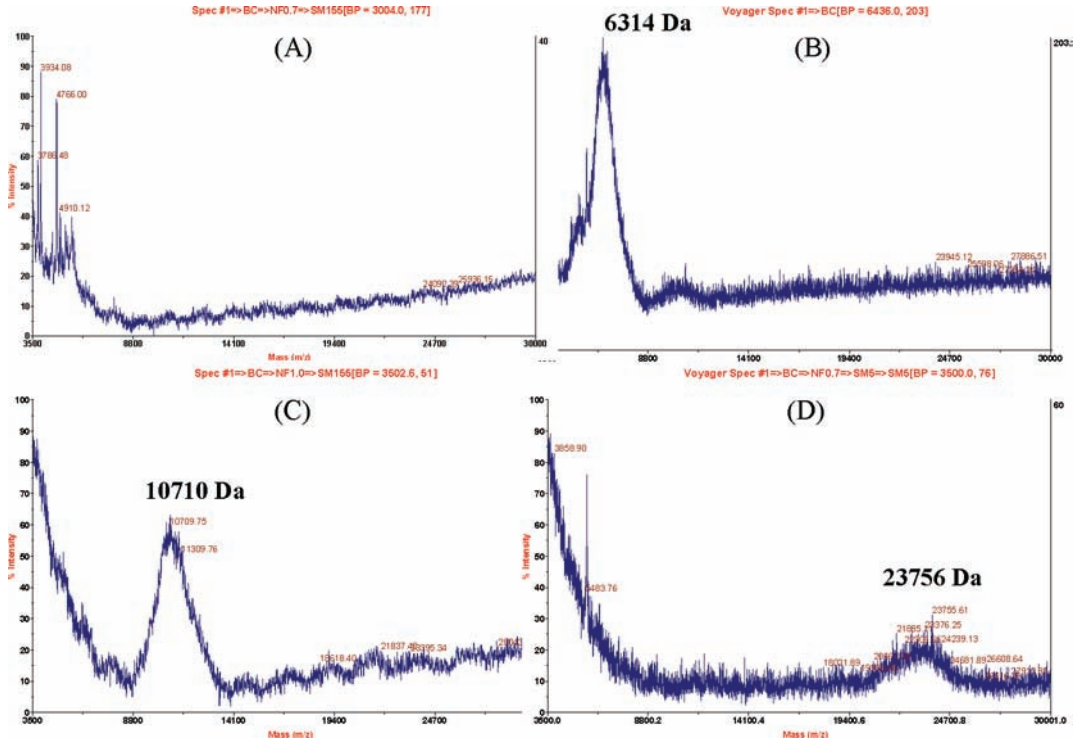


Figure 7. Mass spectra of (A) native IFN, (B) 5 kD mono-PEGylated IFN, (C) 10 kD mono-PEGylated IFN, and (D) 20 kD mono-PEGylated IFN peptide fragments containing N-termini.

Table 1. Biological Activity of IFN and PEGylated IFN

	mean biological activity (MIU/mg)	relative activity (%)	SD ($n = 5$)	CV (%)
IFN	201	100.0	19	9.5
5 kDa PEG-IFN	141	70.6	37	26
10 kDa PEG-IFN	110	55.3	38	26
20 kDa PEG-IFN	43	21.3	37	26

Table 2. Immunoreactivity of IFN and PEGylated IFN

	relative immunogenicity (%)	SD ($n = 4$)	CV (%)
IFN	100.0	1.51	0.01
5 kDa PEG-IFN	48.0	0.25	
10 kDa PEG-IFN	23.0	0.35	
20 kDa PEG-IFN	15.0	0.43	

PEG (*35*). The MS data combined with the Edman degradation results strongly indicated the attachment of a PEG molecule to the N-terminus.

When Monkarsh et al. performed solid-phase PEGylation on IFN α-2a (*20*), however, the PEGylation pH was 10, which would cause an amine coupling reaction for nonsite-specificity. As a result, Monkarsh et al. obtained 11 positional, isomeric mono-PEGylates. To obtain a single species of mono-PEGylate, multiple separation steps would be required. By using reductive alkylation at a lower pH, we were able to obtain a single species of mono-PEGylate and circumvent the multistep separation.

***In Vitro* Bioactivity Analysis of the Mono-PEGylated IFN.** It is well documented that the *in vitro* bioactivity of a protein decreases after PEGylation and decreases further as the PEG MW increases. We observed the same phenomenon with the IFN. As shown in Table 1, the antiviral activity of the mono-PEGylated IFN with 5, 10, and 20 kDa PEG was approximately 71%, 55%, and 21% of the native IFN, respectively. The significant loss of *in vitro* bioactivity could be outweighed by such pharmacokinetic benefits as improved stability (*30*).

Immunoreactivity of the PEGylates was indirectly evaluated by antibody binding activity. Table 2 shows that the immunoreactivity of the mono-PEGylated IFN with 5, 10, and 20 kDa PEG was approximately 48%, 23%, and 15% of the native IFN, respectively. Antibody binding activity corroborates the intrinsic *in vitro* bioactivity of the protein, which decreased in proportion to the MW of the conjugated PEG. It was previously reported that the monoclonal antibody epitope consists of three sites located between Leu 30 and Ile 53 (*16*, *17*). The antibody binding activity of the PEGylate could be significantly affected by the conjugation because of the location of the epitope near the N-terminus.

Stability Analysis of the Mono-PEGylated IFN. Most of the injected biopharmaceutical proteins are degraded in the blood stream from various serum proteases (*14*, *17*), and the protein stability could be significantly improved by PEGylation. In this study, we evaluated the enhanced stability of the mono-PEGylates by measuring and comparing trypsin resistance *in vitro*. Theoretically, there should be a difference in the amount of degradation between the native and mono-PEGylated IFNs because of PEG interference of the trypsin cleavage process (*17*). Assuming that the degradation follows first-order kinetics, the reaction rate constant was calculated to quantitatively assess the stability enhancement effect. Figure 8 shows the rate constant (k) decreasing from 0.82×10^{-2} min^{-1} to 0.50×10^{-2} min^{-1} upon mono-PEGylation with 5 kDa PEG. The stability could be further improved by conjugating a higher MW PEG with potentially improved stability in the blood stream (*36*).

Improvement of the mono-PEGylate thermal stability was evaluated by monitoring the aggregation decrease at 50 °C. As shown in Figure 9, the native IFN aggregated rapidly in 100 min, whereas the mono-PEGylates showed no aggregation for 240 min. The aggregation at an elevated temperature may be explained by reduced thermodynamic stability of the altered protein structures and an increased hydrophobic interaction from exposed hydrophobic patches. The conjugated PEG might swim around the hydrophobic patches to suppress hydrophobic interactions. This hydrophobic mechanism might be similar to

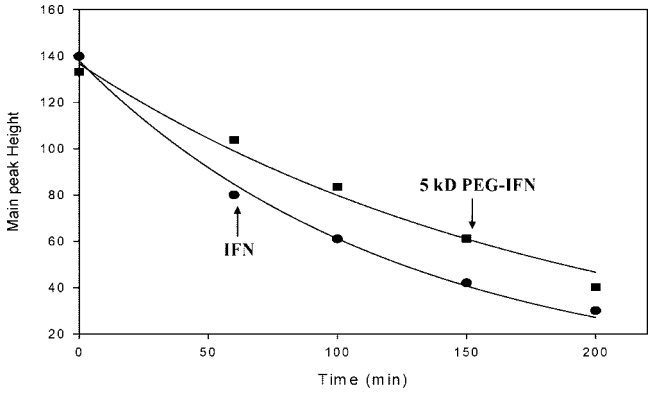


Figure 8. Time course profiles of trypsin digestion of native (●) and mono-PEGlated (■) IFNs.

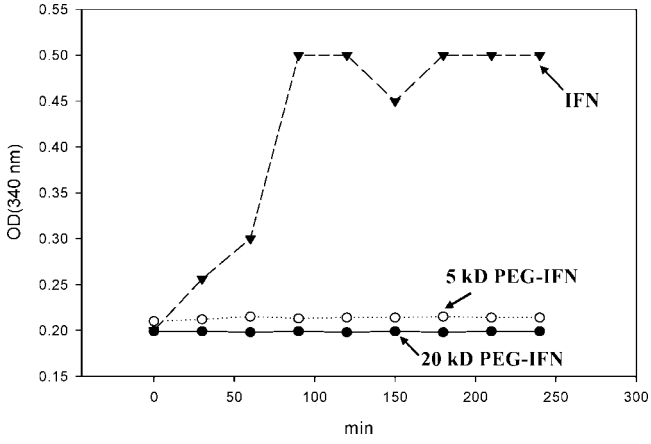


Figure 9. Thermal stability of the native (▼) and modified IFNs conjugated by 5 kD PEG (○) and 20 kD PEG (●).

hydrophobic interactions suppressing the aggregation of *in vitro* refolding enhancements (*31*). The effect of the conjugated PEG on the maintenance of protein structure is still not fully understood, though both antitrypsin and thermal stabilities were significantly improved by N-terminus mono-PEGylation.

CONCLUSIONS

To improve blood circulation stability and reduce immunoreactivity, rhIFN α-2a was modified with solid-phase conjugation of mPEG aldehyde and N-terminus amine. A cation-exchange resin, CM-Sepharose, was used as the solid matrix, and the mono-PEGylate was separated from the unmodified protein. It is suggested that the advantages of solid-phase PEGylation, such as site-specific PEGylation and primary isolation of the mono-PEGylate, can be achieved in a single unit operation. The site-specificity was confirmed by mass spectrometry of the peptide digests and also by N-terminus sequencing using Edman degradation. The mono-PEGylate exhibited reduced antiviral activity and immunoreactivity, and the degree of reduction was proportional to the MW of the conjugated mPEG. The trypsin resistance and thermal stability were significantly improved by mono-PEGylation. Compared to the conventional solution-phase process, solid-phase PEGylation has the potential to avoid multi-PEGylation and minimize post-PEGylation purification.

LITERATURE CITED

(1) Corssmit, E. P. M., Metz, J. D., Sauerwein, H. P., and Romun, J. A. (2000) Biologic responses to IFN-a administration in humans. *J. Interferon Cytokine Res. 20*, 1039–1047.
(2) Potera, C. (2003) Pegylation for improving polypeptide drugs. *Genet. Eng. News 23*, 58–60.
(3) Perry, C. M., and Blair, J. (2001) Peginterferon-alpha-2a (40kD). *Drugs 61*, 2263–2288.
(4) Bailon, P., Palleroni, A., Schaffer, C. A., Spence, C. L., Fung, W. J., Porter, J. E., Ehrlich, G. K., Pan, W., Xu, Z. X., Modi, M. W., Farid, A., and Berthold, W. (2001) Rational design of a potent, long-lasting form of interferon: A 40 kDa branched polyethylene glycol-conjugated interferon alpha 2a for the treatment of Hepatitis C. *Bioconjugate Chem. 12*, 195–202.
(5) Harris, J. M., Martin, N. E., and Modi, M. (2001) PEGylation: A novel process for modifying pharmacokinetics. *Clin. Pharmacokinet. 40*, 539–551.
(6) Liptakova, H., and Kontsek, P. (1990) Problem of recombinant interferon alpha 2-immunogenicity in therapy. *Do Redakcie Doslo 100*, 139–143.
(7) Reddy, K. R., Wright, T. L., Pockros, P. J., Shiffman, M., Eversom, G., Reindollar, R., Fride, M. W., Purdum III, P. P., Jensen, D., Smith, C., Lee, W. M., Boyer, T. D., Lin, A., Pedder, S., and Depamphilis, J. (2001) Efficacy and safety of PEGylated (40 kDa) interferon alpha 2a compared with interferon alpha 2a in noncirrhotic patients with chronic Hepatitis C. *Hepatology 33*, 433–438.
(8) Pepinsky, R. B., Doreen, J. L., and Alan, G. (2001) Improved pharmacokinetic properties of a polyethylene glycol modified form of interferon-beta-1a with preserved in vitro bioactivity. *J. Pharmacol. Exp. Ther. 297*, 1059–1066.
(9) Bailon, P., and Berthold, W. (1998) Polyethylene glycol-conjugated pharmaceutical proteins. *P. S. T. T. 1*, 352–356.
(10) Hinds, K. D., and Kim, S. W. (2002) Effect of PEG conjugation on insulin properties. *Adv. Drug Delivery Rev. 54*, 505–530.
(11) Kodera, Y., Matsushima, A., Hiroto, M., Nishimura, H., Ishii, A., Ueno, T., and Inada, Y. (1998) PEGylation of proteins and bioactive substances for medical and technical applications. *Prog. Polymer. Sci. 23*, 1233–1271.
(12) Zalipsky, S. (1995) Chemistry of polyethylene glycol conjugates with biologically active molecules. *Adv. Drug Delivery Rev. 16*, 157–182.
(13) Conover, C. D., Greenwald, R. B., Pendri, A., and Shum, K. L. (1999) Camptothecin delivery systems: the utility of amino acid spacers for the conjugation of camptothecin with polyethylene glycol to create prodrugs. *Anti-Cancer Drug Des. 14*, 499–506.
(14) Means, G. E., and Feeney, R. E. (1995) Reductive alkylation of proteins. *Anal. Biochem. 224*, 1–16.
(15) Kinstler, O. B., Brems, D. N., Lauren, S. L., Paige, A. G., Hamburger, J. B., and Treuheit, M. J. (1996) Characterization and stability of N-terminally PEGylated rhG-CSF. *Pharmacol. Res. 13*, 996–1002.
(16) Kinstler, O. B. (1998) U.S. Patent 19, 5824784.
(17) Kinstler, O., Molineux, G., Treuheit, M., Ladd, D., and Gegg, C. (2002) Mono-N-terminal poly(ethylene glycol)-protein conjugates. *Adv. Drug Delivery Rev. 54*, 477–485.
(18) Yamamoto, Y., Tsutsumi, Y., Yoshioka, Y., Nishibata, T., Kobayashi, K., Okamoto, T., Mukai, Y., Shimizu, T., Nakagawa, S., Nagata, S., and Mayumi, T. (2003) Site-specific PEGylation of a lysine-deficient TNF-alpha with full bioactivity. *Nat. Biotechnol. 21*, 546–552.
(19) Fee, C. J., and Alstine, J. M. V. (2006) PEG-protein: reaction engineering and separation issues. *Chem. Eng. Sci. 61*, 924–939.
(20) Harris, J. M. and Zalipsky, S. (1997) *Poly(ethylene glycol) Chemistry and Biological Application*, pp 207–216, American Chemical Society, Washington, DC,
(21) Lee, B. K., Lee, J. D. and Lee, E. K. (2004) Solid-Phase, N-Terminus-Specific, Mono-PEGylation of Recombinant Interferon-α-2a: Purification, Characterization, and Bioactivity, presented at ISPPP 2004, Aachen, Germany.
(22) Lee, E. K. (2004) Korean Patent #0453185.
(23) Takacs, M. A., Jacobs, S. J., Bordens, R. M., and Swanson., S. J. (1999) Detention and characterization of antibodies to PEG-

IFN-alpha 2b using surface plasmon resonance. *J. Interferon Cytokine Res. 19*, 781–789.
(24) Rubinstein, S., Familletti, P. C., and Pestaka, S. (1981) Convenient assay for interferons. *J. Virol. 37*, 755–758.
(25) Gillis, E. H., Gosling, J. P., Sreenan, J. M., and Kane, M. (2002) Development and validation of a biosensor-based immunoassay for progesterone in bovine milk. *J. Immunol. Methods 267*, 131–138.
(26) Lofas, S., Malmqvist, M., Ronnberg, I., and Stenberg, E. (1991) Bioanalysis with surface plasmon resonance. *Sens. Actuators, B 5*, 79–84.
(27) Hellman, U., Wernstedt, C., Gonez, J., and Heldin, C. (1995) Improvement of an "In-Gel" digestion procedure for the micropreparation of internal protein fragments for amino acid sequencing. *Anal. Biochem. 224*, 451–455.
(28) Ghorbel, B., Kamoun, A. S., and Nasri, M. (2003) Stability studies of protease from bacillus cereus BG1. *Enzyme Microb. Technol. 6261*, 1–6.
(29) Allen, D., Baffi, R., Bausch, J., Bongers, J., Costello, M., Dougherty, J., Federici, M., Jr., Garnick, R., Peterson, S., Riggins, R., Sewerin, K., and Tuls, J. (1996) Validation of peptide mapping for protein identity and genetic stability. *Biologicals 24*, 255–275.
(30) Seely, J. E., Buckel, S. D., Green, P. D., and Richey, C. W. (2005) Making site-specific PEGylation work. *BioPharm Int. March*, 30–41.
(31) Kim, C. S., and Lee, E. K. (2000) Effects of operating parameters in in vitro renaturation of a fusion protein of human growth hormone and glutathione S transferase from inclusion body. *Process Biochem. 36*, 111–117.
(32) Fee, C. J. and Mason, S. (2004) Charge-pH Behaviour of PEGylated Proteins: Consequences for Downstream Processing, Bioseparation, 2004, Uminonakamichi, Japan, Oct 15–16.
(33) Fee, C. J. (2003) Size-exclusion reaction chromatography (SERC): A new technique for protein PEGylation. *Biotechnol. Bioeng. 82*, 200–206.
(34) Foster, S., Schacher, A., Weyer, K. A., Brugger, D., Dietel, E., Marti, S., and Schreitmuller, T. (2003) Isolaration, Structural characterization, and antiviral activity of positional isomers of monopegylated interferon α-2a (PEGASYS). *Protein Expression Purif. 30*, 78–87.
(35) Monkaesh, S. P., Ma, Y., Aglione, A., Bailon, P., Ciolek, D., Barbieri, B. D., Graves, M. C., Hollfelder, K., Michel, H., Palleroni, A., Porter, J. E., Russoman, E., Roy, S., and Pan, Y. E. (1996) Positional isomers of monopegylated interferon α-2a: Isolation, characterization, and biological activity. *Anal. Biochem. 247*, 434–440.
(36) Yamaoka, T., Tabata, Y., and Ikada, Y. (1994) Distribution and tissue uptake of poly(ethylene) glycol with different molecular weights after intravenous administration to mice. *J. Pharm. Sci. 83*, 601–606.

BC060245M

Synthesis and *in vitro* Behavior of Multivalent Cationic Lipopeptide for DNA Delivery and Release in HeLa Cells

Kewei Wang,[†] Xuehai Yan,[†] Yue Cui,[†] Qiang He,[†,‡] and Junbai Li*[,†]

Beijing National Laboratory for Molecular Sciences (BNLMS), International Joint Lab, CAS Key Lab of Colloid and Interface Science, Institute of Chemistry, Chinese Academy of Sciences, Beijing 100080, People's Republic of China, and Max Planck Institute of Colloids and Interfaces, Golm/Potsdam D-14476, Germany. Received October 8, 2006; Revised Manuscript Received August 7, 2007

We report here that a synthesized multivalent cationic lipopeptide can be used for the delivery and release of gene assembled into lipopeptide vesicles. It is found experimentally that the synthesized lipopeptide is safe for gene therapy because of its biocompatibility and the innocuity of the hydrolysis products, such as lipids and amino acids. The experimental results also show that the assembled DNA/lipopeptide complex has high transfection efficiency in HeLa cells compared to that of the selected commercial reagent, which represents a novel vector for the delivery of therapeutic DNA.

INTRODUCTION

Somatic gene therapy is becoming attractive in medical diagnosis and treatment of various inherited diseases and cancers (*1, 2*). The viral and synthetic vectors for gene delivery are the most common methods (*3–10*), with viral vectors being remarkably efficient in transfecting mammalian cells. These methods have the disadvantage of a lack of biosafety (*11–13*), with recent clinical trials showing that the viral vectors cause a severe inflammatory response and insertional mutagenesis (*14, 15*). Synthetic cationic lipids are attracting considerable attention as gene vectors because of their biosafety and other inherent advantages over viral vectors. Pioneering research indicates that synthetic vectors have the advantage of ease and variability of preparation, lack of immunogenicity, and a capacity to deliver large pieces of DNA, thus allowing for the delivery of artificial chromosomes (*16–18*).

The design of safe and effective gene transfection reagents is still a challenge in gene therapy. Gene transfection with cationic lipids needs to overcome a mass of cellular barriers, including the formation of synthetic vector/DNA complexes and their initial binding to the cell surface, endocytosis, endosomal escape, nuclear entry, and final expression. Herein, we report on the design and synthesis of a novel multivalent cationic lipopeptide (MCL) (Scheme 1). The MCL displays a distinct advantage in gene therapy in view of its biocompatibility, functional expansibility, relative ease of synthesis, and controllable charge density. When hydrolyzed by trypsin, the MCL becomes negative, and the vesicles undergo a charge-reversal process. The bound DNA by MCL vesicles is then excluded from the anionic productions, thus enhancing gene transfection efficiency. This process is obviously different from the previous vectors (*19–24*). The present findings are expected to broaden the application of cationic amphiphiles with peptide headgroups in nonviral gene therapy.

* Corresponding author: Institute of Chemistry, Chinese Academy of Sciences, Zhong Guan Cun, Bei Yi Jie 2, Beijing 100080, China. Tel: +86 10 82614087. Fax: +86 10 82612629. E-mail: jbli@iccas.ac.cn.

[†] Chinese Academy of Sciences.

[‡] Max Planck Institute of Colloids and Interfaces.

EXPERIMENTAL PROCEDURES

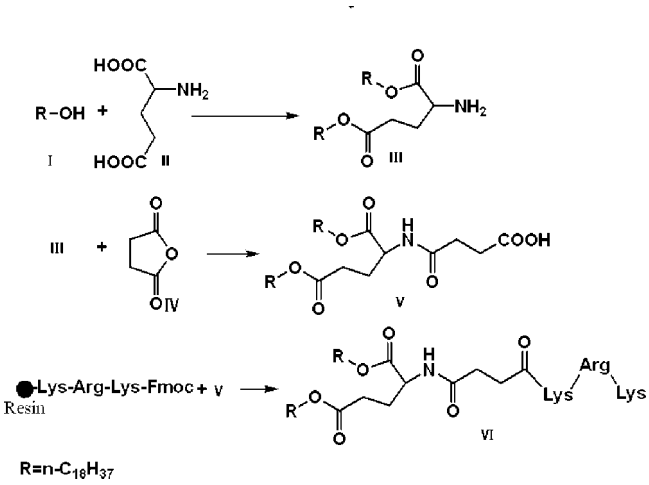
Materials. Ethidiium bromide (EtBr), Trypan blue, trypsin and *N,N*-diisopropylethylamine were purchased from Sigma. The reference transfection reagent (frequently used for control experiments) containing 1,2-dioleoyl-3-trimethylammoniopropane (DOTAP) and dioleoylphosphotidyl-ethanolamine (DOPE) (1:1 w/w) were obtained from Avanti (*25, 26*). Monster green fluorescent protein phGFP vector (phGFP) was from Promega. All chemicals were used as received without further purification. The water used through out all of the experiments was purified with a Milli-Q system from Millipore Co.

Synthesis. The lipopeptide was synthesized on the basis of a previously reported protocol (Scheme 1) (*27*). Briefly, *n*-octadecanol (I) was esterified with equivalent L-glutamic acid (II) to obtain dialkyl L-glutamate (III), under the action of a catalytic amount of *p*-toluene-sulfonic acid in toluene, and refluxed for 2 h. Then the amino group of compound III was coupled with succinic anhydride (IV) by ring opening. Equivalent molar amounts of succinic anhydride and III were added into anhydrous THF (refluxed over Na) and refluxed for 3 h under catalysis by *N,N*-diisopropylethylamine. Solvent THF was removed under vacuum. The residue was recrystallized from acetone to get V with a yield of 85.6%. The tripeptide was synthesized using standard solid-phase 9-fluorenylmethoxycarbonyl (Fmoc) chemistry by Shanghai Sangon Co. (China). The peptide was assembled on Wang resin, incorporating a linker to generate the C-terminal amide upon cleavage of the peptide from the resin. The resin-bound peptide was N-terminally acetylated by reaction with amphiphile V to get the lipopeptide (VI). The target compound was purified to 95% with HPLC on a reversed-phase C18 column, with gradients of acetonitrile in water containing 0.1% TFA to obtain a white powder. The structure of the target molecule was confirmed by ^{1}H NMR spectra (300 M), elemental analysis, and mass spectroscopy (MS). ^{1}H NMR ($CDCl_3$, 300M) δ ppm 0.88 (t, 6H), 1.25 (s, 66H), 1.55–1.66 (m, 10H), 1.95–2.05 (m, 3H), 2.10–2.21 (m, 3H), 2.30–2.45 (m, 7H), 2.48–2.63 (m, 6H), 2.64–2.83 (m, 6H), 4.06 (t, 4H), 4.14 (t, 4H), 4.56–4.67 (m, 2H), 6.51–6.64 (m, 2H), 11.05 (s, 1H). MALDI-MS: Calcd for $[C_{63}H_{121}N_9O_{10}+H]^+$1164.9; found, 1165.2. Elemental analysis: C, 64.68%; H, 10.10%; N, 11.03% (theory: C, 64.97%; H, 10.47%; N,10.82%).

Liposome Preparation. A chloroform solution of the MCL (1 mg/mL) was dried by rotary evaporation to form a thin film. The film was kept under vacuum for 4 h to ensure the complete

10.1021/bc060315p CCC: $37.00 © 2007 American Chemical Society
Published on Web 09/26/2007

Scheme 1. Synthesis Scheme of Multivalent Cationic Lipopeptide



removal of the residual solvent. The dried lipid was hydrated at 37 °C under a N_2 stream with the appropriate amount of deionized water. The final concentration was 1 mM, and the solution was stored at 4 °C. The morphology of the liposome negatively stained by uranyl acetate was observed by transmission electron microcopy (TEM).

Characterization of MCL/DNA Complexes. MCL/DNA complexes were formed by adding DNA solution to MCL liposome dispersion at a charge ratio of 1:2. The obtained samples are also used for the transfection experiments. The morphology of the complex was observed by laser scanning confocal microscopy (LSCM, Olympus FV500). For the measurements of fluorescence microscopy, liposome stock solutions were stained with 0.2 mol % DOPC-NBD, and DNA was labeled using the 5′TAMRA probe. The zeta-potential of the complexes were measured by the ZetaPALS (phase analysis light scattering) technique at pH 7.4 at room temperature (25 °C).

DNA Binding Affinities. DNA binding studies were achieved using competitive displacement fluorometric assay using EtBr as previously reported (*28*). MCL liposome dispersion was mixed with DNA (prestained with EtBr) at different charge ratios of MCL/DNA (0.1:1 to 2:1). A serial of MCL/DNA complexes were obtained for the purpose of DNA binding tests. It is noted that each sample contains 24 μg of calf thymus DNA, 2.8 μg of EtBr, and the appropriate amount of cationic lipid. Water was added to each well in the array, achieving a final volume of 2 mL per well. Fluorescence intensity was measured on a fluorescence spectrophotometer (Hatchi F4500) after incubation at room temperature for 20–25 min.

DNA Release. The above obtained EtBr-DNA/MCL complex was hydrolyzed by trypsin at room temperature for 5 h. The fluorescence intensity was recorded with a fluorescence spectrophotometer (Hatchi F4500) in real time. The variation of the fluorescence intensity reflects the amount of free DNA in the system.

Cell Culture and Transfection Experiments. HeLa cells were cultured in Dulbecco's modified Eagle's medium (DMEM, Gibco BRL) supplemented with 1% penicillin and streptomycin at 37 °C in a humid 5% CO_2 environment, reseeding the cells every 2–4 days to maintain subconfluency. When the HeLa cells reached about 90% confluency, they were split into 24-well plates with a 1:4 ratio using a standard trypsin-based technique. MCL liposome with GFP plasmid DNA was diluted in DMEM at the charge ratio 2:1. The mixture was incubated for 15 min at room temperature before being added to the cells. Transfections were performed over 16 h referencing previously reported methods (*29, 30*). The amount of DNA was the same as that used in the naked DNA control and positive control experiments (commercially available transfection reagents). After incubation

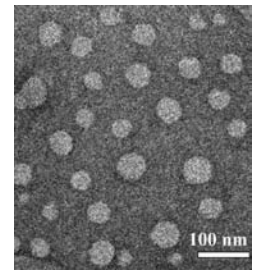


Figure 1. TEM Image of the MCL liposomes.

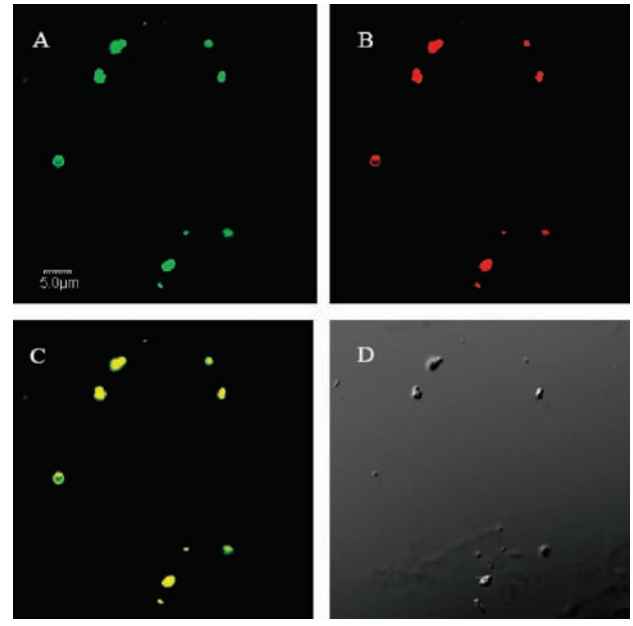


Figure 2. LSCM image of MCL/DNA complexes determined in (A) MCL fluorescence mode; (B) DNA fluorescence mode; (C) overlay fluorescence mode; and (D) transmission mode.

at 37 °C and 5% CO_2 for 2 h, the medium in the wells was gently removed, and fresh growth medium was added. Naked DNA controls were carried out with 0.1 mL of serum-free DMEM medium with 0.5 μg of plasmid DNA. Positive controls were carried out with the reference transfection reagent at the same charge ratio. The transfected cells were observed by fluorescence microscopy (Olympus IX 70). Transfection efficiencies were assessed by a flow cytometer (FCM) at 48 h post-transfection. The parallel samples of MCL, negative control, naked DNA, and positive control were dyed with Trypan blue in order to detect the viability of cells.

RESULTS AND DISCUSSION

The synthesized MCL comprises a hydrophobic moiety with a cationic peptide headgroup, as shown in Scheme 1 (*27*). The headgroup bears two positive charges at pH 7.4 resulting in a high membrane charge density, which enables a high binding affinity with DNA. In addition, the peptide group can be easily degraded by enzymes, allowing DNA to escape from the complex. This design allows lipids to exhibit different charges, spacers, chain lengths, and functional groups.

The TEM image in Figure 1 shows that the MCL can form well dispersed vesicles in the solution. The diameter of the vesicles is about 60 ± 20 nm. The laser scanning confocal microscopy (LSCM) measurement (Figure 2) shows that the addition of DNA into MCL solution results in the coexistence of MCL liposomes with DNA. Figure 2A displays the NBD-labeled vesicles that are shown in green. Figure 2B displays

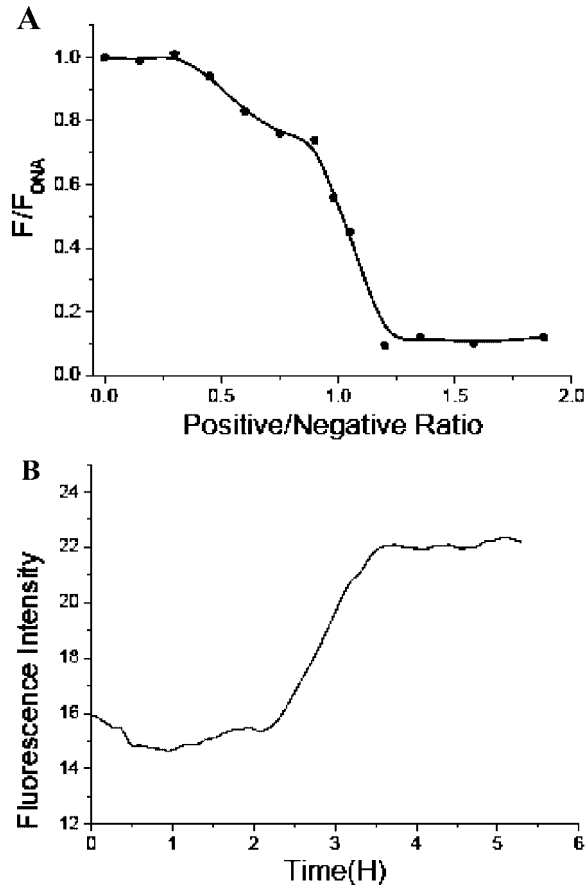


Figure 3. (A) EtBr displacement assay showing the fluorescence intensity as a function of MCL/DNA charge ratio. (B) EtBr displacement assay showing the fluorescence intensity as a function of time after adding the trypsin into the MCL/DNA complexes.

the TAMRA-labeled DNA as red dots by detecting the same sample using another filter. As can be seen, the two images are consistent in both the shape and area of the aggregates. Figure 2C gives the double contributions of NBD-labeled liposomes and TAMRA-labeled DNA. The image in Figure 2D shows the morphology of the complex in transmission mode.

The transfection efficiency of lipoplexes was known to depend strongly on the surface charge of the lipoplex (*31, 32*). We measured the surface potential of MCL liposomes and MCL/DNA complexes (2:1 in charge ratio). The data for the zeta-potential is +31.5 (±0.8 mV) for MCL and +22.3 (±1.6 mV) for MCL/DNA complexes, respectively. It shows that the zeta-potential values for both surfaces are positive, which will increase the ability of the MCL/DNA complexes to adhere to the membrane surface of the cells.

To further verify the binding of DNA with MCL liposomes, we performed the experiments with a standard EtBr-DNA fluorescence quenching exclusion assay. Fluorescence intensity was collected at various charge ratios of MCL to DNA. The results are shown in Figure 3A. EtBr will fluoresce as it intercalates in the middle of the base pairs of DNA and self-quench in solution. When DNA binds with MCL liposomes, EtBr will be displaced. Consequently, the intensity of fluorescence will decrease until all DNA is incorporated into the MCL/DNA complexes at the isoelectronic point. Figure 3A shows that the fluorescence intensity indeed decreases at the isoelectronic region. It means that the MCL liposome and DNA have formed vectors of MCL/DNA complexes.

The change of fluorescence intensity was recorded in real time, while the EtBr-DNA/MCL solution was incubated with trypsin at pH 7.2 at room temperature. Figure 3B shows the

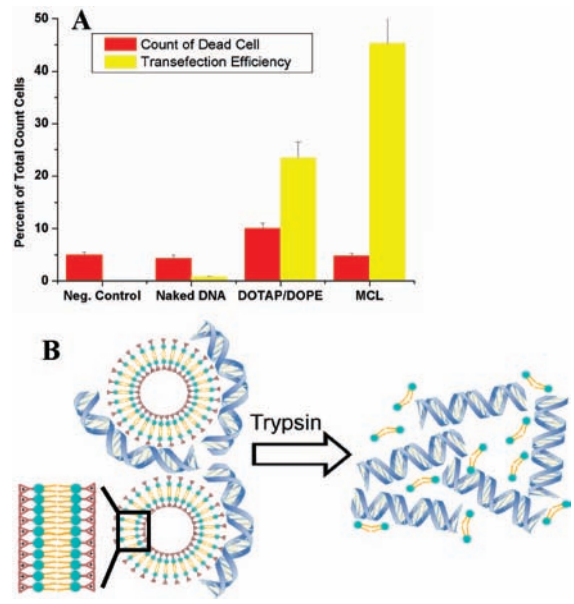


Figure 4. (A) Experimental results of gene transfection efficiency and cytotoxicity in HeLa cells. (B) Proposed mechanism of the DNA release from the MCL/DNA complex after trypsin hydrolysis.

change of the fluorescence intensity of the EtBr-DNA/MCL solution after adding trypsin to the complex. An increase of fluorescence intensity over time is observed. It indicates that EtBr is re-intercalated in base pairs of DNA since the hydrolysis of peptide results in the charge reversal of the lipid headgroups. The fluorescence data also shows that DNA is released from the complexes accompanied by enzymatic hydrolysis.

HeLa cells were split into 24 wells and incubated for 16 h. MCL and the commercial transfection reagent were separately mixed with a plasmid DNA, which contained a reporter gene of phMGFP. Then the plasmid DNA and its mixture with MCL and commercial transfection reagent were added into the HeLa cell wells for the transfection measurements. The fluorescence microscopy images displayed that a great deal of GFP was generated in the transfected cells (see Supporting Information). In order to quantify the ability of MCL to enter cells, flow cytometry was employed to precisely determine the transfection efficiency. As shown in Figure 4A, the transfection efficiency of MCL is about two times that of the commercial transfection reagent, which serves as a reference system. For the naked plasmid DNA, the transfection efficiency is essentially negligible. However, in the presence of MCL, the transfection efficiency is about 45 ± 5%.

To investigate the toxicity of MCL, the ratio of dead cells was detected by cell counters. The total number of dead cells in the negative control (red bar in Figure 4A) is similar to that containing plasmid DNA and MCL, which means that the MCL has no influence upon cell growth. However, the number of dead cells increases after the addition of the commercial transfection reagent. The above results suggest that the MCL has innocuity for cell transfection.

Through the above experiments, we propose that the transfection of DNA/MCL complexes in cells will undergo the following process, as shown in Figure 4B. First, the plasmid DNA binds to the headgroups of the cationic peptide of MCL vesicles. Then, the MCL/DNA vesicles will enter the HeLa cells (e.g., via endocytosis), and trypsin in the cell will hydrolyze the peptide of the plasmid DNA/MCL complexes. The charge reversal of the vesicles will repel DNA and assist DNA to escape from the endosome for the subsequent transcription (*33, 34*). This process is readily performed and thus enhances DNA transfection efficiency.

CONCLUSIONS

In conclusion, we demonstrate that the synthesized multivalent cationic lipopeptide (MCL) can be safely used for the delivery and release of genes. The assembled MCL vesicles have high affinity to bind with DNA through electrostatic interaction. This peptide is biocompatible, and the hydrolytic products, such as lipids and amino acids, are also innoxious. The transfection experiments show that the lipopeptide as vesicles can enhance gene transfection efficiency compared to that of the commercial reagent. Therefore, such a synthesized multivalent cationic lipopeptide represents a new type of vector for the delivery of therapeutic DNA.

ACKNOWLEDGMENT

This work was financially supported by the National Science Foundation of China (Project No. 20403022 and 20520130213), the Chinese Academy of Sciences, and Germany Max Planck Society. Q.H. is grateful to Dr. John Dunlop for critically reading the manuscript and the Alexander von Humboldt foundation for a research fellowship.

Supporting Information Available: The fluorescence images of the transfected cells. This information is available free of charge via the Internet at http://pubs.acs.org.

LITERATURE CITED

(1) Felgner, P. L., and Rhodes, G. (1991) Gene therapeutics. *Nature 349*, 351–352.

(2) Lasic, D. D., Strey, H., Stuart, M. C. A., Podgornik, R., and Frederik, P. M. (1997) The structure of DNA-liposome complexes. *J. Am. Chem. Soc. 119*, 832–833.

(3) Robbins, P. D., Tahara, H., and Ghivizzani, S. C. (1998) Viral vectors for gene therapy. *Trends Biotechnol. 16*, 35–40.

(4) Marshall, E. (2000) Clinical research - FDA halts all gene therapy trials at Penn. *Science 287*, 565–567.

(5) Luo, D., and Saltzman, W. M. (2000) Synthetic DNA delivery systems. *Nat. Biotechnol. 18*, 33–37.

(6) Behr, J. P. (1993) Synthetic gene-transfer vectors. *Acc. Chem. Res. 26*, 274–278.

(7) DeRouchey, J., Walker, G. F., Wagner, E., and Radler, J. O. (2006) Decorated rods: A "bottom-up" self-assembly of monomolecular DNA complexes. *J. Phys. Chem. B 110*, 4548–4554.

(8) Davis, M. E. (2002) Non-viral gene delivery systems. *Curr. Opin. Biotechnol. 13*, 128–131.

(9) Felgner, P. L. (1990) Particulate systems and polymers for in vitro and in vivo delivery of polynucleotides. *Adv. Drug Delivery Rev. 5*, 163–187.

(10) Miller, A. D. (1998) Cationic liposomes for gene therapy. *Angew. Chem., Int. Ed. 37*, 1769–1785.

(11) Verma, I. M., and Somina, N. (1997) Gene therapy - promises, problems and prospects. *Nature 389*, 239–242.

(12) Anderson, W. F. (1998) Human gene therapy. *Nature 392*, 25–30.

(13) Yla-Herttuala, S., and Martin, J. F. (2000) Cardiovascular gene therapy. *Lancet 355*, 213–222.

(14) Raper, S. E., Chirmule, N., Lee, F. S., Lee, F. S., Wivel, N. A., Bagg, A., Gao, G. P., Wilson, J. M., and Batshaw, M. L. (2003) Fatal systemic inflammatory response syndrome in a ornithine transcarbamylase deficient patient following adenoviral gene transfer. *Mol. Genet. Metab. 80*, 148–158.

(15) Hacein-Bey-Abina, S., von Kalle, C., Schmidt, M., Le Deist, F., Wulffraat, N., and McIntyre, E. (2003) A serious adverse event after successful gene therapy for X-linked severe combined immunodeficiency. *N. Engl. J. Med. 348*, 255–256.

(16) Benns, J. M., Choi, J. S., Mahato, R. I., Park, J. S., and Kim, S. W. (2000) pH-Sensitive cationic polymer gene delivery vehicle: N-ac-poly(L-histidine)-graft-poly(L-lysine) comb shaped polymer. *Bioconjugate Chem. 11*, 637–645.

(17) Ahmad, A., Evans, H. M., Ewert, K., George, C. X., Charles, E., Samuel, C. E., and Safinya, C. R. (2005) New multivalent cationic lipids reveal bell curve for transfection efficiency versus membrane charge density: lipid-DNA complexes for gene delivery. *J. Gene Med. 7*, 739–748.

(18) Willard, H. F. (2000) Genomics and gene therapy: artificial chromosomes coming to life. *Science 290*, 1308–1309.

(19) Wang, J. K., Guo, X., Xu, Y. H., Barron, L., and Szoka, F. C. (1998) Synthesis and characterization of long chain alkyl acyl carnitine esters. Potentially biodegradable cationic lipids for use in gene delivery. *J. Med. Chem. 41*, 2207–2215.

(20) Akinc, A., Lynn, D. M., Anderson, D. G., and Langer, R. (2003) Parallel synthesis and biophysical characterization of a degradable polymer library for gene delivery. *J. Am. Chem. Soc. 125*, 5316–5323.

(21) Wang, C., Ge, Q., Ting, D., Nguyen, D., Shen, H. R., Chen, J., Eisen, H. N., Heller, J., Langer, R., and Putnam, D. (2004) Molecularly engineered poly(ortho ester) microspheres for enhanced delivery of DNA vaccines. *Nat. Mater. 3*, 190–196.

(22) Zhu, J., Munn, R. J., and Nantz, M. H. (2000) Self-cleaving ortho ester lipids: A new class of pH-vulnerable amphiphiles. *J. Am. Chem. Soc. 122*, 2645–2646.

(23) Jones, R. A., Cheung, C. Y., Black, F. E., Zia, J. K., Stayton, P. S., Hoffman, A. S., and Wilson, M. R. (2003) Poly(2-alkylacrylic acid) polymers deliver molecules to the cytosol by pH-sensitive disruption of endosomal vesicles. *Biochem. J. 372*, 65–75.

(24) Miyata, K., Kakizawa, Y., Nishiyama, N., Harada, A., Yamasaki, Y., Koyama, H., and Kataoka, K. (2004) Block catiomer polyplexes with regulated densities of charge and disulfide cross-linking directed to enhance gene expression. *J. Am. Chem. Soc. 126*, 2355–2361.

(25) Ewert, K., Ahmad, A., Evans, H. M., Schmidt, H. W., and Safinya, C. R. (2002) Efficient synthesis and cell-transfection properties of a new multivalent cationic lipid for nonviral gene delivery. *J. Med. Chem. 45*, 5023–5029.

(26) Cheung, C. Y., Murthy, N., Stayton, P. S., and Hoffman, A. S. (2001) A pH-sensitive polymer that enhances cationic lipid-mediated gene transfer. *Bioconjugate Chem. 12*, 906–910.

(27) Hachisako, H., Motozato, Y., Murakami, R., and Yamada, K. (1992) Extraordinary monomer-dimer transition of methylene blue induced by the phase transition of Telomer-bilayer membranes formed from dialkyl L-glutamate amphiphiles with oligoacrylic acid-head group. *Chem. Lett. 21*, 219–222.

(28) Gershon, H., Ghirlando, R., Guttman, S. B., and Minsky, A. (1993) Mode of formation and structural features of DNA-cationic liposome complexes used for transfection. *Biochemistry 32*, 7143–7151.

(29) Luo, D., Haverstick, K., Belcheva, N., Han, E., and Saltzman, W. M. (2002) Poly(ethylene glycol)-conjugated PAMAM dendrimer for biocompatible, high-efficiency DNA delivery. *Macromolecules 35*, 3456–3462.

(30) Luo, D., Woodrow-Mumford, K., Belcheva, N., and Saltzman, W. M. (1999) Controlled DNA delivery systems. *Pharm. Res. 16*, 1300–1308.

(31) Miller, A. D. (2004) Nonviral liposomes. *Methods Mol. Med. 90*, 107–137.

(32) Nishikawa, M., and Huang, L. (2001) Nonviral vectors in the new millennium: delivery barriers in gene transfer. *Hum. Gene Ther. 12*, 861–870.

(33) Xu, Y. H., and Szoka, F. C. (1996) Mechanism of DNA release from cationic liposome/DNA complexes used in cell transfection. *Biochemistry 35*, 5616–5623.

(34) Prata, C. A. H., Zhao, Y. X., Barthelemy, P., Li, Y., Luo, D., McIntosh, T. J., Lee, S. J., and Grinstaff, M. W. (2004) Charge-reversal amphiphiles for gene delivery. *J. Am. Chem. Soc. 126*, 12196–12197.

BC060315P

Phage Display Library Derived Peptides that Bind to Human Tumor Melanin as Potential Vehicles for Targeted Radionuclide Therapy of Metastatic Melanoma

Robertha C. Howell,[†] Ekaterina Revskaya,[†] Valeria Pazo,[‡] Joshua D. Nosanchuk,[§,||] Arturo Casadevall,[§,||] and Ekaterina Dadachova*[,†,§]

Department of Nuclear Medicine, Department of Microbiology and Immunology, and Department of Medicine, Albert Einstein College of Medicine of Yeshiva University, Bronx, New York 10461, Jacobi Medical Center, Bronx, New York 10461. Received October 22, 2006; Revised Manuscript Received July 31, 2007

Metastatic melanoma remains an incurable disease, and there is a great need for novel therapeutic modalities. We have recently identified melanin as a target for radionuclide therapy of melanoma and demonstrated the feasibility of this approach using a 188-rhenium (^{188}Re)-radiolabeled melanin-binding decapeptide to fungal melanin known as 4B4. Although the results indicated that radiolabeled melanin-binding decapeptide had activity against melanoma, that peptide also manifested high kidney uptake and this might become a concern during clinical trials. We hypothesized that by identifying peptides with different amino acid composition against tumor melanin we might be able to decrease their kidney uptake. Using the Heptapeptide Ph.D.-7 Phage Display Library, we identified three heptapeptides that bind to human tumor melanin. These peptides were radiolabeled with ^{188}Re via HYNIC ligand, and their comprehensive biodistribution in A2058 human metastatic melanoma tumor-bearing nude mice was compared to that of ^{188}Re-4B4 decapeptide. While tumor uptake of heptapeptides was quite similar to that of ^{188}Re-4B4 decapeptide, there was dramatically less uptake in the kidneys at both 3 h (6% ID/g vs 38%) and 24 h (2% ID/g vs 15%) postinjection. Administration of one of the generated heptapeptides, ^{188}Re-HYNIC-AsnProAsnTrpGlyProArg, to A2058 human metastatic melanoma-bearing nude mice resulted in significant retardation of the tumor growth. Immunofluorescence showed that in spite of their relatively small size heptapeptides were not able to penetrate through the membranes of viable melanoma cells and bound only to extracellular melanin, which provides assurance that they will be safe to healthy melanin-containing tissues during radionuclide therapy. Thus, these heptapeptides appear to have potentially significant advantages for targeted therapy of melanoma relative to existing melanin-binding peptides.

INTRODUCTION

The incidence of melanoma is rising (*1*), and it is an important cause of cancer among young patients (30–50 years). This disease currently affects ~40 000 new patients each year in the US, and there are an estimated 100 000 cases worldwide (*2, 3*). Metastatic melanoma is almost always fatal (*4*) with the median survival time of 8.5 months and an estimated 5 year survival of 6% (*4*). Therapeutic options for metastatic melanoma are limited, and there has been little change in the prognosis for this disease in the past 25 years (*5*).

Most melanomas are pigmented by the presence of melanin. Some melanomas are called "amelanotic" because they are not black or darkly pigmented. However, even amelanotic melanomas contain some melanin (*6, 7*), which makes this pigment a convenient target for the development of radionuclide therapy of metastatic melanoma. The multiplicity of compounds which could potentially serve as "delivery vehicles" of radionuclides to melanoma tumors can be divided into three groups: molecules that bind to melanin, molecules that are melanin precursors, and molecules that bind to melanogenesis-related proteins (reviewed in ref (*8*)).

We have recently demonstrated the feasibility of targeting melanin, an intracellular melanocyte pigment, to deliver cytotoxic radiation to human melanoma cells *in vivo* using a fungal melanin-binding monoclonal antibody (mAb 6D2) with promising therapeutic results (*9*). Later, we expanded this approach to peptides by performing experimental melanoma therapy with 188-rhenium (^{188}Re)-labeled fungal melanin-binding decapeptide 4B4 (*10*) and carried out a comprehensive safety evaluation of this treatment (*11*). The results indicated that radiolabeled melanin-binding peptides have activity against melanoma and that these reagents could be potentially useful against this tumor. Peptides are attractive antitumor agents because they are easily synthesized, are nonimmunogenic, provide rapid clearance from the circulation, and penetrate tissues more thoroughly than larger molecules such as antibodies (*12*). On the other hand, peptides are rapidly degraded by the enzymes in the bloodstream and lack the effector functions conferred by an antibody constant region. The problem of rapid clearance can be ameliorated somewhat by synthesis using D-amino acids, but there is always a concern that peptides can bind to kidney cells and produce nephrotoxicity. This is a particular concern for melanin-binding peptides, because these are usually cationic (*10*), and thus can bind to the negatively charged kidney basement membrane. Clinical trials of radiolabeled peptides suggest that the risk of nephrotoxicity is a function of such characteristics of a peptide molecule as its mass, charge, and clearance pathways as well

* Ekaterina Dadachova PhD, Department of Nuclear Medicine, 1695A Eastchester Road, Bronx, NY 10461, Ph: 718-405-8485; FAX: 718-405-8457; E-mail: edadacho@aecom.yu.edu.

[†] Department of Nuclear Medicine,Albert Einstein College of Medicine of Yeshiva University.

[‡] Jacobi Medical Center.

[§] Department of Microbiology and Immunology, Albert Einstein College of Medicine of Yeshiva University.

[||] Department of Medicine, Albert Einstein College of Medicine of Yeshiva University.

10.1021/bc060330u CCC: $37.00 © 2007 American Chemical Society
Published on Web 10/02/2007

as the chemical and physical characteristics of the radionuclide (*13*). When radiolabeled fungal melanin-binding peptides were used for experimental melanoma therapy, they showed high kidney uptake (*11*). Although there was no long-term nephrotoxicity, this issue could become a concern during clinical trials. Thus, there is a clear need to improve melanin-binding peptides by decreasing their kidney uptake. Here, we describe the isolation and characterization of melanin-binding peptides from peptide libraries with dramatically reduced kidney-binding capacity.

EXPERIMENTAL PROCEDURES

Reagents and Cells. The Ph.D.-7 Phage Display library Kit including the Heptapeptide Phage Display Library, −28 gIII sequencing primer, −96 gIII sequencing primer, and *E. coli* ER2738 host strain were purchased from New England Biolabs. The library has complexity in excess of two billion independent clones, which is sufficient to contain most if not all of the $20^7 = 1.28 \times 10^9$ possible heptapeptide sequences. The Detection Module Recombinant Phage Antibody System used to quantify bound phage was purchased from Amersham Biosciences. QIAPrep Spin M13 Prep columns were purchased from Qiagen. HRP-labeled anti-M13 monoclonal conjugate was purchased from GE Healthcare. HRP-labeled Streptavidin for quantification of the biotinylated peptides and subsequent binding strength determination was purchased from Fisher Scientific. Highly pigmented human melanoma cells MNT1 (*14*) were a gift from Dr. V. Hearing (NIH, Bethesda, MD). Human metastatic pigmented melanoma cells A2058 cells (ATCC, Mannassas, VA) were grown in Dulbecco's Modified Eagle's Medium with 4 mM L-glutamine, 4.5 g/L glucose, and 1.5 g/L sodium bicarbonate. This medium was supplemented with a 10% fetal bovine serum and 5% penicillin–streptomycin solution. Cells were grown at 37 °C in 75 cm^2 cell culture flasks. Subculturing was done at 80–95% confluence at subcultivation ratios of 1:6 and 1:12. Cell layers were dispersed with 0.25% (w/v) Trypsin–EDTA (1×). The cell line Hep 3B2.1–7 (*Homo sapiens* hepatatocellular carcinoma) was purchased from ATCC (cat no HB-8064). Cells were grown routinely in Eagle's Minimum Essential Medium (EMEM) (ATCC) containing 10% FBS (Sigma) at 37 °C in 5% CO_2 incubator.

Preparation of Plates for Melanin-Specific ELISA. Melanin from MNT-1 human melanoma cells was purified as in ref (*11*), and suspended at 2 mg/mL concentration in deionized H_2O. Approximately 150 μL was added to each well of 96 well plates and the solution gently agitated overnight. The melanin-coated wells were then baked at 80 °C for ½ h and blocked with 2% dry milk for 1 h followed by 5 mg/mL BSA in deionized H_2O.

Panning Procedure. Ten microliters of the original phage library (New England Biolabs) was diluted to 100 μL with TBST (TBS + 0.1% [v/v] Tween-80) and the resulting 110 μL pipeted onto one melanin-coated well. The plate was incubated at room temperature for 1 h with gentle agitation. The phages were then discarded and the well washed, to remove nonbinders, 10 times with TBST and excess liquid blotted after each wash. The bound phage was eluted with 0.2 M glycine–HCl (pH 2.2) in 1 mg/mL BSA by rocking the plate gently at room temperature for 10 min. The eluate was pipeted into a microcentrifuge tube, neutralized with 15 μL of 1 M Tris–HCl (pH 9.1) and titered onto LB/IPTG/Xgal plates to determine the concentration of the phage eluate. It was amplified by incubating at 37 °C with vigorous shaking with an early log phase ER2738 culture for 4.5 h. Purification was performed by first centrifuging the culture at 9000 rpm at 4 °C to pellet the ER2738 cells. The supernantant was removed and treated with 1/6 equivalent volume of PEG/NaCl. After cooling overnight at 4 °C, the resulting suspension was again centrifuged at 9000 rpm. The resulting pellet was collected and resuspended in 1 mL TBS. Further centrifugation pelleted residual cells, and 80% of the suspension was collected. One-sixth of equivalent volume of PEG/NaCl was added and the solution incubated on ice for 1 h. The suspension was microcentrifuged at 4 °C for 20 min and the supernatant removed and discarded. The pellet was resuspended in 200 μL TBS. The concentration of the phage was determined by titering onto LB/IPTG/Xgal plates. The process was repeated twice using the obtained eluate (volume-corrected to yield 2×10^{11} phages) for panning with reduced panning time and increasing Tween concentration).

Isolating Clones. The final eluate was plated onto a LB/IPTG/Xgal plate to yield approximately 50 individual clones. Twenty-four clones from the plate were chosen at random and amplified by incubation with 1 mL of early log phase ER2738 culture. The resulting amplified eluates were purified as described above and each plated titered and plated again to yield a plate with approximately 20 individual plaques. Four plaques from each plate were amplified in 1 mL of early log phase ER2378 and the 4 resulting cultures pooled. The cultures were centrifuged at 9000 rpm for 10 min and 80% of the supernatant was removed. The removed supernatant was centrifuged again and 80% of the supernatant removed for extraction of phage DNA. The phage DNA was extracted by elution on QIAPrep Spin M13 Prep. The resulting DNA was amplified by standard molecular biology techniques. Twenty-four phages were selected for DNA sequencing, which was performed at the AECOM DNA Sequencing Core Facility.

Selection of Phages with the Best Melanin-Binding Properties. The phages with the best melanin-binding properties were selected by analyzing the concentration of the phages in the wells coated with melanin as compared to the concentrations in the noncoated wells. To obtain the concentrations of phage, the wells were first treated with an HRP/anti-M13 monoclonal antibody conjugate over a period of 1 h until binding had occurred. Subsequently, the excess conjugate was removed and the wells were washed. Quantitative amounts of HRP substrate (ABTS) and peroxide were added, and after a period of 10 to 30 min, changes in the color of the solution were analyzed for absorbance at 492 nm. The changes in absorbance at 492 nm are directly related to the amount of HRP enzyme present and as such to the amount of bound phage.

Synthesis of Biotinylated and HYNIC-Conjugated Heptapeptides. The best phage binders were selected as above, and the displayed heptapeptides were synthesized from L-amino acids with biotin at the N terminus by Peptides International (KY) for immunofluorescence experiments. To minimize enzymatic degradation *in vivo*, for radiolabeling purposes the same heptapeptides were synthesized by Anaspec from D-amino acids with a hydrazinonicotinamide (HYNIC) chelate appended to the N terminus. An additional heptapeptide, AspGlyAlaTrpMetGlyAla, whose sequence was derived from the sequence of previously described irrelevant decapeptide P601G AspGlyAlaSerTyrSer-TrpMetTyrGlyAla (*10*), was also synthesized in a biotinylated form and with HYNIC ligand as a random control. Biotinylated and HYNIC-conjugated heptapeptides were analyzed by HPLC on a VYDAC 250 mm analytical column equipped with a supporting guard column using the following gradient (A, 0.05% TFA in H_2O; B, 0.05% TFA in acetonitrile; 10–60% A over 50 min at 1 mL/min). The resulting HPLC confirmed the HPLC data obtained from the manufacturers.

Immunofluorescence of A2058 Melanoma Cells. The binding of the biotinylated heptapeptides to A2058 melanoma cells *in vitro* was analyzed by immunofluorescence as in ref (*10*). Approximately 10^6 melanoma cells were blocked for nonspecific binding by incubation in SuperBlock (Pierce, Rockford, IL) for 1 h at 37 °C. Biotinylated heptapeptides were then incubated with the cells for 1 h followed by addition of streptavidin

conjugated to fluorescein isothiocyanate (FITC). The slides were viewed with an Olympus AX70 microscope (Melville, NY) equipped with a FITC filter. Irrelevant biotinylated heptapeptide AspGlyAlaTrpMetGlyAla was used as a negative control.

Radiolabeling of Heptapeptides. The ^{188}Re-perrhenate eluted in saline from ^{188}W/^{188}Re generator was reduced by adding $SnCl_2$ (20 μL of 20 mg/mL 0.1 M HCl) to a suspension of 20 mg sodium glucoheptonate and 400 μL ^{188}Re-perrhenate. The resulting suspension was thoroughly mixed and incubated for 1 h at 37 °C. The reduction was assessed by SG-ITLC in dry acetone. One hundred microliters of a freshly prepared solution of 2 mg HYNIC–heptapeptide dissolved in 1 mL NH_4OAc (0.15 M, pH 4) was placed in a 1.5 mL microcentrifuge tube. To this solution was added approximately 600 μCi of reduced ^{188}Re (up to 400 μL). The resulting solution was incubated in the dark at room temperature for 1 h. The extent of radiolabeling was checked by SG-ITLC developed in 0.15 M NH_4OAc, pH 4. If necessary, the ^{188}Re-HYNIC–heptapeptides were purified from unreacted ^{188}Re on the reverse-phase C18 column. The column was primed with methanol followed by equilibration with NH_4OAc. The sample was then loaded onto the column and the column washed with 5 × 250 μL 0.125 M NH_4OAc followed by 2 × 250 μL 0.5 M NH_4OAc. The radiolabeled HYNIC–heptapeptides were eluted with 2 × 3 mL MeOH. The methanol was removed by evaporation under a nitrogen stream. SG- ITLC (0.15 M NH_4OAc, pH 4) was used to confirm the radiochemical purity of ^{188}Re-HYNIC–heptapeptides.

Binding of ^{188}Re-HYNIC–Heptapeptides to MNT1 and A2058 Melanoma Cells. To investigate the binding of radiolabeled heptapeptides to MNT1 human pigmented melanoma cells, the whole cells in increasing amounts from 1.3 to 15 million per sample were placed into the microcentrifuge tubes preblocked with 1% BSA to prevent nonspecific protein binding in 0.5 mL PBS, and radiolabeled heptapeptides in 0.19 nM concentration were added. In blocking experiments, the cells were preblocked with 10 μg per sample of the respective "cold" heptapeptide. The samples were incubated at 37 °C for 1 h. The suspensions were centrifuged at 1500 rpm for 20 min to pellet the cells, the supernatant was transferred into a different tube, and the radioactivity of the cells and of the supernatant was then counted in a gamma counter. For measuring the binding of heptapeptides to the lysed cells, the experiments were conducted as above, but MNT1 or A2058 cells were osmotically lysed immediately before the binding experiment. For estimation of association equilibrium constants K_a, the radiolabeled heptapeptides were added in increasing amounts (from 0.053 nM to 0.53 nM) to the lysed MNT1 or A2058 lysed cells (5×10^6 cells per centrifuge tube). After 1 h incubation at 37 °C, the activity in the tubes was counted in a gamma counter, the cells were collected by centrifugation, and the pellets were counted. Scatchard analysis was used to compute the heptapeptide association equilibrium constants K_a as in ref (*15*).

Biodistribution of ^{188}Re-HYNIC–Heptapeptides. All animal studies were carried out in accordance with the guidelines of the Institute for Animal Studies at the Albert Einstein College of Medicine. For biodistribution in tumor-bearing mice, melanoma tumors were induced by injecting approximately 8×10^6 A2058 human melanoma cells in 100 μL of the cell-growing medium into the right flank of female nude mice. Ten days after implantation, the tumors reached 0.3–0.7 cm in diameter. To study the biodistribution of four different ^{188}Re-HYNIC–heptapeptides and ^{188}Re-HYNIC–4B4 decapeptide (*11*) as a control, 30 tumor-bearing mice were divided into 5 groups of 6 mice each. Each group was further subdivided into 2 groups of 3 mice each. Each radiolabeled peptide was administered to 2 groups of mice at a dosage of 40 μCi (50 μg) in 100 μL via the tail vein. After 3 h and 24 h, respectively, the first and second groups of each set of mice were sacrificed and internal organs and the tumor taken, blotted from blood, weighed, counted in a gamma counter, and percent Injected dose per gram calculated.

To prove the specificity of peptide uptake in melanoma tumors, the biodistribution of ^{188}Re-HYNIC-AsnProAsnTrpGlyProArg was studied in nude mice bearing two different xenografts—human hepatocellular carcinoma and A2058 metastatic melanoma. For this purpose, 8×10^6 A2058 human melanoma cells and 10^7 Hep 3B human hepatocellular carcinoma cells in 100 μL of the cell-growth medium were injected into the right and left flanks, respectively, of female nude mice. The biodistribution experiment was performed essentially as above except that only tumors, blood, and muscle were taken.

To investigate the influence of D-lysine coinjection on the uptake of ^{188}Re-HYNIC–heptapeptides in kidneys and other major organs, one group of six female CD-1 mice were injected with 40 μCi (50 μg) of ^{188}Re-HYNIC-ThrThrHisGlnPheProPhe in 100 μL via the tail vein, while another group received the same heptapeptide coinjected with D-lysine (400 mg/kg body weight). Three mice from each group were sacrificed at 3 and 24 h, and the biodistribution was performed as above.

Therapy of A2058 Tumor-Bearing Mice with ^{188}Re-HYNIC-AsnProAsnTrpGlyProArg Heptapeptide. The A2058 tumors were initiated in nude mice as described above. When the tumors reached 0.7–0.8 cm in diameter, the mice were randomized into four groups of six mice. Groups 1–3 received IP injections of 1.0 mCi ^{188}Re-HYNIC-AsnProAsnTrpGlyProArg heptapeptide, a matching amount of "cold" HYNIC-AsnProAsnTrpGlyProArg heptapeptide (0.2 μg), or 1.0 mCi ^{188}Re-HYNIC-4B4 decapeptide, respectively. Control group # 4 was left untreated. On day 7, the treatment of animals in groups 1–3 was repeated with the same doses. The size of the tumors was measured in three dimensions with calipers immediately before administration of peptides and on days 3, 6, 14, 17, 21, 25, 32, and 35. The tumor volume was calculated by multiplying the product of the three perpendicular diameters by 0.5.

Correlative Histology/Immunofluorescence of A2058 Melanoma Tumors. To establish the colocalization of heptapeptides with melanin in melanoma tumors, consecutive slides of A2058 melanoma tumors were stained with hematoxylin and eosin (H&E) or were incubated with the biotinylated AsnProAsnTrpGlyProArg heptapeptide for 1 h followed by addition of streptavidin conjugated to fluorescein isothiocyanate (FITC). The slides were viewed with an Olympus AX70 microscope (Melville, NY) equipped with a FITC filter. Irrelevant biotinylated heptapeptide AspGlyAlaTrpMetGlyAla was used as a negative control.

Scintigraphic Imaging. Two mice out of each group treated with radiolabeled peptides in therapy experiments were anesthetized with Isoflurane and scintigraphically imaged for 2 min on a Siemens gamma camera equipped with *ICON* image processing software.

Statistical Analysis. The nonparametric Wilcoxon rank sum test was used to compare organs uptake in biodistribution studies and tumor sizes in therapy studies. The Student's *t* test for unpaired data was employed to analyze differences in binding between heptapeptides. The differences were considered statistically significant when P values were <0.05.

RESULTS

Selection of Tumor Melanin-Binding Phages and Synthesis of Heptapeptides. Twenty-four unique peptides from 24 individually isolated clones were identified (Table 1). Although no consensus sequence was identified throughout these peptides, the sequence "aromatic"−*−* "aromatic" occurred in approximately 25% of the peptides (where * represents an

Table 1. Amino Acid Sequences of Peptides from Isolated M13 Clones[a]

Clone ID		AA Sequence	Single Letter Sequence	Features of Constituent Amino Acids in Peptides of Isolated Clones (aromaticity and charge)	
1	A8	ThrHisPheAlaThrMetPhe	THFATMF	*+*****	*aa***a
2	A4	LeuGlnProThrMetHisLys	LQPTMHK	*****++	*****a*
4	A9	PheLysProProAlaSerLeu	FKPPASL	*+*****	a******
5	A2	AlaGluPheAlaPheAsnPhe	AEFAFNF	*-*****	**a*a*a
6	B6	AsnAlaProSerArgAsnGln	NAPSRNQ	****+**	*******
7	B3	AsnProArgProLeuSerIle	NPRPLSI	**+****	*******
8	A6	SerHisTyrValAsnSerGln	SHYVNSQ	*+*****	*aa****
9	2C	GluGlyLeuHisGlnArgLys	EGLHQRK	***+*++	***a***
10	1A	HisProGlnHisAlaGlyGly	HPQHAGG	+**+***	a**a***
11	4B	HisThrSerHisLeuSerCys	HTSHLSC	+**+***	a**a***
12	*3A*	*TrpProSerPheProIlePro*	*WPSFPIP*	*******	*a**a***
13	3C	ThrProAlaLeuGlnPhePro	TPALQFP	*******	*****+*
14	2D	SerPheThrTrpAlaProAsp	SFTWAPD	******-	*a*a***
15	*2A*	*AlaProProTyrThrAlaTyr*	*APPYTAY*	*******	***a**a
16	4C	SerTrpProSerHisValPro	SWPSHVP	****+**	*a**a**
17	1D	HisProAsnLeuLeuSerPro	HPNLLSP	+******	a******
18	4A	AsnGluSerProProAsnPro	NEYPPNP	*-*****	*******
19	3D	AsnProAsnTrpGlyProArg	NPNWGPR	******+	***a***
20	1B	ThrArgArgGluThrProAla	TRRETPA	*++_***	*******
21	4D	HisThrThrHisHisArgAsn	HTTHHRN	+**+++*	a**aa**
22	2B	ValGluThrTrpArgProAsn	VETWRPN	*-**+**	***a***
23	3B	GluArgPheIleAspThrGln	ERFIDTQ	-+**-**	**a****
24	*1C*	*ThrThrHisGlnPheProPhe*	*TTHQFPF*	**+***	**a*a*a

[a] The peptides with the best binding are highlighted in green, "a" represents an aromatic amino acid, +/− the charge of the amino acid, and * an irrelevant amino acid.

irrelevant amino acid and "aromatic" an aromatically based amino acid). More specifically, the aromatic amino acids were represented by histidine, a positively charged amino acid, in 50% of these cases. Histidine was also found extensively throughout the majority of the other peptide sequences. The best tumor melanin-binding phages were identified by comparing the binding of the phages to the melanin-coated well versus the non-melanin-coated wells (first round of selection, Figure 1a). From this group of clones, 8 of the best binders were chosen for further study (selected phages are highlighted in green in Table 1). These phages were then subjected to the second round of selection by performing ELISA for fourfold serial dilutions of the phage starting from 1.2×10^{12} pfu/mL. Of 8 phages, the 3 best binding phages were identified on the basis of comparison of the binding curves obtained from the melanin-coated wells and the uncoated wells (Figure 1b). As a result, 3 heptapeptides—HisThrThrHisHisArgAsn, AsnProAsnTrp GlyProArg, and ThrThrHisGlnPheProPhe—identified as 4D, 3D, and 1C in Table 1, respectively, were synthesized in biotinylated form and HYNIC-conjugated form for further in vitro and in vivo evaluation.

Heptapeptides Binding To Melanoma Cells *in Vitro.* The binding of heptapeptides to A2058 melanoma cells in culture was studied by immunofluorescence. Figure 2a shows that the biotinylated HisThrThrHisHisArgAsn heptapeptide bound only to nonviable melanoma cells. Nonviable cells apparently released their melanin or had permeable cell membranes that allowed access of the peptide to melanin (Figure 2a, right panel). No binding was observed to viable cells with intact cell membranes (Figure 2a, left panel). Control biotinylated hep-

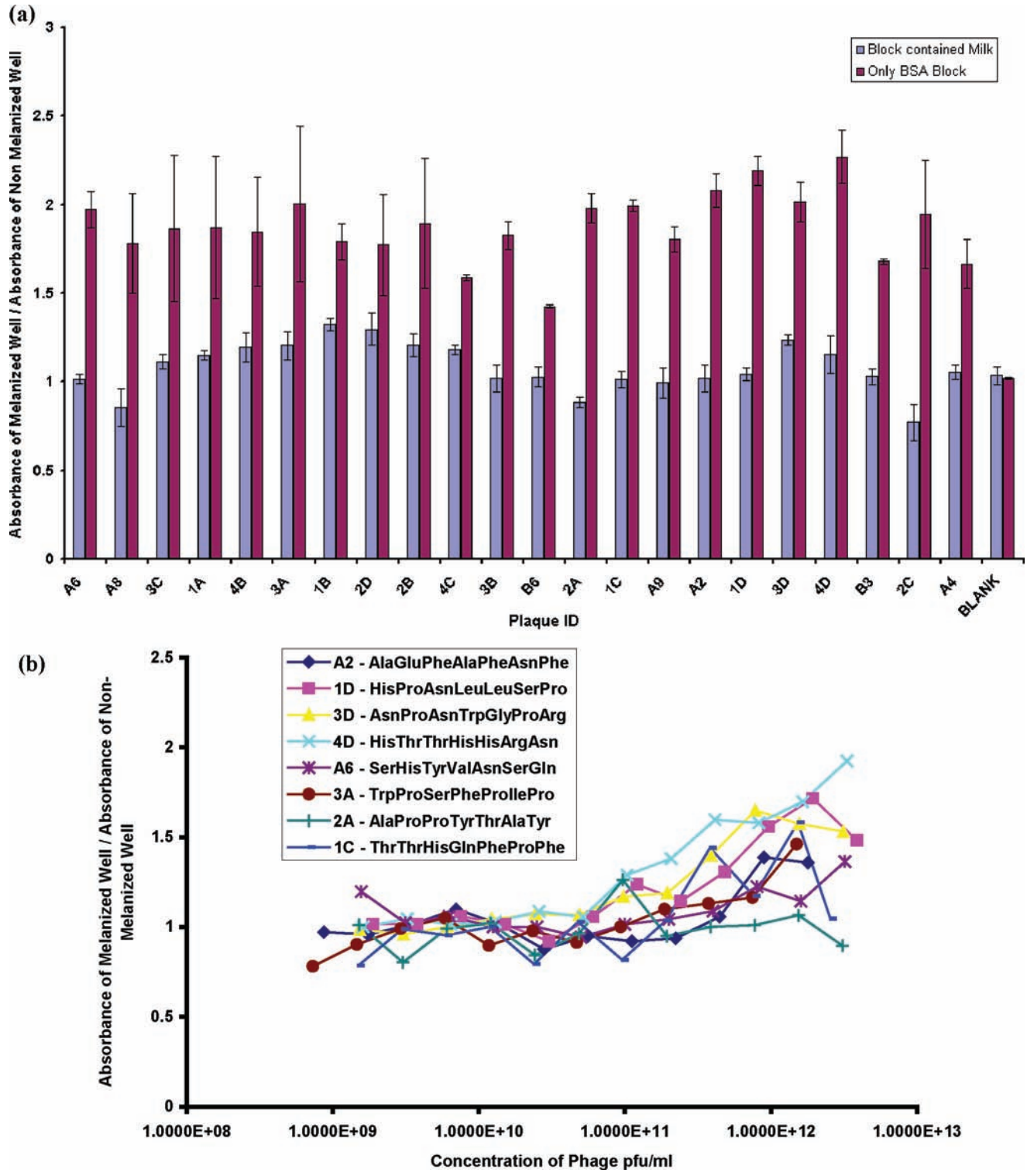


Figure 1. Selection of human tumor melanin binding phages from PhD-7 library. (a) First round of selection: plot of the absorbance ratios for the phages in melanized to nonmelanized wells. The wells were coated with melanin derived from MNT1 melanoma cells. Different blocking conditions were employed to ensure maximal blocking of nonspecific binding. (b) Second round of selection: binding curves resulting from ELISA of the best binding phages showing the ratio of the absorbance of the melanized to nonmelanized wells. Dilutions were fourfold starting at 1×10^{12} pfu/mL.

tapeptide AspGlyAlaTrpMetGlyAla did not bind to either viable or dead A2058 cells (results not shown).

Radiolabeling of HYNIC-Conjugated Heptapeptides. Labeling of HYNIC-conjugated heptapeptides with ^{188}Re resulted in an average of 92% yields for HisThrThrHisHisArgAsn, ThrThrHisGlnPheProPhe, AsnProAsnTrpGlyProArg, and Asp GlyAlaTrpMetGlyAla heptapeptides allowing for their use in cell binding and biodistribution experiments without further purification.

Binding of Radiolabeled Heptapeptides To Mnt1 and A2058 Melanoma Cells. First, we investigated whether ^{188}Re-labeled AsnProAsnTrpGlyProArg, ThrThrHisGlnPheProPhe,

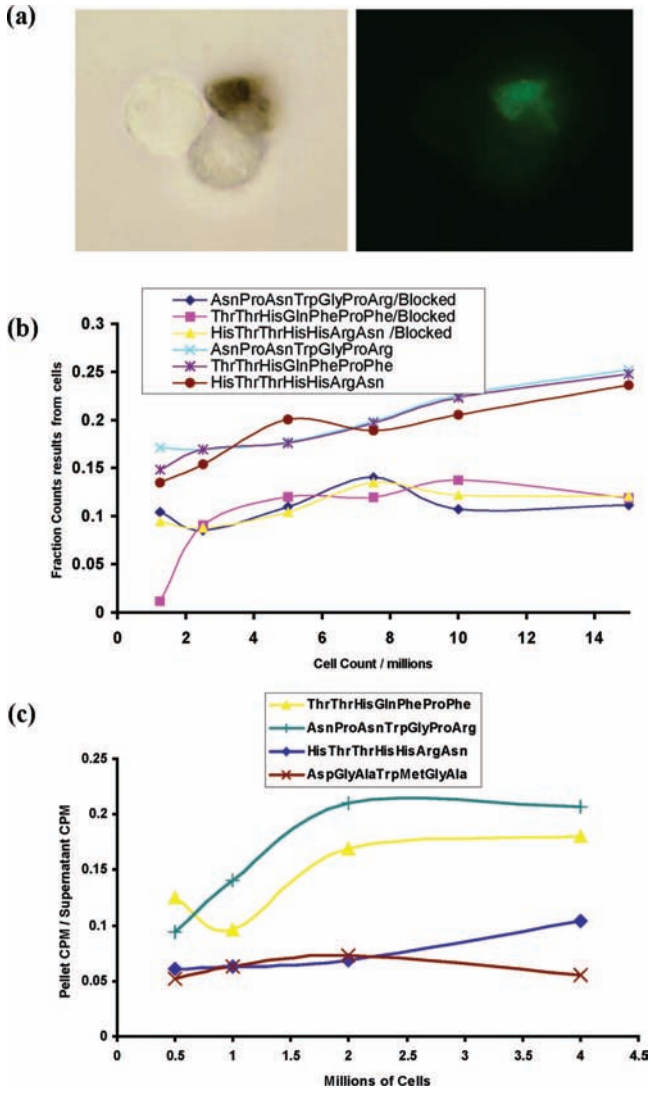


Figure 2. Binding of the heptapeptides to MNT1 and A2058 human melanoma cells. (a) Immunofluorescence image of biotinylated HisThrThrHisHisArgAsn heptapeptide binding to A2058 melanoma cells in culture. (b) Binding of heptapeptides to the whole MNT1 highly melanized melanoma cells. In blocking experiments, the MNT1 cells were preblocked with 10 μg per sample of the respective "cold" heptapeptide. (c) Binding of ^{188}Re-labeled HYNIC–heptapeptides to lysed A2058 cells.

and HisThrThrHisHisArgAsn heptapeptides would bind to whole highly melanized with eumelanin MNT1 melanoma cells (*11*), as melanin from those cells was used for selection of phages. The preparations of whole MNT1 cells contain approximately 10% nonviable cells (as per Trypan blue dye assay) in which melanin is accessible to the peptides. The binding to the MNT1 cells was proportional to the overall number of cells per sample and was decreased 2-fold by preblocking the cells with an excess of "cold" heptapeptides, proving that the binding of ^{188}Re-labeled peptides was specific (Figure 2b). Interestingly, the binding of all three of the above heptapeptides to MNT1 cells was very similar. The osmotic lysis of MNT1 released melanin from all cells in preparations, which increased the percentage binding to almost 100% (results not shown). Scatchard analysis of the binding to the lysed cells allowed estimation of the K_a for AsnProAsnTrpGlyProArg, ThrThrHisGlnPheProPhe, and HisThrThrHisHisArgAsn as $(7.1 \pm 0.5) \times 10^7$ M^{-1}. As A2058 metastatic melanoma cells are only slightly pigmented with pheomelanin, the binding of peptides to the lysed A2058 cells was significantly lower than binding to the

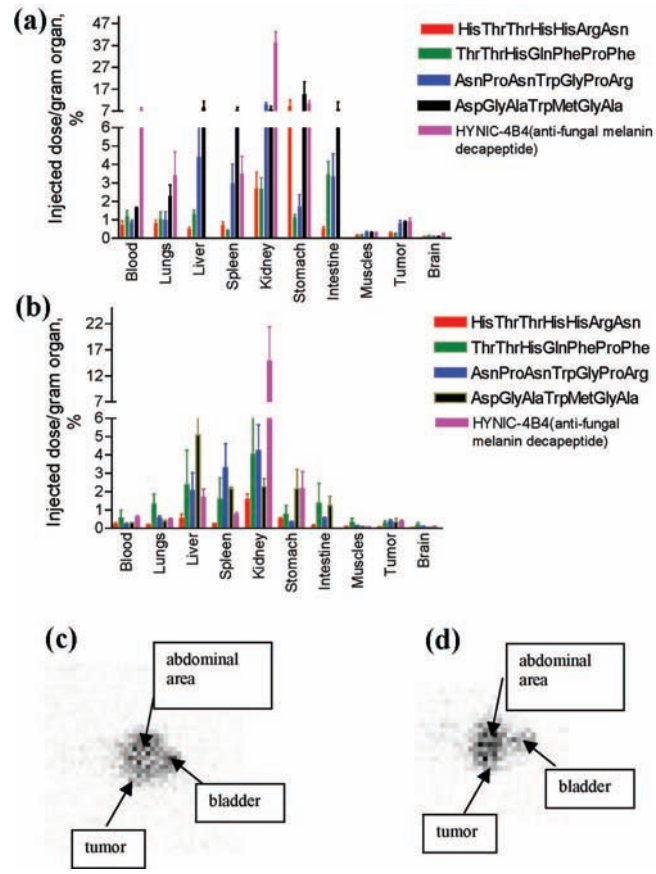


Figure 3. Biodistribution and scintigraphic imaging of ^{188}Re-labeled HYNIC–heptapeptides and ^{188}Re-labeled HYNIC–4B4 decapeptide in nude mice bearing A2058 human melanoma tumors (a) 3 h biodistribution post IV injection; (b) 24 h biodistribution post IV injection; (c) 1 h scintigraphic image of a mouse injected IP with ^{188}Re-HYNIC-AsnProAsnTrpGlyProArg; (d) 3 h scintigraphic image of a mouse injected IP with ^{188}Re-HYNIC-AsnProAsnTrpGlyProArg. The mice were imaged laying on their backs.

lysed MNT1 cells with the highest value of 20% observed for AsnProAsnTrpGlyProArg (Figure 2c). The unrelated control peptide AspGlyAlaTrpMetGlyAla practically did not bind to A2058 cells, while HisThrThrHisHisArgAsn binding reached only 10% at the high cell number (Figure 2c). The two best binders to the A2058 cell line, AsnProAsnTrpGlyProArg and ThrThrHisGlnPheProPhe, had K_a values of 1.5 and 1.1×10^7 M^{-1}, respectively.

Biodistribution and Scintigraphic Imaging of ^{188}Re-HYNIC–Heptapeptides in A2058 Melanoma Tumor-Bearing Mice. The biodistribution of AsnProAsnTrpGlyProArg, ThrThrHisGlnPheProPhe, and HisThrThrHisHisArgAsn heptapeptides and irrelevant AspGlyAlaTrpMetGlyAla was compared to that of fungal melanin-binding decapeptide 4B4 (Figure 3a,b). A dramatic difference in kidney uptake was observed between heptapeptides and 4B4 decapeptide at both 3 h (2.5–12% ID/g vs 38%) and 24 h (1.8–2.4% ID/g vs 15%) postinjection ($P = 0.001$). Melanin-specific heptapeptides showed greater stability *in vivo* than irrelevant heptapeptide AspGlyAlaTrpMetGlyAla or 4B4 decapeptide as judged by the lower stomach uptake of tumor melanin-specific heptapeptides ($P = 0.02$). Though the tumor to blood ratios were less than 1 for the heptapeptides used in biodistribution, for AsnProAsnTrpGlyProArg peptide tumor to blood ratio was almost 1 (0.92), which was a significant improvement in comparison to 4B4 decapeptide (tumor to blood ratio 0.12). Tumor uptake of both heptapeptides and decapeptide was modest at 0.5–1% ID/g at 3 h and decreased approximately 5-fold to 0.1–0.2% ID/g at

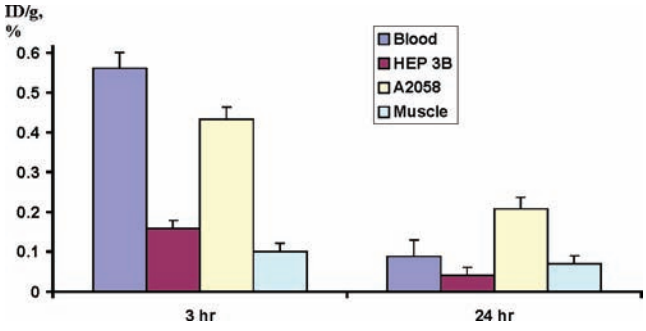


Figure 4. Comparative biodistribution at 3 and 24 h of ^{188}Re-HYNIC-AsnProAsnTrpGlyProArg heptapeptide in nude mice bearing two different xenografts: hepatocellular carcinoma and A2058 melanoma.

24 h. Importantly for therapy, however, the tumor to muscle uptake for these subcutaneous tumors was around 3. Overall, the best biodistribution pattern in terms of low kidney uptake, high stability, and relatively stable tumor uptake was observed for AsnProAsnTrpGlyProArg and ThrThrHisGlnPheProPhe heptapeptides, which was consistent with their higher binding to A2058 melanoma cells *in vitro*. In order to visualize tumor uptake, we imaged mice injected with the ^{188}Re-HYNIC-AsnProAsnTrpGlyProArg peptide on a gamma camera (Figure 3c,d). At both 1 and 3 h postinjection, most of the activity was localized to the abdominal cavity with practically no activity in the blood pool, thus confirming very fast clearance of the peptide from the blood. The tumor was visible at both 1 h (Figure 3c) and 3 h images (Figure 3d).

Biodistribution of ^{188}Re-HYNIC-AsnProAsnTrpGlyProArg in Nude Mice with Hepatocellular Carcinoma and A2058 Melanoma Xenografts. To confirm the specificity of heptapeptide uptake in melanoma tumors, the biodistribution of ^{188}Re-HYNIC-AsnProAsnTrpGlyProArg heptapeptide was also performed in mice bearing two different tumor xenografts on their flanks. The uptake of heptapeptide in A2058 melanoma tumors was 3 times higher than in hepatocellular carcinoma at 3 h postinjection and 5 times higher at 24 h (Figure 4).

Effect of D-Lysine Coinjection on Biodistribution of Heptapeptides. Co-injection of ThrThrHisGlnPheProPhe with D-lysine (400 mg/kg) did not reduce kidney uptake of the peptide. In fact, lysine coinjection was found to increase kidney uptake: At 3 h postinjection, there was 4 times more peptide in the kidneys of mice coinjected with D-lysine compared to control mice ($P = 0.003$) (Figure 5). Even after 24 h, the profound effect was still evident in the mice to whom D-lysine was administered compared to controls (3-fold difference).

Correlative Histology/Immunofluorescence of A2058 Melanoma Tumors. In order to establish the colocalization of heptapeptides with melanin in melanoma tumors, consecutive slides of A2058 melanoma tumors were stained with H&E or were incubated with the biotinylated AsnProAsnTrpGlyProArg heptapeptide. Biotin-AsnProAsnTrpGlyProArg localized in the melanin-rich areas of A2058 tumors (Figure 6a), while irrelevant control heptapeptide did not (results not shown).

Therapy of A2058 Tumor-Bearing Mice with ^{188}Re-HYNIC-AsnProAsnTrpGlyProArg Heptapeptide. To examine the effects of radiolabeled melanin-binding heptapeptides on A2058 tumors, we selected ^{188}Re-HYNIC-AsnProAsnTrpGlyProArg, as this peptide showed the best biodistribution pattern in terms of relatively high tumor uptake, low kidney uptake, and good stability *in vivo*. Three groups of six A2058 tumor-bearing nude mice with tumors of 0.7–0.8 cm in diameter were treated IP with (1) 2 × 1.0 mCi ^{188}Re-HYNIC-AsnProAsnTrpGlyProArg; (2) 2 × "cold" HYNIC-AsnProAsnTrpGlyProArg (0.2 μg each injection); or (3) 2 × 1.0 mCi ^{188}Re-HYNIC–4B4 decapeptide 7 days apart. Mice in the control group were left untreated. Two treatments with peptides were given because this regimen proved effective in the earlier study with ^{188}Re-HYNIC–4B4 decapeptide in MNT1 melanoma tumor-bearing mice (*11*). ^{188}Re-HYNIC–4B4 decapeptide was used as a control because of its success in treatment of MNT1 tumors (*11*) and comparability to ^{188}Re-HYNIC-AsnProAsnTrpGlyProArg uptake in A2058 tumors in this study. The A2058 tumors grew aggressively in the untreated group, and the last surviving mouse had to be sacrificed on day 35 because of the size of its tumor. Significantly slower ($P << 0.01$) tumor growth was observed in all treatment groups with ^{188}Re-HYNIC-AsnProAsnTrpGlyProArg slowing the tumor growth more efficiently ($P = 0.02$) than "cold" HYNIC-AsnProAsnTrp GlyProArg or ^{188}Re-HYNIC–4B4 decapeptide from day 25 posttreatment. Interestingly, "cold" HYNIC-AsnProAsnTrp GlyProArg was almost as efficient in slowing down tumor growth as ^{188}Re-HYNIC–4B4 decapeptide.

DISCUSSION

During the past decade, radiolabeled peptides that bind to different receptors on a variety of tumors have been investigated as potential therapeutic agents in both the preclinical and clinical settings (*16*). Preclinical studies of the radiolabeled peptides in melanoma treatment have concentrated on melanocyte-stimulating hormone (MSH) receptor with efforts directed primarily at the synthesis of metal-cyclized α-MSH peptide analogues such as Re-(Arg(11))CCMSH (*17*). The first therapy with ^{188}Re-(Arg(11))CCMSH in B16/F1 murine melanoma and TXM13 human melanoma-bearing mouse models was reported to result in the reduction of the tumor growth rate and prolonged survival in the treatment groups (*18*). We have recently demonstrated that ^{188}Re-labeled fungal melanin-binding decapeptide 4B4 was effective against experimental MNT1 human melanoma and was safe for normal melanized tissues (*11*). As no human melanin-binding peptides have been reported, for the proof-of-principle experiments targeting melanin in the tumors with radiolabeled melanin-binding peptides (*11*), we utilized the peptides that were originally generated to fungal melanin for purposes unrelated to cancer research (*10*). Although no nephrotoxicity was noted in those studies, the high kidney uptake of the 4B4 fungal melanin-binding peptide prompted the search for the peptides with lower kidney uptake. In this study, we generated the peptides to human melanin in an attempt to provide the structural solution to the problem of high kidney uptake.

During the past decade, phage display has been extensively used in cancer research (reviewed in ref (*19*)). Phage display can be utilized for the fast identification of biologically active ligands for molecules already determined to be important in cancer development, for creating a profile of peptide ligands for a particular cancer cell type, and for the identification of organ and tumor homing peptides. The limitations of the phage display approach are conformational differences between the peptides fused to phage coat proteins and chemically synthesized peptides, which can result in inferior binding of chemically synthesized peptides to their target when compared to the original phages (*20*).

The availability of the commercially available PhD-7 phage display library allowed us to generate heptapeptides that were subsequently selected for their tumor melanin-binding properties by ELISA. These heptapeptides were less aromatic and less positively charged than melanin-binding decapeptides recovered by screening on fungal melanin (*10*). Surprisingly, in spite of their small size, the heptapeptides were not able to penetrate through the membranes of viable A2058 human melanoma cells and bound only to the melanin in nonviable cells or released from the dead cells as demonstrated by immunofluorescence.

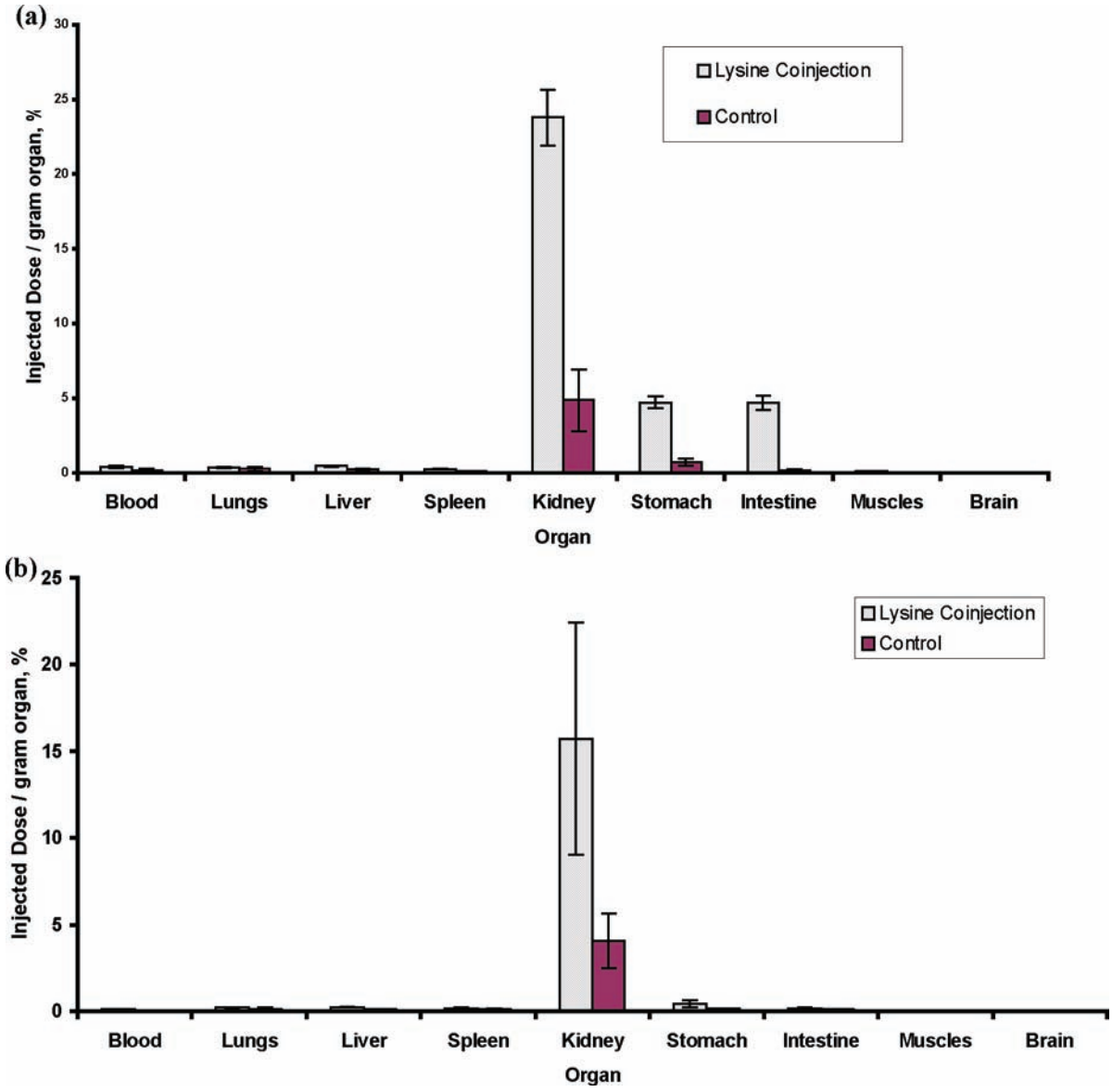


Figure 5. Comparative biodistribution of ^{188}Re-labeled HYNIC-ThrThrHisGlnPheProPhe heptapeptide in non-tumor-bearing CD-1 mice injected IV with peptide alone or coinjected with D-lysine (400 mg/kg body weight): (a) 3 h postinjection; (b) 24 h postinjection.

This result is encouraging, as the inability of heptapeptides to penetrate through cell membranes will minimize toxicity to healthy melanized cells during therapy.

When administered to tumor-bearing mice, both ^{188}Re-labeled heptapeptides and ^{188}Re-labeled decapeptide 4B4 exhibited tumor uptake in A2058 human metastatic melanoma tumors. This is encouraging, as the panel of heptapeptides was developed against black eumelanin from MNT1 melanoma tumors (*8*) and decapeptide 4B4 against black fungal melanin (*10*). In contrast, A2058 tumor cells are pigmented with pheomelanin, a yellow or reddish-brown melanin-type pigment. Both pheomelanin and eumelanin are negatively charged and share some structural similarity, with both types found in melanomas where eumelanin is the predominant pigment in primary tumors, while pheomelanin is associated with metastatic melanomas and progression of the disease (*21*). The predominance of pheomelanin in A2058 cells resulted in relatively low binding of heptapeptides to the tumors. Since melanoma is a very heterogeneous disease, melanin in the patients' tumors will be most likely represented by both eumelanin and pheomelanin, and even so called "amelanotic" melanomas do contain some melanin to ensure targeting with heptapeptides (*22, 23*). In addition, it is worthwhile to note that in a very recent study Newton et al. used phage display methodology to generate α-MSH peptide analogues for the purpose of imaging melanoma tumors (*24*) and observed relatively low uptake of peptides and phages in the tumors. The unrelated control peptide AspGlyAlaTrpMetGlyAla also showed some tumoral accumulation in our biodistribution study. However, it was unstable *in vivo*, which was manifested by high stomach, liver, and intestine uptake. Its high stomach uptake was most likely due to ^{188}Re-perrhenate presence resulting from *in vivo* decomposition of peptide. As pigmented cells can express sodium iodide symporter (NIS) (*25*), the uptake in the tumor seen for AspGlyAlaTrpMetGlyAla may actually be the binding of ^{188}Re-perrhenate to NIS. The specificity of heptapeptides for tumor melanin was proven by preferential uptake of ^{188}Re-HYNIC-AsnProAsnTrpGlyProArg in A2058 melanoma xenografts in mice bearing hepatocellular carcinoma and melanoma xenografts simultaneously and by colocalization of biotin-AsnProAsnTrpGlyProArg with melanin on tumor slides.

In our earlier studies, we estimated the number of nonviable cells in experimental melanoma tumors by subjecting the cells from melanoma tumors grown in nude mice to Trypan blue

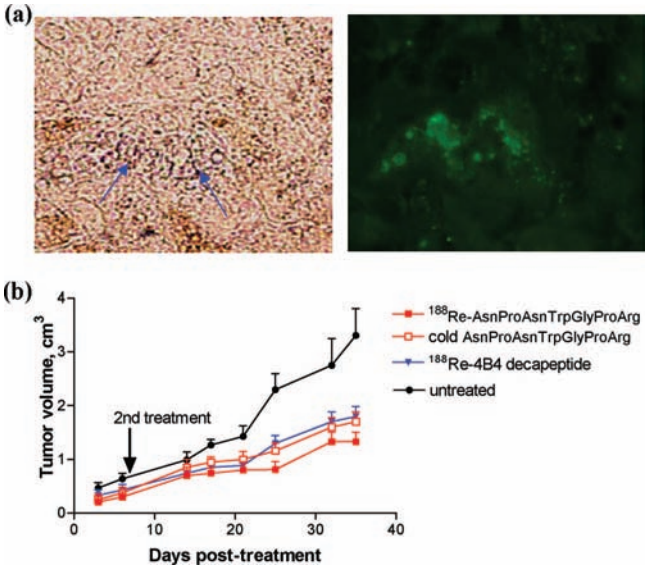


Figure 6. Colocalization of ^{188}Re-HYNIC-AsnProAsnTrpGlyProArg heptapeptide with melanin in melanoma tumors and therapy of A2058 tumor-bearing mice with the same heptapeptide. (a) Left: H&E stained A2058 melanoma tumor slide. Melanin deposits are shown with blue arrows. Right: immunofluorescence with biotinylated AsnProAsnTrp GlyProArg. (b) A2058 tumor-bearing nude mice with tumors of 0.7–0.8 cm in diameter were treated IP with (1) 2 × 1.0 mCi ^{188}Re-HYNIC-AsnProAsnTrpGlyProArg; (2) 2 × "cold" HYNIC-AsnProAsnTrpGlyProArg (0.2 μg each injection); or (3) 2 × 1.0 mCi ^{188}Re-HYNIC–4B4 decapeptide 7 days apart. Mice in the control group were left untreated. Points represent means of tumor size of 6 mice. The bars represent standard deviation.

assay. Approximately 7% of all cells (melanoma and connective tissue) turned to be nonviable in non-necrotic tumors, and up to 40% of cells were nonviable in necrotic tumors (Dadachova et al., unpublished observations). Apparently, this number of cells was sufficient to provide the target for the radiolabeled peptides. In spite of modest tumor uptake, significantly slower ($P << 0.01$) tumor growth was observed in all treatment groups with ^{188}Re-HYNIC-AsnProAsnTrpGlyProArg slowing the tumor growth more efficiently ($P = 0.02$) than "cold" HYNIC-AsnProAsnTrpGlyProArg or ^{188}Re-HYNIC–4B4 decapeptide from day 25 posttreatment. "Cold" HYNIC-AsnProAsnTrp GlyProArg was almost as efficient in slowing down tumor growth as ^{188}Re-HYNIC–4B4 decapeptide, suggesting that the peptide has a therapeutic effect independent of the attached radionuclide. The mechanism for this phenomenon is unknown, but in prior studies, we also observed that "cold" melanin-binding mAb 6D2 had some therapeutic effect on melanoma tumors (*9*). We speculate that melanin-binding peptides and mAbs might be absorbed into the surface of melanin where they become immunogenic and elicit an immune response that triggers localized inflammation that produces an antitumor effect. The explanation for higher efficacy of the radiolabeled heptapeptide may be the combination of the biological effect of the peptide with the deep penetration of the small peptide into the tumor and "cross-fire" irradiation of distant cells by the energetic β-emissions of ^{188}Re providing relatively homogenous irradiation of the tumor. Also, in the future, it might be possible to increase tumor uptake of these heptapeptides using site-directed mutagenesis or peptide arrays.

Since the purpose of the study was to generate melanin-binding peptides with low kidney uptake, we paid particular attention to uptake of radiolabeled heptapeptides in this organ. The kidney uptake of heptapeptides described in this study was on average 7 times less than that for ^{188}Re-labeled decapeptide 4B4. This is a dramatic improvement in the biodistribution pattern of melanin-binding peptides, given that kidneys are a major concern for toxicity during therapy with radiolabeled peptides (*13*). Interestingly, an attempt to further decrease kidney uptake of the ^{188}Re-labeled heptapeptide pharmacologically by coadministration of positively charged amino acid D-lysine, which was supposed to block the negative charge on cell membranes in the proximal tubules and thus prevent heptapeptide retention after glomerular filtration, paradoxically increased its uptake by several fold. Interestingly, the same phenomenon was observed when ^{188}Re-labeled decapeptide 4B4 was coadministered to mice with D-lysine (E. Dadachova, unpublished observations). The explanation of this phenomenon is yet to be found, as molecular mechanisms of renal reabsorption of peptides used in radionuclide therapy have not been clarified. For example, radiolabeled somatostatin peptide analogues have been used in clinical practice since the late 1980s, but only very recently has evidence been presented to suggest that the molecular mechanism of [^{111}In-DTPA]octreotide uptake in renal proximal tubules involves multiligand scavenger receptor megalin (*26*).

In conclusion, by utilizing phage display technique, we generated a panel of tumor melanin-binding heptapeptides which when radiolabeled with ^{188}Re demonstrated 7-fold lower kidney uptake in mice than previously reported ^{188}Re-labeled fungal melanin-binding decapeptide. Administration of one of the generated heptapeptides, ^{188}Re-HYNIC-AsnProAsnTrpGlyProArg, to A2058 human metastatic melanoma-bearing nude mice resulted in significant retardation of the tumor growth. In spite of their relatively small size, heptapeptides were not able to penetrate through the membranes of viable melanoma cells and bound only to extracellular melanin, which provides assurance that they will be safe to healthy melanin-containing tissues during radionuclide therapy of melanoma. Thus, these heptapeptides can be potentially developed into efficient and safe delivery vehicles for targeted radionuclide therapy of melanoma.

ACKNOWLEDGMENT

The authors would like to thank NIH-designated Albert Einstein College of Medicine Cancer Center for providing funding for this work; Dr. M. Torres for help with the phage display library; Dr. L. Mintz for advice on the peptides synthesis; and Dr. X-G. Wang for supplying hepatocellular carcinoma cells.

LITERATURE CITED

(1) Rigel, D. S. (1997) Malignant melanoma: Incidence, issues and their effect on diagnosis and therapy in the 1990s. *Mayo Clin. Proc. 72* (4), 367–371.
(2) Grin-Jorgensen, C. M., Rigel, D. S., and Friedman, R. J. (1992) The worldwide incidence of malignant melanoma. In *Cutaneous Melanoma*, 2nd ed. (Balch C. M., Houghton A. N., Milton G. W., Sober A. J., and Soong S. J., Eds.) pp 27–39, Lippincott Co., Philadelphia
(3) Liu, T., and Soong, S. J. (1996) Epidemiology of malignant melanoma. *Surg Clin. N. Am. 76* (6), 1205–1222.
(4) Sun, W., and Schuchter, L. M. (2001) Metastatic melanoma. *Curr. Treat. Options Oncol. 2* (3), 193–202.
(5) Schuchter, L. (2004) Are we at a turning point for melanoma therapy? 2nd International Melanoma Research Congress, Phoenix, Arizona, November 13–16, 2004; p 2.
(6) Cohen-Solal, K. A., Crespo-Carbone, S. M., Namkoong, J., Mackason, K. R., Roberts, K. G., Reuhl, K. R., and Chen, S. (2002) Progressive appearance of pigmentation in amelanotic melanoma lesions. *Pigment Cell Res. 15* (4), 282–289.
(7) Busam, K. J., Hester, K., Charles, C., Sachs, D. L., Antonescu, C. R., Gonzalez, S., and Halpern, A. C. (2001) Detection of clinically amelanotic malignant melanoma and assessment of its

margins by in vivo confocal scanning laser microscopy. *Arch. Dermatol. 137* (7), 923–929.
(8) Dadachova, E., and Casadevall, A. (2005) Melanin as a potential target for radionuclide therapy of metastatic melanoma. *Future Oncol. 1* (4), 541–549.
(9) Dadachova, E., Nosanchuk, J. D., and Shi, L., et al. (2004) Dead cells in melanoma tumors provide abundant antigen for targeted delivery of ionizing radiation by a monoclonal antibody to melanin. *Proc. Natl. Acad. Sci. U.S.A. 101* (41), 14865–14870.
(10) Nosanchuk, J. D., Valadon, P., Feldmesser, M., and Casadevall, A. (1999) Melanization of Cryptococcus neoformans in murine infection. *Mol. Cell Biol. 19* (1), 745–750.
(11) Dadachova, E., Moadel, T., Schweitzer, A. D., Bryan, R. A., Zhang, T., Mints, L., Revskaya, E., Huang, X., Ortiz, G., Nosanchuck, J. S., Nosanchuck, J. D., and Casadevall, A. (2006) Radiolabeled melanin-binding peptides are safe and effective in treatment of human pigmented melanoma in a mouse model of disease. *Cancer Biother. Radiopharm. 21* (2), 117–129.
(12) Blok, D., Feitsma, R. I., Vermeij, P., and Pauwels, E. J. (1999) Peptide radiopharmaceuticals in nuclear medicine. *Eur. J. Nucl. Med. 26* (11), 1511–1519.
(13) Lambert, B., Cybulla, M., Weiner, S. M., Van De Wiele, C., Ham, H., Dierckx, R. A., and Otte, A. (2004) Renal toxicity after radionuclide therapy. *Radiat. Res. 161* (5), 607–611.
(14) Kushimoto, T. A., Basrur, V., Valencia, J., Matsunaga, J., Viera, W. D., Ferrans, V. J., Muller, J., Appella, E., and Hearing, V. J. (2001) A model for melanosome biogenesis based on the purification and analysis of early melanosomes. *Proc. Natl. Acad. Sci. U.S.A. 98*, 10698–10703.
(15) Lindmo, T., Boven, E., and Cuttitta, F. (1984) Determination of the immunoreactive fraction of radiolabeled monoclonal antibodies by linear extrapolation to binding at infinite antigen excess. *J. Immunol. Methods 72*, 77–89.
(16) Krenning, E. P., Kwekkeboom, D. J., Valkema, R., Pauwels, S., Kvols, L. K., and de Jong, M. (2004) Peptide receptor radionuclide therapy. *Ann. N.Y. Acad. Sci. 1014*, 234–245.
(17) Miao, Y., Whitener, D., Feng, W., Owen, N. K., Chen, J., and Quinn, T. P. (2003) Evaluation of the human melanoma targeting properties of radiolabeled alpha-melanocyte stimulating hormone peptide analogues. *Bioconjugate Chem. 14* (6), 1177–1184.
(18) Miao, Y., Owen, N. K., Fisher, D. R., Hoffman, T. J., and Quinn, T. P. (2005) Therapeutic efficacy of a 188Re-labeled alpha-melanocyte-stimulating hormone peptide analog in murine and human melanoma-bearing mouse models. *J. Nucl. Med. 46* (1), 121.
(19) Romanov, V. I. (2003) Phage display selection and evaluation of cancer drug targets. *Curr. Cancer Drug Targets 3* (2), 119–129.
(20) Landon, L. A., Zou, J., and Deutscher, S. L. (2004) Is phage display technology on target for developing peptide-based cancer drugs? *Curr. Drug Discovery Technol. 1* (2), 113–32.
(21) Hearing, V. (2000) The melanosome: the perfect model for cellular responses to the environment. *Pigment Cell Res. 13* (Suppl 8), 23–34.
(22) Cohen-Solal, K. A., Crespo-Carbone, S. M., and Namkoong, J., et al. (2002) Progressive appearance of pigmentation in amelanotic melanoma lesions. *Pigment Cell Res. 15* (4), 282–289.
(23) Busam, K. J., Hester, K., and Charles, C., et al. (2001) Detection of clinically amelanotic malignant melanoma and assessment of its margins by in vivo confocal scanning laser microscopy. *Arch. Dermatol. 137* (7), 923–929.
(24) Newton, J. R., Miao, Y., Deutscher, S. L., and Quinn, T. P. (2007) Melanoma imaging with pretargeted bivalent bacteriophage. *J. Nucl. Med. 48* (3), 429–36.
(25) Slominski, A., Wortsman, J, Kohn, L., Ain, K. B., Venkataraman, G. M., Pisarchik, A., Chung, J. H., Giuliani, C., Thornton, M., Slugocki, G., and Tobin, D. J. (2002) Expression of hypothalamic-pituitary-thyroid axis related genes in the human skin. *J. Invest. Dermatol. 119* (6), 1449–55.
(26) de Jong, M., Barone, R., Krenning, E., Bernard, B., Melis, M., Visser, T., Gekle, M., Willnow, T. E., Walrand, S., Jamar, F., and Pauwels, S. (2005) Megalin is essential for renal proximal tubule reabsorption of (111)In-DTPA-octreotide. *J. Nucl. Med. 46* (10), 1696–1700.

BC060330U

Wheat Germ Agglutinin-Modified Trifunctional Nanospheres for Cell Recognition

Hai-Yan Xie,[†,‡] Min Xie,[‡] Zhi-Ling Zhang,[‡] Yan-Min Long,[‡] Xin Liu,[‡] Ming-Liang Tang,[§] Dai-Wen Pang,*[,‡] Zheng Tan,[§] Calum Dickinson,[||] and Wuzong Zhou*[,||]

School of Life Science and Technology, Beijing Institute of Technology, Beijing 100081, P. R. China; College of Chemistry and Molecular Sciences, State Key Laboratory of Virology and College of Life Sciences, Wuhan University, Wuhan 430072, P. R. China; and EaStChem, School of Chemistry, University of St. Andrews, St. Andrews, Fife KY16 9ST, United Kingdom. Received December 14, 2006; Revised Manuscript Received August 5, 2007

A simple and convenient strategy has been put forward to fabricate smart fluorescent magnetic wheat germ agglutinin-modified trifunctional nanospheres (WGA-TFNS) for recognition of human prostate carcinoma DU-145 cells which are surface-expressed with sialic acid and *N*-acetylglucosamine. These TFNS can be easily manipulated, tracked, and conveniently used to capture and separate target cells. The presence of wheat germ agglutinin on the surface of WGA-TFNS was confirmed by FTIR, biorecognition of carboxymethyl chitin-modified quantum dots (CM-CT-QDs), and bacterium *Staphylococcus aureus*. The success in recognizing DU-145 cells by the WGA-TFNS indicates that WGA-TFNS could be applicable.

INTRODUCTION

Lectins, which can be found in most organisms, ranging from viruses and bacteria to plants and animals (*1*), form a family of natural nonenzymatic proteins/glycoproteins that bind monosaccharides and oligosaccharides with high specificity, although they are not products of an immune response. Each lectin molecule contains typically two or more carbohydrate binding sites. When they interact with cells, they will not only specifically recognize and bind to the carbohydrate residues on the cell surface, but also cause cross-linking of the cells and their subsequent agglutination (*1*). Lectins also have cytoadhesive and cytoinvasive properties, and can initiate vesicular transport processes based on their recognizing and binding to carbohydrate residues on a cell surface (*2*). Therefore, lectins have been widely used in drug delivery systems (*3*).

Wheat germ agglutinin (WGA), derived from cereals and one of the most widely characterized and least immunogenic lectins, is a dimer consisting of two identical 18 kDa subunits and four carbohydrate binding sites. Since WGA receptors, such as *N*-acetylglucosamine (GlcNAc) and sialic acid, are commonly expressed on surface plasma membranes of most types of neurons in the brain, among a number of lectins with different carbohydrate-binding specificities (*4*), WGA can be used as an effective tracer in a variety of neural systems. As WGA can also recognize some types of cancer cells, it has already been used in some drug delivery applications (*5*).

Nanomaterials, especially nanomaterial-based functional nanodevices, are increasing in their popularity with researchers and manufacturers. Among them, magnetic nanoparticles are extensively studied and widely used for drug delivery, magnetic treatment, and magnetic separation due to their small size, single magnetic domain structures, and superparamagnetism (*6–14*). Fluorescent semiconductor quantum dots (QDs) are another important type of nanoparticles, which have broad excitation and size-dependent photoluminescence with narrow emission bandwidth covering a wide spectral range. By using a single wavelength, many particles with different sizes and different compositions can be simultaneously excited. Furthermore, the QDs exhibit unusual photochemical stability and relatively high photoluminescent quantum yields (*15–19*). By embedding QDs with different emission colors into polymer spheres, a large number of encoded and distinguishable microbeads can be obtained. QD-embedded polymer microspheres are expected to be used in gene expression, high-throughput screening, and medical diagnostics (*20*). On the other hand, magnetic nanoparticle filled beads have been used in the biomedical field, such as immunomagnetic separation and nucleic acid hybridization (*11, 21*). However, in many biomedical and clinical diagnostic fields, there has always been some need for materials with the functions of both magnetic separation and fluorescence tracking. The common strategy is to anchor magnetic nanoparticles and organic fluorophores, respectively, to two kinds of molecules that can interact with each other. The method is complicated, time-consuming, and inefficient (*11, 12, 14*). Several new methods have been developed recently based on the use of QDs and magnetic nanoparticles (*22–30*). Among them, the method developed by us is to construct fluorescent–magnetic bifunctional nanospheres by co-embedding the fluorescent quantum dots and γ-Fe_2O_3 magnetic nanoparticles into single swelling-poly(styrene/acrylamide) copolymer nanospheres (*22, 26–28*). The nanospheres are fluorescence-trackable and magneto-manipulatable, and demonstrate their capability of specific cell targeting after surface-modification with some specific reagents such as folic acid (*22, 26, 27*). Subsequently, they were successfully used in apoptotic Hela cell recognition (*28*). Here, we present WGA-modified trifunctional nanospheres for recognition of human prostate carcinoma DU-145 cells based on a new strategy of convenient modification of fluorescent–mag-

* Corresponding authors. Phone 0086-27-68756759; Faxes 0086-27-68754067, +44 1334 463808; E-mail addresses:dwpang@whu.edu.cn or wzhou@st-andrews.ac.uk.

[†] Beijing Institute of Technology.

[‡] College of Chemistry and Molecular Sciences and State Key Laboratory of Virology, Wuhan University.

[§] College of Life Sciences, Wuhan University.

[||] University of St. Andrews.

10.1021/bc060387g CCC: $37.00 © 2007 American Chemical Society
Published on Web 09/26/2007

netic bifunctional nanospheres, which will be universally applicable for GlcNAc and sialic acid recognition.

EXPERIMENTAL PROCEDURES

Fabrication of Fluorescent–Magnetic Bifunctional Nanospheres. In order to fabricate fluorescent–magnetic bifunctional nanospheres (BFNS) (*22, 26, 27*), some related building materials should be first synthesized. CdSe/ZnS QDs, with the diameter between 3 and 6 nm, were synthesized by the method described in a previous report (*31*). The synthesis of nano-γ-Fe_2O_3 (ca. 8 nm in diameter) was as reported (*27, 32*). Poly(styrene/acrylamide) copolymer nanospheres (St-AAm, 100–250 nm in diameter) were produced from styrene (St) and acrylamide (AAm) by means of emulsifier-free polymerization by the previously reported method (*33*). St-AAm was subsequently modified with hydrazine through the surface amide functional groups, producing a reactive nanosphere surface for future modification and attachment (*27*). The hydrazinized St-AAm was denoted as H_2N-St-AAm.

On the basis of the above building materials, the bifunctional nanospheres were fabricated as described below (Scheme 1) (*22, 26, 27*). Both the QDs and the nano-γ-Fe_2O_3 dispersed in hexane were washed several times to remove any impurities, and the nanoparticles and copolymer nanospheres were dried before use. Hydrazinized bifunctional nanospheres (H_2N-BFNS) were produced by swelling the H_2N-St-AAm in a solvent mixture containing 5% (vol) chloroform and 95% (vol) butanol, and adding a controlled amount of CdSe/ZnS QDs and nano-γ-Fe_2O_3 to the mixture. For example, a typical ratio used in the present work was 3:1 QDs/Fe_2O_3. The mixture was then ultrasonicated until it became a well-dispersed suspension. The mixture was ultrasonicated for a further 30 min, centrifuged, and washed with butanol three times. The resultant H_2N-BFNS with both fluorescence and magnetism were dispersed in ultrapure water for use.

Construction of Wheat Germ Agglutinin-Modified Trifunctional Nanospheres. 0.1 g of succinic anhydride was added to 5 mL of 10 mg/mL H_2N-BFNS aqueous solution. The pH of the reaction system was adjusted to 4 with 1 M NaOH. The reaction lasted for 2–3 h. Then, the product was centrifuged at 12 000 rpm for 10 min several times to remove the excess succinic anhydride. The final product HOOC-BFNS was kept in 0.1 M phosphate buffer solution (PBS) (pH 6.5).

The tube with the solution containing the HOOC-BFNS was put onto a magnetic scaffold for ca. 5 min, and then the HOOC-BFNS were attracted by magnetic force, allowing the solvent to be removed easily. The attachment method was similar to that previously reported (*2, 34*). The HOOC-BFNS were thoroughly washed with 0.1 M PBS (pH 6.5). After that, ca. 5 mg of HOOC-BFNS were activated with 100 mM 1-ethyl-3-(3-dimethylaminopropyl)carbodiimide hydrochloride (EDAC) and 100 mM *N*-hydroxysuccinimide (NHS) in l mL of 0.1 M PBS (pH 6.5) for 30 min at room temperature with continuous shaking. The activated HOOC-BFNS were then washed with l mL of 0.1 M PBS (pH 7.4). To covalently immobilize WGA onto the BFNS surface, 90 μL of activated HOOC-BFNS were reacted with 10 μL of WGA (3.6 mg/mL, dissolved in 0.1 M PBS at pH 7.4) for 4 h at room temperature with continuous shaking to form fluorescent magnetic wheat germ agglutinin modified trifunctional nanospheres (WGA-TFNS). The tube containing WGA-TFNS was put onto the magnetic scaffold to remove any unreacted WGA and then washed with 0.1 M Tris–HCl (pH 7.5, containing 1 mM $CaCl_2$ and 1 mM $MgCl_2$). The resultant WGA-TFNS were dispersed in 400 μL of the same Tris–HCl solution.

Because nano-γ-Fe_2O_3 and QDs in WGA-TFNS would influence the characterization of WGA on the surface of WGA-TFNS, WGA-St-AAm was constructed to facilitate the characterization. WGA-St-AAm was prepared according to the procedure similar to that of WGA-TFNS. The washed HOOC-St-AAm was dispersed in 1 mL of 0.1 M PBS (pH 6.5), then activated with 100 mM EDAC and 100 mM NHS in l mL of 0.1 M PBS (pH 6.5) for 30 min at room temperature with continuous shaking, followed by centrifuging at 12 000 rpm for 40 min to remove excess activation reagents and further washing with l mL of 0.1 M PBS (pH 7.4) by centrifuging at 12 000 rpm for 40 min. Subsequently, 950 μL of activated HOOC-St-AAm was reacted with 50 μL of WGA (3.6 mg/mL, dissolved in 0.1 M PBS at pH 7.4) for 4 h at room temperature with continuous shaking to form WGA-St-AAm. WGA-St-AAm was purified by centrifugation at 12 000 rpm for 40 min to remove excess WGA, and finally dispersed in l mL of 0.1 M PBS (pH 7.4).

Characterization. An Acc. V Spot Maqn scanning electron microscope (SEM) operated at 20 kV was used to characterize the surface morphology of the H_2N-St-AAm nanospheres. The size and dispersity of the nano-γ-Fe_2O_3 and H_2N-St-AAm were characterized by transmission electron microscopy (TEM) on a JEOL-JEM 2010 microscope operated at 200 kV using a Gatan Dual Vision 300 W CCD camera. High-resolution TEM (HRTEM) images of BFNS were obtained on a JEOL-JEM 2011 microscope operated at 200 kV. Chemical composition of the products was examined by energy-dispersive X-ray microanalysis (EDX) using an Oxford Link ISIS system attached to the JEM-2011 microscope. A small electron beam (5–10 nm) was normally chosen for the EDX studies. The X-ray diffraction pattern of the nano-γ-Fe_2O_3 was determined on a D/max-RC diffractometer with Cu (40 kV, 50 mA) as the target.

Fluorescence images were recorded with a Zeiss HRC Axiocam (3900 $\times$ 3900 pixels) camera attached to a Zeiss inverted optical microscope (Axiovert 200M) or an Olympus IX70 inverted fluorescence microscope with a 100 W mercury arc lamp, U-MWU (330–385/400/420nm) and U-MWB filters (450–480/500/515 nm) and an oil-immersion objective (100$\times$).

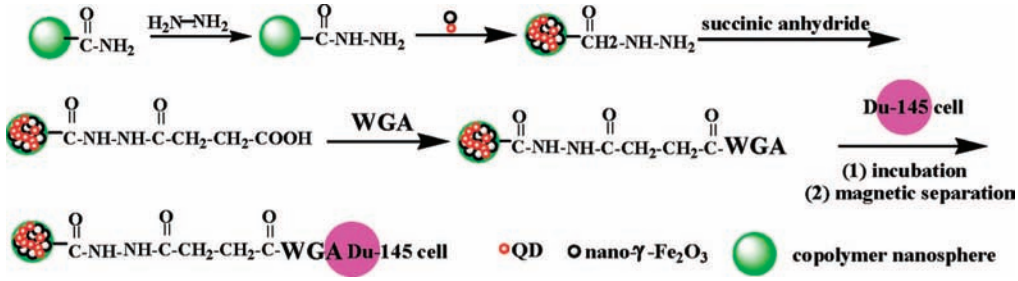
WGA on the surface of WGA-TFNS was characterized by FTIR spectroscopy. H_2N-St-AAm, HOOC-St-AAm, and WGA-St-AAm were lyophilized for FTIR analysis. The infrared spectra of the samples were obtained on a Thermo Nicolet 360 FT-IR spectrophotometer. Pressed pellets were prepared by grinding the powder specimens with KBr in an agate mortar.

Cell Culture and Recognition of Cells by WGA-TFNS. *Staphylococcus aureus* (*S. aureus*) was precultured overnight in 5 mL of Luria-Bertain (LB) culture medium at 37 °C. Then, 100 μL of precultured *S. aureus* suspension was added to 5 mL of LB culture medium, incubated at 37 °C for 6 h with shaking, and kept at 4 °C for further experiments.

S. aureus agglutination was used to confirm the presence of WGA on the WGA-TFNS surface. 0.5 mL of *S. aureus* suspension was harvested by centrifugation at 8000 rpm for 5 min, washed twice with 0.1 M Tris–HCl (pH 7.5, containing 1 mM $CaCl_2$ and 1 mM $MgCl_2$), and resuspended in 400 μL of the same Tris–HCl solution. The mixture of 150 μL of WGA-TFNS and harvested *S. aureus* suspension was incubated at 37 °C for 25 min, magnetically separated on a magnetic scaffold, washed with the 0.1 M Tris–HCl solution, and resuspended in 200 μL of the 0.1 M Tris–HCl solution for imaging.

DU-145 cells (a human prostate carcinoma cell line) were used for the recognition by WGA-TFNS. Cells were routinely cultured at 37 °C in a flask containing RPMI 1640, supplemented with 10% fetal bovine serum (FBS), 100 μg/mL penicillin G, 100 μg/mL streptomycin sulfate, 1.8 mg/mL $NaHCO_3$ and 25 mM HEPES in a humidified atmosphere with 5% CO_2 (in air).

Scheme 1. Construction of a Fluorescent Magnetic Wheat Germ Agglutinin Trifunctional Nanosphere and Its Capturing a Human Prostate Carcinoma Du-145 Cell



Experiments of DU-145 cell capture and separation by WGA-TFNS were carried out as described below. About 1×10^6 DU-145 cells were first cultured in a flask and then detached using trypsin–EDTA solution, and collected by centrifugation at approximately 1000 rpm for 5 min at room temperature. Subsequently, the cells were washed with cold 1 × PBS, resuspended in 900 μL of 1 × PBS and incubated with 100 μL of 5 mg/mL WGA-TFNS for 30 min at room temperature. Besides WGA, Dolichos biflorus agglutinin (DBA), another kind of lectin that can bind with *N*-acetyl-D-galactosamine (GalNAc), was used as a control for WGA. DBA-TFNS were fabricated according to the same procedure as for WGA-TFNS mentioned above.

Examination of the Capacity of WGA-TFNS to Capture DU-145 Cells. DU-145 cells were first cultured in a flask and then detached using trypsin–EDTA solution, and collected by centrifugation at approximately 1000 rpm for 5 min at room temperature. Subsequently, the cells were washed with cold 1 × PBS, resuspended in 1 × PBS, and the cell concentration was determined by hemocytometry. Then, WGA-TFNS were added to DU-145 cell suspension and incubated for 30 min at room temperature and isolated with a magnetic scaffold, and then the uncaptured DU-145 cells in solution were counted.

Cytotoxicity of WGA-TFNS Examined by Trypan Blue Dye Exclusion Assay. DU-145 cells were plated in a 6-well tissue culture plate. After the cells became confluent, the cells were washed twice with 1 × PBS and added with WGA-TFNS, then incubated for 30 min at room temperature. After incubation, DU-145 cells were washed twice with 1 × PBS after redundant WGA-TFNS were removed, then trypsinized and resuspended in RPMI 1640 culture media. DU-145 cells were centrifuged at 1000 rpm for 5 min and dispersed in 1 × PBS, then DU-145 cell solution was mixed with Trypan blue dye (0.8% w/v) in equal volume, staining for 2 min. More than 200 stained and unstained cells (viable cells could not be stained by Trypan blue) were counted by hemocytometry. The cell viability was calculated below.

Cell viability [%] = (number of viable cells/total cell number) × 100

DU-145 cells cultured without WGA-TFNS under the same experimental conditions were used as the control.

RESULTS AND DISCUSSION

Fluorescent Magnetic Bifunctional Nanospheres. Trifunctional nanospheres or smart nanobiodevices simultaneously with fluorescence, magnetism, and biotargeting properties will be a powerful tool for biotracking, bioimaging, bioseparation, clinical diagnosis, and biomedical fundamental research. In view of the structural features (Scheme 1), the formation of the fluorescent magnetic bifunctional nanospheres is an important basis for construction of a variety of smart nanobiodevices.

By our simple and convenient approach (*22*, *26*, *27*), perfect bifunctional nanospheres (Figure 1) can be readily fabricated by embedding both the CdSe/ZnS QDs and the nano-γ-Fe_2O_3 into the swelling H_2N-St-AAm nanospheres simultaneously. The hydrophilic amide (-$CONH_2$) groups of the copolymer tend to be located towards the outer surface of the nanospheres, while the hydrophobic moieties are found in the interior, leading to the formation of hydrophobic hollow cavities, since the copolymer nanospheres are synthesized in an aqueous solution. Both hydrophobic QDs and γ-Fe_2O_3 can be embedded in weakly polar organic solvent (*22*). Therefore, it is believed that the embedment is completed via hydrophobic interactions. As shown in Figure 1, the nanoparticles are widely distributed in the nanospheres. The strong ultrasonication is usually used to prevent the nanoparticles from adsorbing on the surface, and consequently, the surface of the nanospheres is relatively clean as observed from the TEM images. It is reasonable to believe that the particles are actually embedded in the copolymer nanospheres rather than deposited on the surface. When the nanospheres, embedded with QDs and γ-Fe_2O_3, are dispersed in a polar aqueous solution, the embedded hydrophobic nanoparticles are unable to leak from the hydrophobic cavities. No detectable leakage was observed in the resultant H_2N-BFNS, even after 1 week of consecutive ultrasonication. Therefore, the H_2N-BFNS are stable if no chemical that can decompose and denature the nanospheres is present in solution, and any operation, which can denature the nanospheres, is avoided.

H_2N-BFNS were found to have good dispersivity as can be seen from Figure 2. If the numbers of embedded QDs and γ-Fe_2O_3 nanoparticles increase, the fluorescence of the nanospheres will become stronger, and the magneto-manipulation time will be shorter. Strong fluorescence of QDs enables us to observe the light spot from a single QD with the naked eye. Therefore, there are no rigorous requirements for the number of embedded nanoparticles and the reproducibility of the exact embedding amounts.

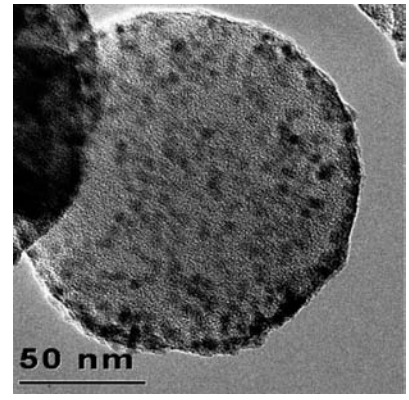


Figure 1. TEM image of a fluorescent magnetic bifunctional nanosphere embedded with both QDs and nano-γ-Fe_2O_3.

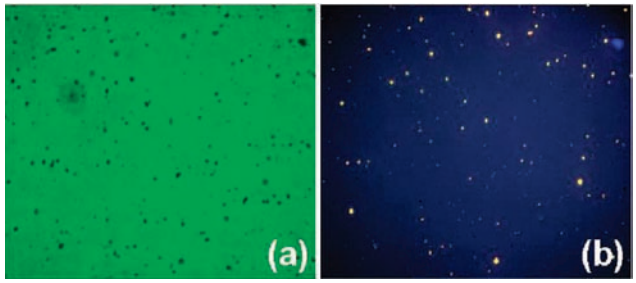


Figure 2. Microscopic images of H_2N-BFNS: (a) bright field and (b) fluorescent. 40× objective.

Strategy for the Modification and Biofunctionalization of the BFNS. As mentioned above, the reactive group of St-AAm for the coupling purpose is the amide on its surface. Since the scheme for the synthesis of the copolymer nanospheres is emulsifier-free, the surface is relatively clean and convenient for conjugating with other molecules. In most cases, it is difficult to anchor any other molecules, especially biomacromolecules, onto the surface of St-AAm, either due to the steric hindrance or due to insufficient reactivity of the amide group on the surface. Therefore, keeping the reactive group away from the surface of St-AAm or converting the amide into another more reactive group is crucial for further biofunctionalization.

As shown in Scheme 1, modification of St-AAm with hydrazine through the surface amide functional groups will produce a relatively reactive nanosphere surface with hydrazide groups. Subsequent co-embedment of CdSe/ZnS QDs and nano-γ-Fe_2O_3 into the H_2N-St-AAm will create H_2N-BFNS to facilitate both future application and construction of trifunctional nanospheres. End carboxyl groups can be readily generated on the surface via another amide linkage to form HOOC-BFNS by reaction of the surface hydrazide of H_2N-BFNS with succinic anhydride. It is due to the magnetism of HOOC-BFNS that the resulting product can be easily separated. The end carboxyl functionalization enables the nanospheres to decrease in steric hindrance and supply a flexible choice of functional groups for attachment to many molecules. The coupling via carboxyl groups can retain the bioactivity of proteins, and the resultant products containing BFNS can be easily separated and purified.

WGA with four carbohydrate binding sites can be conveniently attached to the nanosphere surface through an amide bond between its amino group and the carboxyl on the surface of HOOC-BFNS to produce WGA-TFNS targeting GlcNAc- or sialic acid-containing species.

Characterization of WGA-TFNS. The characterization of nanomaterials, especially nanosized bioconjugates or bioprobes, is extremely important for nanobiotechnology but is also very difficult. Consequently, any attempt to carry this out is highly significant. In the present work, we tried to employ FTIR spectroscopy and also biorecognition assay to characterize the WGA-TFNS.

FTIR Confirmation. FTIR is a powerful characterization tool with the capability of discriminating among various types of covalent bonds. In the present work, FTIR was used to confirm the conjugation of WGA onto the St-AAm surface. As mentioned in the Experimental Procedures, due to the influence of nano-γ-Fe_2O_3 and QDs in WGA-TFNS on the characterization of WGA on the surface of WGA-TFNS, WGA-St-AAm was used as the substitute for WGA-TFNS in the characterization experiments.

Figure 3 gives the FTIR spectra of H_2N-St-AAm, HOOC-St-AAm, and WGA-St-AAm. For H_2N-St-AAm, FTIR spectra showed a broad band near 3442 cm^{-1}, which corresponds to the amine stretching vibration. After pretreating with succinic anhydride (spectrum b), there were two enhanced peaks at 1159 and 1072 cm^{-1} associated with the stretching vibration of the C–N bond of the amide group, showing that succinic anhydride had reacted with H_2N-St-AAm to simultaneously produce HOOC-St-AAm with more amide linkages and carboxyl groups on the surface of the nanospheres for further binding to WGA.

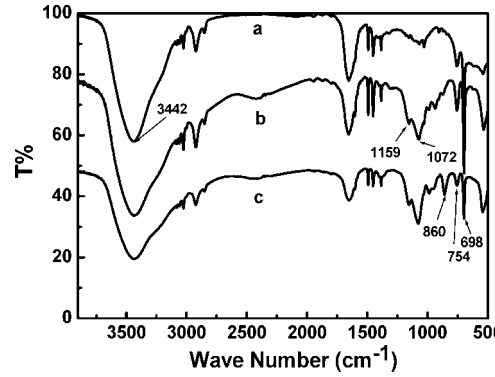


Figure 3. FTIR spectra of H_2N-St-AAm (a), HOOC-St-AAm (b), and WGA-St-AAm (c).

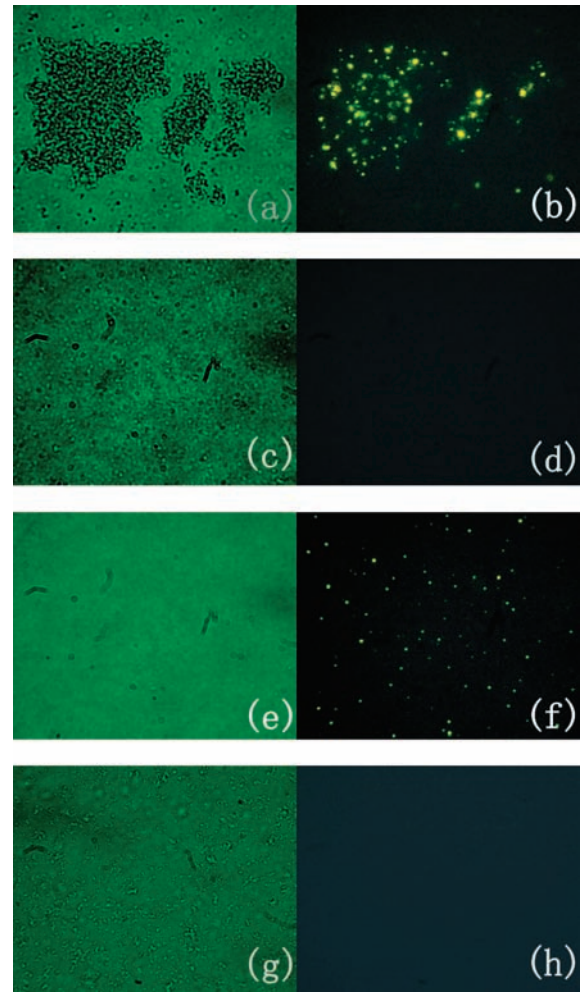


Figure 4. Microscopic images of CM-CT-QDs in the presence of WGA-St-AAm (a,b) or HOOC-St-AAm (c,d), CM-CT-QDs only (e,f) (as the control), and MAA-QDs in the presence of WGA-St-AAm (g,h): bright field (a,c,e,g); fluorescence (b,d,f,h).

For all the three kinds of nanosphere samples, two peaks of phenyl out-of-plane bending vibration at 754 and 698 cm^{-1} could be seen. However, for WGA-St-AAm (spectrum c), the peak at 860 cm^{-1} was obviously enhanced, which may be ascribed to the phenylalanine and tyrosine in the WGA (*35*).

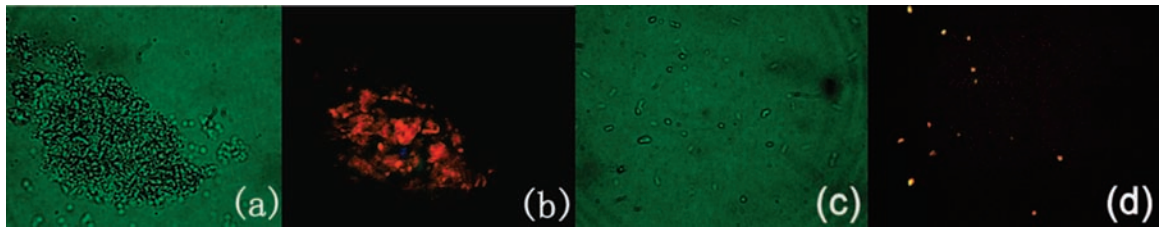


Figure 5. Microscopic images of WGA-TFNS having been incubated with *Staphylococcus aureus* (a,b) at 37 °C for 25 min. Magnetically separated on a magnetic scaffold, washed with 0.1 M Tris–HCl (pH 7.5, containing 1 mM $CaCl_2$ and 1 mM $MgCl_2$), and resuspended in 0.1 M Tris–HCl. Control experiment: WGA-TFNS and *E. coli* were incubated at 37 °C for 30 min. Bright field (a,c); fluorescence (b,d).

Biorecognition Assays. Since WGA can recognize chitin (*36*), which has four carbohydrate binding sites to chitin (*1*), carboxymethyl chitin-modified QDs (*37*) (CM-CT-QDs) can be an ideal probe for the presence of WGA on the surface of WGA-St-AAm. In order to further validate the conjugation of WGA onto the St-AAm surface, CM-CT-QDs were added to WGA-St-AAm and HOOC-St-AAm, respectively (all of them were dispersed in 0.1 M PBS at pH 7.4), and then allowed to react for 30 min. The mixture was centrifuged to remove excess CM-CT-QDs and washed with 0.1 M PBS (pH 7.4). The final product was dissolved in 0.1 M PBS and imaged with a microscope. Because the isoelectric point of WGA is about pH 9, it will be positively charged at pH 7.4, while CM-CT-QDs are negatively charged. In order to confirm that the binding of carboxymethyl chitin to WGA results from specific recognition rather than simply electrostatic interaction, negatively charged mercaptoacetic acid modified QDs (MAA-QDs) was used to examine the electrostatic interaction with WGA-St-AAm.

As shown in Figure 4, when WGA-St-AAm reacted with CM-CT-QDs, the apparent aggregation of WGA-St-AAm was observed in the same field of vision whether in bright or fluorescent field (Figure 4a,b). The pattern (Figure 4b) of fluorescence from CM-CT-QDs evidently indicates that the chitin of CM-CT-QDs had bound to WGA on the WGA-St-AAm surface, further resulting in aggregation due to synchronous exertion of multiple binding sites of WGA. But under the same conditions, no aggregation of HOOC-St-AAm was found (Figure 4c), and also no fluorescence from CM-CT-QDs was observed (Figure 4d), suggesting that CM-CT-QDs could not interact with HOOC-St-AAm without WGA. On the other hand, MAA-QDs could only make WGA-St-AAm slightly aggregate, not so remarkably as with CM-CT-QDs, and no fluorescence from MAA-QDs was observed (Figure 4g,h). This is because MAA-QDs could not strongly bind to WGA-St-AAm and had been washed off. The particle size of CM-CT-QDs was much smaller than WGA-St-AAm. Therefore, CM-CT-QDs could not be observed in bright field. However, the fluorescence of CM-CT-QDs could be seen clearly (Figure 4e,f), implying that CM-CT-QDs were of good dispersivity without aggregation. These experiments confirmed that WGA was indeed present on the surface of WGA-St-AAm, namely, on the surface of WGA-TFNS.

In order to reconfirm the conjugation of WGA onto the surface of WGA-TFNS, *S. aureus* was used. As can be seen from Figure 5a,b, the WGA-TFNS had agglutinated after *S. aureus* suspension was incubated with WGA-TFNS at 37 °C for 25 min, indicative of the presence of WGA on WGA-TFNS surface. It is the multiple binding sites of WGA that one WGA molecule can at most bind to four *S. aureus* cells, resulting in the agglutination. However, this agglutination phenomenon could not be observed with *Escherichia coli* (Figure 5c,d) because no *N*-acetylglucosamine is present on the *Escherichia coli* surface.

Recognition of Human Prostate Carcinoma DU-145 Cells by WGA-TFNS. The four carbohydrate-binding sites of WGA can recognize sialic acid and *N*-acetylglucosamine. Therefore, WGA can accordingly recognize human prostate carcinoma DU-145 cells because they can express sialic acid and *N*-acetylglucosamine on their surface (*38*). Thus, the recognition of DU-145 cells by WGA-TFNS was expected. Figure 6 shows that, after 30 min incubation with WGA-TFNS and subsequent magnetic isolation, the cells had been collected and separated (Figure 6a,b). Accordingly, the cells captured by WGA-TFNS could fluoresce orange (with a maximum emission wavelength of ca. 580 nm), which came from the WGA-TFNS binding to the cancer cells. Dolichos biflorus agglutinin (DBA) was used for the control, which is a glycoprotein with a molecular weight of about 120 000 and consists of 4 subunits of approximately equal size. This lectin has an isoelectric point of about pH 5.5 and 2 binding sites which are specific for glycoconjugates containing *N*-acetyl-D-galactosamine (GalNAc) in the terminal position (*39*). As reported in the literature (*38*), DBA did not have specificity for DU-145 cells; thus, DBA-TFNS could not capture DU-145 cells as shown in Figure 6c and d. At the same time, COOH-BFNS without WGA cannot recognize DU-145 cells as well (Figure 6e,f). Clearly, WGA-TFNS with WGA on the nanosphere surface can indeed recognize specifically DU-145 cells within 30 min. In particular, the cells captured by WGA-TFNS can be isolated readily with

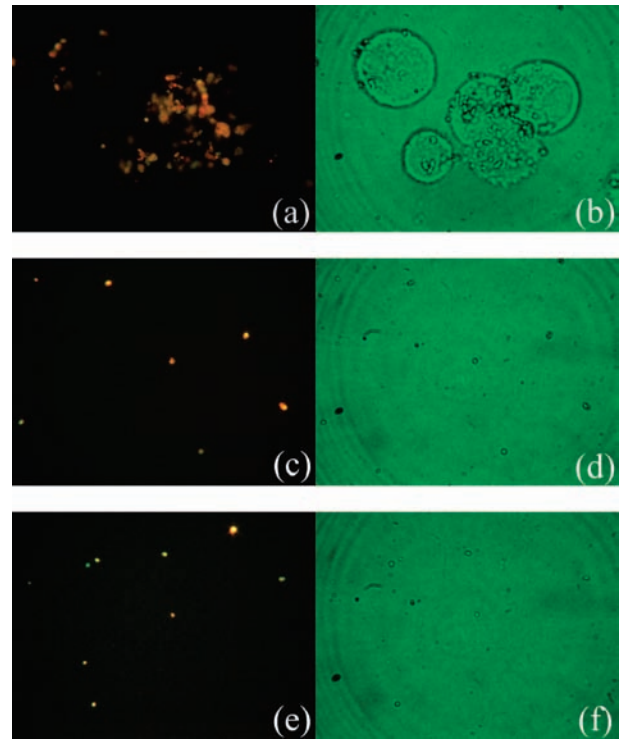


Figure 6. Microscopic images for the recognition of human prostate carcinoma DU-145 cells by WGA-TFNS under an incubation of 30 min with subsequent magnetic scaffold separation (a,b). Control experiment (c–f): DU-145 cells incubated with DBA-TFNS (c,d) and HOOC-BFNS (e,f) for 30 min with magnetic separation. Fluorescence (a,c,e); bright field (b,d,f).

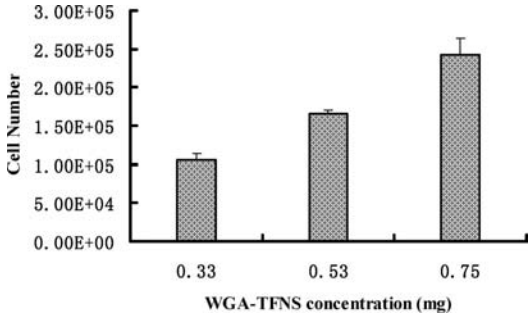


Figure 7. Histogram for capturing capacity of WGA-TFNS.

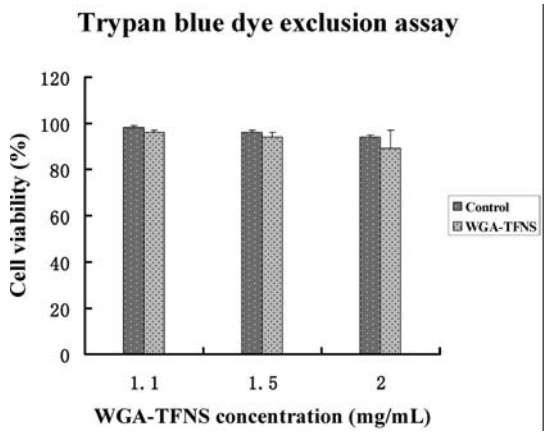


Figure 8. Cytotoxicity of WGA-TFNS examined by Trypan blue dye exclusion assay.

a magnetic scaffold. It is worth pointing out that the magnetic separation is very fast. It only takes tens of seconds to collect the WGA-TFNS-captured cells. The capacity of WGA-TFNS to capture DU-145 cells is shown in Figure 7. About 1.06×10^5 DU-145 cells were captured by only 0.33 mg of WGA-TFNS. By increasing the WGA-TFNS concentration, the number of captured DU-145 cells increased.

The cytotoxicity of WGA-TFNS was examined by Trypan blue dye exclusion assay (*40*). As shown in Figure 8, the cell viability was almost the same both in the presence of WGA-TFNS and in their absence for the control, indicating that WGA-TFNS have scarcely any cytotoxicity on DU-145 cells at WGA concentrations below 2.0 mg/mL and with 30 min incubation.

In general, the relative abundances and branch structures of glycans on the membrane surface of cancer cells are often altered compared with normal cells. These alterations in glycosylation may be indicative of the different stages of the disease, thus being useful for diagnosis. Glycosylation changes in human carcinomas are thought to contribute to the malignant phenotype observed downstream of certain oncogenic events (*41*). Glycans are also the key structures involved in biological processes such as cell attachment, migration, and invasion. Information coded on cell surface glycans is frequently deciphered by proteins, such as lectins, that recognize specific carbohydrate topology (*42*). So, lectins always play an important role in the identification of glycoprotein and the phases of disease, which are very useful for disease diagnosis. Mo and Lim have successfully modified poly(D,L-lactide-*co*-glycolide) particles with WGA to interact with A549 cells (*2*) and made use of lectin receptor-mediated endocytosis for drug release (*5*) based on its capability of binding to membrane-bound carbohydrates. Heinrich et al. (*43*) found that lectin can kill cancer cells, so lectin could be used as a drug candidate for cancer therapy. Hopefully, WGA-TFNS could be used to capture and separate cancer cells, and investigate the mechanism of killing cancer cells by lectin and drug release.

CONCLUSION

A simple and convenient strategy has been put forward to fabricate smart WGA-TFNS with excellent fluorescence, magnetism, and recognition of cancer cells surface-expressed with sialic acid and *N*-acetylglucosamine, which can be easily manipulated, tracked, and conveniently used to capture target cancer cells. WGA-TFNS have the specificity to recognize DU-145 cells, but this is not the case for DBA-TFNS. They have good capture capacity for DU-145 and no cytotoxicity on DU-145 in the present case. The success in capturing DU-145 cells by the WGA-TFNS has opened up a new field: visualizeable and recognizable manipulation and sorting of cells. Alterable functional groups on the BFNS surface such as -NH_2 or -COOH will facilitate their bioconjugation with a variety of biomolecules on demand for the purposes of bioanalysis, biomedical imaging, diagnosis, and combinatorial screening of drugs. Among all the possible applications, simultaneous sorting of different categories of target cells will be the most fascinating, based on multicolor labeling by embedding different sizes and/or types of QDs in different batches of the trifunctional nanospheres.

ACKNOWLEDGMENT

This work was supported by the National Science Fund for Distinguished Young Scholars (no. 20025311), the National Key Scientific Program - Nanoscience and Nanotechnology (no. 2006CB933100), the Science Fund for Creative Research Groups of NSFC (no. 20621502), the 863 Program (no. 2006AA03Z320), the National Natural Science Foundation of China (grant nos. 20505001 and 30570490), the Ministry of Education (nos. 306011 and IRT0543) and Beijing Institute of Technology Fund for Excellent Youth (000Y06-24). The authors thank Professor Dao-Cheng Wu for his helpful discussion and Dr. Wei-Hua Huang for FL imaging. W.Z. thanks EPSRC for a studentship to CD.

Supporting Information Available: A comparison of the difference in recognition of DU-145 cells among WGA-TFNS, DBA-TFNS, and HOOC-BFNS; the cytotoxicity of WGA. This material is available free of charge via the Internet at http://pubs.acs.org/BC.

LITERATURE CITED

(1) Lis, H., and Sharon, N. (1998) Lectins: carbohydrate-specific proteins that mediate cellular recognition. *Chem. Rev. 98*, 637–674.

(2) Mo, Y., and Lim, L.-Y. (2004) Mechanistic study of the uptake of wheat germ agglutinin-conjugated PLGA nanoparticles by A549 cells. *J. Pharm. Sci. 93*, 20–28.

(3) Gabor, F., Bogner, E., Weissenboeck, A., and Wirth, M. (2004) The lectin–cell interaction and its implications to intestinal lectin-mediated drug delivery. *Adv. Drug Delivery Rev. 56*, 459–480.

(4) Yoshihara, Y. (2002) Visualizing selective neural pathways with WGA transgene: combination of neuroanatomy with gene technology. *Neurosci. Res. 44*, 133–140.

(5) Mo, Y., and Lim, L.-Y. (2005) Preparation and in vitro anticancer activity of wheat germ agglutinin WGA.-conjugated PLGA nanoparticles loaded with paclitaxel and isopropyl myristate. *J. Controlled Release 107*, 30–42.

(6) Chemla, Y. R., Grossman, H. L., Poon, Y., McDermott, R., Stevens, R., Alper, M. D., and Clarke, J. (2000) Ultrasensitive magnetic biosensor for homogeneous immunoassay. *Proc. Natl. Acad. Sci. U.S.A. 97*, 14268–14272.

(7) Weizmann, Y., Patolsky, F., Katz, E., and Willner, I. (2003) Amplified DNA sensing and immunosensing by the rotation of

functional magnetic particles. *J. Am. Chem. Soc. 125*, 3452–3454.
(8) Weizmann, Y., Patolsky, F., Lioubashevski, O., and Willner, I. (2004) Magneto-mechanical detection of nucleic acids and telomerase activity in cancer cells. *J. Am. Chem. Soc. 126*, 1073–1080.
(9) Taylor, J. I., Hurst, C. D., Davies, M. J., Sachsinger, N., and Bruce, I. J. (2000) Application of magnetite and silica–magnetite composites to the isolation of genomic DNA. *J. Chromatogr., A 890*, 159–166.
(10) Josephson, L., Tung, C.-H., Moore, A., and Weissleder, R. (1999) High-efficiency intracellular magnetic labeling with novel superparamagnetic-Tat peptide conjugates. *Bioconjugate Chem. 10*, 186–191.
(11) Levison, P. R., Badger, S. E., Dennis, J., Hathi, P., Davies, M. J., Bruce, I. J., and Schimkat, D. (1998) Recent developments of magnetic beads for use in nucleic acid purification. *J. Chromatogr., A 816*, 107–111.
(12) Perrin-Cocon, L. A., Chesne, S., Pignot-Paintrand, I., Marche, P. N., and Villiers, C. L. (2001) Use of magnetic nanobeads to study intracellular antigen processing. *J. Magn. Magn. Mater. 225*, 161–168.
(13) Koelle, D., Kleiner, R., Ludwig, F., Dantsker, E., and Clarke, J. (1999) High-transition-temperature superconducting quantum interference devices. *Rev. Mod. Phys. 71*, 631–686.
(14) Zhang, Y., Kohler, N., and Zhang, M. (2002) Surface modification of superparamagnetic magnetite nanoparticles and their intracellular uptake. *Biomaterials 23*, 1553–1561.
(15) Bruchez, M., Jr., Moronne, M., Gin, P., Weiss, S., and Alivisatos, A. P. (1998) Semiconductor nanocrystals as fluorescent biological labels. *Science 281*, 2013–2016.
(16) Chan, W. C. W., and Nie, S. (1998) Quantum dot bioconjugates for ultrasensitive nonisotopic detection. *Science 281*, 2016–2018.
(17) Michalet, X., Pinaud, F., Lacoste, T. D., Dahan, M., Bruchez, M. P., Alivisatos, A. P., and Weiss, S. (2001) Properties of fluorescent semiconductor nanocrystals and their application to biological labeling. *Single Mol. 2*, 261–276.
(18) Chan, W. C. W., Maxwell, D. J., Gao, X., Bailey, R. E., Han, M., and Nie, S. (2002) Luminescent quantum dots for multiplexed biological detection and imaging. *Curr. Opin. Biotechnol. 13*, 40–46.
(19) Li, J. J., Wang, Y. A., Guo, W., Keay, J. C., Mishima, T. D., Johnson, M. B., and Peng, X. (2003) Large-scale synthesis of nearly monodisperse CdSe/CdS core/shell nanocrystals using air-stable reagents via successive ion layer adsorption and reaction. *J. Am. Chem. Soc. 125*, 12567–12575.
(20) Han, M., Gao, X., Su, J. Z., and Nie, S. (2001) Quantum-dot-tagged microbeads for multiplexed optical coding of biomolecules. *Nat. Biotechnol. 19*, 631–635.
(21) Archer, M. J., Lin, B., Wang, Z., and Stenger, D. A. (2006) Magnetic bead-based solid phase for selective extraction of genomic DNA. *Anal. Biochem. 355*, 285–297.
(22) Pang, D. W., Xie, H. Y., Liu, Y., Zuo, C., and Zhang, Z. L. (2003)Method for the construction of fluorescent magnetic multifunctional nanoparticles. Chinese patent application no. 200310111290.9, Oct. 29.
(23) Hong, X., Li, J., Wang, M., Xu, J., Guo, W., Li, J., Bai, Y., and Li, T. (2004) Fabrication of magnetic luminescent nanocomposites by a layer-by-layer self-assembly approach. *Chem. Mater. 16*, 4022–4027.
(24) Wang, D., He, J., Rosenzweig, N., and Rosenzweig, Z. (2004) Superparamagnetic Fe_2O_3 beads-CdSe/ZnS quantum dots core-shell nanocomposite particles for cell separation. *Nano Lett. 4*, 409–413.
(25) Gaponik, N., Radtchenko, I. L., Sukhorukov, G. B., and Rogach, A. L. (2004) Luminescent polymer microcapsules addressable by a magnetic field. *Langmuir 20*, 1449–1452.
(26) Pang, D. W., Xie, H. Y., Wang, G. P., Zhang, Z. L., Song, E. Q., and Shi, Y. B. (2005)Tri-functional nanospheres. US patent application No.11/135,380, Application date: May 24.
(27) Xie, H. Y., Zuo, C., Liu, Y., Zhang, Z. L., Pang, D. W., Li, X. L., Gong, J. P., Dickinson, C., and Zhou, W. Z. (2005) Cell-targeting multifunctional nanospheres with both fluorescence and magnetism. *Small 1*, 506–509.
(28) Wang, G. P., Song, E. Q., Xie, H. Y., Zhang, Z. L., Tian, Z. Q., Zuo, C., Pang, D. W., Wu, D. C., and Shi, Y. B. (2005) Biofunctionalization of fluorescent-magnetic-bifunctional nanospheres and their applications. *Chem. Commun.* 4276–4278.
(29) Yi, D. K., Selvan, S. T., Lee, S. S., Papaefthymiou, G. C., Kundaliya, D., and Ying, J. Y. (2005) Silica-coated nanocomposites of magnetic nanoparticles and quantum dots. *J. Am. Chem. Soc. 127*, 4990–4991.
(30) Salgueiriño-Maceira, V., Correa-Duarte, M. A., Spasova, M., Liz-Marzán, L. M., and Farle, M. (2006) Composite silica spheres with magnetic and luminescent functionalities. *Adv. Funct. Mater. 16*, 509–514.
(31) Xie, H. Y., Liang, J. G., Liu, Y., Zhang, Z. L., Pang, D. W., He, Z. K., Lu, Z. X., and Huang, W. H. (2005) Preparation and characterization of overcoated II-VI quantum dots. *J. Nanosci. Nanotechnol. 5*, 880–886.
(32) Sun, S., and Zeng, H. (2002) Size-controlled synthesis of magnetite nanoparticles. *J. Am. Chem. Soc. 124*, 8204–8205.
(33) Zhao, X., Liu, Y., and Hui, H. (1997) Preparation of large colored microspheres with carboxyl groups for cell surface labeling. *J. Med. Coll. PLA 12*, 62–65.
(34) Zhao, X., Hilliard, L. R., Mechery, S. J., Wang, Y., Bagwe, R. P., Jin, S., and Tan, W. (2004) A rapid bioassay for single bacterial cell quantitation using bioconjugated nanoparticles. *Proc. Natl. Acad. Sci. U.S.A. 101*, 15027–15032.
(35) Bonnin, S., Besson, F., Gelhausen, M., Chierici, S., and Roux, B. (1999) A FTIR spectroscopy evidence of the interactions between wheat germ agglutinin and N-acetylglucosamine residues. *FEBS Lett. 456*, 361–364.
(36) Kloepfer, J. A., Mielke, R. E., Wong, M. S., Nealson, K. H., Stucky, G., and Nadeau, J. L. (2003) Quantum dots as strain- and metabolism-specific microbiological labels. *Appl. Environ. Microbiol. 69*, 4205–4213.
(37) Xie, M., Liu, H. H., Chen, P., Zhang, Z. L., Wang, X. H., Xie, Z. X., Du, Y. M., Pan, B. Q., and Pang, D. W. (2005) CdSe/ZnS-labeled carboxymethyl chitosan as a bioprobe for live cell imaging. *Chem. Commun.* 5518–5520.
(38) Gabor, F., Klausegger, U., and Wirth, M. (2001) The interaction between wheat germ agglutinin and other plant lectins with prostate cancer cells Du-145. *Int. J. Pharm. 221*, 35–47.
(39) Pramod, S. N., Krishnakantha, T. P., and Venkatesh, Y. P. (2006) Effect of horse gram lectin Dolichos biflorus agglutinin) on degranulation of mast cells and basophils of atopic subjects: Identification as an allergen. *Int. Immunopharmacol. 6*, 1714–1722.
(40) Zhang, C., Wängler, B., Morgenstern, B., Zentgraf, H., Eisenhut, M., Untenecker, H., Krüger, R., Huss, R., Seliger, C., Semmler, W., and Kiessling, F. (2007) Silica- and Alkoxysilane-coated ultrasmall superparamagnetic iron oxide particles: A promising tool to label cells for magnetic resonance imaging. *Langmuir 23*, 1427–1434.
(41) Schulenberg, B., Beechem, J. M., and Patton, W. F. (2003) Mapping glycosylation changes related to cancer using the multiplexed proteomics technology: a protein differential display approach. *J. Chromatogr., B 793*, 127–139.
(42) Irazoqui, F. J., Vozari-Hampe, M. M., Lardone, R. D., Villarreal, M. A., Sendra, V. G., Montich, G. G., Trindade, V. M., Clausen, H., and Nores, G. A. (2005) Fine carbohydrate recognition of Euphorbia milii lectin. *Biochem. Biophys. Res. Commun. 336*, 14–21.
(43) Heinrich, E. L., Welty, L. A. Y., Banner, L. R., and Oppenheimer, S. B. (2005) Direct targeting of cancer cells: A multiparameter approach. *Acta Histochem. 107*, 335–344.

BC060387G

Synthetic PAMAM–RGD Conjugates Target and Bind To Odontoblast-like MDPC 23 cells and the Predentin in Tooth Organ Cultures

Elliott Hill,*,† Rameshwer Shukla,‡ Steve S. Park,‡ and James R. Baker, Jr.‡

Departments of Biologic and Materials Sciences and Internal Medicine, University of Michigan, Ann Arbor, Michigan. Received January 22, 2007; Revised Manuscript Received July 30, 2007

Screening techniques now allow for the identification of small peptides that bind specifically to molecules like cells. However, despite the enthusiasm for this approach, single peptides often lack the binding affinity to target in vivo and regulate cell function. We took peptides containing the Arg-Gly Asp(RGD) motif that bind to the $\alpha_V\beta_3$ integrin and have shown potential as therapeutics. To improve their binding affinity, we synthesized polyamidoamine (PAMAM) dendrimer–RGD conjugates that that contain 12–13 copies of the peptide. When cultured with human dermal microvessel endothelial cells (HDMEC), human vascular endothelial cells (HUVEC), or odontoblast-like MDPC-23 cells, the PAMAM dendrimer conjugate targets this receptor in a manner that is both time- and dose-dependent. Finally, this conjugate selectively targets RGD binding sites in the predentin of human tooth organ cultures. Taken together, these studies provide proof of principle that synthetic PAMAM–RGD conjugates could prove useful as carriers for the tissue-specific delivery of integrin-targeted therapeutics or imaging agents and could be used to engineer tissue regeneration.

INTRODUCTION

Biologically inductive materials have revolutionized our concept of restorative medicine and reconstructive surgery (*1*). This comes from the recognition of the potential of restoring the form and function of lost tissues by engineering approaches using the identical type of functional tissue that was lost. Though relatively few of these materials have been approved by the Food and Drug Administration (FDA), more than 70 companies are spending a total of $600 million per year to develop new products (*2–5*). In the context of oral facial tissues and dentition, a primary effort involves developing materials that do not elicit an immune response or will camouflage structural deficiencies. While some advances in this area have been made with dental filling materials that release fluoride, or wound dressings that release regenerative growth factors, the molecular cues that enhance and maintain a healthy dental pulp and periodontal ligament are largely unknown.

Extensive numbers of studies have introduced the concept that, in general, tissue health and homeostasis are regulated though the interplay of a variety of signals including insoluble signaling molecules, insoluble ligands, mechanical cues, and cell to cell interaction (*6–8*). Integrin adhesion receptors play a crucial role in regulating interactions between cells and the extracellular matrix (ECM) (*9*). Integrin activation initiates multiple intracellular signaling pathways and results in regulation of cell functions such as motility, proliferation, and differentiation (*10*). One such integrin-binding peptide contains the Arg-Gly Asp (RGD) motif that commonly binds to extracellular matrix proteins. Previous studies have demonstrated that proteins modified with RGD peptides bind with high affinity to $\alpha_v\beta_3$ receptors (*11–13*). The $\alpha_v\beta_3$ integrin is found on the luminal surface of endothelial cells only during angiogenesis (*14*). RGD peptides have been used to deliver doxorubicin (*15*) and proapoptotic peptides (*16*) to the tumor vasculature in targeted chemotherapy. Taken together, these data illustrate the important role RGD plays in regulation of normal cell function. In addition, this important ligand can be potentially utilized to target therapeutic molecules to tissues that express the $\alpha_v\beta_3$ receptor. In this regard, antibody and peptide inhibitors of $\alpha_v\beta_3$ integrins are currently in phase I/II clinical trials for the inhibition of angiogenesis in cancer (*17*).

There also has been growing interest in the use of polymers as nonviral vectors for the delivery of targeting and or therapeutic molecules (*18–22*). One such polymer, polyamidoamine (PAMAM) dendrimers, have been synthesized as building blocks for conjugation to biological molecules, including RGD (*23*). PAMAM dendrimers are water-soluble and biocompatible macromolecules that have been coupled to many biological molecules such as proteins, synthetic drugs, and small molecules. These dendrimers can be coupled to multiple $\alpha_V\beta_3$-selective ligands to target tumor-associated capillary beds and allow the delivery of cytotoxic agents to kill the new vessels (*6, 24, 25*). Also, these dendrimer–RGD conjugates may provide useful building blocks for the creation of new biomaterials in dental applications such as adhesive agents for dental implants or delivery vectors for bone morphogenic proteins and transforming growth factors. In the present work, we describe the synthesis and characterization of a generation 5 dendrimer conjugated to c(RGDyK) labeled with fluorescein. In addition, we examine the binding properties and cellular uptake of this conjugate in endothelial cells, and we report unique binding of the dendrimer–RGD conjugate to the predentin of human tooth organs and dental pulp-like MDPC-23 cells.

EXPERIMENTAL PROCEDURES

General. G5-PAMAM dendrimer was prepared at the Michigan Nanotechnology Institute for Medicine and Biological sciences, University of Michigan, and was analyzed extensively by ^{1}H and ^{13}C NMR, matrix-assisted laser desorption–ionization time-of-flight (MALDI-TOF) mass spectrometry, high-performance liquid chromatography (HPLC), gel-permeation chromatography (GPC), and polyacrylamide gel electrophoresis

* Corresponding author. Elliott Hill, Division of Biologic and Materials Sciences, 1011 N. University, University of Michigan, Ann Arbor, MI 48109, Tel: 734-647-2110, e-mail: eehill@umich.edu.

† Department of Biologic and Materials Sciences.

‡ Department of Internal Medicine.

10.1021/bc0700234 CCC: $37.00 © 2007 American Chemical Society
Published on Web 10/31/2007

(PAGE) (*26*). Prepacked Sephadex G-25 PD-10 columns were purchased from Amersham Pharmacia Biotech (Piscataway, NJ) and equilibrated with degassed eluting buffer before sample introduction.

Synthesis of G5-Ac (1). G5 amine dendrimer (0.265 g, 0.0099 mmol) and triethyl amine (0.088 g, 0.8635 mmol) were dissolved in 30 mL anhydrous MeOH and allowed to stir for 30 min. A solution of acetic anhydride (0.076 g, 0.744 mmol) in anhydrous MeOH (15 mL) was added dropwise while stirring. The reaction mixture was allowed to stir overnight at room temperature. After evaporation of the solvent, the residue was dissolved in H_2O and dialyzed in 10 000 MWCO regenerated cellulose dialysis bags initially against PBS buffer, followed by water. The partially acetylated dendrimer was lyophilized to give a colorless powder (0.270 g, 91.2%). The molecular weight of synthesized G5-PAMAM dendrimer was found to be 26 530 g/mol by GPC, and the average number of primary amino groups was estimated to be 108 by potentiometric titration. The average number of acetyl groups (80) has been determined on the basis of a ^{1}H NMR calibration curve drawn by plotting a ratio of acetyl protons and sum of all methylene protons vs degree of actetylation (*27*). ^{1}H NMR (300 MHz, CDCl3): δ = 1.8 (s, 240H), 2.32–2.38 (m, 499H), 2.51–2.52 (m, 260H), 2.65–2.80 (m, 500H), 3.15 (br m, 62H), 3.4 (s,br, 596H), 3.45 (s, 62H). MS (MALDI): 300 050.

G5-Ac-Fl (2). To G5-Ac (102.05 mg, 3.4 mmol) in DMSO (10 mL) was added FITC (5.8 mg, 15.0 mmol) in DMSO (2 mL) dropwise. The reaction was allowed to stir overnight. The reaction mixture was diluted 1:1 in PBS, and free dye was separated from conjugate by gel filtration on a G-25 Sephadex column. The eluted conjugate was concentrated using a centriprep device (MWCO 10 000) and dialyzed against PBS and H_2O before lyophilization. ^{1}H NMR (300 MHz, CDCl3): δ = 1.8 (s, 240H), 2.32–2.38 (m, 499H), 2.51–2.52 (m, 260H), 2.65–2.80 (m, 500H), 3.15 (br m, 62H), 3.4 (s,br, 596H), 3.45 (s, 62H), 6.25 (br s, 16H), 7.02 (br s, 8H), 7.5 (br s, 8H), 7.71 (br s, 8H). MS (MALDI): 34 470.

G5-Ac-Fl-glutarate (3). Glutaric anhydride (0.0029 g, 0.0257 mmol) dissolved in anhydrous MeOH (2 mL) was added dropwise to a solution of G5-Ac80-Fl4 (0.0203 g, 0.0006 mmol) and TEA (0.0026 g, 0.0257 mmol) in anhydrous MeOH (18 mL) while stirring, and the reaction mixture was allowed to stir for another 24 h at room temperature. The solvent was evaporated in vacuo, and the residual material was dissolved in H_2O, purified by extensive ultrafiltration against PBS and H_2O using a centricon device (10k MWCO), then lyophilized. ^{1}H NMR (300 MHz, CDCl3): δ = 1.8 (s, 240H), 1.7 (m, 56h), 2.32–2.38 (m, 499H), 2.2 (m, 112H), 2.51–2.52 (m, 260H), 2.65–2.80 (m, 500H), 3.15 (br m, 62H), 3.4 (s,br, 596H), 3.45 (s, 62H), 6.25 (br s, 16H), 7.02 (br s, 8H), 7.5 (br s, 8H), 7.71 (br s, 8H). MS (MALDI): 38 370.

G5-Ac-Fl-glutarate-c(RGD) (4). An active ester was prepared by reacting G5-Ac80-Fl4-glutarate (12.26 mg, 0.00036 mmol) in H_2O (2.0 mL) with EDC (1.02 mg, 0.00533 mmol) for 3 h. RGD (0.005 g, 0.0036 mmol) in DMSO (0.5 mL) was added dropwise to the above solution and allowed to stir overnight. The product was purified by extensive ultrafiltration against PBS buffer (pH 7.4) and H_2O using a centricon device (10k MWCO), then lyophilized. ^{1}H NMR (300 MHz, CDCl3): δ = 1.8 (s, 240H), 2.32–2.38 (m, 499H), 2.51–2.52 (m, 260H), 2.65–2.80 (m, 500H), 3.15 (br m, 62H), 3.4 (s,br, 596H), 3.45 (s, 62H), 6.25 (br s, 16H), 7.02 (br s, 8H), 7.27 (br, s, 40H), 7.5 (br s, 8H), 7.71 (br s, 8H). MS (MALDI): 42 416.

Cell Cultures. L1210 cell lines were grown in RPMI medium (with folate), supplemented with 10% FBS, 1% penicillin/streptomycin. and 50 nM L-glutamine. These cells were grown in suspension, and the media were changed every other day. MDPC-23 cell cultures were grown in high-glucose DMEM (Gibco) supplemented with 1% P/S and 10% FBS. HDMEC and HUVEC were grown in EGMV-2 media supplemented with 5% FBS, 1% gentamycin, 1% VEGF, 1% ascorbic acid, 0.5% hydrocortisone, 3% hFGF, 1% IGF, and 1% hEGF. HUVEC, HDMEC, and MDPC-23 cells were incubated as a monolayer at 37 °C and 5% CO_2 and grown in 75 cm^3 flasks until 85% confluent (2×10^6 cells/flask). Approximately 0.5×10^6 cells were seeded onto 6 well culture dishes (MatTek Corp., Ashland, MA) and cultured in 3 mL of medium at least 24 h before the initiation of experimental conditions. Samples were examined quantitatively for G5-conjugate uptake via flow cytometry (Coulter-Epiflow) at time points ranging from 1 h to 7 days normalized to controls that were prepared for each time point.

Cell Targeting and Binding Assay. The cellular uptake of G5-Ac-Fl-RGD conjugate was measured in human dermal microvessel endothelial cells (HDMEC), human vascular endothelial cells (HUVEC), fetal mouse molar papillae derived (MDPC-23) cells, and mouse lymphocytic leukemia cell line (L1210) cells. Endothelial cells were cultured in ECM-2 media supplemented with fetal bovine serum, EGF, VEGF, IGF, and IL-8. All other cell lines were cultured in RPMI media (GIBCO) supplemented with 10% FBS/1% P/S. A time course for G5 (100 nM) binding was done, and results were analyzed via flow cytometric analysis (BectonDickinson FACScan analyzer, Fullerton, CA). The mean fluorescence of 10 000 cells was quantified. Confocal microscopic analysis was performed on HDMEC cells cultured in 35 mm glass-bottomed culture dishes (MatTek Corp., Ashland, MA) using a Carl Ziess confocal microscope. Fluorescence and differential interference contrast (DIC) images were collected simultaneously using an argon laser and *Fluoview* software.

Targeting of Tooth Organ Cultures. Adult human molars were extracted, soft tissue was carefully removed, and teeth were stored in 70% ethanol. One millimeter cross sections of medial and distal roots were made with a diamond wheel saw (South Bay Technology Inc., Temple City, CA) at a point 1 mm apical to the cement–enamel junction. Pulp contents were carefully removed, and the sections were placed in 35 mm glass-bottomed culture dishes (MatTek Corp., Ashland, MA). The targeted binding of G5-Ac-Fl-RGD conjugates was examined by coculturing the conjugate with human molar tooth slice sections under three different conditions: (1) tooth slices cocultured with G5-Ac-Fl-glutarate (with out the targeting RGD moiety), (2) tooth slices cocultured with G5-Ac-Fl-RGD, (3) tooth slices preincubated for 1 h with free RGD peptide and then cocultured with G5-Ac-Fl-RGD conjugate. All cocultures were incubated for 3 h; cultures were rinsed with sterile water (3×) and analyzed via confocal microscopic analysis using a Carl Ziess confocal microscope. Fluorescence and differential interference contrast (DIC) images were collected simultaneously using an argon laser and *Fluoview* software.

RESULTS

The conjugate synthesis and characterization was performed as follows: (1) The synthesis and partial surface modification of G5 dendrimer with acetic anhydride (75 mol %) in the presence of triethylamine (Figure 1) was initiated via the use of 75 molar excess of acetic anhydride. This reaction leaves approximately 25% of the primary amines on the surface for further conjugation. In addition, it prevents aggregation, intermolecular interaction, and problems arising from decreased solubility. The degree of acetylation and the purity of the G5 dendrimer conjugate were analyzed using ^{1}H NMR spectroscopy, which shows a distinct signal for the terminal $NHCOCH_3$ protons of the dendrimer. The degree of acetylation was measured by comparing the ratio of $NHCOCH_3$ protons with

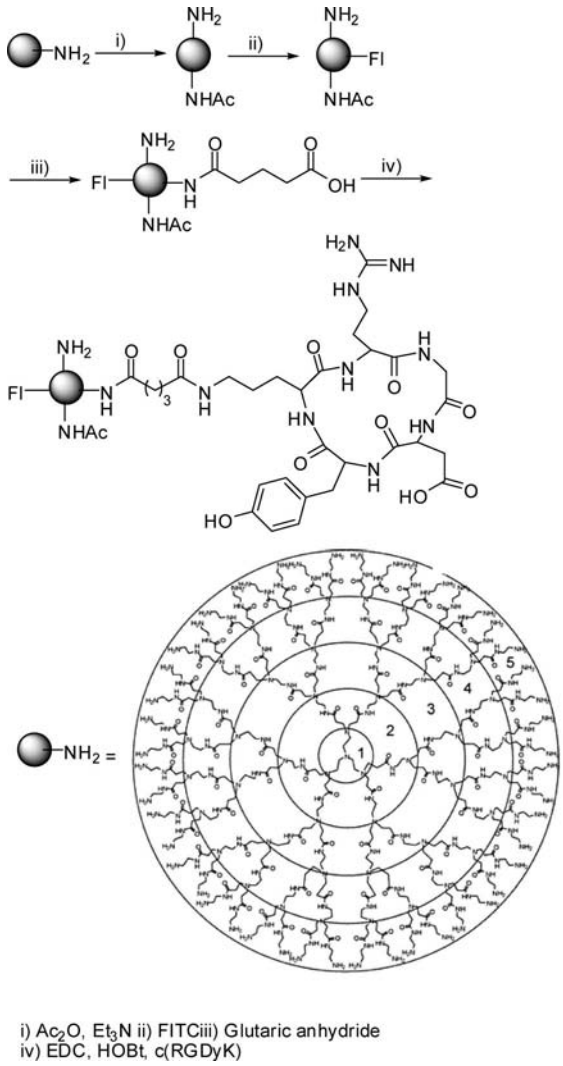


Figure 1. Schematic of PAMAM dendrimer generation 5 (G5)-FL-RGD synthesis.

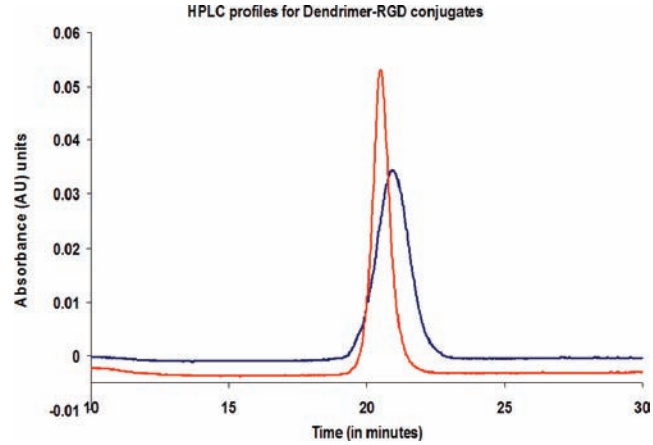


Figure 2. HPLC analysis used to compare G5-FITC to G5-FITC-RGD dendrimer showed a peak typical of a homogeneous peptide conjugate λ max 285 nm. In addition, the difference in retention time between the final conjugate the precursor material gives indirect evidence that RGD peptide conjugation was successful.

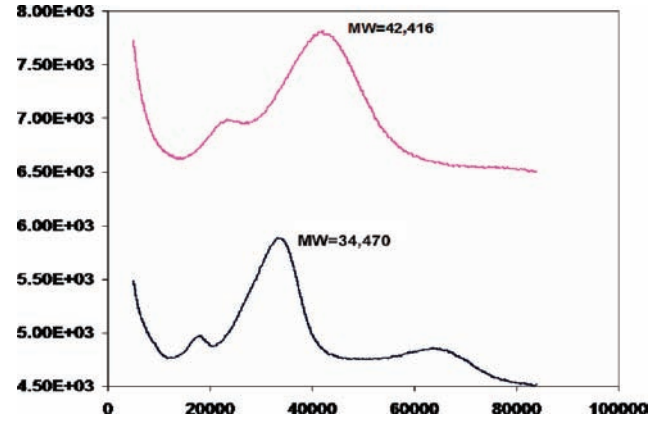


Figure 3. Matrix-assisted laser desorption/ionization time of flight mass spectrometry (MALDI-TOF) analysis of G5-FL conjugate before and after RGD conjugation revealed a difference in mass consistent with the successful conjugation of 13 RGD peptides per G5-FL conjugate.

the sum of all methylene protons in the dendrimer to a calibration curve as described previously (*27*). (2) To detect the conjugate by flow cytometry or for visual imaging via confocal microscopy, a detectable fluorescent probe is required. We labeled the partially acetylated dendrimer with fluorescein isothiocyanate (FITC).

The partially acetylated dendrimer was reacted with 5 mol equiv of FITC dissolved in dimethyl sulfoxide (DMSO). After purification, the conjugate was characterized using ^{1}H NMR spectroscopy and high-performance liquid chromatography (HPLC) (Figure 2). The ^{1}H NMR spectrum of the conjugate shows broad signals in the aromatic region for the FITC (data not shown). The number of dye molecules attached to the dendrimer was calculated to be ~4 based on UV/vis spectroscopy and ^{1}H NMR. (3) Remaining surface amines on the dendrimer were converted to carboxylic acid by reacting with excess glutaric anhydride in MeOH, in the presence of TEA as base. This conversion provides a carboxyl terminal linker while eliminating primary amines that could cause nonspecific charge interactions. The loss of the methylene peaks ($-CH_2CH_2NH_2$) at δ 2.97 and 3.32 ppm and the emergence of the new methylene peaks (-NHCO(CH_2)$_3$COOH) at δ 1.65 and 2.05 ppm indicate complete conversion of the remaining terminal amines to give G5-Ac-Fl-glutarate. (4) Finally, the carboxyl groups were activated by reacting with EDC followed by the addition of 10 equiv of c(RGDyK) to give the dendrimer–RGD conjugate. The dendrimer–RGD conjugate was purified by ultrafiltration and lyophilized. The ^{1}H NMR spectrum of the conjugate shows overlapping signals in the aromatic region for both the FITC and phenyl ring of the peptide apart from the expected aliphatic signals for the dendrimer overlapping with some aliphatic signals from the peptide. The number of peptides was calculated to be 12–13 peptides per dendrimer based on matrix-assisted laser desorption/ionization time of flight (MALDI-TOF) mass spectrometry (Figure 3) and ^{1}H NMR.

The cellular uptake of G5Ac-Fl-RGD examined in MDPC-23 odontoblast-like cells, via flow cytometric analysis, revealed time-dependent uptake of G5 conjugate (Figure 4). Measurable binding was observed at 30 min with an increased uptake beginning at 3 h that seemed to become constant at 6 h. The binding was also dose-dependent with a 10-fold increase seen at 300 nM G5RGD as compared to that seen at 30 nM (Figure 4b).

To examine specific binding of G5-Ac-Fl-RGD to HDMEC, HUVEC, and MDPC-23 cells, these cells were cultured with and without preincubation with free RGD peptide and examined via flow cytometry (Figure 5). This approach also demonstrated that when incubated for 6 h at 37 °C the G5 conjugate exhibited RGD-dependent binding to HDMEC, HUVEC, and MDPC-23 cells. The binding effect was not enhanced by longer incubation times, and binding could be completely inhibited when the cells

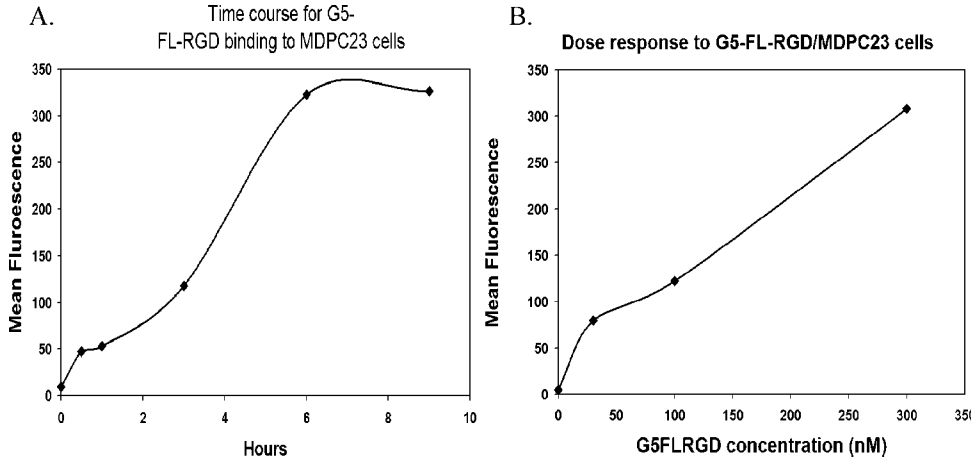


Figure 4. Flow cytometry data of time dependent binding of G5-Ac-Fl-RGD to MDPC-23 (odontoblast like) cells, shows targeted binding after 3 h incubation that increased and stabilized at 6 h (a). The binding demonstrated at 6 h was dose dependent (b).

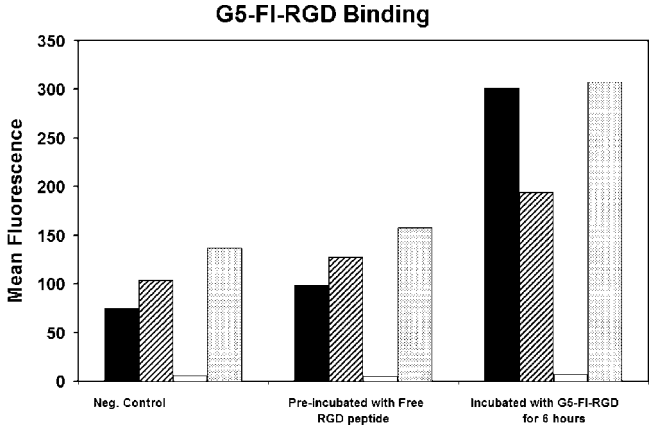


Figure 5. In vitro binding of G5-FL-RGD conjugate to HUVEC (solid block), HDMEC (striped block), or odontoblast-like MDPC-23 (shaded block) cells for 6 h was eliminated by preincubation with free RGD peptide. Negative control L1210 cells exhibited no binding (white block).

were preincubated with free RGD peptide. Finally, no binding was observed when the conjugate was incubated with L1210 cells, cells known to lack RGD binding affinity.

To confirm the flow cytometry data, we repeated the assessment of time-dependent uptake of G5-FL-RGD and its target specific binding to MDPC-23 cells using confocal microscopy. MDPC-23 cells were cultured in 35 cm culture dishes and exposed to 300 nM G5-Fl-RGD conjugate for 30 min, 3 h, or 6 h. The cells demonstrated time-dependent uptake of the conjugate where, at 30 min, the confocal images revealed no apparent internalization of the conjugate (Figure 6a), while after 3 h with the conjugate, the cells showed modest uptake of the G5-FL-RGD (Figure 6b). After 6 h in coculture, the conjugate appears throughout the cytoplasm in a characteristic punctuate pattern (Figure 6c). When HDMEC, HUVEC, and MDPC-23 cells were cultured and exposed to 300 nM G5-FL-RGD with and without preincubation with free RGD peptide, confocal examination confirmed conjugate binding and inhibition by free RGD peptide preincubation (Figure 7).

Finally, when the G5-FL-RGD conjugate was incubated for 3 h in an acellular tooth organ culture, binding to the predentin was clear and robust (Figure 8a–c). This binding was completely eliminated when cultures were preincubated with 300 nM free RGD peptide for 30 min prior to G5 conjugate incubation (Figure 8d–f). Taken together, these data suggest that the G5-FL-RGD conjugate selectively binds to the $\alpha_V\beta_3$ integrin present in the predentin.

DISCUSSION

Tissue engineering is an interdisciplinary field that applies the principles of engineering and the life sciences to the development of biological substitutes that repair, maintain, or improve tissue function that has been lost, impaired, or damaged due to injury, trauma, disease, or cancer (*28*). Currently, in dental medicine, restoration of impaired tooth function depends on materials that share few of the chemical characteristics of natural tooth (*29–31*). About 90% of the organic matrix of tooth structure is type I collagen (*32, 33*). Much work has been done investigating the role of noncollagenous proteins in tooth development (*29, 31, 34, 35*) and pulp biology (*9, 36, 37*). To

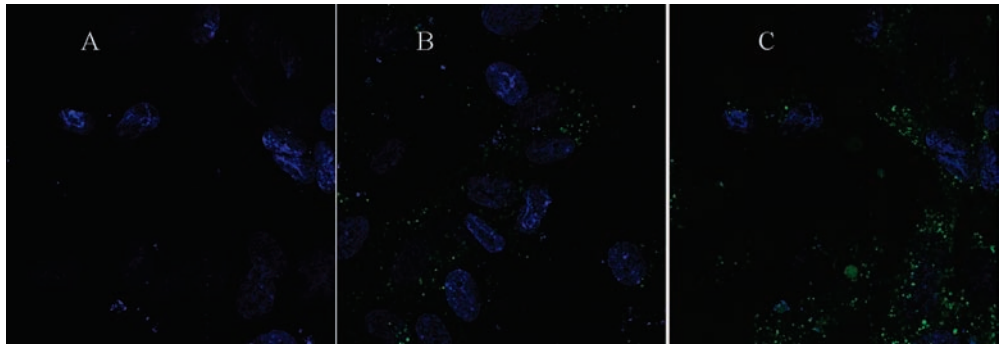


Figure 6. Confocal images of cultured MDPC-23 cells cocultured with G5-Ac-Fl-RGD for 30 min (a), 3 h (b), and 6 h (c) show uptake of this targeted dendrimer in a time-dependent manner.

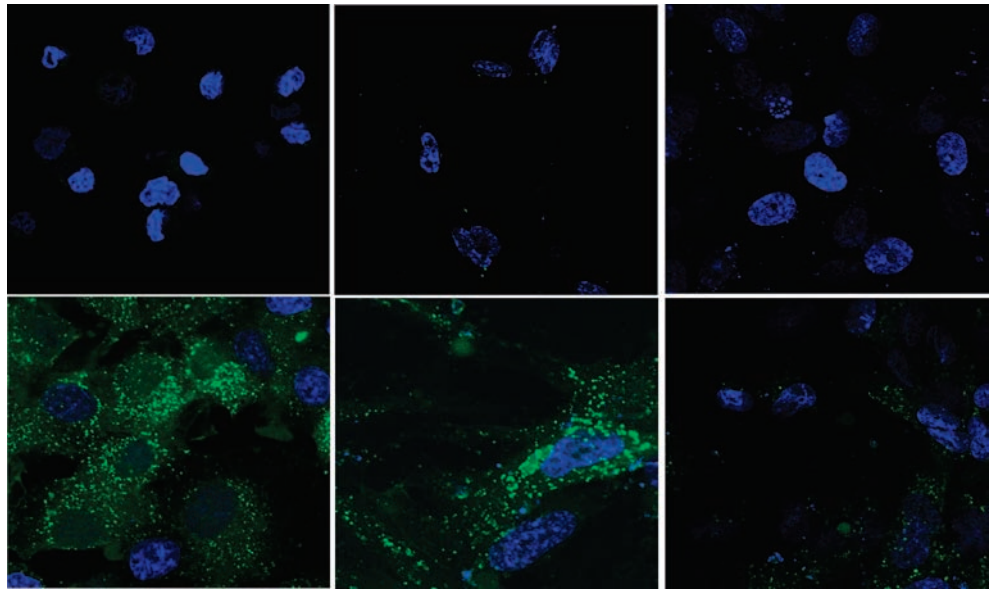


Figure 7. Confocal photomicrographs of odontoblast-like MDPC-23 cells (a,d), human umbilical vein endothelial cells HUVEC (b,e), and human dermal microvascular cells HDMEC (c,f) (60×) show no binding or uptake of G5-Fl-RGD conjugate when cells are preincubated with free RGD peptide (a–c), while binding and uptake of this conjugate are clearly seen in cells not preincubated with free RGD peptide (d–f).

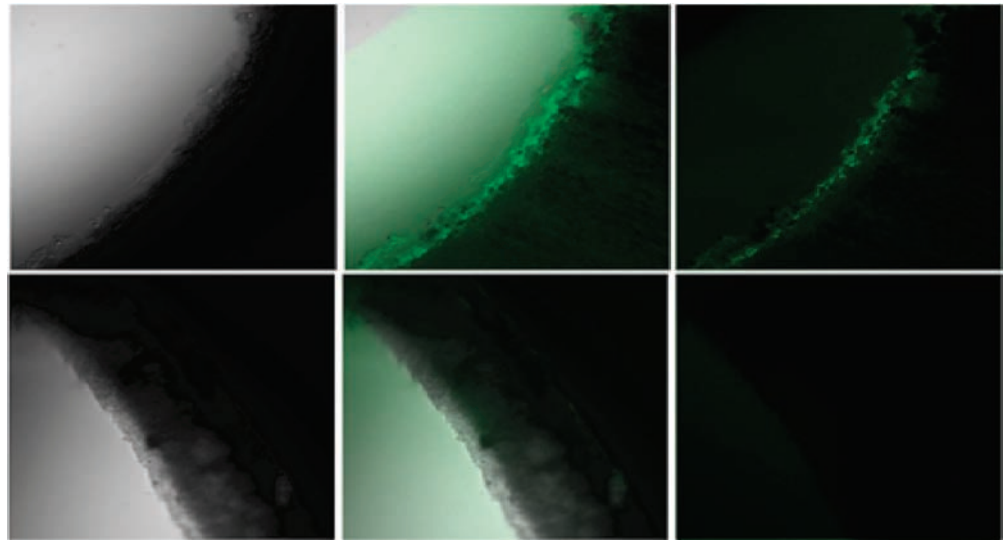


Figure 8. Confocal photomicrographs (20×) of human adult tooth slices (a), when cocultured with RGD targeted G5-Ac-Fl-RGD conjugate (b,c), demonstrate targeted binding of G5-Fl-RGD conjugate to predentin. This effect is not seen in G5-Fl conjugate without the RGD targeting moiety (d,e), and eliminated when coculture of tooth slice and G5-Ac-Fl-RGD was preincubated with free RGD (f) peptide prior to coculture.

build on this work, the present studies examine possible roles for ligands that bind to the organic matrix, specifically the $\alpha_V\beta_3$ integrin.

Integrins constitute a 24-member family of cell adhesion molecules. Each of these molecules consist of two subunits, α and β, which are noncovalently associated (*38*). These subunits bind with specificity to integrin receptors either on extracellular matrix molecules or on the cell surface, thus mediating both cell–cell and cell–matrix interactions (*38*). Strategies focusing on targeting integrin adhesion receptors with short bioadhesive oligopeptides have demonstrated in vitro control of cell adhesion and differentiation. More importantly, these peptides have also demonstrated enhancement of tissue healing responses in vivo including bone formation (*39*), nerve regeneration (*40, 41*) and corneal tissue repair (*42, 43*). Here, we extend this work by showing that synthetic PAMAM–RGD conjugates can be designed to present the RGD motif to cells known to express the $\alpha_V\beta_3$ integrin. By characterizing these conjugates via HPLC, MALDI-TOF, and ^{1}H NMR analysis, we present direct and indirect evidence that RGD peptides were successfully conjugated to a PAMAM-FITC dendrimer platform. In addition, when cultured in vitro with human dermal microvessel endothelial cells (HDMEC), human vascular endothelial cells (HUVEC), and odontoblast-like MDPC-23 cells, we demonstrate both time- and dose-dependent uptake of these conjugates into all three cell types that can be measured quantitatively and visualized via confocal microscopy. We also presented compelling data on the specificity of this binding, which was completely prevented by preincubation with free RGD peptide. Taken together, these data indicate that the G5-FL-RGD conjugate described here selectively binds to cells expressing the $\alpha_V\beta_3$ receptor.

The RGD motif has been widely studied in targeting molecule cancer therapeutics (*11*), and more specifically in targeting the neovasculature of tumor-enhanced angiogenesis (*12, 23, 44*). And, while the role of RGD peptides in angiogenesis is established, the present work is the first study to our knowledge to demonstrate selective binding of a synthetic polymer con-

jugate to the $\alpha_V\beta_3$ integrin binding sites of the predentin matrix of human teeth. The binding, seen via flow cytometry and confirmed by confocal microscopy, suggests robust expression of the $\alpha_V\beta_3$ integrin and uptake of the RGD conjugate in odontoblast-like cells. We further demonstrated that in both the odontoblast-like cells and the predentin of adult tooth organs, this binding is eliminated by preincubation with free RGD peptide. Taken together, these data substantiate a role for this receptor in endothelial cells as well as suggest a possible role in tissue associated with the dental pulp. These data suggest that targeted binding of RGD to tooth predentin may be an important event in pulp biology.

The induction of bone and dentin formation by molecules found in the dental matrix of adult teeth was established several decades ago (*45, 46*). However, the molecular signals responsible for this regenerative response and their signaling pathways are still being studied (*29, 34, 47–50*). In addition, the role of one of the most abundant molecules in the dentin matrix of adult teeth (RGD) is unknown. The current study argues that this often overlooked molecule may play an important role in odontoblast regeneration and/or homeostasis. In addition, we show that synthetic polymers can be used to deliver RGD to both pulplike cells and their mineralized matrix in a way that specifically engages the $\alpha_V\beta_3$ receptor. Since current therapies include mechanical debridment of tooth dentin, diseased via tooth decay or periodontal infection, and this process exposes dentinal tubules and in some cases predentin, the development of functional polymers that can exploit native binding molecules (integrins) for the nonviral delivery of therapeutic drugs makes this therapy a realistic goal for the future.

ACKNOWLEDGMENT

The authors gratefully acknowledge financial support of the National Cancer Institute through contract N01-CM-97065-32.

LITERATURE CITED

(1) Alsberg, E., Anderson, K. W., Albeiruti, A., Rowley, J. A., and Mooney, D. J. (2002) Engineering growing tissues. *Proc. Natl. Acad. Sci. U.S.A. 99*, 12025–30.

(2) Griffith, L. G., and Naughton, G. (2002) Tissue engineering--current challenges and expanding opportunities. *Science 295*, 1009–14.

(3) Payumo, F. C., Kim, H. D., Sherling, M. A., Smith, L. P., Powell, C., Wang, X., Keeping, H. S., Valentini, R. F., and Vandenburgh, H. H. (2002) Tissue engineering skeletal muscle for orthopaedic applications. *Clin. Orthop.* S228–42.

(4) Langer, R., and Vacanti, J. P. (1993) Tissue Engineering. *Science 260*, 920–926.

(5) Saxena, A. K., Marler, J., Benvenuto, M., Willital, G. H., and Vacanti, J. P. (1999) Skeletal muscle tissue engineering using isolated myoblasts on synthetic biodegradable polymers: preliminary studies. *Tiss. Eng. 5*, 525–32.

(6) Albert, J. M., Cao, C., Geng, L., Leavitt, L., Hallahan, D. E., and Lu, B. (2006) Integrin alpha v beta 3 antagonist Cilengitide enhances efficacy of radiotherapy in endothelial cell and non-small-cell lung cancer models. *Int. J. Radiat. Oncol. Biol. Phys. 65*, 1536–43.

(7) Bohl, K. S., Shon, J., Rutherford, B., and Mooney, D. J. (1998) Role of synthetic extracellular matrix in development of engineered dental pulp. *J. Biomater. Sci. Polym. Ed. 9*, 749–64.

(8) Boontheekul, T., and Mooney, D. J. (2003) Protein-based signaling systems in tissue engineering. *Curr. Opin. Biotechnol. 14*, 559–65.

(9) Almushayt, A., Narayanan, K., Zaki, A. E., and George, A. (2006) Dentin matrix protein 1 induces cytodifferentiation of dental pulp stem cells into odontoblasts. *Gene Ther. 13*, 611–20.

(10) Maheshwari, G., Brown, G., Lauffenburger, D. A., Wells, A., and Griffith, L. G. (2000) Cell adhesion and motility depend on nanoscale RGD clustering. *J. Cell Sci. 113*, 1677–86 (Pt 10).

(11) Kok, R. J., Schraa, A. J., Bos, E. J., Moorlag, H. E., Asgeirsdottir, S. A., Everts, M., Meijer, D. K., and Molema, G. (2002) Preparation and functional evaluation of RGD-modified proteins as alpha(v)beta(3) integrin directed therapeutics. *Bioconjugate Chem. 13*, 128–35.

(12) Schraa, A. J., Kok, R. J., Berendsen, A. D., Moorlag, H. E., Bos, E. J., Meijer, D. K., de Leij, L. F., and Molema, G. (2002) Endothelial cells internalize and degrade RGD-modified proteins developed for tumor vasculature targeting. *J. Controlled Release 83*, 241–51.

(13) Schraa, A. J., Kok, R. J., Moorlag, H. E., Bos, E. J., Proost, J. H., Meijer, D. K., de Leij, L. F., and Molema, G. (2002) Targeting of RGD-modified proteins to tumor vasculature: a pharmacokinetic and cellular distribution study. *Int. J. Cancer 102*, 469–75.

(14) Nor, J. E., and Polverini, P. J. (1999) Role of endothelial cell survival and death signals in angiogenesis. *Angiogenesis 3*, 101–16.

(15) Arap, W., Pasqualini, R., and Ruoslahti, E. (1998) Cancer treatment by targeted drug delivery to tumor vasculature in a mouse model. *Science 279*, 377–80.

(16) Ellerby, H. M., Arap, W., Ellerby, L. M., Kain, R., Andrusiak, R., Rio, G. D., Krajewski, S., Lombardo, C. R., Rao, R., Ruoslahti, E., Bredesen, D. E., and Pasqualini, R. (1999) Anti-cancer activity of targeted pro-apoptotic peptides. *Nat. Med. 5*, 1032–8.

(17) Jin, H., and Varner, J. (2004) Integrins: roles in cancer development and as treatment targets. *Br. J. Cancer 90*, 561–5.

(18) Boas, U., and Heegaard, P. M. (2004) Dendrimers in drug research. *Chem. Soc. Rev. 33*, 43–63.

(19) Choi, Y., Thomas, T., Kotlyar, A., Islam, M. T., and Baker, J. R., Jr. (2005) Synthesis and functional evaluation of DNA-assembled polyamidoamine dendrimer clusters for cancer cell-specific targeting. *Chem. Biol. 12*, 35–43.

(20) Khopade, A. J., and Caruso, F. (2002) Stepwise self-assembled poly(amidoamine) dendrimer and poly(styrenesulfonate) microcapsules as sustained delivery vehicles. *Biomacromolecules 3*, 1154–62.

(21) Kobayashi, H., Jo, S. K., Kawamoto, S., Yasuda, H., Hu, X., Knopp, M. V., Brechbiel, M. W., Choyke, P. L., and Star, R. A. (2004) Polyamine dendrimer-based MRI contrast agents for functional kidney imaging to diagnose acute renal failure. *J. Magn. Reson. Imaging 20*, 512–8.

(22) Kukowska-Latallo, J. F., Bielinska, A. U., Johnson, J., Spindler, R., Tomalia, D. A., and Baker, J. R., Jr. (1996) Efficient transfer of genetic material into mammalian cells using Starburst polyamidoamine dendrimers. *Proc. Natl. Acad. Sci. U.S.A. 93*, 4897–902.

(23) Shukla, R., Thomas, T. P., Peters, J., Kotlyar, A., Myc, A., and Baker, J. R., Jr. (2005) Tumor angiogenic vasculature targeting with PAMAM dendrimer-RGD conjugates. *Chem. Commun. (Cambridge)* 5739–41.

(24) Brooks, P. C., Clark, R. A., and Cheresh, D. A. (1994) Requirement of vascular integrin alpha v beta 3 for angiogenesis. *Science 264*, 569–71.

(25) Mitra, A., Mulholland, J., Nan, A., McNeill, E., Ghandehari, H., and Line, B. R. (2005) Targeting tumor angiogenic vasculature using polymer-RGD conjugates. *J. Controlled Release 102*, 191–201.

(26) Shukla, R. T. T. P., Peters, J. L., Desai, A, M., Kukowska-Latallo, J., and Patri, A. K. (2006) HER2 specific tumor targeting with dendrimer conjugated anti-HER2 mAb. *Bioconjugate Chem. 17*, 1109–1115.

(27) Majoros, I. J., Keszler, B., Woehler, S., Bull, T., and Baker, J. R., Jr. (2003) Acetylation of poly(amidoamine) dendrimers. *Macromolecules 36*, 5526–5529.

(28) Langer, R., and Vacanti, J. P. (1993) Tissue engineering. *Science 260*, 920–6.

(29) Nakashima, M. (2005) Bone morphogenetic proteins in dentin regeneration for potential use in endodontic therapy. *Cytokine Growth Factor Rev. 16*, 369–76.
(30) Nakashima, M., and Reddi, A. H. (2003) The application of bone morphogenetic proteins to dental tissue engineering. *Nat. Biotechnol. 21*, 1025–32.
(31) Reddi, A. H. (1998) Role of morphogenetic proteins in skeletal tissue engineering and regeneration. *Nat. Biotechnol. 16*, 247–52.
(32) Gotliv, B. A., Robach, J. S., and Veis, A. (2006) The composition and structure of bovine peritubular dentin: mapping by time of flight secondary ion mass spectroscopy. *J. Struct. Biol. 156*, 320–33.
(33) Linde, A. (1989) Dentin matrix proteins: composition and possible functions in calcification. *Anat. Rec. 224*, 154–66.
(34) Nakashima, M. (1994) Induction of dentine in amputated pulp of dogs by recombinant human bone morphogenetic proteins-2 and −4 with collagen matrix. *Arch. Oral Biol. 39*, 1085–9.
(35) Sloan, A. J., Rutherford, R. B., and Smith, A. J. (2000) Stimulation of the rat dentine-pulp complex by bone morphogenetic protein-7 in vitro. *Arch. Oral Biol. 45*, 173–7.
(36) Kim, J. W., Yamakoshi, Y., Iwata, T., Hu, Y. Y., Zhang, H., Hu, J. C., and Simmer, J. P. (2006) Porcine dentin matrix protein 1: gene structure, cDNA sequence, and expression in teeth. *Eur. J. Oral Sci. 114*, 33–41.
(37) Ye, L., MacDougall, M., Zhang, S., Xie, Y., Zhang, J., Li, Z., Lu, Y., Mishina, Y., and Feng, J. Q. (2004) Deletion of dentin matrix protein-1 leads to a partial failure of maturation of predentin into dentin, hypomineralization, and expanded cavities of pulp and root canal during postnatal tooth development. *J. Biol. Chem. 279*, 19141–8.
(38) Eble, J. A. (2005) Collagen-binding integrins as pharmaceutical targets. *Curr. Pharm. Des. 11*, 867–80.
(39) Ferris, D., Moodie, G., Dimond, P., Gioranni, C., Ehrlich, M., and Valentini, R. (1999) RGD-coated titanium implants stimulate increased bone formation in vivo. *Biomaterials 20*, 2323–2331.
(40) Alsberg, E., Anderson, K., Albeiruti, A., Rowley, J., and Mooney, D. (2002) Engineering growing tissues. *Proc. Natl. Acad. Sci. U.S.A. 99*, 12025–12030.
(41) Elmengaard, B., Bechtold, J., and Soballe, K. (2005) In vivo study of the effect of RGD treatment on bone ongrowth on press-fit titanium alloy implants. *Biomaterials 26*, 3521–3526.
(42) Schense, J., Bloch, J., Aebischer, P., and Hubbell, J. (2000) Enzymatic incorporation of bioactive peptides into fibrin matrices enhances neurite extension. *Nat. Biotechnol. 18*, 415–419.
(43) Yu, X., and Bellamkonda, R. (2003) Tissue-engineered scaffolds are effective alternatives to autografts for bridging peripheral nerve gaps. *Tiss. Eng. 9*, 421–430.
(44) Schraa, A. J., Kok, R. J., Botter, S. M., Withoff, S., Meijer, D. K., de Leij, L. F., and Molema, G. (2004) RGD-modified anti-CD3 antibodies redirect cytolytic capacity of cytotoxic T lymphocytes toward alphavbeta3-expressing endothelial cells. *Int. J. Cancer 112*, 279–85.
(45) Bang, G. (1972) Induction of heterotopic bone formation by demineralized dentin in guinea pigs: antigenicity of the dentin matrix. *J. Oral Pathol. 1*, 172–85.
(46) Bang, G., and Urist, M. R. (1967) Bone induction in excavation chambers in matrix of decalcified dentin. *Arch. Surg. 94*, 781–9.
(47) Hanks, C. T., Fang, D., Sun, Z., Edwards, C. A., and Butler, W. T. (1998) Dentin-specific proteins in MDPC-23 cell line. *Eur. J. Oral Sci. 106*, 260–6. Suppl 1.
(48) Qin, C., Brunn, J. C., Cadena, E., Ridall, A., and Butler, W. T. (2003) Dentin sialoprotein in bone and dentin sialophosphoprotein gene expressed by osteoblasts. *Connect. Tissue Res. 44*, 179–83. Suppl 1.
(49) Sloan, A., and Smith, A. (1999) Stimulation of the dentine-pulp complex of rat incisor teeth by transforming growth factor-beta isoforms 1–3 in vitro. *Arch. Oral Biol. 44*, 149–156.
(50) Sun, Z. L., Fang, D. N., Wu, X. Y., Ritchie, H. H., Begue-Kirn, C., Wataha, J. C., Hanks, C. T., and Butler, W. T. (1998) Expression of dentin sialoprotein (DSP) and other molecular determinants by a new cell line from dental papillae, MDPC-23. *Connect. Tissue Res. 37*, 251–61.

BC0700234

Ultrasmall Mixed Ferrite Colloids as Multidimensional Magnetic Resonance Imaging, Cell Labeling, and Cell Sorting Agents

Ernest V. Groman,* Jacqueline C. Bouchard, Christopher P. Reinhardt, and Dennis E. Vaccaro

BioPhysics Assay Laboratory, Inc., 80 Webster Street, Worcester, Massachusetts 01603. Received January 22, 2007; Revised Manuscript Received August 30, 2007

One area that has been overlooked in the evolution of magnetic nanoparticle technology is the possibility of introducing informational atoms into the iron oxide core of the coated colloid. Introduction of suitable atoms into the iron oxide core offers an opportunity to produce a quantifiable probe, thereby adding one or more dimensions to the magnetic colloid's informational status. Lanthanide-doped iron oxide nanoparticles have been synthesized to introduce informational atoms through the formation of colloidal mixed ferrites. These colloids are designated ultrasmall mixed ferrite iron oxides (USMIOs). USMIOs containing 5 mol % europium exhibit superparamagnetic behavior with an induced magnetization of 56 emu/g Fe at 1.5 T, a powder X-ray diffraction pattern congruent with magnetite, and R_1 and R_2 relaxivity values of 15.4 $(\text{mM s})^{-1}$ and 33.9 $(\text{mM s})^{-1}$, respectively, in aqueous solution at 37 °C and 0.47 T. USMIO can be detected by five physical methods, combining the magnetic resonance imaging (MRI) qualities of iron with the sensitive and quantitative detection of lanthanide metals by neutron activation analysis (NA), time-resolved fluorescence (TRF), X-ray fluorescence, along with detection by electron microscopy (EM). In addition to quantitative detection using neutron activation analysis, the presence of lanthanides in the iron oxide matrix confers attractive optical properties for long-term multilabeling studies with europium and terbium. These USMIOs offer high photostability, a narrow emission band, and a broad absorption band combining the high sensitivity of time-resolved fluorescence with the high spatial resolution of MRI. USMIO nanoparticles are prepared through modifications of traditional magnetite-based iron oxide colloid synthetic methods. A 5 mol % substitution of ferric iron with trivalent europium yielded a colloid with nearly identical magnetic, physical, and chemical characteristics to its magnetite colloid parent.

INTRODUCTION

Since the initial reports of dextran-coated colloidal magnetic iron oxides (*1*), three principal applications for these materials have been reported: magnetic resonance imaging (*2, 3*), cell labeling and tracking (*4–7*), and cell sorting (*8–11*). In these applications, the use of coated magnetic nanoparticles has been conceptually limited by a focus on the iron oxide's surface, i.e., its coating agent, such as dextran, used to stabilize the iron oxide core and covalently bind probes, antibodies, and binding proteins. One area that has been overlooked in the evolution of magnetic nanoparticle technology is the possibility of introducing informational atoms into the iron oxide core of the (dextran-) coated colloid. Introduction of suitable atoms into the iron oxide core offers an opportunity to produce a quantifiable probe, thereby adding one or more dimensions to the magnetic colloid's informational status.

Among the atoms that carry multiple informational packets are those found in the lanthanide series (*12*). Since the chemistry among the lanthanides is so similar (*13*), one would anticipate that introducing one lanthanide element would serve as a guide, through judicious substitutions, for introducing the entire lanthanide series into the iron oxide core of magnetic nanoparticles. Among the informational properties that lanthanide atoms possess (Table 1) are sensitive and quantitative detection by neutron activation (NA) (*14*), detection by time resolved fluorescence (TRF) (*15*), detection by combined X-ray fluorescence/scanning electron microscopy (EM) (*12*), and applications involving neutron capture therapy (*16–18*).

The question that remains is, Can conditions be found whereby lanthanide atoms can be used to form mixed ferrites that simultaneously (i) allow the formation of stable colloids with magnetic properties similar to colloidal magnetite, (ii) allow the conjugation of labels, drugs, and peptides to the dextran surface as previously reported for iron oxide colloids, and (iii) allow efficient cell labeling? In this report, we successfully address this question and describe the synthesis of a family of dextran-coated colloidal mixed ferrites.

MATERIALS AND METHODS

All materials were obtained from commercial sources unless otherwise indicated.

Synthesis of USPIO and USMIO Colloids. Ultrasmall superparamagnetic iron oxide (USPIO) was prepared as follows: $FeCl_3$ $6H_2O$ (15.8g, 58.6 mmol) and $FeCl_2$ $4H_2O$ (6.24 g, 31.6 mmol) were added to 200 mL distilled water, and the resulting solution was filtered through a 0.2 μm filter. Equal volumes of the metal halide solution and a carbohydrate solution [dextran (60 g, Sigma Chemical Co.) in 120 mL distilled water] were then mixed by stirring at ambient temperature. To this mixture was added dropwise a 30% solution of ammonium hydroxide until the pH of the mixture reached 10. At this stage, the mixture was heated to 90 °C for 15 min. The mixture was cooled, resulting in the formation of a black colloidal iron oxide. The pH was adjusted to 7.2–7.5, and excess dextran was removed by ultrafiltration using a 100 kDa molecular weight cutoff membrane. The ultrafiltered product, obtained with a yield in iron of about 90%, was stored at 4 °C.

New nanoparticles (designated USMIO) were made without change in the above procedure other than the removal of various amounts of ferric chloride from the initial starting materials and

* To whom correspondence should be addressed. Tel: 508-770-1190. Fax: 508-770-1191. E-mail: cs@biopal.com.

10.1021/bc070024w CCC: $37.00 © 2007 American Chemical Society
Published on Web 10/18/2007

Table 1. Properties of Specific Lanthanide Isotopes That Relate To Neutron Capture Cross Section, Natural Abundance, Half-Life Decay Times, and Their Applications for Neutron Activation Analysis (NA) (*14*), Time-Resolved Fluorescence (TRF) (*15*), Electron Microscopy (EM) (*12*), and Neutron Capture Therapy (NCT) (*16–18*)

lanthanide	neutron capture reaction	natural abundance[a] (atom %)	NAA cross sections[a] (σ_γ)	half-life (days)[b]	knergy (keV)	NA	TRF	EM	NCT
Sm	$^{152}Sm \rightarrow {}^{153}Sm$	26.70	3210	1.928	103.2	+	+	+	–
Eu	$^{151}Eu \rightarrow {}^{152}Eu$	47.8	5900	0.38	841.6	+	+	+	–
Gd	$^{152}Gd \rightarrow {}^{153}Gd$	0.20	1400	241.6	97.4	–	–	+	–
Gd	$^{157}Gd \rightarrow {}^{158}Gd$	15.65	255000	prompt	n/a	+	–	+	+
La	$^{139}La \rightarrow {}^{140}La$	99.91	21	1.678	1596.2	+	–	+	–
Tb	$^{159}Tb \rightarrow {}^{160}Tb$	100	453.2	72.3	879.4	+	+	+	–
Dy	$^{164}Dy \rightarrow {}^{165}Dy$	28	2700	0.097	94.7	+	+	+	–
Ho	$^{165}Ho \rightarrow {}^{166}Ho$	100	58	1.118	80.6	+	–	+	–
Yb	$^{174}Yb \rightarrow {}^{175}Yb$	31.80	180	4.185	396.3	+	–	+	–
Lu	$^{176}Lu \rightarrow {}^{177}Lu$	2.59	2302	0.153	208	+	–	+	–

[a] Stable isotope. [b] Radioactive isotope.

replacement with equivalent moles of lanthanide chloride. Through this procedure, a series of increasing levels of europium containing ferrites was generated from a substitution of 1–100 mol % of ferric iron with trivalent cationic europium. In a second series, replacement of ferric iron was performed using lanthanum, samarium, terbium, and gadolinium. The final product was tested for the presence of ammonia, iron, and dextran. All products tested negative for ammonia. The product was adjusted for total metals concentration (iron plus lanthanide) to 10 mg/mL. Dextran content varied from 1 to 2.5 mg dextran per milligram of iron.

Dry Weight. Dry weight was recorded in mg/mL. Five milliliters of each sample was dried in a tared container at 105 °C for two days until a constant weight was reached.

Dextran. Dextran concentrations were determined by total organic carbon analysis (Galbraith Laboratories, Knoxville, TN).

Ammonia. USMIO colloids were tested for the presence of ammonia using an ammonium test (EMD Chemicals, Gibbstown, NJ).

Iron Content. Total iron was determined using a 2,2′-bipyridyl photometric method (*19*).

Neutron Activation Analysis (NA). Lanthanide concentrations were measured using neutron activation analysis methods as previously reported (*20*). Samples were placed into contaminant-free sample vials (BioPAL, V-0MS02) and dried at 90 °C prior to neutron activation analysis.

X-ray Powder Diffraction. X-ray powder diffraction was performed by H&M Analytical Services, Inc. (Allentown, NJ). Fine powder samples were mounted on a zero-background holder and tested on a Philips PW1800 diffractometer using Cu radiation at 40 kV/30 mA. Scans were run over the range 15–70° with a step size of 0.05° and counting times of 12–24 h. Once the diffraction patterns were obtained, the phases were identified with the aid of the Powder Diffraction File published by the International Centre for Diffraction Data. The mean crystal size was calculated from the diffraction data by H&M Analytical Services, Inc., using the Scherrer formula.

Magnetization Properties. The magnetization of 5 mol % europium USMIO as a function of applied magnetic field was measured with a Quantum Design physical property measurement system equipped with the vibrating sample magnetometer option (Quantum Design, San Diego, CA). The powdered sample consisting of 5.9 mg of USMIO was press-fit into a polypropylene fixture and secured in a brass trough sample holder. Corrections were applied by subtracting the remanant field of the superconducting magnet.

Magnetic Susceptibility. Magnetic susceptibility was measured as volume susceptibility using a Johnson Matthey magnetic susceptibility balance per the instruction manual. Samples were measured at a concentration of 10 mg/mL (total metals).

MR Relaxometry. MR relaxivity measurements (R_1 and R_2) of USMIO colloids were performed in a 0.47 T Bruker Minispectrometer at 37 °C under the direction of Dr. Craig Ferris, Department of Physiology, University of Massachusetts Medical School (Worcester, MA), following standard procedures (*21*, *22*).

Sizing Methods. Colloids were sized by photon correlation spectroscopy using a 90 *Plus* particle size analyzer (Brookhaven Instruments Company). Samples were diluted to a concentration of 1 mg/mL (total metals) in distilled water (unless otherwise indicated), passed through a 0.1 μm filter, and sonicated for one minute in a water-bath sonicator. A count rate between 50 000 and 500 000 counts per second was obtained. Data were collected for 4 cycles of 15 min and the cumulative results combined. Particle size was calculated by assuming refractive indexes of 1 and 0 for the real and imaginary components, respectively. Typical reproducibility for intra- and interassay variability yielded coefficients of variation of less than 6% and 9%, respectively. Nanoparticle sizes were calculated using an intensity-weighted log normal distribution.

Zeta Potential. Zeta potential measurements for representative colloids were provided courtesy of Brookhaven Instruments Company using a Zeta Potential Analyzer version 3.40. Samples were run at a concentration of 1 mg/mL (total metals) in distilled water (pH 7.2–7.5) under the following instrument parameters: Sample count rate $\sim$ 450 kcps, sampling time = 128 μs, current = 150.00 mA, electric field 27.78 V/cm. Data is reported as the mean zeta potential (mV) of nine measurements.

Cross-Linking and Amination of USMIO Colloids. USMIO colloids were reacted with epichlorohydrin followed by amination using methods previously reported for USPIO iron-based colloids (*23*, *24*). Aminated colloids were further reacted with rhodamine isothiocyanate (RITC) or fluorescein isothiocyanate (FITC) in 0.1 M sodium bicarbonate buffer (pH 8.9) and extensively dialyzed against water.

Time-Resolved Fluorescence (TRF). Time resolved fluorescence spectra were measured using a Varian Cary Eclipse fluorescence spectrophotometer. For TRF measurements, the instrument was set for phosphorescence mode. Spectrophotometer settings for both fluorescence and phosphorescence measurements were as follows: scan control, medium; smoothing, moving average factor 5; excitation filter, auto; emission filter, open; PMT detector voltage, 600 V. Settings for TRF were as follows: total decay time, 0.020 s; number of flashes, 1; delay time, 0.2 ms; gate time, 5 ms. Samples were dissolved in 0.1 N HCl, incubated for 5 min, added to 1 mL of development solution (BioPAL), and incubated for 30 min prior to recording spectra. Excitation and emission wavelengths for europium-doped USMIO colloidal particles were 340 and 615 nm, respectively. Dot blots were performed on standard filter paper and developed by overlaying blotted samples with dicarboxyl

pyridine. Blotted samples were dried at room temperature and visualized under black light (254 nm).

Stability of USMIO Colloid to Chelates and Lysosomal Conditions. One milliliter samples of 5 mol % europium USMIO were dialyzed against 10 mL of the following solutions for the indicated times, using a 12–14K MWCO dialysis membrane: 1 mM EDTA pH 7.4 (24 h), 1 mM DTPA pH 7.4 (24 h), 10 mM succinate pH 7.4 (24 h), 10 mM citrate pH 7.4 (24 h), and 10 mM sodium acetate pH 5.0 (1 h, 3 h, 16 h, 2 days, 5 days). A control sample was dialyzed against PBS pH 7.4 for 24 h. Dialyzed USMIO preparations were compared with untreated starting USMIO for europium by time-resolved fluorescence. Samples were prepared and analyzed by time-resolved fluorescence measurements as described above. Results are reported as the percentage of retained europium compared to the untreated USMIO.

Cell Labeling and Electron Microscopy (EM). Cell labeling and electron microscopy studies were conducted at the University of Massachusetts Medical School (Worcester, MA) under the direction of Dr. Gregory M. Hendricks (Manager Core–Electron Microscopy Facility). Normal murine fibroblasts were grown in Petri dishes. USMIO colloids were diluted (1:10) into cell medium and added to the individual dishes. The cells were incubated with the label for 1 h at room temperature. Unincorporated label was washed off with three changes of fresh PBS. The cells were fixed in 2.5% glutaraldehyde in PBS buffer for 1 h. The cells were then washed in three changes of PBS buffer and postfixed in 1% osmium tetroxide for 20 min at room temperature. Following postfixation, the cells were washed in three changes of PBS buffer and transferred into a 1% aqueous solution of uranyl acetate for 20 min and then left in buffer overnight at 4 °C. The next day, the cells were dehydrated through a graded series of ethanol and transferred into a mixture of epoxy resin (SPI-pon 812/araldite) and ethanol (50:50, v/v) and left overnight to infiltrate. The following day, the cells were transferred through three changes of freshly made whole epoxy resin (SPI-pon 812/araldite) and then into the final embedding mixture of the same epoxy resin and flat-embedded in the dishes and allowed to polymerize for 48 h at 68 °C. Once polymerized, the cells embedded in the epoxy resin were removed from the dishes by immersing the dishes into liquid nitrogen, cracking the dish away from the embedded cells. The cells were then oriented and sectioned (cross sections). Electron micrographs were taken on a Philips CM 10 at 80 kV.

Cell Toxicity. Cell toxicity determination was performed with LinCap cells grown to 60% confluence in cell culture media. The cell culture medium was removed. Five mole percent of europium USMIO was diluted into fresh culture medium to either 0.1 or 1 mg/mL (total metals) and added to the cells and incubated at 5% CO_2 and 37 °C for 24 h. The confluence level of the treated cells was then recorded.

RESULTS

Synthesis. USMIO colloids were synthesized and characterized for size and zeta potential using the lanthanides europium, samarium, and lanthanum (Table 2). The synthetic procedures for each of these three lanthanide-enriched USMIO colloids remained unchanged other than the replacement of ferric iron with trivalent europium in the first synthesis, with trivalent samarium in the second, and trivalent lanthanum in the third. The synthetic procedure proved reproducible. To understand the generality of the synthetic process, other trivalent lanthanides not included in Table 2 were substituted for ferric iron. These elements included terbium, ytterbium, and gadolinium. Each preparation appeared visually identical and had similar sizes. Ytterbium- and gadolinium-containing USMIO colloids were not characterized further. Europium, lanthanum, and samarium were chosen for their excellent properties in detection by neutron activation technology. Europium and terbium were chosen because when combined with suitable enhancers, they produce a strong time-resolved fluorescence signal.

Table 2. Effect of Replacement of Ferric Iron with Trivalent Lanthanides on Colloid Size[a]

lanthanide (%)[b]	effective diameter (nm)	zeta potential (mV)
none	23	−1.54
Eu (1%)	30[c]	-
Eu (1%)	22[c]	-
Eu (5%)	37[c]	5.68
Eu (5%)	44[c]	-
Eu (15%)	35	-
Eu (30%)	26	11.87
Eu (50%)	36	8.03
Eu (100%)	90	-
La (30%)	30	-
Sm (30%)	25	-
Eu (5%)-FITC	49[d]	-
Eu (5%)-FITC	49[e]	-

[a] Samples were prepared for sizing by dilution into water to a concentration of 1 mg/ml for total metals and were then passed through a 0.1 μm filter. Less than 2% of colloid was retained on the filter as assessed by metal analysis (lanthanides by neutron activation analysis and iron by the dipyridyl method) and by absorption spectroscopy at 550 nm. Visual examination of the filters showed a minimal amount of staining indicating small amounts of particulate formation. Eu = europium, La = lanthanum, Sm = samarium. [b] Refers to a mol% replacement of ferric chloride with a trivalent lanthanide metal during synthetic procedures. [c] Represents duplicate synthesis. [d] USMIO colloid cross-linked, aminated and labeled with fluorescein. [e] USMIO colloid cross-linked, aminated and labeled with rhodamine.

Physical Properties. *X-ray Powder Diffraction.* MION and 5 mol % europium USMIO X-ray powder diffraction patterns had all the major peaks associated with authentic magnetite. The X-ray powder diffraction pattern for 5 mol % europium USMIO and the position of the major peaks for magnetite are presented in Figure 1. Small miscellaneous peaks were seen in the 5 mol % europium USMIO preparation and are attributed to the large amounts of dextran present in the dry powder. The crystal type for 50 mol % europium USMIO could not be determined due to its small crystal size. The crystal sizes as determined by X-ray powder diffraction of MION, 5 mol % europium USMIO, and 50 mol % europium USMIO were 7.5, 6.6, and <2 nm, respectively. Crystal dimensions of 5 to 15 nm for USPIO magnetite preparations are reported to all be superparamagnetic (*25*), consistent with magnetization measurements performed on 5 mol % europium USMIO.

Magnetization. The magnetization curve for 5 mol % europium USMIO was obtained by varying the applied magnetic field between −3 and +3 Tesla. At room temperature, 5 mol % europium USMIO exhibited superparamagnetic behavior as shown by a single line with no evidence of hysteresis with an induced magnetization of 56 emu/g Fe at 1.5 T (Figure 2). This compares with the literature value of 68 emu/g iron of MION (*22*).

Magnetic Susceptibility. The effect of increasing substitution of europium (+3) for iron (+3) on susceptibility is shown in Figure 3. At levels of 1 and 5 mol % europium, magnetic susceptibility decreased less than 5%. However, at levels of 50 mol % europium, magnetic susceptibility was lowered by greater than 2 orders of magnitude. The relationship between increasing europium content and decreasing magnetic potency exhibited a semilogarithmic relationship. Since the observed magnetic susceptibility is related to the percentage of iron (+3) in the colloid, the observed decrease in magnetic susceptibility with increasing europium content can be attributed to both disruption of the electronic relationship among the ferric iron components

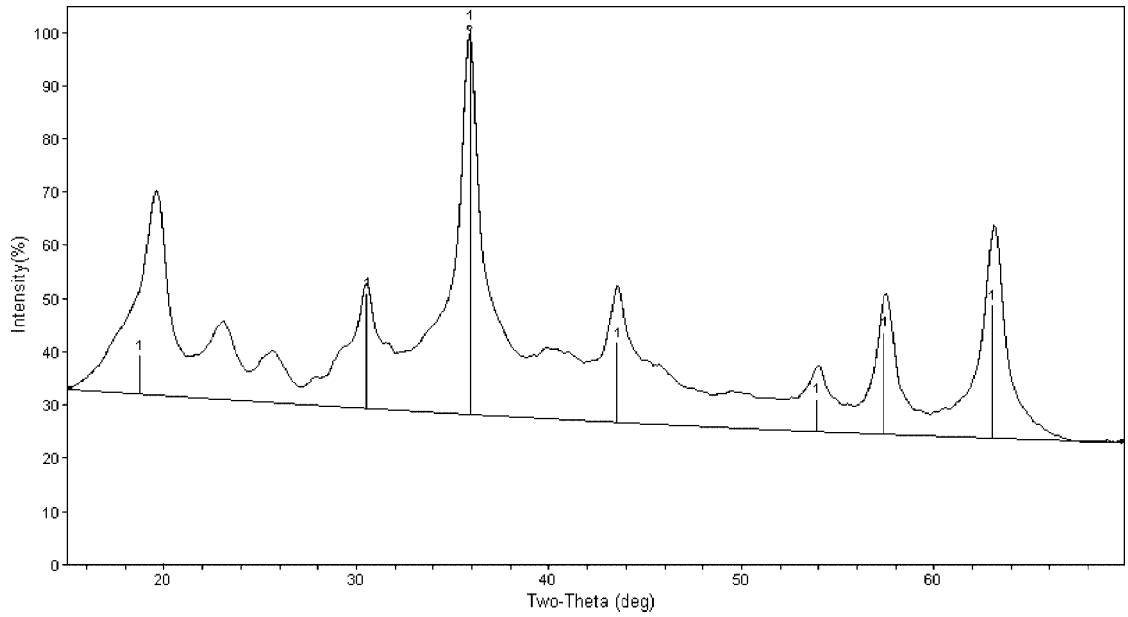


Figure 1. X-ray powder diffraction pattern for 5 mol % europium USMIO. The spectrum was obtained as described in Methods and Materials. The principal peaks for and relative magnitude of magnetite are indicated by the vertical bars labeled 1.

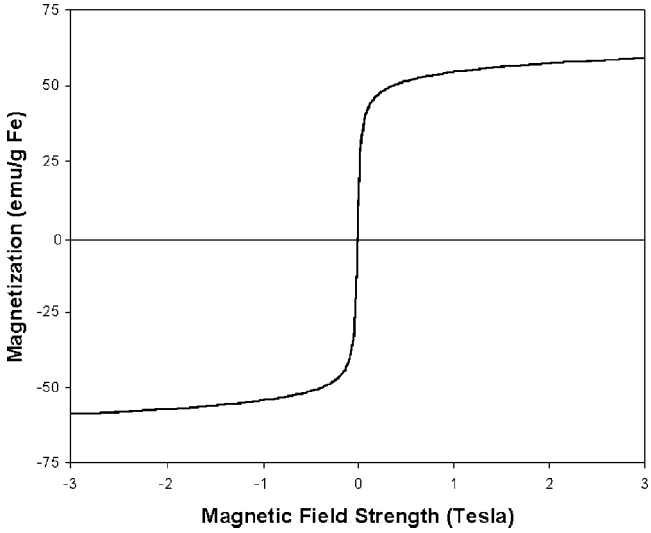


Figure 2. Magnetization vs field strength for 5 mol % europium USMIO at room temperature. The data were acquired between −3 and +3 Tesla and consist of 748 measurements.

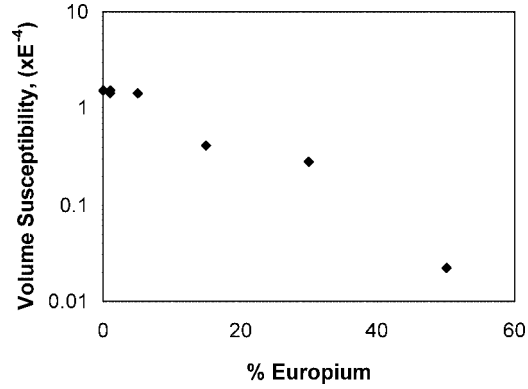


Figure 3. Relationship between magnetic potency (volume susceptibility) and mol % europium replacement of ferric iron in USMIO. Volume susceptibility was determined as described in Methods and Materials section.

Table 3. Relaxivity Values for 5 mol % Europium USMIO and MION

name of contrast agent	mean crystal size (nm)	R_1 (s^{-1} mM^{-1})	R_2 (s^{-1} mM^{-1})	R_2/R_1	refs
AMI-25	7–10	40	160	4	(*21*, *31*, *32*)
Combidex	4.9	23.3	48.9	2.1	(*33*)
MION	4.6[a]	16.5	34.8	2.1	(*22*)
BioPAL MION[b]	17.3	36.1	2.1		
BioPAL USMIO 5%	6.6[b]	15.4	33.9	2.2	

[a] Determined by electron microscopy. [b] Determined by X-ray diffraction.

in the magnetite crystal (responsible for the generation of the magnetic properties of magnetite (*26*)) and decreasing crystal size associated with the increasing europium content (*26, 27*).

Relaxivity. The relaxation constants R_1 and R_2 were measured at 0.47 T and 37 °C. Values for MION and 5 mol % europium USMIO are presented in Table 3. Literature values for R_1 and R_2 for MION and other iron oxides are included in Table 3 for comparison.

Size and Charge. The substitution of trivalent lanthanide metals for ferric iron in the preparation of colloid had minimal effect on colloid size (Table 2). The effective diameters of most USMIO colloids fell between 20 and 40 nm except for one 5 mol % europium USMIO (44 nm) and the 100 mol% europium USMIO (90 nm). No trend exists between colloid size and increasing europium content, as illustrated by the scatter diagram comparing percent europium (abscissa) versus effective diameter (ordinate) (Figure 4). When europium trichloride completely replaced ferric chloride, the colloid size markedly increased. This size increase was accompanied by formation of particulates as indicated by impaired filtration of the colloid. Substitution of ferric iron with 30 mol % samarium or lanthanum also had no effect on colloid size (Table 2).

The size and size distribution of lanthanide-containing magnetite is very close to that found for similar materials consisting exclusively of ferric and ferrous iron. These materials referred to in the literature as SPIO (Feridex) and USPIO (MION) have sizes between 20 and 100 nm with size distribu-

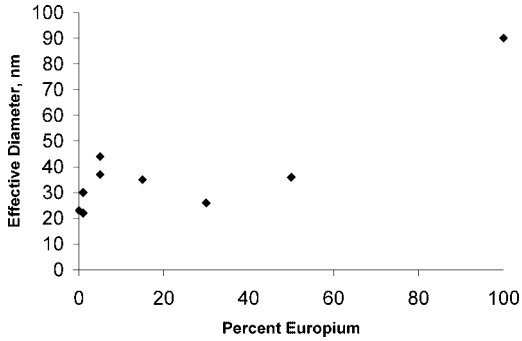


Figure 4. Scattergram of data from Table 2. Percent europium refers to displacement of ferric iron by trivalent europium during synthetic procedures (retention of europium in final colloidal form confirmed by neutron activation analysis; data not shown). The variation in size as a function of increasing lanthanide substitution as illustrated with europium trichloride (through 50 mol % europium) was not statistically significant, as all points fell within 1 standard deviation of the mean effective diameter.

tions that cover a range of a factor of 3 to 4 between the smallest and largest particles (*22*, *28*). USMIO colloid containing 5 mol % europium had an effective diameter of 37 nm with 90% of the particle mass contained between 21 and 64 nm (Figure 5). Similar results were obtained with USMIO colloids containing up to 50 mol % substitution of europium for ferric iron.

The charge of the USMIO colloids was assessed using zeta potential analysis. As shown in Table 2, the zeta potential for colloids containing 0, 5, 30, and 50 mol % europium increases in charge from slightly negative for 0 mol % europium to moderately positive for 50 mol % europium. For comparison, the zeta potential for Feridex, a SPIO, and MION, an USPIO, were measured using the same instrumental system and were −30.97 and −9.16, respectively.

Zeta potentials can vary greatly depending upon the pH and salt concentration. For all zeta potential measurements reported, the samples were diluted 1:10 into distilled water. The pH values of the USMIO, Feridex, and MION were between 7.2 and 7.5. The salt concentration was less than 1 mM. The high negative zeta potential of Feridex can be attributed to its method of synthesis and stabilization with citrate (*29*). The difference in zeta potential between MION and 5 mol % europium USMIO may result from minor variations in synthesis and purification, yielding small differences in binding of chloride and hydroxide ions and loosely associated europium cations to the colloid surface.

Chemical Properties. *Cross-Linking, Amination, and Fluorescence Labeling of USMIO Colloids.* USMIO colloids containing 5 mol % europium were cross-linked with epichlorohydrin. The cross-linking reaction was terminated with ammonia, which introduced amino groups. The presence of amino groups was confirmed by ninhydrin staining. In order to demonstrate the accessibility and reactivity of the amino groups, cross-linked–aminated USMIO was reacted using FITC or RITC as model compounds. Reaction at pH 8.9 led to the covalent attachment of RITC and FITC. In control experiments, RITC and FITC were not retained when incubated with untreated USMIO or cross-linked USMIO not treated with ammonia. Fluorescence of RITC and FITC was clearly apparent in dot blots under black light as well as by detection using conventional instrumental fluorescence detection. The effect of cross-linking, amination, and ligand labeling resulted in a small increase in colloid size consistent with similar reactions reported for colloidal iron oxides. The small size changes strongly indicate that individual colloidal particles do not aggregate during the cross-linking process.

Distinct fluorescence and time-resolved fluorescence spectra were obtained with a cross-linked aminated 5 mol % europium USMIO reacted with RITC (Figure 6). The emission spectrum of rhodamine was clearly apparent when colloid was diluted into either PBS or development solution. The emission spectrum of europium was present only when colloid was diluted into development solution. The absence of an emissions peak for europium (when diluted in PBS) is due to europium's requirement for a chelating antenna in order for its time-resolved properties to be detected (*30*). The fluorescence of rhodamine did not interfere with the acquisition of the time-resolved spectrum for europium for two reasons: (i) Rhodamine does not fluoresce when excited at 340 nm, the excitation wavelength used for europium. (ii) Rhodamine does not yield a signal when excited at 550 nm when its emission spectrum is acquired in phosphorescent mode (time-resolved fluorescence). Therefore, it is possible to acquire the fluorescence spectra of both the organic ligand (rhodamine) and the inorganic element (europium) in the presence of each other without interference from either fluorescent contributor.

USMIO colloids labeled with europium or terbium can be detected by time-resolved fluorescence after treatment with 4,4,4-trifluoro-1-(2-naphthyl)-1,3-butanedione or dicarboxyl pyridine. A representative standard curve is presented in Figure 7 showing the relationship between signal intensity and europium. The minimum level of detection corresponds to about 10^{-14} g of europium.

USMIO colloids labeled with europium or terbium can also be detected using the dot blot technique (Figure 8). Columns 1 and 3 show the visual detection of europium- or terbium-labeled USMIO colloids, which yields a red or green color and a visual detection limit of about 10^{-14} mol. When equal amounts of each USMIO colloid are mixed, a yellow color is obtained (column 2). For comparison, the detection of FITC is shown in column 4, which is minimally visible at 10^{-11} mol.

Europium is Part of the Colloid. The presence of europium in the colloid was demonstrated by passage of europium-containing colloids through a 30K MWCO membrane. Greater than 99% of the europium, as quantified by neutron activation analysis, and 100% of the colloid, as quantified by photon correlation spectroscopy, were retained by the membrane. In a second experiment, after a 10 min treatment of the colloid with 1 mM DTPA (pH 7.4), followed by passage through a 30K MWCO membrane, greater than 98% of the europium was retained by the membrane. As a control experiment, 1 mM europium was treated with 1 mM DTPA (pH 7.4) for 10 min and was found to freely pass through the membrane. In a third experiment using CM-Sephadex (0.01 M Tris buffer pH 7.4) to capture cationic europium, greater than 95% of the europium eluted in the void volume with the colored colloid. In control experiments, cationic europium was quantitatively retained by CM-Sephadex.

In order to additionally demonstrate incorporation of europium into the magnetite crystal structure (fourth experiment), the change in magnetic susceptibility associated with increasing europium substitution for ferric iron in the synthesis of USMIO colloids was examined. A semilogarithmic decline in magnetic potency was associated with increasing europium content consistent with disruption of the crystal structure of the starting magnetite (Figure 3).

In a fifth experiment, the presence of europium in the magnetite crystal was assayed using X-ray powder diffraction. Magnetite samples containing 0 and 5 mol % of europium showed no evidence of europium. This observation was attributed in the 5 mol % europium USMIO to the detection limit of the method. In iron oxide preparations containing 50 mol %

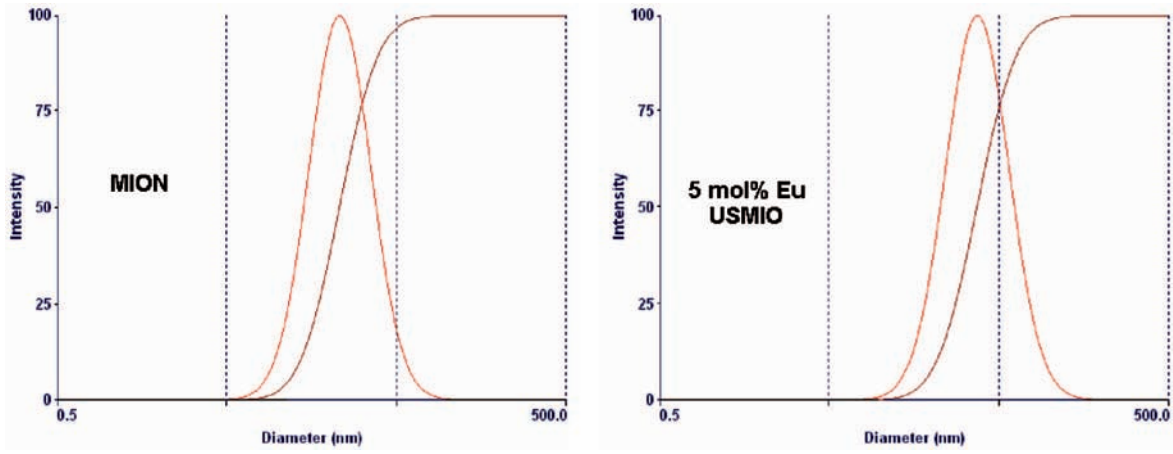


Figure 5. Size distribution of USPIO (MION) colloids and USMIO (5 mol % europium) colloids. MION had an effective diameter of 23 nm and a polydispersity of 0.189. 5 mol % europium USMIO colloids had an effective diameter of 37 nm and a polydispersity of 0.200.

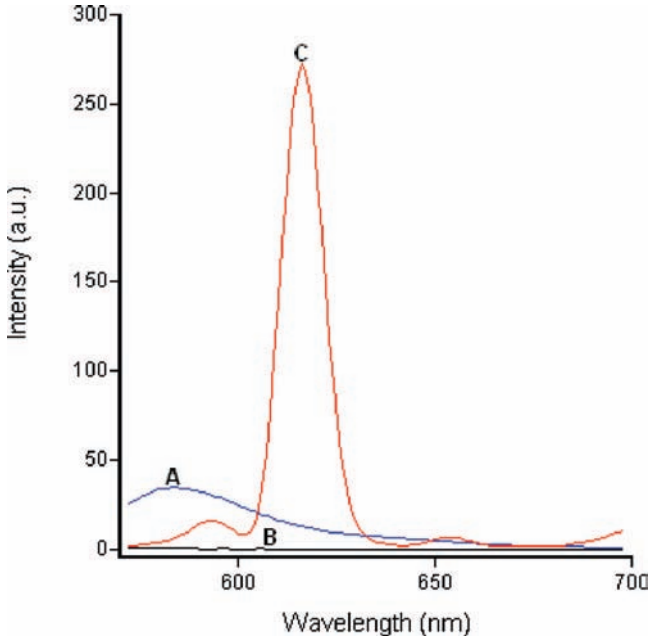


Figure 6. Fluorescence and time-resolved fluorescence spectra of RITC conjugated 5 mol % europium USMIO. USMIO was cross-linked, aminated, and conjugated with RITC. Curve A: Fluorescence of RITC-conjugated USMIO. RITC-conjugated USMIO was diluted 1:10 000 in PBS. The fluorescence spectrum for rhodamine was obtained in fluorescence mode by exciting at 555 nm and scanning emissions between 570 and 700 nm. Curve B: Time-resolved fluorescence of rhodamine-conjugated USMIO without development solution. RITC-conjugated USMIO was diluted 1:10 000 in PBS. Its time-resolved fluorescence spectrum for europium was obtained in phosphorescence mode by exciting at 340 nm and scanning emissions between 570 and 700 nm. Curve C: Time-resolved fluorescence of RITC conjugated USMIO with development solution. RITC-conjugated USMIO was diluted 1:100 into 0.1 N HCl, incubated 5 min, and diluted further 1:100 into development solution. The time-resolved fluorescence spectrum for europium was obtained in phosphorescence mode by exciting at 340 nm and scanning emissions between 570 and 700 nm. Fluorescence spectrum of RITC after acid treatment and incubation in development solution was also obtained in fluorescence mode as described for curve A and presented a nearly identical spectrum to curve A (data not shown).

europium and 100 mol % europium, the presence of characteristic absorption peaks associated with europium oxide were seen.

Stability of USMIO Colloids. The USMIO colloids reported in Table 2 showed no systematic change in size when stored at 4 °C for a period of over a year. Further, 5 mol % europium

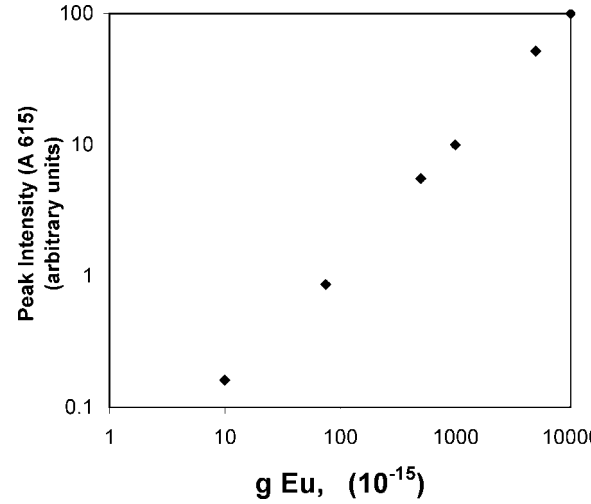


Figure 7. Detection limits for europium in a 5 mol % europium USMIO. Samples were prepared for time-resolved fluorescence measurements as described in Methods and Materials.

USMIO showed no change in size when subjected to autoclaving (121 °C) for 15 min. All colloids reported in Table 2 exhibited no change in size following three freeze–thaw cycles.

The stability of USMIO under physiological conditions between pH 5.0 and 7.4 was studied to simulate stability in serum, cellular cytoplasm, and lysosomal subcompartments (Table 4). At pH 7.4 in the presence of chelating agents (EDTA, DTPA, citrate, succinate), less than 0.2% europium was removed from the colloidal USMIO after 5 days of treatment. This small amount can be attributed to osmotic dilution of the sample during dialysis. At pH 5.0, a time-dependent removal of europium from the colloidal USMIO was observed from 1.40% to 2.04% of total europium. Europium removal plateaued after 2 days, and no additional loss was observed when treatment was extended to 5 days. This small but reproducible loss may be attributed to the removal of surface europium.

Biological Properties. *Cell Labeling with USMIO.* Murine fibroblasts were incubated with 5 mol % europium USMIO suspended in cell medium for 1 h as described in the Methods and Materials section. Cells were then fixed and examined by electron microscopy for the presence of electron dense material. In the image shown in Figure 9, one prominent electron-dense cluster of particles is contained within a vacuole (arrow). Similar electron-dense vacuoles were seen in other fields. In all fields, the particles appeared to be contained within cytoplasmic vacuoles, and no particles were seen adhering to the cell surface.

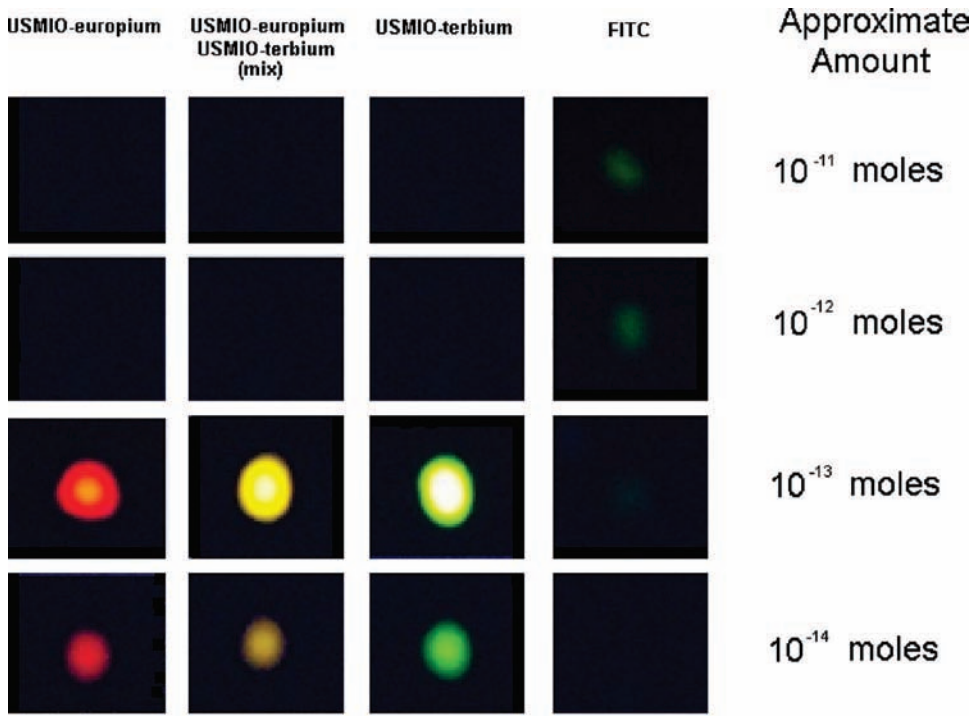


Figure 8. Detection limits and color display of USMIO colloid labeled with europium or terbium. Dot blots of USMIO colloids containing europium and terbium were obtained by pipetting samples containing the indicated amounts of europium or terbium. Samples were dried and then overlaid with dicarboxyl pyridine. No colloid was spotted in rows 1 and 2. Column 4 contains indicated amounts of FITC. Samples were visualized by illumination with a black light set for 254 nm. The approximate amount indicated in the figure represents moles of europium, terbium, or fluorescein contained in the USMIO samples and fluorescein standard, respectively.

Table 4. Stability of USMIO to Chelates and Lysosomal Conditions[a]

dialyzed against:	pH	dialysis (h)	% europium
PBS (control)	7.4	24	99.96
1 mM EDTA	7.4	24	99.91
1 mM DTPA	7.4	24	99.99
10 mM citrate	7.4	24	99.83
10 mM succinate	7.4	24	99.97
10 mM sodium acetate	5.0	1	98.60
10 mM sodium acetate	5.0	3	98.23
10 mM sodium acetate	5.0	16	98.06
10 mM sodium acetate	5.0	48	98.00
10 mM sodium acetate	5.0	120	97.96

[a] 5 mol % europium USMIO was dialyzed against the conditions indicated below. The percent europium retained within the dialysis membrane is shown in column 3.

Close examination of the particle structure reveals multiple groups of smaller irregular shapes that clump together to form the larger particle aggregate. Measurement of the individual "subunits" reveals a size of approximately 4–6 nm consistent with the crystal size measured by X-ray powder diffraction and reported for MION (*22*).

USMIO Cellular Toxicity. There was no suggestion of cell toxicity following a 1 h incubation with USMIO either upon examination of normal murine fibroblasts while in a monolayer or after preparation for electron microscopy (personal communication, Gregory M. Hendricks). Additionally, LinCap cells, when exposed for 24 h to 0.1 and 1 mg/mL (total metals), USMIO showed small declines in confluence falling from a starting level of 60% confluence to 50% and 40% confluence, respectively. The decline in percent confluence may be attributed to cell rounding during the incubation with USMIO.

DISCUSSION

We report the synthesis of a family of mixed ferrite colloidal magnetic iron oxides through the addition of small amounts of non-iron atoms during formation of the iron oxide core. The incorporation of nonferrous atoms to magnetic colloidal iron oxides introduces new reporting properties to these materials while retaining the magnetic potency associated with iron-based MRI contrast agents and cell-sorting magnetic materials. Among the new properties that these atoms confer to the colloidal iron oxides are (i) quantitative detection by neutron activation (Eu, Sm, La, Tb), (ii) quantitative and sensitive detection by time-resolved fluorescence (Eu, Tb), (iii) detection by X-ray fluorescence in conjunction with scanning electron microscopy (all the lanthanides), (iv) simultaneous detection of multiple labeled colloids, e.g., detection of Eu in the presence of La by NA, and (v) applications in neutron capture therapy (Gd). While this report provides data relevant to the incorporation of lanthanides in the ferrite crystal, other elements such as the transition metals scandium, yttrium, cobalt, manganese, and zinc can be introduced using similar synthetic procedures.

Dextran-coated iron oxides containing lanthanides can be prepared using methods that are essentially identical to those used to prepare the analogous iron oxide colloids. Further, these lanthanide-labeled colloids possess nearly identical physical and chemical properties to that of the unlabeled reference material (MION). These properties are manifest in the similarity between the two materials: (i) physical properties including magnetic properties [magnetization (emu/g Fe), superparamagnetism, susceptibility, and relaxivity (R_1 and R_2)], powder X-ray diffraction (crystal size), hydrodynamic size, and size distribution; and (ii) chemical properties including zeta potential (charge), surface chemistry (cross-linking with epichlorohydrin and reaction with low molecular weight ligands), and stability against environmental challenge.

USMIO colloids can be detected by a variety of methods including neutron activation analysis (NA), time-resolved fluorescence (TRF), X-ray fluorescence/scanning electron microscopy (XRF-SEM), and magnetic resonance imaging (MRI). USMIO colloids can be labeled with a number of lanthanides

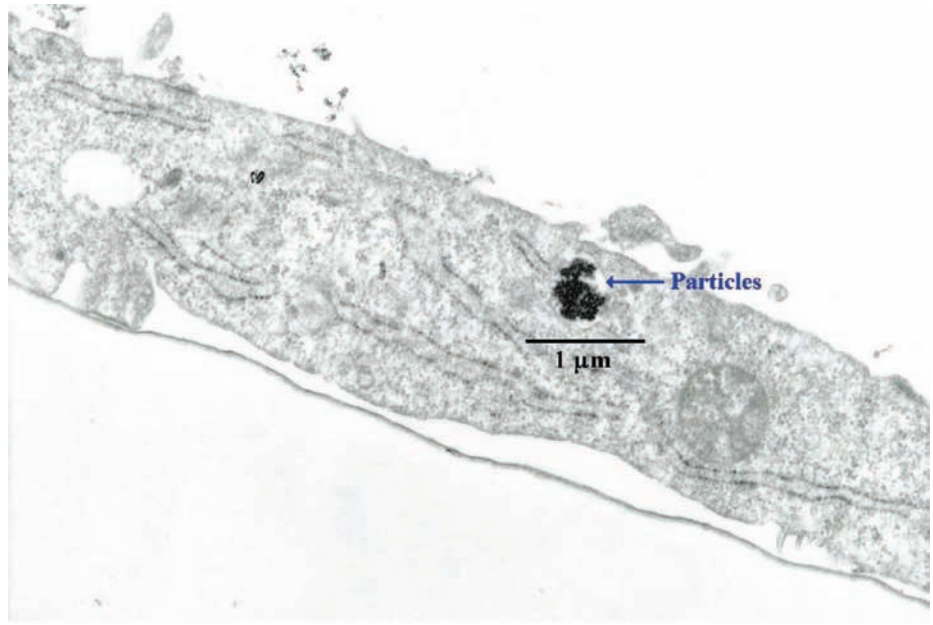


Figure 9. Electron micrograph of 5 mol % europium USMIO in fibroblast cytoplasm. The magnification factor is 25 000.

that can be sensitively detected and quantified by neutron activation analysis (Table 1). The usefulness of any particular lanthanide for NA is determined by its neutron capture cross section of its isotopes, the isotopic abundance of the selected element, and the resulting half-life of the new isotope following neutron capture. On the basis of these requirements, the lanthanides listed in Table 1 have been selected as most useful in neutron activation analysis (*14*).

Neutron activation is a sensitive method of analysis. The limit of detection of europium by NA is 5 ng. Considering the mol % of iron and europium, 95 and 5 mol %, respectively, within an optimized magnetic USMIO colloid, approximately 35 ng of the USMIO colloid can be detected by NA. Similar levels of detection can be achieved with the other lanthanides identified in Table 1.

Neutron activation has the benefits of not requiring sample preparation, correction for differential neutron absorption due to matrix, or processing for quantifying. In addition to labeling iron oxides with europium, other lanthanides can be introduced into the iron oxide core and can be quantified by neutron activation. Since the gamma emission spectra of the various neutron-activated lanthanide elements are both unique and nonoverlapping, these elements can be quantified simultaneously in the presence of other lanthanides. This property allows the design of experiments where similar colloids labeled with different lanthanides are used either sequentially or simultaneously in labeling and tracking cells (*16*).

USMIO colloids labeled with europium or terbium can be detected by time-resolved fluorescence after treatment with 4,4,4-trifluoro-1-(2-naphthyl)-1,3-butanedione or dicarboxyl pyridine. The minimum level of detection corresponds to about 10^{-14} g of europium. USMIO colloids labeled with europium or terbium can also be detected using the dot blot technique with a visual detection limit of about 10^{-14} mol (europium and terbium). The presence of lanthanides in the iron oxide matrix confers attractive optical properties for long-term multilabeling studies with europium and terbium. These USMIOs offer high photostability, a narrow emission band, and a broad absorption band combining the high sensitivity of time-resolved fluorescence with the high spatial resolution of MRI (*15*).

Detection of USMIO colloids using electron microscopy was accomplished after treating cells with colloid added to the cell culture medium. USMIO colloid labeled with 5 mol % europium is strongly magnetic, as indicated from its magnetic susceptibility and magnetization curve. At concentrations of iron equal to approximately 10 mg/mL, the USMIO colloid forms an aqueous ferrofluid consistent with its strong magnetic property. Finally, the USMIO colloid exhibits typical properties of a T2 MRI contrast agent similar to that reported for USPIO (MION) (Table 3) (*21*).

The capability to use neutron activation to quantitate iron oxides and USPIO type materials labeled with lanthanides allows analysis of experimental protocols related to MRI, cell labeling, and cell separation. For instance, when contrast-enhanced MRI experiments are performed with USPIO-type materials labeled with lanthanides, the blood concentration can be followed more accurately and to lower levels of detection than can be achieved using MRI. Further, contrast agent obtained by biopsy, by dissection, or by necropsy can be measured by neutron activation. Similarly, magnetic iron oxides lightly labeled with lanthanides used in cell-sorting experiments can be quantitated to determine the degree of their removal from purified cell preparations. The introduction of gadolinium into USMIO opens the possibility of combining the high spatial resolution of MRI for drug location followed by neutron-capture therapy by exposing the USMIO to thermal neutrons. Therefore, gadolinium-doped USMIO offers an attractive alternative to boron compounds for neutron capture therapy.

Since the initial synthesis of colloidal iron oxides for applications as MR contrast agents, researchers using these materials have arrived at the problem of quantifying the samples containing these colloids in animal models. This problem has been most extreme at low concentrations, particularly in applications of cell labeling and cell tracking. One opportunity to alleviate this difficulty would be to label such colloids with iron-59. However, the use of this isotope in the synthesis of USPIO/USMIO is problematic, especially when the synthesis is performed on the small scale used for trace labeling. A second limitation in using radiolabels is the limited availability of instrumentation suited for quantifying iron-59. Third, a general absence of laboratories prepared to handle iron-59 in the chemical laboratory as well as in animal experimentation has made this solution to quantifying colloidal iron oxides problematic.

We propose a simpler solution to quantifying ferrites as contrast/tracking agents by labeling them with small amounts of stable (nonradioactive) europium. This solution avoids the

introduction of radioactivity into the workplace while minimally affecting the physical and chemical properties of the colloid from that of the unlabeled reference material. Europium can be quantified readily by neutron activation, a well-known and established technique. Neutron activation analysis has several advantages that make it attractive for quantification including sensitive detection, minimal sample preparation, and no quenching of the sample during the activation and counting processes. Further, europium can be sensitively detected by other methods such as time-resolved fluorescence. Thus, through the introduction of europium, USMIO can be quantified by neutron activation, visualized in vivo by MRI, visualized histologically using time-resolved fluorescence, and detected in electron microscopic samples by X-ray fluorescence.

ACKNOWLEDGMENT

This research was supported in part by the National Institute of Health grant no. 1R43AI063731-01A1. Magnetization analysis was kindly provided under the direction of Dr. James O'Brien (Quantum Design, San Diego, CA). The authors thank Dr. Glen Bubbley (Beth Israel Deaconess Medical Center, Boston, MA) and Dr. Gregory M. Hendricks (Manager Core–Electron Microscopy, Facility University of Massachusetts Medical School, Worcester, MA) for their examination of USMIO effects upon cell viability and Dr. Craig Ferris (Department of Physiology, University of Massachusetts Medical School, Worcester, MA) for measuring the relaxivity of USMIO preparations.

LITERATURE CITED

(1) Molday, R. S., and Molday, L. L. (1984) Separation of cells labeled with immunospecific iron dextran microspheres using high gradient magnetic chromatography. *FEBS Lett. 170*, 232–238.

(2) Stark, D. D., Weissleder, R., Elizondo, G., Hahn, P. F., Saini, S., Todd, L. E., Wittenberg, J., and Ferrucci, J. T. (1988) Superparamagnetic iron oxide: clinical application as a contrast agent for MR imaging of the liver. *Radiology 168*, 297–301.

(3) Josephson, L., Groman, E., and Weissleder, R. (1991) Contrast agents for magnetic resonance imaging of the liver. *Targeted Diagn. Ther. 4*, 163–187.

(4) Arbab, A. S., Yocum, G. T., Kalish, H., Jordan, E. K., Anderson, S. A., Khakoo, A. Y., Read, E. J., and Frank, J. A. (2004) Efficient magnetic cell labeling with protamine sulfate complexed to ferumoxides for cellular MRI. *Blood 104*, 1217–1223.

(5) Frank, J. A., Miller, B. R., Arbab, A. S., Zywicke, H. A., Jordan, E. K., Lewis, B. K., Bryant, L. H., Jr., and Bulte, J. W. (2003) Clinically applicable labeling of mammalian and stem cells by combining superparamagnetic iron oxides and transfection agents. *Radiology 228*, 480–487.

(6) Kostura, L., Kraitchman, D. L., Mackay, A. M., Pittenger, M. F., and Bulte, J. W. (2004) Feridex labeling of mesenchymal stem cells inhibits chondrogenesis but not adipogenesis or osteogenesis. *NMR Biomed. 17*, 513–517.

(7) Bulte, J. W. (2006) Intracellular endosomal magnetic labeling of cells. *Methods Mol. Med. 124*, 419–439.

(8) Radbruch, A., Mechtold, B., Thiel, A., Miltenyi, S., and Pfluger, E. (1994) High-gradient magnetic cell sorting. *Methods Cell Biol. 42 Pt B*, 387–403.

(9) Schellenberger, E. A., Reynolds, F., Weissleder, R., and Josephson, L. (2004) Surface-functionalized nanoparticle library yields probes for apoptotic cells. *ChemBioChem 5*, 275–279.

(10) Schellenberger, E. A., Sosnovik, D., Weissleder, R., and Josephson, L. (2004) Magneto/optical annexin V, a multimodal protein. *Bioconjug Chem. 15*, 1062–1067.

(11) Ito, A., Shinkai, M., Honda, H., and Kobayashi, T. (2005) Medical application of functionalized magnetic nanoparticles. *J. Biosci. Bioeng. 100*, 1–11.

(12) Evans, C. H. (1990) *Biochemistry o f the Lanthanides*, Plenum Press, New York.

(13) Cotton, A. F., and Wilkinson, G. (1988) *Advanced Inorganic Chemistry*, John Wiley and Sons, New York.

(14) Parrington, J. R., Knox, H. D., Breneman, S. L., Baum, E. M., and Feiner, F. (1996) *Nuclides and Isotopes*, General Electric Co. and KAPL, Inc., San Jose

(15) Matsumoto, K., and Yuan, J. (2003) In *The Lanthanides and Their Interrelations with Biosystems* (Sigel, A., and Sigel, H., Eds.) p 214, Vol. 40, Marcel Dekker, Inc., New York.

(16) Shih, J. L., and Brugger, R. M. (1992) Neutron induced brachytherapy: a combination of neutron capture therapy and brachytherapy. *Med. Phys. 19*, 369–375.

(17) Shih, J. L., and Brugger, R. M. (1992) Gadolinium as a neutron capture therapy agent. *Med. Phys. 19*, 733–744.

(18) Brugger, R. M., and Shih, J. A. (1989) Evaluation of gadolinium-157 as a neutron capture therapy agent. *Strahlenther Onkol. 165*, 153–156.

(19) ISO 2992: Determination of iron concentraion: 2,2′-Bipyridyl photometric method (1974), www.ios.org.

(20) Reinhardt, C. P., Dalhberg, S., Tries, M. A., Marcel, R., and Leppo, J. A. (2001) Stable labeled microspheres to measure perfusion: validation of a neutron activation assay technique. *Am. J. Physiol. Heart Circ. Physiol. 280*, H108–116.

(21) Josephson, L., Lewis, J., Jacobs, P., Hahn, P. F., and Stark, D. D. (1988) The effects of iron oxides on proton relaxivity. *Magn. Reson. Imaging 6*, 647–653.

(22) Shen, T., Weissleder, R., Papisov, M., Bogdanov, A., Jr., and Brady, T. J. (1993) Monocrystalline iron oxide nanocompounds (MION): physicochemical properties. *Magn. Reson. Med. 29*, 599–604.

(23) Palmacci, S., Josphson, L., and Groman, E. Synthesis of polysaccharide covered superparamagnetic oxide colloids. U.S. Patent 5,262,176, 1993.

(24) Koch, A. M., Reynolds, F., Kircher, M. F., Merkle, H. P., Weissleder, R., and Josephson, L. (2003) Uptake and metabolism of a dual fluorochrome Tat-nanoparticle in HeLa cells. *Bioconjugate Chem. 14*, 1115–1121.

(25) Babes, L., Denizot, B., Tanguy, G., Le Jeune, J. J., and Jallet, P. (1999) Synthesis of iron oxide nanoparticles used as MRI contrast agents: A parametric study. *J. Colloid Interface Sci. 212*, 474–482.

(26) Saebo, K. B. (2004) In *Department of Oncology, Radiology and Clinical Immunology*, p 94, Uppsala University, Uppsala

(27) Zhang, Y., Zhang, H., Xu, Y., and Wang, Y. (2003) Europium doped nanocrystalline titanium dioxide: preparation, phase transformation and photocatalytic properties. *J. Mater. Chem. 13*, 2261–2265.

(28) LaConte, L., Nitin, N., and Bao, G. (2005) Magnetic nanoparticle probes. *Materials Today 8*, 32–38.

(29) Groman, E., Lewis, J., and Josephson, L. Biodegradable superparamagnetic metal oxides as contrast agents for MR imaging. U.S. Patent 4,951,675, 1990.

(30) Picard, C., Geum, N., Nasso, I., Mestre, B., Tisnes, P., Laurent, S., Muller, R. N., and Elst, L. V. (2006) A dual lanthanide probe suitable for optical (Tb3+ luminescence) and magnetic resonance imaging (Gd3+ relaxometry). *Bioorg. Med. Chem. Lett. 16*, 5309–5312.

(31) Rice, H. E., Hsu, E. W., Sheng, H., Evenson, D. A., Freemerman, A. J., Safford, K. M., Provenzale, J. M., Warner, D. S., and Johnson, G. A. (2007) Superparamagnetic iron oxide labeling and transplantation of adipose-derived stem cells in middle cerebral artery occlusion-injured mice. *Am. J. Roentgenol. 188*, 1101–1108.

(32) www.mr-tip.com.

(33) Pannu, H. K., Wang, K. P., Borman, T. L., and Bluemke, D. A. (2000) MR imaging of mediastinal lymph nodes: evaluation using a superparamagnetic contrast agent. *J. Magn. Reson. Imaging 12*, 899–904.

BC070024W

Aequorin-Based Homogeneous Cortisol Immunoassay for Analysis of Saliva Samples

Laura Rowe,[†] Sapna Deo,[‡] Josh Shofner,[†] Mark Ensor,[†] and Sylvia Daunert*[,†]

Department of Chemistry, University of Kentucky, Lexington, Kentucky 40506. Received February 2, 2007; Revised Manuscript Received July 24, 2007

Homogeneous assays are attractive because they are performed in only one phase, namely, the liquid phase, and thus, they do not require separation of phases as their heterogeneous counterparts do. As opposed to heterogeneous assays, the signal generation in a homogeneous assay is a direct result of analyte binding, which allows the multiple washing and incubation steps required in an indirect heterogeneous assay format to be eliminated. Moreover, homogeneous assays are usually fast and amenable to miniaturization and automation. In this article, we describe the development of a homogeneous assay for the hormone cortisol using the bioluminescent photoprotein aequorin as a reporter molecule. A cortisol derivative was chemically conjugated to the lysine residues of a genetically modified aequorin in order to prepare an aequorin–cortisol conjugate capable of binding anticortisol antibodies. The binding of anticortisol antibodies to the aequorin–cortisol conjugate resulted in a linear response reflected in the emission of bioluminescence by aequorin. A competitive binding assay was developed by simultaneously incubating the aequorin–cortisol conjugate, the anticortisol antibodies, and the sample containing free cortisol. Dose–response curves were generated relating the intensity of the bioluminescence signal with the concentration of free cortisol in the sample. The optimized homogeneous immunoassay produced a detection limit of 1×10^{-10} M of free cortisol, with a linear dynamic range spanning from 1×10^{-5} to 1×10^{-9} M. Both serum and salivary levels of cortisol fall well within this assay's linear range (3.0×10^{-7} M to 7.5×10^{-7} M and 1.0×10^{-8} M to 2.5×10^{-8} M, respectively), thereby making this assay attractive for the analysis of this hormone in biological samples. To that end, it was demonstrated that the assay can be reliably used to measure the concentration of free cortisol in saliva without significant pretreatment of the sample.

INTRODUCTION

Homogeneous assays offer the distinct advantage of utilizing relatively simple, "mix and measure" techniques. In a homogeneous assay, the binding of an analyte to its respective binder results in a direct and quantifiable change in signal (*1*). For this reason, homogeneous assays do not require the multiple washing, filtration, and incubation steps that are often required in heterogeneous assays. Therefore, homogeneous assays are more amenable to automation and high-throughput screening adaptation. Traditional enzymatic immunoassays usually do not work in a homogeneous format. Instead, radioisotopic methods, such as scintillation proximity assays, are often employed. However, the use of radioactive substances creates problems in terms of cost, safety, and disposal when dealing with the large reagent volumes necessary for high-throughput screening. In an effort to reduce these problems, there has been a push to increase the availability and practicality of nonisotopic homogeneous assay methods, utilizing techniques such as fluorescence resonance energy transfer (FRET), fluorescence polarization, and fluorescence correlation spectroscopy (*2*).

These homogeneous fluorescence methods have been very successful in reducing the cost and increasing the efficiency of high-throughput drug screening. Problems are encountered, however, as reagent volumes continue to decrease, approaching the sensitivity limit of fluorescence detection. The fluorescent background present in biological fluids can drastically decrease the signal-to-noise ratio when employing fluorescent detection methods in such small sample volumes. In contrast, homogeneous assays based on chemiluminescence or bioluminescence afford the detection limits needed in small volume analysis and are uniquely advantageous in terms of their sensitivity, lack of background noise in biological fluid, and affordability (*3*). Herein, we report the development of such a bioluminescence homogeneous assay for the hormone cortisol employing the recombinant photoprotein aequorin. This assay, in addition to the aforementioned advantages, is also capable of directly detecting cortisol in saliva samples (*4*).

Cortisol is a steroid hormone that is important for the regulation of both metabolic rates and growth rates. Abnormal cortisol levels are indicative of a wide variety of diseases, such as Addison's disease and Cushing's syndrome or the onset of diabetes (*5*). In order to diagnose and properly treat such diseases, a physician must periodically assay a patient's level of free cortisol. However, hormones such as cortisol follow circadian rhythms and require multiple samplings over the course of a day. Noninvasive sampling, such as saliva collection, is therefore preferred over more invasive methods, such as plasma collection. Since the hormone concentration detected in saliva is the nonprotein bound fraction of cortisol, the most important fraction when diagnosing pathological conditions, saliva analysis is as practical as serum analysis for clinical diagnoses (*6*). Another advantage is that the individual concentration of the corticosteroid-binding globulin does not affect the results in salivary cortisol analysis, as it does in serum cortisol analysis. However, the concentration of hormones in saliva is generally 10–50-fold lower than the concentration of hormones in plasma (*7*). For this reason, assays that detect salivary levels of hormones must be more sensitive than the corresponding serum-based assays.

* E-mail address: daunert@uky.edu.
[†] University of Kentucky.
[‡] Current Address: Department of Chemistry, Indiana University Purdue University Indianapolis, Indiana 46202.

10.1021/bc070039u CCC: $37.00 © 2007 American Chemical Society
Published on Web 10/18/2007

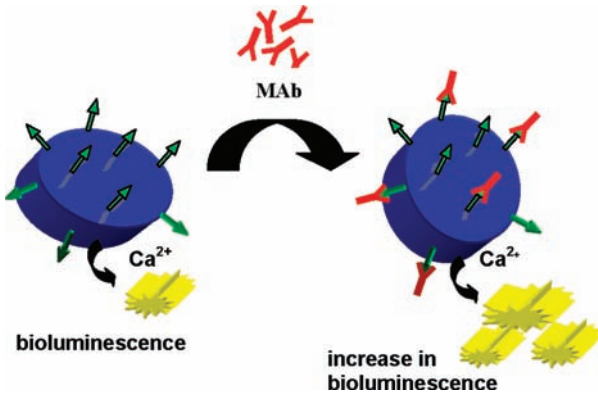


Figure 1. Schematic of how the homogeneous response works in the assay. The bioluminescence intensity of aequorin (blue ball) increases when cortisol Ab (red figures) binds to the cortisol molecules (green arrows) that are conjugated to the aequorin protein via its lysine residues.

In the homogeneous immunoassay described herein, we employed the bioluminescent photoprotein aequorin as a label (Figure 1). Since bioluminescence is a rare phenomenon in terrestrial organisms, there is virtually zero background bioluminescence found in human fluid, and this allows for the highly sensitive detection of the signal emitted by aequorin (*8*). Aequorin is a calcium-activated photoprotein isolated from the jellyfish *Aequorea victoria* that is composed of apoaequorin, coelenterazine, and molecular oxygen (*9*). Coelenterazine, an imdazopyrazinone chromophore, is located in the central, hydrophobic, reaction pocket of apoaequorin. Following the binding of calcium, the protein undergoes a conformational change which leads to the oxidation of coelenterazine to coelenteramide. The relaxation of this excited coelenteramide results in the emission of bioluminescence at 469 nm (*9*). This calcium-induced light emission from aequorin has led to its use as an *in vivo* calcium indicator and as an ultrasensitive label for a variety of immuno- and DNA hybridization assays (*10–19*).

In order to develop a homogeneous assay for cortisol, cortisol-3-*O*-carboxymethyloxime *N*-hydroxysuccinimidyl ester (Cortisol-3-CMO-NHS) was first conjugated to the lysine residues of a cysteine-free aequorin mutant. The cysteine-free mutant of aequorin, in which all three native cysteine residues have been changed to serine residues, was selected on the basis of previous studies performed in our laboratory that demonstrated the higher bioluminescent activity of this mutant, as compared to wild-type aequorin (*20*). Several conjugates were prepared, which differed in their *N*-hydroxysuccinimide cortisol-to-aequorin ratio so that the conjugate that exhibited the largest signal change could be selected for further studies. The conjugate that presented optimal signal generation as well as binding ability to the anticortisol antibody was chosen for the development of the homogeneous assay. The assay was then characterized and optimized in terms of reproducibility, precision, and accuracy in untreated saliva samples in order to establish the analytical performance of the assay. Finally, the assay developed was employed in the determination of cortisol in human saliva samples.

EXPERIMENTAL PROCEDURES

Reagents. Tris (hydroxymethyl) amino methane (Tris) free base, ethylenediaminetetraacetic acid (EDTA) sodium salt, glucose, sodium chloride, calcium chloride, bovine serum albumin, kanamycin, sodium dodecyl sulfate (SDS), and all other reagents were purchased from Sigma (St. Louis, MO). Luria Bertrani (LB) broth was from Gibco BRL (Gaithersberg, MD). Coelenterazine was purchased from Biotium (Hayward, CA). Cortisol-3-CMO-NHS and monoclonal anticortisol antibody were from United States Biological (Swampscott, MA). 96-well polystyrene microtiter plates were purchased from Nunc (Rochester, NY). Bradford assay kits were obtained from Bio-Rad Laboratories (Hercules, CA). The buffers were composed as follows: buffer A, 30 mM Tris, 4 mM EDTA, pH 7.5; buffer B, buffer A with 0.1% Tween-20; buffer C, 30 mM Tris, 100 mM $CaCl_2$, pH:7.5; buffer D, 100 mM $NaHCO_3$, 4 mM EDTA, pH 8.2. Deionized water purified with a Milli-Q System (Waters, Milford, MA) was used to prepare all solutions.

Apparatus. Cell cultures were grown in a Forma Scientific orbital shaker (Marietta, OH), and the optical density was determined using a Milton Roy Spectronic 21D spectrophotometer (Ivyland, PA). Cell cultures were centrifuged using a Beckman J2-M1 centrifuge (Palo Alto, CA). Fractions were lyophilized with a Christ Alpha 2-4 lyophilizer (Osterode am Harz, DE). Triplicate bioluminescence measurements were made on a Dynex MLX Microtiter Plate Luminometer (Vienna, VA). All values reported are the mean of three replicates, which have been background-corrected.

Methods. *Expression and Purification of Apoaequorin.* The plasmid pSD110 was initially constructed in our laboratory to contain the gene for a cysteine-free mutant of apoaequorin in which all three cysteine residues were mutated to serine residues (*19*). This plasmid was transformed into competent *Bacillus subtilis* cells. The cells containing the aequorin gene were then grown to an OD of 0.6, and 1 mM IPTG was added in order to induce the expression of the apoaequorin. The supernatant from the cells was harvested, acid precipitated with glacial acetic acid to a pH of 4.2, and centrifuged for 30 min at 9500 *g*, 4 °C, in order to pelletize the precipitated protein. The protein pellet was resuspended and filtered through a 0.2 μm filter; the pH was then adjusted to 7.5. The resuspended protein was then purified with a HQ ion exchange chromatography column (*18*). Purity of the protein was verified with SDS-PAGE, and concentration was determined with the Bradford Assay.

Conjugation of Aequorin to Cortisol. The apoprotein was dialyzed against buffer D. A solution of cortisol-3-CMO-NHS dissolved in anhydrous dimethyl sulfoxide was then added dropwise to the apoprotein, which was stirring in a 5 mL conical vial, at 4 °C. The reaction was allowed to proceed overnight at 4 °C with slow stirring. The stock solution of the cortisol-3-CMO-NHS in anhydrous dimethyl sulfoxide was prepared immediately prior to use and added to the protein in the following stoichiometric ratios of aequorin/cortisol: 1:1500, 1:2000; 1:2500.

Bioluminescence Emission of the Aequorin–Cortisol Conjugates. The microtiter plate wells for this, and all subsequent experiments, were blocked for nonspecific binding by allowing 300 μL of TE buffer containing 4 mg/mL bovine serum albumin to incubate overnight in the wells at 4 °C. All glass test tubes employed for initial mixing during this, and all subsequent, experiments were also blocked with BSA prior to use in an analogous manner. The wells were then emptied and allowed to air-dry prior to use. The apoaequorin–cortisol conjugates were dialyzed against buffer A and then charged with 100 μg/mL native coelenteraine overnight at 4 °C. Serial dilutions of the conjugates (10^{-8} to 10^{-13} M) were prepared using buffer A. 50 μL of the conjugate dilutions were added to the blocked wells, and signal was collected for 5 s on the luminometer, following the injection of 100 μL of buffer C.

Bioluminescence Half-Life. The conjugates were diluted until total emitted light was less than 5000 RLUs within a 4 s integration time. Ten microliter aliquots of each conjugate were then injected with 100 μL of buffer C, and light measurements were collected every 0.1 s for 4 s on an MGM Optocomp 1 test tube luminometer (Hamden, CT). The linear portion of the decay

kinetics curve was then plotted with time (s) versus ln (intensity). The half-life was then determined using $y = mx + b$, $m = -k$, $t_{1/2} = .697/k$.

Binder Dilution Curves. Anticortisol antibody (330 μg/mL) was serially diluted in buffer A in order to obtain the following dilutions: 33 μg/mL, 3.3 μg/mL, 3.3×10^{-1} μg/mL, 3.3×10^{-2} μg/mL, 3.3×10^{-3} μg/mL, 3.3×10^{-4} μg/mL, 3.3×10^{-5} μg/mL, and 3.3×10^{-6} μg/mL. A volume of 50 μL of the cortisol antibody was incubated with a 50 μL volume of 1×10^{-11} M conjugate (1:1500, 1:2000, 1:2500) for 30 min at room temperature with shaking at 250 rpm. Luminescence measurements were then collected over a 5 s time period following the injection of 100 μL of buffer C.

Dose–Response Curves. A stock solution of 10^{-2} M cortisol was prepared in methanol, and 10^{-3} to 10^{-11} M cortisol dilutions were subsequently made from this stock solution using buffer A. From the binder dilution study, a concentration of 3.3 μg/mL cortisol antibody was selected. A volume of 50 μL of various concentrations of cortisol and a volume of 50 μL cortisol antibody were incubated with 50 μL of the 10^{-11} M 1: 2500 conjugate in blocked microtiter plate wells. The plate was incubated for 30 min at room temperature with shaking at 250 rpm. The luminescence measurements were then collected in a manner identical to the protocol discussed in the binder dilution study. An initial dose–response curve was produced, and the LOD and dynamic range were calculated from this first curve. Subsequent dose–response curves were produced over a period of several days, and these curves were used during the analysis of the saliva samples.

Analysis of Saliva Samples. Saliva samples were collected from six healthy subjects using the following protocol. Subjects rinsed their mouths out with water after they awoke in the morning and collected their saliva 15 min later in two plastic 1.7 mL tubes. Saliva samples were stored at −80 °C until analysis. The samples were thawed and centrifuged at 3000 rpm, 4 °C, just prior to analysis. The supernatant was used for the study. For this study, the buffer used for all dilutions was buffer B. A volume of 50 μL of the 3.3 μg/mL cortisol antibody, 50 μL of the saliva supernatant, and 50 μL of 10^{-11} M 1:2500 conjugate was combined in preblocked wells, incubated at room temperature, with shaking at 250 rpm, for 30 min. Signal was collected from each well for 5 s on the Dynex luminometer following the injection of 100 μL of buffer C. This process was repeated three times, on three separate days, in order to determine the intraassay precision of the salivary cortisol measurements.

Recovery Studies in Saliva. For this study, 1.25 μL of serial dilutions of cortisol standard were added to a pool of saliva (pool 6). Pool 6 refers to the fact that each subject had two separate Eppendorf tubes containing their saliva. The two samples were pooled together to make pool 1 through pool 6. Pool 1 is the combined saliva from subject 1, pool 2 is the combined saliva from subject 2, and so forth. 1.25 μL of 1×10^{-3} to 1×10^{-6} M cortisol standards were added to 250 μL of saliva in order to spike the saliva with 5, 50, 500, and 5000 nmol/L of cortisol. Analysis of the samples was identical to the method detailed in the Analysis of Saliva Samples section.

RESULTS

A cysteine-free mutant of aequorin, in which the cysteines at positions 145, 152, and 180 were all mutated to serine residues, was employed as the label for this assay. This cysteine-free aequorin has been shown to be more active than the wild-type protein. A plasmid was previously constructed in our laboratory that encoded for this apoaequorin mutant (*21*). This plasmid was transformed into *Bacillus subtilis* cells, and the recombinant apoaequorin was then expressed in the cells and purified with ion exchange chromatography. Following purification, the cysteine-free aequorin was chemically conjugated to a cortisol-3-CMO-NHS through the lysine residues of aequorin. Conjugates with aequorin–cortisol derivative initial reaction molar ratios of 1:1500, 1:2000, and 1:2500 were prepared and characterized in terms of their bioluminescent activity and their ability to bind anticortisol antibodies. The bioluminescence of the aequorin–cortisol conjugates was found to be stable for over three months when stored at −80 °C. In order to study the bioluminescent activity of the conjugates, light was collected for 5 s following the addition of a calcium-containing bioluminescence triggering buffer. All three conjugates exhibited acceptable activity, which progressively decreased as the concentration of the cortisol derivative used during conjugation increased. For example, the 1:1500 conjugate exhibited higher activity than the 1:2000 conjugate, and the 1:2000 conjugate was more active than the 1:2500 conjugate. The conjugates were characterized in terms of their half-life to determine whether there were any changes in decay profiles caused by the conjugation. Half-lives were obtained by collecting light for 4 s, at 0.1 s intervals, following the addition of a calcium-containing buffer. The half-life data were analyzed in the same manner as previously described (*12*). The 1:1500, 1:2000, and 1:2500 conjugates gave successively increasing half-lives of 1.48, 1.51, and 1.96 s, respectively.

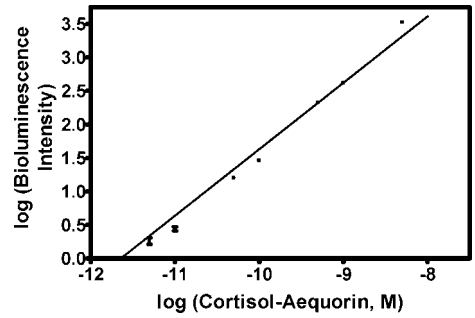


Figure 2. Bioluminescence curve generated by the 1:2500 aequorin–cortisol conjugate. The bioluminescence intensity decreases linearly as the concentration of the conjugate decreases. Data are the mean of three replicates, which have been blank subtracted, ±1 standard deviation.

The aequorin–cortisol conjugates were then characterized in terms of their bioluminescence properties. For that, a curve was generated that related the concentration of the conjugate to the intensity of the bioluminescence signal. From this curve, the lowest possible concentration of the aequorin–cortisol conjugate that could be employed in the development of the assay was determined, i.e., the lowest concentration of conjugate that still exhibited significant bioluminescence emission when compared to a blank control. For this study, the conjugates were first serially diluted with buffer A, and their bioluminescence intensities were then measured over a 5 s time period. From this curve, it was determined that a concentration of 1×10^{-11} M conjugate should be employed in all further studies (Figure 2).

In order to determine the antibody concentration that would produce an optimal change in signal, a binder dilution study was performed employing a 1×10^{-11} M concentration of the aequorin–cortisol conjugate. For this, 50 μL of the conjugate was incubated with 50 μL of different concentrations of anticortisol antibody ranging from 33 to 3.3×10^{-6} μg/mL. Following a 30 min incubation at room temperature with shaking, the bioluminescence intensity of the conjugate–antibody solution was measured over a period of 5 s in a microtiter plate luminometer. Analysis of the binder dilution curve resulted in the selection of the 3.3 μg/mL dilution of anticortisol antibody

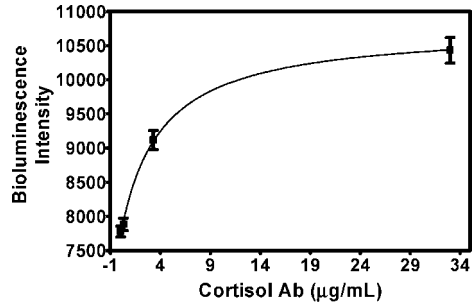


Figure 3. Binder dilution curve for 1:2500 aequorin–cortisol conjugate. The greater the cortisol antibody concentration, the larger the bioluminescent signal from aequorin. Data are the mean of three replicates, which have been blank subtracted, ±1 standard deviation.

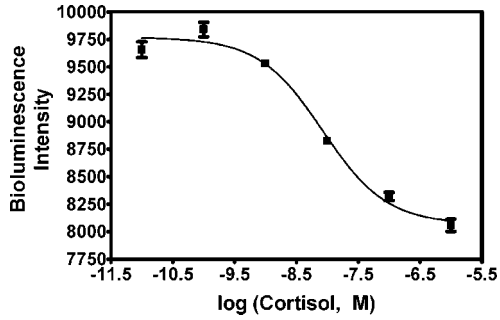


Figure 4. Dose–response curve for cortisol generated using 1:2500 aequorin–cortisol conjugate. Data are the means of three replicates, which have been blank subtracted, ±1 standard deviation.

to be used for the rest of the assay development studies. This concentration was the lowest antibody concentration that caused a significant change in aequorin's signal (Figure 3). Moreover, the results of the binder dilution study indicated that the 1:2500 aequorin–cortisol conjugate yielded the most significant change in signal following anticortisol binding. Therefore, only the 1:2500 aequorin–cortisol conjugate was employed for subsequent dose–response curves and salivary analysis.

Dose–response curves were produced by simultaneously incubating 50 μL of serially diluted cortisol standard, 50 μL of the 1:2500 aequorin–cortisol conjugate, and 50 μL of the anticortisol antibody in a microtiter plate well for 30 min at room temperature, while shaking. Following incubation, light was collected for 5 s after injecting 100 μL of buffer C. The average of three replicates was then plotted (Figure 4). The assay exhibited a sigmoidal response to changing cortisol concentrations with increasing cortisol concentrations resulting in a lower bioluminescence signal. These results corresponded to the data from the binder–dilution curves in that increasing the concentration of anticortisol antibody available to bind the aequorin–cortisol conjugate resulted in an increase in bioluminescent signal. The detection limit for this assay was 1×10^{-10} M of cortisol. The linear dynamic range of the assays spanned over 5 orders of magnitude, from 1×10^{-5} to 1×10^{-9} M of cortisol.

To demonstrate clinical feasibility, we next investigated the ability of this assay to function in untreated biological samples, specifically in human saliva samples. The saliva of six healthy subjects was analyzed, and the concentration of cortisol in the samples fell within, or very close to, the accepted clinical range of morning cortisol saliva levels of 10–25 nmol/L. In order to study the intra-assay precision, the saliva pools of these six subjects were analyzed three times, on subsequent days, and the intra-assay precision was found to be between 0.9% and 6.2% (Table 1). The accuracy of this assay was tested with a percent recovery study. In order to study the performance over a wide range of cortisol concentrations, 5, 50, 500, and 5000 nmol/L samples of cortisol were spiked into the original saliva pool. These spiked samples were then run with the assay, and the results produced an accuracy ranging from 98% to 105% (Table 2).

Table 1. Intra-Assay Precision[a]

saliva pool	observed value 1 (nmol/L)	observed value 2 (nmol/L)	observed value 3 (nmol/L)	mean observed value ± SD (nmol/L)	CV (%)
pool 1	15.6	15.0	15.1	15.2 ± 0.3	2.0
pool 2	5.6	6.0	6.0	5.9 ± 0.2	3.7
pool 3	8.0	7.1	7.7	7.6 ± 0.5	6.2
pool 4	5.3	5.2	5.2	5.3 ± 0.1	1.6
pool 5	7.9	7.8	7.8	7.8 ± 0.1	0.9
pool 6	12.4	11.7	11.7	12.0 ± 0.4	3.5

[a] The saliva of six subjects was analyzed on three subsequent days in order to determine the precision of the assay. Data are the means of three replicates, which have been blank subtracted, ±1 standard deviation.

Table 2. Assay Accuracy[a]

added (nmol/L)	observed value (nmol/L)	expected value (nmol/L)	mean recovery (%)	bias (%)
5.0	18.3 ± 0.2	18.2	100.8 ± 0.9	+ 0.8
50.0	62.0 ± 0.5	63.2	98.1 ± 0.9	− 1.9
500.0	539.4 ± 3.2	513.2	105.1 ± 0.6	+ 5.1
5000.0	5230.5 ± 42.3	5013.2	104.3 ± 0.8	+ 4.3
mean			102.1 ± 0.8	+ 2.1

[a] A saliva pool was spiked with serial dilutions of cortisol standards in order to determine the accuracy of the assay. Data are the means of three replicates, which have been blank subtracted, ±1 standard deviation.

DISCUSSION

In an effort to develop homogeneous assays capable of yielding low detection limits, we selected a bioluminescent photoprotein as the signal-generating label. Other labels commonly employed in these types of assays include enzymes, fluorophores, and radioisotopes. We selected the bioluminescent aequorin over other labeling options because it is nontoxic, very sensitive in biological fluids, does not require long incubation periods, and can be genetically and chemically altered to yield a homogeneous modulation of its bioluminescence signal. The homogeneous, bioluminescence-based assay for cortisol discussed herein represents a distinct advantage over currently available cortisol assays, since it is fast, easy, and has the ability to achieve the very low detection limits that are necessary for salivary analysis.

After conjugating cortisol to aequorin via lysine residues, we determined the decay profile of the conjugates. The results from the activity and half-life studies were similar to the way aequorin responded in previous studies that employed aequorin chemically conjugated to an analyte through its lysine residues (*3*, *10*). In these studies, as in ours, as the molar ratio of analyte to aequorin in the conjugate increased, the bioluminescence activity of the conjugate decreased and the decay half-life of the conjugate increased. We then undertook a calibration study in order to determine the minimum conjugate concentration needed for assay development. From the calibration curves, we selected the 1×10^{-11} M conjugate concentration for a binder dilution study (Figure 2). The binder dilution study was undertaken in order to determine what antibody concentration was optimal for the homogeneous response of the 1×10^{-11} M conjugates. From the binder dilution study, it was determined that a 3.3 μg/mL anticortisol antibody concentration was the minimum antibody concentration required to yield a change in the bioluminescent signal (Figure 3). It was also observed from the binder dilution study that the higher the molar ratio of cortisol

in the conjugate, the more pronounced the homogeneous response following anticortisol antibody binding. In other words, the 1:2000 aequorin–cortisol conjugate gave a better homogeneous response to anticortisol antibodies than the 1:1500 aequorin–cortisol conjugate, and the 1:2500 aequorin–cortisol conjugate exhibited the best homogeneous response, giving the most pronounced change in bioluminescence signal following anticortisol antibody binding. For this reason, the 1:2500 aequorin–cortisol conjugate was selected for the remaining studies, including the dose–response curve and the analysis of saliva samples.

Next, a dose response curve was obtained by incubating the aequorin–cortisol conjugate, the anticortisol antibody, and serially diluted cortisol standards in microtiter plate wells for 30 min. Following incubation, the wells were washed, and the bioluminescence intensity was measured using an automated microtiter plate luminometer. Results of the dose–response curve indicated that decreasing concentrations of cortisol, and corresponding increasing concentrations of free antibody, resulted in an increase in the bioluminescent signal from the conjugate (Figure 4). One may initially assume that increasing the amount of antibody available to bind the conjugate would result in sterically hindering aequorin and, thereby, reduce its bioluminescence, as shown in the homogeneous aequorin-based assay for biotin (*21*). However, a similar homogeneous response to ours, wherein signal increased with increasing antibody concentration, was found by Lewis and colleagues when they studied the response of an aequorin–thyroxine conjugate to increasing concentrations of antithyroxine antibody (*22*). This type of response, seen both here and in Lewis's thyroxine study, is more advantageous than the response found in the biotin assay, since the signal increases as the concentration of free cortisol decreases, thereby allowing a lower detection limit The detection limit of this assay was 1×10^{-10} M cortisol, which is over 1 order of magnitude lower than the detection limit obtained for a heterogeneous bioluminescence aequorin-based cortisol immunoassay, namely, 3.0×10^{-9} M (*4*). The linear range for this assay ranged from 1×10^{-5} M to 1×10^{-9} M, compared to the heterogeneous aequorin-based cortisol assay, whose linear range spanned only 3 orders of magnitude, from 1×10^{-6} to 1×10^{-8} M (*22*). The assay time was 30 min, which is slightly longer than the 18 min time afforded by the Roche Cobas cortisol assay. However, our assay is more sensitive than the Roche assay (0.1 nmol/L vs 0.5 nmol/L) and requires significantly less saliva volume (50 μL vs 500 μL), making our assay more adaptable to miniaturization (*23*). Moreover, the Roche assay utilizes electrochemiluminescence detection, which requires a specialized automated instrument, whereas our assay can be performed using standard luminometers and automated platforms such as Tecan, Hamilton, and so forth.

The low detection limit of the dose–response curve indicated that saliva analysis was possible, due to the fact that salivary levels of free cortisol ranged between 10 and 25 nmol/L. Moreover, salivary cortisol measurements are primarily used to rule out Cushing'syndrome. Cortisol concentrations are very low, generally less than 10 nmol/L, during the standard late-night sampling times used for these Cushing's syndrome tests. Therefore, the 0.1 nmol/L detection limit of this aequorin-based assay suggested that it may be suitable for clinical applications. Also, biological samples generally must be extracted prior to assaying, which is a time-consuming pretreatment. For this assay, the only pretreatment of saliva samples was a brief centrifugation to pellet particulate matter. No extraction or complex pretreatment of biological samples was needed, thereby streamlining the assay. The intra-assay precision with saliva samples was found to be between 0.9% and 6.2%, and the accuracy of the assay was found to be between 98% and 105% using spiked saliva samples. This level of accuracy and precision corresponds to the levels previously reported for cortisol assays, and is a realistic performance for a salivary cortisol assay (*4*).

In summary, we have developed a homogeneous assay using the photoprotein aequorin that can detect physiological levels of cortisol in human saliva. This assay has a dynamic range spanning 5 orders of magnitude and a sub-nanomolar detection limit. Since the level of free cortisol in human saliva ranges from 10 to 25 nmol/L, this assay is also well-suited for real samples, and the analysis of unextracted saliva samples gave acceptable precision and accuracy results. The fact that this homogeneous assay can analyze untreated saliva samples without multiple washing and incubation steps makes it superior to most of the currently commercially available assays for cortisol. Additionally, the low detection limit and long linear range of this assay are sufficient for both serum and saliva analysis. The feasibility of this homogeneous, bioluminescent assay in determining salivary cortisol levels has been clearly demonstrated. However, additional validation methods, such as extensive interference tests, interassay precision, and mass spectrometric confirmation, will be necessary before clinical implementation. However, the speed and simplicity of this homogeneous assay suggests that it may offer a simple alternative for testing salivary cortisol levels in the future, and represent an advance over current technologies by being applicable to both high-throughput screening and on-site monitoring technologies.

ACKNOWLEDGMENT

This study was supported by the National Institutes of Health (CHE 467917) and the National Aeronautics and Space Administration. We thank the Vice President of Research at the University of Kentucky for a University Research Professorship to S.D. S.D. also acknowledges support from a Gill Eminent Professorship. L.R. acknowledges support from Predoctoral Fellowships from the National Institutes of Health and National Science Foundation-IGERT Program at the University of Kentucky.

LITERATURE CITED

(1) Diamandis, W., and Christopoulous, T. (1996) *Immunoassay* (Diamandis, W., Christopoulus, T., Eds.), pp 488–490,Chapter 21, Academic Press, San Diego, CA.

(2) Sittampalam, S., Kahl, S., and Janzen, W. (1997) High throughput screening:advances in assay technology. *Curr. Opin. Chem. Biol. 1*, 384–391.

(3) Desai, U., Deo, S., Hyland, K., Poon, M., and Daunert, S. (2002) Determination of prostacyclin in plasma through a bioluminescent immunoassay for 6-keto-prostaglandin F1α: Implications of dosage in patients with primary hypertension. *Anal. Chem. 74*, 3892–3898.

(4) Mirasoli, M., Deo, S., Lewis, J., Roda, A., and Daunert, S. (2002) Bioluminescence immunoassay for cortisol using recombinant aequorin as a label. *Anal. Biochem. 306*, 204–211.

(5) Tortora, G., and Grabowski, S. *Principles of Anatomy and Physiology* (1996) Harper Collins College Publishers, Menlo Park, CA.

(6) Vining, R. F., McGinley, R. A., and Symons, R. G. (1983) Hormones in saliva: Mode of entry and consequent implications for clinical interpretation. *Clin. Chem. 29*, 1752–1756.

(7) Kahn, J. P., Rubinow, D. R., Davis, C. L., Kling, M., and Post, R. M. (1988) Salivary cortisol: A practical method for evaluation of adrenal function. *Biol. Psychiatry 23*, 335–349.

(8) Daunert, S., and Deo, S. *Photoproteins in Bioanalysis* (2006) Wiley-VCH, Berlin.

(9) Head, J., Inouye, S., Teranishi, K., and Shimomura, O. (2000) The crystal structure of the photoprotein aequorin at 2.3 Å resolution. *Nature (London) 405*, 372–376.
(10) Witkowski, A., Ramanthan, S., and Daunert, S. (1994) Bioluminescence binding assays for biotin with attomole detection based on recombinant aequorin. *Anal. Chem. 66*, 1837–1840.
(11) Feltus, A., Ramanthan, S., and Daunert, S. (1997) Interaction of immobilized avidin with and aequorin-biotin conjugate: An aequorin linked assay for biotin. *Anal. Biochem. 254*, 62–68.
(12) Lewis, J. C., Cullen, L. C., and Daunert, S. (2000) Site-specifically labeled photoprotein-thyroxine conjugates using aequorin mutants containing unique cysteine residues:pplications for binding assays (Part 2). *Bioconjugate Chem. 11*, 140–145.
(13) Hart, R. C., Scheuer, B. L., Rivera, H. N., and Gray, J. (1993) in *Bioluminescene and Chemiluminescence: Status Report* (Szalay, A. A., Kricka, J. L., and Stanley, P., Eds), pp. 320–323, Wiley, Chichester.
(14) Casadie, J., Powell, M. J., and Kenten, J. H. (1990) Expression and secretion of aequorin as a chimeric antibody by means of a mammalian expression vector. *Proc. Natl. Acad. Sci. U.S.A. 87*, 2047–2051.
(15) Zenno, S., and Inouye, S. (1990) Bioluminescent immunoassay using a fusion protein of protein A and the photoprotein aequroin. *Biochem. Biophys. Res. Commun. 171*, 169–174.
(16) Ramanthan, S., Lewis, J. C., Kindy, M. S., and Daunert, S. (1998) Heterogeneous bioluminescence binding assay for an octapeptide using recombinant aequorin. *Anal. Chim. Acta 368*, 181–188.
(17) Witkowski, A., Daunert, S., Kindy, M. S., and Bachas, L. (1993) Enzyme-linked immunosorbent assay for an octapeptide based on a genetically engineered fusion protein. *Anal. Chem. 65*, 1147–1151.
(18) Deo, S. K., and Daunert, S. (2001) An immunoassay for Leu-enkephalin based on a C-terminal aequorin-peptide fusion. *Anal. Chem. 73*, 1903–1908.
(19) Galvan, B., and Christopoulous, T. (1996) Bioluminescence hybridization assays using recombinant aequorin. *Anal. Chem. 68*, 3545–3550.
(20) Lewis, J. C., Lopes-Moya, J. J., and Daunert, S. (2000) Bioluminescence and secondary structure properties of aequorin mutants produced for site-specific conjugation and immobilization. *Bioconjugate Chem. 11*, 65–70.
(21) Grosevnor, A., Feltus, A., Conover, R., Daunert, S., and Anderson, K. (2000) Development of binding assays in microfabricated picoliter vials: an assay for biotin. *Anal. Chem. 72*, 2590–2594.
(22) Lewis, J., and Daunert, S. (2001) Bioluminescence immunoassay for thyroxine employing genetically engineered recombinant aequorin containing unique cysteine residues. *Anal. Chem. 73*, 3227–3233.
(23) Vogeser, M., Durner, J., Seliger, E., and Auernhammer, C. (2006) Measurement of late-night salivary cortisol with an automated immunoassay system. *Clin. Chem. Lab. Med. 44*, 1444–1445.

BC070039U

Site-Specific, Covalent Attachment of Poly(dT)-Modified Peptides To Solid Surfaces for Microarrays

Naoki Kimura,*,† Takashi Okegawa,† Kiyokazu Yamazaki,† and Koji Matsuoka*,‡

Research and Development Center, Nisshinbo Industries Inc., 1-2-3 Onodai, Midori-ku, Chiba 267-0056, Japan, and Area for Molecular Function, Division of Material Science, Graduate School of Science and Engineering, Saitama University, 255 Shimo-okubo, Sakura, Saitama 338-8570, Japan. Received March 13, 2007; Revised Manuscript Received August 30, 2007

The present study reported proof-of-principle for a kinase assay approach that can detect specific peptide phosphorylation events. The method involves attachment of peptides onto commercial aminosilane and polycarbodiimide-coated glass slides, using a newly developed DNattach linker system that consists of a poly(dT) tail (Nisshinbo Industries Inc.), followed by a detection step using fluorescently labeled antiphosphoamino acid antibodies. The linker-modified peptides are efficiently synthesized by Michael addition between maleimido-modified peptides and thiol-containing DNattach. Specific covalent immobilization of the modified peptides onto aminosilane and poly carbodiimide-coated slides is then achieved by short exposure to UV-light. Highly selective and quantitative recognition by standard antiphosphoamino acid antibodies (antiphosphotyrosine and anti-phosphoGFAP) and kinases (c-Src and PKA) to the corresponding modified peptides on the microarray spots is demonstrated. Furthermore, we found that this immobilization method provides greater signal-to-noise ratio and better discrimination ability of phosphorylated amino acids than does the conventional immobilization technique. The phosphorylation pattern of target sequences, detected using fluorescently labeled antiphosphoamino acid antibodies, revealed that the linker system preference of the kinase is determined by its activity profile.

INTRODUCTION

Kinase-catalyzed phosphorylation of proteins is one of the most important mechanisms for the regulation of cell function. Indeed, it has been estimated that more than one third of all mammalian proteins may be subject to modification by phosphorylation *in vivo* (*1, 2*). To date, however, only a limited number of kinases have been identified and fully characterized. One of the most important features of protein kinases is their substrate specificity, which to a large extent is determined by the primary amino acid sequence around the phosphorylation site of the corresponding target protein. As a result, a number of methods have been developed to identify potential kinase substrates, including combinatorial synthesis of peptide libraries on membranes using SPOT technology, one-bead-one-compound peptide libraries, positional-scaling combinatorial libraries, and peptide libraries using affinity-column selection (*3–6*).

More recently, protein- and peptide-based microarrays have also been developed (*7–11*). In comparison to SPOT technology, a much higher density of spots can be attained using a protein array, making it possible to simultaneously screen tens of thousands of kinase substrates on the solid surface. Unfortunately, however, current peptide and protein chip strategies have several limitations. Chemical strategies leading to the oriented immobilization of a polypeptide chain are ideal because this preserves binding capacity and improves the control and reproducibility of the overall process. However, unwanted adsorption of soluble proteins often results in competition with the detection of protein–substrate interactions, leading to a noisy background (*12*). Usually, only a fraction of the immobilized proteins are competent to participate in binding interactions because many of them are immobilized in inaccessible orientations or are partially denatured (*13*). A consequence of these limitations is that most immobilization procedures are not well suited to quantitative assays of protein–substrate interactions. Several immobilization methodologies that involve the modification of peptides prior to spotting onto the solid surface for specific binding events might circumvent these limitations (*7–10, 14–16*). For example, MacBeath et al. (*14*) and Lesaicherre et al. (*15*) independently used slides treated with maleimide and slides treated with glyoxylic acid as platforms, respectively, for the immobilization of N-terminally Cys-containing peptides. Houseman et al. (*7*) reported the fabrication of a peptide microarray by the Diels–Alder-mediated immobilization of the kinase substrate on a self-assembled monolayer of alkanethiolates on gold. Furthermore, Duburcq et al. (*8*) fabricated the peptide microarray using semicarbazide slides that permitted the immobilization of glyoxylyl peptides. However, current methodologies are time-consuming (in the order of hours) and often require relatively large amounts of peptide (i.e., concentrations between 100 μM and 5 mM) for the immobilization procedure (*7–10, 14–16*). In addition, although appropriate for DNA immobilization, additional surface modifications that would make microarray fabrication a laborious and complex procedure are usually required when peptides or very small proteins are printed on commercial DNA microarray slides, and there are only a few commercial slides for fabricating peptide arrays (*17*). Thus, the increased need for simple, robust, and high throughput assays has led us to develop a novel protocol for preparing peptide and protein microarrays.

Over the past few years, we have been developing polycarbodiimide-coated glass and plastic slides for use with DNA microarray substrates (*18–20*). We found that thymine base(s) of DNA efficiently react with the carbodiimide group under UV irradiation (*20*). On the basis of these findings, we have further developed the patented DNattach system (Nisshinbo Industries

* To whom correspondence should be addressed. Phone: +81-43-205-0794. Fax: +81-43-205-0844. E-mail: n-kimu@nisshinbo.co.jp (N.K.). Phone: +81-48-858-3099. E-mail: koji@fms.saitama-u.ac.jp (K.M.).

† Nisshinbo Industries Inc.

‡ Saitama University.

10.1021/bc070083+ CCC: $37.00 © 2007 American Chemical Society
Published on Web 10/23/2007

Inc.), which consists of a poly(dT) tail and spacer group, for immobilizing DNA onto various surfaces including polycarbodiimide, nonmodified metal, and plastic surfaces by UV irradiation (*21*, *22*). Using this system, Takahashi et al. (*22*) successfully detected synaptogenesis in the developing mouse cerebellum on a gold surface. As a first step toward the goal of developing an inexpensive, simple, and robust diagnostic tool for assaying kinase activity, we have further expanded this technology.

Here, we describe a novel, simple, and convenient methodology that uses the DNattach immobilization system to site-specifically immobilize peptides onto commercial aminosilane and polycarbodiimide-coated glass slides by UV irradiation in a microarray format. We have found that the technology is also appropriate for attaching peptide to aminosilane and polycarbodiimide-coated slides by UV irradiation. In this detailed quantitative study, we show that the immobilization system is a simple and rapid technique compared to conventional technologies. Furthermore, the methodology provides a uniform environment for kinase assays, resulting from site-specific immobilization onto the solid surface and the use of a selective immobilization chemistry to prepare the chips. The phosphorylation pattern of target sequences, detected using fluorescently labeled antiphosphoamino acid antibodies, revealed that the linker system preference of the kinase is determined by its activity profile.

EXPERIMENTAL PROCEDURE

Materials and General Methods. β-Alanine and maleic anhydride were purchased from Kanto Chemical Company (Tokyo, Japan). $p60^{c\text{-}src}$ kinase was purchased from Oncogene Science (Cambridge, MA). cAMP-dependent protein kinase (PKA) was purchased from New England BioLabs (Ipswich, MA). AG213 was purchased from Calbiochem-Novabiochem International, Inc. (La Jolla, CA). Anti-phosphoGFAP (YC10) and antiphosphotyrosine (PY20) were purchased from Medical & Biochemical Laboratories (Nagano, Japan) and Exalpha Biologicals (Maynard, MA), respectively. NAP5 columns and the Cy3 and Cy5 mAb Labeling Kits were purchased from GE Healthcare Biosciences (Tokyo, Japan). Thiol-modified DNattach was prepared at Nisshinbo Industries Inc. (Chiba, Japan) as follows (*23*). Poly(dT) (DNattach) modified with a 5′-thiol group and a six-carbon spacer was synthesized on an ABI 3900 DNA synthesizer at a 0.2 μmol scale using the standard phosphoramidite method. The thiol-modified DNattach was then purified on a reverse-phase cartridge following a standard procedure and dried *in vacuo*. All of the amino acids of the peptide sequence that were subsequently coupled on a Wang resin, following the standard procedures of Fmoc solid-phase peptide synthesis, were purchased from Operon (Tokyo, Japan). Peptides modified with biotin and the C_4 alkyl spacer group at the *N*-terminus of the amino acid were also synthesized and purified at Operon. All other chemicals were purchased from Wako Pure Chemical (Tokyo, Japan) and used without further purification.

Synthesis of 3-(Maleimido) Propionic Acid. 3-Maleimido propionic acid was synthesized according to a previous report with some modifications (*24*). Briefly, β-alanine (1 g, 11.2 mmol) and maleic anhydride (1.1 g, 11.2 mmol) in acetic acid (40 mL) were stirred at RT for 15 h under a N_2 atmosphere. The resulting suspension was then heated to 150 °C for 8 h. The solvent was removed *in vacuo*, and the residue was purified by silica gel column chromatography ($CHCl_3$/MeOH = 50:1), affording the compound (1.1 g, 57%) as a colorless solid. ^{1}H NMR (400 MHz, $CDCl_3$): δ 10.30 (1 H, br), 6.73 (2 H, s), 3.84 (2 H, t, J = 7.2 Hz), 2.71 (2 H, t, J = 7.2 Hz). MS (MALDI-TOF): *m*/*z* calcd for $C_{11}H_{10}N_2O_6$ $[M + H]^+$, 267.22; found, 266.7. Alternatively, the title compound is commercially available from Wako Pure Chemical.

Synthesis of Maleimide–Peptide. The Fmoc group of the fully protected peptide on the Wang resin (Operon) was first deprotected with 20% piperidine in DMF for 20 min, and 3-(maleimido) propionic acid was then introduced to the *N*-terminus of the amino acid using 3 equivalents of 3-(maleimido) propionic acid, dichlorohexy carbodiimide, and HOBt in DMF for 1 h. Cleavage and deprotection were effected by reaction with TFA/H_2O = 95:5 or thioanisole/H_2O/1,2-ethanedithiol/triisopropylsilane/TFA = 2.5:2.5:2.5:1:91.5 for 2 h. Cold diethyl ether was added to the reaction mixture, and the resulting pellet was purified using a NAP5 column according to the manufacture's procedure.

Synthesis of DNattach Linker–Peptide Conjugate. One nanomole of the thiol-modified DNattach (Nisshinbo Industries Inc.) and 20 nmol of each maleimide–peptide were dissolved in 100 mM phosphate buffer (pH 7.0) (a total 10 μL of solution) and mixed. The reaction mixtures were stirred at RT for 18 h, and progress of the reaction was monitored at 254 nm by HPLC with a μBondasphere C-8 column (Nihon Waters K.K., Tokyo, Japan). A total of 90–95% conjugate was formed as assessed from the relative areas of the thiol-modified DNattach and the conjugate on the HPLC profile. The resulting conjugate was purified by HPLC. We obtained >90% purity of the conjugates as assessed from the relative areas of the conjugate and the other peaks on the HPLC profile. MS (MALDI-TOF): *m*/*z* calcd for Peptide 1 $[M + 6Na]^+$, 7579.2; found, 7576.2; *m*/*z* calcd for Peptide 2 $[M + 3Na]^+$, 7430.0; found, 7427.4; *m*/*z* calcd for Peptide 3 $[M + 3Na]^+$, 7338.3; found 7338.3; *m*/*z* calcd for Peptide 4 $[M + 3Na]^+$, 7947.3; found, 7951.8; *m*/*z* calcd for Peptide 5 $[M + 4Na]^+$, 7890.2; found, 7894.6; and *m*/*z* calcd for Peptide 6 $[M + 4Na]^+$, 7874.2; found, 7768.3.

Fabrication of Aminosilanized and Polycarbodiimide-Coated Arrays. A polycarbodiimide-coated slide (CarboStation) from Nisshinbo Industries Inc. and a SuparAmine slide from Telechem International, Inc. (Sunnyvale, CA) were used in this study. Both nonmodified and linker-modified peptides were spotted on the slide as spots of ~250 μm in diameter with a spot-to-spot distance of 600 μm using a customized microarray robot (*19*).

After printing, the arrays were irradiated (total 0–0.3 J/cm^2) using a UV Stratalinker 2400 (Stratagene, La Jolla, CA), treated with a blocking solution (3% BSA, 0.2 M NaCl, 0.1 M Tris-HCl at pH 7.5, and 0.05% Triton-X100), then washed with TE buffer (pH 7.2) for 5 min, and dried for storage. UV irradiation was carried out within 3 min.

Fabrication of Streptavidin-Coated Arrays. Streptavidin-coated slides from Greiner Bio-One Co., Ltd. (Tokyo, Japan) were also used in this study. The customized microarray robot was also used to print arrays for the biotinylated peptides (Operon) in phosphate-buffered saline (pH 7.4). After printing, the arrays were incubated at RT for 4 h in a humidified chamber, washed, and treated with the blocking solution according to a previously reported method (*11*).

Kinase Reactions. Protein kinase assays were done according to the manufacturer's procedures with some modifications.

$p60^{c\text{-}src}$ Assay. $p60^{c\text{-}src}$ was added to the reaction buffer (50 mM HEPES-HCl at pH 7.5, 30 mM $MgCl_2$, 0.1 mM EDTA, and 0.015% polyoxyethyl (23) lauryl ether) and 150 μM ATP (final concentration of $p60^{c\text{-}src}$ 0–0.1 U/μL in the reaction buffer in a final volume of 30 μL). The reaction mixture was applied to the slide surface, and the reaction was performed at 37 °C for 240 min. The array was briefly washed with EtOH at RT for 5 min, twice with H_2O at RT for 5 min, and then dried.

Table 1. Peptide Sequences To Be Immobilized onto the Solid Surface

peptide	peptide sequence	kinase	remarks
Peptide 1	NH_2-I**Y**(**PO_3**)GEFKKK-COOH		Y-phosphorylated
Peptide 2	NH_2-I**Y**GEFKKK-COOH	c-Src	
Peptide 3	NH_2-I**A**GEFKKK-COOH		A-substituted
Peptide 4	NH_2-RRRVT**S**(**PO_3**)AARRS-COOH		S-phosphorylated
Peptide 5	NH_2-RRRVT**S**AARRS-COOH	PKA	
Peptide 6	NH_2-RRRVT**A**AARRS-COOH		A-substituted

For inhibition experiments, the inhibitor was included in the reaction mixture, and the concentration of DMSO was adjusted to 2%.

PKA Assay. PKA was added to the reaction buffer (25 mM Tris-HCl at pH 7.5, 2.5 mM $MgCl_2$) and 200 μM ATP (final concentration of PKA 0–5 U/μL in the reaction buffer in a final volume of 30 μL). The reaction mixture was applied to the slide surface, and the reaction was performed at 30 °C for 60 min. The array was briefly washed with EtOH at RT for 5 min, twice with H_2O at RT for 5 min, and then dried.

Detection of Phosphorylated Amino Acids Using Fluorescently Labeled Antiphosphoaminoacid Antibodies. Antiphosphotyrosine and anti-phosphoGFAP antibodies were labeled with either Cy3 or Cy5 using Cy3 or Cy5 mAb Labeling Kit (GE Healthcare Biosciences) and then purified using a NAP5 column according to the manufacturer's procedure. Either fluorescently labeled antiphosphotyrosine or anti-phosphoGFAP antibody, dissolved in PBST containing 1% BSA, was then applied to the array. The array was incubated at RT for 1 h, washed with PBST at RT for 5 min, briefly rinsed with PBS, and then air-dried.

Signal Detection and Data Analysis. A ScanArray 4000 (Packard Biochip, Billerica, MA) or FLA-5100 (Fuji Photo Film, Kanagawa, Japan) instrument was used to detect the signals, with equivalent results. Arrays were scanned with variable photo multiplier tube (PMT) settings to obtain optimum signal intensities. The resulting images were used to generate Tiff data files. Data analysis was done using QuantArray (Packard BioChip) or Science Laboratory (Fuji Photo Film) software, and Microsoft Excel (Microsoft Corp., Redmond, WA). Unless stated otherwise, the average signal values were taken from two spots on two slides processed in parallel. The data were further validated by results from more than five experiments.

RESULTS

Effect of UV Irradiation on Aminosilane and Polycarbodiimide-Coated Glass Surfaces. The goal of the current study was to verify a new method of peptide immobilization onto a solid surface by evaluating the DNA–peptide conjugates for peptide microarray applications. To this end, we prepared six different DNA–peptide conjugates (Table 1), which were easily obtained by Michael addition between maleimide–peptides and thiol–DNattach (Figure 1). In all cases, derivatization was carried out after chain assembly by following standard protocols, thus yielding 5′-modified DNattach and peptides with the maleimide group linked to the *N*-terminus (see Materials and General Methods).

The amount of peptide attached to the solid support and the accessibility of enzymes or antibodies to the immobilized peptide are critical factors in microarray analysis, as they determine both the sensitivity and the dynamic range of measurement. To investigate how UV irradiation during immobilization of peptide via the poly(dT) tail on the surface affects the binding affinity and discriminative ability of the antibody, we first immobilized two different DNA–peptide conjugates (Peptides 1 and 2, Table 1) on the polycarbodiimide-coated glass slide. Peptides 1 and 2 both include a tyrosine residue, although only the tyrosine from the former peptide was phosphorylated. The DNA–peptide conjugates were dissolved in 3× SSC at a concentration of 1 μM and applied to the glass slide in quadruplicate.

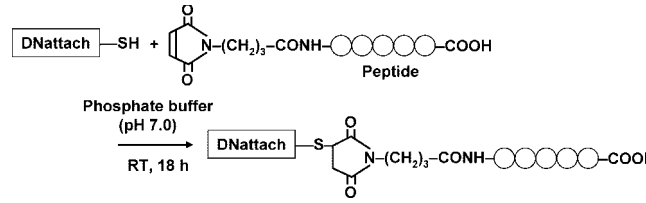


Figure 1. Synthesis of DNattach-induced peptides. The reaction mixture of thiol-modified DNattach and maleimide-modified peptide was incubated at RT for 18 h.

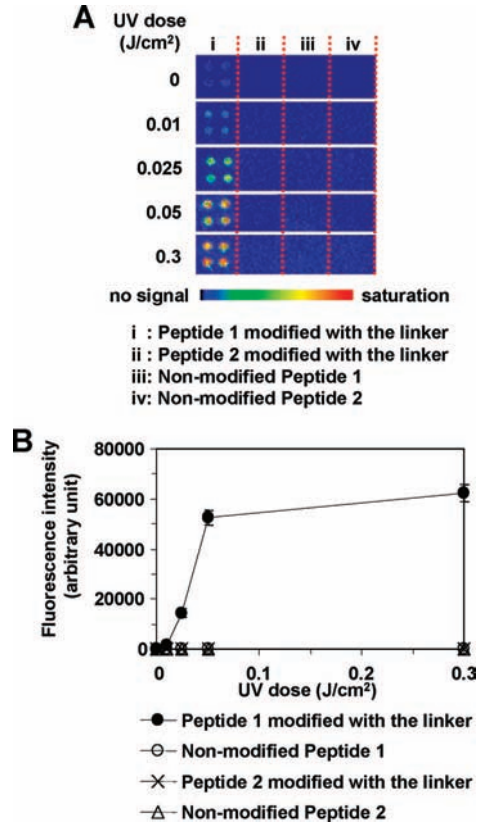


Figure 2. Signal intensities produced upon the interaction of Cy3-labeled antiphosphotyrosine antibody with four different spotted peptides at 0 to 0.3 J/cm^2 of UV irradiation. Peptides 1 and 2 were spotted and immobilized on the polycarbodiimide-coated slide. (A) Spots made with each peptide were present in quadruplicate. (B) The mean signal intensities produced in the experiments are plotted vs UV dose. The error bars indicate standard deviation. Peptide sequences are shown in Table 1. All arrays were scanned with the same PMT setting (600 mV).

In peptide–antibody interaction experiments, Cy3-labeled antiphosphotyrosine antibody, which specifically interacts with the phosphorylated tyrosine in peptide sequences, was used for detection. Figure 2A shows a typical image of fluorescence signal intensities from these experiments. Irrespective of UV dose, peptide–antibody interaction was specific to the phosphorylated tyrosine residue. No signals were obtained from either the non-UV-irradiated arrays or from the UV-irradiated arrays spotted with nonmodified peptides. These results indicate that immobilization of the linker-modified peptide onto the surface by UV irradiation did not originate from residual peptide molecules that were physically absorbed onto the surface. Signal intensities increased with increasing UV dose, whereas non-

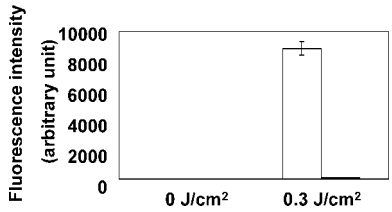


Figure 3. Signal intensities produced upon interaction of Cy5-labeled antiphosphotyrosine antibody with two different spotted peptides at 0 and 0.3 J/cm^2 of UV irradiation. Modified Peptide 1 (white bar) and Peptide 2 (dark bar) at a concentration of 1 μM were spotted and immobilized on the aminosilane slide. The error bars indicate standard deviation. Peptide sequences are shown in Table 1. All arrays were scanned with the same laser power (100%) and PMT setting (50%).

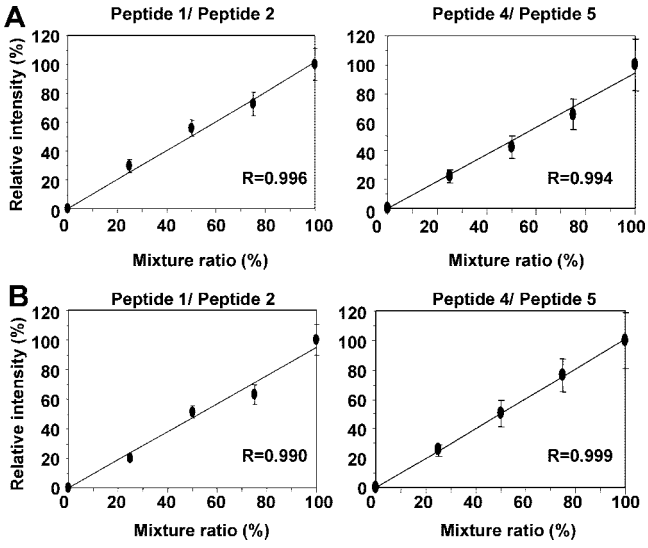


Figure 4. Fluorescent intensity vs amount of phosphorylated substrate. Varied ratios of phosphorylated/nonphosphorylated c-Src (Peptides 1 and 2) and PKA (Peptides 4 and 5) substrates were arrayed onto the polycarbodiimide-coated (A) and aminosilanized (B) slides and probed with the corresponding Cy5-labeled antiphosphoamino acid antibody. The error bars indicate standard deviation. All arrays were scanned with the same laser power (100%) and PMT setting (50%).

specific signals were at background levels. Using a UV dose of up to 0.3 J/cm^2, the signal intensity was 528-fold (Peptide 1) greater for the UV-irradiated array than for the nonirradiated control (Figure 2B). We did not observe an obvious increase in nonspecific signals when the UV dose was increased to 0.3 J/cm^2. A similar trend with the aminosilane slides was also observed (Figure 3).

These results indicate that the modified peptide is immobilized via the poly(dT) attached to the peptide and that the reaction between the DNA–peptide conjugates and polycarbodiimide (aminosilane) on the glass surface is facilitated by UV irradiation.

Detection and Quantification of on-Chip Phosphorylation. We next determined whether the fluorescently labeled antibodies can quantitatively detect phosphorylated peptides on the aminosilanized and polycarbodiimide-coated arrays. Varied ratios of phosphorylated/nonphosphorylated Peptides 1 and 2 (Table 1), with a combined constant concentration (1 μM), were immobilized onto the slide by UV irradiation and then probed with the Cy5-labeled antiphosphotyrosine antibody for 1 h (Figure 4A and B). Figure 4A and B shows that the intensity of the spots increased as the ratio of phosphorylated to nonphosphorylated peptide increased. The graph of fluorescent intensity versus phosphorylated peptide substrate shows a linear correlation for the Peptide 1 ratio, ranging from 0 to 100%, demonstrating the feasibility for on-chip quantification of phosphorylated peptides using this methodology. A similar trend was also observed when we immobilized Peptides 4 and 5 onto the slides by UV irradiation and probed with Cy5-labeled antiphosphoGFAP antibody (Figure 4A and B). Thus, the UV-irradiated DNA–peptide conjugates formed under these conditions are suitable for peptide microarray applications.

Detection Sensitivity. To estimate the detection sensitivity of immunofluorescence detection and laser scanning, modified Peptides 1 and 2 (Table 1) at different concentrations were immobilized onto the aminosilane and polycarbodiimide-coated slides by UV irradiation (0.3 J/cm^2) and then probed with the Cy5-labeled antiphosphotyrosine antibody for 1 h (Figure 5A and B). Figure 5A and B shows that the signal intensity was nearly saturated at a concentration of modified Peptide 1 of only 2.5 μM (carbodiimide) and 5 μM (aminosilane), whereas nonspecific signals were minimal across all DNA–peptide conjugate concentrations. The maximum signal intensity was 1.25-fold (Peptide 1) greater for the carbodiimide slide than for the aminosilane slide. The lowest detection limit was around 0.6 μM, where the signal-to-noise was still around 10 for the aminosilane and 238 for the carbodiimide slide, as shown in Figure 5A and B. These differences most likely arise from different surface conditions, such as loading capacity, charge, hydrophobicity, and efficiency of immobilization and interaction. Further investigation was performed using two different modified peptides (Peptides 4 and 5, Table 1) and the Cy5-labeled anti-phosphoGFAP antibody. A similar trend with these peptides was also observed (Figure 5A and B).

The performance of different attachment chemistry (i.e., most widely used in streptavidin–biotin interaction) was also assessed by testing the detection sensitivity of phosphopeptide, as shown in Figure 5A and B. To this end, we immobilized a total of four different biotinylated peptides (same sequences as those of Peptides 1 and 2, and Peptides 4 and 5 in Table 1) at different concentrations onto streptavidin-coated glass slides and then probed with corresponding Cy5-labeled antiphosphoamino acid antibody (*11*). In our hands, however, we could not detect any signals for the phosphorylated Peptide 1 on the streptavidin slide using interaction and scanning conditions (laser power 100%, PMT 50%) identical to those used in our methodology (data not shown), probably due to the fact that the streptavidin-coated slide has limited peptide binding capacity and/or due to the steric interference of the surface on interaction with the antibody where the phosphorylated tyrosine residue in Peptide 1 is located adjacent to the slide surface (Table 1) (*25*). By contrast, although the streptavidin arrays could discriminate between the phosphorylated Peptide 4 and nonphosphorylated Peptide 5 (the signal intensity for Peptide 4 at a concentration of 5 μM was 17.7-fold greater than that for the Peptide 5 control), quantification revealed lower signals (~9.1-fold) in comparison to those obtained using the poly(dT)-modified peptides and carbodiimide slides (Figure 6).

Thus, we find that DNattach chemistry provides a better substrate for the immobilization of peptides and the interaction with antibody than do conventional biotin–avidine interaction techniques.

Characterization of Kinase Activity. In order to further demonstrate the utility of our methodology for the detection of kinase activity in a microarray format, we next investigated the dose-dependent detection of peptide phosphorylation on a chip. Two different nonphosphorylated substrates at a concentration of 10 μM, Peptide 2 modified with poly(dT) as a substrate for c-Src tyrosine kinase and Peptide 3 modified with poly(dT) as a negative control, were spotted and immobilized onto carbodiimide and aminosilane slides by UV irradiation (Table 1). Nonphosphorylated substrates, Peptide 5 modified with poly(dT) as a substrate of PKA serine kinase and Peptide 6 modified

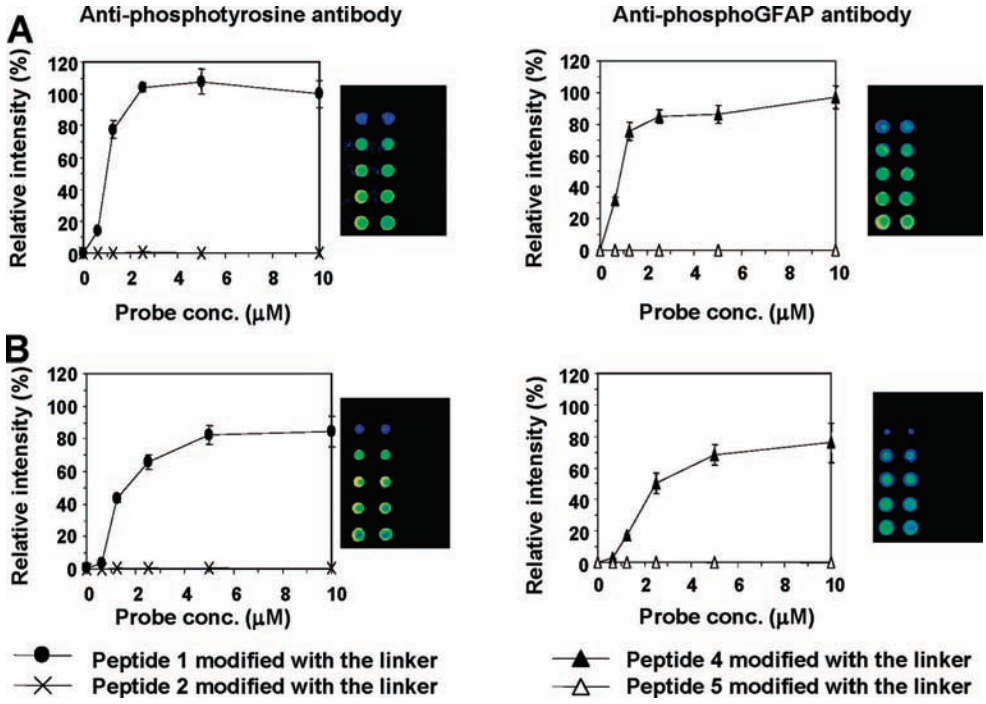


Figure 5. Signal intensities produced upon the interaction of Cy5-labeled antiphosphoaminoacid antibodies. The modified peptides were dissolved in 3× SSC at a concentration of 0–10 μM and spotted on polycarbodiimide (A) and aminosilane (B) in duplicate (see Materials and General Methods). After immobilization, the arrays were probed with the corresponding Cy5-labeled antiphosphoamino acid antibody. Scanned spots and quantitative analysis of spots over interactions with the corresponding antiphosphoamino acid antibody are shown. The error bars indicate standard deviation. All arrays were scanned with the same laser power (100%) and PMT setting (50%). (Note: the maximum mean signal intensity of each specific signal among the different arrays was normalized to 100 (no units); thus, the results represent the relative intensity of the corresponding antiphosphoamino acid antibody.)

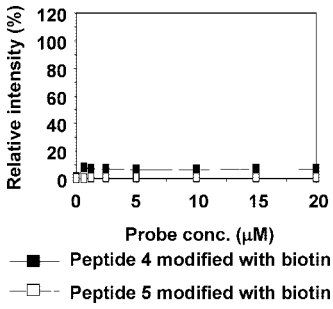


Figure 6. Signal intensities produced upon the interaction of Cy5-labeled anti-phosphoGFAP antibody on the streptavidin arrays. The biotinylated peptides were dissolved in PBS at a concentration of 0–20 μM and spotted on streptavidin slides in duplicate (see Materials and General Methods). After immobilization, the arrays were probed with the Cy5-labeled anti-phosphoGFAP antibody. The error bars indicate standard deviation. All arrays were scanned with the same laser power (100%) and PMT setting (50%). (Note: the maximum mean signal intensity of each specific signal among the different arrays was normalized to 100 (no units) as shown in Figure 5; thus, the results represent the relative intensity of the corresponding antiphosphoamino acid antibody.)

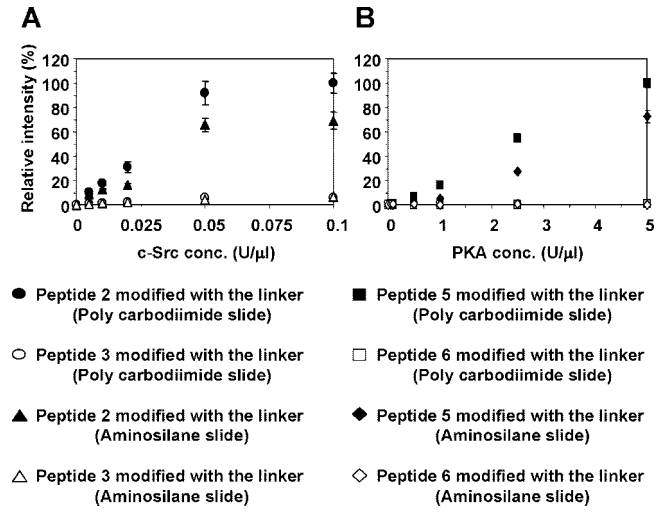


Figure 7. Characterization of c-SRC and PKA kinase activities. The modified Peptide 2, Peptide 3, Peptide 5, and Peptide 6 at the same concentration of 10 μM were immobilized on the slides by UV irradiation (0.3 J/cm^2) and then incubated with (A) c-Src and (B) PKA kinases for 240 or 60 min, respectively. Detection was performed using the corresponding Cy5-labeled antiphosphoamino acid antibody. All arrays were scanned with the same PMT setting (75% and 55% for c-Src and PKA assays, respectively). The error bars indicate standard deviation.

with poly(dT) as a negative control, were also spotted and immobilized onto the same slide (Table 1). The arrays were first incubated with either c-Src or PKA kinase at 5 different kinase concentrations for 240 or 60 min and then incubated with the corresponding fluorescently labeled antiphosphoamino acid antibody for 1 h.

In both cases, Figure 7A and B shows that fluorescent intensities were directly proportional to the concentration of each kinase, whereas nonspecific signals were minimal across all kinase concentrations. In addition, Figure 7A shows that the signal intensity was nearly saturated at a concentration of c-Src kinase of 0.05 U/μL. The CV of intensities for all elements was between 12% and 14% across the entire signal range. As anticipated, the maximum signal intensity was 1.4-fold (Peptide 2) and 1.3-fold (Peptide 5) greater for the carbodiimide slides than for the aminosilane slides (Figure 7A and B). The signal-to-noise ratios for Peptide 2 at a concentration of 0.05 U/μL c-Src kinase were 71.1 (the carbodiimide slide) and 52.5 (the aminsilane slide). In addition, the signal-to-noise ratios for Peptide 5 at a concentration of 5 U/μL PKA kinase were 770

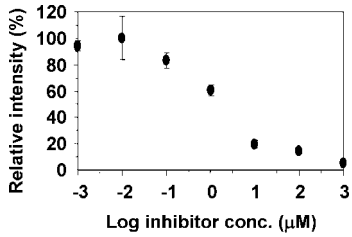


Figure 8. Effect of the AG213 inhibitor upon kinase activity. Modified Peptide 2 was immobilized on the slide by UV irradiation (0.3 J/cm^2) and then incubated with c-Src, ATP, and inhibitor in serial dilutions for 240 min. Detection was performed using the Cy3-labeled antiphosphotyrosine antibody. The error bars indicate standard deviation. All arrays were scanned with the same laser power (100%) and PMT setting (80%).

(the carbodiimide slide) and 678 (the aminsilane slide). These results indicate that, under this immobilization condition, the linker-modified peptide probes are suitable for peptide microarray application.

In order to assess the performance of the different attachment chemistry, again, the biotinytated peptides (Peptides 5 and 6) were spotted and immobilized onto streptavidin slides, and the arrays were incubated with PKA kinase for 60 min and then incubated with the fluorescently labeled anti-phosphoGFAP antibody for 1 h. However, under interaction and scanning conditions (laser power 100%, PMT 55%) identical to those used with the new methodology, we could not detect any signals for the phosphorylation of Peptide 5 (data not shown), probably due to the limited peptide binding capacity on the streptavidin slide and/or due to the steric effect as mentioned above.

Again, we find that DNattach chemistry provides a better substrate for the immobilization of peptides and interaction with kinases than do conventional biotin–avidine interaction techniques.

Evaluation of AG213 Inhibitor of c-Src on the Peptide Arrays. Finally, we used the peptide microarray to evaluate an inhibitor of c-Src, AG213, on substrates. Mixtures containing the kinase, ATP, and inhibitor at concentrations ranging from 1 nM to 1 mM were applied onto the polycarbodiimide surface. After 4 h at 37 °C, the arrays were probed with Cy3-labeled antiphosphotyrosine antibody. When the kinase reactions were performed in the presence of 0.04 U/μL c-Src kinase, an IC_{50} value (1.7 μM) close to the published data in solution-phase assays (8 μM) was obtained (Figure 8) (*7, 26*). The difference observed with this inhibitor may be due to different sources of enzymes or slightly different assay conditions. However, this result is expected since the inhibitor used in this study is known to compete with ATP by binding to the ATP binding site of the kinase (*26*). These results show the feasibility of our methodology for the characterization of inhibitors.

DISCUSSION

The experiments described in this article demonstrate that a combination of modified-peptide and UV irradiation technology can be used to generate an efficient and robust assay for kinases. Nucleases have been studied using peptide–DNA/PNA conjugates by the introduction of a reporter group to investigate DNA–protein interactions (*27–31*). However, this is the first report to demonstrate the utility of UV irradiation of spotted peptides with a poly(dT) tail on commercial aminosilane and polycarbodiimide-coated slides to detect phosphorylation events. The DNA–peptide conjugates are immobilized by UV irradiation to form covalent bonds between the thymidine residues in DNA and the carbodiimide or the amine group on the surface (*20, 32*). On the molecular level, although it is not yet clear how the poly(dT) binds to the substrates by UV irradiation, it can be looked on as any other functional group that is required for efficient immobilization of samples on surfaces (*21, 33, 34*). Polycarbodiimide resin was identified by the presence of absorption at 2145 cm^{-1} in FT-IR assignable to the carbodiimide function. Although the carbodiimide group hydrolyzes very easily at acidic pH around 5 as well as under basic conditions (*18–20, 35*), the polycarbodiimide used in this study was hydrophobic and stable for 12–24 months. In addition, the polycarbodiimide-coated slides can be stored for 6–12 months at room temperature before use (*20*). The presence of carbodiimide groups on the surface was confirmed by X-ray photoelectron spectroscopy. In fact, when fluorescently labeled poly(dT) in 3× SSC were printed on the carbodiimide substrate and the slides were UV-irradiated after 1, 24, 72, and 168 h at RT and then briefly washed, signal intensity from only the slide after 168 h of incubation indicated less signal intensity (1/10-fold) than those obtained from the slides after 1, 24, and 72 h of incubation (data not shown). These results indicate that decomposition of carbodiimide groups on the surface that is involved with the immobilization procedure would dramatically affect immobilization efficiency after 72 h of incubation. The slides should therefore be UV irradiated within 72 h after printing to circumvent this problem. Thus, using this immobilization system, peptides can be reliably and specifically immobilized onto the solid surface. Furthermore, this new immobilization method provides signal intensities greater than those of conventional biotin–avidine interaction techniques. Here, we have demonstrated that this property can be exploited to measure kinase activity. Although the introduction of an additional spacer unit between the biotin and the peptide might avoid steric hindrance and result in facilitating the signal intensity on the streptavidin slide and/or the use of secondary antibody might also facilitate the signal intensity on the streptavidin slide (*25*), the technique described in this study provides three major advantages over those of peptide microarrays that have been reported by other researchers. First, the immobilization reaction involving UV irradiation is both simple and quick, providing a regular, homogeneous environment for immobilized peptide ligands. The peptides therefore have equal activity toward soluble enzyme and are well suited to quantitative assays. Second, a low concentration (up to 10 μM) of modified peptide is sufficient for the kinase assays. By contrast, conventional technologies generally require a peptide concentration of up to 5 mM and a period of several hours for immobilization onto a solid surface (*7–10, 14–16*). Third, using this immobilization method, commercial DNA microarray slides without additional surface modifications can be used for producing peptide microarrays, thereby avoiding making microarray fabrication a laborious and complex procedure.

Mukumoto et al. recently reported that nonmodified DNA could be immobilized onto a carbodiimide-coated gold slide through the covalent bond by a reaction of carbodiimide with the imino moiety of the thymine base in DNA (*35*). Inconsistent with our results, they do not require a UV irradiation procedure for immobilization of DNA. In our studies, however, we could detect only weak signals from Peptide 1 modified with DNattach on non-UV-irradiated slides (Figure 2A and B). These differences may be caused by different surface conditions between our slides treated with polycarbodiimide and their slides treated with the carbodiimide monomer, thereby causing an insufficient amount of immobilized peptides and/or steric effects to detect phosphorylation events on our surface when immobilized peptides on the slides are used in this study without UV irradiation.

One potential drawback of this system is that one has to link the DNattach to the peptides individually followed by multiple purification steps. It might make microarray fabrication a laborious and complex procedure when constructing high-

density peptide microarrays. However, it is possible to synthesize the DNA–peptide conjugates on a solid support and purify the conjugates all together (*36*), and studies to optimize a solid-phase synthesis protocol with DNattach are currently underway. In addition, certain adjustments in the methodology described here will be required if cysteine is to be included in the peptide sequence. The reaction between the free thiol of cysteine and the maleimide group of the peptide conjugate may compete with the reaction between the thiol of DNattach and the maleimide group during the conjugation, yielding side products as a result of Michael additions. To avert the complex mixtures, the conjugate reaction should be carried out using maleimide–peptides with a protected cysteine and followed by unmasking of the thiol group after conjugation. Alternatively, the conjugate reaction may be carried out using 5′-peptide–oligonucleotide conjugates during the conjugation on solid supports as described above (*36*).

In this proof-of-principle study, although we have used a model system consisting of a relatively small number of distinct antiphosphoamino acid antibodies and protein kinases to illustrate the effectiveness of this immobilization methodology, we show that the technique is robust, reliable, and reproducible for generating peptide microarrays. Thus, this method has the potential to provide a key technology for the fabrication of arrays to explore peptides as potential substrates for kinases. This technique might also be applied to high-throughput analysis of various enzyme activity assays and protein expression profiling. In addition, because the linker can be immobilized onto gold surfaces and plastics (*21, 22*), it should be possible to immobilize the modified peptides onto nonmodified gold or plastic surfaces. We are also currently investigating various biological assays, including those for detecting kinase activity, using this system by employing label-free detection methodologies (i.e., SPR and MALDI-TOF Mass). Furthermore, our research group has successfully synthesized poly(dT)-modified carbohydrates and is currently monitoring lectin assays in a carbohydrate microarray format. The results will be reported elsewhere in the near future.

ACKNOWLEDGMENT

We gratefully acknowledge NAI Inc. (Kanagawa, Japan) for their support in proofreading the manuscript and providing valuable suggestions.

LITERATURE CITED

(1) Pawson, T., and Scott, J. D. (1997) Signaling through scaffold, anchoring, and adaptor proteins. *Science 278*, 2075–2080.
(2) Ahn, N. G., and Resing, K. A. (2001) Toward the phosphoproteome. *Nat. Biotechnol. 19*, 317–318.
(3) Dostmann, W. R., Taylor, M. S., Nickl, C. K., Brayden, J. E., Frank, R., and Tegge, W. J. (2000) Highly specific, membrane-permeant peptide blockers of cGMP-dependent protein kinase Iα inhibit NO-induced cerebral dilation. *Proc. Natl. Acad. Sci. U.S.A. 197*, 14772–14777.
(4) Lam, K. S., Lebl, M., and Krchnak, V. (1997) The "One-Bead-One-Compound" combinatorial library method. *Chem. Rev. 97*, 411–448.
(5) Houghten, R. A., Pinilla, C., Blondelle, S. E., Appel, J. R., Dooley, C. T., and Cuervo, J. H. (1991) Generation and use of synthetic peptide combinatorial libraries for basic research and drug discovery. *Nature 354*, 84–86.
(6) Songyang, Z., Carraway, K. L., Eck, M. J., Harrison, S. C., Feldman, R. A., Mohammadi, M., Schlessinger, J., Hubbard, S. R., Smith, D. P., Eng, C., Lorenzo, M. J., Ponder, B. A. J., Mayer, B. J., and Cantley, L. C. (1995) Catalytic specificity of protein-tyrosine kinases is critical for selective signaling. *Nature 373*, 536–539.
(7) Houseman, B. T., Huh, J. H., Kron, S. J., and Mrksich, M. (2002) Peptide chips for the quantitative evaluation of protein kinase activity. *Nat. Biotechnol. 20*, 270–274.
(8) Duburcq, X., Olivier, C., Desmet, R., Halasa, M., Carion, O., Grandidier, B., Heim, T., Stievenard, D., Auriault, C., and Melnyk, O. (2004) Polypeptide semicarbazide glass slide microarrays: characterization and comparison with amine slides in serodetection studies. *Bioconjugate Chem. 15*, 317–325.
(9) Stoevesandt, O., Elbs, M., Kohler, K., Lellouch, A. C., Fischer, R., Andre, T., and Brock, R. (2005) Peptide microarrays for the detection of molecular interactions in cellular signal transduction. *Proteomics 5*, 2010–2017.
(10) Inamori, K., Kyo, M., Nishiya, Y., Inoue, Y., Sonoda, T., Kinoshita, E., Koike, T., and Katayama, Y. (2005) Detection and quantification of on-chip phosphorylated peptides by surface plasmon resonance imaging techniques using a phosphate capture molecule. *Anal. Chem. 77*, 3979–3985.
(11) Uttamchandani, M., Chen, G. Y., Lesaicherre, M. L., and Yao, S. Q. (2004) Site-specific peptide immobilization strategies for the rapid detection of kinase activity on microarrays. *Methods Mol. Biol. 264*, 191–204.
(12) Williams, R. A., and Blanch, H. W. (1994) Covalent immobilization of protein monolayers for biosensor applications. *Biosens. Bioelectron. 9*, 15–167.
(13) Vijayendran, R. A., and Leckband, D. E. (2001) A quantitative assessment of heterogeneity for surface-immobilized proteins. *Anal. Chem. 73*, 471–480.
(14) MacBeath, G., Koehler, A. N., and Schreiber, S. L. (1999) Printing Small Molecules as Microarrays and Detecting Protein-Ligand Interactions en Masse. *J. Am. Chem. Soc. 121*, 7967–7968.
(15) Lesaicherre, M. L., Uttamchandani, M., Chen, G. Y. J., and Yao, S. Q. (2002) Antibody-based fluorescence detection of kinase activity on a peptide array. *Bioorg. Med. Chem. Lett. 12*, 2085–2088.
(16) Falsey, J. R., Renil, M., Park, S., Li, S., and Lam, K. S. (2001) Peptide and small molecule microarray for high throughput cell adhesion and functional assays. *Bioconjugate. Chem. 12*, 346–353.
(17) MacBeath, G., and Schreiber, S. L. (2000) Printing proteins as microarrays for high-throughput function determination. *Science 289*, 1760–1763.
(18) Masson, L., Maynard, C., Brousseau, R., Goh, S. H., Hemmingsen, S. M., Hill, J. E., Paccagnella, A., Oda, R., and Kimura, N. (2006) Identification of pathogenic Helicobacter species by chaperonin-60 differentiation on plastic DNA arrays. *Genomics 87*, 104–112.
(19) Kimura, N., Nagasaka, T., Murakami, J., Sasamoto, H., Murakami, M., Tanaka, N., and Matsubara, N. (2005) Methylation profiles of genes utilizing newly developed CpG island methylation microarray on colorectal cancer patients. *Nucleic Acids Res. 33*, e46.
(20) Kimura, N., Oda, R., Inaki, Y., and Suzuki, O. (2004) Attachment of oligonucleotide probes to poly carbodiimide-coated glass for microarray applications. *Nucleic Acids Res. 32*, e68.
(21) Kimura, N. (2006) One-step immobilization of poly(dT)-modified DNA onto non-modified plastic substrates by UV irradiation for microarrays. *Biochem. Biophys. Res. Commun. 347*, 477–484.
(22) Takahashi, M., Kondoh, Y., Tashiro, H., Koibuchi, N., Kuroda, Y., and Tashiro, T. (2005) Monitoring synaptogenesis in the developing mouse cerebellum with an original oligonucleotide microarray. *J. Neurosci. Res. 80*, 777–788.
(23) Akiyama, M., and Kimura, N. (2005) Immobilized Biomolecule and Method of Detecting Substance Capable of Interacting with Biomolecule, WO2005085857, September 15.
(24) Pearson, R. J., Kassianidis, E., Slawin, A. M., and Philp, D. (2004) Self-replication vs. reactive binary complexes--manipulating recognition-mediated cycloadditions by simple structural modifications. *Org. Biomol. Chem. 2*, 3434–3441.

(25) Lehel, C., Daniel-Issakani, S., Brasseur, M., and Strulovici, B. (1997) A chemiluminescent microtiter plate assay for sensitive detection of protein kinase activity. *Anal. Biochem. 244*, 340–346.

(26) Golomb, G., and Fishbein, I. (1997) Tyrphostins, inhibitors of protein tyrosine kinases in restenosis. *Adv. Drug Delivery Rev. 24*, 53–62.

(27) Mironova, N. L., Pyshnyi, D. V., Ivanova, E. M., Zenkova, M. A., Gross, H. J., and Vlassov, V. V. (2004) Covalently attached oligodeoxyribonucleotides induce RNase activity of a short peptide and modulate its base specificity. *Nucleic Acids Res. 32*, 1928–1936.

(28) Tong, G., Lawlor, J. M., Tregear, G. W., and Haralambidis, J. (1993) The synthesis of oligonucleotide-polyamide conjugate molecules suitable as PCR primers. *J. Org. Chem. 58*, 2223–2231.

(29) Debethune, L., Kohlhagen, G., Grandas, A., and Pommier, Y. (2002) Processing of nucleopeptides mimicking the topoisomerase I-DNA covalent complex by tyrosyl-DNA phosphodiesterase. *Nucleic Acids Res. 30*, 1198–1204.

(30) Hovinen, J., Guzaev, A., Azhayeva, E., Azhayev, A., and Lönnberg, H. (1995) Imidazole tethered oligodeoxyribonucleotides: synthesis and RNA cleaving activity. *J. Org. Chem. 60*, 2205–2209.

(31) Gómez-Pinto, I., Marchán, V., Gago, F., Grandas, A., and González, C. (2003) Solution structure and stability of tryptophan-containing nucleopeptide duplexes. *ChemBioChem. 4*, 40–49.

(32) Wang, H. Y., Malek, R. L., Kwitek, A. E., Greene, A. S., Luu, T. V., Behbahani, B., Frank, B., Quackenbush, J., and Lee, N. H. (2003) Assessing unmodified 70-mer oligonucleotide probe performance on glass-slide microarrays. *Genome Biol. 4*, R5.

(33) Petersen, J., Stangegaard, M., Birgens, H., and Dufva, M. (2007) Detection of mutations in the beta-globin gene by colorimetric staining of DNA microarrays visualized by a flatbed scanner. *Anal. Biochem. 360*, 169–171.

(34) Dufva, M., Petersen, J., Stoltenborg, M., Birgens, H., and Christensen, C. B. (2006) Detection of mutations using microarrays of poly(C)10-poly(T)10 modified DNA probes immobilized on agarose films. *Anal. Biochem. 352*, 188–197.

(35) Mukumoto, K., Ohtsuka, K., Nojima, K., and Takenaka, S. (2006) Preparation of carbodiimide-terminated dithiolane self-assembly monolayers as a new DNA-immobilization method. *Anal. Sci. 22*, 349–355.

(36) Ocampo, S., Albericio, M. F., Fernandez, I., Vilaseca, M., and Eritja, R. (2005) A straightforward synthesis of 5′-peptide oligonucleotide conjugates using *N*α -Fmoc-protected amino acids. *Org. Lett. 7*, 4349–4352.

BC070083+

Development of Albumin-Binding Camptothecin Prodrugs Using a Peptide Positional Scanning Library

Björn Schmid,[†] André Warnecke,[†] Iduna Fichtner,[‡] Manfred Jung,[§] and Felix Kratz*,[†]

Tumor Biology Center, Breisacher Straße 117, 79106 Freiburg, Germany, Max-Delbrück Centrum, Robert-Rössle-Straße 10, 13122 Berlin, Germany, and University of Freiburg, Institute of Pharmaceutical Sciences, Pharmaceutical and Medicinal Chemistry, Albertstraße 25, 79104, Freiburg, Germany. Received March 13, 2007; Revised Manuscript Received July 11, 2007

Designing truly tumor-specific prodrugs remains a challenge in the field of cancer chemotherapy. As a new strategy, we incubated homogenates of a spectrum of human colon tumor xenografts with a fluorogenic positional scanning tetrapeptide library in order to identify peptide sequences that are preferentially cleaved by colon tumors. Our screening experiments at pH 7.4 revealed that Met, Leu, and Lys were preferred amino acids in the position P_1 and Tyr, Phe, and Met in P_2, whereas in P_3 and P_4, the cleavage profiles were less characteristic. However, similar results were obtained when testing breast tumor material and homogenates from healthy murine organs. On the basis of these results, we developed albumin-binding camptothecin (CPT) prodrugs of the general formula EMC-Arg-P_4-P_3-P_2-P_1-Ala-CPT (EMC = 6-maleimidocaproic acid) that incorporated two peptide linkers: H-Arg-Ala-Phe-Met-OH and H-Arg-Phe-Tyr-Met-OH (P_4-P_3-P_2-P_1). The incorporation of two arginine residues rendered the prodrugs water-soluble (>7 mg/mL), while the use of alanine as an amino acid spacer proved to be beneficial for the release of the active agent. Incubation studies with homogenates of HT-29 colon tumor tissue and murine spleen, liver, and kidneys demonstrated cleavage of the peptide linker with CPT–peptide derivatives and CPT being the major cleavage products. Although the peptide sequence is not selectively cleaved in colon tumors, an *in vivo* study in a HT-29 xenograft model showed that the prodrug EMC-Arg-Arg-Ala-Phe-Met-Ala-CPT demonstrated enhanced antitumor efficacy when compared to CPT [(*T*/*C* max: 17% for the prodrug (2 × 12.5 mg/kg CPT equivalents) and 40% for CPT (3 × 12.5 mg/kg)].

INTRODUCTION

One of the major limitations of clinically established anticancer drugs is their lack of tumor selectivity. Cytostatic drugs are evenly distributed in the organism, thus damaging healthy tissue and producing side effects. In order to overcome these drawbacks, a major goal of modern drug development is to provide efficient strategies that enable site-specific delivery of anticancer drugs.

In the past, various low- and high-molecular-weight prodrugs have been evaluated with the aim of improving cancer therapy. Since it has been shown that macromolecules with a molecular weight of >20 kDa accumulate in tumor tissue due to passive targeting almost regardless of their chemical nature (*1*), conjugation of drugs with macromolecules has proved to be a promising and versatile platform technology for tumor targeting (*2*). Typically, the general design of such prodrugs can be formulated as carrier(-spacer-drug)$_n$ wherein *n* describes the number of drugs bound to one carrier molecule.

In the past years, we have developed a macromolecular prodrug concept in which an anticancer agent is functionalized with a thiol-binding maleimide group. After intravenous administration, the prodrug binds rapidly and selectively to the cysteine-34 position of circulating serum albumin, thereby generating a macromolecular transport form of the drug *in situ* (*3–5*). This strategy turned out to be applicable to a number of anticancer drugs such as doxorubicin (*5–8*), carboplatin (*9*), and camptothecin (*10*). These prodrugs demonstrated a lower toxicity combined with a superior *in vivo* efficacy in mice models compared to the respective parent compounds. Our efforts led to the development of DOXO-EMCH, a 6-maleimidocaproic-hydrazone derivative of doxorubicin, which is the first albumin-binding prodrug to enter clinical trials. In animal experiments, DOXO-EMCH was well-tolerated and proved to be superior over doxorubicin in several preclinical tumor models (*3, 4*). In a clinical phase I study, DOXO-EMCH showed promising results (*11*), and a phase II study (with the compound renamed INNO-206) will be initiated at the beginning of 2007.

Although inconspicuously named spacer or linker, the molecule realizing the link between the drug and the carrier plays a crucial role for the prodrug to exert antitumor efficacy. The spacer incorporates a predetermined breaking point and is thus responsible for a site-specific release of the drug after entering tumor cells or tumor tissue, on one hand. On the other hand, the spacer has to ensure the prodrug's stability in the bloodstream and—ideally—healthy tissue. Apparently, a prodrug strategy can only be as effective as its underlying drug release mechanism. It is therefore of special interest to find new release strategies for enhanced tumor specificity and to customize appropriate spacer molecules.

Whereas DOXO-EMCH incorporates an acid-sensitive hydrazone linker that is stable in plasma but is rapidly cleaved after cellular uptake in the acidic environment of endosomes in tumor cells, other strategies for achieving tumor-specific release of drugs are based on the overexpression of certain proteases in tumor tissue. Proteolytic enzymes play a decisive role in metastasis and tumor progression (*12–14*), and elevated levels were reported for cathepsins (*15*), matrix metalloproteases (*16*),

* To whom correspondence should be addressed. Dr. Felix Kratz, Tumor Biology Center, Department of Medical Oncology, Clinical Research, Breisacher Straße 117, D-79106 Freiburg, Federal Republic of Germany. Tel.: +49-761-2062930. Fax: +49-761-2062905. E-mail: felix@tumorbio.uni-freiburg.de.

[†] Tumor Biology Center.

[‡] Max-Delbrück Centrum.

[§] University of Freiburg.

10.1021/bc0700842 CCC: $37.00 © 2007 American Chemical Society
Published on Web 10/05/2007

plasmin (*17*), urokinase-type plasminogen activator (uPA) (*17*), and prostate-specific antigen (PSA) (*18*). In our previous work, we developed a number of albumin-binding prodrugs of doxorubicin that were cleaved by uPA (*8*), PSA (*7*), and the matrix metalloproteases 2 and 9 (*6, 19*). Disadvantages of targeting individual enzymes for cleaving the prodrug are their heterogeneous expression in the tumor and their variability among individual tumors, as well as their expression in healthy tissue.

In the present work, we therefore decided not to focus on individual proteases but instead followed a pragmatic approach at attempting to identify those peptide sequences that are most efficiently cleaved by native tumor material irrespective of whether one or more than one enzyme were involved in the cleavage process. For this purpose, we screened tissue homogenates from colon and breast tumor xenografts as well as healthy murine organs with a positional scanning combinatorial tetrapeptide library. On the basis of these results, we selected two tetrapeptide sequences for the development of albumin-binding prodrugs with the anticancer agent camptothecin (CPT), an alkaloid from the chinese tree *Camptotheca acuminata* first isolated by Wall and co-workers, that shows strong cytotoxic activity (*20*), based on the inhibition of DNA-topoisomerase I (*21*). Due to its poor water-solubility (2.5 μg/mL) (*22*), CPT did not gain any clinical importance, whereas the water-soluble derivatives topotecan and irinotecan have meanwhile been approved for the therapy of colorectal, ovarian, and lung cancer (*23, 24*).

By applying this novel approach, we hoped to obtain selective prodrugs for the treatment of colorectal tumors. Herein, we report on the screening experiments using a positional scanning library, the synthesis of the CPT prodrugs, and their cleavage properties and antitumor activity.

MATERIALS AND METHODS

General. Chemicals and solvents were purchased from Sigma-Aldrich, Fluka, Merck, KMF, LGC Promochem and Roth, and were used without further purification. The Fmoc-protected amino acids were purchased from Bachem AG (Switzerland). For the synthesis of the peptide libraries, polystyrol rink-amide AM-resin [Fmoc-RAM-AM, 100–200 mesh, loading (by Fmoc-determination): 0.65 mmol/g] from RAPP Polymere GmbH (Tübingen, FRG) was used. Camptothecin was purchased from Hande Tech Development, Inc. (USA). H-Ala-CPT was synthesized according to a published procedure (*25*). EMC-Arg-Arg-Ala-Phe-Met-OH was custom-made by JPT Peptide Technologies GmbH (Berlin, Germany). Human serum albumin (5% solution) was purchased from Octapharma GmbH that contained approximately 60% free thiol groups as assessed with the Ellmann's test. The buffers used were vacuum-filtered through a 0.2 μm membrane (Sartorius, Germany) and thoroughly degassed with ultrasound or by purging with nitrogen prior to use. Chemical reactions were carried out under a nitrogen atmosphere. Peptide substances were lyophilized with an Alpha 2–4 lyophilizer (Christ, Germany).

Spectral Analyses. Mass spectra were obtained on a Thermoelectron LCQ Advantage with associated MAT SS 200 data system using electron spray ionization. UV/vis spectrophotometry was carried out with a double-beam spectrophotometer U-2000 from Hitachi. LC-MS-pos ESI spectrometry was carried out on a Finnigan LCQ Advantage mass spectrometer (capillary temperature 300 °C; source-induced dissociation voltage 25 V, Thermo Electron) coupled to a Finnigan Surveyor HPLC system (Thermo Electron, Dreieich, FRG) with a Jupiter C_4 column (300–5, 150 × 2 mm; Phenomenex, Aschaffenburg, FRG). Chromatographic conditions are as follows: flow, 300 μL/min; mobile phase A, 1% MeCN, 99% demin H_2O, 0.06% TFA; mobile phase B, 100% MeCN, 0.06% TFA; gradient 15–20 min increase from 10% mobile phase B to 50% mobile phase B; injection volume, 15 μL.

Chromatography. See Supporting Information for chromatography.

Synthesis of the Peptide Library. The peptides were built up on Rink amide resin (RAM-AM). The synthesis of ACC and P_1-loaded ACC resin (H-P_1-ACC-RAM-AM) was carried out according to a published procedure (*26–28*). We used 18 of the 20 standard amino acids (tryptophane and cysteine were omitted), while the published method used 19 amino acids (cysteine was omitted and norleucine was substituted for methionine), and in contrast to the published procedure, we did not use a fixed P_1-position. The capacity of the resin (0.65 mmol/g) was determined by a spectrophotometric Fmoc quantification assay (*29*). For preparation of the P_1-position of the P_1-library, the H-ACC-RAM-AM-resin was divided into 18 reaction columns (1.30 mmol/column) and was suspended in DMF. Consecutively, each of the 18 Fmoc-amino acids (5 equiv), 1,6-collidine (5 equiv), and HATU (5 equiv) were added to the 18 reaction columns. The mixtures were stirred for 16 h and afterwards thoroughly washed with DMF. The yield of the reaction and the loading of the resin was determined via Fmoc quantitative assay (*29*). If the reaction afforded a yield of <50 %, coupling with HATU was repeated. Fmoc-Thr(OtBu)-OH had to be coupled twice, and Fmoc-Arg(Pbf)-OH, Fmoc-Ile-OH, Fmoc-Pro-OH, and Fmoc-Val-OH even three times, whereby a loading of more than 45% was not obtained for Fmoc-Arg(Pbf)-OH and Fmoc-Ile-OH. For the preparation of the P_2-, P_3-, and P_4- libraries, an isokinetic mixture of 18 Fmoc-P_1-ACC-RAM-AM amino acids was used (*30*). Afterwards, the resin was split in the reaction columns (1.30 mmol/column, 18 columns for each library) and DMF was added to solvate the Fmoc-P_1-ACC-RAM-AM resin under gentle stirring for 30 min. Subsequently, the Fmoc protective group was cleaved by replacing the DMF with 20% piperidine in DMF and agitating for 30 min. The piperidine solution was then filtered off, and the resin was washed several times with DMF.

The P_2-library was synthesized first by preactivating the 18 individual Fmoc-amino acids (10 equiv) in separate vials for 10 min with HOBt (10 equiv) and DIPC (10 equiv) in DMF to define the P_2-position. In a second step, an isokinetic mixture of the 18 Fmoc-amino acids (20 mmol per each library, 10 equiv/column) was preactivated with HOBt (20 mmol) and DIPC (20 mmol) in DMF to couple the randomized P_2-amino acids to the P_1-, P_3-, and P_4-libraries. Subsequently, the solution was added to each column for the P_1-, P_3-, and P_4-libraries and stirred for 3 h. The solution was filtered off, and the resin was washed several times with DMF. The installation of the P_3- and P_4-positions was carried out in the same manner.

After synthesis of the P_4-library was completed, the Fmoc protecting group of the P_4-amino acids was cleaved and the resin was washed with DMF. The resin was then subjected to a capping procedure using 3-nitro-1,2,4-triazole (10 equiv), acetic acid (10 equiv), and DIPC (10 equiv), and was agitated for 16 h at room temperature. Afterwards, DIEA (2 equiv) was added, and agitation continued for 1 h before the resin was washed with DMF. For cleavage of the substrates from the resin and of the protecting groups at the side chain of the amino acids, the resin was treated for 1 h with a mixture consisting of TFA/water/diisopropylsilane 95:2.5:2.5 (v/v) (10 mL/column). Subsequently, the resin was filtered off, and the solutions repeatedly evaporated under addition of 10 mL of ethanol and lyophilized out of an acetonitrile–water mixture (1:5). The final libraries were dissolved in DMSO to a concentration of 2 mM with respect to the fluorophor and were kept frozen at 4 °C and thawed prior to use.

Incubation Studies of Different Tissue Homogenates with the Peptide Libraries P_1–P_4. The incubation studies of the P_1-P_4-tetrapeptide library with different colon (HT-29, 5735, 5854, and 5679) and breast (MCF-7, MDA-MB 435, Breast 6661, and Breast 3366) tumor xenograft homogenates and tissue homogenates of healthy organs from nude mice (liver, kidney, and spleen) and human blood plasma were carried out using a 96-well assay. Preparation of the tissue homogenates was carried out according to two different protocols that were previously reported to preserve the activities of cathepsin B (lysosomally active) (*31*) or matrix metalloproteases 8 and 9 (extracellular) (*32*). We assumed that, following the first protocol (pH 5.0), intracellular proteases would primarily be liberated, whereas the second (pH 7.4) would be appropriate for extracting extracellular proteases. All following steps were carried out on ice. The tissues were cut into small pieces, and 200 mg samples were transferred in a 2 mL Eppendorf tube to which was added 800 μL of buffer (50 mM Tris–HCl buffer, pH 7.4, containing 1 mM monothioglycerol or 50 mM sodium acetate buffer, pH 5.0, containing 100 mM sodium chloride, 4 mM EDTA Na_2, and 0.1% Brij 35). Homogenization was carried out with a micro-dismemberator at 3000 rpm for 3 min with the aid of glass balls (diameter: 3 mm). Afterwards, the samples were centrifuged at 5000 rpm for 10 min at 4 °C. The supernatant was aliquoted and kept frozen at −78 °C prior to use.

The tumor homogenates were diluted 1:10 (75 μL + 675 μL) with buffer pH 7.4 (50 mM Tris–HCl buffer, containing 1 mM monothioglycerol) or buffer pH 5.0 (50 mM sodium acetate buffer, containing 100 mM sodium chloride, 4 mM EDTA-2Na, and 0.1% Brij 35). The ACC–tetrapeptide stock solution (2 mM) in DMSO was diluted 1:200 (10 μL + 1990 μL) with the aforementioned buffers. The 96-well plates were filled according to the following pipette scheme: 50 μL buffer, 25 μL tumor homogenate solution (1:10), shaking for 15 s, 25 μL ACC–tetrapeptide solution (1:200), shaking for 15 s. The fluorescence increase (Ex.: 355 nm, Em.: 460 nm) over a 1 h period was determined at room temperature with a Wallac VICTOR V^2 1420 plate reader.

Synthesis of EMC-Arg-Arg-Ala-Phe-Met-Ala-CPT × 2 TFA (1). HATU (24.2 mg, 0.064 mmol) was added under a nitrogen atmosphere to a solution of camptothecin-20-*O*-(L-alaninate) × TFA (30.8 mg, 0.058 mmol), EMC-Arg-Arg-Ala-Phe-Met-OH × 2 TFA (70 mg, 0.064 mmol), and DIEA (39.9 μL, 0.231 mmol) in 1 mL DMF. The solution was stirred for 1 h at room temperature. Subsequently, the product was precipitated with diethyl ether and purified by preparative C_{18}-RP-HPLC chromatography. Preparative chromatography was carried out on a Nucleosil C18 column (100–7, 250 × 21 mm) with precolumn (100–7, 50 × 21 mm) from Macherey-Nagel. Chromatographic conditions are as follows: flow, 10.0 mL/min; mobile phase A, 30% MeCN, 70% demin. H_2O, 0.1% TFA; mobile phase B, 50% MeCN, 50% demin. H_2O, 0.1% TFA; gradient, 0–43 min 0% to 100% mobile phase B; 43–53 min 100% mobile phase B isocrat.; 53–63 min 0% to 100% mobile phase A; injection volume, 500–1000 μL. After lyophilization, 34 mg (39.6%) of the parent compound was obtained as a bright yellow solid.

ESI-MS dir-pos. (5.0 kV, MeOH): *m*/*z* (%) 1274.3 ($[M]^+$, 100), 1275.4 ($[M + H]^+$, 61) (mass spectrum is included as Supporting Information). HPLC purity (λ = 370 nm): >95%.

Synthesis of the EMC-Arg-Arg-Phe-Tyr-Met-OH Linker. The synthesis of the linker was performed on solid phase using methionine-preloaded Wang resin as the solid support. The Fmoc-amino acids were sequentially coupled following a standard Fmoc protocol (*29*). In a final step, 6-maleimidocaproic acid (EMC: 3.01 g, 14.25 mmol) was dissolved in DMF, and 10 equiv of HOBt and 10 equiv of DIPC were added. After preincubation for 2 min, the solution was added to the reaction vessel containing the resin (total volume of DMF: 25 mL). Afterwards, the resin was treated with a mixture of TFA/water 95:5 (v/v) for 2 h. The resin was separated by filtration, and the filtrate was evaporated three times after addition of 10 mL of ethanol before the residue was dried in high vacuum. 1.624 g of a crude product was obtained. The crude product was dissolved in 15 mL of anhydrous methanol and precipitated with 200 mL anhydrous diethylether, then centrifuged and washed with anhydrous diethyl ether. This purification step yielded 600 mg of an off-white solid. Further purification was achieved by preparative C_{18}-RP-HPLC chromatography. Preparative chromatography was carried out on a Nucleosil C18 column (100–7, 250 × 21 mm) with precolumn (100–7, 50 × 21 mm) from Macherey-Nagel. Chromatographic conditions are as follows: flow, 10.0 mL/min (0–26 min) and 15.0 mL/min (26–57 min); mobile phase A, 10% MeCN, 90% demin H_2O, 0.1% TFA; mobile phase B, 40% MeCN, 60% demin H_2O, 0.1% TFA; gradient, 0–26 min, 100% mobile phase A isocrat.; 26–36 min, 0%–100% mobile phase B; 36–46 min, 100% mobile phase B isocrat.; 46–55 min, 0%–100% mobile phase A; 55–57 min, 100% mobile phase A isocrat.; injection volume, 5 mL. After lyophilization, 243 mg of the parent compound was obtained as a white solid.

ESI-MS dir-pos. (2.5 kV, MeOH): *m*/*z* (%) 965.3 ($[M + H]^+$, 100); HPLC purity (λ = 220 nm): ~98%.

Synthesis of EMC-Arg-Arg-Phe-Tyr-Met-Ala-CPT × 2 TFA (2). HATU (15.5 mg, 0.054 mmol) was added under a nitrogen atmosphere to a solution of camptothecin-20-*O*-(L-alaninate) × TFA (19.8 mg, 0.049 mmol), EMC-Arg-Arg-Phe-Tyr-Met-OH × 2 TFA (65 mg, 0.054 mmol) and DIEA (25.5 μL, 0.198 mmol) in 1 mL DMF. The solution was stirred for 1 h at room temperature. Subsequently, the product was precipitated with diethyl ether, and the crude product was purified by preparative chromatography. Preparative chromatography was carried out in analogy to the isolation of **1**. After lyophilization, 26.3 mg (33.7%) of **2** was obtained as a bright yellow solid.

ESI-MS dir-pos (5.0 kV, 30% MeOH): *m*/*z* (%) 1366.4 ($[M]^+$, 100), 1367.4 ($[M + H]^+$, 70) (mass spectrum is included as Supporting Information); HPLC purity (λ = 370 nm): >95%.

Synthesis of the Albumin Conjugates of 1 (HSA-1) and 2 (HSA-2). 1.5 mg of the albumin-binding prodrug was dissolved in 2 mL of a 5% solution of human serum albumin (HSA) (~100 mg of albumin) and incubated under stirring at 37 °C for 1 h after which no free **1** or **2** was detectable. The HPLC method to determine that the reaction was completed is available as Supporting Information. The sample was kept frozen at −20 °C and thawed prior to use.

Incubation Studies of 1 and 2 with Mouse Blood Plasma. 0.75 mg of the albumin-binding prodrugs were dissolved in 100 μL of sterile-filtered glucose–phosphate buffer (10 mM sodium phosphate/5% D-glucose buffer, pH 5.8). 30 μL aliquots of these solutions were added immediately to 570 μL of mouse plasma (gratefully received from Dr. N. Esser, Tumor Biology Center, Freiburg) and incubated at 37 °C. Samples were collected after 5 min, 4 h, 8 h, and 24 h and were analyzed by HPLC. The decrease in the peak area of the conjugates at 370 nm over time was used to determine the half-lives.

Incubation Studies of HSA-1 and HSA-2 with Tissue Homogenates. 300 μL aliquots of the **HSA-1** and **HSA-2** stock solutions (500 μM) were mixed with 150 μL of TEAA buffer (20 mM, pH 7.4 and pH 5.0) and 150 μL of tissue homogenate (pH 7.4 and pH 5.0). The samples were incubated at 37 °C for 5 min, 4 h, and 24 h and were analyzed by HPLC. 150 μL of the 4 h and 24 h HT-29 samples were kept frozen at −20 °C and thawed prior to analysis by LC-MS spectrometry.

***In Vivo* Efficacy of 1.** For the *in vivo* testing of **1** in comparison with its parent compound, female NMRI: nu/nu mice (inhouse breeding) were used. The mice were held in individually ventilaged cages under sterile and standardized environmental conditions (25 ± 2 °C room temperature, 50 ± 10% relative humidity, 12 h light–dark rhythm). They received autoclaved food and bedding (ssniff, Soest, Germany) and acidified (pH 4.0) drinking water *ad libitum*. All animal experiments were performed under the auspices of the German Animal Protection Law.

10^7 cells of HT-29 were transplanted subcutaneously (s.c.) into the left flank region of anaesthetized (40 mg/kg i.p. Radenarkon, Asta Medica, Frankfurt, Germany) mice on day zero. Mice were randomly distributed to the experimental groups (6 mice per group). When the tumors were grown to a palpable size (90–130 mm^3), treatment was initiated. HT-29 xenografted mice were treated intravenously at day 6, 13, and 20 with 10 mM sodium phosphate/5% D-glucose buffer pH 5.8, camptothecin, or **1** (compound was administered as a solution in 10 mM sodium phosphate/5% D-glucose buffer pH 5.8); for doses, see corresponding tables and figures. The volume of administration was 0.20 mL/20 g body weight.

Tumor size was measured twice weekly with a caliper-like instrument in two dimensions. Individual tumor volumes (V) were calculated by the formula $V = (\text{length} + [\text{width}]^2)/2$ and related to the values on the first day of treatment (relative tumor volume, RTV). At each measurement day, treated/control values (T/C) were calculated as percentage for each experimental group; the optimum (lowest) values obtained within four weeks after treatment were used for evaluating the efficacy of the compounds, and optimum T/C values are presented in the respective tables. Statistical analysis was performed with the U-test (Mann and Whitney) with $p < 0.05$. The body weights of mice were determined every 3 to 4 days.

RESULTS

Positional Scanning Library. The first aim of our work was to assess the proteolytic activity and specificity of selected native tumor tissue homogenates. Generally, for analyzing the substrate specificity of proteases, two different combinatorial strategies have been followed in the past:

1. Fluorogenic libraries of resin-bound peptides (one bead—one peptide) are screened with enzymes. Subsequent Edman degradation or mass spectrometry of selected hits provides exact information about the peptide sequence (*33*).

2. Fluorogenic libraries consist of a defined number of nonimmobilized sublibraries, each having one position fixed with one amino acid while all other positions are randomized (positional scanning (PS) libraries). Incubation of sublibraries with proteases and subsequent measuring of fluorescence provides information on the extent to which a single amino acid in a defined position influences the cleavage rate.

Although screening proteases using the first strategy results in exact information, i.e., concrete peptide sequences which are cleaved by the target enzymes, the selection and analysis of hits is extremely time-consuming when assessing combinatorial peptides consisting of more than two amino acids and becomes nearly impossible when the number of amino acids exceeds four. In contrast, positional scanning—once the library is established—can be easily performed with high throughput and low cost. In addition, positional scanning has the advantage that cleavage studies can be carried out in solution, which allows a kinetic determination of proteolytic processes.

Previously, fluorogenic PS-libraries have been successfully employed to explore the substrate specificity of a variety of proteases (*26, 27, 34, 35*). In our work, we synthesized a tetrapeptide PS-library based on 7-amino-4-carbamoylmethylcoumarin (ACC) as the fluorophor in accordance with a published procedure (*27*). Peptides were built up on solid phase (Rink amide resin) in five subsequent coupling steps: first the dye and then four amino acids were bound to the resin following straightforward Fmoc chemistry. For the randomized positions, an isokinetic mixture of Fmoc-protected amino acids was employed to ensure an even distribution (*30*). In order to provide sufficient structural diversity, we employed all standard amino acids except for tryptophane and cysteine. Hence, after cleaving the peptides from the resin, we obtained 4 × 18 sublibraries each having one position fixed. For instance, 18 sublibraries were obtained comprising the general formula *Xxx*-*Yyy*-*Zzz*-P_1-ACC (P_1-library) with P_1 fixed and positions *Xxx*, *Yyy*, and *Zzz* randomized.

Once the bond between the first amino acid (in position P_1) and the ACC dye is cleaved, a significant increase in fluorescence is observed. Therefore, ACC peptides can serve as model compounds for prodrugs in which peptides are bound to drugs via an amide bond.

Incubation Studies of Different Tumor Homogenates and Tissue Homogenates of Healthy Organs with the PS Library. In a first step, the PS-library was used to study the protease specificity of native tumor tissue. For this purpose, tissue material of four different colon tumors (xenografts of HT-29, 5735, 5854, and 5679) was homogenized according to two different protocols (*31, 32*): while homogenization at pH 5.0 was assumed to preserve activity of lysosomal proteases, a workup at pH 7.4 was performed to target extracellular enzymes.

Figure 1A,B shows the relative increase in fluorescence (F_{1h}/F_{0h}) of the peptide libraries P_1–P_4 after a 1 h incubation with the colon tumor homogenates at pH 7.4 and pH 5.0, respectively. On first inspection, all tissue samples exhibited significant proteolytic activity with the homogenates at pH 7.4 being more active than at pH 5.0. Furthermore, the selectivity of the libraries decreased from P_1 to P_4, and for the positions P_3 and P_4 at pH 5.0, it was not possible to identify specific amino acids that have a positive influence on the cleavage rate. Among the tested colon tumor samples, no significant differences in the overall cleavage profiles were noted, but there were differences in the absolute fluorescence values; e.g., HT-29 and 5735 showed a notably stronger increase in fluorescence than the other tested colon tumor samples within the P_3 and P_4 libraries at pH 7.4.

For P_1 and P_2, a clear preference for the following amino acids can be stated at both pH values:

pH 7.4. P_1: methionine, lysine, and leucine. P_2: tyrosine, methionine, and phenylalanine.

pH 5.0. P_1: methionine, leucine, and tyrosine. P_2: methionine.

This selection is based on an increase in the relative fluorescence value of >3 for P_1 and P_2 at pH 7.4 (Figure 1A) and an increase in the relative fluorescence value of >1.5 for P_1 and P_2 at pH 5.0 (Figure 1B) that was defined as to be able to score amino acids that promote cleavage.

For P_3 and P_4, however, the cleavage profiles are less characteristic. While no preferred amino acid can be identified in these positions at pH 5.0, a marginal positive influence on the cleavage rate for tyrosine, phenylalanine, methionine, and alanine for the P_3-position and for arginine, leucine, methionine, tyrosine, and lysine for P_4 is noted at pH 7.4.

In order to discover whether the cleavage profiles are colon tumor specific, the PS-library was additionally incubated with four different breast carcinoma samples (MCF-7, MDA-MB 435, Breast 6661, Breast 3366) at pH 7.4. The results of this experiment are depicted in Figure 2. On the whole, the cleavage profiles obtained from incubation with these homogenates revealed similar amino acid preferences compared to those of colon tumor homogenates.

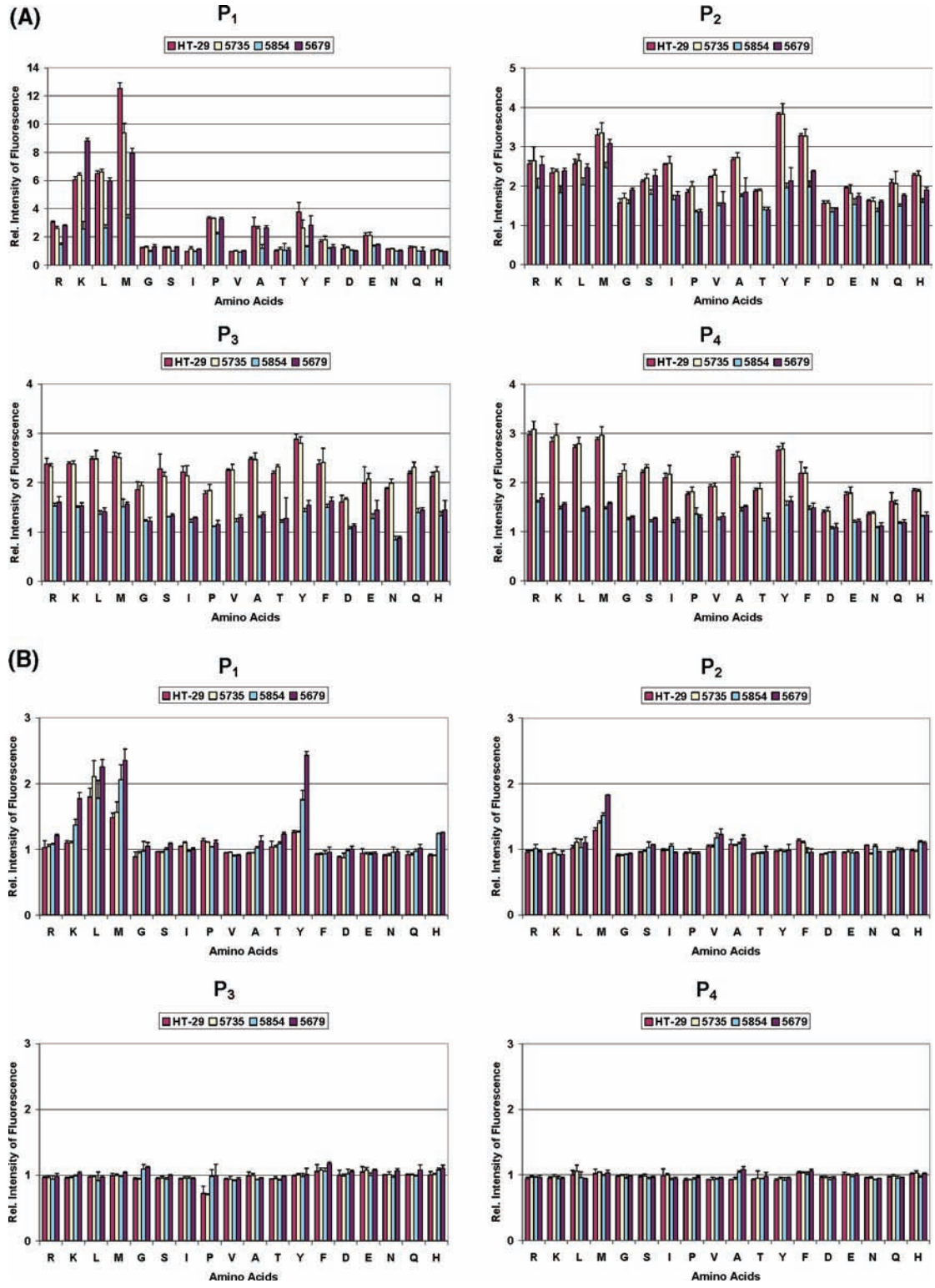


Figure 1. (A) Charts of the P_1–P_4 -libraries incubated with different colon tumor tissue homogenates at pH 7.4. The histograms show the relative increase in fluorescence (F_{1h}/F_{0h}) of the peptide libraries P_1–P_4 after a 1 h incubation with four different colon tumor homogenates at pH 7.4. (number of measurements: $n = 4$). (B) Charts of the P_1–P_4 -libraries incubated with different colon tumor tissue homogenates at pH 5.0. The histograms show the relative increase in fluorescence (F_{1h}/F_{0h}) of the peptide libraries P_1–P_4 after a 1 h incubation with four different colon tumor homogenates at pH 5.0. (number of measurements: $n = 4$.)

To elucidate the ACC–peptides' stability in blood plasma, analogous incubation experiments with the PS libraries P_1–P_4 were carried out using human blood plasma at pH 7.4. The charts in Figure 3 show that no noteworthy increase in fluorescence with human plasma is detected. Hence, in contrast to tumor tissue, the proteolytic activity of plasma seems to be negligible after a 1 h incubation with the library.

Finally, we investigated the proteolytic activity of healthy organs (liver, kidney, and spleen from nude mice). The PS-library was incubated with tissue homogenate samples at pH 5.0 and pH 7.4 (Figures 4 and 5).

At pH 7.4, the cleavage profile was quite similar to that of tumor homogenates with a preference for methionine, lysine, leucine, and additionally alanine in P_1, tyrosine in P_2, and a

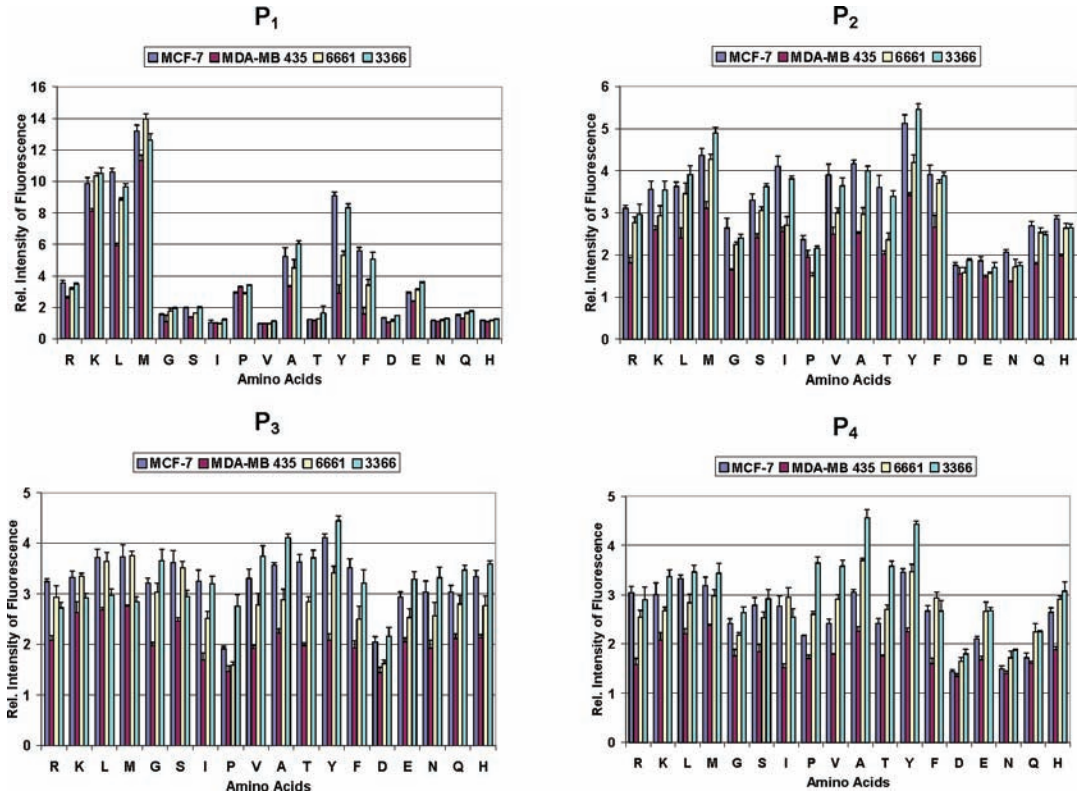


Figure 2. Charts of the P_1–P_4 -libraries incubated with different breast tumor tissue homogenates at pH 7.4. The histograms show the relative increase in fluorescence (F_{1h}/F_{0h}) of the peptide libraries P_1–P_4 after 1 h incubation with four different breast tumor homogenates at pH 7.4. (number of measurements: $n = 4$.)

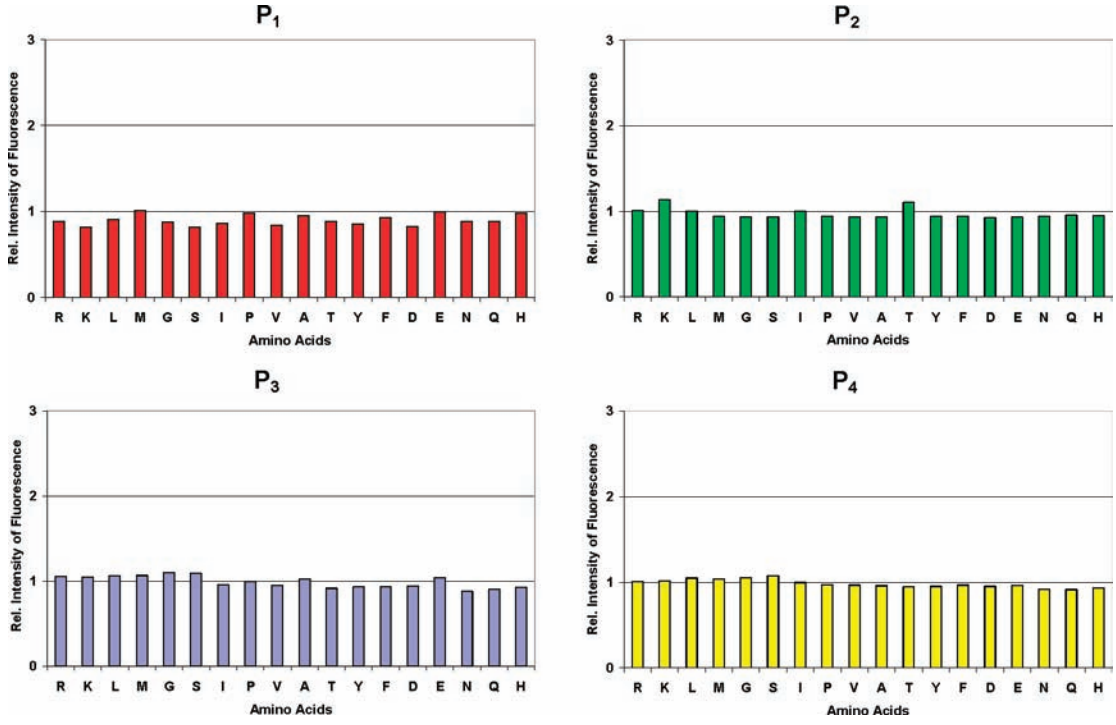


Figure 3. Charts of the P_1–P_4 -library incubated with human blood plasma at pH 7.4. The histograms show the relative increase in fluorescence (F_{1h}/F_{0h}) of the peptide libraries P_1–P_4 after 1 h incubation with human blood plasma at pH 7.4. (number of measurements: $n = 4$.)

less clear picture for P_3 and P_4 (Figure 4). As an exception, the cleavage pattern obtained with kidney homogenate differed markedly from those of liver and spleen. A pronounced cleavage was detected for peptides having arginine, lysine, or glycine in P_1, whereas no clear preference could be seen in P_2–P_4. The overall increase in fluorescence for the P_3- and P_4-libraries was higher in the healthy organs compared to the colon tumor samples.

At pH 5.0, the overall increase in fluorescence was higher in the healthy organs compared to the tumor samples; incubation

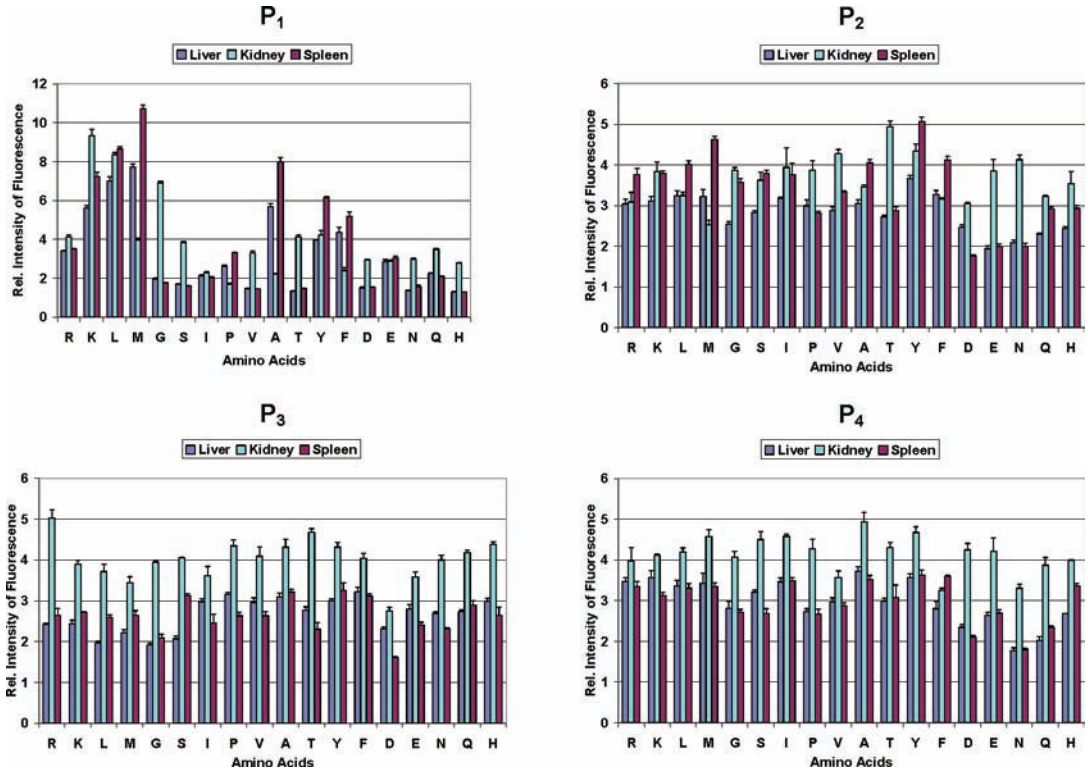


Figure 4. Charts of the P_1–P_4 -library incubated with healthy organs (liver, kidney, and spleen) from nude mice at pH 7.4. The histograms show the relative increase in fluorescence (F_{1h}/F_{0h}) of the peptide libraries P_1–P_4 after 1 h incubation with homogenates of murine healthy organs at pH 7.4. (number of measurements: $n = 4$.)

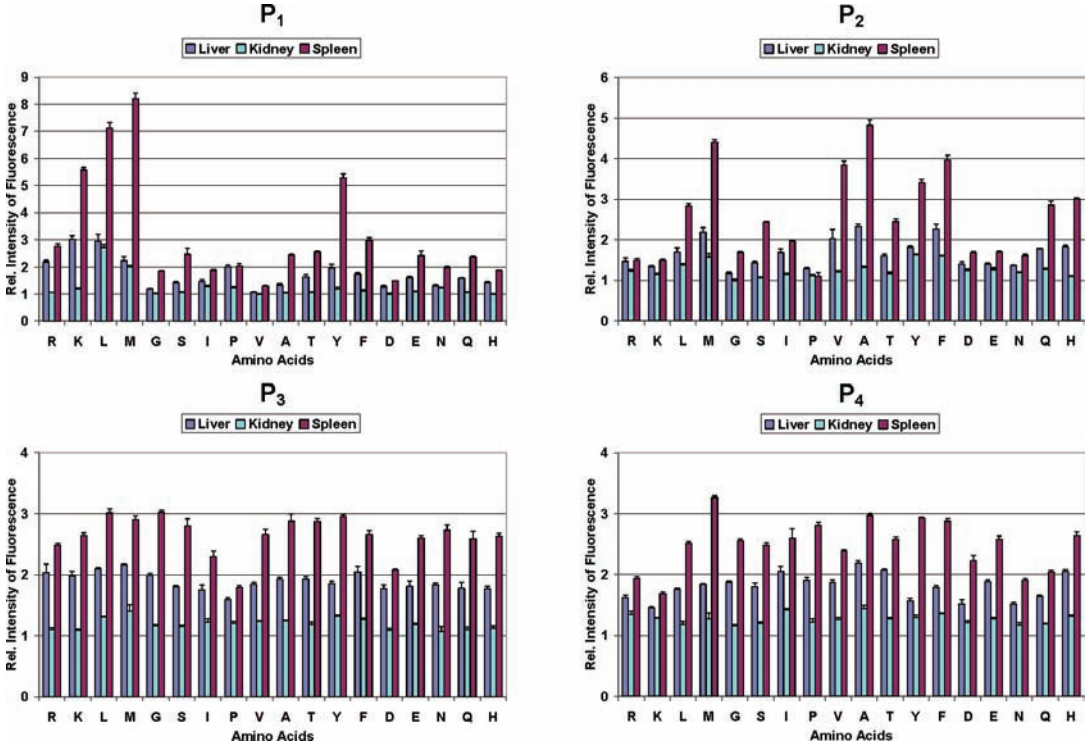
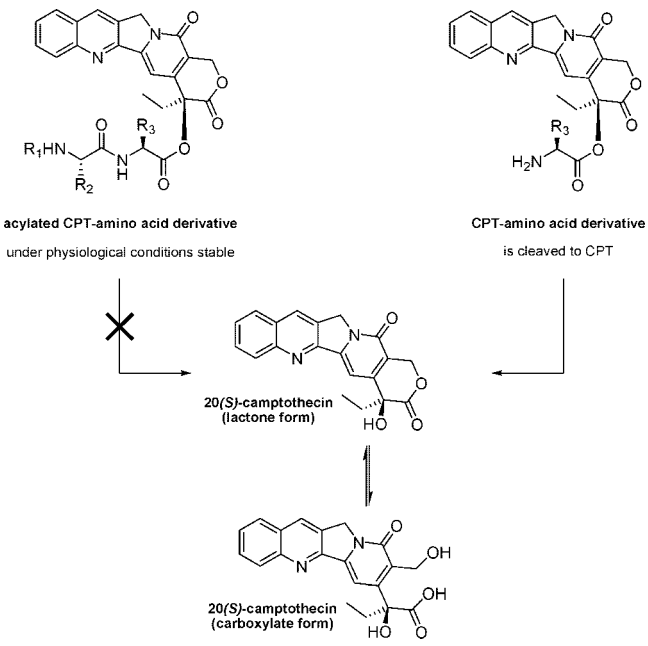


Figure 5. Charts of the P_1–P_4 -library cleaved by healthy organs (liver, kidney, and spleen) from nude mice at pH 5.0. The histograms show the relative increase in fluorescence (F_{1h}/F_{0h}) of the peptide libraries P_1–P_4 after 1 h incubation with homogenates of murine healthy organs at pH 5.0. (number of measurements: $n = 4$.)

studies with spleen homogenate showed the largest increase in fluorescence. For spleen and liver homogenates, a preference for methionine, lysine, leucine, and tyrosine in P_1 and for methionine, valine, alanine, tyrosine, and phenylalanaine in P_2 can be discerned. Incubation studies with kidney homogenates showed a less characteristic picture.

In summary, the cleavage profiles of homogenates from human breast tumors, human colon tumors, and murine organs

Scheme 1. Release of Camptothecin from CPT–Amino Acid Esters

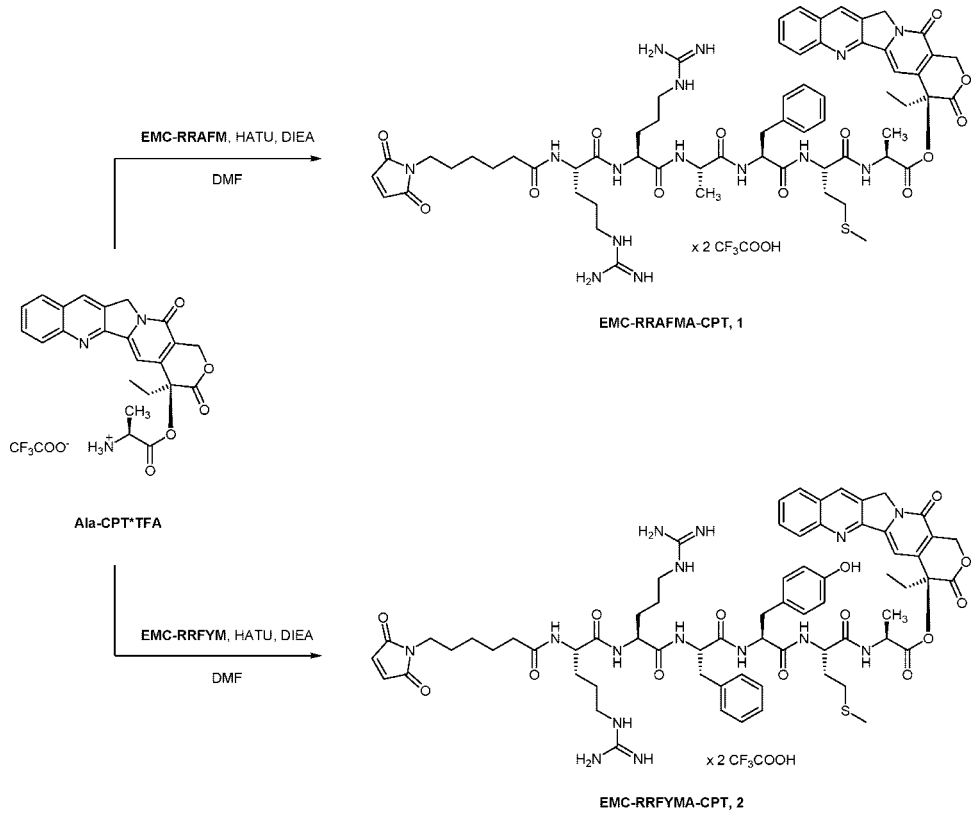


were generally quite similar; albeit, a noteworthy exception was found after incubation with kidney homogenate at pH 7.4. When selecting a peptide sequence that would act as an efficient protease substrate in the prodrugs, we opted to choose and combine those amino acids with a high increase in fluorescence. This was methionine in the P_1-position, either tyrosine or the related phenylalanine in the P_2-position, alanine or phenylalanine the P_3-position, and arginine in the P_4-position, with the latter being chosen to enhance the water solubility of the prodrugs. The syntheses of two prodrugs with camptothecin incorporating the peptide sequences Arg-Ala-Phe-Met or Arg-Phe-Tyr-Met are described below.

Synthesis of the Camptothecin Prodrugs 1 and 2. Camptothecin (CPT), a pentacyclic alkaloid isolated from a Chinese tree, was chosen for the development of albumin-binding prodrugs incorporating the two aforementioned peptide sequences as enzymatically cleavable spacers. Although highly cytotoxic, CPT has not gained any clinical relevance due to its poor water solubility (2.5 μg/mL) (*22*), whereas the hydrophilic derivatives Topotecan and Irinotecan are meanwhile approved for the treatment of colorectal, lung, and ovarian carcinomas. To improve the water solubility and efficacy of CPT, a poly(ethylene glycol) conjugate of CPT (Prothecan) was developed that is currently undergoing phase II clinical trials (*36*). In this macromolecular prodrug, CPT is bound through an alanine spacer to the polymer. Generally, it could be shown that incorporating amino acids between the carrier and CPT turned out to be beneficial for the following reasons (*37*): (a) The ester bond between the amino acid and CPT is relatively stable under physiological conditions as long as the amino acid remains acylated (Scheme 1) (*38*); (b) once the amide bond between the carrier and the amino acid spacer is cleaved, the ester bond between the amino acid and CPT hydrolyzes spontaneously, liberating CPT in its active and less toxic lactone form. However, this in theory simple reaction proved to be quite complex, as previous mechanistic studies on the hydrolysis of H-Gly CPT revealed (*39, 40*).

In our work, we chose to incorporate an alanine spacer between the peptide linker and the drug. Hence, C-terminal cleavage of the peptides results in the release of H-Ala-CPT, which further decomposes to alanine and the free drug. For the synthesis of the albumin-binding prodrugs **1** and **2**, the maleimide-bearing peptides EMC-Arg-Arg-Ala-Phe-Met-OH and EMC-Arg-Arg-Phe-Tyr-Met-OH were reacted with camptothecin-20-*O*-(L-alaninate) (Scheme 2). The latter was readily prepared by a published two-step procedure, in which the first

Scheme 2. Synthesis of the Albumin-Binding CPT Prodrugs 1and 2



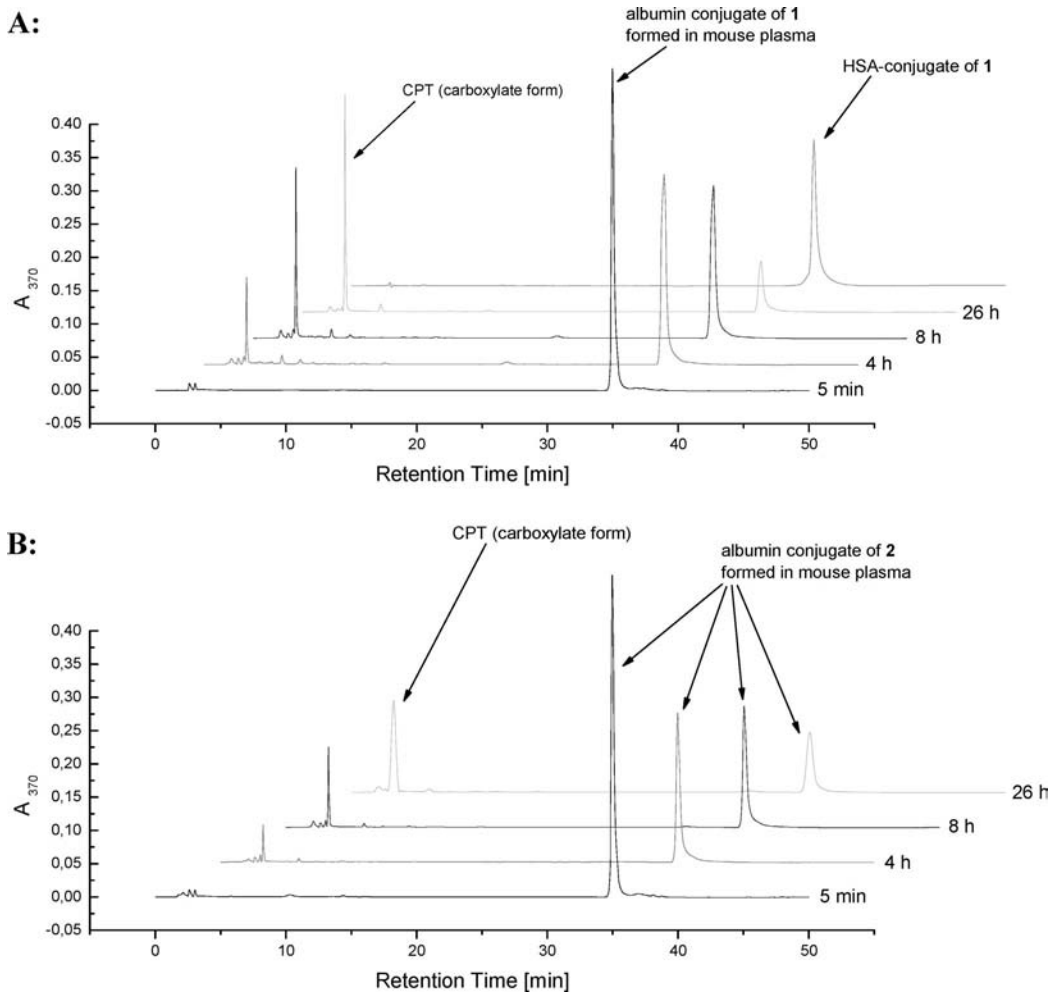


Figure 6. (A,B) Chromatograms of incubation studies of mouse blood plasma after 5 min, 4 h, 8 h, and 26 h with prodrugs **1** (A) and **2** (B) at 37 °C. The chromatograms show the stability of the albumin conjugate of prodrugs **1** and **2** over time, to determine the respective plasma half-lives. In addition, the chromatogram of the HSA-conjugate of **1** is displayed. For chromatographic conditions, see Supporting Information.

step was a stereoselective acylation of 20-(*S*)-camptothecin (*25*). Condensation of camptothecin-20-*O*-(L-alaninate) with the maleimide-bearing peptides was carried out using HATU as the coupling agent. The two prodrugs EMC-Arg-Arg-Ala-Phe-Met-Ala-CPT (**1**) and EMC-Arg-Arg-Phe-Tyr-Met-Ala-CPT (**2**) were purified by preparative HPLC and characterized by mass spectrometry. The incorporation of two arginine moieties in the peptide chain of the linkers of **1** and **2** resulted in excellent solubility in buffer solution (>7 mg/mL), while the parent compound is almost insoluble (CPT: 2.5 μg/mL).

Albumin-Binding Properties and Stability of 1 and 2. In order to show that the prodrugs **1** and **2** bind rapidly and selectively to endogenous serum albumin, incubation with mouse plasma at 37 °C was performed for 5 min and HPLC profiles recorded at $\lambda = 370$ nm, the maximum absorbance of CPT derivatives in the near-UV region.

Figures S1 and S2 in the Supporting Information show the chromatographic profiles of **1** and **2** incubated with mouse blood plasma after 5 min ($\lambda = 370$ nm). While the free prodrugs elute at ~9 min (**1**) and ~11 min (**2**), the signals disappeared almost completely after incubation with mouse plasma, and a single peak eluting at the retention time of mouse serum albumin (MSA) (33–37 min) was observed.

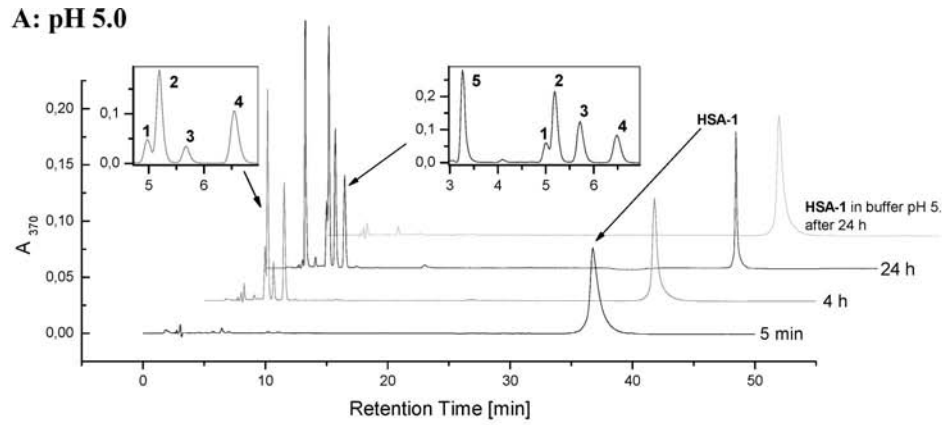
In order to prove that the fast binding results from a Michael addition of the sulfhydryl group of MSA with the maleimide group of the prodrugs, analogous HPLC experiments were carried out in which the cysteine-34 position of MSA was blocked with an excess of ϵ-maleimidocaproic acid (EMC) prior to incubation with **1** and **2** (see Figures S1 and S2 in the Supporting Information). In this case, marginal binding to MSA was observed after incubating plasma with **1** and **2** for 10 min.

This observation is in accordance with our previous work on albumin-binding prodrugs with doxorubicin, camptothecin, and platinum derivatives where we have shown that albumin binding results from a Michael addition between the maleimide group and sulfhydryl group of the cysteine-34 position of serum albumin (*3*, *4*, *8–10*, *41*, *42*).

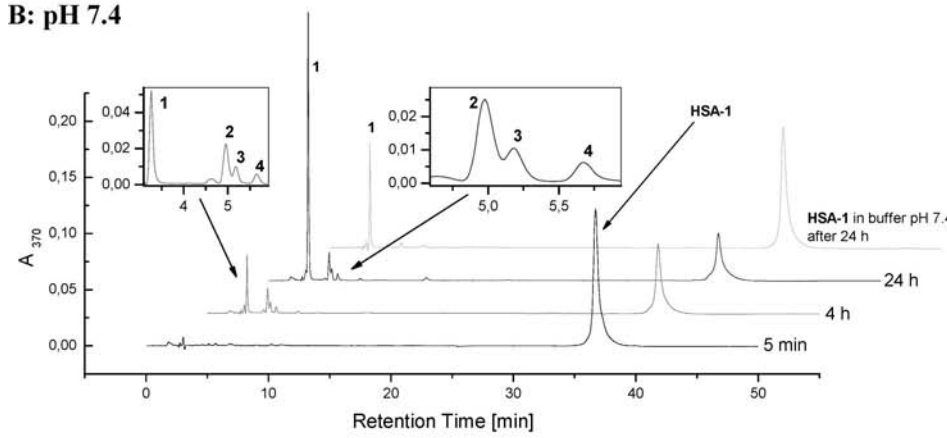
In order to determine the plasma stability of the compounds **1** and **2** bound to albumin, plasma samples with **1** and **2** were analyzed at further time points (4 h, 8 h, and 26 h) by HPLC (Figure 6A,B) in order to obtain a first estimate of their plasma stability. From the decrease of the peak areas of the albumin conjugates of **1** and **2**, the half-lives were approximately $t_{1/2} \sim$ 26 h (**1**) and $t_{1/2} \sim 25$ h (**2**).

Cleavage of HSA-1 and HSA-2 after Incubation with HT-29 Colon Tumor Homogenate and Tissue Homogenates of Healthy Murine Organs (Liver, Kidney, and Spleen). The cleavage properties of the albumin-bound form of **1** and **2** (**HSA-1** and **HSA-2**) were studied in HT-29 colon tumor homogenates at pH 7.4 and 5.0 (Figure 7A,B and Figure 8A,B).

Additionally, buffer stabilities (TEAA, 20 mM) of the albumin conjugates at pH 7.4 and pH 5.0 over 24 h were assessed, demonstrating that a certain degree of unspecific hydrolysis takes place: degradation at pH 7.4 for **HSA-1** <15% and for **HSA-2** <20%; degradation for **HSA-1** and **HSA-2** at pH 5.0 <5%. However, cleavage of **HSA-1** and **HSA-2** in the



Peak number	Retention time [min]	Observed fragment ions [*m/z*]	Peak assignment
1	4.99	589.0 $[M + Na]^+$	H-Met(O)-Ala-CPT
2	5.20	441.9 $[M + Na]^+$, 331.2 [– alanine]$^+$, 303.1 [– alanine – CO]$^+$	H-Ala-CPT
3	5.67	349.1 $[M + H]^+$, 305.1 $[M + H - CO_2]^+$	CPT lactone
4	6.55	573.0 $[M + Na]^+$	H-Met-Ala-CPT
5	3.21	349.1 $[M + H]^+$	CPT carboxylate

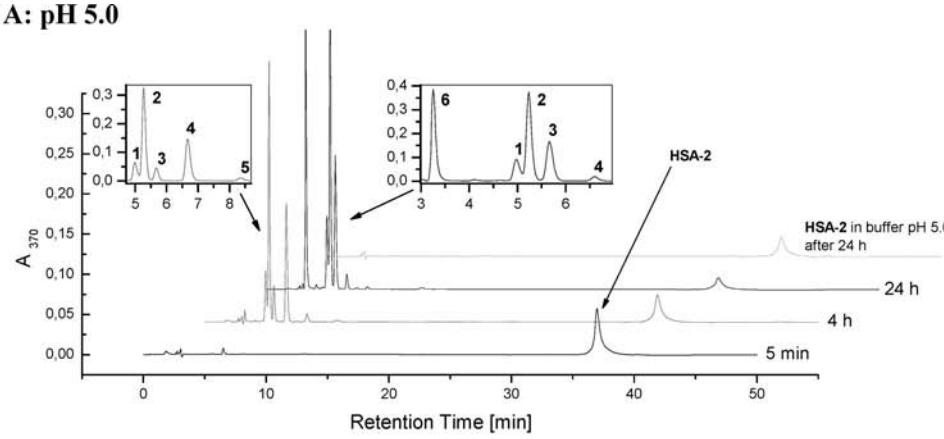


Peak number	Retention time [min]	Observed fragment ions [*m/z*]	Peak assignment
1	3.26	349.1 $[M + H]^+$	CPT carboxylate
2	4.97	589.0 $[M + Na]^+$	H-Met(O)-Ala-CPT
3	5.21	441.9 $[M + Na]^+$, 331.2 [– alanine]$^+$, 303.1 [– alanine – CO]$^+$	H-Ala-CPT
4	5.68	349.1 $[M + H]^+$, 305.1 $[M + H - CO_2]^+$	CPT lactone

Figure 7. (A,B) Chromatograms of incubation studies of the albumin conjugate of prodrug **1** (**HSA-1**) with HT-29 colon tumor homogenate at pH 5.0 (A) and pH 7.4 (B) after 5 min, 4 h, and 24 h at 37 °C. The chromatograms show the enzymatical degradation of **HSA-1** in colon tumor homogenate. The several clustered peaks are highlighted separately and the cleavage products were analyzed via LC-MS. In addition, the chromatograms of **HSA-1** after 24 h in buffer solution pH 5.0 and pH 7.4, respectively, are displayed.

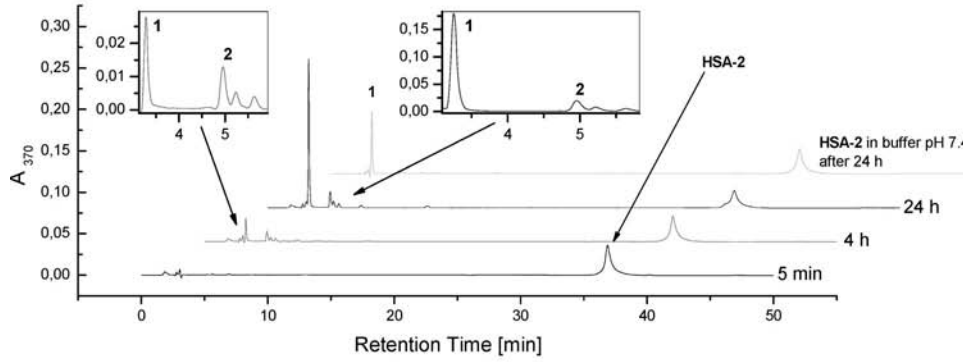
tumor homogenates is more pronounced and specific (Figures 7A,B and 8A,B). The different cleavage products were identified by LC-MS (Figure S7 in Supporting Information) and by use of CPT and CPT-Ala-OH standards. Unfortunately, the HPLC method used for incubation studies could not be transferred one-to-one to the LC-MS investigations. Therefore, the cleavage products could not be identified by retention times but by their peak areas and by the use of reference compounds. For the cleavage of **HSA-1** at pH 7.4, CPT in its hydroxycarboxylate form (as the main product) and in its lactone form as well as H-Met(O)-Ala-CPT (with oxidized methionine) were identified. In contrast, cleavage with HT-29 colon tumor homogenate at pH 5.0 led to a more complex degradation of the albumin conjugate. The identified cleavage products at pH 5.0 were CPT

A: pH 5.0



Peak number	Retention time [min]	Observed fragment ions [*m/z*]	Peak assignment
1	5.03	589.0 $[M + Na]^+$	H-Met(O)-Ala-CPT
2	5.26	441.9 $[M + Na]^+$, 331.2 [– alanine]$^+$, 303.1 [– alanine – CO]$^+$	H-Ala-CPT
3	5.71	349.1 $[M + H]^+$, 305.1 $[M + H - CO_2]^+$	CPT lactone
4	6.64	573.0 $[M + Na]^+$	H-Met-Ala-CPT
5	8.34	736.1 $[M + Na]^+$	H-Tyr-Met-Ala-CPT
6	3.25	349.1 $[M + H]^+$	CPT carboxylate

B: pH 7.4



Peak number	Retention time [min]	Observed fragment ions [*m/z*]	Peak assignment
1	3.25	349.1 $[M + H]^+$	CPT carboxylate
2	4.94	589.0 $[M + Na]^+$	H-Met(O)-Ala-CPT

Figure 8. (A,B) Chromatograms of incubation studies of the albumin conjugate of **2** (**HSA-2**) with HT-29 colon tumor homogenate at pH 5.0 (A) and pH 7.4 (B) after 5 min, 4 h, and 24 h at 37 °C. The chromatograms show the enzymatical degradation of **HSA-2** in colon tumor homogenate. The several clustered peaks are highlighted separately and the cleavage products were analyzed via LC-MS. In addition, the chromatograms of **HSA-2** after 24 h in buffer solution pH 5.0 and pH 7.4, respectively, are displayed.

in its hydroxycarboxylate form and H-Ala-CPT as the main products, and to a lesser extent CPT in its lactone form, H-Met-Ala-CPT and H-Met(O)-Ala-CPT. Overall, the degradation of **HSA-1** in HT-29 tumor homogenate over 24 h was: pH 7.4 >50% and pH 5.0 >70%.

After incubation of **HSA-2** with HT-29 colon tumor homogenate, a similar cleavage pattern was obtained. At pH 7.4, CPT in the carboxylate form (as the main product) and H-Met(O)-Ala-CPT were detected. Cleavage products at pH 5.0 were CPT in the carboxylate form and H-Ala-CPT as the main products, CPT in the lactone form, H-Met-Ala-CPT, H-Met(O)-Ala-CPT, and additionally H-Tyr-Met-Ala-CPT. For **HSA-2**, the following overall degradation in HT-29 tumor homogenate over 24 h could be determined: pH 7.4 >50%, pH 5.0 ~75%.

Interestingly, the cleavage profiles of both **HSA-1** and **HSA-2** at pH 7.4 showed H-Met-Ala-CPT, as well as H-Met(O)-Ala-CPT in which the thiol group of methionine is oxidized.

Table 1. Antitumor Activity of Prodrug 1 against Human Colorectal Xenografts (HT-29) *in Vivo*

compound	dose[a] [mg/kg]	total mortality	body weight change [%] (days 6–9)	*T*/*C* [%] maximal
CPT	3 × 12.5	0/6	−2	40 (day 22)
1	2 × 12.5	1/6 (day 13)	−1	17[b,c] (day 22)

[a] Dose refers to CPT equivalents. [b] Significant to buffer solution. [c] Significant to camptothecin.

Additional cleavage studies were carried out with **HSA-1** and tissue homogenates of healthy, murine organs (liver, kidney, and spleen) at pH 5.0. The cleavage profiles (see Supporting Information Figures S3, S4, and S5) were compared to those of the incubation study with **HSA-1** and HT-29 colon tumor homogenate at pH 5.0 (Figure 7A). The extent of the cleavage is comparable to the tumor homogenate study (overall degradation over 24 h ~75%). The strongest cleavage was obtained with spleen homogenate. Overall, the cleavage profiles are very similar to those of the tumor homogenate study, with the exception of a lower generation of CPT in the carboxylate form.

***In Vivo* Activity of 1.** The *in vivo* efficacy of **1** and CPT was assessed in xenografted nude mice using a human HT-29 colorectal cell line. CPT was evaluated at a dose of 3 × 12.5 mg/kg (i.v.) which was reported to be the maximum tolerated dose (MTD) for camptothecin in nude mice (*43*) and compared to prodrug **1** at the same dose of 3 × 12.5 mg/kg (i.v.) CPT equivalents. As a result of one toxic death that occurred after the second dose (day 13), a third dose of **1** was not administered. Table 1 and Figure 9 summarize the results of this experiment. Besides an acute toxicity, therapy with **1** produced no significant body weight loss (Figure S6 in Supporting Information). Whereas CPT (3 × 12.5 mg/kg) was moderately active (*T*/*C* max 40%), **1** exhibited superior antitumor activity at a lower dose of 2 × 12.5 mg/kg CPT equivalents (*T*/*C* max 17%).

DISCUSSION

In this work, we set out to discover new peptide sequences for the design of prodrugs that are effectively cleaved within the tumor and, if possible, cleaved tumor-selectively. For this purpose, we screened homogenates of native human tumors and healthy murine organs with a positional scanning library. Positional scanning libraries have previously been used to determine the substrate-specificity of proteases such as plasmin or thrombin (*27*) and more recently of cathepsins (*44*).

Although the number of studied biological samples was limited, a first and somewhat disappointing finding was the fact that the cleavage profiles of samples from human breast carcinoma, human colon carcinoma, and murine spleen, kidney, and liver were quite similar. A noteworthy observation is the preference of methionine in P_1, since this amino acid is mostly omitted in the development of peptide libraries and is not commonly found incorporated as an amino acid in protease substrates for ubiquitous enzymes.

Using positional scanning, we were not able to identify amino acids in P_3 and P_4 that had a significant impact on the cleavage rate. Possible explanations are that these positions are variable or the sensitivity of our assay was too low. In theory, a low sensitivity for P_3 and P_4 can result from a high selectivity for P_1 and P_2 due to the small number of cleavable combinations (percentage of all tetrapeptides with the appropriate P_1 and P_2 combinations). Hence, sensitivity for P_3 and P_4 might be improved by developing a new peptide library with fixed P_1 and P_2.

On the basis of the screening results, the selection of amino acids for developing camptothecin prodrugs was explorative in nature, with preference being given to those amino acids which had a significant impact on the cleavage rate at their respective positions.

The resulting prodrugs EMC-Arg-Arg-Ala-Phe-Met-Ala-CPT (**1**) and EMC-Arg-Arg-Phe-Tyr-Met-Ala-CPT (**2**) showed fast albumin binding, acceptable stability in mouse plasma, and a distinct cleavage profile at pH 5.0 and 7.4. Surprisingly, cleavage of the albumin conjugates of **1** and **2** in HT-29 tumor homogenates was far more pronounced at pH 5.0 than at pH 7.4, considering that the reverse order would have been expected on the basis of the results from the screening experiments with our fluorogenic library. Our incubation studies with tumor homogenate revealed that both peptide sequences were primarily cleaved at the scissile bonds in P_1 and P_2.

Results of in vivo studies in the HT-29 xenograft model were encouraging, since EMC-Arg-Arg-Ala-Phe-Met-Ala-CPT (**1**) showed significantly better antitumor activity than CPT at a lower dose. The incorporated peptide sequence in **1** cannot, however, be regarded as a colon tumor selective protease substrate, because a similar cleavage profile was observed with healthy murine organs.

Reasons for the lack of tumor selectivity are manifold: The most obvious explanation is that there are no relevant differences in the expression pattern of proteases between individual tumors and healthy organs that can be detected with any degree of sensitivity using a positional scanning library. A further reason for the lack of tumor selectivity could be that the overall cleavage profile is determined by ubiquitous proteases that

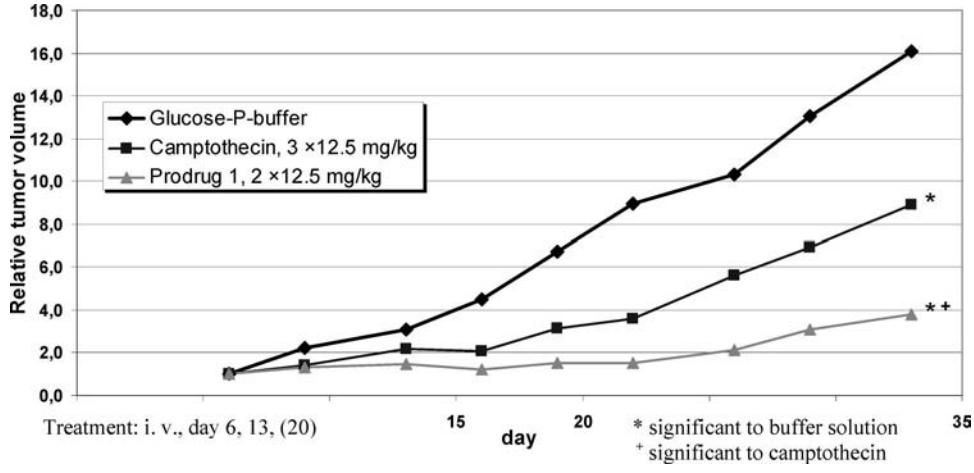


Figure 9. Curves depicting tumor growth inhibition of subcutaneous HT-29 xenografts under therapy with camptothecin and prodrug **1**. The dose of prodrug **1** is given as CPT equivalents. Camptothecin was adminstered at day 6, 13, and 20, whereas prodrug **1** was only administered at day 6 and 13.

overlay finer differences in the expression of proteases in healthy and malignant tissue. Another explanation could be that tumor-associated proteases are deactivated by inhibitors or during homogenate preparation.

An alternative strategy for the evaluation of tumor-selective protease activity would be to consider the cellular pathways for the uptake of macromolecular prodrugs in more detail. In contrast to low-molecular-weight drugs, macromolecular prodrugs are taken up by internalization via the endosomal/lysosomal pathway. As a consequence, assessing the proteolytic activity of pure lysosomal fractions of selected tumors and healthy organs could be an appropriate strategy for future trials in identifying truly tumor-specific peptide sequences.

In summary, we have shown that prodrugs incorporating the peptide sequences Arg-Ala-Phe-Met and Arg-Phe-Tyr-Met that were selected from screening a positional scanning library with colon tumor homogenates were efficiently cleaved in their albumin-bound form after exposure to the initially used colon tumor homogenate. In addition, the antitumor efficacy of prodrug **1** with the Arg-Ala-Phe-Met linker was superior to free camptothecin. However, this sequence is not cleaved selectively in HT-29 colon tumors. It cannot be ruled out that esterases in the acidic milieu of the tumor tissue might be responsible for the cleavage of the ester bond between CPT and the peptide linker and lead to the release of the active compound at the tumor site. The improved activity of the prodrug in comparison to free CPT is presumably based on the much longer circulation of the macromolecular prodrug in the bloodstream due to reduced renal excretion associated with accumulation in the tumor mediated by the EPR effect. Subsequently, the albumin conjugate enters the tumor cell via the endosomal/lysosomal pathway and is presumably enzymatically cleaved to the active lactone form of CPT in the acidic environment of the lysosomes. In contrast, under physiological conditions the major part of free CPT is available in its inactive hydroxycarboxylate form and is rapidly excreted via the kidney.

ACKNOWLEDGMENT

The support of the Wilhelm Sander-Stiftung, Germany, is gratefully acknowledged. We wish to thank Peter Lazar for carrying out the peptide syntheses and Christoph Warth for performing the LC-MS experiments.

Supporting Information Available: Additional experimental data and spectra as described in the text. This material is available free of charge via the Internet at http://pubs.acs.org.

LITERATURE CITED

(1) Matsumura, Y., and Maeda, H. (1986) A new concept for macromolecular therapeutics in cancer chemotherapy: mechanism of tumoritropic accumulation of proteins and the antitumor agent smancs. *Cancer Res. 46*, 6387–6392.

(2) Haag, R., and Kratz, F. (2006) Polymer therapeutics: concepts and applications. *Angew. Chem., Int. Ed. Engl. 45*, 1198–1215.

(3) Kratz, F., Warnecke, A., Scheuermann, K., Stockmar, C., Schwab, J., Lazar, P., Drückes, P., Esser, N., Drevs, J., Rognan, D., Bissantz, C., Hinderling, C., Folkers, G., Fichtner, I., and Unger, C. (2002) Probing the cysteine-34 position of endogenous serum albumin with thiol-binding doxorubicin derivatives: improved efficacy of an acid-sensitive doxorubicin derivative with specific albumin-binding properties compared to that of the parent compound. *J. Med. Chem. 45*, 5523–5533.

(4) Kratz, F., Muller-Driver, R., Hofmann, I., Drevs, J., and Unger, C. (2000) A novel macromolecular prodrug concept exploiting endogenous serum albumin as a drug carrier for cancer chemotherapy. *J. Med. Chem. 43*, 1253–1256.

(5) Kratz, F., Warnecke, A., Scheuermann, K., Stockmar, C., Schwab, J., Lazar, P., Drückes, P., Esser, N., Drevs, J., Rognan, D., Bissantz, C., Hinderling, C., Folkers, G., Fichtner, I., and Unger, C. (2002) Probing the cysteine-34 position of endogenous serum albumin with thiol-binding doxorubicin derivatives. Improved efficacy of an acid-sensitive doxorubicin derivative with specific albumin-binding properties compared to that of the parent compound. *J. Med. Chem. 45*, 5523–5533.

(6) Mansour, A. M., Drevs, J., Esser, N., Hamada, F. M., Badary, O. A., Unger, C., Fichtner, I., and Kratz, F. (2003) A new approach for the treatment of malignant melanoma: enhanced antitumor efficacy of an albumin-binding doxorubicin prodrug that is cleaved by matrix metalloproteinase 2. *Cancer Res. 63*, 4062–4066.

(7) Kratz, F., Mansour, A., Soltau, J., Warnecke, A., Fichtner, I., Unger, C., and Drevs, J. (2005) Development of albumin-binding doxorubicin prodrugs that are cleaved by prostate-specific antigen. *Arch. Pharm. (Weinheim) 338*, 462–472.

(8) Chung, D. E., and Kratz, F. (2006) Development of a novel albumin-binding prodrug that is cleaved by urokinase-type-plasminogen activator (uPA). *Bioorg. Med. Chem. Lett. 16*, 5157–5163.

(9) Warnecke, A., Fichtner, I., Garmann, D., Jaehde, U., and Kratz, F. (2004) Synthesis and biological activity of water-soluble maleimide derivatives of the anticancer drug carboplatin designed as albumin-binding prodrugs. *Bioconjugate Chem. 15*, 1349–1359.

(10) Warnecke, A., and Kratz, F. (2003) Maleimide-oligo(ethylene glycol) derivatives of camptothecin as albumin-binding prodrugs: synthesis and antitumor efficacy. *Bioconjugate Chem. 14*, 377–387.

(11) Kratz, F. (2007) DOXO-EMCH (INNO-206): the first albumin-binding prodrug of doxorubicin to enter clinical trials. *Exp. Opin. Invest. Drugs 16*, 855–866.

(12) Goel, A., and Chauhan, S. S. (1997) Role of proteases in tumor invasion and metastasis. *Ind. J. Exp. Biol. 35*, 553–564.

(13) Ruppert, C., Ehrenforth, S., Scharrer, I., and Halberstadt, E. (1997) Protease levels in breast, ovary, and other gynecological tumor tissues: prognostic importance in breast cancer. *Cancer Detect. Prev. 21*, 452–459.

(14) Decock, J., Paridaens, R., and Cufer, T. (2005) Proteases and metastasis: clinical relevance nowadays? *Curr. Opin. Oncol. 17*, 545–50.

(15) Jedeszko, C., and Sloane, B. F. (2004) Cysteine cathepsins in human cancer. *Biol Chem 385*, 1017–27.

(16) Fingleton, B. (2006) Matrix metalloproteinases: roles in cancer and metastasis. *Front Biosci 11*, 479–91.

(17) Dano, K., Behrendt, N., Hoyer-Hansen, G., Johnsen, M., Lund, L. R., Ploug, M., and Romer, J. (2005) Plasminogen activation and cancer. *Thromb. Haemost. 93*, 676–81.

(18) Partin, A. W., Hanks, G. E., Klein, E. A., Moul, J. W., Nelson, W. G., and Scher, H. I. (2002) Prostate-specific antigen as a marker of disease activity in prostate cancer. *Oncology (Williston Park) 16*, 1218–24, discussion 1224, 1227–8 passim.

(19) Kratz, F., Drevs, J., Bing, G., Stockmar, C., Scheuermann, K., Lazar, P., and Unger, C. (2001) Development and in vitro efficacy of novel MMP2 and MMP9 specific doxorubicin albumin conjugates. *Bioorg. Med. Chem. Lett. 11*, 2001–2006.

(20) Wall, M. E., Wani, M. C., Cook, C. E., and Palmer, K. H. (1966) Plant antitumor agents. I. The isolation and structure of camptothecin, a novel alkaloidal leukemia and tumor inhibitor from camptotheca acuminata. *J. Am. Chem. Soc. 88*, 3888–3890.

(21) Hsiang, Y.-H., Hertzberg, R., Hecht, S., and Liu, L. F. (1985) Camptothecin induces protein-linked DNA breaks via mammalian DNA topoisomerase I. *J. Biol. Chem. 260*, 14873–14878.

(22) Kingsbury, W., Boehm, J., Jakas, D., Holden, K., Hecht, S., Gallagher, G., Caranfa, M., McCabe, F., Faucette, L., Johnson, R., and Hertzberg, R. (1991) Synthesis of water-soluble (aminoalkyl)camptothecin analogues: inhibition of topoisomerase I and antitumor activity. *J. Med. Chem. 34*, 98–107.

(23) Kollmannsberger, C., Mross, K., Jakob, A., Kanz, L., and Bokemeyer, C. (1999) Topotecan - a novel topoisomerase I inhibitor: pharmacology and clinical experience. *Oncology 56*, 1–12.

(24) Rothenberg, M. L. (2001) Irinotecan (CPT-11): recent developments and future directions - colorectal cancer and beyond. *Oncologist 6*, 66–80.

(25) Greenwald, R. B., Pendri, A., and Zhao, H. (1998) Stereoselective acylation of 20-(S)-camptothecin with amino acid derivatives using scandium triflate/DMAP. *Tetrahedron Asymm. 9*, 915–918.

(26) Harris, J. L., Backes, B. J., Leonetti, F., Mahrus, S., Ellman, J. A., and Craik, C. S. (2000) Rapid and general profiling of protease specificity by using combinatorial fluorogenic substrate libraries. *Proc. Natl. Acad. Sci. U.S.A. 97*, 7754–7759.

(27) Backes, B. J., Harris, J. L., Leonetti, F., Craik, C. S., and Ellman, J. A. (2000) Synthesis of positional-scanning libraries of fluorogenic peptide substrates to define the extended substrate specificity of plasmin and thrombin. *Nat. Biotechnol. 18*, 187–193.

(28) Maly, D. J., Leonetti, F., Backes, B. J., Dauber, D. S., Harris, J. L., Craik, C. S., and Ellman, J. A. (2002) Expedient solid-phase synthesis of fluorogenic protease substrates using the 7-amino-4-carbamoylmethylcoumarin (ACC) fluorophore. *J. Org. Chem. 67*, 910–915.

(29) Chan, W. C., and White, P. D. (2000) In *The practical approach series* (Hames, B. D., Ed.).

(30) Ostresh, J. M., Winkle, J. H., Hamashin, V. T., and Houghten, R. A. (1994) Peptide libraries: determination of relative reaction rates of protected amino acids in competitive couplings. *Biopolymers 34*, 1681–1689.

(31) Werle, B., Ebert, W., Klein, W., and Spiess, E. (1994) Cathepsin B in tumors, normal tissue and isolated cells from the human lung. *Anticancer Res. 14*, 1169–1176.

(32) Duffy, M. J., Blaser, J., Duggan, C., McDermott, E., O'Higgins, N., Fennelly, J. J., and Tschesche, H. (1995) Assay of matrix metalloproteases types 8 and 9 by ELISA in human breast cancer. *Br. J. Cancer 71*, 1025–1028.

(33) Richardson, P. L. (2002) The determination and use of optimized protease substrates in drug discovery and development. *Curr. Pharm. Des. 8*, 2559–2581.

(34) Thornberry, N. A., Rano, T. A., Peterson, E. P., Rasper, D. M., Timkey, T., Garcia-Calvo, M., Houtzager, V. M., Nordstrom, P. A., Roy, S., Vaillancourt, J. P., Chapman, K. T., and Nicholson, D. W. (1997) A combinatorial approach defines specificities of members of the caspase family and granzyme B. Functional relationships established for key mediators of apoptosis. *J. Biol. Chem. 272*, 17907–11.

(35) Choe, Y., Leonetti, F., Greenbaum, D. C., Lecaille, F., Bogyo, M., Bromme, D., Ellman, J. A., and Craik, C. S. (2006) Substrate profiling of cysteine proteases using a combinatorial peptide library identifies functionally unique specificities. *J. Biol. Chem. 281*, 12824–32.

(36) Rowinsky, E. K., Rizzo, J., Ochoa, L., Takimoto, C. H., Forouzesh, B., Schwartz, G., Hammond, L. A., Patnaik, A., Kwiatek, J., Goetz, A., Denis, L., McGuire, J., and Tolcher, A. W. (2003) A phase I and pharmacokinetic study of pegylated camptothecin as a 1-hour infusion every 3 weeks in patients with advanced solid malignancies. *J. Clin. Oncol. 21*, 148–157.

(37) Conover, C. D., Greenwald, R. B., Pendri, A., and Shum, K. L. (1999) Camptothecin delivery systems: the utility of amino acid spacers for the conjugation of camptothecin with polyethylene glycol to create prodrugs. *Anti-Cancer Drug Design 14*, 499–506.

(38) Greenwald, R. B., Pendri, A., Conover, C. D., Lee, C., Choe, Y. H., Gilbert, C., Martinez, A., Xia, Y., Wu, D., and Hsue, M. (1998) Camptothecin-20-PEG ester transport forms: the effect of spacer groups on antitumor activity. *Bioorg. Med. Chem. 6*, 551–562.

(39) Liu, X., Zhang, J., Song, L., Lynn, B. C., and Burke, T. G. (2004) Degradation of camptothecin-20(S)-glycinate ester prodrug under physiological conditions. *J. Pharm. Biomed. Anal. 35*, 1113–1125.

(40) Song, L., Bevins, R., and Anderson, B. D. (2006) Kinetics and mechanisms of activation of alpha-amino acid ester prodrugs of camptothecins. *J. Med. Chem. 49*, 4344–4355.

(41) Mansour, A. M., Drevs, J., Esser, N., Hamada, F. M., Badary, O. A., Unger, C., Fichtner, I., and Kratz, F. (2003) A new approach for the treatment of malignant melanoma: enhanced antitumor efficacy of an albumin-binding doxorubicin prodrug that is cleaved by matrix metalloproteinase 2. *Cancer Res. 63*, 4062–4066.

(42) Kratz, F., Mansour, A., Soltau, J., Warnecke, A., Fichtner, I., Unger, C., and Drevs, J. (2005) Development of albumin-binding doxorubicin prodrugs that are cleaved by prostate-specific antigen (PSA). *Arch. Pharm. 338*, 462–472.

(43) Caiolfa, V. R., Zamai, M., Fiorino, A., Frigerio, E., Pellizzoni, C., d'Argy, R., Ghiglieri, A., Castelli, M. G., Farao, M., Pesenti, E., Gigli, M., Angelucci, F., and Suarato, A. (2000) Polymer-bound camptothecin: initial biodistribution and antitumour activity studies. *J. Controlled Release 65*, 105–119.

(44) Choe, Y., Leonetti, F., Greenbaum, D. C., Lecaille, F., Bogyo, M., Bromme, D., Ellman, J. A., and Craik, C. S. (2006) Substrate profiling of cysteine proteases using a combinatorial peptide library identifies functionally unique specificities. *J. Biol. Chem. 281*, 12824–12832.

BC0700842

Targeting Lipopolyplexes Using Bifunctional Peptides Incorporating Hydrophobic Spacer Amino Acids: Synthesis, Transfection, and Biophysical Studies

Michael A. Pilkington-Miksa,[†] Michele J. Writer,[‡] Supti Sarkar,[§] Qing-Hai Meng,[§] Suzie E. Barker,[‡] Parviz Ayazi Shamlou,[¶,§] Helen C. Hailes,[†] Stephen L. Hart,[‡] and Alethea B. Tabor*[,†]

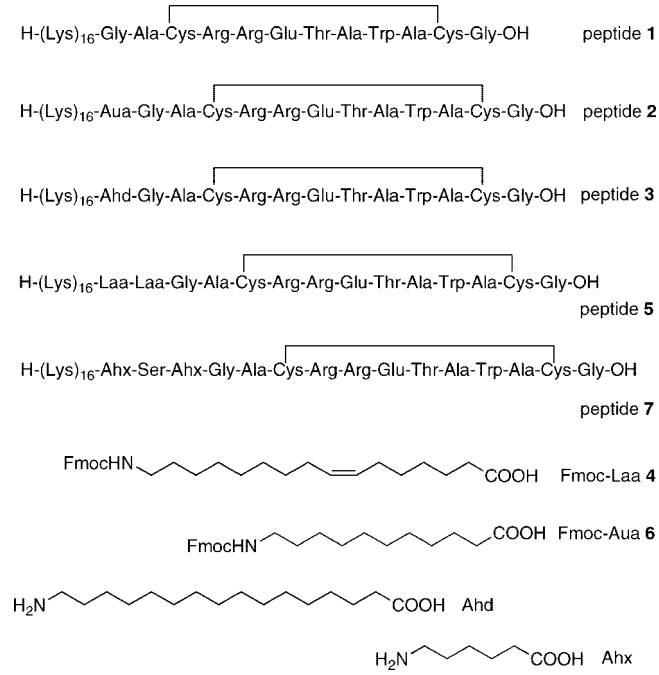
Departments of Chemistry, University College London, Christopher Ingold Laboratories, 20 Gordon Street, London WC1H 0AJ, Wolfson Centre for Gene Therapy of Childhood Disease, UCL Institute of Child Health, 30 Guilford Street, London WC1N 1EH, and Biochemical Engineering, University College London, Torrington Place, London WC1E 7JE, United Kingdom.
Received March 16, 2007; Revised Manuscript Received July 26, 2007

We have developed efficient synthetic routes to two hydrophobic amino acids, suitably protected for solid-phase peptide synthesis, and have successfully synthesized peptides containing these or other hydrophobic amino acids as spacers between a Lys_{16} moiety and an integrin-targeting motif. These peptides have in turn been used to formulate a range of lipopolyplex vectors with Lipofectin and plasmid DNA. The transfection efficiencies of these vectors and their aggregation behavior in buffers and in serum have been studied. We have shown that vectors containing peptides incorporating long linkers that are entirely hydrophobic are less efficient transfection agents. However, linkers of equivalent length that are in part hydrophobic show improved transfection properties, which is probably due to the improved accessibility of the integrin-binding motif.

INTRODUCTION

The development of gene delivery methods for the treatment of various diseases is still limited by the efficiency, reliability, and safety of the vectors used. Although viral vectors frequently exhibit excellent gene transfer efficiencies, recent concerns about their safety and immunogenicity (*1–3*) have led to renewed interest in the design and synthesis of nonviral gene delivery vectors (*4–6*). We are currently investigating the use of a ternary synthetic lipopolyplex vector, the LID vector, for gene delivery. The first generation of these targeted, self-assembling vector complexes (*7*) consisted of plasmid DNA, a lipid component, Lipofectin (a 1:1 mixture of the cationic lipid DOTMA with a co-lipid DOPE), and a cationic peptide (**1**) (comprising a K_{16} domain which binds to the plasmid DNA, a targeting domain (CRRETAWAC), which binds to $\alpha_5\beta_1$ integrins found on cell surfaces, and a flexible spacer sequence (GA)). LID vectors displayed high transfection efficiency and low toxicity *in vitro* and *in vivo*, transfected nondividing cells efficiently, and were well-tolerated upon repeated administration with low immunogenicity *in vivo* (*7–9*).

Our working hypothesis for the transfection pathway is that the LID complexes bind to the $\alpha_5\beta_1$ integrin and are then internalized by receptor-mediated endocytosis. One factor which might have a major effect on the efficiency of vector binding and internalization, therefore, would be the length and structure of the spacer sequence: longer spacers might position the targeting domain away from the vector surface and therefore render it more accessible. We also hypothesized that the condensed DNA was surrounded by a lipid coat and reasoned that hydrophobic spacers might possess the ability to "stack" within the lipid coating, thus simultaneously increasing the stability of the resulting lipopolyplex vector. We have therefore synthesized peptide **2**, containing ll-aminoundecanoic acid (Aua) as a spacer, and peptide **3**, containing 16-aminohexadecanoic acid (Ahd) as spacer. Furthermore, in an attempt to make the spacer amino acid closer in structure to the unsaturated tail of the lipid DOTMA, we have synthesised the novel amino acid **4** (Fmoc-Laa), and used it to prepare peptide **5**. Finally, we have designed and used peptide **7**, incorporating a spacer containing 6-aminohexanoic acid (Ahx) units. We reasoned that the sequence Ahx-Ser-Ahx would be suitably hydrophobic and act



* a.b.tabor@ucl.ac.uk.
[†] Department of Chemistry, University College London.
[‡] Wolfson Centre for Gene Therapy of Childhood Disease, UCL Institute of Child Health.
[§] Department of Biochemical Engineering, University College London.
[¶] Present address: Process Engineering Center, Eli Lilly and Company, Lilly Corporate Center, DC 3127, Indianapolis, Indiana 46285, USA.

10.1021/bc0700943 CCC: $37.00 © 2007 American Chemical Society
Published on Web 10/05/2007

as a longer spacer, but would not be able to stack within a lipid bilayer so efficiently. In this paper, we report the synthesis of amino acids **4** and **6**, and the synthesis of the peptides; we also describe the effect of these spacers on the transfection efficiencies and biophysical properties of lipopolyplex vectors formulated from peptides **2**, **3**, **5**, and **7**.

EXPERIMENTAL PROCEDURES

General Procedures and Materials. All reagents used for synthesis were purchased from commercial suppliers, with the exception of 9-phenylxanthen-9-ol, which was prepared from xanthone and phenylmagnesium bromide following a literature procedure (*10*). Solvents were purified using standard techniques, with the exception of THF, which was distilled from sodium wire without the use of benzophenone for the synthesis of **13**. NMR spectra were recorded on a Bruker AMX300 spectrometer; chemical shifts (δ) are reported in parts per million (ppm) using residual isotopic solvent as an internal reference. Coupling constants (J) are reported in hertz (Hz). Electrospray mass spectra were recorded on Micromass Quattro LC, Thermo Finnegan MAT 900XP, or VG ZAB 2SE instruments, and fast atom bombardment mass spectra on Thermo Finnegan MAT 900XP or VG ZAB 2SE instruments. IR spectra were recorded on a Shimadzu FT-IR 8700.

Solid-phase peptide synthesis was carried out either manually on a Merrifield bubbler or automatically on a peptide synthesizer (MilliGen 9050Plus PepSynthesiser). All reagents used for either manual or automatic synthesis were purchased from commercial suppliers, with the exception of the Fmoc-protected amino acids **4** (Fmoc-Laa) and **6** (Fmoc-Aua). HIPERSOLV DMF of HPLC grade was used straight from the bottle, while dichloromethane and piperidine were freshly distilled over calcium hydride before use. All peptide syntheses were carried out under nitrogen.

Preparative HPLC was carried out on a Waters 600E instrument with Waters 486 UV detector, using a Vydac 218TP reverse-phase HPLC column (25 × 250 mm). Analytical HPLC was carried out on a Varian ProStar 210 with Varian ProStar 320 UV detector, using a Vydac 218TP reverse-phase HPLC column (2.1 × 250 mm). Water/acetonitrile gradients were used as described, with both water and acetonitrile containing 0.1% trifluoroacetic acid and monitoring at 215 nm.

Synthesis of Fmoc-Laa 4. *6-Bromohexanoic Acid tert-Butyl Ester **8** (11).* To 6-bromohexanoic acid (2.50 g, 12.8 mmol) in dry dichloromethane (50 mL) at 0 °C under nitrogen was added *tert*-butyl alcohol (5.5 mL, 66 mmol, 5 equiv) followed by dimethylaminopyridine (0.156 g, 1.28 mmol, 0.1 equiv). After 5 min, dicyclohexylcarbodiimide (2.90 g, 14.08 mmol, 1.1 equiv) was added to this solution at 0 °C. The solution was then left to warm to room temperature and stirred for 12 h. After 12 h, the reaction was filtered and then partitioned with water (50 mL). The organic fraction was dried over anhydrous $MgSO_4$ and concentrated *in vacuo*. The remaining residue was purified by normal-phase silica gel chromatography, eluting with hexane/ethyl acetate (90:10) to give **8** as a clear oil (2.51 g, 78%). ^{1}H NMR (300 MHz, $CDCl_3$) δ 1.45 (9H, s, $C(CH_3)_3$), 1.46 (2H, m, $Br(CH_2)_2CH_2$), 1.62 (2H, quintet, J = 7.1 Hz, $Br(CH_2)_3CH_2CH_2$), 1.88 (2H, quintet, J = 7.1 Hz, $BrCH_2CH_2(CH_2)_3$), 2.23 (2H, t, J = 7.3 Hz, $CH_2COOC(CH_3)_3$), 3.41 (2H, t, J = 6.8 Hz, $BrCH_2$); ^{13}C NMR (75 MHz, $CDCl_3$) δ 24.6, 28.0, 28.5, 32.8, 33.8, 35.7, 80.5, 173.2; IR ν_{max}/cm^{-1} (film) 2977, 2936, 1728; $C_{10}H_{19}O_2Br$ (FAB^+) m/z 253 ($M + H^+$ [^{81}Br], 15%), 251 ($M + H^+$ [^{79}Br], 18%), 197 ([$C_6H_{12}O_2$ ^{81}Br]$^+$, 34%), 195 ([$C_6H_{12}O_2$ ^{79}Br]$^+$, 36%), 57 ([C_4H_9]$^+$, 100%).

*6-Iodohexanoic Acid tert-Butyl Ester **9** (12).* To 6-bromohexanoic acid *tert*-butyl ester **8** (2.30 g, 9.20 mmol) in dry acetone (400 mL) under nitrogen was added sodium iodide (41 g, 275 mmol, 30 equiv). The reaction mixture was left to stir in darkness at room temperature for 6 days, after which time it was filtered. The separated solid was then washed with diethyl ether, which was added to the filtrate. The filtrate was concentrated *in vacuo* and then redissolved in diethyl ether (250 mL). This solution was partitioned with 5% aqueous sodium thiosulfate (100 mL) and saturated aqueous sodium chloride (100 mL). The aqueous phase was back-extracted with diethyl ether (150 mL). The organic solutions were combined, dried over anhydrous $MgSO_4$, and concentrated *in vacuo* to give a yellow oil. This oil was purified by silica gel chromatography, eluting with hexane/ethyl acetate (90:10) to give **9** as a yellow oil (2.53 g, 93%). ^{1}H NMR (300 MHz, $CDCl_3$) δ 1.39–1.49 (2H, m, $I(CH_2)_2CH_2$), 1.45 (9H, s, $C(CH_3)_3$), 1.62 (2H, quintet, J = 7.2 Hz, $I(CH_2)_3CH_2$), 1.84 (2H, quintet, J = 7.2 Hz, ICH_2CH_2), 2.22 (2H, t, J = 7.3 Hz, $CH_2COOC(CH_3)_3$), 3.19 (2H, t, J = 7.0 Hz, $ICH_2(CH_2)_4$); ^{13}C NMR (75 MHz, $CDCl_3$) δ 6.9, 24.4, 28.5, 30.3, 33.6, 35.7, 80.5, 173.2; IR ν_{max}/cm^{-1} (film) 2977, 2933, 1729; $C_{10}H_{19}O_2I$ (FAB^+) m/z 299 ($M + H^+$, 24%), 243 ([$C_6H_{12}O_2I$]$^+$, 55%), 57 ([C_4H_9]$^+$, 100%).

8-Bromooctan-1-ol (13). To 1,8-octanediol (5.96 g, 40.0 mmol) in toluene (350 mL) was added hydrobromic acid (5.25 mL, 48% aq solution). The reaction mixture was heated to reflux for 24 h after which time a further quantity of hydrobromic acid was added (1.5 mL). The reaction mixture was again left to reflux for 24 h. The reaction mixture was then cooled to room temperature, and diethyl ether was added (250 mL). The aqueous hydrobromic acid layer was separated from the organic layer; the organic phase was partitioned with saturated aqueous $NaHCO_3$ (100 mL), then 0.1 M phosphate buffer (pH 7, 100 mL). The aqueous phase was back-extracted with diethyl ether (100 mL); the organic solutions were combined, dried over anhydrous $MgSO_4$, and concentrated *in vacuo* to give a yellow oil (8.56 g). This oil was purified by silica gel chromatography, eluting with hexane/diethyl ether (50:50) to give 8-bromooctan-1-ol as a pale yellow oil (8.29 g, 39.64 mmol, 99%). ^{1}H NMR (300 MHz, $CDCl_3$) δ 1.33–1.59 (10H, m, $BrCH_2CH_2(CH_2)_5$), 1.86 (2H, quintet, J = 7.1 Hz, $BrCH_2CH_2$), 3.40 (2H, t, J = 6.8 Hz, $BrCH_2(CH_2)_5$), 3.63 (2H, t, J = 6.6 Hz, CH_2OH); ^{13}C NMR (75 MHz, $CDCl_3$) δ 26.0, 28.5, 29.1, 29.6, 33.1, 33.2, 34.3, 63.3; IR ν_{max}/cm^{-1} (film) 3333, 2930, 2855; $C_8H_{15}OBr$ (FAB^+) m/z 211 ($M + H^+$ [^{81}Br], 40%), 209 ($M + H^+$ [^{79}Br], 42%), 69 ([C_5H_9]$^+$, 100%), 55 ([C_4H_7]$^+$, 82 %). HRMS (FAB, NOBA matrix): $C_8H_{16}OBr$ calcd for $[MH]^+$ 209.0541, found 209.0550.

*1-Bromo-8-(9-phenyl-xanthen-9-yloxy)octane **10**.* To 8-bromooctan-1-ol (5.41 g, 25.9 mmol) and 9-phenylxanthen-9-ol (*10*) (7.10 g, 25.9 mmol) was added glacial acetic acid (75 mL). Once complete dissolution had occurred, the solution was concentrated *in vacuo*. A further volume of glacial acetic acid (75 mL) was added, and again the resulting solution was concentrated *in vacuo*. This was repeated a further five times. Once all the glacial acetic acid had been removed for the final time, the remaining oil was redissolved in hexane (250 mL). This solution was partitioned with saturated aqueous $NaHCO_3$ and saturated aqueous NaCl, and the aqueous phase was back-extracted with hexane (100 mL). The organic solutions were combined, dried over anhydrous $MgSO_4$, and concentrated *in vacuo* to give **10** as a yellow oil (12.04 g, 100%). ^{1}H NMR (300 MHz, $CDCl_3$) δ 1.20–1.42 (8H, m, $BrCH_2CH_2(CH_2)_4$), 1.51 (2H, m, CH_2CH_2OPx), 1.84 (2H, quintet, J = 7.2 Hz, $BrCH_2CH_2$), 2.96 (2H, t, J = 6.2 Hz, CH_2CH_2OPx), 3.40 (2H, t, J = 6.8 Hz, $BrCH_2$), 7.01–7.41 (13H, m, aromatic); ^{13}C NMR (75 MHz, $CDCl_3$) δ 26.5, 28.5, 29.1, 29.5, 30.2, 33.2, 34.3, 63.4, 75.5, 116.5, 123.7, 124.2, 126.8, 126.9, 128.1, 129.2, 130.0, 149.9, 151.7; IR ν_{max}/cm^{-1} (film) 3033, 2932, 2855,

1603, 1574; $C_{27}H_{29}O_2Br$ (FAB^+) *m/z* 465 ($M + H^+[^{79}Br]$, 1%), 275 ($[C_{19}H_{15}O_2]^+$, 12%), 257 ($[C_{19}H_{13}O]^+$, 100%), 197 ($[C_{13}H_9O_2]^+$, 63%), 181 ($[C_{13}H_8O]^+$, 14%). Anal. Calcd for $C_{27}H_{29}O_2Br$: C, 69.68; H, 6.28; Br, 17.16. Found: C, 69.72; H, 6.20; Br, 17.15.

1-Iodo-8-(9-phenylxanthen-9-yloxy)octane ***11***. To 1-bromo-8-(9-phenyl-xanthenyloxy)octane 10 (12.04 g, 25.9 mmol) in dry acetone (500 mL) was added sodium iodide (155.1 g, 1.03 mol, 40 equiv). The reaction was left stirring under nitrogen, in darkness, and at room temperature for seven days. After seven days, the reaction mixture was concentrated *in vacuo*. The remaining solid was dissolved in diethyl ether (400 mL) and saturated aqueous $NaHCO_3$ (400 mL). The organic phase was then partitioned with 5% aqueous sodium thiosulfate (150 mL) and saturated aqueous NaCl (150 mL). The aqueous solutions were combined and back-extracted with diethyl ether (200 mL). The organic solutions were combined, dried over anhydrous $MgSO_4$, and concentrated *in vacuo* to give a dark yellow oil. This oil was purified by normal-phase silica gel chromatography, eluting with chloroform to give **11** as a pale yellow oil (12.9 g, 97%). ^1H NMR (300 MHz, $CDCl_3$) δ 1.22–1.41 (8H, m, $ICH_2CH_2(CH_2)_4$), 1.54 (2H, m, CH_2CH_2OPx), 1.82 (2H, m, ICH_2CH_2), 2.98 (2H, t, $J = 6.3$ Hz, CH_2OPx), 3.2 (2H, t, $J = 7.0$ Hz, ICH_2CH_2), 7.01–7.41 (13H, m, aromatic); ^{13}C NMR (75 MHz, $CDCl_3$) δ 7.5, 26.5, 28.8, 29.5, 30.2, 30.8, 33.9, 63.4, 75.5, 116.5, 123.7, 124.2, 126.8, 126.9, 128.1, 129.2, 130.0, 149.9, 151.7; IR ν_{max}/cm^{-1} (film) 3033, 2932, 2855, 1603, 1574; $C_{27}H_{29}O_2I$ (FAB^+) *m/z* 535 ($M + Na^+$, 3%), 513 ($M + H^+$, 1%), 257 ($[C_{19}H_{13}O]^+$, 100%), 197 ($[C_{13}H_9O_2]^+$, 47%); HRMS (FAB, NOBA matrix): $C_{27}H_{30}O_2I$ calcd for $[MH]^+$513.1291, found 513.1270.

1-(9-Phenylxanthen-9-yloxy)-dec-9-yne ***12***. To lithium acetylide ethylenediamine (11.5 g, 125 mmol, 40 equiv) under nitrogen was added dry tetrahydrofuran (30 mL). This suspension was cooled to −78 °C, and hexamethylphosphoramide (6 mL) was added. A solution of 1-iodo-8-(9-phenyl-xanthen-9-yloxy)octane 11 (12.8 g, 25.0 mmol) in THF (30 mL) was slowly added to the suspension at −78 °C. Once all the solution had been added to the suspension, the reaction was allowed to warm to room temperature and left stirring overnight. After 24 h, the reaction was concentrated *in vacuo*. The remaining oil was dissolved in diethyl ether (350 mL). This solution was filtered and then partitioned with 5% aqueous sodium thiosulfate (150 mL) and saturated aqueous NaCl (150 mL). The aqueous solutions were combined and back-extracted with diethyl ether (100 mL). The organic solutions were combined, dried over anhydrous $MgSO_4$, and concentrated *in vacuo* to give a brown oil. This oil was purified by normal-phase silica gel chromatography, eluting with hexane/chloroform (50:50) with a few drops of triethylamine, to give **12** as a pale yellow oil (10.05 g, 98%). ^1H NMR (300 MHz, $CDCl_3$) δ 1.24–1.63 (12H, m, $HC{\equiv}CCH_2(CH_2)_6$), 1.95 (1H, t, $J = 2.6$ Hz, $HC{\equiv}CCH_2$), 2.27 (2H, dt, $J = 7.0$ Hz and 2.6 Hz, $HC{\equiv}CCH_2$), 2.98 (2H, t, $J = 6.3$ Hz, CH_2OPx), 7.01–7.41 (13H, m, aromatic); ^{13}C NMR (75 MHz, $CDCl_3$) δ 18.8, 26.6, 28.9, 29.1, 29.4, 29.6, 30.3, 63.4, 68.5, 75.5, 85.1, 116.5, 123.7, 124.3, 126.8, 126.9, 128.1, 129.2, 130.0, 149.9, 151.7; IR ν_{max}/cm^{-1} (film) 3304, 3034, 2932, 2856, 2120, 1603, 1575; $C_{29}H_{30}O_2$ (FAB^+) *m/z* 433 ($M + Na^+$, 2%), 411 ($M + H^+$, 2%), 257 ($[C_{19}H_{13}O]^+$, 100%); HRMS (FAB, NOBA matrix): $C_{29}H_{31}O_2$ calcd for $[MH]^+$ 411.2324, found 411.2300.

2-Methylprop-2-yl 16-(9-phenylxanthen-9-yloxy)hexadeca-7-ynoate ***13***. To freshly purified 1-(9-phenyl-xanthen-9-yloxy)-dec-9-yne **11** (2.05 g, 5.00 mmol) in dry THF (30 mL) under N_2 was added HMPA (4 mL). This solution was cooled to −78 °C, and then *n*-butyl lithium (2.6 mL, 2.5 M, 6.5 mmol, 1.3 equiv) was slowly added. The solution was left to stir for 30 min after which time freshly purified iodohexanoic acid *tert*-butyl ester **9** (1.94 g, 6.5 mmol, 1.3 equiv) in THF (25 mL) was added dropwise. Once this was complete, the reaction was allowed to warm to room temperature and was left to stir for 24 h. The reaction was then concentrated *in vacuo* to yield a brown gum, which was dissolved in diethyl ether (300 mL), and the resulting solution was filtered. The filtrate was partitioned with 5% aqueous sodium thiosulfate (150 mL) and saturated aqueous NaCl (150 mL). The aqueous solutions were combined and back-extracted with diethyl ether (150 mL). The organic solutions were combined, dried over anhydrous $MgSO_4$, and concentrated *in vacuo* to give a brown oil. This oil was purified by normal-phase silica gel chromatography, eluting with hexane/chloroform (40:60) with a few drops of triethylamine, to give **13** as a pale yellow oil (2.03 g, 70%). ^1H NMR (300 MHz, $CDCl_3$) δ 1.18–1.68 (18H, m, $PxOCH_2(CH_2)_6CH_2C{\equiv}CCH_2(CH_2)_3$), 1.45 (9H, s, $C(CH_3)_3$), 2.13–2.16 (4H, m, $PxO(CH_2)_7CH_2C{\equiv}CCH_2$), 2.22 (2H, t, $J = 7.4$ Hz, $CH_2COOC(CH_3)_3$), 2.96 (2H, t, $J = 6.3$ Hz, $PxOCH_2$), 6.99–7.39 (13H, m, H aromatic); ^{13}C NMR (75 MHz, $CDCl_3$) δ 19.0, 19.2, 25.1, 26.6, 28.5, 28.7, 29.2, 29.47, 29.55, 29.61, 30.1, 30.3, 35.9, 63.4, 75.4, 80.3, 80.31, 80.8, 116.5, 123.7, 124.3, 126.8, 126.8, 128.1, 129.2, 130.0, 149.9, 151.7, 173.5; IR ν_{max}/cm^{-1} (film) 2931, 2856, 1733, 1603, 1575; $C_{39}H_{48}O_4$ (FAB^+) *m/z* 603 ($M + Na^+$, 5%), 269 ($[C_{16}H_{29}O_3]^+$, 4%), 257 ($[C_{19}H_{13}O]^+$, 100%).

2-Methylprop-2-yl 16-hydroxyhexadeca-7-ynoate ***14***. To 2-methylprop-2-yl 16-(9-phenylxanthen-9-yloxy)hexadeca-7-ynoate **13** (1.39 g, 2.39 mmol) in dichloromethane (50 mL), under nitrogen was added pyrrole (1.65 mL, 1.6 g, 23.9 mmol, 10 equiv) followed by dichloroacetic acid (1.25 mL, 1.95 g, 15.0 mmol). This solution was left to stir for 10 min at room temperature. An excess of saturated aqueous $NaHCO_3$ was then added, and the reaction was stirred vigorously to ensure mixing of aqueous and organic phases. The organic and aqueous phases were separated, and the aqueous phase was partitioned with dichloromethane (100 mL). The organic solutions were combined, partitioned with saturated aqueous NaCl (50 mL), dried over anhydrous $MgSO_4$, and concentrated *in vacuo* to yield a dark brown oil. This oil was purified by normal-phase silica gel chromatography, using only 60 mm in height of silica and eluting with chloroform with a few drops of triethylamine, to give **14** as a clear oil (0.77 g, 95%). ^1H NMR (300 MHz, $CDCl_3$) δ 1.28–1.68 (18H, m, $HOCH_2(CH_2)_6CH_2C{\equiv}CCH_2(CH_2)_3$), 1.45 (9H, s, $C(CH_3)_3$), 2.15–2.18 (4H, m, $HO(CH_2)_7CH_2C{\equiv}CCH_2$), 2.22 (2H, t, $J = 7.5$ Hz, $CH_2COOC(CH_3)_3$), 3.63 (2H, t, $J = 6.6$ Hz, $HOCH_2$); ^{13}C NMR (75 MHz, $CDCl_3$) δ 19.0, 19.01, 25.1, 26.1, 28.5, 28.7, 29.1, 29.2, 29.5, 29.7, 33.2, 35.9, 63.3, 80.3, 80.4, 80.7, 173.5; IR ν_{max}/cm^{-1} (film) 3419 (broad), 2931, 2856, 1732; $C_{20}H_{36}O_3$ (FAB^+) *m/z* 325 ($M + H^+$, 4%), 269 ($[C_{16}H_{29}O_3]^+$, 27%), 57 ($[C_4H_9]^+$, 100%).

(Z)-2-Methylprop-2-yl 16-hydroxyhexadeca-7-enoate ***15***. A suspension of Lindlar catalyst (500 mg) in hexane/methanol (90:10, 20 mL) was prepared under nitrogen. This suspension was connected to a hydrogenation apparatus and exposed to hydrogen at atmospheric pressure at room temperature until no further change in gas volume was detected. 2-Methylprop-2-yl 16-hydroxy-hexadeca-7-ynoate **14** (0.73 g, 2.26 mmol) in hexane (10 mL) was then added to this suspension, and the reaction was left to absorb approximately 58 cm^3 of hydrogen, at room temperature. Once this had occurred, the reaction mixture was dissolved in dichloromethane (80 mL) and filtered. The filtrate was concentrated *in vacuo* to yield **15** as a yellow oil (0.74 g, 100 %). ^1H NMR (300 MHz, $CDCl_3$) δ 1.23–1.68 (18H, m, $HOCH_2(CH_2)_6CH_2CH{=}CHCH_2(CH_2)_3$), 1.45 (9H, s, $C(CH_3)_3$), 2.02 (4H, m, $HO(CH_2)_7CH_2CH{=}CHCH_2$), 2.22 (2H, t, $J = 7.5$ Hz, $CH_2COOC(CH_3)_3$), 3.65 (2H, t, $J = 6.6$ Hz,

HOCH_2), 5.37 (2H, m, C*H*=C*H*); ^{13}C NMR (75 MHz, $CDCl_3$) δ 25.4, 26.1, 27.5, 27.6, 28.5, 29.2, 29.55, 29.60, 29.8, 29.9, 30.1, 33.2, 36.0, 63.3, 80.3, 130.0, 130.4, 173.7; IR ν_{max}/cm^{-1} (NaCl) 3383 (broad), 3004, 2927, 2855, 1732; $C_{20}H_{38}O_3$ (FAB^+) *m/z* 349 ($M + Na^+$, 1%), 57 ($[C_4H_9]^+$, 100 %); HRMS (FAB, NOBA matrix): $C_{20}H_{38}O_3Na$ calcd for $[M + Na]^+$ 349.2719, found 349.2730.

(Z)-2-Methylprop-2-yl-16-azidohexadeca-7-enoate ***16.*** To (*Z*)-2-methylprop-2-yl-16-hydroxyhexadeca-7-enoate **15** (1.57 g, 4.82 mmol) in dry dichloromethane/triethylamine (1:1, 40 mL) at 0 °C, under nitrogen, was slowly added methanesulfonyl chloride (0.45 mL, 0.66 g, 5.78 mmol, 1.2 equiv). Once addition was complete, the reaction was left to stir for 2 h at room temperature. An excess of saturated aqueous $NaHCO_3$ was then added, and the reaction was stirred vigorously for 10 min. The reaction was then concentrated *in vacuo* until only a small volume of aqueous solution remained. The remaining concentrate was partitioned with dichloromethane (2 × 100 mL). The organic phase was partitioned with saturated aqueous NaCl (75 mL), dried over anhydrous $MgSO_4$, and concentrated *in vacuo* to give the intermediate mesylate as an oil. The recovered oil was immediately dissolved in dry dimethylformamide (20 mL) and sodium azide (1.25 g, 19.3 mmol, 4 equiv) was added. This solution was left to stir under nitrogen at room temperature for five days. The solution was then concentrated *in vacuo* to yield a thick oil, which was dissolved in diethyl ether (200 mL) and filtered. The filtrate was partitioned with water (70 mL) and saturated aqueous NaCl (70 mL). The aqueous solutions were combined and partitioned with diethyl ether (80 mL). The organic solutions were combined, dried over $MgSO_4$, and concentrated *in vacuo* to yield a pale brown oil. This oil was purified by normal-phase silica gel chromatography, eluting with chloroform, to give **16** as a yellow oil (1.52 g, 90%). ^{1}H NMR (300 MHz, $CDCl_3$) δ 1.21–1.41 (14H, m, $N_3CH_2(CH_2)_6CH_2CH$=$CHCH_2(CH_2)_3$), 1.45 (9H, s, $C(CH_3)_3$), 1.58 (4H, m, $N_3CH_2(CH_2)_6CH_2CH$=$CHCH_2(CH_2)_3$-), 2.02 (4H, m, $N_3(CH_2)_7CH_2CH$=$CHCH_2$), 2.21 (2H, t, J = 7.6 Hz, $CH_2COOC(CH_3)_3$), 3.26 (2H, t, J = 6.9 Hz, N_3CH_2), 5.37 (2H, m, $N_3CH_2(CH_2)_7CH$=CH-); ^{13}C NMR (75 MHz, $CDCl_3$) δ 25.4, 27.1, 27.4, 27.6, 28.5, 29.1, 29.2, 29.5, 29.6, 29.75, 29.8, 30.1, 36.0, 51.9, 80.3, 130.0, 130.4, 173.6; IR ν_{max}/cm^{-1} (film) 2929, 2855, 2096, 1732; $C_{20}H_{37}O_2N_3$ (FAB^+) *m/z* 324 ($[C_{20}H_{38}O_2N]^+$, 9%), 57 ($[C_4H_9]^+$, 100 %); HRMS (FAB, NOBA matrix): $C_{20}H_{37}O_2N_3Na$ calcd for $[M + Na]^+$ 374.2783, found 374.2760.

(Z)-2-Methylprop-2-yl-16-aminohexadeca-7-enoate ***17.*** To (*Z*)-2-methylprop-2-yl-16-azidohexadeca-7-enoate **16** (1.28 g, 3.65 mmol) in dry THF (40 mL), under nitrogen was added triphenylphosphine (1.43 g, 5.50 mmol, 1.5 equiv). The solution was left to stir at room temperature for 5 h, after which time water (10 mL) was added and the reaction was left to stir for a further 48 h. The reaction was then concentrated *in vacuo*, redissolved in diethyl ether/hexane (1:1, 60 mL), and filtered. The filtrate was concentrated *in vacuo* to yield an oil, which was purified by normal-phase silica gel chromatography, eluting with a gradient of chloroform and triethylamine (99:1 to 90:10), to give **17** as a pale yellow oil (1.11 g, 93%). ^{1}H NMR (300 MHz, $CDCl_3$) δ 1.24–1.41 (14H, m, $H_2NCH_2(CH_2)_6CH_2CH$=$CHCH_2(CH_2)_3$), 1.45 (9H, s, $C(CH_3)_3$), 1.51–1.66 (4H, m, $H_2NCH_2(CH_2)_6CH_2CH$=$CHCH_2(CH_2)_3$), 2.02 (4H, m, $H_2N(CH_2)_7CH_2CH$=$CHCH_2$), 2.21 (2H, t, J = 7.5 Hz, $CH_2COOC(CH_3)_3$), 2.69 (2H, t, J = 6.9 Hz, $H_2NCH_2(CH_2)_7$), 5.37 (2H, m, $H_2NCH_2(CH_2)_7CH$=$CH(CH_2)_5$); ^{13}C NMR (75 MHz, $CDCl_3$) δ 25.4, 27.3, 27.4, 27.6, 28.50, 29.1, 29.6, 29.79, 29.85, 29.89, 30.0, 30.1, 36.0, 42.6, 80.2, 130.0, 130.4, 173.6; IR ν_{max}/cm^{-1} (film) 3300, 3004, 2926, 2855, 1733; $C_{20}H_{39}O_2N$ (FAB^+) *m/z* 326 ($M + H^+$, 56%), 270 ($[C_{16}H_{32}O_2N]^+$, 87%), 57 ($[C_4H_9]^+$, 100%); HRMS (FAB, NOBA matrix): $C_{20}H_{40}O_2N$ calcd for $[MH]^+$ 326.3059, found 326.3040.

(Z)-2-Methylprop-2-yl-16-(9-fluorenylmethyloxycarbonylamido)hexadeca-7-enoate ***18.*** To (*Z*)-2-methylprop-2-yl-16-aminohexadeca-7-enoate **17** (0.46 g, 1.42 mmol) in dry THF (20 mL), under nitrogen at 0 °C was added *N*-methylmorpholine (0.32 mL, 0.286 g, 2.83 mmol, 2 equiv). This solution was left to stir for 10 min, and then fluorenylmethyl chloroformate (0.73 g, 2.83 mmol, 2 equiv) in dry THF (15 mL) was slowly added. Once addition was complete, the reaction was stirred for a further hour at 0 °C and then left to stir at room temperature overnight. After 24 h, the reaction was concentrated *in vacuo*, redissolved in dichloromethane (150 mL), and filtered. The filtrate was partitioned with 5% aqueous potassium hydrogen sulfate (70 mL) and saturated aqueous NaCl (70 mL). The aqueous solutions were back-extracted with dichloromethane (100 mL). The organic solutions were combined, dried over anhydrous $MgSO_4$, and concentrated *in vacuo* to give a brown solid. This solid was purified by normal-phase silica gel chromatography, eluting with chloroform, to give **18** as a pale brown solid (0.69 g, 89%). ^{1}H NMR (300 MHz, $CDCl_3$) δ 1.20–1.43 (14H, m, $FmocHNCH_2(CH_2)_6CH_2CH$=$CHCH_2(CH_2)_3$), 1.45 (9H, s, $C(CH_3)_3$), 1.57–1.66 (4H, m, $FmocHNCH_2(CH_2)_6CH_2CH$=$CHCH_2(CH_2)_3$), 2.03 (4H, m, $FmocHN(CH_2)_7CH_2CH$=$CHCH_2(CH_2)_4$), 2.21 (2H, t, J = 7.5 Hz, $CH_2COOC(CH_3)_3$), 3.17 (2H, m, J = 6.1 Hz, $FmocHNCH_2$), 4.21 (1H, t, J = 6.7 Hz, $NHCOOCH_2CHC_{12}H_8$), 4.40 (2H, d, J = 6.7 Hz, $NHCOOCH_2C_{13}H_9$), 4.98 (1H, bs, N*H*), 5.37 (2H, m, $FmocHNCH_2(CH_2)_7CH$=CH), 7.31 (2H, t, J = 7.4 Hz, Ar), 7.40 (2H, t, J = 7.4 Hz, Ar), 7.61 (2H, d, J = 7.4 Hz, Ar), 7.77 (2H, d, J = 7.4 Hz, Ar); ^{13}C NMR (75 MHz, $CDCl_3$) δ 25.5, 27.2, 27.5, 27.6, 28.5 ($C(CH_3)_3$), 29.2, 29.6, 29.7, 29.8, 29.9, 30.0, 30.1, 36.0, 41.53, 47.8, 66.9, 80.2 ($C(CH_3)_3$), 120.3, 125.4, 127.4, 128.0, 130.0, 130.4, 141.7, 144.5, 156.9 (*C*=O), 173.6 (*C*=O); IR ν_{max}/cm^{-1} (KBr disc): 3325 (st.), 3005 (wk.), 2926, 2854 (st.), 1730 (st.), 1689 (st.), 1542 (med.), 1266, 1152 (st.); $C_{35}H_{49}O_4N$ (FAB^+) *m/z* 492 ($[C_{31}H_{42}O_4N]^+$, 7%), 270 ($[C_{16}H_{32}O_2N]^+$, 9.6%), 252 ($[C_{16}H_{30}ON]^+$, 5.8%), 179 ($[C_{14}H_{11}]^+$, 100%), 165 ($[C_{13}H_9]^+$, 12%), 57 ($[C_4H_9]^+$, 44.1%); HRMS (FAB, NOBA matrix): $C_{35}H_{49}O_4NNa$ calcd for $[M + Na]^+$ 570.3559, found 570.3580.

(Z) 16-(9-Fluorenylmethyloxycarbonylamido)-hexadeca-7-enoic Acid ***4.*** To (Z)-2-methylprop-2-yl 16-(9-fluorenylmethyloxycarbonylamido)hexadeca-7-enoate **18** (0.75 g, 1.37 mmol) under nitrogen at room temperature was added trifluoroacetic acid/water (95:5, 63 mL). To this solution was immediately added 1,3-propanedithiol (0.693 mL, 0.747 g, 6.9 mmol, 5 equiv). The reaction was left to stir for 1.5 h, after which it was concentrated *in vacuo* to yield a pale brown solid. The solid was purified by normal-phase silica gel chromatography, eluting initially with chloroform (100 %), then gradually changing to chloroform/methanol/acetic acid (92:6:2), to give **4** as an off-white solid (0.64 g, 95 %). ^{1}H NMR (300 MHz, $CDCl_3$) δ 1.27–1.65 (18H, m, $FmocHNCH_2(CH_2)_6CH_2CH$=$CHCH_2(CH_2)_3CH_2CO_2H$), 2.01 (4H, m, $FmocHN(CH_2)_7CH_2CH$=$CHCH_2(CH_2)_4CO_2H$), 2.21 (2H, t, J = 4.9 Hz, -CH_2CO_2H), 3.17 (2H, m, $FmocHNCH_2$), 4.21 (1H, t, J = 6.7 Hz, $NHCOOCH_2CHC_{12}H_8$), 4.40 (2H, d, J = 6.7 Hz, -$NHCOOCH_2C_{13}H_9$), 4.88 (1H, bs, -N*H*-), 5.37 (2H, m, -*CH*=*CH*$(CH_2)_5CO_2H$), 7.31 (2H, dt, J = 7.5 Hz and 0.9 Hz), 7.40 (2H, t, J = 7.4 Hz), 7.61 (2H, d, J = 7.4 Hz), 7.77 (2H, d, J = 7.5 Hz); ^{13}C NMR (75 MHz, $CDCl_3$) δ 25.1, 27.2, 27.4, 27.6, 29.1, 29.6, 29.68, 29.77, 29.83, 30.1, 30.4, 34.5, 41.5, 47.7, 66.9, 120.4, 125.4, 127.4, 128.1, 130.0, 130.1, 141.8, 144.4, 157.0, 179.7; IR ν_{max}/cm^{-1} (KBr) 3325 (st.), 3005 (wk.), 2926, 2854 (st.), 2600–2400 (wk.), 1730 (st.), 1689 (st.), 1542 (med.), 1465 (wk.), 1266, 1152 (st.); $C_{32}H_{41}O_4N$ (FAB^+) *m/z* 492 ($M + H^+$, 3.2%),

270 ($[C_{16}H_{32}O_2N]^+$, 10%), 252 ($[C_{16}H_{30}ON]^+$, 5.3%), 179 ($[C_{14}H_{11}]^+$, 100%), 165 ($[C_{13}H_9]^+$, 12%); HRMS (FAB, NOBA matrix): $C_{32}H_{42}O_4N$ calcd for $[MH]^+$ 492.3114, found 492.3100.

Preparation of Liposomes. Lipopolyplex formulations were prepared by mixing the components in the following order: 50 μL of Lipofectin (InVitrogen Ltd., Paisley, UK: 30 μg/μL in OptiMEM); 70 μL of peptide (at between 0.029 mg/mL and 0.1 mg/mL in OptiMEM, to afford peptide charge ratios of either 4:1 or 1.5:1 (taking into account the TFA counterions associated with each peptide)); followed by 50 μL of the luciferase reporter plasmid pCILux (40 μg/mL in OptiMEM). Plasmid pCILux was prepared by subcloning a luciferase gene from pGL3 Control (Life Technologies, Paisley, UK) into the eukaryotic expression vector pCI (Promega, Southampton, UK). The complex was mixed by pipetting briefly before diluting in OptiMEM to a final volume of 1.57 mL.

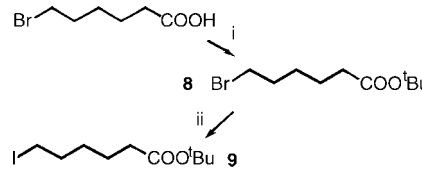
Transfection of Cells. The normal human airway epithelial cell line 1HAEo- (*16*) and the cystic fibrosis (CF) cell line 2CFSMEo- (*17*) (D. Gruenert, University of California, San Francisco) were maintained in Eagle's Minimal Essential Medium (MEM) HEPES modification (Sigma, Poole, UK) containing 10% fetal calf serum (FCS), 100 U/mL penicillin, and 100 μg/mL streptomycin and 2 mM L-glutamine, as described previously (*18*). Neuro-2A cells (ATCC) were maintained in Dulbecco's Modified Eagle Medium (DMEM)-Glutamax-1 (Life Technologies, Paisley, UK) containing 10% fetal calf serum (FCS) (Sigma, Poole, UK), 100 IU/mL penicillin, 100 μg/mL streptomycin, 1% sodium pyruvate, and 1% nonessential amino acids (Life Technologies, Paisley, UK). AJ3.1 is a mouse embryonic fibroblast line derived from A/J embryos 13.5 days postcoitum (Barker et al., manuscript in preparation).

The complete growth medium was removed from cells plated at 2×10^4 cells/well overnight in 96-well plates, and 200 μL of complex (0.25 μg of plasmid DNA) was added to each well, leaving minimal time between preparing the complex and adding to the cells. All transfections were carried out in 6 wells each. The cells were incubated with the complexes for 4 h before replacing with normal media for 24 to 48 h, after which reporter gene expression was analyzed by luciferase assay (Promega, Southampton, UK).

Luciferase assays. Cells were washed twice with PBS before the addition of 100 μl of 1 $\times$ Reporter Lysis Buffer (Promega, Southampton, U. K.) to the cells for 20 min at 4 °C before freezing at −20 °C for at least 30 min followed by thawing at room temperature (±20 °C). Twenty μl of the lysate at room temperature was transferred to a white polystyrene 96-well plate (Porvair Sciences Ltd., Shepperton, U. K.) and the luciferase activity was measured using the Luciferase Assay System (Promega) and a Lucy-1 Luminometer (Anthos Ltd., Saltzburg, Austria). The amount of protein present in each transfection lysate was determined with the Bio-Rad protein assay reagent by the manufacturer's instructions, adding 20 μl from the luciferase test to 200 μl of the reagent diluted 1 in 5 and incubating at room temperature for 10 min before comparing the OD_{590} to a range of BSA standards. Luciferase activity was expressed as Relative Light Units (RLU) per mg of protein (RLU/mg).

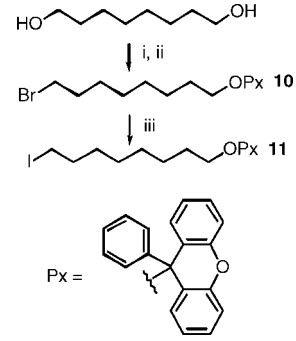
DLS. The complexes were formulated as described above, but using the PSVβ plasmid (a 6.9 kilobase plasmid). All experiments were conducted at a weight ratio of lipid/peptide/DNA 0.75:4:1. This resulted in a 4:1 charge ratio, when the TFA counterions associated with the peptide are taken into account. The DLS measurements were performed using a Malvern Zetasizer 3000 instrument (Malvern Instruments Ltd., UK) operating at a wavelength of 633 nm and a power output of 5 mW. All experiments were conducted at a constant temperature of 25 °C and a scattering angle of 90°, and spectra were collected every 180 s for at least 30 min. For broad, irregularly shaped distributions, where the method of cumulants was inappropriate, the *CONTIN* "constrained regularization" program (*19, 20*) was used for data analysis.

Scheme 1[a]



[a] (i) DCC, DMAP, *tert*-butyl alcohol, CH_2Cl_2, 78%; (ii) NaI, acetone (93%).

Scheme 2[a]



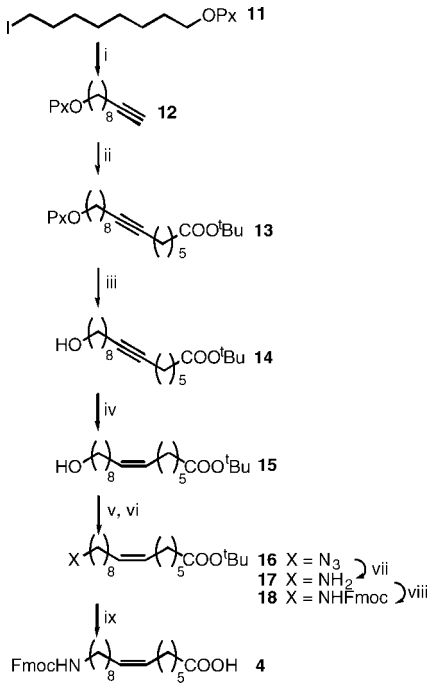
[a] (i) HBr, toluene, rfx (99%); (ii) 9-phenylxanthen-9-ol, AcOH (100%); (iii) NaI, acetone (97%).

RESULTS

Synthesis of the Lipophilic Amino Acids Fmoc-Laa (4) and Fmoc-Aua (6). 6-Aminohexanoic acid is commonly used as a lipophilic spacer in a variety of applications (*21*) and has been shown to increase the serum stability of some bioconjugates in *in vivo* applications (*22*). However, longer or more structurally complex ω-amino acids have not been extensively investigated as spacers or as conformational constraints. The flexible 11-aminoundecanoic acid (Aua) spacer was recently synthesized by the Campbell group as the Fmoc-protected Pfp ester and incorporated into analogues of atrial natriuretic factor (*15*). The only report of a longer, unsaturated linker being used in bioconjugate applications was the use of cis-alkenyl tethers, derived from alkynyl bis-carboxylic acids, as conformationally restricted cross-linked peptide inhibitors of HIV protease (*23*). In order to prepare peptides containing the long-chain ω-amino acids Aua and Laa using solid-phase peptide synthesis techniques, we had to first synthesize the Fmoc-protected amino acids, **4** and **6**, themselves.

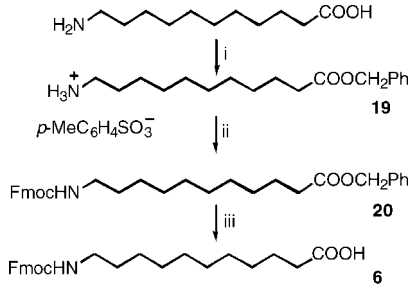
For the cis-alkenyl amino acid Fmoc-Laa **4**, the most efficient synthetic route appeared to be to prepare this from a suitable acetylenic ω-hydroxy acid by selective hydrogenation. This could in turn be synthesized from a protected ω-iodo alcohol, a protected ω-iodo acid, and acetylene. As the other functionality and protecting groups in **4** made it desirable that the protecting group on the ω-iodo acid should not need hydrogenation or base treatment for its removal, we elected to protect the acid as the *tert*-butyl ester. Initial attempts to esterify the available 8-bromohexanoic acid using perchloric acid and *tert*-butyl acetate following a procedure by Jost and Rudinger (*24*) were low-yielding and slow (>5 days), and the low boiling point of the resulting ester **8** made separation from *tert*-butyl acetate difficult. DCC-mediated coupling of *tert*-butyl alcohol (*25*) with the carboxylic acid gave greatly improved yields of the desired ester

Scheme 3[a]



[a] (i) $LiCCH(CH_2NH_2)_2$, HMPA, THF (98%); (ii) n-BuLi, THF/HMPA −78°C, then **9** (70%); (iii) 0.3 M $Cl_2CHCOOH$, pyrrole, CH_2Cl_2 (95%); (iv) Pd/C, H_2, MeOH/hexane (100%); (v) MsCl, Et_3N, CH_2Cl_2; (vi) NaN_3, DMF (90% over 2 steps); (vii) PPh_3, H_2O, THF (93%); (viii) Fmoc-Cl, NMM, THF (89%); (ix) TFA, 5% H_2O, 1,3-propanedithiol (95%).

Scheme 4[a]



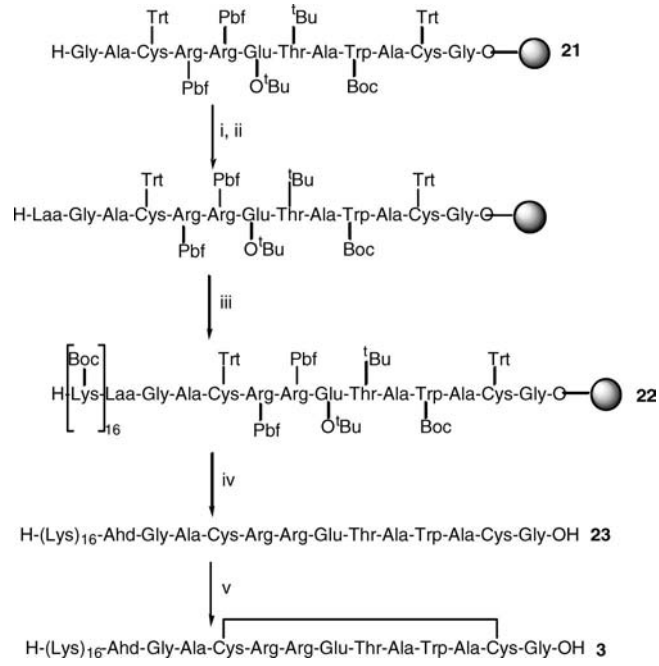
[a] (i) TsOH, $PhCH_2OH$, benzene (91%); (ii) Na_2CO_3 (aq), dioxane, Fmoc-Cl (95%); (iii) H_2, Pd/C, THF (88%).

7 within 24 h; this was then converted to the iodide **9** with sodium iodide (*12*) in 93% yield (Scheme 1).

We elected to protect the ω-iodo alcohol with the highly acid-labile 9-(9-phenyl)xanthenyl group (pixyl, Px), as this could be removed under very mild conditions without deprotection of the *tert*-butyl ester. Selective monopixylation of 1,8-octanediol followed by bromination proved to be unsuccessful as, although the monoprotected diol was effectively synthesized, the 9-phenylxanthyl protecting group proved to be unstable to the conditions required to convert the hydroxyl group to a bromo group (CBr_4, PPh_3 in CH_2Cl_2). 8-Bromooctan-1-ol was therefore synthesized first (Scheme 2) using hydrobromic acid (48%) (*26*). The hydroxy group was then protected with 9-phenylxanthen-9-ol, using glacial acetic acid both as a proton source and for azeotroping off water formed in the reaction, following a procedure by Gaffney and Reese (*27*) to give **10**. Treatment with sodium iodide afforded **11** in 97% yield.

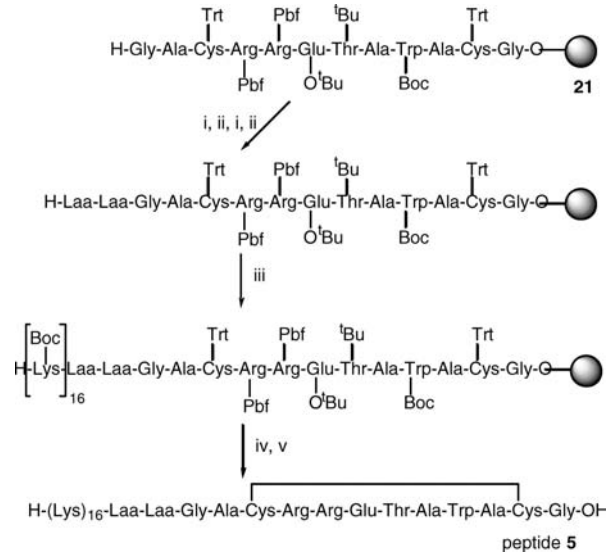
To form the required substituted acetylene, **11** was then reacted with lithium acetylide ethylenediamine complex (LAEDA), using a procedure adapted from DeJarlais and Emken (*28*),

Scheme 5[a]



[a] (i) HOAt, HATU, 1:1 DMF/CH_2Cl_2, **4**; (ii) DBU/piperidine/DMF 1:1:48; (iii) 16 cycles of Fmoc deprotection and coupling of Fmoc-Lys(Boc)-OH, Fmoc deprotection; (iv) TFA (85%), thioanisole (5%), phenol (5%), water (2.5%), and triethylsilane (2.5%); (v) H_2O, 7 d.

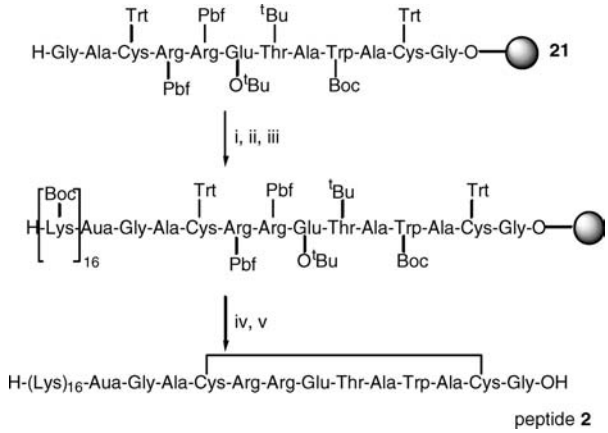
Scheme 6[a]



[a] (i) HOAt, HATU, 1:1 DMF/CH_2Cl_2, **4**; (ii) DBU/piperidine/DMF 1:1:48; (iii) 16 cycles of Fmoc deprotection and coupling of Fmoc-Lys(Boc)-OH, Fmoc deprotection; (iv) TFA (85%), thioanisole (5%), phenol (5%), water (2.5%), and 1,2-ethanedithiol (2.5%); (v) H_2O, 7 d.

to give **12** in excellent yield (Scheme 3). The organolithium derivative of **12** was then prepared by adding *n*-butyl lithium in THF and HMPA at −78 °C; this was followed by addition of **9** to give the desired disubstituted acetylene **13**. Fortuitously, the *tert*-butyl groups of both **13** and **9** appeared to withstand the use of *n*-butyl lithium under the conditions of this reaction. The selective removal of the 9-(9-phenyl)xanthenyl group from **13** was achieved with 0.1 M dichloroacetic acid in dichloromethane using pyrrole as the scavenger (*27*), to give **14**. A small amount (less than 5% by TLC analysis of the crude mixture) of the *tert*-butyl group was removed under these conditions. Catalytic hydrogenation at atmospheric pressure using

Scheme 7[a]



[a] (i) HOAt, HATU, 1:1 DMF/CH_2Cl_2, Fmoc-Aua **6**; (ii) DBU/piperidine/DMF 1:1:48; (iii) 16 cycles of Fmoc deprotection and coupling of Fmoc-Lys(Boc)-OH, Fmoc deprotection; (iv) TFA (85%), thioanisole (5%), phenol (5%), water (2.5%), and triethylsilane (2.5%); (v) H_2O, 7 d.

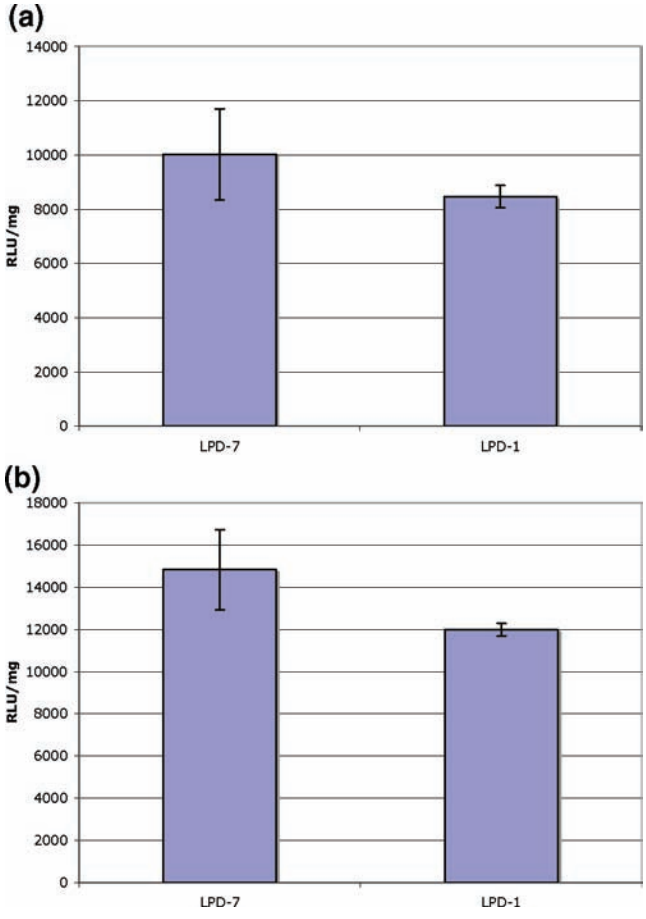


Figure 1. (a) Transfection of 1HAEo- cells with **LPD-1(4:1)** and **LPD-7(4:1)**. (b) Transfection of CFSMEo- cells with **LPD-1(4:1)** and **LPD-7(4:1)**.

Lindlar catalyst in methanol and hexane gave the *cis*-hydroxy compound **15**, which was then mesylated and converted to the azide **16**. Staudinger reduction of **16**, using a procedure originally developed for the synthesis of allylic amines (*29*), gave the amine **17** in 80% yield. A slight modification to the original procedure, adding PPh_3 first and leaving to stir for 5 h before adding water, increased the yield to 93%. Fmoc protection to give **18** (*30*) was followed by removal of the *tert*-butyl

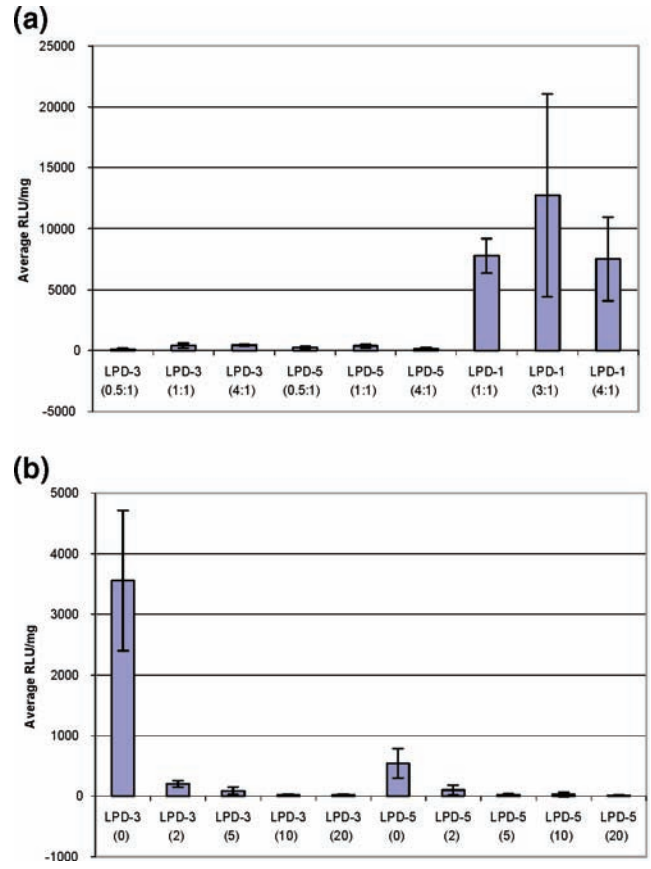


Figure 2. (a) Transfection of 1HAEo- cells with **LPD-3**, **LPD-5**, and **LPD-1** at different charge ratios. (b) Transfection of 1HAEo- cells with **LPD-3** and **LPD-5** at a 4:1 peptide ratio, in varying concentrations of serum.

group (*31*) to give the desired lipophilic amino acid Fmoc-Laa **4** in 46% overall yield from **11**.

For the synthesis of peptide **2**, it was necessary to prepare the Fmoc-derivative of commercially available 11-aminoundecanoic acid. Reaction of the poorly soluble 11-aminoundecanoic acid with fluorenylmethyl chloroformate in water/aqueous sodium hydrogen carbonate failed, and an inseparable mixture of the Fmoc-protected amino acid and the Fmoc-protected dipeptide and tripeptide were recovered. Boumrah et al. (*15*) circumvented the problem of solubility by preparing Fmoc-Aua from 11-(9-fluorenylmethyloxycarbonylamido)undecanoic acid benzyl ester; however, the initial benzyl ester formation was inconvenient because it required the use of dry hydrochloric acid gas. We therefore used a modification (*14*) of a procedure (*32*) for the preparation of amino acid benzyl esters using the less hazardous toluenesulfonic acid to prepare 11-aminoundecanoic acid benzyl ester *p*-toluenesulfonate **19**. Subsequent treatment of **19** with fluorenylmethyl chloroformate in dioxane/aqueous sodium bicarbonate gave 11-(9-fluorenyl-methyloxycarbonylamido)undecanoic acid benzyl ester **20** in 95% yield (Scheme 4). Benzyl deprotection of **20** to give 11-(9-fluorenylmethyloxycarbonylamido)undecanoic acid (Fmoc-Aua, **6**) was accomplished by hydrogenation (*15*) in 88% yield. Thus, **6** was conveniently prepared in three steps in an overall yield of 76%.

Peptide Synthesis. As the integrin-targeting C-terminus is the same for all of the peptides, this sequence was first synthesized on a large scale using automated solid-phase peptide synthesis to give the resin-bound protected peptide **21** (Scheme 5). Incorporation of the lipophilic amino acid Fmoc-Laa **4** using DIC and HOBt in DMF, whether manually or on the peptide synthesizer, was unsuccessful, probably because of the poor

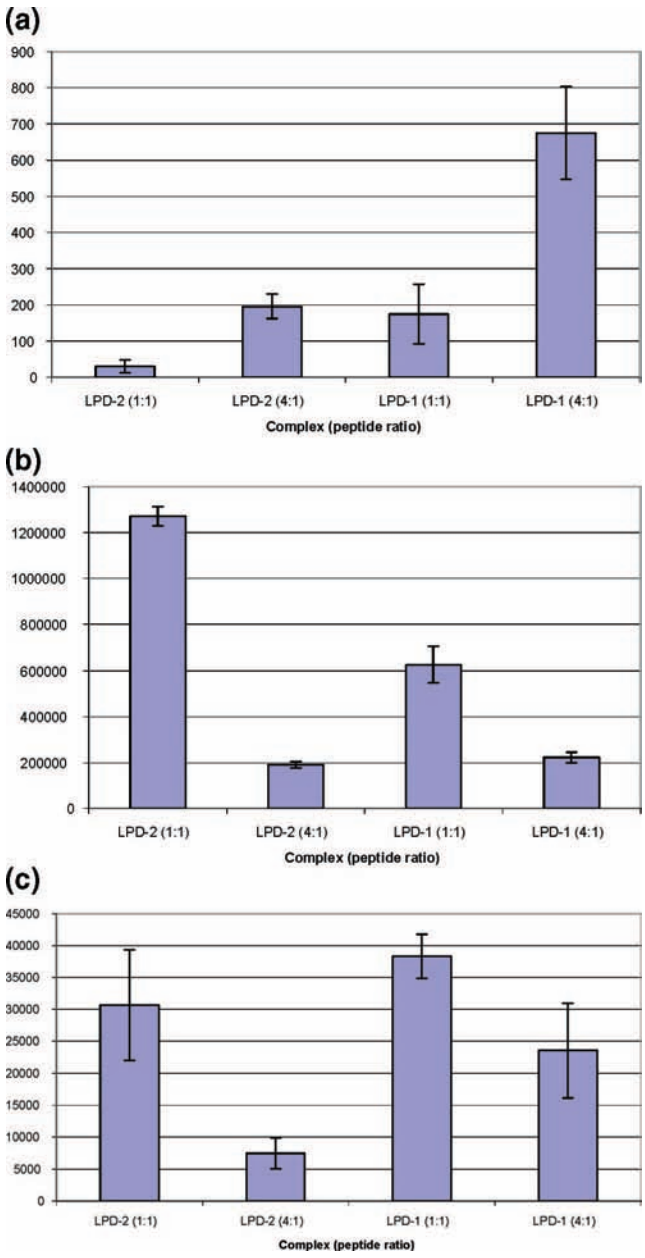


Figure 3. Transfection properties of **LPD-2** and **LPD-1** at 1:1 and 4:1 ratios, in (a) 1HAEo-, (b) N2A, and (c) AJ3.1 cells.

solubility of **4** in DMF. Manual coupling of **4** to **21**, using HATU and HOAt (*33, 34*) in 1:1 CH_2Cl_2/DMF, however, proved successful, and the coupling was confirmed by the Kaiser test and by MS analysis of a cleaved and deprotected sample. As the Laa residue is very hydrophobic, a mixture of DBU and piperidine (*35*) was used for the removal of the Fmoc group. The peptide synthesis was then completed using automated methods to give the resin-bound peptide **22**. Cleavage of **22** from the resin and deprotection, using 85% TFA and thioanisole, phenol, and triethylsilane as scavengers, proved problematic. After purification and MS analysis, it was discovered that reduction of the double bond of Laa had taken place to give peptide **23**, containing the *saturated* Ahd residue. This was surprising, as, although there are instances where double bonds can be reduced with trifluoroacetic acid and an alkylsilane at room temperature, there are very few examples (*36*) of it occurring with nonconjugated alkenes. Aerial oxidiation to form the disulfide bond was then attempted using 0.01 M aqueous ammonium bicarbonate (*37*) or DMSO (*38*). However, both of these methods presented problems in the final HPLC purification

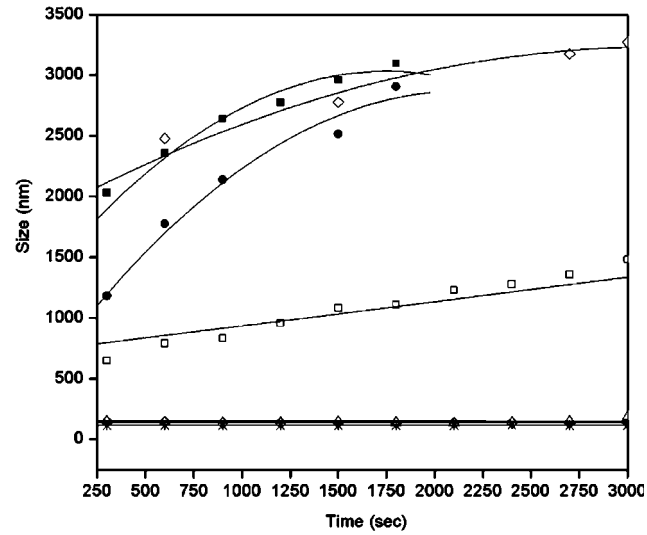


Figure 4. Average aggregate sizes of lipopolyplexes at pH 7.4 as a function of time. Data refer to **LPD-1** in H_2O (♦), **LPD-1** in PBS (■), **LPD-3** in H_2O (△), **LPD-3** in PBS (◇), **LPD-5** in H_2O (*), **LPD-5** in PBS (solid pentagon), **LPD-5** in H_2O + 150 mM NaCl (□). All experiments were conducted at a weight ratio of lipid/peptide/DNA 0.75:4:1 resulting in a +4 charge ratio.

of the peptide, as the excess salts or DMSO led to poor retention of the peptide on the column and hence a very low recovery. The disulfide bond formation was therefore carried out in water at high dilution over 7 days to give complete formation of peptide **3**.

With these observations taken into account, intermediate **21** was then used to prepare peptide **5**. Two Laa residues were incorporated manually using HATU and HOAt, with the Fmoc groups being removed with a mixture of DBU and piperidine. The peptide was completed via automated synthesis and cleaved and deprotected using 85% TFA and thioanisole, phenol, and ethanethiol as scavengers; no reduction of either of the double bonds was detected by MS analysis. Aerial oxidation in water was again carried out to yield peptide **5** (Scheme 6). A similar strategy was used to prepare peptide **2**, using Fmoc-Aua **6** (Scheme 7).

Transfection. A series of lipopolyplexes were formulated, using the previously described procedure (*7*) from Lipofectin, plasmid DNA, and peptides **1**, **2**, **3**, **5**, and **7**, respectively, to give lipopolyplexes **LPD-1** to **LPD-7**. Additionally, each lipopolyplex was formulated at three different peptide/DNA (P/N) charge ratios: 0.5:1; 1:1; and 4:1.

We initially investigated the complex **LPD-7**, with the Ahx-Ser-Ahx spacer. This performed slightly better in transfection than the original LID complex, **LPD-1**, in a range of cell lines (Figure 1). Encouraged by this success, we tested the complexes containing lipid-like spacers, **LPD-3** and **LPD-5**, in 1HAEo- cells (Figure 2). However, the results were disappointing: virtually no transfection was observed with these complexes (Figure 2a) and the complexes showed no stability when placed in even low amounts of serum (Figure 2b).

Peptide **2** contains the 11-aminoundecanoic acid spacer, which is shorter than the other spacer regions but more hydrophobic than the spacer in peptide **7**. The **LPD-2** complexes formulated from this peptide had moderate transfection properties (Figure 3) which were highly dependent on the cell type. In N2A cells, transfection exceeded the original vector (**LPD-1**), whereas in 1HAEo- cells, the transfection was not as good, and in AJ3.1 cells, the transfection was comparable.

Stability Measurements. In order to assess whether the poor transfection results obtained with the lipophilic peptides were

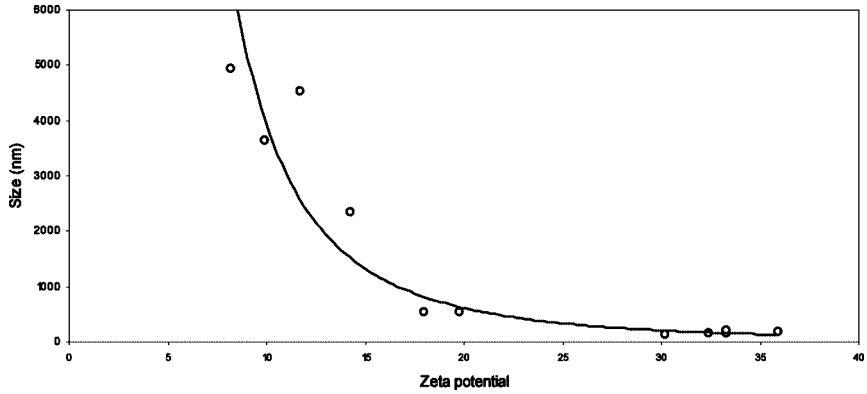


Figure 5. Relationship between zeta potential and particle size. The line represents the Monte Carlo simulation data and the circles the experimental data.

related to aggregation of vector particles, we investigated the aggregation properties of the lipopolyplex complexes containing peptides **3** and **5**. The lipopolyplexes **LPD-1**, **LPD-3**, and **LPD-5** were formulated from Lipofectin, plasmid DNA, and the relevant peptide as described previously (*7*) at 4:1 charge ratios, and the size of the resulting particles measured in water, NaCl solutions, and at different concentrations of phosphate buffered saline (PBS) to mimic physiological conditions. In order to determine the size of the complex, dynamic light scattering (DLS) measurements were made (*39*) and the hydrodynamic radius or diameter of the particles can be calculated (*40*, *41*).

In Figure 4, the changes in size distribution over time of these lipopolyplexes are shown. In water, very little aggregation takes place for any of the complexes; however, when increasing amounts of NaCl are added, the rate of aggregation increases. In PBS, a physiologically relevant buffer, both the original complex and the complexes containing lipophilic spacers aggregate dramatically over time. It is also notable that the starting size of each of the complexes is rather different, with **LPD-3** being the most compact.

DISCUSSION

We have developed efficient routes to two hydrophobic amino acids, suitably protected for solid-phase peptide synthesis. The novel amino acid **4** has been designed to imitate the unsaturated chain of the lipid DOTMA, and we have also developed an improved route to the previously described **6**. We have then successfully synthesized peptides containing these or other hydrophobic amino acids as spacers, for use in nonviral gene delivery studies of targeted ternary lipopolyplex vectors.

Several factors influence the transfection efficiencies of targeted lipopolyplex vectors (*6*). For the present study, three factors could be important. It is probable that a long spacer unit between the DNA-condensation and integrin-targeting moieties of the peptide could lead to better interactions between the vector and the cell surface receptor. We also initially hypothesized that, if these spacer units could be designed to stack within a lipid bilayer, the stability of the vector, and hence its transfection efficiency (*39*), could be enhanced. However, the overall hydrophobicity of the spacer unit will also be important in determining the stability of the resulting vector, and hence the transfection efficiency, as vectors which dissociate rapidly or aggregate in buffer or serum solutions will have greatly reduced transfection efficiencies.

We have previously carried out a theoretical study (*42*) to model the dynamics of vector aggregation. The vectors **LPD-1** and **LPD-3** were studied, using Monte Carlo simulation techniques to model the dynamics of vector aggregation. It was clearly demonstrated, both experimentally and in the simulation, that **LPD-3** aggregated much more rapidly than **LPD-1**. It was shown that the levels of aggregation of vector particles under Brownian motion could be predicted on the basis of the zeta potential of the vector particles. Vector buffer systems with a zeta potential less than 20 mV exhibit significant aggregation (Figure 5).

These results are in agreement with the poor transfection efficiencies of **LPD-3** (Figure 2) and also with the rapid aggregation of **LPD-3** in PBS (Figure 4). The hydrophobicity of the Ahd linker clearly outweighs any beneficial effect of interaction with the hydrophobic portion of either DOTMA or DOPE, although it appears to lead to a structure that is initially more compact than **LPD-1** (Figure 4). Moreover, when two Laa amino acids are used as lipid-like linkers, in peptide **5**, the resulting complex (**LPD-5**) demonstrates equally poor transfection efficiencies (Figure 2) and serum (Figure 2) and buffer (Figure 4) stability. These results suggest three possible alternative hypotheses: either packing of lipid-like linkers within a lipid bilayer is not possible; or it does not result in a more stable vector particle; or ternary lipopolyplex vectors of this type do not have an ordered lipid layer. It is notable that in other, unrelated biological systems where hydrophobic spacers have been employed (*43*) the results have not been as good as with hydrophilic, PEG-based spacers.

In comparison, peptide **7** has a linker sequence of approximately the same length as peptide **5**. However, the transfection efficiency of **LPD-7** is much better than that of **LPD-5**, and also an improvement on the original vector, **LPD-1** (Figures 1 and 2). **LPD-7** is also more efficient than **LPD-2**, with a shorter but equally hydrophobic linker (Figures 1 and 3). We assume that peptide **7** has a spacer unit which is sufficiently long and inflexible to position the integrin targeting motif at the exterior of the vector, rendering it more accessible to cell surface receptors, and that it is the length, rather than the hydrophobicity, of the spacer which is important for efficient transfection. Further biophysical studies into the macromolecular organization and stability properties of ternary targeted lipopolyplex vectors are underway.

ACKNOWLEDGMENT

The EPSRC are thanked for DTA studentships to M.P.M. and S.S. M.W. was supported by a grant from the BBSRC, and S.B. by a studentship from the MRC. The authors thank Dieter Gruenert, California Pacific Medical Center Research Institute, San Francisco, CA, for kindly providing the cell lines CFSMEo- and 1HAEo-.

Supporting Information Available: Experimental details of the synthesis of Fmoc-Aua **6**, and of the synthesis of all peptides described. This material is available free of charge via the Internet at http://pubs.acs.org.

LITERATURE CITED

(1) Somia, N., and Verma, I. M. (2000) Gene therapy: Trials and tribulations. *Nat. Rev. Genet. 1*, 91–99.

(2) Marshall, E. (1999) Clinical trials - gene therapy death prompts review of adenovirus vector. *Science 286*, 2244–2245.

(3) Kang, E. M., and Tisdale, J. F. (2004) The leukaemogenic risk of integrating retroviral vectors in hematopoietic stem cell gene therapy applications. *Curr. Hematol. Rep. 3*, 274–281.

(4) Davis, M. E. (2002) Non-viral gene delivery systems. *Curr. Opin. Biotechnol. 13*, 128–131.

(5) Wolff, J. A. (2002) The "grand" problem of synthetic delivery. *Nat. Biotechnol. 20*, 768–769.

(6) Varga, C. M., Wickham, T. J., and Lauffenburger, D. A. (2000) Receptor-mediated targeting of gene delivery vectors: Insights from molecular mechanisms for improved vehicle design. *Biotechnol. Bioeng. 70*, 593–605.

(7) Hart, S. L., Arancibia-Cárcamo, C. V., Wolfert, M. A., Mailhos, C., O'Reilly, N. J., Ali, R. R., Coutelle, C., George, A. J. T., Harbottle, R. P., Knight, A. M., Larkin, D. F. P., Levinsky, R. J., Seymour, L. W., Thrasher, A. J., and Kinnon, C. (1998) Lipid-mediated enhancement of transfection by a nonviral integrin-targeting vector. *Hum. Gene Ther. 9*, 575–585.

(8) Jenkins, R. G., Herrick, S. E., Meng, Q.-H., Kinnon, C., Laurent, G. J., McAnulty, R. J., and Hart, S. L. (2000) An integrin-targeted non-viral vector for pulmonary gene therapy. *Gene Ther. 7*, 393–400.

(9) Parkes, R., Meng, Q.-H., Siapati, K. E., McEwan, J. R., and Hart, S. L. (2002) High efficiency transfection of porcine vascular cells in vitro with a synthetic vector system. *J. Gene Med. 4*, 292–299.

(10) Weber, E., Dorpinghaus, N., and Csoregh, I. (1990) Versatile and convenient lattice hosts derived from singly bridged triarylmethane frameworks, X-ray crystal structures of 3 inclusion compounds. *J. Chem. Soc., Perkin Trans. 2 12*, 2167–2177.

(11) Spande, T. F. (1980) Synthesis of two novel phosphorylcholine esters for probes in immunological studies. *J. Org. Chem. 45*, 3081–3084.

(12) Castellanos, L., Gateau-Olesker, A., Panne-Jacolot, F., Cleophax, J., and Gero, S. D. (1981) Synthesis of analogs of dioxaprostanoic derivatives from D-xylose and L-xylose. *Tetrahedron 37*, 1691–1696.

(13) Rama Rao, A. V., Pulla Reddy, S., and Rajarathnam Reddy, E. (1986) Short and efficient syntheses of coriolic acid. *J. Org. Chem. 51*, 4158–4159.

(14) Vinogradov, S. A., Lo, L.-W., and Wilson, D. F. (1999) Dendritic polyglutamic porphyrins: probing porphyrin protection by oxygen-dependent quenching of phosphorescence. *Chem.—Eur. J. 5*, 1338–1347.

(15) Boumrah, D., Campbell, M. M., Fenner, S., and Kinsman, R. G. (1997) Spacer molecules in peptide sequences: incorporation into analogues of atrial natriuretic factor. *Tetrahedron 53*, 6977–6992.

(16) Cozens, A. L., Yezzi, M. J., Yamaya, M., Wagner, J. A., Steiger, D., Garber, S. S., Chin, L, Simon, E. M., Cutting, G. R., Gardner, P., Friend, D. S., Basbaum, C. B., and Gruenert, D. C. (2002) A transformed human epithelial cell line that retains tight junctions post crisis. *In Vitro Cell Dev. Biol. 28A*, 735–744.

(17) Cozens, A. L., Yezzi, M. J., Kunzelmann, K., Ohrui, T., Chin, L., Eng, K., Finkbeiner, W. E., Widdicombe, J. H., and Gruenert, D. C. (1994) CFTR expression and chloride secretion in polarized immortal human bronchial epithelial cells. *Am. J. Respir. Cell Mol. Biol. 10*, 38–47.

(18) Meng, Q.-H., Robinson, D., Jenkins, R. G., McAnulty, R. J., and Hart, S. L. (2004) Efficient transfection of non-proliferating human airway epithelial cells with a synthetic vector system. *J. Gene Med. 6*, 210–221.

(19) Provencher, S. W. (1979) Inverse problems in polymer characterisation - direct analysis of polydispersity with photon correlation spectroscopy. *Makromol. Chem. 180*, 201–242.

(20) Provencher, S. W. (1982) CONTIN - A general-purpose constrained regularization program for inverting noisy linear algebraic and integral-equations. *Comput. Phys. Commun. 27*, 229–242.

(21) Lössner, D., Kessler, H., Thumshirn, G., Dahmen, C., Wiltschi, B., Tanaka, M., Knoll, W., Sinner, E.-K., and Reuning, U. (2006) Binding of small mono- and oligomeric integrin ligands to membrane-embedded integrins monitored by surface plasmon-enhanced fluorescence spectroscopy. *Anal. Chem. 78*, 4524–4533.

(22) Youngblood, D. S., Hatlevig, S. A., Hassinger, J. N., Iversen, P. I., and Moulton, H. M. (2007) Stability of cell-penetrating peptide-morpholino oligomer conjugates in human serum and in cells. *Bioconjugate Chem. 18*, 50–60.

(23) Ulysse, L. G., and Chmielewski, J. (1998) Restricting the flexibility of crosslinked, interfacial peptide inhibitors of HIV-1 protease. *Bioorg. Med. Chem. Lett. 8*, 3281–3286.

(24) Jost, K., and Rudinger, J. (1967) Amino acids and peptides. 69. Synthesis of two biologically active analogues of deamino-oxytocin not containing a disulphide bond. *Collect. Czech. Chem. Commun. 32*, 1229–1241.

(25) Li, X., Atkinson, R. N., and King, S. B. (2001) Preparation and evaluation of new L-canavanine derivatives as nitric oxide synthase inhibitors. *Tetrahedron 57*, 6557–6565.

(26) Chong, J. M., Heuft, M. A., and Rabbat, P. (2000) Solvent effects on the monobromination of α,ω-diols: a convenient preparation of ω-bromoalkanols. *J. Org. Chem. 65*, 5837–5838.

(27) Gaffney, P. R. J., and Reese, C. B. (2001) Synthesis of naturally occurring phosphatidylinositol 3,4,5-trisphosphate [PtdIns(3,4,5) P_3] and its diastereoisomers. *J. Chem. Soc., Perkin Trans. I*, 192–205.

(28) DeJarlais, W. J., and Emken, E. A. (1980) A convenient synthesis of ω-acetylenic acids. *Synth. Commun. 10*, 656–660.

(29) Foucaud, A., and ElGuemmout, F. (1989) Preparation of allylic amines from methyl 3-acyloxy 2-methylene propionates 3-substituted by aromatic or heteroaromatic groups. *Bull. Soc. Chim. Fr. 3*, 403–408.

(30) Ayi, A. I., Martos-Alcaniz, M.-L., Condom, R., Frogier, P. R. T., and Guedj, R. (1991) Fluorinated amino acids and peptides. Synthesis of 3,3-difluoro-2-amino acids, peptides and cyclodipeptides incorporating 3,3-difluoro-2-aminobutyric acid or 3,3-difluorophenylalanine residues in their structures. *J. Fluorine Chem. 55*, 13–28.

(31) Wattanasin, S., Weidmann, B., Roche, D., Myers, S., Xing, A., Guo, Q., Sabio, M., von Matt, P., Hugo, R., Maida, S., Lake, P., and Weetall, M. (2001) Design and synthesis of potent and selective inhibitors of integrin VLA-4. *Bioorg. Med. Chem. Lett. 11*, 2955–2958.

(32) Zervas, L., Winitz, M., and Greenstein, J. P. (1957) Studies on arginine peptides. I. Intermediates in the synthesis of N-terminal and C-terminal arginine peptides. *J. Org. Chem., 22*, 1515–1521.

(33) Carpino, L. A. (1993) 1-Hydroxy-7-azabenzotriazole. An efficient peptide coupling additive. *J. Am. Chem. Soc. 115*, 4397–4398.

(34) Carpino, L. A., El-Faham, A., Minor, C. A., and Albericio, F. (1994) Advantageous applications of azabenzotriazole (triazolopyridine)-based coupling reagents to solid-phase peptide synthesis. *J. Chem. Soc.: Chem. Commun.* 201–203.

(35) Wade, J. D., Bedford, J., Sheppard, R. C., and Tregear, G. W. (1991) DBU as an N^{α}-deprotecting reagent for the fluorenylmethoxycarbonyl group in continuous flow solid-phase peptide synthesis. *Peptide Res. 4*, 194–199.

(36) Kursanov, D. N., Parnes, Z. N., Bassova, G. I., Loim, N. M., and Zdanovich, V. I. (1967) Ionic hydrogenation of the ethylene bond and the double bond of the carbonyl group. *Tetrahedron 23*, 2235–2242.

(37) Chan, W. C., and White, P. D. (2001) *Fmoc Solid Phase Peptide Synthesis - A Practical Approach. Practical Approach Series*, Oxford University Press, Oxford.
(38) Otaka, A., Koide, T., Shide, A., and Fujii, N. (1991) Application of dimethylsulphoxide (DMSO)/trifluoroacetic acid (TFA) oxidation to the synthesis of cystine-containing peptide. *Tetrahedron Lett. 32*, 1223–1226.
(39) Lee, L. K., Mount, C. N., and Ayazi Shamlou, P. (2001) Characterisation of the physical stability of colloidal polycation-DNA complexes for gene therapy and DNA vaccines. *Chem. Eng. Sci. 54*, 3171–3178.
(40) Van de Hulst, H. C. (1957) *Light Scattering by Small Particles 1st ed.*, Academic Press, New York.
(41) Kerker, M. (1969) *The Scattering of Light and Other Electromagnetic Radiation*, 1st ed.,Academic Press, New York.
(42) Sarkar, S., Zhang, H., Levy, S. M., Hart, S. L., Hailes, H. C., Tabor, A. B., and Ayazi Shamlou, P. (2003) Prediction of size distribution of lipid-peptide-DNA vector particles using Monte Carlo simulation techniques. *Biotechnol. Appl. Biochem. 38*, 95–102.
(43) Sanchez-Martin, R. M., Muzerelle, M., Chitkul, N., How, S. E., Mittoo, S., and Bradley, M. (2005) Bead-based cellular analysis, sorting and multiplexing. *ChemBioChem 6*, 1341–1345.

BC0700943

Instantaneous Determination via Bimolecular Recognition: Usefulness of FRET in Phosphorylcholine Group Enriched Nanoparticles

Junji Watanabe[†] and Kazuhiko Ishihara*[,‡]

Department of Applied Chemistry and 21st Century COE Program "Center for Integrated Cell and Tissue Regulation", Graduate School of Engineering, Osaka University, 2-1 Yamada-oka, Suita, Osaka 565-0871, Japan, and Department of Materials Engineering, School of Engineering, and Center for NanoBio Integration, The University of Tokyo, 7-3-1 Bunkyo-ku, Hongo, Tokyo 113-8656, Japan. Received March 18, 2007; Revised Manuscript Received July 17, 2007

This paper deals with smart bimolecular recognition for instantaneous determination. In particular, we installed the fluorescence resonance energy transfer (FRET) system in phosphorylcholine (PC) group enriched nanoparticles (NPs). The most favorable characteristics were as follows: (i) the suppression of nonspecific protein adsorption by the PC group enriched surface and (ii) simple bioassay protocol relative to the conventional enzyme-linked immunosorbent assay (ELISA). In the case of immunoassays, nonspecific interaction and complex protocols are known dominant problems. To address these issues, we designed FRET-installed NPs. Agglutination of NPs is a fundamental immunoassay technique; however, it is not quantitative. By evaluating the degree of agglutination based on the fluorescence intensity, the resulting information can be used for diagnosis. Therefore, we installed the FRET system on the surface of the NPs. In this paper, C-reactive protein (CRP) and osteopontin (OPN) were the target biomarkers for instantaneous determination, and the resulting fluorescence intensity correlated well with changes in the concentrations of the target molecules. The immunoassay protocol was quite simple, involving only the mixing of FRET-installed NPs and target molecules, such as CRP and OPN antigens. We successfully evaluated the concentration of the target biomarkers, even when human serum albumin was present as an interference molecule.

INTRODUCTION

Here, we report a new bimolecular recognition system to detect biomarkers using phosphorylcholine (PC) group enriched nanoparticles (NPs). PC group enriched surfaces provide excellent biointerfaces, since they (i) suppress nonspecific protein adsorption (*1–4*) and (ii) stabilize immobilized biomolecules (*5, 6*). PC group enriched surfaces have high hydrophilicities, and the fundamental mechanisms of interactions with proteins are thus investigated in terms of water structure (*7–9*). Therefore, PC group enriched NPs are stable in aqueous solutions without further surface modification. Moreover, PC-introduced polymers have been widely reported using 2-methacryloyloxyethyl phosphorylcholine (MPC) and in hydroxyl group conversions to PC groups via two-step processes. Hilborn et al. reported that PC groups could be incorporated into both terminals of poly(trimethylene carbonate) by using a converting method (*10*). PC-functionalized ionomers showed surface enrichments in PC groups within a few minutes when specimens were soaked in aqueous solutions. Considering these unique properties, PC group enriched surfaces are important materials that form NPs with excellent biointerface properties.

Biomarkers are indicators of biological processes in broad scientific fields, namely, molecular biology; cell biology; and diagnostic, therapeutic, and regenerative medicine. Generally, biomarkers are present in low levels in blood, serum, and cell culture media; thus, amplification and/or highly sensitive methods for detecting trace amounts of biomarkers are major goals when developing immunoassays. Conventional immunosandwich methods, such as enzyme-linked immunosorbent assay (ELISA), are the fundamental protocols for bioassays (*11*). Although the methodology of ELISA is quite simple, unfortunately, it has certain disadvantages in capturing trace biomarker molecules due to the fact that these assays are (i) labor-intensive and time-consuming and (ii) prone to nonspecific protein adsorption. Therefore, to detect low concentrations of biomarkers, assays must be highly sensitive and follow a simple protocol. The latter issue may be improved with the use of PC group enriched surfaces (*1–4*), since nonspecific protein adsorption is suppressed by PC group enriched surfaces that function as blocking biointerfaces. However, even with a decrease in nonspecific protein adsorption, the time-consuming and complicated protocol would continue to be a part of conventional immunoassays. Therefore, instantaneous determination for smart immunoassays is necessary to improve issues regarding complicated protocols.

To improve these issues, we have already proposed a prototype bimolecular recognition system that provides a single protocol that employs fluorescence resonance energy transfer (FRET) on PC group enriched NPs (*12*). The fundamental mechanism of FRET is a distance-dependent interaction between the electronic excited states of two fluorescence molecules in which excitation is transferred from a donor molecule to an acceptor molecule (*13, 14*). Following the capture of a target biomarker by each donor and acceptor molecule-labeled antibody on the NPs, if the FRET phenomenon takes place between donor and acceptor molecules, biomarkers may be detected in the medium. Therefore, we designed dual-bioconjugated NPs covered with PC groups and donor or acceptor molecule labeled antibodies to measure FRET. As a definite plan, each fluorescence molecule was conjugated with a polyclonal antibody, and each fluorescence-labeled antibody was then immobilized onto the PC-covered NPs containing active ester groups for bioconjugation. As a result, the FRET system was installed in the

* Address correspondence to: Tel +81-3-5841-7124, Fax +81-3-5841-8647, E-mail ishihara@mpc.t.u-tokyo.ac.jp (K. Ishihara, Ph.D.).
[†] Osaka University.
[‡] The University of Tokyo.

10.1021/bc070095v CCC: $37.00 © 2007 American Chemical Society
Published on Web 09/18/2007

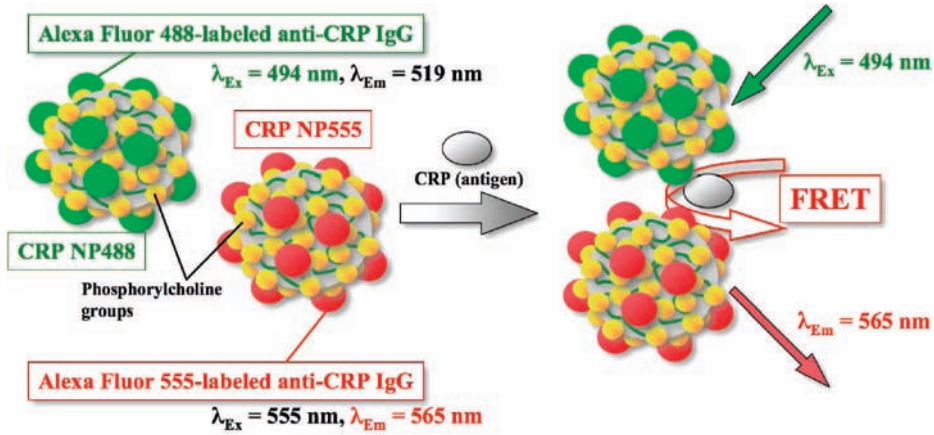


Figure 1. Bimolecular recognition system using PC group enriched NPs by fluorescence resonance energy transfer (FRET). In this illustration, C-reactive protein (CRP) was selected as a target molecule. Two types of NPs could capture the CRP antigen, and FRET was then induced.

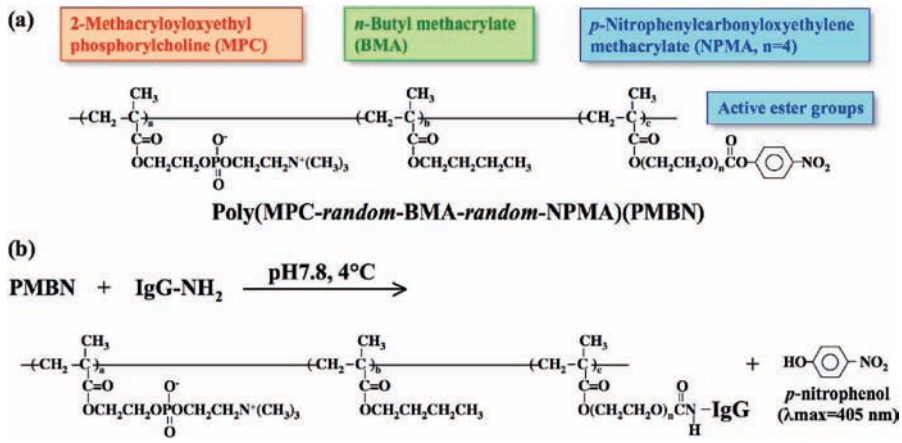


Figure 2. (a) Chemical structure of PC group introduced amphiphilic polymer (PMBN) with active ester groups via oxyethylene spacer (n = 4). (b) Bioconjugation with amino groups in IgG molecule via active ester groups.

bioconjugated PC-covered NPs. Antibody-conjugated NPs could capture specific antigens from sample solutions when the donor and acceptor molecules were in close enough proximity to form antibody–antigen complexes. If FRET occurred by the agglutination of NPs, fluorescence by acceptor molecules would be observed by using a fluorescence spectrometer. The aforementioned reactions are designed to automatically proceed in reaction media when FRET-installed NPs are mixed with blood serum samples. This type of bimolecular recognition system provides a protocol that is rather simple as compared to conventional ELISAs.

Herein, we proposed further improvement of the bimolecular recognition system using FRET-installed NPs and focused on C-reactive protein (CRP) and osteopontin (OPN) as typical target biomarkers for inflammation and differentiation, respectively. Originally, we designed dual-immobilized NPs for bimolecular recognition (*12*). Two types of fluorescence-labeled antibodies were immobilized onto NPs. In the present study, we modified the design of immobilization; mono-immobilized NPs were designed and prepared for bimolecular recognition. Alexa Fluor 488 (donor) and Alexa Fluor 555 (acceptor) were selected as a pair of fluorescence molecules for FRET. Each fluorescent molecule labeled antibody was individually immobilized on the PC group enriched surface (mono-immobilized NPs). For bimolecular recognition using the NPs, the 2 types of mono-immobilized NPs were mixed together, and the addition of an antigen would induce NP agglutination; the FRET phenomenon was then induced quantitatively (Figure 1).

EXPERIMENTAL SECTION

Preparation of PC Group Enriched NPs. PC groups containing polymers (PMBN, Figure 2) for bioconjugation were prepared from MPC, *n*-butyl methacrylate (BMA) (Wako Pure Chemical Co., Ltd., Osaka, Japan), and *p*-nitrophenylcarbonyloxyethylene methacrylate (NPMA). The detailed procedures describing their preparation have been reported elsewhere (*15–17*). PC group enriched NPs were also prepared by a previously reported method (*18*, *19*). The fundamental preparative condition was the solvent evaporation technique via emulsion. PMBN aqueous solution (40 mL, 10 mg/mL) and polystyrene (average molecular weight (MW) = 200 000 g/mol; Kanto Chemicals Co., Ltd., Tokyo, Japan) methylene chloride solution (20 mg, 20 mg/mL) were mixed together. The mixture was treated for 2 min by using a probe-type ultrasonicator (Branson Sonifier 250, Emerson Japan Ltd., Tokyo, Japan). Thus, a finely dispersed emulsion was obtained. After the evaporation of methylene chloride, the resulting NPs were collected using centrifugation. Moreover, the NPs were repeatedly washed by centrifugation and resuspended in ultrapure water. Purified NPs were stored at 4 °C at a concentration of 20 mg/mL until further use.

Preparation of Fluorescence-Labeled Antibodies. For FRET, the distance between the donor and acceptor molecules should be limited, and both must be in close proximity (within 10 nm). The distance at which the energy transfer is 50% efficient is defined by the Förster radius. The magnitude of the radius is dependent on the spectral properties of the donor and

acceptor molecules. In this study, the Förster radius between the Alexa Fluor dye pairs was calculated to be 7 nm (*20*). Antibodies were labeled using the Alexa Fluor labeling kit according to the manufacturer's protocol. In this study, antihuman CRP polyclonal antibodies (CRP-IgG; Oriental Yeast Co., Ltd., Shiga, Japan), recombinant human CRP (Host cell: *Escherichia coli*; Oriental Yeast Co., Ltd.), antimouse OPN polyclonal antibodies (OPN-IgG; R & D Systems, Inc., MN, USA), and recombinant mouse OPN (Host cell: mouse NSO cells; Sigma-Aldrich, Inc., MO, USA) were used without further purification. Alexa Fluor 488 (A-10235, $\lambda_{Ex} = 494$ nm, $\lambda_{Em} = 519$ nm) and Alexa Fluor 555 (A-20174, $\lambda_{Ex} = 555$ nm, $\lambda_{Em} = 565$ nm) labeling kits were purchased from Invitrogen Corp., CA, USA.

In brief, 1 mg CRP-IgG was conjugated with Alexa Fluor 488 dye in sodium bicarbonate buffer (pH 8) for 1 h. To remove the unreacted free dye, the mixture was purified using size-exclusion chromatography (BioGel P-30, Bio-Rad, CA, USA), and Alexa Fluor 488 labeled CRP-IgGs were obtained (CRP IgG488). The resulting conjugates were characterized using UV–vis spectroscopy to calculate the degree of labeling and protein concentration within the samples. The details of the calculation process were referred to from the manufacturer's protocol. OPN-IgG was also labeled with Alexa Fluor dyes, and the samples were referred to as OPN IgG488 and OPN IgG555.

Preparation of Mono-Immobilized NPs. The active ester groups on the NPs could react with the amino groups in IgG (*6*, *16*, *17*, *21*). Therefore, CRP IgG488 (80 μg) solutions were added to NP suspensions (1 mg/mL) using phosphate-buffered saline (PBS, pH 7.8), and the reactions were carried out for 24 h at 4 °C. After the immobilization, the unreacted IgG was removed by centrifugation and re-suspended in ultrapure water. The remaining active ester groups were blocked using glycine for another 24 h at 4 °C. The resulting IgG-immobilized NPs (CRP NP488, concentration of stock solution: 1 mg/mL) were stored at 4 °C until further use. In the same manner, Alexa Fluor 555 dye-labeled anti-CRP IgGs were immobilized to NPs (CRP NP555). Alternatively, OPN NP488 and OPN NP555 were prepared. All the resulting NPs were adjusted to a concentration of 1 mg/mL by using PBS and stored at 4 °C until further use.

Bimolecular Recognition Procedures for Target Biomarkers. The 96-well multiplate for fluorescence measurements (NUNC, Roskilde, Denmark) was used for bimolecular recognition. First, 5 μg each of CRP NP488 and CRP NP555 were simultaneously added to the multiplate, along with 90 μL PBS (pH 7.4) buffer. Basically, the total amount of bioconjugate NPs in each well was adjusted to 10 μg. A target biomarker sample (100 μL), for example, human CRP, was added to each well in various final concentrations ranging from 0.01 to 30 μg/mL. The reaction mixture was mildly rotated for 5 min and maintained at 37 °C for 30 min. Finally, the fluorescence intensity at 590 nm was monitored by excitation at 485 nm by using a multiplate reader (1420 ARVO mx, Perkin Elmer Japan Co. Ltd., Tokyo, Japan).

RESULTS AND DISCUSSION

PC Group Enriched NPs for Bioconjugation. First, we synthesized random copolymers (PMBN) composed of MPC, BMA, and NPMA for bioconjugation as shown in Figure 2b. The monomer composition in the copolymer was determined using ^{1}H nuclear magnetic resonance (^{1}H NMR), and the average molecular weight (Mw) was estimated using gel permeation chromatography (GPC, poly(ethylene glycol) (PEO) standard) as shown in Table 1. Active ester groups on the NPMA units were labile to primary amino groups in biomolecules, and carbamate linkages were produced after the bioconjugation. Interestingly, PMBN was amphiphilic in aqueous solutions, even though the BMA content was approximately 0.43. We believe that hydrophilic PC groups contribute to the amphiphilic property of the molecule. Therefore, PC group enriched NPs could be prepared by a solvent evaporation process using polystyrene (PS), and the resulting NPs were composed of PS cores with PMBN shells (*18*, *19*). Surface elemental analyses on NPs were characterized using X-ray photoelectron spectroscopy (XPS; AXIS-HSi, Shimadzu/Kratos, Kyoto, Japan) (Figure 3). The anode was Mg Kα, and the releasing angle of the photoelectron for each element was fixed at 90°. XPS—an elemental analysis technique—could provide information regarding the outermost surface (within 10 nm). In the case of PC group enriched NPs, O–C–O and C═O peaks from the PMBN were observed at 287.0 and 289.0 eV, respectively. Alternatively, O_{1s} peaks attributed to ether and carbonyl groups were observed at 533.0 and 532.0 eV, respectively. Furthermore, a small broad peak attributed to an aromatic group based on the *p*-nitrophenyl ester group was also observed at 291.5 eV. Additionally, N_{1s} and P_{2p} peaks attributed to trimethyl ammonium (403.0 eV) and phosphate esters (134.0 eV) were observed. We believe that monodispersed NPs covered with PC groups were obtained and that NPs favor the formation of nonspecific interactions with biomolecules. Moreover, the average diameter of the NPs was determined by dynamic light scattering (DLS-7000; Otsuka Electronics Co., Ltd., Tokyo, Japan). On the basis of the Marquadt analysis, the average diameter was approximately 190 nm with a monodispersed size distribution (Figure 4). The average diameter could be changed by altering the PMBN concentration in the feed (*21*). The particle size was crucial in recognizing antigen molecules by using the FRET phenomenon. In the present study, we selected the diameter (190 nm) based on the dispersibility in PBS and its handling of the NPs. The resulting NPs excellently dispersed in PBS due to the hydrophilic surface layer. Moreover, the handling was simple, particularly, the easy sedimentation by

Table 1. Synthetic Result of PC-Based Amphiphilic Polymer[a]

	monomer unit fraction						
	in feed			in polymer[b]			
code	MPC	BMA	NPMA	MPC	BMA	NPMA	Mw[c]
PMBN	0.40	0.50	0.10	0.45	0.43	0.12	5.0×10^4

[a] [Monomer] = 0.5 mol L^{-1}, [AIBN] = 5 mmol L^{-1}. Solvent: ethanol. Polymerization temperature: 60 °C. [b] Determined by ^{1}H NMR. [c] Determined by GPC in water/CH_3OH = 3/7, PEO standards.

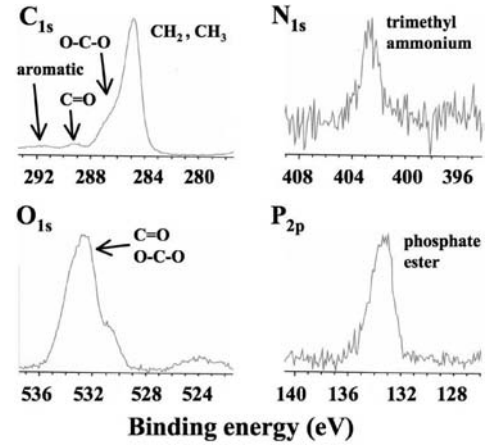


Figure 3. X-ray photoelectron spectroscopy results of phosphorylcholine group enriched nanoparticles.

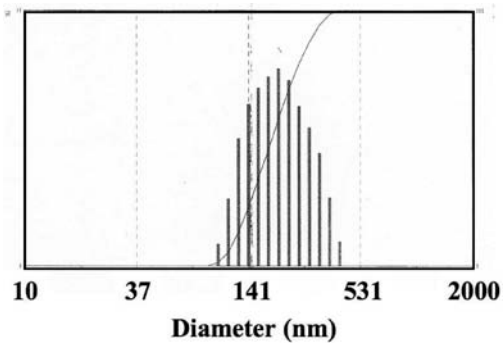


Figure 4. Size distribution of phosphorylcholine group enriched nanoparticles by dynamic light scattering.

Table 2. Results of Labeling Degree Using CRP and OPN

	C-reactive protein IgG		Osteopontin IgG	
	Alexa Fluor dye		Alexa Fluor dye	
	488	555	488	555
concentration (mol/L)	4.4×10^{-6}	4.2×10^{-6}	8.7×10^{-7}	1.1×10^{-6}
labeling degree (mol/mol)	3.2	3.5	3.4	3.5

centrifuging when the NPs were rinsed by repeated centrifugation and dispersion.

Mono-Immobilized PC Group Enriched NPs by Fluorescence-Labeled IgGs. In antibody immobilization, antibody-mediated cross-linking may involve the active ester groups on NPs. Moreover, the epitope region may react with the active ester groups, reducing the efficiency of bimolecular recognition. In our previous report, monodispersed antibody-immobilized NPs were observed using a scanning electron microscope (SEM) (*21*). Further, the NPs could form aggregates upon addition of the target antigen, and this aggregation was also observed using the SEM. Considering these reports, the fluorescence molecule labeled antibody was safely immobilized onto NPs without any antibody-mediated cross-linking, and the resulting NPs could capture the target molecule. To estimate the NP conjugation efficiency, the total amount of active ester groups per milligram of NPs was evaluated by a change in the absorbance of *p*-nitrophenol ($\lambda_{max} = 405$ nm) as a leaving group, following the complete hydrolysis of the ester group by treatment with an aqueous solution of NaOH (0.1 mol/L). Active ester groups were located at a concentration of 1.0 nmol/mg NPs. The conjugation efficiency was estimated using peroxidase-labeled antirabbit IgGs (A6154; Sigma-Aldrich, Inc., MO, USA) as model antibodies. Subsequently, 40% active ester groups were consumed, and the 40% conjugation efficiency was approximately equivalent to that of a monolayer of immobilized antibodies (*6*). The total amount of immobilized antibodies was estimated to be 4×10^{-12} mol (2.4×10^{12} molecules) per 10 μg NPs. If 40% conjugation was performed safely, 1 antibody molecule occupied 70 nm^2. The area was larger than that for saturated immobilization (approximately 15 nm^2). Therefore, intramolecular FRET did not occur due to the long distance of each IgG molecule.

To obtain fluorescence-labeled antibodies, each donor and acceptor molecule were conjugated with each antibody. The conjugation efficiency was calculated from the UV–vis spectrum as shown in Table 2. The resulting labeled CRP or labeled OPN antibodies were recovered at concentrations from 8.7×10^{-7} to 4.4×10^{-6} mol/L (Table 2). Each CRP antibody was labeled with an average of 3.2 donor molecules. Similarly, the conjugation efficiencies of acceptor-labeled CRP and OPN antibodies and donor-labeled OPN antibodies were estimated to be approximately 3.5. Gruber et al. reported that multiple fluorescence labeling on antibodies could cause fluorescence quenching (*22*). In the present study, significant quenching of the fluorescence molecules was not observed. Each fluorescence molecule labeled antibody was immobilized onto NPs. The conjugation efficiency was estimated to be approximately 40% from preliminary tests by using peroxidase-labeled antirabbit IgGs. Thereafter, we obtained 4 types of bioconjugate NPs for bioassays via FRET. The following abbreviations were used as shown in the Experimental Section: CRP NP488, CRP NP555, OPN NP488, and OPN NP555.

FRET Observation by Bimolecular Recognition. First, we evaluated the changes in fluorescence intensities by using bare PC-covered NPs. The resulting fluorescence intensities were monitored using a multiplate reader with adequate filters ($\lambda_{EX} = 485$ nm, $\lambda_{EM} = 590$ nm). NP agglutination reactions were carried out in 96-well plates, and final reaction volumes were adjusted to 200 μL in each well. Furthermore, the final NP concentration was 10 μg in each well. The mole concentration of immobilized antibody on 10 μg NPs was estimated to be approximately 4×10^{-12} mol from our previous report (*6*). On the other hand, 0.1 μg CRP and OPN antigens each approximately equaled 4×10^{-12} mol. Therefore, bimolecular recognition was performed using 0.01–10 μg of each antigen. The NP concentration is important, since fluorescence via FRET was induced by NP agglutination. If the NP concentration was very high, the resulting fluorescence might easily decay by a scattering phenomenon. Fortunately, we did not observe any changes in the fluorescence intensity from bare PC group enriched NPs, even after changing the antigen concentration. We believe that NPs are capable of detecting biomarkers via FRET without any interference. In our previous report, CRP antigens were easily captured by anti-CRP IgG-immobilized PC group enriched NPs (*21*) that agglutinated in the solution and caused turbidity changes via changes in the CRP concentration. In this study, we attempted to install a FRET system at the NP surface in order to achieve a higher sensitivity than that achieved in our previous study. Thus, we first checked the preliminary biorecognition using NPs. The FRET phenomenon is clearly related to the CRP concentration. On the basis of the relationship between the fluorescence and the biomarker concentration, the resulting NPs are capable of detecting target molecules, and thus, FRET took place in the multiwell plates.

In this bimolecular recognition system, target biomarkers were sandwiched in NPs, and fluorescence energy transfer was induced between donor and acceptor molecules. Particularly, the distance between donor and acceptor molecules was strongly regulated by the target antigen. In the present study, CRP (30 kDa) and OPN (120 kDa) were used as the target biomarkers, and the molecular sizes were considered to be approximately 4×4 and 4×12 nm^2, respectively. After complex formation, it is assumed that the donor and acceptor molecules would be in close proximity. Energy transfer may be induced between donor-labeled NPs and acceptor-labeled IgGs (free IgG molecules). Thus, we preliminarily examined the process in detail as shown in Figure 5. NPs and free IgG molecules were combined, and the total amount of each IgG molecule was adjusted as appropriate (4×10^{-12} mol). However, the fluorescence intensity did not precisely correlate with the changes in biomarker concentration. Moreover, the final fluorescence intensity of CRP NP488/CRP IgG555 at 565 nm was significantly higher than that of the alternative combination CRP NP555/CRP IgG488. The dominant reason was the free CRP IgG555 molecules in the former combination. The Alexa Fluor 555 molecules on CRP IgG555 could fluoresce to a small extent due to irradiation with excitation light in the absence of FRET.

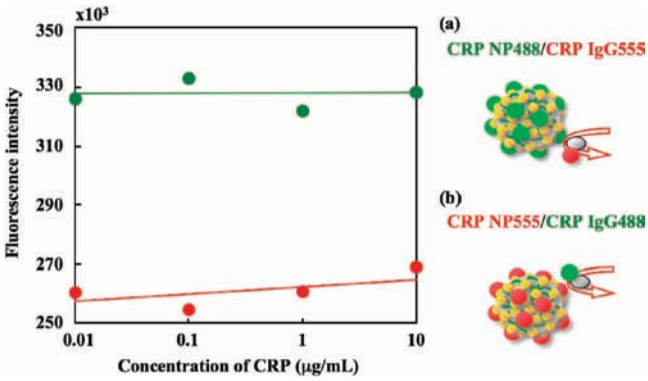


Figure 5. Change in fluorescence intensity by capture of CRP between NPs and free IgG. NPs (10 μg/well) were used: (a) CRP NP488 and CRP IgG555 mixture and (b) CRP NP555 and CRP IgG488 mixture.

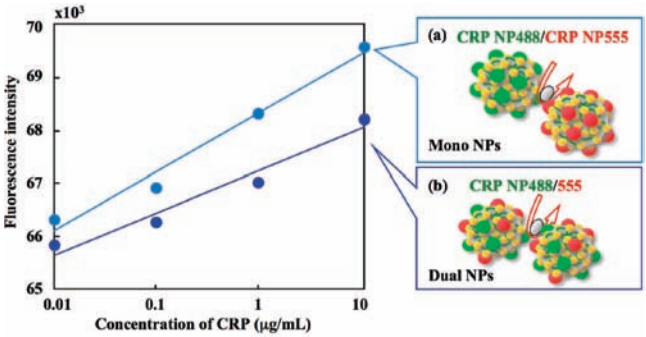


Figure 6. Change in fluorescence intensity. NPs (10 μg/well) were used; (a) mono-immobilized NPs system and (b) dual-immobilized NPs system.

The resulting emission at 590 nm was much higher than that of Alexa Fluor 488 molecules on CRP IgG488. This is the reason for the higher fluorescence intensity of CRP NP488/CRP IgG555. In the case of free IgG, the diffusion coefficient in the solution was very large relative to that of the NPs. Although the fluorescence-labeled IgG might easily capture the target biomarker, the resulting fluorescence intensity did not change. A plausible reason for the insufficient immunoassay is considered to be related to the local concentration of IgG molecules. In the case of bioconjugated NPs, this concentration was quite high relative to the same amount of free IgG molecules in the solution. We have already succeeded in performing a sequential enzymatic reaction on PC group enriched NPs (*6*), and the local concentration is of great importance and governs NP biofunctions. Therefore, target biomarkers should be sandwiched into NPs. Moreover, free IgG molecules interfere with the ideal NP agglutination. Combinations of NPs and free IgG, target molecules were captured in ideal combinations and as products of side reactions. When CRP molecules were sandwiched in CRP NP488 alone, no energy transfer was induced. Furthermore, CRP IgG555 itself could capture CRP molecules, and no FRET was observed. Considering plausible side reactions, target molecules should be captured by a combination of CRP NP488 and CRP NP555.

Optimization of the Bimolecular Recognition System Using NPs. To achieve high-sensitivity bimolecular recognition, two types of bioconjugate NPs were considered, as shown in Figure 6. The fluorescence intensity of mono- or dual-immobilized NPs was lower than that of NPs and free IgG. The NPs and their aggregation by antigen molecules were significantly larger relative to the light source. Therefore, a fair amount of light scattering occurred due to the NPs; the final fluorescence intensity was thus lower relative to the antibody-immobilized NPs and free antibody system. Figure 6a shows mono-immobilized NP bimolecular recognition with donor and acceptor molecules independently immobilized onto NPs. Alternatively, Figure 6b shows both fluorescence molecules immobilized onto NPs (dual-immobilized NP bimolecular recognition). Regarding bimolecular recognition, the question remains whether there is any difference between mono- and dual-immobilized immunoassay systems. To determine whether there was any difference in the dual-immobilized NPs systems, certain experiments were carried out, and the results are summarized in Figure 6. On this basis, it was noted that there was no significant difference in terms of CRP detection. The changes in fluorescence intensity correlated well with CRP concentrations in both bimolecular recognition systems. Moreover, multiparticle clusters may be formed at high concentrations of CRP (*21*). In fact, a mismatched sandwich statistically appeared in the solution. In the case of Figure 6a, the FRET phenomenon was observed only in the sandwich with CRP NP488 and CRP NP555. If the CRP antigen was captured by CRP NP488 alone, the FRET phenomenon could not take place. On the other hand, if the CRP antigen was captured only by the acceptor molecule labeled IgG on CRP NP488/555 (Figure 6b), it was also considered to be a mismatch sandwich (no FRET). The occurrence of these mismatched sandwiches was statistically considered to be 50%. In this mismatch, the FRET phenomenon could not take place; however, the statistical degree of the mismatch was estimated to be 50% in both cases (mono- and dual-immobilized NP immunoassays). Considering these assumptions, there is no difference between both immobilization immunoassay systems. However, the mono-immobilization system is superior to the dual-immobilization system in terms of preparative conditions and storage of NPs. Therefore, the mono-immobilization system was selected for this study.

Diversity of Bimolecular Recognition and Influence of Interference Proteins. The most favorable characteristic of the bimolecular recognition system presented herein is its simplicity, since it involves mixing NPs with sample solutions. A typical simple protocol for the immunoassay is described as follows. First, 5 μL aliquots of CRP NP488 and CRP NP555 are added to the 96-well plate, along with 90 μL PBS (pH 7.4) buffer. A target biomarker, human CRP in this case, is added to each well in various final concentrations ranging from 0.15 to 30 μg/mL. Reaction mixtures are rotated mildly for 5 min by using a plate mixer and maintained at 37 °C for 30 min. After the incubation, the emission fluorescence intensity at 590 nm was monitored by excitation at 485 nm. Excitation and emission wavelengths were regulated using filters. Figure 7a shows the change in the fluorescence intensity by CRP detection. In the reaction medium, NPs covered with donor- or acceptor-labeled CRP antibodies are dispersed. If the CRP antigen was captured by the NPs, the latter could agglutinate within the wells. The antibody is labeled with donor or acceptor molecules, and if the donor and acceptor molecules are close enough to form antigen–antibody complexes, one can observe fluorescence intensity energy transfers. Moreover, the intensity is strongly dependent on the concentration of the target antigen. Therefore, the bioconjugate PC group enriched NPs could specifically detect biomarker molecules. Fortunately, the resulting fluorescence intensity correlated well with the CRP concentration. The aforementioned correlation indicated that ideal agglutination reactions took place when CRP antigen was added to the reaction wells. Additionally, the agglutination was examined using a medium supplemented with protein (4.5 mg/mL human serum albumin (HSA); Sigma-Aldrich Inc.) (Figure 7b). In this study, HSA was added to the reaction media as interference biomolecules. The final result with the HSA-containing system

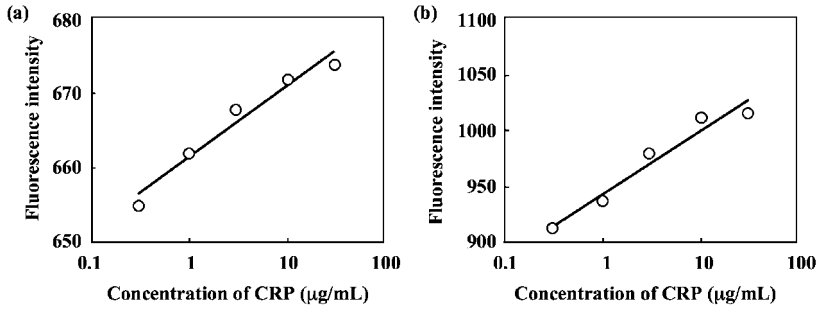


Figure 7. Change in fluorescence intensity by capture of CRP using CRP NP488 and CRP NP555. NPs (each 5 μg/well) were used: (a) without human serum albumin (HSA) and (b) with HSA (4.5 mg/mL).

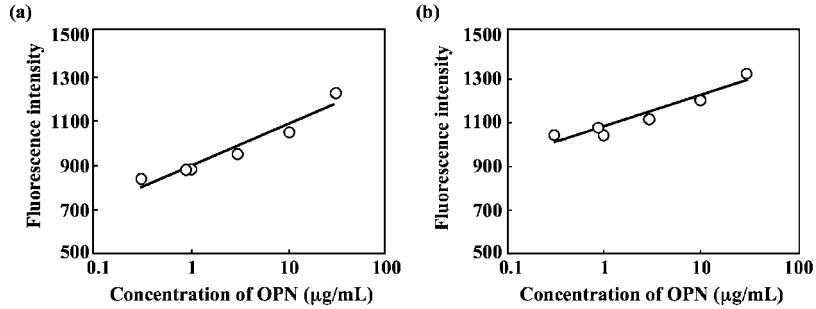


Figure 8. Diversity of immunoassay using FRET system. Change in fluorescence intensity by capture of OPN using OPN NP488 and OPN NP555. NPs (each 5 μg/well) were used: (a) without human serum albumin (HSA) and (b) with HSA (4.5 mg/mL).

correlated with the changes in the CRP concentration. Thus, a FRET system was successfully installed in the bioconjugated PC group enriched NPs, as shown in Figure 1.

OPN was used to obtain more data regarding the diversity of the immunoassay using the FRET system. Figure 8a shows the typical results from the OPN assays using FRET systems. The fluorescence intensity correlates with OPN concentrations ranging from 0.15 to 30 μg/mL. Moreover, the immunoassay was successful even when using HSA-containing media (Figure 8b). Thus, PC group-enriched NPs could capture biomarker molecules on their surfaces without any interference, and fluorescence intensity was observed using FRET. OPN molecules aggregate easily under physiological conditions, because OPN contains dual electric charges due to its cationic and anionic subunits. Therefore, conducting an OPN bioassay by using a conventional ELISA process might be difficult. PC groups contain both electric charges conferred by a trimethylammonium group (cation) and a phosphate group (anion) and show higher free-water contents. Thus, PC group-enriched NPs might easily capture unaggregated OPN molecules. Furthermore, the sensitivity of the present bimolecular recognition was not very high relative to the conventional immunoassay system. However, the recognition protocol was quite easy, and nonspecific protein adsorption was effectively suppressed by the PC group enriched surface. These advantages enable the use of the general methodology in the field of molecular diagnosis.

Our ultimate purpose was to use an immunoassay involving NPs. In particular, a FRET system was used for detection. In this study, target antigens were expected to be captured by NPs. If the antigen was captured only by donor- or acceptor-immobilized NPs, FRET could not take place. However, such specificity was not designed into this NP system. The final result was subject to probability factors. On this basis, we can easily hypothesize that the probability of FRET would be 50%, even when side reactions occurred. With the probability factor taken into account, FRET NPs could precisely read the target antigens. Of course, this immunoassay system is not subject to such types of targets and IgG molecules.

CONCLUSIONS

Improvements in traditional immunoassay systems such as ELISA were designed using PC group-enriched NPs, and these novel bimolecular recognition systems were verified using FRET. Diversity among the target biomarkers was easily designed by changing the fluorescence-labeled antibodies. Additionally, these immunoassays were capable of detecting the existence of interference molecules. Thus, these results suggest that it is possible to tailor the FRET system installed NPs for smart immunoassays as new paradigms.

ACKNOWLEDGMENT

A part of this study was financed by an Industrial Technology Research Grant Program (03A23011a) from the New Energy and Industrial Technology Development Organization (NEDO) of Japan and by a Grant-in-Aid for 21st Century COE “Center for Integrated Cell and Tissue Regulation” from the Ministry of Education, Culture, Sports, Science and Technology of Japan.

LITERATURE CITED

(1) Ishihara, K. (2000) Bioinspired phospholipid polymer biomaterials for making high performance artificial organs. *Sci. Technol. Adv. Mater. 1*, 131–138.

(2) Ishihara, K., Oshida, H., Endo, Y., Ueda, T., Watanabe, A., and Nakabayashi, N. (1992) Hemocompatibility of human whole blood on polymers with a phospholipid polar group and its mechanism. *J. Biomed. Mater. Res. 26*, 1543–1552.

(3) Watanabe, J. and Ishihara, K. (2005) Biointerface, bioconjugation, and biomatrix based on bioinspired phospholipid polymers, In *Handbook of Nanostructured Biomaterials and Their Applications*, Nalwa, H. S. , Ed., American Scientific Publishers, California, 125–149.

(4) Sakaki, S, Iwasaki, Y., Nakabayashi, N., and Ishihara, K. (2000) Water-soluble 2-methacryloyloxyethyl phosphorylcholine copolymer as a novel synthetic blocking reagent in immunoassay system. *Polym. J. 33*, 637–641.
(5) Sakaki, S., Nakabayashi, N., and Ishihara, K. (1999) Stabilization of an antibody conjugated with enzyme by 2-methacryloyloxyethyl phosphorylcholine copolymer in enzyme-linked immunosorbent assay. *J. Biomed. Mater. Res. 47*, 523–528.
(6) Watanabe, J., and Ishihara, K. (2006) Sequential enzymatic reactions and stability of biomolecules immobilized onto phospholipid polymer nanoparticles. *Biomacromolecules 7*, 171–175.
(7) Kitano, H., Imai, M., Mori, T., Ide, G., Yokoyama, Y., and Ishihara, K. (2003) Structure of water in the vicinity of phospholipid analog copolymers as studied by vibrational Spectroscopy. *Langmuir 19*, 10260–10266.
(8) Chen, S., Zheng, J., Li, L., and Jiang, S. (2005) Strong resistance of phosphorylcholine self-assembled monolayers to protein adsorption: insights into nonfouling properties of zwitterionic materials. *J. Am. Chem. Soc. 127*, 14473–14478.
(9) Morisaku, T., Ikehara, T., Watanabe, J., Takai, M., and Ishihara, K. (2005) Design of biocompatible hydrogels with attention to structure of water surrounding polar groups in polymer chains. *Trans. Mater. Res. Soc. Jpn. 30*, 835–838.
(10) Nederberg, F., Bowden, T., Nilsson, B., Hong, J., and Hilborn, J. (2004) Phosphoryl choline introduces dual activity in biomimetic ionomers. *J. Am. Chem. Soc. 126*, 15350–15351.
(11) Knopp, D. (1995) Application of immunological methods for the determination of environmental pollutants in human biomonitoring. A review. *Anal. Chim. Acta 311*, 383–392.
(12) Watanabe, J., and Ishihara, K. Single step diagnosis system by FRET phenomenon induced by antibody-immobilized phosphorylcholine group-covered polymer nanoparticles, *Sens. Actuators, B,*in press.
(13) Stryer, L., and Haugland, R. P. (1967) Energy transfer: a spectroscopic ruler. *Proc. Nat. Acad. Sci. U.S.A. 58*, 719–726.
(14) Berney, C., and Danuser, G. (2003) FRET or no FRET: a quantitative comparison. *Biophys. J. 84*, 3992–4010.
(15) Ishihara, K., Ueda, T., and Nakabayashi, N. (1990) Preparation of phospholipid polymers and their properties as hydrogel membrane. *Polym. J. 22*, 355–360.
(16) Konno, T., Watanabe, J., and Ishihara, K. (2004) Conjugation of enzymes on polymer nanoparticles covered with phosphorylcholine groups. *Biomacromolecules 5*, 342–347.
(17) Takei, K., Konno, T., Watanabe, J., and Ishihara, K. (2004) Regulation of enzyme-substrate complexation by phospholipid polymer conjugates for cell engineering. *Biomacromolecules 5*, 858–862.
(18) Maruyama, A., Ishihara, T., Adachi, N., and Akaike, T. (1994) Preparation of nanoparticles bearing high density carbohydrate chains using carbohydrate-carrying polymers as emulsifier. *Biomaterials 15*, 1035–1042.
(19) Konno, T., Kurita, K., Iwasaki, Y., Nakabayashi, N., and Ishihara, K. (2001) Preparation of nanoparticles composed with bioinspired 2-methacryloyloxyethyl phosphorylcholine polymer. *Biomaterials 22*, 1883–1889.
(20) Haugland, R. P. (2005) *The Handbook, A Guide to Fluorescent Probes and Labeling Technologies*, 10th ed., Invitrogen, CA, p 26.
(21) Park, J.-W., Kurosawa, S., Watanabe, J., and Ishihara, K. (2004) Evaluation of novel 2-methacryloyloxyethyl phosphorylcholine (MPC) polymeric nanoparticles for immunoassay of C-reactive protein detection. *Anal. Chem. 76*, 2649–2655.
(22) Gruber, H. J., Hahn, C. D., Kada, G., Riener, C. K., Harms, G. S., Ahrer, W., Dax, T. G., and Knaus, H.-G. (2000) Anomalous fluorescence enhancement of Cy3 and Cy3.5 versus anomalous fluorescence loss of Cy5 and Cy7 upon covalent linking to IgG and noncovalent binding to avidin. *Bioconjugate Chem. 11*, 696–704.

BC070095V

Fluorescent Diethylcarbamazine Analogues: Sites of Accumulation in *Brugia malayi*

Amy Junnila,[†] D. Scott Bohle,*[,‡] Roger Prichard,*[,†] Inna Perepichka,[‡] and Carla Spina[‡]

Institute of Parasitology and Department of Chemistry, McGill University, 801 Sherbrooke Street West, Montreal, PQ H3A 2K6, Canada. Received March 23, 2007; Revised Manuscript Received July 18, 2007

New fluorescein and rhodamine B-labeled antifilarial drug DEC analogues for use in drug localization studies with confocal microscopy have been prepared by a high-yield three-step synthesis. The resulting β-amine-substituted DEC analogue has a single ethyl substituent which is β-aminated to accommodate the fluorophore of either fluorescein isothiocyananate or rhodamine B. Confocal microscopy is used to show that the drug accumulates in the adult filarial worms in the pharynx, esophagus, and near the nerve ring of all adults, as well as in the uteri and vulva and the testes of the females and males.

INTRODUCTION

Lymphatic filariasis (LF) is a debilitating disease caused by infection with the filarial worms *Wuchereria bancrofti* or *Brugia malayi*. It remains an important disease in tropical areas of Asia, Africa, and the Americas with an estimated 120 million people infected worldwide. LF is caused by the spread of the nematodes by mosquito bites between infected individuals, and its most remarkable symptom is known as elephantiasis which results from the swelling of tissues above infected lymphatic ducts.

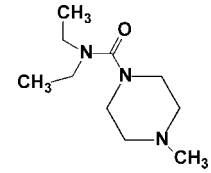
Diethylcarbamazine (DEC) has been the drug of choice in treating LF since its discovery in 1947. (*1–3*) It very rapidly kills circulating first-stage larvae (microfilariae, mf) and may also kill or sterilize adult worms. However, there has been relatively little sustained effort with modern tools to understand its localization and drug targets. Furthermore, there are published (*4*) and preliminary reports of a lack of adequate response to DEC treatment, and drug resistance may be developing. In order to understand the possible mechanisms of resistance to a drug, it is critically important to understand how it works. Fluorescent analogues which share the biological activity of the pharmaceutical would be very useful tools for understanding how DEC works.

Early medicinal chemistry studies identified the fundamental importance of the piperazine ring and the 4-*N*-methyl substituent on the ring (Scheme 1). DEC analogues with a range of substituents for the dialkylcarbamyl group show antifilarial activity, but substitution of the methyl and modification of the ring leads to drug inactivity. (*5, 6*)

In this study, we have synthesized new fluorescein and rhodamine B-labeled DEC analogues for use in drug localization studies with confocal microscopy. A high-yield three-step synthesis (Scheme 2) results in the β-amine-substituted DEC analogue **3** in which only a single ethyl substituent is altered, thus preserving the crucial pharmacophore of DEC. (*5, 6*) Compound **3**, by attachment to its reactive amine group, can be readily conjugated to fluorescein isothiocyanate (FITC) to give **4** or rhodamine B (RHB) to give **5** (Scheme 3).

As **3** is the key intermediate of the new fluorescent probes, it was tested for its antifilarial action in Mongolian gerbils (*Meriones unguiculatus*) infected with *B. malayi* prior to use in drug localization experiments. Solutions of compound **3** which would produce dose rates equivalent to standard dosages of DEC had antifilarial activity comparable to that of DEC, so we proceeded to conjugate **3** to FITC and RHB in order to localize drug accumulation in *B. malayi in vitro*.

Scheme 1. Structure of DEC



EXPERIMENTAL PROCEDURES

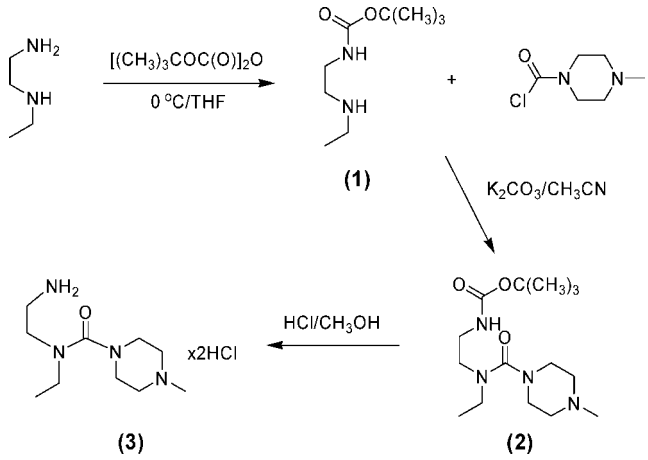
General Experimental. All reagents and solvents were used as supplied commercially, except for tetrahydrofuran (THF) and methylene chloride, which were distilled from Na/Ph_2CO and CaH_2, respectively. *N*-ethylethylenediamine, 4-methyl-1-piperazinecarbonyl chloride hydrochloride, fluorescein isothiocyanate (90%), and rhodamine B isothiocyanate mixture of isomers were purchased from Sigma Chemical Company. ^1H and ^{13}C NMR spectra were measured on a Varian Mercury 300 or 400 MHz spectrometer. All chemical shifts were recorded in δ (ppm) relative to tetramethylsilane (TMS). Melting points were measured with a 2010 differential scanning calorimeter. The IR spectra were taken in KBr disks or as a thin film on a NaCl plate using an ABB Bomem MB Series spectrometer with spectral resolution of 2 cm^{-1}. UV/visible spectra were measured using a Cary 300 Bio UV–visible spectrophotometer from Varian. Fluorescence spectra were recorded on a Varian Cary-Eclipse fluorometer or a FluoroMax 2 (ISA) Jobin Yvon-SPEX spectrofluorometer. The pH values were monitored with Cole Palmer pH meter (model 05669-20) using a Ag/AgCl electrode. The mass spectra analyses were obtained on a Finnigan LCQ-Duo spectrometer operating at 70 eV. Aluminum-backed silica plates with UV indicator and silica gel 60 Å (70–270 mesh) were used in analytical thin-layer chromatography (TLC) and silica gel column chromatography, respectively. Elemental analyses were performed by Quantitative Technologies, Inc.

Synthesis of New DEC Analogues. *tert-Butyl 2-(Ethylamino)ethylcarbamate* **1.** The protected *N*-ethylethylenediamine **1** was prepared by literature methods. (*7*) Recrystallization from pentane with cooling in the freezer led to large crystals of **1**

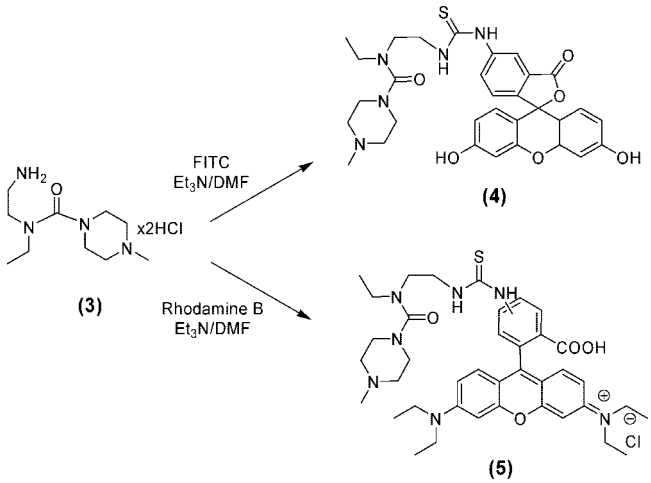
[†] Institute of Parasitology.
[‡] Department of Chemistry.

10.1021/bc0701040 CCC: $37.00 © 2007 American Chemical Society
Published on Web 10/10/2007

Scheme 2. Synthesis of 3 Intermediate Compound



Scheme 3. Synthesis of 4, DEC-FITC and 5, DEC-Rhodamine B



(67%), mp 54–55 °C. ^{1}H NMR ($CDCl_3$, 300 MHz) δ: 1.05 (t, 3H, $J = 7$ Hz), 1.39 (s, 9H), 2.60 (q, 2H, $J = 7$ Hz), 2.67 (t, 2H, $J = 6$ Hz), 3.16 (q, 2H, $J = 6$ Hz), 5.09 (brs, NH). ^{13}C NMR ($CDCl_3$, 300 MHz) δ: 15.7, 28.7, 40.7, 44.1, 49.3, 79.2, 156.2. MS (EI) *m*/*z*: 188 (1.85%), 115 (29.9%), 99 (83.2%), 58 (100%). Anal. Calcd for $C_9H_{20}N_2O_2$ (188.15 g/mol): C, 57.42; H, 10.71; N, 14.88. Found: C, 57.42; H, 10.94; N, 14.81.

tert-Butyl 2-(N-Ethyl-4-methylpiperzaine-1-carboxamido)ethylcarbamate **2.** To a solution of 4-methyl-1-piperazinecarbonyl chloride hydrochloride (2.39 g, 12 mmol) and well-powdered, anhydrous potassium carbonate (4.62 g, 33 mmol) in dry acetonitrile was added **1** (0.90 g, 4.78 mmol) under nitrogen at room temperature. The reaction mixture was stirred overnight, then heated at 60 °C for 3 h. After cooling to room temperature, the precipitate was filtered and washed with acetonitrile (2 × 25 mL). The filtrate was concentrated, and the residue was purified by flash chromatography on silica gel with CH_2Cl_2/methanol (1:0.1 v/v) as an eluent followed by recrystallization from hexane to give **2** as a white solid (1.00 g, 66.5%), mp 70–71 °C. ^{1}H NMR ($CDCl_3$, 400 MHz) δ: 1.14 (t, 3H, $J = 7$ Hz), 1.42 (s, 9H), 2.29 (s, 3H), 2.39 (t, 3H, $J = 5$ Hz), 3.19–3.29 (m, 10H), 5.12 (brs, NH). ^{13}C NMR ($CDCl_3$, 300 MHz) δ: 13.4, 28.4, 38.9, 43.5, 45.7, 46.2, 46.9, 54.7, 79.1, 155.9, 164.6. IR (cm^{-1}): 3330s, 3002m, 2973m, 2942m, 2846m, 2799m, 1705s, 1627s, 1522s, 1448s, 1390m, 1362m, 1283m, 1258m, 1184m, 1164m, 1007m, 976m, 958m, 885m, 774m, 650m, 557m, 529m. MS (EI) *m*/*z*: 314 (2.77%), 240 (17.7%), 126 (100%). Anal. Calcd for $C_{14}H_{30}N_4O_3$ (314.42 g/mol): C, 57.29; H, 9.61; N, 17.81. Found: C, 57.33; H, 9.53; N, 17.76.

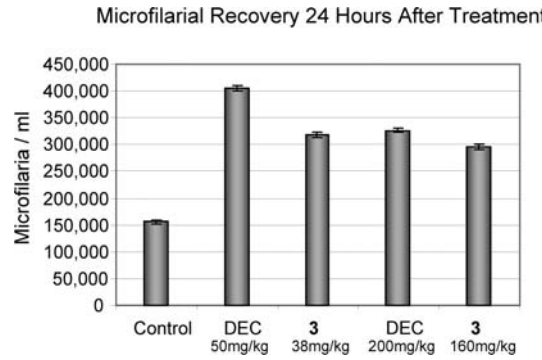


Figure 1. Microfilarial recovery 24 h after treatment. $N = 4$ gerbils per treatment group. Dose levels are shown under each column.

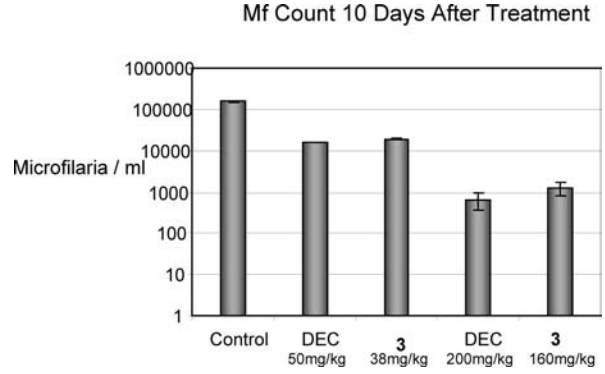


Figure 2. Microfilarial recovery 10 days after treatment. $N = 4$ gerbils per treatment group. Dose levels are shown under each column.

N-(2-Aminoethyl)-N-ethyl-4-methylpiperzaine-1-carboxamide Dihydrochloride **3.** The *tert*-butoxycarbonyl group of **2** was removed by the following procedure: HCl (2.0 M in methanol, 5 mL) was added to a stirred solution of **2** (1.00 g, 3.19 mmol) in methanol (5 mL) at ambient temperature for an additional 3 h. The solvent was evaporated, yielding oil which crystallized after drying *in vacuo* (0.88 g, 97%). ^{1}H NMR (CH_3OH-d_4, 400 MHz) δ: 1.22 (t, 3H, $J = 7$ Hz), 2.94 (s, 3H), 3.12–3.33 (m, 10H), 3.48–3.52 (m, 4H). ^{13}C NMR ($CDCl_3$, 400 MHz) δ: 13.4, 43.6, 45.4, 46.1, 46.8, 49.7, 54.8, 164.4. The resultant product **3** can be stored, at 4 °C, for at least 3 months without decomposition.

1-(Fluorescein-5-yl)-3-(2-N-ethyl-4-methylpiperzaine-1-carboxamido)ethylthiourea **4.** To a solution of **3** (0.187 g, 0.652 mmol) and triethylamine (0.132 g, 1.30 mmol) in anhydrous dimethylformamide was added FITC (0.127 g, 0.326 mmol). The reaction was stirred at room temperature under nitrogen atmosphere with protection from light overnight. The complete removal of FITC was monitored by TLC (eluent CH_2CL_2/methanol 1:0.3 v/v). The solvent was then removed *in vacuo* and the product was purified by flash column chromatography using CH_2Cl_2/methanol (1:0.3 v/v) as an eluent to give **4**, which is isolated as an intense orange powder (0.12 g, 61%). ^{1}H NMR (DMSO-d_6, 400 MHz) δ: 1.06 (t, 3H, $J = 7$ Hz), 2.12 (s, 3H), 2.24 (t, 3H, $J = 5$ Hz), 3.08–3.19 (m, 10H), 6.47–6.63 (m, 6H), 7.11 (d, 1H, $J = 8$ Hz), 7.62 (d, 1H, $J = 8$ Hz), 8.14 (s, 1H), 10.3 (br s, 2H). IR (KBr, cm^{-1}): 3306br, 3146br, 2984br, 1633s, 1581s, 1565s, 1499m, 1465s, 1424m, 1384m, 1366w, 1319s, 1288s, 1255m, 1208m, 1172w, 1111m, 1030w, 966w, 909w, 843w, 802w, 574w, 484w. MS (ESI) $C_{31}H_{33}O_6N_5S$, 603 g/mol) *m*/*z*: found $[M + H]^+$ 604 (29%), $[M + Na]^+$ 626 (35%). Fluorescence (in water): $\lambda_{exc} = 498$ nm, $\lambda_{em} = 520$ nm.

1-(Rhodamine-5(6)-yl)-3-(2-N-ethyl-4-methylpiperzaine-1-carboxamido)ethylthiourea **5.** To a solution of **3** (0.157 g, 0.548 mmol) and triethylamine (0.06 g, 0.60 mmol) in anhydrous

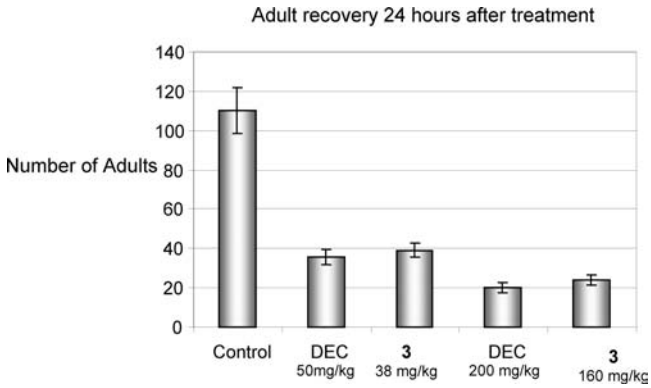


Figure 3. Adult parasite recovery 24 h after treatment. $N = 4$ gerbils per treatment group, with the same dose levels as used in Figures 1 and 2, shown under each column.

dimethylformamide (5 mL) was added rhodamine B isothiocyanate (mixture of isomers, 0.18 g, 0.336 mmol), and the mixture was stirred at room temperature under nitrogen atmosphere with protection from light overnight. Then, the temperature was raised to 70 °C for 10 h (reaction progress was monitored by TLC, eluent CH_2Cl_2/methanol 1:0.3 v/v). The final product **5** was reprecipitated several times from methanol/diethyl ether as a magenta powder (0.11 g, 43.7%) and used without purification for the next analyses. Fluorescence (in methanol): $\lambda_{exc} = 548$ nm, $\lambda_{em} = 570$ nm.

1-(Fluorescein-5-yl)-3-butylthiourea **Control 1.** Under nitrogen, butylamine (0.154 mL, 0.5 M solution in ethanol, 0.077 mmol) was added to a solution of FITC (0.021 g, 0.054 mmol) in dry ethanol (0.1 mL) using a gas-tight microsyringe, and the mixture was stirred at room temperature with protection from light overnight. Progress of the reaction was monitored by TLC (eluent CH_2Cl_2/methanol, 1:0.1 v/v, $R_f = 0.5$). After removal of the solvent, the crude product was purified by column chromatography on silica gel with CH_2Cl_2/methanol (1:0.05 → 1:0.3 v/v) as an eluent to give a deep yellow–orange powder of **control 1** (0.017 g, 68%) ^{1}H NMR (CH_3OH-d_4, 400 MHz) δ: 1.01 (t, 3H, $J = 10$ Hz), 1.44 (m, 2H), 1.67 (m, 2H), 2.03 (s, 1H), 3.63 (m, 2H), 3.98 (s, 1H), 6.72–7.02 (m, 6H), 7.23 (d, 1H, $J = 8$ Hz), 7.86 (d, 1H, $J = 6$ Hz), 8.25 (s, 1H). IR (KBr, cm^{-1}): 3372br, 3253br, 3065br, 2960s, 2929s, 2873m, 2858m, 1685s, 1593s, 1507s, 1465s, 1384s, 1320s, 1261s, 1208s, 1182s, 1112s, 1026w, 995w, 914w, 850s, 804w, 724w, 602w. Fluorescence (in water): $\lambda_{exc} = 505$ nm, $\lambda_{em} = 526$ nm.

1-(Rhodamine-5(6)-yl)-3-butylthiourea **Control 2.** Under nitrogen atmosphere, butylamine (0.106 mL, 0.5 M in EtOH, 0.053 mmol) was added to the solution of Rhodamine B isothiocyanate (21 mg, 0.039 mmol) in dry ethanol (0.1 mL) using a gas-tight microsyringe. The mixture was stirred at room temperature with protection from light overnight, then heated at 70 °C for 6 h. Progress of the reaction was monitored by TLC (eluent CH_2Cl_2/methanol, 4:0.3 v/v). After removal of the solvent, the final product was achieved by reprecipitation of the reaction mixture dissolved in minimal methanol with the addition of diethyl ether to give a deep purple powder of **control 2** (8.3 mg, 35%) ^{1}H NMR (CH_3OH-d_4, 400 MHz) δ: 0.92 (t, 3H, $J = 7$ Hz), 1.30–1.43 (m, 14H), 1.75 (m, 2H), 2.00 (s, 1H), 2.97 (m, 2H), 3.60 (m, 8H), 6.67–6.93 (m, 6H), (d, 7.17 1H, $J = 10$ Hz), (d, 7.47 1H, $J = 10$ Hz), 8.23 (s, 1H). IR (KBr, cm^{-1}): 3422br, 3213br, 2967s, 2936w, 2878w, 2793m, 2527w, 2416w, 1645ws, 1590s, 1528s, 1466s, 1412s, 1338s, 1274s, 1247s, 1181s, 1133s, 1075s, 1012w, 977w, 923w, 825w, 685w. Fluorescence (in water): $\lambda_{exc} = 553$ nm, $\lambda_{em} = 580$ nm.

Parasite Material. Male Mongolian gerbils (*Meriones unguiculatus*) infected intraperitoneally with 400 L3 infective larvae of *B. malayi* were obtained from Dr. J. McCall, University of Georgia. Microfilariae were obtained from the peritoneal cavities of gerbils by lavage with 5 mL phosphate buffered saline; adults were recovered during the subsequent necropsy. Adult worms were washed 3 times in RPMI 1640 containing 20 mM Hepes pH 7.3 to remove any adhering host cells; this was verified by light microscopy. Microfilariae were concentrated by centrifugation of the peritoneal exudates for 5 min at 12 000 rpm; the supernatant was discarded. The pellet containing microfilariae was washed 3 times by adding 1 mL Hepes-buffered RMPI 1640 followed by gentle agitation and centrifugation. Microfilariae were further separated from host cells by the percoll gradient method.

Antifilarial Activity of 3 in Gerbils. Antifilarial activity of the intermediate compound **3** was assessed by *in vivo* comparison with DEC at two dose rates. Gerbils ($N = 4$ for each treatment group) received one of the following combinations: 200 mg/kg or 50 mg/kg DEC in 200 μL normal saline, or 160 mg/kg or 38 mg/kg compound **3** in 200 μL normal saline, or 200 μL normal saline alone for control. All gerbils received

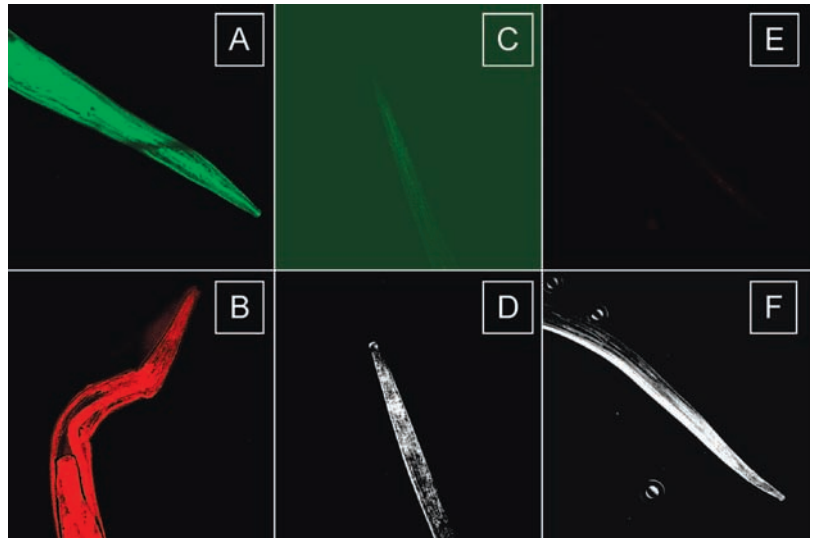
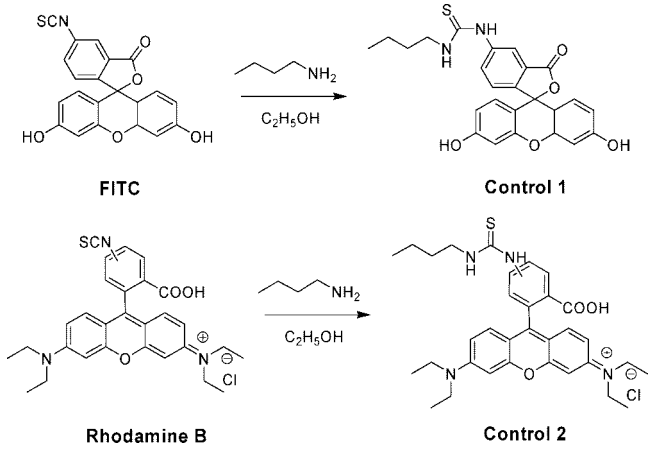


Figure 4. Representative controls. (A) Adult female anterior end stained with unconjugated FITC; (B) adult female posterior end stained with unconjugated RHB; (C) adult female anterior end stained with modified control FITC (**control 1**); (D) light microscope view of C; (E) adult male anterior end stained with modified control RHB (**control 2**); (F) light microscope view of E. All worms were treated for 8 h, either in medium alone in the case of the controls or with the probe at a concentration of 5 μg/mL.

Scheme 4. Synthesis of FITC-Control and Rhodamine-Control 2 Fluorophores



intraperitoneal injections of the specified dose or control for three consecutive days. After necropsy on the third day, adult worms were counted under a dissecting microscope, and larvae were counted using the hemecytometer method. Means +/− standard deviation were calculated, and the difference between the parasites recovered from the treatment groups and control untreated group was assessed statistically.

Statistical Analysis. Data were analyzed using *SPSS* (version 10.0) statistical package (Chicago, IL). Samples were compared with the Kruskal–Wallis rank test. Significance was assessed at $P \leq 0.05$.

***In vitro* Culture of *Brugia malayi* with Experimental Compounds.** Individual adult worms or groups of approximately 10 microfilariae were incubated in 2 mL of standard medium (without fetal calf serum) as previously described in detail. (*8*) Briefly, RPMI 1640 was supplemented with 25 mM Hepes buffer, 2 mM glutamine, 100 U/mL streptomycin, 100 μg/mL penicillin, and 0.25 μg/mL amphotericin B. Cultures were set up in triplicate, and incubated at 37 °C in a 95% air/5% CO_2 atmosphere. An optimal concentration of **4** or **5** (5 μg/mL) was determined by examining worms incubated in concentrations ranging from 0.1 to 20 μg/mL. The optimal concentration was defined as the concentration in which uptake could be detected with the lowest possible amount of background fluorescence. For all subsequent studies, worms received **4** (5 μg/mL), **5** (5 μg/mL), 5 μg/mL native DEC, 5 μg/mL RHB unconjugated mixed isomers, or unconjugated FITC isomer **1** (5 μg/mL) for 8 h. Live stained worms were then washed for 4 h in standard medium (4 changes—1 every hour). Worms were mounted with pro-long antifade kit (Molecular Probes) according to the manufacturer's instructions.

Confocal Microscopy. Confocal images were taken on a Carl Zeiss LSM 510 Laser Scanning System. Images were processed with Zeiss LSM 5 Image Browser (version 3.1.0.99).

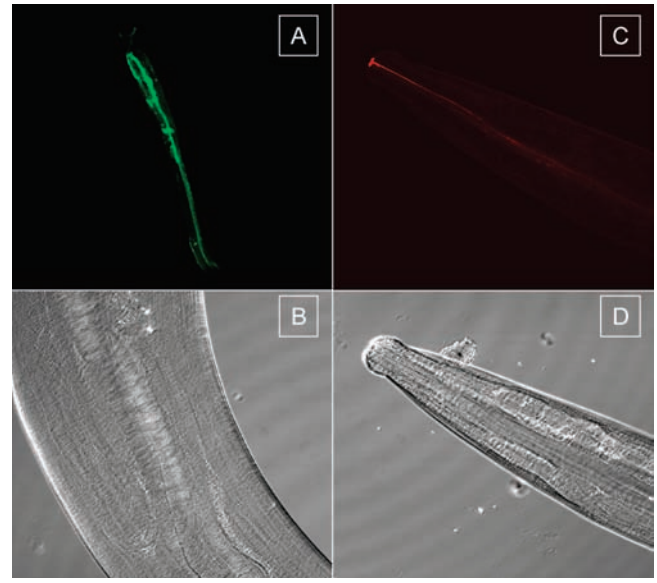


Figure 5. Sites of fluorescent DEC analogue accumulation in adult worms. (A) Adult female esophagus stained with DEC-FITC **4**; (B) light microscopy view of A; (C) adult male pharynx stained with DEC-RHB **5**; (D) light microscopy view of C. Times and probe concentrations used correspond to those used in Figure 4.

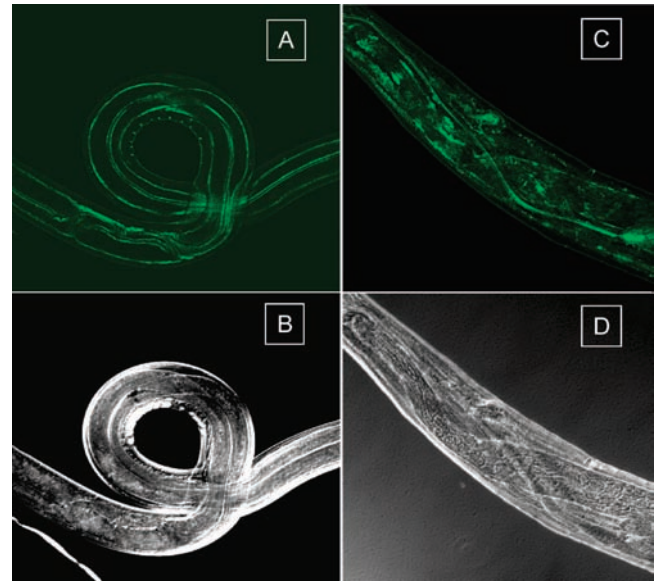


Figure 6. Sites of fluorescent DEC analogue accumulation in adult female worms. (A) Adult female uterus stained with DEC-FITC **4** (mid-body); (B) light microscopy view of A; (C) adult female uterus and vulva stained with DEC-FITC **4** (anterior end); (D) light microscopy view of C. Times and probe concentrations used correspond to those used in Figure 4.

RESULTS

Synthesis of Fluorescent DEC Analogues. The design and synthesis of the DEC fluorescent analogues **4** and **5**, utilized the only site with any flexibility in the molecule, one of the terminal methyls of the diethylamino group. From prior structure–activity studies, it was known that the antifilarial activity of DEC was retained when one of the ethyls was replaced with smaller substituents and the other is larger. (*3*) To build the terminal amino substitutent in **3**, the selective protection of the primary amine with a *t*-boc group was used before condensation with the piperazinecarbonyl chloride to give **2** after two steps. Removal of *t*-boc with acid restored the primary amine, which was then immediately condensed with the fluorescent isothiocyanate FITC or Rhodamine B to give the final fluorescent-labeled DEC analogue **4** or **5**. The four step sequence is shown in Schemes 2 and 32 and 3.

Microfilarial Recovery. Within 24 h after treatment, both concentrations of DEC and **3** resulted in a significant increase of microfilarial levels compared to the control ($P < 0.05$). The low dose rate of both compounds demonstrated a significantly higher microfilarial increase than the high dose rate ($P < 0.05$) (Figure 1).

To determine if **4** and **5** required more time to act on mf, the experiment was carried out again with the sacrifice taking place at 10 days posttreatment instead of 24 h. Ten days after DEC or **3** treatment, microfilarial levels were significantly lower (*P*

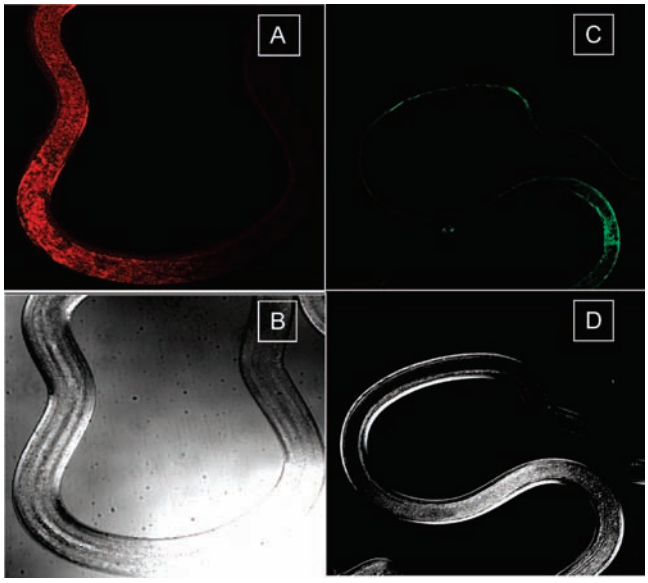


Figure 7. Sites of fluorescent DEC analogue accumulation in adult male worms. (A) Adult male testis stained with DEC-RHB **5** (mid-body), spermatozoa visible; (B) light microscopy view of A; (C) adult male testis stained with DEC-FITC **5** (mid-body), spermatozoa visible; (D) light microscopy view of C. Times and probe concentrations used correspond to those used in Figure 4.

< 0.05) in the treated animals compared with the control, for both compounds and dose rates (Figure 2).

Adult Recovery. At 24 h after treatment, DEC and **3**, at both high and low dose rates, showed adulticidal activity, and adult worm numbers were significantly lower than in the control gerbils ($P < 0.05$). The higher dose rate of both compounds was more effective than the lower dose rate of both compounds ($P < 0.05$) (Figure 3). At 10 days posttreatment, there were very few adults alive, and these were difficult to count, as only parts of worms were visible in clusters of nodules. Adult counts at 10 days are not shown.

Confocal Fluorescence Microscopy. Because **3** and DEC behaved similarly, **3** was conjugated to fluorescent molecules FITC and RHB for further use in confocal fluorescence microscopy. The fluorophores FITC and RHB (used unconjugated as controls) were found to be highly reactive, producing bright and nonspecific staining in the parasites (Figure 4) and were therefore unsuitable as controls. The reactive groups of these fluorophores were modified (Scheme 4) to closely resemble the conjugates used in this study. Control worms treated in media alone (8 h) and worms treated with modified control fluorophores (5 μg/mL for 8 h) showed no significant staining.

At the same concentration (5 μg/mL) and incubation time (8 h), **4** and **5** accumulated in the pharynx, esophagus, and near the nerve ring of all adults (Figure 5), uteri and vulva (Figure 6), and testes (Figure 7). When adult worms were examined by confocal microscopy, the intense staining observed in the uterus, testis, and intestine appeared to be localized to the lining (epithelium) of these organs. Additionally, in a few distinct sections of male testis, the contents of this organ were also stained (Figure 7).

Microfilariae accumulated stain in three distinct body areas (Figure 8); area 1 consisted of the excretory pore and the excretory cell, area 2 was the innerbody, and area 3 consisted of the G2, 3, and 4 cells and possibly the anal pore. As well, it appeared that somatic cell nuclei of microfilaria accumulated stain.

DISCUSSION

Conjugation of DEC to fluorescent molecules required a β-amine substitution. It was therefore necessary to determine

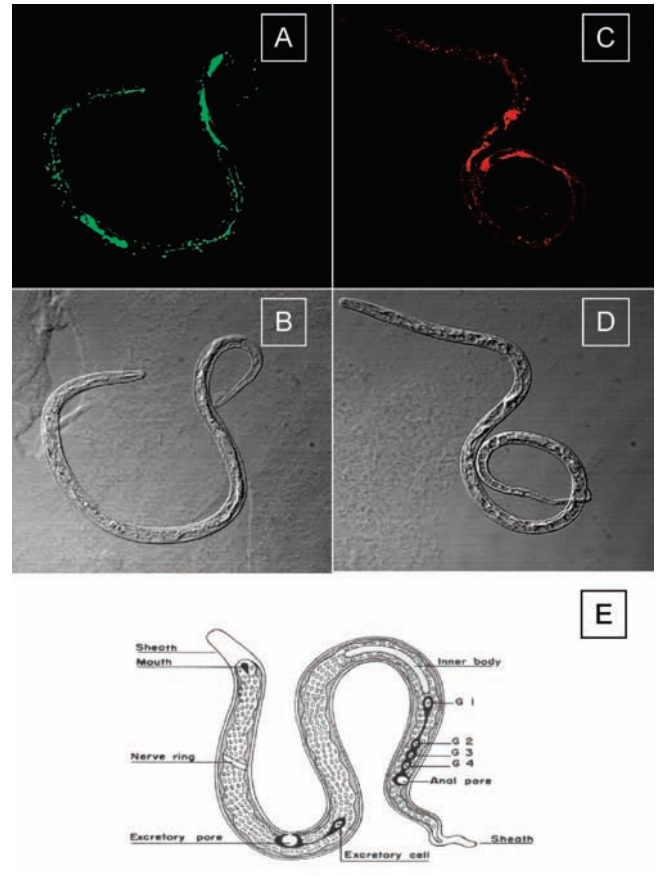


Figure 8. Sites of fluorescent DEC analogue accumulation in microfilariae. (A) Microfilaria stained with **4** DEC-FITC; (B) light microscopy view of A; (C) microfilaria stained with DEC-RHB **5**; (D) light microscopy view of C; (E) reprinted from Noble and Noble (1976) *Parasitology: The Biology of Animal Parasites*, 4th ed., Lea and Febiger, Philadelphia. Times and probe concentrations used correspond to those used in Figure 4.

whether compound **3** would act similarly to DEC in its filaricidal abilities. Similar strategies have been used to determine the subcellular localization of the adrenoceptor inhibitor prazosin when conjugated to BODIPY. (*9*) In survival assays carried out in the gerbil/*Brugia malayi* model, both DEC and **3** caused a surprising initial increase in peritoneal microfilariae 24 h posttreatment. This may be due to toxic effects of these compounds on the adult worms, causing them to release larvae from the uterus. In this particular host/parasite model, DEC and related compounds required several days to effectively reduce microfilariae, so the experiment was carried out again but animals were sacrificed at 10 days posttreatment instead of 24 h. This time, treatment with both DEC and **3** significantly reduced the number of peritoneal microfilariae and further reduced the number of adult worms. In fact, only parts of worms were visible, as they were being broken down in nodules found on the spleen and the liver and free-floating in the peritoneal cavity. Since **3** produced similar antiparasitic activity to DEC, it was conjugated to FITC and RHB for further use in confocal fluorescence microscopy.

In this study, no fluorescence was seen in the muscular system and very little fluorescence was seen in the nervous system (confined only to the area around the anterior nerve ring), which tends to exclude a strictly neuromuscular mode of action of DEC. Adult *Brugia malayi* did, however, strongly accumulate **4** and **5** in the pharynx, esophagus, intestine, and reproductive organs.

The sites of accumulation seen here in adult *Brugia* exposed to the fluorescent DEC analogue together with previous studies

that propose DEC acts by "unmasking previously hidden antigens" could suggest that the drug interferes with either excretion/secretion of a key immunomodulatory factor or with uptake/adsorption of host proteins, for example, serum albumin, which is believed to hide the worms from the immune system. Clearly the drug is accumulating at these sites and this is likely to occur where the drug receptors are localized. What is not observed is a random or diffuse distribution of **3**, which would suggest that it has little specific activity.

Chen and Howells were unable to demonstrate an oral (i.e., pharangeal pumping) uptake *in vitro* of trypan blue, ferritin, or fluorescein conjugated serum proteins by larvae and adults of *Brugia pahangi*. (*10*) It was later demonstrated that the gut of filarial worms is largely nonfunctional and that the cuticle serves as an absorptive as well as excretory surface. (*11*) As no significant fluorescence was detected in the cuticle, it is likely that DEC and DEC analogues are taken up transcuticularly and subsequently accumulate in target tissues.

A study conducted in 1996 provided the first evidence that suggested the existence of an excretory organ in filarial worms in the region of the anterior nerve ring (*12*), and it is believed that the uterus, vas deferens/testis, and intestine are the major organs where excretory proteins, such as superoxide dismutase (*13*) and gluthaione S-transferase (*14*) among others, are synthesized and exported. Our data show fluorescent DEC analogues accumulated in major sites of synthesis of secreted protein (*13*), which lends new evidence to the idea that DEC may be interfering with a key excretory/secretory product.

Microfilariae treated with fluorescent DEC analogues accumulated fluorophore in the inner body, the excretory pore, and the excretory cell, as well as the G-cells. Slight fluorescence was also seen in the pharyngeal thread and some somatic cell nuclei. The microfilariae have a nonfunctional gut (*15, 16*), but they do contain metabolically active sites within the body. (*15*) Feng (1936) demonstrated that the inner body of *Brugia* microfilaria occupies the space that later becomes the intestine in developing larvae. It is interesting to note that DEC analogues accumulate in tissues destined to become those which also accumulate these compounds in the adult worms. The biological significance of these findings is that the drug receptors are most likely localized at the accummulation sites of **3**, and the question we are now determining is the specific protein or receptor target for these drugs.

Advancing knowledge of drug delivery and activity requires an understanding of drug design and drug stability while taking into account the complexities imposed by the biological system (*17*) including cell/tissue penetration, drug-target interaction, and the pharmacodynamic consequences of alterations to native drugs. (*18*) In this study, we developed and synthesized fluorescent drug analogues that helped to address these complexities. The fluorescent DEC analogues synthesized here are small enough to penetrate the filarial cuticle, the crucial pharmacophore is accessible to potential receptors, and the major compound to be attached to the fluorophore **3** retains filaricidal activity.

The use of fluorescent drugs to investigate their targets in cells and tissues continues to expand at a rapid pace. Fluorescence imaging of protein–ligand interactions could provide an important biological context for drugs under study that might be otherwise overlooked by traditional biochemical techniques.

ACKNOWLEDGMENT

The authors gratefully acknowledge support from the FQRNT and the Centre for Host-Parasite Interactions for support in the form of a Centre New Iniative grant. Support from NSERC (to R.P. and D.S.B.) is gratefully acknowledged. In addition, fellowship support for I.P. and C.S. from the CIHR Chemical Biology Traineeship Program is gratefully acknowledged.

LITERATURE CITED

(1) Hewitt, R. I., White, E., Wallace, H. W., Stewart, H. W., Kushner, S., and Subbarow, Y. (1947) Experimental chemotherapy of filariasis. *J. Lab. Clin. Med. 32*, 1304–1313.

(2) Kushner, S., Brancone, L. M, Hewitt, R. I., McEwen, W. L., Subbarow, Y., Stewart, H. W., Turnere, R. J., and Denton, J. J. (1947) Experimental chemotherapy of filariasis. V. The preparation of derivatives of piperazine. *J. Org. Chem. 13*, 144–153.

(3) Stewart, H. W., Turner, R. J., Denton, J. J., Kushner, S., Brancone, L. M., McEwen, W. L., Hewitt, R. I., and Subbarow, Y. (1948) Experimental chemotherapy of filariasis. IV. The preparation of derivatives of piperazine. *J. Org. Chem. 13*, 124–143.

(4) Eberhard, M. L., Lammie, P. J., Dickinson, C. M., and Roberts, J. M. (1991) *J. Infect. Dis. 163*, 1157.

(5) Gayral, P., Gueyouche, C., Bories, C., Loiseau, P., Demerseman, P., Lamotte, G., and Royer, R. (1989) Macrofilaricidal activity of metabolites of diethylcarbamazine. *Arzneim.-Forsh./ Drug Res. 39*, 226–230.

(6) Strum, P. A., Cory, M., and Henry, D. W. (1977) Antifilarial agents. 3-Aminopyrrolidine and 1,4-diazabicyclo[3.2.1]octane derivatives as analogues of diethylcarbamazine. *J. Med. Chem. 20*, 1333–1337.

(7) Krapcho, A. P., Maresch, M. J., and Lunn, J. (1993) Mono-(Boc)-protected diamines. *Syn. Commun. 23*, 2443–2449.

(8) Rao, R., Moussa, H., and Weil, G. J. (2002) Brugia malyai: effects of antibacterial agents on larval viability and develoment in vitro. *Exp. Parasitol. 101*, 77–81.

(9) Sugawara, T., Hirasawa, A., Hashimoto, K., and Tsujimoto, G. (2002) Differences in the subcellular localization of α_1-adrenoceptor subtypes can affect the subtype selectivity of drugs in a study of the fluorescent ligand BODIPY-FL-prazosin. *Life Sci. 70*, 2113–2124.

(10) Chen, S., and Howells, R. (1979) The uptake in birto of dyes, monosacarides and amino acids by the filarial nematode. *Parasitology 78*, 343–354.

(11) Howells, R., and Chen, S. (1981) Brugia pahangi: feeding and nutrient uptake in vitro and in vivo. *Exp. Parasitol. 51*, 42–48.

(12) Strote, G., Bonow, I., and Attah, S. (1996) The ultrastructure of the anterior end of male Onchocerca volvulus: papillae, amphids, nerve ring, and first indiction of an excretory system in the adult filarial worm. *Parasitology 113*, 71–85.

(13) Ou, X., Tang, L., McCrossan, M., Henkle-Duhrsen, K., and Selkirk, M. (1995) Brugia malayi: localization and differential expression of extracellular and cytoplasmic CuZn superoxide dismutase in adults and microfilariae. *Exp. Parasitol. 80*, 515–529.

(14) Salinas, G., Braun, G., and Taylor, D. (1994) Molecular characterization and localization of an Onchocerca volvulus pi-class glutathione transferase. *Mol. Biochem. Parasitol. 66*, 1–9.

(15) Laurence, B., and Simpson, M. (1974) The ultrastructure of the microfilariae of Brugia, Nematoda Filaroidea. *Int. J. Parasitol. 4*, 523–536.

(16) Chen, C., and Chen, C. (1995) Burgia pahangi: effects of melanization on the uptake of nutrients by microfilariae. *Exp. Parasitol. 8*, 72–78.

(17) White, N. S., and Errington, R. J. (2005) Fluorescence techniques for drug delivery research: Theory and practice. *Adv. Drug Delivery Rev. 57*, 17–42.

(18) Gumbelton, M., and Stephens, D. (2005) Coming out of the dark: the evolving role of fluoresecnce imaging in drug delivery research. *Adv. Drug Delivery Rev. 57*, 5–15.

BC0701040

Site-Specific Pegylation of G-CSF by Reversible Denaturation

Francesco M. Veronese,*,† Anna Mero,† Francesca Caboi,‡ Mauro Sergi,‡ Christian Marongiu,‡ and Gianfranco Pasut†

Department of Pharmaceutical Science, University of Padua, via Marzolo 5, 35100 Padua, Italy, and Bio-Ker S.r.l., Piscinamanna 09010 Pula (CA), Italy. Received April 13, 2007; Revised Manuscript Received August 3, 2007

A new strategy has been developed for extending the possibility of poly(ethylene glycol) (PEG) modification to accessible thiol groups of biologically active proteins. In particular, thiol-reactive PEGs have been coupled to the cysteine 17 of granulocyte colony stimulating factor (G-CSF), which is known to be partially buried in a hydrophobic protein pocket. The PEG linking was accomplished by partial protein denaturation with 3 M guanidine·HCl in the absence of any reducing agent in order to preserve the native protein's disulfide bridges. PEG coupling occurred also, but at a lower degree, by using a 3 M solution of urea as the denaturing agent. Following the PEGylation, which was carried out in the unfolded state, the conjugated protein was refolded using dialysis or gel filtration chromatography to eliminate the denaturant. Different thiol-reactive PEGs and polymer molecular weights (5, 10, or 20 kDa) were investigated for G-CSF conjugation under denaturation. The secondary structure of the protein in the G-CSF-PEG conjugates, evaluated using circular dichroism and biological activity assay in cell culture, was maintained with respect to the native protein. Unexpectedly, conjugation enhanced the G-CSF tendency to aggregate, a problem that was overcome by a proper formulation.

INTRODUCTION

Granulocyte colony stimulating factor (G-CSF), the major regulator of granulopoiesis in vivo, represents a pharmaceutically useful protein that stimulates proliferation, differentiation, and survival of cells of the granulocyte lineage (*1, 2*). *E. coli* expressed G-CSF differs from the natural material in its lack of glycosylation and the N-terminal methionyl residue incident to bacterial expression (*3, 4*).

Clinical use of G-CSF (reviewed in refs (*5, 6*)), started in 1986 with the first clinical trials in cancer patients treated with chemotherapy (*7*), and it is now widely used to treat neutropenia, a condition that occurs in a wide variety of disease settings, including congenital defects, bone marrow suppression following pharmacological manipulation, infection, and also in cancer patients undergoing cytotoxic chemotherapy.

In 1991, the United States Food and Drug Administration approved Neupogen (Filgrastim, rh-met-huG-CSF) for use by those patients suffering from neutropenia during or after chemotherapy. Treatment with G-CSF can enable a higher-dose-intensity schedule which may allow better antitumor effects (*8*). It was later approved worldwide for use in bone marrow transplantation and more recently for treatment of severe chronic congenital neutropenia. Neupogen has a potential application in mobilizing peripheral blood progenitor cells for transplantation (*9*), but it presents a short in vivo half-life mainly due to two factors: rapid renal clearance and receptor mediated clearance by granulocytes, the last process that provides a self-regulation control on the G-CSF concentration.

To overcome these shortcomings, some methods have been proposed, and PEGylation is among these. PEGylation is intended to be a chemical linking of poly(ethylene glycol) chains to a drug (*10–13*). PEG conjugation masks the protein's surface and increases the hydrodynamic volume of the polypeptide, thus reducing its renal clearance, preventing the approach of antibodies or antigen processing cells, and decreasing the protein degradation by proteolytic enzymes. Finally, PEG conveys to molecules its physicochemical properties and therefore also modifies the biodistribution and solubility of peptide and nonpeptide drugs.

A PEGylation form of G-CSF, Neulasta, was already introduced in the market in 2002; in this case, PEG chains of 20 kDa have been selectively linked to the G-CSF amino terminus (*14*). The derivative presents a better pharmacokinetic profile and increased patient compliance. Interestingly, a recent study has also highlighted that this conjugate has a lower propensity to aggregate than the native G-CSF (*15*). In particular, the pathway of aggregation is not changed with respect to the native G-CSF, but the kinetic rate is slowed by PEGylation. This means that, after a proper time of incubation, both native G-CSF and PEG–G-CSF reach the same level of aggregation (*15*). The process involves first a conformational change that forms an aggregation-prone protein structure (*16*), which then leads to an initial noncovalent aggregation followed by the formation of covalent dimers and oligomers. These covalently linked forms are due to disulfide bridging and shuffling, which are promoted by the lone free cysteine in the G-CSF sequence (*15, 16*). As a confirmation, a G-CSF mutant obtained by switching the Cys17 with an Ala residue still forms aggregates, but only noncovalent ones.

Starting from these data, we tried to combine the beneficial effects obtained with G-CSF PEGylation (*15*), i.e., the reduction in aggregation kinetic rate, and the elimination of the free thiol of Cys17 that promotes the formation of covalent aggregates (*16*). To reach this goal, we performed the PEGylation of G-CSF selectively at the level of Cys17 using thiol-reactive PEGs. The lone free Cys17 in rhG-CSF, the other four being involved in two disulfide bridges (Cys36-Cys42, Cys64-Cys74), is not accessible in the protein native folding. In fact, Arakawa reported that this cysteine cannot be carboxymethylated by a hydrophilic agent, iodoacetic acid, under native conformation, but it becomes fully reactive when rhG-CSF is denatured (*17*). In other experiments, the free thiol has been shown to react very slowly with a

* Corresponding author. Francesco M. Veronese, Department of Pharmaceutical Science, University of Padua, via Marzolo 5, 35100 Padua, Italy. Phone +39(0)49-8275694; Fax +39(0)49-8275366; E-mail: francesco.veronese@unipd.it.

† University of Padua.

‡ Bio-Ker S.r.l.

10.1021/bc070123+ CCC: $37.00 © 2007 American Chemical Society
Published on Web 10/18/2007

hydrophobic modifying agent, dithiobis-nitrobenzoic acid (DTNB) under nondenaturing conditions. It is postulated that the free cysteine may reside inside a hydrophobic environment of the protein, and therefore, it is inaccessible to chemical modification by hydrophilic agents, whereas it is slightly more accessible to the hydrophobic ones. Conformational studies of G-CSF have also demonstrated that the –SH at position 17 is buried in a cavity of the protein, only partially exposed to solvent.

Therefore, we looked for conditions of specific conjugation between a single chain of PEG and the Cys17 of G-CSF, once this is unmasked by partial denaturation. Furthermore, we tested the different reactivity of three thiol-reactive PEGs: the vinylsulfone–PEG (PEG–VS), the orthopyridyldisulfide–PEG (PEG–OPSS), and the maleimide–PEG (MAL–PEG). Different polymer molecular weights were investigated also.

As a continuation of a preliminary report (*18, 19*), in this paper we describe in more detail the studies involved in the development of this new PEGylation strategy and its application in the preparation of new active PEG–G-CSF conjugates, where only one chain of PEG is bound to the Cys17. Unexpectedly, the obtained conjugates showed a more marked tendency to form soluble aggregates in solution when compared to native G-CSF. Preliminary formulation studies demonstrated that the addition of albumin or β-hydroxypropylcyclodextrin can overcome this aggregation propensity.

MATERIALS AND METHODS

General Methods. A lyophilized powder of rh-G-CSF was supplied by Bioker (Pula, Cagliari, Italy). PEG–OPSS, PEG–VS, and PEG–MAL of different molecular weights were purchased from Nektar (Huntsville, AL). 3-(4,5-Dimethylthiazol)-2-yl-2,5-diphenyl tetrazolium bromide (MTT), 5,5′-dithiobis-(2-nitrobenzoicacid) (DTNB), solvents and denaturing agents, and other chemicals of analytical grade were from Sigma (St. Louis, MO). RPMI medium, fetal bovine serum, and penicillin were from Gibco (Pailey, UK).

Reversed-phase chromatography was performed with a Pharmacia LKB (Gromma, Sweden) analytical HPLC system, using a Vydac C4 column (150 × 4.6 mm, particle size 5 μm) or a Phenomenex C18 column (250 × 4.6 mm, particle size 5 μm). Elution was carried out at a flow rate of 1 mL/min with a linear gradient of acetonitrile in water containing 0.05% (v/v) TFA from 40% to 70% over 25 min. The effluent was monitored by recording the absorbance at 226 nm.

SDS-PAGE was carried out in a vertical slab gel apparatus (Mini-Protean II, Bio-Rad) using an SDS-polyacrylamide gel with a low degree of cross-linking (60% acrylamide, 0.8% bisacrylamide). The gels were stained with Coomassie brilliant blue R-250.

Far-UV circular dichroism (CD) measurements were made at 25 °C on a Jasco J-710 spectropolarimeter (Tokyo, Japan) equipped with a thermostatically controlled cell holder. The instrument was calibrated with D-(+)-10-camphorsulfonic acid. The spectra were recorded in 10 mM acetic acid, 10 mg/mL mannitol, pH 4, at a protein concentration of 0.1 mg/mL, in 1 mm path length quartz cells. Far-UV CD spectra were analyzed in order to estimate the percentage of protein secondary structure from the equation % α-helix = $(\theta_{208\text{nmobs}} - 4000)/(33\,000 - 4000)$ (*20*), where $\theta_{208\ \text{nm,obs}}$ is the observed mean residue ellipticity at 208 nm.

Protein concentrations were determined spectrophotometrically on a Perkin-Elmer Lambda-20 spectrophotometer. The concentrations of stock solutions of G-CSF and G-CSF–PEG conjugates were evaluated from their absorbance at 280 nm. Extinction coefficients at 280 nm for G-CSF (0.88 $mg^{-1}\ cm^2$) were considered unchanged for the G-CSF–PEG conjugates.

Fluorescence emission spectra were recorded at 25 °C on a Perkin-Elmer model LS-50B spectrofluorometer, equipped with a thermostatically controlled cell holder. Spectra were taken in Tris/NaCl buffer, pH 7.5, using 1 cm path length, exciting the samples (1.3 μM) at 295 nm, and recording the emission fluorescence in the wavelength range 303–500 nm, in the presence of different amount of positive (CsCl) and negative (NaI) quenchers.

MALDI Mass Spectrometry. Measurements were performed on a REFLEX time-of-flight instrument (Bruker-Franzen Analytik, Bremen, Germany) equipped with a SCOUT ion source operating in positive linear mode. Ions, formed by a pulsed UV laser beam (nitrogen laser, $\lambda = 337$ nm), were accelerated to 25 kV. Sinapinic acid (saturated solution in acetonitrile/water (50:50 v/v)) was used as a matrix. Samples were dissolved in 0.1% trifluoroacetic acid aqueous solution. Five microliters of the diluted sample solution was mixed with the same volume of matrix solution, and 1 μl of the resulting mixture was deposited on a stainless steel sample holder and allowed to dry before introduction into the mass spectrometer.

Cell Culture. The NSF-60 cell line, which is developed from a mouse myeloblastic leukemia rich in G-CSF receptors, was kindly provided by Dr. William E. Evans St. Jude Children's Research Hospital (USA). Cells were maintained in RPMI medium with 5% fetal bovine serum, 10 U.I./mL penicillin, and 30 U.I./mL Filgrastim at 37 °C, under 5% CO_2 atmosphere.

G-CSF PEGylation under Nondenaturing Conditions. Thiol-reactive PEGs (PEG–OPSS, PEG–VS, or PEG–MAL) were employed. The reactions were carried out in 0.5 M Tris buffer, pH 7.2. At room temperature, one of the active PEGs was added as a powder in a 10-fold molar excess to a rhG-CSF solution (1 mg/mL). The reaction was allowed to proceed for 24 h or in any case until reaching a constant amount of PEG–G-CSF conjugate, which was then analyzed and purified by reverse-phase chromatography according to the conditions reported in Methods and Materials. The purity of the conjugate and the degree of conjugation were determined by SDS-PAGE and DTNB colorimetric assay (*21*).

Control of the Reversibility of G-CSF Denaturation. Solutions of rhG-CSF, at 0.15 mg/mL, were prepared and incubated for 4 h in 2, 3, or 4 M guanidinium chloride (Gu·HCl) in phosphate buffer 0.05 M, pH 7.2. A 5 M solution of urea in the same buffer was also tested as a denaturant. The protein secondary structure recovery was analyzed after dialysis, against sodium acetate 10 mM pH 4.2, to remove the denaturant. The secondary structure was investigated by far-UV CD analysis.

G-CSF PEGylation under Denaturing Conditions. To G-CSF (1.46 mg/mL), dissolved in one of the denaturant solutions reported above, PEG–OPSS (5 kDa), MAL–PEG (5 kDa), or PEG–VS (5 kDa) were added at 10-fold molar excess with respect to the protein. The reaction was allowed to proceed at room temperature, under argon atmosphere, for 4 h. Alternatively, PEG–OPSS at 10 or 20 kDa was used. In this case, the reaction was conducted, under argon atmosphere, for 20 h when using the 10 kDa PEG or at 40 °C for 1 h followed by for 4 h at room temperature when using the 20 kDa PEG.

The reaction mixture was dialyzed against sodium acetate 10 mM pH 4.2, and the conjugate was purified by reverse-phase HPLC using the conditions reported above. The secondary structures of the products were analyzed by far-UV CD.

Evaluation of in Vitro G-CSF Conjugate Activity. NSF-60 cells were seeded in 96 well plates (104 cells/well), and serial dilutions of G-CSF and G-CSF–PEG conjugates were added. The plates were incubated for 67 h at 37 °C before the addition of 20 μL MTT (5 mg/mL in PBS filtered using 0.22 μm filters) to each well. After a further 5 h incubation, the media were removed and optical-grade dimethyl sulfoxide (100 μL) was added to dissolve the formed insoluble formazan dye. Absorbance at 540 nm was measured using an Elisa reader, and the

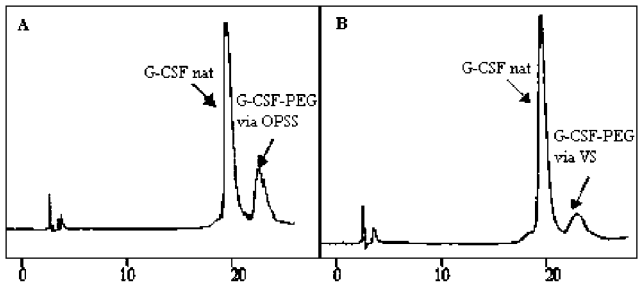


Figure 1. RP-HPLC chromatograms of G-CSF conjugation with thiol-reactive PEGs under physiological conditions after 24 h. (A) reaction mixture of G-CSF and PEG–OPSS (5 kDa); (B) reaction mixture of G-CSF and PEG–VS (5 kDa).

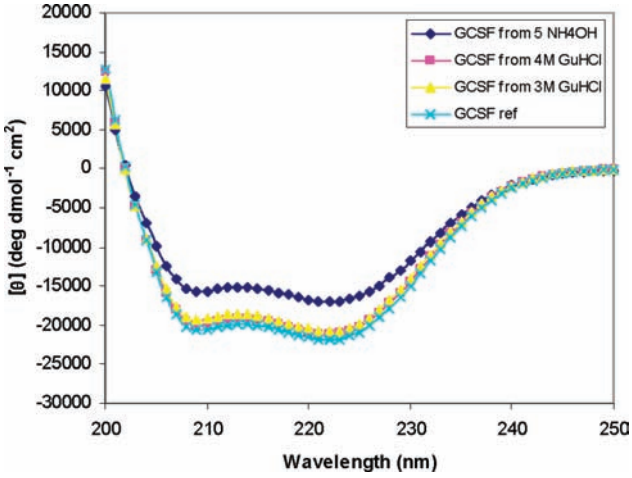


Figure 2. Far-UV CD spectra of native G-CSF in physiological condition (×) and after the denaturation–refolding process. Denaturation was performed using 3 M (▲) or 4 M (■) solutions of guanidine HCI or 5 M (♦) urea. The spectra were obtained at 25 °C in acidic solution at pH 4.2.

cell viability was expressed as a percentage of the viability versus untreated control cells.

RESULTS AND DISCUSSION

G-CSF PEGylation under Nondenaturing Conditions. The direct site-specific conjugation of a linear PEG to the thiol of G-CSF Cys17 was investigated by carrying out the reaction under conditions that maintained the G-CSF tertiary structure. Thiol-reactive PEGs based on double-bond addition (PEG–VS and PEG–MAL) or disulfide exchange (PEG–OPSS) were employed. The reaction was allowed to proceed at room temperature for several hours, until reaching a constant amount of PEG–G-CSF conjugate, as verified by RP-HPLC. In Figure 1 is the RP-HPLC profile of the conjugation mixture of G-CSF and PEG–OPSS (Figure 1A) or PEG–VS (Figure 1B) after 24 h. The degree of conjugation of G-CSF was very limited, thus confirming the difficulty of reaching the buried Cys17. Under these conditions, PEG–OPSS appeared to be slightly more reactive than PEG–VS. PEG–MAL showed a similarly low degree of conjugation (data not shown).

Reversible Denaturation of G-CSF. To overcome the low reactivity of the thiol group of G-CSF in the native state, we studied the conjugation under partially denaturing conditions. For this purpose, urea or Gu·HCl was used as a denaturing agent, while the native protein's disulfide bridges were maintained in order to facilitate the refolding, to prevent PEGylation at unwanted sites, and to avoid S–S scrambling during the refolding.

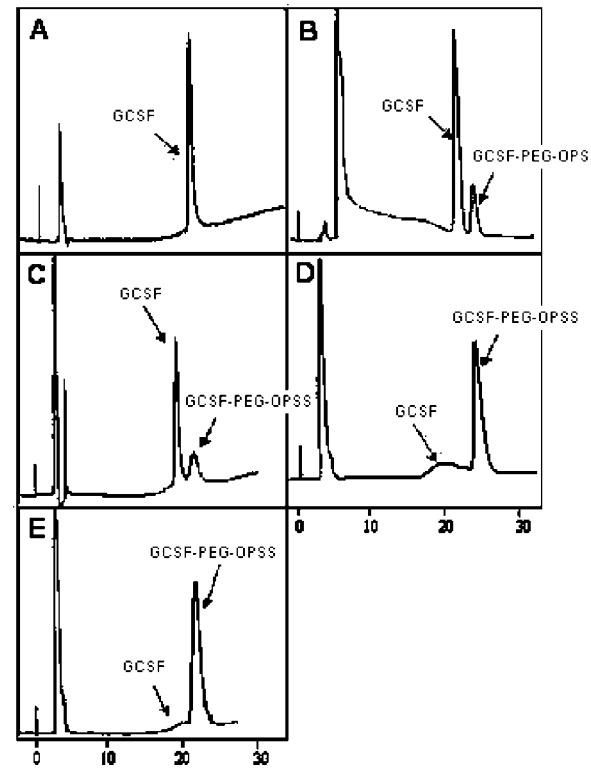


Figure 3. Reaction mixture of G-CSF PEGylated under denaturing conditions. RP-HPLC chromatograms had been obtained using a C4 Vydac column and recorded at 226 nm: (A) native G-CSF; (B) reaction mixture of G-CSF and PEG–OPSS (5 kDa), after 4 h, in the presence of 3 M urea; (C–E) reaction mixture of G-CSF and PEG–OPSS (5 kDa), after 4 h, in the presence of 2, 3, or 4 M guanidine·HCl, respectively.

Table 1. Degree of G-CSF PEGylation after 4 h Using Different PEG Reagents under Different Denaturing Conditions

PEG reagent	percentage of G-CSF conjugation using different denaturing conditions			
	2 M Gu·HCl	3 M Gu·HCl	4 M Gu·HCl	3 M urea
PEG–OPSS (5 kDa)	48	84	95	31
PEG–VS (5 kDa)	15	30	50	11
PEG–MAL (5 kDa)	44	81	91	29

A preliminary study was carried out to evaluate the refolding process of G-CSF after its exposure to different denaturant concentrations. In Figure 2, it is shown that the refolding is complete for concentrations of Gu·HCl up to 4 M. Denaturation using 5 M urea was more critical, and the refolding was incomplete. High salt concentrations interfered with the collection of CD data in the far-UV region. Therefore, spectra of protein samples containing guanidine·HCl could not be obtained below 200 nm.

G-CSF PEGylation under Conditions of Reversible Denaturation. The conjugation of G-CSF by PEG–OPSS 5 kDa, evaluated by reverse-phase HPLC, after 4 h under different denaturing conditions is shown in Figure 3. A fast and high degree of PEGylation at the lone free cysteine residue of G-CSF was successfully reached under the denaturing conditions of 3 or 4 M Gu·HCl. These conjugation data are in good agreement with the cyanylation results of G-CSF Cys17 as a function of Gu·HCl reported by other authors (*16*). PEG linking to denatured G-CSF using a 3 M solution of urea was less effective. Similar results were obtained using PEG–maleimide, while PEG–vinylsulfone had the lowest degree of coupling; in this case, after 4 h only 50% of conjugation was achieved in 4 M

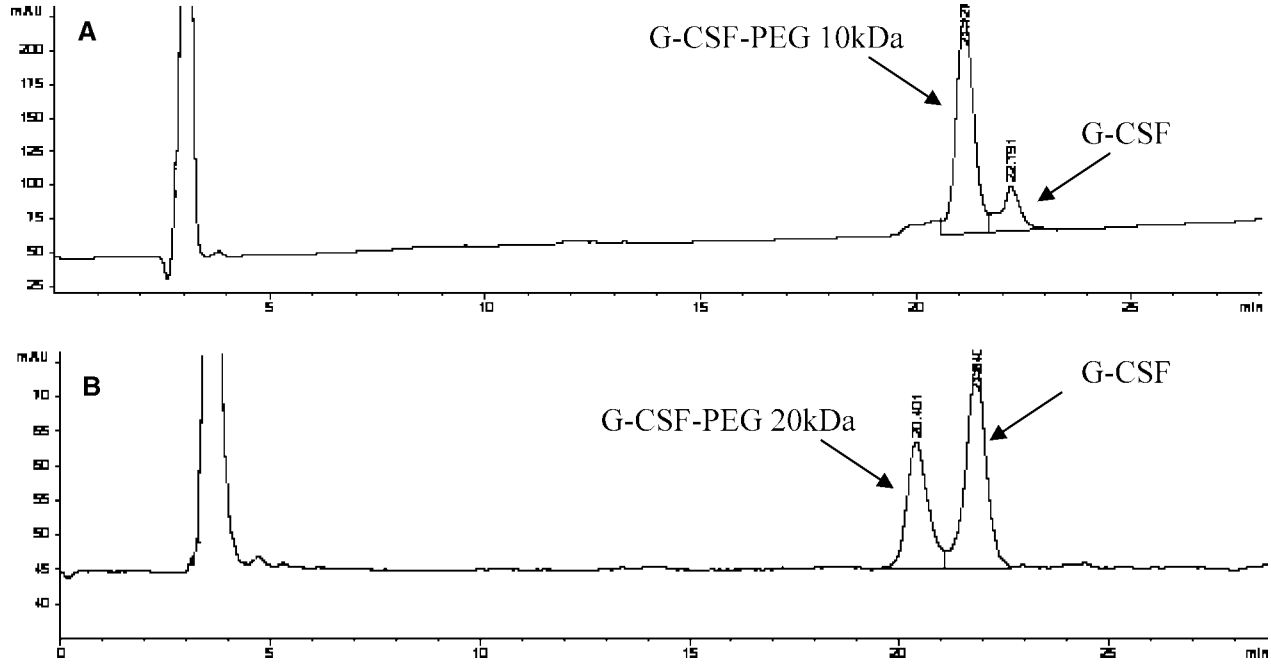


Figure 4. RP-HPLC chromatograms of reaction mixture of G-CSF and PEG–OPSS at different molecular weights, obtained using a C18 Phenomenex column. The spectra were recorded at 280 nm. (A) G-CSF and PEG–OPSS (10 kDa) after 20 h. (B) G-CSF and PEG–OPSS (20 kDa) after 1 h at 40 °C and the following 4 h at room temperature.

of Gu·HCl (Table 1). The denaturant was removed by extensive dialysis towards acetate buffer 10 mM at pH 4.2.

Protein unfolding accompanied by cysteine exposition and reactivity might also be obtained in water/organic solvent solutions. A G-CSF sample dissolved in a 80:20 water/DMSO solution showed a similar reactivity to PEG–OPSS (data not shown). This partial denaturation by DMSO could explain the PEGylation at the level of Cys17 of G-CSF reported by other researchers (*22*).

The conjugation of PEG–OPSS at higher molecular weights, 10 or 20 kDa, was investigated in 4 M guanidinium chloride. Protein modification using these more hindered PEGs was achieved by increasing the reaction time for the 10 kDa polymer and both temperature and time for the 20 kDa PEG. After 4 h at room temperature, the degrees of conjugation were 85% and 45%, respectively (Figure 4A,B). The conjugate G-CSF–PEG (20 kDa), dialyzed and purified as reported above, was characterized by SDS gel electrophoresis (Figure 5). The conjugate appeared as a single band at ∼62 kDa, which does not reflect the sum of G-CSF and polymer molecular weights, because as is known, PEG has a higher hydrodynamic volume than a protein with the same molecular weight (*23*).

The G-CSF–PEG conjugates were further characterized by MALDI-TOF mass spectroscopy, far-UV CD, fluorescence emission and finally by cell proliferative assay.

Structural Characterization of the PEGylated G-CSF. The covalent conjugation was confirmed by MALDI-TOF mass spectroscopy. A broad peak, due to PEG polydispersity, centered at 24 089 kDa, was detected following G-CSF conjugation with PEG 5 kDa. This corresponds to a mono-PEGylated G-CSF (Figure 6A,B).

The near- and far-UV CD spectra of native and PEGylated G-CSF, obtained using mPEG–OPSS 5 kDa, are shown in Figure 7A and B. The observed superimposition of the spectra demonstrates that refolding of PEGylated protein to the native structure took place after PEG linking also. Similar spectra were obtained with G-CSF–PEG–VS and G-CSF–PEG–MAL.

Fluorescence spectra of native and conjugated G-CSF showed a red shift in λ_{max} in the emission spectra, from 344 to 350 nm,

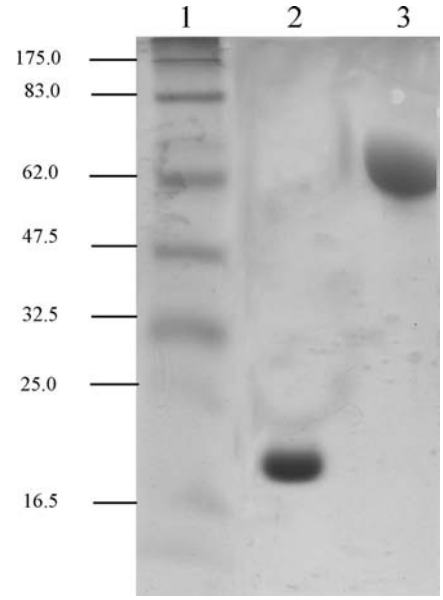


Figure 5. SDS gel electrophoresis of the following: lane 1, low molecular weight standards; lane 2, native G-CSF; lane 3, purified G-CSF–PEG–OPSS (20 kDa).

indicating that tryptophans 58 and 118 are more exposed to solvent in the conjugated protein. These data were confirmed by the tryptophan fluorescence quenching with CsCl and NaI of native G-CSF, G-CSF–PEG–OPSS, and G-CSF–PEG–VS (data not shown). The major solvent exposition of tryptophans in the PEGylated protein can be due to the influence of the highly hydrophilic PEG chain in the surrounding of this amino acid.

In Vitro Cellular Proliferative Activity of G-CSF Conjugates. The activity of conjugated and native G-CSF was evaluated by analyzing the proliferation of a sensitive cell line, which has been developed from a mouse myeloblastic leukemia rich in G-CSF receptors: NFS-60 cells. All of the protein species were found to stimulate cell proliferation, and the final cell

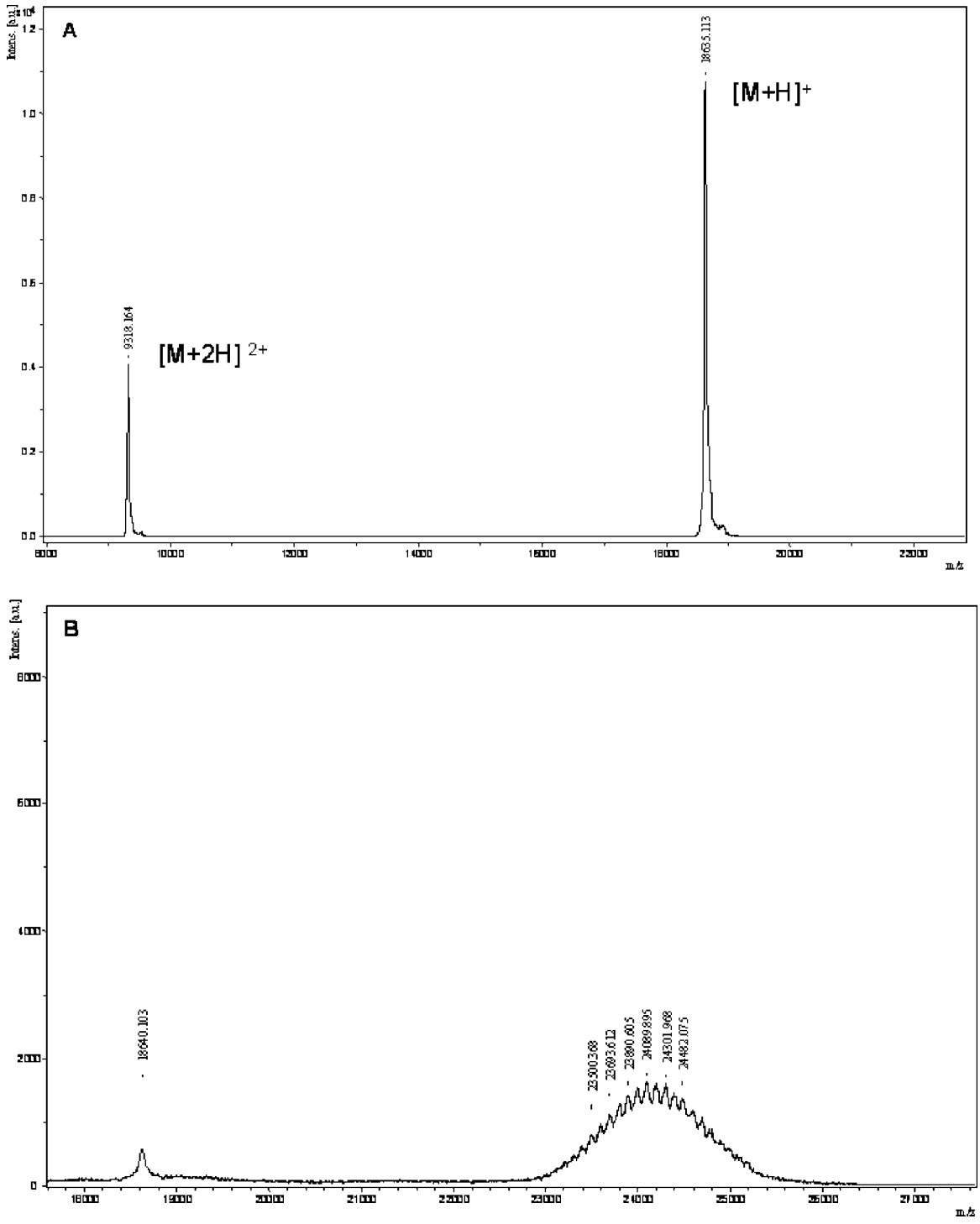


Figure 6. MALDI-TOF mass spectroscopy of (A) native G-CSF; (B) G-CSF–PEG–OPSS (5 kDa); the conjugate was purified from the reaction mixture by RP-HPLC chromatography.

concentration was found to be proportional to the concentration of G-CSF or G-CSF–PEG conjugates present in the cell culture. This allows quantification of the biological potency of G-CSF–PEG conjugates versus a G-CSF reference preparation, applying a dose–reaction ratio.

The IC_{50} values of two G-CSF–PEG conjugates, both prepared using a 5 kDa PEG, are reported in Table 2. The first conjugate was obtained by thiol-exchange reaction using PEG–OPSS and the second by double bond addition using PEG–VS. Both conjugates maintained high biological activity; in particular, the G-CSF–PEG–OPSS was more active than G-CSF–PEG–VS. This may be ascribed to the fact that the more hindered sulfone group of PEG–VS has a negative effect on maintenance of the native protein structure.

Stability of PEGylated G-CSF in Solution. Accelerated stability studies of G-CSF were performed by incubating at 37 °C the PEGylated protein solutions. The aggregation was evaluated on the basis of UV absorption and gel filtration chromatography of the incubated solutions. Figure 8 illustrates that the PEGylated forms unexpectedly undergo more rapid aggregation than the native G-CSF. This result is in contrast to the known drug solubilizing and aggregation prevention properties of PEG. Furthermore, this does not reflect the observations with Neulasta in which PEGylation slowed the rate of aggregate

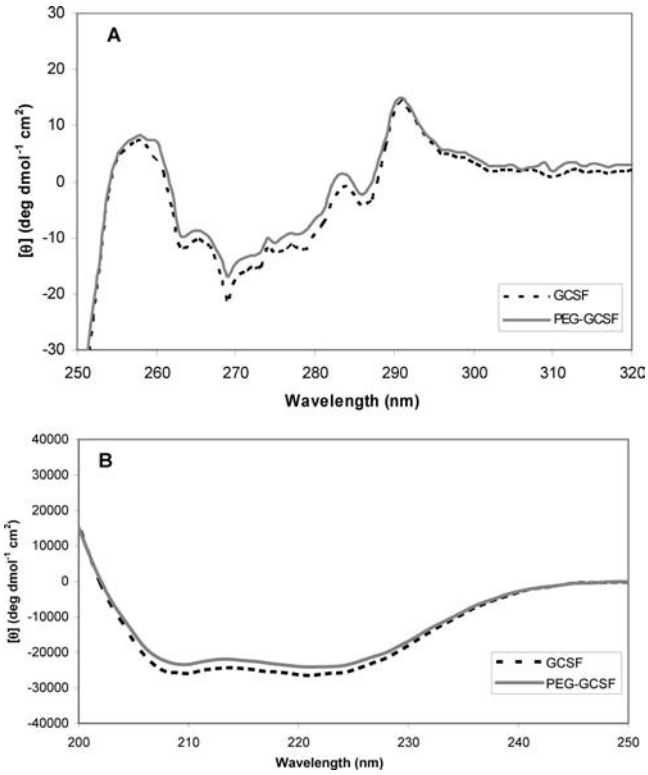


Figure 7. (A) Near-UV CD spectra of native G-CSF, G-CSF–PEG–OPSS (5 kDa). (B) Far-UV CD spectra of native G-CSF, G-CSF–PEG–OPSS (5 kDa). UV-CD spectra were taken at 25 °C in 10 mM acetic acid, 10 mg/mL mannitol, pH 4.2.

Table 2. In Vitro Activity in NSF-60 Cells of Native and Conjugated G-CSF

sample	IC_{50} (pmol/mL)	relative activity
rhG-CSF	0.0096	1
G-CSF–PEG–OPSS (5 kDa)	0.0145	0.66
G-CSF–PEG–VS (5 kDa)	0.039	0.246

formation (*15*). On the other hand, native G-CSF and Neulasta finally lead to covalent aggregates, which are formed as a consequence of disulfide scrambling promoted by the free thiol of Cys17 (*15*). As expected, in our study we did not observe covalent aggregates, since by SDS treatment it was possible to form the monomeric conjugate again. Anyway, preliminary formulation studies demonstrated that it is possible to stabilize the conjugates by adding hydroxypropyl β-cyclodextrin or albumin to G-CSF–PEG solution (Figure 8).

CONCLUSION

We have demonstrated the possibility to get site-specific PEGylation at the level of buried and less-accessible thiol groups of G-CSF cysteine 17. This was achieved by taking advantage of the quantitative reversible G-CSF unfolding by chemical denaturants and maintaining unaltered disulfide bridges to avoid disulfide scrambling. The conjugation was straightforward in the case of 5000 Da PEGs but needed longer time or increased temperature for the higher-molecular-weight PEG (10 and 20 kDa). The structure of the thiol-reactive moiety in the PEG chain plays a role in the biological activity of the final product. In fact, the conjugate G-CSF–PEG–OPSS retains higher activity than the G-CSF–PEG–VS. This may be because PEG, and in particular the steric hindrance of the thiol-reactive moiety, may induce some subtle local changes in the G-CSF three-dimensional structure. This phenomenon was slightly highlighted by fluorescence studies, although it was not evident by CD

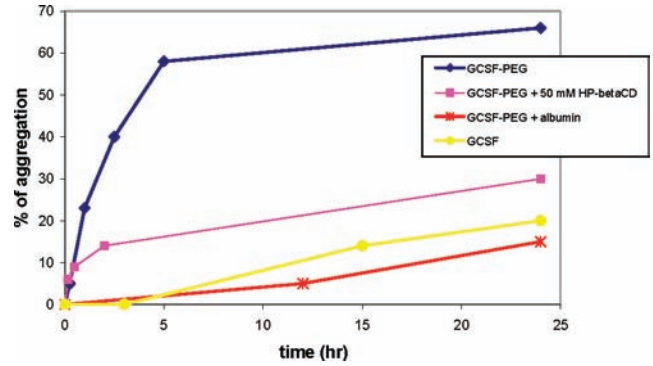


Figure 8. Aggregation profiles of native G-CSF, G-CSF–PEG–OPSS (5 kDa), G-CSF–PEG–OPSS (5 kDa) in 50 mM hydroxypropyl β-cyclodextrin, and G-CSF-PEG-OPSS (5 kDa) in albumin 0.1% (w/v) solution. The samples, all containing 1 mg/mL in G-CSF protein equivalent, were incubated at 37 °C and analyzed at predetermined times by gel filtration chromatography.

analysis. Furthermore, this can be correlated with the increased tendency of PEGylated G-CSF in solution to aggregate with respect to the native protein and the N-terminus PEGylated G-CSF (*15*). The different effect on G-CSF aggregation of this PEGylation strategy can be ascribed to the site of PEG linking. The polymer here is attached to a buried amino acid, and this can cause conformational change that enhances the rate of protein aggregation. We speculate therefore that the faster aggregation may be a consequence of protein hydrophobic residue exposition. In fact, the addition of hydroxypropyl β-cyclodextrin, which is known to mask hydrophobic residues, reduces the aggregation rate (Figure 8). On the other hand, the PEGylation at the level of Cys17 has been performed with the aim of avoiding the formation of covalent aggregates by thiol bridging, a problem faced by both the native and N-terminus PEGylated G-CSF (*15*). As expected, the aggregates, formed by G-CSF PEGylated at the cysteine, are in fact not covalent, and their formation can be totally prevented by a proper formulation by, for instance, using albumin (Figure 8). Therefore, this type of G-CSF–PEG has the advantage of overcoming the problem of covalent aggregation, a drawback presented by both native G-CSF and Neulasta.

This research highlights the possibility of exploiting a protein reversible denaturation for allowing a more selective PEGylation or conjugation of buried residues. Other conditions, which perturb the protein structure, can also enhance the thiol accessibility of G-CSF. In fact, preliminary experiments conducted in our laboratory showed that a complete G-CSF PEGylation at the level of Cys17 could also be achieved by PEG–OPSS during a very short (<30 s) protein exposure to high pH values (~11–12).

The role of protein conformation in influencing the site of PEGylation, as described here, in some way recalls what was done in growth hormone releasing factor (GRF) PEGylation. In this case, structuring solvents allowed a more selective modification, and the change in conformation was exploited to reduce the polymer linking at an unwanted site (*24*).

A final advantage of the procedure reported here is the feasibility of scale-up of the method, as needed for large-scale production of such an important therapeutic protein, because the lone site of modification makes it easier to obtain pure product.

ACKNOWLEDGMENT

The research was supported in part by Bio-Ker.

LITERATURE CITED

(1) Fibbe, W. E., Daha, M. R., Hiemstra, P. S., Duinkerken, N., Lurvink, E., Ralph, P., Altrock, B. W., Kaushansky, K., Willemze, R., and Falkenburg, J. H. (1989) Interleukin 1 and poly(rI).poly(rC) induce production of granulocyte CSF, macrophage CSF, and granulocyte-macrophage CSF by human endothelial cells. *Exp. Hematol. 17* (3), 229–34.

(2) Welte, K., Platzer, E., Lu, L., Gabrilove, J. L., Levi, E., Mertelsmann, R., and Moore, M. A. (1985) Purification and biochemical characterization of human pluripotent hematopoietic colony-stimulating factor. *Proc. Natl. Acad. Sci. U.S.A. 82* (5), 1526–1530.

(3) Lu, H. S., Boone, T. C., Souza, L. M., and Lai, P. H. (1989) Disulfide and secondary structures of recombinant human granulocyte colony stimulating factor. *Arch. Biochem. Biophys. 268* (1), 81–92.

(4) Lu, H. S., Clogston, C. L., Narhi, L. O., Merewether, L. A., Pearl, W. R., and Boone, T. C. (1992) Folding and oxidation of recombinant human granulocyte colony stimulating factor produced in Escherichia coli. Characterization of the disulfide-reduced intermediates and cysteine-serine analogs. *J. Biol. Chem. 267* (13), 8770–8777.

(5) Akbarzadeh, S., and Layton, J. E. (2001) Granulocyte colony-stimulating factor receptor: structure and function. *Vitam. Horm. 63*, 159–194.

(6) Welte, K., Gabrilove, J., and Bronchud, M. H., et al. (1996) Filgrastim (r-metHuG-CSF): the first 10 years. *Blood 88* (6), 1907–1929.

(7) Bronchud, M. H., Scarfee, J. H., and Thatcher, N. (1987) Phase I/II study of recombinant human granulocyte colony-stimulating factor in patients receiving intensive chemotherapy for small cell lung cancer. *Br. J. Cancer 56* (6), 809–813.

(8) Morstyn, G., and Dexter, T. M. (1994) *Neupogen (r-metHuG-CSF) in clinical practice*. Marcel Dekker, New York.

(9) Herman, A. C., Boone, T. C., and Lu, H. S. (1996) Characterization, formulation, and stability of Neupogen (Filgrastim), a recombinant human granulocyte-colony stimulating factor. *Pharm. Biotechnol. 9*, 303–328.

(10) Pasut, G., Guiotto, A., and Veronese, F. M. (2004) Protein, peptide and non-peptide drug PEGylation for therapeutic application: a review. *Exp. Opin. Ther. Patents 14*, 859–894.

(11) Zalipsky, S. (1995) Chemistry of polyethylene glycol conjugates with biologically active molecules. *Adv. Drug Delivery Rev. 16*, 157–182.

(12) Veronese, F. M., and Pasut, G. (2005) PEGylation, successful approach to drug delivery. *Drug Discovery Today 10*, 1451–1457.

(13) Veronese, F. M., and Harris, J. M., Eds. (2002) Theme issue on "Peptide and Protein Pegylation I". *Adv. Drug Delivery Rev. 54*, 453.

(14) Kinstler, O., Molineux, G., Treuheit, M., Ladd, D., and Gegg, C. (2002) Mono-N-terminal poly(ethylene glycol)-protein conjugates. *Adv. Drug Delivery Rev. 54*, 477–486.

(15) Rajan, S. R., Li, T., Aras, M., Sloey, C., Suthrland, W., and Arai, H., et al. (2006) Modulation of protein aggregation by polyethylene glycol conjugation: GCSF as a case study. *Protein Sci. 15*, 1063–1075.

(16) Raso, S. W., Abel, J., Barnes, J. M., Maloney, K. M., Pipes, G., and Treuheit, M. J. (2005) Aggregation of granulocyte-colony stimulating factor in vitro involves a conformationally altered monomeric state. *Protein Sci. 14*, 2246–2257.

(17) Arakawa, T., Prestrelski, S. J., Narhi, L. O., Boone, T. C., and Kenney, W. C. (1993) Cysteine 17 of recombinant human granulocyte-colony stimulating factor is partially solvent-exposed. *J. Protein Chem. 12*, 525–531.

(18) Veronese, F. M., and Berna, M. Novel G-CSF conjugates. Eur. Pat. noEP1737496.

(19) Berna, M., Spagnolo, L., and Veronese, F. M. Site-specific PEGylation of G-CSF by reversible denaturation, 32nd International Symposium on Controlled Release of Bioactive Materials, June 18–22, 2005, Miami, FL,No 415.

(20) Greenfield, N., and Fasman, G. D. (1969) Computed circular dichroism spectra for the evaluation of protein conformation. *Biochemistry 8* (10), 4108–4116.

(21) Ellman, G. L. (1959) Tissue sulphydryl groups. *Arch. Biochem. Biophys. 82*, 70–77.

(22) Hao, Y., Chen, J., Wang, X., Zhu, H., and Rong, Z. (2006) Effects of Site-specific polyethylene glycol modification of recombinant human granulocyte colony-stimulating factor on its biologic activities. *BioDrugs 20* (6), 357–362.

(23) Jørgensen, K. E., and Møller, J. V. (1979) Use of flexible polymers as probes of glomerular pore size. *Am. J. Physiol. 236*, 103–111.

(24) Esposito, P., Barbero, L., and Caccia, P. (2003) PEGylation of growth hormone-releasing hormone (GRF) analogues. *Adv. Drug Delivery Rev. 55*, 1279–1291.

BC070123+

Insulin Receptor Substrate 1 Knockdown in Human MCF7 ER+ Breast Cancer Cells by Nuclease-Resistant *IRS1* siRNA Conjugated To a Disulfide-Bridged D-Peptide Analogue of Insulin-Like Growth Factor 1

Gregory Cesarone,[†] Om Prakash Edupuganti,[†,§] Chang-Po Chen,[†] and Eric Wickstrom*[,‡,†]

Department of Biochemistry and Molecular Biology, and Kimmel Cancer Center, Thomas Jefferson University, Philadelphia, Pennsylvania 19107. Received April 21, 2007; Revised Manuscript Received July 18, 2007

IRS-1 overexpression has been associated with breast cancer development, hormone independence and antiestrogen resistance. IRS-1 is a major downstream signaling protein for insulin and IGF1 receptors, conveying signals to PI-3K/Akt and ERK1/2 pathways. In estrogen-sensitive breast cancer cell lines, the widely used antiestrogen tamoxifen treatment reduces IRS-1 expression and function, thereby inhibiting IRS-1/PI-3K signaling. IRS-1 may serve as an alternative target to overexpressed IGF1R in breast cancer. While siRNA technology has become commonplace in many laboratories for *in vitro* gene knockdown studies, and *in vivo* stability issues are largely solved, its use *in vivo* is limited by an inability to efficiently and specifically deliver it to the intended site of action. We previously reported reduced survival of human MCF7 estrogen receptor positive breast cancer cells treated with a normal *IRS1* siRNA delivered by a cationic lipid, plus an additive effect in combination with tamoxifen. We now report enhanced cellular uptake, relative to the unconjugated serum-stabilized *IRS1* siRNA, of a serum-stabilized *IRS1* siRNA conjugated with our previously characterized peptide mimetic of IGF1, D-(Cys-Ser-Lys-Cys), without the use of cationic lipids or electroporation, in MCF7 cells that overexpress IGF1R. Excess native IGF1 blocked uptake. An *IRS1* siRNA cholesterol conjugate, targeted universally to cell membranes, was taken up by MCF7 cells as much as the peptide mimetic conjugate. *IRS1* mRNA knockdown and IRS-1 protein knockdown were comparable for the IGF1 peptide and cholesterol conjugates. The unconjugated serum-stabilized *IRS1* siRNA control showed negligible effects. Viability assays showed additive effects of siRNA treatment in combination with tamoxifen. In summary, we have taken the first step in converting an siRNA into a pharmacologically active agent for breast cancer.

INTRODUCTION

The crosstalk of ER-α with IGF1R signaling is well-demonstrated and is linked in the proliferation of breast cancer (*1–3*). Estrogens and IGFs act jointly to increase proliferation (*4, 5*); in fact, synergy has been shown between E_2 and IGF-I (*2*). ER-α is able to upregulate the mRNA and protein levels of IGF1R (*6, 7*). These observations illustrate the entwining of signaling between ER-α and IGF1R; yet, in breast cancer, resistance stemming from IGF-IR overexpression and/or prolonged activation leads to protein kinase activation, specifically, by increased pAkt, irrespective of hormone receptor status (*8*).

ER-α has also been shown to enhance the stability of insulin receptor substrate 1 (IRS-1) protein, and to upregulate *IRS1* mRNA (*6, 9, 10*). IRS-1 plays a major role in survival and proliferation signaling as an adaptor of IGF1R, to signal preferentially through the PI3K/Akt pathway for growth, proliferation, and survival (*11*). While IGF1R overexpression on human MCF7 ER+ breast cancer cells does not yield estrogen independence, characterized by reduced estrogen requirements for growth and transformation, IRS-1 seems to play a role in resistance to antiestrogen treatment (*12*). IRS-1 overexpressing MCF7 cells are no longer under ER control; their proliferation is not inhibited by E_2 alone or in combination with IGF1 (*12*). These observations provide a rationale for IRS-1 as the next logical alternative target in attacking breast cancer via a signaling intermediate (*13*). Recently, we reported the ability of *IRS1* siRNA to knock down *IRS1* mRNA, ablate IRS-1 protein, and reduce survival in human MCF7 ER+ breast cancer cells (*14*). siRNA effects were additive with those of tamoxifen (TAM).

Can *IRS1* siRNA, which must be delivered into cells with a cationic lipid, be modified into a pharmacologically active agent for breast cancer? Targeted approaches to therapy in cancer have gained momentum in recent years. The route of delivery for one agent versus another depends on the type or even subtype of cancer targeted (*15*). Recent successes with monoclonal antibody mediated therapy have determined a particular surface receptor to attack, a case of therapeutic agent and delivery vehicle all wrapped into one (*16*). Other solutions represent improvements on more traditional small molecules like taxols with improved delivery schemes to reduce their toxicity (*17*). Perhaps the most simple, yet largely elusive solution, due to delivery issues, is through direct gene targeting with antisense or siRNA.

While a number of reports have described methods of stabilizing these gene-targeting oligonucleotides in serum while retaining their activity (*18*), functionalization for *in vivo* targeted delivery has been a mixed bag. Many attempts have been made to provide siRNAs with the ability to be taken up into cells without the need for liposomal formulations that are fairly toxic *in vivo* but work wonderfully *in vitro*. One example, based on the success of monoclonal antibodies, utilized antibodies against HIV envelope protein and Her2 receptor conjugated to siRNA for cellular uptake *in vitro* and also for *in vivo* mouse studies

* To whom correspondence should be addressed. Tel.: 1.215.955.4578; Fax: 1.215.955.4580; E-mail: eric@tesla.jci.tju.edu.

[†] Department of Biochemistry and Molecular Biology.

[‡] Kimmel Cancer Center.

[§] Current address: BioOnco, Tenali AP 522201, India.

10.1021/bc070135v CCC: $37.00 © 2007 American Chemical Society
Published on Web 10/09/2007

(*19*). A list of other examples, though not exhaustive, includes the use of penetratin (*20*), endogenous *in vivo* knockdown made possible by a cholesterol conjugate (*21*), transportan (*22*), atelocollagen (*23*), and PEG (*24*).

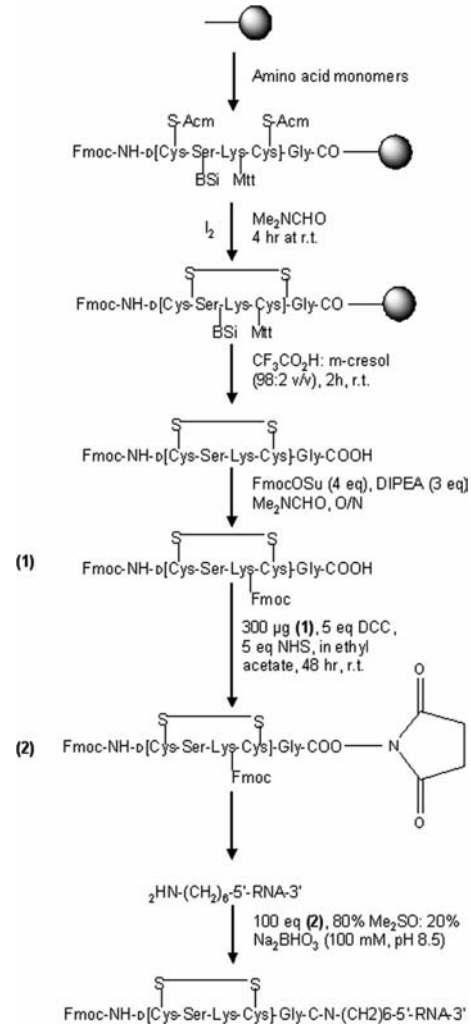
In this work, we tested the hypothesis that a peptide mimetic of IGF1 that has been characterized previously (*25*) would enable *IRS1* siRNA activity, without the need for cationic lipids, in human MCF7 ER+ breast cancer cells that overexpress IGF1R. The Cys-Cys cyclized peptide mimetic D-(Cys-Ser-Lys-Cys) was modeled to emulate an IGF1R binding domain of IGF1 (*25*) and has been used successfully for receptor-mediated endocytosis of peptide nucleic acid (PNA) radiohybridization agents designed to quantitate overexpressed oncogene mRNAs by noninvasive, external imaging *in vivo* (*26*, *27*). We have taken advantage of commercially available modifications to improve the stability of an siRNA that was effective at silencing *IRS1* mRNA in human MCF7 ER+ breast cancer cells (*14*), added a red fluorescent dye to the 3′ end of the antisense siRNA strand to monitor cellular uptake, and added the D-(Cys-Ser-Lys-Cys)-Gly IGF1 peptide analogue to the 5′ end of the sense siRNA strand to enable IGF1R-mediated endocytosis. In MCF7 cells that overexpress IGF1R, we observed enhanced cellular uptake of the serum-stabilized D-(Cys-Ser-Lys-Cys)-Gly-*IRS1* siRNA conjugate, without the use of cationic lipids or electroporation, relative to the unconjugated serum-stabilized *IRS1* siRNA. Excess native IGF1 blocked uptake, implying dependence of uptake on IGF1R. A cholesteryl–*IRS1* siRNA conjugate, targeted universally to cell membranes, displayed similar MCF7 cell uptake. *IRS1* mRNA knockdown and IRS-1 protein knockdown were comparable for the IGF1 peptide and cholesterol conjugates, against a background of minimal effect by the unconjugated serum-stabilized *IRS1* siRNA. Viability assays showed reduced survival of MCF7 cells treated with *IRS1* siRNA-IGF1 peptide conjugate alone or in combination with tamoxifen.

MATERIALS AND METHODS

Solid-Phase Peptide Synthesis of IGF1 Peptide Mimetic. Scheme 1 illustrates our route for solid-phase synthesis of the IGF1 peptide mimetic and its conjugation to the H_2N-Hx-*IRS1* RNA sense strand. The IGF1 mimetic D-(Cys-Ser-Lys-Cys)-Gly (*25*) was synthesized by stepwise Fmoc (9-fluorenylmethoxy carbonyl) coupling of Fmoc-D-Cys(Acm)-OH (Novabiochem, San Diego, CA), Fmoc-D-Lys(Mtt)-OH, and Fmoc-D-Ser(TBDMS)-OH (Bachem, King of Prussia, PA) onto Fmoc-Gly HMP-Tentagel resin (220 μmol/g) (Anaspec, San Jose, CA) using a PS3 peptide synthesizer (Protein Technologies, Phoenix, AZ). Upon completion of coupling, the IGF1 mimetic peptide was cyclized via disulfide bond formation while still on the solid phase support by oxidation with a 10-fold excess of I_2 in $(Me)_2NCHO$ as previously described (*28*). The IGF1 mimetic peptide was then cleaved from its resin using 98% CF_3CO_2H/2% *m*-cresol, followed by reverse-phase HPLC purification on a Microsorb 300 Å pore, 10 μm particle, 10 × 250 mm C_{18} column (Varian, Inc., Palo Alto, CA) eluted with a 40 min gradient from 65% to 100% CH_3CN in aqueous 0.1% CF_3CO_2H at 2 mL/min, at 23 °C, on a SCL-10Avp liquid chromatograph (Shimadzu, Columbia MD) monitored at 260 nm.

The crude product was analyzed by MALDI-TOF mass spectroscopy from an α-cyano-hydroxycinnamic acid matrix excited at 338 nm on a SELDI mass spectrometer (Ciphergen Corp., Fremont, CA) calibrated with porcine neuropeptide Y (Sigma, St. Louis, MO). During cleavage from the resin, the β-TBDMS group of D-Ser(TBDMS) and the ϵ-Mtt group of D-Lys(Mtt) were lost (calculated, 716.8 Da; observed, 716.7 Da). The D-Lys side chain ϵ-NH_2 was then protected again by reaction with FmocOSu (*29*) to yield Fmoc-D-[Cys-Ser-Lys (Fmoc)-Cys]-Gly. Typically, purified Fmoc-D-[Cys-Ser-Lys-Cys]-Gly (1 mg) was dissolved in 50:50 CH_3CN/H_2O (1 mL)

Scheme 1. Synthetic Route to the IGF1 Peptide Mimetic D-(Cys-Ser-Lys-Cys)-Gly and Its Conjugation To the H_2N-Hx-*IRS1* RNA Sense Strand



with 5 equiv FmocOSu (2.35 mg) and 1 equiv iPr_2EtN (0.13 μL). The reaction was followed by subsequent reverse-phase HPLC purification as above to determine the completion time, 15 h. The D-Ser side chain β-OH was not reprotected because it was not likely to compete significantly with the D-Lys side chain ϵ-NH_2 in the succinimidylation reaction.

***IRS1* siRNA.** The *IRS1* siRNA sequence 5′-pCCACGGCGAUCUAGUGCUUUU-3′ was previously found effective and characterized biologically in MCF7 cells (*14*). The three-base mismatch control sequence was 5′-CCACGGCG *GAA* UAGUGCUU-3′. In this study, however, the RNA strands were synthesized with Dharmacon (Lafayette, CO) siSTABLE modifications, which are consistent by MALDI-TOF mass spectroscopy with 2′-O-methyl groups on 11 residues, as well as with 2′-ACE[1] protecting groups to keep the RNA stable until after annealing. The 3′ end of the antisense strand also was modified

[1]Abbreviations: ACE, acetoxyethyl orthoester; Acm, acetoxymethoxy; AEEA, aminoethoxyethoxyacetate; DCC, *N*,*N*′-dicyclohexylcarbodiimide; DCU, *N*,*N*′-dicyclohexylurea; E2, 17-β-estradiol; ER-α, estrogen receptor-α; Fmoc, fluorenylmethoxycarbonyl; Hx, hexyl; IGF1, insulin-like growth factor 1; IGF1R, insulin-like growth factor 1 receptor; IR, insulin receptor; IRS, insulin receptor substrate; Mtt, methyltrityl; MTT, (3-[4,5-dimethylthiazol-2-yl]-2,5-diphenyltetrazolium bromide); NHS, *N*-hydroxysuccinimide; PAGE, polyacrylamide gel electrophoresis; PBS, phosphate-buffered saline; PEG, poly(ethylene glycol); QRT-PCR, quantitative real-time polymerase chain reaction; RNAi, RNA interfer-

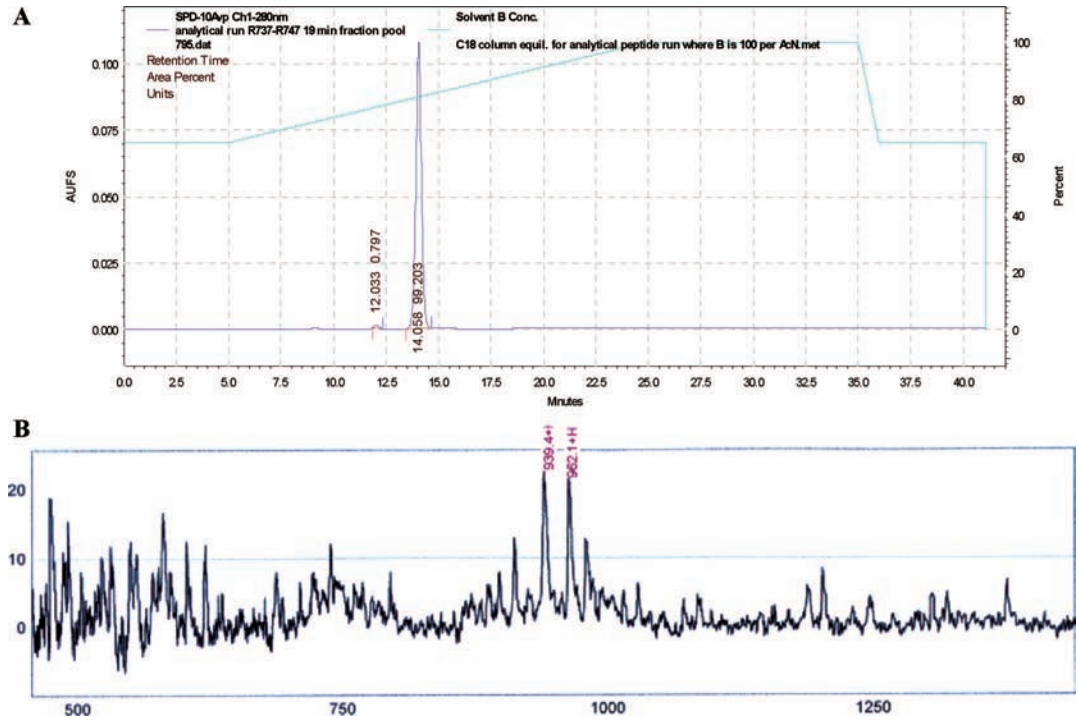


Figure 1. Synthesis, purification, and characterization of IGF1 peptide mimetic. A. Analytical reverse-phase HPLC chromatogram of purified Fmoc-D-[Cys-Ser-Lys(Fmoc)-Cys]-Gly. B. MALDI-TOF mass spectroscopy of purified Fmoc-D-[Cys-Ser-Lys(Fmoc)-Cys]-Gly. Calculated 939.4 Da; observed 939.1 Da.

to include the red fluorescent dye DY547. Finally, the 5′ end of the sense strand was modified to include an H_2N-Hx linker that would permit conjugation to the IGF1 peptide mimetic. A separate siSTABLE *IRS1* siRNA with 5′-sense strand cholesterol and 3′-antisense DY547 was utilized as a positive control, based on a published study with an *APOB* siRNA cholesterol conjugate (*21*). The *IRS1* siRNA sequence and three-base mismatch sequence were analyzed with the *BLASTn* program and found to have no significant homology to other human genes.

Conjugation of IGF1 Peptide to siRNA. Conjugation of Fmoc-D-[Cys-Ser-Lys(Fmoc)-Cys]-Gly to *IRS1* siRNA was achieved in a two-step reaction. First, the Fmoc-D-[Cys-Ser-Lys(Fmoc)-Cys]-Gly C-terminal carboxylate was converted to an NHS ester with 5 equiv of DCC and 5 equiv of NHS to peptide. Fmoc-D-[Cys-Ser-Lys(Fmoc)-Cys]-Gly (300 μg) was dissolved in EtOAc (150 μL), followed by stepwise addition of DCC (330 μg) and NHS (184 μg) stepwise addition at 0 °C on ice, then allowed to reach room temperature and continuously stirred for 48 h. Following the reaction, a white precipitate of DCU was filtered off; Fmoc-D-[Cys-Ser-Lys(Fmoc)-Cys]-Gly NHS ester was concentrated by centrifugal lyophilization and redissolved in Me_2SO.

The reactivity of the Fmoc-D-[Cys-Ser-Lys(Fmoc)-Cys]-Gly NHS ester was tested by reacting 50 μg dissolved in 8 μL Me_2SO, 2 μL 100 mM Na_2HBO_3, pH 8.5, with the free terminal amine on 500 μg AEEA (100 equiv relative to Fmoc-D-[Cys-Ser-Lys(Fmoc)-Cys]-Gly NHS) at room temperature overnight. The products were analyzed by TLC on silica gel plates developed with 60% hexane/40% EtOAc, imaged with ultraviolet light. The migration standards used were Fmoc-D-[Cys-Ser-Lys(Fmoc)-Cys]-Gly NHS ester (Rf 0.40), Fmoc-D-[Cys-Ser-Lys(Fmoc)-Cys]-Gly (Rf 0.38), and AEEA (Rf 0.10).

A parallel test of H_2N-Hx-*IRS1* RNA (20 μg) reactivity with AlexaFluor-532 NHS ester (40 μg, 40 equiv) was carried out in the same solvent mixture as above at room temperature overnight. Reaction products were analyzed by nondenaturing electrophoresis on a 20% polyacrylamide gel in TBE. Bands were visualized by ultraviolet illumination on a 2000R imaging station (Kodak, Rochester, NY).

Conjugation of sense 5′-H_2N-Hx-*IRS1* RNA and Fmoc-D-[Cys-Ser-Lys(Fmoc)-Cys]-Gly NHS was carried out in 80% Me_2SO/20% H_2O (10 μL) to keep both moieties in solution simultaneously (*30*). Sense 5′-H_2N-Hx-*IRS1* RNA (20 μg) was dried by centrifugal lyophilization prior to reaction and resuspended in 2 μL of 100 mM Na_2HBO_3, pH 8.5. Fmoc-D-[Cys-Ser-Lys(Fmoc)-Cys]-Gly NHS (270 μg, 100 equiv relative to sense 5′-H_2N-Hx-*IRS1* RNA) dissolved in 8 μL Me_2SO was added. The reaction was stirred at room temperature overnight. Fmoc protecting groups on the peptide were then removed by the addition of 40 μL of concentrated (28 M) NH_4OH, bringing the total volume to 50 μL. The mixture was reacted at 23 °C for 1.5 h with continuous stirring, followed immediately by addition of another 100 μL of concentrated (28 M) NH_4OH and another 1.5 h incubation at 23 °C, with continuous stirring. NH_3 was then removed by centrifugal lyophilization. D-(Cys-Ser-Lys-Cys)-Gly HN-Hx-*IRS1* RNA was precipitated by addition of 1.5 μL of 10 mg/mL glycogen stock solution as a carrier, followed by 2.5 volumes of EtOH. The mixture was chilled at −20 °C overnight, then sedimentated at 15 000 *g* for 30 min at 4 °C.

Annealing of purified D-(Cys-Ser-Lys-Cys)-Gly HN-Hx-*IRS1* RNA (25 μM) to the antisense-DY547 strand (25 μM) (or 3 mismatch-DY547 strand) with simultaneous removal of RNA 2′-ACE protecting groups was carried out in 2′-O-deprotection buffer (100 mM TEMED–HOAc, pH 3.8) for 45 min at 60 °C followed by cooling at room temperature for 30 min (Dharmacon RNAi Tech. Ref. & App. Guide). Next, the annealed, deprotected D-(Cys-Ser-Lys-Cys)-Gly HN-Hx-*IRS1* RNA was evaporated to dryness and resuspended in H_2O. Concentration was determined by ultraviolet absorbance at 260 nm. Steps from annealing forward were repeated for an *IRS1* siRNA unconju-

ence; siRNA, short interfering RNA; TAM, tamoxifen; TBE, Tris-borate-EDTA; TBDMS, *t*-butyldimethylsilyl.

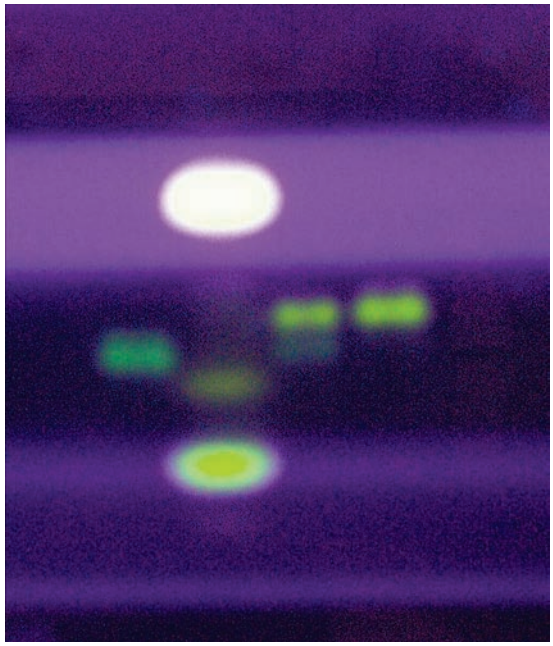


Figure 2. Test of H_2N-Hx-*IRS1* RNA reactivity with AlexaFluor 532-NHS ester. TBE 20% PAGE ran with 250 ng of sample per lane. Lanes from left to right are as follows: 1, H_2N-Hx-*IRS1* RNA alone; 2, AlexaFluor 532-NHS ester alone; 3, H_2N-Hx-*IRS1* RNA reacted with AlexaFluor 532-NHS ester in 80% Me_2SO/20% H_2O with DMAP buffer; 4, H_2N-Hx-*IRS1* RNA reacted with AlexaFluor 532-NHS ester in 80% Me_2SO/20% H_2O with Na_2HBO_3 buffer.

gated control lacking D-(Cys-Ser-Lys-Cys). The extent of annealing was analyzed by native 20% polyacrylamide gel electrophoresis in TBE, followed by staining with Sybr Green II (Molecular Probes, Eugene, OR) and fluorescence observation on a 2000R imaging station (Kodak, Rochester, NY).

Cellular Uptake of siRNA in MCF7 (ER+) Breast Cancer Cells. MCF7 (ATCC, Germantown MD) human breast ER+ epithelial cells were grown in DMEM/F12 medium (Mediatech, Herndon, VA) supplemented with 5% calf serum, 50 U/mL penicillin, 5 μg/mL streptomycin, 2 mM glutamine, and 10 nM 17-β-estradiol under 5% CO_2 in a humidified incubator at 37 °C. MCF7 cells were detached from their flasks with 0.02% EDTA solution (Sigma, St. Louis, MO) and plated 24 h prior to treatment in LabTek 8-well chamber slides (Nalge Nunc International, Naperville, IL) at a concentration of 1.5×10^4 cells/well, such that cells were ~70% confluent at the time of treatment. The cells were then treated for 6 h at 37 °C with D-(Cys-Ser-Lys-Cys)-Gly HN-Hx-*IRS1* siRNA-DY547, cholesteryl-*IRS1*siRNA-DY547, or unconjugated *IRS1* siRNA-DY547, premixed at a final concentration of 1 μM in culture medium. For peptide blocking by human recombinant IGF1 (PeproTech, Rocky Hill, NJ), the culture medium was replaced with serum-free DMEM (Life Technologies, Inc.) containing 0.1% bovine serum albumin, 50 μg/mL holo-transferrin 100 U/mL penicillin, 10 μg/mL streptomycin, 2 mM glutamine, and 10 nM 17-β-estradiol to prevent proteolysis of IGF1, which was added to 10 μM. After 10 min of preblocking, D-(Cys-Ser-Lys-Cys)-Gly HN-Hx-*IRS1* RNA was added to 1 μM as above, and also to a nonblocked serum-free control well, followed by incubation for 6 h at 37 °C. At the end of the uptake period, the cells were washed with serum-free medium to remove fluorescent siRNA probes. Cells were then observed on a CK40 fluorescence microscope (Olympus, Center Valley, PA) with a SPOT color digital camera at 600× magnification through a red filter suitable for the DY547 dye. Uptake images were collected in real time and displayed with *Image Pro Plus 4.5*.

Quantitative Real-Time PCR (QRT-PCR). Quantitation of *IRS1* mRNA levels in treated MCF7 cells was carried out as described previously (*14*). The *IRS1* siRNA forward primer was 5′-CTCCACCTCGGATTGTCTCTTC-3′, the reverse primer was 5′-GAAACCGCCATCGCTGG-3′, and the fluorescent probe was 5′-6FAM-CACGGCGATCTAGTGCTTCGGTGTC-TAMRA-3′. The expression of the endogenous control gene GAPDH was assessed using a premade primer probe set (Applied Biosystems, Foster City, CA).

Western Immunoblot Analysis. At 4 days after siRNA administration, plates were lysed in 50 mM HEPES–KOH, pH 7.5, 150 mM NaCl, 1.5 mM $MgCl_2$, 10 mM EGTA, pH 7.5, 10% glycerin, 1% Triton X-100 with a Complete Mini protease inhibitor cocktail tablet (Roche Applied Science, Piscataway, NJ). Cytoplasmic lysates were electrophoresed on NuPAGE 10% Bis–Tris gels (Invitrogen, San Diego, CA). Antibodies used were anti-IRS-1 (Santa Cruz Biotechnology, Santa Cruz, CA) and anti-GAPDH (Ambion, Austin, TX). The substrate for HRP-conjugated secondary antibodies was SuperSignal West Femto (Pierce, Rockford, IL). Detection and quantitation of protein bands were conducted with a 2000R Image Station (Kodak, Rochester, NY).

Cell Viability Assays. Once stained with 0.4% Trypan blue solution (Mediatech, Herndon, VA) to measure viability, the percentage of dead MCF7 cells from pooled adherent and floating cells was determined by direct cell counting using a hemacytometer. At least 400 cells were counted with each experimental condition performed in triplicate. For the MTT viability assay (Chemicon, Temecula, CA), siRNA treatments were scaled for 96-well plates and assayed colorimetrically according to the manufacturer's instructions at 570 nm vs 630 nm using a μQuant plate reader (Bio-Tek, Winooski, VT), with data collected and analyzed by *KCjunior 1.22*.

RESULTS

IGF1 Peptide Mimetic Synthesis and Purification. In order to synthesize the IGF1 peptide mimetic D-(Cys-Ser-Lys-Cys)-Gly, we used solid-phase peptide synthesis carried out from C-terminus to N-terminus. Following coupling, the D-cysteines were cyclized, the peptide was cleaved from the resin, an initial reverse phase HPLC purification and Fmoc reprotection of D-lysine side chain ϵ-NH_2 was completed, and then finally a second round of purification was performed by reverse-phase HPLC. An analytical chromatogram of this final purified peptide is shown in Figure 1A. The mass of the purified Fmoc-D-[Cys-Ser-Lys(Fmoc)-Cys]-Gly was measured by MALDI-TOF mass spectroscopy and is displayed in Figure 1B: calculated 939.4 Da, observed 939.1 Da.

Reactivity of the IGF1 Peptide and of the H_2N-Hx-*IRS1* RNA Sense Strand. The C-terminal carboxyl group of Fmoc-D-[Cys-Ser-Lys(Fmoc)-Cys]-Gly must first be activated in order for the amino terminus of the H_2N-H_2N-Hx-*IRS1* RNA Hx-*IRS1* RNA sense strand to attack the Fmoc-D-[Cys-Ser-Lys(Fmoc)-Cys] C-terminal carboxylate (*31*). Therefore, we reacted Fmoc-D-[Cys-Ser-Lys(Fmoc)-Cys]-Gly with DCC and NHS to form a Fmoc-D-[Cys-Ser-Lys(Fmoc)-Cys]-Gly NHS ester that would be stable longer than using a carbodiimide alone for an active intermediate.

Prior to conjugation of Fmoc-D-[Cys-Ser-Lys(Fmoc)-Cys]-Gly NHS ester to the H_2N-Hx-*IRS1* RNA sense strand, the reactivity of each was confirmed independently. We tested the reactivity of the Fmoc-D-[Cys-Ser-Lys(Fmoc)-Cys]-Gly NHS ester with that of the free terminal amine on AEEA. TLC showed no Fmoc-D-[Cys-Ser-Lys(Fmoc)-Cys]-Gly NHS ester or Fmoc-D-[Cys-Ser-Lys(Fmoc)-Cys]-Gly in the reaction mixture lane, compared with known lanes. There was, however, a product with higher mobility (Rf 0.92) consistent with the

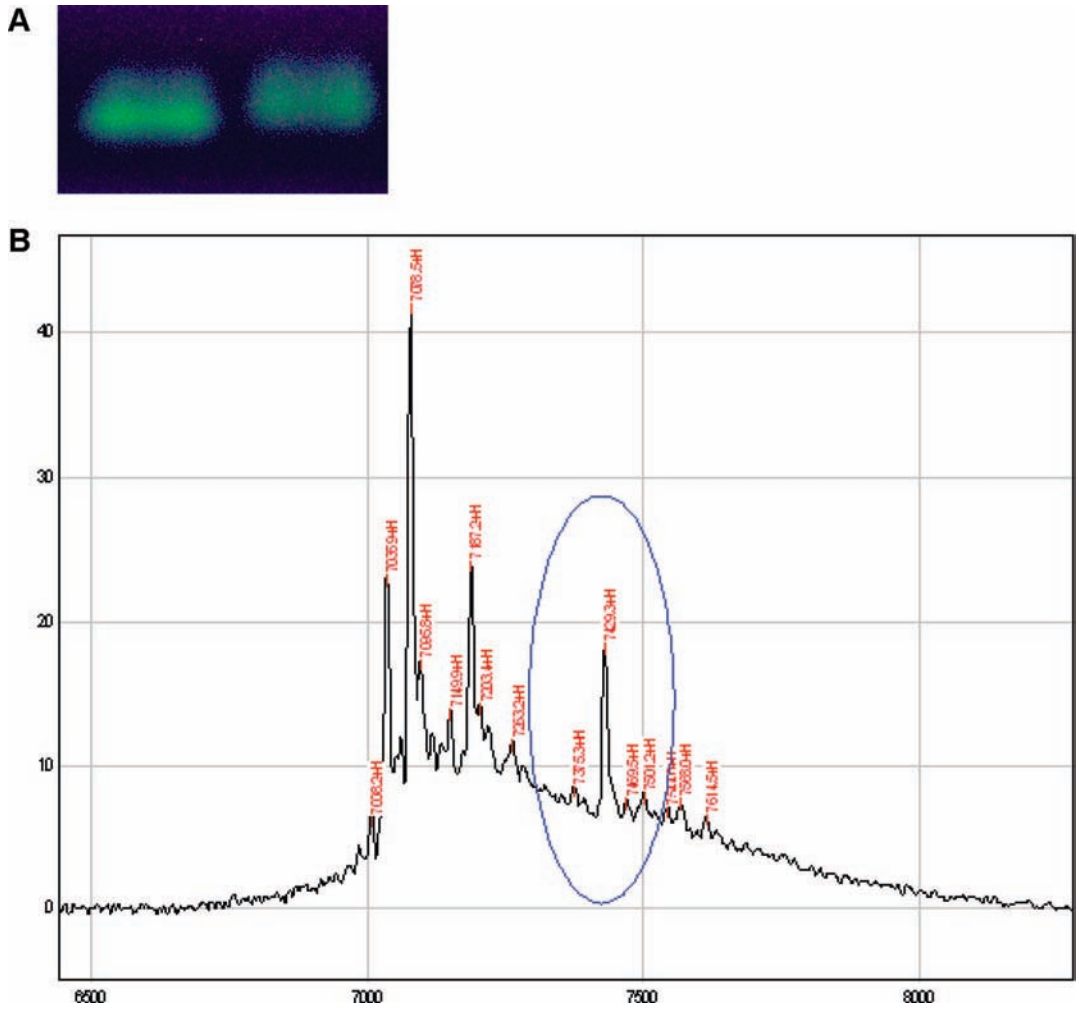


Figure 3. Conjugation of H_2N-Hx-*IRS1* RNA to IGF1 peptide Fmoc-D-[Cys-Ser-Lys(Fmoc)-Cys]-Gly. A. TBE 20% PAGE where left lane is H_2N-Hx-*IRS1* RNA alone unreacted, and right lane is H_2N-Hx-*IRS1* RNA plus Fmoc-D-[Cys-Ser-Lys(Fmoc)-Cys]-Gly NHS ester after reaction and subsequent precipitation. A small shift was observed in the reaction lane as compared to unreacted H_2N-Hx-*IRS1* RNA. B. MALDI-TOF mass spectroscopy of Fmoc-D-[Cys-Ser-Lys(Fmoc)-Cys]-Gly HN-Hx-*IRS1* siRNA. Calculated 7431 Da; observed 7429.3 Da.

predicted Fmoc-D-[Cys-Ser-Lys(Fmoc)-Cys]-Gly AEEA conjugation product, which would be more hydrophobic than either starting material. Because no spots were observed at the Rf of the peptide or peptide–NHS alone, it appeared that all peptide–NHS present in the test reaction was conjugated to peptide–AEEA.

Next, we tested the reactivity of the H_2N-Hx-*IRS1* RNA sense strand with that of a commercially available AlexaFluor 532-NHS ester. Using a fluorescent dye allowed for easy observation of reactivity as well as completeness of reactivity following the reaction due to differential fluorescence intensities and colors upon PAGE analysis (Figure 2). One can observe partial reactivity in the lane where DMAP (pH 8.6) was used as the buffer (orange and green bands) and nearly complete reactivity in the lane where Na_2HBO_3 (pH 8.5) was used as the buffer (orange band only). These separate reactivity tests, plus further optimization trials, formed the basis for optimal conjugation of the Fmoc-D-[Cys-Ser-Lys(Fmoc)-Cys]-Gly NHS ester to the 5′-NH_2-Hx-*IRS1* RNA-3′ sense strand.

Conjugation of IGF1 Peptide to H_2N-Hx-*IRS1* RNA Sense Strand. Following confirmation of individual component reactivities, we then conjugated the H_2N-Hx-*IRS1* RNA sense strand to the Fmoc-D-[Cys-Ser-Lys(Fmoc)-Cys]-Gly NHS ester. A clear upward gel mobility shift of the H_2N-Hx-*IRS1* RNA sense strand band was observed when the reacted RNA was compared to the unreacted RNA by 20% TBE PAGE (Figure 3A). Following the conjugation reaction, cleavage of peptide Fmoc-protecting groups, and precipitation, the molecular mass of the conjugated D-(Cys-Ser-Lys-Cys)-Gly HN-Hx-*IRS1* RNA was measured by MALDI-TOF mass spectroscopy (Figure 3B): calculated 7431.0 Da, observed 7429.3 Da. Annealing yielded only a single significant duplex band upon nondenaturing PAGE (Figure 4), obviating the need for preparative gel electrophoresis.

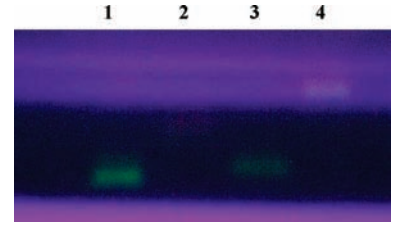


Figure 4. Native 20% polyacrylamide gel electrophoresis in TBE of D-(Cys-Ser-Lys-Cys)-Gly HN-Hx-*IRS1* siRNA duplex. 250 ng of RNA was loaded on each lane. Lane 1, H_2N-Hx-*IRS1* sense RNA; lane 2, *IRS1* antisense RNA-DY547; lane 3, D-(Cys-Ser-Lys-Cys)-Gly HN-Hx-*IRS1* sense RNA; lane 4, annealed duplex. Following TBE PAGE, the gel was stained with Sybr Green II and observed on a Kodak 2000R imaging station.

MCF7 Cellular Uptake of Conjugated siRNAs. The cellular uptake of the D-(Cys-Ser-Lys-Cys)-Gly HN-Hx-*IRS1* siRNA duplex by human MCF7 ER+ breast cancer cells that express high levels of IGF1R was measured by fluorescence microscopy

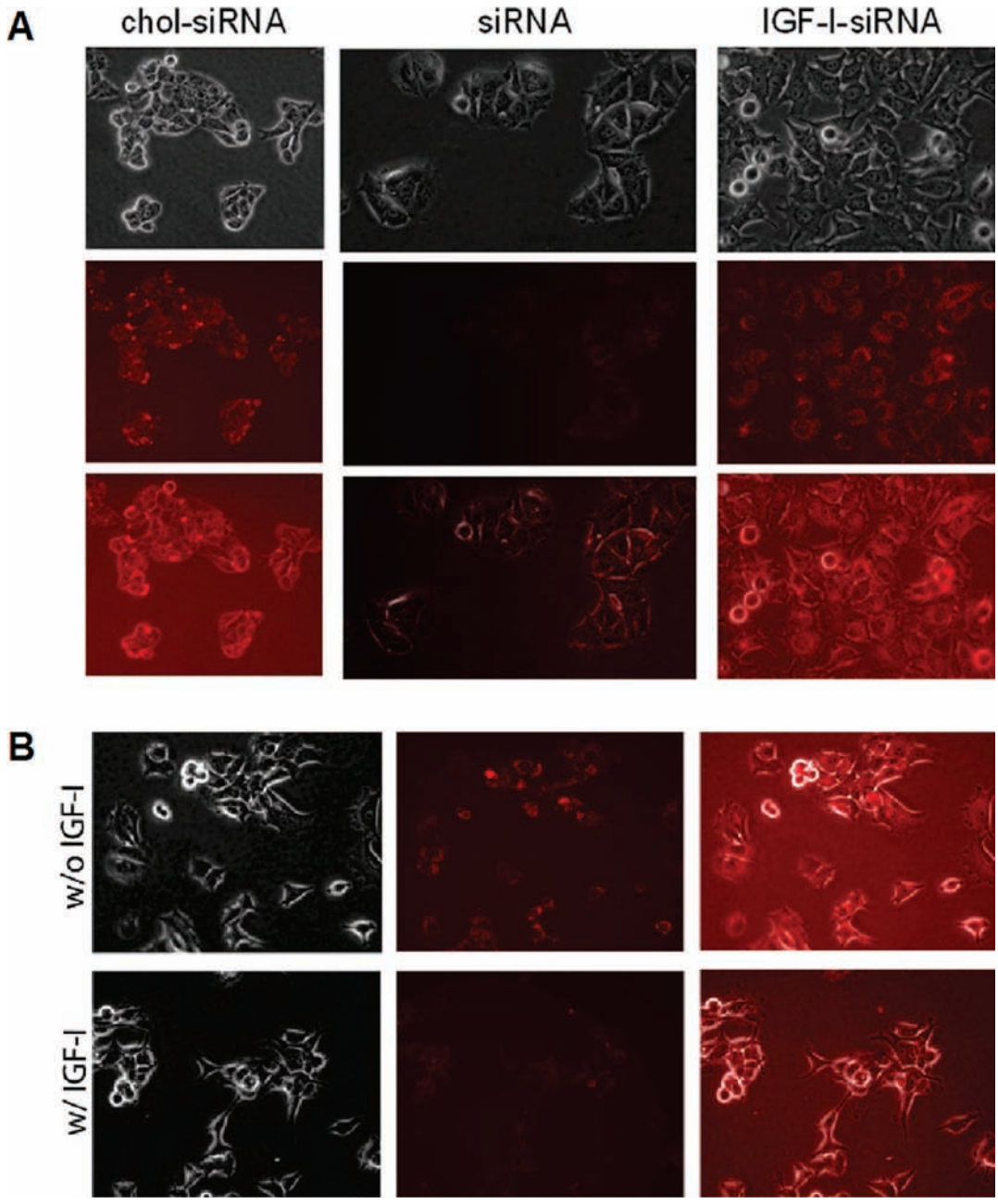


Figure 5. Internalization of siRNA conjugates by human MCF7 ER+ breast cancer cells. A. Cellular uptake of 1 μM cholesteryl–*IRS1* siRNA, D-(Cys-Ser-Lys-Cys)-Gly HN-Hx-*IRS1* siRNA, or unconjugated *IRS1* siRNA, after 6 h. B. Cellular uptake in the absence of serum of 1 μM D-(Cys-Ser-Lys-Cys)-Gly HN-Hx-*IRS1* siRNA after 4 h with or without exogenous full-size recombinant IGF1, 10 μM, added 10 min prior to siRNA.

after 6 h of incubation (Figure 5A). The D-(Cys-Ser-Lys-Cys)-Gly HN-Hx-*IRS1* siRNA and the cholesteryl–*IRS1* siRNA displayed comparable uptake, whereas the unconjugated *IRS1*siRNA was found to have minimal uptake. Preblocking of MCF7 cells with 10 μM full-size IGF1 reduced the uptake of D-(Cys-Ser-Lys-Cys)-Gly HN-Hx-*IRS1* siRNA to the level of the unconjugated *IRS1* siRNA (Figure 5B).

Knockdown Efficacy of Conjugated siRNAs. *IRS1* mRNA levels in treated human MCF7 ER+ breast cancer cells were measured by QRT-PCR over a range of siRNA concentrations (100, 150, 200 nM) (Figure 6A). D-(Cys-Ser-Lys-Cys)-Gly HN-Hx-anti-*IRS1* siRNA lowered the level of *IRS1* mRNA significantly, more and more as the dose increased (55.8 $\pm$ 9.3% at 100 nM, 41.4 $\pm$ 5.4% at 150 nM, 35.8 + 12.7% at 200 nM, relative to untreated). The cholesteryl–anti-*IRS1* siRNA, on the other hand, displayed equal knockdown of *IRS1* mRNA at all three doses. The D-(Cys-Ser-Lys-Cys)-Gly HN-Hx-mismatch siRNA control did not lower *IRS1* mRNA (97.9 $\pm$ 2.7%, 92.4 $\pm$ 14%, 103.9 $\pm$ 1.2% relative to untreated), nor did unconjugated *IRS1* siRNA (100.0 $\pm$ 1.0%, 100.5 $\pm$ 12.9%, 107.4 $\pm$ 19.0% relative to untreated). Mock controls where no siRNA was added also showed no change in *IRS1* mRNA.

IRS-1 protein levels in treated human MCF7 ER+ breast cancer cells were measured by Western blotting (Figure 6B), using the highest treatment concentration (200 nM) tested by QRT-PCR, since no apparent cytotoxic effect was observed, based on negligible change by the D-(Cys-Ser-Lys-Cys)-Gly HN-Hx-mismatch siRNA. Significant IRS-1 protein knockdown was observed when MCF7 cells were treated with D-(Cys-Ser-Lys-Cys)-Gly HN-Hx-*IRS1* siRNA (57.2 $\pm$ 22.8% relative to untreated) or cholesteryl–*IRS1* siRNA (46.1 $\pm$ 2.6% relative to untreated) as compared to nonsignificant knockdown when cells were treated with D-(Cys-Ser-Lys-Cys)-Gly HN-Hx-mismatch siRNA (92.4 $\pm$ 3.3% relative to untreated) and minimal

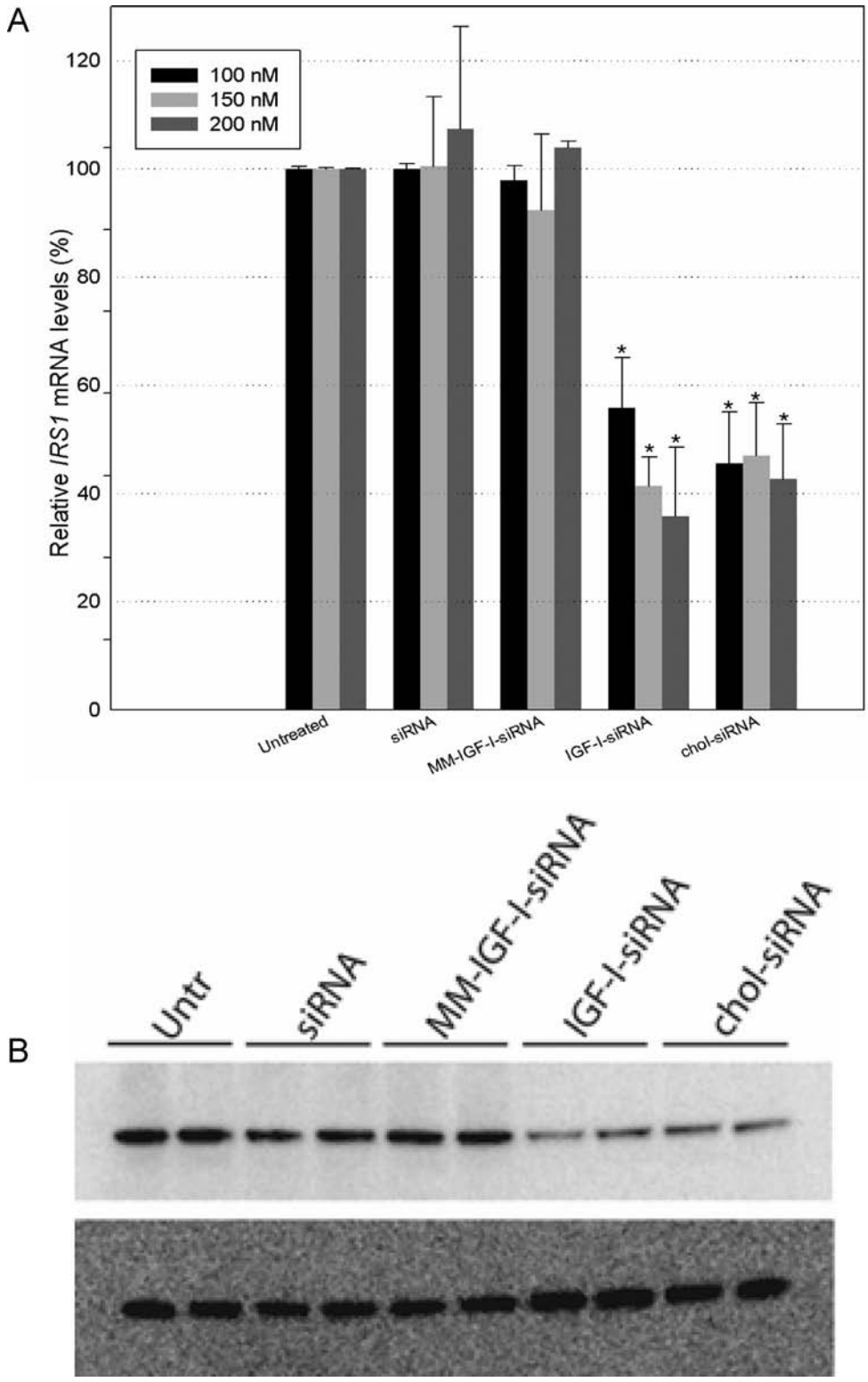


Figure 6. Knockdown efficacy in human MCF7 ER+ breast cancer cells treated with siRNA conjugates. A. QRT-PCR analysis of *IRS1* mRNA levels. Three concentrations of siRNA were tested in MCF7 cells, where total RNA was purified 24 h post-siRNA treatment. Each bar represents the percentage of *IRS1* mRNA expression ± standard deviation relative to untreated cells. * indicates $p < 0.05$ with respect to untreated MCF7 cells. B. Western blot analysis of IRS-1 protein knockdown by 200 nM siRNA of MCF7 cells. Protein was analyzed at a 96 h time point. Expression of IRS-1 was assessed by loading 40 μg of cytoplasmic protein lysate per lane, with the expression of a cytoplasmic enzyme, GAPDH, probed as a loading control following IRS-1 probing and stripping of the blot.

knockdown by unconjugated *IRS1* siRNA (83.6 ± 5.9% relative to untreated).

Viability Following siRNA Treatment Alone or in Combination with TAM. The reasoning behind targeting IRS-1 in breast cancer lies in the previously observed IRS-1 overexpression that correlated with poorer prognosis (*32*) along with estrogen independence (*33*). The IRS-1 phosphorylation level was reduced, causing reduced PI3K activity, with the antiestrogen tamoxifen (*34*). Therefore, we assayed the survival of human MCF7 ER+ breast cancer cells treated with siRNA alone

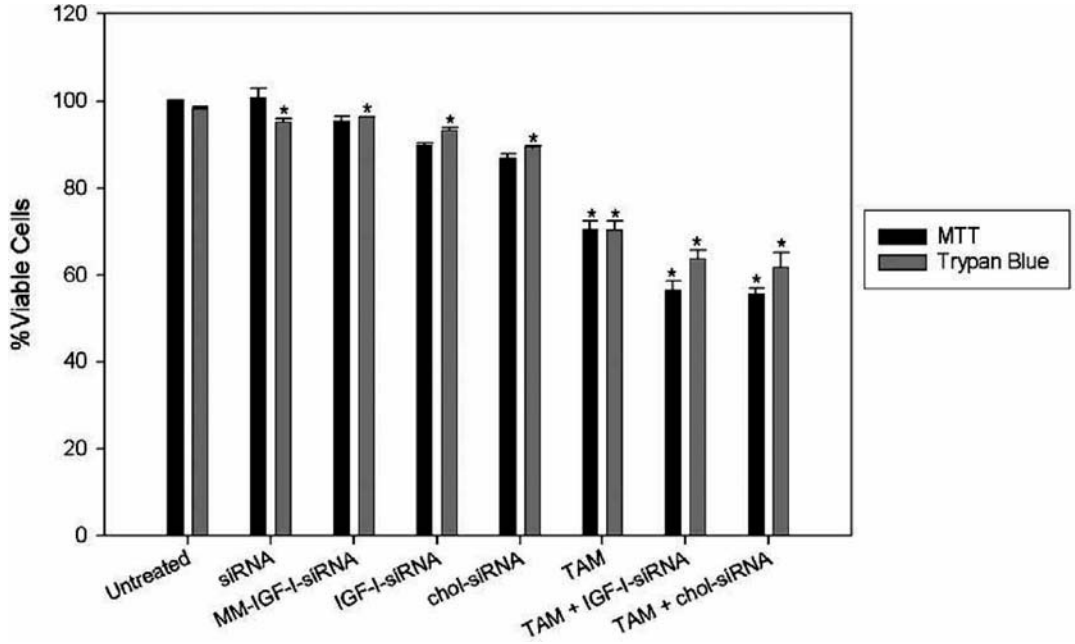


Figure 7. Cell viability of human MCF7 ER+ breast cancer cells following siRNA treatment alone or in combination with the antiestrogen TAM. Percentage of cell death in MCF7 cells after 96 h with a minimum of 400 cells counted for Trypan blue assay. The absorbance was read at 570 nm vs. 630 nm for the MTT assay. Treatment conditions noted on Y-axis. Each bar represents the percentage of viable cells ± standard deviation relative to untreated cells. * indicates $p < 0.05$ with respect to untreated MCF7 cells.

or in combination with TAM, determined by Trypan blue viability staining and the MTT assay (Figure 5B). The decrease in viability for MCF7 cells treated with D-(Cys-Ser-Lys-Cys)-Gly HN-Hx-*IRS1* siRNA (7.7 ± 0.6% by Trypan blue; 10.1 ± 0.5% MTT) was observed to be similar but slightly less than for the cholesteryl-*IRS1* siRNA (10.6 ± 0.3% by Trypan blue; 13.0 ± 0.9% by MTT). The measured decreases in viability are greater than twice the control levels for unconjugated *IRS1* siRNA (4.8 ± 0.7% by Trypan blue; 0% by MTT) or D-(Cys-Ser-Lys-Cys)-Gly HN-Hx-mismatch siRNA (3.7 ± 0.1% by Trypan blue; 4.6 ± 1.1% by MTT). The decreases in viability were similar when TAM treatment alone (29.6 ± 2.0% by Trypan blue; 29.4 ± 1.8% by MTT) was combined with D-(Cys-Ser-Lys-Cys)-Gly HN-Hx-*IRS1* siRNA (37.1 ± 1.8% by Trypan blue; 43.4 ± 2.2% by MTT) or combined with cholesteryl–*IRS1* siRNA (39.2 ± 3.5% by Trypan blue; 44.3 ± 1.3% by MTT).

DISCUSSION

In this study, we tested the hypothesis that conjugation of an siRNA to a cell-targeting ligand, an IGF1 peptide mimetic, would enable cell-specific, receptor-mediated endocytosis and activity of siRNA, without resorting to cationic lipids or electroporation, or a ligand such as cholesterol that directs siRNA uptake by all cells nonspecifically. Other larger versions of the IGF1 ligand were originally utilized to inhibit cancer cells (*25, 35*). We have utilized a smaller disulfide bridged version, D-(Cys-Ser-Lys-Cys), in previous work with PNA radiohybridization probes (*27*).

In this case, the peptide was extended from an HMP-Tentagel resin in order to yield a free C-terminal carboxylate after cleavage. In order to activate the C-terminal carboxylate of D-(Cys-Ser-Lys-Cys)-Gly for attack by the primary amine of the NH_2-Hx-*IRS1* RNA sense strand, the peptide was converted to an NHS ester. 100-fold excesses of peptide–NHS ester were necessary for complete conjugation of the NH_2-Hx-*IRS1* RNA sense strand. During the conjugation, hydrolysis of the NHS ester occurs simultaneously, leading to the need for more equivalents of peptide–NHS ester, compared to the case of NH_2-Hx-*IRS1* RNA conjugation to AlexaFluor 532-NHS ester. Perhaps the commercially obtained AlexaFluor 532-NHS ester was more stable than our IGF1 peptide–NHS ester. It is possible that electron withdrawal by the peptide from the ester linkage enhanced the partial positive charge on the carbonyl carbon, relative to the corresponding alkyl carbonyl carbon in AlexaFluor 532-NHS ester. In reactions utilizing EDC (aqueous) or DCC (organic) coupling reagents, there is a rate of breakdown of the temporary acid anhydride intermediate back to free carboxylates, as well as the effects of pH controlling the rate of hydrolysis (*31*). In this case, pH must be set to balance base-catalyzed ester hydrolysis vs unprotonated NH_2-Hx-*IRS1* RNA attack on the ester.

Upon biological analysis of the siRNA conjugates, we observed cellular uptake in human MCF7 ER+ breast cancer cells. Uptake of the cholesteryl–*IRS1* siRNA and the D-(Cys-Ser-Lys-Cys)-Gly HN-Hx-*IRS1* siRNA was comparable, while unconjugated *IRS1* siRNA showed only a small amount of uptake. siRNA can be taken up into cells independently given ample time, due to the presence of dsRNA-specific receptors, such as TLR3 (*36*). The amount of siRNA taken up in the absence of any other agents was found to be 50 copies per cell when siRNA concentration was 200 nM and cells were incubated with siRNA for 16 h (*37*). If the cellular uptake experiments performed here were extended to a longer time than 6 h, then it may be predicted that the siRNA alone would have been taken up in greater amounts.

When the activity of siRNAs in human MCF7 ER+ breast cancer cells was tested at 100, 150, and 200 nM by QRT-PCR, we observed comparable activity in *IRS1* mRNA knockdown by D-(Cys-Ser-Lys-Cys)-Gly HN-Hx-*IRS1* siRNA and cholesteryl–*IRS1* siRNA. Previous observations have shown that there is a limited capacity to assemble RISC on exogenous siRNA, so that increasing amounts of siRNA beyond saturation will not produce a corresponding increase in RISC activity (*38*). Our dose response likely illustrated this phenomenon. Increasing our siRNA treatment concentrations beyond 200 nM would most likely lead to sequence-independent effects (*39, 40*).

Given that the unconjugated *IRS1* siRNA or the D-(Cys-Ser-Lys-Cys)-Gly HN-Hx-mismatch siRNA were observed to show

negligible change up to 200 nM, that concentration was used for protein analysis and the MCF7 cell viability assays. IRS-1 protein knockdown was matched to viability by the Trypan blue exclusion assay. We observed high variability in D-(Cys-Ser-Lys-Cys)-Gly HN-Hx-*IRS1* siRNA protein knockdown between independent experiments, which may reflect varied efficiency among separate preparations of D-(Cys-Ser-Lys-Cys)-Gly HN-Hx-*IRS1* siRNA. Separately, an MTT assay was utilized as a second method to detect viability. It was apparent that levels of *IRS1* mRNA and IRS-1 protein knockdown, as well as reduced viability, were not as great compared to our previous work using a cationic lipid transfection reagent at 100 nM *IRS1* siRNA (*14*). Modifications made to stabilize siRNA in the presence of serum, as used here, can reduce silencing efficiency compared to unmodified siRNA (*41*). Therefore, it can be assumed that further improvements in the IGF1 peptide mimetic (*25*) for greater internalization, improvements to the conjugation process, a more potent siRNA sequence, or other RNA stabilization modifications for *in vivo* stability are possible.

Nevertheless, we have taken the first step in converting an siRNA into a pharmacologically active agent designed to be specific for human ER+ breast cancer cells that overexpress IGF1R protein and the IGF1R signaling oncogene *IRS1*. However, there are other types of cancer that show overexpression of IGF1R (*42*) and therefore may also benefit from the use of an siRNA against *IRS1*, or another target oncogene of choice, conjugated to an IGF1 peptide mimetic. Still other cancers could be targeted with siRNAs conjugated to different ligand mimetics that target different overexpressed receptors. The conjugation method described above can be generalized to fit both ligand and siRNA targets of choice.

ACKNOWLEDGMENT

We thank Richard Wassell for expert assistance with mass spectroscopy. This work was supported by DOE/BER grant ER63055 to E.W.

LITERATURE CITED

(1) Knowlden, J. M., Hutcheson, I. R., Barrow, D., Gee, J. M. W., and Nicholson, R. I. (2005) Insulin-like growth factor-I receptor signaling in tamoxifen-resistant breast cancer: a supporting role to the epidermal growth factor receptor. *Endocrinology 146*, 4609–4618.

(2) Surmacz, E., Guvakova, M. A., Nolan, M. K., Nicosia, R. F., and Sciacca, L. (1998) Type I insulin-like growth factor receptor function in breast cancer. *Breast Cancer Res. Treat. 47*, 255–67.

(3) Surmacz, E., and Bartucci, M. (2004) Role of estrogen receptor alpha in modulating IGF-I receptor signaling and function in breast cancer. *J. Exp. Clin. Cancer Res. 23*, 385–94.

(4) Song, R. X., Barnes, C. J., Zhang, Z., Bao, Y., Kumar, R., and Santen, R. J. (2004) The role of Shc and insulin-like growth factor 1 receptor in mediating the translocation of estrogen receptor alpha to the plasma membrane. *Proc. Natl. Acad. Sci. U.S.A. 101*, 2076–81.

(5) Yee, D., and Lee, A. V. (2000) Crosstalk between the insulin-like growth factors and estrogens in breast cancer. *J. Mammary Gland Biol. Neoplasia 5*, 107–15.

(6) Lee, A. V., Jackson, J. G., Gooch, J. L., Hilsenbeck, S. G., Coronado-Heinsohn, E., Osborne, C. K., and Yee, D. (1999) Enhancement of insulin-like growth factor signaling in human breast cancer: estrogen regulation of insulin receptor substrate-1 expression in vitro and in vivo. *Mol. Endocrinol. 13*, 787–796.

(7) Stewart, A. J., Johnson, M. D., May, F. E., and Westley, B. R. (1990) Role of insulin-like growth factors and the type I insulin-like growth factor receptor in the estrogen-stimulated proliferation of human breast cancer cells. *J. Biol. Chem. 265*, 21172–8.

(8) Ueda, S., Tsuda, H., Sato, K., Takeuchi, H., Shigekawa, T., Matsubara, O., Hiraide, H., and Mochizuki, H. (2006) Alternative tyrosine phosphorylation of signaling kinases according to hormone receptor status in breast cancer overexpressing the insulin-like growth factor receptor type 1. *Cancer Sci. 97*, 597–604.

(9) Scott, S. J., Hennessey, M. S., Parkinson, R. W., and Molloy, A. P. (2001) Long-term outcome of the 'Beefburger' procedure in patients unsuitable for two-stage revision following infected total knee replacement. *Knee 8*, 281–6.

(10) Mauro, L., Salerno, M., Panno, M. L., Bellizzi, D., Sisci, D., Miglietta, A., Surmacz, E., and Ando, S. (2001) Estradiol increases IRS-1 gene expression and insulin signaling in breast cancer cells. *Biochem. Biophys. Res. Commun. 288*, 685–9.

(11) White, M. F. (2002) IRS proteins and the common path to diabetes. *Am. J. Physiol. Endocrinol. Metab. 283*, E413–22.

(12) Surmacz, E., and Burgaud, J. L. (1995) Overexpression of insulin receptor substrate 1 (IRS-1) in the human breast cancer cell line MCF-7 induces loss of estrogen requirements for growth and transformation. *Clin. Cancer Res. 1*, 1429–36.

(13) Dalmizrak, O., Wu, A., Chen, J., Sun, H., Utama, F. E., Zambelli, D., Tran, T. H., Rui, H., and Baserga, R. (2007) Insulin receptor substrate-1 regulates the transformed phenotype of BT-20 human mammary cancer cells. *Cancer Res. 67*, 2124–30.

(14) Cesarone, G., Garofalo, C., Abrams, M. T., Igoucheva, O., Alexeev, V., Yoon, K., Surmacz, E., and Wickstrom, E. (2006) RNAi-mediated silencing of insulin receptor substrate 1 (IRS-1) enhances tamoxifen-induced cell death in MCF-7 breast cancer cells. *J. Cell. Biochem. 98*, 440–50.

(15) Kaklamani, V. G., and Gradishar, W. J. (2006) Gene expression in breast cancer. *Curr. Treat. Options Oncol. 7*, 123–8.

(16) Bernard-Marty, C., Lebrun, F., Awada, A., and Piccart, M. J. (2006) Monoclonal antibody-based targeted therapy in breast cancer: current status and future directions. *Drugs 66*, 1577–91.

(17) Negishi, T., Koizumi, F., Uchino, H., Kuroda, J., Kawaguchi, T., Naito, S., and Matsumura, Y. (2006) NK105, a paclitaxel-incorporating micellar nanoparticle, is a more potent radiosensitising agent compared to free paclitaxel. *Br. J. Cancer 95*, 601–6.

(18) Jackson, A. L., Burchard, J., Leake, D., Reynolds, A., Schelter, J., Guo, J., Johnson, J. M., Lim, L., Karpilow, J., Nichols, K., Marshall, W., Khvorova, A., and Linsley, P. S. (2006) Position-specific chemical modification of siRNAs reduces "off-target" transcript silencing. *RNA 12*, 1197–205.

(19) Song, E., Zhu, P., Lee, S. K., Chowdhury, D., Kussman, S., Dykxhoorn, D. M., Feng, Y., Palliser, D., Weiner, D. B., Shankar, P., Marasco, W. A., and Lieberman, J. (2005) Antibody mediated in vivo delivery of small interfering RNAs via cell-surface receptors. *Nat. Biotechnol. 23*, 709–17.

(20) Muratovska, A., and Eccles, M. R. (2004) Conjugate for efficient delivery of short interfering RNA (siRNA) into mammalian cells. *FEBS Lett. 558*, 63–8.

(21) Soutschek, J., Akinc, A., Bramlage, B., Charisse, K., Constien, R., Donoghue, M., Elbashir, S., Geick, A., Hadwiger, P., Harborth, J., John, M., Kesavan, V., Lavine, G., Pandey, R. K., Racie, T., Rajeev, K. G., Rohl, I., Toudjarska, I., Wang, G., Wuschko, S., Bumcrot, D., Koteliansky, V., Limmer, S., Manoharan, M., and Vornlocher, H. P. (2004) Therapeutic silencing of an endogenous gene by systemic administration of modified siRNAs. *Nature (London) 432*, 173–8.

(22) El-Andaloussi, S., Holm, T., and Langel, U. (2005) Cell-penetrating peptides: mechanisms and applications. *Curr. Pharm. Des. 11*, 3597–611.

(23) Minakuchi, Y., Takeshita, F., Kosaka, N., Sasaki, H., Yamamoto, Y., Kouno, M., Honma, K., Nagahara, S., Hanai, K., Sano, A., Kato, T., Terada, M., and Ochiya, T. (2004) Atelocollagen-mediated synthetic small interfering RNA delivery for effective gene silencing in vitro and in vivo. *Nucleic Acids Res. 32*, e109.

(24) Kim, S. H., Jeong, J. H., Lee, S. H., Kim, S. W., and Park, T. G. (2006) PEG conjugated VEGF siRNA for anti-angiogenic gene therapy. *J. Controlled Release 116*, 123–9.

(25) Pietrzkowski, Z., Wernicke, D., Porcu, P., Jameson, B., and Baserga, R. (1992) Inhibition of cellular proliferation by peptide analogues of insulin-like growth factor 1. *Cancer Res. 52*, 6447–6451.

(26) Tian, X., Aruva, M. R., Qin, W., Zhu, W., Duffy, K. T., Sauter, E. R., Thakur, M. L., and Wickstrom, E. (2004) External imaging of CCND1 cancer gene activity in experimental human breast cancer xenografts with ^{99m}Tc-peptide-peptide nucleic acid-peptide chimeras. *J. Nucl. Med. 45*, 2070–2082.

(27) Tian, X., Chakrabarti, A., Amirkhanov, N. V., Aruva, M. R., Zhang, K., Mathew, B., Cardi, C., Qin, W., Sauter, E. R., Thakur, M. L., and Wickstrom, E. (2005) External imaging of CCND1, MYC, and KRAS oncogene mRNAs with tumor-targeted radionuclide-PNA-peptide chimeras. *Ann. N.Y. Acad. Sci. 1059*, 106–44.

(28) Tian, X., and Wickstrom, E. (2002) Continuous solid-phase synthesis and disulfide cyclization of peptide-PNA-peptide chimeras. *Org. Lett. 4*, 4013–4016.

(29) Kretsinger, J. K., and Schneider, J. P. (2003) Design and application of basic amino acids displaying enhanced hydrophobicity. *J. Am. Chem. Soc. 125*, 7907–13.

(30) Reuben, M. A., Kusnezov, I. J., and Wickstrom, E. (1979) Inhibition of deacylation and improvement in N-hydroxysuccinimide ester modification of phenylalanyl-tRNA by dimethyl sulfoxide. *Biochim. Biophys. Acta 565*, 219–223.

(31) Sehgal, D., and Vijay, I. K. (1994) A method for the high efficiency of water-soluble carbodiimide-mediated amidation. *Anal. Biochem. 218*, 87–91.

(32) Rocha, R. L., Hilsenbeck, S. G., Jackson, J. G., VanDenBerg, C. L., Weng, C., Lee, A. V., and Yee, D. (1997) Insulin-like growth factor binding protein-3 and insulin receptor substrate-1 in breast cancer: correlation with clinical parameters and disease-free survival. *Clin. Cancer Res. 3*, 103–9.

(33) Surmacz, E. (2000) Function of the IGF-I receptor in breast cancer. *J. Mammary Gland Biol. Neoplasia 5*, 95–105.

(34) Guvakova, M. A., and Surmacz, E. (1997) Overexpressed IGF-I receptors reduce estrogen growth requirements, enhance survival, and promote E-cadherin-mediated cell-cell adhesion in human breast cancer cells. *Exp. Cell Res. 231*, 149–62.

(35) Pietrzkowski, Z., Mulholland, G., Gomella, L., Jameson, B. A., Wernicke, D., and Baserga, R. (1993) Inhibition of growth of prostatic cancer cell lines by peptide analogues of insulin-like growth factor 1. *Cancer Res. 53*, 1102–6.

(36) De Paula, D., Bentley, M. V., and Mahato, R. I. (2007) Hydrophobization and bioconjugation for enhanced siRNA delivery and targeting. *RNA 13*, 431–56.

(37) Overhoff, M., and Sczakiel, G. (2005) Phosphorothioate-stimulated uptake of short interfering RNA by human cells. *EMBO Rep. 6*, 1176–81.

(38) Hutvagner, G., Simard, M. J., Mello, C. C., and Zamore, P. D. (2004) Sequence-specific inhibition of small RNA function. *PLoS Biol. 2*, E98.

(39) Persengiev, S. P., Zhu, X., and Green, M. R. (2004) Nonspecific, concentration-dependent stimulation and repression of mammalian gene expression by small interfering RNAs (siRNAs). *RNA 10*, 12–8.

(40) Semizarov, D., Frost, L., Sarthy, A., Kroeger, P., Halbert, D. N., and Fesik, S. W. (2003) Specificity of short interfering RNA determined through gene expression signatures. *Proc. Natl. Acad. Sci. U.S.A. 100*, 6347–52.

(41) Chiu, Y. L., and Rana, T. M. (2003) siRNA function in RNAi: a chemical modification analysis. *RNA 9*, 1034–48.

(42) Baserga, R., Peruzzi, F., and Reiss, K. (2003) The IGF-1 receptor in cancer biology. *Int. J. Cancer 107*, 873–7.

BC070135V

Synthesis and Biosensor Performance of a Near-IR Thiol-Reactive Fluorophore Based on Benzothiazolium Squaraine

Joseph Thomas,* Douglas B. Sherman, Terry J. Amiss, Sandra A. Andaluz, and J. Bruce Pitner*

BD Technologies, 21 Davis Drive, Research Triangle Park, North Carolina 27709. Received April 24, 2007; Revised Manuscript Received June 29, 2007

Environmentally sensitive near-IR (NIR) dyes are useful fluorophores for various biosensor applications when tissue absorption, scattering, and autofluorescence are a leading concern. Biosensors operating in the NIR region (generally wavelengths >650 nm) would avoid interference from biological media and thereby facilitate relatively interference free sensing. Squaraine dyes are potential candidates to serve as reporter molecules due to their spectral properties in the NIR region, but none is commercially available for site-specific coupling to proteins through native or engineered thiols on cysteine. In this context, we have synthesized a thiol-reactive squaraine that displays fluorescence emission above 650 nm and have coupled the dye site-specifically to various mutants of glucose/galactose binding protein that contained an engineered cysteine for attachment. Mutant E149C/A213R/L238S ISQ GGBP gave a fluorescence change of +50% and a binding constant of 12 mM, which is in the human physiological range for glucose.

INTRODUCTION

Fluorescent dyes that emit in the near-infrared region have been long sought-after for biosensor development due to their specific advantages when operating in biological media. A unique feature that makes the near-IR (NIR) dyes attractive is that their spectral properties are generally independent from biological interferences, such as tissue autofluorescence and scattering. Biological interference is minimized in the 600–900 nm wavelength region (*1–4*). In order for the dye to qualify as a reporter molecule in a fluorescence-based sensor assay, at least one of the fluorescence properties, such as intensity, lifetime, or wavelength, should undergo a significant change in a variety of environments. However, the availability of such dyes is limited for a number of reasons, including poor photostability, solubility, and toxicity. Moreover, the design of these dyes is complicated, since the increased number of conjugated double bonds required to achieve the NIR spectral properties leads to destabilization of the structure.

Squaraines are a class of dyes that could potentially serve as reporter molecules for biosensors in the NIR region. Squaraines are 1,3-disubstituted squaric acid derivatives in which the substituents can be introduced through nucleophilic substitution reactions (*5*). The intense absorption of squaraine dyes arises from charge transfer transitions between the central cyclobutane ring and the oxygen moieties with a minor contribution from the substituents on either side (*6*). Dyes that undergo charge transfer transitions during electronic excitation are generally solvatochromic and environmentally sensitive (*7*). For example, bis(2,4,6-trihydroxy)phenylsquaraine has a fluorescence quantum yield of <0.002 in aqueous media and undergoes a 90-fold enhancement by microencapsulation within β-cyclodextrin (*8*). The fluorescence maximum of squaraine dyes can also be tuned from 550 to 850 nm by the choice of aromatic or heterocyclic substituents (*5, 9–12*). Although the stability of anilinic-type squaraines is limited in water due to reasons not yet identified, the dyes can be stabilized by replacing the anilinic moieties with other heterocycles such as indoles, benzimidazole, benzooxazole, pyrroles, and benzothiazole (*9, 13–16*).

Squaraine dyes are generally not soluble in water; however, they can be made soluble by the introduction of polar functional groups. Moreover, synthetic methods are sufficient to install structural modifications needed for bioconjugation. In a recent study, Oswald et al. modified squaraine dyes with amine-reactive *N*-hydroxysuccinimide (NHS) pendant groups (*1*) and attached these dyes on BSA and HSA proteins. The fluorescence quantum yields of the dyes increased from ca. 0.15 to 0.6–0.7 when attached to protein. The high fluorescence yield of these squaraines allowed measurements in whole blood at detection limits twice as low as alternate assays employing a cyanine-based dye. These studies indicate that squaraines are well-suited for use in implanted fluorescence biosensors.

Periplasmic binding proteins (PBPs) have been the subject of considerable research as reagentless biosensors (*17, 18*). PBPs are composed of two domains that are connected by a hinge, and the proteins undergo a large conformational change at the hinge when they bind their ligands between the two domains (*19, 20*). Attachment of environmentally sensitive fluorophores at engineered cysteines near the binding pocket provides a method to monitor ligand binding as the protein changes from an open, unliganded form to a closed, liganded form (*21–23*). Site-specific attachment also provides greater control of dye placement to maximize the fluorescence response. Nonspecific attachment through amine-reactive groups, such as NHS esters, can result in attachment of multiple dyes to the protein at sites that do not produce a useful response to the binding event (*24*).

We have previously reported the synthesis and biosensor performance of long-wavelength Nile Red derivatives that were conjugated to mutants of maltose binding protein (MBP) (*25*) and to galactose/glucose binding protein (GGBP) (*26*) and displayed fluorescence maxima in the 550–630 nm range. We have also examined the application of a thiol-reactive anilinic squaraine which had a fluorescence maximum near 675 nm when conjugated to GGBP mutants (*27*). Here, we describe the synthesis and biosensor performance of a thiol-reactive derivative of benzothiazolium-based squaraine that demonstrates sensitivity to changes in its environment above 650 nm in the

* Corresponding authors. J.T.: tel 919-597-6617, fax 919-597-6402, e-mail joseph_thomas@bd.com. J.B.P.: tel 919-597-6147, fax 919-597-6402, e-mail bruce_pitner@bd.com.

10.1021/bc700146r CCC: $37.00 © 2007 American Chemical Society
Published on Web 09/12/2007

NIR wavelength range when conjugated to mutants of GGBP containing engineered cysteines.

EXPERIMENTAL PROCEDURES

Materials. Starting materials were products of Sigma-Aldrich unless otherwise indicated. *Eschericia coli* strain Sg13009 was used to prepare GGBP with site-selective cysteine mutations as previously reported (*28*). A Cary 50 Bio UV–vis spectrophotometer was used to record absorption spectra. Fluorescence responses were measured using a PTI QM-4/2003 SE spectrofluorimeter and are uncorrected. A Varian 400 MHz Mercury or Bruker (400 MHz) AMX 400 spectrometer was used to obtain NMR data. A Finnigan-MAT 212 (FAB) or a Sciex 150 Electrospray spectrometer was employed for mass spectral analyses.

Synthesis of ISQ (1). *Intermediate* **1c.** 2-Methylbenzothiazole (1 mM) **1a** and *N*-bromoethylphthalimide **1b** (1 mM) were heated in a round-bottom flask at 100 °C for 24 h. The resultant solids were isolated by filtration and purified by continuous washing with chloroform to obtain the intermediate **1c** in 80% yield. ^{1}H NMR (CD_3OD, TMS) δ ppm: 4.295 (t, CH_2, 2H), 4.871 (s, CH_3, 3H), 5.102 (t, CH_2, 2H), 7.680–7.760 (m, 2H, aromatic), 7.760–7.790 (m, aromatic, 4H), 8.14–8.17 (m, aromatic, 1H), 8.260–8.290 (m, aromatic, 1H). ^{13}C NMR (CD_3OD) δ ppm: 28.091, 35.198, 39.264, 115.946, 123.295, 124.262, 128.607, 129.501, 129.860, 131.574, 134.450, 134.681, 141.656, 168.018. Mol wt calcd for $C_{18}H_{15}N_2O_2S$ is 323 (M+), found 323 (FAB).

Intermediate **1g.** Dibutyl squarate **1e** was reacted with 3-ethyl-2-methyl-benzothiazolium iodide **1d** (1:1 ratio) in ethanol at reflux for 30 min. The reaction mixture was filtered while hot. An orange-colored solid **1f** crystallized out of the filtrate while cooling, which was separated, resuspended in ethanol, and treated with 40% NaOH solution under reflux. After 30 min, the contents were cooled and acidified with 2 N HCl (pH adjusted to 4.0). The product was extracted with chloroform to give intermediate **1g** (97% yield). ^{1}H NMR ($CDCl_3$, TMS) δ ppm: 1.385 (t, CH_3, 3H), 4.150 (q, CH_2, 2H), 5.379 (s, CH, 1H), 7.180–7.200 (m, aromatic, 2H), 7.360–7.400 (m, aromatic, 1H), 7.58–7.595 (d, aromatic, 1H). ^{13}C NMR (CD_3OD) δ ppm: 12.169, 47.836, 48.049, 48.261, 48.466, 48.679, 111.997, 122.958, 123.720, 126.599, 127.684, 141.326, 157.768, 173.967. Mol wt calcd for $C_{14}H_{11}NO_3S$ is 273 (M+), found 273 (FAB).

Intermediate **1h.** Intermediates **1c** and **1g** were reacted in a solvent mixture containing 1:1 (v/v) toluene and *n*-butanol. The reaction mixture was subjected to azeotropic distillation, and the water formed during the reaction was removed using a Dean–Stark trap. After 6 h, the reaction mixture was allowed to cool to room temperature, and the blue product was filtered out. Further purification was carried out using flash column chromatography over silica gel using methanol and chloroform (1:4 ratio) as eluent to obtain dye **1h** in 80% yield. ^{1}H NMR ($CDCl_3$, TMS) δ ppm: 1.439 (t, CH_3, 3H), 4.227 (t, CH_2, 2H), 4.380 (q, CH_2, 2H), 4.581 (t, CH_2, 2H), 6.140 (s, CH, 1H), 6.170 (s, CH, 1H), 7.070–7.823 (m, aromatic, 12H). ^{13}C NMR ($CDCl_3$) δ ppm: 13.122, 35.315, 42.641, 44.495, 104.910, 111.543, 112.686, 122.819, 123.801, 123.918, 124.988, 125.559, 126.424, 126.761, 127.720, 128.006, 128.175, 128.790, 131.648, 131.684, 134.571, 134.674, 134.849, 140.411, 140.550, 140.975, 168.040, 179.242. Mol wt calcd for $C_{32}H_{23}N_3O_4S_2$ is 577 (M+), found 577 (FAB).

Intermediate **1i.** The dye **1h** was dissolved in anhydrous methylene chloride and was treated with hydrazine monohydrate at room temperature. The deprotected squaraine dye precipitated from the reaction mixture and was isolated by filtration, followed by repeated washing with methylene chloride (56% yield). ^{1}H NMR (CD_3OD, TMS) δ ppm: 1.420 (t, CH_3, 3H), 3.780 (t, CH_2, 2H), 4.320 (q, CH_2, 2H), 4.520 (t, CH_2, 2H), 5.924 (s, CH, 1H), 5.964 (s, CH, 1H), 7.200–7.850 (m, aromatic, 8H). Mol wt calcd for $C_{24}H_{21}N_3O_2S_2$ is 447 (M+), found 447 (FAB).

Compound **1.** The intermediate dye **1i** was dissolved in anhydrous methylene chloride, and an equivalent amount of iodoacetic anhydride was added. The mixture was stirred for 3 h at room temperature, and the product was isolated by evaporation of the solvent to obtain the final dye **1**. Purification was carried out by repeated precipitation from hexane/methylene chloride and afforded the product in 48% yield. ^{1}H NMR (CD_3OD, TMS) δ ppm: 1.420 (t, CH_3, 3H), 3.900 (s, CH_2, 2H), 4.300 (q, CH_2, 2H), 4.450 (t, CH_2, 2H), 4.480 (t, CH_2, 2H), 5.820 (s, CH, 1H), 5.980 (s, CH, 1H), 7.200–8.200 (m, aromatic, 8H). Mol wt calcd for $C_{26}H_{22}IN_3O_3S_2$ is 615 (M+), found 615 (FAB).

Preparation of Dye–Protein Conjugates. Dithiothreitol (8 nmol) was added to a solution of GGBP mutant (4 nmol) in PBS (200 uL) in an Eppendorf tube. After mixing for 30 min on a Dynal rotamix (Dynal Inc., New Hyde Park, NY), ISQ (40 nmol) was added from a stock solution of dye in DMSO (approximately 1 mg in 100 uL DMSO). The Eppendorf tube was wrapped in aluminum foil, and mixing continued for 4 h at room temperature. The reaction mixture was purified using a NAP-5 size exclusion column using PBS (pH = 7.4) as the eluent (Amersham-Pharmacia, Uppsula, Sweden). The labeled protein eluted in the second (0.5 mL) fraction. Labeling efficiencies were generally on the order of 20%.

Fluorescence Measurements. The percent change in fluorescence (ΔF) was measured by the relative method using optically dilute solutions of the protein (~2 uM) in the absence and presence of 100 mM glucose unless otherwise noted. Excitation was at 600 nm and emission was measured from 625 to 725 nm. Binding constants were determined using methods as previously described (*26*), which take into account the amounts of labeled and unlabeled protein.

Molecular Modeling. A model of ISQ with methyl groups in place of the ethyl group and the linker was prepared in *Gaussian 98W* (*29*). Geometry optimization was performed using the semiempirical AM1 method, followed by optimization using HF/3-21G and HF/6-31G(d). Following optimization, frequency calculations were performed to confirm that the final geometry was at a stationary point on the potential energy surface. The resulting structure was imported into Sybyl (Tripos, St. Louis, MO) to complete construction of the full dye with linker.

The X-ray crystal structure of closed form *E. coli* GGBP was 2GBP (*30*) taken from the Protein Data Bank (*31*). The open form of GGBP was studied using a homology model created in-house using ribose binding protein (RBP) crystal structure 1URP (*32*) as a template (Sherman et al., unpublished results). The appropriate residues in the GGBP structures were modified to Cys, and the dye was then attached to model the bioconjugate. Genetic algorithm (GA) conformational searches were performed in Sybyl. For ISQ alone, the amide bond was fixed in the trans conformation, and the remaining 7 bonds were defined as rotatable. Default settings in the GA search were generally used with the duplicate window set to 10. For E149C/A213R/L238S ISQ GGBP, the number of rotatable bonds allowed was 14 total (7 in the dye linker, 5 in the A213R side chain, and 2 in the L238S side chain). The population size was increased from 100 to 500, and the number of generations was increased from 5,000 to 15,000. Up to 10 conformers per search were allowed within a 20 kcal/mol energy window.

RESULTS

Synthesis. The synthesis of ISQ (**1**), as shown in Scheme 1, was completed in a total of 6 steps. No base was used for the

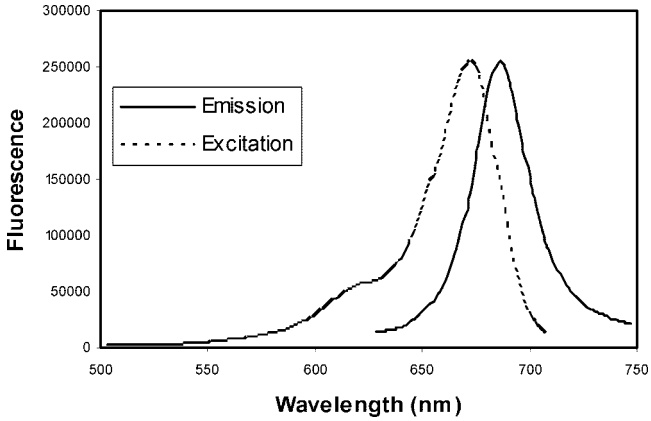
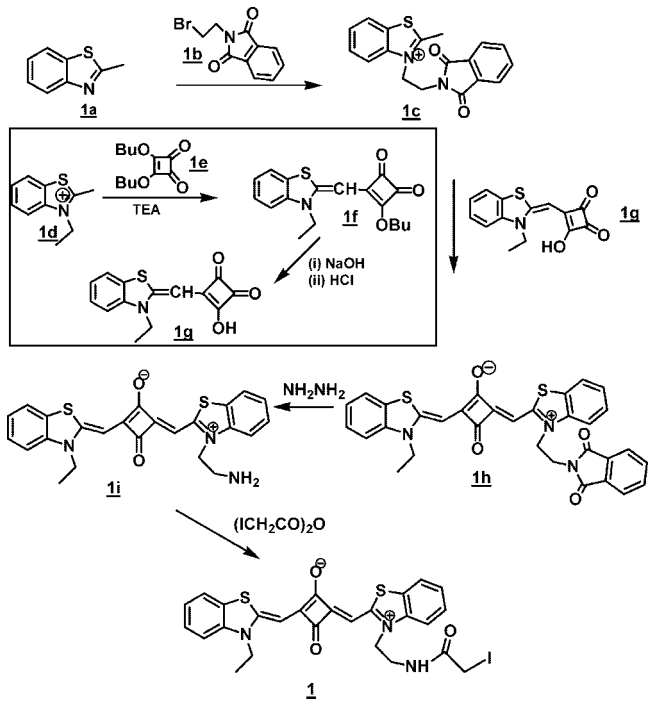


Figure 1. Absorbance and emission spectra of ISQ (**1**) in chloroform.

Scheme 1. Synthesis of ISQ (1)



condensation of **1c** with **1g**, as this reaction takes place spontaneously due to the highly nucleophilic nature of the CH_3 group of **1c**, owing to the presence of the quarternary nitrogen in the ring. The intermediates except for the final dye were purified by flash column chromatography using a mixture of methanol and chloroform with yields of 80% to 97%. The deprotection of the phthalimide group was accomplished using hydrazine in 50% yield. The final thiol-reactive version of the dye was formed under anhydrous conditions using iodoacetic anhydride in the presence of catalytic amounts of pyridine. Purification of the dye was carried out by repeated precipitation using methylene chloride and hexane with a yield of 48%.

Spetrophotometric Properties of ISQ. The excitation and emission spectra of ISQ (**1**) in chloroform is shown in Figure 1. The absorption maximum in chloroform was 680 nm, and it was 652 nm when the dye was attached to E149C GGBP in aqueous medium. The fluorescence maximum was 690 nm in chloroform and 665 nm for the dye–protein conjugate. ISQ (**1**) had a 10 nm Stokes shift in chloroform and a 13 nm shift when attached to the protein. The extinction coefficient was determined to be 51,100 M^{-1} cm^{-1} in chloroform.

Table 1. Summary of the Results for GGBP-NIR Dye Conjugates

GGBP mutation sites	ISQ ΔF^a ($K_d{}^b$, mM)
Y10C	−5
K11C	−5
D14C	−30
V19C	25
K92C	−5
Y107C	−25
T110C	−15
E149C	37 (0.005)
E149C/A213R/L238S	50 (12)
H152C	10
M182C	−14
W183C	17
N211C	−45
D236C	−10

[a] ΔF is the percentage of fluorescence change upon glucose binding by the protein. [b] K_d is the dissociation constant of the binding event expressed in terms of the concentration of glucose.

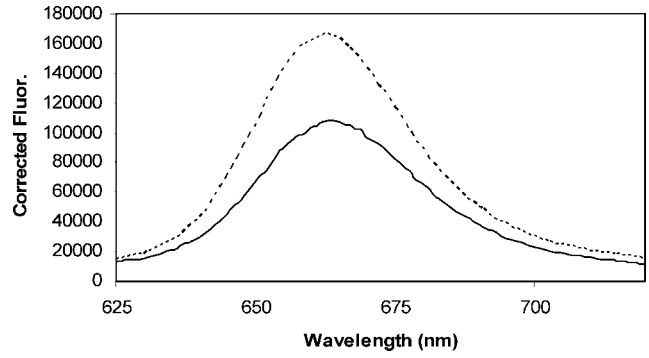


Figure 2. Fluorescence response of E149C/A213R/L238S ISQ GGBP in the absence (solid line) and presence (dotted line) of 200 mM glucose.

Biosensor Responses. ISQ (**1**) was conjugated to GGBP mutants that contained single cysteine mutations at the positions listed in Table 1. The largest changes observed for ISQ (**1**) were with the dye conjugated to D14C (−30%), E149C (37%), E149C/A213R/L238S (50%, Figure 2), and N211C (−45%). Binding constants (K_d) were determined for two of the ISQ-GGBP conjugates. These ranged from 5 uM for E149C-ISQ GGBP to 12 mM for E149C/A213R/L238S ISQ GGBP (Figure 3).

Modeling Analysis. Mutants D14C, K92C, N211C, and E149C/A213R/L238S GGBP were examined by genetic algorithm conformational searches with ISQ conjugated to the cysteine. Searches on the closed forms yielded a single conformation for all protein–dye conjugates except K92C, which produced six conformers that were very similar in dye–protein orientation. ISQ was expelled from the binding pocket and had significant solvent exposure with K92C and N211C (Figure 4a). Only the backbone carbonyl of residue D150 and the side chain of D69 were within 3.7 Å of the dye on K92C-ISQ. Similarly, on N211C-ISQ, only the backbone carbonyl of D13 and the side chain of D184 were within 2 Å of the dye. For D14C, the central four-membered ring of ISQ was within 3.2 Å of the carboxylate group of residue D184. In E149C/A213R/L238S ISQ GGBP (Figure 4c), the dye was parallel to the surface of the N-terminal domain in proximity to the side chains of N43 (3.2 Å), S46 (3.0 Å), D50 (3.8 Å), and T75 (3.5 Å).

The conformational searches on the open forms returned 10 conformers that were within 3 kcal/mol of one another for a given protein–dye conjugate. ISQ was placed inside the open binding pocket in D14C-ISQ approximately 5 Å from the rim of the C-terminal domain. In K92C-ISQ, the dye was solvent-

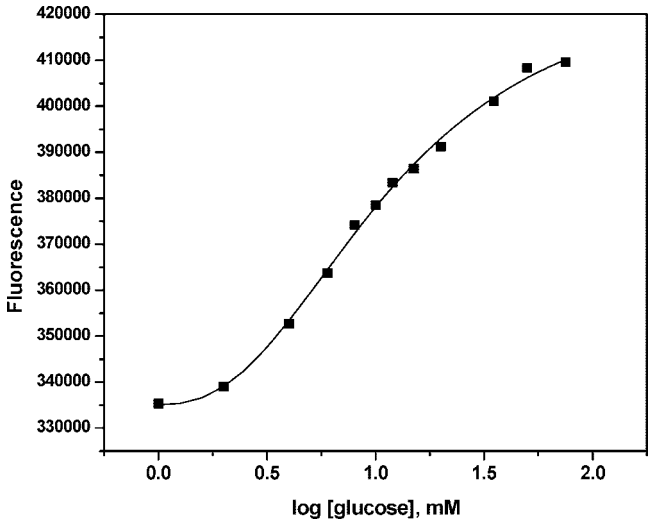


Figure 3. K_d determination for E149C/A213R/L238S ISQ GGBP yielded a 12 mM binding constant.

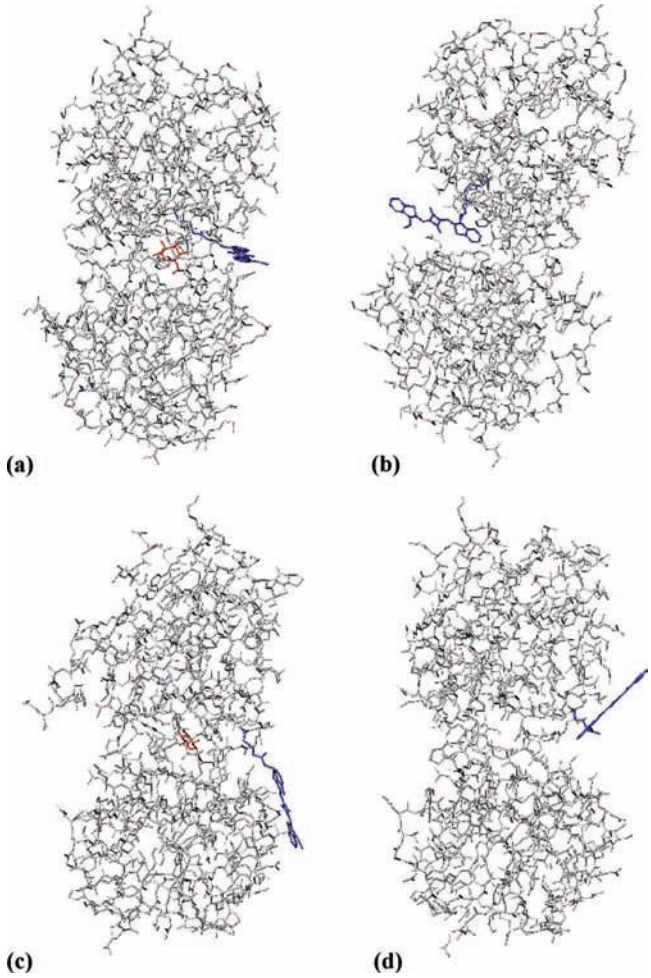


Figure 4. Representative conformers for ISQ attached to N211C GGBP (a and b) and to E149C/A213R/L238S GGBP (c and d). The closed protein conformations are on the left and the open forms on the right. Glucose is in red and the dye is in blue.

exposed or >4 Å from the rim of the binding pocket of the C-terminal domain. For N211C-ISQ, the benothiazolium ring containing the linker was located inside the binding pocket, while the remainder of the dye structure was solvent-exposed (Figure 4b). Finally, the dye in the conformers of E149C/A213R/L238S ISQ GGBP was solvent-exposed with only the side chain of residue Q187 within 3.7 Å of the dye (Figure 4d).

DISCUSSION

The squaraine dye was chosen due to its sharp absorption and fluorescence properties in the >600 nm region, which is highly sensitive to the environment. In general, the synthesis of ISQ (**1**) proceeded smoothly. Deprotection of the phthalimide in **1h** to form **1i** was first attempted using methylamine. This led to a half-protected species as identified by mass spectral and NMR analysis. Using hydrazine in place of methylamine resulted in a cleaner deprotection. In the final step to purify **1**, the high reactivity of the iodoacetamide group prevented purification using column chromatography; thus, the final product was obtained by repeated precipitation from hexane and methylene chloride.

The spectrophotometric properties of ISQ in chloroform and aqueous medium demonstrated the environmental sensitivity of the dye as well as the potential of ISQ for biosensor applications in the NIR region. The dye had Stokes shifts of ≥10 nm, and the absorption maxima in chloroform and aqueous medium were above 650 nm. The fluorescence maxima were also above 665 nm. In addition, ISQ showed remarkable fluorescence properties when conjugated to GGBP, demonstrating that the fluorescence response was significantly affected by the glucose binding event. Of the mutants studied, N211C-ISQ had the largest negative change (−45%). E149C-ISQ had a lower fluorescence change of 37% and a binding constant of 5 uM, which is slightly weaker than the binding constant of wild-type GGBP (0.2 uM) (*33*), but it is consistent with binding constants reported for other dyes (*26*) and bioconjugates (*28*) at this site. As shown in Figure 2, the triple mutant E149C/A213R/L238S ISQ had a larger fluorescence change of +50%, and the binding constant was 12 mM (Figure 3), which is near the midpoint of the human physiological range.

We also wanted to examine molecular models of several dye–protein conjugates to relate the experimental sensor performance to the structures. The chromophoric unit of benzothiazolium squaraine dyes is highly hydrophobic. It tends to be encapsulated within hydrophobic matrices and polymers such as β-cyclodextrin (*8*) and polymers such as polyvinyl pyrrolidone (*34*). Due to this nature, to a first approximation it would be expected that movement of the dye from a more hydrophilic environment to a more hydrophobic environment would result in a positive fluorescence change, whereas movement from a more hydrophobic to a more hydrophilic environment would induce a negative change. Other types of dye–protein interactions, such as hydrogen bonding, can also play an important role in the nature of the fluorescence change (*35*).

Conformational analysis of the dye attached to a number of sites provided qualitative support to this hypothesis. For example, ISQ was solvent-exposed and had very little interaction with the protein in both the open and closed forms of K92C-ISQ, which would be expected to produce little to no change in fluorescence as was observed. D14C-ISQ and N211C-ISQ had significant negative fluorescence changes. For these bioconjugates, the dye was positioned either within the binding pocket near the surface of the C-terminal domain (D14C) or partially buried inside the binding pocket (N211C) of the open form. As with K92C, the dye was solvent-exposed in the closed form for both mutants with only 1 to 2 residues <4 Å from the dye (Figure 4a,c). Such conformational changes would agree with a negative change in fluorescence. In the case of ISQ attached to E149C/A213R/L238S, the dye was solvent-exposed in the open form, but in the closed form, the entire dye was in close proximity to the surface of the N-terminal domain (Figure 4c,d), which agrees qualitatively with the observed positive

change in fluorescence. Thus, the models suggest that the placement of the dye near the protein surface leads to an enhancement in fluorescence by increasing hydrophobic interactions, while increased solvent exposure decreases fluorescence as the dye moves into a hydrophilic environment.

The overall size of the dye may also play a role in the magnitude of the fluorescence response. Greater than 4-fold fluorescence changes have been reported for NBD attached to E149C GGBP (*23*, *36*). NBD is a relatively small molecule that is approximately 6 Å in length. The chromophore of ISQ is approximately 16 Å in length. It is possible that smaller dyes, by virtue of their size, can develop more favorable interactions with the surface of the protein or can enter pockets formed by residue side chains compared to larger dyes such as the squaraines, which in turn would lead to larger fluorescence changes.

In summary, towards the development of reagentless glucose sensors, we have synthesized an NIR fluorescent squaraine dye with a thiol-reactive linker. The dye exhibited fluorescence properties that are highly dependent on the environment. Upon conjugation to glucose binding protein, the fluorescence intensity of the dye underwent significant changes in the presence of glucose. In particular, E149C and E149C/A213R/L238S GGBP showed highly desirable fluorescence intensity changes and could potentially lead to a reagentless glucose monitoring assay. The glucose binding range of ISQ on E149C/A213R/L238S GGBP was in the relevant human physiological range (1–30 mM). Further development of these systems towards a practical glucose sensor is in progress.

ACKNOWLEDGMENT

This work is supported in part by a grant from the Technologies for Metabolic Monitoring (TMM) program, contract number W81XWH-04-1-0076. The authors thank Michael T. Cash (BD Technologies) for obtaining ^{13}C NMR spectra of the compounds and Helen V. Hsieh (BD Technologies) for insightful discussions during the preparation of the manuscript.

LITERATURE CITED

(1) Oswald, B., Patsenker, L., Duschl, J., Szmacinski, H., Wolfbeis, O. S., and Terpetschnig, E. (1999) Synthesis, spectral properties, and detection limits of reactive squaraine dyes, a new class of diode laser compatible fluorescent protein labels. *Bioconjugate Chem. 10*, 925–931.

(2) Buschmann, V., Weston, K. D., and Sauer, M. (2003) Spectroscopic study and evaluation of red-absorbing fluorescent dyes. *Bioconjugate Chem. 14*, 195–204.

(3) Hammer, R. P., Owens, C. V., Hwang, S.-H., Sayes, C. M., and Soper, S. A. (2002) Asymmetrical, water-soluble phthalocyanine dyes for covalent labeling of oligonucleotides. *Bioconjugate Chem. 13*, 1244–1252.

(4) Sophianopoulos, A. J., Lipowski, J., Narayanan, N., and Patonay, G. (1997) Association of near-infrared dyes with bovine serum albumin. *Appl. Spectrosc. 51*, 1511–1515.

(5) Sprenger, H.-E., and Ziegenbein, W. (1968) Cyclobutenediylium dyes. *Angew. Chem., Int. Ed. Engl. 7*, 530–535.

(6) Bigelow, R. W., and Freund, H.-J. (1986) An MNDO and CNDO / S(S + DES CI) study on the structural and electronic properties of a model squaraine dye and related cyanine. *Chem. Phys. 107*, 159–174.

(7) Reichardt, C. (2002) *Solvents and Solvent Effects in Organic Chemistry*, 3rd ed., Wiley-VCH Verlag GmbH & Co. KGaA, Weinheim.

(8) Das, S., Thomas, K. G., George, M. V., and Kamat, P. V. (1992) Fluorescence enhancement of bis(2,4,6-trihydroxyphenyl)squaraine anion by 2:1 host-guest complexation with β-cyclodextrin. *J. Chem. Soc., Faraday Trans. 88*, 3419–3422.

(9) Treibs, A., and Jacob, K. (1965) Cyclotrimethine dyes derived from squaric acid. *Angew. Chem., Int. Ed. Engl. 4*, 694.

(10) Schmidt, A. H. (1980) Reaktionen von quadratsäure und quadratsäure-derivaten. *Synthesis 1980*, 961–994.

(11) Seitz, G., and Imming, P. (1992) Oxocarbons and pseudooxocarbons. *Chem. Rev. 92*, 1227–1260.

(12) Law, K. Y. (1993) Organic photoconductive materials: Recent trends and developments. *Chem. Rev. 93*, 449–486.

(13) Treibs, A., and Jacob, K. (1966) Über tetracylcotrimethinfarbstoffe: Cyclobutenderivate der pyrrolreihe. *Liebigs Ann. Chem. 699*, 153–167.

(14) Ziegenbein, W., and Sprenger, H.-E. (1966) Condensation products of squaric acid and azulenic hydrocarbons. *Angew. Chem., Int. Ed. Engl. 5*, 893–894.

(15) Sprenger, H.-E., and Ziegenbein, W. (1966) Condensation products of tertiary aromatic amines. *Angew. Chem., Int. Ed. Engl. 5*, 894.

(16) Sprenger, H.-E., and Ziegenbein, W. (1967) The cyclobutenediylium cation, a novel chromophore from squaric acid. *Angew. Chem., Int. Ed. Engl. 6*, 553–554.

(17) Dwyer, M. A., and Hellinga, H. W. (2004) Periplasmic binding proteins: A versatile superfamily for protein engineering. *Curr. Opin. Struct. Biol. 14*, 495–504.

(18) Moshou, E. A., Bachas, L. G., Daunert, S., and Deo, S. K. (2006) Hinge-motion proteins: Unraveling their analytical potential. *Anal. Chem. 78*, 6692–6700.

(19) Ames, G. F.-L. (1986) Bacterial periplasmic transport systems: Structure, mechanism, and evolution. *Ann. Rev. Biochem. 55*, 397–425.

(20) Gerstein, M., Lesk, A.M., and Chothia, C. (1994) Structural mechanisms for domain movements in proteins. *Biochemistry 33*, 6739–6749.

(21) Brune, M., Hunter, J. L., Howell, S. A., Martin, S. R., Hazlett, T. L., Corrie, J. E. T., and Webb, M. R. (1998) Mechanism of inorganic phosphate interaction with phosphate binding protein from *Escherichia coli*. *Biochemistry 37*, 10370–10380.

(22) Hellinga, H. W., and Marvin, J. S. (1998) Protein engineering and the development of generic biosensors. *Trends Biotechnol. 16*, 183–189.

(23) de Lorimier, R. M., Smith, J. J., Dwyer, M. A., Looger, L. L., Sali, K. M, Paavola, C. D., Rizk, S. S., Sadigov, S., Conrad, D. W., Loew, L., and Hellinga, H. W. (2002) Construction of a fluorescent biosensor family. *Protein Sci. 11*, 2655–2675.

(24) Zhou, L. Q., and Cass, A. E. G. (1991) Periplasmic binding protein based biosensors. 1. Preliminary study of maltose binding protein as sensing element for maltose biosensor. *Biosens. Bioelectron. 6*, 445–450.

(25) Sherman, D. B., Pitner, J. B., Ambroise, A., and Thomas, K. J. (2006) Synthesis of thiol-reactive, long-wavelength fluorescent phenoxazine derivatives for biosensor applications. *Bioconjugate Chem. 17*, 387–392.

(26) Thomas, K. J., Sherman, D. B., Amiss, T. J., Andaluz, S. A., and Pitner, J. B. (2006) A long-wavelength fluorescent glucose biosensor based on bioconjugates of galactose/glucose binding protein and nile red derivatives. *Diabetes Technol. Ther. 8*, 261–268.

(27) Pitner, J. B., Thomas, J., Sherman, D. B., Alarcón, J., Mohiuddin, G., Kyler, K. S, and Venepalli, B. R. (2005) Design and synthesis of a squaraine dye for long wavelength fluorescence-based biosensors. In *Genetically Engineered and Optical Probes for Biomedical Applications III, Proceedings of SPIE vol. 5704* (Bornhop, D. J., Achilefu, S. I., Raghavachari, R., and Savitsky, A. P., Eds.) pp. 24–29, SPIE, Bellingham, WA.

(28) Hsieh, H. V., Pfeiffer, Z. A., Amiss, T. J., Sherman, D. B., and Pitner, J. B. (2004) Direct detection of glucose by surface plasmon resonance with bacterial glucose/galactose protein. *Biosens. Bioelectron. 19*, 653–660.

(29) Frisch, M. J., Trucks, G. W., Schlegel, H. B., Scuseria, G. E., Robb, M. A., Cheeseman, J. R., Zakrzewski, V. G. , Montgomery, J. A., Jr., Stratmann, R. E., Burant, J. C., Dapprich, S., Millam, J. M., Daniels, A. D., Kudin, K. N., Strain, M. C.,

Farkas, O., Tomasi, J., Barone, V., Cossi, M., Cammi, R., Mennucci, B., Pomelli, C., Adamo, C., Clifford, S., Ochterski, J., Petersson, G. A., Ayala, P. Y., Cui, Q., Morokuma, K., Malick, D. K., Rabuck, A. D., Raghavachari, K., Foresman, J. B., Cioslowski, J., Ortiz, J. V., Stefanov, B. B., Liu, G., Liashenko, A., Piskorz, P., Komaromi, I., Gomperts, R., Martin, R. L., Fox,D. J., Keith, T., Al-Laham, M. A., Peng, C. Y., Nanayakkara, A., Gonzalez, C., Challacombe, M., Gill, P. M. W., Johnson, B. G., Chen, W., Wong, M. W., Andres, J. L., Head-Gordon, M., Replogle, E. S., and Pople, J. A. (2002), *Gaussian 98*, revision A.11.4, Gaussian, Inc., Pittsburgh, PA.

(30) Vyas, N. K., Vyas, M. N., and Quiocho, F.A. (1988) Sugar and signal-transducer binding sites of the *Escherichia coli* galactose chemoreceptor protein. *Science 242*, 1290–1295.

(31) Berman, H. M., Westbrook, J., Feng, Z., Gilliland, G., Bhat, T. N., Weissig, H., Shindyalov, I. N., and Bourne, P. E. (2000) The protein data bank. *Nucl. Acids Res. 28*, 235–242.

(32) Björkman, A. J., and Mowbray, S. L. (1998) Multiple open forms of ribose-binding protein trace the path of its conformational change. *J. Mol. Biol. 279*, 651–664.

(33) Vyas, M. N., Vyas, N. K., and Quiocho, F. A. (1994) Crystallographic analysis of the epimeric and anomeric specificity of the periplasmic transport/chemosensory protein receptor for D-glucose and D-galactose. *Biochemistry 33*, 4762–4768.

(34) Das, S., Thomas, K. G., Thomas, K. J., Madhavan, V., Liu, D., Kamat, P. V., and George, M. V. (1996) Aggregation behaviour of water soluble bis(benzothiazolylidene)squaraine derivatives in aqueous media. *J. Phys. Chem. 100*, 17310–17315.

(35) Dattelbaum, J. D., Looger, L. L., Benson, D. E., Sali, K. M., Thompson, R. B., and Hellinga, H. W. (2005) Analysis of an allosteric signal transduction mechanisms in an engineered fluorescent maltose biosensor. *Protein Sci. 14*, 284–291.

(36) Amiss, T. J., Nycz, C. M. Pitner, J. B. Sherman, D. B. and Wright. D. J. 2003. Binding protein as biosensors. U.S. Patent Application 2003/0134346 A1.

BC700146R

Preparation and Evaluation of Glycosylated Arginine–Glycine–Aspartate (RGD) Derivatives for Integrin Targeting

Brian H. M. Kuijpers,[§] Stan Groothuys,[§] Annemieke C. Soede,[†] Peter Laverman,[†] Otto C. Boerman,[†] Floris L. van Delft,[§] and Floris P. J. T. Rutjes*[,§]

Synthetic Organic Chemistry, Institute for Molecules and Materials, Radboud University Nijmegen, Toernooiveld 1, 6525 ED, Nijmegen, The Netherlands, and Department of Nuclear Medicine, Radboud University Nijmegen Medical Center, P.O. Box 9101, HB Nijmegen 6500, The Netherlands. Received April 27, 2007; Revised Manuscript Received August 9, 2007

Arginine–glycine–aspartate (RGD) derivatives were prepared by a combination of solid-phase and solution-phase synthesis for selective targeting of $\alpha_v\beta_3$ integrin expressed in tumors. In order to evaluate the value of a triazole moiety as a proposed amide isostere, the side chain glycosylated cyclic RGD (*c*RGD) peptides were synthesized with either a natural amide linkage or a triazole. Affinity of the *c*RGD constructs for the $\alpha_v\beta_3$ integrin was determined in a solid-phase competitive binding assay, showing strong similarity in binding affinity for each of the compounds under evaluation. Furthermore, the in vivo tumor targeting potential of glycosylated *c*RGD peptides, linked via amide or triazole, was investigated by determining the biodistribution of ^{125}I-labeled derivatives in mice with tumors expressing $\alpha_v\beta_3$. All of the cyclic RGD derivatives showed preferential uptake in the subcutaneous tumors, with the highest tumor-to-blood ratio measured for the triazole-linked glycosylated derivative. The results of the present study are a clear indication of the value of the triazole moiety as a suitable amide isostere in the development of glycosylated peptides as pharmaceuticals.

INTRODUCTION

In a recent communication, we showed (*1*) that the Cu(I)-catalyzed [3 + 2] cycloaddition (*2, 3*) of an organic azide and an acetylene, one of the most reliable click reactions (*4*), could be used for the synthesis of triazole-linked glycoamino acids. The incorporation of a triazole as a bridging moiety in a glycoamino acid is of particular interest because the triazole function has been postulated as a useful amide isostere (*4, 5*) in terms of electronic properties and atom placement, and the resulting cyclic triazolyl RGD peptides may therefore be of value for a variety of biological or medicinal applications. Thus, it was demonstrated by us, and by others (*6*) that subjection of 1-azidosugars with acetylene-containing amino acids to the standard protocol for copper-catalyzed Huisgen addition leads to triazolylglycoamino acids, with a nitrogen-linked sugar (^{N}TGA), in high yields (Figure 1). Similarly, application of the procedure to 1-acetylenosugar and azide-containing amino acid afforded the corresponding carbon-linked triazole-linked glycoamino acids (^{C}TGA).

The applicability of the triazole-linked glycoamino acids for the preparation of glycopeptides isosteres was inter alia demonstrated by us by incorporation of TGAs into a range of glycopeptides either via standard solution-phase peptide coupling protocols or under the influence of alcalase (*7*). In addition we have shown the possibility of preparing 5-bromo-substituted triazolylglycoamino acids by applying a modified procedure of the Cu(I)-catalyzed Huisgen cycloaddition to azides and bromoacetylenes (*8*).

After suitable technology for the preparation of stable glycopeptides isosteres was established, the present study aimed to investigate the biological relevance of a triazole function as an amide isostere. Some precedence for the isosteric value of a triazole has been provided for true peptide analogues (*4, 5, 9*),

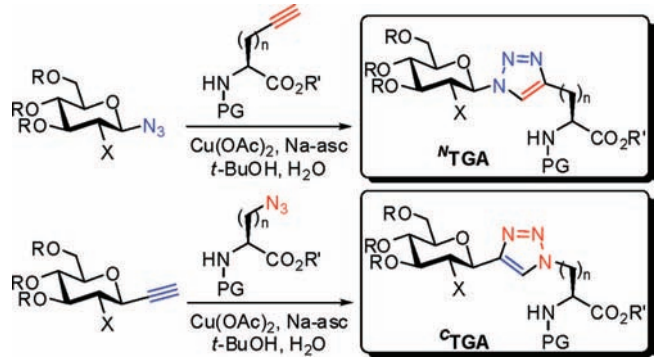


Figure 1. Synthesis of triazolyl glycoamino acids ^{N}TGA and ^{C}TGA.

but the synthesis of triazole-linked glycopeptides with relevant biological activity has hitherto not been reported. Moreover, little was known about the chemical stability of a glycosyl triazole linkage under basic or acidic conditions, with the exception of typical carbohydrate chemistry conditions (*10*). We became intrigued by the covalent attachment of carbohydrates to the so-called arginine–glycine–aspartate (RGD) peptides (*11*), found in proteins of the extracellular matrix such as vitronectin, fibrinogen, and laminin. The RGD motif is specifically recognized by heterodimeric transmembrane proteins called integrins. Integrins link the intracellular cytoskeleton with the extracellular matrix, thereby playing an important role in cell-signaling, cell–cell adhesion, apoptosis, and cell–matrix interactions. More specifically, the $\alpha_v\beta_3$ integrin is expressed on endothelial cells and modulates cell migration and survival during angiogenesis, while the $\alpha_v\beta_3$ integrin expressed on carcinoma cells potentiate metastasis by facilitating extravasation and tissue invasion. As a consequence, the integrin RGD binding site is an attractive pharmaceutical target (*12*) and a large number of RGD analogues have been prepared over the years. For example, Kessler et al. (*13*) showed that cyclo[Arg-Gly-Asp-D-Phe-Val] is one of the most active and selective antagonists for the $\alpha_v\beta_3$

* E-mail: F.Rutjes@science.ru.nl.
[§] Radboud University Nijmegen.
[†] Radboud University Nijmegen Medical Center.

10.1021/bc700154u CCC: $37.00 © 2007 American Chemical Society
Published on Web 10/09/2007

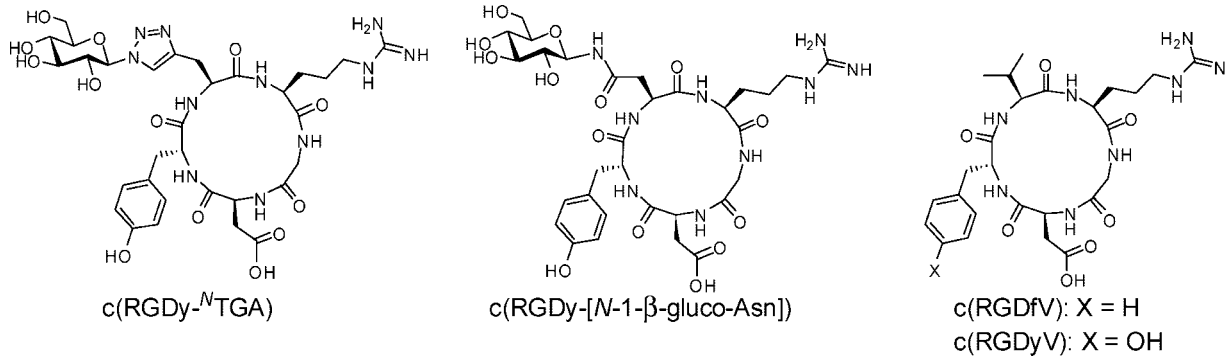
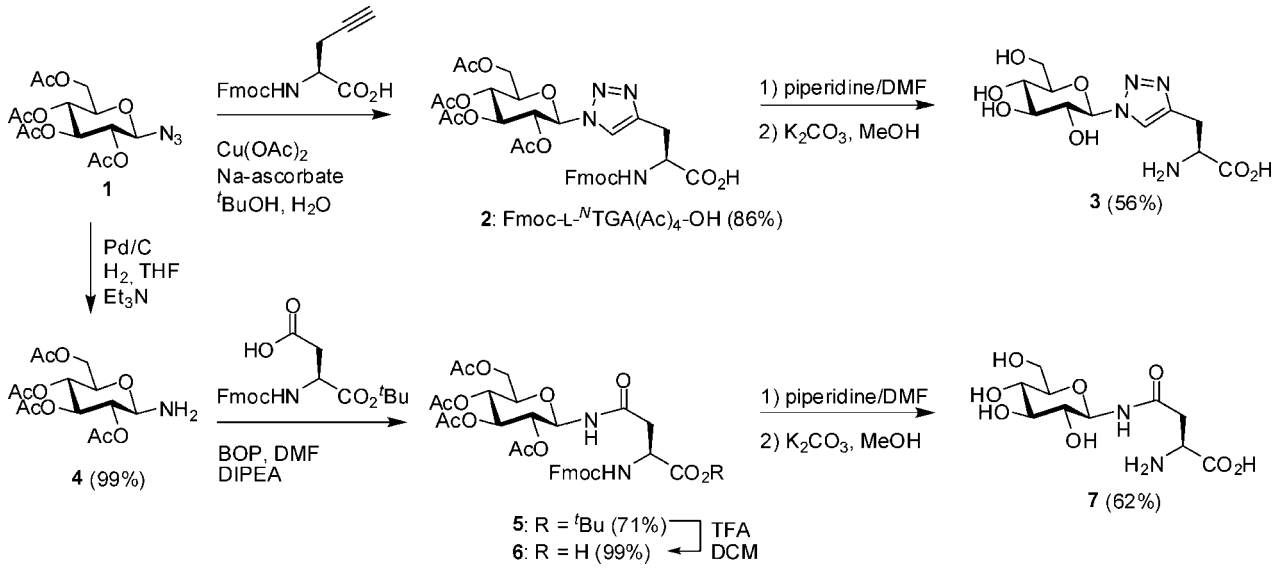


Figure 2. Cyclic RGD peptides for integrin targeting.

Scheme 1. Synthesis of Glycosylated Amino Acids



integrin. Later, it was shown that glycosylation of the side chains of the cyclic RGD (*c*RGD) peptides led to significant improvement of the pharmacokinetic properties of lipophilic peptides (*11*, *14*). Various glycosylated *c*RGD peptides were prepared to elucidate the influence of various substitutions on the biological properties (*15*). On the basis of these studies, we hypothesized that triazole isosteres of such cyclic glyco-RGD peptides would display a comparable pharmaceutical profile. Here, we studied the stability of *N*-triazolylglycoamino acids and the preparation of a representative set of "normal" *c*RGD peptides as well as two glycosylated *c*RGD derivatives (Figure 2) synthesized by a combination of solid phase and solution phase techniques. The *in vitro* and *in vivo* $\alpha_v\beta_3$ binding characteristics of these compounds were investigated.

MATERIALS AND METHODS/EXPERIMENTAL PROCEDURES

All chemicals were used as supplied without further purification. The trityl chloride polystyrene (TCP) resin as well as the 9-fluorenylmethoxycarbonyl (Fmoc) amino acids were purchased from NovaBioChem (Bad Soden, Germany). 1-Hydroxybenzotriazole (HOBt) and diisopropylcarbodiimide (DIPCDI) were purchased from Aldrich (Steinheim, Germany). L-Propargylglycine was purchased from Chiralix (Nijmegen, The Netherlands). All other reagents were purchased from Acros (Geel, Belgium). Low-resolution mass spectra (LRMS) were obtained using a Thermo Scientific Advantage LCQ linear iontrap electrospray mass spectrometer (ESI-MS), and high-resolution mass spectra (HRMS) using electrospray ionization time-of-flight (ESI-TOF) were obtained using a JEOL AccuTOF mass spectometer. ^{1}H and ^{13}C nuclear magnetic resonance (NMR) spectra were recorded on a Varian Inova 400 (400 MHz) or a Bruker DMX300 (300 MHz) spectrometer. The chemical shifts (δ) are given in ppm downfield from tetramethylsilane. Analytical reversed-phase high-performance liquid chromatography (RP-HPLC) was performed on a Merck Hitachi HPLC using an analytical reversed-phase column (Alltech Adsorbosphere C18, 300 Å, 5 μm, 4.6 mm × 250 mm) and a Merck Hitachi (L-4000) UV detector operating at 215 nm. Elution was effected using an appropriate gradient from 0.1% trifluoroacetic acid (TFA) in H_2O/CH_3CN (95/5, v/v) to 0.1% TFA in CH_3CN/H_2O (95/5, v/v). Semipreparative HPLC was performed using an Alltech Adsorbosphere XL C18 column (250 mm × 10 mm, pore size of 100 Å, particle size of 10 μm) at a flow rate of 5.0 mL/min.

Synthesis of Sugar Derivatives (Scheme 1). *2,3,4,6-Tetra-O-acetyl-β-D-glucopyranosylazide (**1**).* The glucopyranosylazide was prepared according to a literature procedure (*16*).

*2,3,4,6-Tetra-O-acetyl-β-D-glucopyranosylamine (**4**).* The glucopyranosylamine was prepared according to a literature procedure (*17*) with slight modification. In an oven-dried Schlenck flask filled with N_2, the azidoglucose **1** (500 mg, 1.3 mmol), Et_3N (140 mg, 1.4 mmol), and Pd/C (14 mg, 0.1 mmol) were suspended in THF (3 mL). Next the Schlenk flask was subjected to a sequence of vacuum and flushing with H_2 (3×), after which it was vigorously stirred while H_2 was bubbled through the solution. After 30 min, the reaction was completed, the slurry was filtered over HyFlo, and THF was evaporated

under reduced pressure to yield **4** as a white solid (99%) sufficiently pure for further reactions.

Synthesis of Fmoc-Protected Glycosidic Amino Acids (Scheme 1). *Fmoc-L-^{N}TGA(Ac)$_4$-OH (2).* The triazole-linked sugar amino acid **2** was prepared according to a procedure reported earlier (*1*). To a solution of glycoside **1** (1 equiv) and Fmoc-protected L-propargylglycine (1 equiv) in *tert*-butanol (0.5 M) was added a solution of $Cu(OAc)_2$ (20 mol %) and sodium ascorbate (40 mol %) in H_2O (0.04 and 0.08 M, respectively). The mixture was stirred overnight, water was added, and the product was extracted with DCM (2×). The combined organic layers were washed with aqueous NaCl, dried over Na_2SO_4, and evaporated in vacuo. The product was purified by flash chromatography using EtOAc/heptane (2/1) to yield a white solid (86%). $R_f = 0.20$ (EtOAc/heptane, 2:1). IR (film): ν 3360, 2950, 2250, 1748, 1221 cm^{-1}. ^{1}H NMR (400 MHz, $CDCl_3$) δ 7.75 (d, J = 7.6 Hz, 1H), 7.70 (s, 1H), 7.61–7.58 (m, 2H), 7.41–7.37 (m, 2H), 7.32–7.28 (m, 2H), 6.00 (d, J = 7.8 Hz, 1H), 5.86–5.83 (m, 1H), 5.48–5.35 (m, 2H), 5.31–5.19 (m, 1H), 4.80–4.67 (m, 1H), 4.38 (d, J = 7.2 Hz, 2H), 4.30 (ABdd, J = 12.6, 5.1 Hz, 1H), 4.23 (t, J = 7.2 Hz, 1H), 4.15–4.09 (m, 1H), 3.99 (ddd, J = 10.2, 4.9, 2.0 Hz, 1H), 3.45–3.30 (m, 2H), 2.10 (s, 3H), 2.07 (s, 3H), 2.02 (s, 3H), 1.84 (s, 3H). ^{13}C NMR (75 MHz, $CDCL_3$) δ 173.2, 170.7, 170.0, 169.8, 169.6, 156.2, 143.9, 143.6, 141.4, 127.9, 127.2, 125.3, 121.4, 120.1, 85.9, 75.4, 72.6, 70.6, 67.9, 67.4, 61.7, 53.4, 47.3, 27.9, 20.8, 20.7, 20.6, 20.2. HRMS (ESI) calculated for $C_{34}H_{37}N_4O_{13}$ $(M + H)^+$ 709.2344, found 709.2357.

^{N}TGA (3). Fmoc-L-^{N}TGA(Ac)$_4$-OH (**2**) (500 mg, 0.70 mmol) was treated with 20% piperidine in DMF (v/v, 5 mL) and stirred for 20 min before concentration of the solvent in vacuo. The crude product was dissolved in MeOH (5 mL), and a catalytic amount of K_2CO_3 was added. The mixture was stirred for 1 h. Purification of the product with a basic ion exchange column (IRA-410) afforded the triazole-linked glycosidic amino acid **3** (125 mg, 56%) as a white solid. IR (film): ν 3309, 2362, 2327, 1623 cm^{-1}. ^{1}H NMR (400 MHz, D_2O) δ 5.01 (d, J = 8.4 Hz, 1H), 4.04 (s, 1H), 3.89 (d, J = 12.2 Hz, 1H), 3.74 (dd, J = 13.0, 4.8 Hz, 1H), 3.46–3.39 (m, 2H), 3.44 (m, 2H), 3.14–2.80 (m, 2H). ^{13}C NMR (75 MHz, $CDCl_3$) δ 172.3, 141.7, 123.3, 86.9, 78.4, 75.4, 71.7, 68.4, 59.9, 53.7, 25.7. HRMS (ESI) calculated for $C_{34}H_{37}N_4O_{13}$ $(M + H)^+$ 709.2357, found 709.2344.

Fmoc-(N-1-Glu(Ac)$_4$-Asn)-OH (6). The triazole-linked sugar amino acid was prepared from glucopyranosylamine **4** and Fmoc-Asp-O^{t}Bu via a procedure reported by van Ameijde et al. (*18*) involving peptide coupling catalyzed by BOP followed by deprotection using TFA/DCM (4 h, room temp) to afford the *N*-glycosylasparagine **6** as a white solid in 71% overall yield. $R_f = 0.12$ (EtOAc/heptane, 2:1). IR (film): ν 3313, 2250, 1740, 1506 cm^{-1}. ^{1}H NMR (400 MHz, $CDCl_3$) δ 7.76 (d, J = 7.5 Hz, 2H), 7.58 (d, J = 7.4 Hz, 2H), 7.40 (t, J = 7.4 Hz, 2H), 7.31 (t, J = 7.4 Hz, 2H), 6.70 (d, J = 8.8 Hz, 1H), 6.16 (d, J = 7.6 Hz, 1H), 5.33 (t, J = 9.5 Hz, 1H), 5.26 (t, J = 9.1 Hz, 1H), 5.08 (t, J = 9.7 Hz, 2H), 4.94 (t, J = 9.5 Hz, 1H), 4.67–4.53 (m, 1H), 4.47–4.34 (m, 2H), 4.30 (dd, J = 12.6, 4.4 Hz, 1H), 4.22 (t, J =7.04 Hz, 1H), 4.08 (dd, J =12.6, 2.0 Hz, 1H), 3.82 (ddd, J =10.1, 4.1, 2.0 Hz, 1H), 2.90 (dd, J =16.3, 2.8 Hz, 1H), 2.76 (dd, J =16.3, 5.2 Hz, 1H), 2.06 (s, 5H), 2.04 (s, 3H), 2.02 (s, 3H). ^{13}C NMR (75 MHz, $CDCl_3$) δ 176.1, 173.9, 171.4, 170.9, 170.2, 169.8, 156.6, 143.7, 141.3, 127.9, 127.2, 125.3, 120.1, 78.0, 73.8, 272.9, 70.8, 68.2, 67.6, 61.8, 50.5, 47.1, 37.7, 20.8, 20.7, 20.7, 20.6. HRMS (ESI) calculated for $C_{33}H_{36}N_2NaO_{14}$ $(M + Na)^+$ 707.2051, found 707.2064.

N-1-Gluco-Asn (7). Fmoc-(*N*-1-Glu(Ac)$_4$-Asn)-OH (**5**) (500 mg, 0.73 mmol) was treated with 20% piperidine in DMF (v/v, 5 mL) and stirred for 20 min before concentration of the solvent in vacuo. The crude product was dissolved in MeOH (5 mL), and a catalytic amount of K_2CO_3 was added. The mixture was stirred for 1 h. Purification of the product with a basic ion exchange column (IRA-410) afforded the amide-linked glycosidic aspargine **7** (133 mg, 62%) as a white solid. ^{1}H NMR (400 MHz, D_2O) δ 8.14 (s, 1H), 5.77 (d, J = 9.2 Hz, 1H), 4.10 (t, J = 5.0 Hz, 1H), 4.02 (t, J = 9.2 Hz, 1H), 3.93 (d, J = 11.4 Hz, 1H), 3.82–3.71 (m, 3H), 3.64 (t, J = 9.1 Hz, 1H), 3.43–3.34 (m, 1H). HRMS (ESI) calculated for $C_{33}H_{36}N_2O_{14}$ $(M + H)^+$ 707.2064, found 707.2051.

Table 1. Stability Tests for ^{N}TGA and *N*-1-β-Glyco-Asn, Respectively

			stability	
conditions	temperature	time	^{N}T GA (**3**)	*N*-1-β-glyco-Asn (**7**)
2 M HCl (aq)	room temp	3 d	++	++
2 M HCl (aq)	reflux	2 h	++	+
4 M HCl (aq)	reflux	3 h	++	− −
2 M NaOH (aq)	room temp	3 d	++	−
2 M NaOH(aq)	reflux	3 h	++	− −
2.6 M HCl/EtOAc	room temp	3 d	++	+
Et_3N	reflux	3 h	++	+

Stability Tests. ^{N}TGA (**3**) (50 mg, 0.07 mmol) or *N*-1-gluco-Asn (**7**) (50 mg, 0.07 mmol) was dissolved in 3 mL of 2 M HCl (aq), 4 M HCl (aq), 2 M NaOH (aq), 2.6 M HCl/EtOAc, or Et_3N and stirred for the time and temperature indicated in Table 1. The relative stability of the substrates was determined by TLC analysis and integration of the ^{1}H NMR signals of the side products and starting material.

General Procedures for the Preparation of the Cyclic RGD Peptides (Scheme 2). Loading of the trityl resin, synthesis of the pentapeptides, cleavage, subsequent cyclization, and deprotection of the cyclic RGD peptides were carried out following standard Fmoc peptide chemistry protocols. Side chains were protected with 2,2,5,7,8-pentamethylchroman (Pmc) for arginine and *tert*-butyl (^{t}Bu) for aspartic acid and tyrosine.

Removal of the Side Chain Protection of the Peptides. The peptides were treated with a solution of 95% trifluoroacetic acid (TFA), 2.5% water, and 2.5% ethanedithiol (EDT) for 4 h at ambient temperature. Next, the glycopeptides were precipitated in diethyl ether. The crude product was isolated by centrifugation and washed three times with diethyl ether.

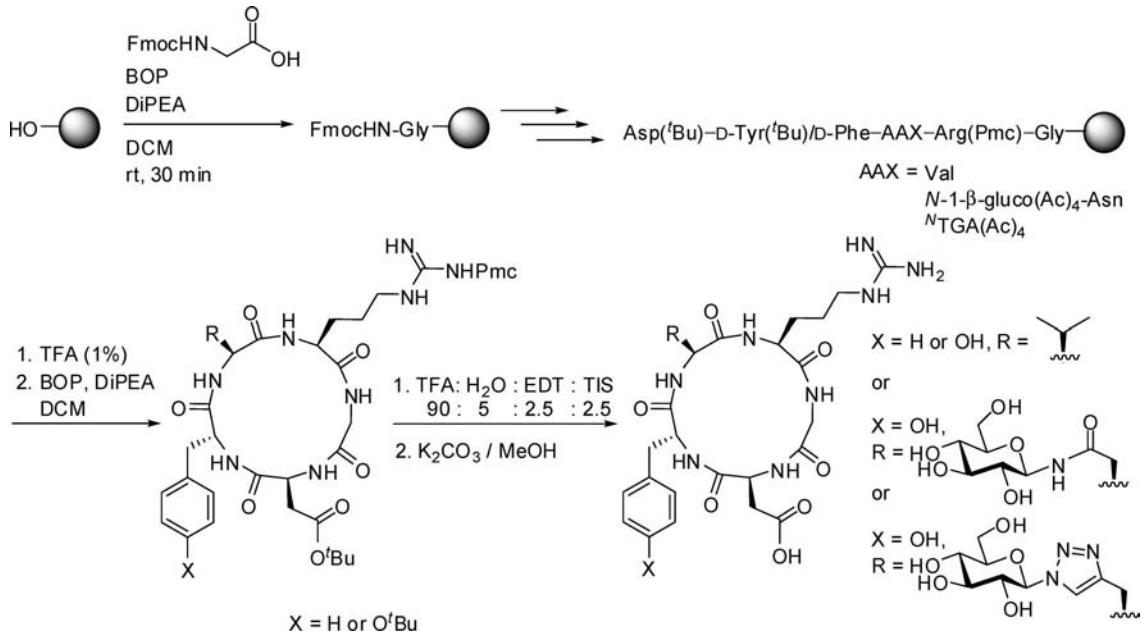
Removal of the Acetyl Protections of the Carbohydrate Bearing Peptides. The crude product was dissolved in MeOH. A catalytic amount of K_2CO_3 was added, and the mixture was stirred for 1 h. Ion exchange resin (Amberlyte IR-120) was added until the solution was neutral, and the ion exchange resin was filtered off. A final purification was done via semipreparative RP-HPLC as described above.

c(RGDfV). Retention time (t_R) (min): 8.1. HRMS (ESI) calculated for $C_{26}H_{39}N_8O_7$ $(M + H)^+$ 575.2914, found 575.2942. For additional data, see ref *14*.

c(RGDyV). t_R (min): 8.2. HRMS (ESI) calculated for $C_{26}H_{39}N_8O_8$ $(M + H)^+$ 591.2891, found 591.2891. For additional data, see ref *19*.

c(RGDy-N-[1-β-gluco(OAc)$_4$]-Asn). t_R (min): 6.3. ^{1}H NMR (400 MHz, MeOD) δ 7.02 (d, J = 8.6 Hz, 2H), 6.70 (d, J = 8.6 Hz, 2H), 5.32 (t, J = 9.5 Hz, 1H), 5.23 (t, J = 9.4 Hz, 1H), 5.04 (t, J = 10.0 Hz, 1H), 4.95 (t, J = 9.5 Hz, 1H), 4.73 (t, J= 6.9 Hz, 1H), 4.57–4.52 (m, 1H), 4.44–4.39 (m, 1H), 4.28–4.23 (m, 3H), 4.11 (dd, J = 12.4, 2.2 Hz, 1H), 3.92 (ddd, J = 10.2, 4.6, 2.4 Hz, 1H), 3.25–3.13 (m, 2H), 3.00–2.95 (m, 1H), 2.86–2.76 (m, 2H), 2.68 (dd, J = 16.1, 6.9 Hz, 1H), 2.57 (dd, J = 16.5, 6.8, 1H), 2.48 (dd, J = 16.1, 5.3 Hz, 1H), 2.03 (s, 3H), 2.03 (s, 3H), 1.99 (s, 3H), 1.98 (s, 3H), 1.98–1.55 (m, 4H). LRMS calculated for $C_{39}H_{54}N_9O_{18}$ $(M + H^+)$ 936.4, found 936.4.

Scheme 2. Preparation of the *c*RGD Peptides



c(RGDy-^{N}TGA(OAc)$_4$). t_R (min): 7.9. ^{1}H NMR (400 MHz, MeOD) δ 7.94 (s, 1H), 6.99 (d, J = 8.5 Hz, 2H), 6.69 (d, J = 8.5 Hz, 2H), 6.09 (d, J = 9.2 Hz, 1H), 5.63 (t, J = 9.4 Hz, 1H), 5.53 (t, J = 9.4 Hz, 1H), 5.27 (t, J = 9.8 Hz, 1H), 4.71 (dd, J = 8.3, 5.7 Hz, 1H), 4.58–4.50 (m, 2H), 4.35–4.24 (m, 3H), 4.17 (dd, J = 12.3, 1.7 Hz, 1 H), 4.13–4.09 (m, 1H), 3.38 (d, J = 15.4 Hz, 1H), 3.26–3.18 (m, 3H), 3.12–3.05 (m, 1H), 2.99–2.94 (m, 1H), 2.84–2.77 (m, 2H), 2.56 (dd, J = 16.6, 5.8 Hz, 1H), 2.06 (s, 3H), 2.00 (s, 3H), 2.00 (s, 3H), 1.83 (s, 3H), 2.00–1.52 (m, 4H). LRMS calculated for $C_{40}H_{54}N_{11}O_{17}$ ($M + H^+$) 960.4, found 960.4.

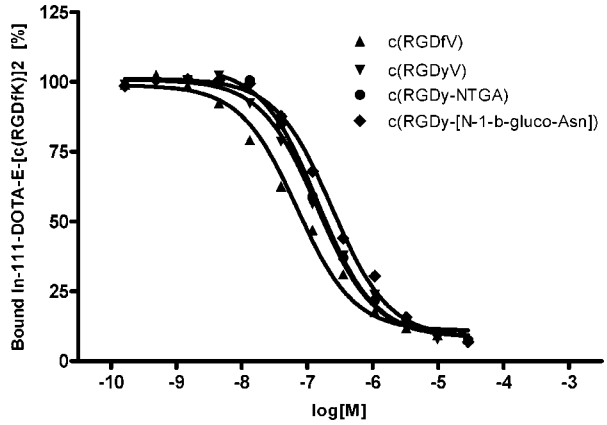
c(RGDy-N-[1-gluco]-Asn). Removal of the acetyl protecting groups as described above afforded 50 mg (0.06 mmol) of the product, 18% relative to the resin. ^{1}H NMR (400 MHz, D_2O/MeOD) δ 7.01 (d, J = 8.4 Hz, 2H), 6.68 (d, J = 8.2 Hz, 2H), 4.88 (ap d, J = 9.5, 1H), 4.70 (t, J = 7.2 Hz, 1H), 4.50 (dd, J = 6.8, 5.0 Hz, 1H), 4.45–4.38 (m, 2H), 4.24 (d, J = 14.5 Hz, 1H), 3.89 (ap d, J = 11.1 Hz, 1H), 3.74 (dd, J = 12.4, 5.1 Hz, 1H), 3.58 (t, J = 9.2, 1H), 3.53–3.40 (m, 3H), 3.38–3.31 (m, 1H), 3.26–3.15 (m, 2H), 2.98 (dd, J = 13.3, 5.9 Hz, 1H), 2.89–2.83 (m, 2H), 2.77 (dd, J = 16.4, 7.2 Hz, 1H), 2.65 (dd, J = 15.6, 6.5 Hz, 1H), 2.55–2.49 (m, 2H), 1.96–1.87 (m, 1H), 1.76–1.67 (m, 1H), 1.65–1.53 (m, 2H). HRMS (ESI) calculated for $C_{31}H_{46}N_9O_{14}$ $(M + H)^+$ 768.3101, found 768.3164.

c(RGDy-^{N}TGA). Removal of the acetyl protections as described above afforded 39 mg (0.05 mmol) of the product, 14% yield relative to the resin. ^{1}H NMR (400 MHz, D_2O) δ 7.83 (s, 1H), 7.01 (d, J = 8.4 Hz, 2H), 6.68 (d, J =8.4 Hz, 2H), 5.72 (d, J = 9.2 Hz, 1H), 4.68 (t, J =7.1 Hz, 1H), 4.51 (dd, J = 9.9, 5.9 Hz, 1H), 4.43 (t, J = 6.9 Hz, 1H), 4.34 (dd, J = 8.9, 5.6 Hz, 1H), 4.21 (d, J = 14.9 Hz, 1H), 3.99 (t, J = 9.2 Hz, 1H), 3.94 (d, J = 10.4 Hz, 1H), 3.68–3.55 (m, 3H), 3.64 (t, J = 9.3 Hz, 1H), 3.50 (d, J = 14.9 Hz, 1H), 3.09–2.95 (m, 3H), 3.04 (dd, J = 15.3, 6.5 Hz, 1H), 2.94 (dd, J = 13.4, 5.9 Hz, 1H), 2.86 (dd, J = 13.2, 10.2 Hz, 1H), 2.67 (dd, J = 15.8, 7.0 Hz, 1H), 2.53 (dd, J = 15.7, 7.3 Hz, 1H), 1.75–1.63 (m, 1H), 1.55–1.42 (m, 1H), 1.35–1.23 (m, 2H). HRMS (ESI) calculated for $C_{32}H_{46}N_{11}O_{13}$ $(M + H)^+$ 792.3210, found 792.3277.

Solid Phase $\alpha_v\beta_3$ Binding Assay. The affinity of *c*(RGDfV), *c*(RGDyV), *c*(RGDy-[*N*-1-β-gluco-Asn]), and *c*(RGDy-^{N}TGA) for the $\alpha_v\beta_3$ integrin was determined in a competitive binding assay using the dimeric peptide ^{111}In-DOTA-E-[*c*(RGDfK)]$_2$ as a tracer. The ^{111}In-labeled peptide (3 MBq/μg) was prepared as described earlier (*20*). Microtiter 96-well vinyl assay plates (Corning B.V., Schiphol-Rijk, The Netherlands) were coated with 100 μL/well of a solution of purified human integrin $\alpha_v\beta_3$ (150 ng/mL) (Chemicon International, Temecula, CA) in coating buffer (25 mM Tris-HCl, pH 7.4, 150 mM NaCl, 1 mM $CaCl_2$, 0.5 mM $MgCl_2$, and 1 mM $MnCl_2$) for 17 h at 4 °C. The plates were washed twice with binding buffer (0.1% bovine serum albumin (BSA) in coating buffer). The wells were blocked for 2 h with 200 μL of blocking buffer (1% BSA in coating buffer) at room temperature. The plates were washed twice with binding buffer. Then 100 μL of binding buffer containing 11 kBq of ^{111}In-DOTA-E-[*c*(RGDfK)]$_2$ and appropriate dilutions of non-labeled *c*(RGDfV), *c*(RGDyV), *c*(RGDy-[*N*-1-β-gluco-Asn]), and *c*(RGDy-^{N}TGA) in binding buffer were incubated in wells at 37 °C for 1 h. After incubation, the plates were washed three times with binding buffer. The retained radioactivity in each well was determined in a γ-counter. IC_{50} values of the *c*RGD peptides were calculated by nonlinear regression using GraphPad Prism (GraphPad Prism 4.0 software, San Diego, CA). Each data point is the average of three determinations.

Radiolabeling of the *c*RGD Peptides. The peptides containing tyrosine, *c*(RGDyV), *c*(RGDy-[*N*-1-β-gluco-Asn]), and *c*(RGDy-^{N}TGA) were labeled with ^{125}I using the iodogen method. The peptide (10–20 μg) was dissolved in 100 μL of phosphate-buffered saline (PBS) (pH 7.4) in a 1.5 mL polypropylene vial coated with 100 μg of iodogen, and [^{125}I]NaI (37 MBq) was added to the vial. After 10 min, the solution was transferred to another vial to terminate the iodination. A sample of the mixture was analyzed by HPLC. Radiochemical purity was always higher than 98%.

Biodistribution Studies. In the right flank of 6–8 week old female nude BALB/c mice, 0.2 mL of a suspension of 15–10^6 cells/mL SK-RC-52 cells was injected subcutaneously (sc). Two weeks after inoculation of the tumor cells, mice were randomly divided into four groups. Mice were injected with ^{125}I-*c*(RGDfV) (0.5 MBq, 0.5 μg), ^{125}I-*c*(RGDyV) (0.5 MBq, 0.5 μg), ^{125}I-*c*(RGDy-[*N*-1-β-gluco-Asn]) (0.5 MBq, 0.5 μg), or ^{125}I-*c*(RGDy-^{N}TGA) (0.5 MBq, 0.5 μg) via the tail vein. Mice were euthanized by CO_2 asphyxiation 2 h postinjection (pi) (four mice per group). Blood, tumor, and all the major organs and tissues were dissected, weighed, and counted in a well-type γ-counter.



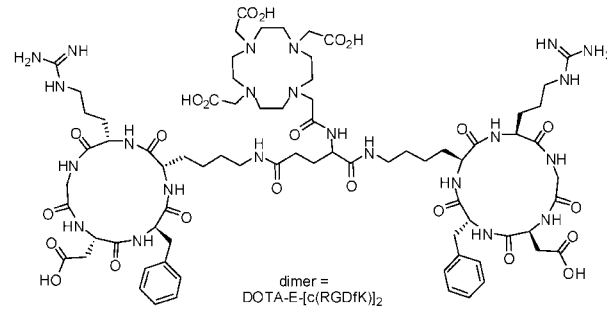


Figure 3. Competition of specific binding of ^{111}In-DOTA-E-[*c*(RGDfK)]$_2$ with *c*(RGDfV) (▲), *c*(RGDyV) (▼), *c*(RGDy-^{N}TGA) (●), and *c*(RGDy-[*N*-1-β-gluco-Asn]) (◆).

The percent injected dose per gram (%ID/g) was determined for each sample. To investigate whether the uptake of each of the four *c*RGD peptides (in the dissected tissues) was $\alpha_v\beta_3$-mediated, a separate group of mice was coinjected with an excess (50 μg) of nonradiolabeled DOTA-E-[*c*(RGDfK)]$_2$ to saturate all the $\alpha_v\beta_3$ integrin receptors, and the biodistribution of the radioiodinated *c*RGD peptide conjugates was determined as described above. All animal experiments were approved by the local animal welfare committee in accordance with the Dutch legislation and carried out in accordance with their guidelines.

RESULTS AND DISCUSSION

Synthesis of Glycoamino Acids. Cyclic RGD peptides represent valuable ligands for selective targeting of $\alpha_v\beta_3$ integrins. Consequently, large numbers of RGD analogues have been prepared (*20–22*) and extensively tested. We have shown that 1-azido sugars and acetylene-modified amino acids readily undergo [3 + 2] cycloaddition via a standard protocol for the copper-catalyzed Huisgen addition to form in high yields triazole isosteres of glycoamino acids (*1*). Although synthetically of interest, here we explored the potential value of triazolyl cyclic glyco-RGD peptides as targeting agents. In this respect, the first relevant question to answer is to what extent the triazole analogues of glycoamino acids have increased stability with respect to the natural compounds. Second, the medicinal value of the triazole compounds as glycoamino acid mimics can only be evaluated by incorporation in biologically active compounds. For this reason, a set of cyclic RGD peptides was chosen to evaluate the binding affinities for $\alpha_v\beta_3$ integrins, including the amide-linked glyco-RGD *c*[RGDy(*N*-1-β-glyco-Asn)], the triazole-linked *c*(RGDy-^{N}TGA) and *c*(RGDyV) and *c*(RGDfV) for reference purposes. D-Tyr was incorporated instead of D-Phe for *c*[RGDy(*N*-1-β-glyco-Asn)], *c*(RGDy-^{N}TGA), and *c*(RGDyV), enabling subsequent iodination for tumor imaging as reported by Haubner et al. (*14*).

The requisite building blocks for solid-phase synthesis, 1-azido-2,3,4,6-tetra-*O*-acetyl-β-D-glucopyranose **1** (*16*) was efficiently condensed with Fmoc-L-propargylglycine under the influence of Cu(OAc)$_2$ and sodium ascorbate in a mixture of ^{t}BuOH and H$_2$O to synthesize fully protected *N*-triazolylglycosidic alanine (*2*), which we refer to as Fmoc-L-^{N}TGA(Ac)$_4$-OH, in a 91% yield. The amide-linked glycoamino acid was prepared by hydrogenation of **1** with hydrogen in the presence of Pd/C and Et$_3$N in MeOH to afford 1-aminoglucose derivative **3**. Subsequent coupling to Fmoc-aspartic acid *tert*-butyl ester yielded acetyl and Fmoc protected glycosidic asparagine *tert*-butyl ester **5** in a yield of 87%. Next, the *tert*-butyl ester was treated with TFA in DCM (1/1, v/v) to afford the free acid Fmoc-[*N*-1-β-glyco(Ac)$_4$-Asn](OH) in near-quantitative yield.

Evaluation of Stability. In order to investigate the chemical stability of the substrates ^{N}TGA(Ac)$_4$-OH, as well as *N*-1-glycosyl(Ac)$_4$-Asn(OH), the protected glycoamino acids **2** and **6** were subjected to treatment with 20% piperidine in DMF (v/v) followed by a saponification of the acetyl esters by K$_2$CO$_3$ in MeOH. The resulting glycoamino acids ^{N}TGA (**3**) and *N*-1-β-glyco-Asn (**7**) were subjected to various acidic and basic conditions as summarized in Table 1. The triazole-linked ^{N}TGA was found to be completely compatible with a range of basic and acidic conditions, whereas the natural amide-linked *N*-1-β-glyco-Asn did not withstand some of the conditions tested. From these results, it can be concluded that triazole-linked substrates are versatile building blocks for the preparation of stable analogues of the common asparagine-linked *N*-glycoproteins.

Solid-Phase Synthesis. For the synthesis of the cyclic RGD peptides, a solid-phase strategy was chosen, followed by cleavage from the resin and cyclization. Thus, in order to avoid racemization of the C-terminal amino acid during the last activation step, Fmoc-glycine was elected as the C-terminal amino acid and coupled to trityl resin with DiPEA in DCM. Subsequent elongation of the peptide was executed by application of standard Fmoc chemistry involving HOBt/DIPCDI-mediated coupling followed by piperidine-induced Fmoc deprotection. Both Fmoc-L-^{N}TGA(Ac)$_4$-OH and Fmoc-[*N*-1-β-glyco(Ac)$_4$]-Asn(OH) were compatible with the conditions applied, although the amide-linked glycoamino acid was incorporated at a much slower rate. After completion of the synthesis, the fully protected pentapeptides were cleaved from the resin using a 1% solution of TFA in DCM and purified by silica gel column chromatography. Next, cyclization of the linear RGD peptides was effected under the influence of BOP to give the protected cyclic peptides in good overall yields (14–18%). Finally, protecting groups were removed under basic conditions and the final product was purified by semipreparative RP-HPLC as described above.

Solid-Phase $\alpha_v\beta_3$ Binding Assay. The affinities of *c*(RGDfV), *c*(RGDyV), *c*(RGDy-[*N*-1-β-gluco-Asn]), and *c*(RGDy-^{N}TGA) for the $\alpha_v\beta_3$ integrin as determined in the competitive binding assay are summarized in Figure 3.

From Figure 3, it becomes clear that binding of ^{111}In-DOTA-E-[*c*(RGDfK)]$_2$ (*23*) to $\alpha_v\beta_3$ was inhibited by each compound in a concentration-dependent manner. In fact, only relatively small differences between the different peptides can be observed, with IC$_{50}$ values of 65 nM for *c*(RGDfV), 144 nM for *c*(RGDyV), 238 nM for *c*(RGDy-[*N*-1-β-gluco-Asn]), and 144 nM for *c*(RGDy-^{N}TGA), indicating that side chain modification had only limited effect on the $\alpha_v\beta_3$ binding affinity of the compounds, which is in agreement with earlier reports (*16, 24, 25*).

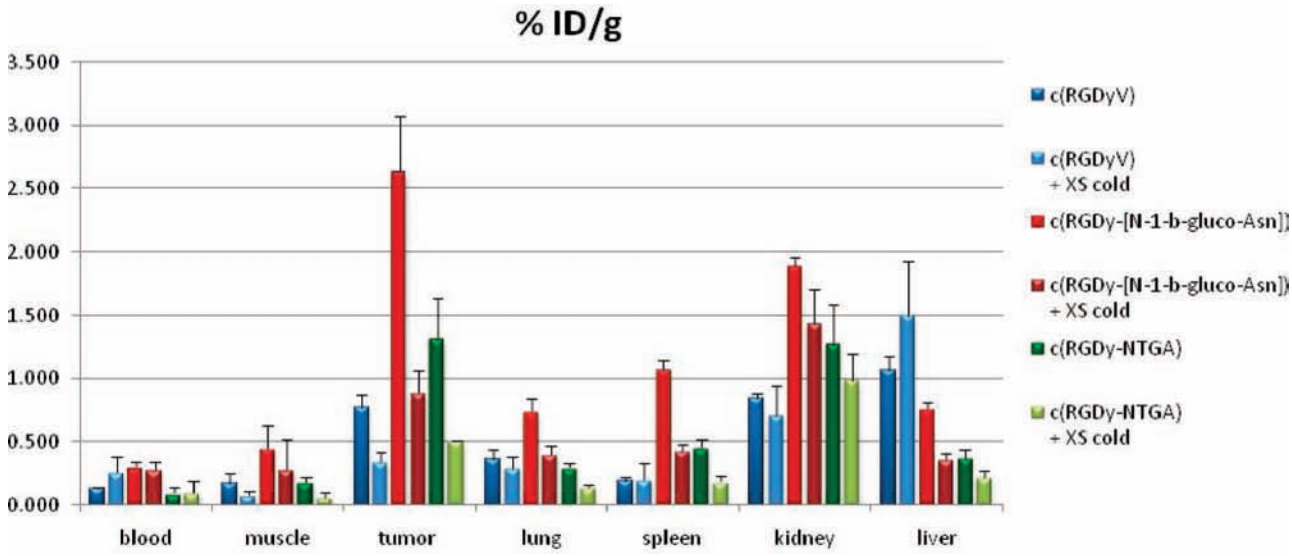


Figure 4. Biodistribution of *c*RGD peptides in athymic mice.

Table 2. Biodistribution Data of ^{125}I-*c*(RGDyV), ^{125}I- *c*(RGDy-[*N*-1-β-gluco-Asn]), and ^{125}I-*c*(RGDy-^{N}TGA) in the Presence and Absence of an Excess of Unlabeled DOTA-E-[*c*(RGDfK)]$_2$ in Athymic Mice with sc SK-RC-52 Tumors 2 h after Injection[a]

	^{125}I-*c*(RGDyV)		^{125}I-*c*[RGDy-(*N*-1-β-gluco-Asn)]		^{125}I-*c*(RGDy-^{N}TGA)	
		nonspecific uptake		nonspecific uptake		nonspecific uptake
blood	0.13 ± 0.01	0.26 ± 0.12	0.30 ± 0.04	0.28 ± 0.06	0.09 ± 0.04	0.10 ± 0.10
muscle	0.17 ± 0.08	0.08 ± 0.03	0.45 ± 0.18	0.28 ± 0.24	0.17 ± 0.04	0.06 ± 0.04
tumor	0.77 ± 0.10	0.34 ± 0.07	2.63 ± 0.45	0.89 ± 0.17	1.31 ± 0.33	0.51 ± 0.01
lung	0.36 ± 0.08	0.29 ± 0.09	0.74 ± 0.1	0.40 ± 0.07	0.29 ± 0.03	0.13 ± 0.02
spleen	0.19 ± 0.02	0.20 ± 0.13	1.07 ± 0.07	0.43 ± 0.05	0.46 ± 0.06	0.18 ± 0.04
kidney	0.84 ± 0.04	0.71 ± 0.24	1.89 ± 0.07	1.43 ± 0.27	1.27 ± 0.32	0.99 ± 0.20
liver	1.07 ± 0.11	1.49 ± 0.44	0.76 ± 0.05	0.36 ± 0.05	0.37 ± 0.07	0.22 ± 0.05
intestine	1.93 ± 1.62	1.82 ± 0.36	2.10 ± 0.44	1.15 ± 0.78	0.8 ± 0.20	0.30 ± 0.13

[a] The organ uptake is expressed as %ID/g.

In addition, these data showed that only a slight difference was noticeable between the carbohydrate containing *c*RGD peptides (*c*[RGDy-^{N}TGA]) and *c*(RGDy-[*N*-1β-gluco-Asn]), which is a first indication that the glycoamino acid binding characteristics are nearly unchanged upon substitution of the amide linkage for a triazole linkage.

Biodistribution Studies. Side chain glycosylation can improve the pharmacological properties of hydrophobic/lipophilic peptides (*26*), which has also been demonstrated for *c*RGD (*14*). In order to validate the potential of the glycoamino acids **3** and **7** for incorporation into glyco-RGD peptides, the biodistribution of ^{125}I-*c*(RGDyV), ^{125}I-*c*(RGDy-[*N*-1-β-gluco-Asn]), and ^{125}I-*c*(RGDy-^{N}TGA) in athymic mice with sc $\alpha_v\beta_3$-expressing tumors was determined (Figure 4). The results of the biodistribution studies of ^{125}I-RGDyV, ^{125}I-*c*(RGDy-[*N*-1-β-gluco-Asn]), and ^{125}I-*c*(RGDy-^{N}TGA) in athymic mice with SK-RC-52 tumors at 2 h pi are summarized in Table 2. In order to determine the nonspecific uptake of the peptides, the biodistribution was also determined in the presence of excess unlabeled *c*RGD compound, i.e., dimeric DOTA-E-[*c*(RGDfK)]$_2$.

All peptides ^{125}I-*c*(RGDyV), ^{125}I-*c*(RGDy-[*N*-1-β-gluco-Asn]), and ^{125}I-*c*(RGDy-^{N}TGA) rapidly cleared from the blood because blood levels at 2 h pi did not exceed 0.3% ID/g. Two hours after injection, the concentration of ^{125}I-*c*(RGDy-[*N*-1-β-gluco-Asn]) and ^{125}I-*c*(RGDy-^{N}TGA in the tumor was the highest of all tissues examined. Coinjection of excess unlabeled DOTA-E-[*c*(RGDfK)]$_2$ (50 μg) along with ^{125}I-*c*(RGDyV), ^{125}I-*c*(RGDy-[*N*-1-β-gluco-Asn]), and ^{125}I-*c*(RGDy-^{N}TGA) indicated that for each of the three compounds, the major part of the uptake in the tumor was $\alpha_v\beta_3$-mediated. In this mouse model, ^{125}I-*c*(RGDy-^{N}TGA) revealed the highest tumor-to-blood ratio (18 at 2 h pi). The carbohydrate-bearing *c*RGD peptides, ^{125}I-*c*(RGDy-[*N*-1-β-gluco-Asn]) and ^{125}I-*c*(RGDy-^{N}TGA), also showed $\alpha_v\beta_3$-mediated uptake in nontarget organs like lung, spleen, and intestine. Specific uptake of *c*RGD analogues in normal tissues has been reported in previous studies and is probably due to $\alpha_v\beta_3$ expression in these tissues (*27, 28*). Furthermore, the conducted studies once more show that tumor uptake is not solely dependent on the binding affinity but relies on many more factors such as blood residence time, molecular weight, structure, charge, etc. These aspects may explain the fact that ^{125}I-*c*(RGDy-[*N*-1-β-gluco-Asn]) displayed the highest tumor uptake while the corresponding monomer failed to provide the highest binding affinity. Although ^{125}I-*c*(RGDy-^{N}TGA) showed the highest tumor-to-blood ratio, it showed a lower tumor uptake than ^{125}I-*c*(RGDy-[*N*-1-β-gluco-Asn]). Therefore, it may be concluded that the high tumor uptake of ^{125}I-*c*(RGDy-[*N*-1-β-gluco-Asn]) can only partially be explained by the presence of the carbohydrate moiety.

CONCLUSION

A high-yielding route for the preparation of Fmoc-L-^{N}TGA(Ac)$_4$-OH starting from azidoglucose and Fmoc-protected propargylglycine is described by application of our technology for the synthesis of triazolylglycoamino acids (*1*). The ^{N}TGA building block was found to display significantly improved chemical stability with respect to the "natural" amide-linked glycoamino acid and is fully compatible with basic and acidic conditions. The incorporation of the Fmoc-

protected ^{N}TGA derivative in an *c*RGD peptide proceeded without incidence, in fact more smoothly than the amide-linked glycoamino acids, with the final yield of the substrate being comparable to the yields of the other cyclic RGD substrates. The solid-phase binding assay revealed no significant differences between the different peptides under evaluation, confirming that modification of the side chain of the cyclic RGD peptide did not affect affinity for $\alpha_v\beta_3$. The ^{125}I-labeled cyclic peptides accumulated specifically in SK-RC-52 tumors. The uptake of the cyclic RGD substrates in the tumor, lung, spleen, and intestine was $\alpha_v\beta_3$-mediated. The biodistribution studies indicated that the side chain glycosylated *c*RGD peptide ^{125}I-*c*(RGDy-^{N}TGA) showed improved pharmacologic properties compared to ^{125}I-*c*(RGDyV), with reduced liver uptake and the highest uptake in the tumor, in accordance with earlier literature reports (*14, 15*) for different glycosylated cyclic RGD peptides. Moreover, the in vitro and in vivo tests indicated that *c*(RGDy-^{N}TGA) to some extent has the same pharmacologic properties as *c*(RGDy-[*N*-1-β-gluco-Asn]), which may be interpreted as one of the first examples of the value of triazoles as amide isosteres. The ease of synthesis of the triazolylglycoamino acids, the improved stability and behavior in solid-phase peptide synthesis, and the similar pharmacologic properties are a demonstration of the potential of ^{N}TGA building blocks as isosteres of amide-linked glycoamino acids for the synthesis of pharmaceutically relevant glycopeptide mimics.

ACKNOWLEDGMENT

SenterNovem (Ministry of Economic Affairs, The Netherlands) is gratefully acknowledged for providing financial support.

Note Added after ASAP Publication: This manuscript was released ASAP on October 9, 2007 with an incorrect definition for (RGD). The correct version was posted on October 17, 2007.

LITERATURE CITED

(1) Kuijpers, B. H. M., Groothuys, S., Keereweer, A. R., Quaedflieg, P. J. L. M., Blaauw, R. H., van Delft, F. L., and Rutjes, F. P. J. T. (2004) Expedient synthesis of triazole-linked glycosyl amino acids and peptides. *Org. Lett. 6*, 3123–3126.

(2) Tornøe, C. W., Christensen, C., and Meldal, M. (2002) Peptidotriazoles on solid phase: 1,2,3-triazoles by regiospecific copper(I)-catalyzed 1,3-dipolar cycloadditions of terminal alkynes to azides. *J. Org. Chem. 67*, 3057–3064.

(3) Rostovtsev, V. V., Green, L. G., Fokin, V. V., and Sharpless, K. B. (2002) A stepwise Huisgen cycloaddition process: copper(I)-catalyzed regioselective "ligation" of azides and terminal alkynes. *Angew. Chem., Int. Ed. 41*, 2596–2599.

(4) Horne, W. S., Stout, C. D., and Ghadiri, M. R. (2003) A heterocyclic peptide nanotube. *J. Am. Chem. Soc. 125*, 9372–9376.

(5) Bock, V. D., Speijer, D., Hiemstra, H., and van Maarseveen, J. H. (2007) 1,2,3-Triazoles as peptide bond isosteres: synthesis and biological evaluation of cyclotetrapeptide mimics. *Org. Biomol. Chem. 5*, 971–975.

(6) Dondoni, A., Giovannini, P. P., and Massi, A. (2004) Assembling heterocycle-tethered C-glycosyl and alpha-amino acid residues via 1,3-dipolar cycloaddition reactions. *Org. Lett. 6*, 2929–2932.

(7) Groothuys, S., Kuijpers, B. H. M., Quaedflieg, P. J. L. M., Roelen, H. C. P. F., Wiertz, R. W., Blaauw, R. H., van Delft, F. L., and Rutjes, F. P. J. T. (2006) Chemoenzymatic synthesis of triazole-linked glycopeptides. *Synthesis* 3146–3152.

(8) Kuijpers, B. H. M., Dijkmans, G. C. T., Groothuys, S., Quaedflieg, P. J. L. M., Blaauw, R. H., van Delft, F. L., and Rutjes, F. P. J. T. (2005) Copper(I)-mediated synthesis of trisubstituted 1,2,3-triazoles. *Synlett* 3059–3062.

(9) Brik, A., Alexandratos, J., Lin, Y. C., Elder, J. H., Olson, A. J., Wlodawer, A., Goodsell, D. S., and Wong, C. H. (2005) 1,2,3-triazole as a peptide surrogate in the rapid synthesis of HIV-1 protease inhibitors. *ChemBioChem 6*, 1167–1169.

(10) Wilkinson, B. L., Bornaghi, L. F., Poulsen, S. A., and Houston, T. A. (2006) Synthetic utility of glycosyl triazoles in carbohydrate chemistry. *Tetrahedron 62*, 8115–8125.

(11) Kessler, H., Diefenbach, B., Finsinger, D., Geyer, A., Gurrath, M., Goodman, S. L., Holzemann, G., Haubner, R., Jonczyk, A., Muller, G., vonRoedern, E. G., and Wermuth, J. (1995) Design of superactive and selective integrin receptor antagonists containing the RGD sequence. *Lett. Pept. Sci. 2*, 155–160.

(12) Kantlehner, M., Finsinger, D., Meyer, J., Schaffner, P., Jonczyk, A., Diefenbach, B., Nies, B., and Kessler, H. (1999) Selective RGD-mediated adhesion of osteoblasts at surfaces of implants. *Angew. Chem., Int. Ed. 38*, 560–562.

(13) Gurrath, M., Muller, G., Kessler, H., Aumailley, M., and Timpl, R. (1992) Conformation activity studies of rationally designed potent antiadhesive RGD peptides. *Eur. J. Biochem. 210*, 911–921.

(14) Haubner, R., Wester, H. J., Burkhart, F., Senekowitsch-Schmidtke, R., Weber, W., Goodman, S. L., Kessler, H., and Schwaiger, M. (2001) Glycosylated RGD-containing peptides, tracer for tumor targeting and angiogenesis imaging with improved biokinetics. *J. Nucl. Med. 42*, 326–336.

(15) Lohof, E., Planker, E., Mang, C., Burkhart, F., Dechantsreiter, M. A., Haubner, R., Wester, H. J., Schwaiger, M., Holzemann, G., Goodman, S. L., and Kessler, H. (2000) Carbohydrate derivatives for use in drug design: cyclic α_v-selective RGD peptides. *Angew. Chem., Int. Ed. 39*, 2761–2764.

(16) Shiozaki, M., Mochizuki, T., Hanzawa, H., and Haruyama, H. (1996) Synthesis of a tetrahydropyrano[2,3-*d*]oxazole analogue of trehazolin. *Carbohydr. Res. 288*, 99–108.

(17) Ichikawa, Y., Nishiyama, T., and Isobe, M. (2001) Stereospecific synthesis of the alpha- and beta-D-glucopyranosyl ureas. *J. Org. Chem. 66*, 4200–4205.

(18) van Ameijde, J., Albada, H. B., and Liskamp, R. M. J. (2002) A convenient preparation of several N-linked glycoamino acid building blocks for efficient solid-phase synthesis of glycopeptides. *J. Chem. Soc., Perkin Trans. 1* 1042–1049.

(19) Haubner, R., Wester, H. J., Reuning, U., Senekowitsch-Schmidtke, R., Diefenbach, B., Kessler, H., Stocklin, G., and Schwaiger, M. (1999) Radiolabeled $\alpha_v\beta_3$ integrin antagonists: a new class of tracers for tumor targeting. *J. Nucl. Med. 40*, 1061–1071.

(20) Dijkgraaf, I., Kruijtzer, J. A. W., Liu, S., Soede, A. C., Oyen, W. J. G., Corstens, F. H. M., Liskamp, R. M. J., and Boerman, O. C. (2007) Improved targeting of the alpha(v)beta(3) integrin by multimerisation of RGD peptides. *Eur. J. Nucl. Med. Mol. Imaging 34*, 267–273.

(21) Dijkgraaf, I., Kruijtzer, J. A. W., Frielink, C., Corstens, F. H. M., Oyen, W. J. G., Liskamp, R. M. J., and Boerman, O. C. (2007) $\alpha_v\beta_3$ integrin-targeting of intraperitoneally growing tumors with a radiolabeled RGD peptide. *Int. J. Cancer 120*, 605–610.

(22) Zhang, X. Z., and Chen, X. Y. (2007) Preparation and characterization of Tc-99m(CO)(3)–BPy–RGD complex as $\alpha_v\beta_3$ integrin receptor-targeted imaging agent. *Appl. Radiat. Isot. 65*, 70–78.

(23) Dijkgraaf, I., Kruijtzer, J. A. W., Frielink, C., Soede, A. C., Hilbers, H. W., Oyen, W. J. G., Corstens, F. H. M., Liskamp, R. M. J., and Boerman, O. C. (2006) Synthesis and biological evaluation of potent $\alpha_v\beta_3$-integrin receptor antagonists. *Nucl. Med. Biol. 33*, 953–961.

(24) Haubner, R., Finsinger, D., and Kessler, H. (1997) Stereoisomeric peptide libraries and peptidomimetics for designing selective inhibitors of the $\alpha_v\beta_3$ integrin for a new cancer therapy. *Angew. Chem., Int. Ed. Engl. 36*, 1375–1389.

(25) Haubner, R., Gratias, R., Diefenbach, B., Goodman, S. L., Jonczyk, A., and Kessler, H. (1996) Structural and functional aspects of RGD-containing cyclic pentapeptides as highly potent and selective integrin $\alpha_v\beta_3$ antagonists. *J. Am. Chem. Soc. 118*, 7461–7472.

(26) Sinclair, A. M., and Elliott, S. (2005) Glycoengineering: the effect of glycosylation on the properties of therapeutic proteins. *J. Pharm. Sci. 94*, 1626–1635.

(27) Janssen, M. L., Oyen, W. J., Dijkgraaf, I., Massuger, L. F., Frielink, C., Edwards, D. S., Rajopadhye, M., Boonstra, H., Corstens, F. H., and Boerman, O. C. (2002) Tumor targeting with radiolabeled $\alpha_v\beta_3$ integrin binding peptides in a nude mouse model. *Cancer Res. 62*, 6146–6151.

(28) Max, R., Gerritsen, R. R. C. M., Nooijen, P. T. G. A., Goodman, S. L., Sutter, A., Keilholz, U., Ruiter, D. J., and DeWaal, R. M. W. (1997) Immunohistochemical analysis of integrin $\alpha_v\beta_3$ expression on tumor-associated vessels of human carcinomas. *Int. J. Cancer 71*, 320–324.

BC700154U

Fabrication of Langmuir–Blodgett Film of a Fullerene Derivative with a Cyclic Peptide as an Anchor

Shigekatsu Fujii, Tomoyuki Morita, and Shunsaku Kimura*

Department of Material Chemistry, Graduate School of Engineering, Kyoto University, Kyoto-Daigaku-Katsura, Nishikyo-ku, Kyoto 615-8510, Japan. Received May 2, 2007; Revised Manuscript Received August 21, 2007

A novel cyclic octapeptide carrying a fullerene unit and poly(ethylene glycol) at the side chain (cyclo8-C_{60} + PEG) was synthesized, and its monolayer formation at the air/water interface and on a substrate was studied. Surface pressure–area per molecule isotherms indicated that cyclo8-C_{60} + PEG formed a stable monolayer at the air/water interface. The cyclo8-C_{60} + PEG monolayers prepared from various spreading volumes (i.e., from various initial areas per molecule) overlapped nicely on a single curve, suggesting that the molecules were uniformly dispersed on the surface without aggregation of the fullerene units. The uniform dispersibility is due to the scaffold effect of the cyclic peptide unit to keep the fullerene units away from each other. The formed monolayer could be quantitatively transferred onto a solid substrate. UV–vis absorption spectroscopy of the Langmuir–Blodgett (LB) monolayer showed that the electronic structure of the fullerene unit was not affected by the formation of the monolayer. Cyclic voltammetry of the LB monolayer in an aqueous solution containing redox species indicated that the LB monolayer was densely packed. Furthermore, reversible redox peaks attributed to the one-electron reduction of the fullerene unit were observed, showing that the redox property of the fullerene unit was also retained in the monolayer. It is thus concluded that the cyclic peptide is a good candidate as a scaffold for stable monolayer formation at the air/water interface and for intact immobilization of the fullerene moiety onto a substrate.

INTRODUCTION

Fullerenes, C_{60} in particular, and their derivatives have attracted much attention because of their special chemical and physical properties (*1–9*). To utilize their unique properties in nanoscale systems, preparation of well-organized thin films of fullerenes on the surface is the first step. So far, monolayers and multilayers have been prepared on various surfaces and their properties have been investigated (*3, 10–15*). The Langmuir–Blodgett (LB) technique has been most widely used as a method for preparation of such ordered thin films. With this technique, a monolayer of organic compounds is first prepared at the air/water interface and the formed monolayer is then transferred onto a solid substrate. However, it is difficult to prepare a stable and uniform monolayer from pristine fullerenes (*16–19*). First, quite low solubility of fullerenes in organic solvents is troublesome in preparation of solutions to be spread on the water surface. Second, even if one finds a good solvent, the fullerene easily self-aggregates at the air/water interface, making the monolayer very stiff and fragile. It is thus hard to transfer the monolayer quantitatively onto a solid substrate. To overcome these problems, chemical modifications of fullerenes are needed. A wide variety of fullerene derivatives have been synthesized by modification with various chemical species such as crown ethers (*12, 20–22*), polyhydroxylates (*23*), oligopeptides (*24, 25*), poly(ethylene glycol)s (*26*), hydrophilic porphyrins (*27, 28*), and so on (*13*). Polymers having fullerenes at the main or side chains (*29, 30*) and dendrimers carrying fullerenes as the dendrons (*31–33*) have been reported as well. In general, attachment of a highly hydrophilic moiety to fullerenes can help the molecule dissolve into solvents and disperse on the surface. Physical prevention of fullerenes from aggregation is also effective. For example, encapsulation of fullerenes by inclusion hosts (e.g., calixarenes (*34–36*) or cyclodextrins (*37, 38*)) has been studied.

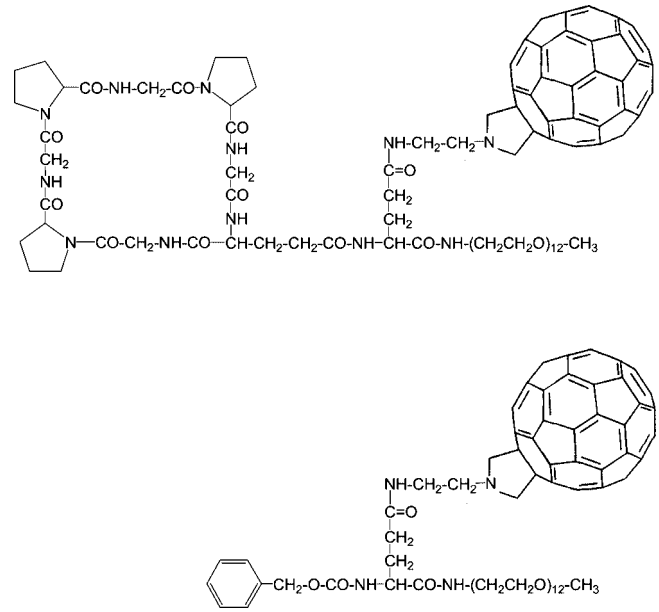


Figure 1. Chemical structures of cyclo8-C_{60}+PEG (top) and C_{60}+PEG (bottom).

In the present study, we synthesized a novel cyclic peptide carrying a fullerene (C_{60}) unit and poly(ethylene glycol) (PEG) chain at the side chain (cyclo8-C_{60} + PEG; Figure 1) for preparation of well-organized monolayers at the air/water interface and on a solid substrate. The PEG chain (the average degree of polymerization is 12) will increase the solubility of the compound to help the C_{60} units disperse in the preparation solution as well as on the water surface. A similar cyclic octapeptide has been shown to have a rigid and flat conformation

* To whom correspondence should be addressed. E-mail: shun@scl.kyoto-u.ac.jp. Phone: (+81)-75-383-2400. Fax: (+81)-75-383-2401.

10.1021/bc700159c CCC: $37.00 © 2007 American Chemical Society
Published on Web 10/18/2007

and to form a stable monolayer at the air/water interface with horizontal orientation to the surface (*39*). Since the molecular area of the cyclic peptide moiety is larger than that of the C_{60} unit, it is expected that aggregation among the C_{60} units is physically suppressed even when the monolayer is compressed. A compound carrying the same fullerene unit and the PEG chain but without the cyclic peptide scaffold (C_{60} + PEG, Figure 1) was also synthesized and used as a control. The formation of the monolayer at the air/water interface was studied by the surface pressure–area per molecule (π–*A*) isotherm analysis. The monolayer was then transferred onto a solid substrate by the vertical dipping method. The electronic property of the C_{60} unit in the LB monolayer was examined by UV–vis absorption spectroscopy, and the packing of the monolayer and the redox property of the C_{60} unit were studied by cyclic voltammetry.

EXPERIMENTAL PROCEDURES

Materials. cyclo8-C_{60} + PEG and C_{60} + PEG, were synthesized by the liquid-phase synthesis. The details in the synthesis are available in Supporting Information.

Monolayer Measurements. A homemade Langmuir film balance with a trough area of 100 mm × 189 mm was used to prepare a monolayer at the air/water interface and to measure the isotherm of the monolayer under linear compression of the molecules spread on the water surface. The subphase temperature was set to 25.0 ± 1.0 °C. Ultrapure water processed by a Millipore Milli-Q system (resistivity of >18 MΩ cm^{-1}) was used as the water subphase. A chloroform solution of the fullerene derivatives was prepared (0.47 mM for cyclo8-C_{60} + PEG and 0.96 mM for C_{60} + PEG), and the solution was spread by a microsyringe onto the water surface. The solvent was allowed to evaporate for 15 min prior to compression, and then the molecules spread on the surface were compressed at a rate of 10 cm^2/min. The monolayer formation was performed at room temperature. The formed monolayer was then transferred onto a solid substrate by the vertical dipping method at a rate of 10 mm/min. Quartz and gold were used as the substrates for UV–vis absorption spectroscopy and cyclic voltammetry, respectively. The gold substrate was prepared by vacuum deposition with chromium (300 Å) as the underlying adhesive layer and gold (2000 Å) on a glass substrate. The glass substrate was cleaned with sulfonic acid and rinsed thoroughly with distilled water and methanol prior to the deposition.

UV–Visible Absorption Spectroscopy. UV–visible absorption spectra were recorded on a Shimadzu UV-2450PC spectrometer at room temperature. The absorption spectrum of the LB monolayer on quartz was measured with a special attachment to hold substrate samples.

Cyclic Voltammetry. Cyclic voltammetry was carried out on a BAS model 604 voltammetric analyzer in a three-electrode system with the gold substrate as the working electrode, Ag/AgCl in 3 M NaCl as the reference electrode, and a platinum wire as the auxiliary electrode. Ultrapure water was used to prepare aqueous solutions for the measurements. All the solutions were deaerated by passing N_2 gas for 10 min prior to the measurements. All the electric potentials reported here were measured with respect to the reference electrode. The experiment to examine the monolayer packing was performed in a 1 mM $K_4[Fe(CN)_6]$ and 1 M KCl aqueous solution at a scan rate of 0.05 V/s. On the other hand, the redox property of the C_{60} unit was investigated in a 1 M *n*-Bu_4NCl aqueous solution at a scan rate of 0.1 V/s. All the measurements were performed at room temperature.

Computational Modeling of Cyclic Peptide Scaffold. The geometry of a model cyclic peptide, cyclo(Pro-Gly)$_4$, was optimized to estimate the molecular area of the cyclic peptide scaffold. The initial geometry was generated by a Fujitsu CAChe WorkSystem software (version 6.1.1). The dihedral angles of the peptide backbone were set $\omega = 180°$, $\varphi = -98°$, and $\psi = 90°$ for the Pro residues while the dihedral angles were set to $\omega = 180°$, $\varphi = -175°$, and $\psi = 178°$ for the Gly residue according to the literature (*40*). The geometry was then optimized by the Molecular Mechanics 2 (MM2) method and the semiempirical Austin Model 1 (AM1) method in the MOPAC 2002 package in the same program.

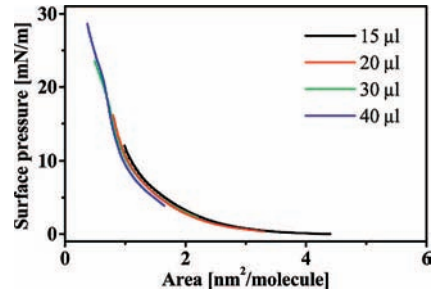


Figure 2. π–*A* isotherms of the cyclo8-C_{60} + PEG monolayer prepared with different spreading volumes.

RESULTS AND DISCUSSION

Monolayer at the Air/Water Interface. The cyclo8-C_{60} + PEG molecule is soluble in many organic solvents because of the modification with the cyclic peptide and the PEG chain. In this study, a chloroform solution of cyclo8-C_{60} + PEG was used for monolayer preparation. The π–*A* isotherms of cyclo8-C_{60} + PEG recorded with various spreading volumes of the solution are shown in Figure 2. With 15 μL of spreading volume (black line), surface pressure was observed at the starting point (~4.5 nm^2/molecule) and increased gradually with compression. Such an expanded isotherm is a typical behavior for monolayers carrying long PEG chains, in which intermolecular interactions among the PEG chains work over a large area (*41–43*). However, since the PEG chain of our compound is relatively short (degree of polymerization is ~12), the behavior at large areas (4–2 nm^2/molecule) might contain the contribution from the interaction among the cyclic peptide moieties. Since the compression ratio is limited to 1/4.5 in our trough, information at smaller areas could not be obtained with this spreading volume. To obtain the information on the C_{60} unit or the cyclic peptide moiety, the spreading volume was increased (Figure 2, red, green, and blue lines). Before the compression, surface pressure more than zero was observed depending on the spreading volume. Despite the separated measurements, the four isotherms overlapped nicely onto one curve; therefore, the behavior of the compound in a wide range of areas can be discussed. This result also suggests that the cyclo8-C_{60} + PEG molecules are uniformly dispersed and the C_{60} units do not aggregate even at small areas. This point will be discussed later. The monolayer did not collapse up to ~30 mN/m, indicating formation of a stable monolayer. The limiting molecular area was estimated to be 1.1 nm^2 by extrapolation of the linear region of the isotherm to the surface pressure of zero. This molecular area is much larger than that of the C_{60} unit (~0.7 nm^2/molecule assuming hexagonal packing of a 0.8 nm diameter sphere). Thus, it should be ascribed to the area of the cyclic peptide moiety. Indeed, a similar cyclic peptide has been reported to form a stable monolayer at the air/water interface. In the case of cyclo[Tyr(X)-Gly-(Pro-Gly)$_3$] (X represents a DR-1 derivative) the molecular area was about 1.0 nm^2 from the π–*A* isotherm (*39*). On the other hand, cyclo(Pro-Gly)$_4$ has a flat square form with a 1.2 nm side estimated by computational geometry optimization. The smaller molecular area of cyclo8-C_{60} + PEG compared with that of cyclo(Pro-Gly)$_4$ suggests that one replacement of the Pro residue in cyclo(Pro-Gly)$_4$ with a Glu

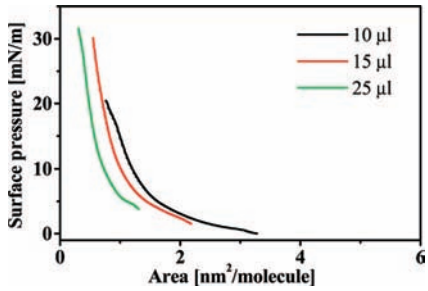


Figure 3. π–A isotherms of the C_{60} + PEG monolayer prepared with different spreading volumes.

or a Tyr derivative should reduce the molecular area because of the reduction of one flat pyrrolidine ring of the Pro residue from the total molecular area. The fact that the limiting molecular area is determined by the cyclic peptide moiety can be interpreted as follows. At large areas, it is unknown whether the C_{60} unit and the cyclic peptide moiety get together or are separated. However, upon compression of the monolayer, the fullerene unit should be physically forced to get on the cyclic peptide moiety because its molecular area is smaller than that of the cyclic peptide moiety with horizontal orientation and the C_{60} unit is hydrophobic. In other words, the cyclic peptide moiety acts as a scaffold to prevent the C_{60} units from aggregation, leading to the formation of a stable monolayer.

To examine the effect of the cyclic peptide moiety on monolayer formation, the control compound without the peptide moiety (C_{60} + PEG) was similarly studied. The isotherms of C_{60} + PEG showed an expanded feature similar to that of cyclo8-C_{60} + PEG (Figure 3). Increase of the surface pressure upon compression is observed even at large areas that can be attributed to the interaction among the PEG chains. However, the dependence on the spreading volume was different. The isotherm is shifted toward the smaller area as the spreading volume is increased. Therefore, the limiting molecular area of C_{60} + PEG could not be obtained. Such behavior is typical for a monolayer composed of molecules with a strong tendency to aggregate (*44*). This result clearly shows that the aggregation among the C_{60} units cannot be suppressed by a PEG chain alone. In other words, the cyclic peptide moiety in the cyclo8-C_{60} + PEG molecule should play an important role as a scaffold to prevent the C_{60} units from the aggregation in a condensed state.

LB Monolayer on a Substrate. The cyclo8-C_{60} + PEG monolayer was transferred onto a solid substrate by the vertical dipping method with the surface pressure maintained at 10 mN/m, resulting in preparation of the LB monolayer on the substrate. Two types of substrates, a quartz substrate and a gold substrate, were used for UV–vis absorption spectroscopy and cyclic voltammety, respectively. The transfer ratio was close to unity at upstroke but nearly zero at downstroke for both substrates. Figure 4 shows the absorption spectra of the cyclo8-C_{60} + PEG LB monolayer and cyclo8-C_{60} + PEG in chloroform. The absorption spectrum in solution shows a typical pattern for fullerene derivatives with four characteristic absorptions at 254, 319, 429, and 699 nm (*45*, *46*). The cyclo8-C_{60} + PEG LB monolayer shows similar absorptions at 252 and 322 nm, but the absorption bands are broadened compared to that in solution. This broadening infers that the C_{60} units electronically interact with each other in a condensed state in the monolayer (*47*). However, the interaction should not be considerable because the peak wavelengths do not shift much. Weak absorption bands at 429 and 699 nm could not be identified because of the lower signal to noise ratio in the monolayer spectrum. It is thus concluded that the electronic structure of the C_{60} unit is not significantly affected upon monolayer formation.

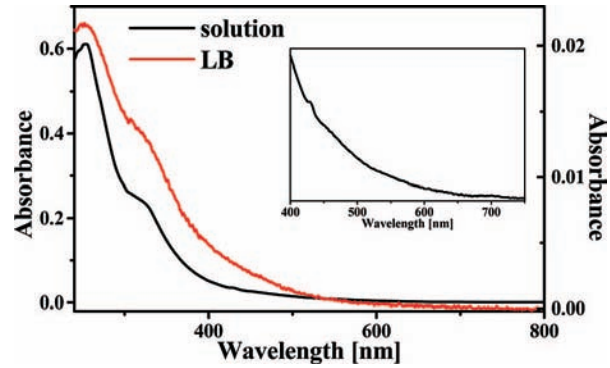


Figure 4. UV–vis absorption spectra of cyclo8-C_{60} + PEG in solution (black) and on a substrate (red). The absorbance of the spectrum in solution is referred to the left vertical axis while that of the LB monolayer to the right axis. The inset shows the magnified view of the spectrum in solution at a wavelength longer than 400 nm.

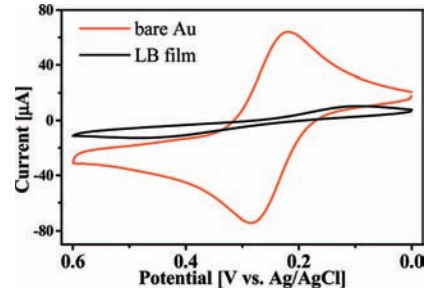


Figure 5. Cyclic voltammograms of a bare gold substrate (red) and the cyclo8-C_{60} + PEG LB monolayer-modified substrate (black) in 1 mM $K_4[Fe(CN)_6]$ and 1 M KCl aqueous solution at a scan rate of 0.05 V/s.

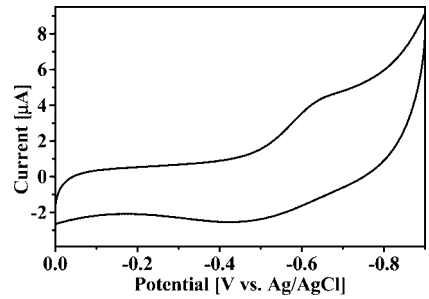


Figure 6. Cyclic voltammogram of the cyclo8-C_{60} + PEG LB monolayer in a 1 M *n*-Bu_4NCl aqueous solution at a scan rate of 0.1 V/s.

To investigate the packing of the cyclo8-C_{60} + PEG LB monolayer, cyclic voltammetry in an aqueous solution containing redox species was carried out using the LB monolayer prepared on a gold substrate. The cyclic voltammograms of a bare gold substrate and the LB monolayer-modified gold substrate in a 1 mM $K_4[Fe(CN)_6]$ solution are shown in Figure 5. Redox peaks of ferrocyanide/ferricyanide were clearly observed in the bare substrate. The peak separation was ~60 mV, showing fast electron transfer at the surface. In contrast, in the cyclo8-C_{60} + PEG LB monolayer, the current of the ferrocyanide/ferricyanide redox reaction was significantly reduced. This result shows that the cyclo8-C_{60} + PEG LB monolayer is well-packed and does not allow the penetration of the redox species to reach the gold surface.

To examine the redox property of the C_{60} unit in the monolayer, cyclic voltammetry in a 1 M *n*-Bu_4NCl aqueous solution was performed (Figure 6). The cyclo8-C_{60} + PEG LB monolayer exhibited reversible redox peaks of one-electron

reduction of the C_{60} unit. The formal potential was −0.53 V (vs Ag/AgCl). The peak separation was relatively large (204 mV), suggesting that the electron transfer between the C_{60} unit and gold is slow. This slow electron transfer can be ascribed to the poor physical contact between the monolayer and gold. Additional reduction peaks typical for C_{60} derivatives were not observed. The surface coverage of the cyclo8-C_{60} + PEG monolayer was estimated to be 0.58×10^{-10} mol cm^{-2} by integration of the area of the reduction peak. This surface coverage is comparable to that of dense C_{60} self-assembled monolayers prepared by covalent linking of molecules to metal ($(0.83–1.6) \times 10^{-10}$ mol cm^{-2}) (*48–50*). It is thus concluded that with modification of C_{60} with a cyclic peptide and PEG, a monolayer with relatively high density of the C_{60} unit can be prepared by the LB method on a surface retaining the C_{60} redox property.

CONCLUSION

In this work, a cyclic peptide carrying a C_{60} unit and a hydrophilic PEG chain at the side chain was synthesized, and its monolayer formation at the air/water interface and on a solid substrate was studied. The molecule formed a stable and uniform monolayer at the air/water interface because of a scaffold effect of the cyclic peptide moiety to prevent the C_{60} units from aggregation. The monolayer at the air/water interface could be successfully transferred onto a solid substrate. Absorption spectroscopy and cyclic voltammetry demonstrated that the electronic and redox properties of the C_{60} unit are preserved even in a condensed state in the monolayer. This method to prepare ordered fullerene thin films will be useful in the development of nanoscale electronics and photonics devices.

ACKNOWLEDGMENT

This work was supported by Grant-in-Aids for Exploratory Research (Grant 17655098) and for Scientific Research B (Grant 18350063) from Japan Society for the Promotion of Science and by the 21st century COE program, COE for a United Approach to New Materials Science, from the Ministry of Education, Culture, Sports, Science, and Technology, Japan.

Supporting Information Available: Details of the synthesis of the compounds. This material is available free of charge via the Internet at http://pubs.acs.org.

LITERATURE CITED

(1) Diederich, F., and Gomez-Lopez, M. (1999) Supramolecular fullerene chemistry. *Chem. Soc. Rev. 28*, 263–277.
(2) Bonifazi, D., Enger, O., and Diederich, F. (2007) Supramolecular [60]fullerene chemistry on surfaces. *Chem. Soc. Rev. 36*, 390–414.
(3) Mirkin, C. A., and Caldwell, W. B. (1996) Thin film, fullerene-based materials. *Tetrahedron 52*, 5113–5130.
(4) Jenekhe, S. A., and Chen, X. L. (1998) Self-assembled aggregates of rod-coil block copolymers and their solubilization and encapsulation of fullerenes. *Science 279*, 1903–1907.
(5) Zhou, S. Q., Burger, C., Chu, B., Sawamura, M., Nagahama, N., Toganoh, M., Hackler, U. E., Isobe, H., and Nakamura, E. (2001) Spherical bilayer vesicles of fullerene-based surfactants in water: a laser light scattering study. *Science 291*, 1944–1947.
(6) Eckert, J. F., Nicoud, J. F., Nierengarten, J. F., Liu, S. G., Echegoyen, L., Barigelletti, F., Armaroli, N., Ouali, L., Krasnikov, V., and Hadziioannou, G. (2000) Fullerene–oligophenylenevinylene hybrids: synthesis, electronic properties, and incorporation in photovoltaic devices. *J. Am. Chem. Soc. 122*, 7467–7479.
(7) Diederich, F., and Kessinger, R. (1999) Templated regioselective and stereoselective synthesis in fullerene chemistry. *Acc. Chem. Res. 32*, 537–545.
(8) Prato, M. (1997) Fullerene chemistry for materials science applications. *J. Mater. Chem. 7*, 1097–1109.
(9) Bonifazi, D., Kiebele, A., Stohr, M., Cheng, F., Jung, T., Diederich, F., and Spillmann, H. (2007) Supramolecular nanostructuring of silver surfaces via self-assembly of [60]fullerene and phorphyrin modules. *Adv. Funct. Mater. 17*, 1051–1062.
(10) Imahori, H., and Sakata, Y. (1999) Fullerenes as novel acceptors in photosynthetic electron transfer. *Eur. J. Org. Chem.* 2445–2457.
(11) Tsukruk, V. V., Lander, L. M., and Brittain, W. J. (1994) Atomic force microscopy of C60 tethered to a self-assembled monolayer. *Langmuir 10*, 996–999.
(12) Arias, F., Godinez, L. A., Wilson, S. R., Kaifer, A. E., and Echegoyen, L. (1996) Interfacial hydrogen bonding. Self-assembly of a monolayer of a fullerene-crown ether derivative on gold surfaces derivatized with an ammonium-terminated alkanethiolate. *J. Am. Chem. Soc. 118*, 6086–6087.
(13) Cardullo, F., Diederich, F., Echegoyen, L., Habicher, T., Jayaraman, N., Leblanc, R. M., Stoddart, J. F., and Wang, S. P. (1998) Stable Langmuir and Langmuir–Blodgett films of fullerene–glycodendron conjugates. *Langmuir 14*, 1955–1959.
(14) Nakanishi, T., Morita, M., Murakami, H., Sagara, T., and Nakashima, N. (2002) Structure and electrochemistry of self-organized fullerene–lipid bilayer films. *Chem.—Eur. J. 8*, 1641–1648.
(15) Nakanishi, T., Ariga, K., Morita, M., Kozai, H., Taniguchi, N., Murakami, H., Sagara, T., and Nakashima, N. (2006) Electrochemistry of fullerene C_{60} embedded in Langmuir–Blodgett films of artificial lipids on electrodes. *Colloids Surf., A 284*, 607–612.
(16) Jehoulet, C., Obeng, Y. S., Kim, Y. T., Zhou, F. M., and Bard, A. J. (1992) Electrochemistry and Langmuir trough studies of fullerene C60 and C70 films. *J. Am. Chem. Soc. 114*, 4237–4247.
(17) Nakamura, T., Tachibana, H., Yumura, M., Matsumoto, M., Azumi, R., Tanaka, M., and Kawabata, Y. (1992) Formation of Langmuir–Blodgett films of a fullerene. *Langmuir 8*, 4–6.
(18) Maliszewskyj, N. C., Heiney, P. A., Jones, D. R., Strongin, R. M., Cichy, M. A., and Smith, A. B. (1993) Langmuir films of C_{60}, $C_{60}O$, and $C_{61}H_2$. *Langmuir 9*, 1439–1441.
(19) Chlistunoff, J., Cliffel, D., and Bard, A. J. (1995) Electrochemistry of fullerene films. *Thin Solid Films 257*, 166–184.
(20) Diederich, F., Jonas, U., Gramlich, V., Herrmann, A., Ringsdorf, H., and Thilgen, C. (1993) Synthesis of a fullerene derivative of benzo[18]crown-6 by Diels–Alder reaction: complexation ability, amphiphilic properties, and X-ray crystal structure of a dimethoxy-1,9 (methano[1,2]benzenomethano)fullerene[60] benzene clathrate. *Helv. Chim. Acta 76*, 2445–2453.
(21) Wang, S. P., Leblanc, R. M., Arias, F., and Echegoyen, L. (1997) Surface and optical properties of Langmuir and LB films of a crown-ether C_{60} derivative. *Langmuir 13*, 1672–1676.
(22) Leigh, D. A., Moody, A. E., Wade, F. A., King, T. A., West, D., and Bahra, G. S. (1995) Second harmonic generation from Langmuir–Blodgett films of fullerene–aza-crown ethers and their potassium ion complexes. *Langmuir 11*, 2334–2336.
(23) Liu, W. J., Jeng, U., Lin, T. L., Lai, S. H., Shih, M. C., Tsao, C. S., Wang, L. Y., Chiang, L. Y., and Sung, L. P. (2000) Adsorption of dodecahydroxylated-fullerene monolayers at the air–water interface. *Physica B 283*, 49–52.
(24) Tundo, P., Perosa, A., Selva, M., Valli, L., and Giannini, C. (2001) Peptide anchored Langmuir–Blodgett films of a fullerene amphiphile. *Colloids Surf., A 190*, 295–303.
(25) Prato, M., Bianco, A., Maggini, M., Scorrano, G., Toniolo, C., and Wudl, F. (1993) Synthesis and characterization of the first fullerene–peptide. *J. Org. Chem. 58*, 5578–5580.
(26) Nierengarten, J. F., Eckert, J. F., Rio, Y., Carreon, M. D., Gallani, J. L., and Guillon, D. (2001) Amphiphilic diblock dendrimers: synthesis and incorporation in Langmuir and Langmuir–Blodgett films. *J. Am. Chem. Soc. 123*, 9743–9748.
(27) Marczak, R., Noworyta, K., Nowakowski, R., Kutner, W., Desbat, B., Araki, Y., Ito, O., Gadde, S., Zandler, M. E., and

D'Souza, F. (2007) Self assembling of porphyrin–fullerene dyads in the Langmuir and Langmuir–Blodgett films: formation as well as spectral, electrochemical and vectorial electron transfer studies. *J. Nanosci. Nanotechnol. 7*, 1455–1471.

(28) Marczak, R., Sgobba, V., Kutner, W., Gadde, S., D'Souza, F., and Guldi, D. M. (2007) Langmuir–Blodgett films of a cationic zinc porphyrin–imidazole-functionalized fullerene dyad: formation and photoelectrochemical studies. *Langmuir 23*, 1917–1923.

(29) Shi, S., Khemani, K. C., Li, Q. C., and Wudl, F. (1992) A polyester and polyurethane of diphenyl C_{61}: retention of fulleroid properties in a polymer. *J. Am. Chem. Soc. 114*, 10656–10657.

(30) Bunker, C. E., Lawson, G. E., and Sun, Y. P. (1995) Fullerene–styrene random copolymers. Novel optical properties. *Macromolecules 28*, 3744–3746.

(31) Wooley, K. L., Hawker, C. J., Frechet, J. M. J., Wudl, F., Srdanov, G., Shi, S., Li, C., and Kao, M. (1993) Fullerene-bound dendrimers: soluble, isolated carbon clusters. *J. Am. Chem. Soc. 115*, 9836–9837.

(32) Brettreich, M., and Hirsch, A. (1998) A highly water-soluble dendro[60]fullerene. *Tetrahedron Lett. 39*, 2731–2734.

(33) Nierengarten, J. F. (2000) Fullerodendrimers: a new class of compounds for supramolecular chemistry and materials science applications. *Chem.—Eur. J. 6*, 3667–3670.

(34) Atwood, J. L., Koutsantonis, G. A., and Raston, C. L. (1994) Purification of C60 and C70 by selective complexation with calixarenes. *Nature 368*, 229–231.

(35) Williams, R. M., Zwier, J. M., Verhoeven, J. W., Nachtegaal, G. H., and Kentgens, A. P. M. (1994) Interactions of fullerenes and calixarenes in the solid state studied with ^{13}C CP-MAS. *J. Am. Chem. Soc. 116*, 6965–6966.

(36) Haino, T., Yanase, M., and Fukazawa, Y. (1998) Fullerenes enclosed in bridged calix[5]arenes. *Angew. Chem., Int. Ed. 37*, 997–998.

(37) Andersson, T., Nilsson, K., Sundahl, M., Westman, G., and Wennerstrom, O. (1992) C-60 embedded in γ-cyclodextrin. A water-soluble fullerene. *J. Chem. Soc., Chem. Commun.* 604–606.

(38) Andersson, T., Westman, G., Wennerstrom, O., and Sundahl, M. (1994) NMR and UV–VIS investigation of water-soluble fullerene-60–γ-cyclodextrin complex. *J. Chem. Soc., Perkin Trans. 2* 1097–1101.

(39) Fujii, S., Morita, T., Umemura, J., and Kimura, S. (2006) Cyclic peptides as scaffold for oriented functional groups on surface. *Thin Solid Films 503*, 224–229.

(40) Madison, V., Deber, C. M., and Blout, E. R. (1977) Cyclic peptides. 17. Metal and amino acid complexes of cyclo(Pro-Gly)$_4$ and analogues studied by nuclear magnetic resonance and circular dichroism. *J. Am. Chem. Soc. 99*, 4788–4798.

(41) Baekmark, T. R., Elender, G., Lasic, D. D., and Sackmann, E. (1995) Conformational transitions of mixed monolayers of phospholipids and poly(ethylene oxide) lipopolymers and interaction forces with solid-surfaces. *Langmuir 11*, 3975–3987.

(42) da Silva, A. M. G., Filipe, E. J. M., d'Oliveira, J. M. R., and Martinho, J. M. G. (1996) Interfacial behavior of poly(styrene)–poly(ethylene oxide) diblock copolymer monolayers at the air–water interface. Hydrophilic block chain length and temperature influence. *Langmuir 12*, 6547–6553.

(43) Naumann, C. A., Brooks, C. F., Fuller, G. G., Knoll, W., and Frank, C. W. (1999) Viscoelastic properties of lipopolymers at the air–water interface: a combined interfacial stress rheometer and film balance study. *Langmuir 15*, 7752–7761.

(44) Marczak, R., Hoang, V. T., Noworyta, K., Zandler, M. E., Kutner, W., and D'Souza, F. (2002) Molecular recognition of adenine, adenosine and ATP at the air–water interface by a uracil appended fullerene. *J. Mater. Chem. 12*, 2123–2129.

(45) Maggini, M., Scorrano, G., and Prato, M. (1993) Addition of azomethine ylides to C-60. Synthesis, characterization, and functionalization of fullerene pyrrolidines. *J. Am. Chem. Soc. 115*, 9798–9799.

(46) An, Y. Z., Anderson, J. L., and Rubin, Y. (1993) Synthesis of α-amino-acid derivatives of C-60 from 1,9-(4-hydroxycyclohexano)-buckminsterfullerene. *J. Org. Chem. 58*, 4799–4801.

(47) Gao, Y., Tang, Z. X., Watkins, E., Majewski, J., and Wang, H. L. (2005) Synthesis and characterization of amphiphilic fullerenes and their Langmuir–Blodgett films. *Langmuir 21*, 1416–1423.

(48) Imahori, H., Azuma, T., Ajavakom, A., Norieda, H., Yamada, H., and Sakata, Y. (1999) An investigation of photocurrent generation by gold electrodes modified with self-assembled monolayers of C-60. *J. Phys. Chem. B 103*, 7233–7237.

(49) Gu, T., Whitesell, J. K., and Fox, M. A. (2004) Electrochemical charging of a fullerene-functionalized self-assembled monolayer on Au(111). *J. Org. Chem. 69*, 4075–4080.

(50) Hoang, V. T., Rogers, L. M., and D'Souza, F. (2002) Synthesis and formation of monolayer self-assembly of thiol appended fullerenes and fullerene–ferrocene dyads on gold electrode. *Electrochem. Commun. 4*, 50–53.

BC700159C

Studies of Luminescent Conjugated Polythiophene Derivatives: Enhanced Spectral Discrimination of Protein Conformational States

Andreas Åslund,[†,§] Anna Herland,[‡,§] Per Hammarström,[†] K. Peter R. Nilsson,[†,||] Bengt-Harald Jonsson,[†] Olle Inganäs,[‡] and Peter Konradsson*[,†]

Chemistry, IFM, Linköping University, SE-581 83 Linköping, Sweden, and Biomolecular and Organic Electronics, IFM, Linköping University, SE-581 83 Linköping, Sweden. Received May 18, 2007; Revised Manuscript Received July 20, 2007

Improved probes for amyloid fibril formation are advantageous for the early detection and better understanding of this disease-associated process. Here, we report a comparative study of eight luminescent conjugated polythiophene derivates (LCPs) and their discrimination of a protein (insulin) in the native or amyloid-like fibrillar state. For two of the LCPs, the synthesis is reported. Compared to their monomer-based analogues, trimer-based LCPs showed significantly better optical signal specificity for amyloid-like fibrils, seen from increased quantum yield and spectral shift. The trimer-based LCPs alone were highly quenched and showed little interaction with native insulin, as seen from analytical ultracentrifugation and insignificant spectral differences from the trimer-based LCP in buffered and native protein solution. Hence, the trimer-based LCPs showed enhanced discrimination between the amyloid-like fibrillar state and the corresponding native protein.

INTRODUCTION

Several human disorders, including Alzheimer's disease, are known to be associated with protein misfolding events and amyloidogenesis. Both *in vivo* deposits and *in vitro* formed amyloid fibrils have a β-sheet-rich fibrillar structure. Although no structural or sequential homology of amyloidogenic proteins is present, the amyloid fibril structure appears generic, showing linear filaments with a diameter of approximately 10 nm (*1*).

For early detection and better understanding of the processes involved in amyloid fibril formation, a sensitive method is fundamental. Traditionally, Congo Red (CR) provides the most standardized way of staining amyloid plaques, showing green birefringence in cross-polarized light (*2*). The binding of CR to amyloid is considered specific but requires good control and experience to be reliable (*3*). The specificity of CR binding to *in vitro* amyloid fibrils has, however, been questioned (*4*), where it was demonstrated that Congo red binds to native, partially folded conformations and amyloid fibrils of several proteins. This finding indicates that CR must be used with caution as a diagnostic test for the presence of amyloid fibrils *in vitro*. Thioflavin T (ThT) and the analogue thioflavin S (ThS) are other small molecules well established for use in analysis of aggregated amyloid proteins formed *in vitro*. The binding of ThT to amyloid is somewhat weaker than CR binding, but upon binding, the dye increases its fluorescence more than 1000-fold (*5*). ThT is a bluegreen-emissive dye, causing interference with autofluorescence from tissue, which is a recurring problem. On the basis of the affinity of CR and ThT, several compounds have been synthesized to increase affinity and contrast, and remove metabolic and toxic liabilities for *in vivo* applications as well as increasing blood- brain barrier permeability (*6–9*). A more novel approach to designing an *in vivo* amyloid imaging probe is the synthesis of a dithienylethenyl compound, on the basis of the empirical experiences of dyes with affinity for amyloid structures performed by Nesterov et al. (*8*).

Luminescent, conjugated polymers (LCPs) have been demonstrated as conformational sensitive optical probes to detect conformal changes in synthetic peptides (*10, 11*) and calcium induced conformal changes in calmodulin (*12*). More recently, we have shown that LCPs can be used to monitor amyloid fibril formation *in vitro* (*13, 14*), for the histological labeling of amyloid deposits in *ex vivo* tissue samples (*15*), and conformal mapping of amyloid deposits (*16*). The electronic structure and thereby the optical processes of LCPs is directly correlated to the conformation of the polymer chains and their organization. If the polymer is governed by a biomolecule capable of folding into several possible conformational states or quaternary organizations, then the optical properties of the polymer will be a spectroscopic signature of the state of the biomolecule.

The chain length of π-conjugated polymers is directly correlated with physical properties such as optical absorption maximum or oxidation potential (*17–20*). Regioregular oligomers of well-defined chain length have been used as model compounds to facilitate the interpretation of physical properties in photonic and electronic applications (*18, 20*). Likewise, in biosensing, a defined conjugated oligomer can give a more specific interaction with the biomolecule, and the correlation between this interaction and the optical properties of the conjugated oligomer would be more easily interpreted.

We have reported the use of a number of polythiophenes with diverse side chain funtionalization for biomolecular interactions (*10, 12–16, 21*), and more recently, we have synthesized trimer-based analogues of these. In this work, we demonstrate two examples of the synthesis of thiophene-based LCPs, PTT, and tPTAA (see Figure 1 and Scheme 1). These two LCPs complete a series of eight, which we have used in this study for structure/functionality evaluation of the properties influencing the interaction between LCPs and amyloid-like fibrils. The LCPs were designed to have different hydrophobic/hydrophilic properties as well as alterations in steric congestion. Interaction with native and fibrillar insulin in solution was studied and evaluated

* Phone: +46- (0)13-28 17 28. Fax: +46- (0)13- 28 13 99. E-mail: petko@ifm.liu.se.

[†] Chemistry.

[‡] Biomolecular and Organic Electronics.

[§] These authors contributed equally to this work.

[||] Current address: UniversitätsSpital Zürich, Institute of Neuropathology, Department of Pathology, Schmelzbergstrasse 12, CH-8091 Zürich, Switzerland.

10.1021/bc700180g CCC: $37.00 © 2007 American Chemical Society
Published on Web 10/17/2007

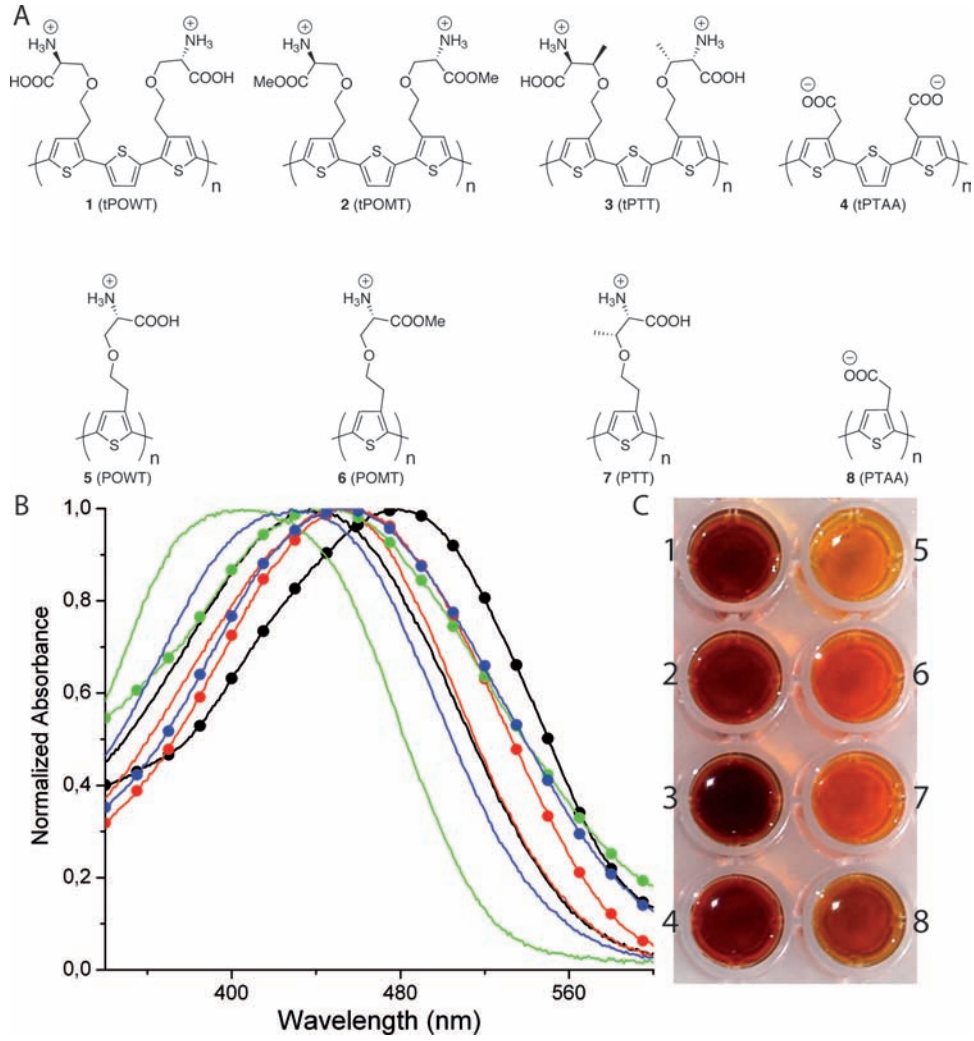


Figure 1. (A) Structures of the eight LCPs: **1** (tPOWT), **2** (tPOMT), **3** (tPTT), **4** tPTAA, **5** (POWT), **6** (POMT), **7** (PTT), and **8** (PTAA). (B) Normalized absorption spectra of LCPs at concentration 25 μg/mL. Filled circles indicate the trimer-based analogue. POWT (green), tPOWT (green), POMT (red), tPOMT (red), PTT (blue), and tPTT (blue) in 50 mM HCl. PTAA (black) and tPTAA (black) are in 100 mM Na_2CO_3. Photograph of the LCPs 1 mg/mL in H_2O; from top to bottom, left row, LCP **1–4**; right row, LCP **5–8**.

by means of their optical properties. The interaction between native/fibrillar insulin and the well-defined trimer-based tPTAA and tPOWT was investigated in more detail.

EXPERIMENTAL PROCEDURES

Polymer Synthesis. Synthesis of PTAA (*22*), POWT (*23*), POMT (*21*), and tPOWT (*13*) has been described elsewhere, and recently, Nilsson et al. (*16*) reported the synthesis of tPOMT and tPTT.

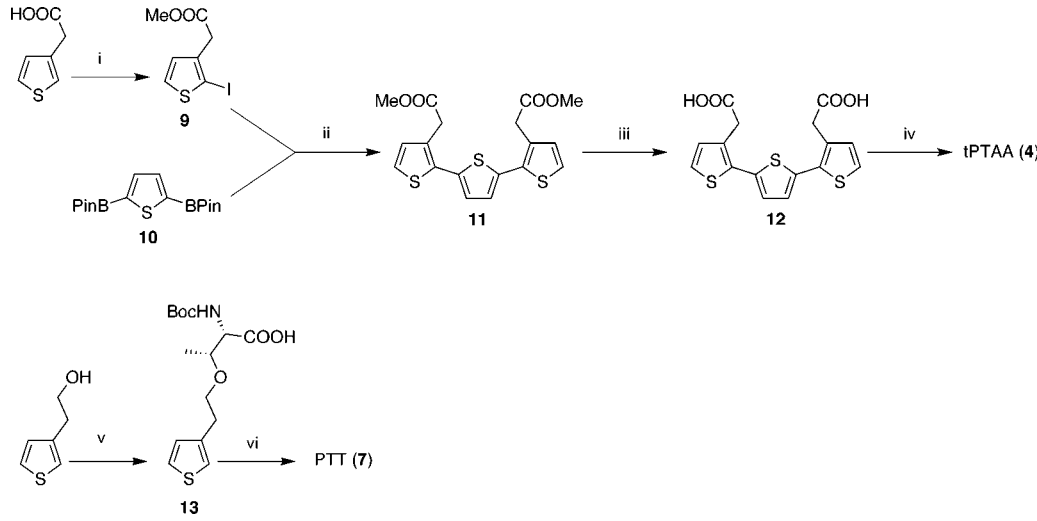
General Methods. Organic extracts were dried over anhydrous magnesium sulfate, filtered, and concentrated in vacuo at 40 °C. 3-Thiopheneethanol, 3-thiopheneacetic acid, and PEPPSI-IPr are commercially available from Sigma-Aldrich Co. Microwave reactions were carried out on a SmithCreator 482 microwave reactor. NMR-spectra were recorded on a Varian 300 MHz instrument. Chemical shifts are given in ppm relative to TMS in $CDCl_3$ (δ 0.00) for ^{1}H and ^{13}C or CD_3OD (δ 3.31) for ^{1}H and CD_3OD (δ 49.0) for ^{13}C NMR. TLC was carried out on Merck precoated 60 F_{254} plates using UV-light and charring with ethanol/sulfuric acid/*p*-anisaldehyde/acetic acid 90:3:2:1 for visualization. Flash column (FC) chromatography was performed using silica gel 60 (0.040–0.063 mm, Merck). Gradient HPLC-MS was performed on a Gilson system (column, Phenomenex C-18 250 × 15 mm and Phenomenex C-18 150 × 4.6 mm for preparative and analytical runs, respectively; pump, Gilson gradient pump 322; UV/vis-detector, Gilson 155; MS detector, Thermo Finnigan Surveyor MSQ; Gilson Fraction Collector FC204) using acetonitrile with 0.1% formic acid and deionized water with 0.1% formic acid as mobile phase. MALDI-TOF MS was recorded in linear positive mode with α-cyano-4-hydroxycinnamic acid matrix (CHCA) or 2,5-dihydroxy benzoic acid (DHB) as matrix.

*(2-Iodo-thiophen-3-yl)-acetic Acid Methyl Ester (***9***).* Acetyl bromide (11.7 mL, 158 mmol) was added slowly to a solution of 3-thiopheneacetic acid (7.51 g, 52.8 mmol) in methanol (60 mL, 0 °C). After 4 h, the mixture was diluted with chloroform (70 mL) and washed twice with $NaHCO_3$ (100 mL, sat, aq.) and once with H_2O (100 mL). After concentration, the product (6.08 g, 39.0 mmol) was dissolved in chloroform/acetic acid (30 mL, 1:1) and cooled to 0 °C, and *N*-iodosuccinimide (11.0 g, 48.8 mmol) was added. Eighteen hours later, water was added to the reaction, and the organic phase was washed twice with KOH (50 mL, 10%, aq.) and H_2O (50 mL). The crude product was purified by vacuum distillation to afford **9** in 43% yield.

^{13}C-NMR($CDCl_3$) δ: 35.9, 52.4, 123.1, 126.0, 128.6, 139.0, 170.9.

^{1}H-NMR($CDCl_3$) δ: 3.63 (s, 2H), 3.78 (s, 3H), 6.93 (d, 1H, J = 5.48 Hz), 7.57 (d, 1H, J = 5.48 Hz). HRMS calcd. for $C_7H_7IO_2S$: $[M]^+$ 281.9211; Found: 281.9209.

Scheme 1[a]



[a] Reagents and conditions: (i) 1. Bromo acetate, methanol; 2. NIS, chloroform/acetic acid (1:1); (ii) K_2CO_3, PEPPSI-IPr, toluene/methanol (1:1); (iii) 1. NaOH, H_2O, dioxane; 2. $FeCl_3$, TBA-triflate, chloroform. (iv) 1. p-TsCl, chloroform/pyridine (7:1); 2. N-t-Boc-Thr, K_2CO_3, DMF; (v) 1. TFA, chloroform; 2. $FeCl_3$, TBA-triflate, chloroform.

*(3″-Methoxycarbonylmethyl-[2,2′;5′,2″]terthiophen-3-yl)-acetic Acid Methyl Ester (***11***).* Compounds **9** (0.185 g, 0.656 mmol), **10** (0.113 g, 0.336 mmol), and K_2CO_3 (0.120 g, 0.868 mmol) were dissolved in degassed toluene/methanol (5 mL, 1:1), and Ar (g) was bubbled for 10 min. PEPPSI-IPr (0.006 mg) was added, and the reaction was subjected to microwave conditions for 10 min at 100 °C. The mixture was diluted with toluene (20 mL) and washed with HCl (10 mL, 1 M, aq.) and H_2O (20 mL). The crude product was further purified by FC (toluene → toluene/ethyl acetate (40:1)) to give the trimer (**11**) (87 mg, 66%) as a pale yellow oil.

^{13}C-NMR($CDCl_3$) δ: 34.7, 52.3, 124.9, 127.5, 130.5, 130.6, 133.0, 135.9, 171.5.

^{1}H-NMR($CDCl_3$) δ: 3.72 (s, 6H), 3.79 (s, 4H), 7.05 (d, 2H, $J = 5.21$), 7.14 (s, 2H), 7.25 (d, 2H, $J = 5.21$). HRMS calcd. for $C_{18}H_{16}O_4S_3$: $[M]^+$ 392.0211; Found: 392.0228.

*tPTAA (***4***).* To a solution of the trimer (**11**) (0.086 g, 0.218 mmol) in dioxane (10 mL), NaOH (5.5 mL, 0.1 M, aq.) was added slowly. When no starting material was seen by TLC, the solution was transferred to an extraction flask, and ethyl acetate (30 mL) was added. The organic phase was washed with HCl (50 mL, 1 M, aq.) subjected to normal workup and used directly in the next step. To a solution of the deprotected trimer and tetrabutylammonium-trifluoromethanesulfonate (0.171 g, 0.436 mmol) in chloroform (5 mL, dry), $FeCl_3$ (0.158 g, 0.981 mmol) was added at 0 °C. After 18 h, methanol was added and the product precipitated as red flakes. The red flakes were collected, dissolved in NaOH (3 M, aq.), neutralized with HCl (conc.), and precipitated with methanol to give tPTAA (**4**) as red crystals (17 mg, 20%).

*(2S,3R)-2-tert-Butoxycarbonylamino-3-(2-thiophen-3-yl-ethoxy)-butyric Acid (***12***).* 3-Thiopheneethanol (7.52 g, 58.7 mmol) and *p*-toluenesulfonic chloride (190.7 g, 16.8 mmol) were added to a solution of chloroform/pyridine (80 mL, 7:1) at 0 °C. After one day, the solution was diluted with diethyl ether and washed twice with HCl (2 M, aq.), twice with $NaHCO_3$ (5%, aq.), and once with H_2O. FC (toluene → toluene/ethyl acetate 3:1) and recrystallization from ethyl acetate/hexane afforded 2-(3-thienyl)ethanol tosylate (16.1 g, 97%) as white crystals. The ^{1}H NMR data was in accordance with that previously reported (*24*). The tosylated product (1.38 g, 4.90 mmol), *N*-t-Boc-Thr (2.15 g, 9.81 mmol), and K_2CO_3 (2.03 g, 14.7 mmol) were added to DMF (90 mL) and heated to 40 °C. After one day, the mixture was poured over HCl/ice (2 M, aq. 1:1) and extracted twice with toluene. The combined extracts were washed twice with H_2O and purified twice on FC (toluene/ethyl acetate 4:1 and toluene/ethyl acetate 6:1) to give **12** (1.16 g, 72%).

^{13}C NMR (CD_3OD) δ: 20.3, 28.7, 30.4, 60.8, 66.4, 68.5, 80.8, 122.7, 126.5, 129.3, 139.4, 158.3, 172.7.

^{1}H NMR (CD_3OD) δ: 1.18 (d, 3H, $J = 6.23$ Hz), 1.46 (s, 9H), 3.00 (t, 2H, $J = 6.78$ Hz), 4.11 (d, 1H, $J = 2.93$), 4.22 (dq, 1H, $J = 2.93$, 6.23 Hz), 4.34 (t, 2H, $J = 6.78$), 7.02 (dd, 1H, $J = 1.47$, 4.95 Hz), 7.15 (dd, 1H, $J = 1.47$, 2.93 Hz), 7.33 (dd, 1H, $J = 2.93$, 4.95). HRMS calcd. for $C_{15}H_{24}NO_5S$: $[M + H]^+$ 330.1375; Found: 330.1303.

*PTT (***7***).* Compound **13** (0.818 g, 2.48 mmol) was added to a solution of dichloromethane/TFA (11 mL, 1:1). After 1 h, the solution was quenched with methanol (3 mL) and coevaporated with toluene three times. The deprotected product and tetrabutylammonium-trifluoromethanesulfonate (1.26 g, 3.22 mmol) were dissolved in chloroform (32 mL, dry) at 0 °C under a N_2 atmosphere. $FeCl_3$ (1.81 g, 11.2 mmol) was added to the solution. After one day, the solution was extracted three times with H_2O. The aqueous solution was diluted with acetone, and conc. HCl (4 mL) was added. When the product had precipitated, it was centrifuged (6 min, 3600 rpm). The collected precipitate was dissolved in water (4 mL) and precipitated from acetone/HCl (40 mL, 25:1). The procedure was repeated twice to afford PTT (**7**) (224 mg, 39%) as red crystals.

Bovine Insulin Preparation. Bovine insulin (Sigma-Aldrich) was dissolved in 2 M guanidine hydrochloride and was dialyzed versus three rounds of 25 mM HCl at 4 °C. The insulin stock solutions ($0.5 \leq 2.0$ mM) were stored at 4 °C and were stable for several weeks. Absorbance at 280 nm was employed for concentration determinations using $\varepsilon^{280} = 5840$ M^{-1}cm for insulin.

Amyloid-Like Fibril Formation. A stock solution containing 320 μM bovine insulin in 25 mM HCl was prepared. The solution was placed in a water bath at 65 °C for at least 13 h to induce amyloid fibril formation. The fibrillated samples were ultra sonicated for at least 10 min prior to optical measurements to avoid sedimentation of large fibril aggregates.

Optical Measurements. Stock solutions of each LCP at a concentration of 1 mg/mL in deionized water were prepared. For fluorescence measurements, 2.5 μL of the LCP solution was diluted with the buffer used: 50 mM HCl and 100 mM Na_2CO_3 at pH 10, to a final volume of 912.5 μL. In the samples where

native and fibrillar insulin were studied, 2.5 μL of the LCP solution was mixed 15 μL of the bovine insulin solution (25 mM HCl) diluted with buffer to a final volume of 912.5 μL. In titration experiments, the concentration of LCP was kept constant, and the concentration of sonicated insulin fibrils was varied between 0 and 105 μM. For the absorption measurements, 5 μL of the LCP solution was diluted to a total volume of 200 μL with buffer.

The samples were incubated for 5 min at RT, and the excitation and emission spectra were recorded with an ISA Jobin-Yvon spex FluoroMax-2 apparatus. For the absorption measurements and the titration experiments, a Tecan Saphire^2 plate reader was used.

Analytical Ultracentrifugation. Weight average molecular weights were determined by analytical ultracentrifugation in Beckman Coulter XL-A/XL-I with an An50Ti rotor and a photoelectric scanner. Equilibrium sedimentation experiments were run at 3000, 7000, 11,000, 15,000, 25,000, 32,000, 40,000, and 45,000 rpm until equilibrium was reached at each speed (20 h) at 20 °C. Five microliters of stock LCP solution was mixed with 30 μL of native or fibrillated bovine insulin solution (320 μM in 25 mM HCl) or 30 μL 25 mM HCl and diluted to 200 μL in buffer. Data was collected at 280 and 446 nm and evaluated using the self-association model in the XL-I, XL-A data analysis software. The solvent density was calculated to be 0.99913 g/cm^3 and 1.00915 g/cm^3 for 50 mM HCl and 100 mM Na_2CO_3, respectively. The partial specific volume (ν) of insulin used was 0.735. ν of the LCPs was determined densiometrically in Anton Paar DMAC02 Precision Density Meter.

RESULTS AND DISCUSSION

Synthesis. *PTT.* 3-Thiopheneethanol was tosylated in chloroform/pyridine, and the tosylate was substituted with *N*-t-Boc-Thr in K_2CO_3 and DMF. Interestingly, the substitution of the tosylate with the secondary alcohol *N*-t-Boc-Thr gave a higher yield of **13** (72%) than that with the primary alcohol *N*-t-Boc-Ser previously reported (57%) (*23*) (see Scheme 1). The functionalized thiophene monomer was subsequently deprotected and polymerized to give PTT (**7**) in 39% yield.

*tPTAA (**4**).* Monohalogenated thiophenes are generally hard to separate from the nonhalogenated thiophene and the dihalogenated one using conventional flush chromatography. Therefore 3-thiopheneacetic acid was protected as a methylester in acetyl bromide and methanol before it was iodinated with NIS in chloroform and acetic acid. This product could be purified by distillation to give **9** in 43% over two steps. The diboronic ester (**10**) used to assemble **11** was made from thiophene with a protocol described by Parakka et al. (*25*). The coupling of **9** and **10** was performed under microwave conditions for 10 min at 100 °C using PEPPSI-IPr as catalyst to afford the trimer (**11**) in 66% yield. Finally, the esters were hydrolyzed under basic conditions, and the deprotected trimer was polymerized using iron(III)chloride to give tPTAA in 20% yield.

Matrix Assisted Laser Desorption/Ionization Time-of-Flight Mass Spectroscopy (MALDI-TOF MS). MALDI-TOF MS has become increasingly important as a convenient method to characterize polymers even though the result often does not reliably show the actual chain length distribution (*26*). PTT (0.5 μL, 1 mg/mL) was mixed with CHCA in 0.1% TFA/acetonitrile (0.5 μL, 1:1) as the matrix. The spectra of the product showed polymers mainly in the range 10 to 18 monomer units following ion series corresponding to the monomer unit $[227n]^+$, $[227n + 35]^+$, and $[227n + 70]^+$, where +35 and +70 correspond to covalent end termination of the polymer by one and two chlorines, respectively (see Figure 2A). There are few references (*27*) in the literature to negatively charged polymers characterized by MALDI-TOF MS, and even the tPTAA-analogue PTAA, synthesized some time ago (*28*), has yet to be characterized this way. Therefore, a new protocol had to be used. tPTAA (0.5 μL) was mixed with DHB (0.5 μL, 10 mg/mL in 10% TFA). The spectra showed two main peaks corresponding to [362n]+, where n corresponds to 4 or 5 units (Figure 2B). The chain distribution of the LCPs varies to some extent depending on the chemical structure of the LCP. However, it seems that the trimer-based LCPs (**1**–**4**) generally have the same molecular weight (around 1500 Da) regardless of the substituent (*13*). The same trend can be observed for the monomer-based LCPs (**5**–**7**), but the molecular weight is higher (around 3000 Da) (*21, 29*).

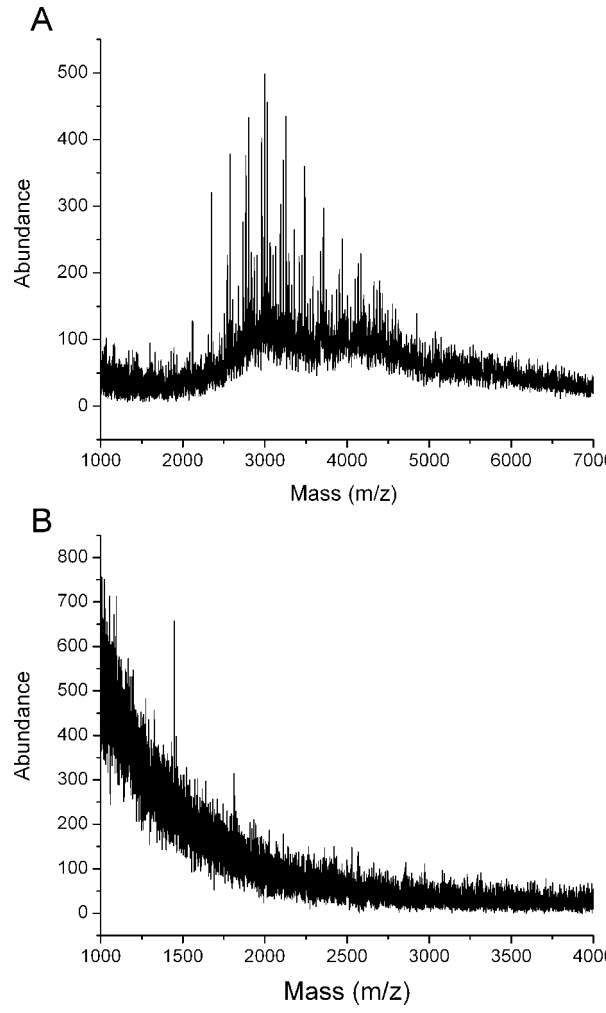


Figure 2. MALDI spectra of (A) PTT and (B) tPTAA.

Optical Characterization of LCPs. The optical properties, measured by absorption, fluorescence, and circular dichroism (CD), of the LCPs in Figure 1 are highly pH-dependent because of the different degree of protonation of the carboxyl and amine groups on the side chains (*13, 30*). The degree of protonation will influence the propensity of the polymer chains to aggregate in water-based solutions. Aggregation will enhance interchain interactions, leading to a red shift in absorption and fluorescence and lower fluorescence intensity due to higher probability of nonradioactive de-excitation pathways. The trimer-based LCPs (compounds **1**–**4**; Figure 1) showed more red-shifted spectra and lower fluorescence intensity (see Table 1 and Figure 1) compared to their monomer-based analogues (compounds **5**–**8**; Figure 1) in the same buffer solution. These differences in optical properties are likely to arise from the lower degree of side-chain substitution along the polymer backbone. The lower

Table 1. Optical properties of LCP values from Figures 1 and 3[a]

LCP	abs λ_{max}	fluor. λ_{max}, I_{max} buffer	fluor. λ_{max}, I_{max} native ins.	fluor. λ_{max}, I_{max} fibrill. ins.
1 (tPOWT)	445	585.5; 8	585; 9	555.5; 84
5 (POWT)	405	552.5; 18	556.5; 28	563; 50
2 (tPOMT)	456	585; 21	586; 21	579.5; 95
6 (POMT)	449	576.5; 57	578; 86	581.5; 95
3 (tPTT)	453	587.5; 13	588; 15	571; 42
7 (PTT)	430	576; 52	579; 48	575; 58
4 (tPTAA)	478	587; 13	586; 12	571; 53
8 (PTAA)	438	561.5; 35	565.5; 57	573.5; 100

[a] The maximum fluorescence intensity was normalized, and the highest intensity of the spectrum PTAA with fibrillar insulin corresponds to 100.

degree of side-chain substitution can enhance interchain backbone interaction and promote aggregation.

Optical Characterization of LCPs Interacting with Native and Fibrillar Insulin. We have shown earlier the characteristic changes in optical properties, in fluorescence–excitation and emission, of LCPs upon interaction with amyloid-like fibrils (*13, 14, 16*), PTAA and tPOWT interacting with insulin fibrils, and PTAA, POMT, tPOMT, and tPTT interacting with fibrils of Aβ 1–42. To further characterize these, we have made a comparison of the monomer- and trimer-based LCPs in fluorescence emission (Figure 3 and Table 1) and fluorescence–excitation spectra of two of the trimer-based LCPs, tPOWT and tPTAA (Figure 4), upon interaction with insulin in native and fibrillar form.

Figure 3 and Table 1 show that there is virtually no difference in the fluorescence emission spectra between buffer and native insulin in the case of the trimer-based LCPs, whereas the monomer-based LCPs show intensity differences and in some cases spectral shifts upon interaction with native insulin. As also seen with fibrillar Aβ (1–42) (*16*), interaction with fibrillar insulin gives a higher quantum yield (QY) for all LCPs, but the relative difference is significantly larger with trimer-based LCPs. All of the emission spectra have been recorded with excitation at 488 nm, which is near the peak maximum of the fluorescence–excitation spectra shown earlier (*16*) and in Figure 4. Also, in these spectra, there is an augmented fluorescence response upon interaction with insulin fibrils. The possibility of exciting these LCPs with 488 nm is advantageous considering that the 488 nm laser line of argon is often used in confocal microscopy. The increased fluorescence emission of the LCPs upon interaction with fibrils was most likely due to polymer chain separation caused by the binding event. Hence, LCPs alone in the corresponding buffer associated into clusters, and notably, the clusters were still in solution. In all cases, except for PTAA, fibril interaction was associated with a blue shift in emission, which is associated with chain separation or an increased twist of the polymer backbone compared to the free LCP cluster.

The spectral discrimination between a LCP in buffered solution, solution with native insulin, or with fibrillar insulin seems to be governed by both the backbone and the side chain of the LCP. It appears important that the backbone is exposed for maximum hydrophobic interaction with fibrillar insulin, while the side chain must remain hydrophilic to ensure water solubility as well as reducing the interaction with native insulin. The six cationic LCPs (**1**–**3** and **5**–**7**) were all buffered at pH 1 and are therefore easily compared with each other. At pH 1, both the LCPs and the protein in its native and fibrillar state were positively charged. Electrostatic repulsion from the charges is likely to occur, and it is reasonable to assume that a trimer-based LCP with every third cationic substituent removed and thereby with a more exposed backbone more easily interacts with the amyloid fibrils. If the three monomer-based cationic LCPs **5**–**7** are compared (Figure 3 and Table 1), there is a relationship between hydrophobicity of the side chain and the spectral discrimination of native and fibrillar insulin. The LCP POWT, substituted with serine, showed a larger shift and higher intensity change than the two methylated species, PTT, methylated at the β-position, and POMT, the methyl ester of serine, when the discrimination between the native and fibrillar state of insulin is compared. Possibly, a more hydrophobic substituent interferes with the fibril/polymer backbone interaction. In the trimer-based LCPs **1**–**3**, the spectral trend as observed with the monomer-based analogues with respect to their side-chain substituents was more pronounced. tPOWT showed almost twice as large a blue-shift and intensity increase as tPOMT and tPTT when comparing spectra from native and fibrillar insulin. Moreover, the spectral difference between the signal of the trimer-based LCPs in buffered solution compared to the signal with native insulin was insignificant. The anionic trimer-based tPTAA (**4**), which was used in a buffered environment at pH 10, shows the same spectral discrepancy as the LCPs **1**–**3**. Compared to the monomer-based **5**–**7**, PTAA showed larger spectral shifts, although not as distinct as for tPTAA. For the application as a probe for amyloid fibril detection, it is clearly advantageous with a low signal toward native protein and buffer. Besides the substitution pattern, there are other differences between the monomer- and trimer-based LCPs that might influence the contrast. The trimer-based LCPs are completely regioregular because of the 2-fold rotational axis in the center thiophene, whereas the monomer-based LCPs do not contain a rotational axis and therefore when polymerized can bind head-to-tail as well as head-to-head. The trimer-based LCPs are also shorter with a more well-defined chain length that could influence the discrimination behavior.

To further evaluate the interaction between LCP and fibrillar insulin, tPTAA and tPOWT were more thoroughly studied. The two LCPs showed the best signal discrepancy and emission enhancement between native and fibrillar insulin. Moreover, tPTAA had so far not been further characterized and was also interesting because of the good tissue staining properties published earlier with its analogue PTAA (*15*).

Titration experiments were performed, where the amount of LCP was kept constant, and the fibril concentration was increased (Figure 5). The titration curve was fitted to a Hill plot cooperative model.

$$Y = B_{max}[X]^{n_H}/(K_{1/2}^{n_H} + [X]^{n_H}) \quad (1)$$

In eq 1, B_{max} is the maximum recorded signal, n_H is the cooperativity value, where a value larger than 1 indicates positive cooperativity, and $K_{1/2}$ is the value where 50% of the maximum signal is reached. At fibril concentration $K_{1/2}$, 50% of the LCP chain population was bound to fibrils.

In the model, tPOWT had a $K_{1/2} = 0.2$ μM and $n = 1.2$, whereas tPTAA had $K_{1/2} = 2.4$ μM and $n = 1$. This indicates that tPTAA (at pH 10) had a lower affinity for fibrils than tPOWT at pH 1. Whether the affinity difference is a side-chain-induced effect or a reduced fibril polymer–backbone interaction at the higher pH is unclear. None of the LCPs showed a clear cooperativity in the interaction event since n was not significantly larger than 1.

To evaluate the interaction between tPTAA and tPOWT with amyloid-like fibrils, we studied the LCP fluorescence response at a constant total protein concentration with increasing fibril content compared to native protein. In Figure 6, the result is presented as the percentage of amyloid-like fibrils in total protein concentration (5.26 μM) as relative change in the fluorescence ratios 550/600 (tPOWT) and 570/670 (tPTAA). Clearly, a small amount of fibrils could be detected in the presence of native protein. The lowest detection level was reached at 0.5% and

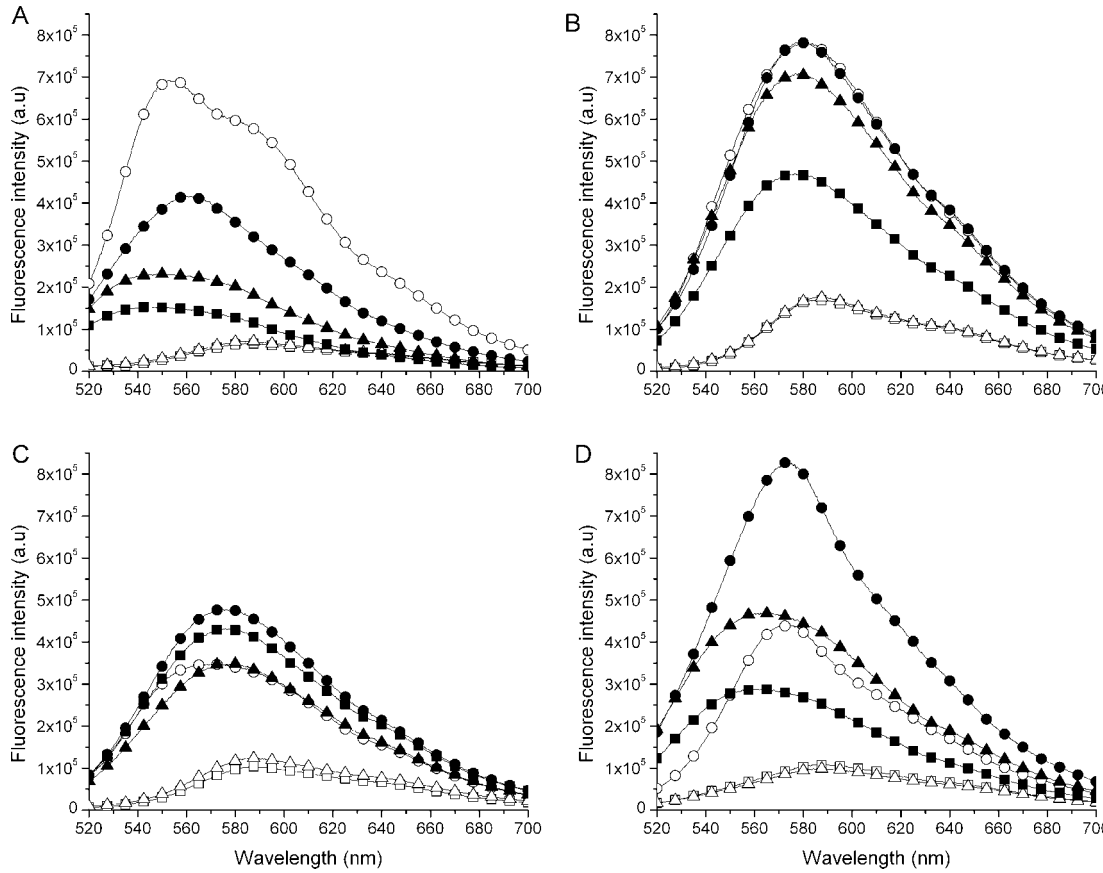


Figure 3. Fluorescence emission spectra. Excitation was at 488 nm. The filled symbols are monomer-based LCPs and the unfilled ones are the trimer-based analogues. ;□ and ;■ are 2.7 μg/mL LCP in buffer. △ and ▲ are 2.7 μg/mL LCP with 5 μM native insulin. ○ and ● are 2.7 μg/mL LCP with 5 μM fibrillar insulin. (A) POWT and tPOWT in 50 mM HCl, (B) POMT and tPOMT in 50 mM HCl, (C) PTT and tPTT in 50 mM HCl, and (D) PTAA and tPTAA in 100 mM Na_2CO_3.

1.4% fibrils for POWT and tPTAA, respectively, corresponding to a 20% relative change in the signal.

Analytical Ultracentrifugation. Along with the limitations of MALDI-TOF MS (vide supra), it is vital to consider that weakly associated assemblies, for example, linked through hydrogen bonding, can easily break during measurements. Analytical ultracentrifugation (AUC) is a nondisruptive solution-based technique, well known for the characterization of proteins and protein complexes and also synthetic macromolecules (*31*). This makes the technique suitable to study the state of LCPs in solutions and the interaction between LCPs and proteins.

AUC experiments were run in equilibrium sedimentation mode at 9 velocities, and absorption was measured at 280 and 445 nm. tPTAA and tPOWT were studied in buffer and with native insulin and fibrillar insulin. tPTAA and tPOWT in buffer were fitted to a single species self-association model as shown in Figure 7.

The main disadvantages of AUC are related to the difficulty in obtaining accurate partial specific volumes in some cases (*31*). The partial specific volume $\bar{\nu}$; is needed to determine the absolute molar mass (M) from the buoyant mass as follows:

$$M_b = M(1 - \bar{\nu}\rho) \qquad (2)$$

$\bar{\nu}$ of tPTAA and tPOWT was determined densiometrically at the concentration (25 μg/mL) used in the AUC experiments in order to avoid the formation of different states of interchain interactions. The low concentration made the measurement of $\bar{\nu}$; difficult, and the obtained value 0.5 for both tPOWT and tPTAA should be seen as a guideline. To our knowledge, there are no values of $\bar{\nu}$; for polythiophenes in the literature, but our value can be compared with the study of Michaels et al., which determined $\bar{\nu}$; of a polyparaphenylene to 0.62, of a polyfluorene to 0.65, and a polydiphenylenevinylene to 0.55 (*32*).

If the sedimentation curves of tPTAA are fitted to a self-association model, the average buoyant mass (M_b) is 25600 ± 1600 g/mol, which gives an molecular mass (M) of 12700 ± 800 g/mol. tPOWT gives a value of M_b of 24800 ± 4000 g/mol, which corresponds to an M of 12400 ± 2000 g/mol. Interestingly, if we compare these values with the MALDI-TOF spectra reported by us earlier (*13*) and in this publication, we can see clear differences since the majority of the tPOWT chains had a mass value of 1509 g/mol and tPTAA had a corresponding value of 1447 g/mol. These values lead us to the conclusion that the studied free LCPs were in a state of small clusters when present in aqueous solution. On average, a cluster of tPTAA consisted of nine polymer chains, and for tPOWT, this value is 8 ± 1. This result could explain the very low fluorescence signal intensity from tPOWT and tPTAA in acidic and basic buffers, respectively, due to intermolecular quenching.

To evaluate the interaction between native insulin and the LCP, an equilibrium sedimentation experiment was run with 48 μM native insulin and 16.6 (tPOWT, 25 μg/mL) and 17.2 (tPTAA, 25 μg/mL) μM LCP. There was no significant difference between the sedimentation profiles at A_{445nm} of the pure LCP samples and those where insulin was present (Figure S1, Supporting Information). The sedimentation profiles of pure insulin measured at A_{280nm} were fitted to the self-association model and resulted in an average weight in 100 mM Na_2CO_3 at pH 10 and in 50 mM HCl at pH 1 of 5700 g/mol and 11500 g/mol, respectively, corresponding to the monomer and dimer weight of insulin. The association state of insulin is highly dependent on pH, ion concentration, and insulin concentration

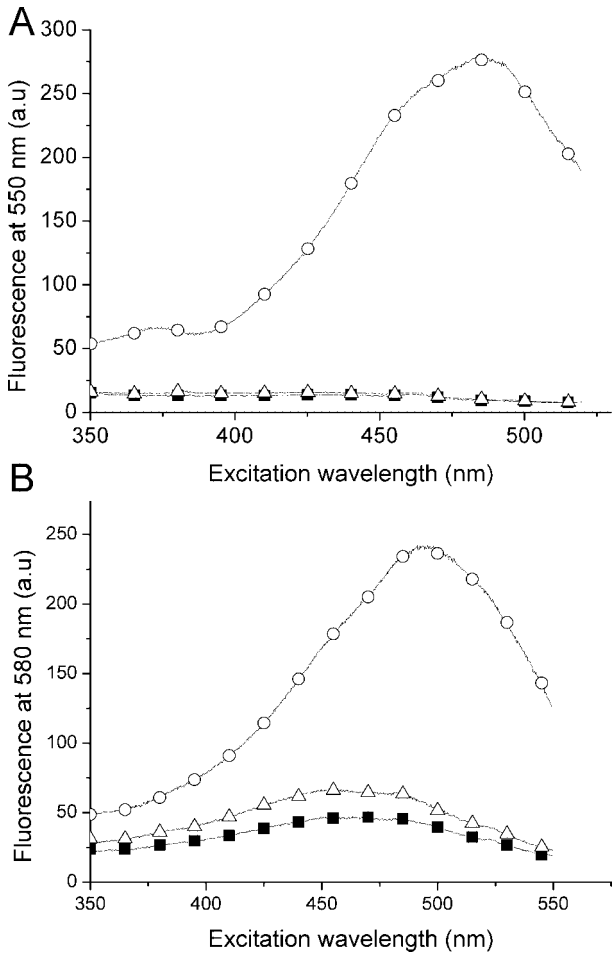


Figure 4. Fluorescence–excitation spectra. (A) Fluorescence emission at 550 nm from 2.7 μg/mL tPOWT in (;■) 50 mM HCl, (;△) 20 mM HCl with 5 μM native insulin, and (○) 50 mM HCl with 5 μM fibrillar insulin. (B) Fluorescence emission at 580 nm from 2.7 μg/mL tPTAA in (;■) 20 mM $NaCaO_3$, (;△) 20 mM $NaCaO_3$ with 5 μM native insulin, and (○) 20 mM $NaCaO_3$ with 5 μM fibrillar insulin.

(*33*). Kadima et al. found that zinc-free insulin was present as monomers at a concentration of 1.9 mg/mL at pH 10.5 (*33*). At an insulin concentration of 2 μM at pH 2.0, Nettleton et al. reported that insulin was to be found mostly in monomeric form but also that dimers were present (*34*). Our results, obtained at pH 1, indicate that the dimerization of insulin increases at lower pH. From the sedimentation curves shown in Figure S1, Supporting Information and the mass determination of native insulin, it can be assumed that the LCPs did not interact with the native protein in the mentioned solution conditions. If one considers the preservation of the fluorescence–excitation and emission properties of the LCP, it is unlikely that the interaction with native insulin led to the disruption of the clusters of LCPs and the formation of a complex of similar mass.

The sedimentation of the ultrasonicated insulin fibrils occurred already before equilibrium at the lowest rotation speed (3000 rpm), indicating that the masses of these fibril fragments are >1000000 g/mol. This result shows that the dissolution of insulin fibrils with aqueous ammonia at pH 10.5 showed by Nilsson et al. (*35*) did not occur in 100 mM Na_2CO_3 at pH 10. In samples with both LCP and sonicated fibrils, the cosedimentation of both species at low rotation speed was obvious, showing interaction between LCP and fibrils.

CONCLUSIONS

From the optical measurements, in absorbance and fluorescence, of the LCP, it was clear that the trimer-based analogues

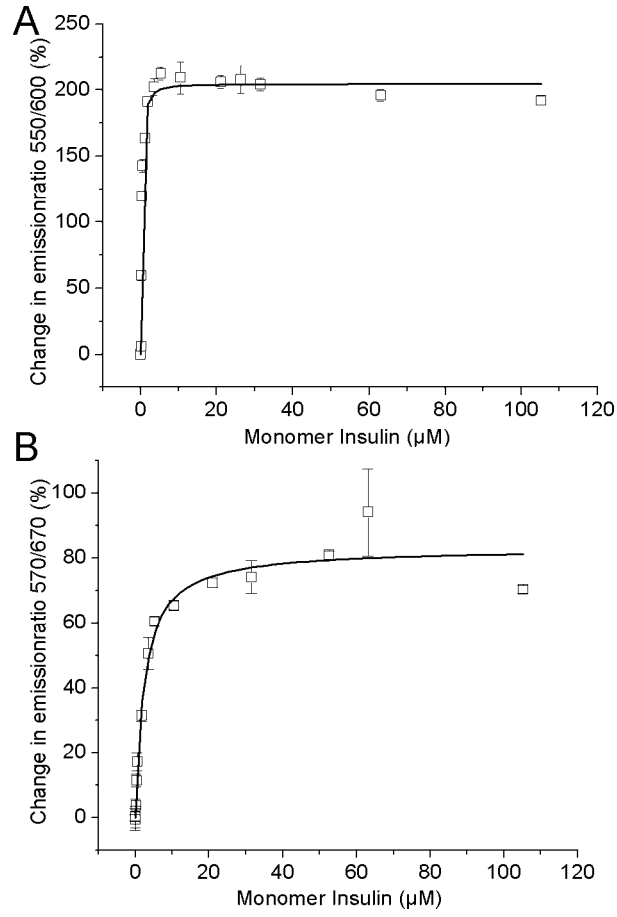


Figure 5. Titration curves of LCP fluorescence. (A) tPOWT (2.7 μg/mL) in 50 mM HCl (B) tPTAA (2.7 μg/mL) in 100 mM Na_2CO_3 at pH 10. Sonicated fibrillated insulin in concentrations given as monomer insulin was added. Excitation was at 488 nm.

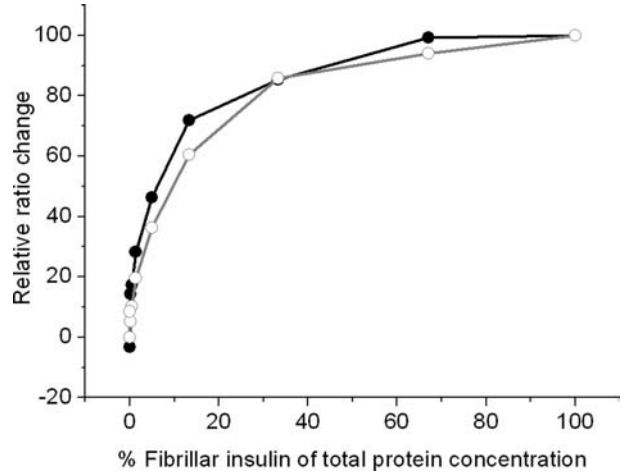


Figure 6. Detection of fibrillar insulin in the presence of native insulin. tPOWT (black) (2.7 μg/mL) in 50 mM HCl. tPTAA (grey) (2.7 μg/mL) in 100 mM Na_2CO_3 at pH 10. The percentage of sonicated fibrillated insulin of the total amount of insulin is shown as the monomer insulin added. Total protein concentration (5.26 μM) was kept constant. Excitation was at 488 nm. The relative change in the emission ratio at 550 nm/600 nm (tPOWT) and 570 nm/670 nm (tPTAA) is shown.

were more quenched in solution, giving lower quantum yields. The trimer-based LCPs showed optical signal specificity for amyloid-like fibrils as seen from increased QY and spectral shift, whereas no spectral changes could be seen with native insulin compared to buffered solution. These results were also supported by the possibility of distinguishing the fibrillar signal in a 70-

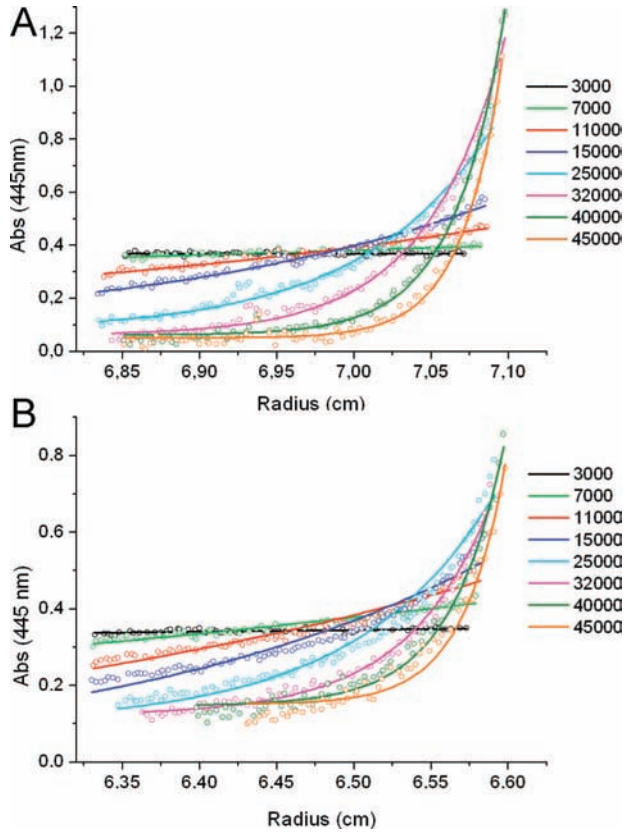


Figure 7. Analytical ultracentrifuge sedimentation curves of absorbance at 445 nm (A) tPOWT (25 μg/mL) in 50 mM HCl. (B) tPTAA (25 μg/mL) in 100 mM Na_2CO_3 at pH 10. Rotation speed in rpm is shown in the legend. Lines are fitted to a self-association model.

fold excess of native insulin. Furthermore, AUC demonstrated that the trimer-based tPTAA and tPOWT showed no interaction with native insulin, whereas they cosediment with fibrils, indicating strong noncovalent binding. We also report that tPTAA and tPOWT form small clusters in solution, likely to avoid exposure of the hydrophobic polythiophene backbone. The LCP/amyloid-like fibril interaction seems to be governed by the backbone of the polymer. If one compare the cationic monomer-based polymers with the trimer-based cationic LCPs, it is apparent that the removal of one out of three side chains and thereby increasing the exposure of the backbone, gave rise to a strong signal enhancement upon interaction with amyloid fibrils compared to monomer-based LCPs. The anionic LCPs PTAA and tPTAA showed the same behavior as their cationic counterparts, even though the pH was changed from acidic to basic. This study verifies our hypothesis that trimer-based LCPs have a better potential than monomer-based LCPs as optical probes for amyloid fibril detection. Moreover, LCPs **2**, **3**, **6**, and **8** have been discussed for use in diagnostics of aggregation proteopathies (*16*), and here, we demonstrate that tPTAA is another potential candidate for these applications.

ACKNOWLEDGMENT

We acknowledge partial funding from VINNOVA and CENANO at LiU (A.H.). Support from the Foundation of Strategic Research (P.H., P.K. and A.Å.), the Wenner-Gren Foundations (P.H.), The Knut and Alice Wallenberg Foundation (K.P.R.N), and the Swedish research council (P.H., P.K, O. I., B-H. J., and A.H) are greatly appreciated.

Supporting Information Available: Analytical ultracentrifugation curves of tPOWT and tPTAA in buffer and in the presence of native insulin. This information is available free of charge via the Internet at http://pubs.acs.org.

LITERATURE CITED

(1) Cohen, A. S., Shirahama, T., and Skinner, M. (1981) Electron microscopy of amyloid, in *Electron Microscopy of Protein* (Harris, I., Ed.), pp 165–205, Academic Press, London.

(2) Glenner, G. G. (1981) The bases of the staining of amyloid fibers: their physico-chemical nature and the mechanism of their dye-substrate interaction. *Prog. Histochem. Cytochem. 13*, 1–37.

(3) Westermark, G. T., Johnson, K. H., and Westermark, P. (1999) Staining methods for identification of amyloid in tissue. *Methods Enzymol. 309*, 3–25.

(4) Khurana, R., Uversky, V. N., Nielsen, L., and Fink, A. L. (2001) Is Congo Red an Amyloid-specific Dye? *J. Biol. Chem. 276*, 22715–22721.

(5) Voropai, E. S., Samtsov, M. P., Kaplevskii, K. N., Maskevich, A. A., Stepuro, V. I., Povarova, O. I., Kuzentsova, I. M., Turoverov, K. K., Fink, A. L., and Uverskii, V. N. (2003) Spectral properites of thioflavin T and its complexes with amyloid fibrils. *J. Appl. Spectrosc. 70*, 868–874.

(6) Crystal, A. S., Giasson, B. I., Crowe, A., Kung, M. P., Zhuang, Z. P., Trojanowski, J. Q., and Lee, V. M. (2003) A comparison of amyloid fibrillogenesis using the novel fluorescent compound K114. *J. Neurochem. 86*, 1359–1368.

(7) LeVine, H. (2005) Mechanism of A beta(1–40) fibril-induced fluorescence of (trans,trans)-1-bromo-2,5-bis(4-hydroxystyryl) benzene (K114). *Biochemistry 44*, 15937–15943.

(8) Nesterov, E. E., Skoch, J., Hyman, B. T., Klunk, W. E., Bacskai, B. J., and Swager, T. M. (2005) In vivo optical Imaging of amyloid aggregates in brain: Design of fluorescent markers. *Angew. Chem., Int. Ed. 44*, 5452–5456.

(9) Styren, S. D., Hamilton, R. L., Styren, G. C., and Klunk, W. E. (2000) X-34, a fluorescent derivative of Congo red: a novel histochemical stain for Alzheimer's disease pathology. *J. Histochem. Cytochem. 48*, 1223–1232.

(10) Nilsson, K. P., Rydberg, J., Baltzer, L., and Inganas, O. (2003) Self-assembly of synthetic peptides control conformation and optical properties of a zwitterionic polythiophene derivative. *Proc. Natl. Acad. Sci. U.S.A. 100*, 10170–10174.

(11) Nilsson, K. P. R., Rydberg, J., Baltzer, L., and Inganas, O. (2004) Twisting macromolecular chains: Self-assembly of a chiral supermolecule from nonchiral polythiophene polyanions and random-coil synthetic peptides. *Proc. Natl. Acad. Sci. U.S.A. 101*, 11197.

(12) Nilsson, K. P. R., and Inganas, O. (2004) Optical emission of a conjugated polyelectrolyte: Calcium-induced conformational changes in calmodulin and calmodulin-calcineurin interactions. *Macromolecules 37*, 9109–9113.

(13) Herland, A., Nilsson, K. P. R., Olsson, J. D. M., Hammarstrom, P., Konradsson, P., and Inganas, O. (2005) Synthesis of a regioregular zwitterionic conjugated oligoelectrolyte, usable as an optical probe for detection of amyloid fibril formation at acidic pH. *J. Am. Chem. Soc. 127*, 2317–2323.

(14) Nilsson, K. P. R., Herland, A., Hammarstrom, P., and Inganas, O. (2005) Conjugated polyelectrolytes: Conformation-sensitive optical probes for detection of amyloid fibril forrnation. *Biochemistry 44*, 3718–3724.

(15) Nilsson, K. P. R., Hammarstrom, P., Ahlgren, F., Herland, A., Schnell, E., Lindgren, M., Westermark, G., and Inganas, O. (2006) Conjugated polyelectrolytes - conformation sensitive optical probes for staining and characterization of amyloid deposits. *ChemBioChem 7*, 1096–1104.

(16) Nilsson, K. P. R., Åslund, A., Berg, I., Nyström, S., Konradsson, P., Herland, A., Inganäs, O., Stabo-Eeg, F., Lindgren, M., Westermark, G. T., Lannfelt, L., Nilsson, L. N. G., and Hammarström, P. (2007) Imaging distinct conformational states of amyloid-beta fibrils in Alzheimer's disease using novel luminescent probes, *ACS Chem. Biol. 2*(8), 553–560.

(17) Frere, P., Raimundo, J. M., Blanchard, P., Delaunay, J., Richomme, P., Sauvajol, J. L., Orduna, J., Garin, J., and Roncali, J. (2003) Effect of local molecular structure on the chain-length dependence of the electronic properties of thiophene-based pi-conjugated systems. *J. Org. Chem. 68*, 7254–7265.

(18) Martin, R. E., and Diederich, F. (1999) Linear Monodisperse π-conjugated Oligomers: Model Componds for Polymers and More. *Angew. Chem., Int. Ed. 38*, 1350–1377.

(19) Meier, H., Stalmach, U., and Kolshorn, H. (1997) Effective conjugation length and UV/vis spectra of oligomers. *Acta Polym. 48*, 379–384.

(20) Müllen, K., and Wegner, G. (1997) *Electronic Materials: The Oligomer Approach*, Wiley-VCH, Weinheim, Germany.

(21) Nilsson, K. P. R., Olsson, J. D. M., Stabo-Eeg, F., Lindgren, M., Konradsson, P., and Inganas, O. (2005) Chiral recognition of a synthetic peptide using enantiomeric conjugated polyelectrolytes and optical spectroscopy. *Macromolecules 38*, 6813–6821.

(22) Ding, L., Jonforsen, M., Roman, L. S., Andersson, M. R., and Inganas, O. (2000) Photovoltaic cells with a conjugated polyelectrolyte. *Synth. Met. 110*, 133–140.

(23) Andersson, M., Ekeblad, P. O., Hjertberg, T., Wennerström, O., and Inganäs, O. (1991) Polythiophene with a free amino acid side chain. *Polymer Commun. 32*, 1991.

(24) Noyce, D. S., and Castenson, R. L. (1973) Participation of heterocyclic moieties in the solvolytic rearrangement of p-arylethyl tosylates. *J. Am. Chem. Soc. 95*, 1247–1253.

(25) Parakka, J. P., Jeevarajan, J. A., Jeevarajan, A. S., Kispert, L. D., and Cava, M. P. (1996) Heterocyclic heptamers containing thiophene and pyrrole units: Synthesis and properties. *Adv. Mater. 8*, 54–59.

(26) Jayakannan, M. v. D., J. L. J., and Janssen, R. A. J. (2001) Mechanistic aspects of the Suzuki polycondensation of thiophene-bisboronic derivatives and diiodobenzenes analyzed by MALDI-TOF mass spectrometry. *Macromolecules 34*, 5386–5393.

(27) Montaudo, G., Samperi, F., and Montaudo, M. S. (2006) Characterization of synthetic polymers by MALDI-MS. *Prog. Polym. Sci. 31*, 277–357.

(28) Kim, B. S., Chen, L., Gong, J. P., and Osada, Y. (1999) Titration behavior and spectral transitions of water-soluble polythiophene carboxylic acids. *Macromolecules 32*, 3964–3969.

(29) Nilsson, K. P. R., Olsson, J. D. M., Konradsson, P., and Inganas, O. (2004) Enantiomeric substituents determine the chirality of luminescent conjugated polythiophenes. *Macromolecules 37*, 6316–6321.

(30) Nilsson, K. P. R., Andersson, M. R., and Inganäs, O. (2002) Conformational transitions of a free amino-acid-functionalized polythiophene induced by different buffer systems. *J. Phys.: Condens. Mater. 14*, 1–10.

(31) Rasa, M., and Schubert, U. S. (2006) Progress in the characterization of synthetic (supramolecular) polymers by analytical ultracentrifugation. *Soft Matter 2*, 561–572.

(32) Michels, J. J., O'Connell, M. J., Taylor, P. N., Wilson, J. S., Cacialli, F., and Anderson, H. L. (2003) Synthesis of conjugated polyrotaxanes. *Chem.–Eur. J. 9*, 6167–6176.

(33) Kadima, W., Øgendal, L., Bauer, R., Kaarsholm, N., Brodersen, K., Hansen, J. F., and Porting, P. (1993) The influence of ionic strength and pH on the aggregation properties of zinc-free insulin studied by static and dynamic laser light scattering. *Biopolymers 33*, 1643–1657.

(34) Nettleton, E. J., Tito, P., Sunde, M., Bouchard, M., Dobson, C. M., and Robinson, C. V. (2000) Characterization of the oligomeric states of insulin in self-assembly and amyloid fibril formation by mass spectrometry. *Biophys. J. 79*, 1053–1065.

(35) Nilsson, M. R., and Dobson, C. M. (2003) Chemical modification of insulin in amyloid fibrils. *Protein Sci. 12*, 2637–2641.

BC700180G

Thiolytically Cleavable Dithiobenzyl Urethane-Linked Polymer–Protein Conjugates as Macromolecular Prodrugs: Reversible PEGylation of Proteins

Samuel Zalipsky,* Nasreen Mullah, Charles Engbers, Maria U. Hutchins, and Radwan Kiwan

ALZA Corporation, 1900 Charleston Road, Mountain View, California 94043. Received May 25, 2007; Revised Manuscript Received August 31, 2007

New thiolytically cleavable dithiobenzyl (DTB) urethane-linked conjugates of methoxypoly(ethylene glycol) (mPEG) and a model protein, lysozyme, were prepared and thoroughly characterized. In contrast to our earlier communication [Zalipsky, et al. (1999) *Bioconjugate Chem. 10*, 703], in the current study we used a more sterically hindered form of *para*-DTB urethane linkage containing a methyl group on the α-carbon to the disulfide moiety. The new reagent for covalent attachment of mPEG-DTB to amino groups of proteins was synthesized via a seven-step process. As a result of PEG conjugation, the lysozyme was shown to completely lose its bacterial cell wall-lysing activity. However, activity was almost fully restored upon cysteine-mediated cleavage of the PEG component. The conjugate decomposition process was monitored by RP-HPLC and by ion spray LC-MS, which showed the formation of the *p*-mercaptobenzyl urethane–lysozyme intermediate, and ultimately its conversion to the unmodified lysozyme as the sole protein component. Pharmacokinetic evaluation of ^{125}I-labeled cleavable and noncleavable PEG-lysozyme given intravenously in rats revealed similar clearance patterns; both cleared in a significantly slower manner compared to that of the native protein. However, subcutaneous administration of the same conjugates showed a significantly larger AUC of the cleavable conjugate, indicating that some cleavage of the DTB urethane may have occurred. Although the DTB-linked PEG-lysozyme exhibited almost the same plasma clearance as the noncleavable counterpart, hinting that methyl-DTB linkage might be stable in the bloodstream, SDS–PAGE examination of the conjugate incubated in plasma showed decomposition at least partially mediated by albumin. These results suggest the potential of PEG-DTB-proteins as macromolecular prodrugs capable of generating fully active native proteins under in vivo conditions.

INTRODUCTION

Covalent linking of proteins with water-soluble biocompatible polymers is often used to modulate the properties of the resulting conjugates in order to make them more amenable to in vivo applications (*1–3*). One of the most popular polymers used for this purpose, polyethylene glycol (PEG[1]) (*4–6*), is known to convey a number of useful properties to its conjugates. Among them are prolonged plasma circulation time, reduced immunogenicity and antigenicity, improved solubility, and resistance to proteolytic degradation (*3, 5–7*). Usually, there is a direct relationship between the amount of the linked polymer and the improvement in the above-listed characteristics. However, covalent attachment of PEG strands to a protein, a process often referred to as PEGylation, is at times accompanied by a substantial loss of the functional biological activity. This is a particularly severe problem for proteins acting on macromolecular substrates (*3, 8, 9*). Most receptor-binding proteins, for example, cytokines and chemokines, fall into this category. Three approaches were applied to deal with the problem of the loss of biological activity as a result of PEGylation: (i) site specific PEGylation, sometimes in combination with site-specific mutagenesis (*10–15*); (ii) protection of receptor-binding site during the conjugation (*16, 17*); and (iii) reversible PEGylation (*18–22*). The latter is essentially a prodrug approach in which one or several PEG chains are acting as pro-moieties. Each of these approaches has its merits and can potentially be effective in some specific situations, and each one of them also presents nontrivial technical obstacles.

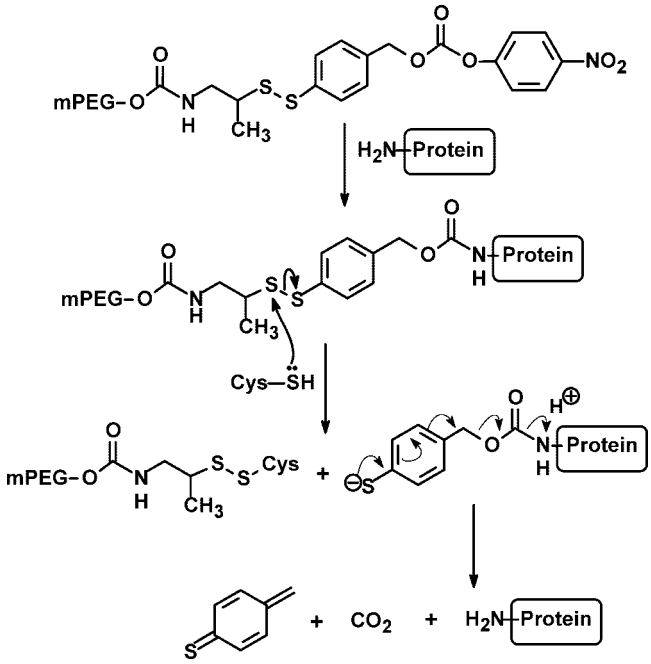
We recently introduced the new PEGylation chemistry depicted in Scheme 1, which was designed to produce gradual in vivo loss of PEG chains from its conjugates (*21, 23, 24*). It is based on benzyl urethane *para*-substituted with a disulfide, dithiobenzyl (DTB) moiety. The urethane formed between an amino group of a protein and the benzyl is quite a stable linkage. However, reductive or thiolytic scission of the disulfide leads to an unstable *p*-mercaptobenzyl urethane intermediate, which breaks down via 1,6-elimination and decarboxylation, and results in the regeneration of the original amino group. To the best of our knowledge, *p*-aryldisulfanyl-substituted benzyloxycarbonyl mitomycin C described by Senter et al. (*25*) constituted the first disclosure of a DTB-urethane derivative. In our laboratory, we used this linkage to prepare a lipid-based anticancer prodrug (*26, 27*) and also thiolytically cleavable lipopolymers (*21, 28*) that were utilized for liposomal and gene delivery. In addition to the thiolytic recovery of the modified amino group, the relative stability of DTB at neutral pH in the absence of redox agents is important for the convenient formulation and storage of the DTB-based conjugates. This feature offers an advantageous distinction from other published approaches to reversible PEGylation (*18–20, 22*) that are triggered by hydrolysis or pH changes. Since reductive scission of disulfide-linked conjugates is known to occur in various physiological environments (*29, 30*), it was envisioned that similarly under in vivo conditions DTB urethane would be cleaved, for example, by cysteine or glutathione-mediated thiolysis or perhaps by an enzymatic

* To whom correspondence should be addressed. Intradigm Corporation, 3350 W. Bayshore Rd., Suite 100, Palo Alto, CA 94303. Tel: (650) 855-1517. Fax: (650) 855-9699. E-mail: szalipsky@intradigm.com.

[1]Abbreviations: DTB, dithiobenzyl; PEG, polyethylene glycol; mPEG, monomethoxy-PEG; mPEG5K, mPEG of molecular weight 5000 Da; NPC, *p*-nitrophenyl carbonate.

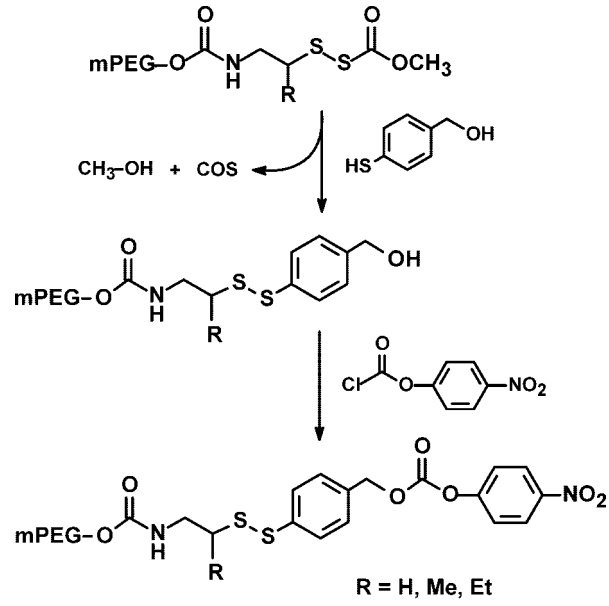
10.1021/bc7001902 CCC: $37.00 © 2007 American Chemical Society
Published on Web 10/13/2007

Scheme 1. Reversible PEGylation of Proteins Using Thiolytically Cleavable DTB Urethane Linker[a]



[a] Sterically hindered DTB containing a methyl group adjacent to the disulfide was utilized in the current study. Note that the thiolytic cleavage shown here for cysteine is equally applicable to any biologically relevant thiol, e.g., glutathione, albumin, etc.

Scheme 2. Synthesis of mPEG-DTB-NPC, Reagent for the Attachment of mPEG-DTB Moieties To Amino Groups on Proteins[a]



[a] Note that the size of the R residue (also shown in Scheme 3) affects the hindrance on the adjacent disulfide and, ultimately, the rate of the PEG detachment from the protein conjugates.

reduction. Thus, in vivo PEG would be present in these reversible conjugates only temporarily, improving such characteristics as pharmacokinetics and biodistribution. As a result of the PEG-chain detachment, the original native protein and its activity would ultimately be regenerated. In essence, the system is intended to work as a macromolecular prodrug, where each PEG chain is acting as a promoiety.

We chose lysozyme as a model protein to perform the initial feasibility studies on conjugate preparation and thiol-mediated decomposition, as well as pharmacokinetic properties of the reversible PEG-DTB-proteins. Lysozyme is a readily available, small protein (14.4 kDa) similar in size to various cytokines and chemokines, and its lytic activity is directed toward a very large substrate, the bacterial cell wall peptidoglycan. Therefore, lysozyme represents a suitable model for a small protein, which is acting on a large substrate to exhibit its biological activity. Herein, we report the results of the lysozyme model studies.

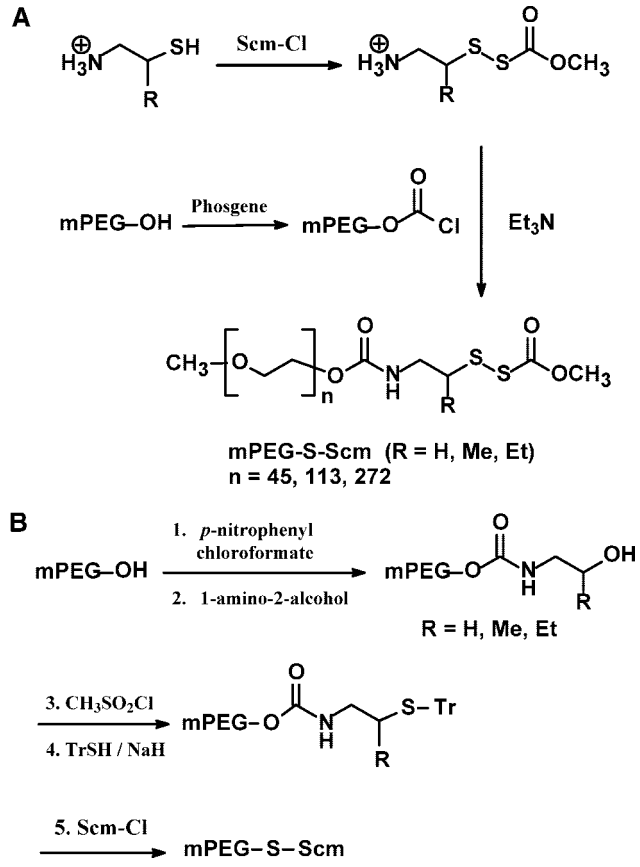
RESULTS AND DISCUSSION

A new reactive polymer derivative, mPEG-DTB-NPC, which is required for the preparation of PEG-DTB-protein conjugates, was synthesized as shown in Scheme 2. This synthesis scheme was applied to mPEG derivatives with molecular weights of 2000, 5000, and 12000 Da with equal success, although the mPEG-2000 derivatives were mainly utilized for the preparation of DTB-linked lipopolymers (*21*, *28*). The R residue, which is intended to regulate the steric hindrance on the disulfide bridge of the DTB urethane linkage and ultimately the rate of the cleavage of this linker was varied from hydrogen to more bulky methyl and ethyl groups. Our earlier experiments with PEG-lipids and PEG-liposomes indicated that when R = Me or Et the liposomes containing these DTB-linked lipopolymers exhibited long persistence in the bloodstream characteristic to STEALTH liposomes, while the analogous preparations with R = H did not (*28*). On the basis of these observations, the protein modifications described herein were performed with the former more stable mPEG-DTB form of the linkage containing a methyl substituent on the disulfide adjacent carbon (Scheme 1).

For the formation of the DTB-mixed disulfide, we relied on the reactivity of the *S*-sulfenylcarbomethoxy (S-Scm) functionality (*21*) (Scheme 2). Facile formation of asymmetrical disulfides via fragmentation of sulfenyl thiocarbonates is known to proceed even with weakly nucleophilic aromatic thiols (*31*). The reaction is driven by the release of COS and methanol. The mPEG-S-Scm was assembled from 1-alkyl-substituted 2-aminothiols (*32*), which were first reacted with methoxycarbonylsulfenyl chloride (Scm-Cl) to form the corresponding ammonium hydrochloride sulfenyl thiocarbonates. The latter were purified and then reacted with mPEG-chloroformate, forming stable carbamate attachments (Scheme 3A). An alternative approach to the *S*-sulfenyl thiocarbonates, prepared by treatment of the corresponding PEG-S-trityl with Scm-Cl by a modification of previously published method (*33*), also worked well. The corresponding S-Tr derivative was prepared in a clean manner from mPEG-OH in four steps as depicted in Scheme 3B. The reaction of mPEG-S-Scm with *p*-mercaptobenzyl alcohol was carried out in methanol at ambient temperature, yielding mPEG-DTB-OH. This reaction was considerably faster for the less-hindered Scm derivatives (R = H), but nevertheless, it was driven to completion with excess *p*-mercaptobenzyl alcohol over 24–48 h in the case of the more hindered analogues (R = Me and Et). To enable alkoxycarbonylation of amino groups, the hydroxyl group of mPEG-DTB-OH was converted into a reactive carbonate form by treatment with nitrophenyl choloroformate (Scheme 2).

This new reagent, mPEG-DTB-NPC (Scheme 1), was utilized in a series of lysozyme modification experiments. The aim of these experiments was to prepare lightly PEGylated species and to study their thiolytic decomposition while comparing the properties to those of the noncleavable analogues of the PEG-lysozyme. The latter were prepared with a known alkoxycarbonylating reagent of proteins, mPEG-NPC (*34*). Our lysozyme modification experiments demonstrated that both reagents, mPEG-DTB-NPC and mPEG-NPC, had similar reactivity

Scheme 3. Synthesis of mPEG-S-Scm by Two Different Approaches: (A) Reacting the Aminothiol Compound with Methoxycarbonylsulfenyl Chloride (Scm-Cl), Followed by Coupling To mPEG-Chloroformate, and (B) Generation of mPEG-S-Tr Followed by Its Conversion To mPEG-S-Scm



toward amino groups on proteins and under the same conditions yielded comparable PEGylated lysozyme mixtures with 1–3 polymer chains per protein molecule. We characterized these conjugates by SDS–PAGE, RP-HPLC, and MALDI-TOF-MS (Figures 1, 2 and 3). We purified the PEG-lysozyme conjugates from the unreacted PEG and protein by cation-exchange chromatography. Baseline separations between the reaction mixture components, PEG-lysozyme, unreacted protein, and excess of PEG reagent, were achievable on the CM-HEMA column. Fractionation on the CM-column also allowed us to obtain pure 1:1 PEG-lysozyme conjugates, which proved to be very useful in our mechanistic studies. MALDI-TOF-MS confirmed the expected molecular masses of $(mPEG)_{1-3}$-lysozyme conjugates in the purified samples. It also showed the presence of the unmodified lysozyme present in the mass spectra of the PEG-DTB-conjugates (Figure 3), even though the preparations were free from the native enzyme by RP-HPLC and SDS–PAGE. This is explained by the partial cleavage of the disulfides linkages under the MALDI conditions, which has been previously reported (*21*, *35*). The conjugate derived from both mPEG-5K and -12K (not shown) produced similar patterns of MALDI spectra.

As illustrated in Scheme 1, the reversibility of the DTB-urethane linkage is based on the thiolytic or reductive cleavage of the disulfide bond. Under in vivo conditions, this can occur via a reaction with any of the thiols present in blood plasma or tissues or by an enzymatic reductive scission of the disulfide. Among the low molecular weight thiols present in the physiological milieu, cysteine is the most reactive. Therefore, to examine the PEG detachment reaction, we used cysteine as the cleaving agent. Upon incubation of the $(mPEG\text{-}DTB)_n$-

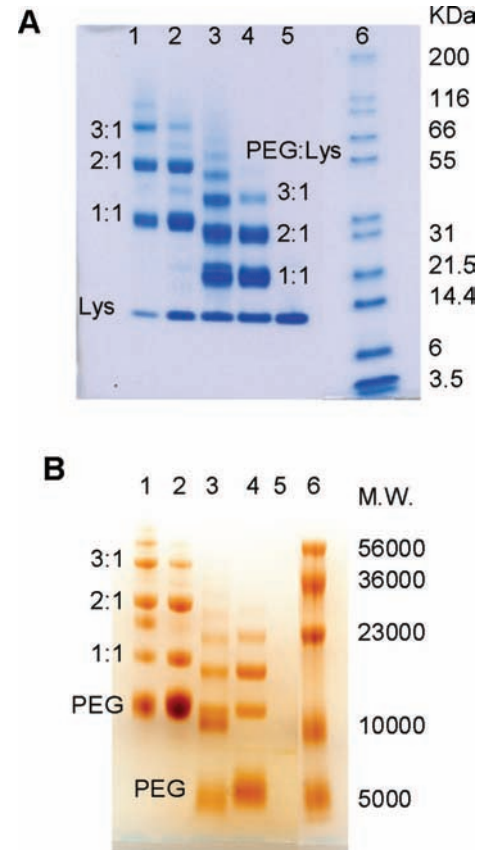


Figure 1. SDS–PAGE showing the content of the conjugate mixtures, using two visualization methods: (A) Coomassie blue detection for protein and (B) iodine staining for PEG species. Lanes: (1) mPEG12K-DTB-lysozyme conjugation, (2) mPEG12K-lysozyme conjugation, (3) mPEG5K-DTB-lysozyme conjugation, (4) mPEG5K-lysozyme conjugation, (5) lysozyme, and (6) molecular weight markers (protein or PEG).

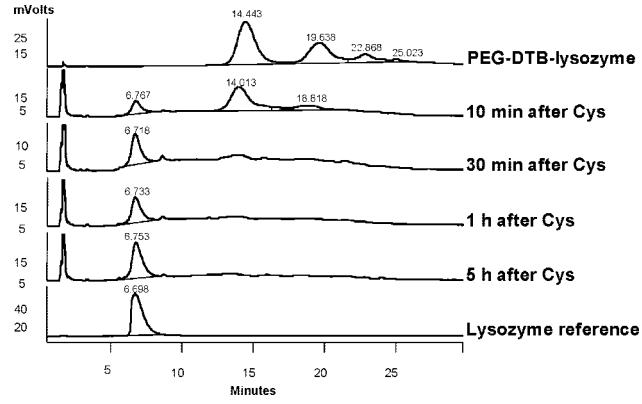


Figure 2. RP-HPLC of $(mPEG5K)_{1-3}$-DTB-lysozyme conjugates and follow-up of their decomposition in 1 mM cysteine solution.

lysozyme–conjugate mixture with cysteine, gradual decomposition and cleavage of the PEG chains took place. Following the de-PEGylation process with RP-HPLC (Figure 2), it was revealed that the heavier PEG-lysozyme species were converted to lighter ones and ultimately formed a sole protein component. The identity of the regenerated protein showing the same elution time on RP-HPLC as lysozyme was corroborated by ion spray LC-MS. Average spectra taken on the peak eluting at 6.7 min were identical to the spectra of the reference lysozyme (Figure 4A and D). LC-MS also confirmed that the main peak of the conjugate mixture eluting at 14.4 min (Figure 4B) was mPEG5K-DTB-lysozyme (calculated molecular mass of 20

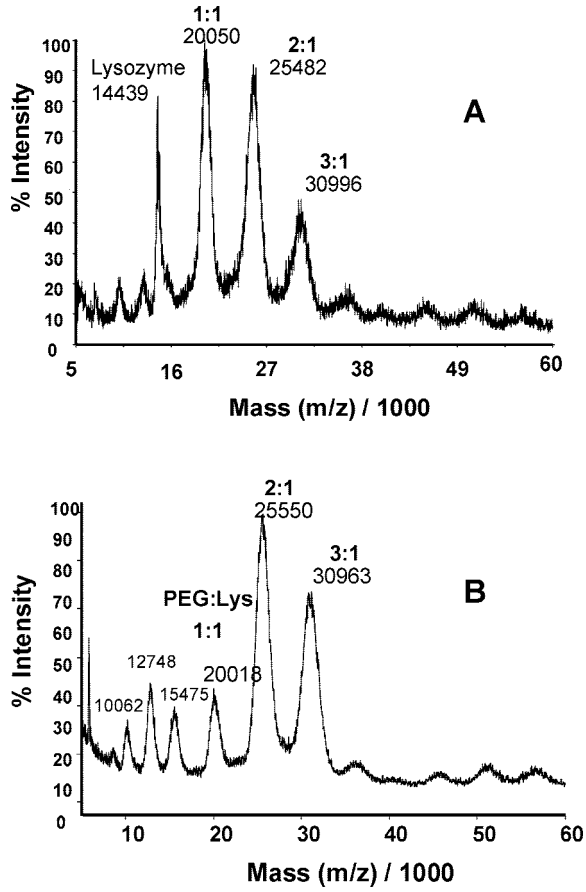


Figure 3. MALDI-TOF spectra of (A) mPEG5K-DTB-lysozyme conjugates and (B) their noncleavable counterparts.

kDa). Two distinct PEG products with bell-shaped distributions centered around 5480 and 5600 Da, differing approximately by the molecular weight of cysteine (121 Da), were observed during the cysteine-mediated cleavage of DTB urethane. The relative amounts of the lighter species (eluting later, less polar mPEG-SH) versus the heavier ones (eluting earlier, more polar mPEG-SS-Cys) increased with the cysteine incubation time, as judged by the ratios of their RP-HPLC peaks (result not shown). This is consistent with the disulfide-linked mPEG-cysteine being the main product (Scheme 1) at the early time points and its conversion to mPEG-thiol with time. For comparison, the ion spray MS of the corresponding mPEG5K-DTB-OH produced a typical bell-shaped distribution of signals centering around 5600 Da. Upon closer examination of the cysteine-mediated de-PEGylation reaction using the 1:1 conjugate of PEG5K-DTB-lysozyme (Figure 5A), we learned that the putative *p*-mercaptobenzyl urethane lysozyme intermediate (confirmed by LC-MS; Figure 4C) was detectable by RP-HPLC. As shown in Figure 5B, the decomposition of this intermediate occurred slower than the initial thiolysis step, which explains why the disappearance of the starting conjugate was faster than the appearance of the free lysozyme product.

One of the characteristics of lysozyme that makes it an excellent model for a large substrate binding protein is the high sensitivity of its cell wall-lysing activity to PEGylation. Consistent with previously reported observations (*36, 37*), we found that attachment of even one PEG chain to lysozyme completely abolishes its enzymatic activity in a *Micrococcus luteus* lysis assay. As illustrated in Figure 6, both cleavable PEG-lysozyme and its noncleavable counterpart showed no activity in this assay. However, in contrast to the noncleavable conjugate, the treatment of PEG-DTB-lysozyme with cysteine restored the lytic activity of the enzyme.

Pharmacokinetic properties of PEG-proteins are mainly governed by the molecular size of the conjugates (*38*). In other words, the results obtained with PEG-lysozyme should be roughly representative of conjugates derived from proteins of size similar to that of lysozyme. We studied the pharmacokinetic properties of the ^{125}I-labeled $(mPEG)_{1-3}$-lysozyme conjugates in rats, comparing the stable urethane analogue to the cleavable DTB-linked counterpart and to the native protein. In order to enhance the contrast between the free protein and its conjugates, we used the higher molecular weight mPEG-12K in these experiments. Following intravenous administration, we observed that both PEG-lysozyme preparations circulated much longer than the native protein (Figure 7A). The DTB-linked conjugate exhibited pharmacokinetic characteristics similar to those of the noncleavable analogue, which hinted at an apparent plasma stability of the DTB-linkage-containing methyl group on the α carbon. This result was consistent with our observations in the liposomal system (*28*), in which the PEG-liposome containing the same sterically hindered DTB linkage also exhibited the same clearance curves as those of the liposome containing the stable urethane-linked lipopolymer analogue. Administration of the same mPEG12K-lysozyme preparations by the subcutaneous route (Figure 7B) resulted in noticeably larger AUC for the DTB-linked conjugate compared to its noncleavable urethane counterpart. Subcutaneous administration is often considered to be a more attractive and less invasive route compared to the intravenous route. Both conjugates exhibited a much longer presence in circulation than the free protein, which rapidly peaked in the bloodstream after subcutaneous administration and also was rapidly cleared. These route-of-administration differences between the results of the two pharmacokinetic experiments and their implications regarding the stability of DTB linker in the relevant environments might be due to the differences in the thiol species and their concentration between plasma and interstitial fluid. It was reported, for example, that the levels of sulfur-containing amino acids are higher in interstitial fluids compared to those in plasma (*39*). However, the albumin concentration in interstitial fluid is significantly lower (*40*) compared to its plasma levels, where it is the most abundant and also the most reactive thiol (*41*).

The latter fact prompted our investigation of the stability of our DTB-linked conjugates in the presence of albumin or plasma. Note that there is a great deal of homology among rat (RSA), human (HSA), and bovine (BSA) albumin, all of which contain a single reactive thiol group, Cys-34. First, we followed the integrity of purified 1:1 PEG5K-lysozyme incubated in BSA solution (4% in PBS, similar to the albumin concentration in plasma) by SDS–PAGE using PEG-sensitive staining. This staining provides information on PEG-containing species, although proteins at high concentrations are also visualized. Conversely, the free lysozyme present at a relatively low concentration was hardly detectable. The results of these experiments are shown in Figure 8. The band of mPEG-DTB-lysozyme completely disappeared from the gel after overnight incubation with albumin (Figure. 8A, lane 9). Under the same conditions, the noncleavable conjugate remained stable (lane 4), excluding the possibility that noncovalent association with albumin was responsible for the disappearance of the cleavable PEG-lysozyme (lane 9). BSA with blocked thiol (pretreated with iodoacetamide) did not react with mPEG-DTB-lysozyme (lane 8), indicating that the thiol group played a role in the decomposition of the conjugate. Finally, when a BSA-decomposed sample of mPEG-DTB-lysozyme was treated with excess DTT, free mPEG5K was readily detectable on the gel (lane 7) to the same extent as cysteine-mediated cleavage product (lane 3). Likewise, mPEG5K-DTB-lysozyme incubations in rat plasma (Figure 8B) produced the same pattern of

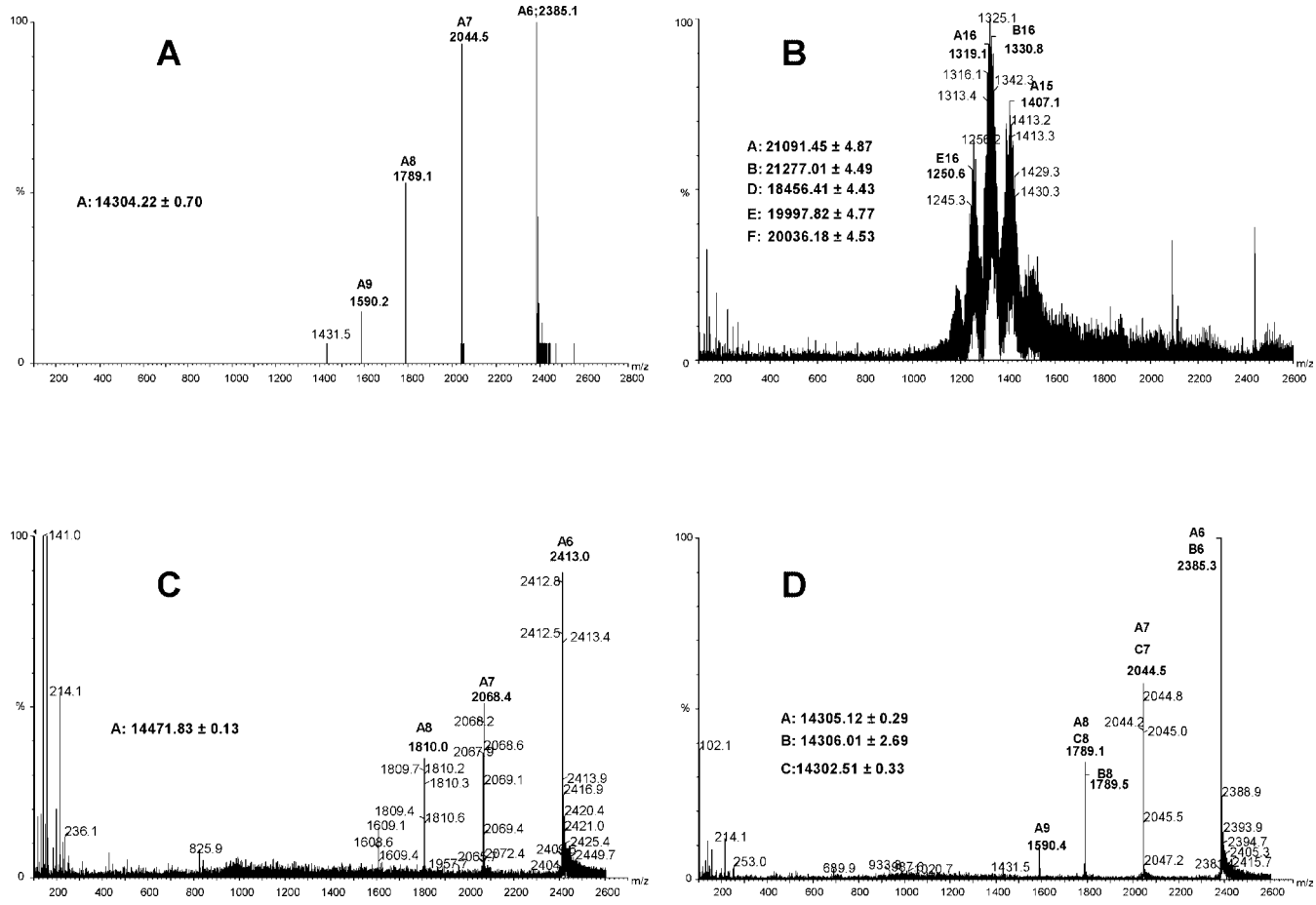


Figure 4. ES-MS spectra of mPEG5K-DTB-lysozyme, the intermediate detected during cysteine-mediated cleavage, and the protein product of this cleavage. (A) Lysozyme reference, (B) mPEG5K-DTB-lysozyme, (C) cleavage intermediate, *p*-mercaptobenzyl urethane lysozyme, and (D) lysozyme regenerated after the decomposition of mPEG5K-DTB-lysozyme.

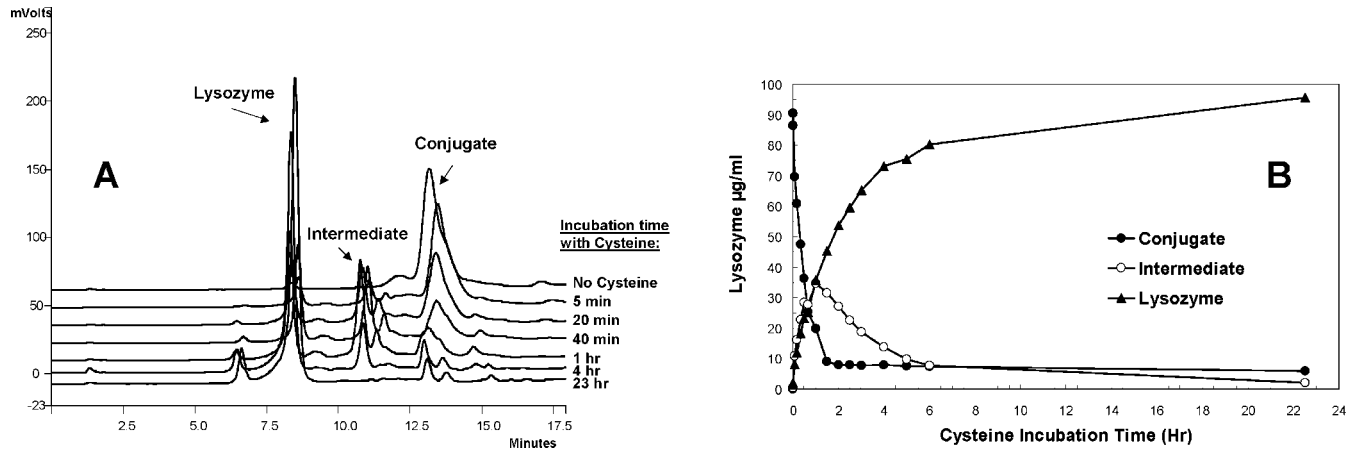


Figure 5. RP-HPLC follow up of 1:1 PEG5K-DTB-lysozyme incubation in cysteine (0.6 mM) solution. (A) Overlay of chromatograms obtained at different time points and (B) time course of the reaction obtained by the integration of the disappearing conjugate, regenerated lysozyme, and the putative *p*-mercaptobenzyl urethane intermediate species.

decomposition as in the albumin solution. These experiments clearly show that albumin cleaves the DTB linkage, and PEG becomes attached to albumin (or another plasma protein), which can be liberated by the excess low molecular weight thiol (DTT). Because of the high concentration of albumin, its oligomers, and other contaminant proteins in the BSA and plasma preparations that we used, in addition to the relatively small shift affected by mPEG5K, the disulfide-linked PEG-albumin species formed during the DTB cleavage were not distinguishable from the background on these gels. In further corroboration of albumin-mediated cleavage, incubation of a model compound, mPEG12K-DTB-Glycine, in excess of HSA, produced facile cleavage accompanied by a clear SDS–PAGE band of mPEG12K-albumin (approximately 100 kDa on a protein molecular weight scale) readily detectable within a few hours and continuing to increase for up to 96 h (result not shown).

In this article, we demonstrate the synthesis of a new PEG-based reagent for the preparation of thiolytically cleavable PEG-DTB-protein conjugates. Using lysozyme as a model, we show that such conjugates are prepared and characterized as their

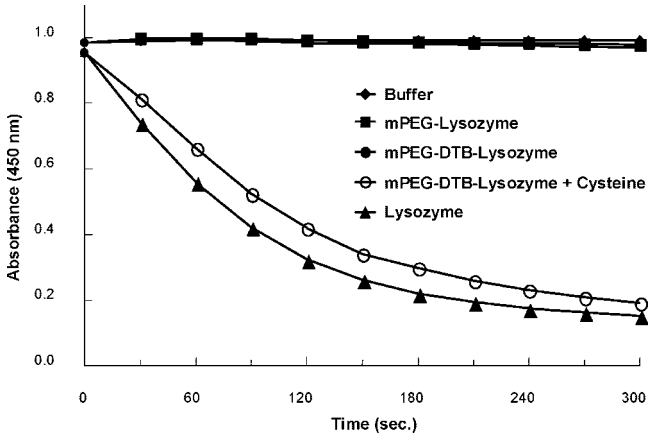


Figure 6. Turbidometric assay of bacterial cell wall lysis of lysozyme and its conjugates. The conjugates and the control samples were treated as described in the Materials and Methods section, under lysozyme activity assay.

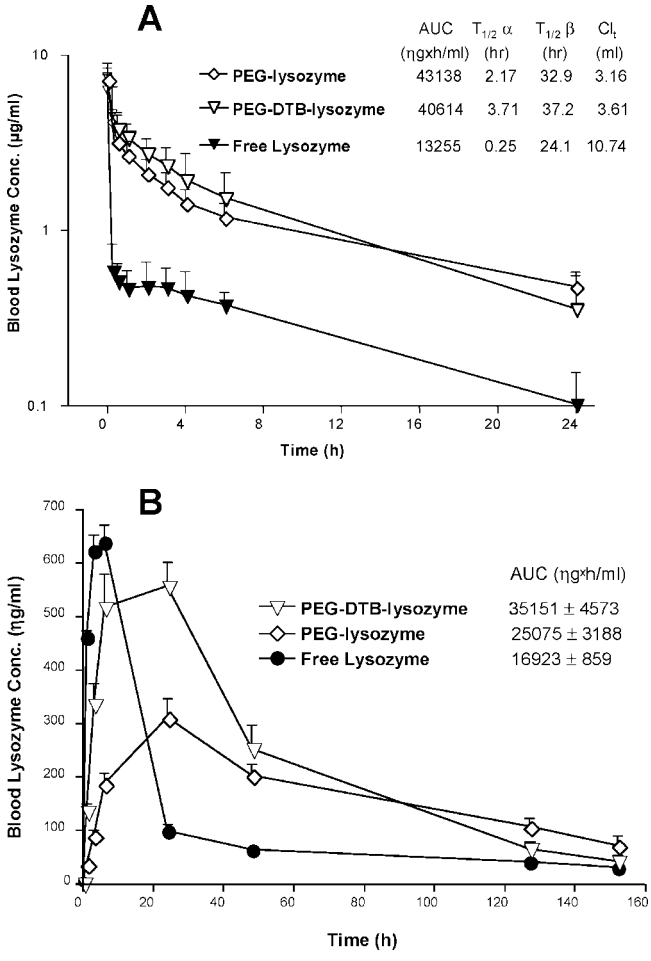


Figure 7. Pharmacokinetics in rats of ^{125}I-labeled mPEG12K-DTB-lysozyme conjugates, its noncleavable analogues, and the free parent protein. Clearance curves were constructed from the radiolabeled detection of ^{125}I after (A) intravenous and (B) subcutaneous administration.

noncleavable counterparts. Thiolytic cleavage occurs under mild conditions achievable in vivo, and most importantly, as expected from a true prodrug, the original native protein is generated as the result. This was demonstrated both by complete recovery of the PEGylation-induced loss of activity and by LC-MS yielding identical spectra of the native and de-PEGylated lysozyme. Furthermore, our studies show that although mPEG12K-DTB-lysozyme exhibited long circulating characteristics similar to its noncleavable counterpart, the DTB linker is clearly vulnerable to both low and high molecular weight biologically relevant thiols, cysteine, and albumin. The latter thiol is the most likely culprit responsible for the decomposition of the conjugate in plasma. The observation of both DTB cleavage and long circulation of mPEG12K-DTB-lysozyme could be the result of a relatively slow breakdown rate; however, alternative explanations are also possible. We investigated, in further detail, the albumin reaction with several PEG-DTB conjugates, and the results as well as the insight into the possible mechanisms involved and the reasons for the long in vivo circulation are presented in a separate paper (Hutchins, M. U., et al., in preparation).

MATERIALS AND METHODS

Lysozyme was obtained from Roche Molecular Biochemicals, Indianapolis, IN. Amino-2-propanethiol hydrochloride (*32*) and 4-mercaptobenzyl alcohol (*42*) were prepared as described elsewhere. All the synthetic procedures below, although written for derivatives of mPEG5K, are equally applicable to the mPEG12K analogues (gifts from Union Carbide and NOF, respectively). All the NMR spectra were acquired in DMSO-d_6/Me_4Si using 360 MHz spectrometer at Acorn NMR, Livermore, CA.

Methoxycarbonyldisulfanyl-2-propylamonium Chloride. The title compound was prepared by reacting methoxycarbonylsulfenyl chloride with an equivalent amount of amino-2-propanethiol hydrochloride according to the previously published procedures (*43*, *44*). Amino-2-propanethiol hydrochloride (1.83 mL, 19.44 mmol) in methanol (15 mL) was added dropwise (~1.0 mL/min) to a cold (4 °C) solution of methoxycarbonylsulfenyl chloride (Scm-Cl, 2.5 g, 19.6 mmol) in methanol (15 mL). The solution was stirred at room temperature for 3 h and then rotary evaporated. The residue was taken up in acetone and then stripped of the solvent two more times, resulting in the formation of a white solid. Silica-C8 (1 g) was added to the product solution in MeOH, which was then evaporated. The product-containing residue was added to the top of the C8-silica column and was eluted with water under N_2 pressure. Fractions containing the pure product were combined, evaporated, and lyophilized from *tert*-butanol (5 mL). It was further dried in vacuo over P_2O_5 to give product as a white solid (2 g, 47% yield). ^{1}H NMR δ: 1.30 (d, C*H*$_3$CH, 3H), 2.94 (br t, C*H*$_2$NH$_3$Cl, 2H), 3.37 (q, CH$_3$C*H*CH$_2$NH$_3$Cl, 1H), 3.88 (s, CH$_3$OCO, 3H), 8.21 (br s, CH$_3$CHCH$_2$N*H*$_3$Cl, 3H) ppm.

MPEG5K-Oxycarbonylaminopropyl-*S*-sulfenylcarbomethoxy (mPEG-S-Scm), Method A. This method is shown in Scheme 3A. mPEG-OH (15 g, 3 mmol) was dried by azeotropic removal of toluene (100 mL). The solution was cooled, diluted with dichloromethane (40 mL), and treated with phosgene (10 mL, 19.3 mmol) at 4 °C. The ice bath was removed, and the reaction was stirred at room temperature overnight and then evaporated to dryness, leaving solid mPEG-chloroformate. Methoxycarbonyldisulfanyl-2-propylamonium chloride (686.7 mg, 3.15 mmol) and then TEA (836.3 μL, 6 mmol) were added to the mPEG-chloroformate in chloroform (30 mL). The reaction mixture was stirred at room temperature overnight and then evaporated. The residue was taken up in warm ethyl acetate (150 mL) and filtered to remove the TEA hydrochloride. The solvent was removed, and the product was purified by recrystallization from ethyl acetate/iso-propanol (100 /100 mL, three times) and dried in vacuo over P_2O_5, yielding a white solid (14.5 g, 93%). ^{1}H NMR δ: 1.18 (d, C*H*$_3$CHSS$_2$, 3H), 3.10 (m, C*H*$_2$NH, 2H), 3.24 (s, CH$_3$O, 3H), 3.50 (s, PEG, ≈520H), 3.86 (s, C*H*$_3$OCOSSCH, 3H), 4.05 (t, OCOC*H*$_2$, 2H), 7.38 (t, OCON*H*, 1H) ppm.

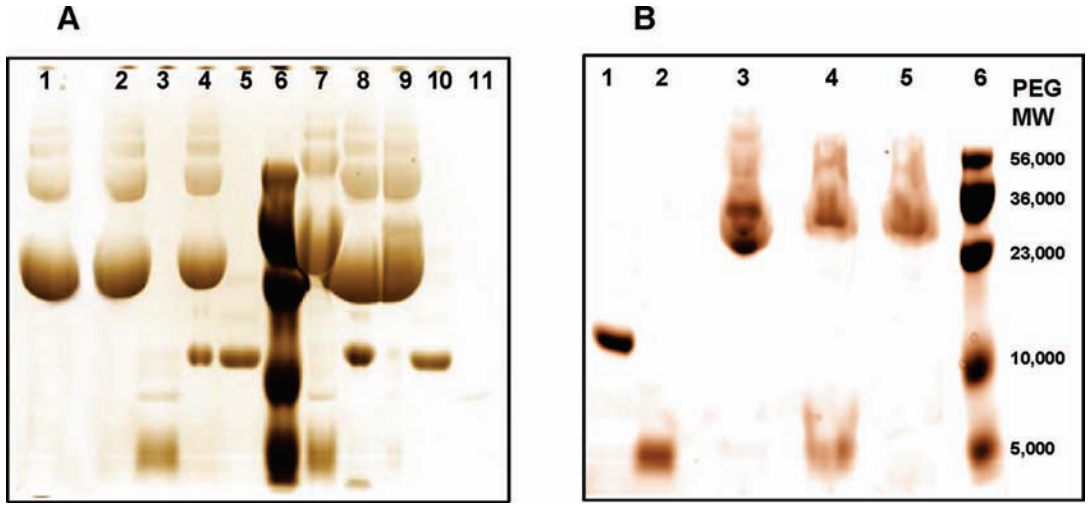


Figure 8. SDS–PAGE gels of samples from an overnight incubation of mPEG5K-DTB-lysozyme and controls in (A) albumin (BSA) solution and in (B) rat plasma. Samples list A: (1) BSA-blocked SH, (2) BSA, (3) mPEG-DTB-lysozyme + cysteine, (4) noncleavable PEG-lysozyme + BSA, (5) noncleavable PEG-lysozyme, (6) PEG MW Markers, (7) mPEG-DTB-lysozyme + BSA, then DTT, (8) mPEG-DTB- lysozyme + BSA-blocked SH, (9) mPEG-DTB-lysozyme + BSA, 16 h, (10) mPEG-DTB-lysozyme, and (11) lysozyme. Samples list B: (1) mPEG-DTB-lysozyme, (2) mPEG-DTB-lysozyme + cysteine, (3) mPEG-DTB-lysozyme in rat plasma, 18 h, (4) mPEG-DTB-lysozyme in rat plasma, then DTT, (5) rat plasma control, and (6) PEG molecular weight markers.

mPEG5K-Nitrophenyl Carbonate (mPEG-NPC). Azeotropically dried mPEG5K-OH (40 g, 8 mmol) in toluene/dichloromethane (20/100 mL) solution was treated with *p*-nitrophenyl chloroformate (2.42 g, 12 mmol) and TEA (3.3 mL, 24 mmol). After the initial cooling (≈15 min) on ice–water during the addition of the reagent, the reaction mixture was stirred at room temperature overnight. The reaction solution was evaporated to dryness, and the residue was taken up in warm ethyl acetate (≈50 °C). TEA hydrochloride was filtered off and washed with a small volume of warm ethyl acetate. The solvent was rotary evaporated, and the residue was recrystallized from iso-propanol twice and then dried in vacuo over P_2O_5, yielding 38.2 g (92%) of white powder. ^{1}H NMR δ: 3.24 (s, CH_3O, 3H), 3.50 (s, PEG, 460H), 4.37 (t, OCOCH_2, 2H), 7.57 (d, C_6H_5, 2H), 8.32 (d, C_6H_5, 2H) ppm.

MPEG5K-Oxycarbonylamino-2-propanol (mPEG-*i*Pr-OH). Amino-2-propanol (1.1 mL, 14.52 mmol) and TEA (2.02 mL, 14.52 mmol) were added to mPEG5K-NPC (25 g, 4.84 mmol) solution in DMF (60 mL) and CH_2Cl_2 (40 mL). The reaction solution turned yellow. It was stirred at room temperature for 30 min. TLC ($CHCl_3$/MeOH = 90:10) showed that the reaction went to completion. Dichloromethane was removed by rotary evaporation, and iso-propanol (250 mL) was added to the concentrated DMF solution. The precipitated product was collected by filtration and further purified by two additional precipitations from iso-propanol. It was then dried in vacuo over P_2O_5, yielding 22.1 g (90%) of white powder. ^{1}H NMR δ: 0.99 (d, CH_3CH, 3H), 2.90 (m, NHCH_2, 2H), 3.24 (s, CH_3O, 3H), 3.50 (s, PEG, ≈480H), 4.04 (t, OCOCH_2, 2H), 4.85 (d, CH_3CHO*H*, 1H), 7.11 (t, NH, 1H) ppm.

MPEG5K-Oxycarbonylamino-2-propyl methanesulfonate (mPEG-OMs). mPEG5K-oxycarbonylamino-2-propanol (22.12 g, 4.34 mmol) was azeotropically dried in its toluene solution (45 mL). The solution was cooled, diluted with dichloromethane (60 mL), and then treated with methanesulfonyl chloride (604.6 μL, 7.81 mmol) and TEA (3.93 mL, 28.21 mmol, 6.5 equiv) while maintaining continuous stirring and cooling (4 °C), and protecting the reaction mixture against air moisture. After 30 min, the cooling bath was removed, and the reaction mixture was stirred at room temperature for 16 h. The solution was rotary evaporated, and the residue was taken up with warm ethyl acetate. TEA salt was removed by filtration. The product was precipitated with iso-propanol and recrystallized with the same solvent two more times, and then dried in vacuo over P_2O_5 yielding 20.27 g (90%) of white powder. ^{1}H NMR δ: 1.28 (d, CH_3CHOMs, 3H), 3.13 (s, CH_3O_2SO, 3H), 3.18 (t, CH_2NH, 2H), 3.24 (s, CH_3O, 3H), 3.50 (s, PEG, ≈480H), 4.08 (t, $OCOCH_2$, 2H), 4.65 (q, C*H*OMs, 1H), 7.51 (t, NH, 1H) ppm.

mPEG5K-Oxycarbonylamino-2-propyl-*S*-triphenylmethane (mPEG-S-Tr). Sodium hydride (60% oil dispersion, 377 mg, 9.4 mmol, 4.75 equiv) was treated with anhydrous toluene (60 mL) at ≈4 °C. Triphenylmethanethiol (3.92 g, 14.6 mmol, 7.15 equiv) was added after 5 min, followed by mPEG-oxycarbonylamino-2-propyl methanesulfone (10.3 g, 1.98 mmol) 10 min later. The reaction turned yellow. After 45 min, acetic acid (440 μL, 7.7 mmol) was added to the reaction mixture to neutralize the excess sodium hydride. A white precipitate was formed. The solution was evaporated to dryness. Warm ethyl acetate (30 mL) and iso-propanol (70 mL) were added to the residue. The solution was filtered while still warm (≈40 °C) and then cooled down to facilitate product precipitation. Then the product was further recrystallized from iso-propanol/tert-butanol (100/20 mL) and dried in vacuo over P_2O_5, yielding 8.87 g (84%) of white powder. ^{1}H NMR δ; 0.75 (d, CH_3CHSTr, 3H), 2.42 (m, CHSTr, 1H); 2.77 (m, CH_2N, 2 H); 3.23 (s, CH_3O, 3H); 3.50 (s, PEG, ≈ 520H), 4.01 (t, OCOCH_2, 2H); 7.24 (t, *p*-H of $SC(C_6H_5)_3$ & NH, 4H); 7.33 (t, *m*-H of $SC(C_6H_5)_3$, 6H); 7.42 (d, *o*-H of $SC(C_6H_5)_3$, 6H) ppm.

MPEG5K-Oxycarbonylaminopropyl-*S*-sulfenylcarbomethoxy (mPEG-S-Scm), Method B. mPEG5K-oxycarbonylamino-2-propyl-*S*-triphenylmethane (8.87 g, 1.65 mmol) was dissolved in TFA/CH_2Cl_2 (10/10 mL) at 4 °C and treated with methoxy carbonylsulfenyl chloride (185.5 μL, 1.99 mmol) while vigorously stirring the solution. The reaction was allowed to proceed at room temperature for 45 min and then evaporated to dryness. The residue was recrystallized with iso-propanol/*tert*-butanol (80/20 mL) twice and then lyophilized from *tert*-butanol (5 mL) and further dried in vacuo over P_2O_5 to yield a white fluffy solid (8.32 g, 97 %). ^{1}H NMR was identical to that of the same derivative obtained in Method A (see above).

MPEG5K-Oxycarbonylaminopropyl-dithiobenzyl Alcohol (mPEG-DTB-OH). mPEG5K-oxycarbonyl-2-(aminopropyl)-*S*-sulfenylcarbomethoxy (8.32 g, 1.6 mmol) was reacted with *p*-mercaptobenzyl alcohol (592 mg, 4 mmol) in methanol/chloroform (25 mL, 90:10) at ambient temperature for 18 h. In

order to drive the reaction to completion, another portion of mercaptobenzyl alcohol (322 mg, 2.2 mmol) was added and allowed to react for 24 h. The reaction solution was evaporated to dryness. The solid residue was recrystallized from ethyl acetate/isopropanol (30/100 mL) three times and then dried in vacuo over P_2O_5, yielding a white powdery material (7.25 g, 94%). ^{1}H NMR δ: 1.17 (d, CH_3CHS$_2$, 3H), 3.02 (m, CH_2NH, 2H), 3.24 (s, CH$_3$O, 3H), 3.50 (s, PEG, ≈470H), 4.05 (br t, CH_2OCO, 2H), 4.48 (d, HOCH_2C$_6$H$_5$, 2H), 5.21 (t, *H*OCH$_2$C$_6$H$_5$, 1H), 7.30(d, C$_6H_5$, 2H), 7.46 (br t, mPEG-OCON*H*, 1H), 7.50 (d, C$_6H_5$, 2H) ppm.

MPEG5K-Oxycarbonylaminopropyl-dithiobenzyl Nitrophenyl Carbonate (mPEG-DTB-NPC). mPEG5K-oxycarbonylamino-2-propyl-dithiobenzyl alcohol (6.75 g, 1.27 mmol) was dissolved in CHCl$_3$ (30 mL) and treated with *p*-nitrophenyl chloroformate (513 mg, 2.54 mmol) and TEA (531 μL, 3.81 mmol) at 4 °C. After 30 min, the ice bath was removed, and the reaction mixture was stirred at room temperature overnight. The reaction solution was rotary evaporated, and the residue was taken up in warm ethyl acetate. TEA hydrochloride was filtered off, and then the solvent was evaporated. The solid residue was recrystallized with ethyl acetate/iso-propanol (30/100 mL) three times and dried in vacuo over P_2O_5, yielding 6.55 g (94%) of white solid. ^{1}H NMR δ: 1.18 (d, CH_3CHSSC$_6$H$_5$, 3H), 3.16 (m, CH$_2$N, 2H), 3.24 (s, CH_3O-PEG, 3H), 3.40 (s, PEG, 180H), 4.03 (br t, OCOCH_2, 2H), 5.28 (s, C$_6$H$_5$CH_2OCO, 2H), 7.45–7.60 (overlapping two types of C$_6$H$_4$ and NH, 7H), 8.31 (d, C$_6$H$_4$NO$_2$, 2H); ^{13}C NMR (DMSO-d_6) δ: 17.5, 45.1, 45.8, 58.0, 63.2, 68.8, 69.7 (PEG), 71.2, 122.5, 125.3, 126.7, 129.3, 137.8, 145.1, 151.9, 155.2, 156.2 ppm.

Preparation and Purification of PEG-Lysozyme Conjugates. Lysozyme (at final concentration of 10 mg/mL) was allowed to react in borate buffer (0.1 M, pH 8.0) at 25 °C for 2–5 h with either mPEG-DTB-NPC or mPEG-NPC, using the feed molar ratio of 3.5 PEG/lysozyme (0.5 PEG/amino group). The conjugation reactions were quenched by the addition of 10-fold excess of glycine.

PEG-lysozyme conjugates were purified on a CM HEMA-IEC Bio 1000 semipreparative HPLC column (7.5 × 150 mm) purchased from Alltech Associates, Deerfield, IL. First, the conjugation reaction was injected into the HPLC column in 10 mM sodium acetate buffer at pH 6. The elution with this buffer was continued until all unreacted PEG was removed. Then, 0.2 M NaCl in 10 mM sodium acetate at pH 6 was applied for 15 min in order to elute the PEGylated-lysozyme. Finally, the native lysozyme was eluted by increasing the salt concentration to 0.5 M NaCl over 20 min. Fractions (1 mL) were collected and assayed for protein and PEG contents. Thus, aliquots (25 μL) of each fraction were reacted with BCA protein assay reagent (200 μL, Pierce Chemical Company, Rockford, IL) in microtiter plate wells at 37 °C for 30 min, and the absorbance was read at 562 nm. Similarly, for PEG determination (*14*), 25 μL aliquots were reacted with 0.1% polymethacrylic acid solution in 1 N HCl (200 μL), in microtiter plate wells, followed by absorbance reading at 400 nm. Fractions containing both protein and PEG were pooled. For the isolation of the PEG-lysozyme containing only one PEG moiety, the same cation-exchange chromatography protocol was repeated and the collected fractions were analyzed by the HPLC reversed-phase assay. Fractions containing the single peak of 1:1 PEG-lysozyme conjugate species were pooled.

SDS–PAGE. Polyacrylamide gel electrophoresis under denaturing conditions was performed for conjugate characterization. Precast 4–12% NuPAGE Bis-Tris gels, MES running buffer, molecular weight protein standards (Mark12), and a Colloidal Coomassie G-250 staining kit, were all obtained from Invitrogen, Carlsbad, CA. In a typical gel, 1 to 3 μg of protein containing sample were loaded per well, then electrophoresed at a constant voltage of 200 mV, and stained for protein according to the manufacturer's instructions. For PEG detection, a duplicate gel was stained with iodine according to Kurfürst (*45*).

Reversed-Phase HPLC Analysis. RP-HPLC separation of PEG-lysozyme conjugates was achieved on a Vydac Protein C4 (4.6 × 150 mm) column eluted at 1 mL/min with an aqueous acetonitrile gradient as follows. Each chromatography run started with mobile phase A (30% acetonitrile, 5% 0.1 M sodium acetate at pH 5, and 65% H_2O) and over a period of 40 min ended with mobile phase B (50% acetonitrile, 50% 0.1 M sodium acetate at pH 5). A UV detector set to 280 nm was used to monitor the chromatography.

De-PEGylation Experiments. A mixture of purified mPEG-DTB-lysozyme conjugates (2 mg/mL protein), containing 1:1, 2:1, and 3:1 conjugate species, was incubated with 1 mM cysteine in 0.1 M sodium phosphate buffer at pH 7.3 containing 5 mM EDTA at 37 °C on a rocking mixer. Aliquots were taken out from the reaction vial at various time points and analyzed by RP-HPLC as described above. These results are shown in Figure 2.

De-PEGylation experiments of the cation-exchange-purified 1:1 PEG-DTB-lysozyme (0.5 mg/mL protein) treated at room temperature with 0.6 mM cysteine (or glutathione (not shown)) were monitored by a modified RP-HPLC method on the same Vydac Protein C4 column and flow rate but under the following elution protocol, which was also suitable for LC-MS. Each chromatography run was conducted with a gradient of 30% to 40% mobile phase B in 18 min. Mobile phase A was composed of 0.1% TFA in 5% acetonitrile and 95% H_2O, while mobile phase B was composed of 0.1% TFA in 95% acetonitrile and 5% H_2O. The fluorescent detector was set at 295 nm excitation and 360 nm emission. The results of these experiments are depicted in Figure 5.

Lysozyme Activity Assay. The enzymatic activity of lysozyme and its conjugates was assessed as previously described (*46*). *Micrococcus luteus* cells were suspended, at 0.3 mg/mL in 0.1 M sodium phosphate buffer at pH 7.3. Test samples were diluted to 0.5 mg/mL (lysozyme equivalent) in the phosphate buffer. Cells suspension and test sample were mixed at a v/v ratio of 1:14 in a 1 cm glass cuvette. Absorbance at 450 nm was immediately recorded for the initial time reading and then for the subsequent 30-s time intervals.

LC-MS. Purified PEG-lysozyme containing only one PEG moiety per lysozyme was treated with 1 mM cysteine, while the reaction was monitored by LC-MS. The HPLC system (HP 1100 LC-102) equipped with the same C4 column as that described above was connected to an electrospray mass spectrometer (Micromass QTOF II), permitting peaks identification by their molecular weights. The sodium acetate in the mobile phase was replaced with ammonium acetate in order to minimize salt interference with electrospray ionization.

Preparation of ^{125}I PEG-Lysozyme. Lysozyme (66 mg in 100 mg/mL in 0.1 M sodium phosphate buffer at pH 7.3) was mixed with 605 μCi of Na^{125}I (ICN Biomedicals, Irvine, CA), in an Iodo-Gen coated tube (Pierce Chemical Company, Rockford, IL), and allowed to react for 1 h at room temperature with mixing at 20 min intervals. The iodination reaction was stopped by removing the free ^{125}I on a Sephadex G-25F gel filtration column (17 mL) and collecting the ^{125}I-lysozyme, which was then reacted with either mPEG-DTB-NPC or mPEG-NPC, and purified by cation exchange chromatography as described above.

Pharmacokinetic Experiments. Male Sprague–Dawley rats (250–330 g each, 3 animals per formulation per experiment) were dosed either by intravenous (via a lateral tail vein) or by

subcutaneous (dorsally above the right rear leg) routes with ^{125}I-labeled lysozyme or its PEG conjugates (0.35 mL, 0.4 mg protein/mL, 4.6×10^6 cpm/mL). Blood samples (0.4 mL) were collected via the retro-orbital sinus. All injections and blood collections were performed while the animals were under inhaled anesthesia (isoflurane/O_2). Samples were collected on heparin into polypropylene tubes and stored on ice for no longer than 1 h before being pipetted in triplicate (0.100 mL) into fresh polypropylene tubes. Blood samples were collected at the following times after dosing (though no single rat had blood collected at all of the following times): 30 s, 15 min, 30 min, and 1, 2, 3, 4, 6, 8, 24, 48, 72, 96, 120, and 168 h post-dose. Note that the last four time points were added for the longer subcutaneous experiments. The samples were then counted for ^{125}I in a Packard 5000 gamma counter. The results are summarized in Figure 7.

ACKNOWLEDGMENT

We would like to thank Union Carbide and NOF Corporation for samples of mPEG5K and mPEG12K, respectively. We are grateful to Katie Zomorodi for her help with processing the pharmacokinetic data and to Bob Suzuki for the acquisition of ES-MS spectra.

LITERATURE CITED

(1) Maeda, H., Seymour, L. W., and Miyamoto, Y. (1992) Conjugates of anticancer agents and polymers: Advantages of macromolecular therapeutics in vivo. *Bioconjugate Chem. 3*, 351–362.

(2) Duncan, R., and Spreafico, F. (1994) Polymer conjugates: Pharmacokinetic considerations for design and development. *Clin. Pharmacokinet. 27*, 290–306.

(3) Zalipsky, S. (1995) Chemistry of polyethylene glycol conjugates with biologically active molecules. *Adv. Drug Delivery Rev. 16*, 157–182.

(4) Harris, J. M., and Zalipsky, S. (1997) *in ACS Symposium Series*, American Chemical Society, Washington, D.C.

(5) Katre, N. V. (1993) The conjugation of proteins with polyethylene glycol and other polymers. Altering properties of proteins to enhance their therapeutic potential. *Adv. Drug Delivery Rev. 10*, 91–114.

(6) Veronese, M. F. (2001) Peptide and protein PEGylation: a review of problems and solutions. *Biomaterials 22*, 405–417.

(7) Delgado, C., Francis, G. E., and Fisher, D. (1992) The uses and properties of PEG-linked proteins. *Crit. Rev. Ther. Drug Carrier Syst. 9*, 249–304.

(8) Caliceti, P., Schiavon, O., Veronese, F. M., and Chaiken, I. M. (1990) Effects of monomethoxypoly(ethylene glycol) modification of ribonuclease on antibody recognition, substrate accessibility and conformational stability. *J. Mol. Recognit. 3*, 89–93.

(9) Chiu, H.-C., Zalipsky, S., Kopeckova, P., and Kopecek, J. (1993) Enzymatic activity of chymotrypsin and its poly(ethylene glycol) conjugates toward low and high molecular weight substrates. *Bioconjugate Chem. 4*, 290–295.

(10) Goodson, R. J., and Katre, N. V. (1990) Site-directed PEGylation of recombinant interleukin-2 at its glycosylation site. *Biotechnology 8*, 343–346.

(11) Sato, H., Ikeda, M., Suzuki, K., and Hirayama, K. (1996) Site-specific modification of interleukin-2 by the combined use of genetic engineering techniques and transglutaminase. *Biochemistry 35*, 13072–13080.

(12) Kinstler, O. B., Brems, D. N., Lauren, S. L., Paige, A. G., Hamburger, J. B., and Treuheit, M. J. (1996) Characterization and stability of N-terminally PEGylated rhG-CSF. *Pharm. Res. 13*, 996–1002.

(13) Gaertner, H. F., and Offord, R. E. (1996) Site-specific attachment of functionalized poly(ethylene glycol) to the amino terminus of proteins. *Bioconjugate Chem. 7*, 38–44.

(14) Zalipsky, S., and Menon-Rudolph, S. (1997) Hydrazide Derivatives of Poly(Ethylene Glycol) and Their Bioconjugates, in Poly(Ethylene Glycol): Chemistry and Biological Applications, *ACS Symposium Series 680* (Harris, J. M., and Zalipsky, S., Eds.) pp 318–341, American Chemical Society, Washington, D.C.

(15) Cazalis, C. S., Haller, C. a., Sease-Cargo, L., and Chaikof, E. L. (2004) C-Terminal site-specific PEGylation of a trancated trombomodulin mutant with retention of full bioactivity. *Bioconjugate Chem. 15*, 1005–1009.

(16) Caliceti, P., Schiavon, O., Sartore, L., Monfardini, C., and Veronese, F. M. (1993) Active site protection of proteolytic enzymes by poly(ethylene glycol) surface modification. *J. Bioact. Compat. Polym. 8*, 41–50.

(17) Caliceti, P., Morpurgo, M., Schiavon, O., Monfardini, C., and Veronese, F. M. (1994) Preservation of thrombolytic activity of urokinase modified with monomethoxypoly(ethylene glycol). *J. Bioact. Compat. Polym. 9*, 251–266.

(18) Garman, A. J., and Kalindjian, S. B. (1987) The preparation and properties of novel reversible polymer-protein conjugates: 2-ω-methoxypolyethylene (5000) glycomethylene-3-methylmaleyl conjugates of plasminogen activators. *FEBS Lett. 223*, 361–365.

(19) Greenwald, R. B., Zhao, H., Yang, K., Reddy, P., and Martinez, A. (2004) A new aliphatic amino prodrug system for delivery of small molecules and proteins utilizing novel PEG derivatives. *J. Med. Chem. 47*, 726–734.

(20) Peleg-Shulman, T., Tsubery, H., Mironchik, M., Fridkin, M., Schreider, G., and Shechter, Y. (2004) Reversible PEGylation: A novel rechnology to release native interferon α2 over a prolonged period. *J. Med. Chem. 47*, 4897–4904.

(21) Zalipsky, S., Qazen, M., Walker II, J. A., Mullah, N., Quinn, Y., and Huang, S. K. (1999) New detachable poly(ethylene glycol) conjugates: Cysteine-cleavable lipopolymers regenerating natural phospholipid, diacyl phosphatidylethanolamine. *Bioconjugate Chem. 10*, 703–707.

(22) Greenwald, R. B., Pendri, A., Choe,Y. H., and Zalipsky, S., (2001) Polymeric prodrugs of amino and hydroxyl-containing bioactive agents, U.S. Patent 6,180,095 B1.

(23) Zalipsky, S., Mullah, N., and Kiwan, R. (2001) Polymer-protein conjugates as macromolecular prodrugs: Reversible PEGylation of proteins. *Proc. Int. Symp. Controlled Release Bioact. Mater. 28*, 73–74.

(24) Zalipsky, S., Kiwan, R., and Mullah, N. (2001) Reversible PEGylation: Thiolytic Regeneration of Active Protein from Its Polymer Conjugates, *in Peptides: The Wave of the Future* (Lebl, M., and Houghten, R. A., Eds.) pp 953–954, American Peptide Society, San Diego, CA.

(25) Senter, P. D., Pearce, W. E., and Greenfield, R. S. (1990) Development of a drug-release strategy based on the reductive fragmentation of benzyl carbamate disulfides. *J. Org. Chem. 55*, 2975–2978.

(26) Zalipsky, S., Saad, M., Kiwan, R., Ber, E., Yu, N., and Minko, T. (2007) Antitumor activity of new liposomal prodrug of mitomycin C in multidrug resistant tumor: Insights on the mechanism of action. *J. Drug Targeting 15*, 518–530.

(27) Gabizon, A. A., Tzemach, D., Horowitz, A. T., Shmeeda, H., Yeh, J., and Zalipsky, S. (2006) Reduced toxicity and superior therapeutic activity of a mitomycin C lipid-based prodrug incorporated in pegylated liposomes. *Clin. Cancer Res. 12*, 1913–20.

(28) Zalipsky, S., Quinn, Y., Jin, B. W. Z., Engbers, C., Mullah, N., Kiwan, R., and Huang, S. K. (2001) New approach to gene delivery mediated by reversible PEGylation of cationic lipid-DNA complexes. *Proc. Int. Symp. Controlled Release Bioact. Mater. 28*, 1177–1178.

(29) Joselyn, P. C. (1972) *Biochemistry of the SH Group*, Academic Press, New York.

(30) Wawrynczak, E. J., and Thorpe, P. E. (1988) Effect of Chemical Linkage upon the Stability and Cytotoxic Activity of A Chain Immunotoxins, in *Immunotoxins* (Frankel, A. E., Ed.), Kluwer, Boston, MA.

(31) Fotouhi, N., Galakatos, N. G., and Kemp, D. S. (1989) Peptide synthesis by prior thiol capture 6: Rates of the disulfide bond forming capture reaction and demonstration of the overall strategy by synthesis of the C-terminal 29-peptide sequence of BPTI. *J. Org. Chem. 54*, 2803–2817.

(32) Owen, T. C. (1967) Amino-alkanethiols from amino-alcohols via aminoalkylsulphates and thiazolidinethiones. *J. Chem. Soc. C*, 1373–1376.

(33) Herman, S., Laccufier, J., and Schacht, E. (1994) End-group modification of α-hydro-ω-methoxy-poly(oxyethylene), 3: Facile methods for the introduction of a thiol-selective end-group. *Macromol. Chem. Phys. 195*, 203–209.

(34) Veronese, F. M., Largajolli, R., Boccu, E., Benassi, C. A., and Schiavon, O. (1985) Surface modification of proteins: Activation of monomethoxy-polyethylene glycols by phenyl-chloroformates and modification of ribonuclease and superoxide dismutase. *Appl. Biochem. Biotechnol. 11*, 141–152.

(35) Patterson, S. D., and Katta, V. (1994) Prompt fragmentation of disulfide-linked peptides during MALDI mass spectrometry. *Anal. Chem. 66*, 3727–3732.

(36) So, T., Ueda, T., Abe, Y., Nakamura, T., and Imoto, T. (1996) Situation of methoxypolyethylene glycol covalently attached to lysozyme. *J. Biochem. 119*, 1086–1093.

(37) Lee, S., Greenwald, R. B., McGuire, J., Yang, K., and Shi, C. (2001) Drug delivery employing 1,6-elimination: Releasable poly(ethylene glycol) conjugates of proteins. *Bioconjugate Chem. 12*, 163–169.

(38) Knauf, M. J., Bell, D. P., Hirtzer, P., Luo, Z.-P., Young, J. D., and Katre, N. V. (1988) Relationship of effective molecular size to systemic clearance in rats of recombinant interleukin-2 chemically modified with water-soluble polymers. *J. Biol. Chem. 263*, 15064–15070.

(39) Robert, M., and Alemany, M. (1982) Lack of uniformity in amino acid distribution in the rat's main liver compartments: Intracellular, interstitial and plasmatic. *IRCS Med. Sci.: Libr. Compend. 10*, 25–6.

(40) Ellmerer, M., Schaupp, L., Brunner, G. A., Sndlhofer, G., Wutte, A., Wach, P., and Pieber, T. R. (2000) Measurement of interstitial albumin in human skeletal muscle and adipose tissue by open-flow microperfusion. *Am. J. Physiol. Endocrinol. Metab. 278*, E352–E356.

(41) Krantz, F., Warnecke, A., Scheuermann, K., Stockmar, C., Schwab, J., Lazar, P., Druckes, P., Esser, N., Drevs, J., Rognan, D., Bissantz, C., Hinderling, C., Folkers, G., Fichtner, I., and Unger, C. (2002) Probing the cysteine-34 position of endogenous serum albumin with thiol-binding doxorubicin derivatives. Improved efficacy of an acid-sensitive doxorubicin derivative with specific albumin-binding properties compared to that of the parent compound. *J. Med. Chem. 45*, 5523–5533.

(42) Itoh, T., Gotoh, K., Ishikawa, N., Hamaguchi, T., and Kubo, M. (1996) 1,9-Dithia[2,2]paracyclophane: Synthesis, molecular structure, and properties. *J. Org. Chem. 61*, 1867–1869.

(43) Brois, S. J., Pilot, J. F., and Barnum, H. W. (1970) A new pathwy to unsymmetrical disulfides. The thiol-induced fragmentation of sulfenylthiocarbonates. *J. Am. Chem. Soc. 92*, 7629–7631.

(44) Koneko, T., Willner, D., Minkovic, I., Knipe, J. O., Braslawsky, G. R., Greenfield, D. M., and Vyas, D. M. (1991) New hydrasone derivatives of adriamycin and their immunoconjugates - a correlation between acid stability and cytotoxisity. *Bioconjugate Chem. 2*, 133–141.

(45) Kurfürst, M. M. (1992) Detection and molecular weight determination of polyethylene glycol-modified hirudin by staining after sodium dodecyl sulfate-polyacrylamide gel electrophoresis. *Anal. Biochem. 200*, 244–248.

(46) Shugar, D. (1952) The measurement of lysozyme activity and the ultra-violet inactivation of lysozyme. *Biochem. Biophys. Acta 8*, 302–9.

BC7001902

Direct Immunofluorescence of Plant Microtubules Based on Semiconductor Nanocrystals

K. Eggenberger,[†] A. Merkulov,[‡] M. Darbandi,[‡] T. Nann,[‡,§] and P. Nick*[,†]

Institut of Botany 1, University of Karlsruhe, Kaiserstrasse 2, D-76128 Karlsruhe, Germany, Freiburg Materials Research Centre, University of Freiburg, Stefan-Meier-Strasse 21, D-79104 Freiburg, Germany, and School of Chemical Sciences and Pharmacy, University of East Anglia (UEA), Norwich NR4 7TJ, U.K. Received May 25, 2007

Fluorescence microscopy in combination with multiple, simultaneous labeling of biomolecules has been a key breakthrough in cell biology. However, the spatiotemporal resolution of this approach is limited by bleaching of the fluorescence label and illegitimate cross-reference of the label. CdSe-based semiconductor nanocrystals with their excellent bleaching stability would be an alternative to overcome this limitation. We therefore explored direct immunofluorescence based on nanocrystal-conjugated antibodies using plant microtubules as model. We compared two strategies of bioconjugation, covalent coupling of antitubulin antibodies to BSA-coated nanocrystals and covalent coupling to nanocrystals that were surrounded by functionalized silica shells. Both nanoparticle–antibody conjugates were used to follow the dynamic reorganization of microtubules through the cell cycle of a tobacco cell culture in double and triple staining with FITC as conventional fluorochrome and Hoechst 33258 as marker for mitotic duplication of DNA. BSA-coated nanocrystals visualized fluorescent dots that decorated the various arrays of microtubules. The specificity of the antibody was maintained after conjugation with the nanocrystals, and the antibodies correctly represented the dynamics of cell-cycle-dependent microtubular reorganization. However, this approach did not yield a contiguous signal. In contrast, silica-shelled nanocrystals visualized contiguous microtubules in the same pattern as found for the conventional fluorochrome FITC and thus can be used as labels for direct immunofluorescence in plant cells.

INTRODUCTION

Luminescent semiconductor nanocrystals with spherical morphology (so called quantum dots or QDs[1]) have attracted enormous interest as labels for bioimaging (for recent reviews, see refs *1* and *2*) because of their increased fluorescence intensity and bleaching resistance. In addition, they can be excited over a broad wavelength range but emit with a narrow band that can be tuned by the size of the particles. Thus, QDs are endowed with optical properties that renders them superior over the organic fluorophores that are used conventionally. However, the application of QDs for cell biology is limited by their potential cytotoxicity (which is discussed controversially (*3–6*)), their large size (*2*), and the challenging task to stabilize those nanoparticles colloidally under the general conditions of biological applications.

To overcome these limitations, QDs have been coated with inert silica shells or, alternatively, by thin layers of organic ligands. The coating protects the QDs from oxidation and prevents the leakage of toxic metal ions, especially Cd^{2+}, that can induce oxidative burst and programmed cell death (*7, 8*). In addition, the coat can be used as platform to generate a surface that is biocompatible and amenable to the coupling with biomolecules of interest.

For biological applications, silica coating has several advantages over alternative coating strategies. Because of the high density of silica, the conjugated particles can be separated easily, during particle preparation and biofunctionalization, from uncoated particles. The silanol groups on the surface decrease hydrophobicity and thus the tendency to agglomerate in aqueous environment. Silica is inert in both aqueous and nonaqueous solvents, which should reduce any noxious effects on the cells hosting the particles as well as microbial degradation (*6*). Silica coats are tighter against leakage of the toxic Cd^{2+} compared to coats made from SH ligands, such as mercaptoacetic acid, 3-mercaptopropionic acid, 11-mercaptoundecanoic acid, or 2-aminoethanethiol. Furthermore, it is possible to introduce specific surface functionalities by modification of surface hydroxyls with amines, thiols, carboxyls, or methacrylate.

The BSA coating provides better electrostatic colloidal stabilization of QDs in water and is more versatile with respect to active groups (i.e., NH_2, COOH, and SH) for the covalent coupling of antibodies to the BSA-coated QDs. Moreover, the coating of QDs with small proteins produces particles of smaller diameter compared to the SiO_2 approach, which improves their suitability for in vivo imaging.

Biology has entered the so-called postgenomic era, where the assignment of gene to function has become a central task. By the use of reverse genetics, expressed sequences of unknown function are analyzed with respect to phenotypes that occur upon overexpression or suppression of the corresponding gene products and with respect to their intracellular localization. Classical light microscopy and electron microscopy have focussed on the visualization of cellular structures. The socalled functional genomics calls for, in addition, reliable information about the molecular nature of these structures. This requirement has stimulated an impressive bloom of fluorescence microscopy that has developed from an exotic technique used by a handful of specialists into a central tool of molecular biology. There are basically three motive forces that drive this development:

* To whom correspondence should be addressed. Phone: +49 721 608 2144. Fax: +49 721 608 4193. E-mail: peter.nick@bio.uni-karlsruhe.de.

[†] University of Karlsruhe.

[‡] University of Freiburg.

[§] University of East Anglia.

[1] Abbreviations: BSA, bovine serum albumin; BY-2, *Nicotiana tabacum* L. cv. Bright Yellow 2 cell line; FITC, fluorescein isothiocyanate; PBS, phosphate buffered saline; QD, quantum dot.

10.1021/bc700188d CCC: $37.00 © 2007 American Chemical Society
Published on Web 09/21/2007

in vivo imaging, spatial (and temporal) resolution, and molecular specificity. To achieve these goals, the technological progress on the side of microscopical devices has to be complemented by advances on the side of the fluorescent label, and it is this point where the QDs have stimulated enormous interest of cell biologists.

So far, the use of QDs for in vivo imaging has been biased toward studies on the organismic level, for instance, when derivatized QDs were successfully targeted to cancer cells (*9, 10*) or when they were targeted to the surface of unicellular spores for the detection of the water-borne pathogen *Cryptosporidium* (*11*). Because of their large size, it is very difficult to exploit the potential of QDs for single-molecule tracking within living cells. Even though it has been published that bona fide labeled kinesins could be tracked in HeLa cells (*12*), the potential of QDs for spatiotemporal resolution has been mainly demonstrated during in vitro studies on single-molecule tracking (for a recent review see ref *13*). For instance, the high bleaching resistance of the QDs made it possible to visualize the hand-over-hand processivity of myosin V during in vitro sliding assays (*14*).

To conjugate QDs to proteins of interest, in most cases the strong binding of streptavidin (coupled to the QDs) and biotin (coupled to the target protein) is utilized. For instance, in a pioneering work, actin was visualized in cellula through a biotinylated version of phalloidin (an actin-binding compound) that was detected by streptavidin-coupled QDs (*15*), or microtubules were visualized simultaneously with nuclei through two different streptavidin-coupled QDs that bound to biotinylated secondary antibodies directed against primary antibodies targeted to tubulin and nuclear epitopes (*16*). A similar approach, where the epitope was visualized by a sandwich composed of three layers (primary antibody, secondary antibody conjugated to biotin, streptavidin-conjugated QDs as tertiary component), was used to visualize chloroplasts in maize leaves in comparison to Alexa 488 as a control fluorophore (*17*). However, the poor quality of the obtained images and the optical setup used in this experiment indicate that the signal might in fact be due to the autofluorescence of chlorophyll. A general problem of the biotin–streptavidin conjugation is the illegitimate cross-reference between different QD–streptavidin conjugates in dual-visualization experiments. The streptavidin is expected to bind to the biotin on both primary antibodies such that the label will not be attributable to the respective epitope. This problem can be somewhat reduced by sequential labeling; however, the second label will still be partitioned between both epitopes, obscuring the specificity of the label. Especially for the discrimination of closely related epitopes (such as differentially modified subpopulations of a given protein), this will seriously impair the feasibility of this approach.

Thus, the best option to obtain specific labeling would be a direct fluorescence, where the QD label is linked to the primary antibody itself. The pronounced bleaching stability of QDs and their brightness is predicted to yield reasonable signals even in the absence of signal amplification through a secondary antibody (and a tertiary streptavidin conjugate). Streptavidin is a very robust biomolecule that tolerates even massive manipulations without a loss of function. This has been the major reason for the wide use of streptavidin as conjugation partner to introduce QDs into the realm of cell biology. Most proteins are much more delicate with respect to their functionality, and it is a challenging task to couple them with QDs in a nondestructive manner. In a previous work we have coupled silica-coated semiconductor nanocrystals directly to the cytoskeletal protein tubulin and were able to demonstrate the specific self-assembly of the QD–tubulin into fluorescent microtubules (*18*). In contrast, antibodies tend to lose their activity when directly coupled to nanoparticles. To date, there is no general solution for coupling biomolecules to nanoparticles under preservation of their biological activity. We therefore ventured to generate biocompatible nanoparticles surfaces that are versatile to be amenable for different kinds of nanoparticles and that are flexible regarding the biological problem. We have chosen two alternative strategies, through a biological surface (bovine serum albumine) and through an inorganic surface (silica), to couple QDs to monoclonal antibodies targeted against tubulin. To challenge the feasibility of this approach for cell-biological applications, we have used the QD-labeled antibodies for direct immunofluorescence following the dynamic reorganization of microtubules during the cell cycle. To our knowledge, this is the first report where QDs have been successfully employed to visualize subcellular details in plant cells.

EXPERIMENTAL PROCEDURES

Synthesis of Luminescent Semiconductor Nanocrystals. The luminescent CdSe/ZnS NPs were synthesized as described elsewhere (*19*) and encapsulated in silica using a water-in-oil microemulsion method at room temperature according to our previous protocol (*20*). Typically, 10 mL of cyclohexane (Roth, Karlsruhe, Germany), 1.3 mL of NP-5 as surfactant (Fluka, Taufkirchen, Germany), and 400 μL of the luminescent CdSe/ZnS NCs (8.72×10^{-7} mol/L) in chloroform (Roth, Karlsruhe, Germany) and 80 μL of tetraethyl orthosilicate (Sigma-Aldrich, Taufkirchen, Germany) as a precursor for silica formation were added in a flask under vigorous stirring. Thirty minutes after formation of the microemulsion, an amount of 150 μL of an aqueous ammonia solution (33 w/v %, Roth, Karlsruhe, Germany) was introduced to initiate the encapsulation process. Subsequently, the reaction mixture was incubated for 24 h at room temperature until completion. Subsequently, the nanoparticles were precipitated from the microemulsion using acetone and were centrifuged and the resultant precipitate of the CdSe/ZnS/SiO_2 composite particles was washed in sequence with butanol, propanol, ethanol (Roth, Karlsruhe, Germany), and water to remove any surfactant and unreacted educts. Finally, the composite particles were dispersed in water. Structure, size, and morphology of the resulting nanoparticles were determined by transmission electron microscopy (TEM; Zeiss LEO 912 Omega operating at 120 kV). For the TEM studies, the specimens were prepared by adding drops of the freshly produced suspension onto a carbon film supported on a Cu grid.

Preparation of Antibody Conjugates with Silica-Shelled Nanocrystals. The silica-encapsulated nanoparticles were briefly spun down, and subjected to three cycles of washing with dry DMSO (Roth, Karlsruhe, Germany), followed by precipitation with dry diethyl ether (Roth, Karlsruhe, Germany). Then, they were redispersed in 1 mL of dry DMSO. A small amount (covering the tip of a spatula) of 1,1′-carbonyldiimidazole (CDI, Fluka, Buchs, Switzerland) was added to the mixture that was then incubated overnight at 4 °C. Subsequently, the nanoparticle dispersion was warmed up to room temperature, incubated for an additional 6 h, and finally centrifuged and resuspended in 1 mL of phosphate buffered saline (PBS). An amount of 200 μL of the primary antibodies at a dilution of 1:10 was added and allowed to bind overnight at 4 °C. The final product was centrifuged and dialyzed against PBS. The resulting conjugates were then used without further purification. As antibodies for the coupling, the mouse monoclonal antibodies DM1A (*21*) and ATT (*22*) specific for the α-tubulin subunit were used in this study.

Preparation of Antibody Conjugates with BSA-Coated NPs. The details for preparation and characterization of BSA-coated CdSe/ZnS core–shell particles will be published else-

where (*23*). Briefly, an amount of 1.5 mL of MeOH was added to 500 μL of CdSe/ZnS nanoparticles in $CHCl_3$ (8.72×10^{-7} mol/L), and the nanoparticles were isolated by centrifugation. Subsequently, 500 μL ofDMSO (Roth, Karlsruhe, Germany) and 10 μL of 2-mercaptoethanol (ME) were added and the sample was heated to 60 °C for 3 h. The nanoparticles were reprecipitated again by addition of 1.3 mL of acetone and 0.2 mL of Et_2O and collected by centrifugation. These hydrophilic nanoparticles were suspended in 500 μL of 2 mg/mL BSA in a Tris-glycine buffer (25 mM Tris, 250 mM glycine, pH 8.3). These BSA-coated nanoparticles were purified by agarose electrophoresis, dialyzed against PBS, and coupled with the target antibodies DM1A and ATT by a standard protocol (*24*) using *N*-(3-dimethylaminopropyl)-*N*′-ethylcarbodiimide hydrochloride (EDC). The resulting conjugates were used without further purification.

Tobacco Cell Cultures. The tobacco cell line BY-2 (*Nicotiana tabacum* L. cv. Bright Yellow 2 (*25*)) was cultivated in liquid medium containing 4.3 g/L Murashige and Skoog salts (Duchefa, Haarlem, The Netherlands), 30 g/L sucrose, 200 mg/L KH_2PO_4, 100 mg/L inositol, 1 mg/L thiamine, and 0.2 mg/L 2,4-dichlorophenoxyacetic acid (2,4-D), pH 5.8. Cells were subcultured weekly, inoculating 1.5–2 mL of stationary cells into 30 mL of fresh medium in 100 mL Erlenmeyer flasks. The cell suspensions were incubated at 25 °C in the dark on an orbital shaker (KS250 basic, IKA Labortechnik, Staufen, Germany) at 150 rpm. Stock BY-2 calli were maintained on media solidified with 0.8% (w/v) agar and subcultured monthly. All experiments were performed 4 days after subcultivation.

Visualization of Microtubules by Indirect Immunofluorescence Using FITC as Label. Microtubules were processed for immunofluorescence in self-made staining chambers using a nylon mesh of 70 μm pore width as published previously (*26*). This allowed fast exchange of media at preventing the loss of cells during the staining. After fixation for 30 min with 3.7% (w/v) paraformaldehyde in microtubule stabilizing buffer (MSB: 50 mM PIPES, 2 mM EGTA, 2 mM $MgSO_4$, 0.1% Triton X-100, pH 6.9), cells were washed in PBS three times for at least 5 min to remove excess paraformaldehyde. Subsequently, the cell wall was digested using 1% (w/v) Macerozym (Duchefa, Haarlem, The Netherlands) and 0.2% (w/v) Pectolyase (Fluka, Taufkirchen, Germany) in MSB for 5 min. Again, excess enzyme was washed out for 5 min with PBS. Unspecific binding sites were blocked for 20 min with 0.5% (w/v) BSA diluted in PBS. Directly after blocking, the cells were transferred into a small volume of the primary antibody. To visualize microtubules, we used a 1:250 dilution in PBS of either DM1A recognizing a conservative epitope near the carboxyterminus of α-tubulin (*21*) or ATT recognizing the carboxyterminal 12 amino acid residues of full-length α-tubulin (*22*), both purchased from Sigma (Taufkirchen, Germany). This primary antibody was allowed to bind overnight at 4 °C. The next day, unbound primary antibody was removed by washing the cells three times for at least 5 min in PBS. The sample was then incubated with a secondary FITC-conjugated antibody targeted against mouse IgG for 1 h at 37 °C in a moist chamber to prevent drying of the specimen. Unbound secondary antibody was removed by washing with PBS, and DNA was stained using 0.1 μg mL^{-1} Hoechst 33258 (2′-(4-hydroxyphenyl)-5-(4-methyl-1-piperazinyl)-2,5′-bi-1*H*-benzimidazole trihydrochloride hydrate) (Sigma, Taufkirchen, Germany).

Visualization of Microtubules by Direct Immunofluorescence Using QDs as Label. The cells were fixed, digested with Macerozyme, blocked, and washed as described above. After the unspecific binding sites were blocked, the cells were incubated overnight at 4 °C with the primary monoclonal antibody against α-tubulin that had been coupled to biofunctionalized, fluorescent CdSe-based semiconductor nanocrystals. The antibody–NC conjugates were adjusted with PBS to a dilution of 1:250 as used in the indirect FITC-based immunofluorescence described above. After unbound particles were washed out the next day, the sample was directly used for the staining of DNA by Hoechst 33258 as described above. To assess the success of bioconjugation for each antibody–NC conjugate batch, a specimen processed in parallel was poststained with a secondary FITC-conjugated antimouse IgG for 1 h at 37 °C and then triple-stained with Hoechst 33258.

Microscopy and Image Analysis. The samples were examined under an AxioImager Z.1 microscope (Zeiss, Jena, Germany) equipped with an ApoTome microscope slider for optical sectioning and a cooled digital CCD camera (AxioCam MRm). For the observation of the QD-antibody conjugates, the filter set 43 HE (excitation at 550 nm, beamsplitter at 570 nm, and emission at 605 nm) was used. The DNA signal and the FITC fluorescence were viewed through filter sets 49 (excitation at 365 nm, beamsplitter at 395 nm, and emission at 445 nm) and 38 HE (excitation at 470 nm, beamsplitter at 495 nm, and emission at 525 nm) (Zeiss, Jena, Germany). A test for potential filter cross-talk, where single-stained samples were viewed with the three filter sets at corresponding exposure conditions, revealed that the filters were tight for the three fluorochromes (data not shown). The images were analyzed using the AxioVision (release 4.5) software and processed for publication using Photoshop (Adobe Systems, San Jose, CA).

RESULTS AND DISCUSSION

Synthesis of CdSe-Based NPs and Their Antibody Conjugates. We used two strategies to prepare the antibody conjugates, which are presented in parts a and b of Figure 1. In the first one the water solubility of NPs has resulted from encapsulation with the hydrophilic SiO_2 layer and the free OH groups on the surface have been used for conjugation of the NPs with tubulin antibody ATT or DM1A via a CDI crosslinker.

In the first strategy (Figure 1a), the CdSe/ZnS nanocrystals were transferred into water by a standard ligand exchange method utilizing 2-mercaptoethanol (ME). In the next step, the product was coated with bovine serum albumine (BSA) to stabilize the nanoparticles against coagulation in water and to provide free chemical groups for improved covalent conjugation (*23*). The covalent coupling between BSA and the antibodies DM1A and ATT occurred via the standard reagent EDC through mutual coupling between free carboxylic and amino side groups on the two respective proteins. The detailed characterization of these particles will be published elsewhere (*23*).

The second strategy (Figure 1b) was based on silica coating as published previously (*20*). Transmission electron micrographs from the resulting CdSe/ZnS nanoparticles and their silica-coated nanocomposites are shown in parts a and b of Figure 2, respectively. Since the electron density of the CdSe/ZnS core is significantly higher than that of silica, the darker and lighter parts of the particles in Figure 2b correspond to the CdSe/ZnS core and the silica shell, respectively. The size distributions of the CdSe/ZnS core particles (Figure 3a), and the CdSe/ZnS/SiO_2 nanocomposites (Figure 3b) were calculated from the micrograph over several hundred individuals. The average diameter of the CdSe/ZnS core particles was 5.8 nm, and the diameter of the silica-coated nanoparticles was 41.6 nm.

The particles obtained by the two approaches were coupled to the monoclonal antitubulin antibodies ATT and DM1A as described in detail in Experimental Procedures. Because of the high affinity and specificity of these antibodies, they are used at highly diluted preparations such that it was not feasible to

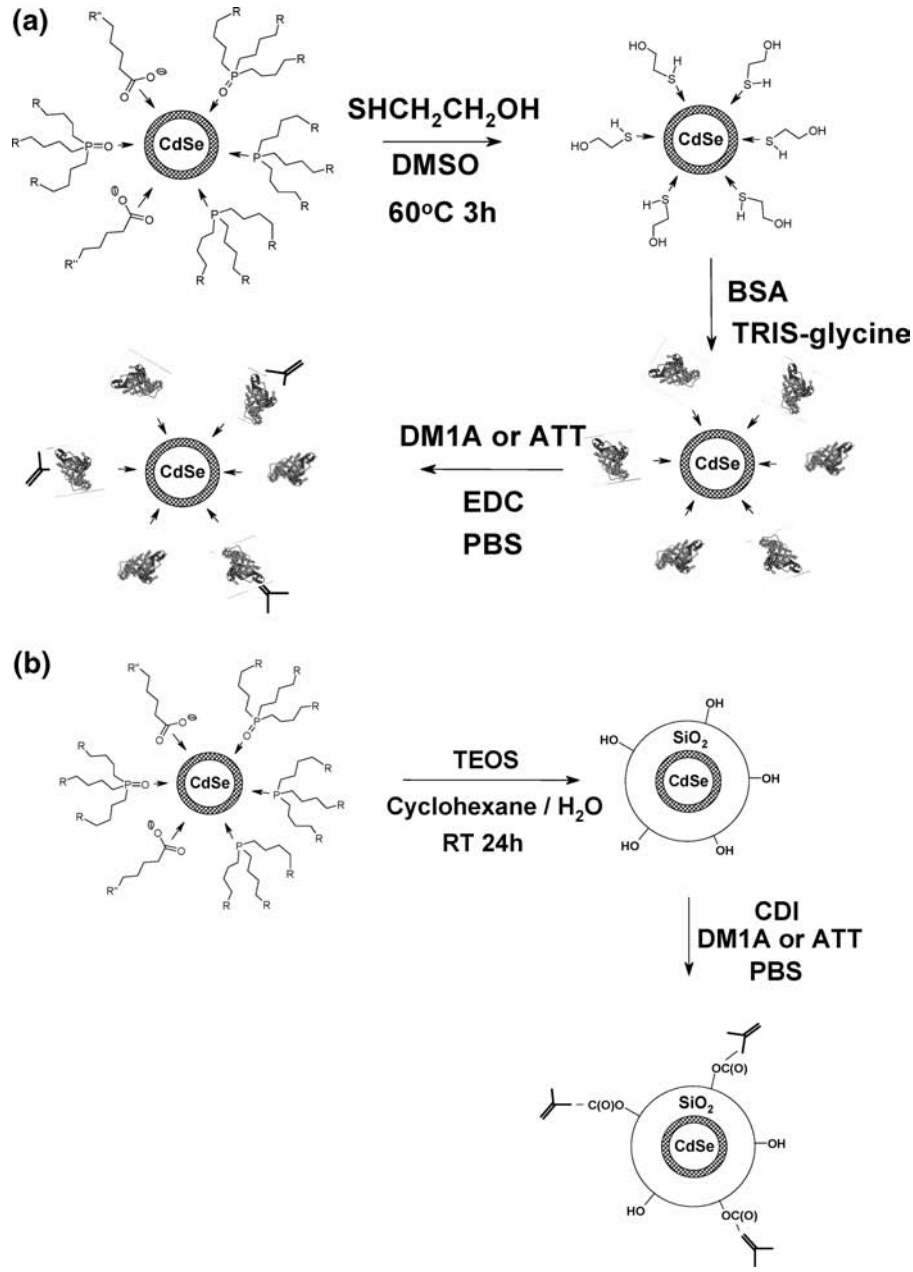


Figure 1. Strategies to conjugate fluorescent CdSe semiconductor nanocrystals to monoclonal antibodies: (a) coupling through coating with bovine serum albumine; (b) coupling through coating with a silica shell with surface functionalities. The black layer around the CdSe core crystal stands for the ZnS shell.

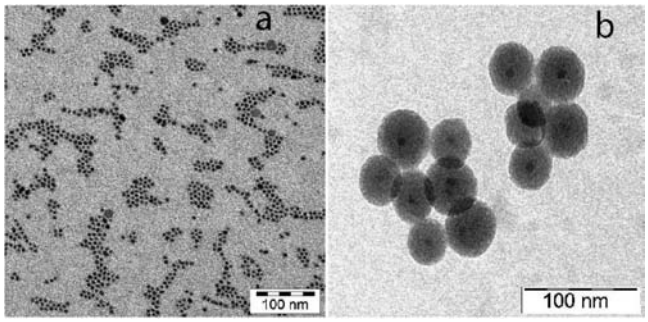


Figure 2. Transmission electron micrographs of (a) the CdSe/ZnS core nanoparticles and (b) the CdSe/ZnS/SiO_2 nanoparticles.

characterize the conjugates by electron microscopy or any other method, such as gel electrophoresis, dynamic light scattering, or size exclusion chromatography. To assess the success of the bioconjugation, we therefore tested the biological functionality (i.e., the immunofluorescence in the target cells) as indicator.

Tubulin Antibodies Conjugated to BSA-Coated Nanocrystals Decorate Microtubules. As the first approach, antibodies conjugated to biofunctionalized, BSA-shelled nanocrystals were used for direct immunofluorescence of microtubules in the tobacco cell line BY-2 (Figure 4). These cells divide readily in suspension culture and are endowed with a clear axis and polarity, which allows very clear identification of the various microtubular arrays that form during the cell cycle.

In premitotic interphase cells, the antitubulin–NC conjugates visualize punctate signals in the cell periphery that are aligned perpendicular to the main axis of the cell file (Figure 4A). This specific orientation, the general appearance, and the localization in the cortical cytoplasm show that these structures correspond to the cortical microtubules typical for this stage of the cell cycle. When confocal sections are recorded from the cell center (parts B1 and B2 of Figure 4), the nanocrystal signal is observed

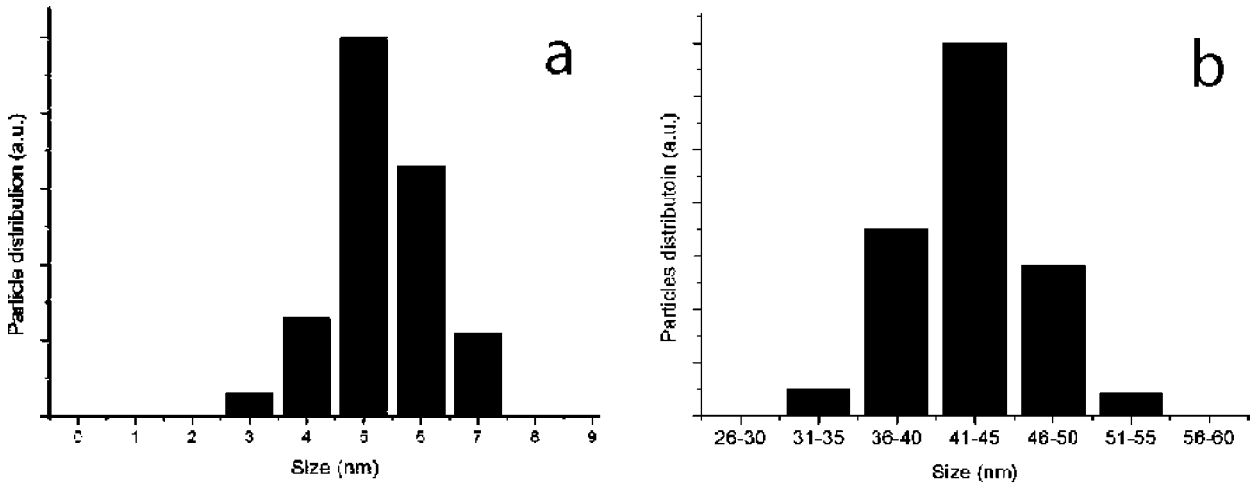


Figure 3. Frequency distribution over particle size for (a) the CdSe/ZnS core particles and (b) the CdSe/ZnS/SiO_2 nanoparticles based on scores of transmission electron micrographs from several hundred individual particles.

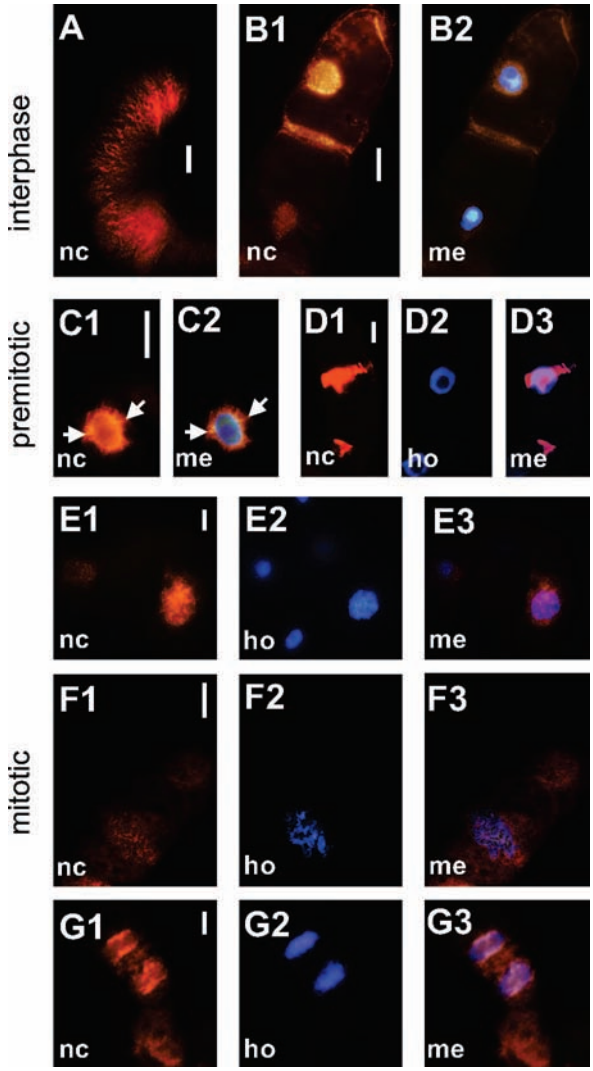


Figure 4. Direct immunofluorescence of tubulin with monoclonal mouse antitubulin antibodies conjugated to BSA-coated QDs followed through different stages of division in tobacco BY-2 cells: (nc) optical setup for the detection of nanocrystals; (ho) optical setup for the detection of DNA (through Hoechst 33258); (me) merge of the two channels to show the QD signal in relation to the DNA. Size of bar is 10 μm.

at the nuclear envelope that ensheaths the DNA. The nuclear envelope is the major microtubule-organizing center in the acentriolar cells of higher plants, and therefore, this nanocrystal signal corresponds to the microtubule-organizing centers that decorate the nuclear surface of plant cells.

Cell division is heralded by a movement of the nucleus into the cell center to the prospective division site and the formation of a microtubular preprophase band from the nuclear envelope that predicts position and orientation of the future cross wall. Both the nuclear envelope (parts C1 and C2 of Figure 4) and the preprophase band that progressively emerges from the nuclear envelope (white arrows in parts C1 and C2 of Figure 4) until a massive band of microtubules is produced (parts D1–D3 of Figure 4) are decorated by the nanocrystal signal.

During the mitotic prophase, when the DNA is condensed into chromosomes (part E2 of Figure 4), the nuclear envelope collapses and the nanocrystals are found to surround the forming spindle (parts E1 and E3 of Figure 4). In the following metaphase, the nanocrystal signal will then attach to the chromosomes spread in the equatorial cell plane (parts F1–F3 of Figure 4) and redistribute to the newly reestablished nuclear envelopes of the daughter nuclei and at the newly forming cross wall in the final telophase (parts G1–G3 of Figure 4).

Thus, the distribution of the nanocrystal–antibody conjugates mirrors exactly the behavior of the microtubular cytoskeleton during the cell cycle. However, the signal obtained by this approach was never contiguous but remained punctate.

As to testing whether the punctate nanocrystal signal was in fact colocalizing with microtubules or whether it was produced by disintegration of microtubules, we counterstained the samples with a FITC-conjugated secondary antibody raised against the primary antitubulin antibody. By dual-channel visualization of the nanocrystal and the FITC signal, it was thus possible to see the context of the nanocrystals with microtubules (Figure 5). To check for a potential filter leakage of the FITC signal upon the nanocrystal signal, we viewed cells, where microtubules had been visualized by a primary antibody that was not conjugated to nanocrystals, as a negative control. When these cells were incubated with the FITC-conjugated secondary antibody (part A1 of Figure 5) and then viewed with the filter used to record the nanocrystal signal, the result was clearly negative (part A1 of Figure 5), demonstrating that the optical setup was tight enough to separate the FITC signal and the nanocrystal signal in dual-channel configurations.

We therefore followed the cell cycle of tobacco cells using triple staining (nanocrystal–antitubulin antibodies, FITC, and Hoechst 33258 for the visualization of DNA). In interphase cells (parts B1–B4 of Figure 5), the cortical microtubules visualized by the secondary antibody (part B2 of Figure 5) were found to

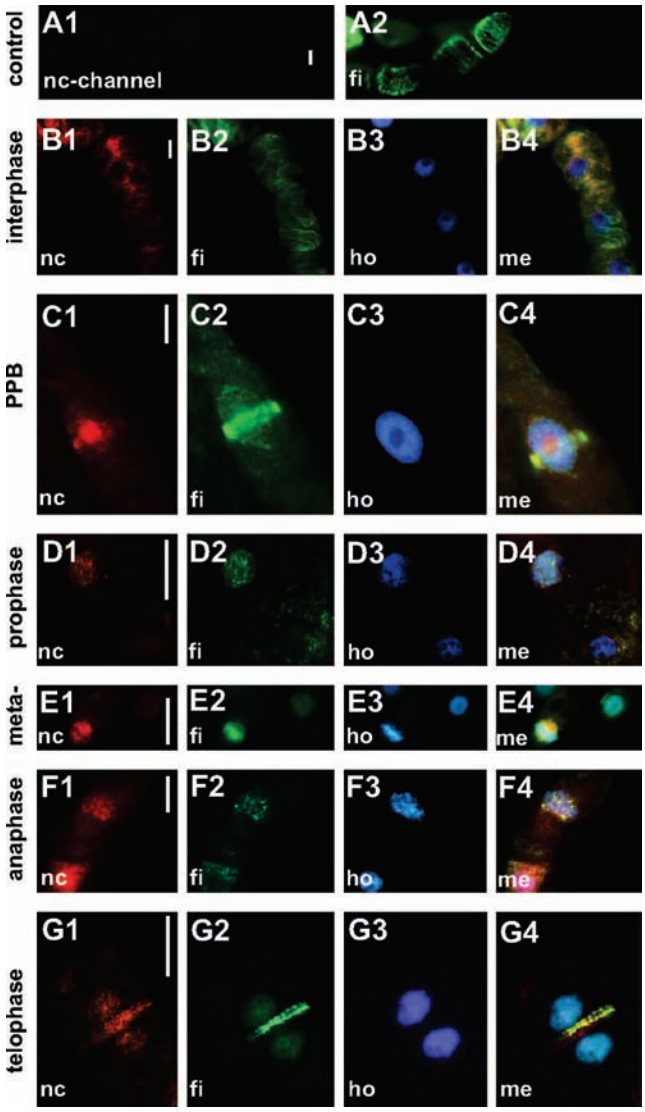


Figure 5. Direct immunofluorescence of tubulin with monoclonal mouse antitubulin antibodies conjugated to BSA-coated QDs and after-staining with FITC-conjugated antimouse IgG followed through different stages of division in tobacco BY-2 cells: (nc) optical setup for the detection of nanocrystals; (fi) optical setup for the detection of the FITC after stain; (ho) optical setup for the detection of DNA (through Hoechst 33258); (me) merge of the three channels to show the QD signal in relation to microtubules and DNA. Size of bar is 10 μm. Parts A1 and A2 show the negative control using unconjugated primary antibody and after stain with FITC-conjugating antimouse IgG (i.e., omitting the QD-conjugated antibodies) to test for potential optical cross-contamination of the nc optical setup through the FITC signal. The negative results show that the optical setup is tight against filter leakage.

be decorated with the nanocrystal signal (part B1 of Figure 5). The merged image exhibited numerous yellow microtubules indicating the high congruence of both signals (part B4 of Figure 5). This congruence was maintained when the cells were prepared for mitosis and generated a preprophase band (parts C1–C4 of Figure 5). Also, the various microtubular arrays characteristic for mitosis such as the nuclear cap in the late prophase (parts D1–D4 of Figure 5), the division spindle in metaphase (parts E1–E4 of Figure 5), and the exploratory microtubules formed at anaphase (parts F1–F4 of Figure 5) were correctly depicted by the two signals. When the microtubular phragmoplast in the late telophase is formed (parts G1–G4 of Figure 5), the nanocrystals decorate the complete region where FITC-labeled microtubules are seen. In addition, the nanocrystal conjugates can be detected in the adjacent cytoplasm and already

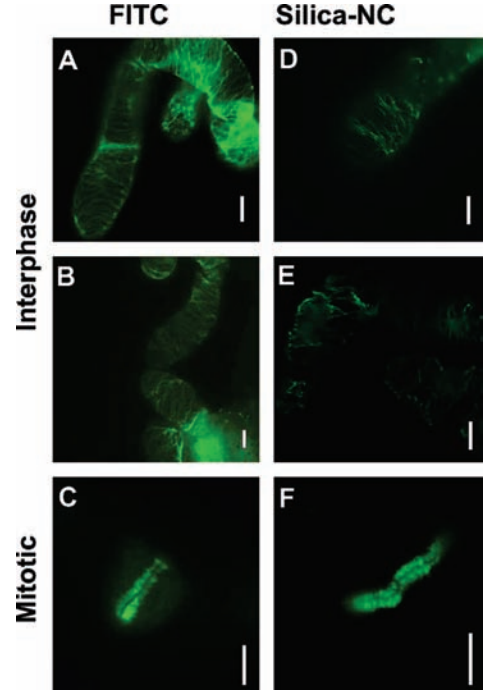


Figure 6. Direct immunofluorescence of tubulin with monoclonal antitubulin antibodies conjugated to silica-coated QDs (D–F) in comparison to the signal obtained by conventional indirect immunofluorescence using secondary antibodies conjugated to FITC (A–C) followed through different stages of division in tobacco BY-2 cells. Size of bar is 10 μm. The two labels are equivalent in terms of specificity, signal-to-noise ratio, intensity, and structural preservation.

very clearly at the nuclear surface of the daughter nuclei (part G1 of Figure 5), where the FITC signal is much weaker (part G2 of Figure 5).

Thus, upon counterstaining with a FITC-conjugated secondary antibody and dual visualization of both signals, the entire dynamics of microtubule arrays characteristic for the plant-cell cycle can be reliably followed. The punctate staining seen for the nanocrystal–antibody conjugates (Figure 4) is therefore not due to microtubules that had been disrupted by the incubation with the nanocrystal–antibody conjugates. Microtubules have remained intact during the labeling procedure and can be contiguously stained by a FITC-conjugated secondary antibody. This indicates that the affinity of the nanocrystal–antibody conjugate for tubulin has been preserved as well as the specificity of binding. However, either a significant proportion of the antitubulin antibody is not conjugated with the nanocrystals or the fluorescence has been lost during the conjugation. These unlabeled primary mouse antibodies are still functional and bind to their cellular target but will not display the fluorescent signal. They can be rendered visible, however, by addition of an antimouse IgG secondary antibody coupled to FITC.

Tubulin Antibodies Conjugated to Silica-Shelled Nanocrystals Label Microtubules. To obtain a contiguous microtubule signal, we therefore tested an alternative approach for the conjugation of the nanocrystals to antitubulin antibodies. The nanocrystals were surrounded by a silica shell that was coated with functional groups that could be used for coupling (*20*). These silica-shelled nanocrystals were then conjugated with antitubulin antibodies and used for direct immunofluorescence in both interphase and mitotic cells of tobacco BY-2 (Figure 6). Conventional labeling of microtubules by indirect immunofluorescence using FITC (parts A–C of Figure 6) was performed in comparison, and both the cortical microtubules (parts A and

B of Figure 6) and mitotic arrays such as the phragmoplasts that organize the new cell plate after completed segregation of the daughter nuclei (part C of Figure 6) were visualized. The silica-shelled nanocrystals (parts D–F of Figure 6) produced a contiguous microtubule signal by direct immunofluorescence that was equivalent, in both the signal amplitude and morphology, to the signal of the conventional label. This signal was now contiguous for both the cortical microtubules (parts D and E of Figure 6) and the phragmoplast (part F of Figure 6) at a simultaneously very low background signal. Thus, the result obtained for the silica-shelled nanocrystals was equivalent to the conventional indirect immunofluorescence.

To summarize our results, we state that both approaches were successful in visualizing the specific epitopes of the antitubulin antibodies through QD-based direct immunofluorescence. However, the conjugation in the BSA-coating approach seemed to be only partial, whereas the SiO_2-coat approach produced a more complete conjugation. This difference might be due to the considerably larger surface of the silica-coated particles at the same concentration of the core CdSe/ZnS Qds. The functionality of the tubulin antibody was maintained in both cases; this is also seen in the FITC-afterstain experiment (Figure 5), where the unconjugated tubulin antibodies were stained by the FITC-labeled secondary antibody and found to be perfectly aligned with microtubules. The signal strengths obtained with direct immunofluorescence using the QDs were absolutely comparable to those resulting from conventional indirect immunofluorescence (Figure 6). Given the fact that up to 50 secondary antibodies bind to one primary antibody in the conventional indirect immunofluorescence, one has to conclude that the fluorescence intensity produced by an individual QD-conjugated antibody is very high.

OUTLOOK

Functional genomics is increasingly extending into the analysis of differentially modified subpopulations of a given protein in order to understand the spatiotemporal dynamics and cell biological function of these modifications (*26*). Double visualization of such subpopulations using highly specific monoclonal antibodies is so far impaired by the fact that these antibodies are almost exclusively available from one animal species (mouse). It is extremely difficult to safeguard against illegitimate cross-reaction of the secondary fluorescent antisera. Direct immunofluorescence would be a good alternative but is limited by low signal strength because the signal amplification due to the labeled secondary antibody is lacking. We could demonstrate in our study that this limitation can be overcome by direct coupling of fluorescent QDs to highly specific antisera while preserving functionality and specificity of the antibody. This should now allow, for instance, visualization of different modifications on the tubulin on the same microtubule. By use of QDs with specific optical properties (such as delayed photostimulated luminescence), it should be possible to obtain higher levels of specificity and better spatiotemporal resolution in confocal applications because a higher number of individual scans can be averaged to increase signal/noise ratios and input amplifications (possible reduced noise/signal ratios). We have demonstrated for the first time that QDs can be successfully utilized in intact, unsectioned plant cells despite the presence of a massive cellulosic cell wall. In the next step we want to extend the use of QDs to the in vivo situation by mild and transient permeabilization of the plasma membrane without infringing viability. In this context it is mainly size that matters such that the BSA-coated particles with their considerably smaller size might become crucial. By use of nanoparticles that are magnetic, it should become possible not only to visualize but also to manipulate specific cellular targets in living plant cells.

ACKNOWLEDGMENT

This work was supported by the Research Priority Programme of the State of Baden-Württemberg (Project LuNaCell) to T.N. and P.N. and by the Center for Functional Nanoscience of the University of Karlsruhe (Project E1.5) to P.N. The authors thank Dr. Jürgen Riegler and Dr. Ralf Thomann for preparation of the CdSe/ZnS nanoparticles and for TEM measurements, respectively. Sabine Purper is ackowledged for the technical assistance in the culture of tobacco cells.

LITERATURE CITED

(1) Michalet, X., Pinaud, F. F., Bentolila, L. A., Tsay, J. M., Doose, S., Li, J. J., Sundaresan, G., Wu, A. M., Gambhir, S. S., and Weiss, S. (2005) Quantum dots for live cells, *in vivo* imaging, and diagnostics. *Science 307*, 538–544.

(2) Medintz, I. L., Uyeda, H. T., Goldman, E. R., and Mattoussi, H. (2005) Quantum dot bioconjugates for imaging, labelling and sensing. *Nat. Mater. 4*, 435–446.

(3) Chen, F., and Gerion, D. (2004) Fluorescent CdSe/ZnS nanocrystal–peptide conjugates for long-term, nontoxic imaging and nuclear targeting in living cells. *Nano Lett. 4*, 1827–1832.

(4) Shibahara, A., Hoshino, A., Hanaki, K. I., Suzuki, K., and Yamamoto, K. (2004) On the cyto-toxicity caused by quantum dots. *Microbiol. Immunol. 48*, 669–675.

(5) Kirchner, C., Liedl, T., Kudera, S., Pellegrino, T., Javier, A. M., Gaub, H. E., Stölzle, S., Fertig, N., and Parak, W. J. (2005) Cytotoxicity of colloidal CdSe and CdSe/ZnS nanoparticles. *Nano Lett. 5*, 331–338.

(6) Zhang, T., Stilwell, J. L., Gerion, D., Ding, L., Elboudwarej, O., Cooke, P. A., Ĝray, J. W., Alivisatos, A. P., and Chen, F. F. (2006) Cellular effect of high doses of silica-coated quantum dot profiled with high throughput gene expression analysis and high content cellomics measurements. *Nano Lett. 6*, 800–808.

(7) Rikans, L. E., and Yamano, T. J. (2000) Mechanisms of cadmium-mediated acute hepatotoxicity. *Biochem. Mol. Toxicol. 14*, 110–117.

(8) Schützendübel, A., and Polle, A. (2002) Plant responses to abiotic stresses: heavy metal-induced oxidative stress and protection by mycorrhization. *J. Exp. Bot. 53*, 1351–1365.

(9) Gao, X., Cui, Y., Levenson, R. M., Chung, L. W. K., and Niel, Sh. (2004) *In vivo* cancer targeting and imaging with semiconductor quantum dots. *Nat. Biotechnol. 22*, 969–976.

(10) Yu, X., Chen, L., Li, K., Li, Y., Luo, S. X. X., Liu, J., Deng, L. Z. Y., Pang, D., and Wang, Q. (2007) Immunofluorescence detection with quantum dot bioconjugates for hepatoma *in vivo*. *J. Biomed. Opt. 12*, 014008.

(11) Lee, L. Y., Ong, S. L., Hu, J. Y., Ng, W. J., Feng, Y., Tan, X., and Wong, S. W. (2004) Use of semiconductor quantum dots for photostable immunofluorescence labeling of *Cryptosporidium parvum*. *Appl. Environ. Microbiol. 70*, 5732–5736.

(12) Courty, S., Luccardini, C., Bellaiche, Y., Cappello, G., and Dahan, M. (2006) Tracking individual kinesin motors in living cells using single quantum-dot imaging. *Nano Lett. 6*, 1491–1495.

(13) Jaiswal, J. K., and Simon, S. M. (2007) Imaging single events at the cell membrane. *Nat. Chem. Biol. 3*, 92–98.

(14) Warshaw, D. M., Kennedy, G. G., Work, S. S., Krementsova, E. B., Beck, S., and Trybus, K. M. (2005) Differential labeling of myosin V heads with quantum dots allows direct visualization of hand-over-hand processivity. *Biophys. J. 88*, L30–L32.

(15) Bruchez, M., Moronne, M., Gin, P., Weiss, Sh., and Alivisatos, A. P. (1998) Semiconductor nanocrystals as fluorescent biological labels. *Science 281*, 2013–2016.

(16) Wu, X., Liu, H., Liu, J., Haley, K. N., Treadway, J. A., Larson, J. P., Ge, N., Peale, F., and Bruchez, M. P. (2002) Immunofluorescent labeling of cancer marker Her2 and other cellular targets with semiconductor quantum dots. *Nat. Biotechnol. 21*, 41–46.

(17) Müller, F., Houben, A., Barker, P. E., Xiao, Y., Käs, J. A., and Melzer, M. (2006) Quantum dots—a versatile tool in plant science? *J. Nanobiotechnol. 4*, 5–10.

(18) Riegler, J., Nick, P., Kielmann, U., and Nann, T. (2003) Visualize the self-assembly of tubulin with luminescent nanorods. *J. Nanosci. Nanotechnol. 3*, 380–385.

(19) Ziegler, J., Merkulov, A., Grabolle, M., Resch, U., and Nann, T. High quality ZnS shells for CdSe nanoparticles—a rapid, low toxic microwave synthesis. *Langmuir* , in press.

(20) Darbandi, M., and Nann, T. (2005) Single quantum dots in silica spheres by microemulsion synthesis. *Chem. Mater. 17*, 5720–5725.

(21) Breitling, F., and Little, M. (1986) Carboxy-terminal regions on the surface of tubulin and microtubules. Epitope locations of YOL1/34, DM1A and DM1B. *J. Mol. Biol. 189*, 367–370.

(22) Kreis, T. E. (1987) Microtubules containing de-tyrosinylated tubulin are less dynamic. *EMBO J. 6*, 2597–2606.

(23) Bücking, W., Merkulov, A., and Nann, T. Manuscript in preparation.

(24) Hermanson, G. T. (1996) *Bioconjugate Techniques* p 785, Academic Press, New York.

(25) Nagata, T., Nemoto, Y., and Hasezawa, S. (1992) Tobacco BY-2 cell line as the "Hela" cell in the cell biology of higher plants. *Int. Rev. Cytol. 132*, 1–30.

(26) Nick, P., Heuing, A., and Ehmann, B. (2000) Plant chaperonins: a role in microtubule-dependent wall-formation? *Protoplasma 211*, 234–244.

(27) Wiesler, B., Wang, Q.Y., and Nick, P. (2002) The stability of cortical microtubules depends on their orientation. *Plant J. 32*, 1023–1032.

BC700188D

Gene Delivery Properties of End-Modified Poly(*β*-amino ester)s

Gregory T. Zugates,[†] Nathan C. Tedford,[‡] Andreas Zumbuehl,[†,§,⊥] Siddharth Jhunjhunwala,[†,#] Christina S. Kang,[†] Linda G. Griffith,[‡,§] Douglas A. Lauffenburger,[†,‡] Robert Langer,[†,‡,||] and Daniel G. Anderson*[,||]

Department of Chemical Engineering, Biological Engineering Division, Department of Mechanical Engineering, and Center for Cancer Research, Massachusetts Institute of Technology, Cambridge, Massachusetts 02139. Received June 10, 2007; Revised Manuscript Received July 19, 2007

Here, we present the synthesis of a library of end-modified poly(*β*-amino ester)s and assess their utility as gene delivery vehicles. Polymers were synthesized using a rapid, two-step approach that involves initial preparation of an acrylate-terminated polymer followed by a postpolymerization amine-capping step to generate end-functionalized polymers. Using a highly efficient poly(*β*-amino ester), C32, we show that the terminal amine can greatly affect and improve polymer properties relevant to gene delivery. Specifically, the *in vitro* transfection levels can be increased by 30% and the optimal polymer:DNA ratio lowered 5-fold by conjugation of the appropriate end group. The most effective modifications were made by grafting primary diamine molecules to the chain termini. The added charge and hydrophobicity of some derivatives enhanced DNA binding and resulted in the formation of polymer–DNA complexes less than 100 nm in diameter. In addition, cellular uptake was improved 5-fold over unmodified C32. The end-modified poly(*β*-amino ester)s presented here are some of the most effective gene-delivery polycations, superior to polyethylenimine and previously reported poly(*β*-amino ester)s. These results show that the end-modification of poly(*β*-amino ester)s is a general strategy to alter functionality and improve the delivery performance of these materials.

INTRODUCTION

Incorporation of new genetic information into cells is a promising strategy for the treatment of many inherited and acquired genetic disorders. In order for gene-based therapeutics to be clinically applicable, a safe and efficient delivery system for DNA needs to be developed. Modified viruses are the most heavily researched agents but continue to be limited by their toxicity, immunogenicity, and low carrying capacity (*1*). As a result, various cationic polymers have been developed as alternative delivery vectors (*2*–*4*).

The most common polycations used for gene delivery are poly(L-lysine) (PLL) and polyethylenimine (PEI) (*3, 5*). High molecular weight derivatives of both polymers have been shown to self-assemble with plasmid DNA to form nanoparticles capable of transfecting a variety of cell types. Furthermore, functionalization of these polymers with PEG chains and targeting ligands has allowed for cell-specific delivery, which is particularly important for cancer gene therapies (*6*–*8*). Despite their widespread use, both PLL and PEI have significant disadvantages that may ultimately limit their clinical utility. In particular, both polymers are known to be very cytotoxic and have relatively low transfection efficiencies compared to viruses, especially in nondividing cells (*9*–*11*).

Poly(*β*-amino ester)s are an alternative class of cationic polymers that have been recently developed and explored as gene delivery vectors (*12*). These polymers are degradable by hydrolysis of backbone ester bonds and contain tertiary amines to facilitate DNA binding (*12*). They are synthesized by Michael addition of bifunctional amines to diacrylates, and can be prepared without solvents, catalysts, or complex protecting-group strategies (*12, 13*). The polymer molecular weight and chain end groups can be easily controlled by adjusting the amine/diacrylate monomer ratio (*14, 15*). Ease of synthesis, along with the commercial availability of many amine and diacrylate monomers, has allowed for the generation of large, structurally diverse libraries of poly(*β*-amino ester)s (*15, 16*). High-throughput transfection screens have identified many polymers that are capable of transfecting cells with much higher efficiencies than PEI, while also demonstrating less toxicity both *in vitro* and *in vivo* (*15, 17*). The polymer libraries have also been useful to elucidate structure–function relationships. These studies have shown that high molecular weight, amine-terminated poly(*β*-amino ester)s with hydroxyl-functionalized side chains are highly efficient polymers for gene delivery (*15*). The most effective polymer discovered, C32, has also been used *in vivo* for the gene-based treatment of prostate cancer (*17*).

The continued development of poly(*β*-amino ester)s for gene therapy and other biomedical applications requires an effective method to chemically modify these materials. As with other polycations, it is necessary to incorporate additional levels of functionality such as serum stability and cell targeting to improve the gene delivery properties of these polymers. The ideal approach to poly(*β*-amino ester) modification would involve a chemistry that is simple, versatile, and adaptable to a high-throughput format. It is important to generate many polymeric derivatives, since any modification has a nontrivial affect on gene delivery. Previous studies have shown that even single carbon or functional group differences between polymer repeat units can drastically affect their transfection efficiencies (*15, 16*).

* To whom correspondence should be addressed. Daniel G. Anderson, Center for Cancer Research, Massachusetts Institute of Technology, 45 Carleton St. Building E25-342, Cambridge, MA 02139. Fax: 617-258-8827. E-mail: dgander@mit.edu.

[†] Department of Chemical Engineering.

[‡] Biological Engineering Division.

[§] Department of Mechanical Engineering.

[||] Center for Cancer Research.

[⊥] Current address: Biozentrum, University of Basel, Klingelbergstrasse 50/70, 4056 Basel, Switzerland.

[#] Current address: Department of Bioengineering, University of Pittsburgh, Pittsburgh, PA 15261.

10.1021/bc7002082 CCC: $37.00 © 2007 American Chemical Society
Published on Web 10/12/2007

We have recently shown that end-modification of poly(β-amino ester)s is a useful approach to improve both the *in vitro* and *in vivo* polymer transfection efficiency (*18*). In this study, we present a rapid, parallel approach to synthesize end-modified poly(β-amino ester)s and explore the effects of end-group structure on polymer gene delivery properties. End-modified polymers were synthesized following a two-step procedure in which an acrylate-terminated base polymer is first prepared by polymerization using excess diacrylate over amine monomer. In a second stage, the base polymer was reacted with various amine reagents to generate amine-capped polymer chains. Following this approach, we have generated a library of end-modified C32 polymers and demonstrate that the terminal amine has a large effect on C32 transfection. Similar to polymer repeat units, end segments differing in a single additional carbon or functional group can drastically affect the polymer delivery properties. In addition, the terminal amine structure has a large influence on cytotoxicity, physical properties, and cellular uptake of polymer–DNA complexes. These results indicate that end-modification is a useful strategy to functionalize poly(β-amino ester)s and improve their gene delivery performance.

EXPERIMENTAL SECTION

Materials. Polyethylenimine (water-free, M_w ~25 kDa, M_n ~10 kDa) was purchased from Sigma-Aldrich (St. Louis, MO). A 25 mM sodium acetate buffer solution pH 5.2 (NaAc buffer) was prepared by diluting a 3 M stock (Sigma-Aldrich). 1,4-Butanediol diacrylate (99%) and 5-amino-1-pentanol (97%) were from Alfa Aesar (Ward Hill, MA). Amine capping reagents were purchased from Sigma-Aldrich, Alfa Aesar, Acros Organics/Fisher Scientific (Pittsburgh, PA), TCI America (Portland, OR), Molecular Biosciences (Boulder, CO), and Toronto Research Chemicals (Ontario, Canada). All chemicals were used as received without any further purification. PicoGreen and Rediplate 96 PicoGreen dsDNA Quantification Kit were purchased from Molecular Probes (Eugene, OR). pCMV-Luc plasmid DNA stock solution (1 mg/mL in water) was obtained from Elim Biopharmaceuticals (Hayward, CA). gWIZ-β-gal plasmid DNA stock solution (5 mg/mL) was obtained from Aldevron (Fargo, ND). The MTT Cell Proliferation Assay and Bright Glo Luciferase Assay Kits were purchased from Promega Corporation (Madison, WI). White and black polystyrene tissue culture treated 96-well plates and half-area polystyrene 96-well plates were obtained from Corning Costar. Clear polystyrene tissue culture treated 96-well plates were obtained from Becton Dickinson (Bedford, MA). Polypropylene 96-well deep-well plates were purchased from Sigma-Aldrich.

Cell Culture. COS-7 cells were obtained from ATCC (Manassas, VA) and maintained in phenol red free DMEM supplemented with 10% fetal bovine serum and 100 units/mL of penicillin/streptomycin. All cell culture reagents were purchased from Invitrogen Corporation (Carlsbad, CA) unless otherwise noted. COS-7 were grown at 37 °C in a 5% CO_2 atmosphere.

Methods. ^{1}H NMR was conducted on a Varian Inova 500 MHz Spectrometer.

Synthesis of Acrylate-Terminated C32 Poly(β-amino ester). Acrylate-terminated C32 polymer was prepared by mixing 793 mg of 1,4-butanediol diacrylate (4 mmol) with 344 mg of 5-amino-1-pentanol (3.3 mmol). Polymerization was performed in a Teflon-lined screw-cap vial under magnetic stirring at 90 °C for 24 h. ^{1}H NMR (d_6-DMSO): δ (ppm) 1.2–1.4 (m, -$NCH_2(CH_2)_3CH_2OH$), 1.6 (bs, -$N(CH_2)_2COOCH_2CH_2$- and $CH_2CHCOOCH_2CH_2$-), 2.3–2.4 (m, -$COOCH_2CH_2N$- and -$NCH_2(CH_2)_4OH$), 2.6–2.7 (m, -$COOCH_2CH_2N$-), 3.4 (bs, -$N(CH_2)_4CH_2OH$), 4.0 (bs, -$N(CH_2)_2COOCH_2CH_2$-), 4.1 (m, $CH_2CHCOOCH_2CH_2$-), 4.4 (bs, -$N(CH_2)_5OH$), 5.9 (m, $CH_2CHCOOCH_2CH_2$-), 6.1–6.2 (m, $CH_2CHCOOCH_2CH_2$-), 6.3–6.4 (m, $CH_2CHCOOCH_2CH_2$-).

Synthesis of Amine-Capped C32 Poly(β-amino ester)s. Acrylate-terminated C32 polymer was dissolved in DMSO at 31.13 wt %/wt. Amine capping reagents were dissolved in DMSO at 0.25 M. End-chain capping reactions were performed by mixing 321 mg of polymer/DMSO solution with 800 μL of amine solution. Reactions were performed in Eppendorf tubes with constant agitation for 24 h. Polymers were stored at −20 °C until use for each experiment. ^{1}H NMR of C32-Ac capped with 5-amino-1-pentanol (i.e., C32–32) (d_6-DMSO): δ (ppm) 1.2–1.4 (m, -$NCH_2(CH_2)_3CH_2OH$), 1.6 (bs, -$N(CH_2)_2COOCH_2CH_2$-), 2.2–2.4 (m, -$COOCH_2CH_2N$- and -$NCH_2(CH_2)_4OH$), 2.4–2.7 (m, -$COOCH_2CH_2N$-), 3.3 (t, J = 6.6 Hz, -$N(CH_2)_4CH_2OH$), 4.0 (bs, -$N(CH_2)_2COOCH_2CH_2$-).

Polymer Transfections. COS-7 cells (15 000 cells/well) were plated in opaque 96-well plates and allowed to adhere overnight. Polymers at 100 mg/mL in DMSO were diluted accordingly into NaAc buffer to concentrations that yield the different polymer:DNA weight ratios. One hundred microliters of diluted polymer solution was mixed vigorously with 100 μL of DNA (60 μg/mL in NaAc buffer) in a 96-well polystyrene plate. The solutions were left undisturbed for 5 min, after which time 120 μL of each was added to 800 μL of cell culture media in a deep-welled polypropylene plate. The media over the cells was then removed with a 12-channel aspirator wand followed by the addition of 150 μL/well of polymer–DNA complex solution. Complexes were incubated over the cells for 1 h after which time they were aspirated off and replaced with 105 μL/well of fresh cell culture media. Cells were allowed to grow for three days at 37 °C, 5% CO_2, and then analyzed for luciferase protein expression.

Luciferase expression was analyzed using Bright-Glo assays kits. Briefly, 100 μL/well of Bright-Glo solution was added to the cell plates. The plates were gently agitated to promote mixing for 2 min Luminescence was then measured on a Perkin Elmer Victor 3 plate luminometer using a 1% neutral density filter and 1 s/well counting time.

Measurements of Polymer Cytotoxicity. Cytotoxicity measurements of polymer–DNA complexes were performed essentially as described for the transfection experiments except that cellular metabolic activity was measured instead of Luciferase protein expression. One day after the transfection, MTT reagent was added to the cell plates at 10 μL/well. The plates were incubated at 37 °C for 2 h. Detergent reagent was then added at 100 μL/well, and the cell plates were left in the dark at room temperature for 4 h. Optical absorbance was measured at 570 nm using a Molecular Devices SPECTRAmax PLUS384 absorbance plate reader and converted to % cell viability relative to untreated cells.

Polymer–DNA Binding Assay with PicoGreen. Polymer solutions at 100 mg/mL in DMSO were diluted into NaAc buffer to a final concentration of 6 mg/mL. In a half-area 96-well plate, 50 μL/well of diluted polymer was added to 50 μL/well of DNA (60 μg/mL in NaAc buffer). The solutions were mixed vigorously and allowed to sit undisturbed for 5 min to allow for polymer–DNA complexation. After this time, 100 μL/well of PicoGreen solution was added. PicoGreen working solution was prepared by diluting 80 μL of the purchased stock into 15.2 mL NaAc buffer. After 5 min, 30 μL/well of polymer–DNA–PicoGreen solution was added to 200 μL/well of DMEM media in black 96-well polystyrene plates. The plate fluorescence was then measured on a Perkin Elmer Victor 3 plate reader using an FITC filter set (excitation 485 nm, emission 535 nm). The relative fluorescence (RF) was calculated using the following relationship

$$\mathrm{RF} = (F_{\mathrm{sample}} - F_{\mathrm{blank}})/(F_{\mathrm{DNA}} - F_{\mathrm{blank}})$$

where F_{sample} is the fluorescence of the polymer–DNA–PicoGreen sample, F_{blank} is the fluorescence of a sample with no

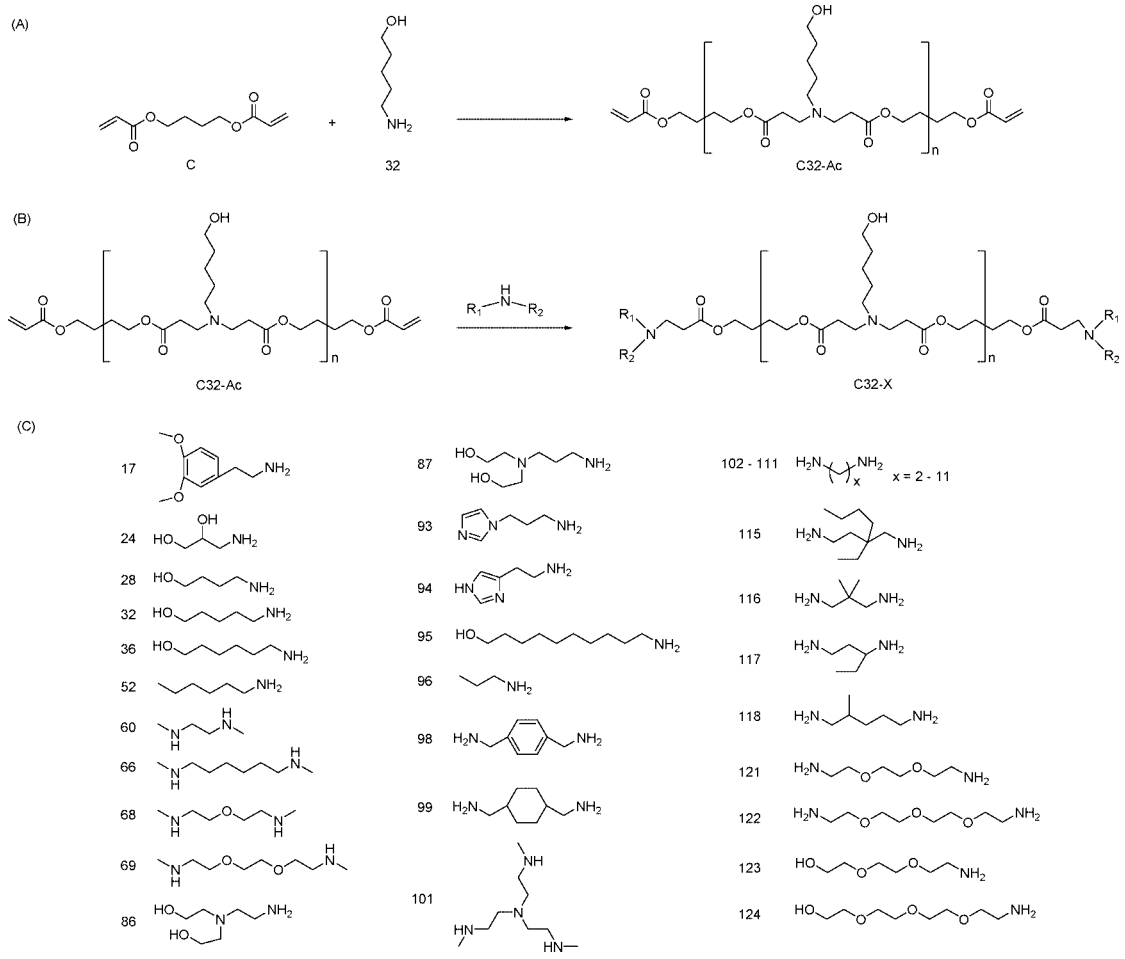


Figure 1. (A) Synthesis of acrylate-terminated C32 polymer (C32-Ac). (B) Synthesis of end-modified C32 polymers (C32-X). (C) Amine capping molecules.

polymer or DNA (only PicoGreen), and F_{DNA} is the fluorescence of DNA–PicoGreen (no polymer).

Polymer–DNA Complex Size. Polymer solutions at 100 mg/mL in DMSO were diluted into NaAc buffer at the appropriate concentration. Concentrations were adjusted for each polymer so that the final polymer:DNA ratio was the same as the ratio that produced the highest transfection. To prepare polymer:DNA complexes, 100 μL of diluted polymer was added to 100 μL of DNA (60 μg/mL in NaAc) and pipetted vigorously. Complexation was allowed to proceed undisturbed for 5 min, after which time 150 μL of the sample was diluted into 1.8 mL of DMEM media. Polymer:DNA complex size was measured on a Zeta-PALS dynamic light scattering detector (Brookhaven Instruments Corporation, Holtsville, NY; 15 mW laser; 676 nm incident beam, 90° scattering angle). Effective particle diameters were calculated from the autocorrelation function using the MAS option of the BIC particle-sizing software assuming a log normal distribution. The solution viscosity and refractive index were assumed equal to those of pure water at 25 °C.

Cellular Uptake Assay. Uptake measurements of polymer–DNA complexes were performed essentially as described for the transfection experiments but using the β-galactosidase (β-gal) plasmid. Instead of quantifying protein expression levels after three days, total cellular DNA was isolated 4 h post-transfection using a DNeasy 96 Tissue Kit (Qiagen; Valencia, CA). DNA isolation was performed according to the supplied instructions and included two PBS washes of the cells before lysis to ensure that surface-bound complexes were removed (*19*). Total DNA was quantified using a Redi-Plate 96 PicoGreen dsDNA Quantification Kit following the supplied instructions. The amount of β-gal DNA delivered was quantified using RT-PCR with a custom Taqman primer and probe set specific for the β-gal plasmid (Applied Biosystems; Foster City, CA). The primers and probe spanned an 80 bp sequence in the β-gal coding region of the plasmid and had the following sequences: forward primer 5′-TTA CAG GGC GGC TTC GTC T-3′, reverse primer 5′-TAA GCC GAC CAC GGG TTG-3′, and the Taqman probe 5′-6FAM-CTG GGT GGA TCA GTC GCT GAT TAA ATA TGA TG-TAMRA-3′. The primers and probes were used at concentrations of 400 nM and 25 nM, respectively. After activating the Taq enzyme at 95 °C for 10 min, 40 cycles of amplification were performed, with each cycle consisting of 95 °C for 15 s, 60 °C for 1 min, followed by a fluorescent plate read using a Chromo4 Continuous Fluorescence Detector (MJ Research; Waltham, MA). Plasmid copy numbers were determined by comparing the RT-PCR cycle threshold values to a plasmid standard curve and analyzed using the *Opticon Monitor 3* sofware package (MJ Research).

RESULTS AND DISCUSSION

Polymer Synthesis. We developed a two-step approach to synthesize end-modified C32 poly(β-amino ester)s, as illustrated in Figure 1A,B (*18*). In the first step, acrylate-terminated C32 polymer was prepared by mixing the corresponding diacrylate and amine monomers in a 1.2:1 molar ratio, as shown previously (Figure 1A) (*14*). This ratio was selected since C32 and many other top-performing, amine-terminated polymers are made at an inverse ratio of 1:1.2 acrylate/amine (*15*). We hypothesized then that the exact opposite ratio may be optimal so that the

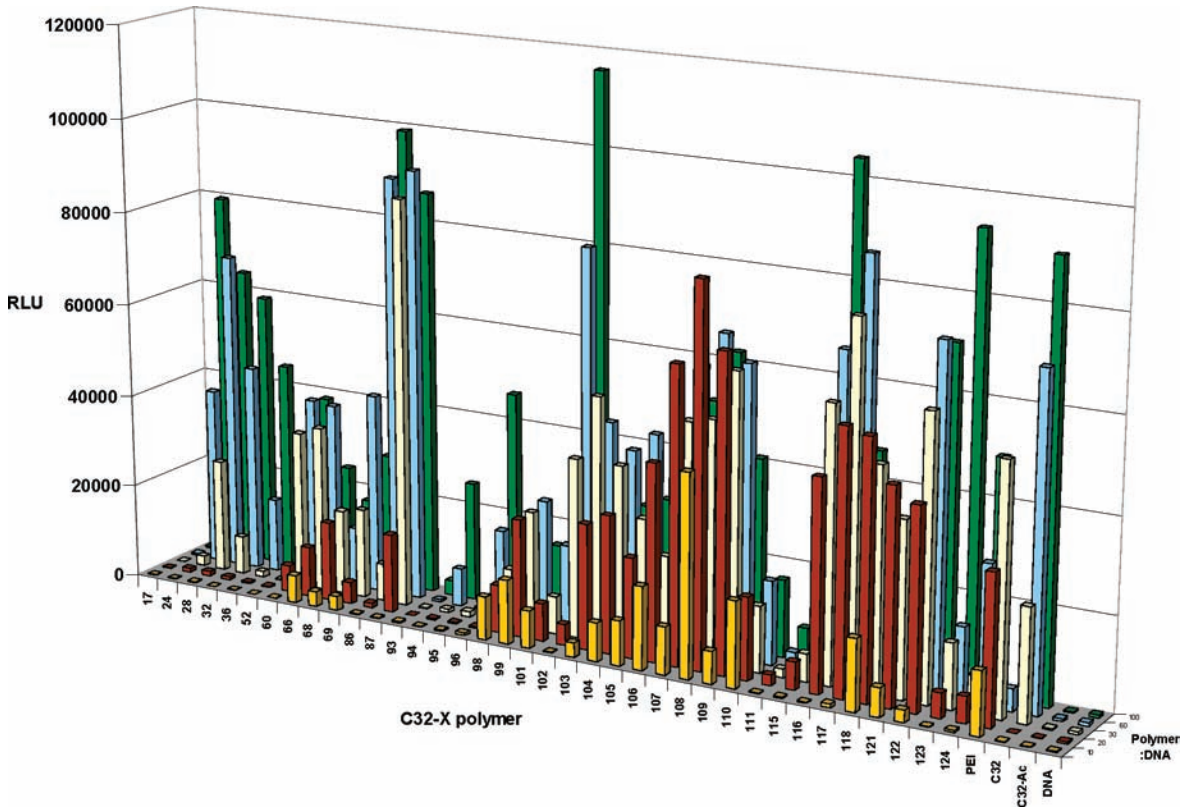


Figure 2. Transfection of COS-7 cells. The relative light units (RLU) from luciferase reporter protein expression are shown for each end-modified C32 polymer (C32-X) at five polymer:DNA weight ratios (10, 20, 30, 60, and 100:1).

relative number of interior to terminal units is approximately preserved, with the end-capping step causing a relatively small change to this balance. Therefore, the diacrylate/amine ratio selected directly controls the final molecular weight. For many poly(β-amino ester)s, molecular weights greater than 10 kDa are usually most effective and can be achieved using a 1.2:1 molar monomer ratio (*15*). For the C32-acrylate polymer (C32-Ac), the weight-average molecular weight is approximately 8800 Da, relative to polystyrene standards, with a 1.9 polydispersity index.

In the second step, acrylate-terminated C32 polymer is reacted with various amine molecules to generate amine-capped polymer chains (Figure 1B). In this way, the chain ends contain amine functionalities different than those present in the interior of the polymer. Most chain-capping reactions are performed using a primary amine molecule, which results in an amine-capped polymer containing secondary amines at the chain end points. Secondary amine molecules are also used but result in tertiary amine groups at the polymer ends. The 37 different amine molecules used for this secondary capping step are shown in Figure 1C. These compounds were selected on the basis of their DMSO solubility, biocompatibility, and ability to assess structure–function relationships. In addition, many of these molecules have proven useful in the synthesis of poly(β-amino ester)s with high transfection efficiencies (*15*).

The end-capping reaction occurs via an amine-acrylate Michael addition, identical to that used in the polymerization. Since acrylates have no detectable reactivity toward hydroxyls, ethers, tertiary amines, amides, aromatics, and some types of heterocycles, all of these functionalities can be incorporated at the chain ends using the appropriate amine reagents (*16*). The reaction is carried out by mixing a concentrated polymer solution with an excess of amine in DMSO at room temperature. The conditions have been optimized with excess amine to fully end-cap all chains without causing any detectable cross-linking or aminolysis of backbone ester bonds, as determined by ^{1}H NMR and GPC analysis (data not shown). Presumably, aminolysis is avoided due to the higher reactivity of acrylates compared to esters and the mild end-capping reaction conditions used. The resulting end-modified polymers can be directly tested for transfection efficiency without prior purification, since the DMSO and excess amine were determined to be nontoxic (data not shown). Therefore, this chemistry permits many polymers with structurally diverse end functionalities to be synthesized and screened in parallel. We show here that such a synthetic method is useful to assess end amine structure–function relationships and improve the gene delivery properties of poly(β-amino ester)s.

For the analysis presented here, we use C32 as a base polymer to examine the effects of the end amine structure on polymer transfection and also explore structure–function relationships. This polymer was identified from previous studies to be the most efficient poly(β-amino ester) for gene delivery (*15*). In principle, other base polymers, diacrylate/amine ratios, and amine-capping agents may be used and could generate more effective polymers for gene delivery.

Cellular Transfections. The DNA delivery efficiency of end-modified poly(β-amino ester)s was evaluated using a high-throughput assay (*20*). Concentrated polymer solutions in DMSO were diluted in sodium acetate buffer and complexed with plasmid DNA to form polymer–DNA nanoparticles. A range of polymer:DNA weight ratios was tested for each polymer, since this parameter is known to have a critical effect on polycation-mediated transfection (*15*). Nanoparticles were then diluted into cell culture media and incubated on COS-7 cells. The diluting media contained 10% serum to account for the effect of serum proteins on polymer transfection.

The transfection efficiencies of amine-terminated C32 polymers are shown in Figure 2. The average luciferase expression levels, measured in relative light units (RLUs), are given for

each polymer at five different polymer:DNA ratios. We have previously shown the transfection data for each end-modified polymer at its optimal ratio and present here the complete data set containing all polymer:DNA ratios (*18*). Also included are the transfection data for 25 kDa branched PEI, one of the most efficient commercially available polycations, and C32, one of the best performing poly(β-amino ester)s synthesized to date. The unmodified, acrylate-terminated C32 polymer is also shown on the far right and demonstrates weak activity that is similar to other acrylate-terminated poly(β-amino ester)s (*14*). While amine-capping reactions of this polymer were verified by ^{1}H NMR analysis, the data in Figure 2 provide functional confirmation by the large increase in transfection between acrylate- and amine-terminated polymers. An overall inspection of the data reveals that the structure of the terminal amine has a dramatic effect on the C32 transfection efficiency. In general, polymers capped with hydrophilic amine end groups containing hydroxyls or additional amines proved most effective. In contrast, chain termination with more hydrophobic amines containing alkyl chains or aromatic rings led to much lower transfection activity.

Perhaps the most important result is that very subtle structural differences in just the terminal amine can have a large effect on polymer transfection efficiency. This is most evident by comparing the C32–36 and C32–52 polymers. The C32–52 polymer, which contains a six-carbon alkyl chain extending from the terminal secondary amine, has a maximum transfection only twice that of naked DNA. In contrast, the C32–36 polymer is 34-fold more effective than C32–52, but only differs in a single hydroxyl group on carbon-6 at the chain end. In fact, the C32–36 polymer is half as effective as C32, demonstrating that a single functional group, in this case a terminal hydroxyl, can significantly alter the polymer delivery properties. A similar effect can be seen between the C32–95 and C32–110 polymers, which consist of terminal decylamines containing either a hydroxyl group or primary amine on carbon-10, respectively. In this case, substituting the terminal hydroxyl for an amine improves the transfection performance by over 1 order of magnitude. This same substitution pattern also changes the optimal polymer:DNA ratio. Comparing two highly efficient polymers, C32–122 and C32–124, the former displays very high RLU output at a 20:1 ratio, whereas the latter requires 5-fold more polymer (i.e., a 100:1 ratio) to achieve the same effect. A similar trend is also seen between the C32–36 and C32–106 polymers. Therefore, amine-capping molecules with hydroxyls and primary amines are most effective, with the latter being optimal at 5-fold lower polymer:DNA ratios in general.

Polymers terminated with primary diamine molecules had the highest transfection efficiency, as determined by both RLU output and lowest optimal polymer:DNA ratio. Specifically, the C32–102 polymer had a very similar transfection profile to that of C32, with a maximum occurring at the highest polymer:DNA ratio of 100:1, but had an overall 30% higher RLU output. This demonstrates that modification at the chain ends can significantly improve the delivery performance. Primary diamine capping also lowered the optimal polymer:DNA ratio substantially in many cases. Seven primary amine-terminated polymers had optimal polymer:DNA ratios of 20:1, while one polymer, C32–110, had a maximum RLU at a 10:1 ratio. The transfection profile at the 20:1 ratio for diamine-capped polymers, C32–102 through C32–111, appears to be a skewed bell-shaped curve with a maximum occurring at the C32–108 polymer. This indicates that larger alkyl chains bridging the diamine functionalities are generally more effective than their short-chain counterparts, with an optimum of eight carbons. The C32–108 polymer had an optimal transfection at a 20:1 ratio that is almost as high as that for C32, which requires a 100:1 ratio. Such a significant reduction in the amount of polymer needed to mediate high levels of transfection has important implications for *in vivo* delivery, where the amount of polymer injected needs to be limited to minimize toxic side effects (*18*).

Cytotoxicity. Many polycations have been shown to elicit considerable cell toxicity that may limit their utility as gene delivery vectors (*10, 11*). The biocompatibility of cationic polymers is determined by a number of factors that include molecular weight, charge density, type of amines, polymer structure (linear, branched, dentritic), and chain flexibility (*21–27*). In general, high molecular weight polymers with a high density of primary and/or secondary amines usually result in substantial cytotoxicity (*28*).

The cytotoxicity of end-modified poly(β-amino ester)s was evaluated using the MTT assay. This colorimetric test is based on the ability of mitochondrial reductase enzymes in viable cells to reduce 3-(4,5-dimethylthiazol-2-yl)-2,5-diphenyl tetrazolium bromide to a purple formazan. Toxicity of end-modified polymers was assessed by performing the same transfection experiment, but assaying for metabolic activity instead of luciferase expression. All polymers were tested at the highest 100:1 polymer:DNA weight ratio, which corresponds to an approximate 400 ug/mL concentration of polymer on the cells. Toxicity analysis at such a high polymer concentration may explain the differences in polymer transfection at high polymer:DNA ratios and simultaneously assess polymer biocompatibility under very aggressive conditions that may be important for their future use and development.

The cytotoxicity levels of end-modified C32 polymers are shown in Figure 3. The percentage of viable cells is displayed as a function of the amine-terminated polymer. Positive and negative control conditions are shown to the far right for PEI and naked DNA. At such high polymer concentrations, PEI is very cytotoxic, as reflected by the low 3% cell viability. In contrast, both C32 and the acrylate-terminated C32 polymer (C32-Ac) show no significant affects on the growth and metabolism of COS-7 cells.

The majority of end-modified C32 polymers show good biocompatibility. This is especially true of all polymers capped with primary monoamine reagents, regardless of the functional groups extending from the amine. Aromatic, alkyl, hydroxyl, secondary and tertiary amines, and imidazole functionalities at the chain end points do not appear to induce any significant adverse effects. Therefore, elevated cytotoxic effects do not sufficiently explain the low transfection ability of polymers terminated with the more hydrophobic amines. In contrast to the polymers capped with monoamines, polymers terminated with primary diamine molecules compromise cell viability to varying extents. While the increased charge is a determining factor, the overall toxicity is also strongly dependent on the hydrophobicity of the end group. In general, increasing the size of the alkyl chain bridging the amine groups increases the toxicity, as is evident by comparing the C32–102 through C32–109 polymers. Furthermore, C32–121, a polymer containing a terminal poly(ethylene glycol amine) with an eight-atom spacer between amine groups, is much less toxic than the corresponding alkyl derivative, C32–108. This indicates that both the spacing between amines and the degree of hydrophobicity in the terminal amine spacer are important determinants of end-amine toxicity.

These significant cytotoxic effects, in large part, explain the decreasing transfection ability of most primary diamine-capped polymers at the higher polymer:DNA ratios. The additional charge, in conjunction with increased hydrophobicity, may be particularly damaging to the cell membranes, since both properties are known to disrupt lipid bilayers (*26*).

DNA Binding. An important requirement for cationic transfection agents is the ability to bind and condense plasmid DNA

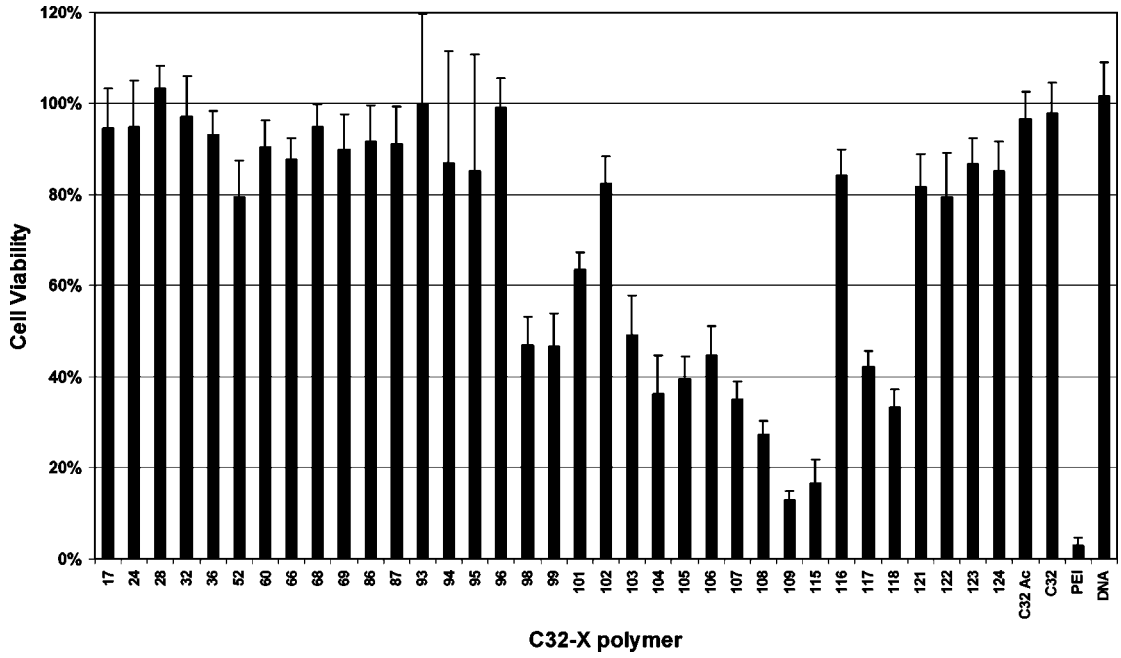


Figure 3. Cytotoxicity levels of end-modified C32 polymers (C32-X) measured using the MTT assay. PEI, C32, C32-Ac, and free DNA toxicity are shown on the far right.

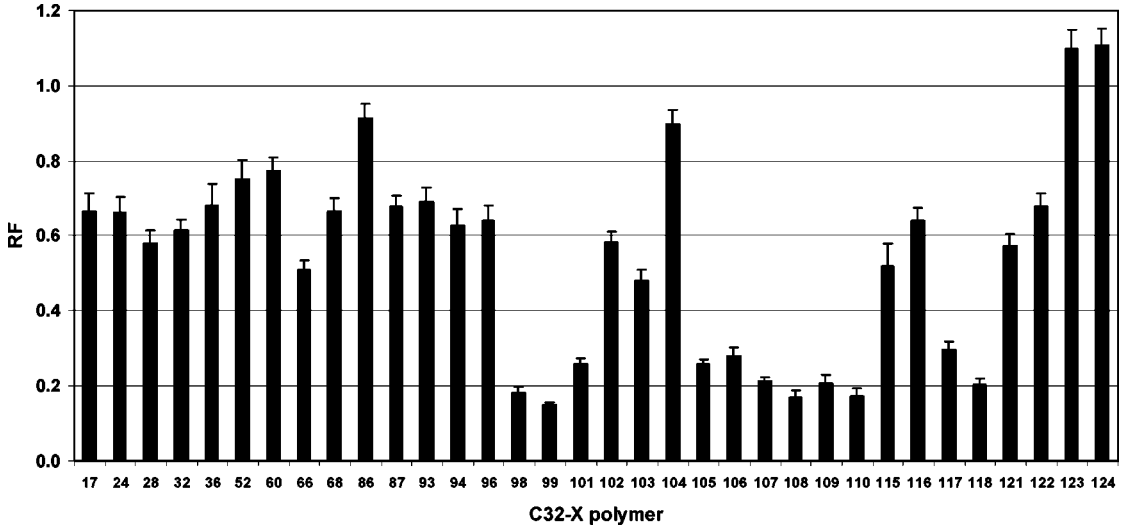


Figure 4. Polymer–DNA binding measured using a PicoGreen assay. Fluorescence reductions relative to free DNA (RF) are shown for each end-modified C32-polymer (C32-X) at the optimal transfecting polymer:DNA ratio for each polymer.

for cell entry (*29*). In general, higher molecular weight polymers with increased cationic charge density display stronger DNA binding at low polymer:DNA ratios (*21, 30, 31*). While strong electrostatic interactions are important to effectively condense and deliver the DNA, the polymer must possess a mechanism to unbind from the DNA once inside the nucleus (*32*). For this reason, the poly(β-amino ester)s may be particularly advantageous, since they undergo hydrolysis with short half-lives (*12*), which may aid in DNA unpackaging.

The binding and condensation of DNA by polycations is often monitored using an agarose gel electrophoresis assay (*33*). This assay can be used to adequately determine the minimum polymer:DNA ratio required for plasmid condensation but does not provide any information on the strength of this interaction. In contrast, dye-binding assays provide a quantitative measure of the polymer–DNA binding event at all polymer:DNA ratios (*34–36*). As a result, we utilized a PicoGreen dye penetration assay to determine the degree of plasmid condensation by the end-modified poly(β-amino ester)s. In this assay, polymer–DNA complexes are formed in a manner similar to their preparation for transfection experiments. The complexes are then mixed with a PicoGreen dye solution, diluted into cell culture media, and the solution fluorescence is measured. The dye exhibits fluorescence only when it intercalates between the DNA base pairs. High fluorescence is typically seen with free plasmid, but significant reductions can occur for polymer–DNA complexes in which the DNA is partially shielded from dye penetration. The magnitude of this fluorescence reduction relative to free DNA correlates to the strength of the polymer–DNA interaction (*14, 37*).

The DNA binding levels for each end-modified polymer are shown in Figure 4. Fluorescence measurements relative to free DNA are given at the optimal transfecting polymer:DNA ratio for each polymer. With the exception of monoamine PEG-terminated polymers, all end-modified materials displayed some level of DNA binding. In general, increased cationic charge at the end groups increased the polymer–DNA binding affinity. This effect is most noticeable by comparing the results of the

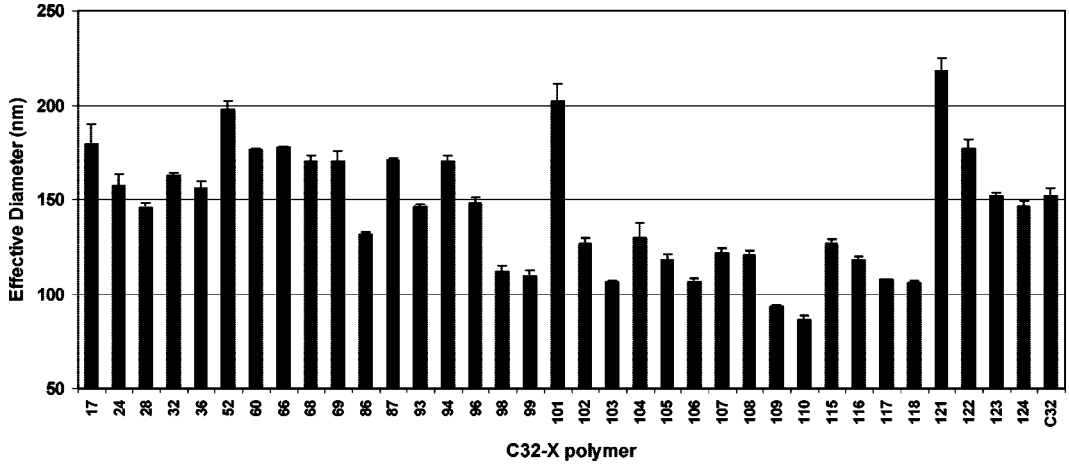


Figure 5. Polymer–DNA complex size measured by dynamic light scattering. The effective diameters of complexes are shown for each end-modified C32 polymer (C32-X) at the optimal transfecting polymer:DNA ratio for each polymer.

PEG amine-capped polymers. The monoamine-capped polymers, C32–123 and C32–124, displayed no measurable binding. However, the substitution of a single primary amine for a hydroxyl at the chain ends (C32–121 and C32–122) leads to increased polymer–DNA binding and less dye penetration. This result indicates that a single functional group only at the very end point of the polymer can bring about large changes in polymer function. Similar conclusions were reached when assessing the overall transfection ability of the polymer but now are seen at just one part of the delivery process.

Perhaps the most noticeable trend in the data is that polymers terminated with primary diamine molecules are most effective at condensing and binding DNA. Additional secondary or tertiary amines at the chain ends were not as effective at increasing the DNA binding ability of the polymer, possibly due to pK_a differences or a more sterically crowded environment that may prevent their electrostatic interaction with DNA (*38, 39*). Similar to the cytotoxicity data, more effect is seen with increased terminal hydrophobicity in addition to the added positive charge. In general, smaller relative fluorescence is seen as the alkyl chain length is increased between terminal amine groups, as is evident by comparing polymers C32–102 through C32–110. These results are supported by lower DNA binding affinity of polymers terminated with the more hydrophilic primary ethylene glycol amine polymers (C32–121 and C32–122).

Polyplex Sizing. Simple electrostatic interactions between the polycation and the negatively charged DNA can often lead to their spontaneous self-assembly into cationic polymer–DNA nanoparticles (*40, 41*). The physical properties of these complexes are particularly important for their subsequent uptake into cells. Complexes with a positive surface charge and a diameter less than 200 nm are usually sufficient for cellular endocytosis (*42*). These properties are dependent upon a number of polymer characteristics and the polymer-DNA mixing technique (*43–47*). Since the terminal amine has demonstrated significant effects on the DNA binding ability of polymers, it should also affect the physical properties of the polymer–DNA complexes.

The effective diameter of complexes formed between end-modified poly(β-amino ester)s and plasmid DNA were measured using dynamic light scattering. Polymer–DNA complexes were formed at the optimal transfecting polymer:DNA ratio for each polycation and then diluted into cell culture media prior to each measurement. Concentrations, solution compositions, and polymer–DNA complexing procedures in each step were identical to those used in the transfection assay. In this way, the nanoparticle physical properties measured in this experiment reflect the actual particle properties in the transfection screen.

Average diameters of the polymer–DNA complexes are presented in Figure 5 for each end-modified C32 polymer. The average diameter varied between 85 to 220 nm, demonstrating the crucial effects of terminal amine structure on the physical properties of polymer–DNA complexes. Also shown on the far right is the average diameter of C32 complexes, which is determined to be 152 nm. In a previous study, C32 complexes were diluted into HEPES buffer and subsequently measured to be 79 nm in diameter (*15*). This difference in particle size illustrates the large effect of serum proteins to disrupt or interact with cationic polymer–DNA complexes. Increases in polymer–DNA complex size in the presence of serum have been seen in our previous studies and with other polycations such as PEI, and have a well-known effect on polymer–DNA properties (*48, 49*). Importantly, the C32 complex diameter is still below the threshold for endocytosis and maintains high transfection levels.

All end-modified polymers formed complexes with effective diameters in a suitable range for cellular uptake. Only two polymers, C32–101 and C32–121, formed complexes with diameters slightly above 200 nm. The former material consists of highly charged chain end groups, whereas the latter contains a short PEG diamine at the chain end points. In general, the PEG-terminated polymers (C32–121 to C32–124) formed larger complexes with diameters between 150 and 220 nm. Despite the large size and weak DNA binding of these polycations, they can still deliver DNA with relatively high efficiencies. This effect is also true of most polymers terminated with monoprimary amine molecules. These polymers, shown on the left side of Figure 5, mostly result in complexes with diameters greater than 150 nm and lower DNA binding ability than primary diamine-capped polymers. Although a general conclusion cannot be made, it is interesting to note that some polymers with very low transfection efficiencies (e.g., C32–117, −52, −101) also form relatively large complexes, suggesting that their physical properties may not be conducive to uptake.

Similar to the DNA binding data, particle sizing appears to be more favorable for polymers capped with primary diamine molecules. For almost all of these polymers, their complexes with DNA have diameters between 85 and 130 nm. The more hydrophilic PEG diamines, C32–121 and C32–122, are the exception, illustrating the importance of a hydrophobic alkyl chain space between amines at the terminus. Although the trend is not as pronounced as that for the DNA binding, it appears that the sizing is somewhat improved by increasing the alkyl chain length. This is especially true at the long chain lengths where C32–109 and C32–110 form the smallest complexes that have diameters less than 100 nm. These polymers assemble into smaller complexes with DNA compared to those terminated with

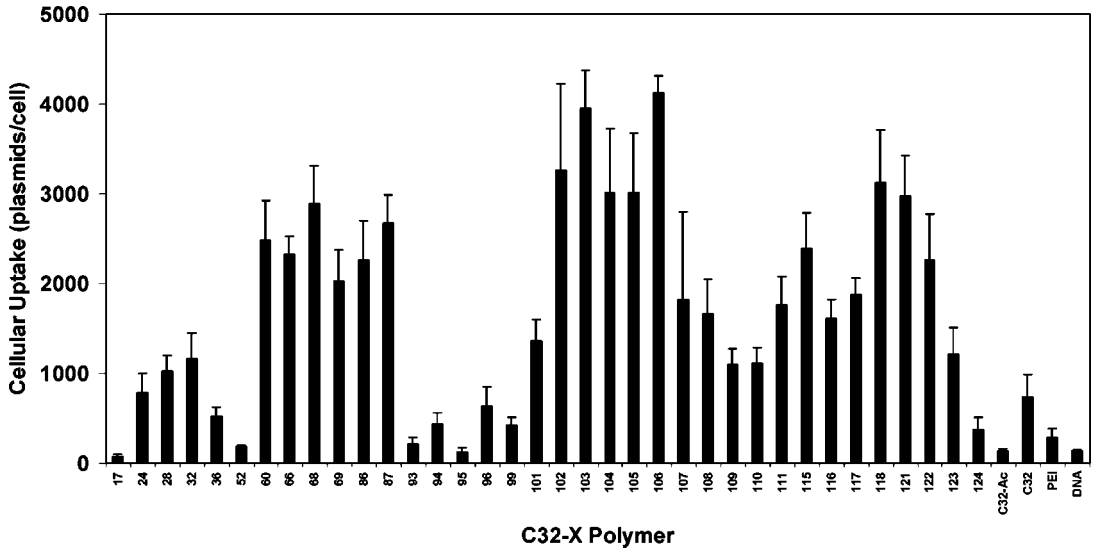


Figure 6. Polymer–DNA uptake into COS-7 cells. DNA uptake levels are shown in the number of plasmids per cell for each end-modified C32 polymer (C32-X).

additional secondary and/or tertiary amines, again illustrating the benefits of primary amines at the chain ends over these other amine functionalities. Consequently, it appears that polymers terminated with alkyl primary diamine molecules have the highest DNA binding affinity and assemble into the smallest polymer–DNA complexes.

DNA Uptake. Differences in the physical properties of polymer–DNA complexes can lead to differences in the rates and levels at which they are endocytosed into cells. Previous studies with poly(β-amino ester)s have shown that smaller complexes with high cationic surface charge are more favorable for cellular uptake (*42*). In addition, amine termination has been shown to promote higher cellular internalization over the corresponding acrylate-terminated polymer (*14*). In light of these findings and the terminal amine affects on polymer–DNA properties, we measured the uptake levels of end-modified C32 polymers. Although previous studies with poly(β-amino ester)s used a novel fluorescence-based technique (*19*), we choose to use a DNA extraction and real-time PCR (RT-PCR) amplification protocol to quantify the amount of endocytosed DNA (*9*). This method provides (1) high sensitivity due to the PCR amplification, (2) linearity over several orders-of-magnitude, (3) the ability to quantify DNA uptake without prelabeling the plasmid, and (4) a high-throughput, 96-well plate format to simultaneously and rapidly analyze all polymers. For this experiment, transfections were performed following the standard protocol using a β-galactosidase (β-gal) plasmid. This DNA was isolated from the cells after a 4 h incubation period, then amplified and quantified using RT-PCR. The total number of β-gal DNA plasmids harvested for each sample was calculated using a standard curve and normalized to the number of COS-7 cells.

The DNA uptake levels for each end-modified polymer are shown in Figure 6. The results are expressed as the number of plasmids endocytosed per cell for each polymer at its optimal transfecting polymer:DNA ratio. Also shown is the low uptake level of free plasmid DNA, which is most likely due to its large size and high anionic charge density that repels the cell surface. Positive control polymers C32 and PEI are also shown to the far right, both of which increase DNA uptake by approximately 5-fold over the free plasmid. In addition to increasing endocytosis, these polycations lead to higher cellular DNA levels by protecting the plasmid from intracellular nucleases. Unlike C32 and PEI, plasmid condensation with the C32-Ac polymer did not improve uptake to any measurable level, which explains the inability of this polymer to mediate transfection. The large difference between C32 and C32-Ac, in terms of both uptake and transfection, highlight the importance of amine termination to improve the C32 polymer delivery properties.

The results in Figure 6 demonstrate that the type of amine at the chain ends has a considerable effect on the endocytosis of C32 polymer–DNA complexes. The uptake levels varied over 2 orders of magnitude among the end-modified polymers, with polymer C32–106 mediating the highest plasmid internalization that is 30-fold greater than free DNA. The most obvious trend in the data is the improved uptake that occurs for polymers with additional terminal amines. This is evident for polymers containing extra secondary and tertiary end amines (C32–60 through C32–87) and mostly for those with an additional primary end amine (C32–102 through C32–122). These results suggest that conjugation of targeting ligands to the chain ends may be a promising strategy to achieve cell-specific delivery.

The differences in uptake between each polymer also explain some important differences in their transfection efficiencies. First, many polymers that are poor transfection agents also displayed very low uptake (e.g., C32–17, −52, −93, −95). This indicates that the extra charge alone at the chain end points (compared to C32-Ac) is not sufficient to promote C32-DNA endocytosis. Specific functional groups at the chain ends, such as hydroxyls and amines, have an enhanced capacity to interact with cell surfaces and increase uptake as compared to more hydrophobic terminal segments. For example, the transfection differences between C32–36 and C32–52 are largely related to their differences in uptake. This comparison demonstrates that a single functional group in the polymer chain, in this case, a terminal hydroxyl, can have a large effect on cell interactions and endocytosis. Extending the comparison further, C32–106 differs from these two materials by a terminal primary amine. The results show that this single substitution at the terminal amine carbon-6 can increase uptake by over 20-fold. This effect is even more surprising considering that the polymer:DNA ratio used for C32–106 is 20:1, 5-fold less than that used for C32–36 and C32–52. In general, the increased uptake by the polymers capped with primary diamines largely explains their increased effectiveness at reduced polymer:DNA ratios. The overall transfection levels may not be substantially improved over C32 and other nonprimary amine polymers because the terminal

functionalities may have important effects on other downstream gene delivery barriers such as endosomal escape, cytosolic trafficking, or nuclear import.

CONCLUSIONS

In this work, we present a fast and simple method to generate end-modified polymer derivatives. Variations in the terminal amine structure are shown to affect many properties that are important for effective polymeric gene delivery. Surprisingly, single carbon and functional group differences only at the chain ends have large effects on the physical properties of polymer–DNA complexes, their cellular uptake, and subsequent transfection. The best results occurred with primary diamine end cappings, which improved transfection of the C32 poly(β-amino ester) and lowered the optimal polymer:DNA ratio by 5-fold. These modifications effectively decreased the polymer–DNA nanocomplex size and increased cellular uptake. This suggests that ligand attachments to the polymer ends may be a promising strategy to achieve cell-specific targeting and improve the *in vivo* biodistribution of polymer–DNA complexes. To our knowledge, the modified poly(β-amino ester)s presented here are some of the most effective and efficient degradable polycations to date, superior to PEI and previously optimized poly(β-amino ester)s. We are currently evaluating the *in vivo* transfection potential of these polymers for the systemic treatment of cancer.

ACKNOWLEDGMENT

G.T.Z thanks the National Science Foundation for a graduate research fellowship. This work was supported by grant EB00244 from the National Institute of Health.

LITERATURE CITED

(1) Kootstra, N. A., and Verma, I. M. (2003) Gene therapy with viral vectors. *Annu. Rev. Pharmacol. Toxicol. 43*, 413–39.
(2) Putnam, D. (2006) Polymers for gene delivery across length scales. *Nat. Mater. 5*, 439–451.
(3) Pack, D. W., Hoffman, A. S., Pun, S., and Stayton, P. S. (2005) Design and development of polymers for gene delivery. *Nat. Rev. Drug Discovery 4*, 581–593.
(4) Wagner, E., and Kloeckner, J. (2006) Gene delivery using polymer therapeutics. *Adv. Polym. Sci. 192*, 135–173.
(5) Thomas, M., and Klibanov, A. M. (2003) Non-viral gene therapy: polycation-mediated DNA delivery. *Appl. Microbiol. Biotechnol. 62*, 27–34.
(6) Kircheis, R., Kichler, A., Wallner, G., Kursa, M., Ogris, M., Felzmann, T., Buchberger, M., and Wagner, E. (1997) Coupling of cell-binding ligands to polyethylenimine for targeted gene delivery. *Gene Ther. 4*, 409–18.
(7) Suh, W., Chung, J. K., Park, S. H., and Kim, S. W. (2001) Anti-JL1 antibody-conjugated poly (L-lysine) for targeted gene delivery to leukemia T cells. *J. Controlled Release 72*, 171–8.
(8) O'Neill, M. M., Kennedy, C. A., Barton, R. W., and Tatake, R. J. (2001) Receptor-mediated gene delivery to human peripheral blood mononuclear cells using anti-CD3 antibody coupled to polyethylenimine. *Gene Ther. 8*, 362–8.
(9) Varga, C. M., Tedford, N. C., Thomas, M., Klibanov, A. M., Griffith, L. G., and Lauffenburger, D. A. (2005) Quantitative comparison of polyethylenimine formulations and adenoviral vectors in terms of intracellular gene delivery processes. *Gene Ther. 12*, 1023–1032.
(10) Brazeau, G. A., Attia, S., Poxon, S., and Hughes, J. A. (1998) *In vitro* myotoxicity of selected cationic macromolecules used in non-viral gene delivery. *Pharm. Res. 15*, 680–4.
(11) Moghimi, S. M., Symonds, P., Murray, J. C., Hunter, A. C., Debska, G., and Szewczyk, A. (2005) A two-stage poly(ethylenimine)-mediated cytotoxicity: Implications for gene transfer/therapy. *Mol. Ther. 11*, 990–995.
(12) Lynn, D. M., and Langer, R. (2000) Degradable poly(β-amino esters): synthesis, characterization, and self-assembly with plasmid DNA. *J. Am. Chem. Soc. 122*, 10761–10768.
(13) Lynn, D. M., Anderson, D. G., Putnam, D., and Langer, R. (2001) Accelerated discovery of synthetic transfection vectors: parallel synthesis and screening of a degradable polymer library. *J. Am. Chem. Soc. 123*, 8155–6.
(14) Akinc, A., Anderson, D. G., Lynn, D. M., and Langer, R. (2003) Synthesis of poly(β-amino ester)s optimized for highly effective gene delivery. *Bioconjugate Chem. 14*, 979–88.
(15) Anderson, D. G., Akinc, A., Hossain, N., and Langer, R. (2005) Structure/property studies of polymeric gene delivery using a library of poly(beta-amino esters). *Mol. Ther. 11*, 426–34.
(16) Anderson, D. G., Lynn, D. M., and Langer, R. (2003) Semi-automated synthesis and screening of a large library of degradable cationic polymers for gene delivery. *Angew. Chem., Int. Ed. Engl. 42*, 3153–8.
(17) Anderson, D. G., Peng, W., Akinc, A., Hossain, N., Kohn, A., Padera, R., Langer, R., and Sawicki, J. A. (2004) A polymer library approach to suicide gene therapy for cancer. *Proc. Natl. Acad. Sci. U.S.A. 101*, 16028–33.
(18) Zugates, G. T., Peng, W., Zumbuehl, A., Jhunjhunwala, S., Huang, Y. H., Langer, R., Sawicki, J. A., and Anderson, D. G. (2007) Rapid optimization of gene delivery by parallel end-modification of poly(b-amino ester)s. *Mol. Ther. 15*, 1306–1312.
(19) Akinc, A., and Langer, R. (2002) Measuring the pH environment of DNA delivered using nonviral vectors: implications for lysosomal trafficking. *Biotechnol. Bioeng. 78*, 503–8.
(20) Zugates, G. T., Anderson, D. G., and Langer, R. (2007). High Throughput Methods for Screening Polymeric Transfection Reagents. In *Gene Transfer: Delivery and Expression of DNA and RNA* (Friedmann, T., and Rossi, J., Eds.) pp 547—554, Cold Spring Harbor Laboratory Press, Woodbury, NY.
(21) Kunath, K., von Harpe, A., Fischer, D., Petersen, H., Bickel, U., Voigt, K., and Kissel, T. (2003) Low-molecular-weight polyethylenimine as a non-viral vector for DNA delivery: comparison of physicochemical properties, transfection efficiency and *in vivo* distribution with high-molecular-weight polyethylenimine. *J. Controlled Release 89*, 113–25.
(22) Kircheis, R., Schuller, S., Brunner, S., Ogris, M., Heider, K. H., Zauner, W., and Wagner, E. (1999) Polycation-based DNA complexes for tumor-targeted gene delivery *in vivo*. *J. Gene Med. 1*, 111–20.
(23) Lv, H., Zhang, S., Wang, B., Cui, S., and Yan, J. (2006) Toxicity of cationic lipids and cationic polymers in gene delivery. *J. Controlled Release 114*, 100–9.
(24) Zhang, X. Q., Wang, X. L., Huang, S. W., Zhuo, R. X., Liu, Z. L., Mao, H. Q., and Leong, K. W. (2005) *In vitro* gene delivery using polyamidoamine dendrimers with a trimesyl core. *Biomacromolecules 6*, 341–50.
(25) Fischer, D., von Harpe, A., Kunath, K., Petersen, H., Li, Y., and Kissel, T. (2002) Copolymers of ethylene imine and N-(2-hydroxyethyl)-ethylene imine as tools to study effects of polymer structure on physicochemical and biological properties of DNA complexes. *Bioconjugate Chem. 13*, 1124–33.
(26) Narita, T., Ohtakeyama, R., Matsukata, M., Gong, J. P., and Osada, Y. (2001) Kinetic study of cell disruption by ionic polymers with varied charge density. *Colloid Polym. Sci. 279*, 178–183.
(27) Godbey, W. T., Wu, K. K., and Mikos, A. G. (1999) Size matters: molecular weight affects the efficiency of poly(ethylenimine) as a gene delivery vehicle. *J. Biomed. Mater. Res. 45*, 268–75.
(28) Fischer, D., Li, Y. X., Ahlemeyer, B., Krieglstein, J., and Kissel, T. (2003) *In vitro* cytotoxicity testing of polycations: influence of polymer structure on cell viability and hemolysis. *Biomaterials 24*, 1121–1131.
(29) Mahato, R. I., Takakura, Y., and Hashida, M. (1997) Nonviral vectors for *in vivo* gene delivery: physicochemical and pharma-

cokinetic considerations. *Crit. Rev. Ther. Drug Carrier Syst. 14*, 133–72.
(30) Chen, D. J., Majors, B. S., Zelikin, A., and Putnam, D. (2005) Structure-function relationships of gene delivery vectors in a limited polycation library. *J. Controlled Release 103*, 273–83.
(31) Rungsardthong, U., Ehtezazi, T., Bailey, L., Armes, S. P., Garnett, M. C., and Stolnik, S. (2003) Effect of polymer ionization on the interaction with DNA in nonviral gene delivery systems. *Biomacromolecules 4*, 683–90.
(32) Schaffer, D. V., Fidelman, N. A., Dan, N., and Lauffenburger, D. A. (2000) Vector unpacking as a potential barrier for receptor-mediated polyplex gene delivery. *Biotechnol. Bioeng. 67*, 598–606.
(33) Parker, A. L., Oupicky, D., Dash, P. R., and Seymour, L. W. (2002) Methodologies for monitoring nanoparticle formation by self-assembly of DNA with poly(l-lysine). *Anal. Biochem. 302*, 75–80.
(34) Welz, C., and Fahr, A. (2001) Spectroscopic methods for characterization of nonviral gene delivery systems from a pharmaceutical point of view. *Appl. Spectros. Rev. 36*, 333–397.
(35) Ramsay, E., Hadgraft, J., Birchall, J., and Gumbleton, M. (2000) Examination of the biophysical interaction between plasmid DNA and the polycations, polylysine and polyornithine, as a basis for their differential gene transfection *in-vitro*. *Int. J. Pharm. 210*, 97–107.
(36) Choi, J. S., Nam, K., Park, J. Y., Kim, J. B., Lee, J. K., and Park, J. S. (2004) Enhanced transfection efficiency of PAMAM dendrimer by surface modification with L-arginine. *J. Controlled Release 99*, 445–56.
(37) Rungsardthong, U., Deshpande, M., Bailey, L., Vamvakaki, M., Armes, S. P., Garnett, M. C., and Stolnik, S. (2001) Copolymers of amine methacrylate with poly(ethylene glycol) as vectors for gene therapy. *J. Controlled Release 73*, 359–80.
(38) Zhong, Z., Song, Y., Engbersen, J. F., Lok, M. C., Hennink, W. E., and Feijen, J. (2005) A versatile family of degradable non-viral gene carriers based on hyperbranched poly(ester amine)s. *J. Controlled Release 109*, 317–29.
(39) Wu, D., Liu, Y., Jiang, X., He, C., Goh, S. H., and Leong, K. W. (2006) Hyperbranched poly(amino ester)s with different terminal amine groups for DNA delivery. *Biomacromolecules 7*, 1879–83.
(40) De Smedt, S. C., Demeester, J., and Hennink, W. E. (2000) Cationic polymer based gene delivery systems. *Pharm. Res. 17*, 113–126.
(41) Elouahabi, A., and Ruysschaert, J. M. (2005) Formation and intracellular trafficking of lipoplexes and polyplexes. *Mol. Ther. 11*, 336–47.
(42) Akinc, A., Lynn, D. M., Anderson, D. G., and Langer, R. (2003) Parallel synthesis and biophysical characterization of a degradable polymer library for gene delivery. *J. Am. Chem. Soc. 125*, 5316–23.
(43) Choosakoonkriang, S., Lobo, B. A., Koe, G. S., Koe, J. G., and Middaugh, C. R. (2003) Biophysical characterization of PEI/DNA complexes. *J. Pharm. Sci. 92*, 1710–22.
(44) Jones, N. A., Hill, I. R., Stolnik, S., Bignotti, F., Davis, S. S., and Garnett, M. C. (2000) Polymer chemical structure is a key determinant of physicochemical and colloidal properties of polymer-DNA complexes for gene delivery. *Biochim. Biophys. Acta 1517*, 1–18.
(45) Wolfert, M. A., Dash, P. R., Nazarova, O., Oupicky, D., Seymour, L. W., Smart, S., Strohalm, J., and Ulbrich, K. (1999) Polyelectrolyte vectors for gene delivery: influence of cationic polymer on biophysical properties of complexes formed with DNA. *Bioconjugate Chem. 10*, 993–1004.
(46) Oupicky, D., Konak, C., Ulbrich, K., Wolfert, M. A., and Seymour, L. W. (2000) DNA delivery systems based on complexes of DNA with synthetic polycations and their copolymers. *J. Controlled Release 65*, 149–71.
(47) Reschel, T., Konak, C., Oupicky, D., Seymour, L. W., and Ulbrich, K. (2002) Physical properties and *in vitro* transfection efficiency of gene delivery vectors based on complexes of DNA with synthetic polycations. *J. Controlled Release 81*, 201–217.
(48) Green, J. J., Shi, J., Chiu, E., Leshchiner, E. S., Langer, R., and Anderson, D. G. (2006) Biodegradable polymeric vectors for gene delivery to human endothelial cells. *Bioconjugate Chem. 17*, 1162–9.
(49) Moret, I., Peris, J. E., Guillem, V. M., Benet, M., Revert, F., Dasi, F., Crespo, A., and Alino, S. F. (2001) Stability of PEI-DNA and DOTAP-DNA complexes: effect of alkaline pH, heparin and serum. *J. Controlled Release 76*, 169–181.

BC7002082

Determination of the Optimized Conditions for Coupling Oligonucleotides with 16-Mercaptohexadecanoic Acid Chemically Adsorbed upon Au

Yi-Te Wu,[†] Jiunn-Der Liao,*[,†,‡] Je-Inn Lin,[†] and Cheng-Chan Lu[§]

Department of Materials Science and Engineering, Center for Micro/Nano Science and Technology, and Department of Pathology, National Cheng Kung University, No. 1, University Road, Tainan 70101, Taiwan. Received June 18, 2007; Revised Manuscript Received September 17, 2007

A specific 5′-modified amino group oligonucleotide (Primer 1), 15-mers in length, is selectively coupled with the carboxyl terminated 16-mercaptohexadecanoic acid (MHDA) chemically adsorbed on Au and subsequently hybridized with Antisense Primer. The amide-coupling process is of significance to create an intermediate structure for the purpose of adding Primer 1, while the hybridization reaction is relevant to various diagnostic purposes to determine the presence in nucleic acids for a target sequence. In this work, the coupling setting was particularly emphasized by varying commonly used temperatures and pH values with a definite concentration of coupling agents (i.e., 10 mM). The recombination with analogous hybridization treatment was investigated using high resolution X-ray photoelectron spectroscopy and a 75° grazing angle Fourier transform infrared spectrometer. On the basis of the spectroscopic studies, the optimized conditions for the coupling process that is also correlated with the molecular density of subsequent hybridization process on MHDA/Au have been proposed at 37 °C and a pH value of 4.5. Therefore, it is pertinent to intensify the joining of short-chain DNA strands by complementary base pairing in diagnostic applications such as the identification of single nucleotide polymorphisms.

1. INTRODUCTION

Single nucleotide polymorphisms (SNPs) are common DNA sequence variations that cause phenotypic differences among individuals. Most SNPs do not lead to physical changes in humans; however, a small part of them may predispose individuals to disease and even influence their complex response to medical treatments or drug regimens (*1–3*). A considerable effort to decode the human genome or to further the understanding of human genetics has been promoted to identify SNPs, for example, SNPs related to drug-metabolizing enzymes (*4*), secretion disorder (*5*), allele-specific extensions (*6*). In particular, only a small percentage of a person's DNA sequence code is necessary for the production of proteins or those involved in transcription regulation (*7*). SNPs found within a coding sequence are therefore of special interest when they are highly associated with the structural and functional properties of proteins. Recent advances in biotechnology have significantly enhanced the process of disease or protein detection (*4–10*) and the practice of preventative and curative medicine. In particular, association study (*11, 12*) can detect and indicate which pattern is most likely associated with the disease-causing genes or complex human disorders. In a recent verification process (*13*), SNP finding is automatically achieved using a combined approach between sequence-specific pattern matching of flanking sequence and a quality assessment of inconsistencies on the average once every kilo-base pair in the human genome.

The use of specific oligonucleotides as therapeutic agents or biomarkers (*14*), for example, lies upon their ability to interfere with the molecular machinery of protein synthesis either by binding to the mRNAs transcribed from a gene or by binding directly to a target gene. In recent years, oligonucleotide hybridization has become relevant to various diagnostic purposes to determine the presence in nucleic acids for a target sequence that is complementary to the oligonucleotide probe (*15–17*). Hybridization on a solid support involves the immobilization of one of the interacting nucleic acids on the surface, while the other is free in solution. For the former, high-density DNA microarrays with the immobilization of aptamers (short, known single-stranded DNA or RNA sequences) are a well-established method capable of measuring gene expression levels (*8, 16*). The chip-based optical detection of the molecular interactions occurring on the immobilized and labeled DNA sequence or functional protein as a probe has been promptly developed (*18–20*). This process combined with a recent technique on microelectronics and rich SNP profiles meets the demands for rapid screening with reduced sample amounts. For the latter, the use of colloidal Au as a color label as bridged between the attached DNA and the oligonucleotides with sequences complementary to either ends of the target DNA is successfully delivered for the detection of DNA hybridization in solution (*21*). However, specific DNA probes attached on magnetic particles are also used for the detection of viable bacteria (*22*).

A perceptive detection of specific molecular binding that is based on optical visualization of the labeled molecules on a microstructured chip surface is still improving. One of the major problems relies on the stability of molecular interactions in varying conditions such as the variation of ionic strengths (*23, 24*), pH values (*23*), and temperatures (*25*). In this study, self-assembled monolayers (SAMs) chemically adsorbed on Au substrates have been introduced for the construction of molecular additions. SAMs are well-ordered and densely packed two-dimensional ensembles of long-chain molecules, which have attracted tremendous attention because of the potential applications in various fields, such as DNA chips, microelectronics, sensors, and nanopatterned SAMs (*26–28*). The SAMs treatment is also one of the proposed methods for extending lithography down to the nanometer scale by applying electron-beam patterning for a new kind of lithography resist (*29, 30*). Much

* Corresponding author. Phone: (886) 6 2757575ext. 62971. Fax: (886) 6 2346290. E-mail: jdliao@mail.ncku.edu.tw.
[†] Department of Materials Science and Engineering.
[‡] Center for Micro/Nano Science and Technology.
[§] Department of Pathology.

10.1021/bc700217n CCC: $37.00 © 2007 American Chemical Society
Published on Web 10/31/2007

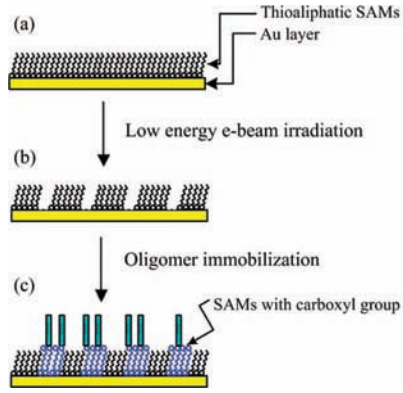


Figure 1. For a practical SAM application, a tailored surface containing $-CH_3$ and carboxyl tail groups can be patterned for the subsequent addition of short-chained oligonucleotides.

attention is devoted to aliphatic SAMs and, above all, to films of *n*-alkanethiol on noble metal substrates. In this study, alkanethiolate monolyers with the carboxyl tail group are chemically adsorbed on Au. A synthesized oligonucleotide with 5′-modified $-NH_2$ or 3′-modified $-OH$ ends on the respective sequences, in association with an allelic polymorphism within the human tumor necrosis factor alpha (TNF-α) promoter region (*31–34*), is subsequently immobilized on SAMs/Au. Optimized conditions for DNA hybridization based on the combination of temperatures, pH values, and the concentration of coupling agents are particularly investigated. As compared with previous measurements using 2D electrospray ionization tandem mass spectroscopy (*35*), this study utilizes surface-sensitive measurements for the identification of chemical bindings in the respective reactions and possibly for subsequent SNPs diagnostic applications.

2. EXPERIMENTAL PROCEDURES

2.1. Preparation of SAMs/Au with Carboxyl Tail Groups. The substrates for thiol-derived SAM fabrication were prepared by thermal evaporation of ≈50 nm of Au onto the polished single crystal silicon (100) wafers (Silicon Sense) primed with a ≈5 nm titanium adhesion layer. The octadecanethiol (ODT, HS-$(CH_2)_{17}$-CH_3) SAMs were formed by standard immersion procedure (*36*), resulting in the homogeneous ODT SAMs on Au (Figure 1a). For the practical applications, a particular part of the ODT SAMs can be easily removed by low-energy electron beam irradiation (Figure 1b), followed by immersion into an ethanolic 1 mM solution of 16-mercaptohexadecanoic acid (MHDA, HS-$(CH_2)_{15}$-COOH, Aldrich) for 1–2 h. A tailored surface with mixed $-CH_3$ and carboxyl tail groups is produced for subsequent treatments (Figure 1c). To investigate the succeeding reactions on the surfaces, a uniform MHDA/Au representing the MHDA-modified part was employed, followed by coupling and hybridizing with the respective oligonucleotides.

2.2. Preparation of the Oligonucleotides. Four types of the oligonucleotides, 15-mers in length, were employed for the experiments.

A digested probe, 5′-GGGCATGGGGACGGG (MDBio Inc., type-1) as an aptamer, with a concentration of 5 μM was synthesized by means of polymerase-mediated single-base primer extension. It was first verified by Dot Hybridization method using Digoxigenin (DIG)-labeled Sequence Specific Oligonucleotide Probe (SSOP, 5′-CCCGTCCCCATGCCC, type-2) with a concentration of 100 μM, followed by dilutions to different concentrations.

The modified amino group at the 5′-end, H_2N-$(CH_2)_6$-5′-GGGCATGGGGACGGG-3′ (MDBio Inc., type-3) as Primer 1, was expected to be amide-bonded on MHDA/Au by adding the coupling agents, 1-ethyl-3-(3-dimethylaminopropyl) carbodiimide (EDC, Sigma) and *N*-hydroxysuccinimide (NHS, Sigma), in PBS or MES buffer solution with various concentrations (1, 10, or 100 mM) and various pH values (4.5, 5.5, 6.5, or 7.4). The Primer 1/MHDA/Au was annealed at 42 °C and thereafter hybridized with the 5′-CCCGTCCCCATGCCC-3′ (MDBio Inc., type-4) as Antisense Probe. The concentration of Primer 1 or Antisense Probe was ≈5 μM, which was first dissolved in deionized water and preserved at −20 °C.

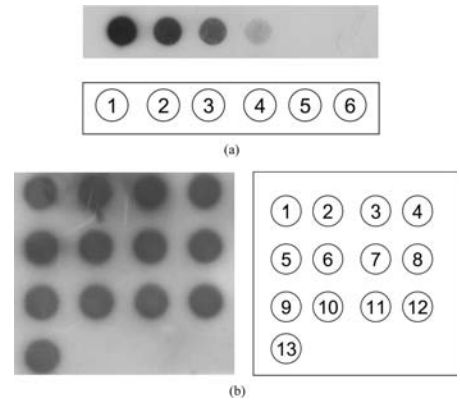


Figure 2. (a) Oligonucleotides were verified by 100 μM SSOP diluted to five different concentrations (i.e., 100, 10, 1.0, 0.1, 0.01, and 0.001 μM, for marks 1–6). (b) Oligonucleotides were assessed in different pH values and reaction times. The pH values of marks 1–4 were 4.5, 5.5, 6.5, and 7.4, respectively (buffered for 6 h). Those of marks 5–8 were analogous in pH values but buffered for 4 h. Those of marks 9–12 were also analogous in pH values but buffered for 2 h. Mark 13 was a control for reference.

2.3. Surface Characterization. Water contact angles were measured immediately after preparing MHDA/Au substrates. The measurements were performed under an argon atmosphere at 22 ± 1 °C. The sessile drop method was used, and a JVC-TK1200 microscope with processing software took the droplet image. A droplet of ≈5 μL was used. For each sample, 10 measurements with a standard deviation below 1° were carried out, and an average value was calculated. Water contact angles of the pristine Au and a uniform MHDA/Au were ≈83.4° and ≈23.2°, respectively. The decrease of contact angle is expected in the presence of the hydrophilic group.

Fourier-transform infrared (FTIR, Bomem DA8.3) with 75° grazing incident angle reflectance (Harrick) was utilized for identifying chemical species in the specific range of 1000–2000 cm^{-1} with 0.5 cm^{-1} resolution and precision of a wavenumber no less than 0.01 cm^{-1}. In this range, positions of the band frequencies were assigned to major IR-active groups in the as-prepared oligonucleotides (*37*).

Synchrotron-based high-resolution X-ray photoelectron spectroscopy (HRXPS) was utilized to characterize the chemical structures of MHDA on Au, amide bonds with Primer 1, and subsequent hybridization with Antisense Probe. HRXPS measurements were carried out at the U5 Undulatory Beam Line of the National Synchrotron Radiation Research Center in Hsinchu, Taiwan. The time for the acquisition of the entire set of the HRXPS spectra for an individual sample was selected as a compromise between spectral quality and the damage induced by X-rays. Details about HRXPS measurements can be found elsewhere (*36*, *38*).

To determine the elemental compositions at the respective surface, the C 1s, S 2p, O 1s, N 1s, and P 2p core level spectra were measured and calculated from HRXPS peak area with correction algorithms and atomic sensitivity factors. The spectra were fitted using Voigt peak profiles and a Shirley background (*38*). The stability of Au–S bonds subsequent to the treatments

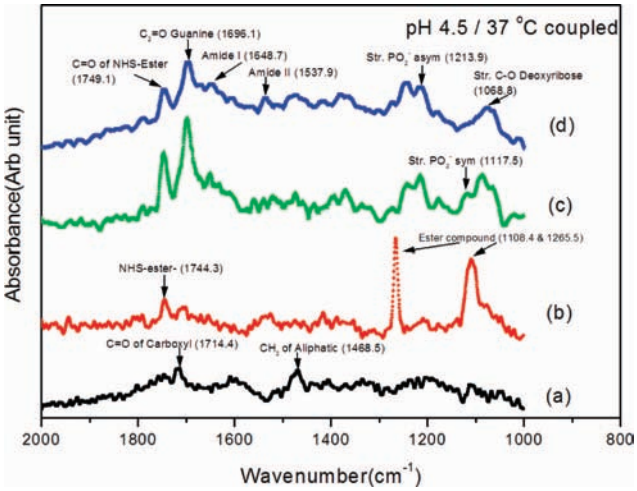


Figure 3. IR absorption spectra of Primer 1/MHDA/Au prepared in different concentrations of EDC and NHS at a pH value of 4.5 at 37 °C. The as-measured surfaces were (a) MHDA/Au and (a) with the concentrations of EDC and NHS at (b) 1 mM, (c) 10 mM, and (d) 100 mM.

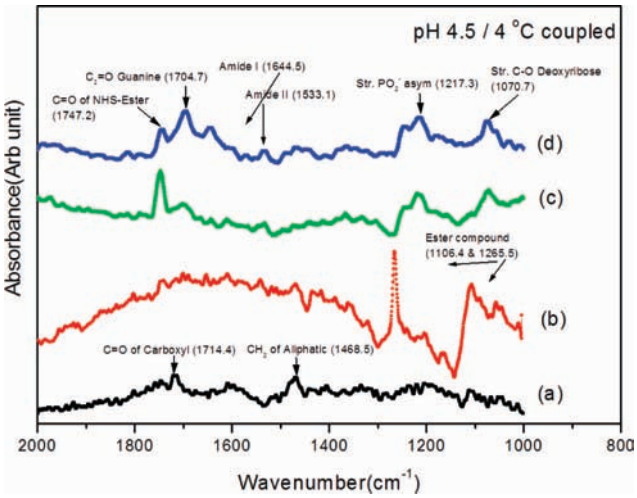


Figure 4. IR absorption spectra of Primer 1/MHDA/Au prepared in different concentrations of EDC and NHS at a pH value of 4.5 at 4 °C. The as-measured surfaces were (a) MHDA/Au and (a) with the concentrations of EDC and NHS at (b) 1 mM, (c) 10 mM, and (d) 100 mM.

was correlated with the S 2p doublet with a binding energy (BE) of ≈162.0 eV. The decrease of the intermediate amide bonds due to the addition of the oligonucleotides was calculated by comparing the intensity of the amide group with that of -N*= from the oligonucleotides (*39*).

3. RESULTS AND DISCUSSION

3.1. Preliminary Tests on the Oligonucleotides Using SSOP Method. The oligonucleotides, Primer 1 and Antisense Probe, with a concentration of 5 μM were first verified by 100 μM SSOP diluted to five different concentrations (Figure 2a). The indications revealed a good relationship with the diluted concentrations. The SSOP diluted to 0.1 μM was still distinguishable (mark 4 in Figure 2a). In Figure 2b, the quality of the oligonucleotides was assessed in different buffer solutions, that is, with MES at pH 4.5, 5.5, and 6.5 or PBS at pH 7.4, with a reaction time of 2, 4, or 6 h. The variations of the buffer solution and the reaction time did not cause structural damage or hydrolysis in the oligonucleotides.

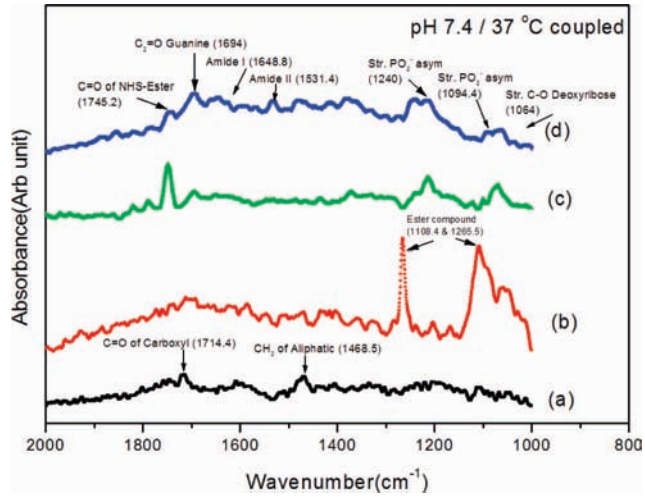


Figure 5. IR absorption spectra of Primer 1/MHDA/Au prepared in different concentrations of EDC and NHS at a pH value of 7.4 at 37 °C. The as-measured surfaces were (a) MHDA/Au and (a) with the concentrations of EDC and NHS at (b) 1 mM, (c) 10 mM, and (d) 100 mM.

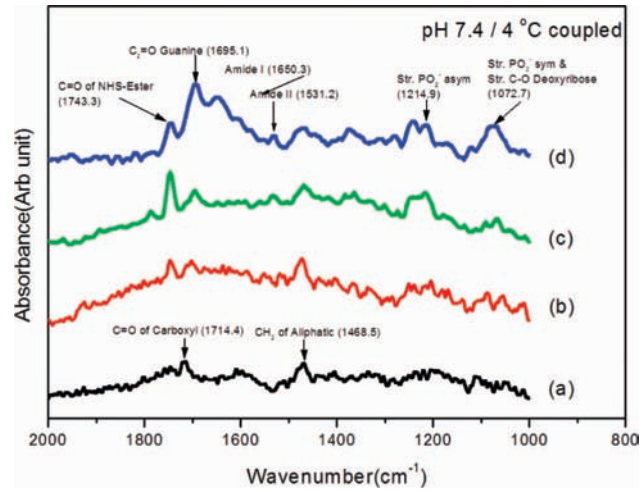


Figure 6. IR absorption spectra of Primer 1/MHDA/Au prepared in different concentrations of EDC and NHS at a pH value of 4.5 at 4 °C. The as-measured surfaces were (a) MHDA/Au and (a) with the concentrations of EDC and NHS at (b) 1 mM, (c) 10 mM, and (d) 100 mM.

3.2. Chemical Structures Examined by FTIR with 75° Grazing Incident Angle Reflectance. An analogous FTIR curve of the pristine surface was taken as the reference and is shown in the bottom curves of Figures 3–6. The characteristic IR peaks for MHDA/Au at 1714.4 cm^{-1} (i.e., C=O in the carboxyl acid) and 1468.5 cm^{-1} (i.e., CH_2 in aliphatic chains) were identified.

The carboxyl tail group of MHDA was anticipated to create an amide bond with the NH_2-modified Primer 1 using EDC and NHS as the coupling agents (*35*, *40*). In the case of the acidic environment at pH 4.5 and 37 °C (Figure 3), the addition of 1 mM EDC and NHS buffered in MES solution (Figure 3b) mainly created ester compounds (1265.5 cm^{-1} and 1108.4 cm^{-1}). The NHS-ester (1744.3 cm^{-1}) was formed transitionally, whereas the coupling of the NH_2-modified Primer 1 was not found. As the buffered concentration of EDC and NHS was increased to 10 mM (Figure 3c), IR absorptions of C-O in deoxyribose of nucleoside (1068.8 cm^{-1}), phosphodiester bond (1117.5 and 1213.9 cm^{-1}), C=O in NHS-ester (1749.1 cm^{-1}), and C=O in Guanine of Purine (1696.1 cm^{-1}), in association with Primer 1, were detected (*40*). Nevertheless, IR absorptions in the range of 1500–1650 cm^{-1}, correlating with the presence

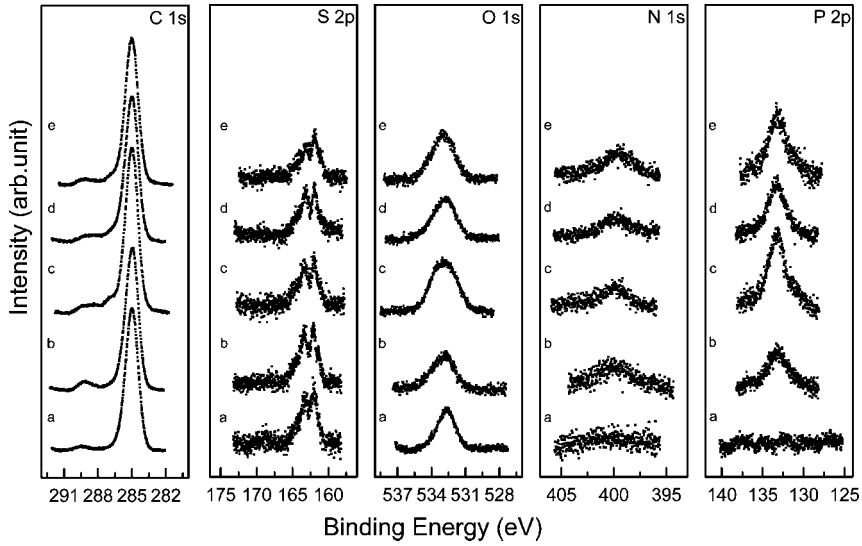


Figure 7. HRXPS spectra of Primer 1/MHDA/Au prepared in 10 mM EDC and NHS at 37 °C. The as-measured surfaces were (a) MHDA/Au, (b) Primer 1 coupled with MHDA/Au at pH 4.5, (c) Primer 1 from (b)/MHDA/Au hybridized with Antisense Probe, (d) Primer 1 coupled with MHDA/Au at pH 7.4, and (e) Primer 1 (from d)/ MHDA/Au hybridized with Antisense Probe. The changes of the intensities of the elements are illustrated in Figure 10.

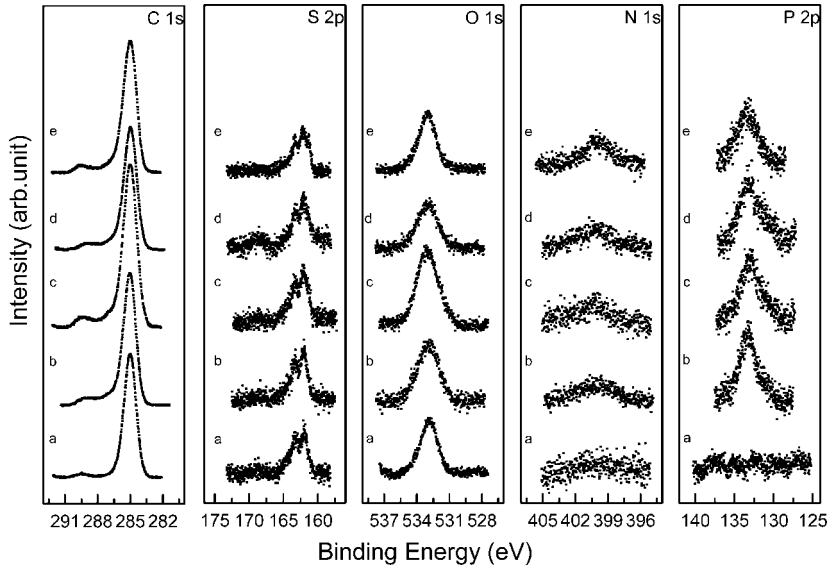


Figure 8. HRXPS spectra of Primer 1/MHDA/Au prepared in 10 mM EDC and NHS at 4 °C. The as-measured surfaces were (a) MHDA/Au, (b) Primer 1 coupled with MHDA/Au at pH 4.5, (c) Primer 1 from (b)/MHDA/Au hybridized with Antisense Probe, (d) Primer 1 coupled with MHDA/Au at pH 7.4, and (e) Primer 1 (from d)/MHDA/Au hybridized with Antisense Probe. The changes of the intensities of the elements are illustrated in Figure 11.

of amide bonds, were considerably weak. It is likely that the sensitivity of the measurement is insufficient to interpret a minor quantity of the intermediate amide bonds. Furthermore, with the addition of 100 mM EDC and NHS in the buffered solution (Figure 3d), the characteristic amide group at 1648.7 (amide I) and 1537.9 cm^{-1} (amide II) and most of the analogous species associated with Primer 1 were simultaneously found.

Analogous results were obtained in the case of the acidic environment at pH 4.5 and 4 °C (Figure 4) and the alkaline environment at 37 °C (Figure 5) and 4 °C (Figure 6). By comparison, the NH_2-modified Primer 1 was well coupled with MHDA/Au in the case of 100 mM EDC and NHS buffered in MES solution at pH 4.5 and 37 °C, while IR intensity of the characteristic amide group and most of the analogous species associated with Primer 1 were clearly found.

From the above measurements, as the coupling agents were buffered to a concentration of 10 mM, the covalently bonded Primer 1 could be identified, whereas the IR intensity correlated with the amide group, the intermediate structure, was relatively insignificant.

3.3. Chemical Bonds Examined by HRXPS. For the pristine MHDA/Au, the characteristic structures of MHDA were determined by HRXPS and presented in the bottom curves of Figures 7 and 8. After carrying out the decompositions of the C 1s, O 1s, and N 1s spectra illustrated in Figure 9, the C 1s spectrum exhibited a major emission peak at a BE of ≈284.8 eV (i.e., C*-C or C*-H) with a fwhms of ≈0.9 eV and chemical shifts at BEs of 285.9 eV (C*-O) and ≈289.2 eV (i.e., O=C*-OH). The S 2p spectrum exhibited a single S 2p doublet with a BE of ≈162.0 eV for the S $2p_{3/2}$ component. This doublet is commonly related to the thiolate species bonded to Au surface (*36, 38, 41, 42*). The O 1s spectrum exhibited the emission peaks at BEs of 532.1 eV (C-O) and 533.4 eV (C=O), resulting from the presence of MHDA. No traces of nitrogen or phosphorus were found.

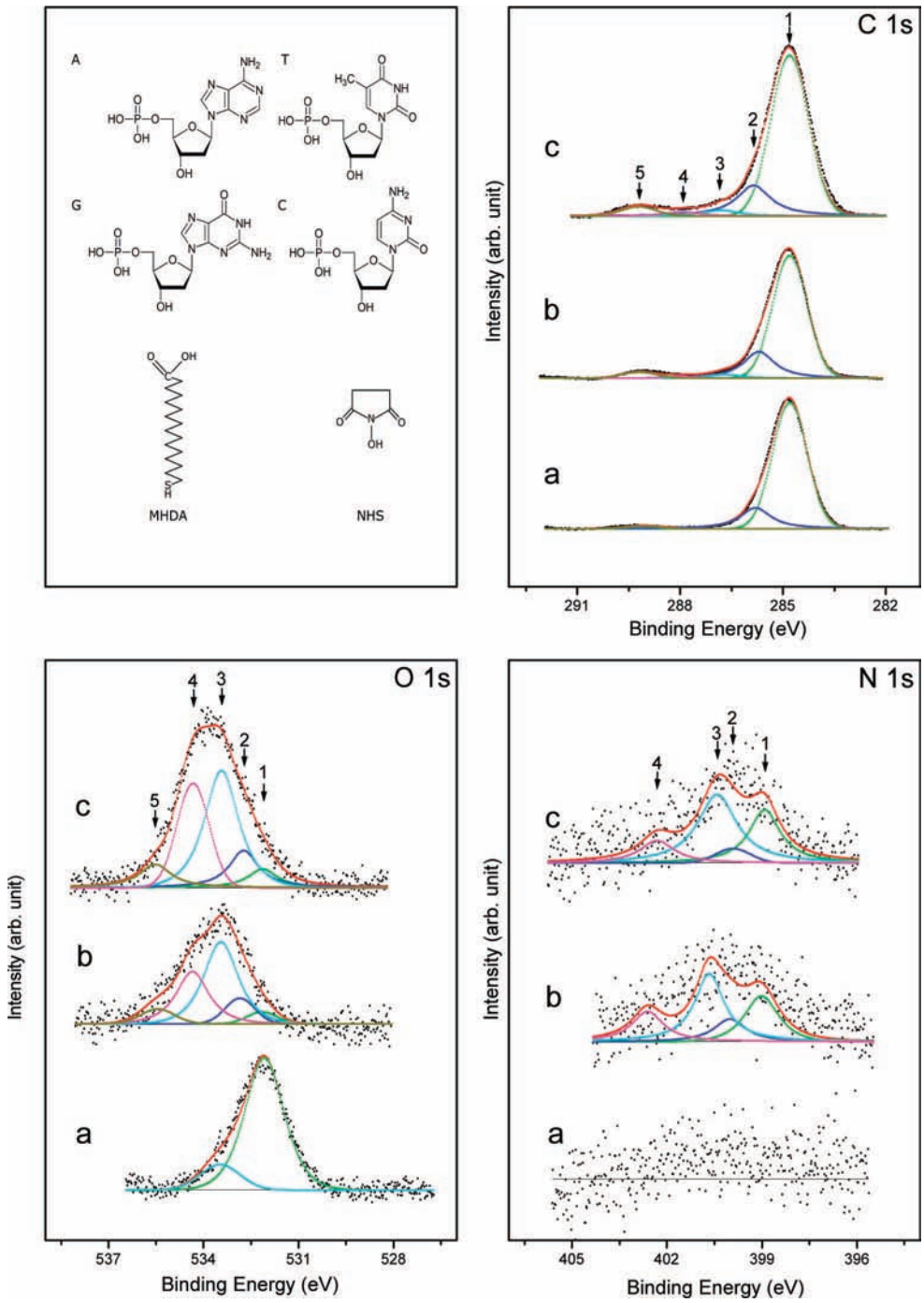


Figure 9. Curve-fitted HRXPS spectra for Primer 1/MHDA/Au prepared in 10 mM of EDC and NHS at 37 °C. The as-measured surfaces were (a) MHDA/Au, (b) Primer 1 coupled with MHDA/Au at pH 4.5, and (c) Primer 1 from (b)/MHDA/Au hybridized with Antisense Probe at 42 °C. The decomposition of the respective C 1s, O 1s, and N 1s spectra is described in section 3.4.

Interfacing of surface characterization with analytical data is not well-developed. Particularly, chemical species of covalent attachment presenting in the multiple linkages are difficult to be defined by configurations. In this section, the respective samples with the coupling agents of 10 mM are purposely studied using HRXPS to gain information of the aptamers upon MHDA/Au under different pH values and coupling or annealing temperatures.

The HRXPS spectra for Primer 1/MHDA/Au, prepared at different pH values or temperatures, are shown in Figures 7b and d and 8b and d, which exhibit analogous BEs. Followed by hybridization with Antisense Probe, their C and O intensities and BEs exhibited variable data (shown in Figures 7c and 7e and 8c and e). Among them, the HRXPS spectra for Primer 1/MHDA/Au prepared in 10 mM EDC and NHS at 37 °C were curve-fitted and studied. In Figure 9, the decompositions of the C 1s spectra were assigned: (1) 284.8 eV, C*-C, (2) 285.9 eV, C*-O, (3) 286.7 eV, amide group or NHS-ester, (4) 287.9 eV, from the oligonucleotide G or C, and (5) 289.1 eV, O=C*-OH or from the oligonucleotide C. The decompositions of the O 1s spectra were assigned: (1) 532.1 eV, C-O*-C from the oligonucleotide G or C, (2) 532.8 eV, amide group or $(N)_2C=O^*$ from the oligonucleotide G, (3) 533.4 eV, C=O* from the oligonucleotide, (4) 534.4 eV, O*=C-OH or C-O-P from the oligonucleotide and (5) 535.6 eV, NHS-ester. The decompositions of the N 1s spectra were assigned: (1) 399.0 eV, -N*= from the oligonucleotide G or C, (2) 400.0 eV, O=C-N*-H from the amide group, (3) 400.5 eV, -N*-, -N*H-, $-N^*H_2$ from the

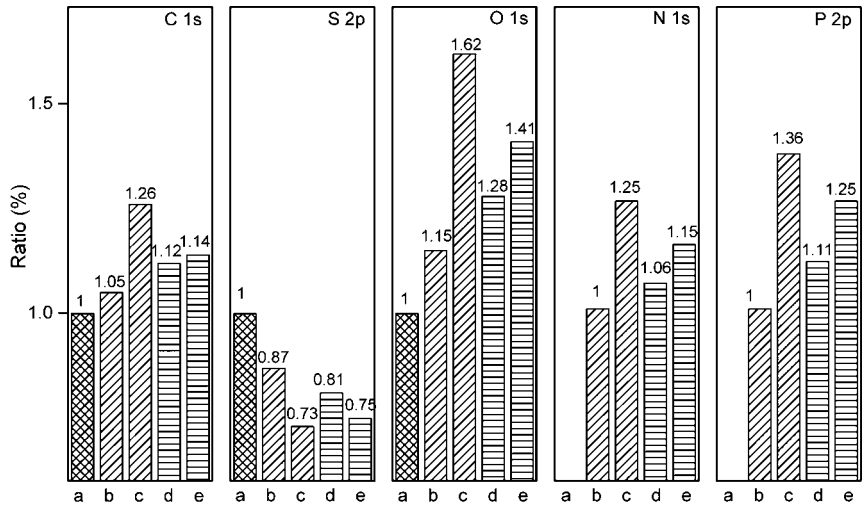


Figure 10. Variations of the content of the elements on Primer 1/MHDA/Au prepared in 10 mM EDC and NHS at 37 °C. The as-measured surfaces were (a) MHDA/Au, (b) Primer 1 coupled with MHDA/Au at pH 4.5, (c) Primer 1 from (b)/MHDA/Au hybridized with Antisense Probe, (d) Primer 1 coupled with MHDA/Au at pH 7.4, and (e) Primer 1 (from d)/ MHDA/Au hybridized with Antisense Probe.

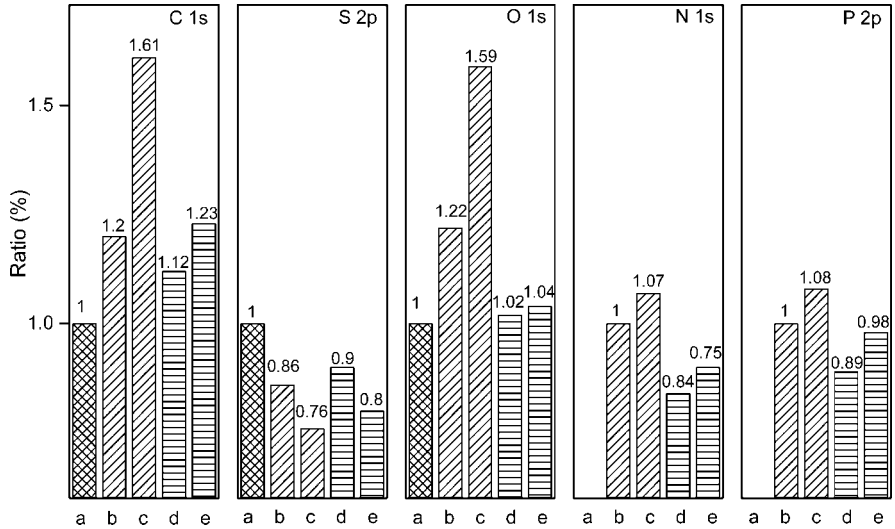


Figure 11. Variations of the content of the elements on Primer 1/MHDA/Au prepared in 10 mM of EDC and NHS at 4 °C. The as-measured surfaces were (a) MHDA/Au, (b) Primer 1 coupled with MHDA/Au at pH 4.5, (c) Primer 1 from (b)/MHDA/Au hybridized with Antisense Probe, (d) Primer 1 coupled with MHDA/Au at pH 7.4, and (e) Primer 1 (from d)/ MHDA/Au hybridized with Antisense Probe.

oligonucleotide G or C, and (4) 402.5 eV, -N*-O from NHS-ester. For the P 2p spectra shown in Figures 7 and 8, the emission peak at a BE of 133.2 eV was associated with the presence of oligonucleotides.

In Figure 9, the ratio of peak 1 over peak 3 at *b* of N1s spectra was close to 2/3, which is identical to the presence of Primer 1 (i.e., mainly from oligonucleotide G), while that at *c* of N 1s spectra was close to 3/5 (*39*), which is approximately the product of Primer 1 in hybridization with Antisense Probe. On the basis of these qualitative measurements, the hybridization between Primer 1 and Antisense Probe noticeably occurred as a result of the particular treatments.

3.4. Semiquantitative Measurements for S–Au and Amide-Coupled Bonds. The addition of Antisense Probe in hybridization with Primer 1 also resulted in decreasing the HRXPS intensity of the amide group, which was associated with the assignments of peak 3 of C 1s, peak 2 of O 1s, and peak 2 of N 1s (Figure 9). In the case of *b* of Primer 1 coupled on MHDA/Au at pH 4.5 and *c* of surface *b* in hybridization with Antisense Probe, the relative intensities of peak 2 over peak 1 in *b* and in *c* were calculated as ≈0.57 for *b* and ≈0.22 for *c*. The spectroscopic result estimated that the intermediate amide bonds significantly decreased from an intensity ratio of ≈0.57 to that of ≈0.22 (or −61.4%) due to the hybridization with Antisense Probe that increased the packing density of the oligonucleotide molecules on Primer 1/ MHDA/Au.

The average thickness of MHDA uultrathin film on Au is ≈19.4 Å, in comparison with ≈18.9 Å for the CH_3 terminated thiols with analogous chain length on Au, whereas a relatively disordered carboxyl terminated SAM on Au is anticipated (*43*). In our previous calculations, the intermolecular spacing of the headgroup S–S for MHDA/Au is presumably larger than that for CH_3 terminated thiols on Au (≈4.97 Å) (*44*) due to the functions and/or the interactions of hydrogen bonds between the tail groups (*43*). As a result, the headgroup (i.e., S adsorbed on Au) of MHDA/Au is not as closely packed as that of CH_3-terminated thiols on Au. As illustrated in Figures 7 and 8, the S–Au bonds kept nearly intact during the coupling and subsequent hybridization processes. It implied that the MHDA uultrathin film on Au was suitable as a molecular support. For a stable coupling process, the bond angle for O=C*−O (≈120°) and that for O=C*−N (≈109°) is changed, which will alter the molecular arrangement as well as the packing density of the oligonucleotide on MHDA/Au. With these calculations, the

photoelectron intensity of the intermediate amide bonds continuously decreases because of the completion of hybridization naturally increases the packing density of the oligonucleotides on MHDA/Au.

The element's ratios calculated from Figures 7 and 8 with respect to the pristine MHDA/Au surface are shown in Figures 10 and 11, respectively. Note that an equal concentration (i.e., 10 mM) of the coupling agent was used. The intensity ratios of the C 1s, O 1s, N 1s, and P 2p spectra increased with the addition of Primer 1 and subsequent to the hybridization of Antisense Probe. Those of the S 2p spectra decreased with the addition of the oligonucleotides because of the increase of molecular density on MHDA/Au. No significant traces of other sulfur-derived species (*45, 46*) were found during the processes. The coupling process in the acid environment (i.e., pH 4.5) either at 37 or 4 °C steadily decreased the S 2p intensities, that is, *c* or *e* with respect to *b* or *d* of S 2p spectra in Figures 10 and 11. In combination with the calculation of molecular density on MHDA/Au, an optimized coupling condition was first suggested at pH 7.4 and 37 °C. However, the increased packing density of the oligonucleotides on MHDA/Au resulted in increasing the elements' ratios of *c* or *e* with respect to *b* or *d* in C 1s, O 1s, N 1s, and P 2p spectra. In combination with the elements' ratio of the oligonucleotide G, C, A, or T, an optimized coupling condition was suggested at pH 4.5 and 37 °C.

Comparing the case of the coupling temperature at 37 °C with that at 4 °C, the former exhibited proficiency in increasing the quantity of the oligonucleotides on MHDA/Au, particularly on the basis of the increased intensity ratios of N 1s and P 2p spectra and the decreased intensity ratios of S 2p spectra. However, comparing the pH value for amide coupling at 4.5 with that at 7.4, the former exhibited values in correlation with the elements' ratio of the oligonucleotide. From these measurements, the optimized coupling conditions in this study were presumably placed at pH 4.5 and 37 °C.

CONCLUSIONS

The use of tailored SAMs chemically adsorbed upon Au is increasingly important for recent techniques in microelectronics. In combination with specific short-chain oligonucleotides along with rich SNP profiles on the microelectronic device, the invention meets the demands for rapid screening with reduced sample amounts. The coupling of the carboxyl tailed MHDA ($\approx$2 nm) with a 5′-modified amino group oligonucleotide 15-mers in length forms an ultra-thin layer. Such a coupled oligonucleotide is relevant to determine the presence of nucleic acids and to act as a diagnostic probe for a target sequence. A perceptive detection for the specific molecular binding on a microstructured chip surface has been highly improved. Therefore, this study particularly emphasizes the stability of molecular interactions under treatment conditions such as pH values and temperatures for the coupling or annealing process. On the basis of the high-resolution spectroscopic studies and the definite concentration of coupling agents (i.e., 10 mM), the optimized conditions for the coupling process have been proposed at pH 4.5 and 37 °C. At the same time, the S–Au bonds and the intermediate amide-coupled structure are considerably resistant to subsequent treatments. Thus, this work provides a method to intensify the joining of short-chain DNA strands with the tailored SAMs/Au prior to completing a hybridization process. It is also promising in creating nanopatterned SAMs/Au for advanced DNA chips, in particular for the detection of SNPs.

ACKNOWLEDGMENT

This work has been supported by the National Science Council of R.O.C under grant No. 95–2621-Z-006–002. The authors would like to thank the Center for Micro/Nano Science and Technology and the Sustainable Environment Research Center, National Cheng Kung University, and National Synchrotron Radiation Research Center, Hsinchu, Taiwan for access to equipment, technical support, and partial financial support.

LITERATURE CITED

(1) Bao, Y. P., Huber, M., Wei, T. F., Marla, S. S., Storhoff, J. J., and Müller, U. R. (2005) SNP identification in unamplified human genomic DNA with gold nanoparticle probes. *Nucleic Acids Res. 33*, e15.

(2) Tsui, C., Colemam, L. E., Griffith, J. L., Bennett, E. A., Goodson, S. G., Scott, J. D., Pittard, W. S., and Devine, S. E. (2003) Single nucleotide polymorphisms (SNPs) that map to gaps in the human SNP map. *Nucleic Acids Res. 31*, 4910–4916.

(3) Hirakawa, M., Tanaka, T., Hashimoto, Y., Kuroda, M., Takagi, T., and Nakamura, Y. (2002) JSNP: a database of common gene variations in the Japanese population. *Nucleic Acids Res. 30*, 158–162.

(4) Hurley, J. D., Engle, L. J., Davis, J. T., Welsh, A. M., and Landers, J. E. (2004) A simple, bead-based approach for multi-SNP molecular haplotyping. *Nucleic Acids Res. 32*, e186.

(5) Osawa, H., Onuma, H., Ochi, M., Murakami, A., Yamauchi, J., Takasuka, T., Tanabe, F., Shimizu, I., Kato, K., Nishida, W., Yamada, K., Tabara, Y., Yasukawa, M., Fujii, Y., Ohashi, J., Miki, T., and Makino, H. (2005) Resistin SNP-420 determines its monocyte mRNA and serum levels inducing type 2 diabetes. *Biochem. Biophys. Res. Commun. 335*, 596–602.

(6) Hultin, E., Käller, M., Ahmadian, A., and Lundeberg, J. (2005) Competitive enzymatic reaction to control allele-specific extensions. *Nucleic Acids Res. 33*, e48.

(7) Ramensky, V., Bork, P., and Sunyaev, S. (2002) Human non-synonymous SNPs: server and survey. *Nucleic Acids Res. 30*, 3894–3900.

(8) Mockler, T. C., and Ecker, J. R. (2005) Applications of DNA tiling arrays for whole-genome analysis. *Genomics 85*, 1–15.

(9) Murphy, M. B., Fuller, S. T., Richardson, P. M., and Doyle, S. A. (2003) An improved method for the *in vitro* evolution of aptamers and applications in protein detection and purification. *Nucleic Acids Res. 31*, e110.

(10) Kohler, N., Sun, C., Wang, J., and Zhang, M. Q. (2005) Methotrexate-modified superparamagnetic nanoparticles and their intracellular uptake into human cancer cells. *Langmuir 21*, 8858–8864.

(11) Olivier, M., Chuang, L. M., Chang, M. S., Chen, Y. T., Pei, D., Ranade, K., de Witte, A., Allen, J., Tran, N., Curb, D., Pratt, R., Neefs, H., Indig, M. A., Law, S., Neri, B., Wang, L., and Cox, D. R. (2002) High-throughput genotyping of single nucleotide polymorphisms using new biplex invader technology. *Nucleic Acids Res. 30*, e53.

(12) Lovmar, L., Fredriksson, M., Liljedahl, U., Sigurdsson, S., and Syvänen, A. C. (2003) Quantitative evaluation by minisequencing and microarrays reveals accurate multiplexed SNP genotyping of whole genome amplified DNA. *Nucleic Acids Res. 31*, e129.

(13) Hoh, J., and Ott, J. (2004) Genetic dissection of diseases: design and methods. *Curr. Opin. Genet. Dev. 14*, 229–232.

(14) Fernet, M., and Hall, J. (2004) Genetic biomarkers of therapeutic radiation sensitivity. *DNA Repair 3*, 1237–1243.

(15) Case-Green, S. C., Mir, K. U., Pritchard, C. E., and Southern, E. M. (1998) Analysing genetic information with DNA arrays. *Curr. Opin. Chem. Biol. 2*, 404–410.

(16) Van Hal, N. L. W., Vorst, O., van Houwelingen, A. M. M., Kok, E. J., Peijnenburg, A., Aharoni, A., van Tunen, A. J., and Keijer, J. (2000) The application of DNA microarrays in gene expression analysis. *J. Biotechnol. 78*, 271–280.

(17) Efimov, V. A., Buryakova, A. A., and Chakhmakhcheva, O. G. (1999) Synthesis of polyacrylamides N-substituted with PNA-like oligonucleotide mimics for molecular diagnostic applications. *Nucleic Acids Res. 27*, 4416–4426.

(18) Reichert, J., Csáki, A., Köhler, J. M., and Fritzsche, W. (2000) Chip-based optical detection of DNA hybridization by means of nanobead labeling. *Anal. Chem. 72*, 6025–6029.
(19) Cuzin, M. (2001) DNA chips: a new tool for genetic analysis and diagnostics. *Transfus. Clin. Biol. 8*, 291–296.
(20) O'Sullivan, P. J., Burke, M., Soini, A. E., and Papkovsky, D. B. (2002) Synthesis and evaluation of phosphorescent oligonucleotide probes for hybridisation assays. *Nucleic Acids Res. 30*, e114.
(21) Cao, Y. C., Jin, R. C., Thaxton, C. S., and Mirkin, C. A. (2005) A two-color-change, nanoparticle-based method for DNA detection. *Talanta 67*, 449–455.
(22) Matsunaga, T., Okochi, M., and Nakayama, H. (1999) Construction of an automated DNA detection system for manipulation of *Microcystis* spp. using specific DNA probe immobilized on magnetic particles. *Electrochim. Acta 44*, 3779–3784.
(23) Yao, G., and Tan, W. H. (2004) Molecular-beacon-based array for sensitive DNA analysis. *Anal. Biochem. 331*, 216–223.
(24) Chandler, D. P., Stults, J. R., Anderson, K. K., and Cebula, S. (2000) Affinity capture and recovery of DNA at femtomolar concentrations with peptide nucleic acid probes. *Anal. Biochem. 283*, 241–249.
(25) McClay, J. L., Sugden, K., Koch, H. G., Higuchi, S., and Craig, I. W. (2002) High-throughput single-nucleotide polymorphism genotyping by fluorescent competitive allele-specific polymerase chain reaction (SNiPTag). *Anal. Biochem. 301*, 200–206.
(26) Sakao, Y., Nakamura, F., Ueno, N., and Hara, M. (2005) Hybridization of oligonucleotide by using DNA self-assembled monolayer. *Colloids Surf., B 40*, 149–152.
(27) Loss, K., Kennedy, S. B., Eidelman, N., Tai, Y., Zharnikov, M., Amis, E. J., Ulman, A., and Gross, R. A. (2005) Combinatorial approach to study enzyme/surface interactions. *Langmuir 21*, 5237–5241.
(28) Veiseh, M., Zareie, M. H., and Zhang, M. Q. (2002) Highly selective protein patterning on gold-silicon substrates for biosensor applications. *Langmuir 18*, 6671–6678.
(29) Klauser, R., Huang, M. L., Wang, S. C., Chen, C. H., Chuang, T. J., Telfort, A., and Zharnikov, M. (2004) Lithography with a focused soft x-ray beam and a monomolecular resist. *Langmuir 20*, 2050–2053.
(30) Tai, Y., Shaporenko, A., Eck, W., Grunze, M., and Zharnikov, M. (2004) Depth distribution of irradiation-induced cross-linking in aromatic self-assembled monolayers. *Langmuir 20*, 7166–7170.
(31) Kroeger, K. M., Carville, K. S., and Abraham, L. J. (1997) The −308 tumor necrosis factor-α promoter polymorphism effects transcription. *Mol. Immunol. 34*, 391–399.
(32) Hajeer, A. H., and Hutchinson, I. V. (2001) Influence of TNFα gene polymorphisms on TNFα production and disease. *Hum. Immunol. 62*, 1191–1199.
(33) Lloyd, B. H., Giles, R. V., Spiller, D. G., Grzybowski, S. J., Tidd, D. M., and Sibson, D. R. (2001) Determination of optimal sites of antisense oligonucleotide cleavage within TNFα mRNA. *Nucleic Acids Res. 29*, 3664–3673.
(34) Yee, L. J., Tang, J., Herrera, J., Kaslow, R. A., and van Leeuwen, D. J. (2000) Tumor necrosis factor gene polymorphisms in patients with cirrhosis from chronic hepatitis C virus infection. *Genes Immunol. 1*, 386–390.
(35) Tyan, Y. C., Jong, S. B., Liao, J. D., Liao, P. C., Yang, M. H., Liu, C. Y., Klauser, R., Himmelhaus, M., and Grunze, M. (2005) Proteomic profiling of erythrocyte proteins by proteolytic digestion chip and identification using two-dimensional electrospray ionization tandem mass spectrometry. *J. Proteome. Res. 4*, 748–757.
(36) Weng, C. C., Liao, J. D., Wu, Y. T., Wang, M. C., Klauser, R., Grunze, M., and Zharnikov, M. (2004) Modification of aliphatic self-assembled monolayers by free-radical-dominant plasma: the role of the plasma composition. *Langmuir 20*, 10093–10099.
(37) Dovbeshko, G. I., Gridina, N. Y., Kruglova, E. B., and Pashchuk, O. P. (2000) FTIR spectroscopy studies of nucleic acid damage. *Talanta 53*, 233–246.
(38) Liao, J. D., Wang, M. C., Weng, C. C., Klauser, R., Frey, S., Zharnikov, M., and Grunze, M. (2002) Modification of alkanethiolate self-assembled monolayers by free radical-dominant plasma. *J. Phys. Chem. B 106*, 77–84.
(39) Saprigin, A. V., Thomas, C. W., Dulcey, C. S., Patteson, C. H., Jr., and Spector, M. S. (2005) Spectroscopic quantification of covalently immobilized oligonucleotides. *Surf. Interface Anal. 37*, 24–32.
(40) Liao, J. D., Lin, S. P., and Wu, Y. T. (2005) Dual properties of the deacetylated sites in chitosan for molecular immobilization and biofunctional effects. *Biomacromolecules 6*, 392–399.
(41) Wang, M. C., Liao, J. D., Weng, C. C., Wu, Y. D., Klauser, R., Frey, S., Heister, K., Zharnikov, M., and Grunze, M. (2002) The effect of the substrate on response of thioaromatic self-assembled monolayers to free radical-dominant plasma. *J. Phys. Chem. B 106*, 6220–6226.
(42) Wang, M. C., Liao, J. D., Weng, C. C., Klauser, R., Shaporenko, A., Grunze, M., and Zharnikov, M. (2003) Modification of aliphatic monomolecular films by free radical dominant plasma: the effect of the alkyl chain length and the substrate. *Langmuir 19*, 9774–9780.
(43) Dannenberger, O., Weiss, K., Himmel, H. J., Jäger, B., Buck, M., and Wöll, Ch. (1997) An orientation analysis of differently endgroup-functionalised alkanethiols adsorbed on Au substrates. *Thin Solid Films 307*, 183–191.
(44) Ulman, A. (1996) Formation and structure of self-assembled monolayers. *Chem. Rev. 96*, 1533–1554.
(45) Yang, Y. W., and Fan, L. J. (2002) High-resolution XPS study of decanethiol on Au(111): single sulfur-gold bonding interaction. *Langmuir 18*, 1157–1164.
(46) Heister, K., Zharnikov, M., Grunze, M., Johannson, L. S. O., and Ulman, A. (2001) Characterization of X-ray induced damage in alkanethiolate monolayers by high-resolution photoelectron spectroscopy. *Langmuir 17*, 8–11.

BC700217N

Optical Antisense Imaging of Tumor with Fluorescent DNA Duplexes

Xinrong Liu,[†,‡] Yi Wang,[†] Kayoko Nakamura,[§] Guozheng Liu,[†] Shuping Dou,[†] Atsushi Kubo,[§] Mary Rusckowski,[†] and Donald J. Hnatowich*[,†,§]

Depatment of Radiology, University of Massachusetts Medical School, Worcester, Massachusetts 01655, and Department of Radiology, Keio University School of Medicine, Tokyo, Japan. Received June 19, 2007; Revised Manuscript Received August 24, 2007

Antisense targeting of tumor with fluorescent conjugated DNA oligomers has the potential of improving tumor/normal tissue ratios over that achievable by nuclear antisense imaging. When administered as a linear duplex of two fluorophore-conjugated oligomers arranged in a manner that inhibits fluorescence as the duplex and designed to dissociate only in the presence of the target mRNA, the fluorescence signal should in principle be inhibited everywhere except in the target cell. Optical imaging by fluorescence quenching using linear fluorophore-conjugated oligomers has not been extensively investigated and may not have been previously considered for antisense targeting. We evaluated in cell culture and in KB-G2 tumor bearing nude mice a 25-mer phosphorothioate (PS) anti-*mdr1* antisense DNA conjugated with the Cy5.5 emitter on its 3′ equivalent end and hybridized as a linear duplex with a shorter 18-mer phosphodiester (PO) complementary DNA (cDNA) with the Black Hole inhibitor BHQ3 on its 5′ end. In serum environments, 90% of the DNA25-Cy5.5 fluorescence was inhibited immediately following addition of the cDNA18-BHQ3 and showed only slight loss of inhibition over 24 h at 37 °C. As evidence of antisense specific binding, when incubated with the DNA25-Cy5.5/cDNA18-BHQ3 duplex, the fluorescence was lower in KB-31 (Pgp +/−) cells compared to KB-G2 (Pgp++) cells, but when incubated with the control cDNA18-Cy5.5/DNA25-BHQ3 duplex in which the fluorophores were reversed, the fluorescence of both cell types was low. As further evidence of specific binding, the fluorescent intensity of total RNA from KB-G2 cells incubated with the study duplex showed evidence of dissociation and hybridization with the target mRNA. Furthermore, the fluorescence microscopy images of KB-G2 cells incubated with DNA25-Cy5.5 as the singlet or study duplex show that migration in both cases is to the nucleus. The animal studies were performed in mice bearing KB-G2 tumor in one thigh and receiving iv the study or control duplexes. The tumor/normal thigh fluorescence ratio was clearly positive as early as 30 min postinjection in the study mice and reached a maximum at 5 h. By contrast, much lower fluorescence was observed in mice receiving the control duplex at the same dosage. Fluorescence microscope imaging showed that the Cy5.5 fluorescence was much higher in tumor sections from the animal that had received the study rather than control duplex. Thus combining a fluorophore-conjugated antisense DNA with an inhibitor-conjugated shorter complementary cDNA inhibited fluorescence both in cell culture and in tumored animals except in the presence of the target mRNA. This proof of concept investigation of optical antisense targeting therefore suggests that further studies including optimization of this approach are appropriate.

INTRODUCTION

Our laboratories now have extensive experience in antisense targeting of a variety of mRNAs with radiolabeled DNAs and other oligomers (*1, 2*). However, our experience and that of other laboratories suggest that achieving adequate tumor/normal radioactivity ratios are often problematic (*3–5*). In the course of our investigations, it became apparent that the hybridization properties of oligomers may have applications in optical imaging as an alternative to nuclear imaging. While nuclear imaging offers many advantages over other imaging modalities including high sensitivity of detection, quantitation accuracy, and the availability of numerous contrast agents (*6*), one disadvantage is the physics of nuclear decay that does not permit manipulation of the γ ray emissions. A property of optical imaging unique among most molecular imaging modalities is the potential to modulate the detectable signal in the target. When two fluorophores are brought into proximity, it is possible to shift the emission fluorescence to a lower energy or higher frequency by fluorescence resonance energy transfer (FRET) or to quench the fluorescence entirely (*7*). Molecular beacons consisting of DNAs in the form of hairpins with fluorophores on each end are already in use in this manner for in vitro assays and for vivo studies as well (*8–12*).

Thus, optical antisense targeting of tumor with fluorescent conjugated DNA oligomers may have the potential of improving tumor/normal tissue ratios. When administered as a linear duplex designed to inhibit fluorescence and to dissociate only in the presence of the target mRNA, the fluorescence signal in principle should be inhibited everywhere except in the target cell. Optical imaging by fluorescence quenching using linear fluorophore-conjugated oligomers has not been extensively investigated and may not have been previously considered for antisense targeting. In this proof of concept study, the target was again the *mdr1* mRNA. We have demonstrated that *mdr1* antisense DNA accumulates in the KB-G2 Pgp++ cells and to a lesser extent in the KB-31 Pgp+/− cells by an antisense mechanism (*13, 14*).

For optical antisense targeting, the properties of the duplex are exacting; the duplex must be sufficiently stable to remain intact in circulation and in normal tissues but yet sufficiently unstable to dissociate in the presence of the target mRNA. Fortunately, we have been able to confirm another essential property of the duplex, namely, that it crosses cell membranes without entrapment (*15*). In this investigation we evaluate a

* To whom correspondence should be addressed. Phone: (508) 856-4256. Fax: (508) 856-4572. E-mail: donald.hnatowich@umassmed.edu.
† University of Massachusetts Medical School.
‡ First author. Phone: (508) 856-3722. Fax: (508) 856-4572 . E-mail: xinrong.liu@umassmed.edu.
§ Keio University School of Medicine.

10.1021/bc700221d CCC: $37.00 © 2007 American Chemical Society
Published on Web 10/17/2007

strategy of delivering a 25-mer phosphorothioate (PS) *mdr1* antisense DNA25 conjugated as a linear duplex with the Cy5.5 emitter on its 3′ equivalent end and complexed with a complementary shorter 18-mer phosphodiester (PO) *mdr1* sense DNA18 with the BHQ3 inhibitor on its 5′ end. The DNA25 emitter and cDNA18 inhibitor are so arranged that fluorescence is effectively inhibited with the DNAs in their duplex form. Once in the vicinity of its mRNA target, a new and stable antisense DNA25-Cy5.5/target mRNA duplex forms spontaneously with the release of the shorter DNA along with its inhibitor. This proof of concept study was conducted in cell culture and in KB-G2 tumor bearing mice.

MATERIALS AND METHODS

The duplex consisted of an *mdr1* uniform PS antisense DNA25 (5′- AAG-ATC-CAT-CCC-GAC-CTC-GCG-CTC-C) and a uniform PO complementary sense cDNA18 (5′-GGA-GCG-CGA-GGT-CGG-GAT). The antisense DNA sequence was elongated from the antisense 20-mer DNA used in these laboratories previously (underlined) (*13*). All DNAs were purchased HPLC purified. The antisense DNAs were obtained with Cy5.5 (Sigma-Proligo, Woodlands, TX) or Black Hole Quencher 3 (BHQ3, Biosearch Technologies, Novato, CA) on the 3′ end (designated herein as DNA25-Cy5.5 and DNA25-BHQ3), and the complementary sense cDNAs were obtained with Cy5.5 or BHQ3 on the 5′ end (designated herein as cDNA18-Cy5.5 and cDNA18-BHQ3). Regardless of whether the DNA was native (i.e., without fluorophore) or whether the attached fluorophore was the Cy5.5 or BHQ3 and regardless of whether the DNA was used as the singlet or duplex, the antisense DNA was always the 25-mer and the sense complementary DNA was always the 18 mer. The KB-G2 (Pgp++) and KB-31 (Pgp+/−) human epidermoid carcinoma cell lines were a gift from Isamu Sugawara (Research Institute of Tuberculosis, Tokyo, Japan) and were cultured in Dulbecco's modified Eagle's medium (DMEM) (Gibco BRL Products, Gaithersburg, MD) containing 10% fetal bovine serum (FBS) for 18–24 h at 37 °C, 5% CO_2. Cells were cultured until about 60–70% confluence was reached. The cells were incubated with DNAs in serum-free DMEM in the cell studies of this investigation.

Duplex Preparation and Stability. Both the study DNA25-Cy5.5/cDNA18-BHQ3 duplex and the control cDNA18-Cy5.5/DNA25-BHQ3 duplexes were prepared by mixing the antisense DNA25 and complementary cDNA18 at a 1:1 molar ratio in 150 mM phosphate buffered saline (PBS). The duplex mixtures were vortexed for 10 s, heated in a boiling water bath for 10 min to dissociate any intrastrand duplexes and allowed to cool to room temperature (25 °C).

To measure stability, the duplexes were added in triplicate at 100 μL per well to a 96-well plate to a final concentration of 0.1 nM in 10% FBS/DMEM and 70% normal mouse serum (Jackson ImmunoResearch Laboratories, Inc., West Grove, PA) and incubated at 37 °C for different times up to 24 h. The control was the singlet free DNA25-Cy5.5 added at the identical molar concentration in the identical manner. The fluorescence intensity (excitation 681 nm/emission 700 nm) was read at each time point on a SpectraMax M5/M5^e Microplate fluorescence plate reader (Molecular Devices Corporation, Sunnyvale, CA).

Cell Studies. Rhodamine 123 (Sigma, St. Louis, MO) was used to confirm that the difference in multidrug resistance (i.e., Pgp expression) between the KB-G2 and KB-31 cells was preserved. Both cells were treated with the study duplex to a final concentration of 0.3 μM, and after 3 h, the cells were trypsinized and suspended in 1% FBS/DMEM. The cells were washed twice and resuspended in the same medium at 37 °C before adding rhodamine 123 at 1 μg/ml. After 1 h at 37 °C, the cells were washed twice and resuspended in ice-cold PBS buffer with 1% BSA. Viable cells were analyzed for rhodamine fluorescence on a Becton Dickinson flow cytometer (BD Biosciences, Franklin Lakes, NJ) using CellQuest software (BD Biosciences).

Two duplex accumulation studies were performed in KB-G2 and KB-31 cells in triplicate in 96-well plates seeded at 5000 cells per well and incubated with 10% FBS/DMEM culture medium overnight. In one study, the DNA25-Cy5.5/cDNA18-BHQ3 duplex and singlet DNA25-Cy5.5 were incubated with KB-G2 cells in serum-free DMEM at dosages of 0.02, 0.1, and 0.3 nmol for 3 h at 37 °C. In the other study, the DNA25-Cy5.5/cDNA18-BHQ3 duplex and the control cDNA18-Cy5.5/DNA25-BHQ3 duplex were incubated with both KB-G2 and KB-31 cells in serum-free DMEM at the same dosage of 0.1 nmol for 3 h at 37 °C. The cells were then washed twice with 10% FBS/DMEM and incubated for 1 h in 10% FBS/DMEM before being washed twice with PBS. The lysis buffer (10 mM Tris-HCl, pH 8.0, 150 mM NaCl, 1% Triton X-100) was then added at 100 μL per well, and the cells were incubated for 1 h at 37 °C. The fluorescence intensity of each lysis solution was measured on the fluorescence plate reader. The data were normalized to the total protein content of each well as determined by the Bradford protein assay (Pierce, Rockford, IL).

To measure total RNA binding, KB-G2 cells were seeded in triplicate in six-well plates at 10 000 cells per well and incubated with 10% FBS/DMEM culture medium overnight. Duplex DNA was added into each well with serum-free DMEM at dosages of 0.9 nmol/well, and the cells were incubated for 3 h at 37 °C. Total RNA was extracted using the RNeasy Mini extraction kit (Qiagen, Valencia, CA). Each sample was then added to the 96-well plate, and fluorescence intensity was measured as above.

The intracellular distribution of fluorescence was measured in KB-G2 cells seeded onto glass bottom culture dishes and incubated in 10% FBS/DMEM overnight. The study duplex DNA was added into each well in serum-free DMEM at a final concentration of 0.3 μM for 3 h at 37 °C. The cells were then washed twice with 10% FBS/DMEM and incubated for 1 h in 10% FBS/DMEM before being washed twice with PBS. For living cell imaging, the cells were directly observed on a Nikon Eclipse TE 2000-S microscope (Nikon Instruments Inc., Melville NY) equipped with a Cy5.5 filter and CCD camera and the images processed using IPLab software (BD Biosciences). For nucleus colocalization analysis, the cells were further incubated with 1 μM Sytox Green (Molecular Probes, Eugene, OR) in 95% ethanol for 15 min to fix and stain the nuclei before being washed twice with PBS and examined under the microscope equipped with a filter (excitation 480 nm/emission 535 nm). In the microscopic images, Cy5.5 and Sytox Green were pseudo-colored red and green, respectively.

Animal Studies. All animal studies were performed with the approval of the UMMS Institutional Animal Care and Use Committee. Male nude mice (NIH Swiss, Taconic Farms, Germantown, NY, 30–40 g) at 7 weeks of age were each injected subcutaneously in the right thigh with a 0.1 mL suspension containing 10^6 KB-G2 cells with greater than 95% viability. Mice were used for imaging studies 14 days later when the tumors reached 0.4–0.6 cm in diameter and were placed on a chlorophyll-free diet (AIN-93G Purified Diet, Harlan Teklad, Madison, WI) for 5 days prior to imaging.

Mice bearing KB-G2 tumor were administered 3 nmol of the control duplex, while additional animals received the study duplex at 1, 3, or 5 nmol in 100 μL of PBS per mouse via a tail vein. Mice were then anesthetized ip with ketamine (8 mg/kg) and xylazine (2 mg/kg). In vivo fluorescence imaging was performed on an IVIS 100 small-animal imaging system

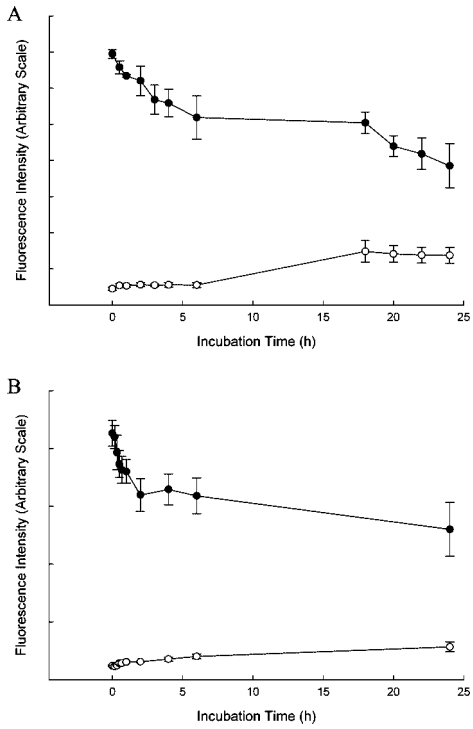


Figure 1. Relative fluorescence intensities of the control singlet PS DNA25-Cy5.5 (closed circles) and the study PS DNA25-Cy5.5/PO cDNA18-BHQ3 duplex (open circles) at 37 °C 10% FBS/DMEM (A) and 70% normal mouse serum (B) over 24 h. Error bars represent 1 sd of the mean ($N = 3$).

(Xenogen, Alameda, CA) using a Cy5.5 filter set. Identical illumination settings (lamp voltage, filters, *f*/stop, field of view, binning) were used for all images, and fluorescence emission was normalized to photons per second per centimeter squared per steradian (p s^{-1} cm^{-2} sr^{-1}). Fluorescence images were acquired at 0.5, 3, 5, and 24 h after injection using 1 s exposure time (*f*/stop 4). Images and measurements of fluorescence signals were acquired and analyzed with Living Image 2.5 software (Xenogen). Regions of interest (ROI) of equal size were centered about the target sites and nontarget sites (i.e., control tumor, contralateral control thigh).

The tumors from mice administered either 3 nmol of the study duplex or the same dosage of control duplex were removed at 24 h, dissected, and treated for fluorescence microscopy imaging. The tumors were placed in tissue holders that were then filled with Tissue-Tek Optimal Cutting Temperature Compound (Sakura Finetek USA, Torrance, CA) and immediately frozen in dry ice. The distribution of the fluoresence within tumor slices of 10 μm thickness was examined, and images were obtained in the GFP channel to locate the cells and in the Cy5.5 channel to show targeting cells. The two images were merged.

Statistical Analysis. Data are presented as the mean ± sd of at least $N = 3$, and statistical analysis was performed using Student's *t* test. A *p* value of less than 0.05 was considered statistically significant.

RESULTS

Duplex Stability. The stability of the DNA25-Cy5.5/cDNA18-BHQ3 duplex was evaluated at 37 °C in 10% FBS/DMEM (Figure 1A) and 70% normal mouse serum (Figure 1B) at 0.1 nM over 24 h and compared to the singlet DNA25-Cy5.5. The fluorescence intensities presented in Figure 1 demonstrate that the duplex is sufficiently stable at least over 24 h in these media. Compared to the fluorescence of the singlet, over 90% of the duplex fluorescence was quenched initially and largely remained

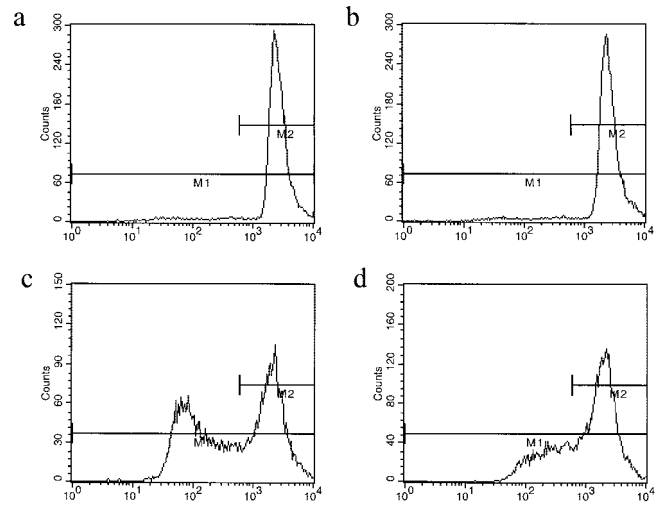


Figure 2. Flow cytometry of KB-31 cells before (a) and after (b) incubation with the study duplex and of KB-G2 cells before (c) and after (d) incubation with the study duplex.

so for about 6 h. Thereafter, the intensity increased but only slowly. The fluorescence intensities of the singlet decreased over this period presumably because of fluorescence decay (*16*).

Cell Studies. *Rhodamine 123 Accumulation.* One major form of multidrug resistance to cancer therapeutic agents is mediated by overexpression of P glycoprotein (Pgp), a membrane protein ATPase that serves as a drug efflux pump (*17, 18*). Rhodamine 123 is a substrate for the Pgp efflux pump and is often used as a surrogate for drug accumulations (*18*). The accumulation of rhodamine 123 by KB-G2 (Pgp++) and KB-31 (Pgp+/−) cells were measured by flow cytometry after incubation with the study duplex at 0.3 μM. Fluorescence intensity was detected in the FL1-H channel. To obtain a histogram from the FACS analysis, the gate M1 was placed to count all cells while gate M2 was placed to count only those cells with high rhodamine 123 fluorescence. Acquisition was set to 20 000 events, and results depict the viable/intact cell population as routinely gated in the forward and side scatter plot. As shown in Figure 2 before incubation with the study duplex, 93% of KB-31 cells showed high accumulations of rhodamine 123 fluorescence (Figure 2a) compared to only 53% of KB-G2 cells (Figure 2c), no doubt because rhodamine 123 was less effectively excreted from KB-31 cells because of a low Pgp expression level in these cells. Thus, these results show that the KB-31 cells used in this investigation were low-level expressors of Pgp compared to KB-G2. As also shown, incubation of KB-G2 cells with the duplex led to a dramatic 35% increase in rhodamine 123 accumulation and therefore a strong inhibition of Pgp expression (Figure 2d compared to Figure 2c). By contrast, incubating KB-31 cells with the duplex had no effect (Figure 2b compared to Figure 2a). Thus, these results also indicate that the duplex is capable of inhibiting Pgp expression by what is almost certainly an antisense effect.

Cellular Accumulation. The KB-G2 cells were incubated with DNA25-Cy5.5 as the singlet and as the study DNA25-Cy5.5/cDNA18-BHQ3 duplex at 0.02, 0.1, or 0.3 nmol for 3 h, and the fluorescence was measured. The histograms of Figure 3A show that the fluorescence intensity of the cells is in all cases significantly higher when incubated with the DNA25-Cy5.5 as the singlet compared to the duplex. The lower fluorescence of cells incubated with the duplex at the same molarity is therefore evidence that the DNA25-Cy5.5/cDNA18-BHQ3 duplex is still largely intact at 3 h, especially given that duplex DNAs appear to accumulate in cells more efficiently than singlet DNAs (*15*).

Both the KB-G2 and KB-31 cells were incubated with both the study DNA25-Cy5.5/cDNA18-BHQ3 and the control

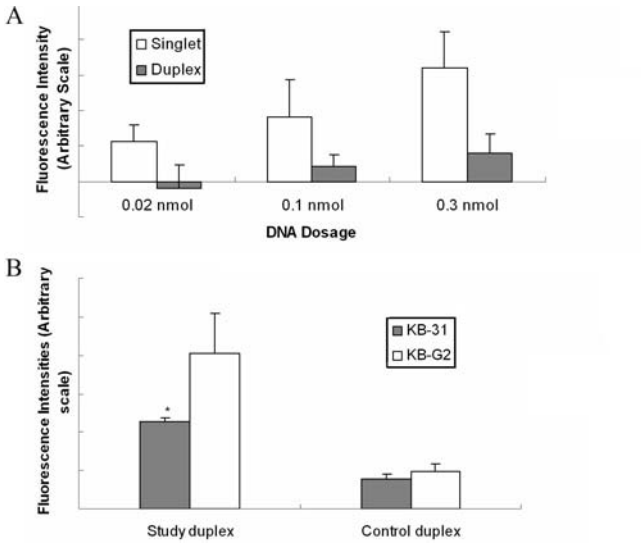


Figure 3. Relative cellular fluorescence intensity at 3 h in KB-G2 cells after incubation with the DNA25-Cy5.5 singlet or the study DNA25-Cy5.5/cDNA18-BHQ3 duplex at three dosages (A) and the relative cellular fluorescence intensity at 3 h in KB-31 and KB-G2 cells after incubation with 0.1 nmol of the study or control duplex (B). Error bars represent 1 sd of the mean ($N = 3$). The higher fluorescence of KB-G2 cells when incubated with the study duplex and the identical fluorescence when incubated with the control duplex are both evidence of antisense binding.

cDNA18-Cy5.5/DNA25-BHQ3 duplex. As shown in Figure 3B, when incubated with the study duplex, the fluorescence was statistically lower ($p = 0.042$) in the KB-31 cells compared to the KB-G2 cells, as expected since the number of mRNA targets in KB-31 cells is limited. However, as also shown in the figure, the fluorescence intensities of the two cell types were statistically identical ($p = 0.211$) when incubated with the control duplex, also as expected since in this case the Cy5.5 fluorophore has been placed on the sense DNA and therefore without affinity for the target mRNA. Both these results provide evidence of antisense binding.

RNA Binding. The KB-G2 cells were incubated with the DNA25-Cy5.5 as the singlet or study duplex at the same molar concentration for 3 h. Total RNA was then extracted and the fluorescence measured. The relative fluorescence intensities in total RNA for cells exposed to the duplex DNA was 189 ± 61 ($N = 3$) and therefore lower than in cells exposed to the singlet DNA at 544 ± 289 ($N = 3$). Under the reasonable assumption that the fluorescence of total RNA is due to specific binding of the DNA25-Cy5.5 to the target mRNA, the higher fluorescence intensity of total RNA incubated with the singlet DNA25-Cy5.5 is not surprising because the duplex requires dissociation before binding. That the RNA binding of the duplex was still about 35% of that of the singlet is therefore promising. The fluorescence intensities of the mRNA themselves were too low to provide a meaningful result.

Intracellular Distribution. The fluorescence images of live and fixed KB-G2 cells are shown in Figure 4 after incubation with the DNA25-Cy5.5 as the singlet or duplex. Live cells (Figure 4A) show similar fluorescence when incubated with the duplex compared to singlet, and in both cases accumulations appear in the nucleus. That the intracellular distributions in fixed cells (Figure 4B) are identical for cells previously incubated with the singlet or duplex and that the accumulations are primarily in the nucleus are obvious by comparison of the Cy5.5 images with that of the nucleus staining Sytox Green. These results suggest that both forms of DNA25-Cy5.5 have the same cellular target and that the target is the nucleus.

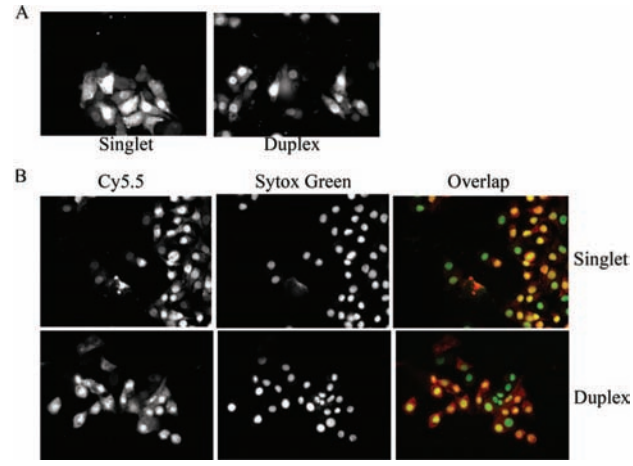


Figure 4. Fluorescence images in live KB-G2 cells incubated with the DNA25-Cy5.5 as the singlet (left) and duplex (right) (A) and the fluorescence images of fixed KB-G2 cells previously incubated with the DNA25-Cy5.5 as the singlet (top row) or duplex (bottom row) (B). The cells were incubated with the DNAs at 0.3 μM for 3 h at 37 °C. Nuclei were labeled with Sytox Green. Fluorescence signal from Cy5.5 was pseudocolored red. Magnification is $\times 400$.

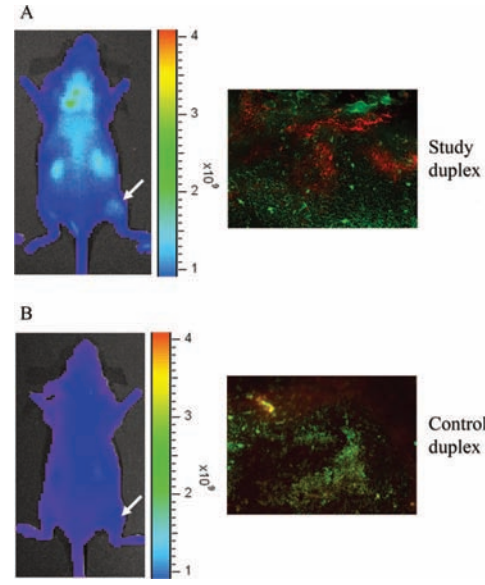


Figure 5. Whole-body fluorescence images of KB-G2 tumor bearing mice in the dorsal view at 5 h following administration of 3 nmol of the study DNA25-Cy5.5/cDNA18-BHQ3 duplex (A) or control cDNA18-Cy5.5/DNA25-BHQ3 duplex (B). The arrow indicates the tumor location. Also presented are microscopic analysis of tissue sections of tumor obtained at 24 h after injection of both study and control duplexes. Magnification is $\times 100$.

Animal Studies. Figure 5 presents whole-body fluorescence images at 5 h in the dorsal view of mice with KB-G2 tumors and images of the sectioned excised tumors in animals receiving the study duplex (Figure 5A) or the control duplex (Figure 5B) at 3 nmol. The whole-body image of the animal receiving the control duplex shows little or no Cy5.5 fluorescence. By contrast, images obtained simultaneously of the animal receiving the study duplex show pronounced whole-body fluorescence and an obvious accumulation in the tumored thigh. The fluorescence in the tumored thigh of mice increased with increasing dosage of study duplex (data not presented); however, the background fluorescence also increased in proportion possibly because of instability of the study duplex toward dissociation in background tissues.

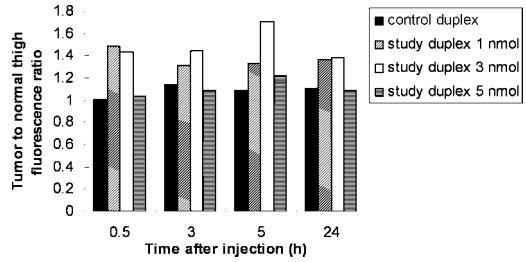


Figure 6. Tumor-to-normal thigh fluorescent ratios at 0.5, 3, 5, and 24 h postadministration in one animal receiving the control duplex and in one study animal receiving 1, 3, or 5 nmol of study duplex. The figure shows higher fluorescence in the tumored thigh in the study animals compared to the control animal.

Further evidence for the preferential targeting of tumor by the study duplex is shown in the ex vivo images of tumor tissue slices from both the study and control animals. In this figure, the green color is due to autofluorescence originating in tumor and muscle tissues and is much weaker than the red Cy5.5 fluorescence due to duplex dissociation. Accordingly, the yellow color that would be expected to show overlap is obscured by the intense red color. Nevertheless, the figure clearly shows the higher Cy5.5 fluorescence in the study tumor compared to the control tumor, in agreement with the animal images.

Regions of interest of equal area were placed over each animal's tumor and contralateral thigh and the fluorescent intensities ratios calculated for all four measurements over the 24 h imaging period. As shown in the histograms of Figure 6, a positive tumor/normal thigh ratio was achieved as early as 30 min postinjection. At all time points, the tumor/normal ratio was never less than about 1.2–1.6 times higher in the animal receiving the study duplex compared to the animal receiving the control duplex.

DISCUSSION

Optical imaging has emerged as an attractive modality capable of investigating biological/molecular events in both cell culture and small living subjects. The modality is noninvasive, highly sensitive, and affordable. Furthermore, the use of fluorescent contrast agents, unlike radiolabeled contrast agents, provides the potential of modulating the detectable signal in the target (*4, 19, 20*). A disadvantage to optical imaging is the much greater influence of tissue absorption and scatter on a fluorescent signal compared to a nuclear signal. Nevertheless, the use of fluorophores emitting in the near-infrared (700–900 nm) range minimizes tissue absorption and also minimizes autofluorescence from nontarget tissues (*21*). Many studies have now demonstrated that optical imaging is practical in small animals (*4, 19, 22*).

These laboratories are investigating antisense DNAs and other oligomers and lately are investigating the use of double-stranded duplexes to improve cellular delivery (*15*). We and others have compared single-stranded and double-stranded DNAs or siRNAs and have shown that double-stranded oligomers (*15, 23, 24*) are stable both in cell culture and in animal (*25*) and appear to show greater accumulates in cells compared to singlet oligomers (*15*). However, a duplex under consideration for antisense targeting must be sufficiently stable to remain intact in circulation and throughout its passage across the cell membrane but not so stable as to interfere with its dissociation and the subsequent binding of the labeled antisense DNA to its mRNA target.

While use of a radiolabeled duplex has now been shown to improve delivery of radiolabeled antisense oligomers, the free duplex in surrounding tissues provide an unwanted background radioactivity level. However, if a fluorescent label were used in place of the radioactivity label and if the complementary oligomer were to contain an inhibiting fluorophore, in principle free duplex would not fluoresce, resulting in an improved target/nontarget ratio. This approach is similar to that already in practice in connection with stem–loop hairpin oligomers (*8, 26*). However, to our knowledge, this report describes the first attempt to use linear duplexes for fluorescent quenching in connection with antisense targeting.

These laboratories and others have observed that the stability of the PS DNA/PO DNA heteroduplex was higher than the stability of an equivalent PS DNA/PS DNA homoduplex (*15, 27, 28*) and that duplexes consisting of two 25-mer phosphorodiamidate morpholino (MORF) oligomers show less evidence of instability in vitro and in vivo compared to duplexes with one or two 15-mer MORF oligomers (*29*). For these reasons a 25-mer PS DNA25/18-mer PO cDNA18 duplex was selected for this study.

The identical antisense DNA sequence used previously in these laboratories (but elongated to 25-mer) and the *mdr1* target mRNA were again used in this investigation. When radiolabeled, successful tumor targeting of this antisense PS DNA by an antisense mechanism was achieved in cell culture (*13*) and in tumored mice (*3*). Furthermore, when the *mdr1* mRNA is targeted, the cells showing high level (KB-G2) and low level (KB-31) *mdr1* mRNA and therefore different Pgp expression may again be used as a study/control pair. Since the *mdr1* mRNA expression of the control Pgp+/– KB-31 cells can be variable and the cells can be inadverently modified to express *mdr1* mRNA and Pgp at levels approaching that of the study Pgp++ KB-G2 cells (*13*), rhodamine 123 was used to confirm that the difference in multidrug resistance (i.e., Pgp expression) between the KB-31 and KB-G2 cells was preserved, as shown in Figure 2.

The Cy5.5 emitter was selected because of its emission in the near-infrared, and BHQ3 was selected as a nonfluorescent quencher both because of its lack of self fluorescence and because it provides spectral overlap over the entire range of Cy5.5 fluorescence. Thus, when the 3′-Cy5.5 conjugated antisense DNA is hybridized with the 5′-BHQ3 complementary DNA, about 90% of the Cy5.5 fluorescence is quenched as shown in Figure 1. As also shown in the figure, the duplex is stable in normal cell media and in 70% serum over 24 h. Furthermore, as shown in Figure 3A, when incubated with KB-G2 cells, the fluorescence intensity of DNA25-Cy5.5 was much lower as the duplex compared to singlet at all dosages as evidence of duplex intracellular stability. To address the question of whether the fluorescence of the duplex is specific and the result of antisense targeting, the identical studies were performed with the Cy5.5 on the complementary sense strand and the BHQ3 on the antisense strand (i.e., cDNA18-Cy5.5/DNA25-BHQ3 duplex) and the results compared with the study duplex (i.e., DNA25-Cy5.5/cDNA18-BHQ3) after incubation in the KB-G2 cells with the high *mdr1* mRNA level and KB-31 cells with a lower *mdr1* mRNA level. As shown in Figure 3B, the cellular accumulations of the control duplex was statistically identical in both cells while the accumulation of the study duplex was statistically higher in the KB-G2 cells as evidence of specific antisense binding.

Further evidence for specific antisense binding of the duplex was obtained in the fluorescent images of KB-G2 cells shown in Figure 4. Evidence from this laboratory (*14*) and other laboratories (*17, 23, 30*) shows that antisense DNAs migrate to the nucleus of target cells. The images in the figure for both the live and fixed KB-G2 cells show similar migration of DNA25-Cy5.5 to the nucleus when incubated as the singlet or duplex. Finally, that incubation of KB-G2 cells with the study duplex increased the accumulation of rhodamine 123 as shown in Figure 2 may also be taken as evidence of specific antisense

targeting because the duplex in this case was apparently interfering with Pgp efflux pump expression and therefore *mdr1* mRNA translation.

The whole-body fluorescent images of KB-G2 tumor bearing mice presented in Figure 5A provide further evidence in support of the hypothesis that the duplex dissociates as expected in the presence of its target mRNA and provides evidence that it does so in vivo at the tumor site. The figure presents images at 5 h of two identical tumored mice receiving either the study or control duplex and at the same 3 nmol dosage and imaged simultaneously. The increased fluorescence in the tumored thigh in the animal receiving the study duplex is apparent in these images as well as in the images obtained following administration of the 1 and 5 nmol dosage of study duplex (data not presented). Regions of interest of equal area were set around both thighs in all animals to generate the ratio of fluorescence in the study thigh compared to normal thigh. As shown in Figure 6, this ratio was never less than 1.2–1.6. Also presented in Figure 5 are fluorescent microscopy images of tumor slices taken from animals receiving either the study or control duplexes. By comparison of the images with that obtained by imaging in the GFP channel, it is apparent that the Cy5.5 fluorescence is emanating from the tumor cells as evidence of tumor targeting.

An interesting observation within Figure 5A is the background fluorescence in animals receiving the study but not the control duplex. Since more than 90% of the Cy5.5 fluorescence may be quenched in the duplex (Figure 1), much lower backgrounds were expected. We hypothesize that the study duplex (PS DNA25-Cy5.5/PO cDNA18-BHQ3) used in this investigation is unstable to dissociation in circulation and/or in normal organs within the 3 h period between administration and imaging. Thus, once the PO DNA-BHQ3 in its singlet form is released, it is expected to rapidly degrade in vivo as any singlet PO DNA (*31*). By contrast, the free PS DNA-Cy5.5 will be stable to enzymatic degradation along with its fluorescence. However, when the control duplex dissociates, the PO DNA-Cy5.5 will be released to be degraded within minutes such that the Cy5.5 may clear the cell and the whole body along with its fluorescence. To investigate this possibility, two tumored animals were imaged immediately following administration of a PO DNA-Cy5.5 or a PS DNA-Cy5.5. At 12 min, the mouse receiving the PO DNA-Cy5.5 showed minimal fluorescence in blood and, in this case, high florescence in kidneys and bladder. By contrast, the mouse receiving the PS DNA-Cy5.5 showed whole-body fluorescence similar to that of Figure 5A (data not presented).

CONCLUSION

In conclusion, our results provide a proof of concept that fluorophore-conjugated linear DNA duplexes may be used to provide a fluorescent image of tumor in mice by an antisense mechanism. We have shown that our selection of Cy5.5 and BHQ3 conjugated DNAs provides efficient fluorescent quenching when hybridized and produces florescence in tumor cells in culture and tumors in vivo when dissociated in the presence of the mRNA target. However, it will be apparent from these results that the selection of a 25-mer antisense PS DNA and an 18-mer complementary sense PO DNA may not be ideal for this application. Additional studies will be needed to investigate the influence of chain length and backbone modifications on future duplexes.

ACKNOWLEDGMENT

We thank Dr. Isamu Sugawara (Research Institute of Tuberculosis, Tokyo, Japan) for providing the KB-G2 and KB-31 cell lines for this investigation. We thank Dr. Alexei Bogdanov, Jr., for assistance with the in vitro fluorescence measurements. This research was supported in part by the Office of Science (BER), U.S. Department of Energy (Grant DE-FG02-03ER63602), the Grant-in-Aid for Scientific Research (Grants 16591225 and 17659374), and the 21st Century Center of Excellence (COE) Program entitled "Establishment of Individualized Cancer Therapy Based on Comprehensive Development of Minimally Invasive and Innovative Therapeutic Methods (Keio University)" from the Japanese Ministry of Education, Science, Sports and Culture.

LITERATURE CITED

(1) Hnatowich, D. J., and Nakamura, K. (2004) Antisense targeting in cell culture with radiolabeled DNAs—a brief review of recent progress. *Ann. Nucl. Med. 18*, 363–368.

(2) Hnatowich, D. J., and Nakamura, K. (2006) The influence of chemical structure of DNA and other oligomer radiopharmaceuticals on tumor delivery. *Curr. Opin. Mol. Ther. 8*, 136–143.

(3) Nakamura, K., Fan, C., Liu, G., Gupta, S., He, J., Dou, S., Kubo, A., Rusckowski, M., and Hnatowich, D. J. (2004) Evidence of antisense tumor targeting in mice. *Bioconjugate Chem. 15*, 1475–1480.

(4) Becker, A., Hessenius, C., Licha, K., Ebert, B., Sukowski, U., Semmler, W., Wiedenmann, B., and Grotzinger, C. (2001) Receptor-targeted optical imaging of tumors with near-infrared fluorescent ligands. *Nat. Biotechnol. 19*, 327–331.

(5) Weissleder, R., Tung, C. H., Mahmood, U., and Bogdanov, A., Jr. (1999) In vivo imaging of tumors with protease-activated near-infrared fluorescent probes. *Nat. Biotechnol. 17*, 375–378.

(6) Hnatowich, D. J. (2002) Molecular imaging and nuclear medicine. *J. Cell. Biochem. Suppl. 39*, 18–24.

(7) Marras, S. A., Kramer, F. R., and Tyagi, S. (2002) Efficiencies of fluorescence resonance energy transfer and contact-mediated quenching in oligonucleotide probes. *Nucleic Acids Res. 30*, e122.

(8) Tyagi, S., and Kramer, F. R. (1996) Molecular beacons: probes that fluoresce upon hybridization. *Nat. Biotechnol. 14*, 303–308.

(9) Silverman, A. P., and Kool, E. T. (2005) Quenched probes for highly specific detection of cellular RNAs. *Trends Biotechnol. 23*, 225–230.

(10) Nitin, N., Santangelo, P. J., Kim, G., Nie, S., and Bao, G. (2004) Peptide-linked molecular beacons for efficient delivery and rapid mRNA detection in living cells. *Nucleic Acids Res. 32*, e58.

(11) McIntyre, J. O., Fingleton, B., Wells, K. S., Piston, D. W., Lynch, C. C., Gautam, S., and Matrisian, L. M. (2004) Development of a novel fluorogenic proteolytic beacon for in vivo detection and imaging of tumour-associated matrix metalloproteinase-7 activity. *Biochem. J. 377*, 617–628.

(12) Zheng, G., Chen, J., Stefflova, K., Jarvi, M., Li, H., and Wilson, B. C. (2007) Photodynamic molecular beacon as an activatable photosensitizer based on protease-controlled singlet oxygen quenching and activation. *Proc. Natl. Acad. Sci. USA 104*, 8989–8994.

(13) Nakamura, K., Kubo, A., and Hnatowich, D. J. (2005) Antisense targeting of P-glycoprotein expression in tissue culture. *J. Nucl. Med. 46*, 509–513.

(14) Liu, X., Nakamura, K., Wang, Y., Wang, Y., Liu, G., He, J., Ding, H., Lu, P., Rusckowski, M., Kubo, A., and Hnatowich, D. J. (2006) Initial mechanistic studies of antisense targeting in cells. *J. Nucl. Med. 47*, 360–368.

(15) Liu, X., Nakamura, K., Wang, Y., Zhang, S., He, J., Liu, G., Dou, S., Kubo, A., Rusckowski, M., and Hnatowich, D. J. (2006) Improved delivery in cell culture of radiolabeled antisense DNAs by duplex formation. *Mol. Imaging Biol. 8*, 278–283.

(16) Eaton, D. F. (1990) Recommended methods for fluorescence decay analysis. *Pure Appl. Chem. 62*, 1631–1648.

(17) Alahari, S. K., Delong, R., Fisher, M. H., Dean, N. M., Viliet, P., and Juliano, R. L. (1998) Novel chemically modified oligonucleotides provide potent inhibition of P-glycoprotein expression. *J. Pharmacol. Exp. Ther. 286*, 419–428.

(18) Kang, H., Fisher, M. H., Xu, D., Miyamoto, Y. J., Marchand, A., Van, Aerschot, A., Herdewijn, P., and Juliano, R. L. (2004) Inhibition of *MDR1* gene expression by chimeric HNA antisense oligonucleotides. *Nucleic Acids Res. 32*, 4411–4419.

(19) Cheng, Z., Levi, J., Xiong, Z., Gheysens, O., Keren, S., Chen, X., and Gambhir, S. S. (2006) Near-infrared fluorescent deoxyglucose analogue for tumor optical imaging in cell culture and living mice. *Bioconjugate Chem. 17*, 662–669.

(20) Ntziachristos, V., Bremer, C., and Weissleder, R. (2003) Fluorescence imaging with near-infrared light: new technological advances that enable in vivo molecular imaging. *Eur. Radiol. 13*, 195–208.

(21) Massoud, T. F., and Gambhir, S. S. (2003) Molecular imaging in living subjects: seeing fundamental biological processes in a new light. *Genes Dev. 17*, 545–580.

(22) Weissleder, R., Tung, C. H., Mahmood, U., and Bogdanov, A., Jr. (1999) In vivo imaging of tumors with protease-activated near-infrared fluorescent probes. *Nat. Biotechnol. 17*, 375–378.

(23) Jekerle, V., Kassack, M. U., Reilly, R. M., Wiese, M., and Piquette-Miller, M. (2005) Functional comparison of single- and double-stranded *mdr1* antisense oligodeoxynucleotides in human ovarian cancer cell lines. *J. Pharm. Pharm. Sci. 8*, 516–527.

(24) Asriab-Fisher, A., Fisher, M., Juliano, R., and Herdewijn, P. (2004) Increased uptake of antisense oligonucleotides by delivery as double stranded complexes. *Biochem. Pharmacol. 68*, 403–407.

(25) Aharinejad, S., Paulus, P., Sioud, M., Hofmann, M., Zins, K., Schäfer, R., Stanley, E. R., and Abraham, D. (2004) Colony-stimulating factor-1 blockage by antisense oligonucleotides and small interference RNAs suppresses growth of human mammary tumor xenografts in mice. *Cancer Res. 64*, 5378–5384.

(26) Bernacchi, S., and Mely, Y. (2001) Exciton interaction in molecular beacons: a sensitive sensor for short range modifications of the nucleic acid structure. *Nucleic Acids Res. 29*, E62-2.

(27) Venkiteswaran, S., Vijayanathan, V., Shirahata, A., Thomas, T., and Thomas, T. J. (2005) Antisense recognition of the HER-2 mRNA: effects of phosphorothioate substitution and polyamines on DNA·RNA, RNA·RNA, and DNA·DNA duplex stability. *Biochemistry 44*, 303–312.

(28) Boczkowska, M., Guga, P., and Stec, W. J. (2002) Stereodefined phosphorothioate analogues of DNA: relative thermodynamic stability of the model PS-DNA/DNA and PS-DNA/RNA complexes. *Biochemistry 41*, 12483–12487.

(29) He, J., Rusckowski, M., Wang, Y., Dou, S., Liu, X., Zhang, S., Liu, G., and Hnatowich, D. J. (2007) Optical pretargeting of tumor with fluorescent MORF oligomers. *Mol. Imaging. Biol. 9*, 17–23.

(30) Toub, N., Bertrand, J. R., Malvy, C., Fattal, E., and Couvreur, P. (2006) Antisense oligonucleotide nanocapsules efficiently inhibit EWS-Fli1 expression in a Ewing's sarcoma model. *Oligonucleotides 16*, 158–168.

(31) Sands, H., Gorey-Feret, L. J., Cocuzza, A. J., Hobbs, F. W., Chidester, D., and Trainor, G. L. (1994) Biodistribution and metabolism of internally 3H-labeled oligonucleotides. I. Comparison of a phosphodiester and a phosphorothioate. *Mol Pharmacol. 45*, 932–943.

BC700221D

Novel Method for *in Vitro* O-Glycosylation of Proteins: Application for Bioconjugation

Boopathy Ramakrishnan,[†,‡] Elizabeth Boeggeman,[†,‡] and Pradman K. Qasba*[,†]

Structural Glycobiology Section, and Basic Research Program, SAIC-Frederick, Inc., Center for Cancer Research Nanobiology Program, Center for Cancer Research, NCI-Frederick, Frederick, Maryland 21702. Received June 23, 2007; Revised Manuscript Received August 27, 2007

Here, we describe a new method for the bioconjugation of a nonglycoprotein with biomolecules. Using polypeptide-α-*N*-acetylgalactosaminyltransferase II (ppGalNAc-T2), we transfer a C2-modified galactose that has a chemical handle, such as ketone or azide, from its respective UDP-sugars to the Ser/Thr residue(s) of an acceptor polypeptide fused to the nonglycoprotein. The protein with the modified galactose is then coupled to a biomolecule that carries an orthogonal reactive group. As a model system for the nonglycoprotein, we engineered glutathione-*S*-transferase (GST) protein with a 17-amino-acid-long fusion peptide at the C-terminal end that was expressed as a soluble protein in *E. coli*. The ppGalNAc-T2 protein, the catalytic domain with the C-terminal lectin domain, was expressed as inclusion bodies in *E. coli*, and an *in vitro* folding method was developed to produce milligram quantities of the active enzyme from a liter of bacterial culture. This ppGalNAc-T2 enzyme transfers from the UDP-sugars not only GalNAc but also C2-modified galactose with a chemical handle to the Ser/Thr residue(s) in the fusion peptide. The chemical handle at the C2 of galactose is used for conjugation and assembly of bionanoparticles and preparation of immuno-liposomes for a targeted drug delivery system. This novel method enables one to glycosylate, using ppGalNAc-T2, the important biological nonglycoproteins, such as single-chain antibodies, growth factors, or bacterial toxins, with an engineered 17-residue peptide sequence at the C-terminus of the molecule, for conjugation and coupling.

Conjugation of monoclonal antibodies with toxins, drugs, and radioisotopes is becoming a new strategy in the diagnosis and treatment of cancer (*1*). A number of such immuno-conjugates are being used to treat cancer (*2–4*). Various methods are being used with mixed success in conjugating antibodies with the cargo molecule. Often, the primary amine groups present on the surface of the protein molecule are used for conjugation; however, since every lysine residue present on the protein molecule would be reactive, this method results in undesirable heterogeneous conjugation and even loss of antibody activity (*5, 6*). Alternatively, the free Cys residue, either naturally present or engineered in the protein molecule, is widely used for conjugation. Since the freely exposed Cys residue is highly reactive in basic pH, these protein molecules require special handling (*7–9*). It has long been demonstrated that the sugar moieties present on the glycoproteins, such as IgG, can be used as a chemical handle for such conjugation (*10–14*). However, the heterogeneous nature of the glycan moiety on the recombinant glycoprotein causes poor coupling. We have recently developed a unique conjugation method that utilizes the *N*-acetylglucosamine residue, (GlcNAc), which is present at the nonreducing end of the glycans of glycoproteins (*15–17*). In this scheme, using the β1,4-galactosyltransferase mutant enzyme, Y298L-Gal-T1, we enzymatically transfer the 2-acetonyl-2-deoxy-galactose (2-keto-Gal) sugar, which has a unique chemical handle, to the GlcNAc residue of the glycoprotein. After the transfer of the sugar residue, this chemical handle can be used for selective conjugation with biologically important molecules (*15, 16*). Using this method, we have shown that even the *N*-glycan moiety of the IgG molecule can be used as the substrate for the transfer of the 2-keto-Gal sugar by the mutant Y298L-Gal-T1 (*17*). However, this method requires the presence of a free GlcNAc moiety on the nonreducing end of the glycan chain of the glycoprotein and cannot be used for nonglycoproteins, such as single-chain antibodies or bacterial toxins expressed in *E. coli*.

Herein we describe a method that takes advantage of the polypeptide-α-*N*-acetylgalactosaminyltransferase enzyme (ppGalNAc-T), which transfers the *N*-acetylgalactosamine sugar (GalNAc) from UDP-GalNAc to Thr/Ser residues on an acceptor polypeptide that is at least 11 amino acids long (*18*). We have engineered an acceptor polypeptide substrate as a fusion peptide at the C-terminus of a nonglycoprotein of interest and used this fusion peptide moiety as an acceptor substrate for the ppGalNAc-T in the transfer of GalNAc residue, thus converting the nonglycoprotein to a glycoprotein. Interestingly, previous *in vivo* studies have shown that ppGalNAc-T can also transfer GalNAc analogue sugars with a unique chemical handle, such as GalNAz, to the acceptor polypeptide (*19*). We show here that the ppGalNAc-T enzyme can also transfer 2-keto-Gal from its UDP-derivative to the acceptor polypeptide. Therefore, it is possible to glycosylate a nonglycoprotein using ppGalNAc-T with a modified sugar carrying a unique chemical handle that can be used for conjugation. Furthermore, in the present study, we have expressed the soluble form of ppGalNAc-T2 in *E. coli* as inclusion bodies and developed an *in vitro* folding method to make large quantities of active ppGalNAc-T2. We have used glutathione-*S*-transferase (GST) protein as a model system for engineering, at its C-terminus, the fusion peptide sequence with a single Thr residue, which is the acceptor substrate for ppGalNAc-T2. We show that ppGalNAc-T2 transfers not only GalNAc or GalNAz, but also 2-keto-Gal, to the single Thr

* Corresponding author. Structural Glycobiology Section, CCRNP, CCR, NCI-Frederick, Building 469, Room 221, Frederick, MD 21702. Phone: (301) 846-1934. Fax: (301) 846-7149. E-mail: qasba@helix.nih.gov.

† Structural Glycobiology Section.

‡ Basic Research Program.

10.1021/bc7002346 Not subject to U. S. Copyright. Published 2007 by American Chemical Society
Published on Web 10/23/2007

residue present in the peptide tag of the GST-tag fusion protein, demonstrating that this method can be used for glycosylating nonglycoproteins, such as single-chain antibodies (scFv), bacterial toxins, and so forth.

EXPERIMENTAL PROCEDURES

Polypeptide-α-*N*-acetylgalactosaminyltransferase-2 Gene Construction and Expression in *E. coli.* The human polypeptide-α-*N*-acetylgalactosaminyltransferase-2 (ppGalNAc-T2) clone (BC041120) was obtained from Open Biosystems. The C-terminal His tag carrying the catalytic and lectin domains of ppGalNAc-T2, coding residues 60 to 583 of the protein, were PCR amplified using the following primers with *Bam*HI and *Eco*RI restriction enzyme sites (shown in italics) at their 5′ terminal: (1) CGC*GGATCC*CGCG GCACAAAGCATGGAGAC-CCTCCCTCCAGGGAAA and (2) GCGCGC C*GAATTC*G-GTCCCTGCTGCAGGTTGAGCGTGAACTTTCCA CTGCTG.

The PCR-amplified product was digested with *Bam*HI and *Eco*RI restriction enzymes and ligated with the pET23a vector digested with the same enzymes. The ligated vector was transfected into XL2 supercompetent cells. The ampicillin-resistant clones were screened for the presence of the ppGalNAc-T2 gene in their plasmid DNA between their *Bam*HI and *Eco*RI restriction sites. The positive clones were sequenced and transfected into Rosetta (DE3) LysS competence cells for the expression of the protein.

In Vitro* Folding of Inclusion Bodies of the ppGalNAc-T2 Protein Produced in *E. coli. The Rosetta (DE3) LysS cells containing the ppGalNAc-T2 cDNA sequence in the pET23a vector were grown to an optical density of 0.7–0.8 and then induced with IPTG. The inclusion bodies were purified from the bacterial pellet as described earlier (*20*). From 1 L of bacterial culture, 60–70 mg of protein were obtained as inclusion bodies. The *in vitro* folding of ppGalNAc-T2 was carried out in a way similar to that of β4Gal-T1 (*20*), with a few modifications. Typically, 100 mg of sulfonated protein were folded for 48 h in 1 L of folding solution that contained oxido-shuffling agents, 500 mM arginine, 10% glycerol, and 10 mM lactose. The presence of glycerol and lactose in the folding solution enhances the folding efficiency of ppGalNAc-T2. After refolding the protein, the folding solution was extensively dialyzed against water. During dialysis, the misfolded protein precipitated out, while the folded protein remained soluble. The soluble protein was concentrated on an Amicon stirred cell using a YM-10 membrane, and further purified on a Ni-column. There was no significant loss of protein observed during concentration and Ni-column purification steps, as estimated by measuring the protein concentration using the Bradford method (BioRad). Nearly 2 mg of folded ppGalNAc-T2 protein wais obtained from 1 L of folding solution. Using the method described previously (*21*), the purified protein was tested for its catalytic activity using a 13-amino-acid peptide, PTTDSTTPAPTTK, as an acceptor. The specific activity of the refolded ppGalNAc-T2 was 20 pmol/min/ng protein.

Construction and Expression of GST Protein with the C-terminal 17-Amino-Acid Glycosylation Tag. The GST gene from the pGEX-2T vector (General Electric (GE)) was amplified first with the 5′-primer and 3′-primer-1, and purified on a low-melt agarose gel. The purified GST gene was further amplified with the 5′-primer and 3′-primer-2, which coded for a 17-amino-acid peptide, GAGGPIMAAATPAPAAK, as a C-terminal extension of GST following a thrombin cleavage site.

5′-Primer: CGC*GGATCC*GCGTCCCCTATACTAGGT-TATTGGAAAATTAAGGGCCTTGTG.

3′-Primer-1: CGCCGGCGTAGCAGCGGCCATGATGGGTC-CGCCGGCTCCACGCGGAACCAGATCCGA.

3′-Primer-2: CCG*GAATTC*CGGCTACTTCGCCGCCG-GCGCCGGCGTAGCAGCGGCCATGATGGG.

The final PCR-amplified DNA fragment was digested with *Bam*HI and *Eco*RI enzymes and ligated with digested pET23a vector with the same enzymes. The ligated vector was transfected into XL2 competent cells. The ampicillin-resistant clones were screened for the presence of the full GST gene between the *Bam*HI and *Eco*RI sites in their plasmid DNA. The positive plasmid DNA was transfected into Rosetta (DE3) LysS cells. The GST-tag protein was expressed as a soluble protein in *E. coli* and purified on a glutathione affinity column (GE). Fifty to sixty milligrams of purified protein were obtained from 1 L of bacterial culture. The C-terminal glycosylation peptide tag was released from a 5 μg protein by thrombin cleavage and analyzed by mass spectrometry. The other GST-tag fusion proteins containing the multiple glycosylation sites were also made using a method similar to that described above. All of the oligonucleotides were synthesized by the Molecular Technology Branch, NCI-Frederick, Frederick, MD.

Glycosylation of the GST-Tag with the *in Vitro* Folded ppGalNAc-T2. Five micrograms of GST-tag protein was incubated overnight at 37 °C with 50 ng of ppGalNAc-T2 in the presence of 25 mM Tris-HCl (pH 8.0), 10 mM $MnCl_2$, and 0.5 mM UDP-sugar (UDP-GalNAc, UDP-2-keto-Gal, or UDP-GalNAz) in a total volume of 25 μL. To remove all of the reaction buffer, the glycosylated GST-tag protein was centrifuged on a centricon filter (10 K molecular weight cutoff) and washed twice with deionized water. The salt-free glycosylated GST-tag was recovered in 20 μL of water, and an aliquot (4 μL) was cut with human thrombin and analyzed by mass spectrometry (MALDI-TOF).

Biotinylation of the Glycosylated GST-Tag and Gel Electrophoresis. The desalted glycosylated GST-tag protein with 2-keto-Gal was biotinylated in 60 μL volume containing 75 mM sodium acetate buffer (pH 5.0) and 3 mM *N*-aminoxymethylcarbonylhydrazino-D-biotin (ARP, Dojindo Laboratories). The reaction was carried out overnight at room temperature. The biotinylated sample was desalted using a centricon filter (10 K molecular weight cutoff) and recovered in 20 μL of water. An aliquot of the sample was cut with thrombin and analyzed using mass spectrometry. The biotinylated proteins uncut and cut with thrombin were analyzed by Western blotting, and they were detected by chemiluminescence using streptavidin–horseradish peroxidase (HRP), as described previously (*17*).

Equal amounts of thrombin-cleaved and -uncleaved GalNAz glycosylated GST-tags were biotinylated using Click-iT Biotin Glycoprotein Detection Kit from Invitrogen, following the manufacturer's instructions. The reaction was carried out for 1 h at room temperature. Since biotinylation was carried out using the unknown components supplied by the manufacturer, it was not possible to simply desalt the protein using centricon filters. Therefore, the mass spectrometry analysis could not be carried out. However, because the Click-iT reaction buffer did not interfere with the protein gel electrophoresis, Western blotting was carried out, and the biotinylated protein was detected by chemiluminescence using HRP, as described earlier (*17*). All of the mass spectroscopic analyses were carried out in the Protein Chemistry Laboratory, NCI-Frederick, Frederick, MD.

RESULTS AND DISCUSSION

The glycoconjugation of a nonglycoprotein was afforded by engineering a C-terminal fusion peptide sequence containing a Thr/Ser residue in the nonglycoprotein (Figure 1a). The fusion peptide can then be glycosylated with ppGalNAc-T, which transfers GalNAc from UDP-α-GalNAc to the Thr/Ser residue

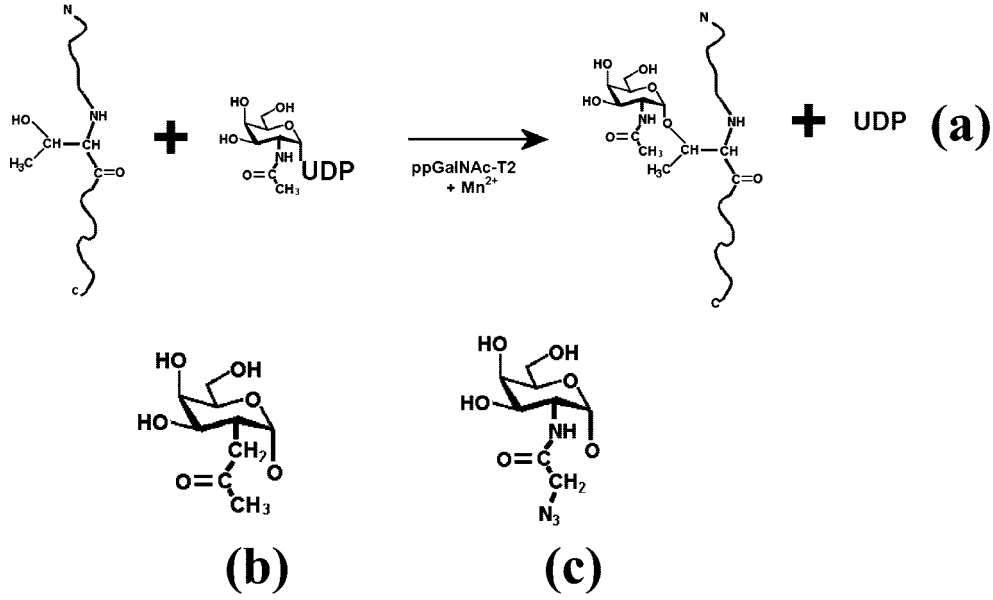


Figure 1. Catalytic reaction of polypeptide-α-*N*-acetylgalactosaminyltransferase (ppGalNAc-T). (a) In the presence of Mn^{2+}, the enzyme transfers GalNAc sugar from its UDP-α-GalNAc donor substrate to the side chain hydroxyl group of the Thr/Ser residue present in a polypeptide acceptor substrate. Here, we show that in addition to transferring GalNAc, the enzyme can transfer (b) 2-keto-Gal and (c) GalNAz from the respective UDP-sugars.

in the fusion peptide. Furthermore, ppGalNAc-T is known to transfer GalNAc analogues with a unique chemical handle (Figure 1b and c) such as the 2-azido-acetyl group. The glycosylated glycoprotein with the modified sugar can then be conjugated through this unique chemical handle to a bioactive molecule, such as immunoglobulin, toxins, and so forth. Although there are 17 homologues in the ppGalNAc-T enzyme family in humans, any one of them, with its preferred acceptor substrate, may be used. Here, we have used ppGalNAc-T2 since its three-dimensional crystal structure and enzymology are well known from previous studies (*21*). We have used GST as a model for a nonglycoprotein because it has been used for the expression of a number of fusion recombinant proteins at its C-terminal end. Here, we have expressed GST-tag protein with a 17-amino-acid fusion peptide with one or many Thr residues at the C-terminal end. These peptides were designed on the basis of a 13-amino-acid peptide, PTTDSTTPAPTTK, known as EA2, which was used for enzymology and crystallographic studies with ppGalNAc-T2 (*21*) and ppGalNAc-T10 (*22*). In the crystal structure of the complex of ppGalNAc-T2 with EA2 acceptor peptide (*21*), only the nanopeptide, STTPAPTTK, was clearly observed, while the N-terminal tetra-peptide, PTTD, was considered to be disordered (*21*). The Thr residue found in the TPAP peptide sequence was found in the ppGalNAc-T2 acceptor binding site, while the remaining N- and C-terminal peptide residues were bound in the extended peptide binding site (*21*). On the basis of these observations, we engineered the peptide tag, SGGPIMDSTTPAPTTK, following the thrombin protease binding sequence found at the C-terminal end of the GST protein (Figure 1a). The hexa-peptide, SGGPIM, was used as a spacer between the protease site and the ppGalNAc-T2 binding peptide, DSTTPAPTTK (Figure 1c). When designing a tag with a single Thr residue, we kept the Thr residue that was found in the acceptor binding site of the ppGalNAc-T2, while the remaining residues were mutated to alanine, thus resulting in a deca-peptide, AAATPAPAAK.

ppGalNAc-T2 Expression in *E. coli* and the *in Vitro* Folding of the Inclusion Bodies. Although the ppGalNAc-T2 enzyme, with a stem region followed by the catalytic domain (CD) and lectin domain (LD), has been expressed previously in various expression systems producing an active soluble protein (*21*), the expression in *E. coli* has produced inactive inclusion bodies. The ppGalNAc-T2 expressed in yeast showed no *N*-glycosylation in the crystal structure and was considered a perfect candidate for expression in *E. coli*, which could be folded from inclusion bodies. Therefore, an *in vitro* folding method was developed to generate active protein. Previously in our laboratory, we have used the S-sulfonation method to produce large quantities of β-1,4-galactosyltransferase (β4Gal-T1) from inclusion bodies (*20*). An active ppGalNAc-T2 can be obtained using this method, albeit at low efficiencies. However, we found that including 10% glycerol and 10 mM lactose during *in vitro* folding increases the folding efficiency of ppGalNAc-T2 to nearly 2 mg of purified protein from 1 L of folding solution containing 100 mg of sulfonated protein obtained from 1.5 L of bacterial culture (Figure 2a and b). The specific activity of the *in vitro*-folded enzyme (20 pmol/min/ng) is comparable to that of the same protein expressed in other systems (*21*). The *in vitro*-folded ppGalNAc-T2 has been used in the experiments described in this article.

Recently, ppGalNAc-T1 has been used for the glycosylation of the nonglycoform of muc1 protein expressed in *E. coli* (*23*). Similarly, ppGalNAc-T2 has been used to construct the *O*-mucin structure on the nonglycoform of the interferon-alpha2b (IFN-alpha2b) expressed in *E. coli* (*24*). Thus, *in vitro* glycosylation of the nonglycoform of glycoproteins is becoming increasingly important. The *in vitro* folding method for ppGalNAc-T2 from inclusion bodies described here shows that large quantities of these glycosyltransferases can be generated from *E. coli* and can be used for such applications as well.

Glycosylation of GST-Tag Protein. GST protein with a 17-amino-acid tag at the C-terminus, following a thrombin cleavage site, has been successfully expressed as a soluble protein from *E. coli* and purified on a glutathione column. First, we expressed the tag with an oligopeptide sequence, SGGPIMDSTTPAPTTK, similar to the one used in the enzyme kinetic studies of ppGalNAc-T2 (*21*). After completion of the enzyme reaction, the 17-amino-acid tag was released by thrombin digestion and analyzed by mass spectrometry (MALDI-TOF) (Figure 3a). The MS analysis of the glycosylated peptide tag showed that it exists as a mixture of three to four glycosylated peptides, suggesting that the four Thr residues present in the peptide tag have been

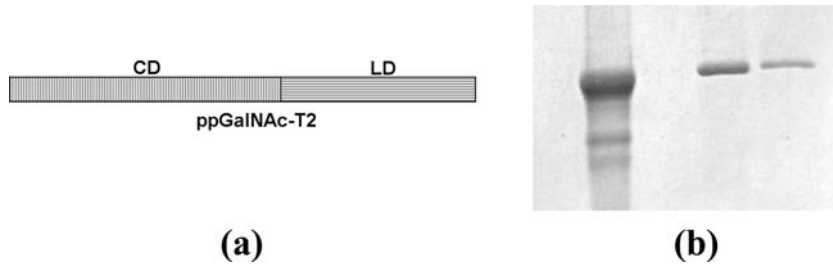


Figure 2. SDS–gel analysis of the inclusion bodies and *in vitro*-folded protein of ppGalNAc-T2. (a) The soluble domain of ppGalNAc-T2, which contains a stem region, catalytic domain (CD), and the lectin domain (LD), is expressed in *E. coli* as inclusion bodies. We have used an *in vitro* folding method to generate active protein. (b) SDS–gel analysis of the inclusion bodies (left lane) and the purified *in vitro* folded active proteins; 1 μg and 0.5 μg, middle and right lanes, respectively.

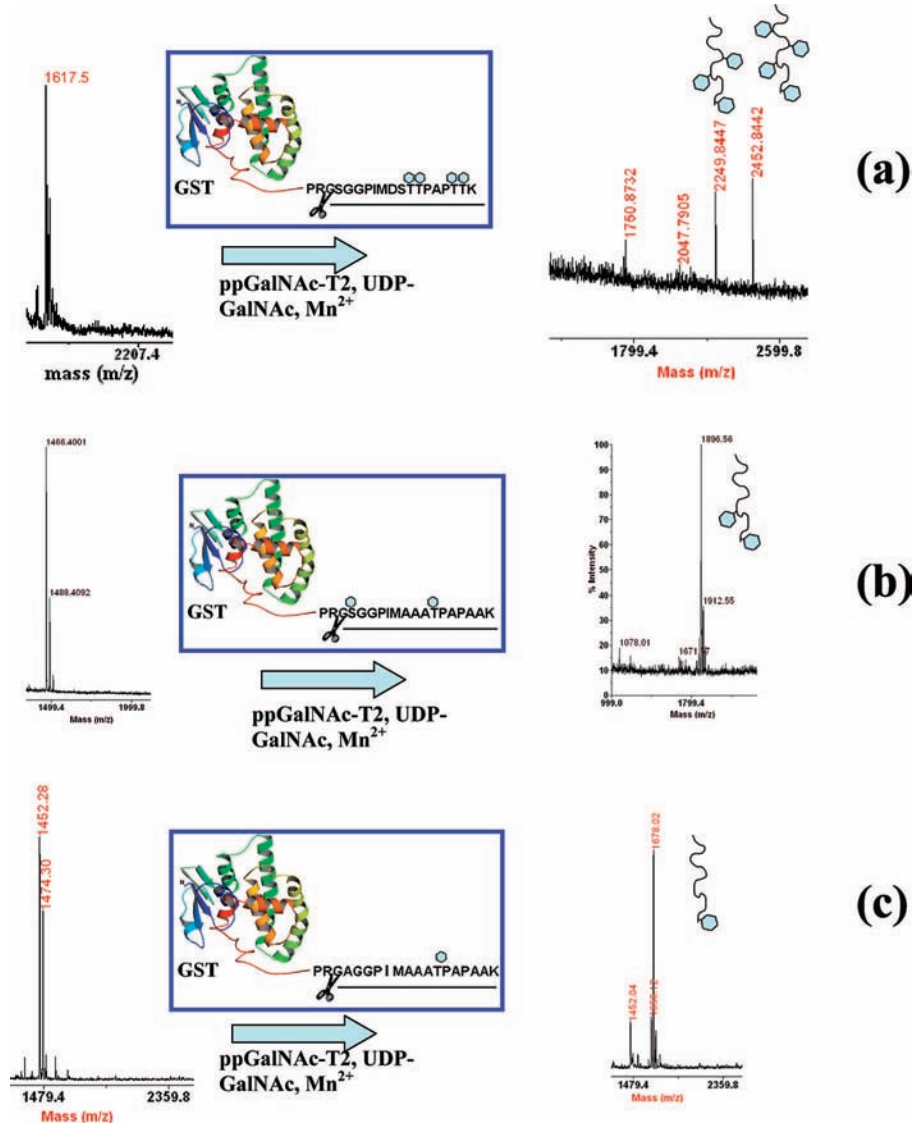


Figure 3. GalNAc transfer by the *in vitro*-folded ppGalNAc-T2 enzyme to GST-tag protein. The glutathione-*S*-transferase protein (shown in the cartoon diagram insert) is expressed with 17 amino acids (in single-letter code) as a fusion peptide at its C-terminus following the thrombin site (RG), shown as cutting scissors. The blue hexagons indicate the potential O-glycosylation residues. The fusion peptides are designed on the basis of the acceptor substrates of ppGalNAc-T2 (*21*). The mass spectrum (MALDI-TOF) of the thrombin-cleaved, nonglycosylated, and glycosylated peptides (panels (a), (b), and (c)) are shown in the left and right side of the arrow, respectively. (a) Although the fusion-peptide tag contains four Thr residues and two Ser residues, the overnight incubation of the GST-tag protein with the ppGalNAc-T2 seems to glycosylate a maximum of four glycosylation sites. (b) When one Thr and one Ser residue are present, they both have been found to be glycosylated. (c) The presence of one Thr residue results in a single glycosylation of the peptide tag; thus, this tag is used for further studies.

glycosylated. Since ppGalNAc-T2 prefers to transfer GalNAc to a Thr residue rather than to a Ser residue, it is expected that all the possible Thr residues present in an acceptor peptide would be glycosylated first, prior to any Ser residues. On the contrary, the redesigned peptide tag, SGGPIMAAATPAPAAK, with one Thr and one Ser residue, was found to have glycosylated with two sugars, suggesting that, in addition to the glycosylation of the single Thr residue, the less-preferred Ser residue is also

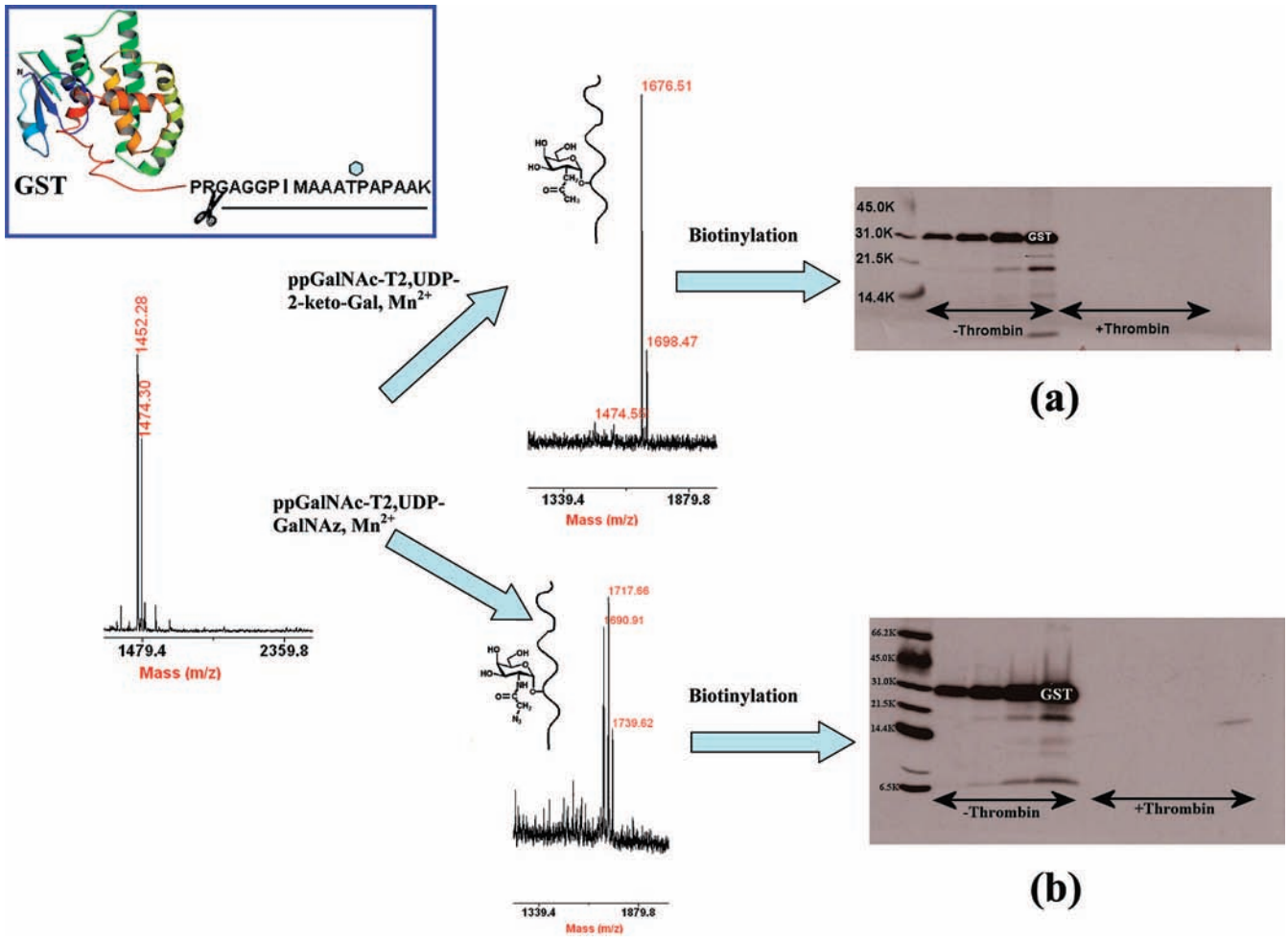


Figure 4. 2-Keto-Gal and GalNAz transfer by the *in vitro*-folded ppGalNAc-T2 enzyme to GST-tag protein. The GST-tag protein with a single Thr residue in its fusion peptide has been used for the transfer of (a) 2-keto-Gal and (b) GalNAz sugars from their respective UDP-derivatives. The mass spectrum (MALDI-TOF) of the nonglycopeptide and glyco-peptide released by thrombin digestion are shown on the left and right sides of the arrows, respectively. The glycosylated protein is biotinylated using the biotin-carrying, appropriate orthogonal reactive group to react with the ketone or azide moiety of the modified sugars. The proteins in the Western blotting were visualized using the streptavidin-HRP chemiluminescence technique. A strong luminescence is observed only for the biotinylated proteins with the fusion peptide (− thrombin), while in the proteins without the fusion peptide (+ thrombin), no trace of chemiluminescence has been observed. This observation indicates that the biotinylation takes place only at the sugar moiety present in the fusion peptide tag.

glycosylated (Figure 3b). The glycosylation of the Ser residue in the second tag, but not in the first tag, could be due to the experimental condition used for glycosylation. Under this condition, the glycosylation of more than three Thr residues in the first tag has been observed (Figure 3a); since the second tag has only one Thr residue, it is not surprising to find that in addition to this single Thr residue, the remaining single Ser residue, though less preferred, is also glycosylated. Mutating the Ser residue to Ala in the peptide tag produced the tagged peptide sequence AGGPIMAATPAPAAK with only one Thr residue, which underwent glycosylation at only one site (Figure 3c). When this Thr was mutated to the Leu residue (AGGPI-MAALPAPAAK), no glycosylation was observed, confirming that the glycosylation takes place at the unique Thr residue (not shown). Although a number of peptides have been previously tested as the acceptor substrates for the ppGalNAc-T2, none of them are presented as a fusion peptide. Thus, these glycosylation studies confirm that the fusion peptide tag can be glycosylated at one or more sites with a Thr, or even Ser, residue present in the fusion peptide tag.

It has been previously shown that ppGalNAc-T enzymes in the live cell can incorporate GalNAz, a modified sugar resembling GalNAc, to the glycan chains (*19*). The incorporation of such unnatural monosaccharides such as azides, which bear a uniquely reactive chemical handle, has enabled the selective labeling of glycoconjugates with a variety of reagents (*19*). Since these studies were carried out *in vivo*, it was not possible to identify the specific ppGalNAc-T that is responsible for the transfer of GalNAz among the 17 family members of ppGalNAc-Ts present in humans. We used ppGalNAc-T2 to transfer a modified galactose that resembles GalNAc, such as 2-keto-galactose or GalNAz, to the fusion peptide in the GST-tag protein. In the present study, we have used the GST-tag protein with only one Thr residue present in its fusion peptide tag.

The catalytic reaction using UDP-α-2-keto-Gal or UDP-α-GalNAz as donor substrates was carried out under the same conditions as the those used for UDP-GalNAc. After catalysis, the thrombin digestion released the glycopeptide that showed the presence of one sugar moiety in the fusion peptide, as indicated by mass spectrometry (Figure 3a). This result suggested that the Thr residue is glycosylated by the ppGalNAc-T2 with modified sugars. To detect the presence of the unique chemical handle, such as the ketone or the azide in the galactose of the peptide tag of GST-tag protein, the samples were biotinylated by appropriate chemical reactions. The biotinylated samples with and without the peptide tag were then subjected to Western blotting, and the proteins were detected by the chemiluminescence technique (*16*, *17*) (Figure 4). The chemi-

luminescence observed only from the protein with the attached peptide tag clearly indicated that the biotinylation was done on the modified sugars of the peptide tag and not on the GST protein, whereas the thrombin-cleaved protein afforded no observable chemiluminescence. Thus, these studies show that ppGalNAc-T2 can efficiently transfer the modified galactose from its UDP derivatives to the fusion peptide and that the chemical handle present in the glycan moiety is readily available for further modification such as biotinylation.

Applications in Glycoconjugation. We have previously shown that the mutant β4Gal-T1 enzyme, Y289L-Gal-T1, can transfer GalNAc from UDP-GalNAc as efficiently as galactose (Gal) from UDP-Gal to the GlcNAc residue present at the nonreducing end (*15*). In addition, we have found that it can also transfer modified sugars, such as 2-keto-galactose, from their UDP-derivative, and this catalytic activity was successfully applied in detecting *O*-GlcNAc modification in the proteins (*16*). The same technique was expanded to other glycoproteins, such as ovalbumin and immunoglobulin IgG, with free GlcNAc at the nonreducing end of their *N*-glycans (*17*). On the basis of the results of these techniques, it was proposed that two glycoproteins with modified sugars with a unique chemical handle such as 2-keto-Gal may be conjugated with chemical cross-linkers, thus enabling the design of novel immunotoxins and MRI contrast agents (*25*). In the present study, we have shown that nonglycoproteins can be glycosylated by engineering a peptide sequence in the protein that can be glycosylated with the modified sugar so that they can also be cross-linked to the other glycoproteins such as IgG with similar modified sugars. Thus, the present study extends our previous technique by showing that an engineered nonglycoprotein with a peptide tag at its C-terminal end can be glycosylated with a modified sugar and coupled to a biomolecule that carries an orthogonal reactive group, making the method very useful in many nanobiological applications. For example, single-chain antibodies (scFv), which are easily expressed in large amounts in *E. coli* as soluble proteins, are increasingly used for immunotherapy compared to their full-length IgG counterparts (*26*). A fusion peptide attached at the C-terminal end of the scFv molecule that can be glycosylated with a modified sugar at a unique site, by the method described here, can be conjugated next with a biomolecule having a corresponding reactive group, such as aminooxy or alkynes, for the assembly of immunoliposome (*27*) or for applications in immunotherapy and targeted drug delivery (*25, 26*).

Although the glycosylation of a surface Thr/Ser residue on the protein by the ppGalNAc-T is possible, the crystal structure of the ppGalNAc-T2 suggests that such a Thr/Ser residue not only has to be present in at least 11-amino-acid-long peptides in the extended conformation but also has to be well exposed to the solvent region. Since cytoplasmic proteins, in contrast to cell-surface proteins, do not get *O*-GalNAc modification, such peptide sequences may not be present on these proteins. However, proteins with a long flexible region that has an accessible Thr/Ser residue may be the candidate acceptors for such undesired glycosylation. In such cases, the O-glycosylation site itself-can be used for glyco-conjugation using modified GalNAc, such as 2-keto-Gal or GalNAz. Although immunogenicity due to the C-terminal tag or the presence of modified sugar is a concern, it may not be well exposed to the environment because of the presence of the bulky conjugating chemical moiety, which may reduce the immunogenic effect. However, such general concerns are associated with most conjugation techniques.

Other recent methods include site-directed introduction and chemoselective ligation of cysteine residues to convert a nonglycoprotein to a glycoprotein (*28*) and site-directed introduction of azido/alkynyl-tagged methionine analogues into proteins (*29*). However, the former method needs special handling of the protein to prevent its free Cys residue from undergoing undesired oxidation, while in the latter method, all the of methionine residues present in the protein are modified. Recently, Carrica et al. (*30*) have described a method for introducing genetically encoded aldehydes at either one of the terminal ends of proteins, which then can be used for conjugation. The present technique demonstrates the fusion of a peptide tag with a single O-glycosylation site, which can be glycosylated with a stable modified sugar moiety with a chemical handle that can be used for linking various biomolecules. These biomolecules, in turn, may be used to design novel nanoparticles for the development of a targeted drug delivery system.

ACKNOWLEDGMENT

We thank Dr. John T. Simpson, Protein Chemistry Laboratory, NCI-Frederick for the mass spectroscopic analysis of the samples. We thank Dr. Linda Hsieh-Wilson, CalTech, for UDP-2-keto galactose; Drs. Tomomi Kubota and Hisashi Narimatsu for providing their ppGalNAc-T2 sample for comparison, and Drs. Maria Manzoni and Marta Pasek for discussions and comments on the manuscript. This project has been funded in part with Federal funds from the National Cancer Institute, National Institutes of Health, under contract No. N01-CO-12400. The content of this publication does not necessarily reflect the view or policies of the Department of Health and Human Services, nor does mention of trade names, commercial products, or organizations imply endorsement by the U.S. Government. This research was supported [in part] by the Intramural Research Program of the NIH, National Cancer Institute, Center for Cancer Research.

LITERATURE CITED

(1) Wu, A. M., and Senter, P. D. (2005) Arming antibodies: prospects and challenges for immunoconjugates. *Nat. Biotechnol. 23*, 1137–1146.

(2) Schrama, D., Reisfeld, R. A., and Becker, J. C. (2006) Antibody targeted drugs as cancer therapeutics. *Nature Rev. Drug Discovery 5*, 147–159.

(3) Lambert, J. M. (2005) Drug-conjugated monoclonal antibodiesfor the treatment of Cancer. *Curr. Opin. Pharmacol. 5*, 543–549.

(4) Garnett, M. C. (2001) Targeted drug conjugates: principles and progress. *Adv. Drug Delivery Rev. 53*, 171–216.

(5) Firestone, R. A., Willner, D., Hofstead, S. J., King, H. D., Kaneko, T., Braslawsky, G. R., Greenfield, R. S., Trail, P. A., Lasch, S. J., Henderson, A. J., Casazza, A. M., Hellström, K. E., and Hellström, I. (1996) Synthesis and antitumour activity of the immunoconjugate BR96-Dox. *J. Controlled Release 39*, 251–259.

(6) Dhawan, S. (2002) Design and construction of novel molecular conjugates for signal amplification (I): conjugation of multiple horseradish peroxidase molecules to immunoglobulin via primary amines on lysine peptide chains. *Peptides 23*, 2091–2098.

(7) Stimmel, J. B., Merrill, B. M., Kuyper, L. F., Moxham, C. P., and Hutchins, J. T. (2000) Site-specific conjugation of serine → cysteine variant monoclonal antibodies. *J. Biol. Chem. 275*, 30445–30450.

(8) Albrecht, H., Burke, P. A., Natarajan, A., Xiong, C. Y., and Kalicinsky, M. (2004) Production of soluble scFvs with C-terminal-free thiol for sitespecific conjugation or stable dimeric scFvs on demand. *Bioconjugate Chem. 15*, 16–26.

(9) Saito, G., Swanson, J. A., and Lee, K. D. (2003) Drug delivery strategy utilizing conjugation via reversible disulfide linkages: role and site of cellular reducing activities. *Adv. Drug Delivery Rev. 55*, 199–215.

(10) O'Shanessy, D. J., Dobersen, M. J., and Quarles, R. H. (1984) A novel procedure for labeling immunoglobulins by conjugation to oligosaccharide moieties. *Immunol. Lett. 8*, 273–277.

(11) O'Shanessy, D. J., and Quarles, R. H. (1987) Labeling of the oligosaccharide moieties of immunoglobulins. *J. Immunol. Methods 99*, 153–161.

(12) Rodwell, D., Alvarez, V. L., Lee, C., Lopes, A. D., Goers, J. W. F., King, H. D., Powsner, H. J., and McKearn, T. J. (1986) Site-specific covalent modification of monoclonal antibodies: in vitro and in vivo evaluations. *Proc. Natl. Acad. Sci. U.S.A. 83*, 2632–2636.

(13) Stan, A. C., Radu, D. L., Casares, S., Bona, C. A., and Brumeanu, T-D. (1999) Antineoplastic efficacy of doxorubicin enzymatically assembled on galactose residues of a monoclonal antibody specific for the carcinoembryonic antigen. *Cancer Res. 59*, 115–121.

(14) Qu, Z., Sharkey, R. M., Hansen, H. J., Shih, L. B., Govindan, S. V., Shen, J., Goldenberg, D. M., and Leung, S.-O. (1998) Carbohydrates engineered at antibody constant domains can be used for site-specific conjugation of drugs and chelates. *J. Immunol. Methods 213*, 131–144.

(15) Ramakrishnan, B., and Qasba, P. K. (2002) Structure-based design of beta 1,4-galactosyltransferase I (beta 4Gal-T1) with equally efficient N-acetylgalactosaminyltransferase activity: point mutation broadens beta 4Gal-T1 donor specificity. *J. Biol. Chem. 277*, 20833–20839.

(16) Khidekel, N., Arndt, S., Lamarre-Vincent, N., Lippert, A., Poulin-Kerstien, K. G., Ramakrishnan, B., Qasba, P. K., and Hsieh-Wilson, L. C. (2003) A chemoenzymatic approach toward the rapid and sensitive detection of O-GlcNAc posttranslational modifications. *J. Am. Chem. Soc. 125*, 16162–16163.

(17) Boeggeman, E., Ramakrishnan, B., Kilgore, C., Khidekel, N., Hsieh-Wilson, L. C., Simpson, J. T., and Qasba, P. K. (2007) Direct identification of nonreducing GlcNAc residues on N-glycans of glycoproteins using a novel chemoenzymatic method. *Bioconjugate Chem. 18*, 806–814.

(18) Ten Hagen, K. G., Fritz, T. A., and Tabak, L. A. (2003) All in the family: the UDP-GalNAc:polypeptide N-acetylgalactosaminyltransferases. *Glycobiology 13*, 1R–16R.

(19) Dube, D. H., Prescher, J. A., Quang, C. N., and Bertozzi, C. R. (2006) Probing mucin-type O-linked glycosylation in living animals. *Proc. Natl. Acad. Sci. U.S.A. 103*, 4819–4824.

(20) Boeggeman, E. E., Ramakrishnan, B., and Qasba, P. K. (2003) The N-terminal stem region of bovine and human beta1,4-galactosyltransferase I increases the in vitro folding efficiency of their catalytic domain from inclusion bodies. *Protein Expression Purif. 30*, 219–229.

(21) Fritz, T. A., Raman, J., and Tabak, L. A. (2006) Dynamic association between the catalytic and lectin domains of human UDP-GalNAc:polypeptide alpha-N-acetylgalactosaminyltransferase-2. *J. Biol. Chem. 281*, 8613–8619.

(22) Kubota, T., Shiba, T., Sugioka, S., Furukawa, S., Sawaki, H., Kato, R., Wakatsuki, S., and Narimatsu, H. (2006) Structural basis of carbohydrate transfer activity by human UDP-GalNAc: polypeptide alpha-N-acetylgalactosaminyltransferase (pp-GalNAc-T10). *J. Mol. Biol. 359*, 708–727.

(23) Freire, T., Lo-Man, R., Piller, F., Piller, V., Leclerc, C., and Bay, S. (2006) Enzymatic large-scale synthesis of MUC6-Tn glycoconjugates for antitumor vaccination. *Glycobiology 16*, 390–401.

(24) DeFrees, S., Wang, Z. G., Xing, R., Scott, A. E., Wang, B. J., Zopf, D., Gouty, D. L., Sjoberg, E. R., Panneerselvam, K., Brinkman-Van der Linden, E. C., Bayer, R. J., Tarp, M. A., and Clausen, H. (2006) GlycoPEGylation of recombinant therapeutic proteins produced in *Escherichia coli*. *Glycobiology 16*, 833–843.

(25) Qasba, P. K., Ramakrishnan, B., and Boeggeman, E. (2006) Mutant glycosyltransferases assist in the development of a targeted drug delivery system and contrast agents for MRI. *Am. Assoc. Pharm. Soc. J. 8*, 190–195.

(26) Hollinger, P., and Hudson, P. J. (2005) Engineered antibody fragments and the rise of single domains. *Nat. Biotechnol. 23*, 1126–1136.

(27) Park, J. W., Banz, C. C., and Martin, F. J. (2004) Future directions of liposome- and immunoliposome-based cancer therapeutics. *Semin. Oncol. 31*, 196–205.

(28) Davis, B. G., Lloyd, R. C., and Bryan Jones, J. (1998) Controlled site-selective glycosylation of proteins by a combined site-directed mutagenesis and chemical modification approach. *J. Org. Chem. 63*, 9614–9615.

(29) Kiick, K. L., Saxon, E., Tirrell, D. A., and Bertozzi, C. R. (2002) Incorporation of azides into recombinant proteins for chemoselective modification by the Staudinger ligation. *Proc. Natl. Acad. Sci. U.S.A. 99*, 19–24.

(30) Carrico, I. S., Carlson, B. L., and Bertozzi, C. R. (2007) Introducing genetically encoded aldehydes into proteins. *Nat. Chem. Biol. 3*, 321–322.

BC7002346

Electrochemically Controllable Conjugation of Proteins on Surfaces

Paula M. Mendes,*[,†,||] Karen L. Christman,[†] Puru Parthasarathy,[‡] Eric Schopf,[‡] Jianyong Ouyang,[§] Yang Yang,[§] Jon A. Preece,[⊥] Heather D. Maynard,[†] Yong Chen,[‡] and J. Fraser Stoddart*[,†]

California NanoSystems Institute and Department of Chemistry and Biochemistry, Department of Mechanical and Aerospace Engineering, and Department of Materials Science and Engineering, University of California, Los Angeles, 405 Hilgard Avenue, Los Angeles, CA 90095-1569 and Department of Chemical Engineering, and School of Chemistry, The University of Birmingham, Edgbaston, Birmingham, B15 2TT, U.K. Received June 21, 2007; Revised Manuscript Received September 5, 2007

The rational design of surfaces for immobilization of proteins is essential to a variety of biological and medical applications ranging from molecular diagnostics to advanced platforms for fundamental studies of molecular and cell biology. We have developed an advanced electrochemically based approach for site-selective and reaction-controlled immobilization of proteins on surfaces. When a molecular monolayer of 4-nitrothiophenol on gold electrode surfaces is reduced electrochemically in a selective fashion at its nitro groups, to afford amino groups by potentiometric scans, the amine can be employed to orchestrate the immobilization of proteins to the surface. This protein immobilization strategy could allow one to fabricate intricate protein structures on surfaces for addressing fundamental and applied problems in biology and medicine.

INTRODUCTION

The controlled immobilization of proteins on surfaces is of paramount importance for a wide variety of applications, ranging from the development of model substrates for mechanistic studies of cell behavior to high-throughput protein assays for drug discovery, clinical diagnostics, and proteomics (*1–7*). In particular, stimulated by the success of DNA arrays in genomics (*1*), substantial scientific and commercial interest has been generated in the use of protein arrays as tools for proteomics (*1, 2*). However, proteins are much more chemically and structurally diverse than nucleic acids, making them intrinsically more complicated to be immobilized on surfaces (*1, 2*). Other difficulties result from the intrinsic fragility of proteins, which have modest conformational stability and can be damaged upon surface immobilization (*1, 2*). Moreover, proteins can adhere and adsorb to most surfaces through a variety of mechanisms (electrostatic interaction, hydrogen bonding, hydrophobic interactions, and/or a combination of these), resulting in nonspecific protein binding (*8*).

Therefore, a primary enabling technology is the ability of controlling the immobilization of proteins on surfaces while avoiding nonspecific protein binding and retaining protein native biological features and properties (*1–3, 5–7*). Molecular surface science has greatly contributed to the advancement of this technology by providing ideal platforms for bioengineering surfaces on a molecular level (*9–15*). For instance, self-assembled monolayers (SAMs), which form spontaneously by the adsorption of an active surfactant onto a solid surface, possess important properties of self-organization and adaptability to a number of technologically relevant surface substrates. The properties of a SAM (thickness, structure, surface energy, stability) can be easily controlled, and specific functionalities can also be introduced into the building blocks. For instance, SAMs of thiols on gold and triethoxysilanes on silicon dioxide (SiO_2) have been exploited (*6, 8, 16–18*) to provide the surfaces not only with active groups that interact with specific moieties of the protein to be immobilized, but also with protein-resistant groups such as poly(ethylene glycol) (PEG).

Proteins have been immobilized onto these surfaces by either adsorption of the proteins (*8*), molecular recognition between the proteins and immobilized ligands (*19*), or covalent coupling to the SAM surface (*16, 17*). The most common conjugation methods rely on the covalent attachment of proteins to "static" (*20*) surfaces chemically modified with different protein-reactive groups, including activated esters (*16*), aldehydes (*21*), or maleimides (*22–24*). On the other hand, strategies for "turning-on" protein reactive groups at SAM surfaces by an "on demand" surface reaction using an external stimulus have great potential as versatile platforms for protein immobilization. Similar strategies have been employed to immobilize urease onto a polymer film (*25*), as well as other biomolecules, such as DNA (*26*) and peptides (*27, 28*) on SAM surfaces, yet protein immobilization onto a SAM using this "on demand" surface reaction approach has not been previously demonstrated.

Here, we report an approach to control protein immobilization on surfaces based on SAMs that can switch from bio-inert to bioactive states in response to an applied electrical potential. The approach we have developed is based on an electrochemical reaction in which aromatic nitro (NO_2) groups, self-assembled on gold surfaces, can be chemically modified by a redox process to amino (NH_2) groups, which can then be used to orchestrate the immobilization of the proteins. Our strategy involves (Figure 1) five steps: (1) functionalization of the electrically addressable gold surfaces with NO_2-terminated SAMs; (2) spatially selective electrochemical reduction (*26, 29–31*) of the NO_2 groups

* Correspondence addresses: Dr. Paula M. Mendes, Department of Chemical Engineering, University of Birmingham, Edgbaston, Birmingham, B15 2TT (UK), Tel: Int. code +(121) 414-5343, Email: p.m.mendes@bham.ac.uk. Dr. J. Fraser Stoddart, Department of Chemistry and Biochemistry, University of California, Los Angeles, 405 Hilgard Avenue, Los Angeles, CA 90095-1569 (USA), Tel: Int. code +(310) 206-7078, Email: stoddart@chem.ucla.edu.

[†] California NanoSystems Institute and Department of Chemistry and Biochemistry, University of California, Los Angeles.

[‡] California NanoSystems Institute and Department of Mechanical and Aerospace Engineering, University of California, Los Angeles.

[§] California NanoSystems Institute and Department of Materials Science and Engineering, University of California, Los Angeles.

[⊥] School of Chemistry, The University of Birmingham.

[||] Present address: Department of Chemical Engineering, The University of Birmingham.

10.1021/bc7002296 CCC: $37.00 © 2007 American Chemical Society
Published on Web 10/26/2007

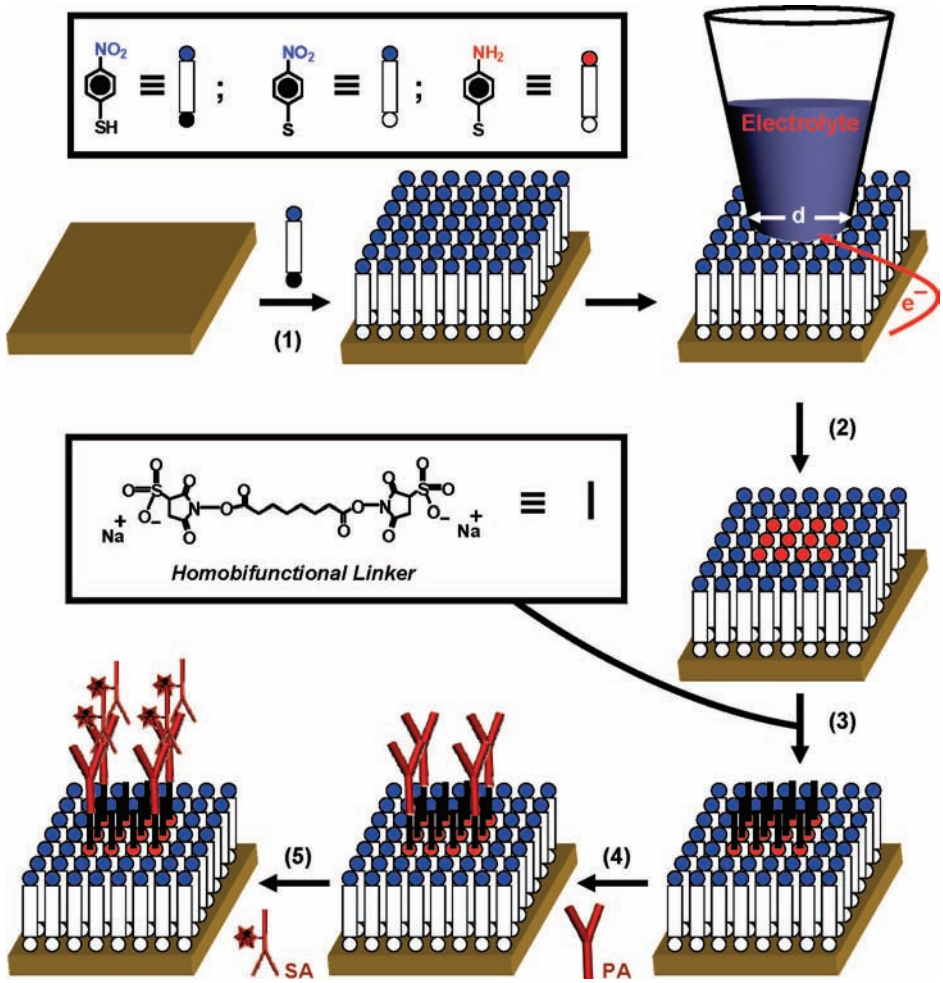


Figure 1. Schematic illustration of the electrochemical conversion from a NO_2 group in the SAMs of 4-nitrothiophenol on an Au electrode to an NH_2 group, which is capable of subsequently inducing the immobilization of primary antibodies, PA (red). Bound primary antibodies are detected using fluorescently labeled secondary antibodies, SA (red). The electrochemical reduction is conducted selectively on the Au electrode area exposed to the electrolyte (diameter (d) = 8 mm).

to primary NH_2 groups; (3) selective reaction of the resulting NH_2-terminated monolayers with a homobifunctional linker; (4) covalent immobilization of primary antibodies; (5) visualization of these bound primary antibodies using fluorescently labeled secondary antibodies. Fluorescence microscopy and surface plasmon resonance (SPR) spectroscopy were employed to characterize the immobilization of antibodies and their selective assembly to the modified areas of the SAM.

EXPERIMENTAL PROCEDURES

SAM Preparation. Substrates with 30 nm thick Au employing a 10 nm thick Ti adhesion layer on an n-type Si wafer were fabricated by electron-beam evaporation. The Au substrates were cleaned with piranha solution (3:1, H_2SO_4/30% H_2O_2), rinsed with ultra high purity (UHP) H_2O (resistivity = 18 MΩ cm) and then HPLC-grade EtOH thoroughly for 1 min. (*Caution: Piranha solution reacts violently with all organic compounds and should be handled with care*). Subsequently, the substrates were immersed in a 0.1 mM ethanolic solution of 4-nitrothiophenol (Sigma-Aldrich) for 12 h to form the SAMs on the Au surfaces. The substrates were rinsed with EtOH and UHP H_2O.

Electrochemical Conversion. The cyclic voltammograms (CVs) of the NO_2-terminated SAMs and their conversion on the Au electrodes were performed using a Princeton Applied Research VMP multichannel potentiostat with a custom-designed Teflon cell, equipped with the functionalized Au substrate as the working electrode, a Pt wire as the counter electrode, and the standard calomel electrode (SCE) as the reference electrode. The planar gold working electrode exposes a circular geometric area of 50 mm^2 to the electrolyte solution. Cyclic voltammetry was carried out at a scan rate of 200 mV/s.

Protein Immobilization. The pristine 4-nitrothiophenol and converted 4-nitrothiophenol SAMs were incubated with a 5 mg/mL solution of bis(sulfosuccinimidyl)suberate (BS^3; Pierce) in phosphate buffered saline pH 7.4 (PBS) for 20 min at room temperature. Samples were rinsed with PBS (~1 min) and incubated with a primary mouse anti-human vascular endothelial growth factor (VEGF) antibody (Biosource) with a concentration of 25 μg/mL in PBS containing 0.1% Triton X-100 (PBS–Triton) for 20 min. The samples were rinsed in PBS buffer solution for 10 min and incubated in the dark for 20 min in a 20 μg/mL PBS–Triton solution of Alexa Fluor 568 goat anti-mouse IgG antibody (Molecular Probes). The substrates were rinsed with PBS for 10 min and mounted for fluorescence microscopy. For the control samples, the pristine 4-nitrothiophenol and converted 4-nitrothiophenol SAMs were stained as described above, without first immobilizing the BS^3 homobifunctional linker.

X-ray Photoelectron Spectroscopy (XPS). XPS experiments were performed in an Omicron XPS/UPS system using a monochromatic Al K_α X-ray source (1486.6 eV) with a pass energy of 50 eV. Fitting of XPS peaks was performed using the *Avantage v2.2* processing software. All spectra were fitted using 30% Lorentzian/70% Gaussian peaks.

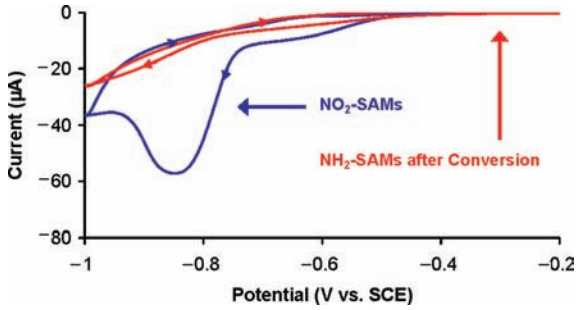


Figure 2. CV (blue curve) of a SAM of 4-nitrothiophenol—the reduction of NO_2 to NH_2 groups appears as a pronounced peak at around −0.85 V. CV (red curve) of the SAM of 4-nitrothiophenol after the reductive scan.

Fluorescence Microscopy. Fluorescence images were collected on a Zeiss Axiovert 200 fluorescent microscope, equipped with an AxioCam MRm monochrome camera. Pictures were acquired using AxioVision LE 4.1 with identical exposure parameters and analyzed using *Image J 1.33u* (NIH). No postexposure image processing was performed.

Surface Plasmon Resonance. SPR spectroscopy experiments were performed with a Biacore X at 25 °C at a flow rate of 2 μL/min. Two different monolayers—pristine 4-nitrothiophenol and converted 4-nitrothiophenol—were prepared on Biacore gold sensor chips. Prior to protein binding studies, 40 μL of a 5 mg/mL solution of the BS^3 homobifunctional linker in PBS, was injected into the gold sensor, followed by a PBS–Triton washing for 10 min. The functionalized gold surfaces (either pristine or converted) were subsequently exposed to a primary antibody by injection of 40 μL of anti-streptavidin produced in rabbit (Sigma) at a concentration of 1.4 mg/mL in PBS–Triton. The protein solution was replaced with the PBS–Triton solution for 25 min to remove any unbound primary antibody. Subsequently, a 40 μL sample of the secondary antibody, Alexa Fluor 488 goat anti-rabbit IgG (Molecular Probes), with a concentration of 20 μg/mL in PBS–Triton was injected, followed by a 10 min PBS–Triton washing.

RESULTS

Cyclic voltammetry (CV) was used to investigate the characteristics of the SAMs and for the chemical conversion ($NO_2 \rightarrow NH_2$) on the gold surfaces. The CV study of the NO_2-terminated SAMs was carried out in three subsequent CV scans. A 0.1 M KCl solution (9:1, EtOH/UHP H_2O) (*26*) was employed as the electrolyte to check the characteristic CV peak that the NO_2 group exhibits (blue curve in Figure 2) (*29*). Next, a second scan was carried out in a 0.1 M KCl aqueous solution to ensure (*29*) an adequate supply of H^+ ions for the complete electrochemical reduction of the NO_2 to NH_2 groups. Finally, the disappearance of the NO_2 group-related peak was observed by running a third scan (red curve in Figure 2) in a 0.1 M KCl solution (9:1, EtOH/UHP H_2O). The potential was swept from 0 to −1.0 V with respect to the SCE. The reductive peak of the NO_2 group was observed at −0.85 V (blue curve in Figure 2). By integrating the area under the reductive peak, the SAMs density was found to be 2.6×10^{14} molecule/cm^2. After the reduction of the NO_2 groups during the second scan, no redox activity was observed (red curve in Figure 2), implying complete conversion of the NO_2-terminated SAMs.

High-resolution XPS spectra were acquired on the gold electrodes before and after surface electrochemical modification. XPS measurements confirmed the conversion of the NO_2 groups (N(1s) binding energy = 405.6 eV; blue curve in Figure 3) to the NH_2 counterparts (N(1s) binding energy = 399.6 eV; red curve in Figure 3). XPS of the pristine 4-nitrothiophenol surfaces also indicated the presence of primary amines. This behavior can be attributed (*32*, *33*) to the gradual reduction of the NO_2 groups to NH_2 groups (Figure 3; blue curve) during X-ray irradiation initiated by the photoelectrons and secondary electrons emitted from the surface. However, in the electrochemically converted NO_2-terminated SAM, the XPS of the N(1s) binding energy region indicated only the presence of the NH_2 group with a strong peak at 399.6 eV.

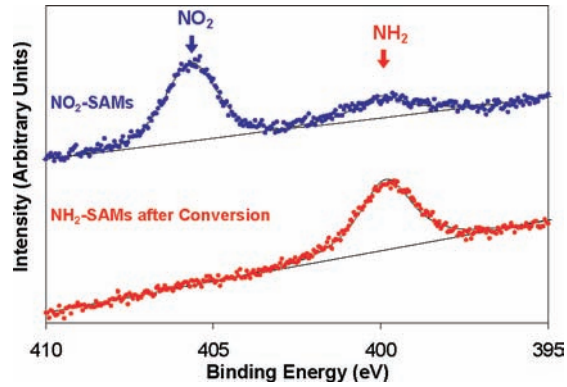


Figure 3. XPS spectra of the N(1s) peak region of a SAM of 4-nitrothiophenol before (blue curve) and after (red curve) the reductive scan. The binding energy of the N (1s) has been shifted by 6 eV, which is consistent with a reduction of NO_2 to NH_2 groups.

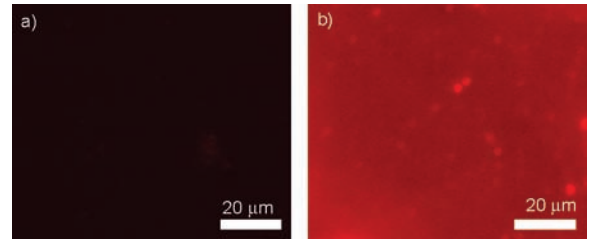


Figure 4. Fluorescence microscope images of a (a) nonconverted and (b) converted NO_2-terminated monolayer region after being sequentially exposed to BS^3, a primary antibody, and a red fluorescent Alexa Fluor 568 conjugated secondary antibody.

Following the XPS confirmation of the efficient electrochemical reduction, the viability of this strategy for the site-selective assembly of proteins on gold surfaces was demonstrated first by fluorescence microscopy. After performing electrochemical conversion on large-scale electrodes (converted area: 50 mm^2 on a 1 cm^2 gold surface area), the electrochemically generated NH_2 groups were activated with the BS^3 homobifunctional linkers to expose amine-reactive *N*-hydroxysulfosuccinimide (Sulfo-NHS) groups. Subsequently, the primary mouse anti-human VEGF antibody was allowed to react with the modified gold surface, followed by incubation with a red fluorescent secondary antibody. Detection of the binding of the primary antibodies to the electrochemically modified surfaces was evaluated by fluorescence microscopy. Figure 4a,4b illustrates the fluorescence microscope images collected from the NO_2- and NH_2-terminated regions of the surface, respectively. The fluorescence images of the regions terminated by the amino groups (Figure 4b) clearly revealed high fluorescence intensity, while the unmodified areas (NO_2 groups) showed minimal fluorescence. The signal-to-noise ratio (specific binding on NH_2-terminated regions/nonspecific binding on NO_2-terminated regions) was determined to be 26, a ratio which demonstrates the high degree of biological specificity to the NH_2 surface over the NO_2 surface.

Control experiments were also established to verify that the selective immobilization of proteins on the NH_2-terminated regions relied on the formation of amide bonds first between

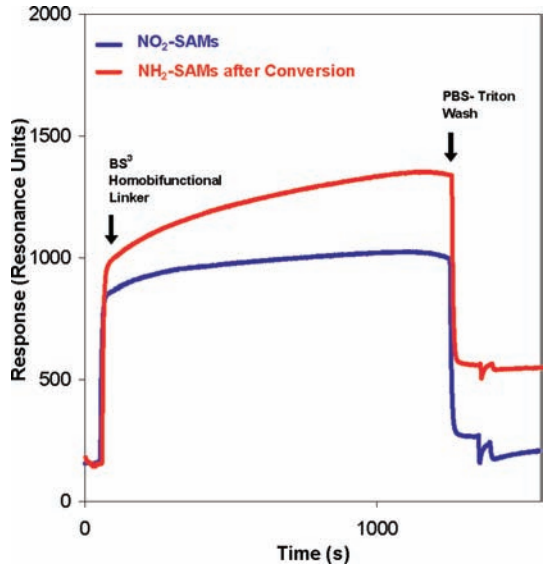


Figure 5. SPR sensorgram traces for the immobilization of BS^3 homobifunctional linker on a SAM of 4-nitrothiophenol (blue curve) and 4-nitrothiophenol after the reductive scan (red curve). SPR spectroscopy data show the selective immobilization of BS^3 to the converted NO_2-terminated monolayers.

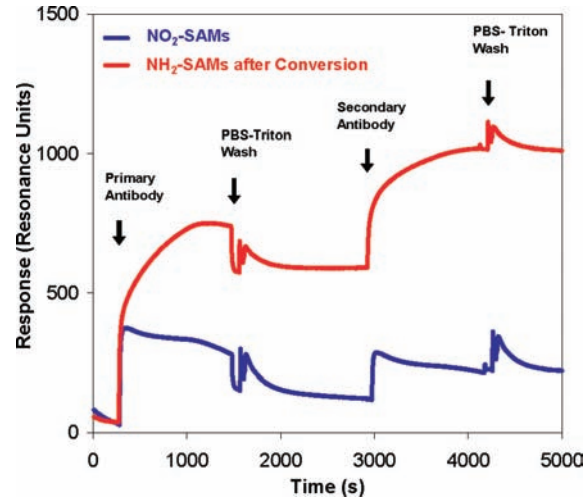


Figure 6. SPR sensorgram traces for the sequential immobilization of a primary antibody followed by a secondary antibody on a SAM of 4-nitrothiophenol (blue curve) and 4-nitrothiophenol after the reductive scan (red curve). The surfaces were washed with PBS–Triton after each protein injection. The antibodies show high binding affinity for converted NO_2-terminated monolayers, whereas negligible antibody adsorption is noted on nonconverted NO_2-terminated monolayers.

the BS^3 homobifunctional linker and the amino groups on the surface, and subsequently between the BS^3 homobifunctional linker and the primary amine groups in the primary antibody. For instance, in the absence of immobilization of the BS^3 homobifunctional linker on the nonconverted and converted NO_2-terminated monolayers, no protein immobilization occurred and no fluorescence was observed. Further evidence of the covalent immobilization of BS^3 on the NH_2 monolayers was obtained by surface plasmon resonance spectroscopy. Nonconverted and converted NO_2-terminated monolayers were exposed to a BS^3 linker solution and their immobilization monitored by SPR (Figure 5). BS^3 was shown to bind irreversibly to the converted NO_2-terminated monolayers, whereas no immobilization was observed for the NO_2-terminated monolayers.

A large SPR response was also observed upon introducing the primary rabbit anti-streptavidin antibody to the NH_2 monolayers activated with succinimidyl esters (Figure 6). When PBS buffer was passed through the system for approximately 30 min, essentially no protein desorbed from the converted monolayer surface. These data establish that the proteins are not nonspecifically adsorbed on the gold surface and thus are likely covalently attached to the surface via the BS^3 linker. These results contrasted with the negligible nonspecific protein binding on pristine NO_2-terminated monolayers, particularly after washing with PBS. Indeed, the protein surface coverage was determined (*34*) to be 56 ng/cm^2 for the NH_2 monolayer regions compared to 8 ng/cm^2 on the pristine NO_2 monolayer regions. The primary antibody immobilized on the NH_2 monolayers was subsequently recognized by the secondary antibody, leading to another sharp increase in the SPR response. After injection of the secondary antibody, the irreversible nature of the protein binding was confirmed by the steady SPR response, following PBS–Triton washing for 10 min. SPR spectroscopy showed that the irreversible immobilization of protein was specific for NH_2 monolayers, and that the pristine NO_2 monolayers effectively prevented unwanted nonspecific binding. This feature is particularly important for binding multiple proteins to a single substrate via the electrochemical activation described herein.

CONCLUDING REMARKS

The NO_2-terminated groups in the SAMs of 4-nitrothiophenol on gold surfaces can be reduced electrochemically and selectively to NH_2 groups by applying a negative voltage between the addressed electrode and its counter electrode in the presence of an electrolyte. By employing the homobifunctional activated ester linker, proteins can then be attached specifically to the NH_2 monolayer region. We have demonstrated that immobilized antibodies exhibit high affinity and selectivity for these NH_2 regions, after activation, as monitored by fluorescence microscopy and surface plasmon resonance spectroscopy. This strategy can potentially be extended to immobilize sequentially a series of different proteins onto selected gold nanoelectrodes by carrying out repeated cycles with the entirely aqueous solution-based, and hence biocompatible, electrochemical and protein immobilization processes. Efforts in this direction are underway.

ACKNOWLEDGMENT

The authors acknowledge support of this work through a Nanoscale Interdisciplinary Research Team (NIRT) Grant (0404458) and through SINAM (DMI-0327077) from the National Science Foundation. KLC would like to thank the NIH NHLBI for a NRSA Postdoctoral Fellowship. JAP would like to thank the European Community for support (NANO3D.NMP-CT-2005-014006).

LITERATURE CITED

(1) Niemeyer, C. M., and Mirkin, C. A. (2004), Wiley-VCH Verlag GmbH & Co. KGaA, Weinheim.
(2) Kambhampati, D. (2004), Wiley-VCH Verlag GmbH & Co. KGaA, Weinheim.
(3) Cui, Y., Wei, Q. Q., Park, H. K., and Lieber, C. M. (2001) Nanowire nanosensors for highly sensitive and selective detection of biological and chemical species. *Science 293*, 1289–1292.
(4) Zheng, G. F., Patolsky, F., Cui, Y., Wang, W. U., and Lieber, C. M. (2005) Multiplexed electrical detection of cancer markers with nanowire sensor arrays. *Nat. Biotechnol. 23*, 1294–1301.
(5) Shekhawat, G., Tark, S. H., and Dravid, V. P. (2006) MOSFET-embedded microcantilevers for measuring deflection in biomolecular sensors. *Science 311*, 1592–1595.
(6) Christman, K. L., Enriquez-Rios, V. D., and Maynard, H. D. (2006) Nanopatterning proteins and peptides. *Soft Matter 2*, 928–939.

(7) Demidov, V. V. (2004) Nanobiosensors and molecular diagnostics: a promising partnership. *Expert Rev. Mol. Diagn. 4*, 267–268.
(8) Mrksich, M. (2005) *MRS Bull. 30*, 180–184.
(9) Sagiv, J. (1980) Organized monolayers by adsorption.1. formation and structure of oleophobic mixed monolayers on solid-surfaces. *J. Am. Chem. Soc. 102*, 92–98.
(10) Maoz, R., and Sagiv, J. (1984) On the formation and structure of self-assembling monolayers.1. a comparative ATR-wettability study of Langmuir-Blodgett and adsorbed films on flat substrates and glass microbeads. *J. Colloid Interface Sci. 100*, 465–496.
(11) Gun, J., Iscovici, R., and Sagiv, J. (1984) On the formation and structure of self-assembling monolayers.2. a comparative-study of Langmuir-Blodgett and adsorbed films using ellipsometry and IR reflection absorption-spectroscopy. *J. Colloid Interface Sci. 101*, 201–213.
(12) Netzer, L., and Sagiv, J. (1983) A new approach to construction of artificial monolayer assemblies. *J. Am. Chem. Soc. 105*, 674–676.
(13) Netzer, L., Iscovici, R., and Sagiv, J. (1983) Adsorbed monolayers versus Langmuir-Blodgett monolayers - why and how.1. from monolayer to multilayer, by adsorption. *J. Am. Chem. Soc. 99*, 235–241.
(14) Nuzzo, R. G., and Allara, D. L. (1983) Adsorption of bifunctional organic disulfides on gold surfaces. *J. Am. Chem. Soc. 105*, 4481–4483.
(15) Mendes, P. M., and Preece, J. A. (2004) Precision chemical engineering: integrating nanolithography and nanoassembly. *Curr. Opin. Colloid Interface Sci. 9*, 236–248.
(16) Lee, S. W., Oh, B. K., Sanedrin, R. G., Salaita, K., Fujigaya, T., and Mirkin, C. A. (2006) Biologically active protein nanoarrays generated using parallel dip-pen nanolithography. *Adv. Mater. 18*, 1133–1136.
(17) Lee, K. B., Park, S. J., Mirkin, C. A., Smith, J. C., and Mrksich, M. (2002) Protein nanoarrays generated by dip-pen nanolithography. *Science 295*, 1702–1705.
(18) Mrksich, M. (2002) What can surface chemistry do for cell biology? *Curr. Opin. Chem. Biol. 6*, 794–797.
(19) Hyun, J., Ahn, S. J., Lee, W. K., Chilkoti, A., and Zauscher, S. (2002) Molecular recognition-mediated fabrication of protein nanostructures by dip-pen lithography. *Nano Lett. 2*, 1203–1207.
(20) Choi, I. S., and Chi, Y. S. (2006) Surface reactions on demand: electrochemical control of SAM-based reactions. *Angew. Chem., Int. Ed. 45*, 4894–4897.
(21) Christman, K. L., and Maynard, H. D. (2005) Protein micropatterns using a pH-responsive polymer and light. *Langmuir 21*, 8389–8393.
(22) Jung, H., Kulkarni, R., and Collier, C. P. (2003) Dip-pen nanolithography of reactive alkoxysilanes on glass. *J. Am. Chem. Soc. 125*, 12096–12097.
(23) Cheung, C. L., Camero, J. A., Woods, B. W., Li, T., Johnson, J. E., and De Yoreo, J. J. (2003) Fabrication of assembled virus nanostructure on templates of chemoselective linkers formed by scanning probe nanolithography. *J. Am. Chem. Soc. 125*, 6848–6849.
(24) Smith, J. C., Lee, K.-B., Wang, Q., Finn, M. G., Johnson, J. E., Mrksich, M., and Mirkin, C. A. (2003) Nanopatterning the chemospecific immobilization of cowpea mosaic virus capsid. *Nano Lett. 3*, 883–886.
(25) Hernández, E. C., Witkowski, A., Daunert, S., and Bachas, L. G. (1995) Potentiometric enzyme electrode for urea based on electrochemically prepared polypyrrole membranes. *Mikrochim. Acta 121*, 63–72.
(26) Lee, C. S., Baker, S. E., Marcus, M. S., Yang, W. S., Eriksson, M. A., and Hamers, R. J. (2004) Electrically addressable biomolecular functionalization of carbon nanotube and carbon nanofiber electrodes. *Nano Lett. 4*, 1713–1716.
(27) Yeo, W.-S., and Mrksich, M. (2006) Electroactive self-assembled monolayers that permit orthogonal control over the adhesion of cells to patterned substrates. *Langmuir 22*, 10816–10820.
(28) Collier, J. H., and Mrksich, M. (2006) Engineering a biospecific communication pathway between cells and electrodes. *Proc. Natl. Acad. Sci. U.S.A. 103*, 2021–2025.
(29) Tsutsumi, H., Furumoto, S., Morita, M., and Matsuda, Y. (1995) Electrochemical-behavior of a 4-nitrothiophenol modified electrode prepared by the self-assembly method. *J. Colloid Interface Sci. 171*, 505–511.
(30) Nielsen, J. U., Esplandiu, M. J., and Kolb, D. M. (2001) 4-Nitrothiophenol SAM on Au(111) investigated by in situ STM, electrochemistry, and XPS. *Langmuir 17*, 3454–3459.
(31) Yang, W. S., Baker, S. E., Butler, J. E., Lee, C. S., Russell, J. N., Shang, L., Sun, B., and Hamers, R. J. (2005) Electrically addressable biomolecular functionalization of conductive nanocrystalline diamond thin films. *Chem. Mater. 17*, 938–940.
(32) Mendes, P., Belloni, M., Ashworth, M., Hardy, C., Nikitin, K., Fitzmaurice, D., Critchley, K., Evans, S., and Preece, J. (2003) A novel example of X-ray-radiation-induced chemical reduction of an aromatic nitro-group-containing thin film on SiO_2 to an aromatic amine film. *ChemPhysChem 4*, 884–889.
(33) Mendes, P. M., Jacke, S., Critchley, K., Plaza, J., Chen, Y., Nikitin, K., Palmer, R. E., Preece, J. A., Evans, S. D., and Fitzmaurice, D. (2004) Gold nanoparticle patterning of silicon wafers using chemical e-beam lithography. *Langmuir 20*, 3766–3768.
(34) Fivash, M., Towler, E. M., and Fisher, R. J. (1998) BIAcore for macromolecular interaction. *Curr. Opin. Biotechnol. 9*, 97–101.

BC7002296

Necrosis Avidity of $^{99m}Tc(CO)_3$-Labeled Pamoic acid Derivatives: Synthesis and Preliminary Biological Evaluation in Animal Models of Necrosis

Humphrey Fonge,[†] Satish K. Chitneni,[†] Jin Lixin,[†] Kathleen Vunckx,[‡] Kristof Prinsen,[†] Johan Nuyts,[‡] Luc Mortelmans,[†] Guy Bormans,[†] Yicheng Ni,[§] and Alfons Verbruggen*[,†]

Laboratory of Radiopharmacy, Faculty of Pharmaceutical Sciences, K.U. Leuven, Herestraat 49, Box 821, BE-3000 Leuven, Belgium, Departments of Nuclear Medicine and Radiology, University Hospital Gasthuisberg, Herestraat 49, BE-3000 Leuven, Belgium. Received June 25, 2007; Revised Manuscript Received August 25, 2007

In a search for an infarct avid tracer agent with improved properties, we have observed that bis-DTPA derivatives of pamoic acid have a high avidity for necrotic tissue. Here, we report the synthesis, radiolabeling, and preliminary evaluation in normal mice and rats with hepatic infarction of the ^{99m}Tc-tricarbonyl complexes of *N*,*N*′-bis(diethylenetriaminopentaacetato)-4,4′-methylene bis(2-hydroxy-3-naphthoic hydrazide) ($^{99m}Tc(CO)_3$-bis-DTPA-pamoate) and [*N*-(5-aminopentyl)pyridin-2-yl-methylamino]methylacetato-4,4′-methylene-2-hydroxy-3-napthalenecarboxamide-(2′-hydroxy-3′-naphthoic acid methyl ester) ($^{99m}Tc(CO)_3$-**12**). Radiolabeling with $^{99m}Tc(CO)_3^+$ was achieved with a radiochemical yield of over 95% for both tracer agents. In normal mice, the polar $^{99m}Tc(CO)_3$-bis-DTPA-pamoate was cleared from plasma via both the liver and the kidneys, while the more lipophilic $^{99m}Tc(CO)_3$-**12** was rapidly cleared via the liver. Blood clearance in mice was faster for $^{99m}Tc(CO)_3$-**12** (0.1% injected dose per gram at 4 h postinjection) than for $^{99m}Tc(CO)_3$-bis-DTPA-pamoate (9.3% injected dose per gram at 4 h postinjection). Affinity and specificity of the tracers for necrotic tissue was studied in rats with hepatic infarction and ethanol-induced necrosis of the liver or muscles. Activity ratios of infarct to viable liver tissue of $^{99m}Tc(CO)_3$-bis-DTPA-pamoate quantified by autoradiography of tissue slices ranged from 4 to 18, depending on the necrosis model and time postinjection of the tracer. Infarcts were also visualized *in vivo* by $^{99m}Tc(CO)_3$-bis-DTPA-pamoate planar gamma imaging. After injection of $^{99m}Tc(CO)_3$-bis-DTPA-pamoate, *in vivo* and *ex vivo* images correlated well with histochemical staining with triphenyltetrazolium chloride and hematoxylin and eosin. $^{99m}Tc(CO)_3$-**12** on the other hand showed no uptake in necrotic tissue. Stability of the tracers was determined *in vitro* after storage at room temperature and by histidine challenge experiments, and *in vivo* in mouse plasma and in urine (for $^{99m}Tc(CO)_3$-bis-DTPA-pamoate). $^{99m}Tc(CO)_3$-bis-DTPA-pamoate was unstable *in vitro* to histidine challenge, while $^{99m}Tc(CO)_3$-**12** was 98% stable *in vitro* in the same conditions. Both tracers showed good *in vivo* stability. $^{99m}Tc(CO)_3$-bis-DTPA-pamoate shows high specificity for necrotic tissue and merits further evaluation as a necrosis avid imaging agent. $^{99m}Tc(CO)_3$-**12** is not useful for visualization of necrotic tissue.

INTRODUCTION

Cell death occurs by two distinct mechanisms: a disorganized nonphysiologic mechanism called necrosis and a well-orchestrated physiologic mechanism termed apoptosis (*1*–*3*). Both forms of cell death have been implicated in many diseases, notably, acute myocardial infarction (AMI), even though it is not very certain which form of death is predominant in the case of AMI (*4, 5*). Therapies aimed at restoring reperfusion to the infarcted organ most often aggravate the injury by shifting the cell towards death by apoptosis (*4, 6, 7*).

Imaging of apoptosis has become a reality with the discovery that annexin-V binds specifically and with nanomolar affinity (K_d = 7 nM) to externalized phosphatidylserine (PS) (*8*–*11*). Targeting of necrosis in AMI has been challenging, given the fact that a multitude of compounds are suddenly released by the dying cells following disintegration of the sarcolemma. A few necrosis avid tracer agents have been in use in nuclear medicine with none having ideal imaging characteristics (*12*). Among these tracers, ^{99m}Tc-glucarate looks the most promising but presents two limitations to its potential clinical applications for imaging AMI (*13*): (1) it is rapidly washed out from the infarcted myocardium and (2) its localization is limited to the early hours of the acute event, thus limiting its potential usefulness to the acute phase of AMI.

In preliminary experiments, we have found that bis-gadolinium *N*,*N*′-bis(diethylenetriaminopentaacetato)-4,4′-methylene bis(2-hydroxy-3-naphthoic hydrazide (bisGd bis-DTPA-pamoate) specifically localizes in necrotic tissue in different animal models of necrosis (*14, 15*). Radiolabeled derivatives of this class of compounds could find more clinical applications in nuclear medicine, e.g., when radiolabeled with technetium-99m, which has almost ideal physical properties for planar and single photon emission computed tomography (SPECT). Classical labeling of diethylene triamine pentaacetate (DTPA) derivatized biomolecules with technetium-99m (^{99m}Tc), i.e., addition of ^{99m}Tc-pertechnetate in the presence of stannous ions, requires a rather large amount of DTPA (5–10 mg) and often results in compounds with rather low stability due to reoxidation of technetium to pertechnetate. Technetium-99m tricarbonyl labeling of biomolecules has the advantage of ease of preparation, efficient complex formation, and inertness of the complex due to the d^6 metal core (*16, 17*). Therefore, we have studied the synthesis and labeling of bis-DTPA pamoate with a $^{99m}Tc(CO)_3^+$ core (Figure 1A) and report here a preliminary evaluation of $^{99m}Tc(CO)_3$-bis-DTPA-pamoate in rats with rep-

* Author for correspondence: Prof. Alfons Verbruggen, Laboratory of Radiopharmacy, Faculty of Pharmaceutical Sciences, K.U. Leuven, Herestraat 49, Onderwijs & Navorsing 2, Box 821, B-3000 Leuven, Belgium. Tel: +32-16-33.04.46. Fax: +32-16-33.04.49. E-mail: alfons.verbruggen@pharm.keuven.be.

[†] Laboratory of Radiopharmacy.

[‡] Department of Nuclear Medicine, University Hospital Gasthuisberg.

[§] Department of Radiology, University Hospital Gasthuisberg.

10.1021/bc700236j CCC: $37.00 © 2007 American Chemical Society
Published on Web 10/12/2007

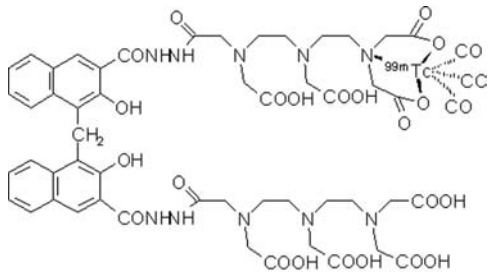


Figure 1. Proposed structures of $^{99m}Tc(CO)_3$-bis-DTPA-pamoate (A) and $^{99m}Tc(CO)_3$-[*N*-(5-aminopentyl)pyridin-2-yl-methylamino]methyl-acetato-4,4′-methylene-2-hydroxy-3-napthalenecarboxamide-(2′-hydroxy-3′-naphthoic acid methyl ester) ($^{99m}Tc(CO)_3$-**12)** (B).

erfused hepatic infarction and ethanol-induced hepatic or muscular necrosis. Necrosis specificity was assessed *in vivo* by planar gamma scintigraphy and *ex vivo* by gamma counting and autoradiography and was compared to TTC and H&E staining techniques at different time points postinjection (p.i.). However, DTPA is not an ideal bifunctional chelating agent for labeling a bioactive compound with a ^{99m}Tc-tricarbonyl core. For this reason, we have derivatized pamoic acid also via a hydrazine spacer with [*N*-(5-aminopentyl)pyridyl-2-yl-amino] methyl acetate (*18*), which is considered an ideal bifunctional chelator for labeling biomolecules with $^{99m}Tc(CO)_3^+$ because of the relatively fast complexation and very high thermodynamic and kinetic stability of a $Tc(CO)_3$ complex with this tridentate system (*17*, *18*). The stability and biological characteristics of the resulting $^{99m}Tc(CO)_3^+$ complex named $^{99m}Tc(CO)_3$-**12** (Figure 1B) have been compared with those of $^{99m}Tc(CO)_3$-bis-DTPA pamoate.

EXPERIMENTAL PROCEDURE

Reagents. 2-Hydroxy-3-naphthoic acid, *N*-ethyldiisopropylamine, *N*,*N*′-dicyclohexylcarbodiimde, *N*-hydroxysuccinimide, N-Boc-1,5-diaminopentane, pyridine, and hydrazine monohydrate were obtained from Sigma Aldrich (Steinheim, Germany); paraformaldehyde and all solvents were obtained from Acros Organics (Geel, Belgium) and were used as purchased. Generator eluate containing $Na^{99m}TcO_4$ was obtained from an Ultratechnekow generator (Tyco Healthcare, Petten, The Netherlands). The Isolink kit used for preparing $^{99m}Tc(CO)_3^+$ was a generous gift from Tyco Healthcare.

Instruments and Methods. ^{1}H NMR spectra were acquired with a Gemini 300 MHz spectrometer (Varian, Palo Alto, CA, USA). Chemical shifts are reported in parts per million (ppm) relative to TMS ($\delta = 0$). Coupling constants are reported in hertz (Hz). Normal-phase column chromatography was performed using silica gel (silica 63–200, 60 Å, MP Biomedicals, Eschwege, Germany). Thin layer chromatography (TLC) was performed on normal-phase 0.2-mm-thick silica gel 60 plates with UV fluorescence (Macherey-Nagel, Düren, Germany), and spots were visualized with UV light (Spectroline, Westbury, NY). TLC plates were developed using one of the following mobile-phase systems: system A, EtOAc/MeOH 70/30 v/v; system B, CH_2Cl_2/hexane 50/50 v/v; system C, $CHCl_3$/hexane 5/95 v/v. High-pressure liquid chromatography (HPLC) analysis was performed on a LaChrom Elite HPLC system (Hitachi, Darmstadt, Germany) using an XTerra RPC_{18} column (5 μm, 4.6 mm $\times$ 250 mm; Waters, Milford, USA). The compounds were eluted from the column using mixtures of 0.05 M ammonium acetate buffer pH 6.8 (solvent A) and acetonitrile (solvent B): 0–8 min, linear gradient from 100% A to 60% A; 8–15 min, 60% A; 15–25 min, linear gradient to 100% B, at a flow rate of 1 mL/min over 30 min. The column effluent was monitored using a UV detector set at 254 nm, and the output signal was acquired on a Laura Lite system (Lablogic, Sheffield, UK). For analysis of radiolabeled compounds, the HPLC eluate was led over a 3 in NaI(Tl) scintillation detector connected to a single-channel analyzer. Radioactivity counting for biodistribution studies was done using an automated system with a gamma counter (3 in NaI(Tl) well crystal) coupled to a multichannel analyzer in a sample changer (Wallac, 1480 Wizard 3", Turku, Finland). The results were corrected for background radiation and physical decay during counting. Accurate mass measurement was performed by coinfusion with a 10 μg/mL solution of a reference as an internal calibration standard on a time-of-flight mass spectrometer (LCT, Micromass, Manchester, UK) equipped with an electrospray ionization (ESI) interface, operated in positive (ES+) or negative (ES−) mode. Samples were infused in acetonitrile/water using a Harvard 22 syringe pump (Harvard instruments, Massachusetts). Acquisition and processing of data was done using *Masslynx* software (Micromass, version 3.5).

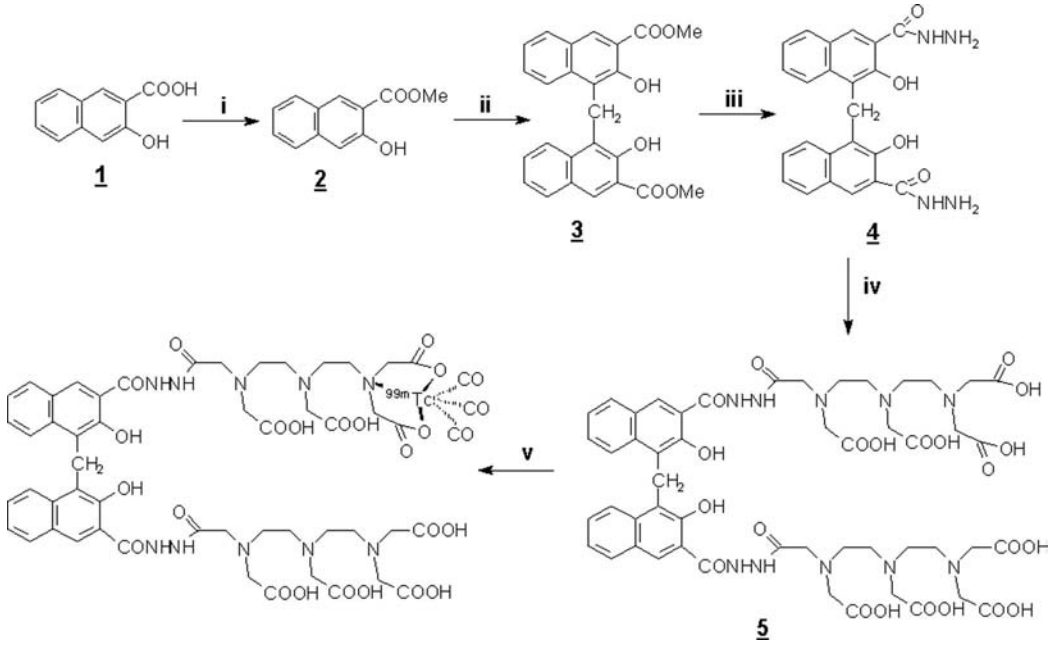
All animal experiments were conducted with the approval of the institutional ethical committee for conduct of experiments on animals.

CHEMISTRY

2-Hydroxy-3-methylnaphthoate (2). To a solution of 2-hydroxy-3-naphthoic acid (19.2 g, 0.094 mol) in acetone (250 mL) was added K_2CO_3 (13 g, 0.1 mol), water (25 mL), and then with stirring over a period of 3.5 h a solution of dimethyl sulfate (11.1 mL, 0.12 mol). The solution was further stirred at room temperature (RT) until all starting material was esterified as judged by TLC (system C, ester (**2**) $R_f = 0.9$). Undissolved K_2CO_3 was filtered off and washed with acetone. The combined filtrates were evaporated *in vacuo* and the residue was dissolved in CH_2Cl_2 and dried over sodium sulfate. The filtrate was concentrated, methanol was added to the warm solution, and the precipitate was filtered off. The resulting yellow powder was purified using column chromatography on silica gel eluted with CH_2Cl_2. Yield 17.8 g (87%). Accurate mass $[C_{12}H_9O_3\text{-}H]^-$: theoretical 201.0557 Da, found 201.0559 Da. ^{1}H NMR ($CDCl_3$, 300 Hz) δ 8.46 (s, 1H, 11-CH), 7.78 (d, 1H, $^3J = 8.3$ Hz, 6-CH), 7.67 (d, 1H, $^3J = 8.4$ Hz, 9-CH), 7.48 (t, 1H, $^3J = 7.4$ Hz, 7-CH), 7.29 (t, 1H, $^3J = 9.1$ Hz, 8-CH), 4.0 (s, 3H, CH_3).

4,4′-Methylene-bis(2-hydroxy-3-methylnaphthoate) (Pamoic Acid Bis-Methyl Ester) (3). To a solution of compound **2** (10.1 g, 46 mmol) in a mixture of acetic acid (80 mL) and sulfuric acid (0.5 mL), paraformaldehyde (2 g, 66.6 mmol) was added, and the mixture was stirred overnight at RT. The yellow precipitate was collected and filtered off, washed with acetic acid and water, and dried. TLC: $R_f = 0.95$ (system C). Yield 9.46 g (97%). Accurate mass $[C_{25}H_{19}O_6\text{-}H]^-$: theoretical 415.1187 Da, found 415.1208 Da. ^{1}H NMR ($CDCl_3$, 300 Hz) δ 8.38.(s, 2H, 11,11′-CH), 8.23 (d, 2H, $^3J = 8.7$ Hz, 9,9′-CH), 7.67 (d, 2H, $^3J = 8.1$ Hz, 6,6′-CH), 7.35 (t, 2H, $^3J = 7.5$ Hz, 7,7′-CH), 7.18 (t, 2H, $^3J = 7.1$ Hz, 8,8′-CH), 4.95 (s, 2H, 4,4′-CH_2), 4.0 (s, 6H, 2 $\times$ CH_3).

Scheme 1[a]



[a] (i) $(CH_3)_2SO_4$, K_2CO_3, RT overnight; (ii) paraformaldehyde, CH_3COOH, H_2SO_4, RT; (iii) NH_2NH_2, reflux (80 °C), 2 h; (iv) DTPA monoanhydride monoethyl ester, DIEA, followed by hydrolysis (NaOH); (v) $^{99m}Tc(CO)_3^+$, pH 11, 70 °C, 20 min.

4,4′-Methylene-bis(2-hydroxy-3-naphthoic hydrazide) (4). A mixture of compound **3** (5.25 g, 12.6 mmol), pyridine (100 mL), methanol (50 mL), and hydrazine monohydrate (16 mL, 1.24 mol) was refluxed for 2 h. Solvents and excess hydrazine were removed azeotropically under reduced pressure with water. The suspension of the residue in methanol was stirred overnight. The hydrazide was collected by filtration and washed with methanol followed by drying over P_2O_5. Yield 5.05 g (97%). TLC: $R_f = 0$ (system B), $R_f = 0.6$ (system A). Accurate mass $[C_{23}H_{19}N_4O_4\text{-}H]^-$: theoretical 415.1412 Da, found 415.1451 Da. ^{1}H NMR (DMSO-d_6, 300 Hz) δ 10.62 (s, 2H, 2 × CONH), 8.38 (s, 2H, 11,11′-CH), 8.14 (d, 2H, $^3J = 8.6$ Hz, 9,9′-CH), 7.68 (d, 2H, $^3J = 8.0$ Hz, 6,6′-CH), 7.31 (t, 2H, $^3J = 7.4$ Hz, 7,7′-CH), 7.19 (t, 2H, $^3J = 7.1$ Hz, 8,8′-CH), 4.99 (s, 4H, NH_2), 4.78 (s, 2H, 4,4′-CH_2).

***N,N′*-Bis(diethylenetriamino pentaacetato)-4,4′-methylene Bis(2-hydroxy-3-naphthoic hydrazide) Sodium Salt (Bis-DTPA-Pamoate) (5).** To a stirred suspension of diethylenetriamine pentaacetic acid monoethyl ester monoanhydride (*15*) (3.4 g, 8.45 mmol) in dry DMF (50 mL), *N*,*N*-diisopropylethylamine (3.7 mL, 21 mmol) and compound **4** (1.5 g, 3.6 mmol) were added and the mixture was stirred at RT for 5 h. Solvents were evaporated under reduced pressure, the oily residue was dissolved in water, and the pH was adjusted to >12 using concentrated NaOH solution. After hydrolysis of the ethyl esters (as judged by HPLC), the volume was reduced at reduced pressure at 60 °C and the pH adjusted to 7.4 with 1 M HCl. The reaction product was purified by reversed-phase adsorption chromatography on silica C-18 stationary phase using a water–acetonitrile gradient. Fractions containing compound **5** were pooled, and the solvents were removed in vacuo. Methanol was added to induce precipitation of compound **5**, and the precipitate was collected by filtration and dried over P_2O_5. Accurate mass $[C_{51}H_{60}N_{10}O_{22}\text{-}2H]^{2-}/2$: theoretical 582.1947 Da, found 582.1916 Da. ^{1}H NMR (DMSO-d_6) δ 8.3 (d, 2H, Ar-H), 8.0 (d, 2H, Ar-H), 7.5 (m, 6H, Ar-H), 4.6 (s, 2H, methylene-H), 4.0 (t, 4H, 2 × CH_2), 2.9–3.4 (m, 36H, methylene of DTPA).

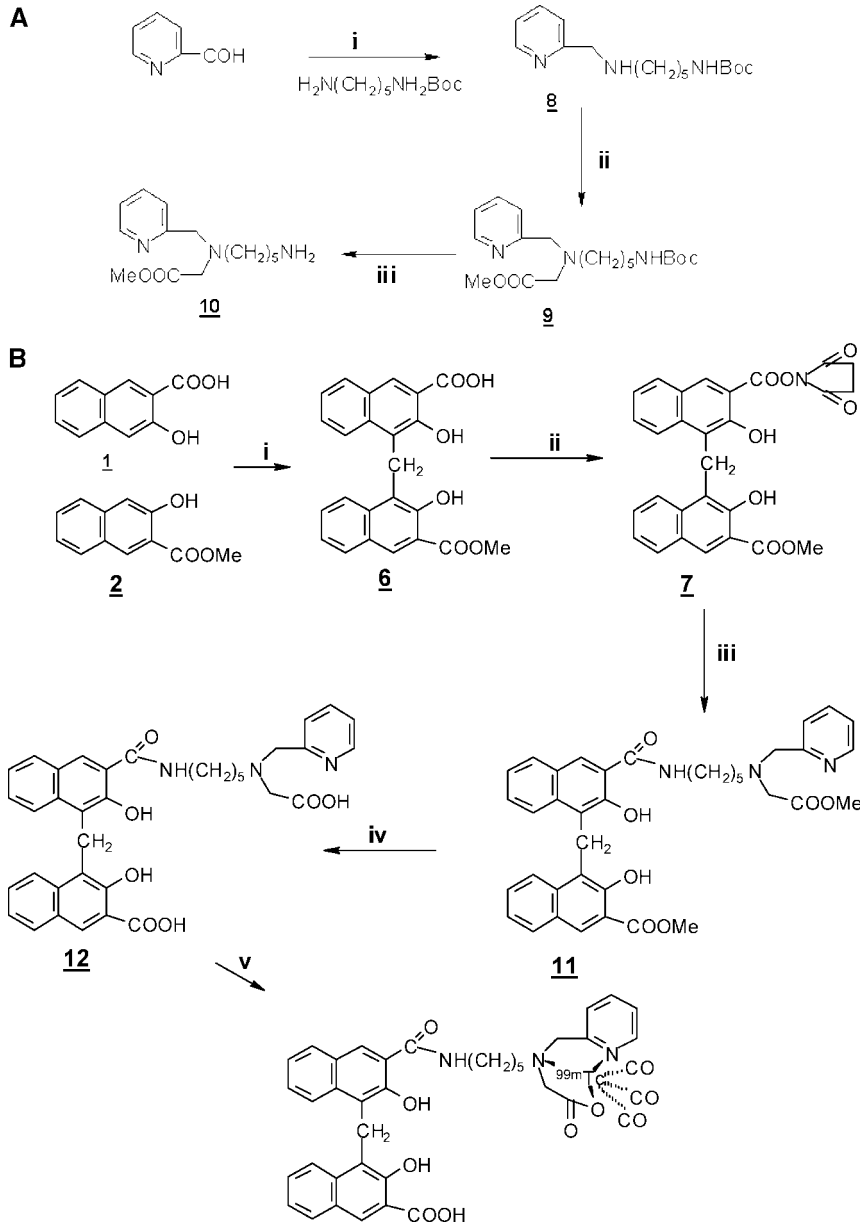
4,4′-Methylene-bis(2-hydroxy-3-naphthalene carboxylic acid) Monomethyl Ester (Pamoic Acid Monomethyl Ester) (6). To a solution of compound **1** (2-hydroxy-3-naphthoic acid, 2 g, 9.8 mmol) and **2** (2-hydroxy-3-methylnaphthoate, 2 g, 9.2 mmol) in a mixture of acetic acid (30 mL) and sulfuric acid (0.2 mL), paraformaldehyde (0.42 g, 14 mmol) was added and stirring was continued for 9 h at RT. The yellow precipitate was collected by filtration, washed successively with acetic acid and water, and dried. The precipitate was then dissolved in $CHCl_3$/hexane (1/3 v/v) and purified by column chromatography on silica gel eluted with a gradient from 100% hexane to 100% $CHCl_3$. The first fraction consisted of pamoic acid bis-methyl ester. Pamoic acid monomethyl ester (purity >80%) was eluted together with pamoic acid using $CHCl_3$/MeOH 95/5 v/v. Pure pamoic acid monomethyl ester was obtained by a second purification on silica gel eluted with $CHCl_3$/MeOH 95/5 v/v. The fractions containing pure pamoic acid monomethyl ester (>95%) were evaporated to give 1.55 g (41%) of a yellow powder. TLC: $R_f = 0.6$ (system A). Accurate mass $[C_{24}H_{17}O_6\text{-}H]^-$: theoretical 401.1031 Da, found 401.1058 Da. ^{1}H NMR (DMSO-d_6, 300 Hz), δ 11.23 (s, 1H, -COOH), 8.49 (s, 2H, 11,11′-CH), 8.12 (t, 2H, $^3J = 9.5$ Hz, 7,7′-CH), 7.9 (d, 2H, $^3J = 7.9$ Hz, 6,6′-CH), 7.43–7.36 (m, 2H, 9.9′-CH), 7.28–7.21 (m, 2H, 8,8′-CH), 4.9 (s, 2H, 4,4′-CH_2), 4.0 (s, 3H, CH_3).

Succinimidyl Pamoic Acid Monomethyl Ester (7). To a solution of compound **6** (0.5 g, 1.24 mmol) and *N*-hydroxysuccinimide (0.143 g, 1.25 mmol) in tetrahydrofuran (THF) (50 mL), dicyclohexylcarbodiimide (DCC, 0.25 g, 1.25 mmol, in 10 mL THF) was added dropwise at 0 °C. The reaction mixture was further stirred at RT overnight, after which it was filtered and washed with THF. The filtrate was evaporated to yield a yellow powder. Yield 85%. TLC: $R_f = 0.85$ (system A). Accurate mass $[C_{28}H_{20}NO_8\text{-}H]^-$: theoretical 498.1194 Da, found 498.1254 Da.

The bifunctional chelator (BFC) [*N*-(5-aminopentyl)pyridin-2-yl-methylamino]methyl acetate (**10**) was synthesized in three steps (**8**, **9**, **10**; Scheme 2A) as previously reported (*18*).

[*N*-(5-Aminopentyl)pyridin-2-yl-methylamino]methylacetato-4,4′-methylene-2-hydroxy-3-napthalenecarboxamide-(2′-hydroxy-3′-naphthoic acid methyl ester) (11). *N*,*N*′ Diisopropylethylamine (171 μL, 1 mmol) was added to a solution of compound **7** (0.32 g, 0.64 mmol) in a mixture dry THF-DMF (1/1 v/v, 20 mL), followed by the dropwise addition of a solution of compound **10** (0.2 g, 0.8 mmol) in dry THF-DMF (1/1 v/v)

Scheme 2[a]



[a] A. (i) (1) 0 °C; (2) $NaBH_4$, RT; (ii) bromomethyl acetate, TEA, RT; (iii) TFA. B. (i) Paraformaldehyde, CH_3COOH, H_2SO_4, RT; (ii) *N*-hydroxysuccinimide, DCC, RT; (iii) bifunctional chelator (**10**), DIEA, RT; (iv) 1 M NaOH; (v) $^{99m}Tc(CO)_3^+$, pH 7.4, 70 °C, 15 min.

under stirring at RT, and stirring was continued for 15 h. The solvents were evaporated and the crude product was purified by column chromatography on silica gel. Lipophilic impurities were washed off with ethyl acetate, and pure compound **11** was eluted with ethyl acetate–methanol (85/15 v/v). The solvents were evaporated to obtain the title compound as a viscous yellow oil (0.25 g, 60%). Its purity was verified by RP-HPLC on an XTerra C_{18} column (5 μm, 4.6 mm × 250 mm) using isocratic elution with acetonitrile–0.05 M NH_4OAc buffer (pH 6.8) (60/40 v/v) at a flow rate of 1 mL/min. The purity was >98%. TLC: $R_f = 0.8$ (system A). Accurate mass $[C_{38}H_{38}N_3O_7\text{-}H]^-$: theoretical 648.2715 Da, found 648.2661 Da. ^1H NMR ($CDCl_3$) δ 8.45 (1H, d, $^3J = 4.8$, 24-CH), 8.40 (s, 1H, 11′-CH), 8.3 (d, 1H, $^3J = 8.7$, 9′-CH), 8.2 (d, 1H, $^3J = 8.7$, 9-CH), 8.0 (s, 1H, 11-CH), 7.7 (d, 1H, $^3J = 8.1$, 6′-CH), 7.5 (d, 1H, $^3J = 8.2$, 6-CH), 7.4 (d, 2H, 21,23-CH), 7.38–7.28 (m, 2H, 7,7′-CH), 7.2–7.1 (m, 2H, 8,8′-CH), 4.9 (s, 2H, 4,4′-CH_2), 4.0 (s, 3H, -CH_3), 3.9 (s, 2H, 19-CH_2), 3.7 (s, 3H, -CH_3), 3.5 (m, 2H, 12-CH), 3.4 (s, 2H, 18-CH_2), 2.7 (t, 2H, 16-CH_2), 1.3 (m, 6H, 13,14,15-CH_2).

[*N*-(5-Aminopentyl)pyridin-2-yl-methylamino]acetato-4,4′-methylene-2-hydroxy-3-napthalenecarboxamide-(2′-hydroxy-3′-naphthoic acid) (12). To a solution of compound **11** (0.1 g, 0.15 mmol) in acetonitrile (10 mL) 1 M NaOH (10 mL) was added. The mixture was stirred at RT for 1 h after which the solution was neutralized with 1 M HCl. The solvents were evaporated, and the crude product was purified using column chromatography on silica gel eluted with ethyl acetate–methanol (70/30 v/v). TLC: $R_f = 0.1$ (system A). Accurate mass $[C_{36}H_{34}N_3O_7\text{-}H]^-$: theoretical 620.2402 Da, found 620.2393 Da.

RADIOCHEMISTRY

$^{99m}Tc(CO)_3(H_2O)_3^+$ Precursor. The technetium-99m tricarbonyl precursor was prepared using an Isolink kit (*19*) by adding 1.1–2.5 GBq of $Na^{99m}TcO_4$ in 1 mL saline to the kit followed by heating at 100 °C for 20 min. After cooling, the pH was adjusted as desired with 1 M HCl. Alternatively, homemade $^{99m}Tc(CO)_3(H_2O)_3^+$ was prepared by bubbling CO gas through a 10 mL sealed vial containing Na_2CO_3 (4.5 mg), Na/K tartrate

(20 mg), and $NaBH_4$ (25 mg) and adding 1.1–2.5 GBq of $Na^{99m}TcO_4$ in 1 mL saline followed by heating at 100 °C for 20 min. The vial was cooled to RT followed by neutralization with 1 M HCl. The precursor solution was then adjusted to the desired pH with 1 M NaOH before use. The yield of the precursor was 99% using the Isolink kit and 90% using the homemade method.

^{99m}Tc(CO)$_3$-bis-DTPA-pamoate. To a 10 mL labeling vial was added 1 mg of bis-DTPA pamoate (**5**) dissolved in 0.2 mL of 0.5 M phosphate buffer pH 11. The vial was purged with nitrogen, and 0.2–1.1 GBq of $^{99m}Tc(CO)_3(H_2O)_3^+$ precursor (0.2–0.5 mL, pH 11) was added. The final pH of the labeling mixture was 11. The mixture was heated at 70 °C for 20 min followed by cooling to RT. The crude labeling reaction mixture was analyzed and purified by RP-HPLC as described above. As the radiolabeled compound was not separated from the ligand bis-DTPA pamoate (**5**) by the HPLC purification, the specific activity of $^{99m}Tc(CO)_3$-bis-DTPA-pamoate was rather low (1 GBq/μmol) if the nonradioactive precursor was taken into account.

^{99m}Tc(CO)$_3$-12. To a 10 mL labeling vial containing 0.5 mg of compound **11** dissolved in 0.5 M phosphate buffer pH 7.4 under nitrogen was added 0.2–1.1 GBq $^{99m}Tc(CO)_3(H_2O)_3^+$ (0.2–0.5 mL, pH 7). The mixture was heated at 70 °C for 15 min followed by cooling and HPLC purification. In this case, the radiolabeled compound was well-separated from the ligand **12** by the HPLC purification; so the specific activity of $^{99m}Tc(CO)_3$-**12** was identical to that of the ^{99m}Tc-pertechnetate eluate, i.e., about 19 350 GBq/μmol.

Octanol/Buffer Partition Coefficient Determination. To 50 μL (74 kBq) of a solution of HPLC-purified radiolabeled compound in a test vial was added 2 mL of 1-octanol and 2 mL of 0.025 M phosphate buffer pH 7.4. The vial was vortexed at room temperature for 2 min and then centrifuged (Centrifuge 4226, Analis, Gent, Belgium) at 1700 g for 10 min. Approximately 50 μL of the 1-octanol phase and 500 μL of the phosphate buffer phase were pipetted and weighed into separate tared test tubes with adequate care to avoid cross contamination between the phases. The volume of fluid pipetted was calculated by dividing the net weight of the fluid by its density. The radioactivity of the test tubes was counted using a 3 in NaI(Tl) scintillation detector mounted in a sample changer. Corrections were made for background radiation and physical decay during counting. The octanol/buffer partition coefficient P was calculated as $P =$ cpm/mL in octanol / cpm/mL in buffer where cpm = counts per min.

***In Vitro* and *in Vivo* Stability of Tracers.** *In vitro* stability of $^{99m}Tc(CO)_3$-bis-DTPA-pamoate and $^{99m}Tc(CO)_3$-**12** at RT was studied by HPLC analysis of the HPLC-purified tracers over a 24 h period and by histidine challenge experiments. 200 μL aliquots (90 MBq) of solutions of the HPLC-purified ^{99m}Tc complexes were incubated with 0.5 mL of a 0.02 M solution of histidine at 37 °C, and the mixtures were analyzed over a 24 h period by RP-HPLC.

In vivo stability of $^{99m}Tc(CO)_3$-bis-DTPA-pamoate was studied in normal mice by determination of the relative amounts of the parent tracer and metabolites in mouse plasma and urine, while *in vivo* stability of $^{99m}Tc(CO)_3$-**12** was only evaluated in mouse plasma since renal excretion was minimal. After tail vein injection of 2.6 MBq of the tracer into mice, the animals were sacrificed by decapitation at 30 min, 4 h, or 24 h postinjection (one mouse per time point). For urine analysis, urine samples were directly injected onto an Oasis HLB column (hydrophilic–lipophilic balanced; 4.6 mm × 20 mm, Waters) in series with a RP-HPLC column (XTerra RPC_{18}, 5 μm, 4.6 mm × 250 mm; Waters, Milford, USA). Blood was collected into a BD vacutainer (containing 7.2 mg K_2EDTA; Beckton Dickinson, Franklin Lakes, USA) and subsequently transferred to a 1.5 mL Eppendorf tube. The blood samples were then centrifuged at 3000 rpm (1837 g) for 5 min to separate plasma. The supernatant plasma sample was injected onto an Oasis column that was preconditioned by successive washings with acetonitrile and water. The proteins of the biological matrix were washed from the Oasis column with 6 mL of water, which was collected in 6 1-mL fractions. The outlet of the Oasis column was then connected to an analytical RP-HPLC column, and both columns in series were then eluted using slightly modified HPLC conditions as compared to the analysis of the intact tracers [0.05 M ammonium acetate buffer (pH 6.8) (solvent A) and acetonitrile (solvent B): 0–8 min, linear gradient from 100% A to 50% A; 8–15 min, 50% A; 15–25 min, linear gradient to 100% B, at a flow rate of 1 mL/min over 30 min]. The HPLC eluate was collected in 35 1-mL fractions, and their radioactivity was measured using a gamma counter.

Biodistribution in Normal Mice. Mice were anesthetized with isoflurane (2%) in oxygen at a flow rate of 1 L/min and then injected via a tail vein with 74 kBq of either $^{99m}Tc(CO)_3$-bis-DTPA-pamoate in 0.1 mL of saline or $^{99m}Tc(CO)_3$-**12** in 0.1 mL of water/poly(ethylene glycol) 400 (PEG 400) 80/20 v/v. They were sacrificed by decapitation under anesthesia at 30 min, 4 h, or 24 h p.i. ($n = 4$ mice per time point). The organs were dissected and weighed in tared tubes, and radioactivity in all organs was counted in a gamma counter. Corrections were made for background radiation and physical decay during counting. Activity in the organs was expressed as % injected dose (I.D.)/organ and % I.D./g of organ. Activity in blood was calculated on the assumption that blood constitutes 7% of total body weight.

Rat Model of Reperfused Hepatic Infarction. Six adult Wistar rats weighing 350–450 g were anesthetized with i.p. injection of pentobarbital at a dose of 40 mg/kg. Under laparotomy, reperfused hepatic infarction was induced by clamping of the hilum of the right liver lobe for 3 h. After reperfusion by declamping hepatic inflow, the abdominal cavity was closed with two layered sutures, and the animals were allowed to recover for at least 8 h (*20*). A solution containing 18.5–74 MBq of $^{99m}Tc(CO)_3$-bis-DTPA-pamoate in 0.5 mL saline was injected via a tail vein, and the rats were sacrificed under anesthesia at 4 h ($n = 3$) or 24 h ($n = 3$) postinjection, followed by *ex vivo* studies.

Rat model of ethanol induced liver or muscular necrosis. Eight adult Wistar rats (body weight 350–450 g) were anesthetized as described above. Under laparotomy necrosis of the liver was induced by slow infusion of 0.2 mL ethanol into the left liver lobe (*21*). The abdominal cavity was closed and the animals were allowed to recover for 8–12 h. A solution containing 18.5–74 MBq of $^{99m}Tc(CO)_3$-bis-DTPA-pamoate or $^{99m}Tc(CO)_3$-**12** in 0.5 mL water/PEG 400 80/20 V/V was injected via a tail vein and the rats were sacrificed under anesthesia at 4 h postinjection ($n = 4$ per tracer) followed by *ex vivo* studies.

Under anesthesia, muscular necrosis was induced in four adult Wistar rats by gradual infusion of 0.2 mL ethanol into the right hind limb. The left hind limb was injected with saline and served as control. The animals were injected via a tail vein with 18.5–74 MBq of $^{99m}Tc(CO)_3$-bis-DTPA-pamoate in 0.5 mL saline and then sacrificed under anesthesia at 5.5 h p.i.. The muscles from the treated and control limbs were then subjected to *ex vivo* studies.

***Ex Vivo* Evaluation of Tracer Uptake.** For *ex vivo* studies, the necrotic tissues (liver and muscle) and healthy control tissues were thoroughly washed with saline (4 °C) to remove blood pool activity. The tissues were then stained separately in TTC solution (1% solution in normal saline) at 37 °C for

Table 1. Biodistribution in Normal Mice ($n \geq 3$ per time point) and in Rats with Reperfused Hepatic Infarction ($n = 3$ per time point) of $^{99m}Tc(CO_3)$-bis-DTPA-Pamoate[a]

	$^{99m}Tc(CO)_3$-bis-DTPA-pamoate expressed as % injected dose/g ± SD				
	normal mice			rats with reperfused hepatic infarction	
organ	30 min	4 h	24 h	4 h	24 h
kidneys	17.6 ± 7.4	25.1 ± 5.1	8.6 ± 1.2	6.1 ± 2.8	6.5 ± 1.6
viable liver lobe	4.5 ± 0.6	4.8 ± 0.3	3.6 ± 0.2	0.7 ± 0.1	0.6 ± 0.1
necrotic liver lobe	NA	NA	NA	1.2 ± 0.2	2.1 ± 0.5
spleen + pancreas	2.0 ± 0.1	1.6 ± 0.1	1.0 ± 0.1	0.6 ± 0.1	0.3 ± 0.0
lungs	8.3 ± 1.8	5.3 ± 1.4	1.9 ± 0.0	0.8 ± 0.1	0.5 ± 0.1
heart	3.8 ± 0.9	2.8 ± 0.7	1.2 ± 0.0	0.7 ± 0.1	0.3 ± 0.0
cerebrum	0.4 ± 0.1	0.3 ± 0.1	0.1 ± 0.0	ND	ND
cerebellum	0.6 ± 0.1	0.4 ± 0.1	0.1 ± 0.0	ND	ND
blood	14.3 ± 2.0	9.3 ± 1.1	2.3 ± 0.4	2.4 ± 0.7	0.8 ± 0.1
	% injected dose ± SD				
urine[b]	15.9 ± 5.6	18.4 ± 1.1	34.6 ± 3.7	5.0 ± 0.5	14.8 ± 0.3
intestines + feces[b]	5.9 ± 0.9	7.9 ± 0.4	24.5 ± 3.1	4.3 ± 0.8	9.4 ± 2.2

[a] NA: not applicable. ND: not determined. SD: standard deviation. [b] Values are shown as % of injected dose due to variability in the content of the bladder and intestines/feces.

Table 2. Biodistribution in Normal Mice ($n = 4$) of $^{99m}Tc(CO)_3$-[*N*-(5-aminopentyl)pyridin-2-yl-methylamino]methylacetato-4,4′-methylene-2-hydroxy-3-napthalenecarboxamide-(2′-hydroxy-3′-naphthoic acid methyl ester) ($^{99m}Tc(CO)_3$-12)[a]

	^{99m}Tc-**12** expressed as % injected dose/g ± SD	
organ	30 min	4 h
kidneys	1.5 ± 0.5	0.3 ± 0.1
liver	24.4 ± 3.0	2.1 ± 0.5
spleen + pancreas	0.6 ± 0.3	0.3 ± 0.1
brain	0.0 ± 0.0	0.0 ± 0.0
lungs	2.4 ± 0.7	0.8 ± 0.2
heart	0.3 ± 0.1	0.1 ± 0.0
blood	0.2 ± 0.0	0.1 ± 0.0
	% injected dose ± SD	
urine[b]	0.4 ± 0.3	0.9 ± 0.3
intestines + feces[b]	51.1 ± 4.8	93.5 ± 2.3

[a] SD: Standard deviation. [b] Values are shown as % of injected dose due to variability of the content of the bladder and intestines/feces.

15 min. Guided by TTC, the necrotic and viable tissue areas were identified, separated, and weighed; and radioactivity in the tissues was immediately counted in a 3 in NaI(Tl) scintillation detector mounted in a sample changer (Wallac Wizard). Corrections were made for background radiation and physical decay during counting, and activity was expressed as % I.D./g tissue. Digital photographs were taken prior to and after staining. The tissues were then quickly frozen in isopentane–liquid nitrogen and cut with a cryotome (Microm HM 550, Walldorf, Germany) into 5–50-μm-thick serial sections mounted on slides. Autoradiograms were obtained from these sections by exposing the slides for 2 days to a high-performance phosphor screen (super resolution screen; Canberra-Packard, Meriden, CT). The images were analyzed with *Optiquant* software (Canberra-Packard), and the radioactivity concentration in the autoradiograms was expressed in digital light units (DLU)/mm^2. Relative tracer concentrations in the necrotic and viable sections of the tissues were estimated by regions of interest (ROIs) analysis of the necrotic and the viable regions of 30 and 50-μm-thick sections of the autoradiograms of all the slices. After exposure for autoradiography, the samples were stained with H&E using a conventional procedure. The stained slices were digitally photographed and contrast enhanced with *Image J* software (NIH, Bethesda, MD). The H&E stained slices were used to examine microscopic evidence of tissue necrosis.

***In Vivo* Detection of Hepatic Infarction by $^{99m}Tc(CO)_3$-bis-DTPA-pamoate Planar Scintigraphy.** Three additional rats with reperfused hepatic infarction and two control rats were used to explore the feasibility of *in vivo* detection of necrosis by $^{99m}Tc(CO)_3$-bis-DTPA-pamoate planar gamma scintigraphy. Rats with reperfused hepatic infarction and a control rat were injected with 53 or 85 MBq of $^{99m}Tc(CO)_3$-bis-DTPA-pamoate followed by 20 min planar imaging at 7 or 23 h p.i. using a parallel hole collimator of a dual-head gamma camera (E-Cam, Siemens Medical Systems, Hoffman Estates, IL) equipped with a pinhole and a parallel hole collimator. Planar imaging was immediately followed by a computed tomography scan (CT, Biograph16, Siemens, Knoxville, TN) for anatomical delineation of the liver.

RESULTS AND DISCUSSION

Chemistry. Bis-DTPA-pamoate (**5**) was synthesized as shown in Scheme 1. Compound **2** was synthesized using dimethyl sulfate in high yield. Coupling of DTPA through one of the terminal carboxylates to pamoic acid bis-hydrazide was realized in good yield using DTPA monoanhydride monoethyl ester (yield 75%). All compounds were characterized by ^{1}H NMR (recorded at 300 Hz).

[*N*-(5-Aminopentyl)pyridin-2-yl-methylamino]acetato-4,4′-methylene-2-hydroxy-3-napthalenecarboxamide-(2′-hydroxy-3′-naphthoic acid) (**12**) was synthesized as shown in Scheme 2B. Synthesis of compound **11** started from pamoic acid monomethyl ester followed by activation of the second carboxylic acid using *N*-hydroxysuccinimide in the presence of DCC as an *in situ* dehydration reagent with a yield of 60%. Ester hydrolysis of compound **11** with 1 M NaOH provided compound **12** with a yield of 85% (HPLC analysis). Labeling of crude **12** or HPLC-purified **12** resulted in similar labeling yields. In all cases, intermediate and final products were purified on normal-phase or reversed-phase silica gel and the purity verified by RP-HPLC to be >95%.

Radiochemistry. Labeling of bis-DTPA-pamoate with a $^{99m}Tc(CO)_3$ core at pH 11 resulted in a main peak (retention time $t_R = 13.5$ min, 1 GBq/μmol) and a slightly more polar peak. The low specific activity of $^{99m}Tc(CO)_3$-bis-DTPA-pamoate resulted from a partial coelution of the unlabeled precursor (bis-DTPA-pamoate) with the labeled compound. However, experience from experiments with Gd-labeled pamoate derivatives for MRI, where milligram amounts are used, and from experiments with derivatives of hypericin, both with low and high specific activity, has shown that specific activity

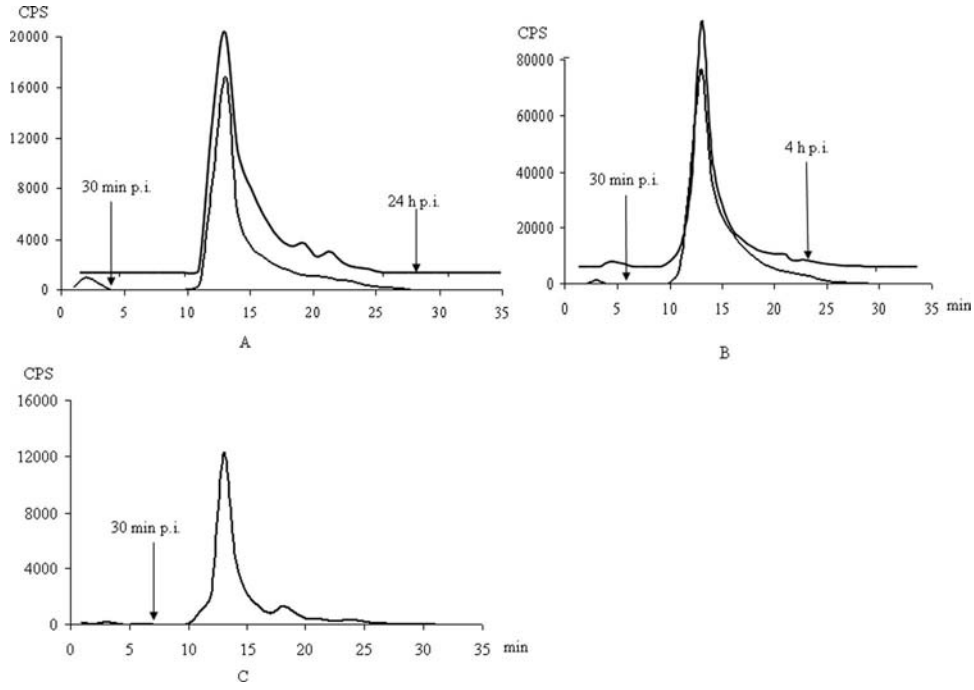


Figure 2. RP-HPLC analysis of mouse plasma (A) and urine (B) after intravenous injection of $^{99m}Tc(CO)_3$-bis-DTPA-pamoate at 30 min p.i. and 24 h p.i. (C) RP-HPLC analysis of mouse plasma after intravenous injection of $^{99m}Tc(CO)_3$-**12** (B) at 30 min p.i.

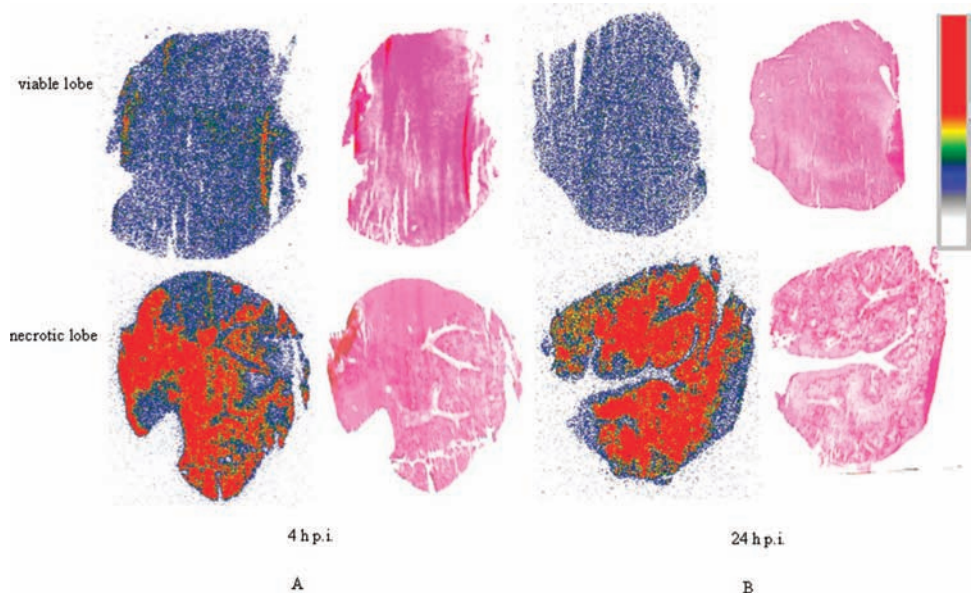


Figure 3. (A) Representative autoradiograms (first and third columns) and corresponding H&E stained sections (second and fourth columns) of 30 μm slices of rat liver with reperfused hepatic infarction. Viable liver lobe (upper row) and necrotic liver lobe (bottom row) at 4 h postinjection of $^{99m}Tc(CO)_3$-bis-DTPA-pamoate and (B) at 24 h postinjection.

is not important with respect to the ability of these agents to localize to a high and sufficient degree in necrotic tissue. A number of isomers could arise from $^{99m}Tc(CO)_3$ labeling of such a bis-DTPA-derivatized compound, including binding of the $^{99m}Tc(CO)_3$ core between the two DTPA ligands or coordination via two amino nitrogens and a carboxylic oxygen, or via three amino nitrogen atoms besides binding in the way suggested in Figure 1A. The main peak containing 95% of the activity was used for the biological evaluation and is thought to consist of a $^{99m}Tc(CO)_3$ core bonded to two carboxylic oxygens and one amino nitrogen of one of the DTPA chains (Figure 1) analogous to the binding of a $^{99m}Tc(CO)_3$ core to iminodiacetic acid (*22*). The structure for the $^{99m}Tc(CO)_3$-DTPA moiety as presented in Figure 1 has also been proposed by a number of other authors (*23*, *24*).

Labeling of compound **12** with technetium-99m tricarbonyl was achieved in very good yield (97%) by heating a buffered solution (pH 7.4) of the precursor and the ^{99m}Tc-tricarbonyl precursor at 70 °C for 15 min. After efficient HPLC purification, a specific activity of about 19 350 GBq/μmol was obtained. Facile labeling of compound **12** is the result of stabilization by π-electrons of the aromatic nitrogen and d^6 electrons of the Tc-metal core (*18*). We also labeled the BFC (**10**) as a reference (HPLC t_R = 12.6 min vs 23.5 min for $^{99m}Tc(CO)_3$-**12**).

Octanol/Phosphate Buffer Partition Coefficient. The log *P* values (±SD) were found to be −1.93 (±0.03) and 2.85

(±0.13) for $^{99m}Tc(CO)_3$-bis-DTPA-pamoate and $^{99m}Tc(CO)_3$-**12,** respectively. Carboxylic acid functions not participating in complex formation account for the hydrophilic nature of $^{99m}Tc(CO)_3$-bis-DTPA-pamoate, but the hydrophilic character may be different in an *in vivo* situation, where there is a possibility of complexation with Ca^{2+} ions in blood, leading to increased lipophilicity and potential retention.

Biodistribution and Stability (*in Vitro* and *in Vivo*) of Tracers. Biodistribution results for $^{99m}Tc(CO)_3$-bis-DTPA-pamoate in normal NMRI mice and in rats with reperfused liver infarction are shown in Table 1 with the results expressed as % injected dose (% I.D.)/g tissue (±SD), except for urine and intestines, where the radioactivity is expressed as % I.D./tissue in view of the variable amount of urine produced and food intake. In normal mice, the tracer was cleared mainly via the kidneys resulting in urine activity of 15.9%, 18.4%, and 34.6% I.D. at 30 min, 4 h, and 24 h p.i., respectively. There was also a significant clearance via the hepatobiliary system resulting in high activity in intestines and feces. Plasma clearance was slow with 6.4% I.D. remaining in blood at 24 h p.i.. Radioactivity in mice carcass was 28.6% and 17.1% I.D. at 30 min p.i. and 24 h p.i., respectively. The reason for the slightly higher carcass activity can be attributed to the slow blood clearance and retention of tracer in muscles. As expected, there was negligible brain uptake of the tracer.

Guided by TTC staining, the necrotic lobes of rats with reperfused liver infarction (TTC negative) were separated from the viable lobes (TTC positive). $^{99m}Tc(CO)_3$-bis-DTPA-pamoate showed higher uptake in liver with reperfused infarction than in normal liver at 4 h and 24 h p.i. At 4 h p.i., the radioactivity concentration was 1.7 times higher in necrotic liver tissue than in normal liver, and this ratio increased to 3.5 at 24 h p.i. Apart from this, biodistribution in rats was similar to that in mice. In rats with ethanol-induced liver necrosis, radioactivity per gram tissue at 4 h p.i. was 1.3 times higher in necrotic liver tissue as compared to normal liver (biodistribution data not shown). The actual ratio was higher, as it appeared impossible to dissect purely necrotic tissue, which always was mixed with some healthy tissue. Therefore, uptake in different areas was more accurately quantified by autoradiography.

Biodistribution results of $^{99m}Tc(CO)_3$-**12** in normal mice are shown in Table 2. The tracer agent showed more rapid clearance from the blood circulation than the more polar $^{99m}Tc(CO)_3$-bis-DTPA-pamoate. Activity of $^{99m}Tc(CO)_3$-**12** in blood was 0.6% and 0.2% I.D at 30 min and 4 h p.i., respectively. The tracer was cleared mainly via the hepatobiliary pathway, resulting in high radioactivity in intestines and feces. Uptake in carcass was negligible at 30 min and 4 h p.i.. Surprisingly, $^{99m}Tc(CO)_3$-**12** did not show any preferential uptake in the necrotic cells in rat studies, both by activity counting (necrotic to viable tissue radioactivity ratio was 0.9 at 4 h p.i.) and by autoradiography (results not shown).

The very high lipophilicity of $^{99m}Tc(CO)_3$-**12** is without doubt the reason for its prominent and fast clearance via liver and intestines and can explain why it is cleared more rapidly from plasma than $^{99m}Tc(CO)_3$-bis-DTPA-pamoate. At this moment, however, no further conclusions can be drawn with respect to a potential relationship between the observed lipophilicity of the complexes and the uptake in necrotic tissue. Both hydrophilic agents (e.g., ^{99m}Tc-glucarate (*25*) and $^{99m}Tc(CO)_3$-bis-DTPA-pamoate) and very lipophilic agents (derivatives of hypericin) (*20, 21*) have shown high avidity for necrotic tissue, so necrosis avidity does not seem to be primarily associated with the lipophilicity of a compound). It is unclear why $^{99m}Tc(CO)_3$-bis-DTPA-pamoate has a higher uptake in necrotic tissue as compared to ^{99m}Tc-**12**. One of the possibilities is that the rapid blood clearance of $^{99m}Tc(CO)_3$-**12** does not allow for time needed for efficient tracer perfusion into the necrotic lesions. On the other hand, the structural differences and the different overall charge and lipophilicity of both tracer agents may contribute to the clearly different biological properties and uptake in necrotic tissue.

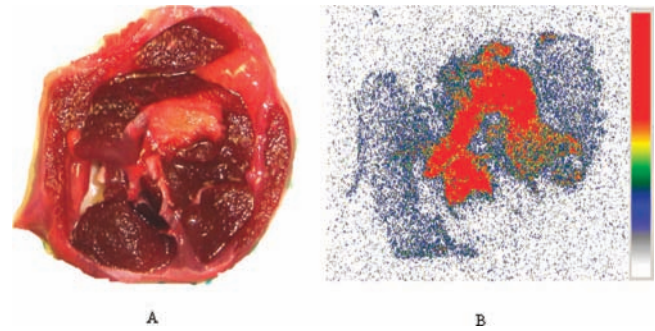


Figure 4. (A) TTC stained muscle after ethanol injection (pale stained, TTC negative area) and adjacent viable muscle tissue (deep red). (B) Autoradiogram of necrotic muscle shows high uptake of $^{99m}Tc(CO)_3$-bis-DTPA-pamoate (5.5 h postinjection) in necrotic area with a necrotic to viable tissue ratio of 18.

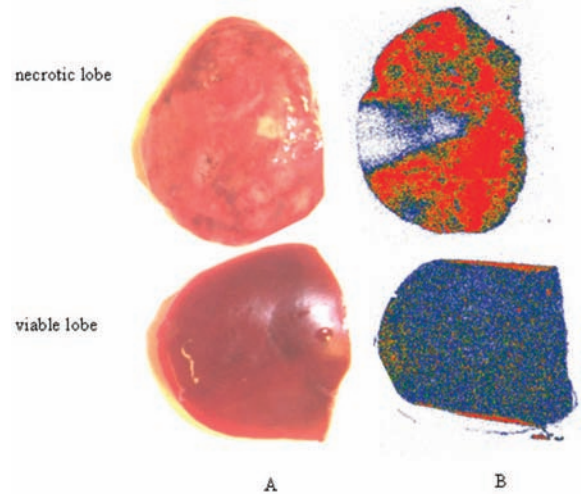


Figure 5. (A) TTC stained liver lobes of rat with ethanol-induced liver necrosis and (B) corresponding autoradiogram of 50 μm slice of the necrotic and viable liver lobes after intravenous injection of $^{99m}Tc(CO)_3$-bis-DTPA-pamoate.

For both tracers, more than 98% of intact tracer was recovered after incubation of the radiolabeled compound for 24 h at room temperature. In challenge experiments with histidine, known to be one of the most potent tridentate chelators for binding of a $^{99m}Tc(CO)_3$ core and often used in tricarbonyl organometallic chemistry to investigate the *in vitro* stability of $^{99m}Tc(CO)_3$ complexes (*18*), $^{99m}Tc(CO)_3$-bis-DTPA-pamoate was less than 50% stable after 24 h in the presence of 0.01 M histidine (>20-fold excess of histidine) at 37 °C, while $^{99m}Tc(CO)_3$-**12** was 98% stable under the same conditions. Results of HPLC analysis of mouse plasma and urine after intravenous injection of $^{99m}Tc(CO)_3$-bis-DTPA-pamoate are shown in Figure 2A,B, respectively. $^{99m}Tc(CO)_3$-bis-DTPA-pamoate showed good stability in plasma and in urine: 98% and 90% of intact tracer were recovered from plasma at 30 min and 24 h p.i., respectively (Figure 2A), while 98% of intact tracer was recovered in urine at 30 min and 4 h p.i. (Figure 2B). This indicates that the *in vivo* stability is sufficient for its use *in vivo* despite its relative instability in histidine-challenging experiments. Less than 10% of lipophilic metabolites were found at 24 h p.i. Such metabolites could result from *in vivo* transchelation of the radiometal to more stable and more lipophilic complexes with plasma proteins.

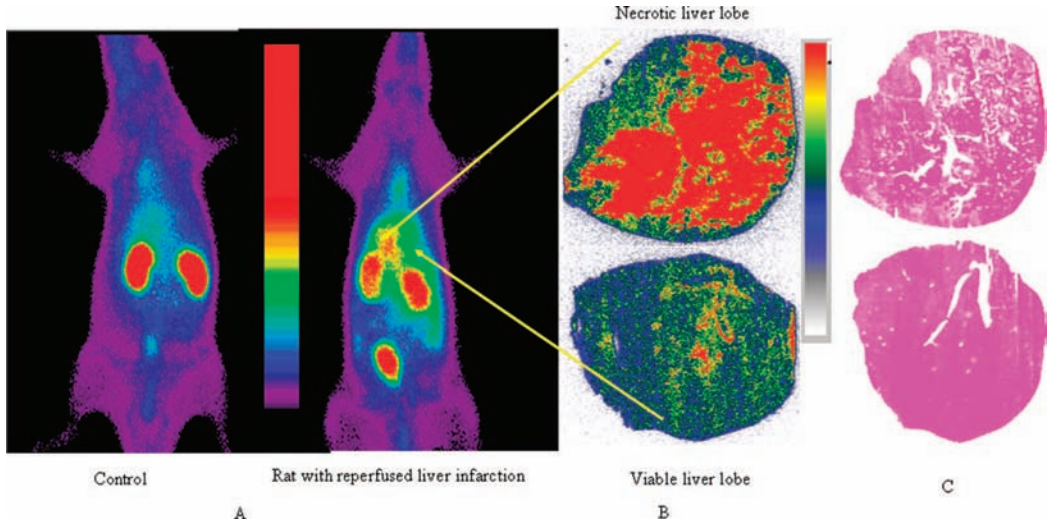


Figure 6. (A) *In vivo* planar image of a control rat and a rat with reperfused hepatic infarction at 7 h postinjection of ^{99m}Tc(CO)$_3$-bis-DTPA-pamoate. (B,C) Autoradiograms of 30 μm liver slices of the same rat after sacrifice (B, top row = necrotic liver and bottom row = viable liver) and scanned photographs of the same slices after H&E staining (C) staining show good correlation with the *in vivo* planar image.

^{99m}Tc(CO)$_3$-**12** was stable in histidine challenge experiments, as 98% of the intact tracer was recovered after 24 h incubation in the presence of excess histidine at 37 °C. The tracer was also stable *in vivo* in mice. At 30 min, there was 97% of intact tracer in plasma (Figure 2C). Plasma stability was not evaluated at later time points, since activity in blood was negligible. For both tracers, however, there was minimal reoxidation to TcO_4^- at all time points examined.

***Ex Vivo* and *in Vivo* Specificity for Necrotic Tissue.** In all rat models, TTC staining confirmed the presence of necrosis. TTC is an avid dye for mitochondrial dehydrogenase activity, and its absence results in pale staining of necrotic tissues by TTC (TTC negative), whereas viable tissues with enzymatic activity would reduce TTC into deep red insoluble formazan (TTC positive) (*26*). Autoradiograms and photographs of the corresponding H&E stained slices of liver of rats with reperfused liver infarction and sacrificed at 4 h or 24 h p.i are shown in Figure 3A,B, respectively. Necrotic to viable tissue activity ratios of ^{99m}Tc(CO)$_3$-bis-DTPA-pamoate in rats with reperfused liver infarction were 7 and 9 at 4 h and 24 h p.i., respectively, as determined by quantitative autoradiography. The contrast ratios at 4 h and 24 h did not differ much because of the rather slow clearance of ^{99m}Tc(CO)$_3$-bis-DTPA-pamoate from liver. Since the tracer is also excreted via the liver, the specificity was further explored in rats with ethanol-induced muscular necrosis (Figure 4). Following infusion of 0.2 mL ethanol (right hind limb) or 0.2 mL saline (left hind limb, control), ^{99m}Tc(CO)$_3$-bis-DTPA-pamoate was administered via i.v.. injection to the rats ($n = 4$) which were sacrificed at 5.5 h p.i.. A TTC negative area was visible in the treated limb (Figure 4A) but not in the control limb (data not shown). Necrotic to viable tissue activity ratios were 15–18 on autoradiography (Figure 4B). The lower necrotic to viable tissue ratio (4:1) observed in the case of ethanol-induced liver necrosis (Figure 5B) could be due to a complete collapse of vasculature following ethanol infusion leading to severe perfusion defects and consequently restricted accessibility of the tracer to necrotic tissue.

In vivo planar imaging was performed in rats with reperfused hepatic infarction at 7 h and 23 h p.i. of ^{99m}Tc(CO)$_3$-bis-DTPA-pamoate. Figure 6A shows representative *in vivo* planar images obtained at 7 h p.i. from a control rat and a rat with hepatic infarction, respectively. Corresponding autoradiograms of 30 μm liver slices of the same rat after sacrifice are shown in Figure 6B (top row = necrotic liver and bottom row = viable liver) and scanned photographs of the same slices after H&E staining in Figure 6C. As can be seen from these images, there was a good match between *in vivo* and *ex vivo* images with high tracer uptake in necrotic liver lobe (hot spots on planar images and autoradiograms). This high uptake was confirmed by gamma counting of dissected liver tissue. For an infarct avid agent to be clinically useful, it should show rapid localization in the infarcted tissue, high avidity and high specificity for necrotic tissue, and a reasonable duration of scan positivity. In the case of AMI, it is important that an infarct avid agent localizes early enough within the time window for thrombolytic therapy (usually <6 h) of the acute event, because delineation and sizing of the infarct is important to determine prognosis and decision making for further therapeutic interventions. A number of infarct avid imaging agents have been used in nuclear medicine for infarct delineation and sizing after AMI with none having all the afore-mentioned optimal imaging characteristics. These include ^{111}In-labeled antimyosin monoclonal antibody (*27*), ^{99m}Tc-pyrophosphate (*28*) and more recently ^{99m}Tc-glucarate (*25*). In the present preliminary evaluation, ^{99m}Tc(CO)$_3$-bis-DTPA-pamoate was localized and retained in the necrotic tissue both early (4 h p.i.) and late (24 h p.i.) in rat liver with reperfused infarction. Late retention in necrotic liver tissue was confirmed by *in vivo* planar imaging, a result which was confirmed by gamma counting and autoradiography (results not shown).

Figure 7 shows a representative photomicrograph of an H&E stained slice of rat liver after reperfused hepatic infarction. Severe tissue thinning and the absence of intact nuclei and cytoplasm are evident in the necrotic regions, while adjacent viable tissue shows intact structures and corresponding low tracer uptake. These necrotic regions are the areas that show high uptake of ^{99m}Tc(CO)$_3$-bis-DTPA-pamoate.

Although the mechanism of uptake of ^{99m}Tc(CO)$_3$-bis-DTPA-pamoate still has to be fully elucidated, one speculative hypothesis is that the tracer binds to Ca^{2+} stores (for which DTPA has a high complexation constant) released during necrotic death, a strong characteristic signal of necrotic cell death (*29*). In addition, ^{99m}Tc-pyrophosphate has been shown to bind to sequestered Ca^{2+} stores that are released during necrotic cell death in the case of AMI (*30*). Ca^{2+} sequestration, however, is

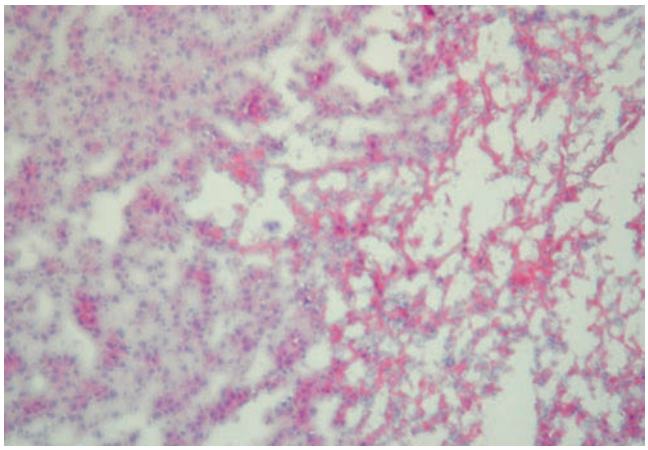


Figure 7. Photomicrograph of rat liver after reperfused hepatic infarction. Disintegrated nuclei and lack of cytoplasm are characteristic evidence of necrosis.

a fairly late but persistent event that occurs during necrotic cell death. This hypothesis remains to be tested.

CONCLUSION

In this study, we have shown that $^{99m}Tc(CO)_3$-bis-DTPA-pamoate is avid for necrotic tissue in three animal models of necrosis, with necrotic to viable tissue activity ratios as high as 18, as determined by quantitative autoradiography. The multiple negative charges of the unbound DTPA chelator at physiological pH could be essential for the *in vivo* binding to necrotic tissue, given the fact that $^{99m}Tc(CO)_3$-**12** did not show avidity for necrotic tissue. To verify this hypothesis, it is our intention to couple different bifunctional chelators (with different charges) to pamoic acid and to evaluate their avidity for necrotic tissue. On the other hand, In^{3+} and Ga^{3+} form more stable complexes with DTPA than technetium-99m. Labeling of $^{99m}Tc(CO)_3$-bis-DTPA-pamoate with $^{111}In^{3+}$ or $^{67/68}Ga^{3+}$could result in radiotracers with versatile imaging properties, a study that is ongoing.

ACKNOWLEDGMENT

The authors would like to thank Peter Vermaelen and Sofie Celen for their contributions to the study. Financial support for the project was obtained from grants awarded by Geconcerteerde Onderzoeksactie (GOA) of the Flemish Government, FWO-Vlaanderen grant G. 0257.05, and in part by the EC - FP6-project DiMI, LSHB-CT-2005-512146.

LITERATURE CITED

(1) Lennon, S. V., Martin, S. J., and Cotter, T. G. (1991) Dose-dependent induction of apoptosis in human tumour cell lines by widely diverging stimuli. *Cell Prolif. 24*, 203–214.

(2) Nagata, S., and Golstein, P. (1995) The Fas death factor. *Science 267*, 1449–1456.

(3) Steller, H. (1995) Mechanisms and genes of cellular suicide. *Science 267*, 1445–1449.

(4) Kajstura, J., Cheng, W., Reiss, K., Clark, W. A., Sonnenblick, E. H., Krajewski, S., Reed, J. C., Olivetti, G., and Anversa, P. (1996) Apoptotic and necrotic myocyte cell deaths are independent contributing variables of infarct size in rats. *Lab. Invest. 74*, 86–107.

(5) Narula, J., Haider, N., Virmani, R., DiSalvo, T. G., Kolodgie, F. D., Hajjar, R. J., Schmidt, U., Semigran, M. J., Dec, G. W., and Khaw, B. A. (1996) Apoptosis in myocytes in end-stage heart failure. *N. Engl. J. Med. 335*, 1182–1189.

(6) Gottlieb, R. A., Burleson, K. O., Kloner, R. A., Babior, B. M., and Engler, R. L. (1994) Reperfusion injury induces apoptosis in rabbit cardiomyocytes. *J. Clin. Invest. 94*, 1621–1628.

(7) Braunwald, E., and Kloner, R. A. (1985) Myocardial reperfusion: a double-edged sword? *J. Clin. Invest. 76*, 1713–1719.

(8) Lahorte, C. M., Vanderheyden, J. L., Steinmetz, N., Van de Wiele, C., Dierckx, R. A., and Slegers, G. (2004) Apoptosis-detecting radioligands: current state of the art and future perspectives. *Eur. J. Nucl. Med. Mol. Imaging 31*, 887–919.

(9) Boersma, H. H., Kietselaer, B. L., Stolk, L. M., Bennaghmouch, A., Hofstra, L., Narula, J., Heidendal, G. A., and Reutelingsperger, C. P. (2005) Past, present, and future of annexin A5: from protein discovery to clinical applications. *J. Nucl. Med. 46*, 2035–2050.

(10) Hofstra, L., Liem, I. H., Dumont, E. A., Boersma, H. H., van Heerde, W. L., Doevendans, P. A., De Muinck, E., Wellens, H. J., Kemerink, G. J., Reutelingsperger, C. P., and Heidendal, G. A. (2000) Visualisation of cell death in vivo in patients with acute myocardial infarction. *Lancet 356*, 209–212.

(11) Maulik, N., Kagan, V. E., Tyurin, V. A., and Das, D. K. (1998) Redistribution of phosphatidylethanolamine and phosphatidylserine precedes reperfusion-induced apoptosis. *Am. J. Physiol. 274*, H242–H248.

(12) Flotats, A., and Carrio, I. (2003) Non-invasive in vivo imaging of myocardial apoptosis and necrosis. *Eur. J. Nucl. Med. Mol. Imaging 30*, 615–630.

(13) Mariani, G., Villa, G., Rossettin, P. F., Spallarossa, P., Bezante, G. P., Brunelli, C., Pak, K. Y., Khaw, B. A., and Strauss, H. W. (1999) Detection of acute myocardial infarction by 99mTc-labeled D-glucaric acid imaging in patients with acute chest pain. *J. Nucl. Med. 40*, 1832–1839.

(14) Ni, Y., Bormans, G., Chen, F., Verbruggen, A., and Marchal, G. (2005) Necrosis avid contrast agents: functional similarity versus structural diversity. *Invest. Radiol. 40*, 526–535.

(15) Marchal, G. J. F., Verbruggen, A., Ni, Y., and Adriaens, P. (2000) Non-porphyrin compounds for use as a diagnosticum and/or pharmaceutical. Patent Number PCT/BE99/00104.

(16) Alberto, R., Schibli, R., Egli, A., Schubiger, A. P., Abram, U., and Kaden, T. A. (1998) A novel organometallic aqua complex of technetium for the labeling of biomolecules: Synthesis of [Tc-99m(OH2)(3)(CO)(3)](+) from [(TcO4)-Tc-99m](−) in aqueous solution and its reaction with a bifunctional ligand. *J. Am. Chem. Soc. 120*, 7987–7988.

(17) Alberto, R., Schibli, R., Waibel, R., Abram, U., and Schubiger, A. P. (1999) Basic aqueous chemistry of [M(OH2)(3)(CO)(3)](+) (M = Re, Tc) directed towards radiopharmaceutical application. *Coord. Chem. Rev. 192*, 901–919.

(18) Stichelberger, A., Waibel, R., Dumas, C., Schubiger, P. A., and Schibli, R. (2003) Versatile synthetic approach to new bifunctional chelating agents tailor made for labeling with the fac-[M(CO)(3)](+) core (M = Tc, Tc-99m, Re): synthesis, in vitro, and in vivo behavior of the model complex [M(APPA)(CO)(3)] (APPA = [(5-amino-pentyl)-pyridin-2-yl-methyl-amino]-acetic acid). *Nucl. Med. Biol. 30*, 465–470.

(19) Alberto, R., Schibli, R., Egli, A., Schubiger, P. A., Herrmann, W. A., Artus, G., Abram, U., and Kaden, T. A. (1995) Metal-carbonyl syntheses.22. Low-pressure carbonylation of [Mocl(4)](−) and [Mo4](−) - the technetium(I) and rhenium(I) complexes [Net(4)](2)[Mcl(3)(Co)(3)]. *J. Organometallic Chem. 493*, 119–127.

(20) Ni, Y., Huyghe, D., Verbeke, K., de Witte, P. A., Nuyts, J., Mortelmans, L., Chen, F., Marchal, G., Verbruggen, A. M., and Bormans, G. M. (2006) First preclinical evaluation of mono-[123I]iodohypericin as a necrosis-avid tracer agent. *Eur. J. Nucl. Med. Mol. Imaging 33*, 595–601.

(21) Fonge, H., Jin, L., Wang, H., Ni, Y., Bormans, G., and Verbruggen, A. (2007) Synthesis and preliminary evaluation of mono-[(123)I]iodohypericin monocarboxylic acid as a necrosis avid imaging agent. *Bioorg. Med. Chem. Lett. 17*, 4001–4005.

(22) Schibli, R., La Bella, R., Alberto, R., Garcia-Garayoa, E., Ortner, K., Abram, U., and Schubiger, P. A. (2000) Influence of

the denticity of ligand systems on the in vitro and in vivo behavior of (99m)Tc(I)-tricarbonyl complexes: a hint for the future functionalization of biomolecules. *Bioconjugate Chem. 11*, 345–351.

(23) Trump, D. P., Mathias, C. J., Yang, Z., Low, P. S., Marmion, M., and Green, M. A. (2002) Synthesis and evaluation of 99mTc(CO)(3)-DTPA-folate as a folate-receptor-targeted radiopharmaceutical. *Nucl. Med. Biol. 29*, 569–573.

(24) Bullok, K. E., Dyszlewski, M., Prior, J. L., Pica, C. M., Sharma, V., and Piwnica-Worms, D. (2002) Characterization of novel histidine-tagged Tat-peptide complexes dual-labeled with (99m)Tc-tricarbonyl and fluorescein for scintigraphy and fluorescence microscopy. *Bioconjugate Chem. 13*, 1226–1237.

(25) Narula, J., Petrov, A., Pak, K. Y., Lister, B. C., and Khaw, B. A. (1997) Very early noninvasive detection of acute experimental nonreperfused myocardial infarction with 99mTc-labeled glucarate. *Circulation 95*, 1577–1584.

(26) Roberts, L. W. (1951) Survey of factors responsible for reduction of 2,3,5-triphenyltetrazolium chloride in plant meristems. *Science 113*, 692–693.

(27) Khaw, B. A., Fallon, J. T., Beller, G. A., and Haber, E. (1979) Specificity of localization of myosin-specific antibody fragments in experimental myocardial infarction. Histologic, histochemical, autoradiographic and scintigraphic studies. *Circulation 60*, 1527–1531.

(28) Keyes, J. W., Leonard, P. F., Brody, S. L., Svetkoff, D. J., Rogers, W. L., and Lucchesi, B. R. (1978) Myocardial infarct quantification in the dog by single photon emission computed tomography. *Circulation 58*, 227–232.

(29) Szabo, C. (2005) Mechanisms of cell necrosis. *Crit. Care Med. 33*, S530–S534.

(30) Buja, L. M., Tofe, A. J., Kulkarni, P. V., Mukherjee, A., Parkey, R. W., Francis, M. D., Bonte, F. J., and Willerson, J. T. (1977) Sites and mechanisms of localization of technetium-99m phosphorus radiopharmaceuticals in acute myocardial infarcts and other tissues. *J. Clin. Invest. 60*, 724–740.

BC700236J

A Multipurpose Receptor Composed of Promiscuous Proteins. Analyte Detection through Pattern Recognition

Johan Viljanen,[†] Jenny Larsson,[†] Andréas Larsson,[†] and Kerstin S. Broo*[,‡]

IFM, Linköping University, S-581 83 Linköping, Sweden, and Department of Chemistry, Göteborg University, S-412 96 Göteborg, Sweden. Received July 5, 2007; Revised Manuscript Received August 17, 2007

A multipurpose receptor akin to the "electronic nose" was composed of coumarin-labeled mutants of human glutathione transferase A1. We have previously constructed a kit for site-specific modification of a lysine residue (A216K) using a thiol ester of glutathione (GSC-Cou_{bio}) as a modifying reagent. In the present investigation, we scrambled the hydrophobic binding site (H-site) of the protein scaffold through mutations at position M208 via random mutagenesis and isolated a representative library of 11 A216K/M208X mutants. All of the double mutants could be site-specifically labeled to form the $K216_{Cou}$ conjugates. The labeled proteins responded to the addition of different analytes with signature changes in their fluorescence spectra resulting in a matrix of 96 data points per analyte. Ligands as diverse as *n*-valeric acid, fumaric acid monoethyl ester, lithocholic acid, 1-chloro-2,4-dinitrobenzene (CDNB), glutathione (GSH), *S*-methyl-GSH, *S*-hexyl-GSH, and GS-DNB all gave rise to signals that potentially can be interpreted through pattern recognition. The measured K_d values range from low micromolar to low millimolar. The cysteine residue C112 was used to anchor the coumarin-labeled protein to a PEG-based hydrogel chip in order to develop surface-based biosensing systems. We have thus initiated the development of a multipurpose, artificial receptor composed of an array of promiscuous proteins where detection of the analyte occurs through pattern recognition of fluorescence signals. In this system, many relatively poor binders each contribute to detailed readout in a truly egalitarian fashion.

INTRODUCTION

The human olfactory system has inspired researchers to develop an electronic nose based on relatively nonspecific sensor electrodes (*1, 2*). The identification of a particular compound is then based on a mathematical interpretation of the signals from the array of electrodes (*3, 4*). Colorimetric sensor arrays for molecular recognition are also common in biosensing applications (*5–8*). We realized that this approach could be extended to utilize proteins as receptors and that the scaffolds we use in our protein reengineering efforts, the glutathione transferases (GSTs,[1] E.C. 2.5.1.18) (*41*) are in fact exceptionally well suited for this type of experiment.

Our previous studies have led us to focus on human glutathione transferase (hGST) A1-1 (Figure 1), a protein that is easy to express and purify, displays a high stability, and is tolerant to mutations (*9–11*). The crystal structure has been solved both with and without ligands (*12, 13*). The GSTs are dimeric detoxication enzymes (phase II) that catalyze the nucleophilic addition of the thiol of glutathione (GSH) to a wide range of hydrophobic electrophilic molecules (*14*). Since they have evolved to function as detoxication enzymes, GSTs have a promiscuous H-site that accepts a large variety of hydrophobic electrophiles (*15–18*), but the glutathione-binding site (G-site) is quite specific (*13, 16*). The modular features of the GSTs are ideal from a protein reengineering aspect with specific binding of GSH in the G-site combined with an adjacent, promiscuous H-site.

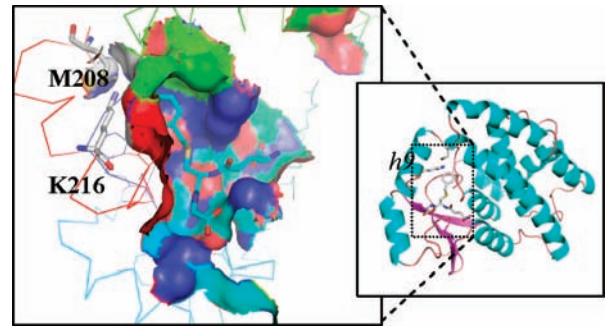


Figure 1. Close-up of the crystal structure (1GUH) of wt hGST A1-1 (A216 replaced with K216) in a complex with *S*-benzyl-GSH. Positions 216 and 208 are shown in "stick" representation, and the flexible helix 9 (h9) is also indicated in the figure. The protein is dimeric but shown here as a monomer for reasons of clarity of presentation. The figure was done with the help of the PyMol (DeLano Scientific LLC) software.

In our previous studies we have extended the repertoire of the protein scaffolds by chemical modifications (*19, 20*). Some of the introduced moieties have fluorescent properties, and we recently developed a method for clean labeling through surface-assisted delivery of fluorescent acyl groups to a specific lysine (K216) introduced through mutation of hGST A1 (*21*) (Scheme 1). The introduced K216 is located in the H-site of the folded

* To whom correspondence should be addressed. Phone: +46-31-772 2745. Fax: +46-31-772 3840. E-mail: brook@chem.gu.se.

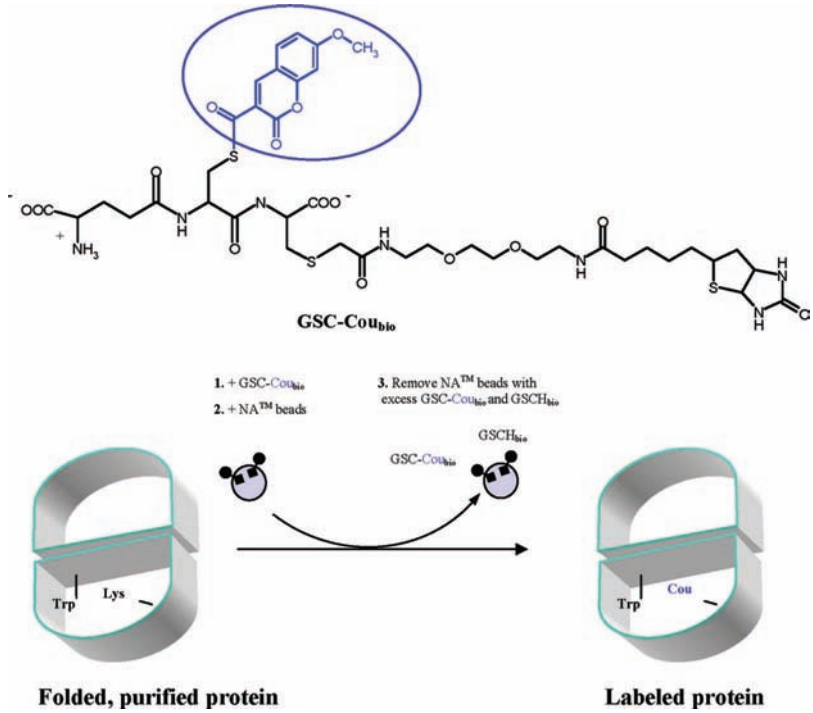
[†] Linköping University.

[‡] Göteborg University.

[1] Abbreviations: $A216K_{Cou}$, coumarin-labeled A216K; C_{18}, octadecyl; CDNB, 1-chloro-2,4-dinitrobenzene; FRET, fluorescence resonance energy transfer; G-site, glutathione-binding site; GS-thiol ester, thiol ester of glutathione; GSC, γ-Glu-Cys-Cys; GS-DNB, the conjugate formed between glutathione and CDNB; GSH, glutathione, γ-Glu-Cys-Gly; GST, glutathione transferase; H-site, hydrophobic electrophile binding site; hGST A1-1, GST A1-1 isoform from human; HPLC, high-performance liquid chromatography; MALDI-MS, matrix assisted laser desorption ionization mass spectrometry; NA, immobilized NeutrAvidin; NaP_i, sodium phosphate; NHS, *N*-hydroxysuccinimide; OD, optical density; PDEA, 2-(2-pyridinyldithio)ethaneamine; PEG, polyethyleneglycol; rt, room temperature; TFA, trifluoroacetic acid; TOF, time of flight; UV, ultraviolet; wt, wild type.

10.1021/bc700247x CCC: $37.00 © 2007 American Chemical Society
Published on Web 10/17/2007

Scheme 1



protein scaffold (Figure 1), and we hypothesized that K216$_{Cou}$ could report changes if the protein scaffold binds a molecule in its vicinity. In analogy to the electronic nose where the electrodes display broad and overlapping binding capacities to a number of substances (*4*), we needed to scramble the binding of different molecules by A216K. However, the overall fold of the protein and thus labeling of K216 by a thiol ester of glutathione (GSC-Cou$_{bio}$) need to be retained. We decided to make a focused library of K216/M208X mutants because position 208 is located in the H-site (Figure 1) and it has previously been shown to be of importance in the binding of the electrophilic substrate (*22*).

MATERIALS AND METHODS

All chemicals and reagents used were of the highest purity available. The tripeptides were synthesized using solid-phase Fmoc chemistry, and protected amino acids were purchased from Novabiochem (Darmstadt, Germany) or Bachem Holding AG (Weil am Rhein, Germany). The fluorescent acyl groups were purchased from Sigma-Aldrich, Inc. (St. Louis, MO) or Molecular Probes, Inc. (Eugene, OR). EZ-Link PEO-iodoacetyl biotin and immobilized NeutrAvidin (NA) gel were purchased from Pierce Biotechnology, Inc. (Rockford, Il). All solid-phase syntheses were carried out in a VacMaster (International Sorbent Technology). The synthesis of GSC-Cou$_{bio}$ has been described elsewhere (*21*). The HPLC experiments were carried out using a Kromasil C_8 column (4.6 mm × 250 mm, Supelco, Inc.) or a Grace Vydac EVEREST C_{18} column (4.6 mm × 150 mm) attached to a Varian system with a ProStar 230 delivery system and a ProStar 330 photodiode array detector, controlled by the Varian LC Software. All mass spectra were recorded using a MALDI-TOF MS (Voyager System 4212, Applied Biosystems) with detection in the positive mode. The UV measurements were performed using a Varian Cay 100 Scan UV–visible spectrophotometer and the results analyzed with the CaryWin UV software. The fluorescence measurements were carried out on a Safire^2 (Tecan), a SpectraMax M2 (Molecular Devices), or a Hitachi F-4500 fluorescence spectrophotometer. The degree of immobilization of labeled A216K on the hydrogel chip was examined with an epifluorescence microscope (Zeiss Axiovert inverted microscope A200 Mot) equipped with a charge coupled device camera (Axiocam HRc, three chips).

Site-Directed Mutagenesis, Protein Expression, and Purification. The vector pET 21 a (+) containing the hGST A1-1 mutant A216K gene was used as a template for replacement of M208 by site-directed mutagenesis using the Quik-Change site directed mutagenesis kit (Stratagene). Oligonucleotide, M208NNN forward (5′-GCCCAAGGAAGCCTCCCNNNGATGAGAAA-TCTTTAGAAG-3′), and its complement (M208NNN reverse) were designed in order to replace codon ATG (M208) with random nucleotide bases to create codons coding for different amino acids. The mutations were checked by DNA sequencing (GATC Biotech, Germany).

From glycerol stocks of the different mutants, an amount of 200 μL of each was plated out on agar plates containing 100 μg/mL ampicillin and incubated at 37 °C over night. The next day the bacteria on the plates were resuspended in a few milliliters of 2YT-medium (16 g/L peptone, 10 g/L yeast extract, 5 g/L NaCl) and approximately half of the bacteria were pored into 1 L of 2YT medium containing 100 μg/mL ampicillin and incubated, shaking at 37 °C until the OD_{600} was about 0.6–0.7. The bacteria were induced to start producing the recombinant protein by adding isopropyl-β-D-thiogalactopyranoside (IPTG) to a final concentration of 1 mM and incubating the mixture at 37 °C with shaking for 3.5 h. The cells were harvested by centrifugation (3000*g*, 30 min, 4 °C), and the pellets were resuspended in a protease inhibitor cocktail (Complete Mini EDTA-free, Roche) containing 20 mM NaP_I, 0.02 % NaN_3, pH 7, with one tablet per 10 mL of buffer. For lysing of the cells, freezing at −80 °C and thawing at 37 °C were performed four times. After the final thawing the lysates were centrifuged at 11000*g* for 30 min at 4 °C.

The supernatants from the different cell lysates were desalted using PD-10 desalting columns (Amersham Biosciences). Purification of the different mutants was performed on a 3 × 5 mL HiTrap SP HP cation exchange column (Amersham Biosciences) attached to an ÄKTA purifier system (Amersham Biosciences). The column was equilibrated with 4 column

volumes of buffer A (20 mM NaP_i, 0.02% NaN_3, pH 7). The eluates from the PD-10 columns were loaded onto the cation exchange column with a flow of 3 mL/min, and thereafter, the column was washed with another 3 column volumes of buffer A. The different recombinant hGST A1-1 mutants were eluted from the column in a linear 13 column volumes gradient at a flow rate of 2 mL/min expanding from 100% buffer A to 100% buffer B (buffer A with 1 M NaCl). From the gradient, 2 mL fractions of the eluted proteins were collected. The peak fractions were pooled and concentrated using Amicon Ultra-15 centrifugal filter units, 10000 MWCO (Millipore). Purity was confirmed by SDS–PAGE, and protein concentrations were determined spectrophotometrically using $\varepsilon_{280} = 24\,700\ M^{-1}\cdot cm^{-1}$ (*23*).

The activities of the GSTs were measured with a standard assay with 1 mM each of 1-chloro-2,4-dinitrobenzene (CDNB) and GSH (pH 6.5 in 0.1 M NaP_i at 30 °C). The proteins were stored in NaP_i buffered solutions containing NaCl and 10% glycerol at −80 or −20 °C until use in the experiments.

Fluorescence measurements were performed on a Hitachi F-4500 fluorescence spectrophotometer, with excitation at 280 nm and emission scanning between 310 and 380 nm. Prior to the measurements, the proteins were diluted to 1 μM in 100 mM NaP_i, pH 7.0, and the fluorescence spectra of A216K and wt hGST A1-1 were also collected for comparison purposes (Supporting Information).

Preparative Labeling of A216K/M208X Mutants. The labeling reactions were performed in 200 μL mixtures of 20 μM protein, 0.1 M NaP_i, pH 7, with 300 μM GSC-Cou_{bio}. The reaction was allowed to proceed at 25 °C for 5 h. For protease treatment, 2 μL of modification reaction mixture was diluted with 17 μL of 75 mM NH_4OAc, pH 4, and the cleavage was started by adding1 μL of *Staphylococcus aureus* protease V-8 (1 μg/μL stock solution in 75 mM NH_4OAc, pH 4). The mixture was then incubated at 25 °C and stopped by adding an equal amount of 0.2% TFA (e.g., 20 μL reaction mixture) after 2 h.

Following incubation, 0.5 μL of the reaction mixture was mixed with 0.5 μL of saturated α-cyano-4-hydroxycinnamic acid matrix, and 0.5 μL of citrate (10 mg/mL) was also added to quench salts from the buffers. The samples were then analyzed by MALDI-MS with detection in the positive mode. Proteolytic digestion with this protease results in K216-containing fragments K_{216}RKIFRF and EK_{216}RKIFRF, corresponding to one missed cleavage.

After modification was complete, 1.1 equiv of NA beads (binding capacity of ≥80 nmol of biotin/mL of gel) was added to the reaction mixture. The gel had been pre-equilibrated in 0.1 M NaP_i, pH 7.1, containing 75 mM NaCl in VacMaster (International Sorbent Technology) tubes. After incubation with the gel (45 min), the labeled protein was eluted by a brief spin in a tabletop centrifuge (Scheme 1).

Array Experiments with Addition of *n*-Valeric Acid, Fumaric Acid Monoethyl Ester, and Lithocholic Acid. A typical array experiment was performed in the following way: 300 μL mixtures of 1 μM labeled protein and 200 μM analyte (0.1 M NaP_i, pH 7) were transferred to a 96-well black microplate (Nunc). A sample of each protein without analyte was also included. Each well was analyzed with respect to direct excitation of the coumarin residue at 355 nm and of the tryptophan residue at 280 nm. The emission was monitored from 370 to 500 nm. The fluorescence intensity at 408 nm was noted and plotted as a function of total analyte concentration. The equivalent parameters were also collected following addition of 200 μM GSH (20 mM stock solution) to each well containing the analytes.

Affinity Determination Using Fluorescence Spectroscopy. Samples of coumarin-labeled mutants (1 μM in 0.1 M NaP_i, pH 7.0) were set up in a 96-well half-area black microplate with a clear bottom (Corning, Inc.). The analytes (GSH, CDNB, GS-DNB, or S-hexyl-GSH) were then added to the wells: GSH, CDNB, and GS-DNB in the range 10 μM to 1.5 mM and *S*-hexyl-GSH in the range 1 nM to 1.5 mM ($V_{tot} = 75\ \mu$L). The optical density (340–500 nm) was recorded for each well. In cases where the optical density exceeded 0.05 at the wavelength of excitation and emission, the fluorescence intensities were corrected according to the following equation (*24*):

$$F_{corr} = F_{obs}\,\mathrm{antilog}\left(\frac{OD_{ex} + OD_{em}}{2}\right) \quad (1)$$

where F_{obs} and F_{corr} are experimental values and corrected fluorescence intensities, respectively, and OD_{ex} and OD_{em} are the optical densities of the sample at the wavelengths of excitation and emission, respectively. The dissociation constant K_d was determined by fitting the following equation to the experimental results under the assumption of a 1:1 binding model:

$$F_{obs} = \frac{F_{bound}[A] + F_{free}K_d}{[A] + K_d} \quad (2)$$

where F_{obs} is the observed fluorescence intensity, F_{bound} is the fluorescence of the protein bound to the analyte, F_{free} is the fluorescence of free protein, and [A] is the concentration of free analyte. The numerical value of [A] can be derived from the following:

$$[A] = \frac{[P]_{tot} + K_d - [A]_{tot}}{2} + \sqrt{\left(\frac{[P]_{tot} + K_d - [A]_{tot}}{2}\right)^2 + K_d[A]_{tot}} \quad (3)$$

where $[P]_{tot}$ is the total concentration of protein and $[A]_{tot}$ is the total concentration of analyte. The fitting of the equations to the experimental values was done with the IGOR Pro 5.0 software (WaveMetrics, Inc.).

Reproducibility of GSH Addition. The reproducibility was checked by splitting a sample of A216K/M208T (1 μM in 0.1 M NaP_i, pH 7.0) in three different wells. As a control, GSH (200 μM) was added and the resulting coumarin fluorescence was recorded. The values differed by less than 5%.

Immobilization of A216Kcou on a PEG-Based Biosensor Chip and Fluorescence Microscopy. A thiol self-assembled monolayer (SAM) was formed by incubating gold-coated silica substrates with 100 μM $HS(CH_2)_{11}CONH(C_2H_4O)_{11}CH_3$ (Polypure AS, Norway) in 99.5% ethanol for at least 24 h at room temperature. The thiol SAM was used as a platform for UV grafted polymerization of a polyethylene glycol (PEG) based matrix, using a process described in detail elsewhere (*25, 26*). By use of masks, arrays of matrix spots were prepared by irradiating the samples with a Philips TUV PL-L 18 W Hg lamp in the presence of a PEG methacrylate monomer (∼10 EG units) (PEG_{10}MA) and 2-hydroxyethyl methacrylate (HEMA). Two different arrays of (i) 200 μm and (ii) 300 μm spots, both with a spacing of 50 μm, were irradiated for 6 and 4 min, respectively. The matrix spots were then carboxylated using bromoacetic acid (*27*). Both samples were activated for 20 min with an aqueous mixture of *N*-ethyl-*N*′-[3-(dimethylamino)propyl]carbodiimide (Biacore AB, Uppsala, Sweden) and *N*-hydroxysuccinimide (Sigma-Aldrich Sweden AB) at 0.2 and 0.05 M, respectively. A216K_{cou} was then immobilized on the hydrogel chip (i) via nucleophilic amino acid residues on the protein and (ii) via Cys112 subsequent to 30 min of incubation in 80 mM 2-(2-pyridinyldithio)ethaneamine in Milli-Q water. The concentration of A216K_{cou} was 0.5–1.0 μM in 10 mM sodium acetate buffer, pH 4.5, and the immobilization time was 60 and 40 min for steps i and ii,, respectively. In addition, sample i was deactivated with 1 M ethanolamine in Milli-Q

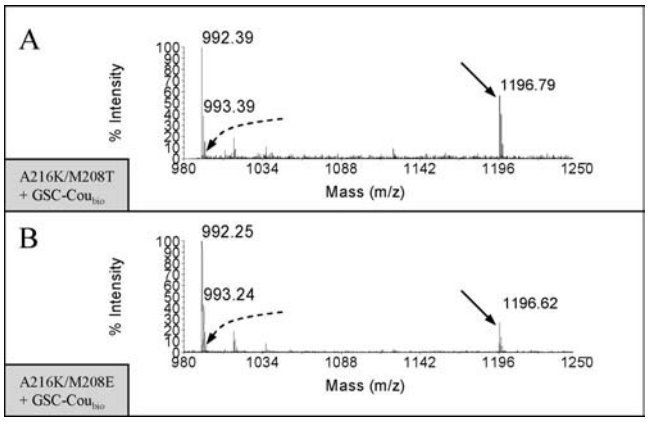


Figure 2. MALDI-MS spectra of proteolytic (*S. aureus* V-8) peptide fragments from (A) A216K/M208T (10 μM) incubated with GSC-Cou$_{bio}$ (100 μM) for 5 h and (B) A216K/M208E (10 μM) incubated with GSC-Cou$_{bio}$ (100 μM) for 5 h. The reaction has gone to completion, but the parent fragments would have an *m*/*z* of 994 g/mol as indicated by a dotted arrow. Modified fragments are highlighted with arrows. The peak at 992 g/mol corresponds to the sodium adduct of GSC-Cou$_{bio}$.

water for 30 min. The arrays were then examined with an epifluorescence microscope (Zeiss Axiovert inverted microscope A200 Mot) equipped with a charge coupled device camera (Axiocam HRc, three chips). A 10× magnification objective was used along with a 365/15 nm band-pass excitation filter and a 397 nm low-pass emission filter. The exposure time was 1.25 s, and the obtained images were enhanced with respect to color and contrast.

RESULTS

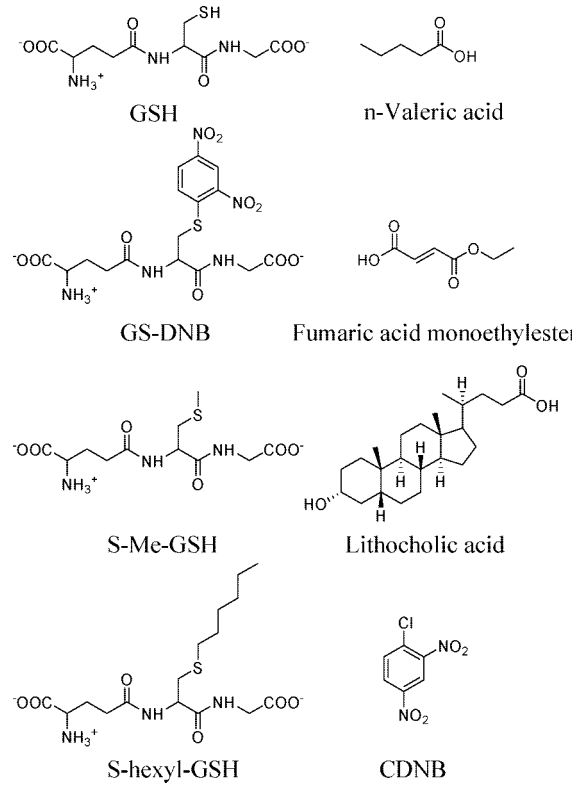
Preparation of the A216K/M208X Library and Pilot Labeling of the Purified A216K/M208X Mutants. Eleven double mutants (A216K/M208L, F, S, Y, A, E, R, T, G, K, and C) were isolated and purified as described elsewhere (*28*). The purities were confirmed by SDS–PAGE, their specific activities toward the standard substrates CDNB and GSH were measured, and their fluorescence spectra resulting from excitation at W21 were recorded and compared to those of wt hGST A1-1 and A216K, respectively (Supporting Information).

Pilot labeling experiments were performed in 20 μL aliquots with GSC-Cou$_{bio}$ (100 μM) and purified protein (10 μM) in buffer (0.1 M NaP$_i$, pH 7.0). The reactions were analyzed by MALDI-MS following proteolytic digestion. To simplify subsequent analyses, we used *S. aureus* V-8 protease because it cleaves after acidic residues and is thus unaffected by lysine modification. For control purposes, the proteins were also digested after incubation in buffer without addition of any reagent. The single mutant A216K was included in all experiments leading to a total of 12 proteins in the receptor family. All mutants became acylated by GSC-Cou$_{bio}$ at residue K216 (Figure 2).

Preparative Labeling of the Receptor Family. The 12 proteins were labeled on a preparative scale in solutions containing 20 μM protein and 300 μM GSC-Cou$_{bio}$ in 0.1 M NaP$_i$, pH 7.0, buffer. On the basis of the results from the pilot experiments, the reactions were allowed to proceed at 25 °C for 5 h. In all subsequent experiments, the labelling reactions were monitored by subjecting 2 μL of the reaction mixtures to proteolytic digestion with subsequent analysis by MALDI-MS.

In order to remove used and excess reagent, an amount of 1.1 equiv of NA beads (binding capacity of ≥80 nmol of biotin/mL of gel) was added to each reaction mixture after 5 h as described previously (*21*) (Scheme 1). After incubation with the gel for 45 min, the labeled protein was eluted by a brief spin in a tabletop centrifuge. We have previously demonstrated that this treatment quantitatively removes residual reagent. After treatment with the NA beads, the fluorescence spectra of the protein eluates displayed the typical coumarin emission (Supporting Information).

Scheme 2



Addition of *n*-Valeric Acid, Fumaric Acid Monoethyl Ester, and Lithocholic Acid to the Receptor Family. In order to explore the signaling potential of the receptor family and find out what kind of information that could be extracted, a screening experiment was set up with 3 analytes (*n*-valeric acid, fumaric acid monoethyl ester, and lithocholic acid) (Scheme 2) and all 12 proteins (the double mutants and A216K) in a microplate format. The chosen analytes do not display any significant absorbance at the measured wavelengths and concentrations (data not shown). The fluorescence spectra of 12 proteins by 3 analytes plus those of the proteins without analytes, the analytes without proteins, and the buffer alone were thus collected (Figure 3). Each well was analyzed with respect to direct excitation of the coumaryl residue at 355 nm and also through excitation at 280 nm (W21) with concomitant FRET to the coumaryl residue. Excitation of GSC-Cou$_{bio}$ at 280 nm did not result in any emission from the coumaryl moiety. In these experiments, both the changes in fluorescence intensities (ΔF_{Cou}) and the positions of the emission maxima ($\Delta\lambda_{em,max}$) were documented. The equivalent parameters were also collected following addition of 200 μM GSH to each sample, resulting in a matrix of eight data points for each analyte and protein combination or 96 data points per analyte (Table 1).

Affinity Studies. In order to investigate the capacity of binding, the K_d values were determined for a subset of analytes. In this experiment, labeled protein was titrated with analytes (all in 0.1 M NaP$_i$ buffer, pH 7.0) (Figures 5 and 6). The fluorescence spectra were recorded using $\lambda_{exc} = 295$ nm (W21) and $\lambda_{exc} = 355$ nm (K216$_{Cou}$). In the case of GSH and *S*-hexyl-GSH, the spectra could be analyzed directly. However, both CDNB and GS-DNB absorb light at the wavelengths used for both excitation and emission. Before the results could be

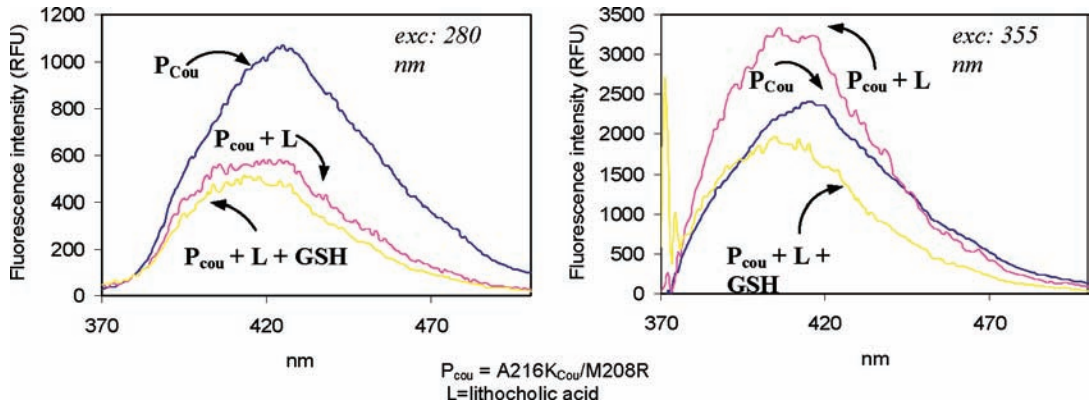


Figure 3. Example of the screening experiment showing changes in fluorescence after addition of first lithocholic acid (200 μM) to wells containing 1 μM labeled A216K$_{Cou}$/M208R followed by GSH (200 μM). For each protein and analyte combination, excitation at 280 nm (W21) with concomitant FRET to the coumaryl residue was followed by direct excitation of the coumaryl residue at 355 nm.

Table 1. Addition of *n*-Valeric Acid, Fumaric Acid Monoethyl Ester, and Lithocholic Acid to the Protein Array

	L	F	S	Y	A	E	R	T	G	K	A216K	C
						n-Valeric Acid						
$\Delta\lambda_{em,max,Cou}$	0	–1	0	0	0	0	0	1	–1	0	0	0
$\Delta\lambda_{em,max,FRET}$	1	–1	0	0	0	0	0	1	0	–1	0	0
$\Delta\lambda_{em,max,Cou,GSH}$	0	0	0	0	0	0	0	0	1	0	0	n.m.[a]
$\Delta\lambda_{em,max,FRET,GSH}$	0	0	0	0	0	0	0	0	2	0	0	n.m.
ΔF_{Cou}	8	9	–1	–1	0	2	–3	–1	21	–8	3	–1
$\Delta F_{Cou,FRET}$	–7	2	–2	–4	–1	1	–2	0	–2	–11	–2	–1
$\Delta F_{Cou,GSH}$	39	44	40	2	37	22	27	35	31	9	66	n.m.
$\Delta F_{Cou,FRET,GSH}$	26	39	35	6	38	17	33	34	25	8	39	n.m.
						Fumaric Acid Monoethyl Ester						
$\Delta\lambda_{em,max,Cou}$	0	0	0	–1	0	0	0	0	0	0	1	0
$\Delta\lambda_{em,max,FRET}$	0	0	0	0	0	0	0	0	0	0	0	0
$\Delta\lambda_{em,max,Cou,GSH}$	0	0	1	0	0	–1	0	0	0	1	0	n.m.
$\Delta\lambda_{em,max,FRET,GSH}$	0	0	0	0	0	0	0	0	0	1	0	n.m.
ΔF_{Cou}	10	14	–2	–3	–1	1	–1	–1	26	–2	4	1
$\Delta F_{Cou,FRET}$	–3	9	8	0	3	4	5	1	4	–5	3	4
$\Delta F_{Cou,GSH}$	39	47	40	4	36	22	28	30	33	15	54	n.m.
$\Delta F_{Cou,FRET,GSH}$	28	43	38	8	39	19	36	35	30	19	39	n.m.
						Lithocholic Acid						
$\Delta\lambda_{em,max,Cou}$	n.m.	n.m.	0	0	–2	1	1	0	0	0	–1	0
$\Delta\lambda_{em,max,FRET}$	n.m.	n.m.	0	0	0	–3	–1	1	0	0	0	0
$\Delta\lambda_{em,max,Cou,GSH}$	n.m.	n.m.	0	0	0	0	–3	–2	0	0	–1	n.m.
$\Delta\lambda_{em,max,FRET,GSH}$	n.m.	n.m.	0	–10	–3	0	–7	0	–1	0	0	n.m.
ΔF_{Cou}	n.m.	n.m.	9	–26	7	0	–34	25	6	1	30	5
$\Delta F_{Cou,FRET}$	n.m.	n.m.	38	–2	48	47	47	44	23	20	55	48
$\Delta F_{Cou,GSH}$	n.m.	n.m.	4	–25	33	29	6	21	–3	–9	43	n.m
$\Delta F_{Cou,FRET,GSH}$	n.m.	n.m.	39	17	52	54	53	53	34	27	60	n.m

[a] n.m. = not measured.

interpreted, the emission intensities were corrected using the approximate correction equation (*24*):

$$F_{corr} = \frac{F_{obs}\,\text{antilog}(OD_{exc} + OD_{em})}{2} \quad (4)$$

We found that the proteins bound GSH, *S*-hexyl-GSH, CDNB, and GS-DNB with K_d values spanning more than 3 orders of magnitude (from 2.5 μM to 6.9 mM) (Table 3).

Immobilization of A216K$_{Cou}$ on a Hydrogel Chip. The cysteine residue C112 (Figure 8) was utilized to couple A216K$_{Cou}$ site specifically to a microarray hydrogel surface (Figure 9). Labeled protein (0.5–1.0 μM) was incubated together with the PDEA activated surface in 10 mM NaOAc buffer, pH 4.5, for 40 min. A216K$_{Cou}$ was also immobilized on a NHS-activated surface via nucleophilic amino acids on the protein. The attachment of protein was verified by MALDI-MS, following direct proteolytic digestion (*S. aureus* V-8) on the array surface (Supporting Information). The arrays were then examined with an epifluorescence microscope equipped with a charge coupled device, and the obtained images were enhanced with respect to color and contrast (Figure 9).

DISCUSSION

This investigation was performed because we wanted to emulate the ideas of the "electronic nose" (*1, 2, 4, 29, 30*) using proteins instead of electrodes, thus getting access to the complex and vast amount of interactions between proteins and small molecules. The idea of having an array of mediocre binders that combine to form a module that can report the presence of a given molecule with a much higher degree of specificity is highly appealing from a scientific point of view, and it can conceivably be of some commercial interest in the future. The inherently relaxed substrate requirements, a hallmark of GST catalysis and a prerequisite for detoxication, together with our newly developed kit for user-friendly protein labeling (*21*) are the perfect combination for building a multipurpose, protein-based sensor of this type.

The task was to deform the binding site (the H-site) of A216K to an appropriate degree, not too much and not too little. Too

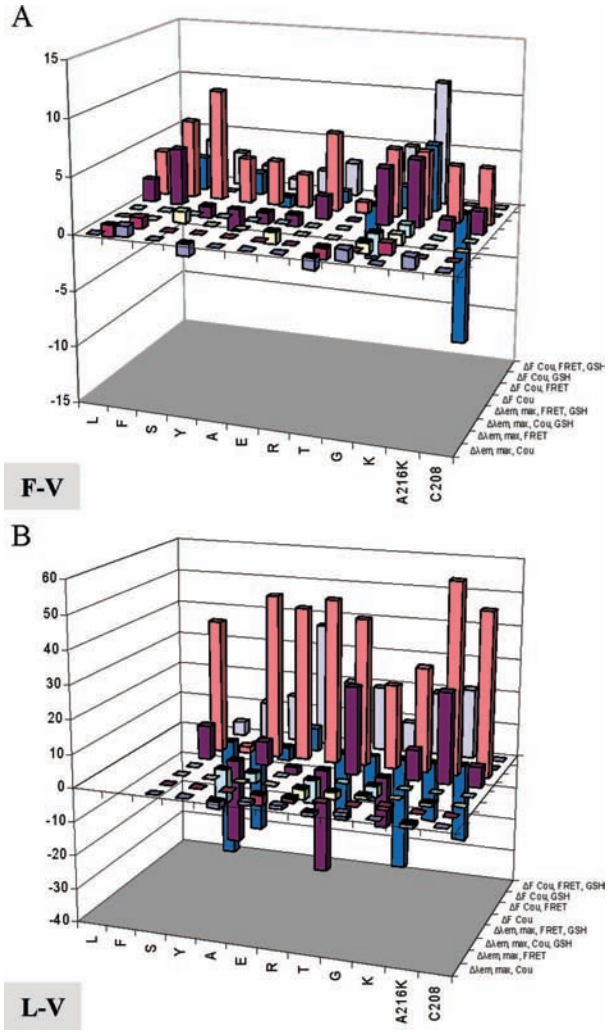


Figure 4. Graphic representation of the changes in fluorescence described in Table 2. Each protein to analyte combination gives rise to eight parameters. In order to simplify the interpretation, the diagrams show the differences in changes between (A) fumaric acid monoethyl ester and *n*-valeric acid and (B) lithocholic acid and *n*-valeric acid. Valeric acid has thus been used as a sort of standard or normalizing substance. The mutants A216K/M208F and L were omitted in the investigation with lithocholic acid.

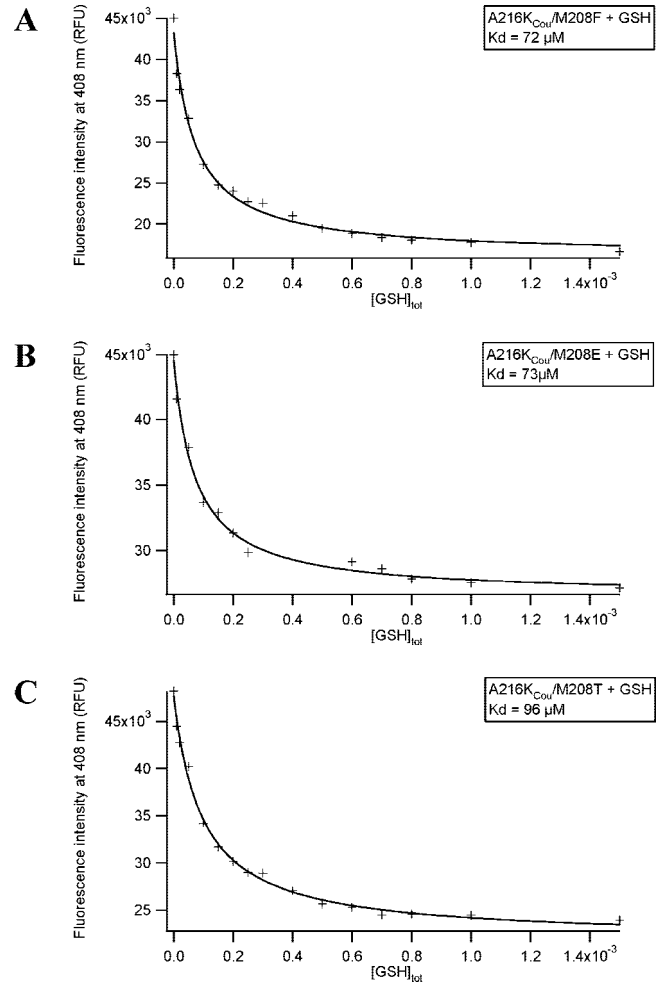


Figure 5. Addition of increasing amounts of GSH to (A) 1 μM A216K$_{Cou}$/M208F, (B) 1 μM A216K$_{Cou}$/M208E, and (C) 1 μM A216K$_{Cou}$/M208T. An equation that describes the dissociation of a bimolecular complex was fitted to the experimental data and gave K_d values of 72, 73, and 96 μM, respectively. Solid lines represent the best fits to the experimental results. The *x*-axis corresponds to the total amount of added GSH ([GSH]$_{tot}$). At the concentrations shown here, [GSH]$_{tot}$ $\approx$ [GSH]$_{free}$.

much would perhaps result in nonexistent binding in the H-site and thus no analyte recognition or spoilage of the G-site with no labeling as a potential outcome. Too little would result in a protein array without binding diversity, somewhat like having an array with just one protein attached to the surface. The mutations also have to be relatively close (in the folded state) to position 216 so that K216$_{Cou}$ can sense and report changes upon binding. In addition, the new mutations also need to be located in or near the H-site where the ligands/analytes are supposed to bind. Previous studies concerning hGST A1-1 have reported that M208 can be mutated with altered substrate preferences as a result (*22, 31*). The side chain of M208 points into the H-site and is located in a region that presumably can undergo changes upon binding of electrophiles because helix9 changes its conformation upon binding of substrates (Figure 1). We wanted a varied panel with mutations ranging from negatively to positively charged, from small to large, from hydrophilic to hydrophobic, and with and without functional groups such as –OH or –SH. We therefore created a A216K/M208X library using a randomized primer and sequenced, expressed, and purified enough clones to obtain 11 double mutants with a wide spread of properties. One of the clones, A216K/M208K, has an additional lysine residue in the H-site, and we therefore studied if that could also become acylated by GSC-Cou$_{bio}$ or if the protein would only become singly labeled.

The double mutants A216K/M208X can react with GSC-Cou$_{bio}$ to form K216$_{Cou}$ conjugates. We have previously shown that A216K can be treated with GSC-Cou$_{bio}$ to form an A216K$_{Cou}$ conjugate and that any used up or excess reagent can be quantitatively removed using NA beads relying on the biotin–streptavidin interaction (*21*) (Supporting Information). Fortunately, the double mutants retained this crucial capacity, enabling us to quick and easy labeling of the receptor family. The speed of the reaction varied, but incubation over 5 h resulted in >85% labeling for all but two mutants (Supporting Information), which we deemed high enough for our needs. We thus have a system where we can start with pure proteins (SDS–PAGE gels, Supporting Information) that can be labeled to more than 85% (Figure 2 and Supporting Information) and where there is no residual fluorescent labeling reagent left in solution after treatment with NA beads (HPLC chromatograms in Supporting Information).

Similar analytes (*n*-valeric acid and fumaric acid monoethyl ester) result in different patterns. In order for this system to work, the receptor must be able to report "signature changes" for different molecules even if they appear similar from the

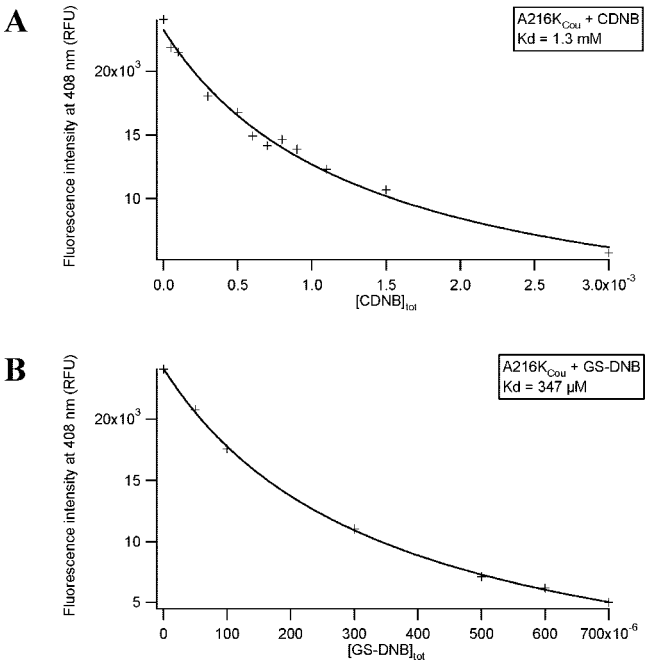


Figure 6. Addition of increasing amounts of (A) CDNB and (B) GS-DNB to the parent protein A216K$_{cou}$ (1 μM). The resulting K_d values were determined by fitting an equation that describes the dissociation of a bimolecular complex, to 1.3 mM and 347 μM, respectively. Solid lines represent the best fits to the experimental results. At the concentrations shown here, [analyte]$_{tot}$ $\approx$ [analyte]$_{free}$.

viewpoint of a promiscuous GST. It is also an advantage if a totally dissimilar molecule (with respect to size, hydrophobicity, charge, etc.) gives a completely dissimilar response. In order to test this and also to obtain information about what parameters are exploitable and how substantial the changes in fluorescence would be, we set up a pilot experiment using all 12 proteins (A216K and the 11 A216K/M208X mutants) and 3 different analytes: *n*-valeric acid, fumaric acid monoethyl ester, and lithocholic acid (Scheme 2). These molecules are all soluble in buffer, and they do not have complicating absorbance spectra at the concentrations used in the experiments. The first two are quite small and have fairly similar structures, and the last one is a large, bulky steroid that is a naturally occurring bile acid known to be a liver-toxic metabolite (*32, 33*) and to probably bind in the groove between the subunits (*34, 35*).

We also wanted to investigate whether W21 that is used to study folding of hGST A1-1 (*11, 36*) could report binding and whether the coumarin that is located in or near the H-site could report binding through direct excitation. The results from the FRET experiments showed competing mechanisms between energy transfer from W21 to the coumarin fluorophore and coumarin quenching. Since the values differ between ΔF_{Cou} and $\Delta F_{Cou,FRET}$ following blank reduction and upon analyte addition (Table 1) and also since the emission intensity influence for the coumarin is much more significant than the emission intensity influence for W21, we concluded that the parameter $\Delta F_{Cou,FRET}$ includes both information contributed from coumarin quenching and distance changes between W21 and coumarin.

Addition of GSH to GSTs can affect the binding of a second substrate in the H-site, and we therefore added GSH to each well after collecting the data in the analyte plus protein experiment. We are of course aware of the fact that GSH alone can cause changes in the fluorescence of the coumarin moiety (*21*) and that the overall signal we observe upon addition of GSH is a combination of both effects. On a cautionary note, GSH can also form adducts with some electrophilic substances, so it should be used with discretion. One final parameter that we were interested in was the change in position of $\lambda_{em,max}$. In the literature, coumarin derivatives are reported to change their emission maxima up to 14 nm going from $CHCl_3$ to MeOH as a solvent (*24*).

In all, this set of parameters ($\Delta\lambda_{em,max,Cou}$, $\Delta\lambda_{em,max,FRET}$, $\Delta\lambda_{em,max,GSH}$, $\Delta\lambda_{em,max,FRET,GSH}$, ΔF_{Cou}, $\Delta F_{Cou,FRET}$, $\Delta F_{Cou,GSH}$, $\Delta F_{Cou,FRET,GSH}$) resulted in a matrix of 12 proteins by 8 data points, or a total of 96 measured parameters for each analyte (Table 1, Figure 4). In an effort to aid visualization, the data from fumaric acid monoethyl ester and lithocholic acid were compared to the changes obtained when *n*-valeric acid was added. This choice was simply based on the fact that *n*-valeric acid is the analyte with the least amount of functional groups in the test set.

We were pleased to observe that the biosensor panel could differentiate between *n*-valeric acid and fumaric acid monoethyl ester (Table 1). The numbers were relatively small, but that is perhaps to be expected when the analytes differ so little. These changes reported by a single protein or just a few proteins in an array would not amount to anything useful, but the combined effect from all 12 proteins is quite promising.

On the other hand, adding lithocholic acid to the panel of proteins resulted in large changes in fluorescence. This molecule definitely affects both W21 and K216$_{Cou}$ in a completely different way than either of the two smaller ligands. Interestingly, we observed wavelength shifts of 10 nm for A216K/M208Y, suggesting a quite substantial change in the hydrophobicity of the microenvironment of the coumarin moiety upon binding of lithocholic acid.

It appears that the most common result when a ligand is added to the panel of labeled proteins is quenching of the fluorescence of coumarin. The most likely cause for this is static quenching; i.e., upon addition of the analyte a nonfluorescent complex is formed between the coumarin and the quencher that serves to limit the absorption by reducing the population of active, excitable molecules. There is a small variation in the degree of quenching of the coumaryl residue between the A216K/M208X mutants, probably resulting from differing microenvironments in the binding site leading to different orientations of K216$_{Cou}$ and analyte. Interestingly, when *S*-hexyl-GSH is added to A216K$_{cou}$, the fluorescence intensity actually increases (Figure 7) but no wavelength shift is observed.

The wavelength shifts upon analyte addition are probably due to solvent or polarity effects. Control experiments demonstrated that GSC-Cou$_{bio}$ in buffer has a significantly lower emission intensity and a $\lambda_{em,\ max}$ that is red-shifted with 17 nm compared to A216K$_{cou}$ (data not shown). This strengthens the notion that the coumaryl group is positioned in a hydrophobic environment in a relatively static manner when attached to K216, since no shift or small wavelength shifts are observed upon analyte addition (Table 1). The small shifts that we do observe in some cases are probably caused by a reorganization of the C-terminal helix upon analyte addition with concomitant alteration of the position of K216$_{Cou}$ from a hydrophobic environment (H-site) to a hydrophilic one (water outside H-site) or vise versa.

No Apparent Correlation between Mutations and Signal Changes. The mutations in position 208 represent a wide range of functionalities. Despite this, there are no striking and consistent trends. In fact, the most striking result seems to be that there are no predictable trends regarding changes in fluorescence. The mutants do not seem to follow any rules, for example adding lithocholic acid to A216K/M208S, T, and Y results in ΔF_{Cou} values of 9, 25, and –26, respectively (Table 1). Another noteworthy example of this is that the ΔF_{Cou} changes recorded for E, R, and K208 are 0, −34, and 1,

Table 2. Differences between Fumaric Acid Monoethyl Ester and *n*-Valeric Acid (Δ F–V) and between Lithocholic Acid and *n*-Valeric Acid (Δ L–V)[a]

	L	F	S	Y	A	E	R	T	G	K	A216K	C
						Δ F–V						
$\Delta\lambda_{em,max,Cou}$	0	1	0	–1	0	0	0	–1	1	0	1	0
$\Delta\lambda_{em,max,FRET}$	–1	1	0	0	0	0	0	–1	0	1	0	0
$\Delta\lambda_{em,max,Cou,GSH}$	0	0	1	0	0	–1	0	0	–1	1	0	n.m.[a]
$\Delta\lambda_{em,max,FRET,GSH}$	0	0	0	0	0	0	0	0	–2	1	0	n.m.
ΔF_{Cou}	2	5	–1	–2	–1	–1	2	0	5	6	1	2
$\Delta F_{Cou,FRET}$	4	7	10	4	4	3	7	1	6	6	5	5
$\Delta F_{Cou,GSH}$	0	3	0	2	–1	0	1	–5	2	6	–12	n.m.
$\Delta F_{Cou,FRET,GSH}$	2	4	3	2	1	2	3	1	5	11	0	n.m.
						Δ L–V						
$\Delta\lambda_{em,max,Cou}$	n.m.	n.m.	0	0	–2	1	1	–1	1	0	–1	0
$\Delta\lambda_{em,max,FRET}$	n.m.	n.m.	0	0	0	–3	–1	0	0	1	0	0
$\Delta\lambda_{em,max,Cou,GSH}$	n.m.	n.m.	0	0	0	0	–3	–2	–1	0	–1	n.m.
$\Delta\lambda_{em,max,FRET,GSH}$	n.m.	n.m.	0	–10	–3	0	–7	0	–3	0	0	n.m.
ΔF_{Cou}	n.m.	n.m.	10	–25	7	–2	–31	26	–15	9	27	6
$\Delta F_{Cou,FRET}$	n.m.	n.m.	40	2	49	46	49	44	25	31	57	49
$\Delta F_{Cou,GSH}$	n.m.	n.m.	–36	–27	–4	7	–21	–14	–34	–18	–23	n.m.
$\Delta F_{Cou,FRET,GSH}$	n.m.	n.m.	4	11	14	37	20	19	9	19	21	n.m.

[a] *n*-Valeric acid acts as a standard comparison. n.m. = not measured.

Table 3. Dissociation Constants of Complexes Formed from Labeled A216K Mutants and a Subset of Analytes, Determined by Fluorescence Spectroscopy

	analyte			
mutant	GSH	CDNB	GS-DNB	*S*-hexyl-GSH
$A216K_{Cou}$	108 μM	1.3 mM	347 μM	2.5 μM
$A216K_{Cou}$/M208A	179 μM	6.8 mM	*a*	*a*
$A216K_{Cou}$/M208S	138 μM	1.2 mM	*a*	*a*
$A216K_{Cou}$/M208Y	*a*	*a*	128 μM	*a*
$A216K_{Cou}$/M208F	72 μM	*a*	*a*	*a*
$A216K_{Cou}$/M208G	99 μM	952 μM	*a*	*a*
$A216K_{Cou}$/M208T	96 μM	775 μM	*a*	*a*
$A216K_{Cou}$/M208L	*a*	2.4 mM	46 μM	*a*
$A216K_{Cou}$/M208E	73 μM	601 μM	*a*	*a*

[a] Not determined.

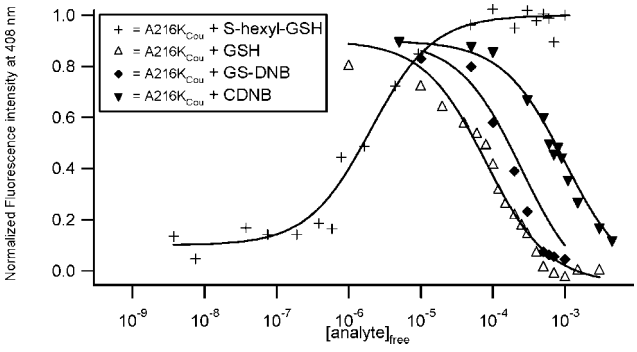


Figure 7. Normalized fluorescence intensity at 408 nm was plotted against the concentration of free analyte, $[analyte]_{free}$. The concentrations were calculated from K_d values. An equation that describes the dissociation of a bimolecular complex was fitted to the experimental data to obtain K_d values: *S*-hexyl-GSH (+, K_d = 2.5 μM), GSH (△, K_d = 108 μM), GS-DNB (◆, K_d = 347 μM), CDNB (▼, K_d = 1.3 mM). The solid lines represent the best fits to the experimental results.

respectively. Here, the negatively charged E208 and the positively charged K yield similar values, whereas R208 is an outsider.

Is one of the proteins more sensitive than the others? Is one of the parameters more sensitive than the others? Upon inspection of Figure 4 (staple F-V and L-V) and Table 2, it is quite clear that the magnitude of changes reported from a protein depends on the ligand it encounters. For example, adding lithocholic acid to A216K/M208T gives rise to large changes in almost all parameters. On the other hand, this particular mutant does not signal any large differences between valeric

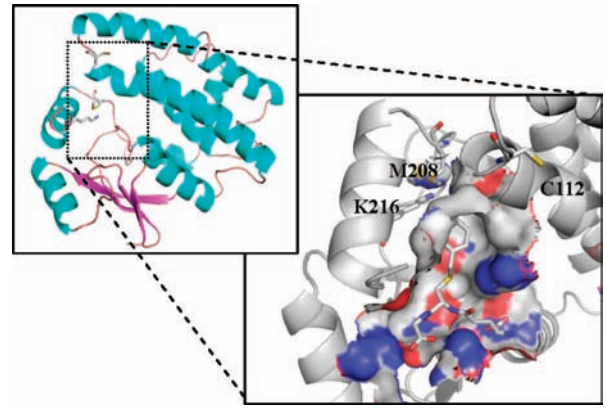


Figure 8. Close-up of the crystal structure (1GUH) of wt hGST A1-1 (A216 replaced with K216) in a complex with *S*-benzyl-GSH. Positions 216, 208, and 112 are shown in "stick" representation. The protein is dimeric but shown here as a monomer for reasons of clarity of presentation. The figure was done with the help of the PyMol (DeLano Scientific LLC) software.

acid and fumaric acid monoethyl ester. One of the weakest candidates is of course A216K/M208C because it is prone to oxidation at the introduced C208 and the stability of this mutant is correspondingly less than that of the others (data not shown). However, from a practical point of view it is the total signature from the panel of proteins that is important, not the behavior of an individual protein.

The related question is of course whether one of the parameters is more sensitive than the others. Again, judging from Figure 4 (staple F-V and L-V) and Table 2, it would appear that perhaps FRET data ($\Delta F_{Cou,FRET}$ and $\Delta F_{Cou,FRET,GSH}$) give rise to relatively large differences. But again, in this case less is not more, since a larger matrix allows for a higher degree of certainty.

The ligands bind in a specific manner to the proteins. In a more quantitative part of the study, we performed titration studies with several molecules: GSH, CDNB, GS-DNB, and *S*-hexyl-GSH. We used a subset of double mutants and included the parent protein A216K as well. The experiments supplied us with information regarding the binding of the ligands (K_d values) and presented an opportunity to work with compounds that have absorbance spectra that interfere with the excitation and emission wavelengths of the probes. Even if it is not ideal,

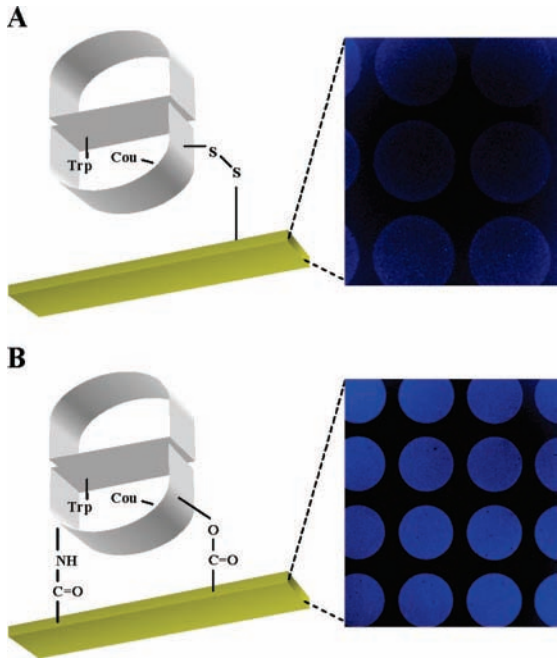


Figure 9. Pictures from epifluorescence microscopy following immobilization of $A216K_{Cou}$ to a PEG-based (hydrogel) surface: (A) site-specific immobilization on a PDEA-activated hydrogel surface through C112 and (B) immobilization on an NHS-activated hydrogel surface through NHS-reactive residues on $A216K_{Cou}$.

the optical density problem can be dealt with using an equation that corrects the fluorescence intensity for inner filter effects (*24*).

The titrations were performed in a black microplate with a clear bottom. Thus, we obtained information regarding the optical density, fluorescence intensity, and wavelength shift in the same experimental setup. The protein concentrations were 1 μM throughout the titrations, since we were expecting affinities in the low micromolar to low millimolar range, based on the K_d for GSH (190 $\pm$ 50 μM) of wild type hGST A1-1 (*37*). The results (Table 3) showed that the affinity for GSH for seven tested mutants varied over quite a narrow range (73–179 μM), in line with our expectations because GSH is known to bind in the G-site. The affinities for CDNB varied between 601 μM for A216K/M208E to 6.8 mM for A216K/M208A. The larger variation for CDNB binding between the mutants was not surprising because position 208 is located in the H-site, where CDNB is known to bind. The nucleophilic aromatic substitution reaction between GSH and CDNB to form GS-DNB is catalyzed by wt hGST A1-1, and the proteins showed affinities for GS-DNB between those for GSH and CDNB, respectively. Also included in the affinity array was *S*-hexyl-GSH, which is a well-known inhibitor of the α class GSTs. This ligand showed the highest affinity, 2.5 μM for A216K. The light-up effect was a positive surprise, enhancing the strength of the biosensor module (Figure 7).

The coumarin-labeled protein scaffold can be anchored to a hydrogel microarray chip using C112 or nucleophilic residues. We used the by now well-studied protein $A216K_{cou}$ to initiate the development of a surface-based biosensing system. The results from IR spectroscopy measurements (data not shown), MALDI-MS measurements following direct proteolytic digestion on the surface (Supporting Information), and fluorescence microscopy studies (Figure 9A), showed that $A216K_{cou}$ could indeed be site-specifically introduced on the hydrogel surface through C112. We also found that $A216K_{cou}$ could be attached to a NHS-activated hydrogel surface (Figure 9B), resulting in an even higher intensity of the emitted light, indicating a higher concentration of $A216K_{cou}$ in the spots. This is not surprising because the protein surface contains many potential NHS-reactive groups. We concluded that an optimization is needed before further development of the surface-based biosensor.

Is this enough? This work constitutes "proof of principle" demonstrating that the ideas of the electronic nose and tongue can be transferred into the protein world. We have no illusions that this array of GST mutants could be used in real life to solve real life problems. Before the step from basic science to a real life application is taken, further diversification of the proteins is necessary as well as screening with real life analytes. However, it is very promising that ligands as diverse as *n*-valeric acid, fumaric acid monoethyl ester, lithocholic acid, CDNB, GSH, *S*-hexyl-GSH, and GS-DNB give rise to different signals that in more mature systems potentially can be distinguished and interpreted through pattern recognition. It is noteworthy that the K_d values we have measured (Table 3) span a range from low micromolar to low millimolar.

The proposed use of our affinity array would in an initial stage be in a relatively controlled environment with a low noise from contributing compounds. This has so far also been true for the electronic nose sensor (*38*), which has for example been employed for quality measurements for commercial cardboard papers (*39*). However, the beauty of the GSTs lies in their promiscuity; it is easy to envision a selection where the scaffold is fine-tuned toward various types of analytes. Indeed, Mannervik et al. (*40*) have already performed a phage-display selection based on hGST A1-1. One can also envision a coupled system wherein GST(s), naturally existent, or mutant(s) attaches GSH to an analyte in situ to hitch a ride with the glutathione backbone and thus lower K_d values. This latter approach is of course only amenable if the analyte is an electrophile. Here also, if there is no GST that can catalyze the desired reaction, one can again think of a selection system to obtain the needed catalyst.

The current system employs probes that are excited at relatively low wavelengths. This causes problems because many substances absorb light in this region and many biologically related solutions absorb or scatter light in this part of the spectrum. This obstacle can also almost certainly be overcome through some sort of selection or screening procedure to obtain mutants that can be labeled at K216 with a fluorescent acyl group that is excited at a higher wavelength.

All of these things are made possible because, amazingly, hGST A1-1 seems to be an almost indestructible parent scaffold. It tolerates double mutations, rt handling over several days, and attachment to a surface without losing its structural integrity or ability to bind its natural substrates.

CONCLUSIONS

We have constructed a multipurpose affinity array composed of a designed family of promiscuous proteins carrying introduced fluorescent residues. It is the pattern of changes generated by binding a specific ligand, i.e., its "signature" that constitutes the readout. This is an approach that turns the aspect of what constitutes a good biosensor upside-down. Here, the strength lies in the numbers; many relatively poor binders each contribute to the overall result.

ACKNOWLEDGMENT

The authors express their sincere gratitude toward Professor Bengt-Harald Jonsson for his kind support. This work was financially supported by The Wenner-Gren Foundation, The Carl-Trygger Foundation, the Knut and Alice Wallenberg Foundation, and the Swedish Research Council.

Supporting Information Available: Stacked fluorescence spectra of the purified A216K/M208X mutants together with A216K and wt hGST A1-1, stacked fluorescence spectra of the coumarin-labeled A216K/M208X mutants together with $A216K_{Cou}$, specific activities toward CDNB and GSH, SDS–PAGE gels of the purified proteins, MALDI-MS spectra showing A216K in buffer before and after labeling with GSC-Cou_{bio}, HPLC chromatograms showing reaction mixtures before and after treatment with NA beads, and direct proteolytic digestion (*Staphylococcus aureus* V-8) on the array surface. This material is available free of charge via the Internet at http://pubs.acs.org.

LITERATURE CITED

(1) Hines, E. L., Llobet, E., and Gardner, J. W. (1999) Electronic noses: a review of signal processing techniques. *IEE Proc: Circuits Devices Syst. 146*, 297–310.

(2) Gardner, J. W., Shin, H. W., and Hines, E. L. (2000) An electronic nose system to diagnose illness. *Sens. Actuators, B 70*, 19–24.

(3) Stetter, J. R., Findlay, M. W., Schroeder, K. M., Yue, C., and Penrose, W. R. (1993) Quality classification of grain using a sensor array and pattern-recognition. *Anal. Chim. Acta 284*, 1–11.

(4) Eklov, T., and Lundstrom, I. (1999) Distributed sensor system for quantification of individual components in a multiple gas mixture. *Anal. Chem. 71*, 3544–3550.

(5) Suslick, K. S., Rakow, N. A., and Sen, A. (2004) Colorimetric sensor arrays for molecular recognition. *Tetrahedron 60*, 11133–11138.

(6) Rakow, N. A., Sen, A., Janzen, M. C., Ponder, J. B., and Suslick, K. S. (2005) Molecular recognition and discrimination of amines with a colorimetric array. *Angew. Chem., Int. Ed. 44*, 4528–4532.

(7) Buryak, A., and Severin, K. (2005) A chemosensor array for the colorimetric identification of 20 natural amino acids. *J. Am. Chem. Soc. 127*, 3700–3701.

(8) Janzen, M. C., Ponder, J. B., Bailey, D. P., Ingison, C. K., and Suslick, K. S. (2006) Colorimetric sensor arrays for volatile organic compounds. *Anal. Chem. 78*, 3591–3600.

(9) Mosebi, S., Sayed, Y., Burke, J., and Dirr, H. W. (2003) Residue 219 impacts on the dynamics of the C-terminal region in glutathione transferase A1-1: implications for stability and catalytic and ligandin functions. *Biochemistry 42*, 15326–15332.

(10) Hederos, S., Broo, K. S., Jakobsson, E., Kleywegt, G. J., Mannervik, B., and Baltzer, L. (2004) Incorporation of a single His residue by rational design enables thiol-ester hydrolysis by human glutathione transferase A1-1. *Proc. Natl. Acad. Sci. U.S.A. 101*, 13163–13167.

(11) Cocco, R., Stenberg, G., Dragani, B., Rossi Principe, D., Paludi, D., Mannervik, B., and Aceto, A. (2001) The folding and stability of human alpha class glutathione transferase A1-1 depend on distinct roles of a conserved N-capping box and hydrophobic staple motif. *J. Biol. Chem. 276*, 32177–32183.

(12) Grahn, E., Novotny, M., Jakobsson, E., Gustafsson, A., Grehn, L., Olin, B., Madsen, D., Wahlberg, M., Mannervik, B., and Kleywegt, G. J. (2006) New crystal structures of human glutathione transferase A1-1 shed light on glutathione binding and the conformation of the C-terminal helix. *Acta Crystallogr., Sect. D: Biol. Crystallogr. 62*, 197–207.

(13) Sinning, I., Kleywegt, G. J., Cowan, S. W., Reinemer, P., Dirr, H. W., Huber, R., Gilliland, G. L., Armstrong, R. N., Ji, X., and Board, P. G., et al. (1993) Structure determination and refinement of human alpha class glutathione transferase A1-1, and a comparison with the Mu and Pi class enzymes. *J. Mol. Biol. 232*, 192–212.

(14) Ketterer, B. (2001) A bird's eye view of the glutathione transferase field. *Chem. Biol. Interact. 138*, 27–42.

(15) Mannervik, B., and Danielson, U. H. (1988) Glutathione transferases—structure and catalytic activity. *CRC Crit. Rev. Biochem. 23*, 283–337.

(16) Sheehan, D., Meade, G., Foley, V. M., and Dowd, C. A. (2001) Structure, function and evolution of glutathione transferases: implications for classification of non-mammalian members of an ancient enzyme superfamily. *Biochem. J. 360*, 1–16.

(17) Armstrong, R. N. (1997) Structure, catalytic mechanism, and evolution of the glutathione transferases. *Chem. Res. Toxicol. 10*, 2–18.

(18) Mannervik, B. (1996) Evolution of glutathione transferases and related enzymes for the protection of cells against electrophiles. *Biochem. Soc. Trans. 24*, 878–880.

(19) Håkansson, S., Viljanen, J., and Broo, K. S. (2003) Programmed delivery of novel functional groups to the alpha class glutathione transferases. *Biochemistry 42*, 10260–10268.

(20) Viljanen, J., Tegler, L., and Broo, K. S. (2004) Combinatorial chemical reengineering of the alpha class glutathione transferases. *Bioconjugate Chem. 15*, 718–727.

(21) Viljanen, J., Tegler, L., Larsson, J., and Broo, K. S. (2006) Surface-assisted delivery of fluorescent groups to hGST A1-1 and a lysine mutant. *Bioconjugate Chem. 17*, 429–437.

(22) Widersten, M., Bjornestedt, R., and Mannervik, B. (1994) Contribution of amino acid residue 208 in the hydrophobic binding site to the catalytic mechanism of human glutathione transferase A1-1. *Biochemistry 33*, 11717–11723.

(23) Gustafsson, A., and Mannervik, B. (1999) Benzoic acid derivatives induce recovery of catalytic activity in the partially inactive Met208Lys mutant of human glutathione transferase A1-1. *J. Mol. Biol. 288*, 787–800.

(24) Lakowicz, J. R. (1999) *Principles of Fluorescence Spectroscopy*, 2nd ed., Kluwer Academic/Plenum, New York.

(25) Larsson, A., Ekblad, T., Andersson, O., and Liedberg, B. (2007) Photografted poly(ethylene glycol) matrix for affinity interaction studies. *Biomacromolecules 8*, 287–295.

(26) Larsson, A., and Liedberg, B. A poly(ethylene glycol) gradient for biochip development. *Langmuir*, submitted.

(27) Löfås, S., and Johnsson, B. (1990) A novel hydrogel matrix on gold surfaces in surface plasmon resonance sensors for fast and efficient covalent immobilization of ligands. *J. Chem. Soc. D* 1526–1528.

(28) Hederos, S., Karlsson, B., Tegler, L., and Broo, K. S. (2005) Ligand-directed labeling of a single lysine residue in hGST A1-1 mutants. *Bioconjugate Chem. 16*, 1009–1018.

(29) Lundstrom, I. (2000) Artificial noses. Picture the smell. *Nature 406*, 682–683.

(30) Jonsson, A., Winquist, F., Schnurer, J., Sundgren, H., and Lundstrom, I. (1997) Electronic nose for microbial quality classification of grains. *Int. J. Food Microbiol. 35*, 187–193.

(31) Hansson, L. O., Widersten, M., and Mannervik, B. (1999) An approach to optimizing the active site in a glutathione transferase by evolution in vitro. *Biochem. J. 344* (Part 1), 93–100.

(32) Hofmann, A. F. (2004) Detoxification of lithocholic acid, a toxic bile acid: relevance to drug hepatotoxicity. *Drug Metab. Rev. 36*, 703–722.

(33) Singh, S. V., Leal, T., and Awasthi, Y. C. (1988) Inhibition of human glutathione-*S*-transferases by bile-acids. *Toxicol. Appl. Pharmacol. 95*, 248–254.

(34) Sayed, Y., Hornby, J. A., Lopez, M., and Dirr, H. (2002) Thermodynamics of the ligandin function of human class alpha glutathione transferase A1-1: energetics of organic anion ligand binding. *Biochem. J. 363*, 341–346.

(35) Kolobe, D., Sayed, Y., and Dirr, H. W. (2004) Characterization of bromosulphophthalein binding to human glutathione *S*-transferase A1-1: thermodynamics and inhibition kinetics. *Biochem. J. 382*, 703–709.

(36) Wallace, L. A., Burke, J., and Dirr, H. W. (2000) Domain–domain interface packing at conserved Trp-20 in class alpha glutathione transferase impacts on protein stability. *Biochim. Biophys. Acta 1478*, 325–332.

(37) Gustafsson, A., Etahadieh, M., Jemth, P., and Mannervik, B. (1999) The C-terminal region of human glutathione transferase A1-1 affects the rate of glutathione binding and the ionization of the active-site Tyr9. *Biochemistry 38*, 16268–16275.

(38) Turner, A. P., and Magan, N. (2004) Electronic noses and disease diagnostics. *Nat. Rev. Microbiol. 2*, 161–166.

(39) Holmberg, M., Winquist, F., Lundstrom, I., Gardner, J. W., and Hines, E. L. (1995) Identification of paper quality using a hybrid electronic nose. *Sens. Actuators, B 27*, 246–249.

(40) Hansson, L. O., Widersten, M., and Mannervik, B. (1997) Mechanism-based phage display selection of active-site mutants of human glutathione transferase A1-1 catalyzing SNAr reactions. *Biochemistry 36*, 11252–11260.

(41) This nomenclature is derived from the following: Mannervik, B., and et al. (1992) *Biochem. J. 282* (Part 1), 305–306.

BC700247X

Cytotoxicity of Polyspermine-Ribonuclease A and Polyspermine-Dimeric Ribonuclease A

Pavla Poučková,[†] Manuela Morbio,[‡] Francesca Vottariello,[‡] Douglas V. Laurents,[§] Josef Matoušek,[||] Josef Souček,[⊥] Giovanni Gotte,[‡] Massimo Donadelli,[‡] Chiara Costanzo,[‡] and Massimo Libonati*[,‡]

Institute of Biophysics and Informatics, 1st Medical Faculty of the Charles University, Prague, Czech Republic, Deptartment of Morphological-Biomedical Sciences, Section of Biological Chemistry, University of Verona, Verona, Italy, Instituto de Química-Física "Rocasolano", C.S.I.C., Madrid, Spain, Institute of Animal Physiology and Genetics, Academy of Sciences of the Czech Republic, Libechov, Czech Republic, and Institute of Hematology and Blood Transfusion, Prague, Czech Republic.
Received July 9, 2007; Revised Manuscript Received August 10, 2007

Polyspermine-ribonuclease A (PS-RNase A) and polyspermine-dimeric ribonuclease A (PS-dimeric RNase A) were prepared by cross-linking ribonuclease A or its covalently linked dimer to polyspermine (PS) using dimethyl suberimidate. The two RNase A derivatives were tested for a possible antitumor action. The *in vitro* and *in vivo* cytotoxic activity of PS-RNase A, although strong, is not higher than that known for free polyspermine. PS-dimeric RNase A, which was characterized by mass spectroscopy, titration of free amine groups, and enzymatic assays, proved instead to be a definitely more efficient antitumor agent, both *in vitro* and *in vivo*. This result could tentatively be explained in view of the importance of positive charges for ribonuclease activity, considering the higher basicity of PS-dimeric RNase A compared to that of PS-(monomeric)RNase A. It must be also taken into account that the dimeric RNase A moiety of PS-dimeric RNase A could evade the cytoplasmic ribonuclease inhibitor, which instead could trap the monomeric RNase A moiety of the other derivative. The two RNase A derivatives degrade poly(A)·poly(U) under conditions where native RNase A is inactive. The results of this work demonstrate once again the importance of positive charges for the functions of mammalian pancreatic type ribonucleases in general, in particular for RNase A derivatives, and the potential therapeutic use of the ribonuclease A derivatives.

INTRODUCTION

Wang and Moore described the preparation of bovine ribonuclease A (RNase A[1]) covalently linked to polyspermine and called the product polyspermine-ribonuclease (*1*). Polyspermine consisted of a chain of spermine residues linked one to another by the bifunctional reagent dimethyl suberimidate. The polyspermine chain, which in the authors' best preparation consisted of eight spermine residues (*1*), was in turn linked, again through dimethyl suberimidate, to a lysine residue of an RNase A molecule (see Figure 1 for the structures of these molecules). The aim of Wang and Moore's work was to obtain ribonuclease A molecules endowed with a definitely higher basicity and higher affinity to nucleic acid molecules than native RNase A within the hypothesis advanced some years before (*2–5*) that pancreatic type ribonucleases are able to degrade not only single-stranded RNA but also double-stranded RNA as well as poly(A) or the RNA moiety of DNA/RNA hybrids (*2*) if they are more basic than bovine RNase A. Although the derivative obtained by Wang and Moore could have been heterogeneous in terms of which amine group on the protein was modified, it was found to maintain the activity on ssRNA but also acquire a very remarkable activity against double-helical polyribonucleotides as substrates (*1*). While the ability of mammalian RNases more basic than RNase A to attack dsRNA is between 10 and 40 times higher than that of RNase A (*2*), except for the special case of human pancreatic RNase, whose activity is very high (*2, 5*), polyspermine-ribonuclease was 115, 176, and 382 times more efficient than RNase A at degrading poly(A)·poly(U), poly(I)·poly(C), and the hybrid molecule poly(rU)·poly(dA), respectively (*1*). Recently, dimers, trimers, tetramers, and higher order oligomers of RNase A, formed by 3D domain swapping of the N-terminus and/or C-terminus of the protein (*6–8*), were shown to be able to remarkably degrade double-stranded polyribonucleotides and poly(A). DsRNA degradation increases as a function of the size of the oligomers, i.e., of the number or density of positive charges available on the oligomers' surface (*6*). Dimers, trimers, and tetramers of RNase A also display interesting biological actions (*9*), such as significant antitumor activity, demonstrated both *in vitro* and *in vivo*, and aspermatogenic action, under conditions where monomeric RNase A is inactive. A possible reason for these activities of the RNase A oligomers is that they could escape, different from native RNase A, interaction with the cytoplasmic ribonuclease inhibitor ((*10*), and references therein). It is worth pointing out that a parallelism exists between the enzymatic activity of the oligomers of RNase A toward dsRNA and its antitumor action. Indeed, both activities increase as a function of the size of the oligomers, and the interpretation of this finding is that both effects might be dependent on the number or density of positive charges present on the protein surface and on their increase (*11*). The high

* Corresponding author. Dipartimento di Scienze Morfologico-Biomediche, Sezione di Chimica Biologica, Università di Verona, Strada Le Grazie 8, I-37134 Verona, Italy. Phone: +39-045-8027166. Fax: +39-045-8027170. E-mail: massimo.libonati@univr.it.

[†] 1st Medical Faculty of the Charles University.

[‡] University of Verona.

[§] C.S.I.C.

[||] Academy of Sciences of the Czech Republic.

[⊥] Institute of Hematology and Blood Transfusion.

[1] Abbreviations: RNase A, bovine pancreatic ribonuclease A; ssRNA, single-stranded RNA; dsRNA, double-stranded RNA; cRI, cytosolic ribonuclease inhibitor; PS-RNase A, polyspermine-RNase A; PS-dimeric RNase A, polyspermine-dimeric RNase A; DMS, dimethyl suberimidate; BS-RNase, bovine seminal ribonuclease.

10.1021/bc700253c CCC: $37.00 © 2007 American Chemical Society
Published on Web 10/04/2007

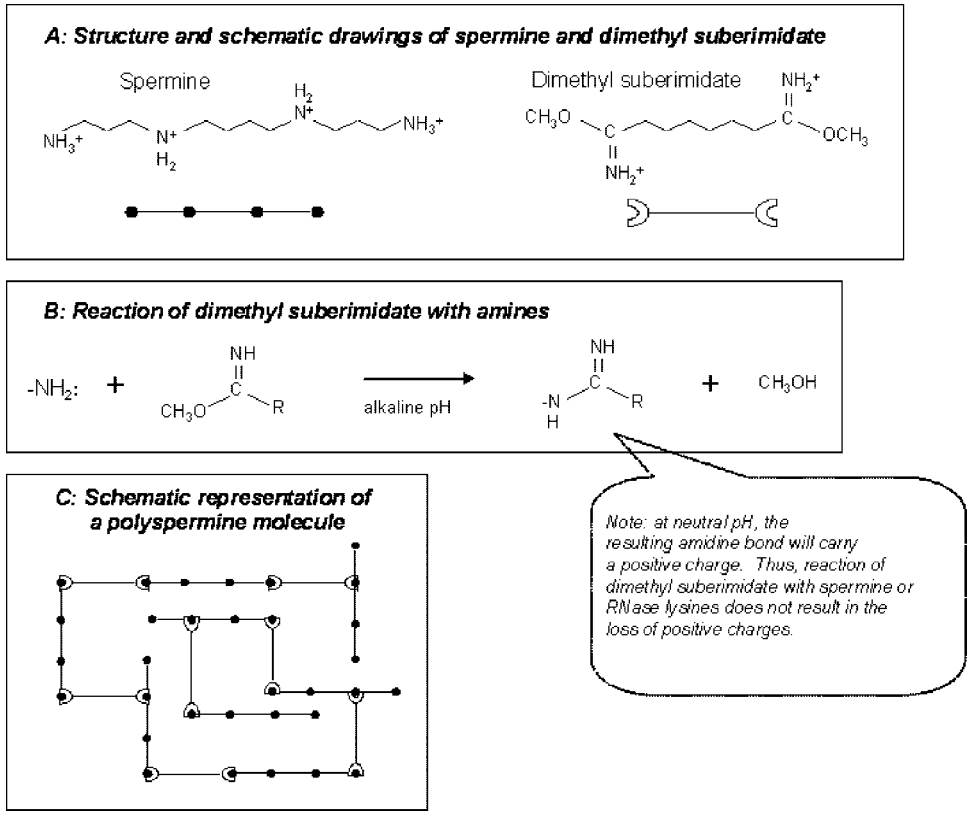


Figure 1. Structure and formation of polyspermine.

number or density of positive charges of an RNase A oligomer would favor the cleavage of dsRNA thanks to, as proposed for basic ribonucleases (*2*), a previous destabilization (*12*) of its secondary structure, thus making available, within the double-helix, single-stranded RNA segments to the action of the RNase. Moreover, the high basicity of an RNase A oligomer could favor its absorbance to and permeation of the cell membrane and enhance, once the oligomer is inside the cell, its enzymatic action toward all RNA secondary structures present in the cell. Besides the double-helical regions of rRNA, mRNA, and tRNA (*9, 11*), transient but important DNA/RNA hybrid structures, such as those occurring during the priming of DNA synthesis by RNA or during the synthesis of mRNA, as well as the polyadenylate tail of mRNA, could become good targets of the catalytic action of oligomeric RNase A (*11*).

In line with these facts, our idea now is to see if the binding of monomeric RNase A or cross-linked RNase A dimers (as the simplest example of oligomeric RNase A) to polyspermine, with the consequent increase of the basicity of the two enzyme species, could evoke a cytotoxicity of the two polyspermine-RNase A complexes higher than the cytotoxicity exerted by free polyspermine or spermine, which is already known (*13, 14*). The cross-linked RNase A dimer, notwithstanding a lower activity towards dsRNA compared to that of aggregated dimers (*15*), has the advantage of being stable, whereas all aggregated oligomers are meta-stable (*11, 16*). Moreover, it should also be able to evade the cRI (*17*). The present investigation, whose results support the ideas advanced (*2–5, 9, 11*) and reported above, is also in line with past work by some of us in searching for ribonuclease derivatives active as antitumor agents (*9, 18–23*).

EXPERIMENTAL PROCEDURES

Preparation of Cross-Linked Dimers of RNase A. To prepare the covalently linked dimer, we followed the procedure outlined by Wilson, Wang, and Moore (*24*). Forty milligrams of RNase A (Type XII-A, purchased from Sigma Chem. Co.) were dissolved in 0.64 mL of 0.2 M sodium phosphate buffer at pH 8.0. One milligram of solid dimethyl suberimidate (Sigma-Aldrich) was added in small aliquots to this solution with stirring. The pH of the solution was adjusted and maintained at 8.0 with 1 M NaOH. The reaction was carried out with stirring for 10 min at room temperature and stopped by adding 0.64 mL of 0.2 M ammonium acetate. The product was then purified and isolated by gel filtration through a Superdex 75 GL 10/300 column in an FPLC system (GE-Healthcare), equilibrated with 0.2 M sodium phosphate buffer at pH 6.7. The flow rate was 0.10 to 0.15 mL/min. The material was concentrated with Millipore Centricon YM-3 and 3000 MW cut-off, the solvent was exchanged to remove dissolved salts, and the sample was finally lyophilized.

Preparation of Polyspermine. One hundred twenty micromoles of spermine (41.78 mg; Sigma-Aldrich) were dissolved in 2 mL of 0.2 M triethanolamine at pH 9.7. To this solution, under stirring, small aliquots of solid dimethyl suberimidate (124 μmol, 33.88 mg) were added, controlling and adjusting the pH to 9.7 with 1 M NaOH. The reaction time was 1 min at room temperature (*1*).

Preparation of (Cross-Linked) Polyspermine-RNase A and Polyspermine-Dimeric RNase A. We cross-linked polyspermine to monomeric RNase A or its dimer following the method described by Wang and Moore (*1*). After the two steps of the previous preparation were completed, 1.1 μmol of monomeric or dimeric RNase A, dissolved in 2 mL of 0.1 M sodium phosphate buffer, pH 9.0, were added to the solution containing 120 μmol of polyspermine + 124 μmol of dimethyl suberimidate (see above). The reaction was carried out, with stirring, for five minutes and stopped by adding 1.5 mL of 2 M ammonium acetate. The products of the mixture were then purified and isolated by gel filtration through a Superdex 75 GL 10/300 column in an FPLC system (GE-Healthcare), equilibrated with

0.2 M sodium phosphate buffer at pH 6.7. The flow rate was 0.1 mL/min. The sample was then concentrated and lyophilized as described above.

Bovine Seminal Ribonuclease (BS-RNase). BS-RNase was isolated from bull seminal plasma obtained from healthy bulls bred in Litohor Insemination Station (Czech Republic). One volume of seminal plasma was diluted with 2.5 volumes of 2% acetic acid. The precipitate was removed by centrifugation and solid ammonium sulfate added to the supernatant up to a concentration of 3 M. After a second centrifugation, the supernatant was dialyzed using the Vivaflow 50 linked module flow system (Vivascience Ltd., Sonehouse, UK) and freeze-dried. For complete purification, chromatographies with CM Sephadex C-50 and Sephadex C-100 columns were used (*25*).

Determination of Free NH_2 Groups on RNase A, Dimeric RNase A, and PS-Dimeric RNase A. One hundred fifty micrograms of protein were dissolved in 1 mL of 0.15 M sodium tetraborate ($Na_2B_4O_7$) at pH 9.5. To this solution, 0.2 mL of 0.015 M trinitrobenzensulfonic acid (Fluka) was added in the dark with stirring. The incubation of this mixture was carried out, without stirring, for 45 min at 37 °C. The reaction was stopped by adding 2 mL of 85–90% formic acid. Finally, the absorbance at 340 nm of the samples and controls of unmodified RNase A was determined. The number of free lysine residues remaining was ascertained using the extinction coefficient of $\varepsilon_{340\ nm} = 12{,}000\ cm^{-1}\ M^{-1}$ per trinitrobenzenyl-lysine. The precision of this assay is ±10% or about one lysine group per RNase A molecule. Unmodified RNase A contains a total of 11 amine groups (10 Lys and one N-terminal amine).

Mass Spectrometry Analyses of the Cross-Linked RNase A Dimer Alone or Conjugated with Polyspermine. Matrix-assisted laser desorption–ionization time-of-flight (MALDI-TOF) mass spectra were recorded with an applied Biosystems Voyager System 6214 mass spectrometer using sinapinic acid in the matrix. The data were analyzed using the software supplied by Applied Biosystems.

Assays of Enzymatic Activity. Enzymatic activity on single-stranded RNA (purified yeast RNA) as substrate was performed according to Kunitz (*26*). The activity toward double-helical polyribonucleotide poly(A)·poly(U) was measured spectrophotometrically according to Libonati and Floridi (*1, 4*).

Assay of Antiproliferative Effect *in Vitro.* (a) ML-2 and K-562 cell lines derived from human leukemias were used for testing the antiproliferative activity of free spermine or polyspermine and the RNase A derivatives, polyspermine-ribonuclease A and polyspermine-dimeric RNase A, side-by-side with bovine seminal ribonuclease, as described previously (*9*). Briefly, ML-2 or K-562 cells (2×10^4) in 0.2 mL of RPMI 1640 medium supplemented with fetal calf serum (10% v/v) were established in microtiter plates (NUNC, FB type) and cultivated in humidified atmosphere, containing 5% CO_2 for 48 h. Four hours before ending cultivation, samples were pulsed with 24 kBq of 6-^{3}H-thymidine (specific activity 980 GBq/mmol, Institute for Research, Development and Application of Radioisotopes, Prague, Czech Republic). Cells were then collected with the Scatron harvester, and the incorporated radioactivity was measured with a Beckman scintillation counter. The mean value of three cultures containing one of the compounds to be tested was compared with the mean value of untreated control cells and the percentage of inhibited proliferation calculated. (b) In addition, human pancreas adenocarcinoma cell lines PaCa44 and PSN1 were used to test the action of the RNase A derivatives or other substances. The cells were grown in RPMI 1640 supplemented with 20 mM glutamine, 10% FBS, and 50 μg/mL gentamicin sulfate (BioWhittaker, Italy). Normal primary fibroblasts (Promocell, PBI Milan) were grown in DMEM supplemented with 10% FBS and 50 μg/mL gentamicin sulfate (BioWhittaker, Italy). All cell lines were incubated at 37 °C with 5% CO_2. Cells were plated in 96-well cell culture plates (4×10^3 cells/well) and treated with the substances to be tested at the concentrations indicated. Treated cells were maintained at 37 °C in the 5% CO_2 atmosphere for 24 h, then stained with Crystal Violet (Sigma). The dye was dissolved with 1% SDS in PBS and measured spectrophotometrically (A_{595}) to determine cell viability. Three independent experiments were performed for each assay condition.

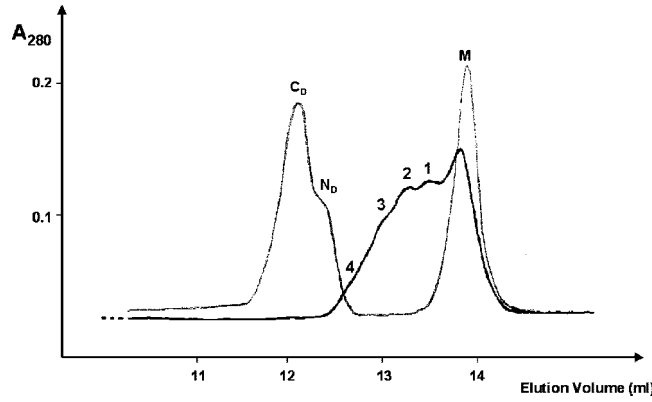


Figure 2. Size exclusion chromatography of polyspermine-ribonuclease A. One-half milligrams of the cross-linking PS-RNase A reaction mixture was applied onto a Superdex 75 GL 10/300 column equilibrated with 0.2 M sodium phosphate buffer, pH 6.7, in a FPLC system (GE-Healthcare). Flow rate was 0.1 mL/min at room temperature. C_D, C-terminal swapped dimeric conformer of RNase A; N_D, N-terminal swapped dimeric conformer of RNase A (*6, 8, 9, 11*). M, monomeric RNase A. 1, 2, 3, and 4, the four detectable PS-RNase A fractions (see text).

Assay of Immunosuppressive Activity on Mixed Lymphocyte Culture (MLC). Immunosuppressive activity of the various compounds was assessed on human lymphocytes stimulated in mixed lymphocyte culture (MLC), as described previously (*18*). Lymphocytes from two unrelated donors were mixed and cultivated in a humidified atmosphere containing CO_2 (5% v/v), at 37 °C, in RPMI 1640 medium supplemented with mixed human AB serum (10% v/v). RNase A derivatives or other substances were added at the beginning of the experiment, and cell mixtures were incubated for six days. Pulsation with (6-^{3}H)-thymidine and calculation of the inhibitory effect were carried out as described above.

Evaluation of the Action of RNase A Derivatives in Nude Mice. The antitumor activity of polyspermine-dimeric RNase A, RNase A cross-linked dimer, or free polyspermine was studied in athymic female nude CD-1 mice (Anlab-Charles River) weighing 18–20 g. Groups of six mice were housed under aseptic conditions (*20*). Human melanoma (tumor line C-32) was obtained from a European tumor bank, ECACC (European Collection of the Cell Cultures, CAMR, Salisbary, Wiltshire SP4 0JG, U.K.). This tumor line was amplified in a tissue culture and was administered subcutaneously to nude mice, on the right flank, with 1×10^7 tumor cells together with 0.1 mL of Matrigel. Intratumoral (i.t.) or intravenuous (i.v.) treatment was initiated when the area of the tumor transplanted in mice reached 5 × 5 mm. The RNase A derivative and other substances were injected (doses specified in Figure legends) three times a week over a period of 18 days. Tumor size was measured twice a week using a slide caliper (length × width × depth) (*9*).

RESULTS

Purification of Polyspermine-Ribonuclease A and Polyspermine-Dimeric Ribonuclease A. PS-RNase A was partly purified by gel filtration (Figure 2). The gel filtration pattern consists of

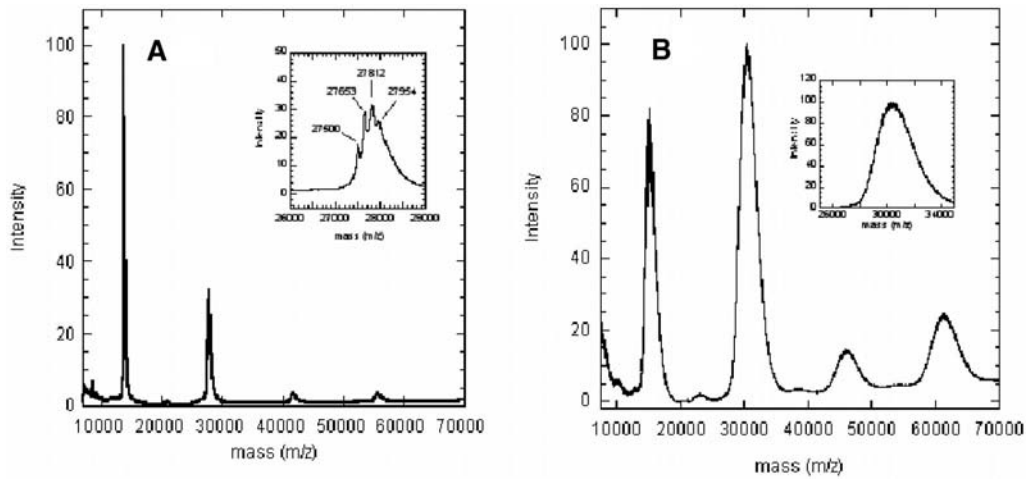


Figure 3. MALDI-TOF mass spectra of (A) cross-linked dimer of RNase A and (B) PS-dimeric RNase A. The fine structure of the dimer peaks is shown in the insets. See Experimental Procedures for details.

a large heterogeneous peak that includes various fractions of monomeric RNase A that reacted with polyspermine. The largest portion of this peak, eluting before the peak corresponding to native, un-reacted RNase A (M in Figure 2), consists of four almost unresolved fractions (indicated as 1, 2, 3, and 4 in Figure 2). Although quite scarcely resolved, fractions 1 and 2 show sufficiently clear apexes (less clear are those of fractions 3 and 4). These apexes were used to calculate the elution volumes, and hence the molecular weight, of the four fractions. The profile of the large peak clearly shows that none of the fractions 1, 2, 3, and 4 elutes in positions similar to or overlapping those of the 3D domain-swapped dimeric RNase A conformers (N_D and C_D) (*11*) used as standards. This is a further indication that the fractions are indeed monomeric variants of RNase A. We assume that the differences in weight between fractions 1, 2, 3, and 4 and native RNase A are due to different amounts of polyspermine bound to the protein, i.e., to the different number of spermine and dimethyl suberimidate residues, whose ratio is always about 1:1, linked to the RNase A molecule. The calculated molecular weight values of the four fractions indicated that sample 1 should contain 2 spermine residues, sample 2 between 2 and 5, sample 3 between 5 and 8, and sample 4 between 9 and 14 spermine residues. An attempt to further purify polyspermine-ribonuclease A by cation exchange chromatography was unsuccessful (data not shown), revealing great heterogeneity, which was already observed by Wang and Moore (*1*) and was also detected in the dimeric RNase A and polyspermine-dimeric ribonuclease A patterns by mass spectra, as described in the next section. This heterogeneity led us to distinguish the eluted fractions of the monomeric RNase A derivative in four final groups that correspond to the four peaks identified in the gel filtration pattern (Figure 2). Fractions that showed, on the basis of the cation exchange chromatography results (not shown), a relatively similar degree of basicity were combined. It must be taken into account that in addition to the number of spermine molecules within the polyspermine moiety, the location of the lysine residues reacting with polyspermine could also influence the elution position. These four PS-RNase A groups have been dialyzed, concentrated, and tested for their enzymatic and biological actions. A similar procedure was followed to isolate PS-dimeric RNase A. A gel filtration analysis, methodologically identical to that used for PS-RNase A, revealed a peak slightly larger than a second, distinct peak of un-reacted dimeric RNase A. The calculation of the molecular weight of the main symmetric peak indicated the presence of about 20–25% of polyspermine and 75–80% of protein, values that are sufficiently close to those calculated by mass spectroscopy (see later). The analysis of PS-dimeric RNase A with cation exchange chromatography did not give a clearer pattern than that obtained with PS-RNase A. We therefore used the total PS-dimeric RNase A peak as such to determine both the enzymatic and antiproliferative activities of PS-dimeric RNase A.

Further Characterization of Polyspermine-Dimeric Ribonuclease A. *(a) Titration of Lysine Groups.* The cross-linked (with dimethyl suberimidate) dimers of RNase A and PS-dimeric RNase A were characterized, side-by-side with native RNase A, by titration of the free amine groups according to Wang and Moore (*1*) (see Experimental Procedures). The number of unmodified amines groups was found to be 9 ± 1 in native RNase A, 8 ± 1 in cross-linked dimeric RNase A, and 6 ± 1 in the PS-dimeric RNase A.

(b) Analysis of Polyspermine-Dimeric Ribonuclease A by Mass Spectroscopy. The mass spectra of the cross-linked RNase A dimers revealed strong peaks with mass/charge ratios corresponding to monomeric and dimeric species and much weaker ones corresponding to trimeric and tetrameric species (Figure 3A). It is important to note that the absolute amount of dimer may actually be as high as that of the monomer since mass spectroscopy tends to exaggerate the intensity of lighter species, which fly better. Both the monomeric and dimeric peaks contain fine peaks with mass/charge values of 13682, 13839, and 14002 (monomer) and 27500, 27653, 27812, and 27954 (dimer) (Figure 3A inset). The lightest monomer has a mass corresponding to native RNase A, and the mass of the lightest dimer is that expected for the dimethyl suberimidate cross-linked dimer of RNase A. The mass/charge increment between the fine peaks observed for both the monomer and dimer is about 153–163 mass units, which corresponds reasonably well to the mass of a molecule of dimethyl suberimidate that has reacted with only one lysine residue (expected mass increase = 170). This increment corresponds even better to the mass of a molecule of dimethyl suberimidate that has reacted with a lysine residue at one end and with a water molecule at the other end to lose a molecule of methanol (expected mass increase = 156). The mass spectrum of PS-dimeric RNase A is shown in Figure 3B. A series of broad peaks can be observed, with masses corresponding approximately to monomer, dimer, trimer, and tetramer. The dimer appears to be the most populated species. The dimer peak is broad; its mass ranges from 28,000 Da (the unmodified dimer) up to 34,000 Da (Figure 3B, inset). This indicates that the number of attached spermine groups present in the dimer varies significantly. The number of spermine groups attached per dimer can be calculated considering that one molecule of dimethyl suberimidate (mass = 138 Da when fully reacted) is required

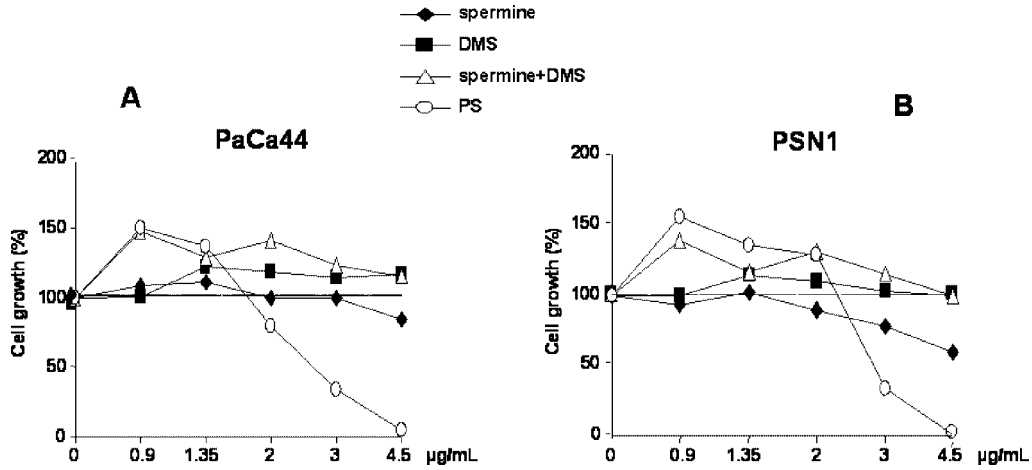


Figure 4. Dose-dependent effects of polyspermine, spermine, and dimethyl suberimidate, alone or mixed together, on two pancreatic adenocarcinoma cell lines. Cells were seeded in 96-well plates and incubated overnight; they were further incubated in the presence of the various substances for 24 h. The concentrations indicated are relative to the concentrations of free polyspermine used. Since the ratio of the amounts of spermine and DMS in polyspermine was about 1:1, the concentrations used of single spermine or DMS were 50% of those indicated on the abscissa. Cell proliferation was determined with the crystal violet colorimetric assay (see Experimental Procedures). The values reported are the means of triplicate wells from three independent experiments. DMS, dimethyl suberimidate. PS, polyspermine.

to couple each spermine molecule (mass = 203 Da). Since the range of dimer peak mass is about 34,000–28,000 Da = 6000 Da, the maximum number of spermine groups attached is about 6000 Da/(138 + 203 Da) = 18.

Taken together, these data suggest (i) that the cross-linked RNase A dimers contain some monomeric species, some of which have half-reacted with additional molecules of dimethyl suberimidate and (ii) that the preparation of PS-dimeric RNase A contains a rich diversity of species bearing from 1 to 18 spermine moieties.

Tests for Possible Biological Actions Displayed by the Single Components of the Polyspermine-RNase A Derivatives. In preliminary *in vitro* experiments, free polyspermine, spermine, the bifunctional reagent dimethyl suberimidate (DMS), and DMS mixed with spermine were tested on two human pancreas adenocarcinoma cell lines, PaCa44 and PSN1, in order to see possible effects that single components of the PS-RNase A complex could evoke in transformed cells. Figure 4A shows that while spermine, DMS, or spermine plus DMS did not show any effect on the two cell lines, and spermine just a small one on PSN1 cells (Figure 4B), the action of polyspermine on both lines was strong, starting at a polyamine concentration between 1 (Figure 4A) and 2 (Figure 4B) μg/mL of culture medium.

Antiproliferative Action *in Vitro* of Polyspermine-Ribonuclease A. The four distinct PS-RNase A fractions eluted in the gel filtration (Figure 2) and grouped on the basis of their basic charge characters (cation exchange chromatography) were tested for their ability to inhibit the proliferation of ML-2 and HT 1197 cell lines side-by-side with spermine, polyspermine, and bovine seminal RNase. Briefly (data not shown), while spermine was only slightly active, the four PS-RNase A fractions, free polyspermine and bovine seminal RNase were found to be efficient antiproliferative agents but without significant differences between PS-RNase A and free polyspermine. Similar results were obtained by testing the immunosuppressive activity of the same substances on mixed lymphocyte cultures (data not shown). Moreover, the PS-RNase A fraction n. 3 (see Figure 2), as one endowed with high basicity and the one showing maximal dsRNase activity (as described later; see Table 1), was also tested on the PaCa44 and SPN1 cell lines, side-by-side with spermine and polyspermine (Figure 5A and B). While free spermine was inactive on PaCa44 cells and just very slightly active on SPN1 cells (in agreement with that shown in Figure 4B), a higher antiproliferative action exerted by free polyspermine relative to that of the PS-RNase A fraction 3 could be observed on PaCa44 cells (Figure 5A). The two agents instead showed similar antiproliferative actions on PSN1 cells (Figure 5B).

Table 1. Enzymatic Activity of the Various Ribonuclease A Species on Single-Stranded RNA and Double-Stranded Poly(A)·Poly(U)[a]

monomeric or dimeric RNase A species	(A) specific activity yeast RNA as substrate	(B) specific activity poly(A)·poly(U) as substrate
native, monomeric RNase A	84.55 ± 6.30	1.55 ± 0.21
DMS-treated monomeric RNase A	49.33 ± 3.06	1.14 ± 0.12
PS-RNase A-1	n.d.	40.25 ± 19.90
PS-RNase A-2	n.d.	76.30 ± 21.70
PS-RNase A-3	n.d.	116.16 ± 39.91
PS-RNase A-4	n.d.	96.73 ± 22.72
domain swapped RNase A C-Dimer	53.46 ± 4.04	12.15 ± 3.04
cross-linked (DMS) RNase A Dimer	12.67 ± 3.02	2.22 ± 0.36
PS-dimeric RNase A	13.33 ± 1.15	25.21 ± 3.88

[a] Incubation mixtures: 0.4 mL of SSC (0.15 M sodium chloride/0.015 M sodium citrate, pH 7.0), containing poly(A)·poly(U), 40 μg, and 1–6 μg of the various RNase A species. Monomeric RNase A, 12 μg. The mixtures were normalized in their sodium phosphate content. (A) Kunitz units. (B) Enzyme units: increase in absorbance at 260 nm/min/total measurable change (*2*). Temperature, 25 °C. PS-RNase A 1, 2, 3, and 4 are the polyspermine-(monomeric) RNase A groups obtained by combining fractions with similar degree of basicity (see text). DMS-treated monomeric RNase A is the ribonuclease A recovered after the cross-linking reaction.

In summary, from this set of experiments, we can conclude that any activity of the polyspermine-ribonuclease A complex should actually be ascribed to the action of polyspermine or, rather, to the polyspermine moiety of the complex.

Antiproliferative Action *in Vitro* of Polyspermine-Dimeric Ribonuclease A. A preliminary experiment was performed by comparing side-by-side the action of the cross-linked RNase A dimers, PS-dimeric RNase A, and free polyspermine on normal primary fibroblast cells (Figure 6A). The RNase A dimers do not show any activity, and the action of free polyspermine is very modest and slightly higher that of PS-dimeric RNase A.

The same substances were then tested for their action on PSN1 cells. As shown in Figure 6B, dimeric RNase A does not show any significant action, while free polyspermine and PS-

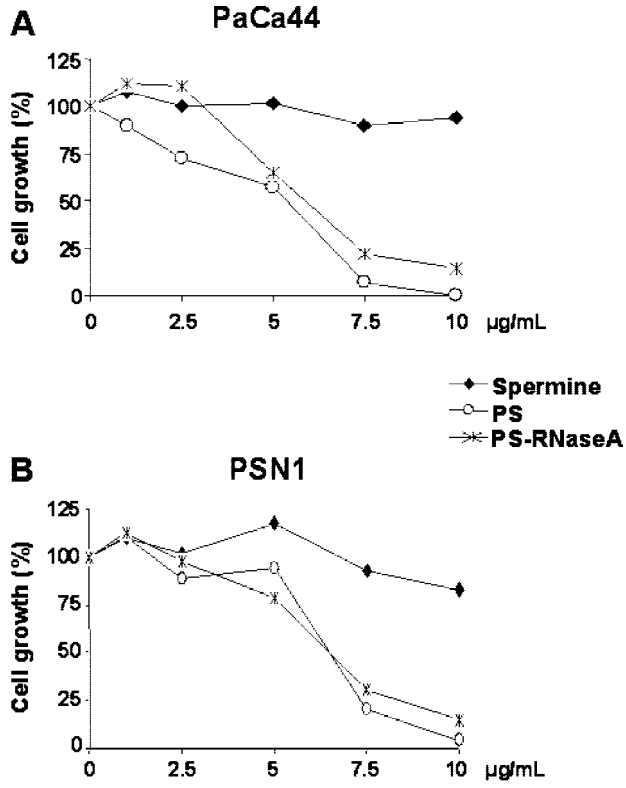


Figure 5. Dose-dependent effects of spermine, polyspermine, or PS-RNase A (group of fractions n. 3) on the two pancreatic adenocarcinoma cell lines, PaCa44 and PSN1. Cells were seeded in 96-well plates and incubated overnight. Cells were further incubated in the presence of the various molecules for 24 h. The concentrations indicated are relative to PS-RNase A. In line with the relative amount of polyspermine present in the RNase A derivative (group n. 3 of eluted fractions) as determined by mass spectroscopy (and gel filtration), the concentrations of single spermine and polyspermine used were 22% and 44%, respectively, of the concentrations of PS-RNase A used. Cell proliferation was determined with the crystal violet colorimetric assay, as described in the Experimental Procedures section. The values are the means of triplicate wells from three independent experiments. PS, polyspermine; PS-RNase A, polyspermine-ribonuclease A (group of fractions n. 3).

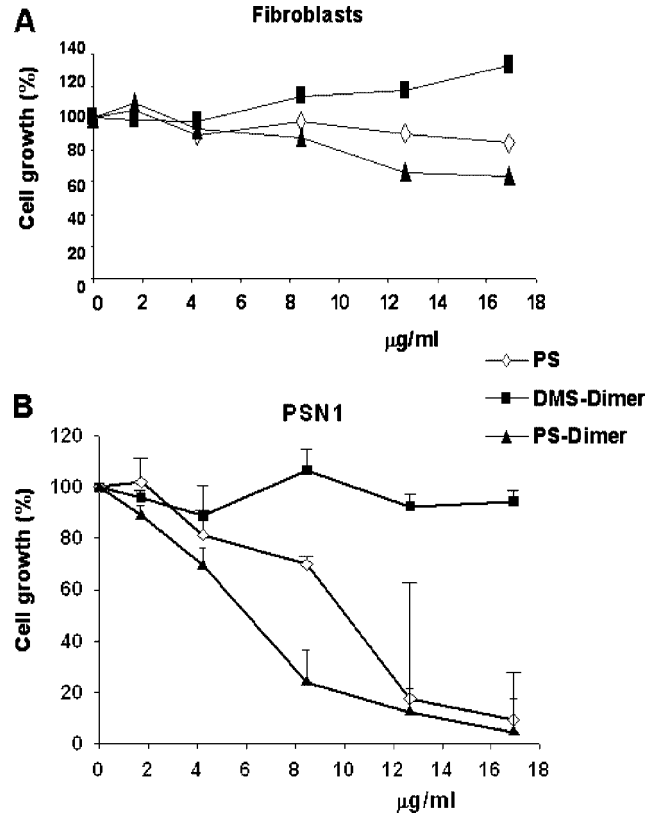


Figure 6. Dose-dependent effects of polyspermine, the cross-linked RNase A dimer, and PS-dimeric RNase A on the growth of (A) normal human fibroblasts and (B) the human pancreatic adenocarcinoma cell line PSN1. Cells were seeded in 96-well plates and incubated overnight. Cells were further incubated in the presence of the various substances for 24 h. The concentrations reported are referred to PS-dimeric RNase A. Considering that this RNase A derivative resulted by mass spectroscopy analyses to be formed by about 20% polyspermine and 80% dimeric RNase A in weight, while calculations by gel filtration were slightly higher, free polyspermine was used in some excess (25%) compared to the calculated concentrations. Cell proliferation was determined using the crystal violet colorimetric assay, as described in the Experimental Procedures section. The values are the means of triplicate wells from three independent experiments. PS, polyspermine; DMS-Dimer, cross-linked dimers of RNase A; PS-Dimer, polyspermine-dimeric ribonuclease A.

dimeric RNase A display a definite antiproliferative activity within almost the entire range of concentrations used, the RNase A derivative appearing to be more efficient than polyspermine alone.

Free polyspermine and PS-dimeric RNase A were also tested side-by-side with bovine seminal RNase on the two tumor cell lines ML-2 and K-562. Quite interestingly (see Figure 7A and B), the antiproliferative effect of free polyspermine on both cell lines is definitely higher than that of bovine seminal RNase, but PS-dimeric RNase A undoubtedly had the strongest antiproliferative action on ML-2 and K 562 cells. Similar results were obtained by assaying polyspermine and PS-dimeric RNase A side-by-side with bovine seminal RNase on the proliferation of a mixed lymphocyte culture (MLC; Figure 7C). Here too, the antiproliferative effect of bovine seminal RNase is remarkably lower than that exerted by the two other agents, and PS-dimeric RNase A is, again, definitely more efficient than polyspermine alone.

Antiproliferative Activity *in Vivo* of Polyspermine-Dimeric RNase A. PS-dimeric RNase A was tested, side-by-side with the cross-linked RNase A dimers and free polyspermine on the growth of a human melanoma (tumor line C-32) transplanted in nude mice. PS-dimeric RNase A was administered either intravenously or intratumorally. The results are shown in Figure 8. When injected intravenously, the inhibiting effect of PS-dimeric RNase A appears to be similar or slightly lower than that of both cross-linked RNase A dimers and free polyspermine. When administered directly into the tumor, although both dimeric RNase A and free polyspermine appear to be quite efficient and similar to each other at inhibiting tumor growth, PS-dimeric RNase A is definitely the most efficient antitumor agent.

Enzymatic Activity of Polyspermine-Ribonuclease A and Polyspermine-Dimeric Ribonuclease A. The ribonuclease activity of the RNase A species of interest was determined on single-stranded RNA according to the method of Kunitz (*26*) and on double-stranded poly(A)·poly(U) using a spectrophotometric assay (*2, 4, 5*). Table 1 (A) shows the activity, expressed in terms of Kunitz specific activity values, of native RNase A, the monomeric RNase A recovered from the cross-linking reaction, the aggregated RNase A C-dimer (formed by the swapping of the C-terminal β-strand of each monomer) (*8, 11*), the cross-linked RNase A dimer, and PS-dimeric RNase A. Both RNase A dimers show less activity against ssRNA compared to that of native, monomeric RNase A. This result, whose interpretation is not straightforward (*2, 11*), agrees with data repeatedly and consistently obtained in a number of assays performed in the past. Indeed, aggregated dimers or oligomers of RNase A, cross-linked oligomers, and even monomeric

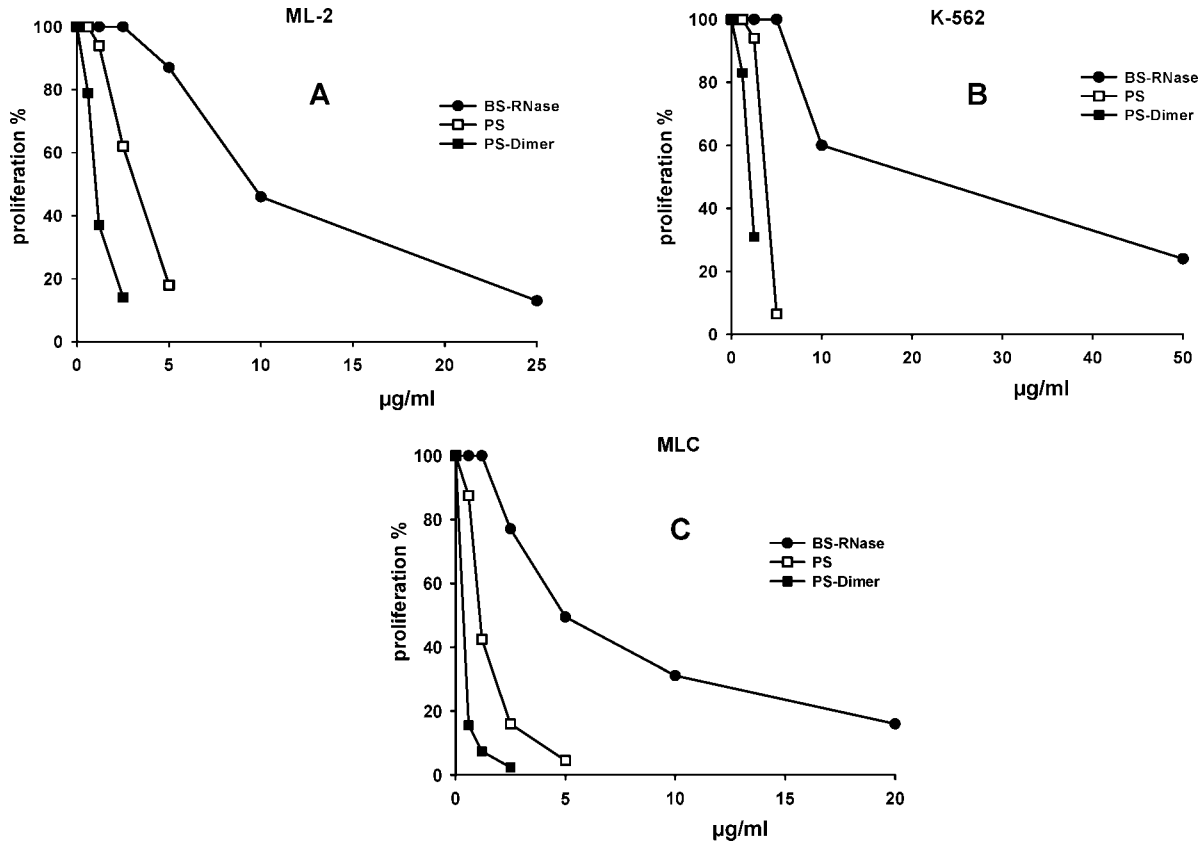


Figure 7. Dose-dependent effects of polyspermine, PS-dimeric RNase A, and bovine seminal RNase on the proliferation of human leukemic cell lines ML-2 (A), K-562 (B), and human lymphocytes stimulated in mixed lymphocytes culture, MLC (C). (A and B) Proliferation was evaluated after two days of incubation by the incorporation of ^{3}H-thymidine into cellular DNA. Each value is the mean of triplicate wells from two experiments and is reported in percent values compared to the value of untreated control samples. (C) Cell proliferation was determined by the incorporation of ^{3}H-thymidine into cellular DNA after six days of incubation. Each value is the mean of three cultures from two experiments and is reported in percent values compared to the value of untreated control cells. As mentioned in the legends to previous Figures, the doses of PS-dimeric RNase A and free polyspermine were calculated by taking into account the actual amount of polyspermine present in the RNase A derivative. BS-RNase, bovine seminal RNase; PS, polyspermine; PS-Dimer, polyspermine-dimeric ribonuclease A.

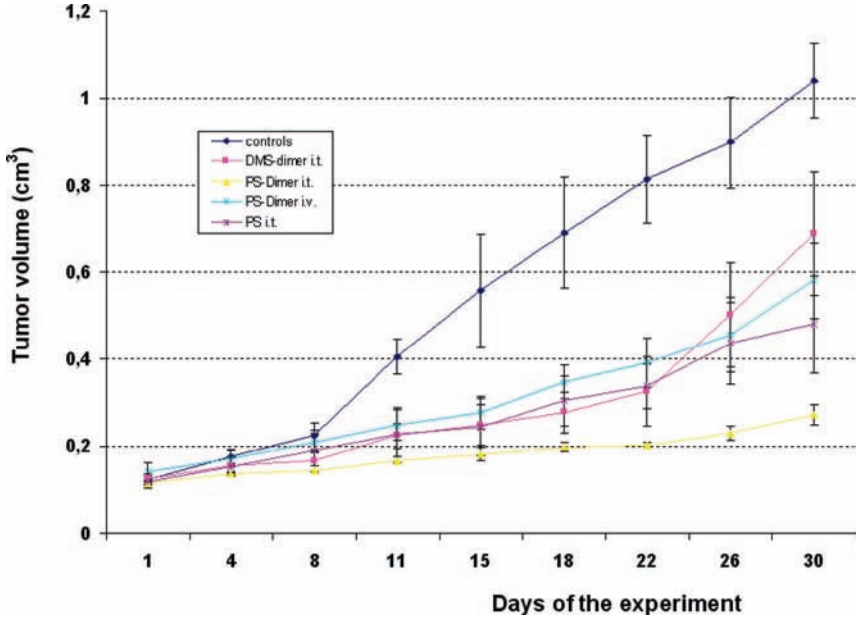


Figure 8. Effects of PS-dimeric RNase A, cross-linked dimers of RNase A, and free polyspermine on the growth of a human melanoma (tumor line C-32) transplanted in nude mice. PS-dimeric RNase A (100 μg/20 g), the cross-linked RNase A dimer (100 μg/20 g), and free polyspermine (25 μg/20 g) were administered intratumorally (i.t.). PS-dimeric RNase A was also administered intravenuously (i.v.) three times a week (total, nine doses). DMS-dimer, cross-linked RNase A dimer; PS-Dimer, PS-dimeric ribonuclease A; PS, free polyspermine.

mammalian ribonucleases endowed with a higher basicity than that of bovine pancreatic RNase A show lower Kunitz specific activity values relative to that of native, monomeric RNase A (*2*, *5*, *11*, *27*, *28*). A remarkably different rank order is

observed for the efficiency of the various RNase A species at cleaving poly(A)·poly(U) (Table 1 (B)). While for native RNase A we obtained a specific activity value that is consistent with values obtained in past experiments (*4, 5, 11, 28*), monomeric RNase A recovered from the cross-linking reaction shows, as already observed (*15*), a slightly lower activity than expected. On the contrary, the four polyspermine-ribonuclease groups, combining fractions endowed with similar degrees of basicity, displayed substantially stronger activity, which for at least three out of the four groups tested appears to be related or dependent on their increased basicity. As for the dimeric RNase A species, the cross-linked dimer shows a significantly lower activity than the C-terminal domain-swapped dimer does, while the action displayed by PS-dimeric RNase A is remarkably higher.

DISCUSSION

The principal aim of this work was to verify whether derivatives of bovine RNase A formed by monomeric or dimeric ribonuclease A cross-linked to polyspermine could display significant *in vitro* and *in vivo* cytotoxic action. Two well-established results provide a basis for expecting PS-RNase A to have strong antitumor activity. The first is that while native, monomeric RNase A is inactive at degrading dsRNA (*2, 29, 30*) and devoid, at least within a reasonable range of concentrations, of any antitumor action, its oligomers formed by simple aggregation (*9*), or dimers and trimers obtained by cross-linkage with dimethyl suberimidate (*15*) show an increased capacity of degrading double-stranded RNA (*11*) as well as remarkable *in vitro* and *in vivo* antitumor activity, which is accompanied by some other biological actions (*9, 11, 15*). The second, well-established finding is that polyspermine-ribonuclease (the product obtained by Wang and Moore (*1*) by cross-linking RNase A to polyspermine) acquires, when compared with that of native RNase A, a very remarkable ability to degrade double-stranded polyribonucleotides (*1*). Wang and Moore also studied the action of spermine or polyspermine added separately to a solution of PS-RNase A and poly(A)·poly(U) as substrate and saw that at concentrations between 1 μM to 0.2 mM the two polyamines increased the catalytic action of the RNase A derivative by less than 10%, while at higher concentrations (0.72 to 2.87 mM), spermine inhibited the enzyme (*1*). The ability to degrade double-helical RNA or DNA/RNA hybrids could be explained, both for RNase A oligomers and PS-RNase A, by the hypothesis ((*2*), and references therein) that the higher basicity of the enzyme molecule (due to its oligomerization, on one side, or to the presence of polyspermine, on the other) could induce, by interacting with dsRNA, a destabilization of the double-helix, with the exposure of single-stranded RNA segments sensitive to ribonucleolytic attack. Also, the biological activity of the RNase A oligomers might be explained with their increased basicity, which could favor their interaction with the cell membrane, their entrance in the cells, and hence their ability to degrade double-helical polyribonucleotide structures vital for the cells (*9, 11*). Moreover, a possible additional reason for the activity of RNase A oligomers is their size, which could ensure their partial or total escape from interaction with the cRI (*8, 11*), which completely inhibits monomeric RNase A.

The results obtained in this work appear to support, at least partly, the original idea. While PS-RNase A does not show an antitumor activity significantly higher than that of polyspermine alone, PS-dimeric RNase A displays both *in vitro* and *in vivo* cytotoxic action definitely higher than that exerted by polyspermine alone. Moreover, it should be taken into account that the activity of polyspermine-dimeric RNase A *in vitro* on several transformed cell lines and *in vivo* against a human melanoma transplanted in nude mice might appear to be lower than it really is because, as indicated by mass spectrometry analyses, some PS-RNase A could be present in the preparation. It is also worth pointing out here that the different effects of the two RNase A derivatives could be partly explained on the basis of a successful interaction of the cRI with the monomeric protein moiety of PS-RNase A. This interaction has been proved to occur also between cRI and the two domain swapped dimers of RNase A (*17*), although, at the same time, these oligomers were found to be biologically active (*9*). In our present case, the cRI could have been unable to interact or able to interact less efficiently with the dimeric protein moiety of PS-dimeric RNase A because of an increased steric hindrance caused by the polyspermine chain(s) linked to the protein. The results presented are also evidence of the already well known antitumor or, more generally, cytotoxic actions of polyamines due to their reaction products, H_2O_2 and aldehyde(s), formed by the oxidative deamination of biogenic amines or polyamines by cellular amine oxidases (*13*). This intrinsic toxicity of spermine and polyspermine may also totally or partially mask the antitumor action of the ribonuclease moiety of the two RNase A derivatives considered here, PS-RNase A and PS-dimeric RNase A. As mentioned above, no antitumor activity significantly higher than that displayed by polyspermine alone could be detected for the former derivative. This might be due not only to the successful intracellular interaction of the monomeric RNase moiety of PS-RNase A with the cytosolic inhibitor but also to the strong cytotoxic action of its polyspermine moiety. Actually, these uncertain results led us to construct the second RNase A derivative. PS-dimeric RNase A in fact shows a definitely higher cytotoxic action than that of polyspermine alone. The divergence in the biological activities of the two polyspermine derivatives of RNase A, partly ascribable to the cytotoxicity intrinsic to the polyspermine moiety, contradicts the fact that the other property, i.e., the ability to degrade *in vitro* double-stranded polyribonucleotides, is shared by both derivatives. This points out, once again, the role of the cRI. As discovered by Wang and Moore (*1*), PS-RNase A is remarkably efficient at degrading double-helical polyribonucleotides. The same is true for PS-dimeric RNase A, although its action on double-stranded poly(A)·poly(U) is lower than expected. This and in general the lower enzymatic activities toward dsRNA shown by cross-linked derivatives of pancreatic ribonuclease A (*15*) compared to that of aggregated dimers is difficult to explain. Indeed, the reaction with dimethyl suberimidate should not change the net charge of the protein since the resulting amidine bond carries a positive charge. However, the loss of enzymatic activity against dsRNA when many lysine-NH_3^+ groups of RNase A were modified was also observed and not explained by Wang, Wilson, and Moore (*24*). A lower activity of the positive charge at the amidine bond as well as the possibility that Lys-41 of some RNase A molecules of the population of reacting ribonuclease A molecules might be modified, or the variable and unspecific location of the dimethyl suberimidate chains on the RNase A surface could be responsible for the reduced enzymatic activity of the RNase A derivatives. The importance of a specific location of positive charges on RNase A for its catalytic activity has been stated, among others (*12, 31*), by McPherson et al. (*32*), who suggested that nine basic amino acid residues can constitute a cationic linear array complementary to the phosphate groups of a polyribonucleotide chain and was also pointed out by some of us for the activity against double-stranded polyribonucleotides shown by mammalian ribonucleases endowed with a higher basicity than bovine RNase A (*2, 5, 11*). In this regard, it is worth mentioning that cationic ribonucleases, such as EDN and ECP, whose positive charges are mainly located far from their active site regions, are inactive on dsRNA (*5, 33*). The same reasons mentioned above could also make polyspermine-monomeric or polyspermine-dimeric ribonuclease A less

efficient in their biological actions. In this regard, the more appropriate dimeric species of RNase A for cross-linking to polyspermine could possibly be the RNase A tandem variants constructed by Leich et al. (*34*) by gene duplication with insertion of the sequence of a peptide linking the C-terminus of an RNase A molecule and the N-terminus of a second RNase A molecule, as well as the new form of RNase A dimer recently described by Simons et al. (*35*). This dimer is stabilized by a single amide bond between the side chain NH_3^+ of Lys-66 and the side chain COO^- group of Glu-9, with no change of the protein net charge.

In conclusion, the results obtained and discussed here support on one side the importance, often pointed out (*1, 2, 11, 24, 27, 36–39*), of the positive charges present on a ribonuclease molecule for its functions and on the other side the potential therapeutic use of ribonucleases and RNase A derivatives (*37, 39–45*).

ACKNOWLEDGMENTS

This work was supported by grants from the Italian M.I.U.R. (P.R.I.N., Progetti di Rilevante Interesse Nazionale, 2004) and Centro Interuniversitario di Biotecnologie (C.I.B.), and grants from the Grant Agency of the Czech Republic No. 523/04/0755 and No. 521/06/1149. We also acknowledge the Spanish "Ministerio de Educación y Ciencia" for additional support via grants CTQ2004-08275 and GEN203-20642.C09-03.

LITERATURE CITED

(1) Wang, D., and Moore, S. (1977) Polyspermine-Ribonuclease prepared by cross-linkage with dimethyl suberimidate. *Biochemistry 16*, 2937–2942.

(2) Libonati, M., and Sorrentino, S. (2001) Degradation of double-stranded RNA by mammalian pancreatic-type ribonucleases. *Methods Enzymol. 341*, 234–248.

(3) Libonati, M., and Floridi, A. (1969) Breakdown of double-stranded RNA by bull semen ribonuclease. *Eur. J. Biochem. 8*, 81–87.

(4) Libonati, M., Furia, A., and Beintema, J. J. (1976) Basic charges on mammalian ribonuclease molecules and the ability to attack double-stranded RNA. *Eur. J. Biochem. 69*, 445–451.

(5) Sorrentino, S., and Libonati, M. (1994) Human pancreatic-type and non-pancreatic-type ribonucleases: a direct side-by-side comparison of their catalytic properties. *Arch. Biochem. Biophys. 312*, 340–348.

(6) Gotte, G., Bertoldi, M., and Libonati, M. (1999) Structural versatility of bovine ribonuclease A. Distinct conformers of trimeric and tetrameric aggregates of the enzyme. *Eur. J. Biochem. 265*, 680–687.

(7) Crestfield, A. M., Stein, W. H., and Moore, S. (1962) On the aggregation of bovine pancreatic ribonuclease. *Arch. Biochem. Biophys. 1*, 217–222.

(8) Gotte, G., Vottariello, F., and Libonati, M. (2003) Thermal aggregation of ribonuclease A. A contribution to the understanding of the role of 3D domain swapping in protein aggregation. *J. Biol. Chem. 278*, 10763–10769.

(9) Matousek, J., Gotte, G., Pouckova, P., Soucek, J., Slavik, T., Vottariello, F., and Libonati, M. (2003) Antitumor and other biological actions of oligomers of ribonuclease A. *J. Biol. Chem. 278*, 23817–23822.

(10) Shapiro, R. (2001) Cytoplasmic ribonuclease inhibitor. *Methods Enzymol. 341*, 611–628. Simons, B. L., Kaplan, H., Fournier, S. M., Cyr, T., and Hefford, M. A. (2007) A novel cross-linked RNase A dimer with enhanced enzymatic properties. *Proteins 66*, 183–195.

(11) Libonati, M., and Gotte, G. (2004) Oligomerization of bovine ribonuclease A: structural and functional features of ist multimers. *Biochem. J. 380*, 311–327.

(12) Jensen, D. E., and von Hippel, P. H. (1976) DNA 'melting' proteins. I. Effects of bovine pancreatic ribonuclease binding on the conformation and stability of DNA. *J. Biol. Chem. 251*, 7198–7214.

(13) Agostinelli, E., Arancia, G., Dalla Vedova, L., Belli, F., Marra, M., Salvi, M., and Toninello, A. (2004) The biological functions of polyamine oxidation products by amine oxydases: perspectives of clinical applications. *Amino Acids 27*, 347–358.

(14) Calcabrini, A., Arancia, G., Marra, M., Crateri, B., Befani, O., Martone, A., and Agostinelli, E. (2002) Enzymatic oxidation products of spermine induce greater cytotoxic effects on human multidrug-resistant colon carcinoma cells (LoVo) than on their wild-type counterparts. *Int. J. Cancer 93*, 43–52.

(15) Gotte, G., Testolin, L., Costanzo, C., Sorrentino, S., Armato, U., and Libonati, M. (1997) Cross-linked trimers of bovine ribonuclease A: activity on double-stranded RNA and antitumor action. *FEBS Lett. 415*, 308–312.

(16) Libonati, M. (2004) Biological actions of the oligomers of ribonuclease A. *Cell. Mol. Life Sci. 61*, 2431–2436.

(17) Naddeo, M., Vitagliano, L., Russo, A., Gotte, G., D'Alessio, G., and Sorrentino, S. (2005) Interactions of the cytotoxic RNase A dimers with the cytosolic ribonuclease inhibitor. *FEBS Lett. 579*, 2663–2668.

(18) Soucek, J., Marinov, I., Benes, J., Hilgert, I., Matousek, J., and Raines, R. T. (1996) Immunosuppressive activity of bovine seminal ribonuclease and its mode of action. *Immunobiology 195*, 271–285.

(19) Soucek, J., Pouckova, P., Strohalm, J., Plocova, D., Hluskova, D., Zadinova, M., and Ulbrich, K. (2002) Poly [N-(2-hydroxypropyl) methacrylamide] conjugates of bovine pancreatic ribonuclease (RNase A) inhibit growth of human melanoma in nude mice. *J. Drug Targeting 10*, 175–183.

(20) Ulbrich, K., Strohalm, J., Plocova, D., Oupicky, D., Subrt, V., Soucek, J., Pouckova, P., and Matousek, J. (2000) Poly[N-(2-Hydroypropyl)Methacrylamide] Conjugates of Bovine Seminal Ribonuclease. Synthesis, Physicochemical, and Preliminary Biological Evaluation. *J. Bioact. Compat. Polym. 15*, 4–26.

(21) Pouckova, P., Soucek, J., Jelinek, J., Zadinova, M., Hluskova, D., Polivkova, J., Navratil, L., Cinatl, J., and Matousek, J. (1998) Antitumor action of bovine seminal ribonuclease. Cytostatic effect on human melanoma and mouse seminoma. *Neoplasma 44*, 30–34.

(22) Soucek, J., Pouckova, P., Matousek, J., Dostal, J., and Zadinova, M. (1996) Antitumor action of bovine seminal ribonuclease. *Neoplasma 43*, 335–340.

(23) Pouckova, P., Skvor, C., Gotte, G., Vottariello, F., Slavik, J. T., Matousek, J., Horak, L., Laurents, D. V., Libonati, M., and Soucek, J. (2006) Some biological actions of PEG-conjugated RNase A oligomers. *Neoplasma 53*, 603–609.

(24) Wang, D., Wilson, G., and Moore, S. (1976) Preparation of cross-linked dimers of pancreatic ribonuclease. *Biochemistry 15*, 660–665.

(25) Dostal, J., and Matousek, J. (1973) Isolation and some chemical properties of aspermatogenic substance from bull seminal vesicle fluid. *J. Reprod. Fertil. 33*, 263–274.

(26) Kunitz, M. (1946) A spectrophotometric method for the measurement of ribonuclease activity. *J. Biol. Chem. 164*, 563–568.

(27) De Prisco, R., Sorrentino, S., Leone, E., and Libonati, M. (1984) A ribonuclease from human seminal plasma active on double-stranded RNA. *Biochim. Biophys. Acta 788*, 356–363.

(28) Libonati, M., Bertoldi, M., and Sorrentino, S. (1996) The activity on double-stranded RNA of aggregates of ribonuclease A higher than dimers increases as a function of the size of the aggregates. *Biochem. J. 318*, 287–290.

(29) Nicholson, A. W. (1996) Structure, reactivity, and biology of double-stranded RNA. *Prog. Nucleic Acid Res. Mol. Biol. 52*, 1–65.

(30) Usher, D. A., Erenrich, E. S., and Eckstein, F. (1972) Geometry of the first step in the action of ribonuclease A (in line-geometry-uridine 2′,3′ thiophosphate-^{31}P NMR). *Proc. Natl. Acad. Sci. U.S.A. 69*, 115–118.

(31) Karpel, R. L., Merkle, D. J., Flowers, B. K., and Delahunty, M. D. (1981) Involvement of basic amino acids in the activity of a nucleic acid helix-destabilizing protein. *Biochim. Biophys. Acta 654*, 42–51.

(32) McPherson, A., Brayer, G., Cascio, D., and Williams, R. (1986) The mechanism of binding of a polynucleotide chain to pancreatic ribonuclease. *Science 232*, 765–768.

(33) Sorrentino, S., and Glitz, D. G. (1991) Ribonuclease activity and substrate preference of human eosinophil cationic protein (ECP). *FEBS Lett. 288*, 23–26.

(34) Leich, F., Koditz, J., Ulbrich-Hofmann, R., and Arnold, U. (2006) Tandemization endows bovine pancreatic ribonuclease with cytotoxic activity. *J. Mol. Biol. 358*, 1305–1313.

(35) Simons, B. L., Kaplan, H., Fournier, S. M., Cyr, T., and Hefford, M. A. (2007) A novel cross-linked RNase A dimer with enhanced enzymatic properties. *Proteins 66*, 183–195.

(36) Futami, J., Maeda, T., Kitazoe, M., Nukui, E., Tada, H., Seno, M., Kosaka, M., and Yamada, H. (2001) Preparation of potent cytotoxic ribonucleases by cationization: enhanced cellular uptake and decreased interaction with ribonuclease inhibitor by chemical modification of carboxyl groups. *Biochemistry 40*, 7518–7524.

(37) Ilinskaya, O. N., Dryer, F., Mitkevitc, V. A., Shaw, K., Pace, C. N., and Makarov, A. A. (2002) Changing the net charge from negative to positive makes ribonuclease Sa cytotoxic. *Protein Sci. 11*, 2522–2525.

(38) Sorrentino, S., Naddeo, M., Russo, A., and D'Alessio, G. (2003) Degradation of double-stranded RNA by human pancreatic ribonuclease: crucial role of noncatalytic basic amino acid residues. *Biochemistry 42*, 10182–10190.

(39) Huang, Y.-C., Lin, Y.-M., Chang, T.-W., Wu, S.-J., Lee, Y.-S., Chang, M. D.-T., Chen, C., Wu, S.-H., and Liao, Y.-D. (2007) The flexible and clustered lysine residues of human ribonuclease 7 are critical for membrane permeability and antimicrobial activity. *J. Biol. Chem. 282*, 4626–4633.

(40) Leland, P. A., and Raines, R. T. (2001) Cancer chemotherapy - ribonucleases to the rescue. *Chem. Biol. 8*, 405–413.

(41) Arnold, U., and Ulbrich-Hofmann, R. (2006) Natural and engineered ribonucleases as potential cancer therapeutics. *Biotechnol. Lett. 28*, 1615–1622.

(42) Makarov, A. A., and Ilinskaya, O. N. (2003) Cytotoxic ribonucleases: molecular weapons and their targets. *FEBS Lett. 540*, 15–20.

(43) Matousek, J. (2001) Ribonucleases and their antitumor activity. *Comp. Biochem. Physiol., C 129*, 175–191.

(44) Youle, R. J., and D'Alessio, G. (1997) Antitumor RNases. *Ribonucleases: Structures and Functions* (D'Alessio, G., and Riordan, J. F., Eds.) pp. 491–514, Academic Press, New York.

(45) Raines, R. T. (1999) Ribonuclease A: From Model System to Cancer Chemotherapeutic, in *Enzymatic Mechanisms*, (Frey, P. A., and Northrop, D. B., Eds.) pp 235–249, IOS Press, Washington, DC.

BC700253C

^{99m}Tc-maEEE-$Z_{HER2:342}$, an Affibody Molecule-Based Tracer for the Detection of HER2 Expression in Malignant Tumors

Thuy Tran,[†] Torun Engfeldt,[‡] Anna Orlova,[†,§] Mattias Sandström,[||] Joachim Feldwisch,[†,§] Lars Abrahmsén,[§] Anders Wennborg,[§] Vladimir Tolmachev,[†,§,⊥] and Amelie Eriksson Karlström*[,‡]

Division of Biomedical Radiation Sciences, Rudbeck Laboratory, Uppsala University, Sweden, School of Biotechnology, Division of Molecular Biotechnology, Royal Institute of Technology, Stockholm, Sweden, Affibody AB, Bromma, Sweden, Medical Radiation Physics, Uppsala University Hospital, Uppsala University, Uppsala, Sweden, and Department of Medical Sciences, Uppsala University, Uppsala, Sweden. Received July 13, 2007; Revised Manuscript Received September 10, 2007

Detection of HER2-overexpression in tumors and metastases is important for the selection of patients who will benefit from trastuzumab treatment. Earlier investigations showed successful imaging of HER2-positive tumors in patients using indium- or gallium-labeled Affibody molecules. The goal of this study was to evaluate the use of ^{99m}Tc-labeled Affibody molecules for the detection of HER2 expression. The Affibody molecule $Z_{HER2:342}$ with the chelator sequences mercaptoacetyl-Gly-Glu-Gly (maGEG) and mercaptoacetyl-Glu-Glu-Glu (maEEE) was synthesized by peptide synthesis and labeled with technetium-99m. Binding specificity, cellular retention, and *in vitro* stability were investigated. The biodistribution of ^{99m}Tc-maGEG-$Z_{HER2:342}$ and ^{99m}Tc-maEEE-$Z_{HER2:342}$ was compared with ^{99m}Tc-maGGG-$Z_{HER2:342}$ in normal mice, and the tumor targeting properties of ^{99m}Tc-maEEE-$Z_{HER2:342}$ were determined in SKOV-3 xenografted nude mice. The results showed that the Affibody molecules were efficiently labeled with technetium-99m. The labeled conjugates were highly stable *in vitro* with preserved HER2-binding capacity. The use of glutamic acid in the chelator sequences for ^{99m}Tc-labeling of $Z_{HER2:342}$ reduced the hepatobiliary excretion 3-fold with a single Gly-to-Glu substitution and 10-fold with three Gly-to-Glu substitutions. ^{99m}Tc-maEEE-$Z_{HER2:342}$ showed a receptor-specific tumor uptake of 7.9 ± 1.0 %IA/g and a tumor-to-blood ratio of 38 at 4 h pi. Gamma-camera imaging with ^{99m}Tc-maEEE-$Z_{HER2:342}$ could detect HER2-expressing tumors in xenografts already at 1 h pi. It was concluded that peptide synthesis for the coupling of chelator sequences to Affibody molecules for ^{99m}Tc labeling is an efficient way to modify the *in vivo* kinetics. Increased hydrophilicity, combined with improved stability of the mercaptoacetyl-triglutamyl chelator, resulted in favorable biodistribution, making ^{99m}Tc-maEEE-$Z_{HER2:342}$ a promising tracer for clinical imaging of HER2 overexpression in tumors.

INTRODUCTION

Malignant transformation of cells may cause altered expression of distinctive molecular features relative to the surrounding tissues. Overexpression of a certain protein is often correlated with tumor progression and/or with tumor response to a certain treatment. Molecular imaging of such protein targets provide important diagnostic information that can influence patient management (*1*). One such target that has been extensively studied is the HER2/*neu* receptor (also known as *erb*B-2), a member of the receptor tyrosine kinase superfamily. HER2 is overexpressed in 20–30% of all breast cancers and in a variety of other tumors of epithelial origin (*2, 3*). Treatment with the humanized antibody trastuzumab (Herceptin, Genentech) improves the survival of patients with HER2-positive breast cancers, likely by the prevention of receptor dimerization and disruption of signaling pathways (*4*). Other anti-HER2 therapeutic agents are under clinical evaluation, including the monoclonal antibody pertuzumab (Omnitarg) (*5*), the heat-shock protein 90 inhibitor 17-AAG (*6*), and the tyrosine kinase inhibitor lapatinib (*7*).

An accurate determination of HER2 status is required in order to select breast cancer patients for Herceptin therapy. Currently, both the American Association of Clinical Oncology (*8*) and the European Group on Tumor Markers (*9*), recommend that HER2 expression should be evaluated on every primary breast cancer in order to identify patients who may benefit from Herceptin treatment. The most widely used methods for the detection of HER2 are immunohistochemical staining (IHC) and fluorescence *in situ* hybridization (FISH) of biopsy samples (*10*). However, these tests have some limitations (*8*), including inability to detect expression heterogeneity within a tumor lesion (*11, 12*) and discordance in HER2 expression between the primary tumor and the metastases (*13*). There is also subjectivity in evaluating the staining score (*11*). In contrast, radionuclide imaging may be applied to visualize HER2 expression in both whole primary tumors and metastatic lesions.

HER2 has no natural ligands (*14*), and monoclonal antibodies have been evaluated as targeting agents for radionuclide imaging (*15*). The general issues associated with the large size of intact IgG (Mw ~150 kDa) are slow blood clearance and slow tumor penetration, leading to low contrast of images (*16*). Reduction of the size of targeting proteins is considered a promising approach to improve the image contrast (*17*) and has generated a number of anti-HER2 antibody fragments such as $F(ab')_2$ (*18*), Fab (*19*), single chain Fv (25–55k Da) (*20*), and diabody (*21*).

Our approach to improve the radionuclide imaging contrast is to create a relatively small HER2-targeting protein by using

* Corresponding author. Amelie Eriksson Karlström, School of Biotechnology, Division of Molecular Biotechnology, Royal Institute of Technology, AlbaNova University Center, Roslagsvägen 30B, S-106 91 Stockholm, Sweden. Tel: +46-8-5537 8333. Fax: +46-8-5537 8481. E-mail: amelie@biotech.kth.se.

[†] Division of Biomedical Radiation Sciences, Uppsala University.

[‡] Royal Institute of Technology.

[§] Affibody AB.

[||] Medical Radiation Physics, Uppsala University.

[⊥] Department of Medical Sciences, Uppsala University.

10.1021/bc7002617 CCC: $37.00 © 2007 American Chemical Society
Published on Web 10/19/2007

Affibody technology, on the basis of the 58 amino acid B-domain of staphylococcal protein A. Randomization of 13 solvent-exposed residues has generated an Affibody library (3×10^9 variants), which has been used for the selection of affinity ligands to a variety of proteins (*22*). Affibody molecules are low molecular weight (7 kDa) and cysteine-free three-helix bundle proteins. The anti-HER2 Affibody molecule $Z_{HER2:342}$ binds to the extracellular domain of HER2 with an affinity of 22 pM (*23*).

Recombinant $Z_{HER2:342}$, labeled with ^{125}I and ^{111}In, demonstrated clear visualization of HER2-expressing SKOV-3 xenografts in mice (*23, 24*). However, the use of peptide synthesis for the production of targeting agents offers the advantage of site-specific incorporation of chelators. $Z_{HER2:342}$ has been produced by peptide synthesis with concomitant coupling of a DOTA chelator to the N-terminus of the protein (*25*). The labeling of this protein with ^{111}In and ^{68}Ga also provided high quality imaging of HER2-expressing tumors in patients (*26*).

One of the most commonly used radionuclides for diagnostics is ^{99m}Tc, as it has favorable photon energy (140 keV), is relatively inexpensive, and readily available. Its physical half-life ($t_{1/2} = 6$ h) is compatible with the rapid kinetics of Affibody molecules. Previously, the synthetic Affibody molecule $Z_{HER2:342}$ has been produced with the chelator maGGG (mercaptoacetyltriglycyl) site-specifically introduced at the N-terminus for the attachment of technetium-99m (*27*). The ^{99m}Tc-maGGG-$Z_{HER2:342}$ specifically targets HER2-expressing tumors in mice, resulting in high tumor-to-nontumor ratios for imaging (*27*). However, this conjugate had predominant hepatobiliary clearance that caused a high radioactivity accumulation in the intestine (intestine plus content contained 30% of the injected activity at 4 h pi). This would restrict its use for the detection of HER2 tumors and metastases in the abdominal area on the day of injection (*27*).

The excretion pathway can be shifted from hepatobiliary to renal if the lipophilicity of the radiolabeled conjugates is reduced (*28, 29*). For example, the use of the aspartic acid-containing chelators MADG and MAD2, for chelation of ^{99m}Tc has clearly increased the renal and decreased the hepatobiliary excretion of ^{99m}Tc-labeled chemotactic peptide conjugates (*30*). Glutamic acid (E) is a polar, negatively charged, and very hydrophilic amino acid (*31*). Moreover, glutamic acid is more suitable for peptide synthesis than aspartic acid since a commonly occurring side reaction under synthetic conditions is the formation of aspartimide by cyclization of aspartyl residues (*32*). We hypothesized that the use of glutamic acid instead of glycine in the chelating sequence of $Z_{HER2:342}$ would decrease the lipophilicity of Affibody molecules enough to suppress hepatobiliary excretion. The goal of this study was to investigate whether the use of mercaptoacetyl-triglutamyl chelator would provide better biodistribution properties of Affibody molecules, resulting in a tracer suitable for imaging on the day of injection. Here, we compare the biodistribution of ^{99m}Tc-labeled mercaptoacetyl-Gly-Gly-Gly-$Z_{HER2:342}$ (^{99m}Tc-maGGG-$Z_{HER2:342}$), mercaptoacetyl-Gly-Glu-Gly-$Z_{HER2:342}$ (^{99m}Tc-maGEG-$Z_{HER2:342}$), and mercaptoacetyl-Glu-Glu-Glu-$Z_{HER2:342}$ (^{99m}Tc-maEEE-$Z_{HER2:342}$) and describe the *in vivo* tumor targeting properties of the best conjugate, ^{99m}Tc-maEEE-$Z_{HER2:342}$.

MATERIALS AND METHODS

Peptide Synthesis. The $Z_{HER2:342}$-sequence was assembled using Fmoc/*t*Bu solid phase peptide synthesis on an Fmoc-amide resin with a substitution of 0.67 mmol/g (Applied Biosystems) as previously described (*27*). 1-Hydroxybenzotriazole (HOBt) and 2-(1*H* -benzotriazol-1-yl)-1,1,3,3-tetramethyluronium hexafluorophosphate (HBTU) (Advanced ChemTech, Louisville, KY) were used to activate equal molar equivalents of Fmoc-protected amino acid.

The Tc-chelating sequences were introduced by step-wise manual synthesis on the N-terminus of the $Z_{HER2:342}$-sequence. Twenty percent piperidine-*N*-methylpyrrolidone (NMP, from VWR) was used for Fmoc deprotection. Acylations were performed with 5 molar equivs of amino acid, HBTU, and HOBt and 10 equivs of *N*-ethyldiisopropylamine (DIEA, from Lancaster Synthesis, Morecambe, England). *S*-trityl-mercaptoacetic acid was from AnaSpec Inc. (San Jose, CA).

Peptides were released from the solid support and permanent protection groups by incubation in trifluoroacetic acid (TFA, Merck international)/H_2O/ethanedithiol (EDT, Aldrich chemical company Inc.)/triisopropylsilane (TIS, Merck International) (94:2.5:2.5:1) for 2 h. The proteins were extracted in *tert*-butyl methyl ether/H_2O (50:50).

Analytical RP-HPLC was run on the crude synthetic product using a 4.5×150 mm polystyrene/divinylbenzene matrix column with 5 μm particles (Amersham Biosciences, Sweden) and a 20 min elution gradient from 20 to 60% B (B, 0.1% TFA-CH_3CN; A, 0.1% TFA-H_2O). The molecular weights of the modified Affibody molecules were confirmed by mass spectrometry, and the proteins were purified on the same column in a 20 min gradient from 25 to 45% B.

Biosensor Analysis. EDC/NHS chemistry was used to immobilize the extracellular domain of HER2 (Fox Chase Cancer Center, Philadelphia, PA) and Human Serum Albumin, HSA, (KabiVitrum, Sweden) on a CM5 sensor chip (Biacore AB, Sweden). HER2 and HSA were diluted to 20 μg/mL in 20 mM NaOAc at pH 4.5, and the immobilization levels reached 500 and 900 response units (RU), respectively. The different Affibody conjugates were diluted to concentrations varying from 0.5 to 10 nM in HBS (10 mM HEPES, 150 mM NaCl, 3.4 mM EDTA, and 0.005% surfactant P20 at pH 7.4), and the binding kinetics were studied in a 5 min association phase and a 10 min dissociation phase, followed by regeneration with 20 mM HCl in HBS.

^{99m}Tc Labeling. For labeling, 20 μL of maGEG-$Z_{HER2:342}$ or maEEE-$Z_{HER2:342}$ (1 mg/mL in deionized degassed water) was mixed with 20 μL of 0.15 M NaOH to obtain a final pH of about 11. A solution of 10 μL of $SnCl_2 \cdot 2\ H_2O$ in 0.01 M HCl (1 mg/mL) was added to the mixture, followed by 100–200 μL of freshly eluted pertechnetate solution. The mixture was slightly vortexed and incubated at room temperature for 60 min. After labeling, ^{99m}Tc-maGEG-$Z_{HER2:342}$ and ^{99m}Tc-maEEE-$Z_{HER2:342}$ were isolated from unreacted technetium and other low-molecular-weight components using size-exclusion chromatography on disposable NAP-5 columns (Amersham Pharmacia Biotech AB, Uppsala, Sweden) pre-equilibrated with PBS. The purity was assessed by analysis with ITLC SG (Gelman Sciences Inc., Ann Arbor), eluted in PBS. Validation experiments demonstrated that in this system, pertechnetate and cysteine complexes of ^{99m}Tc migrate with the eluent front, while labeled Affibody molecules under these conditions remain at the origin. The labeling yield and the stability were determined using ITLC strips, eluted with PBS, and analyzed with Cyclone Storage Phosphor System. To determine the presence of reduced hydrolyzed technetium, ITLC was eluted with pyridine/acetic acid/water (5:3:1.5). In this eluent, the technetium colloids remained at the origin, while the radiolabeled Affibody molecules, pertechnetate and other complexes of ^{99m}Tc, migrated with the solvent front.

Stability Studies. *Cysteine Challenge.* The stability of labeled Affibody conjugates was tested in 300 molar excess of cysteine. A fresh solution of cysteine was prepared (1 mg/mL in PBS at pH 7.0). The radiolabeled conjugates were added to a final molar ratio of cysteine to peptide of 300:1. The test tubes were incubated for 2 h at 37 °C, and the radiochemical purity was analyzed using ITLC.

Plasma Stability Test. Serum samples were prepared as described in ref *27*. Shortly, a serum sample (240 μL) was mixed with freshly labeled ^{99m}Tc-maEEE-$Z_{HER2:342}$ (10 μL) to obtain an Affibody molecule concentration similar to the concentration in blood at the moment of injection. The sample was incubated for 1 h at 37 °C. After incubation, the sample was analyzed on NuPAGE 4–12% Bis-Tris Gel (Invitrogen) in MES buffer (200 V constant). A sample of pertechnetate, not treated in blood serum, was used as reference and run in parallel with the test sample on the same gel. After electrophoresis, the radioactivity distribution along the gel was evaluated using a Cyclone Storage Phosphor System.

***In Vitro* Cell Studies.** The HER2-expressing ovarian carcinoma cell line SKOV-3, displaying approximately 1.2×10^6 HER2 receptors per cell (*33*), was used in this study. The cell line was cultured in McCoy's medium (Flow Irvine, UK). The medium was supplemented with 10% fetal calf serum (Sigma, USA), 2 mM L-glutamine and PEST (penicillin 100 IU/mL and 100 μg/mL streptomycin), all from Biokrom Kg, Germany. The cells were cultured at 37 °C in a humidified incubator with 5% CO_2 and trypsinized using trypsin–EDTA solution (0.25% trypsin and 0.02% EDTA) from Biokrom Kg, Germany. SKOV-3 cells were cultivated on Petri dishes with a diameter of 3.5 cm to a cell density of 2–5 $\times 10^5$ cells per dish.

Binding Specificity Study. To test the binding specificity of the labeled conjugates, one set of SKOV-3 cells was presaturated with a 100-fold excess of nonlabeled Affibody molecules 10 min before the labeled conjugate was added and measured according to Engfeldt et al. (*27*).

Cellular Retention Study. Labeled conjugate (0.8 ng/10^5 cells) was added in 1 mL complete medium to SKOV-3 cells and incubated for 2 h at 37 °C. The incubation medium was removed, and the cells were washed six times with ice-cold serum-free medium, and after the addition of 1 mL of complete medium, the cell dishes were incubated at 37 °C and 5% CO_2 at predetermined time points. The incubation medium was removed, and the dishes were washed six times with 1 mL serum-free medium. The cells were detached with 0.5 mL of trypsin–EDTA for 10 min in 37 °C and resuspended with 0.5 mL of complete medium. The media were collected, and the radioactivity was measured on an automated gamma counter.

Antigen Binding Capacity Study. An assessment of the antigen binding capacity of ^{99m}Tc-labeled conjugates was performed using SKOV-3 cells according to Engfeldt et al. (*27*).

***In Vivo* Animal Studies.** The animal study was approved by the Local Ethics Committee for Animal Research. In comparative biodistribution studies, nontumor-bearing NMRI mice were used. In tumor-targeting and imaging experiments with ^{99m}Tc-maEEE-$Z_{HER2:342}$, female BALB/c *nu/nu* nude mice were used. The animals were acclimatized for one week at the Rudbeck laboratory animal facility before tumor implantation. The tumors were grafted by subcutaneous injection of $\sim 10^7$ SKOV-3 cells in the right hind leg. Xenografts were allowed to develop during 6 weeks. In all biodistribution studies, the mice were euthanized at predetermined time points with an intraperitoneal injection of Ketalar-Rompun solution (20 μL of solution per gram of body weight: Ketalar [ketamine], 10 mg/mL; Rompun [xylazin], 1 mg/mL). The mice were heart-punctured with a 1 mL syringe rinsed with diluted heparin (5,000 IE/mL, Leo Pharma, Copenhagen, Denmark). Blood and organ samples were taken, weighed, and their radioactivity measured using an automatic gamma counter. The organ uptake values were calculated as percent injected activity per gram tissue (% IA/g).

Biodistribution in NMRI Mice. Eight mice were randomly divided into two groups with four animals each. The two groups were subcutaneously injected with ^{99m}Tc-maGEG-$Z_{HER2:342}$ and ^{99m}Tc-maEEE-$Z_{HER2:342}$ (1μg Affibody ligand, $\sim$100 kBq in 100 μL of PBS). The mice were euthanized at 4 h pi; organ samples were collected and measured.

Table 1. Peptide Synthesis and Characterization Data

protein	synthetic yield (%)	theoretical Mw (Da)	experimental Mw (Da)	K_D (pM)
$Z_{HER2:342}$	21	6718	6718	80
maGGG-$Z_{HER2:342}$	16	7021	7020	200
maGEG-$Z_{HER2:342}$	17	7036	7035	360
maEEE-$Z_{HER2:342}$	13	7180	7179	410

Table 2. *In vitro* Data of ^{99m}Tc-labeled Conjugates

conjugate	^{99m}Tc-ma GGG-$Z_{HER2:342}$	^{99m}Tc-ma GEG-$Z_{HER2:342}$	^{99m}Tc-ma EEE-$Z_{HER2:342}$
labeling yield, %	82 ± 12	93 ± 6	90 ± 2
isolated yield, %	76 ± 8	76 ± 3	76 ± 4
radiochemical purity, %	78 ± 1	97 ± 3	98 ± 2
antigen binding capacity, %	86 ± 1	68.7 ± 0.8	66.7 ± 0.3
stability during cysteine challenge, %	88 ± 2	94 ± 3	93 ± 3

Biodistribution in Mice with SKOV-3 Xenografts. The tumor-targeting properties of ^{99m}Tc-maEEE-$Z_{HER2:342}$ were evaluated in female BALB/c *nu/nu* nude mice bearing SKOV-3 xenografts. The mice were subcutaneously co-injected with ^{99m}Tc-maEEE-$Z_{HER2:342}$ and ^{125}I-PIB-$Z_{HER2:342}$ (total of 1 μg Affibody ligand and $\sim$100 kBq in 100 μL of PBS). In previous studies, we have validated that the biodistribution of radiolabeled Affibody molecules 4 h pi is the same for both i.v. and s.c. injection and is independent of the label (*34*, *35*). However, subcutaneous injections are generally more reproducible (smaller errors), which is important for comparative biodistribution studies. After 1, 4, and 6 h pi, the mice were euthanized as described earlier. In the binding specificity study, one group of mice was preinjected with 1,000-fold molar excess of nonlabeled Affibody molecules prior to injection of ^{99m}Tc-maEEE-$Z_{HER2:342}$. At 4 h pi, the mice were sacrificed, and organ samples were collected and measured.

Gamma Camera Imaging with ^{99m}Tc-maEEE-$Z_{HER2:342}$. One group of mice was preinjected through the tail vein with 1000-fold excess of nonlabeled Affibody molecules in order to block the receptors and was imaged after 5 h pi. The other three groups were intravenously injected through the tail vein with 3 MBq of ^{99m}Tc-maEEE-$Z_{HER2:342}$ (10 μg in 100 μL of PBS) and imaged at 1, 2, and 5 h pi. Imaging was performed using a Siemens gamma camera equipped with a LEHR collimator at the Department of Nuclear Medicine of Uppsala University Hospital. Static images were collected for 10 min, and evaluation of the images was performed with a Hermes system (Hermes Medical Solutions).

RESULTS

Peptide Synthesis. The Fmoc solid-phase synthesis of $Z_{HER2:342}$ resulted in a yield of 21% of the full-length peptide, as determined by analytical RP-HPLC. The ^{99m}Tc-chelating sequences of maGEG or maEEE were introduced N-terminally by manual synthesis, resulting in total synthetic yields of 17% and 13%, respectively (Table 1). Following purification by RP-HPLC, the purity was higher than 90%. The molecular weights of the different conjugates were determined by mass spectrometry and correlated well with the theoretically calculated masses, as shown in Table 1.

Biosensor Analysis. The binding kinetics of the different Tc-chelating peptides were compared in a biospecific interaction analysis on a Biacore 2000 instrument. As indicated in Table

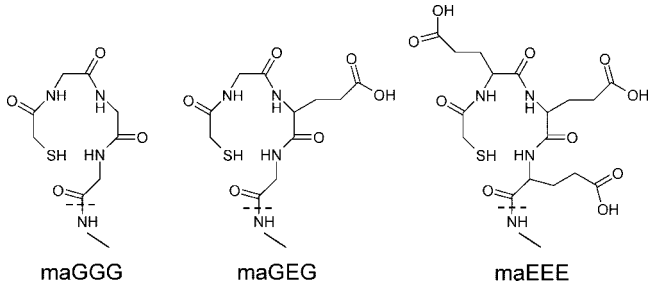


Figure 1. Chelator structures.

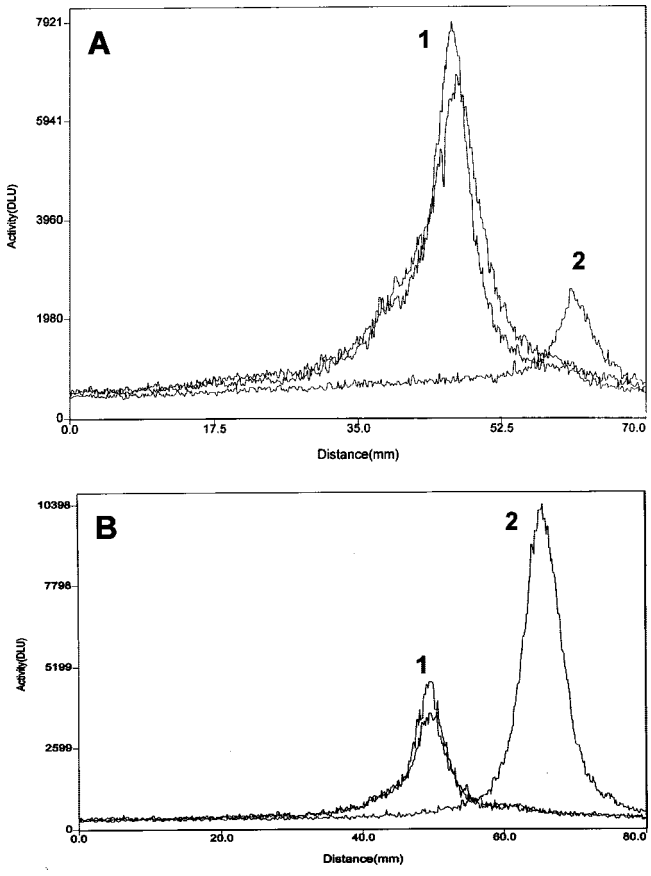


Figure 2. Stability of (A) ^{99m}Tc-maGEG-$Z_{HER2:342}$ and (B) ^{99m}Tc-maEEE-$Z_{HER2:342}$ in mouse serum at 1 h and 37 °C was analyzed using SDS–PAGE. The left peaks (1) represent intact ^{99m}Tc-labeled $Z_{HER2:342}$ (two samples were analyzed). The right peak (2) indicates the reference sample of free pertechnetate.

1, both conjugates showed similar subnanomolar affinities to surface-immobilized HER2 receptors: the dissociation constants (K_D) were 410 pM and 360 pM for maEEE-$Z_{HER2:342}$ and maGEG-$Z_{HER2:342}$, respectively.

^{99m}Tc Labeling. The radiolabeling efficiencies were over 90% for both ^{99m}Tc-maEEE-$Z_{HER2:342}$ and ^{99m}Tc-maGEG-$Z_{HER2:342}$, as shown in Table 2. The isolated yield from size-exclusion chromatography using NAP-5 columns was about 76%, and the radiochemical purity of purified products was typically over 95% for both conjugates. The presence of reduced hydrolyzed technetium was less than 2% in all experiments.

Stability Studies. The *in vitro* stability of the labeled conjugates was evaluated in a cysteine challenge test.

Incubation of the labeled Affibody molecules for 2 h in the presence of a 300-fold molar excess of cysteine demonstrated high stability, with 93% radioactivity still attached to the conjugate (Table 2). The *in vitro* stability of ^{99m}Tc-maGEG-$Z_{HER2:342}$ and ^{99m}Tc-maEEE-$Z_{HER2:342}$ in mouse serum is shown

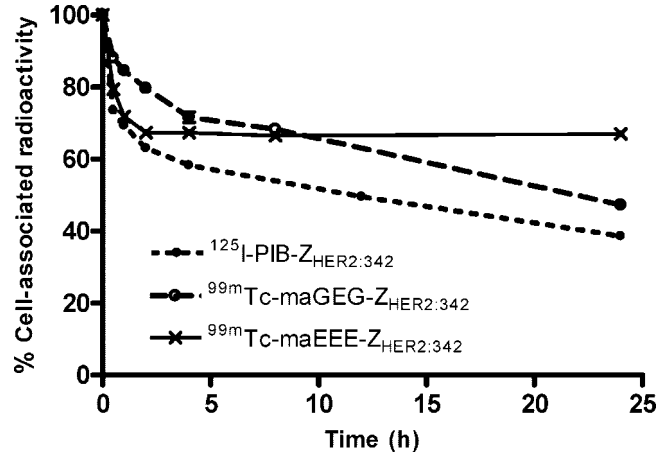


Figure 3. Cellular retention of labeled conjugates in HER2-expressing ovarian carcinoma cells, SKOV-3 cells. ^{125}I-PIB-$Z_{HER2:342}$ (*23*) was included for a comparison.

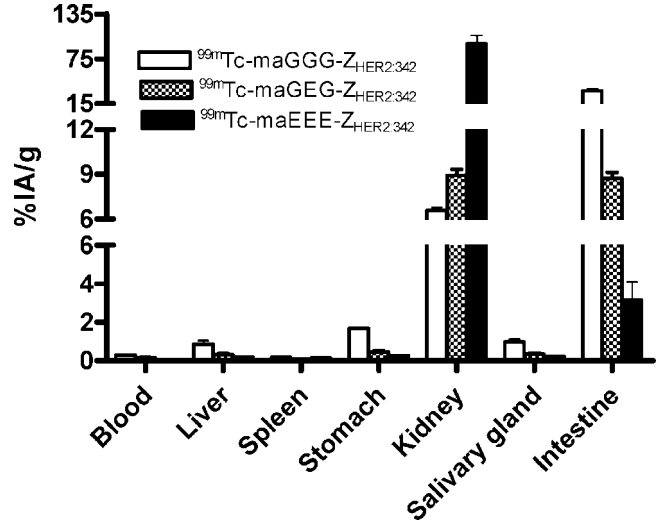


Figure 4. Biodistribution of labeled conjugates in NMRI normal mice at 4 h pi. Data are presented as an average from four animals ± SEM. Uptake in thyroid and muscle were less than 0.08%IA per whole sample and 0.09%IA/g, respectively.

in Figure 2. The radioactivity in the gel showed a single peak of the ^{99m}Tc-labeled $Z_{HER2:342}$ (two samples were analyzed on the same gel), indicating that no detectable transchelation to serum proteins or release of pertechnetate occurred. This experiment also confirmed that Affibody molecules were stable against degradation by blood plasma proteases since no fragments with lower molecular weights were detected.

***In Vitro* Cell Studies.** *Binding Specificity and Antigen Binding Capacity.* The binding specificity of ^{99m}Tc-maEEE-$Z_{HER2:342}$ and ^{99m}Tc-maGEG-$Z_{HER2:342}$ was evaluated in the HER2-expressing ovarian cancer cell line SKOV-3. The binding was specific since it could be blocked with receptor saturation by a 100-fold excess of unlabeled $Z_{HER2:342}$. The antigen binding capacity was estimated to be around 60% for the ^{99m}Tc-maEEE-$Z_{HER2:342}$, indicating that the labeling procedure had a minor effect on the conjugates.

Cellular Retention. The cellular retention of ^{99m}Tc-labeled $Z_{HER2:342}$ and a radioiodinated Affibody molecule, ^{125}I-PIB-$Z_{HER2:342}$, is illustrated in Figure 3. The radioiodinated Affibody molecule was described in earlier studies (*23*) and included here for comparison. ^{99m}Tc-maEEE-$Z_{HER2:342}$ and the radioiodinated conjugate displayed a similar pattern in the beginning, but after 4 h, the iodine label continued to decrease, while the technetium

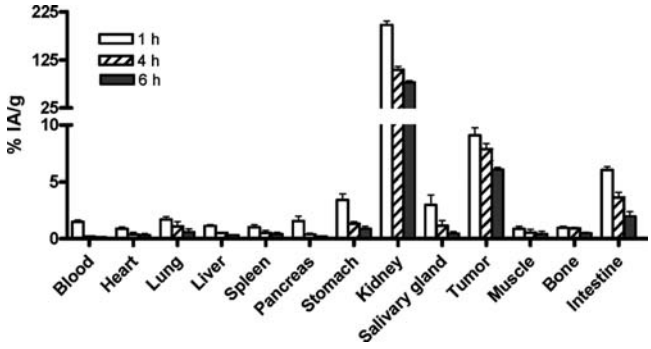


Figure 5. Biodistribution of ^{99m}Tc-maEEE-$Z_{HER2:342}$ in BALB/c *nu/nu* mice with HER2-expressing SKOV-3 xenografts at 1, 4, and 6 h pi. Data are presented as an average from four animals ± SEM. The uptake in thyroid was less than 0.09%IA per whole sample.

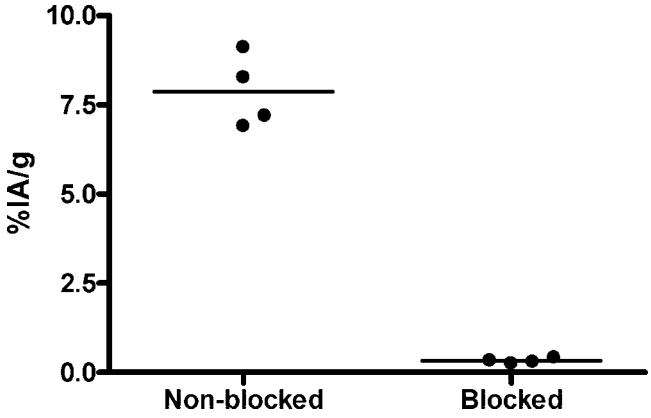


Figure 6. Dot plot of tumor uptake (%IA/g) in BALB/c *nu/nu* mice with SKOV-3 xenografts. Blocked mice received an excess of nonlabeled Affibody molecule prior to the injection of ^{99m}Tc-maEEE-$Z_{HER2:342}$. Student's *t*-test gave $p < 0.0001$.

label showed a discrete slow increase in radioactivity over time. After 24 h, the cell-associated radioactivity retained in the SKOV-3 cells was about 70% for ^{99m}Tc-maEEE-$Z_{HER2:342}$ and 40% for the counterpart, ^{125}I-PIB-$Z_{HER2:342}$ ($p < 0.001$). ^{99m}Tc-maGEG-$Z_{HER2:342}$ possessed higher cell-associated radioactivity retention than ^{99m}Tc-maEEE-$Z_{HER2:342}$ in the first hours but decreased in the same way as that of ^{125}I-PIB-$Z_{HER2:342}$, with 50% of the cell-associated radioactivity retained after 24 h.

***In Vivo* Animal Studies.** *Biodistribution in Normal Mice.* Figure 4 presents the comparative biodistribution of ^{99m}Tc-maGEG- and ^{99m}Tc-maEEE-$Z_{HER2:342}$ in normal NMRI mice at 4 h pi compared to that of ^{99m}Tc-maGGG-$Z_{HER2:342}$. It was shown that the radioactivity uptake was low in all organs, except in the kidneys and intestines. The high uptake in the kidneys is explained by the renal clearance and tubular reabsorption of the small-sized Affibody molecules. A significant difference between the conjugates was observed in the kidneys and intestines. ^{99m}Tc-maEEE-$Z_{HER2:342}$ had 3 times lower radioactivity in the intestines compared to that of ^{99m}Tc-maGEG-$Z_{HER2:342}$ (3.1 ± 1.9%IA/g vs 8.7 ± 0.8%IA/g; $p < 0.001$), while the kidney uptake was 10 times higher (95 ± 23 vs 8.9 ± 0.8 %IA/g; $p < 0.001$). The uptake in the liver, stomach, and salivary glands of ^{99m}Tc-maEEE-$Z_{HER2:342}$ was significantly lower ($p < 0.05$) compared with that of ^{99m}Tc-maGEG-$Z_{HER2:342}$ and ^{99m}Tc-maGGG-$Z_{HER2:342}$ (Figure 4).

Biodistribution in Mice with SKOV-3 Xenografts. The *in vivo* tumor-targeting properties of ^{99m}Tc-maEEE-$Z_{HER2:342}$ were evaluated in BALB/c *nu/nu* mice bearing HER2-expressing SKOV-3 xenografts (Figure 5). The results showed that the radioactivity was cleared rapidly from blood circulation, reaching 0.15 ± 0.05 %IA/g at 6 h pi. The radioactivity clearance from other organs followed the same pattern. Tumor uptake was 9.1 ± 1.4 %IA/g at 1 h pi, 7.9 ± 1.0 %IA/g at 4 h pi, and 6.1 ± 0.4 %IA/g at 6 h pi, indicating a decrease over time.

In the receptor specificity study, one group of mice was preinjected with 1,000-fold molar excess of nonlabeled $Z_{HER2:342}$ in order to saturate the receptors before the administration of ^{99m}Tc-maEEE-$Z_{HER2:342}$. The tumor uptake (Figure 6) in the blocked group was 0.3 ± 0.07 %IA/g and 7.9 ± 1.0 %IA/g in the nonblocked group ($p < 0.0001$), demonstrating that tumor uptake was HER2-specific.

The radioiodinated Affibody molecule ^{125}I-PIB-$Z_{HER2:342}$ (*23*) visualizes HER2-expressing xenografts with high contrast and was therefore co-injected with ^{99m}Tc-maEEE-$Z_{HER2:342}$ as an internal reference for comparison. The tumor-to-organ ratios are listed in Table 3, showing that there was a significant ($p < 0.05$) difference in most organs between the two labels. Especially, the blood radioactivity concentration was much lower for the ^{99m}Tc-label than for the ^{125}I-label at all time points ($p < 0.001$), while the uptake in liver and stomach was lower for the ^{125}I-label. In general, the use of the technetium label provided better tumor-to-organ ratios than the iodine label.

Gamma Camera Imaging with ^{99m}Tc-maEEE-$Z_{HER2:342}$. The tumor-targeting capacity of ^{99m}Tc-maEEE-$Z_{HER2:342}$ was evaluated in BALB/c *nu/nu* mice bearing SKOV-3 tumors. The gamma camera images were acquired 1, 2, and 5 h after the administration of ^{99m}Tc-maEEE-$Z_{HER2:342}$. The tumors could be detected as early as 1 h pi, and the image contrast became better with time (Figure 7A and B). Tumor-to-nontumor ratios for the contralateral thigh were (average ± maximum error) 8.3 ± 0.3, 19 ± 2.1, and 35 ± 0.6 at 1, 2, and 5 h pi, respectively. Two mice were preinjected with nonlabeled Affibody molecules in order to block the receptors, and it was shown clearly that the binding of ^{99m}Tc-maEEE-$Z_{HER2:342}$ was receptor-specific *in vivo* because the tumors were not seen, while the tumors in the nonblocked mice were clearly visualized (Figure 7B). Some radioactivity accumulation is seen in the salivary glands at 1 h pi, which might indicate some release of free pertechnetate. No uptake in any other organs was seen, except in the kidneys, which corresponded well with the biodistribution data. Tumor-to-nontumor ratios for the contralateral thigh were 35 ± 0.6 for the nonblocked mice and 3.6 ± 1.4 for the blocked mice.

DISCUSSION

Affibody molecules are a new class of small targeting proteins displaying optimal biodistribution properties for imaging purposes (*24, 27*). Pilot patient investigations with ^{68}Ga- and ^{111}In-labeled Affibody molecules have demonstrated their utility for the imaging of HER2 expression in metastatic breast cancer (*26*). However, for SPECT imaging, technetium-99m might be the most ideal radioisotope for the labeling of Affibody molecules because of convenient logistics, dosimetric properties, and particularly because the physical half-life ($t_{1/2} \sim 6$ h) matches the quick blood clearance of Affibody molecules.

Earlier studies on a ^{99m}Tc-labeled Affibody molecule, containing a mercaptoacetyltriglycyl chelator (*27*), showed favorable tumor-targeting properties (high tumor-to-blood ratios and excellent binding specificity) of the conjugate. However, this conjugate exhibited high hepatobiliary clearance, making scintigraphic detection of tumors in the abdominal area difficult. It has previously been reported that it is possible to shift the excretion pathway from hepatobiliary to renal by substituting the chelating amino acids with more hydrophilic characters. For this reason, substitution with more hydrophilic chelating residues in the mercaptoacetyl-containing Affibody molecule $Z_{HER2:342}$ was investigated as a strategy for the reduction of abdominal

Table 3. Tumor-to-Organ Ratios of ^{99m}Tc-maEEE-$Z_{HER2:342}$ and ^{125}I-PIB-$Z_{HER2:342}$ in BALB/c *nu/nu* Mice Bearing SKOV-3 Xenografts

	1 h		4 h		6 h	
tumor/organ ratios	^{99m}Tc	^{125}I	^{99m}Tc	^{125}I	^{99m}Tc	^{125}I
T/blood	6.1 ± 0.7^a	2.5 ± 0.3	38 ± 7^a	10 ± 0.8	43 ± 12^a	18 ± 2
T/lung	6 ± 1^a	2.5 ± 0.2	14 ± 12	10 ± 3.6	18 ± 15	27 ± 2
T/kidney	0.050 ± 0.004^a	0.30 ± 0.02	0.08 ± 0.01^a	1.1 ± 0.3	0.08 ± 0.01^a	2.2 ± 0.1
T/liver	8 ± 1^a	2.3 ± 0.2	15 ± 2^a	12 ± 0.7	19 ± 3^a	23 ± 3
T/stomach	3 ± 1	4.5 ± 0.6	6 ± 2^a	15 ± 6	8 ± 3^a	53 ± 23

[a] Significance comparison between ^{99m}Tc- and ^{125}I-label using Student's paired *t*-test; $p < 0.05$.

accumulation. We have found that in the case of the ^{99m}Tc-labeled Affibody molecule $Z_{HER2:342}$, a substitution of the maGGG-chelator with maSSS (mercaptoacetyl-triseryl chelator) caused a clear shift from hepatobiliary to renal excretion (*36*). Still, this conjugate was not optimal for detecting tumors in the abdomen area on the day of injection, thus additional improvement was necessary. One way to further increase the hydrophilicity is to use amino acids with charged side chains such as glutamic acids.

The results from the Biacore experiments showed that the $Z_{HER2:342}$ with the N-terminally incorporated maGEG or maEEE by peptide synthesis bound with high affinity to HER2. Both maGEG-$Z_{HER2:342}$ and maEEE-$Z_{HER2:342}$ were successfully ^{99m}Tc-labeled with a labeling yield of over 90% and a radiochemical purity of more than 95%. Both ^{99m}Tc-maGEG- and ^{99m}Tc-maEEE-$Z_{HER2:342}$ were stable *in vitro* during incubation in 300-fold molar excess of cysteine for 2 h at 37 °C. Furthermore, no evidence of the release of radioactivity from both conjugates or technetium transchelation to blood plasma proteins could be detected after incubation in mouse serum for 1 h, signifying its suitability for *in vivo* use. The labeled conjugates also preserved specific binding to HER2 receptors in SKOV-3 ovarian carcinoma cells *in vitro*. The cellular retention of ^{99m}Tc-maGEG-$Z_{HER2:342}$ in SKOV-3 cells was higher compared with the radioiodinated counterpart, ^{125}I-PIB-$Z_{HER2:342}$. The cell-associated radioactivity of ^{99m}Tc-maEEE-$Z_{HER2:342}$ decreased rapidly in the first 4 h after interrupted incubation and had an appearance similar to that of the radioiodinated one. Surprisingly, the cell-associated radioactivity increased slowly at later time points, indicating some residualizing properties of this conjugate. One possible explanation is that the dissociated conjugate was reabsorbed and internalized, causing the slow increase in the curve. The same phenomenon has been observed earlier with ^{111}In-labelled Affibody molecules (*24*). A possible method to discriminate between the internalized and membrane-bound fractions would be very helpful for a more reliable interpretation of the results of the cellular retention experiment. However, as we have reported earlier (*24*), common methods of internalization assays are inefficient with $Z_{HER2:342}$ because of strong binding to cells, even in an acidic environment.

The substitution of a single glycine with glutamic acid (maGGG vs maGEG) in the chelator showed a clear effect on the excretion pattern in normal mice, with a significant 3-fold reduction of the radioactivity accumulation in the intestines (hepatobiliary excretion). The hepatobiliary clearance was even more reduced when all three glycines in the chelator were replaced by glutamic acids (maGGG to maEEE), resulting in a 10-fold decrease in intestine accumulation. The reduced hepatobiliary excretion, accompanied by the increased kidney uptake, which was especially pronounced in the case of a triple substitution, verified that a clear shift from hepatobiliary to renal excretion occurred. Interestingly, reduction of the radioactivity level in the intestines was not directly translated into an increase of renal accumulation, and the use of the maEEE moiety as chelator caused a higher reabsorption of radioactivity in the kidneys. This effect could be considered as negative per se, but the overall effect on the changed excretion pattern is positive

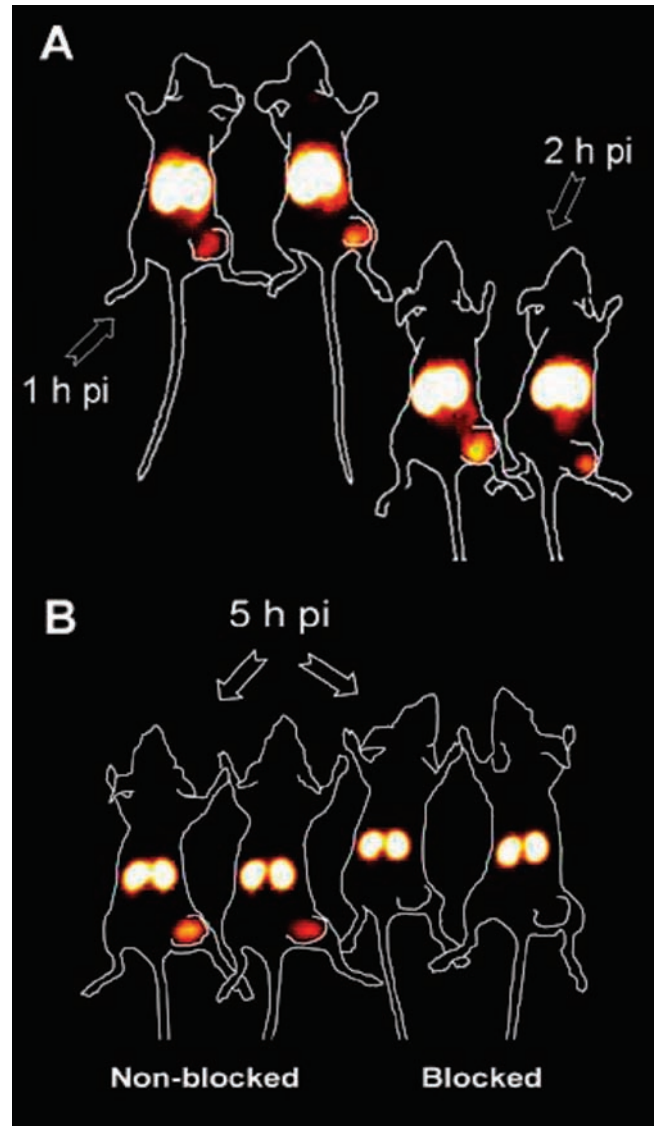


Figure 7. Gamma-camera imaging with ^{99m}Tc-maEEE-$Z_{HER2:342}$ in BALB/c *nu/nu* mice bearing SKOV-3 xenografts. (A) Tumors were well visualized on the right hind legs already at 1 and 2 h pi. (B) The image contrast was better at 5 h pi, and the tumors were blocked with a preinjection of excess of nonlabeled Affibody molecules.

since the position of the kidneys is well-defined, and the use of SPECT/CT makes it possible to distinguish the high radioactivity accumulation in the kidneys from other organs. In contrast, radioactivity in the gastrointestinal tract is more problematic, both by elevated background level and by the occasional formation of hot spots. One concern is the high renal radioactivity accumulation of ^{99m}Tc-maEEE-$Z_{HER2:342}$. This high kidney accumulation could potentially be dose-limiting when using radiolabeled proteins for therapy. In the case of diagnostic applications, the conjugates are labeled with gamma-emitting nuclides, which generate low local doses. The only particulate

Table 4. Biodistribution Data of ^{99m}Tc-labeled $Z_{HER2:342}$, Containing Different Chelators at 4 h pi[a]

	^{99m}Tc-maGGG-$Z_{HER2:342}$	^{99m}Tc-CGG-$Z_{HER2:342}$	^{99m}Tc-CGGG-$Z_{HER2:342}$	^{99m}Tc-maGSG-$Z_{HER2:342}$	^{99m}Tc-maSSS-$Z_{HER2:342}$	^{99m}Tc-maGEG-$Z_{HER2:342}$	^{99m}Tc-maEEE-$Z_{HER2:342}$
blood	0.30 ± 0.03	0.55 ± 0.02	0.52 ± 0.05	0.10 ± 0.02	0.14 ± 0.07	0.15 ± 0.03	0.09 ± 0.02
kidneys	6.6 ± 0.4	51 ± 4	47 ± 7	8 ± 2	18 ± 4	8.9 ± 0.8	95 ± 23
liver	0.9 ± 0.3	0.86 ± 0.09	0.69 ± 0.09	0.2 ± 0.1	0.5 ± 0.3	0.3 ± 0.1	0.21 ± 0.02
intestine[b]	32 ± 4	12.6 ± 0.7	12.0 ± 0.6	17 ± 2	11 ± 2	8.7 ± 0.8	3 ± 2

[a] Data on the chelators maGGG, CGG (cysteinyl-diglycyl), CGGG (cysteinyl-triglycyl) maGSG (mercaptoacetyl-glycyl-seryl-glycyl) and maSSS (mercaptoacetyl-triseryl) are historical controls, taken from refs *34 and 35*. [b] Uptake is presented as %IA/g organ, except for the intestine, where the uptake is for the whole sample.

radiations of such nuclides (^{99m}Tc or ^{111}In) are the Auger and conversion electrons, which are inefficient in causing renal damage. For example, the use of ^{111}In-labeled Octreoscan for therapy demonstrated that renal doses as high as 45 Gy did not cause negative side effects (*37*). Apparently, renal doses in the case of diagnostic application will be much lower.

Another interesting observation is that uptake in the liver, stomach, and salivary glands was significantly lower for ^{99m}Tc-maEEE-$Z_{HER2:342}$ compared with that for ^{99m}Tc-maGEG-$Z_{HER2:342}$ and ^{99m}Tc-maGGG-$Z_{HER2:342}$ (Figure 4). This indicates that the glycine-to-glutamic acid substitution improves the overall *in vivo* stability of the chelates to reoxidation, as these organs are well known to accumulate free pertechnetate. This stabilizing effect on the conjugate is probably contributed from the side chains of the glutamic acid residues in the chelator.

Earlier, the maGGG chelator has been compared with the cysteine-based chelators, cysteine-diglycyl (CGG) and cysteine-triglycyl (CGGG) (*34*). As summarized in Table 4, a comparison with historical data showed a 3-fold reduction of hepatobiliary excretion and a 2-fold increase of renal excretion in the case of the maEEE chelator in comparison with those of cysteine-based chelators. This shift indicates the higher hydrophilicity of the maEEE compared to that of the cysteine-based chelator. A comparison with our previous data (*36*) shows also that the incorporation of glutamic acid in meracaptoacetyl-based chelators shifts the excretion pathway more efficiently to renal than does the incorporation of serine.

^{99m}Tc-maEEE-$Z_{HER2:342}$ was the obvious choice for further evaluation in SKOV-3 xenografted mice because this conjugate showed the best pharmacokinetics properties in normal mice (a low degree of hepatobiliary excretion and the lowest uptake in liver, salivary glands, and stomach). Tumor targeting was efficient, with the highest value of 9.1 ± 1.4 %IA/g reaching 1 h pi. Tumor uptake was HER2-specific since the administration of an excess amount of nonlabeled Affibody molecules could saturate HER2-receptors in the tumors and significantly reduce the uptake of ^{99m}Tc-maEEE-$Z_{HER2:342}$ *in vivo*. The receptor saturation led to a 24-fold decrease in tumor uptake at 4 h pi, from 7.9 ± 1.0 %IA/g to 0.33 ± 0.07 %IA/g ($p < 0.0001$). The accumulated radioactivity in the tumor uptake decreased slowly over time. At the same time, radioactivity in the kidneys and other organs also declined rapidly, resulting in a tumor-to-blood (T/B) ratio of 38 at 4 h pi and 43 at 6 h pi, respectively. It is worthwhile to mention that ^{99m}Tc-maEEE-$Z_{HER2:342}$ seems to be superior in comparison with antibody-based HER2 imaging agents that are under preclinical investigation. For example, the T/B ratio was 3 at 24 h pi for ^{99m}Tc-HYNIC-trastuzumab (*19*), 1.6 at 24 h pi for ^{111}In-DTPA-trastuzumab (*38*), 2.3 at 6 h pi for ^{111}In-T84.66 minibody (*39*), 0.7 at 6 h pi for the ^{111}In-DOTA 10H8 hinge-minibody (*40*), 2.6 at 4 h pi for the ^{125}I-labeled sFv (*21*), and 1.3 at 4 h pi for the ^{125}I-labeled $(sFv')_2$ (*41*).

Gamma camera imaging showed that ^{99m}Tc-maEEE-$Z_{HER2:342}$ accumulated specifically in SKOV-3 tumors since the tumors were blocked with a preinjection of nonlabeled Affibody molecules (right group, Figure 7B). Most interestingly, the tumors were clearly visualized at 1 h pi, and the contrast in the image at 2 h pi did not differ significantly, enabling early detection of HER2-tumors.

The clinical potential of an imaging agent relies on a number of parameters, such as high affinity and selectivity, low nonspecific uptake, and high specific tumor accumulation. Early detection is preferable in patient management, and high tumor-to-organ ratios are crucial. This can be achieved by rapid blood clearance and favorable excretion kinetics (renal clearance being preferred) (*42*). The current study presents an imaging agent that fulfilled these requirements, suggesting a very high potential of ^{99m}Tc-maEEE-$Z_{HER2:342}$ for the detection of HER2 expression. To our knowledge, this is the first time mercaptoacetyl-triglutamyl is being characterized as a chelator for ^{99m}Tc. The results have demonstrated that this chelator decreases the hepatobiliary excretion of peptides and provides a more stable technetium attachment than the mercaptoacetyl-triglycyl chelator.

CONCLUSIONS

The use of peptide synthesis for the coupling of chelator sequences to Affibody molecules for ^{99m}Tc-labeling is an efficient way to modify *in vivo* kinetics of Affibody molecules. Increased hydrophilicity, combined with improved stability of the mercaptoacetyl-triglutamyl chelates, resulted in minimal abdominal accumulation, enabling the rapid detection of HER2-positive tumors and their metastases in the abdominal area. Thus, ^{99m}Tc-maEEE-$Z_{HER2:342}$ appears as a promising tracer for clinical imaging of HER2-overexpression in tumors and metastases.

ACKNOWLEDGMENT

This work was supported by the Swedish Cancer Society (Cancerfonden) and the Swedish Research Council (Vetenskapsrådet).

LITERATURE CITED

(1) Britz-Cunningham, S. H., and Adelstein, S. J. (2003) Molecular targeting with radionuclides: state of the science. *J. Nucl. Med. 44*, 1945–1961.

(2) Stern, D. F., Heffernan, P. A., and Weinberg, R. A. (1986) p185, a product of the neu proto-oncogene, is a receptorlike protein associated with tyrosine kinase activity. *Mol. Cell. Biol. 6*, 1729–1740.

(3) Slamon, D. J., Clark, G. M., Wong, S. G., Levin, W. J., Ullrich, A., and McGuire, W. L. (1987) Human breast cancer: correlation of relapse and survival with amplification of the HER-2/neu oncogene. *Science 235*, 177–182.

(4) Nahta, R., and Esteva, F. J. (2006) Herceptin: mechanisms of action and resistance. *Cancer Lett. 232*, 123–38.

(5) Adams, C. W., Allison, D. E., Flagella, K., Presta, L., Clarke, J., Dybdal, N., McKeever, K., and Sliwkowski, M. X. (2006) Humanization of a recombinant monoclonal antibody to produce a therapeutic HER dimerization inhibitor, pertuzumab. *Cancer Immunol. Immunother. 55*, 717–727.

(6) Beliakoff, J., and Whitesell, L. (2004) Hsp90: an emerging target for breast cancer therapy. *Anti-Cancer Drugs 15*, 651–662.

(7) Reid, A., Vidal, L., Shaw, H., and de Bono, J. (2007) Dual inhibition of ErbB1 EGFR/HER1) and ErbB2 (HER2/neu). *Eur. J. Cancer. 43*, 481–489.
(8) Bast, R. C., Jr., Ravdin, P., Hayes, D. F., Bates, S., Fritsche, H., Jr., Jessup, J. M., Kemeny, N., Locker, G. Y., Mennel, R. G., and Somerfield, M. R. (2001) 2000 update of recommendations for the use of tumor markers in breast and colorectal cancer: clinical practice guidelines of the American Society of Clinical Oncology. *J. Clin. Oncol. 19*, 1865–1878.
(9) Molina, R., Barak, V., van Dalen, A., Duffy, M. J., Einarsson, R., Gion, M., Goike, H., Lamerz, R., Nap, M., Soletormos, G., and Stieber, P. (2005) Tumor markers in breast cancer- European Group on Tumor Markers recommendations. *Tumour Biol. 26*, 281–293.
(10) Bilous, M., Dowsett, M., Hanna, W., Isola, J., Lebeau, A., Moreno, A., Penault-Llorca, F., Ruschoff, J., Tomasic, G., and van de Vijver, M. (2003) Current perspectives on HER2 testing: a review of national testing guidelines. *Mod. Pathol. 16*, 173–82.
(11) Winston, J. S., Ramanaryanan, J., and Levine, E. (2004) HER-2/neu evaluation in breast cancer are we there yet? *Am. J. Clin. Pathol. 121*, S33–S49.
(12) Leong, T. Y., and Leong, A. S. (2006) Controversies in the assessment of HER-2: more questions than answers. *Adv. Anat. Pathol. 13*, 263–269.
(13) Zidan, J., Dashkovsky, I., Stayerman, C., Basher, W., Cozacov, C., and Hadary, A. (2005) Comparison of HER-2 overexpression in primary breast cancer and metastatic sites and its effect on biological targeting therapy of metastatic disease. *Br. J. Cancer 93*, 552–526.
(14) Brennan, P. J., Kumagai, T., Berezov, A., Murali, R., and Greene, M. I. (2000) HER2/neu: mechanisms of dimerization/oligomerization. *Oncogene 19*, 6093–6101.
(15) Goldenberg, D. M., and Nabi, H. A. (1999) Breast cancer imaging with radiolabeled antibodies. *Semin. Nucl. Med. 29*, 41–48.
(16) Reilly, R. M., Sandhu, J., Alvarez-Diez, T. M., Gallinger, S., Kirsh, J., and Stern, H. (1995) Problems of delivery of monoclonal antibodies. Pharmaceutical and pharmacokinetic solutions. *Clin. Pharmacokinet. 28*, 126–142.
(17) Van de Wiele, C., Revets, H., and Mertens, N. (2004) Radioimmunoimaging. Advances and prospects. *Q. J. Nucl. Med. Mol. Imaging 48*, 317–325.
(18) Smith-Jones, P. M., Solit, D. B., Akhurst, T., Afroze, F., Rosen, N., and Larson, S. M. (2004) Imaging the pharmacodynamics of HER2 degradation in response to Hsp90 inhibitors. *Nat. Biotechnol. 22*, 701–706.
(19) Tang, Y., Scollard, D., Chen, P., Wang, J., Holloway, C., and Reilly, R. M. (2005) Imaging of HER2/neu expression in BT-474 human breast cancer xenografts in athymic mice using [(99m)Tc]-HYNIC-trastuzumab (Herceptin) Fab fragments. *Nucl. Med. Commun. 26*, 427–432.
(20) Schier, R., Marks, J. D., Wolf, E. J., Apell, G., Wong, C., McCartney, J. E., Bookman, M. A., Huston, J. S., Houston, L. L., and Weiner, L. M. (1995) In vitro and in vivo characterization of a human anti-c-erbB-2 single-chain Fv isolated from a filamentous phage antibody library. *Immunotechnology 1*, 73–81.
(21) Adams, G. P., McCartney, J. E., Tai, M. S., Oppermann, H., Huston, J. S., Stafford, W. F., 3rd, Bookman, M. A., Fand, I., Houston, L. L., and Weiner, L. M. (1993) Highly specific in vivo tumor targeting by monovalent and divalent forms of 741F8 anti-c-erbB-2 single-chain Fv. *Cancer Res. 53*, 4026–4034.
(22) Nord, K., Gunneriusson, E., Ringdahl, J., Ståhl, S., Uhlén, M., and Nygren, P. Å. (1997) Binding proteins selected from combinatorial libraries of an alpha-helical bacterial receptor domain. *Nat. Biotechnol. 15*, 772–777.
(23) Orlova, A., Magnusson, M., Eriksson, T. L., Nilsson, M., Larsson, B., Höiden-Guthenberg, I., Widström, C., Carlsson, J., Tolmachev, V., Ståhl, S., and Nilsson, F. Y. (2006) Tumor imaging using a picomolar affinity HER2 binding affibody molecule. *Cancer Res. 66*, 4339–4348.
(24) Tolmachev, V., Nilsson, F. Y., Widström, C., Andersson, K., Rosik, D., Gedda, L., Wennborg, A., and Orlova, A. (2006) 111In-benzyl-DTPA-ZHER2:342, an affibody-based conjugate for in vivo imaging of HER2 expression in malignant tumors. *J. Nucl. Med. 47*, 846–853.
(25) Orlova, A., Tolmachev, V., Pehrson, R., Lindborg, M., Tran, T., Sandström, M., Nilsson, F. Y., Wennborg, A., Abrahmsén, L., and Feldwisch, J. (2007) Synthetic affibody molecules: a novel class of affinity ligands for molecular imaging of HER2-expressing malignant tumors. *Cancer Res. 67*, 2178–2186.
(26) Baum, R. P., Orlova, A., Tolmachev, V., and Feldwisch, J. (2006) A novel molecular imaging agent for diagnosis of recurrent HER2 positive breast cancer. First time in human study using an Indium-111- or Gallium-68-labelled Affibody molecule. *Eur. J. Nucl. Med. Mol. Imaging 33*, S91.
(27) Engfeldt, T., Orlova, A., Tran, T., Bruskin, A., Widstrom, C., Eriksson Karlström, A., and Tolmachev, V. (2006) Imaging of HER2-expressing tumours using a synthetic Affibody molecule containing the (99m)Tc-chelating mercaptoacetyl-glycyl-glycyl-glycyl (MAG3) sequence. *Eur. J. Nucl. Med. Mol. Imaging 34*, 722–733.
(28) Zhu, Z., Wang, Y., Zhang, Y., Liu, G., Liu, N., Rusckowski, M., and Hnatowich, D. J. (2001) A novel and simplified route to the synthesis of N3S chelators for 99mTc labeling. *Nucl. Med. Biol. 28*, 703–708.
(29) Decristoforo, C., and Mather, S. J. (2002) The influence of chelator on the pharmacokinetics of 99mTc-labelled peptides. *Q. J. Nucl. Med. 46*, 195–205.
(30) Verbeke, K., Snauwaert, K., Cleynhens, B., Scheers, W., and Verbruggen, A. (2000) Influence of the bifunctional chelate on the biological behavior of (99m)Tc-labeled chemotactic peptide conjugates. *Nucl. Med. Biol. 27*, 769–779.
(31) Kyte, J., and Doolittle, R. F. (1982) A simple method for displaying the hydropathic character of a protein. *J. Mol. Biol. 157*, 105–132.
(32) Nicolas, E., Pedroso, E., and Giralt, E. (1989) Formation of Aspartimide Peptides in Asp-Gly Sequences. *Tetrahedron Lett. 30*, 497–500.
(33) Persson, M., Tolmachev, V., Andersson, K., Gedda, L., Sandström, M., and Carlsson, J. (2005) [(177)Lu]pertuzumab: experimental studies on targeting of HER-2 positive tumour cells. *Eur. J. Nucl. Med. Mol. Imaging 32*, 1457–1462.
(34) Tran, T., Engfeldt, T., Orlova, A., Widström, C., Bruskin, A., Tolmachev, V., and Eriksson Karlström, A. (2007) In vivo evaluation of cysteine-based chelators for attachment of (99m)Tc to tumor-targeting Affibody molecules. *Bioconjugate Chem. 18*, 549–558.
(35) Orlova, A., Rosik, D., Sandström, M., Lundqvist, H., Einarsson, L., and Tolmachev, V. (2007) Evaluation of [(111/114m)In]CHX-A″-DTPA-Z(HER2:342), an Affibody ligand conjugate for targeting of HER2-expressing malignant tumors. *Q. J. Nucl. Med. Mol. Imaging*, in press.
(36) Engfeldt, T., Tran, T., Orlova, A., Widström, C., Feldwisch, J., Abrahmsén, L., Wennborg, A., Eriksson, A. K., and Tolmachev, V. (2007) 99mTc-chelator engineering to improve tumour targeting properties of a HER2-specific Affibody. *Eur. J. Nucl. Med. Mol. Imaging*, in press.
(37) Valkema, R., De Jong, M., Bakker, W. H., Breeman, W. A., Kooij, P. P., Lugtenburg, P. J., De Jong, F. H., Christiansen, A., Kam, B. L., De Herder, W. W., Stridsberg, M., Lindemans, J., Ensing, G., and Krenning, E. P. (2002) Phase I study of peptide receptor radionuclide therapy with [In-DTPA]octreotide: the Rotterdam experience. *Semin. Nucl. Med. 32*, 110–122.
(38) Lub-de Hooge, M. N., Kosterink, J. G., Perik, P. J., Nijnuis, H., Tran, L., Bart, J., Suurmeijer, A. J., de Jong, S., Jager, P. L., and de Vries, E. G. (2004) Preclinical characterisation of 111In-DTPA-trastuzumab. *Br. J. Pharmacol. 143*, 99–106.
(39) Yazaki, P. J., Wu, A. M., Tsai, S. W., Williams, L. E., Ikler, D. N., Wong, J. Y., Shively, J. E., and Raubitschek, A. A. (2001)

Tumor targeting of radiometal labeled anti-CEA recombinant T84.66 diabody and t84.66 minibody: comparison to radioiodinated fragments. *Bioconjugate Chem. 12*, 220–228.

(40) Olafsen, T., Kenanova, V. E., Sundaresan, G., Anderson, A. L., Crow, D., Yazaki, P. J., Li, L., Press, M. F., Gambhir, S. S., Williams, L. E., Wong, J. Y., Raubitschek, A. A., Shively, J. E., and Wu, A. M. (2005) Optimizing radiolabeled engineered anti-p185HER2 antibody fragments for in vivo imaging. *Cancer Res. 65*, 5907–5916.

(41) Tai, M. S., McCartney, J. E., Adams, G. P., Jin, D., Hudziak, R. M., Oppermann, H., Laminet, A. A., Bookman, M. A., Wolf, E. J., and Liu, S. (1995) Targeting c-erbB-2 expressing tumors using single-chain Fv monomers and dimers. *Cancer Res. 55*, 5983s–5989s.

(42) Mariani, G., Erba, P. A., and Signore, A. (2006) Receptor-mediated tumor targeting with radiolabeled peptides: there is more to it than somatostatin analogs. *J. Nucl. Med. 47* 1904–1907.

BC7002617

A Novel G418 Conjugate Results In Targeted Selection of Genetically Protected Hepatocytes without Bystander Toxicity†

Martina Volarevic, Catherine H. Wu, Robert Smolic, John H. Andorfer, and George Y. Wu*

Division of Gastroenterology-Hepatology, Department of Medicine, University of Connecticut Health Center, Farmington, Connecticut. Received July 23, 2007; Revised Manuscript Received September 13, 2007

G418, an aminoglycoside neomycin analogue, is an antimicrobial agent that interferes with protein synthesis and has been used extensively for selection of mammalian cell lines that possess neomycin resistance (NR). It is potent and nonspecific in its effects that occur through tight binding to ribosomal elements. Because of the potent intracellular effect, we wondered whether G418 could be used to select a specific cell type based on receptor-mediated endocytosis. The objective of this study was to target G418 specifically to liver cells via asialoglycoprotein receptors (AsGR) which are known to be highly selective for these cells. A novel G418 conjugate was synthesized chemically by coupling G418 to a galactose-terminating carrier protein, asialoorosomucoid (AsOR), in a molar ratio of 5:1. AsOR–G418 conjugates inhibited viability of AsGR (+) cells by 84.3%, while inhibition in AsGR (–) cells was only by 19%. In AsGR (+) cells, stably transfected with a NR gene, the conjugate decreased viability by less than 9%. Furthermore, incubation of conjugate in cocultures of AsGR (+), and AsGR (–) cells did not result in the loss of viability of neighboring AsGR (–) cells. Our data demonstrate for the first time that G418 can be covalently bound to AsOR to form a conjugate for hepatocyte-specific targeting and toxicity. AsOR–G418 conjugates may be useful tools for genetic manipulation of human liver cells in the presence of nonhepatic cells.

INTRODUCTION

Gentamicin G or G418, a 4,6-disubstituted geneticin, is commonly used to select eukaryotic cells transfected with a neomycin resistance gene (NR) encoding aminoglycoside-modifying enzymes. These enzymes catalyze the covalent modification of specific amino or hydroxyl functional groups leading to inactive drug which binds poorly to ribosomes (*1–4*). G418 inhibitors include a class of aminoglycoside-modifying enzymes, the *O*-phosphotransferases (APH), which use ATP as a donor and modify hydroxyl groups (*5*).

It has been shown previously that high-affinity asialoglycoprotein receptors (AsGR) are predominantly expressed on the sinusoidal surface of mammalian liver cells and represent a useful system for targeting biologically active molecules specifically to the liver (*6, 7*). AsGR allows for efficient uptake of galactose-terminal (asialo)-glycoproteins by receptor-mediated endocytosis. Binding of ligands by the AsGR results in ligand internalization into an endosomal compartment and ultimately to degradation in lysosomes (*8*). This targeting strategy was used for liver-specific delivery of conjugates of antiviral agents (*9, 10*), antimalarial drugs (*11*), foreign genes *in vitro* (*12*), as well as *in vivo* (*13*); in animal models of human diseases (*14, 15*); and recently to systematically induce apoptosis in malignant hepatocytes *in vivo* (*16*). We and others have shown previously that targeted delivery of small molecules can be achieved by direct chemical linkage to an asialoglycoprotein carrier, and those molecules could retain their biological activity (*17, 18*). We wondered whether the potent nonspecific toxicity of G418 could be used to produce specific cell toxicity by taking advantage of receptor-mediated endocytosis, and ultimately to use AsOR–G418 conjugate as a tool for increasing the proportion of human liver cells in the HCV infection rat model recently developed in our laboratory (*19*).

EXPERIMENTAL PROCEDURES

Conjugation of G418 to Asialoorosomucoid. Asialoorosomucoid (AsOR) was produced, as described previously (*20*), by acid hydrolysis of orosomucoid isolated from pooled human serum (American Red Cross) (*21*). Purified AsOR was covalently linked to geneticin (Gibco, Invitrogen Corp.) using 1-ethyl-3 (3-dimethylaminopropyl) carbodiimide (EDC) (Pierce, Rockford, IL) (*22*). Twenty milligrams of AsOR was dissolved in 4 mL of 0.1 M 2-(*N*-morpholino) ethanesulfonic acid (MES), pH 6.0, and filtered through a 0.45 μ syringe-tip filter (Acrodisc, Gelman Sciences, Ann Arbor, MI). Thirty milligrams of geneticin (G418) was dissolved in 1 mL of 0.1 M MES, pH 6.0, and added to AsOR. To this mixture was added 18 mg of EDC, and the solution was incubated with stirring at 25 °C for 4 h followed by dialysis of the reaction mixture through membranes with 12–14 kDa exclusion limits (Spectra/Por, Spectrum Medical Industries, Houston, TX) against 40 L of water at 4 °C for 72 h. The dialyzate was desalted using PD-10 columns (GE Healthcare, Chalf-ont St. Giles, UK). Samples of 2.5 mL were applied on the column and eluted with 3.5 mL water, and samples of 0.5 mL each were collected and absorption at 280 nm monitored. For mass spectrometry analyses, samples were lyophilized and redissolved in water to a concentration of 2 mg/mL, filtered through a 0.45 μm syringe tip, and applied on a Waters RP-HPLC system (Waters, Milford, MA) using semipreparative C-18 polymeric reverse-phase column (Polymer Laboratories Inc., Amherst, MA). Proteins (100 μg) were injected onto the C-18 column, equilibrated with 95% buffer A (0.1% trifluoroacetic acid (TFA)) in H_2O and 5% buffer B (0.085% TFA in acetonitrile), eluted with linear gradients of buffer B at a flow rate of 0.5 mL/min in two phases (5%/min, 0–7 min; 2%/min, 7–27 min). 0.5 mL effluent fractions were collected, and UV absorption was monitored at 280 nm. Fractions with significant 280 nm absorption were analyzed by

* Correspondent mailing address: University of Connecticut Health Center, 263 Farmington Ave., Farmington, CT, 06030. Phone: (860) 679-3158. Fax: (860) 679-3159. E-mail: wu@nso.uchc.edu.

† Presented, in part, at the Annual Meeting of Professional Research Scientists, Experimental Biology 2007, May 2007.

10.1021/bc700277d CCC: $37.00 © 2007 American Chemical Society
Published on Web 10/31/2007

12% SDS PAGE and submitted for identification by matrix assisted laser desorption–ionization (MALDI) mass spectrometer (LCQ-Finnigan Corp., San Jose, CA) (performed at the Albert Einstein College of Medicine, Bronx, NY) to determine the molecular weight and ratios of components present.

As a control for possible nonspecific effects of conjugates in general, a G418 conjugate was prepared with orosomucoid (OR), which does not have exposed terminal galactose residues required for AsGR recognition and uptake. This conjugate was prepared in a manner identical to that for AsOR. To control for possible nonspecific effects of chemical linkage and modification of AsOR, a conjugate was prepared using glycine (Gly) instead of G418 in the same molar ratio. Each was purified and submitted for mass spectrometry analysis.

Cell Lines and Cell Culture. Huh7 [AsGR (+), NR (–)], a well-differentiated human hepatoma cell line that can produce liver-specific enzymes and plasma proteins (*23*), and has asialoglycoprotein receptor activity (*24*) but lacks neomycin resistance (NR), was maintained in Dulbecco's Modified Eagle Medium (DMEM) supplemented with 10% fetal bovine serum (FBS) and antibiotic/antimycotic solution (Invitrogen Corp., Carlsbad, CA). Cells were passaged every 3–4 days to maintain 75% confluent conditions.

GFP-Huh7 [AsGR (+), NR (+)], a hepatocyte-derived cell line that contains both asialoglycoprotein receptors (AsGR) and neomycin resistance (NR) was prepared by stable transfection of Huh7 [AsGR (+)] cells with a green fluorescent protein (GFP) gene and a neomycin resistance gene (NR) in a murine retroviral vector, MG-1 (a generous gift from Dr. David I. Dorsky, University of Connecticut Health Center, Farmington, CT). Viral particles, 3×10^4, in medium were mixed with polybrene (at 8 μg/mL final concentration) and placed in the medium of Huh7 cells at 25% confluency at 37 °C for 2 h. The inoculation medium was exchanged with fresh medium, and after 24 h of viral exposure, cells were trypsinized and replated onto a new dish containing medium with 200 μg/mL G418. Fluorescent cells resistant to G418 toxicity were harvested after 3 weeks.

For additional control experiments, NIH 3T3 [AsGR (–), NR (–)], a mouse fibroblast cell line, was obtained from ATCC and cultured in DMEM supplemented with 10% FBS and 1× antibiotic/antimycotic solution. Cells were grown at 37 °C in a humidified atmosphere of 5% CO_2 (v/v) in air. Cells were passaged every 3–4 days to maintain 75% confluent conditions.

Western Blot Analyses. To determine whether incorporation of GFP and neomycin resistance genes into Huh7 cells had an effect on AsGR expression in GFP-Huh7 cells, total protein extracts of cell lysates were evaluated by Western blot analyses. Cells were harvested in RIPA buffer (50 mM Tris–HCl, pH 7.4, 1% NP-40, 0.25% Na-deoxycholate, 150 mM NaCl, 1 mM EDTA) supplemented with a protease inhibitor cocktail (Roche Applied Science, Indianapolis, IN). Cell debris was removed by centrifugation. Protein concentration was determined with Bio-Rad protein assay. Forty micrograms of protein was resolved by SDS-PAGE and transferred to Hybond nitrocellulose membranes (Amersham Pharmacia, Piscataway, NJ). Membranes were sequentially blocked with 5% nonfat milk in PBS, incubated with a 1:1000 dilution of the polyclonal rabbit AsGR antibody (a gift of Dr. Richard Stockert, Liver Research Center, Albert Einstein College of Medicine, Bronx, NY), washed 3 times with PBS/0.05% Tween 20, incubated with horseradish peroxidase-conjugated goat antirabbit antibody (Pierce, Rockford, IL) at 1:20 000 dilution, and washed again. Bound antibody complexes were detected with SuperSignal chemiluminescent substrate (Pierce, Rockford, IL). To ensure a comparable loading of the samples, blots were incubated with a 1:1000 dilution of a polyclonal rabbit α-tubulin antibody (Abcam Inc., Cambridge, MA) and horseradish peroxidase conjugated goat antirabbit secondary antibody using the same procedures as described above.

Cell-Associated [^{125}I]-AsOR in Huh7 Cells and GFP-Huh7 Cells. To determine whether incorporation of GFP and neomycin resistance genes into Huh7 cells had any effect on AsGR activity, a specific cell-associated ligand was evaluated by assays as described previously (*25*). AsOR (a ligand specific for AsGR) was radiolabeled with carrier-free Na [^{125}I] (Amersham Biosciences) using Iodobeads (Pierce Biotechnologies, Rockford, IL) according to the manufacturer's instructions. [^{125}I]-AsOR at a specific activity of 2×10^6 cpm/μg protein was administered to Huh7 or GFP-Huh7 cells in serum-free DMEM containing 3 mM $CaCl_2$ at 37 °C. The nonspecific uptake was determined by adding unlabeled AsOR in 100-fold molar excess together with [^{125}I]-AsOR. At varying times, radioactive media were removed, cell surfaces washed 5× with ice–cold PBS, and cells solubilized with 0.01 M NaOH. Cell-associated radioactivity was determined in triplicate at varying time points as measured by gamma counting and reported as means ± SD in units of micrograms of AsOR per million cells per hour.

Cell-Associated [^{125}I]-AsOR–G418 in Huh7 Cells. To determine whether covalent binding of G418 to AsOR affected conjugate recognition by the receptor, cell-associated [^{125}I]-AsOR-G418 was compared to that of [^{125}I]-AsOR alone. AsOR–G418 was radiolabeled with carrier-free Na [^{125}I] (Amersham Biosciences) using the method described above. [^{125}I]-AsOR or [^{125}I]-AsOR–G418 at specific activity of 2×10^6 cpm/μg protein was administered to Huh7 cells in serum-free DMEM containing 3 mM $CaCl_2$ at 37 °C. Nonspecific uptake was determined by adding unlabeled AsOR in 100-fold molar excess together with [^{125}I]-AsOR or [^{125}I]-AsOR–G418. At varying times, radioactive medium was removed, cell surfaces washed 5× with ice–cold PBS, and cells solubilized with 0.01 M NaOH. Cell-associated radioactivity was determined by gamma counting and reported as means ± SD in units of nanograms AsOR or [^{125}I]-AsOR–G418 per hour per million cells.

G418 Toxicity Assays. The cytotoxicity of AsOR–G418 conjugate and free G418 against Huh7 [AsGR (+), NR (-)], GFP-Huh7 [AsGR (+), NR (+)], and NIH 3T3 [AsGR (–), NR (–)] cells were determined using TACS-MTT Assay (R&D Systems, Minneapolis, MN) according to the manufacturer's instructions. Cells were plated at a density of 2×10^4 cells/well in flat-bottom 96-well plates as mono- or cocultures. The cells were grown for 24 h and then treated in quadruplicate with 400 μg/mL G418 or AsOR–G418 containing the equivalent number of moles of G418. Cells were continuously incubated at 37 °C under 5% CO_2 for 6 days with the test substances. Following incubation, the media were removed, fresh media containing MTT reagent (0.5 mg/mL) added to the wells, and the incubations continued for 4 h to allow living cells to metabolize MTT to a dark formazan dye. Cell culture media were removed by aspiration, and 100 μL of acidic alcohol (0.04 M HCl–isopropyl alcohol) was added to solubilize the dye. The suspensions were gently mixed for 5 min, and the plates read in a model 680 series microplate reader at 570 nm (BioRad Laboratories, Hercules, CA). The absorbance values provided a direct measure of the number of live cells post-treatment (*26*). Responses were reported as the means ± SD of the numbers of live cells compared to untreated controls (*27*) reported in units of percent.

Coculture Assays for G418 Bystander Toxicity. Equal numbers of GFP- Huh7 [AsGR (+), NR (+)] were cocultured with Huh7 [AsGR (+), NR (–)] or NIH 3T3 [AsGR (–), NR (–)] to provide total cell densities of 2×10^4/mL in 96-well flat-bottom plates and treated as described in G418 toxicity assays. Bystander toxicity was determined using a combination

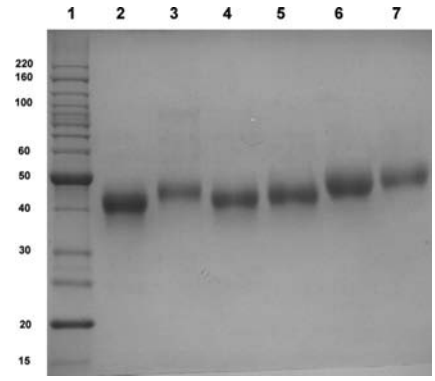


Figure 1. 12.5% SDS–PAGE of purified AsOR-G418 conjugate and controls prepared as described in the Experimental Procedures section. Lane 1, MW marker; lanes 2 and 4, AsOR alone; lane 3, AsOR–G418 conjugate; lane 5, AsOR–Gly conjugate; lane 6, OR; lane 7, OR–G418 conjugate.

Table 1. Mass Spectrometry Analyses of Parent Proteins and Their Conjugates as Determined by MALDI

protein	average most abundant mass peak (kDa)	change in mass from parent protein (kDa)	calculated number of modifications
AsOR	32.371		
AsOR–G418	34.917	2.546	5.20
AsOR–Gly	33.375	0.633	8.46
OR	34.109		
OR–G418	37.260	3.152	6.43

of light and fluorescent microscopy using an Image-iT LIVE Plasma Membrane and Nuclear Labeling Kit (I34406) (Molecular Probes, Invitrogen Corp., Carlsbad, CA) according to the manufacturer's instructions. Briefly, Alexa Fluor 594 WGA and Hoechst 33342 stains provided in the kit were diluted to a concentration of 5 μg/mL with Hanks' Balanced Salt Solution (HBSS) (Invitrogen Corp., Carlsbad, CA). Labeling solution, 100 μL, was applied onto cells and incubated for 10 min at 37 °C. After labeling was complete, the labeling solution was removed, and cells were washed and mounted in HBSS for imaging. Cells were analyzed using an inverted fluorescence microscope with 509 nm filter (Nikon, Avon, MA). Cell images were obtained by using a 10× dry immersion objective without postacquisition enhancement of images.

Statistical Analyses. Statistical analyses were performed using Student's *t* test; *P* values of <0.05 were considered statistically significant.

RESULTS

Elution of AsOR–G418 conjugates during purification by HPLC showed a single peak having absorbance at 280 nm. The AsOR–G418 conjugate migrated slightly slower on 12.5% SDS–PAGE gel compared to AsOR (Figure 1, lanes 3 and 2, respectively), consistent with a molecular weight of 46 000 Da.

From mass spectrometry analyses, the most abundant peak for AsOR had a mass of 32.371 kDa (range 30.473–34.282 kDa), whereas the abundant peak for the AsOR–G418 conjugate had a considerably higher mass of 34.917 kDa (range 34.286–37.461 kDa). From this difference, the G418 to AsOR molar ratio was calculated to be 5:1. For a control conjugate prepared with glycine instead of G418 (AsOR-Gly), the most abundant peak had a mass of 33.375 kDa (range 32.886–33.413 kDa), from which a molar ratio of Gly to AsOR was calculated to be 8:1. For a second control conjugate prepared with OR, OR–G418, the most abundant peak had a mass of 37.260 kDa (range 37.028–37.547 kDa), whereas the mass of the most abundant peak for OR was 34.109 kDa (range 33.848–34.339 kDa) permitting calculation of the molar ratio of G418 to OR to be 6:1. (Table 1).

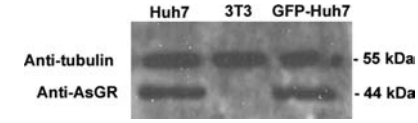


Figure 2. Western blot analysis of AsGR expression in Huh7, GFP-Huh7, and 3T3 cell lines. Cell lysates (40 μg of protein/lane) were resolved by 10% SDS–PAGE and transferred to nitrocellulose. As described in the Experimental Procedures section, prior to probing with anti-AsGR antibody, membranes were probed with antitubulin antibody to assess protein loading. Antibody deposition was detected by chemiluminescence and visualized on XAR film.

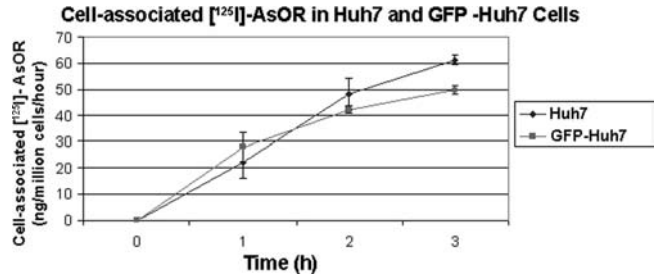


Figure 3. Kinetics of cell-associated [^{125}I]-AsOR in Huh and GFP–Huh7 cells. Confluent dishes of Huh7 cells and GFP–Huh7 cells were incubated with [^{125}I]-AsOR at 37 °C as described in the Experimental Procedures section, in the presence of 3 mM $CaCl_2$ for 1, 2, and 3 h. Nonspecific cell association was determined by the addition of 100-fold molar excess of unlabeled AsOR to medium containing [^{125}I]-AsOR. Cell-associated radioactivity was determined by gamma counting and reported as means ± SD in units of nanograms [^{125}I]-AsOR per hour per million cells.

Western blot analyses of asialoglycoprotein receptor protein from total protein extracts of cell lysates were carried out as described in the Experimental Procedures section. Figure 2 shows that the intensity of the band that migrated as expected for AsGR for a protein of 44.000 kDa, from native Huh7 [AsGR (+)] cells, in lane 1 was not significantly different from that of GFP-Huh 7 [AsGR (+), NR (+)] cells in lane 3. Also, as shown in lane 2, as expected, 3T3 cells, which are nonhepatocellular, lacked the band altogether. The intensities of the tubulin bands were similar in all lanes, indicating that there were no significant differences in the amount of samples loaded.

Figure 3, shows that [^{125}I]-AsOR associated with both Huh7 and GFP–Huh7 cells. The cell-association rate was linear up to 2 h with values of 28.5 ± 5 and 25 ± 2 ng/million cells/h for Huh7 and GFP-Huh7, respectively. The lack of significant difference in AsGR function in this assay suggests that incorporation of GFP and neomycin-resistant genes did not significantly alter the activity of AsGR in GFP–Huh7 cells compared to the original Huh7 cells.

To determine whether conjugation of G418 to AsOR changed asialoglycoprotein recognition by AsGR on liver cells, cell-association studies of labeled AsOR and AsOR–G418 were performed. Figure 4 shows that conjugation of G418 to AsOR did not significantly affect AsOR association by AsG receptors on Huh7 cells. In 1 h, 28.8 ± 5 ng of AsOR–G418 was found to be associated with 1 million Huh7 cells compared to 26.2 ± 6 ng of AsOR. Cell-associated [^{125}I]-AsOR–G418 was competed down to approximately 7% by addition of 100-fold excess of unlabeled AsOR in the medium indicating that internalization of conjugate was mediated by AsGR.

Free G418, AsOR–G418 conjugate, OR–G418 control, and AsOR–Gly control were assessed for their growth inhibitory effects on Huh7 [AsGR (+), NR (–)], GFP–Huh7 [AsGR (+), NR (+)], and NIH 3T3 [AsGR (–), NR (–)] cells. Figure 5

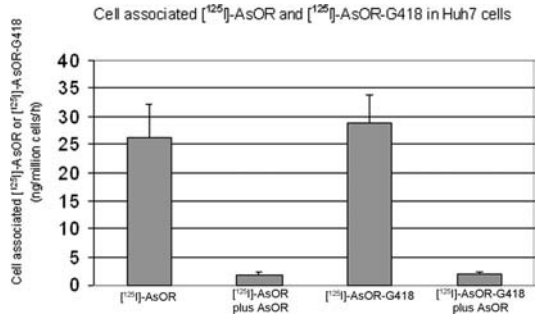


Figure 4. Comparison of cell-associated [^{125}I]-AsOR and [^{125}I]-AsOR–G418 conjugate by Huh7 cells. Confluent dishes of Huh7 cells were incubated with [^{125}I]-AsOR or [^{125}I]-AsOR–G418 at similar specific activity. Nonspecific interaction was determined by addition of 100× molar excess of unlabeled AsOR to the medium. Cell-associated radioactivity was determined by gamma counting and reported as means ± SD in units of nanograms [^{125}I]-AsOR or [^{125}I]-AsOR–G418 per hour per million cells.

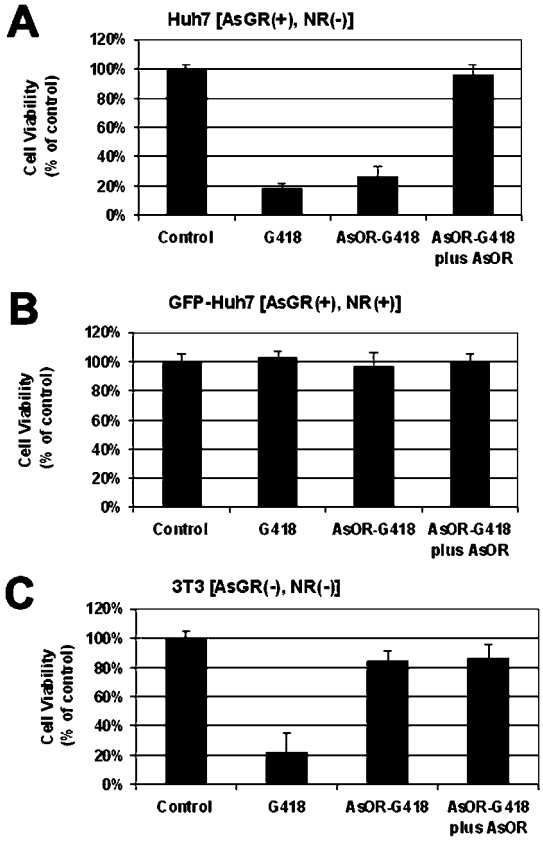


Figure 5. Toxicity of conjugate. Huh7 [AsGR (+), NR (–)], GFP–Huh7 [AsGR (+), NR (+)], and NIH 3T3 [AsGR (–), NR (–)] cells were incubated separately with media alone, AsOR–G418 conjugate, free G418, or AsOR–G418 conjugate in the presence of a 100-fold excess of AsOR as described in the Experimental Procedures section. Cell viability was determined by MTT assay. Panel A, Huh7 [AsGR (+), NR (–)]; Panel B, GFP–Huh7 [AsGR (+), NR (+)]; Panel C, NIH 3T3 [AsGR (–), NR (–)] cell lines. The results represent means ± SD of three independent experiments relative to controls. *$P > 0.05$.

illustrates that after 6 days of AsOR-G418 treatment, Huh7 [AsGR (+), NR (–)] proliferation was inhibited by 84.3% compared to 92% inhibition by G418 alone using molar equivalents of G418 in the media. AsOR–G418 toxicity in Huh7 cells was blocked by excess free AsOR (cell viability was not significantly different from control) in the medium, indicating that the observed toxicity of conjugate was mediated via AsG receptors, and not due to free G418. In contrast, incubation of

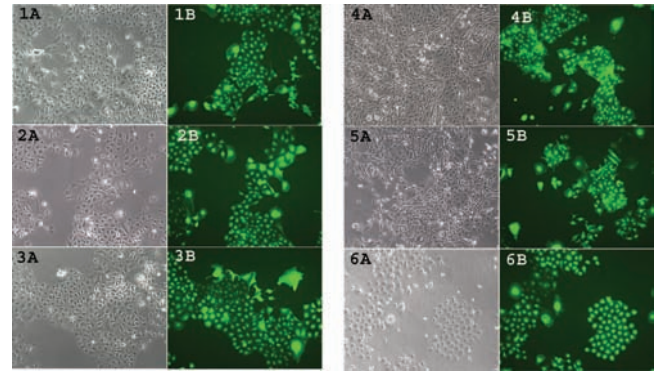


Figure 6. Representative photomicrographs of cells exposed to various agents. Medium alone, panels 1A,B, and 4A,B; medium with AsOR–G418 conjugate, panels 2A,B and 5A,B; or medium with G418 alone, panels 3A,B and 6A,B; 6 days after treatment as described in the Experimental Procedures section. For each pair of photomicrographs, the A panels shows phase contrast results, while the B panels shows fluorescence photomicrographs of the exact same cells. Panels 1A–3B, cocultures of Huh7 [AsGR (+), NR (–)] and GFP–Huh7 [AsGR (+), NR (+)] cells; panels 4A–6B, cocultures of NIH 3T3 [AsGR (–), NR (–)] and GFP–Huh7 [AsGR (+), NR (+)] cells.

3T3 [AsGR (–), NR (–)] cells with free G418 resulted in toxicity, while AsOR–G418 had no effect on 3T3 cell proliferation. GFP–Huh7 cells [AsGR (+) and NR (+)] were not susceptible either to free or conjugated G418, which supports the conclusion that the presence of a neomycin resistance gene in the cells protected them from G418 toxicity. OR–G418 and AsOR–Gly controls did not show significant toxicity to either cell type, indicating that toxicity involved AsGR recognition, was receptor-specific, and required the presence of G418.

To detect possible bystander effects, two pairs of cell lines, Huh7 [AsGR (+), NR (–)] and GFP–Huh7 [AsGR (+), NR (+)] cells; and 3T3 [AsGR (–)] and GFP–Huh7 [AsGR (+), NR (+)] cells were cocultured. The mixed cultures were treated with free G418, AsOR–G418 conjugate, or control media for 6 days. An essential precondition for these experiments was that the cell types could be clearly distinguished from each other by either cell morphology or by an intracellular marker. Because GFP–Huh7 [AsGR (+), NR (+)] express GFP, they can be identified by fluorescence microscopy. Under appropriate UV exposure, GFP-Huh7 cells will emit green fluorescence, while Huh7 and 3T3 do not. 3T3 cells can be distinguished as spindle-shaped cells in contrast to the round Huh7 cells when observed under phase contrast microscopy as described in the Experimental Procedures section. Figure 6 demonstrates the results of cocultures of Huh7 [AsGR (+), NR (–)] and GFP–Huh7 [AsGR (+), NR (+)] cells 6 days after exposure to media alone (panels 1A and 1B). The combined cells reached 100% confluence, and many cells were seen in panel 1A that were not fluorescent, NR (–), in panel 1B. However, after exposure to media containing AsOR–G418 conjugate for 6 days, there were few viable Huh7 [AsGR (+), NR (–)] cells, seen in phase contrast (2A) that were not also fluorescent (panel 2B). The total number of cells were clearly decreased compared to control untreated cells 1A and 1B. In contrast, the morphology of GFP–Huh7 [AsGR (+), NR (+)] cells exposed to conjugated G418 remained normal, and the number of cells attached to the plates visible by phase contrast (panel 2A) were similar compared to the number fluorescent cells (panel 2B). The data support the conclusion that AsGR (+) cells that possessed the NR gene had a selective advantage in the presence of conjugated G418. Cells that had AsGR but lacked an NR gene demonstrated G148-mediated toxicity. The results of exposure of cocultures to free G418 are shown in panels 3A and 3B. As seen before in panels 2A and 2B, the numbers of G418-treated Huh7 cells

lacking NR (nonfluorescent cells in panel 3B) decreased substantially compared to untreated controls, seen by phase contrast (panel 3A) and by fluorescence (panel 3B). Panels 4A and 4B show that cocultures of 3T3 [AsGR(+), NR(–)] and GFP–Huh7 [AsGR (+), NR (+)] cells 6 days after exposure to media alone reached confluency with almost equal representation of nonfluorescent spindle-shaped 3T3 cells and fluorescent GFP–Huh7cells. Panels 5A and 5B show that conjugated G418 had no significant effect on GFP–Huh7 [AsGR (+), NR (+)], (fluorescent) cells, or 3T3 (nonfluorescent spindle-shaped) cells compared to untreated controls (panels 4A and 4B). Because 3T3 cells lack AsG receptors, it was expected that they would not have been affected adversely by the conjugate alone. However, if conjugated G418 taken up by GFP–Huh7 [AsGR (+), NR (+)] had resulted in the release of free G418 into the medium, toxicity to 3T3 cells could have ensued. Panel 5B shows that, although GFP–Huh7 [AsGR (+), NR (+)] cells can take up conjugated G418, they were not only resistant to conjugated G418, but also demonstrated no observable toxicity to neighboring nonfluorescent 3T3 cells (panel 5A). In contrast, free G418-treated 3T3 cells resulted in few viable nonfluorescent cells under identical conditions (panel 6A), demonstrating that those cells were susceptible to free G418. Therefore, the observed survival of those cells following exposure to G418 conjugate suggests that release of free G418 from GFP–Huh7 [AsGR (+), NR (+)] cells, if it occurred, was insufficient to result in bystander toxicity.

DISCUSSION

Our results demonstrate that AsOR–G418 conjugates retain AsGR activity by hepatocyte-derived cells indicating that chemical linkage of G418 to the carrier did not interfere significantly with this biological interaction. Appropriate numbers of exposed terminal galactose residues in close proximity to each other are known to be required for this receptor recognition (*28*). Our results also suggest that five (on average) residues of G418 coupled per AsOR molecule did not significantly affect the interaction of the carbohydrate residues with the membrane-bound cell receptor.

It is well-known that different cell types have differences in sensitivities to G418 (*29*). It could be hypothesized that the differences in AsOR–G418 induced toxicity in different cell lines presented here merely reflected different sensitivities to G418 in each cell line (*29*). However, a G418 dose–response curve was done for each cell line used (data not shown), and 400 μg/mL of free G418 was shown to be the optimal concentration to kill over 90% cells after 6 days of exposure in all cell lines used in our experiments. Furthermore, nearly identical molar ratios of G418 in free and conjugated forms were administered. Therefore, differences in sensitivities or amounts of G418 administered cannot account for the observed differences in toxicity. Lastly, Huh7 cells that lacked the NR gene were highly susceptible to AsOR–G418 conjugates, indicating that the lack of toxicity seen in GFP–Huh7 cells was not due to a lack of activity of the G418 in conjugate form.

Aminoglycosides act by impairing bacterial protein synthesis (*30*) through binding to different regions of the 30 S ribosomal particle based on their chemical structure (*31*). The 4-substituted, 4,5-, and 4,6-disubstituted aminoglycosides are ligands of the eubacterial ribosome decoding aminoacyl-tRNA site (A site) (*32–34*). Among them, the 4,6-disubstituted geneticin, G418, contains three rings that are functionalized by hydroxyl, ammonium, and methyl groups, and has been shown to be toxic to eukaryotic organisms (*35–38*), yeast (*1*), and mammals (*2*) by binding to the 80 S ribosome (*39*). Crystallographic structures of various ribosomal particle complexes revealed the mechanism of action of G418 at the ribosomal level with atomic detail. The two sugar rings constituting the nonamine component common to most of the aminoglycosides bind to the A site. The essential hydrogen bonds involving ring I (to A1408) and ring II (to the phosphate oxygen atoms of a bulge of adenine bases 1492 and 1493, and to G1494) are conserved, and additional contacts are observed from ring III (to phosphate oxygen atoms of G1405 and U1406) (*40*). G418 locks the A site in the open conformation, and by doing so disrupts ribosomal proofreading capability, leading to pretermination or mistranslation (*41*). It is still controversial, however, how G418 reaches its target in the cytosol in sufficient amounts (*42*), because it is too polar to cross mammalian cell membranes by diffusion and is mainly stored in lysosomes of mammalian cells (*43*). However, with some limitations due to its kidney and ear toxicity (*4445*) , geneticin has been used clinically as an antiparasitic agent (*46*). Moreover, administration of geneticin (*47*) has proven helpful in the treatment of patients suffering from some genetic disorders (*48*).

The mechanism by which AsOR–G418 conjugates cause toxicity in target cells has not been elucidated. However, from crystallographic studies of various ribosomal particle complexes which revealed the mechanism of action of G418, it appears clear that toxicity of targeted conjugate depends on retention of G418 structure required for interaction with ribosomes (*40, 41*). Conjugation to a large protein might be expected to interfere with that interaction. However, it has been well-established that the AsGR pathway results in proteolytic degradation of the majority of material taken up by AsGR receptors. Thus, it is possible that G418 is released in the free form following degradation of the protein carrier in lysosomes. The extent to which G418 itself is susceptible to degradation in lysosomes is not known. However, it is known that G418 in the free form after cellular uptake is mostly stored in lysosomes and remains active after this storage (*43*).

Targeting of hepatocytes by the asialoglycoprotein receptors was selected for liver cell targeting based on our previous studies which demonstrated that targeted delivery of small molecules could be achieved by chemical linkage to asialoglycoprotein carriers. As observed in the current study, those small molecules retained their biological activities (*18, 19*).

Collateral toxicity to surrounding tissues, the bystander effect, is a complex phenomenon and appears to be based on different mechanisms, the most important of which is transfer of the toxic metabolite from cells that possess the toxin to their neighbors. This can occur via gap junctions (*49, 50*) consisting of connections that permit the passage of hydrophilic molecules smaller than 1 kDa from one cell to another (*51*). Although genetic resistance to neomycin is known to be due to phosphorylation-mediated inactivation of G418 in surviving cells, it has not been shown previously whether such inactivation is complete or whether free G418-exposed cells could release the toxin to neighboring cells resulting in a bystander effect. The coculture experiments in the current study provide a clear demonstration that, when conjugated G418 is administered to genetically resistant cells, if free G418 is released, the quantities are insufficient to cause toxicity to neighboring cells.

We conclude that chemical coupling of G418 to an asialoglycoprotein results in the targeted delivery of active toxin to cells possessing the appropriate receptor. In the presence of NR, there was no detectable bystander effect. This represents the first description of the use of G418 for targeted selection *in vivo*. While the studies here have focused on liver cells, because many other receptor–ligand combinations are known, the technique may be extended to manipulation of populations of various other non-hepatocellular cell types in cocultures and explants. Indeed, it is possible that such a targeted selection strategy may be applied to animal models to increase the

predominance of one cell type over another. For example, an AsOR–G418 conjugate is being developed to increase the proportion of genetically protected human liver cells at the expense of host rat hepatocytes in an immunocompetent rat model possessing a chimeric human liver (*19*). Such models may be useful in the evaluation of drug toxicity or metabolism in human hepatocytes in animals.

ACKNOWLEDGMENT

Supported in part by grants from NIDDK, RO1- DK042182, and from the Herman Lopata Chair in Hepatitis Research. The authors thank Martha Schwartz for secretarial assistance and Dr. Irving Listowsky and The Laboratory for Macromolecular Analysis and Proteomics Core Facility at the Albert Einstein College of Medicine for arranging the mass spectrometric analyses.

LITERATURE CITED

(1) Jimenez, A., and Davies, J. (1980) Expression of a transposable antibiotic resistance element in Saccharomyces. *Nature (London) 287*, 869–71.

(2) Colbere-Garapin, F., Horodniceanu, F., Kourilsky, P., and Garapin, A. C. (1981) A new dominant hybrid selective marker for higher eukaryotic cells. *J. Mol. Biol. 150*, 1–14.

(3) Xu, M. Z., and Stavnezer, J. (1992) Regulation of transcription of immunoglobulin germ-line gamma 1 RNA: analysis of the promoter/enhancer. *EMBO J. 11*, 145–55.

(4) Moritz, O. L., Biddle, K. E., and Tam, B. M. (2002) Selection of transgenic Xenopus laevis using antibiotic resistance. *Transgenic Res. 11*, 315–9.

(5) Mingeot-Leclercq, M. P., Glupczynski, Y., and Tulkens, P. M. (1999) Aminoglycosides: activity and resistance. *Antimicrob. Agents Chemother. 43*, 727–37.

(6) Virovic, L., Wu, C. H., Konishi, M., and Wu, G. Y. (2005) Novel delivery methods for treatment of viral hepatitis: an update. *Expert Opin. Drug Delivery 2*, 707–17.

(7) Wu, J., Nantz, M. H., and Zern, M. A. (2002) Targeting hepatocytes for drug and gene delivery: emerging novel approaches and applications. *Front. Biosci. 7*, d717–25.

(8) Warren, G. (1990) Cell biology. Trawling for receptors. *Nature (London) 346*, 318–9.

(9) Fiume, L., Mattioli, A., Balboni, P. G., Tognon, M., Barbanti-Brodano, G., de Vries, J., and Wieland, T. (1979) Enhanced inhibition of virus DNA synthesis in hepatocytes by trifluorothymidine coupled to asialofetuin. *FEBS Lett. 103*, 47–51.

(10) Fiume, L., Mattioli, A., Busi, C., Balboni, P. G., Barbanti-Brodano, G., De Vries, J., Altmann, R., and Wieland, T. (1980) Selective inhibition of Ectromelia virus DNA synthesis in hepatocytes by adenine-9-beta-D-arabinofuranoside (ara-A) and adenine-9-beta-D-arabinofuranoside 5′-monophosphate (ara-AMP) conjugated to asialofetuin. *FEBS Lett. 116*, 185–8.

(11) Trouet, A., Masquelier, M., Baurain, R., and Deprez-De Campeneere, D. (1982) A covalent linkage between daunorubicin and proteins that is stable in serum and reversible by lysosomal hydrolases, as required for a lysosomotropic drug-carrier conjugate: in vitro and in vivo studies. *Proc. Natl. Acad. Sci. U.S.A. 79*, 626–9.

(12) Wu, G. Y., and Wu, C. H. (1987) Receptor-mediated in vitro gene transformation by a soluble DNA carrier system. *J. Biol. Chem. 262*, 4429–32.

(13) Wu, G. Y., and Wu, C. H. (1988) Receptor-mediated gene delivery and expression in vivo. *J. Biol. Chem. 263*, 14621–4.

(14) Wilson, J. M., Grossman, M., Wu, C. H., Chowdhury, N. R., Wu, G. Y., and Chowdhury, J. R. (1992) Hepatocyte-directed gene transfer in vivo leads to transient improvement of hypercholesterolemia in low density lipoprotein receptor-deficient rabbits. *J. Biol. Chem. 267*, 963–7.

(15) Chowdhury, N. R., Hays, R. M., Bommineni, V. R., Franki, N., Chowdhury, J. R., Wu, C. H., and Wu, G. Y. (1996) Microtubular disruption prolongs the expression of human bilirubin-uridinediphosphoglucuronate-glucuronosyltransferase-1 gene transferred into Gunn rat livers. *J. Biol. Chem. 271*, 2341–6.

(16) Peng, D. J., Sun, J., Wang, Y. Z., Tian, J., Zhang, Y. H., Noteborn, M. H., and Qu, S. (2007) Inhibition of hepatocarcinoma by systemic delivery of Apoptin gene via the hepatic asialoglycoprotein receptor. *Cancer Gene Ther. 14*, 66–73.

(17) Wu, G. Y., Wu, C. H., and Stockert, R. J. (1983) Model for specific rescue of normal hepatocytes during methotrexate treatment of hepatic malignancy. *Proc. Natl. Acad. Sci. U.S.A. 80*, 3078–80.

(18) Wu, G. Y., Wu, C. H., and Rubin, M. I. (1985) Acetaminophen hepatotoxicity and targeted rescue: a model for specific chemotherapy of hepatocellular carcinoma. *Hepatology 5*, 709–13.

(19) Wu, G. Y., Konishi, M., Walton, C. M., Olive, D., Hayashi, K., and Wu, C. H. (2005) A novel immunocompetent rat model of HCV infection and hepatitis. *Gastroenterology 128*, 1416–23.

(20) Schmid, K., Polis, A., Hunziker, K., Fricke, R., and Yayoshi, M. (1967) Partial characterization of the sialic acid-free forms of alpha-1-acid glycoprotein from human plasma. *Biochem. J. 104*, 361–8.

(21) Whitehead, P. H., and Sammons, H. G. (1966) A simple technique for the isolation of orosomucoid from normal and pathological sera. *Biochim. Biophys. Acta 124*, 209–11.

(22) Habus, I., Xie, J., Iyer, R. P., Zhou, W. Q., Shen, L. X., and Agrawal, S. (1998) A mild and efficient solid-support synthesis of novel oligonucleotide conjugates. *Bioconjugate Chem. 9*, 283–91.

(23) Nakabayashi, H., Taketa, K., Yamane, T., Miyazaki, M., Miyano, K., and Sato, J. (1984) Phenotypical stability of a human hepatoma cell line, HuH-7, in long-term culture with chemically defined medium. *Gann 75*, 151–8.

(24) Liang, T. J., Makdisi, W. J., Sun, S., Hasegawa, K., Zhang, Y., Wands, J. R., Wu, C. H., and Wu, G. Y. (1993) Targeted transfection and expression of hepatitis B viral DNA in human hepatoma cells. *J. Clin. Invest. 91*, 1241–6.

(25) Schwartz, A. L., Fridovich, S. E., Knowles, B. B., and Lodish, H. F. (1981) Characterization of the asialoglycoprotein receptor in a continuous hepatoma line. *J. Biol. Chem. 256*, 8878–81.

(26) Hansen, M. B., Nielsen, S. E., and Berg, K. (1989) Re-examination and further development of a precise and rapid dye method for measuring cell growth/cell kill. *J. Immunol. Methods 119*, 203–10.

(27) Kokoshka, J. M., Ireland, C. M., and Barrows, L. R. (1996) Cell-based screen for identification of inhibitors of tubulin polymerization. *J. Nat. Prod. 59*, 1179–82.

(28) Stockert, R. J. (1995) The asialoglycoprotein receptor: relationships between structure, function, and expression. *Physiol. Rev. 75*, 591–609.

(29) Qian, L., Zhang, Z., Shi, M., Yu, M., Hu, M., Xia, Q., Shen, B., and Guo, N. (2006) Expression and distribution of HSP27 in response to G418 in different human breast cancer cell lines. *Histochem. Cell Biol. 126*, 593–601.

(30) Davies, J., Gorini, L., and Davis, B. D. (1965) Misreading of RNA codewords induced by aminoglycoside antibiotics. *Mol. Pharmacol. 1*, 93–106.

(31) Carter, A. P., Clemons, W. M., Brodersen, D. E., Morgan-Warren, R. J., Wimberly, B. T., and Ramakrishnan, V. (2000) Functional insights from the structure of the 30S ribosomal subunit and its interactions with antibiotics. *Nature (London) 407*, 340–8.

(32) Moazed, D., and Noller, H. F. (1987) Interaction of antibiotics with functional sites in 16S ribosomal RNA. *Nature (London) 327*, 389–94.

(33) Recht, M. I., Fourmy, D., Blanchard, S. C., Dahlquist, K. D., and Puglisi, J. D. (1996) RNA sequence determinants for aminoglycoside binding to an A-site rRNA model oligonucleotide. *J. Mol. Biol. 262*, 421–36.

(34) Ryu, D. H., Litovchick, A., and Rando, R. R. (2002) Stereospecificity of aminoglycoside-ribosomal interactions. *Biochemistry 41*, 10499–509.

(35) Waitz, J. A., Sabatelli, F., Menzel, F., and Moss, E. L., Jr. (1974) Biological activity of antibiotic G-418, a new micromonospora-produced aminoglycoside with activity against protozoa and helminths. *Antimicrob. Agents Chemother. 6*, 579–81.

(36) Wagman, G. H., Testa, R. T., Marquez, J. A., and Weinstein, M. J. (1974) Antibiotic G-418, a new Micromonospora-produced aminoglycoside with activity against protozoa and helminths: fermentation, isolation, and preliminary characterization. *Antimicrob. Agents Chemother. 6*, 144–9.

(37) Loebenberg, D., Counels, M., and Waitz, J. A. (1975) Antibiotic G418, a new micrommomospora-produced aminglycoside with activity apainst protozoa and helminths: antiparasitic activity. *Antimicrob. Agents Chemother. 7*, 811–5.

(38) Eustice, D. C., and Wilhelm, J. M. (1984) Mechanisms of action of aminoglycoside antibiotics in eucaryotic protein synthesis. *Antimicrob. Agents Chemother. 26*, 53–60.

(39) Bar-Nun, S., Shneyour, Y., and Beckmann, J. S. (1983) G-418, an elongation inhibitor of 80 S ribosomes. *Biochim. Biophys. Acta 741*, 123–7.

(40) Vicens, Q., and Westhof, E. (2003) Crystal structure of geneticin bound to a bacterial 16S ribosomal RNA A site oligonucleotide. *J. Mol. Biol. 326*, 1175–88.

(41) Vicens, Q., and Westhof, E. (2003) RNA as a drug target: the case of aminoglycosides. *ChemBioChem 4*, 1018–23.

(42) Buchanan, J. H., Stevens, A., and Sidhu, J. (1987) Aminoglycoside antibiotic treatment of human fibroblasts: intracellular accumulation, molecular changes and the loss of ribosomal accuracy. *Eur. J. Cell Biol. 43*, 141–7.

(43) Tulkens, P., and Trouet, A. (1978) The uptake and intracellular accumulation of aminoglycoside antibiotics in lysosomes of cultured rat fibroblasts. *Biochem. Pharmacol. 27*, 415–24.

(44) Hutchin, T., and Cortopassi, G. (1994) Proposed molecular and cellular mechanism for aminoglycoside ototoxicity. *Antimicrob. Agents Chemother. 38*, 2517–20.

(45) Mingeot-Leclercq, M. P., and Tulkens, P. M. (1999) Aminoglycosides: nephrotoxicity. *Antimicrob. Agents Chemother. 43*, 1003–12.

(46) Griffiths, J. K., Balakrishnan, R., Widmer, G., and Tzipori, S. (1998) Paromomycin and geneticin inhibit intracellular Cryptosporidium parvum without trafficking through the host cell cytoplasm: implications for drug delivery. *Infect. Immun. 66*, 3874–83.

(47) Howard, M. T., Shirts, B. H., Petros, L. M., Flanigan, K. M., Gesteland, R. F., and Atkins, J. F. (2000) Sequence specificity of aminoglycoside-induced stop condon readthrough: potential implications for treatment of Duchenne muscular dystrophy. *Ann. Neurol. 48*, 164–9.

(48) Barton-Davis, E. R., Cordier, L., Shoturma, D. I., Leland, S. E., and Sweeney, H. L. (1999) Aminoglycoside antibiotics restore dystrophin function to skeletal muscles of mdx mice. *J. Clin. Invest. 104*, 375–81.

(49) Vrionis, F. D., Wu, J. K., Qi, P., Waltzman, M., Cherington, V., and Spray, D. C. (1997) The bystander effect exerted by tumor cells expressing the herpes simplex virus thymidine kinase (HSVtk) gene is dependent on connexin expression and cell communication via gap junctions. *Gene Ther. 4*, 577–85.

(50) Mesnil, M., and Yamasaki, H. (2000) Bystander effect in herpes simplex virus-thymidine kinase/ganciclovir cancer gene therapy: role of gap-junctional intercellular communication. *Cancer Res. 60*, 3989–99.

(51) Kumar, N. M., and Gilula, N. B. (1996) The gap junction communication channel. *Cell 84*, 381–8.

BC700277D

1-Phenylethynylpyrene (1-PEPy) as Refined Excimer Forming Alternative to Pyrene: Case of DNA Major Groove Excimer

Irina V. Astakhova,[†] Andrei D. Malakhov,[†] Irina A. Stepanova,[†] Alexey V. Ustinov,[†] Stanislav L. Bondarev,[‡] Alexander S. Paramonov,[†] and Vladimir A. Korshun*[,†]

Shemyakin-Ovchinnikov Institute of Bioorganic Chemistry, Miklukho-Maklaya 16/10, 117997 Moscow, Russia, and Institute of Molecular and Atomic Physics, Nezavisimosti av. 70, 220072 Minsk, Belarus. Received July 24, 2007

1-Phenylethynylpyrene fluorochrome was studied as *meta*- and *para*-derivatives of *arabino*-uridine-2′-carbamates in ss and dsDNA. 1-PEPy showed red-shifted emission and increased fluorescence quantum yield compared to pyrene. Although 1-PEPy has very short excited lifetime (<2.5 ns), it is able to form inter- and intrastrand excimers on DNA, probably resulting from spatial preorganization of two dye molecules.

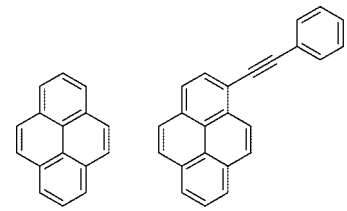
INTRODUCTION

Pyrene (Chart 1) excimer fluorescence (*1, 2*) is a useful tool for structural studies in biochemistry and molecular biology as "a probe of proximity" (*3*). The broad long-wavelength maximum of pyrene excimer emission (typically around 450–500 nm) clearly differs from the structured emission of a single pyrene molecule (370–400 nm). The emission of the pyrene excimer appears as a result of three successive processes: (a) photoexcitation of the pyrene molecule; (b) its reaction with ground-state pyrene and formation of a stacked excited dimer (excimer); (c) emission of a photon with synchronous dissociation of the dimer. The prominent excimer-forming ability of pyrene (among other flat fluorochrome molecules) is determined by its long excited lifetimes (up to hundreds of nanoseconds in several solvents). Thus, an excited pyrene molecule has enough time to meet a spatially reachable ground-state pyrene molecule. Pyrenes in an excimer are coplanar (to a greater or lesser extent) and less than 4 Å apart. Hence, in the case of two pyrenes covalently bound to biomolecule(s), the broad band of excimer emission is unambiguous evidence that the residues are *able* to come into close proximity. The more intense the excimer emission is, the closer the pyrenes are located.

Pyrene excimer on nucleic acids (NA) has been widely studied. It has been applied for the detection of point mutations using tandem hybridization of 5′- and 3′-pyrene-labeled oligonucleotides on complementary targets (*4–9*). Various excimer-forming pyrene bichromophores were used to monitor hybridization (*10–17*). Two or more pyrene residues attached to one (*8, 18–31*) or several different oligonucleotides (*18, 32–43*) were used in studies of NA hybridization, including parallel duplexes (*32, 34*), triplexes (*30, 33, 40, 41, 43*), and quadruplexes (*28*).

However, fluorochromes with excited lifetime of a few nanoseconds are much less prone to forming excimers. For example, perylene displayed a very weak excimer upon tandem hybridization on DNA (*44*). Nevertheless, *preorganized* ethynylpyrene and even ethynylperylene fluorochromes showed explicit excimer fluorescence (*45*).

Chart 1. Structures of Pyrene and 1-PEPy Fluorochromes



Recently, we (*46–50*) and others (*51–53*) introduced 1-PEPy fluorochrome as a label for nucleic acids. It is well-known that introduction of a phenylethynyl group in a fluorescent molecule leads to an increase in absorption together with a bathochromic shift in absorption and emission, a decrease in Stoke's shift and excited lifetime, and an increase in emission quantum yield (fluorescence intensity) (*48* and refererces cited therein). These changes are also the case for pyrene. The parent dye, 1-PEPy (Chart 1), is able to form excimers in THF solution (*47*); the concentration required ($>10^{-2}$ M) is, however, 2–3 orders of magnitude higher compared to pyrene. This correlates with its short excited lifetime (7.72 ns for 1-PEPy in EtOH (*52*)). The absorbance and fluorescence of 1-PEPy derivatives on DNA are approximately 50 nm and 30 nm red-shifted, respectively, in comparison with pyrene derivatives; the first fluorescence maximum of 1-PEPy in oligonucleotides is within 400–405 nm (*48–52*). These spectral features reduce 100-fold the 1-PEPy detection limit with respect to that of pyrene (*52*). 1-PEPy is able to form strong (*48, 50, 51*) or weak (*49, 52*) excimers on DNA.

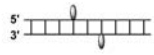
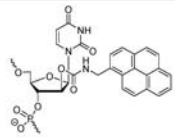
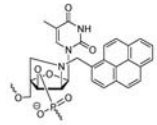
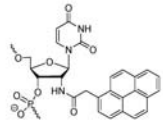
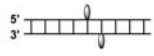
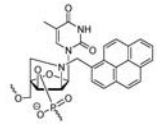
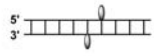
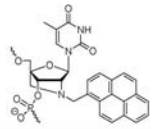
With a short excited lifetime taken into account, the pronounced PEPy excimer should be evidence not only for mutual attainability, but rather preassociation of two PEPy molecules. Thus, an excimer-forming 1-PEPy fluorochrome could become a label of choice for some structural studies of biomolecules. However, photophysical properties of 1-PEPy on nucleic acids have not been reported. Our aim was to explore further 1-PEPy on DNA and to elucidate its potential as an excimer-forming fluorescent probe.

Pyrene attached to the sugar part of a nucleoside in dsDNA can form interstrand excimers located in +2 zipper (*24, 27, 35*), +1 zipper (*27*), or −1 zipper (*8*) mode (Table 1). We have

* Corresponding author. E-mail: korshun@mail.ibch.ru. Tel/Fax: +7-495-330-6738.
[†] Shemyakin-Ovchinnikov Institute of Bioorganic Chemistry.
[‡] Institute of Molecular and Atomic Physics.

10.1021/bc700280h CCC: $37.00 © 2007 American Chemical Society
Published on Web 09/27/2007

Table 1. Reported Examples of Interstrand Pyrene Excimers on DNA from Sugar-Modified Nucleosides

Zipper	Schematic structure	Modified nuleoside	Reference
+2			(*24*)
			(*27*)[a]
			(*35*)
+1			(*27*)
−1			(*8*)

[a]Weak excimer.

chosen the case of the +2 zipper major groove excimer formed by 1-pyrenemethyl *ara*-uridine-2′-carbamate (*24*), replaced pyrene with 1-PEPy, and studied the structural requirements for the 1-PEPy excimer.

EXPERIMENTAL PROCEDURES

General. Reagents obtained from commercial suppliers were used as received; 2′-*O*-(imidazol-1-ylcarbonyl)-3′,5′-*O*-(tetraisopropyldisiloxan-1,3-diyl)uracil-1-*β*-D-arabinofuranoside (*24*), $Pd(PPh_3)_4$ (*54*), 1-ethynylpyrene (*47*), bis(*N*,*N*-diisopropylamino)-2-cyanoethoxyphosphine (*55*), and diisopropylammonium tetrazolide (*56*) were synthesized as described. HPLC-grade DMF was distilled under reduced pressure and stored over 4 Å molecular sieves under nitrogen. DCM was always used freshly distilled over CaH_2. Other solvents were used as received.

500 MHz ^{1}H, 125.7 MHz ^{13}C, and 202.4 MHz ^{31}P NMR spectra were recorded on a Bruker DRX-500 spectrometer at 303 K and referenced to DMSO-d_6 (2.50 ppm for ^{1}H and 39.5 ppm for ^{13}C), MeCN-d_3 (1.96 ppm for ^{1}H) (*57*), and 85% aq H_3PO_4 (0.00 ppm for ^{31}P). ^{1}H–^{13}C gradient-selected HMQC and HMBC spectra were obtained by using 2048 (t_2) × 256 (t_1) complex point data sets, zero-filled to 2048 (F_2) × 1024 (F_1) points. The spectral widths were 13 ppm and 200 ppm for ^{1}H and ^{13}C dimensions, respectively. HMBC spectra were measured with 50 ms delay for evolution of long-range couplings. ^{1}H NMR coupling constants are reported in hertz (Hz) and refer to apparent multiplicities. High-resolution mass spectra were recorded in positive ion mode using IonSpec Fourier Transform ISR mass spectrometer (MALDI) or PE SCIEX QSTAR pulsar mass spectrometer (ESI). Melting points were determined using a Boetius heating table and are uncorrected. Analytical thin-layer chromatography was performed on Kieselgel 60 F_{254} precoated aluminium plates (Merck). Silica gel column chromatography was performed using Merck Kieselgel 60 0.040–0.063 mm. The oligonucleotide synthesis was carried out on a BiosSet ASM-800 instrument in a 200 nmol scale using standard manufacturer's protocols. The coupling step time for modified phosphoramidites was extended to 5 min. Oligonucleotides were isolated using 20% denaturing (7 M urea) PAGE in Tris-borate buffer, pH 8.3, and desalted by gel filtration on a Sephadex G-25 column eluting with saltless buffer. MALDI-TOF mass spectra of oligonucleotides were recorded on Bruker Ultraflex mass spectrometer in positive ion mode; a mixture (1:1 v/v) of 2,6-dihydroxyacetophenone (40 mg/mL in MeOH) and diammonium hydrogen citrate (80 mg/mL in water) was used as a matrix. Theoretical masses of oligonucleotide conjugates were calculated using the monoisotopic element masses. UV spectra were recorded using Beckman DU520 general purpose UV/vis spectrometer. Thermal denaturation experiments were performed on a Perkin Elmer Lambda 40 UV/vis spectrometer with PTP 6 (Peltier temperature programmer) in the medium salt hybridization buffer containing 100 mM NaCl, 10 mM Na_3PO_4, 0.1 mM EDTA, pH 7.0 (concentration of duplex 1.0×10^{-6} M). Fluorescence spectra were obtained in same buffer using a Varian Cary Eclipse fluorescence spectrophotometer (λ_{ex} 360 nm, excitation and emission slits 5 nm, concentrations of each oligonucleotide or duplex 1.0×10^{-7} M). Photophysical studies in the same buffer were performed using a large-aperture apparatus described earlier (*58*). The fluorescence quantum yields Φ_f were measured by the relative method using standards of quinine sulfate in 1 N H_2SO_4 (Φ_f 0.55 (*59*)). The measurements were performed at an angle of 90° to the exciting light beam. The optical density of the solutions in 1-cm quartz cuvettes at the excitation wavelength did not exceed 0.1. The values of Φ_f were corrected with the refractive index of the solvent; the measured refractive indexes of 1 N H_2SO_4 and phosphate buffer were 1.338 and 1.334 at 20 °C, respectively. Fluorescence lifetimes were determined by the method of time-correlated single-photon counting using a PRA model 3000 ns lifetime fluorometer. The parameters of the fluorescence decays were analyzed using T900 software (Edinburgh Instruments). The samples used in quantum yield and lifetime fluorescence measurements were not degassed; concentrations were 3.0×10^{-6} M.

General Procedure for the Preparation of 2′-*O*-(3(4)-Iodobenzylaminocarbonyl)-3′,5′-*O*-(tetraisopropyldisiloxan-1,3-diyl)uracil-1-*β*-D-arabinofuranosides (2a,b). To a solution of 2′-*O*-(imidazol-1-ylcarbonyl)-3′,5′-*O*-(tetraisopropyldisiloxan-1,3-diyl)uracil-1-*β*-D-arabinofuranoside **1** (2.90 g, 5.0 mmol) in THF–MeCN, 1:1 (v/v) (60 mL) 3- or 4-iodobenzylamine (1.63 g, 7.0 mmol) was added, and the mixture was refluxed for 40 h. After conversion of the starting compound **1** is complete (monitoring by TLC, EtOAc–$CHCl_3$, 2:3 v/v), the mixture was diluted with $CHCl_3$ (150 mL), washed with water (100 mL), 5% citric acid (100 mL), and water (100 mL), then dried over Na_2SO_4 and evaporated to dryness. The residue was purified by chromatography on a silica gel column (100 g) with a step gradient of EtOAc (0→5%) in $CHCl_3$ (v/v) as the mobile phase to give carbamates **2a**,**b** as white amorphous foams.

2′-*O*-(3-Iodobenzylaminocarbonyl)-3′,5′-*O*-(tetraisopropyldisiloxan-1,3-diyl)uracil-1-*β*-D-arabinofuranoside (2a). Yield 3.50 g (94%), white foam, R_f 0.52 (EtOAc–$CHCl_3$, 2:3 v/v). MALDI-TOF HRMS: m/z = 768.1642 $[M + Na]^+$, calcd for $[C_{29}H_{44}N_3O_8Si_2 + Na]^+$ 768.1604. ^{1}H NMR (DMSO-d_6, δ): 11.33 (s, 1H, H-3), 7.88 (t, 1H, J = 6.0 Hz, OCON*H*), 7.58 (m, 2H, H-2″, 4″), 7.45 (d, 1H, $J_{5,6}$ = 8.1 Hz, H-6), 7.16–7.05 (m, 2H, H-5″, 6″), 6.12 (m, 1H, H-1′), 5.57 (d, 1H, $J_{5,6}$ = 8.1 Hz, H-5), 5.42 (m, 1H, H-2′), 4.38 (m, 1H, H-3′), 4.17–3.90 (m, 4H, H-5′, NCH_2), 3.86 (m, 1H, H-4′), 1.10–0.92 (m, 28H, Pr^i). ^{13}C NMR (DMSO-d_6, δ): 163.0 (C4), 154.8 (O*C*O), 150.0 (C2), 142.1 (C1″), 140.6 (C6), 135.5 (2C, C2″,4″), 130.5 (C5″), 126.2 (C6″), 101.3 (C5), 94.7 (C3″), 81.0 (C1′), 79.0 (C4′), 76.1 (C2′), 72.6 (C3′), 60.6 (C5′), 43.1 (N*C*H$_2$), 17.3, 17.2 (3C), 16.9, 16.8 (2C), 16.7 (*C*H$_3$), 12.8, 12.4, 12.2, 11.9 (Si*C*).

2′-*O*-(4-Iodobenzylaminocarbonyl)-3′,5′-*O*-(tetraisopropyldisiloxan-1,3-diyl)uracil-1-β-D-arabinofuranoside (2b). Yield 3.14 g (84%), white foam, R_f 0.50 (EtOAc–$CHCl_3$, 2:3 v/v). MALDI-TOF HRMS: m/z= 768.1631 $[M + Na]^+$, calcd for $[C_{29}H_{44}N_3O_8Si_2 + Na]^+$ 768.1604. ^{1}H NMR (DMSO-d_6, δ): 11.38 (s, 1H, H-3), 7.86 (m, 1H, OCON*H*), 7.64 (d, 2H, J = 8.2 Hz, H-3″,5″), 7.45 (d, 1H, $J_{5,6}$ = 8.1 Hz, H-6), 6.94 (d, 2H, J = 8.2 Hz, H-2″,6″), 6.14 (m, 1H, H-1′), 5.59 (d, 1H, $J_{5,6}$ = 8.1 Hz, H-5), 5.38 (m, 1H, H-2′), 4.39 (m, 1H, H-3′), 4.14 (m, 1H, ^2J = 15.9 Hz, J_{NHCH} = 6.4 Hz, NC*H*H), 4.08 (m, 1H, $^2J_{5′a,5′b}$ = 13.0 Hz, $J_{4′,5′a}$ = 3.3 Hz, H-5′a), 4.02 (m, 1H, ^2J = 15.9 Hz, J_{NHCH} = 5.5 Hz, NCH*H*), 3.94 (m, 1H, $^2J_{5′a,5′b}$ = 13.0 Hz, $J_{4′,5′b}$ = 2.7 Hz, H-5′b), 3.86 (m, 1H, H-4′), 1.10–0.93 (m, 28H, Pr^i). ^{13}C NMR (DMSO-d_6, δ): 163.0 (C4), 154.9 (O*C*O), 150.0 (C2), 140.9 (C6), 139.3 (C1″), 137.0 (2C, C3″,5″), 129.0 (2C, C2″,6″), 101.3 (C5), 92.4 (C4″), 81.2 (C1′), 78.8 (C4′), 76.1 (C2′), 72.7 (C3′), 60.7 (C5′), 43.2 (N*C*H$_2$), 17.3, 17.2, 17.1 (2C), 16.9, 16.8 (2C), 16.7 (*C*H$_3$), 12.8, 12.4, 12.2, 11.9 (Si*C*).

General Procedure for the Preparation of 2′-*O*-[3(4)-(Pyren-1-ylethynyl)phenylmethylaminocarbonyl]-3′,5′-*O*-(tetraisopropyldisiloxan-1,3-diyl)uracil-1-β-D-arabinofuranosides (3a,b). To a solution of 2′-*O*-(3(4)-iodobenzylaminocarbonyl)-3′,5′-*O*-(tetraisopropyldisiloxan-1,3-diyl)uracil-1-β-D-arabinofuranoside **2a**(**2b**) (1.49 g, 2.0 mmol), 1-ethynylpyrene (588 mg, 2.4 mmol) and triethylamine (560 μL, 4.0 mmol) in DMF (40 mL) $Pd(PPh_3)_4$ (116 mg, 0.10 mmol) and CuI (38 mg, 0.20 mmol) were subsequently added, and the mixture was stirred under argon for 16 h. After completion of conversion of the starting nucleoside **2** (monitoring by TLC in EtOAc), the mixture was poured into $CHCl_3$ (150 mL). The resulting solution was washed with 3% EDTA-Na_2 (4 × 100 mL) and water (4 × 100 mL), dried over Na_2SO_4, and evaporated to dryness. The residue was purified by chromatography on a silica gel column (150 g) with a step gradient of MeOH (0→3%) in $CHCl_3$ (v/v) as the mobile phase to give 1-PEPy derivatives **3a**,**b** as yellow amorphous foams. Compounds were dissolved in DCM (5 mL), and the solution was added dropwise to hexane (50 mL), the solid precipitated was filtered off, washed with hexane, and dried *in vacuo*.

2′-*O*-[3-(Pyren-1-ylethynyl)phenylmethylaminocarbonyl]-3′,5′-*O*-(tetraisopropyldisiloxan-1,3-diyl)uracil-1-β-D-arabinofuranoside (3a). Yield 1.60 g (95%), yellow amorphous solid, R_f 0.46 (EtOAc–toluene, 1:1 v/v). MALDI-TOF HRMS: m/z = 866.3266 $[M + Na]^+$, calcd for $[C_{47}H_{53}N_3O_8Si_2 + Na]^+$ 866.3263. ^{1}H NMR (DMSO-d_6, δ): 11.37 (s, 1H, H-3), 8.61 (d, 1H, $J_{9‴,10‴}$ = 9.1 Hz, H-10‴), 8.37 (m, 3H, H-6‴,8‴,9‴), 8.33 (m, 1H, $J_{2‴,3‴}$ = 8.0 Hz, H-3‴), 8.26 (m, 2H, H-2‴,5‴), 8.23 (m, 1H, $J_{4‴,5‴}$ = 8.9 Hz, H-4‴), 8.14 (apparent t, 1H, $J_{6‴,7‴}$ = $J_{7‴,8‴}$ = 7.6 Hz, H-7‴), 7.97 (m, 1H, OCON*H*), 7.64 (d, 1H, J = 7.6 Hz), 7.61 (s, 1H), 7.49 (d, 1H, J = 8.0 Hz) (H-6, H-2″, H-4″), 7.44 (apparent t, 1H, J = 7.6 Hz, H-5″), 7.23 (d, 1H, J = 7.6 Hz, H-6″), 6.15 (br.s, 1H, H-1′), 5.60 (d, 1H, $J_{5,6}$ = 8.2 Hz, H-5), 5.46 (m, 1H, H-2′), 4.38 (m, 1H, H-3′), 4.28 (m, 1H, ^2J = 15.9 Hz, J_{NHCH} = 6.4 Hz, NC*H*H), 4.17 (m, 1H, ^2J = 15.9 Hz, J_{NHCH} = 5.8 Hz, NCH*H*), 4.07 (m, 1H, $^2J_{5′a,5′b}$ = 12.8 Hz, $J_{4′,5′a}$ = 3.0 Hz, H-5′a), 3.92 (m, 1H, $^2J_{5′a,5′b}$ = 12.8 Hz, $J_{4′,5′b}$ = 2.4 Hz, H-5′b), 3.86 (m, 1H, H-4′), 1.07–0.87 (m, 28H, Pr^i). ^{13}C NMR (DMSO-d_6, δ): 163.0 (C4), 154.9 (O*C*O), 150.1 (C2), 140.3 (C1″), 140.2 (C6), 131.2 (C10a‴), 131.1 (C3a‴), 130.9 (C5a‴), 130.6 (C8a‴), 130.0 (2C, C2″, C4″), 129.6 (C2‴), 128.9 (2C, C9‴, C5″), 128.5 (C4‴), 127.4 (C5‴), 127.3 (C6″), 126.8 (C7‴), 126.0 (2C, C6‴, C8‴), 125.0 (C3‴), 124.8 (C10′′), 123.7 (C10b‴), 123.5 (C10c‴), 122.4 (C3″), 116.8 (C1‴), 101.4 (C5), 95.2 (Cb), 88.2 (Ca), 80.4 (C1′), 78.7 (C4′), 75.9 (C2′), 72.5 (C3′), 60.6 (C5′), 43.5 (N*C*H$_2$), 17.3, 17.2, 17.1 (2C), 16.8 (3C), 16.7 (*C*H$_3$), 12.8, 12.4, 12.2, 11.8 (Si*C*).

2′-*O*-[4-(Pyren-1-ylethynyl)phenylmethylaminocarbonyl]-3′,5′-*O*-(tetraisopropyldisiloxan-1,3-diyl)uracil-1-β-D-arabinofuranoside (3b). Yield 1.58 g (93%), yellow amorphous solid, R_f = 0.43 (EtOAc–toluene, 1:1 v/v). MALDI-TOF HRMS: m/z= 866.3223 $[M + Na]^+$, calcd for $[C_{47}H_{53}N_3O_8Si_2 + Na]^+$ 866.3263. ^{1}H NMR (DMSO-d_6, δ): 11.44 (s, 1H, H-3), 8.63 (d, 1H, $J_{9‴,10‴}$ = 9.1 Hz, H-10‴), 8.44–8.20 (m, 7H, H-2‴–6‴,8‴,9‴), 8.14 (apparent t, 1H, $J_{6‴,7‴}$ = $J_{7‴,8‴}$ = 7.6 Hz, H-7‴), 7.96 (m, 1H, OCON*H*), 7.71 (d, 2H, $J_{2″,3″}$= $J_{5″,6″}$= 8.1 Hz, H-3″, H-5″), 7.48 (d, 1H, $J_{5,6}$ = 8.0 Hz, H-6), 7.27 (d, 2H, $J_{2″,3″}$ = $J_{5″,6″}$ = 8.1 Hz, H-2″, H-6″), 6.17 (m, 1H, H-1′), 5.64 (d, 1H, $J_{5,6}$ = 8.0 Hz, H-5), 5.42 (m, 1H, H-2′), 4.43 (m, 1H, H-3′), 4.29 (m, 1H, ^2J = 15.9 Hz, J_{NHCH} = 6.4 Hz, NC*H*H), 4.16 (m, 1H, ^2J = 15.9 Hz, J_{NHCH} = 5.5 Hz, NCH*H*), 4.10 (m, 1H, $^2J_{5′a,5′b}$ = 13.1 Hz, $J_{4′,5′a}$ = 3.4 Hz, H-5′a), 3.95 (m, 1H, $^2J_{5′a,5′b}$ = 13.1 Hz, $J_{4′,5′b}$ = 2.7 Hz, H-5′b), 3.88 (m, 1H, H-4′), 1.12–0.92 (m, 28H, Pr^i). ^{13}C NMR (DMSO-d_6, δ): 163.1 (C4), 155.0 (O*C*O), 150.1 (C2), 140.4 (C1″), 140.3 (C6), 131.6 (2C, C3″, C5″), 131.1 (C10a‴), 131.0 (C3a‴), 130.9 (C5a‴), 130.6 (C8a‴), 129.6 (C2‴), 128.9 (C9‴), 128.4 (C4‴), 127.3 (C5‴), 127.0 (2C, C2″, C6″), 126.8 (C7‴), 126.0 (2C, C6‴, C8‴), 125.0 (C3‴), 124.9 (C10′′), 123.8 (C10b‴), 123.5 (C10c‴), 120.8 (C4″), 116.9 (C1‴), 101.4 (C5), 95.4 (Cb), 88.0 (Ca), 81.0 (C1′), 78.6 (C4′), 75.9 (C2′), 72.6 (C3′), 60.6 (C5′), 43.6 (N*C*H$_2$), 17.3, 17.2 (3C), 16.9 (3C), 16.7 (*C*H$_3$), 12.9, 12.4, 12.2, 11.9 (Si*C*).

General Procedure for the Preparation of 2′-*O*-[3(4)-(Pyren-1-ylethynyl)phenylmethylaminocarbonyl]uracil-1-β-D-arabinofuranosides (4a,b). To a solution of 2′-*O*-[3(4)-(pyren-1-ylethynyl)phenylmethylaminocarbonyl]-3′,5′-*O*-(tetraisopropyldisiloxan-1,3-diyl)uracil-1-β-D-arabinofuranoside **3a**(**3b**) (1.69 g, 2 mmol) in THF (5 mL), Et_3N·3HF (0.814 mL, 5 mmol) was added, and the mixture was kept at room temperature overnight. The mixture was diluted with $CHCl_3$ (20 mL), and the title compound was precipitated by addition of Et_2O (20 mL). The solid was filtered off, washed with $CHCl_3$ (15 mL) and Et_2O (2 × 20 mL), and dried *in vacuo* to afford the pure nucleoside **4a**(**4b**).

2′-*O*-[3-(Pyren-1-ylethynyl)phenylmethylaminocarbonyl]-uracil-1-β-D-arabinofuranoside (4a). Yield 1.14 g (95%), yellow crystals, R_f 0.32 (MeOH–toluene, 1:9 v/v), mp 118–121 °C (96% aq ethanol). MALDI-TOF HRMS: m/z = 624.1757 $[M + Na]^+$, calcd for $[C_{35}H_{27}N_3O_7 + Na]^+$ 624.1741. ^{1}H NMR (DMSO-d_6, δ): 11.31 (s, 1H, H-3), 8.63 (d, 1H, $J_{9‴,10‴}$ = 9.1 Hz, H-10‴), 8.39 (m, 3H, H-6‴,8‴,9‴), 8.33 (m, 1H, $J_{2‴,3‴}$ = 8.2 Hz, H-3‴), 8.29 (m, 1H, H-2‴), 8.27 (m, 1H, H-5‴), 8.23 (m, 1H, $J_{4‴,5‴}$ = 8.9 Hz, H-4‴), 8.15 (apparent t, 1H, $J_{6‴,7‴}$ = $J_{7‴,8‴}$ = 7.6 Hz, H-7‴), 7.94 (m, 1H, OCON*H*), 7.65 (m, 3H, H-6, H-2″, H-4″), 7.46 (apparent t, 1H, J = 7.6 Hz, H-5″), 7.25 (d, 1H, J = 7.6 Hz, H-6″), 6.18 (d, 1H, J = 4.9 Hz, H-1′), 5.75 (d, 1H, $J_{3′,OH}$ = 4.9 Hz, 3′-O*H*), 5.62 (d, 1H, $J_{5,6}$ = 8.0 Hz, H-5), 5.09 (m, 1H, H-2′), 5.01 (t, 1H, $J_{5′,OH}$ = 5.5 Hz, 5′-O*H*), 4.23 (m, 2H, NHCH_2), 4.14 (m, 1H, H-3′), 3.80 (m, 1H, H-4′), 3.73–3.59 (m, 2H, H-5′). ^{13}C NMR (DMSO-d_6, δ): 163.1 (C4), 154.9 (O*C*O), 150.1 (C2), 141.6 (C6), 140.1 (C1″), 131.2 (C10a‴), 131.1 (C3a‴), 130.8 (C5a‴), 130.6 (C8a‴), 130.1 (2C, C2″, C4″), 129.7 (C2‴), 129.0 (2C, C5″, C9‴), 128.5 (C4‴), 127.5 (C5‴), 127.3 (C6″), 126.9 (C7‴), 126.1 (3C, C6‴, C8‴), 125.0 (C3‴), 124.9 (C10′′), 123.7 (C10b‴), 123.5 (C10c‴), 122.4 (C3″), 116.8 (C1‴), 100.9 (C5), 95.2 (Cb), 88.3 (Ca), 83.9 (C4′), 82.9 (C1′), 77.2 (C2′), 73.0 (C3′), 60.2 (C5′), 43.6 (N*C*H$_2$).

2′-*O*-[4-(Pyren-1-ylethynyl)phenylmethylaminocarbonyl]-uracil-1-β-D-arabinofuranoside (4b). Yield 1.12 g (93%), yellow crystals, R_f 0.30 (MeOH–toluene, 1:9 v/v), mp 114–115 °C (96% aq ethanol). MALDI-TOF HRMS: m/z = 624.1722 $[M + Na]^+$, calcd for $[C_{35}H_{27}N_3O_7 + Na]^+$ 624.1741. ^{1}H NMR

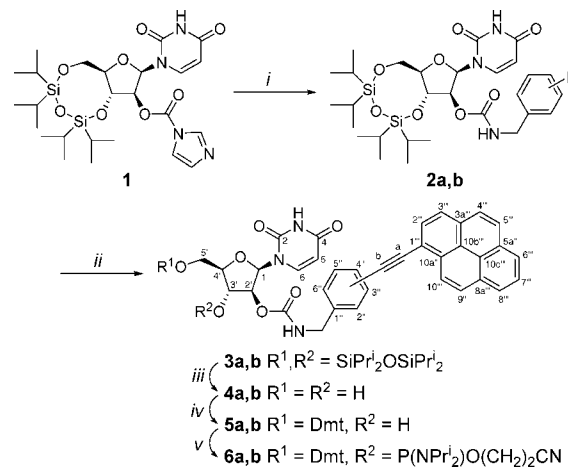
(DMSO-d_6, δ): 11.38 (s, 1H, H-3), 8.63 (d, 1H, $J_{9''',10'''}$ = 8.9 Hz, H-10‴), 8.37 (m, 3H, H-6‴,8‴,9‴), 8.33 (m, 1H, $J_{2''',3'''}$ = 8.0 Hz, H-3‴), 8.27 (m, 2H, H-2‴,5‴), 8.23 (m, 1H, $J_{4''',5'''}$ = 8.9 Hz, H-4‴), 8.15 (apparent t, 1H, $J_{6''',7'''} = J_{7''',8'''}$ = 7.6 Hz, H-7‴), 7.94 (m, 1H, OCON*H*), 7.72 (d, 2H, $J_{2'',3''} = J_{5'',6''}$ = 8.1 Hz, H-3″, H-5″), 7.65 (d, 1H, $J_{5,6}$ = 8.2 Hz, H-6), 7.27 (d, 2H, $J_{2'',3''} = J_{5'',6''}$ = 8.1 Hz, H-2″, H-6″), 6.19 (d, 1H, J = 5.2 Hz, H-1′), 5.75 (d, 1H, $J_{3',OH}$ = 4.9 Hz, 3′-O*H*), 5.65 (d, 1H, $J_{5,6}$ = 8.2 Hz, H-5), 5.11 (m, 1H, H-2′), 5.02 (t, 1H, $J_{5',OH}$ = 5.6 Hz, 5′-O*H*), 4.32 (m, 1H, ^2J = 10.4 Hz, J_{NHCH} = 4.8 Hz, NHC*H*H), 4.19–4.10 (m, 2H, NHCH*H*, H-3′), 3.80 (m, 1H, H-4′), 3.73–3.59 (m, 2H, H-5′). ^{13}C NMR (DMSO-d_6, δ): 163.2 (C4), 155.0 (O*C*O), 150.1 (C2), 141.6 (C6), 140.4 (C1″), 131.6 (2C, C3″, C5″), 131.1 (C10a‴), 131.0 (C3a‴), 130.9 (C5a‴), 130.6 (C8a‴), 129.6 (C2‴), 128.9 (C9‴), 128.4 (C4‴), 127.3 (C5‴), 127.0 (2C, C2″, C6″), 126.8 (C7‴), 126.0 (2C, C6‴, C8‴), 125.0 (C3‴), 124.9 (C10′″), 123.8 (C10b‴), 123.5 (C10c‴), 120.8 (C4″), 116.8 (C1‴), 101.0 (C5), 95.4 (Cb), 88.0 (Ca), 83.6 (C4′), 82.8 (C1′), 77.2 C2′), 72.8 (C3′), 60.1 (C5′), 43.6 (N*C*H$_2$).

General Procedure for the Preparation of 5′-*O*-(4,4′-Dimethoxytrityl)-2′-*O*-[3(4)-(pyren-1-ylethynyl)phenylmethylaminocarbonyl]uracil-1-β-D-arabinofuranosides (5a,b). To a solution of 2′-*O*-[3(4)-(pyren-1-ylethynyl)phenylmethylaminocarbonyl]uracil-1-β-D-arabinofuranoside **4a**(**4b**) (1.004 g, 1.67 mmol) (twice evaporated with Py (2 × 20 mL), dissolved in dried pyridine (15 mL), and cooled to 0 °C), DmtCl (623 mg, 1.84 mmol) was added, and when TLC showed that the reaction was complete (ca. 6–8 h), the mixture was evaporated, diluted with EtOAc (200 mL), and washed with H_2O (200 mL), 5% $NaHCO_3$ (150 mL), H_2O (150 mL), dried, and evaporated. The residue was purified by chromatography on a silica gel column (100 g) with a step gradient of acetone (25→35%) in toluene + 1% NEt_3 v/v/v as the mobile phase to give 5′-*O*-Dmt-protected nucleosides **5a**(**5b**).

5′-*O*-(4,4′-Dimethoxytrityl)-2′-*O*-[3-(pyren-1-ylethynyl)-phenylmethylaminocarbonyl]uracil-1-β-D-arabinofuranoside (5a). Yield 1.28 g (85%), yellow foam, R_f 0.24 (acetone–toluene, 3:7 + 1% Et_3N v/v/v). ESI-TOF HRMS: m/z = 926.3032 $[M + Na]^+$, calcd for $[C_{56}H_{45}N_3O_9 + Na]^+$ 926.3048. ^{1}H NMR (DMSO-d_6, δ): 11.34 (s, 1H, H-3), 8.62 (d, 1H, $J_{9''',10'''}$ = 9.1 Hz, H-10‴), 8.42–8.21 (m, 7H, H-2‴-H-6‴, H-8‴, H-9‴), 8.15 (t, 1H, $J_{6''',7'''} = J_{7''',8'''}$ = 7.6 Hz, H-7‴), 7.87 (br.t, 1H, J = 5.8 Hz, OCON*H*), 7.65 (d, 1H, J = 7.6 Hz, H-4″), 7.63 (s, 1H, H-2″), 7.54 (d, 1H, J = 7.9 Hz, H-6), 7.45 (m, 1H, H-5″), 7.41–7.20 (m, 10H, Ar*H* (Dmt), H-6″), 6.88 (m, 4H, Ar*H* (Dmt)), 6.20 (d, 1H, J = 5.5 Hz, H-1′), 5.81 (d, 1H, $J_{3',OH}$ = 5.5 Hz, 3′-O*H*), 5.43 (d, 1H, $J_{5,6}$ = 8.2 Hz, H-5), 5.11 (m, 1H, H-2′), 4.28–4.15 (m, 3H, NHCH_2, H-3′), 3.89 (m, 1H, H-4′), 3.72 (s, 6H, CH_3), 3.39–3.27 (m, 2H, H-5′).

5′-*O*-(4,4′-Dimethoxytrityl)-2′-*O*-[4-(pyren-1-ylethynyl)-phenylmethylaminocarbonyl]uracil-1-β-D-arabinofuranoside (5b). Yield 1.28 g (85%), yellow foam, R_f 0.24 (acetone–toluene, 3:7 + 1% Et_3N v/v/v). ESI-TOF HRMS: m/z = 926.3057 $[M + Na]^+$, calcd for $[C_{56}H_{45}N_3O_9 + Na]^+$ 926.3048. ^{1}H NMR (DMSO-d_6, δ): 11.41 (s, 1H, H-3), 8.63 (d, 1H, $J_{9''',10'''}$ = 9.1 Hz, H-10‴), 8.42–8.21 (m, 7H, H-2‴-H-6‴, H-8‴, H-9‴), 8.15 (t, 1H, $J_{6''',7'''} = J_{7''',8'''}$ = 7.6 Hz, H-7‴), 7.88 (br.t, 1H, J = 6.0 Hz, OCON*H*), 7.71 (d, 2H, $J_{2'',3''} = J_{5',6''}$ = 8.0 Hz, H-3″, H-5″), 7.55 (d, 1H, $J_{5,6}$ = 8.2 Hz, H-6), 7.37–7.26 (m, 11H, Ar*H* (Dmt), H-2″, H-6″), 6.90 (m, 4H, Ar*H* (Dmt)), 6.22 (d, 1H, J = 5.5 Hz, H-1′), 5.82 (d, 1H, $J_{3',OH}$ = 5.5 Hz, 3′-O*H*), 5.46 (d, 1H, $J_{5,6}$ = 8.2 Hz, H-5), 5.12 (m, 1H, H-2′), 4.31 (m, 1H, ^2J = 16.2 Hz, J_{NHCH} = 6.5 Hz, NHC*H*H), 4.21–4.10 (m, 2H, NHCH*H*, H-3′), 3.89 (m, 1H, H-4′), 3.74 (s, 6H, CH_3), 3.40–3.28 (m, 2H, H-5′).

Scheme 1[a]



[a] Reagents and conditions: (*i*) 3- or 4-iodobenzylamine, THF, MeCN, reflux 40 h, 94% (**2a**), 84% (**2b**); (*ii*) 1-ethynylpyrene, $Pd(PPh_3)_4$, CuI, Et_3N, DMF, rt, 16 h, 95% (**3a**), 93% (**3b**); (*iii*) $Et_3N \cdot 3HF$, THF, overnight, 95% (**4a**), 93% (**4b**); (*iv*) DmtCl, pyridine, 0°C, 6–8 h, 85% (**5a**), 85% (**5b**); (*v*) $(Pr^i_2N)_2POCH_2CH_2CN$, CH_2Cl_2, 2 h, 92% (**6a**), 96% (**6b**).

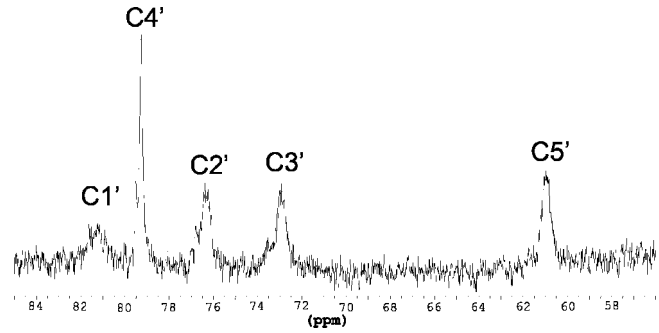


Figure 1. Sugar part of ^{13}C NMR spectrum of compound **2a** (125.7 MHz, 4096 scans).

General Procedure for the Preparation of 3′-*O*-(*N*,*N*-diisopropylamino-2-cyanoethoxyphosphinyl)-5′-*O*-(4,4′-dimethoxytrityl)-2′-*O*-[3(4)-(pyren-1-ylethynyl)phenylmethylaminocarbonyl]uracil-1-β-D-arabinofuranosides (6a,b). 5′-*O*-(4,4′-Dimethoxytrityl)-2′-*O*-[3-(pyren-1-ylethynyl)phenylmethylaminocarbonyl]uracil-1-β-D-arabinofuranoside **5a**(**5b**) (1.00 g, 1.1 mmol) was evaporated with dried DCM (2 × 20 mL), dissolved in dry DCM (25 mL), and *N*,*N*-diisopropylammonium tetrazolide (0.285 g, 1.66 mmol) and bis(*N*,*N*-diisopropylamino)-2-cyanoethoxyphosphine (0.527 mL, 1.66 mmol) were added under argon. The reaction mixture was stirred for 2 h, and then it was diluted with EtOAc (200 mL), washed with H_2O (200 mL), 5% $NaHCO_3$ (150 mL), and H_2O (150 mL), dried, and evaporated. The residue was purified by chromatography on a short silica gel column (50 g) with a step gradient of acetone (25→35%) in toluene + 1% NEt_3 v/v/v as the mobile phase to give phosphoramidites **6a**(**6b**).

3′-*O*-(*N*,*N*-Diisopropylamino-2-cyanoethoxyphosphinyl)-5′-*O*-(4,4′-dimethoxytrityl)-2′-*O*-[3-(pyren-1-ylethynyl)phenylmethylaminocarbonyl]uracil-1-β-D-arabinofuranoside (6a). Yield 1.11 g (92%), yellow foam, R_f 0.52, 0.46 (acetone–toluene, 7:13 + 1% Et_3N v/v/v). ESI-TOF HRMS: m/z = 1126.4137 $[M + Na]^+$, calcd for $[C_{65}H_{62}N_5O_{10}P + Na]^+$ 1126.4126. ^{1}H NMR (MeCN-d_3, δ): 9.05 (br.s, 1H, H-3), 8.71 (m, 1H, H-10‴), 8.37–8.18 (m, 8H, H-2‴–H-6‴, H-8‴, H-9‴), 8.14 (t, 1H, $J_{6''',7'''} = J_{7''',8'''}$ = 7.7 Hz, H-7‴), 7.66 (m, 2H, H-6, H-4″), 7.55 (s, 1H, H-2″), 7.51–7.45 (m, 3H), 7.38–7.28 (m, 10H) (H-6, H-5″, H-6″, OCON*H*, Ar*H* (Dmt)), 6.90 (m, 4H, Ar*H* (Dmt)), 6.28

Table 2. Oligonucleotides Used in This Study[a]

#	sequence, 5′→3′	MALDI MS	calculated mass, $[M + H]^+$
ON1	CTCCCAGGCTCAAAT		
ON2	ATTTGAGCCTGGGAG		
ON3a	CTCCCAGGC**U**CAAAT	4852.1	4857.3
ON3b	CTCCCAGGC**U**CAAAT	4857.2	4857.3
ON4a	C**U**CCCAGGCTCAAAT	4854.4	4857.3
ON4b	C**U**CCCAGGCTCAAAT	4853.4	4857.3
ON5a	C**U**CCCAGGC**U**CAAAT	5212.2	5216.7
ON5b	C**U**CCCAGGC**U**CAAAT	5214.9	5216.7
ON6a	CTCCCAGGCTCAAA**U**CTGG	6108.7	6109.1
ON6b	CTCCCAGGCTCAAA**U**CTGG	6107.8	6109.1
ON7a	A**U**TTGAGCCTGGGAG	5004.9	5008.4
ON7b	A**U**TTGAGCCTGGGAG	5005.5	5008.4
ON8a	AT**U**TGAGCCTGGGAG	5007.7	5008.4
ON8b	AT**U**TGAGCCTGGGAG	5006.0	5008.4
ON9a	ATT**U**GAGCCTGGGAG	5006.0	5008.4
ON9b	ATT**U**GAGCCTGGGAG	5004.7	5008.4
ON10a	CCAGA**U**TTGAGCCTGGGAG	6228.2	6229.2
ON10b	CCAGA**U**TTGAGCCTGGGAG	6226.7	6229.2
ON11a	CCAGAT**U**TGAGCCTGGGAG	6228.2	6229.2
ON11b	CCAGAT**U**TGAGCCTGGGAG	6227.5	6229.2
ON12a	CCAGATT**U**GAGCCTGGGAG	6228.6	6229.2
ON12b	CCAGATT**U**GAGCCTGGGAG	6229.8	6229.2

[a] **U** - modified nucleoside **4a** (for oligonucleotide series **a**) or **4b** (for oligonucleotide series **b**).

Table 3. Thermal Stabilities of Modified Duplexes[a]

#	duplex	T_m (°C)	ΔT_m (°C)	ΔT_m/mod
ON1 × **ON2**	5′-CTC-CCA-GGC-**T**CA-AAT 3′-GAG-GGT-CCG-AGT-TTA	57.6		
ON3a × **ON2**	5′-CTC-CCA-GGC-**U**CA-AAT 3′-GAG-GGT-CCG-AGT-TTA	54.9	−2.7	−2.7
ON4a × **ON2**	5′-C**U**C-CCA-GGC-TCA-AAT 3′-GAG-GGT-CCG-AGT-TTA	54.5	−3.1	−3.1
ON5a × **ON2**	5′-C**U**C-CCA-GGC-**U**CA-AAT 3′-GAG-GGT-CCG-AGT-TTA	55.1	−2.5	−1.3
ON3b × **ON2**	5′-CTC-CCA-GGC-**U**CA-AAT 3′-GAG-GGT-CCG-AGT-TTA	49.6	−8.0	−8.0
ON4b × **ON2**	5′-C**U**C-CCA-GGC-TCA-AAT 3′-GAG-GGT-CCG-AGT-TTA	53.2	−4.4	−4.4
ON5b × **ON2**	5′-C**U**C-CCA-GGC-**U**CA-AAT 3′-GAG-GGT-CCG-AGT-TTA	47.3	−10.3	−5.2

[a] **U** - modified nucleoside **4a** (for oligonucleotide series **a**) or **4b** (for oligonucleotide series **b**).

(m, 1H, H-1′), 5.47 (m, 1H, H-5), 5.41–5.34 (m, 1H, H-2′), 4.63 (m, 0.55H), 4.51 (m, 0.45H) (H-3′, diastereomers), 4.41–4.28 (m, 2H, NCH_2), 4.15–4.08 (m, 1H, H-4′), 3.78 (m, 6H, CH_3), 3.73–3.42 (m, 6H, POCH_2, NC*H*, H-5′), 2.61 (m, 0.90H), 2.51 (t, 1.10H, $J = 6.0$ Hz) (CH_2CN, diastereomers), 1.30–1.04 (m, 12H, CHCH_3). ^{31}P NMR ($CDCl_3$, δ): 151.70, 150.99 (1:0.8).

3′-*O*-(*N,N*-Diisopropylamino-2-cyanoethoxyphosphinyl)-5′-*O*-(4,4′-dimethoxytrityl)-2′-*O*-[4-(pyren-1-ylethynyl)phenylmethylaminocarbonyl]uracil-1-β-D-arabinofuranoside (6b). Yield 1.16 g (96%), yellow foam, R_f 0.38, 0.26 (acetone–toluene, 7:13 + 1% Et_3N v/v/v). ESI-TOF HRMS: $m/z = 1126.4091$ $[M + Na]^+$, calcd for $[C_{65}H_{62}N_5O_{10}P + Na]^+$ 1126.4126. ^{1}H NMR (MeCN-d_3, δ): 9.05 (br.s, 1H, H-3), 8.40–8.19 (m, 7H, H-2‴-H-6‴, H-8‴, H-9‴), 8.15 (t, 1H, $J_{6‴,7‴} = J_{7‴,8‴} = 7.6$ Hz, H-7‴), 7.74 (m, 2H, H-3″, H-5″), 7.57–7.48 (m, 3H), 7.41–7.28 (m, 10H) (H-6, H-2″, H-6″, OCON*H*, Ar*H* (Dmt)), 6.92 (m, 4H, Ar*H* (Dmt)), 6.30 (m, 1H, H-1′), 5.50–5.34 (m, 2H, H-5, H-2′), 4.62 (m, 0.53 H), 4.52 (m, 0.47H) (H-3′, diastereomers), 4.42–4.25 (m, 2H, NCH_2), 4.19–4.08 (m, 1H, H-4′), 3.80 (m, 6H, CH_3), 3.72–3.40 (m, 6H, POCH_2, NC*H*, H-5′), 2.66 (t, 0.94H, $J = 6.1$ Hz), 2.56 (t, 1.06H, $J = 6.0$ Hz) (CH_2CN, diastereomers), 1.27–0.96 (m, 12H, CHCH_3). ^{31}P NMR ($CDCl_3$, δ): 151.57, 151.10 (1:0.9).

RESULTS AND DISCUSSION

The synthesis of reagents for placement of 1-PEPy in a major groove is shown on Scheme 1. The starting imidazolide **1** (*24*) was reacted with 3- or 4-iodobenzylamine to give 3′,5′-Markiewicz-protected iodobenzyl *ara*-uridine-2′-carbamates **2a**,**b**. 1-PEPy fluorochrome was assembled using Sonogashira coupling of iodobenzyl compounds with 1-ethynylpyrene (*47*). Nucleosides **3** contain 1-PEPy unit connected to the sugar part of nucleoside through meta (series **a**) and para (series **b**) positions of a phenyl ring. Silyl protection was removed with triethylamine trihydrofluoride to yield fluorescent nuclesides **4a**,**b** as crystalline solids. These were converted into phosphoramidite reagents using standard methods of nucleoside chemistry—5′-*O*-dimethoxytritylation and 3′-*O*-phosphitylation.

Suddenly, signals from C1′–C5′ and C6 carbons were missing in ^{13}C NMR spectra of 3′,5′-silyl Markiewicz-protected compounds **2a**,**b** and **3a**,**b**. In contrast, nucleosides **4a**,**b** gave normal C1′–C5′ and C6 signals in ^{13}C NMR. Therefore, we repeated

Table 4. Spectroscopic (λ^{abs}_{max}, λ^{fl}_{max}) and Photophysical (Φ_f, τ_f) Properties of Modified Oligonucleotide and Duplexes [a]

#	λ^{abs}_{max}, bands I, II (nm)	λ^{fl}_{max} (nm)	Φ_f	τ_1, (ns)	S_1, (%)	τ_2, (ns)	S_2, (%)	χ^2	$\langle\tau_f\rangle$, (ns)
ON3a	392, 372	402	0.22	0.88	27	2.96	73	1.143	2.40
ON3a × ON2	390, 371	406	0.10	0.59	60	2.19	40	1.040	1.23
ON4a	394, 372	404	0.32	0.88	23	2.64	77	1.022	2.23
ON4a × ON2	393, 371	408	0.09	0.50	82	2.39	18	1.045	0.84
ON3b	394, 372	403	0.16	0.60	35	2.50	65	0.996	1.83
ON3b × ON2	397, 375	408	0.23	0.88	44	2.68	56	1.051	1.89
ON4b	396, 374	404	0.28	0.79	25	2.48	75	1.162	2.06
ON4b × ON2	398, 375	409	0.12	0.59	69	1.77	31	1.047	0.96

[a] S_1 and S_2, contribution of τ_1 and τ_2 components in percentages; χ^2, statistical Pirson criterion associated with the fitted lifetime function and the experimental data; $\langle\tau_f\rangle = \Sigma S_i\tau_i/\Sigma S_i$, average fluorescence lifetime.

Table 5. Fluorescent Properties of *meta*- and *para*-1-PEPy Pairs Located in −1, −2, and −3 Zipper Modes

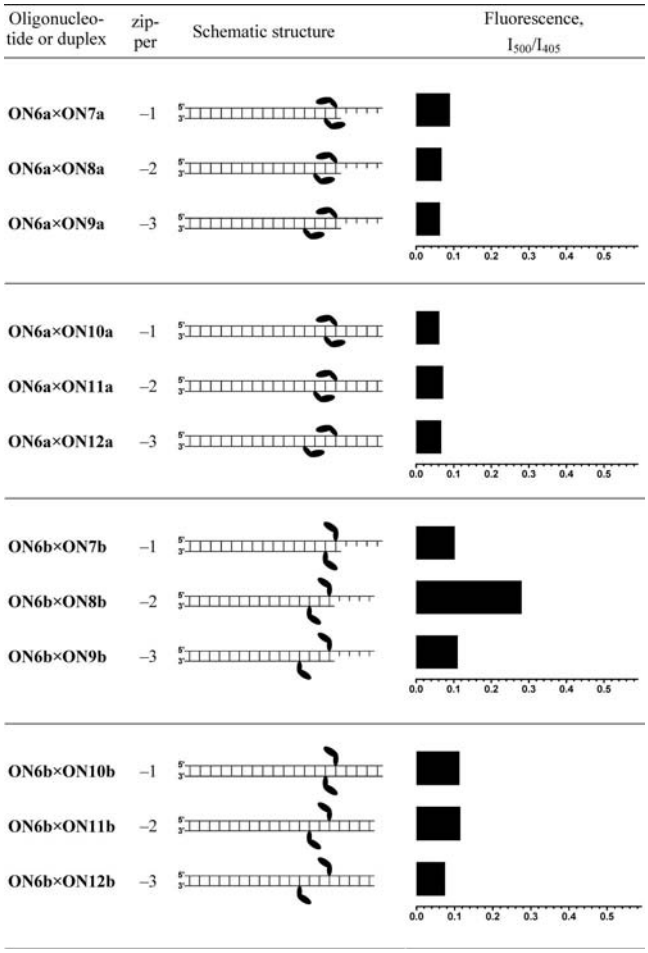
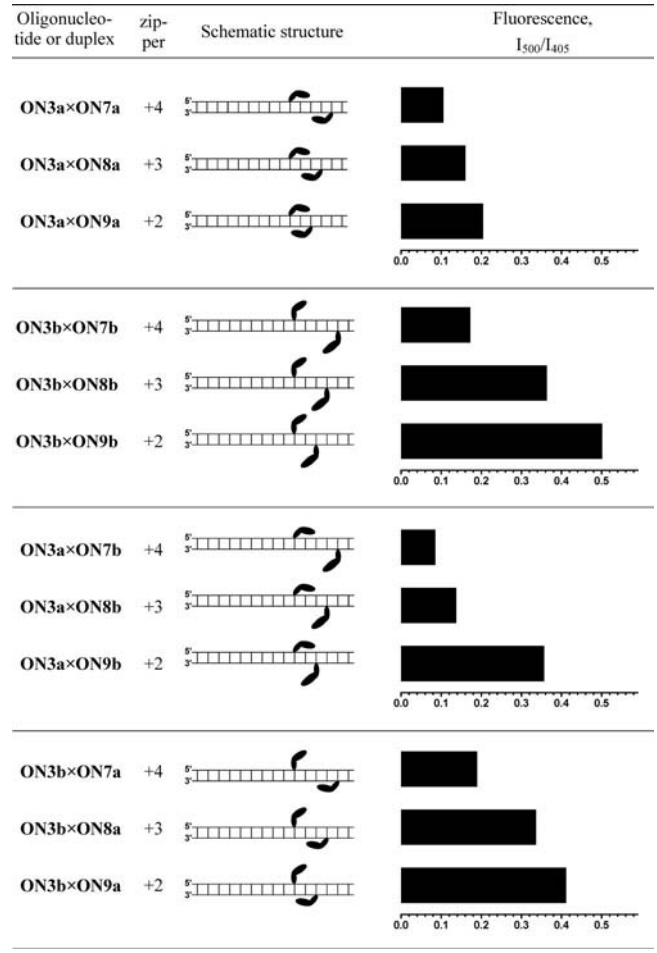


Table 6. Fluorescent Properties of *meta*- and *para*-1-PEPy Pairs Located in +2, +3, and +4 Zipper Modes



^{13}C NMR experiments for compounds **2a**,**b** and **3a**,**b** using 4096 scans. Indeed, broad (up to 200 Hz) signals appeared in expected regions (50–100 ppm for sugar carbons and 140 ppm for C6). Typical sugar carbon signals are shown on Figure 1. The signals gave normal cross-peaks in HMQC spectra and can be easily assigned. The nature of the observed effect is not clear. Evidently, two prerequisites—silyl Markiewicz group and aryl carbamate modification—contribute cooperatively in the unusual shielding of six carbon atoms in compounds **2a**,**b** and **3a**,**b**.

Phosphoramidites **6a**,**b** were used in automated oligonucleotide synthesis to prepare a series of modified oligonucleotides (Table 2) similar to those described for studies of pyrene excimer in DNA major groove (*24*).

It is known that 2′-carbamate modification destabilize dsDNA, but pyrene modification can relieve the negative carbamate influence (*20*, *24*), and *para*-1-PEPy-*ribo*-carbamate even displayed some stabilization of the DNA duplex (*49*). Thermal denaturation studies (Table 3) show that *meta*-1-PEPy-*arabino*-carbamate (series **a**) is similar to pyrene (*24*) in its ability to neutralize the negative carbamate effect. In contrast, PEPy in *para*-1-PEPy-*arabino*-carbamate (series **b**) has no influence on duplex stability: the resulting destabilization is similar to that from aliphatic carbamate (*24*). We speculate that, in the case

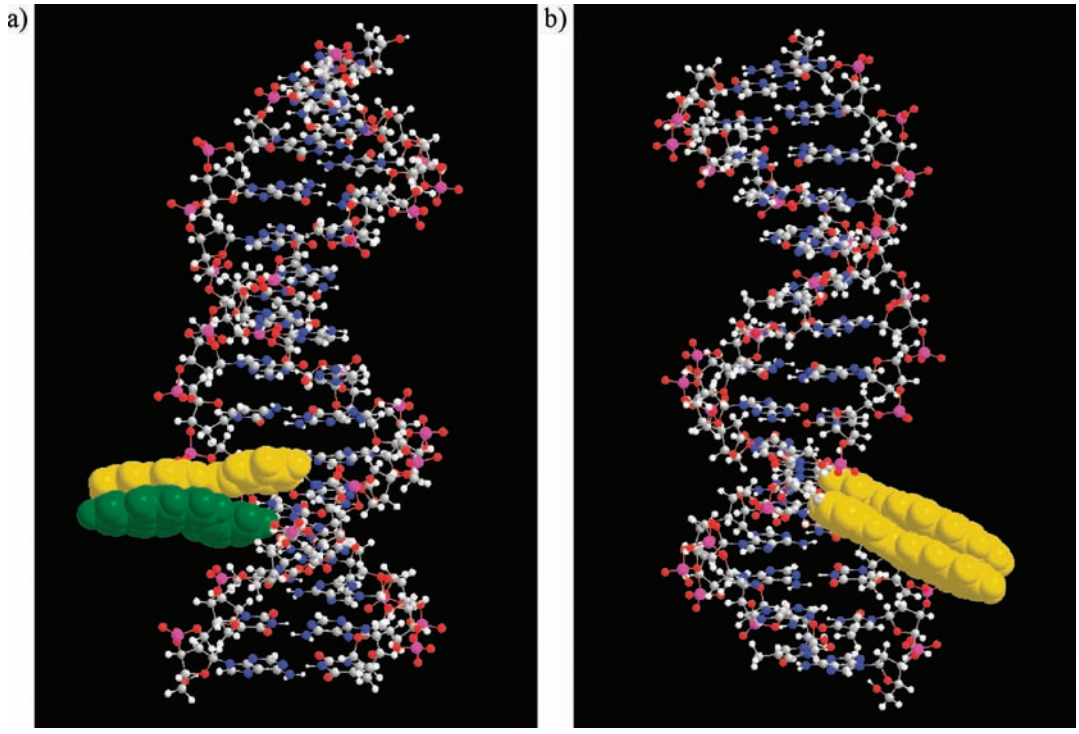


Figure 2. Molecular models of duplexes **ON3b**×**ON9a** (a) and **ON3b**×**ON9b** (b). 1-PEPy residues are shown in space-filling mode and marked in green (meta) and yellow (para attachment). Models constructed in HyperChem 7.5 and GaussView 3.0 with use of standard B-DNA parameters.

of *meta*-1-PEPy-*arabino*-carbamate modification, the aromatic residue fits the major groove of duplex, and in the case of *para*-modification, it is exposed in the environment. There are also no direct data for or against intercalation of PEPy residues into the DNA duplex. The intercalation of PEPy in fully matched duplexes is, however, highly unlikely because of excimer formation in +2 and +3 zipper modes (see below). On the other hand, in mismatched sequences, pyrene can probably replace a nonpairing nucleobase (*20*), and further studies would be useful for 1-PEPy.

Next, we determined spectral and photophysical properties of the *meta*- and *para*-1-PEPy labels as *arabino*-2′-carbamates (Table 4). There are minor variations in absorbances between single-stranded oligonucleotides and their duplexes. Hybridization causes a 4 nm bathochromic shift of fluorescence maximum in the **a** series and a 5 nm shift in the **b** series. The data show that 1-PEPy fluorescence kinetics in ss and dsDNA always fit to two exponential components with different lifetimes, and the average fluorescence lifetime is between 0.84 and 2.40 ns. This is approximately 2 orders of magnitude less than for pyrene derivatives. Not surpisingly, fluorescence quantum yields (9–32%) are much higher than typical quantum yields of pyrene fluorescence on DNA, except for pyrenoyl on amino-LNA (*60*). Hybridization causes a 2–3-fold decrease in average excited lifetime and emission quantum yield for conjugates **ON3a**, **ON4a**, and **ON4b**. In contast, Φ_f and $\langle\tau_f\rangle$ of 1-PEPy fluorochrome in **ON3b** slightly increased in the course of duplex formation.

Further, we studied the possibilities of PEPy interstrand excimer formation in DNA duplexes. In cases of excimer formation, the dye showed a broad emission band around 500 nm. We used the excimer-to-monomer fluorescence intensity ratio, I_{500}/I_{405}, as an excimer formation criterion. In the absence of excimer emission, I_{500}/I_{405} is approximately 0.1. First, we studied a "negative zipper" mode (Table 5). There was no detectable excimer fluorescence in continuous duplexes (**ON6**×**ON10**, **ON6**×**ON11**, **ON6**×**ON12**). In the case of truncated duplexes, an excimer was observed once, for −2 zipper mode in series **b** (**ON6b**×**ON8b**), probably resulting from duplex distortion. Interestingly, pyrene gave −1 zipper excimer in a similar case (*24*).

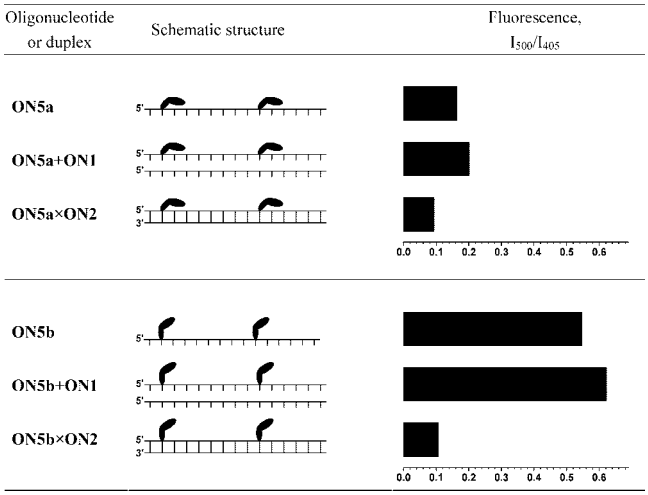
Then, we checked +2, +3, and +4 zippers for *meta*- and *para*- series of 1-PEPy pairs (Table 6). The intensity of excimer fluorescence always increased within the sequence +4 zipper < +3 zipper < +2 zipper. The weakest +2 excimer forms from two *meta*-PEPys, and the strongest from two *para*-compounds. All cases of combinations of **a** and **b** series were studied. The configuration **b** × **a** is always preferable for excimer formation than **a** × **b**. In cotrast to pyrene data (*24*), not only +2, but +3 and even weak +4 zipper excimers were observed in some cases. This can be easily explained by taking into account that the 1-PEPy molecule is approximately 1 nm longer than the pyrene one.

To confirm that the PEPy excimer can be formed in a major groove of a normal B-DNA duplex, molecular models were built (Figure 2). They showed, however, that stacked structures from two spatially accessible PEPy residues are not only located in a major groove, but considerably exposed in a solvent.

In addition, fluorescence data revealed that a doubly labeled oligonucleotide can form a metastable hairpin in aq solutions (Table 7). In the hairpin, two *para*-PEPys are located in close proximity and showed considerable excimer emission. The addition of the same nonlabeled sequence does not decrease the excimer fluorescence. Expectedly, the excimer completely disappears after hybridization with a complementary strand. Thus, the PEPy fluorochrome can be used for preparation of a "molecular beacon"-like excimer-forming probe.

To conclude, we report synthesis of meta and para derivatives of 1-phenylethynylpyrene (1-PEPy) *arabino*-uridine-2′-carbamates, their incorporation into oligonucleotides, spectral and photophysical properties in ss and dsDNA, and stuctural preferences for 1-PEPy major groove excimer. Although the excited lifetime of 1-PEPy derivatives on DNA is ca. 100-fold shorter compared to that of pyrene, PEPy molecules, being

Table 7. Fluorescent Properties of Oligonucleotides Doubly Labeled with *meta*- or *para*-1-PEPy Fluorochromes



located in +2, +3, and even in +4 zipper modes, are able to form a major groove or environmentally exposed interstrand excimer on the DNA duplex. The 1-PEPy excimer, more fastidious about the proximity of fluorochromes, could become a useful tool in structural studies of biomolecules.

ACKNOWLEDGMENT

We thank Maksim Kvach and Youri Habrus for oligonucleotide synthesis, Dmitry Alexeev for mass spectra, Larisa Grusintseva for technical assistance, and Zakhar Shenkarev for helpful advice with NMR spectra. This work was supported by the Russian Foundation for Basic Research (grant no. 06-03-32426).

LITERATURE CITED

(1) Birks, J. B. (1975) Excimers. *Rep. Prog. Phys. 38*, 903–974.
(2) Winnik, F. M. (1993) Photophysics of preassociated pyrenes in aqueous polymer solutions and in other organized media. *Chem. Rev. 93*, 587–614.
(3) Lehrer, S. S. (1997) Intramolecular pyrene excimer fluorescence: a probe of proximity and protein conformational change. *Meth. Enzymol. 278*, 286–295.
(4) Ebata, K., Masuko, M., Ohtani, H., and Kashiwasake-Jibu, M. (1995) Nucleic acid hybridization accompanied with excimer formation from two pyrene-labeled probes. *Photochem. Photobiol. 62*, 836–839.
(5) Paris, P. L., Langenhan, J. M., and Kool, E. T. (1998) Probing DNA sequences in solution with a monomer-excimer fluorescence color change. *Nucleic Acids Res. 26*, 3789–3793.
(6) Masuko, M., Ohtani, H., Ebata, K., and Shimadzu, A. (1998) Optimization of excimer-forming two-probe nucleic acid hybridization method with pyrene as a fluorophore. *Nucleic Acids Res. 26*, 5409–5416.
(7) Dioubankova, N. N., Malakhov, A. D., Stetsenko, D. A., and Korshun, V. A. (2004) Detection of point mutations using pyrene-labeled DNA probes. *Russ. Chem. Bull., Int. Ed., 53*, 463–470.
(8) Hrdlicka, P. J., Babu, B. R., Sørensen, M. D., and Wengel, J. (2004) Interstrand communication between 2′-*N*-(pyren-1-yl)-methyl-2′-amino-LNA monomers in nucleic acid duplexes: directional control and signalling of full complementarity. *Chem. Commun.* 1478–1479.
(9) Bichenkova, E. V., Gbaj, A., Walsh, L., Savage, H. E., Rogert, C., Sardarian, A. R., Etchells, L. L., and Douglas, K. T. (2007) Detection of nucleic acids *in situ*: novel oligonucleotide analogues for target-assembled DNA-mounted exciplexes. *Org. Biomol. Chem. 5*, 1039–1051.
(10) Balakin, K. V., Korshun, V. A., Prokhorenko, I. A., Maleev, G. V., Kudelina, I. A., Gontarev, S. V., and Berlin, Y. A. (1997) A new reagent for labeling macromolecules: an activated derivative of the pyrene bichromophore with excimer fluorescence. *Russ. J. Bioorg. Chem. 23*, 28–36.
(11) Lewis, F. D., Zhang, Y., and Letsinger, R. L. (1997) Bispyrenyl excimer fluorescence: A sensitive oligonucleotide probe. *J. Am. Chem. Soc. 119*, 5451–5452.
(12) Kostenko, E., Dobrikov, M., Pyshnyi, D., Petyuk, V., Komarova, N., Vlassov, V., and Zenkova, M. (2001) 5′-bis-pyrenylated oligonucleotides displaying excimer fluorescence provide sensitive probes of RNA sequence and structure. *Nucleic Acids Res. 29*, 3611–3620.
(13) Yamana, K., Iwai, T., Ohtani, Y., Sato, S., Nakamura, M., and Nakano, H. (2002) Bis-pyrene-labeled oligonucleotides: sequence specificity of excimer and monomer fluorescence changes upon hybridization with DNA. *Bioconjugate Chem. 13*, 1266–1273.
(14) Yamana, K., Ohtani, Y., Nakano, H., and Saito, I. (2003) Bis-pyrene labeled DNA aptamer as an intelligent fluorescent biosensor. *Bioorg. Med. Chem. Lett. 13*, 3429–3431.
(15) Okamoto, A., Ichiba, T., and Saito, I. (2004) Pyrene-labeled oligodeoxynucleotide probe for detecting base insertion by excimer fluorescence emission. *J. Am. Chem. Soc. 126*, 8364–8365.
(16) Novopashina, D. S., Stetsenko, D. A., Totskaya, O. S., Repkova, M. N., and Venyaminova, A. G. (2005) 2′-Bis-pyrene modified oligonucleotides: sensitive fluorescent probes of nucleic acids structure. *Nucleosides, Nucleotides Nucleic Acids 24*, 729–734.
(17) Yamana, K., Fukunaga, Y., Ohtani, Y., Sato, S., Nakamura, M., Kim, W. J., Akaike, T., and Maruyama, A. (2005) DNA mismatch detection using a pyrene–excimer-forming probe. *Chem. Commun.* 2509–2511.
(18) Balakin, K. V., Korshun, V. A., Mikhalev, I. I., Maleev, G. V., Malakhov, A. D., Prokhorenko, I. A., and Berlin, Y. A. (1998) Conjugates of oligonucleotides with polyaromatic fluorophores as promising DNA probes. *Biosens. Bioelectron. 13*, 771–778.
(19) Christensen, U. B., and Pedersen, E. B. (2002) Intercalating nucleic acids containing insertions of 1-O-(1-pyrenylmethyl)glycerol: stabilisation of dsDNA and discrimination of DNA over RNA. *Nucleic Acids Res. 30*, 4918–4925.
(20) Korshun, V. A., Stetsenko, D. A., and Gait, M. J. (2002) Novel uridin-2′-yl carbamates: synthesis, incorporation into oligodeoxyribonucleotides, and remarkable fluorescence properties of 2′-pyren-1-ylmethylcarbamate. *J. Chem. Soc., Perkin Trans. 1*, 1092–1104.
(21) Mahara, A., Iwase, R., Sakamoto, T., Yamana, K., Yamaoka, T., and Murakami, A. (2002) Bispyrene-conjugated 2′-O-methyloligonucleotide as a highly specific RNA-recognition probe. *Angew. Chem. Int. Ed. 41*, 3648–3650.
(22) Michel, J., Bathany, K., Schmitter, J.-M., Monti, J.-P., and Moreau, S. (2002) New ligand combinations for the efficient stabilization of short nucleic acid hairpins. *Tetrahedron 58*, 7975–7982.
(23) Christensen, U. B., and Pedersen, E. B. (2003) Intercalating nucleic acids with pyrene nucleotide analogues as next-nearest neighbors for excimer fluorescence detection of single-point mutations under nonstringent hybridization conditions. *Helv. Chim. Acta 86*, 2090–2097.
(24) Dioubankova, N. N., Malakhov, A. D., Stetsenko, D. A., Gait, M. J., Volynsky, P. E., Efremov, R. G., and Korshun, V. A. (2003) Pyrenemethyl ara-uridine-2′-carbamate: a strong interstrand excimer in the major groove of a DNA duplex. *ChemBioChem 4*, 841–847.
(25) Bryld, T., Højland, T., and Wengel, J. (2004) DNA-selective hybridization and dual strand invasion of short double-stranded DNA using pyren-1-ylcarbonyl-functionalized 4′-C-piperazinomethyl-DNA. *Chem. Commun.* 1064–1065.

(26) Fujimoto, K., Shimizu, H., and Inouye, M. (2004) Unambiguous detection of target DNAs by excimer–monomer switching molecular beacons. *J. Org. Chem. 69*, 3271–3275.
(27) Hrdlicka, P. J., Kumar, T. S., and Wengel, J. (2005) Targeting of mixed sequence double-stranded DNA using pyrene-functionalized 2′-amino-α-L-LNA. *Chem. Commun.*, 4279–4281.
(28) Nagatoishi, S., Nojima, T., Juskowiak, B., and Takenaka, S. (2005) A pyrene-labeled G-quadruplex oligonucleotide as a fluorescent probe for potassium ion detection in biological applications. *Angew. Chem. Int. Ed. 44*, 5067–5070.
(29) Kawai, K., Yoshida, H., Sugimoto, A., Fujitsuka, M., and Majima, T. (2005) Kinetics of transient end-to-end contact of single-stranded DNAs. *J. Am. Chem. Soc. 127*, 13232–13237.
(30) Trkulja, I., Biner, S. M., Langenegger, S. M., and Häner, R. (2007) A molecular probe for the detection of homopurine sequences. *ChemBioChem 8*, 25–27.
(31) Kumar, T. S., Wengel, J., and Hrdlicka, P. J. (2007) 2′-N-(Pyren-1-yl)acetyl-2′-amino-α-L-LNA: synthesis and detection of single nucleotide mismatches in DNA and RNA targets. *ChemBioChem 8*, 1122–1125.
(32) Rippe, K., Fritsch, V., Westhof, E., and Jovin, T. M. (1992) Alternating d(G-A) sequences form a parallel-stranded DNA homoduplex. *EMBO J. 11*, 3777–3786.
(33) Mohammadi, S., Slama-Schwok, A., Leger, G., El Manouni, D., Shchyolkina, A., Leroux, Y., and Taillandier, E. (1997) Triple helix formation and homologous strand exchange in pyrene-labeled oligonucleotides. *Biochemistry 36*, 14836–14844.
(34) Seela, F., He, Y., and Wei, C. (1999) Parallel-stranded oligonucleotide duplexes containing 5-methylisocytosine-guanine and isoguanine-cytosine base pairs. *Tetrahedron 55*, 9481–9500.
(35) Kawai, K., Yoshida, H., Takada, T., Tojo, S., and Majima, T. (2004) Formation of pyrene dimer radical cation at the internal site of oligodeoxynucleotides. *J. Phys. Chem. B 108*, 13547–13550.
(36) Langenegger, S. M., and Häner, R. (2004) Excimer formation by interstrand stacked pyrenes. *Chem. Commun.* 2792–2793.
(37) Filichev, V. V., Vester, B., Hansen, L. H., and Pedersen, E. B. (2005) Easily denaturing nucleic acids derived from intercalating nucleic acids: thermal stability studies, dual duplex invasion and inhibition of transcription start. *Nucleic Acids Res. 33*, 7129–7137.
(38) Langenegger, S. M., and Häner, R. (2006) Selectivity in DNA interstrand-stacking. *Bioorg. Med. Chem. Lett. 16*, 5062–5065.
(39) Malinovskii, V. L., Samain, F., and Häner, R. (2007) Helical arrangement of interstrand stacked pyrenes in a DNA framework. *Angew. Chem., Int. Ed. 46*, 4464–4467.
(40) Trkulja, I., and Häner, R. (2007) Monomeric and heterodimeric triple helical DNA mimics. *J. Am. Chem. Soc. 129*, 7982–7989.
(41) Trkulja, I., and Häner, R. (2007) Triple-helix mediated excimer and exciplex formation. *Bioconjugate Chem. 18*, 289–292.
(42) Samain, F., Malinovskii, V. L., Langenegger, S. M., and Häner, R. (2007) Spectroscopic properties of pyrene-containing DNA mimics. *Bioorg. Med. Chem. 15*, in press (doi: 10.1016/j.bmc.2007.04.052).
(43) Céci, I., Filichev, V. V., and Pedersen, E. B. (2007) Stabilization of parallel triplexes by twisted intercalating nucleic acids (TINAs) incorporating 1,2,3-triazole units and prepared by microwave-accelerated click chemistry. *Chem.—Eur. J. 13*, 6379–6386.
(44) Shimadzu, A., Ohtani, H., Ohuchi, S., Sode, K., and Masuko, M. (1998) Perylene excimer formation by excimer-forming two-probe nucleic acid hybridization method. *Nucl. Acids Symp. Ser. 39*, 45–46.
(45) Chiba, J., Takeshima, S., Mishima, K., Maeda, H., Nanai, Y., Mizuno, K., and Inouye, P. (2007) Artificial DNAs based on alkynyl *C*-nucleosides as a superior scaffold for homo- and heteroexcimer emissions. *Chem.—Eur. J. 13*, in press (doi: 10.1002/chem.200700559).
(46) Korshun, V. A., Prokhorenko, I. A., Gontarev, S. V., Skorobogatyi, M. V., Balakin, K. V., Manasova, E. V., Malakhov, A. D., and Berlin, Y. A. (1997) New pyrene derivatives for fluorescent labeling of oligonucleotides. *Nucleosides Nucleotides 16*, 1461–1464.
(47) Malakhov, A. D., Malakhova, E. V., Kuznitsova, S. V., Grechishnikova, I. V., Prokhorenko, I. A., Skorobogatyi, M. V., Korshun, V. A., and Berlin, Y. A. (2000) Synthesis and fluorescent properties of 5-(1-pyrenylethynyl)-2′-deoxyuridine-containing oligodeoxynucleotides. *Russ. J. Bioorg. Khim. 26*, 34–44.
(48) Malakhov, A. D., Skorobogatyi, M. V., Prokhorenko, I. A., Gontarev, S. V., Kozhich, D. T., Stetsenko, D. A., Stepanova, I. A., Shenkarev, Z. O., Berlin, Y. A., and Korshun, V. A. (2004) 1-(Phenylethynyl)pyrene and 9,10-bis(phenylethynyl)anthracene, useful fluorescent dyes for DNA labeling: excimer formation and energy transfer. *Eur. J. Org. Chem.*, 1298–1307.
(49) Dioubankova, N. N., Malakhov, A. D., Shenkarev, Z. O., and Korshun, V. A. (2004) Oligonucleotides containing new fluorescent 1-phenylethynylpyrene and 9,10-bis(phenylethynyl)anthracene uridine-2′-carbamates: synthesis and properties. *Tetrahedron 60*, 4617–4626.
(50) Prokhorenko, I. A., Malakhov, A. D., Kozlova, A. A., Momynaliev, K., Govorun, V. M., and Korshun, V. A. (2006) Phenylethynylpyrene-labeled oligonucleotide probes for excimer fluorescence SNP analysis of 23S rRNA gene in clarithromycin-resistant *Helicobacter pylori* strains. *Mutat. Res. 599*, 144–51.
(51) Filichev, V. V., and Pedersen, E. B. (2005) Stable and selective formation of Hoogsteen-type triplexes and duplexes using twisted intercalating nucleic acids (TINA) prepared via postsynthetic Sonogashira solid-phase coupling reactions. *J. Am. Chem. Soc. 127*, 14849–14858.
(52) Maeda, H., Maeda, T., Mizuno, K., Fujimoto, K., Shimizu, H., and Inouye, M. (2006) Alkynylpyrenes as improved pyrene-based biomolecular probes with the advantages of high fluorescence quantum yields and long absorption/emission wavelengths. *Chem.—Eur. J. 12*, 824–831.
(53) Filichev, V. V., Nielsen, M. C., Bomholt, N., Jessen, C. H., and Pedersen, E. B. (2006) High thermal stability of 5′−5′-linked alternate Hoogsteen triplexes at physiological pH. *Angew. Chem. Int. Ed. 45*, 5311–5315.
(54) Coulson, D. R. (1972) Tetrakis(triphenylphosphine)palladium(0). *Inorg. Synth. 13*, 121–124.
(55) Bannwarth, W., and Trzeciak, A. (1987) A simple and effective chemical phosphorylation procedure for biomolecules. *Helv. Chim. Acta 70*, 175–186.
(56) Caruthers, M. H., Barone, A. D., Beaucage, S. L., Dodds, D. R., Fisher, E. F., McBride, L. J., Matteucci, M., Stabinsky, Z., and Tang, J.-Y. (1987) Chemial synthesis of deoxyoligonucleotides by the phosphoramidite method. *Methods Enzymol. 154*, 287–313.
(57) Gottlieb, H. E., Kotlyar, V., and Nudelman, A. (1997) NMR chemical shifts of common laboratory solvents as trace impurities. *J. Org. Chem. 62*, 7512–7515.
(58) Borisevich, E. A., Knyukshto, V. N., Kozyrev, A. N., and Solov'ev, K. N. (1993) The influence of external bromine atoms on photophysical processes and NH-shift in porphyrine macrocycle. *Opt. Spectrosc. 74*, 129–135.
(59) Melhuish, W. H. (1961) Quantum efficiencies of fluorescence of organic substances: effect of solvent and concentration of the fluorescent solute. *J. Phys. Chem. 35*, 229–235.
(60) Hrdlicka, P. J., Babu, B. R., Sørensen, M. D., Harrit, N., and Wengel, J. (2005) Multilabeled pyrene-functionalized 2′-amino-LNA probes for nucleic acid detection in homogeneous fluorescence assays. *J. Am. Chem. Soc. 127*, 13293–13299.

BC700280H

Screening of Paclitaxel-Binding Molecules from a Library of Random Peptides Displayed on T7 Phage Particles Using Paclitaxel-Photoimmobilized Resin

Sota Aoki,[†] Kengo Morohashi,[‡,||] Takashi Sunoki,[‡,§] Kouji Kuramochi,[†] Susumu Kobayashi,[‡,§] and Fumio Sugawara*[,†,‡]

Department of Applied Biological Science, Genome and Drug Research Center, and Faculty of Pharmaceutical Sciences, Tokyo University of Science, 2641 Yamazaki, Noda, Chiba 278-8510, Japan. Received July 29, 2007; Revised Manuscript Received September 19, 2007

Paclitaxel (Taxol), an effective anticancer agent, is known to bind to tubulin and induce tubulin polymerization. Several other binding proteins of paclitaxel, such as Bcl-2, heat shock proteins, and NSC-1, have also been reported. Here, we describe a T7 phage-based display to screen for paclitaxel-binding molecules from a random peptide library using paclitaxel-photoimmobilized TentaGel resin. Specific phage particles that bind the paclitaxel-immobilized resin were obtained. Among them, two phage clones included the same consensus amino acid sequence (KACGRTRVTS). Analysis of the protein database using BLAST revealed that a portion of this sequence is conserved in the zinc finger domain of human NFX1. Binding affinity of paclitaxel against the partial recombinant protein of NFX1 (424aa–876aa) was confirmed by pull-down assays and surface plasmon resonance analyses.

INTRODUCTION

Paclitaxel is a highly effective antineoplastic agent used in the treatment of a wide variety of tumors (Figure 1) (*1*).

There are numerous reports in the literature describing the candidate binding proteins of paclitaxel. Paclitaxel promotes tubulin polymerization by binding and stabilizing microtubules (*2–7*). Heat shock proteins 70 and 90 were identified to be paclitaxel-binding proteins from a macrophage cell lysate using biotinylated paclitaxel (*8*). An antiapoptotic protein, Bcl-2, and a neuronal calcium sensor protein, NSC-1, were also recognized as paclitaxel-binding proteins by phage display technology (*9–11*). Bcl-2 was identified from a library of random phage-displayed peptides by an analysis of affinity-selected peptides (*9, 10*). NCS-1 was also found to be a paclitaxel-binding protein using a similar selection procedure from a human brain cDNA phage library (*11*) .

Phage display is one of the best methods for the identification of drug-binding proteins (*12*). Indeed, this method has been successfully applied to the determination of drug-binding proteins for FK506 (*13*), doxorubicin (*14*), HBC (*15*) and paclitaxel (*9–11*). Moreover, phage display technology can be used to efficiently identify the specific drug-binding site within the identified protein (*9, 10*). The combination of screening a library of phage-displayed peptides and the analysis of affinity-selected peptides is anticipated to become a powerful tool for identifying drug-binding sites (*16–21*).

Screening phage display libraries generally entails immobilizing the drug onto a solid surface (*22*). Immobilization of the drug onto an affinity matrix is usually achieved by the formation of a biotinylated derivative, which can then be applied to a streptavidin-coated matrix. Conventional immobilization requires the presence of desirable functional groups within the drug molecule as well as a multistep process to prepare the biotinylated derivatives. However, photoimmobilization makes it possible to covalently immobilize drugs onto the solid surface without the need for derivatization. Kanoh and ourselves have reported the affinity purification of proteins using affinity matrices, in which small molecules were photoimmobilized by photoreaction (*23–25*). Because the photoreaction proceeds in a functional group-independent manner, the molecules are immobilized onto the solid surface in a nonoriented fashion. Thus, photoimmobilization can be a useful tool for the comprehensive analysis of drug-binding proteins.

In this study, paclitaxel-binding molecules were identified from a library of random peptides displayed on T7 phage particles using paclitaxel-photoimmobilized TentaGel.

EXPERIMENTAL PROCEDURES

Materials. Paclitaxel was purchased from Hoechst Marion Roussel (now known as Aventis Pharmaceuticals Inc., Paris, France). Photoaffinity beads were prepared as described previously, and paclitaxel was immobilized on the beads according to the literature (*24*). A 10.2 mg quantity of paclitaxel was used for immobilization onto 30 mg of photoaffinity beads. Photoaffinity beads, which were treated after UV irradiation in the absence of paclitaxel, were used for the control resin. The T7 phage library displaying a random 12 amino acid peptide was prepared as described in our previous paper (*21*). A sensor chip of CM5 and an Amine Coupling Kit were obtained from Biacore AB (now known as GE Healthcare, Amersham, UK). A mouse IgG-κ monoclonal antibody for anti-6His was purchased from Sigma-Aldrich (St Louis, MO). An alkaline phosphatase conjugated with a goat IgG antibody was obtained from Santa Cruz Biotechnology (Santa Cruz, CA).

Panning the Phage Library. A modified version of the biopanning technique given in the manufacturer's instructions (Novagen, Madison, WI) was used in this study (*21*). One milliliter of a random 12 amino acid T7 display library (approximately 9×10^{10} pfu) was added to 100 μg of pretreated

* Corresponding author. Phone: +81-4-7124-1501(ext. 3400). Fax: +81-4-7123-9757., E-mail: sugawara@rs.noda.tus.ac.jp.

[†] Department of Applied Biological Science.

[‡] Genome and Drug Research Center.

[§] Faculty of Pharmaceutical Sciences.

[||] Present address: Department of Plant Cell and Molecular Biology, The Ohio State University, 106 Carmack Road, Columbus, OH 43210.

10.1021/bc700287v CCC: $37.00 © 2007 American Chemical Society
Published on Web 11/03/2007

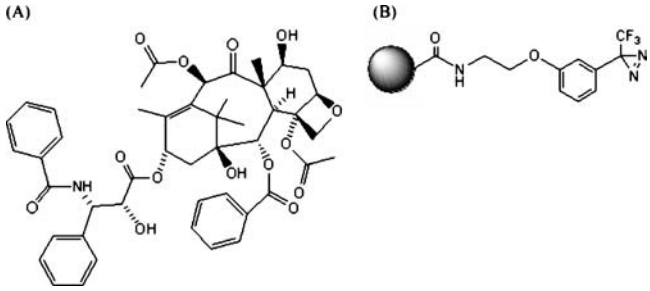


Figure 1. (A) Structure of paclitaxel. (B) Structure of photoaffinity beads (TentaGel).

resin in TBS (50 mM Tris-HCl at pH 8.0 and 150 mM NaCl) for 12 h at room temperature. After incubation at 4 °C for 12 h, the resin was precipitated and the phage solution removed. The resin was then washed 25 times with 1 mL of TBST buffer (50 mM Tris-HCl at pH 8.0, 150 mM NaCl, and 0.1% Tween 20). Adsorbed phage particles were subsequently removed from the resin by 15 min of incubation in 1% SDS solution. The eluted phage particles were amplified after infection into *Escherichia coli* strain BLT5615 as host cells. The amplified phage was applied to the resin, and subsequent rounds of panning were carried out. The titer was monitored at each panning step. The eluted phage solution at each step was used for the immediate infection of 3 mL of host cells. Incubation with shaking at 37 °C was continued until lysis was observed. Amplified phage titers of each round were estimated to be 1–6 $\times$ 10^{10} pfu. After each round, the eluted phage titers were compared to those of the previous round.

Validation of Interaction between Monoclonal T7 Phage and Ligand. The T7 phage mixture from the final round of panning was incubated at low density on an LB plate containing 50 μg/mL of carbenicillin. Individual plaques were randomly picked and diluted into 50 μL of phage extraction buffer (20 mM Tris-HCl at pH 8.0, 100 mM NaCl, and 6 mM $MgSO_4$). To validate the affinity between monoclonal phage and paclitaxel-immobilized resin, the isolated phage particles were amplified with *E. coli* BLT5615. Binding, washing, and elution procedures were carried out as described in the screening procedure. Blank resin, without immobilized paclitaxel, was prepared, and the eluted phage titers were compared to those of the binding phage.

PCR Amplification and Sequencing. For PCR amplification of DNA fragments and sequencing, 5 μL of T7 phage solution was used as the template. T7 UP new (5′-TGCTAACTTC-CAAGCGGACC-3′) and T7 DOWN (5′-AACCCCTCAAGAC-CCGTTA-3′) primers, corresponding to the sequences in the phage vector that flanks the insert, were used to amplify inserted DNA sequences. PCR was performed in a 20 μL of reaction mixture with gene Taq polymerase (Nippon gene, Tokyo, Japan). Amplified fragments were analyzed by agarose gel (1.5%) electrophoresis. After purification of the amplified fragments by ethanol-precipitation, and DNA fragments were sequenced using PRISM BigDye terminator ready reaction kit (version 3.1) (PE-ABI, Foster City, CA) and applied to an ABI3100 sequencer (Applied Biosystems, Foster City, CA). The BLAST program was used for comparing the obtained sequences with sequences in the protein database (*27*).

Protein Expression and Purification. DNA encoding a fragment of the NFX1-type zinc finger domain of NFX1 (424aa–876aa) was amplified from a human leukocyte cDNA library using the forward primer (5′-GGGAATTCTGTGGT-GAGGTTTGTAGAAAG-3′) and the reverse primer (5′-CCCTCGAGACATTCACACTGTAGCTCTACC-3′). The amplified DNA was then cloned into a derivative of pET22b, constructed by insertion of the *E. coli* DsbC chaperone/disulfide isomerase gene. A truncated form of NFX1 (424–876) containing an N-terminal His-tag was coexpressed with DsbC after induction with 0.4 mM IPTG at 16 °C. The harvested cells were lysed by sonication, and cell debris was removed by centrifugation at 12000*g* for 10 min. The crude extract was then loaded onto a Ni-NTA column, and the bound proteins were eluted with a solution of 200 mM imidazole (pH 7.4). The eluted proteins were then dialyzed against PBST buffer.

Table 1. Results of Biopanning with Paclitaxel Immobilized on Photoaffinity Beads

round (th)	input[a] ($\times$ 10^{10})	output[a] ($\times$ 10^{5})	recovery[b] ($\times$ 10^{-6})	enrichment (per round)	enrichment (total)
1	5.00	1.00	2.00		1.00
2	3.20	0.68	2.13	1.07	1.07
3	1.70	1.20	7.06	3.31	3.53

[a] Plaque forming unit. [b] Output/input.

Pull down Assay and Western Blotting. Small molecule pull-down assays were carried out as described previously (*24*). NFX1 adsorbed on the resin was detected using the Bradford assay and Western blot analysis. Western blotting was performed with a mouse IgG monoclonal antibody for anti-6His (used at 1:1000 dilution). A goat antimouse IgG conjugated with alkaline phosphatase was used as the secondary antibody at a dilution of 1:1000. Immunoreacted signals were detected with nitro blue tetrazolium and 5-bromo-4-chloro-3-indolyl phosphate.

Surface Plasmon Resonance (SPR) Analysis. SPR analysis was performed on a BIAcore X (Biacore AB, Sweden, now known as GE Healthcare). The truncated form of NFX1 (424aa–876aa) with an N-terminal His-tag was covalently immobilized to a hydrophilic carboxymethylated dextran matrix on a CM5 sensor chip using a standard amine coupling reaction in 10 mM CH_3CO_2Na (pH 4.0) at a level of approximately 7500 resonance units (RU). Binding analysis was carried out in PBST buffer (20 mM, 150 mM NaCl, 10 μM $ZnCl_2$, and 0.001% Tween 40) containing 8% DMSO at a flow late 20 μL/min. Appropriate concentrations of paclitaxel were injected over the flow cell. The bulk effects of DMSO were subtracted by using reference surfaces. To derive binding constants, data was analyzed by means of global fitting by using the BIA evaluation software (version 3.1).

RESULTS

Selection of T7 Phage Associated with Paclitaxel. A library of random peptides displayed on phage particles was screened for the ability to specifically bind paclitaxel-immobilized resin. Phage particles having affinity for paclitaxel-immobilized resin were efficiently enriched (Table 1). The ratio of eluted phage titer increased in each successive round of screening. We anticipated that the eluted phage particles from the third round would display high affinity for paclitaxel. Thus, 32 phage clones were randomly selected from plates and then sequenced. To estimate the binding specificities of the peptides displayed on phage particles, each single phage clone was amplified, and the resultant phage clones were used for a binding assay (Table 2). The affinity titers of eight selected phage clones (numbers 13, 15, 18, 20, 21, 26, 27, and 29) from paclitaxel-immobilized resins were more than 6.7 times higher than those of the background phage from the control resin. Phage clones 18, 20, and 21 displayed a series of peptides of more than 12 amino acids and had specific affinity for paclitaxel immobilized on the resin. The sequence of clones 20 and 21 were identical for the C-terminal 10 amino acid residues (KACGRTRVTS).

Recombinant Protein Interacts with Paclitaxel. A homology search using the BLAST program demonstrated that the amino acid sequence of the consensus peptide (KACGRTRVTS)

Table 2. Affinity Titers and Selected Amino Acid Sequences of Peptide Displayed on the Phage after the Third Round of Biopanning[a]

clone	sequence	relative enrichment ratio[b]
#13	VYCVL*	12.5
#15	FLFGLFFFTCRS*	9.2
#18	FRIVTCATCVILKAFMGWHYHISRSRS*	11.3
#20	CDSFARSCVRGVGIMKACGRTRVTS*	49.0
#21	LFTDMALSGKVLVKACGRTRVTS*	6.7
#26	LFLCCMGFHGPL*	27.3
#27	LLLSHVSLVCRL*	34.4
#29	CFLLSFVVLGYD*	7.3

[a] Estimation of binding specificities for selected phage clones by affinity titers. The titers of the input phages were adjusted to 1.0×10^{10} cfu/mL. Binding assays were performed on paclitaxel-immobilized resins (paclitaxel +) or control resins (paclitaxel –). [b] The relative enrichment ratio is determined as the output phages from paclitaxel-beads divided by the output phages from control beads.

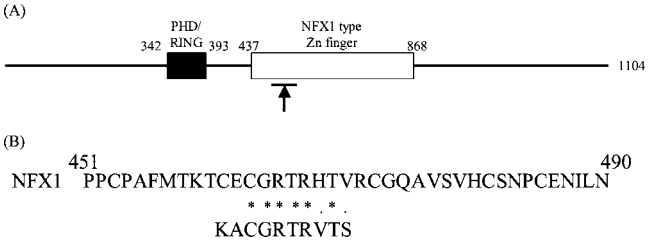


Figure 2. Alignment between obtained amino acid sequence and human NFX1. (A) The similarity site (marked by upward arrow/underline) is contained in the NFX1-type zinc finger domain of NFX1. This region affects the DNA binding of NFX1. (B) The obtained amino acid sequence indicated similarity to C463-T469 of human NFX1. The numbers show amino acid positions in NFX1. The asterisk indicates identical amino acids.

is similar to a part of the zinc finger domain of human NFX1 (Figure 2) (*20, 21, 26*). This region affects the DNA binding of NFX1 (*28*).

A truncated recombinant NFX1 (424aa–876aa) was overexpressed and purified for the binding assays (*28*). The recombinant NFX1 (424aa–876aa) contains an amino acid sequence similar to that of the consensus sequence selected by phage screening.

The amount of truncated NFX1 (424aa–876aa) bound to the paclitaxel-immobilized resin (10 mg) or control resin (10 mg) was determined using the Bradford assay by monitoring absorbance at 595 nm (Figure 3). Approximately 30% of the applied recombinant NFX1 (424aa–876aa) was recovered from the palitaxel-immobilized resin. The recovered NFX1 (424aa–876aa) from the palitaxel-immobilized resin was detected by Western blotting using an anti-6His monoclonal antibody (Figure 3). By contrast, only a small amount of NFX1 bound to the control resin.

Binding analysis between paclitaxel and the truncated form of NFX1 (424aa–876aa) was performed by surface plasmon resonance. The recombinant NFX1 (424aa–876aa) was fixed on a CM5 sensor chip using an amine coupling reaction. The dissociation constant of paclitaxel with NFX1 (424aa–876aa) was determined to be 8×10^{-7} M, using BIA evaluation 3.1 software (Figure 4A). Specificity of binding was confirmed by analyzing the interaction of NFX1 (424aa–876aa) with doxorubicin and ampicillin, whose structures are different from that of paclitaxel. Unlike paclitaxel, neither doxorubicin nor ampicillin showed significant interaction with immobilized NFX1 (424aa–876aa) (Figure 4B).

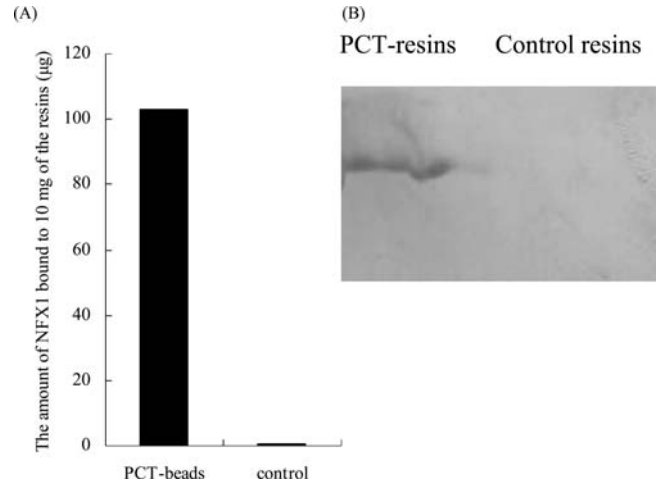


Figure 3. Binding analysis of the recombinant NFX1 (424aa–876aa) with the paclitaxel-immobilized resins (PCT-resins) and control resins (Control resins). (A) Quantitative analysis of proteins bound to 10 mg of resin using the Bradford assay. Note that 348 μg of the recombinant NFX1 (424aa–876aa) was applied to the binding assay. (B) Western blot analysis of the His-tagged zinc finger domain of NFX1 bound to the resin.

DISCUSSION

Identification of binding partners to biologically active small molecules is an important step in elucidating the corresponding mechanism of action. Phage display is a versatile method for the detection of small molecule-binding proteins. One advantage of phage display is that the technique can also be used to identify binding sites within the target protein itself. Indeed, several binding sites for bioactive compounds have been elucidated by screening with phage display.

In the conventional method of phage display, small molecules are usually converted into the biotinylated derivatives and immobilized on a streptavidin-coated matrix. Preparation of biotinylated derivatives can be a laborious and time-consuming process. Furthermore, biotinylation of a small molecule might interfere with binding to the cognate binding partner(s). By contrast, immobilization of small molecules on a solid support using UV irradiation can be readily achieved without the need for derivatization. Using this procedure, the molecules will be immobilized in a nonoriented manner. Therefore, photoimmobilization can eliminate serious problems associated with biotinylation, which could potentially abolish the functional groups required for protein binding.

In the present study, we isolated phage clones that show affinity for paclitaxel-photoimmobilized TentaGel resin. Two of the selected clones have the consensus amino acid sequence KACGRTRVTS. A comparison of this short peptide sequence with the protein database revealed similarity to residues 463–469 of human NFX1. NFX1 is known to be a transcriptional regulator of the human major histocompatibility complex (MHC) class II gene, although it is also expressed in MHC class II-negative cells (*28*). Analysis of NFX1 shows that it possesses a central DNA-binding domain that is subdivided into repeated Cys-rich motifs (437–868 amino acids of NFX1). The motif is similar to, but distinct from, LIM and RING finger domains. NFX1 binds to the conserved X-box motif of MHC class II genes via a repeated zinc finger domain and represses their expression to regulate the duration of an inflammatory response (*28*). The RING-type zinc finger domain also interacts with a ubiquitin-conjugating enzyme (E2) and facilitates ubiquitination (*29*).

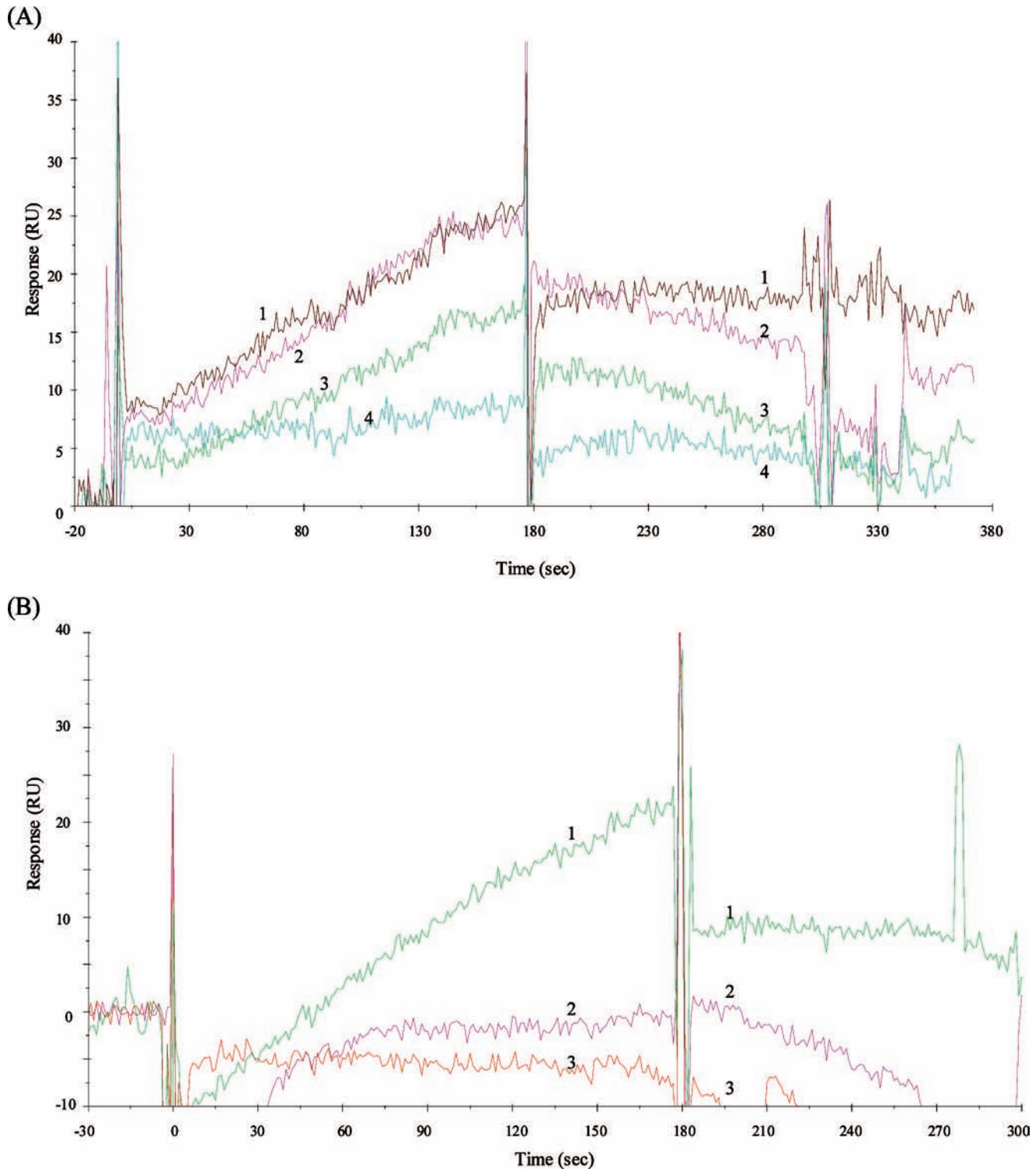


Figure 4. SPR analysis of the binding between paclitaxel and partial recombinant NFX1 (424aa–876aa). Analytes in PBST buffer (containing 8% DMSO) were injected over flow cells on the immobilized NFX1 (424aa–876aa). The background resulting from an injection of running buffer was subtracted from the data before plotting. Response units (RU) were generated by subtraction of the background signal generated simultaneously on the control flow cell. (A) Binding of paclitaxel on immobilized NFX (424aa–876aa) at various concentrations (1, 7.5 μM; 2, 5 μM; 3, 2.5 μM; 4, 1.25 μM). Kinetic studies were performed with BIA evaluation software. (B) Estimation of binding specificity. A 5 μM solution of paclitaxel (1), doxorubicin (2), or ampicillin (3) was loaded.

Interaction between paclitaxel and the partial recombinant NFX1 (424aa–876aa) was confirmed by pull-down assays and surface plasmon resonance analyses. Recombinant NFX1 (424aa–876aa) selectively binds the pactitaxel-photoimmobilized resin by the pull-down assay. Paclitaxel bound the immobilized recombinant NFX1 (424aa–876aa) with a dissociation constant (K_d) of 8×10^{-7} M. By contrast, doxorubicin and ampicillin did not show significant interaction with the immobilized NFX1 (424aa–876aa). Sengupta et al. measured the binding of *N*-dibenzoyl-*N*-[3-(dimethylamino)benzoyl]-paclitaxel, a fluorescent derivative of paclitaxel, to tubulin. Data from these experiments gave an equilibrium dissociation constant of 4.9×10^{-5} M for the binding of paclitaxel to unpolymerized tubulin (*30*). Rodi et al. reported that paclitaxel binds to Bcl-2 with a dissociation

constant of 4×10^{-7} M (*9*). Although we have not examined whether paclitaxel influences the activities of NFX1 and its resultant effects, these results verify that NFX1 is one of the binding proteins of paclitaxel. Interestingly, our experiments established that paclitaxel binds to the zinc finger domain of NFX1, which requires NFX1–DNA interaction. Considering that NFX1 functions as a repressor, paclitaxel might inhibit the repressive effect of NFX1 for MHC class II gene expression, suggesting that paclitaxel activates MHC class II gene expression. Indeed, this hypothesis is consistent with a previous report, which demonstrated that paclitaxel induced MHC class II genes in dendritic cells (*31*).

A homology search of our selected consensus peptide by BLAST gives other candidate binding proteins of paclitaxel. For example, tropoelastin has an amino acid sequence (^{779}KACGRKR^{785}) similar to that of the consensus sequence in the C-terminal region (*32*). Furthermore, placenta-specific 1-like protein precursor contains a segment of sequence (^{76}CGIRTRVVS^{84}) that displays similarity to the selected peptide sequence (*33*). Surprisingly, none of our isolated clones showed similarity to known paclitaxel-binding proteins such as tubulin, heat shock proteins, Bcl-2, or NCS-1. One possible explanation for these results is that our original phage library was not sufficiently diverse. The titer of the primary clones in the library used in this study was 4×10^6 pfu/mL (*21*). The use of a high diversity library would provide a greater amount of information on paclitaxel-binding peptides. Alternatively, interaction of paclitaxel with proteins such as tubulin may involve multiple binding motifs, which despite being far apart in the primary amino acid sequence are spatially close together in the three-dimensional structure. Indeed, paclitaxel binds to a pocket in the second globular domain of β-tubulin facing the microtubule. The use of a highly diverse library would also contribute to more comprehensive information on the binding peptides.

In summary, we have used a T7 phage display screening method to identify paclitaxel-binding molecules from a random peptide library using paclitaxel-photoimmobilized resin. Two of the selected clones have the consensus peptide KACGRTRVTS, which displays similarity to a part of the zinc finger domain of human NFX1. Binding between paclitaxel and recombinant NFX1 was confirmed by pull-down and SPR analyses. Our results demonstrate that this methodology can be used to identify novel binding proteins of small molecules. Studies on the biological effect of paclitaxel on human NFX1 as well as further application and optimization of this methodology are currently underway.

LITERATURE CITED

(1) Mekhail, T. M., and Markmann, M. (2002) Palitaxel in cancer therapy. *Expert. Opin. Pharmacother. 3*, 755–766.

(2) Schiff, P. B., Fant, J., and Horwitz, S. B. (1979) Promotion of microtuble assembly in vitro by taxol. *Nature 277*, 665–667.

(3) Schiff, P. B., and Horwitz, S. B. (1980) Taxol stabilizes microtubles in mouse fibroblast cells. *Proc. Natl. Acad. Sci. U.S.A. 77*, 1561–1565.

(4) Nogales, E., Wolf, S. G., and Downing, K. H. (1998) Structure of the $\alpha\beta$ tubulin dimer by electron crystallography. *Nature 391*, 199–203.

(5) Amos, L. A., and Löwe, J. (1999) How Taxol stabilizes microtubule structure. *Chem. Biol. 3*, R65–R69.

(6) Rao, S., Orr, G. A., Chaudary, A. G., Kingston, D. G., and Horwitz, S. B. (1995) Characterization of the taxol binding site on the microtubule. 2-(m-Azidobenzoyl)taxol photolabels a peptide (amino acids 217–231) of β-tubulin. *J. Biol. Chem. 270*, 20235–20238.

(7) Rao, S., He, L., Chakravary, S., Ojima, I., Orr, G. A., and Horwitz, S. B. (1999) Characterization of the Taxol binding site on the microtubule. Identification of Arg(282) in beta-tubulin as the site of photoincorporation of a 7-benzophenone analogue of Taxol. *J. Biol. Chem. 274*, 37990–37994.

(8) Byrd, C. A., Bornmann, W., Edrjument-Bromage, H., Tempst, P., Pavletich, N., Rosen, N., Nathan, C., and Ding, A. (1999) Heat shock protein 90 mediates macrophage activation by Taxol and bacterial lipopolysaccharide. *Proc. Natl. Acad. Sci. U.S.A. 96*, 5645–5650.

(9) Rodi, D. A., Janes, R. W., Sanganee, H., Holton, R. A., Wallace, B. A., and Makowski, L. (1999) Screening of a library of phage-displayed peptides identifies human bcl-2 as a taxol-binding protein. *J. Mol. Biol. 285*, 197–203.

(10) Rodi, R. J., Agoston, G. E., Manon, R., Lapcevich, R., Green, S. J., and Makowski, L. (2001) Identification of small molecule binding sites within proteins using phage display technology. *Comb. Chem. High Throughput Screening 4*, 553–572.

(11) Boehmerle, W., Splittgerber, U., Lazarus, M. B., Mackenzie, K. M., Johnston, D. G., Austin, D. J., and Ehrlich, B. E. (2006) Paclitaxel induces calcium oscillations via an inositol 1,4,5-trisphosphate receptor and neuronal calcium sensor 1-dependent mechanism. *Proc. Natl. Acad. Sci. U.S.A. 103*, 18356–18361.

(12) Smith, G. P., and Petrenko, V. A. (1997) Phage display. *Chem. Rev. 97*, 391–410.

(13) Sche, P. P., McKenzie, K. M., White, J. D., and Austin, D. J. (1999) Display cloning: functional identification of natural product receptors using cDNA-phage display. *Chem. Biol. 6*, 707–716.

(14) Jin, Y., Yu, J., and Yu, Y. G. (2002) Identification of hNopp140 as a binding partner for doxorubicin with a phage display cloning method. *Chem. Biol. 9*, 157–162.

(15) Shim, J. S., Lee, J., Park, H. J., Park, S. J., and Kwon, H. J. (2004) A new curcumin derivative, HBC, interferes with the cell cycle progression of colon cancer cells via antagonization of the Ca+/calmodulin function. *Chem. Biol 11*, 1455–1463.

(16) Rodi, D. J., Soares, A. S., and Makowski, L. (2004) Quantitative assessment of peptide sequence diversity in M13 combinatorial peptide phage display libraries. *J. Mol. Biol. 322*, 1039–1052.

(17) Mandava, S., Makowski, L., Devarapalli, S., Uzubell, J., and Rodi, D. J. (2004) RELIC-A bioinformatics server for combinatorial peptide analysis and identification of protein-ligand interaction sites. *Proteomics 4*, 1439–1460.

(18) Rodi, D. J., Mandava, S., and Makowski, L. (2004) DIVAA: analysis of amino acid diversity in multiple aligned protein sequences. *Bioinformatics 11*, 3481–3489.

(19) Makowski, L., and Rodi, D. J. (2003) Genome-wide characterisation of the binding repertoire of small molecule drugs. *Hum. Genomics 1*, 41–51.

(20) Aoki, S., Ohta, K., Yamazaki, T., Sugawara, F., and Sakaguchi, K. (2005) Mammalian mitotic centromere-associated kinesin (MCAK): a new molecular target of sulfoquinovosylacylglycerols novel antitumor and immunosuppressive agents. *FEBS J. 272*, 2132–2140.

(21) Morohashi, K., Yoshino, A., Yoshimori, A., Saito, S., Tanuma, S., Sakaguchi, K., and Sugawara, F. (2005) Identification of a drug target motif: an anti-tumor drug NK109 interacts with a PNxxxxP. *Biochem. Pharmacol. 70*, 37–46.

(22) Jin, J. H., and Kwon, H. J. (2006) Chemical genomics with natural products. *J. Microbiol. Biotechnol. 16*, 651–660.

(23) Kanoh, N., Honda, K., Shimizu, S., Muroi, M., and Osada, H. (2005) Photo-cross-linked small-molecule affinity matrix facilitating forward and reverse chemical genetics. *Angew. Chem., Int. Ed. 44*, 3559–3562.

(24) Kuramochi, K., Haruyama, T., Takeuchi, R., Sunoki, T., Watanabe, M., Oshige, M., Kobayashi, S., Sakaguchi, K., and Sugawara, F. (2005) Affinity capture of a mammalian DNA polymerase β by inhibitors immobilized to resins used in solid-phase organic synthesis. *Bioconjugate Chem. 16*, 97–104.

(25) Ito, Y. (2006) Photoimmobilization for microarrays. *Biotechnol Prog. 22*, 924–932.

(26) Morimoto, T., Noda, N., Kato, Y., Watanabe, T., Saitoh, T., Yamazaki, T., Takada, K., Aoki, S., Ohta, K., Oshige, M., Sakaguchi, K., and Sugawara, F. (2006) Identification of antibiotic clarithromycin binding peptide displayed by T7 phage particles. *J. Antibiot. 59*, 625–632.

(27) Altschul, S. F., Madden, T. L., Schaffer, A. A., Zhang, J., Zhang, Z., Miller, W., and Lipman, D. J. (1997) Gapped BLAST and PSI-BLAST: a new generation of protein database search programs. *Nucleic Acids Res. 25*, 3389–3402.

(28) Song, Z., Krushna, S., Thanos, D., Strominger, J. L., and Ono, S. J. (1994) A novel cysteine-rich sequence-specific DNA-binding protein interacts with the conserved X-box motif of the human major histocompatibility complex class 2 genes via a repeated cys-his domain and function as a transcriptional repressor. *J. Exp. Med. 180*, 1763–1774.

(29) Lorick, K. L., Jensen, J. P., Fang, S., Ong, A. M., Hatakeyama, S., and Weissman, A. M. (1999) RING fingers mediate ubiquitin-conjugating enzyme (E2)-dependent ubiquitination. *Proc. Natl. Acad. Sci. U.S.A. 96*, 11364–11369.

(30) Sengupta, S., Boge, T. C., Georg, G., and Himes, R. H. (1995) Interaction of a fluorescent paclitaxel analogue with tubulin. *Biochemistry 34*, 11889–11894.

(31) Joo, H. G. (2003) Altered maturation of dendritic cells by taxol, an anticancer drug. *J. Vet. Sci. 4*, 229–234.

(32) Tamburro, A. M., Bochicchio, B., and Pepe, A. (2003) Dissection of human tropoelastin: exon-by-exon chemical synthesis and related conformational studies. *Biochemistry 42*, 13347–13362.

(33) Mammalian Gene Collection Program Team (2002) Generation and initial analysis of more than 15,000 full-length human and mouse cDNA sequences. *Proc. Natl. Acad. Sci. U.S.A., 99*, 16899–16903.

BC700287V

Click Chemistry for ^{18}F-Labeling of RGD Peptides and microPET Imaging of Tumor Integrin $\alpha_v\beta_3$ Expression

Zi-Bo Li,[†] Zhanhong Wu,[†,‡] Kai Chen,[†] Frederick T. Chin,[†] and Xiaoyuan Chen*[,†]

The Molecular Imaging Program at Stanford (MIPS), Department of Radiology and Bio-X Program, Stanford University School of Medicine, Stanford, California, and Department of Nuclear Medicine, Peking Union Medical College Hospital, Beijing, P.R. China. Received June 20, 2007; Revised Manuscript Received August 3, 2007

The cell adhesion molecule integrin $\alpha_v\beta_3$ plays a key role in tumor angiogenesis and metastasis. A series of ^{18}F-labeled RGD peptides have been developed for PET of integrin expression based on primary amine reactive prosthetic groups. In this study, we report the use of the Cu(I)-catalyzed Huisgen cycloaddition, also known as a click reaction, to label RGD peptides with ^{18}F by forming 1,2,3-triazoles. Nucleophilic fluorination of a toluenesulfonic alkyne provided ^{18}F-alkyne in high yield (nondecay-corrected yield: 65.0 ± 1.9%, starting from the azeotropically dried ^{18}F-fluoride), which was then reacted with an RGD azide (nondecay-corrected yield: 52.0 ± 8.3% within 45 min including HPLC purification). The ^{18}F-labeled peptide was subjected to microPET studies in murine xenograft models. Murine microPET experiments showed good tumor uptake (2.1 ± 0.4%ID/g at 1 h postinjection (p.i.)) with rapid renal and hepatic clearance of ^{18}F-fluoro-PEG-triazoles-RGD$_2$ (^{18}F-FPTA-RGD2) in a subcutaneous U87MG glioblastoma xenograft model (kidney 2.7 ± 0.8%ID/g; liver 1.9 ± 0.4%ID/g at 1 h p.i.). Metabolic stability of the newly synthesized tracer was also analyzed (intact tracer ranging from 75% to 99% at 1 h p.i.). In brief, the new tracer ^{18}F-FPTA-RGD2 was synthesized with high radiochemical yield and high specific activity. This tracer exhibited good tumor-targeting efficacy and relatively good metabolic stability, as well as favorable in vivo pharmacokinetics. This new ^{18}F labeling method based on click reaction may also be useful for radiolabeling of other biomolecules with azide groups in high yield.

INTRODUCTION

The vitronectin receptor integrin $\alpha_v\beta_3$ has been the focus of intensive research because of its major role in several distinct processes, particularly osteoclast-mediated bone resorption (*1*), angiogenesis and pathological neovascularization (*2*), and tumor metastasis (*3*). Integrin $\alpha_v\beta_3$ has distinct functional properties that are mediated through interactions with a variety of extracellular matrix (ECM) proteins (*4, 5*) and a number of important intracellular signaling molecules (including paxillin, focal adhesion kinase caspase-8, and others) (*6–8*). These interactions play a part in regulating intracellular signaling, cell migration, cell proliferation, and cell survival.

Since integrin $\alpha_v\beta_3$ plays a key role in multiple physiological and pathological processes, a method to noninvasively visualize and quantify $\alpha_v\beta_3$ integrin expression levels will provide a means to document integrin levels, wisely choose patients for anti-integrin treatment, and monitor treatment efficacy in integrin-positive patients. Multimodality approaches have been applied to image integrin expression in vivo, including magnetic resonance (MR) (*9, 10*), ultrasound (*11, 12*), near-infrared fluorescence (NIRF) (*13, 14*), single photon emission computed tomography (SPECT), and positron emission tomography (PET) (*15–17*). Due to the high sensitivity and reasonably good spatial/temporal resolution, PET probe development for targeting integrin expression continues to be an area of great interest.

Because ^{18}F is readily available from most small medical cyclotrons and has almost 100% positron efficiency, the physical half-life of ^{18}F (109.7 min) is well-suited for routine clinical use and is well-matched to the biological half-life (blood clearance) of peptides (usually minutes to less than a few hours), ^{18}F-labeled target-specific peptides are becoming widely used as in vivo imaging agents, a few of which have entered early-phase clinical trials (*15*). Different from small organic molecules, direct labeling of peptides via either SN_1 or SN_2 nucleophilic substitution is usually not an option, as peptides will not tolerate the harsh reaction conditions associated with these procedures. Radiofluorination of peptides thus generally uses ^{18}F-prosthetic groups (synthons) that will form stable chemical bonds on the peptides. ^{18}F labeling could be accomplished through the amino group at the N terminus or the lysine side chain using *N*-succinimidyl-4-^{18}F-fluorobenzoate (^{18}F-SFB) (*18, 19*), 4-^{18}F-fluorobenzaldehyde (^{18}F-FBA, via oxime formation and reductive amination) (*20, 21*), 3-^{18}F-fluoro-5-nitrobenzimidate (^{18}F-FNB, via imidation reaction) (*22*), 4-azidophenacyl ^{18}F-fluoride (^{18}F-APF, via photochemical conjugation) (*23*), and 4-^{18}F-fluorophenacyl bromide (^{18}F-FPB, via alkylation reactions) (*22*). ^{18}F labeling of peptide or protein via the carboxylic acid group at the C terminus or glutamic/aspartic acid side chain is less common, and only a few reports exist (*24*). We have previously reported the Michael addition reaction for labeling thiolated RGD peptides (*25*). However, most of these procedures suffer from lengthy and tedious multistep synthetic procedures. As a result, these long, difficult processes make them a challenge to automate and adversely decrease the overall radiolabeling yield.

The recent discovery that Cu(I) catalyzes the Huisgen 1,3-dipolar cycloaddition of organo azides with terminal alkynes to form 1,2,3-triazoles (*26, 27*), often referred to as click chemistry (*28*), has led wide-ranging applications in combinatorial chemistry (*29–31*). This reaction could be carried out in high yields under mild conditions, and the 1,2,3-triazole formed has similar polarity and size with an amide bond (*32*). Due to these favorable aspects with click chemistry, the use of this reaction for making ^{18}F-labeled model peptides have been recently reported (*33, 34*). However, no in vivo PET study has

* E-mail: shawchen@stanford.edu.
[†] Stanford University School of Medicine.
[‡] Peking Union Medical College Hospital.

10.1021/bc700226v CCC: $37.00 © 2007 American Chemical Society
Published on Web 11/21/2007

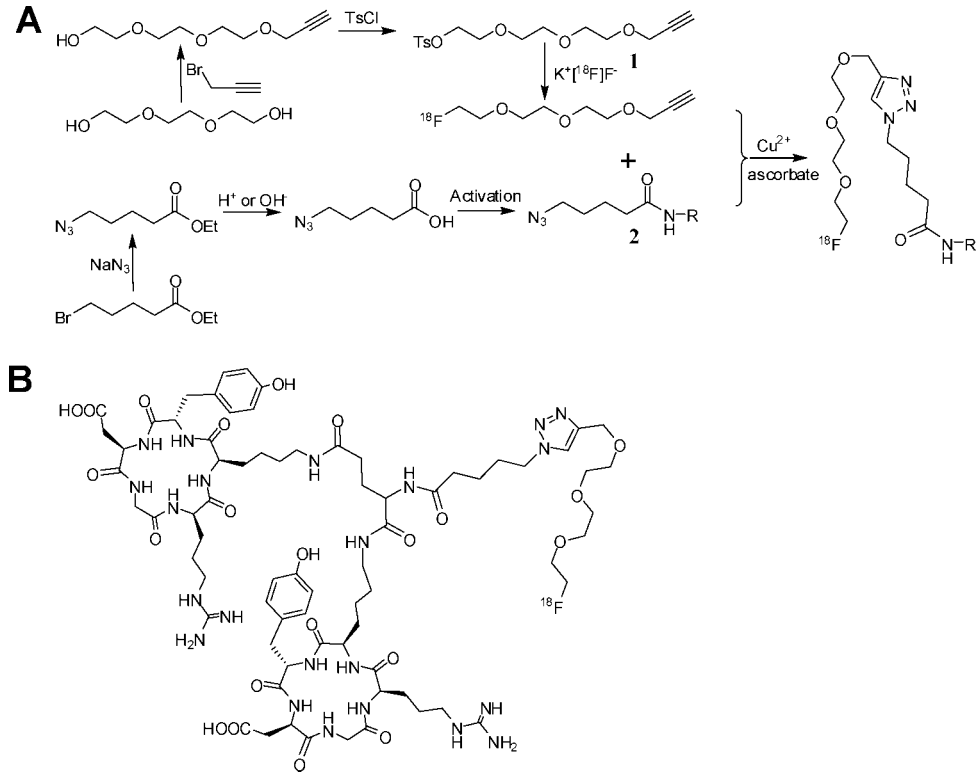


Figure 1. (A) Radiosynthesis of ^{18}F-fluoro-PEG-alkyne intermediate and 1.3-dipolar cycloaddition with terminal azide. R = targeting biomolecule (peptides, proteins, antibodies, etc.). (B) Structure of ^{18}F-fluoro-PEG-alkyne labeled E[c(RGDyK)]$_2$: ^{18}F-fluoro-PEG-triazole-E(RGDyK)$_2$ (^{18}F-FPTA-RGD2).

been reported on ^{18}F-labeled tracers synthesized by click chemistry. Moreover, distillation was required for some of the reported methods (*34*), which is unfortunately difficult to automate. In this study, we labeled dimeric-RGD peptide with our newly developed ^{18}F synthon based on click chemistry and studied the tumor targeting efficacy, in vivo kinetics, and metabolic stability of this tracer in tumor-bearing mice.

MATERIALS AND METHODS

All chemicals obtained commercially were of analytical grade and used without further purification. No-carrier-added ^{18}F–F$^-$ was obtained from a PETtrace cyclotron (GE Healthcare). Reversed-phase extraction C-18 Sep-Pak cartridges were obtained from Waters and were pretreated with ethanol and water before use. The syringe filter and polyethersulfone membranes (pore size, 0.22 μm; diameter, 13 mm) were obtained from Nalge Nunc International. ^{125}I-Echistatin, labeled by the lactoperoxidasemethod to a specific activity of 74 000 GBq/mmol (2000 Ci/mmol), was purchased from GE Healthcare. Analytical as well as semipreparative reversed-phase high-performance liquid chromatography (RP-HPLC) was performed on a Dionex 680 chromatography system with a UVD 170U absorbance detector and model 105S single-channel radiation detector (Carroll & Ramsey Associates). The recorded data were processed using *Chromeleon* v 6.50 software. Isolation of peptides and ^{18}F-labeled peptides was performed using a Vydac protein and peptide column (218TP510; 5 μm, 250 × 10 mm). The flow rate was set at 5 mL/min, with the mobile phase starting from 95% solvent A (0.1% trifluoroacetic acid [TFA] in water) and 5% solvent B (0.1% TFA in acetonitrile [ACN]) (0–2 min) to 35% solvent A and 65% solvent B at 32 min The analytical HPLC was performed using the same gradient system, but with a Vydac column (218TP54, 5 μm, 250 × 4.6 mm) and a flow rate of 1 mL/min. The UV absorbance was monitored at 218 nm, and the identification of the peptides was confirmed by separate standard injection.

Preparation of Alkyne Tosylate (1). The alkyne tosylate (**1**) (Figure 1) was prepared by using the modified method reported by Burgess (*35*). In brief, sodium hydride (1 g, 25 mmol, 60%) was slowly added to the THF solution of triethylene glycol (5.8 g, 38 mmol) at 0 °C. The mixture was stirred for 30 min and propargyl bromide (2.1 mL, 19 mmol) was then added dropwise. The mixture was stirred at room temperature for 18 h, and the triethylene glycol alkyne was obtained as a light yellow oil after purification by chromatography (2.5 g, 70%). ^{1}H NMR (400 MHz, $CDCl_3$) δ 4.13 (d, J = 2.5 Hz, 2H), 3.61–58 (m, 10H), 3.52–3.50 (m, 2H), 2.75 (br, 1H), 2.38 (t, J = 2.5 Hz, 1H). After the triethylene glycol alkyne (1 g, 5.4 mmol) was reconstituted in ACN (15 mL) and triethylamine (2 mL, 14 mmol), *p*-toluenesulfonyl chloride (2.1 g, 11 mmol) was added slowly, and the mixture was stirred at room temperature for 16 h. After the reaction was quenched followed by general workup, the crude product was purified by flash chromatography to afford the alkyne tosylate (**1**) (1.5 g, 81%) as a colorless oil. ^{1}H NMR (400 MHz, $CDCl_3$) δ 7.75 (d, J = 8.4 Hz, 2H), 7.30 (d, J = 8.4 Hz, 2H), 4.14–4.06 (m, 4H), 3.65–3.58 (m, 6H), 3.55–3.52 (m, 4H), 2.38 (s, 3H), 2.37 (t, J = 2.5 Hz, 1H).

Preparation of Azido-RGD2. The 5-azidopentanoic acid was obtained as colorless oil according to the procedure published by Carrié (*36*). ^{1}H NMR (400 MHz, $CDCl_3$) δ 3.25 (t, J = 6.5 Hz, 2H), 2.34 (t, J = 7.1 Hz, 2H), 1.68–1.59 (m, 4H). The azido-RGD2 was prepared from cyclic RGD dimer E[c(RGDyK)]$_2$ (denoted as RGD2). To a solution of 5-azidopentanoic acid (18.6 mg, 0.13 mmol) and 20 μL DIPEA in ACN (0.5 mL), *O*-(*N*-succinimidyl)-1,1,3,3-tetramethyluronium tetrafluoroborate (TSTU, 27 mg, 0.09 mmol) was added. The reaction mixture was stirred at room temperature for 0.5 h and then added to E[c(RGDyK)]$_2$ (20 mg, 14.8 μmol) in *N*,*N*′-dimethylformamide (DMF). The

Table 1. Radiolabeling Yields (decay-corrected) of ^{18}F-Fluoro-PEG-Alkyne Intermediate at Various Conditions ($n = 3$)

entry	solvent	temperature and time	yield (%)
1	ACN	90 °C for 15 min	61.2 ± 2.5
2	ACN	110 °C for 15 min	71.4 ± 3.0
3	ACN/DMSO	110 °C for 15 min	75.0 ± 1.8
4	**DMSO**	**110 °C for 15 min**	**78.5 ± 2.3**
5	DMSO	110 °C for 30 min	84.3 ± 2.1

reaction was stirred at room temperature for another 2 h, and the desired product azido-RGD2 was isolated by preparative HPLC. The collected fractions were combined and lyophilized to give a white fluffy powder (12 mg, 57% yield) with a retention time of 14.8 min on analytical HPLC. MALDI-TOF-MS: *m*/*z* 1475.87 for $[MH]^+$ ($C_{64}H_{95}N_{22}O_{19}$, calculated molecular weight [MW] 1475.71).

Preparation of Fluoro-PEG-Triazole-E(RGDyK)$_2$ (FPTA-RGD2). To a solution of alkyne tosylate (**1**) (6.8 mg, 0.02 mmol) in ACN, powdered potassium fluoride (6 mg, 0.10 mmol), potassium carbonate (3 mg), and Kryptofix 222 (15 mg) were added, and the mixture was heated at 90 °C for 40 min The reaction mixture was evaporated to dryness, and the residue was redissolved in 0.4 mL water and 0.4 mL THF. Azido-RGD2 (1 mg, 0.7 μmol) was then added, followed by $CuSO_4$ (100 μL, 0.1 N) and sodium L-ascorbate (100 μL, 0.3 N) solution. The resulting mixture was stirred at room temperature for 24 h, and the reaction was then quenched and purified by semi-preparative HPLC. The final product fluoro-PEG-triazole-E(RGDyK)$_2$ (FPTA-RGD2) was obtained in 81% yield (0.91 mg) with a retention time of 13.4 min on analytical HPLC. MALDI-TOF-MS: *m*/*z* 1665.82 for $[MH]^+$ ($C_{73}H_{110}FN_{22}O_{22}$, calculated [MW] 1665.81).

Radiochemistry. [^{18}F] Fluoride was prepared by the ^{18}O(p,n)^{18}F nuclear reaction, and it was then adsorbed onto an anion exchange resin cartridge. Kryptofix 222/K_2CO_3 solution (1 mL 9:1 ACN/water, 15 mg Kryptofix 222, 3 mg K_2CO_3) was used to elute the cartridge, and the resulting mixture was dried in a glass reactor. A solution of alkyne tosylate (**1**) (4 mg in 1 mL ACN/DMSO) was then added, and the resulting mixture was heated at the desired temperature (Table 1). After cooling, the reaction was quenched, and the mixture was injected onto a semipreparative HPLC for purification. The collected radioactive peak was diluted in water (10 mL) and passed through a C18 cartridge. The trapped activity was then eluted off the cartridge with 1 mL THF and used for the next reaction. To the reactor vial with azido-RGD2 (1 mg), 37 MBq activity, $CuSO_4$ (100 μL, 0.1 N), and sodium L-ascorbate (100 μL, 0.3 N) were added sequentially. The resulting mixture was heated at 40 °C for 20 min, and the reaction was then quenched and purified by semipreparative HPLC. The final product ^{18}F-FPTA-RGD2 (R_t 13.4 min; decay-corrected yield 69 ± 11%; radiochemical purity >97%) was concentrated and formulated in saline (0.9%, 500 μL) for in vivo studies.

Octanol–Water Partition Coefficient. Approximately 111 kBq of ^{18}F-FPTA-RGD2 in 500 μL of PBS (pH 7.4) were added to 500 μL of octanol in an Eppendorf microcentrifuge tube (model 5415R, Brinkman). The mixture was vigorously vortexed for 1 min at room temperature and centrifuged at 12 500 rpm for 5 min. After centrifugation, 200 μL aliquots of both layers were measured using a γ-counter (Packard Instruments). The experiment was carried out in triplicate.

Cell Line and Animal Models. U87MG human glioblastoma cells were grown in Dulbecco's medium (Gibco) supplemented with 10% fetal bovine serum (FBS), 100 IU/mL penicillin, and 100 μg/mL streptomycin (Invitrogen Co.). Animal procedures were performed according to a protocol approved by the Stanford University Institutional Animal Care and Use Committee. A U87MG xenograft model was generated by subcutaneous (s.c.) injection of 1×10^7 U87MG cells (integrin $\alpha_v\beta_3$-positive) into the front flank of female athymic nude mice. Three to four weeks after inoculation (tumor volume: 100–400 mm^3), the mice (about 9–10 weeks old with 20–25 g body weight) were used for microPET studies.

Cell Integrin Receptor-Binding Assay. In vitro integrin-binding affinity and specificity of E[c(RGDyK)]$_2$ and FPTA-RGD2 were assessed via competitive cell binding assays using ^{125}I-echistatin as the integrin $\alpha_v\beta_3$-specific radioligand (*17*). The best-fit 50% inhibitory concentration (IC_{50}) values for U87MG cells were calculated by fitting the data with nonlinear regression using *GraphPad Prism* (GraphPad Software, Inc.). Experiments were performed with triplicate samples.

In Vivo Metabolic Stability Studies. The metabolic stability of ^{18}F-FPTA-RGD2 was evaluated in an athymic nude mouse bearing a U87MG tumor. 60 min after intravenous injection of 2 MBq of ^{18}F-FPTA-RGD2, the mouse was sacrificed, and relevant organs were harvested. The blood was collected and immediately centrifuged for 5 min at 13 200 rpm. Liver, kidneys, and tumor were homogenized and then centrifuged for 5 min at 13 200 rpm. After removal of the supernatants, the pellets were washed with 1 mL PBS. For each sample, supernatants of both centrifugation steps of blood, liver, and kidneys were combined and passed through C18 Sep-Pak cartridges. The urine sample was directly diluted with 1 mL of PBS and passed through a C18 Sep-Pak cartridge. The cartridges were each washed with 2 mL of water and eluted with 2 mL of ACN containing 0.1% TFA. After evaporation of the solvent, the residues were redissolved in 1 mL PBS and were injected onto the analytical HPLC. The eluent was collected with a fraction collector (0.5 min/fraction), and the radioactivity of each fraction was measured with the γ-counter.

microPET Studies. PET scans and image analysis were performed using a microPET R4 rodent model scanner (Siemens Medical Solutions) as previously reported (*17, 19*). About 2 MBq of ^{18}F-FPTA-RGD2 was intravenously injected into each mouse ($n = 3$) under isoflurane anesthesia (1–3%) and then subjected to a 30-min dynamic scan (1×1 min, 1×1.5 min, 1×3.5 min, 3×5 min, 1×6 min, total of 7 frames) starting from 1 min p.i. 5 min static PET images were also acquired at 1 and 2 h p.i. For each microPET scan, regions of interest (ROIs) were drawn over the tumor, normal tissue, and major organs on decay-corrected whole-body coronal images. The radioactivity concentration (accumulation) within a tumor was obtained from the mean value within the multiple ROIs and then converted to %ID/g (*17*). For a receptor-blocking experiment, mice bearing U87MG tumors on the front left flank were scanned (5 min static) after coinjection with ^{18}F-FPTA-RGD2 (2 MBq) and c(RGDyK) (10 mg/kg).

Statistical Analysis. Quantitative data were expressed as mean ± SD. Means were compared using one-way ANOVA and Student's *t* test. *P* values of <0.05 were considered statistically significant.

RESULTS

Chemistry and Radiochemistry. Both alkyne tosylate (**1**) and azido-RGD2 were obtained in high yields (Figure 1). The alkyne fluoride was prepared in situ and could be used directly for the reaction with azido-RGD2 to make the cold standard, which was purified by HPLC and confirmed by MALDI-TOF mass spectrometry. ^{18}F-alkyne was also obtained in high yield at various conditions (Table 1). The presence of acetonitrile may lower the labeling yield to some extent (Table 1, entries 1–3). Although entry 5 gave the highest decay-corrected yield (84.3 ± 2.1%), the non-decay-corrected yield was 69.8%, which is actually slightly lower than the non-decay-corrected yield from entry 4 (71.4%). Thus, the condition from entry 4 was used for

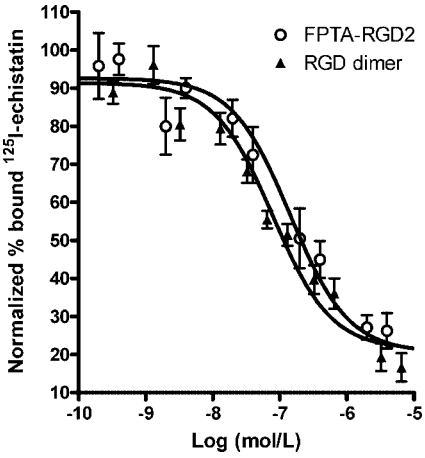


Figure 2. Cell binding assay of E[c(RGDyK)]$_2$ and FPTA-RGD2 using U87MG cells with competitive displacement studies using ^{125}I-echistatin. The IC_{50} values for E[c(RGDyK)]$_2$ and FPTA-RGD2 were 79.2 ± 4.2 and 144 ± 6.5 nM, respectively (n = 3).

the subsequent studies. We also noted that the ^{18}F-alkyne intermediate had to be purified before the conjugation with azido-RGD2 to guarantee high labeling yield (this might due to the removal of a large excess amount of unreacted alkyne). The radiochemical purity of the ^{18}F-labeled peptide ^{18}F-FPTA-RGD2 was higher than 97% according to analytical HPLC. The specific radioactivity of ^{18}F-FPTA-RGD2 was determined to be about 100–200 TBq/mmol based on the labeling agent ^{18}F-SFB, as the unlabeled azido-RGD2 was efficiently separated from the product.

The octanol/water partition coefficient (log P) for ^{18}F-FPTA-RGD2 was −2.71 ± 0.006, indicating that the tracer is slightly more hydrophilic than ^{18}F-FB-RGD2 (^{18}F-FRGD2, −2.103 ± 0.030) and ^{18}F-FB-PEG3-RGD2 (^{18}F-FPRGD2, −2.280 ± 0.054) (*18*).

In Vitro Cell Integrin Receptor-Binding Assay. The receptor-binding affinity of RGD2 and FPTA-RGD2 was determined by performing competitive displacement studies with ^{125}I-echistatin. All peptides inhibited the binding of ^{125}I-echistatin (integrin $\alpha_v\beta_3$-specific) to U87MG cells in a concentration-dependent manner. The IC_{50} values for RGD2 and FPTA-RGD2 were 79.2 ± 4.2 and 144 ± 6.5 nM, respectively (n = 3) (Figure 2). In a parallel experiment, the IC_{50} value for FPRGD2 was 97 ± 4.8 nM. The comparable IC_{50} values of these compounds suggest that the introduction of miniPEG linker and triazole group had little effect on the receptor-binding affinity.

microPET Imaging of U87MG Tumor-Bearing Mice. Dynamic microPET scans were performed on U87MG xenograft model and selected coronal images at different time points after injecting ^{18}F-FPTA-RGD2 were shown in Figure 3A. Good tumor-to-contralateral background contrast was observed as early as 10 min after injection (5.4 ± 0.7%ID/g). The U87MG tumor uptake was 3.1 ± 0.6, 2.1 ± 0.4, and 1.3 ± 0.4%ID/g at 0.5, 1, and 2 h p.i., respectively (n = 3). Most activity in the nontargeted tissues and organs was cleared by 1 h p.i. For example, the uptake values in the kidney, liver, and muscle were as low as 2.7 ± 0.8, 1.9 ± 0.4, and 1.0 ± 0.3%ID/g, respectively, at 1 h p.i. The averaged time–activity curves (TACs) for the U87MG tumor, liver, kidney, and muscle were shown in Figure 4. ^{18}F-FPTA-RGD2 was cleared mainly through the kidneys. Some hepatic clearance was also observed. The integrin $\alpha_v\beta_3$ specificity of ^{18}F-FPTA-RGD2 in vivo was confirmed by a blocking experiment where the tracer was coinjected with c(RGDyK) (10 mg/kg). As can be seen from Figure 3B, the U87MG tumor uptake in the presence of

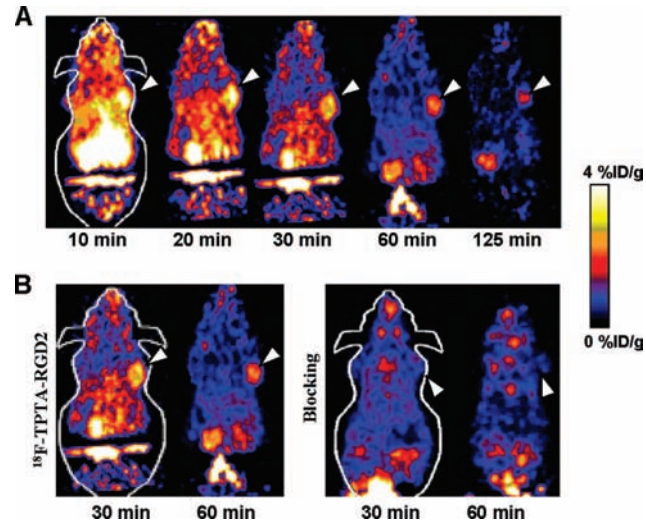


Figure 3. (A) Decay-corrected whole-body coronal microPET images of athymic female nude mice bearing U87MG tumor at 10, 20, 30, 60, and 125 min postinjection (p.i.) of about 2 MBq of ^{18}F-FPTA-RGD2. (B) Coronal microPET images of U87MG tumor-bearing mice at 30 and 60 min p.i. of ^{18}F-FPTA-RGD2 with (denoted as "blocking") and without coinjection of 10 mg/kg mouse body weight of c(RGDyK). Tumors are indicated by arrows.

nonradiolabeled RGD peptide (0.9 ± 0.3%ID/g) is significantly lower than that without RGD blocking (2.1 ± 0.4%ID/g) (P < 0.05) at 1 h p.i.

The comparison of tumor and various organ uptake of ^{18}F-FPTA-RGD2 with ^{18}F-FPRGD2 and ^{18}F-FRGD2 was shown in Figure 5. The uptake in the U87MG tumor was slightly lower for ^{18}F-FPTA-RGD2, which might be caused by integrin $\alpha_v\beta_3$ binding affinity difference (Figure 5A). The kidney uptake for these three tracers was comparable (Figure 5B), and the clearance rate was highest for ^{18}F-FPTA-RGD2. ^{18}F-FPTA-RGD2 had lowest liver uptake, which was consistent with the hydrophilic sequence of these three compounds (Figure 5C). The nonspecific uptake in the muscle was at a very low level for all three compounds (Figure 5D).

In Vivo Metabolic Stability Studies. The metabolic stability of ^{18}F-FPTA-RGD2 was determined in mouse blood and urine and in the liver, kidney, and tumor homogenates at 1 h after intravenous injection of radiotracer into a U87MG tumor-bearing mouse. The extraction efficiency of all organs was between 86% and 99% (Table 2). The lowest extraction efficiency was found for the kidney. 1% to 41% of the total activity could not be trapped on the C-18 cartridges, which can be related to very hydrophilic metabolites and protein-bound activity. After ACN elution, the radioactivity of each sample was injected onto an analytical HPLC, and the HPLC chromatograms are shown in Figure 6. The fraction of intact tracer was between 75% and 99% (Table 2). Although we did not identify the metabolites, we found that all metabolites eluted earlier from the HPLC column rather than the parent compound (Figure 6), which behaved similarly to ^{18}F-FRGD2 (*19*) and ^{18}F-FPRGD2 (*18*).

DISCUSSION

^{18}F-labeling of cyclic RGD peptide was first reported by Haubner et al. (*37*). A monomeric glycopeptide based on c(RGDfK) was ^{18}F-radiolabeled via ^{18}F-2-fluoropropionate prosthetic group and the resulting ^{18}F-galacto-RGD exhibited integrin $\alpha_v\beta_3$ specific tumor uptake in integrin-positive xenograft models. Initial clinical trials in a limited number of cancer patients revealed that this tracer can be safely given to patients and is able to delineate certain lesions that are integrin-positive (*15*). We have ^{18}F-radiolabeled both monomeric and dimeric

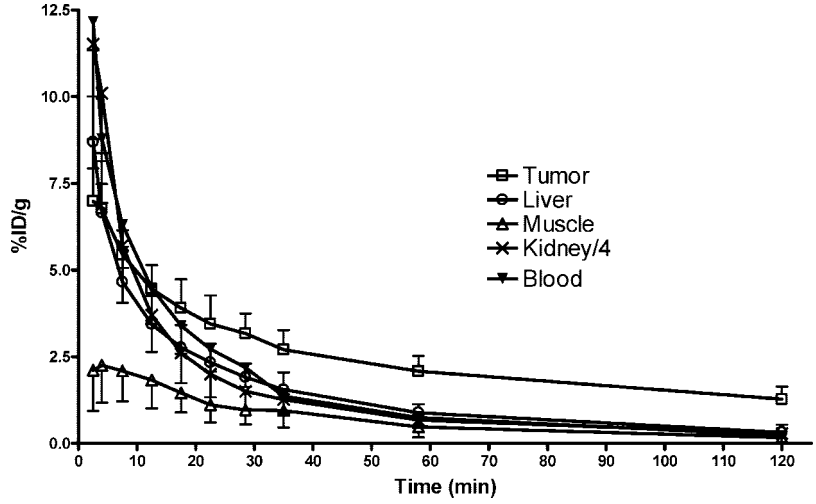


Figure 4. Time–activity curves of the U87MG tumor, liver, kidney, blood, and muscle after intravenous injection of ^{18}F-FPTA-RGD2. Data were derived from multiple time-point microPET study. ROIs are shown as the %ID/g ± SD ($n = 3$). Note that the kidney uptake in the figure is 1/4 of the actual value.

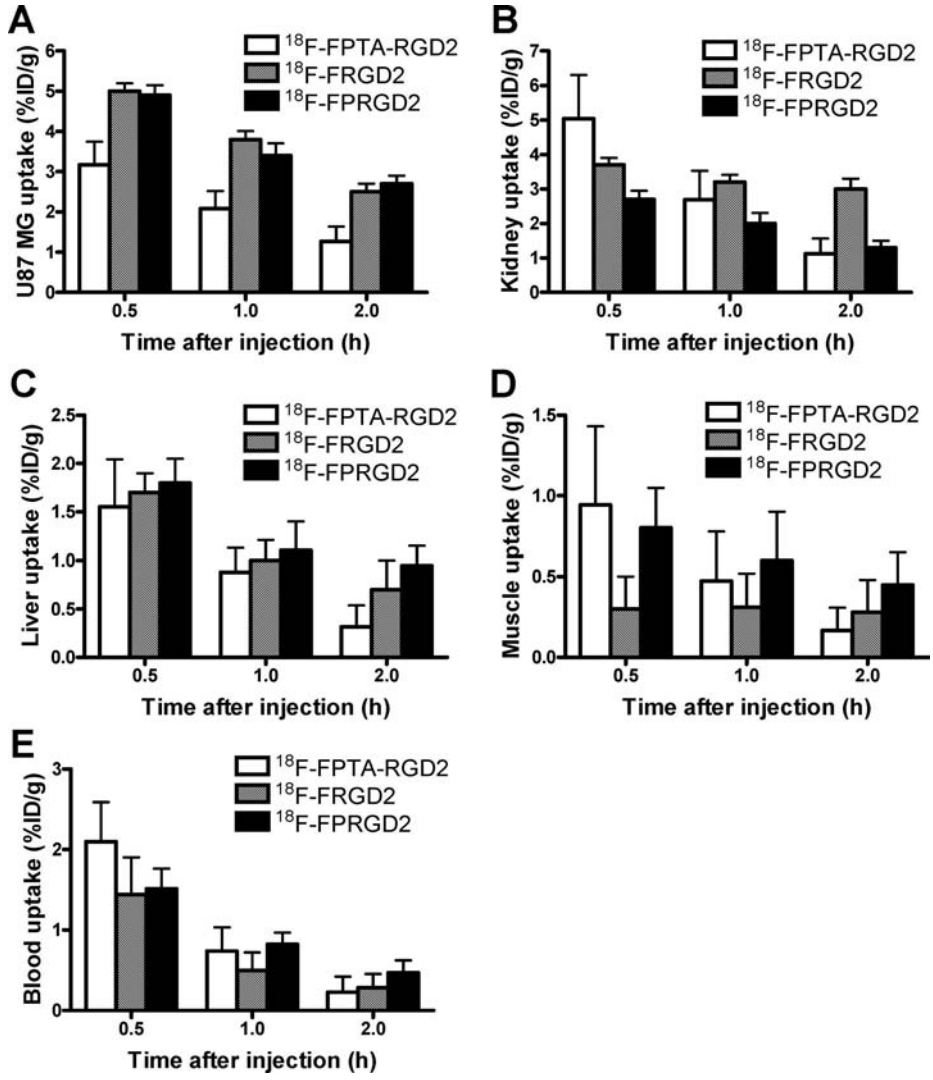


Figure 5. Comparison of ^{18}F-FPTA-RGD2, ^{18}F-FB-RGD2 (^{18}F-FRGD2), and ^{18}F-FB-PEG3-RGD2 (^{18}F-FPRGD2) in U87MG tumor, kidney, liver, muscle, and blood over time.

RGD peptides using an ^{18}F-4-fluorobenzoyl (^{18}F-FB) prosthetic group (*16*, *19*). The dimeric RGD peptide tracer, ^{18}F-FB-E[c(RGDyK)]$_2$ (denoted ^{18}F-FRGD2), exhibited excellent integrin $\alpha_v\beta_3$-specific tumor imaging with favorable in vivo pharmacokinetics (*19*, *38*). The binding potential extrapolated from Logan plot graphical analysis of the PET data correlated well with the receptor density measured by SDS-PAGE/autoradiography in various xenograft models. The tumor-to-

Table 2. Extraction Efficiency, Elution Efficiency, and HPLC Analysis of Soluble Fraction of Tissue Homogenates at 1 h Postinjection of ^{18}F-FPTA-RGD2[a]

fraction	blood	urine	liver	kidney	U87mg
			Extraction Efficiency (%)		
insoluble fraction	0.8	ND	10.3	13.3	7.5
soluble fraction	99.2	ND	89.7	86.7	92.5
			Elution Efficiency (%)		
unretained fraction	2.8	0.4	33.9	12.8	18.5
wash water	8.8	0.5	7.4	3.9	5.2
acetonitrile eluent	88.4	99.1	58.7	83.3	76.4
			HPLC Analysis (%)		
intact tracer	75.9	99.7	81.6	89.1	82.4

[a] ND denotes not determined.

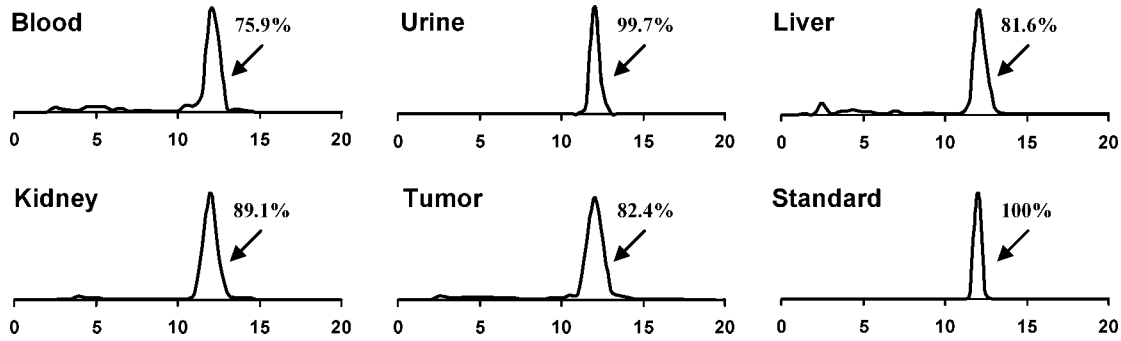


Figure 6. Metabolic stability of ^{18}F-FPTA-RGD2 in mouse blood and urine samples and in liver, kidney, and U87MG tumor homogenates at 1 h after injection. The HPLC profile of pure ^{18}F-FPTA-RGD2 (Standard) is also shown.

background ratio at 1 h after injection of ^{18}F-FRGD2 also gave a good linear relationship with the tumor tissue integrin $\alpha_v\beta_3$ expression level (*19*). We have also reported a thiol-reactive synthon, *N*-[2-(4-^{18}F-fluorobenzamido)ethyl]maleimide (^{18}F-FBEM), for labeling monomeric and dimeric sulfhydryl-RGD peptides (*25*). To extend our efforts of ^{18}F-radiolabeling strategies, we explored and reported the possibility of labeling dimeric RGD peptide E[c(RGDyK)]$_2$ using Hsuigen 1,3-dipolar cycloaddition reaction (one of the click chemistry reactions) and evaluated the ability of the new PET tracer for integrin $\alpha_v\beta_3$ targeting in vitro and in vivo.

Alkyne tosylate (**1**) was designed as the labeling precursor that allowed nucleophilic fluorination and displacement of the tosyl group to occur in high yield under mild conditions (15 min, 78.5 ± 2.3% yield). A triethylene glycol linker was employed in the structure to reduce volatility and obtain water solubility. The azido group was introduced to RGD dimer RGD2 by reacting the glutamate amine group with the azido-NHS ester. A robust catalytic system, Cu^{2+}/ascorbate, was used for the labeling reaction (*27*). In comparison with the SFB labeling procedure (starting from ^{18}F–F$^-$, the total synthesis time of ^{18}F-FPRGD2 was about 180 min with an overall non-decay-corrected yield of 12.9% (decay-corrected yield 40%)) (*18*), click-labeled ^{18}F-FPTA-RGD2 could be obtained in 110 min with 26.9% non-decay-corrected yield (decay-corrected yield 53.8%). The reduced reaction time and increased labeling yield make click chemistry a valuable method for labeling RGD peptide with ^{18}F.

We also studied the application of ^{18}F-FPTA-RGD2 for in vivo imaging. We found that this tracer had good tumor-to-muscle ratio and predominant renal excretion. Compared with ^{18}F-FPRGD2 and ^{18}F-FRGD2, the tumor-targeting efficacy of ^{18}F-FPTA-RGD2 was decreased to some extent, which might be caused by the slightly decreased integrin binding affinity based on cell binding assay. The unspecific blood pool activity could be another factor. However, no significant difference was observed for these compounds ($P > 0.5$) (Figure 5E). ^{18}F-FPTA-RGD2 also had a faster clearance rate and lower liver uptake which might due to the increased hydrophilicity of this tracer ($\log P = -2.710 \pm 0.006$), after the replacement of the benzoic group with a short PEG linker. A metabolic stability study revealed that the triazoles unit, formed by click chemistry in ^{18}F-FPTA-RGD2, has comparable in vivo stability compared with the amide bound made from SFB in the case of ^{18}F-FRGD2 and ^{18}F-FPRGD2 (*18, 19*).

This study demonstrated that RGD peptide can be labeled efficiently through click chemistry. The major advantage of ^{18}F-FPTA-RGD2 would be shortened reaction time, increased labeling yield, and comparable in vivo stability. The tumor-targeting efficacy of this tracer was comparable with SFB-labeled RGD peptides and can be further improved. First, the relatively long linker (triethylene glycol plus four methylene groups) in ^{18}F-FPTA-RGD2 might account for the decreased intergin binding affinity. Our future work will focus on the development of various linkers suitable for this new labeling method and study the in vivo pharmacokinetics of the resulting tracers. Second, high $\alpha_v\beta_3$ binding affinity is needed to afford high tumor uptake and retention. Based on polyvalency effect, tetrameric RGD peptide (*17*), labeled with the synthon described here, would have more effective binding to integrin $\alpha_v\beta_3$ and better tumor targeting efficacy. Third, the click labeling method developed here could also be applied to label a variety of other peptides, proteins, antibodies, or oligonucleotides after the introduction of the azido group. Due to the mild labeling conditions, ^{18}F might be easily engineered to incorporate the organo azide residue without compromising the biological activity.

CONCLUSIONS

The new tracer ^{18}F-FPTA-RGD2 was synthesized with high specific activity based on click chemistry. This tracer exhibited good tumor-targeting efficacy, relatively good metabolic stability, as well as favorable in vivo pharmacokinetics. The new

^{18}F labeling method developed in this study could also have general application in labeling azido-containing bioactive molecules in high radiochemical yield and high specific activity for successful PET applications.

ACKNOWLEDGMENT

This work was supported in part by the National Cancer Institute (NCI) (R21 CA102123, ICMIC P50 CA114747, CCNE U54 CA119367, and SARIP R24 CA93862), Department of Defense (DOD) (W81XWH-04-1-0697, W81XWH-06-1-0665, W81XWH-06-1-0042, DAMD17-03-1-0143, and BC061781), and a Dean's Fellowship (to ZL) from the Stanford University. We thank Dr. David W. Dick from the cyclotron facility for ^{18}F–F$^-$ production.

LITERATURE CITED

(1) Fisher, J. E., Caulfield, M. P., Sato, M., Quartuccio, H. A., Gould, R. J., Garsky, V. M., Rodan, G. A., and Rosenblatt, M. (1993) Inhibition of osteoclastic bone resorption in vivo by echistatin, an "arginyl-glycyl-aspartyl" (RGD)-containing protein. *Endocrinology 132*, 1411–3.

(2) Maeshima, Y., Yerramalla, U. L., Dhanabal, M., Holthaus, K. A., Barbashov, S., Kharbanda, S., Reimer, C., Manfredi, M., Dickerson, W. M., and Kalluri, R. (2001) Extracellular matrix-derived peptide binds to $\alpha_v\beta_3$ integrin and inhibits angiogenesis. *J. Biol. Chem. 276*, 31959–68.

(3) Albelda, S. M. (1993) Role of integrins and other cell adhesion molecules in tumor progression and metastasis. *Lab. Invest. 68*, 4–17.

(4) Ruegg, C., and Mariotti, A. (2003) Vascular integrins: pleiotropic adhesion and signaling molecules in vascular homeostasis and angiogenesis. *Cell. Mol. Life Sci. 60*, 1135–57.

(5) Mizejewski, G. J. (1999) Role of integrins in cancer: survey of expression patterns. *Proc. Soc. Exp. Biol. Med. 222*, 124–38.

(6) Katoh, K., Masuda, M., Kano, Y., Jinguji, Y., and Fujiwara, K. (1995) Focal adhesion proteins associated with apical stress fibers of human fibroblasts. *Cell Motil. Cytoskeleton 31*, 177–95.

(7) Vacca, A., Ria, R., Presta, M., Ribatti, D., Iurlaro, M., Merchionne, F., Tanghetti, E., and Dammacco, F. (2001) $\alpha_v\beta_3$ integrin engagement modulates cell adhesion, proliferation, and protease secretion in human lymphoid tumor cells. *Exp. Hematol. 29*, 993–1003.

(8) Schaller, M. D., Otey, C. A., Hildebrand, J. D., and Parsons, J. T. (1995) Focal adhesion kinase and paxillin bind to peptides mimicking β integrin cytoplasmic domains. *J. Cell Biol. 130*, 1181–7.

(9) Benedetto, S., Pulito, R., Crich, S. G., Tarone, G., Aime, S., Silengo, L., and Hamm, J. (2006) Quantification of the expression level of integrin receptor $\alpha_v\beta_3$ in cell lines and MR imaging with antibody-coated iron oxide particles. *Magn. Reson. Med. 56*, 711–6.

(10) Sipkins, D. A., Cheresh, D. A., Kazemi, M. R., Nevin, L. M., Bednarski, M. D., and Li, K. C. (1998) Detection of tumor angiogenesis in vivo by $\alpha_v\beta_3$-targeted magnetic resonance imaging. *Nat. Med. 4*, 623–6.

(11) Dayton, P. A., Pearson, D., Clark, J., Simon, S., Schumann, P. A., Zutshi, R., Matsunaga, T. O., and Ferrara, K. W. (2004) Ultrasonic analysis of peptide- and antibody-targeted microbubble contrast agents for molecular imaging of $\alpha_v\beta_3$-expressing cells. *Mol. Imaging 3*, 125–34.

(12) Ellegala, D. B., Leong-Poi, H., Carpenter, J. E., Klibanov, A. L., Kaul, S., Shaffrey, M. E., Sklenar, J., and Lindner, J. R. (2003) Imaging tumor angiogenesis with contrast ultrasound and microbubbles targeted to $\alpha_v\beta_3$. *Circulation 108*, 336–41.

(13) Wu, Y., Cai, W., and Chen, X. (2006) Near-infrared fluorescence imaging of tumor integrin $\alpha_v\beta_3$ expression with Cy7-labeled RGD multimers. *Mol. Imaging Biol. 8*, 226–36.

(14) Chen, X., Conti, P. S., and Moats, R. A. (2004) In vivo near-infrared fluorescence imaging of integrin $\alpha_v\beta_3$ in brain tumor xenografts. *Cancer Res. 64*, 8009–14.

(15) Beer, A. J., Haubner, R., Sarbia, M., Goebel, M., Luderschmidt, S., Grosu, A. L., Schnell, O., Niemeyer, M., Kessler, H., Wester, H. J., Weber, W. A., and Schwaiger, M. (2006) Positron emission tomography using [^{18}F]Galacto-RGD identifies the level of integrin $\alpha_v\beta_3$ expression in man. *Clin. Cancer Res. 12*, 3942–9.

(16) Chen, X., Park, R., Khankaldyyan, V., Gonzales-Gomez, I., Tohme, M., Moats, R. A., Bading, J. R., Laug, W. E., and Conti, P. S. (2006) Longitudinal microPET imaging of brain tumor growth with ^{18}F-labeled RGD peptide. *Mol. Imaging Biol. 8*, 9–15.

(17) Wu, Y., Zhang, X., Xiong, Z., Cheng, Z., Fisher, D. R., Liu, S., Gambhir, S. S., and Chen, X. (2005) microPET imaging of glioma integrin $\alpha_v\beta_3$ expression using ^{64}Cu-labeled tetrameric RGD peptide. *J. Nucl. Med. 46*, 1707–18.

(18) Wu, Z., Li, Z., Cai, W., He, L., Chin, F., li, F., and Chen, X. (2007) ^{18}F-labeled mini-PEG spacered RGD dimer (18 F-FPRGD2): synthesis and microPET imaging of $\alpha_v\beta_3$ integrin expression. *Eur. J. Nucl. Med. Mol. Imaging* [Online early access].

(19) Zhang, X., Xiong, Z., Wu, Y., Cai, W., Tseng, J. R., Gambhir, S. S., and Chen, X. (2006) Quantitative PET imaging of tumor integrin $\alpha_v\beta_3$ expression with ^{18}F-FRGD2. *J. Nucl. Med. 47*, 113–21.

(20) Poethko, T., Schottelius, M., Thumshirn, G., Hersel, U., Herz, M., Henriksen, G., Kessler, H., Schwaiger, M., and Wester, H. J. (2004) Two-step methodology for high-yield routine radiohalogenation of peptides: ^{18}F-labeled RGD and octreotide analogs. *J. Nucl. Med. 45*, 892–902.

(21) Schottelius, M., Poethko, T., Herz, M., Reubi, J. C., Kessler, H., Schwaiger, M., and Wester, H. J. (2004) First ^{18}F-labeled tracer suitable for routine clinical imaging of sst receptor-expressing tumors using positron emission tomography. *Clin. Cancer Res. 10*, 3593–606.

(22) Kilbourn, M. R., Dence, C. S., Welch, M. J., and Mathias, C. J. (1987) Fluorine-18 labeling of proteins. *J. Nucl. Med. 28*, 462–70.

(23) Wester, H. J., Hamacher, K., and Stocklin, G. (1996) A comparative study of N.C.A. fluorine-18 labeling of proteins via acylation and photochemical conjugation. *Nucl. Med. Biol. 23*, 365–72.

(24) Wilbur, D. S. (1992) Radiohalogenation of proteins: an overview of radionuclides, labeling methods, and reagents for conjugate labeling. *Bioconjugate Chem. 3*, 433–70.

(25) Cai, W., Zhang, X., Wu, Y., and Chen, X. (2006) A thiol-reactive ^{18}F-labeling agent, N-[2-(4-^{18}F-fluorobenzamido)ethyl]-maleimide, and synthesis of RGD peptide-based tracer for PET imaging of $\alpha_v\beta_3$ integrin expression. *J. Nucl. Med. 47*, 1172–80.

(26) Tornoe, C. W., Christensen, C., and Meldal, M. (2002) Peptidotriazoles on solid phase: [1,2,3]-triazoles by regiospecific copper(I)-catalyzed 1,3-dipolar cycloadditions of terminal alkynes to azides. *J. Org. Chem. 67*, 3057–64.

(27) Rostovtsev, V. V., Green, L. G., Fokin, V. V., and Sharpless, K. B. (2002) A stepwise huisgen cycloaddition process: copper(I)-catalyzed regioselective "ligation" of azides and terminal alkynes. *Angew. Chem., Int. Ed. Engl. 41*, 2596–9.

(28) Kolb, H. C., Finn, M. G., and Sharpless, K. B. (2001) Click chemistry: diverse chemical function from a few good reactions. *Angew. Chem., Int. Ed. Engl. 40*, 2004–2021.

(29) Pagliai, F., Pirali, T., Del Grosso, E., Di Brisco, R., Tron, G. C., Sorba, G., and Genazzani, A. A. (2006) Rapid synthesis of triazole-modified resveratrol analogues via click chemistry. *J. Med. Chem. 49*, 467–70.

(30) Burley, G. A., Gierlich, J., Mofid, M. R., Nir, H., Tal, S., Eichen, Y., and Carell, T. (2006) Directed DNA metallization. *J. Am. Chem. Soc. 128*, 1398–9.

(31) Krasinski, A., Radic, Z., Manetsch, R., Raushel, J., Taylor, P., Sharpless, K. B., and Kolb, H. C. (2005) In situ selection of lead compounds by click chemistry: target-guided optimization of acetylcholinesterase inhibitors. *J. Am. Chem. Soc. 127*, 6686–92.

(32) Bock, V. D., Hiemstra, H., and van Maarseveen, J. H. (2006) Cu^{I}-Catalyzed alkyne-azide "Click" cycloadditions form a mechanistic and synthetic perspective. *Eur. J. Org. Chem.* 51–68.

(33) Marik, J., and Sutcliffe, J. L. (2006) Click for PET: Rapid preparation of [^{18}F]fluoropeptides using Cu^{I}catalyzed 1,3-dipolar cycloaddition. *Tetrahedron Lett. 47*, 6881–84.

(34) Glaser, M., and Arstad, E. (2007) "Click labeling" with 2-[^{18}F]fluoroethylazide for positron emission tomography. *Bioconjugate Chem. 18*, 989–93.

(35) Lu, G., Lam, S., and Burgess, K. (2006) An iterative route to "decorated" ethylene glycol-based linkers. *Chem. Commun. (Cambridge)* 1652–4.

(36) Khoukhi, N., Vaultier, M., and Carrie, R. (1987) Synthesis and reactivity of methyl gama-azido butyrates and ethyl delta-azido valerates and of the corresponding acid chlorides as useful reagents for aminoalkylation. *Tetrahedron 43*, 1811–22.

(37) Haubner, R., Kuhnast, B., Mang, C., Weber, W. A., Kessler, H., Wester, H. J., and Schwaiger, M. (2004) [^{18}F]Galacto-RGD: synthesis, radiolabeling, metabolic stability, and radiation dose estimates. *Bioconjugate Chem. 15*, 61–9.

(38) Chen, X., Tohme, M., Park, R., Hou, Y., Bading, J. R., and Conti, P. S. (2004) Micro-PET imaging of $\alpha_v\beta_3$-integrin expression with ^{18}F-labeled dimeric RGD peptide. *Mol. Imaging 3*, 96–104.

BC700226V

Reductively Aminated D-Xylose–Albumin Conjugate as the Immunogen for Generation of IgG and IgE Antibodies Specific to D-Xylitol, a Haptenic Allergen

Kundimi Sreenath and Yeldur P. Venkatesh*

Department of Biochemistry and Nutrition, Central Food Technological Research Institute (CFTRI), Mysore-570020, Karnataka State, India. Received May 16, 2007; Revised Manuscript Received August 1, 2007

Sugar alcohols are widely used as food additives and drug excipients. Xylitol, a five-carbon sugar alcohol, and a low-calorie alternative sweetener to sucrose (approx 40% fewer calories), has enjoyed an enviable record of safety, and allergic reactions to xylitol are very rare. A case of oral erosive eczema to xylitol has been reported recently [Hanakawa, Y., Hanakawa, Y., Tohyama, M., Yamasaki, K., Hashimoto, K. (2005) Xylitol as a causative agent of oral erosive eczema. *Brit. J. Dermatol. 152*, 821–822]. Xylitol does not contain any reactive groups; hence, it is nonimmunogenic. In order to explain the immunogenicity of xylitol, polyclonal antibodies to xylitol have been raised using the reductive aminated product of D-xylose conjugated to bovine serum albumin (BSA) as the immunogen. Rabbits immunized with xylitol–BSA conjugate (52 haptens/molecule) gave a good antibody response. Purification of antixylitol antibodies was carried out using hapten-affinity chromatography on xylitol–keyhole limpet hemocyanin–Sepharose CL-6B; the yield was ~40 μg/mL of rabbit immune serum. Purified xylitol-specific antibodies appeared to be homogeneous by native PAGE with a pI of ~7.2 by isoelectric focusing. Although the purified antibodies are specific for the xylitoyl moiety of xylitol–protein conjugates, they reacted equally well with the Schiff base conjugate of xylosyl–protein conjugates (68% cross-reactivity) indicating that carbons 2 to 5 of xylitol act as an epitope. Xylitol antibodies showed excellent specificity towards xylitol and <4.4% cross-reactivity with D-xylose and various sugar alcohols except ribitol and galactitol, which showed ~11% and 8% cross-reactivity, respectively. D-Xylitol–BSA conjugate was used to raise IgE antibodies in BALB/c mice by repeated intradermal administration. Passive cutaneous anaphylaxis using the immune sera confirmed the haptenic nature of xylitol.

INTRODUCTION

Sugar alcohols (also known as polyhydric alcohols or polyols) are low-calorie bulk sweeteners. They are being used as food additives and drug excipients, as they are chemically inert, nontoxic, nonhygroscopic, and sweet in taste. Sugar alcohols commonly used as food additives are sorbitol (international numbering system: INS[1] 420), mannitol (INS 421), xylitol (INS 967), and erythritol (INS 968); maltitol (INS 965) and lactitol are used to a lesser extent. Xylitol, a pentitol, has been widely used in foods since its approval by the U.S. Food and Drug Administration (FDA) in 1960, because of its slow absorption, partial utilization, and reduced calories (2.4 calories/g) (*1*). Besides its uses as food additive and sweetener, xylitol has many medical uses such as prevention of dental caries (*2*), middle ear infections (*3*), and experimental osteoporosis (*4*). Xylitol occurs naturally in many fruits and vegetables at concentrations as high as 935 mg (yellow plum) and as low as 14 mg (chestnut) per 100 g dry substance (*5*). Xylitol is a popular sweetener for the diabetic diet in some countries, as it is metabolized independently of insulin and is extremely safe. Xylitol is used in unlimited quantity for foods with special dietary purposes. Sugar-free chewing gums and candies made with xylitol as the principal sweetener have received official endorsements from six national dental associations.

Mannitol, a hexitol, occurs naturally in many plant foods including mushrooms (*6*). The use of mannitol in foods is broadly permitted by the food additive regulations of FDA. In addition, intravenous infusion of 20% (w/v) mannitol (equivalent to 1100 mM) has been used as a therapeutic agent in many clinical situations due to its osmotically active property. Hypersensitivity reactions to 20% mannitol infusion have been reported in a small number of susceptible patients. Recently, mannitol was identified as an allergen for a sensitized subject (*7*, *8*), and mannitol-specific IgE was demonstrated for the first time in the serum of the subject sensitized to mannitol (*9*). Allergic reactions caused by erythritol as a sweetener in processed foods have been reported in three cases (*10*, *11*). On the basis of the inert nature of mannitol and erythritol, a hypothesis has been proposed to explain the mechanism of sensitization and hypersensitivity to these sugar alcohols (*12*). In this hypothesis, the sugar acts as a *prosensitizer*, its Schiff base adduct with proteins acts as a *sensitizer*, and the sugar alcohol acts as a *nonsensitizing elicitor*.

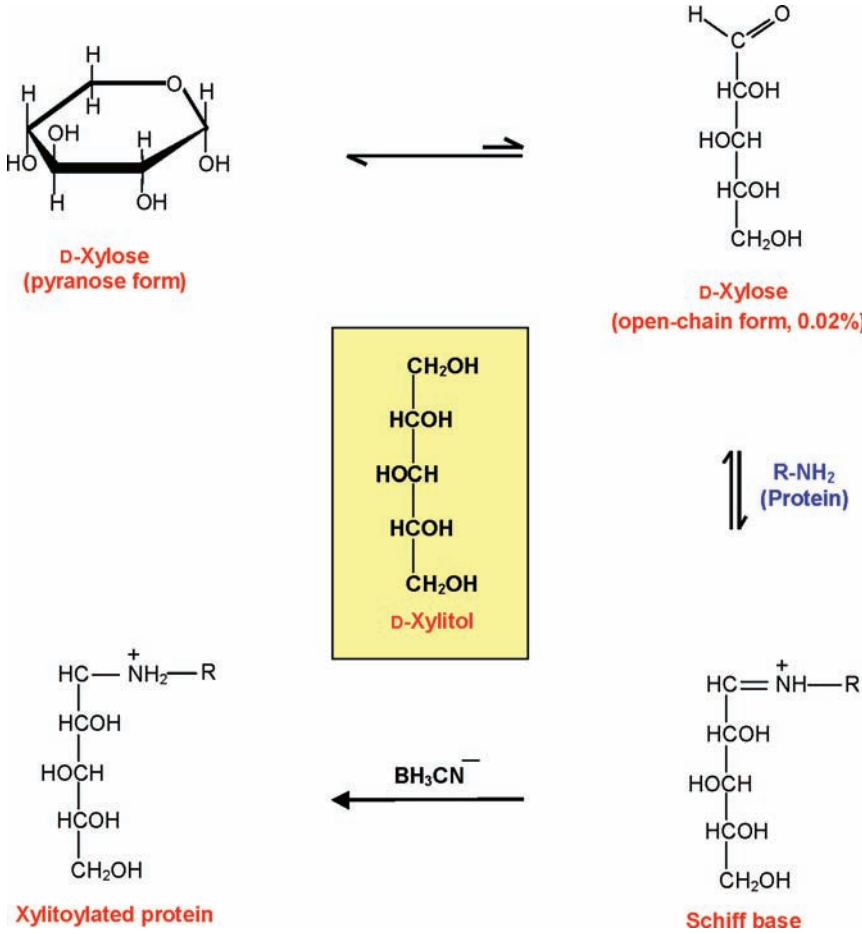
Allergic reactions to xylitol are also rare, similar to the case of mannitol and erythritol. However, one case of oral erosive

* Corresponding author. Dr. Yeldur P. Venkatesh, Ph.D., Department of Biochemistry and Nutrition, Central Food Technological Research Institute (CFTRI), 'Chaluvamba Vilas', KRS Road, Mysore-570020, Karnataka State, India. Tel: +91-821-2514876. Fax: +91-821-2517233. E mail: venkatyp@yahoo.com.

[1]Abbreviations used: INS, international numbering system for food additives; FDA, food and drug administration; IgG, immunoglobulin G; IgE, immunoglobulin E; PCA, passive cutaneous anaphylaxis; BSA, bovine serum albumin; KLH, keyhole limpet hemocyanin; TNBS, trinitrobenzenesulfonic acid; BCIP, 5-bromo-4-chloro-3-indolyl phosphate; NBT, nitro blue tetrazolium; FCA, Freund's complete adjuvant; FIA, Freund's incomplete adjuvant; $NaIO_4$, sodium periodate; M_r, relative molecular mass; SDS-PAGE, sodium dodecyl sulfate-polyacrylamide gel electrophoresis; IEF, isoelectric focusing; pI, isoelectric point; Xyt-BSA, D-xylitol–BSA conjugate; Xyt-KLH, D-xylitol–KLH conjugate; GRAS, generally recognized as safe; HSA, human serum albumin; OVA, ovalbumin.

10.1021/bc700175g CCC: $37.00 © 2007 American Chemical Society
Published on Web 11/03/2007

Scheme 1. Reaction of D-xylose with carrier protein by reductive amination to obtain xylitoyl epitopes. The structure of D-xylitol is shown in the box (carbons C1 to C5 should be viewed from top to bottom. The percentage of open-chain form of D-xylose is based on the circular dichroism study (*22*).



eczema to foods containing xylitol has been reported recently (*13*). Although the skin patch test was positive, the presence of xylitol-specific IgE has not been demonstrated in that study. Therefore, it is likely that the mechanism of formation of IgE antibodies to xylitol (Scheme 1) could follow the general scheme described for mannitol and other sugar alcohols (*12*).

Anticarbohydrate antibodies with specificity towards various monosaccharides, disaccharides, and oligosaccharides have been studied extensively (*14–19*). These are generally specific to *cyclic* pyranose or furanose structures of sugars. Only certain disaccharides have been conjugated to proteins by reductive amination with the aim of obtaining antibodies specific for a terminal nonreducing monosaccharide (cyclic) determinant (*14–16*); however, the acyclic monosaccharide arm formed by the reducing sugar unit was also involved in the antigenic determinant. Unlike saccharides, sugar alcohols possess *acyclic* straight chain structure; they are inert and do not have any reactive aldehyde or ketone groups. Hence, they cannot form conjugates with proteins to mount an immune response. This necessitates an indirect method to obtain sugar alcohol groups on a carrier protein for immunogenicity. Such a strategy was applied for the generation of polyclonal antibodies to erythritol and D-mannitol (*20*, *21*). With this background, it appeared interesting to demonstrate the formation of IgG antibodies to xylitol in rabbits using a xylitol–protein conjugate as the immunogen and characterize the affinity-purified antibodies in terms of specificity and cross-reactivity. The allergenic nature of xylitol was investigated by repeated intradermal administration of xylitol–BSA conjugate in BALB/c mice followed by homologous passive cutaneous anaphylaxis (PCA) assay for the demonstration of xylitol-specific IgE.

EXPERIMENTAL PROCEDURES

Reagents and Chemicals. D-Xylose, Sepharose CL-6B (6% beaded agarose, wet bead diameter: 40–165 μm), bovine serum albumin (BSA), keyhole limpet hemocyanin (KLH), sodium cyanoborohydride, periodic acid, and borane–pyridine complex solution ($C_5H_5N.BH_3$; BH_3 concentration ~8M; excess pyridine ~20%) were obtained from Sigma-Aldrich Chemical Co., St. Louis, MO. Trinitrobenzenesulfonic (TNBS) acid was a product of HiMedia Laboratories, Mumbai, India. Schiff reagent (1-fluoro-2,4-dinitrobenzene) was procured from Sisco Research Laboratories, Mumbai, India. Maxisorp ELISA microtiter plates (flat-bottom) were a product of Nunc A/S, Roskilde, Denmark. Goat antirabbit IgG–alkaline phosphatase conjugate, 5-bromo-4-chloro-3-indolyl phosphate (BCIP)/nitro blue tetrazolium (NBT), Freund's complete adjuvant (FCA), and Freund's incomplete adjuvant (FIA) were products of Bangalore Genei, Bangalore, India. Ampholines (pH 5–8) were procured from Pharmacia, Uppsala, Sweden. All other chemicals were of analytical grade.

Animals. New Zealand white male rabbits (7 months old) and Swiss albino mice (6–8 weeks old) were obtained from the animal house facility of our institute. BALB/c mice aged 6–8 weeks were procured from Central Animal Facility (CAF), Indian Institute of Science, Bangalore, India. Each experimental group consisted of 6 mice.

Preparation of Hapten–Protein Conjugates Containing Xylitol Epitopes. D-Xylose was conjugated to a carrier protein, bovine serum albumin (BSA), or keyhole limpet hemocyanin (KLH), by reductive amination (also termed as reductive alkylation) in the presence of a mild reducing agent, sodium cyanoborohydride, as described earlier for *meso*-erythritol and D-mannitol conjugates (*20, 21*) to obtain stable xylitol epitopes on the conjugated carrier protein.

In a separate experiment, D-xylose (100 mg) was incubated with BSA (68 mg) in the absence of sodium cyanoborohydride to obtain a Schiff base conjugate of D-xylosyl–BSA. The degree of substitution was determined by the decrease in amino groups as quantified by trinitrobenzenesulfonic acid (TNBS) assay. Protein estimation of conjugates was carried out as per the procedure of Bradford (*23*) using BSA as a standard.

Trinitrobenzenesulfonic Acid Assay for Amino Groups. The number of ε-amino groups remaining in conjugated BSA samples was determined using TNBS reagent (*24*). To 1 mL of D-xylitol–BSA conjugate/D-xylosyl–BSA Schiff base conjugate (100 μg protein) solution, 1 mL of 4% $NaHCO_3$ (pH 8.5) and 1 mL of 0.01% freshly prepared aqueous TNBS solutions were added. The reaction was carried out at 42 ± 2 °C for 2 h, followed by the addition of 1 mL of 10% SDS and 0.5 mL of 1 N HCl. The absorbance of the solution was monitored at 335 nm in a spectrophotometer, and a standard curve was obtained with unconjugated BSA (50–200 μg range) after appropriate blank corrections. The percent conjugation for a conjugate at a specified time was calculated from the decrease in absorbance, when compared with that of an identical concentration of standard BSA in the TNBS assay. Percent conjugation was converted to degree of substitution in terms of moles of xylosyl Schiff base or xylitol per mole of carrier, assuming that BSA has 61 TNBS-reactive amino groups (*24, 25*).

Periodic Acid Schiff (PAS) Staining for Glycoconjugates. This was performed to confirm the glycated nature (*26*) of xylitol–BSA conjugate following the reductive amination. Following SDS-PAGE (*27*), the gel was immersed in 12.5% trichloroacetic acid solution for 30 min, transferred to 1% periodic acid solution, and kept in the dark for 50 min. Then, the gel was washed thoroughly with distilled water to remove the periodic acid, followed by the addition of Schiff reagent and incubation at 4 °C for 1 h. After the color development, the reaction was arrested by adding 7% glacial acetic acid.

Immunization and Collection of Antiserum. Three New Zealand white male rabbits (*Oryctolagus cuniculus*), 7 months old, housed in the animal house facility of this institute, were used for the immunization according to standard protocols (*28, 29*), after obtaining approval from the institutional animal ethics committee (IAEC).

Initially, the immunogen, D-xylitol–BSA conjugate (52 mol D-xylitol/mol BSA; 0.5 mL, 1 mg protein) microemulsified with 0.5 mL of 3× concentrated Freund's complete adjuvant, was administered subcutaneously at 8–10 sites on the back of the animal. After 4 weeks, booster doses containing 0.5 mg of the antigen microemulsified with Freund's incomplete adjuvant were administered intramuscularly at 15 day intervals. The animal was bled by marginal ear vein puncture 1 week before the first injection (to obtain preimmune serum) and 1 week after each booster dose (to obtain immune serum). The pooled serum was stored in aliquots below −20 °C.

Titration of Antiserum. To check for the formation of hapten-specific antibodies, the antiserum was analyzed initially by dot-immunoblot assay (*30*) and later by noncompetitive ELISA using the coated antigen format (*31*). The titer of the antiserum was determined by measuring the binding of serial dilutions of the antiserum to coated D-xylitol–KLH (conjugate in which 50% of the amino groups of KLH have been modified with xylitol). Flat-bottom polystyrene microtiter wells were coated with D-xylitol–KLH conjugate at 1000, 100, 50, and 10 ng per well (100 μL volume) in 0.1 M carbonate–bicarbonate buffer, pH 9.6, by incubating at 4 °C overnight. The wells were washed thrice between steps using PBS containing 0.05% Tween-20 (PBS-T). Blocking was done using 0.5% gelatin in PBS-T at 37 °C for 30 min. Antiserum diluted in blocking buffer (1:10 to 1:400 000) was added (100 μL/well) and incubated at 37 °C for 2 h. Goat antirabbit IgG-alkaline phosphatase secondary antibody (1:5000 dilution in blocking buffer; 100 μL/well) was added and incubated at 37 °C for 1 h. Color development was done using *p*-nitrophenyl phosphate (1 mg/mL; 100 μL/well) in 1% diethanolamine buffer, pH 9.8, at 37 °C for 30 min. The reaction was stopped by adding 3 M NaOH (40 μL/well), and the absorbance was read at 405 nm in an ELISA microplate reader.

A positive value in ELISA is defined as the absorbance value obtained with immune serum samples (as measured by absorbance value at 405 nm) 2-fold greater than that obtained in the case of preimmune serum. Antibody titer is defined as the reciprocal of the highest dilution that gave a positive value in ELISA.

Purification of Antixylitol Antibodies. *(a) Preparation of D-Xylitol–Keyhole Limpet Hemocyanin (D-xylitol–KLH)–Sepharose CL-6B Affinity Matrix.* D-Xylitol–KLH conjugate with 50% modification of amino groups was used for immobilization onto Sepharose CL-6B (*32*). Sepharose CL-6B gel was first washed thoroughly with water to remove preservative, and then suspended in water to obtain 0.2 g moist gel/mL (total 10 mL). The washed gel was then oxidized by adding solid sodium periodate ($NaIO_4$) to a final concentration of 25 mM. The mixture was swirled at 25 °C for 30 min; unreacted $NaIO_4$ was inactivated by the addition of an equimolar amount of ethylene glycol. After 15 min, the gel was thoroughly washed with water followed by 0.2 M phosphate buffer, pH 7.0. The moist gel (0.2 g/mL suspension) in phosphate buffer was mixed with D-xylitol–KLH conjugate (2 mg) followed by direct addition of borane–pyridine complex to a final concentration of 25 mM. The reaction mixture was mildly agitated, first at 25 °C for 3 h, and then at 4 °C for 10 h. Next, gel beads were washed extensively with water to remove unreacted borane–pyridine and the ligand. The gel was finally packed into a glass column (2 mL bed volume), and equilibrated with 20 mM phosphate buffer, pH 7.4, containing 140 mM NaCl, and stored at 4 °C in the same buffer with 0.01% merthiolate as a preservative.

(b) Hapten Affinity Chromatography for Purification of Antixylitol Antibodies. Antixylitol–BSA antiserum (6 mL) obtained from the immunized rabbit was diluted 1:1 in PBS (pH 7.4), and passed through the D-xylitol–KLH–Sepharose CL-6B column (0.8 cm id × 4 cm; 2 mL bed volume) that had been pre-equilibrated with PBS at 4 °C. The flowthrough was recycled twice through the column. After washing with 50 mL PBS, the bound antibodies were eluted with 0.1 M glycine–HCl buffer, pH 2.9; the eluate was neutralized immediately using 0.5 M Tris base. The eluate was aliquoted in 200 μL portions and stored below −20 °C. The concentration of specific antibody was calculated on the basis of the reference value of $A^{0.1\%,\ 1\ cm}$ at 280 nm of 1.4 for rabbit IgG (*33*). The affinity-purified antixylitol antibodies were subjected to native-PAGE (basic) using Tris-glycine buffer system, and isoelectric focusing (*29*).

Titration of Hapten Affinity Purified Antibodies and Determination of Cross-Reactivity. The affinity-purified antibodies were tested for their ability to bind to Schiff base conjugate of D-xylosyl–BSA and its reductive aminated product, namely, D-xylitol–BSA conjugate. Therefore, the Schiff base conjugate of D-xylosyl–BSA, or its reduced product (D-xylitol–BSA conjugate) having approximately similar modification of

amino groups was used as the coating antigen; in the case of D-xylosyl–BSA, 20 amino groups had been substituted as compared to 19 amino groups in D-xylitol–BSA. The linear regression analysis was performed using *SigmaStat 3.1* software (Systat Software Asia Pacific Ltd., Bangalore, India).

The affinity-purified antixylitol antibodies were used for noncompetitive ELISA experiments to obtain the binding curves using D-xylitol–KLH (50 ng/well) conjugate as the coating antigen. Specificity and cross-reactivity of the affinity-purified antibodies were studied by inhibition–ELISA experiments. Here, purified antibodies were preincubated with various concentrations (0.01–1000 mM) of test compounds (competitors like D-xylitol, D-mannitol, sorbitol, D-ribitol, L-arabinitol, glycerol, ethylene glycol, D-xylose) and L-lysine at 37 °C for 1 h before adding to coated (D-xylitol–KLH, 50 ng/well) microtiter wells. Other steps were as described in the Titration of Antiserum section. The percent cross-reactivity for various inhibitors was calculated using the formula (IC_{50} for xylitol ÷ IC_{50} for test compound) × 100 where IC_{50} is the concentration required for 50% inhibition in ELISA.

Calculation of Affinity Constant of the Purified Antixylitol Antibodies. The affinity constants of the purified antixylitol antibodies were calculated using a computer program described by Raghava and Agrewala (*34*). This is a simple and reliable method based upon the law of mass action for calculating the affinity constant of a monoclonal antibody directed against the haptenic 2,4,6-trinitrophenyl group using the data obtained from noncompetitive ELISA.

D-Xylitol–KLH conjugate (10 μg/mL) was prepared in 0.1 M carbonate–bicarbonate buffer. A series of 4 doubling dilutions were made so that the final concentration was 1/8 of the starting one. In a 96-well microtiter plate, rows A, B, C, and D were coated with 100 μL D-xylitol–KLH containing 1000, 500, 250, and 125 ng, respectively. KLH (1000 ng in 100 μL) was added in row E that worked as control. After overnight incubation at 4 °C, the plate was washed thrice with PBS-T. The concentration of the affinity-purified antibodies used was 4 ng in 100 μL. All the other steps were followed as described in the Titration of Hapten-Purified Antibodies section.

The menu-driven computer program (Ab_affi program) for calculating the affinity constant of hapten-specific antibody from noncompetitive ELISA data written in GW-BASIC is available from the internet (http://www.imtech.res.in/bic/achsw.html#serv3). Absorbance data obtained from the microtiter plate can be fed to the computer either directly by interfacing or by using the keyboard. Before starting the calculation, a "dilution template" should be defined and the information about the serial dilutions of antibody added to the wells, and antigen coated on the plate must also be supplied.

Induction of Hypersensitivity in BALB/c Mice. BALB/c mice ($n = 6$ in each group) were immunized with 60 μL of saline (negative control), 1 mg/mL ovalbumin (positive control), D-xylitol (1 mg/mL), D-xylitol–BSA conjugates (2 mg/mL), and 2 mg/mL BSA (carrier protein control) by intradermal injection. The use of an adjuvant was avoided in order to assess the inherent allergenicity of the xylitol–BSA conjugate. On days 5, 12, 19, 26, and 33, booster doses were given with 30 μL of each of the antigens mentioned above (*35*). Blood was collected from the retro-orbital vein on days 8 and 22, and finally on day 36, and processed to obtain serum (1.8 mL per collection per group). Serum samples are pooled on a treatment group basis; equal volumes of serum from 3 collections contribute to the pool. Samples were stored at −70 °C until analysis.

Measurement of Serum Antixylitol IgE Antibody by PCA. The antixylitol IgE titer of BALB/c mouse immune serum was measured by the homologous passive cutaneous anaphylaxis (PCA) assay (*36*) performed in Swiss albino mice. For this experiment, 100 μL of 1:1 diluted pooled serum (with saline) obtained from each of the treatment groups (BALB/c mice that were administered separately with different antigens, viz., saline, ovalbumin, D-xylitol–BSA conjugates, BSA, D-xylitol) were injected intradermally on the shaved back of male Swiss albino mice ($n = 5$ for each group). After 24 h, 30 μL of D-xylitol–BSA conjugates having different hapten densities or other antigens (saline, ovalbumin, BSA, D-xylitol) with 0.25% Evans blue were injected intravenously into the respective group ($n = 5$) of animals. The animals were sacrificed 30 min after the i.v. injection, and infiltration of the dye into the skin around the injection sites was observed. A serum sample (representative of a particular antigen) is identified as an IgE responder if the challenge resulted in a blue lesion in the skin with a mean diameter of 3 mm or greater (*37*).

RESULTS

Preparation and Characterization of Xylitol–Protein Conjugates by Reductive Amination. D-Xylose was coupled to BSA by reductive amination (Scheme 1) as described in the Experimental Procedures section. The time course of reductive amination reaction for D-xylose is shown in Figure 1 (panel a). The reaction is faster initially (up to 25 h), and slowly reaches a plateau thereafter. At 20 h of reaction, approximately 32 mol of xylitol have been conjugated per mole of BSA.

The xylitol–BSA conjugate was analyzed by SDS-PAGE (Figure 1, panel b), wherein an increase in molecular mass was apparent for the conjugate as compared to control BSA. The R_f values of the mol wt markers, control (BSA), and D-xylitol–BSA conjugate were calculated (data not shown). The increase in the relative molecular mass (M_r) of xylitol–BSA conjugate when compared to control BSA was ~8 kDa, which translates to 52 mol of xylitol coupled per mole BSA. Since BSA is devoid of glycans, the glycation of D-xylitol–BSA conjugates was detected by PAS staining. The PAS staining (Figure 1, panel c) clearly confirms the addition of glycans by way of xylitoyl groups on the carrier protein, BSA.

D-Xylose was incubated with BSA (without sodium cyanoborohydride) to form Schiff base conjugates. The time course of the reaction is shown in Figure 1, panel d. It is observed that the reaction of D-xylose with BSA is faster initially (up to 3 h) with the availability of almost all the accessible amino groups. As the reaction time progresses, the modification of the amino groups of BSA decreases due to the unstable nature of the Schiff base conjugate and the reversibility of the reaction. TNBS assay showed modification of 20 amino groups at the end of 3 h incubation, and as the time progresses, the rate of conjugation decreases. In the case of the reductive amination reaction (shown for comparison in Figure 1, panel d), the conjugation of D-xylose with BSA gradually increases with time. Approximately 19 and 32 amino groups have been modified in the reductive amination reaction at 3 and 6 h, respectively.

Immunochemical Analyses of Rabbit D-Xylitol–BSA Antiserum. The immunoreactivity of antiserum with D-xylitol–KLH can be detected easily at 1 in 2×10^4 dilution, in the dot-immunoblot analysis, which is shown in Figure 2 (panel A, strip a). The antiserum was positive for D-xylitol–BSA conjugate (Xyt-BSA), D-xylitol–KLH conjugate (Xyt-KLH), and BSA, but was negative for KLH. The highest dilution of antiserum for perceptible detection of dots was found to be 1 in 5×10^4 (strip b). The sensitivity of antixylitol–BSA antiserum was determined by checkerboard analysis of the immune serum where the concentrations of both the antigen and antiserum are varied (Figure 2, panel B). The antiserum titration curves show that the sensitivity of antibodies is seen at 1 in 1×10^4 dilution using 1000 ng per well of coating antigen, D-xylitol–KLH. An optimal titer of 1:100 antiserum dilution was evident at a coating antigen (D-xylitol–KLH) concentration of 100 ng/well.

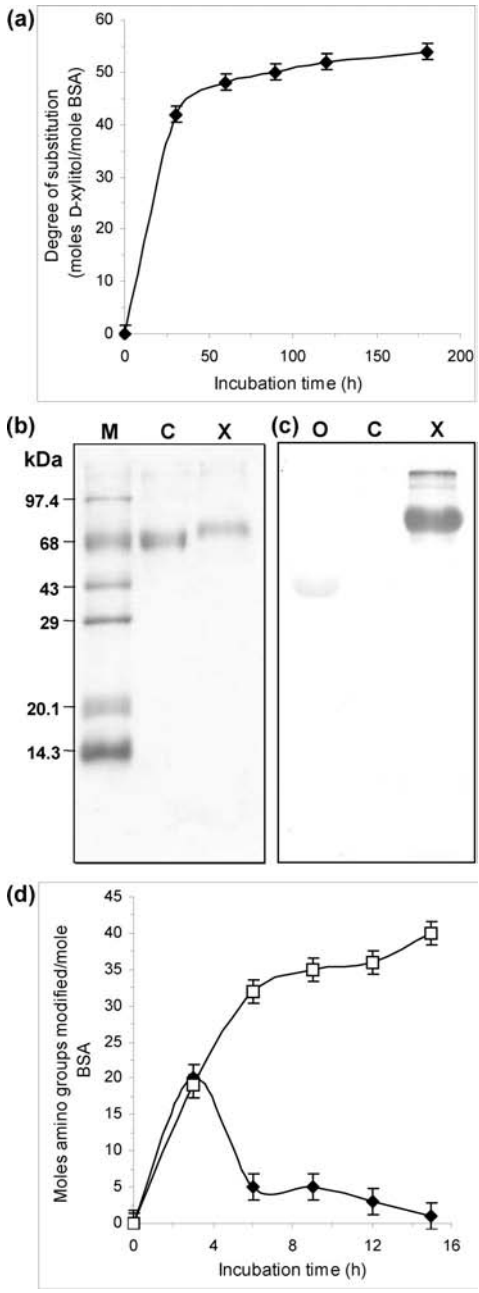


Figure 1. Preparation of D-xylitol–bovine serum albumin (BSA) conjugate by reductive amination at pH 8 and 37 °C. Panel a: Time course of reaction for the formation of D-xylitol–BSA. Panel b: SDS-PAGE (15%; reducing) analysis of D-xylitol–BSA sample from the 180 h reductive amination reaction. Staining: Coomassie blue. Lane M, molecular weight markers in kDa; lane C, control BSA (10 μg); lane X, D-xylitol–BSA conjugate (10 μg). Panel c: Periodic acid–Schiff (PAS) staining of D-xylitol–BSA conjugate analyzed by SDS-PAGE (15%; reducing). Lane O, ovalbumin, a glycoprotein (positive control); lane C, BSA, a nonglycoprotein (negative control); lane X, D-xylitol–BSA conjugate. Protein load: 15 μg in all cases. Panel d: Time course of reaction for the formation of Schiff base conjugate of D-xylose with BSA (♦) or D-xylitol–BSA conjugate by reductive amination (□).

Hapten Affinity Purification of Antixylitol Antibodies. The xylitol-specific antibodies were purified from the antiserum by hapten affinity chromatography on D-xylitol–KLH–Sepharose CL-6B. The elution of bound antibody, after loading the sample and washing, is presented in Figure 3. The antibodies were found to elute in the first 3–4 fractions. The yield of xylitol-specific antibodies was found to be in the range of 36–42 μg per milliliter of rabbit antiserum, based on six chromatographic analyses.

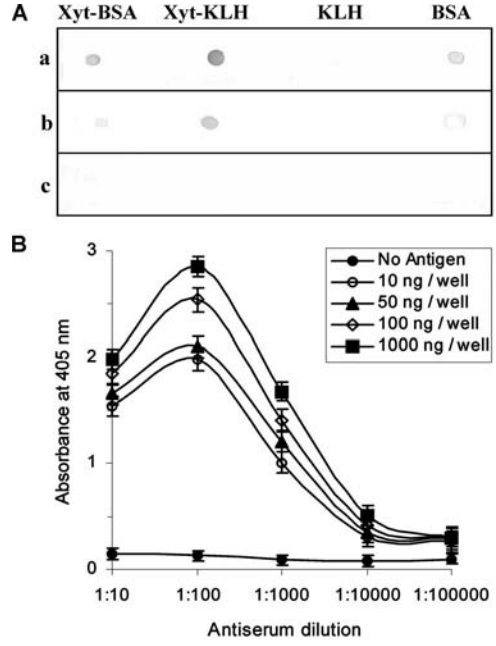


Figure 2. Immunochemical analyses of rabbit antiserum to xylitol–BSA conjugate. Panel A: Dot-immunoblot analysis on nitrocellulose strips. Antigens: 5 μg each of D-xylitol–BSA (Xyt-BSA); D-xylitol–KLH (Xyt-KLH); KLH; BSA. Antixylitol–BSA antiserum dilutions: a, 1:20 000; b, 1:50 000; c, preimmune serum as control (1:2000 dilution). Secondary antibody: goat antirabbit IgG-alkaline phosphatase (1:4000 dilution). Panel B: Checkerboard analysis by ELISA at different coated antigen concentrations and antiserum dilutions. Coating antigen: D-Xylitol–KLH conjugate (concentrations shown as inset). Secondary antibody: goat antirabbit IgG-alkaline phosphatase (1:4000 dilution). The absorbance values are the means of triplicate analysis.

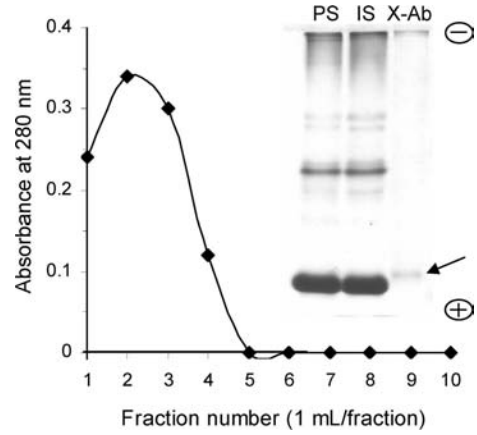


Figure 3. Elution profile of antixylitol antibodies from D-xylitol–KLH–Sepharose CL-6B affinity column (0.8 cm id × 4 cm; 2 mL bed volume). Sample load, 6 mL rabbit antixylitol–BSA antiserum; elution buffer, 0.1 M glycine–HCl, pH 2.9. Inset: Native PAGE (7.5%, basic) analysis of affinity-purified xylitol-specific antibodies. Staining: Coomassie blue. PS, preimmune serum (10 μg); IS, immune serum (10 μg); X-Ab, affinity-purified xylitol-specific antibodies (5 μg); arrow indicates the position.

Affinity-purified antixylitol antibodies were analyzed by native-PAGE (basic), which showed a single band on the gel indicating the homogeneity of the antibodies (Figure 3, inset). Isoelectric focusing (IEF) analysis of affinity-purified antixylitol antibodies showed only a single band at approximately pI 7.2, suggesting a single specific clone and isotype (data not shown).

Characterization of Antixylitol Antibodies. The affinity constant of antixylitol antibodies was calculated using noncom-

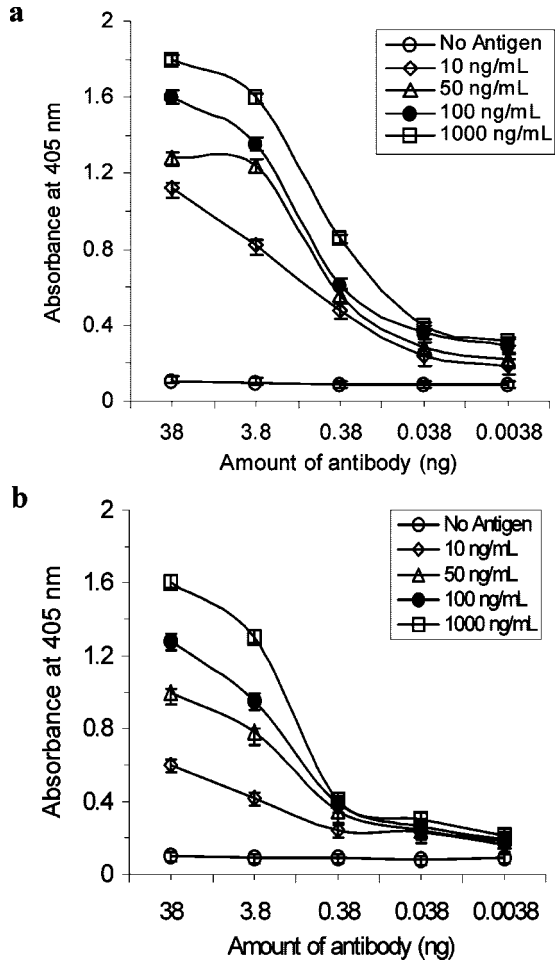


Figure 4. Comparison of binding curves for affinity-purified xylitol antibodies with xylitol–BSA/xylosyl–BSA conjugates. The absorbances at 405 nm for all the antigen concentrations at three different antibody concentrations (38, 3.8, and 0.38 ng) were analyzed between the two data sets by linear regression analysis. The *R* values were found to be 0.979 (at 38 ng), 0.991 (at 3.8 ng), and 0.699 (at 0.38 ng). Panel a: Binding curves obtained with xylitol-specific antibodies as a function of protein concentration and varying coated antigen, D-xylitol–BSA conjugate concentrations. Hapten density: 19 mol/mol BSA. Other details are as given in Figure 2, panel B. Panel b: Binding curves obtained with xylitol-specific antibodies as a function of protein concentration and varying coated antigen, D-xylosyl–BSA (Schiff base conjugate) concentrations. Hapten density: 20 mol/mol BSA.

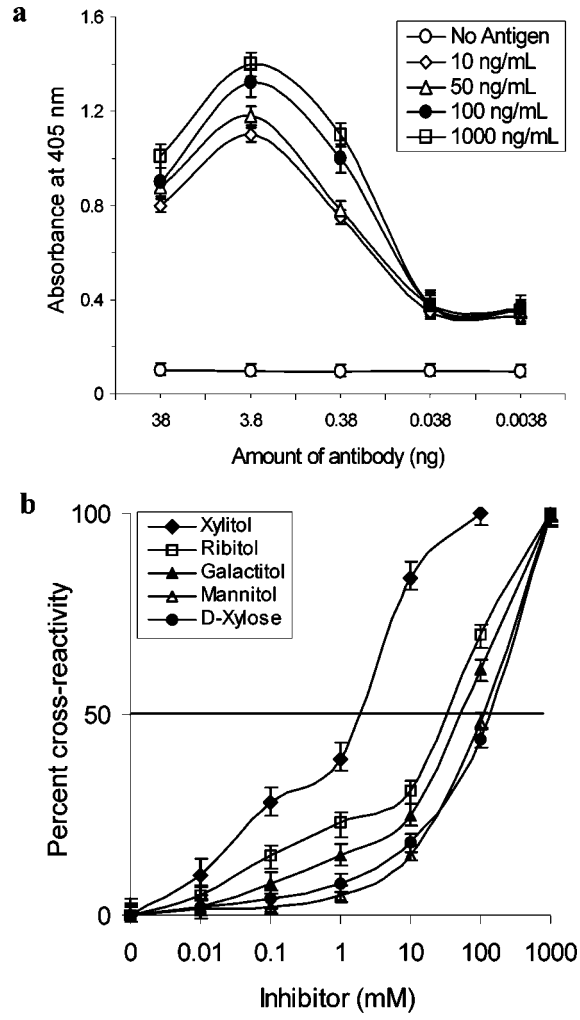


Figure 5. Immunochemical analyses of affinity-purified xylitol antibodies. Panel a: Binding curves of xylitol-specific antibodies as a function of protein concentration and varying coated antigen, D-xylitol–KLH (reductively aminated product) concentrations. Other details are as given in Figure 2, panel B. Panel b: Specificity of purified xylitol antibodies as determined by inhibition ELISA. Coating antigen: D-xylitol–KLH conjugate, 100 ng/well. Purified antixylitol antibodies (~4 ng in 100 μL volume) were preincubated with various concentrations of D-xylitol, ribitol, galactitol, and so forth, at 37 °C for 1 h and then transferred to ELISA wells. Other details are as given in Figure 2, panel B.

petitive ELISA by the method of Raghava and Agrewala (*34*) and was found to be 3.86×10^9.

In order to find out whether the xylitol-specific antibodies can recognize the Schiff base conjugate of xylosyl–BSA, the binding curves with both xylitol–BSA conjugate and xylosyl–BSA conjugate (Schiff base) were examined. The binding curves are shown in Figure 4. It is seen that the affinity-purified antibodies recognize the Schiff base conjugate of xylosyl–BSA (panel b) to a slightly lesser extent—approximately two-thirds the reactivity of xylitol–BSA conjugate (panel a).

Cross-Reactivity of Antixylitol Antibodies. The binding curves obtained with purified xylitol antibodies (Figure 5, panel a) shows that the sensitivity of antibodies can be observed even at ~200 pg (data not shown) for a coating antigen (D-xylitol–KLH) concentration of 100 ng/well. Optimal concentrations of ~4 ng of affinity-purified xylitol antibodies and 100 ng/well of D-xylitol–KLH coating antigen were selected from this checkerboard analysis for the inhibition ELISA studies with various sugars, sugar alcohols, and other small molecules.

Table 1. Specificity and Cross-Reactivity of Affinity-Purified Antixylitol Antibodies

test compound	IC_{50} (mM)	% cross-reactivity
D-xylitol	4.0	100.0
D-ribitol	35.0	11.4
D-galactitol	50.0	8.0
D-mannitol	90.0	4.4
D-xylose	102.5	3.9
L-arabinitol	108.0	3.8
meso-erythritol	108.1	3.8
D-sorbitol	135.1	3.7
D-threitol	350.0	3.0
glycerol	380.0	1.1
ethylene glycol	400.0	1.0
L-lysine	500.0	0.8

Inhibition ELISA was performed to check the cross-reactivity of the purified antixylitol antibodies (Figure 5, panel b). The panel of compounds tested (competitive inhibitors) included sugars like D-xylose and various sugar alcohols (*meso*-erythritol, D-xylitol, L-arabinitol, D-ribitol, D-mannitol, sorbitol, D-galactitol), ethylene glycol, glycerol, and L-lysine. The percent cross-

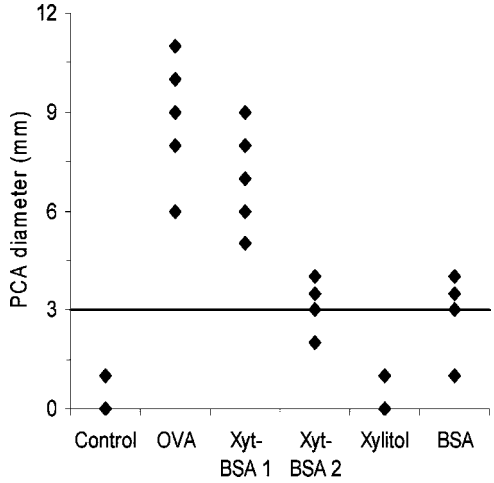


Figure 6. Passive cutaneous anaphylaxis (PCA) assay performed in Swiss albino mice ($n = 5$ per group) of different sera obtained on days 8, 22, and 36 from BALB/c mice ($n = 6$ per treatment group) that received repeated intradermal administration of antigens. The amount of different antigens used for immunization is 60 μg. Xyt–BSA 1, D-xylitol–BSA conjugate with 52 haptens; Xyt–BSA 2, D-xylitol–BSA conjugate with 32 haptens; OVA, ovalbumin; BSA, bovine serum albumin; control, saline. Horizontal line denotes cutoff for positivity at 3 mm. The PCA response from each animal is represented as a data point. Note the overlaps in the data points of control, xylitol, Xyt–BSA 2, and BSA groups.

reactivity for D-xylose and sugar alcohols is summarized in Table 1. Among the sugar alcohols tested, only D-ribitol showed 11.4% and galactitol showed 8% cross-reactivity, whereas for D-xylose and other sugar alcohols, the cross-reactivity ranged from 3.0% to 4.4%. The cross-reactivity was found to be 2–4% in the case of some monosaccharides such as D-glucose, D-mannose, and D-ribose (data not shown). The cross-reactivity was ~1% in the case of ethylene glycol, glycerol, and lysine.

Measurement of Antixylitol–IgE Antibody by Passive Cutaneous Anaphylaxis (PCA). BALB/c mice were immunized with various antigens, saline (negative control), ovalbumin (positive control), D-xylitol–BSA conjugates (Xyt-BSA 1, 52 haptens/mole; Xyt-BSA 2, 32 haptens/mole), D-xylitol, and BSA to evaluate the inherent potential of these antigens to produce IgE response. BALB/c mice immunized with high hapten density D-xylitol–BSA conjugate (Xyt-BSA 1, 60 μg) showed a positive reaction (5–9 mm range) in passive cutaneous anaphylaxis (PCA) when compared to 2–4 mm range seen in mice immunized with moderate hapten density D-xylitol–BSA conjugate (Xyt-BSA 2, 60 μg). Ovalbumin showed a strong positive reaction (6–11 mm range), whereas D-xylitol, BSA, and saline showed a negative reaction (Figure 6).

DISCUSSION

The hypothesis proposed for the mechanism of sensitization as well as IgE-mediated type I (immediate) hypersensitivity to mannitol (*12*) appears to be applicable to xylitol also (Scheme 1). Nearly 52 out of 61 amino groups of BSA can be reductively alkylated with D-xylose. The xylitoylation of BSA was confirmed by an increase in the relative molecular mass as well as positive PAS staining.

D-Xylitol–BSA conjugate as the immunogen produced good antibody response in rabbits, as evidenced by the sensitivity and specificity in dot immunoblots. Xylitol-specific antibodies were purified by affinity chromatography for characterization studies. In order to remove antibodies to BSA from D-xylitol–BSA antiserum, an affinity matrix was prepared by conjugating D-xylose to KLH, a carrier protein other than the one used for immunization, and then covalently coupling this conjugate (D-xylitol–KLH) to Sepharose CL-6B. Another advantage of using KLH for the affinity matrix is its high molecular weight possessing a large number of amino groups (*38*), which are absolutely essential for the coupling of D-xylitol to Sepharose CL-6B, through KLH. The affinity matrix, xylitol–KLH–Sepharose CL-6B, should be of value in purifying xylitol-specific IgE from the serum of allergic subjects sensitized to xylitol. The affinity constant of antixylitol antibodies was 3.86×10^9, which appears to be in the range of affinity constants reported for many monoclonal antibodies raised against haptens.

Interestingly, the affinity-purified antibodies also reacted with the Schiff base conjugate of D-xylosyl–BSA, indicating that antixylitol IgE can react with the Schiff base conjugates of D-xylose with serum proteins which may be formed in vivo by nonenzymic glycation of proteins by xylose. However, the reactivity of purified antibodies with the Schiff base conjugate of D-xylosyl–BSA was roughly two-thirds compared to xylitol–BSA conjugate (Figure 4, panel b).

On the basis of the checkerboard analysis of purified antibodies, the optimal conditions for inhibition ELISA were found to be 100 ng/well coating antigen D-xylitol–KLH, and 4 ng affinity-purified xylitol antibodies in a volume of 100 μL. It is clear from the inhibition ELISA experiments that the antibodies showed the least cross-reactivity with most monosaccharides including D-xylose and sugar alcohols. D-Xylitol showed maximum (100%) cross-reactivity, and among other sugars/sugar alcohols tested, only ribitol and galactitol showed 11.4% and 8% cross-reactivity, respectively. In the reductive amination reaction, the epsilon amino groups of L-lysyl residues of BSA react with the aldehyde group of the sugar D-xylose. Therefore, L-lysine was tested in the cross-reactivity studies to check whether the antibody also recognizes a portion of lysyl residue as an epitope. The results from Table 1 show that the cross-reactivity of L-lysine is only 0.8%, which clearly indicates that the xylitol-specific antibody is not recognizing the lysyl residue. On the basis of the low cross-reactivity of 2-carbon alcohol (ethylene glycol), 3-carbon alcohol (glycerol), and 4-carbon alcohol (*meso*-erythritol), it appears that the portion of xylitol molecule representing carbon atoms 2 to 5 most likely represents a single epitope.

Immunization study using D-xylitol–BSA conjugate in BALB/c mice (without the use of an adjuvant) demonstrated that the conjugate with high hapten density (52 haptens/mole) has the potential to induce IgE response, which is evidenced by the positive reaction in the passive cutaneous anaphylaxis. However, D-xylitol–BSA conjugate with moderate hapten density (32 haptens/mole), D-xylitol, and BSA showed a negative reaction, indicating that they cannot induce IgE response under identical conditions. Thus, the xylitol moiety as a hapten appears to possess allergenicity.

Only a single case of oral erosive eczema to xylitol has been reported so far, based on case history and skin patch test for IgE-mediated hypersensitivity (*13*). However, the presence of xylitol-specific IgE in the serum of the xylitol-sensitized subject has not been demonstrated. Xylitol is currently being used as a low-calorie alternative sweetener, and is listed as a GRAS (generally recognized as safe) substance under food additives. Xylitol and its parent monosaccharide D-xylose are considered safe even at high concentrations as evidenced by several studies (*1–3*, *39–41*). However, the incidence of allergic reactions could slightly increase in the future due to the increased consumption of a variety of processed foods containing D-xylose and/or covalently bound xylitol. Additionally, xylitol may undergo oxidation to xylose in vivo, which can then follow the reactions outlined in Scheme 1. On the basis of the results of our study, it should be possible to demonstrate by ELISA the presence of xylitol-specific IgE in serum using D-xylitol–protein

as the coating antigen. In fact, the presence of mannitol-specific IgE in the serum of the allergic subject sensitized to mannitol has been demonstrated earlier (*9*).

Xylitol conjugate of human serum albumin (HSA) or other endogenous proteins may be formed in vivo, which can give rise to an IgE immune response in humans who are susceptible to sensitization to xylitol. Alternatively, xylitol conjugates or corresponding Schiff bases formed under certain food processing conditions may also act as sensitizing agents. Although not tested, it is possible that the Schiff base conjugate of xylosyl–protein may act as an immunogen to produce antibodies which can recognize both the Schiff base as well as free xylitol, albeit not to a similar extent. In the rare case of oral erosive eczema caused by xylitol as a contact allergen described by Hanakawa et al. (*13*), wherein the presence of xylitol-specific IgE has not been shown, it is highly probable that the afore-mentioned possibilities are operating. On the basis of our earlier hypothesis enunciated for mannitol sensitization and hypersensitivity (*12*), it appears very likely that D-xylose acts as a noneliciting prosensitizer and free D-xylitol acts as a nonsensitizing elicitor. This means that, although xylitol cannot act as a sensitizing agent, it will elicit an allergic reaction in persons sensitized to xylosyl–protein (Schiff base) conjugates. The question of how Schiff base conjugates get reduced in vivo is yet to be investigated.

IgG antibodies specific to xylitol described here should prove useful in developing immunoassays for D-xylitol or D-xylitol epitopes on modified proteins in biological samples, natural and processed foods (*42*), and pharmaceuticals. It is interesting to note in this context that xylosyl–lysyl linkages (aldimine) and xylosyl–seryl linkages are present on core proteins of dermatan sulfate of connective tissues (*43*), and reducible lysine–carbohydrate condensation products have been identified in collagen as a result of age-related changes (*44*).

CONCLUSIONS

The results from this study demonstrate that xylitoyl epitopes can be easily formed on a suitable carrier protein by reductive amination. D-Xylitol–BSA conjugate thus formed (with 52 xylitoyl groups) has been used as an immunogen in rabbits to generate antixylitol antibodies, which have been purified from D-xylitol–BSA antiserum on a hapten-affinity column (D-xylitol–KLH–Sepharose CL-6B) for characterization. The purified antibodies show excellent specificity for xylitol; only ribitol was found to give significant cross-reactivity. Schiff base conjugates of xylosyl–protein are also recognized although to a slightly lesser extent. Immunization study in BALB/c mice has clearly shown that D-xylitol–BSA conjugate with high hapten density induces an IgE response as confirmed by homologous PCA.

ACKNOWLEDGMENT

We wish to thank Dr. V. Prakash, Director, CFTRI, Mysore for his support, keen interest, and constant encouragement in this work. The research work was supported by Council of Scientific and Industrial Research (CSIR), New Delhi (institutional project MLP-1407 to Y.P.V.), and senior research fellowship to K.S. The skillful assistance rendered by Dr. S. P. Muthukumar in animal experiments with BALB/c mice is gratefully acknowledged. We also thank Mr. R. Ravi, Department of Sensory Science, CFTRI, for his valuable assistance in linear regression analysis.

LITERATURE CITED

(1) Bond, M., and Dunning, N., (2006) Xylitol. *Sweeteners and Sugar Alternatives in Food Technology* (Mitchell, H., Ed.) pp 295–324, Chapter 15, Blackwell Publishing, Oxford, U.K.

(2) Mäkinen, K. K., Bennett, C. A., Hujoel, P. P., Isokangas, P. J., Isotupa, K. P., and Pape, H. R., Jr. (1995) Xylitol chewing gums and caries rates: a 40-month cohort study. *J. Dent. Res. 74*, 1904–1913.

(3) Mäkinen, K. K. (2000) The rocky road of xylitol to its clinical application. *J. Dent. Res. 79*, 1352–1355.

(4) Mattila, P., Svanberg, M., and Knuttila, M. (1995) Diminished bone resorption in rats after oral xylitol administration: a dose-response study. *Calcif. Tissue Int. 56*, 232–235.

(5) Jaffe, G. M. (1978) Xylitol-a specialty sweetener. *Sugar y Azucar 93*, 36–42.

(6) Anon. (2004) *Mannitol - A Medical Dictionary, Bibliography, and Annotated Research Guide to Internet References*. Icon Health Publications, San Diego.

(7) Hegde, V. L., Mahesh, P. A., and Venkatesh, Y. P. (2002) Anaphylaxis caused by mannitol in pomegranate (*Punica granatum*). *ACI Int. 14*, 37–39.

(8) Hegde, V. L., Das, J. R., and Venkatesh, Y. P. (2002) Anaphylaxis caused by the ingestion of cultivated mushroom (*Agaricus bisporus*): Identification of allergen as mannitol. *Allergol. Int. 51*, 121–129.

(9) Hegde, V. L., and Venkatesh, Y. P. (2004) Anaphylaxis to excipient mannitol: evidence for an immunoglobulin E-mediated mechanism. *Clin. Exp. Allergy 34*, 1602–1609.

(10) Hino, H., Kasai, S., Hattori, N., and Kenjo, K. (2000) A case of allergic urticaria caused by erythritol. *J. Dermatol. 27*, 163–165.

(11) Yunginger, J. W., Jones, R. T., Kita, H., Saito, K., Hefle, S. L., and Taylor, S. L. (2001) Allergic reactions after ingestion of erythritol-containing foods and beverages. *J. Allergy Clin. Immunol. 108*, 650.

(12) Venkatesh, Y. P., and Hegde, V. L. (2003) A hypothesis for the mechanism of immediate hypersensitivity to mannitol. *Allergol. Int. 52*, 165–170.

(13) Hanakawa, Y., Hanakawa, Y., Tohyama, M., Yamasaki, K., and Hashimoto, K. (2005) Xylitol as a causative agent of oral erosive eczema. *Brit. J. Dermatol. 152*, 821–822.

(14) Schwartz, B. A., and Gray, G. R. (1977) Proteins containing reductively aminated disaccharides: immunochemical characterization. *Arch. Biochem. Biophys. 181*, 542–549.

(15) Gray, G. R. (1978) Antibodies to carbohydrates: preparation of antigens by coupling carbohydrates to proteins by reductive amination with cyanoborohydride. *Methods Enzymol. 55*, 155–160.

(16) Roy, R., Katzenellenbogen, E., and Jennings, H. J. (1984) Improved procedures for the conjugation of oligosaccharides to protein by reductive amination. *Can. J. Biochem. Cell Biol. 62*, 270–275.

(17) Pazur, J. H. (1998) Anti-carbohydrate antibodies with specificity for monosaccharide and oligosaccharide units of antigens. *Advan. Carbohydr. Chem. Biochem. 53*, 201–261.

(18) Pazur, J. H., Reed, A. S., and Scrano, R. S. (2001) Antibodies with specificities for D-xylose and for D-galacturonic acid residues of flaxseed polysaccharides. *Carbohydr. Res. 336*, 195–201.

(19) Pazur, J. H. (2003) The biosynthesis and properties of anti-carbohydrate antibodies. *Studies in Natural Products Chemistry (Series), Bioactive Natural Products, Part J* (Atta-ur Rahman, Ed.), pp 521–565, Vol. 29, Elsevier, Amsterdam.

(20) Sreenath, K., Prabhasankar, P., and Venkatesh, Y. P. (2006) Generation of an antibody specific to erythritol, a non-immunogenic food additive. *Food Addit. Contam. 23*, 861–869.

(21) Hegde, V. L., and Venkatesh, Y. P. (2007) Generation of antibodies specific to D-mannitol, a unique haptenic allergen, using reductively aminated D-mannose-bovine serum albumin conjugate as the immunogen. *Immunobiology 212*, 119–128.

(22) Hayward, L. D., and Angyal, S. J. (1977) A symmetry rule for the circular dichroism of reducing sugars, and the proportion of carbonyl forms in aqueous solutions thereof. *Carbohydr. Res. 51*, 13–20.

(23) Bradford, M. M. (1976) A rapid and sensitive method for the quantitation of microgram quantities of protein utilizing the principle of protein-dye binding. *Anal. Biochem. 72*, 248–254.
(24) Sashidhar, R. B., Capoor, A. K., and Ramana, D. (1994) Quantitation of epsilon-amino group using amino acids as reference standards by trinitrobenzene sulfonic acid: a simple spectrophotometric method for the estimation of hapten to carrier protein ratio. *J. Immunol. Methods 167*, 121–127.
(25) Peters, T., Jr. (1996) *All about albumin-Biochemistry, Genetics and Medical Applications*. Academic Press, San Diego.
(26) Zacharius, R. M., Zell, T. E., Morrison, J. H., and Woodlock, J. J. (1969) Glycoprotein staining following electrophoresis on acrylamide gels. *Anal. Biochem. 30*, 148–152.
(27) Laemmli, U. K. (1970) Cleavage of structural proteins during the assembly of the head of bacteriophage T_4. *Nature (London) 227*, 680–685.
(28) Johnstone, A., and Thorpe, R., (Eds.) (1996) *Immunochemistry in Practice*, 3rd ed., Blackwell Publishing, Oxford, UK.
(29) Howard, G. C., and Kaser, M. R., (Eds.) (2007) *Making and using antibodies: a practical handbook*. pp 1–394, CRC Press, Taylor & Francis Group, Boca Raton, FL.
(30) Hawkes, R. (1986) The dot immunobinding assay. *Methods Enzymol. 121*, 484–491.
(31) Tijssen, P. (1985) *Practice and theory of enzyme immunoassays. Laboratory Techniques in Biochemistry and Molecular Biology*. (Burdon, R. H., van Knippenberg, P. H., Eds.) Elsevier, Amsterdam.
(32) Stults, N. L., Asta, L. M., and Lee, Y. C. (1989) Immobilization of proteins on oxidized crosslinked Sepharose preparations by reductive amination. *Anal. Biochem. 180*, 114–119.
(33) Lüttman, W., Bratke, K., Kupper, M., and Myrtek, D. (2006) *Immunology: The Experimenter Series*, pp 1–41, Elsevier Inc./ Academic Press, Amsterdam.
(34) Raghava, G. P. S., and Agrewala, J. N. (1994) Method for determining the affinity of monoclonal antibody using non-competitive ELISA: a computer program. *J. Immunoassay 15*, 115–118.
(35) Natsuaki, M. (2000) Immediate contact hypersensitivity induced by repeated hapten challenge in mice. *Contact Dermatitis 43*, 267–272.
(36) Ovary, Z. (1958) Passive cutaneous anaphylaxis in the mouse. *J. Immunol. 81*, 355–357.
(37) Dearman, R. J., and Kimber, I. (2007) A mouse model for food allergy using intraperitoneal sensitization. *Methods 41*, 91–98.
(38) Harris, J. R., and Markl, J. (1999) Keyhole limpet hemocyanin (KLH): a biomedical review. *Micron 30*, 597–623.
(39) Bruyland, M., and Ebinger, G. (1994) Beneficial effect of a treatment with xylitol in a patient with myoadenylate deaminase deficiency. *Clin. Neuropharmacol. 17*, 492–493.
(40) Trahan, L. (1995) Xylitol: a review of its action on mutans streptococci and dental plaque-its clinical significance. *Int. Dent. J. 45*, 77–92.
(41) Kuroiwa, Y., Nishikawa, A., Imazawa, T., Kitamura, Y., Kanki, K., Umemura, T., and Hirose, M. (2005) Lack of carcinogenicity of D-xylose given in the diet to F344 rats for two years. *Food Chem. Toxicol. 43*, 1399–1404.
(42) Pazur, J. H., and Li, N. Q. (2004) Application of antibodies for the identification of polysaccharide gum additives in processed foods. *Food Addit. Contam. 21*, 1027–1034.
(43) Longas, M. O., and Meyer, K. (1982) Evidence that a reducible xylosyl-lysine is the protein linkage of dermatan sulfate. *Proc. Natl. Acad. Sci. U.S.A. 79*, 6225–6228.
(44) Robins, S. P., and Bailey, A. J. (1972) Age-related changes in collagen: the identification of reducible lysine-carbohydrate condensation products. *Biochem. Biophys. Res. Commun. 48*, 76–84.

BC700175G

Fluorescent and Affinity-Based Tools To Detect Cysteine Sulfenic Acid Formation in Proteins

Leslie B. Poole,*,† Chananat Klomsiri,† Sarah A. Knaggs,‡ Cristina M. Furdui,|| Kimberly J. Nelson,† Michael J. Thomas,† Jacquelyn S. Fetrow,§ Larry W. Daniel,† and S. Bruce King*,‡

Department of Biochemistry and Section on Molecular Medicine, Wake Forest University School of Medicine, Winston-Salem, North Carolina 27157, and Departments of Chemistry, Physics and Computer Science, Wake Forest University, Winston-Salem, North Carolina 27109. Received July 10, 2007; Revised Manuscript Received September 3, 2007

Cysteine sulfenic acid formation in proteins results from the oxidative modification of susceptible cysteine residues by hydrogen peroxide, alkyl hydroperoxides, and peroxynitrite. This species represents a biologically significant modification occurring during oxidant signaling or oxidative stress, and it can modulate protein function. Most methods to identify such oxidatively modified proteins rely on monitoring the loss of one or more thiol group(s) or on selective labeling of nascent thiol groups following reduction of oxidized proteins. Our previous work reported the direct labeling of these chemically distinct modifications with a dimedone analogue, 1,3-cyclohexadione, to which a linker and functional group (an alcohol) had been added; further addition of a fluorescent isatoic acid or methoxycoumarin reporter allowed detection of the incorporated tag by fluorescence techniques (Poole, L. B., Zeng, B. B., Knaggs, S. A., Yakubu, M., and King, S. B. (2005) Synthesis of chemical probes to map sulfenic acid modifications on proteins. *Bioconjugate Chem. 16*, 1624–1628). We have now expanded our arsenal of tagging reagents to include two fluorescein-, two rhodamine-, and three biotin-conjugated probes based on the original approach. The new tools provide readily detectable fluorescent and affinity probes to identify sulfenic acid modifications in proteins and have been used in subsequent mass spectrometric analyses to confirm covalent attachment of the conjugates and directly determine the site of modification.

INTRODUCTION

Given the significant role played by formation of cysteine sulfenic acid (*S*-hydroxycysteine, R–SOH) in the redox regulation of enzymes and transcription regulators (*1*–*3*) and its general instability toward protein analytical methods (*4*), there is a critical need for better reagents to trap and identify these modifications in proteins. On the basis of a known alkylator of R–SOH, dimedone (5,5-dimethyl-1,3-cyclohexanedione), we previously designed, synthesized, and validated the use of two fluorescent reagents linked to the reactive core of dimedone, 1,3-cyclohexadione, as detectable markers of R–SOH formation in proteins (*5*). These reagents were shown to specifically trap only the R–SOH modification in a test protein, AhpC (a cysteine-based peroxidase from bacteria), leaving underivatized the other protein functional groups (including amines), as well as the thiol, disulfide, or hyperoxidized forms of AhpC. Other oxidized, sulfur-containing functional groups such as *S*-nitrosothiols and sulfoxides were similarly unreactive toward these reagents and dimedone. A limitation of the fluorophores chosen for these initial studies, isatoic acid and 7-methoxycoumarin, is their poor detectability in polyacrylamide gels; they are also not useful as affinity reagents for the isolation of R–SOH forming proteins.

To provide an expanded array of chemical tools to identify and isolate proteins that undergo oxidative modification to form R–SOH, we have implemented a strategy similar to that previously used to incorporate isatoic acid and methoxycoumarin into our dimedone-like reagent. Here, we describe the generation of seven new reagents through the attachment of fluorescein, rhodamine, or biotin moieties to an alcohol functional group on a linker attached to 1,3-cyclohexadione. In related work, generation of a biotinylated, dimedone-like reagent was also very recently reported by another group (*6*); this latter reagent was used to detect and isolate sulfenic acid-modified proteins from cells treated with hydrogen peroxide. Our new compounds are all useful for detecting labeled proteins in polyacrylamide gels; with the fluorescent reagents, a major advantage is that the labeled proteins are directly observable both in solution and after gel electrophoresis. Our data also demonstrate that all of our reagents are compatible with mass spectrometric approaches to confirm covalent attachment and identify the specific site of modification. Three of the reagents with biotin reporter groups offer advantages not only of being detectable through Western blotting type approaches but also of enabling affinity techniques for isolating such modified proteins.

EXPERIMENTAL PROCEDURES

General Synthetic Methods. Glassware was oven-dried before use and cooled to room temperature under N_2. All reagents and solvents were obtained from a commercial source and used without further purification unless noted otherwise. Analytical thin layer chromatography was performed on 250 μm silica gel 60 plates (DC-Fertigplatten Krieselgel 60 F254). Visualization was accomplished with UV light, ethanolic phosphomolybdic acid solution, ethanolic ninhydrin solution,

* To whom correspondence should be addressed. Address: Department of Biochemistry, Center for Structural Biology, Medical Center Boulevard, Winston-Salem, NC 27157. Telephone: 336-716-6711(L.B.P.), 336-758-5774(S.B.K.). Fax: 336-777-3242 (L.B.P.), 336-758-4656 (S.B.K.). E-mail: lbpoole@wfubmc.edu (L.B.P.), kingsb@wfu.edu (S.B.K.).

† Department of Biochemistry, Wake Forest University School of Medicine.

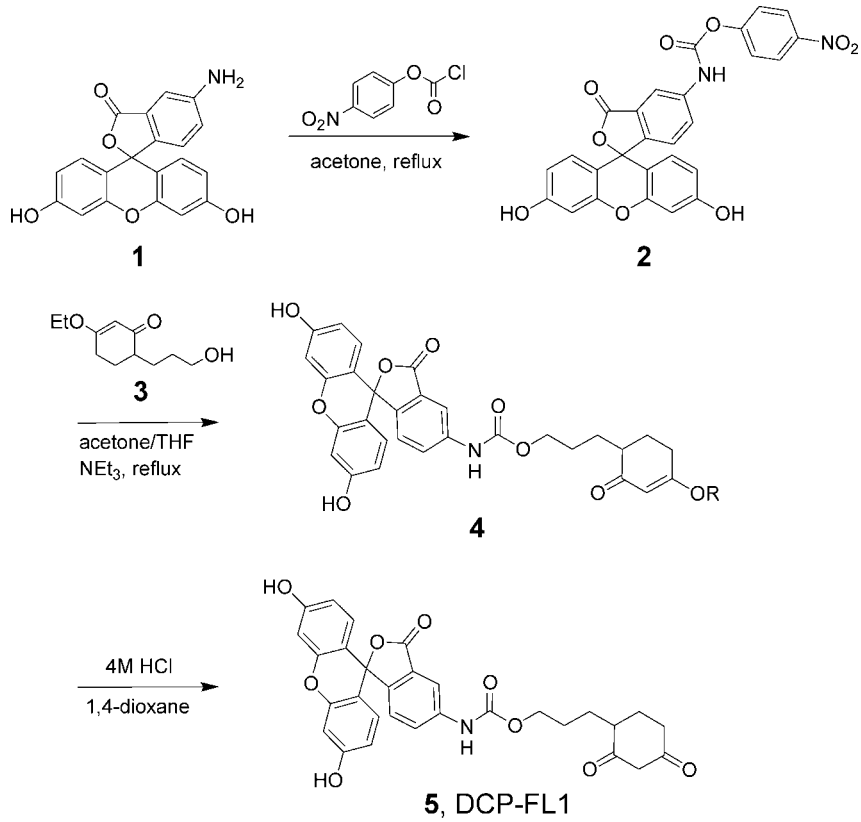
‡ Department of Chemistry, Wake Forest University.

|| Section on Molecular Medicine, Wake Forest University School of Medicine.

§ Departments of Physics and Computer Science, Wake Forest University.

10.1021/bc700257a CCC: $37.00 © 2007 American Chemical Society
Published on Web 11/21/2007

Scheme 1



or aqueous potassium permanganate solution followed by heating. Purification of the reaction products was carried out by flash column chromatography using silica gel 60 (32–63 μm). NMR spectra were recorded on a Bruker DPX 300 spectrometer, operating at 300 MHz (^{1}H NMR) and 75 MHz (^{13}C NMR), with chemical shifts referenced to the residual solvent peak. ^{1}H NMR data are reported as follows: chemical shift, integration, multiplicity (s = singlet, bs = broad singlet, d = doublet, t = triplet, q = quartet, m = multiplet), and coupling constants (Hz). Melting points were determined on a Thomas Hoover Uni-melt capillary melting point apparatus and are uncorrected. Mass spectra of synthesized compounds were obtained as a service by HT Laboratories (San Diego, CA) and are reported as *m/z*. Elemental combustion analysis was performed as a service by Atlantic Microlab Inc. (Atlanta, GA). For log *P* analyses, UV–vis spectra were recorded on a Cary 100 Bio UV–visible spectrophotometer.

Fluoresceinamine 5′-*N*-(*p*-Nitrophenyl)carbamate (2). To a solution of fluoresceinamine isomer I (**1**) (1.0 g, 2.88 mmol) in acetone (40 mL) was added *p*-nitrophenyl chloroformate (638 mg, 3.17 mmol) (Scheme 1). The resultant mixture was refluxed for 4 h and then stirred at room temperature for 24 h. The crude product was filtered from the reaction mixture and washed with dichloromethane (DCM)[1]/acetone (3/1 v/v, 40 mL) to yield a yellow-orange solid (1.42 g, 96.3%). TLC analysis and NMR indicated adequate purity for use in the next step: mp 186–189 °C (dec); R_f = 0.30 (hexanes/EtOAc/MeOH, 5/4/1); ^{1}H NMR (300 MHz, DMSO-d_6, δ) 11.05 (1H, bs), 8.34 (2H, d, J = 9.3 Hz), 8.18 (1H, s), 7.87 (1H, dd, J = 1.5, 8.1 Hz), 7.60 (2H, d, J = 9.0 Hz), 7.29 (1H, d, J = 8.4 Hz), 6.77 (2H, d, J = 1.5 Hz), 6.67–6.60 (4H, m); ^{13}C NMR (75 MHz, DMSO-d_6, δ) 168.7, 160.7, 155.7, 152.7, 151.2, 145.1, 140.4, 129.6, 127.9, 126.2, 125.7, 125.5, 123.3, 113.9, 113.5, 110.4, 102.6; ESI MS *m/z* 513 $(M + H)^+$.

Fluoresceinamine 5′-*N*-[3-(4-Ethoxy-2-oxocyclohex-3-enyl)-propyl)]carbamate (4). To a suspension of fluoresceinamine-5′-*N*-(*p*-nitrophenyl)carbamate (**2**) (500 mg, 0.91 mmol) in THF (10 mL) was added NEt_3 (130 μL, 0.91 mmol) and a solution of 3-ethoxy-6-(3-hydroxypropyl)-cyclohex-2-enone (**3**) (343 mg, 1.73 mmol) in THF (2 mL) (Scheme 1). Alcohol **3** was prepared by previously reported methods (*5*). The resultant mixture was stirred at reflux for 48 h. When the mixture was cooled, MeOH (10 mL) was added. The mixture was filtered, and the filtrate was reduced to dryness to yield an orange oil that was purified by flash column chromatography (hexanes/EtOAc/MeOH, 4/2/1). The pure product (**4**) was obtained as an orange solid (350 mg, 68.4%): mp 172–174 °C (dec); R_f = 0.28 (hexanes/EtOAc/MeOH, 4/2/1); ^{1}H NMR (300 MHz, MeOH-d_4, δ) 7.96 (1H, s), 7.52 (1H, dd, J = 2.9, 8.5 Hz), 6.90 (1H, d, J = 8.4 Hz), 6.46–6.41 (4H, m), 6.32 (2H, dd, J = 2.3, 8.7 Hz), 5.13 (1H, s), 4.40 (2H, t, J = 6.3 Hz), 3.75 (2H, q, J = 6.3 Hz), 2.29 (2H, t, J = 5.7 Hz), 2.23–2.04 (1H, m), 1.96–1.87 (1H, dq, J =

[1]Abbreviations used: DCM, dichloromethane; DMSO, dimethyl sulfoxide; DMAP, 4-(dimethylamino)pyridine; THF, tetrahydrofuran; DCC, dicyclohexylcarbodiimide; BOC, *tert*-butoxycarbonyl; GABA, γ-aminobutyric acid; HOBt, 1-hydroxybenzotriazole; DCP-FL1, fluoresceinamine 5′-*N*-[3-(2,4-dioxocyclohexyl)propyl)]carbamate; DCP-FL2, fluoresceinamine-5′-*N*-[3-((1-(3-(2,4-dioxocyclohexyl)propyl)-1*H*-1,2,3-triazol-4-yl)methyl]urea; DCP-Bio1, 3-(2,4-dioxocyclohexyl)propyl 5-((3a*R*,6*S*,6a*S*)-hexahydro-2-oxo-1*H*-thieno[3,4-*d*]imidazol-6-yl)pentanoate; DCP-Bio2, 5-((3a*R*,6*S*,6a*S*)-hexahydro-2-oxo-1*H*-thieno[3,4-*d*]imidazol-6-yl)-*N*-((1-(3-(2,4-dioxocyclohexyl)propyl)-1*H*-1,2,3-triazol-4-yl)methyl)pentanamide; DCP-Bio3, 3-(2,4-dioxocyclohexyl)propyl 4-(5-((3a*R*,6*S*,6a*S*)-hexahydro-2-oxo-1*H*-thieno[3,4-d]imidazol-6-yl)-pentanamido)butylcarbamate; DCP-Rho1, rhodamine B [4-[3-(2,4-dioxocyclohexyl)propyl]carbamate]piperazine amide; DCP-Rho2, rhodamine B 3-(2,4-dioxocyclohexyl)propyl 4-oxo-4-(piperazin-1-yl)-butylcarbamate; TOF, time of flight; ESI-MS, electrospray ionization mass spectrometry.

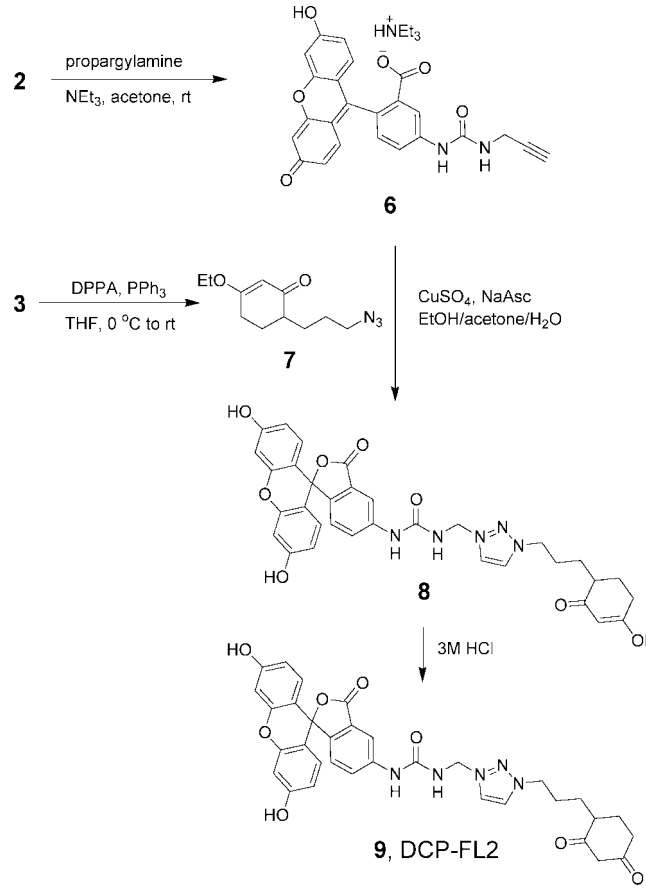
5.0 Hz), 1.79–1.68 (1H, m), 1.65–1.44 (3H, m), 1.38–1.20 (1H, m), 1.14 (3H, t, $J = 7.1$ Hz); ^{13}C NMR (75 MHz, acetone-d_6, δ) 199.9, 177.0, 169.4, 160.2, 154.6, 153.4, 147.6, 142.1, 142.0, 130.2, 128.9, 126.1, 126.0, 125.2, 113.4, 113.2, 111.9, 103.2, 102.5, 83.6, 65.9, 64.8, 45.5, 27.4, 27.3, 26.8, 14.4; ESI MS *m/z* 594 $(M + Na)^+$, 572 $(M + H)^+$. Anal. Calcd for $C_{32}H_{29}NO_9 \cdot H_2O$: C, 65.19; H, 5.30; N, 2.38. Found: C, 65.08; H, 5.30; N, 2.40.

Fluoresceinamine 5′-*N*-[3-(2,4-Dioxocyclohexyl)propyl)]-carbamate (5, DCP-FL1). Fluoresceinamine 5′-*N*-[3-(4-ethoxy-2-oxocyclohex-3-enyl)propyl)]carbamate (**4**) (60 mg, 0.1 mmol) was stirred in a mixture of acetone (10 mL) and 3 N HCl (200 μL) (Scheme 1) until TLC analysis showed complete conversion. The reaction mixture was carefully neutralized (with either 10% NaOH solution or solid Na_2CO_3 followed by filtration) and reduced to dryness. The crude product (**5**) was purified by flash column chromatography (DCM/Et_2O/^{i}PrOH, 8/8/1) to yield the pure product as a yellow solid (54 mg, 94.7%): mp 239 °C (dec); $R_f = 0.19$ (hexanes/EtOAc/MeOH, 4/2/1); log *P* (octan-1-ol/phosphate buffer, pH 7.2) $= -0.89 \pm 0.20$; ^{1}H NMR (300 MHz, MeOH-d_4, δ) 8.23 (1H, s), 7.75 (1H, dd, $J = 1.9$, 8.4 Hz), 7.14 (1H, d, $J = 8.3$ Hz), 6.73–6.69 (4H, m), 6.58 (2H, dd, $J = 2.3$, 8.7 Hz), 4.27 (2H, t, $J = 6.2$ Hz), 2.45 (2H, q, $J = 6.1$ Hz), 2.41–2.34 (1H, m), 2.20–2.10 (1H, m), 2.00–1.75 (3H, m), 1.67–1.57 (1H, m); ^{13}C NMR (75 MHz, acetone-d_6, δ) 202.7, 169.8, 160.6, 155.1, 153.8, 148.1, 142.5, 130.6, 129.3, 126.6, 126.5, 125.7, 113.6, 112.4, 105.1, 103.7, 84.0, 66.3, 66.2, 50.0, 40.7, 27.8, 27.6, 26.1, 24.7; ESI MS *m/z* 544 $(M + H)^+$. Anal. Calcd for $C_{30}H_{25}NO_9 \cdot i$PrOH: C, 65.66; H, 5.51; N, 2.32. Found: C, 64.84; H, 5.38; N, 2.34.

Fluoresceinamine-5′-*N*-(3-propargyl)urea Triethylamine Salt (6). To a suspension of fluoresceinamine 5′-*N*-(*p*-nitrophenyl)carbamate (**2**) (160 mg, 0.31 mmol) in acetone/THF (2/1 v/v, 8 mL) was added propargylamine (21 μL, 0.34 mmol) and NEt_3 (44 μL, 0.31 mmol) (Scheme 2). The resultant solution was stirred at room temperature for 3 h during which the product (**6**) precipitated from the reaction mixture. This was filtered off and washed with DCM/acetone (2/1 v/v, 30 mL) to yield **6** as an orange solid (132 mg, 80.0%). TLC analysis and NMR indicated adequate purity for use in the next step: mp 187–189 °C (dec); $R_f = 0.56$ (EtOAc/hexanes/MeOH, 6/3/1); ^{1}H NMR (300 MHz, MeOH-d_4, δ) 7.96 (1H, d, $J = 2.0$ Hz), 7.79 (1H, dd, $J = 2.1$, 8.3 Hz), 7.13 (1H, d, $J = 8.3$ Hz), 7.06 (2H, d, $J = 8.9$ Hz), 6.64 (2H, dd, $J = 2.2$, 5.4 Hz), 6.61 (2H, d, $J = 2.2$ Hz), 4.03 (2H, q, $J = 2.4$ Hz), 3.07 (6H, q, $J = 7.3$ Hz), 2.62 (1H, t, $J = 2.4$ Hz), 1.22 (9H, t, $J = 7.3$ Hz); ^{13}C NMR (75 MHz, MeOH-d_4, δ) 173.0, 157.9, 157.4, 142.4, 132.1, 129.6, 122.6, 119.8, 118.9, 114.5, 103.9, 81.6, 72.0, 47.6, 30.2; ESI MS *m/z* 429 $(M + H)^+$.

3-Ethoxy-6-(3-azidopropyl)cyclohex-2-enone (7). To a cooled solution of 3-ethoxy-6-(3-hydroxylpropyl)cyclohex-2-enone (**3**) (2.0 g, 10.0 mmol) in THF (40 mL) at 0 °C was added triphenylphosphine (2.91 g, 11.0 mmol), diisopropyl azodicarboxylate (DIAD, 2.15 mL, 11.0 mmol), and diphenylphosphorylazide (DPPA, 2.4 mL, 11.0 mmol) sequentially (Scheme 2). The resultant mixture was stirred at 0 °C and then at room temperature for 16 h before being partitioned between DCM (100 mL) and water (50 mL). The aqueous phase was extracted with DCM (100 mL), and the organic phases were combined, washed with brine (50 mL), dried over anhydrous Na_2SO_4, filtered, and reduced to dryness. The resultant oil was purified by flash column chromatography (2×, hexanes/EtOAc, 2/1, and hexanes/EtOAc/MeOH, 12/2/1) to yield the pure product (**7**) as a pale-yellow liquid (1.6 g, 71.3%). $R_f = 0.31$ (EtOAc/hexanes/MeOH 12/2/1); ^{1}H NMR (300 MHz, $CDCl_3$, δ) 5.31 (1H, s), 3.89 (2H, q, $J = 6.9$ Hz), 3.30 (2H, dt, $J = 1.6$, 6.8 Hz), 2.44 (2H, t, $J = 5.9$ Hz), 2.25–2.16 (1H, dpentet, $J = 1.8$, 5.2 Hz), 2.12–2.03 (1H, dq, $J = 5.0$, 13.2 Hz), 1.95–1.80 (1H, m), 1.78–1.59 (3H, m), 1.53–1.41 (1H, m), 1.36 (3H, t, $J = 7.0$ Hz); ^{13}C NMR (75 MHz, $CDCl_3$, δ) 201.2, 117.2, 102.5, 64.6, 51.9, 45.1, 28.5, 27.2, 26.9, 14.5.

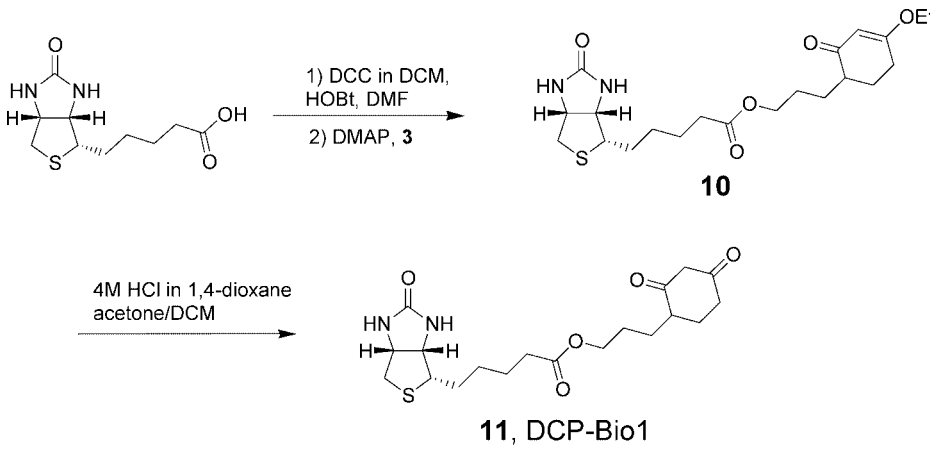
Scheme 2



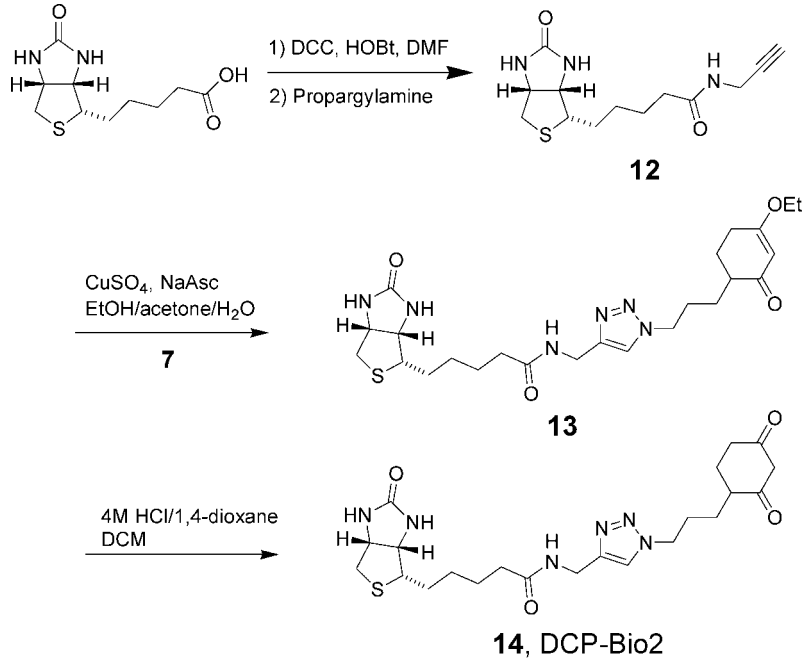
Fluoresceinamine-5′-*N*-[3-((1-(3-(4-ethoxy-2-oxocyclohex-3-enyl)propyl)-1*H*-1,2,3-triazol-4-yl)methyl]urea (8). Fluoresceinamine-5′-*N*-(3-propargyl)urea triethylamine salt (**6**) (132 mg, 0.25 mmol) and 3-ethoxy-6-(3-azidopropyl)cyclohex-2-enone (**7**) (139 mg, 0.62 mmol) were solubilized in a mixture of acetone/EtOH/H_2O (1/2/1 v/v, 4 mL). Sodium ascorbate (12 mg, 0.062 mmol) and $CuSO_4 \cdot 5H_2O$ (156 μL of a 0.1 M solution in H_2O, 0.0156 mmol) were added, and the resultant solution stirred at room temperature for 16 h (Scheme 2). The solvent was removed under reduced pressure and the resultant orange oil purified by flash column chromatography (gradient elution with EtOAc/hexanes/MeOH, 6/3/1, to EtOAc/MeOH, 7/1) to yield the pure product (**8**) as a bright-yellow foam (151 mg, 71.4 %): mp 157 °C (dec); $R_f = 0.14$ (EtOAc/hexanes/MeOH 6/3/1); ^{1}H NMR (300 MHz, MeOH-d_4, δ) 8.10 (1H, s), 7.85 (1H, s), 7.56 (1H, d, $J = 8.3$ Hz), 6.96 (1H, d, $J = 8.3$ Hz), 6.59 (2H, d, $J = 2.0$ Hz), 6.53 (2H, d, $J = 8.7$ Hz), 6.44 (2H, dd, $J = 2.0$, 8.7 Hz), 5.19 (1H, s), 4.43 (2H, s), 4.28 (2H, t, $J = 6.7$ Hz), 3.80 (2H, q, $J = 7.1$ Hz), 2.38–2.21 (2H, m), 2.16–2.08 (1H, m), 1.97–1.78 (3H, m), 1.72–1.61 (1H, m), 1.59–1.48 (1H, m), 1.22 (3H, t, $J = 7.0$ Hz); ^{13}C NMR (75 MHz, acetone-d_6) δ 200.8, 177.9, 170.5, 160.6, 156.5 (x2), 156.4, 153.8, 147.0, 143.6 (x2), 130.6, 129.1, 126.5, 126.4, 125.4, 123.7, 113.6, 112.4, 103.7, 102.9, 84.1, 65.4, 51.2, 45.6, 36.6 (×2), 29.1, 27.7, 14.9; ESI MS *m/z* 652 $(M + H)^+$, 674 $(M + Na)^+$. Anal. Calcd for $C_{35}H_{33}N_5O_8 \cdot 2$MeOH: C, 62.09; H, 5.77; N, 9.78. Found: C, 62.07; H, 5.46; N, 9.65.

Fluoresceinamine-5′-*N*-[3-((1-(3-(2,4-dioxocyclohexyl)propyl)-1*H*-1,2,3-triazol-4-yl)methyl]-urea (DCP-FL2, 9). Fluoresceinamine-5′-*N*-[3-((1-(3-(4-ethoxy-2-oxocyclohex-3-enyl)-

Scheme 3



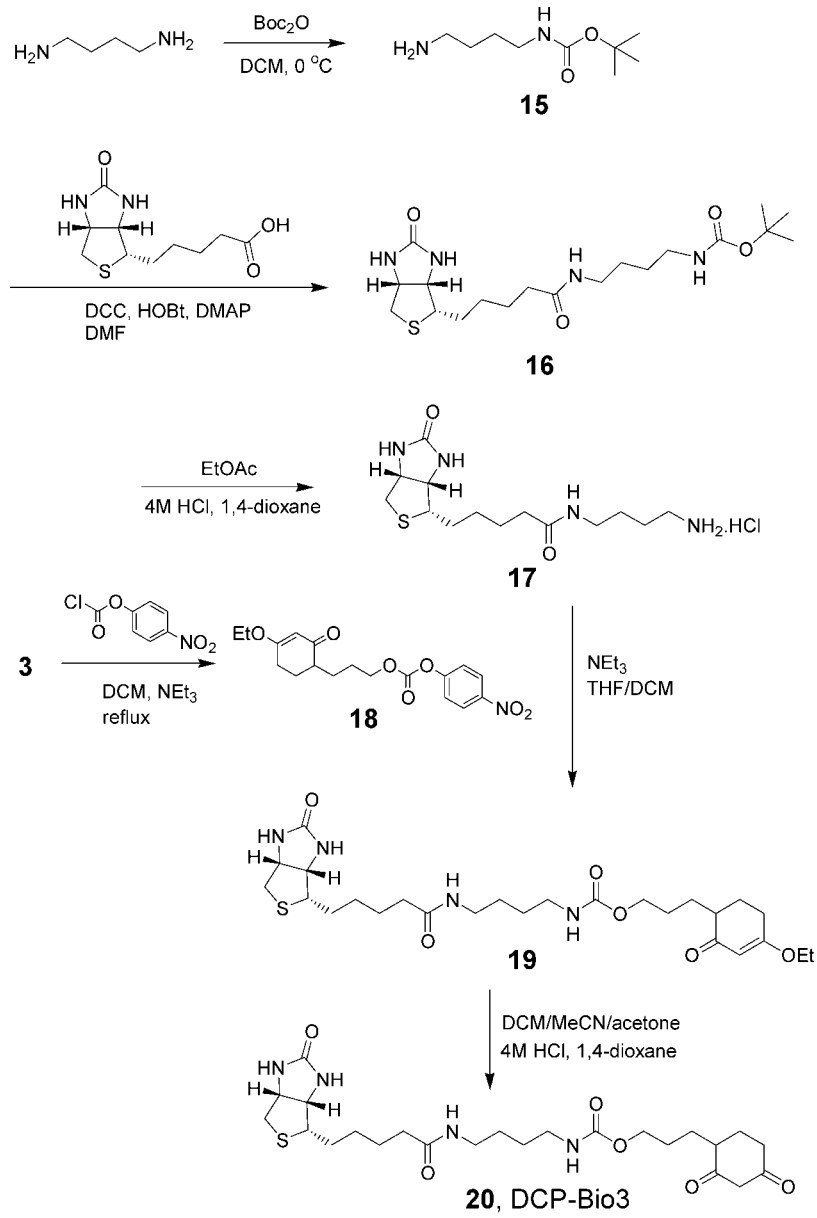
Scheme 4



propyl)-1*H*-1,2,3-triazol-4-yl)methyl]urea (**8**) (70 mg, 0.11 mmol) was stirred in a mixture of THF/acetone/H_2O (4/4/1 v/v/v, 9 mL) and treated with 3 N HCl (500 μL) (Scheme 2). The solution was stirred until TLC analysis indicated near complete conversion of **8** to **9** (3 h to 3 days). The reaction mixture was neutralized and then reduced to dryness. The resulting solids were washed with MeOH and filtered, and the filtrate was concentrated. The crude product was purified by flash column chromatography (gradient elution with DCM/MeOH, 8/2 to 6/4) to yield the pure product (**9**) as a yellow solid (64 mg, 95.5%): mp 224 °C (dec); $R_f = 0.31$ (DCM/MeOH 8/2); log *P* (octan-1-ol/phosphate buffer, pH 7.2) = -1.61 ± 0.24; ^{1}H NMR (300 MHz, MeOH-d_4, δ) 8.10 (1H, d, $J = 1.7$ Hz), 7.86 (1H, s), 7.55 (1H, dd, $J = 2.0$, 8.4 Hz), 6.95 (1H, d, $J = 8.3$ Hz), 6.57 (4H, d, $J = 2.2$ Hz), 6.45 (2H, dd, $J = 2.2$, 8.7 Hz), 4.40 (2H, s), 4.30 (2H, t, $J = 6.9$ Hz), 2.26 (2H, t,$J = 7.0$ Hz), 2.21–2.13 (1H, m), 2.05–1.80 (3H, m), 1.69–1.55 (2H, m), 1.37–1.28 (1H, m), 1.27–1.17 (2H, m); ^{13}C NMR (75 MHz, MeOH-d_4, δ) 204.4, 181.6, 173.0, 172.2, 170.9, 168.5, 167.3, 161.2, 160.8, 144.6, 144.5, 134.7, 134.5, 133.2, 132.4, 131.9, 127.5, 123.6, 122.0, 121.6, 118.9, 118.6, 103.7, 52.5, 52.2, 36.3, 29.2, 29.0, 27.9, 27.7, 27.2; ESI MS *m/z* 624 $(M + H)^+$, 646 $(M + Na)^+$.

3-(4-Ethoxy-2-oxocyclohex-3-enyl)propyl 5-((3a*R*,6*S*,6a*S*)-Hexahydro-2-oxo-1*H*-thieno[3,4-*d*]imidazol-6-yl)pentanoate (10). D-(+)-Biotin (600 mg, 2.46 mmol) and hydroxybenzotriazole (HOBt, 66 mg, 0.49 mmol) were suspended in anhydrous DMF (20 mL) with 4 Å molecular sieves and heated until a clear solution was obtained. When the mixture was cooled, a solution of dicyclohexylcarbodiimide (DCC) in DCM (2.7 mL of a 1.0 M solution in DCM, 2.70 mmol) was added dropwise and the mixture stirred at room temperature for 3 h (solution goes cloudy). 3-Ethoxy-6-(3-hydroxypropyl)cyclohex-2-enone (584 mg, 2.95 mmol) and *N*,*N*-dimethylaminopyridine (DMAP, 30 mg, 0.025 mmol) were added, and the mixture was stirred at 60 °C for 4 h and then at room temperature for 24 h. The mixture was filtered and washed with DCM/MeOH (1/1 v/v, 20 mL), and the filtrate was reduced to dryness and purified by column chromatography (2×, DCM/MeOH, 92/8, then DCM/MeOH, 95/5). The pure product was obtained as white foam (805 mg, 77.2%): mp 164–166 °C; $R_f = 0.43$ (DCM/MeOH 9/1); ^{1}H NMR (300 MHz, $CDCl_3$, δ) 6.14 (1H, s), 5.70 (1H, s), 5.29 (1H, s), 4.49–4.45 (1H, m), 4.27 (1H, dd, $J = 4.7$, 7.2 Hz), 4.04 (2H, t, $J = 6.5$ Hz), 3.85 (2H, q, $J = 7.0$ Hz), 3.12 (1H, q, $J = 4.6$, 7.2 Hz), 2.87 (1H, dd, $J = 4.9$, 12.8 Hz), 2.71

Scheme 5

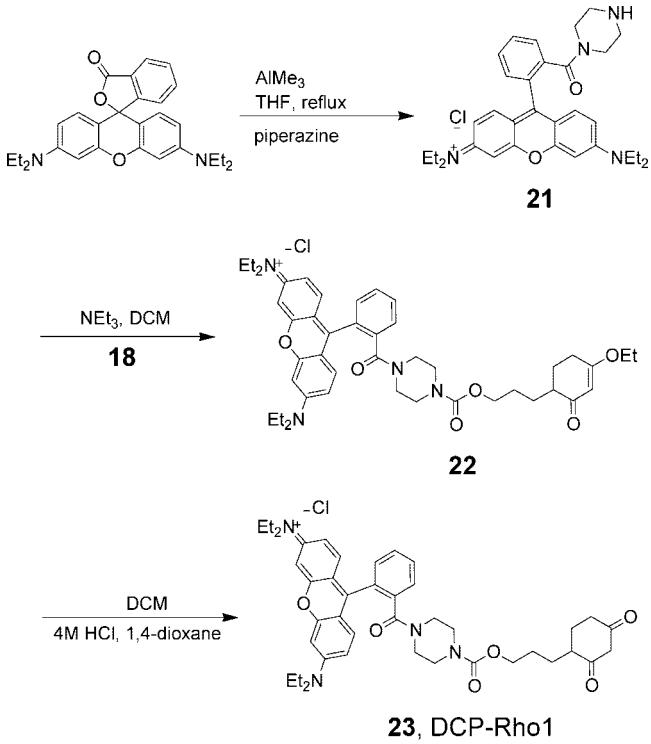


(1H, d, J = 12.7 Hz), 2.40 (2H, t, J = 5.8 Hz), 2.29 (2H, t, J = 7.4 Hz), 2.23–2.12 (1H, m), 2.09–2.00 (1H, dq, J = 5.0, 13.1 Hz), 1.93–1.81 (1H, m), 1.76–1.57 (6H, m), 1.46–1.36 (4H, m), 1.32 (3H, t, J = 7.1 Hz); ^{13}C NMR (75 MHz, $CDCl_3$, δ) 201.5, 177.3, 174.2, 164.3, 102.6, 64.7 (×2), 62.3, 60.5, 55.9, 50.4, 45.1, 34.4, 28.7, 28.6, 28.5, 26.8, 26.6 (×2), 26.4, 25.2, 14.5; ESI MS m/z 425 $(M + H)^+$.

3-(2,4-Dioxocyclohexyl)propyl 5-((3a*R*,6*S*,6a*S*)-Hexahydro-2-oxo-1*H*-thieno[3,4-*d*]imidazol-6-yl)pentanoate (DCP-Bio1, 11). 3-(4-Ethoxy-2-oxocyclohex-3-enyl)propyl 5-((3a*R*,6*S*,6a*S*)-hexahydro-2-oxo-1*H*-thieno[3,4-*d*]imidazol-6-yl)pentanoate (**10**) (600 mg, 1.41 mmol) was solubilized in acetone/DCM (3/1 v/v, 24 mL) and treated with 4 M HCl in 1,4-dioxane (2 mL) (Scheme 3). The mixture was stirred at room temperature for 5 h and then carefully neutralized by the addition of solid Na_2CO_3. The inorganic solids were filtered off and washed with 10% MeOH in DCM, and the combined filtrates were reduced to dryness. The crude yellow oil was purified by flash column chromatography (gradient elution, DCM/MeOH, 90/10 to 89/11) to yield the pure product (**11**) as a glassy solid (390 mg, 69.6% [83.5% based on recovery of **3**]): mp 90–91 °C; R_f = 0.25 (DCM/MeOH 9/1); ^{1}H NMR (300 MHz, MeOH-d_4, δ) 4.74 (1H, dd, J = 5.0, 7.4 Hz), 4.55 (1H, dd, J = 4.4, 7.6 Hz), 4.35 (2H, t, J = 6.1 Hz), 3.46 (1H, m), 3.18 (1H, dd, J = 4.9, 12.8 Hz), 2.96 (1H, d, J = 12.7 Hz), 2.69–2.52 (5H, m), 2.44–2.29 (1H, m), 2.16–1.68 (12H, m); ^{13}C NMR (75 MHz, $CDCl_3$, δ) 204.8, 204.2, 174.1, 164.4 (163.9), 104.6, 64.6 (64.5), 62.5 (62.4), 60.7 (60.6), 58.7, 55.8 (×2), 53.8, 51.2, 49.3, 40.9, 40.1, 34.5 (34.3), 33.5, 30.1 (29.7), 28.7, 27.1, 26.7, 26.6, 26.4, 26.0, 25.3 (25.1); ESI MS m/z 419 $(M + Na)^+$. Anal. Calcd for $C_{19}H_{28}N_2O_5S \cdot 0.5$MeOH: C, 56.77; H, 7.33; N, 6.79. Found: C, 56.91; H, 7.27; N, 6.78.

5-((3a*R*,6*S*,6a*S*)-Hexahydro-2-oxo-1*H*-thieno[3,4-*d*]imidazol-6-yl)-*N*-(prop-2-ynyl)pentanamide (12). When D-(+)-biotin (400 mg, 1.64 mmol), HOBt (44 mg, 0.33 mmol), DCC (1.8 mL of a 1.0 M solution in DCM), and propargyamine (170 μL, 2.46 mmol) were used, the pure product (**12**, Scheme 4) was obtained after flash column chromatography (gradient elution, DCM/MeOH, 92/8 to 90/10) as a white solid (395 mg, 85.7%): mp 169–170 °C; R_f = 0.24 (DCM/MeOH, 9/1); ^{1}H NMR (300 MHz, MeOH-d_4, δ) 4.28 (1H, dd, J = 4.9, 7.9 Hz), 4.10 (1H, dd, J = 4.4, 7.9 Hz), 3.04–2.97 (1H, m), 2.73 (1H, dd, J = 4.9, 12.7 Hz), 2.50 (1H, d, J = 12.7 Hz), 2.38 (2H, t, J = 2.5 Hz), 2.02 (2H, t, J = 7.4 Hz), 1.60–1.31 (4H, m), 1.25 (2H, q, J =

Scheme 6



7.3 Hz); ^{13}C NMR (75 MHz, MeOH-d_4, δ) 176.1, 166.5, 81.1, 72.5, 63.8, 62.0, 57.4, 41.5, 36.9, 30.1, 29.9, 29.8, 27.1; ESI MS *m/z* 282 $(M + H)^+$, 304 $(M + Na)^+$.

***N*-((1-(3-(4-Ethoxy-2-oxocyclohex-3-enyl)propyl)-1*H*-1,2,3-triazol-4-yl)methyl)-5-((3a*R*,6*S*,6a*S*)-hexahydro-2-oxo-1*H*-thieno[3,4-*d*]imidazol-6-yl)pentanamide (13).** 5-((3a*R*,6*S*,6a*S*)-Hexahydro-2-oxo-1*H*-thieno[3,4-*d*]imidazol-6-yl)-*N*-(prop-2-ynyl)pentanamide (**12**) (500 mg, 1.78 mmol) and 3-ethoxy-6-(3-azidopropyl)cyclohex-2-enone (**7**) (397 mg, 1.78 mmol) were solubilized in a mixture of acetone/EtOH/H_2O (1/2/2 v/v/v, 20 mL) (Scheme 4). Sodium ascorbate (70 mg, 0.35 mmol) and $CuSO_4$ (890 μL of a 0.1 M solution in H_2O) were then added, and the resultant solution was stirred at room temperature for 16 h. During this time the product (**13**) precipitated out of solution and was filtered off and washed with acetone to yield a white solid (690 mg). The filtrate was reduced to partial dryness, and EtOAc was added and filtered to yield a second crop (144 mg). Combined yield was 834 mg, 93%: mp 215–217 °C; R_f = 0.5 (DCM/MeOH 8/2); ^{1}H NMR (300 MHz, MeOH-d_4, δ) 7.97 (1H, s), 5.43 (1H, s), 4.64–4.58 (1H, m), 4.54 (2H, s), 4.49 (2H, d, J = 7.0 Hz), 4.40 (1H, dd, J = 4.4, 7.9 Hz), 4.04 (2H, q, J = 7.0 Hz), 3.34–3.27 (1H, m), 3.03 (1H, dd, J = 4.9, 12.9 Hz), 2.81 (1H, d, J = 12.7 Hz), 2.62–2.56 (2H, m), 2.42–2.33 (3H, m), 2.23–2.12 (1H, m), 2.11–2.02 (3H, m), 1.92–1.63 (6H, m), 1.58–1.50 (2H, m), 1.46 (3H, t, J = 7.0 Hz); ^{13}C NMR (75 MHz, $CDCl_3$, δ) 203.8, 180.1, 176.4, 167.1, 104.7, 64.5 (64.4), 62.9 (62.8), 58.4, 54.1, 47.1, 43.2, 38.3 (×2), 37.2 (37.1), 35.5 (35.3), 32.3, 30.9 (30.8), 30.6, 30.5, 29.3 (29.2), 28.1, 27.1, 16.8; ESI MS *m/z* 539 $(M - Na)^-$.

5-((3a*R*,6*S*,6a*S*)-Hexahydro-2-oxo-1*H*-thieno[3,4-*d*]imidazol-6-yl)-*N*-((1-(3-(2,4-dioxocyclohexyl)propyl)-1*H*-1,2,3-triazol-4-yl)methyl)pentanamide (DCP-Bio2, 14). *N*-((1-(3-(4-ethoxy-2-oxocyclohex-3-enyl)propyl)-1*H*-1,2,3-triazol-4-yl)methyl)-5-((3a *R*,6 *S*,6a *S*)-hexahydro-2-oxo-1*H*-thieno[3,4-*d*]imidazol-6-yl)pentanamide (**13**) (88 mg, 0.174 mmol) was solubilized in hot DCM (15 mL) and treated with a 4 M solution of HCl in 1,4-dioxane (0.1 mL) and stirred at room temperature for 72 h. The mixture was then neutralized with solid Na_2CO_3, washed with MeOH, filtered, and reduced to dryness. The pure product (**14**) was obtained after column chromatography (DCM/MeOH, 8/2) as a tan foamy solid (69 mg, 83.1%): mp 176 °C (dec); R_f = 0.21 (DCM/MeOH, 8/2); ^{1}H NMR (300 MHz, MeOH-d_4, δ) 8.02 (1H, s), 4.64 (1H, dd, J = 4.4, 7.8 Hz), 4.54 (2H, bs), 4.43 (2H, dd, J = 4.4, 7.8 Hz), 3.36–3.30 (1H, m), 3.06 (1H, dd, J = 4.9, 12.7 Hz), 2.83 (1H, d, J = 12.7 Hz), 2.53 (2H, t, J = 5.9 Hz), 2.48–2.44 (1H, m), 2.38 (2H, t, J = 7.3 Hz), 2.24–2.05 (2H, m), 1.95–1.64 (6H, m), 1.62–1.52 (4H, m); ^{13}C NMR (75 MHz, MeOH-d_4, δ) 198.5, 189.0, 176.4, 166.4, 146.8, 124.7, 104.7, 63.8, 62.1 57.4, 51.8, 43.5, 41.5, 37.0, 36.0, 31.1, 30.1, 29.9, 29.4, 28.5, 27.2; ESI MS *m/z* 499 $(M + Na)^+$.

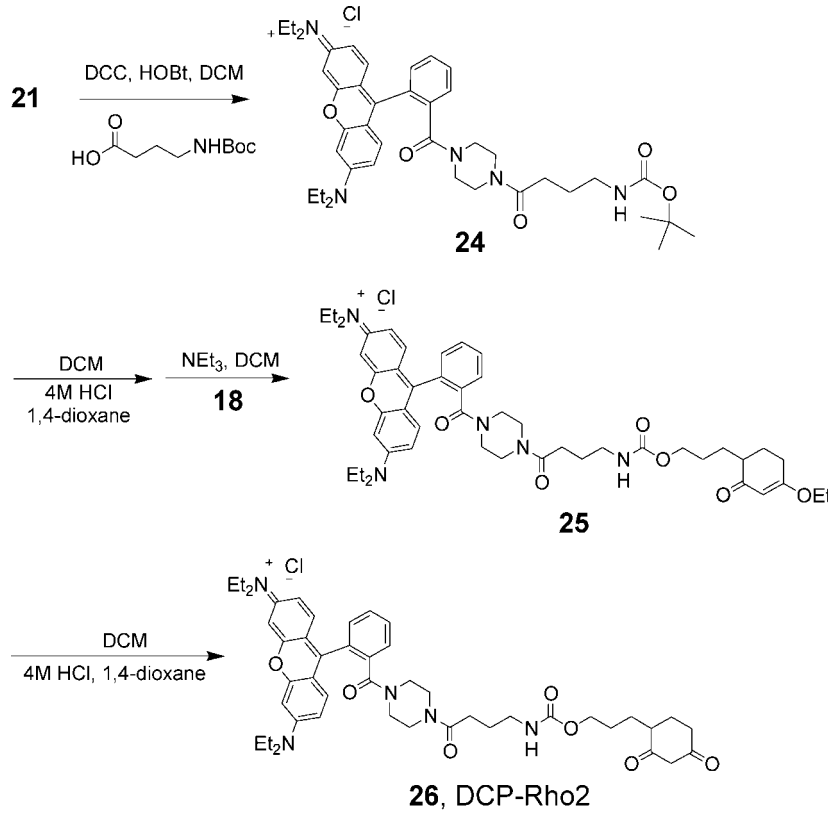
***tert*-Butyl 4-Aminobutylcarbamate (15).** To a solution of 1,4-diaminobutane (11.17 g, 0.127 mol) in DCM (170 mL) at 0 °C was added a solution of di-*tert*-butyl dicarbonate (2.77 g, 12.7 mmol) in DCM (50 mL) dropwise over 50 min (Scheme 5). The mixture was stirred at 0 °C for 2 h and then at room temperature for 16 h before being washed with water (100 mL) and brine (100 mL), dried over anhydrous Na_2SO_4, and reduced to dryness. The crude oil was purified by column chromatography (gradient elution with a 1% NEt_3 saturated solution of DCM/MeOH, 9/1 to 8/2) to yield the pure product (**15**) as a waxy yellow solid (2.217 g, 92.8%). R_f = 0.16 (DCM/MeOH/NEt_3, 90/10/1); ^{1}H NMR (300 MHz, $CDCl_3$, δ) 4.91 (1H, bs), 3.01 (2H, t, J = 6.0 Hz), 2.62 (2H, t, J = 6.6 Hz), 1.65 (2H, bs), 1.55–1.41 (4H, m), 1.32 (9H, s); ^{13}C NMR (300 MHz, $CDCl_3$, δ) 156.01, 78.9, 41.6, 40.4, 30.5, 28.4, 27.5.

***tert*-Butyl 4-(5-((3a*R*,6*S*,6a*S*)-Hexahydro-2-oxo-1*H*-thieno[3,4-*d*]imidazol-6-yl)pentanamido)butylcarbamate (16).** When D-(+)-biotin (500 mg, 2.05 mmol), HOBt (55 mg, 0.41 mmol), DCC (2.25 mL of a 1.0 M solution in DCM), and *tert*-butyl 4-aminobutylcarbamate (**15**) (578 mg, 3.07 mmol) were used, the pure product (**16**) was obtained after flash column chromatography (gradient elution with DCM/MeOH, 9/1 to 85/15) as a white solid (656 mg, 77.4 %; Scheme 5): mp 178–180 °C; R_f = 0.13 (DCM/MeOH, 9/1); ^{1}H NMR (300 MHz, MeOH-d_4, δ) 4.48 (1H, dd, J = 7.9, 4.2 Hz), 4.30 (1H, dd, J = 4.5, 7.9 Hz), 3.23–3.14 (3H, m), 3.03 (2H, t, J = 6.5 Hz), 2.91 (1H, dd, J = 5.0, 12.7 Hz), 2.69 (1H, d, J = 12.7 Hz), 2.18 (2H, t, J = 7.3 Hz), 1.76–1.55 (4H, m), 1.53–1.45 (6H, m), 1.42 (9H, s); ^{13}C NMR (75 MHz, MeOH-d_4, δ) 176.4, 166.5, 159.0, 80.3, 63.8, 62.0, 57.4, 41.5, 40.5, 37.3, 30.2, 29.9 (×2), 28.8, 28.1, 27.3, 26.6; ESI MS *m/z* 415 $(M + H)^+$, 437 $(M + Na)^+$.

***N*-(4-Aminobutyl)-5-((3a*R*,6*S*,6a*S*)-hexahydro-2-oxo-1*H*-thieno[3,4-*d*]imidazol-6-yl)pentanamide Hydrochloride Salt (17).** To a suspension of *tert*-butyl 4-(5-((3a*R*,6*S*,6a*S*)-hexahydro-2-oxo-1*H*-thieno[3,4-*d*]imidazol-6-yl)pentanamido)butylcarbamate (**16**) (370 mg, 0.89 mmol) in EtOAc (15 mL) was added a solution of HCl in 1,4-dioxane (2 mL of a 4 M solution) (Scheme 5). The mixture was stirred at room temperature for 1 h and then reduced to dryness. The crude product (**17**) was recrystallized to purity (MeOH/Et_20) to yield an off-white solid (289 mg, 92.3%): mp 50–51 °C (hygroscopic); ^{1}H NMR (300 MHz, MeOH-d_4, δ) 4.62 (1H, dd, J = 4.7, 7.9 Hz), 4.43 (1H, dd, J = 4.4, 7.9 Hz), 3.31–3.23 (3H, m), 3.03–2.95 (3H, m), 2.77 (1H, d, J = 12.9 Hz), 2.27 (2H, t, J = 7.4 Hz), 1.84–1.54 (8H, m), 1.45 (2H, q, J = 7.1 Hz); ^{13}C NMR (75 MHz, MeOH-d_4, δ) 174.0, 166.2, 64.7, 63.1, 57.3, 41.1, 40.8, 40.2, 36.9, 30.2, 29.8, 27.7, 27.3, 26.3.

3-(4-Ethoxy-2-oxocyclohex-3-enyl)propyl 4-Nitrophenylcarbonate (18). To a solution of 3-ethoxy-6-(3-hydroxylpropyl)cyclohex-2-enone (**3**) (500 mg, 2.52 mmol) in anhydrous DCM (10 mL) was added NEt_3 (0.39 mL, 2.77 mmol) and *p*-nitrophenyl chloroformate (559 mg, 2.77 mmol) (Scheme 5). The mixture was stirred at reflux for 4 h, then at room temperature for 72 h, before being washed with water (20 mL)

Scheme 7



and brine (20 mL). The organic phase was dried, reduced to dryness, and purified by column chromatography (gradient elution with hexanes/EtOAc, 6/4 to 1/1) to yield the pure product (**18**) as a white solid (706 mg, 77.0%): mp 83–85 °C; R_f = 0.35 (hexanes/EtOAc, 1/1); ^{1}H NMR (300 MHz, $CDCl_3$, δ) 8.27 (2H, dt, J = 9.3, 3.2, 2.3 Hz), 7.40 (2H, dt, J = 9.3, 3.2, 2.3 Hz), 5.33 (1H, s), 4.31 (2H, t, J = 6.5 Hz), 3.88 (2H, q, J = 6.9 Hz), 2.48–2.43 (2H, dt, J = 5.6Hz), 2.29–2.18 (1H, m), 2.14–2.05 (1H, dq, J = 4.9 Hz), 2.01–1.71 (4H, m), 1.60–1.47 (1H, m), 1.36 (3H, t, J = 7.0 Hz); ^{13}C NMR (75 MHz, $CDCl_3$, δ) 201.2, 177.2, 156.0, 152.9, 145.7, 125.7, 122.2, 102.6, 69.9, 64.7, 45.0, 28.6, 26.9, 26.5, 26.2, 14.5; ESI MS *m/z* 364 $(M + H)^+$, 386 $(M + Na)^+$.

3-(4-Ethoxy-2-oxocyclohex-3-enyl)propyl 4-(5-((3a*R*,6*S*,6a*S*)-Hexahydro-2-oxo-1*H*-thieno[3,4-*d*]imidazol-6-yl)pentanamido)butylcarbamate (19). To a suspension of *N*-(4-aminobutyl)-5-((3a*R*,6*S*,6a*S*)-hexahydro-2-oxo-1*H*-thieno[3,4-*d*]imidazol-6-yl)pentanamide hydrochloride salt (**17**) (300 mg, 0.83 mmol) in THF/DCM (1/1 v/v, 8 mL) was added 3-(4-ethoxy-2-oxocyclohex-3-enyl)propyl 4-nitrophenylcarbonate (**18**) (245 mg, 0.78 mmol) and NEt_3 (110 μL, 0.83 mmol) (Scheme 5). The mixture was stirred at room temperature for 72 h and filtered, and the solids were washed with MeOH/DCM (1/1 v/v, 20 mL). The filtrate was reduced to dryness to yield a yellow oil that was purified by column chromatography (DCM/MeOH, 85/15). The pure product (**19**) was obtained as a white solid (200 mg, 48.8%): mp 191–192 °C; R_f = 0.13 (DCM/MeOH, 9/1); ^{1}H NMR (300 MHz, $CDCl_3$/MeOH-d_4, δ) 5.05 (1H, s), 4.05 (1H, dd, J = 4.5, 7.8 Hz), 3.78 (2H, t, J = 6.3 Hz), 3.69 (2H, q, J = 7.1 Hz), 2.96–2.91 (3H, m), 2.87 (2H, t, J = 6.8 Hz), 2.67 (1H, dd, J = 4.9, 12.9 Hz), 2.47 (1H, d, J = 12.9 Hz), 2.21 (2H, t, J = 5.8 Hz), 2.00–1.98 (1H, m), 1.94 (2H, t, J = 7.2 Hz), 1.89–1.81 (1H, m), 1.66–1.52 (1H, m), 1.50–1.33 (6H, m), 1.30–1.18 (6H, m), 1.12 (3H, t, J = 7.0 Hz); ^{13}C NMR (75 MHz, $CDCl_3$/MeOH-d_4, δ) 207.2, 205.5, 182.8, 178.7, 168.6, 162.0, 105.9, 105.6, 68.8, 66.3, 64.5, 61.7, 59.9, 48.9, 44.5, 43.2, 40.0, 32.7, 32.4, 32.2, 31.4, 30.8, 30.7, 30.4, 30.2, 29.8, 21.9, 18.1, 12.8; ESI MS *m/z* 561 $(M + Na)^+$.

3-(2,4-Dioxocyclohexyl)propyl 4-(5-((3a*R*,6*S*,6a*S*)-Hexahydro-2-oxo-1 *H*-thieno[3,4-*d*]imidazol-6-yl)pentanamido)butylcarbamate (DCP-Bio3, 20). 3-(4-Ethoxy-2-oxocyclohex-3-enyl)propyl 4-(5-((3a*R*,6*S*,6a*S*)-hexahydro-2-oxo-1*H*-thieno[3,4-*d*]imidazol-6-yl)pentanamido)butylcarbamate (**19**) (110 mg, 0.20 mmol) was solubilized in DCM/MeCN/acetone (2/1/1 v/v/v, 12 mL) and treated with a 4 M solution of HCl in 1,4-dioxane (0.5 mL) (Scheme 5). The mixture was stirred at room temperature for 4 h and then neutralized by the addition of solid sodium carbonate. The mixture was then filtered and washed with DCM/MeOH (3/1 v/v, 20 mL). The filtrate was reduced to dryness and purified by flash column chromatography (gradient elution with DCM/MeOH, 90/10 to 80/20) to yield the pure product (**20**) as a tan foamy solid (82 mg, 78.8%): mp 155 °C (dec); R_f = 0.42 (DCM/MeOH, 80/20); ^{1}H NMR (300 MHz, MeOH-d_4, δ) 4.60 (1H, dd, J = 4.8, 7.4 Hz), 4.40 (1H, dd, J = 4.4, 7.8 Hz), 4.13 (2H, t, J = 5.8 Hz), 3.28 (2H, bd, J = 3.7 Hz), 3.20 (2H, m), 3.02 (1H, dd, J = 4.9, 12.7 Hz), 2.80 (1H, d, J = 12.7 Hz), 2.50 (2H, m), 2.42–2.39 (1H, m), 2.30 (2H, t, J = 7.2 Hz), 2.25–2.15 (1H, m), 1.96–1.50 (16H, m); ^{13}C NMR (75 MHz, MeOH-d_4, δ) 176.5, 166.4, 159.7, 66.2, 63.8, 62.1, 57.4, 53.0, 43.6, 41.8, 41.5, 40.4, 37.3, 34.3, 31.1, 30.2, 29.9, 28.7, 28.3, 28.1, 27.7, 27.3, 26.7, 26.6; ESI MS *m/z* 533 $(M + Na)^+$.

Rhodamine B Piperazine Amide (21). To a solution of piperazine (4.67 g, 54 mmol) in anhydrous DCM (50 mL) was added trimethylaluminum (13.6 mL of a 2 M solution in toluene) dropwise. The resulting mixture was stirred at room temperature for 1 h, and then a solution of rhodamine B base (6.0 g) in DCM (15 mL) was added dropwise (Scheme 6). The reaction mixture was refluxed for 72 h. Upon cooling, the mixture was carefully neutralized by the dropwise addition of a 0.1 M HCl aqueous solution. The heterogeneous mixture was filtered, and the inorganics salts were washed sequentially with DCM (100

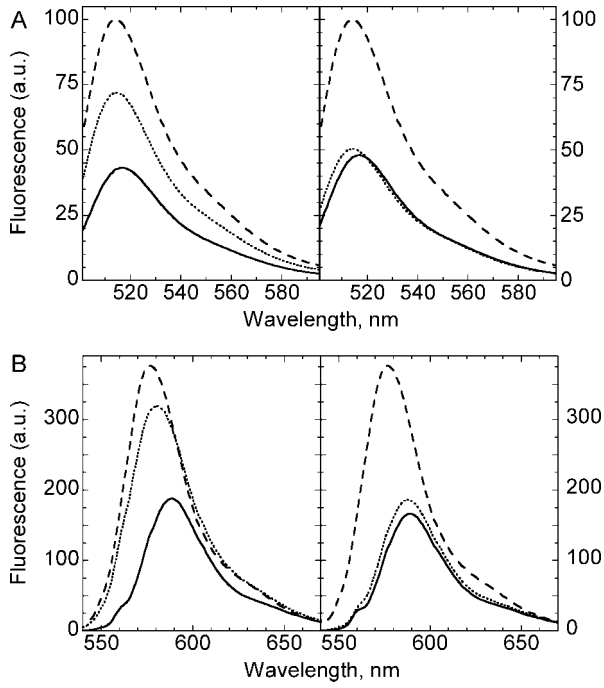


Figure 1. Fluorescence spectra of fluorescein- (A) and rhodamine-linked (B) reagents before (dotted) and after (solid) reaction with cysteine sulfenic acid-containing AhpC. Free fluorescein (A) and rhodamine B (B) are shown as the dashed spectra for comparison. Labeled C165S AhpC was prepared as described in the Experimental Procedures with the cysteine sulfenic acid form of the protein incubated anaerobically with 5 mM **5** (DCP-FL1), **9** (DCP-FL2), **23** (DCP-Rho1), or **26** (DCP-Rho2) for 60 min and then washed free of the unreacted reagent and buffer components into a final buffer of 50 mM Tris-HCl at pH 8 (fluorescein) or 50 mM potassium phosphate buffer at pH 7 (rhodamine) using an Apollo concentrator. Samples in panel A at ~0.5 absorbance (491 nm excitation) were analyzed on a Tecan Safire 2 monochromator-based microplate reader with a gain of 68. Samples in panel B at an absorbance of 0.14 (560 nm excitation) were analyzed on a Varian Cary Eclipse fluorescence spectrophotometer at medium sensitivity, with 5 nm bandwiths for both excitation and emission wavelengths in both instruments.

mL) and DCM/MeOH (4/1 v/v, 150 mL). The filtrate was reduced to partial dryness and partitioned between EtOAc (3 × 200 mL) and saturated $NaHCO_3$ solution (300 mL). The aqueous phase was saturated with NaCl, acidified with 1 M HCl, and extracted with *i*PrOH/DCM (2/1 v/v, 5 × 150 mL). The organic phase was dried over $MgSO_4$, filtered, and reduced to dryness to yield a purple oil. This was solubilized in a minimal amount of MeOH and added dropwise to Et_2O (500 mL), and the crude product (**21**) was filtered off and obtained as a purple-gold solid (5.88 g, 79.3%). ^{1}H NMR (300 MHz, $CDCl_3$, δ) 7.59–7.53 (2H, m), 7.46–7.41 (1H, m), 7.25–7.17 (1H, m), 7.10 (1H, d, J = 9.5 Hz), 7.02 (1H, d, J = 9.5 Hz), 6.84–6.79 (2H, m), 6.64 (2H, dd, J = 2.3, 6.2 Hz), 3.78 (2H, bd, J = 14.1 Hz), 3.63–3.40 (8H, m), 3.32–3.18 (4H, bs), 3.25 (4H, m), 2.98 (2H, bd, J = 20.4 Hz), 2.42 (1H, bs), 1.20 (12H, t, J = 7.0 Hz); ^{13}C NMR (75 MHz, $CDCl_3$, δ) 167.5, 158.0, 156.0, 155.9, 155.8, 134.6, 132.4, 131.7, 131.4, 131.0, 130.7, 130.6, 130.4, 130.3, 127.9, 114.7, 114.4, 96.7, 58.1, 50.4, 46.6, 46.5, 18.7, 13.0; ESI MS *m/z* 511 $(M + H)^+$.

Rhodamine B [4-[3-(4-Ethoxy-2-oxocyclohex-3-enyl)propyl]carbamate]piperazine Amide (22). To a solution of rhodamine B piperazine amide (**21**) (434 mg, 0.79 mmol) in anhydrous DCM (10 mL) was added NEt_3 (180 μL, 1.32 mmol) and 3-(4-ethoxy-2-oxocyclohex-3-enyl)propyl 4-nitrophenylcarbonate (**18**) (240 mg, 0.66 mmol) (Scheme 6). The reaction mixture was stirred at reflux for 6 h and then at room temperature for 16 h, reduced to dryness, and purified by flash column chromatography (2×, DCM/MeOH, 90/10 and then 91/9) to yield the pure product (**22**) as a purple foam (300 mg, 58.8%). R_f = 0.25 (DCM/MeOH 9/1); ^{1}H NMR (300 MHz, $CDCl_3$, δ) 7.64 (2H, m), 7.48 (1H, dd, J = 2.8, 6.8 Hz), 7.30 (1H, dd, J = 2.6, 5.9 Hz), 7.16 (2H, q, J = 9.5 Hz), 6.89 (2H, d, J = 7.6 Hz), 6.74 (2H, bs), 5.24 (1H, s), 3.99 (2H, t, J = 6.5 Hz), 3.80 (2H, q, J = 7.0 Hz), 3.59 (8H, q, J = 7.1 Hz), 3.32 (4H, bs), 3.25 (4H, bs), 2.34 (2H, d, J = 5.3 Hz), 2.15–2.06 (1H, m), 2.04–196 (1H, m), 1.84–1.75 (1H, m), 1.69–1.49 (3H, m), 1.38–1.18 (16H, m); ^{13}C NMR (75 MHz, $CDCl_3$, δ) 201.4, 201.3, 177.4, 168.0, 158.0, 156.0, 155.9, 155.5, 135.3, 132.3, 131.0, 130.8, 130.6, 127.9, 114.5, 114.0, 102.4, 96.8, 66.1, 64.6, 53.9, 46.5, 45.0, 28.5, 26.8, 26.7, 26.2, 14.5, 13.0.

Rhodamine B [4-[3-(2,4-Dioxocyclohexyl)propyl]carbamate]piperazine Amide (DCP-Rho1, 23). Rhodamine B [4-[3-(4-ethoxy-2-oxocyclohex-3-enyl)propyl]carbamate]piperazine amide (**22**) (280 mg, 0.36 mmol) was solubilized in DCM (16 mL) and treated with 4 M HCl in 1,4-dioxane (1 mL) (Scheme 6). The mixture was stirred at room temperature for 16 h, then carefully neutralized by the addition of solid Na_2CO_3. The inorganic solids were filtered off and washed with 10% MeOH in DCM, and the combined filtrates were reduced to dryness. The crude purple oil was purified by flash column chromatography (gradient elution, DCM/MeOH, 92/8 to 90/10) to yield the pure product (**23**) as a purple solid (215 mg, 79.6%): log *P* (octan-1-ol/phosphate buffer, pH 7.2) = 1.026 ± 0.113; ^{1}H NMR (300 MHz, $CDCl_3$, δ) 7.62 (2H, d, J = 3.3 Hz), 7.48 (1H, d, J = 3.0 Hz), 7.29 (1H, d, J = 3.0 Hz), 7.17 (2H, d, J = 9.0 Hz), 6.90 (2H, bs), 6.75 (2H, bs), 5.24 (1H, bs), 3.99 (2H, t, J = 6.0 Hz), 3.82 (8H, t, J = 7.8 Hz), 3.32 (4H, bs), 3.26 (4H, bs), 2.35 (2H, d, J = 5.4 Hz), 2.14–2.08 (1H, m), 2.03–1.98 (1H, m), 1.79–1.75 (1H, m), 1.74–1.62 (3H, m), 1.61–1.44 (1H, m), 1.26 (12H, t, J = 6.6 Hz); ^{13}C NMR (75 MHz, $CDCl_3$, δ) 201.3, 178.2, 168.1, 158.1, 156.1, 155.6, 135.4, 132.4, 131.1, 130.8, 130.6, 128.0, 114.6, 114.1, 102.4, 96.9, 66.2, 66.0, 56.1, 46.6, 45.1, 28.4, 27.7, 27.1, 26.8, 26.7, 26.4, 26.2, 13.1; ESI MS *m/z* 708 $(M + H)^+$.

Rhodamine B *tert*-Butyl 4-oxo-4-(piperazin-1-yl)butylcarbamate (24). *N*-Boc GABA-OH (149 mg, 0.73 mmol) in anhydrous DCM/THF/acetone (1/1/3 v/v/v, 10 mL) was treated with DCC (0.8 mL of 1.0 M solution in DCM). After the mixture was stirred at room temperature for 2 h, rhodamine B piperazine amide (**21**) (400 mg, 0.73 mmol) was added. The mixture was stirred at room temperature for 16 h and reduced to dryness. The residue was purified by flash column chromatography (DCM/MeOH, 90/10) to yield the pure product (**24**) as a purple foam (351 mg, 65.6%). ^{1}H NMR (300 MHz, $CDCl_3$, δ) 7.76 (2H, bs), 7.63 (1H, bs), 7.41–7.01 (5H, m), 6.98 (1H, bs), 6.78 (1H, bs), 3.82–3.57 (10H, m), 3.51–3.36 (5H, m), 3.25–3.18 (3H, m), 2.62–2.57 (1H, m), 1.92–1.88 (4H, m), 1.51 (9H, d, J = 5.0 Hz), 1.42 (12H, t, J = 7.0Hz); ^{13}C NMR (75 MHz, $CDCl_3$, δ) 172.6, 168.0, 158.1, 156.7, 156.6, 156.1, 135.6, 132.5, 131.4, 131.3, 130.6, 130.5, 128.0, 115.3, 114.2, 96.9, 96.4, 79.2, 78.9, 53.9, 48.5, 46.5 (46.3, 42.1, 41.3, 40.5, 32.6, 31.5, 30.7), 28.8, 25.8, 13.0.

Rhodamine B 3-(4-Ethoxy-2-oxocyclohex-3-enyl)propyl 4-Oxo-4-(piperazin-1-yl)butylcarbamate (25). Rhodamine B *tert*-butyl 4-oxo-4-(piperazin-1-yl)butylcarbamate (**24**) (350 mg, 0.48 mmol) in DCM (6 mL) was treated with 4 M HCl in 1,4-dioxane (0.5 mL). The mixture was stirred at room temperature until TLC showed no starting material remaining (5 h), and the mixture was reduced to dryness to yield the crude product as a purple solid (320 mg, 100%). This was directly used in the next step without purification, resolubilized in DCM (10 mL), and treated with NEt_3 (133 μL, 0.96 mmol) and 3-(4-ethoxy-2-oxocyclohex-3-enyl)propyl 4-nitrophenylcarbonate (**18**) (174 mg, 0.48 mmol). The mixture was stirred at room temperature

Table 1. Mass and Spectral Information for Sulfenic Acid-Directed Reagents and Their Adducts with AhpC

reagent	empirical formula	monoisotopic molecular mass	average molecular weight (g/mol)	characteristic ion mass ($[M + H]^+$, Da)[a]	mass of AhpC protein adduct (Da)[b]	$\lambda_{max,ex}$ and $\lambda_{max,em}$ of free reagent (nm)	λ_{max} and $\lambda_{max,em}$ of protein adduct (nm)
DCP-FL1	$C_{30}H_{25}NO_9$	543.15	543.5	576.13	21142.9 ± 2.1	490, 514	493, 517
DCP-FL2	$C_{33}H_{29}N_5O_8$	623.20	623.6	656.18	21223.3 ± 2.1	491, 514	494, 517
DCP-Bio1	$C_{19}H_{28}N_2O_5S$	396.17	396.5	429.14	20996.1 ± 2.1	NF[c]	NF[c]
DCP-Bio2	$C_{22}H_{32}N_6O_4S$	476.22	476.6	509.20	21076.6 ± 2.1	NF[c]	NF[c]
DCP-Bio3	$C_{24}H_{38}N_4O_6S$	510.25	510.7	543.23	21112.5 ± 2.7	NF[c]	NF[c]
DCP-Rho1	$C_{42}H_{51}N_4O_6$	707.38	707.9	739.38[d]	21304.9 ± 2.1	560, 581	570, 588
DCP-Rho2	$C_{46}H_{58}N_5O_7$	792.43	793.0	824.38[d]	21389.6 ± 2.1	570, 588	570, 589

[a] *m/z* value of ion released during MS–MS analysis of the labeled peptide from AhpC, as described in the text. [b] Mass of adduct by electrospray ionization mass spectrometry in a triple quadrupole mass spectrometer. For comparison, the underivatized sulfenic acid form of the C165S mutant of AhpC analyzed under these conditions gave a major peak at 20648.7 Da, accounting for the addition of three oxygen atoms to the protein (presumably the sulfonic acid form at the active site cysteine). The errors listed reflect the hardware accuracy of ±0.01%. Where the MaxEnt error was greater than the instrument error, this number was used instead. [c] NF = nonfluorescent. [d] $[M^+]$, positively charged without the addition of H^+.

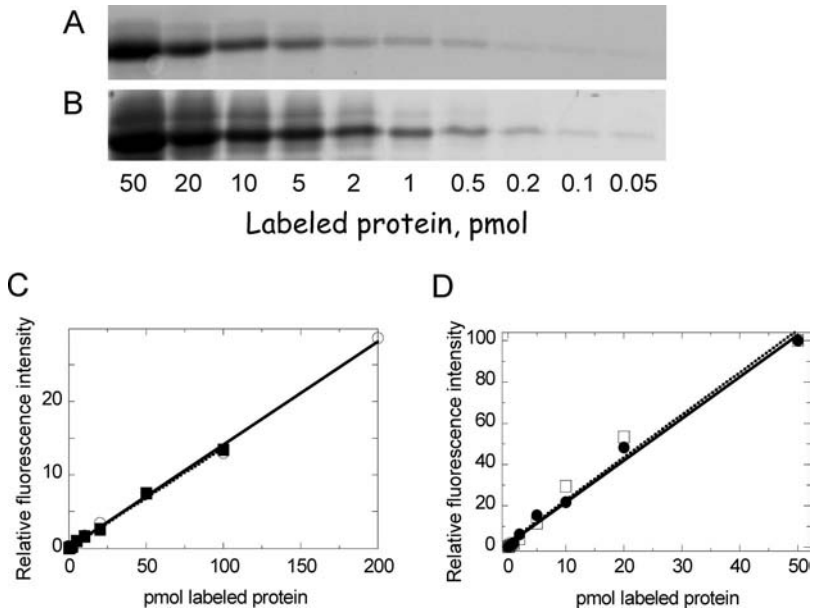


Figure 2. Visualization of labeled AhpC proteins after 1D gel electrophoresis. Varying amounts of AhpC C165S labeled with DCP-FL1 (A) or DCP-Rho1 (B) were loaded onto SDS–polyacylamide gels and resolved by electrophoresis. Gels were washed in deionized water for 30 min and then imaged on an Amersham Storm 840 for fluorescein reagents (using a 450 nm LED at normal sensitivity) or on a Typhoon 8600 fluorescence imager for rhodamine reagents (with a 633 nm red laser and Tamara 580 BP 30 filter at normal sensitivity). Relative fluorescence intensity was determined using ImageQuant software and plotted vs pmol of labeled protein for (C) DCP-FL1 (■) and DCP-FL2 (○) or for (D) DCP-Rho1 (●) and DCP-Rho2 (□).

for 16 h, reduced to dryness, and purified by flash column chromatography (gradient elution, DCM/MeOH, 93/7 to 90/10) to yield the pure product (**25**) as a purple foam (229 mg, 55.9%). R_f = 0.35 (DCM/MeOH 9/1); ^{1}H NMR (300 MHz, $CDCl_3$, δ) 7.61 (2H, bs), 7.48 (1H, bs), 7.27–7.16 (4H, m), 6.85–6.37 (3H, m), 5.20 (1H, s), 3.93 (2H, bs), 3.79 (2H, q, J = 7.0 Hz), 3.57–3.50 (10H, m), 3.34–3.23 (6H, m), 3.13 (2H, bs), 2.68 (2H, bs), 2.48 (1H, bs), 2.35 (2H, t, J = 5.7 Hz), 2.10–1.97 (2H, m), 1.75–1.57 (5H, m), 1.30–1.23 (12H, m); ^{13}C NMR (75 MHz, $CDCl_3$, δ) 201.7, 177.3, 172.7, 168.0, 158.0, 157.5, 156.3, 156.0, 135.6, 132.5, 131.4, 130.5, 130.4, 130.3, 128.0, 115.2, 114.4, 114.1, 102.4, 96.8, 96.4, 64.8, 64.5, 48.5, 46.5, 46.3, 45.1, (42.1, 41.3, 40.9, 31.6, 31.3, 30.0), 28.4, 27.0, 26.6, 26.2, 25.7, 14.5, 13.0; ESI MS *m/z* 821 $(M + H)^+$.

Rhodamine B 3-(2,4-Dioxocyclohexyl)propyl 4-Oxo-4-(piperazin-1-yl)butylcarbamate (DCP-Rho2, 26). Rhodamine B 3-(4-ethoxy-2-oxocyclohex-3-enyl)propyl 4-oxo-4-(piperazin-1-yl)butylcarbamate (**25**) (200 mg, 0.23 mmol) was solubilized in DCM (10 mL) and treated with 4 M HCl in 1,4-dioxane (1 mL). The mixture was stirred at room temperature for 6 h and then carefully neutralized by the addition of solid Na_2CO_3. The inorganic solids were filtered off and washed with 10% MeOH in DCM, and the combined filtrates were reduced to dryness. The residue was purified by flash column chromatography (2×, DCM/MeOH, 86/14 and then 88/12) to yield the product (**26**) as a purple foam (99 mg, 51.3%). ^{1}H NMR (300 MHz, $CDCl_3$, δ) 7.64 (2H, m), 7.48 (1H, dd, J = 2.8, 6.8 Hz), 7.30 (1H, dd, J = 2.6, 5.9 Hz), 7.16 (2H, q, J = 9.5 Hz), 6.89 (2H, d, J = 7.6 Hz), 6.74 (2H, bs), 5.24 (1H, s), 3.99 (2H, t, J = 6.5 Hz), 3.80 (2H, q, J = 7.0 Hz), 3.59 (8H, q, J = 7.1 Hz), 3.32 (4H, bs), 3.25 (4H, bs), 2.34 (2H, d, J = 5.3 Hz), 2.15–2.06 (1H, m), 2.04–196 (1H, m), 1.84–1.75 (1H, m), 1.69–1.49 (3H, m), 1.38–1.18 (16H, m); ^{13}C NMR (75 MHz, $CDCl_3$, δ) 201.7, 177.3, 172.7, 168.0, 158.0, 157.5, 156.3, 156.0, 135.6, 132.5, 131.4, 130.5, 130.4, 130.3, 128.0, 115.2, 114.4, 114.1, 102.4, 96.8, 96.4, 64.8, 64.5, 48.5, 46.5, 46.3, 45.1, (42.1, 41.3, 40.9, 31.6, 31.3, 30.0), 28.4, 27.0, 26.6, 26.2, 25.7, 14.5, 13.0; ESI MS *m/z* 793 $(M + H)^+$.

Generation and Labeling of Sulfenic Acid-Containing C165S AhpC and Papain for Spectral and Mass Spectrometric Analysis. The C165S mutant of AhpC, stored in 5 mM 1,4-dithiothreitol (DTT) but washed free of DTT prior to use, was purified essentially as described previously (*7*). Papain was purchased from Sigma-Aldrich and subjected to concentration and redilution in Apollo concentrators (Orbital Biosciences, Topsfield, MA; 20 kDa cutoff) before use to remove low

molecular weight contaminants. Generation of the sulfenic acid form of AhpC followed earlier procedures (*5*). The corresponding oxidized form of papain was generated by addition of 2 equiv of hydrogen peroxide under anaerobic conditions (in a 10 mL pear-shaped flask subjected to a gentle vacuum and flushed with argon multiple times).

Labeling procedures for generating the alkylated forms of AhpC and papain for subsequent mass spectrometric (MS) analysis were performed with approximately 6 nmol of the sulfenic acid-containing protein under anaerobic conditions. Reactions in either an anaerobic flask or argon-flushed Eppendorf tubes were started with the addition of 5 mM (final concentration) of the reagent of choice in a final volume of 50–100 μL. Reagents were added from a 250 mM stock predissolved in dimethyl sulfoxide (DMSO). Following incubation at room temperature for 60 min or overnight, samples were concentrated and rediluted (at least 3 times, 6 times or more for sticky fluorescein and rhodamine-based reagents) into the buffer of choice using 20 kDa cutoff Apollo ultrafiltration devices. Samples were stored at −20 °C until further use.

Spectral and Gel Analysis of Reagents and Labeled Proteins. UV–visible absorbance spectra were acquired with either an Agilent HP8452A UV–vis diode array spectrophotometer or a Beckman DU-7500 diode array spectrophotometer. Fluorescence measurements were made with either a Varian Cary Eclipse fluorescence spectrophotometer or a Tecan Safire 2 monochromator-based microplate reader. Approximate 100 or 250 mM stock solutions of DCP-FL1 or DCP-FL2 (**5** or **9**, respectively) in DMSO were in some cases standardized using the published extinction coefficient of ∼75 000 M^{-1} cm^{-1} for free fluorescein in pH 9 buffer at 491 nm (*8*). By use of this value and by comparison of the free reagents in pH 9 ammonium bicarbonate and pH 7 phosphate buffers, these reagents and presumably their protein-bound counterparts exhibited average extinction coefficients of ∼67 000 M^{-1} cm^{-1} for both fluorescein reagents. For the rhodamine-linked reagents DCP-Rho1 and DCP-Rho2 (**23** and **26**, respectively), the extinction coefficient for free rhodamine B in methanol (90 000 M^{-1} cm^{-1} at 554 nm) was used (Sigma-Aldrich data sheet); in neutral pH phosphate buffer, this extinction coefficient decreases to about 80 000 M^{-1} cm^{-1} for rhodamine B. Again, assuming the same extinction coefficient for both rhodamine reagents as for rhodamine B in methanol, DCP-Rho1 and DCP-Rho2 exhibited extinction coefficients of approximately 70 000 and 61 000 M^{-1} cm^{-1} in neutral pH phosphate buffer, respectively.

One-dimensional 12% SDS–polyacrylamide gels were electrophoresed using a BioRad Mini-PROTEAN 3 system and standard procedures. Two-dimensional gels used the Bio-Rad Protean IEF cell and Criterion gel systems from Bio-Rad, including 11 cm, pH 3–10 NL IPG strips and 8–16% gradient gels, and methods recommended by the manufacturer. Various amounts of DCP-FL1 labeled C165S AhpC were loaded onto separate strips and focused for ∼5½ h. After focusing, each strip was trimmed to within about 2 cm of the protein band (as estimated from one control strip that was stained with Coomassie blue) and then three different strips were loaded onto the top of each Criterion gel to run the second dimension. All gels were soaked in water for 30 min and then imaged for fluorescence on either an Amersham Storm 840 or a Typhoon 8600 fluorescence imager. Data were analyzed either with ImageQuant software (for 1D gels) or by direct analysis of the images with MATLAB (for 2D gels). Amounts of labeled protein loaded onto each gel were determined using the absorbance of the chromaphores attached to the protein (at 491 and 570 nm for fluorescein- and rhodamine-labeled samples, respectively) and the approximate extinction coefficients, given above. A completely independent calculation was conducted in each case using the known amount of protein and the percent modified based on mass spectral analysis of the intact protein (and an assumed recovery of 100% from the Apollo concentrators) and gave a difference in amounts of ∼10% or less.

Mass Spectrometric Analysis of Labeled Proteins and Peptides. To confirm the size and covalent attachment of each adduct, 1–2 nmol of labeled or unlabeled protein (∼60 μL) in 10 mM ammonium bicarbonate was submitted to the Analytical Chemistry Core Laboratory at Wake Forest University School of Medicine for infusion analysis on a Micromass Quattro II triple quadrupole mass spectrometer equipped with a Z-spray source. Just prior to analysis, samples were diluted 1:1 with acetonitrile and 1% formic acid was added. The data were processed and analyzed using MassLynx, version 3.5.

For MS–MS analysis of alkylated peptides, 0.5 nmol of labeled AhpC proteins was digested in 25 mM ammonium bicarbonate with 50 ng of AspN for ∼16 h at 37 °C. Peptide mixtures were analyzed with a Waters/Micromass Q-TOF API US tandem mass spectrometer equipped with a nanospray source interfaced to a Waters CapLC to detect labeled peptides and reagent-specific ions released by fragmentation. AhpC labeled with DCP-Bio1 and digested as above was also analyzed on a Thermo LTQ ion-trap mass spectrometer coupled with an Ultimate 3000 nano-HPLC system. A typical gradient was run for 60 min from 0% to 100% solvent B (80% acetonitrile, 20% H_2O, and 0.1% formic acid). Solvent A consists of 5% acetonitrile, 95% H_2O, and 0.1% formic acid. The flow rate was set at 200 nL/min on a 75 μm × 10 cm fused silica capillary column (New Objectives) in-house-packed with Michrom Magic C18AQ (200 Å, 5 μm). The analysis was performed in SIM mode where the DCP-Bio1-labeled peptide (*m*/*z* 811.77, +2 charge) was isolated for further fragmentation. Peptide identification was performed using the SEQUEST module in Bioworks suite 3.1 software.

Kinetic Studies of Reagents Reacting with Sulfenic Acid-Containing Proteins. To 5 nmol of papain in 25 mM potassium phosphate buffer at pH 7.0, with 1 mM EDTA, was added DCP-Bio1 (from a 250 mM stock solution in DMSO) at final concentrations of 0.5–5 mM and a total volume of 50 μL. The reaction was initiated with the addition of 2 equiv of hydrogen peroxide. At the appropriate incubation time, each sample was applied to a Bio-Gel P6 spin column to remove small molecules and exchange the buffer into 50 mM ammonium bicarbonate, and then the mass spectra were obtained after rapid addition of acetonitrile and formic acid and injection into an Agilent electrospray ionization (ESI)-TOF mass spectrometer. Fits of the data were carried out using KinTekSim using the model A → B → C, where A is the R–SH form, B the R–SOH form, and C the biotinylated form of papain. The pseudo-first-order rate of A → B was considered unchanging at all concentrations of DCP-Bio1 used, and the rate of B → C varied with the amount of reagent added.

RESULTS AND DISCUSSION

Synthesis of Two Fluorescein Derivatives, DCP-FL1 and DCP-FL2. Initial synthetic approaches involving the synthesis of 5(6)carboxyfluorescein did not yield separable derivatives, which prompted us to explore a different synthetic strategy utilizing commercially available fluoresceinamine isomer I (**1**). Treatment of **1** with *p*-nitrophenyl chloroformate in refluxing acetone gave carbamate derivative (**2**) in near-quantitative yield (Scheme 1). The product could be filtered from the reaction mixture and separated from unreacted starting material. TLC and NMR analyses indicated that this material could be used without additional purification. Reaction with our protected alcohol derivative of 1,3-cyclohexadione (**3**) yielded the protected fluorescein–carbamate conjugate (**4**) in moderate

yield (Scheme 1). Deprotection of the enol ether proceeded cleanly using 4 M HCl in 1,4-dioxane without concomitant carbamate cleavage to give the desired fluorescein derivative (DCP-FL1, **5**; note that the use of this abbreviation is carried over from the nomenclature previously introduced (*5*)).

Synthesis of a more stable urea derivative (DCP-FL2, **9**) involved the introduction of a urea "linker", which began with the reaction of the *p*-nitrophenyl carbamate of fluoresceinamine (**2**) with propargylamine (Scheme 2). Careful addition of 1 equiv of triethylamine induced salt formation, and the product (**6**) could be simply filtered from the reaction mixture, thus obviating the need for purification by column chromatography. Utilization of "click" chemistry (*9*) enabled us to couple the propargylurea (**6**) with the azide derivative (**7**) of our alcohol (synthesized using Mitsunobu conditions; Scheme 2) to form triazole (**8**, Scheme 2). Acid deprotection yielded the urea-linked fluorescein conjugate (DCP-FL2, **9**) in near-quantitative yield.

Synthesis of Three Biotin Derivatives: DCP-Bio1, DCP-Bio2, and DCP-Bio3. To generate the first biotinylated derivative, D-(+)-biotin was coupled with alcohol (**3**) under standard dicyclohexylcarbodiimide (DCC) coupling conditions to yield ester **10** in good yield (Scheme 3). Acid deprotection using anhydrous HCl followed by silica gel column chromatography reproducibly gave the deprotected biotin probe (DCP-Bio1, **11**) in >60% yield (Scheme 3).

Other synthetic strategies were tried to link D-(+)-biotin to our sulfenic acid-reactive compound, as the lability of the ester linkage in **11** was expected to preclude its use in cellular assays because of nonspecific esterase cleavage. On the basis of the "click" chemistry utilized in the synthesis of the fluorescein triazole conjugate (**9**), we applied this strategy to the synthesis of a biotin amide derivative (DCP-Bio2, **14**, Scheme 4). Finally, a further biotin derivative incorporating a longer linker was synthesized as depicted in Scheme 5. Mono *N*-Boc protection of 1,4-diaminobutane was carried out as previously described (*10*), followed by DCC coupling to D-(+)-biotin and Boc deprotection to give the amine hydrochloride salt (**17**, Scheme 5). Coupling of the free amine of **17** with the *p*-nitrophenyl carbonate derivative (**18**) of alcohol **3** gave the protected version of this biotin derivative (**19**, Scheme 5). Similar deprotection methods yielded the extended biotin derivative as before (DCP-Bio3, **20**, Scheme 5).

Synthesis of Two Rhodamine Derivatives: DCP-Rho1 and DCP-Rho2. The utility of cell-permeable fluorophores with spectral profiles different from that of fluorescein may permit future multiplex, differential labeling of protein sulfenic acids. The synthesis of rhodamine B derivatives was explored because rhodamine B is known to be cell-permeable (*11*), absorbs and emits at a longer wavelength than fluorescein, and has a large extinction coefficient.

The synthesis and spectral properties of rhodamine B piperazine amide (**21**) have previously been described (*12*), and this was used as a starting point in our syntheses of rhodamine B probes. Rhodamine B piperazine amide was synthesized as described and isolated as a crude iridescent purple-gold solid in 57–79% yield (**21**, Scheme 6). Coupling of compound **18** and deprotection proceeded smoothly to give the rhodamine derivative (DCP-Rho1, **23**, Scheme 6). The synthesis of a second rhodamine B derivative was undertaken as outlined in Scheme 7. The piperazine amide (**21**) was coupled, using DCC, to *N*-Boc GABA to give the extended protected derivative (**24**, Scheme 7). Deprotection of the *N*-Boc group and further coupling to the carbonate derivative (**18**) followed by enol ether deprotection yielded the second rhodamine probe (DCP-Rho2, **26**, Scheme 7).

Reactivity of Cyclohexadione-Linked Reagents toward Cysteine Sulfenic Acid. Spectroscopic Properties of Free Reagents and Protein Adducts. As described previously, the C165S mutant of AhpC, a cysteine-based peroxidase enzyme (peroxiredoxin) from *Salmonella typhimurium*, is a good test protein because of its rapid formation of the sulfenic acid intermediate at the active site (Cys46) upon oxidation by peroxides and the relative stability of this species under anaerobic condtions when the resolving cysteine (Cys165) is not present to generate the disulfide bond (*4*, *13*). By use of AhpC, all seven conjugates linked to the alcohol functional group of **3** were shown to possess approximately the same reactivity and specificity toward the cysteine sulfenic acid form of C165S AhpC as dimedone and the two conjugates previously synthesized (*5*). Papain (a cysteine-based protease) has also been used as a test protein in the studies described below because of its known propensity to form sulfenic acid at the active site cysteine (*14*, *15*).

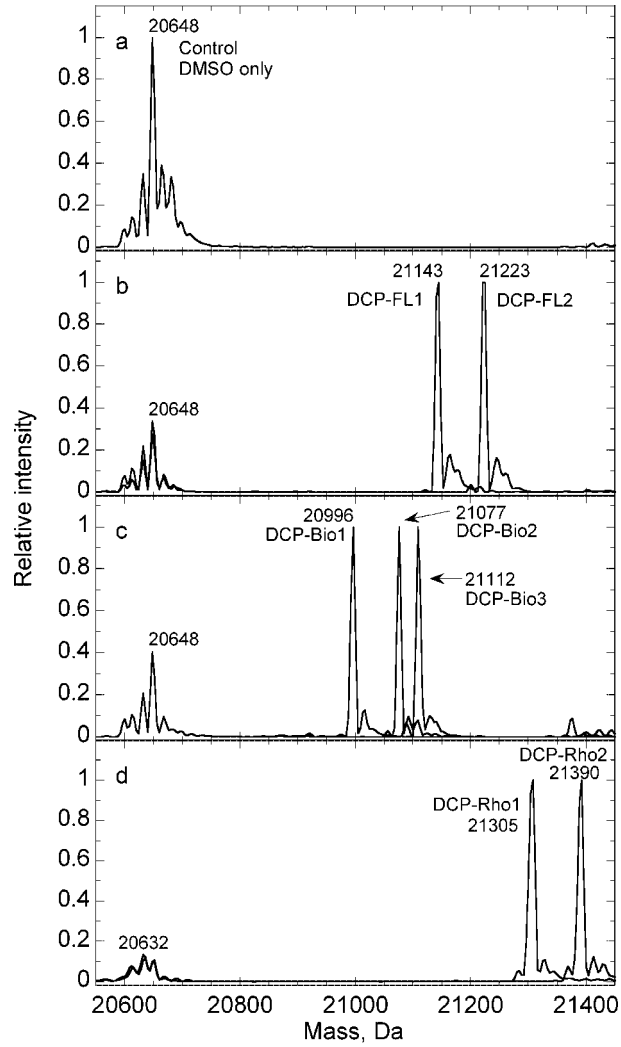


Figure 3. Electrospray ionization mass spectrometry analysis of adducts with the sulfenic acid form of C165S AhpC. The mutant of the bacterial peroxidase AhpC (C165S) containing only the peroxidatic cysteine (Cys46) but not the resolving cysteine (Cys165) that participates in disulfide bond formation was treated with hydrogen peroxide to yield the relatively stabilized sulfenic acid form of the protein under anaerobic conditions, then incubated with DMSO (a) or DMSO containing DCP-FL1 or DCP-FL2 (b), DCP-Bio1, DCP-Bio2, or DCP-Bio3 (c), or DCP-Rho1 or DCP-Rho2 (d) to yield the covalent protein adduct. The treated protein samples were washed, diluted with acetonitrile and formic acid, and analyzed by electrospray ionization mass spectrometry. Shown are the transformed data that represent the relative abundance of the prominent species of C165S AhpC. The peaks observed at 20 632 and 20 648 amu represent the protein with the active site Cys46 in the sulfinic and sulfonic acid states, respectively. Exact masses of the covalent adducts are listed in Table 1.

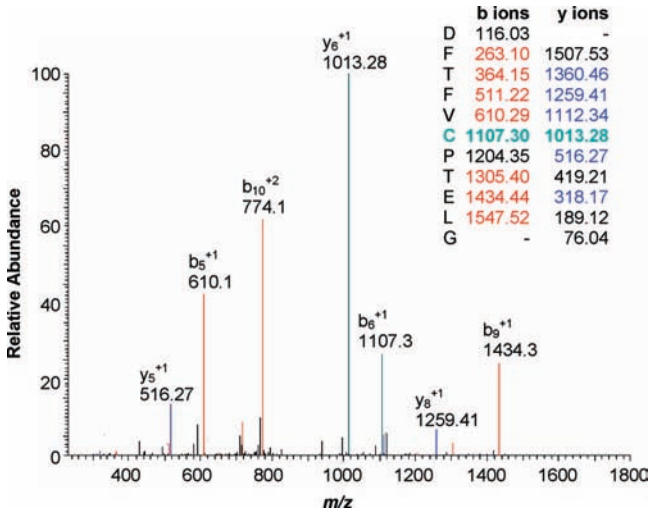


Figure 4. Nano-LC–MS/MS spectrum of the DCP-Bio1-labeled peptide of C165S AhpC containing an adduct at Cys46. The covalent adduct with DCP-Bio1 was prepared from the R–SOH form of the AhpC mutant and digested with AspN in order to generate an 11-residue peptide. The AspN digest was separated by nano-HPLC coupled to a Thermo LTQ ion trap mass spectrometer. The analysis was performed in SIM mode where the DCP-Bio1-labeled peptide (*m/z* 811.77, +2 charge) was isolated for further fragmentation. Cleavage of the amide bond results in N-terminal fragments designated as "b" and C-terminal fragments designated as "y". The masses of both sets of ions are consistent with DCP-Bio1 linked covalently to Cys46 (b6 – b5 = y6 – y5 = 497.1 *m/z*).

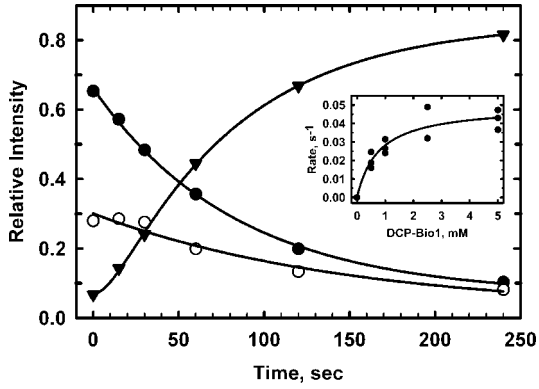


Figure 5. Kinetic studies of modification rates of sulfenic acid-containing papain with DCP-Bio1. Papain in 25 mM potassium phosphate buffer, pH 7, with 1 mM EDTA was incubated with DCP-Bio1 and 2 equiv of hydrogen peroxide, with the time of reaction taken after addition of the oxidant. At each time point a 50 μL sample containing 5 nmol of papain was applied to a Bio-Gel P6 spin column to remove small molecules and exchange the buffer into 10 mM ammonium bicarbonate. Then the mass spectra were obtained after rapid addition of acetonitrile and formic acid and injection into an an Agilent LC/MSD TOF mass spectrometer. Data plotted from one reaction with 5 mM DCP-Bio1 show the loss of the thiol form of papain (closed circles), the appearance of the covalent adduct with DCP-Bio1 (inverted triangles), and the putative sulfenic acid form (open circles) over time. Data from multiple concentrations of reagent and three independent experiments were fit to a A → B → C kinetic model as described in the text, giving a single first-order rate in this experiment of 0.024 ± 0.007 s^{-1} for formation of the sulfenic acid form of papain, and a second, saturable step with a maximal rate of 0.050 ± 0.005 s^{-1} and apparent K_m = 0.77 ± 0.24 mM for reaction of DCP-Bio1 with the sulfenic acid of papain.

The fluorescein- and rhodamine-linked reagents possess highly fluorescent chromophores that are incorporated into the target protein upon modification. Compared with free fluorescein, the DCP-FL1 and DCP-FL2 (**5** and **9**, respectively) reagents in 50 mM Tris-HCl buffer, pH 8, are partially quenched in their emission (Figure 1A) but are not shifted in their absorbance maxima (Table 1). Upon covalent attachment to protein, DCP-FL1 yields a conjugate that is further quenched in emission intensity at the peak by about 40% relative to the free reagent; under these same conditions, DCP-FL2 is not further quenched upon attachment to protein (Figure 1A). Reaction of DCP-FL1 with papain leads to even greater quenching of the fluorophore (by about 75% compared with free DCP-FL1, data not shown). For rhodamine compounds compared with rhodamine B, DCP-Rho1 (**23**) is slightly quenched in its free form but significantly quenched when covalently attached to AhpC (Figure 1B, left panel) and papain (data not shown). DCP-Rho2 (**26**) fluorescence is already significantly quenched (by about 50%) for the free reagent and largely unchanged upon attachment to either AhpC or papain proteins (Figure 1B, right panel and not shown). The quenching of fluorescence in bound DCP-Rho1 and in free and bound DCP-Rho2 is accompanied by a shift in the λ_{max} of both the excitation and emission to longer wavelengths (Table 1).

To evaluate the limit of detection and the linearity of response for the fluorophore-labeled AhpC protein, various amounts of C165S AhpC protein labeled with the different fluorescein- and rhodamine-linked reagents were analyzed in 1D and 2D polyacrylamide gels. For fluorescein, amounts as low as 0.1–0.2 pmol of protein were still detectable using a Storm 840 imager with a 450 nm LED for excitation (Figure 2A) (no improvement in sensitivity was observed using the Typhoon 8600 imager with a 532 nm laser for excitation). Furthermore, quantitation of the signal indicated linearity over at least 4 orders of magnitude (Figure 2C), even though the protein on the gel was significantly overloaded at 100 and 200 pmol (~2 and 4 μg). For comparison, 0.5 pmol was readily detected in a two-dimensional gel spot with good linearity up to at least 5 pmol (see Supporting Information, Figure S1). Gels with rhodamine-labeled AhpC showed similar, but perhaps slightly enhanced, sensitivity of detection (with a Typhoon 8600 imager and a 633 nm laser for excitation) and a reasonable degree of linearity of the signal with the amount of labeled protein loaded (parts B and D of Figure 2).

Because the biotin reagents cannot be directly observed, biotinylated protein was visualized by a Western blotting-like technique that involved transfer of the labeled proteins in the gel to nitrocellulose, addition of a 1:20000 dilution of HRP-conjugated streptavidin, and detection of HRP using the Pico chemiluminescence kit from Pierce. The limit and range of linearity for detection are thus highly dependent on the efficiency of transfer, the chemiluminescence substrate added, and the amount of time the blot is exposed to film. As with Western blots, linearity of signal with the applied biotinylated protein is over a limited range for any one exposure to a chemiluminescent reporter substrate but might be extended by obtaining multiple different exposures of a single gel. In our studies, an approximate lower limit of 0.2–0.5 pmol is typically achievable (e.g., with the Supersignal West Dura HRP detection kit from Pierce), but linearity of response must be established each time (data not shown).

Mass Spectrometry Analysis of Labeled Protein Conjugates, Intact and Proteolytically Digested. Collision-Induced Fragmentation of Label to Trigger MS–MS Sequencing. Covalent adducts of each of the probes were observed only with the sulfenic acid form of AhpC and were not generated with sulfhydryl or disulfide-containing forms of the protein; the covalent modification of AhpC with each probe was confirmed using ESI-MS analysis of the intact, labeled proteins (Figure 3 and Table 1). In each case, the higher molecular weight adduct gave a mass within 1–2 Da of the calculated masses of reduced protein (20 600 Da) plus reagent minus 2 H atoms (as expected

when the covalent bond forms) (Table 1). As shown previously, if not trapped with one of these reagents, the sulfenic acid form of AhpC undergoes further oxidation to sulfinic and sulfonic acids, presumably during incubation of the sample in acetonitrile and formic acid before MS analysis or during the analytical procedure itself (*5, 13*).

To confirm the site of AhpC modification with different probes, AspN digestion of the labeled AhpC was also carried out to generate an 11-residue peptide containing the expected cysteine site susceptible to oxidation. The peptide mixtures were analyzed using liquid chromatography and either a Q-TOF or an LTQ MS. As shown in Figure 4 and in Figure S2 of the Supporting Information, MS–MS analysis of the parent peptides gives high-quality spectra that accurately sequence the labeled peptide and confirm the presence of the covalent adduct on Cys46 of this AhpC peptide. Furthermore, for each of the fluorescein-, biotin- and rhodamine-linked adducts, a characteristic ion is detected of a mass that suggests fragmentation during collision-induced decay between the sulfur and β-carbon of the adducted cysteinyl residue (Table 1). For appropriately equipped mass spectrometers, this specific ion can be used to trigger MS–MS analysis, as was carried out for the DCP-FL1-modified peptide analyzed in the Q-TOF (Supporting Information, Figure S2). Alternatively, several analyses can be conducted with different collision energies, first to identify those peptides giving rise to the characteristic ion of interest and then in a second pass to carry out MS–MS analysis of that set of peptides.

MS-Linked Kinetic Studies of the Reactivity of DCP-Bio1 with Sulfenic Acid-Containing Proteins. To determine the rate of reaction of our reagents with the sulfenic acid forms of AhpC or papain, we used an Agilent ESI-TOF spectrometer to monitor the appearance of sulfenic acid and alkylated protein after the addition of DCP-Bio1 (or dimedone) and hydrogen peroxide. Our initial studies of C165S AhpC indicated a surprisingly slow reaction of the sulfenic acid-containing protein with dimedone; in the presence of 5 mM dimedone, the alkylated protein was generated at an initial rate of about 0.1 min^{-1}, slowing to about 0.009 min^{-1} in a second phase. During this extended incubation, the aerobic sample was also generating the further oxidized sulfinic and sulfonic acid-containing protein, complicating the kinetic analysis. On the basis of what is already known about the active site cysteine group of AhpC, the reactivity of the R–SOH group may be restricted in its "fully folded" form where the active site pocket acts as a shield against modification (*16, 17*).

We then used the same approaches to monitor the reaction of commercially available papain with hydrogen peroxide and DCP-Bio1 and discovered the alkylation reaction to be far faster than that observed between dimedone and AhpC (Figure 5). The reaction in this case is essentially complete within 5 min in the presence of 5 mM DCP-Bio1 and a 2-fold excess of hydrogen peroxide. While additional oxidized species are formed to a limited extent, these species are present at levels of less than 10% at the start of the reaction and at less than 20% at the final time point for concentrations of DCP-Bio1 down to 0.5 mM. The kinetic fits of the data are not significantly affected by ignoring these additional species; from these, the rate constant for formation of the sulfenic acid was determined to be 0.024 $\pm$ 0.007 s^{-1} in 200 μM hydrogen peroxide and potassium phosphate buffer at neutral pH and room temperature (from three independent experiments). This value (translating to a second-order rate constant of 7.2×10^3 M^{-1} min^{-1}) is in very good agreement with a previous determination, where activity loss of papain in the presence of hydrogen peroxide at pH $\sim$6 and 23 °C was found to occur with a second-order rate constant of 3.7×10^3 M^{-1} min^{-1} (*15*). As shown in Figure 5 (inset), the rate constant for modification of the sulfenic acid of papain by DCP-Bio1 increased with reagent concentration to a maximal value of $\sim$0.05 s^{-1} at 5 mM reagent. These data, from multiple reagent concentrations and three independent experiments, fit a Michaelis–Menten type of saturation curve, as is sometimes observed with irreversible inhibitors, with an apparent K_m of 0.77 ± 0.24 mM for DCP-Bio1 and a maximal rate of 0.050 ± 0.005 s^{-1} (Figure 5, inset). This implies a reversible binding step prior to irreversible modification of papain. If this represents pre-equilibrium binding followed by a slow chemical step, 0.77 mM is the K_i of the inhibitor. We had anticipated a simple bimolecular process of sulfenic acid alkylation but instead saw saturation kinetics; whether or not saturable kinetics are typically observed or are unique to papain and/or other cysteine-based proteases remains to be determined. Regarding the differences we observed between AhpC and papain reactivity, it is not surprising to find different rates of reaction in different proteins because the accessibility and stability of the sulfenic acid will vary greatly depending on its microenvironment; this species in papain appears to be far more accessible and/or reactive than that in C165S AhpC.

CONCLUSIONS

Seven new reagents bearing fluorescein, biotin, or rhodamine as detectable tags have now been generated for detection and isolation of proteins or peptides that form sulfenic acids at susceptible cysteinyl residues. These labeled species can be detected at high sensitivity upon gel analysis or can be shown by mass spectrometric analyses to incorporate the covalent label in each case. A further feature of these conjugates is their ability to release specific, detectable fragments upon fragmentation during mass spectrometric analyses that can be used to trigger MS–MS analysis for sequence determination of labeled peptides. Modification of sulfenic acids in the presence of 5 mM reagents can occur within as little as 5 min, as shown in this study for papain. These sulfenic acid-reactive reagents provide a diverse set of new tools with which we can greatly enhance our understanding of the contributions of sulfenic acid formation to protein function and cellular processes like redox signaling.

ACKNOWLEDGMENT

The authors thank Laura Soito for technical assistance and Mike Samuel for mass spectrometry analyses and acknowledge financial support from the American Heart Association Established Investigatorship program (to both L.B.P., Grant 0140175N, and S.B.K., Grant 0140020N), from the Cross Campus Collaborative Research Program at Wake Forest University (to S.B.K. and L.B.P.), and from the National Institutes of Health to L.B.P., with S.B.K., L.W.D., and J.S.F. as coinvestigators (Grant R21 CA112145). Support from the NSF-NIGMS Program in Mathematical Biology through a grant to J.S.F., with L.B.P. and L.W.D. as coinvestigators (Grant RO1 GM075304), is also acknowledged. The Quattro II tandem mass spectrometer was purchased and updated with funds from National Science Foundation (Grant BIR-9414018), the North Carolina Biotechnology Center (Grant 9903IDG-1002), and the Winston-Salem Foundation. The Waters Q-TOF mass spectrometer was purchased with funds from the National Institutes Health (Grant 1S10RR017846). The maintenance of these instruments was supported in part by the Comprehensive Cancer Center of Wake Forest University. A donation from the Dorothy Rhyne and Willard Duke Kimbrell family supported the purchase of the mass spectrometers in the CMF laboratory. The NMR spectrometers used in this work were purchased with partial support from NSF (Grant CHE-9708077) and the North Carolina Biotechnology Center (Grant 9703-IDG-1007).

Supporting Information Available: Experimental details for 2D gel analyses of DCP-FL1 modified AhpC, MS–MS analysis of the labeled peptide from that protein, and log *P* analyses for the compounds synthesized. This material is available free of charge via the Internet at http://pubs.acs.org.

LITERATURE CITED

(1) Claiborne, A., Yeh, J. I., Mallett, T. C., Luba, J., Crane, E. J., 3rd, Charrier, V., and Parsonage, D. (1999) Protein–sulfenic acids: diverse roles for an unlikely player in enzyme catalysis and redox regulation. *Biochemistry 38*, 15407–15416.

(2) Poole, L. B. (2003) Formation and function of sulfenic acids in proteins. In *Current Protocols in Toxicology* (Maines, M. D., Ed.) pp 17.1.1–17.1.17, John Wiley & Sons, Inc., New York.

(3) Poole, L. B., Karplus, P. A., and Claiborne, A. (2004) Protein sulfenic acids in redox signaling. *Annu. Rev. Pharmacol. Toxicol. 44*, 325–347.

(4) Poole, L. B., and Ellis, H. R. (2002) Identification of cysteine sulfenic acid in AhpC of alkyl hydroperoxide reductase. *Methods Enzymol 348*, 122–136.

(5) Poole, L. B., Zeng, B. B., Knaggs, S. A., Yakubu, M., and King, S. B. (2005) Synthesis of chemical probes to map sulfenic acid modifications on proteins. *Bioconjugate Chem. 16*, 1624–1628.

(6) Charles, R. L., Schröder, E., May, G., Free, P., Gaffney, P. R., Begum, S., Wait, R., Heads, R. J., and Eaton, P. (2007) Protein sulfenation as a redox sensor: proteomic studies using a novel biotinylated dimedone analogue, *Mol. Cell Proteomics. 6*, 1473–1484.

(7) Poole, L. B., and Ellis, H. R. (1996) Flavin-dependent alkyl hydroperoxide reductase from *Salmonella typhimurium*. 1. Purification and enzymatic activities of overexpressed AhpF and AhpC proteins. *Biochemistry 35*, 56–64.

(8) Haugland, R. P. (2002) *Handbook of Fluorescent Probes and Research Products*, 9th ed., Molecular Probes, Inc., Eugene, OR.

(9) Kolb, H. C., Finn, M. G., and Sharpless, K. B. (2001) Click chemistry: diverse chemical function from a few good reactions. *Angew. Chem., Int. Ed. 40*, 2004–2021.

(10) Pons, J.-F., Fauchère, J.-L., Lamaty, F., Molla, A., and Lazaro, R. (1998) A constrained diketopiperazine as a new scaffold for the synthesis of peptidomimetics. *Eur. J. Org. Chem.* 853–859.

(11) Toropainen, E., Ranta, V. P., Talvitie, A., Suhonen, P., and Urtti, A. (2001) Culture model of human corneal epithelium for prediction of ocular drug absorption. *Invest. Ophthalmol. Visual Sci. 42*, 2942–2948.

(12) Nguyen, T., and Francis, M. B. (2003) Practical synthetic route to functionalized rhodamine dyes. *Org. Lett. 5*, 3245–3248.

(13) Ellis, H. R., and Poole, L. B. (1997) Novel application of 7-chloro-4-nitrobenzo-2-oxa-1,3-diazole to identify cysteine sulfenic acid in the AhpC component of alkyl hydroperoxide reductase. *Biochemistry 36*, 15013–15018.

(14) Allison, W. S. (1976) Formation and reactions of sulfenic acids in proteins. *Acc. Chem. Res. 9*, 293–299.

(15) Lin, W. S., Armstrong, D. A., and Gaucher, G. M. (1975) Formation and repair of papain sulfenic acid. *Can. J. Biochem. 53*, 298–307.

(16) Wood, Z. A., Poole, L. B., and Karplus, P. A. (2003) Peroxiredoxin evolution and the regulation of hydrogen peroxide signaling. *Science 300*, 650–653.

(17) Parsonage, D., Youngblood, D. S., Sarma, G. N., Wood, Z. A., Karplus, P. A., and Poole, L. B. (2005) Analysis of the link between enzymatic activity and oligomeric state in AhpC, a bacterial peroxiredoxin. *Biochemistry 44*, 10583–10592.

BC700257A

A Novel Functional Translocator Protein Ligand for Cancer Imaging

Mingfeng Bai,[†] Malena B. Rone,[‡] Vassilios Papadopoulos,[‡] and Darryl J. Bornhop*[,†]

Department of Chemistry, Vanderbilt University, VU Station B 351822, Nashville, Tennessee 37235-1822, and Department of Biochemistry and Molecular and Cellular Biology, Georgetown University Medical Center, BSB Rm 315 3900 Reservoir Rd NW, Washington, D.C. 20057. Received July 6, 2007; Revised Manuscript Received September 20, 2007

The translocator protein (TSPO) is an attractive target for tumor imaging due to its up-regulation in numerous cancer cell types. Here, we report a series of functional TSPO ligands, n-TSPOmbb732, which can be conjugated to a variety of signaling moieties and are widely applicable in TSPO-targeted molecular imaging. Two fluorescent dye-labeled 6-TSPOmbb732 displayed nanomolar binding affinities to TSPO and were successfully imaged in vitro.

INTRODUCTION

The 18 kDa translocator protein (TSPO)[1] , previously known as the peripheral-type benzodiazepine receptor (PBR), has become an attractive target for cancer imaging (*1*). Overexpression of TSPO has been observed in a variety of cancers, including brain, breast, colorectal, prostate, and ovarian cancers, astrocytomas, and hepatocellular and endometrial carcinomas (*2*). TSPO is associated with a number of biological processes, such as cell proliferation, apoptosis, steroidogenesis, and immunomodulation; however, its exact physiological role still is not clear.

Several TSPO-selective ligands have been developed, including the diazepam derivative (Ro5–4864), the isoquinoline derivative (PK11195), the 2-acryl-3-indoleacetamide derivative (FGIN-1), and the phenoxyphenyl–acetamide derivative (DAA-1106) (*3, 4*). DAA1106 has become an attractive TSPO ligand, because it has higher binding affinity for TSPO than PK11195, Ro5–4864, and FGIN1. DAA1106 has been shown to displace TSPO-complexed PK11195 and Ro5–4864 at a very low concentration (10^{-15}–10^{-12} M), however, 0.1–1 μM amounts of PK11195, Ro5–4864, or FGIN1 were necessary to displace DAA1106 (*5*). Although promising, TSPO studies using DAA1106 have been limited because the molecule is not easily functionalized.

A conjugable analogue of DAA1106, which can be coupled to a variety of signaling moieties, would be a valuable tool for studying TSPO function. Even though DAA1106 labeled with ^{11}C, ^{3}H, and ^{18}F have been used to study TSPO activity, these labels are limited by their short half-lives and low surface resolution during imaging (*6–8*). Furthermore, biological studies using tritium are cumbersome, expensive, time-consuming, and create radioactive waste. Conjugable analogues of PK11195 and Ro5–4864 were developed previously and labeled with a fluorescent dye (*9–11*). Unfortunately, the binding affinities of the imaging agents were rather low (1 μM for PK11195 analogue and 2.6 μM for Ro5–4864 analogue).

* Corresponding author. VU Station B 351822, 7300 Stevenson Center, Nashville, TN 37235-1822 Tel: 615.322.4226. Fax: 615 0.343.1234. E-mail: Darryl.Bornhop@Vanderbilt.Edu.

[†] Vanderbilt University.

[‡] Georgetown University Medical Center.

[1]Abbreviations: TSPO, translocator protein; PBR, peripheral-type benzodiazepine receptor; NIR6T, IRDyeTM 800CW-6-TSPOmbb732; Liss6T, LissamineTM-6-TSPOmbb732.

Table 1. *n*-TSPOmbb732 Reactions Summary

n-TSPOmbb732	reaction time (h)	yield (%)
3-TSPOmbb732	3	12.7
4-TSPOmbb732	2	7.9
5-TSPOmbb732	2	10
6-TSPOmbb732	6	33
7-TSPOmbb732	2.5	12
8-TSPOmbb732	2.5	5.8
9-TSPOmbb732	2.5	11

In the current study, a conjugable analogue of DAA1106, *n*-TSPOmbb732 (*n* is the number of carbons on the linker) was synthesized and characterized. The analogue has a terminal amino group that facilitates coupling reactions. Two fluorescent dyes, IRDye 800CW NHS ester (LI-COR Biosciences, ε =300 000 L/mol cm in methanol) and Lissamine rhodamine B sulfonyl chloride (Invitrogen, ε =88 000 L/mol cm in methanol) were selected as signaling moieties for conjugation to *n*-TSPOmbb732. As presented here, the resulting molecules have nanomolar binding affinities to TSPO and target TSPO in vitro.

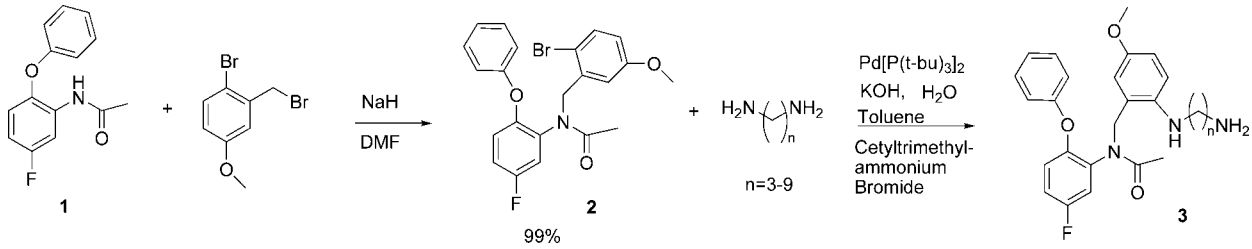
EXPERIMENTAL PROCEDURES

Synthesis. *N-(2-Bromo-5-methoxybenzyl)-N-(5-fluro-2-phenoxphenyl)acetamide (***2***).* To a dry round-bottom flask was added anhydrous DMF (10 mL) and sodium hydride (100 mg), followed by *N*-(5-fluoro-2-phenoxyphenyl)acetamide **1** (1.08 g, 4.4 mmol). After the solution was stirred for 15 min, 2-bromo-5-methoxybenzyl bromide (1.4 g, 5.0 mmol) was added. After another 30 min, the reaction was added to stirring water chilled to 0 °C (60 mL). The mixture was extracted with dichloromethane three times. The organic solutions were combined, dried over sodium sulfate, and evaporated to dryness. The residue was chromatographed (silica gel) using 1:3 ethyl acetate/hexanes as the eluent to yield compound **2** as a yellow oil (1.94 g, 99%). ^{1}H NMR 300 MHz ($CDCl_3$) δ 7.29–7.33 (m, 3H), 7.12 (t, J = 7.6 Hz, 1H), 7.02 (d, J = 3.2 Hz, 1H), 6.80–6.96 (m, 5H), 6.62 (dd, J = 8.4, 2.8 Hz, 1H), 4.96 (AX, J = 15.2 Hz, $\Delta\nu$ = 178 Hz, 2H), 3.66 (s, 3H), 2.00 (s, 3H). MS $(ESI)^+$ $[M + H]^+$ calcd 444.1, found 444.3.

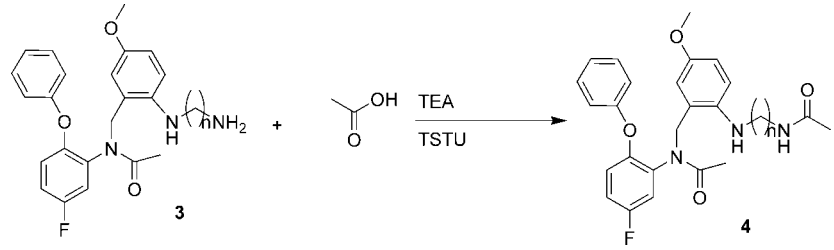
*General Method for n-TSPOmbb732 (***3***) Synthesis.* Pd[P(t-Bu)$_3$]$_2$ (102 mg, 0.2 mmol), cetyltrimethylammonium bromide (36 mg, 0.1 mmol), potassium hydroxide (842 mg, 15 mmol), and diamine (30 mmol) were mixed in toluene (4 mL) under argon. **2** (4.44 g, 10 mmol) in toluene (6 mL) and water (270

10.1021/bc700251e CCC: $37.00 © 2007 American Chemical Society
Published on Web 11/03/2007

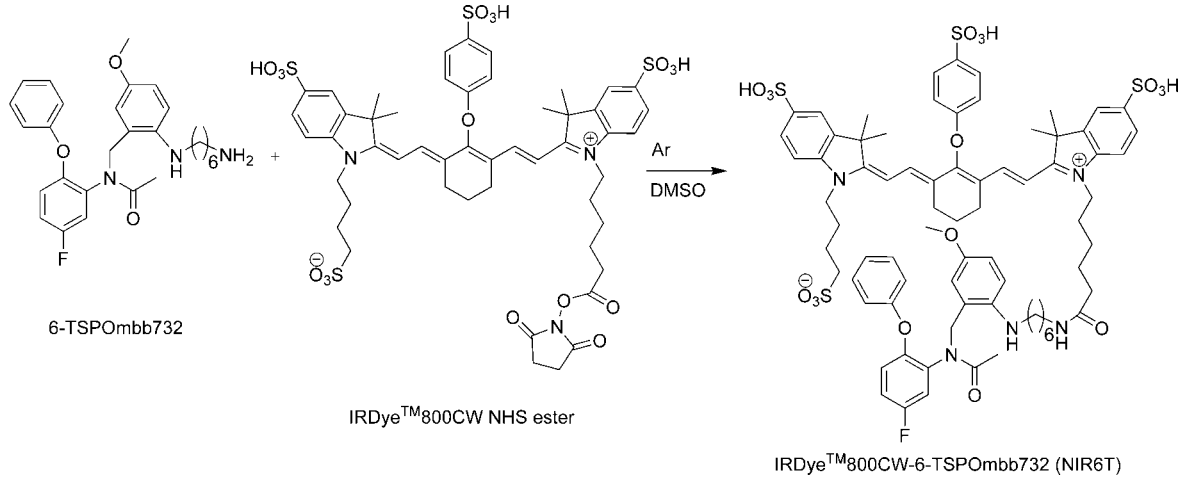
Scheme 1. *n*-TSPOmbb732 Syntheses



Scheme 2. Capped *n*-TSPOmbb732 Synthesis



Scheme 3. IRDye^{TM}800CW-6-TSPOmbb732 (NIR6T) Reaction Scheme



μL, 15 mmol) were added to the mixture by syringe. The flask was sealed with a septum, and the reaction mixture was stirred vigorously at 90 °C for 2–6 h, depending on the length of linker. The reaction then was concentrated by vacuum and purified by column chromatography using 9:1:0.1 methylene chloride/methanol/ammonium hydroxide on silica gel to yield *n*-TSPOmbb732 as a colorless oil. The optimal reaction time and yields of each *n*-TSPOmbb732 are listed in Table 1.

3-TSPOmbb732 (Y = 8.7%). NMR data are not shown because diastereomers could not be separated. MS (ESI)$^+$ [M + H]$^+$ calcd 438.2, found 438.2.

4-TSPOmbb732 (Y = 7.9%). NMR data are not shown because diastereomers could not be separated. MS (ESI)$^+$ [M + H]$^+$ calcd 452.2, found 452.3.

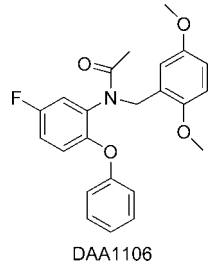


Figure 1. DAA1106 structure.

5-TSPOmbb732 (Y = 10%). ^{1}H NMR 400 MHz ($CDCl_3$) δ 7.27 (t, J = 8.4 Hz, 2H), 7.09 (t, J = 7.6 Hz, 1H), 6.91–6.96 (m, 1H), 6.79–6.83 (m, 1H), 6.69–6.75 (m, 4H), 6.39 (d, J = 8.8 Hz, 1H), 6.19 (d, J = 2.8 Hz, 1H), 4.75 (AX, J = 9.6 Hz, $\Delta\nu$ = 79.2 Hz, 2H), 3.60 (s, 3H), 2.86–3.03 (m, 2H), 2.77 (t, J = 5.1 Hz, 2H), 1.94 (s, 5H), 1.50–1.62 (m, 2H), 1.40–1.45 (m, 5H). MS (ESI)$^+$ [M + H]$^+$ calcd 466.3, found 466.3.

6-TSPOmbb732 (Y = 33%). ^{1}H NMR 300 MHz ($CDCl_3$) δ 7.28 (t, J = 8.1 Hz, 2H), 7.10 (t, J = 7.5 Hz, 1H), 6.91–6.95 (m, 1H), 6.79–6.84 (m, 1H), 6.70–6.75 (m, 4H), 6.40 (d, J = 8.7 Hz, 1H), 6.20 (d, J = 3.0 Hz, 1H), 4.76 (AX, J = 14.7 Hz, $\Delta\nu$ = 95.1 Hz, 2H), 3.61 (s, 3H), 2.87–3.03 (m, 2H), 2.66 (t, J = 6.9 Hz, 2H), 1.94 (s, 3H), 1.54–1.61 (m, 2H), 1.28–0.48 (m, 9H). MS (ESI)$^+$ [M + H]$^+$ calcd 480.3, found 480.2.

7-TSPOmbb732 (Y = 12%). ^{1}H NMR 300 MHz ($CDCl_3$) δ 7.28 (t, J = 7.5 Hz, 2H), 7.10 (t, J = 7.5 Hz, 1H), 6.91–6.98 (m, 1H), 6.80–6.85 (m, 1H), 6.70–6.75 (m, 4H), 6.41 (d, J = 9.0 Hz, 1H), 6.20 (d, J = 3.0 Hz, 1H), 4.76 (AX, J = 14.7 Hz, $\Delta\nu$ = 103.2 Hz, 2H), 3.60 (s, 3H), 2.84–3.06 (m, 2H), 2.68 (t, J = 7.2 Hz, 2H), 1.94 (s, 3H), 1.53–1.60 (m, 2H), 1.31–1.46 (m, 11H). MS (ESI)$^+$ [M + H]$^+$ calcd 494.3, found 494.3.

8-TSPOmbb732 (Y = 5.8%). ^{1}H NMR 400 MHz ($CDCl_3$) δ 7.28 (t, J = 8.4 Hz, 2H), 7.10 (t, J = 7.6 Hz, 1H), 6.92–6.97 (m, 1H), 6.81–6.84 (m, 1H), 6.71–6.74 (m, 4H), 6.41 (d, J = 8.8 Hz, 1H), 6.20 (d, J = 2.8 Hz, 1H), 4.76 (AX, J = 14.4 Hz,

Scheme 4. Lissamine-6-TSPOmbb732 (Liss6T) Reaction Scheme

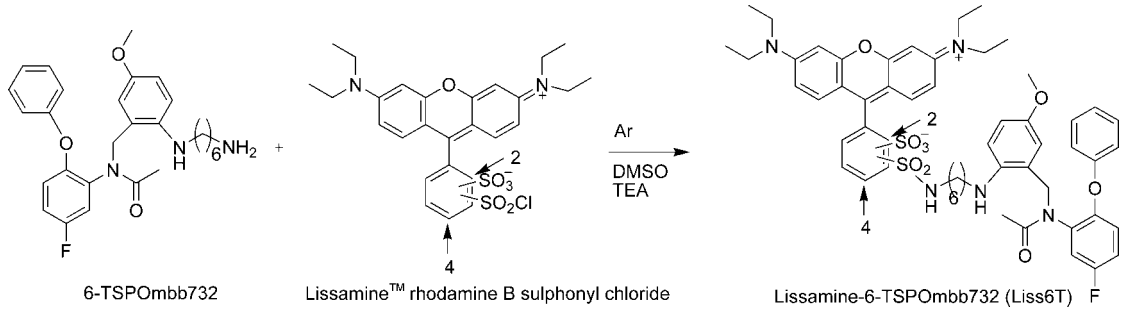


Table 2. TSPO Targeted Agents Binding Studies

TSPO ligands	IC50 (μM)	K_i (nM)
3-TSPOmbb732	0.39 ± 0.13	68 ± 23
4-TSPOmbb732	0.80 ± 0.21	141 ± 36
5-TSPOmbb732	0.84 ± 0.28	149 ± 49
6-TSPOmbb732	0.35 ± 0.22	52 ± 30
7-TSPOmbb732	0.40 ± 0.19	71 ± 33
8-TSPOmbb732	0.24 ± 0.11	43 ± 19
9-TSPOmbb732	0.29 ± 0.09	51 ± 17
NIR6T	0.24 ± 0.13	42 ± 23
Liss6T	0.0051 ± 0.0017	0.91 ± 0.32

$\Delta\nu$ = 140.4 Hz, 2H), 3.60 (s, 3H), 2.85–3.04 (m, 2H), 2.72 (t, J = 7.2 Hz, 2H), 1.94 (s, 3H), 1.44–1.59 (m, 6H), 1.30–1.37 (m, 9H). MS (ESI)$^+$ [M + H]$^+$ calcd 508.3, found 508.3.

9-TSPOmbb732 (Y = 11%). ^{1}H NMR 300 MHz ($CDCl_3$) δ 7.29 (t, J = 7.5 Hz, 2H), 7.10 (t, J = 7.5 Hz, 1H), 6.92–6.97 (m, 1H), 6.80–6.85 (m, 1H), 6.71–6.75 (m, 4H), 6.41 (d, J = 9.0 Hz, 1H), 6.20 (d, J = 3.0 Hz, 1H), 4.76 (AX, J = 14.4 Hz, $\Delta\nu$ = 105.3 Hz, 2H), 3.61 (s, 3H), 2.84–3.06 (m, 2H), 2.72 (t, J = 6.9 Hz, 2H), 2.51 (s, 2H), 1.94 (s, 3H), 1.45–1.62 (m, 5H), 1.19–1.36 (m, 10H). MS (ESI)$^+$ [M + H]$^+$ calcd 522.3, found 522.3.

*General Method for n-TSPOmbb732 Amide (**4**) Synthesis.* A mixture of acetic acid (1.6 μL, 27.5 μmol), triethylamine (TEA) (50 μL) and 2-succinimido-1,1,3,3,-tetramethyluronium tetrafluoroborate (TSTU) (8.3 mg, 27.5 μmol) in anhydrous methylene chloride (1 mL) was stirred at room temperature under argon for 3 h. A solution of **3** (25 μmol) in anhydrous methylene chloride (1 mL) was added to the mixture, and the mixture was stirred for another 2.5 h. The reaction solution was then concentrated by vacuum rotary evaporation, and the product was purified via silica gel column chromatography using 3% methanol in methylene chloride as eluent. *n*-TSPOmbb732 amide was collected as a colorless oil.

3-TSPOmbb732 Amide. ^{1}H NMR 300 MHz ($CDCl_3$) δ 7.27 (t, J = 7.5 Hz, 2H), 7.10 (t, J = 7.2 Hz, 1H), 6.71–6.84 (m, 3H), 6.63 (d, J = 7.5 Hz, 2H), 6.40 (d, J = 8.7 Hz, 1H), 6.19 (d, J = 2.7 Hz, 1H), 6.04 (br s, 1H), 5.12 (br s, 1H), 4.77 (AX, J = 14.4 Hz, $\Delta\nu$ = 36.9 Hz, 2H), 3.61 (s, 3H), 3.29 (q, J = 6.3 Hz, 2H), 2. 94–3.13 (m, 2H), 1.97 (br s, 6H), 1.75–1.79 (m, 2H), 1.67 (br s, 1H). MS (ESI)$^+$ [M + Na]$^+$ calcd 502.2, found 502.1.

4-TSPOmbb732 Amide. ^{1}H NMR 300 MHz ($CDCl_3$) δ 7.27 (t, J = 7.5 Hz, 2H), 7.10 (t, J = 7.2 Hz, 1H), 6.92–6.99 (m, 1H), 6.65–6.84 (m, 5H), 6.56 (br s, 1H), 6.34 (d, J = 8.7 Hz, 1H), 6.20 (d, J = 3.0 Hz, 1H), 4.78 (AX, J = 14.7 Hz, $\Delta\nu$ = 36.0 Hz, 2H), 3.61 (s, 3H), 3.28 (m, 2H), 2.81–3.05 (m, 2H), 2.01 (s, 3H), 1.96 (s, 3H), 1.63–1.68 (m, 5H). MS (ESI)$^+$ [M + H]$^+$ calcd 494.2, found 494.2.

5-TSPOmbb732 Amide. ^{1}H NMR 300 MHz ($CDCl_3$) δ 7.28 (t, J = 7.5 Hz, 2H), 7.10 (t, J = 7.5 Hz, 1H), 6.92–6.99 (m, 1H), 6.80–6.85 (m, 1H), 6.68–6.76 (m, 4H), 6.47 (br s, 1H), 6.39 (d, J = 8.7 Hz, 1H), 6.20 (d, J = 3.0 Hz, 1H), 4.81 (br s, 1H), 4.78 (AX, J = 14.4 Hz, $\Delta\nu$ = 73.5 Hz, 2H), 3.61 (s, 3H), 3.28 (q, J = 6.0 Hz, 2H), 2.82–3.08 (m, 2H), 1.95 (s, 3H), 1.95 (s, 3H), 1.44–1.65 (m, 6H). MS (ESI)$^+$ [M + H]$^+$ calcd 508.3, found 508.2.

6-TSPOmbb732 Amide. ^{1}H NMR 400 MHz ($CDCl_3$) δ 7.28 (t, J = 7.6 Hz, 2H), 7.10 (t, J = 7.2 Hz, 1H), 6.9–6.97 (m, 1H), 6.80–6.84 (m, 1H), 6.70–6.75 (m, 4H), 6.40 (d, J = 8.8 Hz, 1H), 6.19 (d, J = 2.8 Hz, 1H), 5.90 (br s, 1H), 4.87 (br s, 1H), 4.76 (AX, J = 14.4 Hz, $\Delta\nu$ = 114.0 Hz, 2H), 3.60 (s, 3H), 3.24 (q, J = 6.0 Hz, 2H), 2.86–3.06 (m, 2H), 1.97 (s, 3H), 1.94 (s, 3H), 1.48–1.59 (m, 4H), 1.33–1.41 (m, 4H). MS (ESI)$^+$ [M + H]$^+$ calcd 522.3, found 522.2.

7-TSPOmbb732 Amide. ^{1}H NMR 300 MHz ($CDCl_3$) δ 7.28 (t, J = 7.5 Hz, 2H), 7.10 (t, J = 7.2 Hz, 1H), 6.92–6.98 (m, 1H), 6.80–6.85 (m, 1H), 6.70–6.75 (m, 4H), 6.40 (d, J = 8.7 Hz, 1H), 6.19 (d, J = 2.7 Hz, 1H), 5.64 (br s, 1H), 4.87 (br s, 1H), 4.76 (AX, J = 14.4 Hz, $\Delta\nu$ = 100.2 Hz, 2H), 3.60 (s, 3H), 3.23 (q, J = 6.0 Hz, 2H), 2.86–3.03 (m, 2H), 1.96 (s, 3H), 1.94 (s, 3H), 1.45–1.60 (m, 4H), 1.31–1.36 (m, 6H). MS (ESI)$^+$ [M + H]$^+$ calcd 536.3, found 536.4.

8-TSPOmbb732 Amide. ^{1}H NMR 300 MHz ($CDCl_3$) δ 7.29 (t, J = 7.5 Hz, 2H), 7.10 (t, J = 7.2 Hz, 1H), 6.91–6.98 (m, 1H), 6.80–6.85 (m, 1H), 6.70–6.74 (m, 4H), 6.41 (d, J = 8.7 Hz, 1H), 6.20 (d, J = 3.0 Hz, 1H), 5.60 (br s, 1H), 4.86 (br s, 1H), 4.76 (AX, J = 14.4 Hz, $\Delta\nu$ = 113.1 Hz, 2H), 3.61 (s, 3H), 3.23 (q, J = 6.0 Hz, 2H), 2.84–3.06 (m, 2H), 1.96 (s, 3H), 1.94 (s, 3H), 1.46–1.59 (m, 4H), 1.31–1.37 (m, 8H). MS (ESI)$^+$ [M + H]$^+$ calcd 550.3, found 550.5.

9-TSPOmbb732 Amide. ^{1}H NMR 300 MHz ($CDCl_3$) δ 7.29 (t, J = 7.5 Hz, 2H), 7.10 (t, J = 7.2 Hz, 1H), 6.91–6.98 (m, 1H), 6.80–6.85 (m, 1H), 6.70–6.74 (m, 4H), 6.41 (d, J = 9.0 Hz, 1H), 6.20 (d, J = 3.0 Hz, 1H), 5.31 (br s, 1H), 4.86 (br s, 1H), 4.76 (AX, J = 14.4 Hz, $\Delta\nu$ = 110.1 Hz, 2H), 3.61 (s, 3H), 3.23 (q, J = 6.0 Hz, 2H), 2.84–3.05 (m, 2H), 1.97 (s, 3H), 1.94 (s, 3H), 1.46–1.59 (m, 4H), 1.31–1.37 (m, 10H). MS (ESI)$^+$ [M + H]$^+$ calcd 564.3, found 564.5.

IRDye 800CW-6-TSPOmbb732 (NIR6T). IRDye 800CW NHS ester (3 mg, 2.6 μmol) and 6-TSPOmbb732 (3 mg, 6.3 μmol) were mixed in DMSO (7 mL) in a round-bottom flask and stirred under argon flow for 1 h. HPLC analysis was performed on a Varian Polaris C-18 column (250 × 4.6 mm) at a flow rate of 0.8 mL/min. Flow A was 0.1% TEA in water and flow B was 0.1% TEA in acetonitrile. The elution method for analytical HPLC started with a linear gradient from 100% to 70% A over 20 min, continued to 50% A over 5 min, arrived at 20% A in another 10 min, held at 20% A for 3 min, and finally returned to 100% A over 1 min. The elution profile was monitored by UV absorbance at 254 and 780 nm. The product was purified by preparative HPLC using a Varian Polaris C-18 column (250 × 21.2 mm) at 12 mL/min. The collected solution was concentrated by vacuum rotary evaporation, frozen to −78 °C, and dried using a freeze–dry system. NIR6T was collected as a dark green solid (1.2 mg, 31%). ^{1}H NMR 500 MHz (MeOD) δ 7.99–7.91 (m, 3H), 7.86–7.78 (m, 6H), 7.34 (d, J = 8.0 Hz,

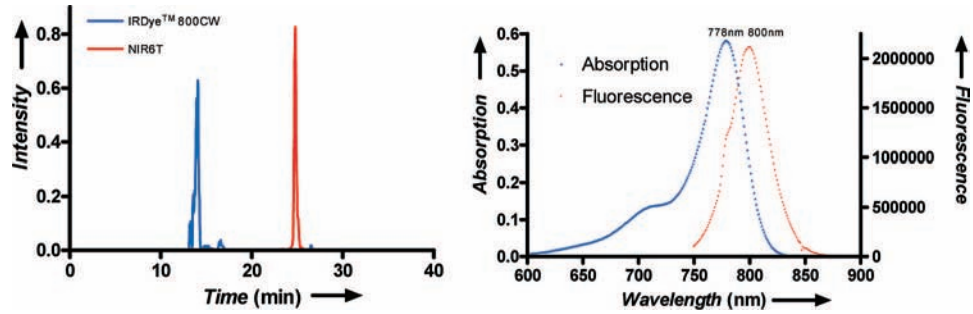


Figure 2. Left: HPLC chromatograph of IRDye 800CW and NIR6T at 780 nm. Right: absorption and emission spectra of NIR6T in methanol.

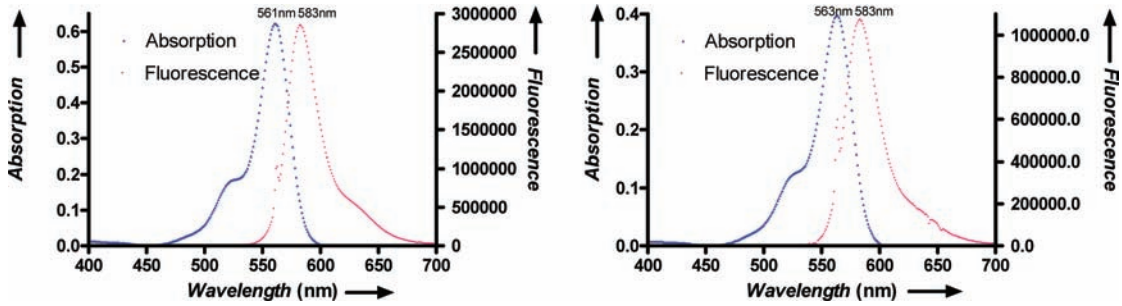


Figure 3. Liss6T isomer I (left) and isomer II (right) absorption and fluorescence.

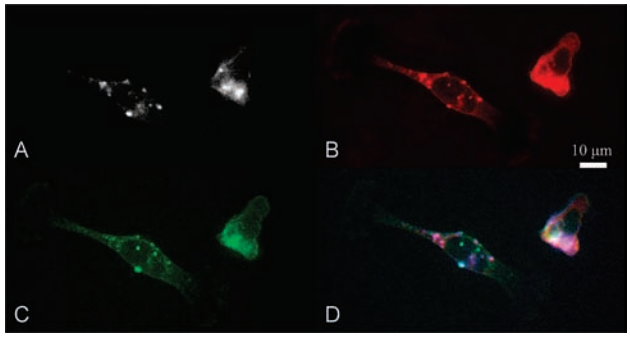


Figure 4. MDA-MB-231 cells fluorescence images. White (blue in overlaid picture) (A): 1 μM NIR6T. Red (B): 1 μM Liss6T. Green (C): 1 nM Mitotracker. Mixed colors (D): overlaid picture of A, B, and C.

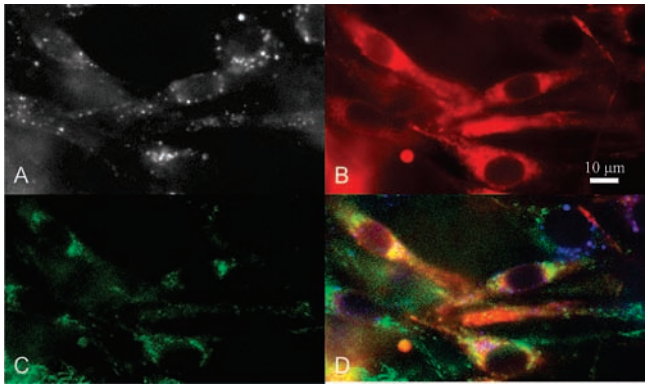


Figure 5. C6 cells fluorescence images. White (blue in overlaid picture) (A): 1 μM NIR6T. Red (B): 1 μM Liss6T. Green (C): 1 nM Mitotracker. Mixed colors (D): overlaid picture of A, B, and C.

1H), 7.27–7.23 (m, 3H), 7.17 (d, J = 8.5 Hz, 1H), 7.10–7.01 (m, 3H), 6.77–6.74 (m, 1H), 6.70 (dd, J = 9.0, 3.0 Hz, 1H), 6.59 (d, J = 8.5 Hz, 2H), 6.42 (d, J = 9.0 Hz, 1H), 6.26 (d, J = 14.0 Hz, 1H), 6.20 (d, J = 3.0 Hz, 1H), 6.15 (d, J = 14.0 Hz, 1H), 4.96 (d, J = 14.5 Hz, 1H), 4.60 (d, J = 14.5 Hz, 1H),

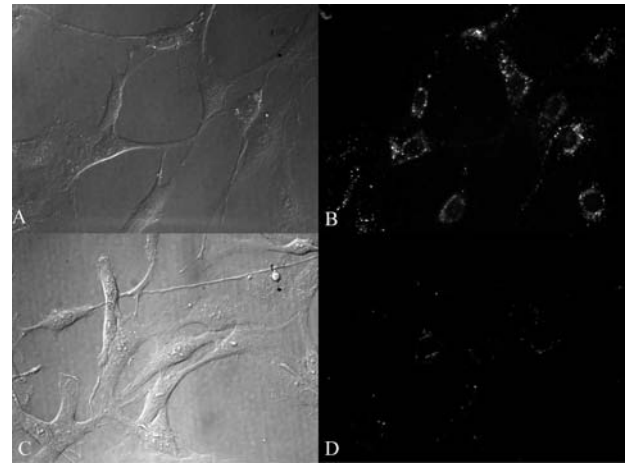


Figure 6. Fluorescence imaging of C6 glioma cells: (A) phase contrast microscopy of cells dosed with 1 μM NIR6T; (B) fluorescence imaging of cells dosed with 1 μM NIR6T; (C) phase contrast microscopy of cells dosed with 1 μM NIR6T and 10 μM DAA1106; (D) fluorescence imaging of cells dosed with 1 μM NIR6T and 10 μM DAA1106.

4.15–4.10 (m, 2H), 4.08–4.05 (m, 2H), 3.52 (s, 3H), 3.43–3.39 (m, 2H), 3.14–3.11 (m, 2H), 3.04–2.93 (m, 2H), 2.89–2.86 (m, 2H), 2.82–2.72 (m, 5H), 2.17 (t, J = 7.0 Hz, 2H), 2.05–2.02 (m, 2H), 1.96–1.91 (m, 8H), 1.79–1.76 (m, 3H), 1.68–1.63 (m, 3H), 1.53–1.41 (m, 6H), 1.37 (d, J = 4.0 Hz, 12H). MS (ESI)$^-$ [M – H]$^-$ calcd 1462.5, found 1462.4.

Lissamine-6-TSPOmbb732 (Liss6T). A mixture of Lissamine rhodamine B sulfonyl chloride (10 mg, 17 μmol), 6-TSPOmbb732 (10 mg, 20 μmol), and triethylamine (15 μL) in dichloromethane (1.6 mL) was stirred under argon at room temperature for 1 h. The reaction solution was concentrated by vacuum rotary evaporation, and the crude product was purified through column chromatography (silica gel) using a 19:1 dichloromethane/methanol solution to yield Liss6T as a pink solid (isomer I, 5.7 mg, 32%; isomer II, 4.7 mg, 27%). ^{1}H NMR 400 MHz ($CDCl_3$) isomer I: δ 8.84 (s, 1H), 7.98 (d, J = 7.6 Hz, 1H), 7.30–7.24 (m, 3H), 7.19 (d, J = 7.6 Hz, 1H), 7.08 (t, J = 7.2 Hz, 1H), 6.93–6.90 (m, 2H), 6.78 (t, J = 8.8 Hz, 3H), 6.70 (dd, J = 8.4,

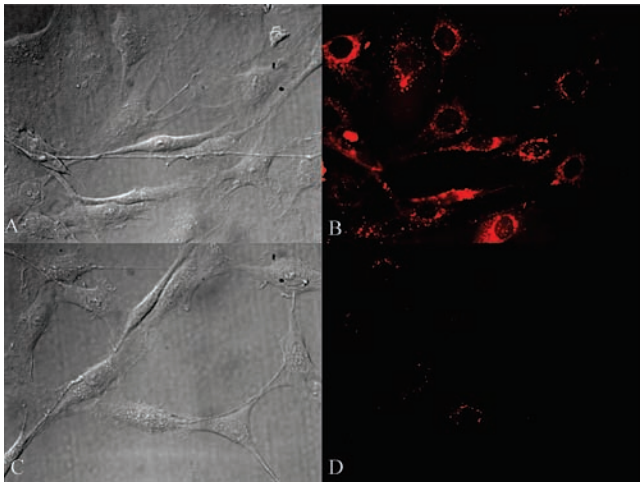


Figure 7. Fluorescence imaging of C6 glioma cells: (A) phase contrast microscopy of cells dosed with 1 μM Liss6T; (B) fluorescence imaging of cells dosed with 1 μM Liss6T; (C) phase contrast microscopy of cells dosed with 1 μM Liss6T and 10 μM DAA1106; (D) fluorescence imaging of cells dosed with 1 μM Liss6T and 10 μM DAA1106.

2.0 Hz, 1H), 6.66–6.63 (m, 3H), 6.37 (d, J = 8.4 Hz, 1H), 6.19 (s, 1H), 5.61 (t, J = 5.2 Hz, 1H), 4.78 (d, J = 6.4 Hz, 1H), 3.59 (s, 3H), 3.56–3.45 (m, 7H), 3.10 (q, J = 6.4 Hz, 2H), 3.02–2.96 (m, 1H), 2.87–2.81 (m, 1H), 2.01 (s, 2H), 1.72–1.50 (m, 12H), 1.44–1.37 (m, 4H), 1.29–1.25 (m, 10H). Isomer II: δ 8.72 (s, 1H), 8.36 (d, J = 7.2 Hz, 1H), 7.27–7.18 (m, 5H), 7.08 (t, J = 7.6 Hz, 1H), 6.95–6.89 (m, 2H), 6.87–6.85 (m, 3H), 6.79–6.76 (m, 1H), 6.71 (d, J = 2.4 Hz, 2H), 6.65 (d, J = 8.0 Hz, 2H), 6.20 (d, J = 2.8 Hz, 1H), 6.05–6.00 (m, 1H), 4.77 (s, 2H), 3.62–3.56 (m, 11H), 3.32–3.27 (m, 1H), 3.02–2.96 (m, 1H), 2.96–2.91 (m, 3H), 2.85–2.79 (m, 2H), 1.95 (s, 3H), 1.52–1.42 (m, 4H), 1.32 (t, J = 7.2 Hz, 12H), 1.15–1.11 (m, 3H). MS (ESI)$^+$ $[M + H]^+$ calcd 1020.4, found1020.4. R_f 0.39 (isomer I), 0.32 (isomer II) (6% methanol in dichloromethane).

Spectroscopic Characterization. Upon preparing NIR6T and Liss6T, absorption and emission spectra were obtained at room temperature with a Shimadzu 1700 UV–vis spectrophotometer and ISS PTI spectrofluorometer, respectively. NIR6T was found to have an absorption maximum at 778 nm and fluorescence maximum at 800 nm in methanol. The two isomers of Liss6T have similar absorption maxima (isomer I at 561nm and isomer II at 563nm) and that same fluorescence maximum at 583 nm.

Binding Studies. C6 glioma cells were cultured in Dulbecco's modified Eagle medium (DMEM)-F12 medium (Gibco/Invitrogen) supplemented with 0.5% FBS and 2.5% horse serum (HS) at 3.7% CO_2. Cells were scraped from 150 mm culture dishes into 5 mL phosphate buffered saline (PBS), dispersed by trituration, and centrifuged at 500× g for 15 min. Cell pellets were resuspended in PBS and assayed for protein concentration. [^{3}H]PK 11195 binding studies on 30 μg of protein from cell suspensions were performed as previously described (*15*). Displacement studies using increasing concentrations of synthesized TSPO ligands were performed in the presence of 15 nM [^{3}H]PK11195. Data were analyzed using *PRISM* software (v 4.0, GraphPad, Inc., San Diego, CA).

Cell Imaging. MDA-MB-231 mammary adenocarcinoma breast cancer cells or C6 rat glioma cells in MaTek dishes were incubated with 1 μM NIR6T and 1 μM Liss6T in culture media for 30 min. 1 nM MitoTracker Green was then added to the plate and incubated for another 10 min. Cells were rinsed and reincubated with saline before imaging using a Nikon epifluorescence microscope equipped with a Hamamatsu C4742–98 camera, Nikon Plan Apo 60×/1.40 oil objective, a mercury lamp, an ICG filter set (excitation 750–800 nm; emission 815–875 nm), a Texas Red filter set (emission 600–660 nm), and a FITC filter set (emission 513–548 nm). Cell uptake of NIR6T and Liss6T was observed in fluorescence images of both cell lines (Figures 5 and 6), while the controls exhibited no significant fluorescence (Supporting Information Figures S1 and S2).

In Vitro Competition. C6 glioma cells were plated in MaTek dishes. The growth media was removed and replaced with media containing the contrast agent. Unchallenged C6 cells were dosed with 1 μM NIR6T or Liss6T. Challenged cells were dosed with 1 μM NIR6T/Liss6T and 10 μM DAA1106. DAA1106 was synthesized in our laboratory as reported (*12*). All cells were incubated for 30 min at 37 °C under 5% CO_2. At the end of the incubation time, cells were rinsed with cell media three times and imaged under a Nikon Eclipse TE2000-U microscope (Lewisville, TX).

RESULTS AND DISCUSSION

The *n*-TSPOmbb732 synthetic pathway is shown in Scheme 1 Compound **1** was synthesized as previously reported (*12*). The alkylation reaction of **1** with 2-bromo-5-methoxybenzyl bromide was straightforward and produced compound **2** at 99% yield. The following aromatic substitution of a diamine (with a 3–9 carbon linker) resulted in relatively low yield (6–33%). This was due to several byproducts and decomposition of the desired product prior to reaction completion. The optimal reaction time for the *n*-TSPOmbb732 reaction is listed in Table 1.

The effect of spacer length on the binding affinity of the *n*-TSPOmbb732 was also investigated. More specifically, *n*-TSPOmbb732 with 3–9 carbon spacers was synthesized, characterized, and used in a competitive binding assay. The amino group was capped by an acetyl group to reduce nonspecific binding (Scheme 2). The binding affinity data are shown in Table 2. *n*-TSPOmbb732 with a three-carbon linker (3-TSPOmbb732) (IC_{50} = 0.39 μM) and 7-TSPOmbb732 (IC_{50} = 0.40 μM) have higher binding affinities than 4-TSPOmbb732 (IC_{50} = 0.80 μM) and 5-TSPOmbb732 (IC_{50} = 0.84 μM), but relatively low binding affinities compared to 6-TSPOmbb732 (IC_{50} = 0.29 μM), 8-TSPOmbb732 (IC_{50} = 0.24 μM) and 9-TSPOmbb732 (IC_{50} = 0.29 μM). Even though these binding affinities are much lower than DAA1106 (IC_{50} = 0.28 nM) and [^{11}C]DAA1106 (IC_{50} = 0.91 nM), the nanomolar binding affinities (K_i = 43–149 nM) appeared rather promising (*12, 13*). A six-carbon linker seemed to be the most optimal due to its relatively high binding affinity and yield (33%) of 6-TSPOmbb732.

NIR probes capable of targeting specific receptors are attractive noninvasive imaging tools for preclinical diagnosis (*14*); therefore, we conjugated our relatively high binding affinity TSPO-targeted ligand, 6-TSPOmbb732, to IRDye 800CW NHS ester. The reaction was straightforward, but the dye conjugation reaction yield was relatively low (31%), mainly due the impurities in the dye sample and side reactions.

HPLC was used to monitor the production of IRDye 800CW-6-TSPOmbb732 (NIR6T). The chromatographs for both the NIR dye and NIR6T at 780 nm are shown in Figure 2 (left). Figure 2 (right) shows the excitation and emission spectra. The excitation of NIR6T at 778 nm and its subsequent NIR emission at 800 nm allow deep tissue penetration with reduced absorption and scattering for in vivo imaging.

Lissamine rhodamine B sulfonyl chloride also was used to conjugate 6-TSPOmbb732 (Liss6T). Lissamine is optimized for the commonly used Texas Red filter set and is well-known for providing high-quality images. Since the commercially available Lissamine dye has two isomers, the conjugation reaction yielded two isomers as well. The spectroscopy curves are shown in Figure 3. Isomer I, which has a higher molar extinction coefficient (ε = 124 000 L/mol cm in methanol) than isomer II (ε = 80 000 L/mol cm in methanol), was selected for imaging.

Both NIR6T ($K_i = 42$ nM) and Liss6T ($K_i = 0.91$ nM) have nanomolar binding affinities to TSPO (Table 2). Conjugation of NIR dye to 6-TSPOmbb732 did not seem to affect the binding affinity significantly; however, Liss6T has significantly higher binding affinity than both NIR6T and 6-TSPOmbb732 amide. This is probably because lissamine dye contributed in the binding mode of Liss6T to TSPO whereas NIR dye did not.

Two cell lines we chose for in vitro imaging are MDA-MB-231 (human metastatic mammary adenocarcinoma) and C6 (rat glioma) cells. Both types of cells overexpress TSPO. Glioma is a type of primary central nervous system (CNS) tumor that arises from glial cells. Currently, surgery is the most effective treatment for glioma. However, unlike most other types of tumors, glioma is infiltrated, which makes it extremely challenging to determine the diseased area. Glioma cell targeted molecular imaging agent that can specifically label glioma cells would be important to guide surgery. Breast cancer is the second most commonly diagnosed cancer among women. Early detection of breast cancer is very important for survival. Currently, breast cancer is usually screened by X-ray. In this process, the breast has to be compressed very hard. In addition, the breast will be exposed to high radiation. Breast cancer targeted optical probe would make optical mammography possible, which does not require breast compression and involves no radiation.

Fluorescence microscopy imaging studies were then performed to investigate the cellular uptake of NIR6T and Liss6T in MDA-MB-231and C6 cells. Accumulation of both agents in these cells was observed (Figures 4 and 5). To demonstrate mitochondrial binding of the dyes, cultures were coincubated with MitoTracker Green, a mitochondrial marker, and our two molecules. Overlaid pictures demonstrate colocalization of all three molecules, which suggested that the optical probes preferentially bind to mitochondria, the primary site of TSPO expression. Furthermore, cells incubated with free dyes (IRDye 800CW acid or Lissamine rhodamine B sulfonyl chloride) did not show significant fluorescence (data shown in Supporting Information). The nanomolar binding affinities of NIR6T and Liss6T provided further evidence for the selective binding.

The specificity of NIR6T and Liss6T to TSPO is further verified by in vitro competition study. In this experiment, C6 glioma cells were treated with 1 μM NIR6T/Liss6T and 10 μM DAA1106 as competitor. Challenged cells showed reduced fluorescence signal compared to unchallenged cells (Figure 6 and 7). Taken together, these data suggest that NIR6T and Liss6T are promising TSPO targeted MI agents.

CONCLUSION

In conclusion, we have synthesized a functional TSPO ligand, *n*-TSPOmbb732, which can be conjugated to a variety of signaling moieties and widely applied for TSPO targeted cancer imaging. In addition, this DAA1106 analogue has been labeled with two fluorescent dyes, and the resulting imaging probes, NIR6T and Liss6T, display nanomolar binding affinities to TSPO and have been successfully imaged in vitro.

ACKNOWLEDGMENT

We thank Department of Defense (grant no. W81XWH-04-1-0432) and NIH (grant no. 5PG20 GM072048-04) for providing funding for this work. We thank A. Coe Foutch and Kathryn Stinson for assistance with cell preparation.

Supporting Information Available: Fluorescence imaging of C6 and MDA-MB-231 cells dosed with NIR6T, Liss6T, and free dyes. This material is available free of charge via the Internet at http://pubs.acs.org.

LITERATURE CITED

(1) Papadopoulos, V., Baraldi, M., Guilarte, T. R., Knudsen, T. B., and Lacapere, J. J., et al. (2006) Translocator protein (18 kDa): new nomenclature for the peripheral-type benzodiazepine receptor based on its structure and molecular function. *Trends Pharmacol. Sci. 27*, 402–409.

(2) Decaudin, D., Castedo, M., Nemati, F., Beurdeley-Thomas, A., and De Pinieux, G., et al. (2002) Peripheral benzodiazepine receptor ligands reverse apoptosis resistance of cancer cells in vitro and in vivo. *Cancer Res. 62*, 1388–1393.

(3) Romeo, E., Auta, J., Kozikowski, A. P., Ma, D., and Papadopoulos, V., et al. (1992) 2-Aryl-3-Indoleacetamides (Fgin-1) - a new class of potent and specific ligands for the mitochondrial dbi receptor (Mdr). *J. Pharmacol. Exp. Therapeutics 262*, 971–978.

(4) Kozikowski, A. P., Ma, D., Brewer, J., Sun, S., and Costa, E., et al. (1993) Chemistry, binding affinities, and behavioral properties of a new class of antineophobic mitochondrial dbi receptor complex (Mdrc) ligands. *J. Med. Chem. 36*, 2908–2920.

(5) Culty, M., Silver, P., Nakazato, A., Gazouli, M., and Li, H., et al. (2001) Peripheral benzodiazepine receptor binding properties and effects on steroid synthesis of two new phenoxyphenylacetamide derivatives, DAA1097 and DAA1106. *Drug Dev. Res. 52*, 475–484.

(6) Zhang, M. R., Maeda, J., Furutsuka, K., Yoshida, Y., and Ogawa, M., et al. (2003) [F-18]FMDAA1106 and [F-18]FEDAA1106: Two positron-emitter labeled ligands for peripheral benzodiazepine receptor (PBR). *Bioorg. Med. Chem. Lett. 13*, 201–204.

(7) Maeda, J., Suhara, T., Zhang, M. R., Okauchi, T., and Yasuno, F., et al. (2004) Novel peripheral benzodiazepine receptor ligand [C-11]DAA1106 for PET: An imaging tool for glial cells in the brain. *Synapse 52*, 283–291.

(8) Chaki, S., Funakoshi, T., Yoshikawa, R., Okuyama, S., and Okubo, T., et al. (1999) Binding characteristics of [H-3]DAA1106, a novel and selective ligand for peripheral benzodiazepine receptors. *Eur. J. Pharmacol. 371*, 197–204.

(9) Manning, H. C., Goebel, T., Marx, J. N., and Bornhop, D. J. (2002) Facile, efficient conjugation of a trifunctional lanthanide chelate to a peripheral benzodiazepine receptor ligand. *Org. Lett. 4*, 1075–1078.

(10) Manning, H. C., Smith, S. M., Sexton, M., Haviland, S., and Bai, M. F., et al. (2006) A peripheral benzodiazepine receptor targeted agent for in vitro imaging and screening. *Bioconjugate Chem. 17*, 735–740.

(11) Bai, M., Wyatt, S., Han, Z., Papadopoulos, V., and Bornhop, D. J. (2007) A novel conjugable translocator protein ligand labeled with a fluorescence dye for in vitro imaging. *Bioconjugate Chem. 18*, 1118–1122.

(12) Okubo, T., Yoshikawa, R., Chaki, S., Okuyama, S., and Nakazato, A. (2004) Design, synthesis and structure-affinity relationships of aryloxyanilide derivatives as novel peripheral benzodiazepine receptor ligands. *Bioorg. Med. Chem. 12*, 423–438.

(13) Zhang, M. R., Kida, T., Noguchi, J., Furutsuka, K., and Maeda, J., et al. (2003) [C-11]DAA1106: Radiosynthesis and in vivo binding to peripheral benzodiazepine receptors in mouse brain. *Nucl. Med. Biol. 30*, 513–519.

(14) Mahmood, U., and Weissleder, R. (2003) Near-infrared optical imaging of proteases in cancer. *Mol. Cancer Therapeutics 2*, 489–496.

(15) Garnier, M., Dimchev, A. B., Boujrad, N., Price, J. M., and Musto, N. A. (1994) In-vitro reconstitution of a functional peripheral-type benzodiazepine receptor from mouse leydig tumor-cells. *Mol. Pharmacol. 45*, 201–211.

BC700251E

Magnetic Relaxation Switch Detection of Human Chorionic Gonadotrophin

Grace Y. Kim,[†,△] Lee Josephson,[‡] Robert Langer,[§] and Michael J. Cima*[,△]

Harvard–MIT Division of Health Sciences and Technology, Cambridge, Massachusetts, Center for Molecular Imaging Research, Massachusetts General Hospital and Harvard Medical School, Boston, Massachusetts, Department of Chemical Engineering and Department of Materials Science and Engineering, Massachusetts Institute of Technology, Cambridge, Massachusetts. Received April 2, 2007; Revised Manuscript Received June 14, 2007

Functionalized nanoparticle contrast agents, also known as magnetic relaxation switches (MRS), were prepared to detect protein A and the β subunit of human chorionic gonadotrophin (hCG-β). Antibodies were attached to cross-linked iron oxide (CLIO) nanoparticles using standard peptide chemistry. Protein A was used as a simple model analyte, as it is naturally multivalent and can bind multiple CLIO-IgG simultaneously. The addition of PA to CLIO-IgG resulted in transverse relaxation time (T_2) shortening compared to a blank control as seen by NMR relaxometry measurements. Analyte-induced aggregation was confirmed by light scattering particle size analysis. A two-particle system was designed to measure hCG-β, as it is not multivalent and requires conjugation of a matched pair of monoclonal antibodies to CLIO (referred to as C95 and C97). Measurement of hCG-β is important, as elevated serum levels are associated with malignancies including testicular and ovarian cancers. The addition of hCG-β to C95 and C97 resulted in T_2 shortening with a linear dynamic concentration range of 0.1 to 1 molecules of analyte per nanoparticle. Similar data were obtained for the hCG dimer. Observations with higher stoichiometric ratios of analyte to nanoparticle and increased nanoparticle valency were also made. This method can potentially be adapted to detect other biomarkers in solution.

INTRODUCTION

Magnetic resonance imaging (MRI) has an important clinical role in the detection and monitoring of cancerous masses. Molecular imaging contrast agents have enhanced these abilities beyond imaging shrinking and growing tumor borders to reporting on the presence and state of additional targets of interest (*1*). Recently, a modification of paramagnetic nanoparticle contrast agents has been used for diagnostic measurements of specific targets, including DNA (*2*), viruses (*3*), cells (*4*), and ions (*5*). The sensitivity of detection varies from 10^{-21} M for DNA to 10^{-6} M for Ca^{2+} depending on a variety of factors, including binding affinity, particle concentration, and sensor format. These particles are called magnetic relaxation switches (MRS) because they "switch" from dispersed to aggregated in the presence of a target molecule or analyte. The aggregation is accomplished by the presence of functional groups on the particle surface that have an affinity for the analyte. The change of state from dispersed to aggregated affects the transverse relaxation time (T_2) of the aqueous medium that surrounds the particles. Thus, aggregation can be detected by magnetic means, enabling measurements in turbid and opaque solutions as well as real-time measurements in patients. Magnetic detection, therefore, has a distinct advantage over optical or electrochemical assays (*6, 7*).

Here, we report the detection of protein A (PA) and human chorionic gonadotrophin (hCG) by functionalized magnetic cross-linked iron oxide nanoparticles (CLIO). PA is a stable cell surface receptor that is naturally multivalent and serves as a simple model system for aggregation. One PA molecule can bind to the Fc portion of least two molecules of IgG at the same time, and thus forms a simple aggregating system. Other proteins, however, may not naturally be multivalent and require a matched pair of antibodies to form a "sandwich"with the analyte in the middle, similar to an ELISA. Detection of hCG requires such a strategy to form networked aggregates, since hCG is not multivalent (Figure 1a). hCG is a heterodimer, consisting of an α and β subunit. Many other hormones share a similar structure to hCG-α, whereas the hCG-β serum level is elevated in testicular and ovarian cancers and locally elevated in cystic fluid and ascites often to concentrations greater than in serum (*8, 9*). It is one of the more well-characterized soluble cancer biomarkers, as it is also a pregnancy marker.

Aggregation of multivalent systems is actively being studied (*10–12*). Functional group balance is important in the formation of aggregates (*12*). An optimum ratio of particle to analyte exists where the analytes form interparticle bridges between two nanoparticles. A network or branched aggregate can be created if the nanoparticle has more than one receptor (Figure 1c). In the low analyte regime, there is insufficient analyte to cause aggregation and very few bridges are created (Figure 1b). High concentrations of analyte will, however, saturate the receptors and prevent cross-linking of nanoparticles (Figure 1d). This phenomenon is known as the prozone effect or high-dose hook effect and is a limitation of all agglutination assays.

MATERIALS AND METHODS

Nanoparticle Conjugation. Magnetic iron oxide nanoparticles with amine-terminated dextran shell (CLIO-NH_2) were produced as described previously (*13*). CLIO-NH_2 was treated with sulfo-succinimidyl-4-(*N*-maleimidomethyl)cyclohexane-1-carboxylate (Sulfo-SMCC, Pierce, Rockford, IL) to create a maleimide functional group. Antibodies (Mouse IgG, Sigma;

* Corresponding author. Michael J. Cima, Ph.D., Department of Materials Science and Engineering, Massachusetts Institute of Technology, 77 Massachusetts Ave., Room 12-011, Cambridge, MA 02139, Tel: 617-253-6877, Fax: 617-258-6936, mjcima@mit.edu.

[†] Harvard–MIT Division of Health Sciences and Technology.

[‡] Massachusetts General Hospital and Harvard Medical School.

[§] Department of Chemical Engineering, Massachusetts Institute of Technology.

[△] Department of Materials Science and Engineering, Massachusetts Institute of Technology.

10.1021/bc070110w CCC: $37.00 © 2007 American Chemical Society
Published on Web 09/25/2007

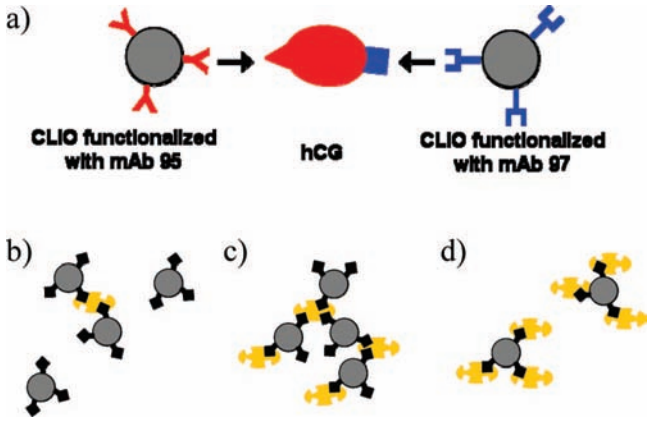


Figure 1. (a) Schematic of hCG aggregation. C95 and C97 recognize a separate epitope on hCG. Aggregation also occurs with hCG-β subunit. (b−d) Schematics of the effect of increasing analyte to particle ratio. Adapted from Costanzo (*12*). (b) Low analyte to particle ratio causes insufficient aggregation for detection. (c) The range of aggregate formation relies on a stoichiometric balance of analyte to particle. (d) The prozone effect is seen at high analyte to particle ratio, where analytes have saturated the particles such that cross-linking of particles is impaired.

anti-HCG-β, Scripps Laboratories, San Diego, CA) were activated with *N*-succinimidyl-*S*-acetylthioacetate (SATA, Pierce) to generate a blocked sulfanyl group which was deprotected with hydroxylamine. The CLIO-SMCC was incubated with the prepared antibody solutions for 4 to 8 h at 4 °C. The reaction was quenched with 2-sulfanylethanol and purified with a Sephacryl 300 column (Sigma). Iron concentrations were determined by absorbance at 410 nm after 1 h incubation in 6 N HCl and H_2O_2 to dissolve CLIO. Protein concentrations were determined by bicinchoninic acid assay (Pierce). The protein concentration was divided by the iron concentration to estimate the number of antibody conjugated to each nanoparticle, assuming 8000 iron molecules per CLIO (*14*). Anti-hCG-β monoclonal antibody-conjugated CLIO are referred to by a shortened form of their product numbers, C95 and C97. The antibodies for C95 and C97 are a matched pair to separate, nonoverlapping epitopes on hCG-β, with K_d values of 10^{-10} M and 5×10^{-9} M, respectively. A second batch of each conjugate, C95–2 and C97–2, was produced by starting with a 3-fold volumetric scaleup of reactants.

Determination of Proton Relaxation Times. Proton relaxation time measurements were performed at 0.47 T and 40 °C (Bruker NMR Minispec, Billerica, MA). Samples were incubated at 40 °C for 1 h for thermal equilibration before measurements were taken. Relaxivities were determined as the slope of a plot of $1/T_2$ or $1/T_1$ (s^{-1}) as a function of the iron concentration (mM).

Aggregation experiments were performed by mixing equal volumes of nanoparticle solutions and analyte solutions. The mixture was incubated at 40 °C for 1 h for thermal equilibration before measurements were taken. CLIO-IgG nanoparticles were mixed with various PA concentrations. An equal mixture of C95 and C97 (C95/C97) or C95–2 and C97–2 (C95–2/C97–2) solutions were used for hCG-β and hCG detection. Analyte dilutions of PA (Sigma, 45 kDa), hCG-β (Scripps Laboratories, 28 kDa), or hCG (Sigma, 37.9 kDa) were prepared in phosphate buffered saline pH 7.4 with 1% penicillin−streptomycin and 0.1% or 1% bovine serum albumin (PBS) to reduce nonspecific adsorptive loss of analyte. Reported concentrations are the final analyte concentrations obtained after mixing. Stability measurements were obtained by measuring relaxation times after incubation at room temperature. Data were plotted as average relaxation time ± standard deviation.

Table 1. Characterization of CLIO Conjugates

sample	analyte	R_2 relaxivity $(mM \cdot s)^{-1}$	R_1 relaxivity $(mM \cdot s)^{-1}$	valency (# Ab per CLIO)
CLIO	n/a[a]	54.2	21.53	n/a
CLIO-IgG	Protein A	47.0	n/m[b]	3.6
CLIO-95 (C95)	hCG-β, hCG	44.1	n/m	2.2
CLIO-97 (C97)	hCG-β, hCG	44.9	n/m	3.1
CLIO-95–2 (C95–2)	hCG-β, hCG	67.9	17.8	4.1
CLIO-97–2 (C97–2)	hCG-β, hCG	76.4	20	4.5

[a] n/a - not applicable. [b] n/m - not measured.

Dynamic Light Scattering. Particle sizes were determined using a 90 Plus Particle Size Analyzer (Brookhaven Instrument Corporation, Holtsville, NY). Samples were measured at 37 °C in PBS, $\lambda = 658$ nm, 90° fixed angle. The log-normal intensity-weighted effective diameter was reported. Population distribution was determined by peak integration of the volume-weighted scattering intensity.

RESULTS

CLIO Conjugation and Characterization. Five batches of CLIO-NH_2 were conjugated with antibodies. The relaxivity and valency of the unconjugated CLIO-NH_2 and conjugated CLIO are reported in Table 1. The relaxivities of conjugated CLIO are similar to those of unconjugated CLIO-NH_2. The same initial concentration of antibody was used in all conjugations. No specific attempt was made to increase the degree of conjugation; however, C95–2 and C97–2 resulted in higher valencies than C95 and C97, yielding approximately 1 to 2 more antibodies per nanoparticle.

CLIO-IgG + Protein A Aggregation. CLIO-IgG was used as a simple model system to assess the conjugation scheme and aggregate formation without the need for a matched pair of antibodies to two nonoverlapping epitopes on the analyte. CLIO-IgG were mixed with PA solutions. The T_2 relaxation time of a CLIO-IgG + PBS control was 101 ± 7 ms. Lower T_2 values were observed when CLIO-IgG was mixed with PA solutions varying from 0.1 to 8 μg/mL. T_2 decreased with PA concentration, and the largest change was seen at 2 μg/mL PA (27%) (Figure 2a). Concentrations between 0.1 and 2 μg/mL correlate with the dynamic concentration range of CLIO-IgG for the given CLIO concentration (Figure 1c). The response flattens at the higher concentrations tested. CLIO-IgG of a higher nanoparticle concentration resulted in the same trend with T_2 decreases up to 40% (data not shown).

The change in T_2 upon addition of PA was attributed to PA-induced aggregation of CLIO-IgG. The formation of aggregates was confirmed by measurements of the particle size (Table 2). The mean particle size of the CLIO-IgG was 52.3 nm. PA solution alone showed no detectable particles by light scattering. Two peaks were observed 2 min after mixing CLIO-IgG and PA to a final PA concentration of 2 μg/mL. The major particle population with a size of 76.1 nm comprised 90% of the volume-weighted scattering efficiency, and the remainder of the population was a size of 620 nm. The initial bimodal distribution formed indicates that some particles react extensively to create large aggregates while the smaller 76.1 nm population may comprise single CLIO-IgG nanoparticles or CLIO-IgG:PA complexes. The time for temperature equilibration required for accuracy precludes rapid T_2 measurements with the current benchtop NMR relaxometer setup; however, uncalibrated measurements of room-temperature samples suggest that T_2 is sensitive to the formation of small populations of aggregates as quickly as it can be measured. This further implies that the small aggregates formed in the initial minutes to hours contribute to the majority of the T_2 changes. The aggregates grow such that nearly half of the particles were in an aggregate at 24 h. These aggregates remain stable up to 5 days at room temperature

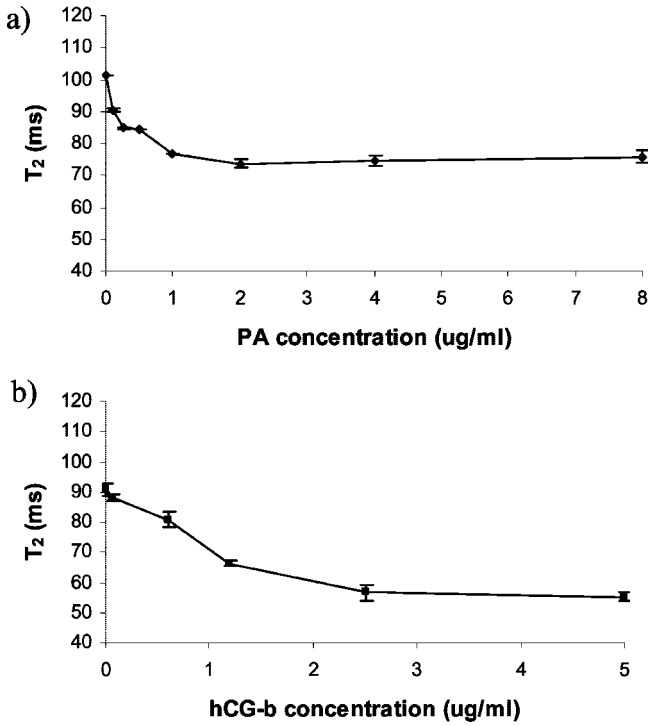


Figure 2. (a) CLIO-IgG's were incubated with various concentrations of protein A. Aggregation of CLIO-IgG is indicated by the decrease in T_2. (b) C95/C97 were incubated with various concentrations of hCG-β. T_2 decreased with increasing concentrations of hCG-β. The data are plotted as averages ± standard deviation ($n = 4$). All concentrations refer to final concentrations after incubation.

Table 2. Particle Size Measurements of CLIO-IgG + Protein A[a]

time	population 1		population 2	
	size (nm)	percent of sample	size (nm)	percent of sample
no analyte	52.3	100	–	–
2 min	76.1	89.7	619.8	10.3
1 day	97.9	58.7	375.5	41.3
5 days	63.4	55.1	551.9	44.9

[a] Particle size analysis of CLIO-IgG upon addition of protein A (final concentration 2 μg/mL). Population distribution was determined by peak integration of the volume-weighted scattering intensity. No particles were detected in PA solution alone.

as confirmed by particle size measurements and NMR relaxometry. T_2 values varied by 6% for 2 μg/mL PA concentration examined by particle sizing (Table 2) over this time period. A variation in T_2 of 6–12% was observed for all other PA samples.

SATA, a nonsite-specific coupling agent, has the potential to interfere with some antibody functionality, but the formation of PA-induced aggregates confirms that sufficient antibody functionality is retained with this conjugation reaction. Higher antibody functionality may be achieved with site-specific coupling such as mercaptoethylamine, which directs modification away from the antibody binding region.

CLIO-95/CLIO-97 Aggregation. CLIO-95/CLIO-97 blends were mixed with various hCG-β concentrations. The T_2 relaxation time of C95/C97 + PBS control was 91 ± 2 ms (Figure 2b). T_2 varied inversely with the amount of hCG-β, with the largest decrease observed at a concentration of 5 μg/mL ($T_2 = 55 \pm 2$ ms, 40% decrease). The change in T_2 was attributed to hCG-β induced aggregation with an apparent dynamic concentration range of 1 order of magnitude. These aggregates were stable over 6 days at room temperature (data not shown). A change in T_2 was found with the addition of hCG-β or hCG. Furthermore, hCG added to C95 alone or C97

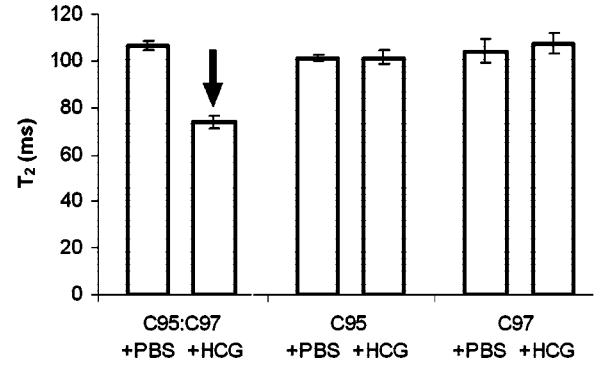


Figure 3. C95/C97 solutions were incubated with PBS or hCG. T_2 shortening is observed with the addition of hCG to C95/C97. Both C95 and C97 are required for hCG induced T_2 changes. Similar results are observed with hCG-β.

alone did not cause a change in T_2 from the respective PBS control (Figure 3), supporting the hypothesis that both antibody-conjugated nanoparticles are required to form an aggregate (Figure 1a). Control solutions contained dispersed nanoparticles as confirmed by DLS. The addition of analyte to CLIO conjugated to a monoclonal antibody can produce analyte:antibody−CLIO complexes, but this is not sufficient to induce a measurable T_2 change. MRS assays require agglomeration of at least two CLIO for "switching" of this sensor.

A larger concentration range was studied to estimate the dynamic range. Responses to the hCG-β subunit and hCG dimer were evaluated. Analyte concentrations were converted to molecular equivalents per CLIO nanoparticle using the theoretical molecular weight and the CLIO concentration. This conversion facilitates the comparison between hCG and hCG-β and interpretation of the stoichiometric nature of this sensor. The C95/C97 mixture was sensitive to both the hCG heterodimer and the hCG-β subunit with a linear dynamic concentration range of 1 order of magnitude (Figure 4a). The decrease in T_2 was much more significant in response to equivalent numbers of hCG molecules as compared with hCG-β. This may be due to stronger avidity and cooperative binding of the antibodies to the hCG molecule over hCG-β alone.

Aggregation behavior with the second, higher-valency CLIO mixture (C95–2/C97–2) was compared to the initial lot of lower-valency C95/C97 (Figure 4b). Similar trends were observed in both lots. The linear dynamic concentration range was the same, with the largest T_2 changes for both C95–2/C97–2 and C95/C97 lots observed at 2.5 molecules of hCG-β per CLIO and 1 molecule of hCG per CLIO. The magnitude of changes in T_2 was larger with hCG over that observed for hCG-β. A decrease in T_2 was, however, not observed at the higher hCG analyte concentrations (2.5, 5, and 10 analyte molecules per CLIO) with C95–2/C97–2. Repeated measurements of these samples yielded a T_2 that was rapidly changing, and in certain cases, a precipitate could be seen to settle overnight. These data are in agreement with a recent study that found the largest stable T_2 change at approximately 1.2 equiv of avidin per biotin-functionalized nanoparticle (*15*). Coefficients of variation above 2% were seen when larger equivalents of avidin were added. Thus, it seems that solution stable CLIO agglutination is subject to an upper limit of approximately 1 equiv of analyte per nanoparticle and that lower valency particles are preferred.

The limit of detection was 0.1 molecules of analyte per CLIO (3.57 nM hCG-β and 3.57 nM hCG) as defined by the concentration where the standard deviation does not overlap with the standard deviation of the PBS control. The limit of detection is an order of magnitude greater than the K_d of the antibody (0.1 nM). Thus, the sensitivity of this stoichiometric sensor at

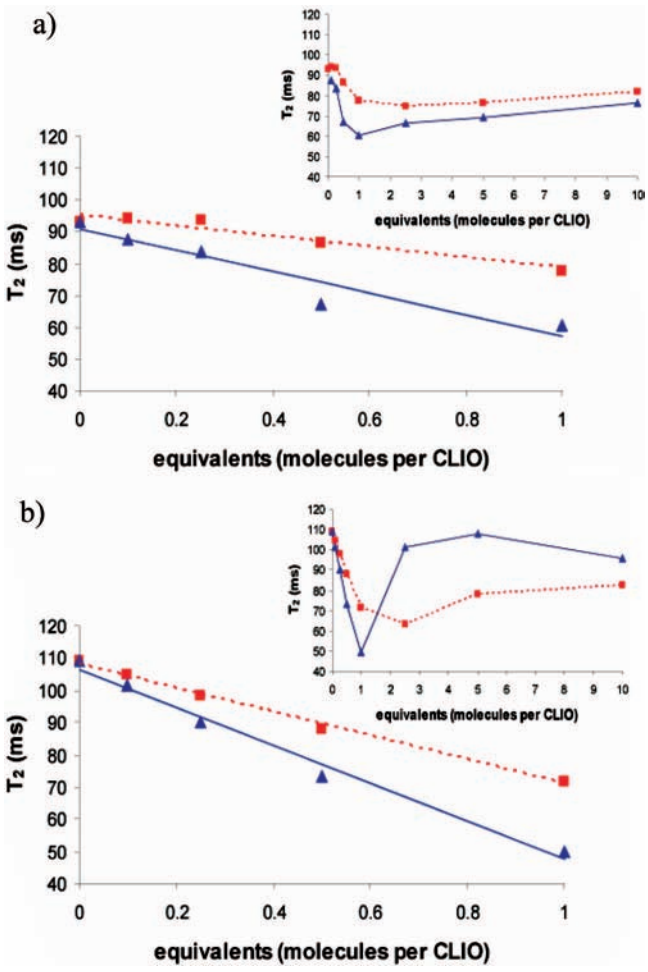


Figure 4. CLIO were incubated with hCG-β (■) and hCG dimer (▲). T_2 varies linearly with analyte concentration between 0.1 and 1 molecules of analyte per CLIO nanoparticle; inset shows the wider concentration range for (a) lower valency C95/C97 mixture and (b) higher valency C95–2/C97–2. Both show enhanced T_2 shortening with hCG compared to hCG-β. The higher valency C95–2/C97–2 particles show larger differences in T_2 and instabilities at the higher analyte regime, which becomes more pronounced with additional incubation time. Error bars are of similar size as the symbols.

the given CLIO concentrations is not limited by the dissociation constant of the antibody. Sensitivity can be enhanced by using a lower CLIO concentration, as fewer total analyte molecules are needed to induce a T_2 change.

Kinetics of Aggregation. The kinetics of aggregation were examined by particle size analysis (Figure 5). It has been suggested that the aggregates are of a fractal nature (*10*), whereas dynamic light scattering assumes a hard-sphere hydrodynamic model. Nevertheless, the effective diameter produces a convenient, single value which represents relative changes in the entire particle population. The effective diameter was approximately 140 nm for the unaggregated C95–2/C97–2 particles and increased with the addition of hCG. The initial rates of increase were 17 ± 1 nm/hr and 21 ± 1 nm/hr for 0.5 and 2.5 μg/mL hCG, respectively. The effective diameter of the aggregates reached 1 μm in hours. Particle size measurements at that size are imprecise due to the heterogeneous population of aggregates formed and the settling of precipitates. Indeed, precipitates can be observed at the bottom of some cuvettes after incubation overnight. Measurements of these settled solutions show that the autocorrelation function has difficulty establishing a baseline and no particles are detected. Micrometer-sized particles are observed upon resuspension of the particles by mixing. Samples

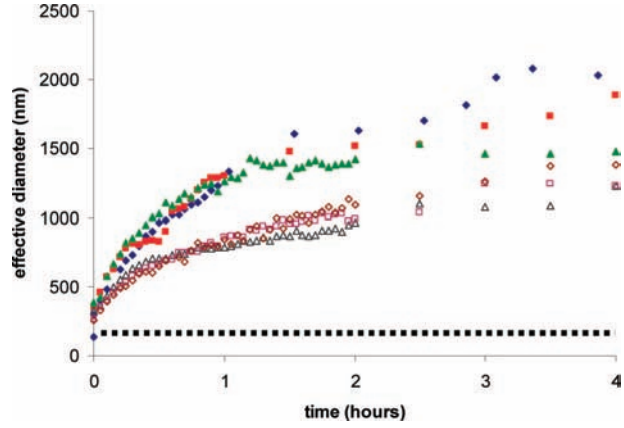


Figure 5. Particle aggregation kinetics as measured by dynamic light scattering. Effective diameter of the C95–2/C97–2 aggregates forming in 2.5 μg/mL hCG (solid symbols, ♦ ■ ▲) and 0.5 μg/mL hCG (open symbols, ◇ □ △). Unaggregated particles show no change in size (dotted line).

were not available for aggregation kinetics with the C95/C97 mixture, but measurements of similar lower-valency conjugate lots show the effective diameter increases to a lower plateau value of less than 200 um in size for all hCG concentrations tested. Particle sizing supports the stable T_2 measurements that were made with CLIO-IgG and C95/C97 days later and the rapidly changing measurements made with C95–2/C97–2.

Agglutination-based assays are subject to the prozone effect when analyte excess results in the formation of analyte/antibody−CLIO complexes without cross-linking (Figure 1d). It is of particular concern for false-negative assay results in syphilis and HIV/AIDS testing (*16, 17*). Measurements are typically repeated with a one-tenth dilution when a false negative is suspected to obtain values in the dynamic range of the assay.

Solution-based magnetic aggregation measurements have an additional limitation due to precipitation. Higher-valency particles produced more pronounced changes in T_2 and have been predicted to aggregate faster (*10*). Higher valency may also be a disadvantage, especially in the higher analyte regime, wherein a greater degree of aggregation may form much larger networks that are prone to insolublity and precipitation. It is interesting that the addition of approximately one antibody more per CLIO has a dramatic effect on aggregation kinetics under these experimental conditions. Thus, both the prozone and insolubility effects may be occurring above the one analyte per nanoparticle ratio to various extents depending on the nanoparticle (size, density, and valency), extent of analyte excess, K_d, and kinetics of aggregate growth. Stabilization of nanoparticle aggregates and control of aggregate growth in favor of nucleation of smaller aggregates will be important to the further development of these types of assays.

The sequential sample analysis format of the benchtop relaxometer and the need for thermal equilibration of samples impede measurements of large sample numbers and relaxation time kinetics. Custom instruments, such as one featuring a microfabricated coil (*18*), a portable sensor (*19*), or the ex situ NMR plate reader being developed in our laboratory, allow these dilute nanoparticle solutions to be measured with more compact instrumentation in small volumes for higher throughput screening and research purposes than is possible with conventional methods. This one-pot sensor system has the advantages of being able to work with an opaque sample with a single mixing step at the expense of the sensitivity that can be obtained by ELISA. This may be useful in instances where fast or sequential measurements are required. Additional applications may exploit the reversible nature of antibody/analyte binding by removal

of analyte, such as through dialysis (*20*). Thus, the same nanoparticle solution can be used for continuous measurements if a fixed volume container is used to achieve a constant nanoparticle concentration.

CONCLUSION

Monoclonal antibodies against hCG-β were attached to each nanoparticle using standard peptide chemistry. The addition of hCG-β or hCG to the MRS resulted in T_2 shortening compared to a blank control value as seen by NMR relaxometry. The size of the particles increased with the addition of hCG, independently confirming that aggregation was occurring. Particle size measurements also suggest that control of aggregate size will be important in enhancing the dynamic range and stability of this type of assay. This method can potentially be adapted to detect other biomarkers in solution.

ACKNOWLEDGMENT

This work was supported by NCI Centers of Cancer Nanotechnology Excellence No. 5 U54 CA119349-12 grant.

LITERATURE CITED

(1) Weissleder, R. (2006) Molecular imaging in cancer. *Science 312*, 1168–71.

(2) Nam, J. M., Stoeva, S. I., and Mirkin, C. A. (2004) Bio-barcode-based DNA detection with PCR-like sensitivity. *J. Am. Chem. Soc. 126*, 5932–3.

(3) Perez, J. M., Simeone, F. J., Saeki, Y., Josephson, L., and Weissleder, R. (2003) Viral-induced self-assembly of magnetic nanoparticles allows the detection of viral particles in biological media. *J. Am. Chem. Soc. 125*, 10192–3.

(4) Schellenberger, E. A., Reynolds, F., Weissleder, R., and Josephson, L. (2004) Surface-functionalized nanoparticle library yields probes for apoptotic cells. *ChemBioChem 5*, 275–9.

(5) Atanasijevic, T., Shusteff, M., Fam, P., and Jasanoff, A. (2006) Calcium-sensitive MRI contrast agents based on superparamagnetic iron oxide nanoparticles and calmodulin. *Proc. Natl. Acad. Sci. U.S.A. 103*, 14707–12.

(6) von Lode, P., Rainaho, J., and Pettersson, K. (2004) Quantitative, wide-range, 5-minute point-of-care immunoassay for total human chorionic gonadotropin in whole blood. *Clin. Chem. 50*, 1026–35.

(7) Chen, J., Tang, J., Yan, F., and Ju, H. (2006) A gold nanoparticles/sol-gel composite architecture for encapsulation of immunoconjugate for reagentless electrochemical immunoassay. *Biomaterials 27*, 2313–21.

(8) Hoermann, R., Gerbes, A. L., Spoettl, G., Jungst, D., and Mann, K. (1992) Immunoreactive human chorionic gonadotropin and its free beta subunit in serum and ascites of patients with malignant tumors. *Cancer Res. 52*, 1520–4.

(9) Grossmann, M., Hoermann, R., Gocze, P. M., Ott, M., Berger, P., and Mann, K. (1995) Measurement of human chorionic gonadotropin-related immunoreactivity in serum, ascites and tumour cysts of patients with gynaecologic malignancies. *Eur. J. Clin. Invest. 25*, 867–73.

(10) Shapiro, M. G., Atanasijevic, T., Faas, H., Westmeyer, G. G., and Jasanoff, A. (2006) Dynamic imaging with MRI contrast agents: quantitative considerations. *Magn. Reson. Imaging 24*, 449–62.

(11) Gillis, P., Moiny, F., and Brooks, R. A. (2002) On T(2)-shortening by strongly magnetized spheres: a partial refocusing model. *Magn. Reson. Med. 47*, 257–63.

(12) Costanzo, P. J., Patten, T. E., and Seery, T. A. (2004) Protein-ligand mediated aggregation of nanoparticles: A study of synthesis and assembly mechanism. *Chem. Mater. 16*, 1775–1785.

(13) Josephson, L., Tung, C. H., Moore, A., and Weissleder, R. (1999) High-efficiency intracellular magnetic labeling with novel superparamagnetic-Tat peptide conjugates. *Bioconjugate Chem. 10*, 186–91.

(14) Reynolds, F., O'Loughlin, T., Weissleder, R., and Josephson, L. (2005) Method of determining nanoparticle core weight. *Anal. Chem. 77*, 814–7.

(15) Taktak, S., Sosnovik, D., Cima, M. J., Weissleder, R., and Josephson, L. (Submitted) Smart, self-reporting nanoparticle sensors using MRI.

(16) Bermes, E. W., Jr., and, and Isaacs, J. H. (1969) Evaluation of a direct agglutination latex particle test for human chorionic gonadotropin. *Am. J. Obstet. Gynecol. 104*, 865–70.

(17) Taborda, C. P., Rivera, J., Zaragoza, O., and Casadevall, A. (2003) More is not necessarily better: prozone-like effects in passive immunization with IgG. *J. Immunol. 170*, 3621–30.

(18) Sillerud, L. O., McDowell, A. F., Adolphi, N. L., Serda, R. E., Adams, D. P., Vasile, M. J., and Alam, T. M. (2006) 1H NMR detection of superparamagnetic nanoparticles at 1T using a microcoil and novel tuning circuit. *J. Magn. Reson. 181*, 181–90.

(19) Perlo, J., Demas, V., Casanova, F., Meriles, C. A., Reimer, J., Pines, A., and Blumich, B. (2005) High-resolution NMR spectroscopy with a portable single-sided sensor. *Science 308*, 1279.

(20) Sun, E. Y., Weissleder, R., and Josephson, L. (2006) Continuous analyte sensing with magnetic nanoswitches. *Small 2*, 1144–7.

BC070110W

Dexamethasone-Conjugated Low Molecular Weight Polyethylenimine as a Nucleus-Targeting Lipopolymer Gene Carrier

Yun Mi Bae,[†] Hye Choi,[†] Seungah Lee,[‡] Seong Ho Kang,[‡] Young Tae Kim,[§] Kihoon Nam,[⊥] Jong Sang Park,[⊥] Minhyung Lee,[||] and Joon Sig Choi*[,†]

Department of Biochemistry, Chungnam National University, Daejeon, 305-764, Korea, Department of Chemistry and Research Institute of Physics and Chemistry (RINPAC), Chonbuk National University, Jeonju, 561-756, Korea, Department of Thoracic and Cardiovascular Surgery, Xenotransplantation Research Center, Seoul National University Hospital, Cancer Research Institute, Seoul National University College of Medicine, Seoul, 110-744, Korea, Department of Bioengineering, Hanyang University, Seoul, 133-791, Korea, and School of Chemistry, Seoul National University, 151-742, Korea. Received January 12, 2007; Revised Manuscript Received July 9, 2007

Dexamethasone, a glucocorticoid steroid, can dilate the nuclear pore complexes and translocate into the nucleus when it is bound to its glucocorticoid receptor, suggesting that the transport of DNA into the nucleus may be facilitated by the reagent. In this research, dexamethasone was conjugated to low molecular weight polyethylenimine (2kDa) for efficient translocation of the polymer/DNA complex into the nucleus. Polyethylenimine (PEI)–dexamethasone (PEI–Dexa) was synthesized by one-step reaction using the Traut's reagent. In gel retardation assay, the PEI–Dexa/DNA complex was completely retarded at or above 0.3/1 weight ratio (polymer/DNA). The average size distributions and ζ-potential values of the complexes were measured at various weight ratios. In vitro transfection assay showed that the PEI–Dexa/DNA complex had higher gene delivery efficiency compared to PEI 2kDa/DNA complex. The localization of PEI–Dexa/plasmid DNA complexes in the nucleus was confirmed by using total internal reflection fluorescence and Nomarski differential interference contrast microscope as well as confocal microscope. Therefore, with efficient nuclear translocation and low cytotoxicity, PEI–Dexa may be useful for nonviral gene therapy.

INTRODUCTION

Gene therapy is an interdisciplinary field, including basic sciences, engineering, pharmacology, and medicines. For more than two decades, it has been gaining interests and prospects as one of the most promising custom-made platform therapeutic technologies in the post-genomic era. The vehicle for encapsulation and delivery of therapeutic genes is either viral vectors or nonviral synthetic vectors, such as cationic liposomes and cationic polymers or the combination of both vectors (*1*). In the view of targeting and transfection efficiency, viral vectors are better than nonviral vectors, but their inevitable problems, such as immune response and possible tumorigenesis, are still difficult barriers to overcome. As an alternative, nonviral synthetic vectors have been actively studied and developed over the past decade, and some recent studies showed promising results for future clinical applications with DNA and RNA delivery (*2, 3*). For the synthetic vectors, the liposome system is one of the most promising carriers for delivering therapeutic genes as well as biologically active molecules into mammalian cells (*4*). The application of such synthetic nonviral vectors is dependent on several factors, such as the solubility in water, the size and surface charge of the complexes, and the lipid composition of liposomes. Therefore, it is necessary to control such conditions and to check every preparation step to get optimal transfection efficiency in vitro and/or in vivo.

Glucocorticoid receptor is an intracellular receptor, which regulates gene expression in the presence of specific ligands. In the presence of glucocorticoid, the receptor binds to the ligand and the receptor–ligand complex is translocated into the nucleus (*5*). It is also reported that the nuclear pore complexes were dilated by the glucocorticoid receptor in the presence of dexamethasone, a potent glucocorticoid (*6, 7*). This dilation effect is considered to be helpful for nonviral gene delivery, which is favorable for translocation of polymer/DNA complex into the nucleus. Also, it was suggested that the transport of the polymer/DNA complex into the nucleus may be facilitated by the ligand–receptor-mediated transport when glucocorticoid is conjugated to the polymer. It was successfully verified in some reports using dexamethasone-mediated gene delivery (*8–10*), and we recently reported that the conjugation of dexamethasone to polyamidoamine dendrimer (PAMAM) increased the transfection efficiency of the polymer (*11*).

The goal of this study is to synthesize and characterize a lipopolymer composed of nontoxic small molecular weight polyethylenimine (PEI) (2kDa) and dexamethasone. We synthesized dexamethasone conjugated PEI with a Traut's coupling reagent. PEI–Dexa might have improved transfection efficiency due to efficient translocation of PEI–Dexa/DNA complex into the nucleus. To prove the hypothesis, we characterized physicochemical properties, cytotoxicity, and in vitro transfection efficiency of PEI–Dexa. Also, the localization of the PEI–Dexa/DNA complex in the nucleus was verified by confocal, total internal reflection fluorescence (TIRF), and Nomarski differential interference contrast (DIC) microscopy.

EXPERIMENTAL METHODS

Materials. Polyethylenimine (branched, 2kDa, and 25kDa), polyamidoamine dendrimer (PAMAM, generation 4), ethidium

* To whom correspondence should be addressed. E-mail: joonsig@cnu.ac.kr. Tel: 82-42-821-5489. Fax: 82-42-822-7548.
[†] Chungnam National University.
[‡] Chonbuk National University.
[§] Seoul National University College of Medicine.
[||] Hanyang University.
[⊥] Seoul National University.

10.1021/bc070012a CCC: $37.00 © 2007 American Chemical Society
Published on Web 09/13/2007

bromide, and 3-[4,5-dimethylthiazol-2-yl]-2,5-diphenyltetrazolium bromide (MTT) were purchased from Sigma-Aldrich Korea. Dexamethasone-21-mesylate was purchased from Steraloids Inc. Luciferase 1000 assay kit and reporter lysis buffer were purchased from Promega (Madison, WI). The luciferase expression plasmid (pCN-Luci) was prepared as reported previously (*12*). HepG2 and 293 cell lines were obtained from Korean Cell Line Bank. PicoGreen reagent and Alexa Fluor 488 protein labeling kit were purchased from Invitrogen. Fetal bovine serum (FBS), Dulbecco's modified Eagle's medium (DMEM), and 100× antibiotic-antimycotic reagent were purchased from GIBCO (Gaithersburg, MD). Micro BCA protein assay kit and 2-iminothiolane (Traut's reagent) were purchased from Pierce (Rockford, IL).

Synthesis of PEI–Dexa. The conjugation reaction was performed as reported previously with some modification (*8, 11*). Low molecular weight PEI (2 kDa) was dissolved in 1.8 mL of anhydrous dimethyl sulfoxide (DMSO) with 2-fold molar excess of Traut's reagent and dexamethasone-21-mesylate. To minimize the crosslinking side reaction, we used anhydrous DMSO and tried to keep away humidity during the reaction. The reaction was allowed to proceed for 4 h at room temperature and was quenched by the addition of an excess amount of cold ethyl acetate. The precipitated product was solubilized in water and dialyzed for 1 day against pure water using dialysis membrane (MWCO 1000). It was further freeze-dried and a white product was obtained (60% yield). The product was solubilized in DMSO-d_6/D_2O for ^1H NMR analysis (300 MHz, Korea Basic Science Institute).

Gel Retardation Assay and PicoGreen Assay. Polymer/plasmid complexes were prepared at various weight ratios ranging from 0.1 to 0.5 in Hepes-buffered saline (20 mM Hepes, 150 mM NaCl, pH 7.4). After 30 min incubation at room temperature for complex formation, the samples were subject to electrophoresis on a 0.7% (w/v) agarose gel containing ethidium bromide (0.5 μg/mL of the gel). After electrophoresis, the gel was analyzed on a UV illuminator to show the location of the DNA. PicoGreen assay for complex formation was also performed as reported previously (*12*).

Dynamic Light Scattering and ζ-Potential Measurements. The hydrodynamic diameters and ζ-potential values of polyplexes at various weight ratios were determined by the Zetasizer Nano ZS system (Malvern Instruments, UK) (*12*). After 30 min incubation, the complex solution was diluted to a final volume of 2 mL prior to measurements. The complex size was measured using Dispersion Technology Software 4.30, and data analysis was performed in automatic mode. The refractive index (n = 1.33) and the viscosity (0.89) of ultrapure water were used at 25 °C for measurements. The measured value is presented as the average size plus or minus a standard deviation of three runs.

Cell Culture and in vitro Transfection. Human embryonic kidney 293 cells and human liver carcinoma HepG2 cells were grown in DMEM with 10% FBS. The cells were routinely maintained on plastic tissue culture dishes at 37 °C in an incubator with a humidified atmosphere containing 5% CO_2/95% air. All media routinely contained antibiotic–antimycotic agent. For the transfection studies, cells were seeded at a density of 2×10^5 cells/well in 24 well flat-bottomed microassay plates 24 h before transfection. Polyplexes were prepared at various weight ratios and added to the cells. For competition assay, dexamethasone stock solution prepared in ethanol was added to each well (final ethanol concentration was 1.6%, v/v) and incubated for 30 min before polyplexes were added. The dexamethasone and polyplexes were incubated for 24 h in the presence of 10% FBS before assay. The amount of plasmid DNA was fixed at 1 μg/well. The cells were then incubated for 1 day at 37 °C in a 5% CO_2 incubator before assay.

Luciferase Assay. After transfection, the cells were washed with phosphate-buffered saline (PBS), and 150 μL of reporter lysis buffer (Promega, Madison, WI) was added to each well. After 15 min of incubation at room temperature, the cells were harvested and transferred to microcentrifuge tubes. After 15 s of vortexing, the cells were centrifuged at 12 000 rpm for 3 min. The protein concentrations of the extracts were determined by using protein assay kit. Luciferase activity was measured in terms of relative light units (RLU) using a luminometer. The final values of luciferase were reported in terms of RLU/μg total protein.

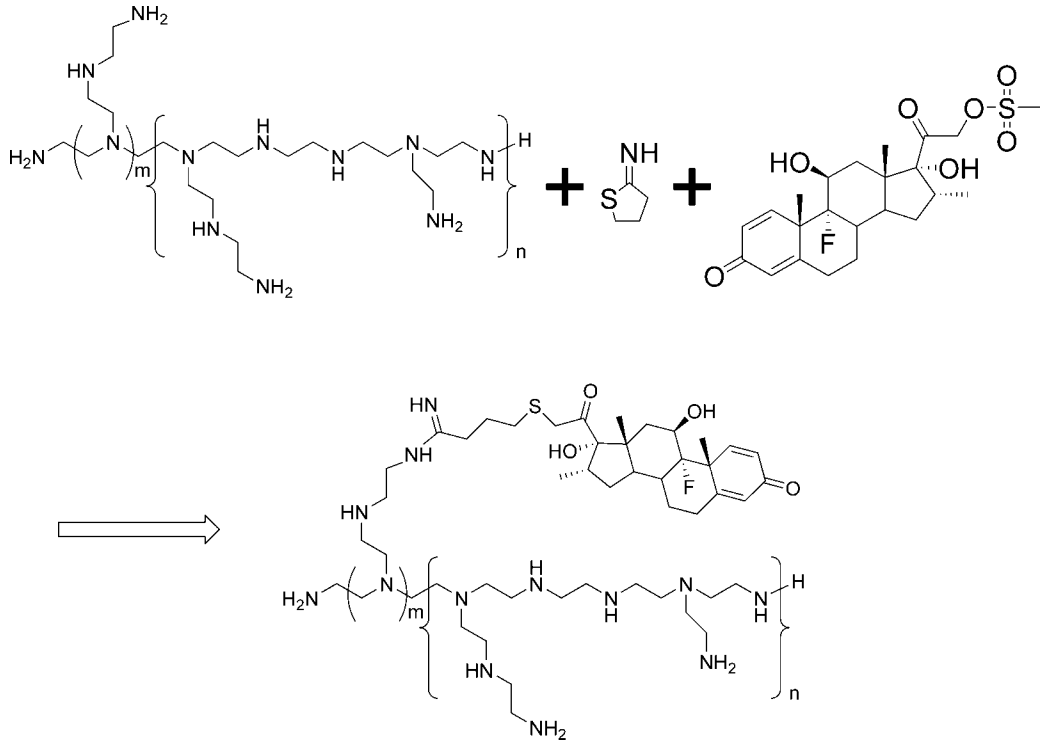
Cytotoxicity Assay. Evaluation of cytotoxicity was performed by the MTT assay (*13*). Cells were seeded at a density of 2×10^4 cells/well in 96 well microassay plates and were incubated for 1 day before adding the polymers. After the addition of each polymer, cells were further incubated for 24 h at 37 °C. After the incubation, 24 μL of 2 mg/mL MTT solution in DPBS was added. The cells were incubated for 4 h at 37 °C and then MTT-containing medium was removed, and 150 μL of DMSO was added to dissolve the formazan crystal formed by live cells. Absorbance was measured at 570 nm using a microplate reader (VersaMax, Molecular Devices).

Fluorescence Labeling of PEI and PEI–Dexa and Complex Formation with Plasmid DNA. PEI and PEI–Dexa (2 mg/mL) were prepared in 0.1 M sodium bicarbonate and mixed with the reactive Alexa Fluor 488 dye followed by stirring for 1 h at room temperature. Each reaction mixture was dialyzed (MWCO 1000) against pure water and freeze-dried yielding a fluorescent product. The Alexa488-labeled PEI or PEI–Dexa and 1.0 μg of plasmid DNA were mixed in 200 μL of FBS-free DMEM (GIBCO, Gaithersburg, MD) to form complexes at a charge ratio of 4. The mixture was incubated for 30 min at room temperature. DNA-linked dendrimer solution was then added to the cells and incubated for the indicated time prior to imaging. The complexes were added to the cells and incubated for 24 h before imaging experiments.

Cell Culture Preparation for Microscopy. 293 cells were grown in a cell culture dish (T25, Falcon), in a DMEM medium supplemented with antibiotic–antimycotic agent (GIBCO) and 10% FBS (GIBCO). The cells were maintained in an incubator with a humidified atmosphere containing 5% CO_2/95% air. Approximately 2×10^4 cells per well were seeded in bare cover glass (22 mm sq, No. 1 Dow Corning, Corning, NY) the day before the experiment, and the cells were maintained with serum-free DMEM. The luciferase expression plasmid (pCN-Luci) was used to prove that the dynamics and localization of polyethyleneimine (PEI) dendrimer and PEI–dexamethasone (PEI–Dexa) conjugated fluorescent dye Alexa 488. HEK 293 cells were examined by adding the DNA-linked functional dendrimer in cover glass before 24 h. Before initiating an experiment, the medium was then removed, and the adherent cells were rinsed twice with DPBS to remove the unbound complexes. A cover glass was placed on the all-side polished dove prism (BK7, 15 mm × 63 mm × 15 mm, n = 1.522, Korea Electro-Optics Co., Ltd., Korea). Surface and interior localization of the polymer/DNA complexes were detected using the epifluorescence and TIRF microscope. Nomarski DIC imaging was used to examine the details of the living cell structure.

Confocal Microscopy Experiments. 293 cells were seeded at a density of 2×10^5 cells/well on a cover glass (18 mm sq) that was spread in each well of a 6 well plate (Falcon) and incubated at 37 °C for a day. Alexa Fluor 488-labeled PEI–Dexa/plasmid DNA complexes were prepared at a 4/1 weight ratio (polymer/plasmid DNA). The amount of plasmid DNA was

Scheme 1. Synthesis Scheme of Polyethylenimine-Dexamethasone (PEI-Dexa)



fixed at 2 μg per well. The polymer/plasmid DNA complex was added to the cells and incubated for 24 h in 10% FBS-containing media. For nucleus labeling, cells were washed with PBS and further incubated for 30 min with 1.8 mL (4 μM) Hoechst 33342 dye (Molecular Probes, U.S.A.). The cells were then finally washed with PBS, and the cells were observed using confocal laser-scanning microscopy (Radiance 200 MP, Bio-Rad, U.K.).

Combined System of Nomarski DIC and TIRFM. We used a combined system of DIC and TIRF microscope for the real-time detection of polymer/DNA complexes localization in living 293 cells. The combined microscope system was similar to the system reported recently (*14*). A 100× (Olympus UPLFL 100×/1.3 N.A., W.D. 0.1) oil immersion objective lens was used for the image acquisition. A charge-coupled device (CCD) camera (Cascade 512B, Photometrics, Tucson, AZ) was mounted on the top of the microscope. The CCD exposure time was 100 ms. The combined system, which we integrated, consists of an upright Olympus BX51 microscope (Olympus Optical Co., LTD, Shinjuku-ku, Tokyo, Japan) equipped with a DIC slider (U-DICT, Olympus) and a Hg lamp for epifluorescence illumination. DIC imaging was used to examine the image and the details of the living cell structure, and epifluorescence imaging was used to detect the distribution of the polymer/DNA complexes in the bulk. The epifluorescence filter cube consisted of U-MWB2 (excitation filter, 460–490 nm; barrier filter, 520 nm; dichromatic mirror, 500 nm, Olympus Optical Co., Ltd., Shinjuku-ku, Tokyo, Japan). The TIRFM imaging was used to detect complexes within the HEK 293 cells. An argon ion laser at 488 nm with a 30 mW output (model 532-LAP-431–220, Melles Griot, Irvin, CA) was used as the excitation source for TIRF. The bare cover glass (No.1 Corning, 22 mm square) incubating the cells was placed on the all-side polished dove prism (BK7, 15 mm × 63 mm × 15 mm, n =1.522, Korea Electro-Optics Co., Ltd., Korea). The cover glass and the prism were index-matched with a drop of immersion oil (Immersol 518F, Zeiss, n =1.518). The laser beam was directed through the prism toward the cover glass/media interface. The angle of incidence, θ_i, was slightly greater than 72°. The laser beams were transmitted through an optical pinhole to eliminate extraneous light and plasma lines and to reduce the laser diameter. A Uniblitz mechanical shutter (model LS3Z2, Vincent Associates, Rochester, NY) was used to reduce photobleaching. The shutter was controlled by a model VMM-D1 shutter driver. All the experiments were performed on the all-side polished dove prism without moving the sample. MetaMorph 6.3 software (Universal Imaging Co., Downingtown, PA) was used to collect the image of the individual single molecules and to process the data.

RESULTS

Synthesis and Properties of PEI–Dexa. In this report, we conjugated low molecular weight PEI with the nucleus-targeting glucocorticoid dexamethasone and applied it to nonviral gene delivery experiments. PEI–dexamethasone, referred to as PEI–Dexa in this study, is one kind of functional water-soluble lipopolymers with nucleus receptor targeting characteristics. As described in Scheme 1, dexamethasone was efficiently conjugated by using the method recently reported (*8*, *11*). In addition to the pH sensitiveness of the linkage, the benefit of this approach was that there was no cationic charge sacrifice effect. The ^{1}H NMR data of the product is presented and each proton peak is identified (Figure 1). The peak intensity ratio was calculated between the ethyl protons of PEI backbone and the two methyl protons at 13′ and 16′ position of the five-numbered ring of dexamethasone (δ = 0.7–0.9 ppm). From the ^{1}H NMR calculations, it was observed that one mole of dexamethasone was conjugated per 1.3 mol of PEI.

Analysis of Complex Formation by Agarose Gel Electrophoresis and PicoGreen Reagent Assay. The complex formation of PEI–Dexa with plasmid DNA was investigated by agarose gel electrophoresis and PicoGreen reagent assay. Polymer/DNA complexes were prepared at various weight ratios ranging from 0.1 to 0.5. As shown in Figure 2A,B, PEI–Dexa was more effective in retardation of complexes at each weight ratio, and it was further approved by PicoGreen reagent assay. We have already reported the same approach for polyplexes

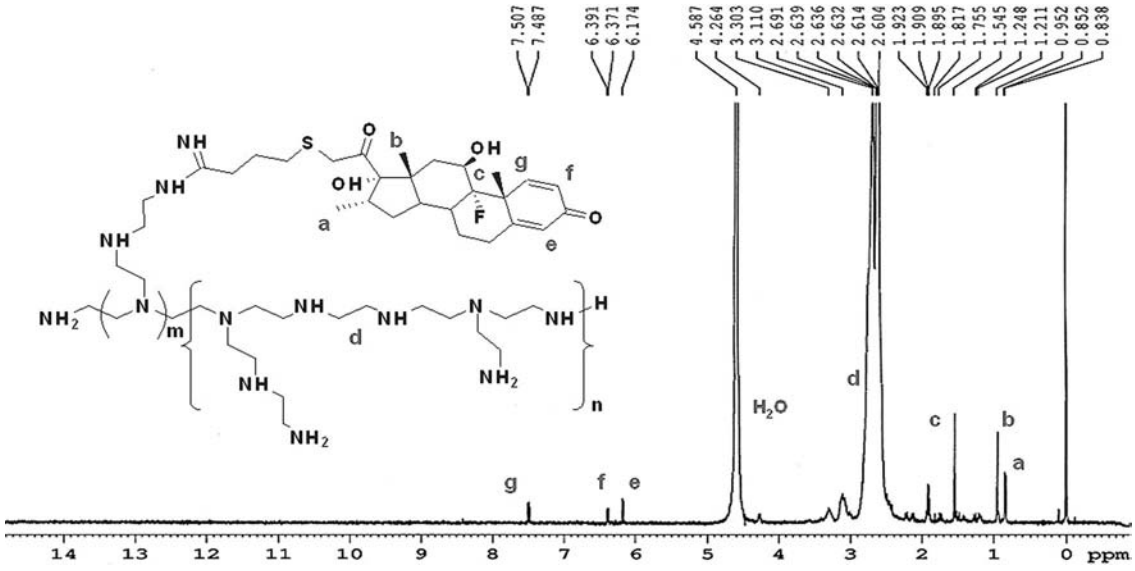


Figure 1. [1]H NMR of PEI–Dexa.

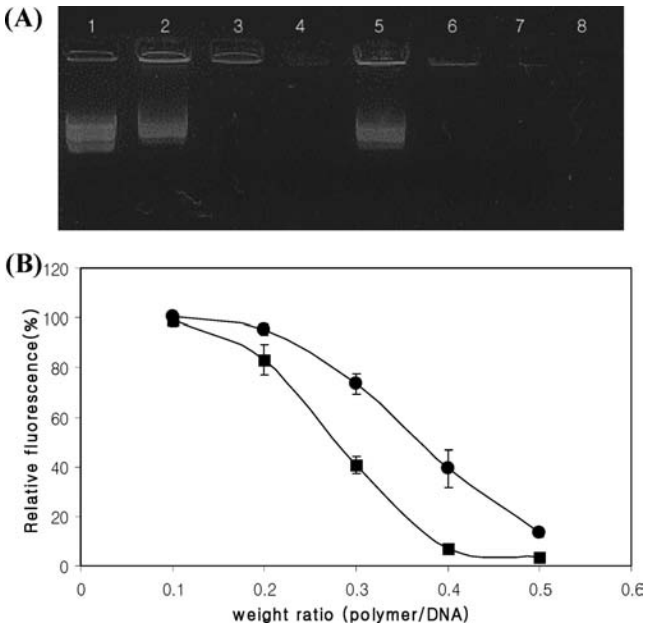


Figure 2. The DNA complexation assay. (A) Agarose gel retardation assay. Plasmid DNA only (lane 1, 5), polymer/DNA weight ratio 0.1 (lane 2, 6), 0.3 (lane 3, 7), 0.5 (lane 4, 8). PEI 2kD (lane 2–4) and PEI–Dexa (lane 6–8). (B) PicoGreen reagent assay at various weight ratios. PEI 2 kDa (●) and PEI–Dexa () ($n = 3$).

and proved that this application is much more effective and sensitive than using EtBr for the characterization of polyplexes (*12*). For PEI–Dexa, the fluorescence intensity decreased more rapidly compared to that of PEI 2kDa, which means that PEI–Dexa can construct more mature complexes inhibiting the PicoGreen reagent from binding the uncomplexed DNA. We think that there is another important factor governing the effective complex formation between PEI–Dexa and DNA compared to PEI. Even though the charge density of PEI–Dexa is lower at the same weight ratio than PEI, the conjugated dexamethasones will function as hydrophobic cores that may facilitate the complex formation in addition to the process of charge neutralization. So it is considered that the presence of hydrophobic dexamethasones may contribute to the complex formation and collapse into complexed particles more effectively with plasmid DNA than PEI.

Size Measurements of the PEI-Dexa/Plasmid DNA Complex. PEI/DNA and PEI–Dexa/DNA complexes were prepared at various weight ratios (polymer/DNA) and the mean particle sizes and the ζ-potential values of polyplexes were measured using the Zetasizer Nano ZS system. As presented in Figure 3, there was no remarkable difference in the mean diameter between PEI/DNA and PEI–Dexa/DNA complexes at the weight ratios tested. In addition, for ζ-potential experiments, PEI–Dexa/DNA complexes showed lower values compared to PEI/DNA complexes. Because the particle sizes of PEI–Dexa/DNA complexes are very similar to those of PEI/DNA complexes and the ζ-potentials of PEI–Dexa/DNA show a few lower values at the same conditions, it is likely that other factors may contribute to the enhanced transfection efficiency of PEI–Dexa compared to PEI.

Transfection Experiments. Low molecular weight PEI (2kDa) or PEI–Dexa was mixed with plasmid DNA at various weight ratios and each complex was evaluated in terms of the transfection efficiency in 293 and HepG2 cells in the presence of 10% FBS (Figure 4A,B). PEI 25kDa and PAMAM polymer was used as positive control reagents. After 24 h of transfection, cells were harvested for assaying the expressed luciferase activity. As in the previous report (*15*), the transfection efficiency of low molecular weight PEI was not remarkable at low weight ratios. In comparison, PEI–Dexa showed a greater increased level of gene expression compared to native PEI 2kDa at all weight ratios tested. As compared with the transfection efficiency of native PEI, the gene expression level of PEI–Dexa increased by 1 order of magnitude for HepG2 and at least 2 orders for 293 cells. Even though the transgene expression level was lower than PEI 25kDa for both cell lines, PEI–Dexa showed comparable transfection efficiency for 293 cells and one order of increased efficiency for HepG2 at weight ratio 8 (polymer/DNA) in comparison with PAMAM. We also studied the effect of dexamethasone incubation on transfection efficiency at different concentration ranges from 10 to 50 nM. As shown in Figure 4C, we observed that the transfection efficiency of PEI–Dexa/DNA constructed at weight ratio 2 apparently decreased to 15%, whereas no competition effects were detected for PEI/DNA.

Cytotoxicity Assay Results. The cytotoxicity of PEI–Dexa was examined and compared with PEI and PAMAM at various concentration ranges for 293 and HepG2 cells. As shown in Figure 5, PEI–Dexa showed no toxicity at the concentration ranges tested in this experiment, whereas PEI 25kDa displayed

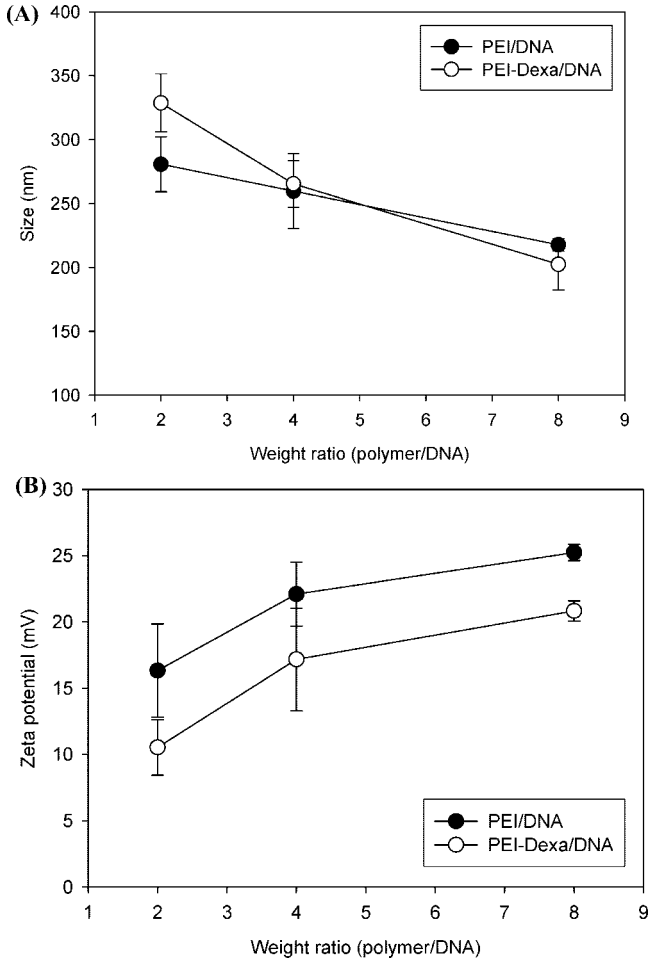


Figure 3. The average size data (A), and ζ-potential values (B) of PEI/DNA and PEI–Dexa/DNA complexes at various weight ratios. Each value is the average plus or minus the standard deviation of three different experiments.

cytotoxicity with increasing concentration levels. This result indicates that dexamethasone conjugated to low molecular weight PEI did not cause any harmful effects at the concentration ranges for the cell lines tested in these experiments.

Confocal Microscopy and TIRFM/DIC Microscopy Experiments. To identify the localization of polyplexes inside cells, confocal microscopy and TIRFM/DIC microscopy experiments were performed in parallel and compared. Each complex constructed at weight ratio 4 (polymer/DNA) was incubated with 293 cells and the difference in cell-associated fluorescence was monitored. Alexa 488 was used to label PEI and PEI–Dexa for complex-mediated fluorescence monitoring. The amount of labeled Alexa 488 for each polymer was calculated using the molar extinction coefficient of the dye at 494 nm (71 000 cm^{-1} M^{-1}), and each value was 2.3×10^{-4} and 4.5×10^{-5} moles of dye per 4.0 μg of PEI and PEI–Dexa, respectively. The labeling efficiency for native PEI was about five times higher than PEI–Dexa.

As shown in Figure 6, many fluorescent complexes were found inside the nucleus in the confocal microscopy image of Alexa 488-labeled PEI–Dexa/plasmid DNA complexes on 293 cells. In addition, in the TIRF/DIC microscopy images, more PEI–Dexa/DNA complexes were found in the nucleus region compared to PEI 2kD/DNA complexes (Figure 7). These results clearly indicate that PEI–Dexa/DNA complexes were more effectively translocated into the nucleus than native PEI 2kDa. This efficient translocation into the nucleus may contribute to the higher transfection efficiency of PEI–Dexa at a lower polymer concentration.

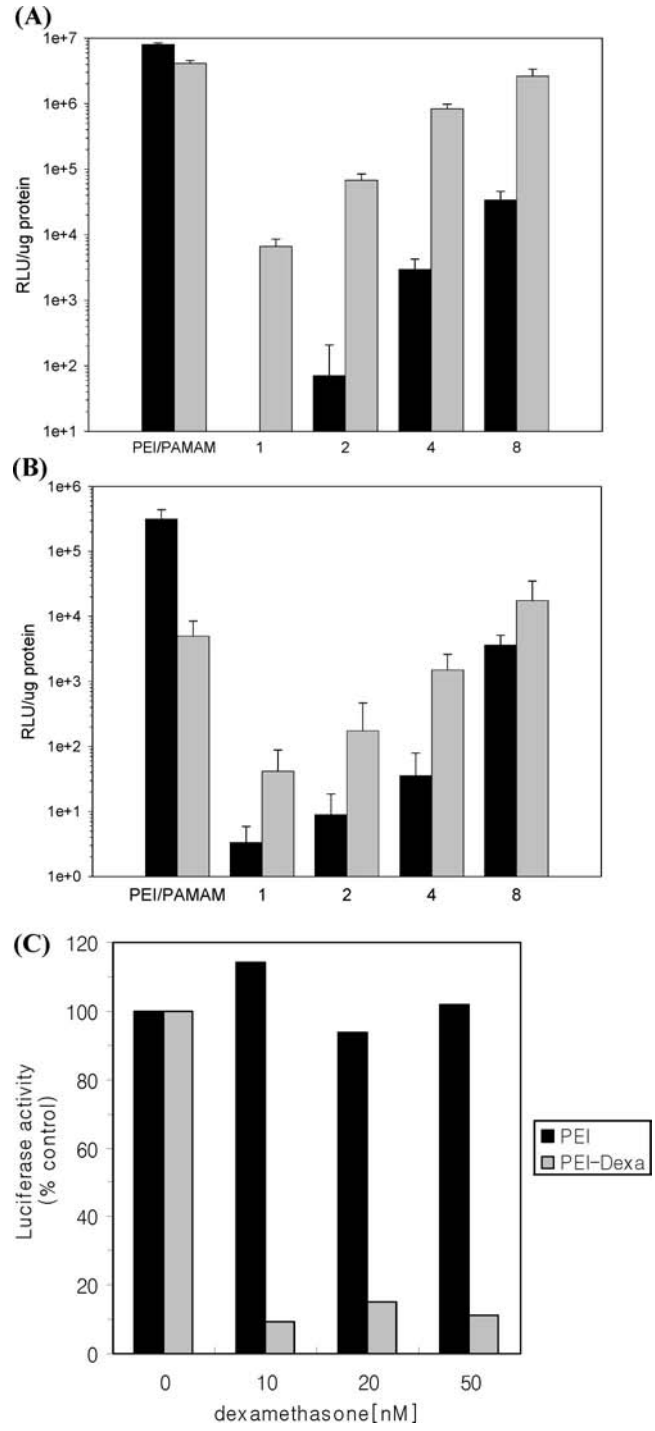


Figure 4. Transfection efficiency of PEI–Dexa for 293 cells (A) and HepG2 cells (B). PEI/PAMAM indicates the control data for PEI 25kDa (black) and PAMAM (gray). The numbers in the *x*-axis are the weight ratios of polymer/DNA complexes for PEI 2kDa (black bars) and PEI–Dexa (gray bars). The competition effects of dexamethasone incubation with each polyplex on transfection efficiency for HepG2 at different nanomolar concentrations (C). Each polyplex was constructed at the weight ratio of 2 and was introduced to cells with dexamethasone. The data are presented as average percent control values of three results of the expressed luciferase activity compared to the nontreated one.

DISCUSSION

The effective cell-specific targeting, endosomal escape, and nuclear localization are key factors for nonviral vectors to

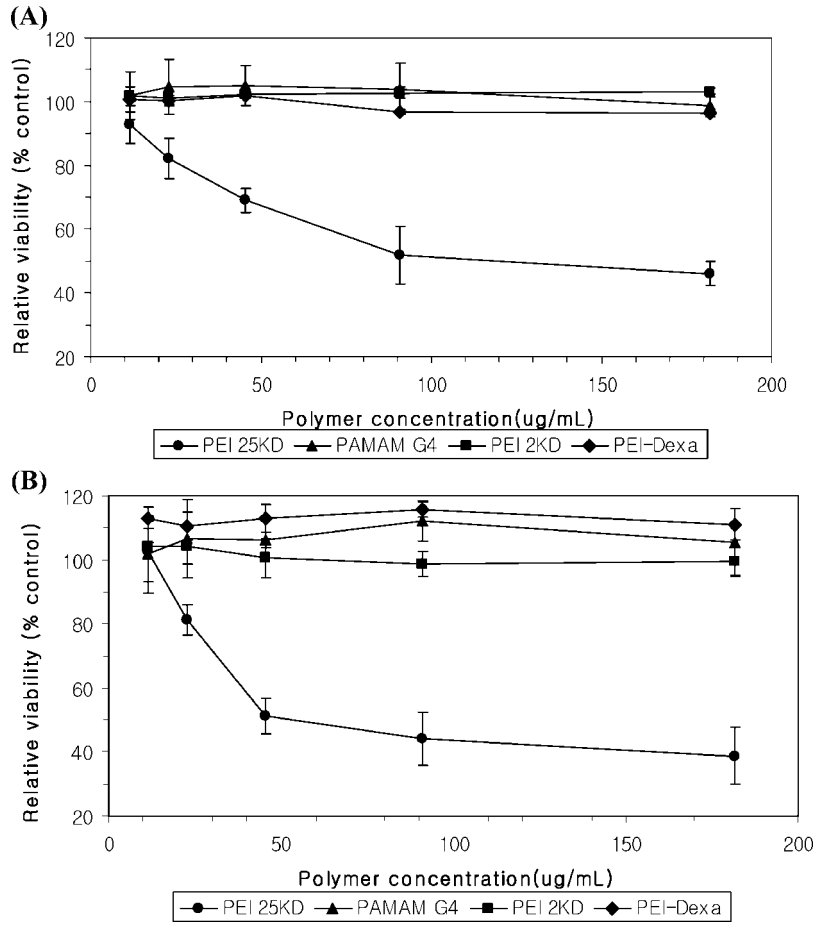


Figure 5. Cytotoxicity assay for 293 cells (A) and HepG2 cells (B) by MTT assay. Relative cell viability was calculated assuming the absorbance at 570 nm of intact control cells to be 100%. Each value is the average plus or minus the standard deviation of three different experiments.

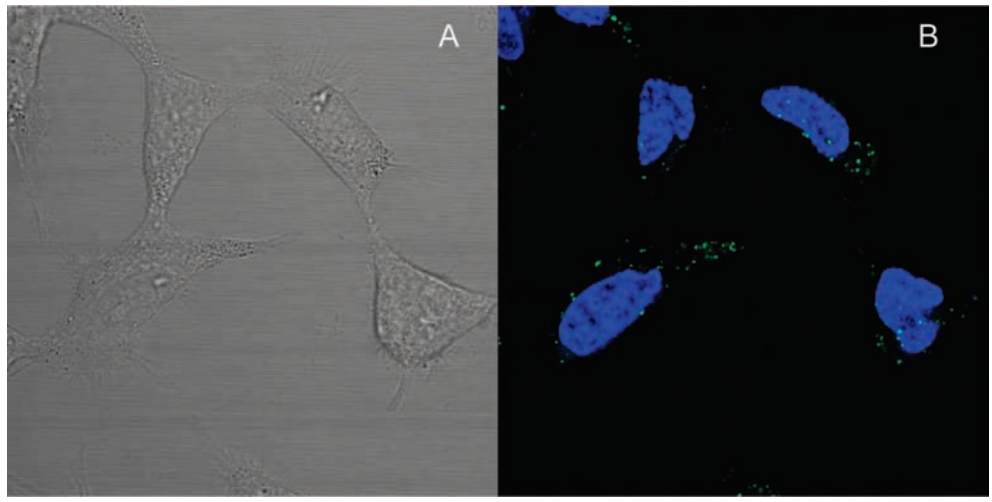


Figure 6. Confocal microscopy images of 293 cells incubated with PEI–Dexa/DNA complexes (B). The complex was prepared as described in Experimental Methods. Hoechst 33342 was used to stain the nucleus (blue) and Alexa 488-labeled polymer was used to localize the complexes (green). The image shown in (A) is the respective transmitted light image of the same field.

improve transfection efficiency (*16–18*). Nuclear localization signal peptides have been employed to increase efficiency for nondividing cells as well as dividing cells (*19, 20*).

PEI 25kDa showed the highest gene transfection efficiency among the polymer vectors that have been reported so far. However, the cytotoxicity of the high molecular weight PEI is a major obstacle in application of the polymer to clinical gene therapy approach. So, low molecular weight PEI 2kDa has been investigated as a gene carrier, because it is relatively nontoxic compared to the higher molecular weight PEI derivatives and it showed remarkable level of transfection efficiency at high polymer/DNA ratios (*15, 21–24*). Many studies have been conducted to modify low molecular weight PEI for enhanced functionality and targeting activity using the polymer as a starting material. In some reports, it was attempted to construct hyperbranched PEI derivatives with high molecular weight using low molecular weight PEI as a building block and to introduce various biodegradable linkages in the backbone (*25–27*). In

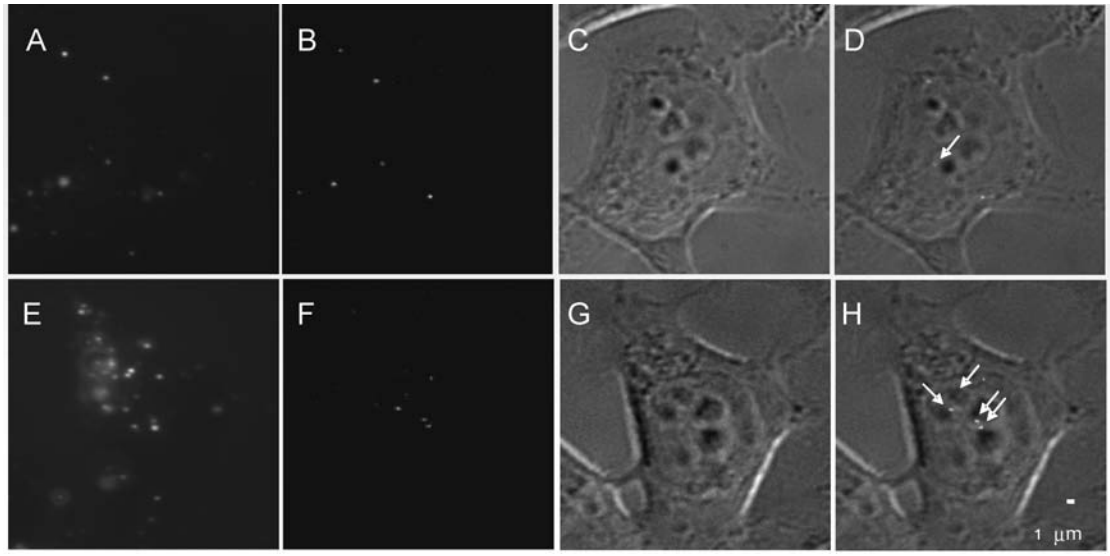


Figure 7. The internalization of polymer/plasmid DNA complexes in living human embryonic kidney 293 cells using various detection techniques of optical microscopes. Epifluorescence: light source, Hg lamp. TIRFM: light source, argon ion laser 488 nm; incident angle θ_i, 72°. DIC: light source, halogen lamp; DIC slider, U–DICT. The images are epifluorescence (A, E), TIRFM (B, F), Nomarski DIC images (C, G), and the merged images of TIRFM and DIC (D, H) of PEI 2kDa/DNA complexes at 4/1 weight ratio (top panels) and PEI–Dexa/DNA complexes at 4/1 weight ratio (bottom panels). The arrows indicate the polymer/DNA complexes.

another study, cholesterol was conjugated to low molecular weight PEI as a hydrophobic moiety to increase membrane perturbation effect leading to enhanced gene delivery, and they named the system as "water-soluble lipopolymer" (*28*).

We reported that the preincubation of free dexamethasone could increase the polyplex-mediated gene transfection efficiency and that it could be attributed to the nuclear pore dilation effect of the drug (*29*). However, due to the reduced solubility of dexamethasone in water, the emulsification step is generally needed using organic solvents and/or other surfactants, which may cause negative effects to cell viability. So it is needed to prepare water-soluble dexamethasone derivatives to make other emulsifying additives unnecessary. The recent development of a novel functional liposomal system known as spermine–dexamethasone provided some valuable characteristics as a nonviral vector system (*8*). The liposome is composed of a cationic spermine headgroup and a nuclear-targeting hydrophobic ligand, dexamethasone, which showed remarkable gene transfection efficiency. Our group also recently reported the synthesis of dexamethasone-conjugated PAMAM, and that the water-soluble conjugate polymer showed higher transfection efficiency than PEI 25kDa in a specific cell line in vitro (*11*).

In line with the previous reports, we attempted to prepare novel functional water-soluble lipopolymeric gene carriers by conjugating nontoxic low molecular weight PEI and dexamethasone. Therefore, PEI–Dexa may be a nuclear-targeting carrier with the functions of carrying the cargo attached to it into the nucleus and dilating nuclear pore complexes. These properties may contribute synergistically to the enhanced transfection efficiency of PEI–Dexa. Indeed, PEI–Dexa showed the enhanced gene transfection efficiency at lower polymer concentrations compared to native PEI, and the transfection efficiency of PEI–Dexa was greatly affected in the presence of dexamethasone for such conditions as presented in Figure 4C.

So, it is presumed that there may be two possible explanations for the enhanced gene transfection efficiency. First, PEI–Dexa is one of the hydrophobic group-containing lipopolymers, which might have membrane perturbation effect like many other cationic liposomes including the water-soluble lipopolymer, PEI–cholesterol. Second, based upon the previous microscope observations that more PEI–Dexa/plasmid DNA complexes were found in the nucleus region compared to PEI 2kDa/DNA complexes, it is possible to propose that PEI-conjugated dexamethasone might have contributed to the enhanced nucleus-localization activity of the complexes causing greater increased transfection efficiency.

Taken together, the results suggest that the conjugation of a glucocorticoid to a polymeric gene carrier may have two favorable effects. First, because dexamethasone is prescribed as a drug for the treatment of inflammation and autoimmune diseases, PEI–Dexa may be a water-soluble lipopolymeric prodrug that enhances the solubility of dexamethasone. Therefore, PEI–Dexa may have dual functions as a water-soluble steroid drug and a gene carrier for combinational approaches of drug/gene therapy. Second, in addition to the nuclear pore complex dilation effect, PEI–Dexa could act as a ligand for intracellular glucocorticoid receptors that are present in mammalian cells. So it is expected that PEI–Dexa may function as a potent nucleus-targeting signal following the ligand–receptor interaction, and the receptor may facilitate the translocation of dexamethasone-decorated complexes into the nucleus and also may function as a reagent that makes the nuclear membrane more vulnerable to the nanoparticles by enlarging the nuclear pores at the same time.

ACKNOWLEDGMENT

This research was supported by the Ministry of Science and Technology (M10534030003-06N3403-00310), by grants from the KBRDG Initiative Research Program (F104AD010011-06A0401-01110), and by the Korea Science and Engineering Foundation (R01-2006-000-10617-0) in Korea.

LITERATURE CITED

(1) Vijayanathan, V., Thomas, T., and Thomas, T. J. (2002) DNA nanoparticles and development of DNA delivery vehicles for gene therapy. *Biochemistry 41,* 14085–94.

(2) Hood, J. D., Bednarski, M., Frausto, R., Guccione, S., Reisfeld, R. A., Xiang, R., and Cheresh, D. A. (2002) Tumor regression by targeted gene delivery to the neovasculature. *Science 296,* 2404–7.

(3) Zhang, Y., Boado, R. J., and Pardridge, W. M. (2003) In vivo knockdown of gene expression in brain cancer with intravenous RNAi in adult rats. *J. Gene Med. 5*, 1039–1045.
(4) Mahato, R. I. (2005) Water insoluble and soluble lipids for gene delivery. *Adv. Drug Delivery Rev. 57*, 699–712.
(5) Adcock, I. M., and Caramori, G. (2001) Cross-talk between proinflammatory transcription factors and glucocorticoids. *Immun. Cell Biol. 79*, 376–84.
(6) Kastrup, L., Oberleithner, H., Ludwig, Y., Schafer, C., and Shahin, V. (2006) Nuclear envelope barrier leak induced by dexamethasone. *J. Cell. Physiol. 206*, 428–34.
(7) Shahin, V., Albermann, L., Schillers, H., Kastrup, L., Schafer, C., Ludwig, Y., Stock, C., and Oberleithner, H. (2005) Steroids dilate nuclear pores imaged with atomic force microscopy. *J. Cell. Physiol. 202*, 591–601.
(8) Gruneich, J. A., Price, A., Zhu, J., and Diamond, S. L. (2004) Cationic corticosteroid for nonviral gene delivery. *Gene Ther. 11*, 668–674.
(9) Rebuffat, A., Bernasconi, A., Ceppi, M., Wehrli, H., Verca, S. B., Ibrahim, M., Frey, B. M., Frey, F. J., and Rusconi, S. (2001) Selective enhancement of gene transfer by steroid-mediated gene delivery. *Nat. Biotechnol. 19*, 1155–61.
(10) Rebuffat, A. G., Nawrocki, A. R., Nielsen, P. E., Bernasconi, A. G., Bernal-Mendez, E., Frey, B. M., and Frey, F. J. (2002) Gene delivery by a steroid-peptide nucleic acid conjugate. *FASEB J. 16*, 1426–8.
(11) Choi, J. S., Ko, K. S., Park, J. S., Kim, Y. H., Kim, S. W., and Lee, M. (2006) Dexamethasone conjugated poly(amidoamine) dendrimer as a gene carrier for efficient nuclear translocation. *Int. J. Pharm. 320*, 171–8.
(12) Choi, J. S., Nam, K., Park, J. Y., Kim, J. B., Lee, J. K., and Park, J. S. (2004) Enhanced transfection efficiency of PAMAM dendrimer by surface modification with L-arginine. *J. Controlled Release 99*, 445–56.
(13) Plumb, J. A., Milroy, R., and Kaye, S. B. (1989) Effects of the pH dependence of 3-(4,5-dimethylthiazol-2-yl)-2,5-diphenyltetrazolium bromide-formazan absorption on chemosensitivity determined by a novel tetrazolium-based assay. *Cancer Res. 49*, 4435–4440.
(14) Lee, S., Choi, J. S., and Kang, S. H. (2007) Combination of DIC with Prism-Type Total Internal Fluorescence Microscope for Direct Observation of PAMAM Dendrimer Nanoparticle as a Gene Delivery in Living Human Cells. *J. Nanosci. Nanotechnol.*, in press.
(15) Fischer, D., Bieber, T., Li, Y. X., Elsasser, H. P., and Kissel, T. (1999) A novel nonviral vector for DNA delivery based on low molecular weight, branched polyethylenimine: Effect of molecular weight on transfection efficiency and cytotoxicity. *Pharm. Res. 16*, 1273–1279.
(16) Dean, D. A., Strong, D. D., and Zimmer, W. E. (2005) Nuclear entry of nonviral vectors. *Gene Ther. 12*, 881–90.
(17) Shea, L. D., and Houchin, T. L. (2004) Modular design of nonviral vectors with bioactive components. *Trends Biotechnol. 22*, 429–31.
(18) Johnson-Saliba, M., and Jans, D. A. (2001) Gene therapy: optimizing DNA delivery to the nucleus. *Curr. Drug Targets 2*, 371–99.
(19) Chan, C. K., and Jans, D. A. (1999) Enhancement of polylysine-mediated transferrinfection by nuclear localization sequences: polylysine does not function as a nuclear localization sequence. *Hum. Gene Ther. 10*, 1695–702.
(20) Morris, M. C., Chaloin, L., Mery, J., Heitz, F., and Divita, G. (1999) A novel potent strategy for gene delivery using a single peptide vector as a carrier. *Nucleic Acids Res. 27*, 3510–7.
(21) Kunath, K., von Harpe, A., Fischer, D., Petersen, H., Bickel, U., Voigt, K., and Kissel, T. (2003) Low-molecular-weight polyethylenimine as a non-viral vector for DNA delivery: comparison of physicochemical properties, transfection efficiency and in vivo distribution with high-molecular-weight polyethylenimine. *J. Controlled Release 89*, 113–25.
(22) Shin, J. Y., Suh, D., Kim, J. M., Choi, H. G., Kim, J. A., Ko, J. J., Lee, Y. B., Kim, J. S., and Oh, Y. K. (2005) Low molecular weight polyethylenimine for efficient transfection of human hematopoietic and umbilical cord blood-derived CD34+ cells. *Biochim. Biophys. Acta 1725*, 377–84.
(23) Morimoto, K., Nishikawa, M., Kawakami, S., Nakano, T., Hattori, Y., Fumoto, S., Yamashita, F., and Hashida, M. (2003) Molecular weight-dependent gene transfection activity of unmodified and galactosylated polyethyleneimine on hepatoma cells and mouse liver. *Mol. Ther. 7*, 254–61.
(24) Lampela, P., Raisanen, J., Mannisto, P. T., Yla-Herttuala, S., and Raasmaja, A. (2002) The use of low-molecular-weight PEIs as gene carriers in the monkey fibroblastoma and rabbit smooth muscle cell cultures. *J. Gene Med. 4*, 205–14.
(25) Ahn, C. H., Chae, S. Y., Bae, Y. H., and Kim, S. W. (2002) Biodegradable poly(ethylenimine) for plasmid DNA delivery. *J. Controlled Release 80*, 273–82.
(26) Forrest, M. L., Koerber, J. T., and Pack, D. W. (2003) A degradable polyethylenimine derivative with low toxicity for highly efficient gene delivery. *Bioconjugate Chem. 14*, 934–40.
(27) Gosselin, M. A., Guo, W., and Lee, R. J. (2001) Efficient gene transfer using reversibly cross-linked low molecular weight polyethylenimine. *Bioconjugate Chem. 12*, 989–94.
(28) Han, S., Mahato, R. I., and Kim, S. W. (2001) Water-soluble lipopolymer for gene delivery. *Bioconjugate Chem. 12*, 337–45.
(29) Choi, J. S., and Lee, M. (2005) Effect of dexamethasone preincubation on polymer-mediated gene delivery. *Bull. Korean Chem. Soc. 26*, 1209–1213.

BC070012A

Synthesis and *in Vitro* Evaluation of Novel Star-Shaped Block Copolymers (Blocked Star Vectors) for Efficient Gene Delivery

Yasuhide Nakayama,*[,†,‡] Chiaki Kakei,[†] Ayaka Ishikawa,[†] Yue-Min Zhou,[†] Yasushi Nemoto,[†,‡,§] and Kingo Uchida[||]

Department of Bioengineering, Advanced Medical Engineering Center National Cardiovascular Center Research Institute, Division of Biotechnology and Macromolecular Chemistry, Faculty of Engineering, Hokkaido University, Chemical Products Division, Development Department, Bridgestone Company, and Department of Materials Chemistry, Faculty of Science and Technology Ryukoku University. Received February 11, 2007; Revised Manuscript Received July 29, 2007

Novel 4-branched diblock copolymers consisting of cationic chains as an inner domain and nonionic chains as an outer domain were prepared by iniferter-based living radial polymerization and evaluated as a polymeric transfectant. The cationic polymerization of 3-(*N*,*N*-dimethylamino)propyl acrylamide (DMAPAAm) using 1,2,4,5-tetrakis(*N*,*N*-diethyldithiocarbamylmethyl)benzene as a 4-functional iniferter followed by the nonionic block polymerization of *N*,*N*-dimethylacrylamide (DMAAm) afforded 4-branched diblock copolymers with controlled compositions. By changing the solution or irradiation conditions, 4-branched PDMAPAAms with molecular weights of 10 000, 20 000, and 50 000 were synthesized. In addition, by graft polymerization, PDMAPAAm–PDMAAm blocked copolymers with copolymer composition (unit ratio of DMAAm/DMAPAAm) ranging from 0.18 to 1.0 for each cationic polymer were synthesized. All polymers were shown to interact with and condense plasmid DNA to yield polymer/DNA complexes (polyplexes). A transfection study on COS-1 cells showed that the polyplexes from block copolymers with cationic chain length of approximately 50 000 and a nonionic chain length of 30 000, which were approximately 200 nm in diameter and very stable in aqueous media, had the most efficient luciferase activity with minimal cellular cytotoxicity under a charge ratio of 20 (vector/pDNA). The PDMAPAAm–PDMAAm-blocked, star-shaped polymers are an attractive novel class of nonviral gene delivery systems.

INTRODUCTION

Cationic polymers such as poly(ethylenimine) (PEI) (*1–4*) and poly(*N*,*N*-dimethylaminopropyl acrylamide) (PDMAPAAm) (*5, 6*), which can generate nanoparticles by the formation of polyion complexes, i.e., "polyplexes" with DNA, are highly expected as one of the major carriers in nonviral gene delivery systems due to the many advantages they offer over viral systems (*7–11*). These advantages include blocking of specific immune responses, no restrictions in the size of DNA, and ease of large-scale production. However, the primary obstacle toward implementing an effective gene therapy using cationic polymers remains their relatively inefficient gene transfection *in vivo* when compared to virus vectors.

Recently, to improve gene transfection efficiency using cationic polymers, we designed a series of branched cationic polymers, linear and 3-, 4-, or 6-branched PDMAPAAm as a novel high-performance gene carrier called star vector (*5*), prepared to have the same molecular weights (Mn 18 000) by iniferter (initiator–transfer agent–terminator)-based photoliving radical polymerization (*12, 13*) from the respective multidithiocarbamate-derivatized benzenes (multifunctional iniferters) and DMAPAAm as a cationic monomer. This experiment revealed that the relative gene expression efficiency increased in the degree of branching that may affect the cationic charge density, and that the compaction of DNA polyplexes was stabilized on an increase in the branch number (*5*). However, the *in vivo* transfection efficiency was not satisfactory because of the high interaction between DNA polyplexes, which was caused by the low colloidal stability of the polyplex particles.

On the other hand, the conjugation of cationic polymers with a hydrophilic and biocompatible polymer such as poly(ethylene glycol) (PEG) (*14–18*) has been reported as a major vector modification strategy to improve transfection efficiency (*19–22*). Surface modification of the cationic polymers with PEG was effective in increasing the long circulation time for DNA delivery system, and PEGylation effect for PEI was studied in detail by Kissel and co-workers (*23, 24*). Kim et al. reported that triblocking by PEG of PEI caused the lack of serum inhibition of transfection activity with low cytotoxicity (*19*).

Therefore, it is highly expected that, by linking the nonionic hydrophilic chains with PDMAPAAm-branched polymers, DNA condensation and gene transfection efficiency will be improved by shielding the particles from unspecific interactions and conferring them stability in a similar fashion as PEGylation of polyplexes. To this end, in this study, we report novel structurally well-defined PDMAPAAm-branched polymers blocked with poly(*N*,*N*-dimethyl acrylamide) (PDMAAm), which is a biocompatible nonionic polymer, as a nonionic chain for *in vitro* gene delivery. The blocked, branched copolymers were synthesized by photoliving radical polymerization of DMAPAAm using benzene derivatized from four dithiocarbamate groups as a 4-functional iniferter followed by block copolymerization of DMAAm. Their DNA-binding properties were studied using dynamic light scattering (DLS). The *in vitro* transfection activity

* To whom correspondence should be addressed. Department of Bioengineering, Advanced Medical Engineering Center, National Cardiovascular Center Research Institute, 5-7-1 Fujishiro-dai, Suita, Osaka 565-8565, Japan. Telephone: (+81) 6-6833-5012(ex. 2624). Fax: (+81) 6-6872-8090 E-mail: nakayama@ri.ncvc.go.jp.

[†] National Cardiovascular Center Research Institute.

[‡] Hokkaido University.

[§] Bridgestone Company.

[||] Ryukoku University.

10.1021/bc070045q CCC: $37.00 © 2007 American Chemical Society
Published on Web 10/09/2007

as well as the cytotoxicity of the block copolymer-based polyplexes was evaluated using COS-1 cells.

EXPERIMENTAL PROCEDURES

Materials. 1,2,4,5-Tetrakis(bromomethyl)benzene was obtained from Sigma-Aldrich (Milwaukee, WI). Sodium *N*,*N*-diethyldithiocarbamate and *N*,*N*-dimethylacrylamide (DMAAm) were purchased from Wako Pure Chemical Ind., Ltd. (Osaka, Japan), and 3-(*N*,*N*-dimethylamino)propyl acrylamide (DMAPAAm) was from Tokyo Kasei Kogyo Co., Ltd. (Tokyo, Japan). Other chemical reagents were commercially obtained from Wako Pure Chemical Ind., Ltd. DMAAm and DMAPAAm were distilled under reduced pressure before use to remove the stabilizer, and other reagents were purified before use according to the requirements.

The luciferase reporter vector plasmid pGL3 control (3.5 MDa, 5256 bp) was purchased from Promega Inc. (Tokyo, Japan) and was amplified with a competent *E. coli* strain DH5α (Promega) and purified using Maxiprep according to a protocol from QIAGEN (Tokyo, Japan). The purity of the plasmid was checked by electrophoresis on a 1% agarose gel, and the concentration was determined by measuring UV absorbance at 260 and 280 nm. Exgen 500 (liner 22 kDa PEI) was obtained from COSMO BIO Co., Ltd. (Tokyo, Japan).

Polymer Synthesis. PDMAPAAm–PDMAAm 4-branched block copolymers were synthesized by iniferter-based photoliving radical polymerization (*12*, *13*) from 1,2,4,5-tetrakis(*N*,*N*-diethyldithiocarbamylmethyl)benzene as a 4-functional iniferter with DMAPAAm and DMAAm as cationic and nonionic monomers, respectively.

*Synthesis of 4-Functional Iniferter (***2***).* We dissolved 1,2,4,5-tetrakis(bromomethyl)benzene (**1**, 5 g) in ethanol (250 mL) and added sodium *N*,*N*-diethyldithiocarbamate (4.8 equiv for **1**) at 0 °C, followed by stirring at room temperature for 24 h. After filtering out the resulting sodium chloride, the filtrate was concentrated, dissolved in water (200 mL), and the extraction was repeated with ether (50 mL × 3). The organic layer was dried using $MgSO_4$ and condensed to yield iniferter **2**. ^{1}H NMR (in D_2O): δ 1.30–1.26 (t, 24H, -CH_2-CH_3), 3.77–3.69 (q, 8H, -N-CH_2-), 4.07–3.99 (q, 8H, -N-CH_2-), 4.57 (s, 8H, Ar-CH_2S), 7.49 (s, 2H, Ar-H).

Synthesis of PDAPAAm 4-Branched Polymer. The iniferter-based photoliving radical reaction of **2** with DMAPAAm was carried out as follows. A methanol solution (20 mL) of **2** (72 mg, 0.1 mmol) and DMAPAAm (3.43 g, 220 equiv) was placed into a 50 mL quartz crystal tube; subsequently, dry N_2 gas was bubbled into the tube to preclude the air gas from solution for 5 min. The mixture solution was then irradiated for 30 min with a 200 W high-pressure mercury lamp (SPOT CURE, USHIO, Tokyo, Japan) under N_2 atmosphere at room temperature, and the light intensity was set to 1 mW/cm^2 at a wavelength of 250 nm (UVR-1; TOPCON, Tokyo, Japan). The reaction mixture was concentrated and adjusted to an appropriate concentration to purify it by precipitation in a large amount of ether. Reprecipitation was carried out in a methanol–ether system. The last precipitate was dried under vacuum to yield PDMAPAAm 4-branched polymer (conv. 40%). The molecular weight was determined by gel permeation chromatography (GPC) analysis: Mn 50 000. ^{1}H NMR: δ 1.7–1.5 (br, 3H, -C<u>H</u>$_2$-CH- and -CH_2-C<u>H</u>$_2$-CH_2-), 2.0–1.8 (br, 1H, -C<u>H</u>-CO), 2.2–2.1 (br, 6H, -N-C<u>H</u>$_3$), 2.4–2.2 (br, 2H, -C<u>H</u>$_2$-N(CH_3)$_2$), 3.2–3.0 (br, 2H, -NH-C<u>H</u>$_2$-), 7.8–7.4 (br, 1H, -NH). Other branched polymers with different number average molecular weights were also synthesized using a similar procedure by changing the monomer concentration (see Table 1).

Synthesis of PDMAPAAm-PDMAAm 4-Branched Copolymer. The general procedure of the synthesis of PDMAPAAm–PDMAAm 4-branched copolymer is described below. A methanol solution (20 mL) of PDMAPAAm 4-branched polymer (Mn 50 000, 125 mg, 2.5 μmol) and DMAAm (2.97 g, 1200 equiv) was placed into a 50 mL quartz crystal tube and deoxygenated by bubbling with dry N_2 gas for 5 min. The mixture solution was then irradiated for 30 min under the above-mentioned conditions. The reaction mixture was concentrated and precipitated in 500 mL of ether. Reprecipitation was carried out in a methanol–ether system. The last precipitate was dried under

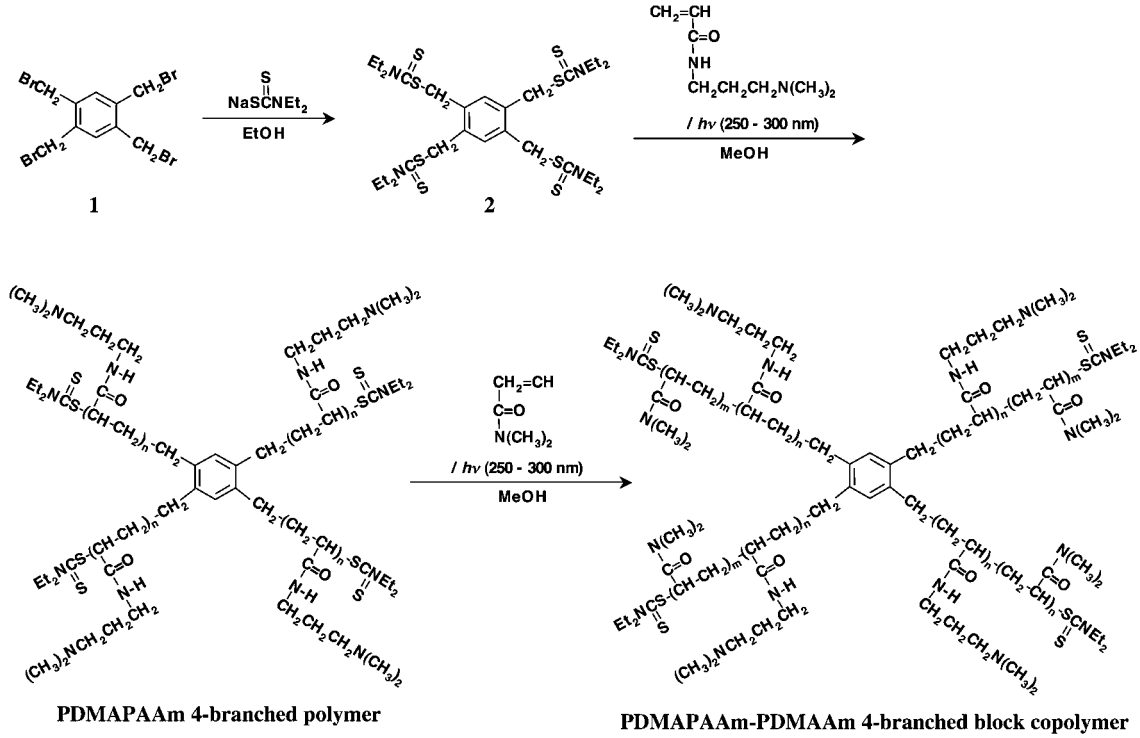


Figure 1. Syntheses of PDMAPAAm 4-branched polymers and PDMAPAAm–PDMAAm 4-branched block copolymers.

Table 1. Reaction Conditions[a] and Molecular Weights of the PDMAPAAm 4-Branched Polymers

			PDMAPAAm 4-branched polymer			
[**2**] (mM)	[DMAPAAm] (M)	irradiation time[b] (min)	conv. (%)	Mn[c] (g/mol)	Mw/Mn[c]	no of DC[d]
5	0.34	30	21	10000	1.3	3.7
5	0.50	30	34	20000	1.4	4.2
5	1.10	30	40	50000	1.4	3.6

[a] Solvent: methanol. [b] Irradiation intensity: 1 mW/cm^2. [c] Setermined by GPC (PEO standard). [d] DC means dithiocarbamate group, and the number of DC was determined by UV spectroscopy.

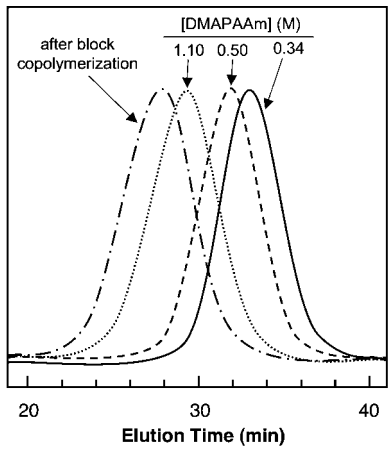


Figure 2. GPC elution curves after polymerization of DMAPAAm from 4-functional iniferter (**2**) as a function of monomer concentration (polymerization conditions were summarized in Table 1) and PDMAPAAm–PDMAAm 4-branched block copolymer (Mn 83 000) obtained after block copolymerization from PDMAPAAm 4-branched polymer (Mn 50 000) under polymerization conditions in Table 2.

vacuum to yield the PDMAPAAm–PDMAAm 4-branched block copolymer (conv. 19%). The total molecular weight was estimated from the integral value of ^{1}H NMR spectra between PDMAPAAm and PDMAAm (see Figure 2): Mn 83 000. ^{1}H NMR (in D_2O): δ 1.0–1.7 (br, 1922H, -C$\underline{H}_2$CH- and -CH$_2$C$\underline{H}_2$CH$_2$-), 1.9 (br, 315H, -CH$_2$C$\underline{H}$- of PDMAPAAm), 2.1 (s, 1890H, -N(C$\underline{H}_3$)$_2$ of PDMAPAAm), 2.3 (br, 630H, -C$\underline{H}_2$N(CH$_3$)$_2$), 2.4–2.7 (br, 331H, -CH$_2$C$\underline{H}$- of PDMAAm), 2.8–2.9 (br, 1986H, -N(C$\underline{H}_3$)$_2$ of PDMAAm), 3.0 (br, 630H, -CONHC$\underline{H}_2$-). Other 4-branched block copolymers with different compositions were also synthesized using a similar procedure by changing the concentrations of PDMAPAAm 4-branched polymer and DMAAm or reaction times (see Table 2).

General Methods. ^{1}H NMR spectra were recorded in D_2O with a 300 MHz NMR spectrometer (Gemini-300; Varian, Palo Alto, CA) at room temperature. GPC analyses in *N*,*N*-dimethylformamide were carried out with a HPLC-8020 instrument (Tosoh, Tokyo, Japan) (column: Tosoh TSKgel α-3000 and α-5000). The columns were calibrated with narrow weight distribution PEG standards (Tosoh). UV–vis spectra in H_2O were recorded with a UV–vis spectrophotometer (UV-1700, Shimadzu Co., Kyoto, Japan).

Preparation of Polymer/Plasmid Complexes. The PDMAPAAm–PDMAAm 4-branched copolymer was dissolved in a saline solution. Aliquots of these solutions (60 μL) were added to the plasmid dissolved in 90 μL of Tris-HCl buffer (pH7.4) to obtain polymer/DNA ratios of 1–20, which correspond to cation/anion (C/A) ratios. The solutions (total volume, 150 μL; plasmid concentration, 20 μg/mL) were mixed using a pipette. After 10 min of complex formation, 25 μL of the complex solutions were added into each well of 24-multiwell dishes for transfection (the amount of DNA added to a well, 0.5 μg/well).

Biophysical Characterization of Polymer/Plasmid Complexes. The ζ-potentials and mean diameters of the polymer/plasmid complexes in a saline solution having the same concentration that was used for transfection at a C/A ratio of 5 were obtained by employing dynamic light scattering (DLS) on an ELS-8000 system (Otuska Co., Osaka, Japan) equipped with a 10 mW He–Ne laser. The mean diameters were determined by cumurant analysis in multimodal setting.

The colloidal stability of polymer/plasmid complexes was studied using DLS at 37 °C and pH 7.4 and 2.0, which was adjusted by 0.1 N HCl solution. The polyplexes were prepared as described above with a C/A ratio of 5. The ionic strength of the suspension was adjusted to 150 mM NaCl.

***In Vitro* Transfection and Cell Viability Assays.** COS-1 cells (approximately 3×10^4 cells per well) were seeded prior to treatment in 24-well plates and grown for 24 h in DMEM (Gibco, Invitrogen Corp., Carlsbad, CA) containing 10% fetal calf serum (Hyclone Laboratories Inc., Logan, UT), penicillin (200 units/mL; ICN Biomedicals Inc., Aurora, OH), and streptomycin (200 mg/mL; ICN) in an atmosphere of 5% CO_2 at 37 °C. Transfections were performed with 0.5 μg of plasmid DNA (pGL3-control) in 24-multiwell dishes in 0.2 mL of OPTI-MEM I (Gibco). After 3 h of incubation, the cells were washed once with PBS(–) and cultured in 1 mL of DMEM containing 10% fetal calf serum for an additional 48 h. The medium was removed and the cells were washed twice with PBS(–). The cells were lysed with 0.2 mL of cell lysis buffer (Promega, Madison, WI) and mixed by vortexing. The lysate was centrifuged at 15 000 rpm for 1 min at 4 °C, and 5 μL of the supernatant was analyzed for luciferase activity using a Luminous CT-9000D (Dia-Iatron, Tokyo, Japan) luminometer. The relative light unit/s (RLU) were converted into the amount of luciferase (pg) using a luciferase standard curve, which was obtained by diluting recombinant luciferase (Promega) in lysis buffer. The protein concentrations of cell lysates were measured by performing a Bio-Rad protein assay (BIO-RAD, Hercules, CA) using bovine serum albumin as a standard. The expressed luciferase represented the amount (mole quantity), which is standardized for the total protein content of the cell lysate. The data are presented as means $\pm$ SD ($n = 5$).

Cytotoxicity was assessed by performing a cell viability assay using the WST-8 method (Dojindo, Kumamoto, Japan). COS-1 cells were seeded 24 h prior to treatment in 96-well plates at 5000 cells per well. Cells were treated under the same conditions used for luciferase assay with 6.2 μL of the transfection mixture including 0.124 μg of pDNA added to each well. They were treated under appropriate conditions for 3 h, washed once with PBS, and cultured in 50 μL of DMEM (Gibco) containing 10% fetal calf serum for an additional 24 h. To each well, 10 μL of WST-8 reagent (5 mmol/L) was added. After 2 h of incubation at 37 °C, absorbance at 450 nm was read in a BIO-RAD microplate reader (model 680). The data are presented as means $\pm$ SD ($n = 5$).

RESULTS AND DISCUSSION

Synthesis and Characterization of the Block Copolymers. The reaction scheme for the preparation of PDMAPAAm–PDMAAm 4-branched block copolymers is depicted in Figure 1. In this reaction, iniferter-based photoliving radical polymerization (*12, 13*), in which chain length can be easily controlled by changing irradiation conditions such as time or

Table 2. Reaction Conditions[a], Molecular Weights, And Composition of PDMAPAAm-PDMAAm 4-Branched Block Copolymers

PDMAPAAm				PDMAPAAm–PDMAAm		
Mn[b] (g/mol)	(mM)	[DMAAm] (M)	irradiation time[c] (min)	conv. (%)	Mn[d] (g/mol)	DMAAm/DMAPAAm[d]
10 000	0.63	0.5	30	6	15 000	0.86
10 000	1.25	0.5	30	5	13 000	0.51
10 000	2.50	0.5	30	3	11 000	0.17
18 000	1.25	0.5	10	7	22 000	0.36
18 000	1.25	0.5	15	8	25 000	0.64
18 000	1.25	0.5	20	9	27 000	0.82
50 000	1.25	0.5	10	13	56 000	0.19
50 000	1.25	1.0	10	15	65 000	0.48
50 000	1.25	1.5	10	19	83 000	1.05

[a] Solvent: methanol. [b] Determined by GPC (PEO standard). [c] Irradiation intensity: 1 mW/cm^2. [d] Polymerization ratios were determined by ^{1}H NMR.

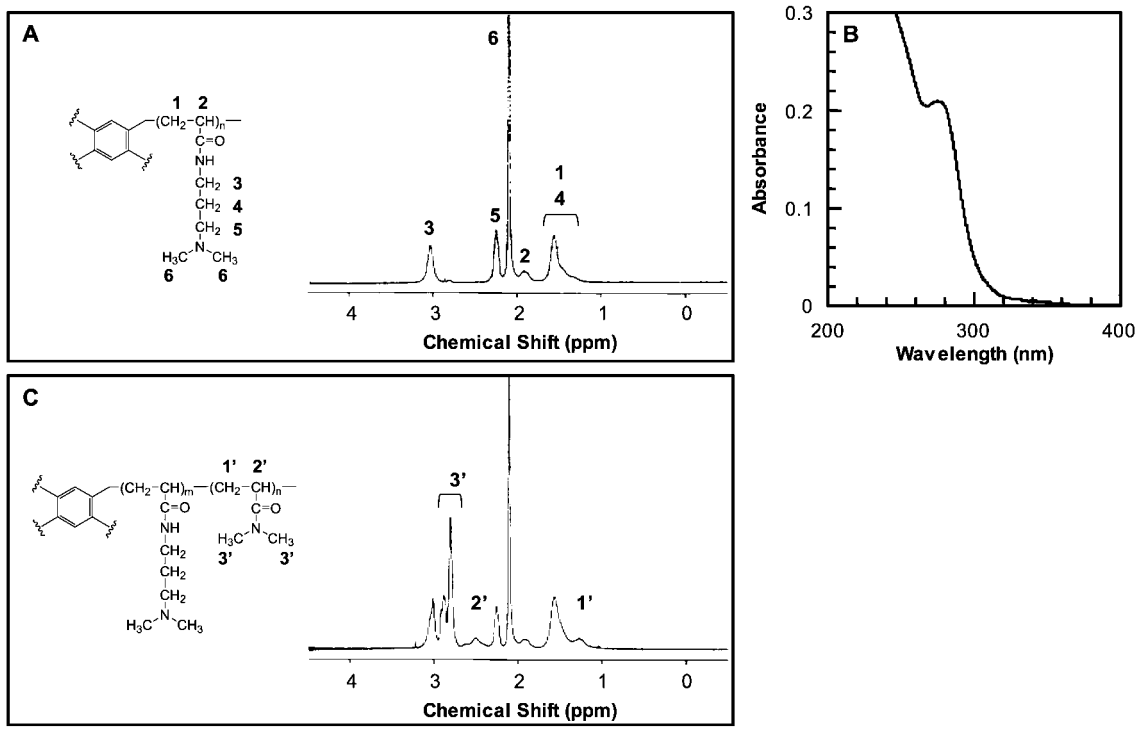


Figure 3. ^{1}H NMR spectra (300 MHz) in D_2O of (A) PDMAPAAm 4-branched polymer and (C) PDMAPAAm–PDMAAm 4-branched block copolymer. (B) Absorption spectrum of PDMAPAAm 4-branched polymer in H_2O. PDMAPAAm 4-branched polymer was prepared by iniferter-based living radical polymerization of 3-(*N*,*N*-dimethylamino)propyl acrylamide initiated from 1,2,4,5-tetrakis(*N*,*N*-diethyldithiocarbamylmethyl)-benzene as a 4-functional iniferter. PDMAPAAm–PDMAAm 4-branched block copolymer was obtained by similar living radical polymerization of *N*,*N*-dimethylacrylamide from PDMAPAAm 4-branched polymer.

light intensity, and solution conditions such as the concentration of iniferter or monomer, was repeated for two different monomers of DMAPAAm and DMAAm. The iniferter-based photoliving radical polymerization was a powerful tool for precise structural design in macromolecules (*5*, *18*, *25*). In a previous paper, we reported that coating materials and surface modification for the improvement of biocompatibility in medical devices were precisely developed (*26*, *27*).

At first, the polymerization of a cationic monomer (DMAPAAm) from 4-functional iniferter (**2**), which was synthesized by the dithiocarbamylation of 1,2,4,5-tetrakis(bromomethyl)benzene (**1**), was performed using a different monomer concentration to obtain PDMAPAAm 4-branched polymers. The preparation conditions are listed in Table 1. Upon 30 min of UV light irradiation at a DMAPAAm concentration of 0.34 M, the initial GPC trace of the iniferter (**2**) with an Mn of 720 g mol^{-1} was completely absent (Figure 2). An increase in the DMAPAAm concentration at a fixed irradiation condition resulted in an increase in the molecular weight with complete shift of the GPC curves toward a high-molecular-weight region, with a narrow polydispersity at 1.3–1.4.

On the other hand, a ^{1}H NMR spectrum showed that no nonreactive monomer and iniferter were detected completely in the all polymers obtained (Figure 3A). In addition, the broad peaks of N-methyl protons originating from the cationic chains were observed at approximately 2.1 ppm. However, the peak of ethyl protons corresponding to the dithiocarbamate group was not detected in the spectrum due to an extremely low existence ratio of the dithiocarbamate group against cationic chains, whereas a UV spectrum showed the remaining dithiocarbamate group (Figure 3B). The number of dithiocarbamate groups in one 4-branched PDMAPAAm molecule ranged from 3.6 to 4.2, which was close to the theoretical value of 4, irrespective of the molecular weigh of PDMAPAAm (Table 1). These results, combined with the afore-mentioned GPC data, indicated that the polymerization of DMAPAAm occurred from iniferter (**2**) via a living radical polymerization mechanism, resulting in the preparation of PDMAPAAm 4-branched cationic polymers. In this reaction, each branch was end-capped almost completely with the dithiocarbamate group, with molecular weights of approximately 10 000, 20 000, and 50 000.

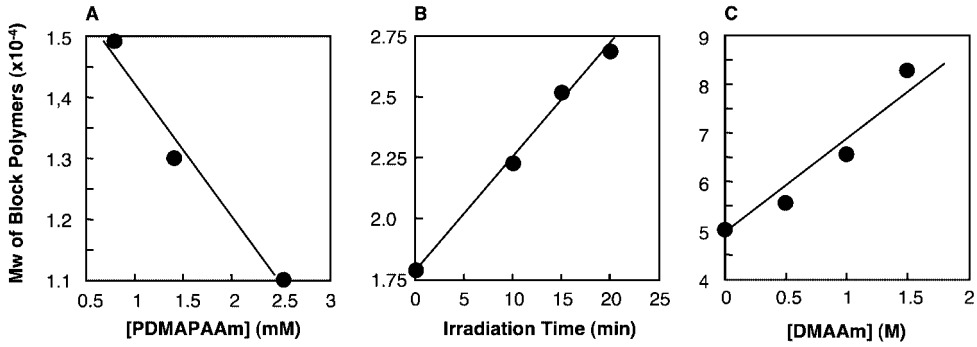


Figure 4. Changes in number average molecular weight (Mn) by changing (A) concentration of macroiniferter (PDMAPAAm 4-branched polymer), (B) irradiation time, and (C) concentration of monomer (*N,N*-dimethylacrylamide). Polymerization conditions were summarized in Table 2.

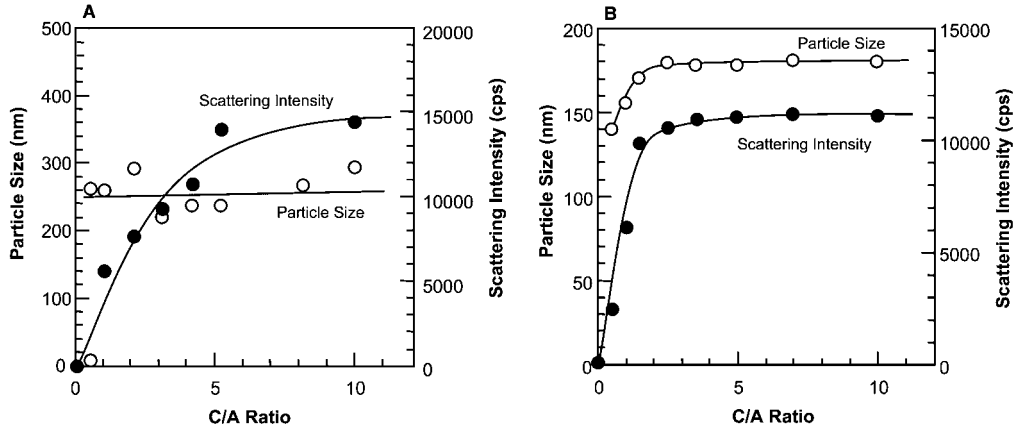


Figure 5. Scattering intensity and cumulant diameter of aqueous solutions of polyplexes prepared by mixing DNA (pGL3-control plasmid, 3 μg) and (A) PDMAPAAm 4-branched polymer with molecular weight of approximately 50 000 or (B) PDMAPAAm–PDMAAm 4-branched block copolymer with molecular weight of approximately 83 000 in different charge ratios.

Second, the photopolymerization of the nonionic monomer, DMAAm, from the obtained PDMAPAAm 4-branched polymers was conducted under a similar UV irradiation condition. Upon UV irradiation, the GPC curves of the polymers were completely shifted to a high-molecular-weight region as shown in Figure 2, indicating that block copolymerization occurred from dithiocarbamated groups located at the terminals of each branch in PDMAPAAm. Narrow polydispersity around 1.4 remained after block copolymerization. Table 2 summarizes the preparation conditions, molecular weight defined by ^{1}H NMR spectra, and the composition of PDMAPAAm–PDMAAm block copolymers. Because the polymerization reactivity of the macroiniferters was very low, it was necessary to raise monomer concentration. Therefore, monomer conversion was controlled at a very low level under 20%. The ^{1}H NMR spectrum of the obtained polymers showed that the peaks of N-methyl protons at approximately 2.8 ppm, carbonyl methyl protons at approximately 2.5 ppm, and methylene protons at approximately 1.3 ppm, all of which originated from the nonionic monomer, were newly detected in the obtained polymers. This indicates that the PDMAPAAm 4-branched polymers could function as a macroiniferter, and the block polymerization of DMAAm occurred from the terminals of each chain of the PDMAPAAm (Fig. 3C).

The dependency of molecular weight on the concentration of the macroiniferters, i.e., PDMAPAAm 4-branched polymers, at a fixed monomer concentration and irradiation time is shown in Figure 4A. The molecular weight of PDMAPAAm–PDMAAm block copolymers that were obtained tended to decrease with an increase in the concentration of the macroiniferter. The molecular weight also increased with irradiation time at a fixed concentration of the macroiniferter and monomer (Figure 4B), and with the concentration of the monomer at a fixed irradiation time and concentration of macroiniferter (Figure 4C). Thus, it can be said that the molecular weight of the PDMAPAAm–PDMAAm block copolymers was precisely controlled by changing the irradiation time and the concentration of the macroiniferter, i.e., PDMAPAAm, and monomer, i.e., DMAAm.

Formation of Polymer/Plasmid Complexes and Their Stability. When a Tris–HCl-buffered solution of pDNA (pGL3-control plasmid) was mixed with a saline solution of the cationic polymers, namely, PDMAPAAm 4-branched polymers, the scattering intensity in DLS measurements was immediately observed regardless of the molecular weight of the cationic polymers, indicating that polymer/plasmid complexes (polyplexes) were formed. Figure 5A shows the typical behavior of the scattering intensity obtained from the cationic polymer with a molecular weight of 50 000, by changing the charge ratio (polymer/pDNA). The intensity increased with the charge ratio and reached a plateau over the ratio of 5, indicating that, for sufficient complex formation, a minimum charge ratio of 5 was required. It was considered that the formation was due to nonspecific electrostatic interaction between the cationic polymers and anionic DNA as previously described in reports (*28, 29*).

The effective diameters of the polyplexes prepared from the cationic polymer (Mn = 50 000), measured by DLS, were approximately 250 nm irrespective of the charge ratio (Figure 5A). The surface charge as revealed by ζ-potential measurements was approximately +30 mV, which was similar to the value observed for the PEI with an Mn of approximately 25 000 (*19*). The size of the formed polyplexes increased upon reduction of the molecular weight of the cationic polymers as shown in Figure 6A. With molecular weight of 10 000, the complex size was approximately 900 nm at a charge ratio of 5. It was

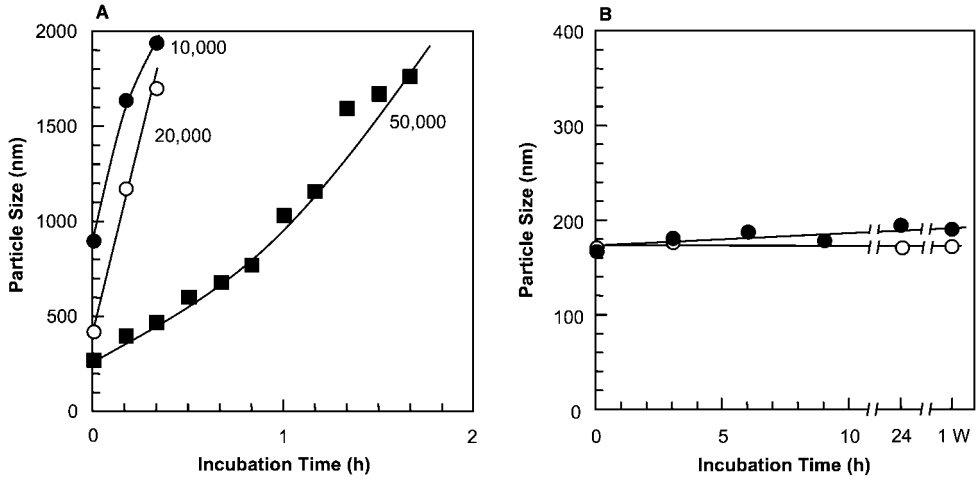


Figure 6. Incubation time dependent cumulant diameter changes in aqueous solutions of polyplexes prepared by mixing DNA (pGL3-control, 3 μg) and (A) PDMAPAAm 4-branched polymer with molecular weights of approximately 10 000, 20 000, and 50 000 at a charge ratio of 5 at pH 7.4 or (B) PDMAPAAm–PDMAAm 4-branched block copolymer with molecular weight of approximately 83 000 at a charge ratio of 5 at pH 7.4 (●) and 2.0 (○).

considered that, in polymers with higher molecular weights, a higher compaction of the polyplexes might occur. In addition, the polyplexes were gradually aggregated with increasing incubation time; that is, the size of the polyplexes formed from cationic polymers with the lowest molecular weight increased to approximately 2000 nm until 20 min after mixing. On the other hand, in the polymer with the highest molecular weight, the increase in the polyplex size was more or less prevented. The stability was higher in the polyplexes formed from polymers with higher molecular weight. Since in those studies the charge ratio was fixed at 5, the outermost surface of the complexes must be completely covered with the cationic polymers. The higher the molecular weigh is, the higher the charge density is. Therefore, it was considered that the electrostatic repulsion power rises with molecular weight, by which the aggregation of the polyplexes might be suppressed in the polymer with highest molecular weight.

On the other hand, in PDMAPAAm–PDMAAm 4-branched block copolymer a similar increase in the scattering intensity was observed immediately after mixing the polymer and DNA. A stable intensity was obtained for charge ratios greater than 2. The formed polyplexes were smaller in size (approximately 180 nm) than the nonblocked polymer. Interestingly, the size remained small even 1 month after complex formation (Figure 6B). The polyplexes were very stable under acidic conditions (Figure 6B) with moderate ζ-potentials of approximately +10 mV, which remained constant over a broad range of charge ratios between 2 and 20. This value was significantly lower than that observed for the cationic homopolymers (~30 mV). This reduced ζ-potential can be ascribed to shielding of the positive surface charge of the polyplexes by the nonionic PDMAAm chains. In addition, there was little change in the size of polyplexes after dilution to 1/20 with saline solution (Figure 7), which may be a great advantage when used for animal application. Obviously, the presence of PDMAAm leads to good colloidal stability of the PDMAPAAm–PDMAAm 4-branched block copolymers.

***In Vitro* Transfection Efficiency.** The transfection efficiency of the two types of cationic polymers—PDMAPAAm 4-branched polymer and PDMAPAAm–PDMAAm 4-branched block copolymer—at the charge ratio of 5 was tested on the model cell line of COS-1 monkey kidney cells. In our previous study, the transfection efficiency was higher in a branching polymer than a linear one (*5*). Therefore, in this study, optimization in 4-branched polymers was performed.

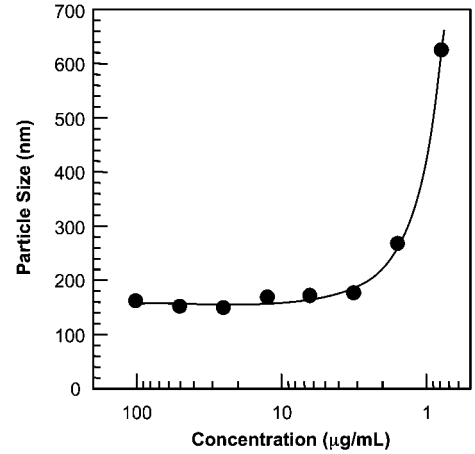


Figure 7. Dilution-dependent cumulant diameter changes in aqueous solutions of polyplexes prepared by mixing DNA (pGL3-control, 3 μg) and PDMAPAAm–PDMAAm 4-branched block copolymer with molecular weight of approximately 83 000 at a charge ratio of 5.

The cells transfected with the luciferase-encoding plasmid (pGL3), in the absence of any polymer, exhibited negligible luciferase expression. On the other hand, in cationic homopolymers the luciferase expression increased with the molecular weight of the polymers (Figure 8). The highest luciferase expression consistently occurred at the highest molecular weight, which may be due to the stability of the polyplexes as shown in Figure 6A.

Figure 9 shows the dependency of the molecular weight of the blocked polymers, which had the same core cationic polymer chain with molecular weight of approximately 50 000 but a nonionic polymer chain with different molecular weights ranging from 0 to approximately 33 000. Blocking resulted in an increase in luciferase activity with the peak transfection activity observed at a total molecular weight of approximately 83 000. The highest activity was approximately 3 times higher than that in PEI (ExGen 500) (*30*), which is a major commercially available typical polymeric vector used as a positive control. It is considered that the DNA expression using the polyplex was observed by the following 5 sequential steps: (1) attachment of the polyplex onto the cell surface, (2) internalization of the polyplex into the cell, (3) endosomal escape of the polyplex, (4) DNA release from the polyplex, and (5) internalization of DNA into the nucleus. Almost all of the cationic homopolymers

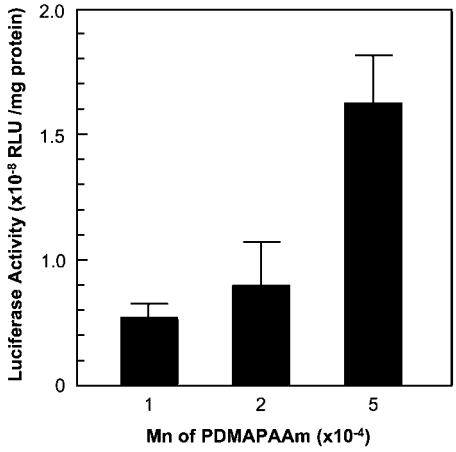


Figure 8. Transfection efficiency of polyplexes prepared by mixing DNA (pGL3-control, 3 μg) and PDMAPAAm 4-branched polymers at a charge ratio of 5.

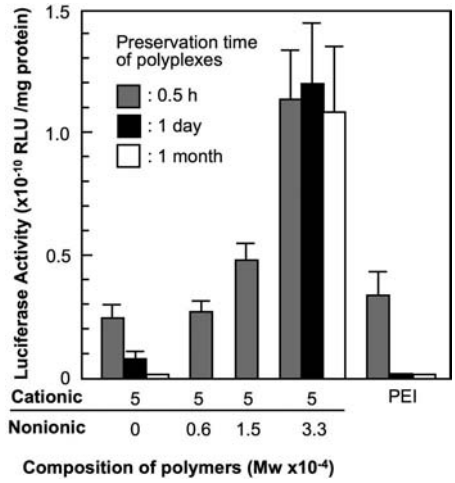


Figure 9. Transfection efficiency of polyplexes prepared by mixing DNA (pGL3-control, 3 μg) and PDMAPAAm–PDMAAm 4-branched block copolymers at a charge ratio of 5 at different preservation times of polyplexes after preparation. For comparison, transfection efficiency data of polyplexes of linear PEI (ExGen 500) at the charge ratio of 5 is also given.

including PEI can conjugate with DNA to prepare nanosized polyplexes immediately after mixing by electrostatic affinity. However, the polyplexes are gradually aggregated with an increase in incubation time to grow to micrometer size by similar electrostatic affinity as demonstrated in Figure 6A. In general, it was reported that transfection efficiency was low in large particles due to difficulty internalizing polyplexes into the cells, which is the afore-mentioned second step. In addition, polyplexes formed from DNA and cationic polymer were relatively rigid compared to those from DNA and block copolymer with a combination of cationic and nonionic chains, because a nonionic chain in the block copolymer can function as a buffer layer to weaken the electrostatic affinity between DNA and polymer. Therefore, it is considered that the only cationic polymer based polyplexes may be not dissociated easily. That is, this may prevent DNA release from the polyplex, which is the afore-mentioned fourth step. For these two reasons it is considered that the 4-branched block copolymer had higher transfection efficiency than linear PEI.

Interestingly, the high activity using the block copolymer was maintained at least 1 month after polyplex formation though the activity markedly decreased with time in nonblocked cationic polymers where approximately 60% of the activity was lost after 1 day (Figure 9). In PEI, little activity remained even 1 day after polyplex formation. In addition, the block copolymer could work as a gene delivery vector in the presence of serum. When serum was present, the transfection activity decreased to approximately 60% at serum concentration of 10%, and approximately 50% at 20%. Even at the serum concentration of 50%, approximately 30% of the initial activity remained.

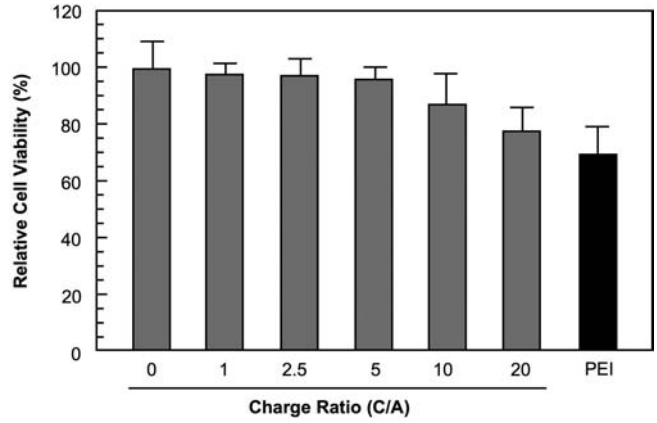


Figure 10. Cytotoxicity of polyplexes prepared by mixing DNA (pGL3-control, 3 μg) and PDMAPAAm–PDMAAm 4-branched block copolymers in different charge ratios. Cell viability was determined by the WST assay.

The *in vitro* cytotoxicity of polyplexes based on the block copolymers was studied as a function of the charge ratio by using the WST assay. The block copolymer with a cationic chain of 50 000 and nonionic chain of 30 000 had little nontoxicity at charge ratios up to 20 (Figure 9B). At high charge ratios of 10 and 20, permissible viability, which was higher than that in PEI at a charge ratio of 6, was observed.

In conclusion, we have demonstrated that nonionic polymer blocked, 4-branched cationic copolymers are a novel class of efficient polymeric carriers for DNA delivery *in vitro*. Excellent colloidal stability with low cytotoxicity of polyplexes based on PDMAPAAm–PDMAAm block copolymer with a cationic chain length of approximately 50 000 and nonionic chain length of approximately 33 000 makes it very promising for *in vivo* gene transfer. The most important advantage of the 4-branched block copolymer is high stability in the formed polyplexes, in which, however, DNA and the polymer were moderately binded. That is, excellent balance between polymer formation and dissociation may be realized in the branched blocked copolymer. In addition, the branched blocked copolymer was applied to an animal model (*31*). Even though the study was limited to only preliminary stages, mice injected with the polyplexes showed a high level of gene expression in liver, kidney, or spleen without any tissue damage. Therefore, in the near future, our research will be directed at verifying the macromolecular structure and molecular weights and the balance of the ratio in the cationic block and the nonionic block with detailed molecular characterization, including mass spectroscopy for several types of cells, for detailed study in *in vitro* and *in vivo* gene delivery.

ACKNOWLEDGMENT

We thank Dr. Mariko Shiba for offering advice regarding this study and Dr. Takeshi Masuda for his excellent technical work.

LITERATURE CITED

(1) Boussif, O., Lezoualc'h, F., Zanta, M., Mergny, M. D., Scherman, D., Demeneix, B., and Behr, J. P. (1995) A versatile vector for gene and oligonucleotide transfer into cells in culture

and *in vivo*: polyethylenimine. *Proc. Natl. Acad. Sci. U.S.A. 92*, 7297–7301.

(2) Godbey, W. T., Wu, K. K., and Mikos, A. G. (1999) Poly(ethylenimine) and its role in gene delivery. *J. Controlled Release 60*, 149–160.

(3) Kichler, A. (2004) Gene transfer with modified polyethylenimines. *J. Gene Med. 6* (Suppl 1), S3–10.

(4) Demeneix, B., Hassani, Z., and Behr, J. P. (2004) Towards multifunctional synthetic vectors. *Curr. Gene Ther. 4*, 445–455.

(5) Nakayama, Y., Masuda, T., Nagaishi, M., Hayashi, M., Ohira, M., and Harada-Shiba, M. (2005) High performance gene delivery polymeric vector: nano-structured cationic star polymers (star vector). *Curr. Drug Delivery 2*, 53–57.

(6) Mizuguchi, I., Ooe, Y., Hoshino, S., Shimura, M., Kasahara, T., Kano, S., Ohta, T., Takaku, F., Nakayama, Y., and Ishizaka, Y. (2005) Improved gene expression in resting macrophages using an oligopeptide derived from Vpr of human immunodeficiency virus type-1. *Biochem. Biophys. Res. Commun. 338*, 1499–1506.

(7) Li, S., and Huang, L. (2000) Gene therapy progress and prospects: non-viral gene therapy by systemic delivery. *Gene Ther. 7*, 31–34.

(8) Luo, D., and Saltzman, W. M. (2000) Enhancement of transfection by physical concentration of DNA at the cell surface. *Nat. Biotechnol. 18*, 33–37.

(9) Gebhart, C. L., and Kabanov, A. K. (2001) Evaluation of polyplexes as gene transfer agents. *J. Controlled Release 73*, 401–416.

(10) Thomas, M., and Klibanov, A. M. (2003) Non-viral gene therapy: polycation-mediated DNA delivery. *Appl. Microbiol. Biotechnol. 62*, 27–34.

(11) Dubruel, P., and Schacht, E. (2006) Vinyl polymers as non-viral gene delivery carriers: current status and prospects. *Macromol. Biosci. 6*, 789–810.

(12) Otsu, T., Yoshida, M., and Tazaki, T. (1982) A model for living radical polymerization. *Makromol. Chem. Rapid Commun. 3*, 133–140.

(13) Otsu, T., Matsunaga, T., Doi, T., and Matsumoto, A. (1995) Features of living radical polymerization of vinyl monomers in homogeneous system using *N,N*-diethyldithiocarbamate derivatives as photoiniferters. *Eur. Polym. J. 31*, 67–78.

(14) Lee, J. K., Kopecek, J., and Andrade, J. D. (1989) Protein-resistant surfaces prepared by PEO-containing block copolymer surfactants. *J. Biomed. Mater. Res. 23*, 351–368.

(15) Maechling-Strasser, C., Dejardin, P., Galin, J. C., and Schmitt, A. (1989) Preadsorption of polymers on glass and silica to reduce fibinogen adsorption. *J. Biomed. Mater. Res. 23*, 1385–1393.

(16) Amiji, M., and Park, K. (1992) Prevention of protein adsorption and platelet adhesion on surfaces by PEO/PPO/PEO triblock copolymers. *Biomaterials 13*, 682–692.

(17) Grainger, D. W., Nojiri, C., Okano, T., and Kim, S. W. (1989) *In vitro* and *ex vivo* platelet interactions with hydrophilic-hydrophobic poly(ethylene oxide)-polystyrene multiblock copolymers. *J. Biomed. Mater. Res. 23*, 979–1005.

(18) Nakayama, Y., Miyamura, M., Hirano, Y., Goto, K., and Matsuda, T. (1999) Preparation of poly(ethylene glycol)-polystyrene block copolymers using photochemistry of dithiocarbamate as a reduced cell-adhesive coating material. *Biomaterials 20*, 963–970.

(19) Zhong, Z., Feijen, J., Lok, M. C., Hennink, W. E., Christensen, L. V., Yockmen, J. W., Kim, Y., and Kim, S. W. (2005) Low molecular weight linear polyethyleninime-b-poly(ethylene glycol)-b-polyethylenimine triblock copolymers; synthesis, characterization, and in vitro gene transfer properties. *Biomacromolecules 6*, 3440–3448.

(20) Brissault, B., Kichler, A., Leborgne, C., Danos, O., Cheradame, H., Gau, J., Auvray, L., and Guis, C. (2006) Synthesis, characterization, and gene transfer application of poly(ethylene glycol-b-ethylenimine) with high molar mass polyamine block. *Biomacromolecules 7*, 2863–2870.

(21) Avgoustakis, K. (2004) Pegylated poly(lactide) and poly(lactid-co-glycolide) nanoparticles: preparation, properties and possible applications in drug delivery. *Curr. Drug. Delivery. 1*, 321–333.

(22) Otsuka, H., Nagasaki, Y., and Kataoka, K. (2003) PEGylated nanoparticles for biological and pharmaceutical applications. *Adv. Drug Delivery Rev. 24*, 403–419.

(23) Patersen, H., Kunath, K., Martin, A. L., Stolnik, S., Roberts, C. J., Davies, M. C., and Kissel, T. (2002) Star-shaped poly(ethylene glycol)-block-polyethylenimine copolymers enhance DNA condensation of low molecular weight polyethylenimines. *Biomacromolecules 3*, 926–936.

(24) Shuai, X., Merdan, T., Unger, F., and Kissel, T. (2005) Supramolecular gene delivery vectors showing enhanced transgene expression and good biocompatibility. *Bioconjugate Chem. 16*, 322–329.

(25) Matsuda, T., Nagase, J., Ghoda, A., Hirano, Y., Kidoaki, S., and Nakayama, Y. (2003) Phosphorylcholine-endcapped oligomer and block co-polymer and surface biological reactivity. *Biomaterials 24*, 4517–4527.

(26) Nakayama, Y., and Matsuda, T. (1996) Surface macromolecular architectural designs using photo-graft copolymerization based on photochemistry of benzyl *N,N*-diethyldithiocarbamate. *Macromolecules 29*, 8622–8630.

(27) Nakayama, Y., and Matsuda, T. (1999) Surface macromolecular microarchitecture design: Biocompatible surfaces via photo-block-graft copolymerization using *N,N*-diethyldithiocarbamate. *Langmuir 15*, 5560–5566.

(28) Xu, B., Wiehle, S., Roth, J. A., and Cristiano, R. J. (1998) The contribution of poly-L-lysine, epidermal growth factor and streptavidin to EGF/PLL/DNA polyplex formation. *Gene Ther. 5*, 1235–1243.

(29) Benns, J. M., and Kim, S. W. (2000) Tailoring new gene delivery designs for specific targets. *J. Drug Target. 8*, 1–12.

(30) Ferrari, S., Moro, E., Pettenazzo, A., Behr, J. P., Zacchello, F., and Scarpa, M. (1997) ExGen 500 is an efficient vector for gene delivery to lung epithelial cells *in vitro* and *in vivo*. *Gene Ther. 4*, 1100–1106.

(31) Zhou, Y., and Nakayama, Y. (2005) Highly effective in vivo gene transfection by blocked star vector. *Conf. Proc. IEEE Eng. Med. Biol. Soc. 1*, 501–503.

BC070045Q

Synthesis of 4-[2-Aminoethyl(nitrosamino)]-1-pyridin-3-yl-butan-1-one, a New NNK Hapten for the Induction of *N*-Nitrosamine-Specific Antibodies

Emmanuel J. F. Prodhomme,[†] Corinne Ensch,[†] Fabienne B. Bouche,[†] Thomas Kaminski,[‡] Sabrina Deroo,[§] Pierre Seck,[||] Gilbert Kirsch,[‡] and Claude P. Muller*[,†]

Institute of Immunology, Laboratoire National de Santé, 20A rue Auguste Lumière, L-1011 Luxembourg, Luxembourg, LIMBP, University Paul Verlaine - Metz, 1 boulevard Arago, F-57070 Metz, France, Laboratoire de Rétrovirologie, CRP-Santé, 84 rue Val Fleuri, L-1526 Luxembourg, Luxembourg, and University of Luxembourg, 162A avenue de la Faïencerie, L-1511 Luxembourg, Luxembourg. Received February 12, 2007; Revised Manuscript Received June 11, 2007

4-(Methylnitrosamino)-1-(3-pyridyl)-1-butanone (NNK) is one of the most abundant and potent procarcinogens in tobacco smoke. In order to induce a strong and substained antibody response against NNK, we developed a functionalized derivative that closely mimicked its structural features, in particular, the pyridyloxobutyl moiety, the adjacent ketone, and the N-nitrosamino group. This hapten was conjugated via a C_2 linker to the highly immunogenic diphteria toxoid licensed as a vaccine in humans to induce polyclonal and monoclonal antibodies. Two monoclonal antibodies were obtained with K_d values of 45.8 nM (P9D5) and 37.6 nM (P7H3), respectively, for NNK-C_2. Both the monoclonal (P9D5 and P7H3) and polyclonal antibodies reacted strongly with NNK (IC_{50} = 80 μM or 160 μM) and NNAL (IC_{50} = 29 μM or 93 μM) and to a lesser extent with some of the metabolites of NNK. Interestingly, the mAbs did not react with the metabolites of the detoxification pathways such as NNK-N-Oxide and NNAL-N-Oxide (IC_{50} > 512 μM). Therefore, such antibodies detect NNK and NNAL and may have the potential to modulate their redistribution in vivo, perhaps reducing some detrimental effects of smoking.

INTRODUCTION

4-(Methylnitrosamino)-1-(3-pyridyl)-1-butanone (NNK)[1] is one of the most abundant and potent procarcinogens in tobacco and tobacco smoke. It results from the nitrosation of nicotine and exhibits lung-selective toxicity in several species (*1*). In vivo, NNK is metabolized, either to detoxified species or to activated metabolites responsible for its carcinogenic effect (*2*). The metabolic pathways are similar in rodents and humans although with some quantitative differences (*3, 4*).

NNK is first converted by carbonyl reduction to 4-(methylnitrosamino)-1-(3-pyridyl)-1-butanol (NNAL). NNK and NNAL are then further metabolized by α-hydroxylation of both carbons adjacent to the N-nitroso group by cytochrome P450 enzymes (*5*). During this activation process, several reactive electrophilic intermediates are generated that methylate and pyridyloxobutylate DNA (*6*). These DNA adducts may, for instance, inactivate the *p*53 tumor-suppressor gene (*7, 8*) or activate the *k-ras* protooncogene (*9–11*) both responsible for NNK carcinogenesis. Two other main metabolic pathways include pyridine N-oxidation to NNK-N-oxide and NNAL-N-oxide, both of which are significantly less tumorigenic than their parent compounds and are therefore regarded as detoxification products (*1, 2*). Glucuronidation of NNAL generates species that can be excreted via bile and urine; it is the main pathway for NNK detoxification in humans (*12*).

The risk for cancers related to NNK depends on the dose, the individual activation and detoxification capacity, and the extent of DNA adduct formation. Many agents have been tested for their ability to inhibit carcinogenesis by chemoprevention (*13, 14*), and some, such as phenethyl isothiocyanate (PEITC), showed some benefit in preliminary studies (*15*). Vaccination against nicotine has spurred renewed interest in prophylactic strategies against low molecular weight compounds, and several vaccines are currently under development (*16–20*). The aim of such prophylactic vaccines is to interrupt the drug-induced dependency of nicotine by preventing the molecule from reaching the central nervous system (*21–24*). Similarly, antibodies against NNK may affect the redistribution of the NNK and its metabolites and reduce their carcinogenicity, but an immunoprophylactic approach against NNK has never been explored.

In order to induce sustained and specific antibodies, a functionalized derivative of NNK must be conjugated to a carrier protein providing the T cell epitopes to activate T helper cells. Here, we show that a conjugate vaccine based on a hapten closely mimicking the structure of NNK and coupled to a protein carrier induces polyclonal and monoclonal antibodies reacting with NNK and NNAL, two major procarcinogens in cigarette smoke.

MATERIALS AND METHODS

Synthesis of NNK Haptens. *Synthesis of the Common Intermediate* **4.** *Preparation of 4-Oxo-4-pyridin-3-yl-butyronitrile (***2***).* A suspension of finely ground sodium cyanide (490 mg, 10 mmol) in 50 mL dry *N*,*N*-dimethylformamide was vigorously stirred at 35 °C for 15 min before undiluted 3-pyridinecarboxaldehyde (**1**, 98%, 10.93 g, 100 mmol) was added dropwise over a period of 30 min. The dark brown

* Corresponding author. E-mail: Claude.Muller@LNS.ETAT.LU. Phone: +352 490604. Fax: +352 490686.
[†] Laboratoire National de Santé.
[‡] University Paul Verlaine - Metz.
[§] Laboratoire de Rétrovirologie.
[||] University of Luxembourg.

[1] Abbreviations: NNK, 4-(methylnitrosamino)-1-(3-pyridyl)-1-butanone; NNAL, 4-(methylnitrosamino)-1-(3-pyridyl)-1-butanol; NNK-N-ox, 4-(methylnitrosamino)-1-(3-pyridyl-*N*-oxide)-1-butanone; NNAL-N-ox, 4-(methylnitrosamino)-1-(3-pyridyl-*N*-oxide)-1-butanol; keto acid, 4-oxo-4-(3-pyridyl)-butanoic acid; hydroxy acid, 4-hydroxy-4-(3-pyridyl)-butanoic acid; keto alcohol, 4-hydroxy-1-(3-pyridyl)-1-butanone; diol, 1-(3-pyridyl)-1-butanediol; DT, diphtheria toxoid; OVA, ovalbumin; NNK-C_2, 4-[2-amino-ethyl(nitrosamino)]-1-pyridin-3-yl-butan-1-one; IC50, 50% inhibiting concentration; O.D., optical density.

10.1021/bc070046i CCC: $37.00 © 2007 American Chemical Society
Published on Web 10/17/2007

solution was stirred for another 30 min, after which acrylonitrile (5.31 g, 100 mmol, 1 equiv) was added over 1 h. The red–orange, viscous solution was mixed for 3 h before glacial acetic acid (629 μl, 11 mmol) was added. After stirring the solution for 5 more minutes, the solvent was partially removed under vacuum and the residue quenched with sat aq NH_4Cl soln. The aq phase was extracted 4 times with $CHCl_3$, then twice with EtOAc, and then mixed with CH_2Cl_2 overnight. The pooled organic extracts were dried ($MgSO_4$), the solvents evaporated *in vacuo*, and the residual oil purified by column chromatography (CC) on SiO_2 (EtOAc/PET 4:1 → 6:1 → 1:0). Recrystallization of the obtained orange-colored solid from 2-propanol yielded product **2** as yellow crystals (11.0 g, 69%). R_f 0.47 (EtOAc); ^{1}H NMR (250 MHz, $CDCl_3$) δ 9.16 (1H, d, J = 2.0 Hz), 8.82 (1H, dd, J = 2.0 Hz), 8.24 (1H, dt, J = 2.0, 7.3 Hz), 7.49 (1H, dd, J = 4.4, 7.3 Hz), 3.40 (2H, t, J = 6.6 Hz, CH_2CH$_2$CN), 2.84 (2H, t, J = 6.6 Hz, CH$_2$CH_2CN) ppm; ^{13}C NMR (63 MHz, $CDCl_3$) δ 198.3, 154.2, 149.4, 135.4, 131.8, 124.0, 118.8, 34.5, 11.6 ppm; *m/z* (ES$^+$) 161.1 ([M + H]$^+$, 100%).

*Preparation of 3-(2-Pyridin-3-yl-[1,3]dioxolan-2-yl)-propionitrile (**3**).* A mixture of 4-oxo-4-pyridin-3-yl-butyronitrile (**2**, 16 g, 0.1 mol), ethylene glycol (100 mL), and *p*-toluenesulfonic acid (20.9 g, 0.11 mol, 1.1 equiv) in 150 mL dry toluene was refluxed for 2 days using a Dean–Stark apparatus. The oily reaction mixture was subsequently evaporated to dryness, and the residue taken up in $CHCl_3$ and washed with sat aq K_2CO_3 soln and ddH_2O. Purification of the crude product by CC (DCM/MeOH 50:1) yielded **3** as a yellow oil (10.6 g, 52%). R_f 0.25 (92:8 DCM/MeOH); ^{1}H NMR (250 MHz, $CDCl_3$) δ 8.7 (1H, s), 8.6 (1H, d, J = 4.7 Hz), 7.7 (1H, dd, J = 7.8, 1.8 Hz), 7.3 (1H, dd, J = 8.1, 5.1 Hz), 4.1 (2H, m), 3.8 (2H, m), 2.5 (2H, t, J = 7.5 Hz), 2.25 (2H, t, J = 7.5 Hz) ppm; ^{13}C NMR (63 MHz, $CDCl_3$) δ 149.9, 147.4, 136.7, 133.4, 123.3, 119.3, 107.3, 64.9, 35.6, 11.4 ppm; *m/z* (ES$^+$) 205.1 ([M + H]$^+$, 100%), 227.1 ([M + Na]$^+$, 15%), 243.0 ([M + K]$^+$, 20%).

*Preparation of 3-(2-Pyridin-3-yl-[1,3]dioxolan-2-yl)-propylamine (**4**).* Nitrile **3** (4.1 g, 20.0 mmol, 1 equiv) was dissolved in 40 mL methanolic ammonia (MeOH sat with gaz NH_3) and hydrogenated with H_2 in the presence of Raney-Ni (ca. 410 mg, 10 wt %) at 10 bar and 40 °C for 3 days in a Parr hydrogenation apparatus. The catalyst was then removed by filtration on Celite and the filter cake extensively washed with MeOH to release the product trapped on the catalyst surface. The filtrate was evaporated *in vacuo* and the residue purified by CC on SiO_2 (DCM/MeOH/25% aq NH_3 soln 90:10:2) to yield amine **20** as a yellow oil (3.3 g, 79%). R_f 0.31 (90/10/2 DCM/MeOH/NH_4OH); ^{1}H NMR (250 MHz, $CDCl_3$) δ 8.7 (1H, s), 8.6 (1H, d, J = 5.5 Hz), 8.0 (1H, d, J = 7.9 Hz), 7.5 (1H, dd, J = 7.8, 5.7 Hz), 4.1 (2H, m), 3.75 (2H, m), 3.6 (2H, t, J = 6 Hz), 2.3 (2H, m), 2.0 (2H, t, J = 7.5 Hz), 1.60 (2H, q, J = 6.5 Hz) ppm; ^{13}C NMR (63 MHz, $CDCl_3$) δ 149.3, 147.7, 137.9, 133.6, 123.0, 109.2, 64.7, 42.1, 37.8, 27.7 ppm; *m/z* (ES$^+$) 209.1 ([M + H]$^+$, 100%).

Synthesis of Linker Molecules **10.** *Preparation of tert-Butyl (3-Hydroxyethyl)carbamate (**9**).* A soln of aminoalcohol **8** in dry DCM was treated with Et_3N (1.1 equiv) at rt for 30 min before a solution of Boc_2O (1.1 equiv) in DCM was slowly added. The mixture was stirred at room temperature overnight and quenched with sat aq NH_4Cl soln. The aq phase was extracted twice with DCM and the combined organic extracts washed with brine, dried ($MgSO_4$), and concentrated *in vacuo* to give crude product **9** as a colorless oil (91–99 %). ^{1}H NMR of the raw (*N*-Boc)-protected product showed that it was generally pure enough to be used in the next step without further purification. R_f 0.68 (20/1 DCM/MeOH); ^{1}H NMR (250 MHz, $CDCl_3$) δ 4.96 (1H, br), 3.70 (2H, dt, J = 11.6, 5.8 Hz), 3.29 (2H, dt, J = 12.45, 6.2 Hz), 2.52 (br, OH), 1.44 (9H, s) ppm; ^{13}C NMR (63 MHz, $CDCl_3$): δ 159.0, 80.0, 62.6, 43.2, 28.3 ppm.

*Preparation of tert-Butyl (2-Iodoethyl)carbamate (**10**).* Iodine (1.2 equiv) was added portionwise to a soln of imidazole (1.2 equiv) and PPh_3 (1.2 equiv) in DCM (50 mL) at 0 °C. The resulting, deeply yellow colored suspension was warmed to rt before a soln of **9** (1 equiv) in DCM was added. The reaction mixture was stirred at rt for 24 h, filtered over Celite, and washed twice with 5% aq $Na_2S_2O_3$ soln. The aq washing phases were extracted with DCM and the organic phases dried ($MgSO_4$) and evaporated *in vacuo*. The residual yellow-colored oil was subjected to purification by CC (ether/EtOAc 1:1) and yielded desired iodide **10** as a pale yellow oil (81%). R_f 0.51 (5/1 PET/EtOAc); ^{1}H NMR (250 MHz, $CDCl_3$) δ 4.95 (1H, br), 3.50 (2H, m), 3.20 (2H, m), 1.47 (9H, s) ppm. ^{13}C NMR (63 MHz, $CDCl_3$) δ 155.8, 79.3, 43.0, 28.3, 5.9 ppm.

N-Alkylation of **4** *with Linkers* **10.** *Preparation of {3-[3-(2-Pyridin-3-yl-[1,3]dioxolan-2-yl)propylamino]ethyl}-carbamic Acid tert-Butyl Ester (**5**).* A soln of amine **4** (1 equiv) in dry DMF (10 mL/mmol) was treated with Cs_2CO_3 (1.2 equiv, dried *in vacuo* prior to use) at rt for 30 min before a soln of **10** (0.99–1.0 equiv) in DMF (2 mL/mmol) was added dropwise. The pale yellow suspension was heated to 60 °C, vigorously stirred overnight, and the solvent evaporated under vacuum. The crude product was redissolved in DCM and washed with sat aq NH_4Cl soln and H_2O. The combined aq phases were extracted with DCM (3×) and EtOAc (1×) and the collected organic layers washed with 5% aq $Na_2S_2O_3$ soln, dried ($MgSO_4$), and evaporated *in vacuo*. The residual oil was subjected to CC (DCM/MeOH 98:2 → 95:5 → 92:8 → 90:10) to separate the monoalkylation product **5** (40%) from the overalkylated material. R_f 0.29 (92/8 DCM/MeOH); ^{1}H NMR (300 MHz, $CDCl_3$) δ 8.66 (1H, s), 8.53 (1H, d, J = 4.3 Hz), 7.73 (1H, d, J = 7.8 Hz), 7.27 (1H, t, J = 7.8 Hz), 6.26 (1H, br), 4.07 (2H, t, J = 6.8 Hz), 3.73 (2H, t, J = 6.8 Hz), 3.54 (2H, m), 3.09 (2H, m), 3.03 (2H, m), 1.99 (4H, m), 1.41 (9H, s) ppm; ^{13}C NMR (75 MHz, $CDCl_3$) δ 157.5, 150.4, 148.3, 138.4, 134.5, 124.0, 109.2, 80.5, 65.2, 48.7, 48.4, 43.5, 37.1, 28.5, 20.3 ppm; *m/z* (ES$^+$) 252.1 ([M + H]$^+$, 100%).

Acid-Catalyzed Nitrosation of **5.** *Preparation of {3-[3-(2-Pyridin-3-yl-[1,3]dioxolan-2-yl)propyl(nitrosamino)]ethyl}-carbamic Acid tert-Butyl Ester (**6**).* Compound **5** (1 equiv) was suspended in ddH_2O (2.5 mL/mmol), the oily droplets dissolved through addition of 1 N aq HCl soln, and the pH of the resulting homogenous layer adjusted to 5–6 with 25% aq NaOH soln. After cooling the solution to 0 °C, an aq soln of $NaNO_2$ (2 equiv) was added dropwise over 20 min. The reaction was allowed to proceed at rt overnight, then diluted with DCM and alkalinized with sat aq $NaHCO_3$. The basic aq layer was extracted with DCM (3×) and EtOAc (1×), the combined organic layers dried ($MgSO_4$), evaporated, and purified by CC on SiO_2 (DCM/MeOH 98:2 → 95:5). Product **6** was obtained as a yellow oil (53–75%). R_f 0.47 (95/5 DCM/MeOH); ^{1}H NMR (250 MHz, $CDCl_3$) δ 8.70 (1H, s), 8.59 (1H, d, J = 4.5 Hz), 7.79 (1H, d, J = 7.8 Hz), 7.32 (1H, t, J = 5.1 Hz), 4.79 (1H, br), 4.12 (2H, m), 4.06 (2H, m), 3.78 (2H, m), 3.36 (2H, m), 3.19 (2H, m), 1.92 (2H, t, J = 7.8 Hz), 1.59 (2H, m), 1.44 (9H, s) ppm; ^{13}C NMR (63 MHz, $CDCl_3$) δ 155.8, 149.5, 147.5, 137.7, 133.5, 123.3, 108.7, 82.4, 64.7, 52.1, 51.8, 43.8, 37.2, 27.7, 22.4 ppm; *m/z* (ES$^+$) 381.0 ([M + H]$^+$, 100%).

*Cleavage of Protection Groups. Preparation of 4-[2-Aminoethyl(nitrosamino)]-1-pyridin-3-yl-butan-1-one (**7**).* Nitrosation product **6** (1 equiv) was dissolved in EtOAc (1 mL/mmol) and treated with a 5-fold excess of conc aq HCl (10 N, 5 equiv) at reflux overnight. The cloudy reaction mixture was then cautiously alkalinized to pH 14 with 25% aq NaOH soln,

and the aq phase vigorously extracted with DCM (3×) and EtOAc (2×). The combined organic phases were washed with brine, dried ($MgSO_4$), and evaporated *in vacuo*. The residual oil was purified by CC (DCM/MeOH/25% aq NH_3 soln 90:10:3) to give the free amine **7** as a yellow oil (40–45%), which was stored at −20 °C under argon. The free amine **7** was then converted into a stable hydrochloride salt by HCl/MeOH-treatment for 2 h at rt and subsequent drying under vacuum. R_f 0.27 (90/10/3 DCM/MeOH/NH_4OH); ^{1}H NMR (200 MHz, D_2O) δ 9.22 (1H, s), 8.97 (1H, d, $J = 6.8$ Hz), 8.88 (1H, d, $J = 4.5$ Hz), 8.10 (1H, dd, $J = 6.8, 4.5$ Hz), 3.34 (1H, q, $J = 2.6$ Hz), 3.26 (2H, t, $J = 5$ Hz), 3.14 (2H, q, $J = 5$ Hz), 3.03 (2H, t, $J = 6.2$ Hz), 2.1 (2H, q, $J = 5$ Hz) ppm; ^{13}C NMR (50 MHz, D_2O) δ 197.0, 145.2, 144.9, 142.06, 134.6, 127.7, 48.9, 47.2, 38.7, 35.6, 20.6 ppm.

Conjugation of Hapten 7 to Proteins. A two-step zero-length cross-linking procedure using active esters was adopted for conjugating amine **7** to ovalbumin (OVA, MW 45 000 g/mol), and diphtheria toxoid (DT, 63 000 g/mol), a kind of gift from the Serum Institute of India (Hadapsar, India). OVA (10 mg mL^{-1}) was dissolved in 100 mM TrisHCl buffer pH 7.5. Crude DT was purified by buffer exchange using a 10K Da cutoff amicon (Millipore, Marlborough, USA) in 100 mM TrisHCl buffer pH 7.5 and the solution adjusted to 10 mg mL^{-1} concentration. 1 mL aliquots of both protein solutions were then reduced by treatment with 1 mL of DTT (2 mg mL^{-1}) in 100 mM TrisHCl buffer pH 7.5 and 7 mL of ddH_2O at 50 °C for 15 min. The reduced proteins were subsequently alkylated without further purification by addition of 1 mL of iodoacetamide (5 mg mL^{-1}) in 100 mM TrisHCl buffer pH 7.5 After stirring the mixture for 15 min at rt, the reduced and alkylated protein solutions were purified by buffer exchange in 100 mM MES buffer pH 6 using a 10K Da cutoff amicon cell. The solution titer were determined by standard protein quantification assays kit (BC-Uptima, Amersham Biosciences, San Francisco, CA). and the concentration adjusted to 10 mg mL^{-1} by dilution.

In a second step, 100 μL of the reduced and alkylated proteins solutions (10 mg mL^{-1}) were activated for 15 min at rt with a mixture of 200 μL of sulfo-NHS (8 mg mL^{-1}, Pierce Rockford, USA; in 100 mM MES buffer pH 6), 200 μL of EDC (2.75 mg mL^{-1} in 100 mM MES buffer pH 6) and 400 μL of ddH_2O. After activation, the excess reagents were quenched at rt for 10 min with 100 μL of β-mercaptoethanol (20 mg mL^{-1} in 100 mM MES buffer pH 6). Finally, 1 mL of NNK hapten **7** (20 mg mL^{-1}) in PBS (0.1 M sodium phosphate, 0.15 M NaCl at pH 7.5) was added to the activated protein solutions and the mixtures left to react overnight in the dark.

The bioconjugate solutions were purified by buffer exchange with 50 mM ammonium bicarbonate buffer pH 7.8 using a 10K Da cutoff amicon cell and quantified through standard protein quantification kit (BC-Uptima, Amersham Biosciences, San Francisco, CA).

Mass Spectroscopy. Positive ion MALDI-TOF mass spectrometry was performed on the [NNK-C_2] conjugates using a Bruker Daltonics ULTRAFLEX TOF/TOF equipped with a 337 nm, 50 Hz N_2 laser of 100 μJ. The crystal matrix, 3,5-dimethoxy-4-hydroxycinnamic acid (sinapinic acid) from Bruker Daltonics (Leipzig, Germany), was prepared at a concentration of 10 mg mL^{-1} in TFA 0.2%/acetonitrile 75:25. Protein samples were 1 mg mL^{-1} in 50 mM ammonium bicarbonnate buffer pH 7.8. 0.5 μL sample and 1 μL matrix solutions were mixed directly on the stainless steel probe and allowed to dry (10 min) at rt. Spectra were recorded in the linear mode, and the resulting data were analyzed using the software supplied by Bruker Daltonics. The instrument was calibrated using a 10 mg mL^{-1} BSA solution in ddH_2O.

Monoclonal antibody production. *Immunization.* Groups of five 8–10-week-old pathogen-free BALB/c mice were primed intraperitoneally (i.p.) with 25 μg of [NNK-C_2]-DT using complete Freund's adjuvant (v/v) (Sigma). Mice were boosted by gastric intubation on day 14, 16, 28, 30, 42, and 44 with the same dose of antigen in the presence of 5 μg cholera toxin (Sigma). Sera were drawn on day 0, 14, 28, 42, 55, and 84 and the anti-NNK-C_2 antibody titer was measured by direct ELISA. Three days prior to the hybridoma fusion, a final boost was performed i.p. with incomplete Freund's adjuvant (v/v) (Sigma) to two mice with the highest NNK-C_2 specific antibody titers.

Hybridoma Production. Hybridomas were produced using ClonaCell-HY complete kit (StemCell Technologies). Briefly, from immunized mice spleen, 10^8 splenocytes were washed and incubated in PEG-containing medium with 2.10^7 parental myeloma cells, SP2/0 for 5 min at 37 °C. After a 24 h expansion, cells were mixed with a methylcellulose-based HAT (hypoxanthine, aminopterin, and thymine) selective medium for hybridomas, and the mixture was plated on dishes and incubated at 37 °C, allowing fused cells to grow for 14 days. Hybridoma colonies were picked and transferred into 96-well plates with growth medium. After 4 days of growth at 37 °C, each supernatant was tested for the presence of specific [NNK-C_2]-antibodies by direct ELISA. Positive clones were further adapted to RPMI-1640 supplemented with HyClone HyQ PF-Mab (Perbio Sciences), a protein-free nutrient supplement for mAb production.

Enzyme-Linked Immunoassays (ELISA). *Indirect ELISA.* 384-well microtiter plates (Microlon, Greiner) were coated overnight with 20 μL of 0.125 μM [NNK-C_2]-OVA in 0.1 M bicarbonate buffer (pH 9.6). After washing, free binding sites were saturated with 1% BSA in Tris-buffered (15 mM) saline (TBS, pH 7.4). 20 μL of diluted mouse serum in TBS containing 0.1% Tween-20 or nondiluted supernatants was incubated for 90 min at rt. Alkaline phosphatase-conjugated goat antimouse mAb (1:750; Southern Biotechnology Associates) and a substrate solution of 0.05% *p*-nitrophenyl phosphate in 1 mM 2-amino-2-methyl-1-propanol (Sigma) and 0.1 mM $MgCl_2$ (pH 10.2) were used to detect antibody binding. Optical density (O.D.) was measured after 60 min at 405 nm. Net OD was calculated by subtraction of the relevant background as described in each figure.

Competition ELISA. In all competition experiments, optimal antigen coating conditions and serum dilutions were determined by direct ELISA. 384-well plates were coated with the minimal amount of antigen required for maximal signal. Sera or mAb supernatants were diluted to obtain 70% binding and a signal of 1.0 to 1.5 O.D. at 0% competition (highest signal). The competitors (NNK metabolites or derivatives, from Toronto Research Chemicals Inc., Canada, and Acros Organics, Geel, Belgium) were resuspended in 100% DMSO, and stock solutions of 100 μM were frozen at −80 °C. Competitors were mixed 1:1 with sera or mAb supernatants to final concentrations of 0 to 512 μM for mAbs or 0 to 1024 μM for serum. Zero (highest signal) and 100% competition (background signal) were determined using no or NNK-C_2 as competitor. The difference between these two values corresponds to the dynamic range of the assay. For each competitor concentration, 50% of the inhibitory concentration, IC_{50}, was calculated. Experiments were independently repeated three times, and data were analyzed used *SigmaStat* software. Net OD was calculated by subtraction of the relevant background as described in each figure.

Affinity Measurements by Surface Plasmon Resonance. BIACORE 3000 instrument, CM5 sensor chip, HBS-EP buffer [10 mmol/L HEPES, 0.15 mol/L NaCl, 3 mmol/L EDTA, and 0.005% surfactant P20 (pH 7.4)], amine coupling kit (*N*-hydroxysuccinimide; *N*-ethyl-*N*′-dimethylaminopropylcarbodi-

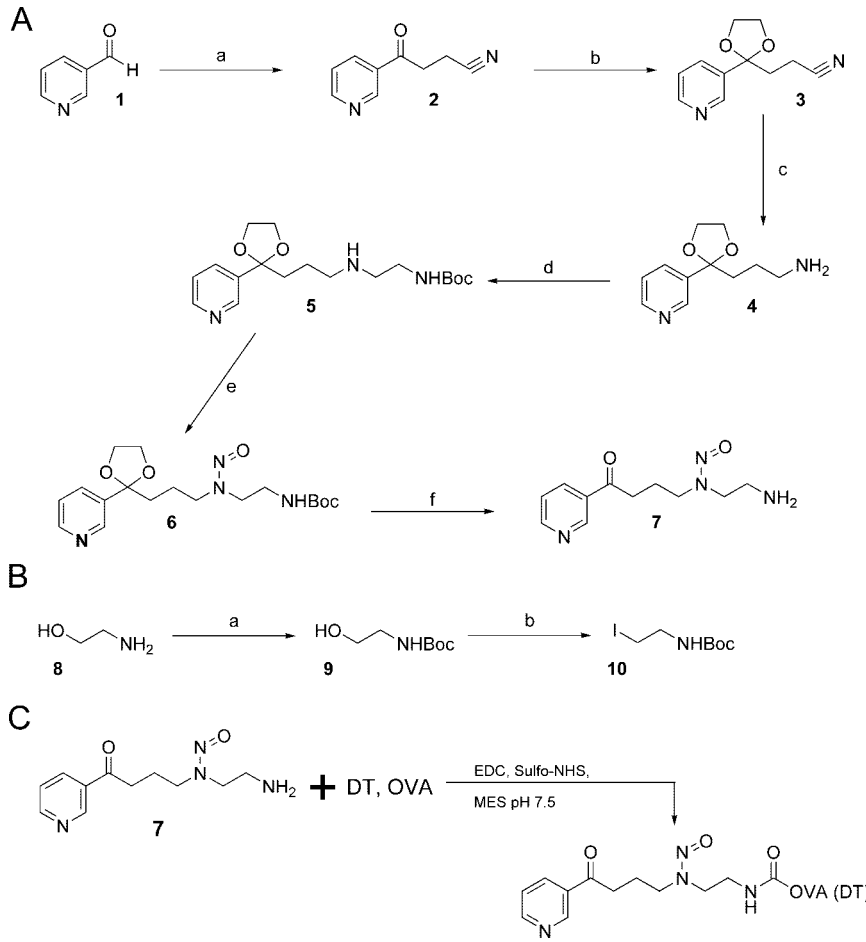


Figure 1. (A) Synthesis of NNK haptens: (a) NaCN, acrylonitrile, DMF, 35 °C, 69%; (b) $OH(CH_2)_2OH$, p-TsOH, toluene, reflux, 2 days, 52%; (c) H_2, Ni-Raney, gaz NH_3/MeOH, 40 °C, 3 days, 79%; (d) $I(CH_2)_2NHBoc$, DIPEA, CH_3CN dry, 55 °C, 18 h, 40%; (e) $NaNO_2$, CH_2Cl_2/H_2O, 1 N aq HCl, rt, overnight, 53%; (f) conc HCl, EtOAc, reflux, overnight. (B) Synthesis of linkers: (a) Boc_2O, Et_3N, CH_2Cl_2, rt, overnight, 91%; (b) I_2, imidazole, PPh_3, CH_2Cl_2, rt, 24 h, 81%. (C) NNK conjugate formation via O-acylisourea intermediates.

imide), and ethanolamine were all obtained from GE Healthcare (Diegem, Belgium). [NNK-C2]-DT and DT were immobilized on CM5 sensor chips according to standard amino coupling procedure. Briefly, the carboxymethylated dextran-coated surface was activated by a 7 min injection of a solution containing 200 mmol/L EDC and 50 mmol/L NHS; then, [NNK-C2]-DT or DT (10μg/mL in 10 mmol/L sodium acetate pH 4.5) was injected. A continuous flow of HBS-EP at 5 μL/min was maintained, and capping of unreacted sites was achieved by injecting 1 mol/L ethanolamine–HCl (pH 8.5). Final immobilization responses of 500 resonance units were achieved. Sensorgrams for kinetic measurements were generated by injection of mAbs at concentrations ranging from 0 to 100 nM in HBS-EP at a flow rate of 30 μL/min. The association and dissociation times were 120 and 900 s, respectively. The chip was regenerated by injection of consecutive pulses of 10 mM glycine pH 1.5 for 30 s and 10 mM glycine pH 2 for 60 s until the difference between the baselines before and after injection was <10 resonance units. Biosensor data were prepared, modeled, and fitted by means of the *BIAevaluation 4.1* software. Data from the reference surface were subtracted to remove the effects of unspecific binding in order to calculate the specific binding. The presence of mass transfer phenomena were excluded by performing the control assays as recommended by BIACORE. Evaluation of the data was done using a bivalent-analyte model with simultaneous determination of association and dissociation constants. The quality of the fitted data was evaluated by comparing the calculated and experimental curves (residual values) and by the $\chi 2$ parameter.

RESULTS

Synthesis of the Hapten. Retrosynthetic analysis of the pyridyl–oxobutyl structure of NNK guided our synthetic effort towards the nitrile route (Figure 1A). This approach took advantage of the commercially available nicotine aldehyde, which already contains the carbonyl function of the hapten. Condensing nicotine aldehyde **1** with acrylonitrile according to Stetter's procedure (*25*) gave the nitrile intermediate **2**, whose carbonyl function was subsequently protected by a 1,3-dioxolane group through treatment with ethylene glycol in boiling toluene. Once the carbonyl was safely masked, the nitrile was catalytically reduced with H_2/Raney-nickel as described by Soyka et al. (*26*). An aliphatic linker chain was then attached on the free amine terminus of **4** using a classical nucleophilic substitution with electrophilic partner **10**. The electrophilic linker chain was constructed by *N*-Boc protection of a commercial aminoalcohol followed by iodination (Figure 1B). The coupling product **5** was obtained with moderate yields and subsequently nitrosated with $NaNO_2$ and cat HCl under biphasic conditions to give compound **6**, which shows all the required structural similarities with NNK, except for the protective groups.

Simultaneous cleavage of the Boc-group and the 1,3-dioxolane was not possible under standard Boc-deprotection conditions (15 equiv CF_3COOH in boiling $CHCl_3$), and compound **6** was dissolved in boiling EtOAc and stirred with conc

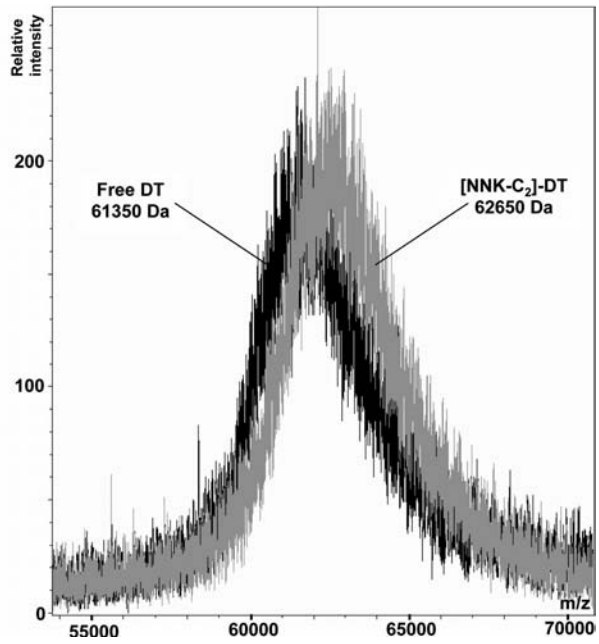


Figure 2. MALDI-TOF mass spectrograms of [NNK-C_2]-DT and free DT.

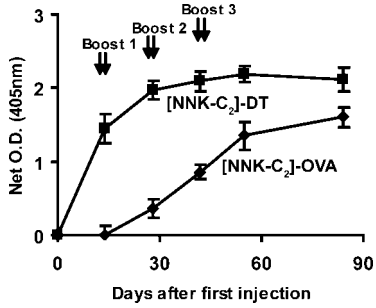


Figure 3. Reactivity of anti-[NNK-C_2]-DT sera with coated [NNK-C_2]-DT or [NNK-C_2]-OVA. Mice were primed with an ip injection and boosted by gastric intubation. Serum dilution 1/1500. Mean ± SD of reactivity of two duplicate experiments after subtraction of background reactivity against irrelevant antigen (DT 0.084 ± 0.05 or OVA 0.077 ± 0.01).

aq HCl overnight. The deprotected compound **7** was extracted in low yields from the aq layer at pH 14. After purification, the substance was redissolved in 1 N aq HCl; the water was eliminated with MeOH as dragging agent and by drying under high vacuum. The resulting hydrochloride salt of compound **7** was deep-frozen until used for bioconjugation.

Conjugation of Hapten To Carrier Proteins. The small synthetic hapten NNK-C_2 **7** was coupled to the large carrier proteins OVA and DT using a standard active ester procedure (*27*) as described in Materials and Methods (Figure 1C). Before conjugation, the native proteins were reduced and alkylated with iodoacetic acid. In all cases, a minimum of a 120-fold molar excess of hapten over the protein carboxylic reactive groups was used. After the coupling reactions, the protein conjugates were purified by dialysis.

MWs of protein conjugates were determined by MALDI-TOF MS, and the average unit of hapten per carrier estimated by mass difference. The typical mass difference between free (61 350 Da) and conjugated DT ([NNK-C_2]-DT, 62 650 Da) of 1.3 KDa (Figure 2) corresponds to an average number of approximately 5.5 NNK-C_2 molecules (235.1 Da) per molecule of carrier. Analysis of OVA conjugate gave very similar estimated numbers of hapten per protein (data not shown).

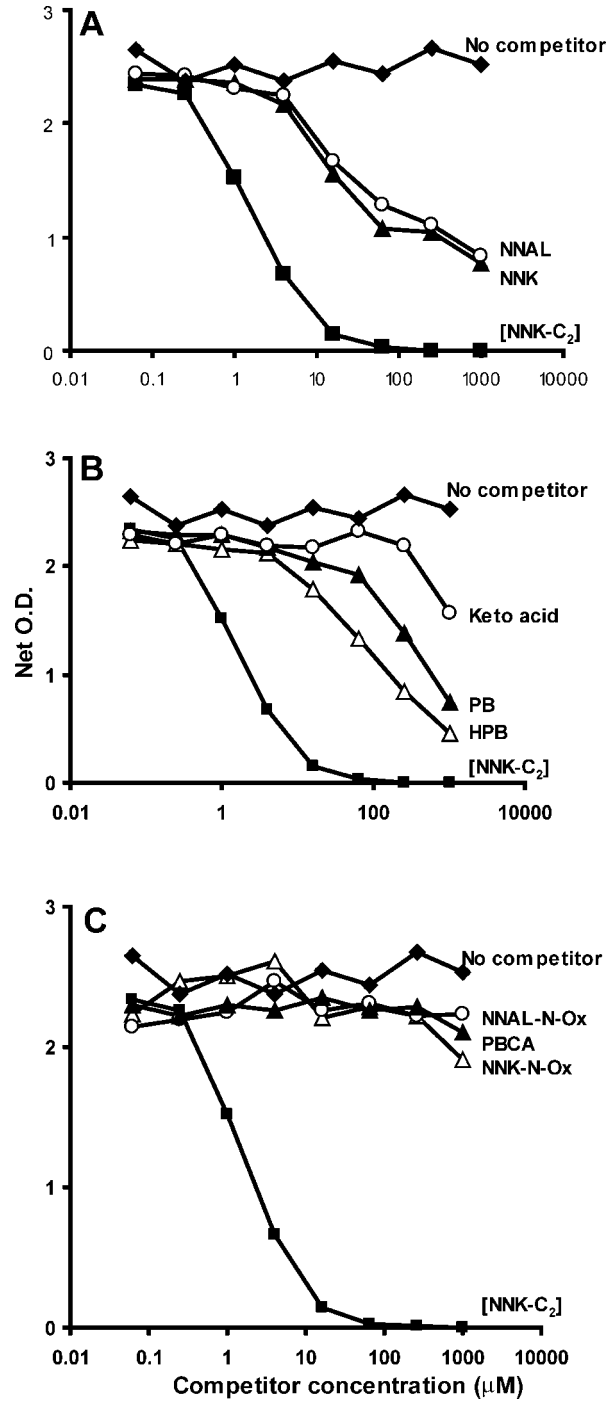


Figure 4. Binding inhibition of mouse anti-[NNK-C_2]-DT sera (1/2500) to coated [NNK-C_2]-OVA by increasing concentration of competitors. (A) NNK, NNAL, NNK-C_2. (B) PB, HPB, keto acid. (C) NNK-N-Ox, NNAL-N-Ox, PBCA. No competitor and NNK-C_2 are shown for comparison in each panel. Reactivity of serum tested after subtraction of background (0.077) corresponding to maximal competition with the highest NNK-C_2 concentration (1024 μM).

Induction of NNK-Specific Antibodies. Specific antibodies were monitored after each injection of [NNK-C_2]-DT (Figure 3). Antibodies against the homologous conjugate appeared within two weeks after the first injection. Significant levels of NNK-C_2 specific antibodies were detected with [NNK-C_2]-OVA after the second injection and increased with each boost (Figure 3). No specific IgA antibodies were detected despite the partially oral route (data not shown). NNK-specific antibodies were monitored by competition ELISA by adding increasing concentrations of NNK as competitors (0–256 μM) (Figure 4) to

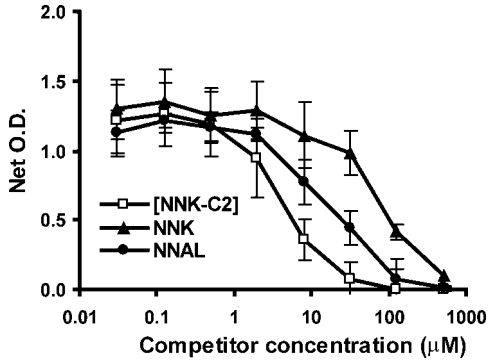


Figure 5. Inhibition of binding of P9D5 to coated [NNK-C_2]-OVA by increasing concentration of NNK, NNAL, and NNK-C_2. Mean ± SD of triplicates is shown. The background corresponding to maximal competition with NNK-C_2 at the highest concentration (512 μM) is 0.079 ± 0.007.

measure their capacity to inhibit the binding of serum antibodies to coated [NNK-C_2]-OVA. The IC_{50} of NNK and NNAL was 26 and 80 μM, respectively, while the IC_{50} of the hapten NNK-C_2 was 16–50-fold lower (Figure 4A). Also, HPB (80 μM) and PB (230 μM) were recognized by mouse sera, while essentially no specific reactivity was detected against NNK-N-Ox, NNAL-N-Ox, PBCA, and keto acid (Figure 4B,C).

Characterization of Monoclonal Antibodies. The spleen of a mouse with high levels of specific antibodies to NNK-C_2 and NNK was used for the production of mAbs. We described here two IgG1 mAbs (P9D5; Figure 5 and P7H3) that reacted strongly with [NNK-C2]-OVA.

The affinity of P9D5 and P7H3 toward the hapten [NNK-C2] was estimated by surface plasmon resonance (BiaCore) following the bivalent analyte model evaluation (Figure 6). K_d of P9D5 was 45.8 nM ($k_{a1} = 1.11 \times 10^5 \pm 202$; $k_{d1} = 5.09 \times 10^{-3} \pm 4.25 \times 10^{-5}$; $\chi^2 = 7.07$); K_d of P7H3 was 37.6 nM ($k_{a1} = 1.99 \times 10^5 \pm 334$; $k_{d1} = 7.49 \times 10^{-3} \pm 8.38 \times 10^{-5}$; $\chi^2 = 5.68$).

The reactivity of P9D5 and P7H3 was also assessed by competition ELISA using NNK metabolites and other derivatives as competitors. Binding was inhibited by NNK-C_2 (range of IC_{50}: 4.4–12 μM), NNAL (range of IC_{50}: 29–93 μM), and NNK (range of IC_{50}: 80–160 μM) (Table 1). Furthermore, the binding of P9D5 was strongly inhibited by HPB ($IC_{50} = 50$ μM), PB ($IC_{50} = 72$ μM), and ENAT ($IC_{50} = 49$ μM). A moderate inhibition of P9D5 binding was observed with keto acid and with PBCA. Weak or no competition was measured with the other metabolites and derivatives. P7H3 showed a similar reactivity: its binding was strongly inhibited by ENAT ($IC_{50} = 80$ μM); moderately inhibited by HPB, PB, keto acid, and PBCA; and weakly or not inhibited by the other metabolites and derivatives.

DISCUSSION

To induce specific antibodies against tobacco smoke associated nitrosamines, we developed a hapten, which closely mimics the common structural features of NNK and NNAL. Both parent molecules share the pyridyl–oxobutyl structure and the N-nitroso functional group responsible for the formation of DNA adducts. Our synthetic route was designed to include the 3-pyridyl group common to all activated NNK metabolites, as well as the possibility of nitrosation of the secondary amine later during the synthesis, while N-oxide groups characteristic of detoxified metabolites were avoided. As a result of our choice of 3-pyridinecarboxaldehyde as the starting material, the ketone differentiating NNK from NNAL was preserved and the N-nitroso functional group was added. In order to elicit a sustained immune response, T cell epitopes were added to the final immunogen by coupling the hapten to carrier proteins, and the tertiary amine was chosen to mediate this conjugation via a C_2 linker. Diphtheria toxoid was selected as a carrier protein, because it is highly immunogenic and is licensed in humans as a vaccine. It has also been extensively used as a carrier in a number of highly successful human conjugate vaccines, e.g., against *Haemophilus influenza* (*28, 29*), *Streptococcus pneumoniae* (*30, 31*), and meningococcal infections (*32, 33*). OVA was used as a control protein carrier to produce the antigen used in the immunoassays.

Thus, our synthetic approach and the final conjugate vaccine differ considerably from that of Talbot et al. (*34*), who used the 4-(carbethoxynitrosamino)-1-(3-pyridyl)-1-butanone, lacking in particular the tertiary amine with its nitroso group and bovine serum albumin as a protein carrier.

The resulting conjugate was successfully used to generate specific polyclonal and monoclonal antibodies. The small size of the hapten molecule, the limited number of specific structural features, and the need for a generic linker directly affected the specificity and the affinity of the antibodies obtained. After immunization with [NNK-C_2]-DT, the antibodies were selected against the heterologous antigen [NNK-C_2]-OVA.

Both conjugates share the NNK-C_2 motif, which was preferentially recognized by both polyclonal and monoclonal antibodies with K_d of 37–46 nM. Because of the 300-fold mass difference, direct binding of NNK to mAbs was not measurable by surface plasmon resonance; therefore, the relative specificity of some structurally and metabolically related molecules were ranked by competition ELISA. In contrast to the antibodies induced against the pyridyl–oxobutyl moiety by Talbot et al. (*34*), our antibodies recognized NNK and, even better, NNAL. The competition capacity of the pyridyl ring ($IC_{50} = 400$ μM

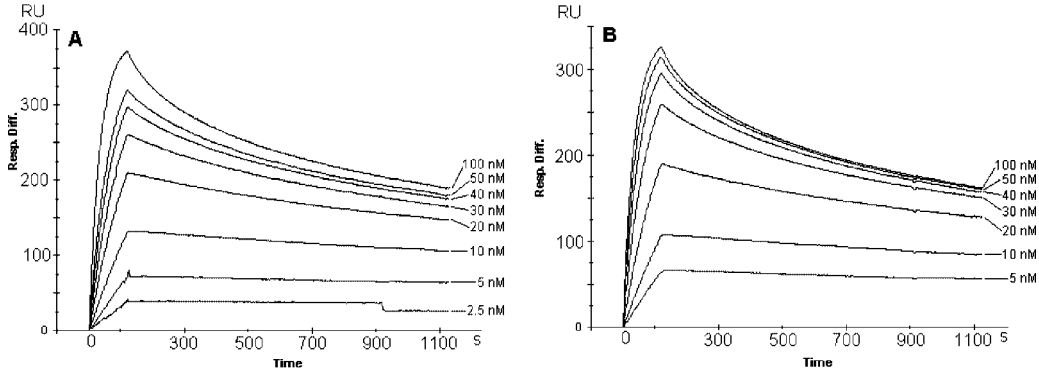
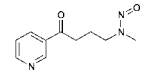
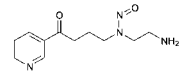
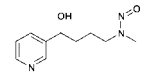
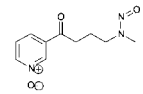
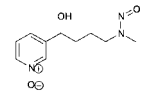
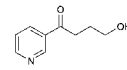
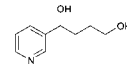
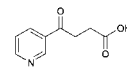
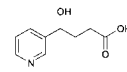
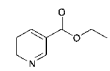


Figure 6. Sensorgrams from the kinetic analysis of binding between mAbs and immobilized [NNK-C2]-DT. Serially diluted mAbs were injected into a reference surface coated with DT and a [NNK-C2]-DT coated surface. (A) IgG mAb P9D5. (B) IgG mAb P7H3.

Table 1. IC50 of Each Competitor (NNK Metabolites and Derivates) for the Binding of P7H3 and P9D5 to the Coated Antigen [NNK-C_2]-OVA

Chemicals Name	Abbreviation	Formula	IC50 (μM) P7H3	IC50 (μM) P9D5
4-(methylnitrosamino)-1-(3-pyridyl)-1-butanone	NNK		160	80
4-[2-Amino-ethyl(nitrosamino)]-1-pyridin-3-yl-butan-1-one	NNK-C_2		12	4.4
NNK metabolites				
4-(methylnitrosamino)-1-(3-pyridyl)-1-butanol	NNAL		93	29
4-(methylnitrosamino)-1-(3-pyridyl-N-oxide)-1-butanone	NNK-N-Ox		>512	>512
4-(methylnitrosamino)-1-(3-pyridyl-N-oxide)-1-butanone	NNAL-N-Ox		>512	>512
4-Hydroxy-1-(3-pyridyl)-1-butanone	HPB		210	50
1-(3-pyridyl)-1-butanediol	PB		500	72
1-(3-pyridyl)-1-butanone-4 carboxylic acid	Keto Acid		270	210
1-(3-pyridyl)-1-butanol-4 carboxylic acid	PBCA		500	190
NNK derivatives				
Ethyl nicotinate	ENAT		80	49
Nicotinamide	NAD		>512	>512
Nicotinic acid	NIA		>512	>512
3-acetyl pyridine	AcP		500	>512
3-picoline	PC		400	320
Nicotinamide-N-oxide	NAD-N-Ox		>512	>512
Nicotinic acid-N-oxide	NIA-N-Ox		>512	>512

or 320 μM for 3-picoline) corresponded to 25–40% of the competition capacity of NNK (IC_{50} = 80 μM or 160 μM) for P9D5 or P7H3 calculated from the OD using the dynamic range of the assay. The N-oxidation of the pyridyl ring (e.g., NAD-N-Ox, NIA-N-Ox, NNK-N-Ox and NNAL-N-Ox) totally oblitterated antibody binding. This shows that the pyridyl ring is an important part of the epitope but the antibody paratope cannot accommodate the bulkier charged groups of the N-Ox species. The side chain in position 3 of the pyridine ring improved the recognition as exemplified by the efficient binding of ethyl nicotinate (IC_{50} = 49–80 μM); however, both mAbs showed some differential sensitivity to functional groups on the side chain. P7H3 required the nitroso group absent in HPB, PB, the ketoacid, and PBCA. In contrast, P9D5 was less sensitive to modification at the nitroso end, with the IC_{50} of HPB and PB being similar to that of NNK, but this mAb was sensitive to the acid moiety in the keto acid and PBCA with a significant increase of the IC_{50}. Surprisingly, the carbonyl reduction of

NNK to NNAL improved the binding by 2–3-fold, although this was not the case for their acid endpoint metabolites. Furthermore, the polyclonal antibodies generated in the serum after vaccination exhibited a very similar recognition pattern with a preferential reactivity toward NNK and NNAL, a low reactivity toward the end point metabolites (HPB, PB, PBCA, and the keto acid) and no reactivity with the detoxified species (NNK-N-Ox, NNAL-N-Ox).

Both the polyclonal and monoclonal antibodies induced by our conjugate vaccine showed an excellent selectivity for NNK and the activated metabolite NNAL but did not recognize the detoxified N-oxide derivatives. It is also reasonable to assume that they will not recognize the NNAL-glucuronidate (generated by the main detoxification pathway in humans) because of steric hindrance of the bulky glucuronic acid moiety adjacent to the pyridyl ring. Also, as a result of the low reactivity of the endpoint metabolites (HPB, PB, PBCA, and the keto acid), these would not compete effectively for the antibodies against activated NNK metabolites. Finally, in contrast to the antibodies induced by the pyridyl–oxobutyl hapten of Talbot et al. (*34*), our antibodies would not only bind to NNK but also to NNAL, the two most carcinogenic species of the metabolic cascade.

In summary, we describe the chemical synthesis of a novel functionalized NNK derivative, which was conjugated to diphtheria toxoid, a highly immunogenic antigen in humans to induce sustained and specific polyclonal and monoclonal antibodies against activated NNK and NNAL nitrosamines but not against their detoxified metabolites. Our results show that these antibodies can be used to detect these two main activated metabolites. Similarly, the concept of a conjugate vaccine against benzo[a]pyrene has previously been discussed (*35*–*37*).

Further in vitro and in vivo studies will be necessary to estimate whether a conjugate vaccine against cigarette smoke associated nitrosamines could potentially alleviate some of the detrimental effects of smoking and ultimately reduce the risk of chemical carcinogenesis in self-exposing individuals. However, the use of such a vaccine would have to be critically assessed to avoid misleading consumers about the many other health risks associated with cigarette smoking.

ACKNOWLEDGMENT

We are grateful to S. Farinelle, S. Willième, and D. Revets for technical assistance. This research was supported by the Fonds National de Recherche of Luxembourg (project FNR01/04/11). Thomas Kaminski was supported by a BFR fellowship of the Ministry of Research, Luxembourg (BFR03/085).

LITERATURE CITED

(1) Hecht, S. S. (1998) Biochemistry, biology and carcinogenicity of tobacco-specific N-nitrosamines. *Chem. Res. Toxicol. 11*, 560–603.

(2) Hecht, S. S. (1994) Metabolic activation and detoxification of tobacco-specific nitrosamines--a model for cancer prevention strategies. *Drug Metab. Rev. 26*, 373–90.

(3) Prokopczyk, B., Trushin, N., Leszczynska, J., Waggoner, S. E., and El-Bayoumy, K. (2001) Human cervical tissue metabolizes the tobacco-specific nitrosamine, 4-(methylnitrosamino)-1-(3-pyridyl)-1-butanone, via alpha-hydroxylation and carbonyl reduction pathways. *Carcinogenesis 22*, 107–14.

(4) Staretz, M. E., Murphy, S. E., Patten, C. J., Nunes, M. G., Koehl, W., Amin, S., Koenig, L. A., Guengerich, F. P., and Hecht, S. S. (1997) Comparative metabolism of the tobacco-related carcinogens benzo[a]pyrene, 4-(methylnitrosamino)-1-(3-pyridyl)-1-butanone, 4-(methylnitrosamino)-1-(3-pyridyl)-1-butanol, and N′- nitrosonornicotine in human hepatic microsomes. *Drug Metab. Dispos. 25*, 154–62.

(5) Jalas, J. R., Hecht, S. S., and Murphy, S. E. (2005) Cytochrome P450 enzymes as catalysts of metabolism of 4-(methylnitrosamino)-1-(3-pyridyl)-1-butanone, a tobacco specific carcinogen. *Chem. Res. Toxicol. 18*, 95–110.

(6) Hecht, S. S. (1999) DNA adduct formation from tobacco-specific N-nitrosamines. *Mutation Research/Fundamental and Molecular Mechanisms of Mutagenesis 424*, 127–142.

(7) Pfeifer, G. P., Denissenko, M. F., Olivier, M., Tretyakova, N., Hecht, S. S., and Hainaut, P. (2002) Tobacco smoke carcinogens, DNA damage and p53 mutations in smoking-associated cancers. *Oncogene 21*, 7435–51.

(8) Cloutier, J.-F., and Castonguay, A. (1998) Modulation of DNA repair by various inhibitors of DNA synthesis following 4-(methylnitrosamino)-1-(3-pyridyl)-1-butanone (NNK) induced DNA damage. *Chem. Biol. Interactions 110*, 7–25.

(9) Hecht, S. S., Carmella, S. G., Foiles, P. G., Murphy, S. E., and Peterson, L. A. (1993) Tobacco-specific nitrosamine adducts: studies in laboratory animals and humans. *Environ. Health Perspect. 99*, 57–63.

(10) Peterson, L. A., Thomson, N. M., Crankshaw, D. L., Donaldson, E. E., and Kenney, P. J. (2001) Interactions between methylating and pyridyloxobutylating agents in A/J mouse lungs: implications for 4-(methylnitrosamino)-1-(3-pyridyl)-1-butanone-induced lung tumorigenesis. *Cancer Res. 61*, 5757–63.

(11) Hashimoto, K., Ohsawa, K. i., and Kimura, M. (2004) Mutations induced by 4-(methylnitrosamino)-1-(3-pyridyl)-1-butanone (NNK) in the lacZ and cII genes of Muta(TM) mouse. *Mutation Research/Genetic Toxicology and Environmental Mutagenesis 560*, 119.

(12) Ren, Q., De Roo, G., Kessler, B., and Witholt, B. (2000) Recovery of active medium-chain-length-poly-3-hydroxyalkanoate polymerase from inactive inclusion bodies using ion-exchange resin. *Biochem. J. 349*, 599–604.

(13) Li, L., Xie, Y., El-Sayed, W. M., Szakacs, J. G., Franklin, M. R., and Roberts, J. C. (2005) Chemopreventive activity of selenocysteine prodrugs against tobacco-derived nitrosamine (NNK) induced lung tumors in the A/J mouse. *J. Biochem. Mol. Toxicol. 19*, 396–405.

(14) Lippman, S. M., and Spitz, M. R. (2001) Lung cancer chemoprevention: an integrated approach. *J. Clin. Oncol. 19*, 74S–82S.

(15) Hecht, S. S. (1997) Approaches to cancer prevention based on an understanding of N-nitrosamine carcinogenesis. *Proc. Soc. Exp. Biol. Med. 216*, 181–91.

(16) Cerny, E. H., Levy, R., Mauel, J., Mpandi, M., Mutter, M., Henzelin-Nkubana, C., Patiny, L., Tuchscherer, G., and Cerny, T. (2002) Preclinical development of a vaccine 'against smoking'. *Onkologie 25*, 406–11.

(17) Cerny, T. (2005) Anti-nicotine vaccination: where are we? *Recent Results Cancer Res. 166*, 167–75.

(18) Hall, W. (2002) The prospects for immunotherapy in smoking cessation. *Lancet 360*, 1089–91.

(19) Maurer, P., Jennings, G. T., Willers, J., Rohner, F., Lindman, Y., Roubicek, K., Renner, W. A., Muller, P., and Bachmann, M. F. (2005) A therapeutic vaccine for nicotine dependence: preclinical efficacy, and Phase I safety and immunogenicity. *Eur. J. Immunol. 35*, 2031–40.

(20) Kantak, K. M. (2003) Vaccines against drugs of abuse: a viable treatment option? *Drugs 63*, 341–52.

(21) Hieda, Y., Keyler, D. E., Ennifar, S., Fattom, A., and Pentel, P. R. (2000) Vaccination against nicotine during continued nicotine administration in rats: immunogenicity of the vaccine and effects on nicotine distribution to brain. *Int. J. Immunopharmacol. 22*, 809–19.

(22) Malin, D. H., Lake, J. R., Lin, A., Saldana, M., Balch, L., Irvin, M. L., Chandrasekara, H., Alvarado, C. L., Hieda, Y., Keyler, D. E., Pentel, P. R., Ennifar, S., Basham, L. E., Naso, R., and Fattom, A. (2001) Passive immunization against nicotine prevents nicotine alleviation of nicotine abstinence syndrome. *Pharmacol. Biochem. Behav. 68*, 87–92.

(23) Pentel, P., and Malin, D. (2002) A vaccine for nicotine dependence: targeting the drug rather than the brain. *Respiration 69*, 193–7.

(24) Pentel, P. R., Malin, D. H., Ennifar, S., Hieda, Y., Keyler, D. E., Lake, J. R., Milstein, J. R., Basham, L. E., Coy, R. T., Moon, J. W., Naso, R., and Fattom, A. (2000) A nicotine conjugate vaccine reduces nicotine distribution to brain and attenuates its behavioral and cardiovascular effects in rats. *Pharmacol. Biochem. Behav. 65*, 191–8.

(25) Stetter, H., Kuhlmann, H., and Lorenz, G. (1980) Cyanide catalyzed conjugate addition of aryl aldehydes: 4-(3-pyridyl)-4-oxobutyronitrile. *Org. Synth. 59*, 53.

(26) Soyka, R., Heckel, A., Nickel, J., Eisert, W., Müller, T. H., and Weisenberger, H. (1994) 6,6-Disubstituted hex-5-enoic acid derivatives as combined thromboxane A_2 receptor antagonists and synthetase inhibitors. *J. Med. Chem. 37*, 26–39.

(27) Grabarek, Z., and Gergely, J. (1990) Zero-length crosslinking procedure with the use of active esters. *Anal. Biochem. 185*, 131–5.

(28) Chu, C., Schneerson, R., Robbins, J. B., and Rastogi, S. C. (1983) Further studies on the immunogenicity of Haemophilus influenzae type b and pneumococcal type 6A polysaccharide-protein conjugates. *Infect. Immunol. 40*, 245–56.

(29) Schneerson, R., Barrera, O., Sutton, A., and Robbins, J. B. (1980) Preparation, characterization, and immunogenicity of *Haemophilus influenzae* type b polysaccharide-protein conjugates. *J. Exp. Med. 152*, 361–76.

(30) Eby, R. (1995) Pneumococcal conjugate vaccines. *Pharm. Biotechnol. 6*, 695–718.

(31) Kayhty, H., and Eskola, J. (1996) New vaccines for the prevention of pneumococcal infections. *Emerg. Infect. Dis. 2*, 289–98.

(32) Lieberman, J. M., Chiu, S. S., Wong, V. K., Partidge, S., Chang, S. J., Chiu, C. Y., Gheesling, L. L., Carlone, G. M., and Ward, J. I. (1996) Safety and immunogenicity of a serogroups A/C Neisseria meningitidis oligosaccharide-protein conjugate vaccine in young children. A randomized controlled trial. *J. Am. Med. Soc. 275*, 1499–503.

(33) Plotkin, S. A., and Orenstein, W. A. (1999) *Vaccines*, 3rd ed. Saunders Company, Philadelphia, http://www.us.elsevierhealth.com/index.jsp.

(34) Talbot, B., Desnoyers, S., and Castonguay, A. (1990) Immunoassays for proteins alkylated by nicotine-derived N-nitrosamines. *Arch. Toxicol. 64*, 360–364.

(35) De Buck, S. S., Augustijns, P., and Muller, C. P. (2005) Specific antibody modulates absorptive transport and metabolic activation of benzo[a]pyrene across Caco-2 monolayers. *J. Pharmacol. Exp. Ther. 313*, 640–6.

(36) De Buck, S. S., Bouche, F. B., Brandenburger, A., and Muller, C. P. (2005) Modulation of the metabolism and adverse effects of benzo[a]pyrene by a specific antibody: a novel host factor in environmental carcinogenesis? *Carcinogenesis 26*, 835–44.

(37) De Buck, S. S., and Muller, C. P. (2005) Immunopropylactic approaches against chemical carcinogenesis. *Vaccine 23*, 2403–6.

BC070046I

Surface Acetylation of Polyamidoamine (PAMAM) Dendrimers Decreases Cytotoxicity while Maintaining Membrane Permeability

Rohit B. Kolhatkar, Kelly M. Kitchens, Peter W. Swaan, and Hamidreza Ghandehari*

Center for Nanomedicine and Cellular Delivery, Department of Pharmaceutical Sciences, University of Maryland, Baltimore, Baltimore, Maryland. Received December 18, 2006; Revised Manuscript Received September 13, 2007

Improving the oral bioavailability of therapeutic compounds remains a challenging area of research. Polyamidoamine (PAMAM) dendrimers are promising candidates for oral drug delivery due to their well-defined compact structure, versatility of surface functionalities, low polydispersity, and ability to enhance transepithelial transport. However, potential cytotoxicity has hampered the development of PAMAM dendrimers for in vivo applications. In this article, we have systematically modified the surface groups of amine-terminated PAMAM dendrimers with acetyl groups. The effect of this modification on cytotoxicity, permeability, and cellular uptake was investigated on Caco-2 cell monolayers. Cytotoxicity was reduced by more than 10-fold as the number of surface acetyl groups increased while maintaining permeability across the cell monolayers. Furthermore, a decrease in nonspecific binding was evident for surface-modified dendrimers compared to their unmodified counterparts. These studies point to novel strategies for minimizing PAMAM dendrimer toxicity while maximizing their transepithelial permeability.

INTRODUCTION

Polymeric drug delivery systems generally entail improved efficacy while concomitantly decreasing the dose limiting toxicity of therapeutically active compounds (*1, 2*). Due to ease of administration and patient compliance, oral delivery remains the preferred route of drug intake; however, the macromolecular nature of polymers oftentimes necessitates their administration by intravenous injection. Polyamidoamine (PAMAM) dendrimers, owing to their unique characteristics such as nanoscopic size range, high drug-loading capacity, low polydispersity, and predictable size and surface charge, have shown promise in drug delivery (*1, 3–5*). Depending on their surface properties and size, PAMAM dendrimers are transported across epithelial barriers to a higher extent than some of the conventional linear water-soluble polymers (*6*). Our recent data suggest that cationic PAMAM dendrimers may permeate across Caco-2 cells to a higher extent than their neutral and anionic counterparts (*7*). However, an important element limiting the clinical application of cationic dendrimers is their cytotoxicity, which is dependent on concentration, generation, and exposure time to the cellular barriers (*8–12*). Studies using epithelial cell lines have shown that the cytotoxicity of cationic dendrimers can be reduced by functionalizing their surface amine groups (*13, 14*). In this article, a small acetyl group was used for neutralization of surface amines to avoid the influence of molecular weight on the properties of the polymer. Other factors that prompted the use of acetyl groups for surface functionalization were as follows: (1) an increasing interest in surface-modified dendrimers for drug delivery; (2) ease of controlling the degree of acetylation by controlling stoichiometry; (3) mild reaction conditions required for acetylation; and (4) increased solubility of acetylated dendrimers. Two different generations of PAMAM dendrimers, namely, G2 and G4, were acetylated and the effect of surface modification on cytotoxicity, permeability, and uptake on Caco-2 epithelial cells was studied.

* Author for correspondence: Hamidreza Ghandehari, Ph.D., University of Maryland School of Pharmacy Center for Nanomedicine and Cellular Delivery, Department of Pharmaceutical Sciences, 20 Penn Street, HSFII Room 625, Baltimore, MD 21201-1075, USA. Telephone: (410) 706-8650. Fax: (410) 706-5017. E-mail address: hghandeh@rx.umaryland.edu.

EXPERIMENTAL PROCEDURES

Materials. PAMAM-G2NH_2 (molecular weight = 3214, 16 amine end groups), PAMAM-G4NH_2 (molecular weight = 14215, 64 amine end groups), Acetic anhydride, [^{14}C]-mannitol (specific activity 50 mCi/mmol), D_2O, and Triton X-100 were purchased from Sigma-Aldrich Co. (St. Louis, MO). ^{3}H-Acetic anhydride was purchased from American Radiolabeled Chemicals Incorporation. Superose 12 HR 16/50 column was purchased from Amersham Pharmacia Biotech (Piscataway, NJ). Caco-2 cells were purchased from American Type Cell Culture (ATCC, Rockville, MD). WST-1 cell proliferation reagent was purchased from Roche Applied Science (Indianapolis, IN). Precast 4–20% gradient express gels for PAGE were obtained from ISC Bioexpress (Kaysville, UT). Tris-glycine-SDS (TGS) buffer (pH = 8.3) was purchased from Invitrogen (Carlsbad, CA). ^{1}H NMR and ^{13}C NMR spectra were obtained using Varian 500 MHz FT NMR. The NMR solvent used was D_2O unless otherwise indicated. All other chemicals used were analytical grade.

Surface Acetylation of PAMAM Dendrimers. Conjugates are designated as G*x*A*y* where *x* represents the PAMAM dendrimer generation and *y* represents the number of acetamide groups on the surface (number of amine groups functionalized). PAMAM dendrimers were reacted with different molar ratios of acetic anhydride in the presence of excess triethylamine to quench acetic acid which was formed as a side product during the reaction (Figure 1) (*15*). A typical procedure for the synthesis of acetylated PAMAM dendrimers (G2A16) was as follows. G2-PAMAM dendrimer (0.100 g, 0.03 mmol) was dissolved in dry methanol (10 mL) followed by addition of acetic anhydride (0.062 g, 0.61 mmol) and triethylamine (0.12 g, 1.2 mmol). The solution was stirred for 12 h at room temperature, and methanol was then evaporated to obtain crude acetylated PAMAM dendrimers. The crude product was redissolved in water and purified by extensive dialysis against distilled water using dialysis membrane of 500 MWCO (Spectrum Laboratories, Inc., Rancho Dominguez, CA). Purified acetylated PAMAM

10.1021/bc0603889 CCC: $37.00 © 2007 American Chemical Society
Published on Web 10/26/2007

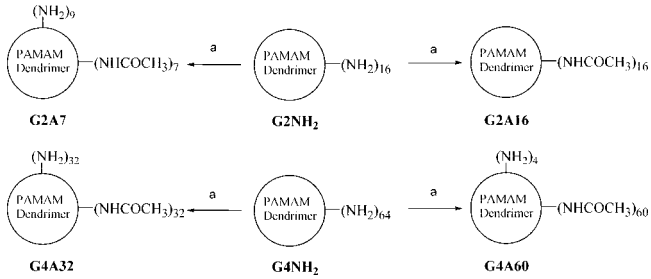


Figure 1. Synthetic scheme for acetylation of PAMAM dendrimers.

dendrimer was then freeze-dried, and solid product was stored in a refrigerator. G2A7, G4A32, and G4A60 were synthesized following a similar procedure with different molar equivalents of acetic anhydride.

Characterization of Acetylated PAMAM Dendrimers. Acetylated PAMAM dendrimers were characterized by size exclusion chromatography (SEC) on a Superpose 12 column (Amersham Biosciences, Piscataway, NJ) using a fast protein liquid chromatography (FPLC) system with phosphate buffer (pH 7.4) as the mobile phase. Eluting molecules were detected using UV detector at 280 nm. The number of surface amine groups modified was determined from ^{1}H NMR by calculating the ratios of integral values of the signal for upfield CH_3 protons (1.8 ppm) and integral values of the signal for -CH_2- protons from PAMAM dendrimer (2.2–4 ppm) (*15*). Figure 2A shows a typical NMR spectrum for acetylated PAMAM dendrimer. ^{1}H-NMR (D_2O, 500 MHz) values for the surface-modified polymers were as follows:

G2A16. δ = 1.89 (48H, s, $COCH_3$), 2.30–2.40 (56H, m, C-C$\underline{H_2}$-CONH), 2.53–2.58 (28H, m, N-C$\underline{H_2}$-CH_2NH), 2.70–2.78 (56H, m, N-CH_2-C$\underline{H_2}$-CO), 3.18–3.25 (88H, CONH-C$\underline{H_2}$).

G2A7. δ = 1.88 (21H, s, $COCH_3$), 2.28–2.42 (56 H, m, C-C$\underline{H_2}$CONH), 2.50–2.60 (28H, m, N-C$\underline{H_2}$-CH_2NH), 2.68–2.80 (56H, m, N-CH_2-C$\underline{H_2}$-CO), 2.96–3.06 (18H, C$\underline{H_2}$$NH_2$), 3.18–3.38 (70H, CONH-C$\underline{H_2}$).

G4A60. δ = 1.89 (180H, s, $COCH_3$), 2.30–2.42 (248H, m, C-C$\underline{H_2}$-CONH), 2.56–2.68 (124H, m, N-C$\underline{H_2}$-CH_2NH), 2.74–2.88 (248H, m, N-CH_2-C$\underline{H_2}$-CO), 3.18–3.30 (376H, CONH-C$\underline{H_2}$).

G4A32. δ = 1.88 (96H, s, $COCH_3$), 2.30–2.42 (248 H, m, C-C$\underline{H_2}$CONH), 2.50–2.60 (124H, m, N-C$\underline{H_2}$-CH_2NH), 2.68–2.80 (248H, m, N-CH_2-C$\underline{H_2}$-CO), 2.96–3.06 (64H, C$\underline{H_2}$$NH_2$), 3.18–3.38 (312H, CONH-C$\underline{H_2}$).

The dendrimers were further characterized using matrix assisted laser desorption–ionization-time of flight mass spectrometry (MALDI-TOF MS) on a Bruker Omniflex (Bruker Daltonics, Billerica, MA) to determine their molecular weights. A stock solution of the dendrimer was prepared by dissolving 1 mg of the sample in methanol. A 1 μL aliquot of the stock solution was mixed with 9 μL of matrix solution. The matrix solution used for characterizing G2 analogues consisted of saturated solution of α-hydroxycinnamic acid, and the matrix solution used for G4 analogues consisted of 10 mg/mL 2,5-dihydroxybenzoic acid in 20:80 acetonitrile/ water containing 0.1% trifluoroacetic acid. The dendrimer matrix mixture was spotted on the target plate (1 μL per spot), and the solvent was allowed to evaporate under ambient conditions. Analysis was performed in the linear mode.

The variations in charge ratio of the dendrimers were analyzed by native polyacrylamide gel electrophoresis (PAGE) and SDS PAGE on a BioRad vertical electrophoresis system (Power Pac 200, BioRad, CA, USA). For SDS PAGE analysis, TGS buffer (10×, pH = 8.3) was diluted with water by a factor of 10 to prepare the running buffer. Each well was loaded with 2.0 μL sample solution comprising 1.0 μL of 1.0 mg/mL PAMAM dendrimer and 1.0 μL sample buffer Laemmli (Sigma, MO). Developed gels were stained with Bio-Safe Coomassie Blue and destained with water. Native PAGE analysis was performed following similar procedures but with reverse polarity, Tris–glycine buffer (pH = 8.3) and methylene blue sucrose dye solution (50% sucrose, 1% methylene blue) were used as the loading buffer.

The surface density of amine groups, SD_a (i.e., the number of amine groups/nm^2 of the surface), was calculated by dividing the number of amine groups on each dendrimer by its surface area. Surface area was calculated by assuming a spherical shape for the dendrimer and the R_G (radius of gyration) values obtained from molecular modeling calculations for different-generation dendrimers (*16*).

Synthesis and Characterization of Radiolabeled PAMAM Dendrimers. The surface modified G4 analogues (G4A32, G4A60) as well as unmodified $G4NH_2$ PAMAM dendrimers were reacted with [^{3}H]-labeled acetic anhydride (5 mCi/mmol of the polymer) as described above to obtain [^{3}H]-labeled G4A32 and G4A60 PAMAM dendrimers. The crude product was purified by dialysis against distilled water for 48 h using dialysis membranes of 1000 MWCO (Spectrum Laboratories, Inc., Rancho Dominguez, CA). The polymers did not show any small molecular weight impurities as examined by size exclusion chromatography using a PD-10 column while measuring the radioactivity of the fractions collected. The specific activity for each radiolabeled polymer was in the range 2–3 mCi/mmol.

Cell Culture. Caco-2 cells (passages 30–60) were grown at 37 °C in an atmosphere of 5% CO_2 and 95% relative humidity. Cells were maintained in T-75 flasks using Dulbecco's Modified Eagle's Medium (DMEM) supplemented with 10% fetal bovine serum, 1% nonessential amino acids, 10 000 units/mL penicillin, 10 000 μg/mL streptomycin, and 25 μg/mL amphotericin. Medium was changed every other day, and cells were passaged at 70–90% confluency using 0.25% trypsin/ethylenediamine tetraacetic acid (EDTA) solution. Incubation buffer consisted of Hank's balanced salt solution (HBSS) supplemented with 10 mM *N*-(2-hydroxyethyl)piperazine-*N*′-(2-ethanesulfonic acid) hemisodium salt (HEPES) buffer (pH 7.4).

Cytotoxicity Assay. Caco-2 cells were seeded (50 000 cells/well) in 96-well cell culture plates (Corning, Inc., Corning, NY) and maintained for 48 h. The cells were washed twice with HBSS and incubated with 100 μL of unmodified and modified PAMAM dendrimer solutions in HBSS. After 3 h, the cells were washed with HBSS to remove the dendrimers and replaced with 100 μL HBSS. Thereafter, 10 μL of cell proliferation reagent WST-1 was added to each well, followed by an incubation period of 4 h. Absorbance was measured at 440 nm using a SpectraMax 384 Plus plate reader (Molecular Devices, Sunnyvale, CA). HBSS was used as a negative control. The experiment was repeated 3 times in triplicate for each concentration of the PAMAM dendrimer.

Cellular Uptake of PAMAM Dendrimers. To determine cellular uptake of radiolabeled PAMAM dendrimer, Caco-2 cells were seeded with a cell density of 80 000 cells per well on cell culture-treated 12-well plates (Becton Dickinson). After 48 h, cells were washed with HBSS and incubated with 0.01 mM radiolabeled PAMAM dendrimers for 30, 60, and 120 min, respectively. At the end of the incubation period, 20 μL of the sample of donor dendrimer solution was collected for measuring radioactivity, and the cells were washed twice with ice–cold HBSS buffer to stop the uptake process. The cells were then lysed with 1 N NaOH solution which was then neutralized with HCl. The cell-associated radioactivity was determined using liquid scintillation counting (Beckman Coulter, Fullerton, CA). The uptake data was normalized to total protein content determined using BCA protein assay kit (Pierce, Evanston, IL).

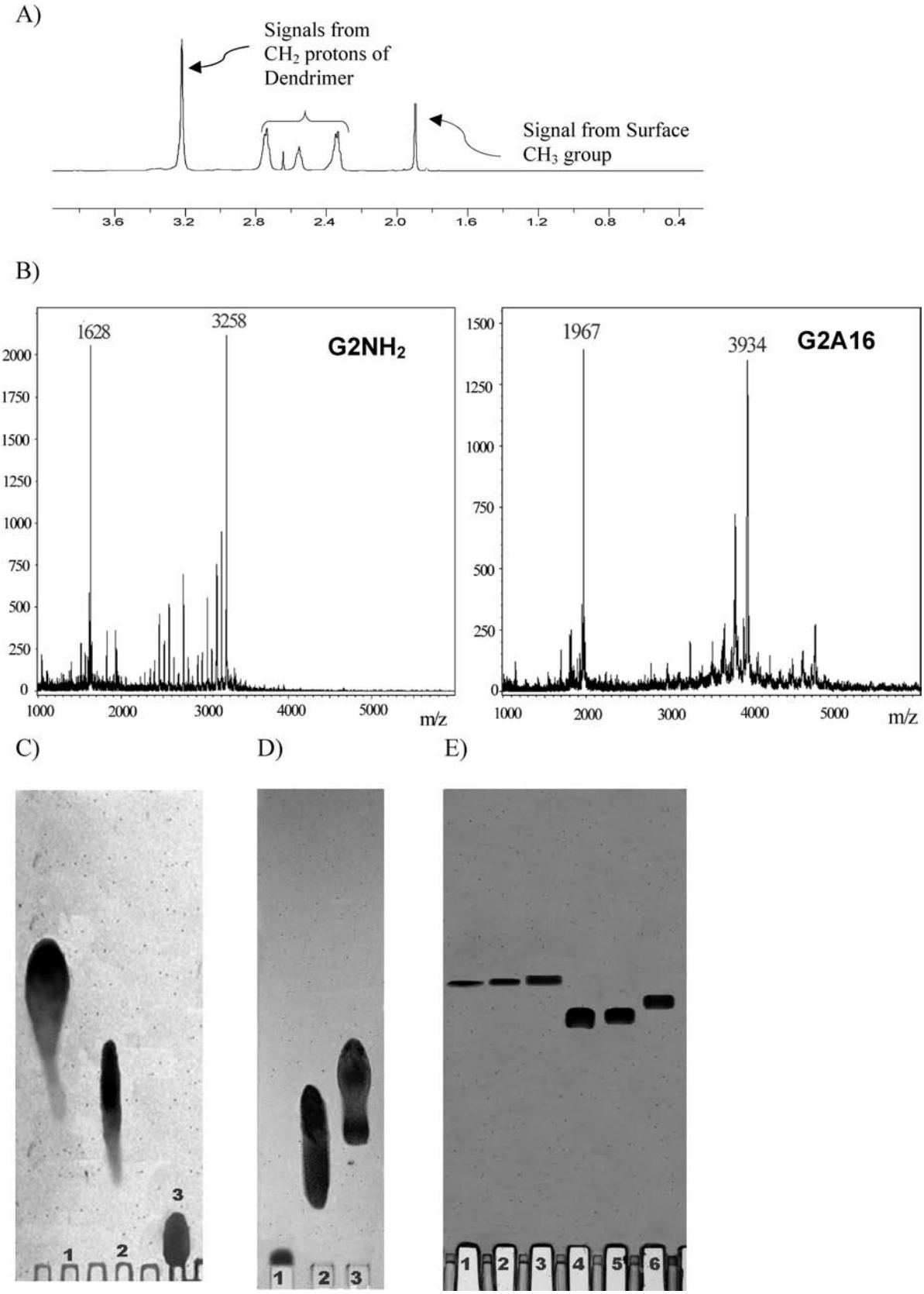


Figure 2. (A) ^{1}H NMR of G2A16. (B) MALDI TOF MS spectra for unmodified G2 (left) and G2A16 (right). (C) Native PAGE analysis of G2, G2A7, and G2A16 in lanes 1, 2, and 3, respectively. (D) Native PAGE analysis of G4A60, G4A32, and G4 in lanes 1, 2, and 3, respectively. (E) SDS PAGE analysis of G2, G2A7, G2A16, G4, G4A32, and G4A60 in lanes 1, 2, 3, 4, 5, and 6, respectively.

Transepithelial Transport Studies. Caco-2 cell monolayers were seeded (80 000 cells/well) on 12-well Transwell cell culture inserts (3 μM pore size). After the cells reach confluency (21–28 days in culture), the transport of PAMAM dendrimers from the apical to the basolateral direction was investigated at donor concentrations of 0.01 mM for G4, 0.01 mM and 0.1 mM for G4A32, and 0.01 mM, 0.1 mM, and 1 mM for G4A60. Prior to experiments, the cells were washed with HBSS buffer, and then

500 μL of the [^{3}H]-labeled polymer was added to the apical side of each insert while 1500 μL of the HBSS buffer was added on the basolateral side. Samples were collected at 0, 30, 60, 90, and 120 min from the basolateral compartment and analyzed for accumulated radiolabel using a liquid scintillation counter (Beckman Coulter, Fullerton, CA). The activity of the apical donor solution was also measured at $t = 0$ and 120 to assess mass balance and determine accurate donor concentrations. The apparent permeability (P_{app}) coefficients for PAMAM dendrimers were calculated as follows:

$$P_{app} = \frac{dM}{C_0 \cdot S \cdot dt} \quad (1)$$

where dM represents the change in dendrimer accumulation on the basolateral side, C_0 the concentration on the apical side of the membrane, S the surface area of the insert (1.12 cm^2), and dt the change in time. Monolayers were considered to be confluent when P_{app} for mannitol was less than $2 \cdot 10 \cdot 10^{-6}$ cm/s.

Additionally, cell monolayer integrity was monitored during transport studies by using an epithelial voltohmmeter (EVOM) (World Precision Instruments, Inc., Sarasota, FL) to measure the transepithelial electrical resistance (TEER) at time points coinciding with sample collection. TEER values (Ω cm^2) were corrected for background (obtained from inserts without cells) and normalized to untreated inserts (% control). After 120 min, the dosing solution was removed, and cells were washed with HBSS. Subsequently, cells were incubated in DMEM and placed at 37 °C overnight. After 24 h, TEER was measured to assess reversibility of tight junctional perturbance.

In a different set of experiments using a similar procedure, the relative integrity of the paracellular (tight junctional) pathway was assessed by evaluating [^{14}C]-mannitol (2.0 μM) permeability in the presence of PAMAM dendrimer.

Statistical Analysis. Statistical analysis was carried out using Student's t-test with a probability value $p < 0.05$ considered statistically significant.

RESULTS AND DISCUSSION

Synthesis and Characterization of Acetylated PAMAM Dendrimers. This study is a logical extension of our previous investigation in which we demonstrated that the permeability of amine-terminated PAMAM dendrimers across Caco-2 cell monolayers is controlled by size, molecular weight, and concentration (*4, 11*). Subsequent studies indicated that cationic PAMAM dendrimers modulate tight junctions of Caco-2 cells, thereby enhancing the transepithelial transport of mannitol (*7*). However, the surface amine groups also render cationic PAMAM dendrimers cytotoxic, limiting their utility as safe and effective drug delivery systems (*7, 12*). With the hypothesis that surface modification can reduce cytotoxicity while maintaining optimal cellular uptake as well as transepithelial permeability, in this study 47% and 100% of the surface amine groups of G2 were functionalized to acetamide to yield G2A7 and G2A16, respectively. Likewise, 50% and 94% of the surface amine groups of G4 were functionalized to acetamide to yield G4A32 and G4A60, respectively. A typical ^{1}H NMR spectrum obtained for completely modified G2A16 dendrimer is shown in Figure 2A. In the ^{1}H NMR spectra, a downfield shift of the signal for CH_2-NH$_2$ and the appearance of a new signal for CH$_3$ protons at 1.89 ppm, as well as the appearance of a new peak at 21.94 ppm corresponding to CO$\underline{C}$H$_3$ in ^{13}C NMR spectra (data not shown) indicate the formation of a covalent bond between surface amine and carbonyl carbon from acetic anhydride. MALDI-TOF MS analysis (Figure 2B) demonstrated an increase in the molecular weight of the polymer as the number of surface acetyl groups increased, suggesting the formation of a covalent bond rather than a complex. Similar MALDI-TOF spectra were obtained for all other unmodified and surface-modified PAMAM dendrimers. The estimated molecular weights (Table 1) were in good agreement with the NMR data obtained.

Table 1. Characteristics of PAMAM Dendrimers Studied

PAMAM dendrimer	no. of surface NH$_2$/acetyl groups[a]	Mw calcd	Mw (MALDI)	elution volume (FPLC) ml	surface density of amine groups[b]
G2NH$_2$	16/0	3250	3258	14.85	0.60
G2A7	9/7	3550	3563	14.77	0.34
G2A16	0/16	3928	3934	14.74	0
G4NH$_2$	64/0	14215	13337	13.10	0.71
G4A32	32/32	15559	14782	12.94	0.35
G4A60	4/60	16735	15887	12.76	0.04

[a] Determined from NMR data. [b] Calculated by dividing number of surface amine groups by surface area (nm^2).

Size exclusion analysis of the polymers showed the absence of small molecular weight impurities. A decrease in the elution volume of the polymers was observed as the number of surface acetyl groups increased (Table 1). Native PAGE analysis with reverse polarity showed that gel migration slowed as the positive charge on the polymer reduced (Figure 2C,D), whereas SDS-PAGE analysis revealed that fully acetylated dendrimers migrated farther as compared to unmodified and partially acetylated dendrimers (Figure 2E). No differences were observed in bands of unmodified and partially acetylated dendrimers (Figure 2E). The bands in native page analysis were broad when compared to the narrow bands obtained from SDS-PAGE. The reason for this is that the native page separated compounds on the basis of charge and molecular weight whereas in SDS-PAGE separation is achieved on the basis of molecular weight only. Thus, in both native PAGE and SDS-PAGE analyses lower-generation smaller dendrimers (G2) migrated farther than higher-generation dendrimers (G4). Interestingly, in a subset of one generation subjected to native PAGE analysis, dendrimers with more positive charge showed farther migration as compared to dendrimers with a lower number of positively charged amine groups. As expected, fully acetylated dendrimers remained at the base due to lack of surface charge.

Acetylation of PAMAM Dendrimers Reduces Cytotoxicity. An evaluation of the effect of dendrimer concentration and the relative degree of surface amine group acetylation on cell viability (Figure 3A) revealed a complete absence of cytotoxicity at the lowest concentration of all PAMAM dendrimers tested (0.01 mM). Increasing the concentration to 0.1 mM significantly decreased cell viability for unmodified dendrimers; however, cell incubation with either partially or fully acetylated PAMAM dendrimers resulted in greater than 90% cell viability. These data suggest that even partial surface modification at this concentration reduces cytotoxicity. Another 10-fold increase in dendrimer concentration (1 mM) demonstrated a concomitant drop in cell viability for unmodified dendrimers. Interestingly, cytotoxicity was absent in cells incubated with PAMAM dendrimers exhibiting the highest degree of acetylation, suggesting a linear relationship between the number of amine groups and cellular cytotoxicity. In fact, a simple plot of cell viability vs the number of surface amine groups (Figure 3B) suggests that cytotoxicity is dependent on the dendrimer generation, probably due to the intrinsic toxicity associated with higher generation dendrimers. However, when cell viability was plotted as a function of surface density (SD_a), a linear correlation was observed irrespective of dendrimer generation (Figure 3C). Overall, G4 dendrimers showed lower cell viability (27%) as compared to G2 (56%) because of an increase in the surface density of amine groups, whereas G2A7 and G4A32 showed similar cell viability (73% vs 70%) due to

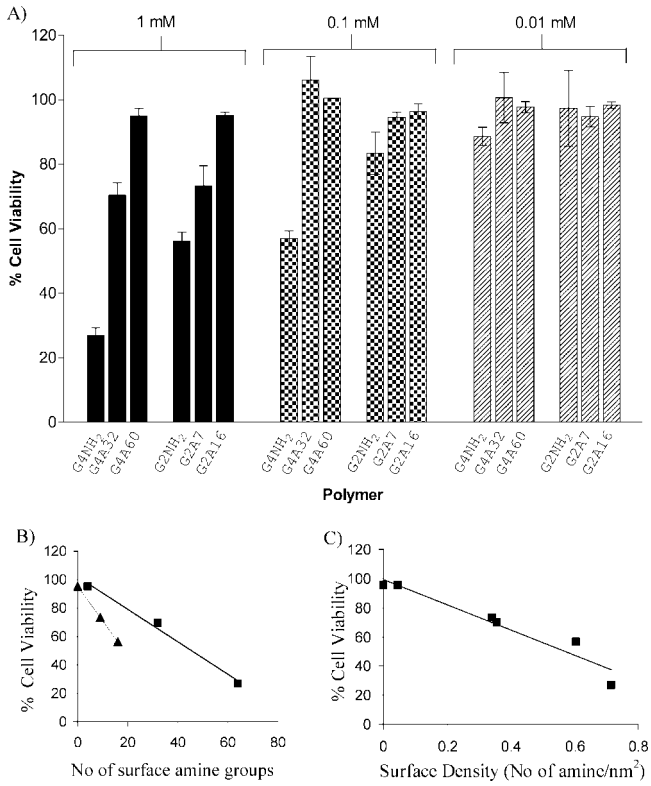


Figure 3. (A) Viability of Caco-2 cells after incubation for 3 h with dendrimers at 1 mM, 0.1 mM, and 0.01 mM. Results are expressed as mean ± SEM ($n = 9$). (B) Relationship between cell viability and number of surface amine groups for (■) G4 ($R^2 = 0.99$) and (▲) G2 analogues ($R^2 = 1$). (C) Relationship between cell viability and surface density ($R^2 = 0.93$).

similar surface density (0.34 vs 0.35) of amine groups. Previously, various investigators (*17–19*) found that cytotoxicity of water-soluble cationic polymers is governed by molecular weight, charge density, and the type of amine functionality (primary vs tertiary). Ryser (*18*) suggested a three-point attachment for eliciting a biological response on the cell membrane and speculated that the cytotoxicity of a polymer will decrease when the space between reactive amine groups is increased. In the current report, we have tried to quantify these observations with PAMAM dendrimers. A multiregressional analysis ($F < 0.001$; $R^2 = 0.7$) using cell viability, %CV, as a dependent variable with surface density, SD_a, and concentration, *C*, as independent variables revealed the following relationship:

$$\%CV = -15.5 \log C - 50.9SD_a + 87.6 \qquad (2)$$

Equation 2 suggests that cell viability in the presence of amine-terminated PAMAM dendrimers is influenced by concentration, size, and number of surface amine groups. This mathematical expression can be useful in predicting the appropriate surface modification required to minimize toxicity of PAMAM dendrimers in the size range studied.

Acetylated PAMAM Dendrimers Retain Cellular Permeability Comparable to Unmodified Dendrimers. The permeability of native and surface-modified G4 analogues was evaluated across Caco-2 cell monolayers (Figure 4A). At previously determined nontoxic concentrations (0.01 and 0.1 mM; Figure 3A), we observed a significant increase in [^{14}C]-mannitol permeability (Figure 4B) and a reduction in TEER values (Figure 4C). Since mannitol is a compound that exclusively traverses the cell monolayer via the paracellular pathway, these data indicate that PAMAM dendrimer incubation led to modulation of the epithelial tight junctions. As further evidence that incubation with acetylated PAMAM dendrimers

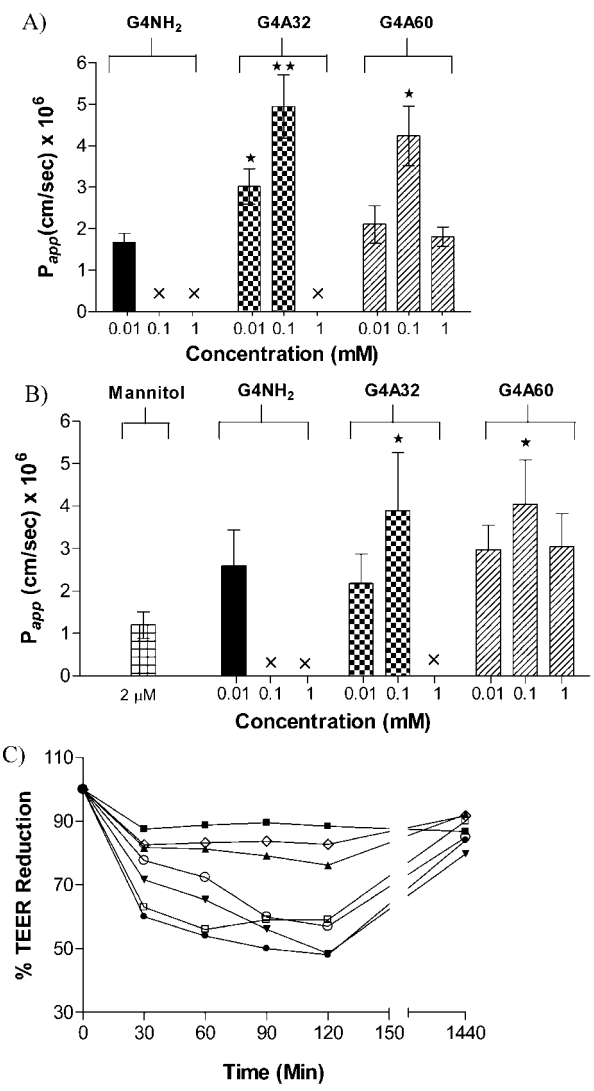


Figure 4. (A) Permeability of $G4NH_2$, G4A32, and G4A60 across Caco-2 cell monolayers after 120 min. Results are reported as mean ± SEM ($n = 6$). (*) ($p < 0.05$) and (**) ($p < 0.01$) denote a significant difference in permeability when compared to permeability of unmodified PAMAM dendrimer at 0.01 mM. (×) Permeability is not evaluated due to cytotoxicity. (B) Permeability of [^{14}C]-mannitol across Caco-2 cell monolayer in the absence and presence of $G4NH_2$, G4A32, and G4A60 dendrimers. Results expressed as mean ± SEM ($n = 6$). (×) Permeability is not evaluated due to cytotoxicity. (C) Effect of unmodified and surface-modified PAMAM dendrimers on transepithelial electrical resistance (TEER): (■) control, (▼), $G4NH_2$ (0.01 mM), (▲) G4A32 (0.01 mM), (○) G4A32 (0.1 mM), (◊) G4A60 (0.01 mM), (□) G4A60 (0.1 mM), (•) G4A60 (1 mM). Results expressed as mean ± SEM ($n = 6$). For clarity, error bars are not shown in the figure.

does not lead to permanent cell damage, we observed the full reversal of tight junctional modulation, as demonstrated by cellular TEER values, after a 24 h equilibration period (Figure 4C).

Permeability enhancement was a function of both dendrimer surface acetylation and donor concentration. At 0.01 mM, a significant increase in the permeability ($p < 0.05$) of G4A32 was observed when compared to unmodified G4 dendrimer. However, an additional increase in acetylation levels (e.g., G4A60) did not further enhance permeability. Although unmodified G4 is toxic at 0.1 mM, 1.5- and 2-fold enhancements of cellular permeability can be achieved by increasing the G4A32 and G4A60 concentration from 0.01 to 0.1 mM, respectively (Figure 4B). Paradoxically, permeability at 1 mM G4A60 led to a significant decrease in its permeability, which

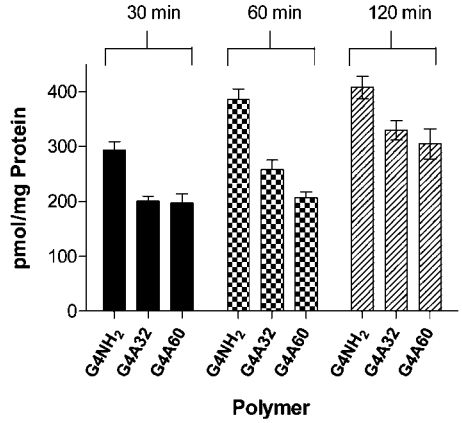


Figure 5. Cellular uptake (pmol of dendrimer/mg of protein) of 0.01 mM G4, G4A32, and G4A60 at 30, 60, and 120 min.

cannot be ascribed to intrinsic cytotoxicity and needs to be further addressed. Overall, the highest level of permeation enhancement was achieved at 0.1 mM with partially acetylated G4. It is interesting to note that the permeation enhancement of acetylated dendrimer is strongly correlated with [^{14}C]-mannitol permeability, but not to concomitant linear changes in TEER values. This would suggest that surface-modified PAMAM dendrimers do not enhance their permeability via the tight junctional route alone, but their enhanced cellular translocation may entail a combined effect on paracellular as well as transcellular permeation pathways.

Previous observations have shown that positively charged dendrimers exert higher permeability when compared to neutral and negatively charged dendrimers. Contrary to expectations, however, surface-modified dendrimers retained their permeability relative to unmodified dendrimers. Whereas this observation is unexpected, it should be noted that the effect of charge on permeability of dendrimer generation is generally more pronounced for lower-generation dendrimers (G2) (*7*). Alternatively, sustained permeability of surface-modified PAMAM dendrimers could be the result of a decrease in hydrophilicity of the polymers and/or conformational changes. Modification of the amine groups to amides renders the dendrimer surface neutral, thereby reducing the repulsive forces between amine groups and potentially leading to a more compact structural assembly. Another possible explanation for the increase in the permeability of G4A32 could be a reduction in nonspecific binding. Quintana and co-workers (*20*) reported that acetylation can be used to reduce nonspecific binding associated with amine-terminated nanoparticles. A decrease in the number of positively charged surface groups may reduce the nonspecific interaction of acetylated PAMAM dendrimers with the negatively charged cell membrane. This, in turn, may result in a relatively higher concentration of free dendrimer at the apical side of the membrane contributing to increased permeability through the paracellular route. These data are in good agreement with studies by Wiwattanapattapee and colleagues (*6*), who observed higher tissue uptake and lower serosal transfer rate for cationic dendrimers compared to anionic dendrimers. In addition, higher-generation dendrimers (G4) used in the current study will still carry a large number of internal tertiary amine groups, which can potentially interact with negatively charged cell membranes, enhancing permeability.

To further investigate their cellular entry mechanism, the uptake into Caco-2 cells of G4 surface-modified dendrimers was determined at nontoxic concentrations (0.01 mM). Assuming steady-state conditions after 30 min of equilibration, we found linear cellular accumulation of dendrimer with increasing incubation time (Figure 5), with a P_{app} (cm/s) of $1.7 \cdot \times 10^{-6}$, $3.0 \cdot \times 10^{-6}$, and $2.1 \cdot \times 10^{-6}$ for $G4NH_2$, G4A32, and G4A60, respectively. Although a significant decrease ($p < 0.05$) in initial uptake for acetylated G4 dendrimer was observed when compared to native dendrimer, there was no apparent decrease in permeability for G4A32 and G4A60, respectively. These data indicate that surface modification of cationic PAMAM dendrimers leads to only modest decreases in cellular uptake compared to native dendrimer, but results in a significant decrease in dendrimer-associated cytotoxicity.

Therapeutic agents are often conjugated to PAMAM dendrimers to gain an overall improvement of their bioavailability. Such surface modification can change cellular permeability characteristics and contribute to changes in the transepithelial transport of PAMAM dendrimers across intestinal cell lines. The remaining surface amine groups available on partially acetylated dendrimers can be used for drug loading and conjugation of targeting moieties to the PAMAM dendrimers while effectively reducing their cytotoxicity in parallel. Thus, the observations from the current study indicate that surface modification of PAMAM dendrimers is a strategy that can be utilized for oral drug delivery.

CONCLUSIONS

In this study, we differentially surface modified a series of cationic amine-terminated PAMAM dendrimers with acetyl groups. Although cationic dendrimers display concentration-dependent cytotoxicity, we observed a significant reduction of cellular toxicity with an increase in surface modification. Cell viability was strongly correlated with surface density of amine groups regardless of dendrimer generation. Surface-modified PAMAM dendrimers displayed permeability and uptake profiles similar to those of unmodified (native) dendrimer. Thus, acetylated PAMAM dendrimers feature reduced cytotoxicity while maintaining appreciable permeability. Taken together, these results suggest that it is possible to tailor-make surface-modified PAMAM dendrimers for specific oral drug delivery needs.

ACKNOWLEDGMENT

Authors appreciate the efforts of Dr. Julie A. Ray for assisting with MALDI-TOF MS experiments. Financial support for Rohit Kolhatkar was made possible by Department of Defense (Multidisciplinary Postdoctoral Fellowship W81XWH-06-1-0698) and for Kelly Kitchens from National Institute of General Medical Sciences (Predoctoral National Research Service Award F31-GM67278). Support was also provided by NIH R01 EB007470.

LITERATURE CITED

(1) Duncan, R. (2006) Polymer conjugates as anticancer nanomedicines. *Nat. Rev. Cancer 6*, 688–701.

(2) Rosen, H., and Abribat, T. (2005) The rise and rise of drug delivery. *Nat. Rev. Drug Discovery 4*, 381–385.

(3) Najlah, M., and D'Emanuele, A. (2006) Crossing cellular barriers using dendrimer nanotechnologies. *Curr. Opin. Pharmacol. 6*, 522–7.

(4) Kitchens, K. M., El-Sayed, M. E., and Ghandehari, H. (2005) Transepithelial and endothelial transport of poly (amidoamine) dendrimers. *Adv. Drug Delivery Rev. 57*, 2163–76.

(5) Duncan, R., and Izzo, L. (2005) Dendrimer biocompatibility and toxicity. *Adv. Drug Delivery Rev. 57*, 2215–2237.

(6) Wiwattanapatapee, R., Carreno-Gomez, B., Malik, N., and Duncan, R. (2000) Anionic PAMAM dendrimers rapidly cross adult rat intestine in vitro: A potential oral delivery system? *Pharm. Res. 17*, 991–998.

(7) Kitchens, K. M., Kolhatkar, R. B., Swaan, P. W., Eddington, N. D., and Ghandehari, H. (2006) Transport of poly(amidoamine) dendrimers across Caco-2 cell monolayers: influence of size, charge and fluorescent labeling. *Pharm. Res. 23*, 2818–26.

(8) Roberts, J., Bhalgat, M., and Zera, R. (1996) Preliminary biological evaluation of polyamidoamine (PAMAM) Starburst-(TM) dendrimers. *J. Biomed. Mater. Res. 30*, 53–65.

(9) Malik, N., Wiwattanapatapee, R., Klopsch, R., Lorenz, K., Frey, H., Weener, J., Meijer, E., Paulus, W., and Duncan, R. (2000) Dendrimers: Relationship between structure and biocompatibility in vitro, and preliminary studies on the biodistribution of I-125-labelled polyamidoamine dendrimers in vivo. *J. Controlled Release 65*, 133–148.

(10) Jevprasesphant, R., Penny, J., Jalal, R., Attwood, D., McKeown, N., and D'Emanuele, A. (2003) The influence of surface modification on the cytotoxicity of PAMAM dendrimers. *Int. J. Pharm. 252*, 263–266.

(11) El-Sayed, M., Ginski, M., Rhodes, C., and Ghandehari, H. (2002) Transepithelial transport of poly(amidoamine) dendrimers across Caco-2 cell monolayers. *J. Controlled Release 81*, 355–65.

(12) El-Sayed, M., Ginski, M., Rhodes, C., and Ghandehari, H. (2003) Influence of surface chemistry of poly(amidoamine) dendrimers on Caco-2 cell monolayers. *J. Bioact. Compat. Polym. 18*, 7–22.

(13) Jevprasesphant, R., Penny, J., Attwood, D., McKeown, N., and D'Emanuele, A. (2003) Engineering of dendrimer surfaces to enhance transepithelial transport and reduce cytotoxicity. *Pharm. Res. 20*, 1543–1550.

(14) Majoros, I. J., Myc, A., Thomas, T., Mehta, C. B., and Baker, J. R., Jr. (2006) PAMAM dendrimer-based multifunctional conjugate for cancer therapy: synthesis, characterization, and functionality. *Biomacromolecules 7*, 572–9.

(15) Majoros, I., Keszler, B., Woehler, S., Bull, T., and Baker, J. (2003) Acetylation of poly(amidoamine) dendrimers. *Macromolecules 36*, 5526–5529.

(16) Lee, I., Athey, B., Wetzel, A., Meixner, W., and Baker, J. (2002) Structural molecular dynamics studies on polyamidoamine dendrimers for a therapeutic application: Effects of pH and generation. *Macromolecules 35*, 4510–4520.

(17) Singh, A. K., Kasinath, B. S., and Lewis, E. J. (1992) Interaction of polycations with cell-surface negative charges of epithelial cells. *Biochim. Biophys. Acta 1120*, 337–42.

(18) Ryser, H. J. (1967) A membrane effect of basic polymers dependent on molecular size. *Nature 215*, 934–6.

(19) Fischer, D., Li, Y., Ahlemeyer, B., Krieglstein, J., and Kissel, T. (2003) In vitro cytotoxicity testing of polycations: influence of polymer structure on cell viability and hemolysis. *Biomaterials 24*, 1121–31.

(20) Quintana, A., Raczka, E., Piehler, L., Lee, I., Myc, A., Majoros, I., Patri, A., Thomas, T., Mule, J., and Baker, J. (2002) Design and function of a dendrimer-based therapeutic nanodevice targeted to tumor cells through the folate receptor. *Pharm. Res. 19*, 1310–1316.

BC0603889

Enhanced Retention of the α-Particle-Emitting Daughters of Actinium-225 by Liposome Carriers

Stavroula Sofou,*,†,§ Barry J. Kappel,† Jaspreet S. Jaggi,† Michael R. McDevitt,† David A. Scheinberg,† and George Sgouros‡

Molecular Pharmacology and Chemistry, Memorial Sloan-Kettering Cancer Center, 1275 York Avenue, New York, New York 10021, and Department of Radiology, Division of Nuclear Medicine, Johns Hopkins Medicine, 4M61 Cancer Research Building II, 1550 Orleans Street, Baltimore, Maryland 21231. Received March 6, 2007; Revised Manuscript Received July 30, 2007

Targeted α-particle emitters hold great promise as therapeutics for micrometastatic disease. Because of their high energy deposition and short range, tumor targeted α-particles can result in high cancer-cell killing with minimal normal-tissue irradiation. Actinium-225 is a potential generator for α-particle therapy: it decays with a 10-day half-life and generates three α-particle-emitting daughters. Retention of ^{225}Ac daughters at the target increases efficacy; escape and distribution throughout the body increases toxicity. During circulation, molecular carriers conjugated to ^{225}Ac cannot retain any of the daughters. We previously proposed liposomal encapsulation of ^{225}Ac to retain the daughters, whose retention was shown to be liposome-size dependent. However, daughter retention was lower than expected: 22% of theoretical maximum decreasing to 14%, partially due to the binding of ^{225}Ac to the phospholipid membrane. In this study, Multivesicular liposomes (MUVELs) composed of different phospholipids were developed to increase daughter retention. MUVELs are large liposomes with entrapped smaller lipid-vesicles containing ^{225}Ac. PEGylated MUVELs stably retained over time 98% of encapsulated ^{225}Ac. Retention of ^{213}Bi, the last daughter, was 31% of the theoretical maximum retention of ^{213}Bi for the liposome sizes studied. MUVELs were conjugated to an anti-HER2/neu antibody (immunolabeled MUVELs) and were evaluated *in vitro* with SKOV3-NMP2 ovarian cancer cells, exhibiting significant cellular internalization (83%). This work demonstrates that immunolabeled MUVELs might be able to deliver higher fractions of generated α-particles per targeted ^{225}Ac compared to the relative fractions of α-particles delivered by ^{225}Ac-labeled molecular carriers.

INTRODUCTION

Targeted α-particle emitters hold great promise as therapeutic agents for micrometastases (*1*). Alpha-particles are highly potent cytotoxic agents, potentially capable of killing tumor cells without limiting morbidity. The increased effectiveness of α-particles is due to the amount of energy deposited per unit distance traveled (high LET), which is of the order of approximately 80 keV/μm. Cell survival studies have shown that α-particle-induced killing is independent of oxygenation state or cell-cycle during irradiation and that as few as 1–3 tracks across the nucleus may result in cell death (*2–4*). In addition, the 50- to 100-μm range of α-particles is consistent with the dimensions of micrometastatic disseminated disease, allowing for localized irradiation of target cells with minimal normal-cell irradiation. Actinium-225 (^{225}Ac) is an α-particle emitter with increased cell killing efficacy (*5–7*) because each actinium-225 decay ($t_{1/2}$ = 10 d) generates three α-particle-emitting daughters (^{221}Fr ($t_{1/2}$ = 4.9 min), ^{217}At ($t_{1/2}$ = 32.3 ms), and ^{213}Bi ($t_{1/2}$ = 45.59 min)) and a total of 4 α -particles per decay. Thus, ^{225}Ac is an attractive candidate for α-particle therapy.

However, the optimal increase in the cell killing efficacy of ^{225}Ac will occur only if all (or most of the) α-emissions occur at the tumor site; otherwise, toxicity may be potentially increased. This is a fundamental difficulty if antibodies or other molecules with attached chelating ligands are to be used as the cell targeting vehicle since the coordination bonds from the chelate to the ^{225}Ac atom will not be retained after the decay of ^{225}Ac. This will leave the first daughter in the decay-chain free to distribute throughout the body where it and the resulting daughters will decay and increase toxicity. Thus, confinement of the intermediate radioactive daughters within the delivery carrier (during circulation) and at the tumor (after targeting) is desirable.

Liposomes have been previously considered for diagnostic and therapeutic delivery of radionuclides (*8–10*). We have previously investigated the encapsulation of ^{225}Ac in liposomes as a means of retaining the α-particle-emitting daughters within liposomes during delivery (*11*). Because of their high kinetic energy, α-particle emissions will escape the liposomal phospholipid membrane to irradiate the targeted cells. Similarly, daughter atoms, during their recoil trajectory (80 to 90 nm), can also penetrate the phospholipid membranes. Because the newly produced daughter atoms are charged, after losing their recoil energy, they cannot diffuse freely across the hydrophobic compartment of the phospholipid bilayer. Consequently, if the end point of a radioactive daughter's recoil trajectory is located within a liposome, the lipid membrane will inhibit free diffusion of the radioactive daughters, thereby retaining them at the site of liposome delivery. The probability of daughter retention is greater for larger liposomes, assuming homogeneous distribution of the parent radionuclides within the liposomal aqueous core.

Our theoretical calculations (*11*) predicted negligible, <0.001 %, (last) daughter retention for 100 nm diameter liposomes and more than 50% retention (of the last daughter) for liposomes larger then 650 nm (in diameter). For giant liposomes with 1 μm diameter, the maximum calculated retention of the last

* Corresponding author. Phone: (718) 260-3863. Fax: (718) 260-3327. E-mail: ssofou@poly.edu.

† Memorial Sloan-Kettering Cancer Center.

‡ Johns Hopkins Medicine.

§ Present address: Othmer-Jacobs Department of Chemical and Biological Engineering, Polytechnic University, 6 MetroTech Center, Brooklyn, New York 11201.

10.1021/bc070075t CCC: $37.00 © 2007 American Chemical Society
Published on Web 10/13/2007

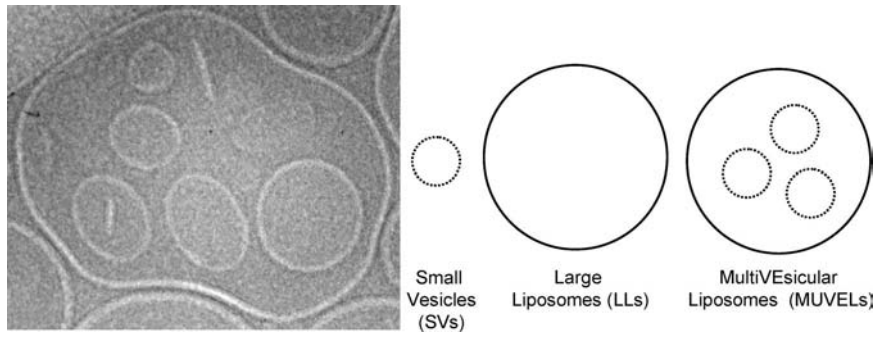


Figure 1. Cryo-TEM image of multivesicular liposomes (horizontal edge is approximately 400 nm), and schematic representation of Multivesicular liposomes (MUVELs) and their components.

daughter does not exceed 65%. However, the measured last daughter retention (11 % decreasing to 7% after 10 days) of 650 nm diameter liposomes was not consistent with the theoretical prediction (50%), and this was shown to be caused, in part, by the binding of ^{225}Ac to the phospholipid membrane. Actinium-225 localization at the liposomal membrane increases daughter loss after nuclear recoil, compared to daughter loss from uniformly distributed ^{225}Ac atoms within the liposomal aqueous core. In this work, we describe and characterize a construct designed to overcome this problem.

To increase daughter retention during circulation, ^{225}Ac was passively entrapped in multivesicular liposomes (MUVELs) (Figure 1). MUVELs are large liposomes (LLs) with entrapped small vesicles (SVs). Actinium-225 was only contained in the small vesicles. This strategy provides (1) confinement of entrapped ^{225}Ac within the aqueous compartment of the large liposomes (LLs) where the small vesicles are contained and thus away from the membrane of large liposomes, and (2) decreased radionuclide partition to the external membrane (large liposome membrane), due to increased internal membrane because of the encapsulated small vesicles. Retention of ^{225}Ac and its last radioactive daughter ^{213}Bi by MUVEL was evaluated over time. In these studies, MUVELs were PEGylated to assure long blood circulation times (*12*). MUVELs were then labeled with the monoclonal anti-HER2/neu antibody Trastuzumab (immunolabeled MUVELs) and were evaluated *in vitro* for targeted delivery of ^{225}Ac to ovarian carcinoma cells (SKOV3-NMP2).

EXPERIMENTAL PROCEDURES

Reagents. The lipids 1,2-dimyristoyl-*sn*-glycero-3-phosphocholine (DMPC), 1,2-diheneicosanoyl-*sn*-glycero-3-phosphocholine (21:0 PC), 1,2-dipalmitoyl-sn-glycero-3-phosphoethanolamine-*N*-[methoxy(polyethyleneglycol)-2000] (ammonium salt) (PEG-labeled lipid), L-α-phosphatidylethanolamine-*N*-(lissamine rhodamine B sulfonyl) (egg) (rhodamine-PE), and 1,2-distearoyl-*sn*-glycero-3-phosphoethanolamine-*N*-[maleimide (polyethylene glycol) 2000] (ammonium salt) (maleimide-PE) (purity >99%) were purchased from Avanti Polar Lipids (Alabaster, Al). Cholesterol, phosphate buffered saline (PBS), fluorexon (calcein), Sephadex G-50, diethylenetriaminepentaacetic acid (DTPA), ascorbic acid, and Triton X-100 were purchased from Sigma-Aldrich (St. Louis, MO). *p*-Isothiocyanatobenzyl-1,4,7,10-tetraazacyclododecane-1,4,7,10-tetraacetic acid (DOTA) was purchased from Macrocyclics (Dallas, TX). Traut's reagent (2-Iminothiolane-HCl) was purchased from Pierce (Rockford, IL). Actinium-225 nitrate was purchased from the Department of Energy, Oak Ridge National Laboratories (Oak Ridge, TN).

Liposome Preparation. The protocol to prepare MUVELs involves passive entrapment of small vesicles (SVs) into large liposomes (LLs). The phospholipid-cholesterol combinations chosen for the encapsulated small vesicles (SVs) and the large liposomes (LLs) were those that resulted in (1) the lowest release of contents by SVs after annealing at 40 °C (40 °C annealing is required for the hydration of the membranes of the LLs that contain encapsulated SVs), (2) the greatest passive entrapment efficacy by the LLs, and (3) the minimum fraction of fusion between lipids of SVs and LLs.

To make small vesicles, mixtures of phosphatidyl choline (21:0 PC), cholesterol (1:1 molar ratio), and PEG-labeled lipids (5.3 mol % of total lipid) in $CHCl_3$ were dried in a rotary evaporator. For ^{225}Ac passive entrapment, the lipids (30 mM final concentration) were resuspended in PBS (1 mM EDTA, pH 7.4) containing the chelated actinium complex (^{225}Ac-DOTA, 3.7–37.0 MBq, depending on radionuclide availability) and DTPA (1 mM). DTPA was used to potentially chelate free ^{225}Ac and ^{213}Bi. The protocol for ^{225}Ac-DOTA chelation is published elsewhere (*5*). The lipid suspension was then annealed to 55 °C for 2 h. Small vesicles were prepared by brief sonication (1–2 min) of the lipid suspension in a bath sonicator (Branson, Danbury, CT) at 75–80 °C until the appearance of a clear solution. The vesicle suspension was then incubated at room temperature for 15 min with 0.050 mL of externally added 10 mM DTPA to complex any free metals before purification during size-exclusion chromatography (SEC) in a Sephadex G-50 (Aldrich, St. Louis, MO) packed 1 × 10 cm column, eluted with sucrose isotonic PBS.

Then to prepare MUVELs, small vesicles were passively encapsulated into large liposomes (LLs). For LLs, mixtures of phosphatidyl choline (DMPC), cholesterol (2:1 molar ratio), maleimide-PEG-labeled lipids (1 mol % of total lipid) and PEG-labeled lipids (4.3 mol % of total lipid) in $CHCl_3$ were dried in a rotary evaporator. For passive entrapment of small vesicles, the dry lipids (60 mM final lipid concentration) were resuspended in the isosmolar sucrose–PBS suspension containing small vesicles (described above). The lipid suspension was then annealed to 40 °C for 2 h. MUVELs were prepared by the extrusion method. The lipid suspension was taken through 21 cycles of extrusion (LiposoFast, Avestin, Ontario, Canada) through two stacked polycarbonate filters (800 nm filter pore diameter) and then diluted in sucrose-free isosmotic PBS solution. Unentrapped small vesicles were removed by centrifugation, and the majority of MUVELs (90% as calculated by the fluorescent intensity of rhodamine-labeled lipids in parallel measurements) were collected in the pellet.

Plain large liposomes (LLs) were prepared as described above, without encapsulating small vesicles.

In all preparations, ascorbic acid (8 mmol/L) was coentrapped to minimize lipid oxidation due to gamma- (*13*) and beta-radiation (*14*), and possibly due to alpha-emissions (*15, 16*).

Liposome Size Distribution Determination. For dynamic light scattering (DLS), an N4 Plus autocorrelator (Beckman-Coulter) was used, equipped with a 632.8 nm He-Ne laser light source. The measurement protocol is published elsewhere (*11*).

Cryo-TEM. MUVELs were imaged using a FEI Tecnai 20 cryo-TEM. Measurements were performed by the staff of the Analytical Imaging Facility at the Albert Einstein College of Medicine, Yeshiva University. Samples were frozen, and thin frozen sections were imaged without staining.

Retention of Entrapped Contents by Liposomes. The protocol to measure the retention of ^{225}Ac and its last radioactive daughter ^{213}Bi by liposomes is described in detail elsewhere (*11*). Briefly, the γ-emissions (radioactivity increase over time and equilibrium values) of ^{213}Bi were measured in liposome fractions, which were separated, at different times, from the parent liposome population and the free radionuclides by SEC (Sephadex G-50). The samples were counted using a Cobra γ-counter (Packard Instrument Co., Inc.). For monitoring ^{213}Bi, the energy window 360–480 keV was used, and for ^{225}Ac, the window 150–600 keV was used, which includes the chief ^{221}Fr and ^{213}Bi photopeaks. Repeated measurements were performed on three different preparations of each liposome structure.

Liposome Immunolabeling. The protocol to immunolabel liposomes is described elsewhere (*17*). Briefly, Trastuzumab purified from Herceptin (Genentech, South San Francisco, CA) or Rituximab (used as isotype-matched control mAb to Trastuzumab in the flow cytometry studies) was activated with Traut's reagent, and was reacted with maleimide-lipids contained in liposomes (1 mol % of total lipid). In purified immunoliposome suspensions (after SEC in 4B Sepharose, 1 × 10 cm), a protein assay was used to quantify the concentration of antibodies, and lipid concentration was determined by the fluorescence intensity of rhodamine-lipids contained in liposomes (0.5–1 mol % of total lipid). Using the measured values of conjugated antibodies per lipid, the average number of antibodies per liposome was calculated (*17*) using for input values the mean size of liposomes (as measured by DLS) and the head group surface area per lipid (70 Å^2) (*18*).

Trastuzumab was also directly radiolabeled with ^{225}Ac. This preparation protocol is published elsewhere (*5, 19*). Conventional labeling of a DOTA-IgG construct does not yield stable product in high yield under any conditions (*19, 20*), which led to the development of the 2-step labeling method. Briefly, the antibody was radiolabeled in 2-steps: the first step entails ^{225}Ac + DOTA-NCS, which proceeded to >95% completion in 30 min; the second step involves the conjugation of the reactive isothiocyanate moiety on the ^{225}Ac -DOTA-NCS product with lysines on the Trastuzumab. This synthetic path was used as the ^{225}Ac + DOTA chelation only goes to completion at elevated temperatures, 55–60 °C, a temperature that will denature the IgG.

Immunoreactivity. Cells were washed twice with ice-cold PBS and blocked by incubation on ice with 2% BSA. Then, ^{225}Ac-labeled antibody (2.6 ng) in 1% HSA, small vesicles, and liposomes (LLs and MUVELs) at 1.0–1.9 μg and 100–190 μg total lipid were added to 10^7 cells and incubated on ice for 30 min. Cells were then washed twice with ice-cold PBS and centrifuged. Twenty-four hours later, supernatants and pellets were counted by scintigraphy (Beckman-Coulter, Fullerton, CA).

Cell Line. The metastatic ovarian carcinoma cell line, SKOV3-NMP2, was derived from serial passage of the parental SKOV3 cell line in nude mice (*21*) and used. Stock T-flask cultures (*20*) were propagated at 37 °C, in 5% CO_2 in RPMI 1640 media supplemented with 10% fetal calf serum (Sigma-Aldrich), 100 units/mL penicillin, and 100 μg/mL streptomycin. Cell concentration was determined by counting trypsinized cells with a hemocytometer.

Cell Binding and Internalization of Liposomes and Radiolabeled Antibody. Harvested SKOV3-NMP2 cells were washed twice with ice-cold media (RPMI 1640/10% FBS/2% BSA) and then resuspended in ice-cold media at a density of 10^6 cells/mL. Radiolabeled liposomes (0.1–1.8 μM lipid, final concentration) or antibody (25 ng) were added to 3.5 mL of cell suspension, and two 200 μL samples were immediately taken and processed as described below. The cells were then placed in a humidified 37 °C incubator with 5% CO_2, where they were periodically swirled and sampled at 0.5, 1, 2, 4, and 24 h. The cells were washed three times with 2 mL of ice-cold PBS, and then 1 mL of an acidic striping buffer (50 mM glycine and150 mM NaCl, pH 2.8) was added for 10 min at room temperature to eliminate the charge-specific binding of membrane-bound conjugates and to remove the surface-bound immunoliposomes or antibodies. After centrifugation, supernatants and pellets were allowed to reach equilibrium before counting (20h).

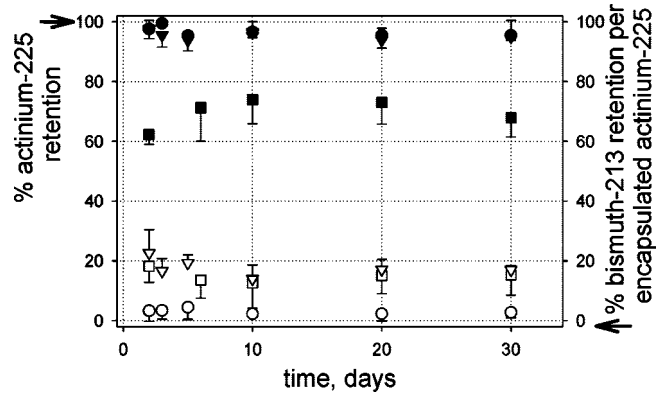


Figure 2. Fraction of ^{225}Ac retention (upper left, closed symbols) and ^{213}Bi retention per encapsulated ^{225}Ac (lower right, open symbols) by multivesicular liposomes (MUVELs) (triangles), large liposomes (LLs) (squares), and small vesicles (SVs) (circles) during 30 days. The error bars correspond to standard deviations of measurements performed on three different preparations of each liposome structure.

Flow Cytometry. Liposomal membranes were labeled with the fluorescent lipid rhodamine-PE (excitation, 550 nm; emission, 590 nm). Harvested cells (ovarian cancer SKOV3-NMP2 cells and fibroblast AL67 cells) were washed three times with ice-cold buffer (PBS/0.5% BSA/0.02% NaN_3) and then resuspended at a density of 5.6 × 10^6 cells/mL. Then 10^6 cells were incubated on ice with liposomes for 25 min (3.3 mM final lipid concentration), washed three times, and finally resuspended at a density of 2.5 × 10^6 cells/mL. To determine the extent of specific binding of immunoliposomes to the HER2/neu antigen receptor, cells were also preincubated with Trastuzumab at 5 μg of antibody per one million cells for 25 min on ice. Cells were then washed twice with ice-cold buffer and incubated with liposomes as above. Fluorescence counting of cell suspensions (50,000 events) was measured using a Beckman-Coulter Cytonics FC500 flow cytometer (Fullerton, CA), and analyzed with the software FlowJo (Tree Star, Inc., Ashland, OR).

RESULTS

Retention of ^{225}Ac by Liposomal Structures. In multivesicular liposomes (MUVELs), ^{225}Ac was encapsulated only into small vesicles (SVs). For 30 days (Figure 2, upper part), more than 95% of the encapsulated ^{225}Ac activity was retained by MUVELs (black triangles) and SVs (black circles). In large liposomes (LLs), only 70% of ^{225}Ac was retained stably over time (black squares).

The retention of ^{225}Ac by liposomes depends on the permeability of the liposomal membrane to the ^{225}Ac–DOTA complex and is not dependent on the radioactive character of ^{225}Ac, which after its recoil may eject the next daughter out of the physical boundaries of liposomes (as is the case for ^{213}Bi). The results on ^{225}Ac retention are identical for both MUVELs and the small

vesicles (SVs) (Figure 2). In both of these cases, ^{225}Ac is encapsulated into the same rigid membranes composed of diheneicosanoyl phosphocholine (21:0 PC, $T_g = 72$ °C) and cholesterol. Small vesicles (SVs) comprised this lipid composition. In MUVELs, the encapsulated small vesicles (SVs) that contain ^{225}Ac also comprise exactly this lipid composition. However, large liposomes (LLs) are made up of more fluid lipids (dimyristoyl phosphocholine (16:0, $T_g = 23$ °C) and cholesterol) that appear to have more permeable membranes to ^{225}Ac–DOTA complexes.

Retention of ^{213}Bi by Liposomal Structures. MUVELs (white triangles) and LLs (white squares) retained over a period of 30 days (Figure 2, lower part), 17 ± 3% and 15 ± 7% of ^{213}Bi, respectively (approximately one-third of the theoretical maximum) (*11*). Both MUVELs and LLs exhibited almost identical ^{213}Bi retention profiles per encapsulated ^{225}Ac nucleus, suggesting that the particular composition of the (external) liposomal membrane does not promote radionuclide localization as opposed to the lipid composition chosen in our first studies (*11*). However, as shown above (Figure 2, upper part), LLs failed to adequately retain the parent ^{225}Ac. Therefore, MUVELs increase the fraction of overall delivered daughters. For example, on day 20, the retention of ^{213}Bi by MUVELs is 17% and by LLs is 15% of the total ^{213}Bi per encapsulated ^{225}Ac. The retention of ^{225}Ac by MUVELs is 94% and by LLs is 73% of the initially encapsulated radioactivity. Therefore, in terms of the initially encapsulated ^{225}Ac radioactivity, $0.17 \times 0.94 = 16\%$ and $0.15 \times 0.73 = 11\%$ of ^{213}Bi is delivered at the site of MUVELs and LLs, respectively.

Also, the insignificant retention of ^{213}Bi (white circles) by small vesicles with sizes comparable to the recoil range of the α-emitting daughters is consistent with our previous theoretical predictions (*22*).

Liposome and Antibody Radiolabeling and Quality Control. More than 95% of ^{225}Ac was chelated to DOTA. The maximum encapsulation efficiency of ^{225}Ac by the liposomal structures using passive entrapment did not exceed 10% of the total initial activity.

The efficiency of radioconjugation to antibody was low with a radiochemical yield of 3% (of the total activity applied) and resulted in radiolabeled antibodies with low specific activity, 1.406 KBq/μg. The radiosynthesis of the ^{225}Ac–DOTA-IgG constructs has been described (*19*), and while the products were radiochemically pure and biologically reactive, the yields were low (<10%). The antibody was radiolabeled in 2-steps, and the specifications and yields of the ^{225}Ac–DOTA-Trastuzumab construct were similar (*20, 23*) to those of the other constructs tested (*19*). The low yield in the second step results from the competing hydrolysis reaction of the isothiocyanate moiety. The mass amounts of DOTA and IgG as well as the activity amount of ^{225}Ac were optimized (*19*), and adding more or less of any of these components will not significantly improve the overall yield. The reported specific activity 1.406 kBq/μg (0.038 Ci/g) was on the same order as the specific activities used clinically with the ^{225}Ac–DOTA-HuM195 therapeutic drug (*24*), and these small doses have demonstrated antileukemic effects.

The conjugation reaction resulted in 937 ± 110 antibodies per liposome. Leakage of entrapped radioactive or fluorescent (calcein) content due to conjugation was not detected (data not shown). The measured average large liposome size for MUVELs was 758 ± 287 nm.

The Her2/neu cell-surface density of $1–3 \times 10^5$ per cell was used (*25*), and approximately one Trastuzumab molecule per 100–300 cell receptors were mixed. The immunoreactivity of radiolabeled Trastuzumab was 65.74 ± 7.51%. For liposomes, two ratios were tested: (a) 100 liposomes per cell (or one liposome-conjugated antibody per 1–3 receptors) and (b) one liposome per cell (or one liposome-conjugated antibody per 100–300 receptors). The antigen binding activity of liposomes was similar for both ratios tested: 4.40 ± 0.89% of immunolabeled MUVELs and 1.83 ± 0.52% of immunolabeled LLs were bound to cells at both lipid-to-cell ratios. Small vesicles (SVs) that were not immunolabeled bound nonspecifically at a low extent (0.75 ± 0.02%).

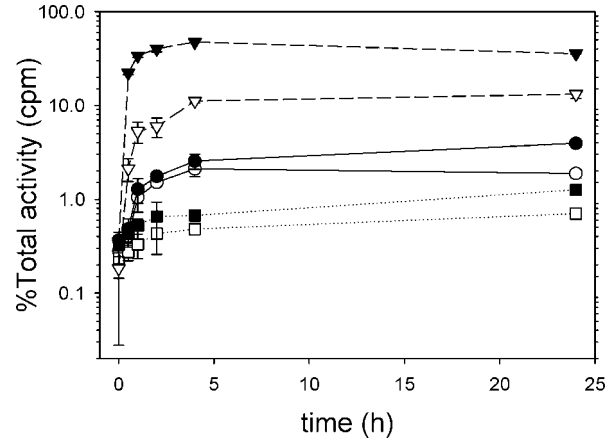


Figure 3. Cell binding and internalization of immunolabeled lipid-structures with encapsulated ^{225}Ac, and ^{225}Ac-conjugated antibody. Closed symbols: fraction of the total initial-activity that became cell-associated. Open symbols: fraction of cell-internalized activity. Triangles, radiolabeled antibody; circles, immunolabeled MUVELs; squares, immunolabeled LLs. The error bars correspond to standard deviations of measurements performed in duplicate.

Cell Binding and Internalization. After 4 h of incubation, the relative total cell-associated radioactivities (Figure 3, closed symbols), compared to $t = 0$, were 2-, 7-, and 135-fold higher for LLs (closed squares), MUVELs (closed circles), and the radiolabeled antibody (closed triangles), respectively. Both types of immunoliposomes (MUVELs and LLs) internalized to a greater extent than the antibody: 83% of the activity of bound immunolabeled MUVELs and 70% of the activity of bound immunolabeled LLs were internalized (4 h incubation) as opposed to only 23% of bound antibody. Also, the fraction of total cell-associated activity (^{225}Ac) delivered by immunolabeled MUVELs (2.5 ± 0.5%) was 3.8 times greater than the fraction of total associated radioactivity delivered by immunolabeled LLs (0.7 ± 0.1%), probably due to the less stable retention of the parent nuclide by LLs (Figure 2, upper part). For the same incubation time, the fraction of total cell-associated activity for nonimmunolabeled MUVELS, LLs, and SVs was 0.47%, 0.61%, and 0.16% of the total added radioactivity, respectively (data not shown). Cell uptake kinetics was significantly slower for all liposome structures compared to that of the radiolabeled antibody.

Using flow cytometry, a significant shift in fluorescence counts (one log unit) was detected only when anti-HER2/neu-immunoliposomes were incubated with SKOV3-NMP2 cells with unblocked HER2/neu receptors (Figure 4A, thick line). Neither specific nor nonspecific binding of liposomes to AL67 (fibroblast cells not expressing the HER2/neu receptor) was detected. The specificity of binding of Trastuzumab-conjugated liposomes to SKOV3-NMP2 cells was also compared to the binding of liposomes conjugated to Rituximab, an anti-CD20 antibody that was used as the isotype-matched control to Trastuzumab. Trastuzumab-labeled liposomes resulted in a shift of fluorescence counts of SKOV3-NMP2 cells that was more

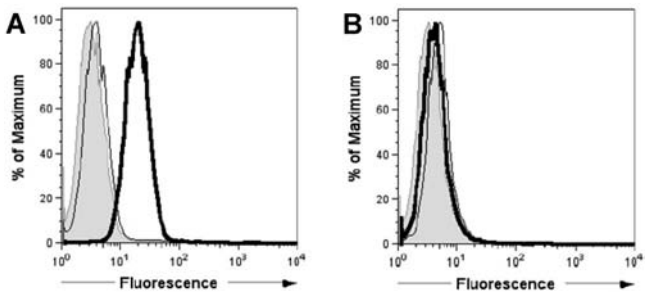


Figure 4. Binding of rhodamine-lipid-containing Trastuzumab-labeled liposomes to SKOV3-NMP2 (A) and AL67 cells (B). Area shaded gray, cells; thin line, cell fluorescence due to immunoliposomes bound to cells that have been preincubated with Trastuzumab; thick line, cell fluorescence due to immunoliposomes bound to cells with unblocked receptors.

than one log unit greater than the shift measured for Rituximab-labeled liposomes. (flow data shown in Supporting Information).

DISCUSSION

Multivesicular liposomes (MUVELs) result in minimal leakage of ^{225}Ac and in significant retention of the α-emitting daughters. MUVELs with encapsulated ^{225}Ac deliver 2.8 out of 4 α-particles emitted per ^{225}Ac decay. This ratio is calculated on the basis of the assumption that the last two radioactive daughters have the same probability x to be retained within liposomes after decay. Assuming probability one for the first daughter ^{221}Fr since ^{225}Ac should be confined close to the core of the large liposomes with a radius larger than the daughter's recoil distance, for the four decays (^{225}Ac to ^{221}Fr, ^{221}Fr to ^{217}At, ^{217}At to ^{213}Bi, and ^{213}Bi to stable ^{209}Pb) the probability of daughter retention (and thus targeted delivery of the subsequently emitted alphas) is x^2. From Figure 2, $1 \times x^2$ is approximately 0.18, x should be equal to 0.42, and the total alphas retained should equal to $1 + 1 + 0.42 \times 2 = 2.8$.

We have previously calculated that for liposomes as large as 750 nm in diameter (similar to the sizes of MUVELs and LLs) not more than 55% of generated ^{213}Bi from the total ^{213}Bi generated by the encapsulated ^{225}Ac is retained by liposomes and can therefore be expected to decay at the cite of the liposome carriers (*11*). These calculations were based on the average recoil trajectory of each daughter (80–90 nm) that is comparable to the size of the liposomal carriers. For this geometry, the probability that a generated daughter would be retained within a liposome decreases as the previous radioactive daughter's location approaches the liposome membrane at the time point of radionuclide decay. In addition, for every subsequent radioactive daughter, the probability of remaining within the physical limits of the liposomal carrier is decreasing compared to the probability corresponding to the previous radioactive daughter. MUVELs exhibit retention of ^{213}Bi that is 17–18% of the total ^{213}Bi generated by the encapsulated ^{225}Ac. In other words, these values correspond to 31–33 % of the theoretical maximum retention for this size of delivery carriers.

In vitro, immunolabeled MUVELs demonstrated greater specific binding to human ovarian carcinoma cells (SKOV3-NMP2) compared to nontargeted liposomes but showed lower immunoreactivity compared to that of the radiolabeled antibody. This result could be due to the relatively large size of liposomes that may interfere with the extracellular matrix by obstructing free diffusion towards the cell surface. The targeting antibodies were conjugated on the free ends of surface-grafted PEG chains of the same length (*26*) to exclude steric hindrance to targeting from neighboring grafted PEG chains. Also, cell uptake kinetics was slower for immunoliposomes compared to that of the free antibody, which could be justified by the different diffusibilities of each structure studied. Measured diffusion coefficients of free IgGs are of the order of 10^{-7} cm^2/s in water at 20 °C (*27*). At the same conditions, the calculated values for liposomes (using the Stokes–Einstein equation for spherical objects) are two orders of magnitude lower (10^{-9} cm^2/s).

In ^{225}Ac-radioimmunotherapy, renal toxicity can become a major dose constraint because of the localization of escaped ^{213}Bi in the kidneys (*28, 29*). MUVELs are proposed for retaining the radioactive daughters at the site of the carrier for the interval between the administration of the carriers and before the carriers are internalized by the targeted cancer cells. Such radioimmunoliposomes would reduce the fraction of escaped radioactive daughters and could potentially be used for the therapy of disseminated micrometastatic tumors in the peritoneal cavity using direct intraperitoneal administration. This approach could combine the following beneficial features: (a) targeting efficacy and specificity due to surface-conjugated tumor-specific antibodies (*17, 30*); (b) long retention times in the peritoneal cavity (*31, 32*) due to large liposome sizes; (c) direct tumor access (*20, 33, 34*) combined with a radiation dose range tailored to micrometastases that do not have developed vasculature (*35*) and cannot be differently accessed; and (d) minimal irradiation of the surrounding healthy tissues because of the α-particles' comparatively short range.

The stable retention of ^{225}Ac by MUVELs will probably be challenged in the presence of serum proteins *in vivo* since proteins are known to interact with the lipid membrane of these carriers in a variety of ways (*36*). Preliminary *in vivo* biodistributions of ^{225}Ac-loaded immunolabeled-liposomes (MUVELs and LLs) that were administered intraperitoneally in BALB/c nude mice bearing intraperitoneally disseminated SKOV3-NMP2 tumors resembling micrometastatic disease (*37*) suggest that *in vivo* MUVELs retain ^{225}Ac to a larger extent than LLs and therefore deliver higher activities of ^{213}Bi to the tumor sites. In addition, both types of immunoliposome compositions exhibit significant hepatic and splenic uptake that is characteristic of this size of drug carriers and could determine the maximum tolerated dose. The short range of α-particles emitted at the sites of normal organs could, however, result in relatively low toxicities at these organs because of the short range of α-particles.

Finally, immunolabeled MUVELs may be particularly useful in delivering lethal radiation doses to cancer cells with low expression levels of molecular targets (*38*). Actinium-225 labeled antibodies generally have low specific activity (1.406 MBq/mg in this study) that corresponds to one conjugated ^{225}Ac atom per 2,300 antibodies. For MUVELs, two passive entrapment steps are required (each with a maximum of 10% encapsulation efficiency). Thus, for 370 MBq (10 mCi) ^{225}Ac initial activity and 1% actinium overall entrapment efficacy, we can encapsulate one actinium nuclide per MUVEL and two actinium nuclides in every 8 MUVELs (for 4×10^{12} liposomes with a mean diameter of 750 nm). Our current work is focused on increasing the encapsulated ^{225}Ac activity within small vesicles using active (ionophore-driven) loading (*39*). Additional structural optimization of MUVELs is also required to further increase ^{213}Bi retention at the liposome sites.

Intraperitoneal micrometastatic disease constitutes a treatment challenge and is common among patients with advanced gynecological and gastrointestinal cancers. In this work, the ovarian carcinoma cells SKOV3-NMP2 were selected to prove the feasibility of targeted delivery *in vitro* of the α-particle nanogenerator ^{225}Ac and its radioactive daughters using immunolabeled MUVELs that can potentially be used against disseminated intraperitoneal micrometastases following locoregional administration. Our findings show that immunolabeled MUVELs retain a third of the theoretical maximum of the

radioactive daughters and that the cell-bound structures become considerably more internalized by ovarian cancer cells than the radiolabeled antibody. These results suggest that the effective numbers of α-particles emitted at the target per delivered ^{225}Ac using MUVELs could be significant, thus providing a promising therapeutic modality for disseminated micrometastatic disease. Additional optimization of MUVELs is necessary to increase the encapsulated radioactivity of ^{225}Ac in order to enable the evaluation of the potential of these liposomes for therapeutic use. Additional increase in daughter retention could be achieved by further increasing the size of the delivery carrier (to 1 μm diameter), but given the limitations of stable intact liposomes of such large diameters, different materials could probably be evaluated to form the outer large shell encapsulating Small Vesicles (SVs) with entrapped ^{225}Ac.

ACKNOWLEDGMENT

This work was supported by the USAMRMC Concept Award DAMD170010657, USAMRMC IDEA Award DAMD170310755, NIH R01 CA55349, the Experimental Therapeutics Center, and the Goodwin Commonwealth Foundation for Cancer Research. D.A.S. is a Doris Duke Distinguished Science Professor. S.S. is the recipient of Dr. Frederick E.G. Valergakis Graduate Research Grant of the Hellenic University Club of New York.

Supporting Information Available: Binding of rhodamine-lipid-containing immuno-liposomes to HER2/neu expressing SKOV3-NMP2 cells by flow cytometry. This information is available free of charge via the Internet at http://pubs.acs.org.

LITERATURE CITED

(1) Couturier, O., Supiot, O., Degraef-Mougin, M., Faivre-Chauvet, A., Carlier, T., Chatal, J. F., and Cherel, M. (2005) Cancer radioimmunotherapy with alpha-emitting nuclides. *Eur. J. Nucl. Med. Imaging 32*, 601–614.

(2) Humm, J. L. (1987) A microdosimetric model of astatine-211 labeled antibodies for radioimmunotherapy. *Int. J. Radiat. Oncol. Biol. Phys. 13*, 1767–1773.

(3) Humm, J. L., and Chin, L. M. (1993) A model of cell inactivation by alpha-particle internal emitters. *Radiat. Res. 134*, 143–150.

(4) Macklis, R. M., Kinsey, B. M., Kassis, A. I., Ferrara, J. L., Archer, R. W., Hines, J. J., Coleman, C. N., Adelstein, S. J., and Burakoff, S. J. (1988) Radioimmunotherapy with alpha-particle-emitting immunoconjugates. *Science 240*, 1024–1026.

(5) McDevitt, M. R., Ma, D., Lai, L. T., Simon, J., Borchardt, P., Frank, R. K., Wu, K., Pellegrini, V., Curcio, M. J., Miederer, M., Bander, N. H., and Scheinberg, D. A. (2001) Tumor therapy with targeted atomic nanogenerators. *Science 294*, 1537–1540.

(6) Kennel, S. J., Brechbiel, M. W., Milenic, D. E., Schlom, J., and Mirzadeh, S. (2002) Actinium-225 conjugates of MAb CC49 and humanized delta CH2CC49. *Cancer Biother. Radiopharm. 17*, 219–231.

(7) Kennel, S. J., Chappell, L. L., Dadachova, K., Brechbiel, M. W., Lankford, T. K., Davis, I. A., Stabin, M., and Mirzadeh, S. (2000) Evaluation of Ac-225 for vascular targeted radioimmunotherapy of lung tumors. *Cancer Biother. Radiopharm. 15*, 235–244.

(8) Emfietzoglou, D., Kostarelos, K., Papakostas, A., Yang, W. H., Ballangrud, A., Song, H., and Sgouros, G. (2005) Liposome-mediated radiotherapeutics within avascular tumor spheroids: comparative dosimetry study for various radionuclides, liposome systems, and a targeting antibody. *J. Nucl. Med. 46*, 89–97.

(9) Kostarelos, K., Emfietzoglou, D., Papakostas, A., W.H., Y., Ballangrud, A. M., and Sgouros, G. (2005) Engineering lipid vesicles of enhanced intratumoral transport capabilities: correlating liposome characteristics with penetration into human prostate tumor spheroids. *J. Liposome Res. 15*, 15–27.

(10) Zielhuis, S. W., Nijsen, J. F. W., Seppenwoodle, J. H., Zonnenberg, B. A., Bakker, C. J. G., Hennink, W. E., van Rijk, P. P., and van het Schip, A. D. (2005) Lanthanide bearing microparticulate systems for multi-modality imaging and targeted therapy of cancer. *Curr. Med. Chem: Anti-Cancer Agents 5*, 303–313.

(11) Sofou, S., Thomas, J. L., Lin, H.-Y., McDevitt, M. R., Scheinberg, D. A., and Sgouros, G. (2004) Engineered liposomes for potential α-particle therapy of metastatic cancer. *J. Nucl. Med. 45*, 253–260.

(12) Allen, C., Dos Santos, N., Gallagher, R., Chiu, G. N. C., Shu, Y., Li, W. M., Johnstone, S. A., Janoff, A. S., Mayer, L. D., Webb, M. S., and Bally, M. B. (2002) Controlling the physical behavior and biological performance of liposome formulations through use of surface grafted polyethylene glycol). *Biosci. Rep. 22*, 225–250.

(13) Stensrud, G., Redford, K., Smistad, G., and Karlsen, J. (1999) Effects of gamma irradiation on solid and lyophilised phospholipids. *Radiat. Phys. Chem. 56*, 611–622.

(14) Chakrabarti, M. C., Le, N., Paik, C. H., De Graff, W. G., and Carrasquillo, J. A. (1996) Prevention of radiolysis of monoclonal antibody during labeling. *J. Nucl. Med. 37*, 1384–1388.

(15) McDevitt, M. R., Finn, R. D., Sgouros, G., Ma, D., and Scheinberg, D. A. (1999) An Ac-225/Bi-213 generator system for therapeutic clinical applications: construction and operation. *Appl. Radiat. Isot. 50*, 895–904.

(16) Nikula, T. K., McDevitt, M. R., Finn, R. D., Wu, C., Kozak, R. W., Garmestani, K., Brechbiel, M. W., Curcio, M. J., Pippin, C. G., Tiffany-Jones, L., Geerlings, S. M. W., Apostolidis, C., Molinet, R., Geerlings, J. M. W., Gansow, O. A., and Scheinberg, D. A. (1999) Alpha-emitting bismuth cyclohexylbenzyl DTPA constructs of recombinant humanized anti-CD33 antibodies: pharmacokinetics, bioactivity, toxicity and chemistry. *J. Nucl. Med. 40*, 166–176.

(17) Kirpotin, D. B., Park, J. W., Hong, S. K., Zalipsky, S., Li, W.-L., Carter, P., Benz, C. C., and Papahadjopoulos, D. (1997) Sterically stabilized anti-HER2 immunoliposomes: design and targeting to human breast cancer cells. *in vitro. Biochemistry 36*, 66–75.

(18) Lasic, D. D. (1993) *Liposomes from Physics to Applications*, Elsevier, Amsterdam.

(19) McDevitt, M. R., Ma, D., Simon, J., Frank, R. K., Kiefer, G. E., and Scheinberg, D. A. (2002) Design and synthesis of actinium-225 radioimmunopharmaceuticals. *Appl. Radiat. Isot. 57*, 841–847.

(20) Borchardt, P., Yuan, R., Miederer, M., McDevitt, M., and Scheinberg, D. (2003) Targeted actinium-225 in vivo generators for therapy of ovarian cancer. *Cancer Res. 63*, 5084.

(21) Mujoo, K., Maneval, D. C., Anderson, S. C., and Gutterman, J. U. (1996) Adenoviral-mediated p53 tumor suppressor gene therapy of human ovarian carcinoma. *Oncogene 12*, 1617–1623.

(22) Ziegler, J. (1996) *Stopping and Range of Ions in Matter (SRIM96)*, IBM, Yorktown, New York.

(23) Ballangrud, Å., Yang, W.-H., Palm, S., Enmon, R., Borchardt, P., Pellegrini, V., McDevitt, M., Scheinberg, D., and Sgouros, G. (2004) Alpha-particle emitting atomic generator (actinium-225)-labeled Trastuzumab (herceptin) targeting of breast cancer spheroids: efficacy versus HER2/neu expression. *Clin. Cancer Res. 10*, 4489–4497.

(24) Jurcic, J., McDevitt, M., Divgi, C., Pandit-Taskar, N., Finn, R., Sgouros, G., Chanel, S., Larson, S., and Scheinberg, D. (2006) Alpha-particle immunotherapy for acute myeloid leukemia (AML) with bismuth-213 and actinium-225. *Cancer Biother. Radiopharm. 21*, s396.

(25) Dean, G. S., Pusztai, L., Xu, F. J., O'Briant, K., DeSombre, K., Conaway, M., Boyer, C. M., Mendelsohn, J., and Bast, R. C. J. (1998) Cell surface density of p185c-erbB-2 determines susceptibility to anti-p185c-erbB-2-Ricin A chain (RTA) immunotoxin therapy alone and in combination with anti-p170EGFR-RTA in ovarian cancer cells. *Clin. Cancer Res. 4*, 2545–2550.

(26) Maruyama, K., Takizawa, T., Yuda, T., Kennel, S. J., Huang, L., and Iwatsuru, M. (1995) Targetability of novel immunoliposomes modified with amphipathic poly(ethylene glycol)s conjugated at their distal terminals to monoclonal antibodies. *Biochim. Biophys. Acta 1234*, 74–80.

(27) Saltzman, W. M., Radomsky, M. L., Whaley, K. J., and Cone, R. A. (1994) Antibody diffusion in human cervical mucus. *Biophys. J. 66*, 508–515.

(28) Jaggi, J., Seshan, S. V., McDevitt, M. R., LaPerle, K., Sgouros, G., and Scheinberg, D. A. (2005) Renal tubulointerstitial changes after internal irradiation with alpha-particle-emitting actinium daughters. *J. Am. Soc. Nephrol. 16*, 2677–2689.

(29) Jaggi, J., Kappel, B. J., McDevitt, M. R., Sgouros, G., Flombaum, C. D., Cabassa, C., and Scheinberg, D. A. (2005) Efforts to control the errant products of a targeted in vivo generator. *Cancer Res. 65*, 4888–4895.

(30) Sapra, P., and Allen, T. M. (2003) Ligand-targeted liposomal anticancer drugs. *Prog. Lipid Res. 42*, 439–462.

(31) Sadzuka, Y., Hirota, S., and Sonobe, T. (2000) Intraperitoneal administration of doxorubicin encapsulating liposomes. *Toxicol. Lett. 116*, 51–59.

(32) Verschraegen, C., Kumagai, S., Davidson, R., Feig, B., Mansfield, P., Lee, S., Maclean, D., Hu, W., Khokhar, A., and Siddik, Z. (2003) Phase I clinical and pharmacological study of intraperitoneal cis-bis-neodecanoato(trans- R, R-1, 2-diaminocyclohexane)-platinum II entrapped in multilamellar liposome vesicles. *J. Cancer Res. Clin. Oncol. 129*, 549–555.

(33) Buijs, W. C. A. M., Tibben, J. G., Boerman, O. C., Molthoff, C. F. M., Massuger, L. F. A. G., Koenders, E. B., Schijf, C. P. T., Siegel, J. A., and Corstens, F. H. M. (1998) Dosimetric analysis of chimeric monoclonal antibody cMOv18 IgG in ovarian carcinoma patients after intraperitoneal and intravenous administration. *Eur. J. Nucl. Med. 25*, 1552–1561.

(34) Markman, M. (2003) Role of intraperitoneal chemotherapy in the front-line setting. *J. Clin. Oncol. 21*, 145s–148s.

(35) Li, C.-Y., Shan, S., Huang, Q., Braun, R. D., Lanzen, J., Hu, K., Lin, P., and Dewhirst, M. W. (2000) Initial stages of tumor cell-induced angiogenesis: evaluation via skin window chambers in rodent models. *J. Natl. Cancer Inst. 92*, 143–147.

(36) Lasic, D. D., and Martin, F. (1995) *Stealth Liposomes*, pp 289, CRC Press, Boca Raton, FL.

(37) Sofou, S., Enmon, R. M., McDevitt, M. R., Jaggi, J., Thomas, J. L., Scheinberg, D. A., and Sgouros, G. (2004) Multivesicular radioimmunoliposomes with encapsulated Actinium-225 for targeted alpha-particle therapy of intraperitoneal micrometastatic cancer. *Cancer Biother. Radiopharm. 19*, s518–519.

(38) McQuarrie, S. A., Mercer, J. R., Syme, A., Suresh, M. R., and Miller, G. G. (2004) Preliminary results of nanopharmaceuticals used in the radiotherapy of ovarian cancer. *J. Pharm. Sci. 7*, 29–34.

(39) Chang, M.-Y., Sgouros, G., and Sofou, S. (2006) Enhanced liposomal encapsulation of actinium-225: High loading activities and stable retention for potential therapeutic use. *Cancer Biother. Radiopharm. 21*, s394.

BC070075T

Conjugation of Polyamidoamine Dendrimers on Biodegradable Microparticles for Nonviral Gene Delivery

Xue-Qing Zhang, Janjira Intra, and Aliasger K. Salem*

Division of Pharmaceutics, College of Pharmacy, University of Iowa, Iowa City, Iowa 52242. Received April 5, 2007; Revised Manuscript Received May 30, 2007

We report on the preparation and characterization of poly(D,L-lactide-*co*-glycolide) (PLGA) microparticles with surface-conjugated polyamidoamine (PAMAM) dendrimers of varying generations. The buffering capacity and zeta-potential of the PLGA PAMAM microparticles increased with increasing generation level of the PAMAM dendrimer conjugated. Conjugation of the PAMAM dendrimer to the surface of the PLGA microparticle removed generation-dependent cytotoxicity in HEK293 and COS7 cell lines. PLGA PAMAM pDNA microparticles displayed similar cytotoxicity profiles to unmodified PLGA pDNA microparticles in COS7 cells. A generation three PAMAM dendrimer conjugated to PLGA microparticles significantly increased transfection efficiencies in comparison to unmodified PLGA microparticles.

1. INTRODUCTION

Delivery of plasmid DNA (pDNA) using biodegradable microparticles has shown significant potential for improving the efficacy of transgene expression (*1*). These microparticles are commonly prepared from poly (D,L-lactide-*co*-glycolide) (PLGA), a polymer that is biodegradable and biocompatible and has FDA approval for use in the clinic (*1–8*). Delivery of pDNA using PLGA microparticles can be achieved using two approaches. In the first approach, pDNA is entrapped into the matrix of the microparticle, allowing for sustained release. Drawbacks to this approach include inactivation of the pDNA during the harsh manufacturing conditions of the microparticles. These conditions include exposure to organic solvents and shear forces associated with the homogenization and sonication steps (*3, 5, 8*). Several approaches have sought to overcome these limitations. These approaches include incorporating cationic excipients that condense and protect the pDNA during entrapment or minimizing shear stress during homogenization by using a cryopreparation modification of the double emulsion method (*9*). In the second approach, pDNA is adsorbed onto the surface of the microparticles after they have been prepared (*3, 10–13*). This method prevents pDNA damage due to microparticle preparation techniques. This approach has found the most promise in genetic vaccination applications (*11, 13, 14*). In addition, microparticles can be loaded with drugs or proteins that complement or enhance the efficacy of the surface-bound pDNA. To bind the pDNA to the surface of the microparticles, a cationic agent is typically incorporated into the formulation method to prepare microparticles that have a net positive charge (*3, 10–13*). This facilitates binding of the negatively charged pDNA to the surface of the microparticles by electrostatic interactions. Approaches to date for preparing cationic microparticles have included the use of cationic surfactants such as cetyltrimethylammoniumbromide (CTAB) (*15*) or cationic polymers such as polyethyleneimine (PEI) that are adsorbed, blended, or covalently attached to the microparticles (*3, 10, 13, 16, 17*). In this study, we prepare PLGA microparticles that have cationic polyamidoamine (PAMAM) dendrimers covalently attached to the surface of the PLGA microparticles. PAMAM dendrimers have several advantages over linear cationic polymers (*18, 19*). Similar to polymers such as PEI, PAMAM dendrimers have both primary and secondary amines that generate significant buffering capacity (*18, 19*). This imparts the carriers with the ability to release from the endosomes into the cytoplasm via the proton sponge mechanism (*19,20*). In comparison to PEI, however, dendrimers are nanoscale, spherical, monodisperse polymers that display lower cytotoxicity and reduced structural density in the intramolecular core (*19*). As the generation of the PAMAM dendrimer increases, the transfection efficiency increases (*21, 22*). A drawback to PAMAM dendrimers, however, is their generation-dependent cytotoxicity (*21–23*). As the generation of the PAMAM molecule increases, its cytotoxicity increases proportionally. In this study, we show, for the first time, that conjugation of PAMAM dendrimers onto the surface of PLGA microparticles imparts the microparticles with generation-dependent buffering capacity and net positive charge while removing generation-dependent cytotoxicity. PLGA microparticles with PAMAM conjugated to the surface produce significantly higher transgene expression than unmodified PLGA microparticles. These results will have considerable potential for a wide variety of applications in microparticle-based nonviral DNA, RNA, and oligonucleotide delivery.

2. MATERIALS AND METHODS

2.1. Materials. D,L-Lactide/glycolide copolymer (PLGA, molar ratio with acid terminal group 50:50, inherent viscosity 0.54 dL/g) was purchased from Absorbable Polymers International (Pelham, AL). PAMAM dendrimers from generations 3–6 (G3, G4, G5, and G6, ethylenediamine core), PEI (25 kDa), and poly(vinyl alcohol) (PVA, MW 30–70 kDa) were purchased from Sigma-Aldrich (St. Louis, MO). 1-Ethyl-3-(3-dimethylaminopropyl)carbodiimide hydrochloride (EDC), *N*-hydroxysulfosuccinimide (Sulfo-NHS), and bicinchoninic acid (BCA) protein assay kit were purchased from Pierce Biotechnology Inc. (Rockford, IL). Dulbecco's Modified Eagle's Medium (DMEM) was obtained from Gibco BRL (Grand Island, NY). The luciferase assay system was purchased from Promega (Madison, WI). For cellular uptake studies, FITC (fluorescein isothiocyanate, Sigma-Aldrich)-labeled dendrimers G3–G6 were prepared by reaction of FITC and PAMAM dendrimers in 0.1

* To whom correspondence should be addressed: aliasger-salem@uiowa.edu.

10.1021/bc070116l CCC: $37.00 © 2007 American Chemical Society
Published on Web 09/12/2007

M sodium carbonate buffer (pH 9) at 4 °C in darkness overnight. FITC-conjugated dendrimers were purified by dialysis (MWCO 7000, Pierce Biotechnology Inc., Rockford, IL) and then lyophilized (Labconco FreeZone 4.5, Kansas City, MO). The level of fluorescein in the dendrimers was determined by measuring their absorbance at 498 nm using standard curves for FITC. Spectrofluorometric analysis (Spectramax M5 Microplate reader, Molecular Device) revealed that approximately 3% of the dendrimer amino groups were attached with FITC.

2.2. Cell Culture. Human embryonic kidney cells (HEK293) and monkey African green kidney fibroblast-like cell line (COS7) were obtained from the American Type Culture Collection (ATCC, Rockville, MD). The cells were maintained in DMEM supplemented with 10% FBS, streptomycin at 100 μg/mL, penicillin at 100 U/mL, and 4 mM L-glutamine at 37 °C in a humidified 5% CO_2-containing atmosphere.

2.3. Amplification and Purification of Plasmid DNA. VR1255 plasmid is a 6.4-kb cDNA encoding firefly luciferase driven by the cytomegalovirus (CMV) promoter/enhancer. The plasmid was transformed in *Escherichia coli* DH5α and amplified in Terrific Broth media at 37 °C overnight with a shaking speed of 300 rpm. The plasmid was purified by an endotoxin-free QIAGEN Giga plasmid purification kit (QIAGEN, Valencia, CA) according to the manufacturer's protocol. Purified pDNA was dissolved in saline, and its purity and concentration were determined by UV absorbance at 260 and 280 nm.

2.4. Preparation of PLGA pDNA and PLGA PAMAM pDNA Microparticles. *2.4.1. PLGA pDNA Microparticles.* PLGA microparticles were prepared using a water in oil in water (w/o/w) double emulsion, solvent evaporation technique. Briefly, 100 mg of 50:50 PLGA was dissolved in 5 mL of dichloromethane (DCM). VR1255 pDNA in 0.5% (w/v) PVA solution was prepared at a concentration of 4mg/mL. Using a microtip probe sonicator set at level 2 (Sonic Dismembrator model 100, Fisher Scientific, Pittsburgh, PA), 500 μL of the PVA solution containing 2 mg of VR1255 pDNA was mixed with the PLGA/DCM solution for 20 s to form the first emulsion. This emulsion was then rapidly added to 50 mL of 0.5% (w/v) PVA solution with stirring at 13,500 rpm for 30 s using an IKA Ultra-Turrax T25 basic homogenizer (IKA, Wilmington, NC). The second emulsion was stirred overnight during which time the DCM solvent was evaporated. The microparticles were then washed 3 times with deionized water and then lyophilized (Labconco FreeZone 4.5, Kansas City, Missouri). The supernatant was collected and analyzed spectrophotometrically at 260 nm using a SpectraMax Plus^{384} microplate spectrophotometer (Molecular Device) for pDNA content. Plasmid DNA entrapped in the PLGA microparticles was calculated by subtracting the pDNA content in the supernatant from the initial concentration of pDNA added. Microparticles were stored at −20 °C until use. For *in vitro* microparticle uptake studies, PLGA microparticles loaded with Rhodamine 123 were prepared using a single emulsion evaporation methodology. Briefly, 100 mg of 50:50 PLGA and 2 mg of Rhodamine 123 (Sigma-Aldrich, St. Louis, MO) were dissolved in 5 mL of DCM. This was then rapidly added to 50 mL of 0.5% (w/v) PVA in deionized water with stirring at 13,500 rpm for 30 s. After evaporation overnight, the rhodamine-labeled microparticles were washed and collected as described above.

2.4.2. PLGA PAMAM pDNA Microparticles. A modified EDC/NHS chemistry was used to conjugate PAMAM dendrimers to the surface of PLGA microparticles to obtain cationic microparticles. Blank PLGA microparticles were prepared with 500 μL of the 0.5% (w/v) PVA solution and 5 mL of DCM containing 200 mg of 50:50 PLGA–COOH using a w/o/w double emulsion, solvent evaporation technique as described above. 100 mg of the PLGA–COOH microparticles were then suspended in 10 mL of 0.1 M MES (2-(*N*-morpholino)ethanesulfonic acid) buffer, pH 5.1. 1 mL of EDC solution (60 mM) in 0.1 M MES buffer and 1 mL of Sulfo-NHS solution (60 mM) in 0.1 M MES buffer were added dropwise to the PLGA microparticle suspension. EDC activation was carried out for 2 h at room temperature. A 10 molar excess of dendrimers G3, G4, G5, G6 or 25 kDa branched PEI was dissolved in 5 mL of 0.1 M MES buffer, respectively. Activated PLGA microparticles were added dropwise to the G3, G4, G5, G6 dendrimer or 25 kDa branched PEI solutions with magnetic stirring and incubated for another 4 h at room temperature. Dendrimer-conjugated PLGA microparticles were washed twice in 1 M NaCl to remove physically adsorbed polymer and twice with deionized water. The resulting microparticles, which were thereafter named PG3, PG4, PG5, PG6, and P-PEI were lyophilized and stored at −20 °C until use. Fluorescamine (4-phenylspiro[furan-2(3H),1′-phthalan]-3,3′-dione) has been used for colorimetric quantification of primary amines and to quantify dendrimers associated with microparticles (*24*). Microparticles PG3, PG4, PG5, PG6, or P-PEI were hydrolyzed in 0.1 N NaOH overnight, and the dendrimer content was measured using spectrofluorometric analysis (Spectramax M5 microplate reader, Molecular Device). Fluorescamine reacts with primary amines in dendrimers to form pyrrolinones, which are excited at 390 nm and have peak emission at 475–490 nm. Quantification of dendrimer conjugated to the PLGA microparticles (w/w) was estimated using standard curves of dendrimer with corresponding generation.

2.5. Microparticle Size and Surface Morphology Analysis. Microparticle size and zeta potential measurements were conducted using the Zetasizer Nano ZS (Malvern, Southborough, MA). Briefly, the microparticles were suspended in deionized water at a concentration of 1 mg/mL. The size measurements were performed at 25 °C at a 173° scattering angle. The mean hydrodynamic diameter was determined by cumulative analysis. The zeta potential determinations were based on electrophoretic mobility of the microparticles in the aqueous medium, which was performed using folded capillary cells in automatic mode. Microparticle morphology was assessed by scanning electron microscopy (SEM, Hitachi S-4000). Briefly, air-dried microparticles were placed on adhesive carbon tabs mounted on SEM specimen stubs. The specimen stubs were coated with approximately 5 nm of gold by ion beam evaporation before examination in the SEM operated at 5 kV accelerating voltage.

2.6. Buffering Capacity of PLGA pDNA and PLGA PAMAM pDNA Microparticles. The ability of PLGA PAMAM microparticles (PG3 to PG6) to resist acidification was tested using the acid titration assay as described by Tang et al. (*24*) Briefly, 10 mg/mL PG3, PG4, PG5, or PG6 microparticles were suspended in 150 mM NaCl, respectively. The pH was first adjusted to ∼9.0 and then titrated in small increments with 0.1 N HCl until a pH of 3.0 was reached. The slope of the pH versus HCl added graph provides an indication of the intrinsic buffering capacity of the delivery vehicles.

2.7. Plasmid DNA Loading on Dendrimer-Conjugated Cationic Microparticles. VR1255 pDNA was loaded on the surface of cationic microparticles PG3, PG4, PG5, or PG6 as described by Singh et al. (*11*) Plasmid DNA was incubated with PG3, PG4, PG5, or PG6 suspensions in PBS (pH adjusted to 6.5) at a concentration of 20 μg pDNA/mg microparticles at 4 °C for 6 h, respectively. The resulting microparticles were centrifuged at 13,200 rpm for 5 min on a microcentrifuge and washed twice with the loading buffer to obtain PG3 pDNA, PG4 pDNA, PG5 pDNA, or PG6 pDNA microparticles. The supernatant was collected and analyzed spectrophotometrically at 260 nm using a SpectraMax Plus^{384} microplate spectrophotometer (Molecular Device) for pDNA content. Plasmid DNA

loading on the cationic microparticles was calculated by subtracting the pDNA content in the supernatant from the initial concentration of pDNA added.

2.8. Cytotoxicity Evaluation using the MTT Assay. The cytotoxicity of the PLGA pDNA, PLGA PAMAM pDNA microparticles, PLGA PEI pDNA microparticles, and PEI pDNA was evaluated using the MTT (3-[4,5-dimethylthiazol-2-yl]-2,5-diphenyltetrazolium bromide) assay (*25*). COS7 and HEK293 cells were seeded in a 96-well plate at a density of 1×10^4 cells/well. Twenty-four hours later, cells were incubated with 200 μL of complete DMEM containing PLGA pDNA or PLGA PAMAM pDNA microparticles at various concentrations. After 4 h of incubation, the medium in each well was replaced with 100 μL of fresh complete medium. Twenty-five microliters of 5 mg/mL MTT solution in PBS was added to each well and incubated with cells for additional 2 h. Cells were lysed with 100 μL of the extraction buffer (20% SDS in 50% DMF, pH 4.7) overnight. The optical density of the lysate was measured at 550 nm using a Spectramax Plus^{384} microplate spectrophotometer (Molecular Device). Values were expressed as a percentage of the control to which no microparticles were added.

2.9. Cellular Uptake of PLGA pDNA and PLGA PAMAM pDNA Microparticles. Dendrimer-conjugated PLGA microparticles PG3, PG4, PG5, and PG6 were prepared using FITC-labeled dendrimers. HEK293 cells were seeded into 12-well plates at a density of 1×10^6/well 24 h before transfection. After 24 h incubation, the medium was replaced with fresh DMEM containing 10% FBS. 0.5 mg/well PLGA/Rhodamine 123, FITC-labeled PG3, PG4, PG5, or PG6 microparticles with and without loaded pDNA were incubated with HEK293 cells for 16 h. Then, the cells were vigorously washed with PBS three times to remove free fluorescent-labeled microparticles and the microparticles adsorbed on the cells surface. Samples were then assessed using flow cytometry (Becton Dickinson). Dot plots were gated on FSC/SSC properties of HEK293 cells to exclude free fluorescent-labeled microparticles. Data was analyzed using *Cell-Quest^{Pro}* software. All samples were tested in triplicate. To confirm that fluorescence would be detectable in the acidic environment of the endosomes, FITC was dissolved into a 150 mM NaCl aqueous solution. When the solution was adjusted to pH 4–5 using 0.1 N HCl, fluorescence could still be clearly detected in comparison to FITC at pH 7.4. To confirm that FITC-labeled particles had been internalized, cells were viewed under a confocal microscope (Bio-Rad Radience 2100MP). Orthogonal sections from stacked images confirmed that particles were predominantly located inside the cell and not just on the surface (data not shown).

2.10. Evaluation of Luciferase Expression in COS7 and HEK293 Cells. COS7 and HEK293 cells were seeded into 24-well plates at a density of 8×10^4/well 24 h before transfection. 0.2 mg/well PLGA pDNA and PLGA PAMAM pDNA microparticles were added to the cells in transfection medium (serum-free) and incubated for 4 h at 37 °C, followed by further incubation in serum-containing medium for 44 h. The concentration of the microparticles was selected on the basis of a target pDNA loading of 5 μg/mg microparticles and an equivalent pDNA dose of 1 μg/well. After the incubation, cells were treated with 200 μL of lysis buffer (Promega). The lysate was subjected to two cycles of freezing and thawing, then transferred into tubes and centrifuged at 13,200 rpm for 5 min. Twenty microliters of supernatant was added to 100 μL of luciferase assay reagent (Promega), and samples were measured on a luminometer for 10 s (Lumat LB 9507, EG&G Berthold, Bad Wildbad, Germany). The relative light units (RLU) were normalized against protein concentration in the cell extracts, measured by a micro BCA protein assay kit (Pierce). Luciferase activity was expressed as relative light units (RLU/mg protein in the cell lysate). The data were reported as mean ± standard deviation for triplicate samples. Every transfection experiment was repeated at least twice.

2.11. Statistical Analysis. Group data were reported as mean ± SD. Differences between groups were analyzed by one-way analysis of variance with a Tukey post-test analysis. Levels of significance were accepted at the $P < 0.05$ level. Statistical analyses were performed using *Prism 3.02* software (Graphpad Software, Inc., San Diego, CA.)

3. RESULTS

3.1. PAMAM Dendrimers Can Be Conjugated To the Surface of PLGA Microparticles Using EDC/NHS Chemistry. Figure 1 schematically shows our approach for preparing unmodified PLGA pDNA microparticles and dendrimer-conjugated PLGA microparticles. PLGA pDNA microparticles were prepared using a w/o/w double emulsion, solvent evaporation technique. 0.5% (w/v) PVA solution was chosen to prepare PLGA microparticles based on results of a previous optimization study on microparticle fabrication processes. Rhodamine 123 is soluble in DCM. Therefore, PLGA microparticles loaded with Rhodamine 123 were prepared using a single emulsion technique that used identical stirring and PVA concentration conditions to the PLGA pDNA microparticles.

For dendrimer-conjugated PLGA microparticles, PAMAM dendrimers from generations 3–6 were covalently attached to the surface of PLGA microparticles using EDC/NHS chemistry. Each of the PAMAM dendrimers from G3 to G6 was conjugated to PLGA microparticles prepared from the same batch. The conjugation of dendrimers was quantified using a fluorescamine assay, which indicated that the amounts of G3, G4, G5, and G6 present on the microparticle surfaces were 5.0, 5.5, 4.6, and 5.4 μg per milligram of microparticles, respectively (Table 1).

3.2. Microparticles Size, Zeta Potential, and Morphology of Microparticles. Figure 2a shows the microparticle size of the PLGA and PLGA PAMAM microparticles. Unmodified PLGA microparticles had an average size of 2.2 μm. After conjugation of PAMAM dendrimers onto the PLGA microparticles surface, the average PLGA microparticle size ranged from 2.3 to 3.2 μm. Figure 2b shows the zeta potential of these PLGA microparticles before and after loading with pDNA. Blank PLGA microparticles with carboxyl groups displayed a net negative surface charge of approximately −50 mV. After the conjugation of PAMAM dendrimers, the surface charge of PLGA microparticles turned positive with values ranging from +20 to +40 mV. After pDNA was electrostatically bound to the PAMAM-conjugated microparticle surface, the zeta potential was reduced to values ranging from +0.5 to +13.5 mV. Furthermore, both before and after pDNA binding, the surface charge of the dendrimer-conjugated PLGA microparticles increased in the order PG6 > PG5 > PG4 > PG3. SEM images (figure 2c) demonstrated that all the PLGA microparticles had a smooth morphology and spherical shape.

3.3. Increases in Buffering Capacity of PLGA PAMAM Microparticles Are Dependent on the Generation of the Conjugated PAMAM Dendrimer. Covalent attachment of PAMAM to PLGA microparticles is expected to provide the microparticles with tertiary and secondary amines that impart endolysosomal pH buffering capacity. This could lead to increased phagoendosomal escape of the carrier microparticles (proton sponge mechanism) (*21*). The buffering capacity of the dendrimer-conjugated PLGA microparticles was assessed by measuring the change in pH of a microparticle suspension (10 mg/mL) upon addition of increasing amounts of 0.1 N HCL. As shown in figure 3, buffering capacity of PAMAM PLGA microparticles is directly correlated with the generation level. The higher the generation level of the PAMAM

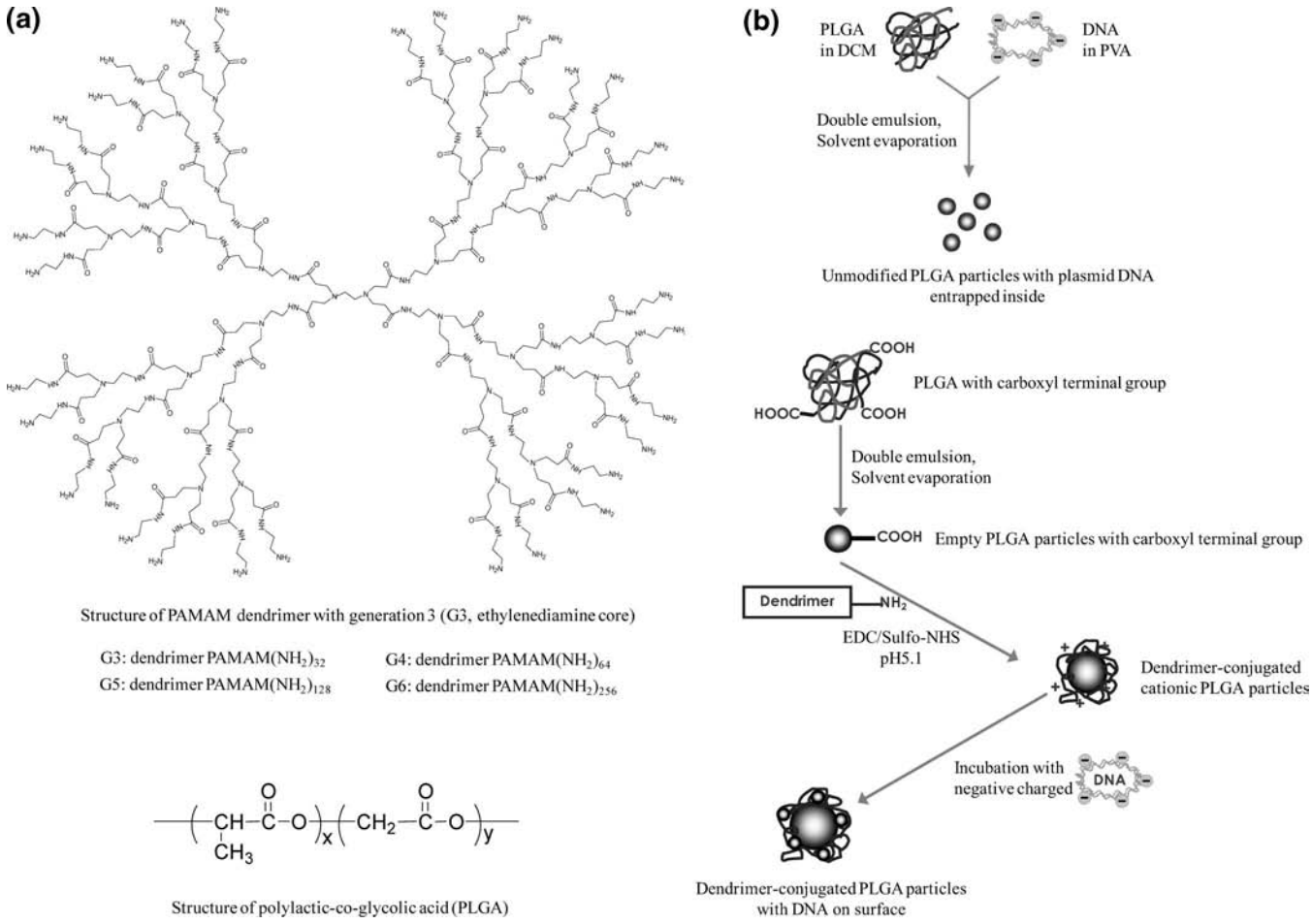


Figure 1. (a) Structure of poly(lactic-*co*-glycolic acid) (PLGA) and PAMAM dendrimers with ethylenediamine core. (b) Schematic of preparation of dendrimer-conjugated PLGA microparticles and unmodified PLGA microparticles.

Table 1. PAMAM Dendrimer Conjugation Efficiency and pDNA Loading Efficiency of PLGA and PAMAM-Conjugated PLGA Microparticles[a]

	dendrimer-conjugation efficiency (μg dendrimer/mg particles)	DNA-loading efficiency (μg pDNA/mg particles)
PLGA/pDNA		3.5 ± 0.1
PG3	5.0	4.0 ± 0.1
PG4	5.5	4.2 ± 0.5
PG5	4.6	4.1 ± 0.1
PG6	5.4	4.8 ± 0.2

[a] Averages representative of 3 measurements $\pm$ standard deviation.

dendrimer conjugated to the PLGA microparticle, the more effective it is at buffering against pH changes. This is indicated by the shift and decrease in the slope of the titration curves.

3.4. PAMAM Conjugation to PLGA Microparticles Significantly Increases pDNA Loading. Covalent attachment of cationic PAMAM dendrimers to the surface of PLGA microparticles significantly increases the efficacy of pDNA binding in comparison to PLGA microparticles entrapping pDNA using a double emulsion, solvent evaporation technique. Plasmid DNA loading on the surface of PG3 microparticles was 15% higher than pDNA entrapment in unmodified PLGA microparticles. Increasing the generation of the PAMAM dendrimer conjugated to the PLGA microparticle from 3 to 6 increased pDNA loading from 4.0 μg to 4.8 μg pDNA/mg particles, respectively. This was 37% higher than the pDNA loading in PLGA microparticles using the double emulsion, solvent evaporation technique and 540% higher than pDNA adsorbed onto the surface of unmodified PLGA microparticles ($\sim$1 μg pDNA/mg particles).

3.5. PAMAM Conjugation to PLGA Microparticles Removes Generation-Dependent Toxicity. *In vitro* cytotoxicity was evaluated in COS7 and HEK293 cells with increasing doses of PLGA pDNA and PLGA PAMAM pDNA microparticle concentrations (from 7.8 to 250 μg of microparticles per milliliter of DMEM). As shown in figure 4, PLGA PAMAM pDNA microparticles had similar cytotoxicity profiles to unmodified PLGA pDNA microparticles in COS7 cells. Cytotoxicity of PLGA PAMAM dendrimers was moderately higher than unmodified PLGA pDNA microparticles in HEK293 cells. No significant difference in the toxicity of PLGA PAMAM pDNA microparticles was observed in either cell line for increasing generation levels of the PAMAM dendrimer conjugated. No significant difference was observed in cytotoxicity between PLGA PAMAM pDNA microparticles and PLGA PEI pDNA microparticles. PLGA PAMAM microparticles were significantly less toxic than PEI alone.

3.6. PAMAM Dendrimer-Conjugated PLGA Microparticles Could Be Efficiently Taken Up by HEK293 Cells. Figure 5 shows cellular uptake data of fluorescence-labeled microparticles incubated with HEK293 cells. PLGA PAMAM pDNA microparticles displayed 6–7-fold higher uptake in cells than unmodified PLGA microparticles. No significant difference in the cell uptake of PLGA PAMAM pDNA microparticles was observed for increasing generation levels of the conjugated PAMAM dendrimer.

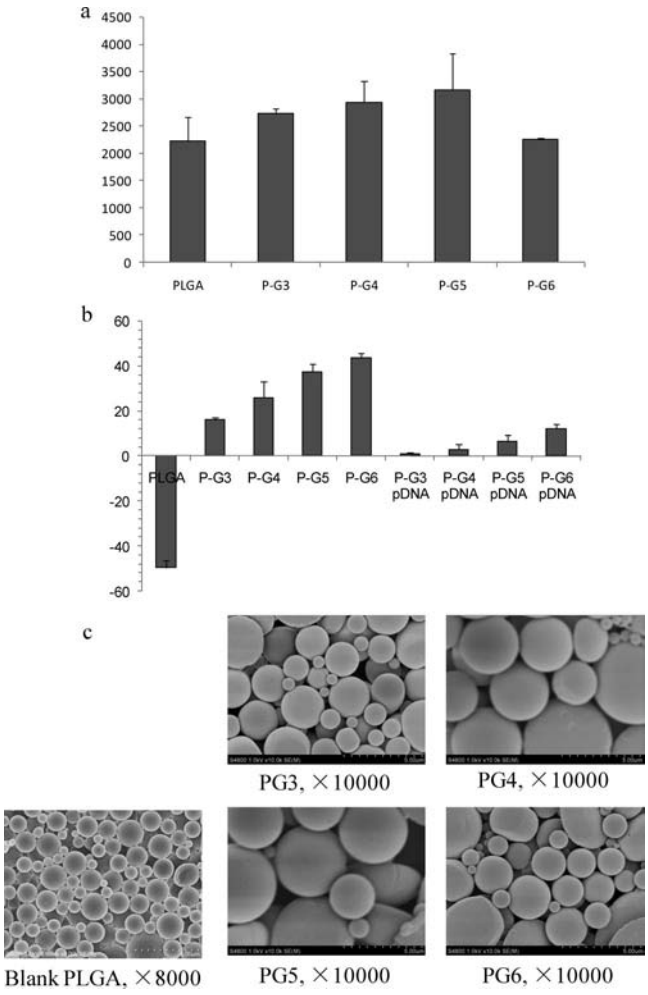


Figure 2. Size (a) and zeta potential (b) of PLGA PAMAM microparticles before and after pDNA binding. Data are represented as the mean ± standard deviation ($n = 3$). SEM images (c) show that the morphology of all the PLGA particles is smooth and spherical in appearance.

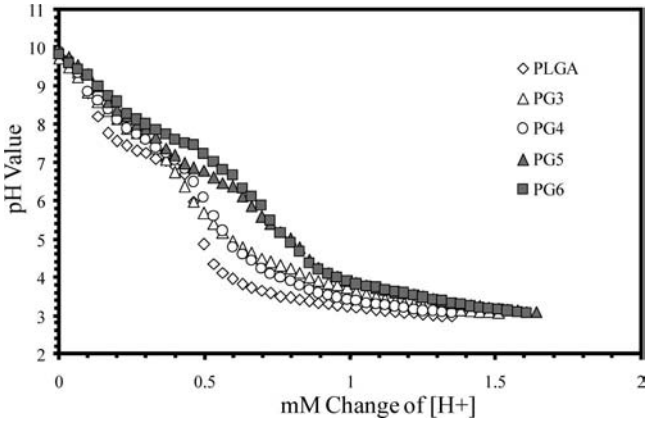


Figure 3. Acid titration experiments with 0.1 N HCL demonstrate the buffering capacity of PAMAM-conjugated and unmodified PLGA microparticles. The data show significantly increased buffering by PAMAM-conjugated PLGA microparticles in comparison to unmodified PLGA microparticles.

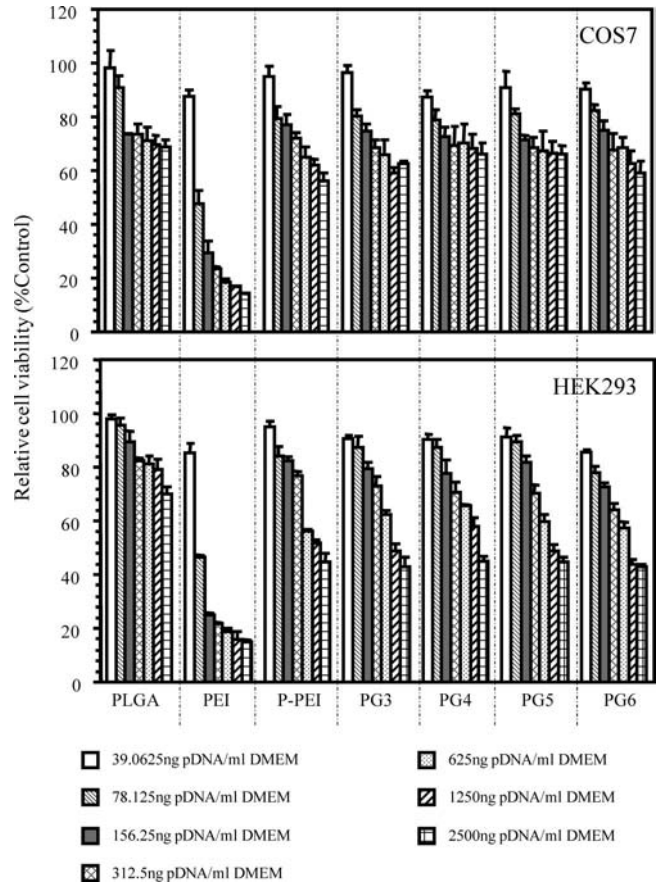


Figure 4. Cytotoxicity of dendrimer-conjugated PLGA pDNA microparticles in COS7 and HEK293 cells in comparison with PEI-conjugated PLGA pDNA microparticles, unmodified PLGA pDNA microparticles, and PEI alone. PEI amounts were selected on the basis of an estimated pDNA dose using an N/P ratio of 10:1. Cell viabilities were evaluated by MTT assay as described in the Materials and Methods section. Data is represented as the mean ± standard deviation ($n = 6$).

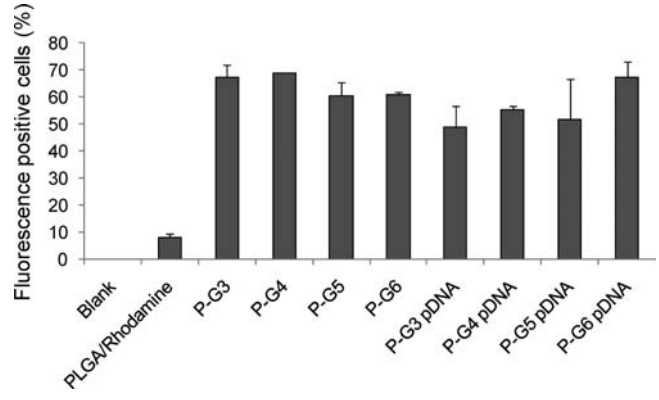


Figure 5. Flow cytometry data of fluorescence-labeled PLGA microparticles that have been incubated with HEK293 cells. The cellular uptake of the PLGA formulations is presented as a percentage of fluorescence-labeled cells ($n = 3$ per group). PLGA microparticle formulations were added at doses of 0.5 mg/well in HEK293 cells. The concentrations of PLGA particles were chosen from an estimated pDNA loading of 5 μg/mg particles and a target pDNA dose of 2.5 μg/well.

3.7. Dendrimer Conjugation Enhanced the Gene Transfection Mediated by PLGA Microparticles in COS7 and HEK293 Cells. Gene transfection mediated by PLGA pDNA and PLGA PAMAM pDNA microparticle formulations was evaluated in COS7 and HEK293 cells (Figure 6). All PLGA PAMAM microparticles showed significantly higher transgene expression than unmodified PLGA microparticles. In contrast with zeta potential and buffering capacity measurements, transfection efficiencies with PLGA PAMAM pDNA microparticles were not dependent on the generation of conjugated

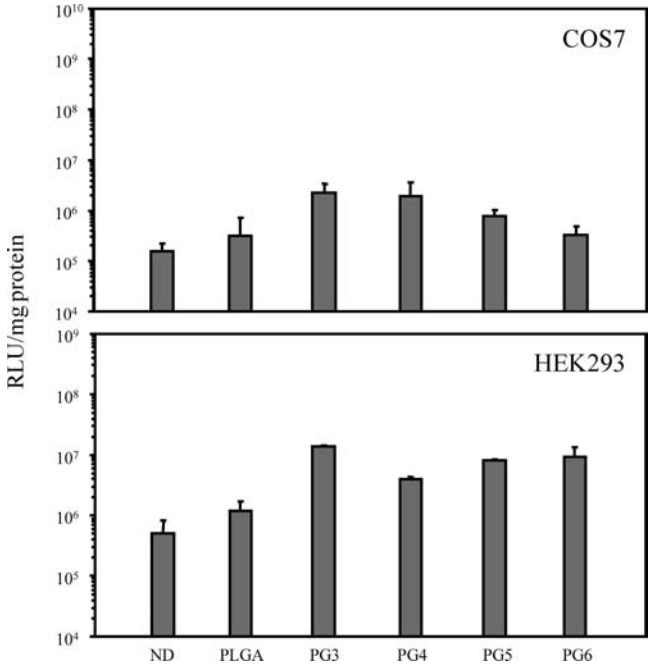


Figure 6. PLGA pDNA and PLGA PAMAM pDNA microparticle mediated gene transfection in COS7 and HEK293 cells. Microparticles were incubated with cells at a concentration of 0.2 mg/well with a target pDNA dose of 1 μg/well. Cell harvesting and luciferase assays were performed 48 h after transfection as described in the Materials and Methods section. Data are represented as mean ± standard deviation ($n = 3$). All the dendrimer-conjugated PLGA microparticles exhibited efficient gene delivery.

PAMAM. PG3 pDNA microparticles mediated the highest luciferase expression in both cell lines, which was 11-fold or 7-fold higher than unmodified PLGA pDNA microparticles in HEK293 or COS7 cells, respectively.

4. DISCUSSION

Delivery of pDNA from PLGA microparticles has shown significant potential in nonviral gene delivery. Entrapping pDNA in PLGA microparticles exposes the pDNA to potentially inactivating solvents and shear forces. (*3, 5, 8*). In addition, the local acidic microenvironment of PLGA microparticles has been reported to nick and subsequently inactivate pDNA (*5, 8*). Loading pDNA onto microparticles after they have been prepared overcomes several of these barriers for efficient pDNA delivery. However, PLGA microparticles are typically prepared using poly(vinyl alcohol) (PVA) surfactants. PVA surfactants impart a negative surface charge on the microparticles because of physical entrapment in the surface of the microparticles (*11,12,26,27*). As a result, pDNA, which has a net negative charge, does not bind efficiently to the PLGA microparticle surface. Several investigators have sought to overcome this limitation by preparing cationic microparticles that bind pDNA electrostatically. Methodologies that have been developed for preparing cationic PLGA microparticles include the use of cationic agents such as cetyltrimethylammoniumbromide (CTAB) (*15*), cetyldimethylethylammonium bromide (CDAB), dimethyldioctadecylammonium bromide (DDA) (*28*), 1,2-dioleoyl-1,3-trimethylammoniopropane (DOTAP), cationic DDAB (*28*), poly(L-lysine) (PLL), (*29–32*) chitosan (*33*) and polyethyleneimine (PEI) (*10, 34*). Preparation of the cationic microparticles has included blending, surface coating, and covalent attachment of these agents (*3, 10, 13, 16, 17*). Each method has its attributes and drawbacks. However, covalent attachment of cationic agents to the surface of microparticles is particularly advantageous because it minimizes toxicity associated with noncovalently attached cationic polymers or surfactants. This method also provides a method for more reliable loading levels—a prerequisite for the pharmaceutical industry (*10*). A significant advantage of these systems is the ability to instantaneously deliver DNA/RNA-based material followed by sequential delivery of complementary agents such as antigens, chemokines, or cytokines entrapped in the PLGA microparticle matrix (*10, 11*). In this study, we evaluated the impact of conjugating PAMAM dendrimers onto the surface of PLGA microparticles for enhanced pDNA delivery. SEM analysis showed that covalent attachment of PAMAM dendrimers to the surface of PLGA microparticles resulted in a smooth and spherical appearance at all generation levels of the PAMAM dendrimer. No statistical difference was observed in particle size after PAMAM conjugation ($P > 0.05$). Covalent attachment of G3 PAMAM dendrimers onto PLGA microparticles (PG3) increased the zeta potential from −50 mV to +20 mV ($P < 0.001$). The zeta potential of the PAMAM dendrimer-conjugated microparticle significantly decreased to values ranging from +0.5 mV to 13.5 mV after pDNA binding. This is most likely because pDNA has a net negative charge that neutralizes the positive charges associated with PAMAM dendrimer when binding electrostatically. Increasing the generation of the PAMAM dendrimer conjugated to the PLGA microparticle surface increased the zeta potential proportionally both before and after plasmid binding. For example, PG6 microparticles displayed zeta potentials of approximately +40 mV before pDNA binding and +12.2 mV after pDNA binding. This presumably relates to the fact that dendrimers at higher generations have more surface amine groups and a higher positive charge density. This change from negative to positive zeta potential increased the ability of pDNA to bind to the surface of the microparticles. PLGA microparticles with PAMAM conjugated to the surface displayed on average 5-fold higher pDNA loading levels in comparison to unmodified PLGA microparticles ($P < 0.001$). PG6 microparticles had significantly higher pDNA loadings than PG3, PG4, and PG5 microparticles ($P < 0.05$). No significant difference in pDNA loading was observed among PG3, PG4, and PG5 ($P > 0.05$). The presence of secondary and tertiary amines on the PAMAM dendrimer structures enabled the PAMAM-modified PLGA microparticles to resist acidification in acid titration experiments ($P < 0.001$ in comparison to unmodified PLGA microparticles). This ability to buffer against pH changes is believed to contribute to endophagosomal escape into the cytoplasm as described by the proton sponge hypothesis (*20, 24*). Increases in the generation level of the PAMAM conjugated to the PLGA microparticles correlated to increases in buffering capacity. The buffering capacity of PLGA PAMAM microparticles also correlated to zeta potential values. Dose-dependent toxicity measurements were made using the MTT assay (*21*). PLGA PAMAM microparticles could be incubated at concentrations as high as 500 μg of particles per milliliter of DMEM with more than 50% of the cells still viable. Several investigators have reported that PAMAM dendrimers alone display generation-dependent toxicity. For example, Duncan and colleagues reported that PAMAM dendrimers display concentration- and generation-dependent cytotoxicity and hemolysis as observed by changes in red cell morphology (*22*). The mechanism by which PAMAM dendrimers induce cytotoxicity is apoptosis involving a caspase-dependent pathway (*35*). Of notable interest in this study is that no significant differences in cytotoxicity were observed for PG3 pDNA, PG4 pDNA, PG5 pDNA, and PG6 pDNA microparticles. PLGA PAMAM microparticles retained the low cytotoxicity properties of unmodified PLGA microparticles in COS7 cells ($P > 0.05$). In the HEK293 cell line, cytotoxicity of PLGA PAMAM microparticles was mod-

erately higher than unmodified PLGA microparticles. This result suggests that cytotoxicity is cell-type dependent, and for certain applications that target specific tissues or cells, PAMAM conjugation to PLGA microparticles could completely remove the undesirable toxicity associated with PAMAM dendrimers alone. These results are consistent with the reduced cytotoxicity that is observed when PEI (25 kDa) is attached to PLGA microparticles in comparison to PEI alone (Figure 4) (*10*). Flow cytometry studies showed that conjugation of PAMAM to the PLGA microparticles significantly enhanced cell uptake by 6–7-fold in comparison to unmodified PLGA microparticles ($P < 0.001$). Changes in particle size were not significant between each group ($P > 0.05$) and were therefore not responsible for this increase in cell uptake. The zeta potential of PLGA PAMAM microparticles was significantly higher than unmodified PLGA microparticles even after pDNA binding. Cationic microparticles demonstrate an enhanced interaction with the negatively charged cellular membranes that is most likely responsible for the enhanced cell uptake. However, increasing the generation of the PAMAM dendrimer conjugated to the PLGA microparticles had no impact on increasing cell uptake further.

Gene transfection experiments were carried out on two model cell lines commonly used to evaluate transfection efficiency. Conjugation of PAMAM dendrimers to PLGA microparticles significantly enhanced luciferase expression in comparison to unmodified PLGA microparticles in both COS7 and HEK293 cell lines. G3 dendrimers covalently attached to PLGA microparticles generated the highest transgene luciferase expression. In contrast to dendrimers alone, however, increasing the generation of the dendrimer conjugated to the PLGA microparticle did not increase luciferase transgene expression. This result was consistent in both HEK293 and COS7 cell lines. This observation is important with respect to the manufacture of the PLGA PAMAM microparticles because G3 PAMAM dendrimers are easier to synthesize (*23*) and four times cheaper than G6 PAMAM dendrimers when purchased commercially (Dendritech). In addition, lower generation number PAMAM dendrimers have longer circulation times (*22*). Lower-generation PAMAM dendrimers that would eventually become free from the microparticle are also substantially less cytotoxic than higher-generation PAMAM dendrimers (*21–23, 35, 36*). Lin and colleagues have shown that G2 dendrimer conjugated to mesoporous silica nanoparticles can generate transfection efficiencies that are significantly higher than commercial transfection reagents because of a sedimentation effect previously described by Luo et al. *(37)* Given that we have observed generation-dependent increases in the buffering capacity and zeta potential for PLGA PAMAM microparticles, we would have expected corresponding transfection efficiency increases. However, in our studies, increases in zeta potential and buffering capacity do not correlate to further increases in transfection efficiency. This is consistent with a number of studies that have shown that zeta potential of dendrimers and transfection efficiency do not necessarily correlate (*38, 39*). The increase in transfection efficiency of PLGA PAMAM pDNA microparticles in comparison to PLGA pDNA microparticles is therefore related to the increased pDNA loading and increased interaction of microparticles with the cell surface. The existence of some buffering capacity may enhance transfection, but this study suggests that further promotion of the proton sponge effect does not further enhance transfection efficiency with this delivery system.

Conjugating PAMAM dendrimers to the surface of PLGA microparticles reveals a number of options for further exploration. The PAMAM dendrimers impart the PLGA microparticles with a much greater proportion of reactive surface functional groups. These could be used for efficient pegylation (*40, 41*), conjugation of cell targeting ligands to the microparticle surface (*42*), or a combination of both (*43*). Loading of the PLGA microparticles with radioisotopes or fluorescent dyes also provides the potential for combined imaging and delivery of biomolecules (*23*).

5. CONCLUSION

We have prepared PLGA microparticles with PAMAM dendrimers conjugated to the surface. The buffering capacity and zeta potential of the microparticles increases with increasing generation level of the conjugated PAMAM dendrimer. Conjugation of the PAMAM dendrimer to the surface of the PLGA microparticle removes generation-dependent toxicity. PLGA PAMAM microparticles displayed similar cytotoxicity profiles to unmodified PLGA microparticles. A G3 PAMAM dendrimer conjugated to PLGA microparticles significantly increased transfection efficiencies in comparison to unmodified PLGA microparticles. Further increases in the generation level of the PAMAM did not increase transfection efficiency. Plasmid DNA entrapped in PLGA microparticles has shown *in vivo* efficacy in animal models and phase II clinical trials (*44–47*). Therefore, the development of PLGA polymers with optimized cationic surfaces should have significant potential for enhancing the response of these systems further.

ACKNOWLEDGMENT

We gratefully acknowledge support aided by grant number IRG-77-004-28 from the American Cancer Society, and the Pharmaceutical Research and Manufacturers of America Foundation. J. Intra acknowledges support from the Parenteral Drug Association for a predoctoral fellowship.

LITERATURE CITED

(1) O'Hagan, D. T., Singh, M., and Ulmer, J. B. (2004) Microparticles for the delivery of DNA vaccines. *Immunol. Rev. 199*, 191–200.

(2) Eldridge, J. H., Staas, J. K., Meulbroek, J. A., Tice, T. R., and Gilley, R. M. (1991) Biodegradable and biocompatible poly(DL-lactide-co-glycolide) microspheres as an adjuvant for staphylococcal enterotoxin-B toxoid which enhances the level of toxin-neutralizing antibodies. *Infect. Immun. 59*, 2978–2986.

(3) Oster, C. G., and Kissel, T. (2005) Comparative study of DNA encapsulation into PLGA microparticles using modified double emulsion methods and spray drying techniques. *J. Microencapsul. 22*, 235–244.

(4) Panyam, J., and Labhasetwar, V. (2003) Biodegradable nanoparticles for drug and gene delivery to cells and tissue. *Adv. Drug Delivery Rev. 55*, 329–347.

(5) Tinsley-Bown, A. M., Fretwell, R., Dowsett, A. B., Davis, S. L., and Farrar, G. H. (2000) Formulation of poly(D,L-lactic-co-glycolic acid) microparticles for rapid plasmid DNA delivery. *J. Controlled Release 66*, 229–241.

(6) Walter, E., Dreher, D., Kok, M., Thiele, L., Kiama, S. G., Gehr, P., and Merkle, H. P. (2001) Hydrophilic poly(DL-lactide-co-glycolide) microspheres for the delivery of DNA to human-derived macrophages and dendritic cells. *J. Controlled Release 76*, 149–168.

(7) Walter, E., and Merkle, H. P. (2002) Microparticle-mediated transfection of non-phagocytic cells in vitro. *J. Drug Targeting 10*, 11–21.

(8) Walter, E., Moelling, K., Pavlovic, J., and Merkle, H. P. (1999) Microencapsulation of DNA using poly(DL-lactide-co-glycolide):

stability issues and release characteristics. *J. Controlled Release 61*, 361–374.

(9) Ando, S., Putnam, D., Pack, D. W., and Langer, R. (1999) PLGA microspheres containing plasmid DNA: preservation of supercoiled DNA via cryopreparation and carbohydrate stabilization. *J. Pharm. Sci. 88*, 126–30.

(10) Kasturi, S. P., Sachaphibulkij, K., and Roy, K. (2005) Covalent conjugation of polyethyleneimine on biodegradable microparticles for delivery of plasmid DNA vaccines. *Biomaterials 26*, 6375–6385.

(11) Singh, M., Briones, M., Ott, G., and O'Hagan, D. (2000) Cationic microparticles: A potent delivery system for DNA vaccines. *Proc. Natl. Acad. Sci. U.S.A. 97*, 811–816.

(12) Singh, M., Fang, J. H., Kazzaz, J., Ugozzoli, M., Chesko, J., Malyala, P., Dhaliwal, R., Wei, R., Hora, M., and O'Hagan, D. (2006) A modified process for preparing cationic polylactide-co-glycolide microparticles with adsorbed DNA. *Int. J. Pharm. 327*, 1–5.

(13) Oster, C. G., Kim, N., Grode, L., Barbu-Tudoran, L., Schaper, A. K., Kaufmann, S. H. E., and Kissel, T. (2005) Cationic microparticles consisting of poly(lactide-co-glycolide) and polyethylenimine as carriers systems for parental DNA vaccination. *J. Controlled Release 104*, 359–377.

(14) Kasturi, S. P., Qin, H., Thomson, K. S., El-Bereir, S., Cha, S. C., Neelapu, S., Kwak, L. W., and Roy, K. (2006) Prophylactic anti-tumor effects in a B cell lymphoma model with DNA vaccines delivered on polyethylenimine (PEI) functionalized PLGA microparticles. *J. Controlled Release 113*, 261–270.

(15) Singh, M., Ugozzoli, M., Briones, M., Kazzaz, J., Soenawan, E., and O'Hagan, D. T. (2003) The effect of CTAB concentration in cationic PLG microparticles on DNA adsorption and in vivo performance. *Pharm. Res. 20*, 247–251.

(16) Bivas-Benita, M., Romeijn, S., Junginger, H. E., and Borchard, G. (2004) PLGA-PEI nanoparticles for gene delivery to pulmonary epithelium. *Eur. J. Pharm. Biopharm. 58*, 1–6.

(17) Nam, Y. S., Kang, H. S., Park, J. Y., Park, T. G., Han, S. H., and Chang, I. S. (2003) New micelle-like polymer aggregates made from PEI-PLGA diblock copolymers: micellar characteristics and cellular uptake. *Biomaterials 24*, 2053–2059.

(18) Zhou, J. H., Wu, J. Y., Hafdi, N., Behr, J. P., Erbacher, P., and Peng, L. (2006) PAMAM dendrimers for efficient siRNA delivery and potent gene silencing. *Chem. Commun*, 2362–2364.

(19) Esfand, R., and Tomalia, D. A. Poly(amidoamine) (PAMAM) dendrimers: from biomimicry to drug delivery and biomedical applications. *Drug Discovery Today* (2001) *6*, 427–436.

(20) Lee, C. C., MacKay, J. A., Frechet, J. M. J., and Szoka, F. C. (2005) Designing dendrimers for biological applications. *Nat. Biotechnol. 23*, 1517–1526.

(21) Zhang, X. Q., Wang, X. L., Huang, S. W., Zhuo, R. X., Liu, Z. L., Mao, H. Q., and Leong, K. W. (2005) In vitro gene delivery using polyamidoamine dendrimers with a trimesyl core. *Biomacromolecules 6*, 341–350.

(22) Malik, N., Wiwattanapatapee, R., Klopsch, R., Lorenz, K., Frey, H., Weener, J. W., Meijer, E. W., Paulus, W., and Duncan, R. (2000) Dendrimers: Relationship between structure and biocompatibility in vitro, and preliminary studies on the biodistribution of I-125-labelled polyamidoamine dendrimers in vivo. *J. Controlled Release 65*, 133–148.

(23) Radu, D. R., Lai, C. Y., Jeftinija, K., Rowe, E. W., Jeftinija, S., and Lin, V. S. Y. (2004) A polyamidoamine dendrimer-capped mesoporous silica nanosphere-based gene transfection reagent. *J. Am. Chem. Soc. 126*, 13216–13217.

(24) Tang, M. X., and Szoka, F. C. (1997) The influence of polymer structure on the interactions of cationic polymers with DNA and morphology of the resulting complexes. *Gene Ther. 4*, 823–832.

(25) Hansen, M. B., Nielsen, S. E., and Berg, K. (1989) Re-examination and further development of a precise and rapid dye method for measuring cell-growth cell kill. *J. Immunol. Methods 119*, 203–210.

(26) Evora, C., Soriano, I., Rogers, R. A., Shakesheff, K. M., Hanes, J., and Langer, R. (1998) Relating the phagocytosis of microparticles by alveolar macrophages to surface chemistry: the effect of 1,2-dipalmitoylphosphatidylcholine. *J. Controlled Release 51*, 143–152.

(27) Shakesheff, K. M., Evora, C., Soriano, I., and Langer, R. (1997) The adsorption of poly(vinyl alcohol) to biodegradable microparticles studied by x-ray photoelectron spectroscopy (XPS). *J. Colloid Interface Sci. 185*, 538–547.

(28) Wasan, E. K., Reimer, D. L., and Bally, M. B. (1996) Plasmid DNA is protected against ultrasonic cavitation-induced damage when complexed to cationic liposomes. *J. Pharm. Sci. 85*, 427–33.

(29) Capan, Y., Woo, B. H., Gebrekidan, S., Ahmed, S., and DeLuca, P. P. (1999) Influence of formulation parameters on the characteristics of poly(D, L-lactide-co-glycolide) microspheres containing poly(L-lysine) complexed plasmid DNA. *J. Controlled Release 60*, 279–86.

(30) Capan, Y., Woo, B. H., Gebrekidan, S., Ahmed, S., and DeLuca, P. P. (1999) Preparation and characterization of poly (D,L-lactide-co-glycolide) microspheres for controlled release of poly(L-lysine) complexed plasmid DNA. *Pharm. Res. 16*, 509–13.

(31) Capan, Y., Woo, B. H., Gebrekidan, S., Ahmed, S., and DeLuca, P. P. (1999) Stability of poly(L-lysine)-complexed plasmid DNA during mechanical stress and DNase I treatment. *Pharm. Dev. Technol. 4*, 491–498.

(32) Gebrekidan, S., Woo, B. H., and DeLuca, P. P. (2000) Formulation and in vitro transfection efficiency of poly (D,L-lactide-co-glycolide) microspheres containing plasmid DNA for gene delivery. *AAPS Pharm. Sci. Technol. 1*, E28.

(33) Ravi Kumar, M. N., Bakowsky, U., and Lehr, C. M. (2004) Preparation and characterization of cationic PLGA nanospheres as DNA carriers. *Biomaterials 25*, 1771–7.

(34) Manuel, W. S., Zheng, J., and Hornsby, P. J. (2001) Transfection by polyethyleneimine-coated microspheres. *J. Drug Targeting 9*, 15.

(35) Kuo, J. H. S., Jan, M. S., and Chu, H. W. (2005) Mechanism of cell death induced by cationic dendrimers in RAW 264.7 murine macrophage-like cells. *J. Pharm. Pharmacol. 57*, 489–495.

(36) Duncan, R., and Izzo, L. (2005) Dendrimer biocompatibility and toxicity. *Adv. Drug Delivery Rev. 57*, 2215–2237.

(37) Luo, D., and Saltzman, W. M. (2000) Enhancement of transfection by physical concentration of DNA at the cell surface. *Nat. Biotechnol. 18*, 893–895.

(38) Braun, C. S., Vetro, J. A., Tomalia, D. A., Koe, G. S., Koe, J. G., and Middaugh, C. R. (2005) Structure/function relationships of polyamidoamine/DNA dendrimers as gene delivery vehicles. *J. Pharm. Sci. 94*, 423–436.

(39) Zinselmeyer, B. H., Mackay, S. P., Schatzlein, A. G., and Uchegbu, I. F. (2002) The lower-generation polypropylenimine dendrimers are effective gene-transfer agents. *Pharm. Res. 19*, 960–967.

(40) Kim, T., Seo, H. J., Choi, J. S., Jang, H. S., Baek, J., Kim, K., and Park, J. S. (2004) PAMAM-PEG-PAMAM: Novel triblock copolymer as a biocompatible and efficient gene delivery carrier. *Biomacromolecules 5*, 2487–2492.

(41) Luo, D., Haverstick, K., Belcheva, N., Han, E., and Saltzman, W. M. (2002) Poly(ethylene glycol)-conjugated PAMAM dendrimer for biocompatible, high-efficiency DNA delivery. *Macromolecules 35*, 3456–3462.

(42) Costantino, L., Gandolfi, F., Bossy-Nobs, L., Tosi, G., Gurny, R., Rivasi, F., Vandelli, M. A., and Forni, F. (2006) Nanoparticulate drug carriers based on hybrid poly(D,L-lactide-co-glycolide)-dendron structures. *Biomaterials 27*, 4635–4645.

(43) Sakhalkar, H. S., Dalal, M. K., Salem, A. K., Ansari, R., Fu, A., Kiani, M. F., Kurjiaka, D. T., Hanes, J., Shakesheff, K. M., and Goetz, D. J. (2003) Leukocyte-inspired biodegradable particles that selectively and avidly adhere to inflamed endo -

thelium in vitro and in vivo. *Proc. Natl. Acad. Sci. U.S.A. 100*, 15895–15900.

(44) Garcia, F., Petry, K. U., Muderspach, L., Gold, M. A., Braly, P., Crum, C. P., Magill, M., Silverman, M., Urban, R. G., Hedley, M. L., and Beach, K. J. (2004) ZYC101a for treatment of high-grade cervical intralepithelial neoplasia: A randomized controlled trial. *Obstet. Gynecol. 103*, 317–326.

(45) Klencke, B., Matijevic, M., Urban, R. G., Lathey, J. L., Hedley, M. L., Berry, M., Thatcher, J., Weinberg, V., Wilson, J., Darragh, T., Jay, N., Da Costa, M., and Palefsky, J. M. (2002) Encapsulated plasmid DNA treatment for human papillomavirus 16-associated anal dysplasia: A phase I study of ZYC101. *Clin. Cancer Res. 8*, 1028–1037.

(46) McKeever, U., Barman, S., Hao, T., Chambers, P., Song, S., Lunsford, L., Hsu, Y. Y., Roy, K., and Hedley, M. L. (2002) Protective immune responses elicited in mice by immunization with formulations of poly (lactide-co-glycolide) microparticles. *Vaccine 20*, 1524–1531.

(47) Sheets, E. E., Urban, R. G., Crum, C. P., Hedley, M. L., Politch, J. A., Gold, M. A., Muderspach, L. I., Cole, G. A., and Crowley-Nowick, P. A. (2003) Immunotherapy of human cervical high-grade cervical intraepithelial neoplasia with microparticle-delivered human papillomavirus 16 E7 plasmid DNA. *Am. J. Obstet. Gynecol. 188*, 916–926.

BC070116L

Degradable-Brushed pHEMA–pDMAEMA Synthesized via ATRP and Click Chemistry for Gene Delivery

Xulin Jiang,[†,‡] Martin C. Lok,[†] and Wim E. Hennink*[,†]

Department of Pharmaceutics, Utrecht Institute for Pharmaceutical Sciences (UIPS) Utrecht University, P.O. Box 80 082, 3508 TB Utrecht, The Netherlands, and Key Laboratory of Biomedical Polymers of Ministry of Education and Department of Chemistry, Wuhan University, Wuhan 430072, P.R. China. Received April 7, 2007; Revised Manuscript Received August 20, 2007

Brushed polymers composed of a backbone of poly(hydroxyethyl methacrylate) (pHEMA) onto which poly(2-(dimethylamino)ethyl methacrylate)s (pDMAEMAs) was grafted via a hydrolyzable linker were synthesized and evaluated as nonviral gene delivery vectors. Both pDMAEMA and pHEMA polymers with controlled molecular weights and narrow distributions were synthesized by controlled atom transfer radical polymerization (ATRP). The azide initiator was used to ensure complete and monoazide functionalization of the pDMAEMA polymer chains. Click reaction between pHEMA with alkyne side groups and the azide end group in the pDMAEMA resulted in a high-molecular-weight polymer composed of low-molecular-weight constituents via an easily degradable carbonate ester linker. The length of the pDMAEMA grafts as well as the number of grafts of the brushed pHEMA–pDMAEMA can be easily varied. At physiological conditions (pH 7.4 and 37 °C), the brushed polymer degraded by hydrolysis of the carbonate ester with a half-life of 96 h. The molecular weights of the formed degradation products was very close to that of the starting pDMAEMA, which is likely below the renal excretion limit (<30 kDa). It was shown that the degradable brushed pHEMA–pDMAEMAs were able to condense plasmid DNA into positively charged nanosized particles. The resulting polyplexes were able to transfect cells efficiently in the presence of the endosomal membrane disrupting INF-7 peptide, and all these degradable polymers showed lower cellular toxicity compared to a high-molecular-weight pDMAEMA reference. On the other hand, the low-molecular-weight pDMAEMA used for the grafting to pHEMA was neither able to condense the structure of DNA nor able to transfect cells. This study demonstrates that grafting a low-molecular-weight cationic polymer via a hydrolyzable linker to a neutral hydrophilic polymer is an effective approach to modulate the transfection activity and toxicity profile of gene delivery polymers.

INTRODUCTION

Gene therapy is considered to be a very promising approach to tackle genetic diseases, slow the progression of tumors, fight viral infections, and stop neurodegeneration (*1–3*). The major challenge in gene therapy is to design vector systems that are able to deliver therapeutic genes efficiently and specifically to the target site (*4*). The gene delivery strategies currently used include viral and nonviral systems. Although viral vectors, such as retroviruses, adenoviruses, and adeno-associated viruses, show efficient delivery and expression of genes, they possess some serious disadvantages, such as the possible introduction of immunogenic and inflammatory response, random DNA insertion, size limitations of the DNA, and problems with pharmaceutical-grade productions (*5–8*). Over the past decades, cationic polymers have been receiving much attention as nonviral gene delivery vectors, because they offer good biosafety and biocompatibility, a high flexibility regarding the size of the DNA that they can deliver, and can be produced relatively easily (*3*). For effective gene delivery, polymer carriers have to meet a series of requirements for the extracellular and intracellular transport of the DNA vector. First of all, the polymers have to be able to bind to and compact the DNA into small particles, called polyplexes. Therefore, the polymers have to be positively charged under physiological conditions. Second, the polyplexes have to be able to target specific cells, facilitating endosomal escape and localizing in the nucleus as well as vector unpacking (*3*, *9*). Third, the polymers should be nontoxic, nonimmunogenic, and preferably biodegradable in a controlled way to yield low-molecular-weight compounds that can be further metabolized or degradation products with molecular weight lower than 30 kDa, which can be excreted by the kidneys (*10*). However, none of the well-known polymers as nonviral carriers that have been evaluated so far, such as poly(L-lysine) (PLL) (*11*), poly(ethylene imine) (PEI) (*5*), chitosan and its derivatives (*12*, *13*), and poly(2-(dimethylamino)ethyl methacrylate) (pDMAEMA) and other cationic polymethacrylates (*14–16*), fulfills all the above functions. The major drawbacks of the generation of cationic gene delivery polymers are their relatively low transfection efficiency and significant cytotoxicity (*17–20*). In order to reduce the cytotoxicity and enhance vector unpacking into the cytosol and/or nucleus, degradable polymeric vectors have been recently investigated for gene delivery. These encompass polymers which degrade via chemical hydrolysis such as poly(4-hydroxy-L-proline ester) (*21*), poly[α-(4-aminobutyl)-L-glycolic acid] (*22*), poly(amino ester)s (*23*, *24*), polyphosphazenes (*9*), and degradable PLL (*25*) and PEI derivatives (*10*, *26*). In recent years, cationic polymers that contain disulfide bridges in the main chain (*27–29*) or in their cross-links (*30–32*) have been investigated for gene delivery. These bonds are reduced in the cytosol by which the polyplex destabilizes and DNA is released.

The transfection efficiency and cytotoxicity of cationic polymers complexed with plasmid DNA are strongly dependent

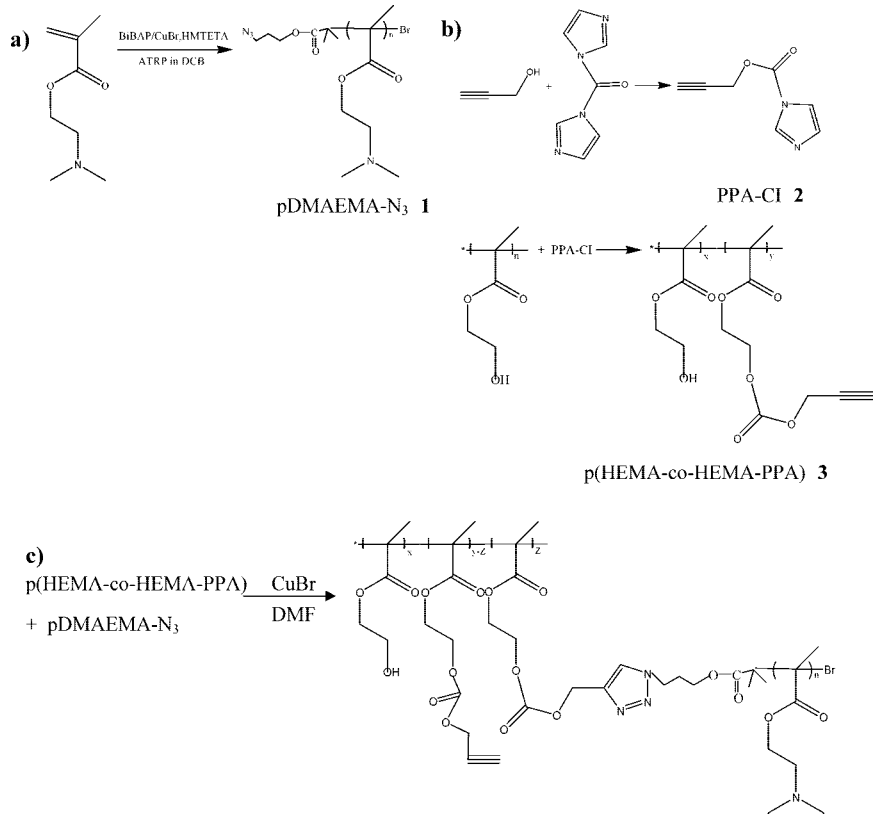
* Corresponding author: W.E. Hennink, Utrecht University, Utrecht Institute for Pharmaceutical Sciences, Department of Pharmaceutics, P.O. Box 80.082, 3508 TB Utrecht, The Netherlands, Phone +31-30-253 6964/7306, Fax + 31-30-251 7839, Email: W.E.Hennink@uu.nl.

[†] Utrecht University.

[‡] Wuhan University.

10.1021/bc0701186 CCC: $37.00 © 2007 American Chemical Society
Published on Web 10/10/2007

Scheme 1. (a) ATRP of 2-(Dimethylamino)ethyl Methacrylate (DMAEMA) Using N_3-Functionalized Initiator in Dichlorobenzene (DCB); (b) pHEMA with Side Chain of Alkynes; (c) Click Chemistry To Form Degradable Brushed pHEMA–pDMAEMA



on their molecular weights. Generally speaking, both the transfection efficiency and the cytotoxicity increase with increasing molecular weight of the cationic polymer, as reported for pDMAEMA (*33*, *34*), PLL (*35*), and PEI (*36*, *37*). In the present study, we therefore designed a high-molecular-weight polymer composed of a low-molecular-weight cationic polymer (pDMAEMA) that is grafted via a degradable linker to a hydrophilic, uncharged polymer (pHEMA). It is expected that these polymers show transfection efficiency comparable to that of high-molecular-weight polymers and degrade to low-molecular-weight cationic polymers, which are less cytotoxic than their high-molecular-weight counterparts.

The synthetic strategy we followed is depicted in Scheme 1. Degradable-brushed pHEMA–pDMAEMA polymers were synthesized via atom transfer radical polymerization (ATRP) (*38*, *39*) of HEMA and DMAEMA and click chemistry between azide-telechelic pDMAEMA and pHEMA with alkyne side groups (*40*–*42*). A carbonate ester, whose hydrolysis rate is higher than that of a "normal" ester (*43*, *44*), was selected as a degradable linker to couple pDMAEMA to the pHEMA backbone. This paper describes the synthesis and degradation of the brushed pHEMA–pDMAEMA polymers and the gene transfection activities of the corresponding polyplexes.

EXPERIMENTAL PROCEDURES

Materials. All chemicals were purchased from Sigma-Aldrich at the highest available purity and used as received, unless stated otherwise. 2-(Dimethylamino)ethyl methacrylate (DMAEMA) and hydroxyethyl methacrylate (HEMA) were obtained from Fluka (Buchs Switzerland). These monomers were distilled over calcium hydride prior to polymerization. Water purified by reverse osmosis was used throughout the study. The plasmid pCMVLacZ, containing a bacterial LacZ gene preceded by a nuclear localization signal under control of a CMV promoter, was purchased from Sanvertech (Heerhugowaard, The Netherlands). An ethidium bromide (EtBr) stock solution was obtained from Sigma (Zwijndrecht, The Netherlands). INF-7, a 24 amino acid containing peptide with fusogenic activity derived from the influenza virus, was synthesized via standard Fmoc solid-phase synthesis (*45*, *46*). The reference poly((dimethylamino)-ethyl methacrylate) (pDMAEMA, $M_n = 200$ kDa, $M_w = 1300$ kDa,) was synthesized via radical polymerization (*33*), and linear PEI (22 kDa, ExGen 500) was purchased from Fermentas (Burlington, Ontario, Canada).

Synthesis of 2-Bromo-Isobutyric Acid 3-Azidopropylester (BiBAP). BiBAP was synthesized from azidopropanol and 2-bromoisobutyryl bromide essentially reported as previously with some slight modifications (*39*). Azidopropanol (*47*) was synthesized as follows. 3-Bromo-1-propanol (3.58 g, 25.8 mmol) and sodium azide (6.71 g, 103.2 mmol) were dissolved in a mixture of 24 mL ethanol and 24 mL water. The solution was stirred at 70 °C in an oil bath for 24 h. Ethanol was then removed by evaporation under reduced pressure, and the product was extracted with dichloromethane (DCM, 3 × 20 mL). The organic layer was dried over Na_2SO_4, filtered, and evaporated to obtain a colorless oil (yield: 1.55 g, 60%). ^{1}H NMR (Gemini 300-MHz spectrometer, Varian, Palo Alto, CA, USA, $CDCl_3$, 298 K), $\delta = 3.76$ (t, $J = 6.0$ Hz, 2H, CH_2O), 3.45 (t, $J = 6.0$ Hz, 2H, CH_2N$_3$), and 1.83 (app. quint, $J = 6.1$ Hz, 2H, CCH_2C). No unreacted 3-bromo-1-propanol was detected by NMR. IR spectrum (neat): 3351 (broad, $\nu_{O\text{-}H}$), 2948, 2882, and 2099 cm^{-1} (ν_{N3}).

A solution of azidopropanol (1.28 g, 12.7 mmol) and triethylamine (3.9 mL, 28 mmol) in Et_2O (40 mL) was cooled to 0 °C in an ice bath, and 2-bromoisobutyryl bromide (3.12 mL, 25.3 mmol) was added dropwise. After stirring the mixture for 1 h at 0 °C, it was stirred for another 17 h at room temperature. Next, the resulting white suspension was filtered, and the filtrate was washed 3 times with 50 mL of a saturated $NaHCO_3$ aqueous solution. The organic layer was dried over

Table 1. Polymerization Conditions and Characteristics of N_3-Telechelic pDMAEMAs and pHEMAs Synthesized via ATRP

name	temp (°C)	[M]:[I] (mol/mol)	time (h)	conversion (%)	$M_{n(SEC)}$[a] (kDa)	$M_{w(SEC)}$ (kDa)	$PDI_{(SEC)}$ (kDa)	M_{nNMR} (kDa)
pDMAEMA-1	20	40	4	78	9.4	11.1	1.18	9.9
pDMAEMA-2	50	25	1.75	96	8.7	10.0	1.15	8.6
pHEMA-1	50	60	3	52	13.2	18.7	1.41	
pHEMA-2	50	30	3	64	6.9	8.2	1.20	

[a] SEC method as described previously (*48*).

Na_2SO_4, filtered, and evaporated to obtain a yellow oily crude residue, in which no unreacted azidopropanol was detected by ^{1}H NMR. The resulting oil was purified by versa flash chromatography (silica column, petroleum ether/Et_2O 20:1) to obtain a colorless oil (yield: 1.98 g, 63%). ^{1}H NMR (300.10 MHz, $CDCl_3$, 298 K), $\delta = 4.28$ (t, $J = 6.1$ Hz, 2H, C*H*$_2$OCO), 3.45 (t, $J = 6.6$ Hz, 2H, C*H*$_2$N$_3$), 1.97 (app. quint, $J = 6.5$ Hz, 2H, CC*H*$_2$C), and 1.94 (s, 6H, C*H*$_3$). IR spectrum (neat): 3005, 2978, 2933, and 2101 cm^{-1} (ν_{N3}).

ATRP of DMAEMA. Following the literature (*38*), ligand 1,1,4,7,10,10-hexamethyltriethylenetetramine (HMTETA), DMAEMA, CuBr, dichlorobenzene (DCB), and initiator BiBAP were introduced in a reaction flask and subjected to five vacuum-N_2 cycles. Polymerizations with 1 g of monomer dissolved in 2 mL DCB were done using different ratios of monomer to initiator (Table 1). The monomer conversion was determined on the basis of the ratio of the polymer protons at 4.25 ppm (2*H*) to the corresponding monomer protons at 4.03 ppm (2*H*) by ^{1}H NMR (300.10 MHz, $CDCl_3$, 298 K). The polymerization was done at room temperature or 50 °C while stirring. After different times, hexane (~20 mL) was added to stop the polymerization and precipitate the polymers. The precipitated polymers were washed with hexane and dried at room temperature. Next, the polymers were dissolved in 10 mL water, extensively dialyzed against water (dialysis tube MWCO 1 kDa), and collected by lyophilization. The ^{1}H NMR spectra of the obtained pDMAEMAs with an azide functional group on the α-terminus and Br atom at the ω-terminus (pDMAEMA-N_3, **1**, Scheme 1) were recorded, and their number-average molecular weight (M_n) was calculated on the basis of the ratio of the polymer protons at 4.03 ppm (2*H*) to the initiator protons at 3.37 ppm (2 *H*, next to azide group). IR spectrum of the polymer: 2947, 2820, 2770, 2099 (ν_{N3}), 1729, 1459, 1269, 1151 cm^{-1}. The molecular weight and the distribution of the pDMAEMA were determined using the SEC method reported previously (*48*).

Synthesis of Propargyl Ester of Carbonyl Imidazole (PPA-CI, 2, Scheme 1). 1,1′-Carbonyldiimidazole (CDI, 29.19 g, 0.18 mol) and 200 mL dichloromethane (DCM) were loaded into a dry round-bottom flask. Then, propargyl alcohol (PPA, 5.82 mL, 0.1 mol) was added dropwise. The obtained clear solution was stirred at room temperature for 1 h, washed with water (3 × 70 mL), dried over sodium sulfate, and evaporated to obtain a white solid (yield: 13.0 g, 87%). ^{1}H NMR (300.10 MHz, $CDCl_3$, 298 K), $\delta = 8.19$ (s, 1H, NC*H*N), 7.45 (s, 1H, NC*H*CHN), 7.10 (s, 1H, NCHC*H*N), 5.0 (s, 2H, OC*H*$_2$C), and 2.63 (s, 1H, CC*H*).

ATRP of HEMA. Following the literature (*49*), 3 mL HEMA (3.21 g, 24.7 mmol), the initiator ethyl 2-bromoisobutyrate (79 or 158 mg, 0.405 or 0.81 mmol), 2,2′-dipyridyl (63 or 126 mg, 1.21 or 2.42 mmol), and CuBr (58 or 166 mg, 0.405 or 0.81 mmol) were dissolved into 3 mL of a mixture of acetone and 1-propanol (2:1, v/v). Then, the reaction mixture was cooled in an ice bath, and oxygen was removed by three vacuum nitrogen cycles. The polymerizations were conducted at 50 °C while stirring for 3 h. The solutions were diluted with about 30 mL methanol and passed over an alumina column to remove the copper. The polymers were precipitated using an excess of diethylether, washed with the same solvent, and dried at room temperature. The obtained colorless polymers were subjected to SEC analysis (2 PLgel Mixed-D columns, mobile phase DMF with 0.02 M LiCl) to obtain their molecular weights and distributions using PEG standards.

Table 2. HEMA–PPA Content of the Copolymers p(HEMA-*co*-HEMA-PPA)

name	pHEMA used	aimed HEMA–PPA content, %	HEMA–PPA content, %
p(HEMA-*co*-HEMA-PPA) **1**	pHEMA-2	50	52
p(HEMA-*co*-HEMA-PPA) **2**	pHEMA-1	50	45
p(HEMA-*co*-HEMA-PPA) **3**	pHEMA-1	25	23

Synthesis of p(HEMA-*co*-HEMA-PPA) (3, Scheme 1). pHEMA (1.0 g; 7.7 mmol OH groups) and PPA-CI (575 mg, 3.8 mmol, OH/CI ratio 2:1; or 285 mg, 1.9 mmol, OH/CI ratio 4:1; see Table 2) were dissolved in 16 g DMSO and stirred overnight at 50 °C under a nitrogen atmosphere. Next, the DMSO solution was dropped into 300 mL diethyl ether to precipitate the polymer, which was dissoved in chloroform after filtration and precipitated twice to yield a white solid (yields about 90%) after drying at room temperature. No peaks above 5 ppm were observed in the ^{1}H NMR spectrum of the resulting polymers (300 MHz, DMSO-d_6, 298 K), which shows that PPA-CI was not present in the isolated polymers. The HEMA–PPA content of the polymer was determined using ^{1}H NMR analysis (ratio of integral between 4.0 and 4.5 ppm (the -COO-C$\underline{H}_2$C$\underline{H}_2$-OCOO- protons of the carbonate ester group) to that of 3.4–4.0 ppm (the -COO-C$\underline{H}_2$C$\underline{H}_2$-OH protons of the hydroxy ethyl group)).

Synthesis of Brushed pHEMA–pDMAEMA by Conjugation of pDMAEMA-N_3 to Polyalkynes via Click Chemistry. Azide-functional pDMAEMA **1** and polyalkynes, p(HEMA-*co*-HEMA-PPA) **3**, were dissolved in DMF and reacted in the presence of a copper(I) catalyst under a nitrogen atmosphere (Scheme 1c). The general procedures involved pDMAEMA-N_3 (1 equiv of N_3), p(HEMA-*co*-HEMA-PPA) (0.8–8 equiv of alkyne), and CuBr (1 equiv) being dissolved in DMF, and the resulting solution (200 mg pDMAEMA in 4 mL DMF) was subjected to five vacuum N_2 cycles. Then, the reaction mixtures were stirred at different temperatures (room temperature up to 80 °C). At regular time intervals, aliquots (10 μL containing about 1 mg of polymer) were withdrawn with a syringe, and added to 1 mL aqueous solution of 0.3 M NaAc (pH 4.4) for SEC molecular weight analysis (*48*). In some reactions, after 4 h, an extra amount of p(HEMA-*co*-HEMA-PPA) was added to consume remaining nonreacted pDMAEMA. If SEC analysis showed the absence of unreacted pDMAEMA, the solutions were extensively dialyzed (dialysis tube MWCO 12–14 kDa) against an NH_4Ac buffer pH 5.0 (10 mM, last step 5 mM). Water was removed by evaporation until about 10 mL remained, and the solutions with the brushed polymers were frozen and stored at −25 °C. The concentration of the brushed polymers was measured by SEC analysis with RI detection (*48*).

Hydrolysis of the Brushed pHEMA–pDMAEMAs. The brushed pHEMA–pDMAEMA polymers were dissolved in 10 mL buffer solutions at a concentration of 2 mg/mL. Buffers used were 0.1 M HEPES (pH 7.4) and 0.2 M NaAc (pH 5.0). These solutions were incubated at 37 °C, and at regular time intervals, 100 μL samples were withdrawn and added to 100 μL of aqueous solution of 0.3 M NaAc (pH 4.4), and stored at

−25 °C. After thawing, the samples were analyzed by SEC as described previously (*48*).

Particle Size and Zeta Potential of Polyplexes. The *Z*-average diameter and polydispersity of the polymer/DNA complexes were measured by dynamic light scattering (DLS) using a Malvern ALV CGS-3 system equipped with an argon-ion laser (488 nm, 10.4 mW) (Uniphase). The ALV correlator software in combination with DTS (Nano) and *ALVFilereader* software was used. Viscosity and refractive index of water at 25 °C were used. The instrument was calibrated with 100 nm polystyrene particles dispersed in water. In a typical experiment, 800 μL of buffer (5 mM HEPES, pH 7.4, or 20 mM HEPES, pH 7.4, adjusted to 150 mM with NaCl (HBS)) with various amounts of polymer was added to 200 μL of the same buffer containing 10 μg of plasmid DNA. The resulting solution was vortexed for 5 s, and after 30 min of incubation time at room temperature, the size of the polyplexes was determined using DLS at 25 °C.

The zeta potential of the polyplexes was measured at 25 °C using a Zetasizer 2000 unit (Malvern) equipped with a DTS5001 cell. The instrument was calibrated using a polystyrene dispersion with a known zeta potential. In a typical experiment, 800 μL of HEPES buffer (5.0 mM, pH 7.4) with various amounts of polymer was added to 200 μL of the same buffer containing 10 μg of plasmid DNA. The resulting solution was vortexed for 5 s, and after 30 min of incubation time at room temperature, the zeta potentials of the polyplexes were determined.

DNA Binding. The binding of the cationic polymers to DNA was examined by the fluorescence-quenching assay of ethidium bromide (EtBr), at a DNA concentration of 10 μg/mL in 20 mM HBS buffer (*9*). EtBr was added at a 1:10 molar ratio to DNA phosphates in 20 mM HBS buffer. Then, the polymer in 20 mM HBS was added to the DNA/EtBr solution to form the polyplexes at different polymer/DNA ratios, followed by vortexing and incubation at room temperature for 30 min. The fluorescence was measured using a Fluorstar Optima plate reader (BMG Laboratory Tech, Germany) at excitation/emission wavelengths of 500 and 600 nm, respectively. The relative fluorescence (F_r) values were calculated as follows:

$$F_r = (F_{obs} - F_e)/(F_0 - F_e)$$

where F_{obs} is the measured fluorescence, F_e is the fluorescence of EtBr in the absence of DNA, and F_0 is the initial fluorescence of DNA/EtBr in the absence of a cationic polymer.

In Vitro Transfection and Toxicity. Transfection and toxicity studies were done in COS-7 cells as described previously using plasmid pCMVLacZ as reporter gene (*33*). Two parallel experimental series, one for the determination of reporter gene expression and the other for the evaluation of number of viable cells using an XTT colorimetric assay, were carried out in separate 96-well plates with cells at a density of 3×10^4 cm^{-2}. Polyplexes were prepared as follows: 150 μL of polymer solution (various concentrations) in HBS was added to 50 μL of 50 μg/mL plasmid solution in HBS buffer. After shaking and incubation for 30 min at room temperature, 50 μL solution of the endosomal membrane disrupting INF-7 peptide (150 μg/mL) was added, and the polyplexes were incubated for another 15 min before addition to the cells. After the cells were rinsed with HBS, 100 μL of the polyplex dispersion and 100 μL of serum-free culture medium were incubated with the cells for 1 h. After removal of the polyplex dispersion, fresh culture medium was added, and the cells were incubated for another 48 h. The transfection efficiency was determined by the activity of β-galactosidase using an ONPG colorimetric assay, of which the value was normalized to that of reference pDMAEME polyplexes (polymer/DNA ratio of 3/1) in the absence of serum. For comparison, the transfection activity of polyplexes of linear PEI (22 kDa, ExGen 500) in the absence of serum was also measured. The cell toxicity was measured using the XTT assay. The XTT value for the untreated cells (without polymer and DNA) was taken as 100% cell viability. All the transfection and toxicity assays were carried out in triplicate.

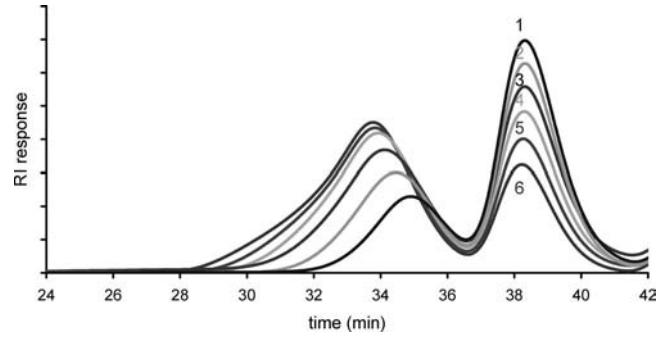


Figure 1. Kinetics of the click reaction of pDMAEMA-N_3 and p(HEMA-*co*-HEMA-PPA) in DMF at a molar ratio of alkyne to azide 1:0.8 at room temperature as followed by SEC. Trace 1 (SEC method as described previously (*48*)), 10 min; 2, 25 min; 3, 50 min; 4, 90 min; 5, 150 min; 6, 240 min. Remark: p(HEMA-*co*-HEMA-PPA) is not detected because it is not soluble in the SEC mobile phase; pDMAEMA-1 and pHEMA-1 were used.

RESULTS AND DISCUSSION

Synthesis of N_3-Telechelic pDMAEMA Using ATRP. Using the azide-initiator (2-bromo-isobutyric acid 3-azidopropylester, BiBAP), ATRP of DMAEMA gave a monoazido-functionalized polymer (Scheme 1). The polymerization kinetics (data not shown) indicated negligible termination and controlled/"living" characteristics of the DMAEMA polymerization under the selected conditions. Further, ^{1}H NMR analysis of the obtained polymer showed the presence of the protons (2*H*, 3.37 ppm) originating from the used initiator, whereas IR analysis showed an absorption peak at 2099 cm^{-1} corresponding to the asymmetric stretching vibration of the azide group. The number-average molecular weights (M_n) of the pDMAEMAs as determined by NMR (e.g., $M_{n(NMR)} = 8.7$ kDa for pDMAEMA-2) are in excellent agreement with those obtained by SEC (for the same polymer, $M_{n(SEC)} = 8.6$ kDa). SEC analysis also showed that the polydispersities are low (PDI = 1.15–1.18), as expected for polymers prepared with ATRP. From these analyses, it is concluded that N_3-telechelic pDMAEMAs have been obtained.

Synthesis of pHEMA with Alkyne Side Groups. pHEMAs with alkyne side groups were synthesized in two steps. First, pHEMAs were synthesized by ATRP (pHEMA-1, insoluble in water; pHEMA-2, water-soluble). The SEC results are shown in Table 1. Second, propargyl alcohol activated with 1,1′-carbonyldiimidazole (PPA-CI) was reacted with pHEMA. The HEMA-PPA contents of the polymers as measured by ^{1}H NMR are shown in Table 2. It can be seen from this table that the HEMA-PPA contents were close to the desired values.

Brushed pHEMA–pDMAEMA Synthesized by Click Reaction. At room temperature, N_3-telechelic pDMAEMA (pDMAEMA-N_3) was coupled to p(HEMA-*co*-HEMA-PPA) in DMF with CuBr as catalyst. A slight molar excess of alkyne to azide groups (1/0.8 mol/mol) was used. The coupling progress was monitored by SEC analysis (Figure 1). This figure shows that the (pDMAEMA-N_3) fraction (retention time ~36.5–41 min) decreased, whereas a high-molecular-weight fraction (retention time ~28–36 min), consisting of brushed pHEMA–pDMAEMA, was formed in time. When no copper catalyst was used, no high-molecular-weight fraction was observed within the investigated time (15 h). This demonstrates that the high-molecular-weight fraction as observed in Figure 2 consisted of brushed pHEMA–pDMAEMA "clicked" via a triazole group

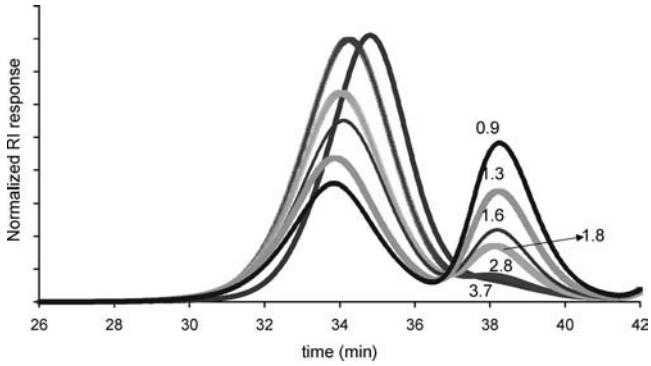


Figure 2. SEC profiles of various brushed pHEMA–pDMAEMA polymers synthesized at different alkyne/azide ratios in DMF at 50 °C for 3 h (SEC method as described previously (*48*)); molar ratios of azide to alkyne are indicated, pDMAEMA-1 and pHEMA-1 were used.

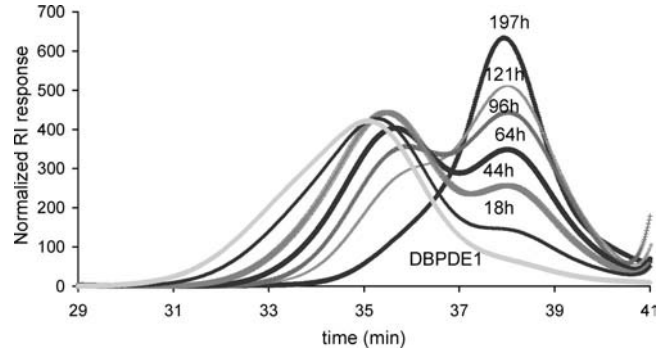


Figure 3. SEC profiles of pHEMA–pDMAEMA-1 incubated for various times at pH 7.4 and 37 °C.

that was formed by the Cu(I)-catalyzed reaction of the terminal azide group of pDMAEMA and the alkyne side groups of p(HEMA-*co*-HEMA-PPA). Figure 1 also shows that after 90 min reaction time almost half of the pDMAEMA-N_3 was coupled to p(HEMA-*co*-HEMA-PPA). However, the click reaction slowed down at the later stages, likely because the grafted pDMAEMA hindered the coupling of pDMAEMA-N_3 to unreacted propagyl groups. After 4 h, prolongation of the reaction time did not decrease the fraction of nonreacted (pDMAEMA-N_3). To optimize the click reaction conditions, different brushed pHEMA–pDMAEMA polymers were synthesized at different alkyne/azide ratios at 50 °C. As seen in Figure 2, the fraction of nonreacted pDMAEMA-N_3 decreased with an increasing alkyne/azide ratio. At the highest alkyne/azide ratio (3.7/1 mol/mol) investigated, hardly any unreacted pDMAEMA-N_3 was detected with SEC after 3 h reaction time at 50 °C. Figure 2 also shows that the molecular weight of the synthesized brushed pHEMA–pDMAEMA decreased with increasing alkyne/azide ratio. This is expected, since with an increasing alkyne/azide ratio the grafting density of the brushed pHEMA–pDMAEMA decreases. The SEC results of the synthesized brushed pHEMA–pDMAEMAs are summarized in Table 3.

Hydrolytic Degradation of Brushed pHEMA–pDMAEMA. The pDMAEMA chains are coupled via a carbonate ester and a "normal" ester to pHEMA (Scheme 1). In previous studies, it has been shown that, in particular, carbonate esters are sensitive towards hydrolysis under physiological conditions (*43, 45*). SEC was used to monitor the hydrolytic degradation of brushed pHEMA–pDMAEMA. As an example, Figure 3 shows the SEC profiles of the brushed pHEMA–pDMAEMA-1 incubated at 37 °C and pH 7.4. This figure clearly demonstrates that the high-molecular-weight brushed pHEMA–pDMAEMA decreases in time with a concomitant increase of a low-molecular-weight fraction (retention time ~36.5–41 min). The molecular weight of the formed polymers after a degradation time of 197 h is very close to that of the starting pDMAEMA, which was coupled to p(HEMA-*co*-HEMA-PPA) via the click reaction. The half-life time (*50*) of the degradable brushed pHEMA–pDMAEMA-1 polymer is about 96 h under the tested conditions. Once pHEMA–pDMAEMA-1 had been incubated for 10 days at pH 5.0 and 37 °C, no degradation was seen with SEC. At this pH, esters have the highest resistance toward chemical hydrolysis. Taken together, the data demonstrate that brushed pHEMA–pDMAEMA most likely degrades by chemical hydrolysis of the carbonate ester bonds via which the pDMAEMA are grafted to p(HEMA-*co*-HEMA-PPA), yielding pDMAEMA and pHEMA as degradation products with a molecular weight allowing excretion via the kidneys.

DNA Condensation and Polyplex Stability. The DNA binding and condensation properties of the starting pDMAEMA and the degradable brushed pHEMA–pDMAEMAs were investigated by dynamic light scattering (DLS) and zeta potential measurement. Once pDMAEMA (pDMAEMA-1, M_w 11.1 kDa) was added to a solution of DNA, only large polymer/DNA polyplex particles (size above 1000 nm) were formed, of which the size did not decrease with increasing polymer concentration, although a positive zeta potential of 28 mV was obtained. However, all the synthesized brushed pHEMA–pDMAEMA polymers (M_w >75 kDa) were able to condense DNA into small particles (90–190 nm, at a polymer to plasmid mass ratio ≥6). This is in agreement with a previous report in which it was demonstrated that only high-molecular-weight pDMAEMA is able to condense the structure of plasmid DNA effectively (*33*). As can be seen in Figure 4, the size of the pHEMA–pDMAEMA-1 based polyplexes is smaller than that of the pHEMA–pDMAEMA-3-based polyplexes when the polymer/DNA mass ratio is >3, although the weight-average molecular weight of pHEMA–pDMAEMA-1 is lower than that of pHEMA–pDMAEMA-3. This implies that the size of the polyplexes does not increase with the molecular weight of the polymer anymore when the molecular weight is high enough (M_w above 75 kDa). The zeta potentials of the brushed pHEMA–pDMAEMA-based polyplexes were independent of the molecular weight of pHEMA–pDMAEMA. The binding of polymers to plasmid DNA was also studied by ethidium bromide fluorescence measurement in HBS buffer (Table 4). This table shows that all tested polymers quenched the plasmid DNA/ethidium bromide fluorescence. The brushed pHEMA–pDMAEMAs showed more quenching than the starting pDMAEMA, indicating a weaker binding of this low-molecular-weight polymer to the plasmid DNA. However, the brushed pHEMA–pDMAEMAs

Table 3. SEC Results of Brushed pHEMA–pDMAEMA Copolymers (Alkyne/Azide Molar Ratio 4:1)[a]

name	p(HEMA-*co*-HEMA-PPA) used	M_n, kDa	M_w, kDa	PDI
pDMAEMA-2		8.7	10.0	1.15
pHEMA-pDMAEMA-1	p(HEMA-co-HEMA-PPA)1	45.2	79.3	1.75
pHEMA-pDMAEMA-2	p(HEMA-co-HEMA-PPA)2	50.9	158	3.10
pHEMA-pDMAEMA-3	p(HEMA-co-HEMA-PPA)3	52.7	589	11.2

[a] SEC method as described previously (*48*).

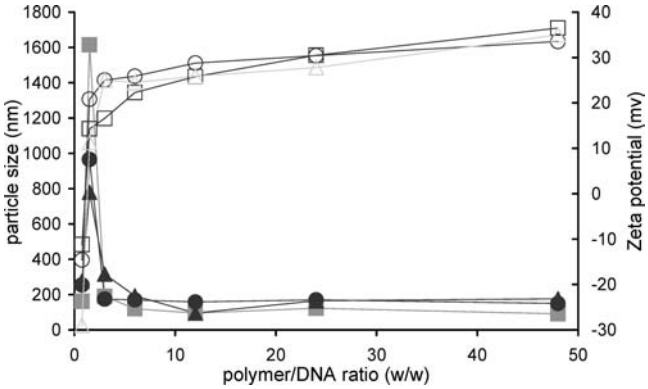


Figure 4. Particle size and zeta potential of brushed pHEMA–pDMAEMA-based polyplexes as a function of polymer/DNA ratio. Square, size of pHEMA–pDMAEMA-1-based polyplexes; circle, size of pHEMA–pDMAEMA-2-based polyplexes; triangle, size of pHEMA–pDMAEMA-3-based polyplexes; open square, zeta potential of pHEMA–pDMAEMA-1-based polyplexes; open circle, zeta potential of pHEMA–pDMAEMA-2-based polyplexes; open triangle, zeta potential of pHEMA–pDMAEMA-3-based polyplexes.

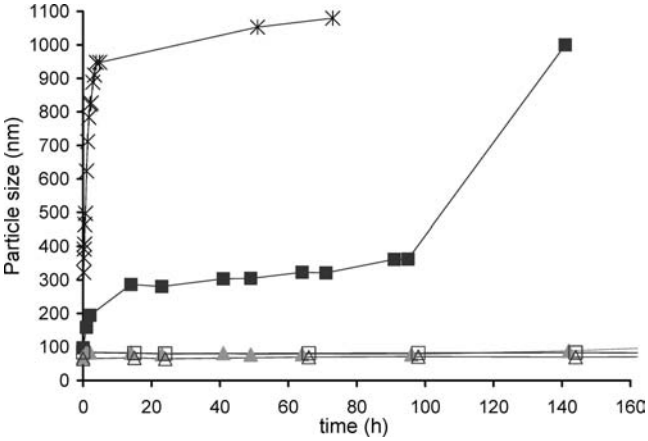


Figure 5. Polyplex (polymer/DNA mass ratio 3:1) destabilization studied by DLS. Square, pHEMA–pDMAEMA-1-based polyplexes at pH 7.4 and 5 mM HEPES; triangle, pHEMA–pDMAEMA-3-based polyplexes at pH 7.4 and 5 mM HEPES; open square, pHEMA–pDMAEMA-1-based polyplexes at pH 5 and 10 mM NaAc; open triangle, pHEMA–pDMAEMA-3-based polyplexes at pH 5 and 10 mM NaAc; star, pHEMA–pDMAEMA-1-based polyplexes at pH 7.4 and HBS.

showed similar quenching as high-molecular-weight pDMAEMA. This is in agreement with the DLS results.

The destabilization of pHEMA–pDMAEMA polyplexes was investigated by DLS. Figure 5 shows the particle size of pHEMA–pDMAEMA-1 and pHEMA–pDMAEMA-3 polyplexes (with the polymer to DNA mass ratio of 3) as a function of time at 37 °C and at pHs 5.0 and 7.4. The size of the polyplexes was constant at pH 5.0 in 10 mM NaAC over the investigated time period (7 days), while the size of the pHEMA–pDMAEMA-1-based polyplexes incubated at pH 7.4 increased substantially over time (Figure 5). The size of pHEMA–pDMAEMA-3 (relatively higher molecular weight) based polyplexes in 10 mM HEPES at pH 7.4 increased very

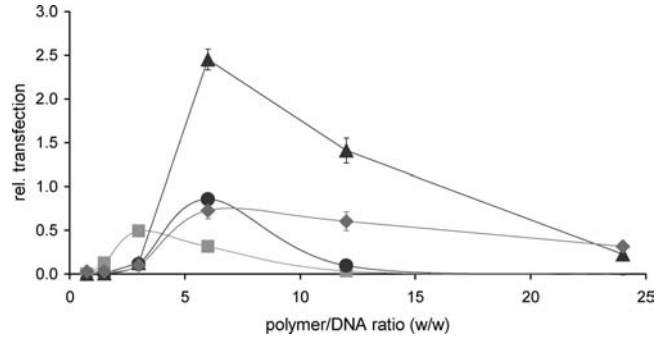


Figure 6. β-Galactosidase expression after incubation of COS-7 cells with polyplexes based on the degradable brushed pHEMA–pDMAEMA polymers and the reference polymer linear PEI in the presence of INF-7 peptide. Square, pHEMA–pDMAEMA-1; circle, pHEMA–pDMAEMA-2; triangle, pHEMA–pDMAEMA-3; diamond, linear PEI.

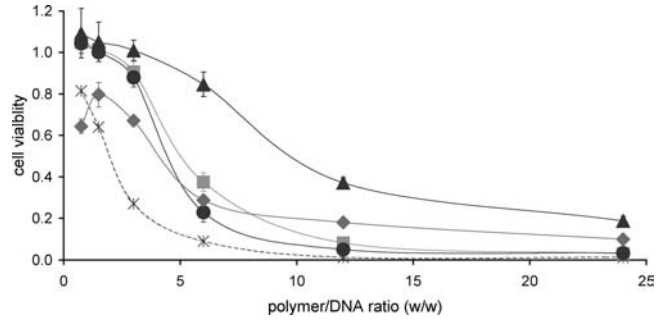


Figure 7. Relative cell viability of polyplexes based on the degradable brushed pHEMA–pDMAEMA polymers and the reference polymers pDMAEMA and linear PEI in the presence of INF-7 peptide in COS-7 cells. Square, pHEMA–pDMAEMA-1; circle, pHEMA–pDMAEMA-2; triangle, pHEMA–pDMAEMA-3; star, reference pDMAEMA; diamond, linear PEI.

slowly, and the size of the polyplexes based on high-molecular-weight pDMAEMA was very stable under the same conditions (data not shown). Likely, the higher-molecular-weight brushed pHEMA–pDMAEMA needs more time to degrade completely than the lower-molecular-weight ones. The observation that polyplexes based on high-molecular-weight pDMAEMA are stable over time after incubation at physiological conditions is in agreement with previous data that this polymer is very stable at pH 7.4 and 37 °C (*51*). The time period in which aggregation of the polyplexes occurred is on the same order of magnitude as pHEMA–pDMAEMA-1 polymer hydrolysis (compare Figure 5 (95 h) with Figure 3 (96 h)), which indicates that the degradation of brushed pHEMA–pDMAEMA polymers is hardly influenced by the complexation with DNA (*45*). The polyplexes in HBS buffer aggregated much more quickly than those in 5 mM HEPES buffer, especially for low polymer/DNA ratio or for polymers with low molecular weight (Figure 5). Obviously, chemical degradation results in a decrease in the colloidal stability of the polyplexes in HEPES-buffered saline.

In Vitro Transfection Efficiency and Cytotoxicity Studies. The transfection activity and toxicity of the different polyplexes was studied in vitro in COS-7 cells (Figures 6 and 7). Figure 6 shows the expression levels of β-galactosidase after incubation of COS-7 cells for 1 h with polyplexes based on the

Table 4. Relative fluorescence of ethidium bromide/plasmid DNA incubated with different cationic polymers in HBS buffer (DNA concentration, 10 μg/mL; ethidium bromide/plasmid DNA, 1:10 (mol/mol))

polymer/DNA (w/w)	pDMAEMA-2	pHEMA–pDMAEMA-1	pHEMA–pDMAEMA-2	pHEMA–pDMAEMA-3	pDMAEMA ref
12	0.50 ± 0.01	0.33 ± 0.02	0.31 ± 0.02	0.34 ± 0.05	0.33 ± 0.07
6	0.50 ± 0.02	0.36 ± 0.01	0.33 ± 0.03	0.36 ± 0.05	0.36 ± 0.04
3	0.51 ± 0.01	0.39 ± 0.02	0.38 ± 0.02	0.45 ± 0.03	0.38 ± 0.05

three degradable brushed pHEMA–pDMAEMA polymers and the reference polymer, linear PEI, as a function of the polymer to DNA ratio in the presence of INF-7 peptide. The transfection efficiency of the polyplexes based on high-molecular-weight pDMAEMA at a polymer/DNA ratio of 3/1 (w/w) was set at 1.0 (*33*). The highest transfection was observed for the polyplexes based on the highest-molecular-weight pHEMA–pDMAEMA-3 at a polymer/DNA mass ratio of 6/1, with a tranfection efficiency about 2.5 times higher than that of the polyplexes based on the reference pDMAEMA and about 3.1 times higher than that of the polyplexes based on linear PEI (Exgen 500). The polyplexes based on lower-molecular-weight brushed pHEMA–pDMAEMA showed lower transfection, which is in agreement with the results reported previously (*33*). The transfection of the pDMAEMA-2-based polyplexes was negligible (data not shown). We also studied the transfection activity of the polyplexes without addition of the INF peptide. In line with previous data (*52*), the transfection was lower (3–4 times), but the observed trends were the same as those observed for the polyplexes with INF.

Importantly, the brushed pHEMA–pDMAEMAs showed lower cellular toxicity as compared to reference pDMAEMA (Figure 7). Of the investigated brushed polymers, pHEMA–pDMAEMA-3-based polyplexes showed the highest transfection efficiency and the lowest toxicity, making this polymer an interesting candidate for future studies.

CONCLUSION

A new degradable brushed pHEMA–pDMAEMA was synthesized via ATRP and click chemistry for gene delivery. The click reaction and the degradation process were monitored clearly by aqueous SEC. The molecular weight of the final main degradation product pDMAEMA was very close to that of the starting pDMAEMA, which was coupled to p(HEMA-*co*-HEMA-PPA) via the click reaction and is likely below the renal excretion range (<30 kDa). It was shown that all the degradable brushed pHEMA–pDMAEMA polymers were able to condense DNA into small particles (90–190 nm) and were able to quench the plasmid DNA/ethidium bromide fluorescence. The resulting polyplexes were able to transfect cells efficiently in the presence of INF-7 peptide and showed lower toxicity compared to high-molecular-weight pDMAEMA. Future work will be focused on the coupling of PEG to prevent nonspecific interactions and of targeting moieties to introduce cell specificity into the systems.

LITERATURE CITED

(1) Verma, I. M., and Weitzman, M. D. (2005) Gene therapy: twenty-first century medicine. *Annu. Rev. Biochem. 74*, 711–738.

(2) Parekh-Olmedo, H., Ferrara, L., Brachman, E., and Kmiec, E. B. (2005) Gene therapy progress and prospects: targeted gene repair. *Gene Ther. 12*, 639–646.

(3) Wagner, E., and Kloecker, J. (2006) Gene delivery using polymer therapeutics. *Adv. Polym. Sci. 192*, 135–173.

(4) Hunt, K. K., and Vorburger, S. A. (2002) Gene therapy: hurdles and hopes for cancer treatment. *Science 297*, 415–416.

(5) Neu, M., Fischer, D., and Kissel, T. (2005) Recent advances in rational gene transfer vector design based on poly(ethylene imine) and its derivatives. *J. Gene Med. 7*, 992–1009.

(6) Smith, A. E. (2006) Viral vectors in gene therapy. *Ann. Rev. Microbiol. 49*, 807–838.

(7) Park, T. G., Jeong, J. H., and Kim, S. W. (2006) Current status of polymeric gene delivery systems. *Adv. Drug Delivery Rev. 58*, 467–486.

(8) Nadeau, I., and Kamen, A. (2003) Production of adenovirus vectors for gene therapy. *Biotechnol. Adv. 20*, 475–489.

(9) Luten, J., van Steenis, J. H., van Someren, R., Kemmink, J., Schuurmans-Nieuwenbroek, N. M. E., Koning, G. A., Crommelin, D. J. A., van Nostrum, C. F., and Hennink, W. E. (2003) Water-soluble biodegradable cationic polyphosphazenes for gene delivery. *J. Controlled Release 89*, 483–497.

(10) Petersen, H., Merdan, T., Kunath, K., Fischer, D., and Kissel, T. (2002) Poly(ethylenimine-co-L-lactamide-co-succinamide): a biodegradable polyethylenimine derivative with an advantageous pH-dependent hydrolytic degradation for gene delivery. *Bioconjugate Chem. 13*, 812–821.

(11) Curiel, D. T., Wagner, E., Cotton, M., Birnstiel, M. L., Agarwal, S., Li, C. M., Loechel, S., and Hu, P. C. (1992) High-efficiency gene transfer mediated by adenovirus coupled to DNA-polylysine complexes. *Hum. Gene Ther. 3*, 147–154.

(12) Borchard, G. (2001) Chitosans for gene delivery. *Adv. Drug Delivery Rev. 52*, 145–150.

(13) Kean, T., Roth, S., and Thanou, M. (2005) Trimethylated chitosans as non-viral gene delivery vectors: Cytotoxicity and transfection efficiency. *J. Controlled Release 103*, 643–653.

(14) Cherng, J. Y., Van de Wetering, P., Talsma, H., Crommelin, D. J. A., and Hennink, W. E. (1996) Effect of size and serum proteins on transfection efficiency of poly((2-dimethylamino) ethyl methacrylate)-plasmid nanoparticles. *Pharm. Res. 13*, 1038–1042.

(15) Luten, J., Akeroyd, N., Funhoff, A., Lok, M. C., Talsma, H., and Hennink, W. E. (2006) Methacrylamide polymers with hydrolysis-sensitive cationic side groups as degradable gene carriers. *Bioconjugate Chem. 17*, 1077–1084.

(16) Dubruel, P., and Schacht, E. (2006) Vinyl polymers as non-viral gene delivery carriers: current status and prospects. *Macromol. Biosci. 6*, 789–810.

(17) De Smedt, S. C., DeMeester, J., and Hennink, W. E. (2000) Cationic polymer based gene delivery systems. *Pharm. Res. 17*, 113–125.

(18) Merdan, T., Kopecek, J., and Kissel, T. (2002) Prospects for cationic polymers in gene and oligonucleotide therapy against cancer. *Adv. Drug Delivery Rev. 54*, 715–758.

(19) Anwer, K., Rhee, B. G., and Mendiratta, S. K. (2003) Recent progress in polymeric gene delivery systems. *Crit. Rev. Ther. Drug Carr. Syst. 20*, 249–293.

(20) Fischer, D., Li, Y.-X., Ahlemeyer, B., Krieglstein, J., and Kissel, T. (2003) In vitro cytotoxicity testing of polycations: influence of polymer structure on cell viability and hemolysis. *Biomaterials 24*, 71121–71131.

(21) Lim, Y. B., Choi, Y. H., and Park, J. S. (1999) A self-destroying polycationic polymer: biodegradable poly(4-hydroxy-l-proline ester). *J. Am. Chem. Soc. 121*, 5633–5639.

(22) Lim, Y.-B., Kim, C.-H., Kim, K., Kim, S. W., and Park, J.-S. (2000) Development of a safe gene delivery system using biodegradable polymer, poly[α-(4-aminobutyl)-L-glycolic acid]. *J. Am. Chem. Soc. 122*, 6524–6525.

(23) Lynn, D. M., and Langer, R. (2000) Degradable poly(β-amino esters): synthesis, characterization, and self-assembly with plasmid DNA. *J. Am. Chem. Soc. 122*, 10761–10768.

(24) Zhong, Z., Song, Y., Engbersen, J. F. J., Lok, M. C., Hennink, W. E., and Feijen, J. (2005) A versatile family of degradable non-viral gene carriers based on hyperbranched poly(ester amine)s. *J. Controlled Release 109*, 317–329.

(25) Pichon, C., LeCam, E., Guerin, B., Coulaud, D., Delain, E., and Midoux, P. (2002) Poly[Lys-(AEDTP)]: A cationic polymer that allows dissociation of pDNA/cationic polymer complexes in a reductive medium and enhances polyfection. *Bioconjugate Chem. 13*, 76–82.

(26) Forrest, M. L., Koerber, J. T., and Pack, D. W. (2003) A degradable polyethylenimine derivative with low toxicity for highly efficient gene delivery. *Bioconjugate Chem. 14*, 934–940.

(27) Lee, Y., Koo, H., Jin, G. W., Mo, H., Cho, M. Y., Park, J.-Y., Choi, J. S., and Park, J. S. (2005) Poly(ethylene oxide sulfide): New PEG derivatives degradable in reductive conditions. *Biomacromolecules 6*, 24–26.

(28) Lin, C., Zhong, Z., Lok, M. C., Jiang, X.-L., Hennink, W. E., Feijen, J., and Engbersen, J. F. J. (2006) Linear poly(amido amine)s with secondary and tertiary amino groups and variable amounts of disulfide linkages: Synthesis and in vitro gene transfer properties. *J. Controlled Release 116*, 130–137.

(29) Lin, C., Zhong, Z., Lok, M. C., Jiang, X.-L., Hennink, W. E., Feijen, J., and Engbersen, J. F. J. (2007) Novel bioreducible poly(amido amine)s for highly efficient gene delivery. *Bioconjugate Chem. 18*, 138–145.

(30) Gosselin, M. A., Guo, W., and Lee, R. J. (2001) Efficient gene transfer using reversibly cross-linked low molecular weight polyethylenimine. *Bioconjugate Chem. 12*, 989–994.

(31) Gosselin, M. A., Guo, W., and Lee, R. J. (2002) Incorporation of reversibly cross-linked polyplexes into LPDII vectors for gene delivery. *Bioconjugate Chem., 13*, 1044–1053.

(32) Miyata, K., Kakizawa, Y., Nishiyama, N., Harada, A., Yamasaki, Y., Koyama, H., and Kataoka, K. (2004) Block catiomer polyplexes with regulated densities of charge and disulfide cross-linking directed to enhance gene expression. *J. Am. Chem. Soc. 126*, 2355–2361.

(33) van de Wetering, P., Cherng, J. Y., Talsma, H., and Hennink, W. E. (1997) Relation between transfection efficiency and cytotoxicity of poly(2-(dimethylamino)ethyl methacrylate/plasmid complexes. *J. Controlled Release 49*, 59–69.

(34) Arigita, C., Zuidam, N. J., Crommelin, D. J. A., and Hennink, W. E. (1999) Association and dissociation characterics of polymer/DNA complexes used for gene delivery. *Pharm. Res. 16*, 1534–1541.

(35) Choksakulnimitr, S., Masuda, S., Tokuda, H., Takakura, Y., and Hashida, M. (1995) In vitro cytotoxicity of macromolecules in different cell culture systems. *J. Controlled Release 34*, 233–241.

(36) Kim, Y. H., Park, J. H., Lee, M., Kim, Y.-H., Park, T. G., and Kim, S. W. (2005) Polyethylenimine with acid-labile linkages as a biodegradable gene carrier. *J. Controlled Release 103*, 209–219.

(37) Godbey, W. T., Wu, K. K., and Mikos, A. G. (1999) Size matters: molecular weight affects the efficiency of poly(ethylenimine) as a gene delivery vehicle. *J. Biomed. Mater. Res. 45*, 268–275.

(38) Zhang, X., Xia, J.-H., and Matyjaszewski, K. (1998) Controlled/"living" radical polymerization of 2-(dimethylamino)ethyl methacrylate. *Macromolecules 31*, 5167–5169.

(39) Mantovani, G., Ladmiral, V., Tao, L., and Haddleton, D. M. (2005) One-pot tandem living radical polymerisation-Huisgens cycloaddition process (click) catalysed by N-alkyl-2-pyridylmethanimine/Cu(I)Br complexes. *Chem. Commun. 2005*, 2089–2091.

(40) Hawker, C. J., and Wooley, K. L. (2005) The convergence of synthetic organic and polymer chemistries. *Science 309*, 1200–1205.

(41) Srinivasachari, S., Liu, Y., Zhang, G., Prevette, L., and Reineke, T. M. (2006) Trehalose click polymers inhibit nanoparticle aggregation and promote pDNA delivery in serum. *J. Am. Chem. Soc. 128*, 8176–8184.

(42) van Dijk, M., Mustafa, K., Dechesne, A. C., van Nostrum, C. F., Hennink, W. E., Rijkers, D. T. S., and Liskamp, R. M. J. (2007) Synthesis of peptide-based polymers by microwave-assisted cycloaddition backbone polymerization. *Biomacromolecules 8*, 327–330.

(43) van Dijk-Wolthuis, W. N. E., van Steenbergen, M. J., Underberg, W. J. M., and Hennink, W. E. (1997) Degradation kinetics of methacrylated dextrans in aqueous solution. *J. Pharm. Sci. 86*, 413–417.

(44) D'Souza, A. J. M., and Topp, E. M. (2004) Release from polymeric prodrugs: Linkages and their degradation. *J. Pharm. Sci. 93*, 1962–1979.

(45) Funhoff, A. M., van Nostrum, C. F., Janssen, A. P. C. A., Fens, M. H. A. M., Crommelin, D. J. A., and Hennink, W. E. (2004) Polymer side-chain degradation as a tool to control the destabilization of polyplexes. *Pharm. Res. 21*, 170–176.

(46) Plank, C., Oberhauser, B., Mechtler, K., Koch, C., and Wagner, E. (1994) The influence of endosome-disruptive peptides on gene-transfer using synthetic virus-like gene-transfer systems. *J. Biol. Chem. 269*, 12918–12924.

(47) Scheel, A. J., Komber, H., and Voit, B. I. (2004) Novel hyperbranched poly([1,2,3]-triazole)s derived from AB2 monomers by a 1,3-dipolar cycloaddition. *Macromol. Rapid Commun. 25*, 1175–1180.

(48) Jiang, X.-L., van der Horst, A., van Steenbergen, M. J., Akeroyd, N., van Nostrum, C. F., Schoenmakers, P. J., and Hennink, W. E. (2006) Molar-mass characterization of cationic polymers for gene delivery by aqueous size-exclusion chromatography. *Pharm. Res. 23*, 595–603.

(49) Beers, K. L., Boo, S., Gaynor, S. G., and Matyjaszewski, K. (1999) Atom transfer radical polymerization of 2-hydroxyethyl methacrylate. *Macromolecules 32*, 5772–5776.

(50) Bikram, M., Ahn, C. H., Chae, S. Y., Lee, M., Yockman, J. W., and Kim, S. W. (2004) Biodegradable poly(ethylene glycol)-co-poly(l-lysine)-g-histidine multiblock copolymers for nonviral gene delivery. *Macromolecules 37*, 1903–1916.

(51) van de Wetering, P., Zuidam, N. J., van Steenbergen, M. J., van der Houwen, O. A. G. J., Underberg, W. J. M., and Hennink, W. E. (1998) A mechanistic study of the hydrolytic stability of poly(2-(dimethylamino)ethyl methacrylate). *Macromolecules 31*, 8063–8068.

(52) Zuidam, N. J., Posthuma, G. V., De Else, T. J., Crommelin, D. J. A., Hennink, W. E., and Storm, G. (2000) Effects of physicochemical characteristics of poly(2-(dimethylamino)ethyl methacrylate)-based polyplexes on cellular association and internalization. *J. Drug Target. 8*, 51–66.

BC0701186

Synthesis of *p*-(Di-*tert*-butyl[^{18}F]fluorosilyl)benzaldehyde ([^{18}F]SiFA-A) with High Specific Activity by Isotopic Exchange: A Convenient Labeling Synthon for the ^{18}F-Labeling of N-amino-oxy Derivatized Peptides

Esther Schirrmacher,*[,∇,†] Björn Wängler,[∇,‡,§] Marek Cypryk,[||] Gerrit Bradtmöller,[⊥] Martin Schäfer,[‡] Michael Eisenhut,[‡] Klaus Jurkschat,[⊥] and Ralf Schirrmacher*[,#]

Lady Davis Institute, Jewish General Hospital, and Montreal Neurological Institute, McGill University, Montreal, Canada, Department of Radiopharmaceutical Chemistry, German Cancer Research Center, Heidelberg, Germany, Department of Nuclear Medicine, Hospital of the Ludwig-Maximilians-University, Munich, Germany, Center of Molecular and Macromolecular Studies, Polish Academy of Science, Lodz, Poland, and Department of Inorganic Chemistry II, University of Dortmund, Dortmund, Germany. Received May 30, 2007; Revised Manuscript Received August 14, 2007

The syntheses of different ^{18}F-labeled peptides using the highly effective labeling synthon *p*-(di-*tert*-butylfluorosilyl) benzaldehyde ([^{18}F]SiFA-A) for the development of ^{18}F-radiopharmaceuticals for oncological positron emission tomography (PET) is reported. The novel and mild labeling technique for the radiosynthesis of [^{18}F]SiFA-A, based on an unexpectedly efficient isotopic ^{19}F–^{18}F exchange, yielded the ^{18}F-synthon [^{18}F]SiFA-A in almost quantitative yields in high specific activities between 225 and 680 GBq/μmol (6081–18 378 Ci/mmol) without applying HPLC purification. The [^{18}F]SiFA-A was finally used to label the N-terminal amino-oxy (N-AO) derivatized peptides AO-Tyr^3-octreotate (AO-TATE), *cyclo*(fK(AO-N)RGD and N-AO-PEG$_2$-[D-Tyr-Gln-Trp-Ala-Val-βAla-His-Thi-Nle-NH$_2$] (AO-BZH3, a bombesin derivative) in high radiochemical yields. Density functional theory (DFT) calculations confirmed high efficiency of the isotopic exchange, which is predicted to proceed via a pentacoordinate siliconate intermediate dissociating immediately to form the radiolabeled [^{18}F]SiFA-A.

INTRODUCTION

Due to the high dissemination of positron emission tomography (PET) (*1*), an imaging modality investigating the distribution of radioactively labeled biomarkers *in vivo*, the synthesis of radiolabeled peptides with the radiohalide fluorine-18 for the detection of cancer of various origins has gained widespread interest in nuclear medicine oncology (*2*). The labeling methods for peptides so far are characterized by multistep synthetic pathways using secondary labeling precursors (prostetic groups) which have to be prepared prior to final bioconjugation to the peptide of interest (*3, 4*). Even novel methods such as chemoselective bioconjugation of aldehydes (*5–7*), solid-phase ^{18}F-fluoropropionylation (*8*), thiol-reactive ^{18}F-labeling agents (*9–12*), and the most recently introduced "click-chemistry" approach for the ^{18}F-labeling of peptides (*13, 14*), although great improvements, still suffer from drawbacks. The need to use HPLC or distillation for purification of the ^{18}F-synthon for final peptide coupling or time-consuming workup often reduce the final preparative yields and are cumbersome for automation. As a completely new labeling method and in addition to other recently published Si-^{18}F chemistry (*15*), our group has introduced an organosilicon-containing fluoride acceptor (Silicon Fluoride Acceptor, SiFA) conjugated to the peptide Tyr^3-octreotate (TATE) as the first practical example applying an ^{18}F-labeling chemistry based on isotopic ^{19}F for ^{18}F-exchange at a silicon atom (*16*). Although the final radiolabeling of SiFA-TATE is easy, the specific activities (SA) so far obtained (3–5 GBq/μmol) are unsatisfying and encouraged us to establish a complementary labeling approach where the *p*-(di-*tert*-butylfluorosilyl) benzaldehyde, hereafter referred to as SiFA-A (**1**), is ^{18}F-labeled in high SAs prior to solution-phase chemoselective conjugation to amino-oxy (AO) derivatized peptides (Figure 1). The fluorosilane [^{18}F]fluorodi-*t*-butylphenylsilane has previously been proven to be stable in human serum at 37 °C as well as under *in vivo* conditions in healthy rats and is therefore suited to be conjugated to peptides (*16*). We applied this two-step ^{18}F-labeling approach to N-terminal AO-derivatized peptides such as AO-Tyr^3-octreotate, AO-poly(ethylene glycol) (PEG)-conjugated bombesin (BN6-14) analogue (BZH3), and a small cyclic peptide containing the Arg-Gly-Asp (RGD) sequence *cyclo*(fK(AO-N)RGD) to cover a wide range of biologically interesting peptides for tumor imaging. Additional DFT calculations on the isotopic ^{19}F–^{18}F isotopic exchange reaction of three different model fluorosilicon compounds gave further insight into this new and exciting radiochemistry. We could demonstrate for the first time that highest SAs of ^{18}F-labeled compounds can be achieved by a simple isotopic exchange using a minimum amount of precursor in the lower nanomolar range.

EXPERIMENTAL SECTION

Materials. Amino acids and resins for Fmoc SPPS were purchased from Novabiochem (Germany). The Rink amide resin and solid-phase C18 cartridges were obtained from Merck (Germany). All other chemicals were obtained from Sigma-Aldrich. HPLC columns: the Chromolith SemiPrep (RP-18e 100–10mm) was purchased from Merck (Germany) and the PerfectSil column (120 C4 5μm, 100 × 4.0 mm) was obtained from MZ-ANALYTICAL (Germany).

* To whom correspondence should be addressed. (E.S.) Tel: (514) 340 8222 3912; fax: (514) 340 8716; E-mail: esther.schirrmacher@mcgill.ca. (R.S.) Tel: (514) 340 8222 5212; fax: (514) 340 7502; E-mail: ralf.schirrmacher@mcgill.ca.

[∇] Esther Schirrmacher and Björn Wängler contributed equally.

[†] Jewish General Hospital, McGill University.

[‡] German Cancer Research Center.

[§] Hospital of the Ludwig-Maximilians-University.

[||] Polish Academy of Science.

[⊥] University of Dortmund.

[#] Montreal Neurological Institute, McGill University.

10.1021/bc700195y CCC: $37.00 © 2007 American Chemical Society
Published on Web 11/21/2007

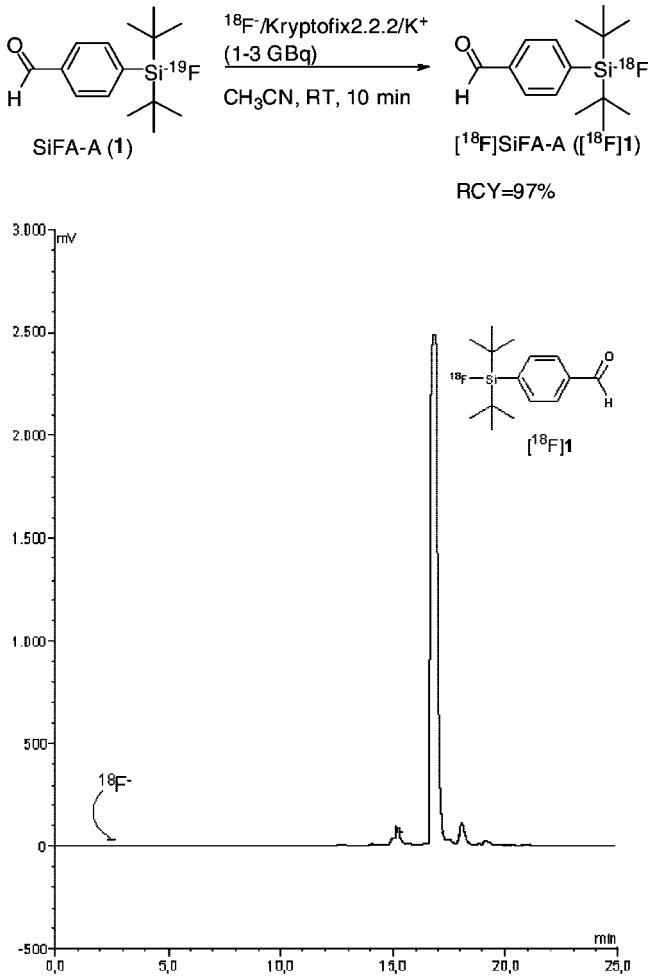


Figure 1. (top) Highly efficient isotopic exchange ^{18}F-radiofluorination of SiFA-A (**1**) (1 μg, 3.75 nmol) with $^{18}F^-$/Kryptofix 2.2.2./K^+ complex (1–3 GBq) in acetonitrile (200 μL) at room temperature yielding [^{18}F]SiFA-A (**1**) with high specific activity (~225–680 GBq/μmol). (bottom) Radio-HPLC chromatogram (HPLC system 1) of the crude reaction mixture.

Instruments. MALDI-TOF molecular weight determination of all peptide conjugates were carried out using a Kratos Kompact MALDI-III apparatus. For AO-derivatized peptide purification, an Agilent 1100 series liquid chromatograph with UV detection (Agilent 1100 multiple wavelength detector G1365B) was used. For radioactivity detection, an HPLC system (Dionex P680 HPLC) with UV detection (Dionex UVD 170U/340U) and radioactivity detector (Raytest, chromatography software *Gabi Star*) was used for the determination of radiochemical yields.

Synthesis of Amino-Oxy(AO)-Derivatized Peptides. The peptide synthesis was conducted using manual Fmoc solid-phase techniques. As for the chain elongation of peptides, N^{α}-(9-fluorenylmethyloxycarbonyl) (Fmoc)-protected aminoacids were used. Amino-oxy derivatized Tyr^3-octreotate (AO-TATE) was synthesized as previously described (*16*).

cyclo(fK(AO-N)RGD). The peptide (0.1 mmol) was synthesized according to a published procedure (*17*). Briefly, the peptide was derivatized on resin with bis-boc-amino-oxyacetic acid (123.7 mg, 0.4 mmol) on the deprotected lysine side chain according to standard Fmoc SPPS coupling procedures (0.98 equiv HBTU/1.0 equiv DIPEA) and subsequently cleaved from the resin (TFA/TIS/H_2O 95/2.5/2.5). For purification, reversed-phase semipreparative HPLC separations were carried out on an Agilent 1100 series liquid chromatograph with UV detection (Agilent 1100 multiple wavelength detector G1365B). HPLC runs were performed using a linear AB gradient (0% A to 100% B in 12 min) where solvent A was 0.1% aq TFA and solvent B was 0.1% TFA in acetonitrile using a Chromolith SemiPrep RP-18e 100-10 mm column at a flow rate of 8 mL/min. The preparative yield after purification and freeze-drying was 10%. MALDI-TOF-MS: *m/z* 676.33 M^+.

Table 1. Retention Times of [^{18}F]SiFA-A ([^{18}F]1) and ^{18}F-Labeled Peptides

compound	retention time [min] HPLC system 1 for preparative HPLC purification	retention time [min] HPLC system 2
[^{18}F]SiFA-A ([^{18}F]**1**)	16.8	31.5
[^{18}F]SiFA-TATE	14.1	28.4
[^{18}F]SiFA-BZH3	13.9	27.8
cyclo(fK([^{18}F]SiFA-AO-N)RGD)	13.9	27.7

N-AO-PEG$_2$-[D-Tyr-Gln-Trp-Ala-Val-βAla-His-Thi-Nle-NH$_2$] (AO-BZH3, a bombesin derivative). The bombesin derivative was synthesized by standard Fmoc solid-phase peptide synthesis (SPPS) using a Rink amide AM resin (200–400 mesh, Merck, 0.15 mmol). Bis-Boc-amino-oxyacetic acid (4.0 equiv, 185.6 mg, 0.6 mmol) was coupled to the N-terminal end of the peptide on resin after N-terminal derivatization with 8-(Fmoc-amino)-3,6-dioxaoctanoic acid using standard Fmoc-SPPS procedures. After cleavage from the resin, the peptide was purified analogously to the procedure described above for *cyclo*(fK(AO-N)RGD) to give a preparative yield of 25% after freeze-drying. MALDI-TOF-MS: *m/z* 1356.63 M^+.

SiFA–Peptide Conjugates. The corresponding SiFA-derivatized peptides *cyclo*(fK(SiFA-AO-N)RGD), MALDI-TOF-MS *m/z* 938.5 M^+; SiFA-BZH3 (N-SiFA-AO-PEG$_2$-[D-Tyr-Gln-Trp-Ala-Val-βAla-His-Thi-Nle-NH$_2$]), MALDI-TOF-MS *m/z* 1618.8 M^+; SiFA-TATE, MALDI-TOF-MS *m/z* 1369.9 M^+ as ^{19}F-standard compounds for HPLC evaluation of the conjugation of [^{18}F]**1** and AO-derivatized peptides were synthesized following a general procedure (*16*).

Radiosynthesis of [^{18}F]SiFA-A ([^{18}F]1) with [^{18}F]F$^-$/Kryptofix 2.2.2./K$^+$-Complex in Acetonitrile. To SiFA-A (**1**) (1 μg, 3.75 nmol; from stock solution in acetonitrile) the [^{18}F]F$^-$/Kryptofix 2.2.2./K^+ complex (~1.5–3.5 GBq, cf. Supporting Information) in acetonitrile (0.2 mL) was added and reacted for 10 min at rt without stirring. Two milliliters of water were added, and the resulting mixture was loaded onto a small solid-phase C18 cartridge (C18, Merck). The trapped [^{18}F]SiFA-A ([^{18}F]**1**) was washed with water (5 mL) and then eluted with hot (60 °C) acetonitrile (1 mL, elution efficiency >98%) to obtain a stock solution (~1–3 GBq, [^{18}F]**1**) for further peptide labeling.

Coupling of ([^{18}F]1) to Amino-oxy (AO)-derivatized peptides. To AO-derivatized peptide (20–100 μg, 0.014–0.147 μmol) dissolved in a minimum amount of water with trifluoroacetic acid at pH4 was added [^{18}F]SiFA-A (170–500 MBq; from stock solution in acetonitrile) and the appropriate amount of water (pH 4, TFA) to obtain a 90/10 acetonitrile/water solution (~150–200 μL). The solution was kept at room temperature for 10 min and injected into an HPLC system (column: PerfectSil 120 C4 5μm, 100 × 4.0 mm, MZ-ANALYTICAL, Germany. HPLC system 1: linear gradient, 30/70 CH_3CN/H_2O over 20 min to 100% CH_3CN; flow, 1 mL/min; Table 1). The peaks corresponding to the peptides (Table 1) were collected, water (10 mL) was added, and the mixture was loaded onto a solid-phase cartridge (C18, Merck). After washing the column with water (10 mL), the purified peptide was eluted with ethanol (0.5 mL, elution efficiency 85%) and diluted with physiological saline (5 mL) to obtain an injectable solution. The overall radiochemical yields (RCY) of the procedure were 50–55 % (referring to the starting activity of

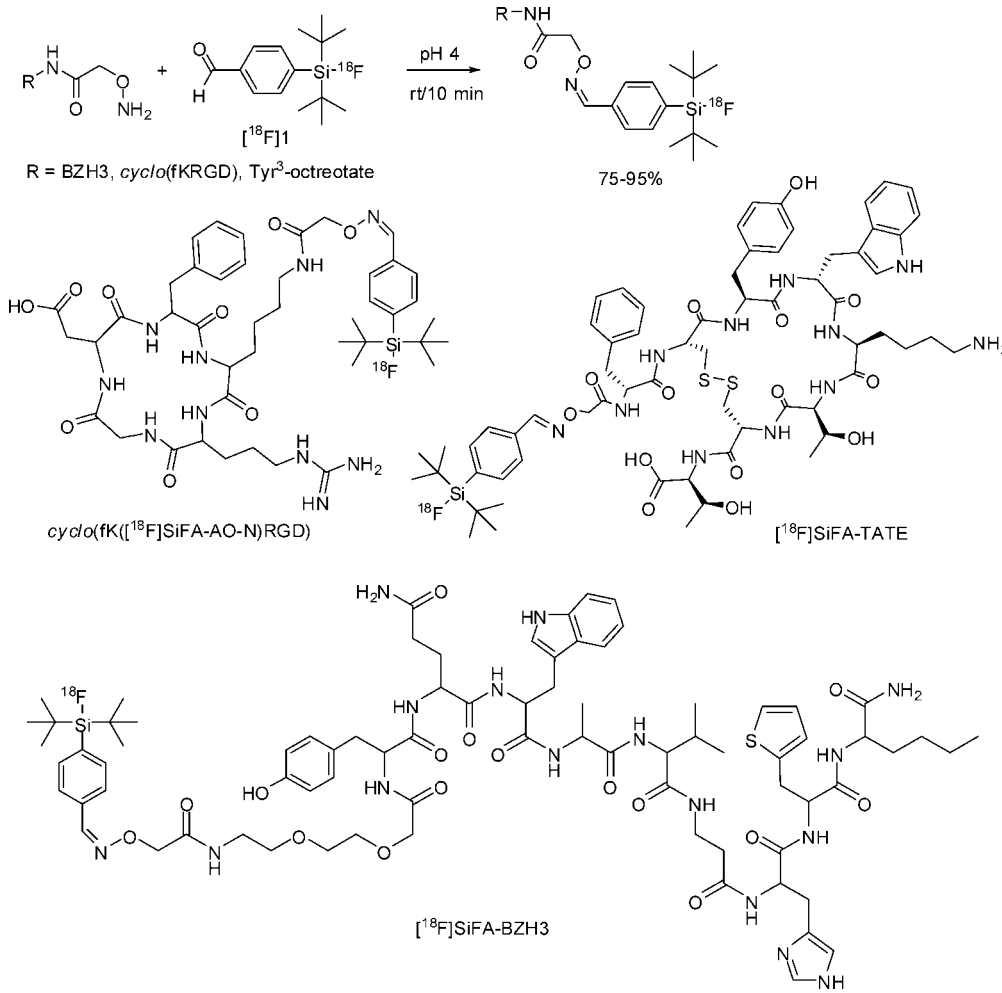


Figure 2. Chemoselective conjugation of [^{18}F]SiFA-A ([^{18}F]**1**) to three AO derivatized peptides (20–100 μg, 14–147 mol) at rt and pH 4 within 10 min in 150–200 μL acetonitrile/H_2O–TFA solution (90:10) and structures of *cyclo*(fK([^{18}F]SiFA-AO-N)RGD), [^{18}F]SiFA-TATE, and [^{18}F]SiFA-BZH3.

[^{18}F]F^-/Kryptofix 2.2.2./K^+ complex) after a total synthesis time of ~40 min (including azeotropic drying of $^{18}F^-$ and synthesis of [^{18}F]**1**). Isolated yields of all [^{18}F]SiFA derivatized peptides were between 110 and 400 MBq. A second HPLC system (HPLC system 2: linear gradient, 100% H_2O over 30 min to 100% CH_3CN; flow, 0.7 mL/min) was used to confirm the experimental outcome obtained with HPLC system 1 for preparative purification (Table 1).

RESULTS AND DISCUSSION

For the synthesis of [^{18}F]**1** by isotopic exchange (Figure 1), the precursor amount of **1** for the reaction with "dried" $^{18}F^-$/Kryptofix 2.2.2./K^+ complex (1.5–3.5 GBq) in acetonitrile (200 μL) to obtain radiochemical yields (RCY) up to 97% of [^{18}F]**1** within 10 min could be downscaled to 1 μg (3.75 nM). This is about 20 times less than the previously published amount of SiFA–peptide conjugate (SiFA-TATE) (*16*) resulting in extraordinarily high SAs. When 1.5–3.5 GBq of the ^{18}F-complex were used, the SAs obtained were between 225–680 GBq/μmol (6,081–18,378 Ci/mmol) which is unexpectedly high for an isotopic exchange reaction. Taking into account that the theoretical SA for cyclotron produced $^{18}F^-$ from the irradiated [^{18}O]water target is 63,270 GBq/μmol (1.71×10^6 Ci/mmol), the loss in SA during synthesis of [^{18}F]**1** is relatively low. The theoretical value of the SA can not be reached in practice. The obtained SA for ^{18}F is always lower due to dilution with the stable element and the SA of applied ^{18}F-labeled PET tracers normally varies between 100–10,000 Ci/mmol. For purification of [^{18}F]**1**, no HPLC is needed because the $^{19}F^-$ for $^{18}F^-$ exchange is highly selective and proceeds without formation of any by-products at room temperature. Solid phase cartridge extraction was performed by diluting with water (5 mL) to dispose of the un-reacted $^{18}F^-$ as well as the Kryptofix 2.2.2. and potassium ions followed by elution with acetonitrile (1 mL) of the purified [^{18}F]**1**. Thus, a stock solution of [^{18}F]**1** for labeling (c[^{18}F]**1**: 1–3 GBq/mL) was obtained for further experiments. The procedure including azeotropic drying of aqueous $^{18}F^-$ took 15 min only. This is in contrast to other one-step labeling synthons for peptides such as 4-[^{18}F]fluorobenzaldehyde ([^{18}F]FB-CHO) (*6*) and N-succinimidyl 4-([^{18}F]fluoromethyl)-benzoate, (*18*) the syntheses of which require more than 30 min and, in addition, still need HPLC purification. To use [^{18}F]SiFA-A ([^{18}F]**1**) as a labeling synthon for chemoselective oxime formation, three different N-terminal modified peptides, namely the AO-derivatized bombesin analog BZH3 (N-AO-PEG_2-[D-Tyr-Gln-Trp-Ala-Val-βAla-His-Thi-Nle-NH_2; PEG_2 is ethyleneglycol (2-aminoethyl)carboxymethyl ether), *cyclo*(fK(AO-N)RGD) (*17*) and AO-Tyr^3-octreotate (N-AO-D-Phe-Cys-Tyr-D-Trp-Lys-Thr-Cys-Thr) (*16*) for the potential use as imaging agents in nuclear medicine oncology were synthesized by means of Fmoc-solid phase peptide synthesis (SPPS). These peptides, radio-labeled mostly with indium-111 (for Single Photon Emission Tomo-

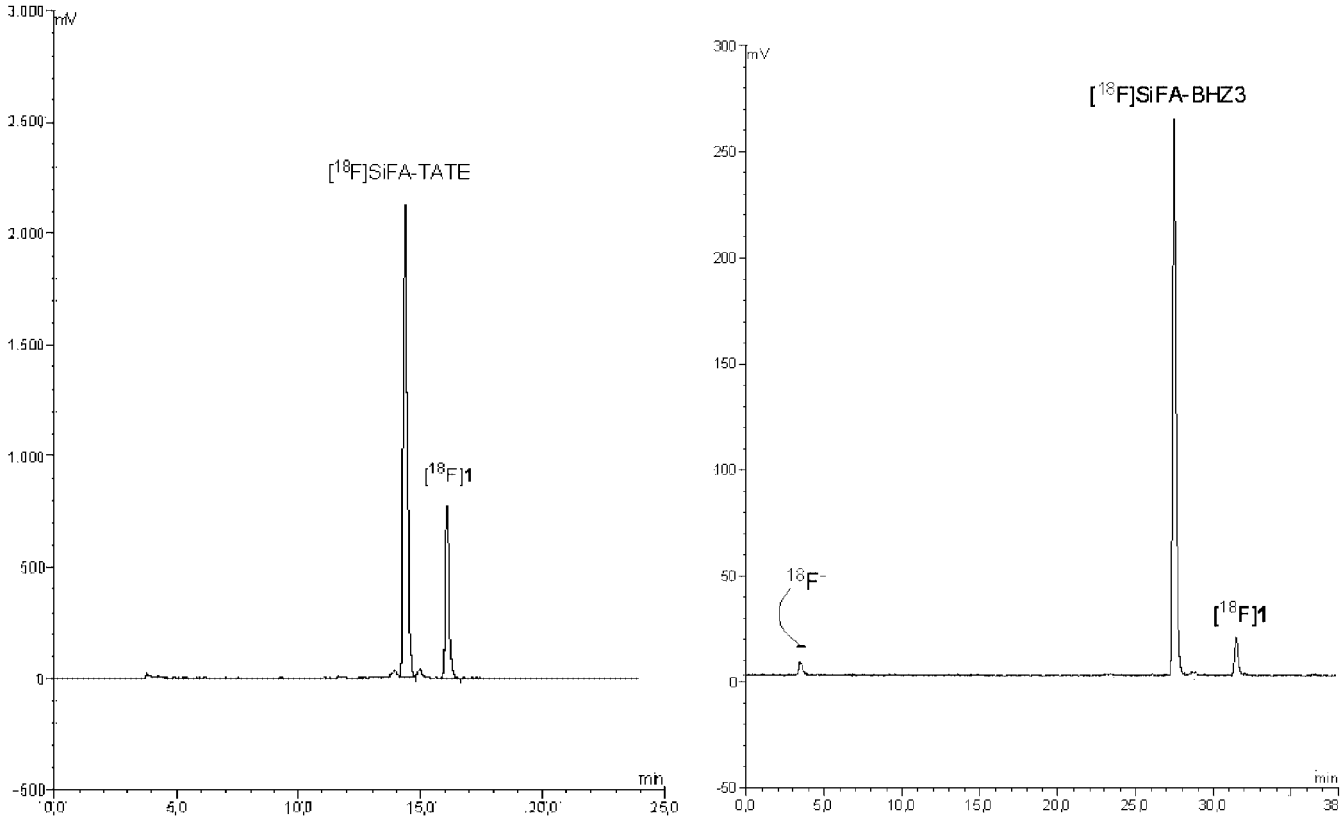


Figure 3. Two exemplary radio-HPLC chromatograms of the reaction of [^{18}F]**1** with AO-Tyr^3-octreotate (AO-TATE) (rt, acetonitrile/water 90/10, pH 4, HPLC system 1 for preparative HPLC conditions, RCY 75%) and the bombesin derivative AO-BZH3 (rt, acetonitrile/water 90/10, pH4, HPLC system 2, RCY 95%) showing the radiolabeled peptides, unreacted [^{18}F]**1**, and, in the case of AO-BZH3 labeling, trace amounts of $^{18}F^-$ (<1%) which could not be separated from [^{18}F]**1** during solid-phase extraction.

graphy (SPECT), gallium-68 (for PET) and therapeutic radionuclides (*19*, *20*) are gaining more and more importance in nuclear medicine and belong now to the more frequently applied imaging agents. Due to the physical properties of ^{18}F (lowest available positron energy of 635 keV), which result in images of higher resolution, the usefulness of these peptides labeled with ^{18}F would increase considerably. [^{18}F]**1** can be coupled to the N-terminal AO-moiety by selective oxime formation, a method described by Thumshirn et al. (*5*) This coupling method has been successfully employed for the syntheses of radiolabeled bioconjugates. Poethko et al. reported the labeling of cyclic RGD peptides as well as octreotide analogs with [^{18}F]FB-CHO in methanolic solution at 60 °C (*6*). We found that the conjugation step applying [^{18}F]**1** and the above mentioned AO-derivatized peptides (20–100 μg, 0.014–0.147 μmol) in acetonitrile/H_2O-TFA solution at pH 4 (total volume of 150–200 μL) proceeds even at room temperature within 10 min thus providing an even milder labeling approach. The yields of the coupling reaction were generally between 75–95% (Figure 3), and the final ^{18}F-labeled peptide conjugates could easily be separated by fast gradient HPLC giving an overall RCY of 50–55% after a total synthesis time of 40 min. In some rare cases, unreacted $^{18}F^-$ from the first reaction step could not be completely removed (<1%) by solid-phase extraction and appears in the final HPLC chromatogram (Figure 3). Although the use of HPLC for final purification is an inevitable shortcoming, one advantage is that the precursor peptide (AO-derivatized peptide), the ^{18}F-labeled conjugate, and the labeling synthon [^{18}F]**1** display very different retention times on the HPLC, making purification extremely simple and fast. Only one HPLC purification is necessary to obtain the ^{18}F-labeled

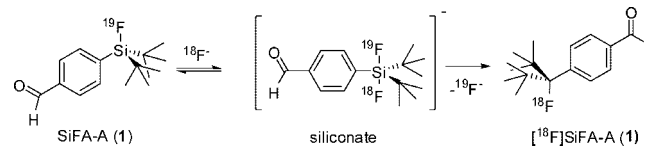


Figure 4. Formation of a pentacoordinate silicon intermediate and further elimination of either $^{19}F^-$ or $^{18}F^-$. As result of the calculated positive Gibbs energy in acetonitrile, the equilibrium concentration of the siliconate is predicted to be low, perhaps undetectable.

peptides, whereas most current methods require at least two HPLC purifications (one for the labeling synthon and one for the labeled peptide). Moreover, this efficient one-column separation gives rise to extraordinarily high SAs of the labeled peptide conjugates, which are in the same range as the SA of [^{18}F]**1** used as a labeling synthon. The question of why the isotopic ^{19}F–^{18}F exchange reaction proceeds so efficiently was further elucidated by conducting DFT calculations on three model fluorosilanes ($R'_nR''_{3-n}SiF$, R′=Ph, R″=*tert*-Bu; n = 1–3) reacting with $^{18}F^-$. According to our calculations, the fluorine exchange reaction in the gas phase should result in a thermodynamically stable pentacoordinated silicon intermediate, in accordance with the known mechanism of nucleophilic substitution at Si (Figure 4) (*21*, *22*). Similar siliconates have been isolated and characterized (*23*). Gibbs free energies of their formation in the gas phase are in the range of −50 to −40 kcal/mol. In acetonitrile, however, the formation of organosiliconates is much less favored. The enthalpies range from −5 to 2 kcal/mol and Gibbs free energies from 5 to 10 kcal/mol. The difference between the thermodynamics in the gas phase and in solution is mainly the result of a dramatically reduced basicity of the fluoride

anion. The energy of $R_3SiF_2^-$ formation increases in the series Ph_3SiF < Ph_2t-$BuSiF$ < Pht-Bu_2SiF, being in line with decreasing Lewis acidity of the silicon atoms and increasing steric hindrance of the organic substituents. Assuming that the changes in solvent effects upon fluoride exchange are similar for all organofluorosilanes, it is reasonable to suppose that the energy barriers are rather low, and in the series of organofluorosilanes studied, they are proportional to the relative energies of the intermediate organosiliconates. These data are in agreement with the high rate of fluorine exchange observed in acetonitrile, meaning that the equilibrium is reached very rapidly (Figure 4). The only detectable ^{18}F-labeled compounds by HPLC were unreacted $^{18}F^-$ (<5%) and [^{18}F]**1**, suggesting that the ^{18}F-siliconate is formed very quickly and eliminates fluoride ($^{18}F^-$ or $^{19}F^-$) immediately. Furthermore, as a result of the very low concentration of both $^{19}F^-$ and [^{18}F]**1** (the compound in excess is nonradioactive SiFA-A (**1**)), there is only a minor probability that the liberated $^{19}F^-$ will collide again with a formed [^{18}F]**1**, making this isotopic exchange statistically virtually irreversible.

In conclusion, the outlined ^{18}F-labeling procedure was shown to be applicable to the syntheses of various AO-derivatized peptides, which in turn are currently used as tumor imaging agents in nuclear medicine. The concept can be further expanded to all sorts of AO-derivatized peptides. The synthesis of [^{18}F]**1** provides the first example of an isotopic exchange reaction leading to SAs which even surpass SAs in conventional nca ^{18}F-radiochemistry. The usefulness of the ^{18}F-labeled peptides as tumor imaging agents is currently under investigation. Due to the demand for easy ^{18}F-labeling techniques in PET radiochemistry, we furthermore anticipate that the SiFA labeling approach will become a useful method in ^{18}F-radiochemistry.

ACKNOWLEDGMENT

This work was supported by the International Isotope Society, Central European Division to R.S.

Supporting Information Available: Preparation of azeotropic dried [^{18}F]F^-/Kryptofix 2.2.2./K^+ complex, DFT calculations of isotopic exchange reaction. This material is available free of charge via the Internet at http://pubs.acs.org.

LITERATURE CITED

(1) Glaser, M., Luthra, S. K., and Brady, F. (2003) Applications of positron-emitting halogens in PET oncology. *Int. J. Oncol. 22*, 253–267.

(2) Snyder, S. E., and Kilbourn, M. (2003) Chemistry of Fluorine-18 Radiopharmaceuticals. *Handbook of Radiopharmaceuticals, Radiochemistry and Applications* (Welch, M., Redvanly, C. S., Eds.) pp 195–227, Chapter 6, Wiley, Chichester.

(3) Blower, P. (2006) Towards molecular imaging and treatment of disease with radionuclides: the role of inorganic chemistry. *Dalton Trans.* 1705–1711.

(4) Knight, L. C. Radiolabeled Peptides for Tumor Imaging. *Handbook of Radiopharmaceuticals, Radiochemistry and Applications* (Welch, M., Redvanly, C. S., Eds) pp 643–684, Chapter 23, Wiley, Chichester.

(5) Thumshirn, G., Hersel, S. L., Goodman, H., and Kessler, H. (2003) Multimeric cyclic RGD peptides as potential tools for tumor targeting: solid-phase peptide synthesis and chemoselective oxime ligation. *Chem. Eur. J. 9*, 2717–2725.

(6) Poethko, T., Schottelius, M., Thumshirn, G., Hersel, U., Herz, M., Henriksen, G., Kessler, H., Schwaiger, M., and Wester, H. J. (2004) Two-step methodology for high-yield routine radiohalogenation of peptides: ^{18}F-labeled RGD and octreotide analogs. *J. Nucl. Med. 45*, 892–902.

(7) Chang, Y. S., Jeong, J. M., Lee, Y.-S., Kim, H. W., Rai, G. B., Lee, S. J., Lee, D. S., Chung, J.-K., and Lee, M. C. (2005) Preparation of ^{18}F-human serum albumin: A simple and efficient protein labeling method with ^{18}F using a hydrazone-formation method. *Bioconjugate Chem. 16*, 1329–1333.

(8) Marik, J., Hausner, S. H., Fix, L. A., Gagnon, K. J., and Sutcliffe, J. L. (2006) Solid-phase synthesis of 2-[^{18}F]fluoropropionyl peptides. *Bioconjugate Chem. 17*, 1017–1021.

(9) Toyokuni, T., Walsh, J. C., Dominguez, A., Phelps, M. E., Barrio, J. R., Gambhir, S. S., and Satyamurthy, N. (2003) Synthesis of a new heterobifunctional linker, N-[4-(aminooxy) butyl]maleimide, for facile access to a thiol-reactive ^{18}F-labeling agent. *Bioconjugate Chem. 14*, 1253–1259.

(10) de Bruin, B., Kuhnast, B., Hinnen, F., Yaouancq, L., Amessou, M., Johannes, L., Samson, A., Boisgard, R., Tavitian, B., and Dollé, F. (2005) 1-[3-(2-[^{18}F]Fluoropyridine-3-yloxy)propyl]pyrrole-2,5-dione: design, synthesis, and radiosynthesis of a new [^{18}F]fluoropyridine-based maleimide reagent for the labeling of peptides and proteins. *Bioconjugate Chem. 16*, 406–420.

(11) Cai, W., Zhang, X., Wu, Y., and Chen, X. (2006) A thiol-reactive ^{18}F-labeling agent, N-[2-(4-^{18}F-fluorobenzamido)ethyl]maleimide, and synthesis of RGD peptide-based tracer for PET imaging of $\alpha_v\beta_3$ integrin expression. *J. Nucl. Med. 47*, 1172–1180.

(12) Prante, O., Einsiedel, J., Haubner, R., Gmeiner, P., Wester, H.-J., Kuwert, T., and Maschauer, S. (2007) 3,4,6-Tri-O-acetyl-2-deoxy-2-[^{18}F]fluoroglucopyranosyl phenylthiosulfonate: a thiol-reactive agent for the chemoselective ^{18}F-glucosylation of peptides. *Bioconjugate Chem. 18*, 254–262.

(13) Marik, J., and Sutcliffe, J. L. (2006) Click for PET: rapid preparation of [^{18}F]fluoropeptides using CuI catalyzed 1,3-dipolar cycloaddition. *Tetrahedron Lett. 47*, 6681–6684.

(14) Glaser, M., and Årstad, E. (2007) "Click Labeling" with 2-[^{18}F]fluoroethylazide for positron emission tomography. *Bioconjugate Chem. 18*, 989–993.

(15) Ting, R., Adam, M. J., Ruth, T. J., and Perrin, D. M. (2005) Arylfluoroborates and alkylfluorosilicates as potential PET imaging agents: high-yielding aqueous biomolecular ^{18}F-labeling. *J. Am. Chem. Soc. 127*, 13094–13095.

(16) Schirrmacher, R., Bradtmöller, G., Schirrmacher, E., Thews, O., Tillmanns, J., Siessmeier, T., Buchholz, H. G., Bartenstein, P., Wängler, B., Niemeyer, C. M., and Jurkschat, K. (2006) ^{18}F-labeling of peptides by means of an organosilicon-based fluoride acceptor. *Angew. Chem., Int. Ed. 45*, 6047–6050.

(17) Wängler, B., Beck, C., Wagner-Utermann, U., Schirrmacher, E., Bauer, C., Rosch, F., Schirrmacher, R., and Eisenhut, M. (2006) Application of tris-allyl-DOTA in the preparation of DOTA-peptide conjugates. *Tetrahedron Lett. 47*, 5985–5988.

(18) Lang, L., and Eckelman, W. C. (1997) Labeling proteins at high specific activity using N-succinimidyl-4-[^{18}F](fluoromethyl)benzoate. *Appl. Radiat. Isot. 48*, 169–173.

(19) Liu, S., and Edwards, D. S. (2001) Bifunctional chelators for therapeutic lanthanide radiopharmaceuticals. *Bioconjugate Chem. 12*, 7–34.

(20) Volkert, A. W., and Hoffman, T. (1999) Therapeutic radionuclides. *Chem. Rev. 99*, 2269–2292.

(21) Bassindale, A. R., Taylor, P. G. (1989) Reaction mechanisms of nucleophilic attack at silicon, *The Chemistry of Organic Silicon Compounds.* (Patai, S., and Rappoport, Z., Eds.) pp 839–892, Chapter 13, Part 1, John Wiley & Sons, New York.

(22) Corriu, R. J. P., and Young, J. C. (1989) Hypervalent silicon compounds, *The Chemistry of Organic Silicon Compounds.* (Patai, S., and Rappoport, Z., Eds.) pp 1241–1288, Chapter 20, Part 2, John Wiley & Sons, New York.

(23) Bréfort, J. L., Corriu, R. J. P., Guérin, C., Henner, B. J. L., and Wong Chi Man, W. W. C. (1990) Pentacoordinated silicon anions: synthesis and reactivity. *Organometallics 9*, 2080–2085.

BC700195Y

Oligonucleotide-Coated Metallic Nanoparticles as a Flexible Platform for Molecular Imaging Agents

Nitin Nitin, David J. Javier, and Rebecca Richards-Kortum*

Department of Bioengineering, Rice University. Received April 13, 2007; Revised Manuscript Received August 14, 2007

Targeted metallic nanoparticles have shown promise as contrast agents for molecular imaging. To obtain molecular specificity, the nanoparticle surface must be appropriately functionalized with probe molecules that will bind to biomarkers of interest. The aim of this study was to develop and characterize a flexible approach to generate molecular imaging agents based on gold nanoparticles conjugated to a diverse range of probe molecules. We present two complementary oligonucleotide-based approaches to develop gold nanoparticle contrast agents which can be functionalized with a variety of biomolecules ranging from small molecules, to peptides, to antibodies. The size, biocompatibility, and protein concentration per nanoparticle are characterized for the two oligonucleotide-based approaches; the results are compared to contrast agents prepared using adsorption of proteins on gold nanoparticles by electrostatic interaction. Contrast agents prepared from oligonucleotide-functionalized nanoparticles are significantly smaller in size and more stable than contrast agents prepared by adsorption of proteins on gold nanoparticles. We demonstrate the flexibility of the oligonucleotide-based approach by preparing contrast agents conjugated to folate, EGF peptide, and anti-EGFR antibodies. Reflectance images of cancer cell lines labeled with functionalized contrast agents show significantly increased image contrast which is specific for the target biomarker. To demonstrate the modularity of this new bioconjugation approach, we use it to conjugate both fluorophore and anti-EGFR antibodies to metal nanoparticles, yielding a contrast agent which can be probed with multiple imaging modalities. This novel bioconjugation approach can be used to prepare contrast agents targeted with biomolecules that span a diverse range of sizes; at the same time, the bioconjugation method can be adapted to develop multimodal contrast agents for molecular imaging without changing the coating design or material.

1. INTRODUCTION

The aim of this study is to develop and characterize a bioconjugation approach which combines the flexibility and specificity of oligonucleotide hybridization with the excellent optical contrast properties of gold nanoparticles to develop biocompatible molecular imaging agents. Gold nanoparticles provide strong contrast when imaged in reflectance mode based on their unique optical absorption and scattering properties (*1–5*). In current clinical practice, reflectance imaging is used to aid in the diagnosis of various cancers and precancers based on differences in the native optical properties of neoplastic and normal epithelial tissue (*6–8*). The development of molecular-specific contrast agents which can be imaged in reflectance mode has the potential to improve the sensitivity and specificity of detection of early-stage precancers and cancers by providing the ability to noninvasively image the molecular changes associated with early neoplastic transformation.

Studies by Sokolov et al. (*4*) and El-Sayed et al. (*3*) have shown the potential of using gold nanoparticles to image receptor overexpression in various tumor model systems. Gold nanoparticle-based contrast agents have distinct advantages due to their biocompatibility, photostability, and ease of coating with proteins and polymers. In these studies, gold nanoparticles were linked to antibodies by direct absorption of protein on the surface of the nanoparticle. It has been established that electrostatically adsorbed gold–protein conjugates are stable only in the presence of excess protein in solution (*9*). This result suggests that there is a dynamic exchange between coated protein molecules and excess proteins in solution. This exchange is not desired for biological applications, as targeting proteins may be displaced by the high concentration of native proteins in biological samples. In addition, electrostatic protein adsorption offers very little control over the orientation of bound molecules; inappropriate orientation and conformational changes in antibodies during adsorption can reduce their binding affinities (*10*). Further, this approach cannot be easily extended to other potential probe biomolecules of interest including peptides and small molecules; small biomolecules cannot provide enough surface coverage to prevent the aggregation of gold nanoparticles in physiological buffers.

As an alternative to direct protein adsorption, other polymeric coatings including dextran, chitosan (*1, 11*), and self assembled monolayers (SAM) have been developed for surface modifications of nanoparticles. In the case of dextran- and chitosan-based coatings, typically large molecular weight polymers (>50 000 MW) are required to coat nanoparticles. This limitation is due to small numbers of reactive groups present on polymer chains with lower molecular weight. The use of large MW polymers leads to coated nanoparticles with a large effective size. In the case of SAM-based coatings, the solubility of the resulting nanoparticle in an aqueous environment is limited by the hydrophobic nature of the coating polymer, leading to aggregation in high-salt solutions.

In addition, various other chemical functionalization techniques have been developed for coating gold nanoparticles in aqueous settings, but in many cases, this has led to aggregation (*12*). This limitation has been overcome by adding various polymeric stabilizers which nonspecifically interact with the particle surface, but these stabilizers can potentially limit the biological applications as well as interfere with surface conjugations (*13*). Further disulfide-modified polymer (e.g., OPSS-PEG) coatings may also absorb nonspecifically on the surface of gold nanoparticles, as the affinities for some of these polymer

* Corresponding author. E-mail: rkortum@rice.edu. Ph.: 713-348-3823. Fax: 713-348-5877.

10.1021/bc0701242 CCC: $37.00 © 2007 American Chemical Society
Published on Web 10/09/2007

backbones are only slightly less than the specific gold–disulfide interactions (*12*). Thus, the functional groups in these coatings will have very limited accessibility for further surface bioconjugation to probe biomolecules. In some cases, polymer molecules with bifunctional ends have been linked to antibodies or other biomolecules before coating the gold nanoparticles. In this case, it is expected that nonspecific adsorption will play a significant role as compared to the single thiol interaction with the gold nanoparticle.

To overcome these limitations, we have developed a bioconjugation approach which combines the stability of thiol-modified oligonucleotide coatings for gold nanoparticles with the ease of bioconjugation using bifunctionally modified oligonucleotides to develop gold-based reflectance contrast agents. This coating approach has been optimized for various analytical assays (*14*) (*15*) and is stable at high salt conditions as well as in the presence of other proteins and biomolecules. The approach provides flexibility to conjugate a variety of biomolecules, to control the orientation of conjugated biomolecules, and to control the size of the functionalized particles. Further, the sequence specificity of oligonucleotides can be exploited to develop flexible approaches for assembly of contrast agents and the development of multifunctional contrast agents, with either multiple targeting moieties or multiple reporting agents.

2. EXPERIMENTAL PROCEDURES

2.1. Materials. Gold nanoparticles (~25 nm) were synthesized using gold chloride ($HAUCl_4$, >99.999% purity, Sigma) and sodium citrate (Sigma). The gold nanoparticles were coated with 19-mer oligonucleotides (MWG, 5′-thiol-AAAAAAAAAA**ATCCTTTAC**-amine) functionalized with a thiol group on the 5′ end and an amino group at the 3′ end. The oligonucleotide was first reduced with TCEP·HCl (Tris(2-carboxyethyl) phosphine hydrochloride, Pierce) before adding it to the gold nanoparticles. Its complementary sequence was also used (MWG, 3′-**TAGGAAATG**TTATAA-amine) for the conjugation of targeting molecules. Targeting molecules were chosen to represent a wide range of molecular weight molecules which include a 165 kD EGFR antibody (epidermal growth factor receptor antibody, Baylor College of Medicine antibody facility), a short 5.5 kD peptide EGF (epidermal growth factor peptide, US Biological), and a small 0.5 kD molecule (folate, Sigma). The following reagents and cross-linkers were used for bioconjugation of the targeting molecules to the oligonucleotide-coated gold nanoparticles: C6-SANH (C6-SANH (C6-succinimidyl 4-hydrazinonicotinate acetone hydrazone, Pierce), C6-SFB (C6-succinimidyl 4-formylbenzoate, Pierce), DMSO (Sigma), 2-mercaptoethanol (Sigma), EDAC (1-ethyl-3-[3-dimethylaminopropyl]carbodiimide hydrochloride, Pierce), and sulfo-NHS (Pierce). For characterization, sodium cyanide (Sigma) was used to dissolve the gold nanoparticles. Purification columns that were used include a Zeba desalting column (Pierce), a YM-3 Microcon spin column (Millipore), and an S-400 spin column (GE Healthcare). For cellular targeting, various cancer cell lines obtained from ATCC were cultured using DMEM (Dulbecco's minimum essential media) or MEM with 5% FBS (fetal bovine serum) with antibiotics as recommended by ATCC. The cell lines include 1483 cells and SiHa cells for EGFR targeting with antibodies and EGF peptides, and Kb cells for targeting folate receptors. A Cy5 dye modified complementary oligonucleotide (MWG) was used to demonstrate the flexibility of the coating and conjugation approach to develop multimodal/multifunctional contrast agents.

2.2. Methods. *2.2.1. Synthesis and Coating of Gold Nanoparticles.* Gold nanospheres (~25 nm) were synthesized using the sodium citrate reduction of gold ions developed by Frens et al. (*16*). The size of the nanospheres was controlled by adjusting the ratio of Au ions ($HAuCl_4$) and sodium citrate. The procedure for coating gold nanoparticles with oligonucleotides was adapted from Mirkin et al. (*14*). This protocol is based on the Au–S interaction between the gold lattice and thiol-functionalized oligonucleotides. The colloidal gold nanoparticles were first stabilized and coated using chemisorption of thiol-modified oligonucleotides (*14*). These oligonucleotides were also modified with NH_2 reactive group at the 3′-terminus. Briefly, 100 μL of 30 μM oligonucleotide was reduced with ~1 mM TCEP for 15 min. The reduced oligonucleotide containing free thiol was then added to 900 μL of gold nanoparticles (~0.1 nM concentration) and aged for 24–48 h with increasing salt concentration (until 1× PBS concentration is reached). The resulting oligonucleotide-coated nanoparticles were concentrated 10-fold by centrifugation at 6000 rpm for 30 min. To illustrate the flexibility of the approach, oligonucleotide-coated nanoparticles were then functionalized with several types of probe molecules, including anti-EGFR antibodies, EGF peptide, and folate.

2.2.2. Bioconjugation of Oligonucleotides and Targeting Molecules To Gold Nanoparticles. a. Direct Approach. In this method, the targeting molecules were directly incorporated onto the oligonucleotide-coated Au nanoparticles. After first coating the gold nanoparticles with oligonucleotides, complementary oligonucleotides (~3 uM) were hybridized to increase the number of amino functional sites. Anti-EGFR (1 mg/mL) or EGF (200 ug/mL) proteins were conjugated to oligonucleotide-coated Au (~1 nM) using heterobifunctional cross-linkers, SANH and SFB. The amino groups present on proteins were functionalized with SFB (20× molar excess), while amino groups present on the oligonucleotide–Au were functionalized with SANH (20× molar excess) for 1–2 h. Excess SANH and SFB were removed by passage on a Zeba desalting column twice. The SFB-modified protein and SANH-modified oligonucleotide Au were then mixed overnight (pH 7.0) at room temperature. The unreacted anti-EGFR or EGF proteins were removed by spinning the gold nanoparticles at 6000 rpm for 30 min. For folate-functionalized nanoparticles, the direct conjugation of folate to oligonucleotide–Au was accomplished using EDAC chemistry. The COOH group present on folate (1 mg/mL, 1 mL) was reacted with EDAC (0.6 mg) and sulfo-NHS (1.1 mg) for 15 min. After quenching the reaction with mercaptoethanol, an aliquot of the highly reactive NHS–folate (~20 uM) was added to oligonucleotide–Au for 2–3 h. Excess NHS–folate was also removed by centrifuging the gold nanoparticles at 6000 rpm for 30 min.

b. Indirect Approach. In this method, complementary oligonucleotides and the targeting molecules were conjugated first before hybridizing them to the oligonucleotide-coated gold nanoparticles. Similar to the direct approach, anti-EGFR or EGF proteins were reacted with SFB, while complementary oligonucleotides (~3 uM) were reacted with SANH. The resulting oligonucleotide–protein was purified using an S-400 spin column and then hybridized to its corresponding oligonucleotide-coated Au nanoparticles overnight at room temperature. For folate conjugation, folate was first added to EDAC/sulfo-NHS, before mixing with complementary oligonucleotides. The oligonucleotide folate conjugate was purified using a YM-3 column and hybridized to its corresponding oligonucleotide–Au. The excess oligonucleotide–protein and oligonucleotide–folate were removed by spinning the gold nanoparticles at 6000 rpm for 30 min.

c. Adsorption of Antibodies on Gold Nanoparticle Surface. For the development of antibody-coated gold nanoparticle-based contrast agents using adsorption of biomolecules on the surface, we followed the procedure developed by Slot and Geuze (1985) (*17*) and adapted by Sokolov et al. (*4*) and

El-Sayed et al. (*3*). Briefly, in this procedure the anti-EGFR antibody was incubated with gold nanoparticles for ~30 min in a salt-free environment. After incubation, the gold nanoparticles were centrifuged to remove excess antibodies in the presence of 1% PEG (10 000 MW). After centrifugation and decantation of solution, the pellet of gold nanoparticles was dispersed in 1× PBS (phosphate buffered saline) and tested for colloidal stability using the conventional salt test. In this test, the gold nanoparticle solution was tested using 10% NaCl solution, and stability was determined by visual assessment of color change. In the case of antibody-coated particles, we did not observe any color change, indicating colloidal stability based on this salt test procedure.

2.2.3. Characterization. Various qualitative and quantitative approaches were used to characterize the gold nanoparticle conjugates.

a. Size Characterization. Dynamic light scattering (DLS, Brookhaven) was used to measure the size of the oligonucleotide-coated nanoparticles, with and without the targeting molecules, and also gold nanoparticles with physically adsorbed antibodies. To evaluate the colloidal stability of gold nanoparticle conjugates, the size measurements were repeated 24 h postsynthesis of contrast agents.

b. Biocompatibility. The biocompatibility of oligonucleotide-coated nanoparticles was determined using the MTT assay following the procedure recommended by ATCC. Briefly, cells were cultured in 90-well plates for 24 h prior to incubation with oligonucleotide-conjugated gold nanoparticles. In each experiment, three wells were incubated with oligonucleotide-coated gold nanoparticles along with triplicate control wells. The experiment was carried out using SiHa and 1483 cell lines. Coated gold nanoparticles were incubated at twice the concentration levels used for cell labeling experiments. After 24 h of incubation, the plates were assayed using reagents provided with the MTT kit. The results were analyzed using absorbance measurements at 570 nm. The background level was determined using cells without any treatment and MTT reagents.

c. Concentration Estimation for Conjugated Antibodies and Peptides on Oligonucleotide-Coated Gold Nanoparticles. To determine the estimated concentration of antibodies and peptides conjugated to oligonucleotide coated gold nanoparticles, we used a protein quantification assay kit based on Coomassie staining. Prior to staining with Coomassie dye, the gold nanoparticles were dissolved using 100 mM potassium cyanide (KCN). This step was essential to remove the contribution from the gold nanoparticle plasmon band during the absorbance assay. Coomassie staining was carried out using the procedure recommended by the Pierce Protein Quantification kit. In addition, we used known concentrations of antibodies and peptides respectively as standards to establish the linear range for the assay and to calculate the concentration of conjugated proteins/peptides on gold nanoparticles.

2.2.4. Reflectance Imaging Using Oligonucleotide-Coated Nanoparticles. Oligonucleotide-coated nanoparticles functionalized with the targeting molecules were incubated with different cancer cell lines (1483 and SiHa for EGFR and EGF targeting, and Kb for folate targeting) at 37 °C for 30 min. 1483 and SiHa are oral and cervical cancer cell lines, respectively, which overexpress the EGF receptor (*18*). Kb cell is an oral cancer cell line which overexpresses the folate receptor (*19*). The cells were washed three times and centrifuged to remove unbound conjugate. Confocal reflectance images were obtained from the resulting cell pellet using a Zeiss LSM 510 microscope in reflectance mode. All images were acquired under the same imaging conditions. Postacquisition, the image contrast was adjusted in images of the folate-targeted cells to facilitate comparison with images acquired from cells labeled with EGF- and EGFR-targeted contrast agents.

2.2.5. Bimodal Contrast Agents and Imaging. To demonstrate the flexibility of the coating approach to develop multifunctional contrast agents, we used the indirect method to develop a contrast agent which combines both reflectance and fluorescence imaging capabilities in a single contrast agent. To develop this bimodal contrast agent, gold nanoparticles coated with oligonucleotides were hybridized overnight with complementary oligonucleotides modified with Cy5 dyes and complementary oligonucleotides conjugated with EGFR antibody. To provide efficient hybridization for antibody-conjugated complementary oligonucleotides, an excess of antibody-conjugated oligonucleotide (5:1 ratio) was used as compared with dye-labeled oligonucleotide. The use of a near-IR dye can be potentially useful for *in vivo* imaging as well as reduce the quenching effects due to gold nanoparticles. After the hybridization step and removal of excess complementary oligonucleotide, the purified product was used to label 1483 cancer cells. Labeled cells were imaged using both fluorescence and reflectance confocal microscopy.

3. RESULTS AND DISCUSSION

Figure 1 shows a schematic representation of the two complementary oligonucleotide-based bioconjugation approaches to develop gold nanoparticle based molecular contrast agents. In the direct approach, a complementary oligonucleotide was hybridized with the oligonucleotide coating on the surface of the gold nanoparticles (Figure 1). This stabilized and extended double-stranded DNA was then further conjugated with target protein or biomolecules of interest using bifunctional cross-linkers. In the indirect approach, a complementary oligonucleotide was first conjugated to targeting molecules (Figure 1). These modified oligonucleotides were then hybridized with the coated oligonucleotides on the surface of gold nanoparticles to generate a molecular contrast agent. These bioconjugation approaches have different advantages for developing molecular contrast agents. In the direct approach, the significant advantage is the ease of separation of small molecules and peptides after a conjugation reaction. In this case, a series of simple centrifugation steps can remove excess unbound targeting molecules from gold-conjugated molecules. In the indirect approach, the significant advantage is the ease with which multifunctional contrast agents can be developed. Using this approach, we can place multiple targeting moieties or multiple reporting moieties on the surface of gold nanoparticles by ratiometric mixing of oligonucleotides conjugated to different moieties. To further enhance the specificity of this process and provide ratiometric control over conjugation processes, different sequences of oligonucleotides can be coated on the surface of gold nanoparticles. These sequences can be hybridized with their respective complementary sequences modified with multiple reporting or targeting agents. In this study, we evaluated contrast agents produced with both the direct and indirect approaches as outlined above.

After developing gold nanoparticle conjugates, our next step was to characterize the bioconjugates and compare their size and stability with conjugates made using absorption of antibodies. We used dynamic light scattering (DLS) to analyze the diameter of the conjugated gold nanoparticles with anti-EGFR, EGF peptide, and folate-based targeting. Results for conjugates prepared using the direct approach are shown in Figure 2a; similar results were obtained using indirect conjugates. The size of the contrast agent increased as the size of the conjugated probe molecule was increased from a small molecule (folate) to a peptide (EGF) to an antibody (anti-EGFR). For example, antibody-conjugated gold nanoparticles prepared using oligo-

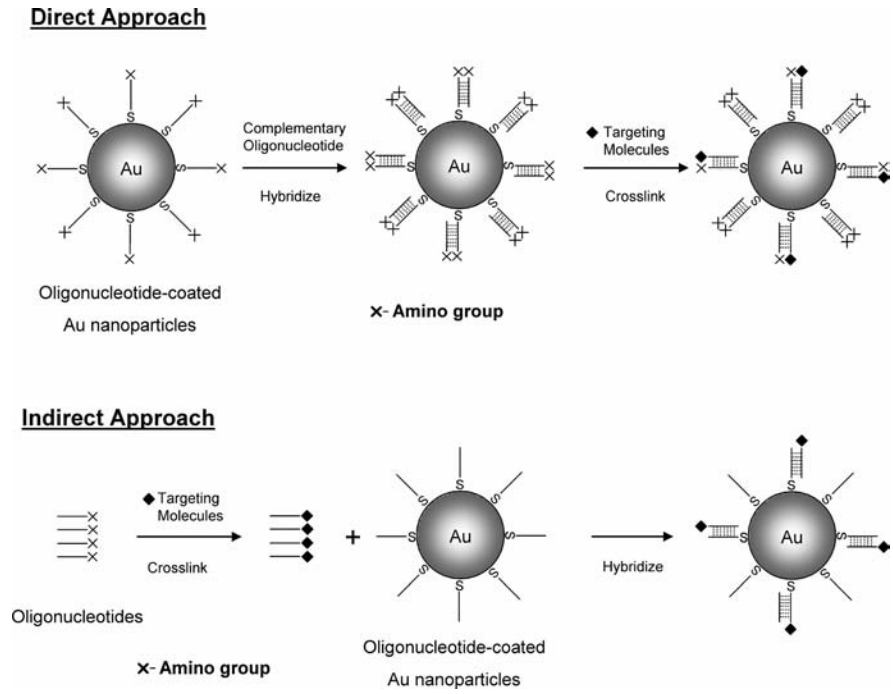


Figure 1. Schematic outline of conjugation of biomolecules to the oligonucleotide-functionalized gold nanoparticles. In the direct approach, the complementary oligonucleotides are first hybridized to the surface of the oligonucleotide-coated gold nanoparticles followed by conjugation of targeting molecules using hetero-bifunctional cross-linkers. In the indirect approach, the targeting biomolecules are first conjugated to the complementary oligonucleotides, which are then hybridized to oligonucleotides coated on the surface of gold nanoparticles. The conjugation approaches offer flexibility in processing and developing a molecular-specific contrast agent.

nucleotide coatings show an increase of approximately ~15–20 nm in diameter as compared with bare gold nanoparticles; this is consistent with an approximate antibody size of 15 nm. In contrast, antibody-targeted contrast agents prepared using adsorption are significantly larger (~80 nm) and show a wide distribution in size as compared to oligonucleotide-conjugated antibodies (~40 nm). These results suggest that the adsorption process leads to larger conjugates either as a result of multiple protein layers per nanoparticle or due to aggregation of nanoparticles.

To characterize and compare the stability of gold nanoparticle conjugates prepared using the adsorption and oligonucleotide procedure, we measured the change in size of anti-EGFR conjugates at 24 h postsynthesis. Results for conjugates prepared using direct oligonucleotide conjugation are shown in Figure 2b; again, similar results were obtained for those prepared using the indirect method. While the sizes of the oligonucleotide-coated, antibody-targeted contrast agents were stable over this time period, we observed a significant increase in the size of the adsorbed conjugates, suggesting that aggregation occurs over time. These results demonstrate the greater stability and smaller size of antibody-targeted, oligonucleotide-coated gold nanoparticles.

To establish biocompatibility of these agents, we carried out the standard MTT-based cytotoxicity assay. Figure 3 shows results of the assay for oligonucleotide-coated gold nanoparticles prepared using the direct method; similar results were obtained for conjugates prepared using the indirect method. No significant change was observed in cell viability even after 24–48 h incubation of these agents with cells, establishing the biocompatibility of oligonucleotide-coated gold nanoparticles in cell culture models. Future studies are warranted to study similar processes in animal models before clinical translation of these contrast agents.

We next estimated the concentration of the proteins or peptides conjugated on the surface of gold nanoparticles using the direct and indirect approaches. The results of this quantification assay are shown in Table 1. Both the direct and indirect methods yield similar concentrations of biomolecules conjugated to the surface of oligonucleotide-coated gold nanoparticles. This indicates that both approaches have similar efficiency for loading probe biomolecules on the surface of gold nanoparticles.

In a next step, we labeled cells in culture with targeted contrast agents; images of labeled cells were obtained using confocal reflectance microscopy. To demonstrate that gold nanoparticles can be conjugated to a wide size range of biomolecules (from antibodies to small molecules), we conjugated gold nanoparticles with anti-EGFR (150 kDa), EGF (6 kDa), and folate (~0.3 Da) using both direct and indirect approaches. To demonstrate the specificity of the resulting contrast agents, we prepared IgG gold nanoparticle conjugates and oligonucleotide-coated particles without any targeting biomolecules as controls. In this study, we used 1483 and SiHa oral and cervical cancer lines to evaluate EGFR-specific contrast and KB cancer cells for folate-specific imaging. Representative confocal reflectance images obtained from cells labeled with direct and indirect conjugates are shown in Figure 4a,b, respectively. Results show strong reflectance signal from the cell membrane of SiHa cells labeled with both anti-EGFR-targeted gold nanoparticles and EGF peptide-based targeting. Images obtained from cells targeted with both direct and indirect conjugates are similar, indicating that effective contrast agents can be generated with either conjugation approach. With targeting of folate overexpression using folate-conjugated gold nanoparticles, we also obtained similar results with both direct and indirect conjugates. The specificity in this case was evaluated using oligonucleotide-modified gold nanoparticles without any targeting molecules.

Based on these results, we have demonstrated that gold nanoparticles can be modified with variety of biomolecules including antibodies, peptides, and small molecules to develop effective reflectance contrast agents for molecular imaging applications. Thus, with this bioconjugation platform, molecular imaging applications with gold nanoparticles are no longer

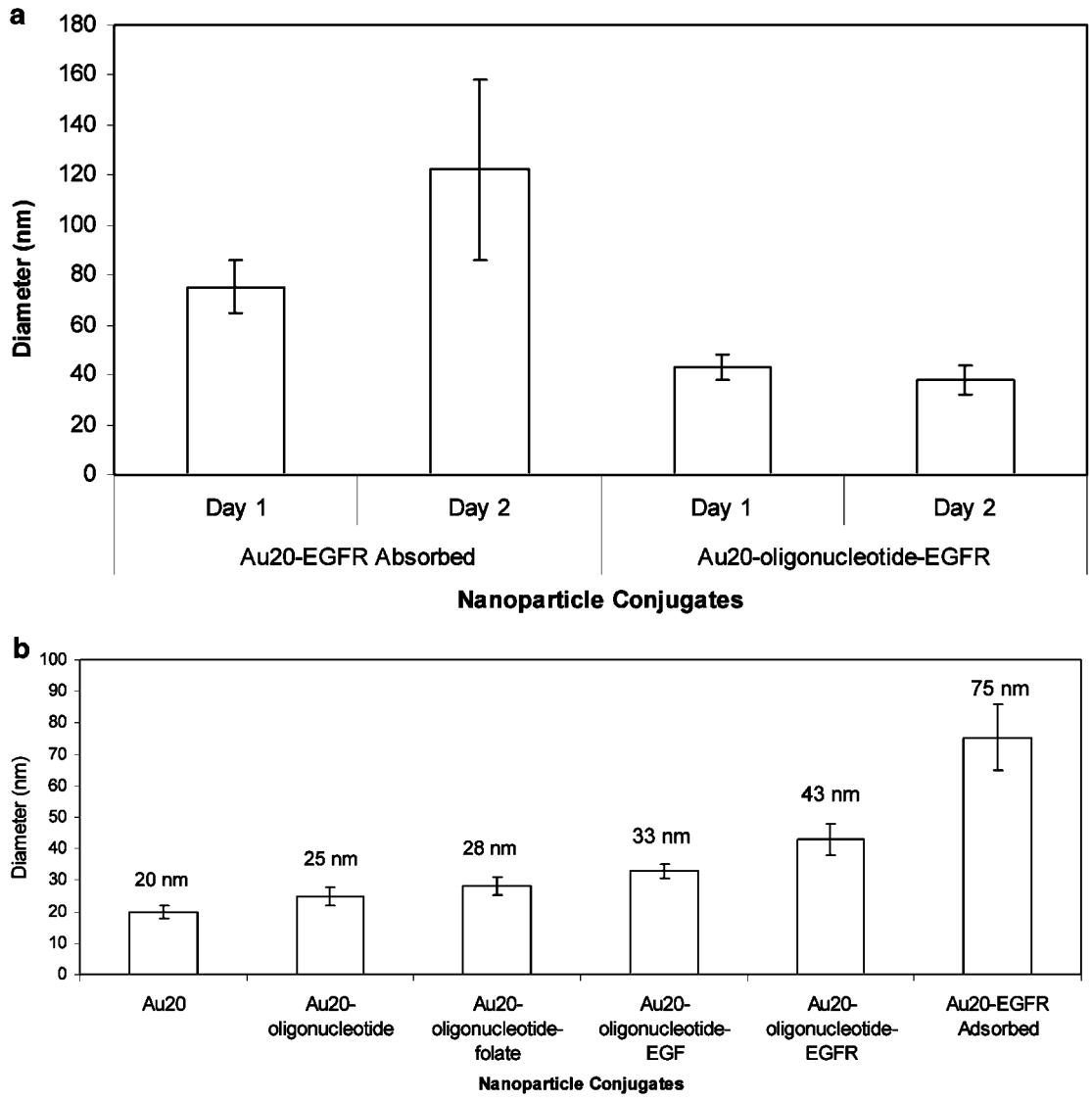


Figure 2. (a) Size measurements of oligonucleotide-coated gold nanoparticles and their conjugates using dynamic light scattering (DLS). The conjugates were prepared using the direct approach. Similar sizes were observed for conjugates prepared using the indirect approach (data not shown). Conjugation using the oligonucleotide approach was compared with methods of directly adsorbing large biomolecules on the surface of gold nanoparticles. (2) Size stability of gold nanoparticle conjugates measured using dynamic light scattering (DLS). Over a period of 24 h, results show an increase in size of gold conjugates with adsorbed antibodies as compared to antibodies chemically conjugated to the surface of gold nanoparticles using the direct approach. Conjugates prepared using the indirect approach showed similar size stability (data not shown).

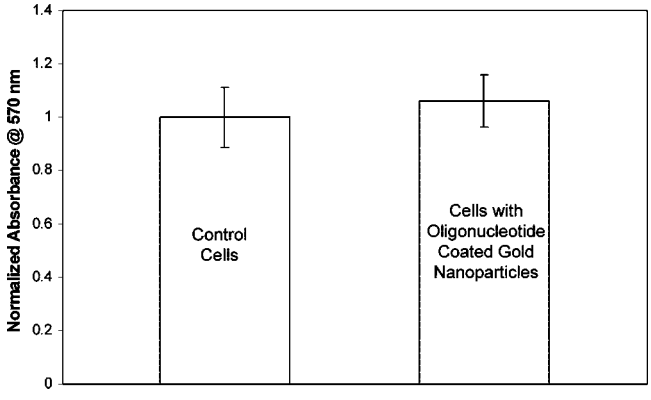


Figure 3. Biocompatibility studies of oligonucleotide-coated gold nanoparticles using standard MTT assay. Cells were incubated for 48 h with gold nanoparticles coated with oligonucleotides and analyzed by measuring absorbance at 570 nm using a standard plate reader.

limited to antibody-based approaches for targeting, and these designs can be easily extended to a variety of biomolecules.

Table 1. Estimated Concentration of Conjugated EGFR Antibodies and EGF Peptide on Surface of Gold Nanoparticles[a]

[protein]	direct μg/mL	indirect μg/mL
anti-EGFR	3.6	4.6
EGF	3.3	4.3

[a] Protein concentration was measured using Coomassie stain after dissolution of protein-conjugated gold nanoparticles in KCN.

To demonstrate the flexibility of this platform to develop bimodality contrast agents, we used the indirect approach to develop a single contrast agent capable of simultaneous reporting in both fluorescence and reflectance modes. The development of multimodality reporting is of significant interest in the area of molecular imaging, as multiple reporters can extend the range of sensitivity, penetration depth, and resolution for reporting molecular events. Figure 5a illustrates the approach to develop a dual-reporting contrast agent directed by the hybridization of complementary oligonucleotides. The cellular assay of this contrast agent was carried under similar conditions as for the direct and indirect conjugates in Figure 4. After

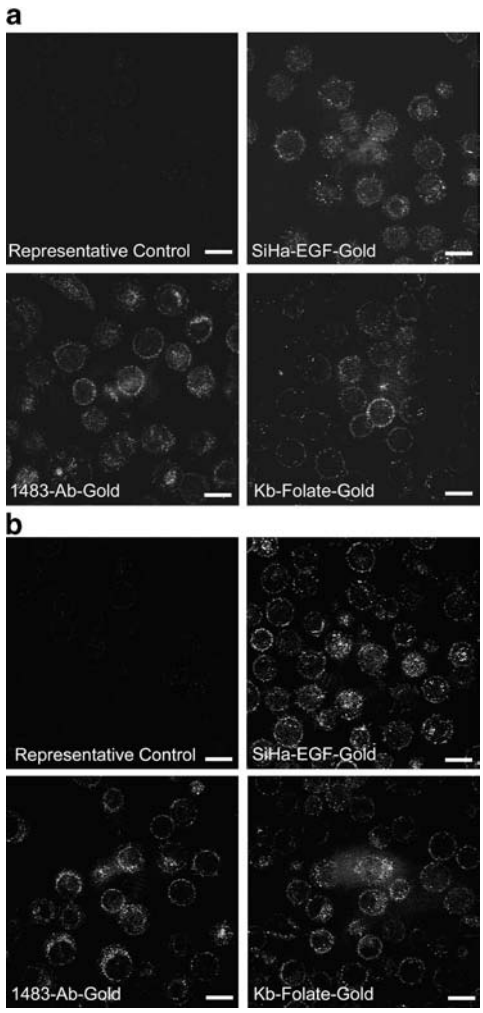


Figure 4. (a) Evaluation of molecular specific targeting of direct conjugates using confocal reflectance imaging. The contrast agents were prepared by conjugating different size-targeting molecules (antibody, peptides, and small molecules) to oligonucleotide-coated gold nanoparticles in various cancer cell lines. IgG-conjugated gold nanoparticles were used as controls in these cell lines (representative control image is shown). The scale bar represents 15 μm. (b) Evaluation of molecular-specific targeting of indirect conjugates using confocal reflectance imaging. The contrast agents were prepared by conjugating different size targeting molecules (antibody, peptides, and small molecules) to oligonucleotide-coated gold nanoparticles in various cancer cell lines. IgG-conjugated gold nanoparticles were used as controls in these cell lines (representative control image is shown). The scale bar represents 15 μm.

incubation with the contrast agent, cells were imaged using both reflectance and fluorescence confocal microscopy. Since the reflectance signal is significantly stronger than the fluorescence signal, the pinhole size and laser power used in reflectance imaging were significantly smaller than that used for fluorescence imaging. Results are shown in Figure 5b and show a similar distribution of reflectance and fluorescence signal on the surface of the cells. The reflectance image collected with a smaller confocal pinhole shows a significantly sharper image than the fluorescence image. This study demonstrates the concept for dual modality imaging, which can be extended to a variety of reporting schemes including MR contrast agents such as Gd^{3+} or PET contrast agents based on modification of oligonucleotides with chelating groups.

4. SUMMARY AND CONCLUSIONS

In this study, we have developed and characterized a bioconjugation approach which combines the flexibility and specificity of oligonucleotide hybridization with the excellent optical contrast properties of gold nanoparticles. The approach yields biocompatible molecular imaging agents which can be targeted with a wide variety of probe molecules to yield high-contrast molecular images in cell model systems. The stability and size distribution of the contrast agents produced using this approach are superior to those of contrast agents based on protein absorbed gold nanoparticles, which have been previously been used to produce targeted gold nanoparticles for use as molecular contrast agents. To demonstrate the flexibility of the conjugation approach, we illustrate the development of multimodal contrast agents which can be imaged in both reflectance and fluorescence modes. The results highlight the potential of oligonucleotide coatings for development of multifunctional molecular contrast agents.

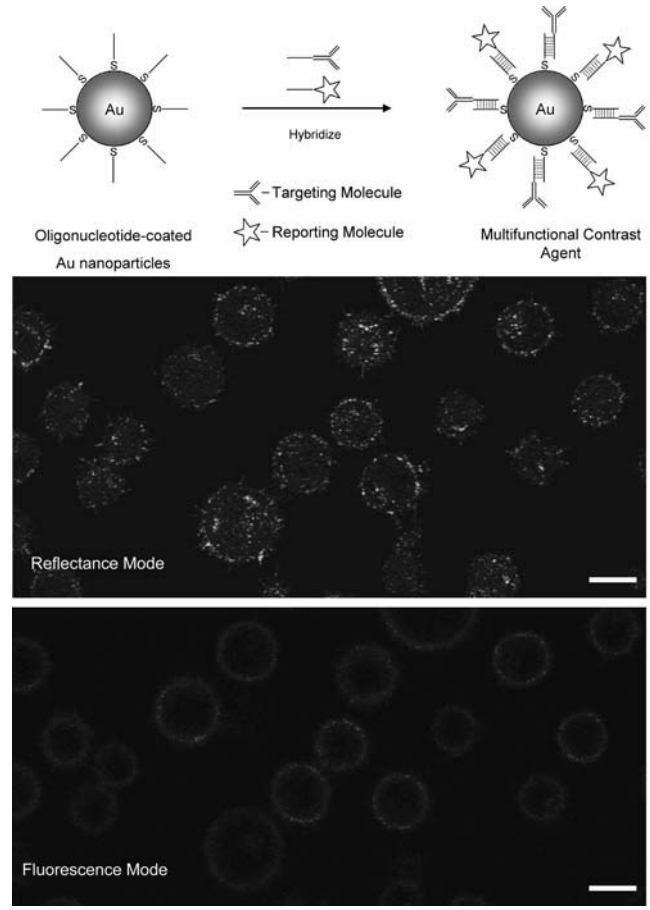


Figure 5. (a) A conceptual approach of using oligonucleotide-coated gold nanoparticles to develop multifunctional contrast agents for targeting, reporting, and delivery. In this example, the ratio of targeting and reporting molecules on the surface of gold nanoparticles can be controlled by controlling the ratio of modified oligonucleotides during the hybridization step. (b) Proof of concept study to illustrate development of bimodal reporting molecular contrast agents. Fluorescence and reflectance confocal images of SiHa cells labeled with bimodal contrast agent targeting the EGF receptor. The scale bar represents 15 μm.

LITERATURE CITED

(1) Aslan, K., Lakowicz, J. R., and Geddes, C. D. (2004) Nanogold-plasmon-resonance-based glucose sensing. *Anal. Biochem. 330*, 145–155.

(2) Chen, J., Saeki, F., Wiley, B. J., Cang, H., Cobb, M. J., Li, Z. Y., Au, L., Zhang, H., Kimmey, M. B., Li, X., and Xia, Y. (2005) Gold nanocages: bioconjugation and their potential use as optical imaging contrast agents. *Nano Lett. 5*, 473–7.

(3) El-Sayed, I. H., Huang, X. H., and El-Sayed, M. A. (2005) Surface plasmon resonance scattering and absorption of anti-EGFR antibody conjugated gold nanoparticles in cancer diagnostics: Applications in oral cancer. *Nano Lett. 5*, 829–834.

(4) Sokolov, K., Follen, M., Aaron, J., Pavlova, I., Malpica, A., Lotan, R., and Richards-Kortum, R. (2003) Real-time vital optical imaging of precancer using anti-epidermal growth factor receptor antibodies conjugated to gold nanoparticles. *Cancer Res. 63*, 1999–2004.

(5) Yguerabide, J., and Yguerabide, E. E. (1998) Light-scattering submicroscopic particles as highly fluorescent analogs and their use as tracer labels in clinical and biological applications - II. Experimental characterization. *Anal. Biochem. 262*, 157–176.

(6) Clark, A., Collier, T., Lacy, A., Follen, M., Malpica, A., Gillenwater, A., and Richards-Kortum, R. (2002) Detection of dysplasia with near real time confocal microscopy. *Biomed. Sci. Instrum. 38*, 393–8.

(7) Collier, T., Follen, M., Malpica, A., and Richards-Kortum, R. (2005) Sources of scattering in cervical tissue: determination of the scattering coefficient by confocal microscopy. *Appl. Opt. 44*, 2072–81.

(8) Drezek, R., Guillaud, M., Collier, T., Boiko, I., Malpica, A., Macaulay, C., Follen, M., and Richards-Kortum, R. (2003) Light scattering from cervical cells throughout neoplastic progression: influence of nuclear morphology, DNA content, and chromatin texture. *J. Biomed. Opt. 8*, 7–16.

(9) Xie, H., Tkachenko, A. G., Glomm, W. R., Ryan, J. A., Brennaman, M. K., Papanikolas, J. M., Franzen, S., and Feldheim, D. L. (2003) Critical flocculation concentrations, binding isotherms, and ligand exchange properties of peptide-modified gold nanoparticles studied by UV-visible, fluorescence, and time-correlated single photon counting spectroscopies. *Anal. Chem. 75*, 5797–5805.

(10) Brandes, N., Welzel, P. B., Werner, C., and Kroh, L. W. (2006) Adsorption-induced conformational changes of proteins onto ceramic particles: Differential scanning calorimetry and FTIR analysis. *J. Colloid Interface Sci. 299*, 56–69.

(11) Lee, S., and Perez-Luna, V. H. (2005) Dextran-gold nanoparticle hybrid material for biomolecule immobilization and detection. *Anal. Chem. 77*, 7204–7211.

(12) Mangeney, C., Ferrage, F., Aujard, I., Marchi-Artzner, V., Jullien, L., Ouari, O., Rekai, E. D., Laschewsky, A., Vikholm, I., and Sadowski, J. W. (2002) Synthesis and properties of water-soluble gold colloids covalently derivatized with neutral polymer monolayers. *J. Am. Chem. Soc. 124*, 5811–5821.

(13) Sato, T. a. R., R. (1980) *Stabilization of Colloidal Dispersions by Polymer Adsorption*, Marcel Dekker, New York.

(14) Elghanian, R., Storhoff, J. J., Mucic, R. C., Letsinger, R. L., and Mirkin, C. A. (1997) Selective colorimetric detection of polynucleotides based on the distance-dependent optical properties of gold nanoparticles. *Science 277*, 1078–1081.

(15) Han, M. S., Lytton-Jean, A. K. R., Oh, B. K., Heo, J., and Mirkin, C. A. (2006) Colorimetric screening of DNA-binding molecules with gold nanoparticle probes. *Angew. Chem., Int. Ed. 45*, 1807–1810.

(16) Frens, G. (1973) Controlled nucleation for regulation of particle-size in monodisperse gold suspensions. *Nat. Phys. Sci. 241*, 20–22.

(17) Slot, J. W., and Geuze, H. J. (1985) A new method of preparing gold probes for multiple-labeling cyto-chemistry. *Eur. J. Cell Biol. 38*, 87–93.

(18) Hsu, E. R., Anslyn, E. V., Dharmawardhane, S., Alizadeh-Naderi, R., Aaron, J. S., Sokolov, K. V., El-Naggar, A. K., Gillenwater, A. M., and Richards-Kortum, R. R. (2004) A far-red fluorescent contrast agent to image epidermal growth factor receptor expression. *Photochem. Photobiol. 79*, 272–9.

(19) Mchugh, M. M., and Cheng, Y. C. (1977) Demonstration of a high affinity folate binder in cultured human Kb cells. *Fed. Proc. 36*, 992–992.

BC0701242

Synthesis, Analysis, in Vitro Characterization, and in Vivo Disposition of a Lamivudine–Dextran Conjugate for Selective Antiviral Delivery to the Liver

Krishna C. Chimalakonda,[†] Hitesh K. Agarwal,[‡] Anil Kumar,[‡] Keykavous Parang,*[,‡] and Reza Mehvar*[,†]

Department of Pharmaceutical Sciences, School of Pharmacy, Texas Tech University Health Sciences Center, 1300 Coulter, Amarillo, Texas 79106, and Department of Biomedical and Pharmaceutical Sciences, College of Pharmacy, University of Rhode Island, Kingston, Rhode Island 02881. Received May 29, 2007; Revised Manuscript Received August 18, 2007

A liver-selective prodrug (3TCSD) of the antiviral drug lamivudine (3TC) was developed and characterized. 3TC was coupled to dextran (~25 kDa) using a succinate linker, and the in vitro and in vivo behavior of the conjugate was studied using newly developed size-exclusion and reversed-phase analytical methods. Synthesized 3TCSD had a purity of >99% with a degree of substitution of 6.5 mg of 3TC per 100 mg of the conjugate. Furthermore, the developed assays were precise and accurate in the concentration ranges of 0.125–20, 0.36–18, and 1–50 μg/mL for 3TC, 3TC succinate (3TCS), and 3TCSD, respectively. In vitro, the conjugate slowly released 3TC in the presence of rat liver lysosomes, whereas it was stable in the corresponding buffer. In vivo in rats, conjugation of 3TC to dextran resulted in 40- and 7-fold decreases in the clearance and volume of distribution of the drug, respectively. However, the accumulation of the conjugated 3TC in the liver was 50-fold higher than that of the parent drug. The high accumulation of the conjugate in the liver was associated with a gradual and sustained release of 3TC in the liver. These studies indicate the feasibility of the synthesis of 3TCS–dextran and its potential use for the selective delivery of 3TC to the liver.

INTRODUCTION

Lamivudine (β-L-2′,3′-dideoxy-3′-thiacytidine, 3TC) is a deoxycytidine nucleoside analogue that inhibits hepatitis B virus (HBV) replication and is used in the treatment of chronic hepatitis B infection (*1*). In addition to the efficacy of antiviral drugs against HBV, treatment of HBV infection is significantly dependent on the pharmacokinetics of these drugs, in particular their distribution and accumulation in the liver. To be effective, 3TC needs to enter liver cells and be phosphorylated to its active form 3TC 5′-triphosphate intracellularly before incorporation into DNA of HBV by DNA polymerase (*2, 3*). Therefore, strategies that direct the drug to its site of action (liver) may increase the effectiveness of the drug and decrease its potential side effects in other nontarget organs. Indeed, several studies (*4–10*) have attempted to target antiviral drugs to the liver for the treatment of HBV infection.

Dextrans are glucose polymers, which are under investigation as macromolecular carriers for delivery of drugs and other therapeutic agents, such as proteins, after the systemic administration of the dextran–drug conjugates (*11–14*). Additionally, conjugates of dextrans with nonsteroidal (*15, 16*) and steroidal (*17, 18*) anti-inflammatory drugs have been studied for local delivery of these drugs to the colon. In a series of studies (*19–21*), we previously showed that the plasma kinetics and tissue distribution of dextran carriers are dependent on the M_w of the polymer. Therefore, dextrans of different M_w may be useful for the delivery of drugs to different tissues after the systemic administration of the conjugate. For example, dextrans with M_w values of 20–70 kDa showed a high degree of selectivity for the liver when the liver/plasma area under the concentration–time curve (AUC) ratio was considered (*21*). The liver selectivity of these dextrans was attributed to their sizes, which restrict their passage through most vascular bed pores while allowing unrestricted passage through the substantially larger pore sizes of the liver sinusoids (*21, 22*).

In addition to the molecular weight, both the electric charge (*23, 24*) and chemical modification (*25, 26*) of dextrans may affect their organ and cellular distribution. For example, it has been reported that positively charged dextrans are taken up by the liver more rapidly and extensively than neutral or negatively charged dextrans (*23, 24*). Additionally, whereas unmodified dextrans distribute to both parenchymal and nonparenchymal cells of the liver (*27*), galactosylation or mannosylation of dextrans results in selective delivery of the macromolecule to the parenchymal and nonparenchymal cells, respectively (*25, 26*). Because electrical or chemical modifications of dextrans may alter their safety profiles (*28*), we have recently used unmodified neutral dextrans for delivery of methylprednisolone to the liver for local immunosuppression (*29–32*). These studies showed that after systemic administration, the conjugate selectively accumulates in the liver, where it gradually releases the active drug, resulting in more intense and sustained pharmacologic effects. Collectively, the above studies suggest that both unmodified and glycosylated dextrans may be suitable for systemic delivery of therapeutic agents to the liver.

The aim of the present study was to synthesize and characterize a conjugate of 3TC with dextran, ~25 kDa, intended for selective delivery of the anti-HBV drug to the liver. The conjugation of 3TC to dextran was achieved through a succinate linker, resulting in a macromolecular prodrug, potentially releasing 3TC and 3TC succinate (3TCS). Therefore, analytical methods were also developed for quantitation of the intact prodrug and simultaneous quantitation of its potential release products (3TC and 3TCS) in biological samples. In addition to in vitro characterization, the plasma pharmacokinetics and tissue disposition of the prodrug and parent drug were also studied in

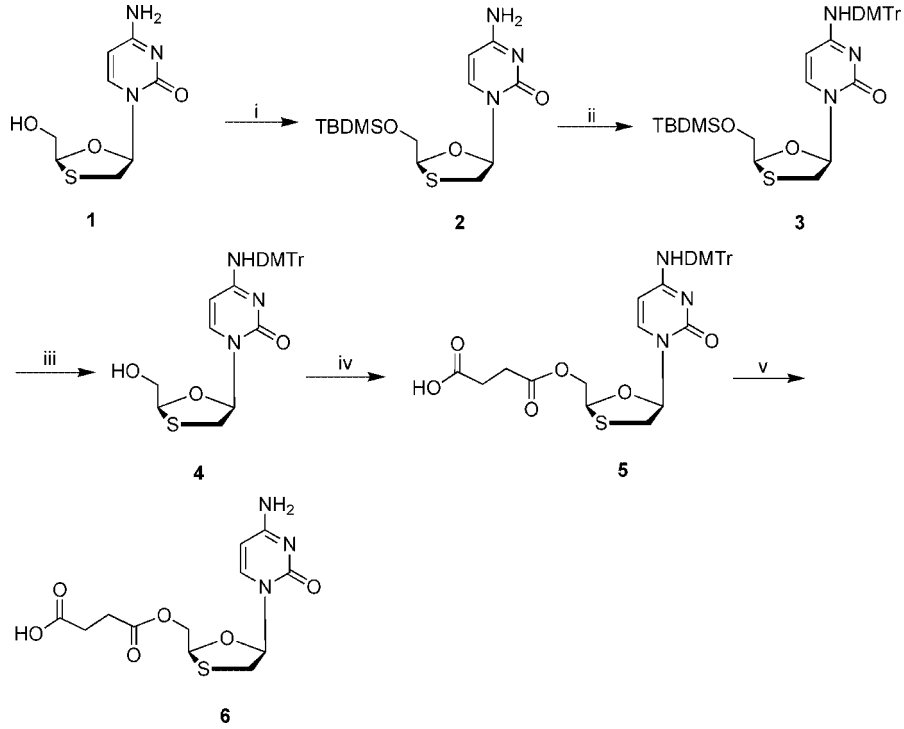
* To whom correspondence should be addressed. For K.P.: phone, (401) 874-4471; fax, (401) 874-5787; e-mail, kparang@uri.edu. For R.M.: phone, (806) 356-4015, extension 337; fax, (806) 356-4034; e-mail, reza.mehvar@ttuhsc.edu.

[†] Texas Tech University Health Sciences Center.

[‡] University of Rhode Island.

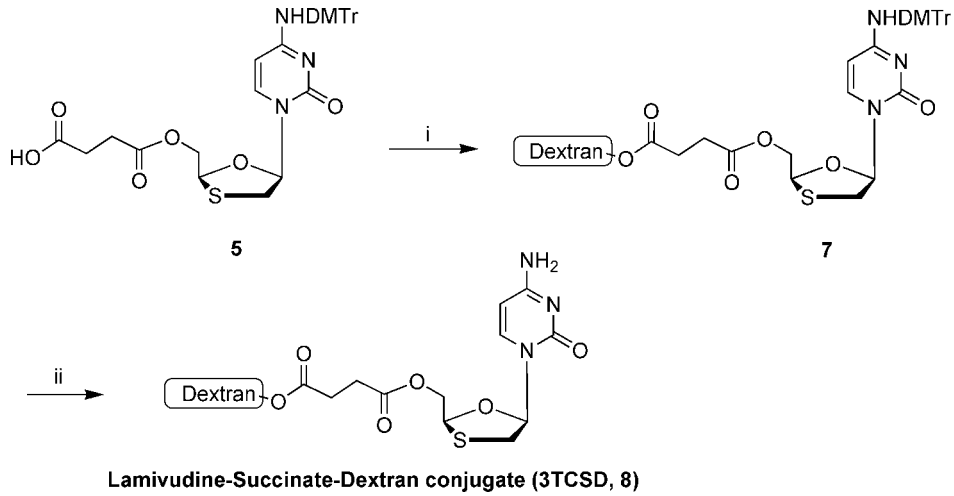
10.1021/bc700193d CCC: $37.00 © 2007 American Chemical Society
Published on Web 10/09/2007

Scheme 1. Synthesis of 4-*N*-(4,4′-Dimethoxytrityl)-5′-*O*-(succinate)-2′,3′-dideoxy-3′-thiacytidine (4-*N*-(4,4′-Dimethoxytrityl)lamivudine succinate, 5) [a]



[a] Reagents: (i) TBDMSCl, imidazole, DMF; (ii) DMTrCl, pyridine; (iii) TBAF, molecular sieves (4 Å); (iv) succinic anhydride, DMF, pyridine, DMAP; (v) AcOH (80%).

Scheme 2. Synthesis of 3TCS–Dextran (3TCSD, 8)[a]



[a] Reagents: (i) dextran 25 kDa, DIC, DMAP, DMSO, DIPEA; (ii) AcOH (80%).

rats, a species that has recently been used as a model for human HBV infection (*33–35*). To the best of our knowledge, this is the first report of designing a macromolecular prodrug of anti-HBV drug lamivudine for targeted delivery to the liver.

EXPERIMENTAL PROCEDURES

Chemicals. Dextran with an average M_w of ~25 kDa (actual M_w = 23 500 Da) was purchased from Dextran Products (Scarborough, Ontario, Canada). Lamivudine (3TC) was purchased from Kemprotec (Middlesbrough, U.K.). Stavudine and kits for liver lysosomal isolation and acid phosphatase were purchased from Sigma Chemical (St. Louis, MO). For chromatography, HPLC grade acetonitrile (Mallinckrodt Chromar HPLC) was obtained from VWR Scientific (Minneapolis, MN). All other reagents were analytical grade and obtained through commercial sources.

Animals. Adult male Sprague-Dawley rats were used in this study for in vitro blood and liver lysosome and in vivo disposition studies as outlined in the subsequent sections. All the procedures involving animals in this study were consistent with the "Principles of Laboratory Animal Care" (NIH Publication Vol. 25, No. 28, revised 1996) and approved by the Texas Tech University Health Sciences Center Institutional Animal Care and Use Committee.

Synthesis of 3TCS–Dextran (3TCSD) Conjugate. The complete procedure for the synthesis of 3TCSD conjugate is depicted in Schemes 1 and 2 and described in detail below. The chemical structures of the intermediates and the final

product were determined by nuclear magnetic resonance spectroscopy (^{1}H NMR) on a Bruker NMR spectrometer (400 MHz) and/or a high-resolution PE Biosystems Mariner API time-of-flight electrospray mass spectrometer.

*1. (–)-5′-O-(tert-Butyldimethylsilyloxy)-2′,3′-dideoxy-3′-thiacytidine (***2***).* *tert*-Butyldimethylsilyl chloride (TBDMSCl) (2.0 g, 13.27 mmol) and imidazole (360 mg, 5.29 mmol) were added to a solution of 3TC (**1**, 1.0 g, 4.36 mmol) in dry *N*,*N*-dimethylformamide (DMF) (50.0 mL). The reaction mixture was stirred at room temperature for 18 h. After completion of the reaction, the solvent was removed under reduced pressure, and the crude compound was purified by column chromatography over silica gel using hexane/dichloromethane as the eluents to afford **2** (1.47 g, 98%). ^{1}H NMR (400 MHz, CD_3OD, δ ppm): 8.21 (d, $J = 7.7$ Hz, 1H, H-6), 6.32 (dd, $J = 5.8$, 2.8 Hz, 1H, H-1′), 6.02 (d, $J = 7.7$ Hz, 1H, H-5), 5.26 (t, $J = 3.0$ Hz, 1H, H-4′), 4.18 (dd, $J = 11.8$, 3.0 Hz, 1H, H-5′), 3.96 (dd, $J = 11.8$, 3.0 Hz, 1H, H-5″), 3.54 (dd, $J = 12.5$, 5.8 Hz, 1H, H-2′), 3.19 (dd, $J = 12.5$, 2.8 Hz, 1H, H-2″), 0.95 (s, 9H, $C(CH_3)_3$), 0.15 (s, 6H, CH_3-Si). HR-MS (ESI-TOF) (*m/z*): $C_{14}H_{25}N_3O_3SSi$ calcd, 343.1386; found 344.3933 [M + H$^+$], 686.4590 [2M$^+$].

*2. (–)-4-N-(4,4′-Dimethoxytrityl)-5′-O-(tert-butyldimethylsilyloxy)-2′,3′-dideoxy-3′-thiacytidine (***3***).* Compound **2** (1.0 g, 2.91 mmol) and 4,4′-dimethoxytrityl chloride (DMTrCl, 1.08 g, 3.19 mmol) were dissolved in dry pyridine (80 mL) and stirred for 4 h at 0 °C and then for an additional 16 h at room temperature. The solution was then neutralized with aqueous sodium bicarbonate (5.0%) and extracted with dichloromethane (3 × 100 mL). The organic layer was dried with anhydrous sodium sulfate, and the solvent was removed under reduced pressure. The crude compound was purified by column chromatography over silica gel using hexane/dicloromethane containing 1.0% triethylamine as the eluents to yield **3** (1.79 g, 95%). ^{1}H NMR (400 MHz, $CDCl_3$, δ ppm): 7.81 (d, $J = 7.7$ Hz, 1H, H-6), 7.74 (dd, $J = 5.7$, 3.3 Hz, 1H, aromatic hydrogen, DMTr), 7.55 (dd, $J = 5.7$, 3.2 Hz, 1H, aromatic hydrogen, DMTr), 7.12–7.33 (m, 7H, aromatic hydrogens, DMTr), 6.82–6.88 (m, 4H, aromatic hydrogens, DMTr), 6.33 (dd, $J = 5.2$, 3.1 Hz, 1H, H-1′), 5.19 (t, $J = 3.1$ Hz, 1H, H-4′), 5.03 (d, $J = 7.7$ Hz, 1H, H-5), 4.30–4.45 (m, 1H, H-5′), 4.00–4.20 (m, 1H, H-5″), 3.81 (s, 6H, DMTr-OCH_3), 3.52 (dd, $J = 12.2$, 5.2 Hz, 1H, H-2′), 3.17 (dd, $J = 12.2$, 3.1 Hz, 1H, H-2″), 0.80 (s, 9H, $C(CH_3)_3$), 0.06 (s, 6H, CH_3–Si). HR-MS (ESI-TOF) (*m/z*): $C_{35}H_{43}N_3O_5SSi$ calcd, 645.2693; found 686.4634 [M + K + 2H]$^+$, 1289.3676 [2M – 1]$^+$.

*3. (–)-4-N-(4,4′-Dimethoxytrityl)-2′,3′-dideoxy-3′-thiacytidine (***4***).* Compound **3** (1.10 g, 1.70 mmol) was stirred with 1 M solution of *tert*-butylammonium fluoride (TBAF) in THF (5.0 mL) in the presence of molecular sieves (4 Å) at room temperature for 12 h. The reaction mixture was concentrated under reduced pressure and dried under vacuum. The crude compound was purified by column chromatography over silica gel using hexane/dichloromethane containing 1.0% triethylamine as the eluents to yield **4** (0.89 g, 98%). ^{1}H NMR (CD_3OD, δ ppm): 8.53 (d, $J = 7.8$ Hz, 1H, H-6), 7.32–7.34 (m, 2H, aromatic hydrogens, DMTr), 7.17–7.23 (m, 6H, aromatic hydrogens, DMTr), 7.11–7.13 (m, 1H, aromatic hydrogen, DMTr), 6.75–7.78 (m, 4H, aromatic hydrogens, DMTr), 6.22 (dd, $J = 5.3$, 2.5 Hz, 1H, H-1′), 6.01 (d, $J = 7.8$ Hz, 1H, H-5), 5.25 (t, $J = 3.1$ Hz, 1H, H-4′), 3.99 (dd, $J = 12.8$, 3.1 Hz, 1H, H-5′), 3.84 (dd, $J = 12.8$, 3.1 Hz, 1H, H-5″), 3.69 (s, 6H, DMTr-OCH_3), 3.51 (dd, $J = 12.6$, 5.3 Hz, 1H, H-2′), 3.27 (dd, $J = 12.6$, 2.5 Hz, 1H, H-2″). HR-MS (ESI-TOF) (*m/z*): $C_{29}H_{29}N_3O_5S$ calcd, 531.1828; found 531.9215 [M + H]$^+$, 632.6915 [M + TEA]$^+$.

*4. (–)-4-N-(4,4′-Dimethoxytrityl)-5′-O-(succinate)-2′,3′-dideoxy-3′-thiacytidine (***5***).* 4-Dimethylaminopyridine (DMAP, 100 mg, 0.82 mmol) and succinic anhydride (290 mg, 2.90 mmol) were added to a solution of compound **4** (770 mg, 1.45 mmol) in dry pyridine (15.0 mL). The reaction mixture was stirred at room temperature overnight. After completion of the reaction, the solvent was evaporated under reduced pressure and the crude compound was purified by column chromatography over silica gel using dichloromethane/methanol containing 1% triethylamine as the eluent to yield **5** (0.82 g, 90%). ^{1}H NMR (400 MHz, DMSO-d_6, δ ppm): 8.56 (br s, 1H, NH), 7.60–7.70 (d, $J = 7.8$ Hz, 1H, H-6), 7.14–7.24 (m, 9H, aromatic hydrogens, DMTr), 6.72–6.84 (m, 4H, aromatic hydrogens, DMTr), 6.30–6.38 (m, 1H, H-1′), 6.10 (d, $J = 7.8$ Hz, 1H, H-5), 5.25–5.35 (m, 1H, H-4′), 4.22–4.34 (m, 2H, H-5′ and H-5″), 3.71 (s, 6H, DMTr-OCH_3), 3.58–3.63 (m, 2H, H-2′ and H-2″), 3.00–3.10 (m, 4H, CH_2CH_2). HR-MS (ESI-TOF) (*m/z*): $C_{33}H_{33}N_3O_8S$ calcd, 631.1988; found 632.1715 [M + H]$^+$, 654.1472 [M + Na]$^+$.

5. (–)-5′-O-(Succinate)-2′,3′-dideoxy-3′-thiacytidine (3TCS, **6***).* Acetic acid (AcOH, 10 mL, 80%) was added to compound **5** (100 mg, 0.16 mmol). The reaction mixture was heated at 80 °C for 30 min. The solvent was removed under reduced pressure and the crude compound was purified by HPLC (acetonitrile/water gradient) to yield **6** (47 mg, 90%). ^{1}H NMR (400 MHz, DMSO-d_6, δ ppm): 12.29 (s, 1H, COOH), 9.50–9.80 (br s, 2H, NH_2), 7.60–7.70 (m, 1H, H-6), 6.20–6.32 (m, 1H, H-1′), 5.81–5.93 (m, 1H, H-5), 5.30–5.36 (m, 1H, H-4′), 4.30–4.40 (m, 2H, H-5′ and H-5″), 3.71–3.80 (m, 2H, H-2′), 3.00–3.200 (m, 5H, H-2″, and CH_2CH_2). HR-MS (ESI-TOF) (*m/z*): $C_{12}H_{15}N_3O_6S$ calcd, 329.0682; found 330.3316 [M + H]$^+$, 658.3471 [2M]$^+$.

6. (–)-Dextran-5′-O-(succinate)-2′,3′-dideoxy-3′-thiacytidine (3TCS–Dextran Conjugate, 3TCSD, **8***).* DMAP (70.0 mg, 0.57 mmol), *N*,*N*′-diisopropylethylamine (DIPEA, 100 μL, 0.61 mmol), and *N*,*N*′-diisopropylcarbodiimide (DIC) (50 μL, 0.32 mmol) were added to a solution of compound **5** (275.0 mg, 0.44 mmol) and dextran (20 kDa, 130 mg) in dry dimethyl sulfoxide (DMSO, 3.0 mL) under nitrogen atmosphere. The reaction mixture was stirred at 40 °C for 48 h. After the completion of the reaction, the reaction mixture was cooled to room temperature and cold diethyl ether/ethanol (45 mL, 50:50 v/v) was added. The mixture was washed twice with cold ethanol/diethyl ether (50:50, v/v) and finally with cold ethanol/acetonitrile (70:30, v/v) and centrifuged. The precipitate was dried under vacuum to give (−)-dextran-4-*N*-(4,4′-dimethoxy trityl)-5′-*O*-(succinate)-2′,3′-dideoxy-3′-thiacytidin [4-*N*-(4′-dimethoxytrityl)lamivudine succinate–dextran conjugate, **7**].

Acetic acid (AcOH, 10 mL, 80%) was added to compound **6**. The reaction mixture was stirred at room temperature for 3 h and then heated at 80 °C for 30 min. The solvent was removed under reduced pressure, and the residue was washed three times with cold diethyl ether/ethanol (45 mL, 50:50 v/v) and centrifuged to give 3TCS–dextran conjugate (3TCSD, **8**). ^{1}H NMR (400 MHz, D_2O, δ ppm): 7.88–8.04 (br s, 1H, H-6), 6.25–6.35 (m, 1H, H-1′), 6.05–6.15 (br s, 1H, H-5), 5.41–5.50 (m, 1H, H-4′), 4.85–5.05 (m, anomeric hydrogen of dextran, H-1), 4.28–4.58 (m, 2H, H-5′ and H-5″), 3.40–4.10 (m, H-2′ and H-2″ of 3TC, H-2, H-3, H-4, H-5, and H6 of dextran), 3.30–3.38 (m, 4H, CH_2CH_2 of succinate).

Further Characterization of 3TCS–Dextran Conjugate (3TCSD, 8). The purity of the powder was determined using both the size-exclusion (SEC) and reversed-phase (RPC) chromatographic methods. The degree of substitution of 3TC in 3TCSD was determined by hydrolysis of the conjugate under basic conditions. To 1 mg of the conjugate were added 1 mL of 0.1 N NaOH and 0.6 mL of methanol. After the mixture was left at room temperature for 5 min, 30 min, and 24 h, 100 μL of the sample was micropipetted into a microcentrifuge tube containing 100 μL of 0.1 M HCl. An aliquot (50 μL) was then

injected into an HPLC instrument. The concentration of the released 3TC was determined using a reversed-phase method based on 3TC standard solutions as described below.

High Performance Liquid Chromatography. Size-exclusion and reversed-phase chromatographic methods were developed and validated for quantitation of the conjugate (3TCSD) and its potential hydrolysis products (3TC and 3TCS), respectively, in buffers or biological samples.

1. Size-Exclusion Liquid Chromatography (SEC). Lamivudine succinate–dextran conjugate (3TCSD) was analyzed in nonbiological and biological (plasma and tissue) samples at ambient temperature using a 30 cm × 7.8 mm analytical gel chromatography column (PolySep-GFC 3000; Phenomenex, Torrance, CA). The mobile phase consisted of water/acetonitrile/acetic acid (75:25:0.2, v/v/v) and was pumped at a flow rate of 1.0 mL/min.

2. Reversed-Phase Liquid Chromatography (RPC). A reversed-phase chromatographic method was developed to quantitate the concentrations of 3TC and 3TCS in aqueous and biological samples. The separation of 3TC, 3TCS, and internal standard (stavudine, IS) was achieved on a 250 mm × 4.6 mm C_{18} column (Microsorb-MV, Varian, Lake Forest, CA) preceded by a 5 cm guard column. The mobile phase consisted of KH_2PO_4 (50 mM)/methanol/triethylamine (90:10:0.1, v/v, pH 7.0), which was pumped at a flow rate of 1.0 mL/min.

3. HPLC System. The HPLC instrument consisted of a 510 pump (Waters; Milford, MA), a 717 plus autosampler (Waters; Milford, MA), and a 486 UV detector (Waters) set at a wavelength of 276 nm. The chromatographic data were managed using Empower, version 2, software. Calibration curves were constructed by plotting the peak areas of 3TCSD or peak area ratios of 3TC or 3TCS over IS against the concentration in the sample using a weight of 1 per concentration.

4. Sample Preparation. For the size exclusion chromatography, to 100 μL of plasma in microcentrifuge tubes were added 20 μL of methanol and 20 μL of 20% (w/v) trichloroacetic acid. After being vortex-mixed for 5 s, the samples were centrifuged in a microcentrifuge at 16 000 rpm for 5 min. A 100 μL aliquot of the supernatant was mixed with 50 μL of 0.5 M phosphate buffer (pH 6.0), and a 75 μL aliquot was injected into the HPLC.

To determine the concentrations of 3TCSD in the tissues by the SEC method, tissues were homogenized in three volumes of water using a homogenizer at a rate of 10 000 rpm. To 100 μL of the whole homogenate in siliconized microcentrifuge tubes were added 50 μL of 0.5 M phosphate buffer (pH 7.0) and 50 μL of cold methanol. Samples were then briefly vortex-mixed, and 40 μL of trichloroacetic acid (40%) was added to precipitate proteins. After being vortex-mixed for 5 s, the samples were centrifuged in a microcentrifuge at 10 000 rpm for 3 min A 100 μL aliquot of the supernatant was mixed with 50 μL of 1 M sodium acetate, and a 75 μL aliquot was injected into the HPLC.

The preparation of plasma samples for reversed-phase chromatography was similar to that for the SEC method with one exception; for the reversed-phase system, 50 μL of 50 μg/mL stavudine was added as an internal standard to the plasma sample before protein precipitation. Similarly, the tissue samples for reversed-phase chromatography were prepared as described above for the SEC method but without the addition of 0.5 M phosphate buffer.

5. Validation of Assays. The inter-run precision (% CV) and accuracy (% error) of the assays were determined from the analysis of quality control samples ($n = 5$) based on reported guidelines (*36*). The concentrations of quality control samples were 1.0, 10, or 50 μg/mL for 3TCSD (SEC method), 0.125, 5.0, and 20 μg/mL for 3TC (RPC method), and 0.36, 5.4, and 18 μg/mL for 3TCS (RPC method). Calibration curves for SEC of 3TCSD contained 0, 1, 2, 5, 10, 15, 25, or 50 μg/mL of the prodrug (3TC equivalent). For RPC, calibration curves consisted of 0, 0.125, 0.25, 0.5, 1.0, 2.0, 5.0, 10, or 20 μg/mL 3TC and 0, 0.36, 0.72, 1.80, 3.6, 5.4, 9.0, or 18 μg/mL 3TCS as 3TC equivalents.

To determine the recovery of 3TCSD, 3TC, and 3TCS from plasma after protein precipitation, plasma samples ($n = 5$) containing 5 or 100 μg/mL 3TCSD, 5 or 50 μg/mL 3TC, or 1.8 or 18 μg/mL 3TCS were subjected to the above assays and the peak areas were determined. The peak areas of these samples were then compared with those containing an equal concentration of each analyte in distilled water, injected directly into the HPLC. Similarly, the recoveries of 3TCSD and 3TC from the liver samples ($n = 5$) containing 5 μg/mL 3TCSD or 0.5 μg/mL of 3TC were determined.

In Vitro Release Characterization. *1. Release Characteristics in Buffers.* The prodrug (3TCSD), at a concentration equivalent to 100 μg/mL 3TC, was dissolved in 10 mM KH_2PO_4 (pH 4.4) or phosphate buffer (pH 7.4). The solutions were then incubated at 37 °C ($n = 3$). Samples (100 μL) were taken at 0, 3, 6, 12, and 24 h and subjected to the above HPLC methods for the quantitation of intact 3TCSD (SEC method) and released 3TC or 3TCS (RPC method).

2. Release Characteristics in Rat Blood. Blood was obtained from rats by cardiac puncture. Approximately 4 IU of heparin was added to each mL of blood to prevent coagulation. Immediately after the collection of blood, 3TCSD conjugate (in 10 mM isotonic phosphate buffer at pH 7.4) was added to produce a blood concentration of 100 μg/mL (3TC equivalent) ($n = 3$). The solution was then incubated at 37 °C. Blood samples (1 mL) were collected at 0, 3, 6, and 12 h in heparinized microcentrifuge tubes. After centrifugation of the blood, the plasma samples (100 μL) were subjected to the assays described above for the determination of 3TC, 3TCS, and/or intact 3TCSD.

3. Release Characteristics in Rat Liver Lysosomes. Crude lysosomal fractions were prepared from the liver of untreated rats according to the procedure described in the lysosome isolation kit (Sigma). Briefly, the rat livers were perfused with ice-cold PBS before removal of the livers. The livers were then homogenized in four volumes of the extraction buffer, followed by differential centrifugation for isolating the lysosomal fraction. The protein concentrations in lysosomal preparations were determined by Bio-Rad protein assay (Bio-Rad, Herecules, CA). The activity of acid phosphatase, a lysosomal marker, in the preparation was tested using a commercial kit (Sigma). The specific enzyme activity in the lysosomal fraction was >9-fold that in the liver homogenate.

For lysosomal hydrolysis studies, 3TCSD (100 μg/mL, 3TC equivalent) was incubated at 37 °C in 50 mM acetate buffer (pH 4.0) in the presence of 5 mM reduced glutathione and 5 mg/mL lysosomal protein ($n = 3$). Samples (100 μL) were then taken at 0, 3, 6, 9, 12, and 24 h and treated as described above for size-exclusion and reversed-phase HPLC analysis.

In Vivo Disposition. A total of 42 adult male Sprague-Dawley rats were divided equally into two groups of 21 rats each, treated with 3TCSD or 3TC. The mean ± SD of the body weights of rats were 241 ± 8 and 240 ± 6 g for the 3TCSD- and 3TC-injected groups, respectively. The animals had free access to drinking water and rat chow before and during the course of experiments.

Single iv bolus doses (5 mg/kg, 3TC equivalent) of 3TCSD or the parent drug 3TC were injected into the penile vein of the animals under isoflurane anesthesia. Different groups of rats ($n = 3$/group per time point) were euthanized at 0 (before drug administration), 5, 15, 60, 120, or 180 min following drug administration, and tissues (liver, spleen, kidneys, heart, lungs, and brain) and blood (cardiac puncture) were collected. Ad-

ditionally, total urine output was collected from zero to 180 min or to 24 h for the 3TC- or 3TCSD-injected group (n = 3/group).

Immediately after excision, the tissues were rinsed in ice-cold saline solution to remove excess blood. Afterward, the tissues were blotted dry and kept frozen until analysis. After centrifugation of the blood in a prechilled and heparin-coated microcentrifuge tube, the plasma was collected. To prevent in vitro hydrolysis of 3TCSD during storage, plasma (500 μL) was mixed with a 10% acetic acid solution (100 μL). Plasma, tissue, and urine samples were kept frozen at −80 °C until analysis.

Pharmacokinetic Analysis. Noncompartmental analysis was performed by using WinNonlin5.0.1 computer program (Pharsight Co.; Mountain View, CA). Terminal elimination rate constant (λ_z) was estimated from the log-linear portion of the plasma or tissue concentration–time courses. Area under the plasma or tissue concentration–time curve (AUC) was estimated from the average plasma or tissue concentrations at different time points using a linear trapezoidal rule with extrapolation to infinity only for the plasma profiles. For tissues, AUCs were not extrapolated beyond the quantifiable samples because of uncertainty about the terminal half-lives. Other estimated pharmacokinetic parameters included apparent total body clearance (CL), renal clearance (CL_R), volume of distribution at steady state (V_{ss}), terminal volume of distribution (V_z), fraction of the drug excreted unchanged in urine (f_e), mean residence time (MRT), and maximum observed drug concentration (C_{max}). The maximum concentrations of 3TCSD or 3TC in plasma (C_0) after the injection of the conjugate or parent drug were estimated by the program. The concentrations of drugs in the tissues were corrected (*21*) for the residual blood using the blood volume fraction of different tissues.

Statistical Analysis. Because of the destructive sampling procedure used for the collection of blood and tissues from different animals at each time point, the composite kinetic parameter AUC could not be obtained for individual rats (*21*). Therefore, the variance of AUC was estimated by a reported (*37*, *38*) procedure based on the standard error of mean and number of samples at each time point. The pairwise comparison of AUCs was then carried out at an α level of 0.05 and a Bonferroni adjusted α of 0.05 or 0.0167 for pairwise comparison of two (one comparison) or three (three comparisons) mean values, respectively. The critical values of Z (Z_{crit}) for the two-sided test using the Bonferroni adjusted α of 0.05 and 0.0167 were 1.96 and 2.39, respectively, and the observed Z (Z_{obs}) was calculated as reported before (*37*, *38*). A Z_{obs} value greater than Z_{crit} was used as an indication of a significant difference between the AUCs.

The differences between groups in their kinetic parameters that could be estimated for individual rats (e.g., C_{max} and CL_R) were determined using a two-tailed unpaired t test at a significance level (α) of 0.05. When possible, data are presented as the mean ± SD.

RESULTS

Synthesis and Characterization of 3TCSD. Lamivudine (3TC) was conjugated to dextran using a succinate linker in two major steps by synthesis of 5′-*O*-succinate ester of the drug (Scheme 1), followed by the reaction of the ester conjugate with dextran (Scheme 2). Lamivudine was initially reacted with TBDMSCl in the presence of imidazole to yield 5′-*O*-TBDMS-lamivudine **2**. The protection of the *N*4-amino group of 5′-*O*-protected lamivudine was carried out in the presence of DMTr-Cl and pyridine to give *N*4-DMTr-5′-*O*-TBDMS-lamivudine **3**. The deprotection of 5′-*O*-TBDMS in the presence of tetrabutylammonium fluoride afforded the *N*4-DMTr derivative of lamivudine **4**, which was used in the reaction with succinic anhydride to generate the *N*4-DMTr-5′-*O*-succinate ester conjugate of lamivudine **5** (Scheme 1). Compound **5** was reacted with dextran in the presence of DIC and DMAP to afford the *N*4-(DMTr)lamivudine succinate–dextran conjugate **7** that was deprotected in the presence of acetic acid to afford the lamivudine succinate–dextran conjugate (3TCSD, **8**) (Scheme 2).

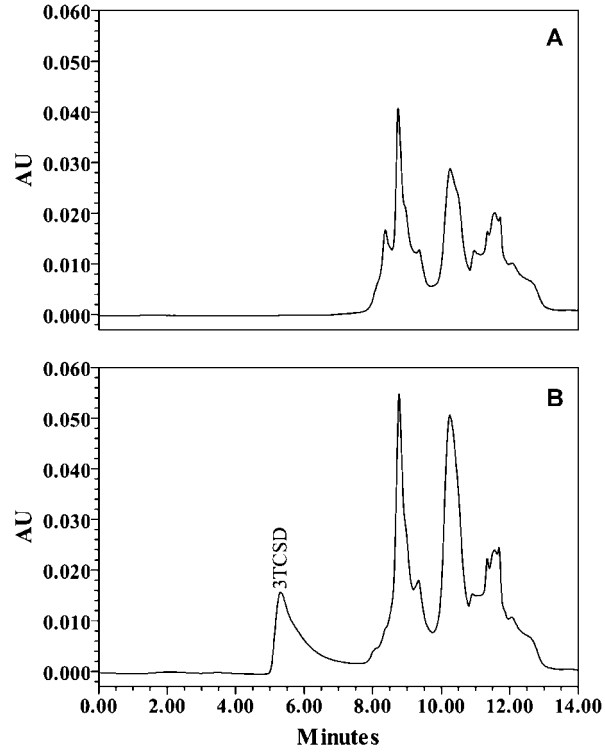


Figure 1. Chromatograms of plasma samples taken from a rat before (A) and 180 min after (B) the administration of a single 5 mg/kg dose (3TC equivalent) of 3TCSD, subjected to the size-exclusion chromatographic method. The 180 min sample contained 9.70 μg/mL 3TCSD.

The purity of the conjugate was >99% as determined by the reversed-phase analysis of a 100 μg/mL solution of the conjugate (n = 3), which contained only 0.296 ± 0.041 μg/mL 3TC without any measurable peak of 3TCS. The degree of substitution of the final product, which was obtained by the base hydrolysis of 3TCSD to 3TC followed by reversed-phase quantitation of the released 3TC, was 6.5 mg of lamivudine in 100 mg of 3TCSD powder. The complete hydrolysis of 3TCSD was confirmed by a complete disappearance of the 3TCSD peak in the SEC method. Additionally, the area of the unhydrolyzed 3TCSD peak in the SEC method was the same as the area of the released 3TC peak in the reversed-phase method after appropriate volume correction, indicating that the degree of substitution may be determined directly from the area of 3TCSD peak without hydrolysis. In terms of size, the peak of 3TCSD in the SEC chromatogram was slightly shifted to the left compared with the peak of the unconjugated dextran carrier, suggesting an increase in the size upon conjugation of dextran with 3TC.

Size-Exclusion Chromatographic Method. Chromatograms of plasma samples taken from a rat before (blank) and 180 min after the administration of a single 5 mg/kg dose (3TC equivalent) of 3TCSD are demonstrated in Figure 1. Dextran–lamivudine succinate eluted at ~5.3 min and was well separated from the endogenous peaks in plasma, which eluted after the conjugate peak (Figure 1). Additionally, the relationship between the peak area of 3TCSD and the detector response was linear ($r^2 \geq 0.998$) over the studied range 1–50 μg/mL.

Table 1. Inter-Run Accuracy and Precision for Quantitation of 3TCSD Using the SEC Assay ($n = 5$)

added concn (μg/mL)	calcd concn (μg/mL)	CV (%)	error (%)
1	0.992	12.8	−0.84
10	10.1	2.34	0.70
50	49.6	1.60	−0.80

The results of the assay validation in plasma are presented in Table 1. Excellent accuracy of the assay is demonstrated by error values of <1% for all the concentrations (even at the lowest concentration of 1 μg/mL). The assay is also deemed precise because the CV values are <13% for the inter-run data (Table 1). On the basis of the data presented in Table 1, the limit of quantitation of the assay is at least equal to 1 μg/mL.

The recovery of 3TCSD from plasma was 88.0 ± 4.2% and 94.1 ± 4.6% at concentrations of 5 and 50 μg/mL, respectively. The recovery of 3TCSD from liver was 94.2 ± 9.5% at a concentration of 5 μg/mL.

Reversed-Phase Chromatographic Method. Figure 2 depicts the chromatograms of plasma samples at zero (blank) and 15 min after the administration of a single 5 mg/kg dose of 3TC to rats and at 3 h after the in vitro incubation of 3TCSD in blood. Lamivudine, internal standard (stavudine), and 3TCS eluted at ∼11, 17, and 26 min, respectively, and were well separated from the endogenous peaks in plasma (Figure 2). Additionally, the relationship between the peak area ratios of 3TC and 3TCS and the sample concentrations was linear ($r^2 \geq$ 0.998) over the studied concentration ranges of 0.125–20 μg/mL for 3TC and 0.36–18 μg/mL (3TC equivalent) for 3TCS.

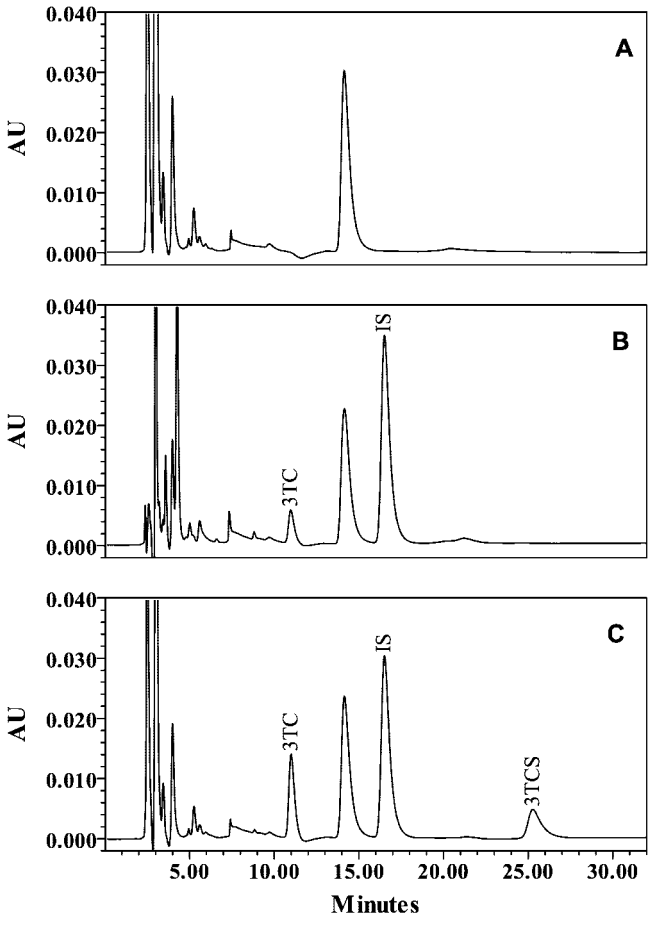


Figure 2. Chromatograms of plasma samples taken from a rat before (A) and 15 min after (B) the administration of a single 5 mg/kg dose of 3TC to rats and at 3 h after in vitro incubation of 3TCSD with rat blood (C), subjected to the reversed-phase chromatographic method. Sample B contained 1.84 μg/mL 3TC, and sample C contained 3.97 and 5.12 μg/mL 3TC and 3TCS, respectively.

Table 2. Inter-Run Accuracy and Precision for Quantitation of 3TC and 3TCS in Plasma Using the Reversed-Phase Assay ($n = 5$)

analyte	added concn (μg/ml)	calcd concn (μg/ml)	CV (%)	error (%)
3TC	0.125	0.138	16.8	10.9
3TC	5.0	4.75	3.15	−5.04
3TC	20	20.8	5.83	4.00
3TCS	0.36	0.378	8.33	5.14
3TCS	5.4	5.18	4.18	−3.73
3TCS	18	18.8	3.93	4.32

Validation results for the reversed-phase assay of 3TC and 3TCS in plasma are presented in Table 2. Excellent accuracy of the assay is demonstrated by error values of <11% for all the concentrations. The assay is also deemed precise because the CV values are <9% for all the concentrations except for the lowest concentration of 3TC, which showed an acceptable CV of 16.8% (Table 2). On the basis of the data presented in Table 2, the limit of quantitation of the assay is 0.125 and 0.36 μg/mL for 3TC and 3TCS, respectively.

For 3TC, the degrees of recovery from plasma were 101 ± 1.8% and 104 ± 1.8% at concentrations of 5 and 50 μg/mL, respectively. For 3TCS, the values were 89.7 ± 8.5% and 85.7 ± 2.6% at concentrations of 1.8 and 18 μg/mL, respectively. The recovery of 3TC from the liver samples at a concentration of 0.5 μg/mL was 95.7 ± 5.25%.

Release Characteristics in Buffers. The SEC and reversed-phase HPLC assays described above were used to investigate the stability of 3TCSD and formation of 3TC and 3TCS at 37 °C at pH 4.4 (Figure 3) or 7.4 (Figure 4). The conjugate was very stable at pH 4.4 as demonstrated by both SEC (Figure 3, top) and reversed-phase (Figure 3, bottom) assays. The concentrations of 3TCSD did not significantly change over 24 h of incubation at 37 °C at pH 4.4 (Figure 3, top). Additionally, reversed-phase analysis showed minor concentrations (<1% of

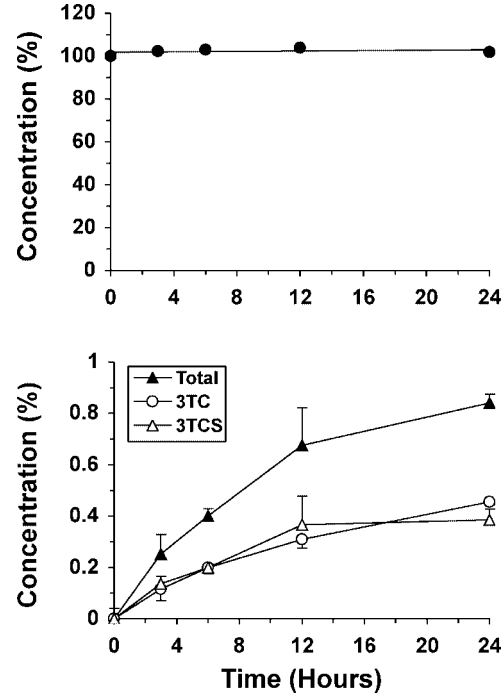


Figure 3. Average concentration–time courses of the intact 3TCSD (top) and released 3TC, 3TCS, and total 3TC (3TC plus 3TCS) (bottom) after incubation of the conjugate at pH 4.4 (37 °C). Error bars represent SD values ($n = 3$). Error bars for 3TCSD are too small to be observable.

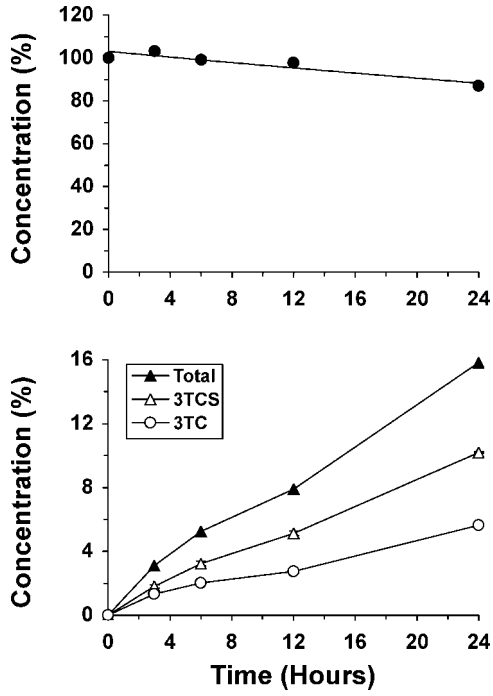


Figure 4. Average concentration–time courses of the intact 3TCSD (top) and released 3TC, 3TCS, and total 3TC (3TC plus 3TCS) (bottom) after incubation of the conjugate at pH 7.4 (37 °C). Error bars represent SD values ($n = 3$). In most cases, error bars are too small to be observable.

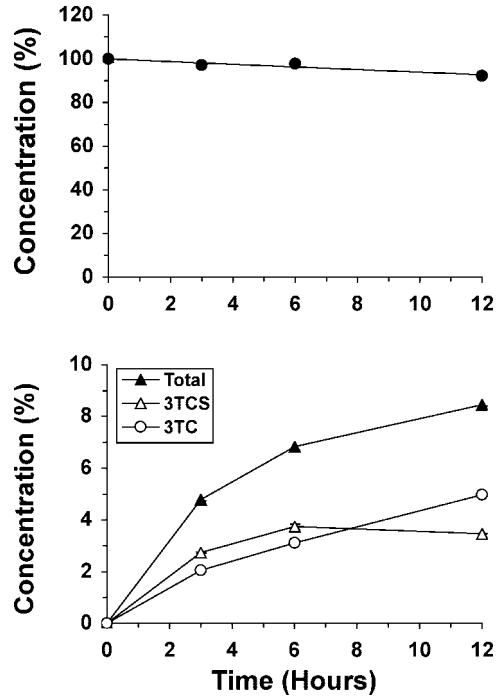


Figure 5. Average concentration–time courses of the intact 3TCSD (top) and released 3TC, 3TCS, and total 3TC (3TC plus 3TCS) (bottom) after incubation of the conjugate in rat blood (37 °C). Error bars represent SD values ($n = 3$). In most cases, error bars are too small to be observable.

the initial concentration of 3TCSD) of 3TC and 3TCS released over the incubation time of 24 h (Figure 3, bottom). On the other hand, measurable hydrolysis of 3TCSD occurred at pH 7.4 (Figure 4). In the SEC method, the concentrations of 3TCSD declined ~16% during 24 h of incubation at pH 7.4 and 37 °C, with an apparent first-order half-life of 108 h (Figure 4, top). The decline in the concentration of 3TCSD (Figure 4, top) was associated with an almost identical increase in the concentrations of free 3TC and 3TCS in the sample analyzed by the reversed-phase method (Figure 4, bottom).

Release Characteristics in Rat Blood. Figure 5 shows the decline in the 3TCSD concentration (top) and associated increases in the concentrations of 3TC and 3TCS (bottom) after incubation of the conjugate in rat blood at 37 °C. The total 3TC (3TC plus 3TC succinate) released during 12 h of incubation in blood was 8.45 ± 0.04% (Figure 5, bottom), in agreement with an equivalent decline (7.75 ± 0.80%) in the concentration of the prodrug in the SEC assay (Figure 5, top). The first-order half-life of the decline in the 3TCSD concentration in plasma was 110 h.

Release Characteristics in Rat Liver Lysosomes. The concentration–time courses of 3TC release following incubation of 3TCSD in the presence and absence of rat liver lysosomes are depicted in Figure 6. The presence of lysosomes in the medium induced a slow release of 3TC (7.36 ± 0.30 μg/mL after 24 h) without any detectable 3TCS. In contrast, the release of 3TC or 3TCS in the same medium in the absence of lysosomes was negligible (Figure 6).

In Vivo Disposition. Plasma concentration–time courses of 3TCSD and 3TC after the injection of single 5 mg/kg (3TC equivalent) doses of the prodrug or the parent drug are depicted in Figure 7. After the injection of unconjugated 3TC, the drug was eliminated relatively rapidly and could not be detected at the last sampling time of 3 h (Figure 7). In contrast, the concentrations of 3TCSD were several-fold higher than those of 3TC and remained high even at the last sampling time after the injection of the conjugate. The plasma concentrations of

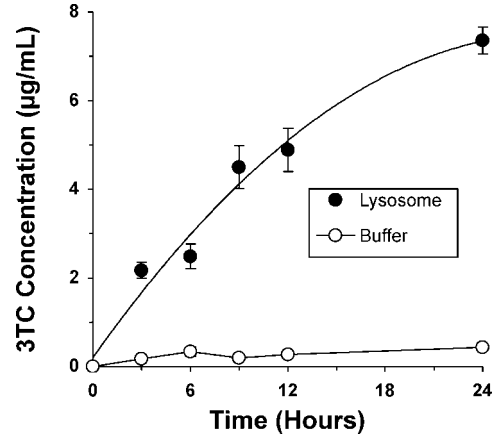


Figure 6. Average concentration–time courses of released 3TC after incubation of the conjugate in rat liver lysosomes or buffer (37 °C). Error bars represent SD values ($n = 3$). In most cases, error bars are too small to be observable.

both 3TC and 3TCSD declined multiexponentially (Figure 7). Additionally, no quantifiable concentrations of 3TC or 3TCS were detected in plasma of 3TCSD-injected rats.

The plasma pharmacokinetic parameters of 3TC and 3TCSD after the injection of the parent drug or the prodrug are listed in Table 3. Conjugation of 3TC to dextran resulted in an almost 40-fold decrease in the total CL of the drug and a similar degree of increase in its plasma AUC. The decrease in total CL was associated with an 80-fold decrease in the CL_R of the drug when conjugated to dextran. Consequently, the fraction of the drug excreted unchanged into urine decreased from 65% for the parent drug to 31% for the conjugate (Table 3). Additionally, dextran conjugation decreased the extent of distribution of the drug as reflected in V_{ss} and V_z values (Table 3), although to a lesser degree than that seen with the CL values (7- to 12-fold versus 40- to 80-fold, respectively). The declines in both the

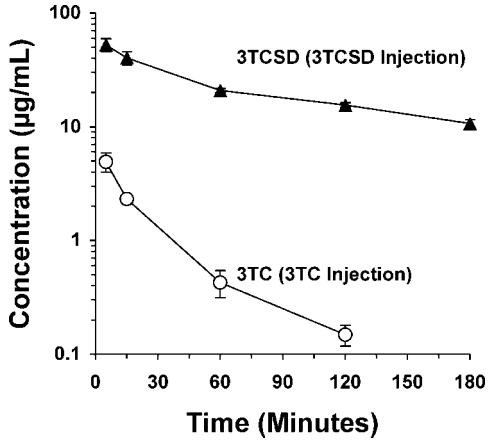


Figure 7. Plasma concentration–time courses of the conjugated (3TCSD) and unconjugated (3TC) lamivudine after iv administration of single 5-mg/kg doses (3TC equivalent) of 3TC or 3TCSD to rats. Standard deviation values are shown as error bars ($n = 3$ rats for each point).

Table 3. Plasma Pharmacokinetic Parameters (Mean ± SD) of Unconjugated (3TC) and Dextran-Conjugated (3TCSD) Lamivudine after a Single iv Dose (5 mg/kg, 3TC Equivalent) of 3TC or 3TCSD

parameter	3TC-injected rats, 3TC	3TCSD-injected rats, 3TCSD[a]
C_{max}, μg mL^{-1}	4.94 ± 0.93[c]	52.5 ± 6.5
AUC, μg min mL^{-1}	153 ± 7[c]	5930 ± 153
CL, mL min^{-1} kg^{-1}	32.6[b]	0.844[b]
CL_R, mL min^{-1} kg^{-1}	21.3 ± 2.1[c]	0.263 ± 0.089
f_e, %	65.3 ± 6.5[c]	31.2 ± 10.6
V_z, mL kg^{-1}	1786[b]	152[b]
V_{ss}, mL kg^{-1}	930[b]	135[b]
λ_z, min^{-1}	0.0183[b]	0.00554[b]
$t_{1/2}(\lambda_z)$, min	37.9[b]	125[b]
MRT, min	28.5[b]	160[b]

[a] No quantifiable concentrations of 3TC or 3TCS were detected in plasma after 3TCSD injection. [b] Standard deviations could not be determined because of destructive sampling method. [c] Significantly different ($P < 0.05$) from the corresponding value for the 3TCSD-injected rats.

clearance and volume of distribution upon conjugation resulted in longer terminal half-lives and MRT values for the conjugate, compared with the parent drug (Table 3).

The hepatic concentration–time courses (top) and AUC values (bottom) of the conjugate and regenerated 3TC after the administration of the conjugate and those of 3TC after the injection of the parent drug itself are depicted in Figure 8. After the injection of 3TC, the hepatic concentrations of the drug were measurable only in the first two samples; no detectable 3TC levels were found in the liver beyond 15 min following the administration of the parent drug (Figure 8, top). However, relatively high concentrations of 3TCSD were detected until the last sampling point. This resulted in >50-fold higher ($P < 0.0001$) AUCs for the conjugated 3TC, compared with the parent drug (Figure 8, bottom). Additionally, the conjugated 3TC slowly released 3TC in the liver (Figure 8, top) with an AUC that was approximately 2.5-fold larger ($P < 0.0001$) than that of the parent drug during the sampling time (Figure 8, bottom). No measurable concentrations of 3TCS were found in the liver.

The kidney concentration–time courses (top) and AUC values (bottom) of the conjugate and regenerated 3TC after the administration of the conjugate and those of 3TC after the injection of the parent drug itself are depicted in Figure 9. In addition to the liver (Figure 8), the kidney was the only other organ where high concentrations of the conjugated and regenerated 3TC were found (Figure 9). In contrast to the liver (Figure 8), however, relatively high and persistent concentrations of 3TC

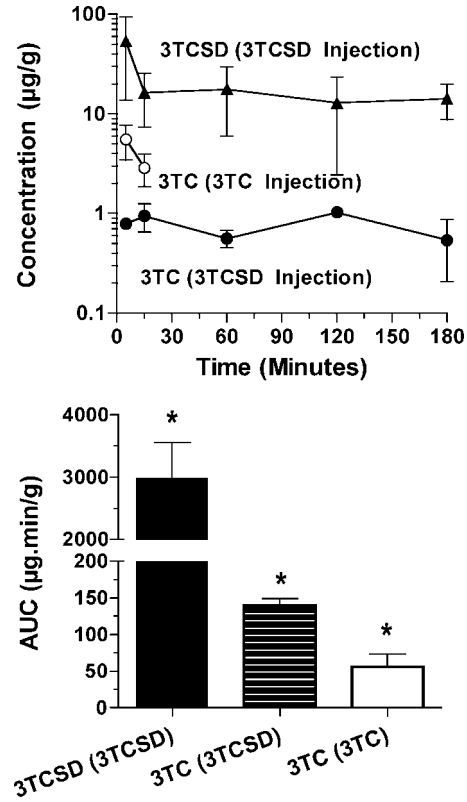


Figure 8. Liver concentration–time courses (top) and AUC values (bottom) of parent (3TC) and/or conjugated (3TCSD) lamivudine after iv administration of single 5 mg/kg doses (3TC equivalent) of 3TC or 3TCSD to rats. Standard deviation values are shown as error bars ($n = 3$ rats for each time point). Asterisks indicate significant differences from the other two groups.

were found in the kidney even after the injection of the parent drug (Figure 9). Therefore, conjugation of 3TC with dextran did not increase the availability of free 3TC in the kidneys, as the AUCs of the regenerated and parent 3TC were not significantly different (Figure 9).

In contrast to the liver (Figure 8) and kidneys (Figure 9), the concentrations of the conjugate and/or regenerated 3TC were very low or undetectable in the lungs, spleen, heart, and brain after 3TCSD injection (data not shown). Additionally, no released 3TC could be detected in these tissues. The concentrations of 3TC after 3TC injection in organs other than kidney were also low or below the limit of detection in most of the samples.

DISCUSSION

Targeted delivery of anti-HBV drugs to the liver, for the treatment of viral hepatic diseases, has attracted the attention of scientists for several years. In one of the first publications on this subject, Balboni et al. (*39*) showed that conjugation of cytosine arabinoside and 5-fluorodeoxyuridine to albumin resulted in accumulation of these antiviral drugs in the mouse liver cells, increasing the effectiveness of the drugs in comparison with the free drugs. Further work by Fiume and colleagues (*6*) modified this strategy by the use of lactosaminated albumin as the carrier, selectively targeting the asialoglycoprotein receptors on the hepatocytes with the galactose moiety of lactose. Additionally, conjugates of antiviral drugs with galactosylated poly-L-lysine, instead of albumin, have been synthesized and tested by the same group (*40, 41*). Others have used arabinogalactan (*42*) or glycosylated lipoproteins (*4, 7*), as liver-accumulating carriers, or prodrugs that release the active drug based on metabolism by hepatic cytochrome P450 (*9, 10*) for

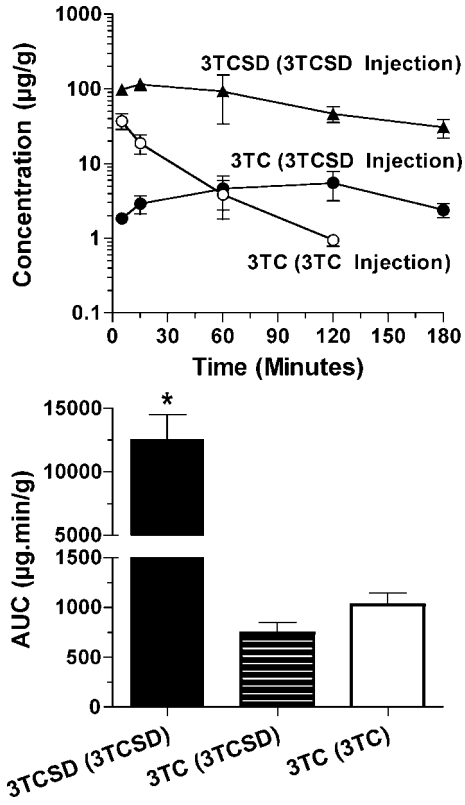


Figure 9. Kidney concentration–time courses (top) and AUC values (bottom) of parent (3TC) and/or conjugated (3TCSD) lamivudine after iv administration of single 5 mg/kg doses (3TC equivalent) of 3TC or 3TCSD to rats. Standard deviation values are shown as error bars (n = 3 rats for each time point). Asterisk indicates significant differences from the other two groups.

targeted delivery of antiviral drugs to the liver. These studies support the general concept that targeted delivery of antiviral drugs to the liver potentially increases the efficacy of these drugs in the treatment of viral liver infections while, at the same time, decreasing their toxic effects in other tissues. However, the choice of carrier and targeting moieties needs optimization to reduce carrier-related side effects, such as increased alkaline phosphatase levels seen with lactosylated human serum albumin (*6*), or to mitigate drawbacks associated with variability in density and affinity seen with the asialoglycoprotein receptors (*5*).

In the present study, we used dextran with a M_w of ~25 kDa as an alternative to the currently studied carriers for the selective delivery of 3TC to the liver in HBV treatment. The synthesis of the conjugate was challenging because of the presence of the free *N*4-amino group in the structure of 3TC, which had to be protected before the reaction of 3TC with succinic anhydride for the synthesis of 3TCS (Scheme 1). Therefore, additional protection/deprotection steps were used by the synthesis of intermediates **2**–**4** to selectively protect the *N*4-amino group before the 5′-O-esterification reaction to afford *N*4-protected 3TCS (Scheme 1). Furthermore, one additional step was used in the deprotection of the *N*4-amino group in the synthesis of the final conjugate 3TCSD (Scheme 2). These extra steps are not needed for the synthesis of the dextran conjugates of other nucleosides such as zidovudine and alovudine, which do not possess a free amino group (*43*). Nevertheless, the synthetic strategy (Schemes 1 and 2) described here afforded a conjugate with a reasonable degree of 3TC substitution (6.5%, w/w).

In addition to our study, we are aware of only one other study that used dextran as a macromolecular prodrug of antiviral agents (*8*). In that study, acyclovir was conjugated to dextran with a M_w of 40 kDa. However, to synthesize the conjugate, dextran was first oxidized to dextran aldehyde before direct reaction of the aldehyde groups of dextran with the amine group of acyclovir to produce a Schiff's base, without any spacer between acyclovir and dextran. Modification of dextrans, including their oxidation, may alter the degradation and safety profiles of native dextrans, which have been used clinically for almost 6 decades as plasma volume expanders (*44*). Therefore, we designed a strategy for conjugation of 3TC to dextran to minimize changes of the structure of native dextran molecule. Consequently, 3TC was coupled to dextran through a succinate linker (Scheme 2), thus avoiding the need for oxidation of dextran as previously reported (*8*).

Lamivudine succinate–dextran (3TCSD) has two ester bonds in its structure (Scheme 2), whose hydrolysis potentially releases 3TC or 3TCS. Therefore, to completely determine the fate of the conjugate and its potential release products in both in vitro and in vivo experiments, analytical methods capable of measurement of all three moieties are needed. To quantitate 3TCSD in both aqueous and biological samples, a SEC assay was developed. The method is capable of separating the conjugate peak from the endogenous peaks (Figure 1) and of accurately and precisely quantitating the conjugate (Table 2).

Several HPLC assays are currently available for the determination of 3TC in plasma and/or tissues (*45–50*). These assays use either solid-phase extraction (*46, 47, 49*) or protein precipitation (*45, 48, 50*) for sample preparation. Additionally, all of them use reversed-phase chromatography with C_{18} (*45, 46, 49*), C_8 (*50*), or phenyl (*47, 48*) columns for separation of 3TC from the endogenous peaks. To quantitate both 3TC and 3TCS simultaneously in our samples, we had to modify these assays. We found that a protein precipitation method with a combination of methanol and trichloroacetic acid resulted in the highest recovery (≥86%) for both 3TC and 3TCS from biological samples. Additionally, our chromatographic conditions resulted in complete separation of 3TC, 3TCS, and IS from the endogenous peaks (Figure 2) and in accurate and precise quantitation of 3TC and 3TCS (Table 2).

The results of our in vitro studies in buffers with different pH (Figures 3 and 4) and rat blood (Figure 5) suggest that the conjugate is relatively stable in buffers and blood. The conjugate was almost completely stable at a pH of 4.4, which was used to simulate any chemical hydrolysis at a pH similar to that of lysosomes, where the conjugate is expected to end up. Also, a comparison of 24 h degradation data at pH 7.4 (Figure 4) with 12 h degradation data in blood (Figure 5) suggests that the degradation of 3TCSD in blood is only due to a slow chemical hydrolysis of the conjugate. This is because the degradation half-lives of 3TCSD in buffer at pH 7.4 and in blood are almost identical (108 and 110 h, respectively), indicating lack of enzymatic hydrolysis of the conjugate in blood. These data are consistent with our previous report on a dextran conjugate of methylprednisolone succinate, which similarly showed little, if any, enzymatic hydrolysis in blood (*51*). Nevertheless, the relatively long half-life of 3TCSD in blood in vitro (110 h) indicates that the conjugate is stable in blood long enough for the uptake by the liver.

Previous studies (*16, 52*) on other ester conjugates of dextrans have proposed that the intact conjugates are resistant to the effects of esterases because of steric hindrance of dextrans. However, after exposure of the conjugate to dextranases, which depolymerize dextrans, esterases can hydrolyze the ester bonds in the conjugate. It has been reported (*11*) that dextranases are present in lysosomes, predominantly in the liver. Additionally, dextrans enter cells via endocytosis, which results in their accumulation in the lysosomal compartments (*53, 54*). Therefore, lysosomal exposure of dextran conjugates to dextranases

may facilitate their further enzymatic hydrolysis. Indeed, our previous work with dextran carriers showed that the M_w of the macromolecule found in the liver slowly decreased over a period of 96 h after its in vivo administration to rats (*20*). Because of our short sampling time of 3 h, we could not detect a significant change in the M_w (retention time in SEC assay) of the 3TCSD conjugate in the liver samples in our current study. However, our in vitro data showing significant amounts of 3TC released at pH 4.0 only in the presence of rat liver lysosomes (Figure 6) are in agreement with these reports.

The literature information about the pharmacokinetics of 3TC in rats is limited. We are aware of only one study reporting the plasma concentration–time course and AUC of the drug after a 230 mg kg^{-1} iv dose (*10*). However, no other pharmacokinetic parameters were reported in that study. We estimated a CL value of 27.1 mL min^{-1} kg^{-1} from the AUC and dose values reported in that study. This value is very close to our value of 32.6 mL min^{-1} kg^{-1} after a much smaller dose of 5 mg kg^{-1} (Table 3), suggesting linear pharmacokinetics of 3TC in the dosage range of 5–230 mg kg^{-1}.

In our study, conjugation of 3TC to dextran substantially decreased both the CL and volume of distribution of 3TC (Table 3) while at the same time increasing the accumulation of the drug in the liver (Figure 8). A similar disposition pattern was also observed for a dextran prodrug of methylprednisolone with a succinate linker (*30*). The simultaneous decrease in volume of distribution and increase in liver accumulation upon dextran conjugation is due to the relatively large pore sizes of the liver sinusoids in comparison with those in the vascular beds of most other organs, allowing unrestricted access of the conjugate to the space of Disse and internalization of the conjugate (*21*).

Because of the limited number of liver samples with quantifiable 3TC concentrations after 3TC injection and slow apparent declines in the liver concentrations of the conjugate and regenerated 3TC after conjugate injection (Figure 8, top), terminal half-lives were not estimated for the liver. Consequently, liver AUC values depicted in Figure 8 (bottom panel) are related to the sampling period without extrapolation to infinity. However, the significant differences between the liver AUCs after 3TC and 3TCSD injections would be expected to be even larger if extrapolated AUCs were used. This is because the apparent decline in the 3TCSD or regenerated 3TC concentrations was substantially slower than that in the liver concentrations of the parent drug (Figure 8, top).

The slow decline in the 3TCSD concentrations in the liver (Figure 8, top) is in agreement with previous ex vivo studies using isolated perfused rat livers (*19*) showing that, once in the liver, the rate of exocytosis of dextrans from the liver cells is negligible. Therefore, the main reason for the decline in the liver concentrations of the conjugate is its elimination by the liver, which is relatively slow based on the in vitro studies in lysosomes (Figure 6). Nevertheless, in contrast to undetectable concentrations of 3TC in the liver beyond 15 min after the parent drug injection, high concentrations of the conjugate in the liver were associated with a gradual and sustained generation of the parent drug in this tissue (Figure 8).

Other than the liver, the conjugate accumulated to a substantial degree and released 3TC only in the kidneys (Figure 9). The substantial accumulation of the conjugate in the kidneys is consistent with the M_w dependency of the renal excretion of the carrier dextrans in rats (*22*). Whereas a significant portion of the dose of dextrans with M_w values of 4 and 20 kDa was excreted into urine, renal excretion of dextrans with M_w values of 70 and 150 kDa was negligible. Interestingly, kidneys have been suggested as an extrahepatic site for virus replication in different models of HBV infection (*55, 56*). Therefore, accumulation of the conjugate and release of 3TC in this organ, in addition to that in the liver, may be of potential therapeutic benefit in chronic HBV infection.

The tissue exposure to 3TC after the administrations of the equivalent doses of the conjugate and the parent drug is the most relevant parameter in terms of targeting index. The ratios of 3TC AUCs after the conjugate and parent drug administration were 2.41 for the liver and 0.721 for the kidneys (see Results). These data clearly show that the conjugation of 3TC to dextran only increased the targeting of the drug to the liver. The significantly higher accumulation of 3TC in the liver is in conformity with the hypothesis of the study; i.e., conjugation of 3TC with dextran allows preferential accumulation of the drug in the liver.

Although our conjugate released both 3TC and 3TCS in vitro in buffers (Figures 3 and 4) and rat blood (Figure 5), only 3TC was observed in biological samples after in vivo administration of the conjugate (Figures 8 and 9). This suggests rapid conversion of any released 3TCS to 3TC in vivo. Our previous work on a methylprednisolone succinate–dextran conjugate (*30*) also showed similar results in that no measurable concentrations of methylprednisolone succinate were found in biological samples after the administration of the conjugate to rats. The rapid conversion of 3TCS to 3TC in vivo is advantageous because 3TCS is not expected to have any biological effects by itself. This is due to the fact that to be effective, 3TC should undergo stepwise phosphorylation at the 5′-position to monophosphate, diphosphate, and triphosphate forms before 5′-triphosphate 3TC is incorporated into the viral DNA (*57*). Therefore, 3TCS, which has a succinate moiety at the 5′-position (Scheme 1, **6**), cannot be converted to the active 5′-triphosphate 3TC without first being converted to 3TC.

In conclusion, a method is presented for the synthesis of a conjugate of native dextran with the antiviral drug 3TC using a succinate linker. Additionally, validated size-exclusion and reversed-phase assays are developed for the determination of purity, in vitro release characteristics, and in vivo disposition of 3TCSD. By use of these methods, the parent conjugate and its degradation products, 3TC and 3TCS, may be quantitated in nonbiological and biological samples. In vitro studies indicate evidence of lysosomal degradation and relative stability of the conjugate in buffers and blood. Additionally, in vivo studies after the administration of the conjugate or the parent drug to rats suggest that the conjugation increases the delivery of the drug to the liver, resulting in higher exposure of the liver to the regenerated antiviral drug.

LITERATURE CITED

(1) Jarvis, B., and Faulds, D. (1999) Lamivudine. A review of its therapeutic potential in chronic hepatitis B. *Drugs 58*, 101–141.
(2) Shaw, T., and Locarnini, S. A. (1999) Preclinical aspects of lamivudine and famciclovir against hepatitis B virus. *J. Viral Hepatitus 6*, 89–106.
(3) Younger, H. M., Bathgate, A. J., and Hayes, P. C. (2004) Nucleoside analogues for the treatment of chronic hepatitis B. *Aliment. Pharmacol. Ther. 20*, 1211–1230.
(4) Bijsterbosch, M. K., van de Bilt, H., and van Berkel, T. J. (1996) Specific targeting of a lipophilic prodrug of iododeoxyuridine to parenchymal liver cells using lactosylated reconstituted high density lipoprotein particles. *Biochem. Pharmacol. 52*, 113–121.
(5) Rensen, P. C. N., Devrueh, R. L. A., and Vanberkel, T. J. C. (1996) Targeting hepatitis B therapy to the liver: clinical pharmacokinetic considerations. *Clin. Pharmacokinet. 31*, 131–155.
(6) Fiume, L., Di Stefano, G., Busi, C., Mattioli, A., Bonino, F., Torrani-Cerenzia, M., Verme, G., Rapicetta, M., Bertini, M., and Gervasi, G. B. (1997) Liver targeting of antiviral nucleoside analogues through the asialoglycoprotein receptor. *J. Viral Hepatitus 4*, 363–370.

(7) de Vrueh, R. L., Rump, E. T., van De Bilt, E., van Veghel, R., Balzarini, J., Biessen, E. A., van Berkel, T. J., and Bijsterbosch, M. K. (2000) Carrier-mediated delivery of 9-(2-phosphonylmethoxyethyl)adenine to parenchymal liver cells: a novel therapeutic approach for hepatitis B. *Antimicrob. Agents Chemother. 44*, 477–483.

(8) Tu, J., Zhong, S., and Li, P. (2004) Studies on acyclovir–dextran conjugate: synthesis and pharmacokinetics. *Drug Dev. Ind. Pharm. 30*, 959–965.

(9) Erion, M. D., van Poelje, P. D., Mackenna, D. A., Colby, T. J., Montag, A. C., Fujitaki, J. M., Linemeyer, D. L., and Bullough, D. A. (2005) Liver-targeted drug delivery using HepDirect prodrugs. *J. Pharmacol. Exp. Ther. 312*, 554–560.

(10) Reddy, K. R., Colby, T. J., Fujitaki, J. M., van Poelje, P. D., and Erion, M. D. (2005) Liver targeting of hepatitis-B antiviral lamivudine using the HepDirect prodrug technology. *Nucleosides Nucleotides Nucleic Acids 24*, 375–381.

(11) Larsen, C. (1989) Dextran prodrugs—structure and stability in relation to therapeutic activity. *Adv. Drug Delivery Rev. 3*, 103–154.

(12) Takakura, Y., and Hashida, M. (1995) Macromolecular drug carrier systems in cancer chemotherapy: macromolecular prodrugs. *Crit. Rev. Oncol. Hematol. 18*, 207–231.

(13) Mehvar, R. (2000) Dextrans for targeted and sustained delivery of therapeutic and imaging agents. *J. Controlled Release 69*, 1–25.

(14) Mehvar, R. (2003) Recent trends in the use of polysaccharides for improved delivery of therapeutic agents: pharmacokinetic and pharmacodynamic perspectives. *Curr. Pharm. Biotechnol. 4*, 283–302.

(15) Harboe, E., Larsen, C., Johansen, M., and Olesen, H. P. (1989) Macromolecular prodrugs. XV. Colon-targeted delivery—bioavailability of naproxen ester prodrugs varying in molecular size in the pig. *Pharm. Res. 6*, 919–923.

(16) Larsen, C., Harboe, E., Johansen, M., and Olesen, H. P. (1989) Macromolecular prodrugs. XVI. Colon-targeted delivery—comparison of the rate of release of naproxen from dextran ester prodrugs in homogenates of various segments of the pig gastrointestinal tract. *Pharm. Res. 6*, 995–999.

(17) McLeod, A. D., Friend, D. R., and Tozer, T. N. (1993) Synthesis and chemical stability of glucocorticoid–dextran esters: potential prodrugs for colon-specific delivery. *Int. J. Pharm. 92*, 105–114.

(18) McLeod, A. D., Friend, D. R., and Tozer, T. N. (1994) Glucocorticoid–dextran conjugates as potential prodrugs for colon-specific delivery: hydrolysis in rat gastrointestinal tract content. *J. Pharm. Sci. 83*, 1284–1288.

(19) Mehvar, R. (1997) Kinetics of hepatic accumulation of dextrans in isolated perfused rat livers. *Drug Metab. Dispos. 25*, 552–556.

(20) Mehvar, R., Robinson, M. A., and Reynolds, J. M. (1995) Dose dependency of the kinetics of dextrans in rats: effects of molecular weight. *J. Pharm. Sci. 84*, 815–818.

(21) Mehvar, R., Robinson, M. A., and Reynolds, J. M. (1994) Molecular weight dependent tissue accumulation of dextrans: in vivo studies in rats. *J. Pharm. Sci. 83*, 1495–1499.

(22) Mehvar, R., and Shepard, T. L. (1992) Molecular weight-dependent pharmacokinetics of fluorescein-labeled dextrans in rats. *J. Pharm. Sci. 81*, 908–912.

(23) Nakane, S., Matsumoto, S., Takakura, Y., Hashida, M., and Sezaki, H. (1987) The accumulation mechanism of cationic mitomycin c–dextran conjugates in the liver: in-vivo cellular localization and in-vitro interaction with hepatocytes. *J. Pharm. Pharmacol. 40*, 1–6.

(24) Nishida, K., Tonegawa, C., Nakane, S., Takakura, Y., Hashida, M., and Sezaki, H. (1990) Effect of electric charge on the hepatic uptake of macromolecules in the rat liver. *Int. J. Pharm. 65*, 7–17.

(25) Vansteenkiste, S., Schacht, E., Duncan, R., Seymour, L., Pawluczyk, I., and Baldwin, R. (1991) Fate of glycosylated dextrans after in vivo administration. *J. Controlled Release 16*, 91–100.

(26) Nishikawa, M., Kamijo, A., Fujita, T., Takakura, Y., Sezaki, H., and Hashida, M. (1993) Synthesis and pharmacokinetics of a new liver-specific carrier, glycosylated carboxymethyl-dextran, and its application to drug targeting. *Pharm. Res. 10*, 1253–1261.

(27) Nishikawa, M., Yamashita, F., Takakura, Y., Hashida, M., and Sezaki, H. (1992) Demonstration of the receptor-mediated hepatic uptake of dextran in mice. *J. Pharm. Pharmacol. 44*, 396–401.

(28) Yamaoka, T., Kuroda, M., Tabata, Y., and Ikada, Y. (1995) Body distribution of dextran derivatives with electric charges after intravenous administration. *Int. J. Pharm. 113*, 149–157.

(29) Mehvar, R., and Hoganson, D. A. (2000) Dextran–methylprednisolone succinate as a prodrug of methylprednisolone: immunosuppressive effects after in vivo administration to rats. *Pharm. Res. 17*, 1402–1407.

(30) Zhang, X., and Mehvar, R. (2001) Dextran–methylprednisolone succinate as a prodrug of methylprednisolone: plasma and tissue disposition. *J. Pharm. Sci. 90*, 2078–2087.

(31) Chimalakonda, A. P., Montgomery, D. L., Weidanz, J. A., Shaik, I. H., Nguyen, J. H., Lemasters, J. J., Kobayashi, E., and Mehvar, R. (2006) Attenuation of acute rejection in a rat liver transplantation model by a liver-targeted dextran prodrug of methylprednisolone. *Transplantation 81*, 678–685.

(32) Chimalakonda, A. P., and Mehvar, R. (2003) Dextran–methylprednisolone succinate as a prodrug of methylprednisolone: local immunosuppressive effects in liver after systemic administration to rats. *Pharm. Res. 20*, 198–204.

(33) Wu, C. H., Ouyang, E. C., Walton, C., Promrat, K., Forouhar, F., and Wu, G. Y. (2003) Hepatitis B virus infection of transplanted human hepatocytes causes a biochemical and histological hepatitis in immunocopetentent rats. *World J. Gastroenterol. 9*, 978–983.

(34) Takahashi, H., Fujimoto, J., Hanada, S., and Isselbacher, K. J. (1995) Acute hepatitis in rats expressing human hepatitis B virus transgenes. *Proc. Natl. Acad. Sci. U.S.A. 92*, 1470–1474.

(35) Wu, C. H., Ouyang, E. C., Walton, C., and Wu, G. Y. (2001) Liver cell transplantation—novel animal model for human hepatic viral infections. *Croat. Med. J. 42*, 446–450.

(36) Shah, V. P., Midha, K. K., Dighe, S., McGilveray, I. J., Skelly, J. P., Yacobi, A., Layoff, T., Viswanathan, C. T., Cook, C. E., McDowall, R. D., Pittman, K. A., and Spector, S. (1992) Analytical methods validation: bioavailability, bioequivalence, and pharmacokinetics. *J. Pharm. Sci. 81*, 309–312.

(37) Bailer, A. J. (1988) Testing for the equality of area under the curves when using destructive measurement techniques. *J. Pharmacokinet. Biopharm. 16*, 303–309.

(38) Yuan, J. (1993) Estimation of variance for AUC in animal studies. *J. Pharm. Sci. 82*, 761–763.

(39) Balboni, P. G., Minia, A., Grossi, M. P., Barbanti-Brodano, G., Mattioli, A., and Fiume, L. (1976) Activity of albumin conjugates of 5-fluorodeoxyuridine and cytosine arabinoside on poxviruses as a lysosomotropic approach to antiviral chemotherapy. *Nature 264*, 181–183.

(40) Fiume, L., Bassi, B., Busi, C., Mattioli, A., Spinosa, G., and Faulstich, H. (1986) Galactosylated poly(L-lysine) as a hepatotropic carrier of 9-beta-D-arabinofuranosyladenine 5′-monophosphate. *FEBS Lett. 203*, 203–206.

(41) Fiume, L., Di Stefano, G., Busi, C., Mattioli, A., Battista Gervasi, G., Bertini, M., Bartoli, C., Catalani, R., Caccia, G., Farina, C., Fissi, A., Pieroni, O., Giuseppetti, R., D'Ugo, E., Bruni, R., and Rapicetta, M. (1997) Hepatotropic conjugate of adenine arabinoside monophosphate with lactosaminated poly-L-lysine. Synthesis of the carrier and pharmacological properties of the conjugate. *J. Hepatol. 26*, 253–259.

(42) Enriquez, P. M., Jung, C., Josephson, L., and Tennant, B. C. (1995) Conjugation of adenine arabinoside 5′-monophosphate to arabinogalactan: synthesis, characterization, and antiviral activity. *Bioconjugate Chem. 6*, 195–202.

(43) Agarwal, H. K.; Kumar, A.; Mehvar, R., and Parang, K. Presented at the 233rd National Meeting of the American Chemical Society, Chicago, IL, March 25–29, 2007.
(44) Thoren, L. (1981) The dextrans-clinical data. *Dev. Biol. Stand. 48*, 157–167.
(45) Zhou, X. J., and Sommadossi, J. P. (1997) Rapid quantitation of (–)-2′-deoxy-3′-thiacytidine in human serum by high-performance liquid chromatography with ultraviolet detection. *J. Chromatogr., B: Biomed. Sci. Appl. 691*, 417–424.
(46) Kenney, K. B., Wring, S. A., Carr, R. M., Wells, G. N., and Dunn, J. A. (2000) Simultaneous determination of zidovudine and lamivudine in human serum using HPLC with tandem mass spectrometry. *J. Pharm. Biomed. Anal. 22*, 967–983.
(47) Zheng, J. J., Wu, S. T., and Emm, T. A. (2001) High-performance liquid chromatographic assay for the determination of 2′-deoxy-3′-thiacytidine (lamivudine) in human plasma. *J. Chromatogr., B: Biomed. Sci. Appl. 761*, 195–201.
(48) Alnouti, Y., White, C. A., and Bartlett, M. G. (2004) Determination of lamivudine in plasma, amniotic fluid, and rat tissues by liquid chromatography. *J. Chromatogr., B: Anal. Technol. Biomed. Life Sci. 803*, 279–884.
(49) Bezy, V., Morin, P., Couerbe, P., Leleu, G., and Agrofoglio, L. (2005) Simultaneous analysis of several antiretroviral nucleosides in rat plasma by high-performance liquid chromatography with UV using acetic acid/hydroxylamine buffer. Test of this new volatile medium-pH for HPLC-ESI-MS/MS. *J. Chromatogr., B: Anal. Technol. Biomed. Life Sci. 821*, 132–143.
(50) Kano, E. K., dos Reis Serra, C. H., Koono, E. E., Andrade, S. S., and Porta, V. (2005) Determination of lamivudine in human plasma by HPLC and its use in bioequivalence studies. *Int. J. Pharm. 297*, 73–79.
(51) Mehvar, R., Dann, R. O., and Hoganson, D. A. (2000) Kinetics of hydrolysis of dextran–methylprednisolone succinate, a macromolecular prodrug of methylprednisolone, in rat blood and liver lysosomes. *J. Controlled Release 68*, 53–61.
(52) Zhang, X., and Mehvar, R. (2001) Dextran–methylprednisolone succinate as a prodrug of methylprednisolone: dose-dependent pharmacokinetics in rats. *Int. J. Pharm. 229*, 173–182.
(53) Lake, J. R., Licko, V., Van Dyke, R. W., and Scharschmidt, B. F. (1985) Biliary secretion of fluid-phase markers by the isolated perfused rat liver. Role of transcellular vesicular transport. *J. Clin. Invest. 76*, 676–684.
(54) Stock, R. J., Cilento, E. V., and McCuskey, R. S. (1989) A quantitative study of fluorescein isothiocyanate–dextran transport in the microcirculation of the isolated perfused rat liver. *Hepatology 9*, 75–82.
(55) Di Bisceglie, A. M., and Hoofnagle, J. H. (1990) Hepatitis B virus replication within the human spleen. *J. Clin. Microbiol. 28*, 2850–2852.
(56) Ogston, C. W., Schechter, E. M., Humes, C. A., and Pranikoff, M. B. (1989) Extrahepatic replication of woodchuck hepatitis virus in chronic infection. *Virology 169*, 9–14.
(57) Johnson, M. A., Moore, K. H., Yuen, G. J., Bye, A., and Pakes, G. E. (1999) Clinical pharmacokinetics of lamivudine. *Clin. Pharmacokinet. 36*, 41–66.

BC700193D

Intermolecular Interaction of Avidin and PEGylated Biotin

Shan Ke,[†,‡] John C. Wright,[†] and Glen S. Kwon*[,‡]

Department of Chemistry, University of Wisconsin—Madison, 1101 University Avenue, Madison, Wisconsin 53706-1322, and Division of Pharmaceutical Sciences, School of Pharmacy, University of Wisconsin—Madison, 777 Highland Avenue, Madison, Wisconsin 53705-2222. Received June 6, 2007; Revised Manuscript Received July 19, 2007

The equilibrium binding constants and stoichiometries between PEGylated biotins and avidin have been studied for a range of PEGylated biotin molecular weights. These studies show that as the molecular weight of PEG (polyethylene glycol) increases over the range 588, 3400, and 5000 g/mol, the equilibrium dissociation constants of PEGylated biotins with avidin increase to $\sim 10^{-8}$ M compared with 10^{-15} M for the biotin–avidin complex. The stoichiometries of PEGylated biotins with avidin are 4:1 for 588 and 3400 g/mol PEG and 1:1 for 5000 g/mol PEG. The data demonstrate that the equilibrium binding constant and the stoichiometry of the avidin–biotin–PEG complex system can be adjusted by the length of PEG chains. This approach may be used with PEGylated biotin analogues for pretargeting in drug delivery, such as a biotin-PEGylated enzyme for converting an inactive prodrug into a cytotoxin. When a PEG chain is chosen as an appropriate spacer, the length of the PEG chain must be considered because PEG can block the binding sites on avidin.

INTRODUCTION

We have attempted to modify therapeutic proteins with PEG (polyethylene glycol) and deliver the PEGylated proteins to tumor tissues through the enhanced permeability and retention (EPR) effect (*1*). The EPR effect results in the selective sequestration of the therapeutic proteins in tumors. After administration of prodrugs, the therapeutic proteins can convert the prodrugs into toxic forms that kill tumor cells. The efficacy of this process depends on optimizing the delivery of the therapeutic proteins to the tumor while eliminating the proteins from the plasma before administration of the prodrug. The enhancement of the plasma half-life of a PEGylated protein is an important prerequisite for EPR targeting tumor tissues and the size of a PEGylated protein is a crucial factor to keep the PEGylated protein circulating in the plasma. It is generally recommended that the size of a therapeutic protein should be larger than the glomerular filtration threshold in order to avoid being cleared too quickly by the renal system (*2*). We believe that an ideal avidin–biotin–PEG–enzyme complex has a molecular weight higher than the glomerular filtration threshold and can increase the EPR tumor targeting. At the same time, this complex must dissociate into avidin and biotin–PEG–CPA (CPA, carboxypeptidase A) in the circulation system so that it can be cleared by the renal system before administration of the prodrug. Once the glomerular filtration threshold is reached, the half-life of the avidin–biotin–PEG–CPA complex in the plasma is primarily dependent on the dissociation kinetics of the complex that allows it to be removed by the renal system. The half-life of the avidin–biotin–PEG–CPA complex must be sufficiently long for significant tumor accumulation but short enough to allow the prodrug administration.

The avidin–biotin technology has been an essential tool in modern bioscience (*3*). The unusually strong interaction of avidin and biotin is often the basis for pretargeting strategies in cancer treatments. For example, avidin or streptavidin has been employed as a bridge between a biotinylated target protein and a biotinyl anticancer reagent (*4–7*). However, the binding between avidin and biotin is so strong that the unmodified avidin–biotin system has a dissociation half-life of ~200 days, a period that is too long to have any potential for our enzyme delivering strategy. The avidin–biotin system has to be modified to reduce the affinity. For this goal we chose biotinylated PEGs, which not only form a complex with avidin with a reduced affinity but also protects the enzyme during delivery (*8*, *9*). Before the synthesis and characterization of the complete avidin–biotin–PEG–enzyme complex, this study examines the intermolecular interaction between avidin and PEGylated biotin as a function of the PEG molecular weight. The work focuses on three areas. (1) One area is affinity. How does the length of PEG chain affect the affinity of biotinylated PEG for avidin? (2) Another area is stoichiometry. Avidin has four binding sites for biotin with a stoichiometry of 1:4 of avidin/biotin. It was reported that PEGylated biotin has a lower affinity for avidin than biotin (*10*), but it is important to learn whether a PEG chain blocks the biotin terminus from binding with avidin/streptavidin and reduces the effective stoichiometry of the complex. (3) Does a long PEG chain envelop avidin in the complex or is the PEGylated biotin preferentially excluded from the avidin?

EXPERIMENTAL PROCEDURES

Materials. The reagents used in this study were commercially available analytical or higher grade materials except for PEGylated biotins, which have a purity ranging from 80% to 98%. 2-Iminobiotin and D-biotin were obtained from Sigma (St. Louis, MO). Avidin and Immuno Pure 2-(4′-hydroxyazobenzene)benzoic acid (HABA) were purchased from Pierce (Rockford, IL). Biotin–PEG(3400) and biotin–PEG(5000) were obtained from Nektar (Huntsville, AL). Biotin–PEG(588) was purchased from Quanta BioDesign (Powell, OH). 2,6-Anilinonaphthalene sulfonate (2,6-ANS) was obtained from Molecular Probes (Carlsbad, CA).

Buffer. The PBS buffer was prepared with 8.00 g of NaCl, 0.20 g of KCl, 2.68 g of $Na_2HPO_4 \cdot 7H_2O$ and 0.24 g of KH_2PO_4, diluted to 1 L with Millipore water, pH 7.4. If necessary, the pH was adjusted using NaOH or HCl. The stability of the

* To whom correspondence should be addressed. Telephone: 608-265-5183. Fax: 608-262-5345. E-mail: gskwon@pharmacy.wisc.edu.
† Department of Chemistry.
‡ School of Pharmacy.

10.1021/bc700204k CCC: $37.00 © 2007 American Chemical Society
Published on Web 10/19/2007

avidin–biotin complex is insensitive to the ionic strength unless a very low ionic strength solution (<20 mM) is used (*11*). The ionic strengths of the solutions in the present study were kept higher than 100 mM.

Quantitative Fluorometric Assay for Binding Sites of Avidin with PEGylated Biotin. The stoichiometry of the binding between a PEGylated biotin and avidin was determined by a dye displacement assay, using 2,6-anilinonaphthalene sulfonate (2,6-ANS) as a fluorescent probe (*12*). Without biotin or biotinylated derivatives, the pseudoligand 2,6-ANS weakly binds to all four functional biotin binding sites on avidin, resulting in the strongly fluorescent 2,6-ANS–avidin complex. Introducing D-biotin or a PEGylated biotin displaces the bound 2,6-ANS from avidin, and the fluorescence decreases to the background fluorescence intensity at the equivalence point. The equivalence point defines the stoichiometry of D-biotin or PEGylated biotin per functional avidin tetramer. It provides a more definitive measure of the stoichiometry than measurements that rely on the magnitude of the fluorescence. D-Biotin solution was used as the primary standard to titrate the avidin solution. The avidin solution was then used as the secondary standard to titrate the unknown PEGylated biotin solution. During the titration, the standard D-biotin solution or the PEGylated biotin solution was added in increments into the 2 mL PBS buffer containing 0.5 nmol of avidin and 50 nmol of 2,6-ANS. After each addition, the fluorescence intensity was measured at 408 nm (slit, 10 nm) with excitation at 328 nm (slit, 10 nm) using a Shimadzu RF-1501 spectrofluorophotometer (Shimadzu, Tokyo 101-8448, Japan). A typical systematic titration took ~1.5 h. The PEGylated biotins in this work had molecular weights of 588, 3400, and 5000 g/mol.

Quantitative Absorbance Assay for Equilibrium Binding Constant of PEGylated Biotin with Avidin. The equilibrium association constant of a PEGylated biotin with avidin, K_a, was also determined by a dye displacement assay, using 2-(4′-hydroxyazobenzene)benzoic acid (HABA). HABA has a large association constant ($K_a' = 1.7 \times 10^5\ M^{-1}$) and competes effectively with PEGylated biotin for avidin (*13, 14*). Introduction of a PEGylated biotin to an avidin–HABA complex solution displaces HABA from avidin, and the absorbance at 500 nm (A_{500}) decreases because of the loss of the avidin–HABA complex. The avidin–complex is the only species that absorbs at 500 nm. Uncomplexed HABA has negligible absorption at 500 nm compared with that of the HABA–avidin complex, and its absorbance was removed by using the same concentration of HABA in PBS buffer as the reference during absorbance measurements.

We assumed that the four biotin-binding sites on avidin are equivalent and do not interact (*15*), so the equilibrium association constant K_a represents the binding of an avidin binding site with a PEGylated biotin. The relationship between A_{500} and the concentrations of PEGylated biotin (S), avidin binding site (P), HABA (I), and their complexes (SP and IP) is defined by the following equilibria and mass balance relationships:

$$S + P \leftrightarrow SP \qquad K_a$$

$$I + P \leftrightarrow IP \qquad K_a'$$

We make the following definitions: S_t, total concentration of PEGylated biotin; [*SP*], concentration of avidin (one binding site) PEGylated biotin complex; [*S*], concentration of the uncomplexed PEGylated biotin; I_t, total concentration of HABA; [*IP*], concentration of avidin (one binding site) HABA complex; [*I*], concentration of the uncomplexed HABA; P_t, total concentration of avidin binding site; [*P*], concentration of the uncomplexed avidin binding site.

At thermodynamic equilibrium,

$$K_a = \frac{[SP]}{[S][P]} \tag{1}$$

$$K_a' = \frac{[IP]}{[I][P]} \tag{2}$$

If S_t, P_t, and I_t represent the total concentrations, the mass balances relations are

$$S_t = [SP] + [S] \tag{3}$$

$$P_t = [P] + [SP] + [IP] \tag{4}$$

$$I_t = [IP] + (I) \tag{5}$$

When eqs 1–5 are combined, the following is obtained:

$$P_t = [P] + \frac{K_a[P]S_t}{1 + K_a[P]} + \frac{K_a'[P](I_t)}{1 + K_a'[P]} \tag{6}$$

The indicator ratio Q is defined as

$$Q = \frac{[I]}{[IP]} \tag{7}$$

where I_P is directly proportional to A_{500}. When eqs 6 and 7 are combined, the following equation results:

$$P_t = \frac{1}{QK_a'} + \frac{K_aS_t}{QK_a' + K_a} + \frac{I_t}{1 + Q} \tag{8}$$

We define the R factor as

$$R = P_t - \frac{1}{QK_a'} - \frac{I_t}{1 + Q} \tag{9}$$

Combining eqs 8 and 9, we obtain the following relationship:

$$\frac{S_t}{R} = \frac{K_a'}{K_a}Q + 1$$

In our experiments, the HABA–avidin solution was prepared by adding HABA and avidin into the PBS buffer. It was followed by the introduction of different amounts of PEGylated biotins (or iminobiotin). The concentrations of avidin and PEGylated biotin solutions were determined by the D-biotin standard titration 2,6-ANS method described above using the stoichiometries defined by the fluorescence assay. The HABA was weighed and quantitatively diluted to a known concentration. After the solution was allowed to reach equilibrium over 5 days, A_{500} was monitored for both the HABA–avidin solution and the HABA–avidin–biotin–PEG solutions. The solution with the same concentration of HABA in PBS buffer was used as the reference to subtract the absorbance from HABA in the sample. All values of A_{500} in the present paper are the absorbance average from at least 10 measurements using an Ultrospec 4000 UV/visible Spectro (Amersham Pharmacia Biotech, Piscataway, NJ) instrument.

Surface Plasmon Resonance (SPR) Measurements of the PEGylated Biotin Binding Constant with Streptavidin. SPR measurements were taken using a Biacore 2000 and the Biacore SA gold film sensor chip where streptavidin is immobilized on the gold surface (Biacore, NJ). Avidin sensor chips were not available. The analysis was performed by injecting the analyte solution so that it flowed over the modified surface of a gold film sensor chip from the instrument (*16*). Prior to use, the biosensor SA chips were preconditioned by applying three consecutive 1 min injections of 1.0 M NaCl in 50 mM NaOH with running PBS buffer at 20 μL/min. The flow rate was then adjusted to 10 μL/min, and 10 μL of ~10^{-6} M PEGylated biotin in PBS buffer was injected. SPR measurements were made using standard procedures (*16*).

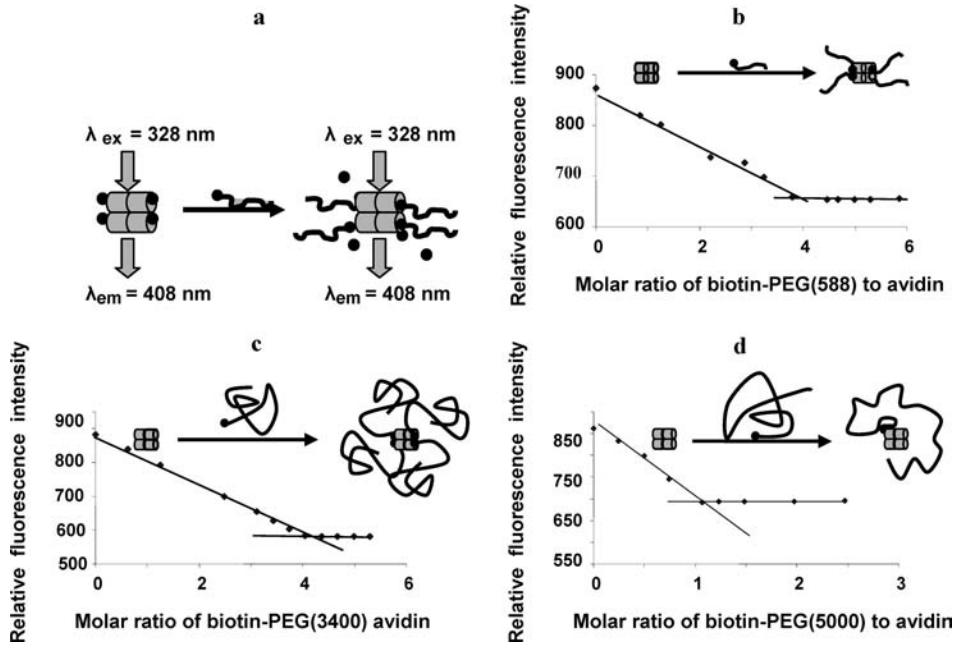


Figure 1. (a) 2,6-ANS fluorometric assay for measuring the avidin–biotin–PEG stoichiometry. The titration curves correspond to (b) biotin–PEG(588), (c) biotin–PEG(3400), and (d) biotin–PEG(5000) with avidin/2,6-ANS in PBS buffer (pH 7.4).

Previous research shows that the binding between avidin and a polymer with a biotin terminus is temperature-dependent (*17*). All the data in the present study were collected at 24 °C.

RESULTS

Stoichiometry of Avidin–Biotin–PEG Complex. Avidin has four binding sites for biotin, two each located at opposite sides of the tetrameric structure of avidin (*18, 19*). Figure 1 shows the 2,6-ANS fluorescence assay that defines the stoichiometry of PEGylated biotin with avidin. If we assume that the PEGylated biotin purity is 100%, the measured stoichiometries of biotin–PEG(588) and biotin–PEG(3400) with avidin are 4.09:1 and 4.56:1, respectively. However, the PEGylated biotin solutions have purities ranging from 80% to 98%. If we assume that the stoichiometry of the PEGylated biotin–avidin complexes is 4:1, the purity of biotin–PEG(588) and biotin–PEG(3400) is 98% and 88%. Similarly, the measured stoichiometry of biotin–PEG(5000) with avidin is 1.11:1, indicating that the stoichiometry is 1:1 and the biotin–PEG(5000) purity is 90%. These results demonstrate that PEGylated biotins of 588 and 3400 g/mol access all four sites on avidin. In contrast, PEGylated biotin of 5000 g/mol accesses only one site on avidin, presumably because of steric hindrance. It appears that at 5000 g/mol, PEGylated biotin bound on avidin sterically hinders the binding to both adjacent and oppositely located biotin binding sites on avidin.

Test Competitive Binding Method Using Small-Molecule Iminobiotin–Avidin System. To test our competitive binding method, we first applied it to the iminobiotin–avidin complex, a small molecule system where the binding between iminobiotin and avidin and its pH dependence has been systematically studied (*20*). PBS buffers with pH 9.0, pH 7.4, and pH 5.4 were chosen for this investigation, and the results are shown in Figure 2. The plot of S_t/R versus Q is linear as our method predicts. The determined K_d values are similar to those obtained by Green using a conventional radiation titration method (*20*).

Equilibrium Binding Constant of Avidin–Biotin–PEG Complex. This competitive binding method was then applied to the systems of avidin with three PEGylated biotins with molecular weights of 588, 3400, and 5000 g/mol, respectively. The analytical measurements of the avidin–biotin–PEG(3400) complex is shown in Table 1, and the determined binding constants are shown in Figure 3. For all three PEGylated biotins, a plot of S_t/R versus Q is linear, and K_a is $\sim 10^8$ M^{-1}, decreasing slightly with molecular weight (Table 2). The K_a of PEGylated biotin with avidin is similar to that of antibody–antigen interactions but much less than the value of biotin. However, the strength of interaction of PEGylated biotin with avidin is sufficient to consider use in pretargeting work.

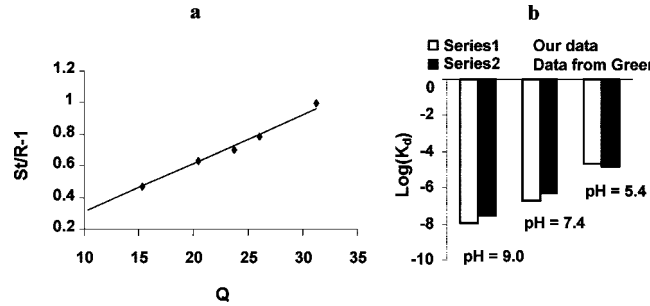


Figure 2. (a) Equilibrium association constant assay for iminobiotin with avidin in a PBS buffer (pH 7.4) and (b) comparison between values thus determined with those obtained by Green using a conventional titration method.

Equilibrium binding constants for the PEGylated biotins with streptavidin were calculated from SPR analysis using an SA sensor chip, and these results are shown in Table 2.

DISCUSSION

Concentration of HABA. To get a measurable change in the absorbance at 500 nm, it is necessary to control the concentration of HABA in order to make the binding of HABA and the binding of biotin–PEG (or iminobiotin) compatible. We controlled the binding ability of two ligands to lie within the range 10^{-2}–10^2 by adjusting the ratio of the concentrations of the two ligands. For example, the concentration of HABA in the biotin–PEG–avidin–HABA system was as high as 1.32×10^{-3} M in order to make HABA binding similar to the binding of biotin–PEG. In contrast, it was 1×10^{-5} M in the iminobiotin–avidin–HABA system with pH 5.42. In both cases, the avidin concentrations were $\sim 10^{-6}$ M.

Table 1. Measurement for Competitive Binding of Biotin–PEG(3400) with HABA Avidin at 24 °C[a]

C_{av} (M)	C_{S_t} (M)	S_t/av	A_{500}	A'_{500}	Q	$S_t/R - 1$	$(S_t/R - 1)/Q$
1.609×10^{-6}	4.887×10^{-7}	3.047×10^{-1}	0.3250	0.3035	2.215×10^{2}	2.942×10^{-1}	1.328×10^{-3}
1.609×10^{-6}	7.804×10^{-7}	4.876×10^{-1}	0.3250	0.2917	2.305×10^{2}	3.015×10^{-1}	1.308×10^{-3}
1.608×10^{-6}	9.742×10^{-7}	6.095×10^{-1}	0.3248	0.2840	2.368×10^{2}	3.089×10^{-1}	1.304×10^{-3}
1.608×10^{-6}	1.470×10^{-6}	9.142×10^{-1}	0.3248	0.2669	2.521×10^{2}	3.113×10^{-1}	1.235×10^{-3}
1.608×10^{-6}	1.959×10^{-6}	1.219×10^{0}	0.3248	0.2503	2.688×10^{2}	3.520×10^{-1}	1.309×10^{-3}
1.607×10^{-6}	2.936×10^{-6}	1.828×10^{0}	0.3245	0.2176	3.094×10^{2}	4.015×10^{-1}	1.298×10^{-3}
1.606×10^{-6}	4.887×10^{-6}	3.047×10^{0}	0.3244	0.1670	4.034×10^{2}	5.800×10^{-1}	1.438×10^{-3}
1.604×10^{-6}	7.804×10^{-6}	4.876×10^{0}	0.3240	0.1096	6.152×10^{2}	8.483×10^{-1}	1.379×10^{-3}

[a] C_{av}, concentration of avidin; C_{S_t}, concentration of biotin–PEG(3400); S_t/av, molar ratio of biotin–PEG(3400) vs avidin; A_{500}, absorbance of avidin–HABA without biotin–PEG(3400) at 500 nm; A'_{500}, absorbance of avidin–HABA with biotin–PEG(3400) at 500 nm.

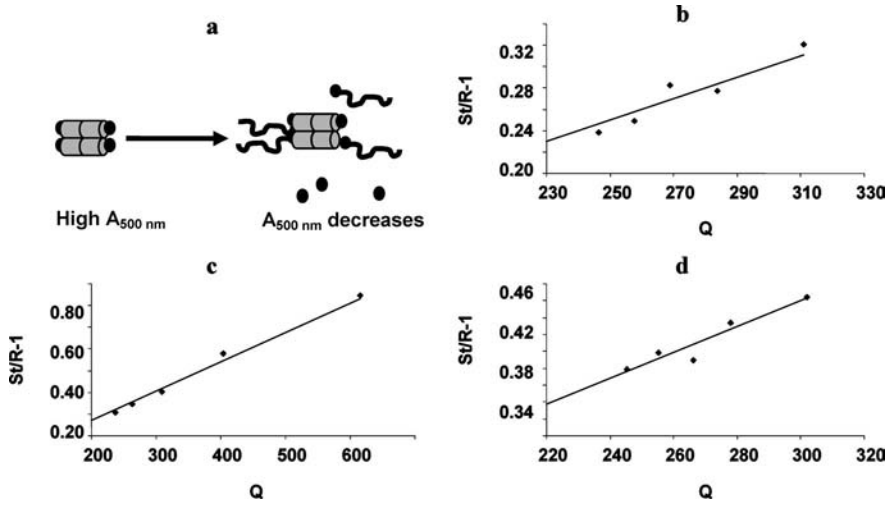


Figure 3. (a) HABA absorbance assay for equilibrium association constant of avidin–biotin–PEG complex and the equilibrium association constant assay curves for (b) biotin–PEG(588), (c) biotin–PEG(3400), and (d) biotin–PEG(5000) with avidin at PBS buffer (pH 7.4).

Table 2. Stoichiometry and Equilibrium Association Constant of PEGylated Biotin with Avidin[a]

	Flory radius R_F (Å)	stoichiometry with avidin	K_a (competitive binding) (M^{-1})	K_a (SPR) (M^{-1})
biotin–PEG(588)	17	4:1	1.7×10^{8}	3.0×10^{8}
biotin–PEG(3400)	48	4:1	1.3×10^{8}	2.6×10^{8}
biotin–PEG(5000)	60	1:1	1.1×10^{8}	1.8×10^{8}

[a] R_F, Flory radius, obtained by using $R_F = aN^{0.6}$, with a (the persistence length of PEG) = 3.5 Å and N = number of ethylene glycol monomer unit in polymer (*37*).

Competitive Binding for Avidin and PEGylated Biotin Complex. The method we presented here relies on the changes of the absorption of the avidin–HABA complex when the protein undergoes competitive binding with biotin–PEG. The advantages of this solution-based method are (1) eliminating the complexity and instability from the attached label groups, (2) rapidly screening the binding ability of the biotinylated derivatives with avidin without requiring expensive instrumentation, and (3) approximating real physiological conditions (*21–23*). To accurately estimate the binding equivalency of a competing PEGylated biotin, it is important that equilibrium is achieved for both competing ligands. The time required to achieve equilibrium binding is a function of the dissociation rate constant of the slower dissociating ligand. Since PEGylated biotin has a higher affinity for avidin than HABA, we assumed that an equilibration time equal to 5 times the half-life of its dissociation is adequate. Gruber reported that the half-life time of 1:3 complex is 10 h for avidin–biotin–PEG(800 and 1900) conjugate complexes (*10*). In our case, full binding of avidin with either HABA or biotin–PEG only resulted in the 1:4 complex, which dissociates more quickly than the 1:3 complex. Considering the stability of avidin (*24*) and the weaker steric blocking effects of HABA compared with PEG, we chose a 5 day equilibration period. This result is reinforced because the same results were observed for a 3 day equilibration period, so it is clear that equilibrium was reached.

Avidin has four binding sites for biotin. We assumed that the four biotin-binding sites on an avidin are almost equivalent or do not interact for the avidin–biotin–PEG(3400) or biotin–PEG(588) complexes (*10*). This assumption is based on the values of $(S_t/R - 1)/Q$ in Table 1, which is constant around 1.35×10^{-3} against the molar ratio of biotin–PEG(3400)/avidin-binding-site of 0.076–1.22 (*25*). Simulations show that differences in the binding constants for the 1:1, 1:2, 1:3, and 1:4 avidin–biotin–PEG complexes change the shape of the curve in Figure 3 and the $(S_t/R - 1)/Q$ values are no longer constant. For the avidin–biotin–PEG(5000) complex, the stoichiometry is defined and there is only a single equilibrium binding constant corresponding to its 1:1 avidin complex.

The Biacore surface plasmon resonance (SPR) based biosensor is used extensively to measure the binding constants for macromolecular interactions (*26, 27*). To check our solution-based competitive binding measurements, we attempted to obtain the equilibrium binding constants of the avidin–biotin–PEG complexes on a Biacore 2000. Since avidin chips were not available through Biacore, we used the SA sensor chip, where streptavidin (SA) is immobilized on the surface. Like avidin, streptavidin also has a high affinity with biotin ($K_d = 10^{-14}$ M) that makes it difficult to regenerate the SA chip surface (*3*). Therefore, our chips were used once, and we have only a single SPR value for K_a. The binding constants determined from the SPR Biacore are similar to those determined by the solution-based competitive binding method (see Table 2). Except for the variation between avidin and streptavidin, this difference also reflects a variety of potential artifacts in surface-based measurements that may create differences between SPR bio-

sensor-based and solution-based measurements (*28, 29*). The data from our solution-based method have been used for further study.

Effects of PEG on Binding Sites of Avidin. The use of PEG as a spacer has been reported to create a high affinity of biotin derivatives with avidin because PEG reduces the steric interaction of all interconnected elements and relieves any nonspecific binding of attached functional groups. More importantly, it is hypothesized that any PEG can be used and the longer PEG chains are advantageous if steric hindrance is not reduced by 7–27 atom spacers (*30–33*). Beyond these broad considerations, it is still not clear whether using the PEG chain as a spacer would block the biotin terminus from binding to avidin/streptavidin. The decreased affinity of PEGylated biotin with avidin in the present study is ascribed to steric hindrance because the bound PEG chain prevents a close approach of biotin to the binding sites of avidin. Nevertheless, the $\sim 10^8$ M^{-1} affinity is still strong enough for a PEG to function as an effective spacer or linker. However, for applications where two binding sites are required, the 1:1 stoichiometry of the avidin–biotin–PEG(5000) complex shows that the PEG(5000) chain is not an effective spacer, since the PEG(5000) chain can block the biotin binding sites on avidin. This blocking may occur because the secondary biotin–PEG(5000) cannot bind an avidin molecule firmly enough to displace 2,6-ANS during the titration. However, biotin–PEG(3400) binds all four sites on avidin and indicates that the subsequent equilibrium association constant of PEGylated biotin is much higher than that of 2,6-ANS (about 10^3 M^{-1}) (*34*). Although PEG–PEG repulsion could allow the exploitation of only one site per pair at opposite sides of the tetrameric structure of avidin, the result from the 1:1 stoichiometry of the avidin–biotin–PEG(5000) complex demonstrates that at 5000 g/mol, PEGylated biotin hinders the binding to not only adjacent but also oppositely located biotin binding sites on avidin. It seems appropriate to speculate that a bound and heavily hydrated PEG chain can surround the avidin and effectively block all other binding sites. If so, the lengths of PEG chains play an important role in such blocking (*35, 36*). The Flory radius of PEG in the bulk solution indicates that 588, 3400, and 5000 Da PEGs occupy spheres with radius of 17, 48, and 60 Å, respectively (*37*), while avidin has dimensions of approximately 56 Å × 50 Å × 40 Å (*38*). Our study shows that biotin–PEG(3400) and biotin–PEG(588) bind to avidin with the same 4:1 ratio as D-biotin. Biotin–NH–PEG1900–$NH_3^+Cl^-$ and biotin–PEG1900–PDP also bind avidin with a 4:1 stoichiometry (*19*). However, in the case of biotin–PEG(5000), even with the preferential exclusion between PEG and avidin (*39*), biotin–PEG(5000) can quickly envelop the avidin after first binding by the biotin terminus and can block further binding of biotin–PEG(5000) by PEG–PEG steric repulsion. Further study on the stoichiometry of avidin and PEGylated biotin with molecular weights varying from 3400 to 5000 Da may lead to a PEG chain that allows the formation of 1:2 avidin–biotin–PEG complex as well.

CONCLUSIONS

The solution-based competitive binding method was successfully applied to the HABA–avidin–biotin–PEG system and used to measure the equilibrium binding constant of PEGylated biotin with avidin. The equilibrium association constants of PEGylated biotin (588, 3400, and 5000 g/mol) are on the order of 10^8 M^{-1} and vary slightly with molecular weight of PEG. The stoichiometries of PEGylated biotins with avidin are 4:1 for 588 and 3400 g/mol PEG and 1:1 for 5000 g/mol PEG. The results demonstrate that the equilibrium binding constant and the stoichiometry of the avidin–biotin–PEG complex system can be adjusted by varying the lengths of PEG chains. Another essential point in the present study is that a long PEG chain could block further binding of biotin-PEGylated derivatives with avidin. On the basis of the binding constant and stoichiometry, the avidin–biotin–PEG complex and their analogues have potential as carriers for pretargeting drug delivery. For example, ref 4 describes how biotin or biotin derivatives can be conjugated with many possible therapeutic molecules, including small molecules, DNA, and larger proteins. We have conjugated bovine carboxypeptidase A (CPA) with biotin–PEG–NHS and obtained a novel and reversible avidin–biotin–PEG–CPA complex system with potential as a therapeutic protein delivery system for solid tumor prodrug targeting (*40*).

ACKNOWLEDGMENT

We thank Dr. McClain for his assistance in the fluorometric assay for the stoichiometry quantitative evaluation and helpful discussion of the paper.

LITERATURE CITED

(1) Ton, G. N., Weichert, J. P., Longino, M. A., and et al. (2005) Methoxypoly(ethylene glycol)-conjugated carboxypeptidase A for solid tumor targeting. Part II: Pharmacokinetics and iodistribution in normal and tumor-bearing rodents. *J. Controlled Release 104*, 155–166.

(2) Maedaa, H., Wua, J., Sawaa, T., Matsumurab, Y., and Horic, K. (2000) Tumor vascular permeability and the EPR effect in macromolecular therapeutics: a review. *J. Controlled Release 65*, 271–284.

(3) Wilchek, M., and Bayer, E. A. (1990) In *Avidin–Biotin Technology* (Wilchek, M., and Bayer, E. A. , Eds.) Methods in Enzymology, Vol. 184, Academic Press, San Diego, CA.

(4) Diamandis, E. P., and Christopoulos, T. K. (1991) The biotin–(strept) avidin system: principles and applications in biotechnology. *Clin. Chem. 37*, 625–636.

(5) Schechter, B., Arnon, R., Wilchek, M., Schlessinger, J., Hurwitz, E., Aboud-Pirak, E., and Sela, M. (1991) Indirect immunotargeting of cis-Pt to humanepidermoid carcinoma KB using the avidin biotin system. *Int. J. Cancer. 48*, 167–172.

(6) Marshall, D., Pendey, R. B., Melton, R. G., Boden, J. A., Boden, R., and Begent, R. H. G. (1995) Galactosylated streptavidin for improved clearance of biotinylated intact and F(ab′)2 fragments of an anti tumor antibody. *Br. J. Cancer 71*, 18–24.

(7) Kassis, A. I., Jones, P. L., Matalka, K. Z., and Adelstein, S. J. (1996) Antibody-dependent signal amplification in tumor xenografts after pretreatment with biotinylated monoclonal antibody and avidin or streptavidin. *J. Nucl. Med. 37*, 343–352.

(8) Yuji, I., Ayako, M., Yoh, K., and Hiroyuki, N. (1990) Review: polyethylene glycol(PEG)–protein conjugates: application to biomedical and biotechnological processes. *J. Bioact. Compat. Polym. 5*, 343–364.

(9) Veronese, F. M. (2001) Peptide and protein PEGylation: a review of problems and solutions. *Biomaterials 22*, 405–417.

(10) Kaiser, K., Marek, M., Haselgruebler, T., Schindler, H., and Gruber, H. J. (1997) Basic studies on heterobifunctional biotin–PEG conjugates with a 3-(4-pyridyldithio)propionyl marker on the second terminus. *Bioconjugate Chem. 8*, 545–551.

(11) Wei, R., and Wright, L. D. (1964) Heat stability of avidin and avidin–biotin complex and influence of ionic strength on affinity of avidin for biotin. *Proc. Soc. Exp. Biol. Med. 117*, 341–344.

(12) Mock, D. M., and Horowitz, P. (1990) Fluorometric assay for avidin–biotin interaction. *Methods Enzymol. 184*, 234–240.

(13) Green, N. M. (1970) Spectrophotometric determination of avidin and biotin. *Methods. Enzymol. 18A*, 418–422.

(14) Green, N. M. (1965) A spectrophotometric assay for avidin and biotin based on binding of dyes by avidin. *Biochem. J. 94*, 23–24.

(15) Green, N. M. (1975) Avidin. *Adv. Protein Chem. 29*, 85–133.

(16) Boozer, C., Kim, G., Cong, S., Guan, H., and Londergan, T. (2006) Looking towards label-free biomolecular interaction analysis in a high throughput format: a review of new surface plasmon resonance technologies. *Curr. Opin. Biotechnol. 17*, 400–405.

(17) Ding, Z., Shimoboji, T., Stayton, P. S., and Hoffman, A. S. (2001) A smart polymer shield that controls the binding of different size biotinylated proteins to streptavidin. *Nature 411*, 59–62.

(18) Finn, F. M., Titus, G., Montibeller, J. A., and Hofmann, K. (1980) Hormone-receptor studies with avidin and biotinylinsulin–avidin complexes. *J. Biol. Chem. 255*, 5742–5746.

(19) Green, N. M., Konieczny, L., Toms, E. J., and Valentine, R. C. (1971) The use of bifunctional biotinyl compounds to determine the arrangement of subunits in avidin. *Biochem. J. 25*, 781–791.

(20) Green, N. M. (1966) Thermodynamics of the binding of biotin and some analogues by avidin. *Biochem. J. 101*, 774–778.

(21) Taylor, I. A., and Kneale, G. C. (2001) A competition assay for DNA binding using the fluorescent probe ANS. *Methods Mol. Biol. 148*, 265–274.

(22) Bradfield, C. A., and Poland, A. A. (1988) Competitive binding assay for 2,3,7,8-tetrachlorodibenzo-*p*-dioxin and related ligands of the Ah receptor. *Mol. Pharmacol. 34*, 682–688.

(23) Motulsky, H. J., and Mahan, L. C. (1984) The kinetics of competitive radioligand binding predicted by the law of mass action. *Mol. Pharmacol. 25*, 1–9.

(24) Gyorgy, P., Rose, C. S., and Tomarelli, R. (1942) Investigations on the stability of avidin. *J. Biol. Chem. 144*, 169–173.

(25) Sinha, B. K., and Chignell, C. F. (1979) The synthesis and use of spin-labeled analogs of biotin in the study of avidin. *Methods Enzymol. 62*, 295–308.

(26) He, J., Liu, X., Zhang, S., Liu, G., and Hnatowich, D. J. (2005) Affinity enhancement bivalent morpholinos for pretargeting: surface plasmon resonance studies of molecular dimensions. *Bioconjugate Chem. 16*, 1098–1104.

(27) Pattnaik, P. (2005) Surface plasmon resonance: applications in understanding receptor–ligand interaction. *Appl. Biochem. Biotechnol. 126*, 79–92.

(28) Myszka, D. G. (1997) Kinetic analysis of macromolecular interactions using surface plasmon resonance biosensors. *Curr. Opin. Biotechnol. 8*, 50–57.

(29) O'Shannessy, D. J., and Winzor, D. J. (1996) Interpretation of deviations from pseudo-first-order kinetic behavior in the characterization of ligand binding by biosensor technology. *Anal. Biochem. 236*, 275–283.

(30) Lim, K., and Herron, J. N. (1992) Molecular simulation of protein–PEG interaction. In *Poly(ethylene glycol) Chemistry: Biotechnical and Biomedical Applications* (Harris, J. M., Ed.) pp 29–56, Plenum Press, New York.

(31) Finn, F. M., Titus, G., and Hofmann, K. (1984) Ligands for insulin receptor isolation. *Biochemistry 23*, 2554–2558.

(32) Hofmeier, H., Pahnke, J., Weidl, C. H., and Schubert, U. S. (2004) Combined biotin–terpyridine systems: a new versatile bridge between biology, polymer science and metallo-supramolecular chemistry. *Biomacromolecules 5*, 2055–2064.

(33) Marek, M., Kaiser, K., and Gruber, H. J. (1997) Biotin–pyrene conjugates with poly(ethylene glycol) spacers are convenient fluorescent probes for avidin and streptavidin. *Bioconjugate Chem. 8*, 560–566.

(34) Mock, D. M., Lankford, G., and Horowitz, P. (1988) A study of the interaction of avidin with 2-anilinonaphthalene-6-sulfonic acid as a probe of the biotin binding site. *Biochim. Biophys. Acta 956*, 23–29.

(35) Kaasgaard, T., Mouritsen, Ole, G., and Jorgensen, K. (2001) Screening effect of PEG on avidin binding to liposome surface receptors. *Int. J. Pharm. 214*, 63–65.

(36) Noppl-Simson, D. A., and Needham, D. (1996) Avidin–biotin interactions at vesicle surfaces: adsorption and binding, cross-bridge formation, and lateral interactions. *Biophys. J. 70*, 1391–1401.

(37) Jeppesen, C., Wong, J. Y., Kuhl, T. L., Israelachvili, J. N., Mullah, N., and Marques, C. M. (2001) Impact of polymer tether length on multiple ligand–receptor bond formation. *Science 293*, 465–468.

(38) Pugliese, L., Coda, A., Malcovati, M., and Bolognesi, M. (1993) Three-dimensional structure of the tetragonal crystal from egg-white avidin in its functional complex with biotin at 2.7 Å resolution. *J. Mol. Biol. 231*, 698–710.

(39) Kerwin, B. A., Chang, B. S., Gegg, C. V., Gonnell, M., Li, T., and Strambini, G. B. (2002) Interactions between PEG and type I soluble tumor necrosis factor receptor: modulation by pH and by PEGylation at the N terminus. *Protein Sci. 11*, 1825–1833.

(40) Ke, S., Wright, J. C., and Kwon, G. S. Avidin–biotin–PEG–CPA complexes as potential EPR directed therapeutic protein carriers: preparation and characterization. *Bioconjugate Chem.*, in press.

BC700204K

Conjugation to Increase Treatment Volume during Local Therapy: A Case Study with PEGylated Camptothecin

Kraig Haverstick,[†] Alison Fleming,[‡] and W. Mark Saltzman*[,‡]

Department of Chemical and Biomolecular Engineering, Cornell University, and Department of Biomedical Engineering, Yale University. Received June 16, 2007

Controlled release of chemotherapy drugs from polymer implants placed directly at the tumor site is a proven method for treatment of cancers of the brain. Although this method provides high doses of drug at the tumor site, the drug does not penetrate far enough into the brain for optimum treatment in most cases. Rapid drug elimination leads to more than a 10-fold drop in concentration within 2 mm of the implant. Conjugation to water-soluble polymers, such as poly(ethylene glycol) (PEG) or dextran, has the potential to increase drug distribution in the brain. We have recently PEGylated the chemotherapy drug camptothecin and found a large increase in the extent of distribution of camptothecin in the rat brain, but most of the drug in tissue was in the less-active conjugated form. Stability of the conjugation bond, activity of the drug–polymer conjugate, solubility of the conjugate relative to the drug, and molecular weight of the polymer must all be considered in the design of a conjugate to maximize drug distribution. Therefore, to optimize the PEGylated system, we have developed a pharmacokinetic model to determine the relative importance of parameters involved in the distribution of drug–polymer conjugates after release from a polymer implant. Our modeling shows that PEGylation has the potential to increase treatment distances to more than a centimeter, which may be sufficient to prevent the recurrence of human brain tumors.

INTRODUCTION

Drug–polymer conjugation is a promising approach for improving systemic and targeted drug delivery. Systemic delivery of camptothecin, an antitumor, topoisomerase I inhibiting drug, has been enhanced by conjugation to dextran (*1*), poly(2-hydroxypropyl) methacrylamide (*2*, *3*), and poly(ethylene glycol) (*4*). Conjugation extends circulation time in the bloodstream, and additional attachment of protease-specific sequences can target release of the free drug. Recently, we have shown that conjugation of camptothecin to PEG can dramatically improve solubility and penetration through tissue (*5*).

Drug delivery to the brain faces challenges not present for delivery to other parts of the body. The blood–brain barrier limits systemic delivery of most drugs (*6*). Local administration by direct injection or controlled-release implantation overcomes this obstacle, but since diffusion becomes the primary means of distribution in the brain, the drug moves slowly from the initial injection or implantation site (*7*). The treatment volume is limited by rapid drug elimination, primarily through capillaries for small, hydrophobic molecules, relative to the rate of diffusion.

The pharmacokinetics of a number of therapeutic drugs in the brain has been studied with the general result being that rapid elimination quickly produces a steady-state profile, where drug concentration decreases sharply with distance from the implant site: the extent of penetration—or the characteristic distance for the drop in concentration—depends on the rate of diffusion of drug in the brain and the rate of elimination (for a review of this literature, see (*8*)). Diffusion and elimination properties in brain tissue have previously been reported for a variety of compounds, including our recent measurements for camptothecin (*5*). These drugs have low molecular weights (below 500, except for paclitaxel), and are fairly hydrophobic (except sucrose), making them susceptible to rapid elimination through capillaries. The dimensionless coefficient, ϕ, analogous to the Thiele modulus in reaction catalysis (*9*), has been previously defined as

$$\varphi = a\sqrt{\frac{k}{D}} \tag{1}$$

where a is the radius of porous catalyst particles, k is the first-order reaction rate, and D is the rate of diffusion of reactant in the catalyst pores. For low values of ϕ, reactant penetrates throughout the catalyst, and reaction efficiency is high; for high values of ϕ, reactant does not penetrate, and the reaction efficiency is low.

This same coefficient can be used to predict the extent of penetration in the brain; in this case, a is the characteristic implant length, k is the first-order rate of elimination in the brain, and D is the effective diffusion coefficient in the brain (*7*). For most drugs, the value for ϕ is greater than 1 (see (*8*)).

Previous modeling results, which assume the presence of only diffusion and first-order elimination, predict that ϕ values in this range lead to a distribution where the drug does not penetrate very far from the surface of a spherical implant. Figure 1 illustrates the steady-state concentration profile of drug around a spherical implant. As ϕ decreases, drug distribution improves, but for ϕ greater than 1, drug concentrations decrease by an order of magnitude within 2 mm of the implant. To improve the distribution of a particular drug, its ϕ value in the brain must be reduced. Since the rate of diffusion cannot be increased, it is necessary to find a way to slow the rate of drug elimination. This can be accomplished by attachment of a polymer. Another factor working against many drugs is their low solubility in water; conjugation to a water-soluble polymer has an additional advantage, since it can significantly increase the maximum achievable concentration of a poorly soluble drug in the brain.

Although elimination is not solely driven by molecular size, larger molecules tend to be retained in the brain for longer

* Address correspondence to Professor W. Mark Saltzman, Department of Biomedical Engineering, P.O. Box 208260, Yale University, New Haven, CT 06520, E-mail:mark.saltzman@yale.edu, Phone: 203-432-4262, Fax:203-432-0030.

[†] Cornell University.

[‡] Yale University.

10.1021/bc700214h CCC: $37.00 © 2007 American Chemical Society
Published on Web 10/13/2007

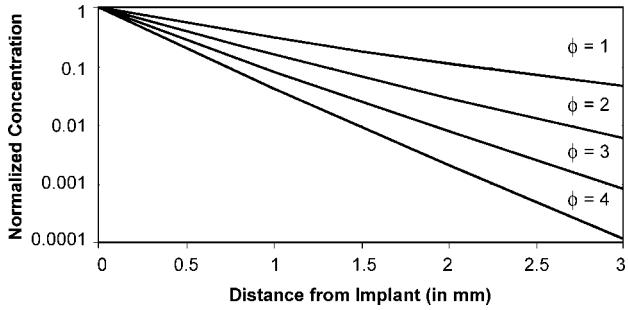


Figure 1. Steady state profiles of drug concentration as a function of distance from the implant.

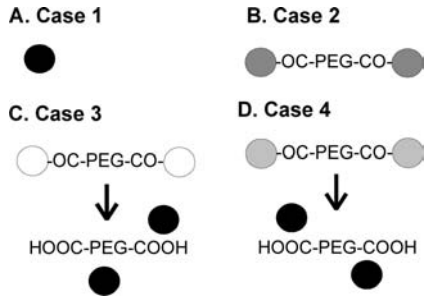


Figure 2. Drug delivery systems. (A) Drug is released in its free state. (B) Moderate-activity conjugate is released and remains in its conjugated form. (C) Inactive conjugate is released, and drug is fully active after hydrolysis. (D) Low-activity conjugate is released, and drug is fully active after hydrolysis. Circles represent drug with shading indicative of the degree of activity.

periods of time. While most drugs have half-lives in the ranges of minutes, larger polymers such as dextran are retained with half-lives of 15 h or more (*10*). Since poly(ethylene glycol) is known for its biocompatibility and its ability to solubilize hydrophobic molecules in water, we believe that PEG–drug conjugates show great potential for improving the brain distribution of drug released from controlled-release polymers.

Since the ultimate goal in improving the distribution of chemotherapy drug is to increase the volume of tissue treated, the potency of the drug must also be considered. The form of the drug is often critical to its potency. When paclitaxel, methotrexate, and doxorubicin were permanently modified with PEG, the toxicity of the conjugates was found to be lower than the toxicity of the free drugs by a factor of 50 to 1000 (*11*). Therefore, as drug–polymer conjugates are evaluated, the toxicity of the conjugate in comparison to the free drug must also be considered in order to determine the relative value of conjugation.

Finally, the time of exposure can be just as important as the level of exposure in the treatment of tumors. A low dose of drug over a long period of time can be more effective than a high dose for a short period for certain kinds of agents. Use of a controlled release implant can provide low levels of chemotherapy drug for periods of weeks or longer. Since conjugation of drug to a polymer will reduce the rate of elimination, residence time in the brain will increase, and dosing with conjugates over a longer time course may be possible.

We have investigated three different types of model drug–polymer systems to compare to a free drug system (Figure 2). In the first case, we looked at release of drug alone as a basis for comparison with conjugates. In the second case, the drug is attached permanently to the diffusable polymer, but the potency of the drug is reduced in conjugated form. In the third case, the drug is coupled by an ester bond, which hydrolyzes under physiological conditions with a half-life of 1 to 3 days. While the drug is attached to the polymer, it is not active. After

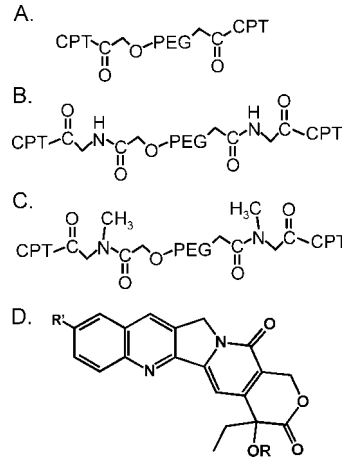


Figure 3. Camptothecin–poly(ethylene glycol) drug–polymer conjugates. (A) PEG-CPT. (B) PEG-Gly CPT. (C) PEG-Sar-CPT. (D) R = R′ = H, Camptothecin: Drug is conjugated at the R site to PEG. R′ = OH, 10-hydroxycamptothecin: Drug is conjugated at the R′ site to PEG.

hydrolysis, the free drug is released and biologically active. Therefore, we initially implant an inactive species, which travels away from the implant site, becomes hydrolyzed in water, and releases the free drug in its active form. In the final case, the drug–polymer conjugate is active but at a lower level than the free drug, and the bond can be hydrolyzed to release the free drug. Each of these systems has the potential to improve distribution of active drug in the brain; our goal in this present study was to determine essential characteristics of PEGylated camptothecin and to model each of these cases to determine which system would be more effective.

EXPERIMENTAL SECTION

Materials. Carboxymethyl poly(ethylene glycol), molecular weight 3400, was purchased from Shearwater Polymers. 10-hydroxycamptothecin was purchased from NetQem. All other reagents and solvents were acquired from Aldrich Chemical Company.

Methods. *Synthesis of Poly(ethylene glycol)–Camptothecin Conjugates.* These procedures were modified from previously published protocols (*12*), as described completely earlier (*5*). The structures of these conjugates appear in Figure 3, and their physical properties are listed in Table 1.

Determination of Solubility. For CPT, excess CPT was added to a PBS solution (pH 7.4). The container was sealed and placed at 37 °C overnight. The UV absorbance of the solution at 369 nm was measured and compared to a calibration curve for CPT to determine the saturated concentration. A Hitachi U-2001 spectrophotometer was used for all UV measurements. For conjugates, approximately 10 mg of conjugate was weighed in a vial. PBS was added in 10 μL increments until all conjugate was dissolved.

Determination of Hydrolysis Rate. Conjugate was weighed and dissolved at a concentration of 9 mg/L in phosphate-buffered saline at 37 °C. The solution was capped and stored in a 37 °C shaker. At increasing intervals of 1 h to a half-day, a 1 mL sample was taken for HPLC analysis. A Waters 2690 Separation module with photodiode array detector was used with a Zorbax 300SB-CN column. A 10 μL volume was injected into a solvent gradient of 80:0:20 to 40:40:20 (water/acetonitrile/0.5% TFA in water) over 20 min to elute the free camptothecin in 12.9 min. The areas under the absorbance curve at 254 nm, 354 nm, and 369 nm were compared to a calibration curve from injected known concentrations of camptothecin to determine the concentration of free camptothecin in the sample. Concentrations

Table 1. Model Parameters from Drug-Polymer Conjugates[a]

drug form	solubility (mg/L)	IC_{50}, 72 h (μg/L)	k_h (h^{-1})	k_e (h^{-1})	D (mm^2/hr)	ϕ (a = 1.5 mm)
Camptothecin	27.5	12.9	N/A	1.28	0.282	3.20
PEG3400-CPT	>1000	ND	0.018	0.017	0.14	0.75
PEG3400-Gly CPT	>1000	ND	0.012	0.017	0.14	0.68
PEG3400-Sar-CPT	>1000	ND	0.0085	0.017	0.14	0.64

[a] ND = not determined. N/A = not applicable.

were plotted versus time and fitted to a first-order curve to determine the hydrolysis rate and initial loading of CPT.

Determination of IC_{50} Values. IC_{50} values were determined for free CPT, PEG3400-Sar-CPT, and PEG3400-Gly CPT using rat 9L glioma cells. Values were based on different exposure times in culture. Experiments were repeated four times for each condition. Conjugates showed activity that was time-delayed by the hydrolysis required to produce active free drug.

Determination of Elimination Rate. Elimination rate was assumed to be first-order. For camptothecin, the elimination rate was determined in rat brains by measuring the total amount of CPT released from a biodegradable polymer implant and remaining in the brain at various time points after implantation. Elimination of PEG4000 and PEG900 has been previously studied in the rat brain (*13*). We have estimated the conjugate elimination rate in a human brain based on these rat data. The overall rate of 1.5×10^{-5} s^{-1} includes 0.2×10^{-5} s^{-1} across the blood–brain barrier and 1.3×10^{-5} s^{-1} from elimination at structural boundaries. Since the length scale of the human brain is ten times that of the rat brain, we estimated conservatively a boundary rate 1/5 the rate in the rat. This gives a total human elimination rate of $(0.2 + 0.26) \times 10^{-5}$ s^{-1} or 0.017 h^{-1}, which we have used in our modeling.

Determination of Effective Diffusion Coefficient. Diffusion coefficients in the brain were calculated empirically using the Wilke–Chang equation (*14*) and multiplying by 0.4 to account for tortuosity in the brain (*7*).Brain diffusion coefficients were also determined experimentally in a previous report (*5*). For CPT, this experimentally determined diffusion coefficient (0.282 mm^2/h) was significantly lower than what we empirically calculated (0.825 mm^2/h) both from Wilke–Chang and from molecules of comparable molecular weights (*15*). Lower-than-expected experimental diffusion coefficients have been reported for other small molecules such as paclitaxel (*16*) and fluorescein (*10*). Experimental PEG3400 conjugate diffusion coefficients (0.14 mm^2/h) in rat brains, assuming an elimination rate of 1.5×10^{-5} s^{-1}, were also found to be lower than expected for PEG based on Wilke–Chang and aqueous experimental values (*17*) (0.18 mm^2/h) for equivalent PEG molecular weight. We have chosen to use the more conservative experimentally determined values.

Model. To predict the effect of different conjugate parameters on distribution of drug in the brain, we have modified a previously established model (*7*) to estimate the treatment volume surrounding a conjugate-loaded polymer implant. This model assumes that drug moves only by simple diffusion and is removed by first-order elimination. Treatment distance and volume will be defined as the brain space, which receives an IC_{50} concentration of chemotherapy drug for 72 h. Treatment distance is measured from the surface of the implant, which is assumed to be stationary and to maintain a constant conjugate concentration. Since drug–polymer conjugates in cases 3 and 4 can be hydrolyzed to release free drug, the model is designed to monitor the distribution of both conjugate and free drug.

For the conjugate, the governing equation in spherical coordinates for distribution after release from a sphere is

$$\frac{\partial C_c}{\partial t} = D_c\left(\frac{\partial^2 C_c}{\partial r^2} + \frac{2}{r}\frac{\partial C_c}{\partial r}\right) - (k_{e,c} + k_h)C_c \qquad (2)$$

and for the free drug, when it is generated only by hydrolysis of the conjugate

$$\frac{\partial C_d}{\partial t} = D_d\left(\frac{\partial^2 C_d}{\partial r^2} + \frac{2}{r}\frac{\partial C_d}{\partial r}\right) + k_h C_c - k_{e,d}C_d \qquad (3)$$

where C_c = concentration of the conjugate; C_d = concentration of the free drug; D_c = effective diffusion coefficient of the conjugate; D_d = effective diffusion coefficient of the drug; $k_{e,c}$ = elimination rate of the conjugate; $k_{e,d}$ = elimination rate of the drug; k_h = hydrolysis rate of the conjugate; t = time; r = radial distance from the center of the implant.

These equations were implemented with the following initial and boundary conditions: When $t = 0$, $C = 0$ for all $r > a$. When $t > 0$, $C \rightarrow 0$ as $r \rightarrow \infty$.

For the conjugate: When $t > 0$, $C = C_0$ at $r = \infty$.

For the free drug: When $t > 0$, $\partial C / \partial r = 0$ at $r = a$ where a is the radius of the implant.

When we are simply releasing free drug or stable drug-polymer conjugate from a polymer, the governing equation is

$$\frac{\partial C_d}{\partial t} = D_d\left(\frac{\partial^2 C_d}{\partial r^2} + \frac{2}{r}\frac{\partial C_d}{\partial r}\right) - k_{e,d}C_d \qquad (4)$$

where the same boundary conditions are applied as for eq 2 for the hydrolyzing conjugate.

The transient solution to eqs 2 and 4 has been obtained and published previously

$$\frac{C}{C_0} = \frac{a}{2r}\left\{\exp\left[-(r-a)\sqrt{\frac{k}{D}}\right]\left[1 - \mathrm{erf}\left(\frac{r-a}{2\sqrt{Dt}} - \sqrt{kt}\right)\right] + \exp\left[(r-a)\sqrt{\frac{k}{D}}\right]\left[1 - \mathrm{erf}\left(\frac{r-a}{2\sqrt{Dt}} + \sqrt{kt}\right)\right]\right\} \qquad (5)$$

where $k = k_{e,c} + k_h$ for the released conjugate and $k = k_{e,d}$ for the released drug (*18*). Therefore, in both of these cases we can easily calculate the distribution of the released material at a given time.

Since eq 3 is coupled to eq 2 by a conjugate concentration term, hydrolyzed drug distribution cannot be determined explicitly. We have used two different approximations to calculate the distribution of drug that has been hydrolyzed from the conjugate. For one approximation, the drug does not diffuse after hydrolysis and goes to steady state. Therefore, eq 3 reduces to

$$\frac{\partial C_d}{\partial t} = k_h C_c - k_{e,d}C_d = 0 \qquad (3a)$$

A second way to simplify eq (3 is to assume that the drug does diffuse and goes rapidly to steady state, or

$$0 = D_d\left(\frac{\partial^2 C_d}{\partial r^2} + \frac{2}{r}\frac{\partial C_d}{\partial r}\right) + k_h C_c - k_{e,d}C_d \qquad (3b)$$

Both approximations simplify calculation of the profile of hydrolyzed drug concentration. Equation 3a greatly overestimates drug concentration close to the implant but slightly underestimates drug concentration far from the site. Equation 3b slightly overestimates drug concentration far from the site. The true transient concentration at the treatment distance should

Table 2. Modeling Values for Determination of Treatment Distances

	conjugate				free CPT			
	C_0 mg/L	D (mm^2/hr)	k_e (hr^{-1})	1/A	k_h (hr^{-1})	D (mm^2/hr)	k_e (hr^{-1})	IC_{50} (μg/L)
case 1	1–25					0.282	1.28	12.9
case 2	1–1000	0.14–0.18	0.017	0.002–0.02				
case 3	1–1000	0.14–0.18	0.017	0	0.005–0.035	0.282	1.28	12.9
case 3	1–1000	0.14–0.18	0.017	0.002–0.02	0.005–0.035	0.282	1.28	12.9

fall between the treatment distances estimated by eqs 3a and 3b. In practice, we found a minimal difference between calculated treatment distances from eqs 3a and 3b for the model parameters used for CPT and PEG-CPT, and therefore eq 3a was used to give the results presented.

RESULTS

Three PEG-camptothecin conjugates were synthesized as described in the Experimental Section. They differed in the stability of the linkage between the polymer and the 20-hydroxyl group of camptothecin. In a previous report, we provided analysis by MALDI-TOF to confirm the chemical modifications (*5*); those results were verified for all of the preparations used here. Table 1 lists the relevant physical properties in the brain for these three compounds in comparison to camptothecin. Solubilities were measured in phosphate-buffered saline at 37 °C, and the CPT solubility is consistent with a previously reported value of 25 mg/L (*18*). An additional benefit of CPT conjugation is stabilization of the active lactone form to higher pH values (*19*). Conjugate concentrations in Table 1 and future discussions refer to the free drug equivalent concentration of the conjugate. For example, 1 mg/L of conjugate has 1 mg/L of CPT attached to PEG. Diffusion coefficients were determined experimentally for CPT and conjugates and are slightly lower than empirically expected. Hydrolysis rates, elimination rates, and IC_{50} values were determined as described in the Experimental Section.

Modeling incorporated simple diffusion, first-order hydrolysis and elimination, and several constraints on the physical system. A spherical polymer implant 3 mm in diameter was assumed. This is the average size of the implants used in typical experiments. PEGs of molecular weights 2000 and 3400 were modeled with the assumption that PEG 2000 will have the same rate of elimination and solubility as PEG 3400. Our model assumes that release from the implant occurs with a constant concentration maintained at the implant surface. Since a homogenous environment was assumed, the concentration of drug varied only with radial distance from the center of the implant. The treatment area, therefore, was a sphere surrounding the implant site.

Four different systems were modeled. Relevant parameters and variables for modeling of these systems are listed in Table 2. In the first case, unconjugated drug is released. A permanent conjugate with reduced cytotoxicity of the conjugate relative to the drug itself is released in case 2. In case 3, the conjugate is assumed to have no toxicity, and the hydrolysis-released drug has the same properties as the drug itself. Case 4 is identical to case 3, except that the conjugate form has cytotoxicity in the range 50–500 times less than the free drug. Variables for the different cases consisted of the C_0 value, hydrolysis rate (0.05–0.035 h^{-1}), conjugate diffusion coefficient (PEG2000 or PEG3400), and IC_{50} value of the conjugate.

The drug and conjugate profiles at 96 h, with a $C_{0,CPT}$ of 25 and a $C_{0,conj}$ of 500 mg/L, appear in Figure 4. These profiles assume a conjugate diffusion coefficient of 0.14 mm^2/h (PEG3400) and, for case 3 (lines 3a and 3b), a hydrolysis rate of 0.018 h^{-1}. The slope of the CPT (line 1) in the semilog plot is very steep, as the drug is eliminated quickly. Released CPT in Figure 4 (line 3b) was calculated using a numerical solution to eq (3b. Although the concentration of CPT released from conjugate (line 3b) is clearly lower at the implant surface than what can be achieved with CPT alone, drug concentration has a much smaller slope in the semilog plot. With no hydrolysis (line 2), the conjugate can reach higher concentrations farther from the implant, but this is offset by the lower cytotoxicity of the conjugate relative to the free drug. Optimization of treatment becomes a balance of these effects.

For all cases, concentration profiles were computed at 96 h after implantation. At this time, concentration profiles were close to steady-state values, and enough drug was present to maintain C_0 values for at least 72 more hours. "Treatment distances" were determined as the farthest distances from the implant surface at which the concentration at 96 h was above the IC_{50} value. For unconjugated drug, this IC_{50} value was 0.0129 mg/L. For conjugated drug, it was A multiplied by 0.0129 mg/L, where A is the toxicity reduction factor for the conjugated form. When both unconjugated and conjugated forms of the drug were present and active (case 4), they were assumed to have an additive effect toward achieving an IC_{50} concentration.

Samples of treatment distance results for cases 2, 3, and 4 appear in Figures 5, 6, and 7, where C_0 = 500 mg/L for all curves in Figure 7. Treatment distances for case 1 were 0.235, 0.264, 0.281, 0.293, and 0.303 cm for C_0 values of 5, 10, 15, 20, and 25 mg/L, respectively. Concentration profiles, and hence treatment distances, for the first two cases were determined exactly using eq 5. Figure 5 shows that increasing the toxicity

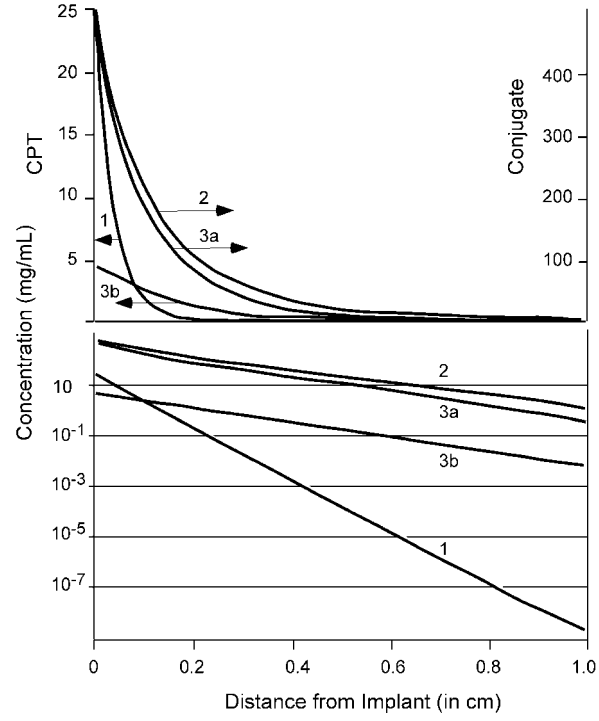


Figure 4. Concentration profiles at 96 h. 1 = CPT (case 1, C_0 = 25 mg/L); 2 = PEG3400═CPT (case 2, C_0 = 500 mg/L); 3a = PEG3400—CPT (case 3/4, C_0 = 500 mg/L); and 3b = CPT released (case 3/4, from PEG3400—CPT). (A) Direct plot. (B) Semilog plot.

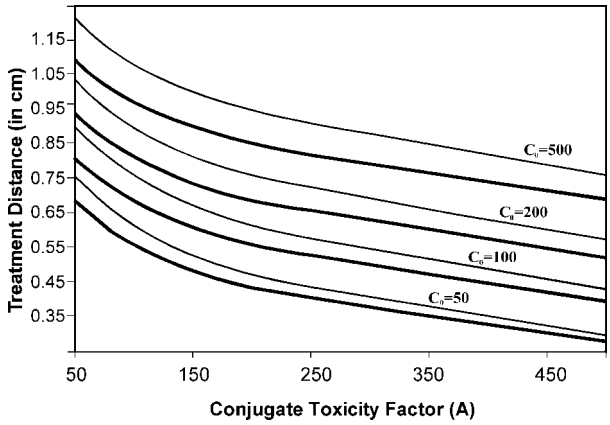


Figure 5. Treatment distances of permanent conjugates (case 2). Thin = PEG2000. Bold = PEG3400.

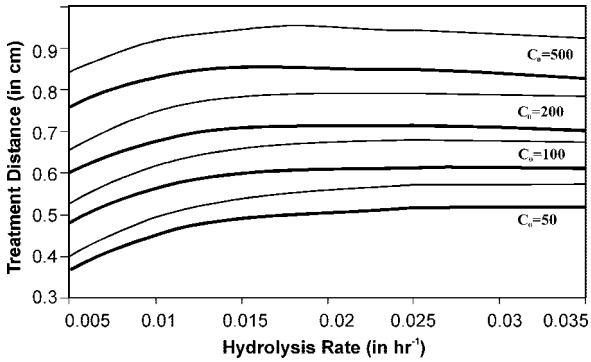


Figure 6. Treatment distances of inert hydrolyzable conjugates (case 3). Thin = PEG2000. Bold = PEG3400.

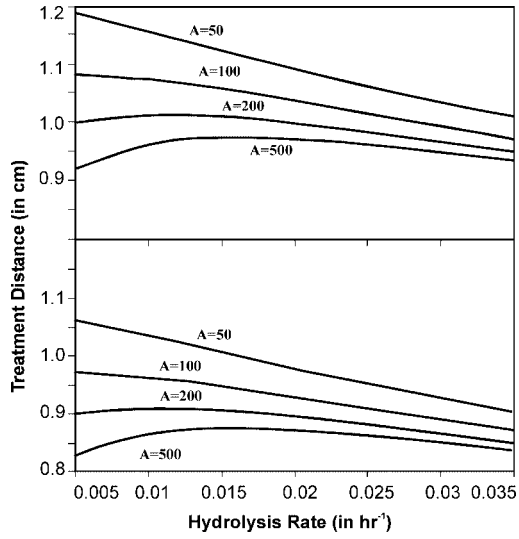


Figure 7. Treatment distances of active, hydrolyzable conjugates (case 4, C_0 = 500 mg/L). (A) PEG2000. (B) PEG3400.

of the conjugate, the C_0 concentration, and the effective diffusion coefficient all lead to larger treatment distances for a case 2 conjugate. For cases 3 and 4, concentration profiles of conjugate were determined exactly with eq 5. Equation 3a was used to get drug concentrations for treatment distance calculations for cases 3 and 4. The results of these calculations appear in Figures 6 and 7. Figure 6 illustrates that, as C_0 decreases for a case 3 conjugate, the optimal hydrolysis rate increases from about 0.018 h^{-1} for $C_0 = 500$ to about 0.035 h^{-1} for $C_0 = 50$ mg/L. Finally, in Figure 7, if A is 100 or less, a nearly permanent conjugate gives the largest treatment distance. The optimal hydrolysis rate increases as A increases to 200 and higher.

DISCUSSION

PEG–CPT conjugates were synthesized and characterized as drug–polymer conjugates to determine appropriate parameters for modeling of drug distribution in the human brain. Our goal was to determine the potential advantage of a drug–polymer conjugate over drug alone in terms of distribution from a controlled-release polymer and tumor treatment. This would allow rational design of future conjugates with optimal physical properties for treatment of a cancer site. Although these equations can be applied to other drug conjugate systems, our results are specific for PEG–camptothecin conjugates.

Case 1 serves as a baseline for comparison to conjugate systems. The C_0 value for camptothecin is severely limited by low water solubility, and camptothecin is rapidly eliminated from the brain. If a saturated concentration can be maintained at the implant surface, a treatment distance of 0.3 cm is achieved. Experimentally, C_0 values as high as 20 mg/L have been maintained in a rat brain for several days after implantation. (*5*) Although the IC_{50} value may not be the critical concentration necessary for effective tumor site treatment, we believe it to be a more appropriate choice than the $C_0/10$ value often used, since it does account for the toxicity of the drug. As a result of the high diffusion and elimination rates, free drug approaches a steady-state profile within a matter of minutes.

The two major advantages of the PEG conjugates are a much greater solubility in water than the drug itself and a much slower rate of elimination. Obviously, increasing the C_0 value increases the treatment distance. Additionally, since we assume PEG2000 differs from PEG3400 only in having a larger diffusion coefficient, a PEG2000 system will give a larger treatment distance than an otherwise equivalent PEG3400 system. Finally, a decrease in A, the toxicity reduction factor, always leads to an increase in treatment distance. The most interesting of the variables is the hydrolysis rate of the conjugate, which will show an internal optimum for treatment distance under most of our conditions.

While a conjugate system allows for considerably more design freedom than a drug alone, we still face physical limitations. We assume that PEG2000 stands at the low molecular weight end for conjugate, or else we risk lower conjugate solubility. Although PEG as low as 900 has been shown to have the same elimination rate as PEG4000, (*13*) we expect the solubilizing power, and hence potential C_0, to be reduced. Therefore, diffusivity of the conjugate has an upward bound of $\sim$0.18 mm^2/h. Depending on the drug, some flexibility in the A factor of the conjugate is possible by using different linkages, such as a 10-hydroxy linkage for CPT, but it is unlikely that a factor less than 50 will be achieved. Additionally, variation of the linkage can be used to produce a range of hydrolysis rates. Within the parameter space we investigated, the largest treatment distance was 1.343 cm for a case 2 PEG2000 conjugate with $A = 50$ and $C_0 = 1000$ mg/L. We have found it difficult to determine A experimentally for our conjugates, because the experimental error is greater than the difference we would predict in the cytotoxicity assays between $A = \infty$ and $A = 50$.

The modeling results can be applied to the CPT conjugates that we synthesized, assuming $C_0 = 500$ mg/L and $1/A = 0$. These cases led to treatment distances of 0.817 cm for the sarcosine conjugate, 0.842 cm for the glycine conjugate, and 0.855 cm for the ester conjugate. The ester conjugate had the optimal hydrolysis rate for these conditions. Although these conjugates already show a significant improvement over the 0.3 cm treatment distance of camptothecin alone, we discuss approaches that might increase treatment distances further in the next few paragraphs.

Decreasing the surface concentration, C_0, decreases the treatment distance. The treatment distance relative to that for $C_0 = 1000$ seems to be fairly independent of the other variables, and doubling C_0 from 500 to 1000 increases the treatment distance an average of 14% for case 2 and 12% for cases 3 and 4. We set 500 mg/L as a practical C_0 limit, which should be achievable *in vivo*. Advantages for further increases are tempered with a very high conjugate loading requirement and concentrations that may be difficult to sustain.

Although drug conjugates have a greatly reduced cytotoxicity relative to the native drug, they have been found to be active at concentrations 50 to 1000 times greater than their parent drug. We assumed an initial $1/A$ value of zero, meaning that the conjugate is completely inert. Increasing conjugate activity in our models with A values of 500, 200, 100, and 50 will lead to an increase in treatment distance and will also decrease the optimum hydrolysis rate. We have found that increases in treatment distance with decreasing A are approximately independent of C_0. As the hydrolysis rate increases, the benefit of increasing $1/A$ to 0.02 decreases from 0.31 to 0.075 cm for PEG3400 and from 0.35 to 0.085 cm for PEG2000.

Increasing the rate of diffusion will also increase the treatment distance. This can only be done by decreasing the molecular weight of PEG, which may have implications for the solubility and elimination rate. Decreasing PEG from 3400 to 2000 increases the conjugate diffusion coefficient from 0.14 to 0.18 mm^2/h. This leads to an average increase of 10.9% in the treatment distance for cases 3 and 4 and an average increase of 9.5% for case 2.

Finally, we can control the hydrolysis rate through the conjugation linkage, so that this variable can be adjusted to maximize treatment distance for a given set of conditions. The optimal hydrolysis rate balances the properties of the conjugate with the properties of the released drug. Increasing the cytotoxicity of the conjugate shifts the optimum hydrolysis rate to lower values, as does increasing the implant surface concentration. Optimizing over the range 0–0.035 h^{-1} can increase treatment distance by as much as 0.287 cm. As conjugate toxicity decreases, increasing the C_0 value leads to an improvement in the treatment distance.

On the basis of our modeling results, the PEG3400–CPT conjugate version gives the greatest treatment distance of the conjugates we have synthesized. On the assumption that it is a case 3 conjugate with no cytotoxicity in the conjugated form and a C_0 value of 500 mg/L, this version gives a treatment distance of 0.855 cm. This value is significantly greater than the 0.3 cm that we calculate for release of unconjugated drug. Released conjugate should treat a volume of 4.24 cm^3, which is 11 times the 0.37 cm^3 treated by unconjugated drug. Reducing to PEG2000–CPT improves the treatment distance to 0.950 cm.

Producing an implant that can sustain a C_0 value as high as 500 mg/L requires some special consideration. As an estimate of total conjugate required, a steady-state profile of PEG3400–CPT with $C_0 = 500$ mg/L contains 0.44 mg of conjugate (with 15 wt % CPT/conjugate). Therefore, the rate of loss of conjugate is 0.44 mg $\times$ 0.035 h^{-1}, or 0.0154 mg/h, for 168 h requires 2.59 mg of conjugate. Placing this mass into a 0.15 cm radius pellet at a density of 1.5 g/cm^3 requires a loading of 12.2%. Several controlled-release polymers have been used for implants of this kind including nonbiodegradable EVAc (polyethylene-*co*-vinyl acetate) (*20, 21*) and biodegradable p(CPP:SA) (poly(1,3-bis(p-carboxyphenoxy)propane/sebacic acid)). (*16, 22*) On the basis of our experience, both EVAc and p(CPP:SA) could be loaded at 15% (or more) and could be designed to maintain such a high C_0. Since PEG–CPT conjugate could be thought of as a "controlled release" device on its own, another possibility would be to create an implant of pure conjugate. A final consideration would be to include free CPT along with conjugate in the loaded implant. This free CPT should be more soluble in the presence of conjugate and may slow hydrolysis when present in high concentrations near the implant.

These calculations help in the interpretation of our previous experimental results with conjugate penetration in the brain (*5*) and also point toward approaches that might improve conjugate design for this application. We note that this study has limitations: in particular, we have made assumptions about the rate of elimination of PEG from the brain and about the relationship between conjugate diffusion and PEG diffusion that need to be verified. In addition, we note that it is difficult to estimate actual values for the parameter A.

CONCLUSIONS

Low solubility and rapid elimination in the brain prevent most drugs from diffusing more than a few millimeters away from an implant site. Poly(ethylene glycol)–drug conjugates have much longer residence times and higher solubilities than their free drug counterparts. For the chemotherapy drug camptothecin, these improvements allow greater distribution of the drug in the brain. This translates into a greater volume of tissue receiving a therapeutic dose of drug and, therefore, a greater likelihood of prevention of tumor recurrence. Specifically, if a therapeutic dose is defined as the IC_{50} concentration of 0.0129 mg/L for 72 h, we predict a 3 mm diameter PEG3400–CPT implant to treat 4.24 cm^3, more than 11 times the volume treated by a CPT implant of the same diameter. This increase in treatment volume may be sufficient to improve the clinical effectiveness of controlled-release implants on human brain tumors.

ACKNOWLEDGMENT

This work was supported by grants from NIH (CA52857 and NS045236).

LITERATURE CITED

(1) Harada, M., Murata, J., Sakamura, Y., Sakakibara, H., Okuno, S., and Suzuki, T. (2001) Carrier and dose effects on the pharmacokinetics of T-0128, a camptothecin analog-carboxymethyl dextran conjugate, in non-tumor and tumor-bearing rats. *J. Controlled Release 71*, 71–86.

(2) Caiolfa, V. R., Zamai, M., Fiorino, A., Frigerio, E., Pellizzoni, C., d'Argy, R., Ghiglieri, A., Castelli, M. G., Farao, M., Pesenti, E., Gigli, M., Angelucci, F., and Suarato, A. (2000) Polymer-bound camptothecin: initial biodistribution and antitumour activity studies. *J. Controlled Release 65*, 105–119.

(3) Sakuma, S., Lu, Z. R., Kopeckova, P., and Kopecek, J. (2001) Biorecognizable HPMA copolymer-drug conjugates for colon-specific delivery of 9-aminocamptothecin. *J. Controlled Release 75*, 365–379.

(4) Conover, C. D., Pendri, A., Lee, C., Gilbert, C. W., Shum, K. L., and Greenwald, R. B. (1997) Camptothecin delivery systems: the antitumor activity of a camptothecin 20-0-polyethylene glycol ester transport form. *Anticancer Res. 17*, 3361–3368.

(5) Fleming, A. B., Haverstick, K., and Saltzman, W. M. (2004) In vitro cytotoxicity and in vivo distribution after direct delivery of PEG-camptothecin conjugates to the rat brain. *Bioconjugate Chem. 15*, 1364–75.

(6) Begley, D. J., Bradbury, M. W., and Kreuter, J. (2000) *The Blood-Brain Barrier and Drug Delivery to the CNS*, Dekker, New York.

(7) Saltzman, W. M., and Radomsky, M. L. (1991) Drugs released from polymers: diffusion and elimination in brain tissue. *Chem. Eng. Sci. 46*, 2429–2444.

(8) Saltzman, W. M. (2000) Interstitial transport in the brain: principles for local drug delivery, In *Handbook of Biomedical*

Engineering (Bronzino, J., Ed.)pp 99–1 to 99–14, CRC Press, Boca Raton, FL.

(9) Thiele, E. W. (1939) Relation between catalytic activity and size of particle. *Ind. Eng. Chem. 31*, 916–920.

(10) Dang, W., and Saltzman, W. M. (1992) Dextran retention in the rat brain following controlled release from a polymer. *Biotechnol. Prog. 8*, 527–532.

(11) Pendri, A., Gilbert, C. W., Soundararajan, S., Bolikal, D., Shorr, R. G. L., and Greenwald, R. B. (1996) PEG Modified Anticancer Drugs: Synthesis and Biological Activity. *J. Bioactive Compat. Polym. 11*, 122–135.

(12) Greenwald, R., Pendri, A., Conover, C., Lee, C., Choe, Y., Gilbert, C., Martinez, A., Xia, J., Wu, D., and Hsue, M. (1998) Camptothecin-20-PEG ester transport forms: the effect of spacer groups on antitumor activity. *Bioorg. Med. Chem. 6*, 551–562.

(13) Cserr, H. F., Cooper, D. N., Suri, P. K., and Patlak, C. S. (1981) Efflux of radiolabeled polyethylene glycols and albumin from rat brain. *Am. J. Physiol. 240*, F319–F328.

(14) Wilke, C. R., and Chang, P. (1955) Correlation of diffusion coefficients in dilute solutions. *AIChE J. 1*, 264–270.

(15) Yaws, C. W. (1995) *Handbook of Transport Property Data: Viscosity, Thermal Conductivity, and Diffusion Coefficients of Liquids and Gases*, Gulf Publishing Company, Houston.

(16) Fung, L. K., Ewend, M. G., Sills, A., Sipos, E. P., Thompson, R., Watts, M., Colvin, O. M., Brem, H., and Saltzman, W. M. (1998) Pharmacokinetics of interstitial delivery of carmustine, 4-hydroperoxycyclophosphamide, and paclitaxel from a biodegradable polymer implant in the monkey brain. *Cancer Res. 58*, 672–684.

(17) Waggoner, R., Blum, F., and Lang, J. (1995) Diffusion in aqueous solutions of poly(ethylene glycol) at low concentrations. *Macromolecules 28*, 2658–2664.

(18) Mahoney, M. J., and Saltzman, W. M. (1996) Controlled release of proteins to tissue transplants for the treatment of neurodegenerative disorders. *J. Pharm. Sci. 85*, 1276–1281.

(19) Zhao, H., Lee, C., Sai, P. K., Choe, Y. H., Boro, M., Pendri, A., Guan, S. Y., and Greenwald, R. B. (2000) 20-O-acylcamptothecin derivatives: evidence for lactone stabilization. *J. Org. Chem. 65*, 4601–4606.

(20) Powell, E. M., Sobarzo, M. R., and Saltzman, W. M. (1990) Controlled release of nerve growth factor from a polymeric implant. *Brain Res. 515*, 309–311.

(21) Reinhard, C., Radomsky, M. L., Saltzman, W. M., Hilton, J., and Brem, H. (1991) Polymeric controlled release of dexamethasone in normal rat brain. *J. Controlled Release 16*, 331–340.

(22) Fung, L., Shin, M., Tyler, B., Brem, H., and Saltzman, W. M. (1996) Chemotherapeutic drugs released from polymers: distribution of 1,3-bis(2-chloroethyl)-1-nitrosourea in the rat brain. *Pharm. Res. 13*, 671–682.

BC700214H

A Radioiodinated MIBG–Octreotate Conjugate Exhibiting Enhanced Uptake and Retention in SSTR2-Expressing Tumor Cells

Ganesan Vaidyanathan,*[,†] Donna J. Affleck,[†] Joseph Norman,[†] Susan O'Dorisio,[‡] and Michael R. Zalutsky[†]

Department of Radiology, Duke University Medical Center, Durham, North Carolina, and Division of Pediatric Hematology/Oncology, University of Iowa, Iowa City, Iowa. Received June 28, 2007; Revised Manuscript Received September 11, 2007

Several neuroendocrine tumors are known to express both the somatostatin receptor subtype 2 (SSTR2) and the norepinephrine transporter (NET), and radiopharmaceuticals directed toward both these targets such as MIBG and octreotide derivatives are routinely used in the clinic. To investigate the possibility of targeting both NET and SSTR2 conjointly, a conjugate of radioiodinated MIBG and octreotate was synthesized. Attempts to synthesize the radioiodinated target compound (MIBG-octreotate; [^{131}I]**12a**) from a tin precursor were futile; however, it could be accomplished from a bromo precursor by exchange radioiodination in 3–36% ($n = 10$) radiochemical yields. The total uptake of [^{131}I]**12a** in SK-N-SH human neuroblastoma cells transfected to express SSTR2 (SK-N-SHsst2) was similar to that for [^{125}I]MIBG at all time points (34.9 ± 2.4% vs 43.8 ± 1.2% at 4 h; $p < 0.05$), while it was substantially lower (5.4 ± 0.3% vs 35.9 ± 1.2%) in the SH-SY5Y cell line, a subclone of SK-N-SH line that is known to express SSTR2. The NET blocker desipramine reduced the uptake of [^{131}I]**12a** only to a small extent, further suggesting a limited role of NET in its binding and accumulation. Uptake of [^{131}I]**12a** in SK-N-SHsst2 cells was 8–10-fold higher ($p < 0.05$) than that of [^{125}I]I-Gluc-TOCA, an octreotide analogue, at all time points over a 4 h period and was reduced to about 20% by 10 μM octreotide demonstrating that the uptake of [^{131}I]**12a** in this cell line is predominantly mediated by SSTR2. The intracellularly trapped radioactivity in SK-N-SHsst2 cells was substantially higher for [^{131}I]**12a** compared to that for [^{125}I]OIBG-octreotate, an isomeric congener of **12a**. Because MIBG has more specific NET-mediated uptake than OIBG, this suggests at least a partial role for NET-mediated uptake of [^{131}I]**12a** in this cell line. While further refinement in the structure of the conjugate—probably interposition of a flexible and/or cleavable linker between the MIBG and octreotate moieties—may be necessary to make it a substrate/ligand for both NET and SSTR2, this conjugate is demonstrated to be much superior than I-Gluc-TOCA with respect to the uptake in SSTR2-expressing cells.

INTRODUCTION

Neuroblastoma (NB) and other neuroendocrine tumors accumulate *meta*-iodobenzylguanidine (MIBG), an analogue of the neurotransmitter norepinephrine, via the norepinephrine transporter (NET), which is also known as the uptake-1 pump (*1, 2*). MIBG, labeled with the β-particle-emitter ^{131}I, has been used extensively in the treatment of NB (*3*). However, responses were not of long duration even when targeted [^{131}I]MIBG therapy was combined with other modalities (*4*). Many neuroblastomas and other neuroendocrine tumors express somatostatin receptors as well (*5–7*), and a number of radiolabeled derivatives of octreotide, an octapeptide ligand for somatostatin receptor subtype 2, have been developed for diagnosis and targeted therapy of these tumors (*8–11*). The complementary role of [*I]MIBG and ^{111}In-pentetreotide in the imaging of neuroendocrine tumors has been demonstrated (*12–14*). For imaging, while tumor foci of certain cancers have been visualized by both labeled radiopharmaceuticals, there are cases in which one of these radiopharmaceuticals and not the other is sequestered in the tumors. In general, ^{111}In-labeled octreotide was found to be more sensitive; however, it was also less selective (*15–20*). For therapy, the combined use of [^{131}I]MIBG and ^{90}Y-labeled octreotide derivatives has been recommended (*12, 21, 22*).

We hypothesized that a radiopharmaceutical derived by combining the structural elements of MIBG and octreotide may have an additive, if not synergistic, effect with respect to uptake and retention in a neuroendocrine tumor that expressed both somatostatin receptor and NET; in addition, it could limit false negative lesion detection because the hybrid radiopharmaceutical might be taken up by tumors via either mechanism. Another impetus for developing such a reagent is that it could overcome the fast washout of labeled MIBG from tumors, presumably also mediated by NET, that likely contributes to the mismatch between [^{131}I]MIBG tumor pharmacokinetics and the 8.1-day half-life of ^{131}I. Our working hypothesis was that a chimeric molecule containing both SSTR2 and NET binding elements could have higher tumor retention. Octreotide derivatives undergo endocytosis after receptor binding, translocating the receptor–ligand complex to lysosomes wherein they undergo extensive catabolism (*23*) with polar and charged catabolites generally being retained in lysosomes. Attempts have been made to exploit this property of octreotide derivatives in order to increase the tumor specificity and intracellular bioavailability of various pharmaceuticals by conjugating them with octreotide analogues. For example, oligonucleotides (*24*), peptide nucleic acids (*25*), as well as the chemotherapeutic agents doxorubicin (*26*) and paclitaxel (*27*) have been conjugated to somatostatin analogues for such a purpose. Recently, hybrid molecules derived by covalent conjugation of an octreotate (Thr-ol at the C-terminus in octreotide replaced with Thr; Chart 1) derivative and the $\alpha_v\beta_3$-targeting RGD peptide also have been described (*28, 29*). In addition, simultaneous targeting of multiple receptors has become an emerging paradigm in drug discovery (*30–35*).

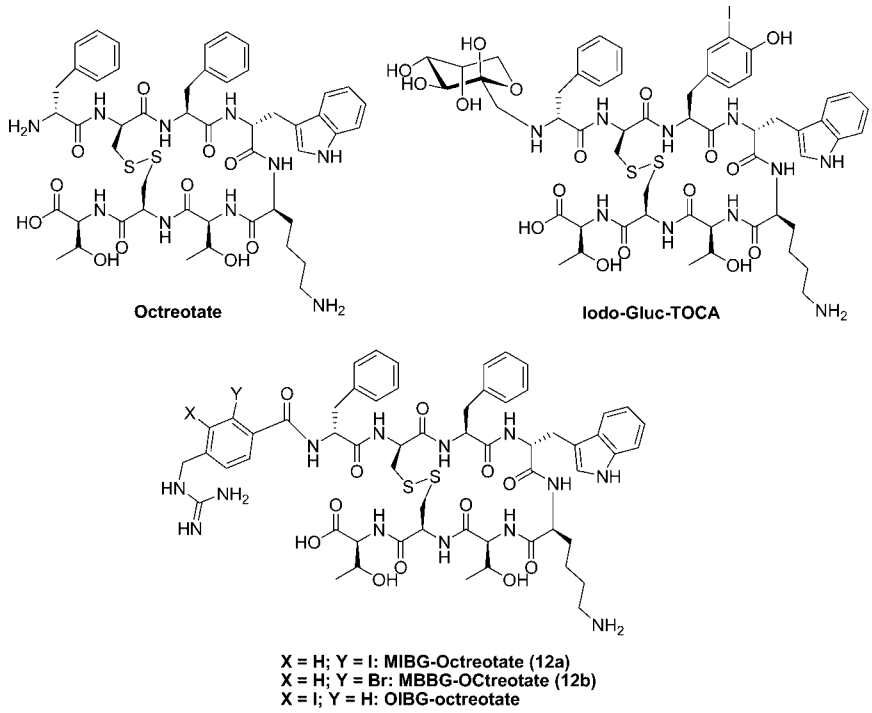
* Correspondence to Ganesan Vaidyanathan, Ph.D., Box 3808, Radiology, Duke University Medical Center, Durham, North Carolina 27710. Phone: (919) 684-7811. Fax: (919) 684-7122. E-mail: ganesan.v@duke.edu

† Duke University Medical Center.

‡ University of Iowa.

10.1021/bc700240r CCC: $37.00 © 2007 American Chemical Society
Published on Web 11/03/2007

Chart 1. Chemical Structures of Octreotate, Iodo-Gluc-TOCA, MIBG-Octreotate, MBBG-Octreotate, and OIBG-Octreotate



Herein, we describe the synthesis of a conjugate of [^{131}I]MIBG and octreotate and its evaluation in human tumor cell lines expressing both SSTR2 and NET. This chimeric conjugate demonstrated superior targeting to SSTR2 receptors compared to one of the best-known SSTR2 targeting peptides; however, unexpectedly, NET-mediated binding of the conjugate was only moderate.

EXPERIMENTAL PROCEDURES

General. All chemicals were purchased from Sigma-Aldrich unless otherwise noted. Sodium [^{125}I]iodide and sodium [^{131}I]iodide with specific activities of 2200 Ci/mmol and 1200 Ci/mmol, respectively, were obtained from Perkin Elmer Life and Analytical Sciences (Boston, MA). N^{ϵ}-Dde-Lys^5-octreotate (**9**), *N*-(4-guanidinomethyl-3-[^{125}I]iodobenzoyl)-D-Phe^1-octreotate ([^{131}I]OIBG-octreotate), and [*I]Iodo-Gluc-TOCA were synthesized as reported earlier (*36*). No-carrier-added [*I]MIBG was synthesized from a silicon precursor (*37*).

Aluminum-backed sheets (Silica gel 60 F254) were used for analytical TLC, and normal-phase column chromatography was performed using silica gel 60, both obtained from EM Science (Gibbstown, NJ). Preparative thick-layer chromatography was performed using 20 × 20 cm, 1000 μm plates (Whatman, Clifton, NJ). Before applying the sample, the plates were run in ethyl acetate to remove any adsorbed impurities. Radio-TLC was initially analyzed using a System 200 Imaging Scanner (BioScan, Washington, DC); sheets were then cut into strips and counted using an automated gamma counter (LKB 1282, Wallac, Finland). High-pressure liquid chromatography was performed using a Beckman System Gold HPLC equipped with a model 126 programmable solvent module, a model 168 diode array detector, a model 170 radioisotope detector, and a model 406 analogue interface module. Reversed-phase chromatography utilized a Waters XTerra C18 column (4.6 × 250 mm, 5 μ) and a Waters XTerra C18 column (19 × 50 mm) for analytical and semipreparative runs, respectively. Proton NMR spectra were obtained on a Varian Mercury 300 spectrometer. Chemical shifts are reported in δ units; solvent peaks are referenced appropriately. Mass spectra were obtained on a JEOL SX-102 high-resolution mass spectrometer (FAB, EI, and GC-MS), an Applied Biosystems Voyager DE Pro (MALDI), or an Agilent 1100 LC/MSD Trap SL (electrospray). High-resolution mass spectra were obtained using a JEOL SX-102 high-resolution mass spectrometer.

Cells and Culture Conditions. SH-SY5Y (*38*), a thrice-cloned subline of the NET-expressing human neuroblastoma cells SK-N-SH (*39*), was obtained from American type Culture Collection (Manassas, VA). Evidence for the presence of somatostatin receptors in the SH-SY5Y cell line has been reported (*40–42*). The incubation medium for these cells was made by mixing 500 mL of RPMI 1640 (GIBCO), 55 mL of fetal calf serum, and 2.7 mL of penicillin-G/streptomycin (10 000 U of penicillin and 10 000 μg of streptomycin in 1 mL of 0.85% saline). SK-N-SH cells stably transfected with SSTR2 (SK-N-SHsst2) were derived as described previously (*5*). The mRNA level in these cells, relative to that in parent SK-N-SH line, was 28.3 ± 5.8 as determined by quantitative RT-PCR (*5*). A medium consisting of 500 mL MEM, 15% FBS, 12 mL penicillin/streptomycin (200 U/mL penicillin and 200 μg/mL streptomycin), 6 mL nonessential amino acids, 6 mL L-glutamine, and 300 mg G418 was used for the culturing these cells. The cells were grown at 37 °C in a humidified incubator containing 5% CO_2. Cell viability was evaluated prior to each experiment by trypan blue dye exclusion (*43*), and was 95–98% for all studies.

2-Iodo-4-methylbenzoic Acid (1a). A solution of sodium nitrite (747 mg; 10.8 mmol) in 6 mL of water was added to a suspension of 2-amino-3-methylbenzoic acid [(Ryan Scientific, Isle of Palms, SC, or Maybridge Building Blocks, Cornwall, UK) 1.51 g; 10 mmol] in cold dilute sulfuric acid (2 mL conc H_2SO_4, 12 g ice, and 18 mL water) at 2–3 °C over a period of 10 min. The mixture was stirred for 2 h at 2–3 °C, and a solution of KI (2.28 g; 10.8 mmol) in 5 mL of water was then added over a period of 15 min while maintaining the temperature at 2–3 °C. The mixture was subsequently heated in an oil bath maintained at 60 °C for 1 h. The reaction mixture was partitioned between ethyl acetate and water, and the aqueous layer was washed twice with ethyl acetate. The combined ethyl acetate layer was washed twice with saturated sodium thiosulfate solution and once with brine. The dried ethyl acetate layer was

evaporated, and the crude product was chromatographed on silica gel using 70:30:0.1 ethyl acetate/hexanes/acetic acid to yield 1.5 g solid (57%). It was further purified by precipitation from an ethyl acetate solution by hexanes: mp 134–136 °C [lit. (*44*) mp 128–130 °C]. The melting point was similar to that of a commercial sample (Maybridge Building Blocks, Cornwall, UK)—individually and mixed.

2-(Trimethylsilyl)ethyl 2-iodo-4-methylbenzoate (2a). Polymer-bound DCC [(Argonaut Technologies, Inc., San Carlos, CA, now a division of Biotage, Uppsala, Sweden), 5.0 g; 5 mmol] was added to a stirred solution of **1a** (930 mg, 3.6 mmol), DMAP (45 mg; 0.4 mmol), and trimethylsilylethanol (570 mg; 4.8 mmol) in 35 mL of dry ethyl acetate. The heterogeneous mixture was stirred at 20 °C under argon atmosphere for 3–4 h. The polymer was filtered and washed with ethyl acetate, which was evaporated from the combined filtrate using a rotary evaporator under aspirator vacuum. The residual oil was chromatographed using a gradient of 0–5% ethyl acetate/hexanes to yield 1.0 g (77%) of **2a** as an oil: ^{1}H NMR ($CDCl_3$) 0.07 (s, 9H), 1.15 (m, 2H), 2.33 (s, 3H), 4.41 (m, 2H), 7.18 (ddd, 1H), 7.72 (dd, 1H), 7.83 (dd, 1H). MS (EI^+), *m*/*z*: 362 (M^+), 245. HRMS (EI^+) Calcd for $C_{13}H_{19}IO_2Si$ (M^+): 362.0199. Found: 362.0197 ± 0.0004 ($n = 2$).

2-(Trimethylsilyl)ethyl 2-bromo-4-methylbenzoate (2b). The title compound was synthesized from 2-bromo-4-methylbenzoic acid similar to **2a** above but using DCC (not polymer-supported). Starting from 2.15 g (10 mmol) of 2-bromo-4-methylbenzoic acid, 2.5 g (80%) of **2b** was obtained as an oil: ^{1}H NMR ($CDCl_3$) 0.07 (s, 9H), 1.15 (m, 2H), 2.36 (s, 3H), 4.42 (m, 2H), 7.15 (ddd, 1H), 7.49 (m, 1H), 7.71 (dd, 1H). MS (GC-EI^+), *m*/*z*: 313 and 315 (M^+), 299 and 301 $(M - CH_3)^+$, 271 and 273 (100%), 227 and 229, 197 and 199 ($M - OCH_2CH_2SiMe_3$).

2-(Trimethylsilyl)ethyl 4-Bromomethyl-2-iodobenzoate (3a). A mixture of **2a** (1.02 g; 2.82 mmol), *N*-bromosuccinimide (473 mg; 2.66 mmol), 1,1′-azo-biscyclohexanenitrile, and 1,2-dichloroethane (DCE; 25 mL) was heated at reflux under an incandescent lamp for 3 h. DCE was evaporated from the cooled mixture, and the residue was partitioned between ethyl acetate and water. The aqueous layer was extracted twice with ethyl acetate, and the pooled ethyl acetate solution was washed with sodium thiosulfate solution and dried. The ethyl acetate was evaporated, and the residual oil was chromatographed on silica gel using a gradient of 0–3% ethyl acetate in hexanes to yield 541 mg (44%) of an oil: ^{1}H NMR ($CDCl_3$) 0.08 (s, 9H), 1.15 (m, 2H), 4.39 (s, 2H), 4.43 (m, 2H), 7.42 (ddd, 1H), 7.76 (dd, 1H), 8.00 (ddd, 1H). MS (EI^+), *m*/*z*: 440 and 442 (M^+), 412 and 414, 397 and 399 (100%), 361, 334. HRMS (EI^+) Calcd for $C_{13}H_{17}BrIO_2Si$ $(M - H)^+$: 438.9226. Found: 438.9231. This compound was contaminated with less than 10% of the dibromo derivative (based on NMR data) and was used as such for the synthesis of **4a**.

2-(Trimethylsilyl)ethyl 2-Bromo-4-bromomethylbenzoate (3b). This compound was synthesized from **2b** following the procedure described for the preparation of **3a**. Starting from 670 mg (2.13 mmol) of **2b**, 526 mg (63%) of **3b** was obtained as an oil: ^{1}H NMR ($CDCl_3$) 0.08 (s, 9H), 1.15 (m, 2H), 4.42 (s, 2H), 4.43 (m, 2H), 7.37 (ddd, 1H), 7.68 (ddd, 1H), 7.74 (dd, 1H).

2-(Trimethylsilyl)ethyl 4-[N^1,N^2-Bis-(*tert*-butyloxycarbonyl)guanidinomethyl]-2-iodobenzoate (4a). N^1,N^2-bis-(*tert*-butyloxycarbonyl)guanidine (412 mg; 1.6 mmol) was added to a stirred suspension of sodium hydride (60% dispersion in mineral oil) (62.5 mg; 1.6 mmol) in 6 mL of dry DMF under argon and the mixture stirred at room temperature for 5 min, whereby a homogenous solution was obtained. A solution of **3a** (504 mg; 1.14 mmol actual) in 2.3 mL of DMF was added to the above solution of the guanidine derivative and the reaction mixture stirred at room temperature for 10–15 min The reaction mixture was partitioned between water and ethyl acetate and the aqueous layer extracted a couple of times with ethyl acetate. The pooled ethyl acetate solution was washed once with brine, dried, and evaporated. The crude mixture was chromatographed on silica gel with a gradient of 5–20% ethyl acetate in hexanes to yield 591 mg (83%) of a white solid: m.p. 103–105 °C. ^{1}H NMR ($CDCl_3$) 0.08 (s, 9H), 1.15 (m, 2H), 1.38 (s, 9H), 1.48 (s, 9H), 4.43 (m, 2H), 5.17 (s, 2H), 7.32 (dd, 1H), 7.75 (dd, 1H), 7.91 (dd, 1H). MS (FAB^+), *m*/*z*: 620 $(M + H)^+$, 564, 508, 436, and 392. HRMS (FAB^+) Calcd for $C_{24}H_{39}IN_3O_6Si$ $(M + H)^+$: 620.1653. Found: 620.1654 ± 0.0016 ($n = 2$).

2-(Trimethylsilyl)ethyl 2-Bromo-4-[N^1,N^2-bis-(*tert*-butyloxycarbonyl)guanidinomethyl]benzoate (4b). This compound was prepared following a procedure similar to that used for the synthesis of **4a**. Starting with 820 mg (2.1 mmol) of **3b**, 551 mg (46%) of a white solid was obtained. ^{1}H NMR ($CDCl_3$) 0.06 (s, 9H), 1.12 (m, 2H), 1.35 (s, 9H), 1.47 (s, 9H), 4.41 (m, 2H), 5.13 (s, 2H), 7.24 (dd, 1H), 7.55 (d, 1H), 7.73 (dd, 1H). MS (FAB^+), *m*/*z*: 572 and 574 $(M + H)^+$, 516 and 518, 460 and 462, 388 and 390, and 344 and 346. HRMS (FAB^+) Calcd for $C_{24}H_{39}{}^{79}BrN_3O_6Si$ $(M + H)^+$: 572.1792. Found: 572.1786 ± 0.0021 ($n = 2$).

4-[N^1,N^2-Bis-(*tert*-butyloxycarbonyl)guanidinomethyl]-2-iodobenzoic Acid (5a). Tetrabutyl ammonium fluoride (0.18 mL of 1 M solution in THF; 0.18 mmol) was added dropwise to a solution of **4a** (40 mg; 0.06 mmol), and the mixture was stirred at 20 °C for 3–4 h. THF was evaporated, and the residue was partitioned between ethyl acetate and 1 N HCl. The aqueous layer was extracted twice with ethyl acetate, and the pooled ethyl acetate solution was washed with brine and dried. Evaporation of ethyl acetate yielded 30 mg (89%) of an oil: ^{1}H NMR ($CDCl_3$) 1.35 (s, 9H), 1.49 (s, 9H), 5.15 (s, 2H), 7.29 (dd, 1H), 7.87 (d, 1H), 7.92 (d, 1H), 9.28 (br d; 2H). MS (FAB^+), *m*/*z*: 520 $(M + H)^+$, 408. HRMS (FAB^+) Calcd for $C_{19}H_{27}IN_3O_6$ $(M + H)^+$: 520.0945. Found: 520.0931 ± 0.0000 ($n = 2$). This compound was carried to the next step without further purification.

4-[N^1,N^2-Bis-(*tert*-butyloxycarbonyl)guanidinomethyl]-2-bromobenzoic Acid (5b). This compound was prepared from **4b** (30 mg; 0.05 mmol) in a fashion similar to the preparation of **5b** in an almost quantitative yield and was used for the next step without further purification. ^{1}H NMR ($CDCl_3$) 1.36 (s, 9H), 1.49 (s, 9H), 5.18 (s, 2H), 7.25 (dd, 1H), 7.58 (d, 1H), 7.88 (dd, 1H), 9.4 (br d; 2H).

***N*-Succinimidyl 4-[N^1,N^2-Bis-(*tert*-butyloxycarbonyl)guanidinomethyl]-2-iodobenzoate (6a).** Polymer-bound DCC (400 mg; 0.4 mmol) and *N*,*N*-dimethylaminopyridine (3 mg) in that order were added to a solution of **5a** (147 mg; 0.28 mmol) in 3 mL of dry ethyl acetate. The mixture was stirred at 20 °C under a positive pressure of argon for a few minutes after which *N*-hydroxysuccinimide (72 mg; 0.6 mmol) was added and then further stirred for 1 h at 20 °C. The resin was filtered off, washed with ethyl acetate, and the filtrate concentrated. Silica gel chromatography using a gradient of 25–40% ethyl acetate in hexanes yielded 50.8 mg (41%) of a foamy solid: m.p. 79–80 °C. ^{1}H NMR ($CDCl_3$) 1.40 (s, 9H), 1.50 (s, 9H), 2.90 (s, 4H), 5.18 (s, 2H), 7.40 (dd, 1H), 8.02 (d, 1H), 8.08 (d, 1H), 9.36 (br d; 2H). MS (FAB^+), *m*/*z*: 617 $(M + H)^+$, 561, 505, 460. HRMS (FAB^+) Calcd for $C_{23}H_{30}IN_4O_8$ $(M + H)^+$: 617.1108. Found: 617.1104 ± 0.0010 ($n = 2$).

***N*-Succinimidyl 4-[N^1,N^2-Bis-(*tert*-butyloxycarbonyl)guanidinomethyl]-2-bromobenzoate (6b).** This compound was prepared from **5b** (30 mg) in 49% yield following the procedure for the preparation of **6a**. ^{1}H NMR ($(CD_3)_2SO$) 1.32 (s, 9H),

1.39 (s, 9H), 2.90 (s, 4H), 5.10 (s, 2H), 7.45 (dd, 1H), 7.78 (dd, 1H), 8.05 (dd, 1H).

2-(Trimethylsilyl)ethyl 4-[N^1,N^2-Bis-(*tert*-butyloxycarbonyl)guanidinomethyl]-2-trimethylstannylbenzoate (7). The title compound was synthesized from either **3a** or **3b** using similar procedures (procedure using **3a** is given below). A mixture of **3a** (128 mg; 0.21 mmol), hexamethylditin (652 mg; 2 mmol), $(Ph_3)_2PdCl_2$ (100 mg; 0.14 mmol) in 4 mL of dioxane was heated at reflux under argon for 1 h. The mixture was cooled to room temperature and passed over a bed of Celite, which was then washed with ethyl acetate. The solvents from the combined filtrate were evaporated, and the residual oil was loaded onto a silica bed. The nonpolar byproducts were washed out with a large excess of hexanes, and the product and polar byproducts were eluted with ethyl acetate. The ethyl acetate was evaporated from latter fractions and the residue chromatographed on silica gel using 5% ethyl acetate in hexanes to yield 107 mg (79%) of an oil: ^{1}H NMR ($CDCl_3$) 0.07 (s, 9H), 0.24 (s, 9H [^{119}Sn-H, d]), 1.13 (m, 2H), 1.31 (s, 9H), 1.48 (s, 9H), 4.38 (m, 2H), 5.22 (s, 2H), 7.24 (dd, 1H), 7.56 (d, 1H), 8.03 (dd, 1H), 9.40 (br d; 2H). MS (FAB^+), *m/z*: cluster peaks at 658 $(M + H)^+$, 642, 602, 546, 514, 414, 356. HRMS (FAB^+) Calcd for $C_{27}H_{48}N_3O_6Si^{120}Sn$ $(M + H)^+$: 658.2334. Found: 658.2328 ± 0.0000 ($n = 2$).

***N*-Succinimidyl 4-[N^1,N^2-Bis-(*tert*-butyloxycarbonyl)guanidinomethyl]-2-(trimethylstannyl)benzoate (8).** A solution of tetrabutylammonium fluoride (317 μL of 1 M in THF; 0.32 mmol) was added to a solution of **7** (76.1 mg; 0.12 mmol) in 1.73 mL of dry THF, and the mixture was stirred at 20 °C for 1–2 h. THF was evaporated and the residue partitioned between water and ethyl acetate. The aqueous layer was extracted twice with ethyl acetate, and the combined ethyl acetate fractions were washed with brine and dried. Ethyl acetate was evaporated and the crude product dried. Polymer-bound DCC 163 mg (0.16 mmol) and 1.4 mg of DMAP were added to a solution of the above acid in 1.3 mL of dry ethyl acetate. Five minutes later, *N*-hydroxysuccinimide (31 mg; 0.27 mmol) was added and the mixture stirred at 20 °C under argon for 2–3 h. The resin was filtered and washed with ethyl acetate. Ethyl acetate was evaporated from the filtrate, and the residue was purified by thick-layer chromatography using 25% ethyl acetate in hexanes to yield 36.2 (46%) mg of an oil: ^{1}H NMR ($CDCl_3$) 0.25 (s, 9H [^{119}Sn-H, d]), 1.35 (s, 9H), 1.48 (s, 9H), 2.90 (br s, 4H), 5.22 (s, 2H), 7.30 (dd, 1H), 7.63 (d, 1H), 8.21 (dd, 1H), 9.40 (br d; 2H). MS (FAB^+), *m/z*: cluster peaks at 655.2 $(M + H)^+$, 543. HRMS (FAB^+) Calcd for $C_{26}H_{39}N_4O_8{}^{120}Sn$ $(M + H)^+$: 655.1784. Found: 655.1907 ± 0.0026 ($n = 4$).

***N*-(4-Guanidinomethyl-2-iodobenzoyl)-D-Phe^1-octreotate (12a).** Compound **6a** (3.4 mg; 5.5 μmol) was added to a solution of **9** (6.2 mg; 5.2 μmol) in 0.1 mL of 0.1 M DIEA in NMP. The homogeneous mixture was heated at 45 °C for 30 h. The progression of the reaction was periodically checked by HPLC. For this, the reversed-phase analytical column was eluted with a gradient consisting of 0.1% HOAc (w/v) in each water (solvent A) and acetonitrile (solvent B) at a flow rate of 1 mL/min. The percentage of solvent B was increased from 30% to 60% over 15 min and to 100% in the next 15 min and then held at 100% for 5 min. Under these conditions, the retention times for peptide **9**, compound **6a**, and the product **10a** were 11.3, 25.5, and 29.0 min, respectively. Several analytical HPLC runs of the reaction mixture were performed to yield 3 mg of **10a**. MS *m/z*: Calcd for $C_{78}H_{100}IN_{13}O_{18}S_2$ 1698.7419. Found (LCMS-ESI) 1699.6 (MH^+), 849.7 (MH^{2+}). Ethanolamine (0.98 mL) was added to a solution of **10a** in 0.98 mL of ethanol and left at 20 °C. The removal of the Dde group was complete in 30 min as judged by HPLC. The HPLC was conducted using the same solvents as above at a flow rate of 1 mL/min; the percentage of B was increased from 10% to 40% over a period of 30 min and to 100% in the next 10 min and then held at 100% for 5 min The retention times of **10a** and **11a** under these conditions were 45.5 and 38.6 min, respectively. Several analytical HPLC runs were performed to obtain 2.5 mg of **11a**. MS *m/z*: Calcd for $C_{68}H_{88}IN_{13}O_{16}S_2$: 1534.5408. Found (MALDI): 1356.4 $(M + Na - 2Boc)^+$, 1334.8 $(MH - 2Boc)^+$. A 95:2.5:2.5 (v/v/v) mixture of TFA/water/triisopropylsilane (0.2 mL) was added to the above peptide (**11a**; 2.5 mg), and the mixture left at 20 °C for 30 min. HPLC (conditions as above for the deprotection of **10a**) indicated complete disappearance of **11a** ($t_R = 38.6$ min) and appearance of a peak at 24.8 min. The solvents were evaporated with a stream of argon and the residue redissolved in 0.5 mL of ethanol, and the ethanol evaporated. The process of coevaporation with ethanol was repeated once, and finally the residue was triturated with ether to obtain 1.9 mg of **12a**. MS *m/z*: Calcd for $C_{58}H_{72}IN_{13}O_{12}S_2$: 1334.3092. Found (MALDI): 1356.26 $(M + Na)^+$, 1334.27 $(MH)^+$.

***N*-(2-Bromo-4-(guanidinomethyl)benzoyl)-D-Phe^1-octreotate (12b).** A solution of **9** (3.2 mg; 2.7: mol) and **6b** (4.8 mg; 8.4: mol) in 0.1 mL of 0.1 M DIEA in NMP was incubated at 20 °C for 20 h whereupon HPLC (same conditions as for the synthesis of **10a**; $t_R = 25.0$ and 27.9 min for **6b** and **10b**, respectively) indicated the complete consumption of **9**. Semipreparative HPLC (same conditions as for analytical with a flow rate of 10 mL/min) of the reaction mixture yielded 1–2 mg of **10b** ($t_R = 22.0$ and 24.0 min for **6b** and **10b**, respectively). MS *m/z*: Calcd for $C_{78}H_{100}BrN_{13}O_{18}S_2$ 1651.7414. Found (FAB^+) 1652.5 and 1650.5 $(M)^+$, 1552.5 and 1550.5 $(M - Boc)^+$, 1452.4 and 1450.4 $(M - 2Boc)^+$. Ethanolamine (0.25 mL) was added to a solution of the above peptide (**10b**) in 0.25 mL ethanol, and the deprotection reaction was allowed to proceed at 20 °C. HPLC (same conditions as for the deprotection of **10a**) at 60 min indicated the complete disappearance of **10b** ($t_R = 44.3$ min) and the appearance of a peak at 38.5 min. Semipreparative HPLC of the reaction mixture (same conditions as analytical except for a flow rate of 10 mL/min; $t_R = 35.3$ min) yielded 1.2 mg of **11b**. MS *m/z*: Calcd for $C_{68}H_{88}BrN_{13}O_{16}S_2$ 1487.5403. Found (FAB^+) 1488.5 and 1486.5 $(M)^+$, 1288.5 and 1286.5 $(M - 2Boc)^+$. A 95:2.5:2.5 mixture of TFA/water/triisopropylsilane (0.2 mL) was added to the above peptide and the mixture incubated at 20 °C for 30 min. HPLC (same conditions as used for the conversion of **10b** to **11b**) indicated complete removal of Boc groups (t_R for **12b** = 22 min). MS *m/z*: Calcd for $C_{58}H_{72}BrN_{13}O_{12}S_2$ 1287.3087. Found (MALDI) 1310.5 and 1308.5 $(M + Na)^+$, 1288.5 and 1286.5 $(MH)^+$.

***N*-[4-(N',N''-Bis-*tert*-butyloxycarbonyl)guanidinomethyl-2-(trimethylstannyl)benzoyl]-D-Phe^1-octreotate (11c).** A solution of **8** (13.8 mg; 21.1 μmol) and **9** (9.4 mg; 7.9 μmol) in 0.15 mL of 0.1 M DIEA in NMP was incubated at 20 °C for 7 d. The reaction progress was monitored by the same reversed-phase HPLC conditions that were used for the synthesis of **10a** and **10b**. The retention times of **8** and **10c** were 29.0 and 32.1 min, respectively. The reaction mixture was subjected to semipreparative HPLC using the conditions used for the isolation of **10b** to yield 5.5 mg of **10c**. MS *m/z*: Calcd for $C_{81}H_{109}N_{13}O_{18}S_2Sn$ 1735.6510. Found (MALDI) cluster peaks around 1537.5 $(M - 2Boc)^+$. Ethanolamine (0.25 mL) was added to a solution of the above peptide in ethanol (0.25 mL) and the mixture left at 20 °C. HPLC (same conditions as for the synthesis of **11a** and **11b**) indicated that the removal of the Dde group was complete in about an hour ($t_R = 47.1$ and 39.1 min for **10c** and **11c**, respectively). The reaction mixture was subjected to semipreparative HPLC (same conditions as for **11b**; $t_R = 36.5$ min) to isolate 2.8 mg of **11c**. MS *m/z*: Calcd for $C_{71}H_{97}N_{13}O_{16}S_2Sn$ 1571.4499. Found (MALDI) cluster peaks around 1375.2 $(M - 2Boc)^+$; (FAB) cluster peaks around 1572.0 $(MH)^+$, 1474.1, 1372, 1354.9.

***N*-(4-Guanidinomethyl-2-[^{131}I]iodobenzoyl)-D-Phe^1-octreotate ([^{131}I]12a).** A mixture of **12b** (50 μg), ^{131}I (0.2–4.0 mCi) and 25 μL of glacial acetic acid in a closed ½-dram vial was heated at 100 °C for 20 min The entire reaction mixture was injected into the analytical reversed-phase HPLC column and eluted with the gradient conditions used for the synthesis of **12a**. The HPLC fractions containing [^{131}I]**12a** were isolated and the radioactivity concentrated using a C18 solid-phase cartridge as reported for the isomeric compound (*36*).

Paired-Label Uptake of [^{125}I]MIBG and [^{131}I]12a by SH-SY5Y and SK-N-SH-sst2 cells as a Function of Time. Cells (5×10^5 per well in 2 mL) in 6-well plates in the respective medium was incubated for 24 h. The medium was removed, and the medium containing 100 nCi of each tracer (in 2 mL) was added to the wells. The cells were incubated at 37 °C for 15, 30, 60, 120, and 240 min, and then the medium was aspirated and the cells were washed with the medium and solubilized in 1 N NaOH. Cell-associated radioactivity was determined by counting for both ^{125}I and ^{131}I in an automated gamma counter. For each time point, the assay was performed in triplicate. To determine whether the uptake was NET-mediated, a parallel assay was performed in the presence of 1.5 μM DMI. The results are expressed as the percentage of total activity that was associated with the cells.

Time-Dependent Paired-Label uptake of [^{131}I]12a and [^{125}I]-I-Gluc-TOCA by SK-N-SH-sst2 Cells. This assay was performed essentially like the above except that a different tracer pair was employed and the assay was done using only the transfected cell line. To determine the extent of SSTR-mediated uptake, a parallel assay was performed in the presence of 10 μM octreotide.

Internalization of [^{131}I]12a versus That of [^{125}I]I-Gluc-TOCA and [^{125}I]OIBG-Octreotate by SK-N-SH-sst2 Cells. These assays were performed in a paired-label format following a procedure reported for octreotate derivatives in another cell line (*36*). Briefly, about 200 000 CPM of each tracer was incubated with 5×10^5 cells at 37 °C for 30 min, 1, 2, 3, and 4 h in the presence or absence of 1 μM octreotide. The cell culture supernatants were removed, and the cells were incubated with an acidic (pH 5) buffer to remove surface-bound radioactivity. Cells were finally lysed with 1 N NaOH and counted for radioactivity. The percentage of input radioactivity that was present in the intracellular compartment was determined. Specific internalized radioactivity, defined as the difference in internalized radioactivity in the presence and absence of 1 μM octreotide, was plotted as a function of time.

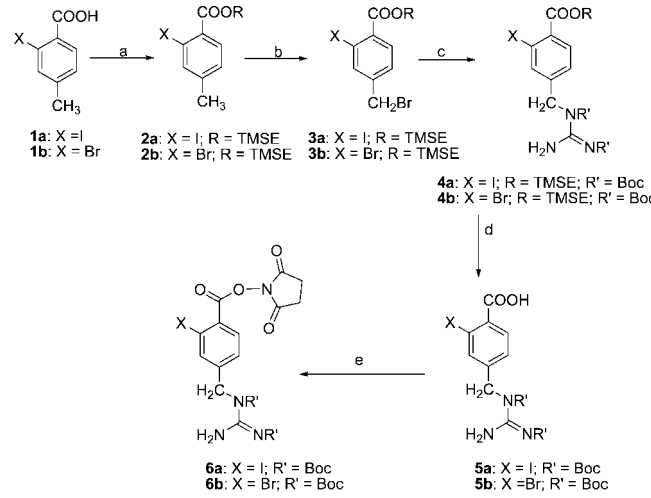
Paired-Label Washout of [^{125}I]MIBG and [^{131}I]12a from SK-N-SH-sst2 Cells. The cells were allowed to take up the tracers for 4 h as in the uptake experiment described above. The medium containing unbound tracers was removed, and the cells were supplemented with fresh medium. Subsequently, the cell-associated radioactivity was determined as above at 0, 4, 8, 16, 24, and 48 h. A paired-label Student's *t* test was used to determine the statistical significance of the difference in the measured values for ^{125}I and ^{131}I.

RESULTS AND DISCUSSION

Radioiodinated MIBG has been widely used for the diagnosis of a number of neuroendocrine tumors as well as imaging the pathophysiology of the heart. MIBG labeled with the β-emitter ^{131}I has been used in the targeted radiotherapy of the above neoplasms. With the hope that a conjugate of [*I]MIBG and an octreotate derivative may deliver a higher cumulative radiation dose to the tumor, we have developed such a fusion molecule and subjected it to preliminary in vitro evaluation of SSTR2- and NET-mediated accumulation in human cancer cells.

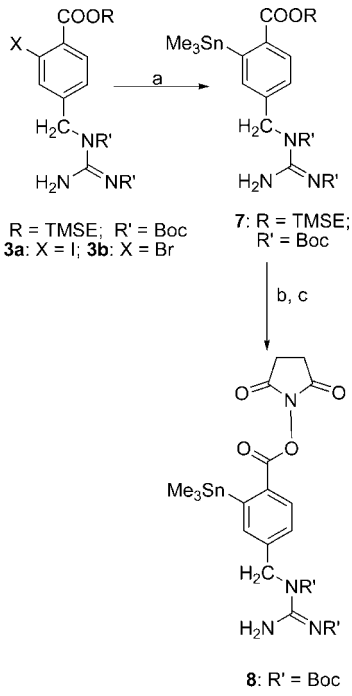
It was envisaged that the easiest way to append an MIBG moiety to a peptide would be to introduce a carboxylic acid function on the MIBG molecule and conjugate it to the N-terminus of the peptide to form an amide bond. We chose to modify MIBG at its 4-position because we showed earlier that the introduction of functional groups at this position did not interfere appreciably with NET-related biological properties of MIBG (*45*). To avoid the potential interference of the carboxyl function present in the peptide in the direct coupling of MIBG derivative with a COOH group, we set forward to synthesize its active ester. Thus, our target was compound **6a** (Scheme 1) wherein the guanidine function of the active ester of an MIBG derivative with an added carboxyl group was protected with Boc groups. Both **6a** and the corresponding trimethylstannyl derivative **8** were prepared as shown in Schemes 1 and 2. The starting material for the iodo derivative, 2-iodo-4-methyl benzoic acid (**1a**), was synthesized from 2-amino-4-methylbenzoic acid. A standard of the final MIBG–octreotate conjugate (**12a**) and the tin precursor (**11c**) were synthesized following protocols reported earlier (*36*) for the isomeric peptide derivatives (Scheme 3). Several sets of different conditions were utilized for the radioiodination of **11c** but less than 1% radiochemical yields of [*I]**11a**, which can be converted to the final target [*I]**12a**, were obtained. Although difficulty in radioiodinating compounds with a carbonyl moiety ortho to the trialkyltin group has been reported, utilizing very harsh conditions has resulted in decent radiochemical yields (*46*). Attempts to radioiodinate **7** to [*I]**4a** under a variety of conditions including those reported by the above authors for their target compound also were futile, and it was not possible to convert the free acid of **7** (R = H) to unlabeled **5a**. Modest radiochemical yields (15–20%) were obtained, however, for the iododestannylation of **8** under relatively mild conditions. It was possible to obtain radioiodinated 4-guanidinomethyl-2-iodobenzoic acid by the nucleophilic iododebromination of the corresponding bromo precursor in 85–90% radiochemical yields (experimental details of the above reactions are not provided). Therefore, a bromo derivative of the peptide conjugate (**12b)** was synthesized (Schemes 1 and 3). Heating a mixture of this peptide and radioiodine in acetic acid yielded the target compound [*I]**12a** (Scheme 4) albeit in modest radiochemical yields (3–36%; $n = 10$). Higher yields might have been obtained with higher amounts of the starting bromo peptide; however, the difference in HPLC retention times between **12a** and **12b** was only 2–3 min, which precluded the use of larger amounts of **12b** for this reaction.

Scheme 1. Synthesis of *N*-Succinimidyl 2-Bromo-4-guanidinomethylbenzoate and *N*-Succinimidyl 4-guanidinomethyl-2-iodobenzoate



a) TMS-ethanol, DCC, DMAP, THF b) NBS, benzoyl peroxide, CCl_4, incandescent light
c) *N,N'*-bis-Boc-guanidine, NaH, DMF d) TBAF, THF e) *N*-hydroxysuccinimide, DCC, THF

Scheme 2. Synthesis of *N*-Succinimidyl 4-(*N*, *N*′-Bis-*tert*-butyloxycarbonyl)guanidinomethyl-2-trimethylstannyl Benzoate

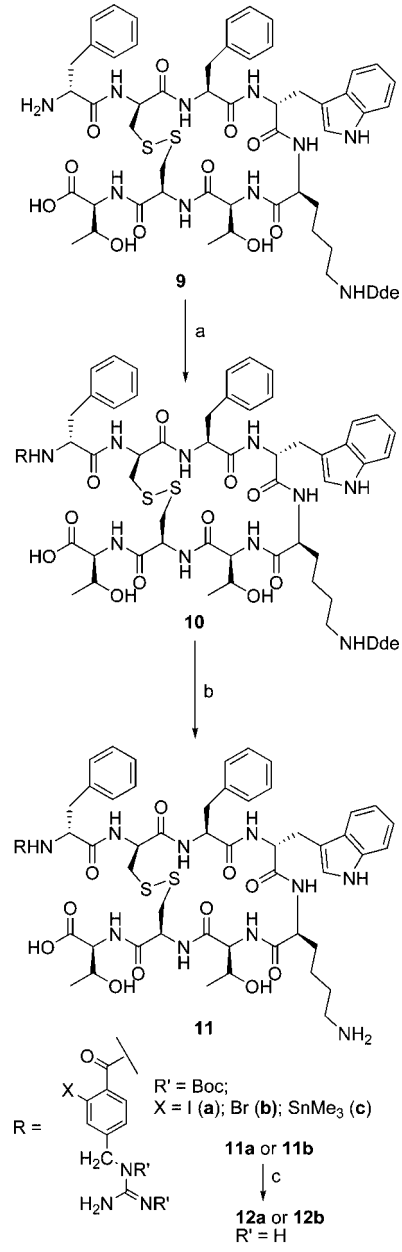


a) Hexamethylditin, $(Ph_3P)_2PdCl_2$, Dioxane b) TBAF, THF c) *N*-hydroxysuccinimide, DCC, THF

The accumulation and retention properties of the MIBG-octreotate ([^{131}I]**12a**) conjugate were evaluated in two cell lines that express both SSTR2 and NET. First, the uptake of [^{125}I]MIBG and [^{131}I]**12a** as a function of time was determined in a paired-label format using SH-SY5Y (*38, 40*) and SK-N-SH-sst2 (*5*) cell lines. Both cell lines demonstrated significant uptake of [^{125}I]MIBG, which appeared to plateau at 4 h (Figure 1). As seen with the wild-type SK-N-SH cells (*2, 47, 48*), the uptake was NET-mediated as shown by its abrogation by DMI treatment. The level of [^{125}I]MIBG uptake in these cell lines was similar to that seen typically in the parental line SK-N-SH (*49*). While specific uptake of radioiodinated MIBG in the SH-SY5Y line has been shown to be similar to the SK-N-SH cell line (*50*), this is the first time the specific uptake of MIBG has been demonstrated in the SSTR2-cloned line. Unlike the case with [^{125}I]MIBG, the uptake of [^{131}I]**12a** did not reach a plateau in either cell line. The total uptake of [^{131}I]**12a** in SK-N-SHsst2 cells was similar to that for [^{125}I]MIBG at all time points (34.9 $\pm$ 2.4% vs 43.8 $\pm$ 1.2% at 4 h; $p < 0.05$), while it was substantially lower in the SH-SY5Y line (5.4 $\pm$ 0.3% vs 35.9 $\pm$ 1.2%). However, DMI did not decrease the uptake of [^{131}I]**12a** in either cell line to the same degree as was seen for [^{125}I]MIBG. This suggests that, while there may be an NET-mediated component to its cell accumulation, the uptake of [^{131}I]**12a** in these cell lines, especially in the SK-N-SH-sst2 cells, might be predominantly related to SSTR2 binding. Although SSTR2 expression in SH-SY5Y cells has been demonstrated (*41*), to our knowledge, its expression level relative to that in SK-N-SH cells has not been reported. On the other hand, quantitative RT-PCR showed that the transfected cells express about a 28-fold higher amount of SSTR2 mRNA than that by the SK-N-SH line.

To investigate the extent of SSTR2 involvement in the uptake of [^{131}I]**12a** by SK-N-SH-sst2 cells, another paired-label assay was performed in which the time-dependent uptake [^{131}I]**12a** was compared to that of [^{125}I]I-Gluc-TOCA. Among various labeled octreotide derivatives, [^{125}I]I-Gluc-TOCA and other sugar-conjugated congeners have demonstrated high accumulation in

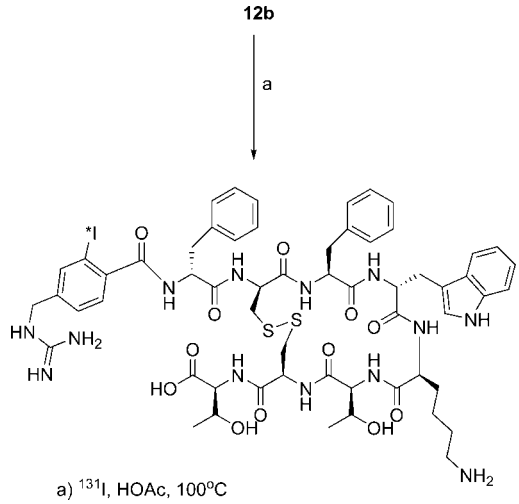
Scheme 3. Synthesis of Octreotate Conjugates 12a, 12b, 12c, 13a, and 13b



a) **6a**, **6b**, or **8**, DIEA/NMP; b) Ethanolamine; c) TFA cocktail

SSTR2-expressing tumor cells and xenografts (*51, 52*). Surprisingly, the uptake of [^{131}I]**12a** was 8–10-fold higher ($p < 0.05$) than that for [^{125}I]I-Gluc-TOCA at all time points (Figure 2). Importantly, the uptake was reduced to about 20% when the cells were coincubated with 10 μM octreotide, demonstrating again that the uptake of [^{131}I]**12a** in this cell line is predominantly mediated by SSTR2. The absolute magnitude of total cellular uptake of [^{131}I]**12a** was lower than that seen in the previous experiment (see Figure 1) and of the intracellularly trapped radioactivity from another experiment (see below; Figure 3). We speculate that this might be due to the use of different passages of cells in different experiments. However, the assays were performed in a paired-label format, and therefore, any changes in receptor and/or transporter expression affected the uptake of both tracers used to the same level, making the comparison meaningful. An exciting observation from these results is that [^{131}I]**12a** exhibits considerably higher SSTR2-mediated cell uptake compared with [^{125}I]I-Gluc-

Scheme 4. Synthesis of Radioiodinated MIBG–Octreotate (12a)



TOCA, which perhaps is one of the best agents for targeting SSTR2-positive tumors.

One of the motivations for development of a hybrid molecule derived from MIBG and octreotate is the feasibility of augmenting the retention of radioactivity in the tumor caused by the possible translocation of the peptide–receptor conjugate to lysosomes after internalization. If the radioactivity were trapped in the lysosomes and, in this manner, NET-mediated egress from the cell was avoided, this could lead to the enhanced residence time in tumor cells, a feature of obvious advantage with such a long-lived radionuclide as ^{131}I. We first determined the extent of internalization of [^{131}I]**12a** by SK-N-SHsst2 cells and compared it to that of [^{125}I]I-Gluc-TOCA and [^{125}I]OIBG-octreotate (*36*)—a position isomer of [^{131}I]**12a**—in two separate paired-label experiments. As depicted in Figure 3, the intracellularly trapped radioactivity from [^{131}I]**12a** steadily increased with time. In concert with the results from the uptake assay, the specific (total minus that in presence of 1 μM octreotide) internalized radioactivity from [^{131}I]**12a** was substantially higher (3–4-fold; $p < 0.05$) than that from [^{125}I]I-Gluc-TOCA. Interestingly, the internalized radioactivity of [^{131}I]**12a** was also higher than that for [^{125}I]OIBG-octreotate. OIBG-octreotate and **12a** differ only in the position of iodine on the aromatic ring (Chart 1). In their seminal work, Wieland and colleagues have shown that, among the three iodobenzylguanidine derivatives, 2-iodobenzylguanidine (OIBG) is the weakest norepinephrine analogue (*53*, *54*). Thus, the above results tempt us to speculate that the enhanced residence time of [^{131}I]**12a** in SK-N-SHsst2 cells is mediated partly by NET.

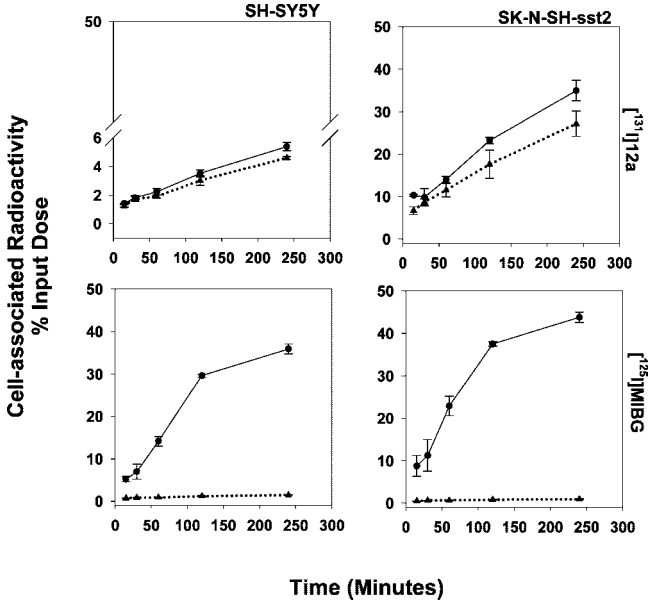


Figure 1. Paired-label time-dependent uptake of [^{125}I]MIBG (bottom panel) and [^{131}I]**12a** (top panel) by SH-SY5Y cells (left panel) and SK-N-SH-sst2 (right panel) in the presence (triangle) and absence (circle) of DMI. Cells (5×10^5 per well) were allowed to take up both tracers in the presence or absence of DMI over various time points, and the cell-associated radioactivity was determined.

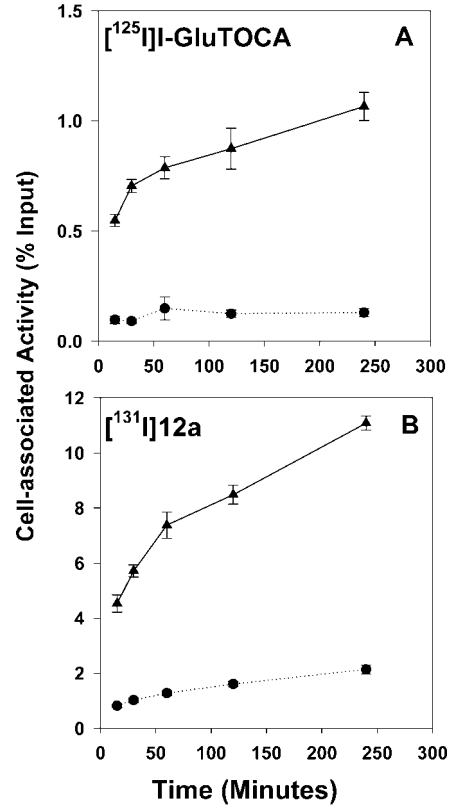


Figure 2. Paired-label uptake of (A) [^{125}I]I-Gluc-TOCA and (B) [^{131}I]**12a** by SK-N-SH-sst2 cells as a function of time in the presence (circle) and absence (triangle) of 1 μM octreotide. The cells were incubated with both tracers for various periods of time in the presence or absence of unlabeled octreotide, and the cell-associated radioactivity was determined. Note that the *Y*-axis scales are not the same for the two plots.

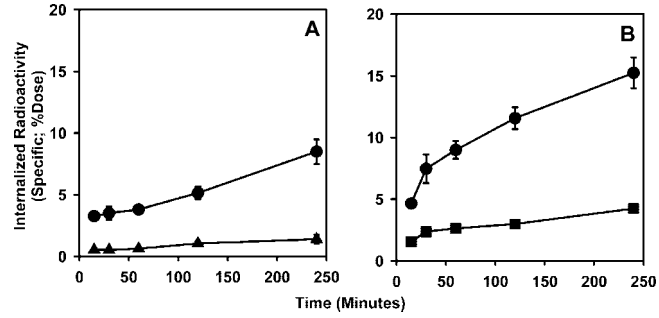


Figure 3. Paired-label specific internalized radioactivity (total minus that in presence of 1 μM octreotide) over a period of 4 h in SK-N-SH-sst2 cells: (A) [^{131}I]**12a** (circle) vs [^{125}I]OIBG-octreotate (triangle) and (B) [^{131}I]**12a** (circle) vs [^{125}I]I-Gluc-TOCA (square). See text for details.

Finally, an assay was performed to determine the extent of egress of [^{131}I]**12a**, in comparison to that of [^{125}I]MIBG, from SK-N-SHsst2 cells. The results from this paired-label study are shown in Figure 4. Up to 24 h, the radioactivity from [^{131}I]**12a** was retained by these cells to a higher extent than from

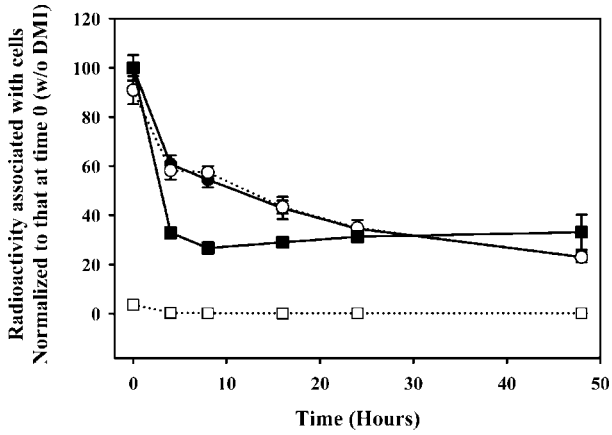


Figure 4. Paired-label washout of [^{125}I]MIBG (square) and [^{131}I]**12a** (circle) from SK-N-SH-sst2 cells in the presence (open) and absence (closed) of 1.5 μM DMI. Cells were allowed to take the two tracers for a period of 4 h; the free radioactivity-containing medium was removed and supplemented with fresh medium with or without DMI. The cell-associated radioactivity was determined periodically afterwards.

[^{125}I]MIBG possibly due to the hypothesized lysosomal trapping. As observed before (*45*), DMI obliterated the retention of [^{125}I]MIBG; on the other hand, it did not have any effect on the retention of [^{131}I]**12a**. Because DMI blocks the NET-mediated uptake, this again demonstrates that NET plays only a minimal role in the uptake of [^{131}I]**12a**.

CONCLUSIONS

In summary, we have developed a method for the synthesis of a conjugate of radioiodinated MIBG and octreotate. While it demonstrated considerable uptake in a tumor cell line expressing both NET and SSTR2, it appears that the predominant pathway for its uptake is via the somatostatin receptor. This might be due to the fact that **12a**, compared to MIBG, lost its affinity to NET due to the presence of the large peptide moiety. MIBG with a COOH function at its 4-position had an uptake 8% that of MIBG in SK-N-SH cells (unpublished results). A conjugate with a long, flexible, and/or cleavable linker may have to be interposed between MIBG and octreotate moieties. On the other hand, the MIBG–octreotate conjugate exhibited excellent retention in these cells that express both NET and SSTR2.

ACKNOWLEDGMENT

This work was supported by grants CA93371 and CA42324 from the National Institutes of Health. The authors want to thank Philip Welsh for his excellent technical assistance.

LITERATURE CITED

(1) Jaques, S., Jr., Tobes, M. C., and Sisson, J. C. (1987) Sodium dependency of uptake of norepinephrine and m-iodobenzylguanidine into cultured human pheochromocytoma cells: evidence for uptake-one. *Cancer Res. 47*, 3920–8.

(2) Smets, L. A., Loesberg, C., Janssen, M., Metwally, E. A., and Huiskamp, R. (1989) Active uptake and extravesicular storage of m-iodobenzylguanidine in human neuroblastoma SK-N-SH cells. *Cancer Res. 49*, 2941–4.

(3) Matthay, K. K., Tan, J. C., Villablanca, J. G., Yanik, G. A., Veatch, J., Franc, B., Twomey, E., Horn, B., Reynolds, C. P., Groshen, S., Seeger, R. C., and Maris, J. M. (2006) Phase I dose escalation of iodine-131-metaiodobenzylguanidine with myeloablative chemotherapy and autologous stem-cell transplantation in refractory neuroblastoma: a new approaches to Neuroblastoma Therapy Consortium Study. *J. Clin. Oncol. 24*, 500–6.

(4) McCluskey, A. G., Boyd, M., Gaze, M. N., and Mairs, R. J. (2005) [^{131}I]MIBG and topotecan: a rationale for combination therapy for neuroblastoma. *Cancer Lett. 228*, 221–7.

(5) Albers, A. R., O'Dorisio, M. S., Balster, D. A., Caprara, M., Gosh, P., Chen, F., Hoeger, C., Rivier, J., Wenger, G. D., O'Dorisio, T. M., and Qualman, S. J. (2000) Somatostatin receptor gene expression in neuroblastoma. *Regul. Pept. 88*, 61–73.

(6) Orlando, C., Raggi, C. C., Bagnoni, L., Sestini, R., Briganti, V., La Cava, G., Bernini, G., Tonini, G. P., Pazzagli, M., Serio, M., and Maggi, M. (2001) Somatostatin receptor type 2 gene expression in neuroblastoma, measured by competitive RT-PCR, is related to patient survival and to somatostatin receptor imaging by indium −111-pentetreotide. *Med. Pediatr. Oncol. 36*, 224–6.

(7) Smitha, M. C., Maggi, M., and Orlando, C. (2004) Somatostatin receptors in non-endocrine tumours. *Dig. Liver Dis. 36*, S78–85 (Suppl. 1).

(8) Pashankar, F. D., O'Dorisio, M. S., and Menda, Y. (2005) MIBG and somatostatin receptor analogs in children: current concepts on diagnostic and therapeutic use. *J. Nucl. Med. 46*, 55S–61S (Suppl. 1).

(9) de Jong, M., Breeman, W. A., Valkema, R., Bernard, B. F., and Krenning, E. P. (2005) Combination radionuclide therapy using ^{177}Lu- and ^{90}Y-labeled somatostatin analogs. *J. Nucl. Med. 46*, 13S–7S (Suppl. 1).

(10) Kwekkeboom, D. J., Mueller-Brand, J., Paganelli, G., Anthony, L. B., Pauwels, S., Kvols, L. K., O'Dorisio, T, M., Valkema, R., Bodei, L., Chinol, M., Maecke, H. R., and Krenning, E. P. (2005) Overview of results of peptide receptor radionuclide therapy with 3 radiolabeled somatostatin analogs. *J. Nucl. Med. 46*, 62S–6S (Suppl. 1).

(11) Valkema, R., Pauwels, S., Kvols, L. K., Barone, R., Jamar, F., Bakker, W. H., Kwekkeboom, D. J., Bouterfa, H., and Krenning, E. P. (2006) Survival and response after peptide receptor radionuclide therapy with [^{90}Y-DOTA^{0},Tyr^{3}]octreotide in patients with advanced gastroenteropancreatic neuroendocrine tumors. *Semin. Nucl. Med. 36*, 147–56.

(12) Kaltsas, G. A., Mukherjee, J. J., and Grossman, A. B. (2001) The value of radiolabelled MIBG and octreotide in the diagnosis and management of neuroendocrine tumours. *Ann. Oncol, 12*, S47–50 (Suppl. 2).

(13) Taal, B. G., Hoefnagel, C. A., Valdes Olmos, R. A., and Boot, H. (1996) Combined diagnostic imaging with ^{131}I-metaiodobenzylguanidine and ^{111}In-pentetreotide in carcinoid tumours. *Eur. J. Cancer 32A*, 1924–32.

(14) van der Harst, E., de Herder, W. W., Bruining, H. A., Bonjer, H. J., de Krijger, R. R., Lamberts, S. W., van de Meiracker, A. H., Boomsma, F., Stijnen, T., Krenning, E. P., Bosman, F. T., and Kwekkeboom, D. J. (2001) [^{123}I]metaiodobenzylguanidine and [^{111}In]octreotide uptake in benign and malignant pheochromocytomas. *J. Clin. Endocrinol. Metab. 86*, 685–93.

(15) Dresel, S., Tatsch, K., Zachoval, R., and Hahn, K. (1996) ^{111}IN-octreotide and ^{123}I-MIBG scintigraphy in the diagnosis of small intestinal carcinoid tumors--results of a comparative investigation. *Nuklearmedizin 35*, 53–8.

(16) Manil, L., Perdereau, B., Barbaroux, C., and Brixy, F. (1994) Strong uptake of ^{111}In-pentetreotide by an MIBG-negative, xenografted neuroblastoma. *Int. J. Cancer 57*, 245–6.

(17) Tenenbaum, F., Lumbroso, J., Schlumberger, M., Mure, A., Plouin, P. F., Caillou, B., and Parmentier, C. (1995) Comparison of radiolabeled octreotide and meta-iodobenzylguanidine (MIBG) scintigraphy in malignant pheochromocytoma. *J. Nucl. Med. 36*, 1–6.

(18) Wiseman, G. A., and Kvols, L. K. (1995) Therapy of neuroendocrine tumors with radiolabeled MIBG and somatostatin analogues. *Semin. Nucl. Med. 25*, 272–8.

(19) Ezziddin, S., Logvinski, T., Yong-Hing, C., Ahmadzadehfar, H., Fischer, H. P., Palmedo, H., Bucerius, J., Reinhardt, M. J., and Biersack, H. J. (2006) Factors predicting tracer uptake in somatostatin receptor and MIBG scintigraphy of metastatic gastroenteropancreatic neuroendocrine tumors. *J. Nucl. Med. 47*, 223–33.

(20) Bombardieri, E., Maccauro, M., De Deckere, E., Savelli, G., and Chiti, A. (2001) Nuclear medicine imaging of neuroendocrine tumours. *Ann. Oncol. 12*, S51–61 (Suppl. 2).

(21) Kaltsas, G., Rockall, A., Papadogias, D., Reznek, R., and Grossman, A. B. (2004) Recent advances in radiological and radionuclide imaging and therapy of neuroendocrine tumours. *Eur. J. Endocrinol. 151*, 15–27.

(22) Madsen, M. T., Bushnell, D. L., Juweid, M. E., Menda, Y., O'Dorisio, M. S., O'Dorisio, T., and Besse, I. M. (2006) Potential increased tumor-dose delivery with combined ^{131}I-MIBG and ^{90}Y-DOTATOC treatment in neuroendocrine tumors: a theoretic model. *J. Nucl. Med. 47*, 660–7.

(23) Geuze, H. J., Slot, J. W., Strous, G. J., Peppard, J., von Figura, K., Hasilik, A., and Schwartz, A. L. (1984) Intracellular receptor sorting during endocytosis: comparative immunoelectron microscopy of multiple receptors in rat liver. *Cell 37*, 195–204.

(24) Mier, W., Eritja, R., Mohammed, A., Haberkorn, U., and Eisenhut, M. (2000) Preparation and evaluation of tumor-targeting peptide-oligonucleotide conjugates. *Bioconjugate Chem. 11*, 855–60.

(25) Sun, L., Fuselier, J. A., Murphy, W. A., and Coy, D. H. (2002) Antisense peptide nucleic acids conjugated to somatostatin analogs and targeted at the n-myc oncogene display enhanced cytotoxity to human neuroblastoma IMR32 cells expressing somatostatin receptors. *Peptides 23*, 1557–65.

(26) Kiaris, H., Schally, A. V., Nagy, A., Szepeshazi, K., Hebert, F., and Halmos, G. (2001) A targeted cytotoxic somatostatin (SST) analogue, AN-238, inhibits the growth of H-69 small-cell lung carcinoma (SCLC) and H-157 non-SCLC in nude mice. *Eur. J. Cancer 37*, 620–8.

(27) Huang, C. M., Wu, Y. T., and Chen, S. T. (2000) Targeting delivery of paclitaxel into tumor cells via somatostatin receptor endocytosis. *Chem. Biol. 7*, 453–61.

(28) Capello, A., Krenning, E. P., Bernard, B. F., Breeman, W. A., Erion, J. L., and de Jong, M. (2006) Anticancer activity of targeted proapoptotic peptides. *J. Nucl. Med. 47*, 122–9.

(29) DeNardo, S. J. (2006) Combined molecular targeting for cancer therapy: a new paradigm in need of molecular imaging. *J. Nucl. Med. 47*, 4–5.

(30) Carlson, C. B., Mowery, P., Owen, R. M., Dykhuizen, E. C., and Kiessling, L. L. (2007) Selective tumor cell targeting using low-affinity, multivalent interactions. *ACS Chem. Biol. 2*, 119–27.

(31) Mammen, M., Choi, S.-K., and Whitesides, G. M. (1998) Polyvalent interactions in biological systems: Implications for design and use of multivalent ligands and inhibitors. *Angew. Chem., Int. Ed. 37*, 2754–2794.

(32) Morphy, R., and Rankovic, Z. (2005) Designed multiple ligands. An emerging drug discovery paradigm. *J. Med. Chem. 48*, 6523–43.

(33) Reubi, J. C., and Waser, B. (2003) Concomitant expression of several peptide receptors in neuroendocrine tumours: molecular basis for in vivo multireceptor tumour targeting. *Eur. J. Nucl. Med. Mol. Imaging 30*, 781–93.

(34) Vagner, J., Handl, H. L., Gillies, R. J., and Hruby, V. J. (2004) Novel targeting strategy based on multimeric ligands for drug delivery and molecular imaging: homooligomers of alpha-MSH. *Bioorg. Med. Chem. Lett. 14*, 211–5.

(35) Qiu, Q., Domarkas, J., Banerjee, R., Merayo, N., Brahimi, F., McNamee, J. P., Gibbs, B. F., and Jean-Claude, B. J. (2007) The combi-targeting concept: in vitro and in vivo fragmentation of a stable combi-nitrosourea engineered to interact with the epidermal growth factor receptor while remaining DNA reactive. *Clin. Cancer Res. 13*, 331–40.

(36) Vaidyanathan, G., Boskovitz, A., Shankar, S., and Zalutsky, M. R. (2004) Radioiodine and ^{211}At-labeled guanidinomethyl halobenzoyl octreotate conjugates: potential peptide radiotherapeutics for somatostatin receptor-positive cancers. *Peptides 25*, 2087–97.

(37) Vaidyanathan, G., and Zalutsky, M. R. (1993) No-carrier-added synthesis of meta-[^{131}I]iodobenzylguanidine. *Appl. Radiat. Isot. 44*, 621–8.

(38) Biedler, J. L., Roffler-Tarlov, S., Schachner, M., and Freedman, L. S. (1978) Multiple neurotransmitter synthesis by human neuroblastoma cell lines and clones. *Cancer Res. 38*, 3751–7.

(39) Biedler, J. L., Helson, L., and Spengler, B. A. (1973) Morphology and growth, tumorigenicity, and cytogenetics of human neuroblastoma cells in continuous culture. *Cancer Res. 33*, 2643–52.

(40) Stirnweis, J., Boehmer, F. D., and Liebmann, C. (2002) The putative somatostatin antagonist, cyclo-(7-aminoheptanoyl-Phe-D-Trp-Lys-Thr[BZL]), may act as potent antiproliferative agonist. *Peptides 23*, 1503–6.

(41) Cattaneo, M. G., Taylor, J. E., Culler, M. D., Nisoli, E., and Vicentini, L. M. (2000) Selective stimulation of somatostatin receptor subtypes: differential effects on Ras/MAP kinase pathway and cell proliferation in human neuroblastoma cells. *FEBS Lett. 481*, 271–6.

(42) Connor, M., Yeo, A., and Henderson, G. (1997) Neuropeptide Y Y2 receptor and somatostatin sst2 receptor coupling to mobilization of intracellular calcium in SH-SY5Y human neuroblastoma cells. *Br. J. Pharmacol. 120*, 455–63.

(43) Kaltenbach, J. P., Kaltenbach, M. H., and Lyons, W. B. (1958) Nigrosin as a dye for differentiating live and dead ascites cells. *Exp. Cell Res. 15*, 112–7.

(44) Panetta, C. A., Garlick, S. M., Durst, H. D., Longo, F. R., and Ward, J. R. (1990) Synthesis of 4-alkyl-2-iodosobenzoic acids - potent catalysts for the hydrolysis of phosphorus esters. *J. Org. Chem. 55*, 5202–5205.

(45) Vaidyanathan, G., Shankar, S., Affleck, D. J., Welsh, P. C., Slade, S. K., and Zalutsky, M. R. (2001) Biological evaluation of ring- and side-chain-substituted m-iodobenzylguanidine analogues. *Bioconjugate Chem. 12*, 798–806.

(46) Zea-Ponce, Y., Baldwin, R. M., Zoghbi, S. S., and Innis, R. B. (1994) Formation of 1-[^{123}I]iodobutane in labeling [^{123}I]iomazenil by iododestannylation: implications for the reaction mechanism. *Appl. Radiat. Isot. 45*, 63–8.

(47) Smets, L. A., Janssen, M., Metwally, E., and Loesberg, C. (1990) Extragranular storage of the neuron blocking agent meta-iodobenzylguanidine (MIBG) in human neuroblastoma cells. *Biochem. Pharmacol. 39*, 1959–64.

(48) Vaidyanathan, G., Welsh, P. C., Vitorello, K. C., Snyder, S., Friedman, H. S., and Zalutsky, M. R. (2004) A 4-methyl-substituted meta-iodobenzylguanidine analogue with prolonged retention in human neuroblastoma cells. *Eur. J. Nucl. Med. Mol. Imaging 31*, 1362–70.

(49) Vaidyanathan, G., Affleck, D. J., and Zalutsky, M. R. (2005) No-carrier-added synthesis of a 4-methyl-substituted meta-iodobenzylguanidine analogue. *Appl. Radiat. Isot. 62*, 435–40.

(50) Iavarone, A., Lasorella, A., Servidei, T., Riccardi, R., and Mastrangelo, R. (1993) Uptake and storage of m-iodobenzylguanidine are frequent neuronal functions of human neuroblastoma cell lines. *Cancer Res. 53*, 304–9.

(51) Vaidyanathan, G., Friedman, H. S., Affleck, D. J., Schottelius, M., Wester, H. J., and Zalutsky, M. R. (2003) Specific and high-level targeting of radiolabeled octreotide analogues to human medulloblastoma xenografts. *Clin. Cancer Res. 9*, 1868–76.

(52) Schottelius, M., Reubi, J. C., Eltschinger, V., Schwaiger, M., and Wester, H. J. (2005) N-terminal sugar conjugation and C-terminal Thr-for-Thr(ol) exchange in radioiodinated Tyr^3-octreotide: effect on cellular ligand trafficking in vitro and tumor accumulation in vivo. *J. Med. Chem. 48*, 2778–89.

(53) Wieland, D. M., Mangner, T. J., Inbasekaran, M. N., Brown, L. E., and Wu, J. L. (1984) Adrenal medulla imaging agents: a structure-distribution relationship study of radiolabeled aralkylguanidines. *J. Med. Chem. 27*, 149–55.

(54) Wieland, D. M., Wu, J., Brown, L. E., Mangner, T. J., Swanson, D. P., and Beierwaltes, W. H. (1980) Radiolabeled adrenergic neuron-blocking agents: adrenomedullary imaging with [^{131}I]iodobenzylguanidine. *J. Nucl. Med. 21*, 349–53.

BC700240R

Temperature-Sensitive Poly(*N*-(2-hydroxypropyl)methacrylamide mono/dilactate)-Coated Liposomes for Triggered Contents Release

Lauri Paasonen,*[,†,‡,§] Birgit Romberg,[†] Gert Storm,[†] Marjo Yliperttula,[‡,§] Arto Urtti,[§] and Wim E. Hennink[†]

Department of Pharmaceutics, Utrecht Institute for Pharmaceutical Sciences, Utrecht University, Sorbonnelaan 16, 3584 CA, Utrecht, The Netherlands, Division of Biopharmacy and Pharmacokinetics, University of Helsinki, P.O. Box 56, 00014 Helsinki, Finland, and Drug Discovery and Development Technology Center, University of Helsinki, P.O. Box 56, 00014 Helsinki, Finland. Received July 4, 2007; Revised Manuscript Received September 13, 2007

We prepared thermosensitive poly(*N*-(2-hydroxypropyl)methacrylamide mono/dilactate) (pHPMA mono/dilactate) polymer and studied temperature-triggered contents release from polymer-coated liposomes. HPMA mono/dilactate polymer was synthesized with a cholesterol anchor suitable for incorporation in the liposomal bilayers and with a cloud point (CP) temperature of the polymer slightly above normal body temperature (42 °C). Dynamic light scattering (DLS) measurements showed that whereas the size of noncoated liposomes remained stable upon raising the temperature from 25 to 46 °C, polymer-coated liposomes aggregated around 43 °C. Also, noncoated liposomes loaded with calcein showed hardly any leakage of the fluorescent marker when heated to 46 °C. However, polymer-coated liposomes showed a high degree of temperature-triggered calcein release above the CP of the polymer. Likely, liposome aggregation and bilayer destabilization are triggered because of the precipitation of the thermosensitive polymer above its CP onto the liposomal bilayers, followed by permeabilization of the liposomal membrane. This study demonstrates that liposomes surface-modified with HPMA mono/dilactate copolymer are attractive systems for achieving temperature-triggered contents release.

INTRODUCTION

Liposomes have been widely studied as nanosized carriers in drug delivery. They are biocompatible, nontoxic, and nonimmunogenic, and they can be used for the delivery of both hydrophilic and hydrophobic drug molecules (*1, 2*). A major challenge in liposomal drug delivery is the triggered release of the drug only at the site of action, resulting in exposure of the target cells to a high concentration of the drug. Several approaches for triggered drug release from liposomes have been investigated. These involve enzyme-activated (*3, 4*), pH-sensitive (*5*), light-sensitive (*6*), ultrasound-triggered (*7*), and temperature-sensitive liposomes (*8, 9*).

Temperature-sensitive liposomes can be prepared from phospholipids that have a sharp gel-to-liquid crystalline transition, but they can be also prepared by functionalizing liposomes with polymers that exhibit a lower critical solution temperature (LCST) (*10*). These polymers are water-soluble below their cloud point (CP) temperature, but they become hydrophobic and subsequently precipitate when the temperature is raised above the CP. Because of the polymer precipitation on the liposome surface, the polymer interacts with the liposomal bilayer resulting in bilayer destabilization, and this feature could be applied for temperature-triggered contents release from the liposomes. Such temperature-sensitive liposomes remain intact at 37 °C and avoid drug leakage in the blood circulation. Heating at the target site (e.g., tumor, skin, back of the eye) subsequently triggers the release of the drug from the liposomes locally, which improves the efficacy of the treatment and reduces side effects. The release temperature should be adjusted to 41–42 °C so that heating does not cause damage to healthy tissues.

Poly(*N*-isopropylacrylamide) [p(NIPAM)] exhibits the CP at 32 °C, and it has been studied as a thermosensitive coating for liposomes by Kono and co-workers (*11–14*). They showed that p(NIPAM) can induce temperature-triggered contents release from liposomes. Hayashi et al. reported that the CP of p(NIPAM) can be increased by copolymerization NIPAM with acrylamide (*12*). This is important because in clinical use the polymer precipitation and drug release from liposomes should occur at a few degrees above normal body temperature. Han and co-workers studied the temperature-triggered release of doxorubicin from liposomes that were coated with p(NIPAM-*co*-acrylamide) and polyethyleneglycol (PEG) (*15*). The major drawback of p(NIPAM) is that it is not biodegradable, and therefore, there is a risk for side effects related to polymer accumulation in the body.

Poly(*N*-(2-hydroxypropyl)methacrylamide) (HPMA) polymers have been widely studied as biodegradable macromolecular carriers for anticancer drugs (*16*). Recently, HPMA-based copolymers with tuneable thermosensitivity were synthesized by free radical polymerization of HPMA monolactate and HPMA dilactate (*17*). It was shown that the CP of HPMA mono/dilactate copolymers can be tailored between 13 and 65 °C by varying the monolactate/dilactate ratio in the copolymer. Importantly, it was also shown that the polymers were biodegradable.

Because of their adjustable thermosensitivity and biodegradability, HPMA mono/dilactate copolymers are a promising tool for temperature-triggered contents release from liposomes. In this study, we synthesized thermosensitive HPMA mono/dilactate copolymers with a cholesterol anchor suitable for incorporation in liposomal bilayers. Liposomes were successfully coated with the polymer, and the temperature-triggered

* To whom correspondence should be addressed. Phone: +358 9 191 59479. Fax: +358 9 191 59725. E-mail: Lauri.Paasonen@helsinki.fi.

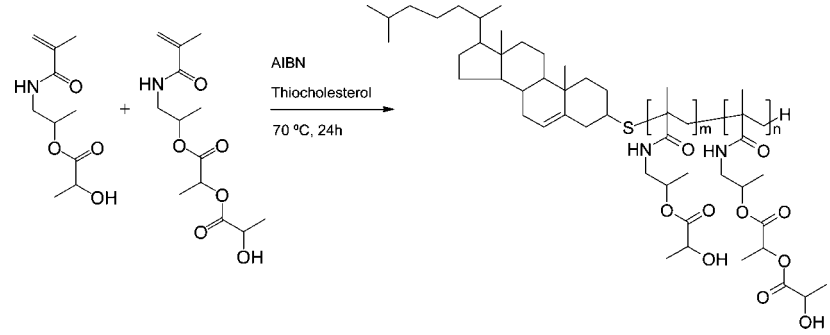
[†] Utrecht University.

[‡] Division of Biopharmacy and Pharmacokinetics, University of Helsinki.

[§] Drug Discovery and Development Technology Center, University of Helsinki.

10.1021/bc700245p CCC: $37.00 © 2007 American Chemical Society
Published on Web 10/27/2007

Scheme 1. Synthesis of Poly(HPMA mono/dilactate)–Cholesterol



liposome aggregation and the release of encapsulated fluorescent marker were determined.

EXPERIMENTAL SECTION

Materials. Thiocholesterol, Ellman's reagent [5,5′-dithiobis(2-nitrobenzoic acid)], cysteine, cholesterol, and calcein were purchased from Sigma-Aldrich Chemie BV, Zwijndrecht, The Netherlands. *N*,*N*′-azobisisobutyronitrile (AIBN) and 1,4-dioxane were purchased from Fluka Chemie AG, Buchs, Switzerland. Egg phosphocholine (EPC), 1,2-dipalmitoyl-*sn*-glycero-3-phosphocholine (DPPC), and 1,2-dioleoyl-*sn*-glycero-3-phosphoethanolamine (DOPE) were purchased from Lipoid GmbH, Ludwigshafen, Germany.

Synthesis of HPMA Mono/Dilactate Copolymers with Cholesterol Anchor. The synthetic route to poly(HPMA mono/dilactate) with a cholesterol anchor is illustrated in Scheme 1. HPMAm monolactate and HPMAm dilactate monomers were synthesized as reported earlier (*18*), and copolymers were prepared by radical polymerization using thiocholesterol as a chain transfer agent (CTA). Thiol compounds act as CTA in radical polymerization (*19*). The molar ratios between HPMAm monolactate and HPMAm dilactate used in polymerization ranged from 70/30 to 85/15. Monomers were dissolved in freshly distilled 1,4-dioxane at the concentration of 100 mg/mL. *N*,*N*′-azobisisobutyronitrile was used as radical initiator at a molar ratio of 500/1 (monomers/AIBN), and thiocholesterol as chain transfer agent was used at a molar ratio of 50/1 (monomers/thiocholesterol). Desired amounts of monomers, AIBN, and thiocholesterol were transferred into sealable glass vial, followed by five freeze–thaw cycles under a nitrogen atmosphere in order to remove oxygen. Polymerization was carried out at 70 °C for 24 h. The obtained polymers were precipitated dropwise into an excess of diethyl ether under vigorous stirring. After centrifugation, the supernatants were discarded and traces of diethyl ether were removed in vacuo. The prepared polymers were dissolved in water, freeze-dried, and stored in a freezer.

Characterization of the Polymers. Traces of unreacted thiocholesterol in the crude polymers were determined by Ellman's assay (*20*). A calibration curve was obtained with cysteine standards (0.25–1.5 mM) by measuring UV absorbance at 412 nm (Perkin Elmer Lambda 2 UV/vis spectrometer, Überlingen, Germany). The molecular weights and their distributions were determined by gel permeation chromatography (GPC). Analysis was performed with a Waters GPC system (Waters Associates Inc., Milford, MA) at 40 °C in Plgel 3 μm MIXED-D column (Polymer Laboratories), using poly(ethylene glycol) standards. The eluent was DMF containing 10 mM LiCl, and the elution rate was 0.7 mL/min.

The polymers were characterized by ^{1}H NMR (Gemini 300 MHz spectrometer, Varian Associates Inc., NMR Instruments, Palo Alto, CA) using $CDCL_3$ as a solvent. The ratios of monolactate to dilactate side chains in the polymers were determined from the peaks at 5.0 and 4.3 ppm as described earlier (*17*), and the cholesterol peak was observed at 0.7 ppm.

The cloud point (CP) temperature of the polymers was measured by static light scattering (SLS) using a temperature gradient (approximately 1 °C/min). The polymers were dissolved in 120 mM ammonium acetate buffer (pH 5) at a concentration of 1, 2, or 5 mg/mL, and the scattering was measured with a fluorometer (Fluorolog Horiba, Edison, NJ) in a quartz cuvette at 650 nm. The samples were under constant stirring during the experiment. The onset of transition from a scattering intensity–temperature curve was considered as the CP temperature.

Preparation of Polymer-Coated Liposomes. Two different liposome formulations were coated with 5 mol % poly(HPMA mono/dilactate)–cholesterol. With this method, polymer chains are expected to be located both on the outer and on the inner surface of the liposomes. One formulation was prepared from DPPC, cholesterol, and the polymer with a molar ratio of 100:42.5:7.5 (DPPC/cholesterol/polymer). The polymers used for coating were 49/51 (monolactate/dilactate) and 71/29, respectively. Another liposome formulation was prepared from DOPE, EPC, and the polymer (71/29) with a molar ratio of 70:25:5 (DOPE/EPC/polymer). Lipids and polymer were dissolved in chloroform in a 50 mL round bottom flask, and the solvent was evaporated in a rotating vacuum evaporator at 35 °C. The resulting lipid–polymer film was further dried under a nitrogen stream and then hydrated with 3 mL of isotonic 20 mM HEPES buffer (pH 7.4) to obtain a final lipid concentration of 30 μmol/mL. For calcein-loaded liposome preparation, the lipid–polymer film was hydrated with 3 mL of calcein solution (60 mM, 280 mOsm). This solution was prepared by dissolving 374 mg of calcein and 17 mg of NaCl in 10 mL of water, and the pH was adjusted to 7.4 with NaOH. The DPPC/cholesterol liposomes were sized by multiple extrusions through two stacked polycarbonate filters with a pore size of 100 nm, and the DOPE/EPC liposomes were extruded through filters with pore sizes of 100 and 50 nm. In the case of calcein-loaded liposomes, free calcein was removed by column filtration using a Sephadex G-50 (Pharmacia Fine Chemicals AB, Uppsala, Sweden) column; samples (500 μL liposomes) were eluted with 20 mM HEPES buffer. The same protocol was used to prepare control liposomes (DPPC/cholesterol (molar ratio 2:1) and DOPE/EPC (molar ratio 7:3)) without polymer coating.

Characterization of Polymer-Coated Liposomes. The amount of incorporated polymer on the DPPC/cholesterol liposome surface was estimated with ^{1}H NMR using a method described earlier (*21*). Briefly, part of the polymer-coated liposome dispersion was subjected to ultracentrifugation (Optima LE-80K, Beckman Instruments, Inc.) at 200000*g* for 1 h to separate liposomes from nongrafted polymer molecules. The supernatant was removed, and the liposome pellet was dispersed in 20 mM HEPES buffer. Subsequently, liposomes were freeze-dried and the cake was dissolved in $CDCl_3$ and analyzed with ^{1}H NMR. The amount of polymer associated with the liposomes

Table 1. Poly(HPMA mono/dilactate)–Cholesterol Copolymer Characteristics

copolymer feed ratio (monolactate/dilactate)	C	yield (%)	M_n (Da)	PDI (M_w/M_n)	CP (°C)
70/30	49/51	60	6200	1.44	36
75/25	55/45	61	5850	1.47	37.5
80/20	71/29	56	5800	1.46	42
85/15	79/21	59	5600	1.42	44

was estimated by comparing the polymer peak (5.0 ppm)/DPPC peak (5.2 ppm) ratio between liposomes before and after ultracentrifugation.

The mean particle size of the liposomes was evaluated by dynamic light scattering (DLS). Liposome samples were diluted with 20 mM HEPES buffer (30 μL of liposomes + 1 mL of buffer) and measured with a Malvern ALV/CGS-3 goniometer (Malvern, U.K.). Also, the polydispersity index (PDI), a value indicating the size distribution of the liposomes, was determined. Measurements were done at different temperatures between 25 and 46 °C in order to investigate the temperature-dependent behavior of the liposomes.

Temperature-Triggered Calcein Release. The release of calcein from liposomes was studied fluorometrically. Calcein does not show fluorescence emission when entrapped at high concentration (60 mM) inside the liposomes but gives strong fluorescence when it is released from the liposomes and diluted in the surrounding buffer. Different calcein concentrations were measured to determine the linear part of the fluorescence signal, and all the subsequent sample measurements were performed in the range 0.01–2 μM. Excitation and emission wavelengths were 490 and 520 nm, respectively. DPPC/cholesterol/polymer liposomes containing calcein were diluted 1:40 in 20 mM HEPES buffer, and the calcein fluorescence was monitored with Fluorolog Horiba by heating the samples from 25 to 50 °C with a heating rate of approximately 1 °C/min. The calcein-loaded DOPE/EPC/polymer liposomes were diluted 1:400 in 20 mM HEPES buffer, and the fluorescence was determined with Fluostar Optima fluorometer (BMG Labtech, Offenburg, Germany) after incubation of the samples in different temperatures. The percent release was then calculated as follows:

$$\% \text{ calcein release} = \frac{F - F_I}{F_T - F_I} \times 100$$

where F is the sample fluorescence at certain temperature, F_I is the initial fluorescence, and F_T is the fluorescence of calcein after solubilization of liposomes by addition of 50 μL of 10% Triton X-100 (Sigma-Aldrich).

RESULTS AND DISCUSSION

Polymer Synthesis and Characterization. Poly(HPMA mono/dilactate)–cholesterol copolymers were synthesized by free radical polymerization using thiocholesterol as a CTA. Ellman's assay showed less than 1% free thiol goups of the original amount in the crude reaction mixture. This suggests that thiocholesterol was built in the polymer. The characteristics of the cholesterol-containing copolymers are summarized in Table 1. The yield of all copolymers was around 60%. Figure 1 shows a ^{1}H NMR spectrum of poly(HPMA mono/dilactate)–cholesterol with a monomer ratio of 71/29 (monolactate/dilactate). The copolymer composition (C) was determined from ^{1}H NMR analysis, and it was observed that the amounts of HPMA monolactate in the products were slightly lower when compared to the feed ratios, suggesting that HPMA dilactate is more reactive than HPMA monolactate under the used polymerization conditions. The peak at 0.7 ppm (Figure 1) indicates the presence of the cholesterol in the copolymer, but because of peak overlap, quantitative analysis of the cholesterol amount could not be performed. GPC results showed that the number average molecular weight (M_n) of the copolymers ranged from 5600 to 6300 Da, depending on the monomer ratio. The polydispersity index (M_w/M_n) of all the copolymers was below 1.5, which indicates a relatively narrow size distribution (Table 1).

Static light scattering measurements showed that the aggregation onset of all the copolymers was sharp; aggregation did not occur below the CP. The CP of the different copolymers in 1 mg/mL solution could be adjusted between 36 and 44 °C by changing the monolactate/dilactate ratio (Table 1). In agreement with previous data (*17*), the CP of the polymer decreased when the concentration of the polymer solution was increased to 2 and 5 mg/mL (Figure 2). The CP of the copolymers increased with higher monolactate content in the copolymer. The increase of the CP is due to the higher hydrophilicity of the monolactate side group. The CPs of the cholesterol anchor containing 71/29 polymer and 79/21 polymer (Table 1) were approximately 4 °C lower than those without anchor (*17*). This can be explained in that the hydrophobicity of the polymers is increased because of the cholesterol anchor. The CPs of cholesterol containing 49/51 polymer and 55/45 polymer were close to the CP of polymer without cholesterol. In these polymers the hydrophobicity of cholesterol is probably masked under hydrophobic dilactate side groups and does not decrease the CP.

Polymer-Coated Liposomes. ^{1}H NMR analysis showed that approximately 60% of the copolymer (copolymer composition of 71/29, Table 1) that was added at the start of the liposome preparation became associated with the liposomes. Probably not all polymer chains contain a cholesterol anchor and therefore were not grafted onto the liposomal bilayers. It is also possible that the longer polymer chains containing the anchor may have been extracted out of the liposomes during extrusion and/or ultracentrifugation.

Dynamic light scattering measurements showed that the mean size and the polydispersity index (PDI) of noncoated liposomes were stable upon heating of the liposome dispersion from 25 to 46 °C (Figure 3). However, both the mean size and the PDI of the DPPC/cholesterol/polymer liposomes were strongly increased at 43 °C (Figure 3A), which corresponds with the CP of the 71/29 polymer (42 °C). Also, when polymers with different CPs were used for coating, DPPC/cholesterol liposomes showed aggregation at the polymer CP (data not shown). When the coating polymer chains become hydrophobic and precipitate above the CP, they interact with the liposomal bilayers and cause liposome aggregation. It was also observed that liposome aggregation was reversible. When the temperature was set back to 25 °C, the mean diameter of the liposomes decreased to 200 nm.

Noncoated DOPE/EPC liposomes were stable between 25 and 46 °C. The mean size and the PDI of DOPE/EPC/polymer liposomes did not increase upon heating to 43 °C, but aggregation was observed at 46 °C (Figure 3B). The size increase was not as pronounced as with DPPC/cholesterol/polymer liposomes, but substantial increase in the PDI indicated liposome aggregation. These findings are likely related to the properties of the lipids. DOPE alone does not form liposomes because it has a tendency to take a hexagonal II phase at 3 °C (*22*). However, liposomes can be prepared by mixing DOPE with stabilizing components, such as cholesterol or phosphocholines. EPC is a natural mixture of saturated and unsaturated phosphocholines with gel-to-liquid crystalline transition temperatures ranging from −70 to 55 °C.

Temperature-Triggered Calcein Release. Uncoated DPPC/cholesterol liposomes remained intact and did not release calcein when the dispersion was heated from 25 to 50 °C. Temperature-triggered calcein release was observed when poly(HPMA mono/dilactate)–cholesterol (monolactate/dilactate ratio of 49/51) was

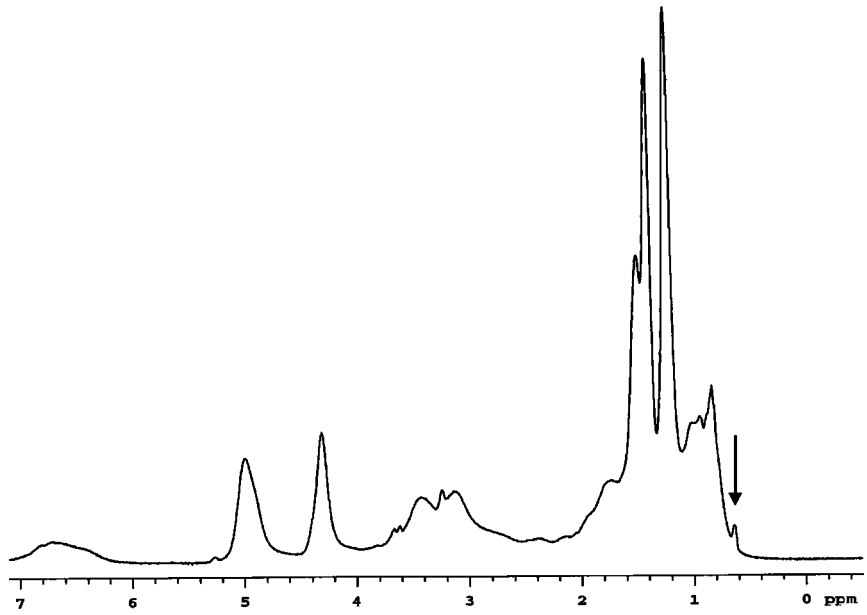


Figure 1. NMR spectrum of poly(HPMA mono/dilactate)–cholesterol (monolactate/dilactate side chain ratio of 71/29). The copolymer composition was calculated from the peak integrals at 5.0 and 4.3 ppm as described earlier (*17*). The arrow indicates the peak at 0.7 ppm that can be ascribed to the cholesterol anchor. This peak is present in cholesterol-containing polymers and absent in a control polymer synthesized without thiocholesterol.

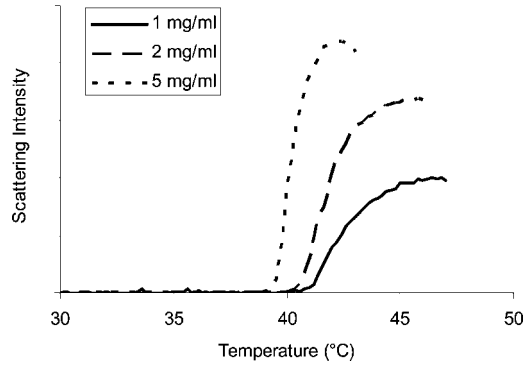


Figure 2. Temperature-dependent precipitation of poly(HPMA mono/dilactate)–cholesterol (71/29) at different polymer concentrations.

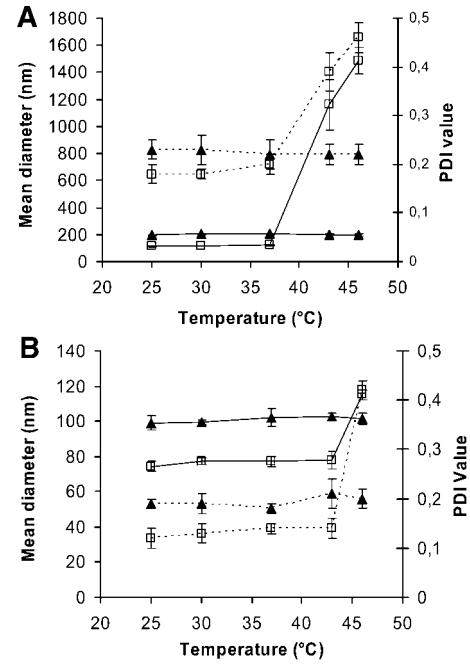


Figure 3. Mean size (solid line) and polydispersity (dashed line) of (A) poly(HPMA mono/dilactate)–cholesterol (71/29) coated DPPC/cholesterol liposomes (open square) and uncoated DPPC/cholesterol liposomes (triangle) and (B) poly(HPMA mono/dilactate)–cholesterol (71/29) coated DOPE/EPC liposomes (open square) and uncoated DOPE/EPC liposomes (triangle). Each data point represents the average ± SE, $n = 4$.

used as coating polymer (Figure 4A). The calcein release onset temperature corresponds with the CP of the coating polymer (36 °C). As mentioned, once the CP is passed, the polymer molecules become hydrophobic, precipitate, and interact with the liposome surface. As a consequence, they destabilize the bilayer and facilitate the release of calcein by disturbing the ordered structure of the lipid bilayer. Aggregation of the liposomes was reversible, which suggests that liposomal bilayers are not decomposed when the polymer precipitates. However, when the 71/29 polymer with a CP of 42 °C was used as coating polymer, no temperature-triggered contents release was observed even when the temperature was increased to 50 °C. It is well-known that DPPC has a transition temperature from the gel to the liquid crystalline phase at 41.5 °C. Probably the interaction between the polymer and the lipid bilayer above the transition temperature of DPPC is not effective enough to induce calcein release because of the higher fluidity of the lipid bilayer.

For many clinical applications it is desirable to prepare drug-containing liposomes that remain intact at 37 °C but will release their contents within the target site when the temperature is locally increased by a few degrees. Kono et al. reported that incorporation of DOPE into the liposome composition increased the temperature-triggered contents release from poly(NIPAM) coated liposomes (*14*). The enhancement of the temperature sensitivity is thought to result from the hydrogen bonding between DOPE and the coating polymer. We determined the temperature-triggered calcein release from poly(HPMA mono/dilactate)–cholesterol (71/29) coated DOPE/EPC liposomes. The CP of the coating polymer was 42 °C, and calcein release was observed above this temperature (Figure 4B). After the polymer-coated liposomes were incubated at 46 °C, almost 90% of the calcein was released, while temperature-triggered release enhancement from uncoated liposomes was not observed. It is

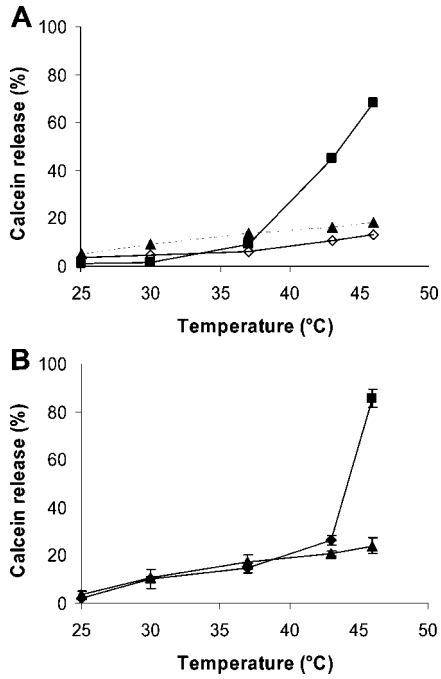


Figure 4. (A) Calcein release from DPPC/cholesterol liposomes coated with 49/51 polymer (square) and 71/29 polymer (open diamond) and from uncoated liposomes (triangle). (B) Calcein release from DOPE/EPC liposomes coated with 71/29 polymer (square) and from uncoated liposomes (triangle) at temperatures between 25 and 46 °C.

likely that the interaction between precipitated polymer and DOPE/EPC liposomes is effective enough to induce calcein release because of the hydrogen bonding. The release temperature (46 °C) is likely too high for clinical applications and should be decreased to ~42 °C. This can be done by using a polymer with lower CP but also by modifying the liposome composition to be more responsive to the phase transition of the polymer.

In conclusion, this study introduces a temperature-sensitive HPMA based copolymer with a cholesterol anchor suitable for incorporation in liposomal bilayers, which is able to mediate temperature-triggered liposome aggregation and contents release. Biodegradability and adjustable release temperature make this system attractive for numerous medical applications in the future, e.g., for targeted anticancer therapy to enhance the efficacy. Such temperature-sensitive liposomes can be prepared to remain intact at 37 °C to avoid drug leakage in the blood circulation and to accumulate in tumor tissue by virtue of the enhanced permeation and retention (EPR) effect. Pegylation or other similar protective coating is probably needed to shield the liposomes against plasma proteins and to extend the liposome half-life in bloodstream. Local heating of the tumor with external heating device can subsequently trigger the drug release because of the aggregation of the thermosensitive polymer, followed by permeabilization of the liposomal membrane.

ACKNOWLEDGMENT

The authors thank Dr. Tina Vermonden and Mr. Najim el Morabit for providing the monomers. This work was supported by the Galenos Network/Euro-PhD program and the Marie Curie EST program (Grant 504992). This work was also supported by the Commission of the European Communities, Priority 3 "Nanotechnologies and Nanosciences, Knowledge Based Multifunctional Materials, New Production Processes and Devices" of the Sixth Framework Programme for Research and Technological Development (Targeted Delivery of Nanomedicine, Grant NMP4-CT-2006 026668). It does not necessarily reflect its views and in no way anticipates the Commission's future policy in this area.

LITERATURE CITED

(1) Torchilin, V. P. (2005) Recent advances with liposomes as pharmaceutical carriers. *Nat. Rev. Drug Discovery 4*, 145–160.
(2) Metselaar, J. M., and Strom, G. (2005) Liposomes in the treatment of inflammatory disorders. *Expert Opin. Drug Delivery 2*, 465–476.
(3) Meers, P. (2001) Enzyme-activated targeting of liposomes. *Adv. Drug Delivery Rev. 53*, 265–272.
(4) Andersen, T. L., Davidsen, J., Begtrup, M., Mouritsen, O. G., and Jorgensen, K. (2004) Enzymatic release of antitumor ether lipids by specific phospholipase A_2 activation of liposome-forming products. *J. Med. Chem. 47*, 1694–1703.
(5) Drummond, D. C., Zignani, M., and Leroux, J. C. (2000) Current status of pH-sensitive liposomes in drug delivery. *Prog. Lipid Res. 39*, 409–460.
(6) Mueller, A., Bondurant, B., and O'Brien, D. F. (2000) Visible-light-stimulated destabilization of PEG-liposomes. *Macromolecules 33*, 4799–4804.
(7) Huang, S.-L., and MacDonald, R. C. (2004) Acoustically active liposomes for drug encapsulation and ultrasound-triggered release. *Biochim. Biophys. Acta 1665*, 134–141.
(8) Needham, D., and Dewhirst, M. W. (2001) The development and testing of a new temperature-sensitive drug delivery system for the treatment of solid tumors. *Adv. Drug Delivery Rev. 53*, 285–305.
(9) Lindner, L. H., Eichhorn, M. E., Eibl, H., Teichert, N., Schmitt-Sody, M., Issels, R. D., and Dellian, M. (2004) Novel temperature-sensitive liposomes with prolonged circulation time. *Clin. Cancer Res. 10*, 2168–2178.
(10) Kono, K. (2001) Thermosensitive polymer-modified liposomes. *Adv. Drug Delivery Rev. 53*, 307–319.
(11) Kono, K., Hayashi, H., and Takagishi, T. (1994) Temperature-sensitive liposomes: liposomes bearing poly(*N*-isopropylacrylamide). *J. Controlled Release 30*, 69–75.
(12) Hayashi, H., Kono, K., and Takagishi, T. (1999) Temperature sensitization of liposomes using copolymers of *N*-isopropylacrylamide. *Bioconjugate Chem. 10*, 412–418.
(13) Kono, K., Henmi, H., Yamasita, H., Hayashi, H, and Takagishi, T. (1999) Improvement of temperature-sensitivity of poly(*N*-isopropylacryamide)-modified liposomes. *J. Controlled Release 59*, 63–75.
(14) Yoshino, K., Kadowaki, A., Takagishi, T., and Kono, K. (2004) Temperature sensitization of liposomes by use of *N*-isopropylacrylamide copolymers with varying transition endotherms. *Bioconjugate Chem. 15*, 1102–1109.
(15) Han, H. D., Shin, B. C., and Choi, H. S. (2006) Doxorubicin-encapsulated thermosensitive liposomes modified with poly(*N*-isopropylacrylamide-*co*-acrylamide): drug release behaviour and stability in the presence of serum. *Eur. J. Pharm. Biopharm. 62*, 110–116.
(16) Kopecek, J., Kopeckova, P., Minko, T., and Lu, Z. (2000) HPMA copolymer–anticancer drug conjugates: design, activity, and mechanism of action. *Eur. J. Pharm. Biopharm. 50*, 61–81.
(17) Soga, O., van Nostrum, C. F., and Hennink, W. E. (2004) Poly(*N*-(2-hydroxypropyl)methacrylamide mono/di lactate): a new class of biodegradable polymers with tuneable sensitivity. *Biomacromolecules 5*, 818–821.
(18) Neradovic, D., van Steenbergen, M. J., Vansteelant, L., Meijer, Y. J., van Nostrum, C. F., and Hennink, W. E. (2003) Degradation mechanism and kinetics of thermosensitive polyacrylamides containing lactic acid side chains. *Macromolecules 36*, 7491–7498.
(19) Kaneko, Y., Sakai, K., Kikuchi, A., Yoshida, R., Sakurai, Y., and Okano, T. (1995) Influence of freely mobile grafted chain length on dynamic properties of comb-type grafted poly(*N*-isopropylacrylamide) hydrogels. *Macromolecules 28*, 7717–7723.

(20) Ellman, G. L. (1959) Tissue sulfhydryl groups. *Arch. Biochem. Biophys. 80*, 70–77.

(21) Romberg, B., Kettenes-van den Bosch, J., de Vringer, T., Storm, G., and Hennink, W. E. (2006) ^{1}H NMR spectroscopy as a tool for determining the composition of poly(hydroxyethyl-L-asparagine)-coated liposomes. *Bioconjugate Chem. 17*, 860–864.

(22) Toombes, G. E., Finnefrock, A. C., Tate, M. W., and Gruner, S. M. (2002) Determination of Lα-HII phase transition temperature for 1,2-dioleoyl-*sn*-glycero-3-phosphatidylethanolamine. *Biophys. J. 82*, 2504–2510.

BC700245P

Ultrastructural Study on the Specific Binding of Genetically Engineered Epidermal Growth Factor to Type I Collagen Fibrils

Koichi Kato, Hideki Sato, and Hiroo Iwata*

Institute for Frontier Medical Sciences, Kyoto University, 53 Kawahara-cho, Shogoin, Sakyo-ku, Kyoto 606-8507, Japan.
Received July 12, 2007; Revised Manuscript Received August 10, 2007

In an attempt to develop collagen-growth factor composites for use in tissue engineering, chimeric proteins consisting of epidermal growth factor and collagen binding domains derived from von Willebrand factor or fibronectin were synthesized by means of recombinant technology. These chimeric proteins were bound to type I collagen fibrils, and the ultrastructures of composites were analyzed by transmission electron microscopy combined with the gold nanoparticle labeling technique. The results of the ultrastructural study revealed that chimeric proteins were densely assembled on collagen fibrils through the specific recognition of binding sites, producing the ordered array of chimeric proteins.

INTRODUCTION

Collagen is the most abundant and ubiquitous extracellular matrix in mammals and has been utilized as biomaterials in a variety of medical applications (*1, 2*). More recently, collagen-based hydrogels and porous materials have been used as scaffolds for tissue regeneration (*3*). In these tissue engineering approaches, signaling molecules such as growth factors have been frequently incorporated into collagen-based scaffolds for optimizing cellular responses (*4*). However, growth factors physically entrapped in scaffolds are rapidly released in an uncontrollable manner, reducing the efficacy of growth factors. To overcome this limitation, several attempts have been made to develop collagen binding growth factors by combining growth factors with polypeptide domains or short peptide sequences having an affinity for collagen α chains (*5–8*).

Collagen-binding chimeric proteins have been rationally designed by means of recombinant technology. Using a bacterial expression system, Tuan et al. (*5*) synthesized biologically active transforming growth factor-β1 fused with a collagen-binding peptide. The research group extended this technology to prepare various growth factors having an affinity for collagen (*6*). Nishi et al. (*7*) and Ishikawa et al. (*8*) developed epidermal growth factor (EGF) that was fused with collagen binding domains (CBDs) derived from *Clostridium histolyticum* collagenase and human fibronectin, respectively. It was shown that these fusion proteins have potential for use in the controlled delivery of growth factors (*7, 8*), especially for accelerating wound-healing processes (*8*).

Collagen also provides attractive materials for neural progenitor cell (NPC) transplantation that aims at the structural and functional restoration of the central nervous system suffering from degenerative diseases and traumatic injuries. In an attempt to provide favorable microenvironments for the survival and the controlled differentiation of NPCs, several groups utilized collagen hydrogels as scaffolds (*9–12*). However, current technologies have limited effects of scaffolding, probably due to the low availability of external signals for adhesion, proliferation, and differentiation. To address this limitation, we are currently involved in the development of collagen binding growth factors that improve their availability for NPCs enclosed in collagen-based materials.

Our previous studies (*13, 14*) revealed that neural stem cells recognized histidine-tagged EGF anchored to the surfaces of culture substrates through coordination of the histidine tag with surface-immobilized metal ions. We found that the density of specifically anchored EGF was one of the most important factors for the attachment of neural stem cells mediated by EGF–EGF receptor interactions. This finding led us to suppose that the density of growth factors on collagen-based materials and their binding specificity play an important role in the successive signal transduction into cells. Therefore, the present study is undertaken to explore the spatial distribution of collagen binding EGF on the surface of type I collagen fibrils. We prepared EGF fused with CBD and labeled the chimeric proteins with gold nanoparticles (GNPs) to study the ultrastructure of the composites consisting of chimeric proteins and collagen fibrils by transmission electron microscopy (TEM).

EXPERIMENTAL PROCEDURES

Construction of Recombinant Plasmids. A bacterial expression system was used to prepare two chimeric proteins consisting of human EGF, CBD derived from either the human von Willebrand factor (vWFCBD; 189 aa, residues 922−1110, A3 domain) (*15*) or human fibronectin (FNCBD; 340 aa, residues 260−599) (*16*), and the hexahistidine tag (6 × His). Control protein lacking CBD (EGF having 6 × His) was prepared as before (*13*). The structures of these proteins are shown in Figure 1.

For the preparation of chimeric genes, the overlap extension method was employed (*17–19*). Primers used in polymerase chain reaction (PCR) are shown in Table 1. Forward primers for EGF (**P1** and **P3**; identical to each other) contained an Nde I restriction site in the 5′ region, while reverse primers for vWFCBD (**P6**) and FNCBD (**P8**) contained, respectively, Xho I and Not I sites in the 5′ region. For subsequent overlap extension, reverse primers for EGF (**P2** and **P4**) contained sequences complementary to the 5′-region of vWFCBD and FNCBD (21 bases in **P2** and 19 bases in **P4**), whereas forward primers for vWFCBD (**P5**) and FNCBD (**P7**) contained sequences complementary to the 3′-region of EGF (21 bases in **P5** and 19 bases in **P7**). Thus, **P2** and **P4** were exactly complementary to **P5** and **P7**, respectively. In addition, six bases

* To whom correspondence should be addressed. Phone and fax: +81-75-751-4119. E-mail: iwata@frontier.kyoto-u.ac.jp.

10.1021/bc700259g CCC: $37.00 © 2007 American Chemical Society
Published on Web 09/26/2007

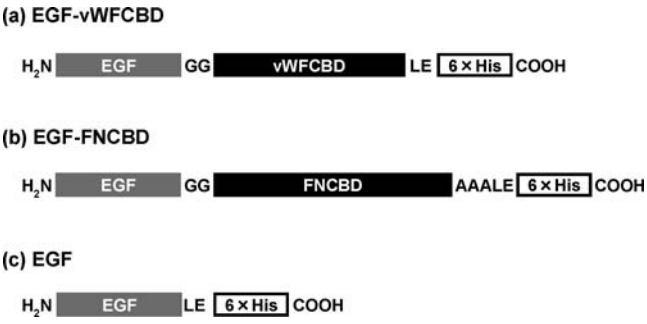


Figure 1. Structure of chimeric and control proteins synthesized in this study. The number of amino acid residues is (EGF) 53, (vWFCBD) 189, (FNCBD) 340, and (6 × His) 6.

were inserted between EGF and CBD to add Gly-Gly as a linker in between (GGTGGT in **P5** and **P7**; ACCACC in **P2** and **P4**).

The cDNA of EGF and CBD were separately amplified from human cDNA libraries of the pancreas (for EGF and vWFCBD) and placenta (for FNCBD) (both from Takara Bio, Inc., Otsu, Japan), using **P1** and **P2** for EGF to be fused with vWFCBD, using **P3** and **P4** for EGF to be fused with FNCBD, using **P5** and **P6** for vWFCBD, and using **P7** and **P8** for FNCBD. An amount of 100 ng of DNA was used as templates in a 100 μL reaction volume that contained 2.5 units of DNA polymerase (Ex Taq, Takara), 0.2 mM dNTP mixture, and 0.4 μM primers. PCR was performed using a thermal cycler (Gene Amp PCR 9700G, Applied Biosystems) under the following cycling conditions: for EGF and vWFCBD, 30 cycles, denaturation at 94 °C for 30 s, annealing at 60 °C for 30 s, extension at 72 °C for 60 s; for FNCBD, 35 cycles, denaturation at 94 °C for 30 s, annealing at 55 °C for 30 s, extension at 72 °C for 90 s. DNA fragments thus obtained were separated by 2% agarose gel electrophoresis and purified using a gel extraction kit (Qiagen).

An amount of 100 ng of each DNA obtained by PCR was mixed (EGF + vWFCBD or EGF + FNCBD) in a solution (100 μL) containing 2.5 units of DNA polymerase (Takara Ex Taq) and 0.2 mM dNTP mixture. These overlapping fragments were denatured, annealed to generate heteroduplexes, and extended to obtain full-length DNA. For the fill-in reaction, the following thermal cycling conditions were employed: seven cycles, denaturation at 94 °C for 1 min, and annealing and extension at 63 °C for 4 min. In the second PCR, 50 μL of reaction products from the above fill-in reaction was used to amplify full-length DNA by priming with **P1** and **P6** for EGF–vWFCBD and with **P3** and **P8** for EGF–FNCBD under the following cycling conditions: for EGF–vWFCBD, 30 cycles, denaturation at 94 °C for 30 s, annealing at 55 °C for 30 s, extension at 72 °C for 120 s; for EGF–FNCBD, 30 cycles, denaturation at 94 °C for 30 s, annealing at 60 °C for 30 s, extension at 72 °C for 90 s.

Chimeric genes thus obtained were purified by gel electrophoresis and subjected to digestion with restriction enzymes, Nde I and Xho I for EGF–vWFCBD and Nde I and Not I for EGF–FNCBD, followed by gel purification to obtain inserts with cohesive ends. These inserts were ligated using T4 ligase (Ligation High, Toyobo, Osaka, Japan) to the upstream of the 6 × His tag in pET-22b(+) plasmid (Novagen) previously linearized by digestion with the same restriction enzymes and transformed to *Escherichia coli* (*E. coli*) strain DH5α (Toyobo). Colonies were randomly picked up, and the presence of the plasmid was verified by colony PCR. Plasmid-containing colonies were then amplified in Luria–Bertani (LB) medium containing 100 μg/mL ampicillin, and plasmids were isolated by the QIAprep Spin Miniprep kit (Qiagen) and ethanol precipitation. After sequence verification, the plasmids obtained were transformed into the *E. coli* host strain BL21(DE3)pLysS (Novagen), and one of the colonies containing plasmids, checked by colony PCR, was amplified in LB medium containing 100 μg/mL ampicillin to obtain glycerol stocks.

Protein Expression and Purification. The expression, purification, and refolding of chimeric proteins were carried out as before (*13*). In brief, the *E. coli* strain BL21(DE3)pLysS harboring recombinant plasmids were grown in 100 mL of LB medium containing 100 μg/mL ampicillin for 1 h. Then, 1 mM isopropyl β-D-thiogalactoside (IPTG) was added to the culture to induce gene expression. After 4 h of additional culture, cells were collected by centrifugation and chilled at –80 °C for 24 h. The cells were thawed and lysed in BugBuster protein extraction reagent (Novagen) containing 25 unit/mL Benzonase nuclease (Novagen). The inclusion bodies containing expressed proteins were purified according to the manufacture's instructions and were solubilized in 20 mM PBS (pH 7.4) containing 8 M urea, 20 mM imidazole, and 5 mM 2-mercaptoethanol. After removal of insoluble particles by centrifugation and filtration, affinity purification was performed using His Trap HP column (Amersham). Trapped proteins were eluted with 20 mM PBS (pH 7.4) containing 8 M urea and 500 mM imidazole. Purified proteins were analyzed by sodium dodecyl sulfate–polyacrylamide gel electrophoresis (SDS–PAGE) using 16% polyacrylamide gel with Tris/tricine/SDS buffer and visualized by staining with Coomassie brilliant blue. The refolding of proteins was performed by the stepwise dialysis method using dialysis membranes with a molecular weight cutoff of 3.5 kDa. Dialysis was performed sequentially against the following buffers: (i) 20 mM Tris-HCl, 0.2 mM dithiothreitol (pH 8.5), (ii) 20 mM Tris-HCl (pH 8.5), (iii) 20 mM Tris-HCl, 0.2 mM oxidized glutathione, 2 mM reduced glutathione (pH 8.0), and (iv) PBS (pH 7.4). Finally, PBS solutions of the refolded proteins were aliquoted and stored at –80 °C until use.

Affinity Precipitation Assay. After being washed with pure water, Speharose CL-6B microbeads (Pharmacia) were suspended in 0.6 M epichlorohydrin in a 1:1 mixture of 0.4 M NaOH and bis(2-methoxyethyl) ether and kept at room temperature for 1 h to introduce epoxides to the beads (*20*). After being washed with water, the beads were transferred to 1 mM 11-mercapto-1-undecanoic acid in a 1:1 mixture of ethanol and PBS and kept overnight at room temperature to allow the reaction of epoxide with nucleophilic thiol (*21*). The resulting

Table 1. Primers Used in Overlap Extension PCR

cDNA	code		DNA sequence of forward (FW) and reverse (RV) primers[c]
EGF[a]	**P1**	FW	GGTCGTCATATGAATAGTGACTCTGAATGTCCCCTG
	P2	RV	GTCCAGGGGCTGGCTGCAGTC*ACCACC*GCGCAGTTCCCACCACTTCAG
EGF[b]	**P3**	FW	GGTCGTCATATGAATAGTGACTCTGAATGTCCCCTG
	P4	RV	GCGGTTGGTAAACAGCTGC*ACCACC*GCGCAGTTCCCACCACTTCAG
vWFCBD	**P5**	FW	CTGAAGTGGTGGGAACTGCGC*GGTGGT*GACTGCAGCCAGCCCCTGGAC
	P6	RV	TCCTCGAGAGAGCACAGTTTGTGGAGGAAGG
FNCBD	**P7**	FW	CTGAAGTGGTGGGAACTGCGC*GGTGGT*GCAGCTGTTTACCAACCGC
	P8	RV	GAGTGCGGCCGCCCACTGGATGGGGTGGGAGTTGGGC

[a] Used for preparing EGF–vWFCBD. [b] Used for preparing EGF–FNCBD. [c] Restriction sites are underlined. Bases for Gly-Gly insertion are written in italics.

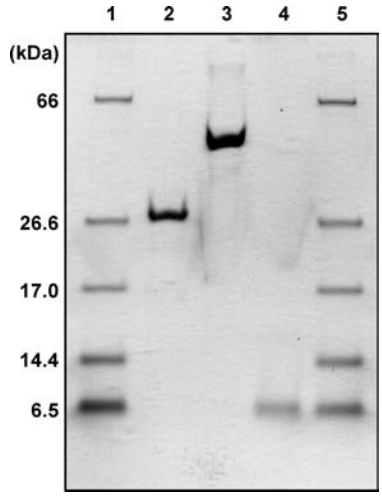


Figure 2. SDS–PAGE analysis results of chimeric and control proteins: (lanes 1 and 5) molecular weight standard; (lane 2) EGF–vWFCBD; (lane 3) EGF–FNCBD; (lane 4) EGF.

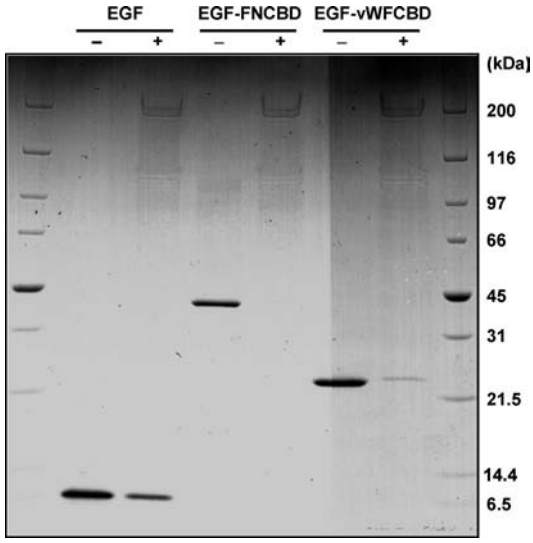


Figure 3. SDS–PAGE analysis results of chimeric and control proteins before (−) and after (+) contact with collagen-adsorbed gel beads.

beads presenting carboxylic acid were washed with water and suspended in 1 mg/mL type I collagen solution (Collagen I-PC, Koken, Tokyo, Japan) in 1×10^{-2} M HCl and kept at room temperature for 3 h to physically adsorb collagen to the beads. Then the beads were washed extensively with 1×10^{-2} M HCl to remove weakly adsorbed collagen. The adsorption of collagen was confirmed by micro-BCA protein assays (Pierce). The suspension of collagen-adsorbed beads (total volume of 100 μL with a bed volume of ~70 μL) was mixed with an equal volume of PBS containing 0.2 mg/mL chimeric proteins or native EGF and kept at 37 °C for 20 min. Then the microbeads were separated from protein solutions by centrifugation. Supernatants and original protein solutions were analyzed by SDS–PAGE to assess concentration depletion due to adsorption to collagen-modified beads.

Enzyme-Linked Immunosorbent Assay (ELISA). An amount of 100 μL microliter of 0.1 mg/mL type I collagen solution (I-PC, Koken) was added to each well of a 96-well polystyrene plate and incubated for 1 h at room temperature to allow the adsorption of collagen. Then the solution was aspirated, and the plate was washed with PBS. After blocking with Blocking One (Nacalai Tesque, Kyoto, Japan), 50 μL of PBS containing chimeric protein or CBD-deficient EGF at 0–50 μg/mL was

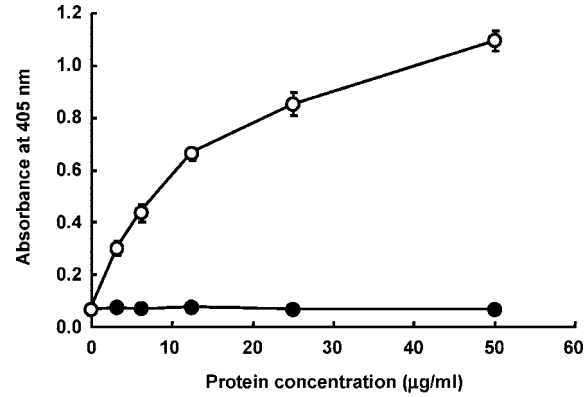


Figure 4. Enzyme-linked immunosorbent assays for the binding of (open circle) EGF–vWFCBD and (closed circle) wild-type EGF onto collagen-coated surfaces. Data are expressed as the mean ± standard deviation for $n = 4$.

added to each well in quadruplicate and incubated at room temperature for 30 min to allow the binding of these proteins to preadsorbed collagen. The solution was aspirated, and the plate was extensively washed with PBS containing 0.05% Tween-20 (PBS-Tween20) followed by binding of goat anti-EGF antibody [1:100, EGF (C20) sc-1341, Santa Cruz] and subsequently rabbit antigoat IgG (1:500, Molecular Probes). The plate was washed with PBS-Tween20. Then a solution of alkaline phosphatase-conjugated antirabbit IgG (Sigma) was added to the plate to allow binding of the antibody at room temperature for 30 min. After the plate was washed with PBS-Tween20, 100 μL of *p*-nitrophenyl phosphate solution (pNPP, Sigma) was added to the wells. The coloring reaction was allowed to proceed at 37 °C for 15 min and was stopped by adding NaOH solution. Finally, the optical density of the solution was recorded at 405 nm with a plate reader.

GNP Labeling. GNPs were prepared according to the reported methods in which $HAuCl_4$ was reduced by sodium citrate (*22*) or sodium borohydride (*23*). The average diameter of GNPs was 15 nm by citrate reduction and 5 nm by $NaBH_4$ reduction when determined by TEM. The suspension of GNPs was centrifuged at 17000*g* for 1 h, and the pellet obtained was washed with water. This procedure was repeated two times, and then GNPs were suspended in H_2O of $^1/_5$ volume relative to the volume of the original suspension. To the suspension, a solution of EGF–vWFCBD, EGF–FNCBD, or EGF was added to a final concentration of 20 μg/mL, and the mixture was incubated at room temperature to physically adsorb these proteins to GNPs. After 2 h of incubation, the suspension was centrifuged at 17000*g* for 15 min and the pellet obtained was suspended in H_2O. EGF–vWFCBD, EGF–FNCBD, and EGF possess intramolecular disulfide bonds and no free cysteine in their folded state. We consider that these proteins are adsorbed to GNPs primarily through nonspecific interactions, as in the case of bovine serum albumin (*24*). Although we have no experimental data that show the efficiency of the interactions for each protein, most of the GNPs are expected to adsorb nonspecifically these proteins from solutions at relatively high concentration.

Binding to Collagen Fibrils. The tail tendon obtained from Fisher344 rats of 12 weeks old was cut into pieces with a length of approximately 1 mm, unraveled using fine forceps, and deposited onto a Cu grid that had been laminated with a polyvinylformal membrane, reinforced with a thin carbon layer, and treated with oxygen plasma. It is reported that the rat tail tendon mostly consists of type I collagen (*25*). To the grid, a drop of 2% Pluronic F-127 (Sigma) solution in water was pipetted and kept at room temperature for 6 h to block the

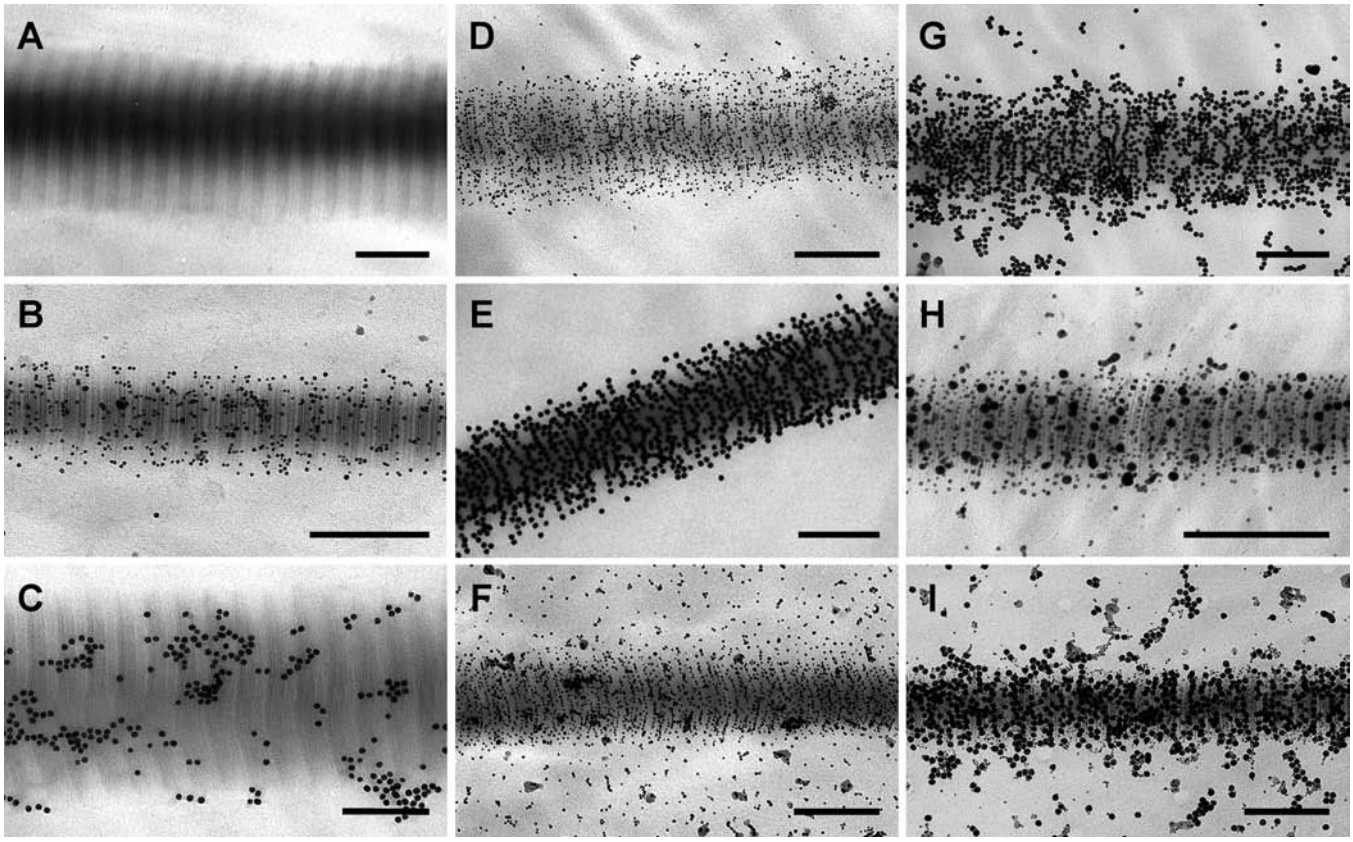


Figure 5. TEM images of (A) a negatively stained collagen fibril and (B–I) a collagen fibril bound with GNP-labeled chimeric proteins. A single chimeric protein was used in parts B–G, whereas two different chimeras were (H) simultaneously or (I) sequentially bound to the fibrils. Parts B and C show the result of control experiments in which (B) nontreated GNPs and (C) GNPs with CBD-deficient EGF (control EGF) were adsorbed. Protein and diameter of GNPs in nm are as follows: (B) no protein, 5; (C) EGF (control), 15; (D) EGF–vWFCBD, 5; (E) EGF–vWFCBD, 15; (F) EGF–FNCBD, 5; (G) EGF–FNCBD, 15; (H, I) EGF–FNCBD, 5, and EGF–vWFCBD, 15. Scale bar is 200 nm.

nonspecific adsorption of GNPs. Then Pluronic solution was removed by absorbing with lint-free paper, and an aliquot of GNP-labeled protein solutions was pipetted to the grid to allow the binding of chimeric proteins to collagen fibrils at 4 °C overnight. When the assembly of two different proteins was studied, chimeric proteins (EGF–vWFCBD or EGF–FNCBD) labeled with different diameters of GNPs (5 or 15 nm) were applied in a mixture or in a sequential manner. The grid was washed with PBS–Tween20 and then fixed with 4% glutaraldehyde solution in PBS. Finally the grid was washed with water and air-dried.

TEM. The grid with collagen fibrils and GNP-labeled chimeric protein was immersed in a 1:1 mixture of ethanol and water, saturated with uranyl acetate, and kept at room temperature for 30 min for negatively staining collagen fibrils. Then the grid was extensively washed with water and finally air-dried. TEM observation was carried out using Hitachi H-7000 operating at an accelerate energy of 75 kV and a typical magnification of 30000× to 60000×.

Two-Dimensional Fast Fourier Transform. Digitized TEM images were rotated using Adobe Photoshop 5.0 to align a fibril of interest with the *y*-axis for the simplicity of later analyses and further transformed to binary images for avoiding interference by the banding patterns of negatively stained collagen fibrils. In addition, surrounding areas around fibrils were masked to eliminate noise originating from nonspecific GNPs. The images were trimmed into 1 μm × 1 μm and adjusted to 512 pixels × 512 pixels. The modified images thus obtained were analyzed by two-dimensional fast Fourier transform (2D-FFT) using the Scion Image software (Scion Corp., MD).

RESULTS

Chimeric Proteins. Figure 2 shows the result of SDS–PAGE analysis for proteins synthesized in this study. As can been seen, three proteins were separated as single bands. Estimated molecular weights are 7 kDa for EGF–His, 28 kDa for EGF–vWFCBD, and 44 kDa for EGF–FNCBD, and they are in accordance with those expected from the number of amino acids contained.

Affinity for Collagen. The results of precipitation assays are shown in Figure 3. The bands of EGF–vWFCBD and EGF–FNCBD were significantly weakened after the compounds made contact with collagen-adsorbed gel beads, while the band of CBD-deficient control EGF remained almost unchanged. These results suggest that CBD-containing chimeric proteins have an affinity for type I collagen. The slight reduction in band intensity observed with control EGF is probably due to its nonspecific adsorption to the beads. To verify further an affinity for collagen, chimeric proteins were subjected to ELISA. As shown in Figure 4, EGF–vWFCBD was bound to the collagen-coated surface. This is in marked contrast to CBD-deficient EGF that exhibited no sign of collagen binding. The results of precipitation assays and ELISA demonstrate that the chimeric proteins, EGF–vWFCBD and EGF–FNCBD, bind to collagen through collagen–CBD interactions.

TEM Observation. The TEM image of negatively stained collagen fibrils (Figure 5A) exhibited a clear banding pattern along the fibril axis with a period of 67 nm, representing the

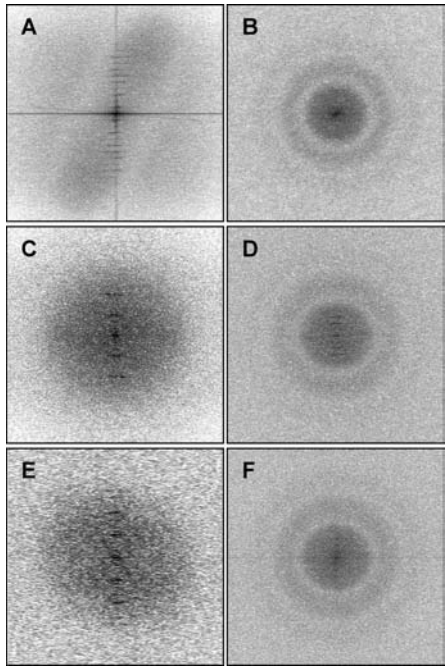


Figure 6. Power spectra obtained by 2D-FFT of TEM images: (A) a negatively stained collagen fibril; (B–F) collagen fibrils with GNP-labeled chimeric or control proteins. Protein and diameter of GNP (nm) are as follows: (B) EGF, 15; (C) EGF–vWFCBD, 5; (D) EGF–vWFCBD, 15; (E) EGF–FNCBD, 5; (f) EGF–FNCBD, 15.

ordered assembly of collagen molecules according to the D-staggered model (*26*).

As shown in Figure 5D–G, GNPs with CBD-containing chimeric proteins are observed selectively and tightly on collagen fibrils. In both cases with EGF–vWFCBD and EGF–FNCBD, it is frequently seen that the strings of GNPs are aligned perpendicular to the fibril axis. We could not observe clear difference between vWFCBD- and FNCBD-chimeras regarding the alignment of GNPs. The difference in the diameter of GNPs had small effects on the formation of strings, exhibiting a similar center-to-center distance between neighboring strings. In contrast, nontreated GNPs (Figure 5B) and GNPs with control EGF (Figure 5C) are seen sparsely on the fibril surface without noticeable ordered structure, suggesting no specific interactions operated between GNPs and collagen. Adsorption of GNPs occasionally took place at the surrounding regions around fibrils. The aggregation of GNPs was also observed especially for GNPs with EGF–FNCBD. These results are likely due to the strong propensity of GNPs for aggregation and adsorption.

Attempts were further made to assemble two types of chimeric proteins carrying different CBDs on the same collagen fibril. vWFCBD and FNCBD are expected to recognize different binding sites on the collagen fibrils (*27*). It is seen that the ordered assembly is clear for smaller GNPs. On the other hand, a smaller number of larger GNPs is seen on the collagen fibrils, with much disordered arrangements compared to the case with smaller GNPs (Figure 5H). This is probably due to steric hindrance because similar results were obtained when EGF–FNCBD and EGF–vWFCBD were labeled with smaller and larger GNPs, respectively. Sequential binding of larger GNPs with EGF–vWFCBD and smaller GNPs with EGF–FNCBD resulted in the improved order of GNP arrangements (Figure 5I).

2D-FFT. To assess the periodical appearance of the strings, 2D-FFT was performed on the TEM images modified as described in the Experimental Procedures. The power spectra are shown in Figure 6. The meridional profiles (corresponding to the fibril axis) were obtained from the power spectra to extract

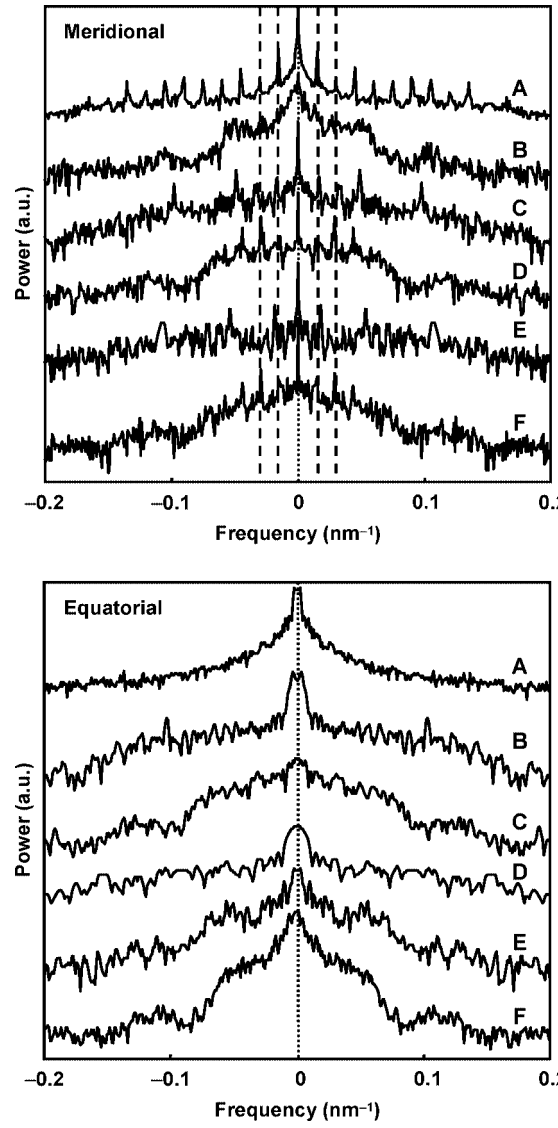


Figure 7. Meridional and equatorial profiles of the power spectra obtained by 2D-FFT of TEM images: (A) a negatively stained collagen fibril; (B–F) collagen fibrils with GNP-labeled chimeric or control proteins. The dashed lines in the meridional profiles indicate the position of lower-order diffraction peaks. Protein and diameter of GNP (nm) are as follows: (B) EGF, 15; (C) EGF–vWFCBD, 5; (D) EGF–vWFCBD, 15; (E) EGF–FNCBD, 5; (F) EGF–FNCBD, 15.

information about periodicity of the strings (Figure 7). Sharp peaks appearing in the meridional profile for a collagen fibril represent the periodic appearance of banding patterns with a frequency of 0.015 nm^{-1} [period = 67 nm, identical to the D-period (*26*)], while no peaks were observed in the equatorial profile (corresponding to the transversal direction of collagen fibrils). In the case of collagen with EGF–vWFCBD, line profiles exhibited characteristic peaks representing the periodic appearance of strings along the longitudinal fibril axis with a frequency of 0.015 nm^{-1} (period = 67 nm). Similar results were obtained for the case with EGF–FNCBD. In contrast, the profile for CBD-deficient EGF had no evident peaks. Alternatively, equatorial profiles exhibited no noticeable peaks in all the GNP–chimeric protein combinations.

DISCUSSION

Collagen-based materials loaded with growth factors are expected to provide artificial microenvironments that mimic a natural extracellular matrix. In the present study, we utilized

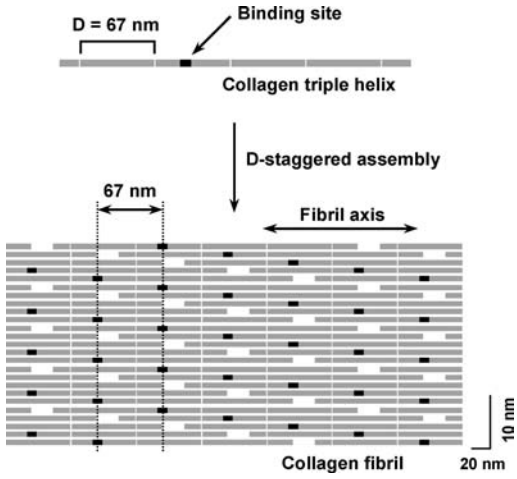


Figure 8. Illustration of the expected distribution of binding sites on the surface of a collagen fibril. When a binding site for CBD (marked in black) is located at a certain region in a collagen triple helix, the D-staggered assembly of collagen monomers produces an array of binding sites on the fibril surface. CBD contained in the EGF chimera recognizes these binding sites to present densely EGF on the fibril surface with nanometer-scale periodicity.

CBDs for the efficient loading of EGF to fibrillar collagen. Because the nanometer scale spatial distribution of surface-immobilized EGF is anticipated to have an influence on its recognition by cell surface receptors (*13*, *14*), we studied here the ultrastructure of composites consisting of collagen fibrils and CBD-containing EGF.

It is known that a collagen fibril is formed by the D-staggered arrangement of collagen molecules (*26*). According to the previous studies on 3D molecular packing by computational modeling (*28*, *29*) and on surface microstructure by scanning electron microscopy (*25*) and atomic force microscopy (*30*), it seems that the D-staggered arrangement also explains in essence the assembled structure at the fibril surface. Because the extended form of a collagen triple helices laterally aligns with D-staggered arrangements, generating a fibril in which individual helices are aligned in the same or slightly declined (*25*) direction as the longitudinal fibril axis, any peptide segments in the collagen α chains are expected to appear periodically with an interval of 67 nm along the longitudinal fibril axis (*26*). This interval is identical to the observed periods of GNP strings, suggesting that the chimeric proteins recognized specific binding sites for CBD involved in the collagen α chains (Figure 8).

However, it is further observed in the TEM images (Figure 5D–G) that the apparent interval of strings is smaller than 67 nm, with at least one more intermitting string. We speculate that this finding accounts for the existence of multiple binding sites on a single α chain for both vWFCBD (*31*, *32*) and FNCBD (*33*) (Figure 8). It is also predicted that the binding sites are periodically distributed in the transversal direction on the fibril surface. However, there is not enough evidence to show the periodical distribution of chimeric proteins along the transversal axis. This is probably because of the small interhelix distance (1.5 nm) (*26*) compared to the size of GNPs (5 or 15 nm in diameter), which might hamper the binding of the GNP-labeled proteins to the neighboring sites by steric hindrance.

In summary, EGF genetically engineered to carry CBDs recognizes their specific binding sites distributed on collagen fibrils. This produces a nanometer-scale molecular assembly, although the minor disorder of assembly was observed occasionally even in single-component systems. The utilization of different CBD-binding sites has potential for loading multiple growth factors in a single matrix. Further study is currently underway to design collagen-growth factor composites that optimize proliferation and differentiation of neural stem/progenitor cells.

ACKNOWLEDGMENT

We thank Makio Fujioka, Central Laboratory for Electron Microscopy, Faculty of Medicine, Kyoto University, for his assistance with TEM. This study was supported by Kobe Cluster, the Knowledge-Based Cluster Creation Project, and Grants-in-Aid for Scientific Research (Grant 19659364), the Ministry of Education, Culture, Sports, Science and Technology (MEXT).

LITERATURE CITED

(1) Patino, M. G., Neiders, M. E., Andreana, S., Noble, B., and Cohen, R. E. (2002) Collagen as an implantable material in medicine and dentistry. *J. Oral Implantol. 28*, 220–225.
(2) Lee, C. H., Singla, A., and Lee, Y. (2001) Biomedical applications of collagen. *Int. J. Pharm. 221*, 1–22.
(3) Ikada, Y. (2006) Scope of tissue engineering. *Tissue Engineering: Fundamentals and Applications* Chapter 1, pp 1–89, Elsevier, Oxford, U.K.
(4) Boontheekul, T., and Mooney, D. J. (2003) Protein-based signaling systems in tissue engineering. *Curr. Opin. Biotechnol. 14*, 559–565.
(5) Tuan, T. L., Cheung, D. T., Wu, L. T., Yee, A., Gabriel, S., Han, B., Morton, L., Nimni, M. E., and Hall, F. L. (1996) Engineering, expression and renaturation of targeted TGF-beta fusion proteins. *Connect. Tissue Res. 34*, 1–9.
(6) Hall, F. L., Kaiser, A., Liu, L., Chen, Z. H., Hu, J., Nimni, M. E., Beart, R. W., Jr., and Gordon, E. M. (2000) Design, expression, and renaturation of a lesion-targeted recombinant epidermal growth factor–von Willebrand factor fusion protein: efficacy in an animal model of experimental colitis. *Int. J. Mol. Med. 6*, 635–643.
(7) Nishi, N., Matsushita, O., Yuube, K., Miyanaka, H., Okabe, A., and Wada, F. (1998) Collagen-binding growth factors: production and characterization of functional fusion proteins having a collagen-binding domain. *Proc. Natl. Acad. Sci. U.S.A. 95*, 7018–7023.
(8) Ishikawa, T., Terai, H., and Kitajima, T. (2001) Production of a biologically active epidermal growth factor fusion protein with high collagen affinity. *J. Biochem. (Tokyo) 129*, 627–633.
(9) O'Connor, S. M., Stenger, D. A., Shaffer, K. M., Maric, D., Barker, J. L., and Ma, W. (2000) Primary neural precursor cell expansion, differentiation and cytosolic Ca(2+) response in three-dimensional collagen gel. *J. Neurosci. Methods 102*, 187–195.
(10) Chen, S. S., Revoltella, R. P., Papini, S., Michelini, M., Fitzgerald, W., Zimmerberg, J., and Margolis, L. (2003) Multilineage differentiation of rhesus monkey embryonic stem cells in three-dimensional culture systems. *Stem Cells 21*, 281–295.
(11) Itoh, T., Satou, T., Dote, K., Hashimoto, S., and Ito, H. (2005) Effect of basic fibroblast growth factor on cultured rat neural stem cell in three-dimensional collagen gel. *Neurol. Res. 27*, 429–432.
(12) Brannvall, K., Bergman, K., Wallenquist, U., Svahn, S., Bowden, T., Hilborn, J., and Forsberg-Nilsson, K. (2007) Enhanced neuronal differentiation in a three-dimensional collagen-hyaluronan matrix. *J. Neurosci. Res. 85*, 2138–2146.
(13) Kato, K., Sato, H., and Iwata, H. (2005) Immobilization of histidine-tagged recombinant proteins onto micropatterned surfaces for cell-based functional assays. *Langmuir 21*, 7071–7075.
(14) Nakaji-Hirabayashi, T., Kato, K., Arima, Y., and Iwata, H. (2007) Oriented immobilization of epidermal growth factor onto culture substrates for the selective expansion of neural stem cells. *Biomaterials 28*, 3517–3529.
(15) Huizinga, E. G., Martijn van der Plas, R., Kroon, J., Sixma, J. J., and Gros, P. (1997) Crystal structure of the A3 domain of human von Willebrand factor: implications for collagen binding. *Structure 5*, 1147–1156.

(16) Skorstengaard, K., Thogersen, H. C., and Petersen, T. E. (1984) Complete primary structure of the collagen-binding domain of bovine fibronectin. *Eur. J. Biochem. 140*, 235–243.

(17) Higuchi, R., Krummel, B., and Saiki, R. K. (1981) A general method of in vitro preparation and specific mutagenesis of DNA fragments: study of protein and DNA interactions. *Nucleic Acids Res. 16*, 7351–7367.

(18) Ho, S. N., Hunt, H. D., Horton, R. M., Pullen, J. K., and Pease, L. R. (1989) Site-directed mutagenesis by overlap extension using the polymerase chain reaction. *Gene 77*, 51–59.

(19) Sambrook, J., and Russell, D. W. (2001) Mutagenesis. *Molecular Cloning. A Laboratory Manual* 3rd ed., Chapter 13, Vol. 2, pp 1–105, Cold Spring Harbor Laboratory Press, New York.

(20) Löfås, S., and Johnsson, B. (1990) A novel hydrogel matrix on gold surfaces in surface plasmon resonance sensors for fast and efficient covalent immobilization of ligands. *J. Chem. Soc., Chem. Commun.* 1526–1528.

(21) Hermanson, G. T., Mallia, A. K., and Smith, P. K. (1992) Activation methods. *Immobilized Affinity Ligand Techniques* Chapter 2, pp 51–136, Academic Press, San Diego, CA.

(22) Turkevich, J., Stevenson, P. G., and Hillier, J. (1951) A study of the nucleation and growth processes in the synthesis of colloidal gold. *Discuss. Faraday Soc. 11*, 55–75.

(23) Grabar, K. C., Allison, K. J., Baker, B. E., Bright, R. M., Brown, K. R., Freeman, R. G., Fox, A. P., Keating, C. D., Musick, M. D., and Natan, M. J. (1996) Two-dimensional arrays of colloidal gold particles: a flexible approach to macroscopic metal surfaces. *Langmuir 12*, 2353–2361.

(24) Brewer, S. H., Glomm, W. R., Johnson, M. C., Knag, M. K., and Franzen, S. (2005) Probing BSA binding to citrate-coated gold nanoparticles and surfaces. *Langmuir 21*, 9303–9307.

(25) Raspanti, M., Ottani, V., and Ruggeri, A. (1989) Different architectures of the collagen fibril: morphological aspects and functional implications. *Int. J. Biol. Macromol. 11*367–371.

(26) Ottani, V., Martini, D., Franchi, M., Ruggeri, A., and Raspanti, M. (2002) Hierarchical structures in fibrillar collagens. *Micron 33*, 587–596.

(27) Di Lullo, G. A., Sweeney, S. M., Korkko, J., Ala-Kokko, L., and San Antonio, J. D. (2002) Mapping the ligand-binding sites and disease-associated mutations on the most abundant protein in the human, type I collagen. *J. Biol. Chem. 277*, 4223–4231.

(28) Silver, D., Miller, J., Harrison, R., and Prockop, D. J. (1992) Helical model of nucleation and propagation to account for the growth of type I collagen fibrils from symmetrical pointed tips: a special example of self-assembly of rod-like monomers. *Proc. Natl. Acad. Sci. U.S.A. 89*, 9860–9864.

(29) Hulmes, D. J., Wess, T. J., Prockop, D. J., and Fratzl, P. (1995) Radial packing, order, and disorder in collagen fibrils. *Biophys. J. 68*, 1661–1670.

(30) Kato, K., Bar, G., and Cantow, H.-J. (2001) The interplay between surface micro-topography and -mechanics of type I collagen fibrils in air and aqueous media: an atomic force microscopy study. *Eur. Phys. J. E 6*, 7–14.

(31) Fitzsimmons, C. M., Cockburn, C. G., Hornsey, V., Prowse, C. V., and Barnes, M. (1988) The interaction of von Willebrand factor (vWf) with collagen: investigation of vWf-binding sites in the collagen molecule. *J. Thromb. Haemostasis 59*, 186–192.

(32) Nishida, N., Sumikawa, H., Sakakura, M., Shimba, N., Takahashi, H., Terasawa, H., Suzuki, E., and Shimada, I. (2003) Collagen-binding mode of vWF-A3 domain determined by a transferred cross-saturation experiment. *Nat. Struct. Biol. 10*, 53–58.

(33) Ingham, K. C., Brew, S. A., and Migliorini, M. (2002) Type I collagen contains at least 14 cryptic fibronectin binding sites of similar affinity. *Arch. Biochem. Biophys. 407*, 217–223.

BC700259G

Effect of the Hydrocarbon Chain and Polymethylene Spacer Lengths on Gene Transfection Efficacies of Gemini Lipids Based on Aromatic Backbone

Avinash Bajaj,[†] Bishwajit Paul,[†] S. S. Indi,[‡] Paturu Kondaiah,[§] and Santanu Bhattacharya*[,†,||]

Department of Organic Chemistry, Department of Microbiology and Cell Biology, and Department of Molecular Reproduction, Development and Genetics, Indian Institute of Science, Bangalore 560 012, India, and Chemical Biology Unit of JNCASR, Bangalore 560 064, India. Received May 18, 2007; Revised Manuscript Received August 27, 2007

Design, syntheses, and gene delivery efficacies of fifteen novel gemini (dimeric) and three monomeric cationic lipids anchored on an aromatic backbone have been described. Each new lipid has been used for liposome formation, and optimal formulations were used to determine the structure–activity correlation of the gene transfection efficacies of these lipids in HeLa and HT1080 cells. The results of the present investigation bring out the effect of hydrocarbon chain lengths and the length of the spacer between the headgroups on gene transfection efficiencies of the cationic gemini lipids based on aromatic backbone. The lipids bearing *n*-$C_{14}H_{29}$ hydrocarbon chain lengths have been found to be the best transfecting agents compared to their counterparts with *n*-$C_{16}H_{33}$ and *n*-$C_{12}H_{25}$ chains in HeLa cells. On the other hand, in HT1080 cells, the lipids based on *n*-$C_{12}H_{25}$ and *n*-$C_{14}H_{29}$ chains were found to be more potent transfecting agents than lipids possessing *n*-$C_{16}H_{33}$ chains. Transmission electron microscopy examination revealed the existence of spherical lipid–DNA complexes.

INTRODUCTION

Over the years, the definition of a "drug molecule" has changed considerably. Drugs have emerged from active components of certain natural products, or via the design of specific enzyme inhibitors. The recent realization of using the genetic material, DNA as a potential drug has led to the development of gene therapy (*1*). Gene therapy can be envisaged as an attempt to cure a disease by supplementing the aberrant gene with a functional one or by the delivery of a suicide gene (*2*) or by transfer of a gene for the production of a therapeutic protein (*3, 4*).

In recent years, many cationic lipid based formulations have been developed to aid the delivery of DNA, *m*RNA, *si*RNA, antisense oligonucleotide, proteins and even drugs into eukaryotic cells. Because of low levels of toxicity and very low immunogenicity, their ability to deliver large pieces of DNA, and ease of preparation, cationic lipids are increasingly used as the nonviral transfection vectors as compared to viral vectors, which have several limitations (*5–13*). In addition, viral vectors add complications during gene transfer by generating adverse immunogenic responses through recombination events with the host genome (*14*).

Cationic lipid and polymeric suspensions readily form complexes with the negatively charged DNA (gene) under ambient conditions (*15*). The molecular structure of cationic lipids is an important parameter that controls their DNA complexation and gene transfection activity (*16*). Accordingly, we have investigated the role of various molecular-level modifications in different synthetic lipids on their membrane-forming properties (*17, 18*) and further influence on gene delivery events (*19–22*). For instance, the functional group that links the polar headgroup and the hydrocarbon chains of such lipid molecules plays a crucial role in their utilization in gene transfer events. Thus, *N*-[1-(2,3-dioleyloxy)propyl)]-*N*,*N*,*N*-trimethylammonium chloride (DOTMA), which contains an ether linkage between the headgroup and the long oleyl chains shows greater *in vivo* transfection efficiency than the corresponding ester analogue *N*-[1-(2,3-dioleoyloxy)propyl)]-*N*,*N*,*N*-trimethylammonium chloride (DOTAP) (*23*). Similarly, cholesterol-based lipids (*24*) and lipopolymers (*25, 26*) are also known as potent transfection agents. Here also, the role of functional group that connects cationic headgroup with a cholesteryl backbone assumes importance (*19*).

Gemini surfactants, i.e. amphiphiles molecules containing two head groups and two aliphatic chains, linked by a rigid or flexible spacer, show more interesting surfactant properties in solution compared to their monomeric counterparts. Recently, a number of reports appeared in the literature which describe the aggregation and transfection properties of gemini surfactants (*27–30*). We reported, for the first time, the synthesis and aggregation behavior of gemini pseudoglyceryl lipids (*31, 32*). It was shown that the aggregation properties of the gemini lipids could be modulated by the length of the spacer (*33*). Recently, the role of the oxyethylene-type spacer between the cationic headgroups on membrane aggregation and hydration properties was also investigated (*34*). Ahmad and co-workers showed the transfection properties of the cardiolipin-based cationic lipids (*35*). Cholesterol-based gemini lipids have been shown to deliver the DNA into the mammalian cells very efficiently and even in the presence of serum (*36, 37*). The gene delivery efficiencies strongly depend on the length of the spacer between the headgroups.

Although there is no systematic study on the use of gemini lipids for gene transfer that are based on aromatic units, there are a few reports in the literature that describe the transfection activities of cationic liposomes based on aromatic headgroups or backbones. Hoekstra et al. showed the gene delivery properties of certain pyridinium surfactants (*38*). Balaban and co-workers reported the transfection properties of various pyridinium based cationic Monomeric, gemini, and oligomeric

* Corresponding author. Phone: (91)-80-2293-2664. Fax: (91)-80-2360-0529. Email: sb@orgchem.iisc.ernet.in.

[†] Department of Organic Chemistry, Indian Institute of Science.

[‡] Department of Microbiology and Cell Biology, Indian Institute of Science.

[§] Department of Molecular Reproduction, Development and Genetics, Indian Institute of Science.

[||] Chemical Biology Unit of JNCASR.

10.1021/bc700181k CCC: $37.00 © 2007 American Chemical Society
Published on Web 11/21/2007

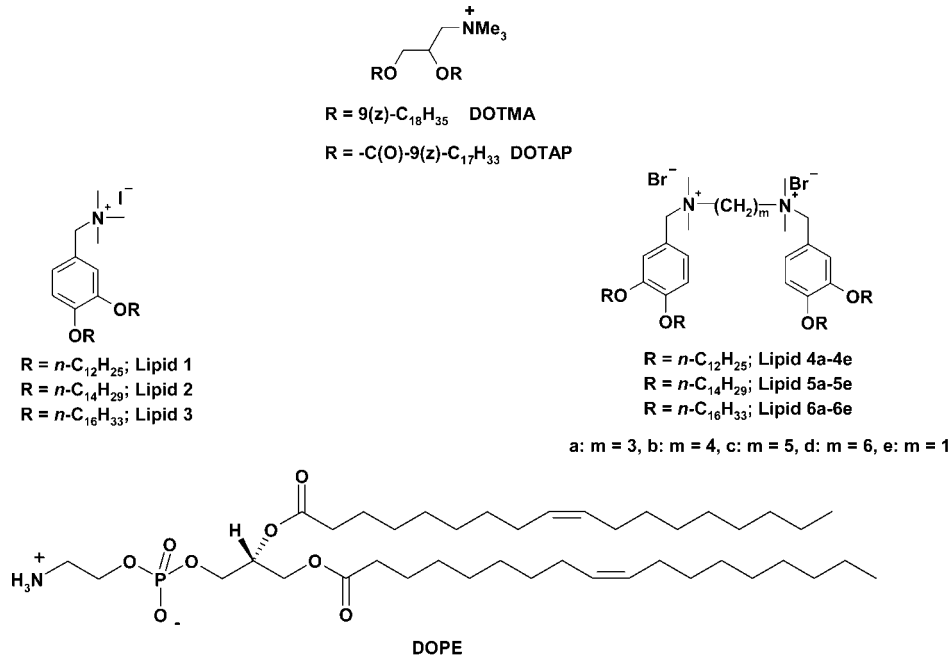


Figure 1. Molecular structures of the monomeric lipids **1**–**3**, gemini lipids **4**–**6** synthesized and studied in this work, and structures of DOTMA, DOTAP, and DOPE.

surfactants having structural variations at the level of hydrophobic segment, linker, and counter ions (*39*). Safinya and co-workers have shown that multivalent cationic lipids with an aromatic backbone hold promise for superior gene transfection (*40*). Aromatic cationic lipids (TRX) possessing amidine headgroup have been developed by Sakurai and co-workers (*41*). Recently, Phanstial and co-workers reported the transfection properties of aromatic lipophilic polyamines (*42*). However, there is no systematic study that examines the transfection activities of a series of gemini lipids based on an aromatic backbone. In addition, none of above reports addressed the important issue of serum compatibility of the liposomal formulations.

We previously reported the aromatic backbone based gemini lipids (*43*). Subsequently, we described the synthesis of aromatic lipids bearing *n*-$C_{16}H_{33}$ hydrocarbon chains that differ from each other in the length of the polymethylene spacer (*44*). Herein, we present the synthesis of two analogous series of gemini lipids based on aromatic backbone bearing *n*-$C_{12}H_{25}$ and *n*-$C_{14}H_{29}$ hydrocarbon chains (Figure 1). We also report the transfection properties of these new gemini and three monomeric cationic lipids based on an aromatic backbone that differ in the hydrocarbon chain lengths and the length of the spacer between the headgroups. We investigated their transfection properties in detail in HeLa and HT1080 cells in the absence and presence of serum conditions. Gemini lipids showed enhanced transfection as compared to Lipofectin, which is a monomeric lipid, structurally related to the present set of gemini lipids, and commercially available reagent based on a 1:1 (w/w) ratio of DOTMA/DOPE[1] formulation. The gemini lipids bearing *n*-$C_{14}H_{29}$ chain lengths have been found to be more effective transfecting agents than their analogues with *n*-$C_{16}H_{33}$ and *n*-$C_{12}H_{25}$ chains in HeLa cells, whereas in HT1080 cells, we observed that the lipids based on *n*-$C_{12}H_{25}$ and *n*-$C_{14}H_{29}$ chains were more effective than lipids bearing *n*-$C_{16}H_{33}$ chains.

EXPERIMENTAL DETAILS

Materials and Methods. All reagents, solvents, and chemicals used in this study were of the highest purity available. The solvents were dried prior to use. Column chromatography was performed using 60–120 mesh silica gel. NMR spectra were recorded using a Jeol JNM λ-300 (300 MHz for ^{1}H) spectrometer. The chemical shifts (δ) are reported in ppm downfield from the internal standard, TMS, for ^{1}H NMR. Mass spectra were recorded on a Kratos PCKompact SEQ V1.2.2 MALDI-TOF spectrometer or on a MicroMass ESI-TOF spectrometer or Shimadzu tabletop GC-MS or ESI-MS (HP1100LC-MSD). Infrared (IR) spectra were recorded on a Jasco FT-IR 410 spectrometer using KBr pellets or neat. Lipids were synthesized as described below and were characterized fully by their ^{1}H NMR, mass spectra, and elemental analysis.

Synthesis. *Methyl-3,4-dihydroxybenzoate (***8***) (45).* To a solution of 2 g (12.98 mol) of 3,4-dihydroxy benzoic acid (**7**) in dry MeOH (8 mL) was added conc HCl dropwise in ice–cold conditions with constant stirring. The resultant mixture was then refluxed at 70 °C for 12 h. After that, the solution was concentrated and extracted using EtOAc, and the pure product was isolated as a brown solid in 90% yield upon rotary evaporation. IR (neat, cm^{-1}): 3351, 1696, 1603, 1532, 1435. ^{1}H NMR ($CDCl_3$, 300 MHz): δ 3.87 (s, 3H, -O-*CH*$_3$), 5.52 (s, 1H, -*OH*), 5.77 (s, 1H, -*OH*), 6.89–6.92 (d, 1H, J = 9.0 Hz, ArH), 7.57–7.59 (m, 2H, ArH).

*Methyl-3,4-dialkyloxybenzoate (***9a**–**9c***).* A mixture of 1.84 g (11.2 mmol) of **8**, 28 mmol of appropriate alkyl bromide, and 33.6 mmol of K_2CO_3 in acetone was refluxed at 70 °C for 3 days. After that, the solution was concentrated, and the reaction mixture was taken in EtOAc. The organic layer was washed with water, brine, and then dried over anhydrous Na_2SO_4. The resulting solution was concentrated, and the residue was purified by chromatography over silica gel column using *n*-hexane/EtOAc as eluent. The pure product was isolated as a white solid in 70–75% yield.

[1]Abbreviations: DOPE, 1,2-dioleoyl-L-α-glycero-3-phosphatidylethanolamine; DOTMA, *N*-[1-(2,3-dioleoyloxypropyl)]-*N*,*N*,*N*-trimethylammonium chloride; DOTAP, *N*-[1-(2,3-dioleoyloxy)propyl]-*N*,*N*,*N*-trimethylammonium chloride; MFI, mean fluorescence intensity; FACS, fluorescence-activated cell sorting.

*Methyl-3,4-didodecyloxybenzoate (***9a***) (46).* IR (neat, cm^{-1}): 2910, 2848, 1712, 1590, 1517, 1467. ^1H NMR ($CDCl_3$, 300 MHz): δ 0.86–0.90 (t, 6H, J = 6Hz, 2× -CH_3), 1.26–1.46 (br m, 36H, 2× -$(CH_2)_9$), 1.78–1.86 (m, 4H, 2× -O-CH_2-CH_2), 3.88 (s, 3H, -O-CH_3), 4.01–4.06 (m, 4H, 2× -O-CH_2), 6.84–6.87 (d, 1H, J = 9.0 Hz, ArH), 7.53 (s, 1H, ArH), 7.61–7.65 (m, 1H, ArH). LRMS: 505 ($M + H^+$). HRMS: Calcd 505.4257 ($M + H^+$); found 505.4253.

*Methyl-3,4-ditetradecyloxybenzoate (***9b***) (46).* IR (neat, cm^{-1}): 2917, 2850, 1712, 1598, 1517, 1467. ^1H NMR ($CDCl_3$, 300 MHz): δ 0.86–0.90 (t, 6H, J = 6Hz, 2× -CH_3), 1.26–1.46 (br m, 44H, 2× -$(CH_2)_{11}$), 1.82 (m, 4H, 2× -O-CH_2-CH_2), 3.88 (s, 3H, -O-CH_3), 4.04 (m, 4H, 2× -O-CH_2), 6.84–6.88 (d, 1H, J = 9.0 Hz, ArH), 7.54 (s, 1H, ArH), 7.64 (m, 1H, ArH). LRMS: 561 ($M + H^+$). HRMS: Calcd 561.4883 ($M + H^+$); found 561.4871.

*Methyl-3,4-dihexadecyloxybenzoate (***9c***) (46).* IR (neat, cm^{-1}): 2910, 2848, 1712, 1590, 1517, 1467. ^1H NMR ($CDCl_3$, 300 MHz): δ 0.86–0.90 (t, 6H, J = 6Hz, 2× -CH_3), 1.26–1.46 (br m, 52H, 2× -$(CH_2)_{13}$), 1.78–1.86 (m, 4H, 2× -O-CH_2-CH_2), 3.88 (s, 3H, -O-CH_3), 4.01–4.06 (m, 4H, 2× -O-CH_2), 6.84–6.87 (d, 1H, J = 9.0 Hz, ArH), 7.53 (s, 1H, ArH), 7.61–7.65 (1H, m, ArH), LRMS: 656 ($M + K^+$).

*3,4-Dialkyloxybenzyl aAlcohol (***10a**–**10c***).* To a suspension 0.6 g (5 mmol) of $LiAlH_4$ in dry THF (5 mL) was added a solution of 3.24 mmol of **9a**–**9c** dropwise in ice–cold conditions with constant stirring under a nitrogen atmosphere. The ice bath was removed, and the resultant was refluxed at 70 °C overnight. Then, moist EtOAc (20 mL) was added slowly and stirred for 10 min at room temperature. The solvent was removed under vacuum, and then the reaction mixture was taken in $CHCl_3$ and washed with saturated Na, K-tartrate solution (50 mL). The aqueous layer was extracted twice with $CHCl_3$. All organic layers were collected together and dried over anhydrous Na_2SO_4, and the solvent was evaporated to leave a solid, which was purified by column chromatography using *n*-hexane/EtOAc as eluent. The pure product was isolated as a white solid in 90–95% yield.

*3,4-Didodecyloxybenzyl Alcohol (***10a***).* IR (neat, cm^{-1}): 3332, 2956, 2917, 2850, 1590, 1517, 1467. ^1H NMR ($CDCl_3$, 300 MHz): δ 0.86–0.90 (t, 6H, J = 6Hz, 2× -CH_3), 1.26–1.46 (br m, 36H, 2× -$(CH_2)_9$) 1.79 (m, 4H, 2× -O-CH_2-CH_2), 3.96–4.02 (m, 4H, 2× -O-CH_2), 4.60 (s, 2H, -CH_2-Ar), 6.85 (s, 2H, ArH), 6.92 (s, 1H, ArH). LRMS: 499 ($M + Na^+$). HRMS: Calcd 499.4127 ($M + Na^+$); found 499.4231.

*3,4-Ditetradecyloxybenzyl Alcohol (***10b***).* IR (neat, cm^{-1}): 3342, 2917, 2850, 1590, 1517, 1467. ^1H NMR ($CDCl_3$, 300 MHz): δ 0.86–0.90 (6H, t, J = 6Hz, 2× -CH_3), 1.26–1.46 (br m, 44H, 2× -$(CH_2)_{11}$), 1.79 (m, 4H, 2× -O-CH_2-CH_2), 3.96–4.02 (m, 4H, 2× -O-CH_2), 4.60 (s, 2H, -CH_2-Ar), 6.85 (s, 2H, ArH), 6.92 (s, 1H, ArH). LRMS: 555 ($M + Na^+$). HRMS: Calcd 555.4753 ($M + Na^+$); found 555.4743.

*3,4-Dihexadecyloxybenzyl Alcohol (***10c***).* IR (neat, cm^{-1}): 3348, 2954, 2916, 2849, 1518, 1466. ^1H NMR ($CDCl_3$, 300 MHz): δ 0.86–0.90 (t, 6H, J = 6Hz, 2× -CH_3), 1.26–1.46 (br m, 52H, 2× -$(CH_2)_{13}$), 1.80 (m, 4H, 2× -O-CH_2-CH_2), 3.96–4.02 (m, 4H, 2× -O-CH_2), 4.6 (s, 2H, -CH_2-Ar), 6.86 (s, 2H, ArH), 6.92 (s, 1H, ArH). LRMS: 612 ($M + Na^+$). HRMS: Calcd 611.5379 ($M + Na^+$); found 611.5370.

*1-(3,4-Dialkanoyloxyphenylmethyl) Dimethylamine (***11a**–**11c***).* To a stirring solution of 0.76 mmol of the benzyl alcohol (**10a**–**10c**), 0.620 g (3 mmol) of PBr_3 in dry DCM was added dropwise in ice–cold conditions. Slowly, the resultant was allowed to rise to room temperature, and the mixture continued to stir for 24 h. Since the bromo compound was unstable, no isolation was attempted. The subsequent step was done *in situ* by adding excess Me_2NH in MeOH and again kept for 12 h. The mixture was concentrated, and the residue was dissolved in $CHCl_3$. The organic mixture was washed with 1 N HCl (2 × 50 mL) followed by water, saturated $NaHCO_3$, and brine, and then dried over anhydrous Na_2SO_4. The organic solvent was removed and then subjected to column chromatography over silica gel using MeOH/$CHCl_3$as an eluent. The pure compound was isolated as a white solid in 80–85% yield.

*1-(3,4-Didodecyloxyphenylmethyl) Dimethylamine (***11a***).* IR (neat, cm^{-1}): 2921, 2852, 1589, 1513, 1467. ^1H NMR ($CDCl_3$, 300 MHz): δ 0.86–0.90 (t, J = 6Hz, 6H, 2× -CH_3), 1.26–1.46 (br m, 36H, 2× -$(CH_2)_9$), 1.79–1.82 (m, 4H, 2× -O-CH_2-CH_2), 2.23 (s, 6H, 2× -N-CH_3), 3.78 (s, 2H, -CH_2-Ar), 3.95–4.01 (m, 4H, 2× -O-CH_2), 6.78–6.87 (m, 3H, ArH). LRMS: 504 ($M + H^+$). HRMS: Calcd 504.4780 ($M + H^+$); found 504.47.

*1-(3,4-Ditetradecyloxyphenylmethyl) Dimethylamine (***11b***).* IR (neat, cm^{-1}): 2923, 2854, 1590, 1511, 1467. ^1H NMR ($CDCl_3$, 300 MHz): δ 0.86–0.90 (t, 6H, J = 6Hz, 2× -CH_3), 1.26–1.46 (br m, 44H, 2× -$(CH_2)_{11}$), 1.80 (m, 4H, 2× -O-CH_2-CH_2), 2.21 (s, 6H, 2× -N-CH_3), 3.33 (s, 2H, -CH_2-Ar), 3.97 (m, 4H, 2× -O-CH_2), 6.79 (m, 3H, ArH). LRMS: 561 ($M + H^+$). HRMS: Calcd 560.5406 ($M + H^+$); found 560.5416.

*1-(3,4-Dihexadecyloxyphenylmethyl) Dimethylamine (***11c***).* IR (neat, cm^{-1}): 2917, 2850, 1590, 1517, 1467. ^1H NMR ($CDCl_3$, 300 MHz): δ 0.86–0.90 (t, 6H, J = 6Hz, 2× -CH_3), 1.26–1.46 (br m, 52H, 2× -$(CH_2)_{13}$), 1.79 (m, 4H, 2× -O-CH_2-CH_2), 2.56 (s, 6H, 2× -N-CH_3), 3.78 (s, 2H, -CH_2-Ar), 3.92–3.98 (m, 4H, 2× -O-CH_2), 6.80 (s, 2H, ArH), 6.93 (s, 1H, ArH). LRMS: 617 ($M + H^+$). HRMS: Calcd 616.6032 ($M + H^+$); found 616.5940.

*1-(3,4-Dialkyloxyphenylmethyl)- N,N,N-trimethyl Ammonium Iodide (***1**, **2**, **3***).* To a solution of **11a–c** (0.11 mmol) in dry EtOH, MeI (excess) was added in a screw-top pressure tube. The resulting mixture was heated to reflux at 80 °C for 24 h. The removal of solvent and subsequent washing with EtOAc–MeOH (9:1) produced a yellowish–white compound. The compound was isolated in quantitative yield.

Lipid **1.** ^1H NMR (300 MHz, $CDCl_3$): δ 0.86–0.90 (t, 6H, J = 6.0 Hz, 2× -CH_3), 1.26–1.46 (m, 36H, 2× -$(CH_2)_9$), 1.75–1.87 (m, 4H, 2× -O-CH_2-CH_2-), 3.35 (s, 9H, 3× -N^+-CH_3), 3.98–4.06 (m, 4H, 2× -O-CH_2-CH_2-), 4.87 (s, 2H, -N^+-CH_2-Ar), 6.88 (d, 1H, J = 9.0 Hz, ArH), 7.11 (d, 1H, J = 9.0 Hz, ArH), 7.20 (s, 1H, ArH). ESI-MS: 519.2 (M^+). Anal. ($C_{34}H_{64}NO_2I \cdot 2H_2O$) C, H, N.

Lipid **2.** ^1H NMR (300 MHz, $CDCl_3$): δ 0.86–0.90 (t, 6H, J = 6.0 Hz, 2× -CH_3), 1.26–1.46 (m, 44H, 2× -$(CH_2)_{11}$), 1.80 (m, 4H, 2× -O-CH_2-CH_2-), 3.36 (s, 9H, 3× -N^+-CH_3), 3.98–4.06 (m, 4H, 2× -O-CH_2-CH_2-), 4.92 (s, 2H, -N^+-CH_2-Ar), 6.86–6.89 (d, 1H, J = 9.0 Hz, ArH), 7.10–7.13 (d, 1H, J = 9.0 Hz, ArH), 7.23 (m, 1H, ArH). ESI-MS: 574.5 (M^+). Anal. ($C_{38}H_{72}NO_2I$) C, H, N.

Lipid **3.** ^1H NMR (300 MHz, $CDCl_3$): δ 0.85 (t, 6H, J = 7.0 Hz, 2× -CH_3), 1.25–1.46 (m, 52H, 2× -$(CH_2)_{13}$), 1.78–1.80 (m, 4H, 2× -O-CH_2-CH_2-), 3.35 (s, 9H, 3× -N^+-CH_3), 3.97–4.05 (m, 4H, -O-CH_2-CH_2-), 4.91 (s, 2H, -N^+-CH_2-Ar), 6.87 (d, 1H, J = 8.1 Hz, ArH), 7.11 (d, 1H, J = 8.1 Hz, ArH), 7.21 (s, 1H, ArH). ESI-MS: 631 (M^+). Anal. ($C_{42}H_{80}NO_2I \cdot 2H_2O$) C, H, N.

*General Method for the Synthesis of Gemini Lipids (***4**, **5**, **6***).* A solution of **11a–c** (0.24 mmol) and appropriate α,ω-dibromoalkane (0.080 mmol) in dry MeOH/EtOAc mixture was refluxed over a period of 48–96 h. It was cooled, and solvent was evaporated to produce a crude solid. It was repeatedly washed with dry EtOAc to remove unreacted starting material and finally subjected to repeated crystallization from a mixture of EtOAc and MeOH (9:1), which gives white solid. Yield 40–50%.

Lipid **4a.** ^1H NMR (300 MHz, $CDCl_3$): δ 0.86–0.90 (t, J = 6.0 Hz, 12H, 4× -CH_3), 1.26–1.46 (m, 72H, 4× -$(CH_2)_9$), 1.80

(m, 8H, 4× -O-CH_2-CH_2), 3.07 (br m, 2H, -N^+-CH_2-CH_2-), 3.22 (s, 12H, 4× -N^+-CH_3), 3.98–4.01 (m, 12H, 4× -O-CH_2-CH_2- and 2× -N^+-CH_2-CH_2), 4.71 (s, 4H, 2× -N^+-CH_2-Ar), 6.86 (d, J = 9.0 Hz, 2H, ArH), 7.08 (m, 4H, ArH). ESI-MS: 459.4 (($C_{12}H_{25}O)_2C_6H_3CH_2^+$), 589.5 (($C_{12}H_{25}O)_2C_6H_3CH_2N^+(CH_3)_2(CH_2)_3N(CH_3)_2$). Anal. ($C_{69}H_{128}N_2O_4Br_2 \cdot 2H_2O$) C, H, N.

Lipid **4b.** ^{1}H NMR (300 MHz, $CDCl_3$): δ 0.86–0.90 (t, J = 6.0 Hz, 12H, 4× -CH_3), 1.25–1.46 (m, 72H, 4× -$(CH_2)_9$), 1.77 (m, 12H, 4× -O-CH_2-CH_2- and 2× -N^+-CH_2-CH_2-), 3.12 (s, 12H, 4× -N^+-CH_3), 3.96–4.02 (m, 12H, 4× -O-CH_2-CH_2- and -N^+-CH_2-CH_2), 4.67 (s, 4H, 2× -N^+-CH_2-Ar), 6.88 (d, J = 9.0 Hz, 2H, ArH), 7.11 (m, 4H, ArH). ESI-MS: 459.4 (($C_{12}H_{25}O)_2C_6H_3CH_2^+$), 603.5 (($C_{12}H_{25}O)_2C_6H_3CH_2N^+(CH_3)_2(CH_2)_4N(CH_3)_2$). Anal. ($C_{70}H_{130}N_2O_4Br_2 \cdot 3H_2O$) C, H, N.

Lipid **4c.** ^{1}H NMR (300 MHz, $CDCl_3$): δ 0.86–0.90 (t, J = 6.0 Hz, 12H, 4× -CH_3), 1.25–1.47 (m, 74H, 4× -$(CH_2)_9$ and -N^+-CH_2-CH_2-CH_2-), 1.80 (m, 8H, 4× -O-CH_2-CH_2), 2.23 (m, 4H, 2× -N^+-CH_2-CH_2-), 3.18 (s, 12H, 4× -N^+-CH_3), 3.99 (m, 12H, 4× -O-CH_2-CH_2- and 2× -N^+-CH_2-CH_2), 4.75 (s, 4H, 2× -N^+-CH_2-Ar), 6.89 (d, 2H, J = 9.0 Hz, ArH), 7.13 (m, 4H, ArH). ESI-MS: 459.4 (($C_{12}H_{25}O)_2C_6H_3CH_2^+$), 617.6 (($C_{12}H_{25}O)_2C_6H_3CH_2N^+(CH_3)_2(CH_2)_5N(CH_3)_2$). Anal. C, H, N, ($C_{71}H_{132}N_2O_4Br_2$).

Lipid **4d.** ^{1}H NMR (300 MHz, $CDCl_3$): δ 0.86–0.90 (t, J = 6.0 Hz, 12H, 4× -CH_3), 1.26–1.46 (m, 76H, 4× -$(CH_2)_9$ and 2× -N^+-CH_2-CH_2-CH_2-), 1.79 (m, 12H, 4× -O-CH_2-CH_2- and 2× -N^+-CH_2-CH_2-CH_2-), 3.23 (s, 12H, 4× -N^+-CH_3), 3.82 (m, 4H, -N^+-CH_2-CH_2), 3.96–4.03 (m, 8 H, 4× -O-CH_2-CH_2-), 4.78 (s, 4H, 2× -N^+-CH_2-Ar), 6.85–6.88 (d, J = 9.0 Hz, 2H, ArH), 7.12–7.16 (m, 4H, ArH). ESI-MS: 547.5 (M^{+2}/2). Anal. ($C_{72}H_{134}N_2O_4Br_2$) C, H, N.

Lipid **4e.** ^{1}H NMR (300 MHz, $CDCl_3$): δ 0.86 (t, J = 6.0 Hz, 12H, 4× -CH_3), 1.26 (m, 92H, 4× -$(CH_2)_9$ and 2× -N^+-CH_2-CH_2-CH_2-CH_2-CH_2-), 1.79 (m, 8H, 4× -O-CH_2-CH_2-), 3.05 (s, 12H, 4× -N^+-CH_3), 3.73 (m, 4H, 2× -N^+-CH_2-CH_2), 3.98 (m, 8H, 4× -O-CH_2-CH_2-), 4.82 (s, 4H, 2× -N^+-CH_2-Ar), 6.84–6.87 (d, J = 9.0 Hz, 2H, ArH), 7.14–7.18 (m, 4H, ArH). ESI-MS: 588 (M^{+2}/2). Anal. ($C_{78}H_{146}N_2O_4Br_2$) C, H, N.

Lipid **5a.** ^{1}H NMR (300 MHz, $CDCl_3$): δ 0.86–0.90 (t, 12H, J = 6.0 Hz, 4× -CH_3), 1.25–1.47 (m, 88H, 4× -$(CH_2)_{11}$), 1.83 (m, 8H, 4× -O-CH_2-CH_2-), 3.05 (m, 2H, -N^+-CH_2-CH_2-), 3.22 (s, 12H, 4× -N^+-CH_3), 4.00 (m, 12H, 4× -O-CH_2-CH_2- and 2× -N^+-CH_2-CH_2), 4.68 (s, 4H, 2× -N^+-CH_2-Ar), 6.88–6.91 (d, 2H, J = 9.0 Hz, ArH),7.06 (m, 4H, ArH). ESI-MS: 515.5 (($C_{14}H_{29}O)_2C_6H_3CH_2^+$), 557.5 (($C_{14}H_{29}O)_2C_6H_3CH_2N^+(CH_3)_2$), 645.6 (($C_{14}H_{29}O)_2C_6H_3CH_2N^+(CH_3)_2(CH_2)_3N(CH_3)_2$), 1241.9 ($M^{+2}$ + Br^-). Anal. ($C_{77}H_{144}N_2O_4Br_2$) C, H, N.

Lipid **5b.** ^{1}H NMR (300 MHz, $CDCl_3$): δ 0.86–0.90 (t, 12H, J = 6.0 Hz, 4× -CH_3), 1.25–1.46 (m, 88H, 4× -$(CH_2)_{11}$), 1.80 (m, 8H, 4× -O-CH_2-CH_2-), 2.31 (m, 4H, 2× -N^+-CH_2-CH_2-), 3.13 (s, 12H, 4× -N^+-CH_3), 3.98 (t, 8H, J = 6.0 Hz, 4× -O-CH_2-CH_2-), 4.12 (m, 4H, -N^+-CH_2-CH_2), 4.63 (s, 4H, 2× -N^+-CH_2-Ar), 6.88–6.90 (d, 2H, J = 6.0 Hz, ArH), 7.04 (m, 4H, ArH). ESI-MS: 515.5 (($C_{14}H_{29}O)_2C_6H_3CH_2^+$), 659.7 (($C_{14}H_{29}O)_2C_6H_3CH_2N^+(CH_3)_2(CH_2)_3N(CH_3)_2$). Anal. ($C_{78}H_{146}N_2O_4Br_2 \cdot 2H_2O$) C, H, N.

Lipid **5c.** ^{1}H NMR (300 MHz, $CDCl_3$): δ 0.86–0.90 (t, 12H, J = 6.0 Hz, 4× -CH_3), 1.25–1.47 (m, 90H, 4× -$(CH_2)_{11}$ and -N^+-CH_2-CH_2-CH_2-), 1.80 (m, 8H, 4× -O-CH_2-CH_2), 2.23 (m, 4H, 2× -N^+-CH_2-CH_2-), 3.18 (s, 12H, 4× -N^+-CH_3), 3.99 (m, 12H, 4× -O-CH_2-CH_2- and 2× -N^+-CH_2-CH_2), 4.75 (s, 4H, 2× -N^+-CH_2-Ar), 6.87–6.89 (d, 2H, J = 6.0 Hz, ArH), 7.13 (m, 4H, ArH). ESI-MS: 515.5 (($C_{14}H_{29}O)_2C_6H_3CH_2^+$), 595.0 ($M^{+2}$/2), 673.7 (($C_{14}H_{29}O)_2C_6H_3CH_2N^+(CH_3)_2(CH_2)_3N(CH_3)_2$), 1270 ($M^{+2}$ + Br^-). Anal. ($C_{79}H_{148}N_2O_4Br_2$) C, H, N.

Lipid **5d.** ^{1}H NMR (300 MHz, $CDCl_3$): δ 0.86–0.90 (t, 12H, J = 6.0 Hz, 4× -CH_3), 1.26–1.46 (m, 92H, 4× -$(CH_2)_{11}$ and 2× -N^+-CH_2-CH_2-CH_2-), 1.79 (m, 8H, 4× -O-CH_2-CH_2-), 2.17 (m, 4H, 2× -N^+-CH_2-CH_2-), 3.21 (s, 12H, 4× -N^+-CH_3), 3.83 (m, 4H, 2× -N^+-CH_2-CH_2), 4.02 (m, 8H, 4× -O-CH_2-CH_2-), 4.72 (s, 4H, 2× -N^+-CH_2-Ar), 6.86–6.89 (d, 2H, J = 8.1 Hz, ArH), 7.12 (m, 4H, ArH). ESI-MS: 602.0 (M^{+2}/2). Anal. ($C_{80}H_{150}N_2O_4Br_2$) C, H, N.

Lipid **5e.** ^{1}H NMR (300 MHz, $CDCl_3$): δ 0.86–0.90 (t, 12H, J = 6.0 Hz, 4× -CH_3), 1.26–1.40 (m, 108H, 4× -$(CH_2)_{11}$ and 2× -N^+-CH_2-CH_2-CH_2-CH_2-CH_2-CH_2-), 1.82 (m, 8H, 4× -O-CH_2-CH_2-), 3.21 (s, 12H, 4× -N^+-CH_3), 3.72 (m, 4H, 2× -N^+-CH_2-CH_2), 4.01 (m, 8H, 4× -O-CH_2-CH_2-), 4.13 (s, 4H, -N^+-CH_2-Ar), 6.84–6.87 (d, 2H, J = 8.1 Hz, ArH), 7.14–7.18 (m, 4H, ArH). ESI-MS: 644.0 (M^{+2}/2). Anal. ($C_{86}H_{162}N_2O_4Br_2 \cdot 2H_2O$) C, H, N.

Lipid **6a.** ^{1}H NMR (300 MHz, $CDCl_3$): δ 0.87 (t, 12H, J = 7.0 Hz, 4× −CH_3), 1.25–1.46 (m, 104H, 4× -$(CH_2)_{13}$), 1.82–1.86 (m, 8H, 4× -O-CH_2-CH_2-), 3.01–3.10 (br m, 2H, -N^+-CH_2-CH_2-), 3.21 (s, 12H, 4× -N^+-CH_3), 3.96–4.01 (m, 12H, 4× -O-CH_2-CH_2- and 2× -N^+-CH_2-CH_2), 4.72 (s, 4H, 2× -N^+-CH_2-Ar), 6.85–6.88 (d, 2H, J = 8.1 Hz, ArH), 7.07–7.10 (m, 4H, ArH). ESI-MS: 637 (M^{2+}/2). Anal. ($C_{85}H_{160}N_2O_4Br_2$) C, H, N.

Lipid **6b.** ^{1}H NMR (300 MHz, $CDCl_3$): δ 0.87 (t, 12H, J = 7.0 Hz, 4× -CH_3), 1.25–1.46 (m, 104H, 4× -$(CH_2)_{13}$), 1.76–1.86 (m, 8H, 4× -O-CH_2-CH_2-), 2.29–3.10 (m, 4H, 2× -N^+-CH_2-CH_2-), 3.12 (s, 12H, 4× -N^+-CH_3), 3.99 (t, 8H, J = 6.0 Hz, 4× -O-CH_2-CH_2-), 4.02–4.11 (m, 4H, 2× -N^+-CH_2-CH_2), 4.62 (s, 4H, 2× -N^+-CH_2-Ar), 6.88 (d, 2H, J = 8.1 Hz, ArH), 7.05–7.12 (m, 4H, ArH). ESI-MS: 644 (M^{2+}/2). Anal. ($C_{86}H_{162}N_2O_4Br_2 \cdot 3H_2O$) C, H, N.

Lipid **6c.** ^{1}H NMR (300 MHz, $CDCl_3$): δ 0.88 (t, 12H, J = 7.0 Hz, 4× -CH_3), 1.25–1.47 (m, 106H, 4× -$(CH_2)_{13}$ and -N^+-CH_2-CH_2-CH_2-), 1.79–1.85 (m, 8H, 4× -O-CH_2-CH_2-), 2.10–2.24 (br m, 4H, 2× -N^+-CH_2-CH_2-), 3.18 (s, 12H, 4× -N^+-CH_3), 3.99–4.01 (m, 12H, 4× -O-CH_2-CH_2- and 2× -N^+-CH_2-CH_2), 4.75 (s, 4H, 2× -N^+-CH_2-Ar), 6.87 (d, 2H, J = 8.1 Hz, ArH), 7.13 (m, 4H, ArH). ESI-MS: 650 (M^{2+}/2). Anal. ($C_{87}H_{164}N_2O_4Br_2$) C, H, N.

Lipid **6d.** ^{1}H NMR (300 MHz, $CDCl_3$): δ 0.88 (t, 12H, J = 7.0 Hz, 4× -CH_3), 1.25–1.46 (m, 108H, 4× -$(CH_2)_{13}$ and 2× -N^+-CH_2-CH_2-CH_2-), 1.78–1.82 (m, 8H, 4× -O-CH_2-CH_2-), 2.24–2.40 (m, 4H, 2× -N^+-CH_2-CH_2-), 3.21 (s, 12H, 4× -N^+-CH_3), 3.84–3.95 (m, 4H, 2× -N^+-CH_2-CH_2), 3.97–4.03 (m, 8H, 4× -O-CH_2-CH_2-), 4.62 (s, 4H, -N^+-CH_2-Ar), 6.87 (d, 2H, J = 8.1 Hz, ArH), 7.13–7.19 (m, 4H, ArH). ESI-MS: 657 (M^{2+}/2). Anal. ($C_{88}H_{166}N_2O_4Br_2$) C, H, N.

Lipid **6e.** ^{1}H NMR (300 MHz, $CDCl_3$): δ 0.86 (t, 12H, J = 7.0 Hz, 4× -CH_3), 1.16–1.40 (m, 124H, 4× -$(CH_2)_{13}$ and 2× -N^+-CH_2-CH_2-CH_2-CH_2-CH_2-CH_2-), 1.76–1.78 (m, 8H, 4× -O-CH_2-CH_2-), 3.17 (s, 12H, 4× -N^+-CH_3), 3.62–3.70 (m, 4H, 2× -N^+-CH_2-CH_2), 3.94–3.99 (m, 8H, 4× -O-CH_2-CH_2-), 4.79 (s, 4H, 2× -N^+-CH_2-Ar), 6.82 (d, 2H, J = 8.1 Hz, ArH), 7.09 (d, 2H, J = 8.1 Hz, ArH), 7.15–7.21 (m, 2H, ArH). ESI-MS: 700 (M^{2+}/2). Anal. ($C_{94}H_{178}N_2O_4Br_2$) C, H, N.

Liposome Preparation. Individual lipid or its mixture with DOPE in the desired mole ratio was dissolved in chloroform in autoclaved Wheaton glass vials. Thin films were made by evaporation of the organic solvent under a steady stream of dry nitrogen. Last traces of organic solvent were removed by keeping these films under vacuum overnight. Freshly autoclaved water (Milli-Q) was added to individual film such that the final concentration of the cationic lipid was 0.5 mM. The mixtures were kept for hydration at 4 °C for 10–12 h and subjected to repeated freeze–thaw cycles (ice–cold water to 70 °C) with intermittent vortexing to ensure hydration. Sonication of these

suspensions for 15 min in a bath sonicator at 70 °C afforded closed cationic liposomes as evidenced from transmission electron microscopy. Liposomes were prepared and kept under sterile conditions. Formulations were stable and, if stored frozen, possessed long shelf life.

Transmission Electron Microscopy. Freshly prepared aqueous suspensions of lipoplexes were examined under transmission electron microscopy by negative staining using 1% uranyl acetate. A 10 μL sample of the suspension was loaded onto Formvar-coated, 400 mesh copper grids and allowed to remain for 1 min. Excess fluid was wicked off the grids by touching their edges to filter paper, and 10 μL of 1% uranyl acetate was applied on the same grid, after which the excess stain was similarly wicked off. The grid was air-dried for 30 min, and the specimens were observed under TEM (JEOL 200-CX) operating at an acceleration voltage of 120 keV. Micrographs were recorded at a magnification of 5000–20 000×.

Plasmid DNA. pEGFP-c3 (Clontech, USA), which encodes for an enhanced green fluorescence protein (GFP) under a CMV promoter, was amplified in *Escherichia coli* (DH5α) and purified using Qiagen Midi Prep Plasmid Purification protocol (Qiagen, Germany). Purity of the plasmid was checked by electrophoresis on 1.0% agarose gel. Concentration of the DNA was estimated spectroscopically by measuring the absorption at 260 nm and confirmed by gel electrophoresis. The plasmid preparations showing a value of $OD_{260}/OD_{280} > 1.8$ were used.

Cell Culture. Cells (HeLa or HT1080) were cultured in Dulbecco's Modified Eagle's Medium (DMEM; Sigma) supplemented with 10% fetal bovine serum (FBS) in T25 culture flasks (Nunc, Denmark) and were incubated at 37 °C in a humidified atmosphere containing 5% CO_2. Cells were regularly passaged by trypsinization with 0.1% trypsin (EDTA 0.02%, dextrose 0.05%, and trypsin 0.1%) in PBS (pH 7.2).

Cytotoxicity. Toxicity of each cationic lipid formulation towards HeLa cells was determined using 3-(4,5-dimethylthiazole-2-yl)-2,5-diphenyltetrazolium bromide reduction assay following the literature procedures (*47*). MTT is converted to an insoluble blue dye, formazan, in actively respiring cells. The assay estimates the concentration of the formazan formed, which in turn gives a measure of the population of cells that are metabolically active.

Cytotoxicity of the lipid formulations optimal for transfection experiments were found out under conditions exactly similar for transfection conditions. Nearly 12 000 cells/well were plated in a 96 well plate. After 24 h, optimized lipid/DOPE formulations were complexed with 0.2 μg of the DNA at an N/P ratio of 0.75 for 30 min. DNA–lipid complexes were added to the cells in the absence of serum. After 4 h of incubation, lipoplexes were removed and 200 μL of media with 10% FBS was added. After 42 h, 20 μL of MTT solution was added and the cells were incubated further for 4 h. Blue formazan crystals were seen as well when checked under the microscope. Media was removed and 200 μL of DMSO was added per well. The absorbance was measured using a microtiter plate reader. The % viability was then calculated as $[\{A_{590}(\text{treated cells}) - \text{background}]/[A_{590}(\text{untreated cells}) - \text{background}\}] \times 100$.

Transfection Procedure. All transfection experiments were carried out in HeLa or HT1080 cells in antibiotic-free media unless specified otherwise. In a typical experiment, 24 well plates were seeded with 45 000 cells/well in antibiotic-free media 24 h before transfection such that they were at least ~70% confluent at the time of transfection. For transfection, to have the required working stocks lipid formulation and DNA were serially diluted separately in DMEM containing no serum. DNA was used at a concentration of 0.8 μg/well unless specified otherwise. The lipid and DNA were complexed in a volume of 200 μL by incubating the desired amount of lipid formulation and DNA together at room temperature for about 30 min. The lipid concentrations were varied so as to obtain the required lipid/DNA (N/P) charge ratios. Charge ratios here represent the ratio of charge on cationic lipid (in mol) to nucleotide base molarity and were calculated by considering the average nucleotide mass of 330. After 30 min of complexation, 200 μL of media were added to the complexes (final DNA concentration = 12.12 μM). Old medium was removed from the wells, cells were washed with DMEM, and lipid–DNA complexes in 200 μL media were added to the cells. The plates were then incubated for 4 h at 37 °C in a humidified atmosphere containing 5% CO_2. At the end of incubation period, medium was removed and cells were washed with DMEM, 500 μL of DMEM containing 10% FBS was added per well. Plates were further incubated for a period of 44 h before checking the reporter gene expression. GFP expression was examined by fluorescence microscopy and was quantified by flow cytometry analysis. Control transfections were performed in each case using a commercially available transfection reagent Lipofectin based on the standard conditions specified by the manufacturer. All the experiments were done in duplicates, and results presented are the average of at least two such independent experiments done on two different days.

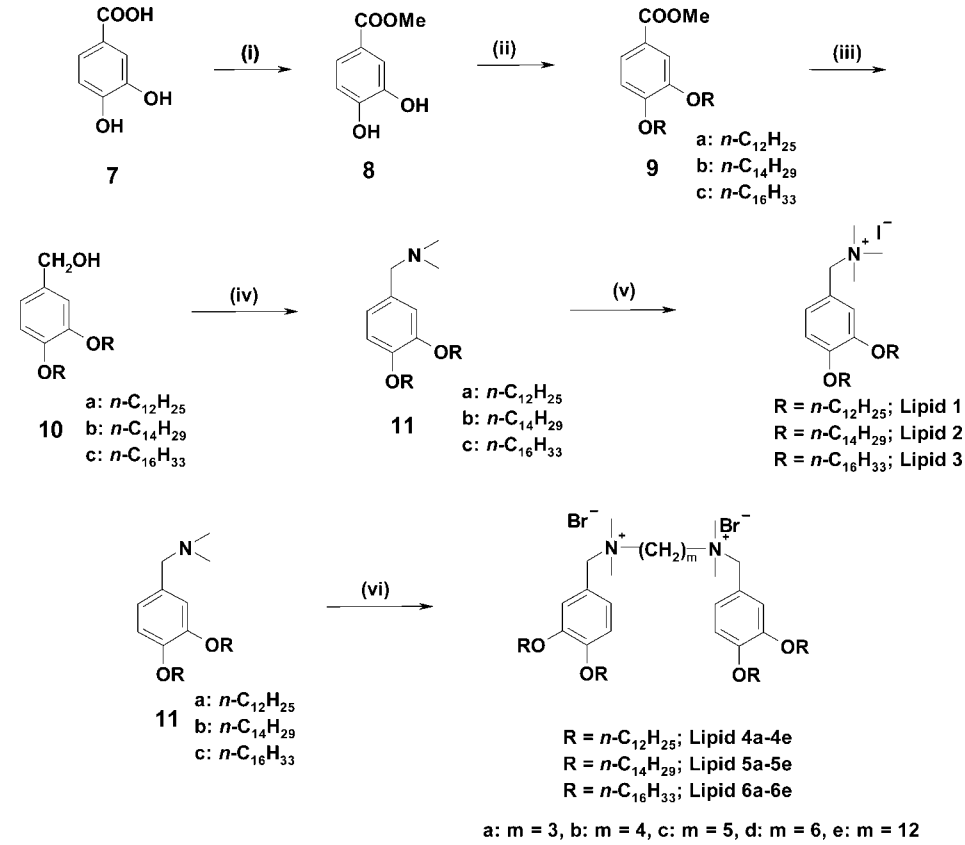
For transfections in the presence of serum, lipid and DNA were separately diluted in serum-free media as already mentioned, and the complexation was done in serum-free media (200 μL) for 30 min. The complex was then diluted to 400 μL with DMEM containing 20% FBS so as to achieve a final serum concentration of 10%. The cells were then incubated with these complexes for 4 h. At the end of the incubation period, medium was removed and cells were washed with DMEM; 500 μL of DMEM containing 10 % FBS was added per well. For transfections at 30% and 50% of serum concentrations, complexes were diluted with DMEM containing 60% FBS or with neat FBS, respectively.

Gel Electrophoresis. To examine the complexation of DNA with cationic lipid suspensions at different lipid–DNA ratios, we prepared lipid–DNA complexes at different lipid–DNA charge ratios in an identical manner as was done with the transfection experiments. After 30 min of incubation, these complexes were electrophoretically run on a 1.0% agarose gel. The uncomplexed DNA moved out of well, but the DNA that was complexed with lipid remained inside the well (*7*).

Flow Cytometry. The reporter gene expression was examined by fluorescence microscopy at regular intervals and was quantified 48 h post-transfection by flow cytometry. The percentage of transfected cells was obtained by determining the statistics of cells fluorescing above the control level wherein nontransfected cells were used as the control. Approximately 10 000 cells were analyzed to achieve the statistical data, which have been presented as the average of at least two such independent measurements. For flow cytometry analysis, ~48 h post-transfection, old medium was removed from the wells; cells were washed with PBS and trypsinized by adding 100 μL of 0.1% trypsin. To each well, 200 μL of PBS containing 20% FBS was added. Duplicate cultures were pooled and analyzed by flow cytometry immediately using a Becton and Dickinson flow cytometer equipped with a fixed laser source at 488 nm.

FACS Analysis. FACS data were analyzed by public domain *WinMDI* software to eliminate data from cell debris (particles smaller than cells), dead cells, and clumps of two or more cells. Subcellular debris and clumps can be distinguished from single cells by size (estimated by the intensity of low angle forward scatter). Dead cells have lower forward-scatter and higher side-scatter than living cells. The FACS scans had been configured to display the fluorescence signals only from those particles with a specified set of scatter properties, namely, living single cells.

Scheme 1[a]



[a] Reagents, conditions, and yields: (i) HCl, MeOH, 80 °C, 12 h, 90%; (ii) RBr, K_2CO_3, dry acetone, 70 °C, 72–86 h, 70–75%; (iii) $LiAlH_4$, dry THF, 70 °C, 12 h, 90–95%; (iv) (a) PBr_3, CH_2Cl_2, rt, 24 h; (b) Me_2NH (excess), MeOH, rt, 12 h (overall yield = 80–85% for steps (a) and (b)); (v) MeI, EtOH, 80 °C, 24 h, screw-top pressure tube, quantitative yields; (vi) $Br(CH_2)_mBr$, MeOH–EtOAc (2:1), 80 °C, screw-top pressure tube, 2–4 days, 40–50%.

This is called a scatter-gated fluorescence analysis. Therefore, the data from dead cells had been eliminated by gating out brightly fluorescent cells.

RESULTS AND DISCUSSION

Chemistry. Fifteen new gemini cationic lipids (**4**–**6**) of different hydrocarbon chain lengths have been synthesized. For comparison of their transfection properties with those of their monomeric counterparts, lipids **1**–**3** were also synthesized (Figure 1). Each of these lipids possesses an aromatic backbone which anchors the linkage between the hydrocarbon chains and the charged headgroup. Two cationic ammonium headgroups are joined through flexible polymethylene spacers.

For the synthesis, first the 3,4-dihydroxy benzoic acid (**7**) was esterified in the presence of conc HCl and dry MeOH under reflux conditions to protect the -COOH moiety (Scheme 1). The corresponding ester (**8**) was obtained in 90% yield. The ester (**8**) was then subjected to alkylation with appropriate *n*-alkyl bromide under reflux conditions in dry acetone in the presence of K_2CO_3 to furnish the dialkylated products (**9a**–**9c**) in 70–75% yields. The ester group of the product (**9a**–**9c**) was then reduced with $LiAlH_4$ in dry THF, under reflux conditions over a period of 12 h, to afford **10a**–**10c** in 90–95% isolated yields. Next, the conversion of **10a**–**10c** to corresponding benzylic bromide was attempted. However, under Appel conditions (CBr_4/PPh_3 in CH_2Cl_2), although TLC indicated satisfactory conversion, during the isolation, a significant part of the product decomposed. The conversion of the alcohol to the corresponding bromide by PBr_3 in CH_2Cl_2 appeared to be complete by TLC. However, again it was not possible to isolate the corresponding bromide presumably because of its high instability. Therefore, upon confirming the formation of the bromide after reaction with PBr_3 in CH_2Cl_2 for 24 h by TLC, a methanolic solution of dimethylamine was introduced directly into the reaction mixture, and the mixture was stirred at room temperature for 12 h. After the usual workup, compounds **11a**–**11c** were obtained in 80–85% yields. Lipids **1**–**3** were prepared upon refluxing the tertiary amines **11a**–**11c** with an excess of MeI in EtOH in quantitative yields (Scheme 1). The gemini cationic lipids with polymethylene spacers, **4**–**6**, were synthesized by heating **11a**–**11c** with the appropriate α,ω-dibromoalkanes to 80 °C in a mixture of MeOH–EtOAc (1:1) for 48–96 h in a screw-top pressure tube (Scheme 1). After repeated crystallizations from a mixture of MeOH-EtOAc, the isolated yields of the gemini lipids ranged from 40% to 50%. All the gemini lipids were adequately characterized by ^{1}H NMR, mass spectra, and elemental analysis.

Aggregate Formation from Cationic Gemini Lipids. Upon hydration, all the cationic lipids were dispersed in water at ~70 °C. The suspensions formed from lipids were found to be translucent. Lipids bearing *n*-$C_{14}H_{29}$ and *n*-$C_{16}H_{33}$ chains were found to be dispersed with difficulty even at ~80 °C. Therefore, we also did not observe their thermal phase transition temperature, whereas lipids bearing *n*-$C_{12}H_{25}$ chains were found to form suspensions easily at ~70 °C and they afforded detectable phase transition temperatures. TEM examination of air-dried, aqueous suspensions of each lipid revealed the existence of vesicular aggregate structures (not shown).

Mixed Liposome Formation with 1,2-dioleoyl-L-α-glycero-3-phosphatidyl Ethanolamine (DOPE). Liposomes could be conveniently prepared from each lipid with naturally occurring lipid (1,2-dioleoyl-L-α-glycero-3-phosphatidyl ethanolamine

Table 1. Optimized Lipid/DOPE Mole Ratios for Cationic Lipids for Transfection Studies

lipid	lipid/DOPE	lipid	lipid/DOPE	lipid	lipid/DOPE
1	1:1	**2**	1:2	**3**	1:2
4a	1:2	**5a**	1:8	**6a**	1:4
4b	1:2	**5b**	1:6	**6b**	1:4
4c	1:2	**5c**	1:2	**6c**	1:4
4d	1:2	**5d**	1:2	**6d**	1:8
4e	1:2	**5e**	1:2	**6e**	1:8

(DOPE)) by first subjecting the films of lipid mixtures to hydration, repeated freeze–thaw cycles, followed by sonication at 70 °C for 15 min. All the DOPE doped lipids formed optically transparent suspensions. The vesicular suspensions were sufficiently stable and no precipitation was observed within three months if stored at 4 °C.

TRANSFECTION BIOLOGY

Optimization of the Lipid/DOPE Ratio. Incorporation of the helper lipid DOPE is known to enhance the transfection efficiencies of many of the cationic lipid-based formulations (*48*). Therefore, we first decided to investigate the optimized lipid/DOPE mole ratio for our newly developed cationic lipids in HeLa cells, as their neat lipid suspensions were found to show very low transfection efficacies (not shown). To find out the optimized transfection efficiency, both the number of transfected cells and mean fluorescence intensity were considered. The mean fluorescence intensities (MFI) defined for GFP-positive cells reveal that the level of GFP expression with a higher MFI value correlate positively with a high GFP expression (*49*). These data were obtained from the flow cytometric analysis. In order to determine the most effective formulations, transfections were performed with identical amounts of the DNA (0.8 μg) and lipid (2.5 μg) upon variation of the mole ratios of cationic lipids in DOPE. Optimized lipid/DOPE ratios were found to vary with different cationic lipids depending upon the hydrocarbon chain lengths and the spacer segment between the cationic headgroups. The optimized lipid/DOPE ratios for all cationic lipids are given in Table 1. Monomeric lipids **2** and **3** showed the maximum transfection at optimized lipid/DOPE ratio of 1:2, whereas monomeric lipid **1** showed the optimum activity at a lipid/DOPE ratio of 1:1. Gemini lipids (**4a**–**4d**) bearing *n*-$C_{12}H_{25}$ hydrocarbon chains showed the maximum transfection efficiency at lipid/DOPE ratio of 1:2. In the case of the other gemini lipids, optimized lipid/DOPE ratios differed depending on both the length of the spacer and the hydrocarbon chain lengths. Lipids **5a**, **6d**, and **6e** showed transfections at the highest optimized lipid/DOPE ratios of 1:8, whereas lipids **5c** and **5d** showed the best activity at lipid/DOPE ratio of 1:2. These differences in the optimized lipid/DOPE ratios could be attributed to their different interaction behavior with DNA and the cell membranes, depending upon the lipid chain lengths and spacers between the headgroups.

Optimization of Lipid/DNA Charge Ratio. After the optimization of the lipid/DOPE ratios for lipids, we performed transfection studies in HeLa cells at different lipid/DNA charge ratios using optimized lipid/DOPE ratios. Monomeric lipid **1** formulation showed 30–40 % GFP cells with MFI of ∼40 by FACS analysis. With the introduction of the spacer between the two monomeric lipid **1** molecules, transfection efficiency increased especially in the number of cells getting transfected (Figure 2). Gemini lipid formulations based on **4a**–**4e** were able to transfect 60–80% of the cells, but the MFI values observed in all the formulations were very low. This suggests that these gemini lipid (**4a**–**4e**) formulations were able to transfect a large number of cells, but the amount of the DNA delivered was low. All these gemini lipid formulations (**4a**–**4e**) were found to be better than the monomeric lipid **1** formulation in terms of their ability to gene transfer. These gemini lipid formulations showed maximum transfection at an N/P ratio of 0.75–1.0 and followed a bell-shaped graph (Figure 2).

The formulation based on monomeric lipid **2** was able to transfect nearly 40% of cells with MFI of ∼75 as compared to the monomeric lipid **1** formulation, which transfected 40% of cells with MFI of ∼40 (Figure 3). This shows that the tetradecyl chain based monomeric lipid **2** is nearly two times better than the monomeric lipid **1** with dodecyl chains especially in terms of the MFI. On dimerization of lipid **2** with -$(CH_2)_3$- propanediyl spacer (lipid **5a**), the transfection efficiency decreased in terms of the number of transfected cells, while the MFI remained nearly the same. This indicates that propanediyl spacer based lipid (**5a**) aggregates were able to transfer nearly the same amount of the DNA but the efficiency reduced to nearly 30%. With an increase in the spacer length to -$(CH_2)_5$- pentanediyl, the transfection efficacy increased dramatically. Lipid **5c** was able to transfect ∼60% of the cells with high MFI of ∼100 at an N/P ratio of 1.0 as compared to its monomeric lipid counterpart **2**, which transfected only 40% of cells with MFI of ∼75. In the case of lipid **5d** and **5e** formulations, the transfection efficacies, however, decreased. The lipid **5d** formulation transfected nearly 40% of the cells with an MFI of ∼75, and lipid **5e** was able to transfect only 30% of the cells with MFI of ∼70. Therefore, among the *n*-$C_{14}H_{29}$ chain-based gemini lipids, lipid **5c** bearing -$(CH_2)_5$- showed maximum transfection efficiency.

Gemini lipid formulations based on hexadecyl chains were found to show the lowest transfection efficiency, in terms of both the number of transfected cells and the MFI. The monomeric lipid **3** formulation was able to transfect nearly 30% of the cells with an MFI of ∼40 (Figure 4). The maximum transfection was observed with the lipid **6d** formulation, transfecting nearly 20% of the cells with an MFI of ∼60, whereas the lipid **6e** formulation transfected ∼20% of the cells with a high MFI of ∼80.

The overall analysis of the data clearly shows that cationic lipids based on *n*-$C_{12}H_{25}$ and *n*-$C_{14}H_{29}$ hydrocarbon chains are better transfecting agents than the lipids possessing *n*-$C_{16}H_{33}$ chains in HeLa cells (Figure 5). Lipids possessing *n*-$C_{12}H_{25}$ chains (**1**, **4a**–**4e**) were able to transfect the highest number of cells with a low MFI, whereas *n*-$C_{14}H_{29}$ chain based lipids (**2**, **5a**–**5e**) transfected cells with a high MFI. This indicates that lipids **2** and **5a**–**5e** were able to deliver a larger amount of the DNA as indicated from MFI as compared to that delivered by lipid **1** and **4a**–**4e** based formulations. Gemini lipids possessing *n*-$C_{16}H_{33}$ chains were found to be the least effective. Formulations based on lipid **5c** possessing the *n*-$C_{14}H_{29}$ chain and the pentamethylene -$(CH_2)_5$- spacer were found to be the best recipe, which transfected nearly 60% of the cells with an MFI of ∼100, which was nearly three times more than a commercially available Lipofectin in terms of the number of cells and four times more efficient in terms of the MFI.

Transfection Studies in HT 1080 Cells. To assess the general utility of these new lipid formulations, transfection studies with optimized lipid formulations were performed in HT1080 cells as well. Nearly 70% of the cells were transfected with the monomeric lipid **1** formulation with an MFI of ∼45 at an N/P ratio of 1.5 as observed by FACS analysis (Supporting Information Figure S-1). Gemini lipid formulations based on **4a** and **4d** were able to transfect 60–80% of the cells with MFI values of ∼40 and 50, respectively, whereas lipid **4b**, **4c,** and **4d** formulations showed ∼40–50% transfection activity.

Monomeric lipid **2** based formulations were able to transfect nearly 50% of cells with MFI ∼35 (Supporting Information Figure S-2). Lipid **5a** and **5b** formulations bearing -$(CH_2)_3$- and

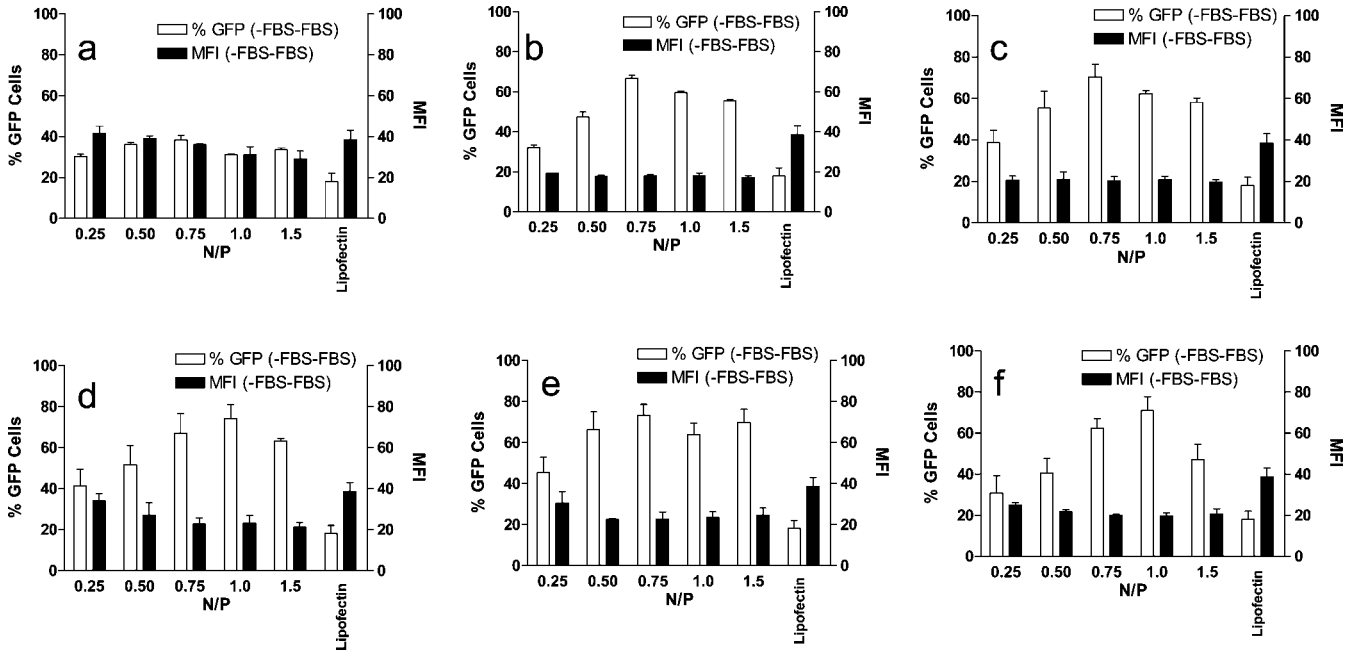


Figure 2. Transfection efficiencies of cationic lipids using optimized lipid/DOPE formulations at various N/P ratios in the absence of serum (−FBS−FBS) in HeLa cells: (a) lipid **1**; (b) lipid **4a**; (c) lipid **4b**; (d) lipid **4c**; (e) lipid **4d**; (f) lipid **4e**. Concentration of the DNA = 0.8 μg/well. Data are expressed as number of transfected cells and MFI as obtained from flow cytometry analysis.

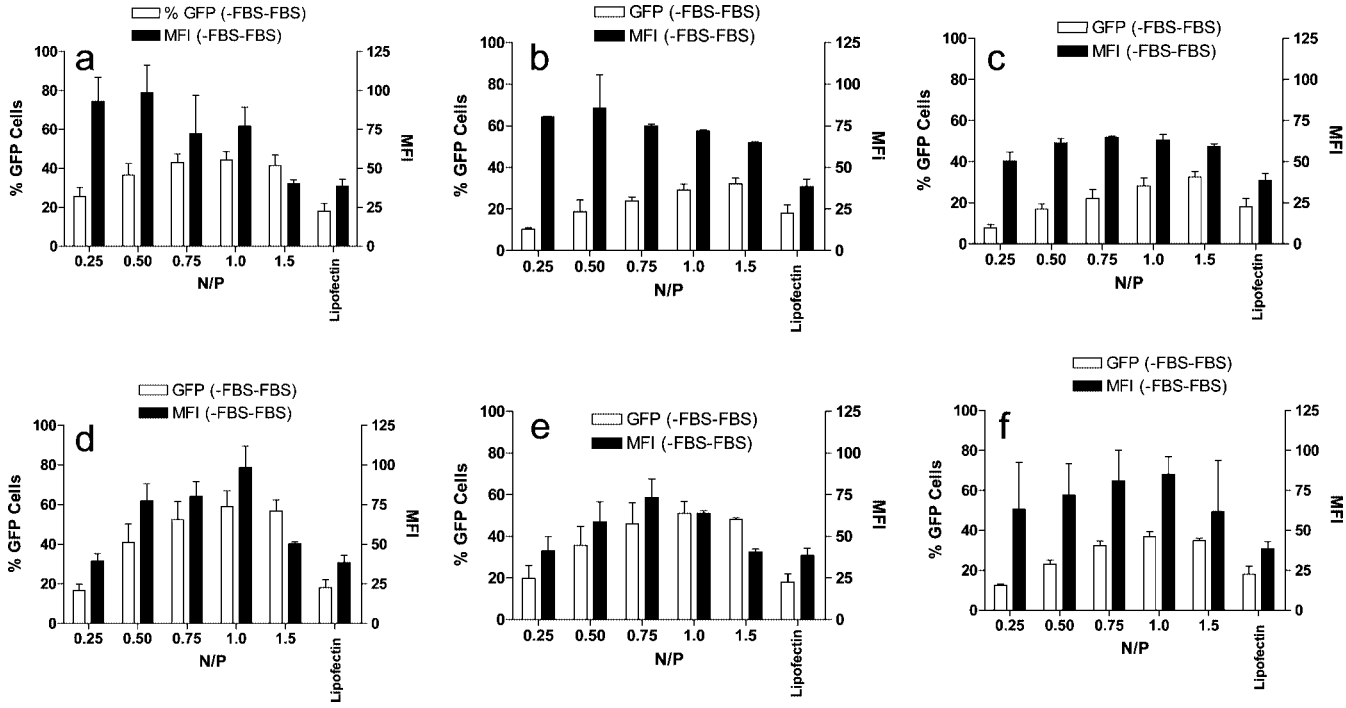


Figure 3. Transfection efficiencies of cationic lipids using optimized lipid/DOPE formulations at various N/P ratios in the absence of serum (−FBS−FBS) in HeLa cells: (a) lipid **2**; (b) lipid **5a**; (c) lipid **5b**; (d) lipid **5c**; (e) lipid **5d**; (f) lipid **5e**. Concentration of the DNA = 0.8 μg/well. Data are expressed as the number of transfected cells and MFI as obtained from flow cytometry analysis.

-$(CH_2)_4$- spacers are not very effective, transfecting ∼20% cells with MFI of ∼20, whereas the lipid **5c** formulation with a -$(CH_2)_5$- spacer showed ∼50% transfection efficacy with MFI of ∼35. Nearly 40% of the cells with an MFI of ∼20 were transfected with lipid **5d** formulations. The lipid **5e** formulation was found to be highly effective with more than 80% transfection efficiency with an MFI of ∼40. Gemini lipid formulations based on *n*-$C_{16}H_{33}$ chains were found to show the least transfection activity, in terms of both the number of transfected cells and MFI even in HT1080 cells, as was seen with HeLa cells (Supporting Information Figure S-3).

Figure 6 presents the comparative transfection efficacies of all lipid formulations at N/P ratio of 0.75 in HT1080 cells. Lipid formulations **1**, **4a**, **4c**, **4d**, and **5c** were found to be the best transfecting agents among all lipid formulations. Formulations of lipids possessing *n*-$C_{16}H_{33}$ chains were not found to be effective at all. Comparing the transfection efficacies of lipid formulations in HeLa and HT1080 cell lines showed interesting features. Overall, the MFI observed in HT1080 cell lines was lower compared to HeLa cells, which indicates that the release of the DNA from lipoplexes in HT1080 is not as easy as in HeLa cells where high MFI was observed.

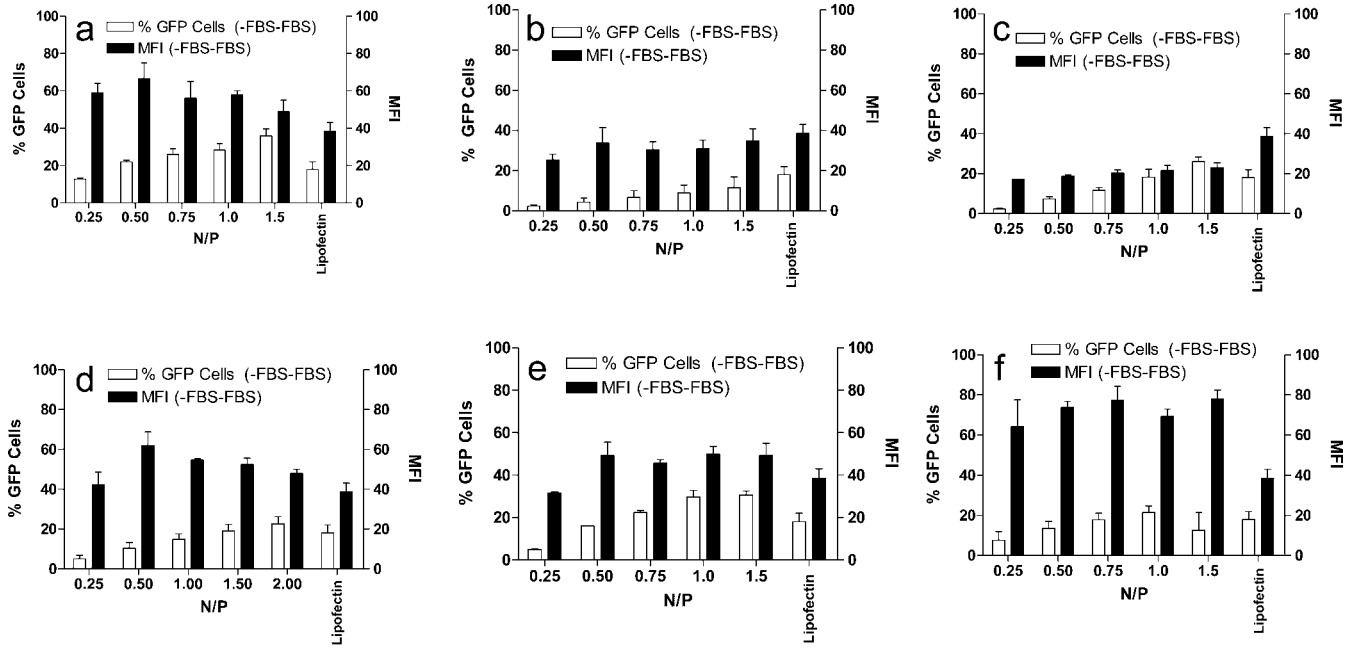


Figure 4. Transfection efficiencies of cationic lipids using optimized lipid/DOPE formulations at various N/P ratios in the absence of serum (−FBS−FBS) in HeLa cells: (a) lipid **3**; (b) lipid **6a**; (c) lipid **6b**; (d) lipid **6c**; (e) lipid **6d**; (f) lipid **6e**. Concentration of the DNA = 0.8 μg/well. Data are expressed as the number of transfected cells and MFI as obtained from flow cytometry analysis.

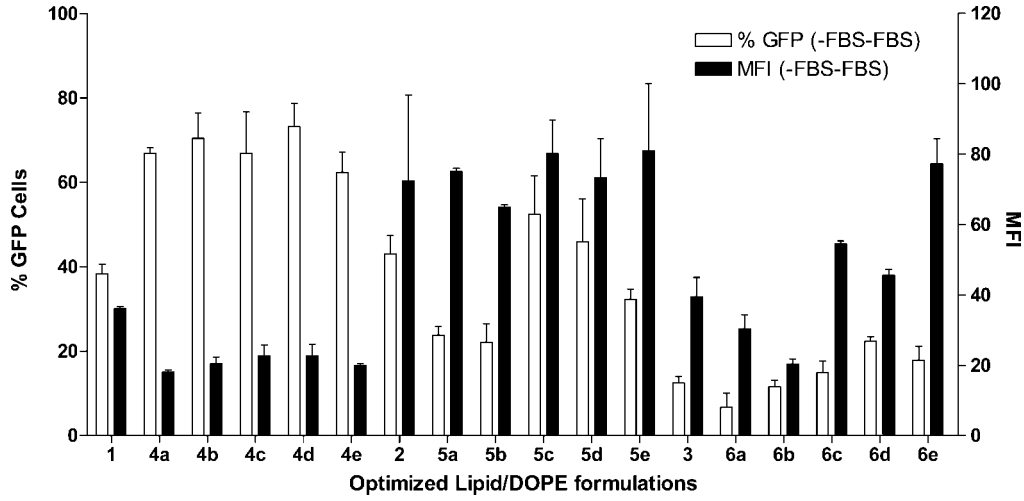


Figure 5. A comparative study showing the effect of the spacer length and hydrocarbon chain lengths on gene transfection efficiencies of gemini lipids based on aromatic backbone in the absence of serum (−FBS−FBS) at an N/P ratio of 0.75 in HeLa cells.

Effect of the Serum. One of the serious limitations of the cationic lipid-mediated gene delivery, especially involving *in vivo* trials, is that the transfection is inefficient particularly in the presence of serum proteins. Transfections in the absence of serum even for *in vitro* experiments are also cumbersome due to the increased toxicity of cationic lipid formulations. To have better potential especially in gene therapy, it is important to develop lipids that are capable of delivering and expressing an external gene inside a cell in the presence of serum (*13, 21, 50*). To have a clear understanding of the effect of the serum in the present set of cationic lipid mediated gene delivery, we performed transfections with our optimized lipid formulations in the presence of serum in HeLa and HT1080 cells.

Monomeric lipid **1/DOPE** was able to transfect nearly 30% of the cells with a low MFI of ∼30 in the presence of 10% serum (Figure 7). With the introduction of the spacer, the transfection efficiency increased in the presence of serum especially in the number of cells. Lipid **4b**–**4d** formulations were able to transfect nearly 60% of the cells in the presence of 10% serum with low MFI, whereas the lipid **4e/DOPE** formulation transfected only 20% of cells. A closer examination of these results suggests that lipid dimerization increases the transfection efficiency in the presence of 10% serum conditions, and this efficiency depends on the length of the spacer. The maximum transfection efficiency was achieved at N/P ratio of 0.75–1.5. The transfection efficiency observed in the presence of serum is comparable to that observed in the absence of serum, which clearly shows that serum does not inhibit the transfection efficacy of these formulations.

The monomeric lipid **2/DOPE** formulation in the presence of 10% serum was able to transfect nearly 40% of cells at N/P ratio of 1.0–1.5 (Figure 8). The lipid **5a/DOPE** formulation was able to transfect nearly 30% of the cells with an MFI of ∼80 at N/P ratio of 1.5. Lipid **5c** and **5d** formulations in the presence of DOPE showed maximum transfection efficiency in the presence of serum, transfecting nearly 60% of cells with MFI which was nearly two times more than that observed in the case of **4b**–**4d/DOPE** formulations. This indicates that the *n*-$C_{14}H_{29}$

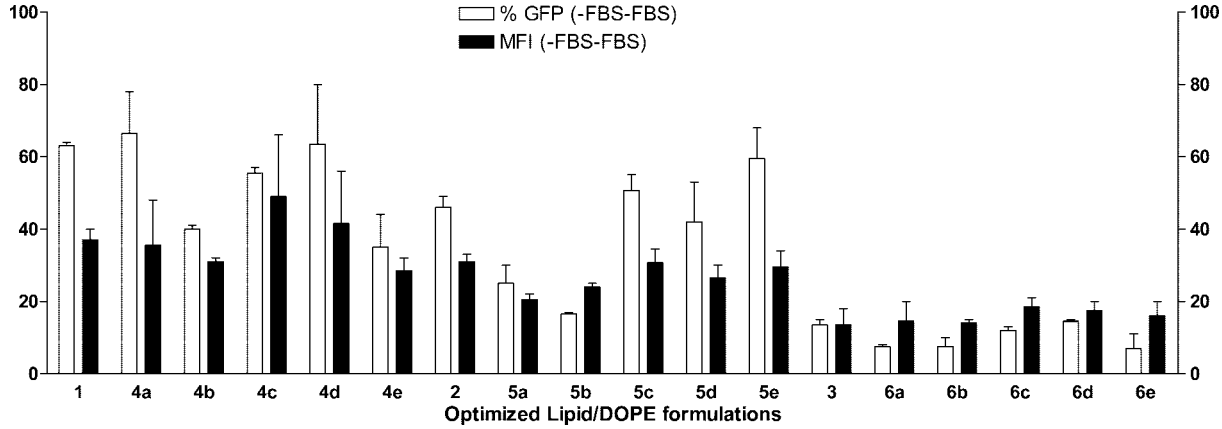


Figure 6. A comparative study showing the effect of the spacer length and hydrocarbon chain lengths on gene transfection efficiencies of gemini lipids based on aromatic backbone in the absence of serum (−FBS−FBS) at N/P ratio of 0.75 in HT 1080 cells.

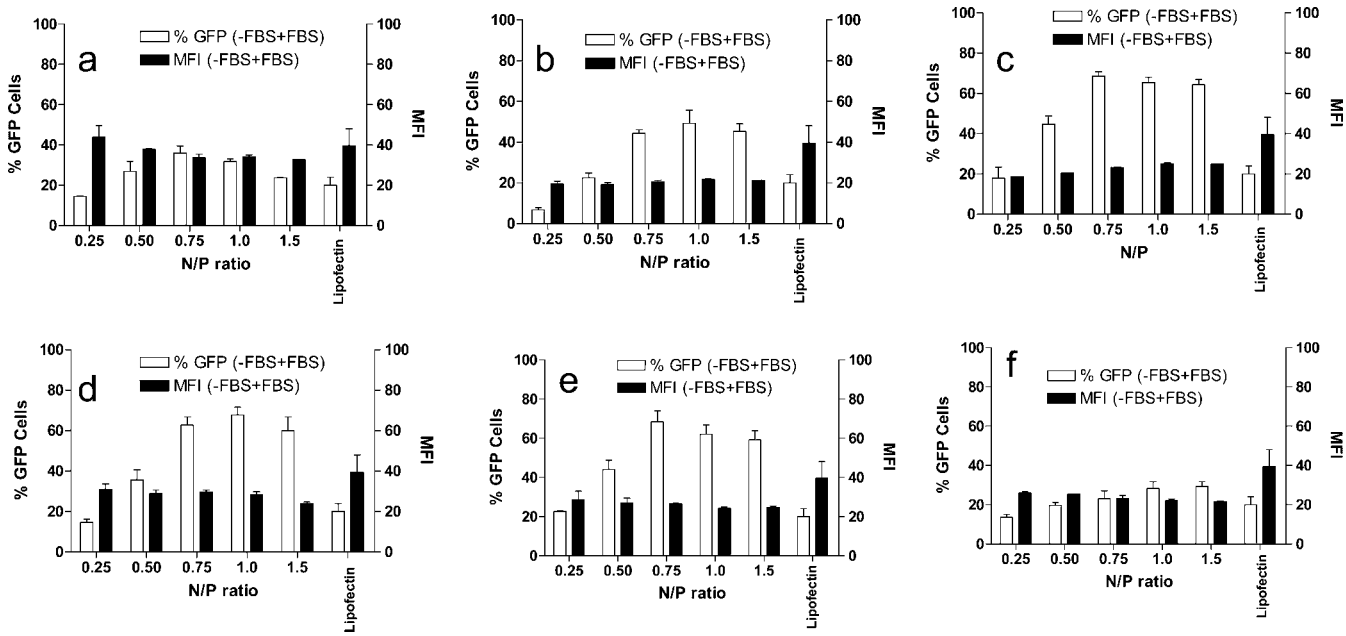


Figure 7. Transfection efficiencies of cationic lipids using optimized lipid/DOPE formulations at various N/P ratios in the presence of serum (−FBS + FBS) in HeLa cells: (a) lipid **1**; (b) lipid **4a**; (c) lipid **4b**; (d) lipid **4c**; (e) lipid **4d**; (f) lipid **4e**. Concentration of the DNA = 0.8 μg/well. Data are expressed as the number of transfected cells and MFI as obtained from flow cytometry analysis.

chain based lipid **5c** and **5d** formulations are two times better in transfection activity as compared to *n*-$C_{12}H_{25}$ chain based lipid **4c** and **4d** formulations in terms of MFI. This means that lipid **5c** and **5d** formulations are able to transfect a greater amount of the DNA into the cells in the presence of serum as well. As observed in the absence of serum conditions, *n*-$C_{16}H_{33}$ chain based lipids (**3**, **6a**–**6e**) were again less efficient in the presence of serum as compared to other lipids (Figure 9).

Effect of Serum on the Transfection in HT1080 Cells. We also performed transfection studies in the presence of 10% serum conditions in HT1080 cells. In the presence of serum, as expected, there is little decrease in the transfection activities of all the lipid formulations in terms of both the number of transfected cells and the MFI. Among the dodecyl chain based lipid formulations, monomeric lipid **1** and gemini lipid **4d** formulations showed maximum activities transfecting ∼60% cells with MFI of ∼40 (Supporting Information Figure S-4). The gemini lipid **5e** formulation was found to be the best among all the formulations in HT1080 cells (Supporting Information Figure S-5). Lipids (**3**, **6a-6e**) with *n*-$C_{16}H_{33}$ were found to be the least efficient even in the presence of serum as compared to other analogues in HT1080 cells. (Supporting Information Figure S-6).

Effect of High Percentage of Serum. To approach the realistic *in vivo* conditions, we performed transfections in the presence of high percentages of serum using the lipid **5c** formulation at different N/P ratios in HeLa cells. We performed transfection in the presence of 10%, 30%, and 50% serum conditions using the optimized lipid/DOPE formulation of **5c**. The transfection profiles are shown in Figure 10. In the presence of 10% serum, nearly 60% of the cells were found to get transfected at an N/P ratio of 4.5 with MFI of 40. The decrease in MFI in the presence of serum is because of the delivery of a low amount of the plasmid DNA. In the presence of serum, negatively charged serum proteins start competing with cationic lipids for negatively charged plasmid DNA, which leads to the delivery of less amount of the DNA inside the cells, because of which the MFI decreased.

In the presence of 30% serum, the lipid **5c** formulation was able to transfect nearly 50% of the cells with MFI of 40. To

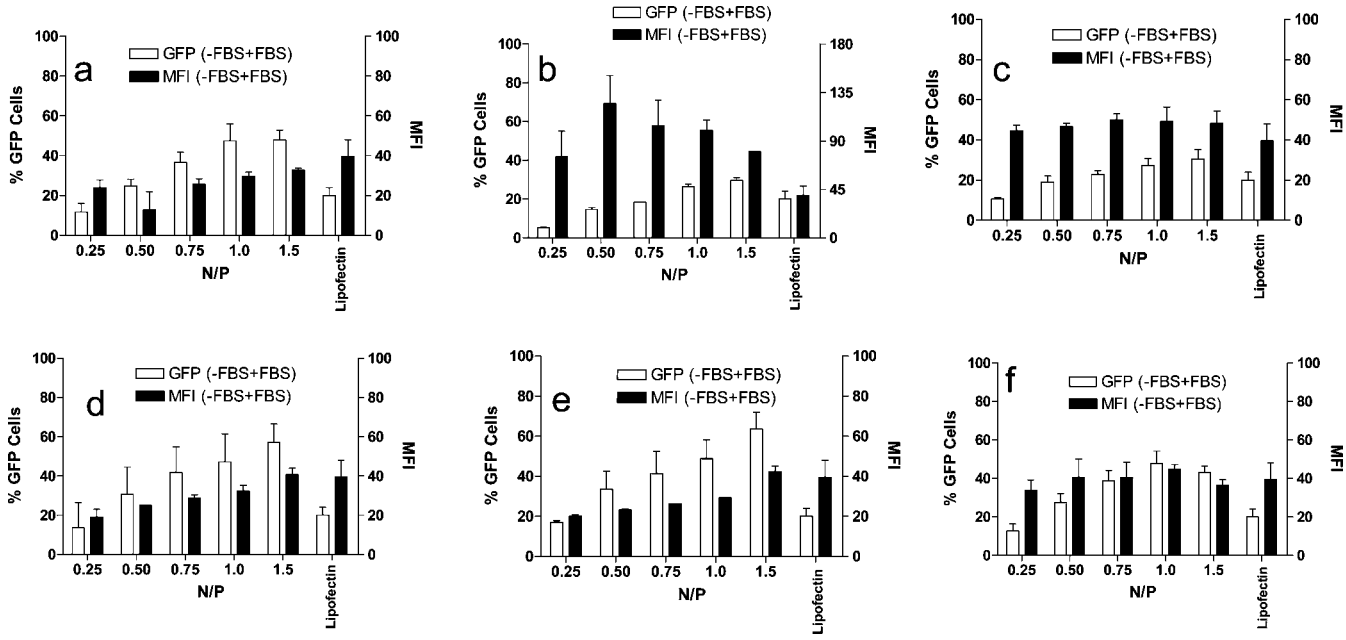


Figure 8. Transfection efficiencies of cationic lipids using optimized lipid/DOPE formulations at various N/P ratios in the presence of serum (−FBS + FBS) in HeLa cells: (a) lipid **2**; (b) lipid **5a**; (c) lipid **5b**; (d) lipid **5c**; (e) lipid **5d**; (f) lipid **5e**. Concentration of the DNA = 0.8 μg/well. Data are expressed as the number of transfected cells and MFI as obtained from flow cytometry analysis.

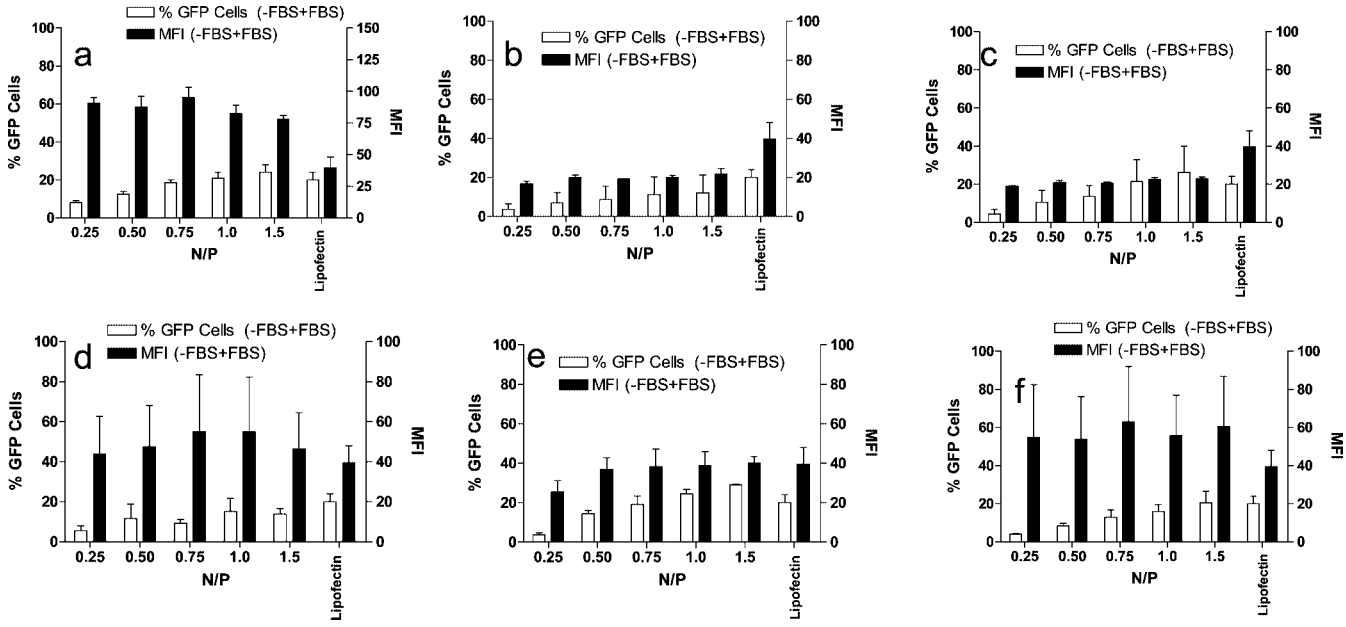


Figure 9. Transfection efficiencies of cationic lipids using optimized lipid/DOPE formulations at various N/P ratios in the presence of serum (−FBS + FBS) in HeLa cells: (a) lipid **3**; (b) lipid **6a**; (c) lipid **6b**; (d) lipid **6c**; (e) lipid **6d**; (f) lipid **6e**. Concentration of the DNA = 0.8 μg/well. Data are expressed as number of transfected cells and MFI as obtained from flow cytometry analysis.

our pleasant surprise, nearly 40% of the cells have been found to be GFP positive in the presence of 50% serum conditions, with very little decrease in MFI. These results showed the unusual behavior of the lipid **5c** formulation, transfecting as many as 40 % of the cells in the presence of 50% serum conditions, where the commercially available formulation Lipofectin failed to transfect.

Cytotoxicity. We performed the MTT-based cell viability assays for all the lipid–DNA complexes in HeLa cells. The cell viability results shown in Figure 11 clearly demonstrate that all the formulations showed more than 80% cell viability except the **4d**, **5d**, and **6d** lipid (based on -$(CH_2)_6$- hexanediyl spacer between the headgroups) based lipid–DNA complexes. The best lipid formulation **5c** showed more than 90% cell viability.

CHARACTERIZATION OF LIPID–DNA COMPLEXES

Gel Electrophoresis. Electrostatic interactions between the plasmid DNA and cationic liposomes as a function of lipid/DNA charge (N/P) ratios were determined by electrophoretic gel retardation assay. Gel electrophoretic patterns for all lipid formulations have been shown in Figures 12 and 13. All lipid formulations showed more than 90% DNA retardation at an N/P ratio of 1.0. Nearly 50% retardation was observed at an N/P ratio of 0.75. The best lipid **5c** formulation showed DNA

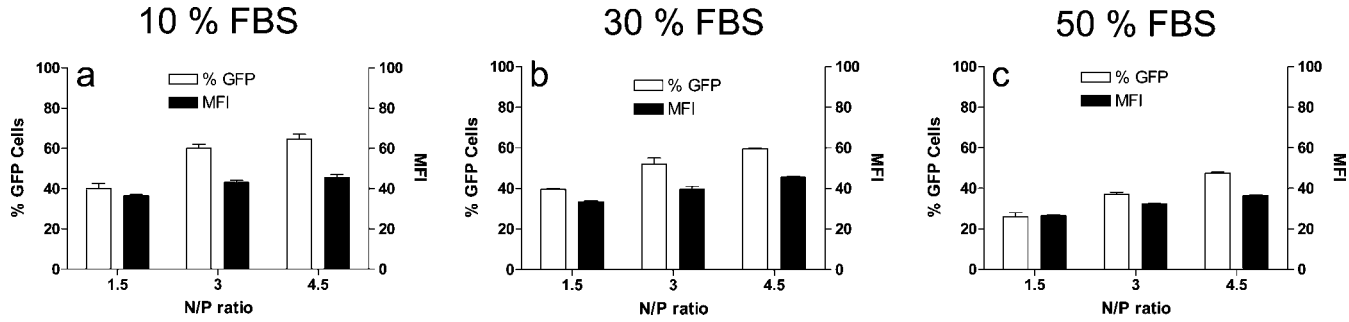


Figure 10. Transfection efficiencies using the optimized lipid **5c**/DOPE formulation at various N/P ratios in the 10%, 30 %, and 50% serum conditions (−FBS + FBS) in HeLa cells: (**a**) 10% FBS; (**b**) 30% FBS; (**c**) 50% FBS. Concentration of the DNA = 0.8 μg/well. Data are expressed as the number of transfected cells and MFI as obtained from flow cytometry analysis.

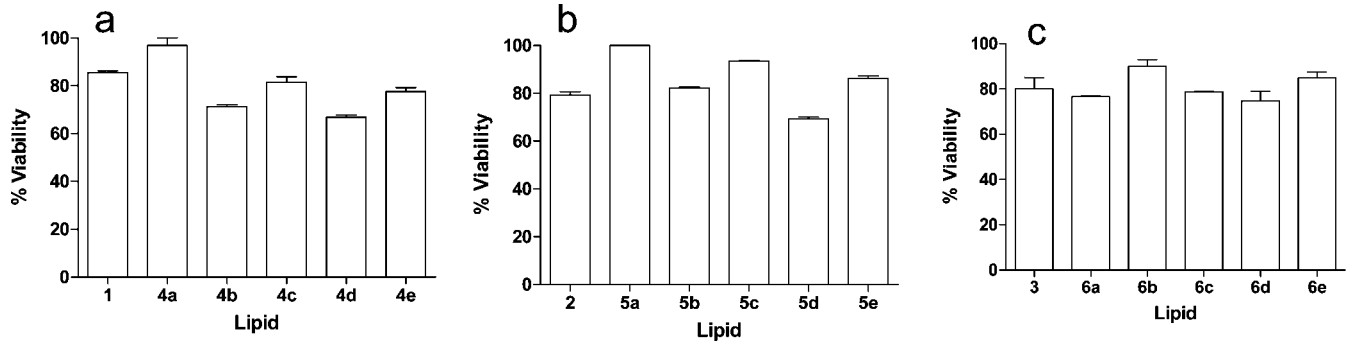


Figure 11. MTT-assay based cellular cytotoxicities of cationic lipid/DNA complexes at their optimized lipid/DNA ratios in HeLa cells: (a) lipids **1**, **4a**–**4e**; (b) lipids **2**, **5a**–**5e**; (c) lipids **3**, **6a**–**6e**.

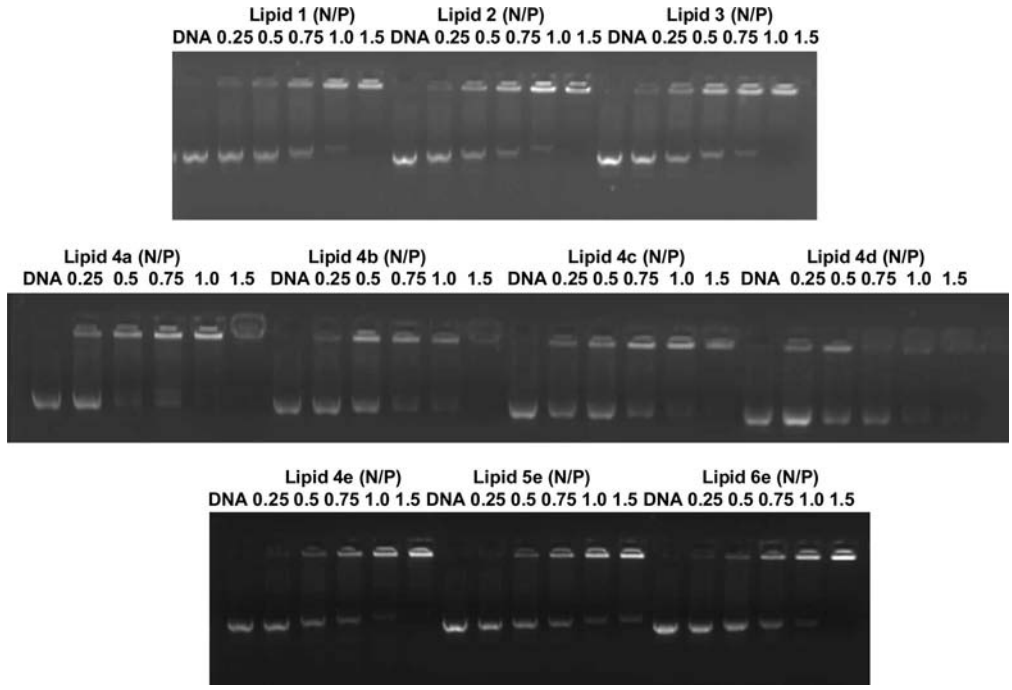


Figure 12. Electrophoretic gel patterns for lipoplex-associated DNA in gel retardation for cationic lipid formulations. The N/P ratios are indicated at the top of each lane.

retardation at an N/P ratio of 1.0, and more than 50% DNA was retarded at an N/P ratio of 0.75. At an N/P ratio of 1.0, maximum transfection had been achieved with this formulation.

Electron Microscopy. To get further insights into the lipid–DNA complexes, we performed electron microscopy of the lipid–DNA complexes using the optimized lipid/DOPE formulations. (*51–56*) Representive electron micrographs of lipid–DNA complexes have been shown in Figure 14. Most of the lipid formulations formed spherical lipid–DNA complexes. Lipid–DNA complexes from lipid **3a** formulations were very uniform and small in size with diameters of ∼150 nm, whereas other lipid–DNA complexes (**4b**, **4c**, **4d**, **4e**) in this series were considerably larger in size ranging from 200 to 400 nm. Lipid **5a** and **5c** formulations showed irregular morphologies, whereas the **5d** formulation showed spherical lipid–DNA complexes. The lipid **5e** formulation formed thread-like lipid–DNA complexes.

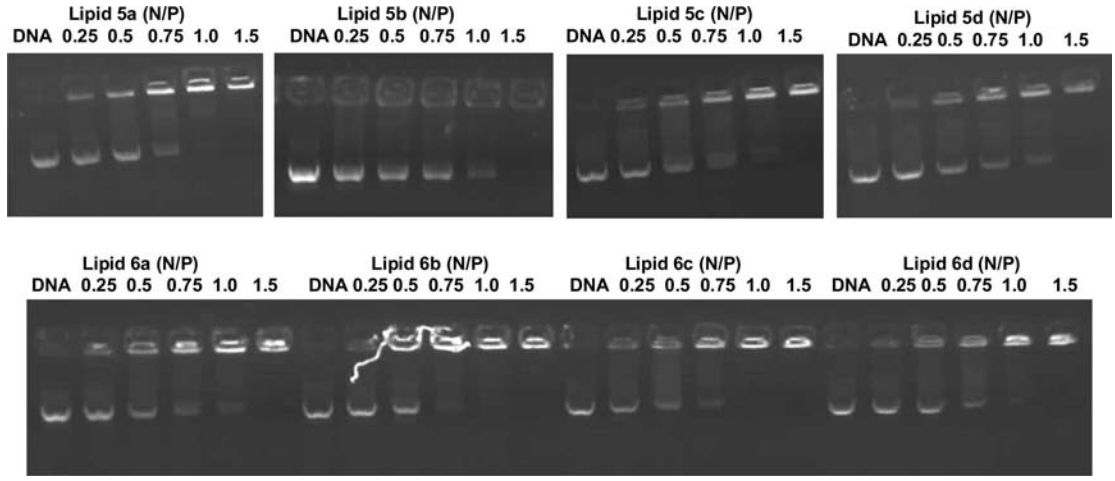


Figure 13. Electrophoretic gel patterns for lipoplex-associated DNA in gel retardation for cationic lipid formulations. The N/P ratios are indicated at the top of each lane.

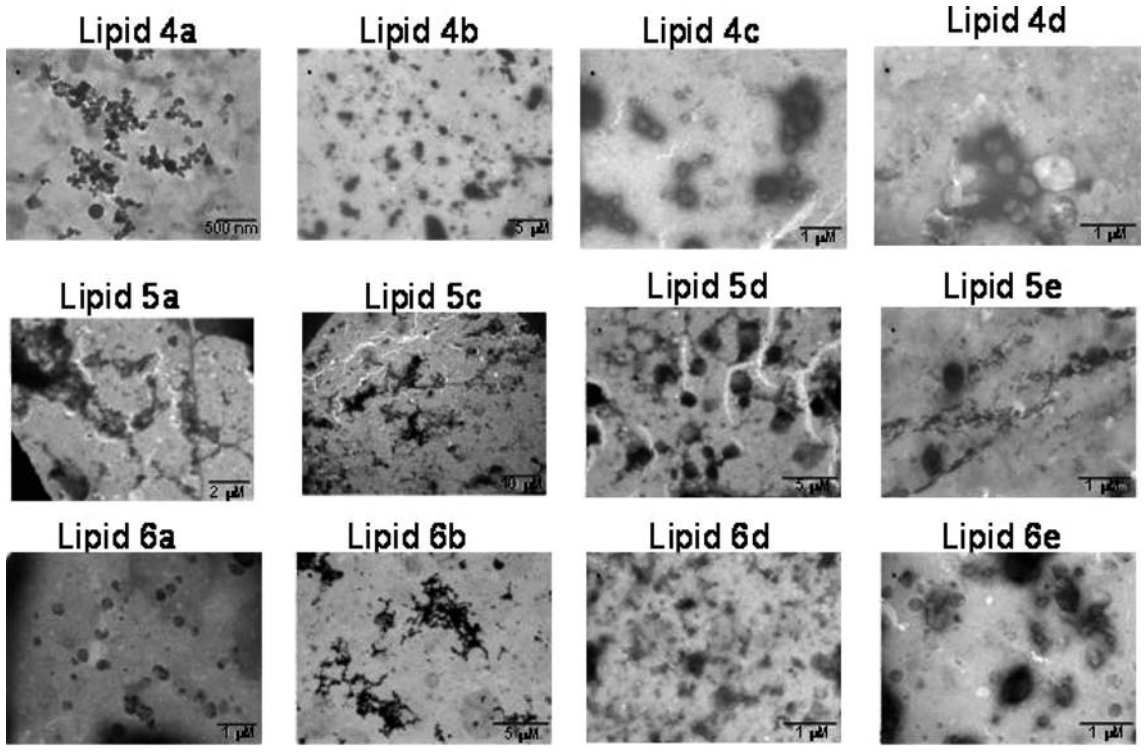


Figure 14. Transmission electron micrographs for the lipoplexes prepared from most effective gemini lipid/DOPE liposome/DNA complexes at the optimized N/P ratio.

Similar observation were also noted by Mahato and co-workers. (*57*) Among *n*-$C_{16}H_{33}$ chain based lipid formulations, lipids **6a** and **6e** formed spherical structures, whereas lipid **6b** formed condensed DNA structures and lipid **6d** afforded small rodlike structures in their electron micrographs.

CONCLUSIONS

Although diverse kinds of cationic lipids have been designed and tested as gene delivery vehicles, there remains a need for continuous improvement in the design of lipids for gene transfer. Keeping these targets in mind, we designed and synthesized a new kind of gemini lipid molecule based on aromatic backbone. Three series of gemini lipids differing in the length of the hydrocarbon chains have been synthesized. Polymethylene spacers of varying length were incorporated between the headgroups. In HeLa cells, gemini lipids bearing *n*-$C_{12}H_{25}$ chains were found to transfect a greater number of cells with low MFI intensity, whereas *n*-$C_{14}H_{29}$ chain based lipids showed transfection with high MFI, and lipids based on *n*-$C_{16}H_{33}$chains were found to be the least effective. Lipid formulation **5c**, possessing tetradecyl chains and pentamethylene spacers, showed the highest gene transfection efficacy in this series. A major characteristic feature of the lipid **5c** formulation is its high serum compatibility, which is one of the major challenges in the lipid-mediated gene delivery. In HT1080 cells, lipid formulations **1**, **4a**, **4c**, **4d**, and **5c** were found to be the best transfecting agents among all lipid formulations. MFI observed in HT1080 cell lines was lower compared to that in HeLa cells, which indicates that the release of the DNA from lipoplexes in HT1080 is more difficult than in HeLa cells where a high MFI was observed. Transmission electron microscopy revealed spherical lipid–DNA complexes for most of the formulations. Regardless of the actual

mechanism (*58–62*) for transfection mediated by this class of gemini lipid formulations, the interesting and meaningful results obtained with these novel aromatic gemini lipids should be of interest to researchers working in the field of gene therapy using nonviral vectors.

ACKNOWLEDGMENT

This work was supported by Department of Biotechnology, Government of India, New Delhi, India. Avinash Bajaj is thankful to the CSIR for senior research fellowship. We thank Dr. Omana Joy, Ms. Padmini, and Mr. Vamsi for their help during the work.

Supporting Information Available: Elemental analysis, transfection studies in HT1080 cells, and FACS details. This material is available free of charge via the internet at http://pubs.acs.org.

LITERATURE CITED

(1) Verma, I. M., and Somia, N. (1997) Gene therapy - promises, problems and prospects. *Nature 389*, 239–242.

(2) Hattori, Y., and Maitani, Y. (2005) Folate-linked nanoparticle-mediated suicide gene therapy in human prostate cancer and nasopharyngeal cancer with herpes simplex virus thymidine kinase. *Cancer Gene Ther. 12*, 796–809.

(3) Miller, A. D. (1992) Human gene therapy comes of age. *Nature 357*, 455–460.

(4) Friedmann, T. (1996) Human gene therapy - an immature genie, but certainly out of the bottle. *Nat. Med. 2*, 144–147.

(5) Guenin, E., Herve, A.-C., Floch, V., Loisel, S., Yaouanc, J.-J., Clement, J.-C., Ferec, C., and Des Abbayes, H. (2000) Cationic phosphonolipids containing quaternary phosphonium and arsonium groups for DNA transfection with good efficiency and low cellular toxicity. *Angew. Chem., Int. Ed. 39*, 629–631.

(6) Zhu, J., Munn, R. J., and Nantz, M. H. (2000) Self-cleaving ortho ester lipids: a new class of pH-vulnerable amphiphiles. *J. Am. Chem. Soc. 122*, 2645–2646.

(7) Choi, J. S., Lee, E. J., Jang, H. S., and Park, J. S. (2001) New cationic liposomes for gene transfer into mammalian cells with high efficiency and low toxicity. *Bioconjugate Chem. 12*, 108–113.

(8) Heyes, J. A., Niculescu-Duvaz, D., Cooper, R. G., and Springer, C. J. (2002) Synthesis of novel cationic lipids: effect of structural modification on the efficiency of gene transfer. *J. Med. Chem. 45*, 99–114.

(9) Hulst, R., Muizebelt, I., Oosting, P., Van der Pol, C., Wagenaar, A., Smisterova, J., Bulten, E., Driessen, C., Hoekstra, D., and Engberts, J. B. F. N. (2004) Sunfish amphiphiles: conceptually new carriers for DNA delivery. *Eur. J. Org. Chem.* 835–849.

(10) Majeti, B. K., Singh, R. S., Yadav, S. K., Bathula, S. R., Ramakrishna, S., Diwan, P. V., Madhavendra, S. S., and Chaudhuri, A. (2004) Enhanced intravenous transgene expression in mouse lung using cyclic-head cationic lipids. *Chem. Biol. 11*, 427–437.

(11) Chittimalla, C., Zammut-Italiano, L., Zuber, G., and Behr, J.-P. (2005) Monomolecular DNA nanoparticles for intravenous delivery of genes. *J. Am. Chem. Soc. 127*, 11436–11441.

(12) Jewell, C. M., Hays, M. E., Kondo, Y., Abbott, N. L., and Lynn, D. M. (2006) Ferrocene-containing cationic lipids for the delivery of DNA: Oxidation state determines transfection activity. *J. Controlled Release 112*, 129–138.

(13) Matsui, K., Sando, S., Sera, T., Aoyama, Y., Sasaki, Y., Komatsu, T., Terashima, T., and Kikuchi, J.-I. (2006) Cerasome as an infusible, cell-friendly, and serum-compatible transfection agent in a viral size. *J. Am. Chem. Soc. 128*, 3114–3115.

(14) Yang, Y., Nunes, F. A., Berencsi, K., Goenczoel, E., Engelhardt, J. F., and Wilson, J. M. (1994) Inactivation of E2a in recombinant adenoviruses improves the prospect for gene therapy in cystic fibrosis. *Nat. Genet. 7*, 362–369.

(15) Liu, L., Zern, M. A., Lizarzaburu, M. E., Nantz, M. H., and Wu, J. (2003) Poly(cationic lipid)-mediated in vivo gene delivery to mouse liver. *Gene Ther. 10*, 180–187.

(16) Nakanishi, M. (2003) New strategy in gene transfection by cationic transfection lipids with a cationic cholesterol. *Curr. Med. Chem. 10*, 1289–1296.

(17) Bhattacharya, S., and Haldar, S. (1996) The effects of cholesterol inclusion on the vesicular membranes of cationic lipids. *Biochim. Biophys. Acta Biomem. 1283*, 21–30.

(18) Bhattacharya, S., and Haldar, S. (2000) Interactions between cholesterol and lipids in bilayer membranes. Role of lipid headgroup and hydrocarbon chain-backbone linkage. *Biochim. Biophys. Acta Biomem. 1467*, 39–53.

(19) Ghosh, Y. K., Visweswariah, S. S., and Bhattacharya, S. (2000) Nature of linkage between the cationic headgroup and cholesteryl skelton controls gene transfection efficiency. *FEBS Lett. 473*, 341–344.

(20) Ghosh, Y. K., Visweswariah, S. S., and Bhattacharya, S. (2002) Advantage of the ether linkage between the positive charge and the cholesteryl skeleton in cholesterol-based amphiphiles as vectors for gene delivery. *Bioconjugate Chem. 13*, 378–384.

(21) Dileep, P. V., Antony, A., and Bhattacharya, S. (2001) Incorporation of oxyethylene units between hydrocarbon chain and pseudoglyceryl backbone in cationic lipid potentiates gene transfection efficiency in the presence of serum. *FEBS Lett. 509*, 327–331.

(22) Bhattacharya, S., and Dileep, P. V. (2004) Cationic oxyethylene lipids. synthesis, aggregation, and transfection properties. *Bioconjugate Chem. 15*, 508–519.

(23) Song, Y. K., Liu, F., Chu, S., and Liu, D. (1997) Characterization of cationic liposome-mediated gene transfer in vivo by intravenous administration. *Hum. Gene Ther. 8*, 1585–1594.

(24) Gao, X., and Huang, L. (1991) A novel cationic liposome reagent for efficient transfection of mammalian cells. *Biochem. Biophys. Res. Commun. 179*, 280–285.

(25) Han, S.-o., Mahato, R. I., and Kim, S. W. (2001) Water-soluble lipopolymer for gene delivery. *Bioconjugate Chem. 12*, 337–345.

(26) Wang, D.-a., Narang, A. S., Kotb, M., Gaber, O. A., Miller, D. D., Kim, S. W., and Mahato, R. I. (2002) Novel branched poly(ethylenimine)-cholesterol water-soluble lipopolymers for gene delivery. *Biomacromolecules 3*, 1197–1207.

(27) Kirby, A. J., Camilleri, P., Engberts, J. B. F. N., Feiters, M. C., Nolte, R. J. M., Soderman, O., Bergsma, M., Bell, P. C., Fielden, M. L., Garcia Rodriguez, C. L., Guedat, P., Kremer, A., McGregor, C., Perrin, C., Ronsin, G., and van Eijk, M. C. P. (2003) Gemini surfactants: New synthetic vectors for gene transfection. *Angew. Chem. Int. Ed. 42*, 1448–1457.

(28) Bell, P. C., Bergsma, M., Dolbnya, I. P., Bras, W., Stuart, M. C. A., Rowan, A. E., Feiters, M. C., and Engberts, J. B. F. N. (2003) Transfection mediated by gemini surfactants: engineered escape from the endosomal compartment. *J. Am. Chem. Soc. 125*, 1551–1558.

(29) Bombelli, C., Faggioli, F., Luciani, P., Mancini, G., and Sacco, M. G. (2005) Efficient transfection of DNA by liposomes formulated with cationic gemini amphiphiles. *J. Med. Chem. 48*, 5378–5382.

(30) Bello, C., Bombelli, C., Borocci, S., di Profio, P., and Mancini, G. (2006) Role of the spacer stereochemistry on the aggregation properties of cationic gemini surfactants. *Langmuir 22*, 9333–9338.

(31) Bhattacharya, S., De, S., and George, S. K. (1997) Synthesis and vesicle formation from novel pseudoglyceryl dimeric lipids. Evidence of formation of widely different membrane organizations with exceptional thermotropic properties. *Chem. Commun.* 2287–2288.

(32) Bhattacharya, S., and De, S. (1999) Synthesis and vesicle formation from dimeric pseudoglyceryl lipids with $(CH_2)_m$ spacers: pronounced m-value dependence of thermal properties,

vesicle fusion, and cholesterol complexation. *Chem.-Eur. J. 5*, 2335–2347.

(33) Bhattacharya, S., and Bajaj, A. (2007) Thermotropic and hydration studies of membranes formed from gemini pseudoglyceryl lipids possessing polymethylene spacers. *Langmuir 23*, 8988–8994.

(34) Bhattacharya, S., and Bajaj, A. (2007) Membrane forming properties of pseudoglyceryl backbone based gemini lipids possessing oxyethylene spacers. *J. Phys. Chem. B 111*, 2463–2472.

(35) Chien, P.-Y., Wang, J., Carbonaro, D., Lei, S., Miller, B., Sheikh, S., Ali, S. M., Ahmad, M. U., and Ahmad, I. (2005) Novel cationic cardiolipin analog-based liposome for efficient DNA and small interfering RNA delivery in vitro and in vivo. *Cancer Gene Ther. 12*, 321–328.

(36) Bajaj, A., Kondiah, P., and Bhattacharya, S. (2007) Design, synthesis and in vitro gene transfection efficacies of cholesterol based gemini lipids and their serum compatibility: a structure activity relationship. *J. Med. Chem. 50*, 2432–2442.

(37) Bajaj, A., Kondaiah, P. and Bhattacharya, S. (2007) Synthesis and gene transfer activities of novel serum compatible cholesterol based gemini lipids possessing oxy-ethylene type spacers. *Bioconjugate Chem. 18*, 1537–1546.

(38) Woude, I. v. d., Wagennar, A., Meekal, A. A. P., Beest, M. B. A. t., Ruiters, M. H. J., Engberts, J. B. F. N., and Hoekstra, D. (1997) Novel pyridinium surfactants for efficient, nontoxic in vitro gene delivery. *Proc. Nat. Acad. Sci. U.S.A. 94*, 1160–1165.

(39) Ilies, M. A., Johnson, B. H., Makori, F., Miller, A., Seitz, W. A., Thompson, E. B., and Balaban, A. T. (2005) Pyridinium cationic lipids in gene delivery: an in vitro and in vivo comparison of transfection efficiency versus a tetraalkylammonium congener. *Arch. Biochem. Biophys. 435*, 217–226.

(40) Ewert, K. K., Evans, H. M., Zidovska, A., Bouxsein, N. F., Ahmad, A., and Safinya, C. R. (2006) A columnar phase of dendritic lipid-based cationic liposome-DNA complexes for gene delivery: hexagonally ordered cylindrical micelles embedded in a DNA honeycomb lattice. *J. Am. Chem. Soc. 128*, 3998–4006.

(41) Koiwai, K., Tokuhisa, K., Karinaga, R., Kudo, Y., Kusuki, S., Takeda, Y., and Sakurai, K. (2005) Transition from a normal to inverted cylinder for an amidine-bearing lipid/pDNA complex and its excellent transfection. *Bioconjugate Chem. 16*, 1349–1351.

(42) Gardner, R. A., Belting, M., Svensson, K., and Phanstiel, O. (2007) Synthesis and transfection efficiencies of new lipophilic polyamines. *J. Med. Chem. 50*, 308–318.

(43) Bhattacharya, S., Subramanian, M., and Hiremath, U. S. (1995) Surfactant lipids containing aromatic units produce vesicular membranes with high thermal stability. *Chem. Phys. Lipids 78*, 177–188.

(44) Paul, B., Bajaj, A., Indi, S. S., and Bhattacharya, S. (2006) Synthesis of novel dimeric cationic lipids based on an aromatic backbone between the hydrocarbon chains and headgroup. *Tetrahedron Lett. 47*, 8401–8405.

(45) Stéphane, S., Olimpia, M., Rosario, S., Bertrand, D., Daniel, G., Emmanuel, T., Piguet, C., and Bünzli, J.-C. G. (2005) Lanthanide luminescent mesomorphic complexes with macrocycles derived from diaza-18-crown-6. *New J. Chem. 29*, 1323–1334.

(46) Percec, V., Rudick, J. G., Peterca, M., Wagner, M., Obata, M., Mitchell, C. M., Cho, W.-D., Balagurusamy, V. S. K., and Heiney, P. A. (2005) Thermoreversible cis-cisoidal to cis-transoidal isomerization of helical dendronized polyphenylacetylenes. *J. Am. Chem. Soc. 127*, 15257–15264.

(47) Hansen, M. B., Nielsen, S. E., and Berg, K. (1989) Re-examination and further development of a precise and rapid dye method for measuring cell growth/cell kill. *J. Immunol. Methods 119*, 203–210.

(48) Felgner, J. H., Kumar, R., Sridhar, C. J., Wheeler, Y. J., Tsai, R., Border, P., Ramsey, M., Martin, C. N., and Felgner, P. L. (1994) Enhanced gene delivery and mechanism studies with a novel series of cationic lipid formulations. *J. Biol. Chem. 269*, 2550–2561.

(49) Chabaud, P., Camplo, M., Payet, D., Serin, G., Molreau, L., Barthelemy, P., and Grinstaff, M. W. (2006) Cationic nucleoside lipids for gene delivery. *Bioconjugate Chem. 17*, 466–472.

(50) Karmali, P. P., Majeti, B. K., Sreedhar, B., and Chaudhuri, A. (2006) In vitro gene transfer efficacies and serum compatibility profiles of novel mono-, di-, and tri-histidinylated cationic transfection lipids: a structure-activity investigation. *Bioconjugate Chem. 17*, 159–171.

(51) May, S., and Ben-Shaul, A. (1997) DNA-lipid complexes: stability of honeycomb-like and spaghetti-like structures. *Biophys. J. 73*, 2427–2440.

(52) Huebner, S., Battersby, B. J., Grimm, R., and Cevc, G. (1999) Lipid-DNA complex formation: reorganization and rupture of lipid vesicles in the presence of DNA as observed by cryoelectron microscopy. *Biophys. J. 76*, 3158–3166.

(53) Smisterova, J., Wagenaar, A., Stuart, M. C. A., Polushkin, E., Brinke, G. t., Hulst, R., Engberts, J. B. F. N., and Hoekstra, D. (2001) Molecular shape of the cationic lipid controls the structure of cationic lipid/dioleylphosphatidylethanolamine-DNA complexes and the efficiency of gene delivery. *J. Biol. Chem. 276*, 47615–47622.

(54) Simberg, D., Danino, D., Talmon, Y., Minsky, A., Ferrari, M. E., Wheeler, C. J., and Barenholz, Y. (2001) Phase behavior, DNA ordering, and size instability of cationic lipoplexes. *J. Biol. Chem. 276*, 47453–47459.

(55) Jennings, K. H., Marshall, I. C. B., Wilkinson, M. J., Kremer, A., Kirby, A. J., and Camilleri, P. (2002) Aggregation properties of a novel class of cationic gemini surfactants correlate with their efficiency as gene transfection agents. *Langmuir 18*, 2426–2429.

(56) Bombelli, C., Borocci, S., Diociaiuti, M., Faggioli, G., Galantini, L., Luciani, P., Mancini, G., and Sacco, M. G. (2005) Role of the spacer of cationic gemini amphiphiles in the condensation of DNA. *Langmuir 21*, 10271–10274.

(57) Narang, A. S., Thoma, L., Miller, D. D., and Mahato, R. I. (2005) cationic lipids with increased DNA binding affinity for nonviral gene transfer in dividing and nondividing cells. *Bioconjugate Chem. 16*, 156–168.

(58) Zabner, J., Fasbender, A. J., Moninger, T., Poellinger, K. A., and Welsh, M. J. (1995) Cellular and molecular barriers to gene transfer by a cationic lipid. *J. Biol. Chem. 270*, 18997–19007.

(59) Xu, Y., and Szoka, F. C., Jr (1996) Mechanism of DNA release from cationic liposome/DNA complexes used in cell transfection. *Biochemistry 35*, 5616–5623.

(60) Bhattacharya, S., and Mandal, S. S. (1997) Interaction of surfactants with DNA. Role of hydrophobicity and surface charge on intercalation and DNA melting. *Biochim. Biophys. Acta. Biomem. 1323*, 29–44.

(61) Bhattacharya, S., and mandal, S. S. (1998) Evidence of interlipidic ion-pairing in anion-induced DNA release from cationic amphiphile-DNA complexes. Mechanistic implications in transfection. *Biochemistry 37*, 7764–7777.

(62) Hasegawa, S., Hirashima, N., and Nakanishi, M. (2001) Microtubule involvement in the intracellular dynamics for gene transfection mediated by cationic liposomes. *Gene Ther. 8*, 1669–1673.

BC700181K

Metallo-Phthalocyanine Near-IR Fluorophores: Oligonucleotide Conjugates and Their Applications in PCR Assays

Irina V. Nesterova,[†] Vera T. Verdree,[†] Serhii Pakhomov,[†] Karen L. Strickler,[†] Michael W. Allen,[||] Robert P. Hammer,[†] and Steven A. Soper*[,‡,§]

Department of Chemistry, Louisiana State University, Baton Rouge, Louisiana 70803, Department of Mechanical Engineering, Louisiana State University, Baton Rouge, Louisiana 70803, Center for BioModular Multi-Scale Systems, Louisiana State University, Baton Rouge, Louisiana 70803, and Thermo Electron Corporation, 5225 Verona Road, Madison, Wisconsin 52711.
Received June 22, 2007; Revised Manuscript Received September 5, 2007

Water soluble, metallo-pthalocyanine (MPc) near-IR fluorophores were designed, synthesized, and evaluated as highly stable and sensitive reporters for fluorescence assays. Their conjugation to oligonucleotides was achieved via succinimidyl ester-amino coupling chemistry with the conditions for conjugation extensively examined and optimized. In addition, various conjugate purification and isolation techniques were evaluated as well. Results showed that under proper conditions and following purification using reverse-phase ion-pair chromatography, labeling efficiencies near 80% could be achieved using ZnPc (Zn phthalocyanine) as the labeling fluorophore. Absorption and fluorescence spectra accumulated for the conjugates indicated that the intrinsic fluorescence properties of the MPc's were not significantly altered by covalent attachment to oligonucleotides. As an example of the utility of MPc reporters, we used the MPc–oligonucleotide conjugates as primers for PCR (polymerase chain reaction) amplifications with the products sorted via electrophoresis and detected using near-IR fluorescence ($\lambda_{ex} = 680$ nm). The MPc dyes were found to be more chemically stable under typical thermal cycling conditions used for PCR compared to the carbocyanine-based near-IR reporter systems typically used and produced single and narrow bands in the electrophoretic traces, indicative of producing a single PCR product during amplification.

INTRODUCTION

Because of a number of compelling advantages associated with near-IR fluorescence ($\lambda > 650$ nm), such as low scattering cross sections, reduced autofluorescence, lower radiation energy, and readily available diode lasers as excitation sources, it can provide better overall detection sensitivity compared to the visible and/or UV regions of the electromagnetic spectrum using rather simple instrumentation, especially when analyzing complex biological systems (*1*–*3*). Applications where the viability of near-IR fluorescence has been demonstrated include DNA sequencing (*4*–*6*), detecting DNA restriction fragments (*7*) and adducts (*8*), analysis of PCR products (*9*), DNA microarrays (*10*), mutation detection (*11*), enzymatic substrate monitoring (*12*), and various fluorescence resonance energy transfer (FRET)-based assays (*11, 13*).

Unfortunately, hurdles still exist, hampering the widespread utilization of near-IR fluorescence. The primary challenge is the limited set of fluorophores available for deep-red excitation that possess favorable chemical and photophysical properties for applications requiring covalent or noncovalent labeling of targets. Despite the growing number of fluorophores that show absorbing properties in the near-IR (*14, 15*), the demands of modern multiplexed, ultrasensitive analyses require the development of new bright fluors with the following properties: (a) a diverse range of photophysical and spectral characteristics that can be easily tuned; (b) good chemical, thermal, and light stability; (c) availability of a wide range of functional groups for covalent conjugation to a variety of targets; and (d) narrow emission envelopes to minimize spectral leakage into various detection channels required for spectral multiplexing.

Phthalocyanines (Pc's) and metallo-phthalocyanines (MPc's) are well-known near-IR absorbing/fluorescing dyes (*16*). Various MPc's have been extensively studied, and many display photophysical properties that are comparable or even superior to those of the most commonly used near-IR reporter systems. These properties include high extinction coefficients ($>10^5$ M^{-1} cm^{-1}) (*17, 18*), favorable fluorescence quantum yields (>0.6) (*19*–*21*), excellent photostability with photobleaching quantum yields as low as 10^{-7} (*17, 22, 23*), and good chemical and thermal stabilities. Another appealing feature of MPc's is that their photophysical properties can be tuned by simply varying peripheral substitution patterns around the macrocycle (*17, 22, 24*) and/or altering the identity of the metal center (*25, 26*).

Covalent attachment of MPc's with various biomolecules that have been reported include those with nucleobases (*27*), oligonucleotides (*28*–*31*), proteins (*23, 32*–*35*), peptides (*36*), or monoclonal antibodies (*35, 37*–*39*) as targets. However, in spite of the impressive photophysical and spectral properties associated with these near-IR dye systems, the analytical utility of MPc's when covalently attached to biomolecular targets have not been extensively reported.

The first commercially available MPc-based reporters were SiPc's (La Jolla Blue), which contained axial polyethylene glycol ligands used to prevent self-aggregation and improve water solubility. Oligonucleotides conjugated to La Jolla Blue were utilized for homogeneous hybridization assays of DNA and RNA targets with the hybridions monitored via transient-state polarized fluorescence with a detection limit reported to be 1 fmol (*28, 29*). Peng and co-workers (*35*) developed another SiPc dye with highly charged axial ligands,

* Corresponding author. Phone: 225-578-1527. Fax: 225-578-3458. E-mail: chsope@lsu.edu.
[†] Department of Chemistry, Louisiana State University.
[‡] Department of Mechanical Engineering, Louisiana State University.
[§] Center for BioModular Multi-Scale Systems, Louisiana State University.
[||] Thermo Electron Corporation.

10.1021/bc700233w CCC: $37.00 © 2007 American Chemical Society
Published on Web 11/21/2007

Scheme 1. Molecular Structures of the ZnPc's Used in These Studies

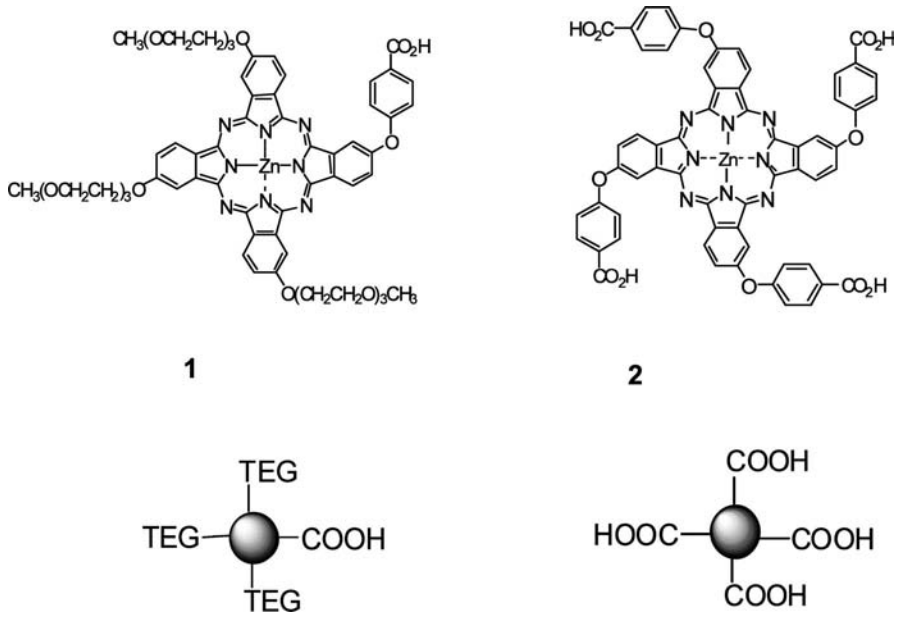


Table 1. Sequences of Oligonucleotides Used for Labeling Reactions, Hybridizations, and PCRs

oligos	sequence (5′→3′)	T_m (°C)
M13mp18 primer1[a] (**O1**)	GTA AAA CGA CGG CCA GT	52.6 °C
M13mp18 primer2 for 381 bp product	CAA CTC TCT CAG GGC CAG	55.0 °C
M13mp18 primer2 for 272 bp product	GGC CGA TTC ATT AAT GCA GC	54.8 °C
M13mp18 primer2 for 185 bp product	ACT CTA TAG GCA CCC CGA	54.2 °C
CFTR1 primer1[b]	GTT GGC ATG CTT TGA TGA CGC TTC	59.4 °C
CFTR1 primer2	GTT TTC CTG GAT TAT GCC TGG GCA C	60.3 °C
Template 1[c] (**O2**)	ACT GGC CGT CGT TTT ACA ACG TCG TGA CTG GGA AAA CCC TGG	70.1 °C

[a] These primers were modified with an amino-group attached to its 5′ end and were labeled with either ZnPc **1** (**1-C12-O1**, using a $C_{12}H_{24}$ linker) or **2** (**2-C12-O1** or **2-C6-O1**, using a $C_{12}H_{24}$ or C_6H_{12} linker, respectively). [b] This primer was modified with an amino-group attached to its 5′ end via a C_6H_{12} linker and was labeled with ZnPc **2**. [c] The underlined sequence is complementary to **O1**.

IRD700DX, and demonstrated its applicability as a bright and photostable near-IR fluorescent label (fluorescence quantum yield of 0.14 in PBS and photobleaching quantum yield of 1.6×10^{-7}) for antibody conjugation.

Duan et al. (*37*) reported on the conjugation of ZnPc, which lacks axial ligands to the metal center, to monoclonal antibodies used to bind to cells bearing the relevant antigenic species. We have previously reported the design, synthesis, and conjugation of MPc's and naphthalocyanines to proteins and oligonucleotides in which two water-soluble asymmetric ZnPc- and naphthalocyanine-based near-IR labeling dyes with isothiocyanate functional groups were conjugated to primary amine-containing targets (*30*). Conjugates of a water soluble ZnPc (**2**, Scheme 1) to streptavidin were prepared and the properties of the conjugates studied (*23*).

The limited use of *Pc*-based labeling fluors have resulted from the lack of (a) appropriately designed molecules that are soluble, possess favorable photophysical properties in aqueous media, and bear functional groups for conjugation; (b) documented labeling conditions that result in the facile and high yield conjugation to biomolecules; and (c) simple and efficient purification protocols for isolating the conjugate.

Herein we report on two water-soluble MPc's, asymmetrical and symmetrical ZnPc's with no axial ligands (**1** and **2**, respectively, see Scheme 1), for conjugation to targets containing primary amine groups. To demonstrate the utility of these labeling fluorophores, the conditions for highly efficient labeling of oligonucleotide targets and robust approaches for the effective isolation and purification of the conjugates are provided as well as the spectral and photophysical properties of the conjugates. Finally, we evaluate the use of these ZnPc-oligonucleotide conjugates as primers for PCR amplifications as analyzed by the gel electrophoretic sorting of the generated amplicons with near-IR fluorescence detection.

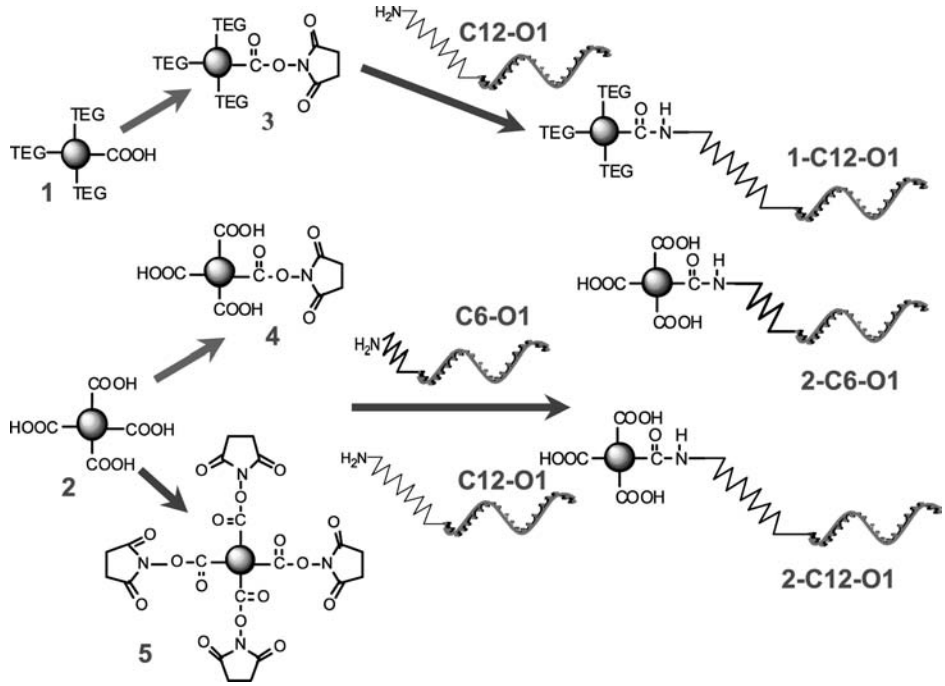
EXPERIMENTAL PROCEDURES

Materials. All materials were of reagent grade and were purchased from commercial suppliers, such as Sigma-Aldrich, EMD or Fisher, and used as received unless otherwise noted. Anhydrous DMF (*N*,*N*-dimethylformamide) and ether were dried before use by passing through columns with molecular sieves and activated alumina. Milli Q water (18 mΩ) produced in-house was used for all solution preparations. Oligonucleotide sequences modified with an amino group at their 5′-end via aliphatic (C_6H_{12} or $C_{12}H_{24}$) linkers or unmodified were obtained from IDT (Coralville, IA). Their sequences and melting temperatures (T_m) for fully matched duplexes are listed in Table 1. Precast agarose gel plates (3%) were purchased from BioRad (Hercules, CA). dNTPs (deoxynucleotides triphosphates) and PCR buffers were purchased from Applied Biosystems (Foster City, CA).

Synthesis of ZnPc's 1, 2, and Succinimidyl Ester 5 (Scheme 2). The preparation of these compounds has been reported elsewhere (*23, 40*).

Synthesis of Succinimidyl Ester 3. The synthesis of this compound was adapted from published procedures with slight modifications (*41*). A mixture of DCC (6 mg, 0.029 mM) and NHS (4 mg, 0.035 mM) was added to ZnPc **1** (12.6 mg, 0.010 mM) dissolved in anhydrous DMF (2 mL). The reaction was

Scheme 2. Conjugation Chemistries of ZnPc 1 and 2 and Their Corresponding Succinimidyl Esters to Oligonucleotide Targets



stirred for 18 h at room temperature in an argon atmosphere while protecting it from light. After the reaction, diethyl ether (approximately 20 mL) was added to the reaction mixture. The sample was centrifuged and the supernatant discarded. The residue was dissolved in acetone, filtered through a 0.2 μm Teflon filter, and evaporated, which afforded 8 mg (59% yield) of succinimidyl ester **3** as a dark-blue powder. MS *m/z* ($M + H^+$) 1296.481, calculated for $C_{64}H_{66}N_9O_{17}Zn$ 1296.387.

Synthesis of Succinimidyl Ester 4. The synthesis of this compound was adapted from published procedures with slight modifications (*41*). A solution of ZnPc **2** (42 mg, 0.037 mmol), NHS (*N*-hydroxysuccinimide) (4.7 mg, 0.041 mmol), and DCC (*N*,*N*′-dicyclohexylcarbodiimide) (8.4 mg, 0.041 mmol) in anhydrous DMF (1.5 mL) was stirred at room temperature in an argon atmosphere for 60 h. The reaction mixture was filtered, the precipitate washed with DMF (5 mL), and the clear filtrate diluted with ether (70 mL) inducing precipitation of the product, which was then centrifuged and the supernatant discarded. The crude product was redissolved in DMF (3 mL) and reprecipitated with ether. After centrifugation, the product was dried *in vacuo*, which afforded 25 mg (56% yield) of succinimidyl ester **4** as a dark-blue powder. ^{1}H NMR (400 MHz, DMSO-d_6) δ 9.10–8.80 (br. s, 4H), 8.75–8.40 (m, 4H), 8.37–8.18 (m, 2H), 8.20–8.00 (m, 6H), 7.90–7.74 (m, 4H), 7.70–7.35 (m, 8H), 2.92 (br. s, 4H). MS *m/z* 1217.09, calcd for $C_{64}H_{35}N_9O_{14}Zn$, 1217.16.

Oligonucleotide–ZnPc Conjugation Reactions. The labeling procedure used was adapted from Molecular Probe's (Carlsbad, CA) standard protocol for amino-reactive Alexa Fluor succinimidyl esters. Stock solutions of **3**–**5** (5–10 mM) were prepared in DMSO (dimethyl sulfoxide). Labeling buffers were prepared in-house by dissolving the appropriate amount of the corresponding salts in water and adjusting the pH using HCl and/or NaOH. The amino-modified oligonucleotide was purified by ethanol precipitation before the conjugation reaction to remove any amino-containing impurities. The purified oligonucleotide was redissolved in water to yield a solution with a concentration of ~25 μg/mL (5 mM).

Unless otherwise noted, the reaction mixture included (in order of addition) succinimidyl ester **3**, **4**, or **5** (200 nmol), water (7 μL), labeling buffer (75 μL), and oligonucleotide (20 nmol). The reaction was incubated at room temperature for 15–18 h. Labeled oligonucleotides were purified by ethanol precipitation (to partially remove excess unreacted dye) using 250 μL of cold absolute ethanol and 10 μL of 3 M NaCl added to the reaction mixture. The solutions were mixed and kept at −20 °C for 30–60 min and centrifuged at 12,000 rpm with the supernatant discarded. The precipitate was dried on air and reconstituted in 100 μL of 0.1 M TEAA (triethylammonium acetate) for chromatographic analysis and purification. The isolated fractions were combined and concentrated in a rotary evaporator. The excess TEAA was removed by drying in high vacuum (<0.01 mmHg) at room temperature.

High Performance Liquid Chromatography (HPLC). The HPLC separations were performed using a JASCO (Easton, MD) 2000-series HPLC equipped with a quaternary gradient pump, autosampler, and fluorescence and diode-array detectors. The analytical column (Zorbax C18, 5 μm, 4.6 mm × 150 mm) was purchased from Agilent Technologies (Santa Clara, CA). The following gradient was used (flow rate = 1.0 mL/min): initial hold at 95% 0.1 M TEAA/5% MeOH for 5 min; ramp up to 5% 0.1 M TEAA/95% MeOH in 30 min; hold for 5 min; and wash for 15 min with 100% MeOH at 1.5 mL/min. The column was allowed to equilibrate at the initial mobile phase conditions for 20 min before the next injection. Typically, two wavelengths were monitored using the diode-array detector: 260 and 680 nm. The fluorescence detector was set to an excitation wavelength of 677 nm, and the emission wavelength was set to 687 nm, the corresponding maxima for ZnPc **2** absorption and emission (*23*).

Determination of Conjugate Concentrations. The concentrations of the ZnPc-labeled oligonucleotides were determined by HPLC against a calibration curve obtained using solutions of the corresponding ZnPc at various concentrations (0.5&–100 μM) when monitoring absorption at 680 nm, where the oligonucleotide offered little if any absorption.

Absorption and Fluorescence Measurements. All absorption spectra were acquired using an Ultrospec 4000 spectrophotometer (Pharmacia Amersham Biosciences, Piscataway, NJ) or Cary 50 UV&–vis (Varian, Palo Alto, CA) with 10 mm path length quartz cuvettes. Emission spectra were acquired using a FLUOROLOG-3 spectrofluorometer (Horiba Jobin Yvon, Edison, NJ) equipped with a 450 W xenon lamp and a cooled

Hamamatsu R928 photomultiplier operated at 900 V in the photon-counting mode. All spectral measurements were performed under ambient conditions within 3 h of solution preparation.

DNA Hybridization. The hybridization of conjugate **2-C6-O1** (here and elsewhere, **1** or **2** represents ZnPc label (Scheme 1, **1** or **2**); **C6** or **C12**, aliphatic linker containing 6 or 12 carbon atoms, respectively; **O1** or **O2**, oligonucleotide sequence (see Table 1)) with complement **O2** was performed by incubating 1 μM solutions of both the labeled oligonucleotide (**2-C6-O1**) and its complement **O2** at equal molar concentrations in a buffer containing 10 mM Tris-HCl, 4 mM $MgCl_2$, and 15 mM KCl at pH 8.5 for 2 h at 30 °C.

Polymerase Chain Reactions (PCRs). PCRs were performed on M13mp18 DNA (USB, Cleveland, OH) or human placental DNA (Sigma-Aldrich, St. Louis, MO) targets. PCR primers (see Table 1 for sequences) were designed to amplify 185 bp, 272 bp, and 381 bp regions of the M13mp18 DNA target and a 98 bp region of human placental DNA. PCRs were performed using a GeneAmp reagent kit with AmpliTaq DNA polymerase (Applied Biosystems, Foster City, CA). PCR cocktails consisted of 1 μL of each of the primers ($\sim$1 μM whenever known), 2 μL of dNTPs (0.2 mM), 10 μL of 10$\times$ PCR buffer, 1 μL of Taq DNA Polymerase (0.5 unit/μL), 1 μL of DNA template (2 ng/μL), and 84 μL of PCR qualified water. PCR was carried out using a commercial thermal cycling instrument (Eppendorf, Hamburg, Germany or Techne, Burlington, NJ). M13mp18 amplifications consisted of the following (30 cycles): 94 °C for 30 s; 57 °C for 40 s; 72 °C for 60 s; and a final extension at 72 °C followed by a cooling step at 4 °C. Thermal cycling of the human placental DNA was designed to amplify the CFTR (cystic fibrosis transmembrane conductance regulator) gene and consisted of an initial denaturation step at 94 °C for 5 min followed by (30 cycles) 94 °C for 40 s; 62 °C for 40 s; 72 °C for 60 s; and a final extension at 72 °C followed by a cooling step to 4 °C. PCRs were also conducted using unlabeled primers of the same sequence as those of the labeled primers to evaluate PCR performance in the presence of the MPc dye reporter.

Gel Electrophoresis. PCR products were electrophoresed either in a 3% precast agarose gel (Bio-Rad Laboratories, Hercules, CA) or a 5.5% (w/v) cross-linked polyacrylamide gel (Li-COR Biosciences, Lincoln, Nebraska). For the agarose gel, separation was performed at 140 mV in 1 $\times$ TAE buffer (Bio-Rad Laboratories, Hercules, CA). Amplicons were indexed against a DNA sizing ladder (50–1000 bp, Promega, Madison, WI). After separation, the gels were stained with ethidium bromide ($\sim$0.3 μL/mL), and images were collected using a Logic Gel imaging system (Eastman Kodak Company, Rochester, NY).

The polyacrylamide gel was polymerized between two borofloat glass plates (21 cm $\times$ 25 cm) and placed in the Global IR^2DNA analysis system (Li-COR Biosciences, Lincoln, NE). The electrophoresis was typically run at 1,500 V for 2.5 h. Amplicons were indexed against a 50–350 bp IRD700-labeled size standard (Li-COR Biosciences, Lincoln, NE). The fluorescence detector contained in this instrument consisted of a scanning laser (λ = 680 nm), an avalanche photodiode detector, and a bandpass filter (preset center wavelength = 720 nm; pass band $\sim$20 nm) situated in front of this detector to isolate the monitored fluorescence.

RESULTS AND DISCUSSION

ZnPc's **1** and **2** (asymmetrical and symmetrical, respectively; see Scheme 1) possess photophysical properties that are comparable or superior to those of commercially available near-IR dyes (e.g., ZnPc **2**: extinction coefficient = 2.9×10^5, fluorescence quantum yield = 0.41, and photobleaching quantum yield = 5.0×10^{-7}; commercially available near-IR dye IRD700: fluorescence quantum yield = 0.70; photobleaching quantum yield = 4.6×10^{-6} (*23*)), are chemically, thermally, and light stable, and are fairly water-soluble, which was achieved by decorating the macrocycle periphery with polar solubilizing groups (triethylene glycols (TEG) or carboxylates). These ZnPc's have narrower absorption and emission envelopes compared to those of the carbocyanine-based near-IR dyes (see Figure 1), making them particularly attractive for spectral multiplexing applications. Additionally, these dyes contained at least one carboxylic group, a convenient and common functionality that can be used for robust labeling of amino-modified biomolecules such as oligonucleotides via succinimidyl ester chemistry (*43*).

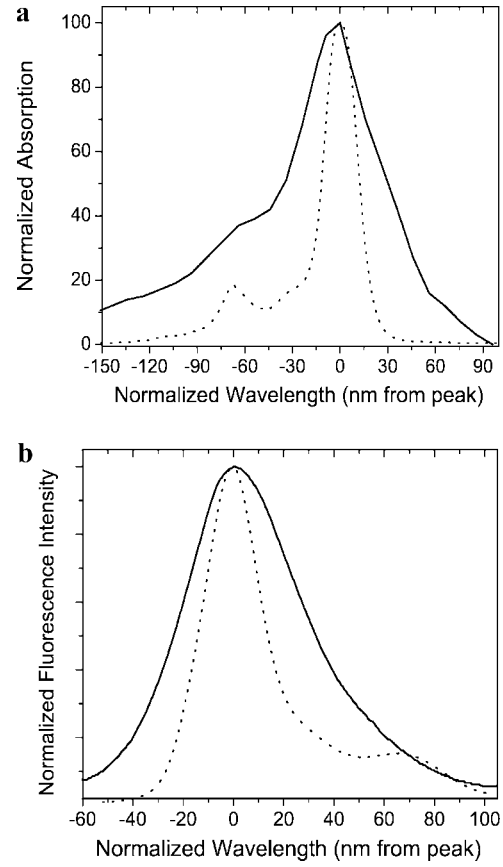


Figure 1. Electronic absorption (a) and emission (b) spectra of a cyanine dye, Cy7 (—), and ZnPc **2** (---). All spectra were acquired using the dyes at a concentration of approximately 1 μM and placed in a DMSO solvent. The spectra were normalized to the absorption or emission maxima.

Two types of MPc's were evaluated in this study: an asymmetric ZnPc **1** containing three triethylene glycol groups to provide solubility in aqueous media and a functional carboxylic group that could be used for labeling reactions, and a symmetric ZnPc **2**, which contained four carboxylic groups that provided both solubilization of the dye in aqueous media and a functional handle to covalently attach the fluorophore to a target.

Conjugation Reactions. The use of succinimidyl esters and their reaction with primary amines has been reported for several MPc's (*28, 29, 31*). We applied this coupling approach to amino-modified oligonucleotides, and ZnPc's **1** and **2** converted into succinimidyl esters **3**–**5** (see Scheme 2). The conjugates, **1-C12-O1**, **2-C12-O1**, and **1-C6-O1**, were isolated using ion-pair reverse-phase chromatography. The chromatographic separation was achieved using a 0.1 M TEAA/CH_3OH gradient (see Figure 2a and Figure S1 in Supporting Information). Using similar

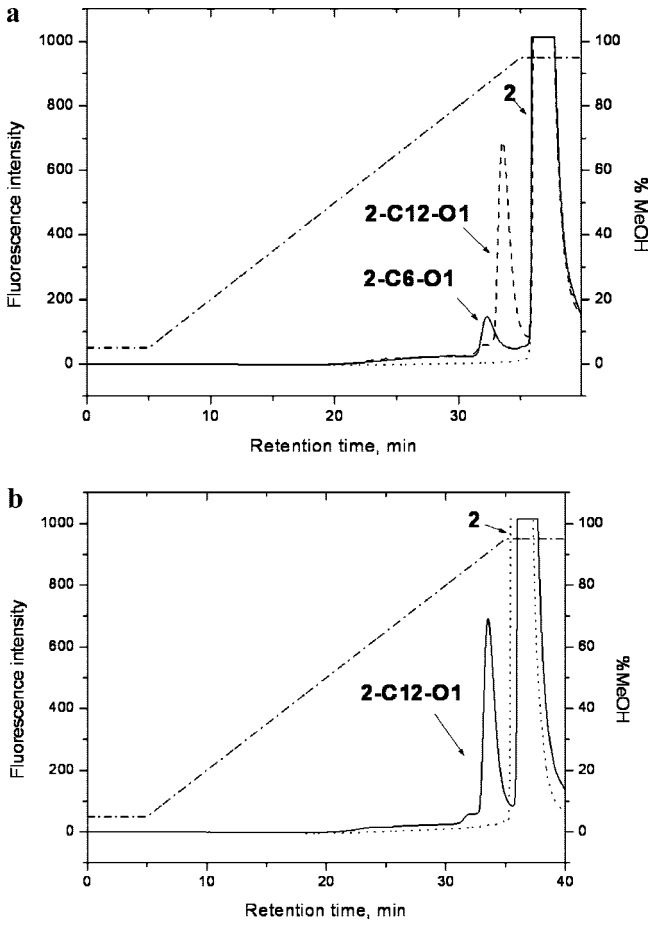


Figure 2. Ion pair, reverse-phase chromatograms of reaction mixtures consisting of a ZnPc succinimidyl ester and an oligonucleotide along with control reactions consisting of the native ZnPc dye and an oligonucleotide. (a) Reactions with succinimidyl ester **4** (—, reaction with **C6-O1**; ---, **C12-O1**; ···, ZnPc **2**; •—•—•, gradient composition). (b) Reaction with succinimidyl ester **4** and a control reaction with the native ZnPc **2** dye (—, reaction with succinimidyl ester **4**; ···, reaction with ZnPc **2**; •—•—•, gradient composition).

gradients with CH_3CN rather than CH_3OH did not result in complete separation of the labeled conjugates from excesses of the corresponding MPc's.

As a control, it was necessary to demonstrate that conjugations were not simply noncovalent associations between the MPc dye and the oligonucleotide. To verify this, a reaction involving a nonreactive MPc (carboxylic acid **2** instead of succinimidyl ester **4** or **5**) and the amino-modified oligonucleotide **O1** was conducted. Inspection of the control chromatograms (Figure 2b) showed no evidence of the MPc's nonspecifically associating with the oligonucleotides; no peak for an association complex was detected in the chromatographic trace. Similar data was also obtained for PEG-modified ZnPc **1** (data not shown).

Experiments were then conducted to optimize the extent of the conjugation reaction by altering reaction conditions, such as pH, buffer composition, and the dye-to-oligonucleotide molar ratio. The labeling efficiencies were evaluated by monitoring the decrease in the original oligonucleotide content observed from the chromatographic traces (details are included in the Supporting Information; see Figure S2). The labeling efficiencies were estimated for various conditions, the results of which are summarized in Tables 2 and 3.

For molecules containing more than one carboxylic group (e.g., ZnPc **2**), several types of succinimidyl esters with different numbers of carboxylic groups converted to succinimidyl esters were possible. Two activated esters of ZnPc **2** were obtained

Table 2. Estimated Labeling Efficiencies at Different MPc/oligonucleotide Molar Concentration Ratios Using Different Dyes, Linkers, and Succinimidyl Esters[a]

Linker[b]	MPc	succinimidyl ester	MPc/oligonucleotide	labeling efficiency
$C_{12}H_{24}$	**1**	**3**	5:1	<5%
$C_{12}H_{24}$	**1**	**3**	10:1	24 ± 6%
$C_{12}H_{24}$	**1**	**3**	18:1	48 ± 2%
$C_{12}H_{24}$	**2**	**5**	11:1	78 ± 5%
$C_{12}H_{24}$	**2**	**5**	21:1	56 ± 3%
$C_{12}H_{24}$	**2**	**5**	38:1	39 ± 2%
C_6H_{12}	**2**	**4**	1:1	<5%
C_6H_{12}	**2**	**4**	4:1	28 ± 3%
C_6H_{12}	**2**	**4**	9:1	38 ± 6%
$C_{12}H_{24}$	**2**	**4**	1:1	33 ± 6%
$C_{12}H_{24}$	**2**	**4**	4:1	47 ± 3%
$C_{12}H_{24}$	**2**	**4**	11:1	53 ± 4%

[a] Conjugation reactions were performed in borate buffer at pH 8.5 and using an oligonucleotide concentration of 20 nM. [b] The aliphatic linker used to attach the amino group to the 5′end of the oligonucleotide.

Table 3. Labeling Efficiencies of an Oligonucleotide with ZnPc 2 at Different Buffer and pH Conditions[a]

pH	borate	carbonate
7.5		67 ± 2%
8.0	26 ± 3%	
8.5	38 ± 6%	59 ± 2%
9.5	15 ± 1%	36 ± 2%

[a] The conjugation reactions used a C_6H_{12} linker, ZnPc **2**, succinimidyl ester **4**, and an MPc/oligonucleotide molar ratio of 9:1.

and used for the labeling evaluation: the tetra-succinimidyl ester **5** (all four carboxylic groups are converted to the succinimidyl esters) and the monosuccinimidyl ester **4** (only one carboxylic group is converted to the succinimidyl ester). As seen in Table 2, tetra-succinimidyl ester **5** resulted in better labeling efficiencies (78%) compared to that of the monosuccinimidyl ester **4** (53%) when using an MPc/oligonucleotide molar ratio of 11:1. This may have resulted from a higher effective concentration of the succinimidyl ester groups associated with the tetra-succinimidyl ester **5** compared to that of the monosuccinimidyl ester **4**. However, multiple targets may become attached to the same fluorophore when using labeling fluors that have several functional groups, as in the case of tetra-ester **5** compared to the monoester **4**, which can complicate the purification step. Indeed, multiple products were observed in the chromatogram when the succinimidyl ester **5** was used. At least two products were observed in the chromatogram when an 11-fold molar excess of the ester was used (see Figure S3 in Supporting Information), one which could be ascribed to the 1:1 MPc/oligonucleotide conjugate and another to a conjugate in which two oligonucleotides were linked to the same dye. The use of molar excesses below 11:1 (MPc/oligonucleotide) when using succinimidyl ester **5** yielded appreciable levels of the tri- and tetra-substituted products (data not shown).

It was generally observed that the labeling efficiency improved with increases in the MPc-to-oligonucleotide molar concentration ratio up to 11:1 (see Table 2), irrespective of the identity of the dye or succinimidyl ester used. The use of an excess of succinimidyl ester was necessary to overcome competing hydrolysis reactions of these functional groups. However, increasing the MPc/oligonucleotide molar ratio beyond approximately 11:1 reduced the extent of labeling (see Table 2). For example, succinimidyl ester **5** showed decreases in the reaction yield from 78% to 39% when the MPc/oligonucleotide molar ratio changed from 11:1 to 38:1, respec-

tively. At higher dye concentrations, aggregation effects between MPc dyes began to dominate (*44*), which reduced the number of monomeric molecules available for the conjugation reaction. Thus, an MPc/oligo molar concentration ratio of approximately 10:1 was found to be optimal for these conjugation reactions.

We also investigated the effect of different aliphatic linker lengths used to tether the functional group (i.e., primary amine) to the oligonucleotide on the MPc-oligonucleotide labeling efficiency. As noted for ZnPc **2** and the monosuccinimidyl ester **4** (see Table 2), better overall labeling efficiencies were observed for oligonucleotides containing a $C_{12}H_{24}$ linker compared to those with C_6H_{12} linkers. The improved labeling efficiency for the $C_{12}H_{24}$ linker may be explained by reductions in electrostatic interactions between the anionic MPc and oligonucleotides when compared to that in the C_6H_{12} linker.

Various buffer compositions and pH values were also investigated as to their effects on the extent of labeling oligonucleotides with these ZnPc dyes. Inspection of Table 3 shows that for the labeling conditions tested (C_6H_{12} linker, ZnPc **2**, succinimidyl ester **4**, and MPc/oligonucleotide molar ratio of 9:1), better labeling was achieved at pH 7.5 when using the carbonate buffer (67%), while for the borate buffer, higher labeling efficiencies were obtained at a pH value of 8.5 (38%). It was also observed that at all pH values, carbonate buffers yielded higher labeling efficiencies. The effects of pH on labeling efficiency most likely resulted from the necessary balance between three factors: succinimidyl ester group hydrolyzis rate, amine group reactivity, and solubility of **1** and **2** in aqueous media. All of these parameters are known to increase with increasing pH (*43*). The enhancement of the labeling efficiency when carbonate buffer was used compared to that with borate (59% vs 38% at pH 8.5; see Table 3) agreed with similar observations reported in the literature using succinimidyl chemistry (*45*).

Conjugate Purification and Isolation. The standard protocols used to purify oligonucleotides from low molecular weight components, SEC filtration, ethanol precipitation, and HPLC, were evaluated for the isolation of MPc–oligonucleotide conjugates. Sephadex G25 size-exclusion columns were found to retain not only ZnPc **2** but also conjugate **2-C6-O1** (see HPLC traces in Figure S4 in Supporting Information), indicating that the separation was not exclusively based on size but also partially on interactions of the dye with the solid support. Ethanol precipitation, an approach based on the limited solubility of oligonucleotides in cold ethanol, also did not provide adequate purification of the conjugates to allow it to be used exclusively. ZnPc's **1** and **2** have limited solubility in EtOH, which results in only ~40% of the unreacted dye being removed in the ethanol supernatant (see HPLC traces in Figure S5 in Supporting Information). A combination of ethanol precipitation followed by reverse-phase ion pair chromatography was found to give the most efficient isolation/purification approach for the MPc–oligonucleotide conjugates. It allowed for pure conjugates to be isolated, even when 10-fold molar excesses of the dye were used; no residual MPc's and/or unlabeled oligonucleotide were observed in chromatograms of the isolated conjugates when subjected to a precleanup with cold ethanol followed by reverse-phase chromatography (data now shown).

Spectral Properties of the MPc–Oligonucleotide Conjugates. Electronic absorption spectra of the conjugate **2-C12-O1** (Figure 3a) contained features characteristic of both domains, MPc and the oligonucleotide, including absorption bands at ~360 and 680 nm associated with the ZnPc and strong absorption between 250 and 260 nm indicating the presence of the oligonucleotide. Also, strong fluorescence was observed around 690 nm from the ZnPc moiety. The fluorescence emission profiles of the isolated conjugates and the corresponding MPc's were similar with no spectral feature changes observed in the conjugates compared to the corresponding ZnPc dyes (see Figure 3b).

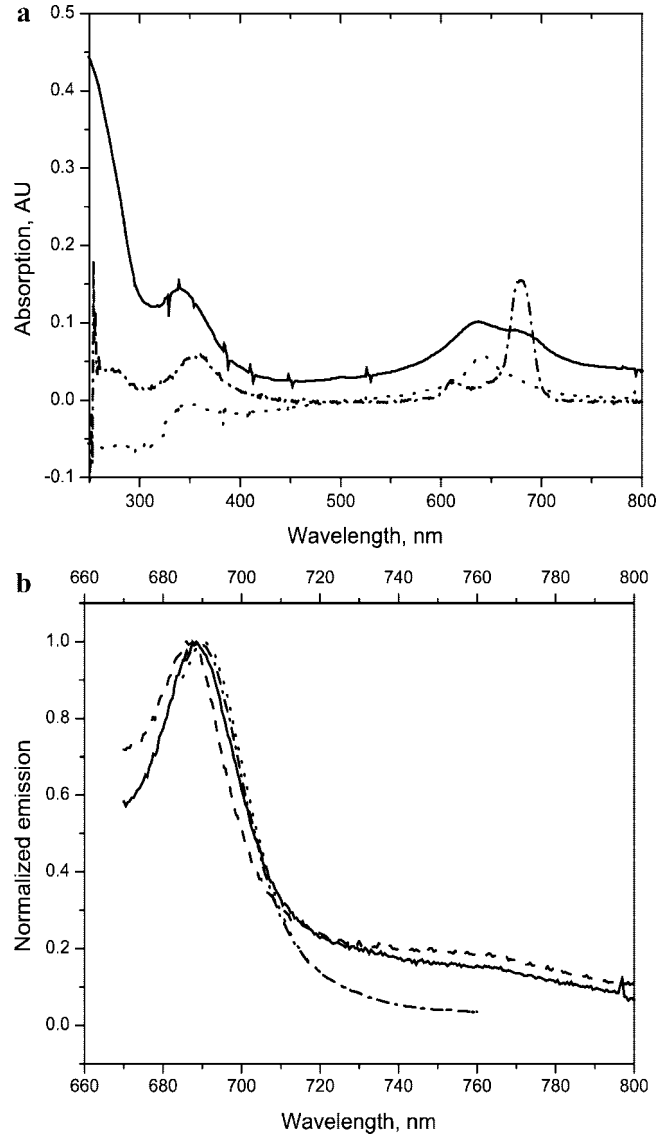


Figure 3. Absorption and emission spectra of purified conjugates and the native MPc dyes. (a) Electronic absorption spectra of **2** (2 μM) in NH_4OH (pH 11) (•••), **2-C12-O1** (concentration unknown) in NH_4OH (pH 11) (—), and **2** (2 μM) in DMSO (•−•−•); (b) Fluorescence emission spectra (λ_{ex} = 650 nm) of **1** (100 nM) in NH_4OH at pH9/MeOH (50/50) (•−•−•), conjugate **1-C12-O1** (concentration unknown) in NH_4OH at pH9/MeOH (50/50) (•••), **2** (100 nM) in carbonate buffer at pH11/MeOH (50:50) (---) and **2-C12-O1** (concentration unknown) in carbonate buffer at pH11/MeOH (50:50) (—).

One of the important intrinsic properties of *Pc*'s and MPc's is their high propensity to aggregate in aqueous solutions (*21*, *26*) with dimerization constants as high as 10^{-9} M^{-1} (*46*). With very few exceptions, neither MPc dimers nor higher order cofacial aggregates fluoresce (*47–49*). Electronic adsorption spectra of MPc's can provide insight into ground-state aggregation processes (*50*); a split and blue-shifted Q-band typically indicates cofacial ground-state aggregation of *Pc* rings (*19*, *44*, *46*, *51*, *52*). Both the free ZnPc **2** and its conjugate **2-C12-O1** showed various degrees of ground-state aggregation in aqueous media as noted from blue-shifts in the absorption maximum, generating a broadband as compared to the molecule in DMSO, where aggregation is expected to be minimal (see Figure 3a).

The absorption spectra of **2-C6-O1** and **2-C6-O1** hybridized to a 42-bp complement oligonucleotide **O2** (see Table 1) were

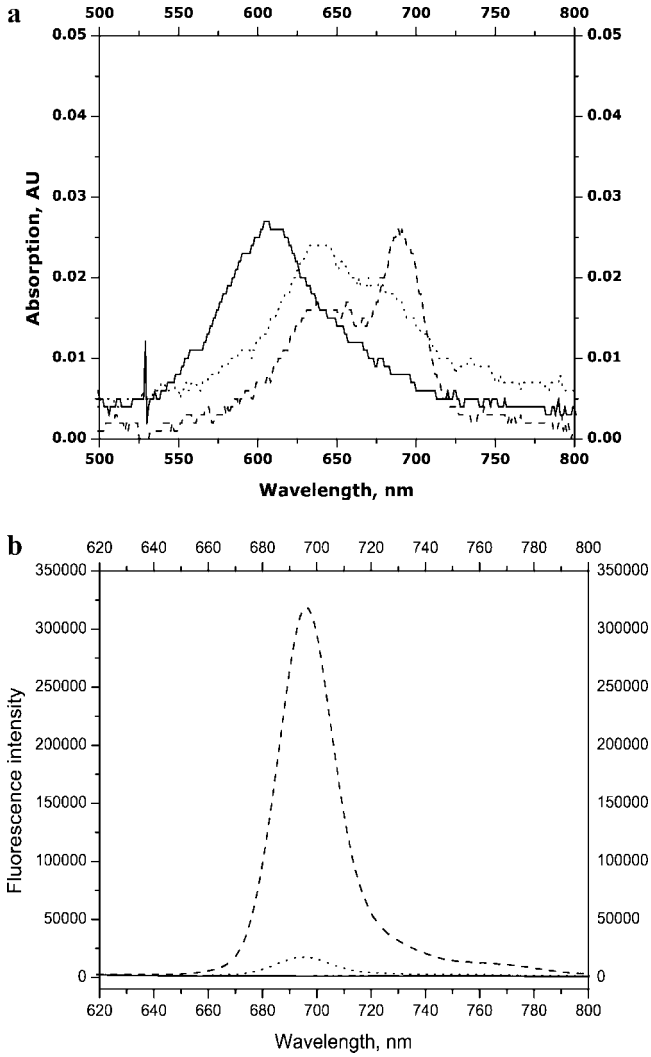


Figure 4. Absorption (a) and emission (b) spectra of solutions of ZnPc **2** (—), conjugate **2-C6-O1** (···), and the hybrid of **2-C6-O1** and **O2** (---). The spectra were measured in a buffer containing 10 mM Tris-HCl, 4 mM $MgCl_2$, and 15 mM KCl at pH 8.5.

also interrogated. The electronic absorption spectra (Figure 4a) indicated almost complete aggregation of ZnPc **2**, partial aggregation of conjugate **2-C6-O1**, and significant reductions in aggregation for the hybrid of **2-C6-O1** with **O2**. The fluorescence results correlated well with the adsorption spectra (see Figure 4b); no detectable fluorescence was observed for ZnPc **2** with a 13-fold increase in fluorescence for the **2-C6-O1**/**O2** hybrid compared to that for **2-C6-O1** alone. These results indicate that MPc aggregation can be substantially diminished when the MPc reporter is part of relatively large oligonucleotide constructs. Similar phenomena have been observed for MPc aggregation upon conjugation to monoclonal antibodies (*37*). However, for the tricarbocyanine near-IR dyes, complete deaggregation effects were observed when this dye was attached to a single nucleotide base (*53*) consistent with the fact that the carbocyanines have low aggregation propensities compared to those of the MPc-based dye systems.

PCR-Based Applications. The ZnPc–oligonucleotide conjugates were next evaluated as potential reagents/reporters for PCR by amplifying different sized regions of an M13mp18 DNA template and a 98 bp region of the exon-10 CFTR gene containing the δF508 mutation, which can provide a high diagnostic value for cystic fibrosis (*54*). The amplicons were sorted by gel electrophoresis using either an agarose gel with

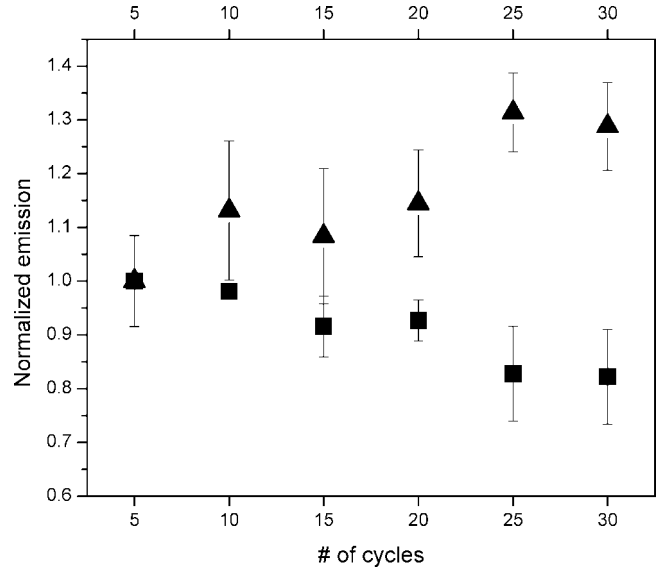


Figure 5. Fluorescence emission intensity of near-IR dye-labeled oligonucleotides (■, IRD700; ▲, ZnPc **2**) as a function of thermal cycle number. The reactions did not contain a target DNA or DNA polymerase. Thermal cycling conditions: 94 °C for 1 min; 55 °C for 40 s; 72 °C for 1 min. Emission wavelengths used were 700 nm for IRD700 and 690 nm for ZnPc **2**. Emission intensities were normalized to the intensity secured after 5 thermal cycles.

UV detection after staining with ethidium bromide or a polyacrylamide gel with near-IR fluorescence detection at ~700 nm.

A comparison of the chemical/thermal stability of ZnPc- and carbocyanine-based near-IR fluorophores was first investigated using PCR, which contained all reagents except the amplification target and polymerase, and was carried through typical thermal cycling conditions. The results of this investigation are shown in Figure 5. (The fluorescence measurements were performed at room temperature following thermal cycling.) As can be seen in the results in Figure 5, the emission intensities for the carbocyanine-labeled oligonucleotide showed incremental decreases with increasing thermal cycle number, while the ZnPc **2** reporter showed modest increases in its fluorescence intensity with increasing thermal cycle number. The loss in fluorescence intensity for the carbocyanine is indicative of chemical changes in the chromophore induced by thermally activated reactions, which result in decreases in the fluorescence of this molecule. In the case of ZnPc **2**, no such reactions were found to occur at the conditions used herein. We also note that the slight increases in the fluorescence observed for the ZnPc **2** chromophore as a function of cycle number could have resulted from deaggregation of the ZnPc-oligonucleotide conjugate (see results in Figures 3 and 4).

We next performed PCR amplification of an M13mp18 or human genomic DNA target using the ZnPc **1** (asymmetrical) and **2** (symmetrical) reporter dyes. The size of the PCR amplicons obtained using both *Pc*-based dye/oligonucleotide conjugates correlated well with their expected sizes based on the known sequences of the test templates and the primer sequences when referenced against standard DNA ladders (see Figure 6). Another important conclusion is that no erroneous bands were detected in either of the PCRs, indicating that the ZnPc-based fluorophores did not perturb the PCR process. The results in Figure 6a show agarose gel electropherograms of PCR amplicons (381 bp) generated using **1**- and **2**-labeled primers or an unlabeled DNA primer. Qualitatively, the correct amplicons were generated for PCRs using the MPC-labeled primers when compared to the same PCRs using the unlabeled primers based on product size.

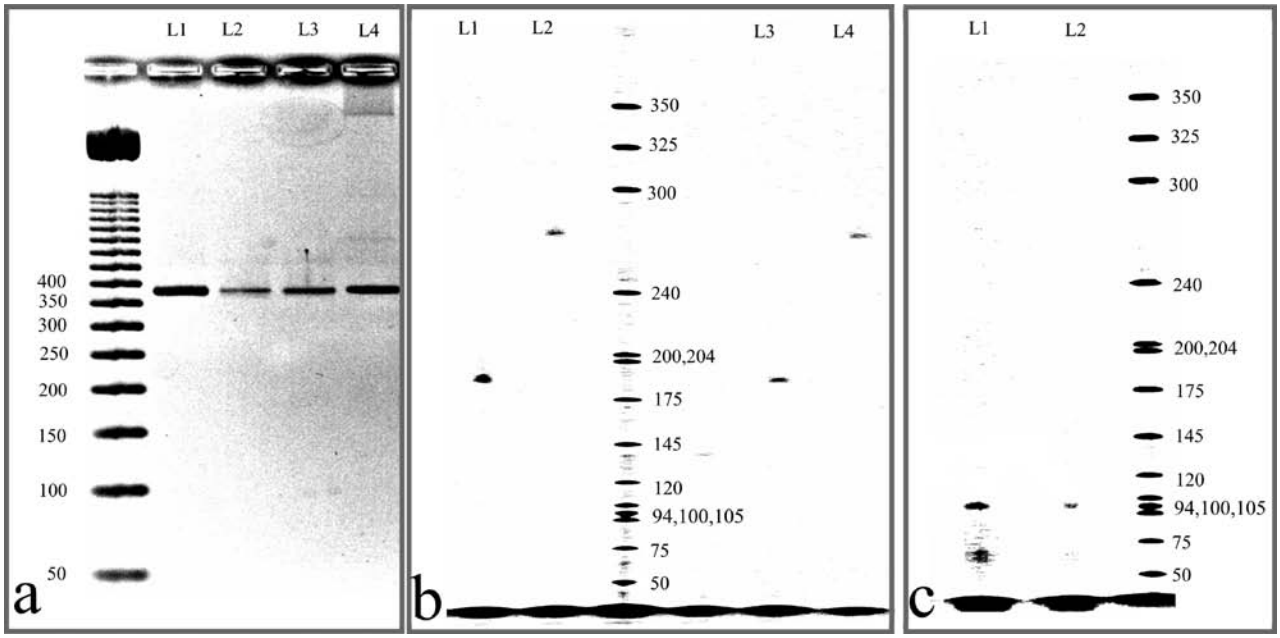


Figure 6. Images of agarose (a) and polyacrylamide (b and c) gels after electrophoresis of PCR products. Detection was accomplished using UV absorption at 254 nm after staining the gel with ethidium bromide (a) or near-IR fluorescence at 700 nm (b and c). (a) 381 bp regions of M13mp18 amplified using primers **1-C12-O1** (L2), **2-C12-O1** (L3), **2-C6-O1** (L4), and unlabeled primer (L1). (b) 185 bp (L1, L3) and 272 bp (L2, L4) amplicons of a M13mp18 template amplified via PCR using primers **2-C6-O1** (L1, L2) or **1-C12-O1** (L3, L4). (c) (L1 and L2), 98 bp region of CFTR gene amplified via PCR using primer labeled with ZnPc **2**.

From the polyacrylamide gel electropherogram shown in Figure 6b, single bands were observed irrespective of amplicon size (185 or 272 bp) with similar amplicon yields using either **1** or **2** as the fluorescent label. The lack of smearing in the electrophoretic bands or the presence of phantom bands indicated that the dye–oligonucleotide constructs did not interact due to dye/dye-induced aggregation to either the amplicons or unconsumed primers following PCR.

As a demonstration of the ability to use these labels for the analysis of PCR products with diagnostic value, human genomic DNA was amplified using primers specific for exon-10 of the CFTR gene, which contains a mutation that provides molecular diagnostic information for cystic fibrosis. As can be seen from the image displayed in Figure 6c, 98 bp amplicons were clearly visible. It should be noted that the fluorescence detector used in this electrophoresis unit was not optimized for the MPc dye systems; the filter system installed in the instrument was designed for dicarbocyanine dyes, which have comparatively larger Stoke's shifts and broader excitation/emission envelopes compared to those of the ZnPc dyes (see Figure 1).

CONCLUSIONS

ZnPc's **1** and **2** (asymmetrical and symmetrical, respectively) were designed to provide water solubility and carboxylic groups that could be used for labeling biomolecules through succinimide-based chemistry. The ZnPc's afforded labeling efficiencies of 80% of target oligonucleotides using optimized conditions, including proper pH (7.5), buffer composition (carbonate), linker structure ($C_{12}H_{24}$), and stoichiometry between the MPc and oligonucleotide (~10:1, respectively). In addition, facile purification strategies were reported on the basis of ion-pair reverse-phase chromatography preceded by cold ethanol precipitation.

Spectroscopic investigations indicated that the conjugation of ZnPc's **1** and **2** to oligonucleotides did not alter their intrinsic fluorescence emission properties but affected the aggregation properties of the MPc's when placed in aqueous media. Partial deaggregation of ZnPc **2** was observed when this dye was attached to a 17mer oligonucleotide as revealed from its ground-state spectrum with slight fluorescence noted for the conjugate compared to that for the native dye in aqueous buffer. When the conjugate was hybridized to its complement, creating a double-stranded 42mer, a 13-fold increase in the fluorescence was observed compared to that in the dye/17mer construct. Because most molecular biology applications, such as PCR and cycle sequencing, create constructs that are larger than the starting primer and the primers are used in large molar excesses, this property could potentially reduce interferences from unextended primers when fluorescence is used for readout.

Another attractive feature of the MPc dyes compared to other near-IR dyes is their superior thermal/chemical stability. These features along with their outstanding photostability (photobleaching quantum yield of 5×10^{-7} (*23*)), narrow absorption/emission envelopes (see Figure 1), and near-IR excitation/emission properties will make *Pc* dyes very attractive candidates for a variety of highly sensitive and multiplexed biomolecular applications (*55*).

ACKNOWLEDGMENT

We thank the National Institutes of Health (National Human Genome Research Institute, Grants HG001499 and CA099246), the National Science Foundation (Grant Numbers CHE-0304833 and EPS-0346411), and the Louisiana Board of Regents for the financial support of this work.

Supporting Information Available: HPLC separation of ZnPc **1** and conjugate **1-C12-O1**, procedure used for calculation of labeling efficiency, multiple conjugation products and their separation, purification of conjugation reaction using G25 microspin columns, and purification of conjugation reaction using ethanol precipitation. This material available free of charge via the Internet at http://pubs.acs.org.

LITERATURE CITED

(1) Williams, D. C., and Soper, S. A. (1995) Ultrasensitive near-Ir Fluorescence Detection for Capillary Gel-Electrophoresis

and DNA-Sequencing Applications. *Anal. Chem. 67*, 3427–3432.
(2) Soper, S. A., and Mattingly, Q. L. (1994) Steady-State and Picosecond Laser Fluorescence Studies of Nonradiative Pathways in Tricarbocyanine Dyes - Implications to the Design of near-Ir Fluorochromes with High Fluorescence Efficiencies. *J. Am. Chem. Soc. 116*, 3744–3752.
(3) Soper, S. A., Mattingly, Q. L., and Vegunta, P. (1993) Photon Burst Detection of Single near-Infrared Fluorescent Molecules. *Anal. Chem. 65*, 740–747.
(4) McWhorter, S., and Soper, S. A. (2000) Near-infrared laser-induced fluorescence detection in capillary electrophoresis. *Electrophoresis 21*, 1267–1280.
(5) Zhu, L., Stryjewski, W., Lassiter, S., and Soper, S. A. (2003) Fluorescence multiplexing with time-resolved and spectral discrimination using a near-IR detector. *Anal. Chem. 75*, 2280–2291.
(6) Lassiter, S. J., Stryjewski, W. J., Wang, Y., and Soper, S. A. (2002) Shedding light on DNA analysis - Multiplexed detection and identification using fluorescence lifetime methods. *Spectroscopy 17*, 14–23.
(7) Owens, C. V., Davidson, Y. Y., Kar, S., and Soper, S. A. (1997) High resolution separation of DNA restriction fragments using capillary electrophoresis with near-IR, diode-based, laser-induced fluorescence detection. *Anal. Chem. 69*, 1256–1261.
(8) Li, G. D., Gao, J. X., Zhou, X. J., Shimelis, O., and Giese, R. W. (2003) Handling and detection of 25 amol of near-infrared dye deoxynucleotide conjugates by capillary electrophoresis with laser-induced fluorescence detection. *J. Chromatogr., A 1004*, 47–50.
(9) Peter, C., Meusel, M., Grawe, F., Katerkamp, A., Cammann, K., and Borchers, T. (2001) Optical DNA-sensor chip for real-time detection of hybridization events. *Fresenius' J. Anal. Chem. 371*, 120–127.
(10) Lassiter, S. J., Stryjewski, W., Legendre, B. J., Erdmann, R., Wahl, M., Wurm, J., Peterson, R., Middendorf, L., and Soper, S. A. (2000) Time resolved fluorescence imaging of slab gels for lifetime base-calling in DNA sequencing applications. *Anal. Chem. 72*, 5373–5382.
(11) Wabuyele, M. B., Farquar, H., Stryjewski, W., Hammer, R. P., Soper, S. A., Cheng, Y. W., and Barany, F. (2003) Approaching real-time molecular diagnostics: Single-pair fluorescence resonance energy transfer (spFRET) detection for the analysis of low abundant point mutations in K-ras oncogenes. *J. Am. Chem. Soc. 125*, 6937–6945.
(12) Chen, X. L., Li, D. H., Yang, H. H., Zhu, Q. Z., Zheng, H., and Xu, J. G. (2001) A new red-region substrate, tetra-substituted amino aluminium phthalocyanine, for the fluorimetric determination of H_2O_2 catalyzed by mimetic peroxidases. *Analyst 126*, 523–527.
(13) Kurner, J. M., Klimant, I., Krause, C., Pringsheim, E., and Wolfbeis, O. S. (2001) A new type of phosphorescent nanospheres for use in advanced time-resolved multiplexed bioassays. *Anal. Biochem. 297*, 32–41.
(14) Kricka, L. J. (2002) Stains, labels and detection strategies for nucleic acids assays. *Ann. Clin. Biochem. 39*, 114–129.
(15) Gomez-Hens, A., and Aguilar-Caballos, M. P. (2004) Long-wavelength fluorophores: new trends in their analytical use. *TrAC, Trends Anal. Chem. 23*, 127–136.
(16) Fabian, J., Nakazumi, H., and Matsuoka, M. (1992) Near-Infrared Absorbing Dyes. *Chem. Rev. 92*, 1197–1226.
(17) Ogunsipe, A., Chen, J. Y., and Nyokong, T. (2004) Photophysical and photochemical studies of zinc(II) phthalocyanine derivatives - effects of substituents and solvents. *New J. Chem. 28*, 822–827.
(18) Kobayashi, N., Ogata, H., Nonaka, N., and Luk'yanets, E. A. (2003) Effect of peripheral substitution on the electronic absorption and fluorescence spectra of metal-free and zinc phthalocyanines. *Chem.–Eur. J. 9*, 5123–5134.
(19) Dhami, S., and Phillips, D. (1996) Comparison of the photophysics of an aggregating and non-aggregating aluminium phthalocyanine system incorporated into unilamellar vesicles. *J. Photochem. Photobiol., A 100*, 77–84.
(20) Ambroz, M., Beeby, A., Macrobert, A. J., Simpson, M. S. C., Svensen, R. K., and Phillips, D. (1991) Preparative, Analytical and Fluorescence Spectroscopic Studies of Sulfonated Aluminum Phthalocyanine Photosensitizers. *J. Photochem. Photobiol., B 9*, 87–95.
(21) Kobayashi, N., Higashi, R., Ishii, K., Hatsusaka, K., and Ohta, K. (1999) Aggregation, complexation with guest molecules, and mesomorphism of amphiphilic phthalocyanines having four- or eight tri(ethylene oxide) chains. *Bull. Chem. Soc. Jpn. 72*, 1263–1271.
(22) Ogunsipe, A., and Nyokong, T. (2004) Effects of substituents and solvents on the photochemical properties of zinc phthalocyanine complexes and their protonated derivatives. *J. Mol. Struct. 689*, 89–97.
(23) Verdree, V. T., Pakhomov, S., Su, G., Allen, M. W., Countryman, A. C., Hammer, R. P., and Soper, S. A. (2007) Water soluble metallo-phthalocyanines: the role of the functional groups on the spectral and photophysical properties. *J. Fluoresc. 17*, 547–563
(24) Cook, M. J., Dunn, A. J., Howe, S. D., Thomson, A. J., and Harrison, K. J. (1988) Octa-Alkoxy Phthalocyanine and Naphthalocyanine Derivatives - Dyes with Q-Band Absorption in the Far Red or near-Infrared. *J. Chem. Soc., Perkin Trans. 1*, 2453–2458.
(25) Ogunsipe, A., and Nyokong, T. (2005) Effects of central metal on the photophysical and photochemical properties of non-transition metal sulfophthalocyanine. *J. Porphyrins. Phthalocyanines 9*, 121–129.
(26) Ogunsipe, A., and Nyokong, T. (2005) Photophysical and photochemical studies of sulphonated non-transition metal phthalocyanines in aqueous and non-aqueous media. *J. Photochem. Photobiol., A 173*, 211–220.
(27) Li, X. Y., and Ng, D. K. P. (2001) Synthesis and spectroscopic properties of the first phthalocyanine-nucleobase conjugates. *Tetrahedron Lett. 42*, 305–309.
(28) Devlin, R., Studholme, R. M., Dandliker, W. B., Fahy, E., Blumeyer, K., and Ghosh, S. S. (1993) Homogeneous Detection of Nucleic-Acids by Transient-State Polarized Fluorescence. *Clin. Chem. 39*, 1939–1943.
(29) Walker, G. T., Nadeau, J. G., Linn, C. P., Devlin, R. F., and Dandliker, W. B. (1996) Strand displacement amplification (SDA) and transient state fluorescence polarization detection of *Mycobacterium tuberculosis* DNA. *Clin. Chem. 42*, 9–13.
(30) Hammer, R. P., Owens, C. V., Hwang, S. H., Sayes, C. M., and Soper, S. A. (2002) Asymmetrical, water-soluble phthalocyanine dyes for covalent labeling of oligonucleotides. *Bioconjugate Chem. 13*, 1244–1252.
(31) Koval, V. V., Chernonosov, A. A., Abramova, T. V., Ivanova, T. W., Fedorova, O. S., Derkacheva, V. M., and Lukyanets, E. A. (2001) Photosensitized and catalytic oxidation of DNA by metallophthalocyanine-oligonucleotide conjugates. *Nucleosides Nucleotides Nucleic Acids 20*, 1259–1262.
(32) Ogunsipe, A., and Nyokong, T. (2005) Photophysicochemical consequences of bovine serum albumin binding to non-transition metal phthalocyanine sulfonates. *Photochem. Photobiol. Sci. 4*, 510–516.
(33) Huang, J. D., Wang, S. Q., Lo, P. C., Fong, W. P., Ko, W. H., and Ng, D. K. P. (2004) Halogenated silicon(IV) phthalocyanines with axial poly(ethylene glycol) chains. Synthesis, spectroscopic properties, complexation with bovine serum albumin and in vitro photodynamic activities. *New J. Chem. 28*, 348–354.
(34) Chen, X. L., Li, D. H., Zhu, Q. Z., Yang, H. H., Zheng, H., Wang, Z. H., and Xu, J. G. (2001) Determination of proteins at nanogram levels by a resonance light-scattering technique with tetra-substituted sulphonated aluminum phthalocyanine. *Talanta 53*, 1205–1210.
(35) Peng, X., Draney, D. R., Volcheck, W. M., Bashford, G. R., Lamb, D. T., Grone, D. L., Zhang, Y., and Johnson, C. M. (2006) Phthalocyanine dye as an extremely photostable and highly

fluorescent near-infrared labeling reagent. *Proc. SPIE Int. Soc. Opt. Eng. 6097*, 60970E/160970E/12.

(36) Sibrian-Vazquez, M., Ortiz, J., Nesterova, I. V., Fernandez-Lazaro, F., Sastre-Santos, A., Soper, S. A., and Vicente, M. G. H. (2007) Synthesis and properties of cell-targeted Zn(II)-phthalocyanine-peptide conjugates. *Bioconjugate Chem. 18*, 410–420.

(37) Duan, W. B., Smith, K., Savoie, H., Savoie, H., Greenman, J., and Boyle, R. W. (2005) Near IR emitting isothiocyanato-substituted fluorophores: their synthesis and bioconjugation to monoclonal antibodies. *Org. Biomol. Chem. 3*, 2384–2386.

(38) Vrouenraets, M. B., Visser, G. W. M., Stigter, M., Oppelaar, H., Snow, G. B., and van Dongen, G. (2001) Targeting of aluminum (III) phthalocyanine tetrasulfonate by use of internalizing monoclonal antibodies: Improved efficacy in photodynamic therapy. *Cancer Res. 61*, 1970–1975.

(39) Carcenac, M., Dorvillius, M., Garambois, V., Glaussel, F., Larroque, C., Langlois, R., Hynes, N. E., van Lier, J. E., and Pelegrin, A. (2001) Internalisation enhances photo-induced cytotoxicity of monoclonal antibody-phthalocyanine conjugates. *Br. J. Cancer 85*, 1787–1793.

(40) Hammer, R. P., Soper, S. A., Pakhomov, S., Jensen, T. J., Allen, M., Nesterova, I. V., and Vicente, M. D. G. H. (2007) Board of Supervisors of LA State University and Agricultural and Mechanical College, Application: WO, pp 75

(41) Koval, V. V., Chernonosov, A. A., Abramova, T. V., Ivanova, T. M., Fedorova, O. S., and Knorre, D. G. (2000) The synthesis of a cobalt(II) tetracarboxyphthalocyanine-deoxyribooligonucleotide conjugate as a reagent for the directed DNA modification. *Bioorg. Khim. 26*, 118–125.

(42) Deleted in proof.

(43) Hermanson, G. T., Ed. (1995) *Bioconjugate Techniques*.

(44) Yang, Y. C., Ward, J. R., and Seiders, R. P. (1985) Dimerization of cobalt(II) tetrasulfonated phthalocyanine in water and aqueous alcoholic solutions. *Inorg. Chem. 24*, 1765–1769.

(45) Cox, W. G., and Singer, V. L. (2004) Fluorescent DNA hybridization probe preparation using amine modification and reactive dye coupling. *Biotechniques 36*, 114–122.

(46) Lebedeva, N. S. (2004) Aggregation properties of water-soluble metal phthalocyanines: effect of ionic strength of solution. *Russ. Chem. Bull. 53*, 2674–2683.

(47) Li, X. Y., He, X., Ng, A. C. H., Wu, C., and Ng, D. K. P. (2000) Influence of surfactants on the aggregation behavior of water-soluble dendritic phthalocyanines. *Macromolecules 33*, 2119–2123.

(48) Howe, L., and Zhang, J. Z. (1997) Ultrafast studies of excited-state dynamics of phthalocyanine and zinc phthalocyanine tetrasulfonate in solution. *J. Phys. Chem. A 101*, 3207–3213.

(49) Dhami, S., Demello, A. J., Rumbles, G., Bishop, S. M., Phillips, D., and Beeby, A. (1995) Phthalocyanine Fluorescence at High-Concentration - Dimers or Reabsorption Effect. *Photochem. Photobiol. 61*, 341–346.

(50) Ferencz, A., Neher, D., Schulze, M., Wegner, G., Viaene, L., and Deschryver, F. C. (1995) Synthesis and Spectroscopic Properties of Phthalocyanine Dimers in Solution. *Chem. Phys. Lett. 245*, 23–29.

(51) Boguta, A., Wojcik, A., Ion, R. M., and Wrobel, D. (2004) Photothermal methods as tools for investigation of weakly interacting non-fluorescent phthalocyanines. *J. Photochem. Photobiol., A 163*, 201–207.

(52) Schutte, W. J., Sluytersrehbach, M., and Sluyters, J. H. (1993) Aggregation of an octasubstituted phthalocyanine in dodecane solution. *J. Phys. Chem. 97*, 6069–6073.

(53) Flanagan, J. H., Khan, S. H., Menchen, S., Soper, S. A., and Hammer, R. P. (1997) Functionalized tricarbocyanine dyes as near-infrared fluorescent probes for biomolecules. *Bioconjugate Chem. 8*, 751–756.

(54) Dork, T., Macek, M., Mekus, F., Tummler, B., Tzountzouris, J., Casals, T., Krebsova, A., Koudova, M., Sakmaryova, I., Macek, M., Vavrova, V., Zemkova, D., Ginter, E., Petrova, N. V., Ivaschenko, T., Baranov, V., Witt, M., Pogorzelski, A., Bal, J., Zekanowsky, C., Wagner, K., Stuhrmann, M., Bauer, I., Seydewitz, H. H., Neumann, T., Jakubiczka, S., Kraus, C., Thamm, B., Nechiporenko, M., Livshits, L., Mosse, N., Tsukerman, G., Kadasi, L., Ravnik-Glavac, M., Glavac, D., Komel, R., Vouk, K., Kucinskas, V., Krumina, A., Teder, M., Kocheva, S., Efremov, G. D., Onay, T., Kirdar, B., Malone, G., Schwarz, M., Zhou, Z. Q., Friedman, K. J., Carles, S., Claustres, M., Bozon, D., Verlingue, C., Ferec, C., Tzetis, M., Kanavakis, E., Cuppens, H., Bombieri, C., Pignatti, P. F., Sangiuolo, F., Jordanova, A., Kusic, J., Radojkovic, D., Sertic, J., Richter, D., Rukavina, A. S., Bjorck, E., Strandvik, B., Cardoso, H., Montgomery, M., Nakielna, B., Hughes, D., Estivill, X., Aznarez, I., Tullis, E., Tsui, L. C., and Zielenski, J. (2000) Characterization of a novel 21-kb deletion, CFTRdele2,3(21 kb), in the CFTR gene: a cystic fibrosis mutation of Slavic origin common in Central and East Europe. *Hum. Genet. 106*, 259–268.

(55) Michalet, X., Pinaud, F. F., Bentolila, L. A., Tsay, J. M., Doose, S., Li, J. J., Sundaresan, G., Wu, A. M., Gambhir, S. S., and Weiss, S. (2005) Quantum dots for live cells, in vivo imaging, and diagnostics. *Science 307*, 538–544.

BC700233W

Novel Polymerizable Surfactants with pH-Sensitive Amphiphilicity and Cell Membrane Disruption for Efficient siRNA Delivery

Xu-Li Wang, Sergej Ramusovic, Thanh Nguyen, and Zheng-Rong Lu*

Department of Pharmaceutics and Pharmaceutical Chemistry, University of Utah, Salt Lake City, Utah 84108. Received July 27, 2007; Revised Manuscript Received September 4, 2007

Small interfering RNA (siRNA) is a promising new therapeutic modality that can specifically silence disease-related genes. The main challenge for successful clinical development of therapeutic siRNA is the lack of efficient delivery systems. In this study, we have designed and synthesized a small library of novel multifunctional siRNA carriers, polymerizable surfactants with pH-sensitive amphiphilicity based on the hypothesis that pH-sensitive amphiphilicity and environmentally sensitive siRNA release can result in efficient siRNA delivery. The polymerizable surfactants comprise a protonatable amino head group, two cysteine residues, and two lipophilic tails. The surfactants demonstrated pH-sensitive amphiphilic hemolytic activity or cell membrane disruption with rat red blood cells. Most of the surfactants resulted in low hemolysis at pH 7.4 and high hemolysis at reduced pH (6.5 and 5.4). The pH-sensitive cell membrane disruption can facilitate endosomal–lysosomal escape of siRNA delivery systems at the endosomal–lysosomal pH. The surfactants formed compact nanoparticles (160–260 nm) with siRNA at N/P ratios of 8 and 10 via charge complexation with the amino head group, lipophilic condensation, and autoxidative polymerization of dithiols. The siRNA complexes with the surfactants demonstrated low cytotoxicity. The cellular siRNA delivery efficiency and RNAi activity of the surfactants correlated well with their pH-sensitive amphiphilic cell membrane disruption. The surfactants mediated 40–88% silencing of luciferase expression with 100 nM siRNA and 35–75% with 20 nM siRNA in U87-luc cells. Some of the surfactants resulted in similar or higher gene silencing efficiency than TransFast. EHCO with no hemolytic activity at pH 7.4 and 6.5 and high hemolytic activity at pH 5.4 resulted in the best siRNA delivery efficiency. The polymerizable surfactants with pH-sensitive amphiphilicity are promising for efficient siRNA delivery.

INTRODUCTION

RNA interference (RNAi) is a natural biological process involving gene silencing or regulation with small interfering RNA (siRNA) (*1, 2*). siRNA is a double-stranded RNA molecule (dsRNA) with approximately 20 to 25 nucleotides. The function of siRNA involves specific incorporation into the RNA-induced silencing complex (RISC) and guiding the RNAi machinery to destroy a target mRNA containing complementary sequences (*3*). It has been demonstrated that siRNA is effective to silence specific genes in mammalian cells and nonhuman primates. It is believed that siRNA can target every gene in the human genome and has unlimited potential to treat human disease with RNAi (*4–9*). However, the challenge for successful clinical applications of RNAi remains the *in vivo* delivery of therapeutic siRNAs into target cells with high efficiency.

Systemic *in vivo* siRNA delivery is a complicated process, which involves protecting siRNA from enzymatic degradation, preventing rapid elimination from the body, and facilitating specific tissue and cell uptake, endosomal–lysosomal escape, and siRNA release in cytoplasm. Although various systems have been reported for siRNA delivery, most of these delivery systems are developed based on the concept for the delivery of plasmid DNA, using cationic lipids (*10, 11*) or polymers (*12–14*). These cationic materials form stable nanoparticles with anionic siRNA via charge complexation and protect siRNA from degradation. These siRNA delivery systems are either toxic or inefficient for specific siRNA delivery (*15*). Innovative approaches are needed to design and develop safe and efficient siRNA delivery systems. New siRNA delivery systems should be safe and have a comprehensive multifunctionality to address the complexity of *in vivo* delivery of therapeutic siRNA.

One of the challenges for efficient siRNA delivery is the escape of siRNA delivery systems from the endosomal–lysosomal compartments and siRNA release in cytoplasm after the systems are internalized through endocytosis. We hypothesize that the incorporation of pH-sensitive amphiphilicity and environmentally sensitive siRNA release will result in efficient siRNA delivery systems that facilitate endosomal–lysosomal escape and cytoplasmic siRNA release. Numerous amphiphilic materials present in nature are able to disrupt cell membranes (*16–18*). The pH-sensitive amphiphilicity of an siRNA carrier will allow the carrier to change its amphiphilic structure at endosomal–lysosomal pH (5.0–6.0), resulting in disruption of endosomal–lysosomal membranes and escape of siRNA delivery systems. It has been shown that the incorporation of degradable disulfide bonds into cationic polymeric delivery systems promotes the release of nucleic acids in the reductive environment of cytosol (*19–21*). According to the hypothesis, we have designed polymerizable surfactants containing dithiol groups, protonatable amines with different pK_a's and lipophilic units as novel multifunctional carriers for siRNA delivery. The surfactants can readily form compact nanoparticles with siRNA via charge–charge complexation and hydrophobic interaction. The dithiol groups in the surfactants in the nanoparticles can be polymerized by forming disulfide bonds via autoxidation to further stabilize siRNA nanoparticles. The pH-sensitive amphiphilicity of the carriers can be tuned by modifying the structures of the protonatable amines and lipophilic groups to allow the nanoparticles escaping from endosomal–lysosomal compartments via amphiphilic membrane disruption. The disulfide bonds will be

* Correspondence to Dr. Zheng-Rong Lu, 421 Wakara Way, Suite 318, Salt Lake City, UT 84108. Phone: 801 587-9450. Fax: 801 585-3614. E-mail: zhengrong.lu@utah.edu.

10.1021/bc700285q CCC: $37.00 © 2007 American Chemical Society
Published on Web 10/17/2007

reduced in the cytoplasm to facilitate the dissociation of nanoparticles and the release of siRNA.

We report here the synthesis and evaluation of a small library of polymerizable surfactants with pH-sensitive amphiphilicity for efficient siRNA delivery. The surfactants were synthesized using combinatorial solid-phase chemistry. The pH-sensitive amphiphilic cell membrane disruption of the surfactants was investigated using hemolysis assay of rat red blood cells at different pH values. The cellular siRNA delivery efficiency of the novel surfactants was evaluated with an antiluciferase siRNA in U87-luc cells with constitutive firefly luciferase expression.

EXPERIMENTAL SECTION

Materials. 2-Chlorotrityl chloride resin, *N*-fluorenylmethoxycarbonyl-*N*-im-trityl-L-histidine, *N*-fluorenylmethoxycarbonyl-*S*-trityl-L-cysteine, 2-(1*H*-benzotriazole-1-yl)-1,1,3,3-tetramethyluronium tetrafluoroborate (TBTU), *N*-hydroxybenzotriazole (HOBt), and 2-acetyldimedone (Dde-OH) were purchased from EMD Biosciences (San Diego, CA). Ethylenediamine, pentaethylenehexamine, spermine, triethylenetetraamine, *N*,*N*-diisopropylethylamine (DIPEA), methyl acrylate, hydrazine, 4-dithiothreitol (DTT), piperidine, trifluoroacetic acid (TFA), hyperbranched PEI (Mw = 25 KDa), *N*-(2,3-dioleoyloxy-1-propyl)trimethylammonium methyl sulfate (DOTAP), bovine serum albumin (BSA), and 2,5-diphenyl-3-(4,5-dimethyl-2-thiazolyl)tetrazolium bromide (MTT) were purchased from Sigma-Aldrich (St. Louis, MO). Anhydrous dimethyl sulfoxide (DMSO), *N*,*N*-dimethylformamide (DMF) and dichloromethane (DCM) were purchased from Acros (Pittsburgh, PA). ISOLUTE column reservoirs (Charlottesville, VA) were used for the solid-phase synthesis. The amines were purified by distillation under reduced pressure before they were used for synthesis. All other materials and solvents were used without additional purification. 5,5′-Dithiobis-(2-nitrobenzoic acid) (DTNB) was purchased from Pierce Inc. (Rockford, IL). TransFast that is formulated with *N*,*N*-[bis-(2-hydroxyethyl)-*N*-methyl-*N*-[2,3-di(tetradecanoyloxy)propyl] ammonium iodide and dioleoyl phosphatidylethanolamine (DOPE) was purchased from Promega. siRNA targeting firefly luciferase was purchased from Dharmacon (Chicago, IL). The sequence of antisense is 5′-UCGAAGUACUCAGCGUAAGdTdT-3′ and that of sense is 3′-dTdTAGCUUCAUGAGUCGCAUUC-5′.

Synthesis of Polymerizable Surfactants. The polymerizable surfactants were synthesized by solid-phase chemistry. The synthetic procedure of (1-aminoethyl)imino-bis[*N*-(oleicyl-cysteinyl-histinyl-1-aminoethyl)propionamide] (EHCO) is described as the representative procedure for the synthesis of the library.

2-Chlorotrityl chloride resin (300 mg) was extensively washed with anhydrous DCM. A mixture of ethylenediamine (1.0 mL, excess) and DIPEA (64 mg) in DCM was added to the resin, and the suspension was shaken for 2 h. The solvent was drained, and the resin was washed with DCM and MeOH. The resin was further shaken with 10 mL DCM/MeOH/DIPEA (17/2/1, v/v/v) for 20 min. The resin was then mixed with methyl acrylate (50 mL, excess) in 10 mL DMF to introduce methyl carboxylate via Michael addition. The reaction was carried out in a rotary evaporator at 50 °C with continuous rotating. A solution of 1,2-ethylenediamine (50 mL, excess) in 10 mL DMF was then mixed with the resin methyl carboxylate. The mixture was rotated in a rotary evaporator at 50 °C for 5 days. The resin containing primary amines was transferred into an ISOLUTE column, mixed with a solution of activated N-α-Fmoc-N-im-trityl-L-histidine (2.0 g, excess) with TBTU/HOBt/DIPEA (excess) in DMF and shaken for 2 h. The resin was subjected to a washing cycle, and the Fmoc protecting group was removed with 20% piperidine in DMF (20 min × 3) to give a resin containing histidine residues. Cysteine residues were similarly incorporated by reacting the resin with N-α-Fmoc-S-trityl-L-cysteine (2.0 g, excess) and TBTU/HOBt/DIPEA (excess) in DMF, followed by removal of Fmoc protecting groups. Finally, oleicyl groups were incorporated by reacting the resin with oleic acid (2 g) in the presence of TBTU/HOBt/DIPEA in DMF for 2 h. The quality of each coupling reaction involving primary amino groups was monitored with the Kaiser test. The resin in each reaction cycle was extensively washed with DMF, MeOH, and DCM and dried under reduced pressure before proceeding to the next reaction. The final resin was then suspended in a solution of TFA/H_2O/EDT/TIBS (94/2.5/2.5/1) and shaken for 3 h at room temperature. The solution was collected and concentrated under reduced pressure. The residue was washed with cold diethyl ether (40 mL × 5) and dried. The final product EHCO was purified by preparative HPLC equipped with a ZORBAX PrepHT C-18 column using an Agilent 1100 series purification system. Product fractions were collected and lyophilized. The purity of the final product was verified by analytic HPLC. The structure of the compound was analyzed by ^{1}H NMR spectroscopy using a Varian Mercury 400 (Palo Alto, CA) and matrix-assisted laser desorption–ionization (MALDI) time-of-flight (TOF) mass spectrometry.

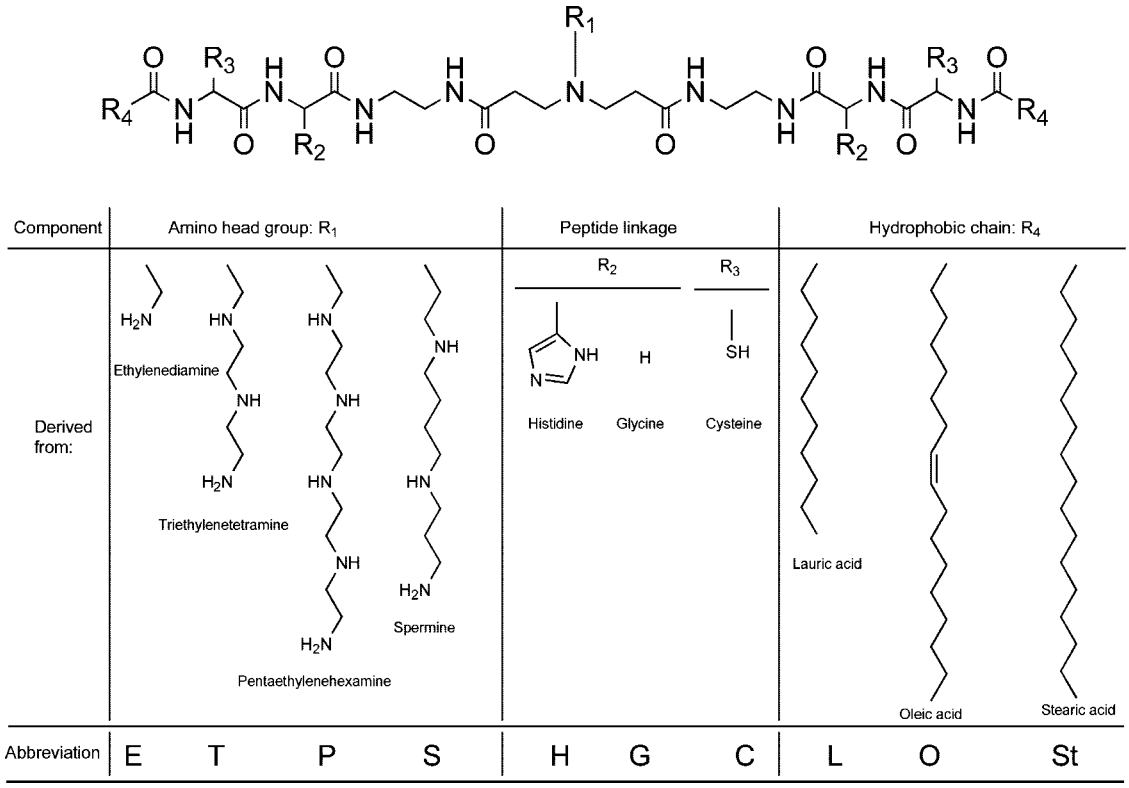
Hemolysis Assay. The surfactants (16.7 μM), DOTAP (16.7 μM), and Triton X-100 (1%, w/v) were dissolved in phosphate buffered saline (PBS) with pH adjusted to 7.4, 6.5, or 5.4 as stock solutions. Rat erythrocytes (RBC) were suspended in prechilled PBS at a concentration of 2 % (w/v) RBC at appropriate pH values and then seeded (100 μL) into a 96-well plate. The sample solutions (100 μL) were added to each well of the RBC suspensions and incubated for 1 h at 37 °C. The absorbance of the supernatant from each sample was measured at 550 nm using a microplate reader to determine the released hemoglobin. The relative hemolysis efficiency was calculated as the percentage of released hemoglobin by the surfactants or DOTAP to that by Triton X-100.

Formation and Size Measurement of Surfactant/siRNA Nanoparticles. Surfactant/siRNA nanoparticulate complexes were prepared by mixing siRNA solution with an equal volume of surfactant solutions at predetermined N/P ratios, followed by 30 min incubation. The size of the nanoparticles was analyzed using a Brookhaven Instruments BI-200SM system equipped with a 5 mW helium neon laser with a wavelength output of 633 nm. The effective diameter and population distribution were computed from the diffusion coefficient. Measurements were made at 25 °C at an angle of 90°, and each sample was analyzed in triplicate.

Autoxidation of the Polymerizable Surfactants. The polymerizable surfactants were diluted from stock solutions (N_2-protected, 2 mg/mL) to an initial thiol concentration of 150 μM in Tris buffer (10 mM pH 8.0). The autoxidation of the dithiols in the surfactants was performed with the working solutions (400 μL) in the absence or presence of 10 μg siRNA (N/P = 10). For each predetermined time point, an aliquot was taken and mixed with an equal volume of Ellman's solution (2 mM DTNB in 50 mM NaOAc solution), and the free thiol concentration was determined by Ellman assay using UV–vis spectrophotometry (Cary-300 Bio).

Polymerizable Surfactant Mediated *in Vitro* Gene Silence with siRNA. U87-luc cells with constitutive expression of firefly luciferase were maintained in minimal essential medium (ATCC) containing 10% FBS, G418 (300 μg/mL), streptomycin (100 μg/mL), and penicillin (100 units/mL). U87-Luc cells were seeded 24 h prior to transfection into a 96-well plate at a density of 5000 cells/well. At the time of siRNA transfection, the medium in each well was replaced with fresh serum-free medium. Antiluciferase siRNA was complexed with the polymerizable surfactants, TransFast, or DOTAP and in-

Scheme 1. General Structure of Polymerizable Surfactants



cubated for 30 min before use. Complexes were incubated with the cells for 4 h at 37 °C. The medium was then replaced with 100 μL of fresh complete medium, and cells were incubated for an additional 44 h. The cells were then washed with prewarmed PBS, treated with 200 μL cell lysis buffer, and subjected to a freeze–thaw cycle. Cellular debris was removed by centrifugation at 14 000 g for 5 min. The luciferase activity in the cell lysate (20 μL) was measured using a luciferase assay kit (100 μL luciferase assay buffer) on a luminometer for 10 s (Lumat 9605, EG&G Wallac). The gene silencing efficiency was normalized against the luciferase expression of untreated cells.

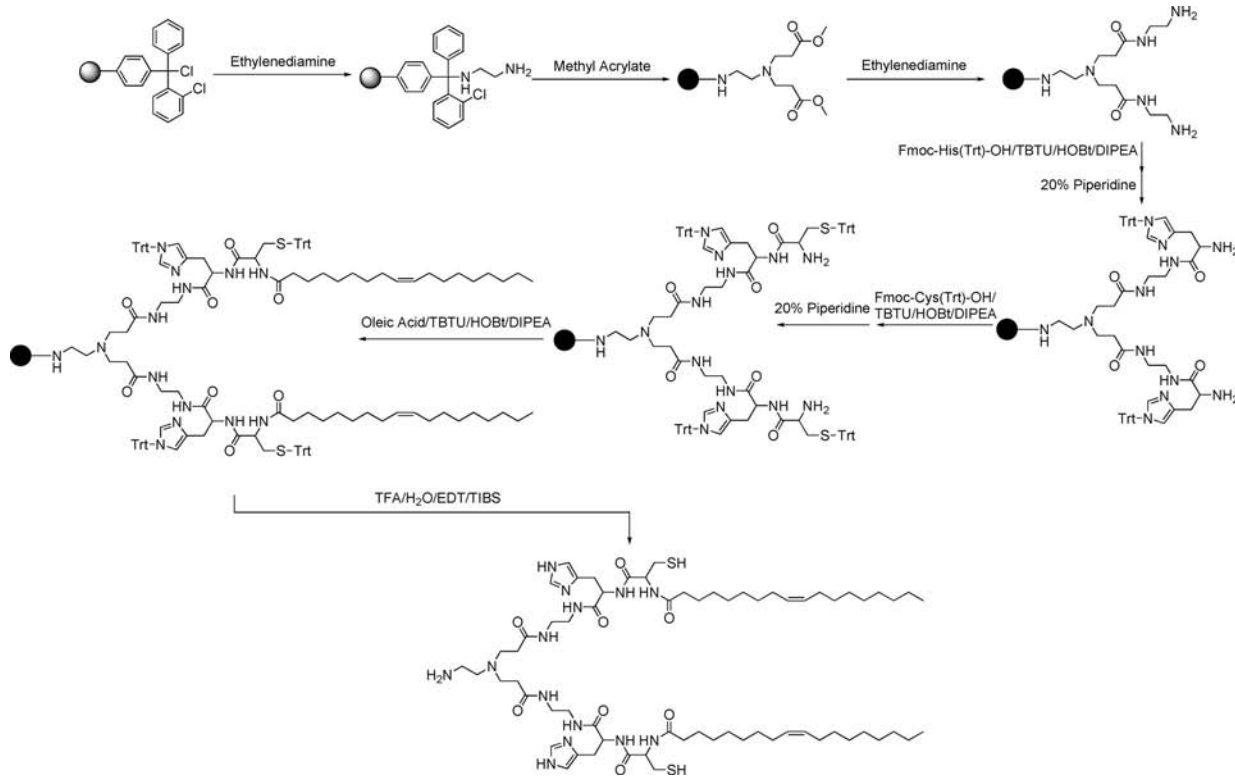
Cytotoxicity of Surfactant/siRNA Complexes. U87-luc cells were incubated with siRNA complexes of different carriers according to the protocol described above. MTT in PBS (5 mg/mL, 25 μL) was added to each well after incubation, and cells were incubated for another 2 h. After cell culture medium was removed, 200 μL DMSO was added to each well, and cells were incubated at 37 °C for 5 min. The optical absorption was measured at 570 nm using a microplate reader (model 550, Bio-Rad Laboratory. Hercules, CA). The relative cell viability was calculated with the equation $([Abs]_{sample} - [Abs]_{blank})/([Abs]_{control} - [Abs]_{blank}) \times 100\%$.

RESULTS AND DISCUSSION

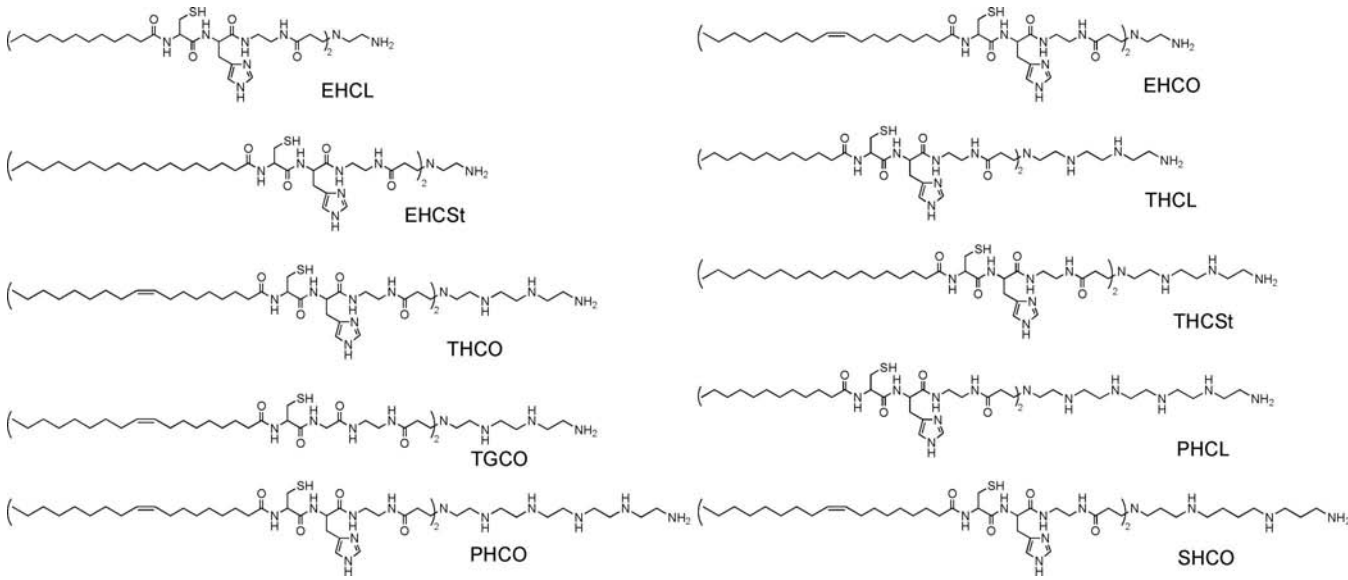
Design and Synthesis of Polymerizable and pH-Sensitive Amphiphilic Surfactants. The polymerizable surfactants with pH-sensitive amphiphilicity are designed based on the hypothesis that pH-sensitive amphiphilicity can facilitate the escape of siRNA delivery systems from endosomal–lysosomal compartments and environmentally sensitive disulfide cross-linking can stabilize the siRNA delivery system in the plasma and facilitate the release of siRNA in cytoplasm for efficient siRNA delivery and effective RNAi. The general structure of the designed polymerizable surfactants is shown in Scheme 1. Each surfactant is composed of three key components in its structure, including a protonatable amino head group, dual cysteine residues, and lipophilic tails. The protonatable amino head group comprises primary, secondary, tertiary, and aromatic amino groups of various pK_a's, which is designed to complex with siRNA and alter the pH-sensitive amphiphilicity of the surfactants. Lipophilic tails are designed to introduce lipophilicity in the surfactants and to condense the nanoparticulate siRNA complexes though hydrophobic interactions. Cysteine residues are designed to further stabilize nanoparticles through polymerization of the surfactants by forming disulfide bonds via autoxidation of thiols. The disulfide bonds are relatively stable in the plasma during the delivery process and can be reduced in the reductive cytosolic environment to facilitate siRNA release. The pH-sensitive amphiphilicity of the surfactants can be tuned by varying the composition of amino groups of different pK_a's and structures of the lipophilic groups.

Different polyamines, including ethylenediamine, triethylenetetraamine, pentaethylenehexamine, and spermine, and histidine have been chosen to build the protonatable head groups. Fatty acids of different chain lengths and structures, including lauric acid, stearic acid, and unsaturated oleic acid, have been used as the hydrophobic units. The small library of surfactants with different combinations of protonatable head groups and lipophilic tails were synthesized using resin-supported solid-phase chemistry. Scheme 2 shows the synthetic procedure of EHCO. The structures of the polymerizable surfactants and their abbreviated names, according to their head group, peptide linkage, and tail chains (Scheme 1), are shown in Scheme 3. For triethylenetetraamine, pentaethylenehexamine, and spermine, their primary and secondary amines were selectively protected by 2-acetyldimedone (Dde-OH) and *tert*-butyloxycarbonyl (Boc) groups, respectively, as described in our previous publication . The polymerizable surfactants with high purity were obtained after purification with preparative HPLC and characterized by ^{1}H NMR and mass spectrometry. The ^{1}H NMR spectrum of EHCO is shown in Figure 1 as a representative example. The

Scheme 2. Synthetic Procedure of EHCO



Scheme 3. Chemical Structures and Abbreviated Names of Different Polymerizable Surfactants with pH-Sensitive Amphiphilicity



calculated mass and measured mass of the polymerizable surfactants are summarized in Table 1. No evidence of oligomers or cyclic byproducts was observed in the mass spectra of the compounds. Over 98% of thiol groups remained in a reduced state as determined by Ellman's assay. TGCO with glycine replacing histidine was prepared to study the impact of imidazole groups on the pH-sensitive amphiphilicity and cell membrane disruption of the surfactants.

pH-Sensitive Hemolysis. Amphiphilic cell membrane disruption is a common phenomenon in nature. Numerous amphiphilic materials have been found to have a fusogenic property of mediating material transport across cell membranes (*22–24*). Amphiphilic peptide sequences are used by viruses, the highly efficient gene delivery systems, in their membrane surface protein to facilitate cell entry or endosomal–lysosomal escape (*25–27*). Several amphiphilic lipids, e.g., DOPE, have been used to enhance the fusion of nucleic acid lipoplexes with cellular membrane for gene delivery (*28, 29*). However, these lipids may not have the ability of selective amphiphilic membrane disruption at the endosomal–lysosomal pH. It is critical for siRNA delivery if siRNA delivery systems have low amphiphilicity at the physiological pH and high amphiphilicity at the endosomal–lysosomal pH, which will only cause selective endosomal–lysosomal membrane disruption. The polymerizable surfactants may not have strong amphiphilicity before the amino head groups are completely protonated at neutral pH. The amphiphilicity of the surfactants may increase with increasing protonation degrees of the head groups at reduced pH.

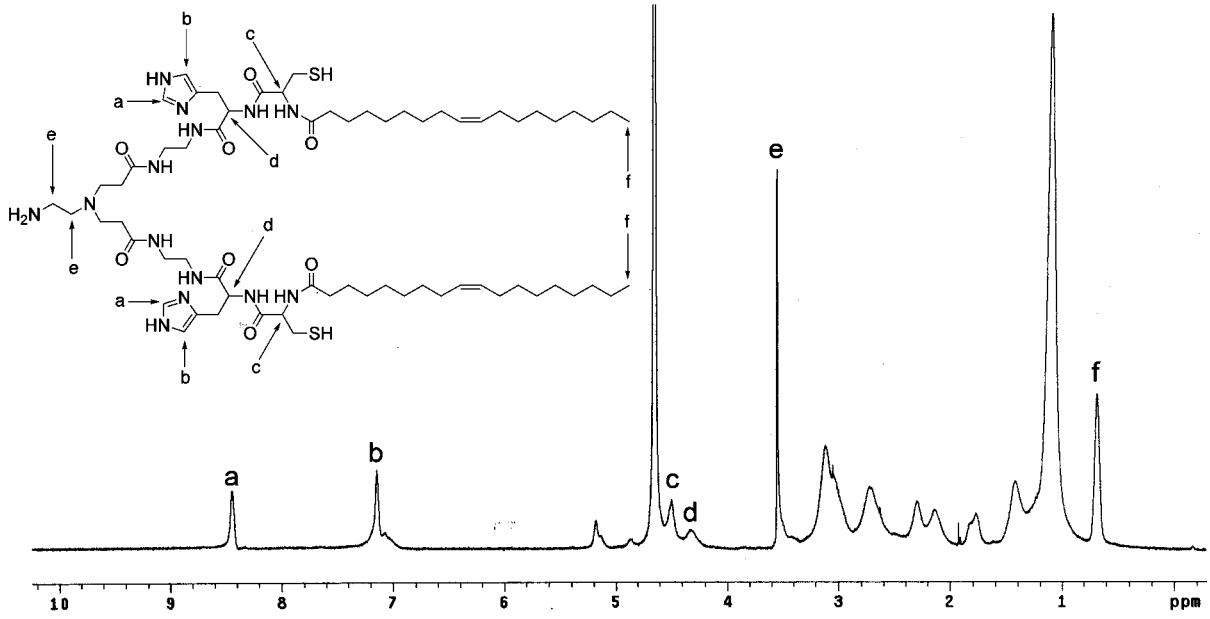


Figure 1. ^{1}H NMR Spectra of EHCO.

Table 1. Measured Mass of the Polymerizable Surfactants by Mass Spectroscopy

entry	MFC abbr	formula	Mw (calcd) *m/e*	Mw (found) $[M + 1]^+$
1	EHCL	$C_{54}H_{96}N_{14}O_8S_2$	1132.70	1133.65
2	EHCO	$C_{66}H_{116}N_{14}O_8S_2$	1296.85	1297.90
3	EHCSt	$C_{66}H_{120}N_{14}O_8S_2$	1300.89	1301.87
4	THCL	$C_{58}H_{106}N_{16}O_8S_2$	1218.78	1219.79
5	THCO	$C_{70}H_{126}N_{16}O_8S_2$	1382.94	1383.94
6	THCSt	$C_{70}H_{130}N_{16}O_8S_2$	1386.97	1387.97
7	TGCO	$C_{62}H_{118}N_{12}O_8S_2$	1222.86	1223.86
8	PHCL	$C_{62}H_{116}N_{18}O_8S_2$	1304.87	1305.87
9	PHCO	$C_{74}H_{136}N_{18}O_8S_2$	1469.02	1470.94
10	SHCO	$C_{74}H_{134}N_{16}O_8S_2$	1439.00	1439.97

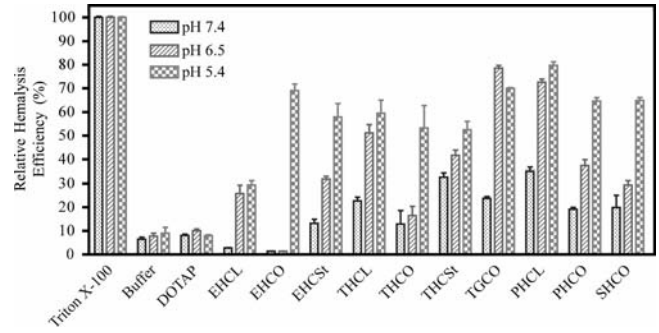


Figure 2. Hemolytic activity of polymerizable surfactants (8.3 μM) and DOTAP (8.3 μM) at pHs of 7.4, 6.5, and 5.4, respectively. Triton X-100 (1%, w/v) and PBS were used as controls.

The pH-sensitive amphiphilic cell membrane disruption of the polymerizable surfactants was evaluated by hemolysis assay with rat red blood cells at different pHs. Figure 2 shows the hemolytic activity of the compounds at pHs 7.4, 6.5, and 5.4 in PBS buffer. The positive control Triton X-100 (1%, w/v) resulted in complete hemolysis. Little hemolysis was shown with the buffer and DOTAP in all cases. The polymerizable surfactants showed various pH-dependent hemolytic activities. Generally, all surfactants had lower hemolytic activity at pH 7.4 than at pHs 6.5 and 5.4. At pH 7.4, EHCL and EHCO resulted in negligible hemolysis, while the rest of the surfactants showed moderate hemolytic activities with 10–35% hemolysis. At pH 6.5, hemolytic activity of the surfactants increased except for EHCO, which still showed negligible hemolysis. At pH 5.4, all surfactants exhibited high hemolysis, and the surfactants except EHCL resulted in 50–80% hemolysis.

The pH-sensitive hemolysis of the surfactants is clearly governed by their structural characteristics. For the surfactants containing histidine residues and the same lipophilic tails, the hemolytic activity increased with increasing number of protonatable amino groups in the head group at pHs 7.4 and 6.5. More protonatable amino groups could result in more charges in the head groups and higher amphiphilicity for the surfactants at neutral pH. For the EHC and THC series, the unsaturated oleicyl group resulted in less hemolysis than the saturated lipophilic tails in the same series at pHs 7.4 and 6.5 except for EHTL at pH 7.4. The comparison between THCO and TGCO suggests that the histidine residues are critical for pH-sensitive amphiphilicity of the surfactants. Overall, the pH-sensitive hemolysis, disruption of membrane of red blood cells, is caused by the pH-sensitive amphiphilicity of the surfactants derived from the combination of protonatable amino head groups and lipophilic tails. When more amino groups are protonated, the surfactants become more amphiphilic and result in more significant hemolysis. The protonation and pH-sensitive amphiphilicity may be governed by the overall pK_a of the head groups of the surfactants. As we have shown here, they can be tuned by using amino groups with different pK_a's.

The pH-sensitive amphiphilicity of the surfactants is critical for efficient cellular siRNA delivery. It is known that pH in the late endosomal compartment is in the range 5.0–6.0 and pH in the lysosomal compartment is 5.0–5.5. Therefore, the pH-responsive amphiphilicity and membrane disruption of the polymerizable surfactants is an ideal feature to trigger endosomal–lysosomal membrane destabilization. Low amphiphilicity of the surfactants at physiological pH will minimize nonspecific cell membrane disruption and nonspecific tissue uptake of siRNA delivery systems. To this end, EHCO with no hemolytic activity at pHs 7.4 and 6.5 and high membrane disruption activity at pH 5.4 could be a suitable carrier for siRNA delivery.

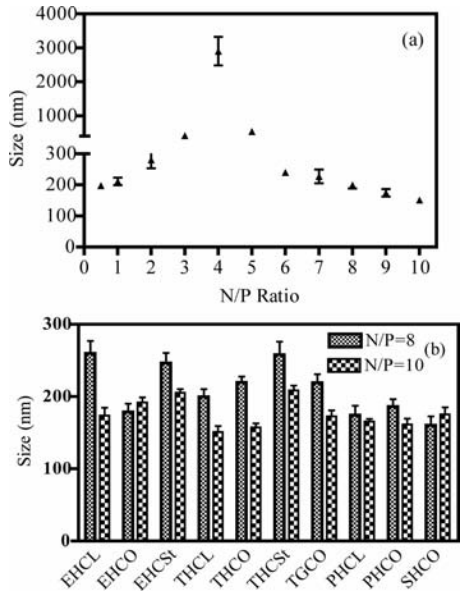


Figure 3. Particle size of the siRNA complexes with the polymerizable surfactants: (a) size of EHCO/siRNA complexes at different N/P ratios; (b) sizes of siRNA complexes with the polymerizable surfactants at N/P ratios of 8 and 10.

Formation of Nanoparticles of the Polymerizable Surfactants with siRNA. The complexation of the polymerizable surfactants with siRNA and formation of nanoparticles of the complexes were investigated by dynamic light scattering. EHCO was first used to study the complexation with siRNA and the impact of N/P ratios on the complexation and formation of nanoparticles. No nanoparticulate formation was detected in either EHCO or siRNA solutions. When EHCO was mixed with siRNA and incubated for 30 min, the formation of nanoparticulate complexes was observed with an N/P ratio as low as 0.5. The particle size changed with N/P ratios of the complexes (Figure 3a). The initial size was approximately 200 nm in diameter at an N/P ratio of 0.5, and the size then increased with increasing N/P ratio up to an N/P ratio of 4. The particle size was as large as about 3 μm at the N/P ratio of 4, possibly due to aggregation of relatively neutral complex particles. The particle size decreased to approximately 240, 200, and 151 nm at the N/P ratios of 6, 8, and 10, respectively. The particle size of siRNA complexes with other polymerizable surfactants was measured at the N/P ratios of 8 and 10 based on the observation with EHCO. As shown in Figure 3b, the average particle sizes of the complexes were in the ranges of 160–260 nm at N/P ratio of 8 and 160–210 nm at N/P ratio of 10. The sizes of most complexes were under the reported cutoff size of 250 nm for efficient cellular uptake (*30*).

The polymerizable surfactants formed relatively compact and small nanoparticles as compared to other reported siRNA delivery systems (*21*). It is speculated that complexes were formed by charge interaction between the carriers and siRNA. Hydrophobic interaction of lipophilic tails and polymerization of dithiols facilitated the formation of stable compact nanoparticles. The polymerization of the surfactants via oxidation was confirmed by the disappearance of thiols after they were mixed with siRNA, as determined by Ellman's assay (Figure 4). The autoxidation rate of thiols was faster in the presence of siRNA than that in the absence of siRNA, possibly because the complexation with siRNA facilitated autoxidation. These disulfide linkages could further stabilize the nanopaticulate complexes. Due to the significant difference of thiol/disulfide redox potential between the extracellular space and the intracellular environment, the disulfide bonds would be stable in the extracellular space during the delivery process and then reduced in cytosol, facilitating the disassociation of nanoparticles and the release of siRNA. A number of recent reports have shown that incorporation of disulfide cross-linking in the siRNA/cationic polymers can stabilize the siRNA nanoparticles and facilitate siRNA release into the reductive cytoplasm, resulting in high transfection efficiency (*19–21*).

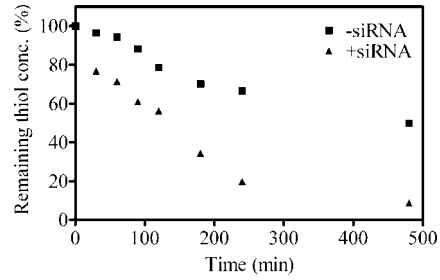


Figure 4. Autoxidation profile of EHCO in the absence or presence of siRNA based on thiol concentration measured by Ellman's assay.

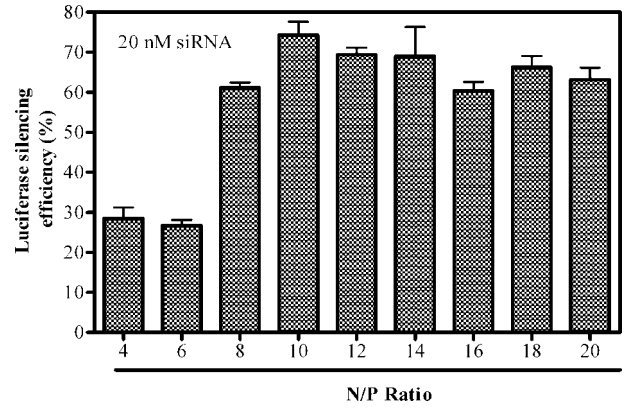


Figure 5. EHCO-mediated luciferase gene silencing efficiency in U87-luc cells at different N/P ratios.

Cellular siRNA Delivery. The efficacy of the polymerizable surfactants for cellular siRNA delivery was evaluated using an antiluciferase siRNA in U87-luc cell line with stable expression of firefly luciferase. Commercial transfection agents TransFast and DOTAP were used as controls. The silencing efficiency of luciferase expression mediated by the surfactants was first evaluated with EHCO at different N/P ratios to obtain the best N/P ratios for effective siRNA delivery. High luciferase expression knockdown efficiency was observed with N/P ratios ranging from 8 to 20 for EHCO (Figure 5). The peak silencing efficiency was observed at the N/P ratio of 10 for the surfactants. The silencing efficiency of luciferase expression mediated by the polymerizable surfactants was evaluated at the fixed N/P ratio of 10. Viability of cells incubated with the siRNA complexes was also investigated at the same time by MTT assay to assess the cytotoxicity of the surfactants. As shown in Figure 6a, TransFast resulted in an 89.6 $\pm$ 5.6% knockdown of luciferase expression as compared to untreated cells with 100 nM siRNA, but significant cellular cytotoxicity was observed with a cell viability of only 57.6 $\pm$ 2.2%. The relatively high gene silencing efficiency of TransFast with 100 nM siRNA could also be the result of low cell viability. DOTAP/siRNA complexes at the same siRNA concentration had higher viability (85.8 $\pm$ 1.6%), but resulted in significantly lower luciferase knockdown efficiency (56.7 $\pm$ 3.1%). The cells incubated with the siRNA complexes of the polymerizable surfactants had a relatively high viability ranging from 78.6 $\pm$ 5.7% to 88.2 $\pm$ 1.3%. The luciferase expression knockdown efficiencies varied from 47.8 $\pm$ 4.2% to 88.4 $\pm$ 3.1%. EHCO resulted in the highest

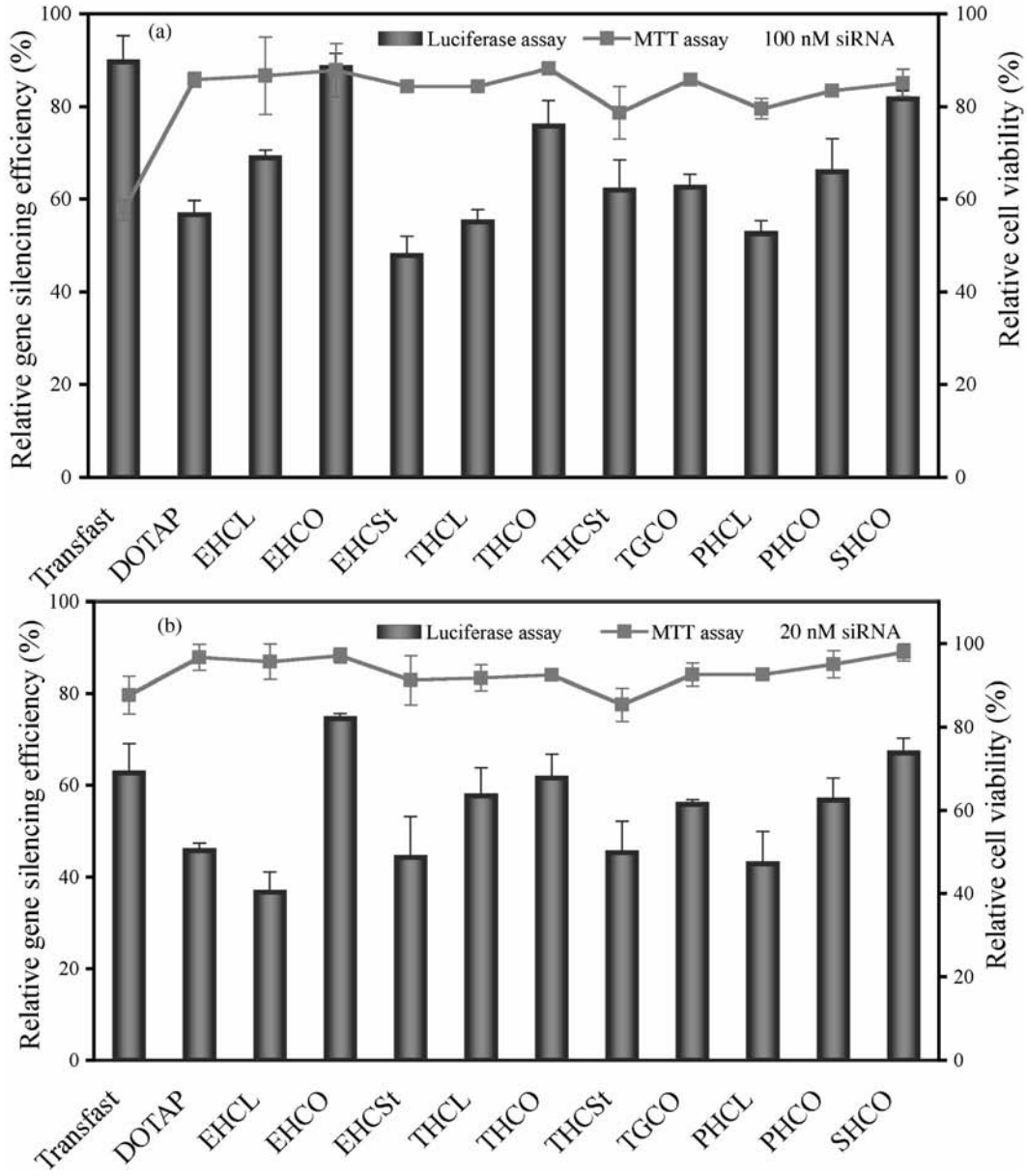


Figure 6. The polymerizable surfactants mediated luciferase gene silencing efficiency and the viability of cells incubated with MFC/siRNA complexes in U87-Luc cells. Transfast and DOTAP were used as controls. Transfection experiments were performed at siRNA concentration of 100 nM (a) or 20 nM (b).

gene silencing efficiency (88.4 ± 3.1%) with high cell viability (86.7 ± 8.3%) among the polymerizable surfactants.

All of the siRNA complexes demonstrated low cytotoxicity at a low siRNA concentration (20 nM), (Figure 6b). Cell viability was high in all cases including Transfast (87.6 ± 4.6%). Under this condition, the polymerizable surfactants except EHCL resulted in higher luciferase silencing efficiency than DOTAP. THCL, THCO, TGCO, PHCO, and SHCO resulted in comparable transfection efficiency to that of TransFast (62.6 ± 6.4%). EHCO (74.5 ± 1.0%) resulted in significantly higher transfection efficiency than TransFast. The cellular siRNA delivery efficiency correlated well to the pH-sensitive hemolytic activity and amphiphilicity of the polymerizable surfactants. EHCO exhibited the highest gene silencing efficiency at both siRNA concentrations. THCO and SHCO with relatively low hemolysis at pHs 7.4 and 6.5 also showed relatively high gene silencing efficiency among the surfactants.

Although the polymerizable surfactants have similar gemini lipid tails to other commercial lipid transfection agents, e.g., DOTAP, no helper molecule like DOPE or cholesterol is needed to achieve high siRNA delivery efficiency. This is an advantageous feature for the polymerizable surfactants as ready-to-use carriers compared to the commercially available liposome or lipid-based transfection agents. To the best of our knowledge, this is the first example of lipid-containing siRNA carriers achieving high siRNA delivery efficiency without a helper lipid. However, helper molecules are required for commercially available lipid-based siRNA carriers, including TransIT-siQUEST and X-tremeGENE, to enhance delivery efficiency (*15*). Some of helper molecules may introduce cytotoxicity in formulations. It is reported that DOTAP was nontoxic as a siRNA carrier, but the formulation of DOTAP with DOPE resulted in significant toxicity (*31*).

It is speculated that the polymerizable surfactants form compact nanoparticles with siRNA through charge–charge complexation, lipophilic condensation, and oxidative polymerization. The lipophilic chains may facilitate lipophilic condensation rather than forming lipid bilayers, because they are further

apart in the polymerizable surfactants as compared to the gemini lipophilic chains in commercial lipids. The cellular siRNA delivery efficiency clearly correlates to pH-sensitive amphiphilicity and pH-sensitive cell membrane disruption of the surfactants. EHCO with no hemolytic activity at pHs 7.4 and 6.5 and high hemolytic activity at the endosomal–lysosomal pH (5.4) has shown the highest cellular siRNA delivery efficiency among the tested polymerizable surfactants. The polymerizable surfactants may have another advantage in that the surface of their siRNA nanoparticles can be readily modified by reacting the unreacted thiols at the surface for various purposes, including pegylation and incorporation of targeting agents. Further study is ongoing to expand the library of the polymerizable surfactants, to develop targeted siRNA delivery systems with the surfactants and to study the factors, including formation of disulfide bonds and polymerization degree of the surfactants, on siRNA delivery efficiency and the mechanism of cellular uptake and intracellular siRNA release with the novel carriers.

CONCLUSION

We have designed and synthesized a small library of novel polymerizable surfactants as multifunctional siRNA carriers based on the hypothesis that pH-sensitive amphiphilicity and environmentally sensitive siRNA release of siRNA delivery systems will result in efficient siRNA delivery and effective RNAi. The polymerizable surfactants showed pH-sensitive amphiphilic hemolysis or cell membrane disruption of rat red blood cells. They formed compact nanoparticles with siRNA. The siRNA delivery and gene silencing efficiency of the surfactants correlated well to their pH-sensitive amphiphilicity. EHCO with low hemolytic activity at the physiological pH and high hemolytic activity at pH 5.4 showed the best gene silencing efficiency in U87-luc cells. The polymerizable surfactants with pH-sensitive amphiphilicity are promising multifunctional carriers for siRNA delivery.

ACKNOWLEDGMENT

We thank Mr. Shawn Owen for his technical support in the synthesis of some of the compounds and Dr. Randy Jensen for providing the U87-luc cells.

LITERATURE CITED

(1) Fire, A., Xu, S. Q., Montgomery, M. K., Kostas, S. A., Driver, S. E., and Mello, C. C. (1998) Potent and specific genetic interference by double-stranded RNA in Caenorhabditis elegans. *Nature 391*, 806–811.

(2) Hannon, G. J. (2002) RNA interference. *Nature 418*, 244–251.

(3) Sontheimer, E. J. (2005) Assembly and function of RNA silencing complexes. *Nat. Rev. Mol. Cell Biol. 6*, 127–138.

(4) Caplen, N. J., and Mousses, S. (2003) Short interfering RNA (siRNA)-mediated RNA interference (RNAi) in human cells. *Therapeut. Oligonucleotides 1002*, 56–62.

(5) Filleur, S., Courtin, A., Ait-Si-Ali, S., Guglielmi, J., Merle, C., Harel-Bellan, A., Clezardin, P., and Cabon, F. (2003) SiRNA-mediated inhibition of vascular endothelial growth factor severely limits tumor resistance to Antiangiogenic thrombospondin-1 and slows tumor vascularization and growth. *Cancer Res. 63*, 3919–3922.

(6) Kim, B., Tang, Q. Q., Biswas, P. S., Xu, J., Schiffelers, R. M., Xie, F. Y., Ansari, A. M., Scaria, P. V., Woodle, M. C., Lu, P., and Rouse, B. T. (2004) Inhibition of ocular angiogenesis by siRNA targeting vascular endothelial growth factor pathway genes - Therapeutic strategy for herpetic stromal keratitis. *Am. J. Pathol. 165*, 2177–2185.

(7) Ralph, G. S., Mazarakis, N. D., and Azzouz, M. (2005) Therapeutic gene silencing in neurological disorders, using interfering RNA. *J. Mol. Med. 83*, 413–419.

(8) Zhang, W. D., Yang, H., Kong, X. Y., Mohapatra, S., San Juan-Vergara, H., Hellermann, G., Behera, S., Singam, R., Lockey, R. F., and Mohapatra, S. S. (2005) Inhibition of respiratory syncytial virus infection with intranasal siRNA nanoparticles targeting the viral NS1 gene. *Nat. Med. 11*, 56–62.

(9) Zimmermann, T. S., Lee, A. C. H., Akinc, A., Bramlage, B., Bumcrot, D., Fedoruk, M. N., Harborth, J., Heyes, J. A., Jeffs, L. B., John, M., Judge, A. D., Lam, K., McClintock, K., Nechev, L. V., Palmer, L. R., Racie, T., Rohl, I., Seiffert, S., Shanmugam, S., Sood, V., Soutschek, J., Toudjarska, I., Wheat, A. J., Yaworski, E., Zedalis, W., Koteliansky, V., Manoharan, M., Vornlocher, H. P., and MacLachlan, I. (2006) RNAi-mediated gene silencing in non-human primates. *Nature 441*, 111–114.

(10) Li, W. J., and Szoka, F. C. (2007) Lipid-based nanoparticles for nucleic acid delivery. *Pharm. Res. 24*, 438–449.

(11) Li, S. D., and Huang, L. (2006) Targeted delivery of antisense oligodeoxynucleotide and small interference RNA into lung cancer cells. *Mol. Pharm. 3*, 579–88.

(12) Segura, T., and Hubbell, J. A. (2007) Synthesis and in vitro characterization of an ABC triblock copolymer for siRNA delivery. *Bioconjugate Chem. 18*, 736–745.

(13) Grayson, A. C. R., Doody, A. M., and Putnam, D. (2006) Biophysical and structural characterization of polyethylenimine-mediated siRNA delivery in vitro. *Pharm. Res. 23*, 1868–1876.

(14) Mao, S. R., Neu, M., Germershaus, O., Merkel, O., Sitterberg, J., Bakowsky, U., and Kissel, T. (2006) Influence of polyethylene glycol chain length on the physicochemical and biological properties of poly(ethylene imine)-graft-poly(ethylene glycol) block copolymer/SiRNA polyplexes. *Bioconjugate Chem. 17*, 1209–1218.

(15) Grayson, A. C., Ma, J., and Putnam, D. (2006) Kinetic and efficacy analysis of RNA interference in stably and transiently expressing cell lines. *Mol. Pharm. 3*, 601–13.

(16) Legendre, J. Y., and Szoka, F. C., Jr. (1993) Cyclic amphipathic peptide-DNA complexes mediate high-efficiency transfection of adherent mammalian cells. *Proc. Natl. Acad. Sci. U.S.A. 90*, 893–7.

(17) Vergne, I., and Cezanne, L. (1999) Alteration of the lateral organization of the plasma membrane of Chinese hamster ovary cells by synthetic lipopeptide, Pam(3)Cys-Ser-Lys(4). *Eur. J. Biochem. 264*, 369–373.

(18) Kamper, N., Day, P. M., Nowak, T., Selinka, H. C., Florin, L., Bolscher, J., Hilbig, L., Schiller, J. T., and Sapp, M. (2006) A membrane-destabilizing peptide in capsid protein L2 is required for egress of papillomavirus genomes from endosomes. *J. Virol. 80*, 759–768.

(19) Manickam, D. S., and Oupicky, D. (2006) Multiblock reducible copolypeptides containing histidine-rich and nuclear localization sequences for gene delivery. *Bioconjugate Chem. 17*, 1395–1403.

(20) Lin, C., Zhong, Z. Y., Lok, M. C., Jiang, X. L., Hennink, W. E., Jan, F. J., and Engbersen, J. F. J. (2006) Linear poly(amido amine)s with secondary and tertiary amino groups and variable amounts of disulfide linkages: Synthesis and in vitro gene transfer properties. *J. Controlled Release 116*, 130–137.

(21) Wang, X. L., Jensen, R., and Lu, Z. R. (2007) A novel environment-sensitive biodegradable polydisulfide with protonatable pendants for nucleic acid delivery. *J. Controlled Release 120*, 250–8.

(22) Bonev, B., Gilbert, R., and Watts, A. (2000) Structural investigations of pneumolysin/lipid complexes. *Mol. Membr. Biol. 17*, 229–235.

(23) Chattopadhyay, K., Bhattacharyya, D., and Banerjee, K. K. (2002) Vibrio cholerae hemolysin - Implication of amphiphilicity and lipid-induced conformational change for its pore-forming activity. *Eur. J. Biochem. 269*, 4351–4358.

(24) Geisler, I., and Chmielewski, J. (2007) Probing length effects and mechanism of cell penetrating agents mounted on a polyproline helix scaffold. *Bioorg. Med. Chem. Lett. 17*, 2765–2768.

(25) Eisenberg, D., and Wesson, M. (1990) The most highly amphiphilic alpha-helices include two amino acid segments in human immunodeficiency virus glycoprotein 41. *Biopolymers 29*, 171–7.

(26) Janshoff, A., Bong, D. T., Steinem, C., Johnson, J. E., and Ghadiri, M. R. (1999) An animal virus-derived peptide switches membrane morphology: Possible relevance to nodaviral transfection processes. *Biochemistry 38*, 5328–5336.

(27) von Messling, V., and Cattaneo, R. (2002) Amino-terminal precursor sequence modulates canine distemper virus fusion protein function. *J. Virol. 76*, 4172–4180.

(28) Wasungu, L., and Hoekstra, D. (2006) Cationic lipids, lipoplexes and intracellular delivery of genes. *J. Controlled Release 116*, 255–264.

(29) Koynova, R., Wang, L., Tarahovsky, Y., and MacDonald, R. C. (2005) Lipid phase control of DNA delivery. *Bioconjugate Chem. 16*, 1335–1339.

(30) Wood, K. C., Little, S. R., Langer, R., and Hammond, P. T. (2005) A family of hierarchically self-assembling linear-dendritic hybrid polymers for highly efficient targeted gene delivery. *Angew. Chem., Int. Ed. 44*, 6704–6708.

(31) Bouxsein, N. F., McAllister, C. S., Ewert, K. K., Samuel, C. E., and and Safinya, C. R. (2007) Structure and gene silencing activities of monovalent and pentavalent cationic lipid vectors complexed with siRNA. *Biochemistry 46*, 4785–4792.

BC700285Q

TECHNICAL NOTES

Synthesis and Properties of Phosphonic Acid Containing Cyanine and Squaraine Dyes for Use as Fluorescent Labels

Mark V. Reddington[†]

Biosearch Technologies, Inc., 81 Digital Drive, Novato, California 94949. Received March 14, 2007; Revised Manuscript Received August 24, 2007

Cyanine and squaraine dyes that contain one or two phosphonate groups attached directly to the aromatic residues of the dyes were synthesized. Absorption and fluorescence properties of the dyes were determined. Succinimidyl active esters were prepared from the dyes and were used to label proteins and oligonucleotides. Some of the dyes permit the preparation of brighter conjugates than do commercially available analogues such as Cy3 and Cy5.

INTRODUCTION

Fluorescent reporters are widely used as labels in biology and medicine (*1*, *2*). As researchers seek to interrogate smaller sample volumes and fewer molecules of analyte, the requirements for the reporter become more demanding. In the case of fluorescent dyes, certain properties have been found to be advantageous. These include (1) high extinction coefficients, (2) high fluorescence quantum yields, (3) low nonspecific binding, (4) high photostability, and (5) ease of chemical modification to permit the ready incorporation of different reactive functionalities and the tuning of absorption and emission wavelengths. For many applications, good water solubility and resistance to the formation of dimers and higher aggregates are essential to prevent adverse effects upon substrate solubility and to prevent quenching of fluorescence through dye–dye ground-state interactions (*1*–*5*). Generally, these latter properties are achieved by attaching charged or neutral water-solubilizing residues to the dye. Subtle differences in the position, the hydrophilicity, and the charge of the water-solubilizing group often result in vastly different performance of a dye as a label (*1*). The sulfonate group is one of the most commonly used water solubilizing groups for commercial fluorescent labels (e.g., Alexa and Cy dyes) in applications where high labeling densities are required because electronic repulsion of the negatively charged dyes inhibits dye–dye contact and quenching interactions (*3*–*6*). To a lesser degree, quaternary ammonium groups (*7*), carbohydrates (*8*), oligonucleotides (*9*), polyethylene glycol residues (*10*), and phosphonate monoesters (*11*) have also been considered for this purpose but have yet to find wide-scale commercial acceptance. Except in the cases of porphyrins (*12*) and cyanines (*13*), where aliphatic phosphonates were used, the phosphonic acid group has remained largely ignored as a means to provide water solubility, resistance to aggregation, and other useful properties for fluorescent labels. Since the phosphonate group may carry two negative charges at some biologically relevant pH values, compared to one charge for the sulfonate group, it offers the possibility of water-soluble labels with enhanced resistance to aggregation and fluorescence quenching and therefore to more brightly labeled substrates. Herein, the synthesis, the photophysical properties, and the protein and oligonucleotide labeling capabilities of some representative examples of phosphonic acid containing cyanine and squarane dyes are presented and discussed. These new dyes have phosphonic acid groups attached directly to the aromatic residues of the dyes rather than through aliphatic linkers because this approach was proven to be more advantageous in the case of analogous sulfonated cyanine dyes (*4*, *5*).

EXPERIMENTAL PROCEDURES

General Methods. All reagents and solvents were either ACS reagent grade or HPLC/spectroscopy grade and were obtained from Sigma-Aldrich, Acros, TCI, or Burdick & Jackson unless otherwise noted. Cy3 monofunctional and Cy5 monofunctional active esters were obtained from Amersham Pharmacia Biotech. Quasar 570 amidite and Quasar 670 amidite were obtained from Biosearch Technologies, Inc. Analytical TLC was performed on EM Biosciences 5534-3 aluminum-backed silica-254 plates or Analtech RPS-F hydrocarbon impregnated silica gel plates. Column chromatography was performed on either Merck silica gel 60 or Analtech bonded C18 reversed-phase (RP) silica gel. For RP column chromatography compressed air was applied to the top of the column to achieve convenient flow rates. For RP column chromatography of dyes, movement of dyes through the column was monitored qualitatively by eye. Deionized (DI) water was used in the preparation of all solvent mixtures used for RP and ion exchange chromatography. Preparative HPLC was run on a Waters HPLC system with a 600E controller, a 600 pump, and a 490E detector using either a Dionex DNAPac (9 × 250 mm) PA-100 column or a Hamilton PRP-1 column. Analytical HPLC was performed on a Waters 2795 system with a 996 photodiode array detector using either a Dionex DNAPac (4 × 250 mm) PA-100 column or a Higgins Haisil HL C18 column. Buffers used for preparative and analytical HPLC were AXA (15% acetonitrile, 0.038 M Tris), AXB (15% acetonitrile, 0.038 M Tris, 1.0 M sodium bromide), RPA (5% acetonitrile, 0.05 M triethylammonium acetate), and RPB (acetonitrile). MALDI mass spectrometry was performed on a Bruker Biflex III MALDI-TOF instrument. Electrospray mass spectrometry was performed on a Finnigan LC Q, and LC–MS was

[†] Telephone: 415-883-8400. Fax: 415-883-8488. E-mail mark@biosearchtech.com.

10.1021/bc070090y CCC: $37.00 © 2007 American Chemical Society
Published on Web 10/11/2007

performed on a Micromass LCT ESI mass spectrometer coupled with a Waters 2790 HPLC and a 996 PDA detector. NMR analysis (^{1}H, 400 Mz; ^{13}C, 100 Mz) was performed by Acorn NMR (Livermore, CA). ^{13}C NMR spectra were acquired with broadband proton–carbon decoupling. Coupling constants reported for ^{13}C NMR spectra are for phosphorus–carbon coupling. Elemental analysis was performed by Desert Analytics (Tucson, AZ). UV–vis spectra were recorded on a Hewlett-Packard 8453 spectrophotometer. Fluorescence spectra were recorded on a PTI spectrofluorometer and were corrected for instrument response characteristics. DNA synthesis was performed on a Biosearch 8700 DNA synthesizer using fast-deprotecting phosphoramidites from Pierce (Milwaukee, WI). Phosphate buffered saline (PBS), pH 7.3 (137 mM NaCl, 2.7 mM KCl, 4.3 mM $Na_2HPO_4 \cdot 7H_2O$, 1.4 mM KH_2PO_4), borate buffered saline (BBS), pH 8.1 (12.5 mM $Na_2B_4O_7 \cdot 10H_2O$, 0.25 mM $HCl_{(aq)}$), carbonate–bicarbonate buffer, pH 9.3 (0.1 M Na_2CO_3, 0.1 M $NaHCO_3$), and PCR buffer (50 mM KCl, 10 mM Tris-HCl, 1.5 mM $MgCl_2$) were prepared according to standard methods.

***p*-Bromophenylhydrazine Hydrochloride (3).** To a 1 L flask were added finely powdered *p*-bromoaniline (69 g, 0.4 mol), water (200 mL), and concentrated hydrochloric acid (100 mL, 1.2 mol). The mixture was cooled in an ice bath to less than 5 °C. A solution of sodium nitrite (30 g, 0.43 mol) in water (90 mL) was added dropwise to the aniline suspension over approximately 1 h while maintaining the temperature at less than 5 °C. The mixture was stirred for a further 0.5 h and then was gravity-filtered through a no. 1 paper into a chilled flask. The solution was added in small portions to a solution of 92% ammonium sulfite (118 g, 0.8 mol) in water (250 mL), which had been chilled to 0 °C, at a rate such that the temperature remained at less than 5 °C (approximately 1 h). During the addition, a yellow solid formed in the mixture. After the addition was completed, stirring was continued for 1 h at 0 °C and then the mixture was allowed to warm to room temperature. The solid was filtered off, and the filtrate was treated with concentrated hydrochloric acid (120 mL). The solution was heated to reflux, during which time a solid formed and then mostly dissolved. The hot solution was filtered and then allowed to cool to room temperature before being chilled in a refrigerator overnight. The crystals that formed were filtered off, washed with 1.0 M hydrochloric acid (60 mL), and dried under vacuum to afford **3** (54.3 g, 60%).

5-Bromo-2,3,3-trimethyl-3*H*-indole (4). To a 500 mL flask were added **3** (40.0 g, 0.179 mol), glacial acetic acid (250 mL), and 3-methylbutanone (50 mL, 0.36 mol). The mixture was heated at reflux for 3 h and then was cooled to room temperature. The volatile components were removed under vacuum, and the residue was partitioned between ether (350 mL) and water (100 mL). The aqueous phase was washed again with petroleum ether (2 × 100 mL), and then the combined organic solutions were dried ($MgSO_4$), filtered, and evaporated under vacuum to afford **4** (35 g, 82%). The bulk of the material was used without further purification. A sample of the oil was distilled on a Kugelrohr to yield a colorless oil: bp, 75 °C at 0.20 mmHg; R_f = 0.62 (SiO_2, dichloromethane (DCM)/methanol, 19:1); ^{1}H NMR ($CDCl_3$) δ 1.29 (s, 6H), 2.26 (s, 3H), and 7.36–7.44 (m, 3H); ^{13}C NMR δ 15.5, 23.0, 54.2, 118.9, 121.4, 124.9, 130.7, 147.9, 152.7, 188.5; ESI-MS obsd (+) 238.0 $(M + H)^+$, calcd 237.02 ($M = C_{11}H_{12}NBr$).

5-Bromo-1-ethyl-2,3,3-trimethyl-3*H*-indolium Iodide (5). To a 250 mL flask were added **4** (12 g, 50.4 mmol), acetonitrile (25 mL), and ethyl iodide (20 mL). The mixture was heated at reflux under argon for 40 h, and then most of the volatile components were removed by distillation. The residue was triturated with ether (100 mL) to give a powder. The solid was filtered off, washed with ether (2 × 150 mL), and dried under high vacuum to afford **5** as a solid (17.3 g, 87%): R_f = 0.70 (SiO_2, DCM/methanol, 9:1); ^{1}H NMR (DMSO-d_6) δ 1.42 (t, J = 7.3 Hz, 3H), 1.55 (s, 6H), 2.84 (s, 3H), 4.48 (quartet, J = 7.3 Hz, 2H), 7.84 (dd, J = 1.9 Hz and J = 8.6 Hz, 1H), 7.96 (d, J = 8.6 Hz, 1H) and 8.19 (d, J = 1.9 Hz, 1H); ^{13}C NMR δ 12.8, 14.3, 21.8, 43.5, 54.6, 117.5, 122.9, 127.1, 132.0, 140.2, 144.4, 196.8; ESI-MS obsd (+) 266.1 $(M - I)^+$, calcd 392.96 ($M = C_{13}H_{17}NBrI$). Anal. Calcd for $C_{13}H_{17}NBrI$: C, 39.62; H, 4.35; N, 3.55. Found: C, 39.56; H, 4.28; N, 3.57.

5-Bromo-1-(5-carboxypentyl)-2,3,3-trimethyl-3*H*-indolium iodide (6). To a 250 mL flask were added **4** (5.8 g, 24 mmol), acetonitrile (25 mL), and 6-iodohexanoic acid (5.1 g, 21 mmol). The mixture was heated at reflux under argon for 40 h. Most of the volatile components were removed by distillation, and then the mixture was heated at 140 °C for 2 h. The mixture was cooled and was triturated with DCM (100 mL) to give a powder. The solid was filtered off, washed with DCM (2 × 50 mL), and dried under high vacuum to afford **6** (8.7 g, 87 %): R_f = 0.38 (SiO_2, DCM/methanol, 9:1); ^{1}H NMR (DMSO-d_6) δ 1.43–1.48 (m, 2H), 1.50–1.55 (m, 8H), 1.82 (quintet, J = 7.5 Hz, 2H), 2.22 (t, J = 7.1 Hz, 2H), 2.83 (s, 3H), 4.44 (t, J = 7.6 Hz, 2H), 7.82–7.85 (m, 1H), 7.95 (d, J = 8.5 Hz, 1H) and 8.19 (d, J = 1.7 Hz, 1H); ^{13}C NMR δ 14.4, 22.0, 24.2, 25.6, 27.1, 33.5, 47.8, 54.6, 117.7, 123.0, 127.1, 132.0, 140.6, 144.3, 174.5, 197.62; ESI-MS obsd (+) 352.2 $(M - I)^+$, calcd 479.00 ($M = C_{17}H_{23}NO_2BrI$). Anal. Calcd for $C_{19}H_{27}NO_2BrI$: C, 42.52; H, 4.83; N, 2.92. Found: C, 42.34; H, 4.78; N, 2.94.

5-Bromo-1-(5-ethoxycarbonylpentyl)-2,3,3-trimethyl-3*H*-indolium iodide (7). To a 250 mL flask were added **6** (2.00 g, 4.17 mmol), ethanol (60 mL), and concentrated sulfuric acid (0.2 mL). The mixture was heated at reflux for 2 h and then was cooled to room temperature. The ethanol was removed under vacuum, and the residue was partitioned between water (40 mL) and DCM (80 mL). The organic layer was washed with 1 M HCl (40 mL), water (40 mL), and a saturated solution of sodium iodide (40 mL). It was dried ($MgSO_4$) and was evaporated under vacuum to afford **7** as a brown solid (1.74 g, 82 %): R_f = 0.79 (SiO_2, DCM/methanol, 9:1); ^{1}H NMR (DMSO-d_6) δ 1.15 (t, J = 7.1 Hz, 3H), 1.43–1.48 (m, 2H), 1.53–1.60 (m, 8H), 1.82 (quintet, J = 7.5 Hz, 2H), 2.29 (t, J = 7.3 Hz, 2H), 2.84 (s, 3H), 4.02 (quartet, J = 7.1 Hz, 2H), 4.44 (t, J = 7.5 Hz, 2H), 7.83–7.86 (m, 1H), 7.95 (d, J = 8.6 Hz, 1H), and 8.19 (d, J = 1.7 Hz, 1H); ^{13}C NMR δ 14.3, 14.4, 22.0, 24.2, 25.4, 27.0, 33.4, 47.8, 54.6, 59.9, 117.6, 123.0, 127.1, 132.0, 140.6, 144.3, 172.9, 197.2; ESI-MS obsd (+) 380.3 $(M - I)^+$, calcd 507.03 ($M = C_{19}H_{27}NO_2BrI$).

(1-Ethyl-3,3-dimethyl-2-methylene-2,3-dihydro-1*H*-indol-5-yl)-phosphonic Acid Diethyl Ester (8). To a dry three-neck 500 mL flask were added **5** (9.6 g, 20 mmol) and nickel chloride (0.52 g, 4.0 mmol). The flask was fitted with a dropping funnel and a condenser and then was lowered into an oil bath. The mixture was heated to 175 °C. At approximately 165 °C triethyl phosphite (15 mL, 86 mmol) was added dropwise over 0.5 h. The mixture fizzed and became dark at first before turning a dark straw color. After the mixture was heated at 175 °C for 0.5 h, a second portion of nickel chloride (0.52 g, 4.0 mmol) was added. The mixture fizzed vigorously, gave off much vapor, and became dark gray-green in color. Heating was continued for 0.5 h, and then the mixture was cooled to room temperature. The mixture was treated with methanol (100 mL) and was filtered through a bed of Celite. The methanol was evaporated under vacuum to leave an oil that was distilled on a Kugelrohr to afford **8** as a colorless liquid that was stored under argon (4.0 g, 62%): bp 155–165 °C at 0.4 mmHg; R_f = 0.67 (SiO_2,

DCM/methanol, 9:1); ESI-MS obsd (+) 324.2 $(M + H)^+$, calcd 323.17 ($M = C_{17}H_{26}NO_3P$).

(1-(5-Ethoxycarbonylpentyl)-3,3-dimethyl-2-methylene-2,3-dihydro-1*H*-indol-5-yl)phosphonic Acid Diethyl Ester (9). To a dry three-neck 500 mL flask were added **7** (11.2 g, 22.1 mmol) and nickel chloride (0.72 g, 5.6 mmol). The flask was fitted with a dropping funnel and a condenser. The mixture was heated to 170 °C, and then triethyl phosphite (30 mL, 173 mmol) was added dropwise over 0.5 h. The temperature was raised to 180 °C, and then a second portion of nickel chloride (0.72 g, 5.6 mmol) was added. After about 20 s, rapid fizzing occurred and the mixture turned grey-green in color. After heating for a further 0.5 h, the mixture was cooled to room temperature and was treated with DCM (200 mL). The mixture was filtered through a fiberglass filter pad, and then the DCM was removed under vacuum. The excess triethyl phosphite and volatile components were removed using a Kugelrohr (110 °C at 0.4 mmHg), and the residue was subjected to column chromatography on silica gel (6 cm × 14 cm) using 2.5–10 % (v/v) methanol in DCM as an eluent. Fractions containing the required compound had a tendency to turn pink upon exposure to air. Evaporation of the fractions afforded **9** as a pink oil that was stored under argon (8.0 g, 86 %): $R_f = 0.68$ (SiO_2, DCM/methanol, 9:1); ESI-MS obsd (+) 438.2 $(M + H)^+$, calcd 437.23 ($M = C_{23}H_{36}NO_5P$).

1-Ethyl-2,3,3-trimethyl-5-phosphono-3*H*-indolium (1). To a 250 mL flask were added **8** (4.8 g, 14.8 mmol) and 6 M hydrochloric acid (60 mL). The mixture was stirred at room temperature until the oil dissolved and then was heated at reflux overnight. After cooling, the mixture was filtered and was evaporated to dryness under vacuum. The residue was treated with water (100 mL) and, after the mixture was stirred for 30 min, was filtered. The aqueous solution was washed with DCM (2 × 60 mL), filtered, and concentrated under vacuum to approximately 4–6 mL. The solution was loaded onto a column of RP silica gel (7 cm × 15 cm) in water, and then the column was eluted with water. Pure fractions (by RP HPLC) were evaporated under vacuum to afford **1** as an off-white solid that was dried over phosphorous pentoxide and stored under argon (3.67 g, 80%): $R_f = 0.50$ (C18-SiO_2, water/methanol, 3:1); ^{1}H NMR (D_2O) δ 1.54 (t, $J = 7.4$ Hz, 3H), 1.60 (s, 6H), 4.52 (quartet, $J = 7.4$ Hz, 2H), 7.86–7.90 (m, 1H), 7.94–8.01 (m, 1H), and 8.03–8.08 (m, 1H). ^{13}C NMR δ 15.1, 15.9, 24.4, 46.5, 57.6, 118.1 (d, $J = 15$ Hz), 128.2 (d, $J = 12$ Hz), 134.4 (d, $J = 11$ Hz), 138.5 (d, $J = 178$ Hz), 144.9 (d, $J = 15$ Hz), 145.6 (d, $J = 3$ Hz), 200.6; ESI-MS obsd (+) 268.2 $(M + H)^+$, 534.7 $(2M + H)^+$, (–) 532.9 $(2M - H)^-$, 799.5 $(3M - H)^-$ 266.1 $(M - H)^-$, calcd 267.10 ($M = C_{13}H_{18}NO_3P$).

1-(5-Carboxypentyl)-2,3,3-trimethyl-5-phosphono-3*H*-indolium (2). Procedure is as for **1** using **9** (8.0 g, 18.3 mmol) and 6 M hydrochloric acid (280 mL) to afford **2** (5.3 g, 76%): $R_f = 0.54$ (C18-SiO_2, water/methanol, 3:1); ^{1}H NMR (D_2O) δ 1.42–1.51 (m, 2H), 1.58–1.72 (m, 8H), 2.04 (quintet, $J = 7.8$ Hz, 2H), 2.38 (t, $J = 7.2$ Hz, 2H), 4.52 (t, $J = 7.4$ Hz, 2H), 7.83–7.87 (m, 2H), 7.93–7.98 (m, 1H), and 8.02–8.06 (m, 1H); ^{13}C NMR δ 15.9, 24.6, 26.7, 28.2, 29.8, 36.4, 50.9, 57.6, 118.1 (d, $J = 15$ Hz), 128.1 (d, $J = 11$Hz), 134.2 (d, $J = 12$ Hz), 140.3 (d, $J = 176$ Hz), 144.7 (d, $J = 15$ Hz), 145.4 (d, $J = 4$ Hz), 181.6, 200.7; ESI-MS obsd (+) 354.3 $(M + H)^+$, 706.9 $(2M + H)^+$, (–) 705.0 $(2M - H)^-$, 352.2 $(M - H)^-$, calcd 353.14 ($M = C_{17}H_{24}NO_5P$).

1-Ethyl-5-formylaminomethyl-2,3,3-trimethyl-3*H*-indolium iodide (13). 4-Aminomethylindole (*18*) (21.4 g, 0.114 mol) was dissolved in methyl formate (60 mL), and the mixture was heated at reflux for 2 days. The volatile components were evaporated under vacuum to leave the formamide as a pale-yellow oil. The bulk of the material was used without further purification. A sample of the oil was distilled on a Kugelrohr to afford the formamide as a colorless oil: bp 182 °C at 0.15 mmHg: $R_f = 0.28$ (SiO_2, DCM/methanol, 19:1); IR (film, ν_{max} cm^{-1}) 1668, 3256; ^{1}H (DMSO-d_6) 1.20 (s, 6H), 2.18 (s, 3H), 4.37 and 4.42 (2 × d, $J = 6$ Hz, 2H), 6.81 and 6.48 (2 × s, 1H), 7.11–7.16 (m, 2H), 7.32–7.40 (m, 1H), and 8.18 (s, 1H); ^{13}C NMR δ 15.4, 23.1, 42.1, 53.7, 119.8, 121.1, 127.3, 134.7, 146.4, 153.1, 161.3, 188.7; ESI-MS obsd (+) 217.1 $(M + H)^+$, calcd 216.13 ($M = C_{13}H_{16}N_2O$). The amide (10.8 g, 50 mmol) was dissolved in acetonitrile (25 mL), and ethyl iodide (25 mL) was added. The mixture was heated at reflux for 40 h, and then the volatile components were removed under vacuum. The residue was dissolved in methanol (20 mL), and this solution was added dropwise to stirred ether (700 mL). After the mixture was stirred for 1.5 h, the solid was filtered off and was washed with ether to afford **13** as a pale-pink solid (17.8 g, 96%): $R_f = 0.25$ (SiO_2, DCM/methanol, 9:1); ^{1}H (DMSO-d_6) δ 1.43 (t, $J = 7.3$ Hz, 3H), 1.52 (s, 6H), 2.84 (s, 3H), 4.42 (d, $J = 6.1$ Hz, 2H), 4.48 (quartet, $J = 7.0$ Hz, 2H), 7.48–7.51 (m, 1H), 7.72 (d, $J = 1.1$ Hz, 1H), 7.94 (d, $J = 8.4$ Hz, 1H), 8.17 (m, 1H), and 8.62 (t, $J = 5.3$ Hz, 1H); ^{13}C NMR δ 12.9, 14.1 22.3, 40.3, 43.7, 54.2, 115.8, 122.5, 127.9, 139.8, 141.1, 142.4, 161.4, 195.8; ESI-MS obsd (+) 245.2 $(M - I)^+$, calcd 372.07 ($M = C_{15}H_{21}N_2OI$). Anal. Calcd for $C_{15}H_{21}N_2OI$: C, 48.4; H, 5.69; N, 7.53. Found: C, 48.35; H, 5.39; N, 7.29.

Dye 14. To a 100 mL flask were added **2** (0.37 g, 1.04 mmol), diphenylformamidine (0.10 g, 0.5 mmol), sodium acetate (0.13 g, 1.6 mmol), and acetic anhydride (5 mL). The mixture was heated at 110 °C for 4.5 h and then was cooled to room temperature. The volatile components were removed under vacuum to leave a tar that was dissolved in concentrated hydrochloric acid (20 mL). The solution was stirred for 3 h and then was diluted by addition to water (500 mL). The mixture was loaded onto a column of RP silica gel (3 cm × 12 cm) in water. The column was washed with water (approximately 1 L) to load all of the compound onto the column and to remove the excess acid. Gradient elution from 0% to 40% (v/v) methanol in water (the methanol was increased in steps of 5%, and volumes from 300 mL to 1 L of eluent were used for each step) eluted the dye. Fractions were evaporated under vacuum to leave a red residue that was treated with the minimum 20% (v/v) water in methanol to dissolve the dye. The solution was filtered through a medium frit and then was evaporated under vacuum. The residue was dried under vacuum to afford **14** (0.080 g, 22%): $R_f = 0.56$ (C18-SiO_2, water/methanol, 3:1), 0.22 (C18-SiO_2, RPA/methanol, 3:1); ^{1}H NMR (D_2O + 2% (v/v) of 30% NaOD) δ 1.42–1.50 (m, 4H), 1.64 (quintet, $J = 7.5$ Hz, 4H), 1.78 (s, 12H), 1.88 (quintet, $J = 7.5$ Hz, 4H), 2.20 (t, $J = 7.4$ Hz, 4H), 4.12 (t, $J = 7.3$ Hz, 4H), 6.33 (d, $J = 13.7$ Hz, 2H), 7.30 (dd, $J = 1.6$ and 8.3 Hz, 2H), 7.72–7.78 (m, 2H), 7.81 (d, $J = 11$ Hz, 2H) and 8.56 (t, $J = 13.6$ Hz, 2H); ^{13}C NMR δ 28.6, 29.0, 29.5, 30.1, 40.3, 46.9, 42.1, 105.1, 113.2 (d, $J = 14$ Hz), 127.0 (d, $J = 9$ Hz), 133.5 (d, $J = 10$ Hz), 140.8 (d, $J = 168$ Hz), 143.3 (d, $J = 13$ Hz), 145.3 (d, $J = 3$ Hz), 153.7, 178.0, 186.6; ESI-MS obsd (+) 717.3 $(M + H)^+$, (–) 715.1 $(M - H)^-$, calcd 716.26 ($M = C_{35}H_{46}N_2O_{10}P_2$). Anal. Calcd for $C_{35}H_{46}N_2O_{10}P_2 \cdot H_2O$: C, 57.22; H, 6.59; N, 3.81; P, 8.43. Found: C, 57.18; H, 6.38; N, 4.08; P, 7.90.

Dye 15. To a 100 mL flask were added **2** (0.37 g, 1.04 mmol), pyridine (25 mL), and triethyl orthoformate (0.28 mL). The mixture was heated at 110 °C for 1.5 h. Triethyl orthoformate (0.25 mL) was added, and heating was continued for 2.5 h. After the mixture was cooled to room temperature, the volatile components were removed under vacuum to leave a tar. The tar was worked up as described for compound **14** (concentrated hydrochloric acid (20 mL), RP column chromatography (3 cm × 12 cm), 0–40% (v/v) methanol in water) to afford **15** as a red solid (0.195 g, 24 %): $R_f = 0.56$ (C18-SiO_2, water/methanol,

3:1), 0.55 (C18-SiO_2, RPA/methanol, 3:1); ^{1}H NMR (D_2O + 2% (v/v) of 30% NaOD) δ 1.21 (t, J = 7.2 Hz, 6H), 1.41–1.49 (m, 4H), 1.64 (quintet, J = 7.4 Hz, 4H), 1.75 (s, 12H), 1.86 (quintet, J = 7.3 Hz, 4H), 2.20 (t, J = 7.5 Hz, 4H), 3.85 (quintet, J = 7.2 Hz, 4H), 4.11 (t, J = 7.2 Hz, 4H), 6.38 (d, J = 13.4 Hz, 2H), 7.40 (dd, J = 1.3 and 8.1 Hz, 2H), 7.74–7.82 (m, 4H) and 8.55 (t, J = 13.4 Hz, 1H); ^{13}C NMR δ 18.6, 28.5, 28.9, 29.5, 30.0, 40.2, 47.0, 52.0, 64.0, 105.9, 114.0 (d, J = 15 Hz), 127.5 (d, J = 11 Hz), 132.6 (d, J = 181 Hz), 134.7 (d, J = 12 Hz), 143.9 (d, J = 15 Hz), 147.0 (d, J = 3 Hz), 154.4, 178.3, 186.4; ESI-MS obsd (+) 773.4 $(M + H)^+$, (–) 771.3 $(M - H)^-$, calcd 772.33 ($M = C_{39}H_{54}N_2O_{10}P_2$).

Dye 16. To a 50 mL flask were added **1** (0.31 g, 1.16 mmol), diphenylformamidine (0.30 g, 1.53 mmol), acetic acid (2 mL), and acetic anhydride (2 mL). The mixture was heated at 120 °C for 1.5 h and then was cooled to room temperature. The volatile components were removed under vacuum to leave a tar that was washed with ether (2 × 30 mL). The residue was dissolved in acetic acid (2 mL), and then pyridine (4 mL) and **10** (0.40 g, 1.14 mmol) were added. The mixture was heated at 120 °C for 0.75 h and then was cooled to room temperature. The volatile components were removed under vacuum, and the residue was dissolved in concentrated hydrochloric acid (30 mL). After being stirred for 3 h, the mixture was diluted by addition to water (200 mL) and then was basified, first by addition of 4 M sodium hydroxide solution until the pH was approximately 4 and then with saturated sodium bicarbonate solution. Initially dye was precipitated from the mixture, but then it redissolved. The aqueous solution was filtered and was loaded onto a column of RP silica gel (4 cm × 15 cm) in water. The column was washed with water (200 mL), 1 M hydrochloric acid (100 mL), and water until the pH of the effluent was neutral. Gradient elution from 0% to 50% (v/v) methanol in water (the methanol was increased in steps of 5% and volumes from 300 mL to 1 L of eluent were used for each step) eluted the symmetrical diphosphonate dye first and then the unsymmetrical dye. The fractions were evaporated under vacuum to leave a red residue that was taken up in methanol. The solution was filtered through a medium frit, and the methanol was removed under vacuum. The residue was washed with acetonitrile and was dried under vacuum to give dye **16** as a red solid (0.32 g, 51%): R_f = 0.26 (C18-SiO_2, water/methanol, 3:1), 0.17 (C18-SiO_2, RPA/methanol, 3:1); ^{1}H NMR (CD_3OD) δ 1.42 (t, J = 7.3 Hz, 3H), 1.51–1.58 (m, 2H), 1.71 (quintet, J = 7.3 Hz, 2H), 1.78 (s, 14H), 1.88 (quintet, J = 7.4 Hz, 2H), 2.33 (t, J = 7.4 Hz, 2H), 4.18–4.24 (m, 4H), 6.48–6.56 (m, 2H), 7.32–7.50 (m, 4H), 7.58 (d, J = 7.0 Hz, 1H), 7.86–7.93 (m, 2H), and 8.57 (t, J = 13.4 Hz, 1H). ^{13}C NMR δ 12.5, 25.7, 27.3, 28.2, 28.3, 34.6, 40.3, 45.3, 50.4, 50.9, 103.5, 104.6, 111.5 (d, J = 16 Hz), 112.8, 123.6, 125.9 (d, J = 12 Hz), 127.2, 130.1, 132.8 (d, J = 194 Hz), 133.2 (d, J = 11 Hz), 141.8 (d, J = 16 Hz), 142.4, 143.2, 145.0 (d, J = 3 Hz), 152.5, 175.4, 176.8, 177.2; ESI-MS obsd (+) 551.4 $(M + H)^+$, (–) 549.3 $(M - H)^-$, calcd 550.26 ($M = C_{31}H_{39}N_2O_5P$). Anal. Calcd for $C_{31}H_{39}N_2O_5P$: C, 67.62; H, 7.14; N, 5.09; P, 5.63. Found: C, 67.25; H, 6.87; N, 5.01; P, 5.6.

Dye 17. To a 100 mL flask were added **1** (0.29 g, 1.08 mmol), diphenylformamidine (0.40 g, 2.0 mmol), acetic acid (5 mL), and acetic anhydride (5 mL). The mixture was heated at 125 °C for 3 h and then was cooled to room temperature. The volatile components were removed under vacuum to leave a tar that was washed with ether (2 × 30 mL) and ethyl acetate (2 × 50 mL). The residue was dissolved in acetic acid (5 mL), and then pyridine (8 mL) and **11** (0.370 g, 1.0 mmol) were added. The mixture was heated at 125 °C for 3 h. The volatile components were removed under vacuum to leave a tar. The tar was worked up as described for compound **16** (concentrated hydrochloric acid (30 mL), RP column chromatography (3 cm × 15 cm), 0–55% (v/v) methanol in water) to afford **17** as a red solid (0.072 g, 14%): R_f = 0.19 (C18-SiO_2, water/methanol, 3:1), 0.24 (C18-SiO_2, RPA/methanol, 3:1); ^{1}H NMR (CD_3OD) δ 1.40–1.46 (m, 6H), 1.78 (s, 6H), 1.79 (s, 6H), 3.73 (s, 2H), 4.18–4.30 (m, 4H), 6.48 (d, J = 13.2 Hz, 1H), 6.58 (d, J = 13.6 Hz, 1H), 7.38–7.44 (m, 3H), 7.53 (s, 1H), 7.85–7.91 (m, 2H), and 8.57 (t, J = 13.4 Hz, 1H); ^{13}C NMR δ 12.5, 12.8, 28.1, 28.3, 40.2, 40.8, 41.5, 50.2, 51.1, 103.3, 104.9, 111.6 (d, J = 15 Hz), 112.7, 124.9, 125.9 (d, J = 12 Hz), 129.2 (d, J = 190 Hz), 131.3, 133.4 (d, J = 11 Hz), 134.8, 141.7, 142.0 (d, J = 15 Hz), 142.9, 145.9 (d, J = 3 Hz), 152.5, 174.9, 175.1, 176.9; ESI-MS obsd (+) 523.3 $(M + H)^+$, 545.3 $(M + Na)^+$, calcd 522.3 ($M = C_{29}H_{35}N_2O_5P$).

Dye 18. To a 250 mL flask were added **12** (0.60 g, 2.04 mmol), diphenylformamidine (0.50 g, 2.6 mmol), acetic acid (21 mL), and acetic anhydride (15 mL). The mixture was heated at 115 °C for 3 h and then was cooled to room temperature. The volatile components were removed under vacuum, and the residue was washed with ethyl acetate (3 × 100 mL) to give a powder. To the powder were added **2** (0.70 g, 2.0 mmol) and acetic acid (25 mL). The mixture was warmed until the solids dissolved, and then pyridine (35 mL) was added. The mixture was heated to 115 °C for 0.5 h and then acetic anhydride (15 mL) was added. The mixture was heated for a further 2 h during which time the mixture became deep-red. The mixture was cooled to room temperature, and then the volatile components were removed under vacuum. The residue was treated with saturated aqueous sodium bicarbonate solution (250 mL) to dissolve the dye. The solution was filtered and was loaded onto a column of RP silica gel (4 cm × 20 cm) in water. The column was washed with water (approximately 200 mL) and 0.5 M hydrochloric acid (approximately 500 mL), RPA buffer (500 mL) and then was eluted with a gradient from 0 to 30% (v/v) methanol in RPA buffer (the methanol was increased in steps of 5%, and volumes from 500 mL to 1 L of eluent were used for each step). The fractions were evaporated under vacuum to leave a red residue that was dissolved in 1 M hydrochloric acid (approximately 100 mL). The solution was loaded onto a column of RP silica gel (3 cm × 10 cm) in water. The column was washed with 1.0 M hydrochloric acid (200 mL) and then with water until the pH of the effluent was neutral. The column was eluted with a sharp gradient from 0 to 50% (v/v) methanol in water. The dye-containing fractions were evaporated under vacuum to afford **18** as a red solid (0.45 g, 34%): R_f = 0.62 (C18-SiO_2, water/methanol, 3:1), 0.55 (C18-SiO_2, RPA/methanol, 3:1); ^{1}H NMR (D_2O) δ 1.38–1.47 (m, 2H), 1.59–1.72 (m, 14H), 1.78–1.94 (m, 6H), 2.20 (t, J = 7.4 Hz, 2H), 2.95 (t, J = 7.5 Hz, 2H), 4.03–4.09 (m, 4H), 6.27–6.32 (m, 2H), 7.24–7.38 (m, 4H), 7.50 (d, J = 7.0 Hz, 1H), 7.75–7.80 (m, 2H), and 8.43 (t, J = 13.5 Hz, 1H); ^{13}C NMR δ 24.4, 28.4, 28.9, 29.4, 29.9, 30.0, 40.1, 40.2, 46.3, 46.9, 51.8, 52.0, 53.2, 105.3, 113.6 (d, J = 15 Hz), 114.0, 125.1, 126.9 (d, J = 11 Hz), 128.3, 131.5, 133.8 (d, J = 11 Hz), 136.3 (d, J = 175 Hz), 143.4 (d, J = 14 Hz), 143.7, 144.5, 146.2, 153.8, 177.7, 177.8, 186.2; ESI-MS obsd (+) 681.3 $(M + Na)^+$, (–) 657.2 $(M - H)^-$, calcd 658.25 ($M = C_{33}H_{43}N_2O_8PS$). Anal. Calcd for $C_{33}H_{43}N_2O_8PS \cdot H_2O$: C, 58.57; H, 6.70; N, 4.14; P, 4.58. Found: C, 58.78; H, 6.83; N, 4.41; P, 4.80.

Dye 18 Disodium Salt. Dye **18** (0.40 g) was dissolved in a mixture of deionized (DI) water (200 mL) and methanol (50 mL). The solution was passed through a column (2.5 cm × 10 cm) of Dowex 50-8X anion exchange resin, sodium form. After the remaining dye was washed off the column with DI water, the solution was concentrated to approximately 20 mL, filtered through a medium frit, and then evaporated under vacuum to afford the disodium salt of **18** as a red solid (0.41 g, 97%). Anal. Calcd for $C_{33}H_{41}N_2O_8PSNa_2 \cdot H_2O$: C, 54.99; H, 6.01; N,

3.89; P, 4.30; Na, 6.38. Found: C, 54.15; H, 6.03; N, 4.03; P, 3.90; Na, 6.30.

Dye 19. To a 100 mL flask were added **2** (0.41 g, 1.15 mmol), malonaldehyde dianilide hydrochloride (0.142.g, 0.55 mmol), acetic anhydride (5 mL), and sodium acetate (0.13 g). The mixture was heated at 110 °C for 4.5 h and then was cooled to room temperature. The volatile components were removed under vacuum to leave a tar. The tar was worked up as described for compound **14** (concentrated hydrochloric acid (30 mL), RP column chromatography (4 cm × 15 cm), 0–40% (v/v) methanol in water) to afford **19** as a blue solid (0.23 g, 51%): $R_f = 0.$ 36 (C18-SiO_2, water/methanol, 3:1), 0.17 (C18-SiO_2, RPA/methanol, 3:1); ^{1}H NMR (D_2O + 2% (v/v) of 30% NaOD) δ 1.41–1.47 (m, 4H), 1.59–1.66 (m, 16H), 1.83 (quintet, $J = 7.3$ Hz, 4H), 2.20 (t, $J = 7.5$ Hz, 4H), 4.07 (t, $J = 7.4$ Hz, 4H), 6.28 (d, $J = 13.6$ Hz, 2H), 6.57 (t, $J = 12.5$ Hz, 1H), 7.26 (dd, $J = 1.9$ and 8.3 Hz, 2H), 7.64–7.67 (m, 2H), 7.75 (d, $J = 11.5$ Hz, 2H), and 7.99 (t, $J = 13.1$ Hz, 2H); ^{13}C NMR δ 28.6, 29.0, 29.5, 29.7, 40.2, 46.7, 51.8, 106.3, 113.2 (d, $J = 15$ Hz), 126.9 (d, $J = 11$ Hz), 127.6, 133.5 (d, $J = 11$ Hz), 136.9 (d, $J = 175$ Hz), 143.8 (d, $J = 15$ Hz), 146.2 (d, $J = 3$ Hz), 156.3, 176.3, 186.5; ESI-MS obsd (+) 743.3 $(M + H)^+$, (–) 741.3 $(M - H)^-$, calcd 742.28 ($M = C_{37}H_{48}N_2O_{10}P_2$). Anal. Calcd for $C_{37}H_{48}N_2O_{10}P_2 \cdot (H_2O)_2$: C, 57.06; H, 6.73; N, 3.60; P, 7.95. Found: C, 56.70; H, 6.62; N, 3.67; P, 7.4.

Dye 20. To a 50 mL flask were added **1** (0.36 g, 1.34 mmol), malonaldehyde dianilide hydrochloride (0.36 g, 1.40 mmol), acetic acid (4 mL), and acetic anhydride (4 mL). The mixture was heated at 110 °C for 1.5 h and then was cooled to room temperature. The volatile components were removed under vacuum to leave a tar. The tar was dissolved in acetic acid (4 mL), and then pyridine (5 mL) and compound **2** (0.46 g, 1.30 mmol) were added. The mixture was heated at 110 °C for 3 h and then was cooled to room temperature. The volatile components were removed under vacuum to leave a dark-blue tar. The tar was worked up as described for **14** (concentrated hydrochloric acid (30 mL), RP column chromatography (4 cm × 15 cm), 0–45% (v/v) methanol in water) to afford **20** as a blue solid (0.205 g, 24%): $R_f = 0.46$ (C18-SiO_2, water/methanol, 3:1), 0.31 (C18-SiO_2, RPA/methanol, 3:1); ^{1}H NMR (CD_3OD) δ 1.43 (t, $J = 7.2$ Hz, 3H), 1.51–1.57 (m, 2H), 1.69–1.89 (m, 16H), 2.35 (t, $J = 7.1$ Hz, 2H), 4.14–4.23 (m, 4H), 6.27–6.37 (m, 2H), 6.68 (t, $J = 12.4$ Hz, 1H), 7.31–7.34 (m, 2H), 7.87–7.95 (m, 4H) and 8.24–8.36 (m, 2H); ESI-MS obsd (+) 657.3 $(M + H)^+$, (–) 655.3 $(M - H)^-$, calcd 656.24 ($M = C_{33}H_{42}N_2O_8P_2$).

Dye 21. To a 100 mL flask were added **1** (1.87 g, 7.0 mmol), malonaldehyde dianilide hydrochloride (2.0 g, 7.73 mmol), acetic acid (20 mL), and acetic anhydride (20 mL). The mixture was heated at 110 °C for 2.5 h and then was cooled to room temperature. The volatile components were removed under vacuum to leave a tar that was washed with ether (2 × 60 mL). The tar was dissolved in acetic acid (30 mL), and then pyridine (40 mL) and **10** (2.5 g, 7.1 mmol) were added. The mixture was heated at 110 °C for 1 h and then was cooled to room temperature. The volatile components were removed under vacuum to leave a tar. The tar was worked up as described for compound **16** (concentrated hydrochloric acid (70 mL), RP column chromatography (4 cm × 20 cm), 0–50% (v/v) methanol in water) to afford a **21** as a blue solid (1.54 g, 38%): $R_f =$ 0.09 (C18-SiO_2, water/methanol, 3:1), 0.10 (C18-SiO_2, RPA/methanol, 3:1); ^{1}H NMR (CD_3OD) δ 1.37 (t, $J = 7.4$ Hz, 3H), 1.46–1.55 (m, 2H), 1.64–1.75 (m, 14H), 1.84 (quintet, $J = 7.4$ Hz, 2H), 2.32 (t, $J = 7.3$ Hz, 2H), 4.11–4.17 (m, 4H), 6.26–6.34 (m, 2H), 6.64 (t, $J = 12.4$ Hz, 1H), 7.25–7.33 (m, 3H), 7.39–7.44 (m, 1H), 7.50 (d, $J = 7.2$, 1H), 7.84–7.90 (m, 2H), and 8.22–8.31 (m, 2H); ^{13}C NMR δ 12.5, 25.7, 27.4, 27.9, 28.2, 34.7, 39.9, 44.9, 50.4, 50.7, 104.0, 104.8, 110.8 (d, $J = 15$ Hz), 112.2, 123.5, 125.9 (d, $J = 10$ Hz), 126.5, 126.8, 129.8, 132.8 (d, $J = 9$ Hz), 135.7 (d, $J = 181$ Hz), 141.9 (d, $J = 15$ Hz), 142.8, 143.5, 144.2 (d, $J = 3$ Hz), 155.5, 155.8, 174.2, 175.2, 177.4; ESI-MS obsd (+) 577.4 $(M + H)^+$, (–) 575.4 $(M - H)^-$, calcd 576.28 ($M = C_{33}H_{41}N_2O_5P$). Anal. Calcd for $C_{33}H_{41}N_2O_5P \cdot (H_2O)_2$: C, 64.69; H, 7.40; N, 4.57; P, 5.06. Found: C, 64.34; H, 7.44; N, 4.66; P, 5.0.

Dye 22. To a 50 mL flask were added **11** (0.387 g, 1.04 mmol), malonaldehyde dianilide hydrochloride (0.321 g, 1.24 mmol), acetic acid (5 mL), and acetic anhydride (5 mL). The mixture was heated at 110 °C for 1 h and then was cooled to room temperature. The volatile components were removed under vacuum to leave a tar that was washed with ether (2 × 60 mL). The tar was dissolved in acetic acid (5 mL), and then pyridine (10 mL) and **1** (0.27 g, 1.0 mmol) were added. The mixture was heated at 110 °C for 1 h and then was cooled to room temperature. The volatile components were removed under vacuum to leave a tar. The tar was worked up as described for compound **16** (concentrated hydrochloric acid (30 mL), RP column chromatography (4 cm × 15 cm), 0–60% (v/v) methanol in water) to afford **22** as a blue solid (0.176 g, 31%): $R_f = 0.19$ (C18-SiO_2, water/methanol, 3:1), 0.20 (C18-SiO_2, RPA/methanol, 3:1); ^{1}H NMR (CD_3OD) δ 1.32–1.41 (m, 6H), 1.72 (s, 6H), 1.73 (s, 6H), 3.70 (s, 2H), 4.10–4.20 (m, 4H), 6.26 (d, $J = 13.6$ Hz, 1H), 6.33 (d, $J = 14.0$ Hz, 1H), 6.62 (t, $J = 12.4$ Hz, 1H), 7.24–7.29 (m, 2H), 7.34–7.37 (m, 1H), 7.45 (d, $J =$ 1.4 Hz, 1H), 7.83–7.90 (m, 2H), and 8.21–8.30 (m, 2H); ^{13}C NMR δ 12.5, 12.6, 27.7, 28.9, 39.9, 40.2, 41.6, 50.3, 50.8, 103.8, 104.6, 110.7 (d, $J = 14$ Hz), 111.9, 124.7, 125.9 (d, $J = 10$ Hz), 126.8, 131.0, 132.8 (d, $J = 10$ Hz), 133.9, 134.9 (d, $J =$ 175 Hz), 141.8 (d, $J = 14$ Hz), 141.9, 143.2, 144.3, 155.3, 155.9, 173.9, 174.9, 175.5; ESI-MS obsd (+) 549.3 $(M + H)^+$, (–) 547.3 $(M - H)^-$, calcd 548.24 ($M = C_{31}H_{37}N_2O_5P$).

Dye 23. To a 250 mL flask were added **12** (0.60 g, 2.04 mmol), malonaldehyde dianilide hydrochloride (0.60 g, 2.3 mmol), acetic acid (25 mL), and acetic anhydride (25 mL). The mixture was heated at 115 °C for 2 h and was cooled to room temperature, and then the volatile components were removed under vacuum. The residue was washed with ethyl acetate (3 × 100 mL) to give a powder. To the powder were added **2** (0.70 g, 2.0 mmol) and acetic acid (25 mL). The mixture was warmed until the solids dissolved, and then pyridine (35 mL) was added. The mixture was heated to 115 °C for 3 h during which time the mixture became deep-blue. The mixture was cooled to room temperature, and the volatile components were removed under vacuum. The residue was worked up as described for compound **18** (RP column chromatography (4 cm × 20 cm, 0–30% (v/v) methanol in RPA) to afford **23** as a blue solid (0.95 g, 69 %): $R_f = 0.46$ (C18-SiO_2, water/methanol, 3:1), 0.41 (C18-SiO_2, RPA/methanol, 3:1); ^{1}H NMR (D_2O) δ 1.38–1.46 (m, 2H), 1.50 (s, 6H), 1.54–1.66 (m, 8H), 1.73–1.97 (m, 6H), 2.21 (t, $J = 7.4$ Hz, 2H), 2.96 (t, $J = 7.4$ Hz, 2H), 4.00 (t, $J =$ 7.4 Hz, 2H), 4.11 (t, $J = 7.4$ Hz, 2H), 6.10 (d, $J = 13.6$ Hz, 1H), 6.24 (d, $J = 13.8$ Hz, 1H), 6.48 (t, $J = 12.5$ Hz, 1H), 7.11–7.16 (m, 1H), 7.24–7.29 (m, 3H), 7.44 (d, $J = 7.5$ Hz, 1H), 7.68–7.74 (m, 2H), and 7.82–7.95 (m, 2H). ^{13}C NMR δ 24.7, 28.6, 28.8, 29.1, 29.6, 29.9, 40.2, 46.5, 46.8, 51.8, 52.2, 53.5, 106.0, 106.7, 113.4 (d, $J = 15$ Hz), 114.1, 125.4, 127.1 (d, $J = 9$ Hz), 127.8, 128.2, 131.5, 133.9 (d, $J = 13$ Hz), 134.7 (d, $J = 179$ Hz), 143.9 (d, $J = 14$ Hz), 144.4, 144.9, 146.9 (d, $J = 2$ Hz), 156.3, 156.9, 176.0, 176.8, 186.2; ESI-MS obsd (+) 729.3 $(M - H + 2Na)^+$, 707.3 $(M + Na)^+$, (–) 683.2 $(M - H)^-$, calcd 684.26 ($M = C_{35}H_{45}N_2O_8PS$). Anal. Calcd for $C_{35}H_{45}N_2O_8PS$: C, 61.39; H, 6.62; N, 4.09; P, 4.52; S, 4.68. Found: C, 61.03; H, 6.62; N, 3.91; P, 4.4; S, 5.64.

Dye 23 Disodium Salt. Dye **23** (0.50 g, 0.73 mmol) was dissolved in a mixture of DI water (200 mL) and methanol (50 mL). The solution was passed through a column (2.5 cm × 10 cm) of Dowex 50-8X anion exchange resin, sodium form. After the remaining dye was washed off the column with DI water, the aqueous solution was concentrated to approximately 20 mL. The solution was filtered through a medium frit and was evaporated under vacuum to afford the sodium salt of dye **23** as a blue solid (0.49 g, 92%). Anal. Calcd for $C_{35}H_{43}N_2O_8PSNa_2 \cdot (H_2O)_2$: C, 54.97; H, 6.19; N, 3.66; P, 4.05; Na, 6.01. Found: C, 54.66; H, 5.97; N, 3.66; P, 3.90; Na, 6.30.

Dye 24. To a 100 mL flask were added **1** (0.50 g, 1.87 mmol), malonaldehyde dianilide hydrochloride (0.50 g, 1.93mmol), acetic acid (6 mL), and acetic anhydride (6 mL). The mixture was heated at 110 °C for 2.5 h and then was cooled to room temperature. The volatile components were removed under vacuum to leave a tar that was washed with ether (2 × 40 mL). The tar was dissolved in acetic acid (4 mL), and then pyridine (5 mL) and **13** (0.75 g, 2.0 mmol) were added. The mixture was heated at 110 °C for 1 h and then was cooled to room temperature. The volatile components were removed under vacuum to leave a dark-blue tar. The tar was worked up as described for compound **16** (concentrated hydrochloric acid (30 mL), RP column chromatography (4 cm × 15 cm), 0–55% (v/v) methanol in water) to afford **24** as a blue solid (0.47 g, 46%): R_f = 0.26 (C18-SiO_2, water/methanol, 1:1), 0.18 (C18-SiO_2, RPA/methanol, 3:1); ^{1}H NMR (CD_3OD) δ 1.36–1.40 (m, 6H), 1.73 (s, 12H), 4.12–4.18 (m, 4H), 4.47 (s, 2H), 6.27–6.32 (m, 2H), 6.62 (t, J = 12.4 Hz, 1H), 7.25–7.29 (m, 2H), 7.36–7.39 (m, 1H), 7.46 (d, J = 1.2 Hz, 1H), 7.83–7.90 (m, 2H), 7.18 (s, 1H) and 8.22–8.30 (m, 2H); ^{13}C NMR δ 12.5, 12.6, 27.7, 27.9, 39.9, 40.2, 42.6, 50.4, 50.7, 104.0, 104.4, 110.8 (d, J = 14 Hz), 111.9, 123.0, 125.9 (d, J = 10 Hz), 126.8, 129.3, 132.8 (d, J = 12 Hz), 135.7 (d, J = 192 Hz), 137.2, 141.9 (d, J = 15 Hz), 142.4, 143.3, 144.2 (d, J = 3 Hz), 155.5, 155.9, 163.8, 174.2, 174.7; ESI-MS obsd (+) 548.4 $(M + H)^+$, (–) 546.4 $(M - H)^-$, calcd 547.26 ($M = C_{31}H_{38}N_3O_4P$).

Dye 25. To a 500 mL flask were added dye **24** (0.39 g, 0.713 mmol), methanol (100 mL), and concentrated HCl (10 mL). The mixture was stirred at room temperature for 40 h. The mixture was diluted with water (200 mL) and then was basified by addition of saturated sodium bicarbonate solution. The aqueous solution was filtered and was loaded onto a column of RP silica gel (3 cm × 10 cm) in water. The column was washed with water to remove the salts and excess base, 1.0 M HCl (50 mL) and finally with water (500 mL) to remove the excess acid. Gradient elution from 0% to 80 % (v/v) methanol in water (the methanol was increased in steps of 10% and volumes from 500 mL to 1 L of eluent were used for each step) first eluted residual starting material and then **25**. The fractions were evaporated under vacuum to leave a blue residue that was taken up in methanol (10 mL). The solution was filtered through a medium frit, and the methanol was removed under vacuum to afford **25** as a blue solid (0.266 g, 72%): R_f = 0.12 (C18-SiO_2, water/methanol, 1:1), 0.12 (C18-SiO_2, RPA/methanol, 3:1); ^{1}H NMR (CD_3OD) δ 1.23–1.33 (m, 6H), 1.63 (s, 12H), 4.00–4.12 (m, 6H), 6.20 (d, J = 13.8 Hz, 1H), 6.28 (d, J = 13.8 Hz, 1H), 6.56 (t, J = 12.3 Hz, 1H), 7.19–7.25 (m, 2H), 7.41–7.43 (m, 1H), 7.53 (s, 1H), 7.72–7.84 (m, 2H), and 8.12–8.22 (m, 2H); ^{13}C NMR δ 12.5, 12.6, 27.8, 27.9, 40.0, 40.2, 42.3, 50.4, 50.7, 104.0, 104.9, 111.2 (d, J = 14 Hz), 111.9, 124.4, 126.0 (d, J = 11 Hz), 127.1, 130.8, 132.3, 132.8 (d, J = 10 Hz), 136.7 (d, J = 177 Hz), 142.1 (d, J = 15 Hz), 143.4, 143.7, 144.0 (d, J = 3 Hz), 155.5, 156.2, 173.9, 175.3; ESI-MS obsd (+) 520.3 $(M + H)^+$, 542.3 $(M + Na)^+$, calcd 519.27 ($M = C_{30}H_{38}N_3O_3P$).

Dye 26. To a 100 mL flask were added **2** (0.41 g, 1.15 mmol), squaric acid (0.063 g, 0.54 mmol), *n*-butanol (50 mL), and toluene (30 mL). The flask was fitted with a Dean–Stark trap, and then the mixture was heated at reflux overnight. After the mixture was cooled to room temperature, the solid was filtered off, washed with DCM (3 × 30 mL), and dried. The solid was dissolved in 0.2 M potassium carbonate solution (150 mL), and the solution was stirred for 6 days. Hydrochloric acid (1.0 M) was added to lower the pH to approximately 1–2. A suspension formed that was stirred for a further 1 h. The solid was filtered off and was washed with water (2 × 3 mL). The solid was dried under vacuum to afford dye **26** as a blue solid (0.32 g, 72%): R_f = 0.11 (C18-SiO_2, water/methanol, 3:1), 0.16 (C18-SiO_2, RPA/methanol, 3:1); ^{1}H NMR (DMSO-d_6) δ 1.35–1.42 (4H, m), 1.56 (quintet, J = 7.3 Hz, 4H), 1.65–1.75 (m, 16H), 2.21 (t, J = 7.2 Hz, 4H), 4.07–4.14 (m, 4H), 5.85 (s, 2H), 7.39–7.42 (m, 2H), 7.63–7.69 (m, 2H), 7.73 (d, J = 11.8 Hz, 2H); ^{13}C NMR δ 24.4, 26.0, 26.5, 26.7, 33.7, 43.2, 48.8, 87.1, 110.2 (d, J = 16 Hz), 124.4 (d, J = 12 Hz), 129.1 (d, J = 184 Hz), 131.3 (d, J = 11 Hz), 141.2 (d, J = 16 Hz), 144.5 (d, J = 3 Hz), 169.5, 174.5, 179.9, 180.8; ESI-MS obsd (–) 783.2 $(M - H)^-$, 805.3 $(M + Na - 2H)^-$, calcd 784.26 ($M = C_{38}H_{46}N_2O_{12}P_2$). Anal. Calcd for $C_{38}H_{46}N_2O_{12}P_2$: C, 58.16; H, 5.91; N, 3.27; P,7.89. Found: C, 57.84; H, 6.13; N, 3.60; P, 7.70.

Dye 14-(NHS Ester)$_2$. To a 25 mL flask were added **14** (44.8 mg, 0.059 mmol), water (0.3 mL), DMF (3 mL), and diisopropylethylamine (DIEA) (0.2 mL). The mixture was stirred until the solid dissolved, and then succinimidotetramethyluronium tetrafluoroborate (TSTU) (35.8 mg, 0.119 mmol) was added. Stirring was continued for 1 h, and then the volatile components were removed under high vacuum without heating. The residue was washed with ethyl acetate (2 × 20 mL), THF (2 × 20 mL), and acetonitrile (2 × 20 mL). The residue was dried under high vacuum overnight with phosphorus pentoxide to afford **14**-(NHS ester)$_2$ as a dark-red solid (48.1 mg). Dye content by RP HPLC was 71% **14**-(NHS ester)$_2$, 24% **14**-NHS ester, and 5% **14**. ESI-MS obsd (–) 909.2 $(M - H)^-$, calcd 910.3 ($M = C_{43}H_{52}N_4O_{14}P_2$).

Dye 16-NHS Ester. To a 25 mL flask were added **16** (89.5 mg, 0.161 mmol), water (0.7 mL), and DMF (1.4 mL). The mixture was stirred until the solid dissolved, and then DIEA (0.24 mL) and DMF (4.8 mL) were added. After the mixture was stirred for 10 min, TSTU (50.3 mg, 0.167 mmol) was added. Stirring was continued for 1 h, and then the volatile components were removed under high vacuum without heating. The residue was dissolved in DCM, and the solution was filtered through a medium frit. The DCM was evaporated under vacuum without heating, and the residue was dried under high vacuum overnight with phosphorus pentoxide to afford **16**-NHS ester as a dark-red solid (147 mg). Dye content by RP HPLC was 96% **16**-NHS ester and 4% **16**. ESI-MS obsd (–) 646.2 $(M - H)^-$, calcd 647.3 ($M = C_{35}H_{42}N_3O_7P$).

Dye 18-NHS Ester. To a 50 mL flask were added **18** (102.5 mg, 0.150 mmol), water (0.8 mL), and DMF (1.8 mL). The mixture was stirred until the solid dissolved, and then DIEA (0.16 mL) and DMF (3.6 mL) were added. After the mixture was stirred for 10 min, TSTU (70 mg, 0.23 mmol) was added. Stirring was continued for 1 h, and then the volatile components were removed under high vacuum without heating. The residue was washed with DCM (3 × 30 mL) to afford a solid. The solid was filtered off, washed with acetonitrile (3 × 20 mL), and dried under high vacuum overnight with phosphorus pentoxide to afford **18**-NHS ester as a dark-red solid (109 mg). Dye content by RP HPLC was 92% **18**-NHS ester and 8% **18**. ESI-MS obsd (–) 754.1 (M – H), calcd 755.3 ($M = C_{37}H_{46}N_3O_{10}PS$).

Dye 20-NHS Ester. To a 25 mL flask were added **20** (42 mg, 0.064 mmol), water (0.3 mL), DMF (3 mL), and DIEA

(0.2 mL). The mixture was stirred until the solid dissolved, and then TSTU (19 mg, 0.119 mmol) was added. Stirring was continued for 1 h, and then the volatile components were removed under high vacuum without heating. The residue was washed with ethyl acetate (2 × 20 mL), THF (2 × 20 mL), and acetonitrile (2 × 20 mL). The residue was dried under high vacuum overnight with phosphorus pentoxide to afford **20**-NHS ester as a dark-blue solid (37.2 mg). Dye content by RP HPLC was 82% **20**-NHS ester and 18% **20**. ESI-MS obsd (–) 752.1 $(M - H)^-$, calcd 753.3 ($M = C_{37}H_{45}N_3O_{10}P_2$).

Dye 21-NHS Ester. Procedure as for compound **16**-NHS ester with **21** (93 mg, 0.163 mmol), water (0.7 mL), DMF (1.4 mL), DIEA (0.20 mL), DMF (4.9 mL), and TSTU (50 mg, 0.166 mmol) gave **21**-NHS ester as a blue solid (137 mg). Dye content by RP HPLC was 90% **21**-NHS ester and 10% **21**. ESI-MS obsd (–) 672.2, calcd 673.3 ($M = C_{37}H_{44}N_3O_7P$).

Dye 23-NHS Ester. Procedure as for compound **18**-NHS ester with **23** (95 mg, 0.161 mmol), water (0.7 mL), DMF (1.4 mL), DIEA (0.14 mL), DMF (2.8 mL), and TSTU (60 mg, 0.20 mmol) gave **23**-NHS ester as a dark-blue solid (101 mg). Dye content by RP HPLC was 94% **23**-NHS ester and 6% **23**. ESI-MS obsd (–) 780.1 (M – H), calcd 781.28 ($M = C_{39}H_{48}N_3O_{10}PS$)

Dye 26-(NHS ester)$_2$. To a 50 mL flask were added **26** (49.7 mg, 0.061 mmol), water (0.3 mL), and DMF (3.0 mL). The mixture was stirred until the solid dissolved, and then DIEA (0.3 mL) was added. After the mixture was stirred for 20 min, TSTU (36.7 mg, 0.121 mmol) was added. Stirring was continued for 1 h, and then the mixture was filtered. The volatile components were removed under high vacuum without heating, and the residue was washed with ethyl acetate (3 × 30 mL), THF (30 mL), and acetonitrile (2 × 30 mL). The solid was dried under high vacuum overnight with phosphorus pentoxide to afford **26**-(NHS ester)$_2$ as a dark-blue solid (109 mg). Dye content by RP HPLC was 83% **26**-(NHS ester)$_2$ and 17% **26**-NHS ester. ESI-MS obsd (–) 977.2 (M – H), calcd 978.3 ($M = C_{46}H_{52}N_4O_{16}P_2$).

Protein Labeling with Dye Succinimidyl Esters. A stock solution of the sheep γ globulin (S-IgG) (Sigma-G9887) was prepared at a concentration of 2 mg/mL (approximately 1.33×10^{-5} M) in carbonate–bicarbonate buffer, pH 9.3. One milliliter aliquots of the stock were dispensed into vials. Stock solutions of the active esters of dyes **16**, **18**, **21**, **23**, and **26** were prepared at a concentration of 0.01 M in DMSO. Saturated solutions of the active esters of dyes **14** and **20** were prepared by adding sufficient material to produce a 0.01 M solution to the appropriate volume of DMSO and shaking the mixture for 2 h at room temperature. Aliquots of the active ester stock solutions were added to the protein solutions to provide a range of starting dye to protein ratios from 0.7:1 to 50:1. The solutions were mixed well and left to stand at room temperature overnight. The samples were divided into two or three equal portions and were purified by size exclusion chromatography on Sephadex G50 (0.7 cm × 12 cm) using either carbonate–bicarbonate buffer, pH 9.3, BBS, pH 8.1, or PBS, pH 7.3, as effluent. The labeled proteins, which eluted from the column prior to the hydrolyzed active esters, were stored at 4 °C. Solutions were warmed to room temperature and were filtered before absorption and fluorescence spectra were recorded. Conjugates of Cy3 and of Cy5 were prepared by following the methods supplied with the products.

Extinction Coefficients and Fluorescence Quantum Yields. Stock solutions of dyes were prepared from weighed samples of dried material and then were serially diluted to provide five solutions with absorbance values in the range 0.2–1. Extinction coefficients (ε) were determined from plots of the absorbance values vs concentration according to Beer's law. Measurements were repeated with fresh solutions, and average values were calculated. Solutions used for absorbance measurements were diluted 20× prior to use in fluorescence measurements. Quantum yields (QYs) were determined relative to standards (rhodamine 6G (QY = 0.86 in ethanol (*14*)) for dyes with absorption maxima in the range 540–560 nm; Cy5.18 (QY = 0.27 in PBS pH 7.3 (*4*)) for dyes with absorption maxima in the range 630–680 nm) and are intended to indicate trends rather than absolute values. For dyes used in labeling experiments, QYs are an average of at least three measurements. Variation between measurements used to calculate extinction coefficients and quantum yields fell within 15% of each other. Values for quantum yields were rounded to two decimal places.

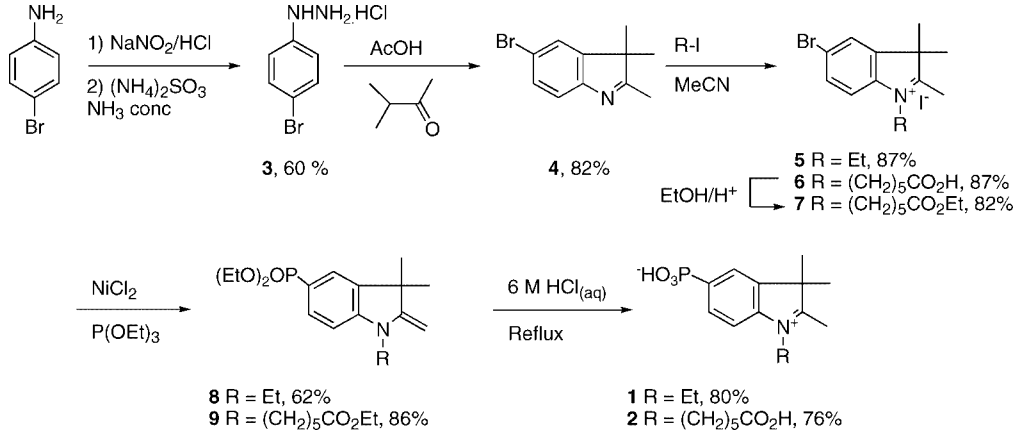
Determination of Dye to Protein Ratios and Conjugate Brightness. Dye to protein (*D*/*P*) ratios were determined as outlined in ref *5*. In cases where absorbance spectra recorded in aqueous solution indicated significant dye aggregation, the solutions were diluted (1:2) with formamide and absorbance spectra recorded again. For each conjugate solution the concentration of dye was estimated using the absorbance of the dye at the peak maximum and the extinction coefficient of free dye according to Beer's law. The absorbance of the conjugated dye at 280 nm was calculated using the ratio of the extinction coefficients of the free dye at 280 nm to that at the peak maximum. (For squarane dye **26**, $\varepsilon_{280nm}/\varepsilon_{peak\ max} = 0.041$. For trimethine cyanine dyes **14**, **16**, and **18**, $\varepsilon_{280nm}/\varepsilon_{peak\ max} = 0.083$. For pentamethine cyanine dyes **20**, **21**, and **23**, $\varepsilon_{280nm}/\varepsilon_{peak\ max} = 0.026$.) The concentration of the protein (MW = 155 000, $\varepsilon_{280nm} = 165\,000$ L mol^{-1} cm^{-1}) was determined from the absorbance value of the solution at 280 nm after correction for the absorbance of the conjugated dye at 280 nm. Conjugate brightness is defined as the product of the extinction coefficient, the quantum yield, and the number of dyes per protein molecule ($(\varepsilon)(QY)(D/P)$). Quantum yields of conjugates were determined in wholly aqueous solutions.

Oligonucleotide Labeling with Dye Succinimidyl Esters. A T_{10} DNA oligonucleotide was prepared using standard automated synthesis regimes on a Biosearch 8700 oligonucleotide synthesizer. For Quasar 570 and Quasar 670, amidites of the dyes were coupled to the DNA fragment on the controlled pore size glass (CPG) solid support. For the other dyes, a monomethoxytrityl (MMT) protected amino C6 functionalized amidite (Biosearch Technologies, Inc.) was manually coupled to the DNA fragment and then the protecting group was removed to afford the amino-modified oligonucleotides still attached to CPG. For cyanine monophosphonates **16**, **18**, **21**, and **23**, the CPG (10 mg) was shaken overnight in a DMSO solution (0.30 mL) of the active ester (3 mg) and *N*-methylmorpholine (0.020 mL). For Cy3 and Cy5, the CPG (10 mg), DMSO (0.3 mL), and *N*-methylmorpholine (0.020 mL) were added to the vial of reactive dye supplied by the manufacturer and the mixtures were shaken overnight. The DNA was cleaved from the CPG using concentrated aqueous ammonia at room temperature for 1 h. The solutions were frozen, and the volatile components were removed using a speed vac. The crude oligonucleotides were purified by a combination of AX and RP HPLC to afford the labeled oligonucleotides that were characterized by electrospray MS. T_{10}-**16**: obsd (–) 3692, calcd 3691. T_{10}-**18**: obsd (–) 3800, calcd 3801. T_{10}-**21**: obsd (–) 3718, calcd 3717. T_{10}-**23**: obsd (–) 3825, calcd. 3827. T_{10}-Q570: obsd (–) 3600, calcd 3601. T_{10}-Q670: obsd (–) 3626, calcd 3627. T_{10}-Cy3.29: obsd (–) 3772, calcd 3771. T_{10}-Cy5.29: obsd (–) 3798 $(M - H)^-$, calcd 3797.

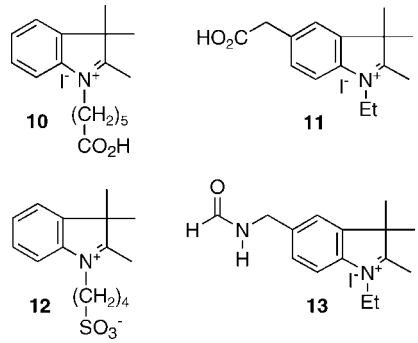
RESULTS AND DISCUSSION

1. Synthesis of Dyes. Key intermediates for the syntheses of the cyanine and squarane dyes are the indolium phosphonates **1** and **2** (Scheme 1). *p*-Bromoaniline was converted into the hydrazine hydrochloride **3**, which was then subjected to Fischer indole condensation with methylbutanone to afford bromoindole

Scheme 1. Synthetic Route To Indolium Phosphonates



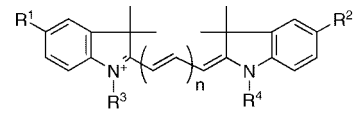
4 (*15*). Preliminary investigation of the nickel-catalyzed substitution reaction of the bromine for phosphonate (*16*) demonstrated that bromoindole **4** could be phosphonated in high yield, but partial ethylation of the indole nitrogen also occurred resulting in a mixture of products. It should be noted that this reaction is extremely vigorous once it begins because of the generation of ethyl bromide in the reaction mixture at temperatures of 160–180 °C. Further study indicated that bromoindolium salts **5** and **6** could be phosphonated with this method. To avoid the possibility of partial ethylation of the carboxylic acid of **6** and a mixture of reaction products, **6** was converted to the ethyl ester **7**. The phosphonation reaction of salts **5** and **7** generated the charge neutral compounds **8** and **9**, which proved to be difficult to isolate in analytically pure form. Hydrolysis of **8** and **9** using refluxing in 6 M hydrochloric acid gave indolium phosphonates **1** and **2** and also small quantities of byproducts in which the phosphonic acid residue was removed from the indolium residue. Compounds **8** and **9** turned pink-red upon exposure to air in a matter of hours, whereas **1** and **2** became colored over a few days. All of these compounds can be stored indefinitely in a desiccator under argon.



Indolium salts **10**–**12** were prepared by literature methods (*17*). Formyl protected aminomethyl indolium salt **13** was prepared from the corresponding aminomethylindole (*18*) by sequential treatment with methyl formate and with ethyl iodide.

Symmetrical and unsymmetrical cyanine dyes and squarane dyes **14**–**25** (Chart 1) were prepared from salts **1** and **2**, and the nonphosphonate indolium salts **10**–**13** were prepared using literature methods with some minor changes as noted below. Attempts to prepare the symmetrical trimethine cyanine dye **14** with the commonly used reaction mixture of triethyl orthoformate in pyridine generated dye **15** in which monophosphonate ethyl esters were formed. Treatment of **15** with refluxing in 6 M hydrochloric acid to hydrolyze these esters resulted in stepwise cleavage of the phosphonate groups from the dye in

Chart 1

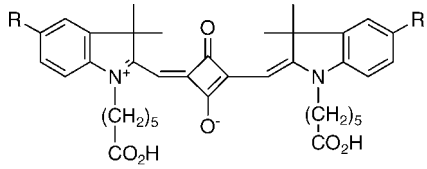


	n	R^1	R^2	R^3	R^4
14	1	PO_3H^-	PO_3H_2	$(CH_2)_5CO_2H$	$(CH_2)_5CO_2H$
15	1	$PO_2(OEt)^-$	PO(OH)(OEt)	$(CH_2)_5CO_2H$	$(CH_2)_5CO_2H$
16	1	PO_3H^-	H	Et	$(CH_2)_5CO_2H$
17	1	PO_3H^-	CH_2CO_2H	Et	Et
18	1	H	PO_3H_2	$(CH_2)_4SO_3^-$	$(CH_2)_5CO_2H$
19	2	PO_3H^-	PO_3H_2	$(CH_2)_5CO_2H$	$(CH_2)_5CO_2H$
20	2	PO_3H^-	PO_3H_2	Et	$(CH_2)_5CO_2H$
21	2	PO_3H^-	H	Et	$(CH_2)_5CO_2H$
22	2	PO_3H^-	CH_2CO_2H	Et	Et
23	2	H	PO_3H_2	$(CH_2)_4SO_3^-$	$(CH_2)_5CO_2H$
24	2	PO_3H^-	CH_2NHCHO	Et	Et
25	2	PO_3H^-	CH_2NH_2	Et	Et
Cy3.18 (*4*)	1	SO_3^-	SO_3H	$(CH_2)_5CO_2H$	$(CH_2)_5CO_2H$
Cy5.18 (*4*)	2	SO_3^-	SO_3H	$(CH_2)_5CO_2H$	$(CH_2)_5CO_2H$
Cy3.29 (*4*)	1	SO_3^-	SO_3H	$(CH_2)_5CO_2H$	Et
Cy5.29 (*4*)	2	SO_3^-	SO_3H	$(CH_2)_5CO_2H$	Et
Quasar 570	1	H	H	R	Et
Quasar 670	2	H	H	R	Et

R =$(CH_2)_5CONH(CH_2)_2O(CH_2)_2OP(NPr_2)(O(CH_2)_2CN)$

addition to phosphonate ester cleavage. Symmetrical trimethine and pentamethine cyanine dyes were prepared in acetic anhydride with sodium acetate as base catalyst using either diphenylformamidine or malonaldehyde dianilide, respectively. Unsymmetrical trimethine and pentamethine cyanine dyes were prepared by first reacting one salt with either diphenylformamidine or malonaldehyde dianilide, respectively, in a mixture of acetic anhydride and pyridine and then treating the resulting intermediate with the second salt in a mixture of pyridine and acetic acid. Analysis of the crude reaction mixtures by RP HPLC indicated that in addition to the desired dyes, significant quantities of byproducts with absorption spectra resembling those of cyanine dye dimers were present. Treatment of the crude reaction mixtures with 1.0 M hydrochloric acid or with 1.0 M sodium carbonate solution for 16 h altered the HPLC trace profile by reducing the products with dimerlike absorption spectra and enhancing those with monomer like spectra. Treatment with concentrated hydrochloric acid for 3 h eliminated these byproducts completely. It seems likely that under the conditions of the condensation reactions dimeric and oligomeric species in which the dyes are connected through the phosphonate groups are formed. These byproducts were more prevalent the longer the phosphonic acid containing salts were heated with acetic anhydride. In the case of some of the unsymmetrical dyes the byproducts were avoided by using the indolium phosphonate in the second step of synthesis rather than the first. In the case of the formyl protected dye **24** partial cleavage of the formyl group was observed during the acid treatment. The formyl group was removed from purified dye **24** using methanolic hydrochloric acid. All of the dyes were isolated by RP column chromatography using gradient elution of methanol in either water or RPA buffer. Elemental analysis indicated that cyanine monophosphonates and diphosphonates were isolated as the zwitterionic forms.

Squaraine diphosphonate **26** was prepared by condensation of indolium salt **2** with squaric acid in a boiling mixture of butanol and toluene (*19, 20*), followed by cleavage of any butyl esters that formed with aqueous potassium carbonate, and was isolated in 72% yield as the zwitterion without the need for chromatography.



26 R = PO_3H_2
Sq 635-b R=SO_3H (*20*)

2. Properties of Dyes. All of the dyes are soluble in water to a greater or lesser degree. The cyanine diphosphonates **14**, **19**, and **20** are readily soluble in aqueous media over a wide range of pH (2–12). In contrast, the zwitterionic cyanine monophosphonates such as **16**, **17**, **21**, and **22** have limited solubility in water and in buffers below pH 7. Sodium salts of cyanine monophosphonates **16** and **21** are highly soluble in water. Cyanine monophosphonates **18**, **23**, and **25**, which have additional water solubilizing groups, maintained good solubility at lower pH (2–7). Cyanine monophosphonates and diphosphonates and squarane diphosphonate **26** may be precipitated from aqueous solution by lowering the pH to 1–2 with hydrochloric acid. After the precipitates were washed with water, the dyes were isolated in their zwitterionic forms.

The cyanine and squaraine phosphonates have similar absorption maxima, emission maxima, and extinction coefficients as their sulfonated analogues (Table 1). In the case of the pentamethine cyanine dyes **19–25**, the pH sensitivity of absorption maxima, emission maxima, and fluorescence quantum yields (QYs) were investigated to determine the effect of the protonation state of the phosphonic acid group on photophysical properties of the dyes. On the basis of the p*K* values for phenylphosphonic acid, 1.83 and 7.07 (*21*), it was assumed that at pH 9.3 the phosphonate group will carry two negative charges; at pH 4 it will have one charge, and at pH 1 it would be neutral. For the pentamethine dyes **19–25** the absorption and emission maxima shift 4–10 nm to the blue when the pH is lowered from 9.3 to 1. The QYs of cyanine diphosphonates **19** and **20** increase slightly as the pH is lowered, whereas those of the cyanine monophosphonates **21–23** decrease dramatically when the pH is lowered from 4 to 1. Comparison of the absorption spectra of **21** at the different pH values shows that at pH 1 the shorter-wavelength shoulder (approximately 605 nm) is significantly higher with respect to the peak maximum than at pH 4. This suggests that aggregation, which usually causes fluorescence quenching, is occurring (Figure 1 in Supporting Information). No such absorption spectrum changes were seen with cyanine diphosphonate **19**. Cyanine monophosphonate **23**, which has the pendent sulfonate group, shows intermediate behavior. The QY of amine containing monophosphonate **25** increases as the pH is lowered presumably because the protonated amine assists

Table 1. Photophysical Data for Cyanine Phosphonates, Squaraine Phosphonates, and Related Dyes

dye	pH[a]	absorption max, nm	emission max, nm	extinction coefficient, [b] L mol^{-1} cm^{-1}	QY[b]
14	9.3	556	571		0.07
	7.3	555	569	133 000	0.07
15	7.3	552	564		0.08
16	9.3	549	564		0.04
	7.3	548	563	133 000	0.04
17	7.3	552	567		0.03
18	9.3	551	565		0.05
	7.3	550	564	133 000	0.05
19	9.3	654	672		0.17
	7.3	652	668		0.17
	4.0	651	666		0.20
	1.0	649	663		0.18
20	9.3	653	669	240 000	0.14
	7.3	651	668	240 000	0.15
	4.0	649	666		0.19
	1.0	647	663		0.19
21	9.3	647	665		0.14
	7.3	646	663	210 000	0.15
	4.0	645	662		0.13
	1.0	643	662		0.05
22	9.3	650	668		0.12
	7.3	649	667		0.11
	4.0	647	665		0.11
	1.0	645	664		0.06
23	9.3	648	666		0.14
	7.3	647	665	220 000	0.16
	4.0	646	663		0.15
	1.0	644	663		0.08
25	9.3	650	668		0.12
	7.3	646	663		0.13
	4.0	645	662		0.15
	1.0	644	661		0.16
26	9.3	637	647		0.04
	7.3	635	644	260 000	0.04
	4.0	634	643		0.04
	1.0	insoluble			
Cy5.18 (*4*)	7.3	649	666	250 000	0.27
Cy5.29 (*4*)	7.3			250 000	0.20
Cy3.18 (*4*)	7.3	550	665	150 000	0.04
					0.07
Sq635-b (*20*)		635	648	140 000	0.15

[a] pH 1, 1.0 M hydrochloric acid; pH 4, 1.0 M NaH_2PO_4; pH 7.3, PBS; pH 9.3, carbonate–bicarbonate buffer. [b] Errors are estimated to be ±10%.

in preventing aggregation. For biological applications, measurements are typically made in the pH range 6–8 within which likely falls the second p*K* of the phosphonic acid group of the dyes. Consequently, the phosphonic acid group should not be considered completely in either the deprotonated or the monoprotonated forms within this pH range.

The cyanine diphosphonates **19** and **20** have lower QYs than do their respective sulfonate analogues Cy5.18 and Cy5.29. Cyanine diphosphonate **14** was found to have similar QY as Cy3.18, although the current study was unable to reproduce the reported QY of 0.04 for Cy3.18 (*4*). Squarane diphosphonate **26** has a higher extinction coefficient but lower QY than its sulfonated analogue Sq635-b (*20*).

3. Synthesis of Succinimidyl Esters. Succinimidyl esters are one of the most commonly used reactive forms of dyes for labeling of amine containing substrates such as proteins and were thought to be a suitable form for the testing of the new dyes. Treatment of the cyanine monophosphonates, such as **16** and **21**, with commonly used activating reagents such as disuccinimidyl carbonate/pyridine, dicyclohexylcarbodiimide/*N*-hydroxysuccinimide, or succinimidotetramethyluronium tetrafluoroborate (TSTU)/diispropylethylamine (DIEA) under anhydrous conditions resulted in mixtures of products some of which exhibited cyanine dimerlike absorption maxima. LC–MS confirmed the presence of dye dimers. Treatment of these mixtures with carbonate-bicarbonate buffer, pH 9.3, for several days did not convert the mixtures back to the starting material, but rather the dimer impurities persisted indicating that the dyes had been linked to each other through the phosphonate groups. The reactivity of phosphonate groups to these activating agents under anhydrous conditions is serious enough to prevent selective activation of carboxylic acid of the dye. Treatment of the cyanine monophosphonates with TSTU/DIEA under partially aqueous (10–15% water) conditions suppressed the formation of the dimer byproducts. It is important to avoid excess TSTU and to ensure that the dye is completely dissolved before the TSTU is added. Active esters of cyanine monophosphonates **16**, **18**, **21**, and **23** were prepared with approximately 90% yield, but separation of the nondye byproducts of the reaction proved to be difficult, and therefore, the crude mixtures were used in labeling experiments without purification. To permit accurate estimation of stoichiometry for labeling experiments, effective molecular weights were calculated on the basis of the mass of starting dye, the mass of final product, and the amount of the dye in the active ester form as determined by RP HPLC at the absorption maximum of the dye. When the disodium salts of dyes **18** and **23** were used, then the active esters were easily separated from the nondye byproducts of the activation reaction. HPLC analysis of the cyanine monophosphonate active esters indicated little decomposition or hydrolysis during storage in a freezer at −8 °C at for at least 3 months.

Application of the partially aqueous activating conditions to the squaraine diphosphonate **26** generated the disuccinimidyl ester in good yield, but activation of cyanine diphosphonates **14**, **19**, and **20** under similar conditions was problematic. After removal of the volatile components from the reaction mixtures and washing, the residues exhibited poor solubility in solvents such as DMSO and DMF. The active esters of **14** and **20** are highly soluble in aqueous media, and solid samples that were added to carbonate–bicarbonate buffer dissolved immediately. RP HPLC analysis of these solutions indicated that the active esters were hydrolyzed back to the starting acids in a few hours. Saturated solutions of the active esters of **14** and **20** in DMSO were used for labeling studies.

4. Protein Labeling Studies. Sheep IgG was labeled in carbonate-bicarbonate buffer at pH 9.3 using the active esters of diphosphonate dyes **14**, **20**, and **26** and of monophosphonate dyes **16**, **18**, **21**, and **23** to produce conjugates with a range of dye to protein (*D*/*P*) ratios. Samples were divided and were purified by G50 size exclusion chromatography using PBS, pH 7.3, BBS, pH 8.1, or carbonate-bicarbonate buffer, pH 9.3. All conjugates remained soluble during labeling at pH 9.3 and during purification in the three buffer systems, but solutions of conjugates of cyanine monophosphonates **16** and **21** with high (>5) *D*/*P* ratios developed precipitates when stored for several days at 4 °C in PBS at pH 7.3. Some of the precipitates dissolved when the solutions were warmed to room temperature. Conjugates of the other dyes did not form precipitates in any of the buffer media. Sheep IgG that was mixed with the parent dyes under conditions identical to those used for labeling separated completely from the dyes when subjected to size exclusion chromatography, indicating that nonspecific binding of the dyes to the protein does not occur. Sheep IgG was also labeled with Cy3.29 and Cy5.29 (known commercially as Cy3 monofunctional and Cy5 monofunctional, respectively) using methods supplied by the manufacturer. Previous studies have determined that labeling of proteins with disuccinimidyl active esters of cyanine and squaraine dyes under conditions similar to those used here does not cause a noticeable amount of protein cross-linking (*17*, *20*). Conjugation of the cyanine dyes and the squaraine dye to the protein resulted in a red shift to the absorption maximum of the dyes by 2–3 and 6 nm, respectively.

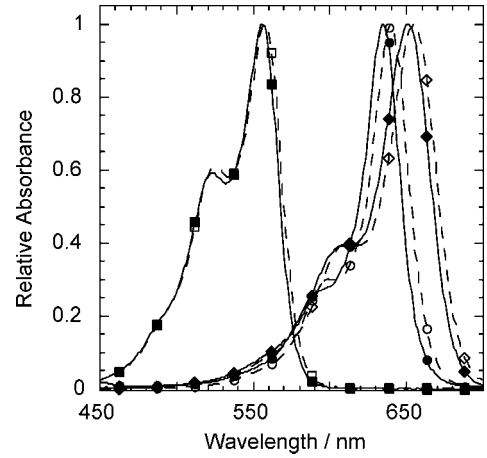


Figure 1. Absorption spectra of dyes (solid lines) and conjugates (dashed lines): **14** (solid squares) and conjugate IgG–(**14**)$_6$ (transparent squares) in BBS, pH 8.1; **20** (solid diamonds) and conjugate IgG–(**20**)$_5$ (transparent diamonds) in BBS, pH 8.1; **26** (solid circles) and conjugate IgG–(**26**)$_3$ (transparent circles) in PBS, pH 7.3.

Typical absorption spectra of the dyes **14**, **20**, and **26** and of their conjugates are shown in Figure 1. Most noticeable is that the absorption spectra of conjugates are almost identical to those of the parent dyes despite the relatively high labeling densities. Usually, in aqueous media, organic dyes held in proximity to each other on the surface of a substrate clump together to form dimers and higher aggregates. Electronic ground-state coupling between the dyes in these aggregates results in different absorption and emission properties than those of the free dye. While some exceptions exist (*5*), it is most common for aggregates of cyanine dyes to show peak maxima that are blue-shifted relative to the free dye. The absorption spectrum of the labeled substrate is the sum of the spectra of the aggregates and of the dye that is still independent. Consequently, aggregation manifests itself in the absorption spectrum as a shoulder on the shorter-wavelength side of the peak maximum of the independent dye, and in extreme cases this shoulder becomes the peak maximum. Thus, the relative height of the shoulder to the peak maximum is an indication of whether aggregation is occurring. Additionally, such aggregates have significantly lower

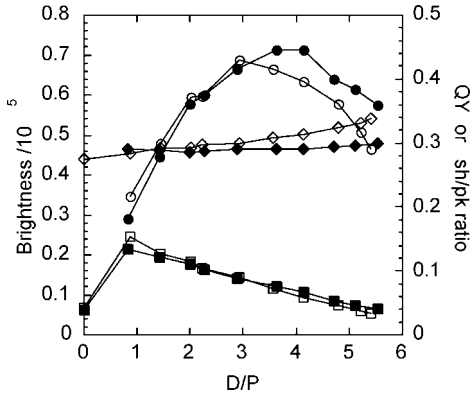


Figure 2. Plots of conjugate brightness (circles), quantum yields (QYs) (squares), and shoulder to peak maximum height (sh/pk) ratio (diamonds) as a function of dye to protein ratio for IgG–**26** conjugates at pH 9.3 (solid symbols) and pH 7.3 (transparent symbols).

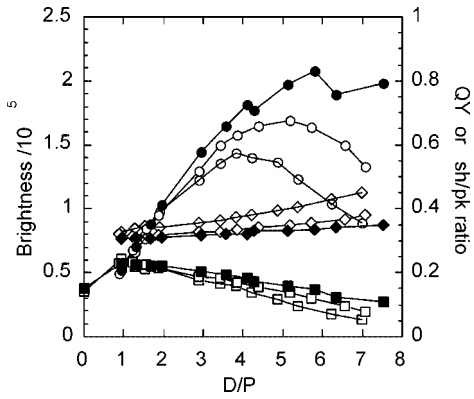


Figure 3. Plots of conjugate brightness (circles), quantum yields (QY) (squares), and shoulder to peak maximum height (sh/pk) ratio (diamonds) as a function of dye to protein ratio for IgG–**20** conjugates at pH 9.3 (solid symbols), pH 8.1 (empty symbols), and pH 7.3 (transparent symbols).

QYs of fluorescence than the free fluorophore and so reduce the QY and the brightness of the labeled substrate (*5, 17, 22*).

At pH 7.3, absorption spectra of the IgG–**26** conjugates show a slight increase in the ratio of the short wavelength shoulder to the peak maximum height (sh/pk ratio) as the *D*/*P* ratio increases, whereas in pH 9.3 buffer there is little change (Figure 2, diamonds). The QY of squaraine **26** increases 4-fold when attached to the protein but then decreases as the dye *D*/*P* ratio increases (Figure 2, squares). The QY is slightly less sensitive to the *D*/*P* ratio at pH 9.3 than at pH 7.3. These differences in the observed absorption and fluorescence properties at the two pH values most likely result from increased ionization of the phosphonic acid residues at the higher pH, with concomitant increases in repulsive dye–dye interactions. The brightness of the conjugates ((ε)(QY)(*D*/*P*)) reaches a maximum with a *D*/*P* ratio of 3 at pH 7.3 and with a *D*/*P* ratio of 4 at pH 9.3 (Figure 2, circles). For comparison, the sulfonate analogue of dye **26**, Sq635-b, was reported to show an increase in QY from 0.15 to 0.68 upon conjugation to bovine serum albumin, but no *D*/*P* ratio for such conjugates was presented (*20*).

The absorption and fluorescence properties of conjugates of cyanine diphosphonate **20** exhibit similar trends as those of squarane diphosphonate **26** (Figure 3). In all three buffers there is a slight increase in the sh/pk ratio and a decrease in QY as the *D*/*P* ratio increases, but at lower pH the changes are more pronounced. The optimal labeling density is pH-dependent with values of 3.5*D*/*P* at pH 7.3, 5*D*/*P* at pH 8.1, and 6*D*/*P* at pH 9.3. For comparison, optimal labeling of IgG with Cy5.29 is

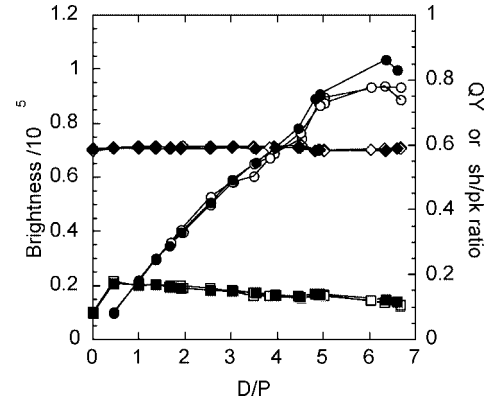


Figure 4. Plots of conjugate brightness (circles), quantum yields (QY) (squares), and shoulder to peak maximum height (sh/pk) ratio (diamonds) as a function of dye to protein ratio for IgG–**14** conjugates at pH 9.3 (solid symbols), pH 8.1 (empty symbols), and pH 7.3 (transparent symbols).

achieved with only 2–3*D*/*P* at which the QY is 0.2 and the conjugate brightness is approximately 1×10^5 (derived from data in ref *22*). Thus, at pH 7.3 the cyanine diphosphonate **20** generates a brighter conjugate than Cy5. If experimental conditions permit the use of media of higher pH, then considerably greater advantage may be gained by use of dye **20**.

Absorption spectra of conjugates of cyanine diphosphonate **14** are relatively insensitive to the *D*/*P* ratio and to pH (Figure 4). The sh/pk ratio remained constant throughout the *D*/*P* range investigated. QY of the dye doubles upon attachment to the protein and then decreases as the *D*/*P* ratio increases. The optimal labeling density with dye **14** is greater than 6*D*/*P* compared 5–6*D*/*P* for Cy3, with the latter having a conjugate brightness of approximately 0.9×10^5 (derived from data in ref *22*). Cyanine diphosphonate **14** offers at least equivalent performance as Cy3.

Cyanine monophosphonates **16**, **18**, **21**, and **23** are more prone to aggregate when attached to sheep IgG than are the cyanine diphosphonates **14** and **20**, as evidenced by the increase of the sh/pk ratio (Figure 2 of Supporting Information). Absorption spectra of dyes **18** and **21**, Cy3 and Cy5, and their conjugates are shown in Figure 5. It is common practice to estimate the concentration of dye in solutions of labeled conjugates through application of Beer's law using the absorbance value at the peak maximum and the extinction coefficient of the free dye. This approach underestimates the *D*/*P* ratio when dye–dye aggregation is significant. Conjugates of the cyanine monophosphonates dyes were diluted with formamide (1:2) to break up the aggregates and permit more accurate estimations of the *D*/*P* ratio. Following the manufacturer's recommended procedures for labeling with Cy3 and Cy5 generated conjugates with 5*D*/*P* and 7*D*/*P*, respectively. In the latter case this *D*/*P* ratio is far from the optimal of 2–3*D*/*P* (*22*).

The absorption and fluorescence properties of conjugates of dyes **16**, **18**, **21**, and **23** followed the same trends as those observed for the conjugates of the cyanine diphosphonates **14** and **20** except that the QY of dye **23** did not increase when the dye was attached to the protein but instead decreased (Figure 6). Optimal labeling densities for the conjugates were determined to be 4*D*/*P* for IgG–**16**, 5*D*/*P* for IgG–**18**, 2–3*D*/*P* for IgG–**21**, and 4*D*/*P* for IgG–**23** (Figure 6). These are lower than for the cyanine diphosphonates **14** and **20** because of increased aggregation and fluorescence quenching of less highly charged dyes. Surprisingly, at optimal labeling densities, dye **21** gives significantly brighter conjugates with 2*D*/*P* than does the sulfonate containing dye **23** with 4*D*/*P*. In all cases, at higher labeling densities the conjugates are brighter at pH 9.3 than at

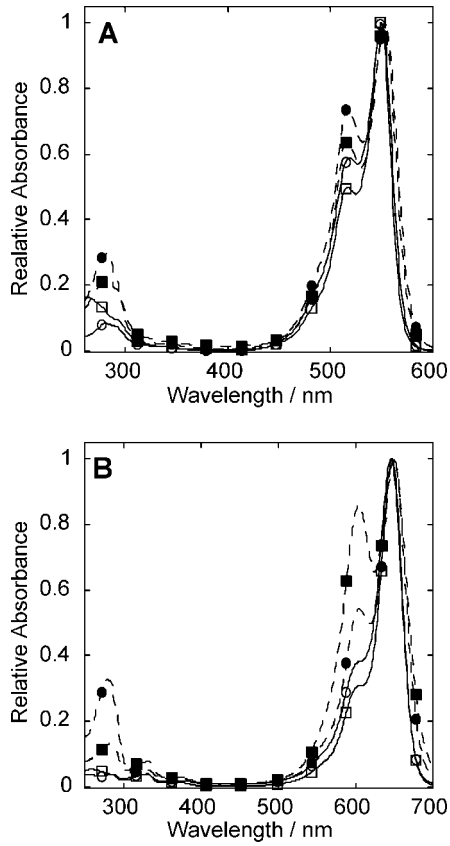


Figure 5. Absorption spectra of dyes (solid lines) and conjugates (dashed lines) in PBS, pH 7.3: (A) **18** (transparent circles), IgG–(**18**)$_4$ (solid circles), Cy3 (transparent squares), IgG–(Cy3) (solid squares); (B) **21** (transparent circles), IgG–(**21**)$_2$ (solid circles), Cy5 (transparent squares), IgG–Cy5 (solid squares).

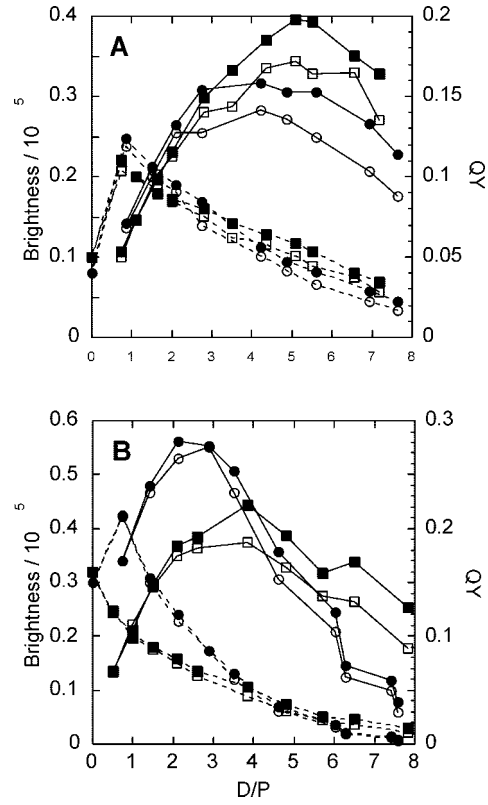


Figure 6. Plots of conjugate brightness (solid lines) and quantum yields (dashed lines) at pH 9.3 (solid symbols) and at pH 7.3 (transparent symbols): (A) IgG–**16** (circles) and IgG–**18** (squares); (B) IgG–**21** (circles) and IgG–**23** (squares).

pH 7.3 whereas at lower labeling densities little difference is seen, again indicating that increased ionization of the phosphonic acid reduces quenching interactions.

The absorption spectra and fluorescence properties of IgG conjugates with cyanine dyes such as Cy3 and Cy5 have been studied at length (*4–6*, *8*, *17, 22*). The initial increase in QY that is seen on conjugation to IgG of the trimethine cyanine dyes such as Cy3, **14**, **16**, and **18** is attributed to a rigidifying effect on the dye caused by association of the dye with the surface of the protein (*4, 22*). In contrast, QYs of pentamethine cyanine dyes, such as Cy5, are less dependent on the environment of the dye, and QYs of conjugates of Cy5 with *D*/*P* ratios less than 1 are similar to those of the free dye (*22*). Labeling of IgG with Cy5 was proposed to proceed in a nonrandom manner with binding of one Cy5 to the protein predisposing the region around the dye to further labeling (*22*), thereby accentuating the likelihood of dye dimer formation on the surface and leading to greater fluorescence quenching than would be seen with random labeling. If this is indeed the case, then labeling with the phosphonated cyanines at pH 9.3, where the phosphonate groups are expected to carry two negative charges, should result in more random labeling and in conjugates that are not so quenched. For cyanine diphosphonate **20**, which is structurally similar to Cy5, the differences between the sh/pk ratios and the large differences in brightness of identical conjugates at pH 9.3 compared to those at pH 7.3 strongly suggest that electronic repulsion between the attached dyes is greater at pH 9.3. Reasons for the differences between the labeling properties of dyes **21** and **23** are not so obvious. The additional sulfonate group of dye **23** has the expected effect of increasing the optimal *D*/*P* ratio, presumably through assisting in solubilizing the dye and offering some inhibition to aggregation. The decrease in QY of dye **23** that is seen when the first dye is attached to the protein is in contrast to all of the other cyanine phosphonates studied here but is commonly seen with cyanine dyes that do not have charges appended to the aromatic residues (*17*). Whatever the mechanisms of labeling and quenching may be, it is clear that the cyanine diphosphonates can produce conjugates that are as bright or brighter than those of commercial Cy3 and Cy5. Conjugates of the monophosphonate cyanines dyes are not as bright as those of Cy3 and Cy5 because of the inherently lower QYs of the parent dyes and because they have a greater tendency to aggregate when attached to the protein.

5. Oligonucleotide Labeling Studies. 5′-Labeled oligodeoxyribonucleotides (ODNs) were prepared by conjugation of the active esters of dyes **16**, **18**, **21**, **23**, Cy3.29, and Cy5.29 to an amino functionalized T_{10}-ODN or by coupling of the amidites of Quasar 570 (Q570) and Quasar 670 (Q670) to a T_{10}-ODN. The pentamethine cyanine dyes **21**, **23**, Q670, and Cy5 in particular decomposed somewhat during the ammonia workup process.

On conjugation to the ODNs, the absorbance maxima of the cyanine monophosphonates are shifted 4 nm to the red and their QYs increase (Table 2), which is consistent with previous observations for cyanine dyes with and without anionic substituents (*9*). ODNs T_{10}-**16** and T_{10}-**18** have similar QYs as ODN T_{10}-Cy3.29, which is lower than that of ODN T_{10}-Q570. ODNs T_{10}-**21** and T_{10}-**23** have lower quantum yields than ODNs T_{10}-Cy5.29 and T_{10}-Q670, which have similar values. The cyanine monophosphonates, and other cyanines that carry anionic charges, such as Cy3 and Cy5, offer no advantage in QY over cyanines that do not carry anionic charges as 5′-fluorescent labels for ODNs, although they may be advantageous when multiple labeling of ODNs or DNA is required.

In conclusion, synthetic methods for the preparation of phosphonic acid containing cyanine and squarane dyes were

Table 2. Photophysical Data for T_{10}-Dye Oligonucleotide Conjugates in PCR Buffer

5′-labeled oligonucleotide	absorption max, nm	emission max, nm	QY
T_{10}-**16**	552	568	0.10
T_{10}-**18**	553	567	0.11
T_{10}-Cy3.29	551	563	0.11
T_{10}-Q570	549	564	0.14
T_{10}-**21**	650	668	0.21
T_{10}-**23**	651	669	0.23
T_{10}-Cy5.29	649	666	0.32
T_{10}-Q670	647	666	0.31

developed. The new dyes have similar spectral properties to existing sulfonic acid containing analogues and can be used to generate brightly labeled dye–protein conjugates. As protein labels, trimethine cyanine diphosphonates, such as dye **14**, are more or less equivalent to the commercial sulfonate analogue Cy3, whereas pentamethine cyanine diphosphonates, such as dye **20**, are superior to the commercial sulfonate analogue Cy5, particularly when used in higher pH environments.

ACKNOWLEDGMENT

The author thanks Alex Herrault for assistance in acquiring LC–MS spectra.

Supporting Information Available: Absorption spectra for dyes **19**, **21**, and **23** and plots of shoulder to peak maximum vs dye to protein ratios for dyes **16**, **18**, **21**, and **23**. This material is available free of charge via the Internet at http://pubs.acs.org.

LITERATURE CITED

(1) Haugland, R. P. (2002) *Handbook of Fluorescent Probes and Research Products*, 9th ed., Molecular Probes, Eugene, OR.
(2) Tsien, R. Y. and Waggoner, A. S. (1995) *Handbook of Biological Confocal Microscopy* (Pawley, J. B., Ed.) Springer, New York.
(3) Panchuk-Voloshine, N., Haugland Rosario, P., Bishop-Stewart, J., Bhalgat, M. K., Millard, P. J., Mao, F., Leung, W.-Y., and Haugland, R. P. (1999) Alexa dyes, a series of new fluorescent dyes that yield exceptionally bright, photostable conjugates. *J. Histochem. Cytochem. 47*, 1179–1188.
(4) Mujumbdar, R. B., Earnst, L. A., Mujumbdar, S. R., Lewis, C. J., and Waggoner, A. S. (1993) Cyanine dye labeling reagents: sulfoindocyanine succinimidyl esters. *Bioconjugate Chem. 4*, 105–111.
(5) Mujumbdar, S. R., Mujumbdar, R. B., Grant, C. M., and Waggoner, A. S. (1996) Cyanine dye labeling reagents: sulfobenzindocyanine succinimidyl esters. *Bioconjugate Chem. 7*, 356–362.
(6) West, R. M., Bosworth, N., and Mujumbdar, R. B. (2005) Cyanine Dye Labeling Reagents. WO 2005/044,923.
(7) Cummins, W., West, R., and Smith, J. A. (2002) Cyanine Dyes. U.S. Patent 6,348,599.
(8) Reddington, M. V. (1998) New glycoconjugated cyanine dyes as fluorescent labeling reagents. *J. Chem. Soc., Perkin Trans. 1*, 143–147.
(9) Gousou, C., Vasseur, J.-J., Bazin, H., Trinquet, E., Maurin, F., and Morvan, F. (2005) Optimized synthesis of functionalized fluorescent oligodeoxynucleotides for protein labeling. *Bioconjugate Chem. 16*, 465–470.
(10) Devlin, R., Studholme, R. M., Dandliker, W. B., Fahy, E., Blumeyer, K., and Ghosh, S. S. (1993) Homogeneous detection of nucleic acids by transient-state polarized fluorescence. *Clin. Chem. 39*, 1939–1943.
(11) Wolfbeis, O. S. (2001) Methods for Solubilizing Optical Markers. WO 01/36,973.
(12) Borbas, K. E., Mroz, P., Hamblin, M., and Lindsey, J. S. (2006) Bioconjugatable porphyrins bearing a compact swallowtail motif for water solubility. *Bioconjugate Chem. 17*, 638–653.
(13) Oswald, B., Gruber, M., Bohmer, M., Lehman, F., Probst, M., and Wolfbeis, O. S. (2001) Novel diode laser-compatible fluorophores and their application to single molecule detection, protein labeling and fluorescence resonance energy transfer immunoassay. *Photochem. Photobiol. 74*, 237–245.
(14) Olmstead, J., III (1979) Calorimetric determinations of absolute fluorescence quantum yields. *J. Phys. Chem. 83*, 2581–2584.
(15) Kawakami, M., and Kitaguchi, H. (2005) Cyanine Dyes. U.S. Patent 6,939,975.
(16) Tavs, P. (1970) Reaction of aryl halides with trialkyl phosphites and dialkyl benzenephosphonites to aromatic phosphonates and phosphinates by nickel salt catalysed arylation. *Chem. Ber. 103*, 2428–2436.
(17) Southwick, P. L., Earnst, L. A., Tauriello, E. W., Parker, S. R., Mujumbdar, R. B., Mujumbdar, S. R., Lewis, H. A., and Waggoner, A. S. (1990) Cyanine dye labeling reagents: carboxymethylindocyanine succinimidyl esters. *Cytometry 11*, 418–430.
(18) Gale, D. J., Lin, J., and Wilshire, J. F. K. (1970) The amidomethylation of Fischer's base. The preparation of some new polymethine dyes. *Aust. J. Chem. 30*, 689–694.
(19) Yee, K.-Y., Bailey, F. C., and Bluett, L. J. (1986) Squaraine chemistry. On the anomalous mass spectra of bis(4-dimethylaminophenyl)squaraine and its derivatives. *Can. J. Chem. 64*, 1607–1619.
(20) Oswald, B., Patsenker, L., Duschl, J., Szmacinski, H., Wolfbeis, O., and Terpetschnig, E. (1999) Synthesis, spectral properties, and detection limits of reactive squaraine dyes, a new class of diode laser compatible fluorescent protein labels. *Bioconjugate Chem. 10*, 925–931.
(21) Albert, A., and Sergent, E. P. (1962) *Ionization Constants of Acids and Bases* Wiley, New York.
(22) Gruber, H. J., Hahn, C. D., Kada, G., Reiner, C. K., Harms, G. S., Ahrer, W., Dax, T. G., and Knaus, H.-G. (2000) Anomalous fluorescence enhancement of Cy3 and Cy3.5 versus anomalous fluorescence loss of Cy5 and Cy7 upon covalent linking to IgG and noncovalent binding to avidin. *Bioconjugate Chem. 11*, 696–704.

BC070090Y

A Facile Synthesis of Azido-Terminated Heterobifunctional Poly(ethylene glycol)s for "Click" Conjugation

Shigehiro Hiki[†] and Kazunori Kataoka*[,†,‡,§]

Department of Materials Engineering, Graduate School of Engineering, and Center for NanoBio Integration, The University of Tokyo, 7-3-1 Hongo, Bunkyo-ku, Tokyo 113-8656, Japan, Core Research Program for Evolutional Science and Technology (CREST), Japan Science and Technology Agency (JST), Tokyo, Japan, and Center for Disease Biology and Integrative Medicine, Graduate School of Medicine, The University of Tokyo, 7-3-1 Hongo, Bunkyo-ku, Tokyo 113-0033, Japan. Received April 27, 2007; Revised Manuscript Received July 26, 2007

New azido-terminated heterobifunctional poly(ethylene glycol) (PEG) derivatives having primary amine and carboxyl end groups, (Azide-PEG-NH_2 and Azide-PEG-COOH, respectively) were synthesized with high efficiency. An α-allyl-ω-hydroxyl PEG was prepared as the first step to Azide-PEG-X (X = NH_2 and COOH) through the ring-opening polymerization of ethylene oxide (EO) with allyl alcohol as an initiator, followed by two-step modification of the hydroxyl end to an azido group. To introduce primary amino or carboxyl functional groups, amination and carboxylation reactions of the allyl terminal ends was then conducted by a radical addition of thiol compounds. Molecular functionalities of both ends of the PEG derivatives thus prepared were characterized by ^1H, ^{13}C NMR, and MALDI-TOF MS spectra, validating that the reaction proceeded quantitatively. The terminal azido functionality is available to conjugate various ligands with an alkyne group through the 1,3-dipolar cycloaddition reaction condition ("click chemistry").

INTRODUCTION

Poly(ethylene glycol) (PEG) conjugation chemistry, termed "PEGylation", has widely been used for the modification of biomolecules such as peptides, proteins, and enzymes (*1–3*), as well as of nanocarriers for drug delivery systems (DDS) such as liposomes and nanoparticles (*4, 5*). The advantages of PEGylation include the improvement of pharmaceutical and pharmacological properties, e.g., increased water solubility and circulatory half-life in vivo, the reduced antigenicity and immunogenicity, and the tolerance of biomolecules against degradation (*1–3*). Actually, several PEG-conjugated proteins have already been available as clinical therapeutics (*6*). Methoxy-terminated monofunctionalized PEG derivatives have mainly been used in these systems. Of further interest from the viewpoint of constructing multifunctionalized biopharmaceutics with PEGylation is the introduction of reactive groups at the α-chain end of PEG to prepare α,ω-heterobifunctional derivatives (heterobifunctional PEG). Heterobifunctional PEG may be useful to install ligands and probes at the distal end of PEGylated liposomes (*7*), polymeric micelles (*8*), synthetic polymers (*9*), and metallic colloids (*10*). So far, several types of heterobifunctional PEG derivatives with reactive groups, such as aldehyde, primary amine, mercapto, and maleimide, have been developed to install a variety of ligands (*8, 11–17*). Nevertheless, to expand the heterobioconjugation through PEG linker into a various combination of ligands and substrates, further improvement in the design of heterobifunctional PEG, particularly from the viewpoint of versatility, is crucial.

Generally, several features such as high yields, chemoselectivity, and the mild reaction condition in aqueous media are indispensable for the bioconjugation. In this regard, the 1,3-dipolar cycloaddition reaction between alkyne and organic azides, yielding the corresponding 1,2,3-triazoles in the mild aqueous condition, has recently received considerable attention in wide areas of chemistry (*18–20*) and has been recognized as particularly useful in the field of bioconjugate chemistry (*21–24*). This Cu(I)-catalyzed 1,3-dipolar cycloaddition reaction (termed "click chemistry") is highly chemoselective and can be performed under mild conditions in aqueous buffers with wide range of pH values. Therefore, the combination of heterobifunctional PEGs with "click chemistry" is a promising approach for bioconjugation (*25*). Indeed, the introduction of biological ligands by "click chemistry" onto the liposomal surface (*26*) and the Au nanoparticle surface (*27*) through the heterobifunctional oligo(ethylene glycol) spacers was recently reported, indicating the high utility of "click"-based bioconjugation.

Nevertheless, little attention has been placed on the novel and versatile method to prepare the azido-terminated heterobifunctional PEGs with a wide range of molecular weight useful for "click"-based bioconjugation. Although, azido-containing oligo(ethylene glycol) derivatives (e.g., N_3-$(CH_2CH_2O)_2$-$CH_2CH_2NH_2$) have been commercialized (*28*), the azido-terminated heterobifunctional PEGs having high molecular weight useful in the bioconjugate chemistry field are not yet available.

Here, we wish to communicate the new synthetic route of azido-terminated heterobifunctional PEGs possessing primary amino and carboxyl groups (Azide-PEG-NH_2 and Azide-PEG-COOH, respectively) with controlled molecular weight through the ring-opening polymerization of ethylene oxide from allyl alcohol as an initiator followed by a quantitative modification of α- and ω-end groups (Scheme 1).

EXPERIMENTAL PROCEDURES

Materials. Ethylene oxide (EO; Sumitomo Seika Chemical, Japan) was dried over calcium hydride and distilled under an argon atmosphere. Allyl alcohol, tetrahydrofuran (THF), *N,N*-

* To whom corresponding should be addressed. Professor Kazunori Kataoka. Tel: +81-3-5841-7138. Fax: +81-3-5841-7139. E-mail: kataoka@bmw.t.u-tokyo.ac.jp.

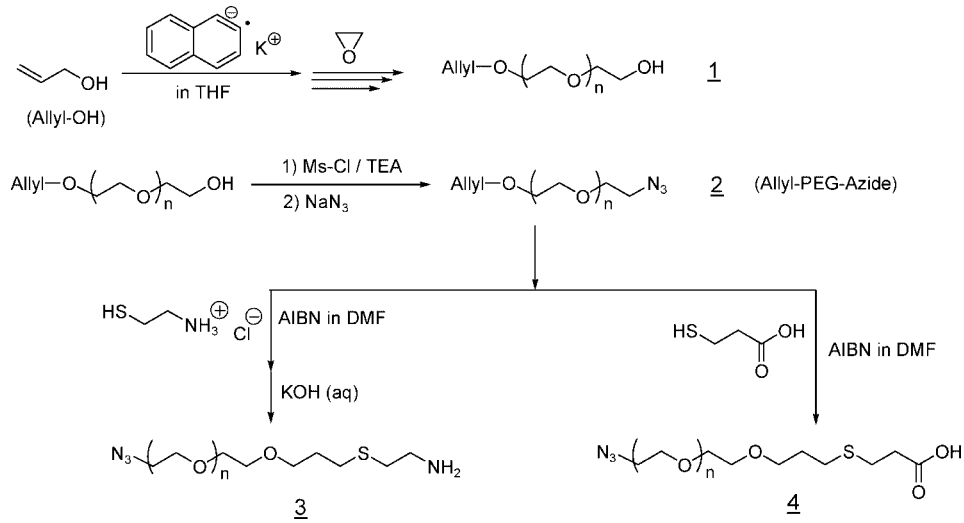
[†] Graduate School of Engineering, The University of Tokyo, and CREST.

[‡] Graduate School of Medicine, The University of Tokyo.

[§] Center for NanoBio Integration, The University of Tokyo.

10.1021/bc700152j CCC: $37.00 © 2007 American Chemical Society
Published on Web 10/25/2007

Scheme 1. Synthetic Route to α-Amino-ω-azido-PEG (3) and α-Carboxy-ω-azide-PEG (4)



dimethylformamide (DMF), triethylamine, 2,2′-azobisisobutyronitrile (AIBN), and methanesulfonyl chloride were purchased from Wako Pure Chemical Industries, Ltd., (Osaka, Japan) and purified by conventional methods. Potassium naphthalene was prepared as a THF solution according to a previous paper (*29*), whose concentration was determined by titration. 2-Aminoethanethiol hydrochloride, mercaptopropionic acid, sodium azide, and other reagents were used as received.

Synthesis of α-Allyl-ω-hydroxyl PEG (1). Allyl alcohol (2.3 mmol, 135 μL) and potassium naphthalene (2 mmol) in 6.6 mL of THF were added to dry THF (75 mL) in a 200 mL flask equipped with a three-way stopcock under argon atmosphere to form potassium allyl alcoholate as an initiator. After stirring for 10 min, liquid EO (302 mmol, 13.3 g) was added to the solution via a cooled syringe. The mixture was allowed to react for 2 days at 25 °C followed by pouring into diethyl ether to precipitate the polymer. The recovered polymer was dried in vacuo and then freeze-dried from benzene. The yield of obtained polymer after purification was 91% (12.1 g). GPC: Number-average molecular weight (M_n) = 5500, M_w/M_n = 1.03. ^{1}H NMR (300 MHz, $CDC1_3$, δ in ppm): 3.63 (m, O-(C$\underline{H}_2$)$_2$-O), 4.02 (d, C$\underline{H}_2$ of allyl group), 5.17–5.30 (dd, C$\underline{H}_2$ of allyl group), 5.87–5.96 (m, C$\underline{H}$ of allyl group).

Synthesis of α-Allyl-ω-azide PEG (2). The azide end group was introduced by the mesylation of the hydroxyl terminus and subsequent substitution with sodium azide, referring to the literature methods (*30*).

Freeze-dried polymer **1** (Allyl-PEG-OH) (2.20 g, 0.40 mmol) from benzene was dissolved in anhydrous THF (15 mL) followed by triethylamine (162 mg, 1.60 mmol) addition. The mixture was then added to a solution of methanesulfonyl chloride (160 mg, 1.40 mmol) in THF (8 mL) under Ar stream, and stirred overnight at room temperature. After the reaction, THF was partially evaporated under reduced pressure. The residue was redissolved in water (40 mL) and extracted with dichloromethane (5 × 100 mL). The organic layers were combined and dried over Na_2SO_4. After filtration and concentration, the polymer was recovered by precipitation into ether and dried in vacuo, yielding a white solid.

This mesylated polymer (620 mg, 0.113 mmol) was dissolved in DMF (12 mL), followed by sodium azide (521 mg, 8.01 mmol) addition, and was stirred for 2 days at 30 °C. Dichloromethane (100 mL) was then added, and the reaction mixture was washed five times with water and brine. The organic layer was dried over Na_2SO_4, filtered, concentrated, and then reprecipitated into ether. The recovered polymer was freeze-dried from benzene (508 mg, 82%). ^{1}H NMR (300 MHz, $CDC1_3$, δ in ppm): 3.46 (t, CH_2-C$\underline{H}_2$-N_3), 3.63 (s, O-(C$\underline{H}_2$)$_2$-O), 4.02 (d, C$\underline{H}_2$ of allyl group), 5.17–5.30 (dd, C$\underline{H}_2$ of allyl group), 5.87–5.96 (m, C$\underline{H}$ of allyl group).

Synthesis of α-Amino-ω-azide PEG (3). Amination of the allyl terminus of polymer **2** was conducted by the radical addition reaction of 2-aminoethanethiol hydrochloride (*31*). Polymer **2** (Allyl-PEG-azide, 502 mg, 0.091 mmol) was freeze-dried from benzene and mixed with the solution in DMF (5 mL) containing 213 mg of 2-aminoethanethiol hydrochloride (1.87 mmol, 20 equiv) and 15 mg of AIBN (0.091 mmol, 1 equiv). The reaction mixture was stirred at 65 °C for 24 h under argon atmosphere. The polymer was precipitated twice in a large excess of ether. The resulting white product was dissolved into methanol, and 5.1 mg (1 equiv) of potassium hydroxide dissolved in water was added. The mixture was stirred for approximately 4 h. Then, methanol was partially evaporated and diluted with water (30 mL), and extracted by dichloromethane (5 × 80 mL). The combined organic layer was dried over Na_2SO_4, filtered, and concentrated to 1/100 of the initial volume. The polymer was reprecipitated from an excess volume of ether and freeze-dried from benzene to lead to a white powder (397 mg, yield = 79%).

Synthesis of α-Carboxy-ω-azide PEG (4). The carboxylation reaction of allyl terminus of polymer **2** was performed in the same manner as described above for the preparation of polymer **3**. Typically, 409 mg of Allyl-PEG-azide, in 4 mL of DMF, was reacted with 159 mg of 3-mercaptopropionic acid (1.50 mmol, 20 equiv) in the presence of 12.2 mg of AIBN (1 equiv). After the reaction, the solution was precipitated into ether twice, and polymer **4** was obtained as a white powder (317 mg, yield = 77%).

Polymer Analysis. ^{1}H and ^{13}C NMR spectra were recorded on a JEOL JNM-AL 300 spectrometer (JEOL, Tokyo, Japan) at 300 and 75.45 MHz, respectively. Chemical shifts are reported in parts per million (ppm) downfield from tetramethylsilane. Number-average molecular weight (M_n) and molecular weight distribution (M_w/M_n) were determined using a GPC (TOSOH HLC-8220) system equipped with two TSK gel columns (G4000HHR and G3000HHR) and an internal refractive index (RI) detector. Columns were eluted with DMF containing lithium chloride (10 mM) at a flow rate of 0.8 mL/min and temperature of 40 °C. Molecular weights were calibrated with poly(ethylene glycol) standards (Polymer Laboratories, Ltd., UK). MALDI-TOF-MS spectra were recorded using Bruker

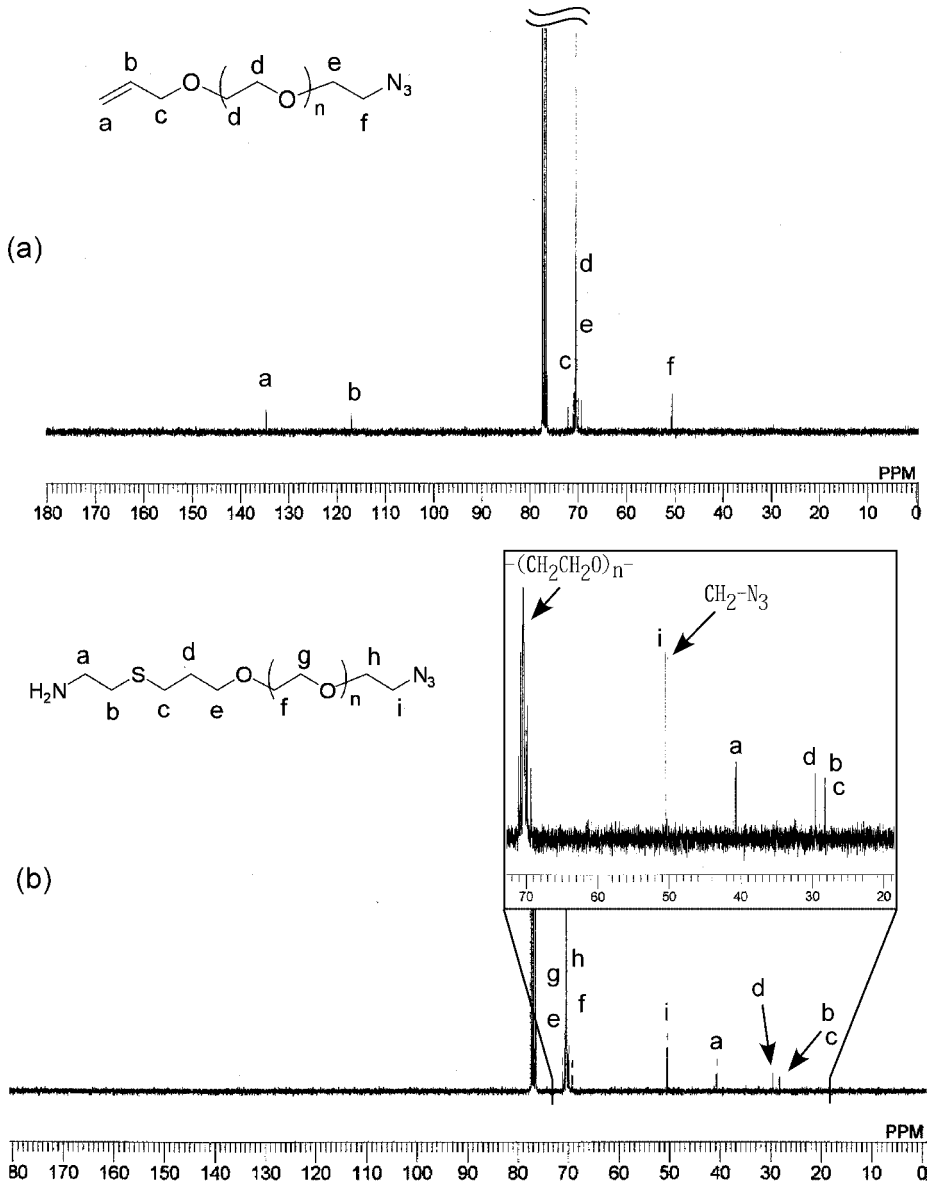


Figure 1. (a) ^{13}C NMR spectrum of Allyl-PEG-Azide ($CDCl_3$ at 20 °C). (b) ^{13}C NMR spectrum of Azide-PEG-NH_2 ($CDCl_3$ at 20 °C).

REFLEX III. α-Cyano-4-hydroxycinnamic acid (CHCA) was used as the matrix for the ionization operated in the reflection mode.

RESULTS AND DISCUSSION

There are several reports on the preparation of oligo(ethylene glycol)s having azido and amino groups from homotelechelic oligo(ethylene glycol)s as the starting materials (*32, 33*). Nevertheless, the synthetic methods involve several complicated reactions as well as separation steps such as chromatographic isolation due to the difficulty of selective monoprotection of the hydroxyl termini. Thus, the application of these synthetic approaches of end-group modification is not expedient for a large-scale synthesis of heterobifunctional PEGs having high molecular weight, giving an impetus to develop a novel synthetic route to the azide-functionalized heterobifunctional PEG with quantitative yields and high specificity under mild reaction conditions.

In this study, allyl alcoholate was selected as an initiator for anionic polymerization of EO, because the allyl end group of the PEG chain allows several kinds of chemical modifications such as addition reactions. To prepare α-allyl-ω-hydroxyl PEG (**1**), the anionic polymerization of EO initiated with potassium allyl alcoholate was carried out in THF solution for 48 h. After precipitation into ether, the product was obtained as white powder. The MW of the polymer **1** (Allyl-PEG-OH) determined from GPC [M_n(GPC) 5500] was close to that from the initial monomer/initiator ratio [M_n(calcd) 5780], indicating an effective initiation efficiency of potassium allyl alcoholate without detrimental side reactions.

α-Allyl-ω-azide PEG (**2**) was obtained through the two-step modification, the mesylation and the subsequent substitution by sodium azide, of hydroxyl function as described in the Experimental Procedures. In the ^{13}C NMR spectrum (Figure 1a), the signals of the carbons of the allyl group are detected at δ 134.7 ppm (a), 117.0 ppm (b), and 72.1 ppm (c), respectively. In addition to these signals, the methylene unit adjacent to the azido group ($CH_2\underline{C}H_2N_3$) was observed at 50.5 ppm (f). Moreover, no signal of the methylene carbon adjacent to the hydroxyl terminus ($CH_2\underline{C}H_2OH$ δ = 61.5 ppm) (*34*) was detected.

Figure 2a shows the MALDI-TOF MS spectra of α-allyl-ω-azide PEG (**2**). In this analysis, although the major peaks of the polymer were detected as the species derived from loss of N_2 from azido group which ascribed to fragmentation due to

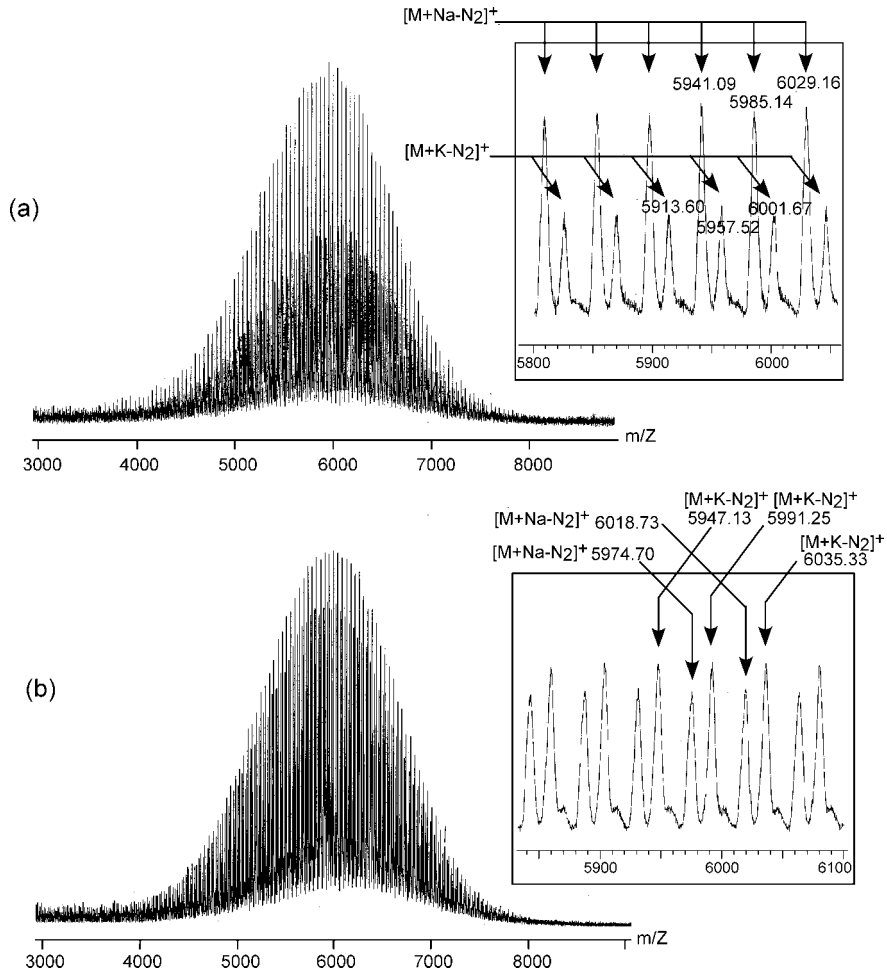


Figure 2. MALDI-TOF Mass Spectrum of Allyl-PEG-Azide (a) and Azide-PEG-NH_2 (b).

the higher laser power during MALDI experiment (*35*), only parent ions of each polymer molecule as planned are observed, without the signal of the side reaction product. From the expanded view of the spectrum in Figure 2a, the mass of the products appears to be around 5900 (M_n = 5670; M_w/M_n = 1.03), which is in a good accordance with the GPC results (M_n = 5500). These data demonstrated that α-allyl-ω-hydroxyl PEG (**1**) was successfully transformed to α-allyl-ω-azide PEG (**2**). Note that there was a report on the chain degradation of tosylate-activated PEG derivatives (*36*). Nevertheless, no sign of degradation was found in the present case of mesylate-activated PEG samples by MALDI-TOF MS spectroscopy, indicating that essentially no degradation of PEG occurred in the activation route via mesylation.

To prepare α-amino-ω-azide PEG, the radical addition reaction of 2-aminoethanethiol hydrochloride to an allyl end group of polymer (**2**) was examined according to the previous method with a slight modification (*31*). The reaction was carried out under the varying ratios of [allyl-PEG-azide]$_0$/[$HSCH_2CH_2NH_3^+Cl^-$]$_0$/[AIBN]$_0$ (=1/5/1, 1/7.5/1, 1/10/1, and 1/20/1 mol equiv) in DMF at 65 °C. The resulting polymer was precipitated twice in ether in order to remove excess of reagents. After the subsequent aqueous workup with potassium hydroxide, the amino-terminated PEG sample was obtained (Scheme 1). The ^{1}H NMR spectrum of the polymer obtained at the conditions of [allyl-PEG-azide]$_0$/[$HSCH_2CH_2NH_3^+Cl^-$]$_0$/[AIBN]$_0$ = 1/10/1 and 1/20/1 revealed the complete disappearance of the signals assigned to the allyl protons at 4.02 (CH_2═$CHC\underline{H_2}$), 5.17–5.30 ($C\underline{H_2}$═$CHCH_2$), and 5.87–5.96 ppm (CH_2═$C\underline{H}CH_2$). Concomitantly, the new signals were clearly observed at 1.82 ($CH_2C\underline{H_2}CH_2S$), 2.60 ($SC\underline{H_2}CH_2NH_2$), 2.62 ($C\underline{H_2}SCH_2CH_2NH_2$), and 2.86 ppm ($CH_2SCH_2C\underline{H_2}NH_2$) corresponding to the resulting structure via the radical addition of 2-aminoethanethiol to allyl group. A decreased ratio of thiol compound in the initial reaction mixture to less than 10 equiv ([allyl-PEG-azide]$_0$/[$HSCH_2CH_2NH_3^+Cl^-$]$_0$/[AIBN]$_0$ = 1/5/1 and 1/7.5/1) resulted in the incomplete amination judged from the observation of the remaining ally protons in the ^{1}H NMR spectra of the obtained polymer samples, suggesting that 10 mol excess equiv of thiol group may be required for the complete amination of allyl group settled at the PEG chin end. No prohibitive effect was observed even at 20 equiv of thiol to allyl groups. In the ^{13}C NMR spectra of the sample obtained at [allyl-PEG-azide]$_0$/[$HSCH_2CH_2NH_3^+Cl^-$]$_0$/[AIBN]$_0$ = 1/20/1 (Figure 1b), no carbon signal corresponding to allyl function remained. The signals detected around δ 40.7 (a), 29.6 (d), and 28.4 ppm (c,d) can be assigned to the $\underline{C}H_2NH_2$, $CH_2\underline{C}H_2CH_2S$, and $CH_2CH_2\underline{C}H_2S\underline{C}H_2$ of the end groups, respectively. Note that no side reaction of the azido group such as a radical scavenging and a subsequent decomposition with denitrogenation occurred, because the signal corresponding to the azido group was detected as intact.

The quantitative conversion of the end allyl group to the primary amino group was also monitored by the MALDI-TOF MS analysis. Figure 2b shows the MALDI-TOF MS spectrum of the reaction product after the radical addition reaction of 2-aminoethanethiol hydrochloride ([allyl-PEG-azide]$_0$/[$HSCH_2CH_2NH_3^+Cl^-$]$_0$/[AIBN]$_0$ = 1/20/1). As mentioned above, the mass distribution of the obtained polymer after the radical addition was the same as that before the reaction, indicating the occurrence of no side reaction. The major series of the molecular masses of the product is expressed in the following equation.

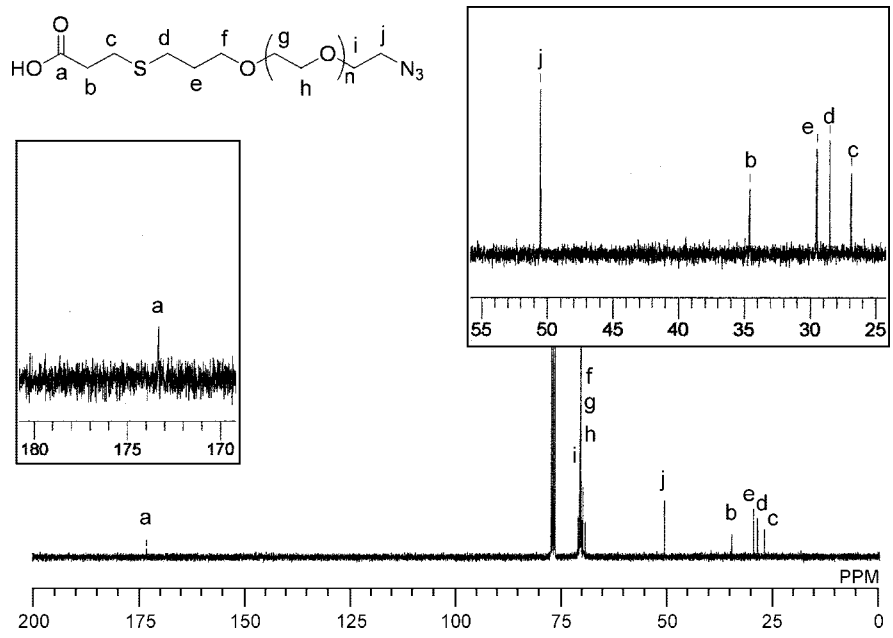


Figure 3. ^{13}C NMR spectrum of Azide-PEG-COOH ($CDCl_3$ at 23 °C).

MW_{MS} = 44.053n (EO) + 70.07 (Azide) + 134.22 ($OCH_2CH_2CH_2SCH_2CH_2NH_2$) + 22.99 (sodium).

These results strongly supported the statement that the novel heterobifunctional PEG possessing an azido group at one end and a primary amino group at the other end was quantitatively prepared.

To demonstrate the versatility of this synthetic route with azido-containing PEG, the carboxylation of α-allyl-ω-azide PEG (**2**) was examined under the same conditions as the amination reaction ([allyl-PEG-azide]$_0$/[$HSCH_2CH_2COOH$]$_0$/[AIBN]$_0$ = 1/20/1). From the ^1H NMR analysis of the resultant polymer, the signals assigned to the allyl group completely disappeared after the reaction, while the methylene protons of the 3-mercaptoacetic acid unit were clearly observed at 1.84 ($CH_2C\underline{H_2}CH_2S$), 2.60 ($SC\underline{H_2}CH_2COOH$), 2.62 ($C\underline{H_2}SCH_2CH_2COOH$), and 2.79 ppm ($CH_2SCH_2C\underline{H_2}COOH$), respectively. In addition, the structure of the resulting polymer after the carboxylation reaction was confirmed by ^{13}C NMR. The corresponding carbon signals of the terminal groups appeared at δ 173.0 ((a) $CH_2\underline{C}OOH$), 50.4; ((j) $\underline{C}H_2N_3$), 34.5; ((b) $\underline{C}H_2COOH$), 29.6; ((e) $CH_2\underline{C}H_2CH_2S$), 28.5; ((d) $CH_2CH_2\underline{C}H_2S$), and 26.9; ((c) $S\underline{C}H_2CH_2COOH$) ppm, respectively, and no signal corresponding to allyl group was detected (Figure 3). These results indicate the successful preparation of heterobifunctional PEG possessing azido and carboxyl groups at the chain ends.

In conclusion, the facile and quantitative synthesis of azido-containing heterobifunctional PEGs via EO polymerization was demonstrated in this study. These azido-containing PEGs can be used to Cu(I)-catalyzed 1,3-dipolar cycloaddition reaction (click chemistry) to introduce versatile biofunctional ligands into the azido terminus, and are thus relevant to a wide range of applications in the field of bioconjugate chemistry. We focused here on the PEG with MW of 5000 because of its versatility in bioconjugate applications, including liposome modification, polymeric micelle formation, and protein conjugation. Basically, chemistry developed here may be applicable to PEG with even higher MW, because the reaction scheme may not be directly influenced by the MW. Nevertheless, the quantitative conversion is still in an issue for the higher MW PEG due to the limited availability of the chain end possibly buried in the coil of PEG strands. We feel that this issue may be better addressed in a future study directly focusing on the reactivity of the allyl group located at the chain end of PEG with different molecular weights.

ACKNOWLEDGMENT

This work was supported by the Core Research for Evolutional Science and Technology (CREST) from the Japan Science and Technology Agency (JST). The authors thank Dr. Darin Y. Furgeson, University of Wisconsin, for his linguistic review of the manuscript.

LITERATURE CITED

(1) Harris, J. M., Ed. (1992) *Poly(ethylene glycol) Chemistry: Biotechnical and Biomedical Applications*, Plenum Press, New York.

(2) Roberts, M. J., Bentley, M. D., and Harris, J. M. (2002) Chemistry for peptide and protein PEGylation. *Adv. Drug Delivery Rev. 54*, 459–476.

(3) Nucci, M. L., Shorr, R., and Abuchowski, A. (1991) The therapeutic value of poly(ethylene glycol) modified proteins. *Adv. Drug Delivery Rev. 6*, 133–151, and references therein.

(4) Gabizon, A., Goren, D., Horowitz, A. T., Tzemach, D., Lossos, A., and Siegal, T. (1997) Long-circulating liposomes for drug delivery in cancer therapy: a review of biodistribution studies in tumor-bearing animals. *Adv. Drug Delivery Rev. 24*, 337–344.

(5) Kataoka, K., Harada, A., and Nagasaki, Y. (2001) Block copolymer micelles for drug delivery: design, characterization and biological significance. *Adv. Drug Delivery Rev. 47*, 113–131.

(6) Duncan, R. (2003) The drawing era of polymer therapeutics. *Nat. Rev. Drug Discovery 2*, 347–360.

(7) Zalipsky, S., Gittelman, J., Mullah, N., Qazen, M. M., and Harding, J. (1998) *Biologically active ligand-bearing polymer-grafted liposomes, Targeting of Drugs 6: Strategies for Stealth Therapeutic Systems*, pp 131–139, Plenum, New York.

(8) Jule, E., Nagasaki, Y., and Kataoka, K. (2002) Surface plasmon resonance study on the interaction between lactose-installed poly(ethylene glycol)-poly(D,L-lactide) block copolymer micelles and lectins immobilized on a gold surface. *Langmuir 18*, 10334–10339.

(9) Ogris, M., Walker, G., Blessing, T., Kircheis, R., Wolschekd, M., and Wagner, E. (2003) Tumor-targeted gene therapy: strategies for the preparation of ligand-polyethylene glycol-polyethylenimine/DNA complexes. *J. Controlled Release 91*, 173–181.

(10) Popielarski, S. R., Pun, S. H., and Davis, M. E. (2005) A nanoparticle-based model delivery system to guide the rational design of gene delivery to the liver. 1. Synthesis and characterization. *Bioconjugate Chem. 16*, 1063–1070.

(11) Nagasaki, Y., Kutsuna, T., Iijima, M., Kato, M., and Kataoka, K. (1995) Formyl-ended heterobifunctional poly(ethylene oxide): Synthesis of poly(ethylene oxide) with a formyl group at one end and a hydroxyl group at the other end. *Bioconjugate Chem. 6*, 231–233.

(12) Yokoyama, M., Okano, T., Sakurai, Y., Kikuchi, A., Ohsako, N., Nagasaki, Y., and Kataoka, K. (1992) Synthesis of poly-(ethylene oxide) with heterobifunctional reactive groups at its terminals by an anionic initiator. *Bioconjugate Chem. 3*, 275–276.

(13) Nagasaki, Y., Iijima, M., Kato, M., and Kataoka, K. (1995) Primary amino-terminal heterobifunctional poly(ethylene oxide). Facile synthesis of poly(ethylene oxide) with a primary amino group at one end and a hydroxyl group at the other end. *Bioconjugate Chem. 6*, 702–704.

(14) Akiyama, Y., Otsuka, H., Nagasaki, Y., Kato, M., and Kataoka, K. (2000) Selective synthesis of heterobifunctional poly(ethylene glycol) derivatives containing both mercapto and acetal terminals. *Bioconjugate Chem. 11*, 947–950.

(15) Gao, X., Tao, W., Lu, W., Zhang, Q., Zhang, Y., Jiang, X., and Fu, S. (2006) Lectin-conjugated PEG-PLA nanoparticles: Preparation and brain delivery after intranasal administration. *Biomaterials 27*, 3482–3490.

(16) Oishi, M., Kataoka, K., and Nagasaki, Y. (2006) pH-Rsponsive three-layered PEGylated polyplex micelle based on a lactosylated ABC triblock copolymer as a targetable and endsome-disruptive nonviral gene vector. *Bioconjugate Chem. 16*, 677–688.

(17) Bae, Y., Jang, W-D., Nishiyama, N., Fukushima, S., and Kataoka, K. (2005) Multifunctional polymeric micelles with folate-mediated cancer cell targeting and pH-triggered drug releasing properties for active intracellular drug delivery. *Mol. BioSyst. 1*, 242–250.

(18) Wu, P., Feldman, A. K., Nugent, A. K., Hawker, C. J., Scheel, A., Voit, B., Pyun, J., Frechet, J. M. J., Sharpless, K. B., and Fokin, V. V. (2004) Efficiency and fidelity in a click-chemistry route to triazole dendrimers by the copper(I)-catalyzed ligation of azides and alkynes. *Angew. Chem., Int. Ed. 43*, 3928–3932.

(19) Malkoch, M., Vestberg, R., Gupta, N., Mespouille, L., Dubois, Ph., Mason, A. F., Hedrick, J. L., Liao, Q., Frank, C. W., Kingsbury, K., and Hawker, C. J. (2006) Synthesis of well-defined hydrogel networks using Click chemistry. *Chem. Commun.* 2774–2776.

(20) Lutz, J. F. (2007) 1,3-Dipolar cycloadditions of azides and alkynes: A universal ligation tool in polymer and materials Science. *Angew. Chem., Int. Ed. 46*, 1018–1025.

(21) Rostovtsev, V. V., Green, L. G., Fokin, V. V., and Sharpless, K. B. (2002) A stepwise Huisgen cycloaddition process: Copper (I)-catalyzed regioselective ligation of azides and terminal alkynes. *Angew. Chem., Int. Ed. 41*, 2596–2599.

(22) Wang, Q., Chan, T. R., Hilgraf, R., Fokin, V. V., Sharpless, K. B., and Finn, M. G. (2003) Bioconjugation by Copper (I)-catalyzed azide-alkyne [3 + 2] cycloaddition. *J. Am. Chem. Soc. 125*, 3192–3193.

(23) Link, A. J., and Tirrell, D. A. (2003) Cell surface labeling of *Escherichia coli* via copper (I)-catalyzed [3 + 2] cycloaddition. *J. Am. Chem. Soc. 125*, 11164–11165.

(24) Deiters, A., Cropp, T. A., Mukherji, M., Chin, J. W., Anderson, J. C., and Schultz, P. G. (2003) Adding amino acids with novel reactivity to the genetic code of *Saccharomyces cerevisiae*. *J. Am. Chem. Soc. 125*, 11782–11783.

(25) Breitenkamp, K., Sill, K., and Skaff, H. Heterobifunctional poly(ethylene glycol), uses thereof and intermediates thereto. PCT Int. Appl. WO 2006047419, 2006

(26) Hassane, F. S., Frisch, B., and Schuber, F. (2006) Targeted liposomes: Convenient coupling of ligands to performed vesicles using "Click Chemistry". *Bioconjugate Chem. 17*, 849–854.

(27) Brennan, J. L., Hatzakis, N. S., Tshikhudo, T. R., Dirvianskyte, N., Razumas, V., Patkar, S., Vind, J., Svendsen, A., Nolte, R. J. M., Rowan, A. E., and Brust, M. (2006) Bionanoconjugation via click chemistry: The creation of functional hybrids of lipases and gold nanoparticles. *Bioconjugate Chem. 17*, 1373–1375.

(28) Fluka Catalogue, #17758. (11-Azido-3,6,9-trioxaundecan-1-amine), >90% (GC).

(29) Szwarc, M., Levy, M., and Milkovich, R. (1956) Polymerization initiated by electron transfer to monomer. A new method of formation of block polymers. *J. Am. Chem. Soc. 78*, 2656.

(30) Garanti, L., and Molteni, G. (2003) MeOPEG-bounded azide cycloadditions to alkynyl dipolarophiles. *Tetrahedron Lett. 44*, 1133–1135.

(31) Cammas, S., Nagasaki, Y., and Kataoka, K. (1995) Heterobifunctional poly(ethylene oxide): synthesis of α-methoxy-ω-amino and α-hydroxy-ω-amino PEOs with the same molecular weights. *Bioconjugate Chem. 6*, 226–230.

(32) Bertozzi, C. R., and Bednarski, M. D. (1991) The synthesis of heterobifunctional linkers for the conjugation of ligands to molecular probes. *J. Org. Chem. 56*, 4326–4329.

(33) Iyer, S. S., Anderson, A. S., Reed, S., Swanson, B., and Schmidt, J. G. (2004) Synthesis of orthogonal end functionalized oligoethylene glycols of defined lengths. *Tetrahedron Lett. 45*, 4285–4288.

(34) Zalipsky, S. (1995) Functionalized poly(ethylene glycol) for preparation of biologically relevant conjugates. *Bioconjugate Chem. 6*, 150–165.

(35) Smith, M. B., March, J., Eds. (2001) *March's Advanced Organic Chemistry. Reactions, Mechanisms, and Structure*, 5 th ed. p 1412, John Wiley & Sons, New York.

(36) McManus, S. P., Karaman, R. M., Sedaghat-Herati, M. R., Shannon, T. G., Hovatter, T. W., and Harris, J. M. (1990) Chain-cleavage and hydrolysis of activated polyethylene glycol derivatives: Evidence for competitive processes. *J. Polym. Sci., Part A: Polym. Chem. 28*, 3337–3346.

BC700152J

Facile and Rapid Direct Gold Surface Immobilization with Controlled Orientation for Carbohydrates

Jeong Hyun Seo,[†] Kyouichi Adachi,[‡,§] Bong Kuk Lee,[‡,§] Dong Gyun Kang,[†] Yeon Kyu Kim,[†] Kyoung Ro Kim,[†] Hea Yeon Lee,*[,‡,§] Tomoji Kawai,[‡,§] and Hyung Joon Cha*[,†]

Department of Chemical Engineering, Pohang University of Science and Technology, Pohang 790-784, Korea, Institute for Scientific and Industrial Research, Osaka University, Osaka 567-0047, Japan, and Core Research for Evolutional Science and technology, Japan Science and Technology Agency, Saitama 332-0012, Japan. Received July 30, 2007; Revised Manuscript Received August 15, 2007

Effective surface immobilization is a prerequisite for numerous carbohydrate-related studies including carbohydrate–biomolecule interactions. In the present work, we report a simple and rapid modification technique for diverse carbohydrate types in which direct oriented immobilization onto a gold surface is accomplished by coupling the amine group of a thiol group-bearing aminophenyl disulfide as a new coupling reagent with an aldehyde group of the terminal reducing sugar in the carbohydrate. To demonstrate the generality of this proposed reductive amination method, we examined its use for three types of carbohydrates: glucose (monosaccharide), lactose (disaccharide), and GM1 pentasaccharide. Through successful mass identifications of the modified carbohydrates, direct binding assays on gold surface using surface plasmon resonance and electrochemical methods, and a terminal galactose-binding lectin assay using atomic force microscopy, we confirmed several advantages including direct and rapid one-step immobilization onto a gold surface and exposure of functional carbohydrate moieties through oriented modification of the terminal reducing sugar. Therefore, this facile modification and immobilization method can be successfully used for diverse biomimetic studies of carbohydrates, including carbohydrate–biomolecule interactions and carbohydrate sensor or array development for diagnosis and screening.

INTRODUCTION

Carbohydrates encode information for specific molecular recognition, help determine protein folding, stability, and pharmacokinetics, play critical roles in determining biological functions, and affect diverse physiological processes (*1–4*). In addition, carbohydrate–protein interactions have been used to elucidate fundamental biochemical processes and identify new pharmaceutical substances in living cell systems (*1–4*). In order to fully study specific carbohydrate interactions with biomolecules such as proteins, DNA, and other carbohydrates in the cell, researchers need effective methods for carbohydrate immobilization (*5–8*).

To date, modification for carbohydrate immobilization has been attempted using several techniques, including copolymerization, coupling with divinyl sulphone, coupling to CNBr-activated substrates, and reductive amination (*9, 10*). However, although these modification methods have demonstrated promising results, general usefulness for diverse carbohydrate types has not been proven (*11, 12*). Previous studies have mainly focused on mono and/or disaccharides, with a few attempts made to immobilize oligo or polysaccharides, because of their structural complexity and problems with severe structural deformity during modification (*13–15*). Therefore, more advanced methods including alternative surface modification have been developed for diverse carbohydrate types (*6, 16–20*). However, these strategies also have tended to be multistep protocols aimed at indirect immobilization. Especially, for biosensor applications, it is desirable to directly and rapidly immobilize various carbohydrates on surfaces by one-step protocols.

Successful surface immobilization of carbohydrates has been further complicated by the need to retain the original structure and expose the functional sites so that the immobilized molecule can mimic the specific biomolecular interactions occurring on the cell surface. Because carbohydrates do not have functional groups for orientation, it has proven technically challenging to immobilize carbohydrates (especially oligo and polysaccharides) in an oriented fashion while retaining their inherent structures and functionalities (*11,12*). Therefore, we sought to develop a method for orienting and immobilizing various carbohydrate types directly and rapidly onto a gold surface that will allow specific carbohydrate–biomolecule recognition. Immobilization of carbohydrates on gold surface can be easily applicable for gold-based biosensors, such as electrochemical (EC) sensors, surface plasmon resonance (SPR), and quartz crystal microbalances (QCM).

We herein report a simple and rapid reductive amination technique by using aminophenyl disulfide as a new coupling reagent for diverse carbohydrate types in which orientation is accomplished by coupling a thiol (-SH) group to the terminal reducing sugar of the carbohydrate, and the oriented carbohydrate is directly immobilized onto a bare gold surface (Scheme 1). To show the generality of our proposed modification/immobilization method, we examined its use for three types of carbohydrates having terminal reducing sugar moieties, namely, glucose (monosaccharide), lactose (disaccharide), and GM1 pentasaccharide. We also demonstrated the interaction of a representative protein with carbohydrates surface-immobilized using our method (Scheme 1).

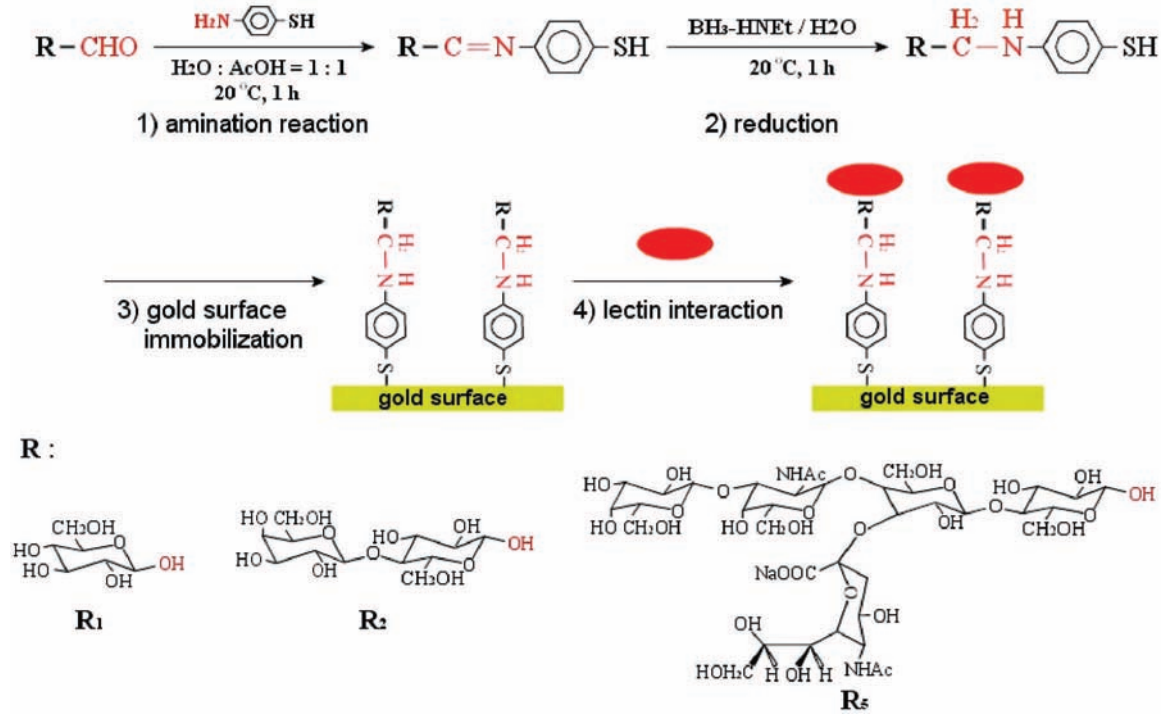
EXPERIMENTAL PROCEDURES

Carbohydrate Modification. Glucose (Sigma), lactose (Sigma), and GM1 pentasaccharide (Alexis Biochemicals) at 100 mM each were separately dissolved in water, and 50 mM aminophenyl disulfide (Aldrich) was dissolved in acetic acid.

* Corresponding author. E-mail: hjcha@postech.ac.kr (H.J.C.). E-mail: hylee@sanken.osaka-u.ac.jp (H.Y.L.).
[†] Pohang University of Science and Technology.
[‡] Osaka University.
[§] Japan Science and Technology Agency.

10.1021/bc700288z CCC: $37.00 © 2007 American Chemical Society
Published on Web 10/05/2007

Scheme 1. Strategy for the Modification and Direct Immobilization of Various Carbohydrate Types[a]



[a] Modified SH-saccharides can be directly immobilized on gold and interact specifically with lectin. R_1, glucose (monosaccharide); R_2, lactose (disaccharide); R_5, GM1 pentasaccharide.

The carbohydrate and aminophenyl disulfide solutions were mixed well and incubated in sealed tubes for 1 h at 20 °C (glucose and lactose) or 30 °C (GM1 pentasaccharide) for the amination reaction step. Then, freshly prepared reducing reagent, 100 mM dimethylamine borane (Fluka), was added to each reaction, and the tubes were incubated unsealed for 1 h at 20 °C for the reduction step. The tubes were then resealed and heated for 1 h at 50 °C under nitrogen gas steaming for the condensation step. All modified carbohydrates were dissolved in 5% acetic acid solution and preserved at −20 °C under light-blocking conditions. Without further purification steps, modified samples were used for MALDI-TOF MS analysis and immobilization.

Mass Identification Using MALDI-TOF MS. To improve the ionization efficiency of MALDI-TOF MS, the samples were desalted using Zip-tip C18 (Millipore) and then eluted onto MALDI target plates using matrix solution (10 mg/mL; α-cyano-4-hydroxycinnamic acid dissolved in a solution consisting of 50% acetonitrile and 0.5% trifluoroacetic acid). All mass spectra were acquired in reflection mode using a 4700 Proteomic Analyzer (Applied Biosystems) at Korea Basic Science Institute. Spectra were obtained in the mass range between 100 to 2000 Da with ~200 laser shots. Internal calibration was performed with 4700 Cal Mix (Applied Biosystems).

SPR-Based Immobilization Analysis. All SPR experiments were performed using a Biacore 2000 instrument (Biacore AB) with a flow system that loaded the solutions as discrete channels. The SIA Kit Au (Biacore AB) was used as the bare gold surface for the direct immobilization of modified SH-containing carbohydrates. The flow rate for binding onto the gold surface was 5 μL/min, and a noninjected channel was used as the baseline. Immobilization was performed by injecting 60 μL of each sample onto the gold surface, and immobilized carbohydrate amounts were measured as RU. All measurements were performed in HEPES-EP buffer (Biacore AB; 10 mM HEPES at pH 7.4, 150 mM NaCl, 3 mM EDTA, and 0.005% surfactant F20).

EC-Based Immobilization Analysis. EC experiments were performed using a BAS 100 B/W potentiostat (Bioanalytical System) at room temperature. The biosensor consisted of an 8-multielectode chip comprising an array of 200-nm diameter gold electrodes on glass (*21–23*). Modified GM1 pentasaccharide (1 μL at 5 mM in HEPES-buffered saline) was directly immobilized onto the multigold electrodes for 1 h at room temperature, and unmodified GM1 pentasaccharide (1 μL at 5 mM) was loaded as a negative control. Electrode pretreatment was carried out for 3 min at 1.8 V in 10 mM H_2SO_4. All CV measurements were performed in solutions containing 5 mM $K_3Fe(CN)_6$ at a scan rate of 100 mV/s. A solid bar of Ag/AgCl in 100 mM KCl and a 5-mm diameter platinum wire were used as the reference and the counter electrode, respectively. The SWV curves were recorded at a 10 mV/s scan rate with a pulse height of 25 mV and a step time of 0.2 s.

Lectin Interaction Analysis Using AFM. We deposited a layer of 99.5% pure Au(111) on a cleaved mica surface using a high speed vacuum (base pressure, 5×10^{-7} Pa) at 450 °C. After the immobilization of SH-GM1 pentasaccharide onto the gold surface, we added 20 mg/mL of galectin (Biovision) and incubated the samples for 1 h. Topology was imaged using Multimode DI AFM (Veeco Instruments).

RESULTS AND DISCUSSION

For the efficient immobilization of diverse carbohydrate types onto a bare gold surface, we used an amination reaction to couple the aldehyde (-CHO) group of the carbohydrate's terminal reducing sugar with the amine ($-NH_2$) group of a thiol-bearing aminophenyl disulfide (Scheme 1). A reductive amination reaction, namely, coupling the aldehyde group of a carbohydrate's terminal reducing sugar with the amine group of 2-aminopyridine, is commonly used for pyridylamination tagging of glycans with 2-aminopyridine in order to facilitate their purification and molecular weight analysis (*13, 14, 24, 25*).

In the present work, we found that mono and disaccharides could be modified at 20 °C reaction temperature, whereas modification of GM1 pentasaccharide was successful at 30 °C. This may suggest that a comparatively higher reaction temper-

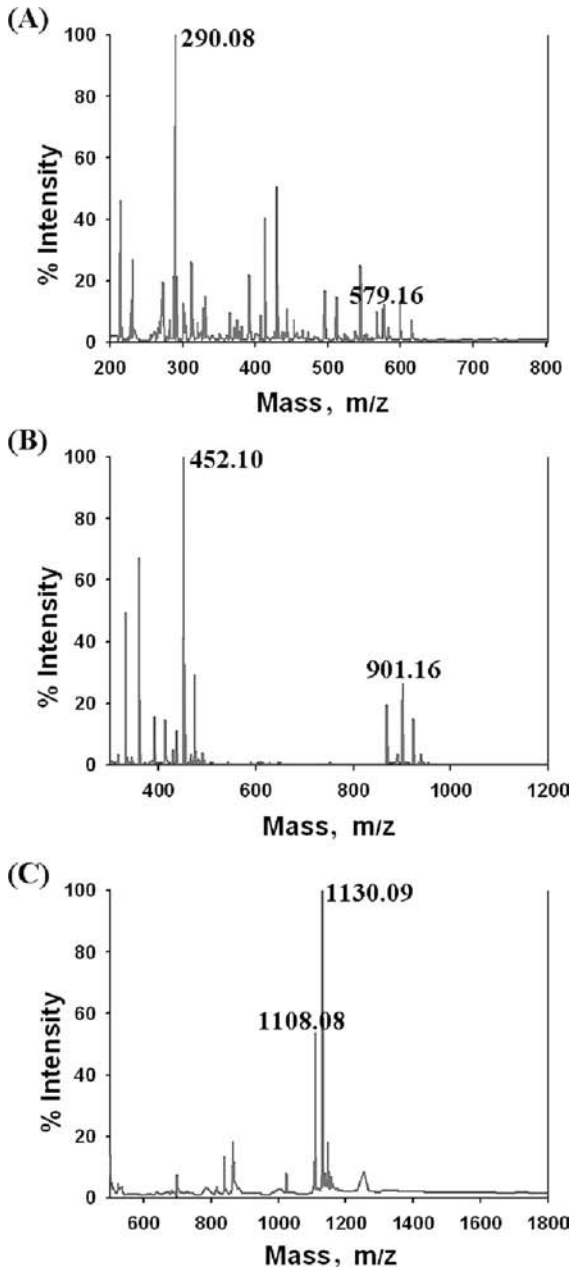


Figure 1. MALDI-TOF MS analysis of SH-modified monosaccharide glucose (A), disaccharide lactose (B), and GM1 pentasaccharide (C).

ature is required to give a higher ratio of an acyclic form of the terminal reducing sugar of complex carbohydrates. We further found that the modification efficiency depended on the concentration of reactants, with experiments containing 100 mM GM1 pentasaccharide showing a higher efficiency than those containing 10 mM of the same carbohydrate at the same concentration (50 mM) of aminophenyl disulfide (data not shown).

To check the feasibility of the modification of target carbohydrates using the proposed reductive amination reaction, we first performed nuclear magnetic resonance spectroscopy (NMR). The NMR spectrum contained features consistent with a -CH_2-NH- moiety (for glucose, ^{1}H NMR [600 MHz, D_2O] δ 3.42–3.48 [3H, m], 3.58–3.62 [5H, m], 6.48 [2H, d, J=8.0 Hz], 7.09 [2H, d, J=8.0 Hz]). We then used matrix-assisted laser desorption–ionization mass spectrometry with time-of-flight (MALDI-TOF MS) analysis to investigate the molecular weights of the modified carbohydrates (Figures 1A–C). Although we used aminophenyl disulfide as the coupling reagent, the modification primarily occurred through the aminophenyl sulfide

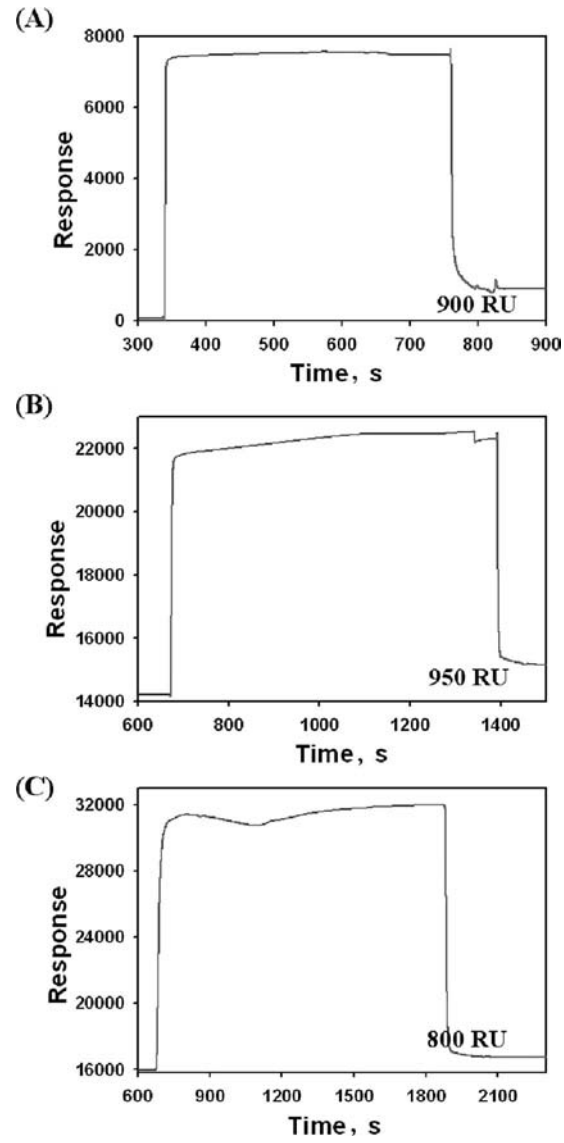


Figure 2. SPR binding assays of SH-modified monosaccharide glucose (A), disaccharide lactose (B), and GM1 pentasaccharide (C).

that might be formed from disulfide bond breakage under acidic (pH 2–3) conditions or reduction of its bond by dimethylamine borane. Therefore, the molecular weights of the modified glucose, lactose, and GM1 pentasaccharide were 290, 452, and 1108 (1130: +Na), respectively. Interestingly, all of the examined samples yielded a double mass value, representing a small peak of modified carbohydrates that had reacted directly with the aminophenyl disulfide. In addition, we also performed the modification of four other types of carbohydrates and confirmed their modifications using mass analyses (data not shown). Overall, these mass analyses confirmed that all of the target carbohydrates were successfully modified.

Without further purification, we then directly immobilized the SH-modified carbohydrates onto a gold surface. All of the SH-modified carbohydrates showed successful binding on the gold surface, as assessed by SPR binding assays (Figure 2A–C). Since the mass of lactose is somewhat higher than that of glucose at the same mole concentration, the resonance unit (RU) value of SH-lactose (950 RUs) was slightly higher than that of SH-glucose (900 RUs). In the case of GM1 pentasaccharide, although we used a carbohydrate concentration of 100 mM for the modification step, we diluted the SH-GM1 pentasaccharide 10-times for immobilization because of its limited available amount. Although GM1 pentasaccharide has a much higher

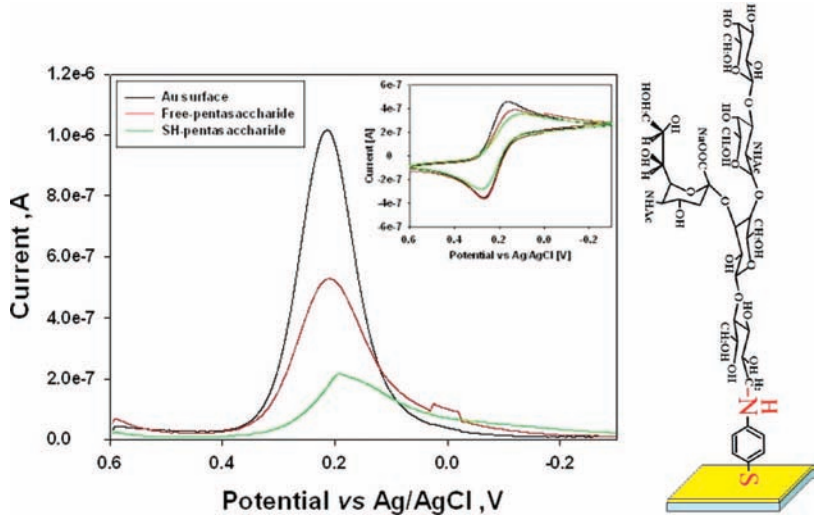


Figure 3. EC response of gold electrodes bound with unmodified GM1 pentasaccharide (red line) and modified SH-GM1 pentasaccharide (green line) compared to that of the bare gold electrode (black line). Inset, CV; main figure, SWV. The schematic illustration represents immobilization of modified SH-GM1 pentasaccharide on the gold surface.

molecular weight than glucose or lactose, the RU value was lower (800 RUs) because the utilized concentration was one-tenth that used in the other experiments. Collectively, these findings indicate that all of the SH-modified carbohydrates were successfully immobilized onto the gold surface without requiring additional treatment steps.

To further evaluate the direct immobilization of SH-modified carbohydrates onto the gold surface, we used EC analysis, which has the advantages of easy detection and high sensitivity at low concentrations (*19–21*) and which might be a useful tool for practical application as a carbohydrate sensor that needs high sensitivity due to very low portion of carbohydrates in the cellular materials. EC analysis was used to obtain the cyclic voltammetry (CV) and square wave voltammetry (SWV) curves from SH-modified and unmodified GM1 pentasaccharide exposed to 200-μm diameter gold electrodes (Figure 3). The CV measurements showed that the EC responses were significantly enhanced for immobilized SH-GM1 pentasaccharide (Figure 3, inset). The peaks and dips in the redox current of the CV signal showed the typical oxidation and reduction responses in the electrolyte of $K_3Fe(CN)_6$. The SWV curves (Figure 3, main figure) revealed that the limiting redox current decreased from 1.05 on the bare gold electrode to 0.2 μA in the presence of immobilized SH-GM1 pentasaccharide. The change ratios of the redox currents of bare gold electrodes in the presence or absence of unmodified or SH-modified GM1 pentasaccharide were ~45% and ~80%, respectively. This clearly showed that the EC signal ratio changed in response to carbohydrate immobilization, indicating that EC could have potential carbohydrate sensor applications. The reduced redox current is due to the decrease in reactive surface area exposed to the electrolyte. Notably, while the current ratio decreased to some extent in the presence of unmodified GM1 pentasaccharide, likely due to physical adsorption from the relatively small carbohydrate size, the redox current was almost completely blocked by the binding of SH-GM1 pentasaccharide to the gold electrode. Future systematic studies may be warranted to examine additional levels of control that may be exerted over this physical adhesion. Therefore, these results collectively indicate that our proposed method is a highly efficient strategy for immobilizing carbohydrates to the tested substrate.

Although the structure of the terminal reducing sugar is changed to the acyclic form by coupling of the aldehyde and amine groups (see Scheme 1), this should not be a problem in long chain carbohydrates such as GM1 pentasaccharide because the generation of the acyclic form only occurred at the surface-linked terminal sugar. A previous study showed that galactose and sialic acid, two terminal sugars of the branched GM1 pentasaccharide, exhibited substantial specific binding interactions (~39% from galactose and ~43% from sialic acid), with a smaller contribution (~17%) arising from the *N*-acetyl galactosamine residue (*26*). However, the central galactose and terminal reducing glucose residues do not appear to make direct interactions with the receptor protein (*26*), indicating that the terminal reducing and central sugars are more likely to act as bridges or linkers. Accordingly, we examined the binding of GM1 pentasaccharide to its terminal galactose-binding lectin, galectin, by topology analysis using atomic force microscopy (AFM) (Figure 4). Our results revealed that galectin did not bind in the case of unmodified, nonimmobilized GM1 pentasaccharide (Figure 4A), whereas galectin was clearly detected as a white spot on SH-GM1 pentasaccharide-immobilized gold

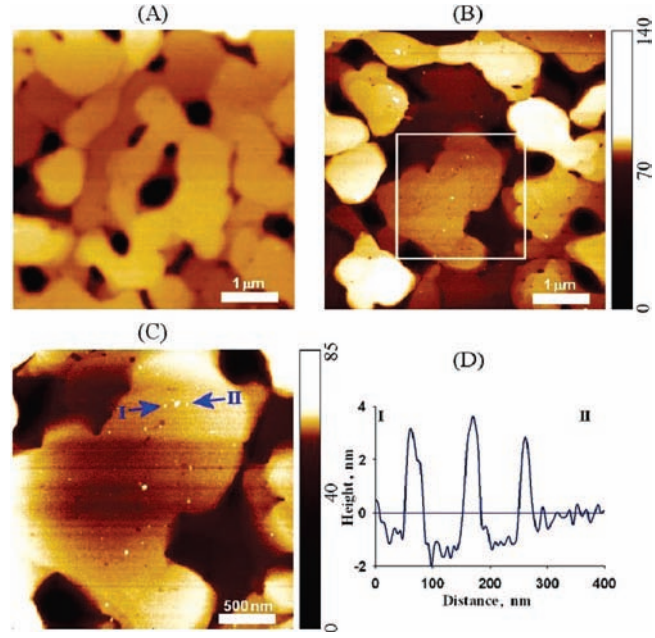


Figure 4. AFM analysis of the GM1 pentasaccharide–galectin interaction on Au(111). (A) Unmodified pentasaccharide, (B) modified SH-pentasaccharide, (C) magnified image of box in B, and (D) line profile of the SH-modified GM1 pentasaccharide–galectin interaction.

(Figure 4B and C). Line profile analysis revealed that the protein spots were 3–4 nm in size (Figure 4D). Importantly, since galectin should interact with only the terminal galactose, these findings confirmed that the modified carbohydrate had been successfully immobilized with the proper orientation.

In the present work, we kept our method simple by using aminophenyl disulfide as both the coupling reagent and the linker. In the future, the use of a longer coupling reagent might help increase the flexibility and receptor binding of the target carbohydrate. However, since increasing the length of the alkyl chain group can change the hydrophobicity of the molecule, the use of an overly long chain could inhibit carbohydrate modification. One of the advantages of our immobilization method is that only the terminal reducing sugar is specifically coupled with the linker reagent, so that the functional sites (e.g., biomolecule recognition or binding sites) of the carbohydrate can be preserved.

In summary, we herein demonstrated that the amine group of thiol-bearing aminophenyl disulfide was successfully coupled with the aldehyde group of the terminal reducing sugar in three types of carbohydrates, namely, glucose (monosaccharide), lactose (disaccharide), and GM1 pentasaccharide. The proposed modification method has several advantages over previously reported methods, including direct and rapid one-step immobilization onto a gold surface without surface pretreatment(s) by thiol group coupling in a mild reaction environment and exposure of functional carbohydrate moieties through oriented immobilization of the terminal reducing sugar. This modification and immobilization method should prove useful for diverse biomimetic studies in carbohydrates, including carbohydrate–biomolecule interaction and carbohydrate sensor or array development for diagnosis and screening.

ACKNOWLEDGMENT

This work was supported by National R&D Project for Nano Science and Technology and Advanced Environmental Biotechnology Research Center at POSTECH from the Korea Science and Engineering Foundation and the Brain Korea 21 Program from the Ministry of Education, Korea.

LITERATURE CITED

(1) Jelinek, R., and Kolusheva, S. (2004) Carbohydrate biosensors. *Chem. Rev. 104*, 5987–6015.

(2) Bertozzi, C. R., and Kiessling, L. L. (2001) Chemical glycobiology. *Science 291*, 2357–2364.

(3) Zachara, N. E., and Hart, G. W. (2002) The emerging significance of O-GlcNAc in cellular regulation. *Chem. Rev. 102*, 431–438.

(4) Ritchie, G. E., Moffatt, B. E., Sim, R. B., Morgan, B. P., Dwek, R. A., and Rudd, P. M. (2002) Glycosylation and the complement system. *Chem. Rev. 102*, 305–320.

(5) Nyquist, R. M., Eberhardt, A. S., Silks, L. A., Li, Z., Yang, X., and Swanson, B. I. (2000) Characterization of self-assembled monolayers for biosensor applications. *Langmuir 16*, 1793–1800.

(6) Park, S. J., and Shin, I. J. (2002) Fabrication of carbohydrate chips for studying protein-carbohydrate interactions. *Angew. Chem., Int. Ed. 41*, 3180–3182.

(7) Lazcka, O., Campo, F. J. D., and Munoz, F. X. (2007) Pathogen detection: A perspective of traditional methods and biosensors. *Biosens. Bioelectron. 22*, 1205–1217.

(8) Ni, J. H., Singh, S., and Wang, L. X. (2003) Synthesis of maleimide-activated carbohydrates as chemoselective tags for site-specific glycosylation of peptides and proteins. *Bioconjugate Chem. 14*, 232–238.

(9) Hermanson, G. T., Mallia, A. K., and Smith, P. K. (1992) *Immobilized Affinity Ligand Techniques*, Vol. 1, pp 137–200, Academic Press, London.

(10) Hatanaka, K., Takeshige, H., and Akaike, T. (1994) Synthesis of a new polymer containing uridine and galactose as pendant groups. *J. Carbohydr. Biochem. 13*, 603–610.

(11) Shin, I., Park, S., and Lee, M. R. (2005) Carbohydrate microarrays: An advanced technology for functional studies of glycans. *Chem.–Eur. J. 11*, 2894–2901.

(12) de Paz, J. L., and Seeberger, P. H. (2006) Recent advances in carbohydrate microarrays. *QSAR Comb. Sci. 25*, 1027–1032.

(13) Kondo, A., Suzuki, J., Kuraya, N., Hase, S., Kato, I., and Ikenaka, T. (1990) Improved method for fluorescence labeling of sugar chains with sialic acid residues. *Agric. Biol. Chem. 54*, 2169–2170.

(14) Hase, S., Ibuki, T., and Ikenaka, T. (1984) Reexamination of the pyridylamination used for fluorescence labeling of oligosaccharides and its application to glycoproteins. *J. Biochem. (Tokyo) 95*, 197–203.

(15) Hase, S., Koyama, S., Daiyasu, H., Takemoto, H., Hara, S., Kobayashi, Y., Kyogoku, Y., and Ikenaka, T. (1986) Structure of a sugar chain of a protease inhibitor isolated from barbados pride (*Caesalpinia pulcherrima Sw.*) seeds. *J. Biochem. (Tokyo) 100*, 1–10.

(16) (a) Wang, D. N., Liu, S. Y., Trummer, B. J., Deng, C., and Wang, A. L. (2002) Carbohydrate microarrays for the recognition of cross-reactive molecular markers of microbes and host cells. *Nat. Biotechnol. 20*, 275–281.

(17) Lee, M., and Shin, I. (2005) Facile preparation of carbohydrate microarrays by site-specific, covalent immobilization of unmodified carbohydrates on hydrazide-coated glass slides. *Org. Lett. 7*, 4269–4272.

(18) Fukui, S., Feizi, T., Galustian, C., Lawson, A. M., and Chai, W. G. (2002) Oligosaccharide microarrays for high-throughput detection and specificity assignments of carbohydrate-protein interactions. *Nat. Biotechnol. 20*, 1011–1017.

(19) Zhi, Z., Powell, A. K., and Turnbull, J. E. (2006) Fabrication of carbohydrate microarrays on gold surfaces: Direct attachment of nonderivatized oligosaccharides to hydrazide-modified self-assembled monolayers. *Anal. Chem. 78*, 4786–4793.

(20) Zhou, X., and Zhou, J. (2006) Oligosaccharide microarrays fabricated on aminooxyacetyl functionalized glass surface for characterization of carbohydrate-protein interaction. *Biosens. Bioelectron. 21*, 1451–1458.

(21) Lee, H. Y., Park, J. W., and Kawai, T. (2004) SNPs feasibility of nonlabeled oligonucletides on using electrochemical sensing. *Electroanalysis 16*, 1999–2002.

(22) Kim, J. M., Jung, H. S., Park, J. W., Yukimasa, T., Oka, H., Lee, H. Y., and Kawai, T. (2005) Spontaneous immobilization of liposomes on electron-beam exposed resist surfaces. *J. Am. Chem. Soc. 127*, 2358–2362.

(23) Lee, H. Y., Park, J. W., Kim, J., Jung, H., and Kawai, T. (2006) Well-oriented nanowell array metrics for integrated digital nanobiosensors. *Appl. Phys. Lett. 89*, 113901.

(24) Takahashi, C., Nakakita, S., and Hase, S. (2003) Conversion of pyridylamino sugar chains to corresponding reducing sugar chains. *J. Biochem. (Tokyo) 134*, 51–55.

(25) Kuraya, N., and Hase, S. (1992) Release of O-linked sugar chains from glycoproteins with anhydrous hydrazine and pyridylamination of the sugar chains with improved reaction conditions. *J. Biochem. (Tokyo) 112*, 122–126.

(26) Merritt, E. A., Sarfaty, S., Vandenakker, F., Lhoir, C., Martial, J. A., and Hol, W. (1994) Crystal-structure of cholera-toxin B-pentamer bound to receptor G(M1) pentasaccharide. *Protein Sci. 3*, 166–175.

BC700288Z

CORRECTIONS

Volume 18, Number 3, 2007.

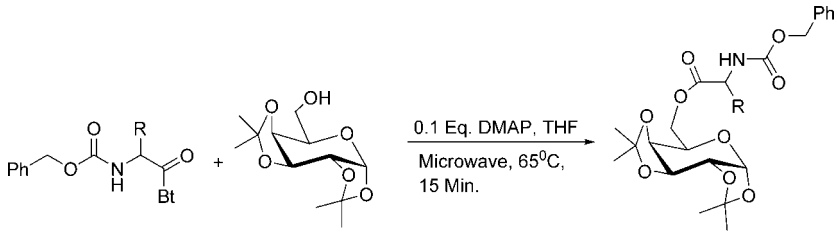
Alan R. Katritzky,* Parul Angrish, and Tamari Narindoshvili

Chiral *O*-(Z-α-Aminoacyl) Sugars: Convenient Building Blocks for Glycopeptide Libraries

The authors regret errors in the stereochemistry shown for the starting carbohydrates **2**, **5**, and **7** and products **3**, **4**, **6**, **8**, **9**, and **10**.

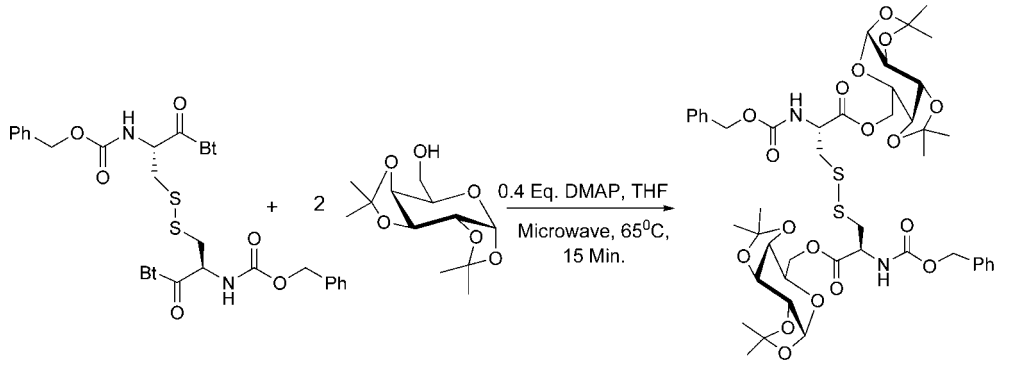
Corrected structures and schemes are shown below:

Scheme 1



1a-d, 1d+1d' **2** **3a-d, 3d+3d'**

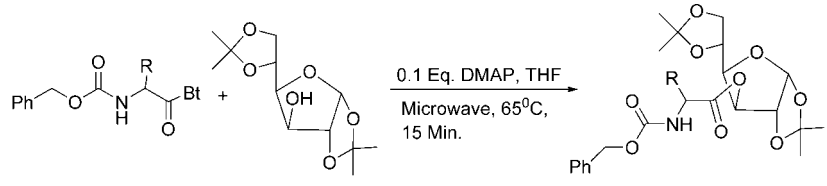
Scheme 2



1d **2** **4 (Yield =96%), HPLC R.T[a]=2.97 min.**

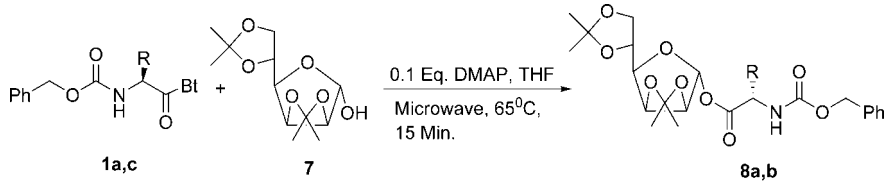
[a](for conditions refer to experimental section)

Scheme 3



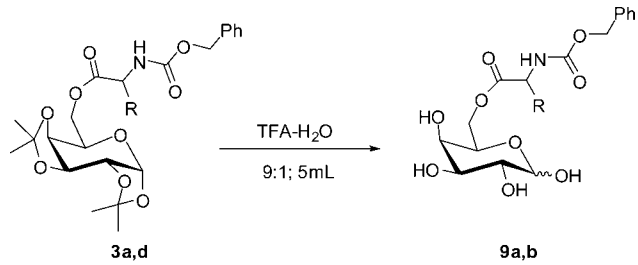
1a-d, (1a+1a'), (1d+1d') **5** **6a-d, (6a+6a'), (6d+6d')**

Scheme 4

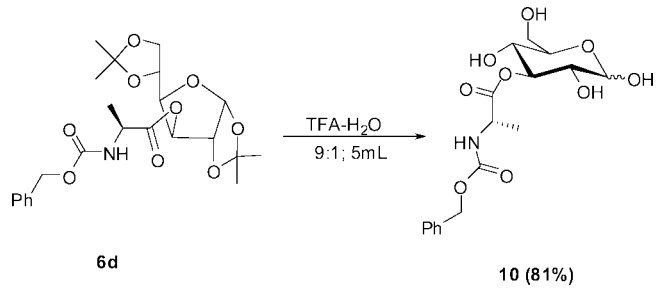


1a,c **7** **8a,b**

Scheme 5



Scheme 6



BC700301B

10.1021/bc700301b
Published on Web 09/14/2007

Volume 17, Number 5, 2006.

Isabelle Tranchant, Anne-Cécile Hervé, Stephen Carlisle, Phillip Lowe, Christopher J. Slevin, Camilla Forssten, John Dilleen, David E. Williams, Alethea B. Tabor, and Helen C. Hailes*

Design and Synthesis of Ferrocene Probe Molecules for Detection by Electrochemical Methods

Since publication of this article, unfortunately we have realized that a co-worker who carried out some experiments in the early studies in this project was inadvertently not included in the list of contributing authors. We would therefore like to acknowledge his contribution with the following correction to the author list (affiliations shown).

Isabelle Tranchant[‡], Anne-Cécile Hervé[†,§], Stephen Carlisle[†], Phillip Lowe[†,¶], Christopher J. Slevin[†,¶], Camilla Forssten[†], John Dilleen[†,¶], Rajiv Bhalla[†,⊥], David E. Williams[†,∥], Alethea B. Tabor, and Helen C. Hailes*

[†]Unipath Ltd., Priory Business Park, Bedford, MK44 3UP, U.K.

[⊥]Current address: GE Healthcare, The Grove Centre, White Lion Road, Amersham, Buckinghamshire, HP7 9LL, U.K.

BC700366D

10.1021/bc700366d
Published on Web 11/21/2007